

Springer
Handbook *of*
Atomic, Molecular,
and Optical Physics

Drake
Editor

2nd Edition

Springer Handbooks

Springer Handbooks provide a concise compilation of approved key information on methods of research, general principles, and functional relationships in physical and applied sciences. The world's leading experts in the fields of physics and engineering will be assigned by one or several renowned editors to write the chapters comprising each volume. The content is selected by these experts from Springer sources (books, journals, online content) and other systematic and approved recent publications of scientific and technical information.

The volumes are designed to be useful as readable desk book to give a fast and comprehensive overview and easy retrieval of essential reliable key information, including tables, graphs, and bibliographies. References to extensive sources are provided.

Gordon W. F. Drake
Editor

Springer Handbook of Atomic, Molecular, and Optical Physics

2nd Edition

With 328 Figures and 125 Tables

 Springer

Editor

Gordon W. F. Drake
Dept. of Physics
University of Windsor
Windsor, Canada

ISSN 2522-8692

ISBN 978-3-030-73892-1

<https://doi.org/10.1007/978-3-030-73893-8>

ISSN 2522-8706 (electronic)

ISBN 978-3-030-73893-8 (eBook)

1st edition: © Springer Science+Business Media New York 2006

2nd edition: © Springer Nature Switzerland AG 2023

This work is subject to copyright. All rights are reserved by the Publisher, whether the whole or part of the material is concerned, specifically the rights of translation, reprinting, reuse of illustrations, recitation, broadcasting, reproduction on microfilms or in any other physical way, and transmission or information storage and retrieval, electronic adaptation, computer software, or by similar or dissimilar methodology now known or hereafter developed.

The use of general descriptive names, registered names, trademarks, service marks, etc. in this publication does not imply, even in the absence of a specific statement, that such names are exempt from the relevant protective laws and regulations and therefore free for general use.

The publisher, the authors and the editors are safe to assume that the advice and information in this book are believed to be true and accurate at the date of publication. Neither the publisher nor the authors or the editors give a warranty, express or implied, with respect to the material contained herein or for any errors or omissions that may have been made. The publisher remains neutral with regard to jurisdictional claims in published maps and institutional affiliations.

This Springer imprint is published by the registered company Springer Nature Switzerland AG.
The registered company address is: Gewerbestrasse 11, 6330 Cham, Switzerland

Foreword

Atomic, molecular, and optical physics (AMO physics) encompasses the foundational knowledge of atomic physics and essential concepts and data for molecular and optical physics. AMO physics provides the tools for understanding the full gamut of atomic, ionic, and molecular collisions that is essential for astronomy and astrophysics. Knowledge from AMO physics overflows into neighboring fields: nuclear physics, material science, biophysics, geo-physics, and atmospheric science. AMO science is crucial to the understanding of climate change.

AMO physics has undergone dramatic advances since the last edition of the AMO Handbook. The discovery of ultracold atoms has led to new tools for many-body physics. Cavity quantum electrodynamics has opened avenues into field theory and quantum information processing. Advances in experimental techniques have revolutionized metrology and enabled a new generation of atomic frequency standards that have reached precision of parts in 10^{19} . A metrological revolution has taken place: all the basic units of science have been redefined in terms of quantum measurements.

Fundamental tests continue to flourish. Atoms now serve as tools for manipulating photons, quantum information theory and quantum communication have advanced, and the search for physics beyond the Standard Model has been carried forward. The discovery of gravitational waves by LIGO was enabled by advances in quantum optics from the AMO community, and the observation of radiation by matter as it falls through the event horizon of a black hole was made possible by synchronizing signals from observatories around the world using atomic clocks at their limit of accuracy.

The Table of Contents of this new edition of the *Springer Handbook of Atomic, Molecular, and Optical Physics* reflects the broad scope of AMO physics today. Its 91 chapters, written by experts and carefully reviewed, are an essential resource for physicists in academic, industrial, and federal research laboratories.

With the changing style in scientific publishing and library practice, browsing has become increasingly difficult. All the more reason to have access to the *Springer Handbook of Atomic, Molecular and Optical Physics*, for which browsing is almost irresistible.

January, 2021

Daniel Kleppner

Foreword to the First Edition by Herbert Walther

The *Handbook of Atomic, Molecular and Optical (AMO) Physics* gives an in-depth survey of the present status of this field of physics. It is an extended version of the first issue to which new and emerging fields have been added. The selection of topics thus traces the recent historic development of AMO physics. The book gives students, scientists, engineers, and other interested people a comprehensive introduction and overview. It combines introductory explanations with descriptions of phenomena, discussions of results achieved, and gives a useful selection of references to allow more detailed studies, making the handbook very suitable as a desktop reference.

AMO physics is an important and basic field of physics. It provided the essential impulse leading to the development of modern physics at the beginning of the last century. We have to remember that at that time not every physicist believed in the existence of atoms and molecules. It was due to Albert Einstein, whose work we commemorate this year with the world year of physics, that this view changed. It was Einstein's microscopic view of molecular motion that led to a way of calculating Avogadro's number and the size of molecules by studying their motion. This work was the basis of his PhD thesis submitted to the University of Zurich in July 1905 and after publication became Einstein's most quoted paper. Furthermore, combining kinetic theory and classical thermodynamics led him to the conclusion that the displacement of a microparticle in Brownian motion varies as the square root of time. The experimental demonstration of this law by Jean Perrin three years later finally afforded striking proof that atoms and molecules are a reality. The energy quantum postulated by Einstein in order to explain the photoelectric effect was the basis for the subsequently initiated development of quantum physics, leading to a revolution in physics and many new applications in science and technology.

The results of AMO physics initiated the development of quantum mechanics and quantum electrodynamics and as a consequence led to a better understanding of the structure of atoms and molecules and their respective interaction with radiation and to the attainment of unprecedented accuracy. AMO physics also influenced the development in other fields of physics, chemistry, astronomy, and biology. It is an astonishing fact that AMO physics constantly went through periods where new phenomena were found, giving rise to an enormous revival of this area. Examples are the maser and laser and their many applications, leading to a better understanding of the basics and the detection of new phenomena, and new possibilities such as laser cooling of atoms, squeezing, and other nonlinear behaviour. Recently, coherent interference effects allowed slow or fast light to be produced. Finally, the achievement of Bose–Einstein condensation in dilute media has opened up a wide range of new phenomena for study. Special quantum phenomena are leading to new applications for transmission of information and for computing. Control of photon emission through specially designed cavities allows controlled and deterministic generation of photons opening the way for a secure information transfer.

Further new possibilities are emerging, such as the techniques for producing attosecond laser pulses and laser pulses with known and controlled phase relation between the envelope and carrier wave, allowing synthesis of even shorter pulses in a controlled manner. Furthermore, laser pulses may soon be available that are sufficiently intense to allow polarization of the vacuum field. Another interesting development is the generation of artificial atoms, e.g.,

quantum dots, opening a field where nanotechnology meets atomic physics. It is thus evident that AMO physics is still going strong and will also provide new and interesting opportunities and results in the future.

Herbert Walther

Preface

The field of atomic, molecular, and optical physics is the oldest part of modern physics, and yet it provides the foundation upon which all the rest is built. The previous edition of the *Springer Handbook of Atomic, Molecular, and Optical Physics* was published in 2005, which was the International Year of Physics celebrating the *Annus mirabilis* of Einstein exactly 100 years earlier. 2005 also marked another in a long sequence of Nobel Prizes awarded for work in the area of AMO physics, this time to Roy Glauber, John Hall, and Ted Hänsch for their work on quantum optics and high-precision measurement. The sequence continued with the 2012 prize being awarded to Serge Haroche and David Wineland for their work on measuring and manipulating individual quantum systems, and the 2018 prize to Arthur Askin for the development of optical tweezers, and Gérard Mourou and Donna Strickland for high-intensity ultrashort laser pulses. Most recently, the Nobel Prize in Physics for 2022 was awarded jointly to Alain Aspect, John F. Clauser and Anton Zeilinger for experiments with entangled photons, establishing the violation of Bell inequalities, and pioneering quantum information science. The 2015 Prize for neutrino oscillations and the 2017 Prize for gravitational waves also made essential use of the techniques of AMO physics for their success. 2015 was also the International Year of Light, where the ever-expanding power and versatility of lasers played a prominent role; this continues to provide a unifying theme for much of AMO physics.

The intent of this Handbook is to provide a ready reference for the principal ideas, techniques, and results that are common to all these areas of research where exciting advances continue apace. The success of the previous 2005 edition and advances in the field provide the motivation for the current revised edition, with the expectation that it will continue as a standard reference source for the field. Many of the topics have not changed significantly since the previous edition was published, such as angular momentum algebra (Chap. 2), perturbation theory (Chap. 5), second quantization (Chap. 6), and the properties of hydrogenic wave functions (Chap. 9), and so these chapters are still the same (except for minor corrections). However, most of the other chapters have been extensively revised, and in some cases completely rewritten. In the search for new physics beyond the Standard Model, it has become increasingly evident that high-precision atomic physics measurements at low energy can be used to supplement, or in some cases extend, what can be learned from high-energy particle accelerators. Entirely new chapters are included on searches for dark matter and an electron electric dipole moment (EDM), and tests of Lorentz invariance and general relativity. The major previous sections on lasers, laser interactions with matter, and quantum optical tests of the foundations of physics remain of central importance in the revised edition, along with the various forms of spectroscopy. The sections on scattering phenomena, both theoretical and experimental, have been augmented to include a new chapter on ultracold Rydberg atom collisions, and another on quantum defect theory. The section on applications remains as important and timely as ever, with extensively updated chapters on aeronomy and global change. Chapter 1 on units and constants has been completely transformed by the redefinition of Planck's constant, Avogadro's number, Boltzmann's constant, and the elementary charge as defined physical constants with zero uncertainty.

The preparation of the original Handbook and the current revision would not have been possible without the help and advice of many people throughout the AMO physics commu-

nity. To name just a few, I am particularly indebted to Thomas Kirchner, Klaus Bartschat, and Jonathan Tennyson for their help and advice on revisions to the section on scattering theory, and to Pierre Meystre and Bruce Shore for their advice and guidance in extending and restructuring the section on quantum optics. Marianna Safronova provided valuable input on searches for new physics beyond the Standard Model.

We regret that the following authors, all giants in the field, from the previous edition are no longer with us. In order of their appearance in the previous edition, they are James D. Louck, Robert N. Hill, William C. Martin, Anthony F. Starace, M. Raymond Flannery, Philip Burke, Bernd Crasemann, Stig Stenholm, Alexander Dalgarno, Alan Garscadden, Hans Bichsel, Mitio Inokuti, John M. Brown, Lorenzo J. Curtis, Kenneth Evenson, Gordon Feldman, Thomas Fulton, Axel Schenzle, Paul Feldman, and Michael R. Strayer.

Work on the current revision project began in February, 2016, and so it has been nearly seven years in the making. Much of the day-to-day work involved corresponding with over 100 authors and keeping track of the status of each of the 91 chapters as they passed through an external review process followed by revisions. In many cases, it also involved actively helping authors solve problems with their \LaTeX source code and establishing good lines of communication with each author concerning the content of other related chapters. All of this would not have been possible without the very capable help of the three Editorial Assistants who worked on various stages of the project: Jacklyn Bizarre, Shawn Steven, and Fatemeh Hamdizadeh. Their tireless efforts and energy contributed greatly to the successful completion of the project. I would also like to acknowledge the very capable assistance of the Springer Handbook Coordinators: Veronika Hamm, Heather King, and Judith Hinterberg. I owe a great debt of gratitude to all of these people in making this revised edition of the *Springer Handbook of Atomic, Molecular and Optical Physics* a reality. I am especially grateful for the love and support of my wife, Mary Louise, and my children Susan and Peter. I hope that the present edition will continue to serve as a valuable resource for many years to come.

November, 2022

Gordon W.F. Drake

Preface to the First Edition

The year 2005 has been officially declared by the United Nations to be the International Year of Physics to commemorate the three famous papers of Einstein published in 1905. It is a fitting tribute to the impact of his work that the *Springer Handbook of Atomic, Molecular, and Optical Physics* should be published in coincidence with this event. Virtually all of AMO Physics rests on the foundations established by Einstein in 1905 (including a fourth paper on relativity and his thesis) and his subsequent work. In addition to the theory of relativity, for which he is best known, Einstein ushered in the era of quantum mechanics with his explanation of the photoelectric effect, and he demonstrated the influence of molecular collisions with his explanation of Brownian motion. He also laid the theoretical foundations for all of laser physics with his discovery (in 1917) of the necessity of the process of stimulated emission, and his discussions of the Einstein–Podolsky–Rosen Gedanken experiment (in 1935) led, through Bell’s inequalities, to current work on entangled states and quantum information. The past century has been a Golden Age for physics in every sense of the term.

Despite this history of unparalleled progress, the field of AMO Physics continues to advance more rapidly than ever. At the time of publication of an earlier Handbook published by AIP Press in 1996 I wrote “The ever increasing power and versatility of lasers continues to open up new areas for study.” Since then, two Nobel Prizes have been awarded for the cooling and trapping of atoms with lasers (Steven Chu, Claude Cohen-Tannoudji, William D. Phillips in 1997), and for the subsequent achievement of Bose–Einstein condensation in a dilute gas of trapped atoms (Eric A. Cornell, Wolfgang Ketterle, Carl E. Wieman in 2001). Although the topic of cooling and trapping was covered in the AIP Handbook, Bose–Einstein condensation was barely mentioned. Since then, the literature has exploded to nearly 2500 papers on Bose–Einstein condensation alone. Similarly, the topics of quantum information and quantum computing barely existed in 1995, and have since become rapidly growing segments of the physics literature. Entirely new topics such as “fast light” and “slow light” have emerged. Techniques for both high precision theory and measurement are opening the possibility to detect a cosmological variation of the fundamental constants with time. All of these topics hold the promise of important engineering and technological applications that come with advances in fundamental science. The more established areas of AMO Physics continue to provide the basic data and broad understanding of a great wealth of underlying processes needed for studies of the environment, and for astrophysics and plasma physics.

These changes and advances provide more than sufficient justification to prepare a thoroughly revised and updated *Atomic, Molecular and Optical Physics Handbook* for the Springer Handbook Program. The aim is to present the basic ideas, methods, techniques and results of the field at a level that is accessible to graduate students and other researchers new to the field. References are meant to be a guide to the literature, rather than a comprehensive bibliography. Entirely new chapters have been added on Bose–Einstein condensation, quantum information, variations of the fundamental constants, and cavity ring-down spectroscopy. Other chapters have been substantially expanded to include new topics such as fast light and slow light. The intent is to provide a book that will continue to be a valuable resource and source of inspiration for both students and established researchers.

I would like to acknowledge the important role played by the members of the Advisory Board in their continuing support of this project, and I would especially like to acknowledge the talents of Mark Cassar as Assistant Editor. In addition to keeping track of the submissions and corresponding with authors, he read and edited the new material for every chapter to ensure uniformity in style and scientific content, and he composed new material to be added to some of the chapters, as noted in the text.

February 2005

Gordon W.F. Drake

Editorial Board

Editor

Gordon W. F. Drake

Department of Physics, University of Windsor, Windsor, Ontario N9B 3P4, Canada
gdrake@uwindsor.ca

Assistant Editors

Jacklyn Bizarre, Shaun Steven, and Fatemeh Hamdizadeh
Department of Physics, University of Windsor, Windsor, ON N9B 3P4, Canada

Advisory Board

Klaus Bartschat
Department of Physics, Drake University, DeMoines, Iowa, USA
klaus.bartschat@drake.edu

Thomas Kirchner
Department of Physics and Astronomy, York University, Toronto, ON M3J 1P3, Canada
tomk@yorku.ca

Pierre Meystre
Optical Sciences Center, The University of Arizona, Tucson, Arizona, USA
pierre@optics.arizona.edu

Marianna Safronova
Department of Physics and Astronomy, University of Delaware, Newark, DE 19716 USA
msafrono@udel.edu

Jonathan Tennyson
Department of Physics and Astronomy, University College London, London WC1E 6BT, UK
j.tennyson@ucl.ac.uk

Contents

Part A Mathematical Methods

1	Units and Constants	3
	Eite Tiesinga	
1.1	Introduction	3
1.2	Atomic Units	3
1.3	Natural Units	5
1.4	Fundamental Constants	5
	References	7
2	Angular Momentum Theory	9
	James D. Louck	
2.1	Orbital Angular Momentum	12
	2.1.1 Cartesian Representation	12
	2.1.2 Spherical Polar Coordinate Representation	14
2.2	Abstract Angular Momentum	15
2.3	Representation Functions	17
	2.3.1 Parametrizations of the Groups $SU(2)$ and $SO(3, \mathbf{R})$	17
	2.3.2 Explicit Forms of Representation Functions	19
	2.3.3 Relations to Special Functions	19
	2.3.4 Orthogonality Properties	20
	2.3.5 Recurrence Relations	21
	2.3.6 Symmetry Relations	21
2.4	Group and Lie Algebra Actions	24
	2.4.1 Matrix Group Actions	24
	2.4.2 Lie Algebra Actions	24
	2.4.3 Hilbert Spaces	25
	2.4.4 Relation to Angular Momentum Theory	25
2.5	Differential Operator Realizations of Angular Momentum	26
2.6	The Symmetric Rotor and Representation Functions	27
2.7	Wigner–Clebsch–Gordan and 3- j Coefficients	29
	2.7.1 Kronecker Product Reduction	30
	2.7.2 Tensor Product Space Construction	31
	2.7.3 Explicit Forms of WCG Coefficients	31
	2.7.4 Symmetries of WCG Coefficients in 3- j Symbol Form	33
	2.7.5 Recurrence Relations	33
	2.7.6 Limiting Properties and Asymptotic Forms	34
	2.7.7 WCG Coefficients as Discretized Representation Functions	34
2.8	Tensor Operator Algebra	35
	2.8.1 Conceptual Framework	35
	2.8.2 Universal Enveloping Algebra of \mathbf{J}	36
	2.8.3 Algebra of Irreducible Tensor Operators	36

2.8.4	Wigner–Eckart Theorem	37
2.8.5	Unit Tensor Operators or Wigner Operators	37
2.9	Racah Coefficients	40
2.9.1	Basic Relations Between WCG and Racah Coefficients	40
2.9.2	Orthogonality and Explicit Form	40
2.9.3	The Fundamental Identities Between Racah Coefficients	41
2.9.4	Schwinger–Bargmann Generating Function and Its Combinatorics	41
2.9.5	Symmetries of $6-j$ Coefficients	42
2.9.6	Further Properties	43
2.10	The $9-j$ Coefficients	44
2.10.1	Hilbert Space and Tensor Operator Actions	44
2.10.2	$9-j$ Invariant Operators	44
2.10.3	Basic Relations Between $9-j$ Coefficients and $6-j$ Coefficients	45
2.10.4	Symmetry Relations for $9-j$ Coefficients and Reduction to $6-j$ Coefficients	46
2.10.5	Explicit Algebraic Form of $9-j$ Coefficients	46
2.10.6	Racah Operators	46
2.10.7	Schwinger–Wu Generating Function and Its Combinatorics	47
2.11	Tensor Spherical Harmonics	48
2.11.1	Spinor Spherical Harmonics as Matrix Functions	49
2.11.2	Vector Spherical Harmonics as Matrix Functions	49
2.11.3	Vector Solid Harmonics as Vector Functions	50
2.12	Coupling and Recoupling Theory and $3n-j$ Coefficients	51
2.12.1	Composite Angular Momentum Systems	51
2.12.2	Binary Coupling Theory: Combinatorics	52
2.12.3	Implementation of Binary Couplings	53
2.12.4	Construction of All Transformation Coefficients in Binary Coupling Theory	54
2.12.5	Unsolved Problems in Recoupling Theory	55
2.13	Supplement on Combinatorial Foundations	56
2.13.1	$SU(2)$ Solid Harmonics	56
2.13.2	Combinatorial Definition of Wigner–Clebsch–Gordan Coefficients	57
2.13.3	Magic Square Realization of the Addition of Two Angular Momenta	59
2.13.4	MacMahon’s and Schwinger’s Master Theorems	60
2.13.5	The Pfaffian and Double Pfaffian	61
2.13.6	Generating Functions for Coupled Wave Functions and Recoupling Coefficients	61
2.14	Author’s Comments	64
2.15	Tables	64
	References	67
3	Group Theory for Atomic Shells	71
	Brian R. Judd	
3.1	Generators	71
3.1.1	Group Elements	71
3.1.2	Conditions on the Structure Constants	72
3.1.3	Cartan–Weyl Form	72
3.1.4	Atomic Operators as Generators	72
3.2	Classification of Lie Algebras	72
3.2.1	Introduction	72
3.2.2	The Semisimple Lie Algebras	72

3.3	Irreducible Representations	73
3.3.1	Labels	73
3.3.2	Dimensions	73
3.3.3	Casimir's Operator	74
3.4	Branching Rules	74
3.4.1	Introduction	74
3.4.2	$U(n) \supset SU(n)$	74
3.4.3	Canonical Reductions	75
3.4.4	Other Reductions	75
3.5	Kronecker Products	75
3.5.1	Outer Products of Tableaux	75
3.5.2	Other Outer Products	75
3.5.3	Plethysms	75
3.6	Atomic States	76
3.6.1	Shell Structure	76
3.6.2	Automorphisms of $SO(8)$	77
3.6.3	Hydrogen and Hydrogen-Like Atoms	77
3.7	The Generalized Wigner–Eckart Theorem	77
3.7.1	Operators	77
3.7.2	The Theorem	77
3.7.3	Calculation of the Isoscalar Factors	78
3.7.4	Generalizations of Angular Momentum Theory	78
3.8	Checks	79
	References	79
4	Dynamical Groups	81
	Josef Paldus	
4.1	Noncompact Dynamical Groups	82
4.1.1	Realizations of $so(2,1)$	82
4.1.2	Hydrogenic Realization of $so(4,2)$	82
4.2	Hamiltonian Transformation and Simple Applications	84
4.2.1	N -Dimensional Isotropic Harmonic Oscillator	84
4.2.2	N -Dimensional Hydrogenic Atom	85
4.2.3	Perturbed Hydrogenic Systems	85
4.3	Compact Dynamical Groups	86
4.3.1	Unitary Group and Its Representations	86
4.3.2	Orthogonal Group $O(n)$ and Its Representations	87
4.3.3	Clifford Algebras and Spinor Representations	87
4.3.4	Bosonic and Fermionic Realizations of $U(n)$	88
4.3.5	The Vibron Model	88
4.3.6	Many-Electron Correlation Problem	89
4.3.7	Clifford Algebra Unitary Group Approach	91
4.3.8	Spin-Dependent Operators	91
	References	92
5	Perturbation Theory	95
	Josef Paldus	
5.1	Matrix Perturbation Theory (PT)	95
5.1.1	Basic Concepts	96
5.1.2	Level-Shift Operators	96
5.1.3	General Formalism	96
5.1.4	Nondegenerate Case	97

5.2	Time-Independent Perturbation Theory	97
5.2.1	General Formulation	97
5.2.2	Brillouin–Wigner and Rayleigh–Schrödinger PT (RSPT)	98
5.2.3	Bracketing Theorem and RSPT	98
5.3	Fermionic Many-Body Perturbation Theory (MBPT)	99
5.3.1	Time-Independent Wick’s Theorem	99
5.3.2	Normal Product Form of PT	99
5.3.3	Møller–Plesset and Epstein–Nesbet PT	100
5.3.4	Diagrammatic MBPT	100
5.3.5	Vacuum and Wave Function Diagrams	101
5.3.6	Hartree–Fock Diagrams	101
5.3.7	Linked and Connected Cluster Theorems	102
5.3.8	Coupled Cluster Theory	103
5.4	Time-Dependent Perturbation Theory	105
5.4.1	Evolution Operator PT Expansion	105
5.4.2	Gell-Mann and Low Formula	105
5.4.3	Potential Scattering and Quantum Dynamics	106
5.4.4	Born Series	106
5.4.5	Variation of Constants Method	107
	References	107
6	Second Quantization	111
	Brian R. Judd	
6.1	Basic Properties	111
6.1.1	Definitions	111
6.1.2	Representation of States	112
6.1.3	Representation of Operators	112
6.2	Tensors	112
6.2.1	Construction	112
6.2.2	Coupled Forms	112
6.2.3	Coefficients of Fractional Parentage	113
6.3	Quasispin	113
6.3.1	Fermions	113
6.3.2	Bosons	113
6.3.3	Triple Tensors	114
6.3.4	Conjugation	114
6.3.5	Dependence on Electron Number	114
6.3.6	The Half-Filled Shell	115
6.4	Complementarity	115
6.4.1	Spin–Quasispin Interchange	115
6.4.2	Matrix Elements	115
6.5	Quasiparticles	116
	References	116
7	Density Matrices	119
	Klaus Bartschat	
7.1	Basic Formulae	120
7.1.1	Pure States	120
7.1.2	Mixed States	120
7.1.3	Expectation Values	120
7.1.4	The Liouville Equation	120
7.1.5	Systems in Thermal Equilibrium	121
7.1.6	Relaxation Processes	121

7.2	Spin and Light Polarizations	121
7.2.1	Spin-Polarized Electrons	121
7.2.2	Light Polarization	122
7.3	Atomic Collisions	122
7.3.1	Scattering Amplitudes	122
7.3.2	Reduced Density Matrices	122
7.4	Irreducible Tensor Operators	123
7.4.1	Definition	123
7.4.2	Transformation Properties	123
7.4.3	Symmetry Properties of State Multipoles	124
7.4.4	Orientation and Alignment	124
7.4.5	Coupled Systems	124
7.5	Time Evolution of State Multipoles	125
7.5.1	Perturbation Coefficients	125
7.5.2	Quantum Beats	125
7.5.3	Time Integration over Quantum Beats	125
7.6	Examples	126
7.6.1	Generalized <i>STU</i> -Parameters	126
7.6.2	Radiation from Excited States: Stokes Parameters	127
7.7	Summary	128
	References	128
8	Computational Techniques	131
	David Schultz and Michael R. Strayer	
8.1	Representation of Functions	132
8.1.1	Interpolation	132
8.1.2	Fitting	133
8.1.3	Fourier Analysis	135
8.1.4	Approximating Integrals	135
8.1.5	Approximating Derivatives	136
8.2	Differential and Integral Equations	137
8.2.1	Ordinary Differential Equations	137
8.2.2	Differencing Algorithms for Partial Differential Equations	138
8.2.3	Variational Methods	140
8.2.4	Finite Elements	140
8.2.5	Integral Equations	142
8.3	Computational Linear Algebra	143
8.4	Monte Carlo Methods	144
8.4.1	Random Numbers	145
8.4.2	Distributions of Random Numbers	145
8.4.3	Monte Carlo Integration	146
	References	147
9	Hydrogenic Wave Functions	149
	Robert N. Hill	
9.1	Schrödinger Equation	149
9.1.1	Spherical Coordinates	149
9.1.2	Parabolic Coordinates	150
9.1.3	Momentum Space	152
9.2	Dirac Equation	153
9.3	The Coulomb Green's Function	154
9.3.1	The Green's Function for the Schrödinger Equation	155
9.3.2	The Green's Function for the Dirac Equation	156

9.4	Special Functions	156
9.4.1	Confluent Hypergeometric Functions	157
9.4.2	Laguerre Polynomials	160
9.4.3	Gegenbauer Polynomials	163
9.4.4	Legendre Functions	163
	References	164
10	Software for Computational Atomic and Molecular Physics	165
	Edmund J. Mansky II	
10.1	Introduction	165
10.2	Software for Atomic Physics	166
10.2.1	Atomic Structure Programs	166
10.2.2	Electron-Atom/Ion Scattering Programs	166
10.3	Software for Molecular Physics	167
10.3.1	Molecular Structure Programs	167
10.3.2	Molecular and Heavy Particle Scattering Programs	167
10.4	Software Libraries and Repositories	168
10.4.1	The CPC Journal and Library	168
10.4.2	Perl and CPAN	168
10.4.3	Python and PyPI	168
10.4.4	C++ and Boost	168
10.4.5	GitHub	168
10.5	General Tools	169
10.5.1	Configuration: GNU Autotools	169
10.5.2	C compilers: gcc	170
10.5.3	FORTRAN Compilers	170
10.5.4	Shell Scripting Languages	170
10.5.5	Mixing Languages	171
10.5.6	Third-Party Libraries and Unit Tests	171
	References	172

Part B Atoms

11	Atomic Spectroscopy	177
	William C. Martin, Wolfgang L. Wiese, and Alexander Kramida	
11.1	Frequency, Wavenumber, Wavelength	178
11.2	Atomic States, Shells, and Configurations	178
11.3	Hydrogen and Hydrogen-Like Ions	178
11.4	Alkalis and Alkali-Like Spectra	178
11.5	Helium and Helium-Like Ions; <i>LS</i> Coupling	179
11.6	Hierarchy of Atomic Structure in <i>LS</i> Coupling	179
11.7	Allowed Terms or Levels for Equivalent Electrons	179
11.7.1	<i>LS</i> Coupling	179
11.7.2	<i>jj</i> Coupling	180
11.8	Notations for Different Coupling Schemes	180
11.8.1	<i>LS</i> Coupling (Russell–Saunders Coupling)	180
11.8.2	<i>jj</i> Coupling of Equivalent Electrons	181
11.8.3	J_1j or J_1J_2 Coupling	181
11.8.4	J_1l or J_1L_2 Coupling (J_1K Coupling)	182
11.8.5	LS_1 Coupling (LK Coupling)	182
11.8.6	Coupling Schemes and Term Symbols	182

11.9	Eigenvector Composition of Levels	182
11.10	Ground Levels and Ionization Energies for Neutral Atoms	183
11.11	Zeeman Effect	183
11.12	Term Series, Quantum Defects, and Spectral-Line Series	185
11.13	Sequences	186
11.13.1	Isoelectronic Sequence	186
11.13.2	Isoionic, Isonuclear, and Homologous Sequences	186
11.14	Spectral Wavelength Ranges, Dispersion of Air	186
11.15	Wavelength Standards	186
11.16	Spectral Lines: Selection Rules, Intensities, Transition Probabilities, f Values, and Line Strengths	187
11.16.1	Emission Intensities (Transition Probabilities)	187
11.16.2	Absorption f -values	187
11.16.3	Line Strengths	187
11.16.4	Relationships Between A , f , and S	188
11.16.5	Relationships Between Line and Multiplet Values	188
11.16.6	Relative Strengths for Lines of Multiplets in LS Coupling	188
11.17	Atomic Lifetimes	189
11.18	Regularities and Scaling	189
11.18.1	Transitions in Hydrogenic (One-Electron) Species	189
11.18.2	Systematic Trends and Regularities in Atoms and Ions with Two or More Electrons	189
11.19	Tabulations of Transition Probabilities	189
11.20	Spectral Line Shapes, Widths, and Shifts	194
11.20.1	Doppler Broadening	194
11.20.2	Pressure Broadening	194
11.21	Spectral Continuum Radiation	195
11.21.1	Hydrogenic Species	195
11.21.2	Many-Electron Systems	196
11.22	Sources of Spectroscopic Data	196
	References	196
12	High Precision Calculations for Helium	199
	Gordon W. F. Drake	
12.1	Introduction	199
12.2	The Three-Body Schrödinger Equation	199
12.2.1	Formal Mathematical Properties	200
12.3	Computational Methods	200
12.3.1	Variational Methods	200
12.3.2	Construction of Basis Sets	201
12.3.3	Calculation of Matrix Elements	202
12.3.4	Other Computational Methods	204
12.4	Variational Eigenvalues	205
12.4.1	Expectation Values of Operators and Sum Rules	205
12.5	Total Energies	205
12.5.1	Quantum Defect Extrapolations	210
12.5.2	Asymptotic Expansions	210
12.6	Radiative Transitions	213
12.6.1	Basic Formulation	213
12.6.2	Oscillator Strength Table	215
12.7	Future Perspectives	215
	References	216

13	Atomic Multipoles	217
	William E. Baylis	
	13.1 Polarization and Multipoles	218
	13.2 The Density Matrix in Liouville Space	219
	13.3 Diagonal Representation: State Populations	219
	13.4 Interaction with Light	220
	13.5 Extensions	221
	References	221
14	Atoms in Strong Fields	223
	S. Pedro Goldman and Mark M. Cassar	
	14.1 Electron in a Uniform Magnetic Field	223
	14.1.1 Nonrelativistic Theory	223
	14.1.2 Relativistic Theory	224
	14.2 Atoms in Uniform Magnetic Fields	225
	14.2.1 Anomalous Zeeman Effect	225
	14.2.2 Normal Zeeman Effect	225
	14.2.3 Paschen–Back Effect	225
	14.3 Atoms in Very Strong Magnetic Fields	226
	14.4 Atoms in Electric Fields	227
	14.4.1 Stark Ionization	227
	14.4.2 Linear Stark Effect	227
	14.4.3 Quadratic Stark Effect	228
	14.4.4 Other Stark Corrections	228
	14.5 Recent Developments	229
	References	229
15	Rydberg Atoms	231
	Thomas F. Gallagher	
	15.1 Wave Functions and Quantum Defect Theory	231
	15.2 Optical Excitation and Radiative Lifetimes	233
	15.3 Electric Fields	234
	15.4 Magnetic Fields	236
	15.5 Microwave Fields	237
	15.6 Collisions	238
	15.7 Autoionizing Rydberg States	239
	References	239
16	Rydberg Atoms in Strong Static Fields	241
	John B. Delos, Thomas Bartsch, and Turgay Uzer	
	16.1 Introduction	241
	16.2 Semiclassical Approximations	242
	16.3 Regular Trajectories and Regular Wave Functions	244
	16.4 Chaotic Trajectories and Irregular Wave Functions	245
	16.4.1 Small-Scale Structure	246
	16.4.2 Large-Scale Structure of Energy Spectra	247
	16.4.3 Chaotic Ionization	250
	16.5 Nuclear-Mass Effects	250
	16.6 Quantum Theories	250
	References	250

17	Hyperfine Structure	253
	Guy T. Emery	
17.1	Splittings and Intensities	254
17.1.1	Angular Momentum Coupling	254
17.1.2	Energy Splittings	254
17.1.3	Intensities	255
17.2	Isotope Shifts	256
17.2.1	Normal Mass Shift	256
17.2.2	Specific Mass Shift	256
17.2.3	Field Shift	256
17.2.4	Separation of Mass Shift and Field Shift	257
17.3	Hyperfine Structure	257
17.3.1	Electric Multipoles	258
17.3.2	Magnetic Multipoles	258
17.3.3	Hyperfine Anomalies	259
	References	259
18	Precision Oscillator Strength and Lifetime Measurements	261
	Lorenzo J. Curtis	
18.1	Introduction	261
18.2	Oscillator Strengths	262
18.2.1	Absorption and Dispersion Measurements	262
18.2.2	Emission Measurements	263
18.2.3	Combined Absorption, Emission and Lifetime Measurements	263
18.2.4	Branching Ratios in Highly Ionized Atoms	264
18.3	Lifetimes	264
18.3.1	The Hanle Effect	264
18.3.2	Time-Resolved Decay Measurements	265
18.3.3	Other Methods	266
18.3.4	Multiplexed Detection	267
	References	267
19	Spectroscopy of Ions Using Fast Beams and Ion Traps	269
	Elmar Träbert and Eric H. Pinnington	
19.1	Spectroscopy Using Fast Ion Beams	269
19.1.1	Beam–Foil Spectroscopy	269
19.1.2	Beam–Gas Spectroscopy	270
19.1.3	Beam–Laser Spectroscopy	271
19.1.4	Other Techniques of Ion–Beam Spectroscopy	272
19.2	Spectroscopy Using Ion Traps	272
19.2.1	Electron Beam Ion Traps	273
19.2.2	Heavy-Ion Storage Rings	277
19.2.3	Conclusions	278
	References	279
20	Line Shapes and Radiation Transfer	283
	Alan Gallagher	
20.1	Collisional Line Shapes	283
20.1.1	Voigt Line Shape	284
20.1.2	Interaction Potentials	284
20.1.3	Classical Oscillator Approximation	284
20.1.4	Impact Approximation	285
20.1.5	Examples: Line Core	286

20.1.6	Δ and γ_c Characteristics	287
20.1.7	Quasistatic Approximation	288
20.1.8	Satellites	289
20.1.9	Bound States and Other Quantum Effects	289
20.1.10	Einstein A and B Coefficients	290
20.2	Radiation Trapping	290
20.2.1	Holstein–Biberman Theory	290
20.2.2	Additional Factors	292
20.2.3	Measurements	293
	References	294
21	Thomas-Fermi and Other Density-Functional Theories	297
	John D. Morgan III	
21.1	Introduction	297
21.2	Thomas–Fermi Theory and Its Extensions	298
21.2.1	Thomas–Fermi Theory	298
21.2.2	Thomas–Fermi–von Weizsäcker Theory	300
21.2.3	Thomas–Fermi–Dirac Theory	301
21.2.4	Thomas–Fermi–von Weizsäcker–Dirac Theory	301
21.2.5	Thomas–Fermi Theory with Different Spin Densities	301
21.3	Nonrelativistic Energies of Heavy Atoms	302
21.4	General Density Functional Theory	302
21.4.1	The Hohenberg–Kohn Theorem for the One-Electron Density	302
21.4.2	The Kohn–Sham Method for Including Exchange and Correlation Corrections	303
21.4.3	Density Functional Theory for Excited States	304
21.4.4	Locality of Density Functional Theory	304
21.4.5	Relativistic and Quantum Field Theoretic Density Functional Theory	304
21.5	Recent Developments	304
	References	306
22	Atomic Structure: Variational Wave Functions and Properties	309
	Charlotte Froese Fischer and Michel Godefroid	
22.1	Nonrelativistic and Relativistic Hamiltonians	309
22.1.1	Schrödinger’s Hamiltonian	310
22.1.2	Dirac–Coulomb(–Breit) Hamiltonian	310
22.1.3	Breit–Pauli Hamiltonian	310
22.2	Many-Electron Wave Functions	311
22.2.1	Nonrelativistic Orbitals and LS Configuration State Functions	311
22.2.2	Relativistic Dirac Orbitals and jj Configuration State Functions	312
22.3	Variational Principle	312
22.4	Hartree–Fock and Dirac–Hartree–Fock Methods	313
22.4.1	Diagonal Energy Parameters and Koopmans’ Theorem	314
22.4.2	Hartree–Fock Operator	314
22.4.3	Brillouin’s Theorem	315
22.4.4	The Dirac–Hartree–Fock Equations	315
22.4.5	Numerical Solution of Variational Equations	315
22.4.6	Properties of Hartree–Fock Solutions	317
22.5	Multiconfiguration (Dirac)-Hartree–Fock Method	318
22.5.1	Z -Dependent Theory	318
22.5.2	The MC(D)HF Approximation	319
22.5.3	Systematic Methods	320

	22.5.4	Excited States	321
	22.5.5	Autoionizing States	321
	22.6	Configuration Interaction Methods	321
	22.7	Atomic Properties	324
	22.7.1	Transition Data—Allowed and Forbidden Lines	324
	22.7.2	Electron Affinities	324
	22.7.3	Metastable States and Autoionization	325
	22.7.4	Nuclear Effects	326
	22.8	Summary	328
		References	328
23		Relativistic Atomic Structure	331
		Ian Grant	
	23.1	Mathematical Basics	332
	23.1.1	Relativistic Notation: Minkowski Space-Time	332
	23.1.2	Lorentz Transformations	332
	23.1.3	Classification of Lorentz Transformations	332
	23.1.4	Contravariant and Covariant Vectors	333
	23.1.5	Poincaré Transformations	333
	23.2	Dirac's Equation	333
	23.2.1	Characterization of Dirac States	334
	23.2.2	The Charge-Current Four-Vector	334
	23.3	QED: Relativistic Atomic and Molecular Structure	335
	23.3.1	The QED Equations of Motion	335
	23.3.2	The Quantized Electron-Positron Field	335
	23.3.3	Quantized Electromagnetic Field	336
	23.3.4	QED Perturbation Theory	336
	23.3.5	Propagators	338
	23.3.6	Effective Interaction of Electrons	339
	23.4	Many-Body Theory For Atoms	339
	23.4.1	Effective Hamiltonians	340
	23.4.2	Nonrelativistic Limit: Breit-Pauli Hamiltonian	340
	23.4.3	Perturbation Theory: Nondegenerate Case	340
	23.4.4	Perturbation Theory: Open-Shell Case	341
	23.4.5	Perturbation Theory: Algorithms	342
	23.5	Spherical Symmetry	342
	23.5.1	Eigenstates of Angular Momentum	342
	23.5.2	Dirac Hamiltonian in Spherical Coordinates	343
	23.5.3	Solutions Near the Nucleus	345
	23.5.4	Bound states: $r \rightarrow \infty$	346
	23.5.5	Hydrogenic Atoms	347
	23.5.6	The Free Electron Problem in Spherical Coordinates	348
	23.6	Numerical Methods for the Radial Dirac Equation	349
	23.6.1	Dirac's Equation on a Finite Domain	349
	23.6.2	Expansion Methods	349
	23.6.3	Finite Basis Set Formalism	350
	23.6.4	Physically Acceptable Basis Sets	350
	23.6.5	Basis Sets Defined on \mathbb{R}^3	352
	23.6.6	B-Splines	353
	23.7	Finite Differences	354

23.8	Many-Electron Atoms	356
23.8.1	Atomic States	356
23.8.2	Atomic Orbitals	356
23.8.3	Slater Determinants	356
23.8.4	Configurational States	356
23.8.5	ASFs and CSF	357
23.8.6	Matrix Construction	357
23.8.7	Dirac–Hartree–Fock–Breit	357
23.8.8	Electron Correlation	359
23.8.9	Electron Self-Energy and Vacuum Polarization	359
23.8.10	Radiative Transitions	360
23.9	GRASP – Information and Software	360
	References	360
24	Many-Body Theory of Atomic Structure and Processes	363
	Miron Y. Amusia	
24.1	Diagrammatic Technique	364
24.1.1	Basic Elements	364
24.1.2	Construction Principles for Diagrams	364
24.1.3	Correspondence Rules	365
24.1.4	Higher-Order Corrections and Summation of Sequences	367
24.2	Calculation of Atomic Properties	368
24.2.1	Electron Correlations in Ground State Properties	368
24.2.2	Characteristics of One-Particle States	369
24.2.3	Electron Scattering	371
24.2.4	Two-Electron and Two-Vacancy States	372
24.2.5	Electron–Vacancy States	373
24.2.6	Photoionization in RPAE and Beyond	374
24.2.7	Photon Emission and Bremsstrahlung	377
24.2.8	RPAE in the Magnetic Channel	378
24.2.9	Consideration of “Big Atoms”	379
24.3	Concluding Remarks	380
	References	381
25	Photoionization of Atoms	383
	Anthony F. Starace	
25.1	General Considerations	383
25.1.1	The Interaction Hamiltonian	383
25.1.2	Alternative Forms for the Transition Matrix Element	384
25.1.3	Selection Rules for Electric Dipole Transitions	385
25.1.4	Boundary Conditions on the Final State Wave Function	385
25.1.5	Photoionization Cross Sections	386
25.2	An Independent Electron Model	386
25.2.1	Central Potential Model	386
25.2.2	High Energy Behavior	387
25.2.3	Near-Threshold Behavior	387
25.3	Particle–Hole Interaction Effects	388
25.3.1	Intrachannel Interactions	388
25.3.2	Virtual Double Excitations	389
25.3.3	Interchannel Interactions	389
25.3.4	Photoionization of Ar	389

25.4	Theoretical Methods for Photoionization	390
25.4.1	Calculational Methods	390
25.4.2	Other Interaction Effects	390
25.5	Related Photoionization Processes	391
25.6	Applications to Other Processes	391
25.6.1	Applications to Two and Three-Photon Ionization Processes	392
25.6.2	Application to High-Order Harmonic Generation	392
25.7	Future Directions	392
	References	393
26	Autoionization	395
	Anand K. Bhatia and Aaron Temkin	
26.1	Introduction	395
26.1.1	Auger Effect	395
26.1.2	Autoionization, Autodetachment, and Radiative Decay	395
26.1.3	Formation, Scattering, and Resonances	396
26.2	Projection Operator Formalism	396
26.2.1	Optical Potential	396
26.2.2	Expansion of V_{op} : The QHQ Problem	396
26.3	Forms of P and Q	396
26.3.1	The Feshbach Form	396
26.3.2	Reduction for the $N = 1$ Target	397
26.3.3	Alternative Projection and Projection-Like Operators	398
26.4	Width, Shift, and Shape Parameter	398
26.4.1	Width and Shift	398
26.4.2	Shape Parameter	398
26.4.3	Relation to Breit–Wigner Parameters	400
26.5	Other Calculational Methods	400
26.5.1	Complex Rotation Method	400
26.5.2	Pseudopotential Method	402
26.5.3	Exact Bound States in Continuum	403
26.6	Related Topics	403
	References	404
27	Green’s Functions of Field Theory	405
	Gordon Feldman and Thomas Fulton	
27.1	Introduction	405
27.2	The Two-Point Green’s Function	406
27.3	The Four-Point Green’s Function	409
27.4	Radiative Transitions	410
27.5	Radiative Corrections	412
	References	414
28	Quantum Electrodynamics	415
	Jonathan R. Sapirstein	
28.1	Introduction	415
28.2	Basic QED Formalism	417
28.3	Perturbation Theory with Green Functions	420
28.4	Two-Particle Bound States	426
28.5	Many-Electron Bound States	428
28.6	Recoil Corrections at High Z	429
28.7	Concluding Remarks	430
	References	431

29	Tests of Fundamental Physics	433
	Eite Tiesinga and Peter J. Mohr	
29.1	Introduction	433
29.2	Consistency of Fundamental Physics	434
29.3	Topics in This Review	436
29.4	Electron g -Factor Anomaly	437
29.5	Atom Recoil Experiments and Mass Spectrometry	438
29.6	Mass-Ratio Measurements Using the g -Factor of Hydrogen-Like Ions	438
29.6.1	Theory for the g -Factor of Hydrogen-Like Ions	439
29.7	Hydrogen Atom Energy levels	441
29.7.1	Theory for the Hydrogen Energy Levels	442
	References	446
30	Atomic Clocks and Constraints on Variations of Fundamental Constants	449
	Savely G. Karshenboim, Victor Flambaum, and Ekkehard Peik	
30.1	Atomic Clocks and Frequency Standards	450
30.1.1	Caesium Atomic Fountain	450
30.1.2	Trapped Ions	451
30.1.3	Laser-Cooled Neutral Atoms	452
30.1.4	Two-Photon Transitions and Doppler-Free Spectroscopy	452
30.1.5	Optical Frequency Measurements	453
30.1.6	Limitations on Frequency Variations	453
30.2	Atomic Spectra and Their Dependence on the Fundamental Constants	454
30.2.1	The Spectrum of Hydrogen and Nonrelativistic Atoms	454
30.2.2	Hyperfine Structure and the Schmidt Model	454
30.2.3	Atomic Spectra: Relativistic Corrections	454
30.3	Laboratory Constraints on Temporal Variations of Fundamental Constants	455
30.3.1	Constraints from Absolute and Relative Optical Measurements	456
30.3.2	Constraints from Microwave Clocks	457
30.3.3	A Model-Independent Constraint on the Variation of the Electron-to-Proton Mass Ratio from Molecular Spectroscopy	457
30.3.4	Other Model-Dependent Constraints	457
30.4	Summary	458
	References	458
31	Searches for New Particles Including Dark Matter with Atomic, Molecular, and Optical Systems	461
	Victor Flambaum and Yevgeny Stadnik	
31.1	Nongravitational Interactions of Spinless Bosons	462
31.2	New Forces	462
31.2.1	Macroscopic-Scale Experiments	463
31.2.2	Atomic-Scale Experiments	463
31.3	Laboratory Sources	464
31.4	Astrophysical Sources	465
31.5	Cosmological Sources	466
31.5.1	Haloscope Experiments	466
31.5.2	Spin-Precession Experiments	466
31.5.3	Time-Varying Physical Constants	467
	References	467

32	Searches for New Physics	471
	Marianna S. Safronova	
32.1	Parity Nonconserving Effects in Atoms	471
32.1.1	Nuclear-Spin-Independent PNC Effects	472
32.1.2	Nuclear-Spin-Dependent PNC Effects	472
32.1.3	PNC in Cesium and Implications for Particle and Hadronic Physics	473
32.1.4	Current PNC Experiments	474
32.2	Electric Dipole Moments and Related Phenomena	475
32.2.1	Experiments with Paramagnetic Systems	475
32.2.2	Experiments with Diamagnetic Systems	476
32.2.3	Impact on Particle Physics	477
32.3	Tests of the CPT Symmetry	477
32.4	Lorentz Symmetry Tests	478
32.4.1	Electron–Photon Sector of SME	478
32.4.2	Proton and Neutron Sectors of SME	480
32.5	AMO Tests of General Relativity	481
32.5.1	Tests of the Einstein Equivalence Principle	481
32.5.2	Other AMO Tests of Gravity	481
32.5.3	Detection of Gravitational Waves	482
	References	482

Part C Molecules

33	Molecular Structure	487
	David R. Yarkony	
33.1	Concepts	488
33.1.1	Nonadiabatic Ansatz: Born–Oppenheimer Approximation	488
33.1.2	Born–Oppenheimer Potential Energy Surfaces and Their Topology	489
33.1.3	Classification of Interstate Couplings: Adiabatic and Diabatic Bases	489
33.1.4	Surfaces of Intersection of Potential Energy Surfaces	490
33.2	Characterization of Potential Energy Surfaces	490
33.2.1	The Self-Consistent Field (SCF) Method	491
33.2.2	Electron Correlation: Wave Function Based Methods	491
33.2.3	Electron Correlation: Density Functional Theory	494
33.2.4	Weakly Interacting Systems	495
33.3	Intersurface Interactions: Perturbations	495
33.3.1	Derivative Couplings	496
33.3.2	Breit–Pauli Interactions	497
33.3.3	Surfaces of Intersection	498
33.4	Nuclear Motion	499
33.4.1	General Considerations	499
33.4.2	Rotational-Vibrational Structure	500
33.4.3	Coupling of Electronic and Rotational Angular Momentum in Weakly Interacting	500
33.4.4	Reaction Path	501
33.5	Reaction Mechanisms: A Spin-Forbidden Chemical Reaction	502
33.6	Recent Developments	504
	References	504

34	Molecular Symmetry and Dynamics	507
	William G. Harter and Tyle C. Reimer	
34.1	Dynamics and Spectra of Molecular Rotors	507
	34.1.1 Rigid Rotors	508
	34.1.2 Molecular States Inside and Out	508
	34.1.3 Rigid Asymmetric Rotor Eigensolutions and Dynamics	509
34.2	Rotational Energy Surfaces and Semiclassical Rotational Dynamics	511
34.3	Symmetry of Molecular Rotors	513
	34.3.1 Asymmetric Rotor Symmetry Analysis	513
34.4	Tetrahedral-Octahedral Rotational Dynamics and Spectra	514
	34.4.1 Semirigid Octahedral Rotors and Centrifugal Tensor Hamiltonians	515
	34.4.2 Octahedral and Tetrahedral Rotational Energy Surfaces	515
	34.4.3 Octahedral and Tetrahedral Rotational Fine Structure	515
	34.4.4 Octahedral Superfine Structure	517
34.5	High-Resolution Rovibrational Structure	518
	34.5.1 Tetrahedral Nuclear Hyperfine Structure	518
	34.5.2 Superhyperfine Structure and Spontaneous Symmetry Breaking	520
	34.5.3 Large Spherical Top Molecules: Cubic-Octahedral Symmetry Effects	521
	34.5.4 Icosahedral Spherical Top Molecules: Extreme Spin Symmetry Effects	523
	34.5.5 $^{12}\text{C}_{60}$ versus $^{13}\text{C}_{60}$: a World of Difference in Spin- $\frac{1}{2}$ Hyperfine Spectroscopy	525
34.6	Composite Rotors and Multiple RES	528
	34.6.1 3-D-Rotor and 2-D-Oscillator Analogy	529
	34.6.2 Gyro-Rotors and 2-D-Local Mode Analogy	530
	34.6.3 Multiple Gyro-Rotor RES and Rotational Energy Eigensurfaces (REES)	531
	34.6.4 Multi-Quantum CF_4 Rovibrational Polyads and REES Visualization	533
	References	534
35	Radiative Transition Probabilities	537
	David L. Huestis	
35.1	Overview	537
	35.1.1 Intensity Versus Line-Position Spectroscopy	537
35.2	Molecular Wave Functions in the Rotating Frame	538
	35.2.1 Symmetries of the Exact Wave Function	538
	35.2.2 Rotation Matrices	539
	35.2.3 Transformation of Ordinary Objects into the Rotating Frame	539
35.3	The Energy–Intensity Model	539
	35.3.1 States, Levels, and Components	539
	35.3.2 The Basis Set and Matrix Hamiltonian	540
	35.3.3 Fitting Experimental Energies	541
	35.3.4 The Transition Moment Matrix	541
	35.3.5 Fitting Experimental Intensities	542
35.4	Selection Rules	542
	35.4.1 Symmetry Types	542
	35.4.2 Rotational Branches and Parity	542
	35.4.3 Nuclear Spin, Spatial Symmetry, and Statistics	543
	35.4.4 Electron Orbital and Spin Angular Momenta	544

35.5	Absorption Cross Sections and Radiative Lifetimes	545
35.5.1	Radiation Relations	545
35.5.2	Transition Moments	545
35.6	Vibrational Band Strengths	546
35.6.1	Franck–Condon Factors	546
35.6.2	Vibrational Transitions	547
35.7	Rotational Branch Strengths	547
35.7.1	Branch Structure and Transition Type	547
35.7.2	Hönl–London Factors	548
35.7.3	Sum Rules	548
35.7.4	Hund’s Cases	549
35.7.5	Symmetric Tops	550
35.7.6	Asymmetric Tops	550
35.8	Forbidden Transitions	551
35.8.1	Spin-Changing Transitions	551
35.8.2	Orbitally-Forbidden Transitions	551
35.9	Recent Developments	552
	References	552
36	Molecular Photodissociation	555
	Abigail J. Dobbyn, David H. Mordant, and Reinhard Schinke	
36.1	Observables	557
36.1.1	Scalar Properties	557
36.1.2	Vector Correlations	557
36.2	Experimental Techniques	558
36.3	Theoretical Techniques	559
36.4	Concepts in Dissociation	561
36.4.1	Direct Dissociation	561
36.4.2	Vibrational Predissociation	561
36.4.3	Electronic Predissociation	562
36.5	Recent Developments	562
36.6	Summary	563
	References	564
37	Time Resolved Molecular Dynamics	565
	Volker Engel and Patrick Nuernberger	
37.1	Introduction	565
37.2	The Principle of Time-Resolved Spectroscopy	566
37.3	Pump-Probe Scheme	568
37.4	Transient Absorption in the Liquid Phase	568
37.5	Further Implementations	570
37.5.1	Coherent Two-Dimensional Spectroscopy	570
37.5.2	Ultrafast Dynamics Studied with X-Ray and Electron Pulses	570
37.5.3	Dynamics and Control	571
	References	572
38	Nonreactive Scattering	575
	Alexandre Faure, Francois Lique, and David R. Flower	
38.1	Definitions	575
38.2	Quantal Method	576
38.3	Symmetries and Conservation Laws	577
38.4	Coordinate Systems	577
38.5	Scattering Equations	578

38.6	Matrix Elements	578
38.6.1	Interaction Potential	578
38.6.2	Centrifugal Potential	579
38.7	Semi and Quasi-Classical Methods	579
38.8	Example: CO–H ₂	579
38.9	New Directions	580
	References	580
39	Gas Phase Reactions	583
	Eric Herbst	
39.1	Introduction	583
39.2	Normal Bimolecular Reactions	585
39.2.1	Capture Theories	585
39.2.2	Phase Space Theories	587
39.2.3	Short-Range Barriers	588
39.2.4	Complexes Followed by Barriers	589
39.2.5	The Role of Tunneling	590
39.3	Association Reactions	591
39.3.1	Radiative Stabilization	591
39.3.2	Complex Formation and Dissociation	592
39.3.3	Competition with Exoergic Channels	593
39.4	Concluding Remarks	593
	References	594
40	Gas Phase Ionic Reactions Abstract	597
	Nigel G. Adams	
40.1	Overview	597
40.2	Reaction Energetics	598
40.3	Chemical Kinetics	599
40.4	Reaction Processes	600
40.4.1	Binary Ion–Neutral Reactions	600
40.4.2	Ternary Ion–Molecule Reactions	603
40.5	Electron Attachment	604
40.6	Recombination	604
40.6.1	Electron–Ion Recombination	604
40.6.2	Ion–Ion Recombination (Mutual Neutralization)	605
	References	606
41	Clusters	609
	Mary L. Mandich	
41.1	Introduction	609
41.2	Metal Clusters	610
41.2.1	Geometric Structures	610
41.2.2	Electronic and Magnetic Properties	610
41.2.3	Chemical Properties	612
41.2.4	Stable Metal Cluster Molecules and Metallocarbohedrenes	612
41.3	Carbon Clusters	613
41.3.1	Small Carbon Clusters	613
41.3.2	Fullerenes	614
41.3.3	Giant Carbon Clusters: Tubes, Capsules, Onions, Russian Dolls, Papier Mâché	615

41.4	Ionic Clusters	615
41.4.1	Geometric Structures	615
41.4.2	Electronic and Chemical Properties	616
41.5	Semiconductor Clusters	616
41.5.1	Silicon and Germanium Clusters	616
41.5.2	Group III–V and Group II–VI Semiconductor Clusters	617
41.6	Noble Gas Clusters	618
41.6.1	Geometric Structures	618
41.6.2	Electronic Properties	618
41.6.3	Doped Noble Gas Clusters	619
41.6.4	Helium Clusters	619
41.7	Molecular Clusters	620
41.7.1	Geometric Structures and Phase Dynamics	620
41.7.2	Electronic Properties: Charge Solvation	621
41.8	Recent Developments	621
	References	622
42	Infrared Spectroscopy	625
	Henry Buijs	
42.1	Introduction	626
42.2	Historical Evolution of Infrared Spectroscopy Practice	626
42.3	Quantitative Analysis by Infrared Spectroscopy	627
42.4	Molecular Spectroscopy	627
42.5	Remote Sensing	628
42.6	The Evolution of Fourier Transform Infrared Spectroscopy (FTIR)	628
42.7	Laser-Based Infrared Spectroscopy	629
42.8	Intensities of Infrared Radiation	629
42.9	Sources for IR Spectroscopy	630
42.10	Relationship Between Source Spectrometer Sample and Detector	630
42.11	Simplified Principle of FTIR Spectroscopy	630
42.11.1	Interferogram Generation: The Michelson Interferometer	630
42.11.2	Description of Wavefront Interference with Time Delay	631
42.11.3	Operation of Spectrum Determination	631
42.11.4	Optical Aspects of FTIR Technology	632
42.12	The Scanning Michelson Interferometer	633
42.13	Infrared Spectroscopy Application Activity 2020	634
42.13.1	Analytical Chemistry Laboratories	634
42.13.2	Biomedical and Pharmaceutical Laboratories	635
42.13.3	Forensic Investigation	635
42.13.4	Infrared Spectroscopy in Quality Assurance Laboratories	636
42.13.5	Process Monitoring by Infrared Spectroscopy	636
42.13.6	Environmental Monitoring	637
42.13.7	Remote Sensing	637
42.14	Conclusion	638
	References	639
43	Laser Spectroscopy in the Submillimeter and Far-Infrared Regions	641
	Kenneth Evenson and John M. Brown	
43.1	Introduction	641
43.2	Experimental Techniques Using Coherent SM-FIR Radiation	642
43.2.1	Tunable FIR Spectroscopy with CO ₂ Laser Difference Generation in a MIM Diode	642

43.2.2	Laser Magnetic Resonance	644
43.2.3	TuFIR and LMR Detectors	645
43.3	Submillimeter and FIR Astronomy	645
43.4	Upper Atmospheric Studies	646
	References	646
44	Spectroscopic Techniques: Lasers	649
	Paul Engelking	
44.1	Laser Basics	649
44.1.1	Stimulated Emission	649
44.1.2	Laser Configurations	649
44.1.3	Gain	650
44.1.4	Laser Light	650
44.2	Laser Designs	651
44.2.1	Cavities	651
44.2.2	Pumping	652
44.3	Interaction of Laser Light with Matter	652
44.3.1	Linear Absorption	652
44.3.2	Multiphoton Absorption	654
44.3.3	Level Shifts	654
44.3.4	Hole Burning	654
44.3.5	Nonlinear Optics	655
44.3.6	Raman Scattering	655
44.4	Recent Developments	656
	References	656
45	Spectroscopic Techniques: Cavity-Enhanced Methods	657
	Barbara Paldus and Alexander A. Kachanov	
45.1	Limitations of Traditional Absorption Spectrometers	657
45.2	Cavity Ring-Down Spectroscopy	658
45.2.1	Pulsed Cavity Ring-Down Spectroscopy	659
45.2.2	Continuous-Wave Cavity Ring-Down Spectroscopy (CW-CRDS)	659
45.3	Cavity-Enhanced Spectroscopy	660
45.3.1	Cavity-Enhanced Transmission Spectroscopy (CETS)	661
45.3.2	Locked Cavity-Enhanced Transmission Spectroscopy (L-CETS)	662
45.4	Extensions to Solids and Liquids	663
45.4.1	Evanescence-Wave Cavity Ring-Down Spectroscopy (EW-CRDS)	663
45.4.2	Cavity Ring-Down of Condensed Media for Analytical Chemistry	663
45.4.3	Cavity Ring-Down Spectroscopy Using Waveguides	663
	References	664
46	Spectroscopic Techniques: Ultraviolet	667
	Glenn Stark, Nelson de Oliveira, and Peter L. Smith	
46.1	Light Sources	668
46.1.1	Synchrotron Radiation	668
46.1.2	Laser-Produced Plasmas	670
46.1.3	Arcs, Sparks, and Discharges	670
46.1.4	Supercontinuum Radiation	670
46.2	VUV Lasers	671
46.2.1	Primary Lasers	671
46.2.2	Nonlinear Techniques	671

46.3	Spectrometers	673
46.3.1	Grating Spectrometers	673
46.3.2	Fourier Transform Spectrometers	674
46.4	Detectors	675
46.4.1	Photomultiplier Tubes	675
46.4.2	Microchannel Plates	675
46.4.3	Silicon Photodiodes	675
46.4.4	Charge-Coupled Devices	676
46.5	Optical Materials	676
46.5.1	Windows	676
46.5.2	Capillaries	676
46.5.3	Thin Films	676
46.5.4	Coatings	677
46.5.5	Interference Filters and Multilayer Coatings	677
46.5.6	Polarizers	677
	References	677

Part D Scattering Theory

47	Classical, Quantal, and Semiclassical Propagators and Applications to Elastic Scattering	685
	Jan-Michael Rost	
47.1	What Is Semiclassics?	685
47.2	Quantum, Classical, and Semiclassical Propagators	686
47.2.1	The Quantum Propagator as a Feynman Path Integral	686
47.2.2	The Classical Propagator	687
47.2.3	The Semiclassical Propagator	687
47.3	Advantages and Disadvantages of Semiclassics	689
47.4	Applications to Elastic Scattering	689
47.4.1	Central Field	689
47.4.2	Center-of-Mass to Laboratory Coordinate Conversion	689
47.5	Quantal Elastic Scattering	690
47.5.1	Scattering Amplitude from the Propagator	690
47.5.2	Partial Wave Expansion	690
47.5.3	Phase Shift and Cross Sections	691
47.5.4	Identical Particles: Symmetry Oscillations	692
47.5.5	Low-Energy $E \rightarrow 0$ Scattering	693
47.5.6	Nonspherical Potentials	695
47.5.7	Reactive Systems	695
47.6	Classical Elastic Scattering	696
47.6.1	Elastic Scattering Cross Section	696
47.6.2	Deflection Functions	696
47.6.3	Glory and Rainbow Scattering	697
47.6.4	Orbiting and Spiraling Collisions	698
47.6.5	Deflection Function and Time Delay from Action	698
47.6.6	Approximate Actions	698
47.7	Semiclassical Elastic Scattering	698
47.7.1	Semiclassical Amplitudes and Cross Sections	698
47.7.2	Diffraction and Glory Amplitudes	700
47.7.3	Small-Angle (Diffraction) Scattering	701
47.7.4	Small-Angle (Glory) Scattering	701

47.7.5	Oscillations in Elastic Scattering	702
47.7.6	Scattering Amplitude in Poisson Sum Representation	702
47.7.7	Semiclassical Phase Shifts	702
47.7.8	Semiclassical Amplitudes: Integral Representation	704
47.8	Coulomb Elastic Scattering	705
47.8.1	Quantum Phase Shift, Rutherford and Mott Scattering	705
47.8.2	Classical Coulomb Scattering	706
47.8.3	Semiclassical Coulomb Scattering	706
47.8.4	Born Approximation for Coulomb Scattering	706
47.9	Results for Model Potentials	707
47.9.1	Classical Deflection Functions and Cross Sections	707
47.9.2	Amplitudes and Cross Sections in Born Approximation	710
	References	711
48	Orientation and Alignment in Atomic and Molecular Collisions	713
	Nils Andersen	
48.1	Introduction	713
48.2	Collisions Involving Unpolarized Beams	714
48.2.1	The Fully Coherent Case	714
48.2.2	The Incoherent Case with Conservation of Atomic Reflection Symmetry	717
48.2.3	The Incoherent Case Without Conservation of Atomic Reflection Symmetry	717
48.3	Collisions Involving Spin-Polarized Beams	718
48.3.1	The Fully Coherent Case	718
48.3.2	The Incoherent Case with Conservation of Atomic Reflection Symmetry	718
48.3.3	The Incoherent Case Without Conservation of Atomic Reflection Symmetry	720
48.4	Example	721
48.4.1	The First Born Approximation	721
48.5	Further Developments	722
48.5.1	$S \rightarrow D$ Excitation	722
48.5.2	$P \rightarrow P$ Excitation	722
48.5.3	Relativistic Effects in $S \rightarrow P$ Excitation	722
48.6	Summary	722
	References	722
49	Electron–Atom, Electron–Ion, and Electron–Molecule Collisions	725
	Klaus Bartschat, Jonathan Tennyson, and Philip Burke	
49.1	Electron–Atom and Electron–Ion Collisions	725
49.1.1	Low-Energy Elastic Scattering and Excitation	725
49.1.2	Relativistic Effects for Heavy Atoms and Ions	728
49.1.3	Multichannel Resonance Theory	729
49.1.4	Solution of the Coupled Integro-Differential Equations	731
49.1.5	Intermediate and High-Energy Elastic Scattering and Excitation	735
49.1.6	Ionization	737
49.2	Electron–Molecule Collisions	741
49.2.1	Laboratory Frame Representation	741
49.2.2	Molecular Frame Representation	742
49.2.3	Inclusion of the Nuclear Motion	742
49.2.4	Electron Collisions with Polyatomic Molecules	744

49.3	Electron–Atom Collisions in a Laser Field	744
49.3.1	Potential Scattering	744
49.3.2	Scattering by Complex Atoms and Ions	746
	References	747
50	Quantum Defect Theory	751
	Chris H. Greene	
50.1	Overview	751
50.2	Conceptual Foundation of QDT	751
50.2.1	Single-Channel Nonrelativistic Quantum Defect Theory	752
50.2.2	Multichannel QDT	753
50.2.3	Molecular Ionization Channels Treated by the Rovibrational Frame Transformation	756
50.2.4	Ultracold Atom–Atom Collisions in MQDT	757
	References	759
51	Positron Collisions	761
	Joshua R. Machacek, Robert P. McEachran, and Allan D. Stauffer	
51.1	Scattering Channels	761
51.1.1	Positronium Formation	762
51.1.2	Annihilation	762
51.2	Theoretical Methods	763
51.3	Particular Applications	765
51.3.1	Atomic Hydrogen	765
51.3.2	Noble Gases	765
51.3.3	Other Atoms	766
51.3.4	Molecular Hydrogen	766
51.3.5	Water	767
51.3.6	Other Molecules	767
51.4	Binding of Positrons to Atoms	768
51.5	Positronium Scattering	768
51.6	Antihydrogen	768
51.7	Reviews	768
	References	769
52	Adiabatic and Diabatic Collision Processes at Low Energies	773
	Evgeny Nikitin and Alexander Kandratsenka	
52.1	Basic Definitions	773
52.1.1	Slow Quasi-Classical Collisions	773
52.1.2	Adiabatic and Diabatic Electronic States	774
52.1.3	Nonadiabatic Transitions: The Massey Parameter	774
52.2	Two-State Approximation	775
52.2.1	Relation Between Adiabatic and Diabatic Basis Functions	775
52.2.2	Coupled Equations and Transition Probabilities in the Common Trajectory Approximation	775
52.2.3	Selection Rules for Nonadiabatic Coupling	777
52.3	Single-Passage Transition Probabilities in Common Trajectory Approximation	778
52.3.1	Transitions Between Noncrossing Adiabatic Potential Energy Curves	778
52.3.2	Transitions Between Crossing Adiabatic Potential Curves	779

52.4	Double-Passage Transition Probabilities	780
52.4.1	Transition Probabilities in the Classically-Allowed and Classically-Forbidden WKB Regimes: Interference and Tunneling	780
52.4.2	Nonadiabatic Transitions near Turning Points	781
52.5	Multiple-Passage Transition Probabilities	782
52.5.1	Multiple Passage in Atomic Collisions	782
52.5.2	Surface Hopping	782
	References	783
53	Ion–Atom and Atom–Atom Collisions	785
	Tom Kirchner, A. Lewis Ford, and John F. Reading	
53.1	Introduction	785
53.2	General Considerations and Formulation of the Problem	785
53.3	Approximate Versus Full Many-Electron Treatments	787
53.4	Computational Techniques	789
53.4.1	Coupled-Channel Methods	789
53.4.2	Numerical Grid Methods	790
53.5	Description of the Ionization Continuum	791
	References	793
54	Ultracold Rydberg Atom–Atom Interaction	795
	Hossein Sadeghpour	
54.1	Zero/Short-Range Neutral Collisions	796
54.2	Low-Energy Phase Shift and Zero-Energy Scattering Length	797
54.3	Ultralong-Range Rydberg Molecules: Fermi’s Idea Redux	798
54.4	Fermi Extended: Do Elastic Collisions Result in Inelastic Chemical Reactions?	798
54.5	Ion-Pair Molecules	799
54.6	Few-Body Short-Range Scattering	800
54.6.1	Additivity of Binary Interactions	800
54.6.2	Three-Body Effective Interactions	800
54.7	Collective Quantum Many-Body Effects	800
54.7.1	Bose and Fermi Polarons	800
54.7.2	Linear Response Absorption	801
	References	802
55	Ion–Atom Charge Transfer Reactions at Low Energies	805
	Bernard Zygelman, Phillip C. Stancil, Muriel Gargaud, and Ronald McCarroll	
55.1	Classical and Semiclassical Treatments	806
55.1.1	Over the Barrier Models	806
55.1.2	Langevin Orbiting	806
55.1.3	Landau–Zener–Rosen Theories	807
55.2	The Molecular Orbital Approach	808
55.2.1	A Gauge Theoretic Framework for the PSS Equations	809
55.3	Cold and Ultracold Charge Exchange and Association	810
55.4	New Developments and Future Prospects	811
	References	811

56	Continuum Distorted Wave and Wannier Methods	813
	Roberto D. Rivarola, Omar A. Fojón, Marcelo Ciappina, and Derrick Crothers	
56.1	Introduction	813
56.2	Continuum Distorted Wave Method	814
	56.2.1 Perturbation Theory	814
	56.2.2 Relativistic Continuum Distorted Waves	816
	56.2.3 Variational CDW	816
	56.2.4 Ionization	817
	56.2.5 Ionization of Molecular Targets	819
56.3	Wannier Method	822
	56.3.1 The Wannier Threshold Law	822
	56.3.2 Peterkop's Semiclassical Theory	822
	56.3.3 The Quantal Semiclassical Approximation	823
	References	827
57	Basic Atomic Processes in High-Energy Ion–Atom Collisions	829
	Alexander Voitkiv	
57.1	Introduction	829
57.2	Atomic Ionization and Projectile-Electron Loss	830
	57.2.1 Atomic Ionization in Collisions with a Bare Nucleus	832
	57.2.2 Projectile-Electron Loss	834
57.3	Electron Transfer Processes	836
	57.3.1 Nonradiative Electron Capture	836
	57.3.2 Radiative Electron Capture	839
57.4	Electron–Positron Pair Production	840
	57.4.1 Free Pair Production	841
	57.4.2 Bound–Free Pair Production	842
	57.4.3 Bound–Bound Pair Production	843
	57.4.4 More Advanced Theoretical Methods	844
	References	844
58	Electron–Ion, Ion–Ion, and Neutral–Neutral Recombination Processes	845
	Edmund J. Mansky II and M. Raymond Flannery	
58.1	Recombination Processes	846
	58.1.1 Electron–Ion Recombination	846
	58.1.2 Positive–Ion Negative–Ion Recombination	846
	58.1.3 Balances	846
	58.1.4 Neutral–Neutral Recombination	847
	58.1.5 N-Body Recombination	848
58.2	Collisional-Radiative Recombination	849
	58.2.1 Saha and Boltzmann Distributions	849
	58.2.2 Quasi-Steady State Distributions	850
	58.2.3 Ionization and Recombination Coefficients	850
	58.2.4 Working Rate Formulae	850
	58.2.5 Computer Codes	850
58.3	Macroscopic Methods	850
	58.3.1 Resonant Capture-Stabilization Model: Dissociative and Dielectronic Recombination	850
	58.3.2 Reactive Sphere Model: Three-Body Electron–Ion and Ion–Ion Recombination	851

58.3.3	Working Formulae for Three-Body Collisional Recombination at Low Density	853
58.3.4	Recombination Influenced by Diffusional Drift at High Gas Densities	853
58.4	Zero-Range Methods	855
58.5	Hyperspherical Methods	856
58.5.1	Three-Body Recombination Rate (Identical Particles)	856
58.5.2	N-Body Recombination Rate (Identical Particles)	857
58.6	Field-Assisted Methods	857
58.7	Dissociative Recombination	857
58.7.1	Curve-Crossing Mechanisms	857
58.7.2	Quantal Cross Section	858
58.7.3	Noncrossing Mechanism	860
58.8	Mutual Neutralization	860
58.8.1	Landau–Zener Probability for Single Crossing at R_X	860
58.8.2	Cross Section and Rate Coefficient for Mutual Neutralization	861
58.9	One-Way Microscopic Equilibrium Current, Flux, and Pair Distributions	861
58.10	Microscopic Methods for Termolecular Ion–Ion Recombination	862
58.10.1	Time-Dependent Method: Low Gas Density	862
58.10.2	Time-Independent Methods: Low Gas Density	863
58.10.3	Recombination at Higher Gas Densities	864
58.10.4	Master Equations	865
58.10.5	Recombination Rate	865
58.11	Radiative Recombination	866
58.11.1	Detailed Balance and Recombination–Ionization Cross Sections	867
58.11.2	Kramers Cross Sections, Rates, Electron Energy-Loss Rates, and Radiated Power for Hydrogenic Systems	867
58.11.3	Basic Formulae for Quantal Cross Sections	869
58.11.4	Bound–Free Oscillator Strengths	871
58.11.5	Radiative Recombination Rate	871
58.11.6	Gaunt Factor, Cross Sections, and Rates for Hydrogenic Systems	872
58.11.7	Exact Universal Rate Scaling Law and Results for Hydrogenic Systems	873
58.12	Useful Quantities	873
	References	873
59	Dielectronic Recombination	875
	Michael Pindzola, Nigel Badnell, and Donald Griffin	
59.1	Introduction	875
59.2	Theoretical Formulation	876
59.3	Comparisons with Experiment	877
59.3.1	Low-Z Ions	877
59.3.2	High-Z Ions and Relativistic Effects	878
59.4	Radiative–Dielectronic Recombination Interference	878
59.5	Dielectronic Recombination in Plasmas	879
	References	879
60	Rydberg Collision Theories	881
	Edmund J. Mansky II	
60.1	Rydberg Collision Processes	882
60.2	General Properties of Rydberg States	882
60.2.1	Dipole Moments	882
60.2.2	Interaction Potentials	884

60.2.3	Radial Integrals	885
60.2.4	Line Strengths	885
60.2.5	Form Factors	886
60.2.6	Impact Broadening	887
60.2.7	Effective Lifetimes and Depopulation Rates	887
60.3	Correspondence Principles	887
60.3.1	Bohr–Sommerfeld Quantization	887
60.3.2	Bohr Correspondence Principle	887
60.3.3	Heisenberg Correspondence Principle	888
60.3.4	Strong Coupling Correspondence Principle	888
60.3.5	Equivalent Oscillator Theorem	888
60.4	Distribution Functions	888
60.4.1	Spatial Distributions	888
60.4.2	Momentum Distributions	889
60.5	Classical Theory	889
60.6	Universality Properties	890
60.6.1	Equal Mass Case	891
60.6.2	Unequal Mass Case	891
60.7	Many-Body and Multiparticle Effects	891
60.7.1	Many-Body Theory	891
60.7.2	Dilute Bose Gas	891
60.8	Working Formulae for Rydberg Collisions	892
60.8.1	Inelastic n, ℓ -Changing Transitions	892
60.8.2	Inelastic $n \rightarrow n'$ Transitions	893
60.8.3	Quasi-Elastic ℓ -Mixing Transitions	894
60.8.4	Elastic $n\ell \rightarrow n\ell'$ Transitions	894
60.8.5	Inelastic $n\ell \rightarrow n\ell'$ Transitions	894
60.8.6	Fine Structure $n\ell J \rightarrow n\ell J'$ Transitions	895
60.9	Impulse Approximation	896
60.9.1	Quantal Impulse Approximation	896
60.9.2	Classical Impulse Approximation	900
60.9.3	Semiquantal Impulse Approximation	901
60.10	Binary Encounter Approximation	903
60.10.1	Differential Cross Sections	903
60.10.2	Integral Cross Sections	904
60.10.3	Classical Ionization Cross Section	906
60.10.4	Classical Charge Transfer Cross Section	906
60.11	Born Approximation	907
60.11.1	Form Factors	907
60.11.2	Hydrogenic Form Factors	907
60.11.3	Excitation Cross Sections	908
60.11.4	Ionization Cross Sections	909
60.11.5	Capture Cross Sections	909
	References	910
61	Mass Transfer at High Energies: Thomas Peak	913
	Jack C. Straton and James H. McGuire	
61.1	The Classical Thomas Process	913
61.2	Quantum Description	914
61.2.1	Uncertainty Effects	914
61.2.2	Conservation of Overall Energy and Momentum	914
61.2.3	Conservation of Intermediate Energy	914
61.2.4	Example: Proton–Helium Scattering	915

61.3	Off-Energy-Shell Effects	916
61.4	Dispersion Relations	916
61.5	Destructive Interference of Amplitudes	916
61.6	Recent Developments	917
	References	917
62	Classical Trajectory and Monte Carlo Techniques	919
	Marcelo Ciappina, Raul O. Barrachina, Francisco Navarrete, and Ronald E. Olson	
62.1	Theoretical Background	919
	62.1.1 Hydrogenic Targets	919
	62.1.2 Nonhydrogenic One-Electron Models	920
	62.1.3 Multiply Charged Projectiles and Many-Electron Targets	920
62.2	Region of Validity	921
62.3	Applications	921
	62.3.1 Hydrogenic Atom Targets	921
	62.3.2 Pseudo-One-Electron Targets	922
	62.3.3 State-Selective Electron Capture	922
	62.3.4 Exotic Projectiles	923
	62.3.5 Heavy-Particle Dynamics	923
	62.3.6 Ion-Molecule Collisions	923
	62.3.7 Strong Laser Field Ionization	924
62.4	Conclusions	925
	References	925
63	Collisional Broadening of Spectral Lines	927
	Gillian Peach	
63.1	Impact Approximation	928
63.2	Isolated Lines	928
	63.2.1 Semiclassical Theory	928
	63.2.2 Simple Formulae	929
	63.2.3 Perturbation Theory	930
	63.2.4 Broadening by Charged Particles	931
	63.2.5 Empirical Formulae	931
63.3	Overlapping Lines	932
	63.3.1 Transitions in Hydrogen and Hydrogenic Ions	932
	63.3.2 Infrared and Radio Lines	933
63.4	Quantum-Mechanical Theory	934
	63.4.1 Impact Approximation	934
	63.4.2 Broadening by Electrons	935
	63.4.3 Broadening by Atoms	936
63.5	One-Perturber Approximation	936
	63.5.1 General Approach and Utility	936
	63.5.2 Broadening by Electrons	937
	63.5.3 Broadening by Atoms and Molecules	938
63.6	Unified Theories and Conclusions	939
	References	939
Part E Scattering Experiment		
64	Photodetachment	943
	David Pegg and Dag Hanstorp	
64.1	Negative Ions	943
64.2	Photodetachment	944

64.2.1	Photodetachment Cross Sections	944
64.2.2	Threshold Behavior	945
64.2.3	Structure in Continuum	946
64.2.4	Photoelectron Angular Distributions	946
64.2.5	Higher-Order Processes	946
64.3	Experimental Procedures	947
64.3.1	Production of Negative Ions	947
64.3.2	Interacting Beams	947
64.3.3	Light Sources	948
64.3.4	Detection Schemes	948
64.4	Measuring Properties of Negative Ions	948
64.4.1	Electron Affinities	948
64.4.2	Bound States	949
64.4.3	Continuum Processes	949
64.5	Investigation of Fundamental Processes	950
64.5.1	Threshold Studies	950
64.5.2	Photodetachment Using Short Laser Pulses	950
64.6	Observations and Applications of Negative Ions	950
64.6.1	Natural Occurrence of Negative Ions	950
64.6.2	Applications of Negative Ions	951
	References	951
65	Photon–Atom Interactions: Low Energy	955
	Denise Caldwell and Manfred Krause	
65.1	Theoretical Concepts	955
65.1.1	Differential Analysis	956
65.1.2	Electron Correlation Effects	958
65.2	Experimental Methods	960
65.2.1	Synchrotron Radiation Source	961
65.2.2	Photoelectron Spectrometry	961
65.2.3	Resolution and Natural Width	963
65.3	Additional Considerations	964
	References	965
66	Photon–Atom Interactions: Intermediate Energies	967
	Michael W. J. Bromley	
66.1	Overview	967
66.2	Scattering Cross Sections	968
66.2.1	Applications of Atomic Cross Sections	970
66.3	Experimental Progress	971
66.3.1	Inelastic Processes	972
66.4	Theory, Computation, and Data	974
66.4.1	Databases	974
66.4.2	Bulk Modeling	974
66.5	Future Directions	975
	References	975
67	Electron–Atom and Electron–Molecule Collisions	981
	Isik Kanik, William McConkey, and Sandor Trajmar	
67.1	Basic Concepts	982
67.1.1	Electron Impact Processes	982
67.1.2	Definition of Cross Sections	982
67.1.3	Scattering Measurements	982

67.2	Collision Processes	984
67.2.1	Total Scattering Cross Sections	984
67.2.2	Elastic Scattering Cross Sections	984
67.2.3	Momentum Transfer Cross Sections	985
67.2.4	Excitation Cross Sections	985
67.2.5	Dissociation Cross Sections	986
67.2.6	Ionization Cross Sections	986
67.3	Coincidence and Superelastic Measurements	987
67.4	Experiments with Polarized Electrons	989
67.5	Electron Collisions with Excited Species	990
67.6	Electron Collisions in Traps	990
67.7	Current Applications	990
67.8	Emerging Applications	991
	References	991
68	Ion–Atom Scattering Experiments: Low Energy	995
	Charles Havener, Ruitian Zhang, and Ronald Phaneuf	
68.1	Low-Energy Ion–Atom Collision Processes	995
68.2	Experimental Methods for Total Cross Section Measurements	997
68.2.1	Gas-Target Beam Attenuation Method	997
68.2.2	Gas-Target Product Growth Method	997
68.2.3	Crossed Ion and Thermal Beams Method	998
68.2.4	Fast Merged Beams Method	998
68.2.5	Trapped Ion Method	999
68.2.6	Swarm Method	999
68.3	Methods for State-Selective Measurements	999
68.3.1	Photon Emission Spectroscopy	999
68.3.2	Translational Energy Spectroscopy	999
68.3.3	Electron Emission Spectroscopy	1000
68.3.4	Recoil-Ion Momentum Spectroscopy	1000
	References	1000
69	Ion–Atom Collisions – High Energy	1003
	Michael Schulz and Lew Cocke	
69.1	Basic One-Electron Processes	1003
69.1.1	Perturbative Processes	1003
69.1.2	Nonperturbative Processes	1009
69.2	Multielectron Processes	1009
69.3	Electron Spectra in Ion–Atom Collisions	1012
69.3.1	General Characteristics	1012
69.3.2	High-Resolution Measurements	1013
69.4	Quasi-Free Electron Processes in Ion–Atom Collisions	1013
69.4.1	Radiative Electron Capture	1014
69.4.2	Resonant Transfer and Excitation	1014
69.4.3	Excitation and Ionization	1014
69.5	Some Exotic Processes	1014
69.5.1	Molecular Orbital X-Rays	1014
69.5.2	Positron Production from Atomic Processes	1015
	References	1015

70	Reactive Scattering	1019
	Hongwei Li, Arthur G. Suits, and Yuan T. Lee	
70.1	Introduction	1019
70.2	Experimental Methods	1020
70.2.1	Molecular Beam Sources	1020
70.2.2	Reagent Preparation	1020
70.2.3	Detection of Neutral Products	1021
70.2.4	A Typical Signal Calculation	1023
70.3	Experimental Configurations	1024
70.3.1	Crossed-Beam Rotatable Detector	1024
70.3.2	Laboratory to Center-of-Mass Transformation	1025
70.3.3	Product Imaging	1026
70.4	Elastic and Inelastic Scattering	1028
70.4.1	The Differential Cross Section	1028
70.4.2	Rotationally Inelastic Scattering	1028
70.4.3	Vibrationally Inelastic Scattering	1029
70.4.4	Electronically Inelastic Scattering	1029
70.5	Reactive Scattering	1029
70.5.1	Harpoon and Stripping Reactions	1029
70.5.2	Rebound Reactions	1030
70.5.3	Long-Lived Complexes	1030
70.6	Recent Developments	1031
	References	1032
71	Ion–Molecule Reactions	1035
	James M. Farrar	
71.1	Introduction	1035
71.2	Specification of Cross Sections	1036
71.3	Instrumentation	1037
71.3.1	Reactant Ion Preparation	1037
71.3.2	Reactant Mass Selection	1037
71.3.3	The Collision Region	1038
71.3.4	Product Detection	1038
71.3.5	Imaging Methods in Velocity Space	1039
71.4	Kinematics	1039
71.5	Recent Examples of State-Resolved Measurements	1040
71.5.1	Velocity-Angle Differential Cross Sections $\sigma(V'_{\text{rel}}, \theta V_{\text{rel}})$	1040
71.5.2	State-Resolved Cross Sections $\sigma(n' n, V_{\text{rel}})$ and Rate Constants $k(n' n, T)$	1040
71.6	The Future of the Field	1042
	References	1042
Part F Quantum Optics		
72	Light-Matter Interaction	1047
	Pierre Meystre	
72.1	Multipole Expansion	1047
72.1.1	Electric Dipole (E1) Interaction	1048
72.1.2	Electric Quadrupole (E2) Interaction	1048
72.1.3	Magnetic Dipole (M1) Interaction	1049

72.2	Lorentz Atom	1049
72.2.1	Complex Notation	1049
72.2.2	Index of Refraction	1049
72.2.3	Beer's Law	1050
72.2.4	Slowly Varying Envelope Approximation	1050
72.3	Two-Level Atoms	1050
72.3.1	Hamiltonian	1050
72.3.2	Rotating Wave Approximation	1051
72.3.3	Rabi Frequency	1051
72.3.4	Dressed States	1051
72.3.5	Optical Bloch Equations	1053
72.4	Relaxation Mechanisms	1053
72.4.1	Relaxation Toward Unobserved Levels	1053
72.4.2	Relaxation Toward Levels of Interest	1053
72.4.3	Optical Bloch Equations with Decay	1054
72.4.4	Density Matrix Equations	1054
72.5	Rate Equation Approximation	1054
72.5.1	Steady State	1055
72.5.2	Saturation	1055
72.5.3	Einstein A and B Coefficients	1055
72.6	Light Scattering	1055
72.6.1	Rayleigh Scattering	1055
72.6.2	Thomson Scattering	1056
72.6.3	Resonant Scattering	1056
	References	1056
73	Absorption and Gain Spectra	1057
	Stig Stenholm	
73.1	Introduction	1057
73.2	Index of Refraction	1057
73.3	Density Matrix Treatment of the Two-Level Atom	1058
73.4	Line Broadening	1059
73.5	The Rate Equation Limit	1060
73.6	Two-Level Doppler-Free Spectroscopy	1062
73.7	Three-Level Spectroscopy	1064
73.8	Special Effects in Three-Level Systems	1065
73.9	Summary of the Literature	1067
	References	1067
74	Laser Principles	1069
	Ralf Menzel and Peter W. Milonni	
74.1	Gain, Threshold, and Matter–Field Coupling	1069
74.2	Continuous Wave, Single-Mode Operation	1071
74.3	Laser Resonators and Transverse Modes	1074
74.4	Photon Statistics	1076
74.5	Multimode and Pulsed Operation	1077
74.6	Instabilities and Chaos	1079
	References	1079

75	Types of Lasers	1081
	Richard S. Quimby and Richard C. Powell	
75.1	Introduction	1081
75.2	Single-Atom Transitions	1082
	75.2.1 Neutral Atom Gas Lasers	1082
	75.2.2 Ion Lasers	1083
	75.2.3 Metal Vapor Lasers	1083
	75.2.4 Rare-Earth Ion Lasers	1083
	75.2.5 Transition Metal Ion Lasers	1086
75.3	Molecular Transitions	1088
	75.3.1 Molecular Vibrational Lasers	1088
	75.3.2 Dye Lasers	1089
	75.3.3 Excimer Lasers	1089
75.4	Solid-State Transitions	1090
	75.4.1 Semiconductor Lasers	1090
	75.4.2 Quantum Cascade Lasers	1091
75.5	Free Electron Lasers	1092
75.6	Nonlinear Optical Processes	1092
	75.6.1 Raman Lasers	1093
	75.6.2 Optical Parametric Oscillators	1093
	75.6.3 Frequency Conversion	1093
	75.6.4 High Harmonic Generation	1094
	References	1094
76	Nonlinear Optics	1097
	Robert W. Boyd, Alexander L. Gaeta, and Enno Giese	
76.1	Nonlinear Susceptibility	1098
	76.1.1 Tensor Properties	1098
	76.1.2 Nonlinear Refractive Index	1098
	76.1.3 Quantum Mechanical Expression for $\chi^{(n)}$	1099
	76.1.4 Hyperpolarizability	1099
76.2	Wave Equation in Nonlinear Optics	1100
	76.2.1 Coupled-Amplitude Equations	1100
	76.2.2 Phase Matching	1100
	76.2.3 Manley–Rowe Relations	1101
	76.2.4 Pulse Propagation	1101
76.3	Second-Order Processes	1101
	76.3.1 Sum-Frequency Generation	1101
	76.3.2 Second Harmonic Generation	1102
	76.3.3 Parametric Amplification and Oscillation	1102
	76.3.4 Difference-Frequency Generation	1102
	76.3.5 Two-Mode Squeezing	1102
	76.3.6 Spontaneous Parametric Down-Conversion	1103
	76.3.7 Focused Beams	1104
76.4	Third-Order Processes	1104
	76.4.1 Third-Harmonic Generation	1104
	76.4.2 Self-Phase and Cross-Phase Modulation	1104
	76.4.3 Four-Wave Mixing	1105
	76.4.4 Self-Focusing and Self-Trapping	1105
	76.4.5 Saturable Absorption	1105
	76.4.6 Two-Photon Absorption	1105
	76.4.7 Nonlinear Ellipse Rotation	1106

76.5	Stimulated Light Scattering	1106
76.5.1	Stimulated Raman Scattering	1106
76.5.2	Stimulated Brillouin Scattering	1106
76.6	Other Nonlinear Optical Processes	1107
76.6.1	High-Order Harmonic Generation	1107
76.6.2	Electro-Optic Effect	1108
76.6.3	Photorefractive Effect	1108
76.7	New Regimes of Nonlinear Optics	1108
76.7.1	Ultrafast and Intense-Field Nonlinear Optics	1108
76.7.2	Nonlinear Plasmonics and Epsilon-Near-Zero Effects	1109
	References	1110
77	Coherent Transients	1111
	Joseph H. Eberly and Carlos R. Stroud Jr.	
77.1	Introduction	1112
77.2	Origin of Relaxation	1112
77.3	State Evolution	1113
77.4	Numerical Estimates of Parameters	1114
77.5	Homogeneous Relaxation	1114
77.5.1	Rabi Oscillations	1114
77.5.2	Bloch Vector and Bloch Sphere	1114
77.5.3	Pi Pulses and Pulse Area	1115
77.5.4	Adiabatic Following	1115
77.6	Inhomogeneous Relaxation	1116
77.6.1	Free Induction Decay	1116
77.6.2	Photon Echoes	1117
77.7	Resonant Pulse Propagation	1117
77.7.1	Maxwell–Bloch Equations	1117
77.7.2	Index of Refraction and Beer’s Law	1117
77.7.3	The Area Theorem and Self-Induced Transparency	1118
77.8	Multilevel Generalizations	1118
77.8.1	Rydberg Packets and Intrinsic Relaxation	1118
77.8.2	Multiphoton Resonance and Two-Photon Bloch Equations	1119
77.8.3	Pump-Probe Resonance and Dark States	1120
77.8.4	Induced Transparency	1121
77.9	Disentanglement and “Sudden Death” of Coherent Transients	1121
	References	1123
78	Multiphoton and Strong-Field Processes	1125
	Marcelo Ciappina, Alexis A. Chacon S., and Maciej Lewenstein	
78.1	Introduction	1125
78.2	Weak-Field Multiphoton Processes	1126
78.2.1	Perturbation Theory	1126
78.2.2	Resonant-Enhanced Multiphoton Ionization	1127
78.2.3	Multielectron Effects	1127
78.2.4	Autoionization	1127
78.2.5	Coherence and Statistics	1127
78.2.6	Effects of Field Fluctuations	1128
78.2.7	Excitation with Multiple Laser Fields	1128
78.2.8	Waveforms	1128
78.3	Strong-Field Multiphoton Processes	1129
78.3.1	Nonperturbative Multiphoton Ionization	1129
78.3.2	Tunneling Ionization	1129

	78.3.3 Multiple Ionization	1130
	78.3.4 Above Threshold Ionization	1130
	78.3.5 High-Order Harmonic Generation	1131
	78.3.6 Stabilization of Atoms in Intense Laser Fields	1133
	78.3.7 Molecules in Intense Laser Fields	1133
	78.3.8 Microwave Ionization of Rydberg Atoms	1134
	78.4 Strong-Field Computational Techniques	1135
	78.4.1 Floquet Theory	1135
	78.4.2 Direct Integration of the TDSE	1135
	78.4.3 Volkov States	1136
	78.4.4 Strong-Field Approximations	1136
	78.4.5 phase-space Averaging Method	1136
	78.5 Atto-Nano Physics	1137
	References	1138
79	Cooling and Trapping	1141
	Juha Javanainen	
	79.1 Notation	1141
	79.2 Control of Atomic Motion by Light	1142
	79.2.1 General Theory	1142
	79.2.2 Two-State Atoms	1144
	79.2.3 Multistate Atoms	1147
	79.3 Magnetic Trap for Atoms	1148
	79.3.1 Evaporative Cooling	1148
	79.4 Trapping and Cooling of Charged Particles	1149
	79.4.1 Paul Trap	1149
	79.4.2 Penning Trap	1150
	79.4.3 Collective Effects in Ion Clouds	1151
	79.5 Experimental	1152
	79.5.1 Free Particles	1152
	79.5.2 Trapped Particles	1152
	79.6 Applications	1153
	79.6.1 Cold Molecules	1153
	79.6.2 Quantum Systems of Internal and CM States	1154
	References	1154
80	Quantum Degenerate Gases	1157
	Juha Javanainen	
	80.1 Introduction	1157
	80.2 Elements of Quantum Field Theory	1158
	80.2.1 Bosons	1158
	80.2.2 Fermions	1159
	80.2.3 Bosons Versus Fermions	1159
	80.3 Basic Properties of Degenerate Gases	1160
	80.3.1 Atoms Are Trapped	1160
	80.3.2 Atom–Atom Interactions	1160
	80.3.3 Model Hamiltonian	1160
	80.3.4 Bosons	1160
	80.3.5 Meaning of the Macroscopic Wave Function	1164
	80.3.6 Fermions	1165

80.4	Experimental	1165
80.4.1	Preparing a BEC	1165
80.4.2	Preparing a Degenerate Fermi Gas	1166
80.4.3	Monitoring Degenerate Gases	1166
80.5	BEC Superfluid	1167
80.5.1	Vortices	1167
80.5.2	Superfluidity	1167
80.6	Optical Lattice as Quantum Simulator	1168
80.6.1	Basics of the Optical Lattice	1168
80.6.2	Strongly Correlated Systems	1169
80.6.3	Topological Phases of Matter	1170
	References	1172
81	De Broglie Optics	1173
	Carsten Henkel and Martin Wilkens	
81.1	Wave-Particle Duality	1173
81.2	The Hamiltonian of de Broglie Optics	1174
81.2.1	Gravitation and Rotation	1174
81.2.2	Charged Particles	1175
81.2.3	Magnetic Moments	1175
81.2.4	Atoms	1175
81.3	Evolution of De Broglie Waves	1177
81.3.1	Light Optics Analogy	1177
81.3.2	WKB Approximation	1177
81.3.3	Phase and Group Velocity	1178
81.3.4	Paraxial Approximation	1178
81.3.5	Raman–Nath Approximation	1178
81.4	Refraction and Reflection	1178
81.4.1	Atomic Mirrors	1179
81.4.2	Atomic Cavities	1179
81.4.3	Atomic Lenses	1180
81.4.4	Atomic Waveguides	1180
81.5	Diffraction	1180
81.5.1	Fraunhofer Diffraction	1180
81.5.2	Fresnel Diffraction	1181
81.5.3	Near-Resonant Kapitza–Dirac Effect	1181
81.5.4	Atom Beam Splitters	1181
81.6	Interference	1182
81.6.1	Interference Phase Shift	1182
81.6.2	Internal-State Interferometry	1184
81.6.3	Manipulation of Cavity Fields by Atom Interferometry	1184
81.7	Coherence of Scalar Matter Waves	1184
81.7.1	Atomic Sources	1185
81.7.2	Atom Decoherence	1185
	References	1186
82	Quantum Properties of Light	1189
	Da-Wei Wang and Girish S. Agarwal	
82.1	Introduction	1189
82.2	Quantization of the Electromagnetic Field	1190
82.3	Quantum States	1190
82.4	Field Observables: Quadratures	1192
82.5	Phase-Space Representations of the Light: P , Q , and Wigner Functions	1192

82.6	Squeezed State	1194
82.7	Detection of Quantum Light by Array Detectors	1196
82.8	Two-Mode Squeezed States	1197
82.9	Quantum Entanglement	1198
82.10	Non-Gaussian Nonclassical States	1199
82.11	Beam Splitter, Interferometer, and Measurement Sensitivity	1200
	References	1203
83	Entangled Atoms and Fields: Cavity QED	1207
	Qiongyi He, Wei Zhang, Dieter Meschede, and Axel Schenzle	
83.1	Introduction	1208
83.2	Atoms and Fields	1208
83.2.1	Two-Level Atoms	1208
83.2.2	Electromagnetic Fields	1208
83.2.3	Dipole Coupling of Fields and Atoms	1209
83.3	Weak Coupling in Cavity QED	1210
83.3.1	Radiating Atoms in Waveguides	1210
83.3.2	Trapped Radiating Atoms and Their Mirror Images	1210
83.3.3	Radiating Atoms in Resonators	1211
83.3.4	Radiative Shifts and Forces	1212
83.3.5	Experiments on Weak Coupling	1213
83.3.6	Cavity QED and Dielectrics	1213
83.4	Strong Coupling in Cavity QED	1213
83.4.1	The Jaynes-Cummings Model	1214
83.4.2	Fock States, Coherent States, and Thermal States	1215
83.4.3	Vacuum Splitting	1216
83.4.4	Strong Coupling in Experiments	1216
83.5	Micromasers	1217
83.5.1	Maser Threshold	1218
83.5.2	Nonclassical Features of the Field	1218
83.5.3	Trapping States	1219
83.5.4	Atom Counting Statistics	1219
83.6	Cavity Cooling	1220
83.6.1	Master Equation	1220
83.6.2	Cavity Cooling Experiments	1221
83.7	Cavity QED for Cold Atomic Gases	1222
83.7.1	Atomic Ensembles in a Cavity	1222
83.7.2	Bose–Einstein Condensate in a Cavity	1223
83.7.3	Cavity Optomechanics with Cold Atoms	1225
83.8	Applications of Cavity QED	1225
83.8.1	Quantum Nondemolition (QND) Counting of Photons	1225
83.8.2	Detecting and Trapping Atoms Through Strong Coupling	1226
83.8.3	Single-Photon Sources	1227
83.8.4	Generation of Entanglement	1227
	References	1228
84	Quantum Optical Tests of the Foundations of Physics	1231
	L. Krister Shalm, Aephraim M. Steinberg, Paul G. Kwiat, and Raymond Y. Chiao	
84.1	Introduction: The Photon Hypothesis	1232
84.2	Quantum Properties of Light	1232
84.2.1	Vacuum Fluctuations: Cavity QED	1232
84.2.2	Two-Photon Light Sources	1233
84.2.3	Squeezed States of Light	1233

- 84.3 Nonclassical Interference 1234
 - 84.3.1 Single-Photon and Matter-Wave Interference 1234
 - 84.3.2 “Nonlocal” Interference Effects and Energy-Time Uncertainty 1235
 - 84.3.3 Two-Photon Interference 1235
- 84.4 Complementarity and Coherence 1236
 - 84.4.1 Wave-Particle Duality 1236
 - 84.4.2 Quantum Eraser 1236
 - 84.4.3 Vacuum-Induced Coherence 1237
 - 84.4.4 Suppression of Spontaneous Parametric Downconversion 1237
- 84.5 Measurements in Quantum Mechanics 1238
 - 84.5.1 Quantum (Anti-)Zeno Effect 1238
 - 84.5.2 Quantum Nondemolition 1238
 - 84.5.3 Quantum Interrogation 1239
 - 84.5.4 Weak Measurements 1239
 - 84.5.5 Direct Measurements of a Wave Function 1240
- 84.6 The EPR Paradox and Bell’s Inequalities 1240
 - 84.6.1 Generalities 1240
 - 84.6.2 Bell’s Inequalities as a Game 1241
 - 84.6.3 Loopholes in Bell Tests 1242
 - 84.6.4 Closing the Loopholes in Bell Tests 1242
 - 84.6.5 Polarization-Based Entangled Sources 1243
 - 84.6.6 Other Entanglement Sources for Bell Tests 1244
 - 84.6.7 Advanced Experimental Tests of Nonlocality 1245
 - 84.6.8 Nonlocality Without Inequalities 1246
 - 84.6.9 Connection to Quantum Information 1246
- 84.7 Single-Photon Tunneling Time 1247
 - 84.7.1 An Application of EPR Correlations to Time Measurements 1247
 - 84.7.2 Superluminal Tunneling Times 1247
 - 84.7.3 Tunneling Delay in a Multilayer Dielectric Mirror 1248
 - 84.7.4 Interpretation of Tunneling Time 1249
 - 84.7.5 Other Fast and Slow Light Schemes 1250
- 84.8 Gravity and Quantum Optics 1250
 - 84.8.1 Gravitational Wave Detection 1250
 - 84.8.2 Gravity and Quantum Information 1251
- References 1251

85 Quantum Information 1259

Daniel F. V. James, Peter L. Knight, and Stefan Scheel

- 85.1 Entanglement and Information 1260
 - 85.1.1 Testing for and Quantifying Entanglement 1260
- 85.2 Simple Quantum Protocols 1262
 - 85.2.1 Quantum Key Distribution 1262
 - 85.2.2 Quantum Teleportation 1262
- 85.3 Quantum Logic 1263
 - 85.3.1 Single-Qubit Operations 1263
 - 85.3.2 Two-Qubit Operations 1264
 - 85.3.3 Multiqubit Gates and Networks 1264
 - 85.3.4 Cluster-State Quantum Computing 1264
- 85.4 Quantum Algorithms 1265
 - 85.4.1 Deutsch–Jozsa Algorithm 1265
 - 85.4.2 Grover’s Search Algorithm 1265
 - 85.4.3 Shor’s Factor-Finding Algorithm 1266
 - 85.4.4 Other Algorithms 1266

85.5	Error Correction	1266
85.6	The DiVincenzo Checklist	1267
85.6.1	Qubit Characterization, Scalability	1267
85.6.2	Initialization	1267
85.6.3	Long Decoherence Times	1268
85.6.4	Universal Set of Quantum Gates	1268
85.6.5	Qubit-Specific Measurement	1268
85.7	Physical Implementations	1268
85.7.1	Linear Optics	1268
85.7.2	Trapped Ions	1269
85.8	Outlook	1269
	References	1270

Part G Applications

86	Applications of Atomic and Molecular Physics to Astrophysics	1275
	Stephen Lepp, Phillip C. Stancil, and Alexander Dalgarno	
86.1	Introduction	1275
86.2	Photoionized Gas	1276
86.3	Collisionally Ionized Gas	1278
86.4	Diffuse Molecular Clouds	1278
86.5	Dark Molecular Clouds	1280
86.6	Circumstellar Shells and Stellar Atmospheres	1281
86.7	Supernova Ejecta	1282
86.8	Shocked Gas	1283
86.9	The Early Universe	1283
86.10	Atacama Large Millimeter/Submillimeter Array	1284
86.11	Recent Developments	1285
86.12	Other Reading	1285
	References	1286
87	Comets	1289
	Paul D. Feldman	
87.1	Introduction	1289
87.2	Observations	1290
87.3	Excitation Mechanisms	1291
87.3.1	Basic Phenomenology	1291
87.3.2	Fluorescence Equilibrium	1292
87.3.3	Swings and Greenstein Effects	1293
87.3.4	Bowen Fluorescence	1294
87.3.5	Electron Impact Excitation	1294
87.3.6	Prompt Emission	1294
87.3.7	OH Level Inversion	1295
87.4	Cometary Models	1295
87.4.1	Photolytic Processes	1295
87.4.2	Density Models	1296
87.4.3	Radiative Transfer Effects	1296
87.5	Summary	1297
	References	1297

88	Aeronomy	1299
	Jane L. Fox	
88.1	Basic Structure of Atmospheres	1299
	88.1.1 Introduction	1299
	88.1.2 Atmospheric Regions	1300
88.2	Density Distributions of Neutral Species	1304
	88.2.1 The Continuity Equation	1304
	88.2.2 Diffusion Coefficients	1305
88.3	Interaction of Solar Radiation with the Atmosphere	1305
	88.3.1 Introduction	1305
	88.3.2 The Interaction of Solar Photons with Atmospheric Gases	1306
	88.3.3 Interaction of Energetic Electrons with Atmospheric Gases	1309
88.4	Ionospheres	1311
	88.4.1 Ionospheric Regions	1311
	88.4.2 Sources of Ionization	1312
	88.4.3 Nightside Ionospheres	1317
	88.4.4 Ionospheric Density Profiles	1320
	88.4.5 Ion Diffusion	1322
88.5	Neutral, Ion, and Electron Temperatures	1323
88.6	Luminosity	1325
88.7	Planetary Escape	1332
	References	1334
89	Applications of Atomic and Molecular Physics to Global Change	1337
	Gonzalo González Abad, Kelly Chance, and Kate P. Kirby	
89.1	Overview	1337
	89.1.1 Global Change Issues	1337
	89.1.2 Structure of the Earth’s Atmosphere	1338
89.2	Atmospheric Models and Data Needs	1339
	89.2.1 Modeling the Thermosphere and Ionosphere	1339
	89.2.2 Heating and Cooling Processes	1339
	89.2.3 Atomic and Molecular Data Needs	1340
89.3	Tropospheric Warming/Upper Atmosphere Cooling	1340
	89.3.1 Incoming and Outgoing Energy Fluxes	1340
	89.3.2 Tropospheric “Global” Warming	1340
	89.3.3 Upper Atmosphere Cooling	1341
89.4	Stratospheric Ozone	1342
	89.4.1 Production and Destruction	1342
	89.4.2 The Antarctic Ozone Hole	1343
	89.4.3 Arctic Ozone Loss	1344
	89.4.4 Global Ozone Depletion	1344
89.5	Atmospheric Measurements	1344
	References	1345
90	Surface Physics	1349
	Erik T. Jensen	
90.1	Low Energy Electrons and Surface Science	1349
90.2	Electron–Atom Interactions	1350
	90.2.1 Elastic Scattering: Low Energy Electron Diffraction (LEED)	1350
	90.2.2 Inelastic Scattering: Electron Energy Loss Spectroscopy	1351
	90.2.3 Auger Electron Spectroscopy	1351

90.3	Photon–Atom Interactions	1352
90.3.1	Ultraviolet Photoelectron Spectroscopy (UPS)	1352
90.3.2	Inverse Photoemission Spectroscopy (IPES)	1353
90.3.3	X-Ray Photoelectron Spectroscopy (XPS)	1353
90.3.4	X-Ray Absorption Methods	1355
90.4	Atom–Surface Interactions	1357
90.4.1	Physisorption	1357
90.4.2	Chemisorption	1357
90.5	Recent Developments	1357
	References	1358
91	Interface with Nuclear Physics	1359
	James S. Cohen and John D. Morgan III	
91.1	Introduction	1359
91.2	Nuclear Size Effects in Atoms	1360
91.2.1	Nuclear Size Effects on Nonrelativistic Energies	1360
91.2.2	Nuclear Size Effects on Relativistic Energies	1361
91.2.3	Nuclear Size Effects on QED Corrections	1362
91.3	Electronic Structure Effects in Nuclear Physics	1362
91.3.1	Electronic Effects on Closely Spaced Nuclear Energy Levels	1362
91.3.2	Electronic Effects on Tritium Beta Decay	1362
91.3.3	Electronic Screening of Low-Energy Nuclear Reactions	1362
91.3.4	Atomic and Molecular Effects in Relativistic Ion–Atom Collisions	1363
91.4	Muon-Catalyzed Fusion	1363
91.4.1	The Catalysis Cycle	1365
91.4.2	Muon Atomic Capture	1365
91.4.3	Muonic Atom Deexcitation and Transfer	1367
91.4.4	Muonic Molecule Formation	1368
91.4.5	Fusion	1370
91.4.6	Sticking and Stripping	1370
91.4.7	Prospectus	1372
	References	1372
	Index	1377

List of Tables

Table 1.1	Exact quantities and their symbols, numerical values, and units in the SI	4
Table 1.2	Selected constants as well as atomic and natural units based on the 2018 CODATA adjustment of the fundamental constants [5]. The first two columns describe the quantity and its mathematical symbol. The third and fourth columns give its numerical value and unit. For quantity X the number in parenthesis in the numerical value is the combined statistical and systematic one-standard-deviation uncertainty $u(X)$ in the last two digits of the numerical value. Finally, the last column gives the relative standard uncertainty $u_r(X) = u(X)/ X $. The unit u is the atomic mass unit, one-twelfth of the mass of a ^{12}C atom	6
Table 2.1	The solid and spherical harmonics \mathcal{Y}_{lm} and the tensor harmonics \mathcal{T}_{μ}^k (labeled by $k = l$ and $\mu = m$) for $l = 0, 1, 2, 3$, and 4	65
Table 2.2	The $3-j$ coefficients for all M 's = 0 or $J_3 = 0, \frac{1}{2}$	65
Table 2.3	The $3-j$ coefficients for $J_3 = 1, \frac{3}{2}, 2$	65
Table 2.4	The $6-j$ coefficients for $d = 0, \frac{1}{2}, 1, \frac{3}{2}, 2$, with $s = a + b + c$	66
Table 3.1	Generators of the Lie groups for the atomic l shell. The subscripts i and j run over all $4l + 2$ states of a single electron	73
Table 3.2	Dimensions D of the irreducible representations (IR's) of various Lie groups	74
Table 3.3	Eigenvalues of Casimir's operator C for groups used in the atomic l shell	74
Table 3.4	The states of the d shell	76
Table 10.1	Atomic structure programs	166
Table 10.2	Atomic scattering programs	166
Table 10.3	Molecular structure programs	167
Table 10.4	Molecular and heavy particle scattering programs	167
Table 10.5	GNU autotools table	169
Table 10.6	Types of FORTRAN compilers	170
Table 10.7	Types of mixing techniques of languages	171
Table 10.8	Types of third-party libraries	172
Table 10.9	Testing harnesses (frameworks)	172
Table 11.1	Atomic structure hierarchy in LS coupling and names for groups of transitions between structural entities	179
Table 11.2	Allowed J -values for l_j^N equivalent electrons (jj) coupling	180
Table 11.3	Ground levels and ionization energies for neutral atoms	184
Table 11.4	Selection rules for discrete transitions	187
Table 11.5	Conversion relations between S and A_{ki} for forbidden transitions	188
Table 11.6	Wavelengths λ , upper energy levels E_k , statistical weights g_i and g_k of lower and upper levels, and transition probabilities A_{ki} for persistent spectral lines of neutral atoms. Many tabulated lines are resonance lines (marked "g"), where the lower energy level belongs to the ground term	190
Table 11.7	Some transitions of the main spectral series of hydrogen	194

Table 11.8	Values of Stark-broadening parameter $\alpha_{1/2}$ of the H_β line of hydrogen (486.1 nm) for various temperatures and electron densities	195
Table 12.1	Formulas for the radial integrals $I_0(a, b, c; \alpha, \beta) = \langle r_1^a r_2^b r_{12}^c e^{-\alpha r_1 - \beta r_2} \rangle_{\text{rad}}$ and $I_0^{\text{log}}(a, b, c; \alpha, \beta) = \langle r_1^a r_2^b r_{12}^c \ln r_{12} e^{-\alpha r_1 - \beta r_2} \rangle_{\text{rad}}$. $\psi(n) = -\gamma + \sum_{k=1}^{n-1} k^{-1}$ is the digamma function, ${}_2F_1(a, b; c; z)$ is the hypergeometric function, and $s = a + b + c + 5$. Except as noted, the formulas apply for $a \geq -1$, $b \geq -1$, $c \geq -1$	203
Table 12.2	Nonrelativistic eigenvalue coefficients ε_0 and ε_1 for helium	206
Table 12.3	Eigenvalue coefficients ε_2 for helium	207
Table 12.4	Values of the reduced electron mass ratio μ/M , including binding energy corrections	207
Table 12.5	Nonrelativistic eigenvalues $E = \varepsilon_0 + (\mu/M)\varepsilon_1 + (\mu/M)^2\varepsilon_2$ for helium-like ions (in units of e^2/a_μ)	208
Table 12.6	Expectation values of various operators for He-like ions for the case $M = \infty$ (in a.u.)	208
Table 12.7	Total ionization energies for ${}^4\text{He}$, calculated with $R_M = 3\,289\,391\,006.600\text{MHz}$	209
Table 12.8	QED corrections to the ionization energy included in Table 12.7 for the S and P -states of helium (in MHz)	210
Table 12.9	Quantum defects for the total energies of helium with the ΔW_n term subtracted [Eq. (12.56)]	211
Table 12.10	Formulas for the hydrogenic expectation value $\langle r^{-j} \rangle \equiv \langle nl r^{-j} nl \rangle$ in terms of $G_p^{nl} = \frac{2^p Z^p (2l-p+2)!}{n^{p+1} (2l+p-1)!}$, $f_p^l = \frac{(l+p)!}{(l-p)!}$	212
Table 12.11	Oscillator strengths for helium. The factor in brackets gives the finite mass correction, with $y = \mu/M$	214
Table 12.12	Singlet-triplet mixing angles for helium	215
Table 14.1	Relativistic ground state binding energy $-E_{\text{gs}}/Z^2$ and finite nuclear size correction $\delta E_{\text{nuc}}/Z^2$ (in a.u.) of hydrogenic atoms for various magnetic fields B (in units of 2.35×10^5 T). δE_{nuc} should be added to E_{gs}	226
Table 14.2	Relativistic binding energy $-E_{2S, -1/2}$ for the $2S_{1/2}$ ($m_j = -\frac{1}{2}$) and $-E_{2P, -1/2}$ for the $2P_{1/2}$ ($m_j = -\frac{1}{2}$) excited states of hydrogen (in a.u.) in an intense magnetic field B (in units of 2.35×10^5 T)	226
Table 14.3	Relativistic corrections $\delta E = (E - E_{\text{NR}})/ E_{\text{R}} $ to the nonrelativistic energies E_{NR} for the ground state and $n = 2$ excited states of hydrogen in an intense magnetic field B (in units of 2.35×10^5 T). The numbers in brackets denote powers of 10	227
Table 14.4	Relativistic dipole polarizabilities for the ground state of hydrogenic atoms	228
Table 18.1	Measured np^2P_J lifetimes	265
Table 22.1	The effective quantum number and quantum defect parameters of the $2snd$ Rydberg series in Be	318
Table 22.2	Observed and Hartree–Fock ionization potentials for the ground states of neutral atoms, in eV.	318
Table 22.3	Classification of replacements from the $1s^2 2s$ ground state of Li. The $1s$ and $2s$ orbitals are occupied, and all the other orbitals are virtual orbitals, vl	319
Table 22.4	Comparison of theoretical and experimental energies for Be $1s^2 2s^2 {}^1S$ in hartrees. All theoretical values include some form of extrapolation	322
Table 22.5	Comparison of CAS-MCHF and PCFI total energies (in hartrees) for the ground state of beryllium with increasing orbital active sets. NCSF corresponds to the size M of the CSF expansion Eq. (22.17)	323
Table 22.6	Convergence of transition data for the $1s^2 2s^2 2p^2 P^\circ \rightarrow 1s^2 2s 2p^2 {}^2D$ transition in boron with increasing active set	324

Table 22.7	Specific mass shift parameter and electron density at the nucleus as a function of the active set	327
Table 22.8	MCHF hyperfine constants (in MHz) for the $1s^2 2s 2p \ ^1P^o$ state of B II . . .	328
Table 23.1	Relativistic angular density functions	344
Table 23.2	Nonrelativistic angular density functions	344
Table 23.3	Spectroscopic labels and angular quantum numbers	345
Table 23.4	Radial moments $\langle \rho^s \rangle$	348
Table 23.5	j^N configurational states in the seniority scheme. The multiplicity of each unresolved degenerate state is indicated by a superscript	357
Table 26.1	Test of sum rule in Eq. (26.15) for the lowest $\text{He}^- (1s 2s^2 \ ^2S)$ autodetachment state [5]. Projection operators are based on a 4 term Hylleraas ϕ_0 and the variational form of v_α given below. Values of other constants are given in [5]	397
Table 26.2	Comparison of methods for calculating the energy of the lowest $\text{He}^- (1s 2s^2 \ ^2S)$ autodetachment state. The QHQ results are denoted $(\hat{E} - E_0)_{\text{Quasi}}$ for the quasi-projection method and $(E - E_0)_{\text{Complete}}$ for the complete projection method [5]. The entries labeled <i>Other results</i> give the full resonant energy. Units are eV	397
Table 26.3	Energies \mathcal{E}_s of the $\text{He}(2s 2p \ ^1P^0)$ autoionization states below $\text{He}^+ (n = 2)$ threshold from the variational calculations of <i>O'Malley</i> and <i>Geltman</i> [11]. Units are Ry; N is the number of terms in the trial function	397
Table 26.4	Comparison of high-precision calculations with the experiment for the resonance parameters of the $\text{He}(^1P^0)$ resonances below the $n = 2$ threshold. For photoabsorption, the appropriate Rydberg constant is $R_M = R_\infty / (1 + m/M)$ [19]. The value used here is $R_M = 13.603833$ eV, and $E_0 = -79.0151$ eV [6]	399
Table 26.5	Comparison of resonance parameters (in eV) obtained from different methods for calculating $^1D^e$ states in H^-	401
Table 26.6	Singlet autoionization states of He of $S, P, D,$ and F angular momentum below the $n = 2$ threshold of He^+ . Results are in eV relative to the ground state energy of $\text{He} = -5.8074475$ Ry	401
Table 26.7	Triplet autoionization states of He of $S, P, D,$ and F angular momentum below the $n = 2$ threshold of He^+ . Results are in eV relative to the ground state energy of $\text{He} = -5.8074475$ Ry	401
Table 26.8	Singlet and triplet autoionization states of Ps^- . Results are in eV relative to the ground state energy of $\text{Ps} = 0.5$ Ry	401
Table 26.9	$^3P^e$ states of Ps^- . Results are in eV relative to the ground state energy of $\text{Ps} = 0.5$ Ry	402
Table 26.10	Odd parity $^{1,3}P$ states of Ps^- . Resonance positions are with respect to the ground state energy of $\text{Ps} = 0.5$ Ry	402
Table 26.11	Resonance energies \mathcal{E}_F (Ry) and widths (eV) for 1P states of He below the $n = 2$ threshold (-1 Ry) of He^+	403
Table 26.12	$^3P^e$ shape resonances in Ps^- . Results are in eV relative to the ground state energy of $\text{Ps}^- = -0.5$ Ry	403
Table 29.1	Coefficients for the QED contributions to the electron anomaly. The coefficients $A_1^{(2n)}$ and functions $A_2^{(2n)}(x)$, evaluated at $x = x_{e\mu} \equiv m_e/m_\mu$ and $x_{e\tau} \equiv m_e/m_\tau$ for the muon and tau leptons, respectively, are listed with two significant digits for ease of comparison; summed values $C_e^{(2n)}$, based on the 2014 CODATA adjustment, are listed as accurately as needed for the tests described in this article. Missing values indicate that their contribution to the electron anomaly is negligible	437

Table 29.2	Theoretical contributions and total value for the g -factor of hydrogenic carbon 12 based on the 2014 CODATA recommended values of the constants and corresponding theory. The total g -factor has a relative uncertainty of 1.3×10^{-11}	441
Table 29.3	Theoretical contributions and total value for the g -factor of hydrogenic silicon 28 based on the 2014 CODATA recommended values of the constants and corresponding theory. The total g -factor has a relative uncertainty of 8.5×10^{-10}	441
Table 29.4	List of contributions and their main dependence on fundamental constants to the hydrogen transition frequencies ordered by appearance in the text. The first two columns give the section in Sec. 29.7.1 in which the contribution is described in detail and the name of the contribution, respectively. The fundamental-constant dependence of a contribution in the third column is given in terms of the Hartree energy $E_h = m_e c^2 \alpha^2$ and four dimensionless variables with values small compared to one: the fine-structure constant α , the proton charge radius divided by the reduced Compton wavelength r_p/λ_C , and the mass ratios m_e/m_μ and m_e/m_p . The last column gives the order of magnitude of each of the contributions in Hz for the $1S_{1/2}-2S_{1/2}$ transition	443
Table 29.5	Values of the Bethe logarithms $\ln k_0(n, \ell)$. Missing entries correspond to states for which no experimental measurements are available	443
Table 29.6	Values of the function $G_{SE}(\alpha)$. Missing entries correspond to states for which no experimental measurements are available	445
Table 29.7	Values of the function $G_{VP}^{(1)}(\alpha)$. No experimental data is available for missing entries. Zero values indicate that their contributions are negligibly small	445
Table 29.8	Values of B_{61} used in the 2014 CODATA adjustment. Zero values indicate that their contributions are negligibly small	445
Table 29.9	Values of B_{60} used in the 2014 CODATA adjustment. The uncertainties of B_{60} for S-states are explained in the text	445
Table 30.1	Accurately measured atomic transition frequencies and their fractional uncertainty ([9, 12] and references therein). These transitions have been used in evaluations of temporal variation of fundamental constants	453
Table 30.2	Magnetic moments and relativistic corrections for atoms involved in microwave standards. The relativistic sensitivity κ is defined in Sec. 30.2.3. Here, μ is an actual value of the nuclear magnetic moment, μ_N is the nuclear magneton, and μ_S stands for the Schmidt value of the nuclear magnetic moment; the nucleon g factors are $g_p/2 \simeq 2.79$ and $g_n/2 \simeq -1.91$	454
Table 30.3	The frequencies of different transitions in neutral atoms and ions, applied or tried for precision spectroscopy, and their sensitivity to variations in α due to relativistic corrections	455
Table 30.4	Model-independent laboratory constraints on the possible time variations of natural constants [41, 42]	457
Table 30.5	Progress in constraining a possible time variation of the fundamental constants: the results of 2004 (following [43, 44]), 2008 (following [45]), and of 2014 using data summarized in [42] but following [43, 44] (see [41] for details). Here, ρ is the correlation coefficient $\rho(\partial \ln \alpha / \partial t, \partial \ln \{R_\infty\} / \partial t)$	457
Table 30.6	Model-dependent laboratory constraints on possible time variations of fundamental constants. The uncertainties here do not include uncertainties from the application of the Schmidt model	458
Table 34.1	Tunneling energy eigensolutions	512
Table 34.2	Character table for symmetry group C_2	513
Table 34.3	Character table for symmetry group D_2	514

Table 34.4	Character table for symmetry group O	516
Table 34.5	$H_{K=28}$ matrix solutions	518
Table 34.6	Hyperfine spin states	520
Table 40.1	Examples illustrating the range of ionic reactions that can occur in the gas phase	598
Table 42.1	Summary of reproducibility, accuracy, and precision of measured components	637
Table 44.1	Fixed frequency lasers	653
Table 44.2	Approximate tuning ranges for tunable lasers	653
Table 46.1	Representative third-order frequency conversion schemes for generation of tunable coherent VUV light	673
Table 47.1	Model interaction potentials	707
Table 48.1	Summary of cases of increasing complexity and the orientation and alignment parameters necessary for unpolarized beams; N_p is the number of independent parameters, and N_d is the number of observation directions required	718
Table 48.2	Summary of cases of increasing complexity for spin-polarized beams. The number of independent dimensionless parameters N_p is listed, along with N_{OA} , the number determined from orientation and alignment only; N_d is the number of observation directions required	721
Table 52.1	Selection rules for the coupling between diabatic and adiabatic states of a diatomic quasi molecule ($w = g, u; \sigma = +, -$)	777
Table 52.2	Selection rules for dynamic coupling between adiabatic states of a system of three atoms	778
Table 58.1	Recombination computer codes	851
Table 60.1	General n -dependence of characteristic properties of Rydberg states. After [4]	883
Table 60.2	Multipoles Q_L for the Stark states $ \pm\rangle$ of $H(n)$	884
Table 60.3	Fit parameters for Cs-Cs and Rb-Rb pseudo-potentials (from [12])	885
Table 60.4	Coefficients $C(n_i l_i \rightarrow n_f l_f)$ in the Born capture cross section formula in Eq. (60.330)	910
Table 60.5	Functions $F(n_i l_i \rightarrow n_f l_f; x)$ in the Born capture cross section formula in Eq. (60.330)	910
Table 70.1	Collision numbers for coupling between different modes. V, R, and T refer to vibrational, rotational, and translational energy, respectively. Each entry is the typical range of Z_{A-B}	1020
Table 75.1	Overview of laser types, organized by the nature of the lasing transition	1082
Table 79.1	Laser cooling parameters for the lowest $S_{1/2}-P_{3/2}$ transition of hydrogen and most alkalis (the D_2 line). Also shown are the nuclear spin I and the ground state hyperfine splitting $\Delta\nu_{\text{hfs}}$	1142
Table 85.1	BB84 protocol for secret key distribution. “Alice” sends information encoded in either of two basis sets. “Bob” randomly chooses a measurement basis that is publicly communicated. For those cases when sender and receiver chose the same basis, the receiver’s measurement yields a secure bit	1262
Table 86.1	Molecules observed in interstellar clouds	1280
Table 88.1	Homopause characteristics of planets and other solar system bodies	1301
Table 88.2	Molecular weights and fractional composition of dry air in the terrestrial atmosphere ^a	1301
Table 88.3	Composition of the lower atmospheres of Mars and Venus	1302
Table 88.4	Composition of the lower atmospheres of Jupiter and Saturn	1303
Table 88.5	Composition of the lower atmospheres of Uranus and Neptune ^a	1303
Table 88.6	Composition of the lower atmosphere of Titan ^a	1303

Table 88.7	Composition of the atmosphere of Triton ^a	1304
Table 88.8	Number densities of neutral and ion species at the surface of Mercury ^a . . .	1304
Table 88.9	Composition of the lower atmosphere of Pluto ^a	1304
Table 88.10	Ionization potentials (I_P) of common atmospheric species (computed with data taken from [56], except as noted)	1313
Table 88.11	Exobase properties of solar system bodies	1333
Table 91.1	Resonant (quasiresonant if negative) collision energies ϵ_{res} (in meV) calculated using Eq. (91.35) ^a	1369
Table 91.2	Comparison of sticking values ^a	1372

About the Authors

Nigel G. Adams

Girish S. Agarwal Institute for Quantum Science and Engineering, Texas A&M University, College Station, USA

Miron Y. Amusia

Nils Andersen The Niels Bohr Institute, University of Copenhagen, Copenhagen, Denmark

Nigel Badnell Dept. of Physics, University of Strathclyde Glasgow, Glasgow, UK

Raul O. Barrachina Bariloche Atomic Centre, National Atomic Energy Commission, Bariloche, Argentina

Thomas Bartsch Mathematical Sciences, Loughborough University, Leicestershire, UK

Klaus Bartschat Dept. of Physics & Astronomy, Drake University, Des Moines, USA

William E. Baylis Department of Physics, University of Windsor, Windsor, ON, Canada

Anand K. Bhatia Laboratory for Astronomy & Solar Physics, NASA Goddard Space Flight Center, Greenbelt, USA

Robert W. Boyd Dept. of Physics, University of Ottawa, Ottawa, Canada, Institute of Optics, University of Rochester, Rochester, USA

Michael W. J. Bromley University of Southern Queensland, Toowoomba, Australia

John M. Brown

Henry Buijs FTS Consulting, Québec, Canada

Philip Burke

Denise Caldwell Physics Division, National Science Foundation, Alexandria, VA, USA

Mark M. Cassar Zekelman School of Information Technology, St. Clair College, Windsor, Canada

Alexis A. Chacon S. Dept. of Physics, Pohang University of Science and Technology and Max Planck Research Initiative/Korea, Pohang, Korea, Republic of

Kelly Chance Harvard-Smithsonian Center for Astrophysics, Cambridge, USA

Raymond Y. Chiao Departments of Physics and Engineering, University of California
Merced, Merced, USA

Marcelo Ciappina Physics Program, Guangdong Technion – Israel Institute of Technology,
Shantou, Guangdong, China

Lew Cocke Dept. of Physics, Kansas State University, Manhattan, USA

James S. Cohen Atomic and Optical Theory, Los Alamos National Laboratory, Los Alamos,
USA

Derrick Crothers

Lorenzo J. Curtis

Alexander Dalgarno

Nelson de Oliveira Ligne DESIRS, Synchrotron Soleil, Gif-sur-Yvette Cedex, France

John B. Delos Butterfly Dynamics LLC, Williamsburg, USA

Abigail J. Dobbyn Göttingen, Germany

Joseph H. Eberly Dept. of Physics and Astronomy, University of Rochester, Rochester,
USA

Guy T. Emery Dept. of Physics, Bowdoin College, Brunswick, USA

Volker Engel Institute of Physical and Theoretical Chemistry, Universität Würzburg,
Würzburg, Germany

Paul Engelking Dept. of Chemistry and Chemical Physics Institute, University of Oregon,
Eugene, USA

Kenneth Evenson

James M. Farrar Dept. of Chemistry, University of Rochester, Rochester, USA

Alexandre Faure Institute of Planetology and Astrophysics of Grenoble (IPAG), University
of Grenoble Alpes (CNRS), Grenoble, France

Gordon Feldman Baltimore, USA

Paul D. Feldman

Victor Flambaum Dept. of Physics, University of New South Wales, Sydney, Australia

M. Raymond Flannery

David R. Flower Dept. of Physics, University of Durham, Durham, UK

Omar A. Fojón Instituto de Física Rosario, Rosario, Argentina

A. Lewis Ford Dept. of Physics, Texas A&M University, College Station, USA

Jane L. Fox Dept. of Physics, Wright State University, Dayton, USA

Charlotte Froese Fischer Dept. of Computer Science, University of British Columbia, Vancouver, Canada

Thomas Fulton

Alexander L. Gaeta Applied Physics and Applied Mathematics, Columbia University, New York, USA

Alan Gallagher Quantum Physics Division, University of Colorado, Boulder, USA

Thomas F. Gallagher Dept. of Physics, University of Virginia, Charlottesville, VA, USA

Muriel Gargaud Observatoire Aquitain des Sciences de l'Univers, Floirac, France

Enno Giese Institut für Angewandte Physik, Technische Universität Darmstadt, Darmstadt, Germany

Michel Godefroid Chemistry Department (SQUARES), Université libre de Bruxelles (ULB), Brussels, Belgium

S. Pedro Goldman Dept. of Physics, Toronto Metropolitan University, Toronto, Canada

Gonzalo González Abad Harvard-Smithsonian Center for Astrophysics, Cambridge, MA, USA

Ian Grant Oxford Mathematical Institute, University of Oxford, Oxford, UK

Chris H. Greene Dept. of Physics & Astronomy, Purdue University, West Lafayette, USA

Donald Griffin Dept. of Physics, Rollins College, Winter Park, USA

Dag Hanstorp Dept. of Physics, University of Gothenburg, Gothenburg, Sweden

William G. Harter Dept. of Physics, University of Arkansas, Fayetteville, USA

Charles Havener Physics Division, Oak Ridge National Laboratory, Oak Ridge, USA

Qiongyi He School of Physics, Peking University, Beijing, China

Carsten Henkel Institute of Physics and Astronomy, University of Potsdam, Potsdam, Germany

Eric Herbst Dept. of Chemistry and Dept. of Astronomy, University of Virginia, Charlottesville, USA

Robert N. Hill

David L. Huestis Molecular Physics Laboratory, SRI International, Menlo Park, USA

Daniel F. V. James Dept. of Physics, University of Toronto, Toronto, Canada

Juha Javanainen Department of Physics, University of Connecticut, Storrs, USA

Erik T. Jensen Dept. of Physics, University of Northern British Columbia, Prince George, Canada

Brian R. Judd Dept. of Physics & Astronomy, The Johns Hopkins University, Baltimore, USA

Alexander A. Kachanov Picarro, Inc., Sunnyvale, USA

Alexander Kandratsenka Dynamics at Surfaces, Max-Planck-Institute for Multidisciplinary Sciences, Göttingen, Germany

Isik Kanik Jet Propulsion Laboratory, California Institute of Technology, Pasadena, USA

Savely G. Karshenboim Faculty of Physics, Ludwig-Maximilians-University, Munich, Germany

Kate P. Kirby American Physical Society, College Park, USA

Tom Kirchner Dept. of Physics & Astronomy, York University, Toronto, Canada

Peter L. Knight Dept. of Physics, Imperial College London, London, UK

Alexander Kramida Physical Measurement Laboratory, National Institute of Standards and Technology, Gaithersburg, MD, USA

Manfred Krause Oak Ridge National Laboratory, Oak Ridge, USA

Paul G. Kwiat Dept. of Physics, University of Illinois at Urbana-Champaign, Urbana, USA

Yuan T. Lee Institute of Atomic and Molecular Science, Academia Sinica, Taipei, Taiwan

Stephen Lepp Dept. of Physics & Astronomy, University of Nevada, Las Vegas, Las Vegas, USA

Maciej Lewenstein The Barcelona Institute of Science and Technology, Quantum Optics Theory, ICFO and ICREA, Castelldefels, Spain

Hongwei Li State Key Laboratory of Molecular Reaction Dynamics, Dalian Institute of Chemical Physics, Chinese Academy of Sciences, Dalian, Liaoning, China

Francois Lique CNRS, IPR (Institut de Physique de Rennes), Université de Rennes 1, Rennes, France

James D. Louck

Joshua R. Machacek Research School of Physics, Australian National University, Canberra, Australia

Mary L. Mandich NOKIA Corp. (retired), Martinsville, USA

Edmund J. Mansky II Eikonol Research Institute, Bend, OR, USA

William C. Martin

Ronald McCarroll Laboratoire de Chimie Physique, Université Pierre et Marie Curie, Paris, France

William McConkey Dept. of Physics, University of Windsor, Windsor, Canada

Robert P. McEachran Research School of Physics, Australian National University, Canberra, Australia

James H. McGuire Dept. of Physics, Tulane University, New Orleans, USA

Ralf Menzel Dept. of Physics, University of Potsdam, Potsdam, Germany

Dieter Meschede Inst. f. Applied Physics, Rheinische Friedrich-Wilhelm Universität Bonn, Bonn, Germany

Pierre Meystre University of Arizona, Tucson, USA

Peter W. Milonni Theoretical Division, Los Alamos National Laboratory, Los Alamos, USA

Peter J. Mohr National Institute of Standards and Technology, Gaithersburg, USA

David H. Mordaunt Göttingen, Germany

John D. Morgan III Dept. of Physics & Astronomy, University of Delaware, Newark, USA

Francisco Navarrete Institute of Physics, University of Rostock, Rostock, Germany

Evgeny Nikitin Dept. of Physics, Technion – Israel Institute of Technology, Haifa, Israel

Patrick Nuernberger Institute of Physical and Theoretical Chemistry, Universität Regensburg, Regensburg, Germany

Ronald E. Olson Physics Dept., University of Missouri-Rolla, Rolla, USA

Barbara Paldus Skymoon Ventures, Palo Alto, USA

Josef Paldus Dept. of Applied Mathematics, University of Waterloo, Waterloo, Canada

Gillian Peach Dept. of Physics and Astronomy, University College London, London, UK

David Pegg Dept. of Physics, University of Tennessee, Knoxville, USA

Ekkehard Peik Physikalisch-Technische Bundesanstalt, Braunschweig, Germany

Ronald Phaneuf Dept. of Physics, University of Nevada, Reno, Reno, USA

Michael Pindzola College of Sciences and Mathematics, Auburn University, Auburn, USA

Eric H. Pinnington Dept. of Physics, University of Alberta, Edmonton, Alberta, Canada

Richard C. Powell Optical Sciences Center, University of Arizona, Tucson, USA

Richard S. Quimby Dept. of Physics, Worcester Polytechnic Institute, Worcester, USA

John F. Reading Dept. of Physics, Texas A&M University, College Station, USA

Tyle C. Reimer University of Arkansas, Fayetteville, USA

Roberto D. Rivarola Instituto de Física Rosario, CONICET – UNR, Rosario, Argentina

Jan-Michael Rost Max Planck Institute for the Physics of Complex Systems, Dresden, Germany

Hossein Sadeghpour Institute for Theoretical Atomic Molecular and Optical Physics (ITAMP), Harvard University, Cambridge, USA

Marianna S. Safronova Dept. of Physics & Astronomy, University of Delaware, Newark, USA

Jonathan R. Sapirstein Department of Physics, University of Notre Dame, Notre Dame, USA

Stefan Scheel Institute of Physics, University of Rostock, Rostock, Germany

Axel Schenzle

Reinhard Schinke Max-Planck-Institute for Dynamics and Self-Organization, Göttingen, Germany

David Schultz Department of Astronomy and Planetary Science, Northern Arizona University, Flagstaff, AZ, USA

Michael Schulz Dept. of Physics, Missouri University of Science & Technology, Rolla, USA

L. Krister Shalm Dept. of Physics, University of Colorado at Boulder, Boulder, USA

Peter L. Smith retired, Cathedral City, USA

Yevgeny Stadnik School of Physics, The University of Sydney, Sydney, Australia

Phillip C. Stancil Dept. of Physics & Astronomy, The University of Georgia, Athens, USA

Anthony F. Starace

Glenn Stark Dept. of Physics, Wellesley College, Wellesley, USA

Allan D. Stauffer Dept. of Physics & Astronomy, York University, Toronto, Canada

Aephraim M. Steinberg Dept. of Physics, University of Toronto, Toronto, Canada

Stig Stenholm

Jack C. Straton Dept. of Physics, Portland State University, Portland, OR, USA

Michael R. Strayer

Carlos R. Stroud Jr. The Institute of Optics, University of Rochester, Rochester, USA

Arthur G. Suits Dept. of Chemistry, University of Missouri, Columbia, USA

Barry N. Taylor Quantum Measurement Division, National Institute of Standards and Technology, Gaithersburg, USA

Aaron Temkin Laboratory for Solar and Space Physics, NASA Goddard Space Flight Center, Greenbelt, USA

Jonathan Tennyson Dept. of Physics & Astronomy, University College London, London, UK

Eite Tiesinga National Institute of Standards and Technology, Gaithersburg, MD, USA

Elmar Träbert Astronomical Institute, Ruhr University Bochum, Bochum, Germany

Sandor Trajmar Jet Propulsion Laboratory, California Institute of Technology, Redwood City, USA

Turgay Uzer School of Physics, Georgia Institute of Technology, Atlanta, USA

Alexander Voitkiv The Institute of Theoretical Physics I, Heinrich-Heine University Düsseldorf, Düsseldorf, Germany

Da-Wei Wang Department of Physics, Zhejiang University, Hangzhou, China

Wolfgang L. Wiese National Institute of Standards and Technology, Gaithersburg, MD, USA

Martin Wilkens Institute of Physics and Astronomy, University of Potsdam, Potsdam, Germany

David R. Yarkony Dept. of Chemistry, The Johns Hopkins University, Baltimore, USA

Ruitian Zhang Institute of Modern Physics, Chinese Academy of Sciences, Lanzhou, China

Wei Zhang Dept. of Physics, Renmin University of China, Beijing, China

Bernard Zygelman Dept. of Physics & Astronomy, University of Nevada, Las Vegas, Las Vegas, USA

Part A
Mathematical Methods

Part A gathers together the mathematical methods applicable to a wide class of problems in atomic, molecular, and optical physics. The application of angular momentum theory to quantum mechanics is presented. The basic tenet that isolated physical systems are invariant to rotations of the system is thereby implemented into physical theory. The powerful methods of group theory and second quantization show how simplifications arise if the atomic shell is treated as a basic structural unit. The well-established symmetry groups of quantum mechanical Hamiltonians are extended to the larger compact and noncompact dynamical groups. Perturbation theory is introduced as a bridge between an exactly solvable problem and a corresponding real one, allowing approx-

imate solutions of various systems of differential equations. The consistent manner in which the density matrix formalism deals with pure and mixed states is developed, showing how the preparation of an initial state, as well as the details regarding the observation of the final state, can be treated in a systematic way. The basic computational techniques necessary for accurate and efficient numerical calculations essential to all fields of physics are outlined, and a summary of relevant software packages is given. The ever-present one-electron solutions of the nonrelativistic Schrödinger equation and the relativistic Dirac equation for the Coulomb potential are then summarized. A summary of the computer software available for atomic and molecular physics calculations is included.



Units and Constants

1

Eite Tiesinga

Contents

1.1	Introduction	3
1.2	Atomic Units	3
1.3	Natural Units	5
1.4	Fundamental Constants	5
	References	7

Abstract

We describe atomic and natural units relevant for the atomic, molecular, and optical physics described in this book. For nonrelativistic models of atoms and molecules absorbing and emitting photons atomic units are appropriate. In this system, energies and lengths are expressed in terms of the Hartree energy and Bohr radius, respectively. Relativistic models are required for precision quantum electrodynamics-based determinations of energy levels of hydrogen and other light atoms and molecules. Natural units are then the most appropriate, and energies and length are expressed in the rest energy of the electron and the reduced Compton wavelength, respectively. Finally, we present values for an abbreviated list of fundamental constants taken from the CODATA (Committee on Data for Science and Technology) adjustment of fundamental constants based on data published or made available before the end of 2018.

Keywords

atomic units · fine structure constant · fundamental constants · International System of Units (SI) · natural units

1.1 Introduction

In science we communicate measurements of quantities or observables in terms of a product of a numerical value and a unit, where the unit is a particular example of the quantity. For example, the spin of an electron is $(1/2)\hbar$, where $1/2$ is the numerical value, and the reduced Planck constant \hbar is the unit or example angular momentum. Equivalently, the spin of the electron is $0.527\,285\dots\times 10^{-34}$ J s in the International System of Units (SI) [1]. More digits for the numerical value can be easily found now that the Planck constant is exactly defined in the SI. In fact, seven exact constants define the seven SI base units second, meter, kilogram, Coulomb, kelvin, and lumen [1]. The names and values of these constants are given in Table 1.1. It was only on World Metrology Day, 20 May 2019, that the Planck constant, elementary charge, Boltzmann constant, and the Avogadro constant were given their exact value in the SI. See [2] for a review of the ideas that led to this redefinition.

The example in the previous paragraph shows that some units are more convenient than others. We tend to prefer units where the numerical value of the measured quantity is of order 1. Preferred units for a system follow from its Hamiltonian H in a process that makes H as well as all operators and constants appearing in H dimensionless. Operators can correspond to particle spins, positions, and momenta but also fields in quantum field theories.

In this chapter, we derive atomic and natural units as they appear in atomic, molecular, and optical physics. For a different view of units in the field of electromagnetism, we recommend the appendix on units and dimensions of [3]. We also present a list of relevant fundamental constants.

1.2 Atomic Units

We derive atomic units starting from the nonrelativistic Hamiltonian for an electron with charge $-e$ and mass m_e

E. Tiesinga (✉)
National Institute of Standards and Technology
Gaithersburg, MD, USA
e-mail: eite.tiesinga@nist.gov

Table 1.1 Exact quantities and their symbols, numerical values, and units in the SI

Quantity	Sym.	Value	Unit
Hyperfine transition frequency of ^{133}Cs	$\Delta\nu_{\text{Cs}}$	9 192 631 770	Hz
Speed of light in vacuum	c	299 792 458	m s^{-1}
Planck constant ^a	h	$6.626\,070\,15 \times 10^{-34}$	J Hz^{-1}
	\hbar	$1.054\,571\,817 \dots \times 10^{-34}$	J s
Elementary charge	e	$1.602\,176\,634 \times 10^{-19}$	C
Boltzmann constant	k	$1.380\,649 \times 10^{-23}$	J K^{-1}
Avogadro constant	N_{A}	$6.022\,140\,76 \times 10^{23}$	mol^{-1}
Luminous efficacy	K_{cd}	683	lm W^{-1}

^a The energy of a photon with frequency ν expressed in unit Hz is $E = h\nu$ in J. The unitary time evolution of the state of this photon is given by $\exp(-iEt/\hbar)|\varphi\rangle$, where $|\varphi\rangle$ is the photon state at time $t = 0$, and time is expressed in unit s. The ratio Et/\hbar is a phase.

bound to an infinitely heavy point-like source with charge $+Ze$, possibly absorbing and emitting transverse photons. Following [4] we use the Coulomb gauge and assume that the charges are contained in a large cubic box with periodic boundary conditions and length L on each side. Here, e is the (positive) elementary charge, and Z is a positive integer. Hence, we have

$$H = \frac{(\vec{p} + e\vec{A}_{\perp}(\vec{r}))^2}{2m_e} - \frac{1}{4\pi\epsilon_0} \frac{Ze^2}{r} + \sum_j \hbar\omega_j \left[a_j^{\dagger} a_j + \frac{1}{2} \right], \quad (1.1)$$

where \vec{r} and \vec{p} are the position and momentum operators of the electron, respectively, and the commutation relations $[r_i, p_j] = i\hbar\delta_{ij}$ for vector components i and j hold. The source is located at $\vec{r} = \vec{0}$, ϵ_0 is the vacuum electric permittivity, and δ_{ij} is the Kronecker delta. For simplicity, we have omitted the Zeeman interaction of the electron spin coupling to a magnetic field.

The last term of Eq. (1.1) describes the photon-field Hamiltonian, where operators a_j and a_j^{\dagger} annihilate and create photons, respectively. For index j , photons are specified by polarization $\vec{\epsilon}_j$ and wavevector \vec{k}_j . The components of the wavevector are integer multiples of $2\pi/L$. By construction $\vec{\epsilon}_j$ and \vec{k}_j are perpendicular to each other, and the frequency of photon j is $\omega_j = c|\vec{k}_j|$, where c is the speed of light in vacuum. Operators a_j and a_j^{\dagger} satisfy the commutation relations $[a_i, a_j^{\dagger}] = \delta_{ij}$. Finally, the transverse vector field operator $\vec{A}_{\perp}(\vec{r})$ ¹ is given by

$$\vec{A}_{\perp}(\vec{r}) = \sum_j \sqrt{\frac{\hbar}{2\epsilon_0\omega_j L^3}} \left[a_j \vec{\epsilon}_j e^{i\vec{k}_j \cdot \vec{r}} + a_j^{\dagger} \vec{\epsilon}_j e^{-i\vec{k}_j \cdot \vec{r}} \right]. \quad (1.2)$$

Similar expressions for the transverse electric $\vec{E}_{\perp}(\vec{r})$ and magnetic $\vec{B}(\vec{r})$ field operators can be written down. The con-

¹ A transverse vector field $\vec{F}_{\perp}(\vec{r})$ in position space \vec{r} is a field such that its Fourier representation $\vec{F}_{\perp}(\vec{k})$ is perpendicular to \vec{k} for all wavevectors \vec{k} . Magnetic fields are transverse vector fields in any gauge and subscript \perp is often dropped.

stants ϵ_0 , c , and the vacuum magnetic permeability μ_0 are not independent. They satisfy

$$c^2 = \frac{1}{\mu_0\epsilon_0}. \quad (1.3)$$

We are now ready to make the Hamiltonian dimensionless. We assume that there exists a convenient length scale a_0 and write for the position operator of the electron $\vec{r} = \vec{x} a_0$, where operator \vec{x} is dimensionless. An equally valid interpretation of $\vec{x} a_0$ is that \vec{x} is a vector of numerical values, and a_0 is the unit for position. The commutation relation for \vec{r} and \vec{p} imply $\vec{p} = -i\hbar\nabla_r$, where ∇_r is the gradient or nabla vector differential operator in \vec{r} , and thus $\vec{p} = -i\nabla_x \hbar a_0^{-1}$. The wavevector and frequency of the photon field are made dimensionless with $\vec{k}_j = \vec{q}_j a_0^{-1}$ and $\omega_j = |q_j| c a_0^{-1}$. The components of \vec{q}_j are integer multiples of $2\pi/\ell$, where $L = \ell a_0$. Thus, the units of electron momentum, photon wavevector, and frequency are $\hbar a_0^{-1}$, a_0^{-1} , and $c a_0^{-1}$, respectively.

To summarize, Eq. (1.1) becomes

$$H = \frac{\hbar^2}{m_e a_0^2} \frac{1}{2} \left(-i\nabla_x + \frac{e a_0}{\hbar} \vec{A}_{\perp}(\vec{x} a_0) \right)^2 - \frac{e^2}{4\pi\epsilon_0 a_0} \frac{Z}{x} + \hbar c a_0^{-1} \sum_j |q_j| \left[a_j^{\dagger} a_j + \frac{1}{2} \right]. \quad (1.4)$$

A comparison of the energies of the first two terms suggests that we choose a_0 such that

$$\frac{\hbar^2}{m_e a_0^2} = \frac{e^2}{4\pi\epsilon_0 a_0} \equiv E_h, \quad (1.5)$$

and, thus,

$$a_0 = \frac{4\pi\epsilon_0 \hbar^2}{m_e e^2}. \quad (1.6)$$

The reference quantities E_h and a_0 or the atomic units of energy and length are better known as the Hartree energy and the Bohr radius, respectively. The Rydberg frequency cR_{∞} is defined by $cR_{\infty} = E_h/2h$.

In atomic units the vector potential is made dimensionless with the choice

$$\vec{A}_\perp(\vec{x} a_0) \equiv \vec{\mathcal{A}}_\perp(\vec{x}) \frac{\hbar}{e a_0}, \quad (1.7)$$

so that the Hamiltonian reads

$$H = \left\{ \frac{1}{2} \left(-i \nabla_x + \vec{\mathcal{A}}_\perp(\vec{x}) \right)^2 - \frac{Z}{x} + \sum_j \frac{1}{\alpha} |q_j| \left[a_j^\dagger a_j + \frac{1}{2} \right] \right\} E_h, \quad (1.8)$$

where the dimensionless fine-structure constant α is

$$\alpha = \frac{e^2}{4\pi\epsilon_0 \hbar c}, \quad (1.9)$$

and $1/\alpha$ is the numerical value of the speed of light in vacuum in atomic units. Specifically, the unit of velocity is $\hbar/m_e a_0$.

1.3 Natural Units

Natural units follow from Dirac's relativistic description of the negatively-charged electron bound to an infinitely-heavy point charge in the presence of transverse photons. Thus, in the Coulomb gauge, we have

$$H_{\text{rel}} = \beta m_e c^2 + c \vec{\alpha} \cdot (\vec{p} + e \vec{A}_\perp(\vec{r})) - I_4 \frac{1}{4\pi\epsilon_0} \frac{Z e^2}{r} + \sum_j \hbar \omega_j \left[a_j^\dagger a_j + \frac{1}{2} \right], \quad (1.10)$$

where $\vec{\alpha}$ and β are four dimensionless mutually anticommuting four-component Dirac matrices with $\alpha_i^2 = \beta^2 = I_4$, and I_4 is the four-component identity matrix. The definition for the transverse vector potential $\vec{A}_\perp(\vec{r})$ remains that of Eq. (1.2). For our purpose of defining natural units, we can ignore interpretations of the positive and negative energy solutions of the Dirac equation as well as effects such as virtual electron-positron pairs, which will be present in the complete quantum electrodynamic (QED) theory.

This relativistic Hamiltonian can be made dimensionless by assuming the length unit λ_C and $\vec{r} = \vec{x} \lambda_C$ with similar expressions for box size L , momentum \vec{p} , and photon wavevector and frequency \vec{k}_j and ω_j . Then we find

$$H_{\text{rel}} = \beta m_e c^2 + \hbar c \lambda_C^{-1} \vec{\alpha} \cdot \left(-i \nabla_x + \frac{e \lambda_C}{\hbar} \vec{\mathcal{A}}_\perp(\vec{x} \lambda_C) \right) - \frac{e^2}{4\pi\epsilon_0 \lambda_C} \frac{Z}{x} + \hbar c \lambda_C^{-1} \sum_j |q_j| \left[a_j^\dagger a_j + \frac{1}{2} \right], \quad (1.11)$$

and, by comparing the energies of the first two terms, choose λ_C such that

$$m_e c^2 = \hbar c \lambda_C^{-1}, \quad (1.12)$$

or

$$\lambda_C = \frac{\hbar}{m_e c}. \quad (1.13)$$

The reference quantities $m_e c^2$ and λ_C or the natural units of energy and length are the energy equivalent of the electron rest mass and the reduced Compton wavelength, respectively. We also note that $\lambda_C = \alpha a_0$ and $E_h = \alpha^2 m_e c^2$.

In natural units the transverse vector potential is not made dimensionless from its appearance in the Hamiltonian but rather from rewriting its definition in Eq. (1.2) in terms of the reduced Compton wavelength. In fact, we choose

$$\vec{A}_\perp(\vec{x} \lambda_C) \equiv \sqrt{4\pi\alpha} \vec{\mathcal{A}}_\perp(\vec{x}) \frac{\hbar}{e \lambda_C}, \quad (1.14)$$

where

$$\vec{\mathcal{A}}_\perp(\vec{x}) = \sum_j \sqrt{\frac{1}{2|q_j| \ell^3}} \left[a_j \vec{\epsilon}_j e^{i \vec{q}_j \cdot \vec{x}} + a_j^\dagger \vec{\epsilon}_j e^{-i \vec{q}_j \cdot \vec{x}} \right] \quad (1.15)$$

by inspection. The transverse vector field $\vec{\mathcal{A}}_\perp(\vec{x})$ only depends on geometric quantities related to the periodic boundary conditions in the cubic box of length $L = \ell \lambda_C$ and not on α or the charge of the electron. Finally, the Hamiltonian in Eq. (1.11) reads

$$H_{\text{rel}} = \left\{ \beta + \vec{\alpha} \cdot \left(-i \nabla_x + \sqrt{4\pi\alpha} \vec{\mathcal{A}}_\perp(\vec{x}) \right) - I_4 \frac{Z\alpha}{x} + \sum_j |q_j| \left[a_j^\dagger a_j + \frac{1}{2} \right] \right\} m_e c^2, \quad (1.16)$$

where the fine-structure constant now appears in the strength of the minimal coupling $\vec{\alpha} \cdot \vec{\mathcal{A}}_\perp(\vec{x})$ of the electron with the photons and in the Coulomb term of the Hamiltonian. The numerical value of the speed of light in vacuum is one in natural units. In fact, the unit of velocity is $\hbar/m_e \lambda_C = c$.

1.4 Fundamental Constants

In Table 1.2 we present an abbreviated list of values for fundamental constants based on the 2018 adjustment of fundamental constants as published by the CODATA taskgroup [5]. The table also gives values for atomic and natural units for a range of quantities, such as charge, speed, and time. The two most accurately known constants are the g -factor of a free electron and the Rydberg frequency $c R_\infty$ (or, equivalently, the Hartree energy) with relative uncertainties of 1.7×10^{-13} and 1.9×10^{-12} , respectively. The least well-known quantity in the table is the proton root-mean-square (rms) charge radius r_p with a relative uncertainty of

Table 1.2 Selected constants as well as atomic and natural units based on the 2018 CODATA adjustment of the fundamental constants [5]. The first two columns describe the quantity and its mathematical symbol. The third and fourth columns give its numerical value and unit. For quantity X the number in parenthesis in the numerical value is the combined statistical and systematic one-standard-deviation uncertainty $u(X)$ in the last two digits of the numerical value. Finally, the last column gives the relative standard uncertainty $u_r(X) = u(X)/|X|$. The unit u is the atomic mass unit, one-twelfth of the mass of a ^{12}C atom

Quantity	Symbol	Numerical value	Unit	Relative std. uncert. u_r
Non-SI units accepted for use within the SI				
Electron volt: (e/C) J	eV	$1.602\,176\,634 \times 10^{-19}$	J	exact
(Unified) atomic mass unit: $m(^{12}\text{C})/12$	u	$1.660\,539\,066\,60(50) \times 10^{-27}$	kg	3.0×10^{-10}
General				
Vacuum magnetic permeability $4\pi\alpha\hbar/e^2c$	μ_0	$1.256\,637\,062\,12(19) \times 10^{-6}$	N A^{-2}	1.5×10^{-10}
$\mu_0/(4\pi \times 10^{-7})$		1.000 000 000 55(15)	N A^{-2}	1.5×10^{-10}
Vacuum electric permittivity $1/\mu_0c^2$	ϵ_0	$8.854\,187\,8128(13) \times 10^{-12}$	F m^{-1}	1.5×10^{-10}
Fine-structure constant $e^2/4\pi\epsilon_0\hbar c$	α	$7.297\,352\,5693(11) \times 10^{-3}$		1.5×10^{-10}
Inverse fine-structure constant	α^{-1}	137.035 999 084(21)		1.5×10^{-10}
Rydberg frequency $\alpha^2m_e c^2/2\hbar = E_h/2h$	cR_∞	$3.289\,841\,960\,2508(64) \times 10^{15}$	Hz	1.9×10^{-12}
Energy equivalent	$hc R_\infty$	$2.179\,872\,361\,1035(42) \times 10^{-18}$	J	1.9×10^{-12}
		13.605 693 122 994(26)	eV	1.9×10^{-12}
Rydberg constant	R_∞	10 973 731.568 160(21)	$[\text{m}^{-1}]^a$	1.9×10^{-12}
Bohr magneton $e\hbar/2m_e$	μ_B	$9.274\,010\,0783(28) \times 10^{-24}$	J T^{-1}	3.0×10^{-10}
	μ_B/h	$1.399\,624\,493\,61(42) \times 10^{10}$	Hz T^{-1}	3.0×10^{-10}
Nuclear magneton $e\hbar/2m_p$	μ_N	$5.050\,783\,7461(15) \times 10^{-27}$	J T^{-1}	3.1×10^{-10}
	μ_N/h	7.622 593 2291(23)	MHz T^{-1}	3.1×10^{-10}
Electron, e				
Electron mass	m_e	$9.109\,383\,7015(28) \times 10^{-31}$	kg	3.0×10^{-10}
		$5.485\,799\,090\,65(16) \times 10^{-4}$	u	2.9×10^{-11}
Energy equivalent	$m_e c^2$	$8.187\,105\,7769(25) \times 10^{-14}$	J	3.0×10^{-10}
		0.510 998 950 00(15)	MeV	3.0×10^{-10}
Electron–muon mass ratio	m_e/m_μ	$4.836\,331\,69(11) \times 10^{-3}$		2.2×10^{-8}
Reduced Compton wavelength $\hbar/m_e c = \alpha a_0$	$\tilde{\lambda}_C$	$3.861\,592\,6796(12) \times 10^{-13}$	m	3.0×10^{-10}
Compton wavelength	λ_C	$2.426\,310\,238\,67(73) \times 10^{-12}$	$[\text{m}]^a$	3.0×10^{-10}
Classical electron radius $\alpha^2 a_0$	r_e	$2.817\,940\,3262(13) \times 10^{-15}$	m	4.5×10^{-10}
Electron magnetic moment	μ_e	$-9.284\,764\,7043(28) \times 10^{-24}$	J T^{-1}	3.0×10^{-10}
to Bohr magneton ratio	μ_e/μ_B	-1.001 159 652 181 28(18)		1.7×10^{-13}
to nuclear magneton ratio	μ_e/μ_N	-1838.281 971 88(11)		6.0×10^{-11}
Electron magnetic moment anomaly $ \mu_e /\mu_B - 1$	a_e	$1.159\,652\,181\,28(18) \times 10^{-3}$		1.5×10^{-10}
Electron g -factor $-2(1 + a_e)$	g_e	-2.002 319 304 362 56(35)		1.7×10^{-13}
Electron–proton magnetic moment ratio	μ_e/μ_p	-658.210 687 89(20)		3.0×10^{-10}
Proton, p				
Proton mass	m_p	$1.672\,621\,923\,69(51) \times 10^{-27}$	kg	3.1×10^{-10}
		1.007 276 466 621(53)	u	5.3×10^{-11}
Energy equivalent	$m_p c^2$	$1.503\,277\,615\,98(46) \times 10^{-10}$	J	3.1×10^{-10}
		938.272 088 16(29)	MeV	3.1×10^{-10}
Proton–electron mass ratio	m_p/m_e	1836.152 673 43(11)		6.0×10^{-11}
Proton rms charge radius	r_p	$8.414(19) \times 10^{-16}$	m	2.2×10^{-3}
Proton magnetic moment	μ_p	$1.410\,606\,797\,36(60) \times 10^{-26}$	J T^{-1}	4.2×10^{-10}
to Bohr magneton ratio	μ_p/μ_B	$1.521\,032\,202\,30(46) \times 10^{-3}$		3.0×10^{-10}
to nuclear magneton ratio	μ_p/μ_N	2.792 847 344 63(82)		2.9×10^{-10}
Proton g -factor $2\mu_p/\mu_N$	g_p	5.585 694 6893(16)		2.9×10^{-10}

^a The full description of m^{-1} is cycles or periods per meter and that of m is meter per cycle (m/cycle). The scientific community is aware of the implied use of these units. It traces back to the conventions for phase and angle and the use of unit Hz versus cycles/s. No solution has been agreed upon.

Table 1.2 (Continued)

Quantity	Symbol	Numerical value	Unit	Relative std. uncert. u_r
Atomic units (a.u.)				
a.u. of charge	e	$1.602\,176\,634 \times 10^{-19}$	C	exact
a.u. of mass	m_e	$9.109\,383\,7015(28) \times 10^{-31}$	kg	3.0×10^{-10}
a.u. of action	\hbar	$1.054\,571\,817 \dots \times 10^{-34}$	J s	exact
a.u. of length: Bohr radius (bohr) $\hbar/\alpha m_e c$	a_0	$5.291\,772\,109\,03(80) \times 10^{-11}$	m	1.5×10^{-10}
a.u. of energy: Hartree energy (Hartree) $\alpha^2 m_e c^2 = e^2/4\pi\epsilon_0 a_0 = 2\hbar c R_\infty$	E_h	$4.359\,744\,722\,2071(85) \times 10^{-18}$	J	1.9×10^{-12}
a.u. of time	\hbar/E_h	$2.418\,884\,326\,5857(47) \times 10^{-17}$	s	1.9×10^{-12}
a.u. of force	E_h/a_0	$8.238\,723\,4983(12) \times 10^{-8}$	N	1.5×10^{-10}
a.u. of velocity: αc	$a_0 E_h/\hbar$	$2.187\,691\,263\,64(33) \times 10^6$	m s^{-1}	1.5×10^{-10}
a.u. of momentum	\hbar/a_0	$1.992\,851\,914\,10(30) \times 10^{-24}$	kg m s^{-1}	1.5×10^{-10}
a.u. of current	$e E_h/\hbar$	$6.623\,618\,237\,510(13) \times 10^{-3}$	A	1.9×10^{-12}
a.u. of charge density	e/a_0^3	$1.081\,202\,384\,57(49) \times 10^{12}$	C m^{-3}	4.5×10^{-10}
a.u. of electric potential	E_h/e	$27.211\,386\,245\,988(53)$	V	1.9×10^{-12}
a.u. of electric field	E_h/ea_0	$5.142\,206\,747\,63(78) \times 10^{11}$	V m^{-1}	1.5×10^{-10}
a.u. of electric dipole moment	ea_0	$8.478\,353\,6255(13) \times 10^{-30}$	C m	1.5×10^{-10}
a.u. of electric quadrupole moment	ea_0^2	$4.486\,551\,5246(14) \times 10^{-40}$	C m^2	3.0×10^{-10}
a.u. of electric polarizability	$e^2 a_0^2/E_h$	$1.648\,777\,274\,36(50) \times 10^{-41}$	$\text{C}^2 \text{ m}^2 \text{ J}^{-1}$	3.0×10^{-10}
a.u. of magnetic flux density	\hbar/ea_0^2	$2.350\,517\,567\,58(71) \times 10^5$	T	3.0×10^{-10}
a.u. of magnetic dipole moment: $2\mu_B$	\hbar/m_e	$1.854\,802\,015\,66(56) \times 10^{-23}$	J T^{-1}	3.0×10^{-10}
a.u. of magnetizability	$e^2 a_0^2/m_e$	$7.891\,036\,6008(48) \times 10^{-29}$	J T^{-2}	6.0×10^{-10}
a.u. of permittivity	$e^2/a_0 E_h$	$1.112\,650\,055\,45(17) \times 10^{-10}$	F m^{-1}	1.5×10^{-10}
Natural units (n.u.)				
n.u. of velocity	c	299 792 458	m s^{-1}	exact
n.u. of action	\hbar	$1.054\,571\,817 \dots \times 10^{-34}$	J s	exact
		$6.582\,119\,569 \dots \times 10^{-16}$	eV s	exact
		$\hbar c$	197.326 980 4 ...	MeV fm
n.u. of mass	m_e	$9.109\,383\,7015(28) \times 10^{-31}$	kg	3.0×10^{-10}
n.u. of energy	$m_e c^2$	$8.187\,105\,7769(25) \times 10^{-14}$	J	3.0×10^{-10}
		0.510 998 950 00(15)	MeV	3.0×10^{-10}
n.u. of momentum	$m_e c$	$2.730\,924\,530\,75(82) \times 10^{-22}$	kg m s^{-1}	3.0×10^{-10}
		0.510 998 950 00(15)	MeV/c	3.0×10^{-10}
n.u. of length: $\hbar/m_e c$	λ_C	$3.861\,592\,6796(12) \times 10^{-13}$	m	3.0×10^{-10}
n.u. of time	$\hbar/m_e c^2$	$1.288\,088\,668\,19(39) \times 10^{-21}$	s	3.0×10^{-10}

2.2×10^{-3} . In fact, r_p extracted from precision spectroscopy on the hydrogen atom and on muonic-hydrogen, where the electron is replaced by a muon, are marginally discrepant.

The fine-structure constant α , vacuum electric permittivity ϵ_0 , and vacuum magnetic permeability μ_0 are dependent. They are related through Eqs. (1.3) and (1.9) and, since in the SI the values for \hbar , e , and c are exact, one of α , ϵ_0 , or μ_0 fixes the other two. In current state-of-the-art experiments that constrain these constants, the dimensionless fine-structure constant is measured or the most conveniently extracted. In fact, the CODATA adjustment uses α as an adjusted constant, and values for ϵ_0 and μ_0 are derived from Eqs. (1.3) and (1.9). Finally, the mass of the electron follows from $m_e = E_h/\alpha^2 c^2$. Its relative uncertainty is twice that of α as the relative uncertainty of the Hartree energy is much better known.

References

1. Bureau International des Poids et Mesures: The official description of the International System of Units (2019). <https://www.bipm.org/en/measurement-units>
2. Mills, I.M., Mohr, P.J., Quinn, T.J., Taylor, B.N., Williams, E.R.: Adapting the international system of units to the twenty-first century. *Phil. Trans. R. Soc. A* **369**, 3907–3924 (2011)
3. Jackson, J.D.: *Classical Electrodynamics*. Wiley, New York, London (1962)
4. Cohen-Tannoudji, C., Dupont-Roc, J., Grynberg, G.: *Atom-Photon Interactions*. Wiley, New York, London (1992)
5. NIST: CODATA internationally recommended values of the fundamental physical constants (2019). <https://physics.nist.gov/constants>



Eite Tiesinga Dr Eite Tiesinga received his PhD from Eindhoven University of Technology in The Netherlands in 1993. He works at the National Institute of Standards and Technology and the University of Maryland in the US. His research focuses on developing clocks and sensors using laser-cooled atoms. He maintains a web-based database of fundamental constants, an initiative by the Committee on Data of the International Science Council (CODATA).



Angular Momentum Theory

2

James D. Louck

Contents

2.1	Orbital Angular Momentum	12	2.9.3	The Fundamental Identities Between Racah Coefficients	41
2.1.1	Cartesian Representation	12	2.9.4	Schwinger–Bargmann Generating Function and Its Combinatorics	41
2.1.2	Spherical Polar Coordinate Representation	14	2.9.5	Symmetries of $6-j$ Coefficients	42
2.2	Abstract Angular Momentum	15	2.9.6	Further Properties	43
2.3	Representation Functions	17	2.10	The $9-j$ Coefficients	44
2.3.1	Parametrizations of the Groups $SU(2)$ and $SO(3, \mathbf{R})$	17	2.10.1	Hilbert Space and Tensor Operator Actions	44
2.3.2	Explicit Forms of Representation Functions	19	2.10.2	$9-j$ Invariant Operators	44
2.3.3	Relations to Special Functions	19	2.10.3	Basic Relations Between $9-j$ Coefficients and $6-j$ Coefficients	45
2.3.4	Orthogonality Properties	20	2.10.4	Symmetry Relations for $9-j$ Coefficients and Reduction to $6-j$ Coefficients	46
2.3.5	Recurrence Relations	21	2.10.5	Explicit Algebraic Form of $9-j$ Coefficients	46
2.3.6	Symmetry Relations	21	2.10.6	Racah Operators	46
2.4	Group and Lie Algebra Actions	24	2.10.7	Schwinger–Wu Generating Function and Its Combinatorics	47
2.4.1	Matrix Group Actions	24	2.11	Tensor Spherical Harmonics	48
2.4.2	Lie Algebra Actions	24	2.11.1	Spinor Spherical Harmonics as Matrix Functions	49
2.4.3	Hilbert Spaces	25	2.11.2	Vector Spherical Harmonics as Matrix Functions	49
2.4.4	Relation to Angular Momentum Theory	25	2.11.3	Vector Solid Harmonics as Vector Functions	50
2.5	Differential Operator Realizations of Angular Momentum	26	2.12	Coupling and Recoupling Theory and $3n-j$ Coefficients	51
2.6	The Symmetric Rotor and Representation Functions	27	2.12.1	Composite Angular Momentum Systems	51
2.7	Wigner–Clebsch–Gordan and $3-j$ Coefficients	29	2.12.2	Binary Coupling Theory: Combinatorics	52
2.7.1	Kronecker Product Reduction	30	2.12.3	Implementation of Binary Couplings	53
2.7.2	Tensor Product Space Construction	31	2.12.4	Construction of All Transformation Coefficients in Binary Coupling Theory	54
2.7.3	Explicit Forms of WCG Coefficients	31	2.12.5	Unsolved Problems in Recoupling Theory	55
2.7.4	Symmetries of WCG Coefficients in $3-j$ Symbol Form	33	2.13	Supplement on Combinatorial Foundations	56
2.7.5	Recurrence Relations	33	2.13.1	$SU(2)$ Solid Harmonics	56
2.7.6	Limiting Properties and Asymptotic Forms	34	2.13.2	Combinatorial Definition of Wigner–Clebsch–Gordan Coefficients	57
2.7.7	WCG Coefficients as Discretized Representation Functions	34	2.13.3	Magic Square Realization of the Addition of Two Angular Momenta	59
2.8	Tensor Operator Algebra	35	2.13.4	MacMahon’s and Schwinger’s Master Theorems	60
2.8.1	Conceptual Framework	35	2.13.5	The Pfaffian and Double Pfaffian	61
2.8.2	Universal Enveloping Algebra of \mathbf{J}	36	2.13.6	Generating Functions for Coupled Wave Functions and Recoupling Coefficients	61
2.8.3	Algebra of Irreducible Tensor Operators	36	2.14	Author’s Comments	64
2.8.4	Wigner–Eckart Theorem	37	2.15	Tables	64
2.8.5	Unit Tensor Operators or Wigner Operators	37	References	67	
2.9	Racah Coefficients	40			
2.9.1	Basic Relations Between WCG and Racah Coefficients	40			
2.9.2	Orthogonality and Explicit Form	40			

Abstract

Angular momentum theory is presented from the viewpoint of the group $SU(1)$ of unimodular unitary matrices of order 2. This is the basic quantum mechanical rotation group for implementing the consequences of rotational symmetry into isolated complex physical systems and gives the structure of the angular momentum multiplets of such systems. This entails the study of representation functions of $SU(2)$, the Lie algebra of $SU(2)$ and copies thereof, and the associated Wigner–Clebsch–Gordan coefficients, Racah coefficients, and $3n-j$ coefficients, with an almost boundless set of interrelations, and presentations of the associated conceptual framework. The relationship of $SU(2)$ to the rotation group in physical 3-space R^3 is given in detail. Formulas are often given in a compendium format with brief introductions on their physical and mathematical content. A special effort is made to interrelate the material to the special functions of mathematics and to the combinatorial foundations of the subject.

Keywords

angular momentum algebra · invariant operator · coupling scheme · symmetry relation · tensor operator · Wigner–Eckart theorem · Lie algebra · Racah coefficients · Clebsch–Gordan coefficients · rotation group

Angular momentum theory in its quantum mechanical applications, which is the subject of this section, is the study of the group of 2×2 unitary unimodular matrices and its irreducible representations. It is the mathematics of implementing into physical theory the basic tenet that isolated physical systems are invariant to rotations of the system in physical 3-space, denoted R^3 , or, equivalently, to the orientation of a Cartesian reference system used to describe the system. That it is the group of 2×2 unimodular matrices that is basic in quantum theory in place of the more obvious group of 3×3 real, orthogonal matrices representing transformations of the coordinates of the constituent particles of the system, or of the reference frame, is a consequence of the Hilbert space structure of the state space of quantum systems and the impossibility of assigning overall phase factors to such states because measurements depend only on the absolute value of transition amplitudes.

The exact relationship between the group $SU(2)$ of 2×2 unimodular unitary matrices and the group $SO(3, R)$ of 3×3 real, proper, orthogonal matrices is an important one for keeping the quantum theory of angular momentum, with its numerous conventions and widespread applications across all fields of quantum physics, free of ambiguities. These notations and relations are fixed at the outset.

Presentation of a point in R^3 :

$$\begin{aligned} \mathbf{x} &= \text{col}(x_1, x_2, x_3) && \text{column matrix,} \\ \mathbf{x}^T &= (x_1, x_2, x_3) && \text{row matrix,} \\ X &= \begin{pmatrix} x_3 & x_1 - ix_2 \\ x_1 + ix_2 & -x_3 \end{pmatrix} && \begin{aligned} &2 \times 2 \text{ traceless Hermitian matrix;} \\ &\text{Cartan's representation.} \end{aligned} \end{aligned}$$

A one-to-one correspondence between the set R^3 of points in 3-space and the set H^2 of 2×2 traceless Hermitian matrices is obtained from $x_i = \frac{1}{2} \text{Tr}(\sigma_i X)$, where the σ_i denote the matrices (Pauli matrices)

$$\sigma_1 = \begin{pmatrix} 0 & 1 \\ 1 & 0 \end{pmatrix}, \quad \sigma_2 = \begin{pmatrix} 0 & -i \\ i & 0 \end{pmatrix}, \quad \sigma_3 = \begin{pmatrix} 1 & 0 \\ 0 & -1 \end{pmatrix}. \quad (2.1)$$

Mappings of R^3 onto itself:

$$\begin{aligned} \mathbf{x} &\rightarrow \mathbf{x}' = R\mathbf{x}, \\ X &\rightarrow X' = UXU^\dagger, \end{aligned}$$

where \dagger denotes Hermitian conjugation of a matrix or an operator.

Two-to-one homomorphism of $SU(2)$ onto $SO(3, R)$:

$$\begin{aligned} R_{ij} &= R_{ij}(U) = \frac{1}{2} \text{Tr}(\sigma_i U \sigma_j U^\dagger), && (2.2) \\ \begin{pmatrix} \xi \\ \mathbf{x}' \end{pmatrix} &= \begin{pmatrix} 1 & 0 & 0 & 0 \\ 0 & & & \\ 0 & R(U) & & \\ 0 & & & \end{pmatrix} \begin{pmatrix} \xi \\ \mathbf{x} \end{pmatrix} \\ &= A^\dagger (U \times U^*) A \begin{pmatrix} \xi \\ \mathbf{x} \end{pmatrix}, && (2.3) \end{aligned}$$

where ξ is an indeterminate, A is the unitary matrix given by

$$A = \frac{1}{\sqrt{2}} \begin{pmatrix} 1 & 0 & 0 & 1 \\ 0 & 1 & -i & 0 \\ 0 & 1 & i & 0 \\ 1 & 0 & 0 & -1 \end{pmatrix},$$

$U \times U^*$ denotes the matrix direct product, and $*$ denotes complex conjugation. There is a simple unifying theme in almost all the applications. The basic mathematical notions that are implemented over and over again in various contexts are: group action on the underlying coordinates and momenta of the physical system and the corresponding group action

in the associated Hilbert space of states; the determination of those subspaces that are mapped irreducibly onto themselves by the group action; the Lie algebra and its actions as derived from the group actions, and conversely; the construction of composite objects from elementary constituents, using the notion of tensor product space and Kronecker products of representations, which are the basic precepts in quantum theory for building complex systems from simpler ones; the reduction of the Kronecker product of irreducible representations into irreducibles with the associated Wigner–Clebsch–Gordan and Racah coefficients determining not only this reduction but also having a dual role in the construction of the irreducible state spaces themselves; and, finally, the repetition of this process for many-particle systems with the attendant theory of $3n-j$ coefficients. The universality of this methodology may be attributed to being able, in favorable situations, to separate the particular consequences of physical law (e.g., the Coulomb force) from the implications of symmetry imposed on the system by our underlying conceptions of space and time. Empirical models based on symmetry that attempt to identify the more important ingredients underlying observed physical phenomena are also of great importance.

The group actions in complex systems are often modeled after the following examples for the actions of the groups $SO(3, \mathbf{R})$ and $SU(2)$ on functions defined over the two-sphere $S^2 \subset \mathbf{R}^3$:

Hilbert space:

$$V = \{f | f \text{ is a polynomial satisfying } \nabla^2 f(\mathbf{x}) = 0\} .$$

Inner or scalar product:

$$(f, f') = \int_{\text{unit sphere}} f^*(\mathbf{x}) f'(\mathbf{x}) dS ,$$

where $f(\mathbf{x}) = f(X)$ for \mathbf{x} presented in the Cartan matrix form X .

Group actions:

$$\begin{aligned} (O_R f)(\mathbf{x}) &= f(R^{-1}\mathbf{x}), & \text{each } f \in V, \\ & & \text{each } \mathbf{x} \in \mathbf{R}^3, \\ (T_U f)(X) &= f(U^\dagger X U), & \text{each } f \in V, \\ & & \text{each } X \in \mathbf{H}^2. \end{aligned}$$

Operator properties:

- O_R is a unitary operator on V ; that is, $(O_R f, O_R f') = (f, f')$.
- T_U is a unitary operator on V ; that is, $(T_U f, T_U f') = (f, f')$.

- $R \rightarrow O_R$ is a unitary representation of $SO(3, \mathbf{R})$; that is, $O_{R_1} O_{R_2} = O_{R_1 R_2}$.
- $U \rightarrow T_U$ is a unitary representation of $SU(2)$; that is, $T_{U_1} T_{U_2} = T_{U_1 U_2}$.
- $O_{R(U)} = T_U = T_{-U}$ is an operator identity on the space V .

One parameter subgroups:

$$\begin{aligned} U_j(t) &= \exp(-it\sigma_j/2), \quad t \in \mathbf{R}, \quad j = 1, 2, 3; \\ R_j(t) &= R(U_j(t)) = \exp(-itM_j), \\ & \quad t \in \mathbf{R}, \quad j = 1, 2, 3; \end{aligned}$$

where

$$\begin{aligned} M_1 &= i \begin{pmatrix} 0 & 0 & 0 \\ 0 & 0 & -1 \\ 0 & 1 & 0 \end{pmatrix}, & M_2 &= i \begin{pmatrix} 0 & 0 & 1 \\ 0 & 0 & 0 \\ -1 & 0 & 0 \end{pmatrix}, \\ M_3 &= i \begin{pmatrix} 0 & -1 & 0 \\ 1 & 0 & 0 \\ 0 & 0 & 0 \end{pmatrix}. \end{aligned} \quad (2.4)$$

Infinitesimal generators:

$$\begin{aligned} L_j &= i(dO_{R_j(t)}/dt)_{t=0}, \\ L_j &= i(dT_{U_j(t)}/dt)_{t=0}, \\ (L_j f)(\mathbf{x}) &= -i \left(x_k \frac{\partial}{\partial x_l} - x_l \frac{\partial}{\partial x_k} \right) f(\mathbf{x}), \\ & \quad j, k, l \text{ cyclic in } 1, 2, 3. \end{aligned} \quad (2.5)$$

Historically, the algebra of angular momentum came about through the quantum rule of replacing the linear momentum \mathbf{p} of a classical point particle, which is located at position \mathbf{r} , by $\mathbf{p} \rightarrow -i\hbar\nabla$, thus replacing the classical angular momentum $\mathbf{r} \times \mathbf{p}$ about the origin of a chosen Cartesian inertial system by the angular momentum operator:

$$\mathbf{L} = -i\mathbf{r} \times \nabla \quad (\text{in units of } \hbar). \quad (2.6)$$

The quantal angular momentum properties of this simple one-particle system are then to be inferred from the properties of these operators and their actions in the associated Hilbert space. This remains the method of introducing angular momentum theory in most textbooks because of its simplicity and historical roots. It also leads to focusing the developments of the theory on the algebra of operators in contrast to emphasizing the associated group transformations of the Hilbert space, although the two viewpoints are intimately linked, as illustrated above. Both perspectives will be presented here.

2.1 Orbital Angular Momentum

The model provided by orbital angular momentum operators is the paradigm for standardizing many of the conventions and relations used in more abstract and general treatments. These basic results for the orbital angular momentum operator $L = -i \mathbf{r} \times \nabla$ acting in the vector space V are given in this section both in Cartesian coordinates $\mathbf{x} = \text{col}(x_1, x_2, x_3)$ and spherical polar coordinates:

$$\mathbf{x} = (r \sin \theta \cos \phi, r \sin \theta \sin \phi, r \cos \theta),$$

$$0 \leq r < \infty, \quad 0 \leq \phi < 2\pi, \quad 0 \leq \theta \leq \pi.$$

2.1.1 Cartesian Representation

Commutation relations:

Cartesian form:

$$[L_1, L_2] = iL_3, \quad [L_2, L_3] = iL_1,$$

$$[L_3, L_1] = iL_2.$$

Cartan form:

$$[L_3, L_+] = L_+, \quad [L_3, L_-] = -L_-,$$

$$[L_+, L_-] = 2L_3.$$

Squared orbital angular momentum:

$$L^2 = L_1^2 + L_2^2 + L_3^2 = L_-L_+ + L_3(L_3 + 1)$$

$$= L_+L_- + L_3(L_3 - 1)$$

$$= -r^2\nabla^2 + (\mathbf{x} \cdot \nabla)^2 + (\mathbf{x} \cdot \nabla).$$

L^2, L_3 form a complete set of commuting Hermitian operators in V with eigenfunctions

$$\mathcal{Y}_{lm}(\mathbf{x}) = \left[\frac{2l+1}{4\pi} (l+m)!(l-m)! \right]^{\frac{1}{2}}$$

$$\times \sum_k \frac{(-x_1 - ix_2)^{k+m} (x_1 - ix_2)^k x_3^{l-m-2k}}{2^{2k+m} (k+m)! k! (l-m-2k)!},$$

where $l = 0, 1, 2, \dots$; $m = l, l-1, \dots, -l$.

Homogeneous polynomial solutions of Laplace's equation:

$$\mathcal{Y}_{lm}(\lambda \mathbf{x}) = \lambda^l \mathcal{Y}_{lm}(\mathbf{x}),$$

$$(\mathbf{x} \cdot \nabla) \mathcal{Y}_{lm}(\mathbf{x}) = l \mathcal{Y}_{lm}(\mathbf{x}),$$

$$\nabla^2 \mathcal{Y}_{lm}(\mathbf{x}) = 0.$$

Complex conjugate:

$$\mathcal{Y}_{lm}^*(\mathbf{x}) = (-1)^m \mathcal{Y}_{l,-m}(\mathbf{x}).$$

Action of angular momentum operators:

$$L_{\pm} \mathcal{Y}_{lm}(\mathbf{x}) = [(l \mp m)(l \pm m + 1)]^{\frac{1}{2}} \mathcal{Y}_{l,m \pm 1}(\mathbf{x}),$$

$$L_3 \mathcal{Y}_{lm}(\mathbf{x}) = m \mathcal{Y}_{lm}(\mathbf{x}),$$

$$L^2 \mathcal{Y}_{lm}(\mathbf{x}) = l(l+1) \mathcal{Y}_{lm}(\mathbf{x}).$$

Highest weight eigenfunction:

$$L_+ \mathcal{Y}_{ll}(\mathbf{x}) = 0, \quad L_3 \mathcal{Y}_{ll}(\mathbf{x}) = l \mathcal{Y}_{ll}(\mathbf{x}),$$

$$\mathcal{Y}_{ll}(\mathbf{x}) = \frac{1}{2^l l!} \left(\frac{(2l+1)!}{4\pi} \right)^{\frac{1}{2}} (-x_1 - ix_2)^l.$$

Generation from highest weight:

$$\mathcal{Y}_{lm}(\mathbf{x}) = \left(\frac{(l+m)}{(2l)!(l-m)!} \right)^{\frac{1}{2}} L_-^{l-m} \mathcal{Y}_{ll}(\mathbf{x}).$$

Relation to Gegenbauer and Jacobi polynomials:

$$\mathcal{Y}_{lm}(\mathbf{x}) = r^{l-|m|} \mathcal{Y}_m(x_1, x_2)$$

$$\times [(2l+1)(l+m)!(l-m)!/2]^{\frac{1}{2}}$$

$$\times H_{l,|m|}(x_3/r),$$

$$H_{l\lambda}(z) = \frac{(2\lambda)!}{2^{\lambda} \lambda!} C_{l-\lambda}^{\lambda+\frac{1}{2}}(z) = \frac{(l+\lambda)!}{2^{\lambda} l!} P_{l-\lambda}^{(\lambda, \lambda)}(z),$$

$$0 \leq \lambda \leq l = 0, 1, 2, \dots,$$

where the $\mathcal{Y}_m(x_1, x_2)$ are homogeneous polynomial solutions of degree $|m|$ of Laplace's equation in 2-space, \mathbf{R}^2 :

$$\mathcal{Y}_m(x_1, x_2) = \begin{cases} (-x_1 - ix_2)^m / \sqrt{2\pi}, & m \geq 0, \\ (x_1 - ix_2)^{-m} / \sqrt{2\pi}, & m \leq 0. \end{cases}$$

(Sect. 2.1.2 for the definition of Gegenbauer and Jacobi polynomials.)

Orthogonal group action:

$$(O_R \mathcal{Y}_{lm})(\mathbf{x}) = \mathcal{Y}_{lm}(R^{-1} \mathbf{x}) = \sum_{m'} \mathcal{D}_{m'm}^l(R) \mathcal{Y}_{lm'}(\mathbf{x}),$$

where the functions $\mathcal{D}_{m'm}^l(R) = D_{m'm}^l(U(R))$ are defined in Sect. 2.3 for various parametrizations of R .

Unitary group action:

$$(T_U \mathcal{Y}_{lm})(X) = \mathcal{Y}_{lm}(U^\dagger X U)$$

$$= \sum_{m'} D_{m'm}^l(U) \mathcal{Y}_{lm'}(X),$$

where the functions $D_{m'm}^l(U)$ are defined in Sects. 2.2 and 2.3.

Orthogonality on the unit sphere:

$$\int_{\text{unit sphere}} \mathbf{Y}_{l'm'}^*(\mathbf{x}) \mathbf{Y}_{lm}(\mathbf{x}) dS = \delta_{l'l} \delta_{m'm} .$$

Product of solid harmonics:

$$\begin{aligned} \mathbf{Y}_{k\mu}(\mathbf{x}) \mathbf{Y}_{lm}(\mathbf{x}) &= \sum_{l'} \langle l' || \mathbf{Y}_k || l \rangle C_{m,\mu,m+\mu}^{lk l'} \mathbf{Y}_{l',m+\mu}(\mathbf{x}) \\ &= \sum_{l'} \langle l' || \mathbf{Y}_k || l \rangle \begin{pmatrix} l & k & l' \\ m & \mu & -m - \mu \end{pmatrix} \\ &\quad \times (-1)^{l'+m+\mu} \mathbf{Y}_{l',m+\mu}(\mathbf{x}) , \\ \langle l' || \mathbf{Y}_k || l \rangle &= r^{l+k-l'} \left(\frac{(2l+1)(2k+1)}{4\pi(2l'+1)} \right)^{\frac{1}{2}} C_{000}^{lk l'} , \\ \langle l' || \mathbf{Y}_k || l \rangle &= r^{l+k-l'} \left(\frac{(2l+1)(2k+1)(2l'+1)}{4\pi} \right)^{\frac{1}{2}} \\ &\quad \times (-1)^{l'} \begin{pmatrix} l & k & l' \\ 0 & 0 & 0 \end{pmatrix} , \end{aligned}$$

where $C_{m_1 m_2 m}^{l_1 l_2 l}$ and

$$\begin{pmatrix} l_1 & l_2 & l \\ m_1 & m_2 & -m \end{pmatrix} = \frac{(-1)^{l_1-l_2+m}}{\sqrt{2l+1}} C_{m_1 m_2 m}^{l_1 l_2 l}$$

denote Wigner–Clebsch–Gordan coefficients and 3– j coefficients, respectively (Sect. 2.7).

Vector addition theorem for solid harmonics:

$$\begin{aligned} \mathbf{Y}_{lm}(\mathbf{z} + \mathbf{z}') &= \sum_{k\mu} \left(\frac{4\pi(2l+1)!}{(2l-2k+1)!(2k+1)!} \right)^{\frac{1}{2}} C_{m-\mu,\mu,m}^{l-k,k,l} \\ &\quad \times \mathbf{Y}_{l-k,m-\mu}(\mathbf{z}) \mathbf{Y}_{k\mu}(\mathbf{z}') , \quad \mathbf{z}, \mathbf{z}' \in \mathbb{C}^3 , \\ C_{m-\mu,\mu,m}^{j-k,k,l} &= \left[\frac{\begin{pmatrix} l+m \\ k+\mu \end{pmatrix} \begin{pmatrix} l-m \\ k-\mu \end{pmatrix}}{\begin{pmatrix} 2l \\ 2k \end{pmatrix}} \right]^{\frac{1}{2}} . \end{aligned}$$

Rotational invariant in two vectors:

$$\begin{aligned} I_l(\mathbf{x}, \mathbf{y}) &= \frac{1}{2^l} \sum_k (-1)^k \begin{pmatrix} l \\ k \end{pmatrix} \begin{pmatrix} 2l-2k \\ l \end{pmatrix} \\ &\quad \times (\mathbf{x} \cdot \mathbf{y})^{l-2k} (\mathbf{x} \cdot \mathbf{x})^k (\mathbf{y} \cdot \mathbf{y})^k \\ &= (\mathbf{x} \cdot \mathbf{x})^{l/2} (\mathbf{y} \cdot \mathbf{y})^{l/2} C_l^{(1/2)}(\hat{\mathbf{x}} \cdot \hat{\mathbf{y}}) \\ &= \frac{4\pi}{2l+1} \sum_m (-1)^m \mathbf{Y}_{lm}(\mathbf{x}) \mathbf{Y}_{l,-m}(\mathbf{y}) , \end{aligned}$$

where $C_l^{(1/2)}(z)$ is a Gegenbauer polynomial (Sect. 2.1.2), and

$$\hat{\mathbf{x}} = \mathbf{x}/|\mathbf{x}| , \quad \hat{\mathbf{y}} = \mathbf{y}/|\mathbf{y}| , \quad \cos \theta = \hat{\mathbf{x}} \cdot \hat{\mathbf{y}} .$$

Legendre polynomials:

$$P_l(\cos \theta) = \frac{4\pi}{2l+1} \sum_m (-1)^m \mathbf{Y}_{l,-m}(\hat{\mathbf{y}}) \mathbf{Y}_{lm}(\hat{\mathbf{x}}) ,$$

$$\begin{aligned} \left(\frac{4\pi}{2l+1} \right)^{\frac{1}{2}} \mathbf{Y}_{l0}(\mathbf{x}) &= \frac{1}{2^l} \sum_k (-1)^k \begin{pmatrix} l \\ k \end{pmatrix} \begin{pmatrix} 2l-2k \\ l \end{pmatrix} \\ &\quad \times x_3^{l-2k} (\mathbf{x} \cdot \mathbf{x})^k \\ &= r^l P_l(x_3/r) . \end{aligned}$$

Rayleigh plane wave expansion:

$$\begin{aligned} e^{i\mathbf{k} \cdot \mathbf{x}} &= 4\pi \sum_{l=0}^{\infty} \sum_{m=-l}^l i^l j_l(kr) \mathbf{Y}_{lm}^*(\hat{\mathbf{k}}) \mathbf{Y}_{lm}(\hat{\mathbf{x}}) , \\ j_l(kr) &= \left(\frac{\pi}{2kr} \right)^{\frac{1}{2}} J_{l+1/2}(kr) . \end{aligned}$$

Relations in potential theory:

$$\begin{aligned} \mathbf{Y}_{lm}(\nabla) \left(\frac{1}{r} \right) &= \frac{(-1)^l (2l)!}{2^l l!} \frac{\mathbf{Y}_{lm}(\mathbf{x})}{r^{2l+1}} , \\ 1/R &= \sum_{l=0}^{\infty} I_l(\mathbf{x}, \mathbf{y}) / r^{2l+1} , \\ I_l(\mathbf{x}, \mathbf{y}) / r^{2l+1} &= \frac{(-1)^l}{l!} (\mathbf{y} \cdot \nabla)^l \left(\frac{1}{r} \right) . \end{aligned}$$

For $\mathbf{R} = \mathbf{x} - \mathbf{y}$, $r = (\mathbf{x} \cdot \mathbf{x})^{\frac{1}{2}}$, $s = (\mathbf{y} \cdot \mathbf{y})^{\frac{1}{2}}$,

$$1/R = \sum_l P_l(\cos \theta) \frac{s^l}{r^{l+1}} , \quad s \leq r , \quad \cos \theta = \hat{\mathbf{x}} \cdot \hat{\mathbf{y}} .$$

Rotational invariants in three vectors:

$$\begin{aligned} I_{(l_1 l_2 l_3)}(\mathbf{x}^1, \mathbf{x}^2, \mathbf{x}^3) &= \frac{(4\pi)^{3/2}}{[(2l_1+1)(2l_2+1)(2l_3+1)]^{\frac{1}{2}}} \\ &\quad \times \sum_{m_1 m_2 m_3} \begin{pmatrix} l_1 & l_2 & l_3 \\ m_1 & m_2 & m_3 \end{pmatrix} \\ &\quad \times \mathbf{Y}_{l_1 m_1}(\mathbf{x}^1) \mathbf{Y}_{l_2 m_2}(\mathbf{x}^2) \mathbf{Y}_{l_3 m_3}(\mathbf{x}^3) , \end{aligned}$$

where $\begin{pmatrix} l_1 & l_2 & l_3 \\ m_1 & m_2 & m_3 \end{pmatrix}$ is a 3– j coefficient (Sect. 2.7).

$$\begin{aligned} I_{(l_1 l_2 l_3)}(\mathbf{x}^1, \mathbf{x}^2, 0) &= \delta_{l_1 l_2} \delta_{l_3 0} (-1)^{l_1} I_{l_1}(\mathbf{x}^1, \mathbf{x}^2) / (2l_1+1)^{\frac{1}{2}} . \end{aligned}$$

Product law:

$$I_{(l)}(\mathbf{x})I_{(k)}(\mathbf{x}) = \sum_{(j)} \left[\prod_{\alpha=1}^3 (-1)^{j_\alpha} (2j_\alpha + 1) \begin{pmatrix} l_\alpha & k_\alpha & j_\alpha \\ 0 & 0 & 0 \end{pmatrix} \times (\mathbf{x}^\alpha \cdot \mathbf{x}^\alpha)^{(l_\alpha + k_\alpha - j_\alpha)/2} \right] \begin{Bmatrix} l_1 & l_2 & l_3 \\ k_1 & k_2 & k_3 \\ j_1 & j_2 & j_3 \end{Bmatrix} I_{(j)}(\mathbf{x}),$$

where $l = (l_1, l_2, l_3)$, etc., $\mathbf{x} = (\mathbf{x}^1, \mathbf{x}^2, \mathbf{x}^3)$.

Coplanar vectors:

$$I_{(l)}(\mathbf{x}^1, \mathbf{x}^2, \alpha \mathbf{x}^1 + \beta \mathbf{x}^2) = \sum_{kl} \left(\frac{(2l_3 + 1)!}{(2l_3 - 2k)!(2k)!} \right)^{\frac{1}{2}} \times \alpha^{l_3 - k} \beta^k (-1)^{l_1 + l_3 + k} (2l + 1) \times \begin{pmatrix} l_3 - k & l_1 & l \\ 0 & 0 & 0 \end{pmatrix} \begin{pmatrix} k & l_2 & l \\ 0 & 0 & 0 \end{pmatrix} \begin{Bmatrix} l_3 - k & l_3 & k \\ l_2 & l & l_1 \end{Bmatrix} \times (\mathbf{x}^1 \cdot \mathbf{x}^1)^{(l_1 + l_3 - l - k)/2} (\mathbf{x}^2 \cdot \mathbf{x}^2)^{(l_2 + k - l)/2} \times I_l(\mathbf{x}^1, \mathbf{x}^2).$$

The bracket symbols in these relations are 6- j and 9- j coefficients (Sects. 2.9, 2.10).

Cartan's vectors of zero length:

$$\begin{aligned} \boldsymbol{\alpha} &= (-z_1^2 + z_2^2, -i(z_1^2 + z_2^2), 2z_1 z_2), \\ \boldsymbol{\alpha} \cdot \boldsymbol{\alpha} &= \alpha_1^2 + \alpha_2^2 + \alpha_3^2 = 0, \\ \mathbf{z} &= (z_1, z_2) \in \mathcal{C}^2. \end{aligned}$$

Solutions of Laplace's equation using vectors of zero length:

$$\nabla^2(\boldsymbol{\alpha} \cdot \mathbf{x})^l = 0, \quad l = 0, 1, \dots$$

Solid harmonics for vectors of zero length:

$$\begin{aligned} (-1)^m Y_{l,-m}(\boldsymbol{\alpha}) &= \frac{(2l)!}{l!} \left(\frac{2l+1}{4\pi} \right)^{\frac{1}{2}} P_{lm}(z_1, z_2), \\ P_{lm}(z_1, z_2) &= \frac{z_1^{l+m} z_2^{l-m}}{\sqrt{(l+m)!(l-m)!}}. \end{aligned}$$

Orbital angular momentum operators for vectors of zero length:

$$\begin{aligned} \mathbf{J} &= -i(\boldsymbol{\alpha} \times \nabla_{\boldsymbol{\alpha}}), \\ J_+ &= z_1 \frac{\partial}{\partial z_2}, \quad J_- = z_2 \frac{\partial}{\partial z_1}, \\ J_3 &= \frac{1}{2} \left(z_1 \frac{\partial}{\partial z_1} - z_2 \frac{\partial}{\partial z_2} \right). \end{aligned}$$

Rotational invariant for vectors of zero length:

$$(\boldsymbol{\alpha} \cdot \mathbf{x})^l = \left(\frac{4\pi}{2l+1} \right)^{\frac{1}{2}} 2^l l! \sum_m P_{lm}(\mathbf{z}) Y_{lm}(\mathbf{x}).$$

Spinorial invariant under $\mathbf{z}^i \rightarrow U \mathbf{z}^i$ ($i = 1, 2, 3$):

$$\begin{aligned} &\sum_{m_1 m_2 m_3} \begin{pmatrix} j_1 & j_2 & j_3 \\ m_1 & m_2 & m_3 \end{pmatrix} P_{j_1 m_1}(\mathbf{z}^1) P_{j_2 m_2}(\mathbf{z}^2) P_{j_3 m_3}(\mathbf{z}^3) \\ &= [(j_1 + j_2 + j_3 + 1)!]^{-1/2} \\ &\quad \times \frac{(z_{12}^{12})^{j_1 + j_2 - j_3} (z_{12}^{31})^{j_3 + j_1 - j_2} (z_{12}^{23})^{j_2 + j_3 - j_1}}{[(j_1 + j_2 - j_3)!(j_3 + j_1 - j_2)!(j_2 + j_3 - j_1)!]^{\frac{1}{2}}}, \\ z_{12}^{ij} &= z_1^i z_2^j - z_1^j z_2^i. \end{aligned}$$

This relation is invariant under the transformation

$$\begin{aligned} \mathbf{z} \rightarrow U \mathbf{z} &= ((U \mathbf{z})_1, (U \mathbf{z})_2) \\ &= (u_{11} z_1 + u_{12} z_2, u_{21} z_1 + u_{22} z_2), \end{aligned}$$

where $U \in SU(2)$. Transformation properties of vectors of zero length:

$$\boldsymbol{\alpha} \rightarrow R \boldsymbol{\alpha}, \quad \boldsymbol{\alpha} = \text{col}(\alpha_1, \alpha_2, \alpha_3),$$

where $\mathbf{z} \rightarrow U \mathbf{z}$ and R is given in terms of U in the beginning of this chapter. Simultaneous eigenvectors of \mathbf{L}^2 and \mathbf{J}^2 :

$$\begin{aligned} \mathbf{L}^2(\boldsymbol{\alpha} \cdot \mathbf{x})^l &= l(l+1)(\boldsymbol{\alpha} \cdot \mathbf{x})^l, \quad l = 0, 1, \dots, \\ \mathbf{J}^2(\boldsymbol{\alpha} \cdot \mathbf{x})^l &= l(l+1)(\boldsymbol{\alpha} \cdot \mathbf{x})^l, \quad l = 0, 1, \dots \end{aligned}$$

2.1.2 Spherical Polar Coordinate Representation

The results given in Sect. 2.1.1 may be presented in any system of coordinates well-defined in terms of Cartesian coordinates. The principal relations for spherical polar coordinates are given in this section, where a vector in \mathbf{R}^3 is now given in the form

$$\begin{aligned} \mathbf{x} = r \hat{\mathbf{x}} &= r(\sin \theta \cos \phi, \sin \theta \sin \phi, \cos \theta), \\ 0 &\leq \theta \leq \pi, \quad 0 \leq \phi < 2\pi. \end{aligned}$$

Orbital angular momentum operators:

$$\begin{aligned} L_1 &= i \cos \phi \cot \theta \frac{\partial}{\partial \phi} + i \sin \phi \frac{\partial}{\partial \theta}, \\ L_2 &= i \sin \phi \cot \theta \frac{\partial}{\partial \phi} - i \cos \phi \frac{\partial}{\partial \theta}, \end{aligned}$$

$$L_3 = -i \frac{\partial}{\partial \phi},$$

$$L_{\pm} = e^{\pm i \phi} \left(\pm \frac{\partial}{\partial \theta} + i \cot \theta \frac{\partial}{\partial \phi} \right),$$

$$L^2 = -\frac{1}{\sin \theta} \frac{\partial}{\partial \theta} \left(\sin \theta \frac{\partial}{\partial \theta} \right) - \frac{1}{\sin^2 \theta} \frac{\partial^2}{\partial \phi^2}.$$

Laplacian:

$$\mathbf{x} \cdot \nabla = r \frac{\partial}{\partial r},$$

$$\nabla^2 = \frac{1}{r^2} \left[\left(r \frac{\partial}{\partial r} \right)^2 + r \frac{\partial}{\partial r} - L^2 \right].$$

Spherical harmonics (solid harmonics on the unit sphere \mathcal{S}^2):

$$Y_{lm}(\theta, \phi) = (-1)^m \left(\frac{2l+1}{4\pi} (l+m)!(l-m)! \right)^{\frac{1}{2}} e^{im\phi}$$

$$\times \sum_k \frac{(-1)^k (\sin \theta)^{2k+m} (\cos \theta)^{l-2k-m}}{2^{2k+m} (k+m)! k! (l-2k-m)!}.$$

Orthogonality on the unit sphere:

$$\int_0^{2\pi} d\phi \int_0^{\pi} d\theta \sin \theta Y_{l'm'}^*(\theta, \phi) Y_{lm}(\theta, \phi) = \delta_{l'l} \delta_{m'm}.$$

Relation to Legendre, Jacobi, and Gegenbauer polynomials:

$$Y_{lm}(\theta, \phi) = (-1)^m \left(\frac{(2l+1)(l-m)!}{4\pi(l+m)!} \right)^{\frac{1}{2}}$$

$$\times P_l^m(\cos \theta) e^{im\phi},$$

$$P_l^m(\cos \theta) = \frac{(l+m)!}{l!} \left(\frac{\sin \theta}{2} \right)^m P_{l-m}^{(m,m)}(\cos \theta).$$

Jacobi polynomials:

$$P_n^{(\alpha,\beta)}(x) = \sum_s \binom{n+\alpha}{s} \binom{n+\beta}{n-s}$$

$$\times \left(\frac{x-1}{2} \right)^{n-s} \left(\frac{x+1}{2} \right)^s,$$

$$n = 0, 1, \dots,$$

where α, β are arbitrary parameters and

$$\binom{z}{k} = \begin{cases} z(z-1)\cdots(z-k+1)/k! & \text{for } k = 1, 2, \dots \\ 1 & \text{for } k = 0 \\ 0 & \text{for } k = -1, -2, \dots \end{cases}$$

Relations between Jacobi polynomials for $n + \alpha, n + \beta, n + \alpha + \beta$ nonnegative integers:

$$P_n^{\alpha,\beta}(x) = \frac{(n+\alpha)!(n+\beta)!}{n!(n+\alpha+\beta)!} \left(\frac{x+1}{2} \right)^{-\beta} P_{n+\beta}^{(\alpha,-\beta)}(x),$$

$$P_n^{\alpha,\beta}(x) = \frac{(n+\alpha)!(n+\beta)!}{n!(n+\alpha+\beta)!} \left(\frac{x-1}{2} \right)^{-\alpha} P_{n+\alpha}^{(-\alpha,\beta)}(x),$$

$$P_n^{\alpha,\beta}(x) = \left(\frac{x-1}{2} \right)^{-\alpha} \left(\frac{x+1}{2} \right)^{-\beta} P_{n+\alpha+\beta}^{(-\alpha,-\beta)}(x).$$

Nonstandard form (α arbitrary):

$$P_n^{(\alpha,\alpha)}(x) = \sum_s \frac{(-1)^s (\alpha+s+1)_{n-s} (1-x^2)^s x^{n-2s}}{2^{2s} s! (n-2s)!},$$

$$(z)_k = z(z+1)\cdots(z+k-1), \quad k = 1, 2, \dots;$$

$$(z)_0 = 1.$$

Gegenbauer polynomials ($\alpha > -1/2$):

$$C_n^{(\alpha)}(x) = \frac{(2\alpha)_n}{(\alpha+1/2)_n} P_n^{(\alpha-\frac{1}{2}, \alpha-\frac{1}{2})}(x)$$

$$= \sum_s \frac{(-1)^s (\alpha)_{n-s} (2x)^{n-2s}}{s! (n-2s)!}.$$

2.2 Abstract Angular Momentum

Abstract angular momentum theory addresses the problem of constructing all finite Hermitian matrices, up to equivalence, that satisfy the same commutation relations

$$[J_1, J_2] = iJ_3, \quad [J_2, J_3] = iJ_1, \quad [J_3, J_1] = iJ_2 \quad (2.7)$$

as some set of Hermitian operators J_1, J_2, J_3 appropriately defined in some Hilbert space; that is, of constructing all finite Hermitian matrices M_i such that under the correspondence $J_i \rightarrow M_i$ ($i = 1, 2, 3$) the commutation relations are still obeyed. If M_1, M_2, M_3 is such a set of Hermitian matrices, then $AM_1A^{-1}, AM_2A^{-1}, AM_3A^{-1}$, is another such set, where A is an arbitrary unitary matrix. This defines what is meant by equivalence. The commutation relations Eq. (2.7) may also be formulated as:

$$[J_3, J_{\pm}] = \pm J_{\pm}, \quad [J_+, J_-] = 2J_3,$$

$$J_{\pm} = J_1 \pm iJ_2, \quad J_+^{\dagger} = J_- \quad (2.8)$$

The squared angular momentum

$$J^2 = J_1^2 + J_2^2 + J_3^2 = J_- J_+ + J_3(J_3 + 1)$$

$$= J_+ J_- + J_3(J_3 - 1) \quad (2.9)$$

commutes with each J_i , and J_3 is, by convention, taken with \mathbf{J}^2 as a pair of commuting Hermitian operators to be diagonalized.

Examples of matrices satisfying relations Eq. (2.7) are provided by $J_i \rightarrow \sigma_i/2$ (the 2×2 Hermitian Pauli matrices defined in Eq. (2.1)) and $J_i \rightarrow M_i$ (the 3×3 matrices defined in Eq. (2.4)), these latter matrices being equivalent to those obtained from the matrices of the orbital angular momentum operators for $l = 1$.

One could determine all Hermitian matrices solving Eqs. (2.7) and (2.8) by using only matrix theory, but it is customary in quantum mechanics to formulate the problem using Hilbert space concepts appropriate to that theory. Thus, one takes the viewpoint that the J_i are linear Hermitian operators with an action defined in a separable Hilbert space \mathcal{H} such that $J_i : \mathcal{H} \rightarrow \mathcal{H}$.

One then seeks to decompose the Hilbert space into a direct sum of subspaces that are irreducible with respect to this action; that is, subspaces that cannot be further decomposed as a direct sum of subspaces that all the J_i leave invariant (map vectors in the space into vectors in the space). In this section, the solution of this fundamental problem for angular momentum theory is given. These results set the notation and phase conventions for all of angular momentum theory, in all of its varied realizations, and the relations are, therefore, sometimes referred to as standard. The method most often used to solve the posed problem is called the method of highest weights.

The solution of this problem is among the most important in quantum theory because of its generality and applicability to a wide range of problems. The space \mathcal{H} can be written as a direct sum

$$\mathcal{H} = \sum_{j=0, \frac{1}{2}, 1, \dots} \oplus n_j \mathcal{H}_j, \quad \text{each } \mathcal{H}_j \perp \mathcal{H}_{j'}, \quad j \neq j', \quad (2.10)$$

in which \mathcal{H}_j denotes a vector space of dimension $2j + 1$ that is invariant and irreducible under the action of the set of operators $J_i, i = 1, 2, 3$, and where the direct sum is over all half-integers $j = 0, \frac{1}{2}, 1, \dots$. There may be multiple occurrences, n_j in number, of the same space \mathcal{H}_j for given j , or no such space, $n_j = 0$, in the direct sum. Abstractly, in so far as angular momentum properties are concerned, each repeated space \mathcal{H}_j is *identical*. Such spaces may, however, be distinguished by their properties with respect to other physical observables, but not by the angular action of momentum operators themselves. The result, Eq. (2.10), applies to any physical system, no matter how complex, in which rotational symmetry, hence $SU(2)$ symmetry, is present, even in situations of higher symmetry where $SU(2)$ is a subgroup. Indeed, the resolution of the terms in Eq. (2.10) for vari-

ous physical systems constitutes *spectroscopy* in the broadest sense.

The characterization of the space \mathcal{H}_j with respect to angular momentum properties is given by the following results, where basis vectors are denoted in the Dirac bra-ket notation.

Orthonormal basis:

$$\{|jm\rangle | m = -j, -j + 1, \dots, j\}. \quad (2.11)$$

$$\langle jm' | jm \rangle = \delta_{m', m}. \quad (2.12)$$

Simultaneous eigenvectors:

$$\mathbf{J}^2 | jm \rangle = j(j + 1) | jm \rangle, \quad J_3 | jm \rangle = m | jm \rangle. \quad (2.13)$$

Action of angular momentum operators:

$$\begin{aligned} J_+ | jm \rangle &= [(j - m)(j + m + 1)]^{1/2} | jm + 1 \rangle, \\ J_- | jm \rangle &= [(j + m)(j - m + 1)]^{1/2} | jm - 1 \rangle. \end{aligned} \quad (2.14)$$

Defining properties of highest weight vector:

$$J_+ | jj \rangle = 0, \quad J_3 | jj \rangle = j | jj \rangle.$$

Generation of general vector from highest weight:

$$| jm \rangle = \left(\frac{(j + m)!}{(2j)!(j - m)!} \right)^{1/2} J_-^{j-m} | jj \rangle.$$

Necessary property of lowest weight vector:

$$J_- | j, -j \rangle = 0, \quad J_3 | j, -j \rangle = -j | j, -j \rangle.$$

Operator in \mathcal{H} corresponding to a rotation by angle ψ about direction $\hat{\mathbf{n}}$ in \mathbf{R}^3 :

$$\begin{aligned} T_{U(\psi, \hat{\mathbf{n}})} &= \exp(-i\psi \hat{\mathbf{n}} \cdot \mathbf{J}), \\ \hat{\mathbf{n}} \cdot \hat{\mathbf{n}} &= n_1^2 + n_2^2 + n_3^2 = 1, \\ \hat{\mathbf{n}} \cdot \mathbf{J} &= n_1 J_1 + n_2 J_2 + n_3 J_3, \\ U(\psi, \hat{\mathbf{n}}) &= \exp(-i\psi \hat{\mathbf{n}} \cdot \boldsymbol{\sigma}/2) \\ &= \sigma_0 \cos(\frac{1}{2}\psi) - i(\hat{\mathbf{n}} \cdot \boldsymbol{\sigma}) \sin(\frac{1}{2}\psi) \\ &= \begin{pmatrix} \cos(\frac{1}{2}\psi) - in_3 \sin(\frac{1}{2}\psi) & (-in_1 - n_2) \sin(\frac{1}{2}\psi) \\ (-in_1 + n_2) \sin(\frac{1}{2}\psi) & \cos(\frac{1}{2}\psi) + in_3 \sin(\frac{1}{2}\psi) \end{pmatrix} \\ &0 \leq \psi \leq 2\pi, \end{aligned} \quad (2.15)$$

where σ_0 denotes the 2×2 unit matrix.

Action of $T_{U(\psi, \hat{\mathbf{n}})}$ on \mathcal{H}_j :

$$T_U | jm \rangle = \sum_{m'} D_{m'/m}^j(U) | jm' \rangle, \quad (2.16)$$

in which $U = U(\psi, \hat{\mathbf{n}})$ and $D_{m'/m}^j(U)$ denotes a homogeneous polynomial of degree $2j$ defined on the elements

$u_{ij} = U_{ij}(\psi, \hat{n})$ in row i and column j of the matrix $U(\psi, \hat{n})$ given by Eq. (2.15). The explicit form of this polynomial is

$$D_{m'm}^j(U) = [(j+m)!(j-m)!(j+m)!(j-m)!]^{\frac{1}{2}} \times \sum_{\boxed{\alpha}} \frac{(u_{11})^{\alpha_{11}}(u_{12})^{\alpha_{12}}(u_{21})^{\alpha_{21}}(u_{22})^{\alpha_{22}}}{\alpha_{11}!\alpha_{12}!\alpha_{21}!\alpha_{22}!}. \quad (2.17)$$

The notation $\boxed{\alpha}$ symbolizes a 2×2 array of nonnegative integers with certain constraints:

$$\begin{array}{cc|cc} \alpha_{11} & \alpha_{12} & j+m' & \\ \alpha_{21} & \alpha_{22} & j-m' & \\ \hline j+m & j-m & & \end{array}.$$

In this array, the α_{ij} are nonnegative integers subject to the row and column constraints (sums) indicated by the (nonnegative) integers $j \pm m$, $j \pm m'$. Explicitly,

$$\begin{aligned} \alpha_{11} + \alpha_{12} &= j + m', & \alpha_{21} + \alpha_{22} &= j - m', \\ \alpha_{11} + \alpha_{21} &= j + m, & \alpha_{12} + \alpha_{22} &= j - m. \end{aligned}$$

The summation is over all such arrays. Any one of the α_{ij} may serve as a single summation index if one wishes to eliminate the redundancy inherent in the square-array notation. The form Eq. (2.17) is very useful for obtaining symmetry relations for these polynomials (Sect. 2.3.6).

Unitary property on \mathcal{H} :

$$\langle T_U \Psi | T_U \Psi \rangle = \langle \Psi | \Psi \rangle, \quad \text{each } \Psi \in \mathcal{H}.$$

Irreducible unitary matrix representation of $SU(2)$:

$$(D^j(U))_{j-m'+1, j-m+1} = D_{m'm}^j(U), \quad m' = j, j-1, \dots, -j; \quad m = j, j-1, \dots, -j, \quad (2.18)$$

denotes the element in row $j-m'+1$ and column $j-m+1$. Then, dimension of $D^j(U) = 2j+1$ and

$$\begin{aligned} D^j(U)D^j(U') &= D^j(UU'), \\ U &\in SU(2), \quad U' \in SU(2), \\ (D^j(U))^\dagger &= (D^j(U))^{-1} = D^j(U^\dagger). \end{aligned}$$

Kronecker (direct) product representation:

$$D^{j_1}(U) \times D^{j_2}(U)$$

is a $(2j_1+1)(2j_2+1)$ dimensional reducible representation of $SU(2)$. One can also effect the reduction of this representation into irreducible ones by abstract methods. The results are given in Sect. 2.7.

2.3 Representation Functions

2.3.1 Parametrizations of the Groups $SU(2)$ and $SO(3, \mathbf{R})$

The irreducible representations of the quantal rotation group, $SU(2)$, are among the most important quantities in all of angular momentum theory. These are the unitary matrices of dimension $2j+1$, denoted by $D^j(U)$, where this notation is used to signify that the elements of this matrix, denoted $D_{m'm}^j(U)$, are functions of the elements u_{ij} of the 2×2 unitary unimodular matrix $U \in SU(2)$. It has become standard to enumerate the rows and columns of these matrices in the order $j, j-1, \dots, -j$ as read from top to bottom down the rows and from left to right across the columns (see also Eq. (2.18)). These matrices may be presented in a variety of parametrizations, all of which are useful. In order to make comparisons between the group $SO(3, \mathbf{R})$ and the group $SU(2)$, it is most useful to parametrize these groups so that they are related according to the two-to-one homomorphism given by Eq. (2.2).

The general parametrization of the group $SU(2)$ is given in terms of the Euler–Rodrigues parameters corresponding to points belonging to the surface of the unit sphere \mathbf{S}^3 in \mathbf{R}^4 ,

$$\alpha_0^2 + \alpha_1^2 + \alpha_2^2 + \alpha_3^2 = 1. \quad (2.19)$$

Each $U \in SU(2)$ can be written in the form:

$$\begin{aligned} U(\alpha_0, \boldsymbol{\alpha}) &= \begin{pmatrix} \alpha_0 - i\alpha_3 & -i\alpha_1 - \alpha_2 \\ -i\alpha_1 + \alpha_2 & \alpha_0 + i\alpha_3 \end{pmatrix} \\ &= \alpha_0 \sigma_0 - i\boldsymbol{\alpha} \cdot \boldsymbol{\sigma}. \end{aligned} \quad (2.20)$$

The $R \in SO(3, \mathbf{R})$ corresponding to this U in the two-to-one homomorphism given by Eq. (2.2) is:

$$\begin{aligned} R(\alpha_0, \boldsymbol{\alpha}) &= \begin{pmatrix} \alpha_0^2 + \alpha_1^2 - \alpha_2^2 - \alpha_3^2 & 2\alpha_1\alpha_2 - 2\alpha_0\alpha_3 & 2\alpha_1\alpha_3 + 2\alpha_0\alpha_2 \\ 2\alpha_1\alpha_2 + 2\alpha_0\alpha_3 & \alpha_0^2 + \alpha_2^2 - \alpha_3^2 - \alpha_1^2 & 2\alpha_2\alpha_3 - 2\alpha_0\alpha_1 \\ 2\alpha_1\alpha_3 - 2\alpha_0\alpha_2 & 2\alpha_2\alpha_3 + 2\alpha_0\alpha_1 & \alpha_0^2 + \alpha_3^2 - \alpha_1^2 - \alpha_2^2 \end{pmatrix}. \end{aligned} \quad (2.21)$$

The procedure of parametrization is implemented uniformly by first parametrizing the points on the unit sphere \mathbf{S}^3 so as to cover the points in \mathbf{S}^3 exactly once, thus obtaining a parametrization of each $U \in SU(2)$. Equation (2.21) is then used to obtain the corresponding parametrization of each $R \in SO(3, \mathbf{R})$, where one notes that $R(-\alpha_0, -\boldsymbol{\alpha}) = R(\alpha_0, \boldsymbol{\alpha})$. Because of this two-to-one correspondence $\pm U \rightarrow R$, the domain of the parameters that cover the unit sphere \mathbf{S}^3 exactly once will cover the group $SO(3, \mathbf{R})$ exactly twice. This is taken into account uniformly by redefining the domain for $SO(3, \mathbf{R})$ so as to cover only the upper hemisphere ($\alpha_0 \geq 0$) of \mathbf{S}^3 .

In the active viewpoint (reference frame fixed with points being transformed into new points), an arbitrary vector $\mathbf{x} = \text{col}(x_1, x_2, x_3) \in \mathbf{R}^3$ is transformed to the new vector $\mathbf{x}' = \text{col}(x'_1, x'_2, x'_3)$ by the rule $\mathbf{x}' = \mathbf{R}\mathbf{x}$, or, equivalently, in terms of the Cartan matrix $X' = UXU^\dagger$. In the passive viewpoint, the basic inertial reference system, which is taken to be a right-handed triad of unit vectors $(\hat{\mathbf{e}}_1, \hat{\mathbf{e}}_2, \hat{\mathbf{e}}_3)$, is transformed by R to a new right-handed triad $(\hat{\mathbf{f}}_1, \hat{\mathbf{f}}_2, \hat{\mathbf{f}}_3)$ by the rule

$$\hat{\mathbf{f}}_j = \sum_i R_{ij} \hat{\mathbf{e}}_i, \quad i = 1, 2, 3,$$

so that $\hat{\mathbf{e}}_i \cdot \hat{\mathbf{f}}_j = R_{ij}$. In this viewpoint, the coordinates of one and the same point P undergo a redescription under the change of frame. If the coordinates of P are (x_1, x_2, x_3) relative to the frame $(\hat{\mathbf{e}}_1, \hat{\mathbf{e}}_2, \hat{\mathbf{e}}_3)$ and (x'_1, x'_2, x'_3) relative to the frame $(\hat{\mathbf{f}}_1, \hat{\mathbf{f}}_2, \hat{\mathbf{f}}_3)$, then

$$x_1 \hat{\mathbf{e}}_1 + x_2 \hat{\mathbf{e}}_2 + x_3 \hat{\mathbf{e}}_3 = x'_1 \hat{\mathbf{f}}_1 + x'_2 \hat{\mathbf{f}}_2 + x'_3 \hat{\mathbf{f}}_3,$$

so that $\mathbf{x}' = \mathbf{R}^T \mathbf{x}$.

Rotation about direction $\hat{\mathbf{n}} \in \mathcal{S}^2$ by positive angle ψ (right-hand rule):

$$(\alpha_0, \boldsymbol{\alpha}) = \left(\cos \frac{1}{2} \psi, \hat{\mathbf{n}} \sin \frac{1}{2} \psi \right), \quad 0 \leq \psi \leq 2\pi,$$

$$\begin{aligned} U(\psi, \hat{\mathbf{n}}) &= \exp\left(-i \frac{1}{2} \psi \hat{\mathbf{n}} \cdot \boldsymbol{\sigma}\right) \\ &= \begin{pmatrix} \cos \frac{1}{2} \psi - in_3 \sin \frac{1}{2} \psi & (-in_1 - n_2) \sin \frac{1}{2} \psi \\ (-in_1 + n_2) \sin \frac{1}{2} \psi & \cos \frac{1}{2} \psi + in_3 \sin \frac{1}{2} \psi \end{pmatrix}, \end{aligned}$$

$$\begin{aligned} R(\psi, \hat{\mathbf{n}}) &= \exp(-i\psi \hat{\mathbf{n}} \cdot \mathbf{M}), \quad 0 \leq \psi \leq \pi \\ &= I_3 - i \sin \psi (\hat{\mathbf{n}} \cdot \mathbf{M}) - (\hat{\mathbf{n}} \cdot \mathbf{M})^2 (1 - \cos \psi) \\ &= \begin{pmatrix} R_{11} & R_{12} & R_{13} \\ R_{21} & R_{22} & R_{23} \\ R_{31} & R_{32} & R_{33} \end{pmatrix}, \end{aligned}$$

$$\begin{aligned} R_{11} &= n_1^2 + (1 - n_1^2) \cos \psi, \\ R_{21} &= n_1 n_2 (1 - \cos \psi) + n_3 \sin \psi, \\ R_{31} &= n_1 n_3 (1 - \cos \psi) - n_2 \sin \psi, \\ R_{12} &= n_1 n_2 (1 - \cos \psi) - n_3 \sin \psi, \\ R_{22} &= n_2^2 + (1 - n_2^2) \cos \psi, \\ R_{32} &= n_2 n_3 (1 - \cos \psi) + n_1 \sin \psi, \\ R_{13} &= n_1 n_3 (1 - \cos \psi) + n_2 \sin \psi, \\ R_{23} &= n_2 n_3 (1 - \cos \psi) - n_1 \sin \psi, \\ R_{33} &= n_3^2 + (1 - n_3^2) \cos \psi. \end{aligned}$$

The unit vector $\hat{\mathbf{n}} \in \mathcal{S}^2$ can be further parametrized in terms of the usual spherical polar coordinates:

$$\begin{aligned} \hat{\mathbf{n}} &= (\sin \theta \cos \phi, \sin \theta \sin \phi, \cos \theta), \\ 0 &\leq \theta \leq \pi, \quad 0 \leq \phi < 2\pi. \end{aligned}$$

Euler angle parametrization:

$$\begin{aligned} U(\alpha\beta\gamma) &= e^{-i\alpha\sigma_3/2} e^{-i\beta\sigma_2/2} e^{-i\gamma\sigma_3/2} \\ &= \begin{pmatrix} e^{-i\alpha/2} \cos(\frac{1}{2}\beta) e^{-i\gamma/2} & -e^{-i\alpha/2} \sin(\frac{1}{2}\beta) e^{i\gamma/2} \\ e^{i\alpha/2} \sin(\frac{1}{2}\beta) e^{-i\gamma/2} & e^{i\alpha/2} \cos(\frac{1}{2}\beta) e^{i\gamma/2} \end{pmatrix}, \end{aligned}$$

$$0 \leq \alpha < 2\pi, \quad 0 \leq \beta \leq \pi \quad \text{or} \quad 2\pi \leq \beta \leq 3\pi, \\ 0 \leq \gamma < 2\pi,$$

$$U(\alpha, \beta + 2\pi, \gamma) = -U(\alpha\beta\gamma);$$

$$R(\alpha\beta\gamma) = e^{-i\alpha M_3} e^{-i\beta M_2} e^{-i\gamma M_3}$$

$$= \begin{pmatrix} \cos \alpha & -\sin \alpha & 0 \\ \sin \alpha & \cos \alpha & 0 \\ 0 & 0 & 1 \end{pmatrix} \begin{pmatrix} \cos \beta & 0 & \sin \beta \\ 0 & 1 & 0 \\ -\sin \beta & 0 & \cos \beta \end{pmatrix}$$

$$\times \begin{pmatrix} \cos \gamma & -\sin \gamma & 0 \\ \sin \gamma & \cos \gamma & 0 \\ 0 & 0 & 1 \end{pmatrix}$$

$$= \begin{pmatrix} \cos \alpha \cos \beta \cos \gamma & -\cos \alpha \cos \beta \sin \gamma & \cos \alpha \sin \beta \\ -\sin \alpha \sin \gamma & -\sin \alpha \cos \gamma & \\ \sin \alpha \cos \beta \cos \gamma & -\sin \alpha \cos \beta \sin \gamma & \sin \alpha \sin \beta \\ +\cos \alpha \sin \gamma & +\cos \alpha \cos \gamma & \\ -\sin \beta \cos \gamma & \sin \beta \sin \gamma & \cos \beta \end{pmatrix}$$

$$0 \leq \alpha < 2\pi, \quad 0 \leq \beta \leq \pi, \quad 0 \leq \gamma < 2\pi.$$

This matrix corresponds to the sequence of frame rotations given by

- rotate by γ about $\hat{\mathbf{e}}_3 = (0, 0, 1)$,
- rotate by β about $\hat{\mathbf{e}}_2 = (0, 1, 0)$,
- rotate by α about $\hat{\mathbf{e}}_3 = (0, 0, 1)$.

Equivalently, it corresponds to the sequence of frame rotations given by

- rotate by α about $\hat{\mathbf{n}}_1 = (0, 0, 1)$,
- rotate by β about $\hat{\mathbf{n}}_2 = (-\sin \alpha, \cos \alpha, 0)$,
- rotate by γ about $\hat{\mathbf{n}}_3 = (\cos \alpha \sin \beta, \sin \alpha \sin \beta, \cos \beta)$.

This latter sequence of rotations is depicted in Fig. 2.1 in obtaining the frame $(\hat{\mathbf{f}}_1, \hat{\mathbf{f}}_2, \hat{\mathbf{f}}_3)$ from $(\hat{\mathbf{e}}_1, \hat{\mathbf{e}}_2, \hat{\mathbf{e}}_3)$.

The four complex numbers

$$\begin{aligned} (a, b, c, d) \\ = (\alpha_0 + i\alpha_3, i\alpha_1 - \alpha_2, i\alpha_1 + \alpha_2, \alpha_0 - i\alpha_3) \end{aligned}$$

are called the Cayley–Klein parameters, whereas the four real numbers $(\alpha_0, \boldsymbol{\alpha})$ defining a point on the surface of the unit sphere in four-space, \mathcal{S}^3 , are known as the Euler–Rodrigues parameters. The three ratios α_i/α_0 form the homogeneous or symmetric Euler parameters.

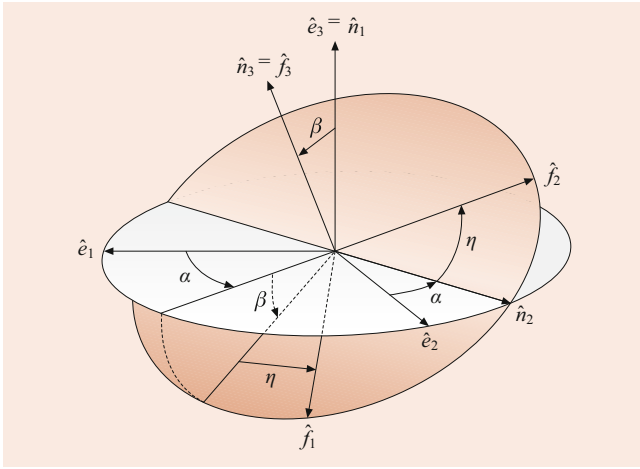


Fig. 2.1 Euler angles. The three Euler angles $(\alpha\beta\gamma)$ are defined by a sequence of three rotations. Reprinted with the permission of Cambridge University Press, after [1]

2.3.2 Explicit Forms of Representation Functions

The general form of the representation functions is given in its most basic and symmetric form in Eq. (2.17). This form applies to every parametrization, it being necessary only to introduce the explicit parametrizations of $U \in SU(2)$ or $R \in SO(3, \mathbf{R})$ given in Sect. 2.3.1 to obtain the explicit results given in this section. A choice is also made for the single independent summation parameter in the α -array. The notation for functions is abused by writing

$$D^j(\omega) = D^j(U(\omega)),$$

$\omega =$ set of parameters of $U \in SU(2)$.

Euler–Rodrigues representation $[(\alpha_0, \boldsymbol{\alpha}) \in \mathcal{S}^3]$:

$$D_{m'm}^j(\alpha_0, \boldsymbol{\alpha}) = [(j+m')!(j-m')!(j+m)!(j-m)!]^{1/2} \\ \times \sum_s \frac{(\alpha_0 - i\alpha_3)^{j+m-s} (-i\alpha_1 - \alpha_2)^{m'-m+s}}{(j+m-s)!(m'-m+s)!} \\ \times \frac{(-i\alpha_1 + \alpha_2)^s (\alpha_0 + i\alpha_3)^{j-m'-s}}{s!(j-m'-s)!}. \quad (2.22)$$

Quaternionic multiplication rule for points on the sphere \mathcal{S}^3 :

$$(\alpha'_0, \boldsymbol{\alpha}')(\alpha_0, \boldsymbol{\alpha}) = (\alpha''_0, \boldsymbol{\alpha}''), \\ \alpha''_0 = \alpha'_0\alpha_0 - \boldsymbol{\alpha}' \cdot \boldsymbol{\alpha}, \\ \boldsymbol{\alpha}'' = \alpha'_0\boldsymbol{\alpha} + \alpha_0\boldsymbol{\alpha}' + \boldsymbol{\alpha}' \times \boldsymbol{\alpha}; \\ D^j(\alpha'_0, \boldsymbol{\alpha}')D^j(\alpha_0, \boldsymbol{\alpha}) = D^j(\alpha''_0, \boldsymbol{\alpha}'').$$

The $(\psi, \hat{\mathbf{n}})$ parameters:

$$\alpha_0 = \cos \frac{1}{2}\psi, \quad \boldsymbol{\alpha} = \hat{\mathbf{n}} \sin \frac{1}{2}\psi.$$

Euler angle parametrization:

$$D_{m'm}^j(\alpha\beta\gamma) = e^{-im'\alpha} d_{m'm}^j(\beta) e^{-im\gamma}, \\ d_{m'm}^j(\beta) = \langle jm' | e^{-i\beta J_2} | jm \rangle \\ = [(j+m')!(j-m')!(j+m)!(j-m)!]^{1/2} \\ \times \sum_s \frac{(-1)^{m'-m+s} (\cos \frac{1}{2}\beta)^{2j+m-m'-2s}}{(j+m-s)!s!(m'-m+s)!} \\ \times \frac{(\sin \frac{1}{2}\beta)^{m'-m+2s}}{(j-m'-s)!}. \quad (2.23)$$

Explicit matrices:

$$d^{1/2}(\beta) = \begin{pmatrix} \cos \frac{1}{2}\beta & -\sin \frac{1}{2}\beta \\ \sin \frac{1}{2}\beta & \cos \frac{1}{2}\beta \end{pmatrix}, \\ d^1(\beta) = \begin{pmatrix} \frac{1+\cos\beta}{2} & \frac{-\sin\beta}{\sqrt{2}} & \frac{1-\cos\beta}{2} \\ \frac{\sin\beta}{\sqrt{2}} & \cos\beta & \frac{-\sin\beta}{\sqrt{2}} \\ \frac{1-\cos\beta}{2} & \frac{\sin\beta}{\sqrt{2}} & \frac{1+\cos\beta}{2} \end{pmatrix}.$$

Formal polynomial form (z_{ij} are indeterminates):

$$D_{m'm}^j(Z) = [(j+m')!(j-m')!(j+m)!(j-m)!]^{1/2} \\ \times \sum_{\boxed{\boldsymbol{\alpha}}} \prod_{i,j=1}^2 (z_{ij})^{\alpha_{ij}} / (\alpha_{ij})!, \quad (2.24)$$

$$D^j(Z')D^j(Z) = D^j(Z'Z).$$

Boson operator form:

Put $a_i^j = z_{ij}$ ($i, j = 1, 2$) in Eq. (2.24). Let \bar{a}_i^j denote the Hermitian conjugate boson so that

$$[a_i^k, a_i^j] = 0, \quad [\bar{a}_i^k, \bar{a}_i^j] = 0, \quad [\bar{a}_i^k, a_i^j] = \delta^{kj} \delta_{li}.$$

Then the boson polynomials are orthogonal in the boson inner product:

$$\langle 0 | D_{\mu'\mu}^{j'}(\bar{A}) D_{m'm}^j(A) | 0 \rangle = (2j)! \delta_{j'j} \delta_{\mu'\mu'} \delta_{\mu\mu}.$$

2.3.3 Relations to Special Functions

Jacobi polynomials (Sect. 2.1.2):

$$d_{m'm}^j(\beta) = \left(\frac{(j+m)!(j-m)!}{(j+m')!(j-m')!} \right)^{1/2} \left(\sin \frac{1}{2}\beta \right)^{m-m'} \\ \times \left(\cos \frac{1}{2}\beta \right)^{m'+m} P_{j-m}^{(m-m', m+m')}(\cos \beta),$$

$$\begin{aligned} d_{m'm}^j(\beta) &= (-1)^{m'-m} d_{-m',-m}^j(\beta) \\ &= (-1)^{m'-m} d_{mm'}^j(\beta) = d_{mm'}^j(-\beta). \end{aligned}$$

Legendre polynomials:

$$\begin{aligned} D_{m0}^l(\beta) &= (-1)^m \left(\frac{(l-m)!}{(l+m)!} \right)^{\frac{1}{2}} P_l^m(\cos \beta) \\ &= \left(\frac{(l+m)!}{(l-m)!} \right)^{\frac{1}{2}} P_l^{-m}(\cos \beta). \end{aligned}$$

Spherical harmonics:

$$\begin{aligned} Y_{lm}(\beta\alpha) &= \left(\frac{2l+1}{4\pi} \right)^{\frac{1}{2}} e^{im\alpha} d_{m0}^l(\beta) \\ &= \left(\frac{2l+1}{4\pi} \right)^{\frac{1}{2}} D_{m0}^{l*}(\alpha\beta\gamma), \\ Y_{lm}^*(\beta\alpha) &= (-1)^m Y_{l,-m}(\beta\alpha). \end{aligned}$$

Gegenbauer polynomials:

$$\begin{aligned} d_{m0}^l(\beta) &= (-1)^m [(l+m)!(l-m)!]^{\frac{1}{2}} \\ &\times \frac{(2m)!}{m!} \left(\frac{\sin \beta}{2} \right)^m C_{l-m}^{(m+1/2)}(\cos \beta), \quad m \geq 0. \end{aligned}$$

Solutions of Laplace's equation in \mathbf{R}^4 (Sect. 2.5):

$$\begin{aligned} \nabla_4^2 D_{m'm}^j(x_0, \mathbf{x}) &= 0, \quad (x_0, \mathbf{x}) \in \mathbf{R}^4, \\ \nabla_4^2 &= \sum_{\mu=0}^3 \frac{\partial^2}{\partial x_\mu^2}. \end{aligned}$$

Replace the Euler–Rodrigues parameters $(\alpha_0, \boldsymbol{\alpha})$ in Eq. (2.22) by an arbitrary point $(x_0, \mathbf{x}) \in \mathbf{R}^4$.

2.3.4 Orthogonality Properties

Inner (scalar) product:

$$\begin{aligned} (\Psi, \Phi) &= \int d\Omega \Psi^*(\mathbf{x}) \Phi(\mathbf{x}), \\ d\Omega &= \text{invariant surface measure for } \mathbf{S}^3, \\ \int_{\mathbf{S}^3} d\Omega &= 2\pi^2. \end{aligned}$$

Spherical polar coordinate for \mathbf{S}^3 :

$$\begin{aligned} (\alpha_0, \boldsymbol{\alpha}) &= \\ (\cos \chi, \cos \phi \sin \theta \sin \chi, \sin \phi \sin \theta \sin \chi, \cos \theta \sin \chi), \\ 0 \leq \theta \leq \pi, \quad 0 \leq \phi < 2\pi, \quad 0 \leq \chi \leq \pi, \end{aligned}$$

$$d\Omega = d\omega \sin^2 \chi d\chi,$$

$$d\omega = d\phi \sin \theta,$$

$$d\theta = \text{invariant surface measure for } \mathbf{S}^2;$$

$$\begin{aligned} \int_0^{2\pi} d\phi \int_0^\pi d\theta \sin \theta \int_0^\pi d\chi \sin^2 \chi D_{m'm}^{j*}(\alpha_0, \boldsymbol{\alpha}) D_{\mu'\mu}^{j'}(\alpha_0, \boldsymbol{\alpha}) \\ = \frac{2\pi^2}{2j+1} \delta_{jj'} \delta_{m'\mu'} \delta_{m\mu}. \end{aligned}$$

Coordinates $(\psi, \hat{\mathbf{n}})$ for \mathbf{S}^3 :

$$\begin{aligned} (\alpha_0, \boldsymbol{\alpha}) &= \left(\cos \frac{\psi}{2}, \hat{\mathbf{n}} \sin \frac{\psi}{2} \right), \\ 0 \leq \psi \leq 2\pi, \quad \hat{\mathbf{n}} \cdot \hat{\mathbf{n}} &= 1, \end{aligned}$$

$$d\Omega = dS(\hat{\mathbf{n}}) \sin^2 \frac{\psi}{2} \frac{d\psi}{2},$$

$$dS(\hat{\mathbf{n}}) = d\omega \text{ for } \hat{\mathbf{n}} = (\sin \theta \cos \phi, \sin \theta \sin \phi, \cos \theta),$$

$$\begin{aligned} \int dS(\hat{\mathbf{n}}) \int_0^{2\pi} \frac{d\psi}{2} \left(\sin \frac{\psi}{2} \right)^2 D_{m'm}^{j*}(\psi, \hat{\mathbf{n}}) D_{\mu'\mu}^{j'}(\psi, \hat{\mathbf{n}}) \\ = \frac{2\pi^2}{2j+1} \delta_{jj'} \delta_{m'\mu'} \delta_{m\mu}, \end{aligned}$$

Euler angles for \mathbf{S}^3 ($SU(2)$):

$$\begin{aligned} (\alpha_0, \boldsymbol{\alpha}) &= \left(\cos \frac{\beta}{2} \cos \frac{1}{2}(\gamma + \alpha), \sin \frac{\beta}{2} \sin \frac{1}{2}(\gamma - \alpha), \right. \\ &\quad \left. \sin \frac{\beta}{2} \cos \frac{1}{2}(\gamma - \alpha), \cos \frac{\beta}{2} \sin \frac{1}{2}(\gamma + \alpha) \right), \end{aligned}$$

$$d\Omega = \frac{1}{8} d\alpha d\gamma \sin \beta d\beta, \quad (2.25)$$

$$\frac{1}{8} \int_0^{2\pi} d\alpha \int_0^{2\pi} d\gamma \int_0^\pi d\beta \sin \beta D_{m'm}^{j*}(\alpha\beta\gamma) D_{\mu'\mu}^{j'}(\alpha\beta\gamma)$$

$$\begin{aligned} + \frac{1}{8} \int_0^{2\pi} d\alpha \int_0^{2\pi} d\gamma \int_{2\pi}^{3\pi} d\beta \sin \beta D_{m'm}^{j*}(\alpha\beta\gamma) D_{\mu'\mu}^{j'}(\alpha\beta\gamma) \\ = \frac{2\pi^2}{2j+1} \delta_{jj'} \delta_{m'\mu'} \delta_{m\mu}. \end{aligned} \quad (2.26)$$

Euler angles for hemisphere of \mathbf{S}^3 ($SO(3, \mathbf{R})$); j' and j both integral):

$$\begin{aligned} \int_0^{2\pi} d\alpha \int_0^{2\pi} d\gamma \int_0^\pi d\beta \sin \beta D_{m'm}^{j*}(\alpha\beta\gamma) D_{\mu'\mu}^{j'}(\alpha\beta\gamma) \\ = \frac{8\pi^2}{2j+1} \delta_{jj'} \delta_{m'\mu'} \delta_{m\mu}. \end{aligned} \quad (2.27)$$

Formal polynomials Eq. (2.24):

$$\left(D_{m'm}^j, D_{\mu'\mu}^{j'} \right) = (2j)! \delta_{jj'} \delta_{m'\mu'} \delta_{m\mu} ,$$

with inner product

$$\langle P, P' \rangle = P^* \left(\frac{\partial}{\partial Z} \right) P'(Z) |_{Z=0} ,$$

where $P^* \left(\frac{\partial}{\partial Z} \right)$ is the complex conjugate polynomial P^* of P in which each z_{ij} is replaced by $\frac{\partial}{\partial z_{ij}}$.

Boson polynomials:

$$\left\langle D_{m'm}^j \left| D_{\mu'\mu}^{j'} \right. \right\rangle = (2j)! \delta_{jj'} \delta_{m'\mu'} \delta_{m\mu} ,$$

with inner product $\langle P | P' \rangle = \langle 0 | P^*(\bar{A}) P'(A) | 0 \rangle$.

2.3.5 Recurrence Relations

Many useful relations between the representation functions may be derived as special cases of general relations between these functions and the WCG coefficients given in Sect. 2.7.1. The simplest of these are obtained from the Kronecker reduction

$$D^j \times D^{\frac{1}{2}} = D^{j+1/2} \oplus D^{j-1/2} .$$

Such relations are usually presented in terms of the Euler angle realization of U , leading to the following relations between the functions $d_{m',m}^j(\beta)$:

$$\begin{aligned} & (j-m+1)^{\frac{1}{2}} \cos\left(\frac{1}{2}\beta\right) d_{m'-1/2,m-1/2}^{j+1/2}(\beta) \\ & + (j+m+1)^{\frac{1}{2}} \sin\left(\frac{1}{2}\beta\right) d_{m'-1/2,m+1/2}^{j+1/2}(\beta) \\ & = (j-m'+1)^{\frac{1}{2}} d_{m',m}^j(\beta) , \\ & - (j-m+1)^{\frac{1}{2}} \sin\left(\frac{1}{2}\beta\right) d_{m'+1/2,m-1/2}^{j+1/2}(\beta) \\ & + (j+m+1)^{\frac{1}{2}} \cos\left(\frac{1}{2}\beta\right) d_{m'+1/2,m+1/2}^{j+1/2}(\beta) \\ & = (j+m'+1)^{\frac{1}{2}} d_{m',m}^j(\beta) , \\ & (j+m)^{\frac{1}{2}} \cos\left(\frac{1}{2}\beta\right) d_{m'-1/2,m-1/2}^{j-1/2}(\beta) \\ & - (j-m)^{\frac{1}{2}} \sin\left(\frac{1}{2}\beta\right) d_{m'-1/2,m+1/2}^{j-1/2}(\beta) \\ & = (j+m')^{\frac{1}{2}} d_{m',m}^j(\beta) , \end{aligned}$$

$$\begin{aligned} & (j+m)^{\frac{1}{2}} \sin\left(\frac{1}{2}\beta\right) d_{m'+1/2,m-1/2}^{j-1/2}(\beta) \\ & + (j-m)^{\frac{1}{2}} \cos\left(\frac{1}{2}\beta\right) d_{m'+1/2,m+1/2}^{j-1/2}(\beta) \\ & = (j-m')^{\frac{1}{2}} d_{m',m}^j(\beta) . \end{aligned}$$

Two useful relations implied by the above are:

$$\begin{aligned} & [(j-m)(j+m+1)]^{\frac{1}{2}} \sin\beta d_{m',m+1}^j(\beta) \\ & + [(j+m)(j-m+1)]^{\frac{1}{2}} \sin\beta d_{m',m-1}^j(\beta) \\ & = 2(m \cos\beta - m') d_{m',m}^j(\beta) , \\ & [(j+m)(j-m+1)]^{\frac{1}{2}} d_{m',m-1}^j(\beta) \\ & + [(j+m')(j-m'+1)]^{\frac{1}{2}} d_{m'-1,m}^j(\beta) \\ & = (m-m') \cot\left(\frac{1}{2}\beta\right) d_{m',m}^j(\beta) . \end{aligned}$$

By considering

$$D^j \times D^1 = D^{j+1} \oplus D^j \oplus D^{j-1} ,$$

one can also readily derive the matrix elements of the direction cosines specifying the orientation of the body-fixed frame $(\hat{f}_1, \hat{f}_2, \hat{f}_3)$ of a symmetric rotor relative to the inertial frame $(\hat{e}_1, \hat{e}_2, \hat{e}_3)$:

$$\lambda_{\mu,\nu} \Psi_{m,m'}^j = \sum_{j'} \left(\frac{2j+1}{2j'+1} \right)^{\frac{1}{2}} C_{m\mu m+\mu}^{j1j'} C_{m'\nu m'+\nu}^{j1j'} \Psi_{m+\mu, m'+\nu}^{j'} ,$$

where the wave functions are those defined for integral j by Eq. (2.37), for half-integral j by Eq. (2.36), and

$$\begin{aligned} \lambda_{\mu,\nu} & = \hat{e}_\mu \cdot \hat{f}_\nu^* = (D_{\mu,\nu}^1)^* , \quad \mu, \nu = -1, 0, +1 ; \\ \hat{e}_{+1} & = -(\hat{e}_1 + i\hat{e}_2)/\sqrt{2} , \quad \hat{e}_0 = \hat{e}_3 , \\ \hat{e}_{-1} & = (\hat{e}_1 - i\hat{e}_2)/\sqrt{2} , \\ \hat{f}_{+1} & = -(\hat{f}_1 + i\hat{f}_2)/\sqrt{2} , \quad \hat{f}_0 = \hat{f}_3 , \\ \hat{f}_{-1} & = (\hat{f}_1 - i\hat{f}_2)/\sqrt{2} . \end{aligned}$$

2.3.6 Symmetry Relations

Symmetry relations for the representation functions $D_{m'm}^j(Z)$ defined by Eq. (2.24) are associated with the action of a finite group G on the set $M(2, 2)$ of complex 2×2 matrices: $g : M(2, 2) \rightarrow M(2, 2)$, $g \in G$. Equivalently, if $Z \in M(2, 2)$ is parametrized by a set Ω of parameters $\omega \in \Omega$ (parameter space), then g may be taken to act directly in the parameter space $g : \Omega \rightarrow \Omega$. The action, denoted

\square , of a group $G = \{e, g, g', \dots\}$ ($e = \text{identity}$) on a set $X = \{x, x', \dots\}$ must satisfy the rules

$$\begin{aligned} g : X &\rightarrow X & e \square x &= x, \text{ all } x \in X, \\ g' \square (g \square x) &= (g'g) \square x, \text{ all } g', g \in G, \text{ all } x \in X. \end{aligned} \quad (2.28)$$

Using \cdot to denote the action of G on $M(2, 2)$ and \square to denote the action of G on Ω , one has the relation:

$$(g \cdot Z)(\omega) = Z(g^{-1} \square \omega).$$

Only finite subgroups G of the unitary group $U(2)$ (group of 2×2 unitary matrices) are considered here: $G \subset U(2)$.

Generally, when G acts on $M(2, 2)$, it effects a unitary linear transformation of the set of functions $\{D_{m'm}^j\}$ (j fixed) defined over $Z \in M(2, 2)$. For certain groups G , or for some elements of G , a single function $D_{\mu'\mu}^j \in \{D_{m'm}^j\}$ occurs in the transformation, so that

$$\begin{aligned} (g \cdot D_{m'm}^j)(Z) &= D_{m'm}^j(g^{-1} \square Z) \\ &= g_{m'm} D_{\mu'\mu}^j(Z), \end{aligned} \quad (2.29)$$

$$(\mu' \mu) \in \{(\lambda' m', \lambda m), (\lambda m, \lambda' m') | \lambda' = \pm 1, \lambda = \pm 1\},$$

where $g_{m'm}$ is a complex number of unit modulus. Relation Eq. (2.29) is called a symmetry relation of $D_{m'm}^j$ with respect to g . Usually, not all elements in G correspond to symmetry relations. In a symmetry relation, the action of the group is effectively transferred to the discrete quantum labels themselves:

$$\begin{aligned} g : m' &\rightarrow \mu' = m'(g), \\ m &\rightarrow \mu = m(g). \end{aligned} \quad (2.30)$$

In terms of a parametrization Ω of $M(2, 2)$, relation Eq. (2.29) is written

$$\begin{aligned} (g D_{m'm}^j)(\omega) &= D_{m'm}^j(g^{-1} \square \omega) \\ &= g_{m'm} D_{\mu'\mu}^j(\omega). \end{aligned} \quad (2.31)$$

In practice, action symbols such as \cdot and \square are often dropped in favor of juxtaposition, when the context is clear. Moreover, the set of complex matrices $M(2, 2)$ may be replaced by $U(2)$ or $SU(2)$ whenever the action conditions Eq. (2.28) are satisfied. Relations (Eqs. (2.29)–(2.31)) are illustrated below by examples.

There are several finite subgroups of interest with various group–subgroup relations between them:

1. Pauli group:

$$\begin{aligned} P &= \{\sigma_\mu, -\sigma_\mu, i\sigma_\mu, -i\sigma_\mu | \mu = 0, 1, 2, 3\}, \\ |P| &= 16. \end{aligned}$$

Each element of this group is an element of $U(2)$. The action of the group P may, therefore, be defined on the group $U(2)$ by left and right actions, as discussed in Sect. 2.4.1.

2. Symmetric group S_4 :

$S_4 = \{p | p \text{ is a permutation of the four Euler–Rodrigues parameters } (\alpha_0, \alpha_1, \alpha_2, \alpha_3)\}$, $|S_4| = 24$. Points in S^3 are mapped to distinct points in S^3 ; hence, one can take $Z \in SU(2)$ and define the group action directly from $U(\alpha_0, \alpha)$ in Eq. (2.20). It is simpler, however, to define the action of the group directly on the representation functions Eq. (2.22). Not all elements of this group define a symmetry in the sense defined by Eq. (2.29) (see below).

3. Abelian group T :

$$\begin{aligned} T &= \{(t_0, t_1, t_2, t_3) | \text{each } t_\mu = \pm 1\}, \\ |T| &= 16. \end{aligned}$$

Group multiplication is component-wise multiplication, and the identity is $(1, 1, 1, 1)$. The action of an element of T is defined directly on the Euler–Rodrigues parameters by component-wise multiplication, thus mapping points in S^3 to points in S^3 ; hence, one can take $Z \in SU(2)$. This group is isomorphic to the direct product group $S_2 \times S_2 \times S_2 \times S_2$, $S_2 = \text{symmetric group on two distinct objects}$.

4. Group G :

$$G = \langle \mathcal{R}, \mathcal{C}, \mathcal{T}, \mathcal{K} \rangle, \quad |G| = 32,$$

where $\mathcal{R}, \mathcal{C}, \mathcal{T}, \mathcal{K}$ denote the operations of row interchange, column interchange, transposition, and conjugation (see below) of an arbitrary matrix.

$$Z = \begin{pmatrix} a & b \\ c & d \end{pmatrix}$$

The notation $\langle \rangle$ designates that the enclosed elements generate G .

It is impossible to give here all the interrelationships among the groups defined in (1)–(4). Instead, some relations are listed as obtained directly from either $D_{m'm}^j(Z)$ defined by Eq. (2.24) or $D_{m'm}^j(\alpha_0, \alpha)$ defined by Eq. (2.22). The actions of the groups T and G defined in (3) and (4) are fully given.

Abelian group T of order 16.

Generators:

$$\begin{aligned} T &= \langle t_0, t_1, t_2, t_3 \rangle, \quad t_0 = (-1, 1, 1, 1), \\ t_1 &= (1, -1, 1, 1), \quad t_2 = (1, 1, -1, 1), \\ t_3 &= (1, 1, 1, -1). \end{aligned}$$

Group action:

$$\begin{aligned} t \cdot a &= (t_0\alpha_0, t_1\alpha_1, t_2\alpha_2, t_3\alpha_3), \\ \text{each } t &= (t_0, t_1, t_2, t_3) \in T, \\ \text{each } a &= (\alpha_0, \alpha_1, \alpha_2, \alpha_3) \in \mathcal{S}^3, \\ (tF)(a) &= F(t \cdot a), \\ t_0 D_{m'm}^j &= (-1)^{m'-m} D_{-m-m'}^j, \\ t_1 D_{m'm}^j &= (-1)^{m'-m} D_{mm'}^j, \\ t_2 D_{m'm}^j &= D_{mm'}^j, \\ t_3 D_{m'm}^j &= D_{-m-m'}^j. \end{aligned}$$

Group G of order 32.

Generators:

$$G = \langle \mathcal{R}, C, \mathcal{T}, \mathcal{K} \rangle.$$

Generator actions:

$$\begin{aligned} (\mathcal{R}F) \begin{pmatrix} a & b \\ c & d \end{pmatrix} &= F \begin{pmatrix} c & d \\ a & b \end{pmatrix}, & \text{row interchange} \\ (\mathcal{C}F) \begin{pmatrix} a & b \\ c & d \end{pmatrix} &= F \begin{pmatrix} b & a \\ d & c \end{pmatrix}, & \text{column interchange} \\ (\mathcal{T}F) \begin{pmatrix} a & b \\ c & d \end{pmatrix} &= F \begin{pmatrix} a & c \\ b & d \end{pmatrix}, & \text{transposition} \\ (\mathcal{K}F) \begin{pmatrix} a & b \\ c & d \end{pmatrix} &= F \begin{pmatrix} d & -c \\ -b & a \end{pmatrix}, & \text{conjugation} \end{aligned}$$

Subgroup H :

$$\begin{aligned} H &= \langle \mathcal{R}, C, \mathcal{T} \rangle \\ &= \{1, \mathcal{R}, C, \mathcal{T}, \mathcal{R}C = \mathcal{C}\mathcal{R}, \mathcal{T}\mathcal{R} = \mathcal{C}\mathcal{T}, \mathcal{T}C \\ &= \mathcal{R}\mathcal{T}, \mathcal{R}\mathcal{C}\mathcal{T}\}, \end{aligned}$$

with relations in H given by

$$\begin{aligned} \mathcal{R}^2 &= \mathcal{C}^2 = \mathcal{T}^2 = 1, \\ \mathcal{T}\mathcal{R}C &= \mathcal{T}C\mathcal{R} = \mathcal{R}\mathcal{C}\mathcal{T} = \mathcal{C}\mathcal{R}\mathcal{T}, \\ \mathcal{R}\mathcal{T}C &= \mathcal{C}\mathcal{T}\mathcal{R} = \mathcal{T}. \end{aligned}$$

Adjoining the idempotent element \mathcal{K} to H gives the group G of order 32:

$$G = \{H, H\mathcal{K}, H\mathcal{K}\mathcal{R}, H\mathcal{K}\mathcal{R}\mathcal{K}\}.$$

Symmetry relations:

$$\begin{aligned} \mathcal{R}D_{m'm}^j &= D_{-m'm}^j, \\ \mathcal{C}D_{m'm}^j &= D_{m'-m}^j, \\ \mathcal{T}D_{m'm}^j &= D_{mm'}^j, \\ \mathcal{K}D_{m'm}^j &= (-1)^{m'-m} D_{-m'-m}^j. \end{aligned} \quad (2.32)$$

These function relations are valid for $D_{m'm}^j$ defined over the arbitrary matrix Z defined by Eq. (2.24). They are also true for $Z = U \in SU(2)$, but now the operations \mathcal{R} and \mathcal{C} change the sign of the determinant of the matrix Z , so that the transformed matrix no longer belongs to $SU(2)$. It does, however, belong to $U(2)$, the group of all 2×2 unitary matrices. The special irreducible representation functions of $U(2)$ defined by Eq. (2.24),

$$D_{m'm}^j(U), \quad U \in U(2),$$

possess each of the 32 symmetries corresponding to the operations in the group G . (There exist other irreducible representations of $U(2)$, involving $\det U$.) The operation \mathcal{K} is closely related to complex conjugation, since for each $U \in U(2)$, $U = (u_{ij})$, one can write

$$\begin{aligned} U^* &= (\det U)^{-1} \begin{pmatrix} u_{22} & -u_{21} \\ -u_{12} & u_{11} \end{pmatrix}, \\ (\mathcal{K}D_{m'm}^j)(U) &= (\det U)^{2j} D_{m'm}^j(U^*) \\ &= (\det U)^{2j} D_{m'm}^{j*}(U) \\ &= (-1)^{m'-m} D_{-m'-m}^j(U). \end{aligned} \quad (2.33)$$

Relations Eqs. (2.32) and (2.33) are valid in an arbitrary parametrization of $U \in U(2)$. In terms of the parametrization

$$U(\chi, \alpha_0, \boldsymbol{\alpha}) = e^{i\chi/2} U(\alpha_0, \boldsymbol{\alpha}), \quad 0 \leq \chi \leq 2\pi,$$

where $U(\alpha_0, \boldsymbol{\alpha}) \in SU(2)$ is the Euler–Rodrigues parametrization, the actions of \mathcal{R} , \mathcal{C} , \mathcal{T} , and \mathcal{K} correspond to the following transformations in parameter space:

$$\begin{aligned} \mathcal{R} : \quad & \chi \rightarrow \chi + \pi, (\alpha_0, \alpha_1, \alpha_2, \alpha_3) \\ & \rightarrow (-\alpha_1, \alpha_0, -\alpha_3, \alpha_2), \\ \mathcal{C} : \quad & \chi \rightarrow \chi + \pi, (\alpha_0, \alpha_1, \alpha_2, \alpha_3) \\ & \rightarrow (-\alpha_1, \alpha_0, \alpha_3, -\alpha_2), \\ \mathcal{T} : \quad & \chi \rightarrow \chi, (\alpha_0, \alpha_1, \alpha_2, \alpha_3) \rightarrow (\alpha_0, \alpha_1, -\alpha_2, \alpha_3), \\ \mathcal{K} : \quad & \chi \rightarrow \chi, (\alpha_0, \alpha_1, \alpha_2, \alpha_3) \\ & \rightarrow (\alpha_0, -\alpha_1, \alpha_2, -\alpha_3). \end{aligned}$$

The new angle $\chi' = \chi + \pi$ is to be identified with the corresponding point on the unit circle so that these mappings are always in the parameter space, which is the sphere \mathcal{S}^3 together with the unit circle for χ . Observe that the following identities hold for functions over $SU(2)$; hence, over $U(2)$:

$$C = T_1 T_3, \quad \mathcal{T} = T_2.$$

Abelian subgroup of S_4 .

Generators:

$K = \langle (0, 3), (1, 2) \rangle$, where $(0, 3)$ and $(1, 2)$ denote transpositions in S_4 , $|K| = 4$.

Group action in parameter space:

$$(0, 3)(\alpha_0, \alpha_1, \alpha_2, \alpha_3) = (\alpha_3, \alpha_1, \alpha_2, \alpha_0) ,$$

$$(1, 2)(\alpha_0, \alpha_1, \alpha_2, \alpha_3) = (\alpha_0, \alpha_2, \alpha_1, \alpha_3) .$$

Symmetry relations:

$$(0, 3)D_{m'm}^j = (-i)^{m'+m} D_{-m-m'}^j ,$$

$$(1, 2)D_{m'm}^j = (-i)^{m'-m} D_{mm'}^j .$$

Diagonal subgroup Σ of the direct product group $P \times P$ ($P = \text{Pauli group}$).

Group elements:

$$\Sigma = \{(\sigma, \sigma) | \sigma \in P\} , \quad |\Sigma| = 16 .$$

Group action:

$$(\sigma, \sigma) : U \rightarrow \sigma U \sigma^T , \quad \text{each } \sigma \in P ,$$

$$[(\sigma, \sigma)F](U) = F(\sigma^T U \sigma) .$$

Example: $\sigma = i\sigma_2$:

$$(\sigma, \sigma) : (\alpha_0, \alpha_1, \alpha_2, \alpha_3) \rightarrow (\alpha_0, -\alpha_1, \alpha_2, -\alpha_3) ,$$

$$[(\sigma, \sigma)F](\alpha_0, \alpha_1, \alpha_2, \alpha_3) = F(\alpha_0, -\alpha_1, \alpha_2, -\alpha_3) ,$$

$$(\sigma, \sigma) = t_1 t_2 \text{ on functions over } U(2) .$$

The relations presented above barely touch on the interrelations among the finite groups introduced in (1)–(4). Symmetry relations Eqs. (2.32) and (2.33), however, give the symmetries of the $d_{m'm}^j(\beta)$ given in Sect. 2.3.3 in the Euler angle parametrization. In general, it is quite tedious to present the above symmetries in terms of Euler angles, with χ adjoined when necessary, because the Euler angles are not uniquely determined by the points of S^3 .

2.4 Group and Lie Algebra Actions

The concept of a group acting on a set is fundamental to applications of group theory to physical problems. Because of the unity that this notion brings to angular momentum theory, it is well worth a brief review in a setting in which a matrix group acts on the set of complex matrices. Thus, let $G \subseteq GL(n, \mathbb{C})$ and $H \subseteq GL(m, \mathbb{C})$ denote arbitrary subgroups, respectively, of the general linear groups of $n \times n$ and $m \times m$ nonsingular complex matrices, and let $M(n, m)$ denote the set of $n \times m$ complex matrices. A matrix $Z \in M(n, m)$ has row and column entries $(z_i^\alpha), i = 1, 2, \dots, n; \alpha = 1, 2, \dots, m$.

2.4.1 Matrix Group Actions

Left and right translations of $Z \in M(n, m)$:

$$L_g Z = g Z , \quad \text{each } g \in G , \quad \text{each } Z \in M(n, m) ,$$

$$R_h Z = Z h^T , \quad \text{each } h \in H , \quad \text{each } Z \in M(n, m) .$$

(T denotes matrix transposition.)

Left and right translations commute:

$$Z' = L_g(R_h Z) = R_h(L_g Z) , \quad \text{each } g \in G, h \in H ,$$

$$Z \in M(n, m) .$$

Equivalent form as a transformation on $\mathbf{z} \in \mathbb{C}^{nm}$:

$$\mathbf{z}' = (g \times h)\mathbf{z} ,$$

where \times denotes the direct product of g and h ; the column matrix \mathbf{z} (respectively, \mathbf{z}') is obtained from the columns of Z (respectively, Z'), $z^\alpha, \alpha = 1, 2, \dots, m$, of the $n \times m$ matrix Z as successive entries in a single column vector $\mathbf{z} \in \mathbb{C}^{nm}$.

Left and right translations in function space:

$$(\mathcal{L}_g f)(Z) = f(g^T Z) , \quad \text{each } g \in G ,$$

$$(\mathcal{R}_h f)(Z) = f(Z h) , \quad \text{each } h \in H ,$$

where $f(Z) = f(z_i^\alpha)$, and the commuting property holds for all well-defined functions f :

$$\mathcal{L}_g(\mathcal{R}_h f) = \mathcal{R}_h(\mathcal{L}_g f) .$$

2.4.2 Lie Algebra Actions

Lie algebra of left and right translations:

$$(D_X f)(Z) = i \frac{d}{dt} f(e^{-itX^T} Z) |_{t=0} ,$$

$$(D^Y f)(Z) = i \frac{d}{dt} f(Z e^{-itY}) |_{t=0} ;$$

$$D_X = \text{Tr}(Z^T X \partial / \partial Z) , \quad \text{each } X \in L(G) ,$$

$$D^Y = \text{Tr}(Y^T Z^T \partial / \partial Z) , \quad \text{each } Y \in L(H) ,$$

$$L(G) = \text{Lie algebra of } G ,$$

$$L(H) = \text{Lie algebra of } H .$$

Linear derivations:

$$D_{\alpha X + \beta X'} = \alpha D_X + \beta D_{X'} , \quad \alpha, \beta \in \mathbb{C} ,$$

$$[D_X, D_{X'}] = D_{[X, X']} ,$$

D^Y obeys these same rules.

Commuting property of left and right derivations:

$$[D_X, D^Y] = 0, \quad X \in L(G), \quad Y \in L(H).$$

Basis set:

$$D_X = \sum_{i,j=1}^n x_{ij} D_{ij}, \quad X = (x_{ij}),$$

$$D^Y = \sum_{\alpha,\beta=1}^m y^{\alpha\beta} D^{\alpha\beta}, \quad Y = (y^{\alpha\beta}),$$

$$D_{ij} = \sum_{\alpha=1}^m z_i^\alpha \frac{\partial}{\partial z_j^\alpha},$$

$$D^{\alpha\beta} = \sum_{i=1}^n z_i^\alpha \frac{\partial}{\partial z_i^\beta}.$$

Commutation rules:

$$[D_{ij}, D_{kl}] = \delta_{jk} D_{il} - \delta_{il} D_{kj},$$

$$[D^{\alpha\beta}, D^{\gamma\epsilon}] = \delta^{\beta\gamma} D^{\alpha\epsilon} - \delta^{\alpha\epsilon} D^{\gamma\beta},$$

$$[D_{ij}, D^{\alpha\beta}] = 0,$$

where $i, j, k, l = 1, 2, \dots, n$, and $\alpha, \beta, \gamma, \epsilon = 1, 2, \dots, m$. The operator sets $\{D_{ij}\}$ and $\{D^{\alpha\beta}\}$ are realizations of the Weyl generators of $GL(n, C)$ and $GL(m, C)$, respectively.

2.4.3 Hilbert Spaces

Space of polynomials with inner product:

$$(P, P') = P^*(\partial/\partial Z)P'(Z)|_{Z=0}.$$

Bargmann space of entire functions with inner product:

$$\langle F, F' \rangle = \int F^*(Z)F'(Z)d\mu(Z),$$

$$d\mu(Z) = \pi^{-nm} \exp\left(-\sum_{i,\alpha} z_i^{\alpha*} z_i^\alpha\right) \prod_{i,\alpha} dx_i^\alpha dy_i^\alpha,$$

$$z_i^\alpha = x_i^\alpha + iy_i^\alpha, i = 1, 2, \dots, n; \alpha = 1, 2, \dots, m.$$

Numerical equality of inner products:

$$(P, P') = \langle P, P' \rangle.$$

2.4.4 Relation to Angular Momentum Theory

Spinorial realization of Sects. 2.4.2 and 2.4.3:

$$G = SU(2), \quad H = (1), \quad Z \in M(2, 1),$$

$$z = \text{col}(z_1, z_2),$$

$$X = \text{set of } 2 \times 2 \text{ traceless, Hermitian matrices,}$$

$$(\mathcal{R}_U f)(z) = f(U^T z),$$

$$D_{\sigma_1/2} = (z^T \sigma_1 \partial/\partial z)/2,$$

$$J_\pm = D_{\sigma_1/2} \pm iD_{\sigma_2/2}, \quad J_3 = D_{\sigma_3/2},$$

$$J_+ = z_1 \partial/\partial z_2, \quad J_- = z_2 \partial/\partial z_1,$$

$$J_3 = (1/2)(z_1 \partial/\partial z_1 - z_2 \partial/\partial z_2),$$

$$(P, P') = P^*(\partial/\partial z_1, \partial/\partial z_2)P(z_1, z_2)|_{z_1=z_2=0}.$$

Orthonormal basis:

$$P_{jm}(z_1, z_2) = z_1^{j+m} z_2^{j-m} / [(j+m)!(j-m)!]^{1/2},$$

$$j = 0, 1/2, 1, 3/2, \dots; \quad m = j, j-1, \dots, -j.$$

Standard action:

$$J^2 P_{jm}(z) = j(j+1)P_{jm}(z),$$

$$J_3 P_{jm}(z) = mP_{jm}(z),$$

$$J_\pm P_{jm}(z) = [(j \mp m)(j \pm m + 1)]^{1/2} P_{j, m \pm 1}(z).$$

Group transformation:

$$(\mathcal{R}_U P_{jm})(z) = \sum_{m'} D_{m'm}^j(U) P_{jm'}(z),$$

where the representation functions are given by Eq. (2.17).

The 2-Spinorial Realization of Sects. 2.4.2 and 2.4.3:

$$G = H = SU(2), \quad Z \in M(2, 2),$$

$$Z = [z^1 z^2], \quad z^\alpha = \text{col}(z_1^\alpha z_2^\alpha),$$

$$X = Y = \text{set of } 2 \times 2 \text{ traceless, Hermitian matrices,}$$

$$(\mathcal{R}_U f)(Z) = f(U^T Z), \quad (\mathcal{L}_V f)(Z) = f(ZV),$$

$$U, V \in SU(2),$$

$$D_{\sigma_1/2} = \text{Tr}(Z^T \sigma_1 \partial/\partial Z)/2,$$

$$D^{\sigma_1/2} = \text{Tr}(\sigma_1 Z^T \partial/\partial Z)/2.$$

$$M_\pm = D_{\sigma_1/2} \pm iD_{\sigma_2/2}, \quad M_3 = D_{\sigma_3/2},$$

$$K_\pm = D^{\sigma_1/2} \pm iD^{\sigma_2/2}, \quad K_3 = D^{\sigma_3/2},$$

$$M_+ = \sum_{\alpha=1}^2 z_1^\alpha \partial/\partial z_2^\alpha, \quad M_- = \sum_{\alpha=1}^2 z_2^\alpha \partial/\partial z_1^\alpha,$$

$$M_3 = \frac{1}{2} \sum_{\alpha=1}^2 (z_1^\alpha \partial/\partial z_1^\alpha - z_2^\alpha \partial/\partial z_2^\alpha),$$

$$K_+ = \sum_{i=1}^2 z_i^1 \partial/\partial z_i^2, \quad K_- = \sum_{i=1}^2 z_i^2 \partial/\partial z_i^1,$$

$$K_3 = \frac{1}{2} \sum_{i=1}^2 (z_i^1 \partial/\partial z_i^1 - z_i^2 \partial/\partial z_i^2).$$

Mutual commutativity of Lie algebras:

$$[M_i, K_j] = 0, \quad i, j = 1, 2, 3.$$

Inner product:

$$(P, P') = P^*(Z)P'(\partial/\partial Z)|_{Z=0},$$

Orthogonal basis Eq. (2.24):

$$\begin{aligned} D_{mm'}^j(Z), \quad j = 0, 1/2, 1, 3/2, \dots, \\ m = j, j-1, \dots, -j; \\ m' = j, j-1, \dots, -j; \\ (D_{mm'}^j, D_{\mu\mu'}^{j'}) = (2j)! \delta_{jj'} \delta_{m\mu} \delta_{m'\mu'} . \end{aligned}$$

Equality of Casimir operators:

$$\mathbf{M}^2 = \mathbf{K}^2 = M_1^2 + M_2^2 + M_3^2 = K_1^2 + K_2^2 + K_3^2.$$

Standard actions:

$$\begin{aligned} M^2 D_{mm'}^j(Z) &= \mathbf{K}^2 D_{mm'}^j(Z) = j(j+1) D_{mm'}^j(Z), \\ M_3 D_{mm'}^j(Z) &= m D_{mm'}^j(Z), \\ K_3 D_{mm'}^j(Z) &= m' D_{mm'}^j(Z), \\ M_{\pm} D_{mm'}^j(Z) &= [(j \mp m)(j \pm m + 1)]^{\frac{1}{2}} D_{m\pm 1, m'}^j(Z), \\ K_{\pm} D_{mm'}^j(Z) &= [(j \mp m')(j \pm m' + 1)]^{\frac{1}{2}} \\ &\quad \times D_{m, m'\pm 1}^j(Z). \end{aligned}$$

Special values:

$$\begin{aligned} D^j \begin{pmatrix} 1 & 0 \\ 0 & 1 \end{pmatrix} &= I_{2j+1} = \text{unit matrix}, \\ D_{mm'}^j \begin{pmatrix} z_1 & 0 \\ z_2 & 0 \end{pmatrix} &= \delta_{jm'} P_{jm}(z_1, z_2), \\ D_{mm'}^j \begin{pmatrix} 0 & z_1 \\ 0 & z_2 \end{pmatrix} &= \delta_{jm} P_{jm'}(z_1, z_2), \\ D_{mm'}^j \begin{pmatrix} z_1 & 0 \\ 0 & z_2 \end{pmatrix} &= \delta_{mm'} z_1^{j+m} z_2^{j-m}, \\ D_{jj}^j(Z) &= (z_1^j)^{2j}. \end{aligned}$$

Symmetry relation:

$$[D^j(Z)]^T = D^j(Z^T).$$

Generation from highest weight:

$$\begin{aligned} D_{mm'}^j(Z) &= \left(\frac{(j+m)!}{(2j)!(j-m)!} \times \frac{(j+m')!}{(2j)!(j-m')!} \right)^{\frac{1}{2}} \\ &\quad \times M_-^{j-m} K_-^{j-m'} D_{jj}^j(Z). \end{aligned}$$

Generating functions:

$$\begin{aligned} (\mathbf{x}^T Z \mathbf{y})^{2j} / (2j)! &= \sum_{mm'} P_{jm}(\mathbf{x}) D_{mm'}^j(Z) P_{jm'}(\mathbf{y}), \\ \exp(t \mathbf{x}^T Z \mathbf{y}) &= \sum_j t^{2j} \sum_{mm'} P_{jm}(\mathbf{x}) D_{mm'}^j(Z) P_{jm'}(\mathbf{y}), \\ \mathbf{x} &= \text{col}(x_1 x_2), \quad \mathbf{y} = \text{col}(y_1 y_2), \\ Z &= (z_i^\alpha), \quad i, \alpha = 1, 2; \quad \text{all indeterminates.} \end{aligned}$$

2.5 Differential Operator Realizations of Angular Momentum

Differential operators realizing the standard commutation relations Eqs. (2.7) and (2.8) can be obtained from the 2-spinorial realizations given in Sect. 2.4.4 by specializing the matrix Z to the appropriate unitary unimodular matrix $U \in SU(2)$ and using the chain rule of elementary calculus. Similarly, one obtains the explicit functions $D_{mm'}^j$ simply by substituting for Z the parametrized U in Eq. (2.24). This procedure is used in this section to obtain all the realizations listed. The notations $\mathbf{M} = (M_1, M_2, M_3)$ and $\mathbf{K} = (K_1, K_2, K_3)$ and the associated M_{\pm} and K_{\pm} refer to the differential operators given by the 2-spinorial realization now transformed to the parameters in question.

Euler angles with $Z = U(\alpha\beta\gamma)$ (Sect. 2.3.1):

$$\begin{aligned} M_3 &= i\partial/\partial\alpha, \quad K_3 = i\partial/\partial\gamma, \\ \frac{1}{2}(e^{i\alpha} M_+ - e^{-i\alpha} M_-) &= \frac{1}{2}(e^{-i\gamma} K_- - e^{i\gamma} K_+) = \frac{\partial}{\partial\beta}, \\ \frac{1}{2}(e^{i\alpha} M_+ + e^{-i\alpha} M_-) &= -(\cot\beta) M_3 + (\sin\beta)^{-1} K_3, \\ \frac{1}{2}(e^{-i\gamma} K_- + e^{i\gamma} K_+) &= (\cot\beta) K_3 - (\sin\beta)^{-1} M_3, \\ M_+ &= e^{-i\alpha} [\partial/\partial\beta - (\cot\beta) M_3 + (\sin\beta)^{-1} K_3], \\ M_- &= e^{i\alpha} [-\partial/\partial\beta - (\cot\beta) M_3 + (\sin\beta)^{-1} K_3], \\ K_+ &= e^{-i\gamma} [-\partial/\partial\beta + (\cot\beta) K_3 - (\sin\beta)^{-1} M_3], \\ K_- &= e^{i\gamma} [\partial/\partial\beta + (\cot\beta) K_3 - (\sin\beta)^{-1} M_3]. \end{aligned}$$

Euler angles with $Z = U^*(\alpha\beta\gamma)$ (replace i by $-i$ in the above relations):

$$\begin{aligned} M_3 &= -i\partial/\partial\alpha, \quad K_3 = -i\partial/\partial\gamma, \\ M_{\pm} &= e^{\pm i\alpha} [\pm\partial/\partial\beta - (\cot\beta) M_3 + (\sin\beta)^{-1} K_3], \\ K_{\pm} &= e^{\pm i\gamma} [\mp\partial/\partial\beta + (\cot\beta) K_3 - (\sin\beta)^{-1} M_3]. \end{aligned} \tag{2.34}$$

Since $D^j(U^*) = (D^j(U))^*$, which is denoted $D^{j*}(U)$, these operators have the standard action on the complex conjugate functions $D_{mm'}^{j*}(U)$.

Quaternionic variables. $(x_0, \mathbf{x}) \in \mathbf{R}^4$:

$$(x'_0, \mathbf{x}') (x_0, \mathbf{x}) = (x'_0 x_0 - \mathbf{x}' \cdot \mathbf{x}, x'_0 \mathbf{x} + x_0 \mathbf{x}' + \mathbf{x}' \times \mathbf{x});$$

$$Z = \begin{pmatrix} z_{11} & z_{12} \\ z_{21} & z_{22} \end{pmatrix} = \begin{pmatrix} x_0 - ix_3 & -ix_1 - x_2 \\ -ix_1 + x_2 & x_0 + ix_3 \end{pmatrix};$$

$$\frac{\partial}{\partial Z} = \begin{pmatrix} \partial/\partial z_{11} & \partial/\partial z_{12} \\ \partial/\partial z_{21} & \partial/\partial z_{22} \end{pmatrix}$$

$$= \frac{1}{2} \begin{pmatrix} \partial/\partial x_0 + i\partial/\partial x_3 & i\partial/\partial x_1 - \partial/\partial x_2 \\ i\partial/\partial x_1 + \partial/\partial x_2 & \partial/\partial x_0 - i\partial/\partial x_3 \end{pmatrix};$$

$$M_i = \frac{1}{2} \text{Tr}(Z^T \sigma_i \partial/\partial Z), \quad K_i = \frac{1}{2} \text{Tr}(\sigma_i Z^T \partial/\partial Z).$$

(The form of $\partial/\partial Z$ is determined by the requirement $(\partial/\partial z_{ij})z_{lk} = \delta_{il}\delta_{jk}$; for example, $\frac{1}{2}(\partial/\partial x_0 + i\partial/\partial x_3)(x_0 - ix_3) = 1$).

Define the six orbital angular momentum operators in \mathbf{R}^4 by

$$L_{jk} = -i(x_j \partial/\partial x_k - x_k \partial/\partial x_j), \quad j < k = 0, 1, 2, 3,$$

which may be written as the orbital angular momentum \mathbf{L} in \mathbf{R}^3 together with the three operators \mathbf{A} given by

$$\mathbf{L} = -i\mathbf{x} \times \nabla, \quad L_1 = L_{23},$$

$$L_2 = L_{31}, \quad L_3 = L_{12},$$

$$\mathbf{A} = (A_1, A_2, A_3) = (L_{01}, L_{02}, L_{03}).$$

Then, we have the following relations:

$$K_1 = (L_1 - A_1)/2, \quad K_2 = (L_2 - A_2)/2,$$

$$K_3 = (L_3 - A_3)/2;$$

$$M_1 = -(L_1 + A_1)/2, \quad M_2 = (L_2 + A_2)/2,$$

$$M_3 = -(L_3 + A_3)/2.$$

Commutation rules:

$$[M_j, K_k] = 0, \quad j, k = 1, 2, 3,$$

$$\mathbf{M} \times \mathbf{M} = i\mathbf{M}, \quad \mathbf{K} \times \mathbf{K} = i\mathbf{K},$$

$$\mathbf{L} \times \mathbf{L} = i\mathbf{L}, \quad \mathbf{A} \times \mathbf{A} = i\mathbf{L},$$

$$[L_j, A_k] = ie_{jkl} A_l,$$

where $e_{jkl} = 1$ for j, k, l an even permutation of 1, 2, 3; $e_{jkl} = -1$ for an odd permutation of 1, 2, 3; $e_{jkl} = 0$, otherwise.

The $\mathbf{M} = (M_1, M_2, M_3)$ and $\mathbf{K} = (K_1, K_2, K_3)$ operators have the standard action given in Sect. 2.2 on the functions

$D_{mm'}^j(x_0, \mathbf{x})$ defined by Eq. (2.22) (Replace α_0 by x_0 and α by \mathbf{x} .) Additional relations:

$$\mathbf{K}^2 = \mathbf{M}^2 = -\frac{1}{4} R^2 \nabla_4^2 + K_0^2 + K_0,$$

$$R^2 = x_0^2 + \mathbf{x} \cdot \mathbf{x},$$

$$\nabla_4^2 = \frac{\partial^2}{\partial x_0^2} + \nabla^2 = \sum_{\mu} \frac{\partial^2}{\partial x_{\mu}^2},$$

$$K_0 = \frac{1}{2} \text{Tr} \left(Z^T \frac{\partial}{\partial Z} \right) = \frac{1}{2} \sum_{\mu=0}^3 x_{\mu} \frac{\partial}{\partial x_{\mu}};$$

$$K_0 D_{mm'}^j(x_0, \mathbf{x}) = j D_{mm'}^j(x_0, \mathbf{x}),$$

$$\nabla_4^2 D_{mm'}^j(x_0, \mathbf{x}) = 0;$$

$$(M_1, -M_2, M_3) = \left(\sum_i R_{i1} K_i, \sum_i R_{i2} K_i, \sum_i R_{i3} K_i \right),$$

$$R_{ij} = \frac{(x_0^2 - \mathbf{x} \cdot \mathbf{x}) \delta_{ij} - 2e_{ijk} x_0 x_k + 2x_i x_j}{x_0^2 + \mathbf{x} \cdot \mathbf{x}},$$

$$\text{each } (x_0, \mathbf{x}) \in \mathbf{R}^4.$$

The relation $R_{ij} = R_{ij}(x_0, \mathbf{x})$ is a mapping of all points of four-space \mathbf{R}^4 (except the origin) onto the group of proper, orthogonal matrices; for $x_0^2 + \mathbf{x} \cdot \mathbf{x} = 1$, it is just the Euler-Rodrigues parametrization, Eq. (2.21).

The operators $\mathbf{R} = (-M_1, M_2, -M_3)$ and $\mathbf{K} = (K_1, K_2, K_3)$ have the standard action on $(-1)^{j+m} D_{-m, m'}^j(x_0, \mathbf{x})$, so that the orbital angular momentum in \mathbf{R}^3 is given by the addition $\mathbf{L} = \mathbf{R} + \mathbf{K}$. Thus, one finds:

$$\sum_{mm'} C_{mm'M}^{jjL} (-1)^{j+m} D_{-mm'}^j(x_0, \mathbf{x})$$

$$= A_{2j, L} R^{2j-L} \mathcal{Y}_{LM}(\mathbf{x}) C_{2j-L}^{(L+1)}(x_0/R),$$

$$A_{2j, L} = (2i)^L (-1)^{2j} L! \left(\frac{4\pi(2j-L)!}{(2j+L+1)!} \right)^{\frac{1}{2}}.$$

2.6 The Symmetric Rotor and Representation Functions

The rigid rotor is an important physical object, and its quantum description enters into many physical theories. This description is an application of angular momentum theory with subtleties that need to be made explicit. It is customary to describe the classical rotor in terms of a right-handed triad of unit vectors $(\hat{f}_1, \hat{f}_2, \hat{f}_3)$ fixed in the rotor and constituting a principal axes system located at the center of mass. The instantaneous orientation of this body-fixed frame relative to a right-handed triad of unit vector $(\hat{e}_1, \hat{e}_2, \hat{e}_3)$ specifying an inertial frame, also located at the center of mass, is then given, say, in terms of Euler angles (for this purpose, one

could use any parametrization of a proper, orthogonal matrix). For Euler angles, the relationship is

$$\hat{\mathbf{f}}_j = \sum_i R_{ij}(\alpha\beta\gamma)\hat{\mathbf{e}}_i . \quad (2.35)$$

The Hamiltonian for the rigid rotor is then of the form

$$H = AP_1^2 + BP_2^2 + CP_3^2 ,$$

\mathbf{J} where $A, B,$ and C are physical constants related to the reciprocals of the principal moments of inertia, and the angular momenta \mathcal{P}_j ($j = 1, 2, 3$) are the components of the total angular momentum \mathbf{J} referred to the body-fixed frame:

$$\mathcal{P}_j = \hat{\mathbf{f}}_j \cdot \mathbf{J} = \sum_i R_{ij}(\alpha\beta\gamma)J_i ,$$

$$\mathbf{J} = \hat{\mathbf{e}}_1 J_1 + \hat{\mathbf{e}}_2 J_2 + \hat{\mathbf{e}}_3 J_3 .$$

For the symmetric rotor (taking $A = B$), the Hamiltonian can be written in the form

$$H = a\mathcal{P}^2 + b\mathcal{P}_3^2 .$$

It is in the interpretation of this Hamiltonian for quantum mechanics that the subtleties already enter, since the nature of angular momentum components referred to a moving reference system must be treated correctly. Relation Eq. (2.35) shows that the body-fixed axes cannot commute with the components of the total angular momentum \mathbf{J} referred to the frame ($\hat{\mathbf{e}}_1, \hat{\mathbf{e}}_2, \hat{\mathbf{e}}_3$). A position vector \mathbf{x} and the orbital angular momentum \mathbf{L} , with components both referred to an inertial frame, satisfy the commutation relations $[L_j, x_k] = ie_{jkl}x_l$, and for a rigid body thought of as a collection of point particles rotating together, the same conditions are to be enforced. Relative to the body-fixed frame, the vector \mathbf{x} is expressed as

$$\sum_k x_k \hat{\mathbf{e}}_k = \sum_h a_h \hat{\mathbf{f}}_h , \quad \text{each } a_h = \text{constant} ,$$

$$x_k = \sum_h a_h R_{kh}(\alpha\beta\gamma) .$$

The direction cosines $R_{kh} = R_{kh}(\alpha\beta\gamma) = \hat{\mathbf{e}}_k \cdot \hat{\mathbf{f}}_h$ and the physical total angular momentum components referred to an inertial frame must satisfy

$$[J_j, R_{kh}] = ie_{jkl}R_{lh} , \quad \text{each } h = 1, 2, 3 ,$$

in complete analogy to $[L_j, x_k] = ie_{jkl}x_l$.

The description of the angular momentum associated with a symmetric rigid rotor and the angular momentum states is summarized as follows [Eq. (2.35)]:

Physical total angular momentum \mathbf{J} with components referred to ($\hat{\mathbf{e}}_1, \hat{\mathbf{e}}_2, \hat{\mathbf{e}}_3$):

$$J_1 = i \cos \alpha \cot \beta \frac{\partial}{\partial \alpha} + i \sin \alpha \frac{\partial}{\partial \beta} - i \frac{\cos \alpha}{\sin \beta} \frac{\partial}{\partial \gamma} ,$$

$$J_2 = i \sin \alpha \cot \beta \frac{\partial}{\partial \alpha} - i \cos \alpha \frac{\partial}{\partial \beta} - i \frac{\sin \alpha}{\sin \beta} \frac{\partial}{\partial \gamma} ,$$

$$J_3 = -i \frac{\partial}{\partial \alpha} .$$

Physical angular momentum \mathbf{J} with components referred to ($\hat{\mathbf{f}}_1, \hat{\mathbf{f}}_2, \hat{\mathbf{f}}_3$):

$$P_1 = -i \cos \gamma \cot \beta \frac{\partial}{\partial \gamma} - i \sin \gamma \frac{\partial}{\partial \beta} + i \frac{\cos \gamma}{\sin \beta} \frac{\partial}{\partial \alpha} ,$$

$$P_2 = i \sin \gamma \cot \beta \frac{\partial}{\partial \gamma} - i \cos \gamma \frac{\partial}{\partial \beta} - i \frac{\sin \gamma}{\sin \beta} \frac{\partial}{\partial \alpha} ,$$

$$P_3 = -i \frac{\partial}{\partial \gamma} .$$

Standard commutation of the J_i :

$$[J_i, J_j] = iJ_k , \quad i, j, k \text{ cyclic} .$$

J_i can stand on either side:

$$P_j = \sum_i R_{ij}(\alpha\beta\gamma)J_i , \quad J_i = \sum_j J_i R_{ij}(\alpha\beta\gamma) .$$

The famous Van Vleck factor of $-i$ in the commutation of the \mathcal{P}_i :

$$[P_i, P_j] = -iP_k , \quad i, j, k \text{ cyclic} .$$

Mutual commutativity of the J_j and \mathcal{P}_i :

$$[P_i, J_j] = 0 , \quad i, j = 1, 2, 3 .$$

Same invariant (squared) total angular momentum:

$$\mathcal{P}_1^2 + \mathcal{P}_2^2 + \mathcal{P}_3^2 = J_1^2 + J_2^2 + J_3^2 = \mathcal{J}^2$$

$$= -\csc^2 \beta \left(\frac{\partial^2}{\partial \alpha^2} + \frac{\partial^2}{\partial \gamma^2} - 2 \cos \beta \frac{\partial^2}{\partial \alpha \partial \gamma} \right)$$

$$- \frac{\partial^2}{\partial \beta^2} - \cot \beta \frac{\partial}{\partial \beta} .$$

Standard actions:

$$\mathcal{J}^2 D_{mm'}^{j*}(\alpha\beta\gamma) = j(j+1)D_{mm'}^{j*}(\alpha\beta\gamma) ,$$

$$J_3 D_{mm'}^{j*}(\alpha\beta\gamma) = m D_{mm'}^{j*}(\alpha\beta\gamma) ,$$

$$P_3 D_{mm'}^{j*}(\alpha\beta\gamma) = m' D_{mm'}^{j*}(\alpha\beta\gamma) ;$$

$$J_{\pm} D_{mm'}^{j*}(\alpha\beta\gamma) = [(j \mp m)(j \pm m + 1)]^{\frac{1}{2}}$$

$$\times D_{m \pm 1, m'}^{j*}(\alpha\beta\gamma) ,$$

$$(P_1 - iP_2) D_{mm'}^{j*}(\alpha\beta\gamma) = [(j - m')(j + m' + 1)]^{\frac{1}{2}}$$

$$\times D_{m, m'+1}^{j*}(\alpha\beta\gamma) ,$$

$$(P_1 + iP_2) D_{mm'}^{j*}(\alpha\beta\gamma) = [(j + m')(j - m' + 1)]^{\frac{1}{2}}$$

$$\times D_{m, m'-1}^{j*}(\alpha\beta\gamma) .$$

Normalized wave functions.

Integral or half-integral j ($SU(2)$ solid body):

$$\left\langle \alpha\beta\gamma \left| \begin{matrix} j \\ m m' \end{matrix} \right. \right\rangle = \sqrt{\frac{2j+1}{2\pi^2}} D_{mm'}^{j*}(\alpha\beta\gamma), \quad (2.36)$$

with inner product

$$\langle F|F' \rangle = \int d\Omega \langle \alpha\beta\gamma|F \rangle^* \langle \alpha\beta\gamma|F' \rangle,$$

where $d\Omega$ is defined by Eq. (2.25), and the integration extends over all α, β, γ given by Eq. (2.26).

Integral j (collection of rigid point particles):

$$\Psi_{mm'}^j(\alpha\beta\gamma) = \sqrt{\frac{2j+1}{8\pi^2}} D_{mm'}^{j*}(\alpha\beta\gamma), \quad (2.37)$$

with inner product

$$\langle \Psi, \Psi' \rangle = \int_0^{2\pi} d\alpha \int_0^\pi d\beta \sin \beta \int_0^{2\pi} d\gamma F^*(\alpha\beta\gamma) F'(\alpha\beta\gamma).$$

The concept of a solid (impenetrable) body is conceptually distinct from that of a collection of point particles moving collectively together in translation and rotation.

2.7 Wigner–Clebsch–Gordan and 3- j Coefficients

Wigner–Clebsch–Gordan (WCG) coefficients (also called vector coupling coefficients) enter the theory of angular momentum in several ways: (1) as the coefficients in the real, orthogonal matrix that reduces the Kronecker product of two irreducible representations of the quantal rotation group into a direct sum of irreducibles; (2) as the coupling coefficients for constructing basis states of sharp angular momentum in the tensor product space from basis states of sharp angular momentum spanning the two constituent spaces; (3) as purely combinatoric objects in the expansion of a power of a 3×3 determinant; and (4) as coupling coefficients in the algebra of tensor operators. These perspectives are intimately connected but have a different focus. The first considers the group itself to be primary and views the Lie algebra as the secondary or derived concept; the second considers the Lie algebra and the construction of the vector spaces that carry irreducible representations as primary and views the representations carried by these spaces as derived quantities; the third is a mathematical construction, at first seeming almost empty of angular momentum concepts, yet the most revealing in showing the symmetry and other properties of the WCG coefficients; and the fourth is the natural extension

of (2) to operators, recognizing that the set of mappings of a vector space into itself is also a vector space. The subject of tensor operator algebra is considered in the next section because of its special importance for physical applications. This section summarizes formulas relating to the first three viewpoints, also giving the explicit mathematical expression of the coefficients in their several forms.

Either viewpoint, (1) or (2), may be taken as an interpretation of the Clebsch–Gordan series, which abstractly expresses the reduction of a Kronecker product of matrices (denoted \times) into a direct sum (denoted \oplus) of matrices:

$$\begin{aligned} [j_1] \times [j_2] &= \sum_{j=|j_1-j_2|}^{j_1+j_2} \oplus [j] \\ &= [|j_1 - j_2|] \oplus [|j_1 - j_2| + 1] \oplus \cdots \oplus [j_1 + j_2]. \end{aligned} \quad (2.38)$$

Given two angular momenta $j_1 \in \{0, \frac{1}{2}, 1, \dots\}$ and $j_2 \in \{0, \frac{1}{2}, 1, \dots\}$, the Clebsch–Gordan (CG) series also expresses the rule of addition of two angular momenta:

$$j = j_1 + j_2, j_1 + j_2 - 1, \dots, |j_1 - j_2|.$$

The integers $\epsilon_{j_1 j_2 j}$ defined by

$$\epsilon_{j_1 j_2 j} = \begin{cases} 1, & \text{for } j_1, j_2, j \text{ satisfying} \\ & \text{the CG-series rule} \\ 0, & \text{otherwise} \end{cases} \quad (2.39)$$

are useful in many relations between angular momentum quantities. The notation $(j_1 j_2 j)$ is used to symbolize the CG-series relation between three angular momentum quantum numbers.

The representation function and Lie algebra interpretations of the CG-series Eq. (2.38) are, respectively:

$$\begin{aligned} C(D^{j_1} \times D^{j_2}) C^T &= \sum_j \oplus \epsilon_{j_1 j_2 j} D^j, \\ C(J_i^{(j_1)} \times J_i^{(j_2)}) C^T &= \sum_j \oplus \epsilon_{j_1 j_2 j} J_i^{(j)}, \\ & i = 1, 2, 3. \end{aligned}$$

The notation $J_i^{(j)}$ denotes the $(2j+1) \times (2j+1)$ matrix with elements

$$\begin{aligned} J_{m',m}^{(j)} &= \langle j m' | J_i | j m \rangle, \\ m', m &= j, j-1, \dots, -j. \end{aligned}$$

The elements of the real, orthogonal matrix C of dimension $(2j_1+1)(2j_2+1)$ that effects these reductions are the WCG coefficients:

$$(C)_{j m_1 m_2} = C_{m_1 m_2}^{j_1 j_2 j}.$$

The pairs, (jm) and (m_1m_2) , index rows and columns, respectively, of the matrix C :

$$\begin{aligned} (jm) : j &= j_1 + j_2, \dots, |j_1 - j_2|, \\ m &= j, \dots, -j; \\ (m_1m_2) : m_1 &= j_1, \dots, -j_1; \\ m_2 &= j_2, \dots, -j_2. \end{aligned}$$

Sum rule on projection quantum numbers:

$$C_{m_1m_2m}^{j_1j_2j} = 0, \quad \text{for } m_1 + m_2 \neq m. \quad (2.40)$$

Clebsch–Gordan series rule on angular momentum quantum numbers:

$$C_{m_1m_2m}^{j_1j_2j} = 0, \quad \text{for } \epsilon_{j_1j_2j} = 0. \quad (2.41)$$

In presenting formulas that express relations relating to the conceptual framework described above, it is best to use a notation for a WCG coefficient giving it as an element of an orthogonal matrix. For the expression of symmetry relations, the $3-j$ coefficient, or $3-j$ symbol notation, is the most convenient. The following notations are used here:

WCG coefficient notation:

$$\begin{aligned} |(j_1j_2)jm\rangle &= \sum_{m_1m_2} C_{m_1m_2m}^{j_1j_2j} |j_1m_1\rangle \otimes |j_2m_2\rangle, \\ |j_1m_1; j_2m_2\rangle &= |j_1m_1\rangle \otimes |j_2m_2\rangle, \\ C_{m_1m_2m}^{j_1j_2j} &= \langle j_1m_1; j_2m_2 | (j_1j_2)jm \rangle, \\ \langle (j_1j_2)j'm' | (j_1j_2)jm \rangle &= \delta_{j'j} \delta_{m'm}. \end{aligned}$$

The $3-j$ coefficient notation:

$$\begin{pmatrix} j_1 & j_2 & j \\ m_1 & m_2 & -m \end{pmatrix} = (-1)^{j_1-j_2+m} (2j+1)^{-1/2} C_{m_1m_2m}^{j_1j_2j}. \quad (2.42)$$

Orthogonality of WCG coefficients:

Orthogonality of rows:

$$\sum_{m_1m_2} C_{m_1m_2m}^{j_1j_2j} C_{m_1m_2m'}^{j_1j_2j'} = \delta_{jj'} \delta_{mm'}. \quad (2.43)$$

Orthogonality of columns (three forms):

$$\begin{aligned} \sum_{jm} C_{m_1m_2m}^{j_1j_2j} C_{m'_1m'_2m}^{j_1j_2j} &= \delta_{m_1m'_1} \delta_{m_2m'_2}, \\ \sum_j C_{m_1m-m_1,m}^{j_1j_2j} C_{m'_1,m-m'_1,m}^{j_1j_2j} &= \delta_{m_1m'_1}, \\ \sum_j C_{m-m_2,m_2,m}^{j_1j_2j} C_{m-m'_2,m'_2,m}^{j_1j_2j} &= \delta_{m_2m'_2}. \end{aligned} \quad (2.44)$$

Orthogonality of $3-j$ coefficients (symbols):

$$\begin{aligned} \sum_{m_1m_2} \begin{pmatrix} j_1 & j_2 & j_3 \\ m_1 & m_2 & m_3 \end{pmatrix} \begin{pmatrix} j_1 & j_2 & j'_3 \\ m_1 & m_2 & m'_3 \end{pmatrix} \\ = \delta_{j_3j'_3} \delta_{m_3m'_3} / (2j_3 + 1), \end{aligned} \quad (2.45)$$

$$\begin{aligned} \sum_{j_3m_3} (2j_3 + 1) \begin{pmatrix} j_1 & j_2 & j_3 \\ m_1 & m_2 & m_3 \end{pmatrix} \begin{pmatrix} j_1 & j_2 & j_3 \\ m'_1 & m'_2 & m_3 \end{pmatrix} \\ = \delta_{m_1m'_1} \delta_{m_2m'_2}. \end{aligned} \quad (2.46)$$

The integers $\epsilon_{j_1j_2j}$ ($j_3 = j$) are sometimes included in the orthogonality relations Eqs. (2.43) and (2.45) to incorporate the extended definition Eq. (2.41) of the WCG coefficients.

2.7.1 Kronecker Product Reduction

Product form:

$$\begin{aligned} D_{m'_1m_1}^{j_1}(U) D_{m'_2m_2}^{j_2}(U) \\ = \sum_j C_{m'_1m'_2,m'_1+m'_2}^{j_1j_2j} C_{m_1m_2,m_1+m_2}^{j_1j_2j} D_{m'_1+m'_2,m_1+m_2}^j(U). \end{aligned}$$

Singly coupled form:

$$\begin{aligned} \sum_{m_1+m_2=m} C_{m_1m_2m}^{j_1j_2j} D_{m'_1m_1}^{j_1}(U) D_{m'_2m_2}^{j_2}(U) \\ = C_{m'_1,m'_2,m'_1+m'_2}^{j_1j_2j} D_{m'_1+m'_2,m}^j(U). \end{aligned}$$

Doubly coupled (reduction) form:

$$\begin{aligned} \sum_{\substack{m'_1+m'_2=m' \\ m_1+m_2=m}} C_{m'_1m'_2m'}^{j_1j_2j} C_{m_1m_2m}^{j_1j_2j} D_{m'_1m_1}^{j_1}(U) D_{m'_2m_2}^{j_2}(U) \\ = \delta_{j'j} D_{m'm}^j(U). \end{aligned}$$

Integral relation:

$$\begin{aligned} \int d\Omega D_{m'_1m_1}^{j_1}(U) D_{m'_2m_2}^{j_2}(U) D_{m'm_1}^{j_3}(U) \\ = \frac{2\pi^2}{2j+1} C_{m'_1m'_2m'}^{j_1j_2j} C_{m_1m_2m}^{j_1j_2j}, \end{aligned}$$

in any parametrization of $U \in SU(2)$ that covers \mathcal{S}^3 exactly once.

Gaunt's integral:

$$\begin{aligned} \int_0^{2\pi} d\alpha \int_0^\pi \sin \beta d\beta Y_{l_1m_1}^*(\beta\alpha) Y_{l_1m_1}(\beta\alpha) Y_{l_2m_2}(\beta\alpha) \\ = \left(\frac{(2l_1+1)(2l_2+1)}{4\pi(2l+1)} \right)^{1/2} C_{000}^{l_1l_2l} C_{m_1m_2m'}. \end{aligned}$$

Integral over three Legendre functions:

$$\begin{aligned} & \int_0^\pi \sin \beta d\beta P_l(\cos \beta) P_{l_1}(\cos \beta) P_{l_2}(\cos \beta) \\ &= \frac{2 \left(C_{000}^{l_1 l_2 l} \right)^2}{2l+1} \\ & C_{000}^{l_1 l_2 l} \\ &= \left(\frac{(2l+1)(l_1+l_2-l)!(l_1-l_2+l)!(-l_1+l_2+l)!}{(l_1+l_2+l+1)!} \right)^{\frac{1}{2}} \\ & \times \frac{(-1)^{L-1} L!}{(L-l_1)!(L-l_2)!(L-l)!}, \\ & L = \frac{1}{2}(l_1+l_2+l), \\ & \text{for } l_1+l_2+l \text{ even} \\ & C_{000}^{l_1 l_2 l} = 0, \quad \text{for } l_1+l_2+l \text{ odd}. \end{aligned}$$

2.7.2 Tensor Product Space Construction

Orthonormal basis of H_{j_1} :

$$\{|j_1 m_1\rangle \mid m_1 = j_1, j_1 - 1, \dots, -j_1\}.$$

Orthonormal basis of H_{j_2} :

$$\{|j_2 m_2\rangle \mid m_2 = j_2, j_2 - 1, \dots, -j_2\}.$$

Uncoupled basis of $H_{j_1} \otimes H_{j_2}$:

$$\{|j_1 m_1\rangle \otimes |j_2 m_2\rangle \mid m_1 = j_1, j_1 - 1, \dots, -j_1; \\ m_2 = j_2, j_2 - 1, \dots, -j_2\}.$$

Coupled basis of $H_{j_1} \otimes H_{j_2}$:

$$\begin{aligned} & \{|(j_1 j_2) j m\rangle \mid j = j_1 + j_2, j_1 + j_2 - 1, \dots, |j_1 - j_2|; \\ & \quad m = j, j - 1, \dots, -j\}, \\ & |(j_1 j_2) j m\rangle = \sum_{m_1 m_2} C_{m_1 m_2}^{j_1 j_2 j} |j_1 m_1\rangle \otimes |j_2 m_2\rangle. \end{aligned}$$

Unitary transformations of spaces:

$$\begin{aligned} T_U |j_1 m_1\rangle &= \sum_{m'_1} D_{m'_1 m_1}^{j_1}(U) |j_1 m'_1\rangle, \\ m_1 &= j_1, j_1 - 1, \dots, -j_1, \quad \text{each } U \in SU(2); \\ T_V |j_2 m_2\rangle &= \sum_{m'_2} D_{m'_2 m_2}^{j_2}(V) |j_2 m'_2\rangle, \\ m_2 &= j_2, j_2 - 1, \dots, -j_2, \quad \text{each } V \in SU(2); \end{aligned}$$

$$\begin{aligned} T_{(U,V)} |j_1 m_1\rangle \otimes |j_2 m_2\rangle &= T_U |j_1 m_1\rangle \otimes T_V |j_2 m_2\rangle \\ &= \sum_{m'_1 m'_2} D_{m'_1 m_1}^{j_1}(U) D_{m'_2 m_2}^{j_2}(V) |j_1 m'_1\rangle \otimes |j_2 m'_2\rangle, \\ & \text{each } U \in SU(2), \quad \text{each } V \in SU(2); \\ T_{(U,U)} |(j_1 j_2) j m\rangle &= \sum_{m'} D_{m' m}^j(U) |(j_1 j_2) j m'\rangle, \\ m &= j, j - 1, \dots, -j; \text{ each } U \in SU(2). \end{aligned}$$

Representation of direct product group $SU(2) \times SU(2)$:

$$T_{(U,V)} T_{(U',V')} = T_{(UU',VV')}.$$

Representation of $SU(2)$ as diagonal subgroup of $SU(2) \times SU(2)$:

$$\begin{aligned} T_{(U,U)} T_{(U',U')} &= T_{(UU',UU')}, \\ T_U &= T_{(U,U)}. \end{aligned}$$

2.7.3 Explicit Forms of WCG Coefficients

Wigner's form:

$$\begin{aligned} & C_{m_1 m_2 m}^{j_1 j_2 j} \\ &= \delta(m_1 + m_2, m) (2j + 1)^{\frac{1}{2}} \\ & \times \left(\frac{(j + j_1 - j_2)!(j - j_1 + j_2)!(j_1 + j_2 - j)!}{(j + j_1 + j_2 + 1)!} \right)^{\frac{1}{2}} \\ & \times \left(\frac{(j + m)!(j - m)!}{(j_1 + m_1)!(j_1 - m_1)!(j_2 + m_2)!(j_2 - m_2)!} \right)^{\frac{1}{2}} \\ & \times \sum_s \frac{(-1)^{j_2 + m_2 + s} (j_2 + j + m_1 - s)!(j_1 - m_1 + s)!}{s!(j - j_1 + j_2 - s)!(j + m - s)!(j_1 - j_2 - m + s)!}. \end{aligned}$$

Racah's form:

$$\begin{aligned} & C_{m_1 m_2 m}^{j_1 j_2 j} \\ &= \delta(m_1 + m_2, m) \\ & \times \left(\frac{(2j + 1)(j_1 + j_2 - j)!}{(j_1 + j_2 + j + 1)!(j + j_1 - j_2)!(j + j_2 - j_1)!} \right)^{\frac{1}{2}} \\ & \times \left(\frac{(j_1 - m_1)!(j_2 - m_2)!(j - m)!(j + m)!}{(j_1 + m_1)!(j_2 + m_2)!} \right)^{\frac{1}{2}} \\ & \times \sum_t \frac{(-1)^{j_1 - m_1 + t} (j_1 + m_1 + t)!(j + j_2 - m_1 - t)!}{t!(j - m - t)!(j_1 - m_1 - t)!(j_2 - j + m_1 + t)!}. \end{aligned}$$

Van der Waerden's form:

$$\begin{aligned} & C_{m_1 m_2 m}^{j_1 j_2 j} \\ &= \delta(m_1 + m_2, m) \\ & \times \left(\frac{(2j + 1)(j_1 + j_2 - j)!(j + j_1 - j_2)!(j + j_2 - j_1)!}{(j_1 + j_2 + j + 1)!} \right)^{\frac{1}{2}} \end{aligned}$$

$$\begin{aligned}
& \times [(j_1 + m_1)!(j_1 - m_1)!(j_2 + m_2)!(j_2 - m_2)!]^{\frac{1}{2}} \\
& \times [(j + m)!(j - m)!]^{\frac{1}{2}} \\
& \times \sum_k (-1)^k [k!(j_1 + j_2 - j - k)!(j_1 - m_1 - k)! \\
& \times (j_2 + m_2 - k)!(j - j_2 + m_1 + k)! \\
& \times (j - j_1 - m_2 + k)!]^{-1}.
\end{aligned}$$

Regge's formula and its combinatoric structure:

$$(\det A)^k = \sum_{\boxed{\alpha}} A(\alpha) \prod_{i,j=1}^3 (a_{ij})^{\alpha_{ij}}, \quad A = (a_{ij}), \quad (2.47)$$

where the summation is over all nonnegative integers α_{ij} that satisfy the row and column sum constraints Eq. (2.17) given by

$$\alpha = \begin{array}{|ccc|} \hline \alpha_{11} & \alpha_{12} & \alpha_{13} \\ \alpha_{21} & \alpha_{22} & \alpha_{23} \\ \alpha_{31} & \alpha_{32} & \alpha_{33} \\ \hline \end{array} \begin{array}{l} k \\ k \\ k \\ k \\ k \\ k \end{array} \quad (2.48)$$

The coefficients $A(\alpha)$ are constrained sums over multinomial coefficients:

$$A(\alpha) = \sum (-1)^{\phi(K)} \binom{k}{k_{123}, k_{132}, k_{231}, k_{213}, k_{312}, k_{321}},$$

where the summation is carried out over all nonnegative integers $k_{i_1 i_2 i_3}$ such that

$$\begin{aligned}
\alpha_{11} &= k_{123} + k_{132}, & \alpha_{12} &= k_{231} + k_{213}, \\
\alpha_{13} &= k_{312} + k_{321}, \\
\alpha_{21} &= k_{312} + k_{213}, & \alpha_{22} &= k_{123} + k_{321}, \\
\alpha_{23} &= k_{231} + k_{132}, \\
\alpha_{31} &= k_{231} + k_{321}, & \alpha_{32} &= k_{312} + k_{132}, \\
\alpha_{33} &= k_{123} + k_{213}, \\
\phi(K) &= \sum_{\pi \in A_3} k_{\pi} = k_{132} + k_{213} + k_{321}.
\end{aligned}$$

The general multinomial coefficient is the integer defined by

$$\binom{k}{k_1, k_2, \dots, k_s} = k! / k_1! k_2! \dots k_s!, \quad k = \sum_i k_i.$$

Relation Eq. (2.47) generalizes in the obvious way to an $n \times n$ determinant, using the symmetric group S_n and its S_{n-1} subgroups $S_{n-1}^{(j)}$, where j denotes that this is the permutation group on the integers $1, 2, \dots, n$ with j deleted [2].

Regge's formula for the $3-j$ coefficient is:

$$\begin{aligned}
& \binom{j_1 \quad j_2 \quad j_3}{m_1 \quad m_2 \quad m_3} \\
& = \delta(m_1 + m_2 + m_3, 0) \left[\prod_{i,j=1}^3 (\alpha_{ij})! \right]^{\frac{1}{2}} \frac{A(\alpha)}{k! [(k+1)!]^{\frac{1}{2}}}, \\
& k = j_1 + j_2 + j_3, \quad (2.49)
\end{aligned}$$

$$\begin{aligned}
\alpha_{11} &= j_1 + m_1, & \alpha_{12} &= j_2 + m_2, & \alpha_{13} &= j_3 + m_3, \\
\alpha_{21} &= j_1 - m_1, & \alpha_{22} &= j_2 - m_2, & \alpha_{23} &= j_3 - m_3, \\
\alpha_{31} &= j_2 + j_3 - j_1, & \alpha_{32} &= j_3 + j_1 - j_2, \\
\alpha_{33} &= j_1 + j_2 - j_3.
\end{aligned}$$

Equation (2.49) shows that WCG coefficients and $3-j$ coefficients are sums over integers, except for a multiplicative normalization factor.

Schwinger's generating function:

$$\exp(t \det A) = \sum_k \frac{t^k}{k!} \sum_{\boxed{\alpha}} A(\alpha) \prod_{i,j} (a_{ij})^{\alpha_{ij}}.$$

The general definition of the ${}_p F_q$ hypergeometric function depending on p numerator parameters, q denominator parameters, and a single variable z is:

$$\begin{aligned}
{}_p F_q \left(\begin{matrix} a_1, \dots, a_p \\ b_1, \dots, b_q \end{matrix}; z \right) &= \sum_{n=0}^{\infty} \frac{(a_1)_n \dots (a_p)_n}{(b_1)_n \dots (b_q)_n} \frac{z^n}{n!}, \\
(a)_n &= a(a+1) \dots (a+n-1), \quad (a)_0 = 1.
\end{aligned}$$

Such a series is terminating if at least one of the numerator parameters is a negative integer (and all other factors are well defined). Both WCG coefficients and Racah $6-j$ coefficients relate to special series of this type, evaluated at $z = 1$. For WCG coefficients, we have for $\alpha + \beta = \gamma$:

$$\begin{aligned}
C_{\alpha\beta\gamma}^{abc} &= [(2c+1)(a+\alpha)!(a-\alpha)!(b+\beta)!(b-\beta)!(c+\gamma)! \\
& \times (c-\gamma)!]^{\frac{1}{2}} (-1)^{a+b+\gamma+\delta_1} \Delta(abc) \\
& \times \frac{{}_3 F_2 \left(\begin{matrix} \epsilon_1 - \delta_1, \epsilon_2 - \delta_1, \epsilon_3 - \delta_1 \\ \delta_2 - \delta_1 + 1, \delta_3 - \delta_1 + 1 \end{matrix}; 1 \right)}{(\delta_2 - \delta_1)!(\delta_3 - \delta_1)!(\delta_1 - \epsilon_1)!(\delta_1 - \epsilon_2)!(\delta_1 - \epsilon_3)!},
\end{aligned}$$

$\delta_1 = \min(a + \alpha + b + \beta, b - \beta + c + \gamma, a + \alpha + c + \gamma)$, $(\delta_1, \delta_2, \delta_3) =$ any permutation of $(a + \alpha + b + \beta, b - \beta + c + \gamma, a + \alpha + c + \gamma)$, after δ_1 is fixed, $(\epsilon_1, \epsilon_2, \epsilon_3) =$ any permutation of $(a + \alpha, b + \alpha + \gamma, c + \gamma)$. A somewhat better form can be found in [2].

The quantity

$$\Delta(abc) = \left(\frac{(a+b-c)!(a-b+c)!(-a+b+c)!}{(a+b+c+1)!} \right)^{\frac{1}{2}}$$

is called a triangle coefficient.

All 72 Regge symmetries are consequences of known properties of the ${}_3F_2$ hypergeometric series.

2.7.4 Symmetries of WCG Coefficients in 3- j Symbol Form

There are 72 known symmetries (up to sign changes) of the 3- j coefficient. There are at least four ways of verifying these symmetries: (1) directly from the van der Waerden form of the coefficients; (2) directly from Regge's generating function; (3) from the known symmetries of the ${}_3F_2$ hypergeometric series; and (4) directly from the symmetries of the representation functions $D_{mm'}^j(U)$. The set of 72 symmetries is succinctly expressed in terms of the coefficient $A(\alpha)$ defined in Sect. 2.8.3 with α_{ij} entries given by Eqs. (2.48) and (2.49) in which $m_1 + m_2 + m_3 = 0$:

$$A \begin{pmatrix} j_1 + m_1 & j_2 + m_2 & j_3 + m_3 \\ j_1 - m_1 & j_2 - m_2 & j_3 - m_3 \\ j_2 + j_3 - j_1 & j_3 + j_1 - j_2 & j_1 + j_2 - j_3 \end{pmatrix}.$$

This coefficient has determinantal symmetry; that is, it is invariant under even permutations of its rows or columns and under transposition, and is multiplied by the factor $(-1)^{j_1+j_2+j_3}$ under odd permutations of its rows or columns. These 72 determinantal operations may be generated from the three operations C_{12}, C_{13}, T consisting of interchange of columns 1 and 2, interchange of columns 1 and 3, and transposition, since the first two operations generate the symmetric group S_3 of permutations of columns, and the symmetric group S'_3 of permutations of rows is then given by TS_3T . The transposition T itself generates a group $\{e, T\}$ isomorphic to the symmetric group S_2 . Thus, the 72 element determinantal group is the direct product group $S_3 \times S'_3 \times \{e, T\}$. The three relations between 3- j coefficients corresponding to the generators C_{12}, C_{13}, T are

$$\begin{aligned} \begin{pmatrix} j_1 & j_2 & j_3 \\ m_1 & m_2 & m_3 \end{pmatrix} &= (-1)^{j_1+j_2+j_3} \begin{pmatrix} j_2 & j_1 & j_3 \\ m_2 & m_1 & m_3 \end{pmatrix}, \\ \begin{pmatrix} j_1 & j_2 & j_3 \\ m_1 & m_2 & m_3 \end{pmatrix} &= (-1)^{j_1+j_2+j_3} \begin{pmatrix} j_3 & j_2 & j_1 \\ m_3 & m_2 & m_1 \end{pmatrix}, \\ \begin{pmatrix} j_1 & j_2 & j_3 \\ m_1 & m_2 & m_3 \end{pmatrix} &= \begin{pmatrix} \frac{j_1+j_2+m_1+m_2}{2} & \frac{j_1+j_2-m_1-m_2}{2} & j_3 \\ \frac{j_1-j_2+m_1-m_2}{2} & \frac{j_1-j_2-m_1+m_2}{2} & j_2-j_1 \end{pmatrix}. \end{aligned}$$

All 72 relations among 3- j coefficients can be obtained from these 3. The 12 classical symmetries of the 3- j symbol

$$\begin{pmatrix} a & b & c \\ \alpha & \beta & \gamma \end{pmatrix}$$

are expressed by:

1. Even permutations of the columns leave the coefficient invariant.
2. Odd permutations of the columns change the sign by the factor $(-1)^{a+b+c}$.
3. Simultaneous sign reversal of the projection quantum numbers changes the sign by $(-1)^{a+b+c}$.

The 72 corresponding symmetries of the WCG coefficients (up to sign changes and dimensional factors) are best obtained from those of the 3- j coefficients by using Eq. (2.42).

2.7.5 Recurrence Relations

Three-term:

$$\begin{aligned} & [(J+1)(J-2j_1)]^{\frac{1}{2}} \begin{pmatrix} j_1 & j_2 & j_3 \\ m_1 & m_2 & m_3 \end{pmatrix} \\ &= [(j_2+m_2)(j_3-m_3)]^{\frac{1}{2}} \begin{pmatrix} j_1 & j_2-\frac{1}{2} & j_3-\frac{1}{2} \\ m_1 & m_2-\frac{1}{2} & m_3+\frac{1}{2} \end{pmatrix} \\ &\quad - [(j_2-m_2)(j_3+m_3)]^{\frac{1}{2}} \begin{pmatrix} j_1 & j_2-\frac{1}{2} & j_3-\frac{1}{2} \\ m_1 & m_2+\frac{1}{2} & m_3-\frac{1}{2} \end{pmatrix}; \\ & [(J-2j_2)(J+1-2j_3)]^{\frac{1}{2}} \begin{pmatrix} j_1 & j_2 & j_3 \\ m_1 & m_2 & m_3 \end{pmatrix} \\ &\quad + [(j_2+m_2+1)(j_3+m_3)]^{\frac{1}{2}} \\ &\quad \times \begin{pmatrix} j_1 & j_2-\frac{1}{2} & j_3+\frac{1}{2} \\ m_1 & m_2-\frac{1}{2} & m_3+\frac{1}{2} \end{pmatrix} \\ &\quad + [(j_2-m_2+1)(j_3-m_3)]^{\frac{1}{2}} \\ &\quad \times \begin{pmatrix} j_1 & j_2-\frac{1}{2} & j_3+\frac{1}{2} \\ m_1 & m_2+\frac{1}{2} & m_3-\frac{1}{2} \end{pmatrix} = 0; \\ & (j_2+m_2)^{\frac{1}{2}} \begin{pmatrix} j_1 & j_2 & j_3 \\ m_1 & m & m_3 \end{pmatrix} \\ &= [(j_3-j_1+j_2)(J+1)(j_3-m_3)]^{\frac{1}{2}} \\ &\quad \times \begin{pmatrix} j_1 & j_2-\frac{1}{2} & j_3-\frac{1}{2} \\ m_1 & m_2-\frac{1}{2} & m_3-\frac{1}{2} \end{pmatrix} \\ &\quad - [(j_1-j_3+j_2)(J-2j_2+1)(j_3+m_3+1)]^{\frac{1}{2}} \\ &\quad \times \begin{pmatrix} j_1 & j_2-\frac{1}{2} & j_3+\frac{1}{2} \\ m_1 & m_2-\frac{1}{2} & m_3+\frac{1}{2} \end{pmatrix}; \end{aligned}$$

$$\begin{aligned} & \begin{pmatrix} j_1 & j_2 & j_3 \\ j_2 - m_3 & -j_2 & m_3 \end{pmatrix} \\ &= - \left(\frac{2j_2(j_3 + m_3)}{(j_3 - j_1 + j_2)(J + 1)} \right)^{\frac{1}{2}} \\ & \quad \times \begin{pmatrix} j_1 & j_2 - \frac{1}{2} & j_3 - \frac{1}{2} \\ j_2 - m_3 & -j_2 + \frac{1}{2} & m_3 - \frac{1}{2} \end{pmatrix}, \\ & j_3 = j_1 + j_2, j_1 + j_2 - 1, \dots, j_1 - j_2 + 1 \quad \text{for } j_1 \geq j_2; \end{aligned}$$

$$\begin{aligned} & \begin{pmatrix} j_1 & j_2 & j_3 \\ j_2 - m_3 & -j_2 & m_3 \end{pmatrix} \\ &= - \left(\frac{2j_2(j_3 - m_3 + 1)}{(j_1 - j_3 + j_2)(J - 2j_2 + 1)} \right)^{\frac{1}{2}} \\ & \quad \times \begin{pmatrix} j_1 & j_2 - \frac{1}{2} & j_3 + \frac{1}{2} \\ j_2 - m_3 & -j_2 + \frac{1}{2} & m_3 - \frac{1}{2} \end{pmatrix}, \\ & j_3 = j_1 + j_2 - 1, j_1 + j_2 - 2, \dots, j_1 - j_2 \quad \text{for } j_1 \geq j_2. \end{aligned}$$

Four-term:

$$\begin{aligned} & [(J + 1)(J - 2j_1)(J - 2j_2)(J - 2j_3 + 1)]^{\frac{1}{2}} \\ & \quad \times \begin{pmatrix} j_1 & j_2 & j_3 \\ m_1 & m_2 & m_3 \end{pmatrix} = [(j_2 - m_2)(j_2 + m_2 + 1) \\ & \quad \times (j_3 + m_3)(j_3 + m_3 - 1)]^{\frac{1}{2}} \\ & \quad \times \begin{pmatrix} j_1 & j_2 & j_3 - 1 \\ m_1 & m_2 + 1 & m_3 - 1 \end{pmatrix} \\ & \quad - 2m_2[(j_3 + m_3)(j_3 - m_3)]^{\frac{1}{2}} \begin{pmatrix} j_1 & j_2 & j_3 - 1 \\ m_1 & m_2 & m_3 \end{pmatrix} \\ & \quad - [(j_2 + m_2)(j_2 - m_2 + 1)(j_3 - m_3)(j_3 - m_3 - 1)]^{\frac{1}{2}} \\ & \quad \times \begin{pmatrix} j_1 & j_2 & j_3 - 1 \\ m_1 & m_2 - 1 & m_3 + 1 \end{pmatrix}. \end{aligned}$$

Five-term:

$$\begin{aligned} & C_{\beta, \delta, \beta + \delta}^{bdf} \\ &= \left(\frac{(b + d - f)(b + f - d + 1)(d - \delta)(f + \beta + \delta + 1)}{(2d)(2f + 1)(2d)(2f + 2)} \right)^{\frac{1}{2}} \\ & \quad \times C_{\beta, \delta + 1/2, \beta + \delta + 1/2}^{bd-1/2f+1/2} \\ & \quad - \left(\frac{(b + d - f)(b + f - d + 1)(d + \delta)(f - \beta - \delta + 1)}{(2d)(2f + 1)(2d)(2f + 2)} \right)^{\frac{1}{2}} \\ & \quad \times C_{\beta, \delta - 1/2, \beta + \delta - 1/2}^{bd-1/2f+1/2} \\ & \quad + \left(\frac{(d + f - b)(b + d + f + 1)(d + \delta)(f + \beta + \delta)}{(2d)(2f + 1)(2d)(2f)} \right)^{\frac{1}{2}} \\ & \quad \times C_{\beta, \delta - 1/2, \beta + \delta - 1/2}^{bd-1/2f-1/2} \end{aligned}$$

$$\begin{aligned} & + \left(\frac{(d + f - b)(b + d + f + 1)(d - \delta)(f - \beta - \delta)}{(2d)(2f + 1)(2d)(2f)} \right)^{\frac{1}{2}} \\ & \quad \times C_{\beta, \delta + 1/2, \beta + \delta + 1/2}^{bd-1/2f-1/2}. \end{aligned}$$

This relation may be used to prove the limit relation Eq. (2.50) from the similar recurrence relation Eq. (2.84c) for the Racah coefficients.

2.7.6 Limiting Properties and Asymptotic Forms

$$\begin{aligned} & \lim_{a \rightarrow \infty} C_{a-\alpha, \beta, a-\alpha+\beta}^{aba+\rho} = \delta_{\rho\beta}, \\ & \lim_{j \rightarrow \infty} (-1)^{a+b+2j-\tau} [(2c + 1)(2j - 2\sigma + 1)]^{\frac{1}{2}} \\ & \quad \times \left\{ \begin{matrix} j - \tau & a & j - \sigma \\ b & j & c \end{matrix} \right\} = C_{\rho\sigma\tau}^{abc}, \end{aligned} \quad (2.50)$$

where the brace symbol is a 6- j coefficient (Sect. 2.9).

$$\begin{aligned} & C_{m, \mu, m+\mu}^{jkj+\Delta} \approx (-1)^{\Delta-\mu} D_{\mu\Delta}^k \begin{pmatrix} \cos \frac{1}{2}\beta & \sin \frac{1}{2}\beta \\ -\sin \frac{1}{2}\beta & \cos \frac{1}{2}\beta \end{pmatrix} \\ & \quad = d_{\mu\Delta}^k(\beta), \quad \text{for large } j; \\ & \cos \frac{1}{2}\beta = \sqrt{\frac{j+m}{2j}}, \quad \sin \frac{1}{2}\beta = \sqrt{\frac{j-m}{2j}}, \\ & C_{m0m}^{jkj} \approx P_k(\cos \beta), \quad \text{for large } j; \end{aligned}$$

$(-1)^k [(2j + 1)(2J + 1)]^{\frac{1}{2}} W(j, k, J + m, J; j, J) \sim P_k(\cos \beta)$,
first for large J , then large j (Sect. 2.9).

2.7.7 WCG Coefficients as Discretized Representation Functions

$$\begin{aligned} & C_{m_1 m_2 m}^{j_1 j_2 j} \\ &= \delta_{m_1 + m_2, m} (-1)^{j_1 - m_1} \\ & \quad \times \left(\frac{(2j + 1)(j_1 + j_2 - j)!}{(j_1 + j_2 + j + 1)!} \right)^{\frac{1}{2}} \\ & \quad \times D_{m, j_1 - j_2}^j \begin{pmatrix} \sqrt{j_1 + m_1} & \sqrt{j_2 + m_2} \\ -\sqrt{j_1 - m_1} & \sqrt{j_2 - m_2} \end{pmatrix} \text{symbolic powers}, \end{aligned} \quad (2.51)$$

where in evaluating this result one first substitutes

$$\begin{aligned} & u_{11} = \sqrt{j_1 + m_1}, \\ & u_{12} = \sqrt{j_2 + m_2}, \\ & u_{21} = -\sqrt{j_1 - m_1}, \\ & u_{22} = \sqrt{j_2 - m_2} \end{aligned}$$

into the form Eq. (2.17), followed by the replacement of ordinary powers by generalized powers:

$$(\pm\sqrt{k})^s \rightarrow (\pm 1)^s \left(\frac{k!}{(k-s)!} \right)^{\frac{1}{2}}.$$

2.8 Tensor Operator Algebra

2.8.1 Conceptual Framework

A tensor operator can be characterized in terms of its algebraic properties with respect to the angular momentum \mathbf{J} or in terms of its transformation properties under unitary transformations generated by \mathbf{J} . Both viewpoints are essential.

A tensor operator \mathbf{T} with respect to the group $SU(2)$ is a set of linear operators

$$\mathbf{T} = \{T_1, T_2, \dots, T_n\},$$

where each operator in the set acts in the space \mathcal{H} defined by Eq. (2.10) and maps this space into itself $T_i : \mathcal{H} \rightarrow \mathcal{H}$, $i = 1, 2, \dots, n$, and where this set of operators has the following properties with respect to the angular momentum \mathbf{J} , which acts in the same space \mathcal{H} in the standard way:

1. Commutation relations with respect to the angular momentum \mathbf{J} :

$$[J_i, T_j] = \sum_{k=1}^n t_{kj}^{(i)} T_k,$$

where the $t_{kj}^{(i)}$ are scalars (invariants) with respect to \mathbf{J} .

2. Unitary transformation with respect to $SU(2)$ rotations:

$$e^{-i\psi\hat{\mathbf{n}}\cdot\mathbf{J}} T_i e^{i\psi\hat{\mathbf{n}}\cdot\mathbf{J}} = \sum_{j=1}^n D_{ji}(U) T_j,$$

$$U = U(\psi, \hat{\mathbf{n}}),$$

where the matrix $D(U)$ is an $n \times n$ unitary matrix representation of $SU(2)$. Reduction of this representation into its irreducible constituents gives the notion of an irreducible tensor operator \mathbf{T}^J of rank J . An irreducible tensor operator \mathbf{T}^J of rank J is a set of $2J + 1$ operators

$$\mathbf{T}^J = \{T_M^J \mid M = J, J-1, \dots, -J\},$$

with the following properties with respect to $SU(2)$.

1. Commutation relations with respect to the angular momentum \mathbf{J} :

$$\begin{aligned} [J_+, T_M^J] &= [(J-M)(J+M+1)]^{\frac{1}{2}} T_{M+1}^J, \\ [J_-, T_M^J] &= [(J+M)(J-M+1)]^{\frac{1}{2}} T_{M-1}^J, \\ [J_3, T_M^J] &= M T_M^J, \\ \sum_i [J_i, [J_i, T_M^J]] &= J(J+1) T_M^J. \end{aligned} \quad (2.52)$$

2. Generation from highest *weight*:

$$T_M^J = \left(\frac{(J+M)!}{(2J)!(J-M)!} \right)^{\frac{1}{2}} [J_-, T_J^J]_{(J-M)},$$

where $[A, B]_{(k)} = [A, [A, B]_{(k-1)}]$, $k = 1, 2, \dots$, with $[A, B]_{(0)} = B$, denotes the k -fold commutator of A with B .

3. Unitary transformation with respect to $SU(2)$ rotations:

$$\begin{aligned} e^{-i\psi\hat{\mathbf{n}}\cdot\mathbf{J}} T_M^J e^{i\psi\hat{\mathbf{n}}\cdot\mathbf{J}} \\ = \sum_{M'} D_{M'M}^J(U) T_{M'}^J, \quad U = U(\psi, \hat{\mathbf{n}}). \end{aligned} \quad (2.53)$$

Angular momentum operators act in Hilbert spaces by acting linearly on the vectors in such spaces. The concept of a tensor operator generalizes this by replacing the irreducible space H_J by the irreducible tensor \mathbf{T}^J , and angular momentum operator action on H_J by commutator action on \mathbf{T}^J , as symbolized, respectively, by

$$\begin{aligned} \mathbf{J} : \{ \text{states} \} &\rightarrow \{ \text{states} \}, \\ \{ \text{commutator action of } \mathbf{J} \} &: \{ \text{tensor operators} \} \\ &\rightarrow \{ \text{tensor operators} \}. \end{aligned}$$

Just as exponentiation of the standard generator action Eqs. (2.13) and (2.14) gives relation Eq. (2.16), so does the exponentiation of the commutator action Eq. (2.52) give relation Eq. (2.53), when one uses the Baker–Campbell–Hausdorff identity:

$$e^{tA} B e^{-tA} = \sum_k \frac{t^k}{k!} [A, B]_{(k)}.$$

Thus, the linear vector space of states is replaced by the linear vector space of operators. Abstractly, relations Eqs. (2.13) and (2.52) are identical: only the rule of action and the object of that action has changed.

An example of an irreducible tensor of rank 1 is the angular momentum \mathbf{J} itself, which has the special property $\mathbf{J} : \mathcal{H}_j \rightarrow \mathcal{H}_j$. Thus, relations Eqs. (2.52) and (2.53) are realized as:

$$\begin{aligned} T_1^1 &= J_{+1} = -(J_1 + iJ_2)/\sqrt{2}, \\ T_0^1 &= J_0 = J_3, \\ T_{-1}^1 &= J_{-1} = (J_1 - iJ_2)/\sqrt{2}; \\ [J_+, T_\mu^1] &= [(1-\mu)(2+\mu)]^{\frac{1}{2}} T_{\mu+1}^1, \\ [J_-, T_\mu^1] &= [(1+\mu)(2-\mu)]^{\frac{1}{2}} T_{\mu-1}^1, \\ [J_3, T_\mu^1] &= \mu T_\mu^1, \quad \mu = 1, 0, -1; \end{aligned}$$

$$\begin{aligned}
e^{-i\psi\hat{\mathbf{n}}\cdot\mathbf{J}}\mathbf{J}e^{i\psi\hat{\mathbf{n}}\cdot\mathbf{J}} &= \mathbf{J}\cos\psi + \hat{\mathbf{n}}(\hat{\mathbf{n}}\cdot\mathbf{J})(1 - \cos\psi) \\
&\quad - (\hat{\mathbf{n}}\times\mathbf{J})\sin\psi, \\
e^{-i\psi\hat{\mathbf{n}}\cdot\mathbf{J}}T_{\mu}^1e^{i\psi\hat{\mathbf{n}}\cdot\mathbf{J}} &= \sum_{\nu} D_{\nu\mu}^1(\psi, \hat{\mathbf{n}})T_{\nu}^1.
\end{aligned}$$

2.8.2 Universal Enveloping Algebra of \mathbf{J}

The universal enveloping algebra $A(\mathbf{J})$ of \mathbf{J} is the set of all complex polynomial operators in the components J_i of \mathbf{J} , or equivalently in (J_+, J_3, J_-) . The irreducible tensor operators spanning this algebra are the analogues of the solid harmonics $\mathcal{Y}_{lm}(\mathbf{x})$ and are characterized by the following properties: Basis set:

$$\begin{aligned}
\mathcal{T}_k^k &= a_k J_+^k, \quad a_k \text{ arbitrary constant}, \\
\mathcal{T}_{\mu}^k &= a_k \left(\frac{(k+\mu)!}{(2k)!(k-\mu)!} \right) [J_-, J_+^k]_{(k-\mu)}, \\
\mu &= k, k-1, \dots, -k; \quad k = 0, 1, 2, \dots
\end{aligned}$$

Standard action with respect to \mathbf{J} :

$$\begin{aligned}
[J_{\pm}, \mathcal{T}_{\mu}^k] &= [(k \mp \mu)(k \pm \mu + 1)]^{\frac{1}{2}} \mathcal{T}_{\mu \pm 1}^k, \\
[J_3, \mathcal{T}_{\mu}^k] &= \mu \mathcal{T}_{\mu}^k, \\
\sum_{i=1}^3 [J_i, [J_i, \mathcal{T}_{\mu}^k]] &= k(k+1) \mathcal{T}_{\mu}^k.
\end{aligned}$$

Unitary transformation:

$$e^{-i\psi\hat{\mathbf{n}}\cdot\mathbf{J}}\mathcal{T}_{\mu}^k e^{i\psi\hat{\mathbf{n}}\cdot\mathbf{J}} = \sum_{\nu} D_{\nu\mu}^k(\psi, \hat{\mathbf{n}})\mathcal{T}_{\nu}^k.$$

2.8.3 Algebra of Irreducible Tensor Operators

Irreducible tensor operators possess, as linear operators acting in the same space, properties 1, 2, and 3 below, and an additional multiplication property 4, which constructs new irreducible tensor operators out of two given ones and is called coupling of irreducible tensor operators. Property 4 extends also to tensor operators acting in the tensor product space associated with kinematically independent systems. It is important that associativity extends to the product Eq. (2.54), as well as to the product Eq. (2.55). Commutativity in these products is generally invalid. The coupling properties given in 4 and 5 are analogous to the coupling of basis state vectors. The operation of Hermitian conjugation of operators, which is the analogue of complex conjugation of states, is also important, and has the properties presented under 5

1. Multiplication of an irreducible tensor operator of rank k by a complex number or an invariant with respect to angular momentum \mathbf{J} gives an irreducible tensor operator of the same rank.
2. Addition of two irreducible tensor operator of the same rank gives an irreducible tensor of that rank.
3. Ordinary multiplication (juxtaposition) of three irreducible tensor operators is associative, but the multiplication of two is noncommutative, in general.
4. Two irreducible tensor operators \mathcal{S}^{k_1} and \mathcal{T}^{k_2} of different or the same ranks acting in the same space may be multiplied to obtain new irreducible tensor operators of ranks given by the angular momentum addition rule (Clebsch-Gordan series):

$$[\mathcal{S}^{k_1} \times \mathcal{T}^{k_2}]_{\mu}^k = \sum_{\mu_1, \mu_2} C_{\mu_1 \mu_2 \mu}^{k_1 k_2 k} \mathcal{S}_{\mu_1}^{k_1} \mathcal{T}_{\mu_2}^{k_2}, \quad (2.54)$$

$$\mu = k, k-1, \dots, -k;$$

$$\text{rank} = k \in \{k_1 + k_2, k_1 + k_2 - 1, \dots, |k_1 - k_2|\}.$$

The following symbol denotes the irreducible tensor operator with the μ -components Eq. (2.54):

$$[\mathcal{S}^{k_1} \times \mathcal{T}^{k_2}]^k.$$

5. Two irreducible tensor operators \mathcal{S}^{k_1} and \mathcal{T}^{k_2} of different or the same ranks acting in different Hilbert spaces, say \mathcal{H} and \mathcal{K} , may first be multiplied by the tensor product rule so as to act in the tensor product space $\mathcal{H} \otimes \mathcal{K}$, that is,

$$S_{\mu_1}^{k_1} \otimes T_{\mu_2}^{k_2} : \mathcal{H} \otimes \mathcal{K} \rightarrow \mathcal{H} \otimes \mathcal{K},$$

and then coupled to obtain new irreducible tensor operators, acting in the same tensor product space $\mathcal{H} \otimes \mathcal{K}$:

$$\begin{aligned}
[\mathcal{S}^{k_1} \otimes \mathcal{T}^{k_2}]_{\mu}^k &= \sum_{\mu_1, \mu_2} C_{\mu_1 \mu_2 \mu}^{k_1 k_2 k} \mathcal{S}_{\mu_1}^{k_1} \otimes \mathcal{T}_{\mu_2}^{k_2}, \\
\mu &= k, k-1, \dots, -k. \quad (2.55)
\end{aligned}$$

The following symbol denotes the tensor operator with the μ -components Eq. (2.55):

$$\begin{aligned}
[\mathcal{S}^{k_1} \otimes \mathcal{T}^{k_2}]^k, \\
k \in \{k_1 + k_2, k_1 + k_2 - 1, \dots, |k_1 - k_2|\}.
\end{aligned}$$

6. The conjugate tensor operator to \mathcal{T}^J , denoted by $\mathcal{T}^{J\dagger}$, is the set of operators with components $T_M^{J\dagger}$ defined by

$$\langle j'm' | T_M^{J\dagger} | jm \rangle = \langle jm | T_M^J | j'm' \rangle^*.$$

These components satisfy the following relations:

$$\begin{aligned}
[J_{\pm}, T_M^{J\dagger}] &= -[(J \pm M)(J \mp M + 1)]^{\frac{1}{2}} T_{M \mp 1}^{J\dagger} \\
[J_3, T_M^{J\dagger}] &= -M T_M^{J\dagger},
\end{aligned}$$

$$\begin{aligned} \sum_i [J_i, [J_i, T_M^{J\dagger}]] &= J(J+1)T_M^{J\dagger}; \\ e^{-i\psi\hat{n}\cdot\mathbf{J}} T_M^{J\dagger} e^{i\psi\hat{n}\cdot\mathbf{J}} &= \sum_{M'} D_{M'M}^{J*}(\psi, \hat{n}) T_{M'}^{J\dagger}; \\ I^J &= \sum_M T_M^J T_M^{J\dagger} = \left(\begin{array}{c} \text{invariant operator to} \\ SU(2) \text{ rotations} \end{array} \right), \\ e^{-i\psi\hat{n}\cdot\mathbf{J}} I^J e^{i\psi\hat{n}\cdot\mathbf{J}} &= I^J. \end{aligned}$$

An important invariant operator is

$$I^{k_1 k_2 k} = \sum_{\mu_1 \mu_2 \mu} C_{\mu_1 \mu_2 \mu}^{k_1 k_2 k} T_{\mu_1}^{k_1} T_{\mu_2}^{k_2} T_{\mu}^{k\dagger}.$$

7. Other definitions of conjugation:

$$T_M^T \rightarrow (-1)^{J-M} T_{-M}^J, \quad T_M^J \rightarrow (-1)^{J+M} T_{-M}^J.$$

2.8.4 Wigner–Eckart Theorem

The Wigner–Eckart theorem establishes the form of the matrix elements of an arbitrary irreducible tensor operator:

$$\begin{aligned} \langle j'm' | T_M^J | jm \rangle &= \langle j' \| \mathbf{T}^J \| j \rangle C_{mMm'}^{jJj'} \\ &= (j' \| \mathbf{T}^J \| j) (-1)^{j+J+m'} \begin{pmatrix} j & J & j' \\ m & M & -m' \end{pmatrix}. \end{aligned}$$

Reduced matrix elements with respect to WCG coefficients:

$$\langle j' \| \mathbf{T}^J \| j \rangle = \sum_{\mu M} C_{\mu M \mu'}^{jJj'} \langle j' \mu' | T_M^J | j \mu \rangle,$$

each $\mu' = j', j' - 1, \dots, -j'$ (the reduced matrix element is independent of μ').

Reduced matrix elements with respect to 3- j coefficients:

$$(j' \| \mathbf{T}^J \| j) = (-1)^{2J} \sqrt{2j'+1} (j' \| \mathbf{T}^J \| j).$$

Examples of irreducible tensor operators include:

1. The solid harmonics with respect to the orbital angular momentum L :

$$\begin{aligned} \mathbf{y}^k(\mathbf{x}) &= \{y_{k\mu}(\mathbf{x}) : \mu = k, \dots, -k\}, \\ y_{k\mu} |lm\rangle &= \sum_{l'} \langle l' \| \mathbf{y}^k \| l \rangle C_{m,\mu,m+\mu}^{l'kl'} |l', m+\mu\rangle, \end{aligned}$$

where

$$\begin{aligned} \langle \mathbf{x} | lm \rangle &= y_{lm}(\mathbf{x}), \\ \langle l' \| \mathbf{y}^k \| l \rangle &= r^{l+k-l'} \left(\frac{(2l+1)(2k+1)}{4\pi(2l'+1)} \right)^{\frac{1}{2}} C_{000}^{l'kl'}, \end{aligned}$$

$$\begin{aligned} y_{k\mu}(\mathbf{x}) y_{lm}(\mathbf{x}) &= \sum_{l'} \langle l' \| \mathbf{y}^k \| l \rangle C_{m,\mu,m+\mu}^{l'kl'} y_{l',m+\mu}(\mathbf{x}), \\ [\mathbf{y}^{k_1}(\mathbf{x}) \otimes \mathbf{y}^{k_2}(\mathbf{x})]_{\mu}^k &= \sum_{\mu_1 \mu_2} C_{\mu_1 \mu_2 \mu}^{k_1 k_2 k} y_{k_1 \mu_1}(\mathbf{x}) y_{k_2 \mu_2}(\mathbf{x}), \\ [\mathbf{y}^{k_1}(\mathbf{x}) \otimes \mathbf{y}^{k_2}(\mathbf{x})]_{\mu}^k &= \langle k \| \mathbf{y}^{k_1} \| k_2 \rangle y_{k\mu}(\mathbf{x}). \end{aligned}$$

2. The polynomial operator \mathcal{T}^k in the components of \mathbf{J} (Sect. 2.8.2):

$$\begin{aligned} \langle j'm' | \mathcal{T}_{\mu}^k | jm \rangle &= \delta_{j'j} \langle j \| \mathcal{T}^k \| j \rangle C_{m\mu m'}^{j k j}, \\ \langle j \| \mathcal{T}^k \| j \rangle &= a_k (-1)^k \left(\frac{(2j+k+1)! k!}{(2j+1)(2j-k)!(2k)!} \right)^{\frac{1}{2}}. \end{aligned}$$

3. Polynomials in the components of an arbitrary vector operator \mathbf{V} , which has the defining relations:

$$\begin{aligned} [J_i, V_j] &= i e_{ijk} V_k, \\ [J_{\pm}, V_{\mu}] &= [(1 \mp \mu)(2 \pm \mu)]^{\frac{1}{2}} V_{\mu \pm 1}, \\ [J_3, V_{\mu}] &= \mu V_{\mu}, \\ V_{+1} &= -(V_1 + iV_2)/\sqrt{2}, \quad V_0 = V_3, \\ V_{-1} &= (V_1 - iV_2)/\sqrt{2}. \end{aligned}$$

This construction parallels exactly that given in Sect. 2.8.2 upon replacing \mathbf{J} by \mathbf{V} . The explicit form of the resulting polynomials may be quite different since no assumptions are made concerning commutation relations between the components V_i of \mathbf{V} . The solid harmonics in the gradient operator ∇ constitute an irreducible tensor operator with respect to the orbital angular momentum L .

2.8.5 Unit Tensor Operators or Wigner Operators

A unit tensor operator is an irreducible tensor operator $\hat{\mathbf{T}}^{J,\Delta}$, indexed not only by the angular momentum quantum number J but also by an additional label Δ , which specifies that this irreducible tensor operator has reduced matrix elements given by

$$\langle j' \| \hat{\mathbf{T}}^{J,\Delta} \| j \rangle = \delta_{j',j+\Delta}.$$

This condition is to be true for all $j = 0, 1/2, 1, \dots$. There is a unit tensor operator defined for each

$$\Delta = J, J-1, \dots, -J.$$

The special symbol

$$\left\langle \begin{array}{ccc} 2J & J+\Delta & \\ & \bullet & \\ & & 0 \end{array} \right\rangle$$

denotes a unit tensor operator, replacing the boldface symbol $\hat{\mathbf{T}}^{J,\Delta}$, while the symbol

$$\left\langle \begin{array}{c} 2J \quad J + \Delta \\ \quad \quad J + M \end{array} \right\rangle, \quad M = J, J - 1, \dots, -J$$

denotes the components. In the same way that abstract angular momentum \mathbf{J} and state vectors $\{|jm\rangle\}$ extract the intrinsic structure of all realizations of angular momentum theory, as given in Sect. 2.2, so does the notion of a unit tensor operator extract the intrinsic structure of the concept of irreducible tensor operator by disregarding the physical content of the theory, which is carried in the structure of the reduced matrix elements. Physical theory is regained from the fact that the unit tensor operators are the basis for arbitrary tensor operators, which is the structural content of the Wigner–Eckart theorem. The concept of a unit tensor operator was introduced by Racah, but it was Biedenharn who recognized the full significance of this concept not only for $SU(2)$, but for all the unitary groups.

All of the content of physical tensor operator theory can be regained from the properties of unit tensor operators or Wigner operators as summarized below.

Notation (double Gel'fand patterns):

$$\left\langle \begin{array}{c} J + \Delta \\ 2J \quad \quad 0 \\ \quad \quad J + M \end{array} \right\rangle, \quad M, \Delta = J, J - 1, \dots, -J \\ 2J = 0, 1, 2, \dots$$

Definition (shift action):

$$\left\langle \begin{array}{c} J + \Delta \\ 2J \quad \quad 0 \\ \quad \quad J + M \end{array} \right\rangle |jm\rangle = C_{m,M,m+M}^{jJj+\Delta} |j + \Delta, m + M\rangle, \quad (2.56)$$

for all $j = 0, \frac{1}{2}, \dots$; $m = j, j - 1, \dots, -j$.

Conjugation:

$$\left\langle \begin{array}{c} J + \Delta \\ 2J \quad \quad 0 \\ \quad \quad J + M \end{array} \right\rangle^\dagger |jm\rangle = C_{m-M,M,m}^{j-\Delta Jj} |j - \Delta, m - M\rangle. \quad (2.57)$$

Orthogonality:

$$\sum_M \left\langle \begin{array}{c} J + \Delta' \\ 2J \quad \quad 0 \\ \quad \quad J + M \end{array} \right\rangle \left\langle \begin{array}{c} J + \Delta \\ 2J \quad \quad 0 \\ \quad \quad J + M \end{array} \right\rangle = \delta_{\Delta'\Delta} \mathbf{I}_\Delta^J, \quad (2.58)$$

$$\sum_\Delta \left\langle \begin{array}{c} J + \Delta \\ 2J \quad \quad 0 \\ \quad \quad J + M' \end{array} \right\rangle \left\langle \begin{array}{c} J + \Delta \\ 2J \quad \quad 0 \\ \quad \quad J + M \end{array} \right\rangle = \delta_{M'M}, \quad (2.59)$$

$$\sum_m \langle jm | \left\langle \begin{array}{c} J' + \Delta' \\ 2J' \quad \quad 0 \\ \quad \quad J' + M' \end{array} \right\rangle \left\langle \begin{array}{c} J + \Delta \\ 2J \quad \quad 0 \\ \quad \quad J + M \end{array} \right\rangle^\dagger |jm\rangle \\ = \frac{2j+1}{2J+1} \delta_{J'J} \delta_{M'M} \delta_{\Delta'\Delta}. \quad (2.60)$$

The invariant operator \mathbf{I}_Δ^J is defined by its action on an arbitrary vector $\psi_j \in \mathcal{H}_j$:

$$\mathbf{I}_\Delta^J \psi_j = \epsilon_{j-\Delta, J, j} \psi_j.$$

Tensor operator property:

$$e^{-i\psi \hat{\mathbf{n}} \cdot \mathbf{J}} \left\langle \begin{array}{c} J + \Delta \\ 2J \quad \quad 0 \\ \quad \quad J + M \end{array} \right\rangle e^{i\psi \hat{\mathbf{n}} \cdot \mathbf{J}} \\ = \sum_{M'} D_{M'M}^J(\psi, \hat{\mathbf{n}}) \left\langle \begin{array}{c} J + \Delta \\ 2J \quad \quad 0 \\ \quad \quad J + M' \end{array} \right\rangle. \quad (2.61)$$

Basis property (Wigner–Eckart theorem):

$$T_M^J |jm\rangle \\ = \left(\sum_\Delta \langle j + \Delta \| \mathbf{T}^J \| j \rangle \left\langle \begin{array}{c} J + \Delta \\ 2J \quad \quad 0 \\ \quad \quad J + M \end{array} \right\rangle \right) |jm\rangle. \quad (2.62)$$

Characteristic null space.

The characteristic null space of the Wigner operator defined by Eq. (2.56) is the set of irreducible subspaces $\mathcal{H}_j \subset \mathcal{H}$ given by

$$\{\mathcal{H}_j : 2j = 0, 1, \dots, J - \Delta - 1\}.$$

Coupling law:

$$\sum_{\alpha\beta} C_{\alpha\beta\gamma}^{abc} \left\langle \begin{array}{c} b + \sigma \\ 2b \quad \quad 0 \\ \quad \quad b + \beta \end{array} \right\rangle \left\langle \begin{array}{c} a + \rho \\ 2a \quad \quad 0 \\ \quad \quad a + \alpha \end{array} \right\rangle \\ = \mathbf{W}_{\rho,\sigma,\rho+\sigma}^{abc} \left\langle \begin{array}{c} c + \rho + \sigma \\ 2c \quad \quad 0 \\ \quad \quad c + \gamma \end{array} \right\rangle, \quad (2.63)$$

where $\mathbf{W}_{\rho\sigma\tau}^{abc}$ is an invariant operator (commutes with \mathbf{J}) and is called a Racah invariant. Its relationship to Racah coefficients and 6- j coefficients is given in Sect. 2.9.

Product law:

$$\left\langle \begin{array}{c} b + \sigma \\ 2b \quad \quad 0 \\ \quad \quad b + \beta \end{array} \right\rangle \left\langle \begin{array}{c} a + \rho \\ 2a \quad \quad 0 \\ \quad \quad a + \alpha \end{array} \right\rangle \\ = \sum_c \mathbf{W}_{\rho,\sigma,\rho+\sigma}^{abc} C_{\alpha,\beta,\alpha+\beta}^{abc} \left\langle \begin{array}{c} c + \rho + \sigma \\ 2c \quad \quad 0 \\ \quad \quad c + \alpha + \beta \end{array} \right\rangle. \quad (2.64)$$

Racah invariant:

$$W_{\rho\sigma\tau}^{abc} = \sum_{\alpha\beta\gamma} C_{\alpha\beta\gamma}^{abc} \times \left\langle \begin{array}{c} b + \sigma \\ 2b \\ b + \beta \end{array} 0 \middle| \begin{array}{c} a + \rho \\ 2a \\ a + \alpha \end{array} 0 \middle| \begin{array}{c} c + \tau \\ 2c \\ c + \gamma \end{array} 0 \right\rangle^\dagger. \quad (2.65)$$

The notation $W_{\rho\sigma\tau}^{abc}$ for a Racah invariant is designed to *match* that of the WCG coefficient on the left, the latter being associated with the lower group theoretical labels, for example,

$$\left(\begin{array}{c} 2a \\ a + \alpha \\ 0 \end{array} \right) \rightarrow |a\alpha\rangle,$$

the state vector having a group transformation law under the action of $SU(2)$, and the former with the shift labels of a unit tensor operator,

$$\left(\begin{array}{c} \alpha + \rho \\ 2\alpha \\ 0 \end{array} \right),$$

and having no associated group transformation law. The invariant operator defined by Eq. (2.65) has real eigenvalues, hence, is a Hermitian operator,

$$W_{\rho\sigma\tau}^{abc\dagger} = W_{\rho\sigma\tau}^{abc}, \quad (2.66)$$

which is diagonal on an arbitrary state vector in \mathcal{H}_j (Sect. 2.9).

The Racah invariant operator does not commute with a unit tensor operator, and it makes a difference whether it is written to the left or to the right of such a unit tensor operator. The convention here writes it to the left.

Relation Eq. (2.65) is taken as the definition of $W_{\rho\sigma\tau}^{abc}$, and the following properties all follow from this expression.

Domain of definition:

$$\begin{aligned} W_{\rho\sigma\tau}^{abc} &: a, b, c \in \{0, 1/2, 1, 3/2, \dots\}; \\ \rho &= a, a - 1, \dots, -a \\ \sigma &= b, b - 1, \dots, -b \\ \tau &= c, c - 1, \dots, -c; \\ W_{\rho\sigma\tau}^{abc} &= \mathbf{0}, \text{ if } \rho + \sigma \neq \tau; \text{ if } \epsilon_{abc} = 0. \end{aligned}$$

Orthogonality relations:

$$\sum_{\rho\sigma} W_{\rho\sigma\tau}^{abc} W_{\rho\sigma\tau'}^{abd} = \delta_{cd} \delta_{\tau\tau'} \epsilon_{abc} \mathbf{I}_\tau^c, \quad (2.67)$$

$$\sum_{c\tau} W_{\rho\sigma\tau}^{abc} W_{\rho'\sigma'\tau}^{abc} = \delta_{\rho\rho'} \delta_{\sigma\sigma'} \mathbf{I}_{\rho\sigma}^{ab}, \quad (2.68)$$

where the \mathbf{I} invariant operators in these expressions have the following eigenvalues on an arbitrary vector $\psi_j \in \mathcal{H}_j$:

$$\begin{aligned} \mathbf{I}_\tau^c \psi_j &= \epsilon_{j-\tau,c,j} \psi_j, \\ \mathbf{I}_{\rho\sigma}^{ab} \psi_j &= \epsilon_{j-\sigma-\rho,a,j-\sigma} \epsilon_{j-\sigma,b,j} \psi_j. \end{aligned}$$

The orthogonality relations for Racah invariants parallel exactly those of WCG coefficients.

Using the orthogonality relations Eq. (2.67) for Racah invariants, the following two relations now follow from Eqs. (2.63) and (2.64), respectively:

WCG and Racah operator coupling:

$$\begin{aligned} &\sum_{\rho\sigma} \sum_{\alpha\beta} W_{\rho,\sigma,\rho+\sigma}^{abd} C_{\alpha,\beta,\alpha+\beta}^{abc} \\ &\times \left\langle \begin{array}{c} b + \sigma \\ 2b \\ b + \beta \end{array} 0 \middle| \begin{array}{c} a + \rho \\ 2a \\ a + \alpha \end{array} 0 \right\rangle \\ &= \delta_{cd} \epsilon_{abc} \mathbf{I}_\tau^d \left\langle \begin{array}{c} c + \tau \\ 2c \\ c + \gamma \end{array} 0 \right\rangle. \end{aligned} \quad (2.69)$$

Racah operator coupling of shift patterns:

$$\begin{aligned} &\sum_{\rho\sigma} W_{\rho\sigma\tau}^{abc} \left\langle \begin{array}{c} b + \sigma \\ 2b \\ b + \beta \end{array} 0 \middle| \begin{array}{c} a + \rho \\ 2a \\ a + \alpha \end{array} 0 \right\rangle \\ &= C_{\alpha,\beta,\alpha+\beta}^{abc} \left\langle \begin{array}{c} c + \tau \\ 2c \\ c + \alpha + \beta \end{array} 0 \right\rangle. \end{aligned} \quad (2.70)$$

Relations (Eqs. (2.56)–(2.70)) capture the full content of irreducible tensor operator algebra through the concept of unit tensor operators that have only 0 or 1 for their reduced matrix elements. Using the Wigner–Eckart theorem Eq. (2.62), the relations between general tensor operators can be reconstructed. Unit tensor operators were invented to exhibit in the most elementary way possible the abstract and intrinsic structure of the irreducible tensor operator algebra, stripping away the details of particular physical applications, thus giving the theory universal application. It accomplishes the same goal for tensor operator theory that the abstract multiplet theory in Sect. 2.2 accomplishes for representation theory.

Physical theory is regained through the concept of reduced matrix element. The coupling rule Eq. (2.54) is now transformed to a rule empty of WCG coefficient content and becomes a rule for coupling of reduced matrix elements using the invariant Racah operators:

$$\begin{aligned} &\langle (\alpha') j' \| [\mathbf{S}^{k_1} \times \mathbf{T}^{k_2}]^k \| (\alpha) j \rangle \\ &= (-1)^{k_1+k_2-k} \sum_{(\alpha'') j''} W_{j''-j, j'-j'', j-j}^{k_2 k_1 k} (j') \\ &\times \langle (\alpha') j' \| \mathbf{S}^{k_1} \| (\alpha'') j'' \rangle \langle (\alpha'') j'' \| \mathbf{T}^{k_2} \| (\alpha) j \rangle. \end{aligned} \quad (2.71)$$

This coupling rule is invariant to all $SU(2)$ rotations and reveals the true role of the Racah coefficients and reduced matrix elements in physical theory as invariant objects under $SU(2)$ rotations. It now becomes imperative to understand Racah coefficients as objects free of their original definition in terms of WCG coefficients.

2.9 Racah Coefficients

Relation Eq. (2.65) is taken, initially, as the definition of the Racah coefficient with appropriate adjustments of notations to conform to Racah's W notation and to Wigner's $6-j$ notation. Corresponding to each of Eqs. (2.63)–(2.65), (2.69), and (2.70), there is a corresponding numerical relationship between WCG coefficients and Racah coefficients. Despite the present day popularity of expressing all such relations in terms of the $3-j$ and $6-j$ notation, this temptation is resisted here for this particular set of relations because of their fundamental origins. The relation between the Racah invariant notation and Racah's original W notation is

$$\begin{aligned} W_{\rho\sigma\tau}^{abc} | jm \rangle &= W_{\rho\sigma\tau}^{abc}(j) | jm \rangle, \\ W_{\rho\sigma\tau}^{abc}(j) &= 0 \quad \text{if } \tau \neq \rho + \sigma, \quad \text{or } \epsilon_{abc} = 0, \\ W_{\rho\sigma\tau}^{abc}(j) &= [(2c+1)(2j-2\sigma+1)]^{1/2} \\ &\quad \times W(j-\tau, a, j, b; j-\sigma, c), \\ [(2e+1)(2f+1)]^{1/2} W(abcd; ef) & \\ &= W_{e-a, c-e, c-a}^{bdf}(c), \end{aligned}$$

$W(abcd; ef) = 0$ unless the triples of nonnegative integers and half-integers (abe) , (cde) , (acf) , and (bdf) satisfy the triangle conditions.

2.9.1 Basic Relations Between WCG and Racah Coefficients

$$\begin{aligned} &\sum_{\beta\delta} C_{\beta\delta\gamma}^{bdf} C_{\alpha+\beta, \delta, \alpha+\gamma}^{edc} C_{\alpha, \beta, \alpha+\beta}^{abe} \\ &= [(2e+1)(2f+1)]^{1/2} W(abcd; ef) C_{\alpha, \gamma, \alpha+\gamma}^{afc}, \\ &\sum_f [(2e+1)(2f+1)]^{1/2} W(abcd; ef) \\ &\quad \times C_{\beta, \delta, \beta+\delta}^{bdf} C_{\alpha, \beta+\delta, \alpha+\beta+\delta}^{afc} \\ &= C_{\alpha+\beta, \delta, \alpha+\beta+\delta}^{edc} C_{\alpha, \beta, \alpha+\beta}^{abe}, \\ \delta_{cc'} [(2e+1)(2f+1)]^{1/2} W(abcd; ef) & \\ &= \sum_{\beta\delta} C_{\beta, \delta, \beta+\delta}^{bdf} C_{\gamma-\delta, \delta, \gamma}^{edc} C_{\gamma-\beta-\delta, \beta, \gamma-\delta}^{abe} \\ &\quad \times C_{\gamma-\beta-\delta, \beta+\delta, \gamma}^{abc'}, \end{aligned}$$

$$\begin{aligned} &\sum_{\beta\delta e} [(2e+1)(2f+1)]^{1/2} W(abcd; ef) \\ &\quad \times C_{\beta\delta\gamma}^{bdf'} C_{\alpha+\beta, \delta, \alpha+\gamma}^{edc} C_{\alpha, \beta, \alpha+\beta}^{abe} \\ &= \delta_{ff'} C_{\alpha, \gamma, \alpha+\gamma}^{afc}, \\ &\sum_e [(2e+1)(2f+1)]^{1/2} W(abcd; ef) \\ &\quad \times C_{\alpha+\beta, \delta, \alpha+\beta+\delta}^{edc} C_{\alpha, \beta, \alpha+\beta}^{abe} \\ &= C_{\beta, \delta, \beta+\delta}^{bdf} C_{\alpha, \beta+\delta, \alpha+\beta+\delta}^{afc}. \end{aligned}$$

2.9.2 Orthogonality and Explicit Form

Orthogonality relations for Racah coefficients:

$$\begin{aligned} &\sum_e (2e+1)(2f+1) W(abcd; ef) W(abcd; ef') \\ &= \delta_{ff'} \epsilon_{acf} \epsilon_{bdf}, \end{aligned} \quad (2.72)$$

$$\begin{aligned} &\sum_f (2e+1)(2f+1) W(abcd; ef) W(abcd; e'f) \\ &= \delta_{ee'} \epsilon_{abe} \epsilon_{cde}. \end{aligned} \quad (2.73)$$

Definition of $6-j$ coefficients:

$$\left\{ \begin{matrix} a & b & e \\ d & c & f \end{matrix} \right\} = (-1)^{a+b+c+d} W(abcd; ef). \quad (2.74)$$

Orthogonality of $6-j$ coefficients:

$$\begin{aligned} &\sum_e (2e+1)(2f+1) \left\{ \begin{matrix} a & b & e \\ d & c & f \end{matrix} \right\} \left\{ \begin{matrix} a & b & e \\ d & c & f' \end{matrix} \right\} \\ &= \delta_{ff'} \epsilon_{acf} \epsilon_{bdf}, \end{aligned} \quad (2.75)$$

$$\begin{aligned} &\sum_f [(2e+1)(2f+1)] \left\{ \begin{matrix} a & b & e \\ d & c & f \end{matrix} \right\} \left\{ \begin{matrix} a & b & e' \\ d & c & f \end{matrix} \right\} \\ &= \delta_{ee'} \epsilon_{abe} \epsilon_{cde}. \end{aligned} \quad (2.76)$$

Explicit form of Racah coefficients:

$$\begin{aligned} W(abcd; ef) &= \Delta(abe) \Delta(cde) \Delta(acf) \Delta(bdf) \\ &\quad \times \sum_k \frac{(-1)^{a+b+c+d+k} (k+1)!}{(k-a-b-e)!(k-c-d-e)!} \\ &\quad \times \frac{1}{(k-a-c-f)!(k-b-d-f)!} \\ &\quad \times \frac{1}{(a+b+c+d-k)!} \\ &\quad \times \frac{1}{(a+d+e+f-k)!(b+c+e+f-k)!}, \end{aligned} \quad (2.77)$$

where $\Delta(abc)$ denotes the triangle coefficient, defined for every triple a, b, c of integers and half-odd integers satisfying the triangle conditions by:

$$\Delta(abc) = \left(\frac{(a+b-c)!(a-b+c)!(-a+b+c)!}{(a+b+c+1)!} \right)^{\frac{1}{2}}. \quad (2.78)$$

2.9.3 The Fundamental Identities Between Racah Coefficients

Each of the three relations given in this section is between Racah coefficients alone. Each expresses a fundamental mathematical property. The Biedenharn–Elliott identity is a consequence of the associativity rule for the open product of three irreducible tensor operators; the Racah sum rule is a consequence of the commutativity of a mapping diagram associated with the coupling of three angular momenta; and the triangle coupling rule is a consequence of the associativity of the open product of three symplection polynomials [1]. As such, these three relations between Racah coefficients, together with the orthogonality relations, are the building blocks on which is constructed a theory of these coefficients that stands on its own, independent of the WCG coefficient origins. Indeed, the latter is recovered through the limit relation Eq. (2.50).

Biedenharn–Elliott identity:

$$W(a'ab'b; c'e)W(a'ed'd; b'c) = \sum_f (2f+1)W(abcd; ef)W(c'bd'd; b'f) \times W(a'ad'f; c'c), \quad (2.79a)$$

$$\begin{aligned} & \begin{Bmatrix} a' & a & c' \\ b & b' & e \end{Bmatrix} \begin{Bmatrix} a' & e & b' \\ d & d' & c \end{Bmatrix} \\ &= \sum_f (-1)^\phi (2f+1) \begin{Bmatrix} a & b & e \\ d & c & f \end{Bmatrix} \begin{Bmatrix} c' & b & b' \\ d & d' & f \end{Bmatrix} \\ & \times \begin{Bmatrix} a' & a & c' \\ f & d' & c \end{Bmatrix}, \\ & \phi = f - e + a' + a + b' + b + c' - c + d' - d. \end{aligned} \quad (2.79b)$$

Racah sum rule:

$$\begin{aligned} & \sum_f (-1)^{b+d-f} (2f+1)W(abcd; ef)W(adcb; gf) \\ &= (-1)^{e+g-a-c} W(bacd; eg), \end{aligned} \quad (2.80a)$$

$$\begin{aligned} & \sum_f (-1)^{e+g+f} (2f+1) \begin{Bmatrix} a & b & e \\ d & c & f \end{Bmatrix} \begin{Bmatrix} a & d & g \\ b & c & f \end{Bmatrix} \\ &= \begin{Bmatrix} b & a & e \\ d & c & g \end{Bmatrix}. \end{aligned} \quad (2.80b)$$

Triangle sum rule:

$$\begin{aligned} & [\Delta(acf)\Delta(bdf)]^{-1} \\ &= (2f+1) \sum_e [\Delta(abe)\Delta(cde)]^{-1} W(abcd; ef), \end{aligned} \quad (2.81a)$$

$$\begin{aligned} & (-1)^{a+b+c+d} [\Delta(acf)\Delta(bdf)]^{-1} \\ &= (2f+1) \sum_e [\Delta(abe)\Delta(cde)]^{-1} \begin{Bmatrix} a b e \\ d c f \end{Bmatrix}. \end{aligned} \quad (2.81b)$$

2.9.4 Schwinger–Bargmann Generating Function and Its Combinatorics

Triangles associated with the 6- j symbol $\begin{Bmatrix} j_1 & j_2 & j_3 \\ j_4 & j_5 & j_6 \end{Bmatrix}$:

$$(j_1 j_2 j_3), \quad (j_3 j_4 j_5), \quad (j_1 j_5 j_6), \quad (j_2 j_4 j_6).$$

Points in \mathbf{R}^3 associated with the triangles:

$$\begin{aligned} & (j_1 j_2 j_3) \rightarrow (x_1, x_2, x_3), \quad (j_3 j_4 j_5) \rightarrow (y_3, x_4, x_5), \\ & (j_1 j_5 j_6) \rightarrow (y_1, y_5, x_6), \quad (j_2 j_4 j_6) \rightarrow (y_2, y_4, y_6). \end{aligned}$$

Tetrahedron associated with the points:

The points define the vertices of a general tetrahedron with lines joining each pair of points that share a common subscript, and the lines are labeled by the product of the common coordinates (Fig. 2.2).

Monomial term:

Define the triangle monomial associated with a triangle $(j_a j_b j_c)$ and its associated point (z_a, z_b, z_c) in \mathbf{R}^3 by

$$(z_a, z_b, z_c)^{(j_a j_b j_c)} = z_a^{j_b+j_c-j_a} z_b^{j_c+j_a-j_b} z_c^{j_a+j_b-j_c}. \quad (2.82)$$

Cubic graph (tetrahedral T_4) functions.

Interchange the symbols x and y in the coordinates of the vertices of the tetrahedron and define the following polynomials on the vertices and edges of the tetrahedron with this modified labeling.

Vertex function: multiply together the coordinates of each vertex and sum over all such vertices to obtain

$$V_3 = y_1 y_2 y_3 + x_3 y_4 y_5 + x_1 x_5 y_6 + x_2 x_4 x_6;$$

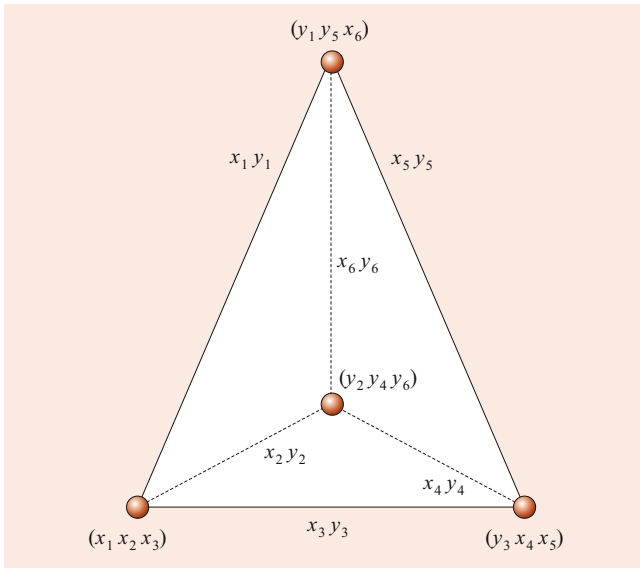


Fig. 2.2 Labeled cubic graph (tetrahedron) associated with $6-j$ coefficients

Edge function: multiply together the coordinates of a given edge and the opposite edge and sum over all such pairs to obtain

$$E_4 = x_1 y_1 x_4 y_4 + x_2 y_2 x_5 y_5 + x_3 y_3 x_6 y_6 .$$

Generating function:

$$(1 + V_3 + E_4)^{-2} = \sum_{\Delta} T(\Delta) Z^{\Delta} , \quad (2.83a)$$

$$Z^{\Delta} = (x_1, x_2, x_3)^{(j_1 j_2 j_3)} (y_3, x_4, x_5)^{(j_3 j_4 j_5)} \\ \times (y_1, y_5, x_6)^{(j_1 j_5 j_6)} (y_2, y_4, y_6)^{(j_2 j_4 j_6)} , \quad (2.83b)$$

$$\Delta = \begin{bmatrix} (j_1 j_2 j_3) \\ (j_3 j_4 j_5) \\ (j_1 j_5 j_6) \\ (j_2 j_4 j_6) \end{bmatrix} ;$$

$$T(\Delta) = \sum_k (-1)^k (k+1) \\ \times \binom{k}{k_1, k_2, k_3, k_4, k_5, k_6, k_7} , \quad (2.83c)$$

$$k_i = k - t_i , \quad i = 1, 2, 3, 4 , \\ k_j = e_j - k , \quad j = 5, 6, 7 ; \\ t_i = \text{triangle sum} = \text{vertex sum}, \\ e_j = \text{opposite edge sum, in pairs}, \\ t_1 = j_1 + j_2 + j_3 , \quad t_2 = j_3 + j_4 + j_5 , \\ t_3 = j_1 + j_5 + j_6 , \quad t_4 = j_2 + j_4 + j_6 ,$$

$$e_1 = (j_2 + j_5) + (j_3 + j_6) , \\ e_2 = (j_1 + j_4) + (j_3 + j_6) , \\ e_3 = (j_1 + j_4) + (j_2 + j_5) .$$

The summation in Eq. (2.83b) is over the infinite set of all tetrahedra, that is, over the infinite set of arrays Δ having nonnegative integral entries. The $6-j$ coefficient is then given by

$$\begin{Bmatrix} j_1 & j_2 & j_3 \\ j_4 & j_5 & j_6 \end{Bmatrix} = \frac{T(\Delta)}{\Delta(j_1 j_2 j_3) \Delta(j_1 j_5 j_6) \Delta(j_2 j_4 j_6) \Delta(j_3 j_4 j_5)} .$$

Since the factor $T(\Delta)$ is an integer in the expansion Eq. (2.83a), this result shows that the $6-j$ coefficient is an integer, up to the multiplicative triangle coefficient factors.

2.9.5 Symmetries of $6-j$ Coefficients

There are 144 symmetry relations among the Racah $6-j$ coefficients. The 24 classical ones, given already by Racah and corresponding to the tetrahedral point group T_d of rotations-inversions (isomorphic to the symmetric group S_4) mapping the regular tetrahedron onto itself, are realized in the $6-j$ symbol

$$\begin{Bmatrix} a & b & e \\ d & c & f \end{Bmatrix}$$

as permutations of its columns and the exchange of any pair of letters in the top row with the corresponding pair in the bottom row. *Regge* discovered the sixfold increase in symmetry by noting that each term in the summation in Eq. (2.77) is invariant not only to the classical 24 symmetries but also under certain linear transformations of the quantum labels. These symmetries are also implicit in Schwinger's generating function.

The full set, including the original 24 substitutions, of linear transformations of the letters a, b, c, d, e, f thus yields a group of linear transformations isomorphic to $S_4 \times S_3$. The column permutations and row-pair interchanges described above applied to each of the 6 symbols in the equalities below yield the set of 144 relationships:

$$\begin{Bmatrix} a & b & e \\ d & c & f \end{Bmatrix} \\ = \begin{Bmatrix} a & \frac{b+c+e-f}{2} & \frac{b+e+f-c}{2} \\ d & \frac{b+c+f-e}{2} & \frac{c+e+f-b}{2} \end{Bmatrix} \\ = \begin{Bmatrix} \frac{a+d+e-f}{2} & b & \frac{a+e+f-d}{2} \\ \frac{a+d+f-e}{2} & c & \frac{d+e+f-a}{2} \end{Bmatrix}$$

$$\begin{aligned}
&= \left\{ \frac{a+b+d-c}{2} \quad \frac{a+b+c-d}{2} \quad e \right\} \\
&= \left\{ \frac{a+b+d-c}{2} \quad \frac{b+c+e-f}{2} \quad \frac{a+e+f-d}{2} \right\} \\
&= \left\{ \frac{a+d+e-f}{2} \quad \frac{a+b+c-d}{2} \quad \frac{b+e+f-c}{2} \right\} \\
&= \left\{ \frac{a+d+f-e}{2} \quad \frac{b+c+d-a}{2} \quad \frac{c+e+f-b}{2} \right\}.
\end{aligned}$$

2.9.6 Further Properties

Recurrence relations:

Three-term:

$$\begin{aligned}
&[(a+b+e+1)(b+e-a) \\
&\quad \times (c+d+e+1)(d+e-c)]^{1/2} \left\{ \begin{matrix} a & b & e \\ d & c & f \end{matrix} \right\} \\
&= -2e[(b+d+f+1)(b+d-f)]^{1/2} \\
&\quad \times \left\{ \begin{matrix} a & b-\frac{1}{2} & e-\frac{1}{2} \\ d-\frac{1}{2} & c & f \end{matrix} \right\} \\
&\quad + [(a+b-e+1)(a+e-b)(c+d-e+1) \\
&\quad \times (c+e-d)]^{1/2} \left\{ \begin{matrix} a & b & e-1 \\ d & c & f \end{matrix} \right\}, \quad (2.84a)
\end{aligned}$$

$$\begin{aligned}
&[(a+c+f+1)(c+e-d) \\
&\quad \times (d+e-c+1)(b+d-f+1)]^{1/2} \left\{ \begin{matrix} a & b & e \\ d & c & f \end{matrix} \right\} \\
&= [(a+c-f)(a+e-b) \\
&\quad \times (b+f+d+2)(b+e-a+1)]^{1/2} \\
&\quad \times \left\{ \begin{matrix} a+\frac{1}{2} & b+\frac{1}{2} & e \\ d+\frac{1}{2} & c-\frac{1}{2} & f \end{matrix} \right\} \\
&\quad + [(c+f-a)(c+e-d)(b-a-c+d+1)]^{1/2} \\
&\quad \times \left\{ \begin{matrix} a & b & e \\ d+\frac{1}{2} & c-\frac{1}{2} & f-\frac{1}{2} \end{matrix} \right\}. \quad (2.84b)
\end{aligned}$$

Five-term:

$$\begin{aligned}
&(2c+1)(2d)(2f+1) \left\{ \begin{matrix} a & b & e \\ d & c & f \end{matrix} \right\} \\
&= [(b+d-f)(b+f-d+1)(d+e-c) \\
&\quad \times (c+e-d+1)(c+f-a+1)(a+c+f+2)]^{1/2}
\end{aligned}$$

$$\begin{aligned}
&\times \left\{ \begin{matrix} a & b & e \\ d-\frac{1}{2} & c+\frac{1}{2} & f+\frac{1}{2} \end{matrix} \right\} + [(b+d-f) \\
&\quad \times (b+f-d+1)(c+d-e)(c+d+e+1) \\
&\quad \times (a+c-f)(a+f-c+1)]^{1/2} \\
&\times \left\{ \begin{matrix} a & b & e \\ d-\frac{1}{2} & c-\frac{1}{2} & f+\frac{1}{2} \end{matrix} \right\} - [(d+f-b) \\
&\quad \times (b+d+f+1)(c+d-e)(c+d+e+1) \\
&\quad \times (c+f-a)(a+c+f+1)]^{1/2} \\
&\times \left\{ \begin{matrix} a & b & e \\ d-\frac{1}{2} & c-\frac{1}{2} & f-\frac{1}{2} \end{matrix} \right\} + [(d+f-b) \\
&\quad \times (b+d+f+1)(d+e-c)(c+e-d+1) \\
&\quad \times (a+f-c)(a+c-f+1)]^{1/2} \\
&\times \left\{ \begin{matrix} a & b & e \\ d-\frac{1}{2} & c+\frac{1}{2} & f-\frac{1}{2} \end{matrix} \right\}. \quad (2.84c)
\end{aligned}$$

Relation to hypergeometric series:

$$\begin{aligned}
\left\{ \begin{matrix} a & b & e \\ d & c & f \end{matrix} \right\} &= (-1)^{a+b+c+d} W(abcd; ef) \\
&= \Delta(abe)\Delta(cde)\Delta(acf)\Delta(bdf) \\
&\quad \times \frac{(-1)^{\beta_1}(\beta_1+1)!}{(\beta_2-\beta_1)!(\beta_3-\beta_1)!} \\
&\quad \times \frac{{}_4F_3\left(\begin{matrix} \alpha_1-\beta_1, & \alpha_2-\beta_1, & \alpha_3-\beta_1, & \alpha_4-\beta_1 \\ -\beta_1-1, & \beta_2-\beta_1+1, & \beta_3-\beta_1+1, & \end{matrix}; 1\right)}{(\beta_1-\alpha_1)!(\beta_1-\alpha_2)!(\beta_1-\alpha_3)!(\beta_1-\alpha_4)!}, \\
\beta_1 &= \min(a+b+c+d, a+d+e+f, b+c+e+f).
\end{aligned}$$

The parameters β_2 and β_3 are identified in either way with the pair remaining in the 3-tuple

$$(a+b+c+d, a+d+e+f, b+c+e+f)$$

after deleting β_1 . The $(\alpha_1, \alpha_2, \alpha_3, \alpha_4)$ may be identified with any permutation of the 4-tuple

$$(a+b+e, c+d+e, a+c+f, b+d+f).$$

The ${}_4F_3$ series is Saalschützian:

$$\begin{aligned}
&1 + \sum (\text{numerator parameters}) \\
&= \sum (\text{denominator parameters}).
\end{aligned}$$

2.10 The 9- j Coefficients

2.10.1 Hilbert Space and Tensor Operator Actions

Let $T^a(1)$ and $T^b(2)$ denote irreducible tensor operators of ranks a and b with respect to kinematically independent angular momentum operators $\mathbf{J}(1)$ and $\mathbf{J}(2)$ that act, respectively, in separable Hilbert spaces $\mathcal{H}(1)$ and $\mathcal{H}(2)$. Let $\mathcal{H}(1)$ and $\mathcal{H}(2)$ be reduced, respectively, into a direct sum of spaces $\mathcal{H}_{j_1}(1)$ and $\mathcal{H}_{j_2}(2)$. The angular momentum $\mathbf{J}(1)$ has the standard action on the orthonormal basis $\{|j_1 m_1\rangle \mid m_1 = j_1, j_1 - 1, \dots, -j_1\}$ of $\mathcal{H}_{j_1}(1)$, and $\mathbf{J}(2)$ has the standard action on the orthonormal basis $\{|j_2 m_2\rangle \mid m_2 = j_2, j_2 - 1, \dots, -j_2\}$ of $\mathcal{H}_{j_2}(2)$. The irreducible tensor operators $T^a(1)$ and $T^b(2)$ also have the standard actions in their respective Hilbert spaces $\mathcal{H}(1)$ and $\mathcal{H}(2)$, as given by the Wigner–Eckart theorem. The total angular momentum \mathbf{J} has the standard action on the coupled orthonormal basis of the tensor product space $\mathcal{H}_{j_1} \otimes \mathcal{H}_{j_2}$:

$$|(j_1 j_2) j m\rangle = \sum_{m_1 m_2} C_{m_1 m_2 m}^{j_1 j_2 j} |j_1 m_1\rangle \otimes |j_2 m_2\rangle. \quad (2.85)$$

The tensor product operator $T^a(1) \otimes T^b(2)$ acts in the tensor product space $\mathcal{H}(1) \otimes \mathcal{H}(2)$ according to the rule:

$$\begin{aligned} (T^a(1) \otimes T^b(2))(|j_1 m_1\rangle \otimes |j_2 m_2\rangle) \\ = T^a(1)|j_1 m_1\rangle \otimes T^b(2)|j_2 m_2\rangle, \end{aligned}$$

so that

$$\begin{aligned} (T^a(1) \otimes T^b(2))|(j_1 j_2) j m\rangle \\ = \sum_{m_1 m_2} C_{m_1 m_2 m}^{j_1 j_2 j} T^a(1)|j_1 m_1\rangle \otimes T^b(2)|j_2 m_2\rangle. \end{aligned} \quad (2.86a)$$

The angular momentum quantities called 9- j coefficients arise when the coupled tensor operators $T^{(ab)c}$ with components γ defined by

$$\begin{aligned} T_{\gamma}^{(ab)c} &= \sum_{\alpha\beta} C_{\alpha\beta\gamma}^{abc} T_{\alpha}^a(1) \otimes T_{\beta}^b(2), \\ \gamma &= c, c-1, \dots, -c, \end{aligned} \quad (2.86b)$$

are considered. The quantity $T^{(ab)c}$ is an irreducible tensor operator of rank c with respect to the total angular momentum \mathbf{J} for all a, b that yield c under the rule of addition of angular momentum.

2.10.2 9- j Invariant Operators

The entire angular momentum content of relation Eq. (2.86b) is captured by taking the irreducible tensor operators $T^a(1)$

and $T^b(2)$ to be unit tensor operators acting in the respective spaces $\mathcal{H}(1)$ and $\mathcal{H}(2)$:

$$\begin{aligned} T_{(\rho\sigma)\gamma}^{(ab)c} \\ = \sum_{\alpha\beta} C_{\alpha\beta\gamma}^{abc} \left\langle \begin{array}{ccc} 2a & \alpha + \rho & 0 \\ & a + \alpha & \end{array} \right\rangle_1 \otimes \left\langle \begin{array}{ccc} 2b & b + \sigma & 0 \\ & b + \beta & \end{array} \right\rangle_2. \end{aligned} \quad (2.87)$$

The placement of the unit tensor operators shows in which space they act, so that the additional identification by indices 1 and 2 could be eliminated. For each given $c \in \{0, 1/2, 1, 3/2, 2, \dots\}$ and all a, b such that the triangle relation (abc) is satisfied, and, for each such pair a, b , all ρ, σ with $\rho \in \{a, a-1, \dots, -a\}$, $\sigma \in \{b, b-1, \dots, -b\}$, an irreducible tensor operator of rank c with respect to the total angular momentum \mathbf{J} with components γ is defined by Eq. (2.87). By the Wigner–Eckart theorem, it must be possible to write

$$\begin{aligned} \sum_{\alpha\beta} C_{\alpha\beta\gamma}^{abc} \left\langle \begin{array}{ccc} 2a & \alpha + \rho & 0 \\ & a + \alpha & \end{array} \right\rangle_1 \otimes \left\langle \begin{array}{ccc} 2b & b + \sigma & 0 \\ & b + \beta & \end{array} \right\rangle_2 \\ = \sum_{\tau} \left[\begin{array}{ccc} abc \\ \rho\sigma\tau \end{array} \right] \left\langle \begin{array}{ccc} c + \tau & & \\ 2c & & 0 \\ c + \gamma & & \end{array} \right\rangle. \end{aligned} \quad (2.88)$$

Where (i) the unit tensor operator on the right-hand side is a irreducible tensor operator with respect to \mathbf{J} ; that is, it has the action on the coupled states given by

$$\begin{aligned} \left\langle \begin{array}{ccc} c + \tau & & \\ 2c & & 0 \\ c + \gamma & & \end{array} \right\rangle |(j_1 j_2) j m\rangle \\ = C_{m, \gamma, m+\gamma}^{j, c, j+\tau} |(j_1 j_2) j + \tau, m + \gamma\rangle; \end{aligned} \quad (2.89)$$

and (ii) the symbol $\left[\begin{array}{ccc} abc \\ \rho\sigma\tau \end{array} \right]$ denotes an invariant operator with respect to the total angular momentum \mathbf{J} . Using the orthogonality of unit tensor operators, we can also write relation Eq. (2.88) in the form:

$$\begin{aligned} \left[\begin{array}{ccc} abc \\ \rho\sigma\tau \end{array} \right] &= \sum_{\alpha\beta\gamma} C_{\alpha\beta\gamma}^{abc} \left\langle \begin{array}{ccc} a + \rho & & \\ 2a & & 0 \\ a + \alpha & & \end{array} \right\rangle_1 \\ &\otimes \left\langle \begin{array}{ccc} b + \sigma & & \\ 2b & & 0 \\ b + \beta & & \end{array} \right\rangle_2 \left\langle \begin{array}{ccc} c + \tau & & \\ 2c & & 0 \\ c + \gamma & & \end{array} \right\rangle^{\dagger}. \end{aligned} \quad (2.90)$$

This form is taken as the definition of the 9- j invariant operator. Its eigenvalues in the coupled basis define the 9- j

coefficient:

$$\begin{aligned}
 & \begin{bmatrix} abc \\ \rho\sigma\tau \end{bmatrix} |(j_1 j_2) j m\rangle \\
 &= \langle (j_1 + \rho, j_2 + \sigma) j + \tau | \begin{bmatrix} abc \\ \rho\sigma\tau \end{bmatrix} |(j_1 j_2) j\rangle \\
 & \quad \times |(j_1 j_2) j m\rangle \\
 &= [(2j + 1)(2c + 1)(2j_1 + 2\rho + 1)(2j_2 + 2\sigma + 1)]^{\frac{1}{2}} \\
 & \quad \times \begin{Bmatrix} j_1 & j_2 & j \\ a & b & c \\ j_1 + \rho & j_2 + \sigma & j + \tau \end{Bmatrix} |(j_1 j_2) j m\rangle. \quad (2.91)
 \end{aligned}$$

The 9- j invariant operators play exactly the same role in the tensor product space of two irreducible angular momentum spaces as do the Racah invariants in one such irreducible angular momentum space.

The full content of the coupling law Eq. (2.86b) for physical irreducible tensor operators is regained in the coupling law for reduced matrix elements:

$$\begin{aligned}
 & \langle (\alpha'_1 \alpha'_2 j'_1 j'_2) j' | [T^a(1) \times T^b(2)]^c | (\alpha_1 \alpha_2 j_1 j_2) j \rangle \\
 &= \begin{bmatrix} j_1 & j_2 & j \\ a & b & c \\ j'_1 & j'_2 & j' \end{bmatrix} \langle (\alpha'_1) j'_1 | T^a(1) | (\alpha_1) j_1 \rangle \\
 & \quad \times \langle (\alpha'_2) j'_2 | T^b(2) | (\alpha_2) j_2 \rangle; \quad (2.92a)
 \end{aligned}$$

$$\begin{aligned}
 & \begin{bmatrix} j_1 & j_2 & j \\ a & b & c \\ j'_1 & j'_2 & j' \end{bmatrix} \\
 &= [(2j'_1 + 1)(2j'_2 + 1)(2j + 1)(2c + 1)]^{\frac{1}{2}} \\
 & \quad \times \begin{Bmatrix} j_1 & j_2 & j \\ a & b & c \\ j'_1 & j'_2 & j' \end{Bmatrix}. \quad (2.92b)
 \end{aligned}$$

2.10.3 Basic Relations Between 9- j Coefficients and 6- j Coefficients

Orthogonality of 9- j coefficients:

$$\begin{aligned}
 & \sum_{hi} (2c + 1)(2f + 1)(2h + 1)(2i + 1) \\
 & \quad \times \begin{Bmatrix} a & b & c \\ d & e & f \\ h & i & j \end{Bmatrix} \begin{Bmatrix} a & b & c' \\ d & e & f' \\ h & i & j \end{Bmatrix} = \delta_{cc'} \delta_{ff'},
 \end{aligned}$$

where this relation is to be applied only to triples (abc) , (def) , (cfj) , (abc') , (def') , $(c'f'j)$ for which the triangle conditions hold.

9- j coefficients in terms of 3- j coefficients:

$$\begin{aligned}
 & \delta_{j_3 j'_3} (2j_3 + 1)^{-1} \begin{Bmatrix} j_{11} & j_{12} & j_{13} \\ j_{21} & j_{22} & j_{23} \\ j_{31} & j_{32} & j_{33} \end{Bmatrix} \\
 &= \sum_{\substack{\text{all } m_{ij} \\ \text{except } m_{33}}} \begin{Bmatrix} j_{11} & j_{12} & j_{13} \\ m_{11} & m_{12} & m_{13} \end{Bmatrix} \begin{Bmatrix} j_{21} & j_{22} & j_{23} \\ m_{21} & m_{22} & m_{23} \end{Bmatrix} \\
 & \quad \times \begin{Bmatrix} j_{31} & j_{32} & j_{33} \\ m_{31} & m_{32} & m_{33} \end{Bmatrix} \begin{Bmatrix} j_{11} & j_{21} & j_{31} \\ m_{11} & m_{21} & m_{31} \end{Bmatrix} \\
 & \quad \times \begin{Bmatrix} j_{12} & j_{22} & j_{32} \\ m_{12} & m_{22} & m_{32} \end{Bmatrix} \begin{Bmatrix} j_{13} & j_{23} & j'_{33} \\ m_{13} & m_{23} & m_{33} \end{Bmatrix}. \quad (2.93)
 \end{aligned}$$

9- j coefficients in terms of 6- j coefficients:

$$\begin{aligned}
 & \begin{Bmatrix} j_{11} & j_{12} & j_{13} \\ j_{21} & j_{22} & j_{23} \\ j_{31} & j_{32} & j_{33} \end{Bmatrix} = \sum_k (-1)^{2k} (2k + 1) \\
 & \quad \times \begin{Bmatrix} j_{11} & j_{21} & j_{31} \\ j_{32} & j_{33} & k \end{Bmatrix} \begin{Bmatrix} j_{12} & j_{22} & j_{32} \\ j_{21} & k & j_{23} \end{Bmatrix} \\
 & \quad \times \begin{Bmatrix} j_{13} & j_{23} & j_{33} \\ k & j_{11} & j_{12} \end{Bmatrix}. \quad (2.94)
 \end{aligned}$$

Basic defining relation for 9- j coefficient from Eq. (2.88):

$$\begin{aligned}
 & (-1)^\phi \begin{Bmatrix} j_{12} & j_{22} & j_{32} \\ j_{11} & j_{21} & j_{31} \\ j_{13} & j_{23} & j_{33} \end{Bmatrix} \begin{Bmatrix} j_{31} & j_{32} & j_{33} \\ m_{31} & m_{32} & m_{33} \end{Bmatrix} \\
 &= \sum_{\text{all } m_{(1i)m_{(2i)}}} \begin{Bmatrix} j_{11} & j_{21} & j_{31} \\ m_{11} & m_{21} & m_{31} \end{Bmatrix} \\
 & \quad \times \begin{Bmatrix} j_{12} & j_{22} & j_{32} \\ m_{12} & m_{22} & m_{32} \end{Bmatrix} \begin{Bmatrix} j_{13} & j_{23} & j_{33} \\ m_{13} & m_{23} & m_{33} \end{Bmatrix} \\
 & \quad \times \begin{Bmatrix} j_{11} & j_{12} & j_{13} \\ m_{11} & m_{12} & m_{13} \end{Bmatrix} \begin{Bmatrix} j_{21} & j_{22} & j_{23} \\ m_{21} & m_{22} & m_{23} \end{Bmatrix}, \\
 & \phi = \sum_{kl} j_{kl}. \quad (2.95)
 \end{aligned}$$

Additional relations:

$$\begin{aligned}
 & \sum_{kl} (-1)^{2b+l+h-f} (2k + 1)(2l + 1) \\
 & \quad \times \begin{Bmatrix} a & b & c \\ e & d & f \\ k & l & i \end{Bmatrix} \begin{Bmatrix} a & e & k \\ d & b & l \\ g & h & i \end{Bmatrix} = \begin{Bmatrix} a & b & c \\ d & e & f \\ g & h & i \end{Bmatrix},
 \end{aligned}$$

$$\begin{aligned}
& \sum_c (2c+1) \begin{Bmatrix} a & b & c \\ d & e & f \\ g & h & i \end{Bmatrix} \begin{Bmatrix} a & b & c \\ f & i & j \end{Bmatrix} \\
&= (-1)^{2j} \begin{Bmatrix} d & e & f \\ b & j & h \end{Bmatrix} \begin{Bmatrix} g & h & i \\ j & a & d \end{Bmatrix}, \\
& \sum_{klm} (2k+1)(2l+1)(2m+1) \\
& \quad \times \begin{Bmatrix} a & b & c \\ d & e & f \\ k & l & m \end{Bmatrix} \begin{Bmatrix} k & l & m \\ a' & b' & c' \\ d' & e' & f' \end{Bmatrix} \\
& \quad \times \begin{Bmatrix} a & d & k \\ a' & d' & k' \end{Bmatrix} \begin{Bmatrix} b & e & l \\ b' & e' & l' \end{Bmatrix} \begin{Bmatrix} c & f & m \\ c' & f' & m' \end{Bmatrix} \\
&= \begin{Bmatrix} a & b & c \\ d' & e' & f' \\ k' & l' & m' \end{Bmatrix} \begin{Bmatrix} k' & l' & m' \\ a' & b' & c' \\ d & e & f \end{Bmatrix}.
\end{aligned}$$

2.10.4 Symmetry Relations for 9- j Coefficients and Reduction to 6- j Coefficients

The 9- j coefficient

$$\begin{Bmatrix} j_{11} & j_{12} & j_{13} \\ j_{21} & j_{22} & j_{23} \\ j_{31} & j_{32} & j_{33} \end{Bmatrix}$$

is invariant under even permutation of its rows, even permutation of its columns, and under the interchange of rows and columns (matrix transposition). It is multiplied by the factor $(-1)^\phi$ Eq. (2.95) under odd permutations of its rows or columns. These 72 symmetries are all consequences of the 72 symmetries of the 3- j coefficient in relation Eq. (2.93).

Reduction to 6- j coefficients:

$$\begin{aligned}
\begin{Bmatrix} a & b & e \\ c & d & e \\ f & f & 0 \end{Bmatrix} &= \begin{Bmatrix} 0 & e & e \\ f & d & b \\ f & c & a \end{Bmatrix} = \begin{Bmatrix} e & 0 & e \\ c & f & a \\ d & f & b \end{Bmatrix} \\
&= \begin{Bmatrix} f & f & 0 \\ d & c & e \\ b & a & e \end{Bmatrix} = \begin{Bmatrix} f & b & d \\ 0 & e & e \\ f & a & c \end{Bmatrix} = \begin{Bmatrix} a & f & c \\ e & 0 & e \\ b & f & d \end{Bmatrix} \\
&= \begin{Bmatrix} b & a & e \\ f & f & 0 \\ d & c & e \end{Bmatrix} = \begin{Bmatrix} e & d & c \\ e & b & a \\ 0 & f & f \end{Bmatrix} = \begin{Bmatrix} c & e & d \\ a & e & b \\ f & 0 & f \end{Bmatrix} \\
&= \frac{(-1)^{b+c+e+f}}{[(2e+1)(2f+1)]^{\frac{1}{2}}} \begin{Bmatrix} a b e \\ d c f \end{Bmatrix}.
\end{aligned}$$

2.10.5 Explicit Algebraic Form of 9- j Coefficients

$$\begin{aligned}
\begin{Bmatrix} a & b & c \\ d & e & f \\ h & i & j \end{Bmatrix} &= (1)^{c+f-j} \frac{(dah)(bei)(jhi)}{(def)(bac)(jcf)} \\
&\times \sum_{xyz} \frac{(-1)^{x+y+z}}{x!y!z!} \\
&\times \frac{(2f-x)!(2a-z)!}{(2i+1+y)!(a+d+h+1-z)!} \\
&\times \frac{(d+e-f+x)!(c+j-f+x)!}{(e+f-d-x)!(c+f-j-x)!} \\
&\times \frac{(e+i-b+y)!(h+i-j+y)!}{(b+e-i-y)!(h+j-i-y)!} \\
&\times \frac{(b+c-a+z)!}{(a+d-h-z)!(a+c-b-z)!} \\
&\times \frac{(a+d+j-i-y-z)!}{(d+i-b-f+x+y)!(b+j-a-f+x+z)!}, \\
(abc) &= \left(\frac{(a-b+c)!(a+b-c)!(a+b+c+1)!}{(b+c-a)!} \right)^{\frac{1}{2}}.
\end{aligned}$$

2.10.6 Racah Operators

A Racah operator is denoted

$$\begin{Bmatrix} a + \rho & & \\ 2a & & 0 \\ & a + \sigma & \end{Bmatrix} \quad \rho, \sigma = a, a-1, \dots, -a, \\
2a = 0, 1, 2, \dots$$

and is a special case of the operator defined by Eq. (2.87):

$$\begin{aligned}
& \begin{Bmatrix} a + \rho & & \\ 2a & & 0 \\ & a + \sigma & \end{Bmatrix} |(j_1 j_2) j m\rangle \\
&= \left(\frac{(2a+1)(2j_2+1)}{(2j_2+2\sigma+1)} \right)^{\frac{1}{2}} \mathbf{T}_{(\rho\sigma)0}^{(aa)0} |(j_1 j_2) j m\rangle. \quad (2.96)
\end{aligned}$$

Thus, a Racah operator is an invariant operator with respect to the total angular momentum \mathbf{J} . Alternative definitions are:

$$\begin{aligned}
& \begin{Bmatrix} a + \rho & & \\ 2a & & 0 \\ & a + \sigma & \end{Bmatrix} \\
&= (-1)^{a+\sigma} \sum_a \begin{Bmatrix} a + \rho & & \\ 2a & & 0 \\ & a + \alpha & \end{Bmatrix} \otimes \begin{Bmatrix} a - \sigma & & \\ 2a & & 0 \\ & a + \alpha & \end{Bmatrix}^\dagger,
\end{aligned}$$

$$\left\{ \begin{array}{ccc} a + \rho & & \\ 2a & & 0 \\ & a + \sigma & \end{array} \right\} |(j_1 j_2) j m\rangle$$

$$= [(2j_1 + 2\rho + 1)(2j_2 + 1)]^{\frac{1}{2}}$$

$$\times W(j, j_1, j_2 + \sigma, a; j_2, j_1 + \rho)$$

$$\times |(j_1 + \rho, j_2 + \sigma) j m\rangle,$$

with conjugate

$$\left\{ \begin{array}{ccc} a + \rho & & \\ 2a & & 0 \\ & a + \sigma & \end{array} \right\}^\dagger |(j_1 j_2) j m\rangle$$

$$= [(2j_1 + 1)(2j_2 - 2\sigma + 1)]^{\frac{1}{2}}$$

$$\times W(j, j_1 - \rho, j_2, a; j_2 - \sigma, j_1)$$

$$\times |(j_1 - \rho, j_2 - \sigma) j m\rangle.$$

Racah operators satisfy orthogonality relations similar in form to Wigner operators. The open product rule is:

$$\left\{ \begin{array}{ccc} b + \sigma & & \\ 2b & & 0 \\ & b + \beta & \end{array} \right\} \left\{ \begin{array}{ccc} a + \rho & & \\ 2a & & 0 \\ & a + \alpha & \end{array} \right\}$$

$$= \sum_c \overline{W}_{\rho, \sigma, \rho + \sigma}^{abc} W_{\alpha, \beta, \alpha + \beta}^{abc} \left\{ \begin{array}{ccc} c + \rho + \sigma & & \\ 2c & & 0 \\ & c + \alpha + \beta & \end{array} \right\}. \quad (2.97)$$

In this result, $\overline{W}_{\rho\sigma\tau}^{abc}$ and $W_{\alpha, \beta, \alpha + \beta}^{abc}$ denote Racah invariants with respect to the angular momenta $\mathbf{J}(1)$ and $\mathbf{J}(2)$, respectively, so that

$$\overline{W}_{\rho\sigma\tau}^{abc} |(j_1 j_2) j m\rangle = W_{\rho\sigma\tau}^{abc}(j_1) |(j_1 j_2) j m\rangle,$$

$$\underline{W}_{\alpha\beta\gamma}^{abc} |(j_1 j_2) j m\rangle = W_{\alpha\beta\gamma}^{abc}(j_2) |(j_1 j_2) j m\rangle.$$

The matrix elements of relation Eq. (2.97) lead to the Biedenharn–Elliott identity. There are five versions of this relationship in complete analogy to relations Eqs. (2.63)–(2.65) and (2.69)–(2.70) for Wigner operators.

Racah operators are a basis for all invariant operators acting in the tensor product space spanned by the coupled basis vectors Eq. (2.85) and are the natural way of formulating interactions in that space. Their algebra is a fascinating study, initiated already in a different guise in the work of Schwinger [3]. Little use has been made of this concept in physical applications.

Additional relations between Racah coefficients or 6– j coefficients may be derived from the various versions of the rule Eq. (2.97) or directly from relation Eq. (2.79b) by using

the orthogonality relations Eq. (2.75). Two of these are:

$$\sum_e (-1)^{a+b+e} (2e + 1)$$

$$\times \left\{ \begin{array}{ccc} a & b & e \\ d & c & g \end{array} \right\} \left\{ \begin{array}{ccc} a' & a & c' \\ b & b' & e \end{array} \right\} \left\{ \begin{array}{ccc} a' & e & b' \\ d & d' & c \end{array} \right\}$$

$$= (-1)^{\phi_1} \left\{ \begin{array}{ccc} c' & b & b' \\ d & d' & g \end{array} \right\} \left\{ \begin{array}{ccc} a' & a & c' \\ g & d' & c \end{array} \right\},$$

$$\phi_1 = g + a' + b' + c' + c + d' + d;$$

$$\sum_{e, e'} (-1)^{a-c'+e-e'} (2e + 1)(2e' + 1)(2f + 1)$$

$$\times \left\{ \begin{array}{ccc} c' & b & e' \\ d & d' & f \end{array} \right\} \left\{ \begin{array}{ccc} a & b & e \\ d & c & g \end{array} \right\} \left\{ \begin{array}{ccc} a' & a & c' \\ b & e' & e \end{array} \right\} \left\{ \begin{array}{ccc} a' & e & e' \\ d & d' & c \end{array} \right\}$$

$$= \delta_{fg} (-1)^{\phi_2} \left\{ \begin{array}{ccc} a' & a & c' \\ g & d' & c \end{array} \right\},$$

$$\phi_2 = g + a' - b + c + d' + d.$$

The W coefficient form of these relations is obtained by deleting all phase factors and making the substitution Eq. (2.74), ignoring the phase factor. There are no phase factors in the corresponding W coefficient relations.

2.10.7 Schwinger–Wu Generating Function and Its Combinatorics

Triangles associated with the 9– j coefficient $\left\{ \begin{array}{ccc} j_1 j_2 j_3 \\ j_4 j_5 j_6 \\ j_7 j_8 j_9 \end{array} \right\}$:

$$(j_1 j_2 j_3), (j_4 j_5 j_6), (j_7 j_8 j_9), (j_1 j_4 j_7),$$

$$(j_2 j_5 j_8), (j_3 j_6 j_9).$$

Points in \mathbf{R}^3 associated with the triangles:

$$(j_1 j_2 j_3) \rightarrow (x_1, x_2, x_3), (j_4 j_5 j_6) \rightarrow (x_4, x_5, x_6),$$

$$(j_7 j_8 j_9) \rightarrow (x_7, x_8, x_9), (j_1 j_4 j_7) \rightarrow (y_1, y_4, y_7),$$

$$(j_2 j_5 j_8) \rightarrow (y_2, y_5, y_8), (j_3 j_6 j_9) \rightarrow (y_3, y_6, y_9).$$

Cubic graph \mathbf{C}_6 in \mathbf{R}^3 associated with the points:

The points define the vertices of a cubic graph \mathbf{C}_6 on six points with lines joining each pair of points that share a common subscript, and the lines are labeled by the products $x_i y_i$, where i is the common subscript (Fig. 2.3).

Cubic graph \mathbf{C}_6 functions:

Interchange the symbols x and y in the coordinates of the vertices of the cubic graph \mathbf{C}_6 and define the following polynomials on the vertices and edges of the \mathbf{C}_6 with this modified labeling.

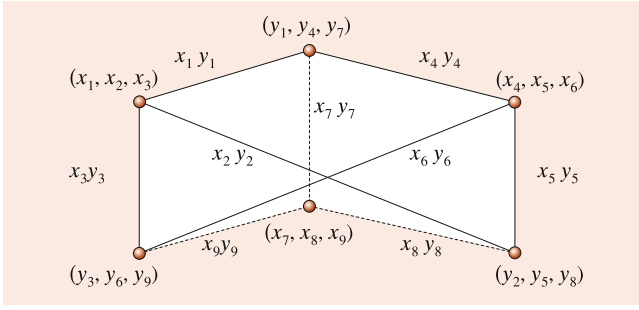


Fig. 2.3 Labeled cubic graph associated with the $9-j$ coefficient

Vertex function: multiply together the coordinates of each pair of adjacent vertices, divide out the coordinates with a common subscript, and sum over all pairs of vertices to obtain

$$V_4 = y_1 y_2 x_6 x_9 + y_1 y_3 x_5 x_8 + y_2 y_3 x_4 x_7 \\ + y_4 y_5 x_3 x_9 + y_4 y_6 x_2 x_8 + y_5 y_6 x_1 x_7 \\ + y_7 y_8 x_3 x_6 + y_7 y_9 x_2 x_5 + y_8 y_9 x_1 x_4 .$$

Edge function:

$$E_6 = \det \begin{bmatrix} x_1 y_1 & x_2 y_2 & x_3 y_3 \\ x_4 y_4 & x_5 y_5 & x_6 y_6 \\ x_7 y_7 & x_8 y_8 & x_9 y_9 \end{bmatrix} .$$

Generating function [4–6]:

$$(1 - V_4 + E_6)^{-2} = \sum_{\Delta} C(\Delta) Z^{\Delta} ,$$

$$Z^{\Delta} = \prod_{\text{all vertices}} (z_a, z_b, z_c)^{(j_a j_b j_c)} \quad (\text{see Eq. (2.82)}) ,$$

$$\Delta = \begin{bmatrix} (j_1 j_2 j_3) \\ (j_4 j_5 j_6) \\ (j_7 j_8 j_9) \\ (j_1 j_4 j_7) \\ (j_2 j_5 j_8) \\ (j_3 j_6 j_9) \end{bmatrix} ,$$

$$C(\Delta) = \sum_k \sum_{\square} \sum_a (-1)^{k_{10} + k_{11} + k_{12}} (k+1) \\ \times \binom{k}{k_1, \dots, k_9, k_{10}, \dots, k_{15}} ,$$

where summation \sum_{\square} is over all 3×3 square arrays of nonnegative integers k_j ($j = 1, 2, \dots, 9$) with fixed row and column sums given by

$$\begin{bmatrix} k_1 & k_2 & k_3 \\ k_4 & k_5 & k_6 \\ k_7 & k_8 & k_9 \end{bmatrix} \quad \begin{matrix} k - t_1 \\ k - t_2 \\ k - t_3 \\ k - t_4 & k - t_5 & k - t_6 \end{matrix}$$

and for each such array the summation \sum_a is over all nonnegative integers a such that the following quantities are nonnegative integers:

$$k_{10} = -a + k_1 - k + j_2 + j_3 + j_4 + j_7 , \\ k_{11} = -a + k_6 - k + j_3 + j_4 + j_5 + j_9 , \\ k_{12} = -a + k_8 - k + j_2 + j_5 + j_7 + j_9 , \\ k_{13} = a + k_5 - k_1 - j_3 + j_6 - j_7 + j_8 , \\ k_{14} = a + k_2 - k_6 + j_1 - j_4 + j_8 - j_9 , \\ k_{15} = a .$$

Note that

$$\sum_{i=10}^{15} k_i = -2k + \sum_{i=1}^9 j_i .$$

The t_i are the following triangle sums:

$$t_1 = j_1 + j_2 + j_3, \quad t_2 = j_4 + j_5 + j_6 , \\ t_3 = j_7 + j_8 + j_9 , \\ t_4 = j_1 + j_4 + j_7, \quad t_5 = j_2 + j_5 + j_8 , \\ t_6 = j_3 + j_6 + j_9 .$$

The $9-j$ coefficient is given by

$$\begin{Bmatrix} j_1 j_2 j_3 \\ j_4 j_5 j_6 \\ j_7 j_8 j_9 \end{Bmatrix} = \Delta(j_1 j_2 j_3) \Delta(j_4 j_5 j_6) \Delta(j_7 j_8 j_9) \\ \times \Delta(j_1 j_4 j_7) \Delta(j_2 j_5 j_8) \Delta(j_3 j_6 j_9) C(\Delta) .$$

The coefficient $C(\Delta)$ is an integer associated with each cubic graph C_6 that counts the number of occurrences of the monomial term Z^{Δ} in the expansion of $(1 - V_4 + E_6)^{-2}$.

2.11 Tensor Spherical Harmonics

Tensor spherical or tensor solid harmonics are special cases of the coupling of two irreducible tensor operators in the tensor product space given in Sect. 2.7.2. They are defined by

$$\mathbf{y}^{(ls)jm} = \sum_v C_{m-v, v, m}^{l s j} \mathbf{y}_{l, m-v} \otimes \xi_v$$

and belong to the tensor product space $\mathcal{H}_l \otimes \mathcal{H}'_s$, where the orthonormal bases of the spaces \mathcal{H}_l and \mathcal{H}'_s are:

$$\{\mathbf{y}_{l\mu} : \mu = l, l-1, \dots, -l\} , \\ \{\xi_v : v = s, s-1, \dots, -s\} .$$

The orbital angular momentum \mathbf{L} has the standard action on the solid harmonics, and a second set of kinematically independent angular momentum operators \mathbf{S} has the standard action on the basis set of \mathcal{H}'_s .

The total angular momentum is:

$$\mathbf{J} = \mathbf{L} \otimes \mathbf{1}' + \mathbf{1} \otimes \mathbf{S},$$

The set of vectors

$$\{ \mathbf{y}^{(ls)jm} : m = j, j-1, \dots, -j; (lsj) \text{ obey the triangle conditions} \}$$

has the following properties:

Orthogonality:

$$\begin{aligned} & \langle \mathbf{y}^{(l's)j'm'}, \mathbf{y}^{(ls)jm} \rangle \\ &= \sum_{vv'} C_{m'-v',v',m'}^{l's j'} C_{m-v,v,m}^{lsj} (\mathbf{y}_{l',m'-v'}, \mathbf{y}_{l,m-v}) \\ & \times (\xi_{v'}, \xi_v)' = \delta_{j'l'} \delta_{l'l} \delta_{m'm}, \end{aligned}$$

where \langle , \rangle denotes the inner product in the space $\mathcal{H}_l \otimes \mathcal{H}_s'$, $(,)$ the inner product in \mathcal{H}_l , and $(,)'$ the inner product in \mathcal{H}_s' .

Operator actions:

$$\begin{aligned} \mathbf{J}^2 \mathbf{y}^{(ls)jm} &= j(j+1) \mathbf{y}^{(ls)jm}, \\ J_3 \mathbf{y}^{(ls)jm} &= m \mathbf{y}^{(ls)jm}, \\ (\mathbf{L}^2 \otimes \mathbf{1}') \mathbf{y}^{(ls)jm} &= l(l+1) \mathbf{y}^{(ls)jm}, \\ (\mathbf{1} \otimes \mathbf{S}^2) \mathbf{y}^{(ls)jm} &= s(s+1) \mathbf{y}^{(ls)jm}, \\ \mathbf{J}^2 &= \mathbf{L}^2 \otimes \mathbf{1}' + \mathbf{1} \otimes \mathbf{S}^2 + 2 \sum_i L_i \otimes S_i, \\ J_{\pm} \mathbf{y}^{(ls)jm} &= [(j \mp m)(j \pm m + 1)]^{\frac{1}{2}} \mathbf{y}^{(ls)j,m \pm 1}. \end{aligned}$$

Transformation property under unitary rotations:

$$\exp(-i \psi \hat{\mathbf{n}} \cdot \mathbf{J}) \mathbf{y}^{(ls)jm} = \sum_{m'} D_{m'm}^j(\psi, \hat{\mathbf{n}}) \mathbf{y}^{(ls)jm'}.$$

Special realization:

The eigenvectors ξ_v are often replaced by column matrices:

$$\begin{aligned} \xi_v &= \text{col}(0 \cdots 0 1 0 \cdots 0), \\ & \text{1 in position } s - v + 1, \quad v = s, s-1, \dots, -s. \end{aligned}$$

The operators $\mathbf{S} = (S_1, S_2, S_3)$ are correspondingly replaced by their standard $(2s+1) \times (2s+1)$ matrix representations $S_i^{(s)}$. The tensor product of operators becomes a $(2s+1) \times (2s+1)$ matrix containing both operators and numerical matrix elements, e.g.,

$$J_i = L_i I_{2s+1} + S_i^{(s)},$$

in which L_i is a differential operator multiplying the unit matrix, that is, L_i is repeated $2s+1$ times along the diagonal.

2.11.1 Spinor Spherical Harmonics as Matrix Functions

Choose $\xi_{+1/2} = \text{col}(1, 0)$, $\xi_{-1/2} = \text{col}(0, 1)$, and $\mathbf{S} = \boldsymbol{\sigma}/2$. The spinor spherical harmonics or Pauli central field spinors are the following, where $j \in \{1/2, 3/2, \dots\}$:

$$\begin{aligned} \mathbf{y}^{(j-\frac{1}{2}, \frac{1}{2})jm} &= \begin{pmatrix} \sqrt{\frac{j+m}{2j}} \mathbf{y}_{j-\frac{1}{2}, m-\frac{1}{2}} \\ \sqrt{\frac{j-m}{2j}} \mathbf{y}_{j-\frac{1}{2}, m+\frac{1}{2}} \end{pmatrix}, \\ \mathbf{y}^{(j+\frac{1}{2}, \frac{1}{2})jm} &= \begin{pmatrix} -\sqrt{\frac{j-m+1}{2j+2}} \mathbf{y}_{j+\frac{1}{2}, m-\frac{1}{2}} \\ \sqrt{\frac{j+m+1}{2j+2}} \mathbf{y}_{j+\frac{1}{2}, m+\frac{1}{2}} \end{pmatrix}. \end{aligned}$$

2.11.2 Vector Spherical Harmonics as Matrix Functions

Choose $\xi_{+1} = \text{col}(1, 0, 0)$, $\xi_0 = \text{col}(0, 1, 0)$, $\xi_{-1} = \text{col}(0, 0, 1)$, and \mathbf{S} the 3×3 angular momentum matrices given by

$$\begin{aligned} S_+ &= \begin{pmatrix} 0 & \sqrt{2} & 0 \\ 0 & 0 & \sqrt{2} \\ 0 & 0 & 0 \end{pmatrix}, \quad S_- = \begin{pmatrix} 0 & 0 & 0 \\ \sqrt{2} & 0 & 0 \\ 0 & \sqrt{2} & 0 \end{pmatrix}, \\ S_3 &= \begin{pmatrix} 1 & 0 & 0 \\ 0 & 0 & 0 \\ 0 & 0 & -1 \end{pmatrix}. \end{aligned}$$

The vector spherical harmonics are the following, where $j \in \{0, 1, 2, \dots\}$:

$$\begin{aligned} \mathbf{y}^{(j-1,1)jm} &= \begin{pmatrix} \sqrt{\frac{(j+m-1)(j+m)}{2j(2j-1)}} \mathbf{y}_{j-1, m-1} \\ \sqrt{\frac{(j-m)(j+m)}{j(2j-1)}} \mathbf{y}_{j-1, m} \\ \sqrt{\frac{(j-m-1)(j-m)}{2j(2j-1)}} \mathbf{y}_{j-1, m+1} \end{pmatrix}, \\ \mathbf{y}^{(j,1)jm} &= \begin{pmatrix} -\sqrt{\frac{(j+m)(j-m+1)}{2j(j+1)}} \mathbf{y}_{j, m-1} \\ \frac{m}{\sqrt{j(j+1)}} \mathbf{y}_{j, m} \\ \sqrt{\frac{(j-m)(j+m+1)}{2j(j+1)}} \mathbf{y}_{j, m+1} \end{pmatrix}, \\ \mathbf{y}^{(j+1,1)jm} &= \begin{pmatrix} \sqrt{\frac{(j-m+1)(j-m+2)}{2(j+1)(2j+3)}} \mathbf{y}_{j+1, m-1} \\ -\sqrt{\frac{(j-m+1)(j+m+1)}{(j+1)(2j+3)}} \mathbf{y}_{j+1, m} \\ \sqrt{\frac{(j+m+2)(j+m+1)}{2(j+1)(2j+3)}} \mathbf{y}_{j+1, m+1} \end{pmatrix}. \end{aligned}$$

Eigenvalue properties:

$$\begin{aligned}\nabla^2 \mathbf{y}^{(l)jm} &= 0, \\ \mathbf{J}^2 \mathbf{y}^{(l)jm} &= j(j+1) \mathbf{y}^{(l)jm}, \\ \mathbf{J}_3 \mathbf{y}^{(l)jm} &= m \mathbf{y}^{(l)jm}, \\ \mathbf{L}^2 \mathbf{y}^{(l)jm} &= l(l+1) \mathbf{y}^{(l)jm}, \\ \mathbf{S}^2 \mathbf{y}^{(l)jm} &= 2 \mathbf{y}^{(l)jm}.\end{aligned}$$

2.11.3 Vector Solid Harmonics as Vector Functions

Vector spherical and solid harmonics can also be defined and their properties presented in terms of the ordinary solid harmonics, using the vectors \mathbf{x} , ∇ , and \mathbf{L} , and the operations of divergence and curl.

Defining equations:

$$\begin{aligned}\mathbf{y}^{(l+1,1)lm} &= -[(l+1)(2l+1)]^{-\frac{1}{2}} [(l+1)\mathbf{x} \\ &\quad + \mathbf{i}\mathbf{x} \times \mathbf{L}] \mathbf{y}_{lm}, \\ \mathbf{y}^{(l,1)lm} &= [l(l+1)]^{-1/2} \mathbf{L} \mathbf{y}_{lm}, \\ r^2 \mathbf{y}^{(l-1,1)lm} &= -[l(2l+1)]^{-\frac{1}{2}} \times (-l\mathbf{x} + \mathbf{i}\mathbf{x} \\ &\quad \times \mathbf{L}) \mathbf{y}_{lm}.\end{aligned}$$

Eigenvalue properties:

$$\begin{aligned}\mathbf{J}^2 \mathbf{y}^{(l)jm} &= j(j+1) \mathbf{y}^{(l)jm}, \\ \mathbf{L}^2 \mathbf{y}^{(l)jm} &= l(l+1) \mathbf{y}^{(l)jm}, \\ \mathbf{S}^2 \mathbf{y}^{(l)jm} &= 2 \mathbf{y}^{(l)jm}, \\ \mathbf{J}_3 \mathbf{y}^{(l)jm} &= m \mathbf{y}^{(l)jm}, \\ \nabla^2 \mathbf{y}^{(l)jm} &= \mathbf{0}, \\ 2i\mathbf{L} \times \mathbf{y}^{(l)jm} &= [j(j+1) - l(l+1) - 2] \mathbf{y}^{(l)jm}.\end{aligned}$$

Orthogonality:

$$\int dS_{\hat{x}} \mathbf{y}^{(l')j'm'*}(\mathbf{x}) \cdot \mathbf{y}^{(l)jm}(\mathbf{x}) = \delta_{l'l} \delta_{j'j} \delta_{m'm} r^{l'+l},$$

where the integration is over the unit sphere in \mathbf{R}^3 .

Complex conjugation:

$$\mathbf{y}^{(l)jm*} = (-1)^{l+1-j} (-1)^m \mathbf{y}^{(l)j,-m}.$$

Vector and gradient formulas:

$$\begin{aligned}\mathbf{x} \mathbf{y}_{lm} &= -\left(\frac{l+1}{2l+1}\right)^{\frac{1}{2}} \mathbf{y}^{(l+1,1)lm} \left(\frac{l}{2l+1}\right)^{\frac{1}{2}} r^2 \mathbf{y}^{(l-1,1)lm}, \\ [(l+1)\nabla + \mathbf{i}\nabla \times \mathbf{L}](F \mathbf{y}_{lm}) \\ &= -[(l+1)(2l+1)]^{\frac{1}{2}} \left(\frac{1}{r} \frac{dF}{dr}\right) \mathbf{y}^{(l+1,1)lm},\end{aligned}$$

$$\begin{aligned}[-l\nabla + \mathbf{i}\nabla \times \mathbf{L}](F \mathbf{y}_{lm}) \\ &= -[l(2l+1)]^{\frac{1}{2}} \left[r \frac{dF}{dr} + (2l+1)F\right] \mathbf{y}^{(l-1,1)lm}, \\ \nabla(F \mathbf{y}_{lm}) &= -\left(\frac{l+1}{2l+1}\right)^{\frac{1}{2}} \left(\frac{1}{r} \frac{dF}{dr}\right) \mathbf{y}^{(l+1,1)lm} \\ &\quad + \left(\frac{l}{2l+1}\right)^{\frac{1}{2}} \left[r \frac{dF}{dr} + (2l+1)F\right] \mathbf{y}^{(l-1,1)lm}, \\ \mathbf{i}\nabla \times \mathbf{L}(F \mathbf{y}_{lm}) &= -l \left(\frac{l+1}{2l+1}\right)^{\frac{1}{2}} \left(\frac{1}{r} \frac{dF}{dr}\right) \mathbf{y}^{(l+1,1)lm} \\ &\quad - (l+1) \left(\frac{l}{2l+1}\right)^{\frac{1}{2}} \left[r \frac{dF}{dr} + (2l+1)F\right] \mathbf{y}^{(l-1,1)lm}.\end{aligned}$$

Curl equations:

$$\begin{aligned}\mathbf{i}\nabla \times (F \mathbf{y}^{(l+1,1)lm}) &= -\left(\frac{l}{2l+1}\right)^{\frac{1}{2}} \\ &\quad \times \left[r \frac{dF}{dr} + (2l+3)F\right] \mathbf{y}^{(l,1)lm}, \\ \mathbf{i}\nabla \times (F \mathbf{y}^{(l,1)lm}) &= -\left(\frac{l}{2l+1}\right)^{\frac{1}{2}} \\ &\quad \times \left(\frac{1}{r} \frac{dF}{dr}\right) \mathbf{y}^{(l+1,1)lm} - \left(\frac{l+1}{2l+1}\right)^{\frac{1}{2}} \\ &\quad \times \left[r \frac{dF}{dr} + (2l+1)F\right] \mathbf{y}^{(l-1,1)lm}, \\ \mathbf{i}\nabla \times (F \mathbf{y}^{(l-1,1)lm}) &= -\left(\frac{l+1}{2l+1}\right)^{\frac{1}{2}} \left(\frac{1}{r} \frac{dF}{dr}\right) \mathbf{y}^{(l,1)lm}.\end{aligned}$$

Divergence equations:

$$\begin{aligned}\nabla \cdot (F \mathbf{y}^{(l+1,1)lm}) &= -\left(\frac{l+1}{2l+1}\right)^{\frac{1}{2}} \left[r \frac{dF}{dr} + (2l+3)F\right] \mathbf{y}_{lm}, \\ \nabla \cdot (F \mathbf{y}^{(l,1)lm}) &= 0, \\ \nabla \cdot (F \mathbf{y}^{(l-1,1)lm}) &= \left(\frac{l}{2l+1}\right)^{\frac{1}{2}} \left(\frac{1}{r} \frac{dF}{dr}\right) \mathbf{y}_{lm}.\end{aligned}$$

Parity property:

$$\mathbf{y}^{(l+\delta,1)lm}(-\mathbf{x}) = (-1)^{l+\delta} \mathbf{y}^{(l+\delta,1)lm}(\mathbf{x}).$$

Scalar product:

$$\begin{aligned}\mathbf{y}^{(l')j'm'} \cdot \mathbf{y}^{(l)jm} \\ &= \sum_{l''} r^{l+l'-l''} \left(\frac{(2j+1)(2j'+1)(2l+1)(2l'+1)}{4\pi(2l''+1)}\right)^{\frac{1}{2}} \\ &\quad \times (-1)^{l+j'+l''} C_{000}^{l'l''} C_{m,m',m+m'}^{j j' l''} \\ &\quad \times \begin{Bmatrix} l' & j' & 1 \\ j & l & l'' \end{Bmatrix} \mathbf{y}_{l'',m+m'}.\end{aligned}$$

Cross product:

$$\begin{aligned} \mathbf{y}^{(l'1)j'm'} \times \mathbf{y}^{(l1)jm} &= (-i\sqrt{2}) \sum_{l''j''} r^{l+l'-l''} \\ &\times \left(\frac{(2j+1)(2j'+1)(3)(2l+1)(2l'+1)}{4\pi} \right)^{\frac{1}{2}} \\ &\times C_{000}^{l'l''} C_{m,m',m+m'}^{j'j''} \begin{Bmatrix} l & 1 & j \\ l' & 1 & j' \\ l'' & 1 & j'' \end{Bmatrix} \mathbf{y}^{(l''1)j''m+m'}. \end{aligned}$$

Conversion to spherical harmonic form:

$$\mathbf{y}^{(l+\delta,1)lm}(\mathbf{x}) = r^{l+\delta} \mathbf{y}^{(l+\delta,1)lm}(\hat{\mathbf{x}}),$$

with appropriate modification of F to account for the factor $r^{l+\delta}$.

2.12 Coupling and Recoupling Theory and 3n-j Coefficients

2.12.1 Composite Angular Momentum Systems

An *elementary* angular momentum system is one whose state space can be written as a direct sum of vector spaces \mathcal{H}_j with orthonormal basis

$$\{|jm\rangle | m = j, j-1, \dots, -j\},$$

on which the angular momentum \mathbf{J} has the standard action, and which under unitary transformation by $\exp(-i\psi\hat{\mathbf{n}} \cdot \mathbf{J})$ undergoes the standard unitary transformation. A composite angular momentum system is one whose state space is a direct sum of the tensor product spaces $\mathcal{H}_{j_1 j_2 \dots j_n}$ of dimension $\prod_{\alpha=1}^n (2j_\alpha + 1)$ with orthonormal basis in the tensor product space of the elementary systems given by

$$|j_1 m_1\rangle \otimes |j_2 m_2\rangle \otimes \dots \otimes |j_n m_n\rangle, \quad (2.98)$$

each $m_\alpha = j_\alpha, j_\alpha - 1, \dots, -j_\alpha$.

The following properties then hold for the composite system.

Independent rotations of the elementary parts:

$$\begin{aligned} &\left\{ \exp[-i\psi_1 \hat{\mathbf{n}}_1 \cdot \mathbf{J}(1)] \otimes \dots \otimes \exp[-i\psi_n \hat{\mathbf{n}}_n \cdot \mathbf{J}(n)] \right\} \\ &\times |j_1 m_1\rangle \otimes \dots \otimes |j_n m_n\rangle \\ &= \exp[-i\psi_1 \hat{\mathbf{n}}_1 \cdot \mathbf{J}(1)] |j_1 m_1\rangle \otimes \dots \\ &\otimes \exp[-i\psi_n \hat{\mathbf{n}}_n \cdot \mathbf{J}(n)] |j_n m_n\rangle \end{aligned}$$

$$\begin{aligned} &= \sum_{m'_1 \dots m'_n} [D^{j_1}(U_1) \times \dots \times D^{j_n}(U_n)]_{m'_1 \dots m'_n; m_1 \dots m_n} \\ &\times |j_1 m'_1\rangle \otimes \dots \otimes |j_n m'_n\rangle, \end{aligned} \quad (2.99)$$

$$\begin{aligned} &[D^{j_1}(U_1) \times \dots \times D^{j_n}(U_n)]_{m'_1 \dots m'_n; m_1 \dots m_n} \\ &= D_{m'_1 m_1}^{j_1}(U_1) \dots D_{m'_n m_n}^{j_n}(U_n), \end{aligned}$$

$$U_\alpha = U(\psi_\alpha, \hat{\mathbf{n}}_\alpha) \in SU(2), \quad \alpha = 1, 2, \dots, n.$$

Multiple Kronecker (direct) product group $SU(2) \times \dots \times SU(2)$.

Group elements:

$$(U_1, \dots, U_n), \quad \text{each } U_\alpha \in SU(2).$$

Multiplication rule:

$$(U'_1, \dots, U'_n)(U_1, \dots, U_n) = (U'_1 U_1, \dots, U'_n U_n).$$

Irreducible representations:

$$D^{j_1}(U_1) \times \dots \times D^{j_n}(U_n). \quad (2.100)$$

Rotation of the composite system as a unit.

Common rotation:

$$U_1 = U_2 = \dots = U_n = U \in SU(2).$$

Diagonal subgroup $SU(2) \subset SU(2) \times \dots \times SU(2)$:

$$(U, U, \dots, U), \quad \text{each } U \in SU(2).$$

Reducible representation of $SU(2)$:

$$D^{j_1}(U) \times \dots \times D^{j_n}(U). \quad (2.101)$$

Total angular momentum of the composite system:

$$\mathbf{J} = \mathbf{J}(1) + \mathbf{J}(2) + \dots + \mathbf{J}(n),$$

in which the k -th term in the sum is to be interpreted as the tensor product operator:

$$\mathbf{I}_1 \otimes \dots \otimes \mathbf{J}(k) \otimes \dots \otimes \mathbf{I}_n, \quad \mathbf{I}_\alpha = \text{unit operator in } \mathcal{H}_{j_\alpha}.$$

The basic problem for composite systems:

The basic problem is to reduce the n -fold direct product representation Eq. (2.101) of $SU(2)$ into a direct sum of irreducible representations, or equivalently, to find all subspaces $\mathcal{H}_j \subset \mathcal{H}_{j_1 j_2 \dots j_n}$, $j \in \{0, 1/2, 1, \dots\}$, with orthonormal bases sets $\{|jm\rangle | m = j, j-1, \dots, -j\}$ on which the total angular momentum \mathbf{J} has the standard action.

Form of the solution:

$$| (j_1 j_2 \cdots j_n)(k) j m \rangle = \sum_{\substack{\text{all } m_\alpha \\ \sum m_\alpha = m}} C_{m_1 m_2 \cdots m_n m}^{j_1 j_2 \cdots j_n j}(k) \\ \times | j_1 m_1 \rangle \otimes | j_2 m_2 \rangle \otimes \cdots \otimes | j_n m_n \rangle, \quad (2.102)$$

$m = j, j-1, \dots, -j$; index set (k) unspecified.

Diagonal operators:

$$\mathbf{J}^2(\alpha) = J_1^2(\alpha) + J_2^2(\alpha) + J_3^2(\alpha), \\ \mathbf{J}^2(\alpha) | (j_1 j_2 \cdots j_n)(k) j m \rangle \\ = j_\alpha(j_\alpha + 1) | (j_1 j_2 \cdots j_n)(k) j m \rangle, \\ \alpha = 1, 2, \dots, n. \quad (2.103)$$

Total angular momentum properties imposed:

$$\mathbf{J}^2 | (j_1 j_2 \cdots j_n)(k) j m \rangle \\ = j(j+1) | (j_1 j_2 \cdots j_n)(k) j m \rangle, \\ J_3 | (j_1 j_2 \cdots j_n)(k) j m \rangle \\ = m | (j_1 j_2 \cdots j_n)(k) j m \rangle, \\ J_\pm | (j_1 j_2 \cdots j_n)(k) j m \rangle \\ = [(j \mp m)(j \pm m + 1)]^{\frac{1}{2}} \\ \times | (j_1 j_2 \cdots j_n)(k) j m \pm 1 \rangle. \quad (2.104)$$

Properties of the index set (k) .

Reduction of Kronecker product Eq. (2.101):

$$D^{j_1} \times D^{j_2} \times \cdots \times D^{j_n} = \sum_j \oplus n_j D^j, \\ \prod_\alpha (2j_\alpha + 1) = \sum_j n_j (2j + 1). \quad (2.105)$$

For fixed j_1, j_2, \dots, j_n , and j , the index set (k) must enumerate exactly n_j perpendicular spaces \mathcal{H}_j .

Incompleteness of set of operators:

There are $2n$ commuting Hermitian operators diagonal on the basis Eq. (2.98):

$$\{ \mathbf{J}^2(\alpha), J_3(\alpha) \mid \alpha = 1, 2, \dots, n \}. \quad (2.106a)$$

There are $n+2$ commuting Hermitian operators diagonal on the basis Eq. (2.102):

$$\{ \mathbf{J}^2, J_3; \mathbf{J}^2(\alpha) \mid \alpha = 1, 2, \dots, n \}. \quad (2.106b)$$

There are $n-2$ additional commuting Hermitian operators, or other rules, required to complete set Eq. (2.106b) and determine the indexing set (k) .

Basic content of coupling and recoupling theory:

Coupling theory is the study of completing the operator set Eq. (2.106b), or the specification of other rules, that

uniquely determine the irreducible representation spaces \mathcal{H}_j occurring in the Kronecker product reduction Eq. (2.105). Recoupling theory is the study of the interrelations between different methods of effecting this reduction; it is a study of relations between the different ways of spanning the multiplicity space

$$\mathcal{H}_j \oplus \mathcal{H}_j \oplus \cdots \oplus \mathcal{H}_j \quad (n_j \text{ terms}).$$

2.12.2 Binary Coupling Theory: Combinatorics

Binary coupling of angular momenta refers to selecting any pair of angular momentum operators from the set of individual system angular momenta

$$\{ \mathbf{J}(1), \mathbf{J}(2), \dots, \mathbf{J}(n) \}$$

and carrying out the *addition of angular momenta* for that pair by coupling the corresponding states in the tensor product space by the standard use of $SU(2)$ WCG coefficients; this is followed by addition of a new pair, which may be a pair distinct from the first pair, or the addition of one new angular momentum to the sum of the first pair, etc. If the order $1, 2, \dots, n$ of the angular momenta is kept fixed in

$$\mathbf{J}_1 + \mathbf{J}_2 + \cdots + \mathbf{J}_n, \quad (2.107)$$

one is led to the problem of parentheses. (To avoid misleading parentheses, the notation $\mathbf{J}_\alpha = \mathbf{J}(\alpha)$ is used in this section.) This is the problem of introducing pairs of parentheses into expression Eq. (2.107) that specify the coupling procedure to be implemented. The procedure is clear from the following cases for $n = 2, 3$, and 4:

$$n = 2: \quad \mathbf{J}_1 + \mathbf{J}_2; \\ n = 3: \quad (\mathbf{J}_1 + \mathbf{J}_2) + \mathbf{J}_3, \\ \mathbf{J}_1 + (\mathbf{J}_2 + \mathbf{J}_3); \\ n = 4: \quad (\mathbf{J}_1 + \mathbf{J}_2) + (\mathbf{J}_3 + \mathbf{J}_4), \\ [(\mathbf{J}_1 + \mathbf{J}_2) + \mathbf{J}_3] + \mathbf{J}_4, \\ [\mathbf{J}_1 + (\mathbf{J}_2 + \mathbf{J}_3)] + \mathbf{J}_4, \\ \mathbf{J}_1 + [(\mathbf{J}_2 + \mathbf{J}_3) + \mathbf{J}_4], \\ \mathbf{J}_1 + [\mathbf{J}_2 + (\mathbf{J}_3 + \mathbf{J}_4)].$$

It is customary to use the ordered sequence

$$j_1 j_2 \cdots j_n \quad (2.108)$$

of angular momentum quantum numbers in place of the angular momentum operators in Eq. (2.107). Thus, the five placement of parentheses for $n = 4$ becomes:

$$(j_1 j_2)(j_3 j_4), [(j_1 j_2) j_3] j_4, [j_1 (j_2 j_3)] j_4, \\ j_1 [(j_2 j_3) j_4], j_1 [j_2 (j_3 j_4)].$$

(It is also customary to omit the last parentheses pair, which encloses the whole sequence.) A sequence Eq. (2.108) into which pairwise insertions of parentheses has been completed is called a binary bracketing of the sequence and is denoted by $(j_1 j_2 \cdots j_n)^B$. This symbol may also be called a coupling symbol. The total number of coupling symbols, that is, the total number of elements a_n in the set

$$\{(j_1 j_2 \cdots j_n)^B | B \text{ is a binary bracketing}\}$$

is given by the Catalan numbers:

$$a_n = \frac{1}{n} \binom{2n-2}{n-1}, \quad n = 2, 3, \dots$$

Effect of permuting the angular momenta:

Since the position of an individual vector space in the tensor product $\mathcal{H}_{j_1} \otimes \cdots \otimes \mathcal{H}_{j_n}$ is kept fixed, the meaning of a permutation of the j_α in the sequence Eq. (2.108) corresponding to a given binary bracketing is to permute the positions of the terms in the summation for the total angular momentum, e.g., $(j_1 j_2) j_3 \rightarrow (j_3 j_1) j_2$ corresponds to

$$\begin{aligned} & (\mathbf{J}_1 \otimes \mathbf{I}_2 \otimes \mathbf{I}_3 + \mathbf{I}_1 \otimes \mathbf{J}_2 \otimes \mathbf{I}_3) + \mathbf{I}_1 \otimes \mathbf{I}_2 \otimes \mathbf{J}_3 \\ &= (\mathbf{I}_1 \otimes \mathbf{I}_2 \otimes \mathbf{J}_3 + \mathbf{J}_1 \otimes \mathbf{I}_2 \otimes \mathbf{I}_3) + \mathbf{I}_1 \otimes \mathbf{J}_2 \otimes \mathbf{I}_3. \end{aligned}$$

Total number of binary bracketing schemes including permutations:

The number of symbols in the set

$$\left\{ (j_{\alpha_1} j_{\alpha_2} \cdots j_{\alpha_n})^B \left| \begin{array}{l} B \text{ is a binary bracketing and} \\ \alpha_1 \alpha_2 \cdots \alpha_n \text{ is a permutation} \\ \text{of } 1, 2, \dots, n \end{array} \right. \right\} \quad (2.109)$$

is $c_n = n! a_n = (n)_{n-1} = n(n+1) \cdots (2n-2)$.

Caution: one should not assign numbers to the symbols j_α , since these symbols serve as noncommuting, nonassociative distinct objects in a counting process.

Binary subproducts:

A binary subproduct in the coupling symbol $(j_{\alpha_1} j_{\alpha_2} \cdots j_{\alpha_n})^B$ is the subset of symbols between a given parentheses pair, say, $\{xy\}$. The symbols x and y may themselves contain binary subproducts. Commutation of a binary subproduct is the operation $\{xy\} \rightarrow \{yx\}$. For example, the coupling symbol $\{(j_1 j_2) j_3\} j_4$ contains three binary subproducts, $\{xy\}$, $[xy]$, (xy) .

Equivalence relation:

Two coupling symbols are defined to be equivalent

$$(j_{\alpha_1} j_{\alpha_2} \cdots j_{\alpha_n})^B \sim (j_{\alpha'_1} j_{\alpha'_2} \cdots j_{\alpha'_n})^B,$$

if one can be obtained from the other by commutation of the symbols in the binary subproducts. Such commutations

change the overall phase of the state vector Eq. (2.102) corresponding to a particular coupling symbol, and such states are counted as being the same (equivalent).

Number of inequivalent coupling schemes:

The equivalence relation under commutation of binary subproducts partitions the set Eq. (2.109) into equivalence classes, each containing 2^{n-1} elements. There are $d_n = c_n / 2^{n-1} = (2n-3)!!$ inequivalent coupling schemes in binary coupling theory. Thus, for $n = 4$, there are $5!! = 5 \times 3 \times 1 = 15$ inequivalent binary coupling schemes.

Type of a coupling symbol:

The type of the coupling symbol $(j_{\alpha_1} j_{\alpha_2} \cdots j_{\alpha_n})^B$ is defined to be the symbol obtained by setting all the j_α equal to a common symbol, say, x . Thus, the type of the coupling symbol $\{(j_1 j_2) j_3\} j_4$ is $\{(x^2)x\}x$.

The Wedderburn–Etherington number b_n gives the number of coupling symbols of distinct types, counting two symbols as equivalent if they are related by commutation of binary subproducts. A closed form of these numbers is not known, although generating functions exist. The first few numbers are:

n	1	2	3	4	5	6	7	8	9	10
b_n	1	1	1	2	3	6	11	23	46	98

There are 15 nontrivial coupling schemes for 4 angular momenta, and they are classified into 2 types, allowing commutation of binary subproducts:

$$\begin{aligned} & \text{Type } [(x^2)x]x \\ & [(j_1 j_2) j_3] j_4, [(j_2 j_3) j_1] j_4, [(j_3 j_1) j_2] j_4 \\ & [(j_1 j_2) j_4] j_3, [(j_2 j_4) j_1] j_3, [(j_4 j_1) j_2] j_3 \\ & [(j_1 j_3) j_4] j_2, [(j_3 j_4) j_1] j_2, [(j_4 j_1) j_3] j_2 \\ & [(j_2 j_3) j_4] j_1, [(j_3 j_4) j_2] j_1, [(j_4 j_2) j_3] j_1 \\ & \text{Type } (x^2)(x^2) \\ & (j_1 j_2)(j_3 j_4), (j_1 j_3)(j_2 j_4), (j_2 j_3)(j_1 j_4) \end{aligned}$$

2.12.3 Implementation of Binary Couplings

Each binary coupling scheme specifies uniquely a set of intermediate angular momentum operators. For example, the intermediate angular momenta associated with the coupling symbol $[(j_1 j_2) j_3] j_4$ are

$$\begin{aligned} \mathbf{J}(1) + \mathbf{J}(2) &= \mathbf{J}(12), \quad \mathbf{J}(12) + \mathbf{J}(3) = \mathbf{J}(123), \\ \mathbf{J}(123) + \mathbf{J}(4) &= \mathbf{J}, \end{aligned}$$

where \mathbf{J} is the total angular momentum. Each coupling symbol $(j_{\alpha_1} j_{\alpha_2} \cdots j_{\alpha_n})^B$ defines exactly $n-2$ intermediate angular momentum operators $\mathbf{K}(\lambda)$, $\lambda = 1, 2, \dots, n-2$. The

squares of these operators completes the set of operators Eq. (2.106b) for each coupling symbol; that is, the states' vectors satisfying Eqs. (2.103)–(2.104) and the following equations are unique, up to an overall choice of phase factor:

$$\begin{aligned} & \mathbf{K}^2(\lambda) | (j_{\alpha_1} j_{\alpha_2} \cdots j_{\alpha_n})^B (k_1 k_2 \cdots k_{n-2}) j m \rangle \\ &= k_\lambda (k_\lambda + 1) | (j_{\alpha_1} j_{\alpha_2} \cdots j_{\alpha_n})^B (k_1 k_2 \cdots k_{n-2}) j m \rangle, \\ & \lambda = 1, 2, \dots, n-2, \quad n > 2. \end{aligned} \quad (2.110)$$

The intermediate angular momentum operators $\mathbf{K}^2(\lambda)$ depend, of course, on the choice of binary couplings implicit in the symbol $(j_{\alpha_1} j_{\alpha_2} \cdots j_{\alpha_n})^B$. The vectors have the following properties.

Orthonormal basis of $\mathcal{H}_{j_1}(1) \otimes \cdots \otimes \mathcal{H}_{j_n}(n)$:

$$\begin{aligned} \langle (j_\alpha)^B (k') j m | (j_\alpha)^B (k) j m \rangle &= \prod_\lambda \delta_{k'_\lambda k_\lambda}, \\ (j_\alpha) &= (j_{\alpha_1}, j_{\alpha_2}, \dots, j_{\alpha_n}), \\ (k) &= (k_1, k_2, \dots, k_{n-2}), \\ (k') &= (k'_1, k'_2, \dots, k'_{n-2}). \end{aligned}$$

The range of each k_λ is uniquely determined by the Clebsch–Gordan series and the binary couplings in the coupling symbol. Together these ranges enumerate exactly the multiplicity n_j of \mathcal{H}_j occurring in the reduction of the multiple Kronecker product.

Uniqueness of state vectors:

$$\begin{aligned} & | (j_{\alpha_1} j_{\alpha_2} \cdots j_{\alpha_n})^B (k_1 k_2 \cdots k_{n-2}) j m \rangle \\ &= \sum_{\sum m_\alpha = m} C \left[\begin{array}{c} j_{\alpha_1} \cdots j_{\alpha_n} \\ m_{\alpha_1} \cdots m_{\alpha_n} \end{array} \right]^B \begin{array}{c} j \\ m \end{array} (k_1, \dots, k_{n-2}) \\ & \times | j_1 m_1 \rangle \otimes \cdots \otimes | j_n m_n \rangle. \end{aligned}$$

In the C coefficient, the $\left(\begin{array}{c} j_\alpha \\ m_\alpha \end{array} \right)$ are paired in the binary bracketing. Each such C coefficient is a summation over a unique product of $n-1$ $SU(2)$ WCG coefficients.

Equivalent basis vectors:

$$\begin{aligned} & | (j_{\alpha_1} j_{\alpha_2} \cdots j_{\alpha_n})^B (k_1 k_2 \cdots k_{n-2}) j m \rangle \\ &= \pm | (j_{\alpha'_1} j_{\alpha'_2} \cdots j_{\alpha'_n})^B (k_1 k_2 \cdots k_{n-2}) j m \rangle, \end{aligned}$$

if and only if $(j_{\alpha_1} j_{\alpha_2} \cdots j_{\alpha_n})^B \sim (j_{\alpha'_1} j_{\alpha'_2} \cdots j_{\alpha'_n})^B$. Inequivalent basis vector are orthonormal in all quantum numbers labeling the state vector.

Recoupling coefficients:

A recoupling coefficient is a transformation coefficient

$$\langle (j_\beta)^{B'} | (l) j m | (j_\alpha)^B (k) j m \rangle$$

relating any two orthonormal bases of the space $\mathcal{H}_{j_1} \otimes \cdots \otimes \mathcal{H}_{j_n}$, say, the one defined by Eqs. (2.103), (2.104), and (2.110) for a prescribed coupling scheme corresponding to a bracketing B , and a second one, again defined by these relations but for a different coupling scheme corresponding to a bracketing B' . For example, for $n=3$, there are three inequivalent coupling symbols and $\binom{3}{2} = 3$ recoupling coefficients; for $n=4$, there are 15 inequivalent coupling symbols and $\binom{15}{2} = 105$ recoupling coefficients. Each coefficient is, of course, expressible as a sum over products of $2(n-1)$ WCG coefficients, obtained simply by taking the inner product:

$$\begin{aligned} & \langle (j_\beta)^{B'} (l) j m | (j_\alpha)^B (k) j m \rangle \\ &= \sum_{\sum m_\alpha = m} C \left[\begin{array}{c} j_{\beta_1} \cdots j_{\beta_n} \\ m_{\beta_1} \cdots m_{\beta_n} \end{array} \right]^{B'} \begin{array}{c} j \\ m \end{array} (l) \\ & \times C \left[\begin{array}{c} j_{\alpha_1} \cdots j_{\alpha_n} \\ m_{\alpha_1} \cdots m_{\alpha_n} \end{array} \right]^B \begin{array}{c} j \\ m \end{array} (k). \end{aligned} \quad (2.111)$$

The fundamental theorem of binary coupling theory states for inequivalent coupling schemes:

Each recoupling coefficient is expressible as a sum over products of Racah coefficients, the only other quantities occurring in the summation being phase and dimension factors.

In every instance, the summation over projection quantum numbers in the right-hand side of Eq. (2.111) is expressible as a sum over Racah coefficients.

2.12.4 Construction of All Transformation Coefficients in Binary Coupling Theory

Augmented notation:

The coupling symbol $(j_{\alpha_1} j_{\alpha_2} \cdots j_{\alpha_n})^B$ contains all information as to how n angular momenta are to be coupled but is not specific in how the intermediate angular momentum quantum numbers $(k_1 k_2 \cdots k_{n-2})$, are to be matched with the binary couplings implicit in the coupling symbol. For explicit calculations, it is necessary to remedy this deficiency in notation. This may be done by attaching the $n-2$ intermediate angular momentum quantum numbers and the total angular momentum j as subscripts to the $n-1$ parentheses pairs in the coupling symbol. For example, for $(j_1 j_2 j_3 j_4 j_5)^B = \{[(j_1 j_2)(j_3 j_4)]j_5\}$, this results in the replacement

$$\begin{aligned} & \{[(j_1 j_2)(j_3 j_4)]j_5\} (k_1 k_2 k_3) \\ & \rightarrow \{[(j_1 j_2)_{k_1} (j_3 j_4)_{k_2}]_{k_3} j_5\}_j. \end{aligned}$$

The basic coupling symbol structure is regained simply by ignoring all inferior letters.

Basic rules for commutation and association:

Let x, y, z denote arbitrary disjoint contiguous subcoupling symbols $\{[(x)(y)](z)\}$ contained in the coupling symbol $(j_{\alpha_1} j_{\alpha_2} \cdots j_{\alpha_n})^B$. Let a, b, c denote the intermediate angular momenta associated with addition of the angular momenta represented in x, y, z , respectively, d the angular momentum representing the sum of a and b , and k the sum of d and c . Symbolically, this subcoupling may be presented as

$$\begin{aligned} \sum \mathbf{J}(x) &= \mathbf{J}(a), & \sum \mathbf{J}(y) &= \mathbf{J}(b), \\ \sum \mathbf{J}(z) &= \mathbf{J}(c), \\ \mathbf{J} &= \cdots \{[\mathbf{J}(a) + \mathbf{J}(b)] + \mathbf{J}(c)\} \cdots; \\ \mathbf{J}(a) + \mathbf{J}(b) &= \mathbf{J}(d); & \mathbf{J}(d) + \mathbf{J}(c) &= \mathbf{J}(k), \end{aligned}$$

with augmented coupling symbol

$$(j_{\alpha_1} j_{\alpha_2} \cdots j_{\alpha_n})^B = \cdots \{[(x)_a(y)_b]_d(z)_c\}_k \cdots.$$

There are only two basic operations in constructing the recoupling coefficient between any two coupling schemes.

Commutation of symbols:

$$(x)_a(y)_b \rightarrow (y)_b(x)_a,$$

with the transformation of state vector given by

$$\begin{aligned} |\cdots [(x)_a(y)_b]_d \cdots\rangle \\ \rightarrow (-1)^{a+b-d} |\cdots [(y)_b(x)_a]_d \cdots\rangle \\ = |\cdots [(x)_a(y)_b]_d \cdots\rangle. \end{aligned}$$

Association of symbols:

$$[(x)_a(y)_b]_d(z)_c \rightarrow (x)_a[(y)_b(z)_c],$$

with the transformation of state vector given by

$$\begin{aligned} |\cdots \{[(x)_a(y)_b]_d(z)_c\}_k \cdots\rangle \\ \rightarrow \sum_e [(2d+1)(2e+1)]^{1/2} W(abkc; de) \\ \times |\cdots \{(x)_a[(y)_b(z)_c]_e\}_k \cdots\rangle \\ = |\cdots \{[(x)_a(y)_b]_d(z)_c\}_k \cdots\rangle. \end{aligned}$$

The basic result for the calculation of all recoupling coefficients:

Each pair of coupling schemes for n angular momenta can be brought into coincidence by a series of commutations and associations performed on either of the set of coupling symbols defining the coupling scheme.

In principle, this result gives a method for the construction of all recoupling transformation coefficients and sets

the stage for the formulation of still deeper questions arising in recoupling theory, as summarized in Sect. 2.12.5. The following examples illustrate the content of the preceding abstract constructions.

Examples:

WCG coefficient form:

$$\begin{aligned} \{[(ab)_e c]_f d\}_g \mid [(ac)_h (bd)_k]_g \\ = \sum_{\alpha+\beta+\gamma+\delta=m} C_{\alpha,\beta,\alpha+\beta}^{abe} C_{\alpha+\beta,\gamma,\alpha+\beta+\gamma}^{ecf} C_{\alpha+\beta+\gamma,\delta,m}^{fdg} \\ \times C_{\alpha,\gamma,\alpha+\gamma}^{ach} C_{\beta,\delta,\beta+\delta}^{bdk} C_{\alpha+\gamma,\beta+\delta,m}^{hkg}. \end{aligned}$$

6- j coefficient as recoupling coefficient:

$$\begin{aligned} (ac)(bd) \xrightarrow{R} [(ac)b]d \xrightarrow{\phi} [b(ac)]d \xrightarrow{R} [(ba)c]d \\ \xrightarrow{\phi} [(ab)c]d, \end{aligned}$$

where ϕ denotes that the communication of symbols effects a phase factor transformation, and R denotes that the associative of symbol effects a Racah coefficient transformation:

$$\begin{aligned} \{[(ab)_e c]_f d\}_g \mid [(ac)_h (bd)_k]_g \\ = (-1)^{e+h-a-f} [(2f+1)(2k+1)]^{1/2} W(hbgd; fk) \\ \times [(2e+1)(2h+1)]^{1/2} W(bafc; eh). \end{aligned}$$

9- j coefficient as recoupling coefficient:

$$\begin{aligned} (ac)(bd) \xrightarrow{R} [(ac)b]d \xrightarrow{\phi} [b(ac)]d \xrightarrow{R} [(ba)c]d \\ \xrightarrow{\phi} [(ab)c]d \xrightarrow{R} (ab)(cd), \\ \{[(ab)_e (cd)_f]_g \mid [(ac)_h (bd)_k]_g\} \\ = [(2e+1)(2f+1)(2h+1)(2k+1)]^{1/2} \\ \times \sum_l (-1)^{2l} (2l+1) \begin{Bmatrix} ach \\ lbe \end{Bmatrix} \begin{Bmatrix} bdk \\ ghl \end{Bmatrix} \begin{Bmatrix} efg \\ dlc \end{Bmatrix} \\ = [(2e+1)(2f+1)(2h+1)(2k+1)]^{1/2} \begin{Bmatrix} abe \\ cdf \\ hkg \end{Bmatrix}. \end{aligned}$$

2.12.5 Unsolved Problems in Recoupling Theory

1. Define a route between two coupling symbols for n angular momenta to be any sequence of transpositions and associations that carries one symbol into the other. Each such route then gives rise to a unique expression for the corresponding recoupling coefficient in terms of 6- j coefficients. In general, there are several routes between the same pair of coupling symbols, leading, therefore, to

identities between $6-j$ coefficients. How many nontrivial routes are there between two given coupling symbols, leading to nontrivial relations between $6-j$ coefficients (trivial means related by a phase factor)?

2. Only $6-j$ coefficients arise in all possible couplings of three angular momenta; only $6-j$ and $9-j$ coefficients arise in all possible couplings of four angular momenta; in addition to $6-j$ and $9-j$ coefficients, two new *classes* of coefficients, called $12-j$ coefficients of the first and second kind, arise in the coupling of five angular momenta; in addition to $6-j$, $9-j$, and the two classes of $12-j$ coefficients, five new classes of $15-j$ coefficients arise in the coupling of six angular momenta, \dots . What are the classes of $3n-j$ coefficients? The nonconstructive answer is that a summation over $6-j$ coefficients arising in the coupling of n angular momenta is of a new class if it cannot be expressed in terms of previously defined coefficients occurring in the recoupling of $n-1$ or fewer angular momenta.
3. Toward answering the question of classes of $3n-j$ coefficients, one is led into the classification problem of planar cubic graphs. It is known that every $3n-j$ coefficient corresponds to a planar cubic graph, but the converse is not true. For small n , the relation between the coupling of n angular momenta, the number of new classes of $3(n-1)-j$ coefficients, and the number of nonisomorphic planar cubic graphs on $2(n-1)$ points is:

n	Classes of $3(n-1)-j$ coefficients	Cubic graphs on $2(n-1)$ points
3	1	1
4	1	2
5	2	5
6	5	19
7	18	87
8	84	?
9	576	?

The geometrical object for $n=3$ is a planar graph isomorphic to the tetrahedron in 3-space. The classification of all nonisomorphic cubic graphs on $2(n-1)$ points is an unsolved problem in mathematics, as is the classification of classes for $3(n-1)-j$ coefficients.

4. There are (at least) two methods of realizing the basic triangles of angular momentum theory in terms of graphs. The fundamental structural element $[(ab)c]$ is represented either in terms of its points or in terms of its lines (Fig. 2.4). The right representation leads to the interpretation of recoupling coefficients as functions defined on pairs of labeled binary trees [1]; the left corresponds to the diagrams of the *Jucys* school [7, 8]. Either method leads to the relationship of recoupling coefficients to cubic graphs.
5. The approach of classifying $3n-j$ coefficients through the use of unit tensor operator couplings, Racah operators,

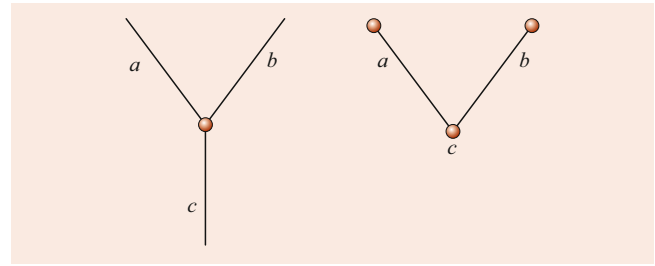


Fig. 2.4 The fundamental triangle $[(ab)c]$ can be realized by lines or points

$9-j$ -invariant operators, and general invariant operators is undeveloped.

2.13 Supplement on Combinatorial Foundations

The quantum theory of angular momentum can be worked out using the abstract postulates of the properties of angular momenta operators and the abstract Hilbert space in which they act. The underlying mathematical apparatus is the Lie algebra of the group $SU(2)$ and multiple copies thereof. An alternative approach is to use special Hilbert spaces that realize all the properties of the abstract postulates and perform calculations within that framework. The framework must be sufficiently rich in structure so as to apply to a manifold of physical situations. This approach has often been used in our treatment; it is an approach that is particularly useful for revealing the combinatorial foundations of quantum angular momentum theory. We illustrate this concretely in this supplementary section. The basic objects are the polynomials defined by Eq. (2.24), which we now call $SU(2)$ solid harmonics, where we change the notation slightly by interchanging the role of m and m' .

2.13.1 $SU(2)$ Solid Harmonics

The $SU(2)$ solid harmonics are defined to be the homogeneous polynomials of degree $2j$ in four commuting indeterminates given by

$$D_{mm'}^j(Z) = \sqrt{\alpha! \beta!} \sum_{(\alpha:A;\beta)} \frac{Z^A}{A!}, \quad (2.112)$$

in which the indeterminates Z and the nonnegative exponents A are encoded in the matrix arrays

$$Z = \begin{pmatrix} z_{11} & z_{12} \\ z_{21} & z_{22} \end{pmatrix}, \quad A = \begin{pmatrix} a_{11} & a_{12} \\ a_{21} & a_{22} \end{pmatrix},$$

$$X^A = \prod_{i,j=1}^2 z_{ij}^{a_{ij}}, \quad A! = \prod_{i,j=1}^2 (a_{ij})!,$$

$$\alpha! = \alpha_1! \alpha_2!, \quad \beta! = \beta_1! \beta_2!.$$

The symbol $(\alpha : A : \beta)$ in Eq. (2.112) denotes that the matrix array A of nonnegative integer entries has row and column sums of its a_{ij} entries given in terms of the quantum numbers j, m, m' by

$$a_{11} + a_{12} = \alpha_1 = j + m, \quad a_{21} + a_{22} = \alpha_2 = j - m,$$

$$a_{11} + a_{21} = \beta_1 = j + m', \quad a_{12} + a_{22} = \beta_2 = j - m'.$$

These $SU(2)$ solid harmonics are among the most important functions in angular momentum theory. Not only do they unify the irreducible representations of $SU(2)$ in any parametrization by the appropriate definition of the indeterminates in terms of generalized coordinates, they also include the popular boson calculus realization of state vectors for quantum mechanical systems, as well as the state vectors for the symmetric rigid rotator.

The realization of the inner product is essential. Physical theory demands an inner product that is given in terms of integrations of wave functions over the variables of the theory, as required by the probabilistic interpretation of wave functions. It is the requirement that realizations of angular momentum operators be Hermitian with respect to the inner product for the spaces being used that assures the orthogonality of functions, so that one is able to take results from one realization of the inner product to another with compatibility of relations. Often, in combinatorial arguments, the inner product plays no direct role.

The nomenclature for $SU(2)$ solid harmonics for the polynomials defined by Eq. (2.112) is by analogy with the term $SO(3, \mathbf{R})$ solid harmonics for the polynomials described in Sect. 2.1.

The polynomials $\mathcal{Y}_{lm}(\mathbf{x})$, $\mathbf{x} = (x_1, x_2, x_3) \in \mathbf{R}^3$ are homogeneous of degree l . The angular momentum operator \mathbf{L}^2 is given by

$$\mathbf{L}^2 = -r^2 \nabla^2 + (\mathbf{x} \cdot \nabla)^2 + (\mathbf{x} \cdot \nabla),$$

which is a sum of two commuting operators $-r^2 \nabla^2$ and $(\mathbf{x} \cdot \nabla)^2 + \mathbf{x} \cdot \nabla$, each of which is invariant under orthogonal transformations. The $SO(3, \mathbf{R})$ solid harmonics are homogeneous polynomials of degree l that solve $\nabla^2 \mathcal{Y}_{lm}(\mathbf{x}) = 0$, so that $\mathbf{L}^2 \mathcal{Y}_{lm}(\mathbf{x}) = l(l+1) \mathcal{Y}_{lm}(\mathbf{x})$. The component angular momentum operators L_i then have the standard action on these polynomials, and under real, proper, orthogonal transformations give the irreducible representations of the group $SO(3, \mathbf{R})$.

The polynomials $D_{mm'}^j(\mathbf{Z})$, $\mathbf{z} = (z_{11}, z_{21}, z_{12}, z_{22}) \in \mathbf{C}^4$ are homogeneous of degree $2j$. The angular momentum op-

erator \mathbf{J}^2 , with $\mathbf{J} = (J_1, J_2, J_3)$, is given by

$$\mathbf{J}^2 = -(\det Z) \left(\det \frac{\partial}{\partial Z} \right) + J_0(J_0 + 1),$$

$$J_0 = \frac{1}{2} \mathbf{z} \cdot \boldsymbol{\partial},$$

$$\boldsymbol{\partial} = \left(\frac{\partial}{\partial z_{11}}, \frac{\partial}{\partial z_{21}}, \frac{\partial}{\partial z_{12}}, \frac{\partial}{\partial z_{22}} \right), \quad (2.113)$$

which is a sum of two commuting operators $-(\det Z) \left(\det \frac{\partial}{\partial Z} \right)$ and $J_0(J_0 + 1)$, each of which is invariant under $SU(2)$ transformations. The $SU(2)$ solid harmonics are homogeneous polynomials of degree $2j$ such that

$$\det \frac{\partial}{\partial Z} D_{mm'}^j(\mathbf{Z}) = 0,$$

$$\mathbf{J}^2 D_{mm'}^j(\mathbf{Z}) = j(j+1) D_{mm'}^j(\mathbf{Z}).$$

The components of the angular momentum operators $\mathbf{J} = (J_1, J_2, J_3) = (M_1, M_2, M_3)$ and $\mathbf{K} = (K_1, K_2, K_3)$ then have the standard action on these polynomials as given in Sect. 2.4.4, and under either left or right $SU(2)$ transformations, these polynomials give the irreducible representations of the group $SU(2)$.

2.13.2 Combinatorial Definition of Wigner–Clebsch–Gordan Coefficients

The $SU(2)$ solid harmonics have a basic role in the interpretation of WCG coefficients in combinatorial terms. We recall from Sect. 2.7.2 that the basic abstract Hilbert space coupling rule for compounding two kinematically independent angular momenta with components $\mathbf{J}_1 = (J_1(1), J_2(1), J_3(1))$ and $\mathbf{J}_2 = (J_1(2), J_2(2), J_3(2))$ to a total angular momentum $\mathbf{J} = (J_1, J_2, J_3) = \mathbf{J}_1 + \mathbf{J}_2$ is

$$|(j_1 j_2) j m\rangle$$

$$= \sum_{m_1+m_2=m} C \begin{matrix} j_1 & j_2 & j \\ m_1 & m_2 & m \end{matrix} |j_1 m_1\rangle \otimes |j_2 m_2\rangle. \quad (2.114)$$

This relation in abstract Hilbert space is realized explicitly by spinorial polynomials as follows:

$$\psi_{(j_1 j_2) j m}(\mathbf{Z}) = \sum_{m_1+m_2=m} C \begin{matrix} j_1 & j_2 & j \\ m_1 & m_2 & m \end{matrix}$$

$$\times \psi_{j_1 m_1}(z_{11}, z_{21}) \psi_{j_2 m_2}(z_{12}, z_{22}), \quad (2.115)$$

$$\psi_{(j_1 j_2) j m}(\mathbf{Z}) = \sqrt{\frac{2j+1}{(j_1+j_2-j)!(j_1+j_2+j+1)!}}$$

$$\times (\det Z)^{j_1+j_2-j} D_{m, j_1-j_2}^j(\mathbf{Z}), \quad (2.116)$$

$$\psi_{jm}(x, y) = \frac{x^{j+m} y^{j-m}}{\sqrt{(j+m)!(j-m)!}}. \quad (2.117)$$

Explicit knowledge of the WCG coefficients is not needed to prove these relationships. The angular momentum operators

$$\begin{aligned} J_+(1) &= z_{11} \frac{\partial}{\partial z_{21}}, & J_-(1) &= z_{21} \frac{\partial}{\partial z_{11}}, \\ J_3(1) &= \frac{1}{2} \left(z_{11} \frac{\partial}{\partial z_{11}} - z_{21} \frac{\partial}{\partial z_{21}} \right); \\ J_+(2) &= z_{12} \frac{\partial}{\partial z_{22}}, & J_-(2) &= z_{22} \frac{\partial}{\partial z_{12}}, \\ J_3(2) &= \frac{1}{2} \left(z_{12} \frac{\partial}{\partial z_{12}} - z_{22} \frac{\partial}{\partial z_{22}} \right) \end{aligned}$$

are Hermitian in the polynomial inner product defined in Sect. 2.4.3 and have the standard action on the polynomials $\psi_{j_1 m_1}(z_{11}, z_{21})$ and $\psi_{j_2 m_2}(z_{12}, z_{22})$, respectively, which are normalized in the inner product (\cdot, \cdot) . The components of total angular momentum operator $\mathbf{J} = \mathbf{M} = \mathbf{J}_1 + \mathbf{J}_2$ have the standard action on the polynomials $\psi_{(j_1 j_2) j m}(Z)$ since they have the standard action on the factor $D_m^{j_1 j_2}(Z)$, as given in Sect. 2.4.4, and $[\mathbf{J}, \det X] = [\mathbf{J}, \det \frac{\partial}{\partial Z}] = 0$. Thus, we have

$$\begin{aligned} \mathbf{J}^2 \psi_{(j_1 j_2) j m}(Z) &= j(j+1) \psi_{(j_1 j_2) j m}(Z), \\ J_{\pm} \psi_{(j_1 j_2) j m}(Z) &= \sqrt{(j \mp m)(j \pm m + 1)} \\ &\quad \times \psi_{(j_1 j_2) j m \pm 1}(Z). \end{aligned}$$

We also note that the two commuting parts of \mathbf{J}^2 are diagonal on these functions:

$$\begin{aligned} J_0(J_0 + 1) \psi_{(j_1 j_2) j m}(Z) &= (j_1 + j_2)(j_1 + j_2 + 1) \psi_{(j_1 j_2) j m}(Z), \\ (\det Z) \left(\det \frac{\partial}{\partial X} \right) \psi_{(j_1 j_2) j m}(Z) &= (j_1 + j_2 - j)(j_1 + j_2 + j_1 + 1) \psi_{(j_1 j_2) j m}(Z). \end{aligned}$$

It is necessary only to verify these properties for the highest weight function $D_j^j(Z) = z_{11}^j / \sqrt{(2j)!}$, for which they are seen to hold.

The angular momentum operators $\mathbf{K} = (K_1, K_2, K_3)$ defined in Sect. 2.4.4 with components that commute with those of $\mathbf{J} = (M_1, M_2, M_3)$ and having $\mathbf{K}^2 = \mathbf{J}^2$ also have a well-defined action on the functions $\psi_{(j_1 j_2) j m}(Z)$. The action of K_+ , K_- , and K_3 on the quantum numbers (j_1, j_2) is to effect the shifts to $(j_1 + \frac{1}{2}, j_2 - \frac{1}{2})$, $(j_1 - \frac{1}{2}, j_2 + \frac{1}{2})$, and (j_1, j_2) , respectively. These actions of Hermitian angular momentum operators satisfying the standard commutation relations $\mathbf{K} \times \mathbf{K} = i\mathbf{K}$ are quite unusual in that they depend only on the angular momentum quantum numbers j_1, j_2, j themselves, which satisfy the triangle rule and give further interesting properties of the modified $SU(2)$ solid harmon-

ics $\psi_{(j_1 j_2) j m}(Z)$. We note these properties in full:

$$\begin{aligned} \mathbf{K}^2 \psi_{(j_1 j_2) j m}(Z) &= j(j+1) \psi_{(j_1 j_2) j m}(Z), \\ K_3 \psi_{(j_1 j_2) j m}(Z) &= (j_1 - j_2) \psi_{(j_1 j_2) j m}(Z), \\ K_+ \psi_{(j_1 j_2) j m}(Z) &= \sqrt{(j - j_1 + j_2)(j + j_1 - j_2 + 1)} \psi_{(j_1 + \frac{1}{2} j_2 - \frac{1}{2}) j m}(Z), \\ K_- \psi_{(j_1 j_2) j m}(Z) &= \sqrt{(j + j_1 - j_2)(j - j_1 + j_2 + 1)} \psi_{(j_1 - \frac{1}{2} j_2 + \frac{1}{2}) j m}(Z). \end{aligned}$$

These relations play no direct role in our continuing considerations of Eq. (2.116) and the determination of the WCG coefficients, and we do not interpret them further.

The explicit WCG coefficients are obtained by expanding the 2×2 determinant in Eq. (2.116), multiplying this expansion into the D -polynomial, and changing the order of the summation. These operations are most succinctly expressed in terms of the umbral calculus of *Roman* and *Rota* [6], using their method of evaluation. The evaluation at y of a divided power $x^k/k!$ of a single indeterminate x to a nonnegative integral power k is defined by

$$\text{eval}_y \frac{x^k}{k!} = \frac{(y)_k}{k!} = \frac{y(y-1) \cdots (y-k+1)}{k!} = \binom{y}{k},$$

where $(y)_k$ is the falling factorial. This definition is extended to products by

$$\text{eval}_{(y_1, y_2, \dots, y_n)} \prod_{i=1}^n \frac{x^{k_i}}{k_i!} = \prod_{i=1}^n \text{eval}_{y_i} \frac{x^{k_i}}{k_i!} = \prod_{i=1}^n \binom{y_i}{k_i}.$$

It is also extended by linearity to sums of such divided powers, multiplied by arbitrary numbers.

The application of these rules to our problem involving four indeterminates gives

$$\begin{aligned} &\frac{(\det X)^n}{n!} \sum_{(\alpha: A: \alpha')} \frac{X^A}{A!} \\ &= \sum_{(\beta: B: \beta')} \text{eval}_B \left(\frac{(\det X)^n}{n!} \right) \frac{X^B}{B!}, \quad (2.118) \\ &\beta = (\alpha_1 + n, \alpha_2 + n), \quad \beta' = (\alpha'_1 + n, \alpha'_2 + n), \\ &\text{eval}_B \frac{(\det X)^n}{n!} \\ &= \sum_{k_1 + k_2 = n} (-1)^{k_2} k_1! k_2! \binom{b_{11}}{k_1} \binom{b_{12}}{k_2} \binom{b_{21}}{k_2} \binom{b_{22}}{k_1}. \quad (2.119) \end{aligned}$$

In this result, we do not identify the labels with angular momentum quantum numbers. Relation Eq. (2.119) is a purely

combinatorial, algebraic identity for arbitrary indeterminates and arbitrary row and column sum constraints on the array A as specified by $\alpha = (\alpha_1, \alpha_2)$ and $\alpha' = (\alpha'_1, \alpha'_2)$. There are no square roots involved.

We now apply relations (Eqs. (2.118)–(2.119)) to the case at hand: $n = j_1 + j_2 - j$, $\alpha = (j + m, j - m)$, $\alpha' = (j + j_1 - j_2, j - j_1 + j_2)$, $\beta = (j_1 + j_2 + m, j_1 + j_2 - m)$, $\beta' = (2j_1, 2j_2)$. This gives the following result for the WCG coefficients:

$$\begin{aligned} & C_{m_1 m_2 m}^{j_1 j_2 j} \\ &= \sqrt{\frac{(j_1 + j_2 - j)!(j_1 - j_2 + j)!(-j_1 + j_2 + j)!}{(j_1 + j_2 + j + 1)!}} \\ & \times \sqrt{\frac{(2j + 1)(j + m)!(j - m)!}{(j_1 + m_1)!(j_1 - m_1)!(j_2 + m_2)!(j_2 - m_2)!}} \\ & \times \text{eval}_A \frac{(\det X)^{j_1 + j_2 - j}}{(j_1 + j_2 - j)!}, \quad (2.120) \\ & \text{eval}_A \frac{(\det X)^{j_1 + j_2 - j}}{(j_1 + j_2 - j)!} \\ &= \sum_{k_1 + k_2 = j_1 + j_2 - j} (-1)^{k_2} k_1! k_2! \binom{j_1 + m_1}{k_1} \binom{j_2 + m_2}{k_2} \\ & \times \binom{j_1 - m_1}{k_2} \binom{j_2 - m_2}{k_1}. \quad (2.121) \end{aligned}$$

In summary, we have the following. Up to multiplicative square-root factors, the WCG coefficient is the evaluation at the point

$$B = \begin{pmatrix} j_1 + m_1 & j_2 + m_2 \\ j_1 - m_1 & j_2 - m_2 \end{pmatrix}$$

of the divided power

$$\frac{(\det X)^{j_1 + j_2 - j}}{(j_1 + j_2 - j)!}$$

of a determinant, which is an integer.

The abstract umbral calculus of Rota thus finds its way, at a basic level, into angular momentum theory. Relation Eq. (2.120) is but a rewriting in terms of evaluations of the well-known Van der Waerden form of the WCG coefficients.

2.13.3 Magic Square Realization of the Addition of Two Angular Momenta

The origin of Eq. (2.114), giving the states of total angular momentum by compounding two angular momenta, is usually attributed to properties of the direct sum of two copies of the Lie algebra of the unitary unimodular group $SU(2)$ and

to the use of differential operators to realize the Lie algebras and state vectors, as was done above. It is an interesting combinatorial result that this structure for adding angular momentum is fully encoded within the properties of magic squares of order 3, and no operators whatsoever are needed, only the condition of being a magic square. We have already noted in Sect. 2.7.4 that Regge observed that the restrictions on the domains of the quantum numbers j_1, m_1, j_2, m_2, j, m are encoded in terms of a magic square A with line sum $J = j_1 + j_2 + j$:

$$A = \begin{pmatrix} j_1 + m_1 & j_2 + m_2 & j - m \\ j_1 - m_1 & j_2 - m_2 & j + m \\ j_2 - j_1 + j & j_1 - j_2 + j & j_1 + j_2 - j \end{pmatrix}. \quad (2.122)$$

The angular momentum quantum numbers are given in terms of the elements of $A = (a_{ij})_{1 \leq i, j \leq 3}$ by the invertible relations

$$\begin{aligned} j_1 &= \frac{1}{2}(a_{11} + a_{21}), & j_2 &= \frac{1}{2}(a_{12} + a_{22}), \\ j &= \frac{1}{2}(a_{13} + a_{23}), \\ m_1 &= \frac{1}{2}(a_{11} - a_{21}), & m_2 &= \frac{1}{2}(a_{12} - a_{22}), \\ m &= \frac{1}{2}(a_{23} - a_{13}). \end{aligned}$$

It follows from these definitions and the fact that A is a magic square of line sum J that the sum rule $m_1 + m_2 = m$ and the triangle condition are fulfilled.

We use the symbol $\langle j_1, j_2, j \rangle$ to denote any triple j_1, j_2, j of angular momentum quantum numbers that satisfy the triangle conditions, where we note that, if a given triple satisfies the triangle conditions, then all permutations of the triple also satisfy the triangle conditions. The number of magic squares for fixed line sum J is obtained as follows. Define $\Delta_J = \{\text{all triangles } \langle j_1, j_2, j \rangle \mid j_1 + j_2 + j = J\}$ and $M(j_1, j_2, j) = \{(m_1, m_2) \mid -j_1 \leq m_1 \leq j_1; -j_2 \leq m_2 \leq j_2; -j \leq m_1 + m_2 \leq j\}$. Then we have the following identity, which gives the number of angular momentum magic squares with line sum J :

$$\sum_{(j_1, j_2, j) \in \Delta_J} |M(j_1, j_2, j)| = \binom{J+5}{5} - \binom{J+2}{5}. \quad (2.123)$$

It is nontrivial to effect the summation on the left-hand side of this relation to obtain the right-hand side, but this expression is known from the theory of magic squares of Stanley [9, 10].

Not only can the addition of two angular momenta in quantum theory, with its triangle rule for three angular momentum quantum numbers and its sum rule on the corresponding projection quantum numbers, be codified in magic

squares of order 3 and arbitrary line sum, but also the content of the abstract state vector of Eq. (2.114) itself can be thus expressed:

$$\begin{aligned} & \left| \frac{1}{2}(a_{11} + a_{21}), \frac{1}{2}(a_{12} + a_{22}); \frac{1}{2}(a_{13} + a_{23}), \frac{1}{2}(a_{23} - a_{13}) \right\rangle \\ &= \sum_{\begin{pmatrix} a_{11} & a_{12} \\ a_{21} & a_{22} \end{pmatrix}} C(A) \left| \frac{1}{2}(a_{11} + a_{21}), \frac{1}{2}(a_{11} - a_{21}) \right\rangle \\ & \quad \otimes \left| \frac{1}{2}(a_{12} + a_{22}), \frac{1}{2}(a_{12} - a_{22}) \right\rangle, \end{aligned}$$

where the summation is over all subsets

$$\begin{pmatrix} a_{11} & a_{12} \\ a_{21} & a_{22} \end{pmatrix}$$

of the magic square of order 3, such that row 3 and column 3 are held fixed. The coefficients $C(A)$ themselves are the WCG coefficients, which may be regarded as a function whose domain of definition is the set of all magic squares of order 3. The triangle rule $\langle j_1, j_2, j \rangle$ and the sum rule on (m_1, m_2, m) are implied by the structure of magic squares of order 3. These rich combinatorial footings of angular momentum theory are completed by the observation that the Clebsch–Gordan coefficients themselves are obtained by the Schwinger–Regge generating function given in Sect. 2.7.3 (see [2] for the relation to ${}_3F_2$ hypergeometric functions).

2.13.4 MacMahon’s and Schwinger’s Master Theorems

Generating functions codify the content of many mathematical entities in a unifying, comprehensive way. These functions are very popular in combinatorics, and Schwinger used them extensively in his treatment of angular momentum theory. In this section, we present a natural generalization of the $SU(2)$ solid harmonics to a class of polynomials that are homogeneous in n^2 indeterminates. While these polynomials are of interest in their own right, it is their fundamental role in the addition of n kinematically independent angular momenta that motivates their introduction here. They bring an unexpected unity and coherence to angular momentum coupling and recoupling theory [11].

We list in compendium format some of the principal results.

Special $U(n)$ solid harmonics:

$$D_{\alpha,\beta}^k(Z) = \sqrt{\alpha!\beta!} \sum_{A \in M(\alpha,\beta)} \frac{Z^A}{A!}, \quad (2.124)$$

$A = (a_{ij})_{1 \leq i, j \leq n}$: matrix of order n in nonnegative integers;

$$A! = \prod_{i,j=1}^n a_{ij}!, \quad Z^A = \prod_{i,j=1}^n z_{ij}^{a_{ij}};$$

where we employ the notations:

$\alpha = (\alpha_1, \alpha_2, \dots, \alpha_n)$: sequence (composition) of nonnegative integers having the sum k , denoted $\alpha \vdash k$;
 $x^\alpha = x_1^{\alpha_1} x_2^{\alpha_2} \dots x_n^{\alpha_n}$, $\alpha! = \alpha_1! \alpha_2! \dots \alpha_n!$;
 $\beta = (\beta_1, \beta_2, \dots, \beta_n)$: second composition $\beta \vdash k$;
 $M(\alpha, \beta)$, the set of all matrices A such that the entries in row i sums to α_i and those in column j to β_j .

The significance of the row-sum vector α is that α_i is the degree of the polynomial in the variables $(z_{i1}, z_{i2}, \dots, z_{in})$ in row i of Z , with a similar interpretation for β in terms of columns.

Matrix of the $D_{\alpha,\beta}^k(Z)$ polynomials:

The number of compositions of the integer k into n nonnegative parts is given by $\binom{n+k-1}{k}$. The compositions in this set may be linearly ordered by the lexicographical rule $\alpha > \beta$, if the first nonzero part of $\alpha - \beta$ is positive. The polynomial $D_{\alpha,\beta}^k(Z)$ is then the entry in row α and column β in the matrix $D^k(Z)$ of dimension $\dim D^k(Z) = \binom{n+k-1}{k}$, where, following the convention for $SU(2)$, the rows are labeled from top to bottom by the greatest to the least sequence, and the columns are labeled in the same manner as read from left to right. There is a combinatorial proof by Chen and Louck [12] that these polynomials satisfy the following multiplication rule for arbitrary matrices X and Y :

$$D^k(XY) = D^k(X)D^k(Y). \quad (2.125)$$

Orthogonality in the inner product $(,)$ defined in Sect. 2.4.3:

$$\langle D_{\alpha,\beta}^k, D_{\alpha',\beta'}^k \rangle = \delta_{\alpha,\alpha'} \delta_{\beta,\beta'} k!.$$

Value on $Z = \text{diag}(z_1, z_2, \dots, z_n)$:

$$\begin{aligned} D_{\alpha,\beta}^k[\text{diag}(z_1, z_2, \dots, z_n)] &= \delta_{\alpha,\beta} z^\alpha, \\ D^k(I_n) &= I_{\binom{n+k-1}{k}}. \end{aligned} \quad (2.126)$$

Transposition property:

$$D^k(Z^T) = [D^k(Z)]^T.$$

Special irreducible unitary representations of $U(n)$:

$$D^k(U)D^k(V) = D^k(UV), \quad \text{all } U, V \in U(n).$$

Schwinger’s Master Theorem: for any two matrices X and Y of order n , the following identities hold:

$$\begin{aligned} e^{(\partial_x: X: \partial_y)} e^{(x: Y: y)} \Big|_{x=y=0} &= \sum_{k=0}^{\infty} \sum_{\alpha, \beta \vdash k} D_{\alpha,\beta}^k(X) D_{\beta,\alpha}^k(Y) \\ &= \frac{1}{\det(I - XY)}, \end{aligned} \quad (2.127)$$

$$(x : Z : y) = xZy^T = \sum_{i,j=1}^n z_{ij}x_iy_j .$$

MacMahon's Master Theorem: let X be the diagonal matrix $X = \text{diag}(x_1, x_2, \dots, x_n)$ and Y a matrix of order n . Then the coefficient of x^α in the expansion of $\frac{1}{\det(I - XY)}$ equals the coefficient of x^α in the product y^α , $y_i = \sum_{j=1}^n y_{ij}x_j$, that is,

$$\frac{1}{\det(I - XY)} = \sum_{k=0}^{\infty} \sum_{\alpha \vdash k} D_{\alpha, \alpha}^k(Y) x^\alpha . \quad (2.128)$$

Basic Master Theorem: let Z be a matrix of order n . Then

$$\frac{1}{\det(I - tZ)} = \sum_{k=0}^{\infty} t^k \sum_{\alpha \vdash k} D_{\alpha, \alpha}^k(Z) . \quad (2.129)$$

Schwinger's relation Eq. (2.127) follows from the basic relation Eq. (2.129) by setting $Z = XY$ and using the multiplication property Eq. (2.125); MacMahon's relation then follows from Schwinger's result by setting $X = \text{diag}(x_1, x_2, \dots, x_n)$ and using property Eq. (2.126). Of course, MacMahon's Master Theorem preceded Schwinger's result by many years [13]. The unification into the single form by using properties of the $D_{\alpha, \beta}^k(Z)$ polynomials was pointed out in [14]. More surprisingly, relation Eq. (2.129) was already discovered for the general linear group in 1897 by *Molien* [15]; its properties are developed extensively in *Michel* and *Zhilinski* [16] in the context of group theory.

For many purposes, it is better in combinatorics to avoid all square roots by using the polynomials

$$L_{\alpha, \beta}(Z) = \sum_{A \in M(\alpha, \beta)} \frac{Z^A}{A!}$$

in place of the $D_{\alpha, \beta}^k(Z)$ defined in Eq. (2.124).

2.13.5 The Pfaffian and Double Pfaffian

Schwinger observed that the calculation of $3n - j$ coefficients involves taking the square root $\sqrt{\det(I - AB)}$, where A and B are skew symmetric (antisymmetric) matrices of order n , but the procedure is rather obscure. The appropriate concepts for taking the square root is that of a Pfaffian and a double Pfaffian, denoted, respectively, by $\text{Pf}(A)$ and $\text{Pf}(A, B)$. The definitions require the concept of a matching of the set of integers $\{1, 2, \dots, n\}$. A matching of $\{1, 2, \dots, n\}$ is an unordered set of disjoint subsets $\{i, j\}$ containing two elements. For example, the matchings of $1, 2, 3$ are $\{1, 2\}$, $\{1, 3\}$, and $\{2, 3\}$. We then have the following constructs.

The Pfaffian and double Pfaffian of skew symmetric matrices $A = (a_{ij})$ and $B = (b_{ij})$ of order n :

$$\text{Pf}(A) = \sum_{\{i_1, i_2\}, \{i_3, i_4\}, \dots, \{i_{n-1}, i_n\}} \varepsilon(i_1 i_2 \cdots i_n) \times a_{i_1, i_2} a_{i_3, i_4} \cdots a_{i_{n-1}, i_n} , \quad (2.130)$$

$$\text{Pf}(A, B) = 1 + \sum_{k \geq 1} \sum_{\substack{\{i_1, i_2\}, \{i_3, i_4\}, \dots, \{i_{2k-1}, i_{2k}\} \\ \{j_1, j_2\}, \{j_3, j_4\}, \dots, \{j_{2k-1}, j_{2k}\}}} \varepsilon(i_1 i_2 \cdots i_{2k}) \varepsilon(j_1 j_2 \cdots j_{2k}) \times a_{i_1, i_2} a_{i_3, i_4} \cdots a_{i_{2k-1}, i_{2k}} \times b_{j_1, j_2} b_{j_3, j_4} \cdots b_{j_{2k-1}, j_{2k}} , \quad (2.131)$$

where $\{i_1, i_2\}, \{i_3, i_4\}, \dots, \{i_{n-1}, i_n\}$ is a matching of $\{1, 2, \dots, n\}$, and $\varepsilon(i_1 i_2 \cdots i_n)$ is the sign of the permutation (number of inversions). Similarly, in the double Pfaffian, the 2-subsets are matchings of a subset of $\{1, 2, \dots, n\}$ of even length.

Relations of skew symmetric matrices A, B to Pfaffians:

$$\sqrt{\det A} = \text{Pf}(A) ; \quad \sqrt{\det(I - AB)} = \text{Pf}(A, B) . \quad (2.132)$$

2.13.6 Generating Functions for Coupled Wave Functions and Recoupling Coefficients

This section is a reformulation, nontrivial extension, and interpretation of results found in *Schwinger* [3]. We first refine the notation used in Sect. 2.12.3.

Set of triangles in the coupling scheme:

Each coupling scheme, as determined by the bracketing B , has associated with it a unique ordered set of $n - 1$ triangles

$$\begin{aligned} T_B(j, k, j) &= \{ \langle a_i, b_i, k_i \rangle \mid i = 1, 2, \dots, n - 1 \} , \\ j &= (j_1, j_2, \dots, j_n) , \\ k &= (k_1, k_2, \dots, k_{n-2}) , \\ k_{n-1} &= j . \end{aligned}$$

The third part k_i of $\langle a_i, b_i, k_i \rangle$ can always be chosen, without loss of generality, as an intermediate angular momentum ($k_{n-1} = j$), and the triangles in the set can be ordered by $\langle a_i, b_i, k_i \rangle < \langle a_{i+1}, b_{i+1}, k_{i+1} \rangle$. The remaining pair of angular momentum labels in the triangle $\langle a_i, b_i, k_i \rangle$ then fall, in general, into four classes: $\langle a_i, b_i, k_i \rangle$ in which a_i can be either a j_r or a k_s , and b_i can be either a $j_{r'}$ or $k_{s'}$. The distribution of the j 's and k 's among the a_i and b_i is uniquely determined by the bracketing B that defines the coupling scheme.

Clebsch–Gordan coefficients for a given coupling scheme:

$$\begin{pmatrix} \mathbf{j} & \mathbf{k} & \mathbf{j} \\ \mathbf{m} & \mathbf{q} & \mathbf{m} \end{pmatrix}^B = \prod_{(a_i, b_i, k_i) \in \mathbf{T}_B(\mathbf{j}, \mathbf{k}, \mathbf{j})} C_{\alpha_i \beta_i q_i}^{a_i b_i k_i}, \quad (2.133)$$

in which the projection quantum numbers α_i and β_i are m 's and q 's that match the a_i and b_i . In the given coupling scheme determined by the bracketing B , only (j_i, m_i) , $i = 1, 2, \dots, n$; (k_i, q_i) , $i = 1, 2, \dots, n-2$, and (j, m) appear in the Clebsch–Gordan coefficients. In fact, if one explicitly implements the sum rule on the projection quantum numbers, it is always possible to express the q_i as sums over the m_i and m .

Coupled angular momentum function for n angular momenta:

$$\Psi_{(\mathbf{j}, \mathbf{k}) \mathbf{j} \mathbf{m}}^B(\mathbf{x}, \mathbf{y}) = \sum_{\mathbf{m}} \begin{pmatrix} \mathbf{j} & \mathbf{k} & \mathbf{j} \\ \mathbf{m} & \mathbf{q} & \mathbf{m} \end{pmatrix}^B \prod_{i=1}^n \psi_{j_i m_i}(x_i, y_i). \quad (2.134)$$

$$\begin{pmatrix} \mathbf{j} \\ \mathbf{m} \end{pmatrix} = \begin{pmatrix} j_1 & j_2 & \cdots & j_n \\ m_1 & m_2 & \cdots & m_n \end{pmatrix},$$

$$\begin{pmatrix} \mathbf{k} \\ \mathbf{q} \end{pmatrix} = \begin{pmatrix} k_1 & k_2 & \cdots & k_{n-2} \\ q_1 & q_2 & \cdots & q_{n-2} \end{pmatrix}. \quad (2.135)$$

$$Z = (z_1 z_2 \dots z_{n+1}) = \begin{pmatrix} x_1 & x_2 & \cdots & x_{n+1} \\ y_1 & y_2 & \cdots & y_{n+1} \end{pmatrix}. \quad (2.136)$$

Only the first n columns of Z enter into Eq. (2.136), but the last column occurs below.

The skew symmetric matrix of a coupling scheme:

The set of triangles $\mathbf{T}_B(\mathbf{j}, \mathbf{k}, \mathbf{j}) = \{(a_i, b_i, k_i) | i = 1, 2, \dots, n-1\}$, which is uniquely defined by the bracketing B , can be mapped to a unique skew symmetric matrix of order $n+1$. This mapping is one of the most important results for obtaining generating functions for the coupled wave functions Eq. (2.134) and the recoupling coefficients given below. The skew symmetric matrix depends on the bracketing B and the detailed manner in which the j 's and k 's are distributed among the triangles in $\mathbf{T}_B(\mathbf{j}, \mathbf{k}, \mathbf{j})$. The rule for constructing the skew symmetric matrix is quite intricate. First, we define a $3 \times (n-1)$ matrix T of indeterminates by

$$T = \begin{pmatrix} t_{11} & t_{12} & \cdots & t_{1,n-1} \\ t_{21} & t_{22} & \cdots & t_{2,n-1} \\ t_{31} & t_{32} & \cdots & t_{3,n-1} \end{pmatrix}. \quad (2.137)$$

Second, we associate with each $(a_i, b_i, k_i) \in \mathbf{T}_B(\mathbf{j}, \mathbf{k}, \mathbf{j})$, a triple of indeterminates (u_i, v_i, w_i) as given by

$$\begin{aligned} (a_1, b_1, k_1) &\mapsto (u_1, v_1, w_1), & \text{with } w_1 &= t_{21}u_1 + t_{11}v_1, \\ (a_2, b_2, k_2) &\mapsto (u_2, v_2, w_2), & \text{with } w_2 &= t_{22}u_2 + t_{12}v_2, \\ &\vdots & & \vdots \end{aligned}$$

$$\begin{aligned} (a_{n-1}, b_{n-1}, k_{n-1}) &\mapsto (u_{n-1}, v_{n-1}, w_{n-1}), \\ \text{with } w_{n-1} &= t_{2,n-1}u_{n-2} + t_{1,n-1}v_{n-1}. \end{aligned} \quad (2.138)$$

The indeterminates u_i and v_i are identified as a column $z_i = (x_i, y_i)$ of the $2 \times (n+1)$ matrix Z defined by Eq. (2.136), or as one of the w 's occurring higher in the display Eq. (2.138). The distribution rule is in one-to-one correspondence with the distribution of j 's and k 's in the corresponding triangle. Thus, we have

$$\begin{aligned} u_i &= z_r, & \text{if } a_i &= j_r; & v_i &= z_s, & \text{if } b_i &= j_s; \\ u_i &= z_r, & \text{if } a_i &= j_r; & v_i &= w_s, & \text{if } b_i &= k_s; \\ u_i &= w_r, & \text{if } a_i &= k_r; & v_i &= z_s, & \text{if } b_i &= j_s; \\ u_i &= w_r, & \text{if } a_i &= k_r; & v_i &= w_s, & \text{if } b_i &= k_s. \end{aligned}$$

The explicit identification of all j 's and k 's is uniquely determined by the bracketing B . Once this identification has been made, the elements a_{ij} , $i < j$ of the skew symmetric matrix A of order $n+1$ are uniquely determined in terms of the elements of T by equating coefficients of $\det(z_i, z_j) = x_i y_j - x_j y_i$ on the two sides of the form

$$\begin{aligned} \sum_{1 \leq i < j \leq n+1} a_{ij} \det(z_i, z_j) \\ = \sum_{i=1}^{n-1} t_{3i} \det(u_i, v_i) + \det(w_{n-1}, z_{n+1}), \end{aligned} \quad (2.139)$$

where (t_{1i}, t_{2i}, t_{3i}) is the i -th column of the $3 \times (n-1)$ matrix T of indeterminates. This relation can be inferred from results given by Schwinger. Since the elements of A are determined as monomials in the elements of T , we sometimes denote A by $A(T)$. It is useful to illustrate the rule for determining A for $n = 2, 3, 4$.

$n = 2$: triangle: $\langle j_1, j_2, k_1 \rangle$:

$$w_1 = t_{21}z_1 + t_{11}z_2$$

$$\begin{aligned} a_{12} \det(z_1, z_2) + a_{13} \det(z_1, z_3) + a_{23} \det(z_2, z_3) \\ = t_{31} \det(u_1, v_1) + \det(w_1, z_3) \\ = t_{31} \det(z_1, z_2) + t_{21} \det(z_1, z_3) \\ + t_{11} \det(z_2, z_3); \end{aligned}$$

$$a_{12} = t_{31}, \quad a_{13} = t_{21}, \quad a_{23} = t_{11}.$$

$n = 3$: ordered triangles: $\langle j_1, j_2, k_1 \rangle, \langle k_1, j_3, k_2 \rangle$:

$$w_1 = t_{21}u_1 + t_{11}v_1, \quad u_1 = z_1, v_1 = z_2;$$

$$w_2 = t_{22}u_2 + t_{12}v_2, \quad u_2 = w_1, v_2 = z_3.$$

$$\begin{aligned} \sum_{1 \leq i < j \leq 4} a_{ij} \det(z_i, z_j) \\ = t_{31} \det(u_1, v_1) + t_{32} \det(u_2, v_2) + \det(w_2, z_4); \end{aligned}$$

$$\begin{aligned} a_{12} &= t_{31}, & a_{13} &= t_{21}t_{32}, & a_{14} &= t_{21}t_{22} \\ a_{23} &= t_{11}t_{32}, & a_{24} &= t_{11}t_{22} \\ a_{34} &= t_{12} \end{aligned}$$

$n = 4$: ordered triangles: $\langle j_3, j_1, k_1 \rangle, \langle j_4, j_2, k_2 \rangle, \langle k_1, k_2, k_3 \rangle$:

$$\begin{aligned} w_1 &= t_{21}u_1 + t_{11}v_1, & u_1 &= z_3, & v_1 &= z_1, \\ w_2 &= t_{22}u_2 + t_{12}v_2, & u_2 &= z_4, & v_2 &= z_2, \\ w_3 &= t_{23}u_3 + t_{13}v_3, & u_3 &= w_1, & v_3 &= w_2; \\ w_3 &= t_{11}t_{23}z_1 + t_{12}t_{13}z_2 + t_{21}t_{23}z_3 + t_{22}t_{13}z_4, \\ \sum_{1 \leq i < j \leq 5} a_{ij} \det(z_i, z_j) &= t_{31} \det(u_1, v_1) + t_{32} \\ &\times \det(u_2, v_2) + t_{33} \det(u_3, v_3) + \det(w_3, z_5); \\ a_{12} &= t_{11}t_{12}t_{33}, & a_{13} &= -t_{31}, & a_{14} &= t_{11}t_{22}t_{33}, \\ a_{23} &= -t_{12}t_{21}t_{33}, & a_{24} &= -t_{32}, \\ a_{34} &= t_{21}t_{22}t_{33}, \end{aligned}$$

$$\begin{aligned} a_{15} &= t_{11}t_{23} \\ a_{25} &= t_{12}t_{13} \\ a_{35} &= t_{21}t_{23} \\ a_{45} &= t_{22}t_{13} \end{aligned}$$

Triangle monomials.

Let $\langle a, b, c \rangle$ be a triangle of quantum numbers (a, b, c) , let (x, y, z) be three indeterminates, and let B denote a binary coupling scheme with the set of triangles $T_B(\mathbf{j}, \mathbf{k}, j)$.

Elementary triangle monomial:

$$\begin{aligned} \Phi_{\langle a, b, c \rangle}(x, y, z) &= \{abc\}^{-1} x^{b+c-a} y^{a+c-b} z^{a+b-c}, \\ \{abc\} &= \frac{(2c+1)(b+c-a)(a+c-b)!(a+b-c)!}{(a+b+c+1)!}^{\frac{1}{2}}. \end{aligned} \quad (2.140)$$

Triangle monomial associated with a given coupling scheme B :

$$\Phi_{\mathbf{j}, \mathbf{k}, j}^B(T) = \prod_{\langle a_i, b_i, k_i \rangle \in T_B(\mathbf{j}, \mathbf{k}, j)} \Phi_{\langle a_i, b_i, k_i \rangle}(t_{1i}, t_{2i}, t_{3i}). \quad (2.141)$$

Using the definitions introduced above, we can now give the generating functions for the coupled wave functions and the recoupling coefficients for each coupling scheme as determined by the bracketing B .

Generating function for coupled wave functions:

$$\begin{aligned} e^{xA(T)y^T} &= e^{\sum_{1 \leq i < j \leq n+1} a_{ij} \det(z_i, z_j)} \\ &= \sum_{\mathbf{j}, \mathbf{k}} \Phi_{\mathbf{j}, \mathbf{k}, j}^B(T) \sum_m (-1)^{j-m} \psi_{j, -m}(x_{n+1}, y_{n+1}) \\ &\quad \times \Psi_{(\mathbf{j}, \mathbf{k})_{jm}}^B(\mathbf{x}, \mathbf{y}), \\ x &= (x_1, x_2, \dots, x_{n+1}), \quad y = (y_1, y_2, \dots, y_{n+1}). \end{aligned} \quad (2.142)$$

Relation to $U(n+1)$ solid harmonics:

$$e^{xA(T)y^T} = \sum_{k=0}^{\infty} \sum_{\alpha, \beta \vdash k} \frac{x^\alpha}{\sqrt{\alpha!}} D_{\alpha, \beta}^k(A(T)) \frac{y^\beta}{\sqrt{\beta!}}. \quad (2.143)$$

Relation of $U(n+1)$ solid harmonics to triangle monomials:

$$D_{\alpha, \beta}^k[A(T)] = (-1)^{j-m} \sum_k \begin{pmatrix} \mathbf{j} & \mathbf{k} & j \\ \mathbf{m} & \mathbf{q} & m \end{pmatrix}^B \Phi_{\mathbf{j}, \mathbf{k}, j}^B(T) \quad (2.144)$$

$$\begin{aligned} \alpha_i &= j_i + m_i, & \beta_i &= j_i - m_i \quad i = 1, 2, \dots, n; \\ \alpha_{n+1} &= j - m, & \beta_{n+1} &= j + m; \\ \sum_i \alpha_i &= \sum_i \beta_i = j_1 + j_2 + \dots + j_n + j. \end{aligned}$$

The relation between the skew symmetric matrix $A(T)$ of order $n+1$ and the elements of the $3 \times (n-1)$ matrix T is that described in relations Eq. (2.138).

Generating function for all recoupling coefficients:

$$\begin{aligned} \frac{1}{[\text{Pf}(A(T), A'(T'))]^2} &= \frac{1}{[\text{Pf}(A(T), A'(T'))]^2} \\ &= \sum_{\mathbf{j}, \mathbf{k}, \mathbf{k}', j} \Phi_{\mathbf{j}, \mathbf{k}, j}^B(T) \Phi_{\mathbf{j}', \mathbf{k}', j}^{B'}(T') \langle \mathbf{j}, \mathbf{k}, j \parallel \mathbf{j}', \mathbf{k}', j \rangle, \end{aligned} \quad (2.145)$$

where $\langle \mathbf{j}, \mathbf{k}, j \parallel \mathbf{j}', \mathbf{k}', j \rangle$ denotes the recoupling coefficient that effects the transformation between the coupling schemes corresponding to the bracketing B and the bracketing B' , and where the sequence \mathbf{j}' is a permutation of \mathbf{j} in accordance with the bracketing B' . We also note that

$$\begin{aligned} \frac{1}{\text{Pf}(A, A')} &= \frac{1}{\sqrt{\det(I - AA')}} \\ &= \left[1 + \sum_{k \geq 1} \sum_{\alpha, \beta \vdash k} D_{\alpha, \beta}^k(A) D_{\beta, \alpha}^k(A') \right]^{\frac{1}{2}}, \end{aligned} \quad (2.146)$$

for arbitrary skew symmetric matrices of order n .

Relation Eq. (2.145) generates all recoupling coefficients, the trivial ones (those differing by signs) and all the complicated ones, that is, those corresponding to $3n-j$ coefficients. It will also be observed that the expansion of the reciprocal of the double Pfaffian effects an infinite sum in which no radicals occur, which in turn implies that the every recoupling coefficient has the form

$$\begin{aligned} \langle \mathbf{j}, \mathbf{k}, j \parallel \mathbf{j}', \mathbf{k}', j \rangle &= \prod_{\langle a_i, b_i, k_i \rangle \in T_B(\mathbf{j}, \mathbf{k}, j)} \{a_i, b_i, k_i\} \\ &\quad \times \prod_{\langle a'_i, b'_i, k'_i \rangle \in T_{B'}(\mathbf{j}', \mathbf{k}', j)} \{a'_i, b'_i, k'_i\} \\ &\quad \times I(\mathbf{j}, \mathbf{k}, j \parallel \mathbf{j}', \mathbf{k}', j), \end{aligned}$$

where $I(j, k, j || j', k', j)$ is an integer. Each recoupling coefficient is an integer multiplied by square-root factors that depend on the triangles associated with the coupling scheme.

Such features can be very useful in the development of algorithms for the calculation of $3n-j$ coefficients, including WCG coefficients [17]. Relation Eq. (2.145) should be useful for the classification of $3n-j$ coefficients.

2.14 Author's Comments

The relationship between the group $SU(2)$ of 2×2 unitary unimodular (determinant 1) matrices under the usual rule of matrix multiplication for multiplying pairs and the group of 3×3 rotation group $SO(3, R)$ of proper (determinant 1) orthogonal matrices under matrix multiplication of pairs most often uses the known fact that $SU(2)$ is the minimal covering group of $SO(3, R)$. This is the method used in the first version of the *Springer Handbook* and the *Revised Springer Handbook* presented here. However, there is another way of viewing the relationship between the two groups as a sort of nonlinear isomorphism. This is the 3×3 Cartan Hermitian matrix representation, which gives a one-to-one correspondence with the fundamental 3×3 representation of the rotation group. This was already initiated in Sect. 2.1 of this chapter. It will not be carried further here. However, it is appropriate to point out that entering into the development will be the domain of definition, which may be taken to be the unit sphere for the rotation group, and to which is adjoined the Euler angle χ for the unitary unimodular group $SU(2)$ (Chap. 2 and, in particular, Sect. 5, of [1]). It is this Cartan representation by Hermitian matrices that is to be compared to the 3×3 representation of the rotation group $SO(3, R)$ by the active rotation of a physical system onto itself. All of this must be woven together in a coherent fashion.

Then, there is always the question of whether or not the electron is a composite object: electron plus spin? (All reasonable questions should be allowed in any reasonable theory.) Can the electron contain within itself a hidden massless object of spin-1/2 that it can cast-off only in a special environment? Surely this is nonsense. Nonetheless, the invisible partner can be there in the above viewpoint.

Quite aside from the above possibilities of structure, there is another feature of angular momentum theory as presented in this article—the use of the covering group $SU(2)$ of $SO(3, R)$. Racah calculated the coefficients in the form given by Eq. (2.77) by summing over four Clebsch–Gordan coefficients as given by the third formula in the collection at the beginning of Sect. 2.9.1. The details of this calculation can be found in Vol. 8 of [1]. What is important about this form is its expression in terms of triangle coefficients. The question is: since the Racah form of angular momentum theory is applicable to both angular momenta with integer and half-odd

integers, and this feature carries forward to the full family of $3n-j$ coefficients constructed from the Clebsch–Gordan and Racah coefficients, how does it happen that only factorials appear in Eq. (2.77), and the occurrence of the gamma function is never an issue? It must be the case that the set of triangle coefficients that occur in the Racah coefficient somehow block out the occurrence of the gamma function. This places the role of triangle coefficients at the basis of the quantum mechanics of physics. *In the development of angular momentum theory, it is triangle coefficients that have a built-in structure that assures that only factorials occur in the expression of its family of $3n-j$ coefficients.*

The author has carried the properties of triangle coefficients forward by showing how to include all triangles into a single comprehensive symbol for every $3n-j$ coefficient. This leads directly to the classification of $3n-j$ coefficients in terms of binary trees and gives many new insights into the tenets of angular momentum theory. The reference to the two books is given here for the benefit of the reader wishing to pursue this subject: James D. Louck, *Unitary Symmetry and Combinatorics*, World Scientific, Singapore, 2008; *Applications of Unitary Symmetry and Combinatorics*, World Scientific, Singapore, 2011.

In pointing out these references, the author is also obligated to mention an error that occurs throughout. The statement that the smallest angular momentum that occurs in implementing the Clebsch–Gordan series into the addition of n angular momenta is the least of all positive angular momenta in the multiset $pmj_1, pmj_2, \dots, pmj_n$ of 2^n angular momenta is wrong. This was pointed out to the author by Dr. Wade Smith about 4 years ago by giving the counterexample $j_1 = 1, j_2 = 1, j_3 = 1, j_4 = 4$. The correct answer is $j(\min) =$ greatest angular momentum in the set j_1, j_2, \dots, j_n of original angular momenta being coupled.

2.15 Tables

Excerpts and Fig. 2.1 are reprinted from *Biedenharn and Louck* [1] with permission of Cambridge University Press. Tables 2.2–2.4 have been adapted from *Edmonds* [18] by permission of Princeton University Press. Thanks are given for this cooperation.

Acknowledgments This contribution on angular momentum theory is dedicated to Lawrence C. Biedenharn, whose tireless and continuing efforts in bringing understanding and structure to this complex subject is everywhere imprinted.

We also wish to acknowledge the many contributions of H. W. Galbraith and W. Y. C. Chen in sorting out the significance of results found in *Schwinger* [3]. The Supplement is dedicated to the memory of Brian G. Wybourne, whose contributions to symmetry techniques and angular momentum theory, both abstract and applied to physical systems, was monumental.

Table 2.1 The solid and spherical harmonics \mathcal{Y}_{lm} and the tensor harmonics \mathcal{T}_μ^k (labeled by $k = l$ and $\mu = m$) for $l = 0, 1, 2, 3$, and 4

l	m	$\sqrt{4\pi}\mathcal{Y}_{lm}(r)$	$\sqrt{4\pi}\mathcal{Y}_{lm}(\theta, \varphi)$	\mathcal{T}_m^l
1	± 1	$\mp\sqrt{\frac{3}{2}}(x \pm iy)$	$\mp\sqrt{\frac{3}{2}}e^{\pm i\varphi}\sin\theta$	$\mp\sqrt{2}J_\pm$
	0	$\sqrt{3}z$	$\sqrt{3}\cos\theta$	$2J_3$
2	± 2	$\frac{1}{2}\sqrt{\frac{15}{2}}(x \pm iy)^2$	$\frac{1}{2}\sqrt{\frac{15}{2}}e^{\pm 2i\varphi}\sin^2\theta$	$\sqrt{6}J_\pm^2$
	± 1	$\mp\sqrt{\frac{15}{2}}(x \pm iy)z$	$\mp\sqrt{\frac{15}{2}}e^{\pm i\varphi}\sin\theta\cos\theta$	$\mp\sqrt{6}J_\pm(2J_3 \pm 1)$
	0	$\frac{1}{2}\sqrt{5}(3z^2 - r^2)$	$\frac{1}{2}\sqrt{5}(3\cos^2\theta - 1)$	$2(3J_3^2 - J^2)$
3	± 3	$\mp\frac{1}{4}\sqrt{35}(x \pm iy)^3$	$\mp\frac{1}{4}\sqrt{35}e^{\pm 3i\varphi}\sin^3\theta$	$\mp 2\sqrt{5}J_\pm^3$
	± 2	$\frac{1}{2}\sqrt{\frac{105}{2}}(x \pm iy)^2z$	$\frac{1}{2}\sqrt{\frac{105}{2}}e^{\pm 2i\varphi}\sin^2\theta\cos\theta$	$2\sqrt{30}J_\pm^2(J_3 \pm 1)$
	± 1	$\mp\frac{1}{4}21(x \pm iy)(5z^2 - r^2)$	$\mp\frac{1}{4}\sqrt{21}e^{\pm i\varphi}\sin\theta(5\cos^2\theta - 1)$	$\mp 2\sqrt{3}J_\pm(5J_3^2 - J^2 \pm 5J_3 + 2)$
	0	$\frac{1}{2}\sqrt{7}(5z^2 - 3r^2)z$	$\frac{1}{2}\sqrt{7}(5\cos^2\theta - 3)\cos\theta$	$4(5J_3^2 - 3J^2 + 1)J_3$
4	± 4	$\frac{3}{16}\sqrt{70}(x \pm iy)^4$	$\frac{3}{16}\sqrt{70}e^{\pm 4i\varphi}\sin^4\theta$	$\sqrt{70}J_\pm^4$
	± 3	$\mp\frac{3}{4}\sqrt{35}(x \pm iy)^3z$	$\mp\frac{3}{4}\sqrt{35}e^{\pm 3i\varphi}\sin^3\theta\cos\theta$	$\mp 2\sqrt{35}J_\pm^3(2J_3 \pm 3)$
	± 2	$\frac{3}{8}\sqrt{10}(x \pm iy)^2(7z^2 - r^2)$	$\frac{3}{8}\sqrt{10}e^{\pm 2i\varphi}\sin^2\theta(7\cos^2\theta - 1)$	$2\sqrt{10}J_\pm^2(7J_3^2 - J^2 \pm 14J_3 + 9)$
	± 1	$\mp\frac{3}{4}\sqrt{5}(x \pm iy)(7z^2 - 3r^2)z$	$\mp\frac{3}{4}\sqrt{5}e^{\pm i\varphi}\sin\theta(7\cos^2\theta - 3)\cos\theta$	$\mp\sqrt{5}J_\pm(28J_3^3 - 12J^2J_3 \pm 42J_3^2 - 6J^2 + 38J_3 \pm 12)$
	0	$\frac{15}{8}(7z^4 - 6z^2r^2 + \frac{3}{5}r^4)$	$\frac{15}{8}(7\cos^4\theta - 6\cos^2\theta + \frac{3}{5})$	$70J_3^4 - 60J^2J_3^2 + 6(J^2)^2 + 50J_3^2 - 12J^2$

Table 2.2 The $3-j$ coefficients for all M 's = 0 or $J_3 = 0, \frac{1}{2}$

$\begin{pmatrix} J_1 & J_2 & J_3 \\ 0 & 0 & 0 \end{pmatrix} = (-1)^{\frac{1}{2}J} \left(\frac{(J_1 + J_2 - J_3)!(J_1 + J_3 - J_2)!(J_2 + J_3 - J_1)!}{(J_1 + J_2 + J_3 + 1)!} \right)^{\frac{1}{2}} \frac{(\frac{1}{2}J)!}{(\frac{1}{2}J - J_1)!(\frac{1}{2}J - J_2)!(\frac{1}{2}J - J_3)!}, \quad J \text{ even}$
$\begin{pmatrix} J_1 & J_2 & J_3 \\ 0 & 0 & 0 \end{pmatrix} = 0, \quad J \text{ odd, where } J = J_1 + J_2 + J_3$
$\begin{pmatrix} J & J & 0 \\ M & -M & 0 \end{pmatrix} = (-1)^{J-M} \frac{1}{(2J + 1)^{1/2}}$
$\begin{pmatrix} J + \frac{1}{2} & J & \frac{1}{2} \\ M & -M - \frac{1}{2} & \frac{1}{2} \end{pmatrix} = (-1)^{J-M-\frac{1}{2}} \left(\frac{J - M + \frac{1}{2}}{(2J + 2)(2J + 1)} \right)^{1/2}$

Table 2.3 The $3-j$ coefficients for $J_3 = 1, \frac{3}{2}, 2$

$\begin{pmatrix} J + 1 & J & 1 \\ M & -M - 1 & 1 \end{pmatrix} = (-1)^{J-M-1} \left(\frac{(J - M)(J - M + 1)}{(2J + 3)(2J + 2)(2J + 1)} \right)^{\frac{1}{2}}$
$\begin{pmatrix} J + 1 & J & 1 \\ M & -M & 0 \end{pmatrix} = (-1)^{J-M-1} \left(\frac{2(J + M + 1)(J - M + 1)}{(2J + 3)(2J + 2)(2J + 1)} \right)^{\frac{1}{2}}$
$\begin{pmatrix} J & J & 1 \\ M & -M - 1 & 1 \end{pmatrix} = (-1)^{J-M} \left(\frac{2(J - M)(J + M + 1)}{(2J + 2)(2J + 1)(2J)} \right)^{\frac{1}{2}}$
$\begin{pmatrix} J & J & 1 \\ M & -M & 0 \end{pmatrix} = (-1)^{J-M} \frac{M}{[(2J + 1)(J + 1)J]^{\frac{1}{2}}}$
$\begin{pmatrix} J + \frac{3}{2} & J & \frac{3}{2} \\ M & -M - \frac{3}{2} & \frac{3}{2} \end{pmatrix} = (-1)^{J-M+\frac{1}{2}} \left(\frac{(J - M - \frac{1}{2})(J - M + \frac{1}{2})(J - M + \frac{3}{2})}{(2J + 4)(2J + 3)(2J + 2)(2J + 1)} \right)^{\frac{1}{2}}$
$\begin{pmatrix} J + \frac{3}{2} & J & \frac{3}{2} \\ M & -M - \frac{1}{2} & \frac{3}{2} \end{pmatrix} = (-1)^{J-M+\frac{1}{2}} \left(\frac{3(J - M + \frac{1}{2})(J - M + \frac{3}{2})(J + M + \frac{3}{2})}{(2J + 4)(2J + 3)(2J + 2)(2J + 1)} \right)^{\frac{1}{2}}$
$\begin{pmatrix} J + \frac{1}{2} & J & \frac{3}{2} \\ M & -M - \frac{3}{2} & \frac{3}{2} \end{pmatrix} = (-1)^{J-M-\frac{1}{2}} \left(\frac{3(J - M - \frac{1}{2})(J - M + \frac{1}{2})(J + M + \frac{3}{2})}{(2J + 3)(2J + 2)(2J + 1)2J} \right)^{\frac{1}{2}}$

Table 2.3 (Continued)

$\begin{pmatrix} J + \frac{1}{2} & J & \frac{3}{2} \\ M & -M - \frac{1}{2} & \frac{1}{2} \end{pmatrix}$	$= (-1)^{J-M-\frac{1}{2}} \left(\frac{J-M+\frac{1}{2}}{(2J+3)(2J+2)(2J+1)2J} \right)^{\frac{1}{2}} \left(J+3M+\frac{3}{2} \right)$
$\begin{pmatrix} J+2 & J & 2 \\ M & -M-2 & 2 \end{pmatrix}$	$= (-1)^{J-M} \left(\frac{(J-M-1)(J-M)(J-M+1)(J-M+2)}{(2J+5)(2J+4)(2J+3)(2J+2)(2J+1)} \right)^{\frac{1}{2}}$
$\begin{pmatrix} J+2 & J & 2 \\ M & -M-1 & 1 \end{pmatrix}$	$= (-1)^{J-M} \left(\frac{(J+M+2)(J-M+2)(J-M+1)(J-M)}{(2J+5)(2J+4)(2J+3)(2J+2)(2J+1)} \right)^{\frac{1}{2}}$
$\begin{pmatrix} J+2 & J & 2 \\ M & -M & 0 \end{pmatrix}$	$= (-1)^{J-M} \left(\frac{6(J+M+2)(J+M+1)(J-M+2)(J-M+1)}{(2J+5)(2J+4)(2J+3)(2J+2)(2J+1)} \right)^{\frac{1}{2}}$
$\begin{pmatrix} J+1 & J & 2 \\ M & -M-2 & 2 \end{pmatrix}$	$= 2(-1)^{J-M+1} \left(\frac{(J-M-1)(J-M)(J-M+1)(J+M+2)}{(2J+4)(2J+3)(2J+2)(2J+1)2J} \right)^{\frac{1}{2}}$
$\begin{pmatrix} J+1 & J & 2 \\ M & -M-1 & 1 \end{pmatrix}$	$= (-1)^{J-M+1} 2(J+2M+2) \left(\frac{(J-M+1)(J-M)}{(2J+4)(2J+3)(2J+2)(2J+1)2J} \right)^{\frac{1}{2}}$
$\begin{pmatrix} J+1 & J & 2 \\ M & -M & 0 \end{pmatrix}$	$= (-1)^{J-M+1} 2M \left(\frac{6(J+M+1)(J-M+1)}{(2J+4)(2J+3)(2J+2)(2J+1)2J} \right)^{\frac{1}{2}}$
$\begin{pmatrix} J & J & 2 \\ M & -M-2 & 2 \end{pmatrix}$	$= (-1)^{J-M} \left(\frac{6(J-M-1)(J-M)(J+M+1)(J+M+2)}{(2J+3)(2J+2)(2J+1)(2J)(2J-1)} \right)^{\frac{1}{2}}$
$\begin{pmatrix} J & J & 2 \\ M & -M-1 & 1 \end{pmatrix}$	$= (-1)^{J-M} (1+2M) \left(\frac{6(J+M+1)(J-M)}{(2J+3)(2J+2)(2J+1)(2J)(2J-1)} \right)^{\frac{1}{2}}$
$\begin{pmatrix} J & J & 2 \\ M & -M & 0 \end{pmatrix}$	$= (-1)^{J-M} \frac{2[3M^2 - J(J+1)]}{[(2J+3)(2J+2)(2J+1)(2J)(2J-1)]^{\frac{1}{2}}}$

Table 2.4 The $6-j$ coefficients for $d = 0, \frac{1}{2}, 1, \frac{3}{2}, 2$, with $s = a + b + c$

$\begin{Bmatrix} a & b & c \\ 0 & e & f \end{Bmatrix}$	$= (-1)^s [(2b+1)(2c+1)]^{\frac{1}{2}} \delta_{bf} \delta_{ce}$
$\begin{Bmatrix} a & b & c \\ \frac{1}{2} & c - \frac{1}{2} & b + \frac{1}{2} \end{Bmatrix}$	$= (-1)^s \left(\frac{(s-2b)(s-2c+1)}{(2b+1)(2b+2)2c(2c+1)} \right)^{\frac{1}{2}}$
$\begin{Bmatrix} a & b & c \\ \frac{1}{2} & c - \frac{1}{2} & b - \frac{1}{2} \end{Bmatrix}$	$= (-1)^s \left(\frac{(s+1)(s-2a)}{2b(2b+1)2c(2c+1)} \right)^{\frac{1}{2}}$
$\begin{Bmatrix} a & b & c \\ 1 & c-1 & b-1 \end{Bmatrix}$	$= (-1)^s \left(\frac{s(s+1)(s-2a-1)(s-2a)}{(2b-1)2b(2b+1)(2c-1)2c(2c+1)} \right)^{\frac{1}{2}}$
$\begin{Bmatrix} a & b & c \\ 1 & c-1 & b \end{Bmatrix}$	$= (-1)^s \left(\frac{2(s+1)(s-2a)(s-2b)(s-2c+1)}{2b(2b+1)(2b+2)(2c-1)2c(2c+1)} \right)^{\frac{1}{2}}$
$\begin{Bmatrix} a & b & c \\ 1 & c-1 & b+1 \end{Bmatrix}$	$= (-1)^s \left(\frac{(s-2b-1)(s-2b)(s-2c+1)(s-2c+2)}{(2b+1)(2b+2)(2b+3)(2c-1)2c(2c+1)} \right)^{\frac{1}{2}}$
$\begin{Bmatrix} a & b & c \\ 1 & c & b \end{Bmatrix}$	$= (-1)^{s+1} \frac{2[b(b+1)+c(c+1)-a(a+1)]}{[2b(2b+1)(2b+2)2c(2c+1)(2c+2)]^{\frac{1}{2}}}$
$\begin{Bmatrix} a & b & c \\ \frac{3}{2} & c - \frac{3}{2} & b - \frac{3}{2} \end{Bmatrix}$	$= (-1)^s \left(\frac{(s-1)s(s+1)(s-2a-2)(s-2a-1)(s-2a)}{(2b-2)(2b-1)2b(2b+1)(2c-2)(2c-1)2c(2c+1)} \right)^{\frac{1}{2}}$
$\begin{Bmatrix} a & b & c \\ \frac{3}{2} & c - \frac{3}{2} & b - \frac{1}{2} \end{Bmatrix}$	$= (-1)^s \left(\frac{3s(s+1)(s-2a-1)(s-2a)(s-2b)(s-2b+1)}{(2b-1)2b(2b+1)(2b+2)(2c-2)(2c-1)2c(2c+1)} \right)^{\frac{1}{2}}$
$\begin{Bmatrix} a & b & c \\ \frac{3}{2} & c - \frac{3}{2} & b + \frac{1}{2} \end{Bmatrix}$	$= (-1)^s \left(\frac{3(s+1)(s-2a)(s-2b-1)(s-2b)(s-2c+1)(s-2c+2)}{2b(2b+1)(2b+2)(2b+3)(2c-2)(2c-1)2c(2c+1)} \right)^{\frac{1}{2}}$

Table 2.4 (Continued)

$\left\{ \begin{matrix} a & b & c \\ \frac{3}{2} & c - \frac{3}{2} & b + \frac{3}{2} \end{matrix} \right\}$	$= (-1)^s \left(\frac{(s-2b-2)(s-2b-1)(s-2b)(s-2c+1)(s-2c+2)(s-2c+3)}{(2b+1)(2b+2)(2b+3)(2b+4)(2c-2)(2c-1)2c(2c+1)} \right)^{\frac{1}{2}}$
$\left\{ \begin{matrix} a & b & c \\ \frac{3}{2} & c - \frac{1}{2} & b - \frac{1}{2} \end{matrix} \right\}$	$= (-1)^s \frac{[2(s-2b)(s-2c) - (s+2)(s-2a-1)][(s+1)(s-2a)]^{\frac{1}{2}}}{[(2b-1)2b(2b+1)(2b+2)(2c-1)2c(2c+1)(2c+2)]^{\frac{1}{2}}}$
$\left\{ \begin{matrix} a & b & c \\ \frac{3}{2} & c - \frac{1}{2} & b + \frac{1}{2} \end{matrix} \right\}$	$= (-1)^s \frac{[(s-2b-1)(s-2c) - 2(s+2)(s-2a)][(s-2b)(s-2c+1)]^{\frac{1}{2}}}{[2b(2b+1)(2b+2)(2b+3)2c(2c+1)(2c+2)(2c+3)]^{\frac{1}{2}}}$
$\left\{ \begin{matrix} a & b & c \\ 2 & c-2 & b-2 \end{matrix} \right\}$	$= (-1)^s \left(\frac{(s-2)(s-1)s(s+1)}{(2b-3)(2b-2)(2b-1)2b(2b+1)} \right)^{\frac{1}{2}} \left(\frac{(s-2a-3)(s-2a-2)(s-2a-1)(s-2a)}{(2c-3)(2c-2)(2c-1)2c(2c+1)} \right)^{\frac{1}{2}}$
$\left\{ \begin{matrix} a & b & c \\ 2 & c-2 & b-1 \end{matrix} \right\}$	$= (-1)^s 2 \left(\frac{(s-1)s(s+1)}{(2b-2)(2b-1)2b(2b+1)(2b+2)} \right)^{\frac{1}{2}} \left(\frac{(s-2a-2)(s-2a-1)(s-2a)(s-2b)(s-2c+1)}{(2c-3)(2c-2)(2c-1)2c(2c+1)} \right)^{\frac{1}{2}}$
$\left\{ \begin{matrix} a & b & c \\ 2 & c-2 & b \end{matrix} \right\}$	$= (-1)^s \left(\frac{6s(s+1)(s-2a-1)(s-2a)}{(2b-1)2b(2b+1)(2b+2)(2b+3)} \right)^{\frac{1}{2}} \left(\frac{(s-2b)(s-2c+1)(s-2c+2)}{(2c-3)(2c-2)(2c-1)2c(2c+1)} \right)^{\frac{1}{2}}$
$\left\{ \begin{matrix} a & b & c \\ 2 & c-2 & b+1 \end{matrix} \right\}$	$= (-1)^s 2 \left(\frac{(s+1)(s-2a)(s-2b-2)(s-2b-1)(s-2b)}{2b(2b+1)(2b+2)(2b+3)(2b+4)} \right)^{\frac{1}{2}} \left(\frac{(s-2c+1)(s-2c+2)(s-2c+3)}{(2c-3)(2c-2)(2c-1)2c(2c+1)} \right)^{\frac{1}{2}}$
$\left\{ \begin{matrix} a & b & c \\ 2 & c-2 & b+2 \end{matrix} \right\}$	$= (-1)^s \left(\frac{(s-2b-3)(s-2b-2)(s-2b-1)(s-2b)}{(2b+1)(2b+2)(2b+3)(2b+4)(2b+5)} \right)^{\frac{1}{2}} \left(\frac{(s-2c+1)(s-2c+2)(s-2c+3)(s-2c+4)}{(2c-3)(2c-2)(2c-1)2c(2c+1)} \right)^{\frac{1}{2}}$
$\left\{ \begin{matrix} a & b & c \\ 2 & c-1 & b-1 \end{matrix} \right\}$	$= (-1)^s \frac{4[(a+b)(a-b+1) - (c-1)(c-b+1)]}{[(2b-2)(2b-1)2b(2b+1)(2b+2)]^{\frac{1}{2}}} \left(\frac{s(s+1)(s-2a-1)(s-2a)}{(2c-2)(2c-1)2c(2c+1)(2c+2)} \right)^{\frac{1}{2}}$
$\left\{ \begin{matrix} a & b & c \\ 2 & c-1 & b \end{matrix} \right\}$	$= (-1)^s 2 \frac{[(a-b+1)(a-b) - c^2 + 1]}{[(2b-1)2b(2b+1)(2b+2)(2b+3)]^{\frac{1}{2}}} \left(\frac{6(s+1)(s-2a)(s-2b)(s-2c+1)}{(2c-2)(2c-1)2c(2c+1)(2c+2)} \right)^{\frac{1}{2}}$
$\left\{ \begin{matrix} a & b & c \\ 2 & c-1 & b+1 \end{matrix} \right\}$	$= (-1)^s \frac{4[(a+b+2)(a-b-1) - (c-1)(b+c+2)]}{[2b(2b+1)(2b+2)(2b+3)(2b+4)]^{\frac{1}{2}}} \left(\frac{(s-2b-1)(s-2b)(s-2c+1)(s-2c+2)}{(2c-2)(2c-1)2c(2c+1)(2c+2)} \right)^{\frac{1}{2}}$
$\left\{ \begin{matrix} a & b & c \\ 2 & c & b \end{matrix} \right\}$	$= (-1)^s \frac{2[3X(X-1) - 4b(b+1)c(c+1)]}{[(2b-1)2b(2b+1)(2b+2)(2b+3)]^{\frac{1}{2}}} \left(\frac{1}{(2c-1)2c(2c+1)(2c+2)(2c+3)} \right)^{\frac{1}{2}}$, where $X = b(b+1) + c(c+1) - a(a+1)$

The author expresses his gratitude to Debi Erpenbeck, whose artful mastery of \TeX and scrupulous attention to detail allowed the numerous complex relations to be displayed in two-column format.

Author's note. It is quite impossible to attribute credits fairly in this subject because of its diverse origins across all areas of physics, chemistry, and mathematics. Any attempt to do so would likely be as misleading as it is informative. Most of the material is rooted in the very foundations of quantum theory itself, and the physical problems it addresses, making it still more difficult to assess unambiguous credit of ideas. Pragmatically, there is also the problem of confidence in the detailed correctness of complicated relationships, which prejudices one to cite those relationships personally checked. This accounts for the heavy use of formulas from [1], which is, by far, the most often used source. But most of that material itself is derived from other primary sources, and an inadequate attempt was made there to indicate the broad base of origins. While one might expect to find in a reference book a comprehensive list of credits for most of the formulas, it has been necessary to weigh the relative merits of presenting a mature subject from a viewpoint of conceptual unity versus credits for individual contributions. The first position was adopted. Nonetheless, there is an obligation to indicate the origins of a subject, noting those works that have been most influential in its developments. The list of textbooks and seminal articles given in the references is intended to serve this purpose, however inadequately.

Excerpts and Fig. 2.1 are reprinted from *Biedenharn and Louck* [1] with permission of Cambridge University Press. Tables 2.2–2.4 have been adapted from *Edmonds* [18] by permission of Princeton University Press. Thanks are given for this cooperation.

References

1. Biedenharn, L.C., Louck, J.D.: In: Rota, G.-C. (ed.) *Encyclopedia of Mathematics and Its Applications* 8 & 9. Addison-Wesley, Reading (1981), presently by Cambridge Univ. Press
2. Louck, J.D.: *J. Math. Math. Sci.* **22**, 745 (1999)
3. Schwinger, J.: On angular momentum. U. S. Atomic Energy Commission Report NYO-3071, 1952 (unpublished). In: Biedenharn, L.C., van Dam, H. (eds.) *Quantum Theory of Angular Momentum*, pp. 229–279. Academic Press, New York (1965)
4. Judd, B.R., Lister, G.M.S.: *J. Phys. A* **20**, 3159 (1987)
5. Judd, B.R.: In: Gruber, B., Millman, R.S. (eds.) *Symmetries in Science*, pp. 151–160. Plenum, New York (1980)
6. Roman, S., Rota, G.-C.: *Adv. Math.* **27**, 95 (1978)
7. Jucys, A.P., Levinson, I.B., Vanagas, V.V.: *The Theory of Angular Momentum*. Israel Program for Scientific Translation, Jerusalem (1962). Translated from the Russian by A. Sen, A. R. Sen (1962)

8. Jucys, A.P., Bandzaitis, A.A.: *Angular Momentum Theory in Quantum Physics*. Moksias, Vilnius (1977)
9. Stanley, R.P.: *Enumerative Combinatorics vol. 1*. Cambridge Univ. Press, Cambridge (1997)
10. Clebsch, A.: *Theorie der binären algebraischen Formen*. Teubner, Leipzig (1872)
11. Louck, J.D., Chen, W.Y.C., Galbraith, H.W.: In: Lulek, T., Lulek, B., Wal, A. (eds.) *Symmetry, Structural Properties of Condensed Matter*, pp. 112–137. World Scientific, Singapore (1999)
12. Chen, W.Y.C., Louck, J.D.: *Adv. Math.* **140**, 207 (1998)
13. MacMahon, P.A.: *Combinatory Analysis*. Cambridge Univ. Press, Cambridge (1960). Originally published in two volumes by Cambridge Univ. Press, Cambridge (1915, 1916)
14. Louck, J.D.: *Adv. Appl. Math.* **17**, 143 (1996)
15. Molien, T.: Über die Invarianten der linearen Substitutionsgruppen. *Sitzungsber. Königl. Preuss. Akad. Wiss.* **52**, 1152 (1897)
16. Michel, L., Zhilinskii, B.I.: *Phys. Rep.* **341**, 11 (2001)
17. Wei, L.: *Comput. Phys. Commun.* **120**, 222 (1999)
18. Edmonds, A.R.: *Angular Momentum in Quantum Mechanics*. Princeton Univ. Press, Princeton (1957)
19. Cartan, E.: Thesis. Paris, Nony (1894). *Oeuvres Complète*, Part 1, pp. 137–287. Gauthier-Villars, Paris (1952)
20. Weyl, H.: *Gruppentheorie und Quantenmechanik*. Hirzel, Leipzig (1928). Translated by H.P. Robertson as: *The Theory of Groups and Quantum Mechanics*. Methuen, London (1931)
21. Dirac, P.A.M.: *The Principles of Quantum Mechanics*, 4th edn. Oxford Univ. Press, London (1958)
22. Born, M., Jordan, P.: *Elementare Quantenmechanik*. Springer, Berlin, Heidelberg (1930)
23. Casimir, H.B.G.: Thesis, University of Leyden. Wolters, Groningen (1931). *Koninkl. Ned. Akad. Wetenschap Proc.* **34**, 844 (1931)
24. van der Waerden, B.L.: *Die gruppentheoretische Methode in der Quantenmechanik*. Springer, Berlin, Heidelberg (1932)
25. Pauli, W.: In: Geiger, H., Scheel, K. (eds.) *Handbuch der Physik*, vol. 24, pp. 83–272. Springer, Berlin, Heidelberg (1933). Chap. 1. Later published in: *Encyclopedia of Physics*, vol. 5, Part 1, pp. 45, 46, ed. by S. Flügge. Springer, Berlin, Heidelberg (1958)
26. Weyl, H.: *The Structure and Representations of Continuous Groups*. Lectures at the Institute for Advanced Study, Princeton. (1935). (unpublished) notes by R. Brauer
27. Condon, E.U., Shortley, G.H.: *The Theory of Atomic Spectra*. Cambridge Univ. Press, London (1935)
28. Kramers, H.A.: *Quantum Mechanics*. North-Holland, Amsterdam (1957). Translation by D. ter Haar of Kramer's monograph published in: *Hand- und Jahrbuch der chemischen Physik* (1937)
29. Szegő, G.: *Orthogonal Polynomials*. Edwards, Ann Arbor (1948)
30. Gel'fand, I.M., Shapiro, Z.Y.: *Am. Math. Soc. Transl.* **2**, 207 (1956)
31. Erdelyi, A., Magnus, W., Oberhettinger, F., Tricomi, G.F.: *Higher Transcendental Functions vol. 1*. McGraw-Hill, New York (1953)
32. Wigner, E.P.: *Application of Group Theory to the Special Functions of Mathematical Physics*. Lecture notes. (1955). (unpublished)
33. Brinkman, H.C.: *Applications of Spinor Invariants in Atomic Physics*. North-Holland, Amsterdam (1956)
34. Rose, M.E.: *Elementary Theory of Angular Momentum*. Wiley, New York (1957)
35. Fano, U., Racah, G.: *Irreducible Tensorial Sets*. Academic Press, New York (1959)
36. Wigner, E.P.: *Group Theory and Its Application to the Quantum Mechanics of Atomic Spectra*. Academic Press, New York (1959). Translation from the 1931 German edition by J.J. Griffin
37. Slater, J.C.: *Quantum Theory of Atomic Structure vol. 2*. McGraw-Hill, New York (1960)
38. Heine, V.: *Group Theory and Quantum Mechanics; An Introduction to Its Present Usage*. Pergamon, New York (1960)
39. Sharp, W.T.: Thesis. Princeton University. (1960). issued as Report AECL-1098, Atomic Energy of Canada, Chalk River, Ontario (1960)
40. Brink, D.M., Satchler, G.R.: *Angular Momentum*. Oxford Univ. Press, London (1962)
41. Hamermesh, M.: *Group Theory and Its Applications to Physical Problems*. Addison-Wesley, Reading (1962)
42. Mackey, G.W.: *The Mathematical Foundations of Quantum Mechanics*. Benjamin, New York (1963)
43. de-Shalit, A., Talmi, I.: *Nuclear Shell Theory*. Pure and Applied Physics Series, vol. 14. Academic Press, New York (1963)
44. Feynman, R.P.: *Feynman Lectures on Physics*. Addison-Wesley, Reading (1963). Chap. 34
45. Judd, R.: *Operator Techniques in Atomic Spectroscopy*. McGraw-Hill, New York (1963)
46. Davydov, A.S.: *Quantum Mechanics*. Pergamon/Addison-Wesley, London/Reading (1965). Translation from the Russian of: *Kvantovaya Mekhanika*. Moscow (1963), with revisions and additions by D. ter Haar
47. Gel'fand, I.M., Minlos, R.A., Shapiro, Z.Y.: *Representations of the Rotation and Lorentz Groups and Their Applications*. Macmillan, New York (1963). Translated from the Russian by G. Cummins and T. Boddington
48. Hagedorn, R.: *Selected Topics on Scattering Theory: Part IV, Angular Momentum*. Lectures given at the Max-Planck-Institut für Physik, Munich. (1963)
49. Naimark, M.A.: *Linear Representations of the Lorentz Group*. Pergamon, New York (1964)
50. Biedenharn, L.C., van Dam, H.: *Quantum Theory of Angular Momentum*. Academic Press, New York (1965)
51. van der Waerden, B.L.: *Sources of Quantum Mechanics*. North-Holland, Amsterdam (1967)
52. Judd, B.R.: *Second Quantization and Atomic Spectroscopy*. Johns Hopkins Press, Baltimore (1967)
53. Vilenkin, N.: *Special Functions and the Theory of Group Representations vol. 22*. Amer. Math. Soc., Providence (1968). Translated from the Russian
54. Talman, J.D.: *Special Functions: A Group Theoretic Approach*. Benjamin, New York (1968). Based on E. P. Wigner's lectures (see Schwinger, 1952)
55. Wybourne, B.G.: *Symmetry Principles and Atomic Spectroscopy*. Wiley, New York (1970)
56. El Baz, E.A., Castel, B.: *Graphical Methods of Spin Algebras in Atomic, Nuclear, and Particle Physics*. Dekker, New York (1972)
57. Gilmore, R.: *Lie Groups, Lie Algebras, and Some of Their Applications*. Wiley, New York (1974)
58. Varshalovich, D.A., Moskalev, A.N., Khersonskii, V.K.: *Quantum Theory of Angular Momentum*. Nauka, Leningrad (1975). (in Russian)
59. Cowan, R.D.: *The Theory of Atomic Structure and Spectra*. Univ. Calif. Press, Berkeley (1981)
60. Zare, R.N.: *Angular Momentum*. Wiley, New York (1988)
61. Andrews, G.E., Askey, R.A., Roy, R.: *Special functions*. In: Rota, G.-C. (ed.) *Encyclopedia of Mathematics and Its Applications*, vol. 71, Cambridge Univ. Press, Cambridge (1999)
62. Gordan, P.: *Über das Formensystem binärer Formen*. Teubner, Leipzig (1875)
63. Heisenberg, W.: *Z. Phys.* **33**, 879 (1925)
64. Born, M., Jordan, P.: *Z. Phys.* **34**, 858 (1925)
65. Dirac, P.A.M.: *Proc. R. Soc. A* **109**, 642 (1925)
66. Born, M., Heisenberg, W., Jordan, P.: *Z. Phys.* **35**, 557 (1926)
67. Pauli, W.: *Z. Phys.* **36**, 336 (1926)
68. Wigner, E.P.: *Z. Phys.* **43**, 624 (1927)

69. Wigner, E.P.: *Z. Phys.* **45**, 601 (1927)
70. Eckart, C.: *Rev. Mod. Phys.* **2**, 305 (1930)
71. Wigner, E.P.: *Göttinger Nachr. Math.-Phys.* **1932**, 546 (1932)
72. Van Vleck, J.H.: *Phys. Rev.* **47**, 487 (1935)
73. Wigner, E.P.: On the matrices which reduce the Kronecker products of representations of S. R. groups, 1940 (unpublished). In: Biedenharn, L.C., van Dam, H. (eds.) *Quantum Theory of Angular Momentum*, pp. 87–133. Academic Press, New York (1965)
74. Racah, G.: *Phys. Rev.* **62**, 438 (1942)
75. Racah, G.: *Phys. Rev.* **63**, 367 (1943)
76. Gel'fand, I.M., Tseitlin, M.L.: *Dokl. Akad. Nauk. SSSR* **71**, 825 (1950)
77. Van Vleck, J.H.: *Rev. Mod. Phys.* **23**, 213 (1951)
78. Jahn, H.A.: *Proc. R. Soc. A* **205**, 192 (1951)
79. Biedenharn, L.C., Blatt, J.M., Rose, M.E.: *Rev. Mod. Phys.* **24**, 249 (1952)
80. Biedenharn, L.C.: Notes on Multipole Fields. Lecture notes at Yale University, New Haven. (1952). (unpublished)
81. Elliott, J.P.: *Proc. R. Soc. A* **218**, 345 (1953)
82. Biedenharn, L.C.: *J. Math. Phys.* **31**, 287 (1953)
83. Jahn, H.A., Hope, J.: *Phys. Rev.* **93**, 318 (1954)
84. Regge, T.: *Nuovo Cimento* **10**, 544 (1958)
85. Regge, T.: *Nuovo Cimento* **11**, 116 (1959)
86. Bargmann, V.: *Commun. Pure Appl. Math.* **14**, 187 (1961)
87. Giovannini, A., Smith, D.A.: In: Block, F., Cohen, S.G., de-Shalit, A., Sambursky, S., Talmi, I. (eds.) *Spectroscopic and Group Theoretic Methods in Physics (Racah Memorial Volume)*, pp. 89–97. Wiley–Interscience, New York (1968)
88. Bargmann, V.: *Rev. Mod. Phys.* **34**, 829 (1962)
89. Michel, L.: In: Bargmann, V. (ed.) *Lecture Notes in Physics: Group Representations in Mathematics and Physics*, Battelle Rencontres, pp. 36–143. Springer, Berlin, Heidelberg (1970)
90. Wu, A.C.T.: *J. Math. Phys.* **13**, 84 (1972)
91. Smorodinskii, Y.A., Shelepin, L.A.: *Sov. Phys. Usp.* **15**, 1 (1972)
92. Smorodinskii, Y.A., Shelepin, L.A.: *Usp. Fiz. Nauk* **106**, 3 (1972)
93. Shelepin, L.A.: Invariant algebraic methods and symmetric analysis of cooperative phenomena. In: Skobel'tsyn, D.V. (ed.) *Group-Theoretical Methods in Physics*, pp. 1–109. Fourth Internat. Collog., Nijmegen (1975). A special research report translated from the Russian by Consultants Bureau, New York, London.
94. Smorodinskii, Y.A.: *Sov. Phys. JETP* **48**, 403 (1978)
95. Gel'fand, I.M., Graev, M.I.: *Dokl. Math.* **33**, 336 (2000). Transl. from *Dokl. Akad. Nauk* **372**, 151 (2000)



James D. Louck James Louck was a Los Alamos National Laboratory Fellow. He earned his PhD in Molecular Physics from The Ohio State University in 1958 and was the coauthor of three books. Except for the years 1960–1963 at Auburn University, his career was in the Theoretical Division at Los Alamos developing symmetry methods for physical systems. He passed away in 2018, just shy of his 90-th birthday.



Group Theory for Atomic Shells

3

Brian R. Judd

Contents

3.1	Generators	71
3.1.1	Group Elements	71
3.1.2	Conditions on the Structure Constants	72
3.1.3	Cartan–Weyl Form	72
3.1.4	Atomic Operators as Generators	72
3.2	Classification of Lie Algebras	72
3.2.1	Introduction	72
3.2.2	The Semisimple Lie Algebras	72
3.3	Irreducible Representations	73
3.3.1	Labels	73
3.3.2	Dimensions	73
3.3.3	Casimir’s Operator	74
3.4	Branching Rules	74
3.4.1	Introduction	74
3.4.2	$U(n) \supset SU(n)$	74
3.4.3	Canonical Reductions	75
3.4.4	Other Reductions	75
3.5	Kronecker Products	75
3.5.1	Outer Products of Tableaux	75
3.5.2	Other Outer Products	75
3.5.3	Plethysms	75
3.6	Atomic States	76
3.6.1	Shell Structure	76
3.6.2	Automorphisms of $SO(8)$	77
3.6.3	Hydrogen and Hydrogen-Like Atoms	77
3.7	The Generalized Wigner–Eckart Theorem	77
3.7.1	Operators	77
3.7.2	The Theorem	77
3.7.3	Calculation of the Isoscalar Factors	78
3.7.4	Generalizations of Angular Momentum Theory	78
3.8	Checks	79
	References	79

Abstract

The basic elements of the theory of Lie groups and their irreducible representations (IRs) are described. The IRs are used to label the states of an atomic shell and also the components of operators of physical interest. Applications of the generalized Wigner–Eckart theorem lead to relations between matrix elements appearing in different electronic configurations. This is particularly useful in the *f* shell, where transformations among the seven orbital states of an *f* electron can be described by the unitary group $U(7)$ and its sequential subgroups $SO(7)$, G_2 , and $SO(3)$ with respective IRs $[\lambda]$, W , U , and L . Extensions to groups that involve electron spin S (like $Sp(14)$) are described, as are groups that do not conserve electron number. The most useful of the latter is the quasispin group whose generators Q connect states of identical W , U , L and seniority v in the *f* shell. The symmetries of products of objects (states or operators) that themselves possess symmetries are described by the technique of plethysms.

Keywords

group theory · atomic shells · Lie groups · irreducible representations · Wigner–Eckart theorem · quasispin

3.1 Generators

3.1.1 Group Elements

An element S_a of a Lie group \mathcal{G} corresponding to an infinitesimal transformation can be written in the form

$$S_a = 1 + \delta a^\sigma X_\sigma, \quad (3.1)$$

where the δa^σ are the infinitesimal parameters and the X_σ are the generators [1]. Summation over the repeated Greek

B. R. Judd (✉)
Dept. of Physics & Astronomy, The Johns Hopkins University
Baltimore, MD, USA
e-mail: juddbr@pha.jhu.edu

index is implied. Transformations corresponding to finite parameters can be found by exponentiation

$$S_a \rightarrow \exp(a^1 X_1) \exp(a^2 X_2) \cdots \exp(a^r X_r). \quad (3.2)$$

The generators necessarily form a Lie algebra, that is, they close under commutation

$$[X_\rho, X_\sigma] = c_{\rho\sigma}^\tau X_\tau. \quad (3.3)$$

In terms of the structure constants $c_{\rho\sigma}^\tau$, the metric tensor is defined as

$$g_{\rho\sigma} = c_{\rho\lambda}^\mu c_{\sigma\mu}^\lambda. \quad (3.4)$$

3.1.2 Conditions on the Structure Constants

For an Abelian group, all the generators commute with one another

$$c_{\rho\sigma}^\tau = 0. \quad (3.5)$$

The operators X_σ ($\sigma = 1, 2, \dots, p < r$) form the generators of a subgroup if [2]

$$c_{\rho\sigma}^\tau = 0, \quad (\rho, \sigma \leq p, \tau > p). \quad (3.6)$$

The subgroup is invariant if the stronger condition

$$c_{\rho\sigma}^\tau = 0, \quad (\rho \leq p, \tau > p) \quad (3.7)$$

is satisfied. A group is *simple* if it contains no invariant subgroup (besides the unit element). A group is *semisimple* if it contains no Abelian invariant subgroup (besides the unit element). A necessary and sufficient condition that a group be semisimple is that

$$\det |g_{\rho\tau}| \neq 0. \quad (3.8)$$

All simple groups are semisimple. For semisimple groups, the inverse tensor $g^{\mu\nu}$ can be formed, thus permitting suffixes to be raised. The quadratic operator

$$C = g^{\rho\sigma} X_\rho X_\sigma \quad (3.9)$$

commutes with all generators of the group and is called Casimir's operator [1]. If the generators of a group \mathcal{G} can be broken up into two sets such that each member of one set commutes with all the members of the other, that is, if

$$c_{\rho\sigma}^\tau = 0, \quad (\rho \leq p, \sigma > p), \quad (3.10)$$

then the two sets form the generators of two invariant subgroups, \mathcal{H} and \mathcal{K} . The group \mathcal{G} is the direct product of \mathcal{H} and \mathcal{K} and is written as $\mathcal{H} \times \mathcal{K}$.

3.1.3 Cartan–Weyl Form

By taking suitable linear combinations H_i and E_α of the generators X_σ , the basic commutation relations Eq. (3.3) can be thrown into the so-called Cartan–Weyl form [1]

$$[H_i, H_j] = 0, \quad (3.11)$$

$$[H_i, E_\alpha] = \alpha_i E_\alpha, \quad (3.12)$$

$$[E_\alpha, E_{-\alpha}] = \alpha^i H_i, \quad (3.13)$$

$$[E_\alpha, E_\beta] = N_{\alpha\beta} E_{\alpha+\beta}. \quad (3.14)$$

The Roman symbols i, j, \dots run over an l -dimensional space (the *weight* space of *rank* l) in which the numbers α_i can be visualized as the components of the vectors (called *roots*). The E_α are shift operators, the displacements being specified by the components of α . The operator $E_{\alpha+\beta}$ in Eq. (3.17) is to be interpreted as 0 if $\alpha + \beta$ is not a root. The coefficient $N_{\alpha\beta}$ depends on the choice of normalization.

3.1.4 Atomic Operators as Generators

The pairs $a_\xi^\dagger a_\eta$ of creation and annihilation operators for either bosons or fermions, as defined in Sect. 6.1.1 close under commutation and form a Lie algebra. The coupled forms $W^{(\kappa k)}$, defined in Sect. 6.2.2, are often used to play the role of the generators for electrons in an atomic shell.

3.2 Classification of Lie Algebras

3.2.1 Introduction

The semisimple Lie algebras have been classified by *Cartan* [3]. They consist of four main classes A_l, B_l, C_l, D_l , and five exceptions G_2, F_4, E_6, E_7, E_8 . Each algebra is characterized by an array of roots in the l -dimensional weight space; they are conveniently specified by a set of mutually orthogonal unit vectors e_i . The total number of generators (those of type E_α plus the l generators of type H_i) gives the *order* of the algebra.

3.2.2 The Semisimple Lie Algebras

A_l . The roots are conveniently represented by the vectors $e_i - e_j$ ($i, j = 1, 2, \dots, l + 1$). They are all perpendicular to Σe_k and do not extend beyond the l -dimensional weight space. The order of the algebra is $l(l + 2)$. The group for which this algebra can serve as a basis is the special unitary group $SU(l + 1)$.

Table 3.1 Generators of the Lie groups for the atomic l shell. The subscripts i and j run over all $4l + 2$ states of a single electron

Group	Generators
$SO(8l + 5)^a$	$a_i^\dagger a_j^\dagger, a_i^\dagger a_j, a_i a_j, a_i^\dagger, a_j$
$SO(8l + 4)^a$	$a_i^\dagger a_j^\dagger, a_i^\dagger a_j, a_i a_j$
$U(4l + 2)^b$	$W^{(\kappa k)}$ ($\kappa = 0, 1; k = 0, 1, \dots, 2l$)
$SU(4l + 2)^b$	$W^{(\kappa k)}$ (as above, with $\kappa = k = 0$ excluded)
$Sp(4l + 2)^c$	$W^{(\kappa k)}$ (as above, with $\kappa + k$ odd)
$U(2l + 1)^d$	$W^{(0k)}$ ($k = 0, 1, \dots, 2l$)
$SU(2l + 1)^d$	$W^{(0k)}$ ($k = 1, 2, \dots, 2l$)
$SO(2l + 1)^d$	$W^{(0k)}$ ($k = 1, 3, 5, \dots, 2l - 1$)
G_2^d	$W^{(01)}, W^{(05)}$ (for $l = 3$)
$SO_L(3)^e$	$W^{(01)}$ (or L)
$SO_S(3)^e$	$W^{(10)}$ (or S)
$U_A(2l + 1) \times U_B(2l + 1)^f$	$W_{0q}^{(0k)} + W_{0q}^{(1k)}, W_{0q}^{(0k)} - W_{0q}^{(1k)}$ ($k = 0, 1, \dots, 2l$)
$SO_\lambda(2l + 1) \times SO_\mu(2l + 1) \times SO_\nu(2l + 1) \times SO_\xi(2l + 1)^g$	$(\theta^\dagger \theta)^{(k)}$ (k odd, $\theta \equiv \lambda, \mu, \nu, \xi$)
$U_\lambda(2^l) \times U_\mu(2^l) \times U_\nu(2^l) \times U_\xi(2^l)^h$	$q_\theta^\dagger q_\theta$ (all components, $\theta \equiv \lambda, \mu, \nu, \xi$)

^a [4, 5]; ^b [1, 6]; ^c [6, 7]; ^d [6]; ^e [8]; ^f [9]; ^g [10, 11] and Eqs. (6.69)–(6.72); ^h [12]

B_l . The roots are $\pm e_i$ and $\pm e_i \pm e_j$ ($i, j = 1, 2, \dots, l; i \neq j$). The order of the algebra is $l(2l + 1)$. A corresponding group is the special orthogonal (or rotation) group in $2l + 1$ dimensions, $SO(2l + 1)$.

C_l . The roots are $\pm 2e_i$ and $\pm e_i \pm e_j$ ($i, j = 1, 2, \dots, l; i \neq j$). The order of the algebra is $l(2l + 1)$. A corresponding group is the symplectic group in $2l$ dimensions, $Sp(2l)$. A rotation of the roots yields $C_2 = B_2$.

D_l . The roots are $\pm e_i \pm e_j$ ($i, j = 1, 2, \dots, l; i \neq j$). The order of the algebra is $l(2l - 1)$. A corresponding group is the special orthogonal (or rotation) group $SO(2l)$. A rotation of the roots yields $D_3 = A_3$. Also, $D_2 = A_1 \times A_1$.

E_6, E_7, E_8 . The roots are given by *Racah* [1]. The respective orders are 78, 133, and 248.

F_4 . The roots consist of the roots of B_4 together with the 16 vectors $\frac{1}{2}(\pm e_1 \pm e_2 \pm e_3 \pm e_4)$. The order of the algebra is 52.

G_2 . The roots consist of the roots of A_2 together with the six vectors $\pm(2e_i - e_j - e_k)$ ($i \neq j \neq k = 1, 2, 3$). The order of the algebra is 14.

Examples of Lie groups used in atomic shell theory, together with their generators, are given in Table 3.1.

3.3 Irreducible Representations

3.3.1 Labels

If n atomic states of a collection transform among themselves under an arbitrary action of the generators of a group \mathcal{G} , then the states form a *representation* of \mathcal{G} . The representation is *irreducible* if n' linear combinations of the states cannot be found that also exhibit that property, where $n' < n$. The commuting generators H_i of \mathcal{G} can be simultaneously diagonalized within the n states: their eigenvalues (m_1, m_2, \dots, m_l) for an eigenstate ψ specify the *weight* of the eigenstate. The weight above is said to be *higher* than $(m'_1, m'_2, \dots, m'_l)$ if the first non-vanishing term in the sequence $m_1 - m'_1, m_2 - m'_2, \dots$ is positive. An irreducible representation (IR) of a semisimple group is uniquely specified (to within an equivalence) by its highest weight [1], which can therefore be used as a defining label.

3.3.2 Dimensions

The dimensions of the IRs of various groups are expressed in terms of the highest weights and set out in Table 3.2. General algebraic expressions have been given by *Wybourne* [13, pp. 137]. Numerical tabulations have been made by Butler in the appendix to another book by *Wybourne* [14], and also by *McKay* and *Patera* [15]. The latter defines the IRs by specifying the coordinates of the weights with respect to the simple roots of *Dynkin* [16].

Table 3.2 Dimensions D of the irreducible representations (IR's) of various Lie groups

Group	IR	D
SO(2)	M	1
SO(3)	D_J	$2J + 1$
SO(4) = SO _A (3) × SO _B (3)	$D_J \times D_K$	$(2J + 1)(2K + 1)$
SO(5)	$(w_1 w_2)$	$(w_1 + w_2 + 2)(w_1 - w_2 + 1)(2w_1 + 3)(2w_2 + 1)/6$
SO(6)	$(w_1 w_2 w_3)$	$(w_1 - w_2 + 1)(w_1 - w_3 + 2)(w_2 - w_3 + 1) \times (w_1 + w_2 + 3)(w_1 + w_3 + 2)(w_2 + w_3 + 1)/12$
SO(7)	$(w_1 w_2 w_3)$	$(w_1 + w_2 + 4)(w_1 + w_3 + 3)(w_2 + w_3 + 2)(w_1 - w_2 + 1)(w_1 - w_3 + 2)(w_2 - w_3 + 1) \times (2w_1 + 5)(2w_2 + 3)(2w_3 + 1)/720$
G ₂	$(u_1 u_2)$	$(u_1 + u_2 + 3)(u_1 + 2)(2u_1 + u_2 + 5)(u_1 + 2u_2 + 4)(u_1 - u_2 + 1)(u_2 + 1)/120$
SU(3) or U(3)	$[\lambda_1 \lambda_2 \lambda_3]$	$(\lambda_1 - \lambda_2 + 1)(\lambda_1 - \lambda_3 + 2)(\lambda_2 - \lambda_3 + 1)/2$
SU(4) or U(4)	$[\lambda_1 \lambda_2 \lambda_3 \lambda_4]$	As for $(w_1 w_2 w_3)$ of SO(6) ^a
Sp(4)	$\langle \sigma_1 \sigma_2 \rangle$	As for $(w_1 w_2)$ of SO(5) ^b
Sp(6)	$\langle \sigma_1 \sigma_2 \sigma_3 \rangle$	$(\sigma_1 - \sigma_2 + 1)(\sigma_1 - \sigma_3 + 2)(\sigma_1 + \sigma_2 + 5)(\sigma_1 + \sigma_3 + 4)(\sigma_2 + \sigma_3 + 3)(\sigma_2 - \sigma_3 + 1) \times (\sigma_1 + 3)(\sigma_2 + 2)(\sigma_3 + 1)/720$

^a Subject to the conditions $w_1 = (\lambda_1 + \lambda_2 - \lambda_3 - \lambda_4)/2$, $w_2 = (\lambda_1 - \lambda_2 + \lambda_3 - \lambda_4)/2$, $w_3 = (\lambda_1 - \lambda_2 - \lambda_3 + \lambda_4)/2$

^b Subject to the conditions $w_1 = (\sigma_1 + \sigma_2)/2$, $w_2 = (\sigma_1 - \sigma_2)/2$

Table 3.3 Eigenvalues of Casimir's operator C for groups used in the atomic l shell

Group	IR	Operator	Eigenvalue
SU($2l + 1$)	$[\lambda]^a$	$\sum_{k>0} (\mathbf{V}^{(k)})^2$	$3N + 2Nl - \frac{1}{2}N^2 - 2S(S + 1) - N^2/(2l + 1)$
SO($2l + 1$)	\mathcal{W}^b	$\sum_{k\text{ odd}} (\mathbf{V}^{(k)})^2$	$\frac{1}{2} \sum_{i=1}^l w_i(w_i + 1 + 2l - 2i)$
G ₂	$(u_1 u_2)$	$\frac{1}{4} [(\mathbf{V}^{(1)})^2 + (\mathbf{V}^{(5)})^2]$	$(u_1^2 + u_2^2 + u_1 u_2 + 5u_1 + 4u_2)/12$

^a Appropriate for terms of l^N with total spin S [7, p. 125]

^b Defined by the l weights $(w_1 w_2 \dots w_l)$

3.3.3 Casimir's Operator

The eigenvalues of Casimir's operator C , defined in Eq. (3.9), can be expressed in terms of the highest weights of an IR [1]. A complete algebraic listing for all the semisimple Lie groups has been given by *Wybourne* [13, p. 140]. Sometimes Casimir's operator is given in terms of the spherical tensors $\mathcal{W}^{(k)}$, or of their special cases $\mathbf{V}^{(k)}$ ($= 2^{\frac{1}{2}} \mathcal{W}^{(0k)}$) for which the single-electron reduced matrix element satisfies

$$(nl \| v^{(k)} \| nl) = (2k + 1)^{\frac{1}{2}}. \quad (3.15)$$

The eigenvalues of several operators of that form are given in Table 3.3.

3.4 Branching Rules

3.4.1 Introduction

If a group \mathcal{H} shares some of its generators with a group \mathcal{G} , the first can be considered a subgroup of the second. That is, $\mathcal{G} \supset \mathcal{H}$. Many of the groups in Table 3.1 can be put in extended group–subgroup sequences. The IRs of a subgroup that together span an IR of the group constitute a *branching* rule.

3.4.2 $U(n) \supset SU(n)$

The group $U(n)$ differs from $SU(n)$ in that the former contains among its generators a scalar such as $(W^{(00)})$ that, by itself, forms an invariant subgroup. Thus $U(n)$ is not semisimple. The scalar in question commutes with all the generators of the group and so is of type H_i . Its presence enlarges the dimension, l , of the weight space by 1, an extension that can be accommodated by the unit vectors \mathbf{e}_i of A_l given in Sect. 3.2.2. The reduction $U(n) \supset SU(n)$ leads to the branching rule

$$[\lambda_1 \lambda_2 \dots \lambda_n] \rightarrow [\lambda_1 - a, \lambda_2 - a, \dots, \lambda_n - a], \quad (3.16)$$

where, in the IR of $SU(n)$ on the right,

$$a = (\lambda_1 + \lambda_2 + \dots + \lambda_n)/n. \quad (3.17)$$

To avoid fractional weights, the IRs of $SU(n)$ are frequently replaced by those of $U(n)$ for which the λ_i are integers. The weights $\lambda_1, \lambda_2, \dots$ can be interpreted as the number of cells in successive rows of a *Young Tableau*. When the n states of a single particle are taken as a basis for the IR $[10 \dots 0]$ of $U(n)$, thus corresponding to a tableau comprising a single cell, the tableaux comprising N cells can be interpreted in two ways, namely, (1) as an IR of $U(n)$ for a system of

N particles, and (2) as an IR of S_N , the finite group of permutations on N objects. A given tableau corresponds to as many permutations as there are ways of entering the numbers $1, 2, \dots, N$ in the cells such that the numbers increase going from left to right along the rows, and from top to bottom down the columns. A tableau possessing cells numbered in this way is called *standard*; it defines a permutation corresponding to a symmetrization with respect to the numbers in the rows, followed by an antisymmetrization with respect to the numbers in the columns [17].

3.4.3 Canonical Reductions

A group–subgroup sequence of the type

$$U(n) \supset U(n-1) \supset U(n-2) \supset \dots \supset U(1) \quad (3.18)$$

is called *canonical* [18]. The branching rules for those IRs $[\lambda'_1 \lambda'_2 \dots \lambda'_{n-1}]$ of $U(n-1)$ contained in $[\lambda_1 \lambda_2 \dots \lambda_n]$ of $U(n)$ have been given by Weyl [19] in terms of the *betweenness* conditions

$$\lambda_1 \geq \lambda'_1 \geq \lambda_2 \geq \lambda'_2 \geq \dots \geq \lambda'_{n-1} \geq \lambda_n. \quad (3.19)$$

The possibility of using the scheme of Eq. (3.18) in the theory of complex atomic spectra has been explored by Harter [20, 21], Harter and Patterson [22], and by Drake and Schlesinger [23, 24] (see also Sect. 4.3.1).

3.4.4 Other Reductions

The algebraic formulae for $U(n) \supset SO(n)$ and $U(n) \supset Sp(n)$ have been given by Littlewood [25] and in a rather more accessible form by Wybourne [14]. Special cases have been tabulated by Butler (in Tables C-1 through C-15 in [14]). Another set of tables, in which Dynkin's labeling scheme is used, has been given by McKay and Patera [15]. Descriptions of how to apply the mechanics of the mathematics to the Young tableaux that describe the IRs of $U(n)$ can be found in the articles of Jahn [26] [with particular reference to $SO(5)$] and Flowers [27] [for $Sp(2j+1)$]. For the atomic l shell, the reductions $SO(2l+1) \supset SO(3)$ and (for f electrons) $SO(7) \supset G_2$ and $G_2 \supset SO(3)$ are important. The sources cited in the previous Section are useful here. It is important to recognize that the embedding of one group in another can often be performed in inequivalent ways, depending on which generators are discarded in the reduction process. Thus the use of $SO(5) \supset SO(3)$ in the atomic d shell involves a different $SO(3)$ group from that derived from the canonical sequence $SO(5) \supset SO(4) \supset SO(3)$.

3.5 Kronecker Products

3.5.1 Outer Products of Tableaux

Consider the tableau $[\lambda_1 \lambda_2 \dots \lambda_n]$, where the total number of cells is N . A preliminary definition is required. If among the first r terms of any permutation of the N factors of the product, $x_1^{\lambda_1} x_2^{\lambda_2} \dots x_n^{\lambda_n}$, the number of times x_1 occurs is \geq the number of times x_2 occurs \geq the number of times x_3 occurs, etc. for all values of r , this permutation is called a *lattice* permutation. The prescription of Littlewood [25] for finding the tableaux appearing in the Kronecker product of $[\lambda_1 \lambda_2 \dots \lambda_n]$ with $[\mu_1 \mu_2 \dots \mu_m]$ is as follows. The acceptable tableaux are those that can be built by adding to the tableau $[\lambda_1 \lambda_2 \dots \lambda_n]$, μ_1 cells containing the same symbol α , then μ_2 cells containing the same symbol β , etc., subject to two conditions:

1. After the addition of each set of cells labeled by a common symbol we must have a permissible tableau with no two identical symbols in the same column;
2. If the total set of added symbols is read from right to left in the consecutive rows of the final tableau, we obtain a lattice permutation of $\alpha^{\mu_1} \beta^{\mu_2} \gamma^{\mu_3} \dots$

Examples of this procedure have been given [25, p. 96; 7, p. 136; 14, p. 24]. An extensive tabulation involving tableaux with $N < 8$ has been calculated by Butler and given by Wybourne [14, Table B-1].

3.5.2 Other Outer Products

The rules for constructing the Kronecker products for $U(n)$ follow by interpreting the Young tableaux of the previous section as IRs of $U(n)$. The known branching rules for reductions to subgroups enable the Kronecker products for the subgroups to be found. Many examples for $SO(n)$, $Sp(n)$, and G_2 can be found in the book by Wybourne [14, Tables D-1–D-15, and E-4].

3.5.3 Plethysms

Sometimes a particle can be thought of as being composite (as when the six orbital states $s+d$ of a single electron are taken to span the IR [200] of $SU(3)$). When the n' component states of a particle form a basis for an IR $[\lambda']$ of $U(n)$ other than $[10 \dots 0]$, the process of finding which IRs of $U(n)$ occur for N -particle states whose permutation symmetries are determined by a given Young tableau $[\lambda]$ with N cells is called a *plethysm* [25, p. 289] and written as $[\lambda'] \otimes [\lambda]$.

The special techniques for doing this have been described by *Wybourne* [14]. An elementary method, which is often adequate in many cases, runs as follows:

1. Expand $[\lambda']^N$ by repeated use of Table B-1 from [14]. The resulting tableaux $[\lambda'']$ are independent of n .
2. Choose a small value of n , and strike out all tableaux from the set $[\lambda'']$ that possess more than n rows (since they are unacceptable as IRs of $U(n)$).
3. Interpret the remaining tableaux $[\lambda'']$ as IRs of $U(n)$ and find their dimensions from Tables A-2 through A-17 of [14]. Check that the sum of the dimensions is $(\dim[\lambda'])^N$.
4. Interpret the various tableaux $[\lambda]$ possessing the same number N of cells as IRs of $U(\dim[\lambda'])$, and find their dimensions from [14].
5. Match the dimensions of parts (3) and (4), remembering that each tableau $[\lambda]$ occurs as often as the number of its standard forms. This determines the possible ways of assigning the IRs $[\lambda'']$ of $U(n)$ to each $[\lambda]$.
6. Proceed to higher n to remove ambiguities and to include the tableaux struck out in step 2.

This procedure can be extended to calculate the plethysms for other groups. Examples of the type $W \otimes [\lambda]$ and $U \otimes [\lambda]$, where W and U are IRs of $SO(7)$ and G_2 , have been given for $[\lambda] \equiv [2]$ and $[11]$ corresponding to the separation of W^2 and U^2 into their symmetric and antisymmetric parts [28]. The technique of plethysm is also useful for mixed atomic configurations (Sect. 3.6.1).

3.6 Atomic States

3.6.1 Shell Structure

The 2^{4l+2} states of the l shell span the elementary spinor IR $(\frac{1}{2}\frac{1}{2}\cdots\frac{1}{2})$ of $SO(8l+5)$, which decomposes into the two IRs $(\frac{1}{2}\frac{1}{2}\cdots\pm\frac{1}{2})$ of $SO(8l+4)$, corresponding to an even and an odd number N of electrons [4]. The states of l^N span the IR $[1^N 0^{4l+2-N}]$ of $U(4l+2)$, corresponding to the antisymmetric Young tableau comprising a single column of N cells. The separation of spin and orbit through the subgroup $U(2) \times U(2l+1)$ yields the tableau products $[\lambda] \times [\tilde{\lambda}]$, where $[\tilde{\lambda}]$ is the tableau obtained by reflecting $[\lambda]$ in a diagonal line [1]. The IRs of the subgroup $U(2) \times SO(2l+1)$ are denoted by S and W [6]. An alternative way of reaching this subgroup from $U(4l+2)$ involves the intermediary $Sp(4l+2)$, whose IRs $\langle 1^v 0^{2l+1-v} \rangle$ possess as a basis the states with seniority v [7]. A subgroup of $SO(2l+1)$ is the $SO(3)$ group whose IRs specify L , the total orbital angular momentum.

Table 3.4 The states of the d shell

d^N	M_Q	$^{2S+1}[\lambda]$	v	W	L	
d^0	$-\frac{5}{2}$	$^1[0]$	0	(00)	S	
d^1	-2	$^2[1]$	1	(10)	D	
d^2	$-\frac{3}{2}$	$^1[2]$	0	(00)	S	
			2	(20)	DG	
d^3	-1	$^3[11]$	2	(11)	PF	
			$^2[21]$	1	(10)	D
				3	(21)	PDFGH
d^4	$-\frac{1}{2}$	$^4[111]$	3	(11)	PF	
			$^1[22]$	0	(00)	S
				2	(20)	DG
		4		(22)	SDFGI	
		$^3[211]$	2	(11)	PF	
			4	(21)	PDFGH	
d^5	0	$^5[1111]$	4	(10)	D	
			$^2[221]$	1	(10)	D
				3	(21)	PDFGH
		5		(22)	SDFGI	
		$^4[2111]$	3	(11)	PF	
			5	(20)	DG	
$^6[11111]$	5	(00)	S			

Alternatives to this classic sequence are provided by the last three groups listed in Table 3.1, together with their respective subgroups. For $U_A(2l+1) \times U_B(2l+1)$, the shell is factored by considering spin-up and spin-down electrons as distinct (and statistically independent) particles [29]. A further factorization by means of the quasiparticles, θ , leads to four independent spaces. The 2^l states in each space span the elementary spinor $(\frac{1}{2}^l)$ of $SO_\theta(2l+1)$, which can be regarded as a fictitious particle (or quark), q_θ [30].

The standard classification of the states of the d-shell is given in Table 3.4. The component M_Q of the quasispin Q (defined in Eqs. (6.33)–(6.35)) is listed, as well as the seniority, $v = 2l + 1 - 2Q$, the IRs W of $SO(5)$, and the value of L (as a spectroscopic symbol). Only states in the first half of the shell appear; the classification for the second half is the same as the first except that the signs of M_Q are reversed. A general rule for arbitrary l is exemplified by noting that every W (the IR of $SO(2l+1)$) occurs with two spins (S_1 and S_2) and two quasispins (Q_1 and Q_2) such that $S_1 = Q_2$ and $S_2 = Q_1$. No duplicated spectroscopic terms appear in Table 3.4. The generators of $SO(5)$ do not commute with the inter-electronic Coulomb interaction; thus the separations effected by $SO(5)$ merely define (to within a phase) a basis. The analog of Table 3.4 has been given by *Wybourne* [31] for the f shell. As *Racah* [6] showed, the group G_2 can be used to help distinguish repeated terms, but a few duplications remain. They are distinguished by *Nielson* and *Koster* [32] in their tables of spectroscopic coefficients by the letters A and B . The scope for applications of group theory becomes enlarged when the states of a single electron embrace more

than one l value. Extensions of the standard model have been made by *Feneuille* [33–36] with particular reference to the configurations $(d + s)^N$, for which quasiparticles have also been considered [37]. The group $SU(3)$ has been used for $(d + s)^N p^M$ [38]. The mixed configurations $(s + f)^4$ have found a use in the quark model of the atomic f shell [30]. A brief description of this model has been given by *Fano* and *Rao* [39].

3.6.2 Automorphisms of $SO(8)$

The quark structure $s + f$ derives from the $SO(3)$ structure of the elementary spinor $(\frac{1}{2}\frac{1}{2}\frac{1}{2})$ of $SO(7)$. Its eight components span the IR (1000) of $SO(8)$, a group that admits automorphisms [40]. This property is exhibited by the existence of the three distinct subgroups $SO(7)$ (Racah's group), $SO(7)'$, and $SO(7)''$, all of which possess the same G_2 and $SO(3)$ as subgroups. A reversal of the relative phase of the s and f quarks takes $SO(7)$ into $SO(7)''$ and vice versa [41]. The generators of $SO(7)'$ are the sums of the corresponding generators of $SO(7)$ and $SO(7)''$. The phase reversal between the s and f quarks, when interpreted in terms of electronic states, explains the unexpected simplifications found by *Racah* [6] in his equation (87) [42], which goes beyond what the Wigner–Eckart theorem for G_2 would predict. Similarly, explanations can be found for some (but not all) proportionalities between blocks of matrix elements of components of the spin–other-orbit interaction for f electrons [43]. *Hansen* and *Ven* have given some examples of still unexplained proportionalities [44]. The group $SO(7)'$ has proved useful in analyses of the effective three-electron operators used to represent weak configuration interaction in the f shell [41].

3.6.3 Hydrogen and Hydrogen-Like Atoms

The nonrelativistic hydrogen atom possesses an $SO(4)$ symmetry associated with the invariance of the Runge–Lenz vector, which indicates the direction of the major axis of the classical elliptic orbit [5]. The quantum-mechanical form of this vector can be written in dimensionless units as

$$\mathbf{a} = \frac{(\mathbf{l} \times \mathbf{p}) - (\mathbf{p} \times \mathbf{l}) + 2Zr\hbar^2/ra_0}{2p_0}, \quad (3.20)$$

where $a_0 = \hbar^2/me^2$ is the Bohr radius, Ze is the nuclear charge, p_0 is related to the principal quantum number n by $p_0 = Z/na_0$, and where the momentum \mathbf{p} and angular momentum \mathbf{l} of the electron in its orbit are measured in units of \hbar . The analysis is best carried out in momentum space [45]. The four coordinates to which $SO(4)$ refers can

be taken from Eqs. (9.43)–(9.46) or directly as kp_x, kp_y, kp_z , and $kp_0(1 - p^2/p_0^2)/2$, where $k = 2p_0/(p^2 + p_0^2)$. The generators of $SO(4)$ are provided by the 6 components of the two mutually commuting vectors $(\mathbf{l} + \mathbf{a})/2$ and $(\mathbf{l} - \mathbf{a})/2$, each of which behaves as an angular momentum vector. The equivalence $SO(4) = SO(3) \times SO(3)$ corresponds to the isomorphism $D_2 = A_1 \times A_1$ of Sect. 3.2.2.

Hydrogenic eigenfunctions belonging to various energies can be selected to form bases for a number of groups. The inclusion of all the levels up to a given n yields the IR $(n - 1, 0)$ of $SO(5)$. Levels of a given l and all n form an infinite basis for an IR of the noncompact group $SO(2, 1)$ [46]. All the bound hydrogenic states span an IR of $SO(4, 2)$, as do the states in the continuum [47]. Subgroups of $SO(4, 2)$ and their generators have been listed by *Wybourne* [13] in his Table 21.2.

To the extent that the central potential of a complex atom resembles the r^{-1} dependence for a bare nucleus, the group $SO(4)$ can be used to label the states [48].

3.7 The Generalized Wigner–Eckart Theorem

3.7.1 Operators

All atomic operators involving only the electrons can be built from their creation and annihilation operators. The appropriate group labels for an atomic operator acting on N electrons, each with n relevant component states, reduces to working out the various parts of the Kronecker products $[10 \dots 0]^N \times [0 \dots 0 - 1]^N$ of $U(n)$. Subgroups of $U(n)$ can further define these parts, which may be limited by Hermiticity constraints. The group labels for the Coulomb interaction for f electrons were first given by *Racah* [6]. Interactions involving electron spin were classified later [49–51]. Operators that represent the effects of configuration interaction on the d and f shells have also been studied [28, 52–56].

3.7.2 The Theorem

Let the ket, operator T , and bra of a matrix element be labeled by an IR (R_a, R_c, R_b) of a group \mathcal{G} , each with a component (i_a, i_c, i_b) . Suppose the supplementary labels γ_k are also required to complete the definitions. The generalized Wigner–Eckart theorem is

$$\begin{aligned} & \langle \gamma_a R_a i_a | T(\gamma_c R_c i_c) | \gamma_b R_b i_b \rangle \\ &= \sum_{\beta} A_{\beta}(\beta R_a i_a | R_b i_b, R_c i_c), \end{aligned} \quad (3.21)$$

where β distinguishes the IRs R_a should they appear more than once in the reduction of the Kronecker product $R_b \times R_c$.

The *reduced* matrix element A_β is independent of the i_k [6, 8]. The second factor on the right-hand side of Eq. (3.21) is a Clebsch–Gordan (CG) coefficient for the group \mathcal{G} .

If the specification Ri can be replaced by $R\tau r_i$, where r denotes an IR of a subgroup \mathcal{H} of \mathcal{G} , and τ is an additional symbol that may be necessary to make the classification unambiguous, the CG coefficient for \mathcal{G} factorizes according to the Racah lemma [6]

$$\begin{aligned} & (\beta R_a \tau_a r_a i_a | R_b \tau_b r_b i_b, R_c \tau_c r_c i_c) \\ &= \sum_{\alpha} (\alpha r_a i_a | r_b i_b, r_c i_c) (\beta R_a \tau_a r_a | R_b \tau_b r_b + R_c \tau_c r_c)_{\alpha}. \end{aligned} \quad (3.22)$$

The first factor on the right is a CG coefficient for the group \mathcal{H} ; the second factor is an *isoscalar* factor [57].

3.7.3 Calculation of the Isoscalar Factors

The group \mathcal{H} above is often $\text{SO}(3)$, whose Clebsch–Gordan coefficients (and their related $3-j$ symbols) are well-known (Chap. 2). The principal difficulty in establishing comparable formulae for the isoscalar factors lies in giving algebraic meaning to β . Several methods are available for obtaining numerical results as follows.

Extraction from Tabulated Quantities

If R_b or R_c correspond to the IRs labeling a single electron, the factorization of the known [32] coefficients of fractional parentage (cfp) according to formulae of the type [6]

$$\begin{aligned} & (d^N SLv \{d^{N-1} S' L' v'\}) \\ &= (d^N S v \{d^{N-1} S' v'\}) (W' L' + (10) d | W L) \end{aligned} \quad (3.23)$$

yields some isoscalar factors. In this example, W and W' are the IRs of $\text{SO}(5)$ defined by the triples NSv and $N'S'v'$ (with $N' = N - 1$) as in Table 3.4. This approach can be applied to the f shell to give isoscalar factors for $\text{SO}(7)$ and G_2 . The many-electron cfp of *Donlan* [58] and the multielectron cfp of *Velkov* [59] further extend the range to IRs R_b and R_c describing many-electron systems. Isoscalar factors found in this way have the advantage that their relative phases as well as the significance of the indices β and τ coincide with current usage.

Evaluation Using Casimir's Operator

Two commuting copies (b and c) are made of the generators of the group \mathcal{G} to form the generators of the direct product $\mathcal{G}_b \times \mathcal{G}_c$ [60]. Corresponding generators of \mathcal{G}_b and \mathcal{G}_c are added to give the generators of \mathcal{G}_a . Each quadratic operator $(T_a)^2$ appearing in the expression for Casimir's operator C_a for \mathcal{G}_a (as listed in Table 3.3) is written as $(T_b + T_c)^2$. On expanding the expressions of this type, the terms $(T_b)^2$ and

$(T_c)^2$ yield Casimir's operators C_b and C_c for \mathcal{G}_b and \mathcal{G}_c . Their eigenvalues can be written down in terms of the highest weights of the IRs appearing in the isoscalar factor of Eq. (3.22). If the cross products of the type $(T_b \cdot T_c)$ can be evaluated within the uncoupled states $|R_b \tau_b r_b, R_c \tau_c r_c\rangle$, then our knowledge of the eigenvalues of C_a for the coupled states $|\beta R_a \tau_a r_a\rangle$ provides the equations for determining (to within the freedom implied by β) the isoscalar factors relating the uncoupled to the coupled states. The evaluation of the cross products is straightforward when $\mathcal{H} = \text{SO}(3)$, since the relevant $6-j$ symbols are readily available [61]. Examples of this method can be found in the literature [52].

3.7.4 Generalizations of Angular Momentum Theory

CG coefficients, $n-j$ symbols, reduced matrix elements, and the entire apparatus of angular momentum theory all have their generalizations to groups other than $\text{SO}(3)$. An interchange of two columns of a $3-j$ symbol has its analog in the interchange of two parts of an isoscalar factor. For IRs W and L of $\text{SO}(2l + 1)$ and $\text{SO}(3)$, there are two possibilities:

1. The interchange of the two parts separated by the plus sign, namely,

$$\begin{aligned} & (W_a \tau_a L_a | W_b \tau_b L_b + W_c \tau_c L_c) \\ &= (-1)^t (W_a \tau_a L_a | W_c \tau_c L_c + W_b \tau_b L_b), \end{aligned} \quad (3.24)$$

where $t = L_a - L_b - L_c + x$, with x dependent on the IRs W only; or,

2. The *reciprocity* relation of *Racah* [6]

$$\begin{aligned} & (W_a \tau_a L_a | W_b \tau_b L_b + W_c \tau_c L_c) \\ &= (-1)^{t'} [(2L_b + 1) \dim W_a / (2L_a + 1) \dim W_b]^{\frac{1}{2}} \\ &\quad \times (W_b \tau_b L_b | W_a \tau_a L_a + W_c \tau_c L_c), \end{aligned} \quad (3.25)$$

where $t' = L_a - L_b - L_c + x'$, with x' dependent on the IRs W , but taken to be l by *Racah* for $W_c = (10 \dots 0)$.

Reduced matrix elements in $\text{SO}(3)$ can be further reduced by the extraction of isoscalar factors. When W_a occurs once in the decomposition of $W \times W_b$ we have

$$\begin{aligned} & (\gamma_a W_a \tau_a L_a || T^{(WL)} || \gamma_b W_b \tau_b L_b) \\ &= [(2L_a + 1) / \dim W_a]^{\frac{1}{2}} (\gamma_a W_a || T^{(W)} || \gamma_b W_b) \\ &\quad \times (W_b \tau_b L_b + W L | W_a \tau_a L_a). \end{aligned} \quad (3.26)$$

Analogous of the $n-j$ symbols are discussed by *Butler* [62].

3.8 Checks

The existence of numerical checks is useful when using group theory in atomic physics. The CG coefficients, isoscalar factors, and the various generalizations of the $n-j$ symbols are often calculated in ways that conceal the simplicity and structure of the answer. Practitioners are familiar with several empirical rules:

1. Numbers with different irrationalities, such as $\sqrt{2}$ and $\sqrt{3}$, are never added to one another.
2. The denominators of fractions seldom involve high primes.
3. High primes are uncommon, but when they appear, it is usually in diagonal matrix elements rather than off-diagonal ones.
4. A sum of a number of terms frequently factors in what appears to be an unexpected way, and similar sums often exhibit similar factors.

Guided by these rules, one will find that such errors as do arise occur with phases rather than with magnitudes.

References

1. Racah, G.: *Group Theory and Spectroscopy*. Springer Tracts in Modern Physics, vol. 37. Springer, New York (1965)
2. Eisenhart, L.P.: *Continuous Groups of Transformations*. Dover, New York (1961)
3. Cartan, E.: *Sur la Structure des Groupes de Transformations Finis et Continus*. Nony, Paris (1894). Thesis
4. Judd, B.R.: In: Loeb, E.M. (ed.) *Group Theory and Its Applications*. Academic Press, New York (1968)
5. Condon, E.U., Odabasi, H.: *Atomic Structure*. Cambridge Univ. Press, Cambridge (1980)
6. Racah, G.: *Phys. Rev.* **76**, 1352 (1949)
7. Judd, B.R.: *Operator Techniques in Atomic Spectroscopy*. Princeton Univ. Press, Princeton (1963)
8. Wigner, E.P.: *Group Theory*. Academic Press, New York (1959)
9. Judd, B.R.: *Phys. Rev.* **162**, 28 (1967)
10. Armstrong, L., Judd, B.R.: *Proc. R. Soc. A* **315**, 27 (1970)
11. Armstrong, L., Judd, B.R.: *Proc. R. Soc. A* **315**, 39 (1970)
12. Judd, B.R., Lister, G.M.S.: *J. Phys. A* **25**, 2615 (1992)
13. Wybourne, B.G.: *Classical Groups for Physicists*. Wiley, New York (1974)
14. Wybourne, B.G.: *Symmetry Principles and Atomic Spectroscopy*. Wiley, New York (1970)
15. McKay, W.G., Patera, J.: *Tables of Dimensions, Indices, and Branching Rules for Representations of Simple Lie Algebras*. Dekker, New York (1981)
16. Dynkin, E.B.: *Am. Math. Soc. Transl. Ser. 2* **6**, 245 (1965)
17. Rutherford, D.E.: *Substitutional Analysis*. Edinburgh Univ. Press, Edinburgh (1948)
18. Moshinsky, M.: *Group Theory and the Many-Body Problem*. Gordon Breach, New York (1968)
19. Weyl, H.: *The Theory of Groups and Quantum Mechanics*. Dover, New York (1950)
20. Harter, W.G.: *Phys. Rev. A* **8**, 2819 (1973)
21. Harter, W.G.: *Principles of Symmetry, Dynamics and Spectroscopy*. Wiley, New York (1993)
22. Harter, W.G., Patterson, C.W.: *A Unitary Calculus for Electronic Orbitals*. Lect. Notes Phys., vol. 49. Springer, Berlin, Heidelberg (1976)
23. Drake, G.W.F., Schlesinger, M.: *Phys. Rev. A* **15**, 1990 (1977)
24. Kent, R.D., Schlesinger, M.: *Phys. Rev. A* **50**, 186 (1994)
25. Littlewood, D.E.: *The Theory of Group Characters*. Clarendon, Oxford (1950)
26. Jahn, H.A.: *Proc. R. Soc. A* **201**, 516 (1950)
27. Flowers, B.H.: *Proc. R. Soc. A* **212**, 248 (1952)
28. Judd, B.R., Wadzinski, H.T.: *J. Math. Phys.* **8**, 2125 (1967)
29. Shudeman, C.L.B.: *J. Frankl. Inst.* **224**, 501 (1937)
30. Judd, B.R., Lister, G.M.S.: *Phys. Rev. Lett.* **67**, 1720 (1991)
31. Wybourne, B.G.: *Spectroscopic Properties of Rare Earths*. Wiley, New York, p 15 (1965)
32. Nielson, C.W., Koster, G.F.: *Spectroscopic Coefficients for the p^n , d^n , and f^n Configurations*. MIT Press, Cambridge (1963)
33. Feneuille, S.: *J. Phys. Fr.* **28**, 61 (1967)
34. Feneuille, S.: *J. Phys. Fr.* **28**, 315 (1967)
35. Feneuille, S.: *J. Phys. Fr.* **28**, 701 (1967)
36. Feneuille, S.: *J. Phys. Fr.* **28**, 497 (1967)
37. Feneuille, S.: *J. Phys. Fr.* **30**, 923 (1969)
38. Feneuille, S., Crubellier, A., Haskell, T.: *J. Phys. Fr.* **31**, 25 (1970)
39. Fano, U., Rao, A.R.P.: *Symmetry Principles in Quantum Physics*. Academic Press, New York (1996). Sect. 8.3.3
40. Georgi, H.: *Lie Algebras in Particle Physics*. Benjamin/Cummings, Reading (1982). Chap. XXV
41. Judd, B.R.: *Phys. Rep.* **285**, 1 (1997)
42. Lo, E., Hansen, J.E., Judd, B.R.: *J. Phys. B* **33**, 819 (2000)
43. Judd, B.R., Lo, E.: *Phys. Rev. Lett.* **85**, 948 (2000)
44. Hansen, J.E., Ven, E.G.: *Mol. Phys.* **101**, 997 (2003)
45. Englefield, M.J.: *Group Theory and the Coulomb Problem*. Wiley, New York (1972)
46. Armstrong, L.: *J. Phys. Fr.* **31**, 17 (1970)
47. Wulfman, C.E.: In: Loeb, E.M. (ed.) *Group Theory and Its Applications*, vol. 2, Academic Press, New York (1971)
48. Herrick, D.R.: *Adv. Chem. Phys.* **52**, 1 (1982)
49. McLellan, A.G.: *Proc. Phys. Soc. Lond.* **76**, 419 (1960)
50. Judd, B.R.: *Physica* **33**, 174 (1967)
51. Judd, B.R., Crosswhite, H.M., Crosswhite, H.: *Phys. Rev.* **169**, 130 (1968)
52. Judd, B.R.: *Phys. Rev.* **141**, 4 (1966)
53. Judd, B.R., Suskin, M.A.: *J. Opt. Soc. Am. B* **1**, 261 (1984)
54. Judd, B.R., Leavitt, R.C.: *J. Phys. B* **19**, 485 (1986)
55. Leavitt, R.C.: *J. Phys. A* **20**, 3171 (1987)
56. Leavitt, R.C.: *J. Phys. B* **21**, 2363 (1988)
57. Edmonds, A.R.: *Proc. R. Soc. A* **268**, 567 (1962)
58. Donlan, V.L.: *Air Force Material Laboratory Report No. AFML-TR-70-249*. Wright-Patterson Air Force Base, Ohio (1970)
59. Velkov, D.D.: *Multi-Electron Coefficients of Fractional Parentage for the p, d, and f Shells*. The Johns Hopkins Univ., Baltimore (2000). Ph.D. Thesis, <http://www.pha.jhu.edu/groups/cfp/>
60. Nutter, P., Nielsen, C.: *Fractional Parentage Coefficients of Terms of f^n , II. Direct Evaluation of Racah's Factored Forms by a Group Theoretical Approach*. Raytheon, Waltham, p 133 (1963). Technical Memorandum T-133
61. Rotenberg, M., Bivins, R., Metropolis, N., Wooten, J.K.: *The 3-j and 6-j Symbols*. MIT Press, Cambridge (1959)
62. Butler, P.H.: *Philos. Trans. R. Soc. A* **277**, 545 (1975)



Brian Judd Brian Judd has had a life-long interest in applying group theory to the spectroscopic properties of the rare earths. He held appointments at Oxford, Chicago, Paris and Berkeley before joining the Physics Department of the Johns Hopkins University in 1966. He received the Spedding Award for Rare-Earth Research in 1988 and is an Honorary Fellow of Brasenose College, Oxford.



Dynamical Groups

4

Josef Paldus

Contents

4.1	Noncompact Dynamical Groups	82
4.1.1	Realizations of $so(2,1)$	82
4.1.2	Hydrogenic Realization of $so(4,2)$	82
4.2	Hamiltonian Transformation and Simple Applications	84
4.2.1	N -Dimensional Isotropic Harmonic Oscillator	84
4.2.2	N -Dimensional Hydrogenic Atom	85
4.2.3	Perturbed Hydrogenic Systems	85
4.3	Compact Dynamical Groups	86
4.3.1	Unitary Group and Its Representations	86
4.3.2	Orthogonal Group $O(n)$ and Its Representations	87
4.3.3	Clifford Algebras and Spinor Representations	87
4.3.4	Bosonic and Fermionic Realizations of $U(n)$	88
4.3.5	The Vibron Model	88
4.3.6	Many-Electron Correlation Problem	89
4.3.7	Clifford Algebra Unitary Group Approach	91
4.3.8	Spin-Dependent Operators	91
	References	92

Abstract

The well-known *symmetry (invariance, degeneracy) groups* or *algebras* of quantum mechanical Hamiltonians provide quantum numbers (conservation laws, integrals of motion) for state labeling and the associated selection rules. In addition, it is often advantageous to employ much larger groups, referred to as the *dynamical groups (noninvariance groups, dynamical algebras, spectrum generating algebras)*, which may or may not be the invariance groups of the studied system [1–7]. In all known cases, they are Lie groups (LGs), or rather corresponding Lie algebras (LAs), and one usually requires that all states of interest of a system be contained

in a single irreducible representation (irrep). Likewise, one may require that the Hamiltonian be expressible in terms of the Casimir operators of the corresponding universal enveloping algebra [8, 9]. In a weaker sense, one regards any group (or corresponding algebra) as a dynamical group if the Hamiltonian can be expressed in terms of its generators [10–12]. In nuclear physics, one sometimes distinguishes *exact* (baryon number preserving), *almost exact* (e.g., total isospin), *approximate* (e.g., $SU(3)$ of the “eightfold way”) and *model* (e.g., nuclear shell model) *dynamical symmetries* [13]. The dynamical groups of interest in atomic and molecular physics can be conveniently classified by their topological characteristic of compactness. Noncompact LGs (LAs) generally arise in simple problems involving an infinite number of bound states, while those involving a finite number of bound states (e.g., molecular vibrations or abinitio models of electronic structure) exploit compact LG’s.

We follow the convention of designating Lie groups by capital letters and Lie algebras by lower case letters, e.g., the Lie algebra of the rotation group $SO(3)$ is designated as $so(3)$.

Keywords

Clifford algebra · spinor representation · Casimir operator · angular momentum vector · molecular electronic structure · special orthogonal Lie algebras (LAs) $so(3)$, $so(4)$, $so(2,1)$, $so(4,2)$ · unitary group $U(n)$ and its LA · Clifford and Grassmann algebras · spinor group · vibron model · N -dim harmonic oscillator · N -dim hydrogenic and relativistic hydrogenic atom · diatomic ions · Zeeman and Lo-Surdo-Stark effect · Laplace-Runge-Lenz vector · unitary group approach (UGA) · Graphical UGA (GUGA) · spin dependent UGA · molecular electronic structure · Gel’fand tableau · Paldus tableau · Shavitt graph · Casimir operator · Gould-Paldus operator

J. Paldus (✉)
Dept. of Applied Mathematics, University of Waterloo
Waterloo, ON, Canada
e-mail: paldus@uwaterloo.ca

4.1 Noncompact Dynamical Groups

As an illustration we present basic facts concerning LAs that are useful for centrosymmetric Kepler-type problems, their realizations and typical applications. Recall that a *realization* of a LA is a homomorphism associating a concrete set of physically relevant operators with each abstract basis of the given LA. The physical operators we will use are general (intrinsic) position vectors $\mathbf{R} = (X_1, X_2, \dots, X_N)$ in \mathbb{R}^N and their corresponding momenta $\mathbf{P} = (P_1, P_2, \dots, P_N)$, satisfying the basic commutation relations ($\hbar = 1$)

$$[X_j, X_k] = [P_j, P_k] = 0, \quad [X_j, P_k] = i\delta_{jk}I. \quad (4.1)$$

4.1.1 Realizations of so(2,1)

This important LA is a simple noncompact analogue of the well-known rotation group LA so(3), (Sect. 2.1 and Sect. 3.2). Designating its three generators by T_j ($j = 1, 2, 3$), its structure constants (Sect. 2.1.1 and Sect. 3.1.1) are defined by

$$\begin{aligned} [T_1, T_2] &= i\gamma T_3, \\ [T_2, T_3] &= iT_1, \\ [T_3, T_1] &= iT_2, \end{aligned} \quad (4.2)$$

with $\gamma = -1$, while $\gamma = 1$ gives so(3). Defining the so-called ladder (raising and lowering) operators

$$T_{\pm} = T_1 \pm iT_2, \quad (4.3)$$

we also have that

$$[T_+, T_-] = 2\gamma T_3, \quad [T_3, T_{\pm}] = \pm T_3. \quad (4.4)$$

The Casimir operator then has the form

$$T^2 = \gamma(T_1^2 + T_2^2) + T_3^2 = \gamma T_+ T_- + T_3^2 - T_3. \quad (4.5)$$

With a Hermitian scalar product satisfying $T_j^\dagger = T_j$ ($j = 1, 2, 3$), so that $T_{\pm}^\dagger = T_{\mp}$, the unitary irreps (unirreps) carried by the simultaneous eigenstates of T^2 and T_3 have the form (Sect. 2.1.1 and Sect. 2.2)

$$\begin{aligned} T^2|kq\rangle &= k(k+1)|kq\rangle, \\ T_3|kq\rangle &= q|kq\rangle, \\ T_{\pm}|kq\rangle &= \sqrt{\gamma(k \mp q)(k \pm q + 1)}|k, q \pm 1\rangle. \end{aligned} \quad (4.6)$$

For so(3), ($\gamma = 1$), only finite dimensional irreps $\mathcal{D}^{(k)}$, $k = 0, 1, 2, \dots$ with $|q| \leq k$ are possible (Sect. 2.2 and Sect. 2.3). In contrast, there are no nontrivial finite dimensional unirreps of so(2,1); (for classification, see e.g., [2, 14, 15]). The

relevant class $\mathcal{D}^+(k)$ of so(2,1) unirreps for bound state problems has a T_3 eigenspectrum bounded from below and is given by $q = -k + \mu$; $\mu = 0, 1, 2, \dots$, and $k < 0$ or, equivalently, $\mathcal{D}^+(-k-1)$ with $q = k+1 + \mu$; $\mu = 0, 1, 2, \dots$; $k > -1$, since $k_1 = -k-1$ defines an equivalent unirrep and $k_1(k_1+1) = k(k+1)$. There exists a similar class of irreps with the T_3 spectrum bounded from above and two classes (principal and supplementary) with unbounded T_3 spectra (which may be exploited in scattering problems).

For problems involving only central potentials, a useful realization is given in terms of the radial distance $R = |\mathbf{R}|$ and the radial momentum

$$\begin{aligned} P_R &= -\frac{i}{R} \frac{\partial}{\partial R} R = -i \left(\frac{\partial}{\partial R} + \frac{1}{R} \right) \\ &= \frac{1}{R} (\mathbf{R} \cdot \mathbf{P} - iI), \end{aligned} \quad (4.7)$$

so that $[R, P_R] = iI$. Recall that

$$P^2 = P_R^2 + \frac{L^2}{R^2}, \quad \mathbf{L} = \mathbf{R} \wedge \mathbf{P}. \quad (4.8)$$

The general form of the desired so(2,1) realization is [2, 14–17]

$$\begin{aligned} \left. \begin{aligned} T_1 \\ T_3 \end{aligned} \right\} &= \frac{1}{2} R^{-\nu} (\nu^{-2} R^2 P_R^2 + \xi \mp R^{2\nu}), \\ T_2 &= \frac{1}{2} [2\nu^{-1} R P_R - i(1 - \nu^{-1})I], \end{aligned} \quad (4.9)$$

where ξ is either a c -number (scalar operator) or an operator that commutes with both R and P_R , and ν is an arbitrary real number.

To interrelate this realization with so(2,1) unirreps $\mathcal{D}^+(k)$ or $\mathcal{D}^+(-k-1)$, we have to establish the connection between the quantum numbers k, q and the parameters ξ and ν . Considering the Casimir operator T^2 in Eq. (4.5), we find that in our realization Eq. (4.9)

$$T^2 = \xi + (1 - \nu^2)/4\nu^2, \quad (4.10)$$

so that

$$k = \frac{1}{2} \left(-1 \pm \sqrt{4\xi + \nu^{-2}} \right), \quad (4.11)$$

and

$$q = q_0 + \mu, \quad \mu = 0, 1, 2, \dots, \quad (4.12)$$

where

$$q_0 = k + 1 = \frac{1}{2} \left(1 \pm \sqrt{4\xi + \nu^{-2}} \right), \quad k > -1. \quad (4.13)$$

4.1.2 Hydrogenic Realization of so(4,2)

To obtain suitable hydrogenic realizations of so(4,2) it is best to proceed from so(4) (the dynamical symmetry group for

the bound states of the nonrelativistic Kepler problem) and merge it with $\text{so}(2,1)$ [2, 14, 15].

The $\text{so}(4)$ LA can be realized either as a direct sum $\text{so}(4) = \text{so}(3) \oplus \text{so}(3)$ or by supplementing $\text{so}(3)$ with an appropriately scaled quantum mechanical analogue of the Laplace–Runge–Lenz (LRL) vector (Sect. 3.6.2). In the first case, we use two commuting angular momentum vectors \mathbf{M} and \mathbf{N} (Sect. 2.5),

$$\begin{aligned} [M_j, M_k] &= i\varepsilon_{jkl}M_\ell, & [N_j, N_k] &= i\varepsilon_{jkl}N_\ell, \\ [M_j, N_k] &= 0, & (j, k, \ell &= 1, 2, 3), \end{aligned} \quad (4.14)$$

while in the second case, we use the components of the total angular momentum vector \mathbf{J} and LRL-like vector \mathbf{V} with commutation relations

$$\begin{aligned} [J_j, J_k] &= i\varepsilon_{jkl}J_\ell, \\ [V_j, V_k] &= i\sigma\varepsilon_{jkl}J_\ell, \\ [J_j, V_k] &= i\varepsilon_{jkl}V_\ell, & (j, k, \ell &= 1, 2, 3), \end{aligned} \quad (4.15)$$

with $\sigma = 1$. For $\sigma = -1$, we obtain $\text{so}(3,1)$ (the LA of the homogeneous Lorentz group), which is relevant to the scattering problem of a particle in the Coulomb (or Kepler) potential (see the text following Eqs. (4.25) and (4.31)). For $\sigma = 0$, we get $\text{e}(3)$ (the LA of the three-dimensional Euclidean group) [18–20]. Note that Eqs. (4.14) and (4.15) are interrelated by

$$\mathbf{M} = \frac{1}{2}(\mathbf{J} + \mathbf{V}), \quad \mathbf{N} = \frac{1}{2}(\mathbf{J} - \mathbf{V}), \quad (4.16)$$

so that $\mathbf{J} = \mathbf{M} \oplus \mathbf{N}$ and $\mathbf{V} = 2\mathbf{M} - \mathbf{J}$. The two Casimir operators C_1 and C_2 are

$$\begin{aligned} C_1 &= \sigma J^2 + V^2 \\ &= \sigma J_+ J_- + V_+ V_- + V_3^2 + \sigma J_3(J_3 - 2), \\ C_2 &= (\mathbf{V} \cdot \mathbf{J}) = (\mathbf{J} \cdot \mathbf{V}) \\ &= \frac{1}{2}(V_+ J_- + V_- J_+) + V_3 J_3, \end{aligned} \quad (4.17)$$

where, again,

$$X_\pm = X_1 \pm iX_2, \quad X = J \text{ or } V. \quad (4.18)$$

For $\text{so}(3,1)$ and $\text{e}(3)$, only infinite dimensional nontrivial irreps are possible, while for $\text{so}(4)$, only finite dimensional ones arise. To get unirreps, we require \mathbf{J} and \mathbf{V} to be Hermitian. Using $\{J^2, J_3, C_1, C_2\}$ as a complete set of commuting operators for $\text{so}(4)$, we label the basis vectors by the four quantum numbers as $|\gamma jm\rangle \equiv |(j_0, \eta) jm\rangle$, so that

$$\begin{aligned} J^2|\gamma jm\rangle &= j(j+1)|\gamma jm\rangle, \\ J_3|\gamma jm\rangle &= m|\gamma jm\rangle, \\ C_1|\gamma jm\rangle &= (j_0^2 - \eta^2 - 1)|\gamma jm\rangle, \\ C_2|\gamma jm\rangle &= j_0\eta|\gamma jm\rangle, \end{aligned} \quad (4.19)$$

with $2|j_0|$ being a nonnegative integer and

$$\begin{aligned} j &= |j_0|, |j_0| + 1, \dots, \eta - 1; \\ \eta &= |j_0| + k, \quad k = 1, 2, \dots \end{aligned} \quad (4.20)$$

(see, e.g., [17] for the action of J_\pm, V_3 and V_\pm).

To obtain the hydrogenic (or Kepler) realization of $\text{so}(4)$, we consider the quantum mechanical analogue of the classical LRL vector

$$\begin{aligned} \tilde{\mathbf{V}} &= \frac{1}{2}(\mathbf{p} \wedge \mathbf{L} - \mathbf{L} \wedge \mathbf{p}) - Zr^{-1}\mathbf{r} \\ &= \frac{1}{2}\mathbf{r}p^2 - \mathbf{p}(\mathbf{r} \cdot \mathbf{p}) + \mathbf{r}H, \\ \mathbf{L} &= \mathbf{r} \wedge \mathbf{p}, \end{aligned} \quad (4.21)$$

which commutes with the hydrogenic Hamiltonian

$$H = \frac{1}{2}p^2 - Zr^{-1}. \quad (4.22)$$

Note that

$$\begin{aligned} [\mathbf{L}, H] &= [\tilde{\mathbf{V}}, H] = 0, \\ (\mathbf{L} \cdot \tilde{\mathbf{V}}) &= (\tilde{\mathbf{V}} \cdot \mathbf{L}) = 0, \\ \tilde{\mathbf{V}}^2 &= 2H(L^2 + 1) + Z^2, \end{aligned} \quad (4.23)$$

while the components of \mathbf{L} and $\tilde{\mathbf{V}}$ satisfy the commutation relations

$$\begin{aligned} [L_j, L_k] &= i\varepsilon_{jkl}L_\ell, \\ [L_j, \tilde{V}_k] &= i\varepsilon_{jkl}\tilde{V}_\ell, \\ [\tilde{V}_j, \tilde{V}_k] &= (-2H)\varepsilon_{jkl}L_\ell. \end{aligned} \quad (4.24)$$

Thus, restricting ourselves to a specific bound state energy level E_n , we can replace H by E_n and define

$$V_j = (-2E_n)^{-1/2}\tilde{V}_j \quad (j = 1, 2, 3), \quad (4.25)$$

obtaining the $\text{so}(4)$ commutation relations Eq. (4.15) (with \mathbf{J} replaced by \mathbf{L}). This is Pauli's hydrogenic realization of $\text{so}(4)$ [21–23]. [In a similar way we can consider continuum states $E > 0$ and define $\mathbf{V} = (2E)^{-1/2}\tilde{\mathbf{V}}$, obtaining an $\text{so}(3,1)$ realization.] The last identity of Eq. (4.23) now becomes

$$V^2 = -(L^2 + 1) - Z^2/2E_n, \quad (4.26)$$

which immediately implies Bohr's formula, since $V^2 + L^2 = 4M^2 = -1 - Z^2/2E_n$, so that

$$E_n = -Z^2/2(2j_1 + 1)^2 = -Z^2/2n^2, \quad (4.27)$$

where $n = 2j_1 + 1$ and j_1 is the angular momentum quantum number for \mathbf{M} , Eq. (4.16). In terms of the irrep labels Eq. (4.20), we have that $j_0 = 0$, $\eta = n$, so that $|\gamma \ell m\rangle = |(0, n)\ell m\rangle \equiv |n\ell m\rangle$, $\ell = 0, 1, \dots, n - 1$.

Using the stepwise merging of $\text{so}(4)$ and $\text{so}(2,1)$ [adding first T_2 , which leads to $\text{so}(4,1)$, and subsequently T_1 and T_3],

we arrive at the hydrogenic realization of $\text{so}(4,2)$ having 15 generators $\mathbf{L}, \mathbf{A}, \mathbf{B}, \mathbf{\Gamma}, T_1, T_2, T_3$, namely ([2, 14, 15, 17])

$$\begin{aligned} \mathbf{L} &= \mathbf{R} \wedge \mathbf{P}, \\ \left. \begin{array}{l} \mathbf{A} \\ \mathbf{B} \end{array} \right\} &= \frac{1}{2} \mathbf{R} \mathbf{P}^2 - \mathbf{P}(\mathbf{R} \cdot \mathbf{P}) \mp \mathbf{R}, \\ \mathbf{\Gamma} &= \mathbf{R} \mathbf{P}, \\ \left. \begin{array}{l} T_1 \\ T_3 \end{array} \right\} &= \frac{1}{2} (\mathbf{R} \mathbf{P}^2 \mp \mathbf{R}) = \frac{1}{2} (\mathbf{R} \mathbf{P}_R^2 + L^2 \mathbf{R}^{-1} \mp \mathbf{R}), \\ T_2 &= \mathbf{R} \cdot \mathbf{P} - iI = \mathbf{R} \mathbf{P}_R. \end{aligned} \quad (4.28)$$

Relabeling these generators by the elements of an antisymmetric 6×6 matrix according to the scheme

$$L_{jk} \leftrightarrow \begin{pmatrix} 0 & L_3 & -L_2 & A_1 & B_1 & \Gamma_1 \\ & 0 & L_1 & A_2 & B_2 & \Gamma_2 \\ & & 0 & A_3 & B_3 & \Gamma_3 \\ & & & 0 & T_2 & T_1 \\ & & & & 0 & T_3 \\ & & & & & 0 \end{pmatrix} \quad (4.29)$$

we can write the commutation relations in the following standard form

$$[L_{jk}, L_{\ell m}] = i(g_{j\ell} L_{km} + g_{km} L_{j\ell} - g_{k\ell} L_{jm} - g_{jm} L_{k\ell}), \quad (4.30)$$

with the diagonal metric tensor g_{jk} defined by the matrix $G = \text{diag}[1, 1, 1, 1, -1, -1]$. The matrix form Eq. (4.29) also implies the subalgebra structure

$$\text{so}(4,2) \supset \text{so}(4,1) \supset \text{so}(4) \supset \text{so}(3), \quad (4.31)$$

with $\text{so}(4,1)$ generated by $\mathbf{L}, \mathbf{A}, \mathbf{B}$ and T_2 , and $\text{so}(4)$ by \mathbf{L}, \mathbf{A} . [\mathbf{L}, \mathbf{B} also generate $\text{so}(3,1)$.]

The three independent Casimir operators (quadratic, cubic, and quartic) are [24] (summation over all indices is implied)

$$\begin{aligned} Q_2 &= \frac{1}{2} L_{jk} L^{jk} \\ &= L^2 + A^2 - B^2 - \Gamma^2 + T_3^2 - T_1^2 - T_2^2, \\ Q_3 &= \frac{1}{48} \varepsilon_{ijklmn} L^{ij} L^{kl} L^{mn} \\ &= T_1(\mathbf{B} \cdot \mathbf{L}) + T_2(\mathbf{\Gamma} \cdot \mathbf{L}) + T_3(\mathbf{A} \cdot \mathbf{L}) \\ &\quad + \mathbf{A} \cdot (\mathbf{B} \wedge \mathbf{\Gamma}), \\ Q_4 &= L_{jk} L^{k\ell} L_{\ell m} L^{mj}. \end{aligned} \quad (4.32)$$

For our hydrogenic realization $Q_2 = -3$, $Q_3 = Q_4 = 0$. Thus, our hydrogenic realization implies a single unirrep of $\text{so}(4,2)$ adapted to the chain Eq. (4.31).

4.2 Hamiltonian Transformation and Simple Applications

The basic idea is to transform the relevant Schrödinger equation into an eigenvalue problem for one of the operators from the complete set of commuting operators in our realizations, e.g., T_3 for $\text{so}(2,1)$. Instead of using a rather involved ‘‘tilting’’ transformation ([1, p. 20], and [2, 14, 15]), we can rely on a simple scaling transformation [16, 25]

$$\mathbf{r} = \lambda \mathbf{R}, \quad \mathbf{p} = \lambda^{-1} \mathbf{P}, \quad r = \lambda R, \quad p_r = \lambda^{-1} P_R, \quad (4.33)$$

where

$$r = \left(\sum_{j=1}^N x_j^2 \right)^{1/2}, \quad (4.34)$$

and

$$p^2 = p_r^2 + r^{-2} \left[\frac{1}{4} (N-1)(N-3) + L^2 \right], \quad (4.35)$$

with p_r defined analogously to P_R in Eq. (4.7); r and p are the physical operators in terms of which the Hamiltonian of the studied system is expressed. Recall that L^2 has eigenvalues [26]

$$\ell(\ell + N - 2), \quad \ell = 0, 1, 2, \dots \quad \text{for } N \geq 2, \quad (4.36)$$

and we can set $\ell = 0$ for $N = 1$ (the angular momentum term vanishes in the one-dimensional case). The units in which $m = e = \hbar = 1$, $c \approx 137$ are used throughout.

4.2.1 N-Dimensional Isotropic Harmonic Oscillator

Considering the Hamiltonian

$$H = \frac{1}{2} p^2 + \frac{1}{2} \omega^2 r^2, \quad (4.37)$$

with p^2 in the form Eq. (4.35), transforming the corresponding Schrödinger equation using the scaling transformation Eq. (4.33) and multiplying by $\frac{1}{4} \lambda^2$, we get for the radial component

$$\frac{1}{2} \left(\frac{1}{4} P_R^2 + R^{-2} \xi + \frac{1}{4} \omega^2 \lambda^4 R^2 - \frac{1}{2} \lambda^2 E \right) \psi_R(\lambda R) = 0, \quad (4.38)$$

with

$$\xi = \frac{1}{16} (N-1)(N-3) + \frac{1}{4} \ell(\ell + N - 2). \quad (4.39)$$

Choosing λ such that $(\omega/2)^2 \lambda^4 = 1$, we can rewrite Eq. (4.38) using the $\text{so}(2,1)$ realization Eq. (4.9) with $\nu = 2$ as

$$\left(T_3 - \frac{1}{4} \lambda^2 E \right) \psi_R(\lambda R) = 0. \quad (4.40)$$

Thus, using the second equation of Eq. (4.6) we can interchange $\psi_{\mathbf{R}}(\lambda R)$ with $|kq\rangle$ and set $\frac{1}{4}\lambda^2 E = q$, so that

$$E = 4q/\lambda^2 = 2q\omega, \quad (4.41)$$

with q given by Eqs. (4.12) and (4.13), i.e.,

$$q = q_0 + \mu, \quad \mu = 0, 1, 2, \dots, \quad (4.42)$$

and

$$q_0 = k + 1 = \frac{1}{2} \left[1 \pm \left(\ell + \frac{1}{2}N - 1 \right) \right]. \quad (4.43)$$

Now, for $N = 1$, we set $\ell = 0$ so that $q_0 = \frac{1}{4}$ and $q_0 = \frac{3}{4}$, yielding for $E = 2q\omega$ the values $(\frac{1}{2} + 2\mu)\omega$ and $(\frac{1}{2} + 2\mu + 1)\omega$, $\mu = 0, 1, 2, \dots$. Combining both sets we thus get for $N = 1$ the well-known result

$$E \equiv E_n = \left(n + \frac{1}{2} \right) \omega, \quad n = 0, 1, 2, \dots \quad (4.44)$$

Similarly, for the general case $N \geq 2$, we choose the upper sign in Eq. (4.43) [so that $k > -1$] and get

$$E \equiv E_n = \left(n + \frac{1}{2}N \right) \omega, \quad n = 0, 1, 2, \dots, \quad (4.45)$$

where we identified $(\ell + 2\mu)$ with the principal quantum number n .

4.2.2 N -Dimensional Hydrogenic Atom

Applying the scaling transformation Eq. (4.33) to the hydrogenic Hamiltonian Eq. (4.22) in N -dimensions, we get for the radial component (after multiplying from the left by $\lambda^2 R$)

$$\left[\frac{1}{2} (R P_{\mathbf{R}}^2 + R^{-1} \xi - 2\lambda^2 E R) - \lambda Z \right] \psi_{\mathbf{R}}(\lambda R) = 0, \quad (4.46)$$

where now

$$\xi = \frac{1}{4} (N-1)(N-3) + \ell(\ell + N - 2). \quad (4.47)$$

In this case, we must set $2\lambda^2 E = -1$ and use realization Eq. (4.9) with $\nu = 1$ to obtain

$$(T_3 - \lambda Z) \psi_{\mathbf{R}}(\lambda R) = 0. \quad (4.48)$$

This immediately implies that

$$\lambda Z = q, \quad (4.49)$$

and

$$q_0 = k + 1 = \frac{1}{2} [1 \pm (2\ell + N - 2)]. \quad (4.50)$$

Choosing the upper sign [since $\ell \geq 0$ and $k > -1$], so that $q_0 = \ell + \frac{1}{2}(N-1)$, and identifying q with the principal quantum number n , we finally have that

$$E \equiv E_n = -\frac{1}{2\lambda^2} = -\frac{Z^2}{2n^2}. \quad (4.51)$$

The N -dimensional relativistic hydrogenic atom can be treated in the same way, using either the Klein–Gordon or Dirac–Coulomb equations [2, 14–17].

4.2.3 Perturbed Hydrogenic Systems

The $\text{so}(4,2)$ based Lie algebraic formalism can be conveniently exploited to carry out large-order perturbation theory ([27–29] and Chap. 5) for hydrogenic systems described by the Schrödinger equation

$$[H_0 + \varepsilon V(\mathbf{r})] \psi(\mathbf{r}) = (E_0 + \Delta E) \psi(\mathbf{r}), \quad (4.52)$$

with H_0 given by Eq. (4.22) and E_0 by E of Eq. (4.51). Applying transformation Eq. (4.33), using Eqs. (4.49), (4.51), and multiplying on the left-hand side by $\lambda^2 R$, we get

$$\left[\frac{1}{2} R P^2 - q + \frac{1}{2} R + \varepsilon \lambda^2 R V(\lambda \mathbf{R}) - \lambda^2 R \Delta E \right] \Psi(\mathbf{R}) = 0, \quad (4.53)$$

where we set $\psi(\lambda \mathbf{R}) \equiv \Psi(\mathbf{R})$. For the important case of a three-dimensional hydrogenic atom [$N = 3$, $\xi = \ell(\ell + 1)$, $q \equiv n$], using the $\text{so}(4,2)$ realization Eq. (4.28) [or $\text{so}(2,1)$ realization Eq. (4.9) with $\nu = 1$] we get

$$(K + \varepsilon W - S \Delta E) \Psi(\mathbf{R}) = 0, \quad (4.54)$$

with

$$\begin{aligned} K &= T_3 - n, \\ W &= \lambda^2 R V(\lambda \mathbf{R}), \\ S &= \lambda^2 R. \end{aligned} \quad (4.55)$$

We also have that $\lambda = n/Z$ and for the ground state case $n = q = 1$. Although Eq. (4.54) has the form of a generalized eigenvalue problem requiring perturbation theory formalism with a nonorthogonal basis (where S represents an overlap), T_3 is Hermitian with respect to a $(1/R)$ scalar product, and the required matrix elements can, therefore, be evaluated easily [2, 14, 15, 17, 27–29].

For central field perturbations, $V(\mathbf{r}) = V(r)$, the problem reduces to one dimension, and since $R = T_3 - T_1$, the $\text{so}(2,1)$ hydrogenic realization ($\nu = 1$) can be employed. For problems of a hydrogenic atom in a magnetic field (Zeeman effect) [27–30] or a one-electron diatomic ion [31], the $\text{so}(4,2)$ formalism is required (note, however, that the LoSurdo–Stark effect can also be treated as a one-dimensional problem using parabolic coordinates [32]).

The main advantage of the LA approach stems from the fact that the spectrum of T_3 is discrete, so that no integration over continuum states is required. Moreover, the relevant perturbations are closely packed around the diagonal in this representation, so that infinite sums are replaced by small finite sums.

For example, for the LoSurdo–Stark problem, when $V(\mathbf{r}) = \mathcal{F}z$, where \mathcal{F} designates electric field strength in the z -direction, we get Eq. (4.54) with $\varepsilon = \mathcal{F}$ and $W = (n/Z)^3 RZ$, $S = (n/Z)^2 R$. Since both R and Z are readily expressed in terms of $\text{so}(4,2)$ generators,

$$Z = B_3 - A_3, \quad R = T_3 - T_1, \quad (4.56)$$

we can easily compute all the required matrix elements [2, 14, 15, 17].

Similarly, considering the Zeeman effect with

$$V(\mathbf{r}) = \frac{1}{2}BL_3 + \frac{1}{8}B^2(r^2 - z^2), \quad (4.57)$$

where B designates magnetic field strength in the z -direction, we have for the ground state when $n = 1$, $\ell = m = 0$ that $\varepsilon = \frac{1}{8}B^2$, $K = T_3 - 1$, $W = Z^{-4}R(R^2 - Z^2)$ and $S = Z^{-2}R$. Again, the matrix elements of W and S are obtained from those of Z and R , Eq. (4.56), by matrix multiplication (for tables and programs, see [17]).

One can treat one-electron diatomic ions [2, 14, 15, 31] and screened Coulomb potentials, including charmonium and harmonium [10–12, 17, 33, 34], in a similar way.

Note, finally, that we can also formulate the perturbed problem Eq. (4.54) in a standard form not involving the “overlap” by defining the scaling factor as $\lambda = (-2E)^{-1/2}$, where E is now the exact energy $E = E_0 + \Delta E$; Eq. (4.54) then becomes

$$(T_3 + \varepsilon W - \lambda Z)\Psi(\mathbf{R}) = 0, \quad (4.58)$$

with the eigenvalue λZ . In this case, any conventional perturbation formalism applies, but the desired energy has to be found from λZ [35].

4.3 Compact Dynamical Groups

Unitary groups $U(n)$ and their LAs often play the role of (compact) dynamical groups since

1. Quantum mechanical observables are Hermitian, and the LA of $U(n)$ is comprised of Hermitian operators [under the $\exp(iA)$ mapping].
2. Any compact Lie group is isomorphic to a subgroup of some $U(n)$.

3. “Nothing of algebraic import is lost by the unitary restriction” [36].

All $U(n)$ irreps have finite dimension and are, thus, relevant to problems involving a finite number of bound states [3–6, 10–12, 36–45].

4.3.1 Unitary Group and Its Representations

The unitary group $U(n)$ has n^2 generators E_{ij} spanning its LA and satisfying the commutation relations

$$[E_{ij}, E_{k\ell}] = \delta_{jk} E_{i\ell} - \delta_{i\ell} E_{kj} \quad (4.59)$$

and the Hermitian property

$$E_{ij}^\dagger = E_{ji}. \quad (4.60)$$

They are classified as *raising* ($i < j$), *lowering* ($i > j$), and *weight* ($i = j$) generators according to whether they raise, lower, and preserve the weight, respectively. The *weight vector* is a vector of the carrier space of an irrep that is a simultaneous eigenvector of all weight generators E_{ii} of $U(n)$ (comprising its Cartan subalgebra), and the vector $\mathbf{m} = (m_1, m_2, \dots, m_n)$ with integer components, consisting of corresponding eigenvalues, is called a *weight*. The *highest weight* \mathbf{m}_n (in lexical ordering),

$$\mathbf{m}_n = (m_{1n}, m_{2n}, \dots, m_{nn}), \quad (4.61)$$

with

$$m_{1n} \geq m_{2n} \geq \dots \geq m_{nn}, \quad (4.62)$$

uniquely labels $U(n)$ irreps, $\Gamma(\mathbf{m}_n)$, and may be represented by a Young pattern. Subducing $\Gamma(\mathbf{m}_r)$ of $U(r)$ to $U(r-1)$, embedded as $U(r-1) \oplus 1$ in $U(r)$, gives [41]

$$\Gamma(\mathbf{m}_r) \downarrow U(r-1) = \bigoplus \Gamma(\mathbf{m}_{r-1}), \quad (4.63)$$

where the sum extends over all $U(r-1)$ weights $\mathbf{m}_{r-1} = (m_{1,r-1}, m_{2,r-1}, \dots, m_{r-1,r-1})$ satisfying the so-called “betweenness conditions” [38]

$$m_{ir} \geq m_{i,r-1} \geq m_{i+1,r} \quad (i = 1, \dots, r-1). \quad (4.64)$$

Two irreps $\Gamma(\mathbf{m}_n)$ and $\Gamma(\mathbf{m}'_n)$ of $U(n)$ yield the same irrep when restricted to $SU(n)$ if $m_i = m'_i + h$, $i = 1, \dots, n$. The $SU(n)$ irreps are thus labeled with highest weights with $m_{nn} = 0$. The dimension of $\Gamma(\mathbf{m}_n)$ of $U(n)$ is given by the Weyl dimension formula [36]

$$\dim \Gamma(\mathbf{m}_n) = \prod_{i < j} (m_{in} - m_{jn} + j - i) / 1!2! \dots (n-1)!. \quad (4.65)$$

The $U(n)$ Casimir operators have the form

$$C_k^{U(n)} = \sum_{i_1, i_2, \dots, i_k=1}^n E_{i_1 i_2} E_{i_2 i_3} \cdots E_{i_{k-1} i_k} E_{i_k i_1}. \quad (4.66)$$

The first-order Casimir operator is given by the sum of weight generators and equals the sum of the highest weight components.

Since $U(1)$ is Abelian, the *Gel'fand-Tsetlin* [42] canonical chain (Sect. 3.4.3)

$$U(n) \supset U(n-1) \supset \cdots \supset U(1) \quad (4.67)$$

can be used to label uniquely the basis vectors of the carrier space of $\Gamma(\mathbf{m}_n)$ by triangular Gel'fand tableaux $[m]$ defined by

$$[m] = \begin{bmatrix} \mathbf{m}_n \\ \mathbf{m}_{n-1} \\ \cdots \\ \mathbf{m}_2 \\ \mathbf{m}_1 \end{bmatrix} = \begin{bmatrix} m_{1n} & m_{2n} & \cdots & m_{nn} \\ m_{1,n-1} & \cdots & m_{n-1,n-1} & \\ & \cdots & & \\ & & \cdots & \\ & & & m_{12} & m_{22} \\ & & & & m_{11} \end{bmatrix}, \quad (4.68)$$

with entries satisfying betweenness conditions Eq. (4.64). Matrix representatives of weight generators are diagonal

$$\langle [m'] | E_{ii} | [m] \rangle = \delta_{[m],[m']} \left(\sum_{j=1}^i m_{ji} - \sum_{j=1}^{i-1} m_{j,i-1} \right), \quad (4.69)$$

while those for other generators are rather involved [42–45]. Note that only elementary ($E_{i,i+1}$) raising generators are required since

$$\langle [m'] | E_{ij} | [m] \rangle = \langle [m] | E_{ji} | [m'] \rangle, \quad (4.70)$$

and

$$E_{ij} = [E_{i,i+1}, E_{i+1,j}]. \quad (4.71)$$

In special cases required in applications ([39, 40] and Sect. 4.3.4) efficient algorithms exist for the computation of explicit representations.

4.3.2 Orthogonal Group $O(n)$ and Its Representations

Since $O(n)$ is a proper subgroup of $U(n)$, its representation theory has a similar structure. The suitable generators are

$$\begin{aligned} F_{ij} &= E_{ij} - E_{ji}, & F_{ji} &= -F_{ij}, \\ F_{ii} &= 0, & F_{ij}^\dagger &= -F_{ji} \end{aligned} \quad (4.72)$$

and satisfy the commutation relations

$$[F_{ij}, F_{k\ell}] = \delta_{jk} F_{i\ell} + \delta_{i\ell} F_{jk} - \delta_{ik} F_{j\ell} - \delta_{j\ell} F_{ik}. \quad (4.73)$$

The canonical chain has the form

$$O(n) \supset O(n-1) \supset \cdots \supset O(2). \quad (4.74)$$

The components of the highest weight \mathbf{m}_n ,

$$\mathbf{m}_n = (m_{1n}, m_{2n}, \dots, m_{kn}), \quad (4.75)$$

satisfy the conditions

$$m_{1n} \geq m_{2n} \geq \cdots \geq m_{kn} \geq 0 \quad \text{for } n = 2k + 1, \quad (4.76)$$

and

$$m_{1n} \geq m_{2n} \geq \cdots \geq |m_{kn}| \quad \text{for } n = 2k, \quad (4.77)$$

where m_{in} are simultaneously integers or half-odd integers. The former are referred to as *tensor representations* (since they arise as tensor products of fundamental irreps), while those with half-odd integer components are called *spinor representations*. Note that for $n = 2k$, we have two lowest (mirror-conjugated) spinor representations, namely $\mathbf{m}^{(+)} = (\frac{1}{2}, \frac{1}{2}, \dots, \frac{1}{2})$ and $\mathbf{m}^{(-)} = (\frac{1}{2}, \dots, \frac{1}{2}, -\frac{1}{2})$. Only tensor representations can be labeled by Young tableaux.

Subducing $O(n)$ to $O(n-1)$, the betweenness conditions (branching rules) have the form

$$m_{in} \geq m_{i,n-1} \geq m_{i+1,n} \quad (i = 1, \dots, k-1) \quad (4.78)$$

together with

$$m_{k,2k+1} \geq |m_{k,2k}|, \quad (4.79)$$

when $n = 2k + 1$. The $m_{i,n-1}$ components are integral (half-odd integral) if the m_{in} are integral (half-odd integral). The $U(n) \supset O(n)$ [or $SU(n) \supset SO(n)$] subduction rules are more involved [46].

4.3.3 Clifford Algebras and Spinor Representations

While all reps of $U(n)$ or $SL(n)$ arise as tensor powers of the standard rep, only half of the reps of $SO(m)$ or $O(m)$ arise this way, since $SO(m)$ is not simply connected when $m > 2$. A double covering of $SO(m)$ leads to *spin groups* $\text{Spin}(m)$. The best way to proceed is, however, to construct the so-called *Clifford algebras* C_m , whose multiplicative group (consisting of invertible elements) contains a subgroup that provides a double cover of $SO(m)$. The key fact is that C_{2k} is

isomorphic with $\mathfrak{gl}(2^k)$ and C_{2k+1} with $\mathfrak{gl}(2^k) \oplus \mathfrak{gl}(2^k)$. The reps of C_m thus provide the required *spinor reps*.

A Clifford algebra C_m is an associative algebra generated by *Clifford numbers* α_i satisfying the anticommutation relations

$$\{\alpha_i, \alpha_j\} = 2\delta_{ij} \quad (i, j = 1, \dots, m). \quad (4.80)$$

Since $\alpha_i^2 = 1$, $\dim C_m = 2^m$, and a general element of C_m is a product of Clifford numbers $\alpha_1^{v_1} \alpha_2^{v_2} \dots \alpha_m^{v_m}$ with $v_i = 0$ or 1.

To see the relation with $\mathfrak{so}(m+1)$ note that

$$F_{0k} = -\frac{1}{2}i\alpha_k, \quad F_{jk} = \frac{1}{4}[\alpha_j, \alpha_k] = \frac{1}{2}\alpha_j\alpha_k, \quad (j \neq k) \quad (4.81)$$

satisfy the commutation relations Eq. (4.73).

As an example, C_2 can be realized by Pauli matrices by setting

$$\alpha_1 = \sigma_1 = \begin{pmatrix} 0 & 1 \\ 1 & 0 \end{pmatrix}, \quad \alpha_2 = \sigma_2 = \begin{pmatrix} 0 & i \\ -i & 0 \end{pmatrix}. \quad (4.82)$$

Clearly, the four matrices $\mathbf{1}_2, \alpha_1, \alpha_2$, and $\alpha_1\alpha_2$ are linearly independent (note that $\sigma_3 = i\sigma_1\sigma_2$), so that C_2 is isomorphic to $\mathfrak{gl}(2, \mathbb{C})$.

Similarly, considering Dirac–Pauli matrices

$$\gamma_0 = \begin{pmatrix} -i\mathbf{1}_2 & \mathbf{0} \\ \mathbf{0} & -i\mathbf{1}_2 \end{pmatrix} = i\gamma_4, \quad \gamma_k = \begin{pmatrix} \mathbf{0} & i\sigma_k \\ -i\sigma_k & \mathbf{0} \end{pmatrix}, \quad (k = 1, 2, 3), \quad (4.83)$$

we have that

$$\{\gamma_i, \gamma_j\} = 2\delta_{ij}, \quad (i, j = 1, \dots, 4), \quad (4.84)$$

so that γ_i ($i = 1, \dots, 4$) or ($i = 0, \dots, 3$) represent Clifford numbers for C_4 and $\mathbf{1}_4, \gamma_i, \gamma_i\gamma_j$ ($i < j$), $\gamma_i\gamma_j\gamma_k$ ($i < j < k$) and $\gamma_5 \equiv \gamma_1\gamma_2\gamma_3\gamma_4 = i\gamma_0\gamma_1\gamma_2\gamma_3$ form an additive basis for $\mathfrak{gl}(4, \mathbb{C})$ (the γ_i themselves are said to form a multiplicative basis). For general construction of C_m Clifford numbers in terms of direct products of Pauli matrices see [47, 48].

4.3.4 Bosonic and Fermionic Realizations of $U(n)$

Designating by b_i^\dagger (b_i) the boson creation (annihilation) operators (Sect. 6.1.1) satisfying the commutation relations $[b_i, b_j] = [b_i^\dagger, b_j^\dagger] = 0$, $[b_i, b_j^\dagger] = \delta_{ij}$, we obtain a possible $U(n)$ realization by defining its n^2 generators as follows

$$G_{ij} = b_i^\dagger b_j. \quad (4.85)$$

The first-order Casimir operator, Eq. (4.66) with $k = 1$, then represents the total number operator

$$\hat{N} \equiv C_1^{U(n)} = \sum_{i=1}^n G_{ii} = \sum_{i=1}^n b_i^\dagger b_i, \quad (4.86)$$

and the physically relevant states, being totally symmetric, carry single row irreps $\Gamma(N\dot{0}) \equiv \Gamma(N0\dots 0)$.

Similarly, for fermion creation (annihilation) operators X_I^\dagger (X_I) that are associated with some orthonormal spin-orbital set $\{|I\rangle\}$, $I = 1, 2, \dots, 2n$, and satisfy the anticommutation relations $\{X_I, X_J\} = \{X_I^\dagger, X_J^\dagger\} = 0$, $\{X_I, X_J^\dagger\} = \delta_{IJ}$, the operators

$$e_{IJ} = X_I^\dagger X_J \quad (4.87)$$

again represent the $U(2n)$ generators satisfying Eqs. (4.59) and (4.60). The first-order Casimir then represents the total number operator $\hat{N} = \sum_I X_I^\dagger X_I$, while the possible physical states are characterized by totally antisymmetric single column irreps $\Gamma(1^N\dot{0}) \equiv \Gamma(11\dots 10\dots 0)$.

4.3.5 The Vibron Model

Similar to the unified description of nuclear collective rovibrational states using the interacting boson model [49–51], one can build an analogous model for molecular rotation-vibration spectra [8]. For diatomics, an appropriate dynamical group is $U(4)$ [8, 52–54] and, generally, for rotation-vibration spectra in r -dimensions, one requires $U(r+1)$. For triatomics, the $U(4)$ generating algebra is generalized to $U(4) \otimes U(4)$, and for the $(k+1)$ atomic molecule to $U^{(1)}(4) \otimes \dots \otimes U^{(k)}(4)$ [8, 52–54].

For the bosonic realization of $U(4)$, we need four creation (b_i^\dagger , $i = 1, \dots, 4$) and four annihilation (b_i) operators (Sect. 4.3.4). The Hamiltonian may be generally expressed as a multilinear form in terms of boson number preserving products ($b_i^\dagger b_j$), so that using Eq. (4.85) we can write

$$H = h^{(0)} + \sum_{ij} h_{ij}^{(1)} G_{ij} + \frac{1}{2} \sum_{ijkl} h_{ijkl}^{(2)} G_{ij} G_{kl} + \dots \quad (4.88)$$

The energy levels (as a function of 0, 1, 2, \dots -body matrix elements $h^0, h_{ij}^{(1)}, h_{ijkl}^{(2)}$, etc.) are then determined by diagonalizing H in an appropriate space, which is conveniently provided by the carrier space of the totally symmetric irrep $\Gamma(N000) \equiv \Gamma(N\dot{0})$ of $U(4)$.

The requirement that the resulting states be characterized by angular momentum J and parity P quantum numbers necessitates that the boson operators involved have definite transformation properties under rotations and reflections [8]. The boson operators are thus subdivided into

the scalar operators (σ^\dagger, σ) , $J = 0$, and vector operators $(\pi_\mu^\dagger, \pi_\mu; \mu = 0, \pm 1)$, $J = 1$ with parity $P = (-)^J$. All commutators vanish except for

$$[\sigma, \sigma^\dagger] = 1, \quad [\pi_\mu, \pi_{\mu'}^\dagger] = \delta_{\mu\mu'}. \quad (4.89)$$

Since H preserves the total number of vibrons $N = n_\sigma + n_\pi$, the second-order Hamiltonian Eq. (4.88) within the irrep $\Gamma(N\dot{0})$ can be expressed in terms of four independent parameters (apart from an overall constant) as

$$\begin{aligned} H = & e^{(0)} + e^{(1)}[\pi^\dagger \times \tilde{\pi}]_0^{(0)} \\ & + e_1^{(2)}\left[[\pi^\dagger \times \pi^\dagger]^{(0)} \times [\tilde{\pi} \times \tilde{\pi}]^{(0)}\right]_0^{(0)} \\ & + e_2^{(2)}\left[[\pi^\dagger \times \pi^\dagger]^{(2)} \times [\tilde{\pi} \times \tilde{\pi}]^{(2)}\right]_0^{(0)} \\ & + e_3^{(2)}\left[[\pi^\dagger \times \pi^\dagger]^{(0)} \times [\tilde{\sigma} \times \tilde{\sigma}]\right]^{(0)} \\ & + [\sigma^\dagger \times \sigma^\dagger]^{(0)} \times [\tilde{\pi} \times \tilde{\pi}]_0^{(0)} + \dots, \quad (4.90) \end{aligned}$$

where $\tilde{\sigma} = \sigma$, $\tilde{\pi}_\mu = (-)^{1-\mu}\pi_{-\mu}$ and square brackets indicate the SU(2) couplings.

In special cases, the eigenvalue problem for H can be solved analytically, assuming that H can be expressed in terms of Casimir operators of a complete chain of subgroups of U(4) (referred to as dynamical symmetries). Requiring that the chain contains the physical rotation group O(3), one has two possibilities

$$\begin{aligned} \text{(I)} \quad & \text{U}(4) \supset \text{O}(4) \supset \text{O}(3) \supset \text{O}(2), \\ \text{(II)} \quad & \text{U}(4) \supset \text{U}(3) \supset \text{O}(3) \supset \text{O}(2). \quad (4.91) \end{aligned}$$

These imply labels (quantum numbers): N [total vibron number defining a totally symmetric irrep of U(4)], $\omega = N, N-2, N-4, \dots, 1$ or 0 [defining a totally symmetric irrep of O(4)] and $n_\pi = N, N-1, \dots, 0$ [defining the U(3) irrep], in addition to the O(3) \supset O(2) labels $J, M; |M| \leq J$. In terms of these labels one finds for the respective Hamiltonians

$$\begin{aligned} H^{(\text{I})} &= F + A C_2^{\text{O}(4)} + B C_2^{\text{O}(3)}, \\ H^{(\text{II})} &= F + \varepsilon C_1^{\text{U}(3)} + \alpha C_2^{\text{U}(3)} + \beta C_2^{\text{O}(3)}, \quad (4.92) \end{aligned}$$

where $F, A, B, \varepsilon, \alpha, \beta$ are free parameters, and $C_i^{\text{U}(k)}, C_i^{\text{O}(k)}$ are relevant Casimir operators, the following expressions [8, 52–54] for their eigenvalues

$$\begin{aligned} E^{(\text{I})}(N, \omega, J, M) &= F + A\omega(\omega + 2) + BJ(J + 1), \\ E^{(\text{II})}(N, n_\pi, J, M) &= F + \varepsilon n_\pi + \alpha n_\pi(n_\pi + 3) \\ &+ \beta J(J + 1). \quad (4.93) \end{aligned}$$

The limit (I) is appropriate for rigid diatomics and limit (II) for nonrigid ones [8, 52–54].

In addition to handling diatomic and triatomic systems, the vibron model was also applied to the overtone spectrum of acetylene [55], intramolecular relaxation in benzene and its dimers [56, 57], octahedral molecules of the XF₆ type (X = S, W, and U) [58], and to linear polyatomics [59]. Most recently, the experimental (dispersed fluorescence and stimulated emission pumping) vibrational spectra of H₂O and SO₂ in their ground states, representing typical local-mode and normal-mode molecules, respectively, have been analyzed, including highly excited levels, by relying on the U(2) algebraic effective Hamiltonian approach [60–62]. The U(2) algebraic scheme [63] also enabled the treatment of Franck–Condon transition intensities [64, 65] in rovibronic spectra. The attempts at a similar heuristic phenomenological description of electronic spectra have so far met with only limited success [66].

4.3.6 Many-Electron Correlation Problem

In atomic and molecular electronic structure calculations one employs a spin-independent model Hamiltonian

$$\begin{aligned} H = & \sum_{i,j} h_{ij} \sum_{\sigma=1}^2 X_{i\sigma}^\dagger X_{j\sigma} \\ & + \frac{1}{2} \sum_{i,j,k,\ell} v_{ij,k\ell} \sum_{\sigma,\tau=1}^2 X_{i\sigma}^\dagger X_{j\tau}^\dagger X_{\ell\tau} X_{k\sigma}, \quad (4.94) \end{aligned}$$

where $X_I^\dagger \equiv X_{i\sigma}^\dagger$ (X_I) designate the creation (annihilation) operators associated with the orthonormal spin orbitals $|I\rangle \equiv |i\sigma\rangle = |i\rangle \otimes |\sigma\rangle; i = 1, \dots, n; \sigma = 1, 2$ [$\sigma = 1, 2$ labeling the spin-up and spin-down eigenstates of S_z], and $h_{ij} = \langle i|\hat{h}|j\rangle$, $v_{ij,k\ell} = \langle i(1)j(2)|\hat{v}|k(1)\ell(2)\rangle$ are the one and two-electron integrals in the orbital basis $\{|i\rangle\}$. As stated in Sect. 4.3.4, $e_{IJ} \equiv e_{i\sigma,j\tau} = X_{i\sigma}^\dagger X_{j\tau}$ may then be regarded as U(2n) generators, and the appropriate U(2n) irrep for N -electron states is $\Gamma(1^N\dot{0})$.

Similar to the nuclear many-body problem [67], one defines mutually commuting partial traces of spin-orbital generators e_{IJ} , Eq. (4.87),

$$\begin{aligned} E_{ij} &= \sum_{\sigma=1}^2 e_{i\sigma,j\sigma} = \sum_{\sigma=1}^2 X_{i\sigma}^\dagger X_{j\sigma}, \\ \mathcal{E}_{\sigma\tau} &= \sum_{i=1}^n e_{i\sigma,i\tau} = \sum_{i=1}^n X_{i\sigma}^\dagger X_{i\tau}, \quad (4.95) \end{aligned}$$

which again satisfy the unitary group commutation relations Eq. (4.59) and property Eq. (4.60), and may thus be considered as the generators of the orbital group U(n) and the spin group U(2). The Hamiltonian Eq. (4.94) is thus expressible

in terms of orbital $U(n)$ generators

$$H = \sum_{i,j} h_{ij} E_{ij} + \frac{1}{2} \sum_{i,j,k,\ell} v_{ij,k\ell} (E_{ik} E_{j\ell} - \delta_{jk} E_{i\ell}) . \quad (4.96)$$

We can thus achieve an automatic spin adaptation by exploiting the chain

$$U(2n) \supset U(n) \otimes U(2) \quad (4.97)$$

and diagonalize H within the carrier space of two-column $U(n)$ irreps $\Gamma(2^a 1^b 0^c) \equiv \Gamma(a, b, c)$ with [39, 68]

$$\begin{aligned} a &= \frac{1}{2}N - S , & b &= 2S , \\ c &= n - a - b = n - \frac{1}{2}N - S , \end{aligned} \quad (4.98)$$

considering the states of multiplicity $(2S + 1)$ involving n orbitals and N electrons. The dimension of each spin-adapted subproblem equals [39, 68]

$$\dim \Gamma(2^a 1^b 0^c) = \frac{b+1}{n+1} \binom{n+1}{a} \binom{n+1}{c} , \quad (4.99)$$

where $\binom{m}{n}$ designate binomial coefficients.

Exploiting simplified irrep labeling by triples of integers (a, b, c) , Eq. (4.98), at each level of the canonical chain Eq. (4.67), one achieves more efficient state labeling by replacing Gel'fand tableaux Eq. (4.68) by $n \times 3$ ABC [68] or Paldus or Gel'fand–Paldus tableaux [40, 69–77]

$$[P] = [a_i b_i c_i] , \quad (4.100)$$

where $a_i + b_i + c_i = i$. Another convenient labeling uses the ternary *step numbers* d_i , $0 \leq d_i \leq 3$ [68–70, 78, 79]

$$d_i = 1 + 2(a_i - a_{i-1}) - (c_i - c_{i-1}) . \quad (4.101)$$

A compact representation of a spin-adapted basis of *configuration state functions* (CSFs) spanning a given $U(n)$ irrep $\Gamma(2^a 1^b 0^c)$ is given by a *distinct row table* (DRT) ([69, 70], cf. also [10–12, 39, 71]). The entire basis is then conveniently described by a *Shavitt graph* [11, 69, 70], providing a compact and transparent representation of the entire basis of CSFs, and the corresponding formalism is referred to as the graphical UGA (GUGA). This facilitates the design of computer codes not only for the full configuration interaction (FCI) calculations ([80]) but mainly for a limited or truncated CI.

The Shavitt graph is a two-rooted graph whose vertices represent distinct rows of the ABC tableaux for each subgroup $U(i)$ ($i = 1, \dots, n$) with the top root representing the highest weight $(a, b, c) \equiv (a_n, b_n, c_n)$ for $U(n)$ and the bottom root the trivial row $(0, 0, 0) \equiv (a_0, b_0, c_0)$. The entire graph is placed on a grid so that the slope of its edges im-

plies the relevant step numbers. Each basis vector or CSF is thus represented by a path interconnecting both roots.

Considering the generator matrix elements, we note that the bra and ket state paths coincide outside the range given by the generator indices, thus forming a loop within this range that can be split into the *segment values* for each elementary step. The explicit form of segment values has been derived in several different ways [10–12, 68–71, 75–77, 79, 81–85] (but not within GUGA per se [82]). However, this factorization into a product of segment values is not unique and can be done in several ways ([79, 84, 85]).

The most efficient way for a derivation of explicit expressions for segment values exploits the *graphical methods of spin algebras* employing Jucys-type angular-momentum diagrams ([86]) while relying on the fact that the $U(n)$ electronic CSFs correspond to the Yamanouchi–Kotani coupling scheme [67]. This approach is particularly efficient for matrix elements involving generator products [79, 87, 88]. Yet another useful approach [84, 85, 89] introduced spin-adapted creation and annihilation operators that in a certain way mimic those of the standard second-quantization formalism ([82]), which also proved to be very useful for spin-dependent formalism (Sect. 4.3.8).

A recent development that exploits GUGA representation of the electronic CSF $U(n)$ basis is the so-called *graphically contracted function* (GCF) method [90, 91], which is based on the graph density concept. This approach enables a comparison of CSFs in terms of nodes and arcs (edges) of the Shavitt graph, thus opening a possibility of handling extremely large CIs exceeding traditional ones by many orders of magnitude. For the most recent development that also introduced a multifacet GCF (MFGCF), see [92].

Finally, we note that the unitary group formalism that is based either on $U(n)$ or on the universal enveloping algebra of $U(n)$ proved to be of great usefulness in various post-Hartree–Fock approaches to molecular electronic structure [93], especially in large-scale CI calculations (cf., the COLUMBUS Program System [94–97]; see also [24–31] in [12]), in MC-SCF approaches [98–101], propagator methods [102], and coupled cluster (CC) methods of both single-reference [103–118] and multi-reference [119–122] type, as well as in various other investigations, such as quantum dots [123], in handling of composite systems [89, 124–126], valence-bond (VB) approaches [127–132], reduced density matrices (RDMs) [105, 133], nuclear magnetic resonance (NMR) [134], or charge migration in fragmentation of peptide ions [135, 136]; see also [10–12] for other references. We should also mention numerous other developments and extensions, such as Clifford algebra UGA (CAUGA) (Sect. 4.3.7), bonded tableau UGA [137], parafermi algebras [138], and related developments ([139]).

Very recently there have been a new, very promising, exploitation of UGA (see recent critical reviews [140–

142]) and GUGA in the FCI-QMC (Quantum Monte Carlo) method [143–145], enabling a very efficient handling of relatively large, complex systems [146–151], as well as an exploitation [152] of eCCSD (*externally corrected* Coupled Cluster methods with Singles and Doubles) ([153] and Sect. 5.3.8).

4.3.7 Clifford Algebra Unitary Group Approach

The Clifford algebra unitary group approach (CAUGA) exploits a realization of the spinor algebra of the rotation group $SO(2n + 1)$ in the covering algebra of $U(2^n)$ to obtain explicit representation matrices for the $U(n)$ [or $SO(2n + 1)$ or $SO(2n)$] generators in the basis adapted to the chain [125, 154–157]

$$U(2^n) \supset \text{Spin}(m) \supset SO(m) \supset U(n) , \\ (m = 2n + 1 \quad \text{or} \quad m = 2n) \quad (4.102)$$

supplemented, if desired, by the canonical chain Eq. (4.67) for $U(n)$.

To realize the connection with the fermionic Grassmann algebra generated by the creation (X_I^\dagger) and annihilation (X_I) operators, $I = 1, \dots, 2n$, note that it is isomorphic with the Clifford algebra C_{4n} when we define [12, 25]

$$\alpha_I = X_I + X_I^\dagger , \quad \alpha_{I+2n} = i(X_I - X_I^\dagger) , \\ (I = 1, \dots, 2n) . \quad (4.103)$$

For practical applications, the most important is the finite imbedding $U(2^n) \supset U(n)$ (for the role of intermediate groups, see [154–156]). All states of an n -orbital model, regardless the electron number N and the total spin S , are contained in a single two-box totally symmetric irrep $\langle 20 \rangle$ of $U(2^n)$ [125, 157]. To simplify the notation, one employs the one-to-one correspondence between the Clifford algebra monomials, labeled by the occupation numbers $m_i = 0$ or $m_i = 1$ ($i = 1, \dots, n$), and “multiparticle” single-column $U(n)$ states labeled by

$$p \equiv p\{m_i\} = 2^n - (m_1 m_2 \cdots m_n)_2 , \quad (4.104)$$

where the occupation number array $(m_1 \cdots m_n)$ is interpreted as a binary integer, which we then regard as one-box states $|p\rangle$ of $U(2^n)$. The orbital $U(n)$ generators A_{ij} may then be expressed as simple linear combinations of $U(2^n)$ generators $E_{pq} = |p\rangle\langle q|$ with coefficients equal to ± 1 [125, 157].

Generally, any p -column $U(n)$ irrep is contained at least once in the totally symmetric p -box irrep of $U(2^n)$. For many-electron problems, one thus requires a two-box irrep $\langle 20 \rangle$. Any state arising in the $U(n)$ irrep $\Gamma(a, b, c)$

can then be represented as a linear combination of two-box states, labeled by the Weyl tableaux $[i|j] \equiv \boxed{i|j}$. In particular, the highest weight state of $\Gamma(a, b, c)$ is represented by $[2^c|2^{b+c}]$. Once this representation is available, it is straightforward to compute explicit representations of $U(n)$ generators, since E_{pq} act trivially on $[i|j]$ [125]. Defining unnormalized states $(i|j)$ as

$$(i|j) = \sqrt{1 + \delta_{ij}} \quad [i|j] , \quad (4.105)$$

we have

$$E_{pq}(i|j) = \delta_{qi}(p|j) + \delta_{qj}(i|p) . \quad (4.106)$$

The main features of CAUGA may, thus, be summarized as follows: CAUGA

1. Effectively reduces an N -electron problem to a number of two-boson problems
2. Enables an exploitation of an arbitrary coupling scheme (being particularly suited for the valence bond method)
3. Can be applied to particle-number nonconserving operators
4. Easily extends to fermions with an arbitrary spin
5. Drastically simplifies evaluation of explicit representations of $U(n)$ generators and of their products
6. Can be exploited in other than shell-model approaches [127–129, 131, 158–160].

4.3.8 Spin-Dependent Operators

The spin-adapted $U(n)$ -based UGA is entirely satisfactory in most investigations of molecular electronic structure. However, when exploring the fine structure in high-resolution spectra, the intersystem crossings, phosphorescent lifetimes, molecular predissociation, spin–orbit interactions in transition metals, and like phenomena, the *explicitly* spin-dependent terms must be included in the Hamiltonian. Since in most cases the total spin S represents a good approximate quantum number, it is advantageous to employ $U(n)$ spin-adapted N -electron states as a point of departure and consider the matrix elements of general spin-orbital $U(2n)$ generators in terms of the $U(2n) \supset U(n) \otimes SU(2)$ basis. Such an approach is generally referred to as a spin-dependent UGA and was first considered in the context of the symmetric group and Racah algebra by Drake and Schlesinger [83] and later on in terms of the *Gel'fand–Paldus tableaux* [82, 161–165].

Now, the segmentation of the matrix elements of spin-dependent one-body operators may be shown to be very similar to that for the two-body operators, which makes it possible to exploit the existing UGA or GUGA codes. However, this necessitates that we employ a larger group, say

$U(n + 1)$, or even $U(n + 2)$ [82, 165], since $U(n + 1)$ generators can change the spin at the $U(n)$ level, as is the case for spin-dependent one-body operators. In fact, the advantage of a large $U(n + 1)$ group follows immediately when we employ the graphical methods of spin algebras ([79]), as was done by Drake and Schlesinger [83]. This fact was also exploited by Yabushita *et al.* [166] and implemented in GUGA codes. However, since this approach [166] relies on Racah–Wigner calculus, it requires six additional steps in order to conform with the standard UGA-based formalism, including the introduction of an additional phase factor and a transformation to a “real spherical” spin function in order to ascertain a real-valued form of the relevant matrix elements. These steps may be avoided using an approach that is based on the spin-free analogues of creation and annihilation operators [84, 85]. Indeed, this approach leads to a simple formalism [82] that enables the evaluation of the required one-electron spin-dependent terms in much the same way as the standard spin-independent two-electron (i.e., Coulomb) matrix elements. Only a few additional expressions had to be derived and all the required segment values are given in [82].

In general, the $U(2n)$ generators $e_{i\sigma,j\tau} \equiv e_{IJ}$ may be resolved into the spin-shift components $e(\pm)_{IJ}$ that increase (+) or decrease (–) the total spin S by one unit and the zero-spin component $e(0)_{IJ}$ that preserves S . The relevant matrix elements can then be expressed in terms of the matrix elements of a single $U(n)$ adjoint tensor operator Δ , which is given by the following second-degree polynomial in $U(n)$ generators,

$$\Delta = \mathbf{E}(\mathbf{E} + N/2 - n - 2), \quad \mathbf{E} = \|E_{ij}\|, \quad (4.107)$$

and by the well-known matrix elements of $U(2)$ or $SU(2)$ generators in terms of the pure spin states [161, 162] ([167, 168]). The operator Eq. (4.107), referred to as the Gould–Paldus operator [169], also plays a key role in the determination of reduced density matrices [105, 133] and has recently been exploited in the multireference spin-adapted variant of the density functional theory [169]. Very recently Robb *et al.* used spin dependent UGA to evaluate spin densities for CI in a basis of S^2 -adapted CSFs [170].

References

1. Barut, A.O.: Dynamical Groups and Generalized Symmetries in Quantum Theory. Vols. 1 and 2. Univ. Canterbury, Christchurch (1971)
2. Bohm, A., Ne’eman, Y., Barut, A.O.: Dynamical Groups and Spectrum Generating Algebras. World Scientific, Singapore (1988)
3. Gilmore, R.: Lie Groups, Lie Algebras, and Some of Their Applications. Wiley, New York (1974)
4. Wybourne, B.G.: Classical Groups for Physicists. Wiley, New York (1974)

5. Chen, J.-Q.: Group Representation Theory for Physicists. World Scientific, Singapore (1989)
6. Chen, J.-Q., Ping, J., Wang, F.: Group Representation Theory for Physicists, 2nd edn. World Scientific, Singapore (2002)
7. Castaños, O., Frank, A., Lopez-Peña, R.: J. Phys. A Math. Gen. **23**, 5141 (1990)
8. Iachello, F., Levine, R.D.: Algebraic Theory of Molecules. Oxford Univ. Press, Oxford (1995)
9. Frank, A., Van Isacker, P.: Algebraic Methods in Molecular and Nuclear Structure. Wiley, New York (1994)
10. Paldus, J.: In: Truhlar, D.G. (ed.) Mathematical Frontiers in Computational Chemical Physics, pp. 262–299. Springer, Berlin, Heidelberg (1988)
11. Shavitt, I.: In: Truhlar, D.G. (ed.) Mathematical Frontiers in Computational Chemical Physics, pp. 300–349. Springer, Berlin, Heidelberg (1988)
12. Paldus, J.: Contemporary Mathematics vol. 160. AMS, Providence, pp 209–236 (1994)
13. Parikh, J.C.: Group Symmetries in Nuclear Structure. Plenum, New York (1978)
14. Adams, B.G., Čížek, J., Paldus, J.: Int. J. Quantum Chem. **21**, 153 (1982)
15. Adams, B.G., Čížek, J., Paldus, J.: Adv. Quantum Chem. **19**, 1 (1988). Also reprinted in: Böhm, A., Ne’eman, Y., Barut, A.O. (eds.): Dynamical Groups and Spectrum Generating Algebras, pp. 103–207. World Scientific, Singapore (1988)
16. Čížek, J., Paldus, J.: Int. J. Quantum Chem. **12**, 875 (1977)
17. Adams, B.G.: Algebraic Approach to Simple Quantum Systems. Springer, Berlin, Heidelberg (1994)
18. Bohm, A.: Nuovo Cimento A **43**, 665 (1966)
19. Bohm, A.: Quantum Mechanics. Springer, New York (1979)
20. Naimark, M.A.: Linear Representations of the Lorentz Group. Pergamon, New York (1964)
21. Pauli, W.: Z. Phys. **36**, 336 (1926)
22. Fock, V.: Z. Phys. **98**, 145 (1935)
23. Barut, A.O.: Phys. Rev. B **135**, 839 (1964)
24. Barut, A.O., Bornzin, G.L.: J. Math. Phys. **12**, 841 (1971)
25. Zaicev, G.A.: Algebraic Problems of Mathematical and Theoretical Physics. Science Publ. House, Moscow (1974). in Russian
26. Joseph, A.: Rev. Mod. Phys. **39**, 829 (1967)
27. Bednar, M.: Ann. Phys. **75**, 305 (1973)
28. Čížek, J., Vrscaj, E.R.: In: Sharp, R., Coleman, B. (eds.) Group Theoretical Methods in Physics, pp. 155–160. Academic Press, New York (1977)
29. Čížek, J., Vrscaj, E.R.: Int. J. Quantum Chem. **21**, 27 (1982)
30. Avron, J.E., Adams, B.G., Čížek, J., Clay, M., Glasser, L., Otto, P., Paldus, J., Vrscaj, E.R.: Phys. Rev. Lett. **43**, 691 (1979)
31. Čížek, J., Clay, M., Paldus, J.: Phys. Rev. A **22**, 793 (1980)
32. Silverstone, H.J., Adams, B.G., Čížek, J., Otto, P.: Phys. Rev. Lett. **43**, 1498 (1979)
33. Vrscaj, E.R.: Phys. Rev. A **31**, 2054 (1985)
34. Vrscaj, E.R.: Phys. Rev. A **33**, 1433 (1986)
35. Silverstone, H.J., Moats, R.K.: Phys. Rev. A **23**, 1645 (1981)
36. Weyl, H.: Classical Groups. Princeton Univ. Press, Princeton (1939)
37. Barut, A.O., Raczka, R.: Theory of Group Representations and Applications. Polish Science Publ, Warszawa (1977)
38. Louck, J.D.: Am. J. Phys. **38**, 3 (1970)
39. Paldus, J.: In: Eyring, H., Henderson, D.J. (eds.) Theoretical Chemistry: Advances and Perspectives, vol. 2, pp. 131–290. Academic Press, New York (1976)
40. Matsen, F.A., Pauncz, R.: The Unitary Group in Quantum Chemistry. Elsevier, Amsterdam (1986)
41. Weyl, H.: The Theory of Groups and Quantum Mechanics. Dover, New York (1964)

42. Gel'fand, I.M., Tsetlin, M.L.: Dokl. Akad. Nauk. SSSR **71**(825), 1070 (1950)
43. Baird, G.E., Biedenharn, L.C.: J. Math. Phys. **4**, 1449 (1963)
44. Biedenharn, L.C., Louck, J.D.: Angular Momentum in Quantum Physics: Theory and Application. Addison-Wesley, Reading (1981)
45. Biedenharn, L.C., Louck, J.D.: The Racah-Wigner Algebra in Quantum Theory. Addison-Wesley, Reading (1981)
46. Deneen, J., Quesne, C.: J. Phys. A **16**, 2995 (1983)
47. Boerner, H.: Representations of Groups, 2nd edn. North-Holland, Amsterdam (1970)
48. Ramakrishnan, A.: L-Matrix Theory or the Grammar of Dirac Matrices. Tata McGraw-Hill, India (1972)
49. Arima, A., Iachello, F.: Phys. Rev. Lett. **35**, 1069 (1975)
50. Iachello, F., Arima, A.: The Interacting Boson Model. Cambridge Univ. Press, Cambridge (1987)
51. Iachello, F., Van Isacker, P.: The Interacting Boson-Fermion Model. Cambridge Univ. Press, Cambridge (2004)
52. Iachello, F.: Chem. Phys. Lett. **78**, 581 (1981)
53. Iachello, F., Levine, R.D.: J. Chem. Phys. **77**, 3046 (1982)
54. van Roosmalen, O.S., Iachello, F., Levine, R.D., Dieperink, A.E.L.: J. Chem. Phys. **79**, 2515 (1983)
55. Hornos, J., Iachello, F.: J. Chem. Phys. **90**, 5284 (1989)
56. Iachello, F., Oss, S.: J. Chem. Phys. **99**, 7337 (1993)
57. Iachello, F., Oss, S.: J. Chem. Phys. **102**, 1141 (1995)
58. Chen, J.-Q., Iachello, F., Ping, J.-L.: J. Chem. Phys. **104**, 815 (1996)
59. Sako, T., Aoki, D., Yamanouchi, K., Iachello, F.: J. Chem. Phys. **113**, 6063 (2000)
60. Sako, T., Yamanouchi, K., Iachello, F.: J. Chem. Phys. **113**, 7292 (2000)
61. Sako, T., Yamanouchi, K., Iachello, F.: J. Chem. Phys. **114**, 9441 (2001)
62. Sako, T., Yamanouchi, K., Iachello, F.: J. Chem. Phys. **117**, 1641 (2002)
63. Iachello, F., Oss, S.: J. Chem. Phys. **104**, 6956 (1996)
64. Iachello, F., Leviatan, A., Mengoni, A.: J. Chem. Phys. **95**, 1449 (1991)
65. Müller, T., Vaccaro, P.H., Pérez-Bernal, F., Iachello, F.: J. Chem. Phys. **111**, 5038 (1999)
66. Frank, A., Lemus, R., Iachello, F.: J. Chem. Phys. **91**, 29 (1989)
67. Moshinsky, M.: Group Theory and the Many-Body Problem. Gordon Breach, New York (1968)
68. Paldus, J.: J. Chem. Phys. **61**, 5321 (1974)
69. Shavitt, I.: Int. J. Quantum Chem. Symp. **11**, 131 (1977)
70. Shavitt, I.: Int. J. Quantum Chem. Symp. **12**, 5 (1978)
71. Hinze, J. (ed.): The Unitary Group for the Evaluation of Electronic Energy Matrix Elements. Lect. Notes Chem., vol. 22. Springer, Berlin, Heidelberg (1981)
72. Pauncz, R.: Spin Eigenfunctions: Construction and Use. Plenum, New York (1979). Chap. 9
73. Wilson, S.: Electron Correlation in Molecules. Clarendon, Oxford (1984). Chap. 5
74. McWeeny, R.: Methods of Molecular Quantum Mechanics, 2nd edn. Academic Press, New York (1989). Chap. 10
75. Gould, M.D., Chandler, G.S.: Int. J. Quantum Chem. **25**(553), 603–1089 (1984)
76. Gould, M.D., Chandler, G.S.: Int. J. Quantum Chem. **26**, 441 (1984)
77. Gould, M.D., Chandler, G.S.: Int. J. Quantum Chem. **27**, 878 (1985). Erratum
78. Paldus, J.: Phys. Rev. A **14**, 1620 (1976)
79. Paldus, J., Boyle, M.J.: Phys. Scr. **21**, 295 (1980)
80. Zarrabian, S., Sarma, C.R., Paldus, J.: Chem Phys Lett **155**, 183 (1989)
81. Robb, M.A., Niazi, U.: Comp. Phys. Rep. **1**, 127 (1984)
82. Li, X., Paldus, J.: Theor. Chem. Acc. **133**, 1467 (2014). Also reprinted in: Shepard, R., Pitzer, R.M., Dunning, T. (eds.): Isaiah Shavitt: A Memorial Festschrift from Theoretical Chemistry Accounts, pp. 45–60. Springer, Berlin, Heidelberg (2014)
83. Drake, G.W.F., Schlesinger, M.: Phys. Rev. A **15**, 1990 (1977)
84. Li, X., Paldus, J.: J. Math. Chem. **4**, 295 (1990)
85. Li, X., Paldus, J.: J. Math. Chem. **13**, 273 (1993)
86. Wormer, P.E.S., Paldus, J.: Adv. Quantum Chem. **51**, 59 (2006)
87. Paldus, J., Boyle, M.J.: Phys. Rev. A **22**, 2299 (1980)
88. Boyle, M.J., Paldus, J.: Phys. Rev. A **22**, 2316 (1980)
89. Li, X., Paldus, J.: J. Math. Chem. **14**, 325 (1993)
90. Shepard, R.: J. Phys. Chem. A. **109**, 11629 (2005)
91. Gidofalvi, G., Shepard, R.: Mol. Phys. **108**, 2217 (2010)
92. Gidofalvi, G., Brozell, S.R., Shepard, R.: Theor. Chem. Acc. **133**, 1512 (2014)
93. Robb, M.A.: Theor. Chem. Acc. **103**, 317 (2000)
94. Shepard, R., Shavitt, I., Pitzer, R.M., Comeau, D.C., Pepper, M., Lischka, H., Szalay, P.G., Ahlrichs, R., Brown, F.B., Zhao, J.-G.: Int. J. Quantum Chem. Symp. **22**, 149 (1988)
95. Lischka, H., Shepard, R., Pitzer, R.M., Shavitt, I., Dallos, M., Müller, T., Szalay, P.G., Seth, M., Kedziora, G.S., Yabushita, S., Zhang, Z.: Phys. Chem. Chem. Phys. **3**, 664 (2001)
96. Shepard, R., Shavitt, I., Lischka, H.: J. Comp. Chem. **23**, 1121 (2001)
97. Lischka, H., Shepard, R., Shavitt, I., Pitzer, R.M., Dallos, M., Müller, T., Szalay, P.G., Brown, F.B., Ahlrichs, R., Böhm, H.J., Chang, A., Comeau, D.C., Gdanitz, R., Dachsel, H., Ehrhardt, C., Ernzerhof, M., Höchtel, P., Irle, S., Kedziora, G., Kovar, T., Parasuk, V., Pepper, M.J.M., Scharf, P., Schiffer, H., Schindler, M., Schüler, M., Seth, M., Stahlberg, E.A., Zhao, J.-G., Yabushita, S., Zhang, Z., Barbatti, M., Matsika, S., Schuurmann, M., Yarkony, D.R., Brozell, S.R., Beck, E.V., Blaudeau, J.-P., Ruckebauer, M., Sellner, B., Plasser, F., Szymczak, J.J.: COLUMBUS, An Ab Initio Electronic Structure Program, release 7.0 (2012)
98. Brooks, B.R., Laidig, W.D., Saxe, P., Schaefer III, H.F.: J. Chem. Phys. **72**, 3837 (1980)
99. Lischka, H., Shepard, R., Brown, F.B., Shavitt, I.: Int. J. Quantum Chem. Symp. **15**, 91 (1981)
100. Shepard, R., Simons, J.: Int. J. Quantum Chem. Symp. **14**, 211 (1980)
101. Evade, R.H.A., Robb, M.A.: Chem. Phys. Lett. **83**, 362 (1981)
102. Born, G., Shavitt, I.: J. Chem. Phys. **76**, 558 (1982)
103. Baker, H., Robb, M.A.: Mol. Phys. **50**, 1077 (1983)
104. Paldus, J., Jeziorski, B.: Theor. Chim. Acta **73**, 81 (1988)
105. Paldus, J., Gould, M.D.: Theor. Chim. Acta **86**, 83 (1993)
106. Li, X., Paldus, J.: J. Chem. Phys. **101**, 8812 (1994)
107. Li, X., Paldus, J.: Chem. Phys. Lett. **231**, 1 (1994)
108. Jeziorski, B., Paldus, J., Jankowski, P.: Int. J. Quantum Chem. **56**, 129 (1995)
109. Li, X., Paldus, J.: J. Chem. Phys. **102**, 8059 (1995)
110. Li, X., Paldus, J.: J. Chem. Phys. **102**, 8897 (1995)
111. Li, X., Paldus, J.: J. Chem. Phys. **103**, 6536 (1996)
112. Li, X., Paldus, J.: J. Chem. Phys. **104**, 9555 (1996)
113. Paldus, J., Li, X.: Can. J. Chem. **74**, 918 (1996)
114. Li, X., Paldus, J.: Recent advances in coupled-cluster methods. In: Bartlett, R.J. (ed.) Recent Advances in Computational Chemistry, vol. 3, pp. 183–219. World Scientific, Singapore (1997)
115. Li, X., Paldus, J.: Int. J. Quantum Chem. **70**, 65 (1998)
116. Li, X., Paldus, J.: Mol. Phys. **94**, 41 (1998)
117. Jankowski, P., Jeziorski, B.: J. Chem. Phys. **111**, 1857 (1999)
118. Li, X., Paldus, J.: J Mol Struct **527**, 165 (2000)
119. Maitra, R., Sinha, D., Mukherjee, D.: J. Chem. Phys. **137**, 024105 (2012)

120. Maitra, R., Sinha, D., Mukherjee, D.: *J Chem Phys* **139**, 229903 (2013). Erratum
121. Sen, S., Shee, A., Mukherjee, D.: *J. Chem. Phys.* **137**, 074104 (2012)
122. Paldus, J., Čárský, P., Pittner, J.: In: Čárský, P., Paldus, J., Pittner, J. (eds.) *Recent Progress in Coupled Cluster Methods: Theory and Applications*, pp. 455–489. Springer, Berlin (2010)
123. Remacle, F., Levin, R.D.: *Chem. Phys. Chem.* **2**, 20 (2001)
124. Gould, M.D., Paldus, J.: *Int. J. Quantum Chem.* **30**, 327 (1986)
125. Paldus, J., Gao, M.-J., Chen, J.-Q.: *Phys. Rev. A* **35**, 3197 (1987)
126. Kent, R.D., Schlesinger, M.: *Phys. Rev. A* **48**, 4156 (1993)
127. Li, X., Paldus, J.: *Int. J. Quantum Chem.* **41**, 117 (1992)
128. Paldus, J., Planelles, J.: *Theor. Chim. Acta* **89**, 13 (1994)
129. Planelles, J., Paldus, J., Li, X.: *Theor. Chim. Acta* **89**(33), 59 (1994)
130. Paldus, J., Li, X.: In: Frank, A., Seligman, T.H., Wolf, K.B. (eds.) *Group Theory in Physics AIP Conference Proceedings*, vol. 266, pp. 159–178. American Institute of Physics, New York (1992)
131. Paldus, J., Li, X.: In: Gruber, B. (ed.) *Symmetries in Science VI: From the Rotation Group to Quantum Algebras*, pp. 573–592. Plenum, New York (1993)
132. Paldus, J.: *J. Math. Chem.* **56**, 1595 (2018)
133. Gould, M.D., Paldus, J., Chandler, G.S.: *J. Chem. Phys.* **93**, 4142 (1990)
134. Kent, R.D., Schlesinger, M., Ponnappalli, P.S.: *Phys. Rev. B* **31**, 1264 (1985)
135. Remacle, F., Levin, R.D.: *J. Chem. Phys.* **110**, 5089 (1999)
136. Remacle, F., Levin, R.D.: *J. Phys. Chem. A* **104**, 2341 (2000)
137. Li, X., Zhang, Q.: *Int. J. Quantum Chem.* **36**, 599 (1989)
138. Gould, M.D., Paldus, J.: *Phys. Rev. A* **34**, 804 (1986)
139. Harter, W.G., Patterson, C.W.: *A Unitary Calculus for Atomic Orbitals. Lecture Notes in Physics*, vol. 49. Springer, Berlin (1976)
140. Paldus, J.: *J. Math. Chem.* **59**, 1 (2021)
141. Paldus, J.: *J. Math. Chem.* **59**, 37 (2021)
142. Paldus, J.: *J. Math. Chem.* **59**, 72 (2021)
143. Dobrautz, W., Smart, S.D., Alavi, A.: *J. Chem. Phys.* **151**, 094104 (2019)
144. Dobrautz, W.: *Development of Full Configuration Interaction Quantum Monte Carlo Methods for Strongly Correlated Electron Systems. PhD Thesis, University of Stuttgart* (2019)
145. Li Manni, G., Guther, K., Ma, D., Dobrautz, W.: In: González, L., Lindh, R. (eds.) *Quantum Chemistry and Dynamics of Excited States: Methods and Applications*, Chap. 6, 133–204. Wiley, New York (2021)
146. Li Manni, G., Dobrautz, W., Alavi, A.: *J. Chem. Theory Comput.* **16**, 2202 (2020)
147. Guther, K., Anderson, R.J., Blunt, N.S., Bogdanov, N.A., Cleland, D., Dattani, N., Dobrautz, W., Ghanem, K., Jeszenszki, P., Liebermann, N., Li Manni, G., Lozovoi, A.Y., Luo, H., Ma, D., Merz, F., Overy, C., Rampp, M., Samantha, P.K., Schwarz, L.R., Shepherd, J.J., Smart, S.D., Vitale, E., Weser, O., Booth, G.H., Alavi, A.: *J. Chem. Phys.* **153**, 034107 (2020)
148. Ghanem, K., Guther, K., Alavi, A.: *J. Chem. Phys.* **153**, 224115 (2020)
149. Li Manni, G., Dobrautz, W., Bogdanov, N.A., Guther, K., Alavi, A.: *J. Phys. Chem. A* **125**, 4727 (2021)
150. Dobrautz, W., Weser, O., Bogdanov, N.A., Alavi, A., Li Manni, G.: *J. Chem. Theory Comput.* **17**, 5684 (2021)
151. Yun, S., Dobrautz, W., Luo, H., Alavi, A.: *Phys. Rev. B* **104**, 235102 (2021)
152. Vitale, E., Alavi, A., Kats, D.S.: *J. Chem. Theory Comput.* **16**(9), 5621 (2020)
153. Paldus, J.: *J. Math. Chem.* **55**, 477 (2017)
154. Nikam, R.S., Sarma, C.R.: *J. Math. Phys.* **25**, 1199 (1984)
155. Sarma, C.R., Paldus, J.: *J. Math. Phys.* **26**, 1140 (1985)
156. Gould, M.D., Paldus, J.: *J. Math. Phys.* **28**, 2304 (1987)
157. Paldus, J., Sarma, C.R.: *J. Chem. Phys.* **83**, 5135 (1985)
158. Paldus, J.: In: Malli, G.L. (ed.) *Relativistic and Electron Correlation Effects in Molecules and Solids NATO ASI Series B*, pp. 207–282. Plenum, New York (1994)
159. Li, X., Paldus, J.: *J. Chem. Phys.* **102**, 8059 (1995)
160. Piecuch, P., Li, X., Paldus, J.: *Chem. Phys. Lett.* **230**, 377 (1994)
161. Gould, M.D., Paldus, J.: *J. Chem. Phys.* **92**, 7394 (1990)
162. Gould, M.D., Battle, J.S.: *J. Chem. Phys.* **99**, 5961 (1993)
163. Kent, R.D., Schlesinger, M.: *Phys. Rev. A* **42**, 1155 (1990)
164. Kent, R.D., Schlesinger, M.: *Phys. Rev. A* **50**, 186 (1994)
165. Kent, R.D., Schlesinger, M., Shavitt, I.: *Int. J. Quantum Chem.* **41**, 89 (1992)
166. Yabushita, S., Zhang, Z., Pitzer, R.M.: *J. Phys. Chem. A* **103**, 5791 (1999)
167. Gould, M.D., Battle, J.S.: *J. Chem. Phys.* **98**, 8843 (1993)
168. Gould, M.D., Battle, J.S.: *J. Chem. Phys.* **99**, 5983 (1993)
169. Khait, Y.G., Hoffmann, M.R.: *J. Chem. Phys.* **120**, 5005 (2004)
170. Polyak, I., Bearpark, M.J., Robb, M.A.: *Int. J. Quantum Chem.* **18**(12), e.25559 (2017); <https://doi.org/10.1002/qua.25559>



Josef Paldus Josef Paldus is Distinguished Professor Emeritus at the Department of Applied Mathematics of the University of Waterloo, Canada. He received his PhD from the Czechoslovak Academy of Sciences and his RNDr and DrSc from the Faculty of Mathematics and Physics of Charles University, Prague, Czech Republic. His research interests are the methodology of quantum chemistry and the electronic structure of molecular systems. He has published over 340 papers, reviews, and chapters.



Perturbation Theory

5

Josef Paldus

Contents

5.1	Matrix Perturbation Theory (PT)	95
5.1.1	Basic Concepts	96
5.1.2	Level-Shift Operators	96
5.1.3	General Formalism	96
5.1.4	Nondegenerate Case	97
5.2	Time-Independent Perturbation Theory	97
5.2.1	General Formulation	97
5.2.2	Brillouin–Wigner and Rayleigh–Schrödinger PT (RSPT)	98
5.2.3	Bracketing Theorem and RSPT	98
5.3	Fermionic Many-Body Perturbation Theory (MBPT)	99
5.3.1	Time-Independent Wick’s Theorem	99
5.3.2	Normal Product Form of PT	99
5.3.3	Møller–Plesset and Epstein–Nesbet PT	100
5.3.4	Diagrammatic MBPT	100
5.3.5	Vacuum and Wave Function Diagrams	101
5.3.6	Hartree–Fock Diagrams	101
5.3.7	Linked and Connected Cluster Theorems	102
5.3.8	Coupled Cluster Theory	103
5.4	Time-Dependent Perturbation Theory	105
5.4.1	Evolution Operator PT Expansion	105
5.4.2	Gell-Mann and Low Formula	105
5.4.3	Potential Scattering and Quantum Dynamics	106
5.4.4	Born Series	106
5.4.5	Variation of Constants Method	107
	References	107

Abstract

Perturbation theory (PT) represents one of the bridges that takes us from a simpler, exactly solvable (unperturbed) problem to a corresponding real (perturbed) problem by expressing its solutions as a series expansion in a suitably chosen “small” parameter ε in such a way that the problem reduces to the unperturbed problem when $\varepsilon = 0$. It originated in classical mechanics and eventually developed into an important branch of applied mathematics

J. Paldus (✉)
 Dept. of Applied Mathematics, University of Waterloo
 Waterloo, ON, Canada
 e-mail: paldus@uwaterloo.ca

enabling physicists and engineers to obtain approximate solutions of various systems of differential equations [1–5]. For the problems of atomic and molecular structure and dynamics, the perturbed problem is usually given by the time-independent or time-dependent Schrödinger equation [6–10].

Keywords

perturbation theory (PT) · level shift operators · Brillouin–Wigner PT · Rayleigh–Schrödinger PT · many-body PT (MBPT) · diagrammatic MBPT · bracketing theorem · Wick’s theorem · Møller–Plesset PT · Epstein–Nesbet PT · linked and connected cluster theorems · coupled cluster (CC) theory · multireference CC (MRCC) methods · state universal and valence universal MRCC · internally and externally corrected CC · time-dependent PT · Gell-Mann and Low formula · Tomonaga–Schwinger equation · Born series · potential scattering

5.1 Matrix Perturbation Theory (PT)

A prototype of a time-independent PT considers an eigenvalue problem for the Hamiltonian H of the form

$$H = H_0 + V, \quad V = \sum_{i=1}^{\infty} \varepsilon^i V_i, \quad (5.1)$$

acting in a (finite-dimensional) Hilbert space \mathcal{V}_n , assuming that the spectral resolution of the unperturbed operator H_0 is known; i.e.,

$$H_0 = \sum_i \omega_i P_i, \quad P_i P_j = \delta_{ij} P_j, \quad \sum_i P_i = I, \quad (5.2)$$

where ω_i are distinct eigenvalues of H_0 , the P_i form a complete orthonormal set of Hermitian idempotents, and I is the identity operator on \mathcal{V}_n . The PT problem for H can then be

formulated within the Lie algebra \mathcal{A} (Sect. 3.2) generated by H_0 and V [11, 12].

5.1.1 Basic Concepts

Define the diagonal part $\langle X \rangle$ of a general operator $X \in \mathcal{A}$ by

$$\langle X \rangle = \sum_i P_i X P_i \quad (5.3)$$

and recall that the adjoint action of $X \in \mathcal{A}$, $\text{ad } X: \mathcal{A} \rightarrow \mathcal{A}$ is defined by

$$\text{ad } X(Y) = [X, Y], \quad (\forall Y \in \mathcal{A}), \quad (5.4)$$

where the square bracket denotes the commutator. The key problem of PT is the ‘‘inversion’’ of this operation, i.e., the solution of the equation [11–13]

$$\text{ad } H_0(X) \equiv [H_0, X] = Y. \quad (5.5)$$

Assuming that $\langle Y \rangle = 0$, then

$$X = R(Y) + \langle A \rangle, \quad (5.6)$$

where $A \in \mathcal{A}$ is arbitrary, and

$$R(Y) = \sum_{i \neq j} \Delta_{ij}^{-1} P_i Y P_j, \quad (5.7)$$

with $\Delta_{ij} = \omega_i - \omega_j$, represents the solution of Eq. (5.5) with the vanishing diagonal part $\langle R(Y) \rangle = 0$.

5.1.2 Level-Shift Operators

To solve the PT problem for H , Eq. (5.1) we search for a unitary level-shift transformation U [11, 12], $U^\dagger U = U U^\dagger = I$,

$$U H U^\dagger = U(H_0 + V)U^\dagger = H_0 + E, \quad (5.8)$$

where the level-shift operator E satisfies the condition

$$E = \langle E \rangle. \quad (5.9)$$

To guarantee the unitarity of U we express it in the form

$$U = e^G, \quad G^\dagger = -G, \quad \langle G \rangle = 0. \quad (5.10)$$

Using the Hausdorff formula

$$e^A B e^{-A} = \sum_{k=0}^{\infty} (k!)^{-1} (\text{ad } A)^k B \quad (5.11)$$

and defining the operator

$$F = [H_0, G], \quad (5.12)$$

we find from Eq. (5.8) that

$$E + F = V + \frac{1}{2}[G, V + E] + \sum_{k=2}^{\infty} (k!)^{-1} B_k (\text{ad } G)^k (V - E), \quad (5.13)$$

where we used the identity [14]

$$\left(\sum_{k=0}^{\infty} \frac{B_k}{k!} X^k \right) \left(\sum_{k=0}^{\infty} \frac{1}{(k+1)!} X^k \right) = I, \quad (5.14)$$

and B_k designates the Bernoulli numbers [15]

$$\begin{aligned} B_0 &= 1, & B_1 &= -\frac{1}{2}, & B_2 &= \frac{1}{6}, \\ B_{2k+1} &= 0 \quad (k \geq 1), \\ B_4 &= \frac{1}{30}, & B_6 &= \frac{1}{42}, & \text{etc.} \end{aligned} \quad (5.15)$$

5.1.3 General Formalism

Introducing the PT expansion for relevant operators,

$$X = \sum_{i=1}^{\infty} \varepsilon^i X_i, \quad X = E, F, G; \quad F_i = [H_0, G_i], \quad (5.16)$$

Eq. (5.13) leads to the following system of equations

$$\begin{aligned} E_1 + F_1 &= V_1, \\ E_2 + F_2 &= V_2 + \frac{1}{2}[G_1, V_1 + E_1], \\ E_3 + F_3 &= V_3 + \frac{1}{2}[G_1, V_2 + E_2] \\ &\quad + \frac{1}{2}[G_2, V_1 + E_1] \\ &\quad + \frac{1}{12}[G_1, [G_1, V_1 - E_1]], \quad \text{etc.}, \end{aligned} \quad (5.17)$$

which can be solved recursively for E_i and G_i by taking their diagonal part and applying operator R , Eq. (5.7), since

$$\begin{aligned} \langle E_i \rangle &= E_i, & \langle G_i \rangle &= \langle F_i \rangle = 0, \\ R F_i &= G_i, & R E_i &= 0. \end{aligned} \quad (5.18)$$

We thus get

$$\begin{aligned} E_1 &= \langle V_1 \rangle, \\ E_2 &= \langle V_2 \rangle + \frac{1}{2} \langle [R V_1, V_1] \rangle, \\ E_3 &= \langle V_3 \rangle + \langle [R V_1, V_2] \rangle \\ &\quad + \frac{1}{6} \langle [R V_1, [R V_1, 2V_1 + E_1]] \rangle, \quad \text{etc.}, \end{aligned} \quad (5.19)$$

and

$$\begin{aligned} G_1 &= RV_1, \\ G_2 &= RV_2 + \frac{1}{2}R[RV_1, V_1 + E_1], \quad \text{etc.} \end{aligned} \quad (5.20)$$

Since

$$\begin{aligned} \langle R(X) \rangle &= R\langle X \rangle = 0, \quad \langle R(X)Y \rangle = -\langle XR(Y) \rangle, \\ R\langle X \rangle &= R(X)\langle Y \rangle, \quad R(\langle X \rangle Y) = \langle X \rangle R(Y), \end{aligned} \quad (5.21)$$

these relationships can be transformed to a more conventional form

$$\begin{aligned} E_2 &= \langle V_2 \rangle - \langle V_1 RV_1 \rangle, \\ E_3 &= \langle V_3 \rangle - \langle V_1 RV_2 \rangle - \langle V_2 RV_1 \rangle \\ &\quad + \frac{1}{6} \langle R(V_1)R(V_1)[2V_1 + \langle V_1 \rangle] \rangle \\ &\quad - \frac{1}{3} \langle R(V_1)[2V_1 + \langle V_1 \rangle]R(V_1) \rangle \\ &\quad + \frac{1}{6} \langle [2V_1 + \langle V_1 \rangle]R(V_1)R(V_1) \rangle, \quad \text{etc.} \end{aligned} \quad (5.22)$$

However, in this way certain nonphysical terms arise that exactly cancel when the commutator form is employed (Sect. 5.3.7).

5.1.4 Nondegenerate Case

In the nondegenerate case, when $P_i = |i\rangle\langle i|$, with $|i\rangle$ representing the eigenvector of H_0 associated with the eigenvalue ω_i , the level-shift operator is diagonal, and its explicit PT expansion (as well as that for the corresponding eigenvectors) is readily obtained from Eqs. (5.19) and (5.20). Writing x_{ij} for the matrix element $\langle i|X|j\rangle$, we get

$$\begin{aligned} (e_1)_{ii} &= (v_1)_{ii}, \\ (e_2)_{ii} &= (v_2)_{ii} - \sum'_j \frac{(v_1)_{ij}(v_1)_{ji}}{\Delta_{ji}}, \\ (e_3)_{ii} &= (v_3)_{ii} - \sum'_j \frac{(v_1)_{ij}(v_2)_{ji} + (v_2)_{ij}(v_1)_{ji}}{\Delta_{ji}} \\ &\quad + \sum'_{j,k} \frac{(v_1)_{ij}(v_1)_{jk}(v_1)_{ki}}{\Delta_{ji}\Delta_{ki}} \\ &\quad - (v_1)_{ii} \sum'_j \frac{(v_1)_{ij}(v_1)_{ji}}{\Delta_{ji}^2}, \quad \text{etc.}, \end{aligned} \quad (5.23)$$

the prime on the summation symbols indicating that the terms with the vanishing denominator are to be deleted.

Note that in contrast to PT expansions, which directly expand the level-shift transformation U , $U = 1 + \varepsilon U_1 + \varepsilon^2 U_2 + \dots$, the above Lie algebraic formulation has the advantage that U stays unitary in every order of PT. This is particularly useful in spectroscopic applications, such as line broadening.

5.2 Time-Independent Perturbation Theory

For stationary problems, particularly those arising in atomic and molecular electronic structure studies relying on ab initio model Hamiltonians, the PT of Sect. 5.1 can be given a more explicit form that avoids a priori the nonphysical, size inextensive terms [7–10, 16–18].

5.2.1 General Formulation

We wish to find the eigenvalues and eigenvectors of the full (perturbed) problem

$$K|\Psi_i\rangle \equiv (K_0 + W)|\Psi_i\rangle = k_i|\Psi_i\rangle, \quad (5.24)$$

assuming we know those of the unperturbed problem

$$K_0|\Phi_i\rangle = \kappa_i|\Phi_i\rangle, \quad \langle \Phi_i|\Phi_j\rangle = \delta_{ij}. \quad (5.25)$$

For simplicity, we restrict ourselves to the nondegenerate case ($\kappa_i \neq \kappa_j$ if $i \neq j$) and consider only the first-order perturbation (Eq. (5.1), $\varepsilon V_1 \equiv W$, $V_i = 0$ for $i \geq 2$). Of course, K and K_0 are Hermitian operators acting in a Hilbert space, which, in ab initio applications, is finite-dimensional.

Using the intermediate normalization for $|\Psi_i\rangle$,

$$\langle \Psi_i|\Phi_i\rangle = 1, \quad (5.26)$$

the asymmetric energy formula gives

$$k_i = \kappa_i + \langle \Phi_i|W|\Psi_i\rangle. \quad (5.27)$$

The idempotent Hermitian projectors

$$P_i = |\Phi_i\rangle\langle \Phi_i|, \quad Q_i = P_i^\perp = 1 - P_i = \sum_{j(\neq i)} |\Phi_j\rangle\langle \Phi_j| \quad (5.28)$$

commute with K_0 , so that

$$(\lambda - K_0)Q_i|\Psi_i\rangle = Q_i(\lambda - k_i + W)|\Psi_i\rangle, \quad (5.29)$$

λ being an arbitrary scalar (note that we write λI simply as λ). Since the resolvent $(\lambda - K_0)^{-1}$ of K_0 is nonsingular on the orthogonal complement of the i -th eigenspace, we get

$$Q_i|\Psi_i\rangle = |\Psi_i\rangle - |\Phi_i\rangle = R_i(\lambda)(\lambda - k_i + W)|\Psi_i\rangle, \quad (5.30)$$

where

$$\begin{aligned} R_i &\equiv R_i(\lambda) = (\lambda - K_0)^{-1}Q_i \\ &= Q_i(\lambda - K_0)^{-1} = \sum_{j(\neq i)} \frac{|\Phi_j\rangle\langle \Phi_j|}{\lambda - \kappa_j}, \end{aligned} \quad (5.31)$$

assuming $(\lambda \neq \kappa_j)$. Iterating this relationship, we get prototypes of the desired PT expansion for $|\Psi_i\rangle$,

$$|\Psi_i\rangle = \sum_{n=0}^{\infty} [R_i(\lambda - k_i + W)]^n |\Phi_i\rangle, \quad (5.32)$$

and, from Eq. (5.27), for k_i ,

$$k_i = \kappa_i + \sum_{n=0}^{\infty} \langle \Phi_i | W [R_i(\lambda - k_i + W)]^n | \Phi_i \rangle. \quad (5.33)$$

5.2.2 Brillouin–Wigner and Rayleigh–Schrödinger PT (RSPT)

So far, the parameter λ was arbitrary as long as $\lambda \neq \kappa_j$ ($j \neq i$). The following two choices lead to the two basic types of many-body perturbation theory (MBPT):

Brillouin–Wigner (BW) PT Setting $\lambda = k_i$ gives

$$k_i = \kappa_i + \sum_{n=0}^{\infty} \langle \Phi_i | W (R_i^{(\text{BW})} W)^n | \Phi_i \rangle, \quad (5.34)$$

$$|\Psi_i\rangle = \sum_{n=0}^{\infty} (R_i^{(\text{BW})} W)^n |\Phi_i\rangle, \quad (5.35)$$

where

$$R_i^{(\text{BW})} = \sum_{j(\neq i)} \frac{|\Phi_j\rangle\langle\Phi_j|}{k_i - \kappa_j}. \quad (5.36)$$

Rayleigh–Schrödinger (RS) PT Setting $\lambda = \kappa_i$ gives

$$k_i = \kappa_i + \sum_{n=0}^{\infty} \langle \Phi_i | W [R_i^{(\text{RS})}(\kappa_i - k_i + W)]^n | \Phi_i \rangle, \quad (5.37)$$

$$|\Psi_i\rangle = \sum_{n=0}^{\infty} [R_i^{(\text{RS})}(\kappa_i - k_i + W)]^n |\Phi_i\rangle, \quad (5.38)$$

where now

$$R_i \equiv R_i^{(\text{RS})} = \sum_{j(\neq i)} \frac{|\Phi_j\rangle\langle\Phi_j|}{\kappa_i - \kappa_j}. \quad (5.39)$$

The main distinction between these two PTs lies in the fact that the BW form has the exact eigenvalues appearing in the denominators and, thus, leads to polynomial expressions for k_i . Although these are not difficult to solve numerically, since the eigenvalues are separated, the resulting energies are never size extensive and, thus, unusable for extended systems. They are also unsuitable for finite systems when the particle number changes, as in various dissociation processes. From now on, we thus investigate only the RSPT, which yields a fully size-extensive theory.

5.2.3 Bracketing Theorem and RSPT

Expressions Eqs. (5.37) and (5.38) are not explicit, since they involve the exact eigenvalues k_i on the right-hand side. To achieve an order-by-order separation, set

$$k_i \equiv k = \sum_{j=0}^{\infty} k^{(j)}, \quad |\Psi_i\rangle \equiv |\Psi\rangle = \sum_{j=0}^{\infty} |\Psi^{(j)}\rangle, \quad (5.40)$$

where the superscript (j) indicates the j -th-order in the perturbation W . We only consider the eigenvalue expressions, since the corresponding eigenvectors are readily recovered from them by removing the bra state and the first interaction W (Eqs. (5.37) and (5.38)). We also simplify the mean value notation writing for a general operator X ,

$$\langle X \rangle \equiv \langle \Phi_i | X | \Phi_i \rangle. \quad (5.41)$$

Substituting the first expansion Eq. (5.40) into Eq. (5.37) and collecting the terms of the same order in W , we get

$$\begin{aligned} k^{(0)} &= \kappa_i, \\ k^{(1)} &= \langle W \rangle, \\ k^{(2)} &= \langle WRW \rangle, \\ k^{(3)} &= \langle W(RW)^2 \rangle - \langle W \rangle \langle WR^2W \rangle, \\ k^{(4)} &= \langle W(RW)^3 \rangle \\ &\quad - \langle W \rangle (\langle WR(RW)^2 \rangle + \langle (WR)^2 RW \rangle) \\ &\quad + \langle W \rangle^2 \langle WR^3W \rangle - \langle WRW \rangle \langle WR^2W \rangle, \quad \text{etc.} \end{aligned} \quad (5.42)$$

The general expression has the form

$$k^{(n)} = \langle W(RW)^{n-1} \rangle + \mathcal{R}^{(n)}, \quad (5.43)$$

the first term on the right-hand side being referred to as the *principal* n -th-order term, while $\mathcal{R}^{(n)}$ designates the so-called *renormalization* terms that are obtained by the *bracketing theorem* [16, 19] as follows:

1. Insert the bracketings $\langle \dots \rangle$ around the $W, WRW, \dots, WR \dots RW$ operator strings of the principal term in all possible ways.
2. Bracketings involving the rightmost and/or the leftmost interaction vanish.
3. The sign of each bracketed term is given by $(-1)^{n_B}$, where n_B is the number of bracketings.
4. Bracketings within bracketings are allowed, e.g., $\langle WR \langle WR \langle W \rangle RW \rangle RW \rangle = \langle W \rangle \langle WR^2W \rangle^2$.
5. The total number of bracketings (including the principal term) is $(2n - 2)! / [n!(n - 1)!]$.

5.3 Fermionic Many-Body Perturbation Theory (MBPT)

5.3.1 Time-Independent Wick's Theorem

The development of an explicit MBPT formalism is greatly facilitated by the exploitation of the time-independent version of Wick's theorem. This version of the theorem expresses an arbitrary product of creation (a_μ^\dagger) and annihilation (a_μ) operators (Chap. 6) as a normal product (relative to $|\Phi_0\rangle$) and as normal products with all possible contractions of these operators [16–18],

$$\begin{aligned} x_1 x_2 \cdots x_k &= N[x_1 x_2 \cdots x_k] + \Sigma N[x_1 \overline{x_2 \cdots x_k}], \\ (x_i &= a_{\mu_i}^\dagger \text{ or } x_i = a_{\mu_i}), \end{aligned} \quad (5.44)$$

where

$$\begin{aligned} \overline{a_\mu^\dagger a_\nu^\dagger} &= \overline{a_\mu a_\nu} = 0, \\ \overline{a_\mu^\dagger a_\nu} &= h(\mu)\delta_{\mu\nu}, \quad \overline{a_\mu a_\nu^\dagger} = p(\mu)\delta_{\mu\nu}, \end{aligned} \quad (5.45)$$

and

$$\begin{aligned} h(\mu) &= 1, \quad p(\mu) = 0 \text{ if } |\mu\rangle \text{ is occupied in } |\Phi_0\rangle \\ &\text{(hole states),} \\ h(\mu) &= 0, \quad p(\mu) = 1 \text{ if } |\mu\rangle \text{ is unoccupied in } |\Phi_0\rangle \\ &\text{(particle states).} \end{aligned} \quad (5.46)$$

The N -product with contractions is defined as a product of individual contractions times the N -product of uncontracted operators (defining $N[\emptyset] \equiv 1$ for an empty set) with the sign given by the parity of the permutation reordering the operators into their final order.

Note that the Fermi vacuum mean value of an N -product vanishes unless all operators are contracted. Thus, $\langle x_1 x_2 \cdots x_k \rangle$ is given by the sum over all possible fully contracted terms (vacuum terms). Similar rules follow for the expressions of the type $\langle x_1 x_2 \cdots x_k \rangle |\Phi\rangle$. Moreover, if some operators on the left-hand side of Eq. (5.44) are already in the N -product form, all the terms involving contractions between these operators vanish.

5.3.2 Normal Product Form of PT

Consider the eigenvalue problem for a general ab initio or semiempirical electronic Hamiltonian H with one and two-body components Z and V , namely,

$$\begin{aligned} H|\Psi_i\rangle &= E_i|\Psi_i\rangle, \\ H &= Z + V = \sum_i z(i) + \sum_{i<j} v(i, j), \end{aligned} \quad (5.47)$$

and a corresponding unperturbed problem

$$\begin{aligned} H_0|\Phi_i\rangle &= \varepsilon_i|\Phi_i\rangle, \\ H_0 &= Z + U, \quad \langle\Phi_i|\Phi_j\rangle = \delta_{ij}, \end{aligned} \quad (5.48)$$

with U representing some approximation to V . In the case that U is also a one-electron operator, $U = \Sigma_i u(i)$, the unperturbed problem Eq. (5.48) is separable and reduces to a one-electron problem,

$$(z + u)|\mu\rangle = \omega_\mu|\mu\rangle, \quad (5.49)$$

which is assumed to be solved. Choosing the orthonormal spin orbitals $\{|\mu\rangle\}$ as a basis of the second quantization representation Sect. 6.1, the N -electron solutions of Eq. (5.48) can be represented as

$$|\Phi_i\rangle = a_{\mu_1}^\dagger a_{\mu_2}^\dagger \cdots a_{\mu_N}^\dagger |0\rangle, \quad (5.50)$$

$$\varepsilon_i = \sum_{j=1}^N \omega_{\mu_j}, \quad (5.51)$$

the state label i representing the occupied spin orbital set $\{\mu_1, \mu_2, \dots, \mu_N\}$, while the one and two-body operators take the form

$$X = \sum_{\mu, \nu} \langle \mu|x|\nu \rangle a_\mu^\dagger a_\nu, \quad X = Z, U; \quad x = z, u, \quad (5.52)$$

$$V = \frac{1}{2} \sum_{\mu, \nu, \sigma, \tau} \langle \mu\nu|v|\sigma\tau \rangle a_\mu^\dagger a_\nu^\dagger a_\tau a_\sigma. \quad (5.53)$$

Considering, for simplicity, a nondegenerate ground state $|\Phi\rangle \equiv |\Phi_0\rangle = a_1^\dagger a_2^\dagger \cdots a_N^\dagger |0\rangle$, referred to as a Fermi vacuum, we define the *normal product form* of these operators relative to $|\Phi\rangle$

$$\begin{aligned} X_N &\equiv X - \langle X \rangle = \sum_{\mu, \nu} \langle \mu|x|\nu \rangle N[a_\mu^\dagger a_\nu], \\ (X &= Z, U, G; \quad x = z, u, g) \end{aligned} \quad (5.54a)$$

$$\begin{aligned} V_N &\equiv V - \langle V \rangle - G_N \\ &= \frac{1}{2} \sum_{\mu, \nu, \sigma, \tau} \langle \mu\nu|v|\sigma\tau \rangle N[a_\mu^\dagger a_\nu^\dagger a_\tau a_\sigma] \\ &= \frac{1}{4} \sum_{\mu, \nu, \sigma, \tau} \langle \mu\nu|v|\sigma\tau \rangle_A N[a_\mu^\dagger a_\nu^\dagger a_\tau a_\sigma], \end{aligned} \quad (5.54b)$$

where

$$\langle \mu|g|\nu \rangle = \sum_{\sigma=1}^N \langle \mu\sigma|v|\nu\sigma \rangle_A, \quad (5.55)$$

$$\langle \mu\nu|v|\sigma\tau \rangle_A = \langle \mu\nu|v|\sigma\tau \rangle - \langle \mu\nu|v|\tau\sigma \rangle, \quad (5.56)$$

$\langle X \rangle = \langle \Phi | X | \Phi \rangle$, and $N[\dots]$ designates the normal product relative to $|\Phi\rangle$ [16–18]. (Recall that $N[x_1 x_2 \dots x_k] = \pm b_{\mu_1}^\dagger \dots b_{\mu_i}^\dagger b_{\mu_{i+1}} \dots b_{\mu_k}$, where $x_i = b_{\mu_i}$ or $b_{\mu_i}^\dagger$ are the annihilation and creation operators of the particle-hole formalism relative to $|\Phi\rangle$, i.e., $b_\mu = a_\mu^\dagger$ for $\mu \leq N$ and $b_\mu = a_\mu$ for $\mu > N$, the sign being determined by the parity of the permutation $p : j \mapsto \mu_j$.)

Defining

$$K = H - \langle H \rangle, \quad K_0 = H_0 - \langle H_0 \rangle = H_0 - \varepsilon_0, \quad (5.57)$$

we can return to Eqs. (5.24) and (5.25), where now

$$\begin{aligned} k_i &= E_i - \langle H \rangle, \quad \kappa_i = \varepsilon_i - \varepsilon_0, \\ \varepsilon_0 &= \sum_{\mu=1}^N \omega_\mu, \end{aligned} \quad (5.58)$$

and

$$W = K - K_0 = V - U - \langle V - U \rangle. \quad (5.59)$$

With this choice, $\langle W \rangle = 0$, so that for the reference state $|\Phi\rangle$, Eq. (5.42) simplify to (we drop the subscript 0 for simplicity)

$$\begin{aligned} k^{(0)} &= 0, \quad k^{(1)} = 0, \\ k^{(2)} &= \langle WRW \rangle, \\ k^{(3)} &= \langle WRWRW \rangle, \\ k^{(4)} &= \langle W(RW)^3 \rangle - \langle WRW \rangle \langle WR^2W \rangle, \quad \text{etc.} \end{aligned} \quad (5.60)$$

Note that W is also in the N -product form,

$$W = W_1 + W_2, \quad W_1 = G_N - U_N, \quad W_2 = V_N. \quad (5.61)$$

5.3.3 Møller–Plesset and Epstein–Nesbet PT

Choosing $U = G$ we have

$$H_0 = Z + G \equiv F, \quad (5.62)$$

so that Eq. (5.49) represent Hartree–Fock (HF) equations, and ω_μ and $|\mu\rangle$ the canonical HF orbital energies and spin orbitals, respectively. Since $\langle H \rangle = \sum_{\mu=1}^N (\langle \mu | z | \mu \rangle + \frac{1}{2} \langle \mu | g | \mu \rangle)$ is the HF energy, $k = k_0$ gives directly the ground state correlation energy. (Note, however, that the N -product form of PT eliminates the first-order contribution $k^{(1)} = \langle W \rangle$ in any basis, even when F is not diagonal.) With this choice, $W_1 = 0$, $W = V_N$, and the denominators in Eq. (5.39) are given by the differences of HF orbital energies

$$\kappa_0 - \kappa_j = \sum_{i=1}^{\lambda} (\omega_{\mu_i} - \omega_{\nu_i}) \equiv \Delta\{\{\mu_i\}; \{\nu_j\}\}, \quad (5.63)$$

assuming that $|\Phi_j\rangle$ is a λ -times excited configuration relative to $|\Phi\rangle$ obtained through excitations $\mu_i \rightarrow \nu_i$, $i = 1, \dots, \lambda$. Using the Slater rules (or the second quantization algebra), we can express the second-order contribution in terms of the two-electron integrals and HF orbital energies as

$$k^{(2)} = \frac{1}{2} \sum_{a,b,r,s} \frac{\langle ab | v | rs \rangle (\langle rs | v | ab \rangle - \langle rs | v | ba \rangle)}{\omega_a + \omega_b - \omega_r - \omega_s}, \quad (5.64)$$

where the summations over $a, b (r, s)$ extend over all occupied (unoccupied) spin orbitals in $|\Phi\rangle$. Obtaining the corresponding higher-order corrections becomes more and more laborious and, beginning with the fourth-order, important cancellations arise between the principal and renormalization terms, even when the N -product form is employed. These will be addressed in Sect. 5.3.7.

The above outlined PT with H_0 given by the HF operator is often referred to as the *Møller–Plesset* PT [20] and, when truncated to the n -th order, is designated by the acronym *MPn*, $n = 2, 3, \dots$. In this version, the two-electron integrals enter the denominators only through the HF orbital energies. In an alternative, less often employed variant, referred to as the *Epstein–Nesbet* PT [21, 22], the whole diagonal part of H is used as the unperturbed Hamiltonian, i.e.,

$$H_0 = \sum_i \langle \Phi_i | H | \Phi_i \rangle P_i. \quad (5.65)$$

With this choice, the denominators are given as differences of the diagonal elements of the configuration interaction matrix.

5.3.4 Diagrammatic MBPT

To facilitate the evaluation of higher-order terms and, especially, to derive the general properties and characteristics of the MBPT, it is useful to employ a diagrammatic representation [7–10, 16–18]. Representing all the operators in Eqs. (5.42) and (5.43) or (5.60) in the second quantized form, we have to deal with the reference state (i.e., the Fermi vacuum) mean values of the strings of annihilation and creation operators (or with these strings acting on the reference in the case of a wave function). This is efficiently done using Wick’s theorem and its diagrammatic representation via a special form of Feynman diagrams. In this representation, we associate with various operators suitable vertices with incident oriented lines representing the creation (outgoing lines) and annihilation (ingoing lines) operators that are involved in their second quantization form. A few typical diagrams representing operators ($-U$), W_1 and V are shown in Fig. 5.1a, Fig. 5.1b and Fig. 5.1c, Fig. 5.1d, respectively. Using the N -product form of PT with HF orbitals (Sect. 5.3.3), we only need the two-electron operator V or V_N , which

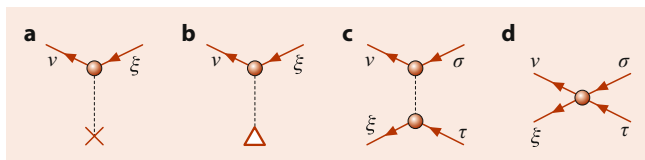


Fig. 5.1 Diagrammatic representation of one and two-electron operators

can be represented using either nonantisymmetrized vertices (Fig. 5.1c), leading to the *Goldstone diagrams* [23], or antisymmetrized vertices (Fig. 5.1d), associated with antisymmetrized two-electron integrals Eq. (5.56) and yielding the *Hugenholtz diagrams* [24].

5.3.5 Vacuum and Wave Function Diagrams

Applying Wick's theorem to the strings of operators involved, we represent the individual contractions, Eq. (5.45), by joining corresponding oriented lines. To obtain a nonvanishing contribution, only contractions preserving the orientation need be considered (Eq. (5.45)). The resulting *internal* lines have either the left–right orientation (*hole* lines) or the right–left one (*particle* lines). Only fully contracted terms, represented by the so-called *vacuum diagrams* (having only internal lines), can contribute to the energy, while those representing wave function contributions have uncontracted or *free* lines extending to the left. When the operators involved are in the N -product form, no contractions of oriented lines issuing from the same vertex are allowed. The projection-like operators R , Eq. (5.39), or their powers, lead to the denominators, Eq. (5.63), given by the difference of hole and particle orbital energies associated with, respectively, hole and particle lines passing through the interval separating the corresponding two neighboring vertices. Clearly, there must always be at least one pair of such lines lest the denominator vanish. Thus, for example, the second-order contribution $\langle WRW \rangle$ is represented either by the two Goldstone diagrams [23] (Fig. 5.2a,b) or by the single Hugenholtz diagram [24] (Fig. 5.2c). The rules for the energy (vacuum) diagram evaluation are as follows:

1. Associate appropriate matrix elements with all vertices and form their product. The outgoing (ingoing) lines

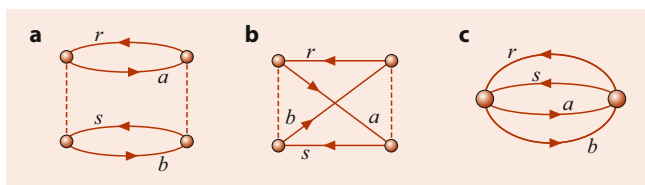


Fig. 5.2 The second-order Goldstone (a), (b) and Hugenholtz (c) diagrams

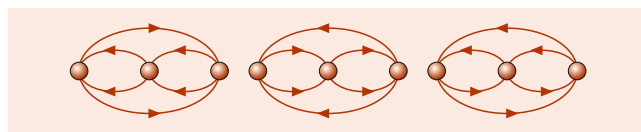


Fig. 5.3 Hugenholtz diagrams for the third-order energy contribution

on each vertex define the bra (ket) states of a given matrix element, and for the Goldstone diagrams, the oriented lines attached to the same node are associated with the same electron number, (e.g., for the leftmost vertex in diagram (a) of Fig. 5.2, we have $\langle ab|v|rs \rangle \equiv \langle a(1)b(2)|v|r(1)s(2) \rangle$).

2. Associate a denominator, Eq. (5.63), or its appropriate power, with every neighboring pair of vertices (and, for the wave function diagrams, also with the free lines extending to the left of the leftmost vertex; with each pair of such free lines associate also the corresponding pair of particle creation and hole annihilation operators).
3. Sum over all hole and particle labels.
4. Multiply each diagram contribution by the weight factor given by the reciprocal value of the order of the group of automorphisms of the diagram (stripped of summation labels) and by the sign $(-1)^{h+\ell}$, where h designates the number of internal hole lines, and ℓ gives the number of closed loops of oriented lines (for Hugenholtz diagrams, use any of its Goldstone representatives to determine the correct phase).

Applying these rules to diagrams (a) and (b) of Fig. 5.2 we clearly recover Eq. (5.64) or, using the Hugenholtz diagram of Fig. 5.2, the equivalent expression

$$k^{(2)} = \frac{1}{4} \sum_{a,b,r,s} \langle ab|v|rs \rangle_A \langle rs|v|ab \rangle_A \Delta^{-1}(a,b;r,s). \quad (5.66)$$

The possible third-order Hugenholtz diagrams are shown in Fig. 5.3 with the central vertex involving particle–particle, hole–hole, and particle–hole interaction [16–18].

5.3.6 Hartree–Fock Diagrams

In the general case (non-HF orbitals and/or not normal product form of PT), the one-electron terms, as well as the contractions between operators associated with the same vertex, can occur (the latter are always the hole lines). Representing the W_1 and $(-U)$ operators as shown in Fig. 5.1, the one-body perturbation W_1 represents in fact the three diagrams as shown in Fig. 5.4. The second-order contribution of this type is then represented by the diagrams in Fig. 5.5, which in fact represents nine diagrams that result when each W_1 vertex is replaced by three vertices as shown in Fig. 5.4.

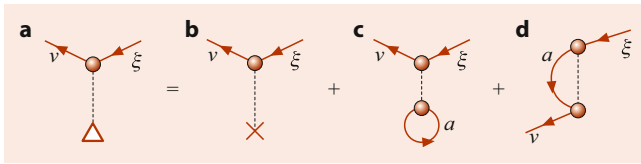
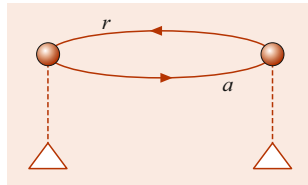


Fig. 5.4 Schematic representation of $W_1 = G_N - U_N$

Fig. 5.5 The second-order, one-particle contribution



Using HF orbitals, all these terms mutually cancel out, as can be seen above. For this reason, the diagrams involving contractions of lines issuing from the same vertex are referred to as *Hartree–Fock diagrams*. Note, however, that even when not employing the canonical HF orbitals, it is convenient to introduce W_1 vertices of the normal product form PT and replace all nine HF-type diagrams by a single diagram of Fig. 5.5. Clearly, this feature provides even greater efficiency in higher orders of PT.

5.3.7 Linked and Connected Cluster Theorems

Using the N -product form of PT, the first nonvanishing renormalization term occurs in the fourth-order (Eq. (5.60)). For a system consisting of N noninteracting species, the energy given by this nonphysical term is proportional to N^2 and, thus, violates the size extensivity of the theory. It was first shown by *Brueckner* [25] that in the fourth order, these terms are in fact exactly canceled by the corresponding contributions originating in the principal term. A general proof of this cancellation in an arbitrary order was then given by *Goldstone* [23] and *Hubbard* [26] using a time-dependent PT based on Gell-Mann and Low adiabatic theorem and evolution operator (Sect. 5.4) and by *Hugenholtz* [24] employing a time-independent PT, relying on Green’s function or the resolvent operator.

To comprehend this cancellation, consider the fourth-order energy contribution arising from the so-called unlinked diagrams (no such contribution can arise in the second or third order) shown in Fig. 5.6. An *unlinked diagram* is defined as a diagram containing a disconnected vacuum diagram (for the energy diagrams, the terms unlinked and disconnected are synonymous). The numerators associated with both diagrams being identical, we only consider the denominators. Designating the denominator associated with the

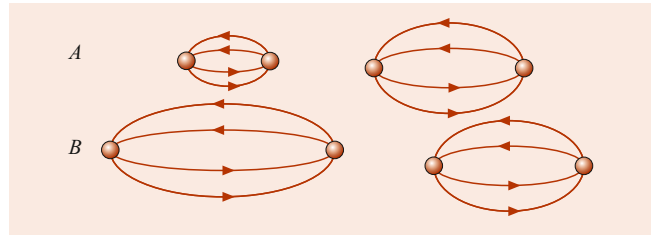


Fig. 5.6 The fourth-order unlinked diagrams

top and the bottom part by A and B , respectively, we find for the overall contribution

$$\frac{1}{B} \cdot \frac{1}{A+B} \cdot \frac{1}{B} + \frac{1}{A} \cdot \frac{1}{A+B} \cdot \frac{1}{B} = \left(\frac{1}{B} + \frac{1}{A} \right) \frac{1}{(A+B)B} = \frac{1}{AB^2}. \quad (5.67)$$

Thus, the contribution from these terms exactly cancels that from the renormalization term $\langle WRW \rangle \langle WR^2W \rangle$.

Generalizing Eq. (5.67) we obtain the *factorization lemma* of *Frantz and Mills* [27], which implies the cancellation of renormalization terms by the unlinked terms originating from the principal term. This result holds for the energy as well as for the wave function contributions in every order of PT, as ascertained by the *linked cluster theorem*, which states that

$$\Delta E = k = \sum_{n=0}^{\infty} \langle \Phi | W | \Psi^{(n)} \rangle = \sum_{n=0}^{\infty} \langle W(RW)^n \rangle_L, \quad (5.68)$$

$$|\Psi\rangle = \sum_{n=0}^{\infty} |\Psi^{(n)}\rangle = \sum_{n=0}^{\infty} \{ (RW)^n |\Phi\rangle \}_L, \quad (5.69)$$

where the subscript L indicates that only linked diagrams (or terms) are to be considered. This enables us to obtain general, explicit expressions for the n -th-order PT contributions by first constructing all possible linked diagrams involving n vertices and by converting them into the explicit algebraic expressions using the rules of Sect. 5.3.5. Note that linked energy diagrams are always connected, but the linked wave function diagrams are either connected or disconnected, each disconnected component possessing at least one pair of particle–hole free lines extending to the left.

To reveal a deeper structure of the result Eq. (5.69) define the *cluster operator* T that generates all connected wave function diagrams,

$$T|\Phi\rangle = \sum_{n=1}^{\infty} \{ (RW)^n |\Phi\rangle \}_C, \quad (5.70)$$

the subscript C indicating that only contributions from *connected* diagrams are to be included. Since the general component with r disconnected parts can be shown to be

represented by the term $(r!)^{-1}T^r|\Phi\rangle$, the general structure of the exact wave function $|\Psi\rangle$ is given by the *connected cluster theorem* [24, 26], which states that

$$|\Psi\rangle = e^T |\Phi\rangle, \quad (5.71)$$

assuming an *intermediate normalization* $\langle\Phi|\Psi\rangle = 1$. In other words, the wave operator \mathcal{W} that transforms the unperturbed independent particle model wave function $|\Phi\rangle$ into the exact one according to

$$|\Psi\rangle = \mathcal{W}|\Phi\rangle \quad (5.72)$$

is given by the exponential of the cluster operator T ,

$$\mathcal{W} = e^T, \quad (5.73)$$

which, in turn, is given by the connected wave function diagrams. This is in fact the basis of the coupled cluster methods [28–33] (Sect. 5.3.8). For recent reviews, see, e.g., [10, 17, 18, 34–41]; for a historical perspective, see [42, 43].

The contributions to T may be further classified by their excitation rank i ,

$$T = \sum_{i=1}^N T_i, \quad (5.74)$$

where T_i designates connected diagrams with i pairs of free particle–hole lines, producing i -times excited components of $|\Psi\rangle$ when acting on $|\Phi\rangle$.

5.3.8 Coupled Cluster Theory

To motivate coupled cluster (CC) approaches we recall that summing all HF diagrams (Sect. 5.3.6) is equivalent to solving the HF equations. Likewise, depending on the average electron density of the system, it may be essential to sum certain types of PT diagrams to infinite order at the post-HF level, namely the ring diagrams (*random phase approximation*) in the case of high-density electron gas and ladder diagrams for low-density systems. An ideal approach that can sum different kinds of diagrams and their combinations, and is thus capable of recovering a large part of the electronic correlation energy, is based on the connected cluster theorem (Sect. 5.3.7), referred to in this context as the *exponential cluster ansatz* Eq. (5.71) for the wave operator. Using this ansatz, one derives a system of energy-independent non-linear coupled cluster (CC) equations [10, 17, 18, 30–33] determining the cluster amplitudes of T . These CC equations can be regarded as recurrence relations generating the MBPT series [17, 18], so that by solving these equations one, in fact, implicitly generates all the relevant MBPT diagrams and sums them to infinite order. Since the solution

of the full CC equations is equivalent to the exact solution of the Schrödinger equation, we must—in all practical applications—introduce a suitable truncation scheme, which implies that only diagrams of certain types are summed. (For different possible truncation schemes, see [44, Sect. 2].)

Generally, using the cluster expansion Eq. (5.71) in the N -product form of the Schrödinger equation,

$$\begin{aligned} H_N|\Psi\rangle &\equiv (H - \langle H \rangle)|\Psi\rangle = \Delta E|\Psi\rangle, \\ \Delta E &= E - E_0, \end{aligned} \quad (5.75)$$

premultiplying with the inverse of the wave operator, and using the Hausdorff formula Eq. (5.11) yields

$$e^{-T} H_N e^T |\Phi\rangle = \sum_{n=0}^{\infty} \frac{[\text{ad}(-T)]^n H_N}{n!} = \Delta E|\Phi\rangle. \quad (5.76)$$

In fact, this expansion terminates, so that using Eq. (5.74) and projecting onto $|\Phi\rangle$ we obtain the energy expression

$$\Delta E = \langle H_N T_2 \rangle + \frac{1}{2} \langle H_N T_1^2 \rangle, \quad (5.77)$$

while the projection onto the manifold of excited states $\{|\Phi_i\rangle\}$ relative to $|\Phi\rangle \equiv |\Phi_0\rangle$ gives the system of CC equations

$$\langle\Phi_i|H_N + [H_N, T] + \frac{1}{2}[[H_N, T], T] + \dots|\Phi\rangle = 0. \quad (5.78)$$

Approximating, e.g., T by the most important pair cluster component $T \approx T_2$ gives the so-called CCD (coupled clusters with doubles) approximation

$$\langle\Phi_i^{(2)}|H_N + [H_N, T_2] + \frac{1}{2}[[H_N, T_2], T_2]|\Phi\rangle = 0, \quad (5.79)$$

the superscript (2) indicating pair excitations relative to $|\Phi\rangle$.

Equivalently, Eqs. (5.77) and (5.78) can be written in the form

$$\Delta E = \langle H_N e^T \rangle_C, \quad (5.80)$$

$$\langle\Phi_i|(H_N e^T)_C|\Phi\rangle = 0, \quad (5.81)$$

the subscript C again indicating that only connected diagrams are to be considered. The general explicit form of CC equations is

$$a_i + \sum_j b_{ij} t_j + \sum_{j \leq k} c_{ijk} t_j t_k + \dots = 0, \quad (5.82)$$

where $a_i = \langle\Phi_i|H_N|\Phi_0\rangle$, $b_{ij} = \langle\Phi_i|H_N|\Phi_j\rangle_C$, $c_{ijk} = \langle\Phi_i|H_N|\Phi_j \otimes \Phi_k\rangle_C$, etc. Writing the diagonal linear term b_{ii} in the form

$$b_{ii} = \Delta_i + b'_{ii}, \quad (5.83)$$

this system can be solved iteratively by rewriting it in the form

$$t_i^{(n+1)} = \Delta_i^{-1} \left(a_i + b'_{ii} t_i^{(n)} + \sum_j b'_{ij} t_j^{(n)} + \sum_{j \leq k} c_{ijk} t_j^{(n)} t_k^{(n)} + \dots \right). \quad (5.84)$$

Starting with the zeroth approximation $t_i^{(0)} = 0$, the first iteration is

$$t_i^{(1)} = \Delta_i^{-1} a_i, \quad (5.85)$$

which yields the second-order PT energy when used in Eq. (5.77). Clearly, the successive iterations generate higher and higher orders of the PT. At any truncation level, a size extensive result is obtained.

The single reference (SR) CC methods continue to be remarkably efficient in handling the dynamic correlation effects and are, thus, widely exploited in computations of molecular electronic structure. Several general-purpose codes are available for this purpose (for reviews: [10, 18, 34–36, 38]). The basic workhorse that provides the required T_1 and T_2 cluster amplitudes results by setting $T_i = 0$ for $i > 2$ in Eq. (5.74) (the CC with singles and doubles (CCSD) method [45]). A small, but often important, T_3 component is usually accounted for perturbatively via the CCSD(T) method [46, 47], which is often referred to as the “gold standard” of quantum chemistry, since it provides very accurate and reliable results. Unfortunately, this is no longer the case in the presence of quasidegeneracy when handling strongly-correlated systems or when breaking chemical bonds as in generating potential energy curves or surfaces. This can to some extent be avoided by employing one of the renormalized versions of CCSD(T) [48] but, in general, requires multireference-type approaches (see below).

In order to compute the excitation, ionization, or electron attachment energies one employs the *equation-of-motion* (EOM) and the *linear-response* formalisms relying on the generalized cluster ansatz [49] $|\Psi\rangle = R e^T |\Phi\rangle$, where R yields an appropriate zero (or first)-order wave function of the open-shell system considered when acting on $|\Phi\rangle$. In general, this leads to a non-Hermitian eigenvalue problem, which requires a computation of the right and left eigenvectors [10]. These developments also enabled calculation of other properties than the energy (dipole and quadrupole moments, polarizabilities, etc.), [10, 18, 34–36]. Here, we should also mention a possibility of using the cluster ansatz based on the *unitary group approach* (UGA) [50, 51] (Sect. 4.3.6).

At this stage it is important to recall that the standard SR MBPT and CC approaches pertain to nondegenerate, lowest-lying closed-shell states of a given symmetry species. Although the CC methods are often used even for open-shell states by relying on the unrestricted HF (UHF) reference (of the different-orbitals-for-different-spins (DODS) type),

a proper description of such states requires a multireference (MR) generalization based on the *effective Hamiltonian* formalism [7, 18, 36, 52–54]. Unfortunately, such a generalization is not unambiguous. The two viable formulations, the so-called *valence universal* (VU) [7, 53] and *state universal* (SU) [54] MR CC methods have enjoyed continued following (see [55] for recent developments), yet are computationally demanding and often plagued with the intruder state and other problems [17, 52]. For these reasons, no general-purpose codes have yet been developed, and only a few actual applications have been carried out [18, 36] (see, however, the recently formulated SU CC approach for *general model spaces* [56–59]).

In view of the ambiguity, complexity, and computational demands of genuine MR CC approaches it is tempting to design SR CC-type methods that are capable of accommodating both the nondynamic and dynamic correlation effects. This may be achieved by exploiting the complementarity of perturbative (i.e., CC) and variational (CI, CAS SCF, etc.)-type approaches, leading to the so-called *externally corrected* (ec) ecCCSD or ecCCSD(T) methods (for an overview, see [44]; see also [60, 61] and the so-called *state selective* or *state specific* (SS) approaches [62]). The basic idea here is to extract a suitable approximation $T_3^{(0)}$ and $T_4^{(0)}$ of, respectively, the T_3 and T_4 clusters from some independent source and account for them in the CCD or CCSD equations, i.e.,

$$\langle \Phi_i | H_N \left(T_2 + \frac{1}{2} T_2^2 + T_3^{(0)} + T_4^{(0)} \right) | \Phi \rangle_C = 0, \quad (5.86)$$

thus achieving a more meaningful decoupling of the CC chain by simply evaluating the $T_3^{(0)}$ and $T_4^{(0)}$ -dependent terms and adding them to the absolute term. Note that using the exact (i.e., *full configuration interaction* (FCI)) T_3 and T_4 amplitudes the ecCCSD equations will recover the exact FCI energy. The most promising version of such an ecCCSD approach employs the three- and four-body amplitudes obtained by a cluster analysis of a small MR CI wave function and is referred to as the reduced MR CCSD (RMR CCSD) method [63–65] (see [44] for a list of numerous applications). Very recently, the required approximate three and four-body clusters were extracted by relying on the (G)UGA based ((graphical) UGA) (see [66–68] for recent reviews) FCI quantum Monte Carlo (FCI-QMC) or *i*-FCI-QMC codes [69–71] yielding encouraging results [61, 72–74]. Very recently, Chan et al. [75] exploited for the same purpose the density matrix renormalization group (DMRG) approach [76–78] in the ecCCSD formalism [44].

The same goal, which simultaneously leads to more efficient SR CC formalisms, may also be achieved via an effective implicit account of higher-order clusters by relying on the role of the EPV (exclusion principle violating) diagrams that are separable over the hole lines, leading to the so-called *internally corrected* (ic) methods, such as approx-

imate coupled pair (ACP-D45) approach, approximate CC with doubles (ACCD) or with approximate quads (ACPQ) methods (see [44] for relevant references). Very recently, similar ideas to the icCCSD approaches [44] were exploited by Kats et al. [79–81] in the so-called *distinguished cluster* (DC) approximations, such as DC with doubles (DCD), DC with singles and doubles (DCSD) and DCSD corrected for triples (DCSD(T)) methods, leading to numerous exploitations in actual systems [82–85], including transcorrelated CC methods [86].

A very recent development [87] exploits the quantum Monte Carlo (MC) formalism in solving the CC equations, resulting in a stochastic CCMC method [87, 88], which was also extended to the *equation of motion* CC (EOMCC) type approaches [89] enabling handling the excited states energetics. This way of solving the CC equations should allow applications to larger systems than do the currently available standard codes.

Finally, note that the CC approach has also been used to handle bosonic-type problems of the vibrational structure in molecular spectra and, generally, multimode dynamics [90].

5.4 Time-Dependent Perturbation Theory

5.4.1 Evolution Operator PT Expansion

By introducing the *evolution operator* $U(t, t_0)$

$$|\Psi(t)\rangle = U(t, t_0)|\Psi(t_0)\rangle, \quad (5.87)$$

the time-dependent Schrödinger equation

$$i\hbar \frac{\partial}{\partial t} |\Psi(t)\rangle = H |\Psi(t)\rangle \quad (5.88)$$

becomes

$$i\hbar \frac{\partial}{\partial t} U(t, t_0) = H U(t, t_0). \quad (5.89)$$

Clearly,

$$\begin{aligned} U(t_0, t_0) &= 1, \\ U(t, t_0) &= U(t, t')U(t', t_0), \\ U(t, t_0)^{-1} &= U(t_0, t) = U^\dagger(t, t_0). \end{aligned} \quad (5.90)$$

If the Hamiltonian is time-independent, then

$$U(t, t_0) = \exp\left[-\frac{i}{\hbar} H(t - t_0)\right]. \quad (5.91)$$

In the *interaction picture* (subscript I),

$$|\Psi(t)\rangle_I = \exp\left(\frac{i}{\hbar} H_0 t\right) |\Psi(t)\rangle, \quad (5.92)$$

where now

$$H = H_0 + V, \quad (5.93)$$

the Schrödinger equation becomes

$$i\hbar \frac{\partial}{\partial t} |\Psi(t)\rangle_I = V(t)_I |\Psi(t)\rangle_I. \quad (5.94)$$

This is known as the *Tomonaga–Schwinger equation* [91]. Analogously, the evolution operator in this picture (we drop the subscript I from now on) satisfies

$$i\hbar \frac{\partial}{\partial t} U(t, t_0) = V(t)U(t, t_0), \quad (5.95)$$

with the initial condition $U(t_0, t_0) = 1$. This differential equation is equivalent to an integral equation

$$U(t, t_0) = 1 - \frac{i}{\hbar} \int_{t_0}^t V(t_1)U(t_1, t_0) dt_1. \quad (5.96)$$

Iterating we get [92, 93]

$$\begin{aligned} U(t, t_0) &= \sum_{n=0}^{\infty} \left(-\frac{i}{\hbar}\right)^n \\ &\quad \times \int_{t_0}^t dt_1 \int_{t_0}^{t_1} dt_2 \cdots \int_{t_0}^{t_{n-1}} dt_n V(t_1)V(t_2) \cdots V(t_n) \\ &= \sum_{n=0}^{\infty} \frac{(-i/\hbar)^n}{n!} \\ &\quad \times \int_{t_0}^t dt_1 \cdots \int_{t_0}^t dt_n T[V(t_1) \cdots V(t_n)], \end{aligned} \quad (5.97)$$

where $T[\cdots]$ designates the time-ordering or chronological operator.

5.4.2 Gell-Mann and Low Formula

For a time-independent perturbation, one introduces the so-called *adiabatic switching* by writing

$$H_\alpha(t) = H_0 + \lambda e^{-\alpha|t|} V, \quad \alpha > 0, \quad (5.98)$$

so that $H_\alpha(t \rightarrow \pm\infty) = H_0$ and $H_\alpha(t \rightarrow 0) = H = H_0 + \lambda V$. Then

$$|\Psi(t)\rangle_I = U_\alpha(t, -\infty|\lambda)|\Phi_0\rangle, \quad (5.99)$$

with $U_\alpha(t, -\infty|\lambda)$ obtained with $V_\alpha(t) = \lambda e^{-\alpha|t|} V$ (all in the interaction picture). The desired energy is then given by the Gell-Mann and Low formula [94]

$$\Delta E = \lim_{\alpha \rightarrow 0^+} i\hbar \alpha \lambda \frac{\partial}{\partial \lambda} \ln \langle \Phi_0 | U_\alpha(0, -\infty|\lambda) | \Phi_0 \rangle, \quad (5.100a)$$

or

$$\Delta E = \frac{1}{2} \lim_{\alpha \rightarrow 0^+} i\hbar \alpha \lambda \frac{\partial}{\partial \lambda} \ln \langle \Phi_0 | U_\alpha(\infty, -\infty|\lambda) | \Phi_0 \rangle, \quad (5.100b)$$

which result from the asymmetric energy formula Eq. (5.27). One can similarly obtain the perturbation expansion for the one or two-particle Green's functions, e.g.,

$$G_{\mu\nu}(t, t') = \lim_{\alpha \rightarrow 0^+} \frac{\langle T \{ a_\mu(t) a_\nu^\dagger(t') U_\alpha(\infty, -\infty | \lambda) \} \rangle}{\langle U_\alpha(\infty, -\infty | \lambda) \rangle}, \quad (5.101)$$

with the operators in the interaction representation and the expectation values in the noninteracting ground state $|\Phi_0\rangle$. Analogous expressions result for $G(\mathbf{r}t, \mathbf{r}'t')$, etc., when the creation and annihilation operators are replaced by the corresponding field operators.

5.4.3 Potential Scattering and Quantum Dynamics

The Schrödinger equation for a free particle of energy $E = \hbar^2 k^2 / 2m$, moving in the potential $V(\mathbf{r})$,

$$\begin{aligned} (\nabla^2 + k^2)\psi(k, \mathbf{r}) &= v(\mathbf{r})\psi(k, \mathbf{r}), \\ v(\mathbf{r}) &= (2m/\hbar^2)V(\mathbf{r}), \end{aligned} \quad (5.102)$$

has the formal solution

$$\psi(k, \mathbf{r}) = \Phi(k, \mathbf{r}) + \int G_0(k, \mathbf{r}, \mathbf{r}') v(\mathbf{r}') \psi(k, \mathbf{r}') d\mathbf{r}', \quad (5.103)$$

where $\Phi(k, \mathbf{r})$ is a solution of the homogeneous equation [$v(\mathbf{r}) \equiv 0$], and $G_0(k, \mathbf{r}, \mathbf{r}')$ is a classical Green's function

$$(\nabla^2 + k^2)G_0(k, \mathbf{r}, \mathbf{r}') = \delta(\mathbf{r} - \mathbf{r}'). \quad (5.104)$$

For an in-going plane wave $\Phi(k, \mathbf{r}) \equiv \Phi_{\mathbf{k}_i}(\mathbf{r}) = (2\pi)^{3/2} \exp(i\mathbf{k}_i \cdot \mathbf{r})$ with the initial wave vector \mathbf{k}_i and appropriate asymptotic boundary conditions (outgoing spherical wave with positive phase velocity), when $G_0(k, \mathbf{r}, \mathbf{r}') \equiv G_0^{(+)}(|\mathbf{r} - \mathbf{r}'|) = -(4\pi|\mathbf{r} - \mathbf{r}'|)^{-1} e^{ik|\mathbf{r} - \mathbf{r}'|}$, Eq. (5.103) is referred to as the *Lippmann–Schwinger equation* [95]. It can be equivalently transformed into the integral equation for Green's function

$$\begin{aligned} G^{(+)}(\mathbf{r}, \mathbf{r}') &= G_0^{(+)}(\mathbf{r}, \mathbf{r}') + \int G_0^{(+)}(\mathbf{r}, \mathbf{r}'') v(\mathbf{r}'') \\ &\times G^{(+)}(\mathbf{r}'', \mathbf{r}') d\mathbf{r}'', \end{aligned} \quad (5.105)$$

representing a special case of the Dyson equation.

In the time-dependent case, considering the scattering of a spinless massive particle by a time-dependent potential $V(\mathbf{r}, t)$, we get similarly

$$\begin{aligned} \psi(\mathbf{r}, t) &= \Phi(\mathbf{r}, t) \\ &+ \int G_0(\mathbf{r}, \mathbf{r}'; t, t') V(\mathbf{r}', t') \psi(\mathbf{r}', t') d\mathbf{r}' dt', \end{aligned} \quad (5.106)$$

where the zero-order time-dependent Green's function now satisfies the equation

$$\left(i\hbar \frac{\partial}{\partial t} - H_0 \right) G_0(\mathbf{r}, \mathbf{r}'; t, t') = \delta(\mathbf{r} - \mathbf{r}') \delta(t - t'). \quad (5.107)$$

Again, for causal propagation one chooses the *time-retarded* or *causal* Green's function or propagator $G_0^{(+)}(\mathbf{r}, \mathbf{r}'; t, t')$.

5.4.4 Born Series

Iteration of Eq. (5.106) gives the *Born sequence*

$$\begin{aligned} \psi_0(\mathbf{r}, t) &= \Phi(\mathbf{r}, t), \\ \psi_1(\mathbf{r}, t) &= \Phi(\mathbf{r}, t) + \int G_0^{(+)}(\mathbf{r}, \mathbf{r}'; t, t') \\ &\times V(\mathbf{r}', t') \Phi(\mathbf{r}', t') d\mathbf{r}' dt', \end{aligned} \quad (5.108a)$$

$$\begin{aligned} \psi_2(\mathbf{r}, t) &= \Phi(\mathbf{r}, t) + \int G_0^{(+)}(\mathbf{r}, \mathbf{r}'; t, t') \\ &\times V(\mathbf{r}', t') \psi_1(\mathbf{r}', t') d\mathbf{r}' dt', \end{aligned} \quad (5.108b)$$

and, generally

$$\begin{aligned} \psi_n(\mathbf{r}, t) &= \Phi(\mathbf{r}, t) + \int G_0^{(+)}(\mathbf{r}, \mathbf{r}'; t, t') \\ &\times V(\mathbf{r}', t') \psi_{n-1}(\mathbf{r}', t') d\mathbf{r}' dt'. \end{aligned} \quad (5.109)$$

Summing individual contributions gives the *Born series* for $\psi(\mathbf{r}, t) \equiv \psi^{(+)}(\mathbf{r}, t)$,

$$\psi(\mathbf{r}, t) = \sum_{n=0}^{\infty} \chi_n(\mathbf{r}, t), \quad (5.110)$$

where

$$\begin{aligned} \chi_0(\mathbf{r}, t) &= \Phi(\mathbf{r}, t), \\ \chi_n(\mathbf{r}, t) &= \int \mathcal{G}_n(\mathbf{r}, \mathbf{r}'; t, t') \Phi(\mathbf{r}', t') d\mathbf{r}' dt', \end{aligned} \quad (5.111)$$

with

$$\begin{aligned} \mathcal{G}_n(\mathbf{r}, \mathbf{r}'; t, t') &= \int \mathcal{G}_1(\mathbf{r}, \mathbf{r}''; t, t'') \\ &\times \mathcal{G}_{n-1}(\mathbf{r}'', \mathbf{r}'; t'', t') d\mathbf{r}'' dt'', \quad (n > 1) \\ \mathcal{G}_1(\mathbf{r}, \mathbf{r}'; t, t') &= G_0^{(+)}(\mathbf{r}, \mathbf{r}'; t, t') V(\mathbf{r}', t'). \end{aligned} \quad (5.112)$$

In a similar way we obtain the Born series for the scattering amplitudes or transition matrix elements.

5.4.5 Variation of Constants Method

An alternative way of formulating the time-dependent PT is the method of variation of the constants [96, 97]. Start again with the time-dependent Schrödinger equation (5.88) with $H = H_0 + V$ and assume that H_0 is time-independent, while V is a time-dependent perturbation. Designating the eigenvalues and eigenstates of H_0 by ε_i and $|\Phi_i\rangle$, respectively (Eq. (5.48)), the general solution of the unperturbed time-dependent Schrödinger equation

$$i\hbar \frac{\partial}{\partial t} |\Psi_0\rangle = H_0 |\Psi_0\rangle \quad (5.113)$$

has the form

$$|\Psi_0\rangle = \sum_j c_j |\Phi_j\rangle \exp\left(-\frac{i}{\hbar} \varepsilon_j t\right), \quad (5.114)$$

with c_j representing arbitrary constants, and the sum indicating both the summation over the discrete part and the integration over the continuum part of the spectrum of H_0 .

In the spirit of the general variation of constants procedure, write the unknown perturbed wave function $|\Psi(t)\rangle$, Eq. (5.88), in the form

$$|\Psi(t)\rangle = \sum_j C_j(t) |\Phi_j\rangle \exp\left(-\frac{i}{\hbar} \varepsilon_j t\right), \quad (5.115)$$

where the $C_j(t)$ are now functions of time. Substituting this ansatz into the time-dependent Schrödinger equation (5.88) gives

$$\dot{C}_j(t) = (i\hbar)^{-1} \sum_k C_k(t) V_{jk} \exp[(i/\hbar) \Delta_{jk} t], \quad (5.116)$$

where

$$\Delta_{jk} = \varepsilon_j - \varepsilon_k, \quad V_{jk} = \langle \Phi_j | V | \Phi_k \rangle. \quad (5.117)$$

Introducing again the “small” parameter λ by writing the Hamiltonian H in the form

$$H = H_0 + \lambda V(t) \quad (5.118)$$

and expanding the “coefficients” $C_j(t)$ in powers of λ ,

$$C_j \equiv C_j(t) = \sum_{k=0}^{\infty} C_j^{(k)}(t) \lambda^k, \quad (5.119)$$

gives the system of first-order differential equations

$$\begin{aligned} \dot{C}_j^{(n+1)} &= (i\hbar)^{-1} \sum_k C_k^{(n)} V_{jk} \exp[(i/\hbar) \Delta_{jk} t], \\ n &= 0, 1, 2, \dots, \end{aligned} \quad (5.120)$$

with the initial condition $\dot{C}_j^{(0)} = 0$, which implies that $C_j^{(0)}$ are time independent, so that $C_j^{(0)} = c_j$, obtaining Eq. (5.114) in the zeroth order. The system Eq. (5.120) can be integrated to any prescribed order. For example, if the system is initially in a stationary state $|\Phi_i\rangle$, then set

$$C_j^{(0)} = \begin{cases} \delta_{ji} & \text{for discrete states,} \\ \delta(j-i) & \text{for continuous states,} \end{cases} \quad (5.121)$$

so that

$$C_{j(i)}^{(1)}(t) = (i\hbar)^{-1} \int_{-\infty}^t V_{ji} \exp[(i/\hbar) \Delta_{ji} t'] dt', \quad (5.122)$$

assuming $C_{j(i)}^{(1)}(-\infty) = 0$. Clearly, $|C_{j(i)}^{(1)}(t)|^2$ gives the first-order transition probability for the transition from the initial state $|\Phi_i\rangle$ to a particular state $|\Phi_j\rangle$. These in turn will yield the first-order differential cross sections [98].

References

1. Kato, T.: Perturbation Theory for Linear Operators. Springer, Berlin, Heidelberg (1966)
2. Baumgärtel, H.: Analytic Perturbation Theory for Matrices and Operators. Akademie, Berlin (1984)
3. Hinch, E.J.: Perturbation Methods. Cambridge Univ. Press, Cambridge (1991)
4. Bogaevski, V.N., Povzner, A.: Algebraic Methods in Nonlinear Perturbation Theory. Springer, Berlin, Heidelberg (1991)
5. Bender, C.M., Orszag, S.A.: Advanced Mathematical Methods for Scientists and Engineers: Asymptotic Methods and Perturbation Theory. Springer, New York (1999)
6. Corson, E.M.: Perturbation Methods in the Quantum Mechanics of n-Electron Systems. Blackie & Son, London (1951)
7. Lindgren, I., Morrison, J.: Atomic Many-Body Theory. Springer, Berlin, Heidelberg (1982)
8. Gross, E.K.U., Runge, E., Heinonen, O.: Many-Particle Theory. Hilger, New York (1991)
9. Harris, F.E., Monkhorst, H.J., Freeman, D.L.: Algebraic and Diagrammatic Methods in Many-Fermion Theory. Oxford Univ. Press, Oxford (1992)
10. Shavitt, I., Bartlett, R.J.: Many-Body Methods in Chemistry and Physics: MBPT and Coupled Cluster Theory. Cambridge Univ. Press, Cambridge (2009)
11. Primas, H.: Helv. Phys. Acta **34**, 331 (1961)
12. Primas, H.: Rev. Mod. Phys. **35**, 710 (1963)
13. Rosenblum, M.: Duke Math. J. **23**, 263 (1956)
14. Arfken, G.: Mathematical Methods for Physicists. Academic Press, New York, p. 327 (1985)
15. Iyanaga, S., Kawada, Y. (eds.): Encyclopedic Dictionary of Mathematics. MIT Press, Cambridge, p. 1494 (1980). Appendix B, Table 3
16. Paldus, J., Čížek, J.: Adv. Quantum Chem. **9**, 105 (1975)
17. Paldus, J.: In: Wilson, S., Diercksen, G.H.F. (eds.) Methods in Computational Molecular Physics. NATO ASI Series B, vol. 293, pp. 99–194. Plenum, New York (1992)
18. Paldus, J.: Chap. 19. In: Wilson, S. (ed.): Handbook of Molecular Physics and Quantum Chemistry, vol. 2, pp. 272–313. Wiley, Chichester (2003)

19. Silverstone, H.J., Holloway, T.T.: *J. Chem. Phys.* **52**, 1472 (1970)
20. Møller, C., Plesset, M.S.: *Phys. Rev.* **46**, 618 (1934)
21. Epstein, P.S.: *Phys. Rev.* **28**, 695 (1926)
22. Nesbet, R.K.: *Proc. R. Soc. Lond. A* **250**, 312 (1955)
23. Goldstone, J.: *Proc. R. Soc. Lond. A* **239**, 267 (1957)
24. Hugenholtz, H.M.: *Physica (Utrecht)* **23**, 481 (1957)
25. Brueckner, K.A.: *Phys. Rev.* **100**, 36 (1955)
26. Hubbard, J.: *Proc. R. Soc. Lond. A* **240**, 539 (1957)
27. Frantz, L.M., Mills, R.L.: *Nucl. Phys.* **15**, 16 (1960)
28. Coester, F.: *Nucl. Phys.* **7**, 421 (1958)
29. Coester, F., Kümmel, H.: *Nucl. Phys.* **17**, 477 (1960)
30. Čížek, J.: *J. Chem. Phys.* **45**, 4256 (1966)
31. Čížek, J.: *Adv. Chem. Phys.* **14**, 35 (1969)
32. Čížek, J., Paldus, J.: *Int. J. Quantum Chem.* **5**, 359 (1971)
33. Paldus, J., Čížek, J., Shavitt, I.: *Phys. Rev. A* **5**, 50 (1972)
34. Bartlett, R.J.: Part I. In: Yarkony, D.R. (ed.) *Modern Electronic Structure Theory*, pp. 47–108. World Scientific, Singapore (1995)
35. Bartlett, R.J. (ed.): *Recent Advances in Coupled-Cluster Methods. Recent Advances in Computational Chemistry*, vol. 3. World Scientific, Singapore (1997)
36. Paldus, J., Li, X.: *Adv. Chem. Phys.* **110**, 1 (1999)
37. Crawford, T.D., Schaefer III, H.F.: In: Lipkowitz, K.B., Boyd, D.B. (eds.) *Reviews of Computational Chemistry*, vol. 14, pp. 33–136. Wiley, New York (2000)
38. Bartlett, R.J., Musiał, M.: *Rev. Mod. Phys.* **79**, 291 (2007)
39. Čárský, P., Paldus, J., Pittner, J. (eds.): *Recent Progress in Coupled Cluster Methods: Theory and Applications. Challenges and Advances in Computational Chemistry and Physics*, vol. 11. Springer, Berlin (2010)
40. Bartlett, R.J.: *Mol. Phys.* **108**, 2905 (2010)
41. Bartlett, R.J.: *Wiley Interdiscip. Rev. Comput. Mol. Sci.* **2**, 126–138 (2012)
42. Paldus, J.: Chap. 7. In: Dykstra, C.E., Frenking, G., Kim, K.S., Scuseria, G.E. (eds.) *Theory and Applications of Computational Chemistry: The First Forty Years*, pp. 115–147. Elsevier, Amsterdam (2005)
43. Bartlett, R.J.: Chap. 42. In: Dykstra, C.E., Frenking, G., Kim, K.S., Scuseria, G.E. (eds.) *Theory and Applications of Computational Chemistry: The First Forty Years*, pp. 1191–1221. Elsevier, Amsterdam (2005)
44. Paldus, J.: *J. Math. Chem.* **55**, 477 (2017)
45. Bartlett, R.J., Purvis, G.D.: *Int. J. Quantum Chem.* **14**, 561 (1978)
46. Raghavachari, K., Trucks, G.W., Pople, J.A., Head-Gordon, M.: *Chem. Phys. Lett.* **157**, 479 (1989)
47. Lee, T.J., Scuseria, G.E.: In: Langhoff, S.R. (ed.) *Quantum Mechanical Electronic Structure Calculations with Chemical Accuracy*, pp. 47–108. Kluwer, Dordrecht (1995)
48. Kowalski, K., Piecuch, P.: *J. Chem. Phys.* **120**, 1715 (2004)
49. Paldus, J., Čížek, J., Saute, M., Laforge, A.: *Phys. Rev. A* **17**, 805 (1978)
50. Li, X., Paldus, J.: *J. Chem. Phys.* **101**, 8812 (1994)
51. Jeziorski, B., Paldus, J., Jankowski, P.: *Int. J. Quantum Chem.* **56**, 129 (1995)
52. Paldus, J.: In: Malli, G.L. (ed.) *Relativistic and Electron Correlation Effects in Molecules and Solids. NATO ASI Series B: Physics*, vol. 318, pp. 207–282. Plenum, New York (1994)
53. Lindgren, I., Mukherjee, D.: *Phys. Rep.* **151**, 93 (1987)
54. Jeziorski, B., Monkhorst, H.J.: *Phys. Rev. A* **24**, 1686 (1981)
55. Paldus, J., Čárský, P., Pittner, J.: Chap. 17. In: Čárský, P., Paldus, J., Pittner, J. (eds.) *Recent Progress in Coupled-Cluster Methods: Theory and Applications*, pp. 455–489. Springer, Berlin (2010)
56. Li, X., Paldus, J.: *J. Chem. Phys.* **119**, 5320 (2003)
57. Li, X., Paldus, J.: *J. Chem. Phys.* **119**, 5334 (2003)
58. Li, X., Paldus, J.: *J. Chem. Phys.* **119**, 5343 (2003)
59. Li, X., Paldus, J.: *J. Chem. Phys.* **120**, 5890 (2004)
60. Margoulas, I., Gururangan, K., Piecuch, P., Deustua, J.E., Shen, J.: *J. Chem. Theory Comput.* **17**, 4006 (2021)
61. Margoulas, I., Shen, J., Piecuch, P.: *Addressing Strong Correlation by Approximate Coupled-Pair Methods with Active-Space Full Treatment of Three-Body Clusters*, arXiv:2111.13787v1 [physics.chem-ph] (2021)
62. Chattopadhyay, S., Pahari, D., Mukherjee, D., Mahapatra, U.S.: *J. Chem. Phys.* **120**, 5968 (2004)
63. Li, X., Paldus, J.: *J. Chem. Phys.* **107**, 6257 (1997)
64. Li, X., Paldus, J.: *J. Chem. Phys.* **108**, 637 (1998)
65. Li, X., Paldus, J.: *J. Chem. Phys.* **129**, 054104 (2004)
66. Paldus, J.: *J. Math. Chem.* **59**, 1 (2021)
67. Paldus, J.: *J. Math. Chem.* **59**, 37 (2021)
68. Paldus, J.: *J. Math. Chem.* **59**, 72 (2021)
69. Dobroutz, W., Smart, S.D., Alavi, A.: *J. Chem. Phys.* **151**, 94104 (2019)
70. Dobroutz, W.: *Development of Full Configuration Interaction Quantum Monte Carlo Methods for Strongly Correlated Electron Systems*. PhD Thesis, University of Stuttgart (2019)
71. Li Manni, G., Guther, K., Ma, D., Dobroutz, W.: In: González, L., Lindh, R. (eds.) *Quantum Chemistry and Dynamics of Excited States: Methods and Applications*, Chap. 6, pp. 133–204. Wiley, New York (2021)
72. Deustua, J.E., Magoulas, I., Shen, J., Piecuch, P.: *J. Chem. Phys.* **149**, 151101 (2018)
73. Deustua, J.E., Shen, J., Piecuch, P.: *J. Chem. Phys.* **154**, 124103 (2021)
74. Gururangan, K., Deustua, J.E., Shen, J., Piecuch, P.: *J. Chem. Phys.* **155**, 174114 (2021)
75. Lee, S., Zhai, H., Sharma, S., Umrigar, C.J., Chan, G.K.-L.: *J. Chem. Theory Comput.* **17**, 3414 (2021)
76. Chan, G.K.-L., Head-Gordon, M.: *J. Chem. Phys.* **116**, 4462 (2001)
77. Chan, G.K.-L.: *J. Chem. Phys.* **120**, 3172 (2003)
78. Olivares-Amaya, R., Hu, W., Nakatani, N., Sharma, S., Yang, J., Chan, G.K.-L.: *J. Chem. Phys.* **142**, 034102 (2015)
79. Kats, D., Manby, F.R.: *J. Chem. Phys.* **139**, 021102 (2013)
80. Kats, D.: *J. Chem. Phys.* **141**, 061101 (2014)
81. Kats, D.: *J. Chem. Phys.* **144**, 044102 (2016)
82. Kats, D., Kreplin, D., Werner, H.-J., Manby, F.R.: *J. Chem. Phys.* **142**, 064111 (2015)
83. Kats, D., Köhn, A.: *J. Chem. Phys.* **150**, 151101 (2019)
84. Vitale, E., Alavi, A., Kats, D.: *J. Chem. Theory Comput.* **16**(9), 5621 (2020)
85. Schraivogel, T., Kats, D.: *J. Chem. Phys.* **155**, 064101 (2021)
86. Schraivogel, T., Cohen, A.J., Alavi, A., Kats, D.: *J. Chem. Phys.* **155**, 191101 (2021)
87. Thom, A.J.W.: *Phys. Rev. Lett.* **105**, 263004 (2010)
88. Deustua, J.E., Shen, J., Piecuch, P.: *Phys. Rev. Lett.* **119**, 223003 (2017)
89. Deustua, J.E., Yuwono, S.H., Shen, J., Piecuch, P.: *J. Chem. Phys.* **150**, 111101 (2019)
90. Christiansen, O.: *J. Chem. Phys.* **120**, 2149 (2004)
91. Dyson, F.J.: *Phys. Rev.* **75**, 486 (1949)
92. Tomonaga, S.: *Prog. Theor. Phys. (Kyoto)* **1**, 27 (1946)
93. Schwinger, J.: *Phys. Rev.* **74**, 1439 (1948)
94. Gell-Mann, M., Low, F.: *Phys. Rev.* **84**, 350 (1951)
95. Lippmann, B.A., Schwinger, J.: *Phys. Rev.* **79**, 469 (1950)
96. Dirac, P.A.M.: *Proc. R. Soc. Lond. A* **112**, 661 (1926)
97. Dirac, P.A.M.: *Proc. R. Soc. Lond. A* **114**, 243 (1926)
98. Joachain, C.J.: *Quantum Collision Theory*. Elsevier, New York (1975)



Josef Paldus Josef Paldus is Distinguished Professor Emeritus at the Department of Applied Mathematics of the University of Waterloo, Canada. He received his PhD from the Czechoslovak Academy of Sciences and his RNDr and DrSc from the Faculty of Mathematics and Physics of Charles University, Prague, Czech Republic.

His research interests are the methodology of quantum chemistry and the electronic structure of molecular systems. He has published over 340 papers, reviews, and chapters.



Second Quantization

6

Brian R. Judd

Contents

6.1	Basic Properties	111
6.1.1	Definitions	111
6.1.2	Representation of States	112
6.1.3	Representation of Operators	112
6.2	Tensors	112
6.2.1	Construction	112
6.2.2	Coupled Forms	112
6.2.3	Coefficients of Fractional Parentage	113
6.3	Quasispin	113
6.3.1	Fermions	113
6.3.2	Bosons	113
6.3.3	Triple Tensors	114
6.3.4	Conjugation	114
6.3.5	Dependence on Electron Number	114
6.3.6	The Half-Filled Shell	115
6.4	Complementarity	115
6.4.1	Spin–Quasispin Interchange	115
6.4.2	Matrix Elements	115
6.5	Quasiparticles	116
	References	116

Abstract

In second quantization, the characteristic properties of eigenfunctions are transferred to operators. This approach has the advantage of treating the atomic shell as the basic unit, as opposed to the electron configuration. The creation and annihilation operators allow one to move from configuration to configuration, exposing an intrinsic shell structure. The introduction of coefficients of fractional parentage (cfp) then allows the calculation of the matrix elements of an operator in one configuration to be expressed in terms of those of the same operator in another configuration; hence the matrix elements of an operator

in all configurations may be determined from the knowledge of its matrix elements in but one. This can be viewed as an extension of the usual Wigner-Eckart theorem. The basic concepts of quasispin and quasiparticle are also introduced within this context.

Keywords

second quantization · intrinsic shell structure · coefficients of fractional parentage · Wigner–Eckart theorem · quasispin

6.1 Basic Properties

6.1.1 Definitions

The creation operator a_{ξ}^{\dagger} creates the quantum state ξ . The annihilation (or destruction) operator a_{η} annihilates the quantum state η . The vacuum (or reference) state $|0\rangle$ satisfies the equation

$$a_{\eta}|0\rangle = 0. \quad (6.1)$$

Bosons satisfy the commutation relations

$$[a_{\xi}^{\dagger}, a_{\eta}^{\dagger}] = 0, \quad (6.2)$$

$$[a_{\xi}, a_{\eta}] = 0, \quad (6.3)$$

$$[a_{\xi}, a_{\eta}^{\dagger}] = \delta(\xi, \eta), \quad (6.4)$$

where $[A, B] \equiv AB - BA$. Fermions satisfy the anticommutation relations

$$[a_{\xi}^{\dagger}, a_{\eta}^{\dagger}]_{+} = 0, \quad (6.5)$$

$$[a_{\xi}, a_{\eta}]_{+} = 0, \quad (6.6)$$

$$[a_{\xi}, a_{\eta}^{\dagger}]_{+} = \delta(\xi, \eta), \quad (6.7)$$

where $[A, B]_{+} \equiv AB + BA$.

B. R. Judd (✉)
Dept. of Physics & Astronomy, The Johns Hopkins University
Baltimore, MD, USA
e-mail: juddbr@pha.jhu.edu

6.1.2 Representation of States

For an electron in an atom, characterized by the quantum number quartet $(n \ell m_s m_\ell)$, the identification $\xi \equiv (n \ell m_s m_\ell)$ for fermions is made. For normalized Slater determinants $\{\alpha\beta \dots v\}$ characterized by the electron states α, β, \dots, v , the equivalences

$$a_\alpha^\dagger a_\beta^\dagger \dots a_v^\dagger |0\rangle \equiv \{\alpha\beta \dots v\}, \quad (6.8)$$

$$\langle 0|a_v \dots a_\beta a_\alpha \equiv \{\alpha\beta \dots v\}^* \quad (6.9)$$

are valid, where the asterisk denotes the complex conjugate.

For a normalized boson state $\{\dots\}$ in which the label ξ appears N_ξ times, the additional factor

$$[N_\alpha! N_\beta! \dots N_v!]^{-\frac{1}{2}} \quad (6.10)$$

must be included on the left-hand sides of the equivalences Eqs. (6.8) and (6.9).

6.1.3 Representation of Operators

For an operator F , consisting of the sum of operators f_i acting on the single electron i ,

$$F \equiv \sum_{\xi, \eta} a_\xi^\dagger \langle \xi | f | \eta \rangle a_\eta. \quad (6.11)$$

For an operator G , consisting of the sum of operators g_{ij} acting on the pair of electrons i and j ,

$$G \equiv \frac{1}{2} \sum_{\xi, \eta, \zeta, \lambda} a_\xi^\dagger a_\eta^\dagger \langle \xi_1 \eta_2 | g_{12} | \zeta_1 \lambda_2 \rangle a_\lambda a_\zeta. \quad (6.12)$$

For an N -particle system $|\Psi\rangle$,

$$\sum_{\xi} a_\xi^\dagger a_\xi |\Psi\rangle = N |\Psi\rangle. \quad (6.13)$$

The representations of single-particle and two-particle operators for bosons are identical to those given above for fermions [1].

6.2 Tensors

6.2.1 Construction

If the description ξ for a single fermion or boson state includes an angular momentum quantum number t and the corresponding magnetic quantum number m_t , then the $2t + 1$ components of a creation operator a_σ^\dagger , where $\sigma \equiv (t, m_t)$ and

$-t \leq m_t \leq t$, satisfy the commutation relations of *Racah* [2] for an irreducible spherical tensor of rank t with respect to the total angular momentum \mathbf{T} , given by

$$\mathbf{T} = \sum_{\xi} a_\xi^\dagger \langle \xi | \mathbf{T} | \eta \rangle a_\eta. \quad (6.14)$$

That is, with the phase conventions of *Condon and Shortley* [3],

$$[T_z, a_\sigma^\dagger] = m_t a_\sigma^\dagger, \quad (6.15)$$

$$[T_x \pm iT_y, a_\sigma^\dagger] = [t(t+1) - m_t(m_t \pm 1)]^{\frac{1}{2}} a_\tau^\dagger, \quad (6.16)$$

where $\tau \equiv (t, m_t \pm 1)$.

A spherical tensor \mathbf{a} constructed from annihilation operators possesses the components \tilde{a}_σ , which satisfy

$$\tilde{a}_\sigma = (-1)^p a_\zeta, \quad (6.17)$$

with $p = t - m_t$ and $\zeta \equiv (t, -m_t)$.

The $4\ell + 2$ components of the creation operator for an electron in the atomic ℓ shell form a double tensor of rank $\frac{1}{2}$ with respect to the total spin \mathbf{S} , and rank ℓ with respect to the total angular momentum \mathbf{L} .

6.2.2 Coupled Forms

Tensors formed from annihilation and creation operators can be coupled by means of the usual rules of angular momentum theory [4]. The double tensor defined for electrons in the ℓ shell by

$$\mathbf{W}^{(\kappa k)} = -(\mathbf{a}^\dagger \mathbf{a})^{(\kappa k)}, \quad (6.18)$$

possesses a rank κ with respect to \mathbf{S} , and rank k with respect to \mathbf{L} . Its reduced matrix element, defined here as in (5.4.1) of *Edmonds* [4], for a single electron in both the spin and orbital spaces, is given by

$$(s \ell || \mathbf{W}^{(\kappa k)} || s \ell) = [(2\kappa + 1)(2k + 1)]^{\frac{1}{2}}. \quad (6.19)$$

The connections to tensors whose matrix elements have been tabulated [5, 6] are

$$\mathbf{W}^{(0k)} = [(2k + 1)/2]^{\frac{1}{2}} \mathbf{U}^{(k)}, \quad (6.20)$$

$$\mathbf{W}^{(1k)} = [2(2k + 1)]^{\frac{1}{2}} \mathbf{V}^{(k1)}. \quad (6.21)$$

For terms with common spin S , say ψ and ψ' ,

$$\begin{aligned} & (\psi || \mathbf{W}^{(0k)} || \psi') \\ &= [(2S + 1)(2k + 1)/2]^{\frac{1}{2}} (\psi || \mathbf{U}^{(k)} || \psi'). \end{aligned} \quad (6.22)$$

This result is obtained because the ranks assigned to the tensors imply that $\mathbf{W}^{(0k)}$ is to be reduced with respect to both

the spin \mathbf{S} and the orbit \mathbf{L} , while $U^{(k)}$ is to be reduced only with respect to \mathbf{L} .

The following relations hold for electrons with azimuthal quantum numbers ℓ [7]:

$$\mathbf{S} = [(2\ell + 1)/2]^{\frac{1}{2}} \mathbf{W}^{(10)}, \quad (6.23)$$

$$\mathbf{L} = [2\ell(\ell + 1)(2\ell + 1)/3]^{\frac{1}{2}} \mathbf{W}^{(01)}, \quad (6.24)$$

$$\sum_i (s_i \mathbf{C}_i^{(2)})^{(1)} = - \left(\frac{\ell(\ell + 1)(2\ell + 1)}{10(2\ell - 1)(2\ell + 3)} \right)^{\frac{1}{2}} \mathbf{W}^{(12)1}, \quad (6.25)$$

$$\sum_i (s_i \cdot \ell_i) = -[\ell(\ell + 1)(2\ell + 1)/2] \mathbf{W}^{(11)0}, \quad (6.26)$$

where the tensor \mathbf{C}^k of Racah [2] is related to the spherical harmonics by

$$\mathbf{C}_q^{(k)} = [4\pi/(2k + 1)]^{\frac{1}{2}} Y_{kq}, \quad (6.27)$$

and where the tensors of the type $\mathbf{W}^{(\kappa k)K}$ indicate that the spin and orbital ranks are coupled to a resultant K .

6.2.3 Coefficients of Fractional Parentage

Let ψ and $\bar{\psi}$ denote terms of ℓ^N and ℓ^{N-1} characterized by (S, L) and (\bar{S}, \bar{L}) . The coefficients of fractional parentage (cfp) $(\psi \{ \bar{\psi})$ of Racah [8] allow one to calculate an antisymmetrized function ψ by vector-coupling $\bar{\psi}$ to the spin and orbit of the N th electron:

$$|\psi\rangle = \sum_{\bar{\psi}} |\bar{\psi}, {}^2\ell, SL\rangle (\bar{\psi} \{ \psi), \quad (6.28)$$

where the sum over $\bar{\psi}$ includes \bar{S}, \bar{L} , and any other quantum numbers necessary to define the spectroscopic terms of ℓ^{N-1} . The cfp's are given by

$$(\psi || a^\dagger || \bar{\psi}) = (-1)^N [N(2S + 1)(2L + 1)]^{\frac{1}{2}} (\psi \{ \bar{\psi}), \quad (6.29)$$

$$(\bar{\psi} || a || \psi) = (-1)^g [N(2S + 1)(2L + 1)]^{\frac{1}{2}} (\bar{\psi} \{ \psi), \quad (6.30)$$

where $g = N + \bar{S} + \bar{L} - s - S - \ell - L$. A tabulation for the p, d, and f shells has been given by Nielson and Koster [5].

Two-electron cfp are given by

$$(\psi || (a^\dagger a^\dagger)^{(\kappa k)} || \bar{\psi}) = [N(N - 1)(2S + 1)(2L + 1)]^{\frac{1}{2}} \times (\psi \{ \bar{\psi}, \ell^2(\kappa k)), \quad (6.31)$$

where $\bar{\psi}$ denotes a term of ℓ^{N-2} , and the symbols κ and k stand for the S and the L of a term of ℓ^2 . A tabulation for the p, d, and f shells has been given by Donlan [9]. An extension to all multielectron cfp has been carried out by Velkov [10].

If, through successive applications of the two-particle operators $(\mathbf{a}\mathbf{a})^{(00)}$, a state of ℓ^N can be reduced to ℓ^v , but no further, then v is the seniority number of Racah [8].

If the ranks s and ℓ of \mathbf{a}^\dagger are coupled to \bar{S} and \bar{L} of $\bar{\psi}$, the term

$$(\mathbf{a}^\dagger | \bar{\psi})^{(SL)} \quad (6.32)$$

either vanishes, or is a term of ℓ^N characterized by S and L . Such a term is said to possess the godparent $\bar{\psi}$. Redmond [11] has used the notion of godparents to generate an explicit formula for the single particle cfp [7].

6.3 Quasispin

6.3.1 Fermions

For electrons, the components $Q_\pm (\equiv Q_x \pm iQ_y)$ and Q_z of the quasispin \mathbf{Q} are defined by [7, 12]

$$Q_+ = [(2\ell + 1)/2]^{\frac{1}{2}} (\mathbf{a}^\dagger \mathbf{a}^\dagger)^{(00)}, \quad (6.33)$$

$$Q_- = -[(2\ell + 1)/2]^{\frac{1}{2}} (\mathbf{a}\mathbf{a})^{(00)}, \quad (6.34)$$

$$Q_z = -[(2\ell + 1)/8]^{\frac{1}{2}} [(\mathbf{a}^\dagger \mathbf{a})^{(00)} + (\mathbf{a}\mathbf{a}^\dagger)^{(00)}]. \quad (6.35)$$

The term quasispin comes from the fact that the components of \mathbf{Q} satisfy the commutation relations of an angular momentum vector. The eigenvalues M_Q of Q_z , for a state of ℓ^N , are given by

$$M_Q = -(2\ell + 1 - N)/2. \quad (6.36)$$

The shift operators Q_+ and Q_- connect states of the ℓ shell possessing the same value of the seniority v of Racah [8]. A string of such connected states defines the extrema of M_Q , from which it follows that

$$Q = (2\ell + 1 - v)/2. \quad (6.37)$$

Rudzikas has placed special emphasis on quasispin in his reworking of atomic shell theory, and he has also introduced isospin to embrace electrons differing in their principal quantum numbers n [13]. Concise tables of one-electron cfp with their quasispin dependence factored out have been given [14], as have the algebraic dependences on v and S of two-electron cfp [15].

6.3.2 Bosons

For real vibrational modes created by $a_v^\dagger (v = 1, 2, \dots, d)$, the analogs of Eqs. (6.33)–(6.35) are

$$P_+ = -\frac{1}{2} \sum_v a_v^\dagger a_v^\dagger, \quad (6.38)$$

$$P_- = \frac{1}{2} \sum_v a_v a_v, \quad (6.39)$$

$$P_z = \frac{1}{4} \sum_v (a_v^\dagger a_v + a_v a_v^\dagger), \quad (6.40)$$

and \mathbf{P} is an angular momentum vector [16]. The eigenvalues M_P for an n -boson state are given by

$$M_P = (2n + d)/4, \quad (6.41)$$

and can therefore be quarter-integral. Successive application of the operator P_+ to a state $|n_0\rangle$, for which $P_-|n_0\rangle = 0$, generates an infinite ladder of states characterized by

$$P = (2n + d - 4)/4. \quad (6.42)$$

6.3.3 Triple Tensors

The creation and annihilation operators a_ξ^\dagger and a_ξ for a given state ξ can be regarded as the two components of a tensor of rank $\frac{1}{2}$ with respect to quasispin (either \mathbf{Q} or \mathbf{P}). For electrons, this leads to triple tensors $\mathbf{a}^{(qs\ell)}$ (for which $q = s = \frac{1}{2}$) satisfying

$$\begin{aligned} a_\lambda^{(qs\ell)} a_\mu^{(qs\ell)} + a_\mu^{(qs\ell)} a_\lambda^{(qs\ell)} \\ = (-1)^{x+1} \delta(m_q, -m'_q) \delta(m_s, -m'_s) \delta(m_\ell, -m'_\ell), \end{aligned} \quad (6.43)$$

where $\lambda \equiv (m_q m_s m_\ell)$, $\mu \equiv (m'_q m'_s m'_\ell)$, and $x = q + s + \ell + m_q + m_s + m_\ell$. In terms of the coupled tensor

$$\mathbf{X}^{(K\kappa k)} = (\mathbf{a}^{(qs\ell)} \mathbf{a}^{(qs\ell)})^{(K\kappa k)}, \quad (6.44)$$

the angular momenta \mathbf{Q} , \mathbf{S} , and \mathbf{L} are given by

$$\mathbf{Q} = -[(2\ell + 1)/4]^{\frac{1}{2}} \mathbf{X}^{(100)}, \quad (6.45)$$

$$\mathbf{S} = -[(2\ell + 1)/4]^{\frac{1}{2}} \mathbf{X}^{(010)}, \quad (6.46)$$

$$\mathbf{L} = -[\ell(\ell + 1)(2\ell + 1)/3]^{\frac{1}{2}} \mathbf{X}^{(001)}. \quad (6.47)$$

Furthermore, the components of $\mathbf{X}^{(K\kappa k)}$ for which $M_K = 0$ are identical to the corresponding components of $2^{\frac{1}{2}} (\mathbf{a}^\dagger \mathbf{a})^{(\kappa k)}$ when $K + \kappa + k$ is odd; and

$$\mathbf{X}^{(K\kappa k)} = -(2\ell + 1)^{\frac{1}{2}} \delta(K, 0) \delta(\kappa, 0) \delta(k, 0) \quad (6.48)$$

when $K + \kappa + k$ is even.

6.3.4 Conjugation

Creation and annihilation operators can be interchanged by the operation of the conjugation operator C [7, 17]. For electrons in the atomic ℓ shell,

$$C a_\xi^{(qs\ell)} C^{-1} = (-1)^{q-m_q} a_\eta^{(qs\ell)}, \quad (6.49)$$

where $\xi \equiv (m_q m_s m_\ell)$ and $\eta \equiv ((-m_q) m_s m_\ell)$. In terms of the tensors \mathbf{a}^\dagger and \mathbf{a} ,

$$C \mathbf{a}^\dagger C^{-1} = \mathbf{a}, \quad C \mathbf{a} C^{-1} = -\mathbf{a}^\dagger. \quad (6.50)$$

Furthermore,

$$C X_\lambda^{(K\kappa k)} C^{-1} = (-1)^{K-M_K} X_\mu^{(K\kappa k)}, \quad (6.51)$$

where $\lambda \equiv (M_K M_\kappa M_k)$ and $\mu \equiv [(-M_K) M_\kappa M_k]$, and

$$C |QM_Q\rangle = (-1)^{Q-M_Q} |Q - M_Q\rangle. \quad (6.52)$$

Thus, from Eq. (6.36), the action of C takes N into $4\ell + 2 - N$; that is, C interchanges electrons and holes. When the case $\kappa = k = 0$ is excluded, application of Eqs. (6.51) and (6.52) yields

$$\begin{aligned} (\ell^N \psi || W^{(\kappa k)} || \ell^N \psi') \\ = (-1)^y (\ell^{4\ell+2-N} \psi || W^{(\kappa k)} || \ell^{4\ell+2-N} \psi'), \end{aligned} \quad (6.53)$$

where $y = \kappa + k + \frac{1}{2}(v' - v) + 1$, and where the seniorities v and v' are implied by ψ and ψ' . A similar application to reduced matrix elements of \mathbf{a}^\dagger and \mathbf{a} gives the following relation between cfp:

$$\begin{aligned} (\ell^{N+1} \psi \{ | \ell^N \psi') \\ = (-1)^z (\ell^{4\ell+1-N} \psi \{ | \ell^{4\ell+2-N} \psi') \\ \times \left(\frac{(4\ell + 2 - N)(2S' + 1)(2L' + 1)}{(N + 1)(2S + 1)(2L + 1)} \right)^{\frac{1}{2}}, \end{aligned} \quad (6.54)$$

where $z = S + S' - s + L + L' - \ell + \frac{1}{2}(v + v' - 1)$. The phases y and z stem from the conventions of angular momentum theory, which enter via quasispin. *Racah* [2, 8] did not use this concept, and his phase choices are slightly different from the ones above.

For a Cartesian component Q_u of the quasispin \mathbf{Q} ,

$$C Q_u C^{-1} = -Q_u. \quad (6.55)$$

Thus, C is the analog of the time-reversal operator T , for which

$$T L_u T^{-1} = -L_u, \quad (6.56)$$

$$T S_u T^{-1} = -S_u. \quad (6.57)$$

Both C and T are antiunitary; thus,

$$C i C^{-1} = -i. \quad (6.58)$$

6.3.5 Dependence on Electron Number

Application of the Wigner–Eckart theorem to matrix elements whose component parts have well-defined quasispin

ranks yields the dependence of the matrix elements on the electron number N [18, 19]. For $\kappa + k$ even and nonzero, the quasispin rank of $W^{(\kappa k)}$ is 1, and

$$\begin{aligned} & (\ell^N \psi || W^{(\kappa k)} || \ell^N \psi') \\ &= \frac{(2\ell + 1 - N)}{(2\ell + 1 - v)} (\ell^v \psi || W^{(\kappa k)} || \ell^v \psi'). \end{aligned} \quad (6.59)$$

For $\kappa + k$ odd, $W^{(\kappa k)}$ is necessarily a quasispin scalar, and the matrix elements are diagonal with respect to the seniority and independent of N . These properties were first stated in Eqs. (69) and (70) of [8].

Application of these ideas to single-electron cfp yields, for states ψ and $\bar{\psi}$ with seniorities v and $v + 1$, respectively,

$$\begin{aligned} & (\ell^N \psi || \ell^{N-1} \bar{\psi}) \\ &= [(N - v)(v + 2)/2N]^{\frac{1}{2}} (\ell^{v+2} \psi || \ell^{v+1} \bar{\psi}). \end{aligned} \quad (6.60)$$

6.3.6 The Half-Filled Shell

Selection rules for operators of good quasispin rank K , taken between states of the half-filled shell (for which $M_Q = 0$), can be found by inspecting the $3-j$ symbol

$$\begin{pmatrix} Q & K & Q' \\ 0 & 0 & 0 \end{pmatrix},$$

which appears when the Wigner-Eckart theorem is applied in quasispin space. This $3-j$ symbol vanishes unless $Q + K + Q'$ is even. An equivalent result can be obtained for $W^{(\kappa k)}$ by referring to Eq. (6.53) and insisting that y be even.

6.4 Complementarity

6.4.1 Spin-Quasispin Interchange

The operator R formally interchanges spin and quasispin. The result for the creation and annihilation operators for electrons can be expressed in terms of triple tensors:

$$Ra_{\xi}^{(qs\ell)} R^{-1} = a_{\eta}^{(qs\ell)}, \quad (6.61)$$

where $\xi \equiv (m_q m_s m_\ell)$ and $\eta \equiv (m_s m_q m_\ell)$. For the tensors $X^{(K\kappa k)}$ defined in Eq. (6.44), we get

$$RX_{\lambda}^{(K\kappa k)} R^{-1} = X_{\mu}^{(\kappa K k)}, \quad (6.62)$$

where $\lambda \equiv (M_K M_{\kappa} M_k)$ and $\mu \equiv (M_{\kappa} M_K M_k)$. For states of the ℓ shell,

$$R|\gamma Q M_Q S M_S\rangle = (-1)^t |\gamma S M_S Q M_Q\rangle, \quad (6.63)$$

where the quasispin of the ket on the right is S and the spin is Q . The phase factor t depends on S and Q and on phase choices made for the coefficients of fractional parentage. The symbol γ denotes the additional labels necessary to completely define the state in question, including L and M_L .

For every γ , Racah [20] observed that there are two possible pairs (v_1, S_1) and (v_2, S_2) satisfying

$$v_1 + 2S_2 = v_2 + 2S_1 = 2\ell + 1. \quad (6.64)$$

From Eq. (6.37) it follows that

$$S_1 = Q_2, \quad S_2 = Q_1. \quad (6.65)$$

6.4.2 Matrix Elements

Application of the complementarity operator R to the component parts of a matrix element leads to the equation

$$\begin{aligned} & \langle \gamma Q M_Q S M_S | X_{\lambda}^{(K\kappa k)} | \gamma' Q' M'_Q S' M'_S \rangle \\ &= (-1)^y \langle \gamma S M_S Q M_Q | X_{\mu}^{(\kappa K k)} | \gamma' S' M'_S Q' M'_Q \rangle, \end{aligned} \quad (6.66)$$

where λ and μ have the same significance as in Eq. (6.62), and where y , like t of Eq. (6.63), depends on the spins and quasispins but not on the associated magnetic quantum numbers. Equation (6.66) leads to a useful special case when $M_K = M_{\kappa} = 0$ and the tensors X are converted to those of type W , defined in Eq. (6.18). The sum $K + \kappa + k$ is taken to be odd, with the scalars $\kappa = k = 0$ and $K = k = 0$ excluded. Application of the Wigner-Eckart theorem to the spin and orbital spaces yields

$$\begin{aligned} & \frac{\langle \gamma Q M_Q S || W^{(\kappa k)} || \gamma' Q' M'_Q S' \rangle}{\langle \gamma S M_S Q || W^{(K k)} || \gamma' S' M'_S Q' \rangle} \\ &= (-1)^z \frac{\begin{pmatrix} Q & K & Q' \\ -M_Q & 0 & M_Q \end{pmatrix}}{\begin{pmatrix} S & \kappa & S' \\ -M_S & 0 & M_S \end{pmatrix}}, \end{aligned} \quad (6.67)$$

where $z = y + Q - M_Q - S + M_S$. An equivalent form is

$$\begin{aligned} & \frac{(\ell^N \gamma v_1 S_1 || W^{(\kappa k)} || \ell^N \gamma' v'_1 S'_1)}{(\ell^{N'} \gamma' v_2 S_2 || W^{(K k)} || \ell^{N'} \gamma' v'_2 S'_2)} \\ &= (-1)^z \frac{\begin{pmatrix} \frac{1}{2}(2\ell + 1 - v_1) & K & \frac{1}{2}(2\ell + 1 - v'_1) \\ \frac{1}{2}(2\ell + 1 - N) & 0 & \frac{1}{2}(N - 2\ell - 1) \end{pmatrix}}{\begin{pmatrix} \frac{1}{2}(2\ell + 1 - v_2) & \kappa & \frac{1}{2}(2\ell + 1 - v'_2) \\ \frac{1}{2}(2\ell + 1 - N') & 0 & \frac{1}{2}(N' - 2\ell - 1) \end{pmatrix}}, \end{aligned} \quad (6.68)$$

where Eq. (6.64) is satisfied both for the unprimed and primed quantities.

6.5 Quasiparticles

Sets of linear combinations of the creation and annihilation operators for electrons in the ℓ shell can be constructed such that every member of one set anticommutes with a member of a different set. To preserve the tensorial character of these quasiparticle operators with respect to \mathbf{L} , it is convenient to define [21, 22]

$$\lambda_q^\dagger = 2^{-\frac{1}{2}} \left[a_{\frac{1}{2},q}^\dagger + (-1)^{\ell-q} a_{\frac{1}{2},-q} \right], \quad (6.69)$$

$$\mu_q^\dagger = 2^{-\frac{1}{2}} \left[a_{\frac{1}{2},q}^\dagger - (-1)^{\ell-q} a_{\frac{1}{2},-q} \right], \quad (6.70)$$

$$\nu_q^\dagger = 2^{-\frac{1}{2}} \left[a_{-\frac{1}{2},q}^\dagger + (-1)^{\ell-q} a_{-\frac{1}{2},-q} \right], \quad (6.71)$$

$$\xi_q^\dagger = 2^{-\frac{1}{2}} \left[a_{-\frac{1}{2},q}^\dagger - (-1)^{\ell-q} a_{-\frac{1}{2},-q} \right]. \quad (6.72)$$

The four tensors θ^\dagger ($\equiv \lambda^\dagger, \mu^\dagger, \nu^\dagger$, or ξ^\dagger) anticommute with each other; the first two act in the spin-up space, the second two in the spin-down space. The tensors θ , whose components $\tilde{\theta}_q$ are defined as in Eq. (6.17) with $t = \ell$ and $m_t = q$, are related to their adjoints by the equations

$$\lambda^\dagger = \lambda, \quad \mu^\dagger = -\mu, \quad (6.73)$$

$$\nu^\dagger = \nu, \quad \xi^\dagger = -\xi. \quad (6.74)$$

Under the action of the complementarity operator R (see Eq. (6.61)) [23],

$$R \lambda R^{-1} = \lambda, \quad R \mu R^{-1} = \mu, \quad (6.75)$$

$$R \nu R^{-1} = \nu, \quad R \xi R^{-1} = -\xi. \quad (6.76)$$

The tensors λ , μ , and ν , for a given component q , form a vector with respect to $\mathbf{S} + \mathbf{Q}$. Every component of ξ is scalar with respect to $\mathbf{S} + \mathbf{Q}$ [24].

The compound quasiparticle operators defined by [21, 22]

$$\Theta_q^\dagger = 2^{-\frac{1}{2}} [\theta_q^\dagger, \theta_0^\dagger], \quad (6.77)$$

where $q > 0$ and $\theta \equiv \lambda, \mu, \nu$, or ξ satisfy the anticommutation relations

$$[\Theta_q^\dagger, \Theta_{q'}^\dagger]_+ = 0, \quad (6.78)$$

$$[\Theta_q, \Theta_{q'}]_+ = 0, \quad (6.79)$$

$$[\Theta_q^\dagger, \Theta_{q'}]_+ = \delta(q, q'), \quad (6.80)$$

for $q, q' > 0$. The Θ_q^\dagger with $q > 0$ can thus be regarded as the creation operators for a fermion quasiparticle with ℓ components.

The connection between the creation and annihilation operators for quasiparticles and for quarks (appearing in the last two rows of Table 3.1) is

$$\theta \rightarrow 2^{(\ell-1)/2} \epsilon_\theta \gamma_\theta (\mathbf{q}_\theta^\dagger \mathbf{q}_\theta)^{(10\dots 0)}, \quad (6.81)$$

where the γ_θ are Dirac matrices satisfying

$$\gamma_\theta \gamma_\phi + \gamma_\phi \gamma_\theta = 2\delta(\theta, \phi), \quad (6.82)$$

and the ϵ_θ are phases, to some extent dependent on the definitions Eqs. (6.69)–(6.72) [25]. The superscript $(10\dots 0)$ indicates that $\mathbf{q}_\theta^\dagger$ and \mathbf{q}_θ each of which belongs to the elementary spinor $(\frac{1}{2}\frac{1}{2}\dots\frac{1}{2})$ of $\text{SO}_\theta(2\ell + 1)$, are to be coupled to the resultant $(10\dots 0)$, which matches the group label for θ . In the quark model, the $2^{4\ell+2}$ states of the atomic ℓ shell are given by

$$\mathbf{q}_\lambda^\dagger \mathbf{q}_\mu^\dagger \mathbf{q}_\nu^\dagger \mathbf{q}_\xi^\dagger |0\rangle_{pp'}, \quad (6.83)$$

where p and p' are parity labels that distinguish the four reference states $|0\rangle$ corresponding to the evenness and oddness of the number of spin-up and spin-down electrons. The scalar nature of ξ (and hence of \mathbf{q}_ξ) with respect to $\mathbf{S} + \mathbf{Q}$ can be used to derive relations between spin-orbit matrix elements that go beyond those expected from an application of the Wigner–Eckart theorem [26].

References

- Gross, E.K.U., Runge, E., Heinenon, O.: Many-Particle Theory. Hilger, New York (1991)
- Racah, G.: Phys. Rev. **62**, 438 (1942)
- Condon, E.U., Shortley, G.H.: The Theory of Atomic Spectra. Cambridge Univ. Press, New York (1935)
- Edmonds, A.R.: Angular Momentum in Quantum Mechanics. Princeton Univ. Press, Princeton (1957)
- Nielson, C.W., Koster, G.F.: Spectroscopic Coefficients for the p^n , d^n , and f^n Configurations. MIT Press, Cambridge (1963)
- Karazija, R., Vizbaraitė, J., Rudzikas, Z., Jucys, A.P.: Tables for the Calculation of Matrix Elements of Atomic Operators. Computing Centre of the Academy of Sciences, Moscow (1967)
- Judd, B.R.: Second Quantization and Atomic Spectroscopy. Johns Hopkins, Baltimore (1967)
- Racah, G.: Phys. Rev. **63**, 367 (1943)
- Donlan, V.L.: Air Force Materials Laboratory Report No. AFML-TR-70-249. Wright-Patterson Air Force Base, Ohio (1970)
- Velkov, D.D.: Multi-Electron Coefficients of Fractional Parentage for the p , d , and f Shells. Ph.D. Thesis. The Johns Hopkins University, Baltimore (2000). <http://www.pha.jhu.edu/groups/cfp/>
- Redmond, P.J.: Proc. R. Soc. A **222**, 84 (1954)
- Flowers, B.H., Szpikowski, S.: Proc. Phys. Soc. **84**, 673 (1964)
- Rudzikas, Z.: Theoretical Atomic Spectroscopy. Cambridge Univ. Press, New York (1997)
- Gaigalas, G., Rudzikas, Z., Froese Fischer, C.: At. Data Nucl. Data Tables **70**, 1 (1998)
- Judd, B.R., Lo, E., Velkov, D.: Mol. Phys. **98**, 1151 (2000). Table 4
- Judd, B.R.: J. Phys. C **14**, 375 (1981)
- Bell, J.S.: Nucl. Phys. **12**, 117 (1959)
- Watanabe, H.: Prog. Theor. Phys. **32**, 106 (1964)
- Lawson, R.D., Macfarlane, M.H.: Nucl. Phys. **66**, 80 (1965)
- Racah, G.: Phys. Rev. **76**, 1352 (1949). Table I
- Armstrong, L., Judd, B.R.: Proc. R. Soc. A **315**, 27 (1970)
- Armstrong, L., Judd, B.R.: Proc. R. Soc. A **315**, 39 (1970)
- Judd, B.R., Li, S.: J. Phys. B **22**, 2851 (1989)
- Judd, B.R., Lister, G.M.S., Suskin, M.A.: J. Phys. B **19**, 1107 (1986)
- Judd, B.R.: Phys. Rep. **285**, 1 (1997)
- Judd, B.R., Lo, E.: Phys. Rev. Lett. **85**, 948 (2000)



Brian Judd Brian Judd has had a lifelong interest in applying group theory to the spectroscopic properties of the rare earths. He held appointments at Oxford, Chicago, Paris and Berkeley before joining the Physics Department of the Johns Hopkins University in 1966. He received the Spedding Award for Rare-Earth Research in 1988 and is an Honorary Fellow of Brasenose College, Oxford.



Density Matrices

7

Klaus Bartschat 

Contents

7.1	Basic Formulae	120
7.1.1	Pure States	120
7.1.2	Mixed States	120
7.1.3	Expectation Values	120
7.1.4	The Liouville Equation	120
7.1.5	Systems in Thermal Equilibrium	121
7.1.6	Relaxation Processes	121
7.2	Spin and Light Polarizations	121
7.2.1	Spin-Polarized Electrons	121
7.2.2	Light Polarization	122
7.3	Atomic Collisions	122
7.3.1	Scattering Amplitudes	122
7.3.2	Reduced Density Matrices	122
7.4	Irreducible Tensor Operators	123
7.4.1	Definition	123
7.4.2	Transformation Properties	123
7.4.3	Symmetry Properties of State Multipoles	124
7.4.4	Orientation and Alignment	124
7.4.5	Coupled Systems	124
7.5	Time Evolution of State Multipoles	125
7.5.1	Perturbation Coefficients	125
7.5.2	Quantum Beats	125
7.5.3	Time Integration over Quantum Beats	125
7.6	Examples	126
7.6.1	Generalized <i>STU</i> -Parameters	126
7.6.2	Radiation from Excited States: Stokes Parameters	127
7.7	Summary	128
	References	128

Abstract

The density operator was first introduced by *J. von Neumann* [1] in 1927 and has since been widely used in quantum statistics. Over the past decades, however, the application of density matrices has spread to many other fields of physics. Density matrices have been used to describe, for example, coherence and correlation phenomena, alignment and orientation and their effect on the polarization of emitted radiation, quantum beat spectroscopy, optical pumping, and scattering processes, particularly when spin-polarized projectiles and/or targets are involved. A thorough introduction to the theory of density matrices and their applications, with an emphasis on atomic physics, can be found in the book by *Blum* [2], from which many equations have been extracted for use in this chapter.

Keywords

density matrix · density operator · reduce density matrix · Stokes parameter · tensor operator

The main advantage of the density matrix formalism is its ability to deal with pure and mixed states in the same consistent manner. The preparation of the initial state as well as the details regarding the observation of the final state can be treated in a systematic way. In particular, averages over quantum numbers of unpolarized beams in the initial state and incoherent sums over nonobserved quantum numbers in the final state can be accounted for via the reduced density matrix. Furthermore, expansion of the density matrix in terms of irreducible tensor operators and the corresponding state multipoles allows for the use of advanced angular momentum techniques, as outlined in Chaps. 2, 3 and 13. More details can be found in textbooks such as [3, 4].

K. Bartschat (✉)
Dept. of Physics & Astronomy, Drake University
Des Moines, IA, USA
e-mail: klaus.bartschat@drake.edu

7.1 Basic Formulae

7.1.1 Pure States

Consider a system in a quantum state that is represented by a single wave function $|\Psi\rangle$. The density operator for this situation is defined as

$$\rho = |\Psi\rangle\langle\Psi|. \quad (7.1)$$

If $|\Psi\rangle$ is normalized to unity, i.e., if

$$\langle\Psi|\Psi\rangle = 1, \quad (7.2)$$

then

$$\rho^2 = \rho. \quad (7.3)$$

Equation (7.3) is the basic equation for identifying *pure* quantum mechanical states represented by a density operator.

Next, consider the expansion of $|\Psi\rangle$ in terms of a complete orthonormal set of basis functions $\{|\Phi_n\rangle\}$, i.e.,

$$|\Psi\rangle = \sum_n c_n |\Phi_n\rangle. \quad (7.4)$$

The density operator then becomes

$$\rho = \sum_{n,m} c_n c_m^* |\Phi_n\rangle\langle\Phi_m| = \rho_{nm} |\Phi_n\rangle\langle\Phi_m|, \quad (7.5)$$

where the star denotes the complex conjugate quantity. Note that the density matrix elements $\rho_{nm} = \langle\Phi_n|\rho|\Phi_m\rangle$ depend on the choice of the basis and that the density matrix is Hermitian, i.e.,

$$\rho_{mn}^* = \rho_{nm}. \quad (7.6)$$

Finally, if $|\Psi\rangle = |\Phi_i\rangle$ is one of the basis functions, then

$$\rho_{mn} = \delta_{ni}\delta_{mi}, \quad (7.7)$$

where δ_{ni} is the Kronecker δ . Hence, the density matrix is diagonal in this representation with only one nonvanishing element.

7.1.2 Mixed States

The above concepts can be extended to treat statistical ensembles of pure quantum states. In the simplest case, such *mixed* states can be represented by a diagonal density matrix of the form

$$\rho = \sum_n w_n |\Psi_n\rangle\langle\Psi_n|, \quad (7.8)$$

where the weight w_n is the fraction of systems in the pure quantum state $|\Psi_n\rangle$. The standard normalization for the trace

of ρ is

$$\text{Tr}\{\rho\} = \sum_n w_n = 1. \quad (7.9)$$

Since the trace is invariant under unitary transformations of the basis functions, Eq. (7.9) also holds if the $|\Psi_n\rangle$ states themselves are expanded in terms of basis functions as in Eq. (7.4). For a pure state and the normalization Eq. (7.9), one finds in an arbitrary basis

$$\text{Tr}\{\rho\} = \text{Tr}\{\rho^2\} = 1. \quad (7.10)$$

7.1.3 Expectation Values

The density operator contains the maximum available information about a physical system. Consequently, it can be used to calculate expectation values for any operator A that represents a physical observable. In general,

$$\langle A \rangle = \text{Tr}\{A\rho\}/\text{Tr}\{\rho\}, \quad (7.11)$$

where $\text{Tr}\{\rho\}$ in the denominator of Eq. (7.11) ensures the correct result even for a normalization that is different from Eq. (7.9). The invariance of the trace operation ensures the same result—independently of the particular choice of the basis representation.

7.1.4 The Liouville Equation

Suppose Eq. (7.8) is valid for a time $t = 0$. If the functions $|\Psi_n(\mathbf{r}, t)\rangle$ obey the Schrödinger equation, i.e.,

$$i\frac{\partial}{\partial t}|\Psi_n(\mathbf{r}, t)\rangle = H(t)|\Psi_n(\mathbf{r}, t)\rangle, \quad (7.12)$$

the density operator at the time t can be written as

$$\rho(t) = U(t)\rho(0)U^\dagger(t). \quad (7.13)$$

In Eq. (7.13), $U(t)$ is the time evolution operator that relates the wave functions at times $t = 0$ and t according to

$$|\Psi_n(\mathbf{r}, t)\rangle = U(t)|\Psi_n(\mathbf{r}, 0)\rangle, \quad (7.14)$$

and $U^\dagger(t)$ denotes its adjoint. Note that

$$U(t) = e^{-iHt}, \quad (7.15)$$

if the Hamiltonian H is time independent.

Differentiation of Eq. (7.13) with respect to time and inserting Eq. (7.14) into the Schrödinger equation (7.12) yields the equation of motion

$$i\frac{\partial}{\partial t}\rho(t) = [H(t), \rho(t)], \quad (7.16)$$

where $[A, B]$ denotes a commutator.

The Liouville equation (7.16) can be used to determine the density matrix and to treat transitions from nonequilibrium to equilibrium states in quantum mechanical systems. Especially for approximate solutions in the presence of small time-dependent perturbation terms in an otherwise time-independent Hamiltonian, i.e., for

$$H(t) = H_0 + V(t), \quad (7.17)$$

the interaction picture is preferably used. The Liouville equation then becomes

$$i\frac{\partial}{\partial t}\rho_I(t) = [V_I(t), \rho_I(t)], \quad (7.18)$$

where the subscript I denotes the operator in the interaction picture. In first-order perturbation theory, Eq. (7.18) can be integrated to yield

$$\rho_I(t) = \rho_I(0) - i \int_0^t [V_I(\tau), \rho_I(0)] d\tau, \quad (7.19)$$

and higher-order terms can be obtained through subsequent iterations.

7.1.5 Systems in Thermal Equilibrium

According to quantum statistics, the density operator for a system that is in thermal equilibrium with a surrounding reservoir \mathcal{R} at a temperature T (canonical ensemble) can be expressed as

$$\rho = \frac{\exp(-\beta H)}{Z}, \quad (7.20)$$

where H is the Hamiltonian, and $\beta = 1/k_B T$ with k_B being the Boltzmann constant. The partition sum

$$Z = \text{Tr}\{\exp(-\beta H)\} \quad (7.21)$$

ensures the normalization condition Eq. (7.9). Expectation values are calculated according to Eq. (7.11), and extensions to other types of ensembles are straightforward.

7.1.6 Relaxation Processes

Transitions from nonequilibrium to equilibrium states can also be described within the density matrix formalism. One of the basic problems is to account for irreversibility in the energy (and sometimes particle) exchange between the system of interest, S , and the reservoir, \mathcal{R} . This is usually achieved by assuming that the interaction of the system with the reservoir is negligible and, therefore, the density matrix

representation for the reservoir at any time t is the same as the representation for $t = 0$.

Another frequently made assumption is the Markov approximation. In this approximation, one assumes that the system *forgets* all knowledge of the past, so that the density matrix elements at the time $t + \Delta t$ depend only on the values of these elements, and their first derivatives, at the time t . When Eq. (7.19) is put back into Eq. (7.18), the result in the Markov approximation can be rewritten as

$$\frac{\partial}{\partial t}\rho_{SI}(t) = -i \text{Tr}_{\mathcal{R}}[V_I(t), \rho_{SI}(0)\rho_{\mathcal{R}}(0)] - \int_0^t d\tau \text{Tr}_{\mathcal{R}}[V_I(t), [V_I(\tau), \rho_{SI}(t)\rho_{\mathcal{R}}(0)]] , \quad (7.22)$$

where $\text{Tr}_{\mathcal{R}}$ denotes the trace with regard to all variables of the reservoir. Note that the integral over $d\tau$ contains the system density matrix in the interaction picture, ρ_{SI} , at the time t , rather than at all times τ that are integrated over (the Markov approximation), and that the density matrix for the reservoir is taken as $\rho_{\mathcal{R}}(0)$ at all times. For more details, see Chap. 7 of *Blum* [2] and references therein.

Equations such as Eq. (7.22) are the basis for the master or rate equation approach used, for example, in quantum optics for the theory of lasers and the coupling of atoms to cavity modes. For more details, see Chaps. 72, 74, 77 and 82.

7.2 Spin and Light Polarizations

Density matrices are frequently used to describe the polarization state of spin-polarized particle beams as well as light. The latter can either be emitted from excited atomic or molecular ensembles or can be used, for example, for laser pumping purposes.

7.2.1 Spin-Polarized Electrons

The spin polarization of an electron beam with respect to a given quantization axis \hat{n} is defined as [5]

$$P_{\hat{n}} = \frac{N_{\uparrow} - N_{\downarrow}}{N_{\uparrow} + N_{\downarrow}}, \quad (7.23)$$

where $N_{\uparrow}(N_{\downarrow})$ is the number of electrons with spin up (down) with regard to this axis. An arbitrary polarization state is described by the density matrix

$$\rho = \frac{1}{2} \begin{pmatrix} 1 + P_z & P_x - iP_y \\ P_x + iP_y & 1 - P_z \end{pmatrix}, \quad (7.24)$$

where $P_{x,y,x}$ are the Cartesian components of the spin polarization vector. The individual components can be obtained

from the density matrix as

$$P_i = \text{Tr}\{\sigma_i \rho\}, \quad (7.25)$$

where σ_i ($i = x, y, z$) are the standard Pauli spin matrices.

7.2.2 Light Polarization

Another important use of the density matrix formalism is the description of light polarization in terms of the so-called Stokes parameters [6]. For a given direction of observation, the general polarization state of light can be fully determined by the measurement of one circular and two independent linear polarizations. Using the notation of *Born and Wolf* [7], the density matrix is given by

$$\rho = \frac{I_{\text{tot}}}{2} \begin{pmatrix} 1 - P_3 & P_1 - iP_2 \\ P_1 + iP_2 & 1 + P_3 \end{pmatrix}, \quad (7.26)$$

where P_1 and P_2 are linear light polarizations, while P_3 is the circular polarization (also Sect. 7.6). In Eq. (7.26), the density matrix is normalized in such a way that

$$\text{Tr}\{\rho\} = I_{\text{tot}}, \quad (7.27)$$

where I_{tot} is the total light intensity. Other frequently used names for the various Stokes parameters are

$$P_1 = \eta_3 = M, \quad (7.28)$$

$$P_2 = \eta_1 = C, \quad (7.29)$$

$$P_3 = -\eta_2 = S. \quad (7.30)$$

The Stokes parameters of electric dipole radiation can be related directly to the charge distribution of the emitting atomic ensemble. As discussed in detail in Chap. 48, one finds, for example,

$$L_{\perp} = -P_3 \quad (7.31)$$

for the angular momentum transfer perpendicular to the scattering plane in collisional (de)excitation, and

$$\gamma = \frac{1}{2} \arg\{P_1 + iP_2\} \quad (7.32)$$

for the alignment angle.

7.3 Atomic Collisions

7.3.1 Scattering Amplitudes

Transitions from an initial state $|J_0 M_0; \mathbf{k}_0 m_0\rangle$ to a final state $|J_1 M_1; \mathbf{k}_1 m_1\rangle$ are described by scattering amplitudes

$$f(M_1 m_1; M_0 m_0) = \langle J_1 M_1; \mathbf{k}_1 m_1 | \mathcal{T} | J_0 M_0; \mathbf{k}_0 m_0 \rangle, \quad (7.33)$$

where \mathcal{T} is the transition operator. Furthermore, J_0 (J_1) is the total electronic angular momentum in the initial (final) state of the target and M_0 (M_1) its corresponding z -component, while \mathbf{k}_0 (\mathbf{k}_1) is the initial (final) momentum of the projectile and m_0 (m_1) its spin component.

7.3.2 Reduced Density Matrices

While the scattering amplitudes are the central elements in a theoretical description, some restrictions usually need to be taken into account in a practical experiment. The most important ones are: (i) there is no *pure* initial state, and (ii) not all possible quantum numbers are simultaneously determined in the final state. The solution to this problem can be found by using the density matrix formalism. First, the complete density operator after the collision process is given by [2]

$$\rho_{\text{out}} = \mathcal{T} \rho_{\text{in}} \mathcal{T}^\dagger, \quad (7.34)$$

where ρ_{in} is the density operator before the collision. The corresponding matrix elements are given by

$$\begin{aligned} (\rho_{\text{out}})_{m'_1 m_1}^{k_1, M'_1 M_1} &= \sum_{m'_0 m_0 M'_0 M_0} \rho_{m'_0 m_0} \rho_{M'_0 M_0} \\ &\times f(M'_1 m'_1; M'_0 m'_0) \\ &\times f^*(M_1 m_1; M_0 m_0), \end{aligned} \quad (7.35)$$

where the term $\rho_{m'_0 m_0} \rho_{M'_0 M_0}$ describes the preparation of the initial state (i). Secondly, *reduced* density matrices account for (ii). For example, if only the scattered projectiles are observed, the corresponding elements of the reduced density matrix are obtained by summing over the atomic quantum numbers as follows:

$$(\rho_{\text{out}})_{m'_1 m_1}^{k_1} = \sum_{M_1} (\rho_{\text{out}})_{m'_1 m_1}^{k_1, M_1 M_1}. \quad (7.36)$$

The differential cross section for unpolarized projectile and target beams is given by

$$\frac{d\sigma}{d\Omega} = C \sum_{m_1} (\rho_{\text{out}})_{m_1 m_1}^{k_1}, \quad (7.37)$$

where C is a constant that depends on the normalization of the continuum waves in a numerical calculation.

On the other hand, if only the atoms are observed (for example, by analyzing the light emitted in optical transitions), the elements

$$(\rho_{\text{out}})_{M'_1 M_1} = \int d^3 \mathbf{k}_1 \sum_{m_1} (\rho_{\text{out}})_{m_1 m_1}^{k_1, M'_1 M_1} \quad (7.38)$$

determine the integrated Stokes parameters [8, 9], i.e., the polarization of the emitted light. They contain information about the angular momentum distribution in the excited target ensemble.

Finally, for electron–photon coincidence experiments without spin analysis in the final state, the elements

$$(\rho_{\text{out}})_{M'_1 M_1}^{k_1} = \sum_{m_1} (\rho_{\text{out}})_{m_1 m_1}^{k_1, M'_1 M_1} \quad (7.39)$$

simultaneously contain information about the projectiles and the target. This information can be extracted by measuring the angle-differential Stokes parameters. In particular, for unpolarized electrons and atoms, the *natural coordinate system*, where the quantization axis coincides with the normal to the scattering plane, allows for a simple physical interpretation of the various parameters [10] (Chap. 48).

The density matrix formalism outlined above is very useful for obtaining a qualitative description of the geometrical and sometimes also of the dynamical symmetries of the collision process [11]. Two explicit examples are discussed in Sect. 7.6.

7.4 Irreducible Tensor Operators

The general density matrix theory can be formulated in a very elegant fashion by decomposing the density operator in terms of irreducible components whose matrix elements then become the state multipoles. In such a formulation, full advantage can be taken of the most sophisticated techniques developed in angular momentum algebra (Chap. 2). Many explicit examples can be found in [3, 4].

7.4.1 Definition

The density operator for an ensemble of particles in quantum states labeled as $|JM\rangle$, where J and M are the total angular momentum and its magnetic component, respectively, can be written as

$$\rho = \sum_{J'JM'M} \rho_{M'M}^{J'J} |J'M'\rangle \langle JM|, \quad (7.40)$$

where

$$\rho_{M'M}^{J'J} = \langle J'M' | \rho | JM \rangle \quad (7.41)$$

are the matrix elements. (For simplicity, interactions outside the single manifold of momentum states $|JM\rangle$ are neglected.) Alternatively, one may write

$$+ \rho = \sum_{J'JKQ} \langle T(J'J)_{KQ}^\dagger \rangle T(J'J)_{KQ}, \quad (7.42)$$

where the irreducible tensor operators are defined in terms of 3- j -symbols as

$$T(J'J)_{KQ} = \sum_{M'M} (-1)^{J'-M'} \sqrt{2K+1} \times \begin{pmatrix} J' & J & K \\ M' & -M & -Q \end{pmatrix} |J'M'\rangle \langle JM|, \quad (7.43)$$

and the state multipoles or statistical tensors are given by

$$\langle T(J'J)_{KQ}^\dagger \rangle = \sum_{M'M} (-1)^{J'-M'} \sqrt{2K+1} \times \begin{pmatrix} J' & J & K \\ M' & -M & -Q \end{pmatrix} \langle J'M' | \rho | JM \rangle. \quad (7.44)$$

Hence, the selection rules for the 3- j -symbols imply that

$$|J - J'| \leq K \leq J + J', \quad (7.45)$$

$$M' - M = Q. \quad (7.46)$$

Equation (7.44) can be inverted through the orthogonality condition of the 3- j -symbols to give

$$\langle J'M' | \rho | JM \rangle = \sum_{KQ} (-1)^{J'-M'} \sqrt{2K+1} \times \begin{pmatrix} J' & J & K \\ M' & -M & -Q \end{pmatrix} \langle T(J'J)_{KQ}^\dagger \rangle. \quad (7.47)$$

7.4.2 Transformation Properties

Suppose a coordinate system (X_2, Y_2, Z_2) is obtained from another coordinate system (X_1, Y_1, Z_1) through a rotation by a set of three Euler angles (γ, β, α) as defined in *Edmonds* [12]. The irreducible tensor operators Eq. (7.43) defined in the (X_1, Y_1, Z_1) system are then related to the operators $\langle T(J'J)_{KQ}^\dagger \rangle$ in the (X_2, Y_2, Z_2) system by

$$T(J'J)_{KQ} = \sum_q T(J'J)_{Kq} D(\gamma, \beta, \alpha)_{qQ}^K, \quad (7.48)$$

where

$$D(\gamma, \beta, \alpha)_{M'M}^J = e^{iM'\gamma} d(\beta)_{M'M}^J e^{iM\alpha} \quad (7.49)$$

is a rotation matrix (Chap. 2). Note that the rank K of the tensor operator is invariant under such rotations. Similarly,

$$\langle T(J'J)_{KQ}^\dagger \rangle = \sum_q \langle T(J'J)_{Kq}^\dagger \rangle D(\gamma, \beta, \alpha)_{qQ}^{K*} \quad (7.50)$$

holds for the state multipoles.

The irreducible tensor operators fulfill the orthogonality condition

$$\text{Tr}\left\{T(J'J)_{KQ} T(J'J)_{K'Q'}^\dagger\right\} = \delta_{K'K} \delta_{Q'Q}. \quad (7.51)$$

With

$$T(J'J)_{00} = \frac{1}{\sqrt{2J+1}} \delta_{J'J} \mathbf{1} \quad (7.52)$$

being proportional to the unit operator $\mathbf{1}$, it follows that all tensor operators have vanishing trace, except for the monopole $T(J'J)_{00}$.

Reduced tensor operators fulfill the Wigner–Eckart theorem (Sect. 2.8.4)

$$\begin{aligned} & \langle J'M' | T(J'J)_{KQ} | JM \rangle \\ &= (-1)^{J'-M'} \begin{pmatrix} J' & K & J \\ -M' & Q & M \end{pmatrix} \langle J' || T_K || J \rangle, \end{aligned} \quad (7.53)$$

where the reduced matrix element is simply given by

$$\langle J' || T_K || J \rangle = \frac{1}{\sqrt{2K+1}}. \quad (7.54)$$

7.4.3 Symmetry Properties of State Multipoles

The Hermiticity condition for the density matrix implies

$$\langle T(J'J)_{KQ}^\dagger \rangle^* = (-1)^{J'-J+Q} \langle T(JJ')_{K-Q}^\dagger \rangle, \quad (7.55)$$

which, for sharp angular momentum $J' = J$, yields

$$\langle T(J)_{KQ}^\dagger \rangle^* = (-1)^Q \langle T(J)_{K-Q}^\dagger \rangle. \quad (7.56)$$

Hence, the state multipoles $\langle T(J)_{K0}^\dagger \rangle$ are real numbers.

Furthermore, the transformation property Eq. (7.50) of the state multipoles imposes restrictions on nonvanishing state multipoles to describe systems with given symmetry properties. In detail, one finds:

1. For spherically symmetric systems,

$$\langle T(J'J)_{KQ}^\dagger \rangle = \langle T(J'J)_{KQ}^\dagger \rangle_{\text{rot}} \quad (7.57)$$

for *all* sets of Euler angles. This implies that only the monopole term $\langle T(J)_{00}^\dagger \rangle$ can be different from zero.

2. For axially symmetric systems,

$$\langle T(J'J)_{KQ}^\dagger \rangle = \langle T(J'J)_{KQ}^\dagger \rangle_{\text{rot}} \quad (7.58)$$

for *all* Euler angles ϕ that describe a rotation around the z -axis. Since this angle enters via a factor $\exp(-iQ\phi)$ into the general transformation formula Eq. (7.50), it follows

that only state multipoles with $Q = 0$, i.e., $\langle T(J'J)_{K0}^\dagger \rangle$, can be different from zero in such a situation.

3. For planar symmetric systems with fixed $J' = J$,

$$\langle T(J)_{KQ}^\dagger \rangle = (-1)^K \langle T(J)_{KQ}^\dagger \rangle^* \quad (7.59)$$

if the system properties are invariant under reflection in the xz -plane. Hence, state multipoles with even rank K are real numbers, while those with odd rank are purely imaginary in this case.

The above results can be applied immediately to the description of atomic collisions where the incident beam axis is the quantization axis (the so-called *collision system*). For example, impact excitation of unpolarized targets by unpolarized projectiles without observation of the scattered projectiles is symmetric both with regard to rotation around the incident beam axis and with regard to reflection in any plane containing this axis. Consequently, the state multipoles $\langle T(J)_{00}^\dagger \rangle$, $\langle T(J)_{20}^\dagger \rangle$, $\langle T(J)_{40}^\dagger \rangle$, ... fully characterize the atomic ensemble of interest. Using Eq. (7.50), similar relationships can be derived for state multipoles defined with regard to other coordinate systems, such as the *natural system* where the quantization axis coincides with the normal vector to the scattering plane (Chap. 48).

7.4.4 Orientation and Alignment

From the above discussion, it is apparent that the description of systems that do not exhibit spherical symmetry requires the knowledge of state multipoles with rank $K \neq 0$. Frequently, the multipoles with $K = 1$ and $K = 2$ are determined via the angular correlation and the polarization of radiation emitted from an ensemble of collisionally excited targets. The state multipoles with $K = 1$ are proportional to the spherical components of the angular momentum expectation value and, therefore, give rise to a nonvanishing circular light polarization (Sect. 7.6). This corresponds to a sense of rotation or an orientation in the ensemble, which is, therefore, called oriented (Sect. 48.1).

On the other hand, nonvanishing multipoles with rank $K = 2$ describe the alignment of the system. Some authors, however, use the terms *alignment* or *orientation* synonymously for all nonvanishing state multipoles with rank $K \neq 0$, thereby describing any system with anisotropic occupation of magnetic sublevels as *aligned* or *oriented*. For details on alignment and orientation, see Chap. 48 and [3, 4].

7.4.5 Coupled Systems

Tensor operators and state multipoles for coupled systems are constructed as direct products (\otimes) of the operators for

the individual systems. For example, the density operator for two subsystems in basis states $|L, M_L\rangle$ and $|S, M_S\rangle$ is constructed as [2]

$$\rho = \sum_{KQkq} \langle T(L)_{KQ}^\dagger \otimes T(S)_{kq}^\dagger \rangle [T(L)_{KQ} \otimes T(S)_{kq}]. \quad (7.60)$$

If the two systems are uncorrelated, the state multipoles factor as

$$\langle T(L)_{KQ}^\dagger \otimes T(S)_{kq}^\dagger \rangle = \langle T(L)_{KQ}^\dagger \rangle \langle T(S)_{kq}^\dagger \rangle. \quad (7.61)$$

More generally, irreducible representations of coupled operators can be defined in terms of a 9- j -symbol as

$$T(J', J)_{K'Q'} = \sum_{KQkq} \hat{K} \hat{k} \hat{J} \hat{J}' (KQ, kq | K'Q') \times \begin{Bmatrix} K & k & K' \\ L & S & J' \\ L & S & J \end{Bmatrix} T(L)_{KQ} \otimes T(S)_{kq}, \quad (7.62)$$

where $\hat{x} \equiv \sqrt{2x+1}$ and $(j_1 m_1, j_2 m_2 | j_3 m_3)$ is a standard Clebsch–Gordan coefficient.

7.5 Time Evolution of State Multipoles

7.5.1 Perturbation Coefficients

From the general expansions

$$\rho(t) = \sum_{j'jkq} \langle T(j'j; t)_{kq}^\dagger \rangle T(j'j)_{kq} \quad (7.63)$$

in terms of irreducible components, together with Eq. (7.42) for time $t = 0$ and Eq. (7.13) for the time development of the density operator, it follows that

$$\langle T(j'j; t)_{kq}^\dagger \rangle = \sum_{J'JKQ} \langle T(J'J; 0)_{KQ}^\dagger \rangle G(J'J, j'j; t)_{Kk}^{Qq}, \quad (7.64)$$

where the perturbation coefficients are defined as

$$G(J'J, j'j; t)_{Kk}^{Qq} = \text{Tr} \left\{ U(t) T(J'J)_{KQ} U(t)^\dagger T(j'j)_{kq}^\dagger \right\}. \quad (7.65)$$

Hence, these coefficients relate the state multipoles at time t to those at $t = 0$.

7.5.2 Quantum Beats

An important application of the perturbation coefficients is the coherent excitation of several quantum states, which sub-

sequently decay by optical transitions. Such an excitation may be performed, for example, in beam-foil experiments or electron–atom collisions where the energy width of the electron beam is too large to resolve the fine structure (or hyperfine structure) of the target states.

Suppose, for instance, that explicitly relativistic effects, such as the spin–orbit interaction between the projectile and the target, can be neglected *during* a collision process between an incident electron and a target atom. In that case, the orbital angular momentum (L) system of the collisionally excited target states may be oriented, depending on the scattering angle of the projectile. On the other hand, the spin (S) system remains unaffected (unpolarized), provided that both the target and the projectile beams are unpolarized. During the lifetime of the excited target states, however, the spin–orbit interaction *within* the target produces an exchange of orientation between the L and the S systems, which results in a net loss of orientation in the L system.

This effect can be observed directly through the intensity and the polarization of the light emitted from the excited target ensemble. The perturbation coefficients for the fine-structure interaction are found to be [2, 13]

$$G(L; t)_K = \frac{\exp(-\gamma t)}{2S+1} \sum_{J'J} (2J'+1)(2J+1) \times \begin{Bmatrix} L & J' & S \\ J & L & K \end{Bmatrix}^2 \cos(\omega_{J'} - \omega_J)t, \quad (7.66)$$

where $\omega_{J'} - \omega_J$ corresponds to the (angular) frequency difference between the various multiplet states with total electronic angular momenta J' and J , respectively. Also, γ is the natural width of the spectral line; for simplicity, the same lifetime was assumed in Eq. (7.66) for all states of the multiplet.

Note that the perturbation coefficients are independent of the multipole component Q in this case, and that there is no mixing between different multipole ranks K . Similar results can be derived [2, 13] for the hyperfine interaction and also to account for the combined effect of fine and hyperfine structure. The cosine terms represent correlation between the signal from different fine-structure states, and they lead to oscillations in the intensity as well as the measured Stokes parameters in a time-resolved experiment.

Finally, generalized perturbation coefficients have been derived for the case where both the L and the S systems may be oriented and/or aligned during the collision process [14]. This can happen when spin-polarized projectiles and/or target beams are prepared.

7.5.3 Time Integration over Quantum Beats

If the excitation and decay times cannot be resolved in a given experimental setup, the perturbation coefficients need

to be integrated over time. As a result, the quantum beats disappear, but a net effect may still be visible through a depolarization of the emitted radiation. For the case of atomic fine structure interaction discussed above, one finds [2, 13]

$$\begin{aligned}\bar{G}(L)_K &= \int_0^\infty G(L; t)_K dt \\ &= \frac{1}{2S+1} \sum_{J'J} (2J'+1)(2J+1) \\ &\quad \times \begin{Bmatrix} L & J' & S \\ J & L & K \end{Bmatrix}^2 \frac{\gamma}{\gamma^2 + \omega_{J'J}^2},\end{aligned}\quad (7.67)$$

where $\omega_{J'J} = \omega_{J'} - \omega_J$. Note that the amount of depolarization depends on the relationship between the fine structure splitting and the natural line width. For $|\omega_{J'J}| \gg \gamma$ (if $J' \neq J$), the terms with $J' = J$ dominate and cause the maximum depolarization; for the opposite case $|\omega_{J'J}| \ll \gamma$, the sum rule for the 6- j -symbols can be applied and no depolarization is observed.

Similar depolarizations can be caused through hyperfine structure effects, as well as through external fields. An important example of the latter case is the Hanle effect (Sect. 18.2.1).

7.6 Examples

In this section, two examples of the reduced density formalism are discussed explicitly. These are: (i) the change of the spin polarization of initially polarized spin- $\frac{1}{2}$ projectiles after scattering from unpolarized targets, and (ii) the Stokes parameters describing the angular distribution and the polarization of light as detected in projectile-photon coincidence experiments after collisional excitation. The recent book by *Andersen and Bartschat* [4] provides a detailed introduction to these topics, together with a thorough discussion of benchmark studies in the field of electronic and atomic collisions, including extensions to ionization processes, as well as applications in plasma, surface, and nuclear physics. Even more extensive compilations of such studies can be found in a review series dealing with unpolarized electrons colliding with unpolarized targets [10], heavy-particle collisions [15], and the special role of projectile and target spins in such collisions [16].

7.6.1 Generalized *STU*-Parameters

For spin-polarized projectile scattering from unpolarized targets, the generalized *STU*-parameters [11] contain information about the projectile spin polarization after the collision.

These parameters can be expressed in terms of the elements Eq. (7.36).

To analyze this problem explicitly, one defines the quantities

$$\begin{aligned}\langle m'_1 m'_0; m_1 m_0 \rangle &= \frac{1}{2J_0+1} \sum_{M_1 M_0} f(M_1 m'_1; M_0 m'_0) \\ &\quad \times f^*(M_1 m_1; M_0 m_0),\end{aligned}\quad (7.68)$$

which contain the *maximum information* that can be obtained from the scattering process, if only the polarization of the projectiles is prepared before the collision and measured thereafter.

Next, the number of independent parameters that can be determined in such an experiment needs to be examined. For spin- $\frac{1}{2}$ particles, there are $2 \times 2 \times 2 \times 2 = 16$ possible combinations of $\{m'_1 m'_0; m_1 m_0\}$ and, therefore, 16 complex or 32 real parameters (in the most general case of spin- S particles, there would be $(2S+1)^4$ combinations). However, from the definition Eq. (7.68) and the Hermiticity of the reduced density matrix contained therein, it follows that

$$\langle m'_1 m'_0; m_1 m_0 \rangle = \langle m_1 m_0; m'_1 m'_0 \rangle^*.\quad (7.69)$$

Furthermore, parity conservation of the interaction or the equivalent reflection invariance with regard to the scattering plane yields the additional relationship [11]

$$\begin{aligned}f(M_1 m_1; M_0 m_0) &= (-1)^{J_1 - M_1 + \frac{1}{2} - m_1 + J_0 - M_0 + \frac{1}{2} - m_0} \\ &\quad \times \Pi_1 \Pi_0 f(-M_1 - m_1; -M_0 - m_0),\end{aligned}\quad (7.70)$$

where Π_1 and Π_0 are ± 1 , depending on the parities of the atomic states involved. Hence,

$$\begin{aligned}\langle m'_1 m'_0; m_1 m_0 \rangle &= (-1)^{m'_1 - m_1 + m'_0 - m_0} \\ &\quad \times \langle -m'_1 - m'_0; -m_1 - m_0 \rangle.\end{aligned}\quad (7.71)$$

Note that Eqs. (7.70) and (7.71) hold for the collision frame, where the quantization axis (\hat{z}) is taken as the incident beam axis and the scattering plane is the xz -plane. Similar formulas can be derived for the natural frame (Sect. 7.3.2).

Consequently, *eight* independent parameters are sufficient to characterize the reduced spin density matrix of the scattered projectiles. These can be chosen as the *absolute* differential cross section

$$\sigma_u = \frac{1}{2} \sum_{m_1, m_0} \langle m_1 m_0; m_1 m_0 \rangle,\quad (7.72)$$

for the scattering of unpolarized projectiles from unpolarized targets and the seven *relative* parameters

$$S_A = -\frac{2}{\sigma_u} \text{Im} \left\{ \left\langle \frac{1}{2} - \frac{1}{2}; \frac{11}{22} \right\rangle \right\}, \quad (7.73)$$

$$S_P = -\frac{2}{\sigma_u} \text{Im} \left\{ \left\langle \frac{11}{22}; -\frac{11}{22} \right\rangle \right\}, \quad (7.74)$$

$$T_y = \frac{1}{\sigma_u} \left[\left\langle -\frac{1}{2} - \frac{1}{2}; \frac{11}{22} \right\rangle - \left\langle -\frac{11}{22}; \frac{1}{2} - \frac{1}{2} \right\rangle \right], \quad (7.75)$$

$$T_x = \frac{1}{\sigma_u} \left[\left\langle -\frac{1}{2} - \frac{1}{2}; \frac{11}{22} \right\rangle + \left\langle -\frac{11}{22}; \frac{1}{2} - \frac{1}{2} \right\rangle \right], \quad (7.76)$$

$$T_z = \frac{1}{\sigma_u} \left[\left\langle \frac{11}{22}; \frac{11}{22} \right\rangle - \left\langle \frac{11}{22}; -\frac{11}{22} \right\rangle \right], \quad (7.77)$$

$$U_{xz} = \frac{2}{\sigma_u} \text{Re} \left\{ \left\langle \frac{11}{22}; -\frac{11}{22} \right\rangle \right\}, \quad (7.78)$$

$$U_{zx} = -\frac{2}{\sigma_u} \text{Re} \left\{ \left\langle \frac{1}{2} - \frac{1}{2}; \frac{11}{22} \right\rangle \right\}, \quad (7.79)$$

where $\text{Re}\{x\}$ and $\text{Im}\{x\}$ denote the real and imaginary parts of the complex quantity x , respectively. Note that normalization constants have been omitted in Eq. (7.72) to simplify the notation.

Therefore, the most general form for the polarization vector after scattering, \mathbf{P}' , for an initial polarization vector $\mathbf{P} = (P_x, P_y, P_z)$ is given by

$$\frac{(S_P + T_y P_y) \hat{y} + (T_x P_x + U_{xz} P_z) \hat{x} + (T_z P_z - U_{zx} P_x) \hat{z}}{1 + S_A P_y}. \quad (7.80)$$

The physical meaning of the above relation is illustrated in Fig. 7.1.

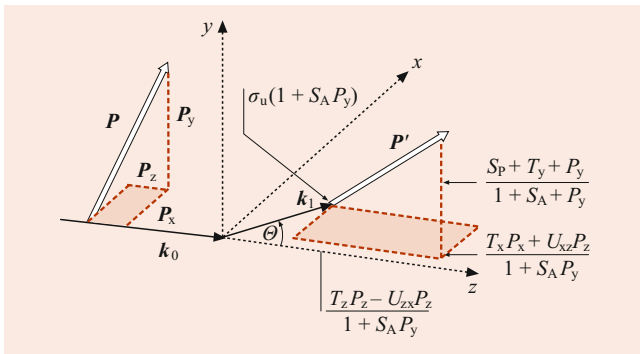


Fig. 7.1 Physical meaning of the generalized *STU*-parameters: the polarization function S_P gives the polarization of an initially unpolarized projectile beam after the collision, while the asymmetry function S_A determines a left–right asymmetry in the differential cross section for the scattering of a spin-polarized beam. Furthermore, the contraction parameters (T_x, T_y, T_z) describe the change of an initial polarization component along the three Cartesian axes, while the parameters U_{xz} and U_{zx} determine the rotation of a polarization component in the scattering plane

The following geometries are particularly suitable for the experimental determination of the individual parameters; σ_u and S_P can be measured with unpolarized incident projectiles. A transverse polarization component perpendicular to the scattering plane ($\mathbf{P} = P_y \hat{y}$) is needed to obtain S_A and T_y . Finally, the measurement of T_x , U_{zx} , T_z , and U_{xz} requires both transverse ($P_x \hat{x}$) and longitudinal ($P_z \hat{z}$) projectile polarization components in the scattering plane.

7.6.2 Radiation from Excited States: Stokes Parameters

The state-multipole description is also widely used for the parametrization of the Stokes parameters that describe the polarization of light emitted in optical decays of excited atomic ensembles. The general case of excitation by spin-polarized projectiles has been treated by *Bartschat* and collaborators [8]. The basic experimental setup for electron–photon coincidence experiments and the definition of the Stokes parameters are illustrated in Figs. 7.2 and 7.3.

For impact excitation of an atomic state with total electronic angular momentum J and an electric dipole transition to a state with J_f , the photon intensity in a direction $\hat{n} = (\Theta_\gamma, \Phi_\gamma)$ is given by

$$I(\Theta_\gamma, \Phi_\gamma) = C \left[\frac{2(-1)^{J-J_f}}{3\sqrt{2J+1}} \langle T(J)_{00}^\dagger \rangle - \begin{Bmatrix} 1 & 1 & 2 \\ J & J & J_f \end{Bmatrix} \times \left(\text{Re} \left\{ \langle T(J)_{22}^\dagger \rangle \right\} \sin^2 \Theta_\gamma \cos 2\Phi_\gamma - \text{Re} \left\{ \langle T(J)_{21}^\dagger \rangle \right\} \sin 2\Theta_\gamma \cos \Phi_\gamma + \sqrt{\frac{1}{6}} \langle T(J)_{20}^\dagger \rangle (3 \cos^2 \Theta_\gamma - 1) - \text{Im} \left\{ \langle T(J)_{22}^\dagger \rangle \right\} \sin^2 \Theta_\gamma \sin 2\Phi_\gamma + \text{Im} \left\{ \langle T(J)_{21}^\dagger \rangle \right\} \sin 2\Theta_\gamma \sin \Phi_\gamma \right) \right], \quad (7.81)$$

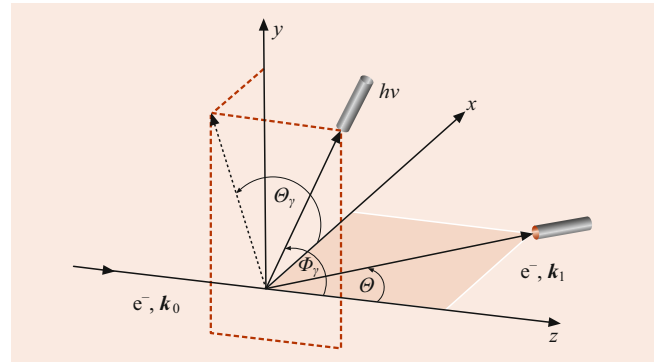


Fig. 7.2 Geometry of electron–photon coincidence experiments

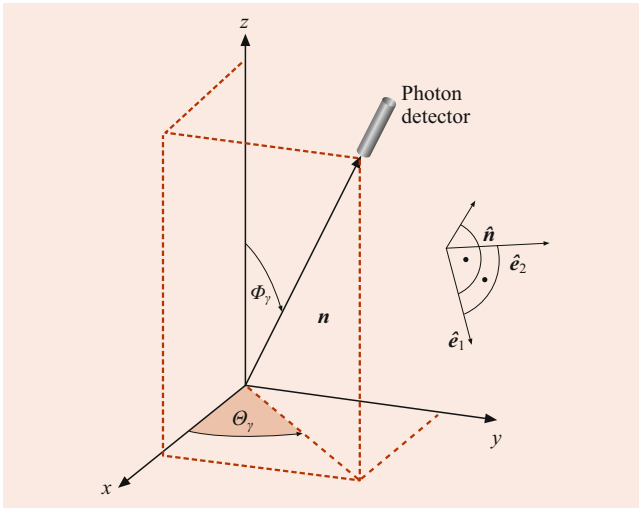


Fig. 7.3 Definition of the Stokes parameters: photons are observed in a direction \hat{n} with polar angles $(\Theta_\gamma, \Phi_\gamma)$ in the collision system. The three unit vectors $(\hat{n}, \hat{e}_1, \hat{e}_2)$ define the helicity system of the photons, $\hat{e}_1 = (\Theta_\gamma + 90^\circ, \Phi_\gamma)$ lies in the plane spanned by \hat{n} and \hat{z} and is perpendicular to \hat{n} , while $\hat{e}_2 = (\Theta_\gamma, \Phi_\gamma + 90^\circ)$ is perpendicular to both \hat{n} and \hat{e}_1 . In addition to the circular polarization P_3 , the linear polarizations P_1 and P_2 are defined with respect to axes in the plane spanned by \hat{e}_1 and \hat{e}_2 . Counting from the direction of \hat{e}_1 , the axes are located at $(0^\circ, 90^\circ)$ for P_1 and at $(45^\circ, 135^\circ)$ for P_2 , respectively

where

$$C = \frac{e^2 \omega^4}{2\pi c^3} |\langle J_f \| \mathbf{r} \| J \rangle|^2 (-1)^{J-J_f} \quad (7.82)$$

is a constant containing the frequency ω of the transition as well as the reduced radial dipole matrix element.

Similarly, the product of the intensity I and the circular light polarization P_3 can be written in terms of state multipoles as

$$\begin{aligned} (I \cdot P_3)(\Theta_\gamma, \Phi_\gamma) = & -C \begin{Bmatrix} 1 & 1 & 1 \\ J & J & J_f \end{Bmatrix} \\ & \times \left(\text{Im} \left\{ \left\langle T(J)_{11}^\dagger \right\rangle \right\} 2 \sin \Theta_\gamma \sin \Phi_\gamma \right. \\ & - \text{Re} \left\{ \left\langle T(J)_{11}^\dagger \right\rangle \right\} 2 \sin \Theta_\gamma \cos \Phi_\gamma \\ & \left. + \sqrt{2} \left\langle T(J)_{10}^\dagger \right\rangle \cos \Theta_\gamma \right), \quad (7.83) \end{aligned}$$

so that P_3 can be calculated as

$$P_3(\Theta_\gamma, \Phi_\gamma) = (I \cdot P_3)(\Theta_\gamma, \Phi_\gamma) / I(\Theta_\gamma, \Phi_\gamma). \quad (7.84)$$

Note that each state multipole gives rise to a characteristic angular dependence in the formulas for the Stokes parameters, and that perturbation coefficients may need to be applied

to deal, for example, with depolarization effects due to internal or external fields. General formulas for $P_1 = \eta_3$ and $P_2 = \eta_1$ can be found in [8] and, for both the natural and the collision systems, in [4].

As was pointed out before, some of the state multipoles may vanish, depending on the experimental arrangement. A detailed analysis of the information contained in the state multipoles and the generalized Stokes parameters (which are defined for specific values of the projectile spin polarization) has been given by *Andersen* and *Bartschat* [4, 17, 18]. They reanalyzed the experiment performed by *Sohn* and *Hanne* [19] and showed how the density matrix of the excited atomic ensemble can be determined by a measurement of the generalized Stokes parameters. In some cases, this will allow for the extraction of a complete set of scattering amplitudes for the collision process. Such a *perfect scattering experiment* was called for by *Bederson* many years ago [20] and is within reach even for fairly complex excitation processes. The most promising cases were discussed by *Andersen* and *Bartschat* [4, 17, 21].

7.7 Summary

The basic formulas dealing with density matrices in quantum mechanics, with particular emphasis on reduced matrix theory and its applications in atomic physics, have been summarized. More details are given in the introductory textbooks by *Blum* [2], *Balashov* et al. [3], *Andersen* and *Bartschat* [4], and the references listed below.

References

1. von Neumann, J.: Göttinger Nachr. **1927**, 245–272 (1927)
2. Blum, K.: Density Matrix Theory and Applications, 3rd edn. Springer, New York (2012)
3. Balashov, V.V., Grum-Grzhimailo, A.N., Kabachnik, N.M.: Polarization and Correlation Phenomena in Atomic Collisions. A Practical Theory Course. Plenum, New York (2000)
4. Andersen, N., Bartschat, K.: Polarization, Alignment, and Orientation in Atomic Collisions, 2nd edn. Springer, New York (2017)
5. Kessler, J.: Polarized Electrons. Springer, New York (1985)
6. Baylis, W.E., Bonenfant, J., Derbyshire, J., Huschilt, J.: Am. J. Phys. **61**, 534 (1993)
7. Born, M., Wolf, E.: Principles of Optics. Pergamon, New York (1970)
8. Bartschat, K., Blum, K., Hanne, G.F., Kessler, J.: J. Phys. B **14**, 3761 (1981)
9. Bartschat, K., Blum, K.: Z. Phys. A **304**, 85 (1982)
10. Andersen, N., Gallagher, J.W., Hertel, I.V.: Phys. Rep. **165**, 1 (1988)
11. Bartschat, K.: Phys. Rep. **180**, 1 (1989)
12. Edmonds, A.R.: Angular Momentum in Quantum Mechanics. Princeton Univ. Press, Princeton (1957)
13. Fano, U., Macek, J.H.: Rev. Mod. Phys. **45**, 553 (1973)

14. Bartschat, K., Andrä, H.J., Blum, K.: *Z. Phys. A* **314**, 257 (1983)
15. Andersen, N., Broad, J.T., Campbell, E.E., Gallagher, J.W., Hertel, I.V.: *Phys. Rep.* **278**, 107 (1997)
16. Andersen, N., Bartschat, K., Broad, J.T., Hertel, I.V.: *Phys. Rep.* **279**, 251 (1997)
17. Andersen, N., Bartschat, K.: *Adv. At. Mol. Phys.* **36**, 1 (1996)
18. Andersen, N., Bartschat, K.: *J. Phys. B* **27**, 3189 (1994). corrigendum: *J. Phys. B* **29**, 1149 (1996)
19. Sohn, M., Hanne, G.F.: *J. Phys. B* **25**, 4627 (1992)
20. Bederson, B.: *Comments At. Mol. Phys.* **1**, 41, 65 (1969)
21. Andersen, N., Bartschat, K.: *J. Phys. B* **30**, 5071 (1997)



Klaus Bartschat Klaus Bartschat is the Levitt Distinguished Professor of Physics at Drake University. His research focuses on the general theory and computational treatment of electron and photon collisions with atoms and ions, including the direct solution of the time-dependent Schrödinger equation for ultrashort intense laser-matter interactions and the use of the R-matrix (close-coupling) method for electron collisions with complex targets.



Computational Techniques

8

David Schultz  and Michael R. Strayer

Contents

8.1	Representation of Functions	132
8.1.1	Interpolation	132
8.1.2	Fitting	133
8.1.3	Fourier Analysis	135
8.1.4	Approximating Integrals	135
8.1.5	Approximating Derivatives	136
8.2	Differential and Integral Equations	137
8.2.1	Ordinary Differential Equations	137
8.2.2	Differencing Algorithms for Partial Differential Equations	138
8.2.3	Variational Methods	140
8.2.4	Finite Elements	140
8.2.5	Integral Equations	142
8.3	Computational Linear Algebra	143
8.4	Monte Carlo Methods	144
8.4.1	Random Numbers	145
8.4.2	Distributions of Random Numbers	145
8.4.3	Monte Carlo Integration	146
	References	147

Abstract

Essential to atomic, molecular, and optical physics is the ability to perform numerical computations accurately and efficiently. Whether the specific approach involves perturbation theory, close coupling expansion, solution of classical equations of motion, or fitting and smoothing of data, basic computational techniques such as integration, differentiation, interpolation, matrix and eigenvalue manipulation, Monte Carlo sampling, and solution of differential equations must be among the standard tool kit.

This chapter outlines a portion of this tool kit with the aim of giving guidance and organization to a wide array

of computational techniques. After having digested the present overview, the reader is then referred to detailed treatments given in many of the large number of texts existing on numerical analysis and computational techniques [1–6], mathematical functions [7–9], and mathematical physics [10–18].

In addition to these excellent general references, in the age of the internet, many resources are also available through free publishing projects or research laboratory resources made public. Many of these resources seek to provide techniques and computer codes of high accuracy, portability, robustness, and efficiency, and often take advantage of modern structured programming and computational parallelism, going beyond the highly accessible, broadly applicable, but simple numerical recipes and codes described in the classic texts. A list of such numerical analysis software is given on the Wikipedia, providing very brief descriptions of the packages available [19], and the journal *Computer Physics Communications* (CPC) publishes computational physics research and applications software with many codes applicable to atomic, molecular, and optical physics (see the CPC program library maintained at Queen’s University Belfast [20]). Especially in the sections that follow on differential equations and computational linear algebra, mention is made of the role of software packages readily available to aid in implementing practical solutions.

Finally, in this brief introduction to computational techniques, we note the existence of commercial packages for mathematics, including those for computer algebra, performing numerical calculations and visualizing results through proprietary programming languages, and even performing simulations through such tools as finite-element analysis, including Mathematica, Maple, MATLAB, Mathcad, and COMSOL, for example.

D. Schultz (✉)
 Department of Astronomy and Planetary Science, Northern Arizona
 University
 Flagstaff, AZ, USA
 e-mail: david.schultz@nau.edu

Keywords

numerical methods · numerical analysis · computational methods · numerical approximation · numerical integration · random numbers · linear algebra · differential equations · interpolation · Fourier analysis

8.1 Representation of Functions

The ability to represent functions in terms of polynomials or other basic functions is the key to interpolating or fitting data, and to approximating numerically the operations of integration and differentiation. In addition, using methods such as Fourier analysis, knowledge of the properties of functions beyond even their intermediate values, derivatives, and antiderivatives may be determined (e.g., the *spectral* properties).

8.1.1 Interpolation

Given the value of a function $f(x)$ at a set of points x_1, x_2, \dots, x_n , the function is often required at some other values between these abscissas. The process known as *interpolation* seeks to estimate these unknown values by adjusting the parameters of a known function to approximate the local or global behavior of $f(x)$. One of the most useful representations of a function for these purposes utilizes the *algebraic polynomials*, $P_n(x) = a_0 + a_1x + \dots + a_nx^n$, where the coefficients are real constants, and the exponents are nonnegative integers. The utility stems from the fact that given any continuous function defined on a closed interval, there exists an algebraic polynomial that is as close to that function as desired (Weierstrass theorem).

One simple application of these polynomials is the power series expansion of the function $f(x)$ about some point, x_0 , i.e.,

$$f(x) = \sum_{k=0}^{\infty} a_k (x - x_0)^k. \quad (8.1)$$

A familiar example is the *Taylor expansion*, in which the coefficients are given by

$$a_k = \frac{f^{(k)}(x_0)}{k!}, \quad (8.2)$$

where $f^{(k)}$ indicates the k -th derivative of the function. This form, although quite useful in the derivation of formal techniques, is not very useful for interpolation, since it assumes the function and its derivatives are known and since it is guaranteed to be a good approximation only very near the point x_0 about which the expansion has been made.

Lagrange Interpolation

The polynomial of degree $n - 1$ that passes through all n points $[x_1, f(x_1)], [x_2, f(x_2)], \dots, [x_n, f(x_n)]$ is given by

$$P(x) = \sum_{k=1}^n f(x_k) \prod_{i=1, i \neq k}^n \frac{x - x_i}{x_k - x_i} \quad (8.3)$$

$$= \sum_{k=1}^n f(x_k) L_{nk}(x), \quad (8.4)$$

where $L_{nk}(x)$ are the *Lagrange interpolating polynomials*. Perhaps the most familiar example is that of linear interpolation between the points $[x_1, y_1 \equiv f(x_1)]$ and $[x_2, y_2 \equiv f(x_2)]$, namely,

$$P(x) = \frac{x - x_2}{x_1 - x_2} y_1 + \frac{x - x_1}{x_2 - x_1} y_2. \quad (8.5)$$

In practice, it is difficult to estimate the formal error bound for this method, since it depends on knowledge of the $(n + 1)$ -th derivative. Alternatively, one uses *iterated interpolation*, in which successively higher-order approximations are tried until appropriate agreement is obtained. *Neville's algorithm* defines a recursive procedure to yield an arbitrary order interpolant from polynomials of lower order. This method and subtle refinements of it form the basis for most recommended polynomial interpolation schemes [3–5].

One important word of caution to bear in mind is that the more points used in constructing the interpolant, and therefore the higher the polynomial order, the greater will be the oscillation in the interpolating function. This highly oscillating polynomial most likely will not correspond more closely to the desired function than polynomials of lower order. As a general rule of thumb, fewer than six points should be used.

Cubic Splines

By dividing the interval of interest into a number of subintervals and in each using a polynomial of only modest order, one may avoid the oscillatory nature of high-order (many-point) interpolants. This approach utilizes *piecewise polynomial functions*, the simplest of which is just a linear segment. However, such a straight line approximation has a discontinuous derivative at the data points – a property that one may wish to avoid, especially if the derivative of the function is also desired – and which clearly does not provide a smooth interpolant. The solution, therefore, is to choose the polynomial of lowest order that has enough free parameters (the constants a_0, a_1, \dots) to satisfy the constraints that the function and its derivative are continuous across the subintervals, as well as specifying the derivative at the endpoints x_0 and x_n .

Piecewise cubic polynomials satisfy these constraints and have a continuous second derivative as well. *Cubic spline interpolation* does not, however, guarantee that the derivatives of the interpolant agree with those of the function at the data

points, much less globally. The cubic polynomial in each interval has four undetermined coefficients,

$$P_i(x) = a_i + b_i(x - x_i) + c_i(x - x_i)^2 + d_i(x - x_i)^3, \quad (8.6)$$

for $i = 0, 1, \dots, n - 1$. Applying the constraints, a system of equations is found that may be solved once the endpoint derivatives are specified. If the second derivatives at the endpoints are set to zero, then the result is termed a *natural spline*, and its shape is like that which a long flexible rod would take if forced to pass through all the data points. A *clamped spline* results if the first derivatives are specified at the endpoints, and is usually a better approximation since it incorporates more information about the function (if one has a reasonable way to determine or approximate these first derivatives).

The set of equations in the unknowns, along with the boundary conditions, constitute a *tridiagonal system or matrix*, and is therefore amenable to solution by algorithms designed for speed and efficiency for such systems (Sect. 8.3; [1–5]). Other alternatives of potentially significant utility are schemes based on the use of rational functions and orthogonal polynomials.

Rational Function Interpolation

If the function that one seeks to interpolate has one or more poles for real x , then polynomial approximations are not good, and a better method is to use quotients of polynomials, so-called *rational functions*. This occurs since the inverse powers of the dependent variable will fit the region near the pole better if the order is large enough. In fact, if the function is free of poles on the real axis but its analytic continuation in the complex plane has poles, the polynomial approximation may also be poor. It is this property that slows or prevents the convergence of power series. Numerical algorithms very similar to those used to generate iterated polynomial interpolants exist [1, 3–5] and can be useful for functions that are not amenable to polynomial interpolation. Rational function interpolation is related to the method of *Padé approximation* used to improve convergence of power series. This is a rational function analog of Taylor expansion.

Orthogonal Function Interpolation

Interpolation using functions other than the algebraic polynomials can be defined and are often useful. Particularly worthy of mention are schemes based on *orthogonal polynomials* since they play a central role in numerical quadrature. A set of functions $\phi_1(x), \phi_2(x), \dots, \phi_n(x)$ defined on the interval $[a, b]$ is said to be orthogonal with respect to a weight function $\mathcal{W}(x)$, if the inner product defined by

$$\langle \phi_i | \phi_j \rangle = \int_a^b \phi_i(x) \phi_j(x) \mathcal{W}(x) dx \quad (8.7)$$

is zero for $i \neq j$ and positive for $i = j$. In this case, for any polynomial $P(x)$ of degree at most n , there exists unique constants α_k such that

$$P(x) = \sum_{k=0}^n \alpha_k \phi_k(x). \quad (8.8)$$

Among the more commonly used orthogonal polynomials are *Legendre*, *Laguerre*, and *Chebyshev* polynomials.

Chebyshev Interpolation

The significant advantages of employing a representation of a function in terms of Chebyshev polynomials, $T_k(x)$, i.e.,

$$f(x) = \sum_{k=0}^{\infty} a_k T_k(x), \quad (8.9)$$

stems from the fact that (i) the expansion rapidly converges, (ii) the polynomials have a simple form, and (iii) the polynomial approximates the solution of the *minimax* problem very closely. This latter property refers to the requirement that the expansion *minimizes* the *maximum* magnitude of the error of the approximation. In particular, the Chebyshev series expansion can be truncated, so that for a given n it yields the most accurate approximation to the function. Thus, Chebyshev polynomial interpolation is essentially as good as one can hope to do. Since these polynomials are defined on the interval $[-1, 1]$, if the endpoints of the interval in question are a and b , the change of variable

$$y = \frac{x - \frac{1}{2}(b + a)}{\frac{1}{2}(b - a)} \quad (8.10)$$

will affect the proper transformation. *Press et al.* [3–5], for example, give convenient and efficient routines for computing the Chebyshev expansion of a function. See [7, 10] for tabulations, recurrence formulas, orthogonality properties, etc., of these polynomials.

8.1.2 Fitting

Fitting of data stands in distinction from interpolation in that the data may have some uncertainty. Therefore, simply determining a polynomial that passes through the points may not yield the best approximation of the underlying function. In fitting, one is concerned with minimizing the deviations of some model function from the data points in an optimal or best-fit manner. For example, given a set of data points, even a low-order interpolating polynomial might have significant oscillation. In fact, if one accounts for the statistical uncertainties in the data, the best fit may be obtained simply by considering the points to lie on a line.

In addition, most of the traditional methods of assigning this quality of best fit to a particular set of parameters of the model function rely on the assumption that the random deviations are described by a Gaussian (normal) distribution. Results of physical measurements, for example the counting of events, is often closer to a Poisson distribution, which tends (not necessarily uniformly) to a Gaussian in the limit of a large number of events, or may even contain *outliers* that lie far outside a Gaussian distribution. In these cases, fitting methods might significantly distort the parameters of the model function in trying to force these different distributions to the Gaussian form. Thus, the *least-squares* and *chi-square* fitting procedures discussed below should be used with this caveat in mind. Other techniques, often termed *robust fitting* [3–5, 21], should be used when the distribution is not Gaussian or replete with outliers.

Least Squares

In this common approach to fitting, we wish to determine the m parameters a_l of some function $f(x; a_1, a_2, \dots, a_m)$, in this example depending on one variable, x . In particular, we seek to minimize the sum of the squares of the deviations

$$\sum_{k=1}^n [y(x_k) - f(x_k; a_1, a_2, \dots, a_m)]^2 \quad (8.11)$$

by adjusting the parameters, where the $y(x_k)$ are the n data points. In the simplest case, the model function is just a straight line, $f(x; a_1, a_2) = a_1x + a_2$. Elementary multivariate calculus implies that a minimum occurs if

$$a_1 \sum_{k=1}^n x_k^2 + a_2 \sum_{k=1}^n x_k = \sum_{k=1}^n x_k y_k, \quad (8.12)$$

$$a_1 \sum_{k=1}^n x_k + a_2 n = \sum_{k=1}^n y_k, \quad (8.13)$$

which are called the *normal equations*. Solution of these equations is straightforward, and an error estimate of the fit can be found [3–5]. In particular, variances may be computed for each parameter, as well as measures of the correlation between uncertainties and an overall estimate of the *goodness of fit* of the data.

Chi-Square Fitting

If the data points each have associated with them a different standard deviation, σ_k , the least-squares principle is modified by minimizing the *chi-square*, defined as

$$\chi^2 \equiv \sum_{k=1}^n \left[\frac{y_k - f(x_k; a_1, a_2, \dots, a_m)}{\sigma_k} \right]^2. \quad (8.14)$$

Assuming that the uncertainties in the data points are normally distributed, the chi-square value gives a measure of the

goodness of fit. If there are n data points and m adjustable parameters, then the probability that χ^2 should exceed a particular value purely by chance is

$$Q = Q\left(\frac{n-m}{2}, \frac{\chi^2}{2}\right), \quad (8.15)$$

where $Q(a, x) = \Gamma(a, x)/\Gamma(a)$ is the incomplete gamma function. For small values of Q , the deviations of the fit from the data are unlikely to be by chance, and values close to one are indications of better fits. In terms of the chi-square, reasonable fits often have $\chi^2 \approx n - m$.

Other important applications of the chi-square method include simulation and estimating standard deviations. For example, if one has some idea of the actual (i.e., non-Gaussian) distribution of uncertainties of the data points, Monte Carlo simulation can be used to generate a set of test data points subject to this presumed distribution, and then the fitting procedure may be performed on the simulated data set. This allows one to test the accuracy or applicability of the model function chosen. In other situations, if the uncertainties of the data points are unknown, one can assume that they are all equal to some value, say σ , fit using the chi-square procedure, and solve for the value of σ . Thus, some measure of the uncertainty from this statistical point of view can be provided.

General Least Squares

The least-squares procedure can be generalized, usually by allowing any linear combination of basis functions to determine the model function

$$f(x; a_1, a_2, \dots, a_m) = \sum_{l=1}^m a_l \psi_l(x). \quad (8.16)$$

The basis functions need not be polynomials. Similarly, the formula for chi-square can be generalized and normal equations determined through minimization. The equations may be written in compact form by defining a matrix \mathbf{A} with elements

$$A_{i,j} = \frac{\psi_j(x_i)}{\sigma_i}, \quad (8.17)$$

and a column vector \mathbf{B} with elements

$$B_i = \frac{y_i}{\sigma_i}. \quad (8.18)$$

Then the normal equations are [3–5]

$$\sum_{j=1}^m \alpha_{kj} a_j = \beta_k, \quad (8.19)$$

where

$$[\alpha] = \mathbf{A}^T \mathbf{A}, \quad [\beta] = \mathbf{A}^T \mathbf{B}, \quad (8.20)$$

and a_j are the adjustable parameters. These equations may be solved using standard methods of computational linear algebra such as Gauss–Jordan elimination. Difficulties involving sensitivity to round-off errors can be avoided by using carefully developed codes to perform this solution [3–5]. We note that elements of the inverse of the matrix α are related to the variances associated with the free parameters and to the covariances relating them.

Statistical Analysis of Data

Data generated by an experiment, or from a Monte Carlo simulation, have uncertainties due to the statistical, or random, character of the processes by which they are acquired. Therefore, one must be able to describe certain features of the data statistically, such as their mean, variance and skewness, and the degree to which correlations exist, either between one portion of the data and another, or between the data and some other standard or model distribution. A very readable introduction to this type of analysis was given by *Young* [22], while more comprehensive treatments are also available [23].

8.1.3 Fourier Analysis

The *Fourier transform* takes, for example, a function of time into a function of frequency, or vice versa, namely

$$\tilde{\varphi}(\omega) = \frac{1}{\sqrt{2\pi}} \int_{-\infty}^{\infty} \varphi(t) e^{i\omega t} dt, \quad (8.21)$$

$$\varphi(t) = \frac{1}{\sqrt{2\pi}} \int_{-\infty}^{\infty} \tilde{\varphi}(\omega) e^{-i\omega t} d\omega. \quad (8.22)$$

In this case, the time history of the function $\varphi(t)$ may be termed the *signal* and $\tilde{\varphi}(\omega)$ the *frequency spectrum*. Also, if the frequency is related to the energy by $E = \hbar\omega$, one obtains an *energy spectrum* from a signal, and thus the name *spectral methods* for techniques based on the Fourier analysis of signals.

The Fourier transform also defines the relationship between the spatial and momentum representations of wave functions, i.e.,

$$\psi(x) = \frac{1}{\sqrt{2\pi}} \int_{-\infty}^{\infty} \tilde{\psi}(p) e^{ipx} dp, \quad (8.23)$$

$$\tilde{\psi}(p) = \frac{1}{\sqrt{2\pi}} \int_{-\infty}^{\infty} \psi(x) e^{-ipx} dx. \quad (8.24)$$

Along with the closely related *sine*, *cosine*, and *Laplace transforms*, the Fourier transform is an extraordinarily powerful tool in the representation of functions, spectral analysis,

convolution of functions, filtering, and analysis of correlation. Good introductions to these techniques with particular attention to applications in physics can be found in [10, 16, 24]. To implement the Fourier transform numerically, the integral transform pair can be converted to sums

$$\tilde{\varphi}(\omega_j) = \frac{1}{\sqrt{2N2\pi}} \sum_{k=0}^{2N-1} \varphi(t_k) e^{i\omega_j t_k}, \quad (8.25)$$

$$\varphi(t_k) = \frac{1}{\sqrt{2N2\pi}} \sum_{j=0}^{2N-1} \tilde{\varphi}(\omega_j) e^{-i\omega_j t_k}, \quad (8.26)$$

where the functions are *sampled* at $2N$ points. These equations define the *discrete Fourier transform* (DFT). Two cautions in using the DFT are as follows.

First, if a continuous function of time is sampled at, for simplicity, uniformly spaced intervals, (i.e., $t_{i+1} = t_i + \Delta$), then there is a critical frequency $\omega_c = \pi/\Delta$, known as the *Nyquist frequency*, which limits the fidelity of the DFT of this function in that it is *aliased*. That is, components outside the frequency range $-\omega_c$ to ω_c are falsely transformed into this range due to the finite sampling. This effect can be remediated by filtering or windowing techniques. If, however, the function is *bandwidth limited* to frequencies smaller than ω_c , then the DFT does not suffer from this effect, and the signal is completely determined by its samples.

Second, implementing the DFT directly from the equations above would require approximately N^2 multiplications to perform the Fourier transform of a function sampled at N points. A variety of *fast Fourier transform* (FFT) algorithms have been developed (e.g., the Danielson–Lanczos and Cooley–Tukey methods) that require only on the order of $(N/2) \log_2 N$ multiplications. Thus, for even moderately large sets of points, the FFT methods are, indeed, much faster than the direct implementation of the DFT. Issues involved in sampling, aliasing, and selection of algorithms for the FFT are discussed in great detail, for example, in [3–5, 15, 25]. In addition to basic computer codes with which to implement the FFT and related tasks, given, for example, in *Numerical Recipes* [3–5], codes for real and complex valued FFTs that have been implemented and benchmarked on a variety of platforms including parallel computer systems are available, for example, the Fastest Fourier Transform in the West (FFTW) [26].

8.1.4 Approximating Integrals

Polynomial Quadrature

Definite integrals may be approximated through a procedure known as numerical quadrature by replacing the integral by

an appropriate sum, i.e.,

$$\int_a^b f(x)dx \approx \sum_{k=0}^n a_k f(x_k) . \quad (8.27)$$

Most formulas for such approximations are based on the interpolating polynomials described in Sect. 8.1.1, especially the Lagrange polynomials, in which case the coefficients a_k are given by

$$a_k = \int_a^b L_{nk}(x_k)dx . \quad (8.28)$$

If first or second degree Lagrange polynomials are used with a uniform spacing between the data points, one obtains the *trapezoidal* and *Simpson's rules*, i.e.,

$$\int_a^b f(x)dx \approx \frac{\delta}{2} [f(a) + f(b)] + \mathcal{O}[\delta^3 f^{(2)}(\zeta)] , \quad (8.29)$$

$$\int_a^b f(x)dx \approx \frac{\delta}{3} \left[f(a) + 4f\left(\frac{\delta}{2}\right) + f(b) \right] + \mathcal{O}[\delta^5 f^{(4)}(\zeta)] , \quad (8.30)$$

respectively, with $\delta = b - a$, and for some ζ in $[a, b]$.

Other commonly used formulas based on low-order polynomials, generally referred to as *Newton-Cotes* formulas, are described and discussed in detail in numerical analysis texts [1, 2]. Since potentially unwanted rapid oscillations in interpolants may arise, it is generally the case that increasing the order of the quadrature scheme too greatly does not generally improve the accuracy of the approximation. Dividing the interval $[a, b]$ into a number of subintervals and summing the result of application of a low-order formula in each subinterval is usually a much better approach. This procedure, referred to as *composite quadrature*, may be combined with choosing the data points at a nonuniform spacing, decreasing the spacing where the function varies rapidly, and increasing the spacing for economy where the function is smooth to construct an *adaptive quadrature*.

Gaussian Quadrature

If the function whose definite integral is to be approximated can be evaluated explicitly, then the data points (abscissas) can be chosen in a manner in which significantly greater accuracy may be obtained than using Newton-Cotes formulas of equal order. *Gaussian quadrature* is a procedure in which the error in the approximation is minimized owing to this freedom to choose both data points (abscissas) and coefficients. By utilizing orthogonal polynomials and choosing the abscissas at the roots of the polynomials in the interval under

consideration, it can be shown that the coefficients may be optimally chosen by solving a simple set of linear equations.

Thus, a Gaussian quadrature scheme approximates the definite integral of a function multiplied by the weight function appropriate to the orthogonal polynomial being used as

$$\int_a^b \mathcal{W}(x)f(x)dx \approx \sum_{k=1}^n a_k f(x_k) , \quad (8.31)$$

where the function is to be evaluated at the abscissas given by the roots of the orthogonal polynomial, x_k . In this case, the coefficients a_k are often referred to as *weights* but should not be confused with the weight function $\mathcal{W}(x)$ (Sect. 8.1.1). Since the Legendre polynomials are orthogonal over the interval $[-1, 1]$ with respect to the weight function $\mathcal{W}(x) \equiv 1$, this equation has a particularly simple form, leading immediately to the *Gauss-Legendre quadrature*. If $f(x)$ contains the weight function of another of the orthogonal polynomials as a factor, the corresponding *Gauss-Laguerre* or *Gauss-Chebyshev* quadrature should be used.

The roots and coefficients have been tabulated [7] for many common choices of the orthogonal polynomials (e.g., Legendre, Laguerre, Chebyshev) and for various orders. Simple computer subroutines are also available that conveniently compute them [3–5]. Since the various orthogonal polynomials are defined over different intervals, use of the change of variables such as that given in Eq. (8.10) may be required. So, for Gauss-Legendre quadrature we make use of the transformation

$$\int_a^b f(x) dx \approx \frac{(b-a)}{2} \int_{-1}^1 f\left(\frac{(b-a)y + b + a}{2}\right) dy . \quad (8.32)$$

Other Methods

Especially for multidimensional integrals that cannot be reduced analytically to separable or iterated integrals of lower dimension, *Monte Carlo* integration may provide the only means of finding a good approximation. This method is described in Sect. 8.4.3. Also, a convenient quadrature scheme can be devised based on the cubic spline interpolation described in Sect. 8.1.1, since in each subinterval, the definite integral of a cubic polynomial of known coefficients is evident.

8.15 Approximating Derivatives

Numerical Differentiation

The calculation of derivatives from a numerical representation of a function is generally less stable than the calculation of integrals, because differentiation tends to enhance fluctuations and worsen the convergence properties of power series.

For example, if $f(x)$ is twice continuously differentiable on $[a, b]$, then differentiation of the linear Lagrange interpolation formula Eq. (8.5) yields

$$f^{(1)}(x_0) = \frac{f(x_0 + \delta) - f(x_0)}{\delta} + \mathcal{O}[\delta f^{(2)}(\zeta)], \quad (8.33)$$

for some x_0 and ζ in $[a, b]$, where $\delta = b - a$. In the limit $\delta \rightarrow 0$, Eq. (8.33) coincides with the definition of the derivative. However, in practical calculations with finite precision arithmetic, δ cannot be taken too small because of numerical cancellation in the calculation of $f(a + \delta) - f(a)$.

In practice, increasing the order of the polynomial used decreases the truncation error, but at the expense of increasing round-off error, the upshot being that three and five-point approximations are usually the most useful. Various three and five-point formulas are given in standard texts [2, 7, 9]. Two common five-point formulas (centered and forward/backward) are

$$f^{(1)}(x_0) = \frac{1}{12\delta} [f(x_0 - 2\delta) - 8f(x_0 - \delta) + 8f(x_0 + \delta) - f(x_0 + 2\delta)] + \mathcal{O}[\delta^4 f^{(5)}(\zeta)] \quad (8.34)$$

$$f^{(1)}(x_0) = \frac{1}{12\delta} [-25f(x_0) + 48f(x_0 + \delta) - 36f(x_0 + 2\delta) + 16f(x_0 + 3\delta) - 3f(x_0 + 4\delta)] + \mathcal{O}[\delta^4 f^{(5)}(\zeta)]. \quad (8.35)$$

The second formula is useful for evaluating the derivative at the left or right endpoint of the interval, depending on whether δ is positive or negative, respectively.

Derivatives of Interpolated Functions

An interpolating function can be directly differentiated to obtain the derivative at any desired point. For example, if $f(x) \approx a_0 + a_1x + a_2x^2$, then $f^{(1)}(x) = a_1 + 2a_2x$. However, this approach may fail to give the best approximation to $f^{(1)}(x)$ if the original interpolation was optimized to give the best possible representation of $f(x)$.

8.2 Differential and Integral Equations

The subject of differential and integral equations is immense in both richness and scope. The discussion here focuses on techniques and algorithms, rather than the formal aspect of the theory. Further information can be found elsewhere under the broad categories of finite-element and finite-difference methods. The *Numerov method*, which is particularly useful in integrating the Schrödinger equation, is described in great detail in [18].

8.2.1 Ordinary Differential Equations

An *ordinary differential equation* is an equation involving an unknown function and one or more of its derivatives that depend on only one independent variable [27]. The *order* of a differential equation is the order of the highest derivative appearing in the equation. A solution of a general differential equation of order n ,

$$f(t, y, \dot{y}, \dots, y^{(n)}) = 0, \quad (8.36)$$

is a real-valued function $y(t)$ having the following properties: (1) $y(t)$ and its first n derivatives exist, so $y(t)$ and its first $n - 1$ derivatives must be continuous, and (2) $y(t)$ satisfies the differential equation for all t . A unique solution requires the specification of n conditions on $y(t)$ and its derivatives. The conditions may be specified as n initial conditions at a single t to give an *initial-value problem*, or at the end points of an interval to give a *boundary value problem*.

First consider solutions to the simple equation

$$\dot{y} = f(t, y), \quad y(a) = A. \quad (8.37)$$

The methods discussed below can be extended to systems of first-order differential equations and to higher-order differential equations. The methods are referred to as *discrete-variable methods* and generate a sequence of approximate values for $y(t)$, y_1, y_2, y_3, \dots at points t_1, t_2, t_3, \dots . For simplicity, the discussion here assumes a constant spacing h between t points. We shall first describe a class of methods known as *one-step methods* [28]. They have no memory of the solutions at past times; given y_i , there is a recipe for y_{i+1} that depends only on information at t_i . Errors enter into numerical solutions from two sources. The first is the *discretization error* and depends on the method being used. The second is the *computational error* that includes such things as round-off error.

For a solution on the interval $[a, b]$, let the t points be equally spaced; so for some positive integer n and $h = (b - a)/n$, $t_i = a + ih$, $i = 0, 1, \dots, n$. If $a < b$, h is positive, and the integration is forward; if $a > b$, h is negative, and the integration is backward. The latter case could occur in solving for the initial point of a solution curve given the terminal point. A general one-step method can then be written in the form

$$y_{i+1} = y_i + h\Delta(t_i, y_i), \quad y_0 = y(t_0), \quad (8.38)$$

where Δ is a function that characterizes the method. Different Δ functions are displayed next, giving rise to the Taylor-series methods and the Runge–Kutta methods.

Taylor-Series Algorithm

To obtain an approximate solution of order p on $[a, b]$, generate the sequence

$$\begin{aligned} y_{i+1} &= y_i + h \left[f(t_i, y_i) + \cdots + f^{(p-1)}(t_i, y_i) \frac{h^{p-1}}{p!} \right], \\ t_{i+1} &= t_i + h, \quad i = 0, 1, \dots, n-1, \end{aligned} \quad (8.39)$$

where $t_0 = a$, and $y_0 = A$. The Taylor method of order $p = 1$ is known as *Euler's method*:

$$\begin{aligned} y_{i+1} &= y_i + hf(t_i, y_i), \\ t_{i+1} &= t_i + h. \end{aligned} \quad (8.40)$$

Taylor-series methods can be quite effective if the total derivatives of f are not too difficult to evaluate. Software packages are available that perform exact differentiation (ADIFOR, Maple, Mathematica, etc.), facilitating the use of this approach.

Runge–Kutta Methods

Runge–Kutta methods are designed to approximate Taylor-series methods [29] but have the advantage of not requiring explicit evaluations of the derivatives of $f(t, y)$. The basic idea is to use a linear combination of values of $f(t, y)$ to approximate $y(t)$. This linear combination is matched up as closely as possible with a Taylor series for $y(t)$ to obtain methods of the highest possible order p . Euler's method is an example using one function evaluation.

To obtain an approximate solution of order $p = 2$, let $h = (b - a)/n$ and generate the sequences

$$\begin{aligned} y_{i+1} &= y_i + h \left[(1 - \gamma)f(t_i, y_i) \right. \\ &\quad \left. + \gamma f \left[t_i + \frac{h}{2\gamma}, y_i + \frac{h}{2\gamma} f(t_i, y_i) \right] \right], \\ t_{i+1} &= t_i + h, \quad i = 0, 1, \dots, n-1, \end{aligned} \quad (8.41)$$

where $\gamma \neq 0$, $t_0 = a$, $y_0 = A$.

Euler's method is the special case, $\gamma = 0$, and has order 1; the improved Euler method has $\gamma = 1/2$, and the Euler–Cauchy method has $\gamma = 1$.

The Adams–Bashforth and Adams–Moulton Formulas

These formulas furnish important and widely used examples of multistep methods [30]. On reaching a mesh point t_i with approximate solution $y_i \cong y(t_i)$, (usually) approximate solutions $y_{i+1-j} \cong y(t_{i+1-j})$ for $j = 2, 3, \dots, p$ are available. From the differential equation itself, approximations to the derivatives $\dot{y}(t_{i+1-j})$ can be obtained.

An attractive feature of the approach is the form of the underlying polynomial approximation, $P(t)$, to $\dot{y}(t)$ because it can be used to approximate $y(t)$ between mesh points

$$y(t) \cong y_i + \int_{t_i}^t P(t) dt. \quad (8.42)$$

The lowest-order Adams–Bashforth formula arises from interpolating the single value $f_i = f(t_i, y_i)$ by $P(t)$. The interpolating polynomial is constant, so its integration from t_i to t_{i+1} results in $hf(t_i, y_i)$, and the first-order Adams–Bashforth formula:

$$y_{i+1} = y_i + hf(t_i, y_i). \quad (8.43)$$

This is just the forward Euler formula. For constant step size h , the second-order Adams–Bashforth formula is

$$y_{i+1} = y_i + h \left[\left(\frac{3}{2} \right) f(t_i, y_i) - \left(\frac{1}{2} \right) f(t_{i-1}, y_{i-1}) \right]. \quad (8.44)$$

The lowest-order Adams–Moulton formula involves interpolating the single value $f_{i+1} = f(t_{i+1}, y_{i+1})$ and leads to the backward Euler formula

$$y_{i+1} = y_i + hf(t_{i+1}, y_{i+1}), \quad (8.45)$$

which defines y_{i+1} implicitly. From its definition it is clear that it has the same accuracy as the forward Euler method; its advantage is vastly superior stability. The second-order Adams–Moulton method also does not use previously computed solution values; it is called the trapezoidal rule, because it generalizes the trapezoidal rule for integrals to differential equations:

$$y_{i+1} = y_i + \frac{h}{2} [f(t_{i+1}, y_{i+1}) + f(t_i, y_i)]. \quad (8.46)$$

The Adams–Moulton formula of order p is more accurate than the Adams–Bashforth formula of the same order. Hence, it can use a larger step size; the Adams–Moulton formula is also more stable. A code based on such methods is more complex than a Runge–Kutta code, because it must cope with the difficulties of starting the integration and changing the step size. Modern Adams codes attempt to select the most efficient formula at each step, as well as to choose an optimal step size h to achieve a specified accuracy.

8.2.2 Differencing Algorithms for Partial Differential Equations

Differencing schemes, based on flux conservation methods [31], are the modern approach to solving partial differential equations describing the evolution of physical systems.

One begins by writing the balance equations for a single cell and subsequently applying quadratures and interpolation formulas. Such approaches have been successful for the full spectrum of hyperbolic, elliptic, and parabolic equations. For simplicity, we begin by discussing systems involving only one space variable.

As a prototype, consider the parabolic equation

$$c \frac{\partial}{\partial t} u(x, t) = \sigma \frac{\partial^2}{\partial x^2} u(x, t), \quad (8.47)$$

where c and σ are constants, and $u(x, t)$ is the solution. We begin by establishing a grid of points on the xt -plane with step size h in the x direction and step size k in the t -direction. Let spatial grid points be denoted by $x_n = x_0 + nh$ and time grid points by $t_j = t_0 + jk$, where n and j are integers, and (x_0, t_0) is the origin of the space–time grid. The points ξ_{n-1} and ξ_n are introduced to establish a *control interval*. We begin with a conservation statement

$$\begin{aligned} & \int_{\xi_{n-1}}^{\xi_n} dx [r(x, t_{j+1}) - r(x, t_j)] \\ &= \int_{t_j}^{t_{j+1}} dt [q(\xi_{n-1}, t) - q(\xi_n, t)]. \end{aligned} \quad (8.48)$$

This equation states that the change in the field density on the interval (ξ_{n-1}, ξ_n) from time $t = t_j$ to time $t = t_{j+1}$ is given by the flux into this interval at ξ_{n-1} minus the flux out of the interval at ξ_n from time t_j to time t_{j+1} . This expresses the conservation of material in the case that no sources or sinks are present. We relate the field variable u to the physical variables (the density r and the flux q). We consider the case in which the density is assumed to have the form

$$r(x, t) = cu(x, t) + b, \quad (8.49)$$

with c and b constants; thus

$$\begin{aligned} & c \int_{\xi_{n-1}}^{\xi_n} dx [u(x, t_{j+1}) - u(x, t_j)] \\ & \approx c [u(x_n, t_{j+1}) - u(x_n, t_j)] h. \end{aligned} \quad (8.50)$$

When developing conservation-law equations, there are two commonly used strategies for approximating the right-hand-side of Eq. (8.48): (i) left-end-point quadrature

$$\begin{aligned} & \int_{t_j}^{t_{j+1}} dt [q(\xi_{n-1}, t) - q(\xi_n, t)] \\ & \approx [q(\xi_{n-1}, t_j) - q(\xi_n, t_j)] k, \end{aligned} \quad (8.51)$$

and (ii) right-end-point quadrature

$$\begin{aligned} & \int_{t_j}^{t_{j+1}} dt [q(\xi_{n-1}, t) - q(\xi_n, t)] \\ & \approx [q(\xi_{n-1}, t_{j+1}) - q(\xi_n, t_{j+1})] k. \end{aligned} \quad (8.52)$$

Combining Eq. (8.48) with the respective approximations yields: from (i) an *explicit* method

$$\begin{aligned} & c [u(x_n, t_{j+1}) - u(x_n, t_j)] h \\ & \approx [q(\xi_{n-1}, t_j) - q(\xi_n, t_j)] k, \end{aligned} \quad (8.53)$$

and from (ii) an *implicit* method

$$\begin{aligned} & c [u(x_n, t_{j+1}) - u(x_n, t_j)] h \\ & \approx [q(\xi_{n-1}, t_{j+1}) - q(\xi_n, t_{j+1})] k. \end{aligned} \quad (8.54)$$

Using centered-finite-difference formulas to approximate the fluxes at the control points ξ_{n-1} and ξ_n yields

$$q(\xi_{n-1}, t_j) = -\sigma \frac{u(x_n, t_j) - u(x_{n-1}, t_j)}{h}, \quad (8.55)$$

and

$$q(\xi_n, t_j) = -\sigma \frac{u(x_{n+1}, t_j) - u(x_n, t_j)}{h}, \quad (8.56)$$

where σ is a constant. We also obtain similar formulas for the fluxes at time t_{j+1} .

We have used a lower case u to denote the continuous field variable, $u = u(x, t)$. Note that all of the quadrature and difference formulas involving u are stated as approximate equalities. In each of these approximate equality statements, the amount by which the right-hand side differs from the left-hand side is called the truncation error. If u is a well-behaved function (has enough smooth derivatives), then it can be shown that these truncation errors approach zero as the grid spacings, h and k , approach zero.

If U_n^j denotes the exact solution on the grid, from (i) we have the result

$$c(U_n^{j+1} - U_n^j)h^2 = \sigma k (U_{n-1}^j + U_{n+1}^j - 2U_n^j). \quad (8.57)$$

This is an *explicit* method, since it provides the solution to the difference equation at time t_{j+1} , knowing the values at time t_j .

If we use the numerical approximations (ii), we obtain the result

$$c(U_n^{j+1} - U_n^j)h^2 = \sigma k (U_{n-1}^{j+1} + U_{n+1}^{j+1} - 2U_n^{j+1}). \quad (8.58)$$

Note that this equation defines the solution at time t_{j+1} *implicitly*, since a system of algebraic equations is required to be satisfied.

8.2.3 Variational Methods

A common problem in atomic, molecular, and optical physics is to find the extrema or the stationary values of functionals. For example, one might seek the eigenvalues and eigenvectors of a Hamiltonian system, such as via the minimization of the expectation value of the energy of a trial wave function to determine the ground state of an atom or molecule, via so-called *variational methods*. We shall outline in detail the Rayleigh–Ritz method [32]. This method is limited to boundary value problems that can be formulated in terms of the minimization of a functional $J[u]$. For definiteness we consider the case of a differential operator defined by

$$Lu(x) = f(x) , \quad (8.59)$$

with $x = x_i, i = 1, 2, 3$ in R , for example, and with $u = 0$ on the boundary of R . The function $f(x)$ is the source. It is assumed that L is always nonsingular, and in addition, for the Ritz method L is Hermitian. The real-valued functions u are in the Hilbert space Ω of the operator L . We construct the functional $J[u]$ defined as

$$J[u] = \int_{\Omega} dx [u(x)Lu(x) - 2u(x)f(x)] . \quad (8.60)$$

The variational ansatz considers a subspace of Ω , Ω_n , spanned by a class of functions $\phi_n(x)$, and we construct the function $u^n \approx u$ as

$$u^n(x) = \sum_{i=1}^n c_i \phi_i(x) . \quad (8.61)$$

We solve for the coefficients c_i by minimizing $J[u^n]$:

$$\partial_{c_i} J[u^n] = 0 , \quad i = 1, \dots, n . \quad (8.62)$$

These equations are cast into a set of well-behaved algebraic equations

$$\sum_{j=1}^n A_{i,j} c_j = g_i , \quad i = 1, \dots, n , \quad (8.63)$$

with $A_{i,j} = \int_{\Omega} dx \phi_i(x)L\phi_j(x)$, and $g_i = \int_{\Omega} dx \phi_i(x)f(x)$.

Under very general conditions, the functions u^n converge uniformly to u . The main drawback of the Ritz method lies in the assumption of hermiticity of the operator L . For the *Galerkin method* we relax this assumption with no other changes. Thus, we obtain an identical set of equations as above, with the exception that the function g is no longer symmetric. The convergence of the sequence of solutions u^n to u is no longer guaranteed, unless the operator can be separated into a symmetric part L_0 , $L = L_0 + K$, so that $L_0^{-1}K$ is bounded.

8.2.4 Finite Elements

As discussed in Sect. 8.2.2, in the finite-difference method for classical partial differential equations, the solution domain is approximated by a grid of uniformly spaced nodes. At each node, the governing differential equation is approximated by an algebraic expression that references adjacent grid points. A system of equations is obtained by evaluating the previous algebraic approximations for each node in the domain. Finally, the system is solved for each value of the dependent variable at each node. The *finite-element method* evolved from computational approaches to implementation of the variational method and of potentially greater accuracy and flexibility.

In the finite-element method [33], the solution domain can be discretized into a number of uniform or nonuniform finite elements that are connected via nodes. The change of the dependent variable with regard to location is approximated within each element by an interpolation function. The interpolation function is defined relative to the values of the variable at the nodes associated with each element. The original boundary value problem is then replaced with an equivalent integral formulation. The interpolation functions are substituted into the integral equation, integrated, and combined with the results from all other elements in the solution domain.

The results of this procedure can be reformulated into a matrix equation of the form

$$\sum_{j=1}^n A_{i,j} c_j = g_i , \quad i = 1, \dots, n , \quad (8.64)$$

with $A_{i,j} = \int_{\Omega} dx \phi_i(x)L\phi_j(x)$, and $g_i = \int_{\Omega} dx \phi_i(x)f(x)$ exactly as obtained in Sect. 8.2.3. The only difference arises in the definitions of the support functions $\phi_i(x)$. In general, if these functions are piecewise polynomials on some finite domain, they are called finite elements or splines. Finite elements make it possible to deal in a systematic fashion with regions having curved boundaries of an arbitrary shape. Also, one can systematically estimate the accuracy of the solution in terms of the parameters that label the finite-element family, and the solutions are no more difficult to generate than more complex variational methods.

In one space dimension, the simplest finite-element family begins with the set of step functions defined by

$$\phi_i(x) = \begin{cases} 1 & x_{i-1} \leq x \leq x_i \\ 0 & \text{otherwise} . \end{cases} \quad (8.65)$$

The use of these simple *hat* functions as a basis does not provide any advantage over the usual finite-difference schemes. However, for certain problems in two or more dimensions, finite-element methods have distinct advantages

over other methods. Generally, the use of finite elements requires complex, sophisticated computer programs for implementation. The use of higher-order polynomials, commonly called splines, as a basis has been extensively used in atomic and molecular physics. An extensive literature is available [34, 35].

We illustrate the use of the finite-element method by applying it to the Schrödinger equation. In this case, the linear operator L is $H - E$, where, as usual, E is the energy, and the Hamiltonian H is the sum of the kinetic and potential energies, that is, $L = H - E = \mathcal{T} + V - E$ and $Lu(x) = 0$. We define the finite elements through support points, or knots, given by the sequence $\{x_1, x_2, x_3, \dots\}$, which are not necessarily spaced uniformly. Since the *hat* functions have vanishing derivatives, we employ the next more complex basis, that is, *tent* functions, which are piecewise linear functions given by

$$\phi_i(x) = \begin{cases} \frac{x - x_{i-1}}{x_i - x_{i-1}} & x_{i-1} \leq x \leq x_i \\ \frac{x_{i+1} - x}{x_{i+1} - x_i} & x_i \leq x \leq x_{i+1} \\ 0 & \text{otherwise} \end{cases} \quad (8.66)$$

and for which the derivative is given by

$$\frac{d}{dx}\phi_i(x) = \begin{cases} \frac{1}{x_i - x_{i-1}} & x_{i-1} \leq x \leq x_i \\ -\frac{1}{x_{i+1} - x_i} & x_i \leq x \leq x_{i+1} \\ 0 & \text{otherwise} \end{cases} \quad (8.67)$$

The functions have a maximum value of 1 at the midpoint of the interval $[x_{i-1}, x_{i+1}]$, with partially overlapping adjacent elements. In fact, the overlaps may be represented by a matrix \mathbf{O} with elements

$$O_{ij} = \int_{-\infty}^{\infty} dx \phi_i(x)\phi_j(x). \quad (8.68)$$

Thus, if $i = j$,

$$\begin{aligned} O_{ii} &= \int_{x_{i-1}}^{x_i} dx \frac{(x - x_{i-1})^2}{(x_i - x_{i-1})^2} + \int_{x_i}^{x_{i+1}} dx \frac{(x - x_i)^2}{(x_{i+1} - x_i)^2} \\ &= \frac{1}{3}(x_{i+1} - x_{i-1}); \end{aligned} \quad (8.69)$$

if $i = j - 1$,

$$\begin{aligned} O_{ij} &= \int_{x_i}^{x_{i+1}} dx \frac{(x - x_i)(x_{i+1} - x)}{(x_{i+1} - x_i)^2} \\ &= \frac{1}{6}(x_{i+1} - x_i); \end{aligned} \quad (8.70)$$

if $i = j + 1$,

$$\begin{aligned} O_{ij} &= \int_{x_{i-1}}^{x_i} dx \frac{(x - x_{i-1})(x_i - x)}{(x_i - x_{i-1})^2} \\ &= \frac{1}{6}(x_i - x_{i-1}); \end{aligned} \quad (8.71)$$

and $O_{ij} = 0$ otherwise.

The potential energy is represented by the matrix

$$V_{ij} = \int_{-\infty}^{\infty} dx \phi_i(x)V(x)\phi_j(x), \quad (8.72)$$

which may be well approximated by

$$\begin{aligned} V_{ij} &\approx V(x_i) \int_{-\infty}^{\infty} dx \phi_i(x)\phi_j(x) \\ &= V(x_i)O_{ij}, \end{aligned} \quad (8.73)$$

if $x_j - x_i$ is small. The kinetic energy, $\mathcal{T} = -\frac{1}{2}d^2/dx^2$, is similarly given by

$$\mathcal{T}_{ij} = -\frac{1}{2} \int_{-\infty}^{\infty} dx \phi_i(x) \frac{d^2}{dx^2} \phi_j(x), \quad (8.74)$$

which we compute by integrating by parts, since the tent functions have a singular second derivative

$$\mathcal{T}_{ij} = \frac{1}{2} \int_{-\infty}^{\infty} dx \left(\frac{d}{dx} \phi_i(x) \right) \left(\frac{d}{dx} \phi_j(x) \right), \quad (8.75)$$

which in turn is evaluated to yield

$$\mathcal{T}_{ij} = \begin{cases} \frac{x_{i+1} - x_{i-1}}{2(x_i - x_{i-1})(x_{i+1} - x_i)} & i = j \\ \frac{1}{2(x_i - x_{i+1})} & i = j - 1 \\ \frac{1}{2(x_{i-1} - x_i)} & i = j + 1 \\ 0 & \text{otherwise} \end{cases} \quad (8.76)$$

Finally, since the Hamiltonian matrix is $H_{ij} = \mathcal{T}_{ij} + V_{ij}$, the solution vector $u_i(x)$ may be found by solving the eigenvalue equation

$$[H_{ij} - EO_{ij}]u_i(x) = 0. \quad (8.77)$$

Going beyond this simple example, discrete variable representation (DVR) methods, also known as pseudospectral methods, and direct solution of the Schrödinger equation

on numeral grids via finite-difference, finite-element, and high-order interpolant methods, have been adopted broadly in atomic, molecular, and optical physics as the power of computational resources has grown in recent decades. An introduction to DVR methods applied to solving the time-dependent Schrödinger equation for quantum dynamics of molecules, as an example, has been given by *Light* [36, 37].

8.2.5 Integral Equations

Central to much of practical and formal scattering theory is the integral equation and techniques of its solution. For example, in atomic collision theory, the Schrödinger differential equation

$$[E - H_0(\mathbf{r})]\psi(\mathbf{r}) = V(\mathbf{r})\psi(\mathbf{r}), \quad (8.78)$$

where the Hamiltonian $H_0 \equiv -(\hbar^2/2m)\nabla^2 + V_0$ may be solved by exploiting the solution for a delta function source, i.e.,

$$(E - H_0)G(\mathbf{r}, \mathbf{r}') = \delta(\mathbf{r} - \mathbf{r}'). \quad (8.79)$$

In terms of this *Green's function* $G(\mathbf{r}, \mathbf{r}')$, and any solution $\chi(\mathbf{r})$ of the homogeneous equation (i.e., with $V(\mathbf{r}) = 0$), the general solution is

$$\psi(\mathbf{r}) = \chi(\mathbf{r}) + \int d\mathbf{r}' G(\mathbf{r}, \mathbf{r}')V(\mathbf{r}')\psi(\mathbf{r}'), \quad (8.80)$$

for which, given a choice of the functions $G(\mathbf{r}, \mathbf{r}')$ and $\chi(\mathbf{r})$, particular boundary conditions are determined. This integral equation is the Lippmann–Schwinger equation of potential scattering. Further topics on scattering theory are covered in other chapters (especially Chaps. 49 to 62) and in standard texts such as those by *Joachain* [38], *Rodberg*, and *Thaler* [39], and *Goldberger* and *Watson* [40]. Owing especially to the wide variety of specialized techniques for solving integral equations, we briefly survey only a few of the most-frequently applied methods.

Integral Transforms

Certain classes of integral equations may be solved using integral transforms such as the Fourier or Laplace transforms. These integral transforms typically have the form

$$f(x) = \int dx' K(x, x')g(x'), \quad (8.81)$$

where $f(x)$ is the integral transform of $g(x')$ by the kernel $K(x, x')$. Such a pair of functions is the solution of the Schrödinger equation (spatial wave function) and its Fourier transform (momentum representation wave function). *Arfken* [10], *Morse*, and *Feshbach* [12], and *Courant*

and *Hilbert* [13] give other examples, as well as being excellent references for the application of integral equations and Green's functions in mathematical physics. In their analytic form, these transform methods provide a powerful method of solving integral equations for special cases. In addition, they may be implemented by performing the transform numerically.

Power Series Solution

For an equation of the form (in one dimension for simplicity)

$$\psi(r) = \chi(r) + \lambda \int dr' K(r, r')\psi(r'), \quad (8.82)$$

a solution may be found by iteration. That is, as a first approximation, set $\psi_0(r) = \chi(r)$ so that

$$\psi_1(r) = \chi(r) + \lambda \int dr' K(r, r')\chi(r'). \quad (8.83)$$

This may be repeated to form a power series solution, i.e.,

$$\psi_n(r) = \sum_{k=0}^n \lambda^k I_k(r), \quad (8.84)$$

where

$$I_0(r) = \chi(r), \quad (8.85)$$

$$I_1(r) = \int dr' K(r, r')\chi(r'), \quad (8.86)$$

$$I_2(r) = \int dr'' \int dr' K(r, r')K(r', r'')\chi(r''), \quad (8.87)$$

$$I_n(r) = \int dr' \dots \int dr^{(n)} K(r, r')K(r, r'') \dots K(r^{(n-1)}, r^{(n)}). \quad (8.88)$$

If the series converges, then the solution $\psi(r)$ is approached by the expansion. When the Schrödinger equation is cast as an integral equation for scattering in a potential, this iteration scheme leads to the *Born series*, the first term of which is the incident, unperturbed wave, and the second term is usually referred to simply as the *Born approximation*.

Separable Kernels

If the kernel is separable, i.e.,

$$K(r, r') = \sum_{k=1}^n f_k(r)g_k(r'), \quad (8.89)$$

where n is finite, then substitution into the prototype integral equation (8.82) yields

$$\psi(r) = \chi(r) + \lambda \sum_{k=1}^n f_k(r) \int dr' g_k(r')\psi(r'). \quad (8.90)$$

Multiplying by $f_k(r)$, integrating over r , and rearranging yields the set of algebraic equations

$$c_j = b_j + \lambda \sum_{k=1}^n a_{jk} c_k, \quad (8.91)$$

where

$$c_k = \int dr' g_k(r') \psi(r'), \quad (8.92)$$

$$b_k = \int dr f_k(r) \chi(r), \quad (8.93)$$

$$a_{jk} = \int dr g_j(r) f_k(r), \quad (8.94)$$

or, if \mathbf{c} and \mathbf{b} denote vectors, and \mathbf{A} denotes the matrix of constants a_{jk} ,

$$\mathbf{c} = (\mathbf{1} - \lambda \mathbf{A})^{-1} \mathbf{b}. \quad (8.95)$$

The eigenvalues are the roots of the determinantal equation. Substituting these into $(\mathbf{1} - \lambda \mathbf{A})\mathbf{c} = 0$ yields the constants c_k that determine the solution of the original equation. This derivation may be found in the text by *Arfken* [10], along with an explicit example. Even if the kernel is not exactly separable, if it is approximately so, then this procedure can yield a result that can be substituted into the original equation as a first step in an iterative solution.

Numerical Integration

Perhaps the most straightforward method of solving an integral equation is to apply a numerical integration formula such as Gaussian quadrature. An equation of the form

$$\psi(r) = \int dr' K(r, r') \chi(r') \quad (8.96)$$

can be approximated as

$$\psi(r_j) = \sum_{k=1}^n w_k K(r_j, r'_k) \chi(r_k), \quad (8.97)$$

where w_k are quadrature weights, if the kernel is well behaved. However, such an approach is not without pitfalls. In light of the previous section, this approach is equivalent to replacing the integral equation by a set of algebraic equations. In this example, we have

$$\psi_j = \sum_{k=1}^n M_{jk} \chi_k, \quad (8.98)$$

so that the solution of the equation is found by inverting the matrix \mathbf{M} . Since there is no guarantee that this matrix is not ill conditioned, the numerical procedure may not produce meaningful results. In particular, only certain classes of integral equations and kernels will lead to stable solutions.

8.3 Computational Linear Algebra

Previous sections of this chapter dealt with interpolation, differential equations, and related topics. Generally, discretization methodologies lead to classes of algebraic equations. In recent decades, enormous progress has been made in developing algorithms for solving linear-algebraic equations [41]. Many of the most widely adopted computational linear algebra routines are available through *Netlib* [42], a portal developed to facilitate the distribution of such software for use in scientific computation. These routines include packages such as the Basic Linear Algebra Subprograms (BLAS) [42, 43], which performs vector addition, dot products, matrix multiplications, etc., and the Linear Algebra Package (LAPACK, and ScaLAPACK its distributed memory implementation) [42, 44], which is used for solving linear systems of equations, eigenvalue problems, factorizations, and decompositions, etc.

Here, we discuss methods for solving systems of equations such as

$$\begin{aligned} a_{11}x_1 + a_{12}x_2 + \cdots + a_{1n}x_n &= b_1, \\ a_{21}x_1 + a_{22}x_2 + \cdots + a_{2n}x_n &= b_2, \\ &\vdots \\ a_{m1}x_1 + a_{m2}x_2 + \cdots + a_{mn}x_n &= b_m. \end{aligned} \quad (8.99)$$

In these equations, a_{ij} and b_i form the set of known quantities, and x_i must be determined. The solution to these equations can be found if they are linearly independent. Numerically, problems can arise due to truncation and round-off errors that lead to an approximate linear dependence [45]. In this case, the set of equations are approximately singular, and special methods must be invoked. Much of the complexity of modern algorithms comes from minimizing the effects of such errors. For relatively small sets of nonsingular equations, direct methods in which the solution is obtained after a definite number of operations can work well. However, for very large systems iterative techniques are preferable [46].

A great many algorithms are available for solving Eq. (8.99), depending on the structure of the coefficients. For example, if the matrix of coefficients \mathbf{A} is dense, using Gaussian elimination takes $2n^3/3$ operations; if \mathbf{A} is also symmetric and positive definite, using the Cholesky algorithm takes a factor of 2 fewer operations. If \mathbf{A} is triangular, that is, either zero above the diagonal or zero below the diagonal, we can solve the above system by simple substitution in only n^2 operations. For example, if \mathbf{A} arises from solving certain elliptic partial differential equations, such as Poisson's equation, then $\mathbf{A}\mathbf{x} = \mathbf{b}$ can be solved using multigrid methods in only n operations.

We shall outline below how to solve Eq. (8.99) using elementary Gaussian elimination. More advanced methods,

such as the *conjugate gradient*, *generalized minimum residuals*, and the *Lanczos method* are treated elsewhere [47].

To solve $A\mathbf{x} = \mathbf{b}$, we first use Gaussian elimination to factor the matrix A as $PA = LU$, where L is lower triangular, U is upper triangular, and P is a matrix that permutes the rows of A . Then we solve the triangular system $L\mathbf{y} = P\mathbf{b}$ and $U\mathbf{x} = \mathbf{y}$. These last two operations are easily performed using standard linear algebra libraries. The factorization $PA = LU$ takes most of the time. Reordering the rows of A with P is called pivoting and is necessary for numerical stability. In the standard partial pivoting scheme, L has 1s on its diagonal and other entries bounded in absolute value by 1. The simplest version of Gaussian elimination involves adding multiples of one row of A to others to zero out subdiagonal entries, and overwriting A with L and U .

We first describe the decomposition of PA into a product of upper and lower triangular matrices,

$$A' = LU, \quad (8.100)$$

where the matrix A' is defined by $A' = PA$. Writing out the indices, we obtain

$$A'_{ij} = \sum_{k=1}^{\min(i,j)} L_{ik}U_{kj}. \quad (8.101)$$

We shall make the choice

$$L_{ii} = 1. \quad (8.102)$$

These equations have the remarkable property that the elements A'_{ij} of each row can be scanned in turn, writing L_{ij} and U_{ij} into the locations A'_{ij} as we go. At each position (i, j) , only the current A'_{ij} and already-calculated values of $L_{i'j'}$ and $U_{i'j'}$ are required. To see how this works, consider the first few rows. If $i = 1$,

$$A'_{1j} = U_{1j}, \quad (8.103)$$

defining the first row of L and U . The U_{1j} are written over the A'_{1j} , which are no longer needed. If $i = 2$,

$$\begin{aligned} A'_{21} &= L_{21}U_{11}, & j &= 1 \\ A'_{2j} &= L_{21}U_{1j} + U_{2j}, & j &\geq 2. \end{aligned} \quad (8.104)$$

The first line gives L_{21} and the second U_{2j} , in terms of existing elements of L and U . The U_{2j} and L_{21} are written over the A'_{2j} . (Remember that $L_{ii} = 1$ by definition.) If $i = 3$,

$$\begin{aligned} A'_{31} &= L_{31}U_{11}, & j &= 1 \\ A'_{32} &= L_{31}U_{12} + L_{32}U_{22}, & j &= 2 \\ A'_{3j} &= L_{31}U_{1j} + L_{32}U_{2j} + U_{3j}, & j &\geq 3, \end{aligned} \quad (8.105)$$

yielding in turn L_{31}, L_{32} , and U_{3j} , which are written over A'_{3j} .

The algorithm should now be clear. At the i -th row,

$$\begin{aligned} L_{ij} &= U_{jj}^{-1} \left(A'_{ij} - \sum_{k=1}^{j-1} L_{ik}U_{kj} \right), & j &\leq i-1 \\ U_{ij} &= A'_{ij} - \sum_{k=1}^{i-1} L_{ik}U_{kj}, & j &\geq i. \end{aligned} \quad (8.106)$$

We observe from the first line of these equations that the algorithm may run into numerical inaccuracies if any U_{jj} becomes very small. Now $U_{11} = A'_{11}$, while in general $U_{ii} = A'_{ii} - \dots$. Thus the absolute values of the U_{ii} are maximized if the rows are rearranged so that the absolutely largest elements of A' in each column lie on the diagonal. Note that the solutions are unchanged by permuting the rows (same equations, different order).

The *LU decomposition* can now be used to solve the system. This relies on the fact that the inversion of a triangular matrix is a simple process of back substitution. We replace Eq. (8.99) by two systems of equations. Written out in full, the equations for a typical column of \mathbf{y} look like

$$\begin{aligned} L_{11}y_1 &= b'_1, \\ L_{21}y_1 + L_{22}y_2 &= b'_2, \\ L_{31}y_1 + L_{32}y_2 + L_{33}y_3 &= b'_3, \\ &\vdots, \end{aligned} \quad (8.107)$$

where the vector \mathbf{b}' is $\mathbf{p}' = P\mathbf{b}$. Thus, from successive rows, we obtain y_1, y_2, y_3, \dots in turn

$$\begin{aligned} U_{11}x_1 &= y_1, \\ U_{12}x_1 + U_{22}x_2 &= y_2, \\ U_{13}x_1 + U_{23}x_2 + U_{33}x_3 &= y_3, \\ &\vdots, \end{aligned} \quad (8.108)$$

and from successive rows of the latter, we obtain x_1, x_2, x_3, \dots in turn.

Software libraries (*Netlib* [42], described above) also exists for evaluating all the error bounds for dense and band matrices. Gaussian elimination with pivoting is almost always numerically stable, so the error bound one expects from solving these equations is of the order of $n\epsilon$, where ϵ is related to the condition number of the matrix A . A good discussion of errors and conditioning is given in [3–5].

8.4 Monte Carlo Methods

Owing to the continuing rapid development of computational facilities and the ever-increasing desire to perform *ab initio* calculations, the use of Monte Carlo methods is becoming widespread as a means to evaluate previously intractable

multidimensional integrals and to enable complex modeling and simulation.

For example, a wide range of applications broadly classified as *quantum Monte Carlo* have been used to compute, for example, the ground-state eigenfunctions of simple molecules. Also, guided random walks have found application in the computation of Green's functions, and variables chosen randomly, subject to particular constraints, have been used to mimic the electronic distribution of atoms. The latter application, used in the *classical trajectory Monte Carlo technique* (CTMC) described in Chap. 62, allows the statistical quasiquantum representation of ion-atom collisions. CTMC is akin to another class of Monte Carlo simulations, classical molecular dynamics, which is used to describe systems ranging from molecules to solids as being composed of atoms whose movement is governed by classical mechanics subject to quantum mechanically derived potentials.

Here, we summarize the basic tools needed in these methods and how they may be used to produce specific distributions and make tractable the evaluation of multidimensional integrals with complicated boundaries. Detailed descriptions of these methods can be found in [3–5, 18, 48].

8.4.1 Random Numbers

An essential ingredient of any Monte Carlo procedure is the availability of a computer-generated sequence of random numbers that is not periodic and is free of other significant statistical correlations. Often, such numbers are termed *pseudorandom* or *quasirandom*, in distinction to truly random physical processes. While the quality of random number generators supplied with computers has greatly improved over time, it is important to be aware of the potential dangers that can be present. For example, many systems are supplied with a random number generator based on the *linear congruential method*. Typically, a sequence of integers n_1, n_2, n_3, \dots is first produced between 0 and $N - 1$ by using the recurrence relation

$$n_{i+1} = (an_i + b) \bmod N, \quad 0 \leq i < N - 1, \quad (8.109)$$

where a, b, N , and the seed value n_0 are positive integers. Real numbers between 0 and (strictly) 1 are then obtained by dividing by N . The period of this sequence is at most N and depends on the judicious choice of the constants, with N being limited by the word size of the computer. A user who is unsure whether the character of the random numbers generated on a particular computer platform is proper can perform additional randomizing shuffles or use a portable random number generator; both procedures are described in detail in the texts by Knuth [6] and Press et al. [3–5], for example. In addition, tests of random number sequences have

been developed, for example, the widely used tests published by L'Ecuyer and Simard [49].

The need for such tests has grown in the present era of parallel computing, relevant not only to use of parallel random number generators on supercomputers and clusters but also the use of personal computers and workstations employing multicore/multithread, computation. In fact, the scale of Monte Carlo calculations possible on contemporary platforms has exposed deficiencies of many commonly used methods of generating random numbers, leading to development of more robust techniques. These new methods seek to ensure the quality of random numbers, first of all for large sequences within a single stream, as well as for multiple streams (other threads on a single processing unit or across nodes within a cluster). A widely used set of parallel random number generators that pass robust tests was developed and described by Srinivasan, Mascagni, and Ceperley [50], for example.

8.4.2 Distributions of Random Numbers

Most distributions of random numbers begin with sequences generated uniformly between a lower and an upper limit, and are therefore called *uniform deviates*. However, it is often useful to draw the random numbers from other distributions, such as the Gaussian, Poisson, exponential, gamma, or binomial distributions. These are particularly useful in modeling data or supplying input for an event generator or simulator. In addition, as described below, choosing the random numbers according to some weighting function can significantly improve the efficiency of integration schemes based on Monte Carlo sampling.

Perhaps the most direct way to produce the required distribution is the *transformation method*. If we have a sequence of uniform deviates x on $(0, 1)$ and wish to find a new sequence y that is distributed with probability given by some function $f(y)$, it can be shown that the required transformation is given by

$$y(x) = \left[\int_0^y f(y) dy \right]^{-1}. \quad (8.110)$$

Evidently, the indefinite integral must be both known and invertible, either analytically or numerically. Since this is seldom the case for distributions of interest, other less direct methods are most often applied. However, even these other methods often rely on the transformation method as one stage of the procedure. The transformation method may also be generalized to more than one dimension [3–5].

A more widely applicable approach is the *rejection method*, also known as *von Neumann rejection*. In this case, if one wishes to find a sequence y distributed according to $f(y)$, one first chooses another function $\tilde{f}(y)$, called the

comparison function, which is everywhere greater than $f(y)$ on the desired interval. In addition, a way must exist to generate y according to the comparison function, such as use of the transformation method. Thus, the comparison function must be simpler or better known than the distribution to be found. One simple choice is a constant function that is larger than the maximum value of $f(y)$, but choices that are *closer* to $f(y)$ will be much more efficient.

To proceed, y is generated uniformly according to $\tilde{f}(y)$, and another deviate x is chosen uniformly on $(0, 1)$. One then rejects or accepts y , depending on whether x is greater than or less than the ratio $f(y)/\tilde{f}(y)$, respectively. The fraction of trial numbers accepted depends on the ratio of the area under the desired function to that under the comparison function. Clearly, the efficiency of this scheme depends on how few of the numbers initially generated must be rejected, and, therefore, on how closely the comparison function approximates the desired distribution. The Lorentzian distribution, for which the inverse definite integral is known (the tangent function), is a good comparison function for a variety of *bell-shaped* distributions such as the Gaussian (normal), Poisson, and gamma distributions.

Especially for distributions that are functions of more than one variable and possess complicated boundaries, the rejection method is impractical, and the transformation method simply inapplicable. In the 1950s, a method to generate distributions for such situations was developed and applied in the study of statistical mechanics, where multidimensional integrals (e.g., the partition function) must often be solved numerically. It is known as the *Metropolis algorithm*. This procedure, or its variants, has more recently been adopted to aid in the computation of eigenfunctions of complicated Hamiltonians and scattering operators. In essence, the Metropolis method generates a random walk through the space of the dependent variables, and in the limit of a large number of steps in the walk, the points visited approximate the desired distribution.

In its simplest form, the Metropolis method generates this distribution of points by stepping through this space, most frequently taking a step *downhill* but sometimes taking a step *uphill*. That is, given a set of coordinates \mathbf{q} and a desired distribution function $f(\mathbf{q})$, a trial step is taken from the i -th configuration \mathbf{q}_i to the next, depending on whether the ratio $f(\mathbf{q}_{i+1})/f(\mathbf{q}_i)$ is greater or less than 1. If the ratio is greater than 1, the step is accepted, but if it is less than 1, the step is accepted with a probability given by the ratio.

8.4.3 Monte Carlo Integration

The basic idea of Monte Carlo integration is that if a large number of points is generated uniformly randomly in some n -dimensional space, the number falling inside a given re-

gion is proportional to the volume, or definite integral, of the function defining that region. Although this idea is as true in one dimension as it is in n , unless there is a large number (*large* could be as little as three) of dimensions or the boundaries are quite complicated, the numerical quadrature schemes described previously are more accurate and efficient. However, since the Monte Carlo approach is based on just sampling the function at representative points rather than evaluating the function at a large number of finely spaced quadrature points, its advantage for very large problems is apparent.

For simplicity, consider the Monte Carlo method for integrating a function of only one variable; the generalization to n dimensions being straightforward. If we generate N random points uniformly on (a, b) , then in the limit of large N , the integral is

$$\int_a^b f(x)dx \approx \frac{1}{N} \langle f(x) \rangle \pm \sqrt{\frac{\langle f^2(x) \rangle - \langle f(x) \rangle^2}{N}}, \quad (8.111)$$

where

$$\langle f(x) \rangle \equiv \frac{1}{N} \sum_{i=1}^N f(x_i) \quad (8.112)$$

is the arithmetic mean. The probable error given is appropriately a statistical one rather than a rigorous error bound and is the one standard error limit. From this, one can see that the error decreases only as $N^{1/2}$, more slowly than the rate of decrease for the quadrature schemes based on interpolation. Also, the accuracy is greater for relatively smooth functions, since the Monte Carlo generation of points is unlikely to sample narrowly peaked features of the integrand well. To estimate the integral of a multidimensional function with complicated boundaries, find an enclosing volume and generate points uniformly randomly within it. Keeping the enclosing volume as close as possible to the volume of interest minimizes the number of points that fall outside, and therefore increases the efficiency of the procedure.

The Monte Carlo integral is related to the techniques for generating random numbers according to prescribed distributions described in Sect. 8.4.2. If we consider a normalized distribution $w(x)$, known as the *weight function*, then with the change of variables defined by

$$y(x) = \int_a^x w(x')dx', \quad (8.113)$$

the Monte Carlo estimate of the integral becomes

$$\int_a^b f(x)dx \approx \frac{1}{N} \left\langle \frac{f[x(y)]}{w[x(y)]} \right\rangle, \quad (8.114)$$

assuming that the transformation is invertible. Choosing $w(x)$ to behave approximately as $f(x)$ allows a more efficient generation of points within the boundaries of the integrand. This occurs since the uniform distribution of points y results in values of x distributed according to w and, therefore, close to f . This procedure, generally termed the *reduction of variance* of the Monte Carlo integration, improves the efficiency of the procedure to the extent that the transformed function f/w can be made smooth, and that the sampled region is as small as possible but still contains the volume to be estimated.

References

1. Stoer, J., Bulirsch, R.: Introduction to Numerical Analysis. Springer, New York (2002)
2. Burden, R.L., Faires, J.D.: Numerical Analysis. Thomson Brooks/Cole, Belmont (2005)
3. Press, W.H., Teukolsky, S.A., Vetterling, W.T., Flannery, B.P.: Numerical Recipes, the Art of Scientific Computing. Cambridge Univ. Press, Cambridge (2007)
4. Press, W.H., Flannery, B.P., Teukolsky, S.A., Vetterling, W.T.: Numerical Recipes in Fortran 77: The Art of Scientific Computing. Cambridge Univ. Press, Cambridge (1992)
5. Press, W.H., Teukolsky, S.A., Vetterling, W.T., Flannery, B.P.: Numerical Recipes in Fortran 90: The Art of Parallel Scientific Computing. Cambridge Univ. Press, Cambridge (1996)
6. Knuth, D.E.: The Art of Computer Programming, Volume 2: Seminumerical Algorithms. Addison-Wesley, Boston (1998)
7. Abramowitz, M., Stegun, I.A. (eds.): Handbook of Mathematical Functions. Applied Mathematics Series, vol. 55. National Bureau of Standards/Dover, Washington/New York (1972). NIST Digital Library of Mathematical Functions: dlmf.nist.gov
8. Gradshteyn, I.S., Ryzhik, I.M.: Tables of Integrals, Series, and Products. Elsevier, Amsterdam (2007)
9. Zwillinger, D.: CRC Standard Mathematical Tables and Formulae. CRC, Boca Raton (2012)
10. Arfken, G.B., Weber, H.J., Harris, F.E.: Mathematical Methods for Physicists. Elsevier, Amsterdam (2013)
11. Whittaker, E.T., Watson, G.N.: A Course of Modern Analysis. Cambridge Univ. Press, Cambridge (2006)
12. Morse, P.M., Feshbach, H.: Methods of Theoretical Physics. McGraw-Hill, Boston (1999)
13. Courant, R., Hilbert, D.: Methods of Mathematical Physics. Interscience, New York (2009)
14. Margenau, H., Murphy, G.M.: The Mathematics of Physics and Chemistry. Van Nostrand, New York (1976)
15. Hamming, R.W.: Numerical Methods for Scientists and Engineers. McGraw-Hill, New York (1973)
16. Jeffreys, H., Jeffreys, B.S.: Methods of Mathematical Physics. Cambridge Univ. Press, Cambridge (1999)
17. Bender, C.M., Orszag, S.: Advanced Mathematical Methods for Scientists and Engineers. Springer, New York (1999)
18. Koonin, S.E., Meredith, D.C.: Computational Physics. Addison-Wesley, Reading (1995)
19. Wikipedia: List of numerical-analysis software (2021). https://en.wikipedia.org/wiki/List_of_numerical_analysis_%software
20. Computer Physics Communications Program Library: www.cpc.cs.qub.ac.uk/
21. Huber, P.J., Ronchetti, E.M.: Robust Statistics. Wiley, Hoboken (2009)
22. Young, H.D.: Statistical Treatment of Experimental Data: An Introduction to Statistical Methods. Waveland Press, Prospect Heights (1996)
23. Bevington, P.R., Robinson, D.K.: Data Reduction and Error Analysis for the Physical Sciences. McGraw-Hill, New York (2003)
24. Champeney, D.C.: Fourier Transforms and Their Physical Applications. Academic Press, London (1988)
25. Elliott, D.F., Rao, K.R.: Fast Transforms: Algorithms, Analyses, Applications. Academic Press, London (1982)
26. FFTW: <https://en.wikipedia.org/wiki/FFTW>; www.fftw.org
27. Lambert, J.D.: Numerical Methods for Ordinary Differential Equations: The Initial Value Problem. Chichester, New York (2000)
28. Shampine, L.F.: Numerical Solution of Ordinary Differential Equations. Chapman Hall, New York (1994)
29. Butcher, J.: The Numerical Analysis of Ordinary Differential Equations: Runge–Kutta and General Linear Methods. Wiley, New York (1987)
30. Hall, G., Watt, J.M.: Modern Numerical Methods for Ordinary Differential Equations. Clarendon, Oxford (1976)
31. Gladwell, I., Wait, R. (eds.): A Survey of Numerical Methods for Partial Differential Equations. Clarendon, Oxford (1979)
32. Rektorys, K.: Variational Methods in Mathematics, Science, and Engineering. Springer Netherlands, Amsterdam (2012)
33. Cook, R.D., Malkus, D.S., Plesha, M.E., Witt, R.J.: Concepts and Applications of Finite Element Analysis. Wiley, New York (2002)
34. Nürnberger, G.: Approximation by Spline Functions. Springer, Berlin, Heidelberg (1989)
35. DeBoor, C.: Practical Guide to Splines. Springer, Berlin (2013)
36. Light, J.C., Carrington, T.: Discrete variable representation and their utilization. Adv. Chem. Phys. **114**, 263 (2000)
37. Light, J.C., Hamilton, I.P., Lill, J.V.: Generalized discrete variable approximation in quantum mechanics. J. Chem. Phys. **82**, 1400 (1985)
38. Joachain, C.J.: Quantum Collision Theory. North Holland, Amsterdam (1987)
39. Rodberg, L.S., Thaler, R.M.: Introduction to the Quantum Theory of Scattering. Academic Press, New York (1970)
40. Goldberger, M.L., Watson, K.M.: Collision Theory. Dover, Mineola (2004)
41. Ciarlet, P.G.: Introduction to Numerical Linear Algebra and Optimisation. Cambridge Univ. Press, Cambridge (2001)
42. Netlib Repository at UTK and ORNL: www.netlib.org
43. en.wikipedia.org/wiki/Basic_Linear_Algebra_Subprograms
44. Wikipedia: LAPACK (2021). <https://en.wikipedia.org/wiki/LAPACK>
45. Golub, G., Van Loan, C.: Matrix Computations. Johns Hopkins Univ. Press, Baltimore (2013)
46. Hackbusch, W.: Iterative Solution of Large Sparse Systems of Equations. Springer, Cham (2016)
47. George, A., Liu, J.: Computer Solution of Large Sparse Positive Definite Systems. Prentice-Hall, Englewood Cliffs (1981)
48. Kalos, M.H., Whitlock, P.A.: The Basics of Monte Carlo Methods. Wiley, Weinheim (2008)
49. L'Ecuyer, P., Simard, R.: TestU01: A C library for empirical testing of random number generators. ACM Trans. Math. Softw. **33**(4), 22 (2007)
50. Srinivasan, A., Mascagni, M., Ceperley, D.: Testing parallel random number generators. Parallel Comput. **29**, 69 (2003)



David Schultz David Schultz is Vice President for Research at Northern Arizona University and has held research and administrative positions at the University of North Texas, Oak Ridge National Laboratory, and the University of Tennessee. His interests are in computational atomic physics, using both molecular dynamics simulation and quantum mechanical, discrete variable representations, and in applications in plasma science and astrophysics.



Hydrogenic Wave Functions

9

Robert N. Hill

Contents

9.1	Schrödinger Equation	149
9.1.1	Spherical Coordinates	149
9.1.2	Parabolic Coordinates	150
9.1.3	Momentum Space	152
9.2	Dirac Equation	153
9.3	The Coulomb Green's Function	154
9.3.1	The Green's Function for the Schrödinger Equation	155
9.3.2	The Green's Function for the Dirac Equation	156
9.4	Special Functions	156
9.4.1	Confluent Hypergeometric Functions	157
9.4.2	Laguerre Polynomials	160
9.4.3	Gegenbauer Polynomials	163
9.4.4	Legendre Functions	163
	References	164

Keywords

hydrogenic wave function · Schrödinger equation · Dirac equation · Coulomb potential · the Coulomb Green's function

9.1 Schrödinger Equation

The nonrelativistic Schrödinger equation for a hydrogenic ion of nuclear charge Z in atomic units is

$$\left(-\frac{1}{2}\nabla^2 - \frac{Z}{r}\right)\psi(\mathbf{r}) = E\psi(\mathbf{r}). \quad (9.1)$$

9.1.1 Spherical Coordinates

The separable solutions of Eq. (9.1) in spherical coordinates are

$$\psi(\mathbf{r}) = Y_{\ell m}(\theta, \phi)R_{\ell}(r), \quad (9.2)$$

where $Y_{\ell m}(\theta, \phi)$ is a spherical harmonic as defined by Edmonds [13] and $R_{\ell}(r)$ is a solution of the radial equation

$$\left[-\frac{1}{2}\left(\frac{d^2}{dr^2} + \frac{2}{r}\frac{d}{dr} - \frac{\ell(\ell+1)}{r^2}\right) - \frac{Z}{r}\right]R_{\ell}(r) = ER_{\ell}(r). \quad (9.3)$$

The general solution to Eq. (9.3) is

$$R_{\ell}(r) = r^{\ell}\exp(ikr)[A_1F_1(a; c; z) + BU(a, c, z)], \quad (9.4)$$

where ${}_1F_1$ and U are the regular and irregular solutions of the confluent hypergeometric equation defined in Eqs. (9.130) and (9.131) below, and

$$k = \sqrt{2E}, \quad (9.5)$$

$$a = \ell + 1 - ik^{-1}Z, \quad (9.6)$$

$$c = 2\ell + 2, \quad (9.7)$$

$$z = -2ikr. \quad (9.8)$$

Abstract

This chapter summarizes the solutions of the one-electron nonrelativistic Schrödinger equation, and the one-electron relativistic Dirac equation, for the Coulomb potential. The standard notations and conventions used in the mathematics literature for special functions have been chosen in preference to the notations customarily used in the physics literature whenever there is a conflict. This has been done to facilitate the use of standard reference works such as Abramowitz and Stegun [1], the *Bateman* project [2, 3], *Gradshteyn and Ryzhik* [4], *Jahnke and Emde* [5], *Luke* [6, 7], *Magnus, Oberhettinger, and Soni* [8], *Olver* [9], *Szegö* [10], and the new NIST Digital Library of Mathematical Functions project, which has prepared a hardcover update [11] of *Abramowitz and Stegun* [1] and an online digital library of mathematical functions [12]. The section on special functions contains many of the formulas which are needed to check the results quoted in the previous sections, together with a number of other useful formulas. It includes a brief introduction to asymptotic methods. References to the numerical evaluation of special functions are given.

A and B are arbitrary constants. The solution given in Eq. (9.4) has an $r^{-\ell-1}$ singularity at $r = 0$ unless $B = 0$ or a is a non-positive integer. The leading term for small r is proportional to r^ℓ when $B = 0$ and/or a is a non-positive integer. The large r behavior of the solution for Eq. (9.4) follows from Eqs. (9.134), (9.135), and (9.164) below. Bound state solutions, with energy

$$E = -\frac{1}{2}Z^2n^{-2} \quad (9.9)$$

are obtained when $a = -n + \ell + 1$ where $n > \ell$ is the principal quantum number. The properly normalized bound state solutions are

$$R_{n,\ell}(r) = \frac{2Z}{n^2} \sqrt{\frac{Z(n-\ell-1)!}{(n+\ell)!}} \left(\frac{2Zr}{n}\right)^\ell \times \exp\left(-\frac{Zr}{n}\right) L_{n-\ell-1}^{(2\ell+1)}\left(\frac{2Zr}{n}\right), \quad (9.10)$$

where $L_{n-\ell-1}^{(2\ell+1)}$ is the generalized Laguerre polynomial defined in Eq. (9.187). The relation in Eq. (9.188) shows that ${}_1F_1$ and U are linearly dependent in this case, so that Eq. (9.4) is no longer the general solution of Eq. (9.3). A linearly independent solution for this case can be obtained by replacing the $L_{n-\ell-1}^{(2\ell+1)}(2Zr/n)$ in Eq. (9.10) by the second (irregular) solution $M_{n-\ell-1}^{(2\ell+1)}(2Zr/n)$ of the Laguerre equation (see Eqs. (9.194), (9.196), and (9.197)). The first three $R_{n,\ell}$ are

$$R_{1,0}(r) = 2Z^{3/2} \exp(-Zr), \quad (9.11)$$

$$R_{2,0}(r) = \left(\frac{1}{2}Z\right)^{3/2} (2 - Zr) \exp\left(-\frac{1}{2}Zr\right), \quad (9.12)$$

$$R_{2,1}(r) = \left(\frac{1}{2}Z\right)^{3/2} \left(\frac{1}{3}\right)^{1/2} Zr \exp\left(-\frac{1}{2}Zr\right). \quad (9.13)$$

Additional explicit expressions, together with graphs of some of them, can be found in *Pauling and Wilson* [14].

The $R_{n,\ell}$ can be expanded in powers of $1/n$ [15]

$$R_{n,\ell}(r) = -\left[\frac{2Z^2(n+\ell)!}{(n-\ell-1)!n^{2\ell+4}}\right]^{1/2} \times r^{-1/2} \sum_{k=0}^{\infty} g_k^{(\ell)} \left[(8Zr)^{1/2}\right] n^{-2k}, \quad (9.14)$$

where the functions $g_k^{(\ell)}(z)$ are finite linear combinations of Bessel functions

$$g_k^{(\ell)}(z) = z^{3k} \sum_{m=0}^k a_{k,m}^{(\ell)} J_{2\ell+2m+k+1}(z). \quad (9.15)$$

The coefficients $a_{k,m}^{(\ell)}$ in Eq. (9.15) are calculated recursively from

$$a_{k,m}^{(\ell)} = \frac{(2\ell+2m+k+1)}{32(2k+m)(2\ell+m+2k+1)} \times \frac{1}{(2\ell+2m+k-1)} \times \left[(2\ell+2m+k-1)a_{k-1,m}^{(\ell)} + 32(k-m+1)(2\ell+m-k)a_{k,m-1}^{(\ell)} \right], \quad (9.16)$$

starting with the initial condition

$$a_{0,0}^{(\ell)} = 1. \quad (9.17)$$

The expansion Eq. (9.14) converges uniformly in r for r in any bounded region of the complex r -plane. However, it converges fast enough so that a few terms give a good description of $R_{n,\ell}$ only if r is small. The square root in Eq. (9.14) has not been expanded in inverse powers of n because it has a branch point at $1/n = 1/\ell$ which would reduce the radius of convergence of the expansion to $1/\ell$. In some cases, large n expansions of matrix elements can be obtained by inserting Eq. (9.14) for $R_{n,\ell}$ and integrating term by term; examples can be found in *Drake and Hill* [15]. An asymptotic expansion in powers of $1/n$, which is valid from r equal to an arbitrary fixed positive number through the turning point at $r = 2n^2/Z$ out to $r = \infty$, can be assembled from Eqs. (9.133), (9.166)–(9.181), and (9.188) below.

The $R_{n,\ell}$ are not a complete set because the continuum has been left out. The *Sturmian* functions $\rho_{k,\ell}$, given by

$$\rho_{k,\ell}(\beta; r) = \sqrt{\frac{\beta^3 k!}{\Gamma(k+2\ell+3)}} (\beta r)^\ell e^{-\beta r/2} \times L_k^{(2\ell+2)}(\beta r), \quad (9.18)$$

do form a complete orthonormal set. The positive constant β , which is independent of k and ℓ , sets the length scale for the basis set Eq. (9.18).

9.1.2 Parabolic Coordinates

The Schrödinger equation (9.1) is separable in parabolic coordinates ξ, η, ϕ , which are related to spherical coordinates r, θ, ϕ via

$$\xi = r + z = r[1 + \cos(\theta)], \quad (9.19)$$

$$\eta = r - z = r[1 - \cos(\theta)], \quad (9.20)$$

$$\phi = \phi. \quad (9.21)$$

This separability in a second coordinate system is related to the existence of a *hidden* $O(4)$ symmetry, which is also responsible for the degeneracy of the bound states [16, 17].

The solutions in parabolic coordinates are particularly convenient for derivations of the Stark effect and the Rutherford scattering cross section. The separable solutions of Eq. (9.1) in parabolic coordinates are

$$\psi(\mathbf{r}) = \exp(im\phi)N(\eta)\mathcal{E}(\xi), \quad (9.22)$$

where

$$\begin{aligned} N(\eta) &= \eta^{|m|/2} \exp\left(\frac{1}{2}ik_1\eta\right) \\ &\quad \times [A_1 F_1(a_1; c; -ik_1\eta) \\ &\quad + BU(a_1, c, -ik_1\eta)], \end{aligned} \quad (9.23)$$

$$\begin{aligned} \mathcal{E}(\xi) &= \xi^{|m|/2} \exp\left(\frac{1}{2}ik_2\xi\right) \\ &\quad \times [C_1 F_1(a_2; c; -ik_2\xi) \\ &\quad + DU(a_2, c, -ik_2\xi)], \end{aligned} \quad (9.24)$$

with ${}_1F_1$ and U defined in Eqs. (9.130), (9.131) below, and

$$k_1 = \pm k_2 = \pm\sqrt{2E}, \quad (9.25)$$

$$a_1 = \frac{1}{2}(|m| + 1) - ik_1^{-1}\mu, \quad (9.26)$$

$$a_2 = \frac{1}{2}(|m| + 1) - ik_2^{-1}(Z - \mu), \quad (9.27)$$

$$c = |m| + 1. \quad (9.28)$$

A , B , C , and D are arbitrary constants; μ is the separation constant. An important special case is the well-known *Coulomb function*

$$\begin{aligned} \psi_C(\mathbf{r}) &= \Gamma(1 - ik^{-1}Z) \exp\left(\frac{1}{2}\pi k^{-1}Z + i\mathbf{k} \cdot \mathbf{r}\right) \\ &\quad \times {}_1F_1[ik^{-1}Z; 1; i(kr - \mathbf{k} \cdot \mathbf{r})], \end{aligned} \quad (9.29)$$

which is obtained by orienting the z -axis in the \mathbf{k} direction and taking $m = 0$, $-k_1 = k_2 = |\mathbf{k}|$, $\mu = Z + \frac{1}{2}i|\mathbf{k}|$. ψ_C is normalized to unit incoming flux [see Eq. (9.34) below]. In applications, Z is often replaced by $-Z_1Z_2$, so that the Coulomb potential in Eq. (9.1) becomes $+Z_1Z_2/r$. Equation (9.232), the addition theorem for the spherical harmonics [13, p. 63 Eq. 4.6.6], and the $\lambda = c = 1$ special case of Eq. (9.163) below can be used to expand ψ_C into an infinite sum of solutions of the form Eq. (9.2)

$$\begin{aligned} \psi_C(\mathbf{r}) &= 4\pi \sum_{\ell=0}^{\infty} \sum_{m=-\ell}^{\ell} \frac{\Gamma(\ell + 1 - ik^{-1}Z)}{(2\ell + 1)!} \\ &\quad \times (-2ik)^\ell e^{\pi k^{-1}Z/2} Y_{\ell m}^*(\theta_k, \phi_k) Y_{\ell m}(\theta, \phi) \\ &\quad \times r^\ell e^{ikr} {}_1F_1(\ell + 1 - ik^{-1}Z; 2\ell + 2; -2ikr), \end{aligned} \quad (9.30)$$

where k , θ_k , and ϕ_k are the spherical coordinates of \mathbf{k} . ψ_C can be split into an incoming plane wave and an outgoing spherical wave with the aid of Eq. (9.134) below

$$\psi_C(\mathbf{r}) = \psi_{\text{in}}(\mathbf{r}) + \psi_{\text{out}}(\mathbf{r}), \quad (9.31)$$

where

$$\begin{aligned} \psi_{\text{in}}(\mathbf{r}) &= \exp\left(i\mathbf{k} \cdot \mathbf{r} - \frac{1}{2}\pi k^{-1}Z\right) \\ &\quad \times U[ik^{-1}Z; 1; i(kr - \mathbf{k} \cdot \mathbf{r})], \end{aligned} \quad (9.32)$$

$$\begin{aligned} \psi_{\text{out}}(\mathbf{r}) &= -\frac{\Gamma(1 - ik^{-1}Z)}{\Gamma(ik^{-1}Z)} \exp\left(ikr - \frac{1}{2}\pi k^{-1}Z\right) \\ &\quad \times U[1 - ik^{-1}Z; 1; -i(kr - \mathbf{k} \cdot \mathbf{r})]. \end{aligned} \quad (9.33)$$

The functions ψ_{in} and ψ_{out} can be expanded for $kr - \mathbf{k} \cdot \mathbf{r}$ large with the aid of Eq. (9.164). The result is

$$\begin{aligned} \psi_{\text{in}}(\mathbf{r}) &\approx \exp[i\mathbf{k} \cdot \mathbf{r} - ik^{-1}Z \ln(kr - \mathbf{k} \cdot \mathbf{r})] \\ &\quad \times \sum_{n=0}^{\infty} \frac{(-i)^n}{n!} \left[\frac{\Gamma(ik^{-1}Z + n)}{\Gamma(ik^{-1}Z)} \right]^2 \\ &\quad \times (kr - \mathbf{k} \cdot \mathbf{r})^{-n}, \end{aligned} \quad (9.34)$$

$$\begin{aligned} \psi_{\text{out}}(\mathbf{r}) &\approx -\frac{i\Gamma(1 - ik^{-1}Z)}{\Gamma(ik^{-1}Z)(kr - \mathbf{k} \cdot \mathbf{r})} \\ &\quad \times \exp[ikr - ik^{-1}Z \ln(kr - \mathbf{k} \cdot \mathbf{r})] \\ &\quad \times \sum_{n=0}^{\infty} \frac{i^n}{n!} \left[\frac{\Gamma(1 - ik^{-1}Z + n)}{\Gamma(1 - ik^{-1}Z)} \right]^2 \\ &\quad \times (kr - \mathbf{k} \cdot \mathbf{r})^{-n}. \end{aligned} \quad (9.35)$$

Because Eq. (9.1) is an elliptic partial differential equation, its solutions must be analytic functions of the Cartesian coordinates (except at $r = 0$, where the solutions have cusps). The $n = 0$ special case of Eq. (9.138) shows that ψ_{in} and ψ_{out} are logarithmically singular at $\mathbf{k} \cdot \mathbf{r} = kr$. Thus ψ_{in} and ψ_{out} are not solutions to Eq. (9.1) at $\mathbf{k} \cdot \mathbf{r} = kr$. The logarithmic singularity cancels when ψ_{in} and ψ_{out} are added to form ψ_C , which is a solution to Eq. (9.1).

Bound state solutions, with energy

$$E = -\frac{1}{2}Z^2(n_1 + n_2 + |m| + 1)^{-2}, \quad (9.36)$$

are obtained when $a_1 = -n_1$ and $a_2 = -n_2$ where n_1 and n_2 are non-negative integers. The properly normalized bound state solutions, which can be put into one-one correspondence with the bound state solutions in spherical coordinates,

are

$$\begin{aligned} \psi_{n_1, n_2, m}(\eta, \xi, \phi) &= \sqrt{\frac{\beta^{2|m|+4} n_1! n_2!}{2\pi Z(n_1 + |m|)! (n_2 + |m|)!}} \\ &\times \exp\left[im\phi - \frac{1}{2}\beta(\eta + \xi)\right] \\ &\times (\eta\xi)^{|m|/2} L_{n_1}^{(|m|)}(\beta\eta) L_{n_2}^{(|m|)}(\beta\xi), \end{aligned} \quad (9.37)$$

where

$$\beta = Z(n_1 + n_2 + |m| + 1)^{-1}. \quad (9.38)$$

9.1.3 Momentum Space

The nonrelativistic Schrödinger equation (9.1) becomes the integral equation

$$\frac{1}{2}p^2\phi(\mathbf{p}) - \frac{Z}{2\pi^2} \int \frac{\phi(\mathbf{p}')}{(\mathbf{p} - \mathbf{p}')^2} d^3\mathbf{p}' = E\phi(\mathbf{p}) \quad (9.39)$$

in momentum space. Its solutions are related to the solutions in coordinate space via the Fourier transforms

$$\psi(\mathbf{r}) = (2\pi)^{-3/2} \int \exp(i\mathbf{p} \cdot \mathbf{r}) \phi(\mathbf{p}) d^3\mathbf{p}, \quad (9.40)$$

$$\phi(\mathbf{p}) = (2\pi)^{-3/2} \int \exp(-i\mathbf{p} \cdot \mathbf{r}) \psi(\mathbf{r}) d^3\mathbf{r}. \quad (9.41)$$

A trick of *Fock's* [16, 18] can be used to expose the *hidden* $O(4)$ symmetry of hydrogen and construct the bound state solutions to Eq. (9.39). Let p, θ_p, ϕ_p and p', θ'_p, ϕ'_p be the spherical coordinates of \mathbf{p} and \mathbf{p}' . Change variables from p, p' to χ, χ' via $p = \sqrt{-2E} \tan(\chi/2)$ and $p' = \sqrt{-2E} \tan(\chi'/2)$. This brings Eq. (9.39) to the form

$$\begin{aligned} 2\pi^2 Z^{-1} \sqrt{-2E} [\sec^4[\chi/2] \phi(\mathbf{p})] \\ = \int \frac{[\sec^4(\chi'/2) \phi(\mathbf{p}')] \sin^2(\chi') d\chi' \sin(\theta_p) d\theta_p d\phi_p}{2 - 2[\cos(\chi) \cos(\chi') + \sin(\chi) \sin(\chi') \cos(\gamma')]}, \end{aligned} \quad (9.42)$$

where γ' is the angle between \mathbf{p} and \mathbf{p}' . Equation (9.42) is solved by introducing spherical coordinates and spherical harmonics in four dimensions via a natural extension of the procedure used in three dimensions. Going to polar coordinates on x and y yields the cylindrical coordinates r_2, ϕ, z ; the further step of going to polar coordinates on r_2 and z yields spherical coordinates r_3, θ, ϕ . If there is a fourth coordinate w , spherical coordinates in four dimensions are obtained via the additional step of going to polar coordinates on r_3 and w . The result is

$$x = r_4 \sin(\chi) \sin(\theta) \cos(\phi), \quad (9.43)$$

$$y = r_4 \sin(\chi) \sin(\theta) \sin(\phi), \quad (9.44)$$

$$z = r_4 \sin(\chi) \cos(\theta), \quad (9.45)$$

$$w = r_4 \cos(\chi). \quad (9.46)$$

The volume element, which is easily obtained via the same series of transformations, is

$$dV = r_4^3 dr_4 d\Omega_4, \quad (9.47)$$

$$d\Omega_4 = \sin^2(\chi) d\chi \sin(\theta) d\theta d\phi. \quad (9.48)$$

The four-dimensional spherical harmonics [2, Vol. 2, Chap. XI] are

$$\begin{aligned} Y_{n, \ell, m}(\chi, \theta, \phi) &= 2^{\ell+1} \ell! \sqrt{\frac{n(n-\ell-1)!}{2\pi(n+\ell)!}} \sin^\ell(\chi) \\ &\times C_{n-\ell-1}^{\ell+1}[\cos(\chi)] Y_{\ell m}(\theta, \phi), \end{aligned} \quad (9.49)$$

where $C_{n-\ell-1}^{\ell+1}$ is a Gegenbauer polynomial and $n \geq \ell + 1$ is an integer. They have the orthonormality property

$$\begin{aligned} \int Y_{n, \ell, m}^*(\chi, \theta, \phi) Y_{n', \ell', m'}(\chi, \theta, \phi) d\Omega_4 \\ = \delta_{n, n'} \delta_{\ell, \ell'} \delta_{m, m'}. \end{aligned} \quad (9.50)$$

Equations (9.229) and (9.230) with $\lambda = 1$, (9.231), and the addition theorem for the three dimensional spherical harmonics $Y_{\ell m}$ can be used to show that

$$\begin{aligned} \{1 - 2[\cos(\chi) \cos(\chi') \sin(\chi) \sin(\chi') \cos(\gamma')]\} t + t^2\}^{-1} \\ = \sum_{n=1}^{\infty} \sum_{\ell=0}^{n-1} \sum_{m=-\ell}^{\ell} \frac{2\pi^2}{n} t^{n-1} Y_{n, \ell, m}(\chi, \theta, \phi) \\ \times Y_{n, \ell, m}^*(\chi', \theta', \phi') \end{aligned} \quad (9.51)$$

holds for $|t| < 1$, where γ' is the angle between \mathbf{p} and \mathbf{p}' . Multiply both sides of Eq. (9.51) by $Y_{n, \ell, m}(\chi', \theta', \phi') d\Omega'_4$ (where $d\Omega'_4$ is $d\Omega_4$ with χ, θ, ϕ replaced by χ', θ', ϕ') and use the orthogonality relation Eq. (9.50). The result can be rearranged to the form

$$\begin{aligned} 2\pi^2 n^{-1} t^{n-1} Y_{n, \ell, m}(\chi, \theta, \phi) \\ = \int \frac{Y_{n, \ell, m}(\chi', \theta', \phi') \sin^2(\chi') d\chi' \sin(\theta) d\theta d\phi}{1 - 2[\cos(\chi) \cos(\chi') + \sin(\chi) \sin(\chi') \cos(\gamma')]\} t + t^2}. \end{aligned} \quad (9.52)$$

Analytic continuation can be used to show that Eq. (9.52) is valid for all complex t despite the fact that Eq. (9.51) is restricted to $|t| < 1$. Comparing the $t = 1$ case of Eq. (9.52) with Eq. (9.42) shows that $E = -\frac{1}{2}Z^2 n^{-2}$ in agreement with Eq. (9.9), and that

$$\begin{aligned} \phi(\mathbf{p}) &= \left\{ \begin{array}{l} \text{normalizing} \\ \text{factor} \end{array} \right\} \cos^4(\chi/2) \\ &\times Y_{n, \ell, m}(\chi, \theta, \phi). \end{aligned} \quad (9.53)$$

Transforming from χ back to p brings these to the form

$$\phi(\mathbf{p}) = Y_{\ell m}(\theta_p, \phi_p) F_{n, \ell}(p), \quad (9.54)$$

where the properly normalized radial functions are

$$F_{n,\ell}(p) = 2^{2\ell+2} n^2 \ell! \sqrt{\frac{2(n-\ell-1)!}{\pi Z^3 (n+\ell)!}} \left(\frac{np}{Z}\right)^\ell \times \frac{Z^{2\ell+4}}{(n^2 p^2 + Z^2)^{\ell+2}} \times C_{n-\ell-1}^{\ell+1} \left(\frac{n^2 p^2 - Z^2}{n^2 p^2 + Z^2}\right). \quad (9.55)$$

The first three $F_{n,\ell}$ are

$$F_{1,0}(p) = 4 \sqrt{\frac{2}{\pi Z^3}} \frac{Z^4}{(p^2 + Z^2)^2}, \quad (9.56)$$

$$F_{2,0}(p) = \frac{32}{\sqrt{\pi Z^3}} \frac{Z^4 (4p^2 - Z^2)}{(4p^2 + Z^2)^3}, \quad (9.57)$$

$$F_{2,1}(p) = \frac{128}{\sqrt{3\pi Z^3}} \frac{Z^5 p}{(4p^2 + Z^2)^3}. \quad (9.58)$$

The $F_{n,\ell}$ satisfy the integral equation

$$\frac{1}{2} p^2 F_{n,\ell}(p) - \frac{Z}{\pi p} \int_0^\infty Q_\ell \left(\frac{p^2 + p'^2}{2pp'}\right) F_{n,\ell}(p') p' dp' = E F_{n,\ell}(p), \quad (9.59)$$

which can be obtained by inserting Eq. (9.54) in Eq. (9.39). Here Q_ℓ is the Legendre function of the second kind, which is defined in Eq. (9.233) below.

9.2 Dirac Equation

The relativistic Dirac equation for a hydrogenic ion of nuclear charge Z can be reduced to dimensionless form by using the Compton wavelength $\hbar/(mc)$ for the length scale and the rest mass energy mc^2 for the energy scale. The result is

$$\left(-i\boldsymbol{\alpha} \cdot \nabla + \beta - \frac{Z\alpha}{r}\right) \psi(\mathbf{r}) = E \psi(\mathbf{r}), \quad (9.60)$$

where $\alpha = e^2/(\hbar c)$ is the fine structure constant, and $\boldsymbol{\alpha}$, β are the usual Dirac matrices

$$\boldsymbol{\alpha} = \begin{pmatrix} 0 & \boldsymbol{\sigma} \\ \boldsymbol{\sigma} & 0 \end{pmatrix}, \quad \beta = \begin{pmatrix} I & 0 \\ 0 & -I \end{pmatrix}. \quad (9.61)$$

Here $\boldsymbol{\sigma}$ is a vector whose components are the two by two Pauli matrices, and I is the two by two identity matrix given by

$$\sigma_x = \begin{pmatrix} 0 & 1 \\ 1 & 0 \end{pmatrix}, \quad \sigma_y = \begin{pmatrix} 0 & -i \\ i & 0 \end{pmatrix}, \\ \sigma_z = \begin{pmatrix} 1 & 0 \\ 0 & -1 \end{pmatrix}, \quad I = \begin{pmatrix} 1 & 0 \\ 0 & 1 \end{pmatrix}. \quad (9.62)$$

The solutions to Eq. (9.60) in spherical coordinates have the form

$$\psi(\mathbf{r}) = \begin{pmatrix} G(r) \chi_\kappa^m(\theta, \phi) \\ iF(r) \chi_{-\kappa}^m(\theta, \phi) \end{pmatrix}, \quad (9.63)$$

where, for positive energy states, $G(r)$ is the radial part of the large component and $iF(r)$ is the radial part of the small component. For negative energy states, $G(r)$ is the radial part of the small component and $iF(r)$ is the radial part of the large component. χ is the two component spinor

$$\chi_\kappa^m = \begin{pmatrix} -\frac{\kappa}{|\kappa|} \left(\frac{\kappa + \frac{1}{2} - m}{2\kappa + 1}\right)^{1/2} Y_{|\kappa + \frac{1}{2}| - \frac{1}{2}, m - \frac{1}{2}} \\ \left(\frac{\kappa + \frac{1}{2} + m}{2\kappa + 1}\right)^{1/2} Y_{|\kappa + \frac{1}{2}| - \frac{1}{2}, m + \frac{1}{2}} \end{pmatrix}. \quad (9.64)$$

The relativistic quantum number κ is related to the total angular momentum quantum number j by

$$\kappa = \pm \left(j + \frac{1}{2}\right). \quad (9.65)$$

Because j takes on the values $\frac{1}{2}, \frac{3}{2}, \frac{5}{2}, \dots$, κ is restricted to the values $\pm 1, \pm 2, \pm 3, \dots$. The spinor χ_κ^m obeys the useful relations

$$\boldsymbol{\sigma} \cdot \hat{\mathbf{r}} \chi_\kappa^m = -\chi_{-\kappa}^m, \quad (9.66)$$

$$\boldsymbol{\sigma} \cdot \mathbf{L} \chi_\kappa^m = -(\kappa + 1) \chi_\kappa^m, \quad (9.67)$$

where $\hat{\mathbf{r}} = \mathbf{r}/r$ and $\mathbf{L} = \mathbf{r} \times \mathbf{p}$ with $\mathbf{p} = -i\nabla$. Equations (9.66), (9.67), and the identity

$$\boldsymbol{\sigma} \cdot \mathbf{p} = (\boldsymbol{\sigma} \cdot \hat{\mathbf{r}}) \left(\hat{\mathbf{r}} \cdot \mathbf{p} + \frac{i\boldsymbol{\sigma} \cdot \mathbf{L}}{r}\right) \quad (9.68)$$

can be used to derive the radial equations, which are

$$\left(\frac{d}{dr} + \frac{1+\kappa}{r}\right) G(r) - \left(1 + E + \frac{Z\alpha}{r}\right) F(r) = 0, \quad (9.69)$$

$$\left(\frac{d}{dr} + \frac{1-\kappa}{r}\right) F(r) - \left(1 - E - \frac{Z\alpha}{r}\right) G(r) = 0. \quad (9.70)$$

Equations (9.158), (9.159), (9.161), and (9.162) below can be used to show that the general solution to Eqs. (9.69) and (9.70) is

$$G(r) = r^\nu \exp(-\lambda r) (1 + E)^{1/2} \{A[f_2(r) + f_1(r)] + B[f_4(r) + f_3(r)]\}, \quad (9.71)$$

$$F(r) = r^\nu \exp(-\lambda r) (1 - E)^{1/2} \{A[f_2(r) - f_1(r)] + B[f_4(r) - f_3(r)]\}, \quad (9.72)$$

where

$$f_1(r) = (Z\alpha\lambda^{-1} - \kappa)_1 F_1(a; c; 2\lambda r), \quad (9.73)$$

$$f_2(r) = a_1 F_1(a + 1; c; 2\lambda r), \quad (9.74)$$

$$f_3(r) = U(a, c, 2\lambda r), \quad (9.75)$$

$$f_4(r) = (Z\alpha\lambda^{-1} + \kappa) U(a + 1, c, 2\lambda r), \quad (9.76)$$

$$\lambda = (1 + E)^{1/2}(1 - E)^{1/2}, \quad (9.77)$$

$$\gamma = -1 + (\kappa^2 - Z^2\alpha^2)^{1/2}, \quad (9.78)$$

$$a = 1 + \gamma - \lambda^{-1}EZ\alpha, \quad (9.79)$$

$$c = 3 + 2\gamma. \quad (9.80)$$

A and B are arbitrary constants. Because γ is in general not an integer, the solutions have a branch point at $r = 0$, and become infinite at $r = 0$ when $\kappa = \pm 1$, which makes γ negative. The solutions for $E < -1$ and $E > +1$ are in the continuum, which implies that one of the factors $(1 + E)^{1/2}$, $(1 - E)^{1/2}$ is real with the other imaginary. Square integrable solutions, with energy

$$E_{n,\kappa} = \frac{Z}{|Z|} \left[1 + \frac{Z^2\alpha^2}{(n+1+\gamma)^2} \right]^{-1/2}, \quad (9.81)$$

are obtained when $a = -n$ where n is a non-negative integer. The properly normalized square integrable solutions are

$$G_{n,\kappa}(r) = C_{n,\kappa}(2\lambda r)^\gamma \exp(-\lambda r)(1 + E_{n,\kappa})^{1/2} \times [g_{n,\kappa}^{(2)}(r) + g_{n,\kappa}^{(1)}(r)], \quad (9.82)$$

$$F_{n,\kappa}(r) = C_{n,\kappa}(2\lambda r)^\gamma \exp(-\lambda r)(1 - E_{n,\kappa})^{1/2} \times [g_{n,\kappa}^{(2)}(r) - g_{n,\kappa}^{(1)}(r)], \quad (9.83)$$

$$g_{n,\kappa}^{(1)}(r) = (Z\alpha\lambda^{-1} - \kappa)^{1/2} L_n^{(2+2\gamma)}(2\lambda r), \quad (9.84)$$

$$g_{n,\kappa}^{(2)}(r) = -(n+2+2\gamma)(Z\alpha\lambda^{-1} - \kappa)^{-1/2} \times L_{n-1}^{(2+2\gamma)}(2\lambda r), \quad (9.85)$$

$$C_{n,\kappa} = \sqrt{\frac{2\lambda^4 n!}{Z\alpha\Gamma(n+3+2\gamma)}}. \quad (9.86)$$

When $n = 0$, $|Z\alpha\lambda^{-1}| = |\kappa|$, and the value of κ whose sign is the same as the sign of $Z\alpha\lambda^{-1}$ is not permitted. Also, $L_{-1}^{(2+2\gamma)}(2\lambda r)$ is counted as zero, so that $g_{0,\kappa}^{(2)}(r) = 0$.

The eigenvalues and eigenfunctions for the first four states for $Z > 0$ will now be written out explicitly in terms of the variable $\rho = Z\alpha r$. For the $1S_{1/2}$ ground state, with $n = 0$, $j = \frac{1}{2}$, $\kappa = -1$, the formulae are

$$E_{0,-1} = \sqrt{1 - Z^2\alpha^2}, \quad (9.87)$$

$$G_{0,-1}(r) = \sqrt{\frac{4Z^3\alpha^3(1 + E_{0,-1})}{\Gamma(1 + 2E_{0,-1})}} (2\rho)^{E_{0,-1}-1} e^{-\rho}, \quad (9.88)$$

$$F_{0,-1}(r) = -\sqrt{\frac{4Z^3\alpha^3(1 - E_{0,-1})}{\Gamma(1 + 2E_{0,-1})}} (2\rho)^{E_{0,-1}-1} e^{-\rho}. \quad (9.89)$$

The formulae for the $2S_{1/2}$ excited state, with $n = 1$, $j = \frac{1}{2}$, $\kappa = -1$, and for the $2P_{1/2}$ excited state, with $n = 1$, $j = \frac{1}{2}$, $\kappa = 1$, can be written together. They are

$$E_{1,\kappa} = \left(\frac{1}{2} + \frac{1}{2} \sqrt{1 - Z^2\alpha^2} \right)^{1/2}, \quad (9.90)$$

$$G_{1,\kappa}(r) = \sqrt{\frac{Z^3\alpha^3(2E_{1,\kappa} - \kappa)(1 + E_{1,\kappa})}{2E_{1,\kappa}^2 \Gamma(4E_{1,\kappa}^2 + 1)}} \times \rho_1^{2E_{1,\kappa}^2 - 2} e^{-\rho_1/2} \times [(2E_{1,\kappa} - \kappa - 1)(2E_{1,\kappa} + \kappa) - \rho_1], \quad (9.91)$$

$$F_{1,\kappa}(r) = -\sqrt{\frac{Z^3\alpha^3(2E_{1,\kappa} - \kappa)(1 - E_{1,\kappa})}{2E_{1,\kappa}^2 \Gamma(4E_{1,\kappa}^2 + 1)}} \times \rho_1^{2E_{1,\kappa}^2 - 2} e^{-\rho_1/2} \times [(2E_{1,\kappa} - \kappa + 1)(2E_{1,\kappa} + \kappa) - \rho_1], \quad (9.92)$$

where $\rho_1 = \rho/E_{1,\kappa}$. For the $2P_{3/2}$ excited state, with $n = 0$, $j = \frac{3}{2}$, $\kappa = -2$, the formulae are

$$E_{0,-2} = \sqrt{1 - \frac{1}{4}Z^2\alpha^2}, \quad (9.93)$$

$$G_{0,-2}(r) = \sqrt{\frac{Z^3\alpha^3(1 + E_{0,-2})}{2\Gamma(1 + 4E_{0,-2})}} \rho^{2E_{0,-2}-1} e^{-\rho/2}, \quad (9.94)$$

$$F_{0,-2}(r) = -\sqrt{\frac{Z^3\alpha^3(1 - E_{0,-2})}{2\Gamma(1 + 4E_{0,-2})}} \rho^{2E_{0,-2}-1} e^{-\rho/2}. \quad (9.95)$$

9.3 The Coulomb Green's Function

The abstract Green's operator for a Hamiltonian H is the inverse $G(E) = (H - E)^{-1}$. It is used to write the solution to $(H - E)|\xi\rangle = |\eta\rangle$ in the form $|\xi\rangle = G|\eta\rangle$. It has the spectral representation

$$G(E) = \sum_j \frac{1}{E_j - E} |e_j\rangle \langle e_j|. \quad (9.96)$$

The sum over j in Eq. (9.96) runs over *all* of the spectrum of H , including the continuum. For the bound state part of the spectrum, the numbers E_j and vectors $|e_j\rangle$ are the eigenvalues and eigenvectors of H . For the continuous spectrum, $|e_j\rangle \langle e_j|$ is a projection valued measure [19]. The representation Eq. (9.96) shows that $G(E)$ has first order poles at the eigenvalues. The reduced Green's operator (also known as the generalized Green's operator), which is the ordinary Green's operator with the singular terms subtracted out, remains finite when E is at an eigenvalue. It can be calculated from

$$G^{(\text{red})}(E_k) = \lim_{E \rightarrow E_k} \left\{ \frac{\partial}{\partial E} [(E - E_k)G(E)] \right\}. \quad (9.97)$$

The coordinate and momentum space representatives of the abstract Green's operator are the Green's functions. The non-relativistic Coulomb Green's function has been discussed by *Hostler and Schwinger* [20–22]. A unified treatment of the Coulomb Green's functions for the Schrödinger and Dirac equations has been given by *Swainson and Drake* [23–25]. Reduced Green's functions are discussed in the third of the Swainson–Drake papers, and in the paper of *Hill and Huxtable* [26].

9.3.1 The Green's Function for the Schrödinger Equation

The Green's function $G^{(S)}$ for the Schrödinger equation (9.98) is a solution of

$$\left(-\frac{1}{2}\nabla^2 - \frac{Z}{r} - E\right)G^{(S)}(\mathbf{r}, \mathbf{r}'; E) = \delta(\mathbf{r} - \mathbf{r}'). \quad (9.98)$$

An explicit closed form expression for $G^{(S)}$ is

$$G^{(S)}(\mathbf{r}, \mathbf{r}'; E) = \frac{\Gamma(1-\nu)}{2\pi|\mathbf{r} - \mathbf{r}'|} \times \left[W_{\nu, \frac{1}{2}}(z_2) \frac{\partial}{\partial z_1} M_{\nu, \frac{1}{2}}(z_1) - M_{\nu, \frac{1}{2}}(z_1) \frac{\partial}{\partial z_2} W_{\nu, \frac{1}{2}}(z_2) \right], \quad (9.99)$$

where $M_{\nu, 1/2}$ and $W_{\nu, 1/2}$ are the Whittaker functions defined in Eqs. (9.132) and (9.133) below, and

$$\nu = Z(-2E)^{-1/2}, \quad (9.100)$$

$$z_1 = (-2E)^{1/2}(r + r' - |\mathbf{r} - \mathbf{r}'|), \quad (9.101)$$

$$z_2 = (-2E)^{1/2}(r + r' + |\mathbf{r} - \mathbf{r}'|). \quad (9.102)$$

The branch on which $(-2E)^{1/2}$ is positive should be taken when $E < 0$. When $E > 0$, the branch which corresponds to incoming (or outgoing) waves at infinity can be selected with the aid of the asymptotic approximation

$$G^{(S)}(\mathbf{r}, \mathbf{r}'; E) \approx \frac{\Gamma(1-\nu)}{2\pi|\mathbf{r} - \mathbf{r}'|} z_2^\nu \exp(-\frac{1}{2}z_2), \quad (9.103)$$

which holds when $z_2 \gg z_1$. This approximation is obtained by using Eqs. (9.130), (9.132), (9.133), and (9.164) in Eq. (9.99). A number of useful expansions for $G^{(S)}$ can be obtained from the integral representation

$$G^{(S)}(\mathbf{r}, \mathbf{r}'; E) = \frac{2Z}{\nu} \int_0^\infty \left[\coth\left(\frac{1}{2}\rho\right) \right]^{2\nu} \sinh(\rho) \times I_0 \left\{ \nu^{-1} Z \sinh(\rho) (2rr')^{1/2} [1 + \cos(\Theta)] \right\} \times \exp[-\nu^{-1} Z (r + r') \cosh(\rho)] d\rho, \quad (9.104)$$

where Θ is the angle between \mathbf{r} and \mathbf{r}' . These expansions, and other integral representations, can be found in [20–25]. The partial wave expansion of $G^{(S)}$ is

$$G^{(S)}(\mathbf{r}, \mathbf{r}'; E) = \sum_{\ell, m} g_\ell^{(S)}(r, r'; \nu) Y_{\ell m}(\theta, \phi) Y_{\ell m}^*(\theta', \phi'). \quad (9.105)$$

The radial Green's function $g_\ell^{(S)}$ is a solution of the radial equation

$$\left[-\frac{1}{2} \left(\frac{d^2}{dr^2} + \frac{2}{r} \frac{d}{dr} - \frac{\ell(\ell+1)}{r^2} \right) - \frac{Z}{r} - E \right] g_\ell^{(S)}(r, r'; \nu) = \frac{\delta(r - r')}{rr'}. \quad (9.106)$$

The standard method for calculating the Green's function of a second order ordinary differential equation [27, pp. 354–355] yields

$$g_\ell^{(S)}(r, r'; \nu) = \frac{(2Z)^{2\ell+2} \Gamma(\ell+1-\nu)}{(2\ell+1)! \nu^{2\ell+1}} \exp[-\nu^{-1} Z (r + r')] \times (rr')^\ell {}_1F_1(\ell+1-\nu; 2\ell+2; 2\nu^{-1} Z r_<) \times U(\ell+1-\nu, 2\ell+2, 2\nu^{-1} Z r_>), \quad (9.107)$$

where $r_<$ is the smaller of the pair r, r' and $r_>$ is the larger of the pair r, r' . Matrix elements of $g_\ell^{(S)}$ can be calculated with the aid of the formula for the double Laplace transform, which is

$$\int_0^\infty dr \int_0^\infty dr' (rr')^{\ell+1} \exp(-\lambda r - \lambda' r') g_\ell^{(S)}(r, r'; \nu) = \frac{2(2\ell+1)!}{\ell-\nu+1} \left(\frac{\nu}{2Z} \right)^{2\ell+3} \left(\frac{4Z^2}{(\nu\lambda+Z)(\nu\lambda'+Z)} \right)^{2\ell+2} \times {}_2F_1(2\ell+2, \ell-\nu+1; \ell-\nu+2; 1-\zeta), \quad (9.108)$$

where

$$\zeta = \frac{2\nu Z(\lambda + \lambda')}{(\nu\lambda + Z)(\nu\lambda' + Z)}, \quad (9.109)$$

Matrix elements with respect to Slater orbitals can be calculated from Eq. (9.108) by taking derivatives with respect to λ and/or λ' to bring down powers of r and r' . Matrix elements with respect to Laguerre polynomials can be calculated by using Eq. (9.108) to evaluate integrals over the generating function Eq. (9.199) for the Laguerre polynomial [26]. Other methods of calculating matrix elements are discussed in *Swainson and Drake* [23–25]. The Green's function $\tilde{G}^{(S)}$ in momentum space is related to the coordinate space Green's function $G^{(S)}$ via the Fourier transforms

$$G^{(S)}(\mathbf{r}, \mathbf{r}'; E) = (2\pi)^{-3} \int \exp[i(\mathbf{p} \cdot \mathbf{r} - \mathbf{p}' \cdot \mathbf{r}')] \times \tilde{G}^{(S)}(\mathbf{p}, \mathbf{p}'; E) d^3 p d^3 p', \quad (9.110)$$

$$\begin{aligned} \tilde{G}^{(S)}(\mathbf{p}, \mathbf{p}'; E) &= (2\pi)^{-3} \int \exp[-i(\mathbf{p} \cdot \mathbf{r} - \mathbf{p}' \cdot \mathbf{r}')] \\ &\quad \times G^{(S)}(\mathbf{r}, \mathbf{r}'; E) d^3\mathbf{r} d^3\mathbf{r}'. \end{aligned} \quad (9.111)$$

The Green's function $\tilde{G}^{(S)}$ is a solution of

$$\begin{aligned} \left(\frac{1}{2}p^2 - E\right) \tilde{G}^{(S)}(\mathbf{p}, \mathbf{p}'; E) - \frac{Z}{2\pi^2} \int \frac{1}{(\mathbf{p} - \mathbf{p}'')^2} \\ \times \tilde{G}^{(S)}(\mathbf{p}'', \mathbf{p}'; E) d^3\mathbf{p}'' = \delta(\mathbf{p} - \mathbf{p}'). \end{aligned} \quad (9.112)$$

An explicit closed form expression for $\tilde{G}^{(S)}$ is

$$\begin{aligned} \tilde{G}^{(S)}(\mathbf{p}, \mathbf{p}'; E) &= \frac{\delta(\mathbf{p} - \mathbf{p}')}{\frac{1}{2}p^2 - E} + \frac{Z}{2\pi^2 |\mathbf{p} - \mathbf{p}'|^2 \left(\frac{1}{2}p^2 - E\right) \left[\frac{1}{2}(p')^2 - E\right]} \\ &\quad \times \left\{ 1 + \frac{\nu q}{1 - \nu} \left[\left(\frac{1 - q}{1 + q}\right) {}_2F_1\left(1, 1 - \nu; 2 - \nu; \frac{1 - q}{1 + q}\right) \right. \right. \\ &\quad \left. \left. - \left(\frac{1 + q}{1 - q}\right) {}_2F_1\left(1, 1 - \nu; 2 - \nu; \frac{1 + q}{1 - q}\right) \right] \right\}, \end{aligned} \quad (9.113)$$

where

$$q = \sqrt{\frac{2E |\mathbf{p} - \mathbf{p}'|^2}{4E^2 - 4E \mathbf{p} \cdot \mathbf{p}' + (pp')^2}}. \quad (9.114)$$

9.3.2 The Green's Function for the Dirac Equation

The Green's function G_D for the Dirac equation (9.60) is a 4×4 matrix valued solution of

$$\begin{aligned} \left(-i\boldsymbol{\alpha} \cdot \nabla + \beta - \frac{Z\boldsymbol{\alpha}}{r} - E\right) G_D(\mathbf{r}, \mathbf{r}'; E) \\ = \delta(\mathbf{r} - \mathbf{r}') I_4, \end{aligned} \quad (9.115)$$

where I_4 is the 4×4 identity matrix. The partial wave expansion of G_D is

$$G_D(\mathbf{r}, \mathbf{r}'; E) = \sum_{\kappa, m} \begin{pmatrix} G_{11}^{\kappa, m} & -iG_{12}^{\kappa, m} \\ iG_{21}^{\kappa, m} & G_{22}^{\kappa, m} \end{pmatrix}, \quad (9.116)$$

where

$$G_{11}^{\kappa, m} = \chi_{\kappa}^m(\theta, \phi) \chi_{\kappa}^{m\dagger}(\theta', \phi') g_{11}(r, r'; E), \quad (9.117)$$

$$G_{12}^{\kappa, m} = \chi_{\kappa}^m(\theta, \phi) \chi_{-\kappa}^{m\dagger}(\theta', \phi') g_{12}(r, r'; E), \quad (9.118)$$

$$G_{21}^{\kappa, m} = \chi_{-\kappa}^m(\theta, \phi) \chi_{\kappa}^{m\dagger}(\theta', \phi') g_{21}(r, r'; E), \quad (9.119)$$

$$G_{22}^{\kappa, m} = \chi_{-\kappa}^m(\theta, \phi) \chi_{-\kappa}^{m\dagger}(\theta', \phi') g_{22}(r, r'; E). \quad (9.120)$$

The identity

$$\begin{aligned} \delta(\mathbf{r} - \mathbf{r}') I_4 &= \frac{\delta(r - r')}{r r'} \\ &\quad \times \sum_{\kappa, m} \begin{pmatrix} \chi_{\kappa}^m(\theta, \phi) \chi_{\kappa}^{m\dagger}(\theta', \phi') & 0 \\ 0 & \chi_{-\kappa}^m(\theta, \phi) \chi_{-\kappa}^{m\dagger}(\theta', \phi') \end{pmatrix} \end{aligned} \quad (9.121)$$

can be used to show that the radial functions $g_{jk}(r, r'; E)$ satisfy the equation

$$\begin{aligned} \begin{pmatrix} \left(1 - E - \frac{Z\alpha}{r}\right) & -\left(\frac{d}{dr} + \frac{1 - \kappa}{r}\right) \\ \left(\frac{d}{dr} + \frac{1 + \kappa}{r}\right) & -\left(1 + E + \frac{Z\alpha}{r}\right) \end{pmatrix} \\ \times \begin{pmatrix} g_{11}(r, r'; E) & g_{12}(r, r'; E) \\ g_{21}(r, r'; E) & g_{22}(r, r'; E) \end{pmatrix} = \frac{\delta(r - r')}{r r'} \begin{pmatrix} 1 & 0 \\ 0 & 1 \end{pmatrix}. \end{aligned} \quad (9.122)$$

The solution to Eq. (9.122) is

$$\begin{aligned} \begin{pmatrix} g_{11}(r, r'; E) & g_{12}(r, r'; E) \\ g_{21}(r, r'; E) & g_{22}(r, r'; E) \end{pmatrix} &= \frac{(2\lambda)^{1+2\gamma} \Gamma(a)}{\Gamma(3 + 2\gamma)} \\ &\quad \times \left[\Theta(r' - r) \begin{pmatrix} G_{<}(r) \\ F_{<}(r) \end{pmatrix} \begin{pmatrix} G_{>}(r') & F_{>}(r') \end{pmatrix} \right. \\ &\quad \left. + \Theta(r - r') \begin{pmatrix} G_{>}(r) \\ F_{>}(r) \end{pmatrix} \begin{pmatrix} G_{<}(r') & F_{<}(r') \end{pmatrix} \right], \end{aligned} \quad (9.123)$$

where a is defined by Eq. (9.79), Θ is the Heaviside unit function, defined by

$$\Theta(x) = \begin{cases} 1, & x > 0, \\ \frac{1}{2}, & x = 0, \\ 0, & x < 0, \end{cases} \quad (9.124)$$

and the functions $G_{<}$, $F_{<}$, $G_{>}$, and $F_{>}$ are special cases of the homogeneous solutions Eq. (9.71)–(9.80)

$$G_{<}(r) = r^\gamma \exp(-\lambda r) (1 + E)^{1/2} [f_2(r) + f_1(r)], \quad (9.125)$$

$$F_{<}(r) = r^\gamma \exp(-\lambda r) (1 - E)^{1/2} [f_2(r) - f_1(r)], \quad (9.126)$$

$$G_{>}(r) = r^\gamma \exp(-\lambda r) (1 + E)^{1/2} [f_4(r) + f_3(r)], \quad (9.127)$$

$$F_{>}(r) = r^\gamma \exp(-\lambda r) (1 - E)^{1/2} [f_4(r) - f_3(r)]. \quad (9.128)$$

The functions $G_{<}(r)$ and $F_{<}(r)$ obey the boundary conditions at $r = 0$. The functions $G_{>}(r)$ and $F_{>}(r)$ obey the boundary conditions at $r = \infty$. Integral representations and expansions for the Dirac Green's function can be found in [23–25, 28]. Matrix element evaluation is discussed in [23–25].

9.4 Special Functions

This section contains a brief list of formulae for the special functions which appear in the solutions discussed above. Derivations, and many additional formulae, can be found in

the standard reference works listed in the bibliography. For numerically useful approximations and available software packages, see *Olver et al.* [12], and *Lozier and Olver* [29].

9.4.1 Confluent Hypergeometric Functions

The confluent hypergeometric differential equation is

$$\left[z \frac{d^2}{dz^2} + (c - z) \frac{d}{dz} - a \right] w(z) = 0. \quad (9.129)$$

Equation (9.129) has a regular singular point at $r = 0$ with indices 0 and $1 - c$ and an irregular singular point at ∞ . The regular solution to Eq. (9.129) is the confluent hypergeometric function, denoted by ${}_1F_1$ in generalized hypergeometric series notation. It can be defined by the series

$${}_1F_1(a; c; z) = \frac{\Gamma(c)}{\Gamma(a)} \sum_{n=0}^{\infty} \frac{\Gamma(a+n)}{\Gamma(c+n)} \frac{z^n}{n!}. \quad (9.130)$$

The series Eq. (9.130) for ${}_1F_1$ converges for all finite z if c is not a negative integer or zero. It reduces to a polynomial of degree n in z if $a = -n$ where n is a positive integer and c is not a negative integer or zero. The function ${}_1F_1(a; c; z)$ is denoted by the symbol $M(a, c, z)$ in *Abramowitz and Stegun* [1], in *Jahnke and Emde* [5], and in *Olver* [9], by ${}_1F_1(a; c; z)$ in both of *Luke's* books [6, 7] and in *Magnus, Oberhettinger, and Soni* [8], and by $\Phi(a, c; z)$ in the *Bateman* project [2, 3] and *Gradshteyn and Ryzhik* [4]. The irregular solution to Eq. (9.129) is

$$\begin{aligned} U(a, c, z) &= \frac{\Gamma(1-c)}{\Gamma(1+a-c)} {}_1F_1(a; c; z) \\ &+ \frac{\Gamma(c-1)}{\Gamma(a)} z^{1-c} \\ &\times {}_1F_1(1+a-c; 2-c; z). \end{aligned} \quad (9.131)$$

The function $U(a, c, z)$ is multiple-valued, with principal branch $-\pi < \arg z \leq \pi$. It is denoted by the symbol $U(a, c, z)$ in *Abramowitz and Stegun* [1], in *Magnus, Oberhettinger, and Soni* [8], and in *Olver* [9], by $\psi(a; c; z)$ in the first of *Luke's* books [6], by $U(a; c; z)$ in the second of *Luke's* books [7], and by $\Psi(a, c; z)$ in the *Bateman* project [2, 3] and *Gradshteyn and Ryzhik* [4].

The Whittaker functions $M_{\kappa, \mu}$ and $W_{\kappa, \mu}$, which are related to ${}_1F_1$ and U via

$$\begin{aligned} M_{\kappa, \mu}(z) &= \exp\left(-\frac{1}{2}z\right) z^{\mu+\frac{1}{2}} \\ &\times {}_1F_1\left(\mu + \frac{1}{2} - \kappa; 2\mu + 1; z\right), \end{aligned} \quad (9.132)$$

$$\begin{aligned} W_{\kappa, \mu}(z) &= \exp\left(-\frac{1}{2}z\right) z^{\mu+\frac{1}{2}} \\ &\times U\left(\mu + \frac{1}{2} - \kappa, 2\mu + 1, z\right), \end{aligned} \quad (9.133)$$

are sometimes used instead of ${}_1F_1$ and U . For numerical evaluation and a program, see [30, 31].

The regular solution can be written as a linear combination of irregular solutions via

$$\begin{aligned} {}_1F_1(a; c; z) &= \frac{\Gamma(c)}{\Gamma(c-a)} e^{i\pi\epsilon a} U(a, c, z) + \frac{\Gamma(c)}{\Gamma(a)} \\ &\times e^{z+i\pi\epsilon(a-c)} U(c-a, c, -z), \end{aligned} \quad (9.134)$$

$$\epsilon = \begin{cases} +1, & \text{Im } z > 0, \\ -1, & \text{Im } z < 0. \end{cases} \quad (9.135)$$

${}_1F_1$ can also be obtained from U as the discontinuity across a branch cut

$$\begin{aligned} &z^{c-1} \exp(-z) {}_1F_1(a; c; z) \\ &= \frac{\Gamma(1-a)\Gamma(c)}{2\pi i} \\ &\times \left[(ze^{-i\pi})^{c-1} U(c-a, c, ze^{-i\pi}) \right. \\ &\quad \left. - (ze^{i\pi})^{c-1} U(c-a, c, ze^{i\pi}) \right]. \end{aligned} \quad (9.136)$$

The Wronskian of the two solutions is

$$\begin{aligned} &{}_1F_1(a; c; z) \frac{d}{dz} U(a, c, z) - U(a, c, z) \frac{d}{dz} {}_1F_1(a; c; z) \\ &= -\Gamma(c) z^{-c} \frac{\exp(z)}{\Gamma(a)}. \end{aligned} \quad (9.137)$$

A formula for $U(a, c, z)$ when c is the integer $n+1$ can be obtained by taking the $c \rightarrow n+1$ limit of the right-hand side of Eq. (9.131) to obtain

$$\begin{aligned} U(a, n+1, z) &= \frac{(-1)^{n+1}}{\Gamma(a-n)} \\ &\times \left[\frac{1}{n!} \ln(z) {}_1F_1(a; n+1; z) \right. \\ &\quad \left. + \sum_{k=-n}^{\infty} \frac{\Gamma(a+k) a_k z^k}{\Gamma(a)(k+n)!} \right], \end{aligned} \quad (9.138)$$

where

$$a_k = \begin{cases} (-1)^{k+1} (-k-1)!, & -n \leq k \leq -1, \\ [\Psi(k+a) - \Psi(k+1) \\ - \Psi(k+n+1)]/k!, & k \geq 0. \end{cases} \quad (9.139)$$

Here Ψ is the logarithmic derivative of the gamma function

$$\Psi(z) = \Gamma'(z)/\Gamma(z). \quad (9.140)$$

n is a non-negative integer. When $n = 0$, the sum from $k = -n$ to -1 is omitted.

The basic integral representations for ${}_1F_1$ and U are

$${}_1F_1(a; c; z) = \frac{\Gamma(c)}{\Gamma(a)\Gamma(c-a)} \times \int_0^1 e^{zt} t^{a-1} (1-t)^{c-a-1} dt, \quad (9.141)$$

$$U(a, c, z) = \frac{1}{\Gamma(a)} \int_0^\infty e^{-zt} t^{a-1} (1+t)^{c-a-1} dt. \quad (9.142)$$

The basic transformation formulae for ${}_1F_1$ and U are

$${}_1F_1(a; c; z) = e^z {}_1F_1(c-a; c; -z), \quad (9.143)$$

$$U(a, c, z) = z^{1-c} U(a-c+1, 2-c, z). \quad (9.144)$$

The recurrence relations among contiguous functions are

$$(z+2a-c) {}_1F_1(a; c; z) = (a-c) {}_1F_1(a-1; c; z) + a {}_1F_1(a+1; c; z), \quad (9.145)$$

$$(z+a-1) {}_1F_1(a; c; z) = (a-c) {}_1F_1(a-1; c; z) + (c-1) {}_1F_1(a; c-1; z), \quad (9.146)$$

$$c {}_1F_1(a; c; z) = c {}_1F_1(a-1; c; z) + z {}_1F_1(a; c+1; z), \quad (9.147)$$

$$(a+1-c) {}_1F_1(a; c; z) = a {}_1F_1(a+1; c; z) + (1-c) {}_1F_1(a; c-1; z), \quad (9.148)$$

$$c(z+a) {}_1F_1(a; c; z) = a c {}_1F_1(a+1; c; z) + (c-a) z {}_1F_1(a; c+1; z), \quad (9.149)$$

$$c(z+c-1) {}_1F_1(a; c; z) = c(c-1) {}_1F_1(a; c-1; z) + (c-a) {}_1F_1(a; c+1; z), \quad (9.150)$$

$$(z+2a-c)U(a; c; z) = U(a-1; c; z) + a(a-c+1)U(a+1; c; z), \quad (9.151)$$

$$(z+a-1)U(a; c; z) = U(a-1; c; z) + (c-a-1)U(a; c-1; z), \quad (9.152)$$

$$(c-a)U(a; c; z) = -U(a-1; c; z) + zU(a; c+1; z), \quad (9.153)$$

$$(a+1-c)U(a; c; z) = aU(a+1; c; z) + U(a; c-1; z), \quad (9.154)$$

$$(z+a)U(a; c; z) = a(a-c+1)U(a+1; c; z) + zU(a; c+1; z), \quad (9.155)$$

$$(z+c-1)U(a; c; z) = (c-a-1)(c-1)U(a; c-1; z) + zU(a; c+1; z). \quad (9.156)$$

Useful differentiation formulae include

$$\frac{d}{dz} {}_1F_1(a; c; z) = a c^{-1} {}_1F_1(a+1; c+1; z), \quad (9.157)$$

$$\frac{d}{dz} [z^a {}_1F_1(a; c; z)] = a z^{a-1} {}_1F_1(a+1; c; z), \quad (9.158)$$

$$\frac{d}{dz} [e^{-z} z^{c-a-1} {}_1F_1(a+1; c; z)] = (c-a-1) e^{-z} z^{c-a-2} {}_1F_1(a; c; z), \quad (9.159)$$

$$\frac{d}{dz} U(a, c, z) = -a U(a+1, c+1, z), \quad (9.160)$$

$$\frac{d}{dz} [z^a U(a, c, z)] = a(a-c+1) z^{a-1} U(a+1, c, z), \quad (9.161)$$

$$\frac{d}{dz} [e^{-z} z^{c-a-1} U(a+1, c, z)] = -e^{-z} z^{c-a-2} U(a, c, z). \quad (9.162)$$

An important multiplication theorem is

$${}_1F_1(a; c; z_1 z_2) = \sum_{k=0}^\infty \frac{\Gamma(a+k)\Gamma(\lambda+2k)}{k!\Gamma(a)\Gamma(\lambda+k)} (-z_1)^k \times {}_2F_1(-k, \lambda+k; c; z_1) \times {}_1F_1(a+k; \lambda+2k+1; z_2). \quad (9.163)$$

The fundamental asymptotic expansion for large z is

$$U(a, c, z) \approx z^{-a} \sum_{n=0}^\infty \frac{\Gamma(a+n)\Gamma(1+a-c+n)}{n!\Gamma(a)\Gamma(1+a-c)} (-z)^{-n}, \quad -\frac{3}{2}\pi < \arg z < \frac{3}{2}\pi. \quad (9.164)$$

The asymptotic expansion of ${}_1F_1$ for large z is obtained by using Eq. (9.164) and

$$\exp[z + i\pi\epsilon(a-c)]U(c-a, c, -z) \approx e^z z^{a-c} \sum_{n=0}^\infty \frac{\Gamma(c-a+n)\Gamma(1-a+n)}{n!\Gamma(c-a)\Gamma(1-a)} z^{-n}, \quad -\frac{5}{2}\pi < \arg z < \frac{5}{2}\pi, \quad (9.165)$$

which is a consequence of Eq. (9.164), on the right-hand side of Eq. (9.134). In the asymptotic expansion Eq. (9.165), and

in the asymptotic expansion for ${}_1F_1$, the change in the factor $\exp[i\pi\epsilon(a-c)]$ as $\arg z$ passes through zero is compensated by the phase change which comes from a factor $(-z)^{a-c}$ in the asymptotic expansion of $U(c-a, c, -z)$. The change in the factor $\exp(i\pi\epsilon a)$ in the first term of Eq. (9.134) as $\arg z$ passes through zero is not compensated by any other phase change. However, this discontinuity occurs in a region in which this first term is negligible compared to the second term. This is an example of the Stokes phenomenon [32], which occurs because the single-valued function ${}_1F_1$ is being approximated by multiple-valued functions. The large z asymptotic expansion of ${}_1F_1$ is valid for $-\frac{3}{2}\pi < \arg z < \frac{3}{2}\pi$, which is the overlap of the domain of validity of the expansions Eqs. (9.164) and (9.165).

Uniform asymptotic expansions for the Whittaker functions $M_{\kappa,\mu}$ and $W_{\kappa,\mu}$ introduced in Eqs. (9.132), (9.133) have been constructed via Olver's method. The following result [9, p. 412, Ex. 7.3], which holds for x positive, κ large and positive, and μ unrestricted, gives the flavor of these approximations

$$W_{\kappa,\mu}(4\kappa x) = \frac{2^{4/3}\pi^{1/2}\kappa^{\kappa+(1/6)}}{\phi_n(\kappa, \mu)\exp(\kappa)} \left(\frac{x\zeta}{x-1}\right)^{1/4} \times \left\{ \text{Ai}\left[(4\kappa)^{2/3}\zeta\right] \sum_{s=0}^n \frac{A_s(\zeta)}{(4\kappa)^{2s}} + \frac{\text{Ai}'\left[(4\kappa)^{2/3}\zeta\right]}{(4\kappa)^{2/3}} + \sum_{s=0}^n \frac{B_s(\zeta)}{(4\kappa)^{2s}} + \epsilon_{2n+1,2}(4\kappa, \zeta) \right\}. \quad (9.166)$$

Here Ai is the Airy function, and $\epsilon_{2n+1,2}$ is an error term which tends to zero faster than the last term kept when $\kappa \rightarrow \infty$ with n fixed. ζ is related to x by

$$\frac{4}{3}\zeta^{3/2} = (x^2 - x)^{1/2} - \ln\left[x^{1/2} + (x-1)^{1/2}\right], \quad x \geq 1, \quad (9.167)$$

$$\frac{4}{3}(-\zeta)^{3/2} = \cos^{-1}(x^{1/2}) - (x - x^2)^{1/2}, \quad 0 < x \leq 1. \quad (9.168)$$

ζ is an analytic function of x in the neighborhood of $x = 1$; conversely, x is an analytic function of ζ in the neighborhood of $\zeta = 0$. The differential form of the relations Eqs. (9.167) and (9.168) is

$$2\zeta^{1/2}d\zeta = x^{-1/2}(x-1)^{1/2}dx \quad x \geq 1, \quad (9.169)$$

$$2(-\zeta)^{1/2}d\zeta = x^{-1/2}(1-x)^{1/2}dx \quad 0 < x \leq 1. \quad (9.170)$$

A Taylor series expansion of ζ about $x = 1$ is most easily constructed by expanding the $x^{-1/2}$ in Eq. (9.169) or (9.170)

about $x = 1$ and integrating term by term. The opening terms of such an expansion are

$$\zeta = 2^{-2/3} \left[(x-1) - \frac{1}{5}(x-1)^2 + \frac{17}{175}(x-1)^3 \right] + O[(x-1)^4]. \quad (9.171)$$

The coefficient functions A_s and B_s are calculated recursively from

$$B_s(\zeta) = \frac{1}{2\zeta^{1/2}} \int_0^\zeta [\psi(\eta)A_s(\eta) - A_s''(\eta)] \frac{d\eta}{\eta^{1/2}}, \quad x \geq 1, \quad (9.172)$$

$$B_s(\zeta) = \frac{1}{2(-\zeta)^{1/2}} \int_\zeta^0 [\psi(\eta)A_s(\eta) - A_s''(\eta)] \frac{d\eta}{(-\eta)^{1/2}}, \quad 0 < x \leq 1, \quad (9.173)$$

$$A_{s+1}(\zeta) = -\frac{1}{2}B_s'(\zeta) + \frac{1}{2} \int \psi(\zeta)B_s(\zeta)d\zeta, \quad (9.174)$$

$$\psi(\zeta) = \frac{(4\mu^2 - 1)\zeta}{x(x-1)} + \frac{(3-8x)\zeta}{4x(x-1)^3} + \frac{5}{16\zeta^2}. \quad (9.175)$$

The functions $A_s(\zeta)$, $B_s(\zeta)$, and $\psi(\zeta)$, which appear to be singular at $\zeta = 0$, are actually analytic functions of ζ at $\zeta = 0$. The first few coefficient functions are

$$A_0(\zeta) = 1, \quad (9.176)$$

$$B_0(\zeta) = \frac{1}{4}\zeta^{-1/2} \left(\frac{x}{x-1}\right)^{3/2} \left[\left(8\mu^2 - \frac{1}{2}\right) \left(\frac{x}{x-1}\right)^2 - \left(\frac{x}{x-1}\right) + \frac{5}{6} \right] - \frac{5}{48}\zeta^{-2}, \quad (9.177)$$

$$A_1(\zeta) = \frac{1}{4}\zeta^{-1} [B_0(\zeta) - \psi(\zeta)] + \zeta [B_0(\zeta)]^2. \quad (9.178)$$

The function ϕ_n is calculated from

$$\phi_n(\kappa, \mu) = \sum_{s=0}^n \frac{A_s(\infty)}{(4\kappa)^{2s}} - \sum_{s=0}^{n-1} \lim_{\zeta \rightarrow \infty} \frac{\zeta^{1/2}B_s(\zeta)}{(4\kappa)^{2s+1}}. \quad (9.179)$$

The first two ϕ_n are

$$\phi_0(\kappa, \mu) = 1, \quad (9.180)$$

$$\phi_1(\kappa, \mu) = 1 - \left(\frac{12\mu^2 - 1}{24\kappa}\right) + \left(\frac{12\mu^2 - 1}{24\kappa}\right)^2. \quad (9.181)$$

A bound for the error term $\epsilon_{2n+1,2}$ has been given by Olver [9, p. 410, Eq. 7.13]. The extension to the complex case can be found in Skovgaard [33]. Skovgaard's expansions are in powers of $(4\kappa)^{-1}$ instead of $(4\kappa)^{-2}$, because the factor $1/\phi_n(\kappa, \mu)$ has been expanded out in inverse powers of 4κ

in his results; as a consequence, his coefficient functions A_s and B_s differ from Olver's. The corresponding asymptotic expansions for $U(\mu + \frac{1}{2} - \kappa, 2\mu + 1, 4\kappa z)$ and for the Laguerre polynomial

$$L_{\kappa-\mu-1/2}^{(2\mu)}(4\kappa z)$$

can be constructed with the aid of Eqs. (9.133) and (9.188).

Formulae for matrix element integrals can be obtained by inserting the integral representation Eq. (9.141) and interchanging the orders of integration. An example is

$$\int_0^\infty z^\mu {}_1F_1(a_1; c_1; \lambda_1 z) {}_1F_1(a_2; c_2; \lambda_2 z) dz = F_2(\mu + 1, a_1, a_2, c_1, c_2; -\lambda_1, -\lambda_2). \quad (9.182)$$

Here F_2 is one of the hypergeometric functions of two variables introduced by Appell, which can be defined either by the integral representation [2, Vol. 1, p. 230, Eq. 2]

$$F_2(\alpha, \beta, \beta', \gamma, \gamma'; x, y) = \frac{\Gamma(\gamma)\Gamma(\gamma')}{\Gamma(\beta)\Gamma(\beta')\Gamma(\gamma-\beta)\Gamma(\gamma'-\beta')} \times \int_0^1 du \int_0^1 dv u^{\beta-1} v^{\beta'-1} (1-u)^{\gamma-\beta-1} \times (1-v)^{\gamma'-\beta'-1} (1-ux-vy)^{-\alpha}, \quad (9.183)$$

or by the series expansion [2, Vol. 1, p. 224, Eq. 7]

$$F_2(\alpha, \beta, \beta', \gamma, \gamma'; x, y) = \sum_{m=0}^\infty \sum_{n=0}^\infty \frac{\Gamma(\alpha+m+n)}{m!n!\Gamma(\alpha)} \times \frac{\Gamma(\beta+m)\Gamma(\beta'+n)\Gamma(\gamma)\Gamma(\gamma')}{\Gamma(\beta)\Gamma(\beta')\Gamma(\gamma+m)\Gamma(\gamma'+n)} x^m y^n, \quad (9.184)$$

which converges for $|x| + |y| < 1$. Numerical evaluation of F_2 is particularly convenient in the special cases where it can be expressed in terms of ordinary hypergeometric functions ${}_2F_1$ [2, Vol. 1, Chap. 2], which are easy to calculate, or in terms of elementary functions. The key is the formula [2, Vol. 1, p. 238, Eq. 3]

$$F_2(\alpha, \beta, \beta', \alpha, \alpha; x, y) = (1-x)^{-\beta} (1-y)^{-\beta'} \times {}_2F_1\left[\beta, \beta'; \alpha; \frac{xy}{(1-x)(1-y)}\right], \quad (9.185)$$

which shows that it is necessary to get Appell functions F_2 in which the first, fourth, and fifth parameters are equal.

This can be achieved by exploiting whatever freedom in the choice of $a_1, a_2, c_1,$ and c_2 is available, and by using identities such as

$$F_2(\alpha + 2, \beta, \beta', \alpha + 1, \alpha + 1; x, y) = (\alpha + 1)^{-1} \beta' y \times F_2(\alpha + 1, \beta, \beta' + 1, \alpha + 1, \alpha + 1; x, y) + [F_2(\alpha + 1, \beta, \beta', \alpha + 1, \alpha + 1; x, y) + 2(\alpha + 1)^{-2} \beta \beta' x y \times F_2(\alpha + 2, \beta + 1, \beta' + 1, \alpha + 2, \alpha + 2; x, y)] + (\alpha + 1)^{-1} \beta x \times F_2(\alpha + 1, \beta + 1, \beta', \alpha + 1, \alpha + 1; x, y), \quad (9.186)$$

to obtain Appell functions F_2 for which the reduction Eq. (9.185) can be used.

9.4.2 Laguerre Polynomials

The Laguerre polynomials $L_n^{(\alpha)}$ are the polynomial solutions of the differential equation

$$\left[z \frac{d^2}{dz^2} + (\alpha + 1 - z) \frac{d}{dz} + n \right] L_n^{(\alpha)}(z) = 0. \quad (9.187)$$

They are a special case of the confluent hypergeometric function

$$L_n^{(\alpha)}(z) = \frac{\Gamma(n + \alpha + 1)}{n! \Gamma(\alpha + 1)} {}_1F_1(-n; \alpha + 1; z) = \frac{(-1)^n}{n!} U(-n, \alpha + 1, z), \quad (9.188)$$

and are given explicitly by

$$L_n^{(\alpha)}(z) = \sum_{k=0}^n \frac{\Gamma(\alpha + n + 1)}{k!(n-k)! \Gamma(\alpha + k + 1)} (-z)^k. \quad (9.189)$$

The $L_n^{(\alpha)}$ are sometimes called generalized Laguerre polynomials, because $L_n^{(0)}$, which is often denoted by L_n , is the polynomial introduced by Laguerre. This Laguerre polynomial differs from the *associated Laguerre function* for which the symbol L_q^p (with p and q both integers) is often used in the physics literature. The relation between the two is

$$\left[L_q^p(z) \right]_{\text{physics}} = (-1)^{p+q} q! L_{q-p}^{(p)}(z). \quad (9.190)$$

The first three $L_n^{(\alpha)}$ are

$$L_0^{(\alpha)}(z) = 1, \quad (9.191)$$

$$L_1^{(\alpha)}(z) = \alpha + 1 - z, \quad (9.192)$$

$$L_2^{(\alpha)}(z) = \frac{1}{2}(\alpha + 1)(\alpha + 2) - (\alpha + 2)z + \frac{1}{2}z^2. \quad (9.193)$$

Equation (9.188) shows that the irregular solution U does not supply a linearly independent second solution. A second solution which remains linearly independent and finite when α is a positive integer is

$$M_n^{(\alpha)}(z) = -\Gamma(\alpha) \left[z^{-\alpha} {}_1F_1(-n-\alpha; 1-\alpha; z) - \cos(\pi\alpha) \Gamma(1-\alpha) L_n^{(\alpha)}(z) \right]. \quad (9.194)$$

The Wronskian of the two solutions is

$$\begin{aligned} L_n^{(\alpha)}(z) \frac{d}{dz} M_n^{(\alpha)}(z) - M_n^{(\alpha)}(z) \frac{d}{dz} L_n^{(\alpha)}(z) \\ = \Gamma(n+\alpha+1) z^{-\alpha-1} \exp(z) / n!. \end{aligned} \quad (9.195)$$

A formula for $M_n^{(\alpha)}(z)$ when α is a positive integer m can be obtained by taking the $\alpha \rightarrow m$ limit of the right-hand side of Eq. (9.194) to obtain

$$M_n^{(m)}(z) = \ln(z) L_n^{(m)}(z) + \sum_{k=-m}^{\infty} \frac{(n+m)!}{(k+m)!} b_k z^k, \quad (9.196)$$

where

$$b_k = \begin{cases} -(-k-1)/(n-k)!, & -m \leq k \leq -1, \\ (-1)^k [\Psi(n+1-k) - \Psi(k+1) \\ - \Psi(k+m+1)] / [k!(n-k)!], & 0 \leq k \leq n, \\ (-1)^n (k-n-1)! / k!, & k \geq n+1. \end{cases} \quad (9.197)$$

The Rodrigues formula is

$$L_n^{(\alpha)}(z) = \frac{1}{n!} z^{-\alpha} \exp(z) \frac{d^n}{dz^n} [z^{n+\alpha} \exp(-z)]. \quad (9.198)$$

The generating function is

$$(1-w)^{-\alpha-1} \exp\left(-\frac{wz}{1-w}\right) = \sum_{n=0}^{\infty} L_n^{(\alpha)}(z) w^n. \quad (9.199)$$

The Christoffel–Darboux formula is

$$\begin{aligned} \sum_{k=0}^n \frac{k!}{\Gamma(k+\alpha+1)} L_k^{(\alpha)}(w) L_k^{(\alpha)}(z) \\ = \frac{(n+1)! \left[L_n^{(\alpha)}(w) L_{n+1}^{(\alpha)}(z) - L_{n+1}^{(\alpha)}(w) L_n^{(\alpha)}(z) \right]}{\Gamma(n+\alpha+1)(w-z)}. \end{aligned} \quad (9.200)$$

The orthonormality relation is

$$\begin{aligned} \int_0^{\infty} x^{\alpha} \exp(-x) L_n^{(\alpha)}(x) L_{n'}^{(\alpha)}(x) dx \\ = (n!)^{-1} \Gamma(n+\alpha+1) \delta_{n,n'}. \end{aligned} \quad (9.201)$$

Other useful integration formulae include

$$\begin{aligned} \int_0^{\infty} x^{\alpha+1} \exp(-x) L_n^{(\alpha)}(x) L_{n'}^{(\alpha)}(x) dx \\ = \frac{\Gamma(n+\alpha+1)}{n!} [-n \delta_{n,n'+1} + (2n+\alpha+1) \delta_{n,n'} \\ - (n+\alpha+1) \delta_{n,n'-1}], \end{aligned} \quad (9.202)$$

$$\begin{aligned} \int_0^{\infty} x^{\alpha-1} \exp(-x) L_n^{(\alpha)}(x) L_{n'}^{(\alpha)}(x) dx \\ = \frac{\Gamma(n_{<}+\alpha+1)}{n_{<}! \alpha}, \quad n_{<} = \min(n, n'), \end{aligned} \quad (9.203)$$

$$\begin{aligned} \int_0^{\infty} x^{\alpha-2} \exp(-x) L_n^{(\alpha)}(x) L_{n'}^{(\alpha)}(x) dx \\ = \frac{\Gamma(n_{<}+\alpha+1)}{n_{<}! \alpha(\alpha+2)} \left\{ \alpha [(\alpha+1)(n+n') + 4\alpha + 5] \right. \\ \left. \times (1-n_{<}) + 2(n+1)(n'+1) + 2\alpha(n+n') \right\}, \\ n_{<} = \min(n, n'). \end{aligned} \quad (9.204)$$

The differentiation and recursion relations are

$$z \frac{d}{dz} L_n^{(\alpha)}(z) = n L_n^{(\alpha)}(z) - (n+\alpha) L_{n-1}^{(\alpha)}(z), \quad (9.205)$$

$$L_{n+1}^{(\alpha)}(z) = (n+1)^{-1} \left[(2n+\alpha+1-z) L_n^{(\alpha)}(z) - (n+\alpha) L_{n-1}^{(\alpha)}(z) \right]. \quad (9.206)$$

Additional relations can be obtained as special cases of the relations listed above for the confluent hypergeometric function by using the relation Eq. (9.188).

The coefficients c_k in a Laguerre polynomial expansion such as

$$\begin{aligned} F(x) = \sum_{k=0}^{\infty} \frac{k!}{\Gamma(k+\alpha+1)} c_k \\ \times (\beta x)^{\alpha/2} \exp\left(-\frac{1}{2}\beta x\right) L_k^{(\alpha)}(\beta x) \end{aligned} \quad (9.207)$$

are given by the integral

$$c_k = \beta \int_0^{\infty} F(x) (\beta x)^{\alpha/2} \exp\left(-\frac{1}{2}\beta x\right) L_k^{(\alpha)}(\beta x) dx. \quad (9.208)$$

The rate of convergence of the expansion Eq. (9.207) is determined by the asymptotic behavior of the integral Eq. (9.208) for large k . A convenient way of extracting this asymptotic behavior will be described with the special case

$$\alpha = 0, \quad (9.209)$$

$$F(x) = (x+c)^{\nu} \exp(-\gamma x), \quad (9.210)$$

as an example. Since the discussion is intended to be illustrative rather than exhaustive, only the case $\gamma < \frac{1}{2}\beta$ will be considered. The method is based on the generating function Eq. (9.199). The generating function $g(z)$ for the coefficients c_k is given in general by

$$g(z) = \sum_{k=0}^{\infty} c_k z^k = \beta^{(2+\alpha)/2} (1-z)^{-\alpha-1} G\left[\frac{\beta(1+z)}{2(1-z)}\right], \quad (9.211)$$

where G is the Laplace transform

$$G(\lambda) = \int_0^{\infty} x^{\alpha/2} F(x) \exp(-\lambda x) dx. \quad (9.212)$$

The asymptotic analysis of the expansion coefficient c_k begins with the Cauchy integral for c_k , which is

$$c_k = \frac{1}{2\pi i} \int_C z^{-k-1} g(z) dz, \quad (9.213)$$

where the contour C is a small circle which runs counter-clockwise around the origin. The contour C is deformed to give integrals which can be evaluated via standard methods for the asymptotic evaluation of integrals [34, 35]. For the example Eqs. (9.209), (9.210),

$$g(z) = \beta c^{\nu+1} (1-z)^{-1} U[1, \nu+2, t(z)], \quad (9.214)$$

$$t(z) = \frac{(\beta+2\gamma)c + (\beta-2\gamma)cz}{2(1-z)}. \quad (9.215)$$

This $g(z)$ has a branch point on the negative real axis at $z = -(\beta+2\gamma)/(\beta-2\gamma)$, and a combination of a branch point and an essential singularity on the positive real axis at $z = 1$. It is convenient to take the associated branch cuts to run from $-\infty$ to $-(\beta+2\gamma)/(\beta-2\gamma)$ on the negative real axis, and from $+1$ to $+\infty$ on the positive real axis. The contour C can be deformed into the sum of two contours which run clockwise around the branch cuts. Then

$$c_k = c_k^{(1)} + c_k^{(2)}, \quad (9.216)$$

where $c_k^{(1)}$ is the contribution from a contour which runs clockwise around the branch cut from $-\infty$ to $-(\beta+2\gamma)/(\beta-2\gamma)$ on the negative real axis, and $c_k^{(2)}$ is the contribution from a contour which runs clockwise around the branch cut from $+1$ to $+\infty$ on the positive real axis. The asymptotic behavior of $c_k^{(1)}$ can be extracted in straightfor-

ward fashion via the method of Darboux [9, pp. 309–315, 321; 35, pp. 116–122]. The result is

$$c_k^{(1)} = \left(\frac{2\beta}{\beta+2\gamma}\right) \left[\frac{4\beta}{(\beta+2\gamma)(\beta-2\gamma)}\right]^{\nu} (-1)^k \times k^{\nu} \left(\frac{\beta-2\gamma}{\beta+2\gamma}\right)^k [1 + O(k^{-1})]. \quad (9.217)$$

The contribution $c_k^{(2)}$ requires a somewhat different strategy. The first step writes it as an integral along the real axis from $+1$ to $+\infty$ of the jump across the branch cut. Evaluating the jump yields

$$c_k^{(2)} = \frac{\beta}{\Gamma(-\nu)} \int_0^{\infty} dx x^{\nu} \left[\beta + \left(\frac{1}{2}\beta - \gamma\right)x\right]^{-\nu-1} \times \exp\left[-\left(\frac{1}{2}\beta - \gamma\right)c - (k+1)\ln(1+x) - \beta c x^{-1}\right]. \quad (9.218)$$

The integrand in Eq. (9.218) has a saddle point at $x \approx [\beta c / (k+1)]^{1/2}$. The asymptotics for $(k+1)c$ large can be extracted via the method of steepest descent (also known as the saddle point method) [9, pp. 136–138; 35, pp. 85–103; 34], (see Chap. 8). However, if $k+1$ is large with $(k+1)c$ small or moderate, the steepest descent approximation breaks down because the saddle point is too close to the branch point of the integrand at $x = 0$. The breakdown can be cured by using the small x approximations $[\beta + (1/2\beta - \gamma)x]^{-\nu-1} \approx \beta^{-\nu-1}$ and $\ln(1+x) \approx x - 1/2(k+1)^{-1}\beta c$ to obtain

$$c_k^{(2)} = \frac{2\beta}{\Gamma(-\nu)} \left(\frac{c}{(k+1)\beta}\right)^{(\nu+1)/2} \exp(\beta c) \times K_{\nu+1}\left[2\sqrt{(k+1)\beta c}\right] [1 + O(k^{-1/2})]. \quad (9.219)$$

The function $K_{\nu+1}$ which appears in Eq. (9.219) is a modified Bessel function of the third kind in standard notation. The large z approximation $K_{\nu+1}(z) \approx \pi^{1/2} (2z)^{-1/2} \exp(-z)$ can be used to recover the result of a steepest descent approximation to Eq. (9.218), which is

$$c_k^{(2)} = \frac{\pi^{1/2} \beta c^{\nu+1}}{\Gamma(-\nu)} [\beta c (k + \frac{1}{2})]^{-(2\nu+3)/4} \times \exp\left\{\gamma c - 2[\beta c (k + \frac{1}{2})]^{1/2}\right\} \times [1 + O(k^{-1})]. \quad (9.220)$$

The approximation Eq. (9.219) remains valid as $c \rightarrow 0$. The approximation Eq. (9.220) does not.

The generating function method outlined above has one very nice feature: if the singularity in the complex z -plane

which dominates the asymptotics is known, the analysis can be inverted to obtain a *convergence acceleration function* which builds in this singularity, and has no other singularities in the finite complex z -plane. The difference between the original $F(x)$ and this convergence acceleration function will have an expansion of the form Eq. (9.207) which converges faster than the expansion of $F(x)$. Examples can be found in [36–39].

The contributions $c_k^{(1)}$ and $c_k^{(2)}$ exhibit two typical features. The most rapidly varying part, which is

$$[(\beta - 2\gamma)/(\beta + 2\gamma)]^k \quad (9.221)$$

for $c_k^{(1)}$, and

$$\exp\left\{-2\left[\beta c\left(k + \frac{1}{2}\right)\right]^{1/2}\right\} \quad (9.222)$$

for the steepest descent approximation to $c_k^{(2)}$, is determined by the location of the associated singularity. The next most important part, which is k^ν for $c_k^{(1)}$, and $(k + 1/2)^{-(2\nu+3)/4}$ for the steepest descent approximation to $c_k^{(2)}$, is determined by the nature of the singularity (i.e., by the value of ν).

9.4.3 Gegenbauer Polynomials

The Gegenbauer polynomials are a special case of the Jacobi polynomial, and of the hypergeometric function

$$\begin{aligned} C_n^\lambda(z) &= \frac{\Gamma(\lambda + \frac{1}{2})\Gamma(2\lambda + n)}{\Gamma(2\lambda)\Gamma(\lambda + n + \frac{1}{2})} P_n^{(\lambda - \frac{1}{2}, \lambda - \frac{1}{2})}(z) \\ &= \frac{\Gamma(2\lambda + n)}{n!\Gamma(2\lambda)} \\ &\quad \times {}_2F_1\left(-n, n + 2\lambda; \lambda + \frac{1}{2}; \frac{1}{2} - \frac{1}{2}z\right), \end{aligned} \quad (9.223)$$

and are given explicitly by

$$C_n^\lambda(z) = \sum_{k=0}^{[n/2]} \frac{(-1)^k \Gamma(\lambda + n - k)}{k!(n - 2k)!\Gamma(\lambda)} (2z)^{n-2k}. \quad (9.224)$$

The first three C_n^λ are

$$C_0^\lambda(z) = 1, \quad (9.225)$$

$$C_1^\lambda(z) = 2\lambda z, \quad (9.226)$$

$$C_2^\lambda(z) = 2\lambda(\lambda + 1)z^2 - \lambda. \quad (9.227)$$

Additional C_n^λ can be obtained with the aid of the recursion relation

$$\begin{aligned} C_{n+1}^\lambda(z) &= (n + 1)^{-1} [2(n + \lambda)z C_n^\lambda(z) \\ &\quad - (n + 2\lambda - 1)C_{n-1}^\lambda(z)], \end{aligned} \quad (9.228)$$

which is valid for $n \geq 1$. A generating function is

$$(1 - 2zt + t^2)^{-\lambda} = \sum_{n=0}^{\infty} C_n^\lambda(z) t^n. \quad (9.229)$$

An important addition theorem, which can be used to derive addition theorems for spherical harmonics in any number of dimensions, is

$$\begin{aligned} C_n^\lambda[\cos(\gamma)] &= \frac{\Gamma(2\lambda - 1)}{[\Gamma(\lambda)]^2} \sum_{\ell=0}^n \frac{2^{2\ell}(2\lambda + 2\ell - 1)}{\Gamma(n + 2\lambda + \ell)} \\ &\quad \times \Gamma(n - \ell + 1) [\Gamma(\lambda + \ell)]^2 \\ &\quad \times \sin^\ell(\chi) \sin^\ell(\chi') \\ &\quad \times C_{n-\ell}^{\lambda+\ell}[\cos(\chi)] C_{n-\ell}^{\lambda+\ell}[\cos(\chi')] \\ &\quad \times C_\ell^{\lambda-\frac{1}{2}}[\cos(\gamma')], \end{aligned} \quad (9.230)$$

$$\begin{aligned} \cos(\gamma) &= \cos(\chi) \cos(\chi') \\ &\quad + \sin(\chi) \sin(\chi') \cos(\gamma'). \end{aligned} \quad (9.231)$$

9.4.4 Legendre Functions

The Legendre polynomials $P_\ell(z)$ are a special case of the Gegenbauer polynomial, and of the hypergeometric function

$$\begin{aligned} P_\ell(z) &= C_n^{1/2}(z) \\ &= {}_2F_1\left(-n, n + 1; 1; \frac{1}{2} - \frac{1}{2}z\right). \end{aligned} \quad (9.232)$$

The second (irregular) solution to the Legendre equation, which appears in Eq. (9.43) above, can be defined by the integral representation

$$Q_\ell(z) = 2^{-\ell-1} \int_{-1}^1 (1 - t^2)^\ell (z - t)^{-\ell-1} dt. \quad (9.233)$$

The first two Q_ℓ are

$$Q_0(z) = \frac{1}{2} \ln\left(\frac{z+1}{z-1}\right), \quad (9.234)$$

$$Q_1(z) = \frac{1}{2} z \ln\left(\frac{z+1}{z-1}\right) - 1, \quad (9.235)$$

Additional Q_ℓ can be obtained with the aid of the recursion relation

$$\begin{aligned} Q_{\ell+1}(z) &= [(2\ell + 1)z Q_\ell(z) \\ &\quad - \ell Q_{\ell-1}(z)] / (\ell + 1), \end{aligned} \quad (9.236)$$

which is valid for $\ell \geq 1$.

References

1. Abramowitz, M., Stegun, I.A.: Handbook of Mathematical Functions. Dover, New York (1965)
2. Erdelyi, A., Magnus, W., Oberhettinger, F., Tricomi, F.G.: Higher Transcendental Functions vol. 1–3. McGraw-Hill, New York, p 1953 (1955)
3. Erdelyi, A., Magnus, W., Oberhettinger, F., Tricomi, F.G.: Tables of Integral Transforms vol. 1 & 2. McGraw-Hill, New York (1954)
4. Gradshteyn, I.S., Ryzhik, I.W.: Tables of Integrals, Series, and Products, 4th edn. Academic Press, New York (1965)
5. Jahnke, E., Emde, F.: Tables of Functions with Formulae and Curves, 4th edn. Dover, New York (1945)
6. Luke, Y.L.: The Special Functions and Their Approximations vol. 1 & 2. Academic Press, New York (1969)
7. Luke, Y.L.: Mathematical Functions and Their Approximations. Academic Press, New York (1975)
8. Magnus, W., Oberhettinger, F., Soni, R.P.: Formulas and Theorems for the Special Functions of Mathematical Physics, 3rd edn. Springer, Berlin, Heidelberg (1966)
9. Olver, F.W.J.: Asymptotics and Special Functions. A.K. Peters, Wellesley (1997). reprint of Academic Press, New York 1974
10. Szegő, G.: Orthogonal Polynomials vol. 23. AMS, Providence (1975)
11. Olver, F.W.J., Lozier, D.W., Boisvert, R.F., Clark, C.W. (eds.): The NIST Handbook of Mathematical Functions. Cambridge University Press, New York, NY (2021)
12. Olver, F.W.J., Lozier, D.W., Boisvert, R.F., Clark, C.W.: NIST Digital Library of Mathematical Functions (2022) (see <http://dlmf.nist.gov/>)
13. Edmonds, A.R.: Angular Momentum in Quantum Mechanics. Princeton Univ. Press, Princeton (1960). Sect. 2.5
14. Pauling, L., Wilson, E.B.: Introduction to Quantum Mechanics With Applications to Chemistry. McGraw-Hill, New York (1935). Sect. 21
15. Drake, G.W.F., Hill, R.N.: J. Phys. B **26**, 3159 (1993)
16. Schiff, L.I.: Quantum Mechanics, 3rd edn. McGraw-Hill, New York, pp 234–239 (1968)
17. Talman, J.D.: Special Functions: A Group Theoretic Approach. W.A. Benjamin, New York, pp 186–188 (1968)
18. Fock, V.: Z. Phys. **98**, 145 (1935). Sect. 3.6.3
19. Reed, M., Simon, B.: Methods of Modern Mathematical Physics. I. Functional Analysis. Academic Press, New York, London, pp 263–264 (1972). Chaps. VII and VIII, see Theorem VIII.6
20. Hostler, L.: J. Math. Phys. **5**(5), 591 (1964)
21. Hostler, L.: J. Math. Phys. **5**(9), 1235 (1964)
22. Schwinger, J.: J. Math. Phys. **5**(11), 1606 (1964)
23. Swainson, R.A., Drake, G.W.F.: J. Phys. A **24**, 79 (1991)
24. Swainson, R.A., Drake, G.W.F.: J. Phys. A **24**, 95 (1991)
25. Swainson, R.A., Drake, G.W.F.: J. Phys. A **24**, 1801 (1991)
26. Hill, R.N., Huxtable, B.D.: J. Math. Phys. **23**, 2365 (1982)
27. Courant, R., Hilbert, D.: Methods of Mathematical Physics vol. 1. Interscience, New York (1953)
28. Hylton, D.J.: J. Math. Phys. **25**, 1125 (1984)
29. Lozier, D.W., Olver, F.W.J.: In: Gautschi, W. (ed.) Mathematics of Computation 1943–1993: A Half-Century of Computational Mathematics Proc. Symp. Appl. Math., vol. 48, AMS, Providence (1994)
30. Thompson, I.J., Barnett, A.R.: J. Comput. Phys. **64**, 490 (1986)
31. Thompson, I.J., Barnett, A.R.: Comput. Phys. Commun. **36**, 363 (1985)
32. Meyer, R.E.: Siam Rev. **31**, 435 (1989)
33. Skovgaard, H.: Uniform Asymptotic Expansions of Confluent Hypergeometric Functions and Whittaker Functions. Gjellerups, Copenhagen (1966)
34. Bleistein, N., Handelsman, R.A.: Asymptotic Expansions of Integrals. Dover, New York (1986). reprint of Holt, Rinehart, & Winston, New York 1975
35. Wong, R.: Asymptotic Approximations of Integrals. SIAM, Philadelphia (2001). reprint of Academic Press, San Diego 1989
36. Forrey, R.C., Hill, R.N.: Ann. Phys. **226**, 88 (1993)
37. Hill, R.N.: Phys. Rev. A **51**, 4433 (1995)
38. Forrey, R.C., Hill, R.N., Sharma, R.D.: Phys. Rev. A **52**, 2948 (1995)
39. Krauthausen, C., Hill, R.N.: Can. J. Phys. **80**, 181 (2002)



Robert Nyden Hill Professor Robert Nyden Hill received his Ph.D. from Yale University in 1962. In 1964, after postdoctoral fellowships at Princeton and Yale, he joined the faculty of the University of Delaware Physics Department, from which he retired in 1997. He published papers in relativistic dynamics, statistical mechanics, mathematical physics, and atomic and molecular physics.



Software for Computational Atomic and Molecular Physics

10

Edmund J. Mansky II

Contents

10.1	Introduction	165
10.2	Software for Atomic Physics	166
10.2.1	Atomic Structure Programs	166
10.2.2	Electron-Atom/Ion Scattering Programs	166
10.3	Software for Molecular Physics	167
10.3.1	Molecular Structure Programs	167
10.3.2	Molecular and Heavy Particle Scattering Programs	167
10.4	Software Libraries and Repositories	168
10.4.1	The CPC Journal and Library	168
10.4.2	Perl and CPAN	168
10.4.3	Python and PyPI	168
10.4.4	C++ and Boost	168
10.4.5	GitHub	168
10.5	General Tools	169
10.5.1	Configuration: GNU Autotools	169
10.5.2	C compilers: gcc	170
10.5.3	FORTRAN Compilers	170
10.5.4	Shell Scripting Languages	170
10.5.5	Mixing Languages	171
10.5.6	Third-Party Libraries and Unit Tests	171
	References	172

Abstract

When the first edition of the Handbook was published, the Internet was just beginning to become commonly used in scientific computing, outside the original Advanced Research Projects Agency Network (ARPANET) community. The landscape of scientific computing today has become much more complex and with many more options. It is timely, therefore, to include a brief discussion of the software currently used in atomic and molecular physics. Collected together in this chapter are a list of essential computer programs in atomic and molecular physics in tables designed for ease of use. Also included

is a guide to the various software libraries and repositories that can serve the atomic and molecular physics communities. Finally, some topics that generally get little explicit discussion in the literature, but are central to setting up and running a computational research group, are discussed.

Keywords

atomic scattering codes · atomic structure codes · molecular scattering codes · molecular structure codes · R-matrix codes · Perl · Python · FORTRAN compilers

10.1 Introduction

In both theoretical and experimental atomic and molecular physics, computers and software are central to the analysis and processing of data. Since the first edition of this Handbook was published in 1996, the growth of Web programming and the Internet has allowed a vast amount of software to be easily downloaded, shared, and used. Many excellent textbooks and monographs on computational physics [1–4], and programming in a large number of computer languages [5–14], are readily available. See, for example, Chap. 8 for additional details on computational techniques. Many excellent books and websites already exist that cover different pieces of information needed by working researchers in atomic and molecular physics who need to find a particular program in a given field, say atomic structure or scattering, or to help in setting up a computational standalone machine, or cluster. None provide an overall guide to finding computer programs in atomic and molecular physics for specific problems, nor a guide to software repositories and the core software most commonly used in scientific computing. This chapter begins to fill that gap by providing to the active researcher, and the new graduate student, a helpful resource that points to key atomic and molecular software and the underlying tools needed to effectively setup a computational machine.

E. J. Mansky II (✉)
Eikonal Research Institute
Bend, OR, USA
e-mail: mansky@mindspring.com

10.2 Software for Atomic Physics

The types of programs for atomic structure calculations range from empirical and semiempirical techniques to a wide variety of *ab initio* techniques. Programs for atomic scattering have similarly ranged from simple potential models to solving coupled sets of differential or integral equations involving thousands of quantal states. The complexity of the physics included in both structure and scattering codes has tracked closely advances in both computer hardware and physical theories.

10.2.1 Atomic Structure Programs

The core list of types of atomic structure programs includes Hartree–Fock, multiconfiguration Hartree–Fock and configuration interaction programs. Also necessarily included are many-body perturbation theory programs and newer tech-

niques using B-splines. We also include a reference to two suites of programs, CHIANTI and ADAS, used widely in the astrophysics and plasma physics communities, respectively. Details on atomic structure theories can be found in Chaps. 5 and 22–24.

Table 10.1 shows a list of atomic structure programs that are available.

10.2.2 Electron-Atom/Ion Scattering Programs

The core list of electron-atom/ion scattering codes necessarily includes multiple versions of the R-matrix suite of codes, the AUTOSTRUCTURE program that employs distorted-waves, and several other distorted-wave and polarized orbital programs. Also included is the NIEM program and some additional codes that compute scattering amplitudes and observables. See Chaps. 7, 47–57 and 60 for details on atomic scattering theories and observables.

Table 10.1 Atomic structure programs

Name	Description	CPC program name	Link/reference
HF86	Hartree–Fock (HF)	AATK	CPC 43 (1987) 355
DBSR_HF	B-spline HF	AEZK	CPC 202 (2016) 287
MCHF_88	Multiconfiguration HF	ABZK	CPC 64 (1991) 431
ATSP2K	MCHF for large-scale calcs.	ADLY	CPC 176 (2007) 559
MCDF	Multiconfiguration Dirac–Fock	ACRV	CPC 9 (1975) 31
GRASP2K	Relativistic MCDHF	ADZL v_1 ADZL v_1_1	CPC 177 (2007) 597 CPC 184 (2013) 2197
CIV3	Configuration interaction (CI)	AAKM	CPC 9 (1975) 141
MBPT	Many-body perturbation theory	ACXF	CPC 14 (1978) 71
CI-MBPT	CI + many-body pert. theory	AEWV	CPC 195 (2015) 199
ba5	Exact hydrogenic to $n \rightarrow 1000$	ADUU	CPC 166 (2005) 191
ADAS	Atomic data and analysis structure		http://www.adas.ac.uk/
CHIANTI	Atomic database for spectroscopic diagnostics of astrophysical plasmas		http://www.chiantidatabase.org/ AASS 125 (1997) 149

The CPC program library is located at <https://data.mendeley.com/journal/00104655>

Table 10.2 Atomic scattering programs

Name	Description	CPC program name	Link/reference
ASYM	Asymptotic solution	ACQE	CPC 1 (1969) 88
POLORB	Polarized orbital	AAGW	CPC 7 (1974) 38
UCLDW	Distorted wave	ADJG	CPC 114 (1998) 243
R-matrix	R-matrix suite	AAHA, AAHB, AAHC AAHF	CPC 8 (1974) 149 CPC 14 (1978) 367
R-matrix + BP	R-matrix + Briet–Pauli	AANS, AANT, AANU	CPC 25 (1982) 347
R-matrix NX	R-matrix + no exchange	ACGP	CPC 69 (1992) 76
R-matrix1	R-matrix (1995)	ADCP	CPC 92 (1995) 290
BSR	B-spline R-matrix	ADWY	CPC 174 (2006) 273
SCATTAMPREL	Scattering amplitudes w/relativistic effects	ACFE	CPC 30 (1983) 369
OBSERVABLES	Calculate observations from scattering amp. (see Chap. 7)	ACFF	CPC 30 (1983) 383
NIEM	Noniterative integral-equation method	AAJG, AAJH	CPC 23 (1981) 233
IMPACT	Coupled integro-differential eqs	ACYE	CPC 15 (1978) 23
AUTOSTRUCTURE	BP distorted wave	AEIV	CPC 182 (2011) 1528

Table 10.2 shows a list of atomic scattering programs that are available.

10.3 Software for Molecular Physics

The rapid advances in computer hardware (CPU design and speed, multicores, multi-GPUs, etc.) has profoundly influenced the size and complexity of the molecules that can now be tackled computationally. Molecular structure programs now routinely include basis sets of many thousands of states and incorporate complex techniques for electron exchange and configuration interaction in a full multicenter setting. Similarly, the molecular and heavy-particle scattering programs, in many cases, incorporate the results of these large-scale molecular structure programs in their scattering calculations. Computational chemistry is a vast field today, and due to space limitations we have selected a subset of the programs that are available based on their utility and widespread usage in molecular physics. In addition to the Computer Physics Communications (CPC) Program Library (discussed in Sect. 10.4.1), additional resources for molec-

ular programs can be found in [15–20]. For those readers interested in further details of computer hardware, see [21].

10.3.1 Molecular Structure Programs

The core list of types of molecular structure programs include the GAUSSIAN and GAMESS suite of programs, as well as HONDO, MOLCAS and others. Also included as an example of a non-FORTRAN program is PySCF, which is a SCF program written in Python. See Chaps. 33–34 for further details on molecular structure theories.

Table 10.3 shows a list of molecular structure programs that are available.

10.3.2 Molecular and Heavy Particle Scattering Programs

The core list of types of molecular and heavy-particle scattering programs includes the POLYRATE suite, inelastic and vibrational collisions, as well as the calculation of quantum

Table 10.3 Molecular structure programs

Name	Description	CPC program name	Link/reference
GAUSSIAN	HF w/Gaussian orbitals		http://www.gaussian.com
GAMESS-US	HF, SCF, MCSCF and others		https://www.msg.chem.iastate.edu/gamess/download.html
GAMESS-UK	HF, MP2, MP3, DFT and others		http://www.csar.cfs.ac.uk/user_information/software/chemistry/gamess_uk.shtml Mol. Phys. 103 (2005) 719
HONDO	HF, SCF and others	ABFS	CPC 52 (1989) 415
MOLCAS	HF, DFT, MCSCF and others		https://www.molcas.org
TRIATOM	Rovibrational level of triatomics	AALO	CPC 42 (1986) 257
DIRAC	HF, MP2, DFT, CC and others		http://www.diracprogram.org/doku.php Theo. Chem. Accounts 116 (2006) 241
PySCF	Python-based SCF		https://github.com/sunqm/pyscf
MOLPRO	MCSCF, CI, CC, MP2, and others		https://www.molpro.net
PQS	MP2, MP3, MP4, SCF, and others		http://www.pqs-chem.com

Table 10.4 Molecular and heavy particle scattering programs

Name	Description	CPC program name	Link/reference
DCS	Differential cross sections for diatomics	ABTG	CPC 60 (1990) 391
POLYDCS	DCS for e^- + polyatomics	ADJB	CPC 114 (1998) 129
POLYRATE	Semiclassical chemical reaction rates	ABBD v_1	CPC 47 (1987) 91
POLYRATE 4	Chemical reaction rates for polyatomics	ABBD v_2	CPC 71 (1992) 235
POLYRATE 6.5		ABBD v_3	CPC 88 (1995) 341
EDWIN	Inelastic molecular collisions	AAJC	CPC 19 (1980) 359
VIBREQ	Collisions w/electronic and vibrational degrees of freedom	AAOX	CPC 28 (1982) 207
SBECROSS	Quantum transport properties in molecular gases	ADFB	CPC 103 (1997) 251
CDW1	Electron capture in ion-atom collisions	AAHL	CPC 23 (1981) 153
ABC	Quantum reactive scattering	ADMX	CPC 133 (2000) 128

transport properties of molecular gases. See Chaps. 36–40 for more details on molecular scattering theories.

Table 10.4 shows a list of molecular structure codes that are available.

10.4 Software Libraries and Repositories

The number and quality of libraries and repositories of scientific and other software has increased greatly over the past 30 years. Originally, only a few scientific journals archived programs and sent to them to users who requested them for distribution. Such distributions from scientific journals, such as *Computer Physics Communications*, were not free due to the cost of producing and shipping magnetic tapes to users. Today, many websites contain high-quality scientific software and other software that complement and extend the functionality of scientific programs. In the following sections some of the core libraries and repositories that are currently available are listed.

10.4.1 The CPC Journal and Library

The journal *Computer Physics Communications* is one of the oldest scientific journals that has been archiving computer programs in all areas of physics since 1969. Currently, the vast majority of programs are in FORTRAN, with a smaller number in C, C++, Python, and Julia [22]. Since 2015, all programs archived at CPC are freely available via the Mendeley Data interface [23] and via their website at Queen's University, Belfast.

The CPC Program Library can be found at <http://www.cpc.cs.qub.ac.uk/>. Currently, over 1800 refereed programs are deposited with the CPC Program Library. The column labeled *CPC Program Name* in Tables 10.1–10.4 is referred to at the CPC website as the *Catalogue ID*. Entering the ID into the search box at the CPC website will allow easy access to the specified program.

10.4.2 Perl and CPAN

Perl is a scripting language [5–9] that comes installed on most new computers and has an extensive library of freely available modules covering the entire field of numerical computing as well as encompassing most topics in software generally.

The main website for Perl is The Comprehensive Perl Archive Network, or CPAN, and is located at <https://www.cpan.org> and currently has over 200 000+ modules, all freely available.

Noteworthy for atomic and molecular computational physics are the Perl Data Language module, the math mod-

ules `Math::BLAS`, `Math::GSL`, which provide the ability to call into the BLAS library or the GNU Scientific Library, respectively; and the `Inline` family of modules that provide the ability to embed calls to other languages into Perl modules. See Sect. 10.5.5 for more details on software bridges and the mixing of languages generally.

10.4.3 Python and PyPI

Python is another popular scripting language [11, 12] and is also generally installed on all new computers. Python is object-oriented in its basic design and has a simpler syntax than that of Perl, and is therefore quite popular. Python also has an extensive library of freely available modules, located at the Python Package Index website <https://pypi.org>, which currently has over 139 000 projects.

Especially noteworthy for computational work are the Python modules `NumPy`, `SciPy` [24], `Pandas` [25, 26], `AstroPy`, `SunPy`, and `Dedalus`. The modules `NumPy`, `SciPy` and `Pandas` are part of the SciPy Stack, which includes methods for basic N-dimensional array manipulation (`NumPy`), data analysis and structure (`Pandas`), and scientific computing (`SciPy`). See <https://scipy.org> for further details on the SciPy stack. The modules `AstroPy` and `SunPy` contain a large number of basic functions and tools used in astronomy and heliophysics, respectively. `Dedalus` is a framework (library) for solving partial differential equations using spectral methods.

Python modules that allow embedding calls to other languages from Python also exist, including `PyInline`, `inline`, and `np_inline`, among others. See Sect. 10.5.5 for more discussion on software bridges and the mixing of languages.

10.4.4 C++ and Boost

C++ is an extension of the C language to include classes [27, 28] and is a widely used language in all areas of scientific computing [29]. Most new computers come with a compiler that can compile C++ code. See Sect. 10.5.2 for more on compilers.

C++ has an extensive list of libraries that are available [30]. The Boost library, located at <https://www.boost.org>, has a large number of modules on linear algebra, multi-precision arithmetic, and numerical analysis [31].

10.4.5 GitHub

GitHub is a website, <https://www.github.com>, where one can freely create a repository (repo) for a software project and upload and share the files in it with others. Private repos can

also be created for a monthly fee. Free repos can be searched by tags or keywords to find ones dealing with specific subject areas. Free repos can be downloaded at no cost. The code uploaded to GitHub is not a refereed code deposited at (for example) the CPC library, yet many high-quality software packages are available at GitHub, in a wide variety of languages. Currently, the total number of repos at GitHub is on the order of 85 million.

10.5 General Tools

We describe here some general tools and topics that have proven essential in configuring and setting up a computational group. Much of the material in this section is generally passed along by word-of-mouth within a research group. Coverage of the topics considered here depends upon the type of computational work a given group is doing, as well as the range of computer skills within the group. By bringing together in one place a discussion of topics such as the configuration of open-source software, compilers, libraries, and the mixing of languages, we hope to bring some coherence and background to help answer common questions such as *Why doesn't X build on my machine?*, *What is gcc?*, or *Where is FORTRAN?*, among others.

10.5.1 Configuration: GNU Autotools

Configuring and installing open-source software has become much more standardized and simplified over the past 20 years. Most open-source software makes use of the GNU autotools (our shorthand) suite of scripts: `aclocal`, `autoconf`, `autoheader`, and `automake`. The purpose of these scripts is to generate the `configure` script and the `Makefile.am` automake Makefile for the machine it is running on. To complete the configuration of a given software project, one then executes `configure config options...`, and then `make` to begin the final compilation of the software. The reason for the complexity of the autotools suite is due to their overall design to be executable on as many different computer systems as possible.

The `configure` script checks for the existence of all system-supplied programs that the given open-source project requires. As `configure` checks the existence of each required component, it will create and execute a small program

to test the required program for correct output. If the output is incorrect, an error is printed in the `config.log` file, and processing continues. Once the set of existence checks are completed, `configure` will then generate the Makefiles in each subfolder of the project. If `configure` exits with an error from the existence check process, the error may be resolved simply by adding a missing header file or library, or adding additional directories to the colon-delimited shell environment variables such as `INC`, `LD_LIBRARY_PATH`, or `PKG_CONFIG_PATH`, so that already installed required programs can be found upon a rerun of `configure`.

In most cases, an open-source software project will already include a `configure` script, and hence there may be no need to run the autotool scripts in full. It is essential to run the autotools in three cases: (a) where no `configure` script is provided; (b) where the `configure` script is badly broken, or out of date, and will not run; or (c) to extend the functionality of an open-source project to include the creation of shared dynamic libraries (for example). For cases (a) and (b), the GNU programs `autoscan` (part of `autoconf` project) and `libtoolize` (part of the `libtool` project) provide a mechanism to generate a `configure.ac` script, or add `libtool` functionality to a project, respectively. Table 10.5 summarizes the execution sequence of the autotool scripts.

Each autotool script has their own GNU project webpage, which can be found at <https://www.gnu.org>. In the case where one is using an older machine, and/or an older operating system, the autotool scripts and the M4 version of the macro processor may need updating *first* to a newer version before running the autotool scripts.

The autotool scripts are designed to be used in conjunction with several other GNU project software: `libtool` and `pkg-config`. Both programs will also usually be installed on new computers, or included in a given Linux distribution, for example. `libtool` provides a very general mechanism to link object modules into a library in a multiplatform manner. `pkg-config` is a program that keeps track of the management of multiple packages installed on a machine, including the location of the libraries that support a given package. Therefore, for open-source projects that are designed to be configured and built using the GNU autotools suite, it is important that *prior* to building a given project, the program `pkg-config` is installed into the folder tree where the target projects will be installed. Hence, as open-source projects are installed into `/usr/local` (say), the

Table 10.5 GNU autotools table

Script name ~>	Input macro/autoconf required ~>	Produces output
<code>aclocal</code>	<code>acinclude.m4</code> and <code>configure.ac</code>	<code>aclocal.m4</code>
<code>autoconf</code>	<code>aclocal.m4</code> , <code>configure.ac</code> and <code>acsite.m4</code>	<code>configure</code>
<code>autoheader</code>	<code>aclocal.m4</code> , <code>configure.ac</code> and <code>acsite.m4</code>	<code>config.h.in</code>
<code>automake</code>	<code>configure.ac</code> and <code>Makefile.am</code>	<code>Makefile.in</code>

program `pkg-config` in that folder tree will keep track of each install, thereby allowing later installs of projects to find earlier dependencies.

As a general rule, when updating such important scripts as the autotools scripts, or compilers, it is safest to install the updated code in `/usr/local`, `/opt`, or some other directory outside of the system directory tree. By installing core scripts and codes in `/usr/local` one avoids breaking any operating system code. Another key point to know about `configure` is that the full set of options `configure` supports for a given open-source project can be found by executing `configure --help`. Examining the full set of options for `configure` is useful to see whether any other open-source project or library should be installed *prior* to running `configure` for the project at hand. In many cases, such project dependencies are not always covered in the README or INSTALL files, but only obtained from `configure --help`.

10.5.2 C compilers: gcc

Central to the development of new scientific software is the compiler. The scope and functionality of compilers has also grown enormously over the past 20 years or so. Many new language concepts have been developed and incorporated into C and C++ compilers, and advances in CPU architecture (massive multicore systems, GPUs, etc.) have resulted in a concomitant increase in compiler options to take advantage of the hardware advances.

Among the most widely used C/C++ compilers used today is gcc from the GNU Foundation. The gcc project has its own website, <https://gcc.gnu.org>, where an extensive amount of documentation can be found for all versions of gcc, as well as details on where one can freely download it. See [32] for further details.

Much depends on the version of gcc on a given computer. If the version of gcc is too old, many open-source packages cannot be built. Generally, one would want gcc with a version 4.2 or greater. Depending upon the manufacturer of the computer one is using, the gcc suite already installed may not be complete. For Linux users this may mean that additional gcc packages will need to be installed, using the appropriate package manager program (e.g., `yum`, `apt`, `rpm`), to get a fully functioning gcc suite. For nonscientific users these omissions are usually never encountered. Scientific soft-

ware using complex library options, or advanced features of optimization may well encounter difficulties with their system-installed gcc if the suite is not complete (missing header files or libraries being the most common omissions). In that case, it is entirely feasible to build and install a complete gcc suite separate from the system supplied one. It is beyond the scope of this chapter to describe how one goes about building gcc in such a case. We point out that the step-by-step building of newer versions of gcc from older ones is routinely done as part of the release testing performed at compiler farms by the gcc as part of their testing prior to a new release of gcc. See the archived email list for gcc for details [33].

LLVM and Clang

Another popular C/C++ compiler suite is the Low-Level Virtual Machine (LLVM) Project with its front-end package Clang. The motivation for creation of the LLVM compiler was a desire for better diagnostics and a license that would allow for commercial development (LLVM underlies much of the development of iPhone apps). Details about LLVM and documentation can be found at their website: <https://llvm.org> and in a number of books [34, 35], for example.

10.5.3 FORTRAN Compilers

Most scientific software is still written in FORTRAN [13, 14]. The FORTRAN compiler that is part of the gcc suite is called `gfortran`. Most computers unfortunately still do not come supplied with a FORTRAN compiler as part of the operating system. One either pays for the installation of FORTRAN from a vendor, or one may install `gfortran` for free from the gcc suite. See the `gfortran` website for further details: <https://gcc.gnu.org/fortran>.

Table 10.6 summarizes some of the most popular FORTRAN compilers currently being used in scientific software.

10.5.4 Shell Scripting Languages

Shell scripting languages such as Perl and Python have advanced far from their roots in `ksh`, `bash`, and `csh`, both in functionality and performance [10]. In many respects, Perl and Python compare quite well in overall performance and optimization to compiled languages such as FORTRAN

Table 10.6 Types of FORTRAN compilers

Name	Type	Description	Link
<code>gfortran</code>	GNU (free)	GCC FORTRAN compiler	https://gcc.gnu.org/fortran
<code>g95</code>	Free	Fortran 95 and later	https://www.g95.org
ProFORTRAN	Commercial	Fortran 95 and later	https://www.absoft.com
PGFORTRAN	Free/commercial (depends on edition)	Fortran 95 and later	https://www.pgroup.com

and C/C++. In fact, depending upon the requirements of the scientific software being used, an efficient partition of problems to Perl/Python for some portion of a problem (say pattern matching of regular expressions or file IO), while the rest can be handled by the compiled program in C/FORTRAN, is entirely feasible by using the many modules available in Perl/Python.

It should be noted that for many years, Perl and Python scripts have been used internally by gcc during its build for precisely the problems described above.

10.5.5 Mixing Languages

Frequently in developing software in a group with backgrounds in various computer languages, the question of rewriting existing code in a different, or newer, language arises. While in many cases there are good reasons for undertaking a rewrite, there are alternatives available that may obviate the need for a complete rewrite.

It is actually a quite commonly used technique to mix the use of two languages to solve a given problem. Software written in one language, which has high performance in tasks such as string manipulation, can be completely integrated with software written in a different language with high performance in numerical processing. In the case just described, we are referring to the mixing of C and FORTRAN, each of which worked on data *shared* between the two languages in the same compiled code. The data is shared in core when the COMMON block in FORTRAN and a C structure have the same name. The two data structures having the same name act then as a bridge between the two languages.

In the second common case, one wants to reuse some existing programs by having the ability to call them from a program written in a different language than the first program. In this latter case, one is sharing or mixing the *code* in various modules. By mixing the code one avoids the need to rewrite an existing library or program.

The two types of mixing, involving the sharing of data or code, are summarized in Table 10.7.

Another technique to facilitate the use of one language from another is through the use of “glue” or hybrid languages. The use of the XS extension to Perl [36] allows computationally intensive calls to be executed in C from Perl and is commonly used in many modules in CPAN. Similarly,

the use of the hybrid compiler and language Cython [37] allows calls to C and C++ code to be made from Python. Both XS and Cython are used extensively in scientific computing.

10.5.6 Third-Party Libraries and Unit Tests

Third-Party Libraries

The use of third-party libraries has long been a standard part of scientific software. The most common types of libraries included in the compilation of a scientific code in C or FORTRAN would bring in functions from linear algebra and numerical analysis. Typical libraries include BLAS, LAPACK, ATLAS, IMSL, and NAG, to name just a few. Table 10.8 collects key information about the most commonly used scientific libraries. Software such as Mathematica or MatLab have not been included here, as they may be considered full, standalone integrated development environments.

Most open-source libraries have had modules written in Perl or Python to permit the easy calling of third-party libraries from within shell scripts, which is an example of the mixing described in Sect. 10.5.5.

Unit Tests

Unit tests in software are small pieces of code that permit the *testing* of a program’s functions with test or mocked data. The phrase *unit* in unit tests refers to the process of gradually building test scripts in each component or unit of the codebase until the entire codebase is covered.

The purpose of testing the program with known data that should produce a known result is to automate the process of finding bugs in code when the codebase has changed. Testing a program for correctness of output is generally unnecessary for small programs. Testing programs for correctness becomes paramount when the codebase is tens of thousands, or even hundreds of thousands of lines of code, spread among hundreds to thousands of individual files. In the case of large codebases, having a mechanism to test the code against a reference (the unit tests) greatly aids finding bugs that occur when changes occur.

The software that links the unit test scripts in a given language with the code being tested are known as testing frameworks or harnesses. See [38] for details in the case of Perl and more generally [39]. Table 10.9 summarizes the harnesses that are currently used for C, C++, FORTRAN, Perl, and Python.

Table 10.7 Types of mixing techniques of languages

Type	Description	Technique/code	Comment
Data sharing	Blocks of data shared between languages	COMMON blocks and C structures have same name	C/FORTRAN
Code sharing	Blocks of code in one language call modules in another language	Inline and inline modules used in Perl, Python, resp.	Perl/Python

Table 10.8 Types of third-party libraries

Library name	Description	Link
BLAS	Linear algebra library	http://www.netlib.org/blas/
LAPACK	Linear algebra library	http://netlib.sandia.gov/lapack/
ATLAS	Automatically tuned linear algebra library	https://sourceforge.net/projects/math-atlas/
GSL	GNU scientific library	https://www.gnu.org/software/gsl/
IMSL	Numerical library (commercial)	https://www.imsl.com
NAG	Numerical library (commercial)	https://www.nag.com/

Table 10.9 Testing harnesses (frameworks)

Harness name	Description	Link/comment
CUnit	Unit testing in C	http://cunit.sourceforge.net/
Check	Unit testing in C	https://libcheck.github.io/check/
CppTest	Unit testing in C++	http://cpptest.sourceforge.net/
CppUnit	Unit testing in C++	https://sourceforge.net/projects/cppunit/
FUnit	Unit testing in FORTRAN	https://github.com/ieyasu/funit
Test::Harness, Test::More, TAP and Test::Simple	Unit testing in Perl	All part of standard Perl
unittest, XPyUnit, Nose and Doctest	Unit testing in Python	All part of standard Python

References

- Thijssen, J.: Computational Physics, 2nd edn. Cambridge Univ. Press, Cambridge (2013)
- Boudreau, J.F., Swanson, E.S.: Applied Computational Physics. Oxford Univ. Press, Oxford (2018)
- Barschat, K.: Computational Atomic Physics. Springer, New York (1996)
- LeBris, C., Ciarlet, P.G.: Special Volume: Computational Chemistry. Handbook of Numerical Analysis, vol. 10. North-Holland, New York (2003)
- Wall, L., Christiansen, T., Orwant, J.: Programming Perl, 3rd edn. O'Reilly, Sebastopol (2000)
- Schwartz, R.L., Foy, B.D., Phoenix, T.: Intermediate Perl, 2nd edn. O'Reilly, Sebastopol (2012)
- chromatic: Modern Perl 2011–2012. Oynx Neon Press, Portland (2012)
- Dominus, M.J.: Higher-Order Perl. Elsevier/Morgan Kaufmann, San Francisco (2005)
- Conway, D.: Object Oriented Perl. Manning, Greenwich (2000)
- Kak, A.: Scripting with Objects: A Comparative Presentation of Object-Oriented Scripting with Perl and Python. Wiley, Hoboken (2008)
- Lutz, M.: Programming Python, 4th edn. O'Reilly, Sebastopol (2010)
- Ramalho, L.: Fluent Python. O'Reilly, Sebastopol (2015)
- Adams, J.C., Brainerd, W.S., Martin, J.T., Smith, B.T., Wagener, J.L.: FORTRAN 95 Handbook: Complete ISO/ANSI Reference. MIT Press, Cambridge (1997)
- Metcalfe, M., Reid, J., Cohen, M.: Modern Fortran Explained. Oxford Univ. Press, Oxford (2011)
- Tannor, D., Machnes, S., Assémat, E., Larsson, H.R.: Phase-space versus coordinate-space methods: prognosis for large quantum calculations. In: Rice, S.A., Dinner, A. (eds.) Advances in Chemical Physics, vol. 163, Wiley, New York (2018)
- Wilson, S.: Methods in Computational Chemistry vol. 1, 2. Plenum Press, New York (1988)
- Olivucci, M.: Computational Photochemistry. Theoretical and Computational Chemistry, vol. 16. Elsevier, New York (2005)
- Papageorgiou, A., Traub, J.F.: In: Rice, S.A., Dinner, A. (eds.) Quantum Information and Computation for Chemistry Advances in Chemical Physics, vol. 154, Academic Press, New York (2014)
- Harris, F.E.: Exponentially correlated wave functions for four-body systems. In: Hoggan, P.E., Ozdogan, T. (eds.) Advances in Quantum Chemistry, vol. 73, Academic Press, New York (2016)
- Harris, F.E., Albert, V.V.: Fully correlated wavefunctions for three- and four-body systems. In: Hoggan, P.E. (ed.) Advances in Quantum Chemistry, vol. 67, Academic Press, New York (2013)
- Mueller, S., Soper, M.E., Sosinsky, B.: Upgrading and Repairing Servers. QUE, Indianapolis (2006)
- Kramer, S., Plankensteiner, D., Ostermann, L., Ritsch, H.: QuantumOptics.jl: A Julia framework for simulating open quantum systems. CPC, vol. 227., pp 109–116 (2018)
- Mendeley: Share and discover datasets (2021). <https://www.mendeley.com/datasets>
- Nunez-Iglesias, J., van der Walt, S., Dashnow, H.: Elegant SciPy. O'Reilly, Sebastopol (2017)
- McKinney, W.: Python for Data Analysis. O'Reilly, Sebastopol (2013)
- Gorelick, M., Ozsvald, I.: High Performance Python. O'Reilly, Sebastopol (2014)
- Stroustrup, B.: The Design and Evolution of C. Addison-Wesley, New York (1994)
- Stroustrup, B.: C++ Programming Language, 4th edn. Addison-Wesley, New York (2013)
- Barton, J.J., Nackman, L.R.: Scientific and Engineering C. Addison-Wesley, New York (1994)
- cppreference.com: A list of open source C++ libraries (2021). <https://en.cppreference.com/w/cpp/links/libs>
- Schaling, B.: The Boost C++ Libraries. XML Press, Laguna Hills (2008)
- Miller, F.P.: GNU Compiler Collection. Alphascript, New York (1994)
- The Gcc Archives: (2021). <https://gcc.gnu.org/ml/gcc>
- Pandey, M.: LLVM Cookbook. pact, New York (2008)

35. Engemann, R., Li, Z., Midkiff, S.P.: Languages and Compilers for High Performance Computing. Springer, New York (2004)
36. Jenness, T., Cozens, S.: Extending and Embedding Perl: The Definitive Guide to XS, Embedding and the Perl Internals. Manning, Greenwich (2003)
37. Smith, K.W.: Cython: A Guide for Python Programmers. O'Reilly, Sebastopol (2015)
38. Langworth, I., chromatic: Perl Testing: A Developer's Notebook. O'Reilly, Sebastopol (2005)
39. Hamill, P.: Unit Test Frameworks: A Language-Independent Overview. O'Reilly, Sebastopol (2005)



Edmund J. Mansky II Edmund J. Mansky II received his PhD from Georgia Institute of Technology in 1985. His theoretical work involves statistical mechanics of dense gases. In addition, his interests are three-body recombination processes and collisions involving Rydberg states of atoms and molecules at thermal and ultracold temperatures. His day job is programming heliophysics data for the scientific community.

Part B
Atoms

Part B presents the main concepts in the theoretical and experimental knowledge of atomic systems, including atomic structure and radiation. Ionization energies for neutral atoms and transition probabilities of selected neutral atoms are tabulated. The computational methods needed for very high precision approximations for helium are summarized. The physical and geometrical significance of simple multipoles is examined. The basic nonrelativistic and relativistic theory of electrons and atoms in external magnetic fields is given. Various properties of Rydberg atoms in external fields and in collisions are investigated. The sources of hyperfine structure in atomic and molecular spectra are outlined, and the resulting energy splittings and isotope shifts given. Precision oscillator strength and lifetime measurements, which provide stringent experimental tests of fundamental atomic structure calculations, are discussed. Ion beam spectroscopy is introduced, and individual applications of ion beam techniques are detailed. A basic description of neutral collisional line shapes is given, along with a discussion of radiation transfer in a confined atomic vapor. Many qualitative features of the Thomas–Fermi model are studied, and its later outgrowth into general density functional theory delineated. The Hartree–Fock and multiconfiguration Hartree–Fock theories, along with configuration interaction methods, are discussed in detail, and their application to the calculation of various atomic properties presented. Relativistic methods for the calculation of the atomic structure for general many-electron atoms are described. A consistent diagrammatic method for

calculating the structure of atoms and the characteristics of different atomic processes is given. An outline of the theory of atomic photoionization and the dynamics of the photon–atom collision process is presented. Those kinds of electron correlation that are most important in photoionization are emphasized. The process of autoionization is treated as a quasi-bound state imbedded in the scattering continuum, and a brief description of the main elements of the theory is given. Green’s function techniques are applied to the calculation of higher-order corrections to atomic energy levels, and also of transition amplitudes for radiative transitions of atoms. Basic quantum electrodynamic calculations, which are needed to explain small deviations from the solution to the Schrödinger equation in simple systems, are presented. Comparisons of precise measurements and theoretical predictions that provide tests of our knowledge of fundamental physics are made, focusing on several quantitative tests of quantum electrodynamics. Precise measurements of parity nonconserving effects in atoms could lead to possible modifications of the Standard Model, and thus uncover new physics. An approach to this fundamental problem is described. The problem of the possible variation of the fundamental constants with time is discussed in relation to atomic clocks and precision frequency measurements. The most advanced atomic clocks are described, and the current laboratory constraints on these variations are listed. Other atomic physics methods currently of interest in the search for new physics beyond the Standard Model are discussed.



William C. Martin, Wolfgang L. Wiese, and Alexander Kramida 

Contents

11.1	Frequency, Wavenumber, Wavelength	178	11.16	Spectral Lines: Selection Rules, Intensities, Transition Probabilities, f Values, and Line Strengths	187
11.2	Atomic States, Shells, and Configurations	178	11.16.1	Emission Intensities (Transition Probabilities)	187
11.3	Hydrogen and Hydrogen-Like Ions	178	11.16.2	Absorption f -values	187
11.4	Alkalis and Alkali-Like Spectra	178	11.16.3	Line Strengths	187
11.5	Helium and Helium-Like Ions; LS Coupling	179	11.16.4	Relationships Between A , f , and S	188
11.6	Hierarchy of Atomic Structure in LS Coupling	179	11.16.5	Relationships Between Line and Multiplet Values	188
11.7	Allowed Terms or Levels for Equivalent Electrons	179	11.16.6	Relative Strengths for Lines of Multiplets in LS Coupling	188
11.7.1	LS Coupling	179	11.17	Atomic Lifetimes	189
11.7.2	jj Coupling	180	11.18	Regularities and Scaling	189
11.8	Notations for Different Coupling Schemes	180	11.18.1	Transitions in Hydrogenic (One-Electron) Species	189
11.8.1	LS Coupling (Russell–Saunders Coupling)	180	11.18.2	Systematic Trends and Regularities in Atoms and Ions with Two or More Electrons	189
11.8.2	jj Coupling of Equivalent Electrons	181	11.19	Tabulations of Transition Probabilities	189
11.8.3	J_1j or J_1J_2 Coupling	181	11.20	Spectral Line Shapes, Widths, and Shifts	194
11.8.4	J_1l or J_1L_2 Coupling (J_1K Coupling)	182	11.20.1	Doppler Broadening	194
11.8.5	LS_1 Coupling (LK Coupling)	182	11.20.2	Pressure Broadening	194
11.8.6	Coupling Schemes and Term Symbols	182	11.21	Spectral Continuum Radiation	195
11.9	Eigenvector Composition of Levels	182	11.21.1	Hydrogenic Species	195
11.10	Ground Levels and Ionization Energies for Neutral Atoms	183	11.21.2	Many-Electron Systems	196
11.11	Zeeman Effect	183	11.22	Sources of Spectroscopic Data	196
11.12	Term Series, Quantum Defects, and Spectral-Line Series	185	References	196	
11.13	Sequences	186			
11.13.1	Isoelectronic Sequence	186			
11.13.2	Isoionic, Isonuclear, and Homologous Sequences	186			
11.14	Spectral Wavelength Ranges, Dispersion of Air	186			
11.15	Wavelength Standards	186			

W. L. Wiese
National Institute of Standards and Technology
Gaithersburg, MD, USA

A. Kramida
Physical Measurement Laboratory, National Institute of Standards and Technology
Gaithersburg, MD, USA
e-mail: alexander.kramida@nist.gov

Abstract

This chapter outlines the main concepts of atomic structure, with some emphasis on terminology and notation. Atomic radiation is discussed, in particular the wavelengths, intensities, and shapes of spectral lines, and a few remarks are made regarding continuous spectra. We include tabulations of ionization energies for neutral atoms and transition probabilities for persistent lines of selected neutral atoms and provide references to sources of atomic spectroscopic data.

Experimental techniques and the details of atomic theoretical methods are not covered in this chapter; these and a number of other subjects pertinent to atomic spectroscopy are treated in one or more of at least fifteen other chapters in this book.

Keywords

quantum number · oscillator strength · orbital angular momentum · coupling scheme · energy level · spectral line · wavelength · line broadening · line intensity · ionization energy · transition probability · reference data

11.1 Frequency, Wavenumber, Wavelength

The photon energy due to an electron transition between an upper atomic level k (of energy E_k) and a lower level i is

$$\Delta E = E_k - E_i = h\nu = hc\sigma = \frac{hc}{\lambda_{\text{vac}}}, \quad (11.1)$$

where ν is the frequency, σ the wavenumber in vacuum, and λ_{vac} the wavelength in vacuum. The most accurate spectroscopic measurements are determinations of transition frequencies, the unit being the hertz ($1 \text{ Hz} = 1 \text{ s}^{-1}$) or one of its multiples. Frequency, wavenumber, and wavelength (in vacuum) have equivalent relative precision, since the speed of light is exactly defined [1]. The most common wavelength units are the nanometer (nm), the angstrom ($1 \text{ \AA} = 10^{-1} \text{ nm}$) and the micrometer (μm , a.k.a. micron). The SI wavenumber unit is the inverse meter, but in practice wavenumbers are usually expressed in inverse centimeters: $1 \text{ cm}^{-1} = 10^2 \text{ m}^{-1}$, equivalent to $2.99792458 \times 10^4 \text{ MHz}$. Energy units and conversion factors are further discussed in Chap. 1.

11.2 Atomic States, Shells, and Configurations

A one-electron atomic *state* is defined by the quantum numbers $nlm_l m_s$ or $nlj m_j$, with n and l representing the principal quantum number and the orbital angular momentum quantum number, respectively. The allowed values of n are the positive integers, and $l = 0, 1, \dots, n - 1$. The quantum number j represents the angular momentum obtained by coupling the orbital and spin angular momenta of an electron, i.e., $\mathbf{j} = \mathbf{l} + \mathbf{s}$, so that $j = l \pm 1/2$. The magnetic quantum numbers m_l , m_s , and m_j represent the projections of the corresponding angular momenta along a particular direction; thus, for example, $m_l = -l, -l + 1, \dots, l$ and $m_s = \pm 1/2$.

The central field approximation for a many-electron atom leads to wave functions expressed in terms of products of such one-electron states [2–4]. Those electrons having the same principal quantum number n belong to the *shell* for that number. Electrons having both the same n value and l value belong to a *subshell*, all electrons in a particular subshell being *equivalent*. The notation for a *configuration* of N equivalent electrons is nl^N , the superscript usually being omitted for $N = 1$. A configuration of several subshells

is written as $n_1 l_1^{N_1} n_2 l_2^{N_2} \dots$. The numerical values of l are replaced by letters in writing a configuration, according to the code s, p, d for $l = 0, 1, 2$ and $f, g, h \dots$ for $l = 3, 4, 5 \dots$, the letter j being omitted.

The Pauli exclusion principle prohibits atomic states having two electrons with all four quantum numbers the same. Thus, the maximum number of equivalent electrons is $2(2l + 1)$. A subshell having this number of electrons is *full*, *complete*, or *closed*, and a subshell having a smaller number of electrons is *unfilled*, *incomplete*, or *open*. The $3p^6$ configuration thus represents a full subshell, and $3s^2 3p^6 3d^{10}$ represents a full shell for $n = 3$.

The *parity* of a configuration is *even* or *odd* according to whether $\sum_i l_i$ is even or odd, the sum being taken over all electrons (in practice only those in open subshells need to be considered).

11.3 Hydrogen and Hydrogen-Like Ions

For these atoms and ions, the quantum numbers n , l , and j adequately describe the energy structure of electronic shells [4, 5]. A particular *level* is denoted either by nl_j or by $nl^2 L_J$ with $L = l$ and $J = j$. The latter notation is somewhat redundant for one-electron spectra but is useful for consistency with more complex structures. The L values are written with the same letter code used for l values, but with capital letters. The *multiplicity* of the L term is equal to $2S + 1 = 2s + 1 = 2$. Written as a superscript, this number expresses the *doublet* character of the structure: each term for $L \geq 1$ has two levels with $J = L \pm 1/2$.

The Coulomb interaction between the nucleus and the single electron is dominant, so that the largest energy separations are associated with levels having different n . The hyperfine splitting of the ^1H $1s$ ground level is $1420405751.768(1) \text{ Hz}$ [6]. It results from the interaction of the proton and electron magnetic moments and gives rise to the famous 21 cm line. The separations of the $2n - 1$ excited levels having the same n are largely determined by relativistic contributions, including the spin–orbit interaction, with the result that each of the $n - 1$ pairs of levels having the same j value is almost degenerate; the separation of the two levels in each pair is mainly due to relatively small Lamb shifts (Sects. 29.7 and 28.3).

11.4 Alkalis and Alkali-Like Spectra

In the central field approximation there exists no angular-momentum coupling between a closed subshell and an electron outside the subshell, since the net spin and orbital angular momenta of the subshell are both zero. The nlj quantum numbers are, then, again appropriate for a single

electron outside closed subshells. However, the electrostatic interactions of this electron with the other electrons and with the nucleus yield a strong l -dependence of the energy levels [7]. The differing extent of *core penetration* for ns and np electrons can, in some cases, for example, give an energy difference comparable to or exceeding the difference between the np and $(n + 1)p$ levels. The spin-orbit fine-structure separation between the nl ($l > 0$) levels having $j = l - 1/2$ and $l + 1/2$ is relatively small.

11.5 Helium and Helium-Like Ions; LS Coupling

The energy structure of the normal $1snl$ configurations is dominated by the electron-nucleus and electron-electron Coulomb contributions [5]. In helium and in helium-like ions of the lighter elements, the separations of levels having the same n and having $l = s, p,$ or d are mainly determined by direct and exchange electrostatic interactions between the electrons, while the spin-orbit, spin-other orbit, and other relativistic contributions are much smaller. This is the condition for LS coupling, in which:

- The orbital angular momenta of the electrons are coupled to give a total orbital angular momentum $\mathbf{L} = \sum_i \mathbf{l}_i$.
- The spins of the electrons are coupled to give a total spin $\mathbf{S} = \sum_i \mathbf{s}_i$.

The combination of a particular S value with a particular L value comprises a spectroscopic *term*, the notation for which is ^{2S+1}L . The quantum number $2S + 1$ is the *multiplicity* of the term. The \mathbf{S} and \mathbf{L} vectors are coupled to obtain the total angular momentum, $\mathbf{J} = \mathbf{S} + \mathbf{L}$, for a *level* of the term; the level is denoted as $^{2S+1}L_J$.

The parity is indicated by appended degree symbols on odd parity terms.

For $1snl$ configurations, $L = l$ and $S = 0$ or 1 , i.e., the terms are *singlets* ($S = 0$) or *triplets* ($S = 1$). As examples of the He I structure, the ionization energy (energy required to remove one of the $1s$ electrons in the $1s^2$ ground configuration) is 24.5874 eV, the $1s2s$ $^3S-^1S$ separation is 0.7962 eV, the $1s2p$ $^3P^o-^1P^o$ separation is 0.2539 eV, and the $1s2p$ $^3P_2^o-^3P_0^o$ fine-structure spread is only 1.32×10^{-4} eV.

11.6 Hierarchy of Atomic Structure in LS Coupling

The centrality of LS coupling in the analysis and theoretical interpretation of atomic spectra has led to the acceptance of notations and nomenclature well adapted to discussions of particular structures and spectra [2]. The main elements

Table 11.1 Atomic structure hierarchy in LS coupling and names for groups of transitions between structural entities

Structural entity	Quantum numbers ^a	Group of all transitions
Configuration	$(n_i l_i)^{N_i}$	Transition array
System	$(n_i l_i)^{N_i} \gamma S$	Intrasystem transitions Intercombination transitions
Term	$(n_i l_i)^{N_i} \gamma SL$	Multiplet
Level	$(n_i l_i)^{N_i} \gamma SLJ$	Line
Level component	$(n_i l_i)^{N_i} \gamma SLJM$	Line component

^a The configuration may include several open subshells, as indicated by the i subscripts. The letter γ represents any additional quantum numbers, such as ancestral terms, necessary to specify a particular term

of the nomenclature are shown in Table 11.1, most of the structural entities having already been defined in the above discussions of simple spectra. The quantum numbers in the table represent a full description for complex configurations, and the accepted names for transitions between the structural elements are also given.

As an example, the Ca I $3d4p$ $^3D_2^o$ level belongs to the $^3D^o$ term. The $3d4s$ $^3D_2-3d4p$ $^3D_3^o$ line belongs to the corresponding $^3D-^3D^o$ triplet *multiplet*, one of those discussed by Russell and Saunders in their classic paper on the alkaline-earth spectra [8]. The $3d4s-3d4p$ transition array includes both the singlet and triplet multiplets, as well as any (LS -forbidden) *intercombination* or *intersystem* lines arising from transitions between levels of the singlet *system* and those of the triplet *system*. The order of the two terms in the transitions as written above, with the lower-energy term on the left, is standard in atomic spectroscopy. Examples of notations for complex configurations are given in Sect. 11.8.

11.7 Allowed Terms or Levels for Equivalent Electrons

11.7.1 LS Coupling

The allowed LS terms of a configuration consisting of two nonequivalent groups of electrons are obtained by coupling the \mathbf{S} and \mathbf{L} vectors of the groups in all possible ways, and the procedure may be extended to any number of such groups. Thus, the allowed terms for any configuration can be obtained from a table of the allowed terms for groups of equivalent electrons.

The configuration l^N has more than one allowed term of certain LS types if $l > 1$ and $2 < N < 4l$ (d^3-d^7 , f^3-f^{11} , etc.). The recurring terms of a particular LS term type from d^N and f^N configurations are assigned sequential index numbers in the tables of Nielson and Koster [9]; the index numbers stand for additional numbers having group-theoretical significance that serve to differentiate the recurring terms. The first of those additional quantum numbers is

Table 11.2 Allowed J -values for l_j^N equivalent electrons (jj) coupling

l_j^N	Allowed J -values
$l_{1/2}$	1/2
$l_{1/2}^2$	0
$l_{3/2}$ and $l_{3/2}^3$	3/2
$l_{3/2}^2$	0, 2
$l_{3/2}^4$	0
$l_{5/2}$ and $l_{5/2}^5$	5/2
$l_{5/2}^2$ and $l_{5/2}^4$	0, 2, 4
$l_{5/2}^3$	3/2, 5/2, 9/2
$l_{5/2}^6$	0
$l_{7/2}$ and $l_{7/2}^7$	7/2
$l_{7/2}^2$ and $l_{7/2}^6$	0, 2, 4, 6
$l_{7/2}^3$ and $l_{7/2}^5$	3/2, 5/2, 7/2, 9/2, 11/2, 15/2
$l_{7/2}^4$	0, 2, 4, 6
$l_{7/2}^8$	0

seniority [10]. It uniquely differentiates all recurring terms of d^N and most of f^N , except for a few terms of f^5 and f^9 , f^6 and f^8 , and f^7 . These remaining terms, which occur only in pairs, are further labeled A or B (in combination with seniority) to indicate Racah's separation of the two terms.

The index numbers of Nielson and Koster are in practice the most frequently used labels for the recurring terms of f^N configurations. Use of their index numbers for the recurring terms of d^N configurations perhaps has the disadvantage of substituting an arbitrary number for a quantum number (the seniority). The actual value of the seniority number is rarely needed, however, and a consistent notation for the d^N and f^N configurations is desirable. A table of the allowed LS terms of the l^N electrons for $l \leq 3$ is given in [10], with all recurring terms having the index numbers of Nielson and Koster as a following on-line integer. The group-theoretical labels are also listed. Thus, the $d^3\ ^2D$ term having seniority 3 is designated 2D_2 , instead of 2_3D , in this scheme; and the level having $J = 3/2$ is designated $^2D_{3/2}$.

11.7.2 jj Coupling

The Pauli exclusion principle restricts the set of possible J -values for a group of N equivalent electrons having the same j -value, l_j^N . The allowed J -values for such groups are given in Table 11.2 for $j = 1/2, 3/2, 5/2$, and $7/2$ (sufficient for $l \leq 3$). The $l_{7/2}^4$ group has two allowed levels for each of the J -values 2 and 4. The subscripts distinguishing the two levels in each case are the seniority numbers [11].

The allowed levels of the configuration nl^N may be obtained by dividing the electrons into sets of two groups

$nl_{l+1/2}^Q nl_{l-1/2}^R$, $Q + R = N$. The possible sets run from $Q = N - 2l$ (or zero if $N < 2l$) up to $Q = N$ or $Q = 2l + 2$, whichever is smaller. The (degenerate) levels for a set with both Q and R nonzero have wave functions defined by the quantum numbers $(\alpha J_1, \beta J_2)J$, with J_1 and J_2 deriving from the Q and R groups, respectively. The symbols α and β represent any additional quantum numbers required to identify levels. The J values of the allowed levels for each $(\alpha J_1, \beta J_2)$ subset are obtained by combining J_1 and J_2 in the usual way.

11.8 Notations for Different Coupling Schemes

In this section, we give enough examples to make clear the meaning of the different coupling-scheme notations. Not all the configurations in the examples have been identified experimentally, and some of the examples of a particular coupling scheme given for heuristic purposes may be physically inappropriate. Cowan [3] describes the physical conditions for the different coupling schemes and gives experimental examples.

11.8.1 LS Coupling (Russell–Saunders Coupling)

Some of the examples given below indicate notations bearing on the order of coupling of the electrons

1. $3d^7\ ^4F_{7/2}$
2. $3d^7(^4F)4s4p(^3P^\circ)\ ^6F_{9/2}^\circ$
3. $4f^7(^8S^\circ)6s6p(^4P)\ ^{11}P_5^\circ$
4. $3p^5(^2P^\circ)3d^2(^1G)\ ^2F_{7/2}^\circ$
5. $4f^{10}(^3K_2)6s6p(^1P^\circ)\ ^3L_6^\circ$
6. $4f^7(^8S^\circ)5d(^7D^\circ)6p\ ^8F_{13/2}$
7. $4f^7(^8S^\circ)5d(^9D^\circ)6s(^8D^\circ)7s\ ^9D_5^\circ$
8. $4f^7(^8S^\circ)5d(^9D^\circ)6s6p(^3P^\circ)\ ^{11}F_8$
9. $4f^7(^8S^\circ)5d^2(^1G)\ (^8G^\circ)6p\ ^7F_0$
10. $4f(^2F^\circ)\ 5d^2(^1G)6s(^2G)\ ^1P_1^\circ$

In the second example, the seven $3d$ electrons couple to give a 4F term, and the $4s$ and $4p$ electrons couple to form the $^3P^\circ$ term; the final $^6F^\circ$ term is one of nine possible terms obtained by coupling the 4F grandparent and $^3P^\circ$ parent terms. The next three examples are similar to the second. The meaning of the index number 2 following the 3K symbol in the fifth example is explained in Sect. 11.7.1.

The coupling in example 6 is appropriate if the interaction of the $5d$ and $4f$ electrons is sufficiently stronger than the $5d-6p$ interaction. The $^7D^\circ$ parent term results from coupling the $5d$ electron to the $^8S^\circ$ grandparent, and the $6p$ electron is then coupled to the $^7D^\circ$ parent to form the final

8F term. A space is inserted between the $5d$ electron and the $^7D^\circ$ parent to emphasize that the latter is formed by coupling a term ($^8S^\circ$) listed to the left of the space. Example 7 illustrates a similar coupling order carried to a further stage; the $^8D^\circ$ parent term results from the coupling of the $6s$ electron to the $^9D^\circ$ grandparent.

Example 8 is similar to examples 2–5, but in 8 the first of the two terms that couple to form the final 1F term, i.e., the $^9D^\circ$ term, is itself formed by the coupling of the $5d$ electron to the $^8S^\circ$ core term. Example 9 shows an $^8G^\circ$ parent term formed by coupling the $^8S^\circ$ and 1G grandparent terms. A space is again used to emphasize that the following ($^8G^\circ$) term is formed by the coupling of terms listed before the space.

A different order of coupling is indicated in the final example, the $5d^2\ ^1G$ term being coupled first to the external $6s$ electron instead of directly to the $4f$ core electron. The $4f$ ($^2F^\circ$) core term is isolated by a space to denote that it is coupled (to the $5d^2(^1G)6s\ ^2G$ term) only after the other electrons have been coupled. The notation in this particular case (with a single $4f$ electron) could be simplified by writing the $4f$ electron after the 2G term to which it is coupled. It appears more important, however, to retain the convention of giving the core portion of the configuration first.

The notations in examples 1–5 are in the form recommended by *Russell et al.* [12] and used in both the Atomic Energy States [13] and Atomic Energy Levels [10, 14] compilations. The spacings used in the remaining examples allow different orders of coupling of the electrons to be indicated without the use of additional parentheses, brackets, etc.

Some authors assign a short name to each (final) term, so that the configuration can be omitted in tables of classified lines, etc. The most common scheme distinguishes the low terms of a particular SL type by the prefixes a, b, c, \dots , and the high terms by z, y, x, \dots [14].

11.8.2 jj Coupling of Equivalent Electrons

This scheme is used, for example, in relativistic calculations. The lower-case j indicates the angular momentum of one electron ($j = l \pm 1/2$) or of each electron in an l_j^N group. Various ways of indicating which of the two possible j -values applies to such a group without writing the j -value subscript have been used by different authors; we give the j -values explicitly in the first four examples below. We use the symbols J_i and j to represent total angular momenta.

1. $(6p_{1/2}^2)_0$
2. $(6p_{1/2}^2\ 6p_{3/2})_{3/2}^\circ$
3. $(6p_{1/2}^2\ 6p_{3/2}^2)_2$

4. $4d_{5/2}^3\ 4d_{3/2}^2\ (9/2, 2)_{11/2}$
5. $4d_+^3\ 4d_-^2\ (9/2, 2)_{11/2}$

The relatively large spin–orbit interaction of the $6p$ electrons produces jj -coupling structures for the $6p^2$, $6p^3$, and $6p^4$ ground configurations of neutral Pb, Bi, and Po, respectively; the notations for the ground levels of these atoms are given as the first three examples above. The configuration in the first example shows the notation for equivalent electrons having the same j value l_j^N , in this case two $6p$ electrons each having $j = 1/2$. A convenient notation for a particular level ($J = 0$) of such a group is also indicated. The second example extends this notation to the case of a $6p^3$ configuration divided into two groups according to the two possible j values. A similar notation is shown for the $6p^4$ level in the third example; this level might also be designated $(6p_{3/2}^{-2})_2$, the negative superscript indicating the two $6p$ holes. The $(J_1, J_2)_J$ term and level notation shown on the right in the fourth example is convenient because each of the two electron groups $4d_{5/2}^3$ and $4d_{3/2}^2$ has more than one allowed total J_i value. The assumed convention is that J_1 applies to the group on the left ($J_1 = 9/2$ for the $4d_{5/2}^3$ group) and J_2 to that on the right. Example 5 shows another possible representation of example 4 using a minus in the subscript to denote $j = l - 1/2$ and a plus to denote $j = l + 1/2$.

11.8.3 J_1j or J_1J_2 Coupling

1. $3d^9(^2D_{5/2})4p_{3/2}\ (5/2, 3/2)_3^\circ$
2. $4f^{11}(^2H_{9/2}^\circ)6s6p(^3P_1^\circ)\ (9/2, 1)_{7/2}$
3. $4f^9(^6H^\circ)5d(^7H_8^\circ)6s6p(^3P_0^\circ)\ (8, 0)_8$
4. $4f^{12}(^3H_6)5d(^2D)6s6p(^3P^\circ)\ ({}^4F_{3/2}^\circ)\ (6, 3/2)_{13/2}^\circ$
5. $5f^4({}^5I_4)6d_{3/2}\ (4, 3/2)_{11/2}^\circ\ 7s7p(^1P_1^\circ)\ (11/2, 1)_{9/2}^\circ$
6. $5f_{7/2}^4\ 5f_{5/2}^5\ (8, 5/2)_{21/2}^\circ\ 7p_{3/2}\ (21/2, 3/2)_{10}$
7. $5f_{7/2}^3\ 5f_{5/2}^3\ (9/2, 9/2)_9\ 7s7p(^3P_2^\circ)\ (9, 2)_7^\circ$
8. $2s\ 2p_- \ 2p_+\ (0, 3/2)_{3/2}$
9. $[(2s\ 2p_-)_0\ 2p_+]_{3/2}$

The first five examples all have core electrons in LS coupling, whereas jj coupling is indicated for the $5f$ core electrons in examples 6 and 7. Since the J_1 and J_2 values in the final (J_1, J_2) term have already been given as subscripts in the configuration, the (J_1, J_2) term notations are redundant in all these examples. Unless separation of the configuration and final term designations is desired, as in some data tables, one may obtain a more concise notation by simply enclosing the entire configuration in brackets and adding the final J value as a subscript. Thus, the level in the first example

can be designated as $[3d^9(2D_{5/2})4p_{3/2}]_3^\circ$. If the configuration and coupling order are assumed to be known, still shorter designations may be used; for example, the fourth level above might then be given as $[(^3H_6)(^3P^\circ)(^4F_{3/2}^\circ)]_{13/2}$ or $(^3H_6, ^3P^\circ, ^4F_{3/2}^\circ)_{13/2}$. Similar economies of notation are of course possible, and often useful, in all coupling schemes. Example 8 shows a somewhat more compact representation of a case similar to example 6 with the j -values of the p electrons ($j = l \pm 1/2$) indicated by the plus and minus symbols in the subscripts. The s subshell does not need a subscript, since it has a unique possible j -value of $1/2$. The parent term $(0, 1/2)$ can be omitted before the last subshell $2p_+$, since the final term gives its J_1 -value, $J_1 = 0$, and the space before the last subshell makes the order of summation unambiguous. Another possible way to designate the same level is shown in example 9.

11.8.4 $J_1 l$ or $J_1 L_2$ Coupling ($J_1 K$ Coupling)

1. $3p^5(2P_{1/2}^\circ)5g^2[9/2]_5^\circ$
2. $4f^2(^3H_4)5g^2[3]_{5/2}$
3. $4f^{13}(^2F_{7/2}^\circ)5d^2(^1D) \ ^1[7/2]_{7/2}^\circ$
4. $4f^{13}(^2F_{5/2}^\circ)5d6s(^3D) \ ^3[9/2]_{11/2}^\circ$

The final terms in the first two examples result from coupling a parent-level J_1 to the orbital angular momentum of a $5g$ electron to obtain a resultant K , the K value being enclosed in brackets. The spin of the external electron is then coupled with the K angular momentum to obtain a pair of J values, $J = K \pm 1/2$ (for $K \neq 0$). The multiplicity (2) of such pair terms is usually omitted from the term symbol, but other multiplicities occur in the more general $J_1 L_2$ coupling (examples 3 and 4). The last two examples are straightforward extensions of $J_1 l$ coupling, with the L_2 and S_2 momenta of the *external* term (1D and 3D in examples 3 and 4, respectively) replacing the l and s momenta of a single external electron.

11.8.5 LS_1 Coupling (LK Coupling)

1. $3s^23p(^2P^\circ)4fG^2[7/2]_3$
2. $3d^7(^4P)4s4p(^3P^\circ)D^\circ \ ^3[5/2]_{7/2}^\circ$

The orbital angular momentum of the core is coupled with the orbital angular momentum of the external electron(s) to give the total orbital angular momentum L . The letter symbol for the final L value is listed with the configuration because this angular momentum is then coupled with the spin of the core (S_1) to obtain the resultant K angular momentum of

the final term (in brackets). The multiplicity of the $[K]$ term arises from the spin of the external electron(s).

11.8.6 Coupling Schemes and Term Symbols

The coupling schemes outlined above include those now most frequently used in calculations of atomic structure [3]. Any term symbol gives the values of two angular momenta that may be coupled to give the total electronic angular momentum of a level (indicated by the J -value). For configurations of more than one unfilled subshell, the angular momenta involved in the final coupling derive from two groups of electrons (either group may consist of only one electron). These are often an inner group of coupled electrons and an outer group of coupled electrons, respectively. In any case, the quantum numbers for the two groups can be distinguished by subscripts 1 and 2, so that quantum numbers represented by capital letters without subscripts are total quantum numbers for both groups. Thus, the quantum numbers for the two vectors that couple to give the final J are related to the term symbol as follows:

Coupling scheme	Quantum numbers for vectors that couple to give J	Term symbol
LS	L, S	^{2S+1}L
$J_1 J_2$	J_1, J_2	(J_1, J_2)
$J_1 L_2(\rightarrow K)$	K, S_2	$^{2S_2+1}[K]$
$LS_1(\rightarrow K)$	K, S_2	$^{2S_2+1}[K]$

11.9 Eigenvector Composition of Levels

The wave functions of levels are often expressed as eigenvectors that are linear combinations of basis states in one of the standard coupling schemes. Thus, the wave function $\Psi(\alpha J)$ for a level labeled αJ might be expressed in terms of LS coupling basis states $\Phi(\gamma SLJ)$

$$\Psi(\alpha J) = \sum_{\gamma SL} c(\gamma SLJ) \Phi(\gamma SLJ) . \quad (11.2)$$

The $c(\gamma SLJ)$ are expansion coefficients, and

$$\sum_{\gamma SL} |c(\gamma SLJ)|^2 = 1 . \quad (11.3)$$

The squared expansion coefficients for the various γSL terms in the composition of the αJ level are conveniently expressed as percentages, whose sum is 100%. Thus, the percentage contributed by the pure Russell–Saunders state γSLJ is equal to $100 \times |c(\gamma SLJ)|^2$. The notation for

Russell–Saunders basis states has been used only for concreteness; the eigenvectors may be expressed in any coupling scheme, and the coupling schemes may be different for different configurations included in a single calculation (with configuration interaction). *Intermediate coupling* conditions for a configuration are such that calculations in both LS and jj coupling yield some eigenvectors representing significant mixtures of basis states. Eigenvectors represented by the above equations are usually given in such a way that all terms in the summation use the same coupling scheme, and all eigenvectors for a given configuration use the same coupling scheme as well.

The largest percentage in the composition of a level is called the *purity* of the level in that coupling scheme. The coupling scheme (or combination of coupling schemes if more than one configuration is involved) that results in the largest average purity for all the levels in a calculation is usually best for naming the levels. With regard to any particular calculation, one does well to remember that, as with other calculated quantities, the resulting eigenvectors depend on a specific theoretical model and are subject to the inaccuracies of whatever approximations the model involves.

Theoretical calculations of experimental energy level structures have yielded many eigenvectors having significantly less than 50% purity in any coupling scheme. Since many of the corresponding levels have nevertheless been assigned names by spectroscopists, some caution is advisable in the acceptance of the level designations found in the literature. Moreover, the level designations, such as configuration and term labels, are not something permanent. Unlike the energy intervals, the wavefunctions and their composition are not directly observable. They are always a product of some theoretical interpretation. As theory evolves and improves with time, so does the interpretation of observed atomic properties, and, thus, some of the level designations are bound to change in the course of the development of the theory.

11.10 Ground Levels and Ionization Energies for Neutral Atoms

Fortunately, most of the ground levels of the neutral atoms have reasonably meaningful LS -coupling names, the corresponding eigenvector percentages lying in the range from $\approx 55\%$ to 100%. These names are listed in Table 11.3 except for Pb, Pa, U, and Np. The lowest few ground-configuration levels of these four atoms comprise better $[core](L_1S_1J_1)[valence]_j (J_1j)$ terms than LS -coupling terms, the $[core]$ and $[valence]$ shells being $6s^2$ and $6p^2$ for Pb and $5f^N$ and $6d7s^2$ for Pa, U, and Np. As noted in Sect. 11.8.2, the jj -coupling names given there for the ground levels of Bi and Po are more appropriate than the

alternative LS -coupling designations in Table 11.3. For the heaviest elements, Sg, Bh, and Hs, only the J -values of the final terms are known.

For brevity, the ionization energies in the table are given with no more than four digits after the decimal point. However, for all of the first 56 atoms, H through Ba, as well as for many of the heavier atoms, they are experimentally known with greater precision. The values in the table are from recent compilations [15, 16]. The National Institute of Standards and Technology (NIST) maintains an online *Atomic Spectra Database* (ASD) [15], which is updated with new and revised data every year. Each year, a few of the ionization energies tabulated here are revised. ASD provides full information about the uncertainties of the data and bibliographic references.

11.11 Zeeman Effect

The Zeeman effect is of special interest because of the importance of Zeeman data in the analysis and theoretical interpretation of complex spectra. In a weak field, the J value remains a valid quantum number, although in general a level is split into magnetic sublevels [3, 17]. The Landé g -value of such a level may be defined by the expression for the energy shift of its magnetic sublevel having magnetic quantum number M , which has one of the $2J + 1$ -values, $-J, -J + 1, \dots, J$

$$\Delta E = gM\mu_B B . \quad (11.4)$$

B is the magnetic flux density, and μ_B is the Bohr magneton ($\mu_B = e\hbar/2m_e$).

The wavenumber shift $\Delta\sigma$ corresponding to this energy shift is

$$\Delta\sigma = gM(0.46686B \text{ cm}^{-1}) , \quad (11.5)$$

with B representing the numerical value of the magnetic flux density in teslas. The quantity in parentheses, the Lorentz unit, is about 1 or 2 cm^{-1} for typical flux densities used to obtain Zeeman-effect data with classical spectroscopic methods. Accurate data can be obtained with much smaller fields, of course, by using higher-resolution techniques such as laser spectroscopy. Most of the g -values now available for atomic energy levels were derived by application of the above formula (for each of the two combining levels) to measurements of optical Zeeman patterns. A single transverse-Zeeman-effect pattern (two polarizations, resolved components, and sufficiently complete) can yield the J -value and the g value for each of the two levels involved.

Neglecting a number of higher-order effects, we can evaluate the g value of a level βJ belonging to a pure LS -

Table 11.3 Ground levels and ionization energies for neutral atoms

Z	Element	Ground configuration ^a			Ground level	Ionization energy (eV)	Z	Element	Ground configuration ^a				Ground level	Ionization energy (eV)		
1	H	1s			$2S_{1/2}$	13.5984	55	Cs	[Xe]			6s	$2S_{1/2}$	3.8939		
2	He	1s ²			$1S_0$	24.5874	56	Ba	[Xe]			6s ²	$1S_0$	5.2117		
3	Li	1s ²	2s		$2S_{1/2}$	5.3917	57	La	[Xe]		5d	6s ²	$2D_{3/2}$	5.5769		
4	Be	1s ²	2s ²		$1S_0$	9.3227	58	Ce	[Xe]	4f	5d	6s ²	$1G_4$	5.5386		
5	B	1s ²	2s ²	2p	$2P_{1/2}^{\circ}$	8.2980	59	Pr	[Xe]	4f ³		6s ²	$4I_{9/2}^{\circ}$	5.4702		
6	C	1s ²	2s ²	2p ²	$3P_0$	11.2603	60	Nd	[Xe]	4f ⁴		6s ²	$5I_4$	5.5250		
7	N	1s ²	2s ²	2p ³	$4S_{3/2}^{\circ}$	14.5341	61	Pm	[Xe]	4f ⁵		6s ²	$6H_{5/2}^{\circ}$	5.5819		
8	O	1s ²	2s ²	2p ⁴	$3P_2$	13.6181	62	Sm	[Xe]	4f ⁶		6s ²	$7F_0$	5.6437		
9	F	1s ²	2s ²	2p ⁵	$2P_{3/2}^{\circ}$	17.4228	63	Eu	[Xe]	4f ⁷		6s ²	$8S_{7/2}^{\circ}$	5.6704		
10	Ne	1s ²	2s ²	2p ⁶	$1S_0$	21.5645	64	Gd	[Xe]	4f ⁷	5d	6s ²	$9D_2^{\circ}$	6.1498		
11	Na	[Ne]	3s		$2S_{1/2}$	5.1391	65	Tb	[Xe]	4f ⁹		6s ²	$6H_{15/2}^{\circ}$	5.8638		
12	Mg	[Ne]	3s ²		$1S_0$	7.6462	66	Dy	[Xe]	4f ¹⁰		6s ²	$5I_8$	5.9391		
13	Al	[Ne]	3s ²	3p	$2P_{1/2}^{\circ}$	5.9858	67	Ho	[Xe]	4f ¹¹		6s ²	$4I_{15/2}^{\circ}$	6.0215		
14	Si	[Ne]	3s ²	3p ²	$3P_0$	8.1517	68	Er	[Xe]	4f ¹²		6s ²	$3H_6$	6.1077		
15	P	[Ne]	3s ²	3p ³	$4S_{3/2}^{\circ}$	10.4867	69	Tm	[Xe]	4f ¹³		6s ²	$2F_{7/2}^{\circ}$	6.1844		
16	S	[Ne]	3s ²	3p ⁴	$3P_2$	10.3600	70	Yb	[Xe]	4f ¹⁴		6s ²	$1S_0$	6.2542		
17	Cl	[Ne]	3s ²	3p ⁵	$2P_{3/2}^{\circ}$	12.9676	71	Lu	[Xe]	4f ¹⁴	5d	6s ²	$2D_{3/2}$	5.4259		
18	Ar	[Ne]	3s ²	3p ⁶	$1S_0$	15.7596	72	Hf	[Xe]	4f ¹⁴	5d ²	6s ²	$3F_2$	6.8251		
19	K	[Ar]		4s	$2S_{1/2}$	4.3407	73	Ta	[Xe]	4f ¹⁴	5d ³	6s ²	$4F_{3/2}$	7.5496		
20	Ca	[Ar]		4s ²	$1S_0$	6.1132	74	W	[Xe]	4f ¹⁴	5d ⁴	6s ²	$5D_0$	7.8640		
21	Sc	[Ar]	3d	4s ²	$2D_{3/2}$	6.5615	75	Re	[Xe]	4f ¹⁴	5d ⁵	6s ²	$6S_{5/2}$	7.8335		
22	Ti	[Ar]	3d ²	4s ²	$3F_2$	6.8281	76	Os	[Xe]	4f ¹⁴	5d ⁶	6s ²	$5D_4$	8.4382		
23	V	[Ar]	3d ³	4s ²	$4F_{3/2}$	6.7462	77	Ir	[Xe]	4f ¹⁴	5d ⁷	6s ²	$4F_{9/2}$	8.9670		
24	Cr	[Ar]	3d ⁵	4s	$7S_3$	6.7665	78	Pt	[Xe]	4f ¹⁴	5d ⁹	6s	$3D_3$	8.9588		
25	Mn	[Ar]	3d ⁵	4s ²	$6S_{5/2}$	7.4340	79	Au	[Xe]	4f ¹⁴	5d ¹⁰	6s	$2S_{1/2}$	9.2256		
26	Fe	[Ar]	3d ⁶	4s ²	$5D_4$	7.9025	80	Hg	[Xe]	4f ¹⁴	5d ¹⁰	6s ²	$1S_0$	10.4375		
27	Co	[Ar]	3d ⁷	4s ²	$4F_{9/2}$	7.8810	81	Tl	[Xe]	4f ¹⁴	5d ¹⁰	6s ²	6p	$2P_{1/2}^{\circ}$	6.1083	
28	Ni	[Ar]	3d ⁸	4s ²	$3F_4$	7.6399	82	Pb	[Xe]	4f ¹⁴	5d ¹⁰	6s ²	6p ²	$(1/2, 1/2)_0$	7.4167	
29	Cu	[Ar]	3d ¹⁰	4s	$2S_{1/2}$	7.7264	83	Bi	[Xe]	4f ¹⁴	5d ¹⁰	6s ²	6p ³	$4S_{3/2}^{\circ}$	7.2855	
30	Zn	[Ar]	3d ¹⁰	4s ²	$1S_0$	9.3942	84	Po	[Xe]	4f ¹⁴	5d ¹⁰	6s ²	6p ⁴	$3P_2$	8.4181	
31	Ga	[Ar]	3d ¹⁰	4s ²	4p	$2P_{1/2}^{\circ}$	5.9993	85	At	[Xe]	4f ¹⁴	5d ¹⁰	6s ²	6p ⁵	$2P_{3/2}^{\circ}$	9.3175
32	Ge	[Ar]	3d ¹⁰	4s ²	4p ²	$3P_0$	7.8994	86	Rn	[Xe]	4f ¹⁴	5d ¹⁰	6s ²	6p ⁶	$1S_0$	10.7485
33	As	[Ar]	3d ¹⁰	4s ²	4p ³	$4S_{3/2}^{\circ}$	9.7886	87	Fr	[Rn]			7s	$2S_{1/2}$	4.0727	
34	Se	[Ar]	3d ¹⁰	4s ²	4p ⁴	$3P_2$	9.7524	88	Ra	[Rn]			7s ²	$1S_0$	5.2784	
35	Br	[Ar]	3d ¹⁰	4s ²	4p ⁵	$2P_{3/2}^{\circ}$	11.8138	89	Ac	[Rn]		6d	7s ²	$2D_{3/2}$	5.3802	
36	Kr	[Ar]	3d ¹⁰	4s ²	4p ⁶	$1S_0$	13.9996	90	Th	[Rn]		6d ²	7s ²	$3F_2$	6.3067	
37	Rb	[Kr]		5s	$2S_{1/2}$	4.1771	91	Pa	[Rn]	5f ²	($3H_4$)	6d	7s ²	$(4, 3/2)_{11/2}$	5.89	
38	Sr	[Kr]		5s ²	$1S_0$	5.6949	92	U	[Rn]	5f ³	($4I_{9/2}^{\circ}$)	6d	7s ²	$(9/2, 3/2)_6^{\circ}$	6.1941	
39	Y	[Kr]	4d	5s ²	$2D_{3/2}$	6.2173	93	Np	[Rn]	5f ⁴	($5I_4$)	6d	7s ²	$(4, 3/2)_{11/2}$	6.2655	
40	Zr	[Kr]	4d ²	5s ²	$3F_2$	6.6341	94	Pu	[Rn]	5f ⁶		7s ²	$7F_0$	6.0258		
41	Nb	[Kr]	4d ⁴	5s	$6D_{1/2}$	6.7589	95	Am	[Rn]	5f ⁷		7s ²	$8S_{7/2}^{\circ}$	5.9738		
42	Mo	[Kr]	4d ⁵	5s	$7S_3$	7.0924	96	Cm	[Rn]	5f ⁷	6d	7s ²	$9D_2^{\circ}$	5.9914		
43	Tc	[Kr]	4d ⁵	5s ²	$6S_{5/2}$	7.1194	97	Bk	[Rn]	5f ⁹		7s ²	$6H_{15/2}^{\circ}$	6.1979		
44	Ru	[Kr]	4d ⁷	5s	$5F_5$	7.3605	98	Cf	[Rn]	5f ¹⁰		7s ²	$5I_8$	6.2819		
45	Rh	[Kr]	4d ⁸	5s	$4F_{9/2}$	7.4589	99	Es	[Rn]	5f ¹¹		7s ²	$4I_{15/2}^{\circ}$	6.3676		
46	Pd	[Kr]	4d ¹⁰		$1S_0$	8.3368	100	Fm	[Rn]	5f ¹²		7s ²	$3H_6$	6.50		
47	Ag	[Kr]	4d ¹⁰	5s	$2S_{1/2}$	7.5762	101	Md	[Rn]	5f ¹³		7s ²	$2F_{7/2}^{\circ}$	6.58		
48	Cd	[Kr]	4d ¹⁰	5s ²	$1S_0$	8.9938	102	No	[Rn]	5f ¹⁴		7s ²	$1S_0$	6.6262		
49	In	[Kr]	4d ¹⁰	5s ²	5p	$2P_{1/2}^{\circ}$	5.7864	103	Lr	[Rn]	5f ¹⁴		7s ²	7p	$2P_{1/2}^{\circ}$	4.96
50	Sn	[Kr]	4d ¹⁰	5s ²	5p ²	$3P_0$	7.3439	104	Rf	[Rn]	5f ¹⁴	6d ²	7s ²	$3F_2$	6.02	
51	Sb	[Kr]	4d ¹⁰	5s ²	5p ³	$4S_{3/2}^{\circ}$	8.6084	105	Db	[Rn]	5f ¹⁴	6d ³	7s ²	$4F_{3/2}$	6.8	
52	Te	[Kr]	4d ¹⁰	5s ²	5p ⁴	$3P_2$	9.0098	106	Sg	[Rn]	5f ¹⁴	6d ⁴	7s ²	$J = 0$	7.8	
53	I	[Kr]	4d ¹⁰	5s ²	5p ⁵	$2P_{3/2}^{\circ}$	10.4513	107	Bh	[Rn]	5f ¹⁴	6d ⁵	7s ²	$J = 5/2$	7.7	
54	Xe	[Kr]	4d ¹⁰	5s ²	5p ⁶	$1S_0$	12.1298	108	Hs	[Rn]	5f ¹⁴	6d ⁶	7s ²	$J = 4$	7.6	

^a An element symbol in brackets represents the electrons in the ground configuration of that element

coupling term using the formula

$$g_{\beta SLJ} = 1 + \left\{ (g_e - 1) \frac{J(J+1) - L(L+1) + S(S+1)}{2J(J+1)} \right\}.$$

The independence of this expression from any other quantum numbers (represented by β) such as the configuration, etc., is important. The expression is derived from vector coupling formulas by assuming a g value of unity for a pure orbital angular momentum and writing the g value for a pure electron spin as g_e [18]. A value of 2 for g_e yields the Landé formula. If the anomaly of the magnetic dipole moment of the electron, arising from small quantum electrodynamics effects [19], is taken into account, the value of g_e is 2.0023193. *Schwinger* g values obtained with this more accurate value for g_e are given for levels of SL terms in [10].

The usefulness of g_{SLJ} -values is enhanced by their relation to the g -values in intermediate coupling. In the notation used in Eq. (11.2) for the wave function of a level βJ in intermediate coupling, the corresponding g -value is given by

$$g_{\beta J} = \sum_{\gamma SL} g_{SLJ} |c(\gamma SLJ)|^2, \quad (11.6)$$

where the summation is over the same set of quantum numbers as for the wave function. The $g_{\beta J}$ -value is, thus, a weighted average of the Landé g_{SLJ} -values, the weighting factors being just the corresponding component percentages.

Formulas for magnetic splitting factors in the J_1J_2 and J_1L_2 coupling schemes are given in [10, 18]. Some higher-order effects that must be included in more accurate Zeeman-effect calculations are treated by *Bethe* and *Salpeter* [5] and by *Wybourne* [18], for example. High-precision calculations for helium are given in [20]. See also Chaps. 14 and 15.

11.12 Term Series, Quantum Defects, and Spectral-Line Series

The Bohr energy levels for hydrogen or for a hydrogenic (one-electron) ion with nuclear charge Z are given by

$$E_n = -\frac{R_Z Z^2}{n^2}, \quad (11.7)$$

where R_Z is the Rydberg constant for the appropriate nuclear mass; R_Z can be found from the infinite-mass Rydberg constant

$$R_Z = \frac{R_\infty}{1 + \frac{m_e}{M_Z}}, \quad (11.8)$$

where m_e is the mass of the electron, and M_Z is the mass of the nucleus. Equation (11.7) gives the energy relative to the ionization limit. For a multielectron atom, the deviations of

a series of (core) nl levels from hydrogenic E_n -values may be due mainly to core penetration by the nl electron (low l -value series), or core polarization by the nl electron (high l -value series), or a combination of the two effects. In either case, it can be shown that these deviations can be approximately represented by a constant quantum defect δ_l in the Rydberg formula,

$$E_{nl} = -\frac{R_Z Z_c^2}{(n - \delta_l)^2} = -\frac{R_Z Z_c^2}{(n^*)^2}, \quad (11.9)$$

where Z_c is the charge of the core and $n^* = n - \delta$ is the effective principal quantum number. If the core includes only closed subshells, the E_{nl} -values are with respect to a value of zero for the (core) 1S_0 level, i.e., the 1S_0 level is the limit of the (core) nl series. If the quantities in Eq. (11.9) are taken as positive, they represent term values or ionization energies; the term value of the ground level of an atom or ion with respect to the ground level of the next higher ion is, thus, the principal ionization energy.

If the core has one or more open subshells, the series limit may be the barycenter of the entire core configuration, or any appropriate sub-structure of the core, down to and including a single level. The E_{nl} -values refer to the series of corresponding (core) nl structures built on the particular limit structure. The value of the quantum defect depends to some extent on which (core) nl structures are represented by the series formula.

The quantum defect in general also has an energy dependence that must be taken into account if lower members of a series are to be accurately represented by Eq. (11.9). For an unperturbed series, this dependence can be expressed by the extended Ritz formula

$$\begin{aligned} \delta &= n - n^* \\ &= \delta_0 + \frac{a}{(n - \delta_0)^2} + \frac{b}{(n - \delta_0)^4} + \dots, \end{aligned} \quad (11.10)$$

with $\delta_0, a, b \dots$ constants for the series (δ_0 being the limit value of the quantum defect for high series members) [21]. The value of a is usually positive for core-penetration series and negative for core-polarization series. A discussion of the foundations of the Ritz expansion and application to high precision calculations in helium is given in [22] (see also Chap. 12).

A spectral-line series results from either emission or absorption transitions involving a common lower level and a series of successive (core) nl upper levels differing only in their n values. The principal series of Na I, $3s^2S_{1/2} - np^2P_{1/2,3/2}^\circ$ ($n \geq 3$) is an example. The regularity of successive upper term values with increasing n (Eqs. (11.9), (11.10)) is, of course, observed in line series; the intervals between successive lines decrease in a regular manner towards higher wavenumbers, and the series of increasing wavenumbers converges towards the term value of the lower level as a limit.

11.13 Sequences

Several types of sequences of elements and/or ionization stages are useful because of regularities in the progressive values of parameters relating to structure and other properties along the sequences. All sequence names may refer either to the atoms and/or ions of the sequence or to their spectra.

11.13.1 Isoelectronic Sequence

A neutral atom and those ions of other elements having the same number of electrons as the atom comprise an isoelectronic sequence. (Note that a negative ion having this number of electrons is a member of the sequence.) An isoelectronic sequence is named according to its neutral member; for example, the Na I isoelectronic sequence.

11.13.2 Isoionic, Isonuclear, and Homologous Sequences

An isoionic sequence comprises atoms or ions of different elements having the same charge. Such sequences have probably been the most useful along the d and f-shell rows of the periodic table. Isoionic analyses have also been carried out along p-shell rows, however, and a fine-structure regularity covering spectra of the p-shell atoms throughout the periodic table is known [23].

The atom and successive ions of a particular element comprise the isonuclear sequence for that element.

The elements of a particular column and subgroup in the periodic table are homologous. Thus, the C, Si, Ge, Sn, and Pb atoms belong to a homologous sequence having np^2 ground configurations (Table 11.3). The singly ionized atoms of these elements comprise another example of a homologous sequence.

11.14 Spectral Wavelength Ranges, Dispersion of Air

The ranges of the most interest for optical atomic spectroscopy are:

~ 2–20 μm	Mid-infrared (IR)
700–2000 nm	Near IR
400–700 nm	Visible
200–400 nm	Near ultraviolet (UV)
100–200 nm	Vacuum UV (VUV) or far UV
10–100 nm	Extreme UV (EUV or XUV)
< 10 nm	Soft X-ray, X-ray

The above correspondence of names to ranges should not be taken as exact; the variation as to the extent of some of the named ranges found in the literature is considerable.

For regions longer than 200 nm, wavelengths in standard air are commonly tabulated. These wavelengths can be related to energy-level differences by conversion to the corresponding (vacuum) wavenumbers or frequencies [24, 25].

11.15 Wavelength Standards

In 2001, the Comité International des Poids et Mesures recommended values for optical frequency standards from stabilized lasers using various absorbing atoms, atomic ions, and molecules [26]. These frequencies range from 29,054,057,446,579 Hz (10.318436884460 μm ; relative standard uncertainty 1.4×10^{-13}) for a transition in OsO₄ to 1,267,402,452,889.92 kHz (236.54085354975 nm; relative standard uncertainty 3.6×10^{-13}) for a transition in the ¹¹⁵In⁺ ion [26].

Extensive tables of wavenumbers for molecular transitions in the mid-IR range of 2.3 to 20.5 μm are included in a calibration atlas published in 1998 [27]. Wavenumbers of Ar I [28] and Ar II [29] emission lines having uncertainties as small as 0.0003 cm^{-1} are included in tables for these spectra covering a broad range from 222 nm to 5.865 μm . Measurements of U and Th lines (575 to 692 nm) suitable for wavenumber calibration at uncertainty levels of 0.0003 or 0.0004 cm^{-1} were reported in [30]. Comprehensive tables of lines for U [31, 32], Th [33], and I₂ [34–37] are useful for calibration at uncertainty levels of 0.00003 to 0.003 cm^{-1} , the line list of the Th spectrum extending down to 235 nm.

A 1974 compilation gives reference wavelengths for some 5400 lines of 38 elements covering the range 1.5 nm to 2.5 μm , with most uncertainties between 10^{-5} and 2×10^{-4} nm [38]. The wavelengths for some 1100 Fe lines selected from the Fe/Ne hollow-cathode spectrum have been recommended for reference standards over the range 183 nm to 4.2 μm , with wavenumber uncertainties 0.001–0.002 cm^{-1} [39]. A comprehensive work on the Fe II spectrum [40] includes about 13,000 lines from VUV to far IR with wavenumber uncertainties between 0.0001 and 0.005 cm^{-1} . Wavelengths for about 3000 VUV and UV lines (110–400 nm) from a Pt/Ne hollow-cathode lamp have been determined with uncertainties of 0.0002 nm or less [15, 41]. More recent high-accuracy measurements of ultraviolet lines of Fe I, Ge I, Kr II, and Pt I, II include some wavelengths with uncertainties smaller than 10^{-5} nm [42]. The wavelengths tabulated for the Kr and Pt lines in [42] extend from 171 nm to 315 nm, and the accuracies of earlier measurements of a number of spectra useful for wavelength calibration are discussed.

11.16 Spectral Lines: Selection Rules, Intensities, Transition Probabilities, f Values, and Line Strengths

The selection rules for discrete transitions are given in Table 11.4.

11.16.1 Emission Intensities (Transition Probabilities)

In the absence of self-absorption and stimulated emission, the total power ϵ radiated in a spectral line of frequency ν per unit source volume and per unit solid angle is

$$\epsilon_{\text{line}} = (4\pi)^{-1} h\nu A_{ki} N_k, \quad (11.11)$$

where A_{ki} is the atomic transition probability and N_k the number per unit volume (number density) of excited atoms in the upper (initial) level k . For a homogeneous light source of length l and for the optically thin case, where all radiation escapes, the total emitted line intensity (SI quantity: radiance) is

$$\begin{aligned} I_{\text{line}} &= \epsilon_{\text{line}} l = \int_0^{+\infty} I(\lambda) d\lambda \\ &= (4\pi)^{-1} \left(\frac{hc}{\lambda_0} \right) A_{ki} N_k l, \end{aligned} \quad (11.12)$$

where $I(\lambda)$ is the specific intensity at wavelength λ , and λ_0 the wavelength at line center.

11.16.2 Absorption f -values

In absorption, the reduction of intensity of light passing through a medium is described by the quantity called the re-

duced absorption

$$W(\lambda) = \frac{[I(\lambda) - I'(\lambda)]}{I(\lambda)}, \quad (11.13)$$

where $I(\lambda)$ is the incident intensity at wavelength λ , e.g., from a source providing a continuous background, and $I'(\lambda)$ the intensity after passage through the absorbing medium. The total reduced absorption of a homogeneous and optically thin absorbing medium of length l for a spectral line arising from a transition between levels i and k is obtained by integrating the above equation

$$\begin{aligned} W_{ik} &= \int_0^{+\infty} W(\lambda) d\lambda \\ &= \frac{e^2}{4\epsilon_0 m_e c^2} \lambda_0^2 N_i f_{ik} l, \end{aligned} \quad (11.14)$$

where f_{ik} is the atomic (absorption) oscillator strength (dimensionless), λ_0 is the central wavelength of the line, N_i is the density of atoms in state i , and the other quantities are fundamental constants.

In astrophysics, the quantity given by the above equation is called the *equivalent width* of a spectral line [43]. Although it is not directly related to the width of the line profile, the term makes sense, as this quantity corresponds to the width of a rectangle having a unit height and the same area as the portion of the continuum absorbed by the spectral line.

11.16.3 Line Strengths

A_{ki} and f_{ik} are the principal atomic quantities related to line intensities. In theoretical work, the *line strength* S is also widely used (Chap. 22)

$$S = S(i, k) = S(k, i) = |R_{ik}|^2, \quad (11.15)$$

$$R_{ik} = \langle \psi_k | P | \psi_i \rangle, \quad (11.16)$$

Table 11.4 Selection rules for discrete transitions

	Electric dipole (E1) (allowed)	Magnetic dipole (M1) (forbidden)	Electric quadrupole (E2) (forbidden)
Rigorous rules	1. $\Delta J = 0, \pm 1$ (except $0 \not\rightarrow 0$)	$\Delta J = 0, \pm 1$ (except $0 \not\rightarrow 0$)	$\Delta J = 0, \pm 1, \pm 2$ (except $0 \not\rightarrow 0, 1/2 \not\rightarrow 1/2, 0 \not\rightarrow 1$)
	2. $\Delta M = 0, \pm 1$ (except $0 \not\rightarrow 0$ when $\Delta J = 0$)	$\Delta M = 0, \pm 1$ (except $0 \not\rightarrow 0$ when $\Delta J = 0$)	$\Delta M = 0, \pm 1, \pm 2$
	3. Parity change	No parity change	No parity change
With negligible configuration interaction	4. One electron jumping, with $\Delta l = \pm 1$, Δn arbitrary	No change in electron configuration; i.e., for all electrons, $\Delta l = 0$, $\Delta n = 0$	No change in electron configuration; or one electron jumping with $\Delta l = 0, \pm 2$, Δn arbitrary
For LS coupling only	5. $\Delta S = 0$	$\Delta S = 0$	$\Delta S = 0$
	6. $\Delta L = 0, \pm 1$ (except $0 \not\rightarrow 0$)	$\Delta L = 0$ $\Delta J = \pm 1$	$\Delta L = 0, \pm 1, \pm 2$ (except $0 \not\rightarrow 0, 0 \not\rightarrow 1$)

where ψ_i and ψ_k are the initial-state wavefunctions and the final-state wavefunctions, and R_{ik} is the *transition matrix element* of the appropriate multipole operator P (computation of R_{ik} involves an integration over spatial and spin coordinates of all N electrons of the atom or ion).

11.16.4 Relationships Between A , f , and S

The relationships between A , f , and S for electric dipole (E1, or “allowed”) transitions in SI units (A in s^{-1} , λ in m, S in $\text{m}^2 \text{C}^2$) are

$$A_{ki} = \frac{2\pi e^2}{m_e c \epsilon_0 \lambda^2} \frac{g_i}{g_k} f_{ik} = \frac{16\pi^3}{3h \epsilon_0 \lambda^3 g_k} S. \quad (11.17)$$

Numerically, in customary units (A in s^{-1} , λ in nm, S in atomic units, i.e., $a_0^2 e^2$),

$$A_{ki} = \frac{6.67025177 \times 10^{13}}{\lambda^2} \frac{g_i}{g_k} f_{ik} = \frac{2.0261269 \times 10^{15}}{\lambda^3 g_k} S, \quad (11.18)$$

and for S and ΔE in atomic units,

$$f_{ik} = \frac{2}{3} \left(\frac{\Delta E}{g_i} \right) S; \quad (11.19)$$

g_i and g_k are the statistical weights, which are obtained from the appropriate angular momentum quantum numbers. Thus, for the lower (upper) level of a spectral line, $g_{i(k)} = 2J_{i(k)} + 1$ and for the lower and upper terms of a multiplet, the g -values are calculated from the corresponding quantum numbers

$$\bar{g}_{i(k)} = \sum_{i(k)} (2J_{i(k)} + 1) = (2L_{i(k)} + 1) (2S_{i(k)} + 1). \quad (11.20)$$

Conversion relations between S and A_{ki} for the most common forbidden transitions are given in Table 11.5. Oscillator strengths f are rarely used for forbidden transitions, i.e., magnetic dipole (M1), electric quadrupole (E2), etc. However, the left-hand parts of Eqs. (11.17) and (11.18) are valid for any transition type and can be used to calculate f_{ik} from the normally tabulated A_{ki} -values.

[Numerical example: for the $1s2p\ ^1P_1^o - 1s3d\ ^1D_2$ (allowed) transition in He I at 667.815 nm (in air): $g_i = 3$; $g_k = 5$; $A_{ki} = 6.3705 \times 10^7 \text{ s}^{-1}$; $f_{ik} = 0.71028$; $S = 46.860 a_0^2 e^2$.]

Table 11.5 Conversion relations between S and A_{ki} for forbidden transitions

	SI units ^a	Numerically, in customary units ^b
Electric quadrupole	$A_{ki} = \frac{16\pi^5}{15h \epsilon_0 \lambda^5 g_k} S$	$A_{ki} = \frac{1.1199500 \times 10^{13}}{g_k \lambda^5} S$
Magnetic dipole	$A_{ki} = \frac{16\pi^3 \mu_0}{3h \lambda^3 g_k} S$	$A_{ki} = \frac{2.6973500 \times 10^{10}}{g_k \lambda^3} S$

^a A in s^{-1} , λ in m. Electric quadrupole: S in $\text{m}^4 \text{C}^2$. Magnetic dipole: S in $\text{J}^2 \text{T}^{-2}$

^b A in s^{-1} , λ in nm; S in atomic units: $a_0^4 e^2 = 2.01291442 \times 10^{-79} \text{ m}^4 \text{C}^2$ (electric quadrupole), $e^2 h^2 / 16\pi^2 m_e^2 = \mu_B^2 = 8.6007261 \times 10^{-47} \text{ J}^2 \text{ T}^{-2}$ (magnetic dipole). μ_B is the Bohr magneton.

11.16.5 Relationships Between Line and Multiplet Values

The relations between the total strength and f value of a multiplet (M) and the corresponding quantities for the lines of the multiplet (allowed transitions) are

$$S_M = \sum S_{\text{line}}, \quad (11.21)$$

$$f_M = (\bar{\lambda} \bar{g}_i)^{-1} \sum_{J_k, J_i} g_i \lambda(J_i, J_k) f(J_i, J_k); \quad (11.22)$$

$\bar{\lambda}$ is the weighted (*multiplet*) wavelength in vacuum

$$\bar{\lambda} = n \bar{\lambda}_{\text{air}} = \frac{hc}{\Delta E}, \quad (11.23)$$

where

$$\begin{aligned} \overline{\Delta E} &= \overline{E_k} - \overline{E_i} \\ &= (\bar{g}_k)^{-1} \sum_{J_k} g_k E_k - (\bar{g}_i)^{-1} \sum_{J_i} g_i E_i, \end{aligned} \quad (11.24)$$

\bar{g}_i and \bar{g}_k are defined by Eq. (11.20), and n is the refractive index of air.

11.16.6 Relative Strengths for Lines of Multiplets in LS Coupling

A general formula for the relative line strengths S_{rel} of fine-structure components of LS multiplets is given by Sobel'man [44]

$$S_{\text{rel}}(i, k, S) = \frac{(2J_i + 1)(2J_k + 1)}{2S + 1} \left\{ \begin{matrix} L_i & J_i & S \\ J_k & L_k & 1 \end{matrix} \right\}, \quad (11.25)$$

where the indexes i and k correspond to the initial and final levels, respectively, S is their common multiplicity, and the matrix in curly brackets is Wigner's 6- j -symbol. The values of S_{rel} in the above equation are normalized so that their sum over all multiplet components is unity. From this expression, it follows that the strongest, or principal, components of a multiplet are those for which the changes in J and L are

equal. The strongest of the principal lines correspond to the largest J -value of the initial level. The other, weaker components of the multiplet are called satellite lines. In order of decreasing intensity they are called the first-order satellites ($\Delta J = 0, \Delta L = \pm 1$) and second-order satellites ($\Delta J = +1, \Delta L = -1$ or $\Delta J = -1, \Delta L = +1$). A discussion of normalization of S_{rel} as well as extensive tables of their values are given in [45].

11.17 Atomic Lifetimes

The radiative lifetime τ_k of an atomic level k is related to the sum of transition probabilities to all levels i lower in energy than k

$$\tau_k = \left(\sum_i A_{ki} \right)^{-1}. \quad (11.26)$$

The *branching* fraction of a particular transition, say to state i' , is defined as

$$\frac{A_{ki'}}{\sum_i A_{ki}} = A_{ki'} \tau_k. \quad (11.27)$$

If only one branch (i') exists (or if all other branches may be neglected), one obtains $A_{ki'} \tau_k = 1$, and

$$\tau_k = 1/A_{ki'}. \quad (11.28)$$

Precision lifetime measurement techniques are discussed in Chaps. 18 and 19.

11.18 Regularities and Scaling

11.18.1 Transitions in Hydrogenic (One-Electron) Species

According to Eqs. (11.1) and (11.7), the nonrelativistic *energy* of a hydrogenic transition is

$$(\Delta E)_Z = (E_k - E_i)_Z = R_Z Z^2 (1/n_i^2 - 1/n_k^2). \quad (11.29)$$

Hydrogenic Z Scaling

The spectroscopic quantities for a hydrogenic ion of nuclear charge Z are related to the equivalent quantities in hydrogen ($Z = 1$) as follows (neglecting small differences in the values of R_Z)

$$(\Delta E)_Z = Z^2 (\Delta E)_H, \quad (11.30)$$

$$(\lambda_{\text{vac}})_Z = Z^{-2} (\lambda_{\text{vac}})_H, \quad (11.31)$$

$$S_Z = Z^{-2} S_H, \quad (11.32)$$

$$f_Z = f_H, \quad (11.33)$$

$$A_Z = Z^4 A_H. \quad (11.34)$$

For large values of Z , roughly $Z > 20$, relativistic corrections become noticeable and must be taken into account.

f -value Trends

f -values for high series members (large n' values) of hydrogenic ions decrease according to

$$f(n, l \rightarrow n', l \pm 1) \propto (n')^{-3}. \quad (11.35)$$

11.18.2 Systematic Trends and Regularities in Atoms and Ions with Two or More Electrons

Atomic quantities for a given state or transition in an *isoelectronic sequence* may be expressed as power series expansions in Z^{-1}

$$Z^{-2} E = E_0 + E_1 Z^{-1} + E_2 Z^{-2} + \dots, \quad (11.36)$$

$$Z^2 S = S_0 + S_1 Z^{-1} + S_2 Z^{-2} + \dots, \quad (11.37)$$

$$f = f_0 + f_1 Z^{-1} + f_2 Z^{-2} + \dots, \quad (11.38)$$

where E_0 , f_0 , and S_0 are hydrogenic quantities. For transitions in which n does not change ($n_i = n_k$), $f_0 = 0$, since states i and k are degenerate.

For equivalent transitions of *homologous atoms*, f values vary gradually. Transitions to be compared in the case of *alkalis* are [46]

$$\begin{aligned} (nl - n'l')_{\text{Li}} &\rightarrow [(n+1)l - (n'+1)l']_{\text{Na}} \\ &\rightarrow [(n+2)l - (n'+2)l']_{\text{Cu}} \rightarrow \dots \end{aligned}$$

Complex atomic structures, as well as cases involving strong cancellation in the integrand of the transition integral, generally do not adhere to this regular behavior.

11.19 Tabulations of Transition Probabilities

The A_{ki} -values for strong lines of selected elements are given in Table 11.6. Data for some lines of the main spectral series of hydrogen are given in Table 11.7.

Experimental and theoretical methods to determine A , f , or S -values, as well as atomic lifetimes are discussed in Chaps. 12, 18, 19, and 22.

Methods for critical evaluation of accuracy of experimental and theoretical transition probabilities have been developed over several decades by the NIST Atomic Spectroscopy Group [47, 48]. Examples of the work of this group can be found in [49, 50]. Comprehensive tables of A , f , and S , including forbidden lines, are collected in the NIST ASD [15].

For references to other sources of transition probability data, see Sect. 11.22.

Table 11.6 Wavelengths λ , upper energy levels E_k , statistical weights g_i and g_k of lower and upper levels, and transition probabilities A_{ki} for persistent spectral lines of neutral atoms. Many tabulated lines are resonance lines (marked “g”), where the lower energy level belongs to the ground term

Element	λ^a (nm)	E_k (cm^{-1})	g_i	g_k	A_{ki} (10^8 s^{-1})	Accuracy ^b
Ag	328.07g	30,473	2	4	1.4	B
	338.29g	29,552	2	2	1.3	B
	520.91	48,744	2	4	0.75	D
	546.55	48,764	4	6	0.86	D
Al	308.22g	32,435	2	4	0.587	B+
	309.27g	32,437	4	6	0.729	B+
	394.40g	25,348	2	2	0.499	B+
	396.15g	25,348	4	2	0.985	B+
Ar	104.82g	95,400	1	3	5.32	AA
	415.86	117,184	5	5	0.0140	B
	425.94	118,871	3	1	0.0398	B+
	763.51	106,238	5	5	0.245	B
	794.82	107,132	1	3	0.186	B
	811.53	105,463	5	7	0.331	B
As	189.04g	52,898	4	6	2.66	C+
	193.76g	51,610	4	4	2.19	C+
	228.81	54,605	6	4	2.8	D
	234.98	53,136	4	2	3.1	D
Au	242.80g	41,175	2	4	1.98	B+
	267.60g	37,359	2	2	1.64	A+
B	182.59g	54,768	2	4	1.70	A
	182.64g	54,768	4	6	2.04	A
	249.68g	40,040	2	2	0.840	A
	249.77g	40,040	4	2	1.68	A
Ba	553.55g	18,060	1	3	1.190	A+
	649.88	24,980	7	7	0.54	C+
	705.99	23,757	7	9	0.50	C
	728.03	22,947	5	7	0.32	C+
Be	234.86g	42,565	1	3	5.52	A
	265.06	59,696	9	9 ^c	4.23	A
Bi	222.82g	44,865	4	4	0.88	C+
	289.80	45,916	4	2	1.53	B
	298.90	44,865	4	4	0.54	C+
	306.77g	32,588	4	2	1.67	B
Br	148.85g	67,184	4	4	2.0	D+
	154.07g	64,907	4	4	2.2	D+
	734.85	78,512	4	6	0.047	C
C	156.14g	64,087	5	7	1.17	A
	165.70g	60,393	5	5	2.61	A
	193.09	61,982	5	3	3.39	A
	247.86	61,982	1	3	0.28	C+
Ca	422.67g	23,652	1	3	2.18	B+
	430.25	38,552	5	5	1.36	C+
	558.88	38,259	7	7	0.49	D
	616.22	31,539	5	3	0.48	C
	643.91	35,897	7	9	0.53	D
Cd	228.80g	43,692	1	3	5.3	C
	346.62	59,498	3	5	1.2	D
	361.05	59,516	5	7	1.3	D
	508.58	51,484	5	3	0.56	C

Table 11.6 (Continued)

Element	λ^a (nm)	E_k (cm^{-1})	g_i	g_k	A_{ki} (10^8 s^{-1})	Accuracy ^b
Cl	134.72g	74,226	4	4	4.19	C+
	135.17g	74,866	2	2	3.23	C+
	452.62	96,313	4	4	0.051	C
	725.66	85,735	6	4	0.15	D
Co	340.51	32,842	10	10	1.0	C+
	345.35	32,431	10	12	1.1	C+
	350.23	32,028	10	8	0.80	C+
	356.94	35,451	8	8	1.5	C
Cr	357.87g	27,935	7	9	1.48	B
	359.35g	27,820	7	7	1.50	B
	360.53g	27,729	7	5	1.62	B
	425.43g	23,499	7	9	0.315	B
	427.48g	23,386	7	7	0.307	B
	520.84	26,787	5	7	0.506	B
Cs	387.61g	25,792	2	4	0.0039	B+
	455.53g	21,946	2	4	0.01836	AA
	459.32g	21,765	2	2	0.00794	A+
	852.11g	11,732	2	4	0.3279	AAA
	894.35g	11,178	2	2	0.2863	AAA
Cu	217.89g	45,879	2	4	0.91	C+
	324.75g	30,784	2	4	1.395	AA
	327.40g	30,535	2	2	1.376	AA
	521.82	49,942	4	6	0.75	C+
F	95.483g	104,731	4	4	5.98	B+
	685.60	116,987	6	8	0.487	C+
	739.87	115,918	6	6	0.353	C
	775.47	117,623	4	6	0.323	C+
Fe	358.12	34,844	11	13	1.02	A
	371.99g	26,875	9	11	0.162	A
	373.49	33,695	11	11	0.901	A
	374.56g	27,395	5	7	0.115	A
	385.99g	25,900	9	9	0.0969	A
	404.58	36,686	9	9	0.862	A
Ga	287.42g	34,782	2	4	1.17	B+
	294.36g	34,788	4	6	1.34	B+
	403.30g	24,789	2	2	0.485	B+
	417.20g	24,789	4	2	0.945	B+
Ge	265.16g	37,702	1	3	0.85	C
	270.96g	37,452	3	1	2.8	C
	275.46g	37,702	5	3	1.1	C
	303.91	40,021	5	3	2.8	C
He	53.703g	186,209	1	3	5.6634	AAA
	58.433g	171,135	1	3	17.989	AAA
	388.86	185,565	3	9 ^c	0.09475	AAA
	402.62	193,917	9	15 ^c	0.1160	AAA
	447.15	191,444	9	15 ^c	0.2458	AAA
	587.57	186,102	9	15 ^c	0.7070	AAA
Hg	253.65g	39,412	1	3	0.0840	A+
	312.57	71,396	3	5	0.66	B+
	435.83	62,350	3	3	0.56	B
	546.07	62,350	5	3	0.49	B

Table 11.6 (Continued)

Element	λ^a (nm)	E_k (cm^{-1})	g_i	g_k	A_{ki} (10^8 s^{-1})	Accuracy ^b
I	178.28g	56,093	4	4	2.71	C
	183.04g	54,633	4	6	0.16	D
In	303.93g	32,892	2	4	1.11	B+
	325.61g	32,916	4	6	1.30	B+
	410.17g	24,373	2	2	0.496	B+
	451.13g	24,373	4	2	0.893	B+
	404.41g	24,720	2	4	0.0115	A
K	404.72g	24,701	2	2	0.0107	B+
	766.49g	13,043	2	4	0.3779	AAA
	769.90g	12,985	2	2	0.3734	AAA
	557.03	97,919	5	3	0.00980	B+
Kr	587.09	97,945	3	5	0.0071	C
	760.15	93,123	5	5	0.2732	AA
	811.29	92,294	5	7	0.3610	AAA
	323.27g	30,925	2	6 ^c	0.01002	AA
Li	460.29	36,623	6	10 ^c	0.2322	AA
	610.36	31,283	6	10 ^c	0.6856	AAA
	670.78g	14,904	2	6 ^c	0.3689	AAA
	202.58g	49,347	1	3	0.612	B+
Mg	285.21g	35,051	1	3	4.91	A
	470.30	56,308	3	5	0.219	B+
	518.36	41,197	5	3	0.561	A
	279.48g	35,770	6	8	3.7	C
Mn	279.83g	35,726	6	6	3.6	C
	280.11g	35,690	6	4	3.7	C
	403.08g	24,802	6	8	0.17	C+
	403.31g	24,788	6	6	0.165	C+
	403.45g	24,779	6	4	0.158	C+
	119.96g	83,365	4	6	4.07	A
N	149.26	86,221	6	4	3.11	B+
	493.51	106,478	4	2	0.0176	B
	746.83	96,751	6	4	0.196	B+
	821.63	95,532	6	6	0.226	B+
	568.26	34,549	2	4	0.101	A
	589.00g	16,973	2	4	0.616	AA
Na	589.59g	16,956	2	2	0.614	AA
	818.33	29,173	2	4	0.429	A+
	73.590g	135,889	1	3	5.88	A
	74.372g	134,459	1	3	0.440	A
Ne	585.25	152,971	3	1	0.615	AA
	607.43	150,917	3	1	0.603	B+
	640.22	149,657	5	7	0.5149	AAA
	310.16	33,112	5	7	0.63	C+
	313.41	33,611	3	5	0.73	C+
Ni	336.96g	29,669	9	7	0.18	C
	341.48	29,481	7	9	0.55	C
	352.45	28,569	7	5	1.0	C
	361.94	31,031	5	7	0.66	C

Table 11.6 (Continued)

Element	λ^a (nm)	E_k (cm^{-1})	g_i	g_k	A_{ki} (10^8 s^{-1})	Accuracy ^b
O	130.22g	76,795	5	3	3.41	A
	436.82	99,681	3	9 ^c	0.00758	B
	543.69	105,019	7	5	0.0180	C+
	715.67	116,631	5	5	0.505	B
	777.19	86,631	5	7	0.369	A
P	177.50g	56,340	4	6	2.17	C
	178.28g	56,091	4	4	2.14	C
	213.62	58,174	6	4	2.83	C
	253.56	58,174	4	4	0.95	C
Pb	280.20	46,329	5	7	1.61	C+
	283.31g	35,287	1	3	0.49	C+
	368.35	34,960	3	1	1.37	B
	405.78	35,287	5	3	0.90	C+
Rb	420.18g	23,793	2	4	0.0177	B+
	421.55g	23,715	2	2	0.0150	B
	780.03g	12,817	2	4	0.3812	AAA
	794.76g	12,579	2	2	0.3614	AAA
S	147.40g	67,843	5	7	1.96	C+
	166.67	69,238	5	5	4.58	C+
	180.73g	55,331	5	3	3.27	C+
	469.41	73,921	5	7	0.0084	D
Sc	390.75g	25,585	4	6	1.66	B+
	391.18g	25,725	6	8	1.79	B+
	402.04g	24,866	4	4	1.63	B+
	402.37g	25,014	6	6	1.65	B+
Si	250.69g	39,955	3	5	0.547	B
	251.61g	39,955	5	5	1.68	B
	288.16	40,992	5	3	2.17	B
	500.61	60,962	3	5	0.028	D
	594.85	57,798	3	5	0.0222	C
Sn	284.00g	38,629	5	5	1.7	D
	303.41g	34,641	3	1	2.0	D
	317.50g	34,914	5	3	1.0	D
	326.23	39,257	5	3	2.7	D
Sr	242.81g	41,172	1	3	0.17	C+
	460.73g	21,698	1	3	2.01	AA
Ti	364.27g	27,615	7	9	0.895	A
	365.35g	27,750	9	11	0.869	A
	399.86g	25,388	9	9	0.481	A
	521.04g	19,574	9	9	0.0389	B
	498.17	26,911	11	13	0.660	C+
Tl	276.79g	36,118	2	4	1.26	C
	351.92g	36,200	4	6	1.24	C
	377.57g	26,478	2	2	0.625	B
	535.05g	26,478	4	2	0.705	B
U	356.66g	28,650	11	11	0.24	B
	357.16	38,338	17	15	0.13	C
	358.49g	27,887	13	15	0.18	B

Table 11.6 (Continued)

Element	λ^a (nm)	E_k (cm^{-1})	g_i	g_k	A_{ki} (10^8 s^{-1})	Accuracy ^b
V	318.34g	31,541	6	8	2.52	B+
	411.18	26,738	10	10	1.00	B+
	437.92	25,253	10	12	1.15	B+
	438.47	25,111	8	10	0.92	B+
Xe	119.20g	83,890	1	3	5.93	B+
	129.56g	77,185	1	3	2.53	A+
	146.96g	68,045	1	3	2.73	A+
	467.12	88,469	5	7	0.0249	B
	711.96	92,445	7	9	0.0839	B
Zn	213.86g	46,745	1	3	7.14	A
	330.26	62,772	3	5	1.20	B
	334.50	62,777	5	7	1.70	B
	636.23	62,459	3	5	0.47	C

^a A “g” following the wavelength indicates that the lower level of the transition belongs to the ground term, i.e., the line is a resonance line. Wavelengths below 200 nm are in vacuum, and those above 200 nm are in air.

^b Accuracy estimates pertain to A_{ki} -values: AAA, uncertainty within 0.3%; AA, within 1%; A+, within 2%; A, within 3%; B+, within 7%; B, within 10%; C+, within 18%; C, within 25%; D+, within 40%; D, within 50%

^c The A_{ki} , λ , g_i , and g_k are multiplet values; see Eq. (11.20) and Sect. 11.16.5

Table 11.7 Some transitions of the main spectral series of hydrogen

$n-n^a$	Customary name ^b	λ^c (nm)	g_i^d	g_k	A_{ki}^e (10^8 s^{-1})	$n-n^a$	Customary name ^b	λ^c (nm)	g_i^d	g_k	A_{ki}^e (10^8 s^{-1})
1–2	L_α	121.56701	2	8	4.6986	2–6	H_δ	410.17415	8	72	9.7320(–3)
1–3	L_β	102.57220	2	18	5.5751(–1)	2–7	H_ϵ	397.00788	8	98	4.3889(–3)
1–4	L_γ	97.25365	2	32	1.2785(–1)	3–4	P_α	1875.0976	18	32	8.9860(–2)
1–5	L_δ	94.97429	2	50	4.1250(–2)	3–5	P_β	1281.8070	18	50	2.2008(–2)
1–6	L_ϵ	93.78033	2	72	1.6440(–2)	3–6	P_γ	1093.8086	18	72	7.7829(–3)
2–3	H_α	656.2819	8	18	4.4101(–1)	3–7	P_δ	1004.9369	18	98	3.3585(–3)
2–4	H_β	486.1333	8	32	8.4193(–2)	3–8	P_ϵ	954.5969	18	128	1.6506(–3)
2–5	H_γ	434.0471	8	50	2.5304(–2)	4–5	Brackett- α	4052.269	32	50	2.6993(–2)

^a Principal quantum numbers of the lower and upper levels

^b L_α is often called Lyman α , H_α = Balmer α , P_α = Paschen α

^c Wavelengths below 200 nm are in vacuum; values above 200 nm are in air

^d For transitions in hydrogen, $g_{i(k)} = 2(n_{i(k)})^2$, where $n_{i(k)}$, is the principal quantum number of the lower (upper) electron shell

^e The number in parentheses indicates the power of 10 by which the value has to be multiplied; uncertainties of these theoretical A-values are smaller than 0.3%

11.20 Spectral Line Shapes, Widths, and Shifts

Observed spectral lines are always broadened. The principal physical causes of spectral line broadening are Doppler and pressure broadening. The theoretical foundations of line broadening are discussed in Chaps. 20 and 63.

11.20.1 Doppler Broadening

Doppler broadening is due to the thermal motion of the emitting atoms. For a Maxwellian velocity distribution, the line shape is *Gaussian*; the full width at half maximum intensity (FWHM) is, in the same units as wavelength (λ),

$$\Delta\lambda_{1/2}^D = (7.16233 \times 10^{-7}) \lambda (T/M)^{1/2}; \quad (11.39)$$

T is the temperature of the emitters in K, and M the atomic weight in atomic mass units (u).

11.20.2 Pressure Broadening

Pressure broadening is due to collisions of the emitters with neighboring particles (also Chaps. 20 and 63). Shapes are often approximately Lorentzian, i.e., $I(\lambda) \propto \{1 + [(\lambda - \lambda_0)/\Delta\lambda_{1/2}]^2\}^{-1}$. In the following formulas, all FWHMs and wavelengths are expressed in nm, particle densities N in cm^{-3} , temperatures T in K, and energies E or I in cm^{-1} .

Resonance broadening (self-broadening) occurs only between identical species and is confined to lines with the upper or lower level having an electric dipole transition (resonance

line) to the ground state. The FWHM may be estimated as

$$\Delta\lambda_{1/2}^R \simeq 8.6 \times 10^{-28} \left(\frac{g_i}{g_k} \right)^{1/2} \lambda^2 \lambda_r f_r N_i, \quad (11.40)$$

where λ is the wavelength of the observed line; f_r and λ_r are the oscillator strength and wavelength of the resonance line, and g_k and g_i are the statistical weights of its upper and lower levels; N_i is the ground state number density.

For the $1s2p\ ^1P_1^o - 1s3d\ ^1D_2$ transition in He I [$\lambda = 667.815$ nm; $\lambda_r(1s^2\ ^1S_0 - 1s2p\ ^1P_1^o) = 58.4334$ nm; $g_i = 1$; $g_k = 3$; $f_r = 0.2762$] at $N_i = 1 \times 10^{18}$ cm $^{-3}$: $\Delta\lambda_{1/2}^R = 0.0036$ nm.

Van der Waals broadening arises from the dipole interaction of an excited atom with the induced dipole of a ground state atom. (In the case of foreign gas broadening, both the perturber and the radiator may be in their respective ground states.) An approximate formula [51] for the FWHM, strictly applicable to hydrogen and similar atomic structures only, is

$$\Delta\lambda_{1/2}^W \simeq 8.5 \times 10^{-11} \lambda^2 C_6^{2/5} (T/\mu)^{3/10} N, \quad (11.41)$$

where μ is the atom-perturber reduced mass in atomic mass units, N the perturber density, and C_6 the interaction constant; C_6 may be roughly estimated as follows

$$C_6 = C_k - C_i, \quad (11.42)$$

with

$$C_{i(k)} \simeq 9.1 \times 10^{-46} \alpha_d R_{i(k)}^2 [\text{m}^6/\text{s}], \quad (11.43)$$

where α_d is the mean dipole polarizability of the perturber atom,

$$\alpha_d \approx 4.5 \left(\frac{3I_H}{4E^*} \right)^2 a_0^3, \quad (11.44)$$

I_H being the ionization energy of hydrogen and E^* the energy of the first excited level of the perturber atom, and $R_{i(k)}^2$ are the mean squared radii of the wavefunctions of the initial and final levels of the transition,

$$R_{i(k)}^2 \approx 2.5 \left[\frac{I_H}{(I - E_{i(k)})} \right]^2 a_0^2, \quad (11.45)$$

where I is the ionization energy of the radiator. Van der Waals broadened lines are redshifted by about one-third the size of the FWHM.

For the $1s2p\ ^1P_1^o - 1s3d\ ^1D_2$ transition in He I, and with He as perturber: $\lambda = 667.815$ nm; $I = 198,311$ cm $^{-1}$; $E^* = E_i = 171,135$ cm $^{-1}$; $E_k = 186,105$ cm $^{-1}$; $\mu = 2$. At $T = 273$ K and $N = 1 \times 10^{18}$ cm $^{-3}$: $\Delta\lambda_{1/2}^W = 0.0012$ nm.

Stark broadening due to charged perturbers, i.e., ions and electrons, usually dominates resonance and van der Waals

Table 11.8 Values of Stark-broadening parameter $\alpha_{1/2}$ of the H β line of hydrogen (486.1 nm) for various temperatures and electron densities

T (K)	N_e (cm $^{-3}$)			
	10^{15}	10^{16}	10^{17}	10^{18}
5000	0.0787	0.0808	0.0765	...
10,000	0.0803	0.0840	0.0851	0.0781
20,000	0.0815	0.0860	0.0902	0.0896
30,000	0.0814	0.0860	0.0919	0.0946

broadening in discharges and plasmas. The FWHM for hydrogen lines is

$$\Delta\lambda_{1/2}^{S,H} = (2.50 \times 10^{-10}) \alpha_{1/2} N_e^{2/3}, \quad (11.46)$$

where N_e is the electron density. The half-width parameter $\alpha_{1/2}$ for the H β line at 486.1 nm, widely used for plasma diagnostics, is tabulated in Table 11.8 for some typical temperatures and electron densities [45]. This reference also contains $\alpha_{1/2}$ parameters for other hydrogen lines, as well as Stark width and shift data for numerous lines of other elements, i.e., neutral atoms and singly charged ions (in the latter, Stark widths and shifts depend linearly on N_e). Other tabulations of complete hydrogen Stark profiles exist. *Griem* [52] gives a theoretical foundation for treatment of Stark broadening of spectral lines in plasmas.

11.21 Spectral Continuum Radiation

11.21.1 Hydrogenic Species

Precise quantum-mechanical calculations exist only for hydrogenic species. The total power ϵ_{cont} radiated (per unit source volume and per unit solid angle, and expressed in SI units) in the wavelength interval $\Delta\lambda$ is the sum of radiation due to the recombination of a free electron with a bare ion (free-bound transitions) and bremsstrahlung (free-free transitions)

$$\begin{aligned} \epsilon_{\text{cont}} = & \frac{e^6}{2\pi c^2 \epsilon_0^3 (6\pi m_e)^{3/2}} N_e N_Z Z^2 \\ & \times \frac{1}{(kT)^{1/2}} \exp\left(-\frac{hc}{\lambda kT}\right) \frac{\Delta\lambda}{\lambda^2} \\ & \times \left\{ \frac{2Z^2 I_H}{kT} \sum_{n \geq (Z^2 I_H \lambda / hc)^{1/2}}^{n'} \frac{\gamma_{\text{fb}}}{n^3} \exp\left(\frac{Z^2 I_H}{n^2 kT}\right) \right. \\ & \left. + \bar{\gamma}_{\text{fb}} \left[\exp\left(\frac{Z^2 I_H}{(n' + 1)^2 kT}\right) - 1 \right] + \gamma_{\text{ff}} \right\}, \quad (11.47) \end{aligned}$$

where N_e is the electron density, N_Z the number density of hydrogenic (bare) ions of nuclear charge Z , I_H the ionization energy of hydrogen, n' the principal quantum number of

the lowest level for which adjacent levels are so close that they approach a continuum, and summation over n may be replaced by an integral (the choice of n' is rather arbitrary; n' as low as 6 can be found in the literature); γ_{fb} and γ_{ff} are the Gaunt factors, which are generally close to unity. (For the higher free-bound continua, starting with $n' + 1$, an average Gaunt factor $\bar{\gamma}_{fb}$ is used.) For neutral hydrogen, the recombination continuum forming H^- also becomes important [53].

In the equation above, the value of the constant factor before N_e is $6.065 \times 10^{-55} \text{ W m}^4 \text{ J}^{1/2} \text{ sr}^{-1}$. [Numerical example: for atomic hydrogen ($Z = 1$), the quantity ϵ_{cont} has the value $2.9 \text{ W m}^{-3} \text{ sr}^{-1}$ under the following conditions: $\lambda = 3 \times 10^{-7} \text{ m}$; $\Delta\lambda = 1 \times 10^{-10} \text{ m}$; $N_e (= N_{Z=1}) = 1 \times 10^{21} \text{ m}^{-3}$; $T = 12,000 \text{ K}$. The lower limit of the summation index n is 2; the upper limit n' has been taken to be 10. All Gaunt factors γ_{fb} , $\bar{\gamma}_{fb}$, and γ_{ff} have been assumed to be unity.]

11.21.2 Many-Electron Systems

For many-electron systems, only approximate theoretical treatments exist, based on the quantum-defect method [54]. For results of calculations for noble gases, see, e.g., [55, 56]. Experimental work is centered on the noble gases [57, 58]. Modifications of the continuum by autoionization processes must also be considered.

Near the ionization limit, the f values for bound-bound transitions of a spectral series ($n' \rightarrow \infty$) make a smooth connection to the differential oscillator strength distribution $df/d\epsilon$ in the continuum [3].

11.22 Sources of Spectroscopic Data

Access to most of the atomic spectroscopic databases currently online is given by links at the Plasma Gate server [59]. Extensive data from NIST compilations of atomic wavelengths, energy levels, and transition probabilities are available from the *Atomic Spectra Database* (ASD) at the NIST site [15]. Section 11.15 includes additional references for wavelength tables. The modern trend of online dissemination of digital data is exemplified by the Virtual Atomic and Molecular Data Centre (VAMDC) Consortium [60], which provides online access to many atomic and molecular spectroscopic databases through a unified portal.

References

1. Taylor, B.N., Thompson, A. (eds.): The International System of Units (SI) (2008) <https://doi.org/10.6028/NIST.SP.330e2008>. NIST Special Publication 330, available online at <https://www.nist.gov/pml/special-publication-330>
2. Condon, E.U., Shortley, G.H.: The Theory of Atomic Spectra. Cambridge Univ. Press, Cambridge (1935)
3. Cowan, R.D.: The Theory of Atomic Structure and Spectra. Univ. California Press, Berkeley (1981)
4. Demtröder, W.: Atoms, Molecules, and Photons. An Introduction to Atomic-, Molecular- and Quantum Physics, 2nd edn. Springer, New York (2006)
5. Bethe, H.A., Salpeter, E.E.: Quantum Mechanics of One- and Two-Electron Atoms. Plenum, New York (1977)
6. Karshenboim, S.G.: Phys. Rep. **422**, 1 (2005). <https://doi.org/10.1016/j.physrep.2005.08.008>
7. Edlén, B.: In: Flügge, S. (ed.) Encyclopedia of Physics, vol. 27, Springer, Berlin, Heidelberg (1964)
8. Russell, H.N., Saunders, F.A.: Astrophys. J. **61**, 38 (1925). <https://doi.org/10.1086/142872>
9. Nielson, C.W., Koster, G.F.: Spectroscopic Coefficients for the p^n , d^n , and f^n Configurations. MIT Press, Cambridge (1963)
10. Martin, W.C., Zalubas, R., Hagan, L.: Atomic Energy Levels – The Rare-Earth Elements. U.S. Government Printing Office, Washington (1978). Nat. Stand. Ref. Data Ser., Nat. Bur. Stand. No. 60
11. de-Shalit, A., Talmi, I.: Nuclear Shell Theory. Academic Press, New York (1963)
12. Russell, H.N., Shenstone, A.G., Turner, L.A.: Phys. Rev. **33**, 900 (1929). <https://doi.org/10.1103/PhysRev.33.900>
13. Bacher, R.F., Goudsmit, S.: Atomic Energy States. McGraw-Hill, New York (1932)
14. Moore, C.E.: Atomic Energy Levels. U.S. Government Printing Office, Washington (1971). Nat. Stand. Ref. Data Ser., Nat. Bur. Stand. No. 35
15. Kramida, A., Ralchenko, Y., Reader, J., NIST ASD Team: NIST Atomic Spectra Database, version 5.9 (2021) <https://doi.org/10.18434/T4W30F>. Available online at <https://physics.nist.gov/asd>; This is one of several online NIST databases referred to in this chapter. The databases are accessible online at <https://www.nist.gov/pml/productsservices/physical-reference-data>
16. Sansonetti, J.E., Martin, W.C.: Handbook of Basic Atomic Spectroscopic Data, NIST (online database). <https://physics.nist.gov/PhysRefData/Handbook>. These tables include selected data on wavelengths, energy levels, and transition probabilities for the neutral and singly-ionized atoms of all elements up through einsteinium ($Z = 1-99$); <https://doi.org/10.18434/T4FW23>
17. Bernath, P.F.: Spectra of Atoms and Molecules, 3rd edn. Oxford Univ. Press, New York (2015)
18. Wybourne, B.G.: Spectroscopic Properties of Rare Earths. Wiley, New York (1965)
19. Schwinger, J.: Phys. Rev. **73**, 416 (1948). <https://doi.org/10.1103/PhysRev.73.416>
20. Yan, Z.C., Drake, G.W.F.: Phys. Rev. A **50**, R1980 (1994). <https://doi.org/10.1103/PhysRevA.50.R1980>
21. Martin, W.C.: J. Opt. Soc. Am. **70**, 784 (1980). <https://doi.org/10.1364/JOSA.70.000784>
22. Drake, G.W.F.: Adv. At. Mol. Opt. Phys. **32**, 93 (1994). [https://doi.org/10.1016/S1049-250X\(08\)60012-9](https://doi.org/10.1016/S1049-250X(08)60012-9)
23. Fano, U., Martin, W.C.: In: Brittin, W.E., Odabasi, H. (eds.) Topics in Modern Physics, A Tribute to E.U. Condon, pp. 147–152. Colorado Associated Univ. Press, Colorado (1971)
24. Edlén, B.: Metrologia **2**, 71 (1966). <https://doi.org/10.1088/0026-1394/2/2/002>
25. Peck, E.R., Reeder, K.: J. Opt. Soc. Am. **62**, 958 (1972). <https://doi.org/10.1364/JOSA.62.000958>
26. Quinn, T.J.: Metrologia **40**, 103 (2003). <https://doi.org/10.1088/0026-1394/40/2/316>
27. Maki, A.G., Wells, J.S.: Wavenumber Calibration Tables from Heterodyne Frequency Measurements, version 1.3. NIST, Gaithersburg (1998) <https://doi.org/10.18434/T49598>. Originally

- published as NIST Special Publication 821 (U.S. Government Printing Office, Washington 1987)
28. Whaling, W., Anderson, W.H.C., Carle, M.T., Brault, J.W., Zarem, H.A.: *J. Res. Natl. Inst. Stand. Technol.* **107**, 149 (2002). <https://doi.org/10.6028/jres.10714>
 29. Whaling, W., Anderson, W.H.C., Carle, M.T., Brault, J.W., Zarem, H.A.: *J. Quant. Spectrosc. Radiat. Transf.* **53**, 1 (1995). [https://doi.org/10.1016/0022-4073\(94\)00102-D](https://doi.org/10.1016/0022-4073(94)00102-D)
 30. Sansonetti, C.J., Weber, K.-H.: *J. Opt. Soc. Am. B* **1**, 361 (1984). <https://doi.org/10.1364/JOSAB.1.000361>
 31. Palmer, B.A., Keller, R.A., Engleman Jr., R.: Los Alamos National Laboratory Report LA-8251-MS, UC-34a (1980)
 32. Redman, S.L., Lawler, J.E., Nave, G., Ramsey, L.W., Mahadevan, S.: *Astrophys. J. Suppl. Ser.* **195**, 24 (2011). <https://doi.org/10.1088/0067-0049/195/2/24>
 33. Redman, S.L., Nave, G., Sansonetti, C.J.: *Astrophys. J. Suppl. Ser.* **211**, 4 (2014). <https://doi.org/10.1088/0067-0049/211/1/4>
 34. Gerstenkorn, S., Luc, P.: *Atlas du Spectre d'Absorption de la Molécule d'Iode entre 14 800–20 000 cm⁻¹*. Editions du CNRS, Paris (1978)
 35. Kato, H., Kasahara, S., Misono, M., Maasaki, B.: *Doppler-Free High Resolution Spectral Atlas of Iodine Molecule 15 000 to 19 000 cm⁻¹*. Japan Society for the Promotion of Science, Tokyo (2000)
 36. Knöckel, H., Bodermann, B., Tiemann, E.: *Eur. Phys. J. D* **28**, 199 (2004). <https://doi.org/10.1140/epjd/e2003-00313-4>
 37. Salami, H., Ross, A.J.: *J. Mol. Spectrosc.* **233**, 157 (2005). <https://doi.org/10.1016/j.jms.2005.06.002>
 38. Kaufman, V., Edlén, B.: *J. Phys. Chem. Ref. Data* **3**, 825 (1974). <https://doi.org/10.1063/1.3253149>
 39. Nave, G., Johansson, S., Learner, R.C.M., Thorne, A.P., Brault, J.W.: *Astrophys. J. Suppl. Ser.* **94**, 221 (1994). and references therein <https://doi.org/10.1086/192079>
 40. Nave, G., Johansson, S.: *Astrophys. J. Suppl. Ser.* **204**, 1 (2013). <https://doi.org/10.1088/0067-0049/204/1/1>
 41. Sansonetti, J.E., Reader, J., Sansonetti, C.J., Acquista, N.: *Atlas of the Spectrum of a Platinum/Neon Hollow-Cathode Lamp in the Region 1130–4330 Å*. *J. Res. Natl. Inst. Stand. Technol.* **97**, 1–212 (1992). <https://doi.org/10.6028/jres.097.002>; online database available at <https://www.nist.gov/pml/ultraviolet-spectrum-platinum-lamp>
 42. Nave, G., Sansonetti, C.J.: *J. Opt. Soc. Am. B* **21**, 442 (2004). <https://doi.org/10.1364/JOSAB.21.000442>
 43. Stahler, S.W., Palla, F.: *The Formation of Stars*. Wiley-VCH, Weinheim (2004)
 44. Sobel'man, I.I.: *Introduction to the Theory of Atomic Spectra*. Pergamon Press, New York (1972)
 45. Cox, A.N. (ed.): *Allen's Astrophysical Quantities*, 4th edn. AIP Press, Springer, New York (2000)
 46. Weiss, A.W.: *J. Quant. Spectrosc. Radiat. Transf.* **18**, 481 (1977). [https://doi.org/10.1016/0022-4073\(77\)90046-2](https://doi.org/10.1016/0022-4073(77)90046-2)
 47. Wiese, W.L.: *Phys. Scr.* **T65**, 188 (1996). <https://doi.org/10.1088/0031-8949/1996/T65/028>
 48. Kramida, A.: *Fusion Sci. Technol.* **63**, 313 (2013). <https://doi.org/10.13182/FST13-A16437>
 49. Wiese, W.L., Fuhr, J.R.: *J. Phys. Chem. Ref. Data* **38**, 565 (2009). <https://doi.org/10.1063/1.3077727>
 50. Fuhr, J.R., Wiese, W.L.: *J. Phys. Chem. Ref. Data* **39**, 013101 (2010). <https://doi.org/10.1063/1.3286088>
 51. Kunze, H.-J.: *Introduction to Plasma Spectroscopy*. Springer, New York (2009)
 52. Griem, H.R.: *Spectral Line Broadening by Plasmas*. Academic Press, New York (1974)
 53. Roberts, J.R., Voigt, P.A.: *J. Res. Natl. Bur. Stand.* **75A**, 291 (1971). <https://doi.org/10.6028/jres.075A.028>
 54. Sobelman, I.I.: *Atomic Spectra and Radiative Transitions*, 2nd edn. Springer, Berlin, Heidelberg (1992)
 55. Schlüter, D.: *Z. Phys.* **210**, 80 (1968). <https://doi.org/10.1007/BF01379872>
 56. Hofsaess, D.: *J. Quant. Spectrosc. Radiat. Transf.* **19**, 339 (1978). [https://doi.org/10.1016/0022-4073\(78\)90068-7](https://doi.org/10.1016/0022-4073(78)90068-7)
 57. Wilbers, A.T.M., Kroesen, G.M.W., Timmermans, C.J., Schram, D.C.: *J. Quant. Spectrosc. Radiat. Transf.* **45**, 1 (1991). [https://doi.org/10.1016/0022-4073\(91\)90076-3](https://doi.org/10.1016/0022-4073(91)90076-3)
 58. Sukhorukov, V.L., Petrov, I.D., Schäfer, M., Merkt, F., Ruf, M.-W., Hotop, H.: *J. Phys. B* **45**, 092001 (2012). <https://doi.org/10.1088/0953-4075/45/9/092001>
 59. Ralchenko, Y., Stambulchik, E.: *Databases for Atomic and Plasma Physics* (2018). Available at <https://doi.org/10.34933/wis.000400>
 60. VAMDC Consortium: <http://www.vamdc.org>



William C. Martin William C. Martin's research included the measurement and energy-level analysis of atomic spectra. He also published a number of critical compilations of atomic spectroscopic data, including a large volume for the rare-earth elements. As a Scientist Emeritus at NIST, Dr. Martin continued to work on internet-accessible atomic spectra databases. He passed away in 2013.



Wolfgang Wiese Wolfgang Wiese is a physicist with extensive research background in atomic spectroscopy and in the critical tabulation of atomic reference data. He has worked at the National Institute of Standards and Technology for more than 40 years and has led the Atomic Physics Division from 1978 to 2004. He has authored 6 data volumes on Atomic Transition Probabilities, 15 book chapters and about 225 shorter research papers.



Alexander Kramida Alexander Kramida received his PhD from the Moscow Institute of Physics and Technology in 1981. He worked at the Institute for Spectroscopy of the Russian Academy of Sciences. Since 2003, he works at the National Institute of Standards and Technology, USA on analysis of atomic spectra and development of databases and tools for research in atomic and plasma physics.



Gordon W. F. Drake

Contents

12.1	Introduction	199
12.2	The Three-Body Schrödinger Equation	199
12.2.1	Formal Mathematical Properties	200
12.3	Computational Methods	200
12.3.1	Variational Methods	200
12.3.2	Construction of Basis Sets	201
12.3.3	Calculation of Matrix Elements	202
12.3.4	Other Computational Methods	204
12.4	Variational Eigenvalues	205
12.4.1	Expectation Values of Operators and Sum Rules	205
12.5	Total Energies	205
12.5.1	Quantum Defect Extrapolations	210
12.5.2	Asymptotic Expansions	210
12.6	Radiative Transitions	213
12.6.1	Basic Formulation	213
12.6.2	Oscillator Strength Table	215
12.7	Future Perspectives	215
	References	216

Abstract

Exact analytic solutions to the Schrödinger equation are known only for hydrogen and other equivalent two-body systems (Chap. 9). However, very high precision approximations are now available for helium and other three-body systems that are essentially exact for all practical purposes. This chapter summarizes the computational methods and tabulates numerical results for the ground state and several excited states up to $n = 10$ and $L = 7$. General formulas are presented for the evaluation of matrix elements in Hylleraas coordinates. Relativistic and quantum electrodynamic effects are included, along with quantum defect extrapolations to states of higher n and

asymptotic expansions to states of higher angular momentum L . Radiative transitions are discussed and oscillator strengths tabulated for a wide variety of transitions.

Keywords

helium · variational methods · Hylleraas coordinates · energies · relativistic and quantum electrodynamic corrections · asymptotic expansions · quantum defects · radiative transitions · oscillator strengths

12.1 Introduction

Exact analytic solutions to the Schrödinger equation are known only for atomic hydrogen and other equivalent two-body systems (Chap. 9). However, very high precision approximations are now available for helium, which are essentially exact for all practical purposes. This chapter summarizes the computational methods and tabulates numerical results for the ground state and several singly excited states. Similar methods can be applied to other three-body problems.

12.2 The Three-Body Schrödinger Equation

The Schrödinger equation for a three-body system consisting of a nucleus of charge Ze , mass M , and two electrons of charge $-e$ and mass m_e is

$$\left[\frac{1}{2M} P_N^2 + \frac{1}{2m_e} \sum_{i=1}^2 P_i^2 + V(\mathbf{R}_N, \mathbf{R}_i) \right] \Psi = E\Psi, \quad (12.1)$$

where $\mathbf{P}_i = (\hbar/i)\nabla_i$ and

$$V(\mathbf{R}_N, \mathbf{R}_i) = -\frac{Ze^2}{|\mathbf{R}_N - \mathbf{R}_1|} - \frac{Ze^2}{|\mathbf{R}_N - \mathbf{R}_2|} + \frac{e^2}{|\mathbf{R}_1 - \mathbf{R}_2|} \quad (12.2)$$

G. W. F. Drake (✉)
Dept. of Physics, University of Windsor
N9B 3P4 Windsor, ON, Canada
e-mail: gdrake@uwindsor.ca

depends only on the relative particle separations. Since the center of mass (c.m.) is then an ignorable coordinate, it can be eliminated by defining the relative particle coordinates

$$\mathbf{r}_i = \mathbf{R}_i - \mathbf{R}_N$$

to obtain

$$\left[\frac{1}{2\mu} \sum_{i=1}^2 \mathbf{p}_i^2 + \frac{1}{M} \mathbf{p}_1 \cdot \mathbf{p}_2 + V(\mathbf{r}_1, \mathbf{r}_2) \right] \Psi = E \Psi, \quad (12.3)$$

where $\mu = m_e M / (m_e + M)$ is the electron reduced mass, and the term $H_{\text{mp}} = \mathbf{p}_1 \cdot \mathbf{p}_2 / M$ is called the mass polarization operator. For computational purposes, it is usual to measure distance in units of $a_\mu = (m_e / \mu) a_0$ and energies in units of $e^2 / a_\mu = 2(\mu / m_e) R_\infty$, so that Eq. (12.3) assumes the dimensionless form

$$\left[-\frac{1}{2} \sum_{i=1}^2 \nabla_{\rho_i}^2 - \frac{\mu}{M} \nabla_{\rho_1} \cdot \nabla_{\rho_2} + V(\rho_1, \rho_2) \right] \Psi = \varepsilon \Psi, \quad (12.4)$$

where $\rho_i = \mathbf{r}_i / a_\mu$, $\varepsilon = E / (e^2 / a_\mu)$, and

$$V(\rho_1, \rho_2) = -\frac{Z}{\rho_1} - \frac{Z}{\rho_2} + \frac{1}{|\rho_1 - \rho_2|}. \quad (12.5)$$

The limit $\mu / M \rightarrow 0$ defines the infinite nuclear mass problem with eigenvalue ε_0 and eigenfunction Ψ_0 . If the mass polarization term is treated as a small perturbation, then the total energy assumes the form

$$E = \left[\varepsilon_0 + \frac{\mu}{M} \varepsilon_1 + \left(\frac{\mu}{M} \right)^2 \varepsilon_2 + \dots \right] \frac{\mu}{m_e} \frac{e^2}{a_0}, \quad (12.6)$$

where $\varepsilon_1 = -\langle \Psi_0 | \nabla_{\rho_1} \cdot \nabla_{\rho_2} | \Psi_0 \rangle$ determines the first-order specific mass shift, and ε_2 is the second-order coefficient. The common $(\mu / m_e) \varepsilon_0$ mass scaling of all eigenvalues determines the normal mass shift. Since $\mu / m = 1 - \mu / M$, the shift is $-(\mu / M) \varepsilon_0$.

12.2.1 Formal Mathematical Properties

Two-particle coalescences. The exact nonrelativistic wave function for any many-body system contains discontinuities or cusps in the spherically averaged radial derivative with respect to r_{ij} as $r_{ij} \rightarrow 0$, where $r_{ij} = |\mathbf{r}_i - \mathbf{r}_j|$ is any interparticle coordinate. If the masses and charges are m_i and q_i , respectively, then the discontinuities are given by the Kato cusp condition [1]

$$\hbar^2 \left(\frac{\partial \bar{\Psi}}{\partial r_{ij}} \right)_{r_{ij}=0} = \mu_{ij} q_i q_j \Psi(r_{ij} = 0), \quad (12.7)$$

where $\mu_{ij} = m_i m_j / (m_i + m_j)$, and $\bar{\Psi}$ denotes the wave function averaged over a sphere centered at $r_{ij} = 0$. If Ψ vanishes at $r_{ij} = 0$, then its leading dependence on r_{ij} is of the form $r_{ij}^l Y_{lm}(\mathbf{r}_{ij})$, for some integer $l > 0$ [2]. Equation (12.7) applies to any Coulombic system. The electron–nucleus cusp in the wave functions for hydrogen provides a simple example.

Three-particle coalescences. Three-particle coalescences are described by the Fock expansion [3], as recently discussed by Myers et al. [4]. For the S -states of He-like ions, the expansion has the form

$$\Psi(\mathbf{r}_1, \mathbf{r}_2) = \sum_{j=0}^{\infty} \sum_{k=0}^{[j/2]} \mathcal{R}^j (\ln \mathcal{R})^k \phi_{j,k}, \quad (12.8)$$

where $[]$ denotes “greatest integer in”, and $\mathcal{R} = (r_1^2 + r_2^2)^{1/2}$ is the hyperradius. The leading coefficients are

$$\begin{aligned} \phi_{0,0} &= 1, \\ \phi_{1,0} &= -(Zr_1 + Zr_2 - \frac{1}{2}r_{12}) / \mathcal{R}, \\ \phi_{2,1} &= -2Z \left(\frac{\pi - 2}{3\pi} \right) \frac{\mathbf{r}_1 \cdot \mathbf{r}_2}{\mathcal{R}^2}. \end{aligned} \quad (12.9)$$

The next term $\phi_{2,0}$ is known in terms of a lengthy expression [4, 5], but higher terms have not yet been obtained in closed form. The Fock expansion has been proved convergent for all $\mathcal{R} < \frac{1}{2}$ [6] and extended to pointwise convergence for all \mathcal{R} [7, 8].

Asymptotic form. The long-range behavior of many-electron wave functions has been studied from several points of view [9–11]. The basic result of [12] is that at large distances, the one-electron density behaves as

$$\rho^{1/2}(r) \approx r^{Z^*/t-1} e^{-tr}, \quad (12.10)$$

where $t = (2I_1)^{1/2}$, I_1 is the first ionization potential (in a.u.), and $Z^* = Z - N + 1$ is the screened nuclear charge seen by the outer most electron. For hydrogenic systems with principal quantum number n , $I_1 = (Z^*)^2 / 2n^2$.

12.3 Computational Methods

12.3.1 Variational Methods

Most high-precision calculations for the bound states of three-body systems such as helium are based on the Rayleigh–Ritz variational principle. For any normalizable trial function Ψ_{tr} , the quantity

$$E_{\text{tr}} = \frac{\langle \Psi_{\text{tr}} | H | \Psi_{\text{tr}} \rangle}{\langle \Psi_{\text{tr}} | \Psi_{\text{tr}} \rangle} \quad (12.11)$$

satisfies the inequality $E_{\text{tr}} \geq E_1$, where E_1 is the true ground-state energy. Thus, E_{tr} is an upper bound to E_1 . The inequality is easily proved by expanding Ψ_{tr} in the complete basis set of eigenfunctions $\Psi_1, \Psi_2, \Psi_3, \dots$ of H with eigenvalues $E_1 < E_2 < E_3 < \dots$, so that

$$\Psi_{\text{tr}} = \sum_{i=1}^{\infty} c_i \Psi_i, \quad (12.12)$$

where the c_i are expansion coefficients. This can always be done in principle, even though the exact Ψ_i are not actually known. If Ψ_{tr} is normalized so that $\langle \Psi_{\text{tr}} | \Psi_{\text{tr}} \rangle = 1$, then $\sum_{i=1}^{\infty} |c_i|^2 = 1$, and

$$\begin{aligned} E_{\text{tr}} &= |c_1|^2 E_1 + |c_2|^2 E_2 + |c_3|^2 E_3 + \dots \\ &= E_1 + |c_2|^2 (E_2 - E_1) + |c_3|^2 (E_3 - E_1) + \dots \\ &\geq E_1, \end{aligned} \quad (12.13)$$

which proves the theorem.

The basic idea of variational calculations, then, is to write Ψ_{tr} in some arbitrarily chosen mathematical form with variational parameters (subject to normalizability and boundary conditions at the origin and infinity) and then adjust the parameters to obtain the minimum value of E_{tr} .

The minimization problem for the case of *linear* variational coefficients can be solved algebraically. For example, let

$$\chi_p(\alpha, \beta) = r_1^i r_2^j r_{12}^k e^{-\alpha r_1 - \beta r_2} \quad (12.14)$$

denote the members of a basis set, where p is an index labeling distinct triplets of nonnegative integer values for the powers $\{i, j, k\}$, and α, β are (for the moment) fixed constants determining the distance scale.

If Ψ_{tr} is expanded in the form

$$\Psi_{\text{tr}} = \sum_{p=1}^N c_p \chi_p(\alpha, \beta), \quad (12.15)$$

then the solution to the system of equations $\partial E_{\text{tr}} / \partial c_p = 0$, $p = 1, \dots, N$, is exactly equivalent to solving the N -dimensional generalized eigenvalue problem

$$\mathbf{H}\mathbf{c} = \lambda \mathbf{O}\mathbf{c}, \quad (12.16)$$

where \mathbf{c} is a column vector of coefficients c_p , and \mathbf{H} and \mathbf{O} have matrix elements $H_{pq} = \langle \chi_p | H | \chi_q \rangle$ and $O_{pq} = \langle \chi_p | \chi_q \rangle$. There are N eigenvalues $\lambda_1, \lambda_2, \dots, \lambda_N$, of which the lowest is an upper bound to E_1 .

Extension to excited states. By the Hylleraas–Undheim–MacDonald (HUM) theorem [13, 14], the remaining eigenvalues $\lambda_2, \lambda_3, \dots$ are also upper bounds to the exact energies E_2, E_3, \dots , provided that the spectrum is bounded from below. The HUM theorem is a consequence of the matrix

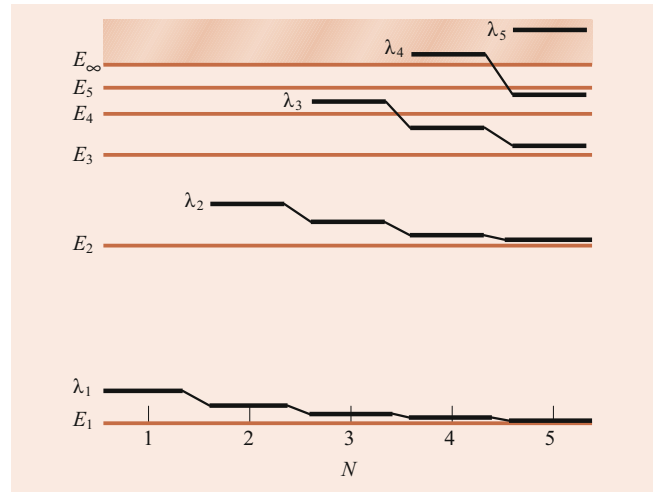


Fig. 12.1 Diagram illustrating the Hylleraas–Undheim–MacDonald Theorem. The λ_p , $p = 1, \dots, N$ are the variational eigenvalues for an N -dimensional basis set, and the E_i are the exact eigenvalues of H . The highest λ_p lie in the continuous spectrum of H

eigenvalue interleaving theorem, which states that as the dimensions of \mathbf{H} and \mathbf{O} are progressively increased by adding an extra row and column, the N old eigenvalues λ_p fall between the $N + 1$ new ones. Consequently, as illustrated in Fig. 12.1, all eigenvalues numbered from the bottom up must move inexorably downward as N is increased. Since the exact spectrum of bound states is obtained in the limit $N \rightarrow \infty$, no λ_p can cross the corresponding exact E_p on its way down. Thus, $\lambda_p \geq E_p$ for every finite N .

12.3.2 Construction of Basis Sets

Since the Schrödinger equation (12.4) is not separable in the electron coordinates, basis sets which incorporate the $r_{12} = |\mathbf{r}_1 - \mathbf{r}_2|$ interelectron coordinate are most efficient. The necessity for r_{12} terms also follows from the Fock expansion in Eq. (12.8). A basis set constructed from terms of the form Eq. (12.14) is called a Hylleraas basis set [15]. (The basis set is often expressed in terms of the equivalent variables $s = r_1 + r_2$, $t = r_1 - r_2$, $u = r_{12}$.)

With $\chi_p(\alpha, \beta)$ defined as in Eq. (12.14), the general form for a state of total angular momentum L is

$$\begin{aligned} \Psi_{\text{tr}} &= \sum_{l_1=0}^{[L/2]} \sum_p C_{p,l_1} \chi_p(\alpha, \beta) r_1^{l_1} r_2^{l_2} \mathcal{Y}_{l_1 L-l_1 L}^M(\hat{\mathbf{r}}_1, \hat{\mathbf{r}}_2) \\ &\quad \pm \text{exchange}, \end{aligned} \quad (12.17)$$

where

$$\begin{aligned} \mathcal{Y}_{l_1 l_2 L}^M(\hat{\mathbf{r}}_1, \hat{\mathbf{r}}_2) &= \sum_{m_1, m_2} Y_{l_1 m_1}(\hat{\mathbf{r}}_1) Y_{l_2 m_2}(\hat{\mathbf{r}}_2) \\ &\quad \times \langle l_1 l_2 m_1 m_2 | LM \rangle \end{aligned} \quad (12.18)$$

is the vector coupled product of angular momenta l_1, l_2 for the two electrons. The sum over p in Eq. (12.17) typically includes all terms in Eq. (12.14) with $i + j + k \leq \Omega$, where Ω is an integer determining a so-called *Pekeris shell* of terms, and the exchange term denotes the interchange of r_1 and r_2 with (+) for singlet states and (−) for triplet states. Convergence is studied by progressively increasing Ω . The number of terms is

$$N = \frac{1}{6}(\Omega + 1)(\Omega + 2)(\Omega + 3).$$

Basis sets of this type were used by many authors, culminating in the extensive high-precision calculations of Pekeris and coworkers [16] for low-lying states, using as many as 1078 terms. Their accuracy is not easily surpassed because of the rapid growth of N with Ω and because of numerical linear dependence in the basis set for large Ω . Recently, their accuracy has been surpassed by two principal methods. The first explicitly includes powers of logarithmic and half-integral terms in χ_p , as suggested by the Fock expansion [17–19]. The most accurate calculation to date is that of Schwartz [20] who obtained 35 significant figures for the nonrelativistic ground-state energy of helium. This is particularly effective for S -states. The second focuses directly on the multiple distance scales required for an accurate representation of the wave function by writing the trial function in terms of the double basis set [21]

$$\begin{aligned} \Psi_{\text{tr}} = & \sum_{l_1=0}^{[L/2]} \sum_p \left[C_{p,l_1}^{(1)} \chi_p(\alpha_1, \beta_1) + C_{p,l_1}^{(2)} \chi_p(\alpha_2, \beta_2) \right] \\ & \times r_1^{l_1} r_2^{l_2} \mathcal{Y}_{l_1 l_2 L}(\mathbf{r}_1, \mathbf{r}_2) \pm \text{exchange}, \end{aligned} \quad (12.19)$$

where each $\chi_p(\alpha, \beta)$ is of the form of Eq. (12.14) but with different values for the distance scales α_1, β_1 and α_2, β_2 in the two sets of terms. They are determined by a complete minimization of E_{tr} with respect to all four parameters, producing a natural division of the basis set into an asymptotic sector and a close-range correlation sector. The method produces a dramatic improvement in accuracy for higher-lying Rydberg states (where variational methods typically deteriorate rapidly in accuracy) and is also effective for low-lying S -states [22, 23]. Nonrelativistic energies accurate to 1 part in 10^{16} are obtainable with modest computing resources.

Another version of the variational method is the quasirandom (or stochastic) method in which nonlinear exponential parameters for all three of r_1, r_2 , and r_{12} are chosen at random from certain specified intervals [24, 25]. The method is remarkably accurate and efficient for low-lying states but subject to severe roundoff error.

12.3.3 Calculation of Matrix Elements

The three-body problem has the unique advantage that the full six-dimensional volume element (in the c.m. frame) can

be transformed to the product of a three-dimensional angular integral (ang) and a three-dimensional radial integral (rad) over r_1, r_2 , and r_{12} . The transformation is

$$\begin{aligned} \iint d\mathbf{r}_1 d\mathbf{r}_2 = & \int_0^{2\pi} d\phi \int_0^{2\pi} d\varphi_1 \int_0^{\pi} \sin\theta_1 d\theta_1 \\ & \times \int_0^{\infty} r_1 dr_1 \int_0^{\infty} r_2 dr_2 \int_{|r_1-r_2|}^{r_1+r_2} r_{12} dr_{12}, \end{aligned} \quad (12.20)$$

where θ_1, φ_1 are the polar angles of \mathbf{r}_1 , and ϕ is the angle of rotation of the triangle formed by $\mathbf{r}_1, \mathbf{r}_2$, and \mathbf{r}_{12} about the \mathbf{r}_1 direction. The polar angles θ_2, φ_2 are then dependent variables. The basic angular integral is

$$\begin{aligned} & \langle Y_{l_1 m_1}^*(\theta_1, \varphi_1) Y_{l_2 m_2}(\theta_2, \varphi_2) \rangle_{\text{ang}} \\ & = 2\pi \delta_{l_1 l_2} \delta_{m_1 m_2} P_{l_1}(\cos\theta), \end{aligned} \quad (12.21)$$

where $\cos\theta \equiv \hat{\mathbf{r}}_1 \cdot \hat{\mathbf{r}}_2$ denotes the radial function

$$\cos\theta = \frac{r_1^2 + r_2^2 - r_{12}^2}{2r_1 r_2}, \quad (12.22)$$

and $P_l(\cos\theta)$ is a Legendre polynomial. The angular integral over vector-coupled spherical harmonics is [26]

$$\begin{aligned} & \langle \mathcal{Y}_{l_1' l_2' L'}^{M'*}(\hat{\mathbf{r}}_1, \hat{\mathbf{r}}_2) \mathcal{Y}_{l_1 l_2 L}^M(\hat{\mathbf{r}}_1, \hat{\mathbf{r}}_2) \rangle_{\text{ang}} \\ & = \delta_{L'L'} \delta_{M,M'} \sum_{\Lambda} C_{\Lambda} P_{\Lambda}(\cos\theta), \end{aligned} \quad (12.23)$$

where

$$\begin{aligned} C_{\Lambda} = & \frac{1}{2} [(2l_1 + 1)(2l_1' + 1)(2l_2 + 1)(2l_2' + 1)]^{1/2} \\ & \times (-1)^{L+\Lambda} (2\Lambda + 1) \\ & \times \begin{pmatrix} l_1' & l_1 & \Lambda \\ 0 & 0 & 0 \end{pmatrix} \begin{pmatrix} l_2' & l_2 & \Lambda \\ 0 & 0 & 0 \end{pmatrix} \begin{Bmatrix} L & l_1 & l_2 \\ \Lambda & l_2' & l_1' \end{Bmatrix}, \end{aligned} \quad (12.24)$$

and the sum over Λ includes all nonvanishing terms. This can be extended to general matrix elements of tensor operators by further vector coupling [26].

Radial integrals. Table 12.1 lists formulas for the radial integrals arising from matrix elements of H , as well as those from the Breit interaction (Sect. 22.1.3). Although they can all be written in closed form, some have been expressed as infinite series in order to achieve good numerical stability. The exceptions are formulas 5 and 10 in the table, which became unstable as $\alpha \rightarrow \beta$. More elaborate techniques for these are discussed in [27]. Other cases can be derived by

Table 12.1 Formulas for the radial integrals $I_0(a, b, c; \alpha, \beta) = \langle r_1^a r_2^b r_{12}^c e^{-\alpha r_1 - \beta r_2} \rangle_{\text{rad}}$ and $I_0^{\log}(a, b, c; \alpha, \beta) = \langle r_1^a r_2^b r_{12}^c \ln r_{12} e^{-\alpha r_1 - \beta r_2} \rangle_{\text{rad}}$. $\psi(n) = -\gamma + \sum_{k=1}^{n-1} k^{-1}$ is the digamma function, ${}_2F_1(a, b; c; z)$ is the hypergeometric function, and $s = a + b + c + 5$. Except as noted, the formulas apply for $a \geq -1, b \geq -1, c \geq -1$

1.	$I_0(-2, -2, -1; \alpha, \beta) = \frac{2}{\alpha} \ln\left(\frac{\alpha + \beta}{\beta}\right) + \frac{2}{\beta} \ln\left(\frac{\alpha + \beta}{\alpha}\right)$
2.	$I_0(a, b, c; \alpha, \beta) = \frac{2}{c+2} \sum_{i=0}^{\lfloor (c+1)/2 \rfloor} \binom{c+2}{2i+1} [F_{a+2i+2, b+c-2i+2}(\alpha, \beta) + F_{b+2i+2, a+c-2i+2}(\beta, \alpha)] \quad (c \geq -1, s \geq 0)$ where $F_{p,q}(\alpha, \beta) = \begin{cases} \frac{q!}{(\alpha + \beta)^{p+1} \beta^{q+1}} \sum_{j=0}^q \frac{(p+j)!}{j!} \left(\frac{\beta}{\alpha + \beta}\right)^j & q \geq 0, p \geq 0 \\ \frac{p!}{\alpha^{p+q+2}} \sum_{j=p+q+1}^{\infty} \frac{j!}{(j-q)!} \left(\frac{\alpha}{\alpha + \beta}\right)^{j+1} & q < 0, p \geq 0 \\ 0^a & p < 0 \end{cases}$
3.	$I_0(a, b, c; \alpha, \alpha) = \frac{2^{c+3} s!}{(c+2)(2\alpha)^{s+1}} \left\{ \sum_{j=0}^{a+1} \binom{a+1}{j} (b+1)! \left[\frac{j!}{(j+b+2)!} - \frac{(j+c+2)!}{(j+b+c+4)!} \right] + (a \leftrightarrow b) \right\}$
4.	$I_0(-1, -1, -2; \alpha, \beta) = \frac{2 \ln(\alpha/\beta)}{\alpha^2 - \beta^2}$
5.	$I_0(a, b, -2; \alpha, \beta) = \frac{(a+1)!}{\alpha^{a+2}} \sum_{j=0}^{a+1} \frac{(b+1+j)!}{j!} \left[\frac{\alpha^j}{(\alpha + \beta)^{b+2+j}} - \frac{(-\alpha)^j}{(\beta - \alpha)^{b+2+j}} \right] \times \left[\ln\left(\frac{2\alpha}{\alpha + \beta}\right) - \psi(a+2-j) + \psi(1) \right] + (a \leftrightarrow b)$
6.	$I_0(a, b, -2; \alpha, \alpha) = \frac{2s!(a+1)!(b+1)!}{(2\alpha)^{s+1}} \left[\sum_{j=0}^{a+1} \frac{\psi(s+1-j) - \psi(a+2-j)}{j!(s-j)!} + (a \leftrightarrow b) \right]$
7.	$I_0(-1, -1, -3; \alpha, \beta) = \frac{2(\beta \ln \beta - \alpha \ln \alpha)}{\alpha^2 - \beta^2} + \frac{2[\psi(2) - \ln \varepsilon]^b}{\alpha + \beta}$
8.	$I_0(a, b, -3; \alpha, \beta) = \left[\frac{(a+1)!}{\alpha^{a+1}(\alpha + \beta)^{b+2}} \sum_{j=0}^a \frac{(b+1+j)!}{j!(a+1-j)} \left(\frac{\alpha}{\alpha + \beta}\right)^j + (a \leftrightarrow b) \right] - \frac{s! [\ln(\alpha\beta\varepsilon^2) - 2\psi(2)]}{(\alpha + \beta)^{s+1}} - \frac{(a+1)!(b+1)!}{(s+1)\alpha^{a+2}\beta^{b+1}} {}_2F_1\left(a+2, 1; s+2; \frac{\alpha-\beta}{\alpha}\right), \quad a \geq -1, b \geq -1$
9.	$I_0^{\log}(-1, -1, c; \alpha, \beta) = \frac{2(c+1)!}{\alpha^2 - \beta^2} \left[\frac{\ln \alpha - \psi(c+2)}{\alpha^{c+2}} - \frac{\ln \beta - \psi(c+2)}{\beta^{c+2}} \right]$
10.	$I_0^{\log}(a, b, c; \alpha, \beta) = \frac{(a+1)!}{(c+2)\alpha^{a+c+4}} \sum_{j=0}^{a+1} \frac{(b+1+j)!(a+c+3-j)!}{j!(a+1-j)!} \left[\frac{\alpha^j}{(\alpha + \beta)^{b+2+j}} - \frac{(-\alpha)^j}{(\beta - \alpha)^{b+2+j}} \right] \times \left[-\psi(a+c+4-j) + \frac{1}{c+2} + \ln \alpha \right] + (a \leftrightarrow b)$
11.	$I_0^{\log}(a, b, c; \alpha, \alpha) = \frac{2^{c+3} s!(b+1)!}{(c+2)(2\alpha)^{s+1}} \sum_{j=0}^{a+1} \binom{a+1}{j} \left\{ \left[\frac{j!}{(j+b+2)!} - \frac{(j+c+2)!}{(j+b+c+4)!} \right] \left[\psi(s+1) - \ln \alpha - \frac{1}{c+2} \right] + \frac{(a+c+3-j)!}{(s+1-j)!} [\psi(s+1-j) - \psi(a+c+4-j)] \right\} + (a \leftrightarrow b)$

^a Terms with $p < 0$ represent divergent parts which cancel from convergent differences between integrals with the same α and β
^b ε is the radius of an infinitesimal sphere about $r_{12} = 0$ which is omitted from the range of integration

use of the formula

$$\langle r_1^{-1} r_2^{-1} f(r_{12}) e^{-\alpha r_1 - \beta r_2} \rangle_{\text{rad}} = \frac{2}{\alpha^2 - \beta^2} \int_0^\infty (e^{-\beta r} - e^{-\alpha r}) r f(r) dr, \quad (12.25)$$

and then differentiating or integrating with respect to α or β to raise or lower the powers of r_1 and r_2 .

Total integral. The angular integral in Eq. (12.23) combined with the radial integrals from Table 12.1 yields the total integral

$$\langle \mathcal{Y}_{l_1 l_2}^{M*} \mathcal{Y}_{l_1' l_2'}^M f(a, b, c; \alpha, \beta) \rangle = \sum_{\Lambda} C_{\Lambda} I_{\Lambda}(a, b, c; \alpha, \beta), \quad (12.26)$$

where

$$I_\Lambda(a, b, c; \alpha, \beta) = \langle f(a, b, c; \alpha, \beta) P_\Lambda(\cos \theta) \rangle_{\text{rad}},$$

$$f(a, b, c; \alpha, \beta) = r_1^a r_2^b r_{12}^c e^{-\alpha r_1 - \beta r_2}.$$

Starting from I_0 and I_1 , the general I_Λ can be efficiently calculated from the recursion relations [26]

$$I_{\Lambda+1}(a, b, c; \alpha, \beta) = \frac{2\Lambda + 1}{c + 2} I_\Lambda(a - 1, b - 1, c + 2; \alpha, \beta) + I_{\Lambda-1}(a, b, c; \alpha, \beta), \quad c \neq -2 \quad (12.27)$$

$$I_{\Lambda+1}(a, b, -2; \alpha, \beta) = (2\Lambda + 1) I_\Lambda^{\text{log}}(a - 1, b - 1, 0; \alpha, \beta) + I_{\Lambda-1}(a, b, -2; \alpha, \beta), \quad c = -2, \quad (12.28)$$

where

$$I_\Lambda^{\text{log}}(a, b, c; \alpha, \beta) = \langle f(a, b, c; \alpha, \beta) \ln r_{12} P_\Lambda(\cos \theta) \rangle_{\text{rad}}.$$

The I_Λ^{log} integrals follow the recursion relation

$$I_{\Lambda+1}^{\text{log}}(a, b, c; \alpha, \beta) = \frac{(2\Lambda + 1)}{c + 2} \left[I_\Lambda^{\text{log}}(a - 1, b - 1, c + 2; \alpha, \beta) - \frac{1}{c + 2} I_\Lambda(a - 1, b - 1, c + 2; \alpha, \beta) \right] + I_{\Lambda-1}^{\text{log}}(a, b, c; \alpha, \beta). \quad (12.29)$$

Hamiltonian matrix elements. The general form of the Laplacian operator in terms of r_1, r_2, r_{12} variables is

$$\nabla_1^2 = \frac{1}{r_1^2} \frac{\partial}{\partial r_1} \left(r_1^2 \frac{\partial}{\partial r_1} \right) + \frac{1}{r^2} \frac{\partial}{\partial r} \left(r^2 \frac{\partial}{\partial r} \right) - \frac{l_1^2}{r_1^2} + \frac{2(r_1 - r_2 \cos \theta)}{r} \frac{\partial^2}{\partial r_1 \partial r} - 2(\nabla_1^Y \cdot \mathbf{r}_2) \frac{1}{r} \frac{\partial}{\partial r}, \quad (12.30)$$

and similarly for ∇_2^2 with subscripts 1 and 2 interchanged. The term ∇_1^Y is understood to act only on the $\mathcal{Y}_{l_1 l_2 L}^M(\hat{\mathbf{r}}_1, \hat{\mathbf{r}}_2)$ part of the wave function. This term in ∇_1^2 can be easily evaluated by means of the effective operator replacement

$$\langle \mathcal{Y}_{l_1' l_2' L'}^{M*} \nabla_1^Y \cdot \mathbf{r}_2 \mathcal{Y}_{l_1 l_2 L}^M \rangle_{\text{ang}} \frac{1}{r_{12}} \frac{\partial g(r_{12})}{\partial r_{12}} \rightarrow \frac{g(r_{12})}{2r_1 r_2} \sum_\Lambda \tilde{C}_\Lambda P_\Lambda(\cos \theta) \quad (12.31)$$

for the angular part of the total integral, where

$$\tilde{C}_\Lambda = [l_1'(l_1' + 1) - l_1(l_1 + 1) - \Lambda(\Lambda + 1)] C_\Lambda. \quad (12.32)$$

The replacement in Eq. (12.31) becomes an equality after radial integration with any function $g(r_{12})$ in the integrand. The matrix elements of H between arbitrary basis functions defined by

$$\chi = r_1^a r_2^b r_{12}^c e^{-\alpha r_1 - \beta r_2} \mathcal{Y}_{l_1 l_2 L}^M(\hat{\mathbf{r}}_1, \hat{\mathbf{r}}_2),$$

$$\chi' = r_1^{a'} r_2^{b'} r_{12}^{c'} e^{-\alpha' r_1 - \beta' r_2} \mathcal{Y}_{l_1' l_2' L}^M(\hat{\mathbf{r}}_1, \hat{\mathbf{r}}_2),$$

can then be written in the explicitly Hermitian form (for infinite nuclear mass)

$$\langle \chi' | H | \chi \rangle = \frac{1}{8} \sum_\Lambda C_\Lambda \sum_{i=0}^2 \left[A_i^{(1)} I_\Lambda(a_+ - i, b_+, c_+; \alpha_+, \beta_+) + A_i^{(2)} I_\Lambda(a_+, b_+ - i, c_+; \alpha_+, \beta_+) + A_i^{(3)} I_\Lambda(a_+, b_+, c_+ - i; \alpha_+, \beta_+) \right], \quad (12.33)$$

where $a_\pm = a \pm a'$, $\alpha_\pm = \alpha \pm \alpha'$ etc., and

$$A_0^{(1)} = -\alpha_+^2 - \alpha_-^2 + 2\alpha_- \alpha_+ (c_-/c_+),$$

$$A_1^{(1)} = 2\{\alpha_+(a_+ + 2) + \alpha_- a_- - [\alpha_+ a_- + \alpha_-(a_+ + 2)](c_-/c_+)\} - 8Z,$$

$$A_2^{(1)} = -a_+^2 - a_-^2 - 2a_+ + 2a_-(a_+ + 1)(c_-/c_+) + 2l_1(l_1 + 1)(1 - c_-/c_+) + 2l_1'(l_1' + 1)(1 + c_-/c_+),$$

$$A_0^{(3)} = 0, \quad A_1^{(3)} = 8,$$

$$A_2^{(3)} = 2(c_+^2 - c_-^2),$$

with $(c_-/c_+) = 0$ for $c_+ = 0$. The $A_i^{(2)}$ are defined similarly to $A_i^{(1)}$ with the replacements $a \rightarrow b$, $\alpha \rightarrow \beta$, $l_1 \rightarrow l_2$. The term $A_1^{(3)} = 8$ corresponds to the electron–electron repulsion term e^2/r in H , and $-8Z$ in $A_1^{(1)}$ is the electron–nucleus attraction term. The overlap integral is

$$\langle \chi' | \chi \rangle = \sum_\Lambda C_\Lambda I_\Lambda(a_+, b_+, c_+; \alpha_+, \beta_+). \quad (12.34)$$

12.3.4 Other Computational Methods

Although not yet at the same level of accuracy as variational methods, certain nonvariational methods, such as finite element methods [28], solutions to the Faddeev equations [29], and the correlated-function hyperspherical-harmonic method [30], have their own advantages of flexibility and/or generality. A characteristic feature of these methods is that they provide direct numerical solutions to the three-body problem, which, in principle, converge pointwise to the exact solution rather than depending upon a globally optimized solution. Other methods particularly suited to doubly-excited states are discussed in Chap. 26 and Sect. 22.7.3.

12.4 Variational Eigenvalues

High-precision variational eigenvalues are available for all states of helium up to $n = 10$ and $L = 7$ [22, 23]. The non-relativistic values of ε_0 , ε_1 and ε_2 [Eq. (12.6)] are listed in Tables 12.2 and 12.3. Values of ε_0 for some of the low-lying states are updated with more recent results by *Aznabaev et al.* [31] as noted in Table 12.2. The ε_0 are the eigenvalues for infinite nuclear mass, and ε_1 and ε_2 , together with Eq. (12.6), give the finite mass corrections for the isotopes ^3He and ^4He . The values of μ/M can be calculated from

$$\frac{\mu}{M} = \left[\frac{M_A}{5.485\,799\,090\,65(16) \times 10^{-4}} - N + 1 \right]^{-1}, \quad (12.35)$$

where M_A is the atomic mass (in amu; see [32] for a tabulation), and N is the number of electrons. (For high-precision work, the helium electronic binding energy of 8.48×10^{-8} amu should be added to M_A .) For ^4He , one can use directly the accurately known value of m_e/m_α to calculate $\mu/M = 1/(m_\alpha/m_e + 1)$. Values of μ/M for the first several isotopes are listed in Table 12.4, and the corresponding energy coefficients for the $1s^2\ ^1S$ ground state are given in Table 12.5. For the higher-lying S -states up to $n = 24$, high precision eigenvalues have been obtained by *Nakashima and Nakatsuji* [33] by their free iterative-complement-interaction-method.

12.4.1 Expectation Values of Operators and Sum Rules

Expectation values for various powers of the radial coordinates, together with operators appearing in the Breit interaction, are listed in Table 12.6 for the ground state of helium and He-like ions. Included are all terms required to calculate $\langle V^2 \rangle$, and the oscillator strength sum rules [34]

$$S(-1) = \frac{2}{3} \langle (\mathbf{r}_1 + \mathbf{r}_2)^2 \rangle, \quad (12.36a)$$

$$S(0) = 2, \quad (12.36b)$$

$$S(1) = -\frac{4}{3}(\varepsilon_0 - \varepsilon_1), \quad (12.36c)$$

$$S(2) = \frac{2\pi Z}{3} \langle \delta(\mathbf{r}_1) + \delta(\mathbf{r}_2) \rangle, \quad (12.36d)$$

where $S(k) = \sum_n [\varepsilon_0(n^1P) - \varepsilon_0(1^1S)]^k f_{0n}$, with energies in a.u., and f_{0n} is the $1^1S - n^1P$ oscillator strength (Sect. 12.6.1).

12.5 Total Energies

As discussed in Chaps. 22 and 28, relativistic and QED corrections must be added to the nonrelativistic eigenvalues of Sect. 12.4 before a meaningful comparison with measured

transition frequencies can be made. The corrections are discussed in detail in [22, 35].

Using the fine-structure constant $\alpha \simeq 1/137$ as an expansion parameter, the terms in order of decreasing size are:

1. Relativistic corrections of $O(\alpha^2)$.

$$\begin{aligned} H_{\text{rel}} &= H_{\text{NFS}} + H_{\text{FS}}, \\ H_{\text{NFS}} &= H_{\text{mass}} + H_{\text{D}} + H_{\text{SSC}} + H_{\text{oo}}, \\ H_{\text{FS}} &= H_{\text{so}} + H_{\text{soo}} + H_{\text{ss}}. \end{aligned}$$

The various nonfine-structure (NFS) and fine-structure (FS) terms are defined in Sect. 22.1. The off-diagonal matrix elements of H_{FS} mix states of different spin and cause a breakdown of LS -coupling.

2. Anomalous magnetic moment corrections of $O(\alpha^3)$.

The general FS matrix elements between states with spins S and S' due to the anomalous magnetic moment a_e are (Sect. 22.7.3)

$$\begin{aligned} \langle \gamma S | H_{\text{FS}}^{\text{anom}} | \gamma' S' \rangle &= 2a_e \langle \gamma S | H_{\text{so}} + \frac{2}{3} \delta_{S,S'} H_{\text{soo}} \\ &\quad + \left(1 + \frac{1}{2} a_e\right) H_{\text{ss}} | \gamma' S' \rangle, \end{aligned} \quad (12.37)$$

where $a_e = (g_e - 2)/2 = \alpha/(2\pi) - 0.328\,479\alpha^2 + \dots$.

3. QED corrections of $O(\alpha^3)$. The lowest order QED corrections (including NFS anomalous magnetic moment terms) can be written in the form $\Delta_{L,1} + \Delta_{L,2}$, where

$$\Delta E_{L,1} = \frac{4}{3} Z \alpha^3 \left[\ln(Z\alpha)^{-2} + \frac{19}{30} - \ln k_0 \right] \langle \delta(\mathbf{r}_1) + \delta(\mathbf{r}_2) \rangle \quad (12.38)$$

$$\Delta E_{L,2} = \alpha^3 \left[\frac{89}{15} + \frac{14}{3} \ln \alpha - \frac{20}{3} \mathbf{s}_1 \cdot \mathbf{s}_2 \right] \langle \delta(\mathbf{r}_{12}) \rangle - \frac{4}{3} \alpha^3 Q, \quad (12.39)$$

$\ln k_0$ is the two-electron Bethe logarithm defined by

$$\ln k_0 = \frac{\sum_i |\langle 0 | \mathbf{p}_1 + \mathbf{p}_2 | i \rangle|^2 (E_i - E_0) \ln |E_i - E_0|}{\sum_i |\langle 0 | \mathbf{p}_1 + \mathbf{p}_2 | i \rangle|^2 (E_i - E_0)} \quad (12.40)$$

summed over all intermediate states and Q is the matrix element defined by

$$Q = \frac{1}{4\pi} \lim_{\epsilon \rightarrow 0} \sum_{i>j} \langle r_{12}^{-3}(\epsilon) + 4\pi(\gamma + \ln \epsilon) \delta(\mathbf{r}_{12}) \rangle \quad (12.41)$$

where γ is Euler's constant, and ϵ is the radius of an infinitesimal sphere about $r_{12} = 0$ that is excluded from the range of integration (i.e. the principal value of the divergent integral). These two-electron QED corrections are known as the Araki-Sucher terms [36, 37].

For a highly excited $1snl$ state, $\Delta E_{L,2} \rightarrow 0$, $\langle \delta(\mathbf{r}_1) + \delta(\mathbf{r}_2) \rangle \rightarrow Z^3/\pi$, $\ln k_0 \rightarrow \ln k_0(1s) = 2.984\,128\,555$, and $\Delta E_{L,1}$ reduces to the Lamb shift of the $1s$ core state

Table 12.2 Nonrelativistic eigenvalue coefficients ε_0 and ε_1 for helium

State	$\varepsilon_0(n^1L)$	$\varepsilon_1(n^1L)$	$\varepsilon_0(n^3L)$	$\varepsilon_1(n^3L)$
1 S	-2.903 724 377 034 119 60 ^a	0.159 069 475 085 84		
2 S	-2.145 974 046 054 417 42 ^a	0.009 503 864 419 28	-2.175 229 378 236 791 31	0.007 442 130 706 04
2 P	-2.123 843 086 498 101 36 ^a	0.046 044 524 937(1)	-2.133 164 190 779 283 21 ^a	-0.064 572 425 024(4)
3 S	-2.061 271 989 740 908 65 ^a	0.002 630 567 097 7(1)	-2.068 689 067 472 457 19	0.001 896 211 617 81
3 P	-2.055 146 362 091 943 54 ^a	0.014 548 047 097(1)	-2.058 081 084 274 275 33 ^a	-0.018 369 001 636(2)
3 D	-2.055 620 732 852 246 49 ^a	-0.000 249 399 992 1(1)	-2.055 636 309 453 261 33 ^a	0.000 025 322 839(1)
4 S	-2.033 586 717 030 725 44 ^a	0.001 073 641 226 6(1)	-2.036 512 083 098 236 30 ^a	0.000 742 661 516 18
4 P	-2.031 069 650 450 240 71 ^a	0.006 254 923 554 3(1)	-2.032 324 354 296 630 33 ^a	-0.007 555 178 98(1)
4 D	-2.031 279 846 178 685 00 ^a	-0.000 129 175 188 7(8)	-2.031 288 847 501 795 54 ^a	0.000 029 442 651(2)
4 F	-2.031 255 144 381 748 61 ^a	-0.000 010 024 269 4(2)	-2.031 255 168 403 245 39 ^a	-0.000 009 669 639 6
5 S	-2.021 176 851 574 363(5)	0.000 538 860 360 5(1)	-2.022 618 872 302 312 27(1)	0.000 363 697 136 49
5 P	-2.019 905 989 900 83(2)	0.003 230 021 84(2)	-2.020 551 187 256 25(1)	-0.003 810 911 035(1)
5 D	-2.020 015 836 159 984(4)	-0.000 071 883 131(6)	-2.020 021 027 446 911(5)	0.000 019 568 85(1)
5 F	-2.020 002 937 158 742 7(5)	-0.000 005 704 294 6(4)	-2.020 002 957 377 369 4(4)	-0.000 005 406 490 0(5)
5 G	-2.020 000 710 898 584 71(1)	-0.000 001 404 413 6	-2.020 000 710 925 343 92(1)	-0.000 001 404 001 3
6 S	-2.014 563 098 446 60(1)	0.000 307 704 277(1)	-2.015 377 452 992 862 19(3)	0.000 204 329 479 10
6 P	-2.013 833 979 671 73(2)	0.001 878 058 536(1)	-2.014 207 958 773 74(1)	-0.002 184 346 463(1)
6 D	-2.013 898 227 424 286(5)	-0.000 043 412 268 9(9)	-2.013 901 415 453 792(7)	0.000 012 742 22(3)
6 F	-2.013 890 683 815 549 7(3)	-0.000 003 482 257(7)	-2.013 890 698 348 532 0(2)	-0.000 003 268 458 6(8)
6 G	-2.013 889 345 387 313 22(3)	-0.000 000 898 579 9(7)	-2.013 889 345 416 952 96(3)	-0.000 000 898 123 7(7)
6 H	-2.013 889 034 754 279 72	-0.000 000 290 347 1	-2.013 889 034 754 301 55	-0.000 000 290 346 7
7 S	-2.010 625 776 210 87(2)	0.000 191 925 025(1)	-2.011 129 919 527 626 21(4)	0.000 125 981 736 89
7 P	-2.010 169 314 529 35(2)	0.001 186 152 30(1)	-2.010 404 960 007 94(2)	-0.001 366 500 8(3)
7 D	-2.010 210 028 457 98(1)	-0.000 028 027 840(2)	-2.010 212 105 955 595(2)	0.000 008 563 121(3)
7 F	-2.010 205 248 074 013(1)	-0.000 002 262 00(4)	-2.010 205 258 374 865(1)	-0.000 002 110 58(3)
7 G	-2.010 204 386 224 772 55(7)	-0.000 000 598 396 3(3)	-2.010 204 386 250 217 93(6)	-0.000 000 598 005(1)
7 H	-2.010 204 182 806 482 04(2)	-0.000 000 201 097 8	-2.010 204 182 806 512 04(1)	-0.000 000 201 097 3
7 I	-2.010 204 120 606 191 32	-0.000 000 077 775 5	-2.010 204 120 606 191 340	-0.000 000 077 775 5
8 S	-2.008 093 622 105 61(4)	0.000 127 650 436(1)	-2.008 427 122 064 721 42(6)	0.000 083 070 552 34
8 P	-2.007 789 127 133 22(2)	0.000 796 195 83(5)	-2.007 947 013 771 12(1)	-0.000 911 053 5(3)
8 D	-2.007 816 512 563 811(7)	-0.000 019 076 181(1)	-2.007 817 934 711 706(3)	0.000 005 971 123 4(3)
8 F	-2.007 813 297 115 014 1(6)	-0.000 001 545 48(1)	-2.007 813 304 535 090 8(5)	-0.000 001 436 452(2)
8 G	-2.007 812 711 494 024 1(1)	-0.000 000 415 004 0(1)	-2.007 812 711 514 424 82(9)	-0.000 000 414 690 4
8 H	-2.007 812 571 828 655 81(1)	-0.000 000 142 649 2(3)	-2.007 812 571 828 685 73(1)	-0.000 000 142 648 7(2)
8 I	-2.007 812 528 549 584 59	-0.000 000 056 935 9	-2.007 812 528 549 584 61	-0.000 000 056 935 9
8 K	-2.007 812 512 570 229 31	-0.000 000 025 111 3	-2.007 812 512 570 229 306	-0.000 000 025 111 3
9 S	-2.006 369 553 107 85(3)	0.000 089 149 638 7(7)	-2.006 601 516 715 010 67(3)	0.000 057 628 311 52
9 P	-2.006 156 384 652 86(5)	0.000 559 978 028(2)	-2.006 267 267 366 41(4)	-0.000 637 531 359(6)
9 D	-2.006 175 671 437 641(6)	-0.000 013 542 185(3)	-2.006 176 684 884 697(2)	0.000 004 306 538(6)
9 F	-2.006 173 406 897 324 6(8)	-0.000 001 099 967 1(3)	-2.006 173 412 365 043 0(7)	-0.000 001 019 651(2)
9 G	-2.006 172 991 627 586 3(2)	-0.000 000 298 267 2(1)	-2.006 172 991 643 665 0(3)	-0.000 000 298 019 8(1)
9 H	-2.006 172 891 903 619 14(2)	-0.000 000 104 002 2	-2.006 172 891 903 645 88(2)	-0.000 000 104 001 9
9 I	-2.006 172 860 732 382 57	-0.000 000 042 313 6	-2.006 172 860 732 382 60	-0.000 000 042 313 6(1)
9 K	-2.006 172 849 096 329 78	-0.000 000 019 151 6	-2.006 172 849 096 329 780	-0.000 000 019 151 6
10 S	-2.005 142 991 748 00(8)	0.000 064 697 214(3)	-2.005 310 794 915 611 3(2)	0.000 041 598 811 52
10 P	-2.004 987 983 802 22(4)	0.000 408 649 426 3	-2.005 068 805 497 8(1)	-0.000 463 433 718(8)
10 D	-2.005 002 071 654 250(6)	-0.000 009 947 506 0(6)	-2.005 002 818 080 232(8)	0.000 003 198 298(8)
10 F	-2.005 000 417 564 668 2(9)	-0.000 000 809 442(9)	-2.005 000 421 686 603 6(7)	-0.000 000 748 926 4(2)
10 G	-2.005 000 112 764 318 0(3)	-0.000 000 220 982(2)	-2.005 000 112 777 003 1(4)	-0.000 000 220 785(3)
10 H	-2.005 000 039 214 394 52(2)	-0.000 000 077 806 7	-2.005 000 039 214 417 41(2)	-0.000 000 077 806 2
10 I	-2.005 000 016 086 516 19	-0.000 000 032 059 0(1)	-2.005 000 016 086 516 22	-0.000 000 032 058 9(2)
10 K	-2.005 000 007 388 375 88	-0.000 000 014 751 4	-2.005 000 007 388 375 88	-0.000 000 014 751 4

^a Aznabaev et al. [31] with a 22000-term basis set.

Table 12.3 Eigenvalue coefficients ε_2 for helium

State	$\varepsilon_2(n^1L)$	$\varepsilon_2(n^3L)$
1 S	-0.470 391 870(1)	
2 S	-0.135 276 864(1)	-0.057 495 847 9(2)
2 P	-0.168 271 22(7)	-0.204 959 88(1)
3 S	-0.058 599 3124(4)	-0.040 455 850 5(5)
3 P	-0.066 047 859(3)	-0.070 292 710(2)
3 D	-0.057 201 299(9)	-0.054 737 73(1)
4 S	-0.032 522 293(2)	-0.025 628 633 8(1)
4 P	-0.035 159 71(6)	-0.036 129 973(2)
4 D	-0.032 150 91(2)	-0.030 747 891(7)
4 F	-0.031 274 336(4)	-0.031 277 992 1(3)
5 S	-0.020 647 26(9)	-0.017 322 734 96
5 P	-0.021 847 6(3)	-0.022 166 61(9)
5 D	-0.020 510 1(2)	-0.019 706 2(2)
5 F	-0.020 013 498(6)	-0.020 016 561(4)
5 G	-0.020 003 560 8	-0.020 003 564 6
6 S	-0.014 261 796(4)	-0.012 411 399 1(3)
6 P	-0.014 902 86(9)	-0.015 033 58(5)
6 D	-0.014 199 4(2)	-0.013 707 27(1)
6 F	-0.013 896 984(2)	-0.013 899 22(3)
6 G	-0.013 891 179(6)	-0.013 891 184(8)
6 H	-0.013 889 619 1	-0.013 889 619 0
7 S	-0.010 438 2(2)	-0.009 304 443 3(3)
7 P	-0.010 818 6(2)	-0.010 879(2)
7 D	-0.010 405 09(3)	-0.010 085 212(1)
7 F	-0.010 209 2(3)	-0.010 210 7(3)
7 G	-0.010 205 61(5)	-0.010 205 61(5)
7 H	-0.010 204 590(2)	-0.010 204 587(2)
7 I	-0.010 204 276 7	-0.010 204 276 8
8 S	-0.007 968 944(3)	-0.007 224 770 5(3)
8 P	-0.008 211 7(5)	-0.008 248 7(6)
8 D	-0.007 950 7(4)	-0.007 731 59(2)
8 F	-0.007 815 9(3)	-0.007 817 0(2)
8 G	-0.007 813 563(1)	-0.007 813 568(3)
8 H	-0.007 812 855(4)	-0.007 812 859(5)
8 I	-0.007 812 642 9	-0.007 812 642 9
8 K	-0.007 812 563 0	-0.007 812 563 0
9 S	-0.006 282 5136(1)	-0.005 768 028 5(1)
9 P	-0.006 445 7(2)	-0.006 464 936 9(1)
9 D	-0.006 270 99(7)	-0.006 115 2(1)
9 F	-0.006 175 20(1)	-0.006 176 025 4(7)
9 G	-0.006 173 579 6(1)	-0.006 173 592(4)
9 H	-0.006 173 104(2)	-0.006 173 101(2)
9 I	-0.006 172 945 9(1)	-0.006 172 946 0(2)
9 K	-0.006 172 887 6	-0.006 172 887 6
10 S	-0.005 079 8362(8)	-0.004 709 453 0(1)
10 P	-0.005 197(1)	-0.005 206 7(1)
10 D	-0.005 072 4(4)	-0.004 958 0(8)
10 F	-0.005 001 76(2)	-0.005 002 386(2)
10 G	-0.005 000 55(2)	-0.005 000 55(2)
10 H	-0.005 000 193 5(2)	-0.005 000 193 5(1)
10 I	-0.005 000 080 3(4)	-0.005 000 081(1)
10 K	-0.005 000 036 9	-0.005 000 036 8

Table 12.4 Values of the reduced electron mass ratio μ/M , including binding energy corrections

Isotope	$\mu/M \times 10^4$
¹ H	5.443 205 7507(5)
² D	2.723 695 0538(2)
³ He	1.819 212 0630(16)
⁴ He	1.370 745 634 66(5)
⁶ Li	0.912 167 5131(2)
⁷ Li	0.782 020 2727(6)
⁹ Be	0.608 820 388(3)

(Sect. 29.7.1). Thus, $\Delta E_{L,1}$ represents the electron–nucleus part of the QED shift with the factor of Z^3/π replaced by the correct electron density at the nucleus. Accurate values of $\ln k_0$ for two-electron atoms and ions are tabulated in [38]. For the low-lying S -states and P -states of helium [25, 39],

$$\ln k_0(1^1S) = 2.983 865 861, \quad (12.42a)$$

$$\ln k_0(2^1S) = 2.980 118 365, \quad (12.42b)$$

$$\ln k_0(2^3S) = 2.977 742 459, \quad (12.42c)$$

$$\ln k_0(2^1P) = 2.983 803 377, \quad (12.42d)$$

$$\ln k_0(2^3P) = 2.983 690 995. \quad (12.42e)$$

For a $1snl$ state with large l , the asymptotic expansion [40, 41]

$$\begin{aligned} \ln k_0(1snl) \approx & \ln k_0(1s) + \frac{1}{n^3} \left(\frac{Z-1}{Z} \right)^4 \ln k_0(nl) \\ & + 0.316 205(6) Z^{-6} \langle r^{-4} \rangle_{nl} \\ & + \Delta\beta(1snl) \end{aligned} \quad (12.43)$$

becomes essentially exact. Here, $\ln k_0(nl)$ is the one-electron Bethe logarithm [42], and

$$\langle r^{-4} \rangle_{nl} = \frac{16(Z-1)^4 [3n^2 - l(l+1)]}{(2l-1)2l(2l+1)(2l+2)(2l+3)}. \quad (12.44)$$

The correction $\Delta\beta(1snl)$ for higher order terms is

$$\begin{aligned} \Delta\beta(1snl \ ^1L) = & 95.8(8) \langle r^{-6} \rangle - 845(19) \langle r^{-7} \rangle \\ & + 1406(50) \langle r^{-8} \rangle, \end{aligned} \quad (12.45)$$

$$\begin{aligned} \Delta\beta(1snl \ ^3L) = & 95.1(9) \langle r^{-6} \rangle - 841(23) \langle r^{-7} \rangle \\ & + 1584(60) \langle r^{-8} \rangle. \end{aligned} \quad (12.46)$$

For example, for the $1s4f \ ^1F$ state, $\beta(4 \ ^1F) = 2.984 127 1493(3)$.

For higher Z , $1/Z$, expansions of [38] should be used.

4. Relativistic finite mass corrections of $O(\alpha^2\mu/M)$.

Relativistic finite mass corrections come from two sources. First, a transformation to relative coordinates as in Eq. (12.3) is applied to the pairwise Breit interactions among the three

Table 12.5 Nonrelativistic eigenvalues $E = \varepsilon_0 + (\mu/M)\varepsilon_1 + (\mu/M)^2\varepsilon_2$ for helium-like ions (in units of e^2/a_μ)

Atom	$\varepsilon_0(1^1S)$	$\varepsilon_1(1^1S)$	$\varepsilon_2(1^1S)$
H ⁻	-0.527 751 016 544 377	0.032 879 781 852 30	-0.059 779 492 64(1)
He	-2.903 724 377 034 119 5	0.159 069 475 085 84	-0.470 391 870(1)
Li ⁺	-7.279 913 412 669 305 9	0.288 975 786 393 99	-1.277 369 377 6(2)
Be ⁺⁺	-13.655 566 238 423 586 7	0.420 520 303 439 44	-2.491 572 858 1(1)

Table 12.6 Expectation values of various operators for He-like ions for the case $M = \infty$ (in a.u.)

Quantity	H ⁻	He	Li ⁺	Be ⁺⁺
$\langle r_1^2 \rangle$	11.913 699 678 05(6)	1.193 482 995 019	0.446 279 011 201	0.232 067 315 531
$\langle r_{12}^2 \rangle$	25.202 025 291 2(1)	2.516 439 312 833	0.927 064 803 063	0.477 946 525 143
$\langle \mathbf{r}_1 \cdot \mathbf{r}_2 \rangle$	-0.687 312 967 569	-0.064 736 661 398	-0.017 253 390 330	-0.006 905 947 040
$\langle r_1 \rangle$	2.710 178 278 444(1)	0.929 472 294 874	0.572 774 149 971	0.414 283 328 006
$\langle r_{12} \rangle$	4.412 694 497 992(2)	1.422 070 255 566	0.862 315 375 456	0.618 756 314 066
$\langle 1/r_1 \rangle$	0.683 261 767 652	1.688 316 800 717	2.687 924 397 413	3.687 750 406 344
$\langle 1/r_{12} \rangle$	0.311 021 502 214	0.945 818 448 800	1.567 719 559 137	2.190 870 773 906
$\langle 1/r_1^2 \rangle$	1.116 662 824 6(1)	6.017 408 867 0(1)	14.927 623 721 4(2)	27.840 105 671 33(2)
$\langle 1/r_{12}^2 \rangle$	0.155 104 152 58(3)	1.464 770 923 350(1)	4.082 232 787 55(2)	8.028 801 781 824(1)
$\langle 1/r_1 r_2 \rangle$	0.382 627 890 340	2.708 655 474 480	7.011 874 111 824(1)	13.313 954 940 144(1)
$\langle 1/r_1 r_{12} \rangle$	0.253 077 567 065	1.920 943 921 900	5.069 790 932 379	9.717 071 116 528
$\langle \delta(r_1) \rangle$	0.164 552 872 86(3)	1.810 429 318 49(3)	6.852 009 434 4(1)	17.198 172 544 74(3)
$\langle \delta(r_{12}) \rangle$	0.002 737 992 3(3)	0.106 345 371 2(2)	0.533 722 537 1(9)	1.522 895 354 1(2)
$\langle p^4 \rangle$	2.462 558 614(3)	54.088 067 230(2)	310.547 150 179(6)	1047.278 491 476(2)
$\langle H_{00} \rangle / \alpha^2$	-0.008 875 022 10(1)	-0.139 094 690 556(1)	-0.427 991 611 178(9)	-0.878 768 694 709(1)

particles, generating the new terms [43]

$$\Delta = \Delta_{00} + \Delta_{\text{so}} + 2\frac{m_e}{M}H_{\text{so}},$$

where

$$\Delta_{00} = \frac{-Z\alpha^2 m_e}{2M} \sum_{i,j} \frac{1}{r_i} [\mathbf{p}_j \cdot \mathbf{p}_i + \hat{\mathbf{r}}_i \cdot (\hat{\mathbf{r}}_i \cdot \mathbf{p}_j) \mathbf{p}_i], \quad (12.47)$$

$$\Delta_{\text{so}} = \frac{Z\alpha^2 m_e}{M} \sum_{i \neq j} \frac{1}{r_i^3} \mathbf{r}_i \times \mathbf{p}_j \cdot \mathbf{s}_i. \quad (12.48)$$

Second, the mass polarization term H_{mp} in Eq. (12.3) generates second-order cross terms between H_{mp} and H_{rel} . If the wave functions are calculated by solving Eq. (12.4) in scaled atomic units, the H_{mp} correction is then automatically included to all orders, and the mass-corrected relativistic energy shift is (in units of e^2/a_0)

$$\Delta E_{\text{rel}} = \left(\frac{\mu}{m_e} \right)^3 \left(\left(\frac{\mu}{m_e} \right) H_{\text{mass}} + H_{\text{D}} + H_{\text{SSC}} + H_{00} + \Delta_{00} + \left(1 + \frac{2m_e}{M} \right) H_{\text{so}} + H_{\text{soo}} + H_{\text{ss}} + \Delta_{\text{so}} \right), \quad (12.49)$$

with $\mu/m_e = 1 - \mu/M$. The difference $\Delta E_{\text{rel}} - \langle H_{\text{rel}} \rangle_\infty$ calculated for infinite nuclear mass is the relativistic finite mass correction.

5. Higher-order corrections. All higher-order terms are now known in their entirety up to order α^4 Ry (or equivalently

$\alpha^6 mc^2$) [44] and the spin-dependent parts up to order α^5 Ry. The theory and a comparison with experiment are reviewed by Pachucki et al. [45]. The more accurate spin-dependent parts are particularly important in connection with the 2^3P_J fine structure splittings [46] and determinations of the fine structure constant from atomic spectroscopy [47]. Recoil terms of order $\alpha^4 m/M$ Ry are of importance in the interpretation of isotope shift measurements. The isotope shift has been extensively used to determine the nuclear charge radii of short-lived species such as the halo nuclei ^6He and ^8He [48].

For the energy terms of order α^4 Ry, the dominant electron–nucleus part is known from the one-electron Lamb shift to be

$$\Delta E'_{L,1} = Z\alpha^3 \left[\pi Z\alpha \left(\frac{427}{96} - 2 \ln 2 \right) + 0.538 931 \frac{\alpha}{\pi} \right] \times \langle \delta(\mathbf{r}_1) + \delta(\mathbf{r}_2) \rangle + O(\alpha^5), \quad (12.50)$$

and the electron–electron logarithmic part is [49]

$$\Delta E'_{L,2} = \pi\alpha^4 \ln \alpha^{-1} \langle \delta(r_{12}) \rangle, \quad (12.51)$$

As an example, $\Delta E'_{L,1}$ contributes -50.336 MHz and -88.267 MHz to the $2^1P - 2^1S$ and $2^3P_J - 2^3S_1$ transition frequencies, respectively, while the differences between theory and experiment are ≈ 1 MHz and ≈ -7 MHz for the two cases [35]. Thus, two-electron corrections (for example, relativistic corrections of relative order $Z\alpha$ to $\Delta E_{L,2}$) are evidently small.

Table 12.7 lists the calculated ionization energies for all states of helium up to $n = 10$ and $L = 7$. Some of the en-

Table 12.7 Total ionization energies for ${}^4\text{He}$, calculated with $R_M = 3\,289\,391\,006.600$ MHz

State	$E(n^1L_L)$	$E(n^3L_{L-1})$	$E(n^3L_L)$	$E(n^3L_{L+1})$
1 S	5 945 204 173.(36) ^a			
2 S	960 332 038.0(1.9) ^a			1 152 842 741.4(1.3) ^a
2 P	814 709 146.46(40) ^a	876 078 646.9428(8) ^b	876 108 263.8953(8) ^b	876 110 555.0742(8) ^b
3 S	403 096 132.(1)	451 903 472.(2)	451 903 472.(2)	451 903 472.(2)
3 P	362 787 968.23(5)	382 109 901.7(1)	382 118 016.86(9)	382 118 676.05(1)
3 D	365 917 748.661(19) ^c	366 018 892.691(23) ^c	366 020 217.716(23) ^c	366 020 292.981(23) ^c
4 S	220 960 311.0(7)	240 210 377.3(7)	240 210 377.3(7)	240 210 377.3(7)
4 P	204 397 210.75(4)	212 658 040.5(2)	212 661 348.0(2)	212 661 617.7(2)
4 D	205 783 935.665(9) ^c	205 842 547.795(11) ^c	205 843 102.990(11) ^c	205 843 138.986(11) ^c
4 F	205 620 797.139 9(15)	205 621 029.597 1(19)	205 621 502.013 5(19)	205 621 287.969 4(15)
5 S	139 318 258.4(3)	148 807 311.8(4)	148 807 311.8(4)	148 807 311.8(4)
5 P	130 955 541.836(19)	135 203 442.99(11)	135 205 105.24(11)	135 205 240.76(11)
5 D	131 680 211.860(5) ^c	131 714 043.872(6) ^c	131 714 327.415(6) ^c	131 714 346.623(6) ^c
5 F	131 595 041.497 5(9)	131 595 195.231 6(12)	131 595 419.737 5(12)	131 595 327.450 6(9)
5 G	131 580 320.128 4(2)	131 580 370.942 0(3)	131 580 529.514 3(3)	131 580 446.456 2(2)
6 S	95 807 681.97(18)	101 166 442.3(2)	101 166 442.3(2)	101 166 442.3(2)
6 P	91 009 810.521(11)	93 472 041.50(6)	93 472 992.51(6)	93 473 070.00(6)
6 D	91 433 655.795(3) ^c	91 454 440.567(4) ^c	91 454 604.438(4) ^c	91 454 615.775(4) ^c
6 F	91 383 852.028 7(5)	91 383 954.298 6(7)	91 384 078.897 4(7)	91 384 030.791 4(5)
6 G	91 374 997.957 91(15)	91 375 027.414 6(2)	91 375 119.133 0(2)	91 375 071.110 59(15)
6 H	91 372 940.609 15(5)	91 372 961.810 38(8)	91 373 021.527 12(8)	91 372 990.223 57(5)
7 S	69 904 819.75(11)	73 222 269.28(12)	73 222 269.28(12)	73 222 269.28(12)
7 P	66 901 127.504(7)	68 452 586.60(4)	68 453 180.90(4)	68 453 229.30(4)
7 D	67 169 717.127 2(20) ^c	67 183 264.565 5(20) ^c	67 183 367.678 1(20) ^c	67 183 374.898 6(20) ^c
7 F	67 138 158.555 3(4)	67 138 228.556 6(5)	67 138 305.063 7(5)	67 138 276.717 8(4)
7 G	67 132 455.945 34(10)	67 132 474.519 29(16)	67 132 532.254 93(16)	67 132 502.034 54(10)
7 H	67 131 109.012 98(4)	67 131 122.364 48(6)	67 131 159.970 01(6)	67 131 140.256 92(4)
7 I	67 130 692.477 700(15)	67 130 702.487 20(3)	67 130 728.912 70(3)	67 130 715.086 086(15)
8 S	53 246 283.07(7)	55 440 834.08(8)	55 440 834.08(8)	55 440 834.08(8)
8 P	51 242 587.369(5)	52 282 092.00(3)	52 282 487.96(3)	52 282 520.19(3)
8 D	51 423 248.121 5(10) ^c	51 432 523.230 4(20) ^c	51 432 592.271 0(20) ^c	51 432 597.142 1(20) ^c
8 F	51 402 021.627 5(3)	51 402 071.108 6(3)	51 402 121.532 8(3)	51 402 103.368 7(3)
8 G	51 398 146.236 30(8)	51 398 158.691 23(12)	51 398 197.358 27(12)	51 398 177.123 47(9)
8 H	51 397 221.577 55(3)	51 397 230.522 15(5)	51 397 255.714 73(5)	51 397 242.508 48(3)
8 I	51 396 931.941 336(10)	51 396 938.646 95(2)	51 396 956.349 94(2)	51 396 947.087 163(10)
8 K	51 396 822.732 870(10)	51 396 827.927 806(10)	51 396 841.051 166(10)	51 396 834.201 597(10)
9 S	41 903 979.20(5)	43 430 382.87(5)	43 430 382.87(5)	43 430 382.87(5)
9 P	40 501 246.374(3)	41 231 283.22(2)	41 231 560.17(2)	41 231 582.71(2)
9 D	40 628 480.253 2(9)	40 635 090.445 8(12)	40 635 138.920 1(11)	40 635 142.359 2(11)
9 F	40 613 531.507 8(2)	40 613 567.554 0(2)	40 613 602.576 6(2)	40 613 590.209 2(2)
9 G	40 610 783.197 32(7)	40 610 791.950 93(9)	40 610 819.102 15(9)	40 610 804.896 07(7)
9 H	40 610 123.034 47(2)	40 610 129.316 61(4)	40 610 147.010 06(4)	40 610 137.734 90(2)
9 I	40 609 914.515 382(10)	40 609 919.224 968(17)	40 609 931.658 315(17)	40 609 925.152 765(10)
9 K	40 609 835.096 177(10)	40 609 838.744 754(10)	40 609 847.961 702(10)	40 609 843.151 026(10)
10 S	33 834 679.62(4)	34 938 883.86(4)	34 938 883.86(4)	34 938 883.86(4)
10 P	32 814 665.300(2)	33 346 784.339(14)	33 346 985.598(13)	33 347 001.972(13)
10 D	32 907 601.904 8(6) ^c	32 912 470.747 1(9) ^c	32 912 506.072 9(9) ^c	32 912 508.586 7(9) ^c
10 F	32 896 683.095 55(13)	32 896 710.066 06(18)	32 896 735.396 13(18)	32 896 726.580 63(14)
10 G	32 894 665.769 82(4)	32 894 672.154 58(6)	32 894 691.944 56(6)	32 894 681.591 36(4)
10 H	32 894 178.908 49(2)	32 894 183.488 20(3)	32 894 196.386 67(3)	32 894 189.625 08(2)
10 I	32 894 024.239 94(1)	32 894 027.673 24(1)	32 894 036.737 13(1)	32 894 031.994 58(1)
10 K	32 893 964.925 90	32 893 967.585 71(1)	32 893 974.304 86(1)	32 893 970.797 88

^a Pachucki, Patkóš and Yerokhin [45].^b Fine structure relative to 2^3P centroid at 876 106 246.0(7) MHz [45].^c Yerokhin et al. [50].

Table 12.8 QED corrections to the ionization energy included in Table 12.7 for the S and P -states of helium (in MHz)

State	$\Delta E_{L,1} + \Delta E'_{L,1}$		$\Delta E_{L,2} + \Delta E'_{L,2}$	
	Singlet	Triplet	Singlet	Triplet
1 S	-41 286(36) ^a		–	
2 S	-2 810(2) ^a	-4 059(1) ^a	–	–
3 S	-858.34	-1 030.29	91.258	8.468
4 S	-349.09	-402.29	37.303	3.203
5 S	-174.93	-196.80	18.735	1.544
6 S	-99.807	-110.505	10.702	0.861
7 S	-62.221	-68.113	6.677	0.528
8 S	-41.369	-44.904	4.441	0.347
9 S	-28.885	-31.147	3.102	0.240
10 S	-20.959	-22.482	2.251	0.173
2 P	-48.9(4) ^a	1 254.3(7) ^{a,b}	–	–
3 P	-35.13	344.96	19.559	12.376
4 P	-15.15	142.33	8.413	5.035
5 P	-7.816	71.911	4.348	2.529
6 P	-4.540	41.256	2.529	1.446
7 P	-2.866	25.824	1.598	0.904
8 P	-1.923	17.223	1.073	0.602
9 P	-1.352	12.055	0.755	0.421
10 P	-0.987	8.764	0.551	0.306

^a Total of $\Delta E_{L,1} + \Delta E_{L,2}$ from [45].

^b Centroid value without fine structure. See [45].

tries have been updated with more recent results by *Pachucki* et al. [45] for the low-lying S and P -states, and by *Yerokhin* et al. [50] for the D -states. As noted in the latter reference, there is evidently a systematic discrepancy between theory and experiment for all the $nD-2S$ and $nD-2P$ transitions. Except for using an updated value for the Rydberg states, the other entries are the same as previously tabulated in [51].

For the D -states and beyond, the uncertainties are sufficiently small that these states can be taken as known points of reference in the interpretation of experimental transition frequencies. However, long-range Casimir–Polder corrections [52] are not included since they still lack experimental confirmation [53]. The QED shifts are the largest for the S and P -states. The contributions from $\Delta E_{L,1} + \Delta E'_{L,1}$ and $\Delta E_{L,2} + \Delta E'_{L,2}$ for these states are listed separately in Table 12.8. Applications to isotope shifts and measurements of the nuclear radius are discussed in Sects. 17.2 and 91.2.

12.5.1 Quantum Defect Extrapolations

As discussed in Sect. 15.1, the ionization energies of an isolated Rydberg series of states can be expressed in the form

$$W_n = R_M(Z-1)^2/n^{*2}, \quad (12.52)$$

where $Z-1$ is the screened nuclear charge, and n^* is the effective principal quantum number defined by an iterative solution to the equation

$$n^* = n - \delta(n^*), \quad (12.53)$$

where $\delta(n^*)$ is the *quantum defect* defined by the Ritz expansion

$$\delta(n^*) = \delta_0 + \frac{\delta_2}{(n-\delta)^2} + \frac{\delta_4}{(n-\delta)^4} + \dots, \quad (12.54)$$

with constant coefficients δ_i . The absence of *odd* terms in this series is a special property of the eigenvalues of Hamiltonians of the form $H_C + V$, where H_C is a pure one-electron Coulomb Hamiltonian, and V is a local, short-range, spherically symmetric potential of arbitrary strength (see [54] for further discussion). For the Rydberg states of helium, odd terms must be included in the Ritz expansion in Eq. (12.54) due to relativistic and mass polarization corrections, but they can be removed again by first adjusting the energies according to

$$W'_n = W_n - \Delta W_n, \quad (12.55)$$

where, to sufficient accuracy [54] [see the discussion following Eq. (12.68)]

$$\Delta W_n = R_M \left\{ \frac{-3\alpha^2(Z-1)^4}{4n^4} + \left(\frac{\mu}{M} \right)^2 \frac{(Z-1)^2}{n^2} \times \left[1 + \frac{5}{6}(\alpha Z)^2 \right] \right\}, \quad (12.56)$$

with $Z=2$ for helium. The quantum defect parameters listed in Table 12.9 provide accurate extrapolations to higher-lying Rydberg states, with

$$W_n = R_M/n^{*2} + \Delta W_n. \quad (12.57)$$

12.5.2 Asymptotic Expansions

The asymptotic expansion method [35, 55] rapidly increases in accuracy with increasing angular momentum L of the Rydberg electron, and can be used to high precision for $L \geq 7$. The method is based on a model in which:

1. The Rydberg electron, treated as a distinguishable particle, moves in the field of the core consisting of the He nucleus and a tightly bound $1s$ electron.
2. The core, as characterized by its various multipole moments, is perturbed by the electric field of the Rydberg electron.

Table 12.9 Quantum defects for the total energies of helium with the ΔW_n term subtracted [Eq. (12.56)]

δ_i	Value			
	1S_0			3S_1
δ_0	0.139 718 064 86(21)			0.296 656 487 71(75)
δ_2	0.027 835 737(18)			0.038 296 666(59)
δ_4	0.016 792 29(41)			0.007 513 1(12)
δ_6	-0.001 459 0(31)			-0.004 547 6(79)
δ_8	0.002 922 7(65)			0.002 180(14)
	1P_1	3P_0	3P_1	3P_2
δ_0	-0.012 141 803 603(64)	0.068 328 002 51(27)	0.068 357 857 65(27)	0.068 360 283 79(23)
δ_2	0.007 519 080 4(59)	-0.018 641 975(24)	-0.018 630 462(24)	-0.018 629 228(21)
δ_4	0.013 977 80(15)	-0.012 331 65(57)	-0.012 330 40(57)	-0.012 332 75(51)
δ_6	0.004 837 3(12)	-0.007 951 5(45)	-0.007 951 2(45)	-0.007 952 7(41)
δ_8	0.001 228 3(29)	-0.005 448(10)	-0.005 450(10)	-0.005 451(9)
	1D_2	3D_1	3D_2	3D_3
δ_0	0.002 113 378 464(49)	0.002 885 580 281(22)	0.002 890 941 493(25)	0.002 891 328 825(26)
δ_2	-0.003 090 051 0(58)	-0.006 357 601 2(27)	-0.006 357 183 6(30)	-0.006 357 704 0(33)
δ_4	0.000 008 27(22)	0.000 336 67(11)	0.000 337 77(11)	0.000 336 70(13)
δ_6	-0.000 309 4(31)	0.000 839 4(16)	0.000 839 2(16)	0.000 839 5(18)
δ_8	-0.000 401(14)	0.000 379 8(72)	0.000 432 3(75)	0.000 381 1(83)
	1F_3	3F_2	3F_3	3F_4
δ_0	0.000 440 294 26(62)	0.000 444 869 89(22)	0.000 448 594 83(28)	0.000 447 379 27(21)
δ_2	-0.001 689 446(65)	-0.001 739 275(24)	-0.001 727 232(30)	-0.001 739 217(23)
δ_4	-0.000 118 3(20)	0.000 104 76(76)	0.000 152 4(9)	0.000 104 78(71)
δ_6	0.000 326(18)	0.000 033 7(69)	-0.000 248 6(83)	0.000 033 1(64)
	1G_4	3G_3	3G_4	3G_5
δ_0	0.000 124 734 490(79)	0.000 125 707 43(12)	0.000 128 713 16(10)	0.000 127 141 67(11)
δ_2	-0.000 796 230(12)	-0.000 796 498(19)	-0.000 796 246(15)	-0.000 796 484(17)
δ_4	-0.000 012 05(53)	-0.000 009 80(81)	-0.000 011 89(66)	-0.000 009 85(75)
δ_6	-0.000 013 6(69)	-0.000 019(11)	-0.000 014 1(85)	-0.000 019(10)
	1H_5	3H_4	3H_5	3H_6
δ_0	0.000 047 100 899(61)	0.000 047 797 067(43)	0.000 049 757 614(51)	0.000 048 729 846(45)
δ_2	-0.000 433 227 7(84)	-0.000 433 232 2(55)	-0.000 433 227 4(65)	-0.000 433 228 1(57)
δ_4	-0.000 008 14(26)	-0.000 008 07(16)	-0.000 008 13(19)	-0.000 008 10(16)
	1I_6	3I_5	3I_6	3I_7
δ_0	0.000 021 868 881(17)	0.000 022 390 759(20)	0.000 023 768 483(14)	0.000 023 047 609(26)
δ_2	-0.000 261 067 3(22)	-0.000 261 068 0(28)	-0.000 261 066 2(18)	-0.000 261 067 2(35)
δ_4	-0.000 004 048(67)	-0.000 004 042(87)	-0.000 004 076(58)	-0.000 004 04(11)

A systematic perturbation expansion yields an asymptotic series of the form

$$\varepsilon_0^{nL} = -2 - \frac{(Z-1)^2}{2n^2} + a_0 \sum_{j=4}^N A_j \langle r^{-j} \rangle_{nL} \frac{e^2}{a_0}, \quad (12.58)$$

where the expectation value $\langle r^{-j} \rangle_{nL}$ is calculated with respect to the hydrogenic nL -electron wave function [56], and the series is truncated at the upper limit N , where the series begins diverging. The leading coefficients A_j are

$$A_4 = -\frac{1}{2}\alpha_1, \quad A_5 = 0, \quad A_6 = -\frac{1}{2}(\alpha_2 - 6\beta_1),$$

where α_k is the 2^k -pole polarizability of the hydrogenic core, and β_k is a nonadiabatic correction. The exact hydrogenic values are

$$\alpha_1 = \frac{9a_0^3}{2Z^4}, \quad \alpha_2 = \frac{15a_0^5}{Z^6}, \quad \beta_1 = \frac{43a_0^5}{8Z^6}.$$

All terms are known up to A_{10} (see [35, 55] for detailed results, and [57] for derivations and corrections to earlier work). The expansions for the terms ε_0 , ε_1 , and ε_2 in Eq. (12.6) for helium are [57]

$$\begin{aligned} \varepsilon_0^{nL} = & -2 - \frac{1}{2n^2} - \frac{9}{64}\langle r^{-4} \rangle + \frac{69}{512}\langle r^{-6} \rangle + \frac{3833}{15360}\langle r^{-7} \rangle \\ & - \left[\frac{55923}{65536} + \frac{957L(L+1)}{10240} \right] \langle r^{-8} \rangle - \frac{908185}{688128}\langle r^{-9} \rangle \\ & + \left[\frac{21035363}{6193152} + \frac{33275L(L+1)}{28672} \right] \langle r^{-10} \rangle \\ & + e^{(1,1)} - \frac{23}{20}e^{(1,2)}, \end{aligned} \quad (12.59)$$

$$\begin{aligned} \varepsilon_1^{nL} = & -\frac{9}{32}\langle r^{-4} \rangle + \frac{249}{256}\langle r^{-6} \rangle + \frac{319}{3840}\langle r^{-7} \rangle \\ & - \left[\frac{34\,659}{16\,384} + \frac{957L(L+1)}{5120} \right] \langle r^{-8} \rangle - \frac{14\,419}{3072} \langle r^{-9} \rangle \\ & + \left[\frac{155\,027\,773}{6\,193\,152} + \frac{24\,155L(L+1)}{8192} \right] \langle r^{-10} \rangle \\ & + 4e^{(1,1)} - \frac{53}{5}e^{(1,2)}, \end{aligned} \quad (12.60)$$

$$\begin{aligned} \varepsilon_2^{nL} = & -\frac{1}{2n^2} - \frac{45}{64}\langle r^{-4} \rangle + \frac{165}{512}\langle r^{-6} \rangle + \frac{2555}{3072}\langle r^{-7} \rangle \\ & - \left[\frac{268\,485}{32\,768} + \frac{957L(L+1)}{2048} \right] \langle r^{-8} \rangle + \frac{598\,909}{172\,032} \langle r^{-9} \rangle \\ & + \left[\frac{1148\,906\,421}{49\,545\,216} + \frac{629\,515L(L+1)}{114\,688} \right] \langle r^{-10} \rangle \\ & + 14e^{(1,1)} - \frac{251}{10}e^{(1,2)}. \end{aligned} \quad (12.61)$$

The terms $e^{(1,1)}$ and $e^{(1,2)}$ are second-order dipole-dipole and dipole-quadrupole perturbation corrections. Defining $f_p^L = (L+p)!/(L-p)!$, they are given by

$$\begin{aligned} e^{(i,j)} = & -\frac{(2-\delta_{j,k})2^{2i+2j+1}(2L-2i)!(2L-2j)!}{n^3(2L+2i+1)!(2L+2j+1)!} \\ & \times \left[\frac{2^{2i+2j}(2L-2i-2j)!A^{(i,j)}}{n^{2i+2j+2}(2L+2i+2j+1)!} + \frac{B^{(i,j)}}{n^{2i+2j+1}} \right], \end{aligned} \quad (12.62)$$

with

$$\begin{aligned} A^{(1,1)} = & 3n^2(3n^2-2f_1)(f_1-2)(45+623f_1^L+3640f_2^L \\ & + 560f_3^L), \\ B^{(1,1)} = & (9n^2-7f_1^L)(3n^2-f_1^L), \\ A^{(1,2)} = & -21n^6(94\,500+122\,850f_1^L-1126\,125f_2^L \\ & -18\,931\,770f_3^L-11\,171\,160f_4^L \\ & -1029\,600f_5^L-18\,304f_6^L) \\ & -15n^4(94\,500-444\,150f_1^L+7747\,425f_2^L \\ & +337\,931\,880f_3^L+375\,290\,190f_4^L \\ & +66\,518\,760f_5^L+2880\,416f_6^L+29\,568f_7^L) \\ & +9n^2f_1^L(90\,300-177\,450f_1^L+1738\,450f_2^L \\ & +133\,125\,575f_3^L+160\,040\,870f_4^L \\ & +29\,322\,216f_5^L+1293\,600f_6^L+13\,440f_7^L) \\ & +2f_1^Lf_2^Lf_3^L(45+252f_1^L-1680f_2^L-2240f_3^L), \\ B^{(1,2)} = & 315n^6+125n^4(3-5f_1^L)-7n^2f_1^L(43-39f_1^L) \\ & -27f_1^Lf_2^L. \end{aligned}$$

The accuracy of the expansion for the ε_0 , ε_1 , and ε_2 can be reliably estimated to be one-half of the last $\langle r^{-j} \rangle$ term included in the sum. Formulas for the $\langle r^{-j} \rangle$ are given in Table 12.10.

Table 12.10 Formulas for the hydrogenic expectation value $\langle r^{-j} \rangle \equiv (nl|r^{-j}|nl)$ in terms of

$$G_p^{nl} = \frac{2^p Z^p (2l-p+2)!}{n^{p+1} (2l+p-1)!}, \quad f_p^l = \frac{(l+p)!}{(l-p)!}.$$

j	$\langle r^{-j} \rangle (a_0)$
2	$\frac{1}{2}G_2^{nl}$
3	nG_3^{nl}
4	$G_4^{nl}(3n^2-f_1^l)$
5	$2G_5^{nl}[5n^3-n(3f_1^l-1)]$
6	$G_6^{nl}[35n^4-5n^2(6f_1^l-5)+3f_2^l]$
7	$2G_7^{nl}[63n^5-35n^3(2f_1^l-3)+n(15f_2^l-20f_1^l+12)]$
8	$G_8^{nl}[462n^6-210n^4(3f_1^l-7)+42n^2(5f_2^l-15f_1^l+14)-10f_3^l]$
9	$2G_9^{nl}[858n^7-462n^5(3f_1^l-10)+42n^3(15f_2^l-75f_1^l+101)-2n(35f_3^l-105f_2^l+252f_1^l-180)]$
10	$G_{10}^{nl}[6435n^8-6006n^6(2f_1^l-9)+1155n^4(6f_2^l-44f_1^l+81)-6n^2(210f_3^l-1365f_2^l+4648f_1^l-4566)+35f_4^l]$

The asymptotic formulas for the NFS relativistic corrections are [35, 58]

$$\begin{aligned} \langle H_{\text{mass}} + H_{\text{D}} \rangle \rightarrow & -\frac{\alpha^2 Z^4}{8} + h_1(nL) + \chi_1(nL) + \frac{(Z\alpha)^2}{2} \\ & \times \left[\frac{14}{3Z^4} \langle r^{-4} \rangle - \frac{5041}{240Z^6} \langle r^{-6} \rangle \right], \end{aligned} \quad (12.63)$$

$$\langle H_{\text{oo}} \rangle \rightarrow \frac{\alpha^2}{Z^2} \left[\langle r^{-4} \rangle + \frac{3(Z-1)}{Z^2} \langle r^{-5} \rangle - \frac{3(f_1^L+8)}{4Z^2} \langle r^{-6} \rangle \right], \quad (12.64)$$

where

$$h_1(nL) = \frac{\alpha^2(Z-1)^4}{2n^3} \left[\frac{3}{4n} - \frac{1}{L+\frac{1}{2}} \right] \quad (12.65)$$

is the leading one-electron Dirac energy, and

$$\begin{aligned} \chi_1(nL) = & \frac{\alpha^2 \alpha_1}{2} \left\{ 3 \left(\frac{Z-1}{n} \right)^2 \langle r^{-4} \rangle - (Z-1) \langle r^{-5} \rangle \right. \\ & - \frac{4(2L-2)!}{(2L+3)!} \left[4 \left(\frac{Z-1}{n} \right)^6 \left(n + \frac{9n^2-5f_1^L}{2L+1} \right) \right. \\ & \left. \left. + (Z-1)^2 \left(\frac{40f_2^L+70f_1^L-3}{2L+1} \right) \langle r^{-4} \rangle \right] \right\} \end{aligned} \quad (12.66)$$

is the correction due to the dipole perturbation of the Rydberg electron. The relativistic recoil terms due to mass polarization are

$$\begin{aligned} \langle H_{\text{mass}} + H_{\text{D}} \rangle_{\text{RR}} \rightarrow & \frac{\mu}{M} \left[\frac{22(Z\alpha)^2(Z-1)}{9Z^4} \langle r^{-4} \rangle + 2(Z-1)\chi_1(nL) \right] \\ & + \left(\frac{\mu}{M} \right)^2 \left[-\frac{5}{12} \left(\frac{\alpha Z(Z-1)}{n} \right)^2 + 4h_1(nL) \right], \end{aligned} \quad (12.67)$$

$$\begin{aligned} & \langle H_{00} \rangle_{RR} + \langle \Delta_{00} \rangle \\ & \rightarrow -\frac{\alpha^2 \mu}{M} \left[Z^4 + \frac{(Z-1)^4}{n^3} \left(\frac{1}{n} - \frac{3}{2L+1} \right) \right. \\ & \quad \left. - \frac{25[1+13f(Z)]}{16Z^2} \langle r^{-4} \rangle \right], \end{aligned} \quad (12.68)$$

with $f(Z) \simeq 1 + (Z-2)/6$. The $-(5/12)[\alpha Z(Z-1)/n]^2$ term in Eq. (12.67) is the dominant contribution in helium for $L \geq 4$. It is included in Eq. (12.56) for ΔW_n , along with the leading $1/n^2$ term from Eq. (12.61), and the $1/n^4$ term from Eq. (12.65). The complete relativistic finite mass correction includes also the mass-scaling terms $-(\mu/M)\langle 4H_{\text{mass}} + 3H_D + 3H_{00} \rangle$ obtained by expanding μ/m_e in Eq. (12.49). The $\langle \delta(\mathbf{r}_1) \rangle$ term is [59]

$$\begin{aligned} \pi \langle \delta(\mathbf{r}_1) \rangle & \rightarrow \frac{Z^3}{2} - \frac{31}{4Z^3} \langle r^{-4} \rangle + \frac{1447}{32Z^5} \langle r^{-7} \rangle \\ & \quad - \frac{31(Z-1)}{2Z^3} \left(\frac{\mu}{M} \right) \langle r^{-4} \rangle + \dots; \end{aligned} \quad (12.69)$$

$\langle \delta(\mathbf{r}_{12}) \rangle$ vanishes exponentially as $1/n^{2L+4}$ with increasing L . The complete asymptotic expressions for the FS matrix elements are summarized by the formulas

$$\begin{aligned} & \langle nL^3L_J | H_{\text{FS}} | nL^3L_J \rangle \\ & \rightarrow T_{nL}(J) \{ Z - 3 + 2S_L(J) + 2a_e[Z - 2 \\ & \quad + (2 + a_e)S_L(J)] + (\mu/M)[2 - 4S_L(J)] \}, \quad (12.70) \\ & \langle nL^3L_J | H_{\text{FS}} | nL^1L_J \rangle \\ & \rightarrow T_{nL}(L)(Z + 1 + 2a_e Z - 2\mu/M) \sqrt{L(L+1)}, \end{aligned} \quad (12.71)$$

where

$$\begin{aligned} T_{nL}(J) & = \begin{cases} -\alpha^2(L+1)\langle r^{-3} \rangle/4 & J = L-1, \\ -\alpha^2\langle r^{-3} \rangle/4 & J = L, \\ \alpha^2 L \langle r^{-3} \rangle/4 & J = L+1, \end{cases} \\ S_L(J) & = \begin{cases} 1 & J = L, \\ \pm 1/(2J+1) & J = L \pm 1. \end{cases} \end{aligned}$$

The asymptotic form for the QED term $\Delta E_{L,1}$ follows from Eq. (12.38) with the use of Eq. (12.69) for $\langle \delta(\mathbf{r}_1) \rangle$ and Eq. (12.43) for $\ln k_0$. The electron–electron part is

$$\Delta E_{L,2} \rightarrow -\frac{7\alpha^3}{6\pi} \left(\langle r^{-3} \rangle + \frac{3}{Z^2} \langle r^{-5} \rangle \right). \quad (12.72)$$

With the use of the formulas in this section, the variationally calculated ionization energies for the K -states ($L=7$) in Table 12.7 can be reproduced to within ± 20 Hz. For $L > 7$, the uncertainty becomes less than 1 Hz, up to the Casimir–Polder retardation effects, which have not been included.

12.6 Radiative Transitions

12.6.1 Basic Formulation

In a semiclassical picture, the interaction Hamiltonian with the radiation field is obtained by making the minimal coupling replacements

$$\begin{aligned} \mathbf{P}_N & \rightarrow \mathbf{P}_N - \frac{Ze}{c} \mathbf{A}(\mathbf{R}_N), \\ \mathbf{P}_i & \rightarrow \mathbf{P}_i + \frac{e}{c} \mathbf{A}_i(\mathbf{R}_i) \end{aligned} \quad (12.73)$$

in Eq. (12.1), where

$$\mathbf{A}(\mathbf{R}) = c \left(\frac{2\pi\hbar}{\omega\mathcal{V}} \right)^{1/2} \hat{\boldsymbol{\epsilon}} e^{i\mathbf{k}\cdot\mathbf{R}} \quad (12.74)$$

is the time-independent part of the vector potential $\mathbf{A}(\mathbf{r}, t) = \mathbf{A}(\mathbf{r})e^{-i\omega t} + \text{c.c.}$ for a photon of frequency ω , wave vector \mathbf{k} , and polarization $\hat{\boldsymbol{\epsilon}} \perp \mathbf{k}$ normalized to unit photon energy $\hbar\omega$ in volume \mathcal{V} . The linear coupling terms then yield

$$H_{\text{int}} = -\frac{Ze}{Mc} \mathbf{P}_N \cdot \mathbf{A}(\mathbf{R}_N) + \frac{e}{m_e c} \sum_{i=1}^2 \mathbf{P}_i \cdot \mathbf{A}(\mathbf{R}_i), \quad (12.75)$$

and from Fermi's Golden Rule, the decay rate for spontaneous emission from state γ to γ' is

$$w_{\gamma,\gamma'} d\Omega = \frac{2\pi}{\hbar} |\langle \gamma | H_{\text{int}} | \gamma' \rangle|^2 \rho_f, \quad (12.76)$$

where $\rho_f = \mathcal{V} \omega^2 d\omega / (2\pi c)^3 \hbar$ is the number of photon states with polarization $\hat{\boldsymbol{\epsilon}}$ per unit energy and solid angle in the normalization volume \mathcal{V} . In the long wavelength and electric dipole approximations, the factor $e^{i\mathbf{k}\cdot\mathbf{R}}$ in Eq. (12.74) is replaced by unity. After integrating over angles $d\Omega$ and summing over polarizations $\hat{\boldsymbol{\epsilon}}$, the decay rate reduces to

$$w_{\gamma,\gamma'} = \frac{4}{3} \alpha \omega_{\gamma,\gamma'} |\langle \gamma | \mathbf{Q}_p | \gamma' \rangle|^2, \quad (12.77)$$

where $\omega_{\gamma',\gamma}$ is the transition frequency and \mathbf{Q}_p is the velocity form of the transition operator

$$\mathbf{Q}_p = \frac{Z}{Mc} \mathbf{P}_N + \frac{1}{m_e c} \sum_{i=1}^N \mathbf{P}_i, \quad (12.78)$$

for the general case of N electrons. From the commutator $[H_0, \mathbf{Q}_r / \hbar \omega_{\gamma,\gamma'}] = \mathbf{Q}_p$, where H_0 is the field-free Hamiltonian in Eq. (12.1), the equivalent length form is

$$\mathbf{Q}_r = -\frac{i}{c} \omega_{\gamma,\gamma'} \left(Z \mathbf{R}_N - \sum_{i=1}^N \mathbf{R}_i \right). \quad (12.79)$$

After transforming to c.m. plus relative coordinates in paral-

Table 12.11 Oscillator strengths for helium. The factor in brackets gives the finite mass correction, with $y = \mu/M$

	1 ¹ S	2 ¹ S	3 ¹ S	4 ¹ S
2 ¹ P	0.276 1647(1 - 2.282y)	0.376 4403(1 + 1.255y)	-0.145 4703(1 + 1.351y)	-0.025 8703(1 + 0.885y)
3 ¹ P	0.073 4349(1 - 1.789y)	0.151 3417(1 - 3.971y)	0.626 1931(1 + 1.234y)	-0.307 5074(1 + 1.097y)
4 ¹ P	0.029 8629(1 - 1.583y)	0.049 1549(1 - 3.235y)	0.143 8889(1 - 4.650y)	0.858 0214(1 + 1.205y)
5 ¹ P	0.015 0393(1 - 1.474y)	0.022 3377(1 - 2.967y)	0.050 4714(1 - 3.764y)	0.146 2869(1 - 5.080y)
6 ¹ P	0.008 6277(1 - 1.407y)	0.012 1340(1 - 2.829y)	0.024 1835(1 - 3.444y)	0.052 7562(1 - 4.105y)
7 ¹ P	0.005 4054(1 - 1.362y)	0.007 3596(1 - 2.75y)	0.013 6794(1 - 3.279y)	0.025 8918(1 - 3.75y)
	2 ³ S	3 ³ S	4 ³ S	5 ³ S
2 ³ P	0.539 0861(1 - 3.185y)	-0.208 5359(1 - 3.773y)	-0.031 7208(1 - 2.819y)	-0.011 3409(1 - 2.609y)
3 ³ P	0.064 4612(1 + 5.552y)	0.890 8513(1 - 2.967y)	-0.435 6711(1 - 3.362y)	-0.067 6073(1 - 2.359y)
4 ³ P	0.025 7689(1 + 3.886y)	0.050 0833(1 + 7.505y)	1.215 2630(1 - 2.878y)	-0.668 3003(1 - 3.185y)
5 ³ P	0.012 4906(1 + 3.332y)	0.022 9141(1 + 5.209y)	0.044 2305(1 + 9.009y)	1.530 6287(1 - 2.827y)
6 ³ P	0.006 9822(1 + 3.063y)	0.011 9933(1 + 4.460y)	0.021 6301(1 + 6.198y)	0.041 5177(1 + 10.215y)
7 ³ P	0.004 2990(1 + 2.908y)	0.007 0772(1 + 4.092y)	0.011 7754(1 + 5.292y)	0.021 1003(1 + 6.981y)
	2 ¹ P	3 ¹ P	4 ¹ P	5 ¹ P
3 ¹ D	0.710 1641(1 - 0.281y)	-0.021 1401(1 + 29.947y)	-0.015 3034(1 - 6.680y)	-0.003 1128(1 - 6.27y)
4 ¹ D	0.120 2704(1 - 1.307y)	0.648 1049(1 + 0.435y)	-0.040 0610(1 + 29.183y)	-0.039 2932(1 - 6.163y)
5 ¹ D	0.043 2576(1 - 1.681y)	0.141 3027(1 - 0.566y)	0.647 6679(1 + 0.817y)	-0.057 3258(1 + 28.903y)
6 ¹ D	0.020 9485(1 - 1.866y)	0.056 2766(1 - 0.936y)	0.152 8104(1 - 0.170y)	0.669 8361(1 + 1.056y)
7 ¹ D	0.011 8970(1 - 1.975y)	0.028 8961(1 - 1.127y)	0.063 5953(1 - 0.538y)	0.163 0272(1 + 0.082y)
8 ¹ D	0.007 4645(1 - 2.046y)	0.017 0777(1 - 1.241y)	0.033 6403(1 - 0.731y)	0.069 3063(1 - 0.26y)
	2 ³ P	3 ³ P	4 ³ P	5 ³ P
3 ³ D	0.610 2252(1 - 2.029y)	0.112 1004(1 + 6.653y)	-0.036 9592(1 + 3.292y)	-0.006 9009(1 + 2.678y)
4 ³ D	0.122 8469(1 - 1.001y)	0.477 5938(1 - 3.059y)	0.200 9498(1 + 6.368y)	-0.088 3017(1 + 2.939y)
5 ³ D	0.047 0071(1 - 0.631y)	0.124 5532(1 - 2.019y)	0.438 3888(1 - 3.607y)	0.280 0558(1 + 6.225y)
6 ³ D	0.023 4692(1 - 0.449y)	0.053 0093(1 - 1.631y)	0.123 9414(1 - 2.555y)	0.429 4411(1 - 3.961y)
7 ³ D	0.013 5638(1 - 0.346y)	0.028 1587(1 - 1.432y)	0.055 2332(1 - 2.153y)	0.125 2389(1 - 2.904y)
8 ³ D	0.008 6047(1 - 0.280y)	0.016 9809(1 - 1.315y)	0.030 2853(1 - 1.94y)	0.057 0589(1 - 2.498y)
	3 ¹ D	4 ¹ D	5 ¹ D	6 ¹ D
4 ¹ F	1.015 0829(1 - 1.010y)	0.002 4920(1 + 3.833y)	-0.012 6968(1 - 0.888y)	-0.002 2631(1 - 0.890y)
5 ¹ F	0.156 8808(1 - 0.993y)	0.886 1343(1 - 1.023y)	0.004 6467(1 + 4.139y)	-0.033 2539(1 - 0.893y)
6 ¹ F	0.054 0508(1 - 0.984y)	0.186 0576(1 - 1.001y)	0.839 1374(1 - 1.031y)	0.006 6028(1 + 4.302y)
7 ¹ F	0.025 6799(1 - 0.978y)	0.072 3229(1 - 0.994y)	0.196 3692(1 - 1.014y)	0.826 9464(1 - 1.039y)
8 ¹ F	0.014 4782(1 - 0.978y)	0.036 6627(1 - 0.987y)	0.080 7847(1 - 1.003y)	0.203 1182(1 - 1.019y)
9 ¹ F	0.009 0730(1 - 0.977y)	0.021 5401(1 - 0.975y)	0.042 4256(1 - 1.000y)	0.086 0955(1 - 1.01y)
	3 ³ D	4 ³ D	5 ³ D	6 ³ D
4 ³ F	1.014 3389(1 - 0.997y)	0.003 3992(1 - 2.166y)	-0.012 8084(1 - 1.042y)	-0.002 2830(1 - 1.044y)
5 ³ F	0.156 9831(1 - 1.004y)	0.884 5767(1 - 0.991y)	0.006 5121(1 - 2.387y)	-0.033 5369(1 - 1.043y)
6 ³ F	0.054 1179(1 - 1.006y)	0.186 0264(1 - 1.003y)	0.837 0221(1 - 0.988y)	0.009 3836(1 - 2.499y)
7 ³ F	0.025 7201(1 - 1.008y)	0.072 3579(1 - 1.003y)	0.196 2031(1 - 0.996y)	0.824 4031(1 - 0.984y)
8 ³ F	0.014 5037(1 - 1.009y)	0.036 6936(1 - 1.004y)	0.080 7712(1 - 1.00y)	0.202 8407(1 - 0.993y)
9 ³ F	0.009 0903(1 - 1.008y)	0.021 5632(1 - 1.011y)	0.042 4344(1 - 0.99y)	0.086 0373(1 - 0.99y)

with Eq. (12.3), the dipole transition operators become

$$\mathbf{Q}_p = \frac{Z_p}{mc} \sum_{i=1}^N \mathbf{p}_i, \quad \mathbf{Q}_r = \frac{i\omega_{\gamma,\gamma'}}{c} Z_r \sum_{i=1}^N \mathbf{r}_i, \quad (12.80)$$

with

$$Z_p = \frac{Zm_e + M}{M}, \quad Z_r = \frac{Zm_e + M}{Nm_e + M},$$

and H_0 now contains the H_{mp} term. If Eq. (12.3) is solved exactly for the states $|\gamma\rangle$ and $|\gamma'\rangle$, then the identity

$$\langle \gamma | \mathbf{Q}_p | \gamma' \rangle = \langle \gamma | \mathbf{Q}_r | \gamma' \rangle \quad (12.81)$$

is satisfied to all orders in m_e/M . For a neutral atom, $N = Z$ and $Z_r = 1$. If the oscillator strength is defined by

$$\begin{aligned} f_{\gamma',\gamma} &= \frac{2m_e\omega_{\gamma',\gamma}}{3\hbar} \left(\frac{Z_r}{Z_p} \right) |\langle \gamma' | \sum_{i=1}^N \mathbf{r}_i | \gamma \rangle|^2 \\ &= \frac{2}{3m_e\hbar\omega_{\gamma',\gamma}} \left(\frac{Z_p}{Z_r} \right) |\langle \gamma' | \sum_{i=1}^N \mathbf{p}_i | \gamma \rangle|^2, \end{aligned} \quad (12.82)$$

then the sum rule $\sum_{\gamma'} f_{\gamma',\gamma} = N$ remains valid, independent of m_e/M . The decay rate, summed over final states and av-

eraged over initial states, is

$$\bar{w}_{\gamma,\gamma'} = -\frac{2\alpha\hbar\omega_{\gamma,\gamma'}}{m_e c^2} Z_p Z_r \bar{f}_{\gamma,\gamma'}, \quad (12.83)$$

where $\bar{f}_{\gamma,\gamma'} = -(g_\gamma/g_{\gamma'})\bar{f}_{\gamma',\gamma}$ is the (negative) oscillator strength for photon emission, and $g_\gamma, g_{\gamma'}$ are the statistical weights of the states.

12.6.2 Oscillator Strength Table

Table 12.11 provides arrays of nonrelativistic oscillator strengths among various states of helium, including the effects of finite nuclear mass as a separate factor. In the absence of mass polarization, the correction factor would be $(1 + \mu/M)^{-1} \simeq 1 - \mu/M$. Mass polarization effects are particularly strong for P -states and for transitions with $\Delta n = 0$.

The largest relativistic correction comes from singlet-triplet mixing between states with the same n, L , and J (e.g. 3^1D_2 and 3^3D_2) due to H_{FS} . The wave functions obtained by diagonalizing the 2×2 matrices $\mathbf{H}_0 + \mathbf{H}_{\text{NFS}} + \mathbf{H}_{\text{FS}}$ are then

$$\begin{aligned} \Psi(n^1L_L) &= \Psi_0(n^1L_L) \cos \theta + \Psi_0(n^3L_L) \sin \theta \\ \Psi(n^3L_L) &= -\Psi_0(n^1L_L) \sin \theta + \Psi_0(n^3L_L) \cos \theta. \end{aligned}$$

Values of $\sin \theta$ are listed in Table 12.12. The corrected oscillator strengths $\tilde{f}_{\gamma,\gamma'}$ for the singlet (s) and triplet (t) components of a $\gamma \rightarrow \gamma'$ transition can then be calculated from the values in Table 12.11 according to

$$\begin{aligned} \tilde{f}_{\gamma,\gamma'}^{\text{ss}} &= \omega_{\gamma,\gamma'}^{\text{ss}} \left(X_{\gamma,\gamma'}^{\text{ss}} \cos \theta_\gamma \cos \theta_{\gamma'} + X_{\gamma,\gamma'}^{\text{tt}} \sin \theta_\gamma \sin \theta_{\gamma'} \right)^2, \\ \tilde{f}_{\gamma,\gamma'}^{\text{tt}} &= \omega_{\gamma,\gamma'}^{\text{tt}} \left(X_{\gamma,\gamma'}^{\text{ss}} \sin \theta_\gamma \sin \theta_{\gamma'} + X_{\gamma,\gamma'}^{\text{tt}} \cos \theta_\gamma \cos \theta_{\gamma'} \right)^2, \\ \tilde{f}_{\gamma,\gamma'}^{\text{st}} &= \omega_{\gamma,\gamma'}^{\text{st}} \left(X_{\gamma,\gamma'}^{\text{ss}} \cos \theta_\gamma \sin \theta_{\gamma'} - X_{\gamma,\gamma'}^{\text{tt}} \sin \theta_\gamma \cos \theta_{\gamma'} \right)^2, \\ \tilde{f}_{\gamma,\gamma'}^{\text{ts}} &= \omega_{\gamma,\gamma'}^{\text{ts}} \left(X_{\gamma,\gamma'}^{\text{ss}} \sin \theta_\gamma \cos \theta_{\gamma'} - X_{\gamma,\gamma'}^{\text{tt}} \cos \theta_\gamma \sin \theta_{\gamma'} \right)^2, \end{aligned}$$

where $X_{\gamma,\gamma'}^{\text{ss}} = (f_{\gamma,\gamma'}^{\text{ss}}/\omega_{\gamma,\gamma'}^{\text{ss}})^{1/2}$, and similarly for $X_{\gamma,\gamma'}^{\text{tt}}$. From Eq. (12.82), $X_{\gamma,\gamma'}$ is proportional to the dipole length form of the transition operator, for which there are no spin-dependent relativistic corrections [60]. The mixing corrections are particularly significant for D - F and F - G transitions, where intermediate coupling prevails. The two-state approximation becomes increasingly accurate with increasing L , but for P -

Table 12.12 Singlet-triplet mixing angles for helium

State	$\sin \theta$	State	$\sin \theta$	State	$\sin \theta$
2 P	0.000 2783				
3 P	0.000 2558	3 D	0.015 6095		
4 P	0.000 2498	4 D	0.011 3960	4 F	0.604 1024
5 P	0.000 2473	5 D	0.010 1143	5 F	0.549 9291
6 P	0.000 2460	6 D	0.009 5289	6 F	0.518 0737
7 P	0.000 2452	7 D	0.009 2067	7 F	0.498 4184
8 P	0.000 2447	8 D	0.009 0087	8 F	0.485 5768
9 P	0.000 2444	9 D	0.008 8777	9 F	0.476 7620
10 P	0.000 2442	10 D	0.008 7862	10 F	0.470 4595
5 G	0.693 4752				
6 G	0.693 1996	6 H	0.696 2385		
7 G	0.692 9889	7 H	0.696 2377	7 I	0.697 9315
8 G	0.692 8356	8 H	0.696 2372	8 I	0.697 9315
9 G	0.692 7195	9 H	0.696 2374	9 I	0.697 9316
10 G	0.692 6329	10 H	0.696 2353	10 I	0.697 9316
8 K	0.699 1671				
9 K	0.699 1671	9 L	0.700 1089		
10 K	0.699 1671	10 L	0.700 1089	10 M	0.700 8507

states, where $\sin \theta$ is small, states with $n' \neq n$ must also be included [61].

12.7 Future Perspectives

The variational calculations, together with quantum defect extrapolations for high n and asymptotic expansions for high L , provide essentially exact results for the entire singly-excited spectrum of helium. In this sense, helium joins hydrogen as a fundamental atomic system. The dominant uncertainties arise from two-electron QED effects beyond the current realm of standard atomic physics. Transition frequencies from the $1s2s^1S_0$ state are now known to better than ± 0.5 MHz (± 1.8 parts in 10^9) [62], and the fine structure intervals in the $1s2p^3P$ state have been measured to an accuracy exceeding 1 kHz [63]. Comparisons with theory [64, 65] hold the promise of determining an “atomic physics” value for the fine structure constant. Transition frequencies among the $n = 10$ states are known even more accurately [53]. Recent progress in the use of the isotope shift to deduce the size of the nucleus from the nuclear volume effect (Sect. 91.2) has attracted a great deal of attention, especially for neutron-rich “halo” nuclei such as ^6He and ^{11}Li .

Acknowledgments The author is grateful to R.N. Hill and J.D. Morgan III for suggesting some of the material in Sect. 12.1. This work was supported by the Natural Sciences and Engineering Research Council of Canada.

References

1. Kato, T.: *Commun. Pure Appl. Math.* **10**, 151 (1957)
2. Hoffmann-Ostenhoff, M., Hoffmann-Ostenhoff, T., Stremmitzer, H.: *Phys. Rev. Lett.* **68**, 3857 (1992)
3. Fock, V.A.: *Izv. Akad. Nauk SSSR Ser. Fiz.* **18**, 161 (1954)
4. Myers, C.R., Umrigar, C.J., Sethna, J.P., Morgan III, J.D.: *Phys. Rev. A* **44**, 5537 (1991)
5. Gottschalk, J.E., Maslen, E.N.: *J. Phys. A* **20**, 2781 (1987) and earlier references therein
6. Macek, J.H.: *Phys. Rev.* **160**, 170 (1967)
7. Leray, J.: In: Ciarlet, P.G., Roseau, M. (eds.) *Trends and Applications of Pure Mathematics to Mechanics*, Lecture Notes in Physics, vol. 195, pp. 235–247. Springer, Berlin (1984)
8. Morgan III, J.D.: *Theor. Chem. Acta* **69**, 181 (1986)
9. Deift, P., Hunziker, W., Simon, B., Vock, E.: *Commun. Math. Phys.* **64**, 1 (1978)
10. Morgan III, J.D.: *J. Phys. A* **10**, L91 (1977)
11. Hoffmann-Ostenhoff, M., Hoffmann-Ostenhoff, T.: *Phys. Rev. A* **16**, 1782 (1977)
12. Ahlrichs, R., Hoffmann-Ostenhoff, T., Hoffmann-Ostenhoff, M., Morgan III, J.D.: *Phys. Rev. A* **23**, 2107 (1981). and earlier references therein
13. Hylleraas, E.A., Undheim, B.: *Z. Phys.* **65**, 759 (1930)
14. MacDonald, J.K.L.: *Phys. Rev.* **43**, 830 (1933)
15. Hylleraas, E.A.: *Z. Phys.* **48**, 469 (1928)
16. Accad, Y., Pekeris, C.L., Schiff, B.: *Phys. Rev. A* **4**, 516 (1971)
17. Frankowski, K., Pekeris, C.L.: *Phys. Rev.* **146**, 46 (1966)
18. Freund, D.E., Huxtable, B.D., Morgan III, J.D.: *Phys. Rev. A* **29**, 980 (1984)
19. Thakkar, A.J., Koga, T.: *Phys. Rev. A* **50**, 854 (1994)
20. Schwartz, C.: *Int. J. Mod. Phys.* **15**, 877 (2006)
21. Drake, G.W.F.: *Nucl. Instrum. Methods Phys. Res. B* **31**, 7 (1988)
22. Drake, G.W.F., Yan, Z.-C.: *Phys. Rev. A* **46**, 2378 (1992)
23. Drake, G.W.F., Yan, Z.-C.: *Chem. Phys. Lett.* **229**, 486 (1994)
24. Frolov, A.M., Smith, V.H.: *J. Phys. B* **37**, 2917 (2004)
25. Korobov, V.: *Phys. Rev. A* **69**, 054501 (2004). The Bethe logarithms calculated by Korobov include an additional $\ln Z^2$ in their definition
26. Drake, G.W.F.: *Phys. Rev. A* **18**, 820 (1978)
27. Yan, Z.-C., Drake, G.W.F.: *Can. J. Phys.* **72**, 822 (1994)
28. Ackermann, J.: *Phys. Rev. A* **52**, 1968 (1995) and earlier references therein
29. Hu, C.-Y., Kvitsinsky, A.A., Cohen, J.S.: *J. Phys. B* **28**, 3629 (1995) and earlier references therein
30. Krivec, R., Mandelzweig, V.B., Varga, K.: *Phys. Rev.* **61**, 062503 (2000) and earlier references therein
31. Aznabaev, D.T., Bekbaev, A.K., Korobov, V.I.: *Phys. Rev. A* **98**, 012510 (2018)
32. Wang, M., Audi, G., Kondev, F.G., Huang, W.J., Naimi, S., Xu, X.: *Chin. Phys. C* **41**, 030003 (2017)
33. Nakashima, H., Nakatsuji, H.: *J. Chem. Phys.* **128**, 154108 (2008)
34. Dalgarno, A., Lynn, N.: *Proc. Phys. Soc. A* **70**, 802 (1957)
35. Drake, G.W.F.: *Adv. At. Mol. Opt. Phys.* **31**, 1 (1993)
36. Araki, H.: *Prog. Theor. Phys.* **17**, 619 (1957)
37. Sucher, J.: *Phys. Rev.* **109**, 1010 (1958)
38. Drake, G.W.F., Goldman, S.P.: *Can. J. Phys.* **77**, 835 (1999)
39. Korobov, V.I.: *Phys. Rev. A* **100**, 012517 (2019)
40. Goldman, S.P., Drake, G.W.F.: *Phys. Rev. Lett.* **68**, 1683 (1992)
41. Drake, G.W.F.: *Phys. Scr.* **T95**, 22 (2001)
42. Drake, G.W.F., Swainson, R.A.: *Phys. Rev. A* **41**, 1243 (1990)
43. Stone, A.P.: *Proc. Phys. Soc.* **77**, 786 (1961)
44. Yerokhin, V.A., Pachucki, K.: *Phys. Rev. A* **81**, 022507 (2010)
45. Pachucki, K., Patkóš, V., Yerokhin, V.A.: *Phys. Rev. A* **95**, 062510 (2017)
46. Yan, Z.-C., Drake, G.W.F.: *Phys. Rev. Lett.* **74**, 4791 (1995)
47. Kato, K., Skinner, T.D.G., Hessels, E.A.: *Phys. Rev. Lett.* **121**, 143002 (2018)
48. Lu, Z.-T., Mueller, P., Drake, G.W.F., Nortershauser, W., Pieper, S.C., Yan, Z.-C.: *Rev. Mod. Phys.* **85**, 1383 (2013)
49. Drake, G.W.F., Khriplovich, I.B., Milstein, A.I., Yelkhovskiy, A.S.: *Phys. Rev. A* **48**, R15 (1993)
50. Yerokhin, V.A., Patkóš, V., Puchalski, M., Pachucki, K.: *Phys. Rev. A* **102**, 01807 (2020)
51. Morton, D.C., Wu, Q.X., Drake, G.W.F.: *Can. J. Phys.* **84**, 83 (2006)
52. Babb, J.F., Spruch, L.: *Phys. Rev. A* **38**, 13 (1988)
53. Storry, C.H., Rothery, N.E., Hessels, E.A.: *Phys. Rev. Lett.* **75**, 3249 (1995) and earlier references therein
54. Drake, G.W.F.: *Adv. At. Mol. Opt. Phys.* **32**, 93 (1994)
55. Drachman, R.J.: *Phys. Rev. A* **47**, 694 (1993) and earlier references therein
56. Drake, G.W.F., Swainson, R.A.: *Phys. Rev. A* **42**, 1123 (1990)
57. Wang, X.-F., Yan, Z.-C.: *Phys. Rev. A* **95**, 022505 (2017)
58. Hessels, E.A.: *Phys. Rev. A* **46**, 5389 (1992)
59. Drake, G.W.F.: *Phys. Rev. A* **45**, 70 (1992)
60. Drake, G.W.F.: *Phys. Rev. A* **5**, 1979 (1972)
61. Drake, G.W.F.: *Phys. Rev. A* **19**, 1387 (1979)
62. Sansonetti, C.J., Gillaspay, J.D.: *Phys. Rev. A* **45**, R1 (1992)
63. George, M.C., Lombardi, L.D., Hessels, E.A.: *Phys. Rev. Lett.* **87**, 173002 (2001)
64. Drake, G.W.F.: *Can. J. Phys.* **80**, 1195 (2002)
65. Pachucki, K., Sapirstein, J.: *J. Phys. B* **36**, 803 (2003) and earlier references therein
66. Fock, V.A.: *D. Kngl. Norske Videnskab. Selsk. Forh.* **31**, 138 (1958)
67. Fock, V.A.: *D. Kngl. Norske Videnskab. Selsk. Forh.* **31**, 145 (1958)
68. Sochilin, G.B.: *Int. J. Quantum Chem.* **3**, 297 (1969)
69. McIsaac, K., Maslen, E.N.: *Int. J. Quantum Chem.* **31**, 361 (1987)
70. Hylleraas, E.A.: *Z. Phys.* **54**, 347 (1929)
71. Frankowski, K., Pekeris, C.L.: *Phys. Rev.* **150**, 366(E) (1966)
72. Drake, G.W.F.: In: Levin, F.S., Micha, D.A. (eds.) *Long Range Casimir Forces: Theory and Recent Experiments in Atomic Systems*, p. 107. Plenum, New York (1993)
73. Stone, A.P.: *Proc. Phys. Soc.* **81**, 868 (1963)
74. Au, C.-K.: *Phys. Rev. A* **39**, 2789 (1989)
75. Au, C.-K., Mesa, M.A.: *Phys. Rev. A* **41**, 2848 (1990)
76. Drake, G.W.F.: *J. Phys. B* **9**, L169 (1976)
77. Lichten, W., Shiner, D., Zhou, Z.-X.: *Phys. Rev. A* **43**, 1663 (1991)



Gordon W.F. Drake, FRSC, FAPS

Gordon W.F. Drake, Professor of Physics (Emeritus) at the University of Windsor and past Editor of *Physical Review A*. He received his BSc degree from McGill University, 1964, MSc from the University of Western Ontario, 1965, and PhD from York University, 1967. He has published 230 refereed research papers and is widely cited for his high-precision calculations for two and three-electron atoms, including relativistic and quantum electrodynamic effects.



Atomic Multipoles

13

William E. Baylis

Contents

13.1	Polarization and Multipoles	218
13.2	The Density Matrix in Liouville Space	219
13.3	Diagonal Representation: State Populations	219
13.4	Interaction with Light	220
13.5	Extensions	221
	References	221

Abstract

Often symmetries in the experiment limit the number of nonvanishing multipoles, and frequently only populations proportional to diagonal elements of the density matrix are significant. This chapter studies the physical and geometrical significance of simple multipoles and examines whether symmetries allow a complete characterization of the ensemble with state populations. More thorough treatments can be found elsewhere [1].

Keywords

density matrix · total angular momentum · multipole moment · atomic ensemble · state manifold

A typical atomic experiment involves the preparation of an atomic or molecular ensemble, its perturbation by a combination of collisions and external fields, and the characterization of the perturbed system through detection of emitted or scattered particles or quanta. The ensemble can be described by its density matrix, whose full specification generally requires elements between every pair of states in a complete basis set, and whose elements generally depend on spatial posi-

tion, velocity, and time. The time development of such an ensemble may depend on interactions among the atoms of the ensemble with each other, with external fields, and with external perturbers. Most problems burdened by this much detail are intractable, but fortunately, significant simplifications can usually be made.

In this chapter, only ensembles of homogeneously excited, independent atoms are considered. The spatial and velocity distribution of the atoms is thus assumed to be independent of the quantum-state distribution, and the total density matrix can be factored into the product of a phase-space distribution with a state density matrix that is independent of position and velocity. The assumption is severe and prevents us from treating cases of radiation transfer (Chap. 20) where the degree of excitation varies as a function of position or problems of velocity-selective laser excitation. Nevertheless, many experiments in atomic physics do use ensembles that are well-described by our assumption, and even in more complex cases, our model can often serve as a starting point for analysis. Typical of the experiments for which our approach is well suited are collisionally induced polarization relaxation experiments in a gas cell, either of an excited state or of an optically pumped ground state. In addition, we shall for the most part focus on a few isolated manifolds, usually a ground-state manifold and one or two excited-state manifolds. Each manifold, we assume, can be described by a given eigenvalue J of the total angular momentum. The qualifier *isolated* means that coherences between manifolds oscillate rapidly in time compared to other processes and can be ignored. These assumptions permit a great simplification and frequently allow a decoupling of the equations of motion, as shown below. The density matrix within each state manifold can be described by multipole moments, which are coefficients of the expansion of the density matrix in irreducible tensor operators, as described in Chap. 7. Each state multipole is associated with a physical electric or magnetic moment in the atom.

The amount of information which can be imparted to, or obtained from, an atomic ensemble is limited by the finite

W. E. Baylis (✉)
 Department of Physics, University of Windsor
 Windsor, ON, Canada
 e-mail: baylis@uwindsor.ca

number of accessible multipole moments. The nature of that information may depend on the time evolution of the multipoles in external fields and their relaxation through collisions. The ideal experiment is a *complete* measurement that determines all the multipoles. Often *over-complete* experiments can be designed, but there is little reason for determining redundant information unless consistency checks are important.

13.1 Polarization and Multipoles

An ensemble is said to be *polarized* if there is a nonstatistical distribution of atoms in magnetic sublevels. The type of polarization can be described by the *multipoles* that exist. In many experiments, symmetries in the preparation or detection of the ensemble limit the detectable polarizations to ones caused by different sublevel populations. One can then employ the relatively simple *population* (or *diagonal*) representation. The more general case is discussed in the next section.

As an introduction to the concepts, consider an atomic manifold of total angular momentum $3/2$, for example an excited alkali $P_{3/2}$ state. There are four magnetic sublevels $|m\rangle$ with $m = \pm 3/2, \pm 1/2$ so that state populations are given by a four-dimensional population–density vector

$$\mathbf{N} = \begin{pmatrix} N_{3/2} \\ N_{1/2} \\ N_{-1/2} \\ N_{-3/2} \end{pmatrix}, \quad (13.1)$$

where N_m is the density of atoms in state $|m\rangle$. If there are no external fields, the time evolution of \mathbf{N} is given by

$$\dot{\mathbf{N}} = \mathbf{S} - \Gamma \mathbf{N} - \boldsymbol{\gamma} \cdot \mathbf{N}, \quad (13.2)$$

where \mathbf{S} is the source vector and gives the excitation rate to the various sublevels, Γ is the radiative decay rate, assumed the same for all levels, and $\boldsymbol{\gamma}$ is the collisional matrix, whose elements $-\gamma_{mn}$ give the collisional transition rate from n to m .

The equation of motion is most easily solved if the basis used for the state space exploits the symmetry. Define the *spherical* orthonormal basis of vectors

$$\hat{\mathbf{T}}_0 = \frac{1}{2} \begin{pmatrix} 1 \\ 1 \\ 1 \\ 1 \end{pmatrix}, \quad \hat{\mathbf{T}}_1 = \frac{1}{\sqrt{20}} \begin{pmatrix} 3 \\ 1 \\ -1 \\ -3 \end{pmatrix}, \quad (13.3)$$

$$\hat{\mathbf{T}}_2 = \frac{1}{2} \begin{pmatrix} 1 \\ -1 \\ -1 \\ 1 \end{pmatrix}, \quad \hat{\mathbf{T}}_3 = \frac{1}{\sqrt{20}} \begin{pmatrix} 1 \\ -3 \\ 3 \\ -1 \end{pmatrix}. \quad (13.4)$$

(These relations follow from the \mathbf{T}_{LM} with $M = 0$. See Sects. 13.2 and 13.3). The population vector \mathbf{N} can be expanded

$$\mathbf{N} = \sum_{L=0}^4 n_L \hat{\mathbf{T}}_L, \quad (13.5)$$

where the coefficients $n_L = \mathbf{N} \cdot \hat{\mathbf{T}}_L$ contain all the knowable information about the population distribution. The coefficient n_L is called the $2L$ multipole moment of the ensemble. In particular,

$$n_0 = \frac{1}{2} \sum_m N_m$$

is twice the population of the entire ensemble;

$$n_1 = 5^{-1/2} \sum_m m N_m = \frac{2n_0 \langle J_z \rangle}{\sqrt{5}}$$

is the *orientation* (associated with a physical magnetic-dipole moment) of the system,

$$n_2 = \frac{1}{3} n_0 \langle 3J_z^2 - J^2 \rangle$$

is the *alignment* (electric quadrupole moment), and

$$n_3 = \frac{2n_0}{\sqrt{45}} \langle J_z(5J_z + 1 - 3J^2) \rangle$$

is the octupole moment of \mathbf{N} . The source vector \mathbf{S} is readily expanded in the same basis.

If the collisions are isotropic, as is usually approximately the case in gas-cell experiments, then the collision matrix $\boldsymbol{\gamma}$ is invariant under rotations and

$$\boldsymbol{\gamma} \cdot \hat{\mathbf{T}}_L = \gamma_L \hat{\mathbf{T}}_L. \quad (13.6)$$

The equation of motion Eq. (13.2) is separated into four uncoupled scalar equations

$$\dot{n}_L = S_L - \Gamma n_L - \gamma_L n_L. \quad (13.7)$$

If the source term $S_L = \mathbf{S} \cdot \hat{\mathbf{T}}_L$ is constant, Eq. (13.7) have the simple solutions

$$n_L(t) = n_L(\infty) + [n_L(0) - n_L(\infty)] \exp[-(\Gamma + \gamma_L)t], \quad (13.8)$$

with the steady-state value

$$n_L(\infty) = \frac{S_L}{\Gamma + \gamma_L}. \quad (13.9)$$

The detection of such multipoles is discussed at the end of Sect. 13.4.

13.2 The Density Matrix in Liouville Space

If in the example of the last section the state basis is changed, say by rotating the axis of quantization, then populations are generally no longer sufficient to characterize the ensemble. In the new basis, the ensemble will have been prepared in a coherent superposition of states. An adequate description for the quantum state of an ensemble in a manifold of n quantum states requires an $n \times n$ density matrix $\rho(t)$ as discussed in Chap. 7.

The density matrix may be considered a vector in a space, called *Liouville space*, of n^2 dimensions. A convenient set of complex orthonormal basis vectors in this space is given by the irreducible tensor operators T_{LM}

$$T_{LM}^* \cdot T_{L'M'} := \text{Tr}\{T_{LM}^\dagger T_{L'M'}\} = \delta_{LL'} \delta_{MM'}, \quad (13.10)$$

where the trace (Tr) expression is appropriate for the usual $n \times n$ matrix representations of the T_{LM} . Every quantum operator on the manifold can be expanded in the basis $\{T_{LM}\}$, and in particular the density matrix has an expansion

$$\rho(t) = \sum_{LM} \rho_{LM}(t) T_{LM}, \quad (13.11)$$

with time-dependent coefficients

$$\begin{aligned} \rho_{LM}(t) &= T_{LM}^* \cdot \rho(t) := \text{Tr}\{T_{LM}^\dagger \rho(t)\} \\ &= N \langle T_{LM}^\dagger \rangle \end{aligned} \quad (13.12)$$

that are identified with the multipole moments of the ensemble. Here, $\langle \dots \rangle$ indicates the average value over the ensemble and $N = \text{Tr}\{\rho\}$ is the normalization of the density matrix ρ , which is often set equal to unity but is sometimes more conveniently set equal to the total density of atoms in the manifold.

The T_{LM} are defined to transform under rotations as spherical harmonics Y_{LM} [2, 3]. The expansion Eq. (13.11) splits the density matrix into basis vectors T_{LM} which contain the geometric information and scalar coefficients (the multipole moments) $\rho_{LM}(t)$ which contain the physical information about state distributions.

The time dependence of $\rho(t)$ is given by the Schrödinger equation and in the interaction picture takes the form

$$i\hbar \dot{\rho} = [V, \rho], \quad (13.13)$$

where V is the interaction due to external fields (including radiation) and collisions. When V is expanded and second-order perturbation theory is applied, the time evolution Eq. (13.13) can be expressed in a form analogous to Eq. (13.2) but with an extra term [1]

$$\dot{\rho} = S - \Gamma \cdot \rho - \gamma \cdot \rho - iL_0 \cdot \rho, \quad (13.14)$$

where L_0 is the *Liouville operator* arising from the interaction V_0 with slowly varying external fields. Its matrix elements with ρ are

$$(L_0 \cdot \rho)_{mn} = \hbar^{-1} [V_0, \rho]_{mn} = (\omega_m - \omega_n) \rho_{mn}, \quad (13.15)$$

where $\omega_m - \omega_n$ are the field-induced frequency splittings between the states.

For example, in a weak magnetic field $B_0 \hat{z}$ oriented along the quantization axis \hat{z} , $V_0 = \omega_0 J_z$ where $\omega_0 = g_j \mu_B B_0 / \hbar$. Since $[J_z, T_{LM}] = M \hbar T_{LM}$ (see Chap. 7, then assuming that the collisions are isotropic and that the radiative decay rate is the same for all states of the manifold, the expansion of ρ in T_{LM} decouples the equation of motion Eq. (13.14) into multipoles

$$\dot{\rho}_{LM} = S_{LM} - \Gamma \rho_{LM} - \gamma_L \rho_{LM} - iM \omega_0 \rho_{LM}, \quad (13.16)$$

with the solution

$$\begin{aligned} \rho_{LM}(t) &= \rho_{LM}(\infty) + [\rho_{LM}(0) - \rho_{LM}(\infty)] \\ &\quad \times \exp[-(\Gamma + \gamma_L + iM \omega_0)t] \end{aligned} \quad (13.17)$$

comprising a transient part that decays as it precesses at the angular rate ω_0 plus a steady-state part that predicts the collisionally broadened Hanle effect (Chap. 18)

$$\rho_{LM}(\infty) = \frac{S_{LM}}{\Gamma + \gamma_L + iM \omega_0}. \quad (13.18)$$

If $M = 0$, the solutions reduce to the field-independent ones given in Eq. (13.9). On the other hand, any stray field that is not aligned with an induced multipole moment can rotate the moment and possibly cause systematic measurement errors if not taken into account. Measurements of γ_L in a gas cell at temperature T are frequently used to determine thermally averaged multipole-relaxation cross sections Q_L , defined by

$$\gamma_L = N \bar{v} Q_L, \quad (13.19)$$

where N is the density of perturbers, and the mean relative velocity is $\bar{v} = 2\pi^{-1/2} (2kT/\mu)^{1/2}$, with μ the reduced mass of the polarized-atom/perturber system. Many semiclassical and full quantum calculations of such cross sections have been made, both for atoms [1, 4] and for molecules [5].

13.3 Diagonal Representation: State Populations

An ensemble is said to be in a *coherent state* when one or more of the off-diagonal elements of the density matrix do not vanish. In a manifold of angular momentum substates of

a single total angular momentum j , the ensemble has coherence if and only if it is not axially symmetric, that is, if and only if $[\rho, J_z] \neq 0$. In an ensemble lacking coherence, or one in which any coherence that is present does not affect the observation, only the $N = 2j + 1$ diagonal elements of the $N \times N$ density matrix, those that represent state populations, need be considered. In terms of multipoles, only the N elements ρ_{L0} then play a role; the ρ_{LM} elements with $M \neq 0$ can be safely ignored. Such a *diagonal representation* is valid whenever (1) the time evolution of the system is axially symmetric and (2) either the preparation of the system or its detection is axially symmetric.

13.4 Interaction with Light

A polarized system can be prepared in a variety of ways, including beam splitting in external fields, collisional excitation (including beam-foil excitation of fast beams), or radiative excitation with directed and/or polarized light. Several options for the detection of multipoles also exist, including the measurement of the anisotropy and/or polarization of scattered particles or photons. In this section, the interaction of the atomic ensemble with dipole radiation is considered.

It is convenient to define a *detection operator* for electric dipole radiation of polarization $\hat{\epsilon}$ by

$$\mathbf{D}_\lambda(\hat{\epsilon}) = \sum_\mu \hat{\epsilon} \cdot \mathbf{d} |\lambda\mu\rangle \langle \lambda\mu| \mathbf{d} \cdot \hat{\epsilon}^* \quad (13.20)$$

for decay to the state λ . Here, $\mathbf{d} = \sum_k e r_k$ is the dipole-moment operator of the atom and μ is a magnetic sublevel of λ . The detection operator is a vector in Liouville space and can be expanded in irreducible tensor operators according to

$$\mathbf{D}_\lambda(\hat{\epsilon}) = \sum_{LM} D_{\lambda LM}(\hat{\epsilon}) \mathbf{T}_{LM}, \quad (13.21)$$

where

$$\begin{aligned} D_{\lambda LM}(\hat{\epsilon}) &= \mathbf{T}_{LM}^* \cdot \mathbf{D}_\lambda(\hat{\epsilon}) \\ &= B_L(\lambda) \Phi_{LM}(\hat{\epsilon}), \end{aligned} \quad (13.22)$$

with the dynamics contained in

$$B_L(\lambda) = (-1)^{\lambda+L+j+1} |d_{j\lambda}|^2 \left\{ \begin{matrix} 1 & L & 1 \\ j & \lambda & j \end{matrix} \right\}, \quad (13.23)$$

and the angular dependence in

$$\begin{aligned} \Phi_{LM}(\hat{\epsilon}) &= (2L+1)^{1/2} \sum_{rs} \hat{\epsilon} \cdot \hat{\mathbf{r}}(\hat{\epsilon} \cdot \hat{\mathbf{s}})^* \\ &\times (-1)^{1-s} \begin{pmatrix} 1 & L & 1 \\ r & \lambda & -s \end{pmatrix}. \end{aligned} \quad (13.24)$$

Here, $\hat{\mathbf{r}}$ and $\hat{\mathbf{s}}$ range over the unit spherical tensors of rank one, namely $\pm \hat{\mathbf{1}} = \mp(\hat{x} \pm i\hat{y})/\sqrt{2}$ and $\hat{\mathbf{0}} = \hat{z}$ (see also *Omont* [6], who gives tables of Φ_{LM}), and $d_{j\lambda}$ is a reduced matrix element of \mathbf{d} .

The intensity of radiation of polarization $\hat{\epsilon}'$ emitted by an excited ensemble of atoms with state density matrix ρ in its radiative decay to level λ is

$$\begin{aligned} \rho^* \cdot \mathbf{D}_\lambda(\hat{\epsilon}') &= \sum_{m,n,\mu} \langle \lambda\mu | \mathbf{d} \cdot \hat{\epsilon}'^* | m \rangle \rho_{mn} \langle n | \mathbf{d} \cdot \hat{\epsilon}' | \lambda\mu \rangle \\ &= \sum_{LM} \rho_{LM} D_{\lambda LM}, \end{aligned} \quad (13.25)$$

and by selection of polarization or spatial distribution, individual multipole components $D_{\lambda LM}$ and hence ρ_{LM} can be determined. The source terms S_{LM} excited by electric-dipole radiation from an isotropic ground state are given by a linear combination of $D_{\lambda LM}$

$$S_{LM} = (2\pi)^2 \sum_{\lambda, \hat{\epsilon}} u_{\hat{\epsilon}}(\lambda) D_{\lambda LM}(\hat{\epsilon}), \quad (13.26)$$

where $u_{\hat{\epsilon}}(\lambda)$ is the energy density of exciting radiation with polarization vector $\hat{\epsilon}$ per unit energy. From the $3-j$ symbol in Eq. (13.24), only the $L = 0, 1,$ and 2 components of ρ are observable unless the splitting of the Zeeman sublevels of λ are spectroscopically resolved. Similarly, if the ground state is unpolarized and its Zeeman sublevels unresolved, then only $L = 0, 1,$ and 2 components of ρ can be excited. To excite higher-order multipoles, the ground state can be polarized by optical pumping [7].

As an example, consider the axially symmetric system discussed in Sect. 13.1 with $j = 3/2$ in the excited state and $\lambda = 1/2$ in the ground state. Only the four diagonal elements of $\mathbf{D}(\hat{\epsilon}')$,

$$\begin{aligned} D_m(\hat{\epsilon}') &= \sum_\mu | \langle jm | \hat{\epsilon}' \cdot \mathbf{d} | \lambda\mu \rangle |^2 \\ &= |d_{j\lambda}|^2 \sum_{\mu r} | \hat{\epsilon}' \cdot \hat{\mathbf{r}} |^2 \begin{pmatrix} \lambda & 1 & j \\ -\mu & r & m \end{pmatrix}^2, \end{aligned}$$

are needed for the $2j + 1$ values of $m = -j, \dots, j$, where μ ranges over the $2\lambda + 1$ values from $-\lambda$ to λ and $r = \pm 1, 0$. One finds directly

$$\begin{aligned} \mathbf{D}(\hat{\epsilon}') &= \frac{|d_{j\lambda}|^2}{12} \\ &\times \left[|\hat{\epsilon}' \cdot \hat{\mathbf{1}}|^2 \begin{pmatrix} 3 \\ 1 \\ 0 \\ 0 \end{pmatrix} + |\hat{\epsilon}' \cdot \hat{\mathbf{0}}|^2 \begin{pmatrix} 0 \\ 2 \\ 2 \\ 0 \end{pmatrix} + |\hat{\epsilon}' \cdot \hat{\mathbf{1}}|^2 \begin{pmatrix} 0 \\ 0 \\ 1 \\ 3 \end{pmatrix} \right]. \end{aligned} \quad (13.27)$$

The detected signal of polarization $\hat{\epsilon}'$ is proportional to $N \cdot \mathbf{D}(\hat{\epsilon}')$, where N is the population–density vector Eq. (13.1). Some of the state polarization can be monitored by looking at polarized dipole radiation. If the emitted light is observed as it propagates perpendicular to the polarization vector, the intensities are given to within an overall constant of proportionality by

$$I_{\sigma\pm} = \mathbf{D}(\pm\hat{\mathbf{i}}) \cdot N, \quad I_{\pi} = \mathbf{D}(\hat{\mathbf{o}}) \cdot N, \quad (13.28)$$

$$I_{\sigma} = \mathbf{D}(\hat{\xi}) \cdot N = \frac{1}{2}(I_{\sigma+} + I_{\sigma-}), \quad (13.29)$$

where $\hat{\xi}$ is any real unit vector (linear polarization vector) in the xy -plane. The intensities of polarized radiation may also be given in terms of Stokes parameters [8] (see also Chap. 7). By expanding N in the spherical basis vectors T_L as in Eq. (13.5), one obtains a detected signal

$$\begin{aligned} N \cdot \mathbf{D}(\hat{\epsilon}') &= \sum_{L=0}^{2j+1} n_L D_{\lambda L 0} & (13.30) \\ &= \frac{|d_{j\lambda}|^2}{12} \left[2n_0 + \sqrt{5} \left(|\hat{\epsilon}' \cdot \hat{\mathbf{i}}|^2 - |\hat{\epsilon}' \cdot -\hat{\mathbf{i}}|^2 \right) n_1 \right. \\ &\quad \left. + \left(3|\hat{\epsilon}' \cdot \hat{\mathbf{o}}|^2 - 1 \right) n_2 \right]. & (13.31) \end{aligned}$$

Thus there is no way to monitor the octupole polarization n_3 from the dipole radiation since $D_{\lambda L M} = 0$ for $L > 2$. To monitor the orientation n_1 , the circular polarization must be measured

$$\frac{\sqrt{5} n_1}{3 n_0} = \frac{I_{\sigma+} - I_{\sigma-}}{2I_{\sigma} + I_{\pi}}, \quad (13.32)$$

since the coefficient $D_{\lambda L 0}$ vanishes for any linear polarization. Conversely, from

$$\frac{n_2}{2n_0} = \frac{I_{\sigma} - I_{\pi}}{2I_{\sigma} + I_{\pi}}, \quad (13.33)$$

alignment is given by linear polarization. However, the denominator in both cases is different from that common in polarization measurements, and indeed, the ratio $(I_{\sigma+} - I_{\sigma-})/(I_{\sigma+} + I_{\sigma-})$ is *not* proportional to the orientation but contains a contribution from the alignment, and $(I_{\sigma} - I_{\pi})/(I_{\sigma} + I_{\pi})$ is not linear in the alignment. The expressions for other total angular momenta j are the same except for the numerical coefficients on the LHS of Eqs. (13.32) and (13.33). Finally, if the desire is to measure the total excited-state population n_0 without any polarization component (which might rotate in stray external fields), one can choose linear polarization at an angle to make $D_{\lambda 2 0}$ disappear, namely at the *magic angle* $\theta = \arccos(3^{-1/2}) = 54.74^\circ$. Of course, the same angle may be chosen to excite an unpolarized population.

13.5 Extensions

Although the discussion here has focused on cell experiments in which collisional perturbations are isotropic and state manifolds with a given total angular momentum j are well isolated, the concept of state multipoles is also useful in many applications where the collision symmetry is lower and where states with different j values interact, possibly due to the presence of fine and hyperfine structure [1]. Applications have been made in electron–atom collisions (Chap. 7), atom–atom collisions [9], and atom–molecule collisions [5].

References

1. Baylis, W.E.: Chap. 28. In: Progress in Atomic Physics, ed. by Hanle, W. and Kleinpoppen, H. (Plenum, New York 1977)
2. Fano, U.: Rev. Mod. Phys. **29**, 74 (1957)
3. Fano, U., Racah, G.: Irreducible Tensorial Sets. Academic Press, New York (1967)
4. Lewis, E.L.: Phys. Rep. **58**, 1 (1980)
5. Baylis, W.E., Pascale, J., Rossi, F.: Phys. Rev. A **36**, 4212 (1987)
6. Omont, A.: Prog. Quantum Electron. **5**, 69 (1977)
7. Happer, W.: Rev. Mod. Phys. **44**, 169 (1972)
8. Baylis, W.E., Bonenfant, J., Derbyshire, J., Huschilt, J.: Am. J. Phys. **61**, 534 (1993)
9. Nikitin, E.E., Umanski, S.Y.: Theory of Slow Atomic Collisions. Springer, Berlin, Heidelberg (1984)



William E. Baylis Professor Baylis earned degrees in physics from Duke (B.Sc.), the University of Illinois (M.Sc.), and the Technical University of Munich (D.Sc.). He has authored two books, edited or co-edited four more, contributed 28 chapters to other volumes, and published over a hundred journal articles. His publications are in theoretical physics and emphasize atomic and molecular structure, atomic collisions, and interactions with radiation. His most recent work concerns relativistic dynamics, the photon position operator and wave function, and applications of Clifford algebra, especially to the quantum–classical interface. He is a fellow of the American Physical Society, past chair of the Divisions of Atomic and Molecular Physics and of Theoretical Physics of the Canadian Association of Physicists, a member of the international editorial boards of the Springer Series of Atomic, Optical, and Plasma Physics and of the journal Advances in Applied Clifford Algebras. He is currently a University Professor emeritus at the University of Windsor.



S. Pedro Goldman and Mark M. Cassar

Contents

14.1	Electron in a Uniform Magnetic Field	223
14.1.1	Nonrelativistic Theory	223
14.1.2	Relativistic Theory	224
14.2	Atoms in Uniform Magnetic Fields	225
14.2.1	Anomalous Zeeman Effect	225
14.2.2	Normal Zeeman Effect	225
14.2.3	Paschen–Back Effect	225
14.3	Atoms in Very Strong Magnetic Fields	226
14.4	Atoms in Electric Fields	227
14.4.1	Stark Ionization	227
14.4.2	Linear Stark Effect	227
14.4.3	Quadratic Stark Effect	228
14.4.4	Other Stark Corrections	228
14.5	Recent Developments	229
References		229

Abstract

Interest in the effect that electric and magnetic fields have on the internal structure of atoms is as old as quantum mechanics itself. In practical terms, an atom’s spectrum acts as its signature, and so it is important to understand how electric and magnetic fields alter this characteristic. In this chapter, a summary of the basic nonrelativistic and relativistic theory of electrons and atoms in external magnetic fields is given. Extensions to the case of very strong fields are then introduced for both types of fields.

S. P. Goldman (✉)
Dept. of Physics, Toronto Metropolitan University
Toronto, Canada
e-mail: goldman@ryerson.ca

M. M. Cassar
Zekelman School of Information Technology, St. Clair College
Windsor, ON, Canada
e-mail: mcassar@stclaircollege.ca

Keywords

neutron star · Landau level · Zeeman effect · Stark shift · field atom

14.1 Electron in a Uniform Magnetic Field

14.1.1 Nonrelativistic Theory

The nonrelativistic Hamiltonian (in Gaussian units) for an electron in an external field \mathbf{A} is [1]

$$H = \frac{1}{2m} \left(\mathbf{p} - \frac{e}{c} \mathbf{A} \right)^2 - \boldsymbol{\mu} \cdot \mathbf{B} + eV, \quad (14.1)$$

where \mathbf{A} is the vector potential and V is the scalar potential. The second term in Eq. (14.1) must be included to account for the interaction of the electron magnetic moment with an external magnetic field. The potentials \mathbf{A} and V are only defined to within a gauge transformation [2]:

$$\mathbf{A}' = \mathbf{A} + \nabla f, \quad V' = V - \frac{1}{c} \frac{\partial f}{\partial t}. \quad (14.2)$$

We choose the gauge $\nabla \cdot \mathbf{A} = 0$ in which the momentum operator $\mathbf{p} = i\hbar \nabla$ and vector potential \mathbf{A} commute. \mathbf{B} is a constant uniform magnetic field with vector potential

$$\mathbf{A} = \frac{1}{2} \mathbf{B} \times \mathbf{r}. \quad (14.3)$$

$\boldsymbol{\mu}$ is the magnetic moment of the electron:

$$\boldsymbol{\mu} = \frac{1}{2} g_e \mu_B \boldsymbol{\sigma}, \quad (14.4)$$

where the σ_i are the Pauli spin matrices, $\mu_B = e\hbar/2m_e c$ is the Bohr magneton and g_e is the electron g -factor which accounts for the anomalous magnetic moment of the electron (see Sect. 29.4).

Consider now the case of a free electron in a constant uniform field in the z -direction with no scalar potential, i.e., $V = 0$ in Eq. (14.1). This case also describes an atom in the limit of strong magnetic fields such that the Coulomb interactions are negligible. In this case, which is different from Eq. (14.3), we have

$$\mathbf{B} = B\hat{z} \text{ with } \begin{cases} A_x = -By \\ A_y = Ax = 0 \end{cases}. \quad (14.5)$$

For this field, the operators μ_z , p_x and p_z commute with the Hamiltonian and are therefore conserved. Calling their respective eigenvalues μ_z , p_x and p_z , with $-\infty \leq p_x, p_y \leq \infty$, the eigenstates are written as

$$\psi = e^{i(p_x x + p_z z)/\hbar} \varphi(y). \quad (14.6)$$

Calling $y_0 = -cp_x/eB$, φ satisfies

$$\begin{aligned} & -\frac{\hbar^2}{2m} \frac{d^2}{dy^2} \varphi + \frac{1}{2} m \omega_B^2 (y - y_0)^2 \varphi \\ & = \left(E + \mu_z B - \frac{p_z^2}{2m} \right) \varphi, \end{aligned} \quad (14.7)$$

which is the Schrödinger equation for a one-dimensional harmonic oscillator with angular frequency $\omega_B = |e|B/mc$, the cyclotron frequency of the electron. The solutions to Eq. (14.7) give the eigenstates for an electron in an external homogeneous magnetic field. They are called *Landau levels* [1] with energies given by

$$E_n = \left(n + \frac{1}{2} + m_s \right) \hbar \omega_B + \frac{p_z^2}{2m}, \quad (14.8)$$

where $\hbar m_s = \pm \hbar/2$ is the eigenvalue of the z -component of the spin operator s , and eigenfunctions given by

$$\begin{aligned} \varphi_n(y) &= \frac{1}{\sqrt{\pi^{1/2} a_B 2^n n!}} \\ &\times \exp\left(-\frac{(y - y_0)^2}{2a_B^2}\right) H_n\left(\frac{y - y_0}{a_B}\right), \end{aligned} \quad (14.9)$$

where $a_B = \sqrt{\hbar/m\omega_B}$ and the H_n are Hermite polynomials [3].

14.1.2 Relativistic Theory

The relativistic analog of Eq. (14.1) is given by the Dirac Hamiltonian

$$H_D = c\boldsymbol{\alpha} \cdot \left(\mathbf{p} - \frac{e}{c} \mathbf{A} \right) + \beta mc^2 + eV, \quad (14.10)$$

where $\boldsymbol{\alpha}$ and β are the 4×4 matrices defined by Eq. (9.61). The eigenfunctions of the Dirac Hamiltonian Eq. (14.10) are written as four-dimensional spinors:

$$\psi_D = \begin{pmatrix} \psi^{(1)} \\ \psi^{(2)} \\ \psi^{(3)} \\ \psi^{(4)} \end{pmatrix} \equiv \begin{pmatrix} \phi_1 \\ \phi_{-1} \\ \chi_1 \\ \chi_{-1} \end{pmatrix} \equiv \begin{pmatrix} \phi \\ \chi \end{pmatrix}, \quad (14.11)$$

where ϕ and χ are two-dimensional (Pauli) spinors and ϕ_i and χ_i are functions of the coordinates of the electron.

In the case $V = 0$, the lower component χ can be eliminated in the eigenvalue equation $H_D \psi = E \psi$ to obtain a Hamiltonian equation for ϕ only, similar to Eq. (14.1) [4]. For a field defined by Eq. (14.5) one writes ϕ in the form (as in the nonrelativistic case)

$$\phi = e^{i(p_x x + p_z z)/\hbar} f(y). \quad (14.12)$$

Here, $f(y)$ satisfies the equation

$$\begin{aligned} & -\frac{\hbar^2}{2m} \frac{d^2}{dy^2} \varphi + \frac{1}{2} m \omega_B^2 (y - y_0)^2 \varphi \\ & = \left(\frac{E^2 - m^2 c^4}{2mc^2} + \mu_z B - \frac{p_z^2}{2m} \right) \varphi, \end{aligned} \quad (14.13)$$

which reduces to the nonrelativistic form Eq. (14.7) in the limit $E \rightarrow mc^2$. In Eq. (14.13), the term involving μ is not included arbitrarily as in Eq. (14.1) but is a consequence of $H_D \phi$, which predicts the value $g = 2$. The value g_e used in Eq. (14.4) includes radiative corrections to the Dirac value.

From Eq. (14.13) we obtain

$$E_n^2 = 2mc^2 \left[\frac{mc^2}{2} + \left(n + \frac{1}{2} + m_s \right) \hbar \omega_B + \frac{p_z^2}{2m} \right], \quad (14.14)$$

and the eigenfunctions $\psi_{m_s}^D$ are

$$\begin{aligned} \psi_{1/2}^D &= N \begin{pmatrix} \frac{E + mc^2}{c} \psi_n \\ 0 \\ p_z \psi_n \\ -\frac{i\hbar}{a_B} \sqrt{2n} \psi_{n-1} \end{pmatrix}, \\ \psi_{-1/2}^D &= N \begin{pmatrix} 0 \\ \frac{E + mc^2}{c} \psi_n \\ \frac{i\hbar}{a_B} \sqrt{2(n+1)} \psi_{n+1} \\ -p_z \psi_n \end{pmatrix}, \end{aligned} \quad (14.15)$$

where ψ_n is defined as in Eqs. (14.6) and (14.9), and N is a normalization constant.

14.2 Atoms in Uniform Magnetic Fields

14.2.1 Anomalous Zeeman Effect

Consider now the nonrelativistic Hamiltonian for a one-electron atom in the presence of an external magnetic field \mathbf{B} . The one-electron Hamiltonian can be written as [5]

$$H = \frac{1}{2m} \mathbf{p}^2 - \frac{1}{4\pi\epsilon_0} \frac{Ze^2}{r} + \xi(r) \mathbf{L} \cdot \mathbf{S} + \frac{\mu_B}{\hbar} (\mathbf{L} + g_e \mathbf{S}) \cdot \mathbf{B} + \frac{e^2}{8mc^2} (\mathbf{B} \times \mathbf{r})^2, \quad (14.16)$$

where

$$\xi(r) = \frac{1}{2m^2 c^2} \frac{Ze^2}{4\pi\epsilon_0} \frac{1}{r^3}. \quad (14.17)$$

The anomalous Zeeman effect corresponds to the case of *weak* magnetic fields such that the magnetic interaction is small compared with the $\mathbf{L} \cdot \mathbf{S}$ spin-orbit term. The energy shifts are obtained from a perturbation of Eq. (14.16) with $\mathbf{B} = 0$. The unperturbed wave functions are eigenfunctions of L^2 , S^2 , J^2 and J_z , with $\mathbf{J} = \mathbf{L} + \mathbf{S}$, but are not eigenfunctions of L_z or S_z . The energy levels with given values of l , s and j split in the presence of a field defined by Eq. (14.5) according to

$$\Delta E_{m_j} = g \mu_B B m_j, \quad (14.18)$$

where g is the *Landé splitting factor* given by

$$g = g_l \frac{j(j+1) - s(s+1) + l(l+1)}{2j(j+1)} + g_e \frac{j(j+1) + s(s+1) - l(l+1)}{2j(j+1)}, \quad (14.19)$$

where g_e is defined by Eq. (14.4), and $g_l = 1 - m_e/M$ to lowest order in m_e/M , where m_e is the electron mass and M is the nuclear mass. To a first approximation, it is often sufficient to take $g_e = 2$ (the Dirac value) and $g_l = 1$. In the case of a many-electron atom, j , l and s are replaced by the *total* angular momenta J , L and S . In the one-electron case (neglecting corrections to g_l or g_e) the g -value is simply

$$g \approx \frac{j + \frac{1}{2}}{l + \frac{1}{2}}, \quad (14.20)$$

which shows that the splitting of the $j = l + \frac{1}{2}$ levels is larger than that of the $j = l - \frac{1}{2}$ levels. The selection rules for the splitting of spectral lines are $\delta m_j = 0$ for components polarized parallel to the field (π components), and $\delta m_j = \pm 1$ for those perpendicular to the field (σ components).

14.2.2 Normal Zeeman Effect

For moderately strong fields up to $B \approx 10^4$ T, the quadratic $(\mathbf{B} \times \mathbf{r})^2$ term in Eq. (14.16) can be neglected. If the spin-

orbit interaction term is also neglected, then the energies relative to the field-free eigenvalues E_n are given by

$$E_n(B) = E_n + \mu_B B (m_l + 2m_s). \quad (14.21)$$

The selection rules for transitions are $\Delta m_s = 0$ and $\Delta m_l = 0, \pm 1$. The transition energy of a spectral line is split into three components, the *Lorentz triplet*

$$\Delta E_n = \Delta E_{n,0} + (\Delta m_l) \hbar \omega_L, \quad (14.22)$$

where $\Delta E_{n,0}$ is the transition energy in the absence of a field, and $\omega_L = |e|B/2m$ is the Larmor frequency. Transitions with $\Delta m_l = 0$ produce the π line at the unshifted transition energy; transitions with $\Delta m_l = \pm 1$ produce the shifted σ lines. Lorentz triplets can be observed in many-electron atoms in which the total spin is zero.

14.2.3 Paschen–Back Effect

We add now to the results of the last section the first-order perturbation caused by the spin-orbit term. The calculation can be performed in closed form for hydrogenic atoms, for which the contribution to the energy of the level n is [6]

$$\begin{aligned} \Delta E_n &= 0, \quad \text{for } l = 0 \\ \Delta E_n &= \frac{\alpha^4 Z^4 \mu c^2}{2n^3} m_l m_s \\ &\quad \times \left[l \left(l + \frac{1}{2} \right) (l + 1) \right], \quad \text{for } l \neq 0 \end{aligned} \quad (14.23)$$

where μ is the reduced mass, $\mu = mM/(m+M)$. A general expression of the relativistic solution for the Paschen–Back effect can be written for the one-electron case in the Pauli approximation in which the eigenstates are given in terms of ϕ in Eq. (14.11). Call ϕ_{\pm}^0 the eigenfunctions with no external field corresponding to $j = l \pm \frac{1}{2}$ with unperturbed energies E_{\pm}^0 respectively. In terms of the dimensionless variables

$$\begin{aligned} \eta &= \frac{\mu_B B}{E_+ - E_-}, \quad \epsilon = \sqrt{1 + \eta \frac{4m_j}{2l+1} + \eta^2}, \\ \gamma &= \frac{1}{\epsilon} \left(1 + \eta \frac{4m_j}{2l+1} \right), \end{aligned} \quad (14.24)$$

the energies E_{\pm} and wave functions ϕ_{\pm} of the states, in the presence of the field B , are

$$E_{\pm} = \frac{E_{\pm}^0}{2} (1 \pm \epsilon + 2m_j \eta) + \frac{E_{\mp}^0}{2} (1 \mp \epsilon - 2m_j \eta) \quad (14.25)$$

and

$$\phi_{\pm} = \pm \sqrt{\frac{1 \pm \gamma}{2}} \phi_+^0 + \sqrt{\frac{1 \mp \gamma}{2}} \phi_-^0. \quad (14.26)$$

14.3 Atoms in Very Strong Magnetic Fields

The case of *very* strong magnetic fields (i.e., $B > 10^4$ T), such as those encountered at the surface of neutron stars, is also called the *quadratic Zeeman effect*, as the last term in Eq. (14.16) is dominant. In this range, perturbation calculations fail to yield good results as the field is too large, and even at fields of the order $B \approx 10^7$ T the Landau high B approximation of Eqs. (14.8) and (14.9) is not adequate.

Very accurate calculations have been performed using variational finite basis set techniques for both the relativistic Dirac and nonrelativistic Schrödinger Hamiltonians. The calculations use the following relativistic basis set [7] that includes nuclear size effects (R is the nuclear size) and contains both asymptotic limits, the Coulomb limit for $B = 0$ and the Landau limit for $B \rightarrow \infty$:

$$\psi_{nl}^{(k,v)} = \begin{cases} r^{q_k-1+2n} e^{-a_{nv}^{(k)} r^2 - \beta \rho^2} \Omega_k & r \leq R \\ b_{nv}^{(k)} r^{\gamma_v-1+n} e^{-\lambda r - \beta \rho^2} \Omega_k & r > R \end{cases} \quad (14.27)$$

with

$$\Omega_k = (\cos \theta)^{l-|m_k|} (\sin \theta)^{|m_k|} e^{im_k \phi} \omega_k, \quad (14.28)$$

where

$$\begin{aligned} n &= 0, 1, \dots, N_r, \quad k = 1, 2, 3, 4, \quad v = 1, 2, 3, 4, \\ q_1 &= q_2 = k_0, \quad q_3 = q_4 = k'_0, \\ m_k &= \mu - \sigma_k/2, \quad \sigma_1 = \sigma_3 = 1, \quad \sigma_2 = \sigma_4 = -1. \end{aligned}$$

Here, k refers to the component $\psi^{(k)}$ in Eq. (14.11), and λ and β are variational parameters. The power of r at the origin is given by

$$k_0 = \begin{cases} |\kappa| & \text{if } \kappa < 0 \\ |\kappa| + 1 & \text{if } \kappa > 0, \end{cases} \quad (14.29)$$

$$k'_0 = \begin{cases} |\kappa| + 1 & \text{if } \kappa < 0 \\ |\kappa| & \text{if } \kappa > 0, \end{cases} \quad (14.30)$$

The index v refers to the two regular and two irregular solutions for $r > R$ that match the corresponding powers at the origin k_0 and k'_0 .

$$\gamma_1 = \gamma_0, \quad \gamma_2 = \gamma_0 + 1, \quad \gamma_3 = -\gamma_0, \quad \gamma_4 = -\gamma_0 + 1, \quad (14.31)$$

$$\gamma_0 = \sqrt{\kappa^2 - (\alpha Z)^2}, \quad \kappa = \mp \left(v \pm \frac{1}{2} \right) + \frac{1}{2}, \quad (14.32)$$

$$\begin{aligned} \omega_1 &= \begin{pmatrix} \vartheta_1 \\ 0 \end{pmatrix}, & \omega_2 &= \begin{pmatrix} \vartheta_{-1} \\ 0 \end{pmatrix}, \\ \omega_3 &= \begin{pmatrix} 0 \\ i\vartheta_{-1} \end{pmatrix}, & \omega_4 &= \begin{pmatrix} 0 \\ i\vartheta_1 \end{pmatrix}, \end{aligned} \quad (14.33)$$

Table 14.1 Relativistic ground state binding energy $-E_{\text{gs}}/Z^2$ and finite nuclear size correction $\delta E_{\text{nuc}}/Z^2$ (in a.u.) of hydrogenic atoms for various magnetic fields B (in units of 2.35×10^5 T). δE_{nuc} should be added to E_{gs}

Z	B	$-E_{\text{gs}}/Z^2$	$\delta E_{\text{nuc}}/Z^2$
1	0	0.50000665659748375	1.55786×10^{-10}
1	10^{-5}	0.5000116564837	1.5579×10^{-10}
1	10^{-2}	0.504981572360	1.5580×10^{-10}
1	10^{-1}	0.5475324083429	1.5718×10^{-10}
1	2	1.0222180290	3.23×10^{-10}
1	10	1.74780068	1.182×10^{-9}
1	20	2.21540091	2.360×10^{-9}
1	200	4.7271233	3.032×10^{-8}
1	500	6.2570326	8.778×10^{-8}
20	0	0.5026913084075098	1.3372×10^{-6}
20	1	0.50393086705	1.34×10^{-6}
20	10	0.514950248	1.3×10^{-6}
20	100	0.61237794	1.4×10^{-6}
40	0	0.511129686143	1.1878×10^{-5}
92	0	0.5743381407377	8.4155×10^{-4}
92	1	0.574386987	8.4155×10^{-4}

Table 14.2 Relativistic binding energy $-E_{2S,-1/2}$ for the $2S_{1/2}$ ($m_j = -\frac{1}{2}$) and $-E_{2P,-1/2}$ for the $2P_{1/2}$ ($m_j = -\frac{1}{2}$) excited states of hydrogen (in a.u.) in an intense magnetic field B (in units of 2.35×10^5 T)

B	$-E_{2S,-1/2}$	$-E_{2P,-1/2}$
10^{-6}	0.125002580164	0.125002283074
10^{-5}		0.125006104950
10^{-4}	0.12505204495	0.12505096792
10^{-3}		0.1254994694
10^{-2}	0.1296536428	0.1298513642
0.05	0.142018956	
0.1	0.1480917386	0.1624110524
0.2	0.14898958	
0.5	0.15081015	
1	0.16047107	0.26000934
10	0.20895591	0.38266318
100	0.256191	0.4636641

where ϑ_k is a two-component Pauli spinor: $\sigma_z \vartheta_k = k \vartheta_i$. For even (odd) parity states, the value of l for the large components ($k = 1, 2$) is an even (odd) number greater than or equal to $|m_k|$ up to $2N_\theta$ (for even parity) or $2N_\theta + 1$ (for odd parity), while for the small components ($k = 3, 4$) it is an odd (even) number greater than or equal to $|m_k|$ up to $2N_\theta + 1$ (for even parity) or $2N_\theta$ (for odd parity), since the small component has a different nonrelativistic parity than the large component. The coefficients $a_{nv}^{(k)}$ and $b_{nv}^{(k)}$ are determined by the continuity condition of the basis functions and their first derivatives at R . For a point nucleus, the section $r \leq R$ is omitted; for a nonrelativistic calculation, take $\alpha = 0$ in the basis set.

Table 14.1 presents relativistic (Dirac) energies for the ground state of one-electron atoms. Values for a point nucleus and finite nuclear size corrections are given. Table 14.2

Table 14.3 Relativistic corrections $\delta E = (E - E_{NR})/|E_R|$ to the non-relativistic energies E_{NR} for the ground state and $n = 2$ excited states of hydrogen in an intense magnetic field B (in units of 2.35×10^5 T). The numbers in brackets denote powers of 10

B	δE_{gs}	B	$\delta E_{2S,-1/2}$	$\delta E_{2P,-1/2}$
0.1	-1.08[-5]	1[-6]	-1.66[-5]	-1.43[-5]
1	-5.21[-6]	1[-4]	-1.66[-5]	-7.86[-6]
2	-4.03[-6]	1[-3]		-7.72[-6]
3	-3.48[-6]	1[-2]	-1.60[-5]	-7.30[-6]
20	-1.09[-6]	0.05	-1.57[-5]	
200	4.61[-6]	0.1	-1.74[-6]	-6.00[-6]
500	8.81[-6]	1	-1.3[-5]	-1.05[-5]
2000	1.85[-5]	10	-2.0[-5]	-3.48[-5]
5000	2.78[-5]	100	-3.9[-5]	-1.0[-4]

presents the relativistic energies for $n = 2$ excited states of hydrogen with the (negligible) finite nuclear size correction included.

Table 14.3, which displays the relativistic corrections of the energies of the previous two tables, presents one of the most interesting relativistic results: the change in sign of the relativistic correction of the energy of the ground state at $B \approx 10^7$ T.

14.4 Atoms in Electric Fields

14.4.1 Stark Ionization

An external electric field \mathbf{F} introduces the perturbing potential

$$V = -\mathbf{d} \cdot \mathbf{F}, \quad (14.34)$$

where

$$\mathbf{d} = \sum_i q_i \mathbf{r}_i \quad (14.35)$$

is the dipole moment of the atom, and i runs over all electrons in the atom. In the case of strong external electric fields, bound states do not exist because the atom ionizes. Consider a hydrogenic atom in a static electric field

$$\mathbf{F} = F \hat{z}. \quad (14.36)$$

The total potential acting on the electron is then

$$V_{\text{tot}}(\mathbf{r}) = -\frac{e^2 Z}{4\pi\epsilon_0 r} + eFz. \quad (14.37)$$

Consider the z -dependence of this potential. Call $\rho = \sqrt{x^2 + y^2}$ and $v(z, \rho) = V(x, y, z)$. Unlike the Coulomb case in which $v_{\text{Coul}}(\pm\infty, \rho) = 0$ resulting in an infinite number of bound states, now $v(\pm\infty, \rho) = \pm\infty$ and v has a local maximum. On the z axis, this maximum occurs at $z_{\text{max}} = -\sqrt{Z|e|/(4\pi\epsilon_0 F)}$ for which $v(z_{\text{max}}, 0) = 0$. There is then a potential barrier through which the electron can tunnel, i.e.,

there are no bound states any longer but *resonances*. The potential barrier is shallower the stronger the field; the well can contain a smaller number of bound states and ionization occurs.

14.4.2 Linear Stark Effect

The electric field Eq. (14.36) produces a dipole potential

$$V_F = eFz = eFr \sqrt{\frac{4\pi}{3}} Y_{10}(\hat{\mathbf{r}}), \quad (14.38)$$

which does not preserve parity. A first-order perturbation calculation for the energy

$$E_n^{(1)} = \langle n | V_F | n \rangle \quad (14.39)$$

yields null results unless the unperturbed states are degenerate with states of opposite parity.

In the remainder of this chapter, atomic units will be used. Final results for energies can be multiplied by $2R_\infty hc$ to translate to SI or other units. The calculation can be carried out in detail for the case of hydrogenic atoms [8]. In this case it is convenient to work in parabolic coordinates: φ denotes the usual angle in the xy -plane, and

$$\begin{aligned} \xi &= r + z, \\ \eta &= r - z. \end{aligned} \quad (14.40)$$

The Hamiltonian for a hydrogenic atom with a field $V_F = \frac{1}{2} F (\xi - \eta)$ from Eq. (14.38) is

$$(\xi + \eta)H = \xi h_+(\xi) + \eta h_-(\eta). \quad (14.41)$$

The wave function is written in the form

$$\Psi(\xi, \eta, \varphi) = \frac{1}{\sqrt{2\pi Z}} \psi_+(\xi) \psi_-(\eta) e^{im_l \varphi}, \quad (14.42)$$

with the ψ_\pm satisfying

$$h_\pm(x) \psi_\pm(x) = E \psi_\pm(x), \quad (14.43)$$

where $x = \xi$ for ψ_+ and $x = \eta$ for ψ_- , and

$$h_\pm(x) = -\frac{2}{x} \frac{d}{dx} \left(x \frac{d}{dx} \right) - \frac{2Z_\pm}{x} + \frac{m_l^2}{2x^2} \mp \frac{1}{2} Fx, \quad (14.44)$$

with

$$Z = Z_+ + Z_-. \quad (14.45)$$

Using the notation

$$\begin{aligned} \epsilon &= \sqrt{-2E}, \\ n_\pm &= Z_\pm / \epsilon - \frac{1}{2} (|m_l| + 1), \\ n &= n_+ + n_- + |m_l| + 1, \end{aligned}$$

$$\begin{aligned} n_+, N_- &= 0, 1, \dots, n - |m_l| + 1, \\ |m_l| &= 0, 1, 2, \dots, n - 1, \\ \delta n &= n_+ - n_-, \end{aligned} \quad (14.46)$$

where n is the principal quantum number, the unperturbed eigenfunctions are

$$\psi_{\pm}(x) = \frac{\epsilon n_{\pm}!^{\frac{1}{2}}}{(n_{\pm} + |m_l|)!^{\frac{1}{2}}} e^{-\frac{1}{2}\epsilon x} (\epsilon x)^{\frac{1}{2}|m_l|} L_{n_{\pm}}^{(|m_l|)}(\epsilon x), \quad (14.47)$$

where the $L_b^{(a)}$ are generalized Laguerre polynomials (Sect. 9.4.2). The zero-order eigenvalues are

$$Z_{\pm}^{(0)} = \left(n_{\pm} + \frac{m_l + 1}{2} \right) \epsilon. \quad (14.48)$$

The first-order perturbation yields

$$\begin{aligned} Z_{\pm}^{(1)} &= \pm \frac{1}{4} \frac{F}{\epsilon^2} [6n_{\pm}(n_{\pm} \\ &+ m_l + 1) + m_l(m_l + 3) + 2]. \end{aligned} \quad (14.49)$$

From these

$$\epsilon = \frac{Z}{n} - \frac{3}{2 F \left(\frac{n}{Z} \right)^2 \delta_n}, \quad (14.50)$$

and to first order in F ,

$$\begin{aligned} E &= -\frac{1}{2}\epsilon^2 \approx E^{(0)} + E^{(1)}, \\ E^{(0)} &= -\frac{1}{2} \frac{Z^2}{n^2}, \\ E^{(1)} &= \frac{3}{2} \frac{F}{Z} n \delta_n. \end{aligned} \quad (14.51)$$

14.4.3 Quadratic Stark Effect

A perturbation linear in the field F yields no contribution to nondegenerate states (e.g., the ground state $n_+ = n_- = m = 0$; $n = 1$). In this case, the lowest order contribution comes from the *quadratic Stark effect*, the contribution of order F^2 . The quadratic perturbation to a level $E_n^{(0)}$ caused by a general electric field \mathbf{F} can be written in terms of the symmetric tensor α_{ij}^n as

$$E_n^{(2)} = -\frac{1}{2} \alpha_{ij}^n F_i F_j, \quad (14.52)$$

with

$$\alpha_{ij}^n = -2 \sum_{m \neq n} \frac{\langle n | d_i | m \rangle \langle m | d_j | n \rangle}{E_n - E_m}, \quad (14.53)$$

where d_i is defined in Eq. (14.35).

Table 14.4 Relativistic dipole polarizabilities for the ground state of hydrogenic atoms

Z	$\alpha_{\text{rel}}^{n=1} Z^4 / (a_0^3)$
1	4.4997515
5	4.4937883
10	4.4751644
20	4.4008376
30	4.2775621
40	4.1062474
50	3.8881792
60	3.6250295
70	3.3188659
80	2.9721524
90	2.5877205
100	2.1686483

For a field Eq. (14.36),

$$\Delta E_n = -\frac{1}{2} \alpha^n F^2, \quad (14.54)$$

where

$$\alpha^n \equiv \alpha_{zz}^n = -2e^2 \sum_{m \neq n} \frac{|\langle n | z | m \rangle|^2}{E_n - E_m}. \quad (14.55)$$

In terms of Eq. (14.46), a general nonrelativistic expression for the *dipole polarizability* of hydrogenic ions is [9]

$$\alpha^n = \frac{a_0^3 n^4}{8Z^4} (17n^2 - 3\delta_n^2 - 9m_l^2 + 19). \quad (14.56)$$

For the ground state of hydrogenic atoms,

$$\alpha^{n=1} = \frac{9a_0^3}{2Z^4}. \quad (14.57)$$

Table 14.4 lists the *relativistic* values for the ground state polarizability $\alpha_{\text{rel}}^{n=1}$, obtained by calculating Eq. (14.55) using relativistic variational basis sets [10]. The values are interpolated by

$$\alpha^{n=1} = \frac{a_0^3}{Z^4} \left[\frac{9}{2} - \frac{14}{3} (\alpha Z)^2 + 0.53983 (\alpha Z)^4 \right]. \quad (14.58)$$

14.4.4 Other Stark Corrections

Third Order Corrections

For the energy correction cubic in the external field Eq. (14.36), one obtains [9]

$$\begin{aligned} E^{(3)} &= \frac{3}{32} F^3 \left(\frac{n}{Z} \right)^7 \\ &\times \delta_n (23n^2 - \delta_n^2 + 11m_l^2 + 39). \end{aligned} \quad (14.59)$$

Relativistic Linear Stark-Shift of the Fine Structure of Hydrogen

For a Stark effect small relative to the fine structure, the degenerate levels corresponding to the same value of j split according to

$$\delta_m E_{nj} = \frac{3}{4} \sqrt{n^2 - \left(j + \frac{1}{2}\right)^2} \frac{nm}{j(j+1)} F. \quad (14.60)$$

Other Stark Corrections in Hydrogen

The expectation value of the delta function, is, in a.u. [11],

$$2\pi \langle 1s | \delta(\mathbf{r}) | 1s \rangle = 2 - 31F^2. \quad (14.61)$$

For the Bethe logarithm β defined by

$$\beta_{1s} = \frac{\sum_n |\langle 1s | \mathbf{p} | n \rangle|^2 (E_n - E_{1s}) \ln |E_n - E_{1s}|}{\sum_n |\langle 1s | \mathbf{p} | n \rangle|^2 (E_n - E_{1s})}, \quad (14.62)$$

the result is [12]

$$\beta_{1s} = 2.290\,981\,375\,205\,552\,301 + 0.316\,205(6) F^2. \quad (14.63)$$

These results are useful in calculating an asymptotic expansion for the two-electron Bethe logarithm [13].

14.5 Recent Developments

The drastic change of an atom's internal structure in the presence of external electric and magnetic fields is shown most clearly through the changes induced in its spectral features. Of these features, avoided crossings are a distinctive example. Recent work in this area by *Férez* and *Dehesa* [14] has suggested the use of Shannon's information entropy [15], defined by

$$S = - \int \rho(\mathbf{r}) \ln \rho(\mathbf{r}) d\mathbf{r}, \quad (14.64)$$

where $\rho(\mathbf{r}) = |\psi(\mathbf{r})|^2$, as an indicator or predictor of such irregular features of atomic spectra. By studying some excited states of hydrogen in parallel fields it was shown that, for the states involved, a marked confinement of the electron cloud and an information-theoretic exchange occurs when the magnetic field strength is adjusted adiabatically through the region of an avoided crossing. The field strengths studied are characteristic of compact astronomical objects, such as white dwarfs and neutron stars.

Although the effects of strong magnetic fields on the structure and dynamics of hydrogen have been known for some time, knowledge of the helium atom in such fields has only recently become sufficient for comparison with astrophysical observations [16–18]. As one example of their importance, such studies have proven critical in showing the

presence of helium in the atmospheres of certain magnetic white dwarfs [19].

In recent years, the increased sophistication and resolution of observation techniques has not only increased the number of known astronomical objects, but also motivated the study of the effects of strong fields on heavier atoms [20].

Another interesting area of current research concerns the relationship between quantum mechanics and classically chaotic systems. For these studies, Rubidium Rydberg atoms are an ideal system since laboratory fields can easily push the atom to the strong-field limit [21–23].

For a very useful review of various topics up to 1998 see [24]; a more concise review, concerning the electronic structure of atoms, molecules, and bulk matter, including some properties of dense plasma, in strong fields, is given in [25].

References

1. Landau, L.D., Lifshitz, E.M.: Quantum Mechanics (Course of Theoretical Physics) vol. 3. Pergamon, Oxford, p 456 (1977)
2. Landau, L.D., Lifshitz, E.M.: The Classical Theory of Fields (Course of Theoretical Physics) vol. 2. Pergamon, Oxford, p 49 (1975)
3. Messiah, A.: Quantum Mechanics. Wiley, New York, p 491 (1999)
4. Itzykson, C., Zuber, J.-B.: Quantum Field Theory. McGraw-Hill, New York, p 67 (1980)
5. Bethe, H.A., Salpeter, E.: Quantum Mechanics of One- and Two-Electron Atoms. Plenum, New York, p 208 (1977)
6. Bethe, H.A., Salpeter, E.: Quantum Mechanics of One- and Two-Electron Atoms. Plenum, New York, p 211 (1977)
7. Chen, Z., Goldman, S.P.: Phys. Rev. A **48**, 1107 (1993)
8. Bethe, H.A., Salpeter, E.: Quantum Mechanics of One- and Two-Electron Atoms. Plenum, New York, p 229 (1977)
9. Bethe, H.A., Salpeter, E.: Quantum Mechanics of One- and Two-Electron Atoms. Plenum, New York, p 233 (1977)
10. Drake, G.W.F., Goldman, S.P.: Phys. Rev. A **23**, 2093 (1981)
11. Drake, G.W.F.: Phys. Rev. A **45**, 70 (1992)
12. Goldman, S.P.: Phys. Rev. A **50**, 3039 (1994)
13. Goldman, S.P., Drake, G.W.F.: Phys. Rev. Lett. **68**, 1683 (1992)
14. González-Férez, R., Dehesa, J.S.: Phys. Rev. Lett. **91**, 113001 (2003)
15. Shannon, C.E.: Bell Syst. Tech. J. **27**, 623 (1948)
16. Becken, W., Schmelcher, P., Diakonov, F.K.: J. Phys. B **32**, 1557 (1999)
17. Becken, W., Schmelcher, P.: Phys. Rev. A **63**, 053412 (2001)
18. Becken, W., Schmelcher, P.: Phys. Rev. A **65**, 033416 (2002)
19. Jordan, S., Schmelcher, P., Becken, W., Schweizer, W.: Astron. Astrophys. **336**, 33 (1998)
20. P. Schmelcher: private communication
21. von Milczewski, J., Uzer, T.: In: Schmelcher, P., Schweizer, W. (eds.) Atoms and Molecules in Strong External Fields, p. 199. Springer, Berlin, Heidelberg (1998)
22. Main, J., Wunner, G.: In: Schmelcher, P., Schweizer, W. (eds.) Atoms and Molecules in Strong External Fields, p. 223. Springer, Berlin, Heidelberg (1998)
23. Guest, J.R., Raithel, G.: Phys. Rev. A **68**, 052502 (2003)
24. Schmelcher, P., Schweizer, W. (eds.): Atoms and Molecules in Strong External Fields. Springer, Berlin (1998)
25. Lai, D.: Rev. Mod. Phys. **73**, 629 (2001)



Pedro Goldman Professor Pedro Goldman completed a Ph.D. in Relativistic Atomic Physics at the University of Windsor. His work in atomic physics includes pioneering work on relativistic variational basis sets, relativistic calculations for many-electron atoms and diatomic molecules, accurate calculations for atoms in strong magnetic fields and accurate calculations of QED energy corrections and of the energy levels of Helium. Presently his research is directed to the optimization of the radiation therapy of tumours. He has as well received numerous teaching awards.



Mark M. Cassar Mark M. Cassar received his Ph.D. from the University of Windsor, Canada in 2003. His past research focused on high-precision theoretical calculations for the energy level structure of three-body atomic and molecular systems. He is currently working on applications of artificial intelligence in medicine.



Thomas F. Gallagher

Contents

15.1	Wave Functions and Quantum Defect Theory	231
15.2	Optical Excitation and Radiative Lifetimes	233
15.3	Electric Fields	234
15.4	Magnetic Fields	236
15.5	Microwave Fields	237
15.6	Collisions	238
15.7	Autoionizing Rydberg States	239
	References	239

Abstract

Rydberg atoms are those in which the valence electron is in a state of high principal quantum number n . They are of historical interest since the observation of Rydberg series helped in the initial unraveling of atomic spectroscopy [1]. Since the 1970s, these atoms have been studied mostly for two reasons. First, Rydberg states are at the border between bound states and the continuum, and any process that can result in either excited bound states or ions and free electrons usually leads to the production of Rydberg states. Second, the exaggerated properties of Rydberg atoms allow experiments to be done that would be difficult or impossible with normal atoms.

Keywords

microwave field · Rydberg state · radiative lifetime · Rydberg atom · photoionization · cross section

T. F. Gallagher (✉)
 Dept. of Physics, University of Virginia
 Charlottesville, VA, USA
 e-mail: tfg@virginia.edu, jbdelos@wm.edu

15.1 Wave Functions and Quantum Defect Theory

Many of the properties of Rydberg atoms can be calculated accurately using quantum defect theory, which is easily understood by starting with the H atom [2]. We shall use atomic units, as discussed in Sect. 1.2. The Schrödinger equation for the motion of the electron in a H atom in spherical coordinates is

$$\left(-\frac{1}{2}\nabla^2 - \frac{1}{r}\right)\Psi(r, \theta, \phi) = E\Psi(r, \theta, \phi), \quad (15.1)$$

where E is the energy, r is the distance between the electron and the proton, and θ and ϕ are the polar and azimuthal angles of the electron's position. Equation (15.1) can be separated, and its solution expressed as the product

$$\Psi(r, \theta, \phi) = R(r)Y_{\ell m}(\theta, \phi), \quad (15.2)$$

where ℓ and m are the orbital and azimuthal-orbital angular momentum (i.e., magnetic) quantum numbers, and $Y_{\ell m}(\theta, \phi)$ is a normalized spherical harmonic; $R(r)$ satisfies the radial equation

$$\frac{d^2R(r)}{dr^2} + \frac{2dR(r)}{rdr} + 2ER(r) + \frac{2R(r)}{r} = \frac{\ell(\ell + 1)R}{r^2}, \quad (15.3)$$

which has the two physically interesting solutions

$$R(r) = \frac{f(\ell, E, r)}{r}, \quad (15.4)$$

$$R(r) = \frac{g(\ell, E, r)}{r}. \quad (15.5)$$

The f and g functions are the regular and irregular Coulomb functions, which are the solutions to a variant of Eq. (15.3). As $r \rightarrow 0$, they have the forms [3]

$$f(\ell, E, r) \propto r^{\ell+1}, \quad (15.6)$$

$$g(\ell, E, r) \propto r^{-\ell}, \quad (15.7)$$

irrespective of whether E is positive or negative. As $r \rightarrow \infty$, for $E > 0$ the f and g functions are sine and cosine waves, i.e., there is a phase shift of $\pi/2$ between them. For $E < 0$, it is useful to introduce ν , defined by $E = -1/2\nu^2$, and for $E < 0$ as $r \rightarrow \infty$

$$f = u(\ell, \nu, r) \sin \pi \nu - v(\ell, \nu, r) e^{i\pi \nu}, \quad (15.8)$$

$$g = -u(\ell, \nu, r) \cos \pi \nu + v(\ell, \nu, r) e^{i\pi(\nu+1/2)}, \quad (15.9)$$

where u and v are exponentially increasing and decreasing functions of r . As $r \rightarrow \infty$, $u \rightarrow \infty$ and $v \rightarrow 0$.

Requiring that the wave function be square integrable means that as $r \rightarrow 0$, only the f function is allowed. Equation (15.8) shows that the $r \rightarrow \infty$ boundary condition requires that $\sin \pi \nu$ be zero or ν an integer n , leading to the hydrogenic Bohr formula for the energies

$$E = -\frac{1}{2n^2}. \quad (15.10)$$

The classical turning point of an s wave occurs at $r = 2n^2$, and the expectation values of positive powers of r reflect the location of the outer turning point, i.e.,

$$\langle r^k \rangle \approx n^{2k}. \quad (15.11)$$

The expectation values of negative powers of r are determined by the properties of the wave function at small r . The normalization constant of the radial wave function scales as $n^{-3/2}$, so that $R(r) \propto n^{-3/2} r^{\ell+1}$ for small r . Accordingly, the expectation values of negative powers of r , except r^{-1} , and any properties that depend on the small r part of the wave function, scale as n^{-3} . Using the properties of the wave function and the energies, the n -scaling of the properties of Rydberg atoms can be determined.

The primary reason for introducing the Coulomb waves instead of the more common Hermite polynomial solution for the radial function is to set the stage for single-channel quantum defect theory, which enables us to calculate the wave functions and properties of one-valence electron atoms such as Na. The simplest picture of an Na Rydberg atom is an electron orbiting a positively charged Na^+ core consisting of 10 electrons and a nucleus of charge +11. The ten electrons are assumed to be frozen in place with spherical symmetry about the nucleus, so their charge cloud is not polarized by the outer valence electron, although the valence electron can penetrate the ten-electron cloud. When the electron penetrates the charge cloud of the core electrons, it sees a potential well deeper than $-1/r$ due to the decreased shielding of the +11 nuclear charge. For Na and other alkali atoms, we assume that there is a radius r_c such that for $r < r_c$ the potential is deeper than $-1/r$, and for $r > r_c$ it is equal to $-1/r$. As a result of the deeper potential at $r < r_c$, the radial wave function is pulled into the core in Na, relative to H, as shown in

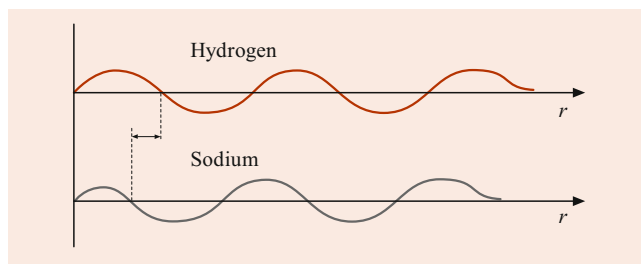


Fig. 15.1 Radial wave functions for H and Na showing that the Na wave function is pulled in toward the ionic core

Fig. 15.1. For $r \geq r_c$, the potential is a Coulomb $-1/r$ potential, and $R(r)$ is a solution of Eq. (15.3), which can be expressed as

$$R(r) = [f(\ell, \nu, r) \cos \tau_\ell - g(\ell, \nu, r) \sin \tau_\ell] / r, \quad (15.12)$$

where τ_ℓ is the radial phase shift.

Near the ionization limit, $E \approx 0$, and as a result, the kinetic energy of the Rydberg electron is greater than $1/r_c$ (≈ 10 eV) when $r < r_c$. As a result, changes in E of 0.10 eV, the $n = 10$ binding energy, do not appreciably alter the phase shift τ_ℓ , and we can assume τ_ℓ to be independent of E . The ℓ dependence of τ_ℓ arises because the centrifugal $\ell(\ell+1)/r$ term in Eq. (15.3) excludes the Rydberg electron from the region of the core in states of high ℓ . Applying the $r \rightarrow \infty$ boundary condition to the wave function of Eq. (15.12) leads to the requirement that the coefficient of u vanish, i.e.,

$$\cos \tau_\ell \sin(\pi \nu) + \sin \tau_\ell \cos(\pi \nu) = 0, \quad (15.13)$$

which implies that $\sin(\pi \nu + \tau_\ell) = 0$ or $\nu = n - \tau_\ell / \pi$. Usually τ_ℓ / π is written as δ_ℓ and termed the quantum defect, and the energies of members of the $n\ell$ series are written as

$$E = -\frac{1}{2(n - \delta_\ell)^2} = -\frac{1}{2n^{*2}}, \quad (15.14)$$

where $n^* = n - \delta_\ell$ is often termed the effective quantum number (Sect. 12.5.1).

Knowledge of the quantum defect δ_ℓ of a series of ℓ states determines their energies, and it is a straightforward matter to calculate the Coulomb wave function specified in Eq. (15.12) using a Numerov algorithm [4, 5]. This procedure gives wave functions valid for $r \geq r_c$, which can be used to calculate many of the properties of Rydberg atoms with great accuracy. The effect of core penetration on the energies is easily seen in the energy level diagram of Fig. 15.2. The Na $\ell \geq 2$ states have the same energies as hydrogen, while the s and p states, with quantum defects of 1.35 and 0.85, respectively, lie far below the hydrogenic energies.

Although it is impossible to discern in Fig. 15.2, the Na $\ell \geq 2$ states also lie below the hydrogenic energies. For these

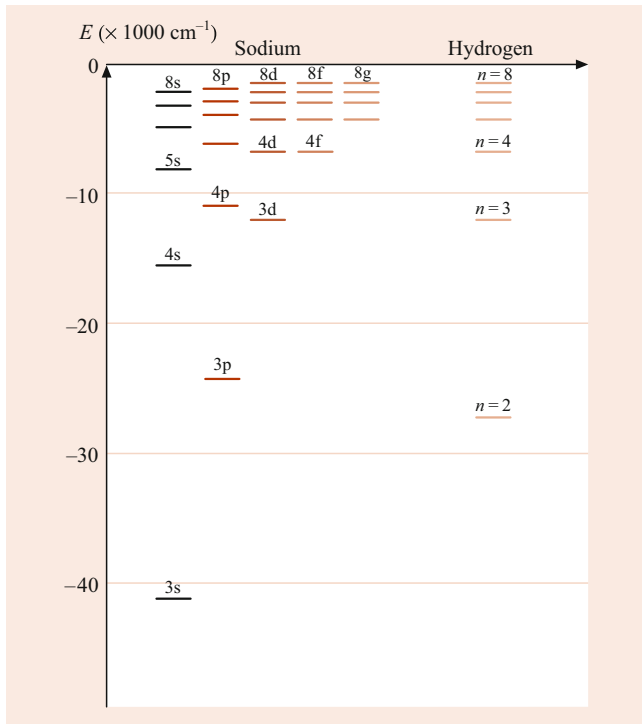


Fig. 15.2 Energy levels of Na and H

states, it is not core penetration but core polarization that is responsible for the shift to lower energy. Contrary to our earlier assumption that the outer electron does not affect the inner electrons if $r > r_c$, the outer electron polarizes the inner electron cloud even when $r > r_c$, and the energies of even the high ℓ states fall below the hydrogenic energies. The leading term in the polarization energy is due to the dipole polarizability of the core, α_d . For high ℓ states, it gives a quantum defect of [6]

$$\delta_\ell = \frac{3\alpha_d}{4\ell^5}. \quad (15.15)$$

Quantum defects due primarily to core polarization rarely exceed 10^{-2} , while those due to core penetration are often greater than 1.

15.2 Optical Excitation and Radiative Lifetimes

Optical excitation of the Rydberg states from the ground state or any other low-lying state is the continuation of the photoionization cross section σ_{PI} below the ionization limit. The photoionization cross section, discussed more extensively in Chap. 25, is approximately constant at the limit. Above and below the limit the average photoabsorption cross section is the same, as evidenced by the fact that a discontinuity is not evident in an absorption spectrum, i.e., it is not possible to see where the unresolved Rydberg states end and the contin-

uum begins. Nonetheless, below the limit the cross section is structured by the Δn spacing of $1/n^3$ between adjacent members of the Rydberg series. In any experiment, there is a finite resolution $\Delta\omega$ with which the Rydberg states can be excited. It can arise, for example, from the Doppler width or a laser linewidth. This resolution determines the cross section σ_n for exciting the Rydberg state of principal quantum number n . Explicitly, σ_n is given by

$$\sigma_n = \frac{\sigma_{PI}}{n^3 \Delta\omega}. \quad (15.16)$$

A typical value for σ_{PI} is 10^{-18} cm^2 . For a resolution $\Delta\omega = 1 \text{ cm}^{-1}$ ($6 \times 10^{-6} \text{ a.u.}$) the cross section for exciting an $n = 20$ atom is $3 \times 10^{-17} \text{ cm}^2$.

From the wave functions of the Rydberg states, we can also derive the n^{-3} dependence of the photoexcitation cross section. The dipole matrix element from the ground state to a Rydberg state only involves the part of the Rydberg state wave function near the core. At small r , the Rydberg wave function only depends on n through the n^{-3} normalization factor, and as a result, the squared dipole matrix element between the ground state and the Rydberg state and the cross section both have an n^{-3} dependence.

Radiative decay, which is covered in Chap. 18, is, to some extent, the reverse of optical excitation. The general expression for the spontaneous transition rate from the $n\ell$ state to the $n'\ell'$ state is the Einstein A coefficient, given by [2]

$$A_{n\ell, n'\ell'} = \frac{4}{3} \mu_{n\ell, n'\ell'}^2 \omega_{n\ell, n'\ell'}^3 \frac{\alpha^3 g_{>}}{2g_n + 1}, \quad (15.17)$$

where $\mu_{n\ell, n'\ell'}$ and $\omega_{n\ell, n'\ell'}$ are the electric dipole matrix elements and frequencies of the $n\ell \rightarrow n'\ell'$ transitions, g_n and $g_{n'}$ are the degeneracies of the $n\ell$ and $n'\ell'$ states, and $g_{>}$ is the greater of g_n and $g_{n'}$. The lifetime $\tau_{n\ell}$ of the $n\ell$ state is obtained by summing the decay rates to all possible lower energy states. Explicitly,

$$\frac{1}{\tau_{n\ell}} = \sum_{n'\ell'} A_{n\ell, n'\ell'}. \quad (15.18)$$

Due to the ω^3 factor in Eq. (15.17), the highest frequency transition usually contributes most heavily to the total radiative decay rate, and the dominant decay is likely to be the lowest lying state possible. For low- ℓ Rydberg states, the lowest lying ℓ' states are bound by orders of magnitude more than the Rydberg states, and the frequency of the decay is nearly independent of n . Only the squared dipole moment depends on n , as n^{-3} , because of the normalization of the Rydberg wave function at the core. Consequently, for low- ℓ states,

$$\tau_{n\ell} \propto n^3. \quad (15.19)$$

As a typical example, the 10f state in H has a lifetime of $1.08 \mu\text{s}$ [7].

The highest ℓ states, with $\ell = n - 1$, have radiative lifetimes with a completely different n dependence. The only possible transitions are $n \rightarrow n - 1$, with frequency $1/n^3$. In this case, the dipole moments reflect the large size of both the n and $n - 1$ states and have the n^2 scaling of the orbital radius. Using Eq. (15.17) for $\ell = n - 1$ leads to

$$\tau_{n(n-1)} \propto n^5. \quad (15.20)$$

Another useful lifetime, τ_n , is that corresponding to the average decay rate of all ℓ, m states of the same n . It scales as $n^{4.5}$ [2, 8].

Equation (15.17) describes spontaneous decay to lower lying states driven by the vacuum. At room temperature, 300 K, there are many thermal photons at the frequencies of the $n \rightarrow n \pm 1$ transitions of Rydberg states for $n \geq 10$, and these photons drive transitions to higher and lower states [9]. A convenient way of describing blackbody radiation is in terms of the photon occupation number \bar{n} , given by

$$\bar{n} = \frac{1}{e^{\hbar\omega/kT} - 1}. \quad (15.21)$$

The stimulated emission or absorption rate $K_{n\ell, n'\ell'}$ from state $n\ell$ to state $n'\ell'$ is given by

$$K_{n\ell, n'\ell'} = \frac{4}{3} \mu_{n\ell, n'\ell'}^2 \omega_{n\ell, n'\ell'}^3 \frac{\alpha^3 \bar{n} g_{>}}{2g_n + 1}. \quad (15.22)$$

Summing these rates over n' and ℓ' gives the total blackbody decay rate $1/\tau_n^{\text{bb}}$. Explicitly,

$$\frac{1}{\tau_n^{\text{bb}}} = \sum_{n'\ell'} K_{n\ell, n'\ell'}. \quad (15.23)$$

The resulting lifetime τ_n^{T} at any given temperature is given by

$$\frac{1}{\tau_n^{\text{T}}} = 1/\tau_{n\ell} + 1/\tau_n^{\text{bb}}. \quad (15.24)$$

For low- ℓ states with $10 < n < 20$, blackbody radiation produces a 10% decrease in the lifetimes, but for high- ℓ states of the same n , it reduces the lifetimes by a factor of 10. Since $1/\tau_n^{\text{bb}} \propto n^{-2}$, this term must dominate normal spontaneous emission at high n .

The above discussion of spontaneous and stimulated transitions is based on the implicit assumption that the atoms are in free space. If the atoms are in a cavity, which introduces structure into the blackbody and vacuum fields, the transition rates are significantly altered [10]. These alterations are described in Chap. 83. If the cavity is tuned to a resonance, it increases the transition rate by the finesse of the cavity (approximately the Q for low-order modes). On the other hand, if the cavity is tuned between resonances, the transition rate is suppressed by a similar factor.

15.3 Electric Fields

As a starting point, consider the H atom in a static electric field \mathcal{E} in the z -direction and focus on the states of principal quantum number n . The field couples ℓ and $\ell \pm 1$ states of the same m by the electric dipole matrix elements. Since the states all have a common zero field energy of $-1/2n^2$, and the off-diagonal Hamiltonian matrix elements are all proportional to \mathcal{E} , the eigenstates are field-independent linear combinations of the zero field ℓ states of the same m , and the energy shifts from $-1/2n^2$ are linear in \mathcal{E} . In this first-order approximation, the energies are given by [2]

$$E = -\frac{1}{2n^2} + \frac{3}{2}(n_1 - n_2)n\mathcal{E}, \quad (15.25)$$

where n_1 and n_2 are parabolic quantum numbers (Sect. 9.1.2), which satisfy

$$n_1 + n_2 + |m| + 1 = n. \quad (15.26)$$

Consider the $m = 0$ states as an example. The $n_1 - n_2 = n - 1$ state is shifted up in energy by $\frac{3}{2}n(n - 1)\mathcal{E}$ and is called the extreme blue Stark state, and the $n_2 - n_1 = n - 1$ state is shifted down in energy by $\frac{3}{2}n(n - 1)\mathcal{E}$ and is called the extreme red Stark state. These two states have large permanent dipole moments, and in the red (blue) state, the electron spends most of its time on the downfield (upfield) side of the proton as shown in Fig. 15.3, a plot of the potential along

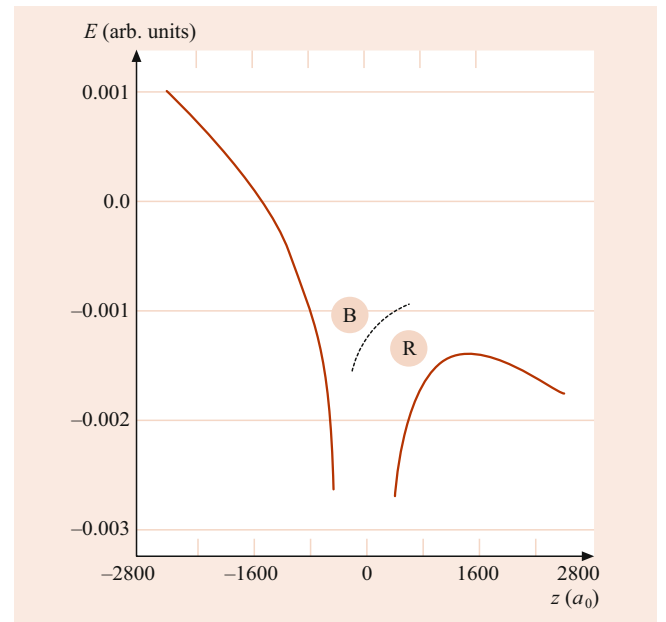


Fig. 15.3 Combined Coulomb–Stark potential along the z -axis when a field of 5×10^{-7} a.u. (2700 V/cm) is applied in the z -direction (solid lines). The extreme red state (R) is near the saddle point, and the extreme blue (B) state is held on the upfield side of the atom by an effective potential (dashed line) roughly analogous to a centrifugal potential

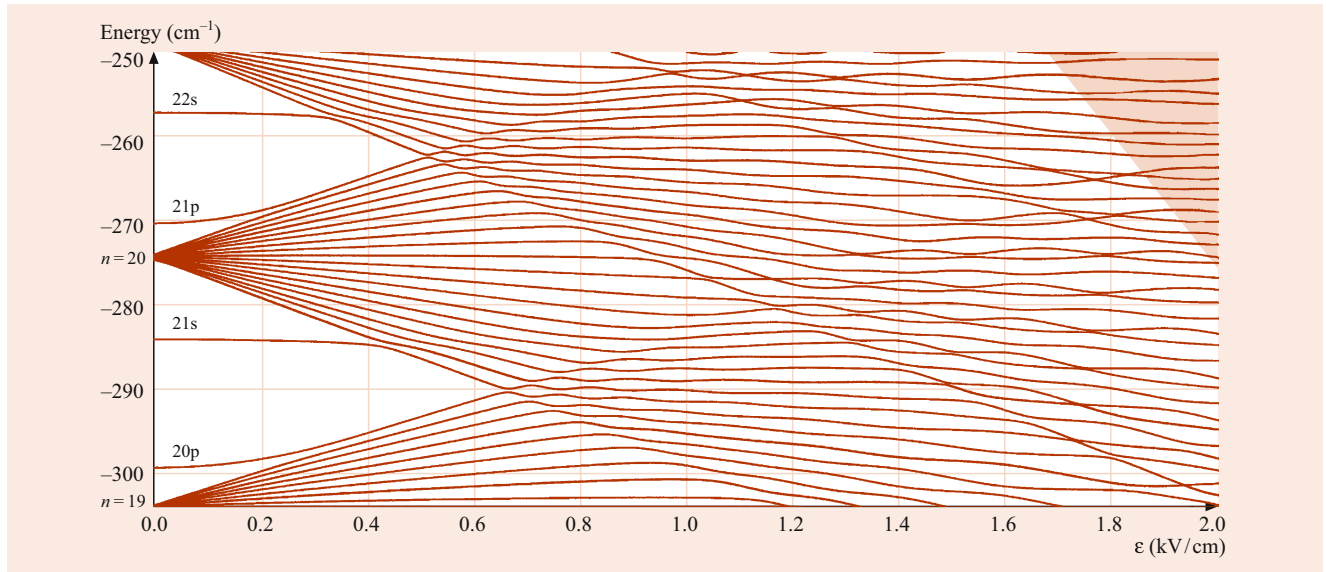


Fig. 15.4 Energies of Na $m = 0$ levels of $n \approx 20$ as a function of electric field. The shaded region is above the classical ionization limit

the z -axis. We have here ignored the electric dipole couplings to other n states, which introduce small second-order Stark shifts to lower energy. As implied by Eq. (15.26), states of higher m have smaller shifts. In particular, the circular $m = \ell = n - 1$ state has no first-order shift since there are no degenerate states to which it is coupled by the field.

The Stark effect in other atoms is similar, but not identical to that observed in H. This point is shown by Fig. 15.4, a plot of the energies of the Na $m = 0$ levels near $n = 20$. The energy levels are similar to those of H in that most of the levels exhibit apparently linear Stark shifts from the zero field energy of the high- ℓ states. The differences, however, are twofold. First, the levels from s and p states with nonzero quantum defects join the manifold of Stark states at some nonzero field, given approximately by [4]

$$\mathcal{E} = \frac{2\delta'_\ell}{3n^5}, \quad (15.27)$$

where δ'_ℓ is the magnitude of the difference between δ_ℓ and the nearest integer. Second, there are avoided crossings between the blue $n = 20$ and red $n = 21$ Stark states. In H, these states would cross, but in Na they do not because of the finite sized Na^+ core, which also leads to the nonzero quantum defects of the ns and np states.

Field ionization is both intrinsically interesting and of great practical importance for the detection of Rydberg atoms [11]. The simplest picture of field ionization can be understood with the help of Fig. 15.4. The potential along the z -axis of an atom in a field \mathcal{E} in the z -direction is given by

$$V = -\frac{1}{r} - \mathcal{E}z. \quad (15.28)$$

If an atom has an energy E relative to the zero field limit, it can ionize classically if the energy E lies above the saddle point in the potential. The required field is given by

$$\mathcal{E} = \frac{E^2}{4}. \quad (15.29)$$

Ignoring the Stark shifts and using $E = -1/2n^2$ yields the expression

$$\mathcal{E} = \frac{1}{16n^4}. \quad (15.30)$$

The H atom ionizes classically as described above or by quantum mechanical tunneling, which occurs at slightly lower fields. Since the tunneling rates increase exponentially with field strength, typically an order of magnitude for a 3% change in the field, specifying the classical ionization field is a good approximation to the field, which gives an ionization rate of practical interest. The red and blue states of H ionize at very different fields, as shown by Fig. 15.5, a plot of the $m = 0$ Stark states out to the fields at which the ionization rates are 10^6 s^{-1} [12]. First, note the crossing of the levels of different n mentioned earlier. Second, note that the red states ionize at lower fields than the blue states do, in spite of the fact that they are lower in energy. In the red states, the electron is close to the saddle point of the potential of Fig. 15.3, and it ionizes according to Eq. (15.29). If the Stark shift of the extreme red state to lower energy is taken into account, Eq. (15.30) becomes

$$\mathcal{E} = \frac{1}{9n^4}. \quad (15.31)$$

In the blue state, the electron is held on the upfield side of the atom by an effective potential roughly analogous to a cen-

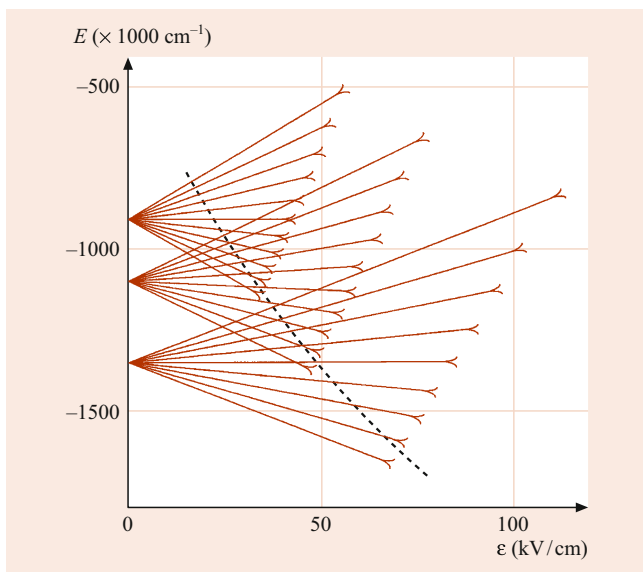


Fig. 15.5 Energies of H $m = 0$ levels of $n = 9, 10,$ and 11 as functions of electric field. The widths of the levels due to ionization broaden exponentially with fields, and the onset of the broadening indicated is at an ionization rate of 10^6 s^{-1} . The broken line indicating the classical ionization limit, $E = E^2/4$, passes near the points at which the extreme red states ionize

trifugal potential, as shown by Fig. 15.3. At the same field, the blue state's energy is lower relative to the saddle point of its potential, shown by the broken line of Fig. 15.3, than is the energy of the red state relative to the saddle point of its potential, given by Eq. (15.28) and shown by the solid line of Fig. 15.3. As shown by the broken line of Fig. 15.5, the classical ionization limit of Eq. (15.29) is simply a line connecting the ionization fields of the extreme red Stark states. All other states are stable above the classical ionization limit. In the Na atom, ionization of $m = 0$ states occurs in a qualitatively different fashion [12]. Due to the finite size of the Na^+ core, crossings are avoided between the blue and red Stark states of different n , as is shown by Fig. 15.4. In the region above the classical ionization limit, shown by the shaded region of Fig. 15.4, the same coupling between hydrogenically stable blue states and the degenerate red continua leads to autoionization of the blue states [13]. As a result, all states above the classical ionization limit ionize at experimentally significant rates. In higher m states, the core coupling is smaller, and the behavior is more similar to H.

Field ionization is commonly used to detect Rydberg atoms in a state selective manner. Experiments are most often conducted at or near zero field, and afterwards the field is increased in order to ionize the atoms. Exactly how the atoms pass from the low field to the high ionizing field is quite important. The passage can be adiabatic, diabatic, or anything in between. The selectivity is best if the passage is purely adiabatic or purely diabatic, for in these two cases, unique paths are followed.

In zero field, optical excitation from a ground s state leads only to final np states. In the presence of an electric field, all the Stark states are optically accessible, because they all have some p character. The fact that all the Stark states are optically accessible from the ground state allows the population of arbitrary ℓ states of nonhydrogenic atoms by a technique called Stark switching [6, 14]. In any atom other than H, the ℓ states are nondegenerate in zero field, and each of them is adiabatically connected to one, and only one, high field Stark state, as shown by Fig. 15.4. If one of the Stark states is excited with a laser and the field reduced to zero adiabatically, the atoms are left in a single zero field ℓ state.

In zero field, the photoionization cross section is structureless. However, in an electric field, it exhibits obvious structure, sometimes termed strong field mixing resonances. Specifically, when ground state s atoms are exposed to light polarized parallel to the static field, an oscillatory structure is observed in the cross section, even above the zero field ionization limit [15]. The origin of the structure can be understood with the aid of a simple classical picture [16, 17]. The electrons ejected in the downfield direction can simply leave the atom, while the electrons ejected in the upfield direction are reflected back across the ionic core and also leave the atom in the downfield direction. The wave packets corresponding to these two classical trajectories are added, and they can interfere constructively or destructively at the ionic core, depending on the phase accumulation of the reflected wave packet. Since the phase depends on the energy, there is an oscillation in the photoexcitation spectrum. This model suggests that no oscillations should be observed for light polarized perpendicular to the static field, and none are. The oscillations can also be thought of as arising from the remnants of quasistable extreme blue Stark states that have been shifted above the ionization limit, and, using this approach or a WKB approach, one can show that the spacing between the oscillations at the zero field limit is $\Delta E = \mathcal{E}^{3/4}$ [18, 19]. Further discussion can be found in Chap. 16.

The initial photoexcitation experiments were done using narrow bandwidth lasers, so that the time dependence of the classical pictures was not explicitly observed. Using mode locked lasers it has been possible to create a variety of Rydberg wave packets [20, 21] and observe, in effect, the classical motion of an electron in an atom. Of particular interest is that it has been possible to directly observe the time delay of the ejection of electrons subsequent to excitation in an electric field [22].

15.4 Magnetic Fields

To first order, the energy shift of a Rydberg atom due to a magnetic field B (the Zeeman effect) is proportional to the angular momentum of the atom. Since the states op-

tically accessible from the ground state have low angular momenta, the energy shifts are the same as those of low-lying atomic states. In contrast, the second-order diamagnetic energy shifts are proportional to the area of the Rydberg electron's orbit and scale as $B^2 n^4$ [23]. The diamagnetic interaction mixes the ℓ states, allowing all to be excited from the ground state, and produces large shifts to higher energies. The energy levels as a function of the magnetic field are reminiscent of the Stark energy levels shown in Fig. 15.5, differing in that the energy shifts are quadratic in the magnetic field.

One of the most striking phenomena in magnetic fields is the existence of quasi-Landau resonances, spaced by $\Delta E = 3\hbar B/2$, in the photoionization cross section above the ionization limit [24]. The origin of this structure is similar to the origin of the strong field mixing resonances observed in electric fields. An electron ejected in the plane perpendicular to the B fields is launched into a circular orbit and returns to the ionic core. The returning wave packet can be in or out of phase with the one leaving the ionic core, and, thus, can interfere constructively or destructively with it. While the electron motion in the xy -plane is bound, motion in the z -direction is unaffected by the magnetic field and is unbounded above the ionization limit, leading to resonances of substantial width. The Coulomb potential does provide some binding in the z -direction and allows the existence of quasi-stable three-dimensional orbits [25].

15.5 Microwave Fields

Strong microwave fields have been used to drive multiphoton transitions between Rydberg states and to ionize them. Here, we restrict our attention to ionization. Ionization by both linearly and circularly polarized fields has been explored with both H and other atoms.

Hydrogen atoms have been studied with linearly polarized fields of frequencies up to 36 GHz [26]. When the microwave frequency $\omega \ll 1/n^3$, ionization of $m = 0$ states occurs at a field of $\mathcal{E} = 1/9n^4(E^2/4)$, which is the field at which the extreme red Stark state is ionized by a static field. Due to the second-order Stark effect, the blue and red shifted states are not quite mirror images of each other, and when the microwave field reverses, transitions between Stark states occur. There is a rapid mixing of the Stark states of the same n and m by a microwave field, and all of them are ionized at the same microwave field amplitude, $\mathcal{E} = 1/9n^4$. Important points are that no change in n occurs, and the ionization field is the same as the static field required for ionization of the extreme red Stark state. As ω approaches $1/n^3$, the field falls below $1/9n^4$ due to Δn transitions to higher lying states, allowing ionization at lower fields. This form of ionization can be well described as the transition to the classically chaotic

regime [27]. For $\omega > 1/n^3$, the ionization field is more or less constant, and for $\omega > 1/2n^2$, the process becomes photoionization.

The ionization of nonhydrogenic atoms by linearly polarized fields has also been investigated at frequencies of up to 30 GHz, but the result is very different from the hydrogenic result. For $\omega \ll 1/n^3$ and low m , ionization occurs at a field of $\mathcal{E} \approx 1/3n^5$ [28]. This is the field at which the $m = 0$ extreme blue and red Stark states of principal quantum number n and $n + 1$ have their avoided crossing. For $n = 20$, this field is ≈ 500 V/cm, as shown by Fig. 15.4. How ionization occurs can be understood with a simple model based on a time-varying electric field. As the microwave field oscillates in time, atoms follow the Stark states of Na shown in Fig. 15.4. Even with very small field amplitudes, transitions between the Stark states of the same n are quite rapid because of the zero field avoided crossings. If the field reaches $1/3n^5$, the avoided crossing between the extreme red n and blue $n + 1$ state is reached, and an atom in the blue n Stark state can make a Landau–Zener transition to the red $n + 1$ Stark state. Since the analogous red–blue avoided crossings between higher lying states occur at lower fields, once an atom has made the $n \rightarrow n + 1$ transition, it rapidly makes a succession of transitions through higher n states to a state that is itself ionized by the field.

The Landau–Zener description given above is somewhat oversimplified in that we have ignored the coherence between field cycles. When it is included, we see that the transitions between levels are resonant multiphoton transitions. While the resonant character is obscured by the presence of many overlapping resonances, the coherence substantially increases the $n \rightarrow n + 1$ transition probability even when $\mathcal{E} < 1/3n^5$. The fields required for ionization calculated using this model are lower than $1/3n^5$, in agreement with the experimental observations. Nonhydrogenic Na states of high m behave like H, because no states with significant quantum defects are included, and the $n \rightarrow n + 1$ avoided crossings are vanishingly small.

Experiments on ionization of alkali atoms by circularly polarized fields of frequency ω show that for $\omega \ll 1/n^3$, a field amplitude of $\mathcal{E} = 1/16n^4$ is required for ionization [29]. This field is the same as the static field required. In a frame rotating with frequency ω , the circularly polarized field is stationary and cannot induce transitions, so this result is not surprising. On the other hand, when the problem is transformed to the rotating frame, the potential of Eq. (15.28) is replaced by

$$V = -\frac{1}{r} - \mathcal{E}x - \frac{\omega^2 \rho^2}{2}, \quad (15.32)$$

where $\rho^2 = x^2 + y^2$, and we have assumed the field to be in the x -direction in the rotating frame. This potential has a saddle point below $\mathcal{E} = 1/16n^4$ [30]. As n , or ω , is raised

so that $\omega \rightarrow 1/n^3$, the experimentally observed field falls below $1/16n^4$, but not so fast as implied by Eq. (15.32). Equation (15.32) is based solely on energy considerations, and ionization at the threshold field implied by Eq. (15.32) requires that the electron escape over the saddle point in the rotating frame at nearly zero velocity. For this to happen, when ω approaches $1/n^3$, more than n units of angular momentum must be transferred to the electron, which is unlikely. Models based on a restriction of the angular momentum transferred from the field to the Rydberg electron are in better agreement with the experimental results. Small deviations of a few percent from circular polarization allow ionization at fields as low as $\mathcal{E} = 1/3n^5$. This sensitivity can be understood as follows. In the rotating frame, a field with slightly elliptical polarization appears to be a large static field with a superimposed oscillating field at frequency 2ω . The oscillating field drives transitions to states of higher energy, allowing ionization at fields less than $\mathcal{E} = 1/16n^4$.

In the regime in which $\omega > 1/n^3$, microwave ionization of nonhydrogenic atoms is essentially the same as it is in H [31]. In this regime, the microwave field couples states differing in n by more than 1, and the pressure or absence of quantum defects is not so important. Consequently, only for $\omega > 1/n^3$ is the microwave ionization of H and other atoms different.

15.6 Collisions

Since Rydberg atoms are large, with geometric cross sections proportional to n^4 , one might expect the cross sections for collisions to be correspondingly large. In fact, such is often not the case. A useful way of understanding collisions of neutral atoms and molecules with Rydberg atoms is to imagine an atom or molecule M passing through the electron cloud of an Na Rydberg atom. There are three interactions

$$e^- - \text{Na}^+, \quad e^- - M, \quad M - \text{Na}^+. \quad (15.33)$$

The long-range $e^- - \text{Na}^+$ interaction determines the energy levels of the Na atom. The short-range of the $e^- - M$ and $M - \text{Na}^+$ interactions makes it likely that only one will be important at any given time. This approximation, termed the binary encounter approximation, is described in Chap. 60. The $M - \text{Na}^+$ interaction can only lead to cross sections of $\approx 10\text{--}100 \text{ \AA}^2$. On the other hand, since the electron can be anywhere in the cloud, the cross sections due to the $e^- - M$ interaction can be as large as the geometric cross section of the Rydberg atom. Accordingly, we focus on the $e^- - M$ interaction.

Consider a thermal collision between M and an Na Rydberg atom. Typically, M passes through the electron cloud slowly compared with the velocity of the Rydberg electron, and it is the $e^- - M$ scattering that determines what happens

in the M -Na collision, as first pointed out by *Fermi* [32]. First, consider the case where M is an atom. There are no energetically accessible states of atom M that can be excited by the low-energy electron, so the scattering must be elastic. The electron can transfer very little kinetic energy to M , but the direction of the electron's motion can change. With this thought in mind, we can see that only the collisional mixing of nearly degenerate ℓ states of the same n has very large cross sections. The ℓ -mixing cross sections are approximately geometric at low n [33]. If the M atom comes anywhere into the Rydberg orbit, scattering into a different ℓ state occurs. At high n , the cross section decreases, because the probability distribution of the Rydberg electron becomes too dilute, and it becomes increasingly likely that the M atom will pass through the Rydberg electron's orbit without encountering the electron. The n at which the peak ℓ -mixing cross section occurs increases with the electron scattering length of the atom. While ℓ -mixing cross sections are large, n changing cross sections are small ($\approx 100 \text{ \AA}^2$) since they cannot occur when the Rydberg electron is anywhere close to the outer turning point of its orbit [34].

If M is a molecule, there are likely to be energetically accessible vibrational and rotational transitions that can provide energy to or accept energy from the Rydberg electron, and this possibility increases the likelihood of n changing collisions with Rydberg atoms [11]. Electronic energy from the Rydberg atom must be resonantly transferred to rotation or vibration in the molecule. In heavy or complex molecules, the presence of many rotational-vibrational states tends to obscure the resonant character of the transfer, but in several light systems, the collisional resonances have been observed clearly [11].

Using the large Stark shifts of Rydberg atoms it is possible to tune the levels so that resonant energy transfer between two colliding atoms can occur [35] by the resonant dipole-dipole coupling,

$$Vd = \frac{\mu_1 \mu_2}{R^3}. \quad (15.34)$$

Here, μ_1 and μ_2 are the dipole matrix elements of the upward and downward transitions in the two atoms, and R is their separation. At room temperature, this process leads to enormous cross sections, substantially in excess of the geometric cross sections. At the low temperatures ($300 \mu\text{K}$) attainable using cold atoms, the atoms do not move, and, therefore, cannot collide. However, resonant dipole-dipole energy transfer is still observed due to the static dipole-dipole interactions of not two but many atoms [36, 37].

Since Rydberg atoms are easily perturbed by electric fields, it is hardly a surprise that collisions of charged particles with Rydberg atoms have large cross sections. In cold Rydberg atom samples, these large cross sections can lead to the spontaneous evolution to a plasma, since the macroscopic positive charge of the cold ions can trap any liberated

electrons, leading to impact ionization for a large part of the Rydberg atom sample [38, 39].

15.7 Autoionizing Rydberg States

The bound Rydberg atoms considered thus far are formed by adding the Rydberg electron to the ground state of the ionic core. It could equally well be added to an excited state of the core [40]. Figure 15.6 shows the energy levels of the ground 5s state of Sr⁺ and the excited 5p state. Adding an $n\ell$ electron to the 5s state yields the bound Sr 5s $n\ell$ state, and adding it to the excited 5p state gives the doubly excited 5p $n\ell$ state, which is coupled by the Coulomb interaction to the degenerate 5s $\epsilon\ell'$ continuum. The 5p $n\ell$ state autoionizes at the rate $\Gamma_{n\ell}$ given by [41]

$$\Gamma_{n\ell} = 2\pi |\langle 5p n \ell | V | 5s \epsilon \ell' \rangle|^2, \quad (15.35)$$

where V denotes the Coulomb coupling between the nominally bound 5p $n\ell$ state and the 5s $\epsilon\ell'$ continuum. A more general description of autoionization can be found in Chap. 26.

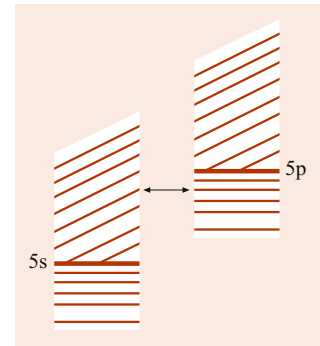
A simple picture, based on superelastic electron scattering from the Sr⁺ 5p state, gives the scaling of the autoionization rates of Eq. (15.35) with n and ℓ . The $n\ell$ Rydberg electron is in an elliptical orbit, and each time it comes near the core it has an n -independent probability γ_ℓ of scattering superelastically from the Sr⁺ 5p ion, leaving the core in the 5s state and gaining enough energy to escape from the Coulomb potential of the Sr⁺ core. The autoionization rate of the 5p $n\ell$ state is obtained by multiplying γ_ℓ by the orbital frequency of the $n\ell$ state, $1/n^3$, to obtain

$$\Gamma_{n\ell} = \frac{\gamma_\ell}{n^3}. \quad (15.36)$$

Equation (15.36) displays the n dependence of the autoionization rate explicitly and the ℓ dependence through γ_ℓ . As ℓ increases, the closest approach of the Rydberg electron to the Sr⁺ is at a larger orbital radius, so that superelastic scattering becomes progressively less probable, and γ_ℓ decreases rapidly with increasing ℓ . The simple picture of autoionization given above implies a finite probability of autoionization each time the $n\ell$ electron passes the ionic core, so the probability of an atom remaining in the autoionizing state should resemble stair steps [42], which can be directly observed using mode locked laser excitation and detection [43].

To a first approximation, the Sr 5p $n\ell$ states can be described by the independent electron picture used above, but in states converging to higher lying states of Sr⁺, the independent electron picture fails. Consider the Sr⁺ $\ell \geq 4$ states of $n > 5$. They are essentially degenerate, and the field due to an outer Rydberg electron converts the zero field ℓ states to superpositions much like Stark states. The outer electron

Fig. 15.6 Sr⁺ 5s and 5p states (—); the Rydberg states of Sr converging to these two ionic states are shown by (—), the continuum above the two ionic levels (///). The 5p $n\ell$ states are coupled to the 5s $\epsilon\ell'$ continua and autoionize



polarizes the Sr⁺ core, so that the outer electron is in a potential due to a charge and a dipole, and the resulting dipole states of the outer electron display a qualitatively different excitation spectrum than do states such as the 5p $n\ell$ states, which are well described by an independent particle picture [44]. When both electrons are excited to very high-lying states, with the outer electron in a state of relatively low ℓ , the classical orbits of the two electrons cross. Time domain measurements, made using wave packets, show that, in this case, autoionization is likely to occur in the first orbit of the outer electron [45].

References

- White, H.E.: Introduction to Atomic Spectra. McGraw-Hill, New York (1934)
- Bethe, H.A., Salpeter, E.A.: Quantum Mechanics of One and Two Electron Atoms. Academic Press, New York (1975)
- Fano, U.: Phys. Rev. A **2**, 353 (1970)
- Zimmerman, M.L., Littman, M.G., Kash, M.M., Kleppner, D.: Phys. Rev. A **20**, 2251 (1979)
- Bhatti, S.A., Cromer, C.L., Cooke, W.E.: Phys. Rev. A **24**, 161 (1981)
- Freeman, R.R., Kleppner, D.: Phys. Rev. A **14**, 1614 (1976)
- Lindgard, A., Nielsen, S.E.: At. Data Nucl. Data Tables **19**, 534 (1977)
- Chang, E.S.: Phys. Rev. A **31**, 495 (1985)
- Cooke, W.E., Gallagher, T.F.: Phys. Rev. A **21**, 588 (1980)
- Haroche, S., Raimond, J.M.: Radiative properties of Rydberg states in resonant cavities. In: Bates, D., Bederson, B. (eds.) Advances in Atomic and Molecular Physics, vol. 20, Academic Press, New York (1985)
- Dunning, F.B., Stebbings, R.F.: Experimental studies of thermal-energy collisions of Rydberg atoms with molecules. In: Stebbings, R.F., Dunning, F.B. (eds.) Rydberg States of Atoms and Molecules. Cambridge Univ. Press, Cambridge (1983)
- Bailey, D.S., Hiskes, J.R., Riviere, A.C.: Nucl. Fusion **5**, 41 (1965)
- Littman, M.G., Kash, M.M., Kleppner, D.: Phys. Rev. Lett. **41**, 103 (1978)
- Jones, R.R., Gallagher, T.F.: Phys. Rev. A **38**, 2946 (1988)
- Freeman, R.R., Economou, N.P., Bjorklund, G.C., Lu, K.T.: Phys. Rev. Lett. **41**, 1463 (1978)
- Reinhardt, W.P.: J. Phys. B **16**, 635 (1983)
- Gao, J., Delos, J.B., Baruch, M.C.: Phys. Rev. A **46**, 1449 (1992)
- Gallagher, T.F.: Rydberg Atoms. Cambridge Univ. Press, Cambridge (1994)

19. Rau, A.R.P.: *J. Phys. B* **12**, L193 (1979)
20. Jones, R.R., Noordam, L.D.: *Adv. At. Mol. Opt. Phys.* **38**, 1 (1997)
21. Alber, G., Zoller, P.: *Phys. Rep.* **199**, 231 (1991)
22. Warntjes, J.B.M., Wesdorp, C., Robicheaux, F., Noordam, L.D.: *Phys. Rev. Lett.* **83**, 512 (1999)
23. Kleppner, D., Littman, M.G., Zimmerman, M.L.: Rydberg atoms in strong fields. In: Stebbings, R.F., Dunning, F.B. (eds.) *Rydberg States of Atoms and Molecules*. Cambridge Univ. Press, Cambridge (1983)
24. Garton, W.R.S., Tomkins, F.S.: *Astrophys. J.* **158**, 839 (1969)
25. Holle, A., Main, J., Wiebusch, G., Rottke, H., Welge, K.H.: *Phys. Rev. Lett.* **61**, 161 (1988)
26. Sauer, B.E., Bellerman, M.R.W., Koch, P.M.: *Phys. Rev. Lett.* **68**, 1633 (1992)
27. Jensen, R.V., Susskind, S.M., Sanders, M.M.: *Phys. Rep.* **201**, 1 (1991)
28. Pillet, P., van Linden van der Heuvell, H.B., Smith, W.W., Kachru, R., Tran, N.H., Gallagher, T.F.: *Phys. Rev. A* **30**, 280 (1984)
29. Fu, P., Scholz, T.J., Hettema, J.M., Gallagher, T.F.: *Phys. Rev. Lett.* **64**, 511 (1990)
30. Nauenberg, M.: *Phys. Rev. Lett.* **64**, 2731 (1990)
31. Krug, A., Buchleitner, A.: *Phys. Rev. A* **66**, 053416 (2002)
32. Fermi, E.: *Nuovo Cimento* **11**, 157 (1934)
33. Gallagher, T.F., Edelstein, S.A., Hill, R.M.: *Phys. Rev. A* **15**, 1945 (1977)
34. Gounand, F., Berlande, J.: Experimental studies of the interaction of Rydberg atoms with atomic species at thermal energies. In: Stebbings, R.F., Dunning, F.B. (eds.) *Rydberg States of Atoms and Molecules*. Cambridge Univ. Press, Cambridge (1983)
35. Gallagher, T.F.: *Phys. Rep.* **210**, 319 (1992)
36. Mourachko, I., Comparat, D., de Tomasi, F., Fioretti, A., Nosbaum, P., Akulin, V.M., Pillet, P.: *Phys. Rev. Lett.* **80**, 253 (1998)
37. Anderson, W.R., Veale, J.R., Gallagher, T.F.: *Phys. Rev. Lett.* **80**, 249 (1998)
38. Robinson, M.P., Laburthe-Tolra, B., Noel, M.W., Gallagher, T.F., Pillet, P.: *Phys. Rev. Lett.* **85**, 4466 (2000)
39. Dutta, S.K., Guest, J.R., Feldbaum, D., Walz-Flannigan, A., Raitel, G.: *Phys. Rev. Lett.* **86**, 3993 (2001)
40. Gallagher, T.F.: *J. Opt. Soc. Am. B* **4**, 794 (1987)
41. Fano, U.: *Phys. Rev.* **124**, 1866 (1961)
42. Wang, X., Cooke, W.E.: *Phys. Rev. Lett.* **67**, 696 (1991)
43. Pisharody, S.N., Jones, R.R.: *Phys. Rev. A* **65**, 033418 (2002)
44. Eichmann, U., Lange, V., Sandner, W.: *Phys. Rev. Lett.* **68**, 21 (1992)
45. Pisharody, S.N., Jones, R.R.: *Science* **303**, 813 (2004)




Thomas F. Gallagher Thomas F. Gallagher received his PhD in Physics in 1971 from Harvard University and is now the Jesse W. Beams Professor of Physics at the University of Virginia. His research is focused on the use of Rydberg atoms to realize novel physical systems.



Rydberg Atoms in Strong Static Fields

16

John B. Delos , Thomas Bartsch, and Turgay Uzer

Contents

16.1	Introduction	241
16.2	Semiclassical Approximations	242
16.3	Regular Trajectories and Regular Wave Functions	244
16.4	Chaotic Trajectories and Irregular Wave Functions	245
16.4.1	Small-Scale Structure	246
16.4.2	Large-Scale Structure of Energy Spectra	247
16.4.3	Chaotic Ionization	250
16.5	Nuclear-Mass Effects	250
16.6	Quantum Theories	250
	References	250

to the large-scale structure of the density of states and the absorption spectrum.

This chapter is restricted to a discussion of Rydberg atoms in strong static fields. Related information on atoms in strong fields, on Rydberg atoms, and on the interaction of atoms with strong laser fields can be found elsewhere in the book.

Keywords

semiclassical methods · quantum chaos · Rydberg states · recurrence spectroscopy · closed orbits · external fields

Abstract

Semiclassical approximations provide a connection between quantum mechanics and classical mechanics. That relationship is problematic when classical orbits are chaotic. Highly excited states of atoms have provided a laboratory for the study of this relationship. When classical trajectories are orderly, corresponding quantum spectra and wave-functions display the same type of order. When they are chaotic, the quantum spectrum is very complex, but short closed classical orbits are connected

16.1 Introduction

Confronting classical and quantum mechanics in systems whose classical motion is chaotic is one of the fundamental problems of physics, as evidenced by the enormous outpouring of research during the last three decades. Introductions to chaotic classical dynamics are given in [1, 2], and detailed discussions of quantum manifestations of classical chaos are given in [3–5]. Highly excited Rydberg atoms in external fields play a prominent role in this quest because they are among the best known examples of quantum systems whose classical counterparts are chaotic [6–11]. For a wide variety of field configurations and field strengths, their spectra can be measured to high precision. At the same time, since their Hamiltonians are known analytically, they are equally amenable to accurate theoretical investigations using either classical or quantum mechanics. This chapter is focused on semiclassical descriptions of Rydberg atoms in strong static fields. Related information on atoms in strong fields can be found in Chap. 14 of this Handbook, on Rydberg atoms in Chap. 15, and on the interaction of atoms with strong laser fields in Chaps. 76 and 78. Atomic units will be used throughout this chapter.

J. B. Delos (✉)
Butterfly Dynamics LLC
Williamsburg, VA, USA
e-mail: jbdelosci@gmail.com

T. Bartsch
Mathematical Sciences, Loughborough University
Leicestershire, UK
e-mail: T.Bartsch@lboro.ac.uk

T. Uzer
School of Physics, Georgia Institute of Technology
Atlanta, GA, USA
e-mail: turgay.uzer@physics.gatech.edu

Various configurations of external fields have been studied:

1. an electric field, which in hydrogen leads to separable and, therefore, integrable classical dynamics;
2. a magnetic field, which produces a transition from regular to chaotic classical dynamics and which sparked the interest in Rydberg atoms as prototype examples for the study of the quantum-classical correspondence [7, 12–14] and references therein;
3. parallel electric and magnetic fields [15];
4. crossed electric and magnetic fields, which break all continuous symmetries of the unperturbed atom and, thus, allow one to study the transition from regularity to chaos in three coupled degrees of freedom [16–20].

The hydrogen atom is the prototype example for states with a single highly excited electron under the influence of strong external fields. For an electron in the hydrogen ground state, the influence of external electric or magnetic fields becomes comparable to that of the nuclear Coulomb field when the field strengths are in the order of the atomic units of electric field strength, $F_0 = e/(4\pi\epsilon_0 a_0) = 5.142\,206\,42(44) \times 10^{11}$ V/m, or magnetic field strength, $B_0 = \hbar/(ea_0^2) = 2.350\,517\,42(20) \times 10^5$ T, which are far beyond experimental reach. However, the relative importance of the external fields scales with the principal quantum number n as $n^4 F$ and $n^3 B$, so that for highly excited atoms, laboratory fields can easily be “strong”. In a nonhydrogenic atom, the influence of the inner-shell electrons can be summarized by means of a short-range effective core potential or a set of quantum defects [21, 22]. For laboratory field strengths, the core is too small to be appreciably influenced by the external fields. For this reason, the field-free quantum defects can be used to model core effects even in the presence of external fields [23].

The Hamiltonian for a hydrogen atom in a \hat{z} -directed magnetic field and an electric field of arbitrary orientation is, in atomic units,

$$H = \frac{\mathbf{p}^2}{2} - \frac{1}{r} + \frac{1}{2} B L_z + \frac{1}{8} B^2 \rho^2 + \mathbf{r} \cdot \mathbf{F} = E, \quad (16.1)$$

where $\rho^2 = x^2 + y^2$ and L_z is the angular momentum component along the magnetic field axis. The dynamics depends on four parameters: the field strengths F and B , the energy E , and the angle between the fields. We can reduce the number of independent parameters by one if we exploit a scaling property of the Hamiltonian. In terms of the scaled quantities

$$\begin{aligned} \tilde{\mathbf{r}} &= w^{-2} \mathbf{r}, & \tilde{\mathbf{p}} &= w \mathbf{p}, \\ \tilde{E} &= w^2 E, & \tilde{F} &= w^4 F, \end{aligned} \quad (16.2)$$

with the scaling parameter

$$w = B^{-1/3}, \quad (16.3)$$

the scaled Hamiltonian reads

$$\tilde{H} = \frac{\tilde{\mathbf{p}}^2}{2} - \frac{1}{\tilde{r}} + \frac{1}{2} \tilde{L}_z + \frac{1}{8} \tilde{\rho}^2 + \tilde{\mathbf{r}} \cdot \tilde{\mathbf{F}} = \tilde{E}. \quad (16.4)$$

The scaled dynamics, thus, depends only on three parameters: the scaled energy \tilde{E} and the scaled electric field strength \tilde{F} and its polar angle. If the fields are parallel, then the scaled angular momentum \tilde{L}_z is conserved, and it can be regarded as another fixed parameter, so, for example, if there is no electric field and $\tilde{L}_z = 0$ the scaled dynamics depends only on the scaled energy \tilde{E} .

16.2 Semiclassical Approximations

In Rydberg states, as in other highly excited quantum states, the deBroglie wavelength of the electron is short compared to the range over which the potential energy varies, so semiclassical approximations are appropriate means for insightful calculations. The semiclassical approximation in one dimension is a standard topic in textbooks on quantum mechanics, but satisfactory treatments in higher dimension are not common in textbooks. Therefore, below we give a brief description of semiclassical theory in two dimensions, which is adequate for many studies of Rydberg atoms in fields.

Semiclassical approximations are typically constructed using numerical computations of classical trajectories. The semiclassical approximation in two dimensions is easiest to explain by thinking about elastic scattering of particles of mass m and energy E from a fixed potential energy $V(r)$ having long-range attraction and short-range repulsion [24]. In Fig. 16.1, a stream of classical particles comes in from the left and interacts with such a potential energy fixed at the ori-

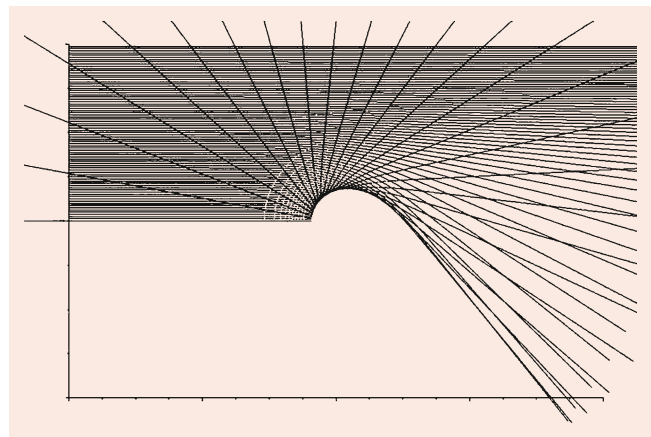


Fig. 16.1 Two-dimensional scattering with long-range attraction and short-range repulsion. (Figure kindly provided by C. Schleif)

gin. The radial (r) and angular (ϕ) motions are described by

$$\begin{aligned} \frac{dr}{dt} &= \left[\left(\frac{2}{m} \right) \left(E - V(r) - \frac{l^2}{2mr^2} \right) \right]^{1/2} \\ \frac{d\phi}{dt} &= \frac{l}{mr^2} \end{aligned} \quad (16.5)$$

(l = angular momentum). Particles having a large impact parameter b are only slightly deflected by the long-range attractive force. For smaller b , there is more deflection downward, which is said to be the negative scattering angle. The deflection reaches an extremum (the negative scattering angle has a minimum, called the “rainbow angle”), and then at smaller b , when the repulsive force dominates, particles are scattered upward, which is the positive scattering angle, until when $b = 0$, the scattering angle equals π (backward scattering).

The complete family of classical paths defines a dynamically allowed region of the plane, and two paths arrive at each point in this allowed region. The boundary between allowed and forbidden regions is called a “caustic”. (The dynamically forbidden region is much larger than the energetically forbidden region; the latter is the interior of a circle around the origin, where the potential energy exceeds the incident kinetic energy. The caustic touches the energetically forbidden region only on the trajectory having $b = 0$ [24]. Paths at larger b never touch the energetically forbidden region because of angular momentum repulsion, $l^2/2mr^2$.)

Two properties of this family of classical trajectories are needed for the calculation of a semiclassical approximation to the quantum wave function, the classical actions and the classical densities. On each path, the position $\mathbf{q}(t, b) = [x(t, b), z(t, b)]$ and the momentum $\mathbf{p}(t, b) =$

$[p_x(t, b), p_z(t, b)]$ are single-valued vector functions of time and of the impact parameter. The classical action is likewise a single-valued function of (t, b) ,

$$S(t, b) = \int_{t_0}^t \left[\mathbf{p}(t, b) \cdot \frac{\partial \mathbf{q}(t, b)}{\partial t} \right] dt. \quad (16.6)$$

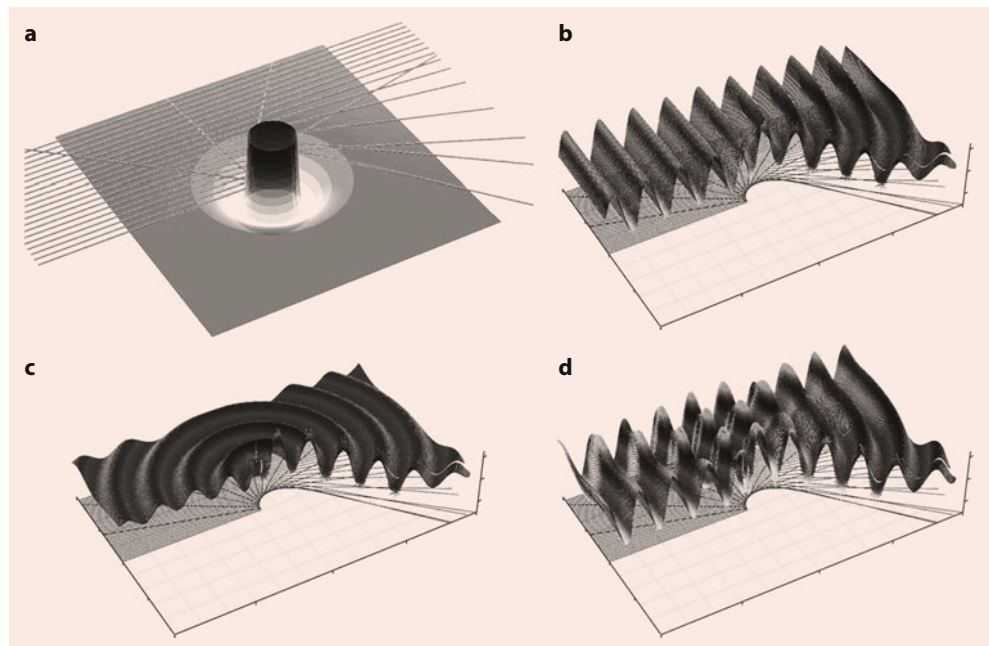
The classical density describes the fact that trajectories approaching the target represent a uniform flow, neighboring paths converge at the caustic, and scattered paths diverge from each other. This density is given by the function

$$\begin{aligned} \rho(t, b) &= \left| \left[\frac{J(t_0, b)}{J(t, b)} \right] \right|, \\ \text{where } J(t, b) &= \frac{\partial \mathbf{q}}{\partial(t, b)} = \frac{\partial(x, z)}{\partial(t, b)}, \end{aligned} \quad (16.7)$$

where t_0 is the initial time on each trajectory.

To construct a semiclassical wave function, we need to express the classical action and density as functions of position \mathbf{q} . Since two paths arrive at each point in the allowed region, these quantities are two-valued functions of \mathbf{q} . Each path that touches the caustic is divided into an “incident” (*Inc*) portion, prior to touching the caustic, and a “scattered” (*Scat*) portion, after touching the caustic. At large b , where paths never touch the caustic, the entire path is regarded as “*Inc*”, even the part that is going away from the target. (Quantum-mechanical descriptions of such collisions use an expansion in radial functions times spherical harmonics, and the radial function is divided into incoming and outgoing waves. The caustic does not coincide with the distance of

Fig. 16.2 Potential energy, trajectories, and wave functions for two-dimensional scattering with long-range attraction and short-range repulsion. (a) The potential energy, with a well and a barrier, and some trajectories from Fig. 16.1 shown in perspective. (b) Trajectories and the “incident” term in the wave function. (c) Trajectories and the “scattered” term in the wave function. (d) The complete wave function in the classically allowed region. (Figure kindly provided by C. Schleich)



closest approach of each trajectory, so our description of “incident” and “scattered” terms in the semiclassical wave function does not correspond directly to radial incoming and outgoing waves.)

Numerical inversion and interpolation of the relationship between \mathbf{q} and (t, b) gives two-valued action and density functions, $S_\alpha(\mathbf{q}), \rho_\alpha(\mathbf{q})$, with $\alpha = (\text{Inc}, \text{Scat})$. Then the semiclassical approximation to the wave function in the allowed region is given by a sum of an “incident” and a “scattered” wave function,

$$\psi_\alpha(\mathbf{q}) = [\rho_\alpha(\mathbf{q})]^{1/2} \exp\left(i\left[\frac{S_\alpha(\mathbf{q})}{\hbar} - \frac{\mu_\alpha\pi}{2}\right]\right),$$

$$\alpha = (\text{Inc}, \text{Scat}). \quad (16.8)$$

The absolute square of each term is the associated classical density, and the phase is the classical action with a correction $\mu_\alpha\pi/2$, where μ_α is called the Maslov index. In this case, $\mu_I = 0, \mu_S = 1$. The incident and scattered and full wave functions are shown in Fig. 16.2b–d. One sees refraction of the *Inc* term following the classical trajectories, and reflection producing the nearly circular outgoing *Scat* term. In the full wave function, one sees interference between these two waves.

Momentum-vector-fields are gradients of the two-valued action function, $\mathbf{p}_\alpha(\mathbf{q}) = \nabla S_\alpha(\mathbf{q})$, so $\nabla \times \mathbf{p}_\alpha(\mathbf{q}) = 0$. Any family of trajectories that forms a momentum-vector field with vanishing curl forms what in optics is called a “normal congruence” (in modern language, such a momentum-vector field defines a “Lagrangian manifold” in phase space). From any such vector field, a corresponding semiclassical wave function Eq. (16.8) can be constructed. Further details and mathematical theory are given in [24–28].

16.3 Regular Trajectories and Regular Wave Functions

We return now to Rydberg states of atoms in fields. At energies below the ionization threshold, there are bound trajectories that stay in a finite region of space. Figure 16.3 shows a path in cylindrical coordinates (ρ, z) followed by an electron in the presence of the attractive Coulomb force of a nucleus at the origin and forces from electric and magnetic fields directed along the z -axis. This is an example of a “regular” trajectory. The path is a perturbed Kepler ellipse; the eccentricity and orientation of the ellipse change continuously with time such that the ellipse does not close on itself. Also, the cylindrical coordinate ρ cannot be negative, so in this picture, the ellipse is folded over across itself.

For weak electric and magnetic fields, the principal action is approximately conserved, and its associated principal quantum number n is a good quantum number. If the fields

are parallel, then the z -component of angular momentum L_z is conserved, and quantized as $m\hbar$. However, the total angular momentum is not conserved, and ℓ is not a good quantum number. It is replaced by an approximately conserved quantity, which can be written in various ways. *Solov’ev* [29] and *Herrick* [30] wrote it as

$$\Lambda = 4A^2 - 5A_z^2, \quad (16.9)$$

where A is the Laplace–Runge–Lenz vector

$$A = \frac{1}{\sqrt{-2E}} \left(\frac{1}{2}(\mathbf{p} \times \mathbf{L} - \mathbf{L} \times \mathbf{p}) - \frac{\mathbf{r}}{r} \right). \quad (16.10)$$

Waterland et al. [15] used hydrogenic action and angle variables and classical perturbation theory to write the conserved quantity in the form

$$F(\text{eccentricity, orientation}) \simeq \text{constant} \equiv f^0. \quad (16.11)$$

Detailed analysis of either of these functions, Eq. (16.9) or Eq. (16.11), gives an understanding of all details of the regular classical trajectories.

This regular path winds around in the (ρ, z) plane such that it forms four well-defined curl-free momentum-vector fields $\mathbf{p}_\alpha(\mathbf{q})$, with each having a well-defined density $\rho_\alpha(\mathbf{q})$. Accordingly, each of these four vector-fields “support” a semiclassical wave function of the form Eq. (16.8), and the full wave function is a linear combination of these four terms. However, it is necessary to combine the terms in such a way that the full semiclassical wave function corresponds to a quantum wave function that satisfies the boundary conditions, $\psi(\rho, z) \rightarrow 0$ as $\rho \rightarrow \infty, z \rightarrow \pm\infty$. This requires quantization conditions.

In the 4-D phase space (\mathbf{q}, \mathbf{p}) , any surface having fixed energy E and satisfying Eq. (16.11) forms a 2-D torus labeled by (E, f^0) , and the exact trajectory lies very close to

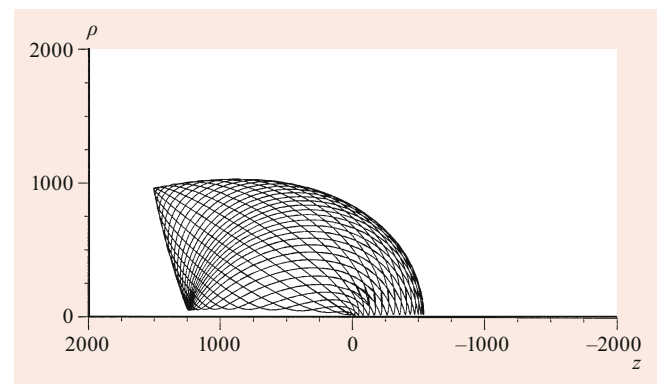


Fig. 16.3 A regular trajectory of an atomic electron in parallel electric and magnetic fields. This one has appropriately quantized action variables, so it is an “eigentrajjectory”, from which a semiclassical eigenfunction can be calculated

this surface. Any 2-D torus (the surface of a donut) has two distinct fundamental loops that cannot be shrunk to a point. Action variables are defined as

$$\mathbf{S}_j(E, f^0) = \int_j \mathbf{p}(\mathbf{q}; E, f^0) \cdot d\mathbf{q}, \quad j = 1, 2 \quad (16.12)$$

around each of the two fundamental loops of each torus [25, 28, 31–33]. The tori form continuous families, since E and f^0 vary continuously. Out of those continuous families of tori, we select a discrete set having appropriately quantized values of action variables

$$\mathbf{S}_j(E, f^0) = \left(k_j + \frac{\mu_j}{4}\right)2\pi\hbar, \quad j = 1, 2; \quad (16.13)$$

k_j is a positive integer, and μ_j is a Maslov index (equal to 2 in this case). Those discrete tori are called “eigentori”, and the trajectories on them are called “eigentrajectories”.

The momentum-vector fields associated with each eigentrajjectory, with their associated densities and action functions, “support” a quantized semiclassical wave function. The local wavelength of the α semiclassical term is $\lambda_\alpha = 2\pi\hbar/|\mathbf{p}_\alpha(\mathbf{q})|$, and the quantization condition ensures that there will be a properly quantized number of wavelengths associated with each fundamental loop of each eigentorus. Thus, the corresponding exact quantum wave function will satisfy the necessary boundary conditions.

In Fig. 16.4 is shown the complete quantum wave function (absolute squared) associated with the eigentrajjectory that was shown in Fig. 16.3. (This eigenfunction was computed by accurate quantum methods, with no reference to the semiclassical wave function.) We see that the wave function primarily occupies the same region of space as the eigentrajjectory, diffracting into the nearby classically forbidden region. The local wavelength and density of the quantum

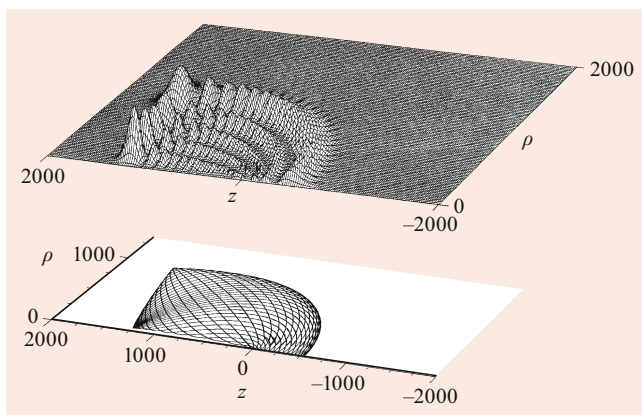


Fig. 16.4 Below is the eigentrajjectory that was shown in Fig. 16.3, and above is an accurate eigenfunction for a Rydberg state of an electron in an atom in parallel electric and magnetic fields

wave function are consistent with the local momentum and density of the eigentrajjectory [15].

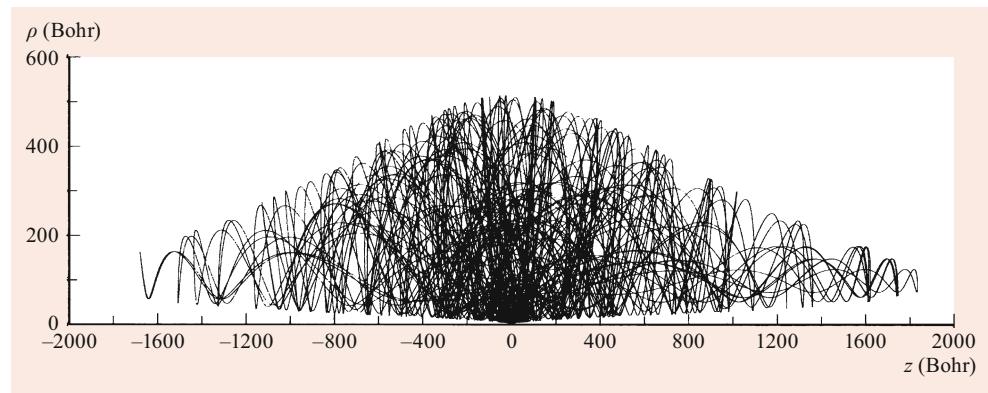
This case illustrates the general principles for systems having regular trajectories [3, 4, 34, 35]. (1) Regular bound trajectories wind around a finite region of space such that they form curl-free momentum-vector fields. In the phase space of dimension $2n$, bound regular trajectories lie on tori of dimension n . (2) Upon an appropriately quantized set of these regular trajectories, one can construct semiclassical wave functions such that the corresponding exact quantum wave function satisfies the necessary boundary conditions. In the simple cases (in the absence of tunneling), there is a one-to-one correspondence between eigentrajectories and eigenfunctions. (3) All trajectories are regular if the equations of motion are separable (i.e., the Hamilton–Jacobi equation is separable), or, more generally, if the system has n degrees of freedom and n conservation laws (technically, n “isolating integrals of the motion”). (4) Analysis of the conservation laws tells us everything we might want to know about the structure of the trajectories. (5) For weak perturbations of a system having regular trajectories, most of the trajectories are regular (Kolmogorov–Arnold–Moser (KAM) theorem [36–38]).

16.4 Chaotic Trajectories and Irregular Wave Functions

An example of a chaotic trajectory is shown in Fig. 16.5. As in Fig. 16.3, this is one continuous curve showing a path in (ρ, z) -space followed by a classical electron in the Coulomb field of a nucleus at the origin and a magnetic field along the z -axis (no applied electric field). In contrast to the curve shown in Fig. 16.3, which is similar to a machine-wound spool of twine, this path looks like a bowl of spaghetti that got dropped on the floor. Nevertheless, there is short-time order in the path: far from the nucleus, the electron’s path is close to a helix, circling around a magnetic field line, while close to the nucleus it is close to a Kepler ellipse. However, we can see no long-time order in this path. If we could draw a curve inside of which the magnetic field were negligible and outside of which the Coulomb field were negligible, we could say that the magnetic field scatters the electron from one Kepler orbit to another, or we could say that the Coulomb field scatters the electron from one helix to another; either way, the long-time behavior is chaotic. Such trajectories arise when magnetic and Coulomb forces compete but neither dominates everywhere [7, 39]. This happens as the energy approaches the ionization limit, or if the magnetic field becomes extremely strong (in the kilotesla range).

There is a second way that chaos arises in Rydberg states of atoms. The quantum or classical Hamiltonian for a hy-

Fig. 16.5 A chaotic trajectory of an atomic electron in a strong magnetic field. (Courtesy of Donald Noid)



drogen atom in an electric field is separable in parabolic coordinates, so all bound trajectories lie on tori. However for all other atoms, the small ion core scatters the electron from one torus to another, and the long-time behavior is chaotic. One may compare the motion to that of a billiard ball on a rectangular table containing a small round barrier [40–43].

Some properties of chaotic trajectories are the following. (1) They have a sensitive dependence on initial conditions: a small displacement of initial conditions grows exponentially, restricting predictability to short times. (2) Even in a chaotic system, there is order on short time scales. The trajectories obey Newton’s laws, and if the forces are smooth functions of position, then the paths are smooth functions of initial conditions (according to property (1), they become horrible and even uncomputable functions, but they are, in principle, smooth – as time increases, the derivative of final position with respect to initial position becomes gargantuan but finite). Thus, chaos is a long-time property of classical trajectories. (3) While regular bound trajectories are restricted to n -dimensional tori in the $2n$ -dimensional phase space, chaotic trajectories may fill the energy shell, in the sense of approaching arbitrarily closely to any point in it. Accordingly, at any spatial point, (ρ, z) , the magnitude of the momentum is determined by conservation of energy, but the direction of the momentum is not. Therefore, a path does not form a curl-free momentum-vector field, indeed, it does not form a momentum-vector field at all. Therefore, we cannot use chaotic trajectories to build quantum wave functions in the way that is done for regular trajectories. This is the “problem of quantum chaos”: if classical trajectories of a given system are chaotic, what can be said about the quantum states? For reviews of this problem see [3, 4, 34, 44]. Here, we discuss only Rydberg atoms in static fields.

Two general principles apply. (A) Long-time chaos in classical mechanics carries over to irregular behavior of individual energy levels and individual eigenfunctions – these are most visible at high resolution of energy. (B) Short-time order in classical mechanics carries over to short-time order in quantum mechanics, and that in turn is connected to the

large-scale structure of the energy spectrum and other quantum properties – these are most visible at low resolution of energy. Thus, different manifestations of chaos appear when we look at the spectrum on different scales [35].

16.4.1 Small-Scale Structure

In Chap. 15, Fig. 15.5 shows energy levels of hydrogen in an electric field. It is seen that energy levels from different values of principal quantum number n cross each other. This is because the Schrodinger equation (as well as the Hamilton–Jacobi equation) is separable in parabolic coordinates. All bound motions are, therefore, regular, and states that cross have different parabolic quantum numbers. Figure 15.4 shows energy levels of sodium in an electric field. Now the states avoid crossing. The ion core scatters the electron from one parabolic state to another, and all eigenstates of the full Hamiltonian are superpositions of many different parabolic states. In this case, the avoided crossings are a quantum manifestation of the classical chaos that arises from core scattering. These figures suggest that regular behavior allows lots of degeneracies and near-degeneracies, but chaotic behavior produces avoided crossings, thus pushing eigenvalues apart.

This repulsion of energy levels shows up in nearest-neighbor statistics of the energies. For each energy eigenvalue, define s to be the absolute value of the energy gap to its nearest neighboring eigenvalue, and then for a large collection of eigenvalues find the probability distribution $P(s)$ of values of s . This is the nearest-neighbor spacing distribution. For Rydberg states of atoms, this nearest-neighbor spacing distribution was computed in [40] and is shown in Fig. 16.6, first for hydrogen, and then for lithium. The stepped line is the histogram, and the two dashed lines are an exponential, which permits lots of near-degeneracies, as is seen in regular spectra, and a Wigner distribution, $P(s) = (\pi/2)s \exp(-\pi s^2/4)$, which goes to zero as $s \rightarrow 0$, consistent with irregular spectra and their avoided crossings.

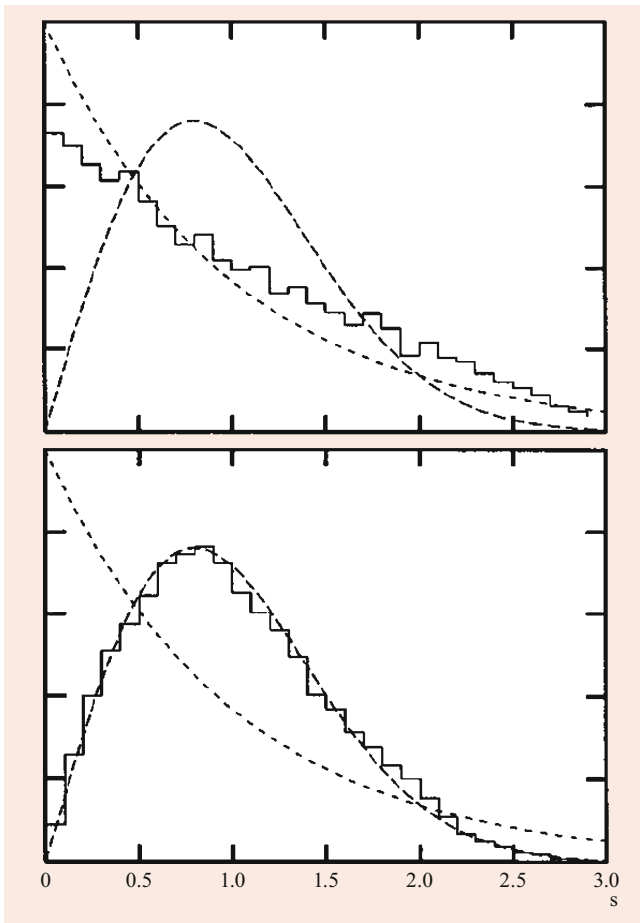


Fig. 16.6 Nearest-neighbor spacing distribution for Rydberg states of hydrogen (*above*) and for lithium (*below*). The stepped curve is the histogram computed from the spectrum; the light and heavy dashed lines are, respectively, an exponential and a Wigner distribution [40]

16.4.2 Large-Scale Structure of Energy Spectra

If instead of looking at individual quantum states, we average the properties of these states over a finite band of energies, then a relationship to classical periodic orbits appears. This connection was first recognized by *Gutzwiller* [4], and experiments and theory on Rydberg states of atoms have shown the connection most clearly [45–47].

The first experimental evidence came from measurements of the absorption spectrum of atoms in magnetic fields [12–14]. At “low” energies, meaning absorption to Rydberg states around $n \approx 30$ in laboratory magnetic fields (≈ 6 T), spectral lines fall into orderly sequences, quantitatively described by the regular trajectories and wave functions discussed above. With increasing energy, the spectrum becomes messier, partly because of chaotic dynamics and partly because levels are not well resolved. Then at higher energies, orderly oscillations appear. The wavelength of these oscillations on the energy axis ΔE_1 is related to the return time T_1 of a closed orbit perpendicular to the magnetic field, $\Delta E_1 = 2\pi\hbar/T_1$.

Later, when the absorption spectrum of a hydrogen atom in a 6 T magnetic field was measured [14], it was found that the spectrum could be Fourier-decomposed into a sum of sinusoidal oscillations,

$$\text{Abs}(E) \simeq \sum_j C_j \sin\left(\frac{T_j E}{\hbar} + \Delta_j^0\right), \quad (16.14)$$

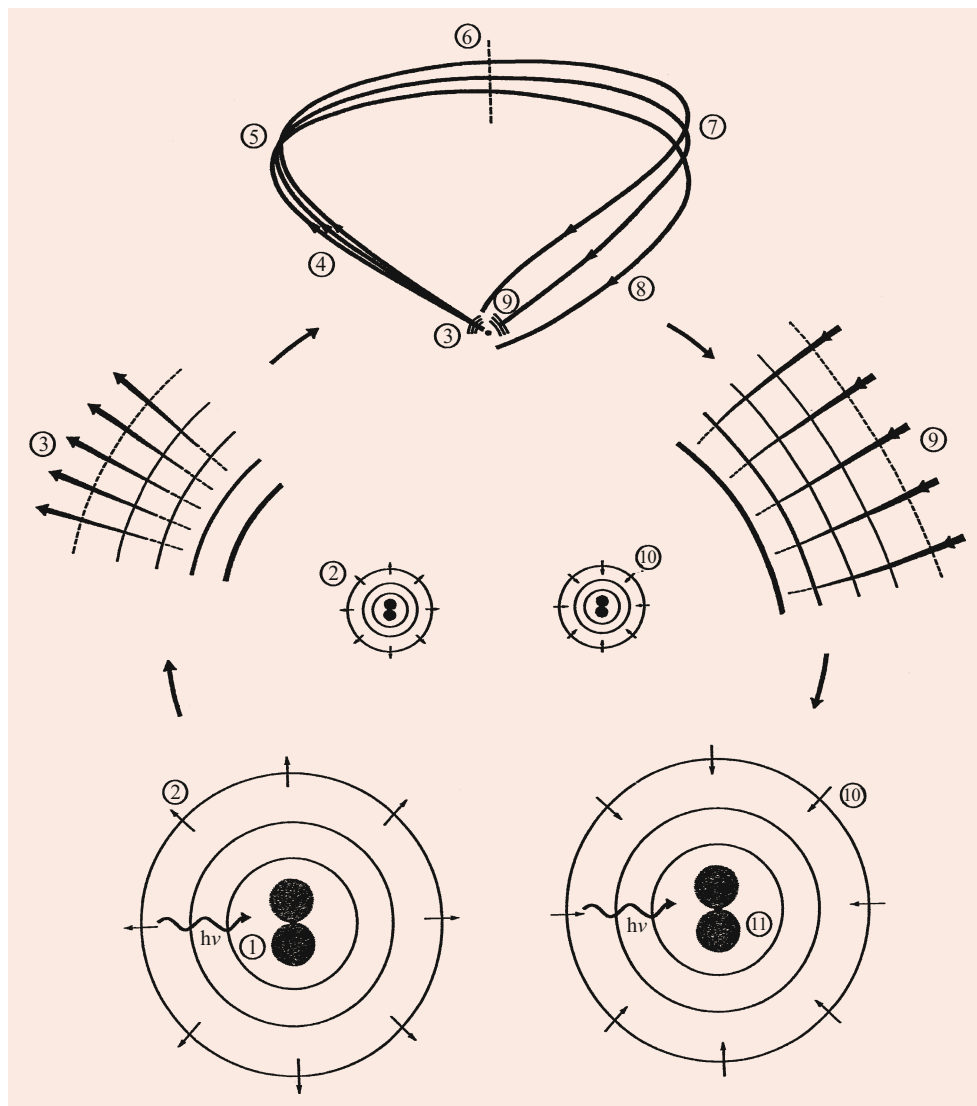
and that these T_j are times of returning classical orbits of the electron. The shortest returning orbits produce oscillations of longest wavelength (on the energy axis), and successively longer returning orbits produce oscillations of successively shorter wavelength. This observation was the birth of recurrence spectroscopy, a different way of thinking about absorption spectra: instead of examining individual energy levels, the Fourier-transform of the absorption spectrum provides measures of closed classical orbits of the electron as it moves in the Coulomb field of the nucleus and the applied electric and magnetic fields [17, 48–53]. (In the case of atomic absorption spectra, the semiclassical connection is to orbits that are closed at the nucleus, not to periodic orbits.)

The physical picture is shown in Fig. 16.7. Light shining on an atom (like a vibrator in a ripple tank, sending out a continuous stream of water waves) produces a continuous stream of electron waves moving out from the atom in all directions, with energy close to the ionization threshold. That is a quantum process. However, when the waves move away, we can follow the waves by following the corresponding “rays”, the outgoing classical trajectories. At large distances, the trajectories and waves are turned around by the applied fields. Some trajectories and waves go out in directions such that they return to the atom after a while. When they do, the waves refract and diffract around the atom, producing a steady stream of incoming waves, which interfere with the steady stream of outgoing waves, producing the oscillations that are visible in the absorption spectrum. This physical picture leads to a quantitative formula,

$$\text{Abs}(E; B, F) = \sum_j C_j(E; B, F) \sin(\Delta_j(E; B, F)). \quad (16.15)$$

Here, j labels the closed orbits, and $\Delta_j(E; B, F)$ is a phase, in which the most important term is the classical action integrated around the closed orbit. The duration of the closed orbit is $T_j = \partial\Delta_j/\partial E$, which recovers the approximate formula Eq. (16.14). The coefficient $C_j(E; B, F)$ is slowly varying with energy and magnetic and electric field strengths; it contains factors representing the angular distribution of outgoing waves, and the (square root of) the classical density associated with the returning trajectories [45, 46]. This coefficient is called the “recurrence amplitude”, and its absolute square is the “recurrence strength”.

Fig. 16.7 Clockwise from *lower left*. Light shining on an atom (1) produces a continuous stream of outgoing electron waves (2), having energy close to the ionization threshold. When those waves get away from the atom, we can follow them by following the corresponding “rays” or classical trajectories (3). These trajectories travel away (4), pass through a caustic (5), a focus (6), and another caustic (7). We have drawn trajectories that return to the vicinity of the nucleus (8). When they do, they refract (9), and the waves diffract (10) around the nucleus, producing a steady stream of incoming waves that overlap the initial state (11) and interfere with the outgoing waves, producing interference oscillations in the absorption spectrum



Scaled-variable methods provide important improvements to the experimental measurements [13]. The structure, size, and return times of orbits change with energy and field strengths, but it turns out that (for $F = 0$ and $L_z = 0$) the shapes of classical orbits depend only on the scaled energy, which is $\varepsilon = EB^{-2/3}$ (Eq. (16.2)). At constant scaled energy, the classical action is proportional to $w = B^{-1/3}$, and the coefficient $C_j(E; B)$ is nearly constant. It follows that if the absorption spectrum is measured varying E and B simultaneously to hold ε fixed, and the absorption is recorded as a function of w , then the oscillations become almost perfectly sinusoidal, and the recurrence spectrum becomes a set of sharp peaks, one at the scaled classical action of each returning orbit. An example of a scaled-variable recurrence spectrum for hydrogen in a magnetic field is shown in Fig. 16.8 [54].

For atoms in an electric field F with no magnetic field present, the scaled energy is $\varepsilon = EF^{-1/2}$. For this case, a family of recurrence spectra is drawn in a single graph in

Fig. 16.9 [55]. At all energies there is a closed orbit of the electron that goes up parallel to the electric field; its recurrence peak is barely visible in the upper left part of the figure. In certain ranges of energies, many other closed orbits are present. Some are shown at the bottom of Fig. 16.9, labeled (m/n) , meaning m cycles of motion transverse to the field during n cycles of motion parallel to the field. The scaled actions of these orbits are close to the scaled action of n cycles of the parallel orbit. If we gradually lower the scaled energy, there is a point at which each of these closed orbits splits (bifurcates) out of the parallel orbit. At that point, orbits neighboring the parallel orbit return strongly focused on the residual ion, and the recurrence strength is large. Such points are marked in the figure.

The detailed analysis of many such experiments has led to advances in classical and semiclassical mechanics. (1) In a magnetic field, one can see bifurcation and proliferation of closed orbits as order changes to chaos with increasing ε .

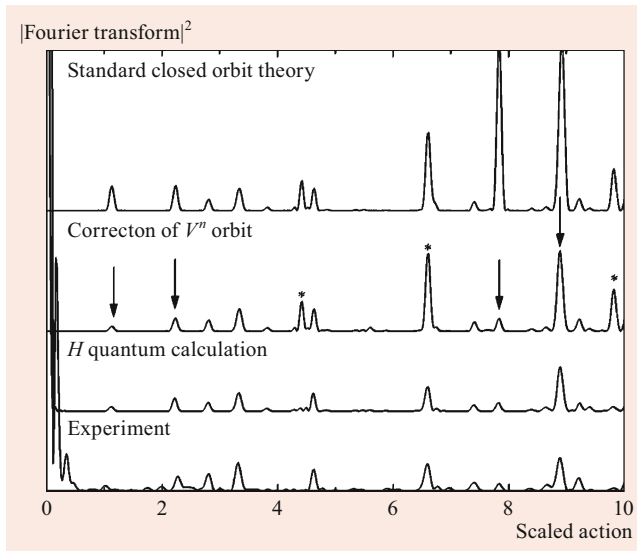


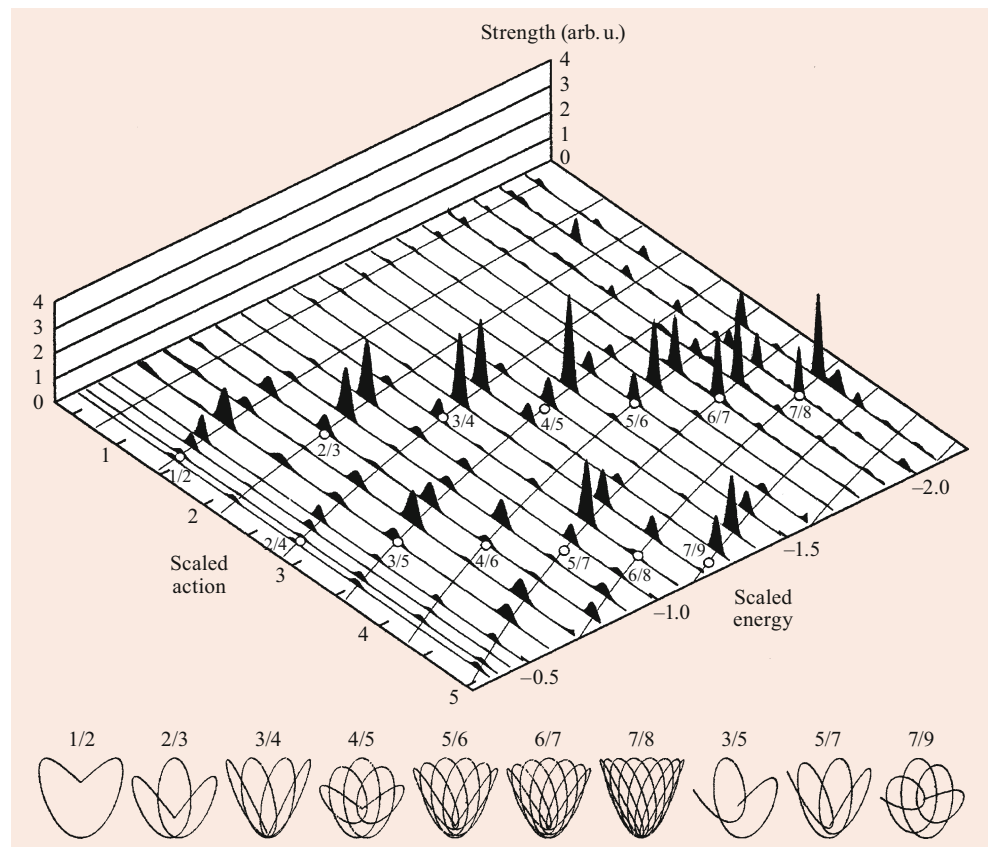
Fig. 16.8 A scaled-variable recurrence spectrum for hydrogen in a magnetic field. The location of each peak is the scaled action of a closed orbit; the height of each is the recurrence strength for that orbit. Arrows and asterisks mark corrections to simple semiclassical theory because of divergences near bifurcations [54]

Mathematical theory shows that there are just five generic patterns of bifurcations of periodic orbits. In atomic systems, these generic patterns are modified by symmetries. Calcula-

tions and theory show the shapes of bifurcated orbits. Also, sequences of bifurcations can be understood by reduction of the Hamiltonian to a local normal form. Measurements of recurrence spectra – intrinsically a quantum wave-interference phenomenon – have provided the most detailed and precise observations of bifurcations of classical periodic orbits and closed orbits [48, 56–63]. (2) Breaking cylindrical symmetry, by varying the angle between applied fields, weakens the recurrences in a systematic way. Breaking time symmetry, by applying a slowly oscillating field, has the same effect, and allows the electron orbit to be reconstructed from the recurrence spectrum [50, 51, 64]. (3) Semiclassical approximations diverge at bifurcations because there are boundaries between classically allowed and forbidden regions. The divergences are repaired by diffraction integrals such as Airy functions or Fresnel-type integrals. Diffraction into forbidden regions and also above-barrier reflection of waves produces “ghost recurrences” [54, 59, 61, 63, 65–71] (4) For nonhydrogenic atoms, the ion core scatters electrons from one returning orbit to another, producing “combination recurrences” [40, 72–75]. (5) Similar concepts give a theory of “width-weighted spectra”, related to energy-averaged decay rates of atoms [76].

Finally, we mention that recurrence spectroscopy associated with Rydberg states helped to stimulate the study of periodic orbits and their bifurcations in molecular systems [77–80].

Fig. 16.9 Many recurrence spectra for an atom in an electric field are drawn in a single graph [55]. The curves in the horizontal plane represent the scaled action of the parallel orbit and its repetitions as a function of scaled energy. Locations of bifurcations are marked with small open circles. New orbits created in bifurcations have almost the same action as the corresponding return of the parallel orbit. Measured recurrence strengths are shown in the vertical direction. Recurrences are especially strong at scaled energies slightly lower than bifurcations. Orbits created by bifurcation of the parallel orbit are shown along the bottom. The 2/4, 4/6, and 6/8 orbits are repetitions of the 1/2, 2/3, and 3/4 orbits, respectively, so their shapes are identical



16.4.3 Chaotic Ionization

At energies high enough that the electron can escape, we have a “chaotic scattering” system, or, for photoionization, a chaotic “half-collision”, or chaotic transport problem. The situation is closely related to the modern version of transition state theory of chemical reaction rates, and also has a connection with asteroid escape rates [81–86]. Consider the following experiment (which, as of this writing, has not yet been performed). An atom in a magnetic (and possibly electric) field is excited by a short laser pulse to an energy that permits escape of the electron. (The ideal experiment will excite to the minimum range of energies allowed by the uncertainty principle.) We might expect that the excited atom would decay by ionization exponentially with time. In fact, however, electrons come out in a chaotic sequence of short pulses. Classical calculations show that a graph of the time required for the electron to escape from the atom versus its initial direction has a fractal structure [87–91]. This fractal does not have the perfectly regular self-similar structure of mathematical fractals such as the Cantor set [92–95], nor is it a fractal with only statistical self-similarity. It is a distinct type, which has been called an “epistrophic” fractal.

The definition and characterization of such fractals is given in [96–99], and application to the chaotic escape of electrons from atoms in fields is given in [100–106]. Quantum calculations [107] verify that the predictions obtained from this fractal description are correct, at least for short times. It appears that epistrophic fractals occur commonly (perhaps generically) in chaotic scattering because they have been identified both theoretically and experimentally in the escape of particles or light or sound from a vase-shaped cavity [108–110], and theoretically in the escape of atoms from a trap [111], ballistic atom pumps [112–114], fluid flow [115, 116], and perhaps also in the dynamics of the buckling of a nanobeam [117].

16.5 Nuclear-Mass Effects

So far, only the relative motion of the electron with respect to the ionic core has been described. This is appropriate if the nucleus can be assumed to be infinitely heavy and, thus, not to take part in the motion. To include the effects of a finite nuclear mass, the description must start from the coupled two-body Hamiltonian and then work toward a separation of the internal dynamics from the center-of-mass (CM) motion.

It turns out that in the presence of a magnetic field, unlike for the field-free two-body problem, a complete separation of the relative and CM motions is impossible. Instead, only a pseudo-separation can be achieved, where the relative and CM motions remain coupled through a new constant of motion called the pseudomomentum \mathbf{K} [118]. This coupling

introduces a number of novel effects into the dynamics [119–123].

The influence of the CM motion on the internal dynamics is twofold. On the one hand, the motion of the atom in the magnetic field causes an induced electric field (motional Stark effect). On the other hand, the kinetic energy of the CM motion gives rise to an additional confining potential for the internal motion that could, in principle, locate the electron at a large distance from the nucleus, and produce atomic states with a huge dipole moment. Conversely, the motion of the CM is driven by the internal motion, the most strongly so in the case of vanishing pseudomomentum. It, thus, reflects the transition from regular to chaotic internal dynamics: regular internal motion leads to regular CM motion, whereas chaotic internal dynamics can give rise to chaotic behavior of the CM.

16.6 Quantum Theories

This chapter has focused on semiclassical theories and the connections between classical trajectories and quantum wave functions in excited states of atoms in fields. For more information on quantum theory of atoms in fields, the reader is referred to [124–126].

References

- Hilborn, R.C.: *Chaos and Nonlinear Dynamics: An Introduction for Scientists and Engineers*, 2nd edn. Oxford Univ. Press, Oxford, New York (2000)
- Jackson, E.A.: *Perspectives of Nonlinear Dynamics*. Cambridge Univ. Press, Cambridge (1990)
- Haake, F.: *Quantum Signatures of Chaos*, 2nd edn. Springer Series in Synergetics, vol. 54. Springer, Berlin, Heidelberg, New York (2013)
- Gutzwiller, M.C.: *Chaos in Classical and Quantum Mechanics*. Interdisciplinary Applied Mathematics, vol. 1. Springer, Berlin, Heidelberg, New York (2013)
- Berggren, K.: *Quantum Chaos Y2K: Proceedings of Nobel Symposium 116, Bäckaskog Castle, Sweden, June 13–17, 2000*. World Scientific, Singapore (2001)
- Bayfield, J.E.: *Phys. Rep.* **51**, 317 (1979)
- Delos, J., Knudson, S., Noid, D.: *Phys. Rev. A* **30**, 1208 (1984)
- Delande, D., Gay, J.: *Comments At. Mol. Phys.* **19**, 35 (1986)
- Casati, G., Chirikov, B.V., Shepelyansky, D.L., Guarneri, I.: *Phys. Rep.* **154**, 77 (1987)
- Hasegawa, H.: *Prog. Theor. Phys. Suppl.* **98**, 198 (1989)
- Friedrich, H., Wintgen, D.: *Phys. Rep.* **183**, 37 (1989)
- Lu, K.T., Tomkins, F.S., Garton, W.R.S.: *Proc. R. Soc. A* **362**, 421 (1978)
- Holle, A., Main, J., Wiebusch, G., Rottke, H., Welge, K.: *Phys. Rev. Lett.* **61**, 161 (1988)
- Main, J., Wiebusch, G., Holle, A., Welge, K.: *Phys. Rev. Lett.* **57**, 2789 (1986)
- Waterland, R., Delos, J., Du, M.: *Phys. Rev. A* **35**, 5064 (1987)
- Raithel, G., Fauth, M., Walther, H.: *Phys. Rev. A* **44**, 1898 (1991)
- Freund, S., Ubert, R., Flöthmann, E., Welge, K., Wang, D., Delos, J.: *Phys. Rev. A* **65**, 53408 (2002)

18. Connerade, J., Zhan, M., Rao, J., Taylor, K.: *J. Phys. B* **32**, 2351 (1999)
19. Bartsch, T., Main, J., Wunner, G.: *Phys. Rev. A* **67**, 063411 (2003)
20. Von Milczewski, J., Uzer, T.: *Phys. Rev. E* **55**, 6540 (1997)
21. Gallagher, T.F.: *Rydberg Atoms*. Cambridge Monographs on Atomic, Molecular and Chemical Physics, vol. 3. Cambridge Univ. Press, Cambridge (2005)
22. Friedrich, H.: *Theoretical Atomic Physics*, 3rd edn. Springer, Berlin, Heidelberg (2006)
23. Rao, J., Taylor, K.: *J. Phys. B* **30**, 3627 (1997)
24. Knudson, S., Delos, J., Bloom, B.: *J. Chem. Phys.* **83**, 5703 (1985)
25. Knudson, S.K., Delos, J.B., Noid, D.W.: *J. Chem. Phys.* **84**, 6886 (1986)
26. Delos, J.B.: *Adv. Chem. Phys.* **65**, 161 (1986)
27. Littlejohn, R.G.: *J. Stat. Phys.* **68**, 7 (1992)
28. Maslov, V.P., Fedoriuk, M.V.: *Semi-Classical Approximations in Quantum Mechanics*. D. Reidel Publishing Company, Dordrecht (1981)
29. Solov'ev, E.: *Sov. Phys. JETP* **55**, 1017 (1982)
30. Herrick, D.R.: *Phys. Rev. A* **26**, 323 (1982)
31. Noid, D.W., Marcus, R.A.: *J. Chem. Phys.* **62**, 2119 (1975)
32. Keller, J.B.: *Ann. Phys.* **4**, 180 (1958)
33. Stone, A.D.: *Phys. Today* **58**, 37 (2005)
34. Berry, M.V.: *Les Houches Lect. Ser.* **36**, 171 (1983)
35. Berry, M.V.: In: *The Wave-Particle Dualism: A Tribute to Louis de Broglie on his 90th Birthday*, p. 231. D. Reidel Publishing Company, Dordrecht, Boston, Lancaster (1984)
36. Arnold, V.I.: *Mathematical Methods of Classical Mechanics*. Springer, New York (1978)
37. Arnold, V., Avez, A.: *Ergodic Problems of Classical Mechanics*. Benjamin Inc., New York (1968)
38. Moser, J.K.: *Stable and Random Motions in Dynamical Systems*. Princeton Univ. Press, Princeton (1973)
39. Hansen, K.T.: *Phys. Rev. E* **51**, 1838 (1995)
40. Courtney, M., Kleppner, D.: *Phys. Rev. A* **53**, 178 (1996)
41. Chernov, N., Markarian, R.: *Chaotic Billiards*. American Mathematical Society, Providence (2006)
42. Doron, E., Smilansky, U.: *Nonlinearity* **5**, 1055 (1992)
43. Sridhar, S., Hogenboom, D., Willemsen, B.A.: *J. Stat. Phys.* **68**, 239 (1992)
44. Berry, M.V.: *R. Soc. Lond. Proc. Ser. A* **413**, 183 (1987)
45. Du, M., Delos, J.: *Phys. Rev. A* **38**, 1896 (1988)
46. Du, M., Delos, J.: *Phys. Rev. A* **38**, 1913 (1988)
47. Bogomol'nyi, E.: *Sov. Phys. JETP* **69**, 275 (1989)
48. Main, J., Wiebusch, G., Welge, K., Shaw, J., Delos, J.: *Phys. Rev. A* **49**, 847 (1994)
49. Gao, J., Delos, J.B.: *Phys. Rev. A* **49**, 869 (1994)
50. Spellmeyer, N., Kleppner, D., Haggerty, M.R., Kondratovich, V., Delos, J.B., Gao, J.: *Phys. Rev. Lett.* **79**, 1650 (1997)
51. Haggerty, M., Delos, J.: *Phys. Rev. A* **61**, 53406 (2000)
52. Jensen, R.V., Flores-Rueda, H., Wright, J.D., Keeler, M.L., Morgan, T.J.: *Phys. Rev. A* **62**, 53410 (2000)
53. Keeler, M.L.: *Phys. Rev. A* **77**, 34503 (2008)
54. Karremans, K., Vassen, W., Hogervorst, W.: *Phys. Rev. A* **60**, 4764 (1999)
55. Courtney, M., Jiao, H., Spellmeyer, N., Kleppner, D., Gao, J., Delos, J.B.: *Phys. Rev. Lett.* **74**, 1538 (1995)
56. Mao, J., Delos, J.: *Phys. Rev. A* **45**, 1746 (1992)
57. Sadvovskii, D.A., Shaw, J.A., Delos, J.B.: *Phys. Rev. Lett.* **75**, 2120 (1995)
58. Sadvovskii, D.A., Delos, J.B.: *Phys. Rev. E* **54**, 2033 (1996)
59. Shaw, J.A., Robicheaux, F.: *Phys. Rev. A* **58**, 3561 (1998)
60. Kips, A., Vassen, W., Hogervorst, W.: *Phys. Rev. A* **59**, 2948 (1999)
61. Gao, J., Delos, J.B.: *Phys. Rev. A* **56**, 356 (1997)
62. Wang, D., Delos, J.: *Phys. Rev. A* **63**, 43409 (2001)
63. Main, J., Wunner, G.: *Phys. Rev. A* **55**, 1743 (1997)
64. Haggerty, M., Spellmeyer, N., Kleppner, D., Delos, J.: *Phys. Rev. Lett.* **81**, 1592 (1998)
65. Peters, A.D., Jaffé, C., Delos, J.B.: *Phys. Rev. Lett.* **73**, 2825 (1994)
66. Shaw, J.A., Robicheaux, F.: *Phys. Rev. A* **58**, 1910 (1998)
67. Bartsch, T., Main, J., Wunner, G.: *J. Phys. A* **32**, 3013 (1999)
68. Bartsch, T., Main, J., Wunner, G.: *Ann. Phys.* **277**, 19 (1999)
69. Bartsch, T., Main, J., Wunner, G.: *Phys. Rev. A* **66**, 033404 (2002)
70. Fabčić, T., Main, J., Bartsch, T., Wunner, G.: *J. Phys. B* **38**, 219 (2005)
71. Kondratovich, V., Delos, J.B., Spellmeyer, N., Kleppner, D.: *Phys. Rev. A* **62**, 043409 (2000)
72. Gao, J., Delos, J.B.: *Phys. Rev. A* **46**, 1455 (1992)
73. Dando, P.A., Monteiro, T.S., Delande, D., Taylor, K.T.: *Phys. Rev. Lett.* **74**, 1099 (1995)
74. Dando, P.A., Monteiro, T.S., Delande, D., Taylor, K.T.: *Phys. Rev. A* **54**, 127 (1996)
75. Matzkin, A., Monteiro, T.S.: *Phys. Rev. Lett.* **87**, 143002 (2001)
76. Beims, M., Kondratovich, V., Delos, J.: *Phys. Rev. A* **62**, 43401 (2000)
77. Johnson, B.R., Kinsey, J.L.: *Phys. Rev. Lett.* **62**, 1607 (1989)
78. Farantos, S.C.: *Laser Chem.* **13**, 87 (1993)
79. Farantos, S.C.: *Int. Rev. Phys. Chem.* **15**, 345 (1996)
80. Prosmiati, R., Farantos, S.C.: *J. Chem. Phys.* **118**, 8275 (2003)
81. Jaffé, C., Farrelly, D., Uzer, T.: *Phys. Rev. Lett.* **84**, 610 (2000)
82. Jaffé, C., Uzer, T.: *Ann. N. Y. Acad. Sci.* **1017**, 39 (2004)
83. Jaffé, C., Ross, S.D., Lo, M.W., Marsden, J., Farrelly, D., Uzer, T.: *Phys. Rev. Lett.* **89**, 11101 (2002)
84. Uzer, T., Jaffé, C., Palacian, J., Yanguas, P., Wiggins, S.: *Nonlinearity* **15**, 957 (2002)
85. Jaffé, C., Farrelly, D., Uzer, T.: *Phys. Rev. A* **60**, 3833 (1999)
86. Müller, S., Heusler, S., Braun, P., Haake, F.: *New J. Phys.* **9**, 12 (2007)
87. Jensen, R.: *Chaos* **1**, 101 (1991)
88. Main, J., Wunner, G.: *Phys. Rev. Lett.* **69**, 586 (1992)
89. Tiyyapan, A., Jaffé, C.: *J. Chem. Phys.* **103**, 5499 (1995)
90. Hansen, K.T., Güttler, S.: *J. Phys. A* **30**, 3421 (1997)
91. Stania, G., Walther, H.: *Phys. Rev. Lett.* **95**, 194101 (2005)
92. Mandelbrot, B.B.: *The Fractal Geometry of Nature*. W.H. Freeman Company, New York (1982)
93. Keen, L., Devaney, R.L., Alligood, K.T.: *Chaos and Fractals: The Mathematics Behind the Computer Graphics*. American Mathematical Society, Providence (1989)
94. Barnsley, M.F.: *Fractals Everywhere*, 2nd edn. Academic Press, Massachusetts (1993)
95. Falconer, K.: *Fractals: A Very Short Introduction*. Oxford Univ. Press, Oxford (2013)
96. Mitchell, K., Handley, J., Tighe, B., Delos, J., Knudson, S.: *Chaos* **13**, 880 (2003)
97. Mitchell, K., Handley, J., Delos, J., Knudson, S.: *Chaos* **13**, 892 (2003)
98. Mitchell, K.A., Delos, J.B.: *Physica D* **221**, 170 (2006)
99. Mitchell, K.A.: *Physica D* **238**, 737 (2009)
100. Mitchell, K., Handley, J., Tighe, B., Flower, A., Delos, J.: *Phys. Rev. Lett.* **92**, 73001 (2004)
101. Mitchell, K., Handley, J., Tighe, B., Flower, A., Delos, J.: *Phys. Rev. A* **70**, 43407 (2004)
102. Delos, J., Mitchell, K.: *Few-Body Syst.* **38**, 181 (2006)
103. Mitchell, K.A., Delos, J.B.: *Physica D* **229**, 9 (2007)
104. Burke, K., Mitchell, K.A.: 2010 Annual Meeting of the California-Nevada Section of the APS, Vol. 55 (2010)
105. Wang, L., Yang, H., Liu, X., Liu, H., Zhan, M., Delos, J.: *Phys. Rev. A* **82**, 22514 (2010)
106. Shan-Hong, D., Song, G., Yong-Ping, L., Xue-You, X., Sheng-Lu, L.: *Chin. Phys. B* **19**, 040511 (2010)

107. Topçu, T.Ü., Robiccheaux, F.: Abstract 5005. In: APS 37th Meeting of the Division of Atomic, Molecular and Optical Physics 2006 (2006)
108. Hansen, P., Mitchell, K.A., Delos, J.B.: Phys. Rev. E **73**, 66226 (2006)
109. Novick, J., Keeler, M.L., Giefer, J., Delos, J.B.: Phys. Rev. E **85**, 016205 (2012)
110. Novick, J., Delos, J.B.: Phys. Rev. E **85**, 016206 (2012)
111. Mitchell, K.A., Steck, D.A.: Phys. Rev. A **76**, 31403 (2007)
112. Ivory, M.K., Byrd, T.A., Pyle, A.J., Das, K.K., Mitchell, K.A., Aubin, S., Delos, J.B.: Phys. Rev. A **90**, 023602 (2014)
113. Byrd, T.A., Das, K.K., Mitchell, K.A., Aubin, S., Delos, J.B.: Phys. Rev. E **90**, 052107 (2014)
114. Byrd, T.A., Delos, J.B.: Phys. Rev. E **89**, 022907 (2014)
115. Budyansky, M.V., Uleysky, M.Y., Prants, S.V.: J. Exp. Theor. Phys. **99**, 1018 (2004)
116. Budyansky, M., Prants, S.: In: Proceedings of the 2005 International Conference of Physics and Control, p. 556. (2005)
117. Collins, P., Ezra, G.S., Wiggins, S.: Phys. Rev. E **86**, 056218 (2012)
118. Avron, J., Herbst, I., Simon, B.: Ann. Phys. **114**, 431 (1978)
119. Schmelcher, P., Cederbaum, L.S.: arXiv preprint physics/9909045 (1999)
120. Schmelcher, P., Cederbaum, L.: Int. J. Quantum Chem. **40**, 371 (1991)
121. Schmelcher, P.: Phys. Rev. A **64**, 063412 (2001)
122. Melezhik, V., Schmelcher, P.: Phys. Rev. Lett. **84**, 1870 (2000)
123. Schmelcher, P., Cederbaum, L.: Struct. Bonding **86**, 27 (1997)
124. Ruder, H., Wunner, G., Herold, H., Geyer, F.: Atoms in Strong Magnetic Fields: Quantum Mechanical Treatment and Applications in Astrophysics and Quantum Chaos. Springer, Berlin (1994)
125. Friedrich, H., Eckhardt, B.: Classical, Semiclassical and Quantum Dynamics in Atoms. Springer, Berlin, Heidelberg (2014)
126. Friedrich, H.: Theoretical Atomic Physics, 4th edn. Springer, Berlin (2017)



John Delos John Delos received a PhD in Chemistry from MIT and spent most of his career in physics at William and Mary. His research interests have been in classical and semiclassical mechanics, atomic collisions, order and chaos, and excited states of atoms in fields. Currently, he studies heart rates and respiration of infants in neonatal intensive care units.



Thomas Bartsch Thomas Bartsch received a PhD in Theoretical Physics from the University of Stuttgart, was a Postdoctoral Fellow at Georgia Tech, and is now Senior Lecturer in Mathematics at Loughboro University, UK. His research is centered on applications of nonlinear dynamics to atomic and molecular processes.



Turgay Uzer Professor Turgay Uzer obtained his doctorate at Harvard and was a Postdoctoral Fellow at CalTech. Currently he is Regent's Professor in Physics at Georgia Institute of Technology. His research interests include: Rydberg atoms and molecules, semiclassical theories, nonlinear dynamics/chaos, intramolecular energy transfer, and chemical reactivity.



Guy T. Emery

Contents

17.1	Splittings and Intensities	254
17.1.1	Angular Momentum Coupling	254
17.1.2	Energy Splittings	254
17.1.3	Intensities	255
17.2	Isotope Shifts	256
17.2.1	Normal Mass Shift	256
17.2.2	Specific Mass Shift	256
17.2.3	Field Shift	256
17.2.4	Separation of Mass Shift and Field Shift	257
17.3	Hyperfine Structure	257
17.3.1	Electric Multipoles	258
17.3.2	Magnetic Multipoles	258
17.3.3	Hyperfine Anomalies	259
	References	259

Abstract

Hyperfine structure in atomic and molecular spectra is a result of the interaction between electronic degrees of freedom and nuclear properties other than the dominant one, the nuclear Coulomb field. It includes splittings of energy levels (and thus of spectral lines) from magnetic dipole and electric quadrupole interactions (and higher multipoles, on occasion). Isotope shifts are experimentally entangled with hyperfine structure, and the so-called field effect in the isotope shift can be naturally included as part of hyperfine structure. Studies of hyperfine structure can be used to probe nuclear properties, but they are an equally important probe of the structure of atomic systems, providing especially good tests of atomic wave functions near the nucleus. There are also isotope shifts owing to the mass differences between different nuclear species, and the study of these shifts provides useful atomic information, especially about correlations between electrons.

G. T. Emery (✉)
Dept. of Physics, Bowdoin College
Brunswick, ME, USA
e-mail: gemery@bowdoin.edu

Hyperfine effects are usually small and often, but not always, it is sufficient to consider only diagonal matrix elements for the atomic or molecular system and for the nuclear system. In some cases, however, matrix elements off-diagonal in the atomic space, even though small, can be of importance; one possible result is to cause admixtures sufficient to make normally *forbidden* transitions possible.

Keywords

hyperfine structure · isotope shift · mass shift · tensor operator · diagonal matrix element

In the diagonal case, one can picture each electron undergoing elastic scattering from the nucleus and returning to its initial bound state. As pointed out by *Casimir* [1, 2], however, the *internal conversion* of nuclear gamma-ray transitions involves the inelastic down-scattering from an excited nuclear state to a lower one as an electron goes from an initial bound state to the continuum. By further conversion of bound to continuum states, one sees the connection with electron scattering from the nucleus – elastic, inelastic, and break-up. Hyperfine structure of outer-shell electronic states is at the low momentum-transfer end of this chain of related processes.

Some of the standard textbooks which discuss hyperfine structure are [3–10] and a few newer texts [11–14]. Especially relevant are [15–19] and the conference proceedings [20–22].

The study of hyperfine structure in free atoms, ions, and molecules is part of the more extensive research area of hyperfine interactions, which includes the study of atoms and molecules in matter, both at rest, for example as part of the structure of a solid, and moving, such as ions moving through condensed or gaseous matter. This more general subject also includes the ways in which atomic electrons shield the nucleus, or anti-shield it, from external or collective fields. Thus nuclear magnetic resonance, nuclear quadrupole reso-

nance, electron-nuclear double resonance, recoilless nuclear absorption and emission, nuclear orientation, production of polarized beams, and many other widely used techniques, are intimately connected with hyperfine effects.

Though hyperfine effects are ordinarily small in electronic systems, they can become much larger in *exotic* atoms: those with a heavier lepton or hadron as the *light* particle. Hyperfine effects are typically related to light particle density at the nucleus, or to expectation values of r^{-3} , and thus scale as the cube of the light particle mass. The study of muonic atoms has contributed importantly to knowledge of the nuclear charge distribution [23–26]. There has been considerable interest in pionic atoms, where the strong interaction also contributes to hyperfine structure (e.g., [27, 28]), and also in kaonic, antiprotonic, and other hadronic *atoms* [29, 30]. See especially [31] for recent work on antiprotonic helium.

Some other examples of interaction between atomic and nuclear degrees of freedom are discussed in Chap. 91.

17.1 Splittings and Intensities

17.1.1 Angular Momentum Coupling

When the nuclear system is in an isotropic environment, each nuclear state β has a definite value of nuclear angular momentum $I_\beta \hbar$, where the possible values of I_β are related to the number of nucleons (protons plus neutrons) in the same way as those for J_α are related to the number of electrons in electronic state $|\alpha\rangle$. The nuclear operators, eigenstates, and eigenvalues are related to each other in the same way as for atomic angular momentum by

$$\begin{aligned} I^2|\beta\rangle &= I_\beta(I_\beta + 1)|\beta\rangle, \\ I_z|\beta\rangle &= M_\beta|\beta\rangle, \end{aligned} \quad (17.1)$$

in units with $\hbar = 1$. Shift operators move the system from one M -value to another, as for the atomic system (see Chap. 2), and the operator I is the generator of rotations. When the combined atomic-nuclear system is considered, in an isotropic environment, it is the total angular momentum of the combined system defined by

$$\mathbf{F} = \mathbf{J} + \mathbf{I}, \quad (17.2)$$

that has definite values. The state of the combined system can be labeled by γ , so that

$$\begin{aligned} F^2|\gamma\rangle &= F_\gamma(F_\gamma + 1)|\gamma\rangle, \\ F_z|\gamma\rangle &= M_\gamma|\gamma\rangle. \end{aligned} \quad (17.3)$$

The shift operators are defined as before, and it is now \mathbf{F} that is the generator of rotations of the (combined) system, or of the coordinate frame to which the system is referred.

By the rules of combining angular momenta, the possible values of the quantum number F are separated by integer steps and run from an upper limit of $J_\alpha + I_\beta$ to a lower limit of $|J_\alpha - I_\beta|$. The number of possible eigenvalues F is the smaller of $2J_\alpha + 1$ and $2I_\beta + 1$. Experimental values of the nuclear quantum number I may be found in a number of compilations [32–34].

17.1.2 Energy Splittings

Electromagnetic interactions between atomic electrons and the nucleus can be expanded in a multipole series

$$\begin{aligned} H_{eN} &= \sum_k \mathbf{T}^k(\mathbf{N}) \cdot \mathbf{T}^k(\mathbf{e}), \\ &\equiv \sum_{k,q} (-1)^q T_q^k(\mathbf{N}) T_{-q}^k(\mathbf{e}) \end{aligned} \quad (17.4)$$

where $\mathbf{T}^k(\mathbf{N})$ is an irreducible tensor operator of rank k operating in the nuclear space, and similarly $\mathbf{T}^k(\mathbf{e})$ operates in the space of the electrons. Since one is taking diagonal matrix elements (in the nuclear space, at least) in states that are to a very good approximation eigenstates of the parity operator, only even electric multipoles (E0, E2, etc.) and odd magnetic multipoles (M1, M3, etc.) contribute to the series. The effects of the parity nonconserving weak interaction are considered in Chap. 28.

The term with $k = 0$ contributes directly to the structure (and fine structure) of atomic systems, and its dominant contributions come from the external r^{-1} electrostatic field of the nucleus. The *hyperfine* Hamiltonian is defined by subtracting that term to obtain

$$\begin{aligned} H_{\text{hfs}} &= \sum_i [T^0(\mathbf{N})T^0(i) - (-Ze^2/r_i)] \\ &+ \sum_{k=1} \mathbf{T}^k(\mathbf{N}) \cdot \mathbf{T}^k(\mathbf{e}), \end{aligned} \quad (17.5)$$

where Z is the nuclear charge number. The difference between the Ze^2/r term(s) and the full monopole term is called the *field effect* or *finite nuclear size effect* in the isotope shift, and the remaining terms contribute dipole ($k = 1$), quadrupole ($k = 2$), and higher multipoles in hyperfine structure.

Since the hyperfine Hamiltonian can be expressed as a multipole expansion, its contributions to the pattern of energy levels for the various F values in a given J_α, I_β multiplet in first-order perturbation theory can be described

relatively simply in terms of $3-j$ and $6-j$ symbols. The contribution of the term which is the scalar product of electron and nuclear operators of multipole k is

$$\begin{aligned} \Delta E_k(JIF, JIF) &= (-)^{J+I+F} \begin{Bmatrix} J & J & k \\ I & I & F \end{Bmatrix} \\ &\times \left[\begin{pmatrix} J & k & J \\ J & 0 & -J \end{pmatrix} \begin{pmatrix} I & k & I \\ I & 0 & -I \end{pmatrix} \right]^{-1} A_k, \quad (17.6) \end{aligned}$$

where for $k \geq 1$,

$$A_k = \langle JJ | \mathbf{T}^k(\mathbf{e}) | JJ \rangle \cdot \langle II | \mathbf{T}^k(\mathbf{N}) | II \rangle. \quad (17.7)$$

The commonly used hfs coefficients A , B , etc., are related to the A_k by

$$A = A_1/IJ, \quad B = 4A_2, \quad C = A_3, \quad D = A_4. \quad (17.8)$$

The isotope shift A_0 is the matrix element of the reduced monopole operator.

The pattern of the splitting depends on the total angular momentum F wholly through the $6-j$ symbol. Since for $k = 0$ the value of the $6-j$ symbol is independent of F , the monopole term shifts all levels of the hyperfine multiplet equally, independent of the value of F .

The F -dependence of the dipole contribution can be found from the fact that the same $6-j$ symbol would appear for any scalar product of $k = 1$ operators, for example $\mathbf{J} \cdot \mathbf{I}$. But in this product space, with J , I , and F all good quantum numbers, the diagonal matrix elements of $\mathbf{J} \cdot \mathbf{I}$ are just

$$\langle \mathbf{J} \cdot \mathbf{I} \rangle = \frac{1}{2} [F(F+1) - J(J+1) - I(I+1)], \quad (17.9)$$

so that

$$\begin{aligned} \Delta E_1(JIF, JIF) &= \frac{1}{2} A [F(F+1) - J(J+1) - I(I+1)], \quad (17.10) \end{aligned}$$

where, in terms of reduced matrix elements according to the convention of *Brink* and *Satchler* [35, p. 152], (the first version given in Sect. 2.8.4)

$$\begin{aligned} A &= [J(J+1)]^{-1/2} \langle J | \mathbf{T}^1(\mathbf{e}) | J \rangle [I(I+1)]^{-1/2} \\ &\times \langle I | \mathbf{T}^1(\mathbf{N}) | I \rangle. \quad (17.11) \end{aligned}$$

A is the magnetic dipole hyperfine structure constant for the atomic level J and nuclear state I . M1 hfs shows the same pattern of splittings as spin-orbit fine structure, described sometimes as the *Landé interval rule*.

Electric quadrupole hfs is described by the quadrupole hyperfine structure constant B . If we define the quantity $K = [F(F+1) - J(J+1) - I(I+1)]$, then

$$\begin{aligned} \Delta E_2(JIF, JIF) &= \frac{(\frac{1}{4}B)[3K(K+1)/2 - 2J(J+1)I(I+1)]}{J(2J-1)I(2I-1)}. \quad (17.12) \end{aligned}$$

The constant B is related to the tensor operators by

$$\begin{aligned} \frac{1}{4}B &= [J(2J-1)/(J+1)(2J+3)]^{-1/2} \\ &\times \langle J | \mathbf{T}^2(\mathbf{e}) | J \rangle \\ &\times [I(2I-1)/(I+1)(2I+3)]^{-1/2} \\ &\times \langle I | \mathbf{T}^2(\mathbf{N}) | I \rangle. \quad (17.13) \end{aligned}$$

For higher multipoles, see [36].

The multipole expansion is important because it is valid for relativistic as well as nonrelativistic situations, and for nuclear penetration effects (hyperfine anomalies discussed in Sect. 17.3.3) as well as for normal hyperfine structure. Its limitation comes from its nature as a first-order diagonal perturbation. Off-diagonal contributions, even when small, can perturb the pattern, but, more importantly, can lead to misleading values for the A_k coefficients, including the isotope shift.

17.1.3 Intensities

When hyperfine structure is observed as a splitting in an optical transition between different atomic levels, there are relations between the intensities of the components. The general rule for reduced matrix elements of a tensor operator operating in the first part of a coupled space is [35, p. 152]

$$\begin{aligned} \langle JIF | Q^\lambda(\mathbf{e}) | J'IF' \rangle &= (-1)^{\lambda+I+F'+J} (2F'+1)^{1/2} \begin{Bmatrix} F & F' & \lambda \\ J' & J & I \end{Bmatrix} \\ &\times (2J+1)^{1/2} \langle J | Q^\lambda(\mathbf{e}) | J' \rangle. \quad (17.14) \end{aligned}$$

For a dipole transition ($\lambda = 1$) connecting atomic states J and J' , with fixed nuclear spin I , the line strength $S_{FF'}$ of the hyperfine component connecting F and F' is related to the line strength $S_{JJ'}$ by

$$S_{FF'} = (2F+1)(2F'+1) \begin{Bmatrix} F & F' & 1 \\ J' & J & I \end{Bmatrix}^2 S_{JJ'}. \quad (17.15)$$

17.2 Isotope Shifts

Two distinct mechanisms contribute to isotope shifts in atomic energy levels and transition energies. First, there are shifts due to the different mass values of the isotopes; these *mass shifts* can again be separated into two kinds, the normal mass shift and the specific mass shift. Second, there are shifts due to different nuclear charge distributions in different isotopes. Shifts of this sort are called *field shifts*, and can be considered to be the monopole part of the hyperfine interaction.

The usual convention is to describe an isotope shift in a transition as positive when the line frequency is greater for the heavier isotope.

17.2.1 Normal Mass Shift

The *normal mass shift* occurs already for one-electron atoms, where the energy scale in the c.m. frame for the electron–nucleus system is directly proportional to the reduced mass of the system, $\mu = mM/(M + m)$, where m is the mass of the electron and M that of the nucleus. The two natural limits are those of an infinitely heavy nucleus, where $\mu = m$, and positronium, where $\mu = \frac{1}{2}m$. The normal mass shift applies to all levels of all atomic systems. The fractional shift in frequency between isotopes of mass M_H and M_L is given by

$$(v_H - v_L)/v_H = m(M_H - M_L)/M_H(M_L + m), \quad (17.16)$$

or

$$(v_H - v_L)/v_L = m(M_H - M_L)/(M_H + m)M_L. \quad (17.17)$$

The normal mass shift between deuterium and protonic hydrogen is $(v_D - v_H)/v_H = 2.721 \times 10^{-4}$, amounting to 4.15 cm^{-1} (0.179 nm) for Balmer α . It decreases rapidly for heavy elements, with $\Delta v/v \approx (A_H - A_L)/(1823A_H A_L)$, where the A -values are the atomic mass numbers; for the pair $^{208}\text{Pb} - ^{206}\text{Pb}$, $\Delta v/v$ is then 2.56×10^{-8} , corresponding to a wavelength shift of 0.000014 nm for a line at 550 nm .

17.2.2 Specific Mass Shift

When the system has more than two particles the situation is more complicated; in particular, the center of mass of any particular electron and the nucleus is no longer the center of mass of the whole system. When c.m. motion is removed from the Hamiltonian, there remains a set of *mass polarization* terms

$$H_{\text{mp}} = \frac{1}{M} \sum_{j < k} \mathbf{p}_j \cdot \mathbf{p}_k, \quad (17.18)$$

where M is the nuclear mass and \mathbf{p}_j is the momentum of the j th electron. The matrix elements of these terms can be strongly state-dependent, and the difference in their contributions for isotopes of different mass is called the *specific mass shift* (SMS). For a transition $a \rightarrow b$, the lowest-order SMS between isotopes A and A' is

$$\Delta v(a, b; A, A') = K^{a,b}(M_A - M_{A'})/M_A M_{A'}, \quad (17.19)$$

where

$$K^{a,b} = \langle a | \sum_{j < k} \mathbf{p}_j \cdot \mathbf{p}_k | a \rangle - \langle b | \sum_{j < k} \mathbf{p}_j \cdot \mathbf{p}_k | b \rangle. \quad (17.20)$$

It was earlier thought that the SMS, like the normal mass shift, was always very small for heavy atoms, but that has turned out not to be the case.

Since the operator $\mathbf{p}_1 \cdot \mathbf{p}_2$ resembles the product of two dipole transition operators, the matrix elements of H_{mp} vanish between simple product-type wave functions unless allowed by dipole selection rules. For example, in the $1s n\ell$ 1L and 3L states of helium, the only nonvanishing diagonal terms are the $\ell = 1$ exchange terms $\pm \langle 1s(1)np(2) | \mathbf{p}_1 \cdot \mathbf{p}_2 | np(2)1s(1) \rangle$, with $(-)$ for singlet states and $(+)$ for triplet states. The resulting Hughes–Eckart level shift [37] is positive for singlets and negative for triplets. For other states, $\langle H_{\text{mp}} \rangle$ acquires a nonzero value due to electron correlation (configuration mixing) effects, but the resulting level shifts are correspondingly smaller. Detailed tabulations for many states of helium, including second-order corrections, are given by Drake and Yan [38].

For other atoms, the diagonal matrix elements of H_{mp} within a single electron configuration are weighted by the same coefficients as those that weight the Slater exchange integral G^1 . Relativistic corrections have been given by Stone [39, 40]. Bauche and Champeau [18] provide a useful discussion of the SMS, as does King [16].

Among recent results, we mention high-precision experimental work on the difference in the splittings $2^3S_1 - 2^3P_J$ between ^4He and ^3He [41–43], which can be compared with theoretical results [43–45], and an extensive multi-isotope study in Sm II, in which isotope-shift results are used to deduce structure information for a number of levels [46].

17.2.3 Field Shift

The field shift is due to different electric monopole interactions within the nucleus for different nuclei. Since the field shift is state-dependent, it contributes to the isotope shift of electronic transition frequencies. When field shifts occur between different isomeric levels of the same nuclear species, they are called *isomer shifts*.

Following *Seltzer* [47], (see also the summary in *Fricke et al.* [48]), a level shift can be written as

$$\Delta E = -e^2 \int [\rho_N(A) - \rho_N(A')] \times \left[r_N^{-1} \int \rho_e d\tau_e - \int r_e^{-1} \rho_e d\tau_e \right] d\tau_N. \quad (17.21)$$

The electronic factor inside the second bracket can be fitted as an even power series in r_N , starting with r_N^{2j+1} . The result is that the field shift for a transition a is

$$\Delta v(a, AA') = F^a \lambda^{AA'}, \quad (17.22)$$

with

$$\lambda^{AA'} = \delta \langle r^2 \rangle_{AA'} + (C_2/C_1) \delta \langle r^4 \rangle_{AA'} + (C_3/C_1) \delta \langle r^6 \rangle_{AA'} + \dots, \quad (17.23)$$

where $\delta \langle r^k \rangle_{AA'} = \langle r^k \rangle_A - \langle r^k \rangle_{A'}$. The term F^a is an electronic factor proportional to the change in electron density at the nucleus between the initial and final electronic states; in the simplest perturbation approach F^a is equal to $-(4\pi/6)Ze^2\Delta\rho_e(0)$, where $\Delta\rho_e(0)$ is the electron density at the nucleus in the lower atomic state minus that in the upper (see Sect. 91.2). The ratios C_2/C_1 etc., which weight the higher even moments, depend only on Z and not on the particular transition; values are tabulated in [47, 49, 50], as are F -factors for K X-ray transitions. This approach has been generalized and reformulated by *Blundell et al.* [50].

Measurements of isotope shifts of optical lines have long played an important role in the determination of nuclear rms radii. A more comprehensive picture of nuclear charge distributions can be found by combining optical isotope shift results with those for X-ray lines and for transitions in muonic atoms, together with results of elastic electron scattering from nuclei; a compilation of the results of such an analysis is to be found in *Fricke et al.* [48].

17.2.4 Separation of Mass Shift and Field Shift

From the measured isotope shift for a spectral line a between a pair of isotopes A and A' , one can define a *residual isotope shift* by subtracting the normal mass shift. The residual shift is the sum of two terms, each with an electronic factor and a nuclear factor

$$\Delta v_{a,AA'} = K^a(M_A - M_{A'})/M_A M_{A'} + F^a \lambda^{AA'}. \quad (17.24)$$

If the field shift is assumed to be negligible, the electronic factor K^a can be extracted. Similarly, if the SMS is assumed to be negligible, from the ratios $\Delta v(a, A_1 A_2)/\Delta v(a, A_3 A_4)$, ratios of $\lambda(A_1 A_2)/\lambda(A_3 A_4)$ can be obtained, and the ratios

$\Delta v(a, A_1 A_2)/\Delta v(b, A_1 A_2)$ give ratios of the electronic factors F^a/F^b .

If both contributions have to be considered, one can gain information from a *King plot* [16, 51] in which a *modified residual shift* $\Delta v'(a, AA')$ for line a is defined as

$$\Delta v'(a, AA') = \Delta v(a, AA') M_A M_{A'} / (M_A - M_{A'}). \quad (17.25)$$

(Some authors modify the whole shift, without subtracting the normal mass shift; since the isotopic mass dependence is the same for the two mass-shift contributions, the separation proceeds as before, but with an altered definition of the constant K .) For each isotope pair AA' , this defines a point in the King plot whose ordinate is, e.g., $\Delta v'(a, AA')$ and whose abscissa is $\Delta v'(b, AA')$. If the assumed additivity is valid, one finds a linear relationship between the modified shifts for line a and those for another line b according to

$$\Delta v'(a, AA') = (F^a/F^b) \Delta v'(b, AA') + K^a - K^b (F^a/F^b). \quad (17.26)$$

From the slope of the line one has the ratio of F -factors for the two lines, and from the intercept a relation between the K -factors. A sometimes useful variant of the King plot involves choosing a pair of isotopes, say B and B' as a reference pair [16, 48]. A *reduced shift* $\Delta v''(a, AA')$ is then defined as

$$\Delta v''(a, AA') = \frac{\Delta v(a, AA') M_A M_{A'} (M_B - M_{B'})}{(M_A - M_{A'}) M_B M_{B'}}, \quad (17.27)$$

and $\Delta v''(a)$ is plotted versus $\Delta v''(b)$.

It is not in general possible to extract F - and K -values for individual transitions from optical isotope shifts alone, unless one has at least one calculated or otherwise reliably known value. Information about nuclear charge distributions, however, and isotopic changes in them, is available from other sources, including X-ray isotope shifts, muonic X-rays, and elastic electron scattering from nuclei. Calculated electronic factors for K X-ray transitions can be expected to be more reliable than those for optical transitions. The effects of finite nuclear size are much bigger in muonic than electronic atoms, and screening effects much smaller. Combined analyses of all four types of data lead to the best current knowledge of changes in nuclear charge parameters, and thus contribute to knowledge of the electronic factors F^a and K^a for optical transitions [48].

17.3 Hyperfine Structure

We discuss first *normal* hyperfine structure, in which terms coming from penetration of electrons into the nuclear charge and current distributions can be neglected; such contributions, the *anomalous* hyperfine structure, are briefly discussed in Sect. 17.3.3. See also Sect. 22.7.4.

17.3.1 Electric Multipoles

The electric quadrupole tensor operators, when penetration is neglected, are

$$\mathbf{T}^2(N) = \rho_N(\mathbf{r}_N)r_N^2\mathbf{C}^{(2)}, \quad (17.28)$$

where ρ_N is the nuclear charge density, and

$$\mathbf{T}^2(e_i) = -er_i^{-3}\mathbf{C}^{(2)}(i). \quad (17.29)$$

The matrix element of $\mathbf{T}^2(N)$ that occurs in the expansion coefficient A_2 is just $e/2$ times the nuclear quadrupole moment Q :

$$eQ = 2\langle II|\mathbf{T}^2(N)|II\rangle. \quad (17.30)$$

Experimental values of Q are tabulated by *Raghavan* [32] and more recently discussed by *Pyykkö* [52]. The matrix element of $\mathbf{T}^2(e)$, summed over all electrons, also has a simple semiclassical interpretation [7];

$$\begin{aligned} \langle JJ|\mathbf{T}^2(e)|JJ\rangle &= (e/2)q_J \\ &= (1/2)\langle\partial^2V/\partial z^2\rangle_{JJ}, \end{aligned} \quad (17.31)$$

where V is the electrostatic potential at the nucleus due to the electrons. The quadrupole splitting constant can thus be expressed as

$$B = 4A_2 = e^2Qq_J = eQ\langle\partial^2V/\partial z^2\rangle_{JJ}. \quad (17.32)$$

Because the matrix elements of spherical harmonics in $l sj$ -coupled states are independent of l (aside from the parity requirement that $l + l' + k$ be even), the one-electron matrix elements of $\mathbf{T}^2(e)$ are [36]

$$\begin{aligned} \langle l sj|\mathbf{T}^2(e)|l' sj'\rangle \\ = -e\langle l sj|\mathbf{C}^{(2)}|l' sj'\rangle \int r^{-3}(gg' + ff')dr, \end{aligned} \quad (17.33)$$

where g and f are the large and small r -multiplied Dirac radial functions, and the right-hand reduced matrix element is equal to $(-1)^{k-1}C_{\frac{1}{2}0\frac{1}{2}}^{jkj'}$ with $k = 2$ [35, p. 153].

Electric hexadecapole hyperfine structure follows similar rules [36]. While there is considerable indirect evidence that many nuclear states have nonzero E4 moments [53], their effect on hyperfine structure has been identified only occasionally [54, 55].

17.3.2 Magnetic Multipoles

For the magnetic multipole modes, when penetration effects are neglected, and when the the nuclear current is taken to be

a sum of the orbital-current and spin-current contributions of individual nucleons, the nuclear tensor operator can be written as the sum

$$\begin{aligned} \mathbf{T}^k(N) &= (e\hbar/2m_p c) \sum_n [k(2k-1)]^{1/2} r_n^{k-1} \\ &\times \left[2g_{ln}(k+1)^{-1}(\mathbf{C}^{(k-1)}\mathbf{L}_n)^{(k)} \right. \\ &\left. + g_{sn}(\mathbf{C}^{(k-1)}\mathbf{S}_n)^{(k)} \right], \end{aligned} \quad (17.34)$$

where $e\hbar/2m_p c$ is the nuclear magneton, and in the extreme single-nucleon model the orbital g -factors g_{ln} are 1 for protons and 0 for neutrons, while the spin g -factors g_{sn} are 5.585694701(56) for protons and $-3.82608546(90)$ for neutrons. Similarly, for electron i , the atomic Mk operator can be written

$$\mathbf{T}^k(e_i) = ie[(k+1)/k]^{1/2} r_i^{-k-1} (\boldsymbol{\alpha}_i \mathbf{C}_i^{(k)})^{(k)}. \quad (17.35)$$

For the magnetic dipole case, the nuclear operator of Eq. (17.29) becomes

$$\mathbf{T}^1(N) = (e\hbar/2m_p c) \sum_n (g_{ln}\mathbf{L}_n + g_{sn}\mathbf{S}_n). \quad (17.36)$$

The nuclear currents, however, are more complicated in the strongly interacting and relatively dense environment of real nuclear systems; renormalized g -factors can be used to take some such effects into account. For the quenching of spin matrix elements, see *Castel* and *Towner* [56]; for the M1 mode, the effective g -factor is typically in the neighborhood of 0.5 or 0.6 of the free-space value. It is also sometimes useful to consider effective orbital g -factors, but the effective value is smaller, with $g_{\text{eff}}/g_{\text{free}} = 1.05 - 1.1$ [57]. The matrix element of $\mathbf{T}^1(N)$ is the nuclear magnetic dipole moment

$$\mu = \langle II|\mathbf{T}^1(N)|II\rangle. \quad (17.37)$$

Experimental values of μ are tabulated by *Raghavan* [32].

In the semiclassical picture where $\Delta E = -\boldsymbol{\mu} \cdot \mathbf{B}(0)$, the contributions to $\mathbf{B}(0)$ from the orbital and spin magnetism of the i -th electron are

$$\mathbf{B}_l(0) = -2\mu_0 r_i^{-3} \mathbf{l}_i, \quad (17.38)$$

$$\mathbf{B}_s(0) = 2\mu_0 r_i^{-3} (10)^{1/2} [\mathbf{s}_i \mathbf{C}_i^{(2)}]^{(1)}, \quad (17.39)$$

while the *contact* term for s-electrons is

$$\mathbf{B}_c(0) = -(16\pi/3)\mu_0 \rho_i(0) \mathbf{s}. \quad (17.40)$$

The one-electron matrix elements of $\mathbf{T}^1(e)$ are [36]

$$\begin{aligned} \langle l sj|\mathbf{T}^1(e)|l' sj'\rangle &= -e(\kappa + \kappa') \langle l sj|\mathbf{C}^{(1)}|l' sj'\rangle \\ &\times \int r^{-2}(fg' + gf')dr, \end{aligned} \quad (17.41)$$

where for a given combination lsj , $\kappa = (l - j)(2j + 1)$, and l_x is the opposite-parity orbital quantum number of the small Dirac component, $l_x = l + 1$ for $j = l + 1/2$, $l_x = l - 1$ for $j = l - 1/2$. Recent high precision calculations for the hyperfine structure of helium and lithium, including relativistic corrections and second-order effects, have recently been done by *Pachucki* [58, 59].

Magnetic octupole hyperfine structure [60, 61] follows similar rules [36, 62]. Systems studied in recent years include Eu I excited states [63].

17.3.3 Hyperfine Anomalies

When the electron density is nonzero inside the nucleus, the interaction with different kinds of nuclear current density is in general different; there is, for example, a sensitivity to differing radial distributions of spin and orbital currents. The result is that the ratio of A -values for two isotopes is not necessarily the same as the ratio of nuclear g -factors [64]. The anomaly for two nuclear species a and b is characterized by

$${}^a\Delta^b = (A_a/A_b)(g_a/g_b) - 1. \quad (17.42)$$

Δ is seldom larger than a few per cent. The theory for the M1 mode was worked out by *Bohr* and *Weisskopf* [65]; there are relatively recent reviews of theory and experiment [66, 67], and an especially clear exposition of the semiclassical limit [68]. Recent experimental results include transitions in isotopes of La II [69], and the ground state of hydrogenlike thallium [70]. Anomalies are expected to be considerably smaller for the electric mode.

References

- Casimir, H.B.G.: On the Interaction Between Atomic Nuclei and Electrons. Teyler's Tweede Genootschap, Haarlem (1963)
- Casimir, H.B.G.: On the Interaction Between Atomic Nuclei and Electrons. Freeman, San Francisco (1936)
- Pauling, L., Goudsmit, S.: The Structure of Line Spectra. McGraw-Hill, New York (1930)
- Herzberg, G.: Atomic Spectra and Atomic Structure, 2nd edn. Dover, New York (1944)
- Herzberg, G.: Molecular Spectra and Molecular Structure, I. Spectra of Diatomic Molecules, 2nd edn. Van Nostrand, Princeton (1950)
- Kopfermann, H.: Nuclear Moments. Academic Press, New York (1958)
- Ramsey, N.F.: Molecular Beams. Clarendon, Oxford (1956)
- Slater, J.C.: Quantum Theory of Atomic Structure vol. II. McGraw-Hill, New York (1960)
- Sobelman, I.I.: Introduction to the Theory of Atomic Spectra. Pergamon, London (1972)
- Kuhn, H.G.: Atomic Spectra, 2nd edn. Academic Press, New York (1969)
- Corney, A.: Atomic and Laser Spectroscopy. Clarendon, Oxford (1977)
- Weissbluth, M.: Atoms and Molecules. Academic Press, New York (1978)
- Sobelman, I.I.: Atomic Spectra and Radiative Transitions. Springer, Berlin, Heidelberg (1979)
- Haken, H., Wolf, H.C.: Atomic and Quantum Physics. Springer, Berlin, Heidelberg (1984)
- Armstrong Jr., L.: Theory of the Hyperfine Structure of Free Atoms. Wiley, New York (1971)
- King, W.H.: Isotope Shifts in Atomic Spectra. Plenum, New York (1984)
- Lindgren, I., Morrison, J.: Atomic Many-Body Theory. Springer, Berlin, Heidelberg (1982)
- Bauche, J., Champeau, R.-J.: Recent progress in the theory of atomic isotope shift. Adv. At. Mol. Opt. Phys. **12**, 39 (1976)
- Heilig, K., Steudel, A.: New developments of classical optical spectroscopy. In: Hanle, W., Kleinpoppen, H. (eds.) Progress in Atomic Spectroscopy, Part A, pp. 263–328. Plenum, New York (1978)
- Hughes, V.W., Bederson, B., Cohen, V.W., Pichanik, F.M.J. (eds.): Atomic Physics. Plenum, New York (1969). articles by H. M. Foley, pp. 509–522, and H. H. Stroke, pp. 523–550
- Zorn, J.C., Lewis, R.R., Weiss, M.K. (eds.): Atomic Physics. AIP Conf. Proc., vol. 233. American Institute of Physics, New York (1991)
- Walther, H., Hänsch, T.W., Neizert, B.: Atomic Physics. AIP Conf. Proc., vol. 275. American Institute of Physics, New York (1993)
- Hüfner, J., Scheck, F., Wu, C.S.: Muonic atoms. In: Hugh, V.W., Wu, C.S. (eds.) Muon Physics, pp. 201–307. (1977)
- Barrett, R.C.: Numerical evaluation of muonic-atom energy levels. In: Hugh, V.W., Wu, C.S. (eds.) Muon Physics, pp. 309–322. (1977)
- Barrett, R.C., Jackson, D.: Nuclear Sizes and Structure. Oxford Univ. Press, Oxford (1977)
- Pachucki, K.: Hyperfine structure of muonic helium. Phys. Rev. A **63**, 032508 (2001)
- Backenstoss, G.: Pionic atoms. Ann. Rev. Nucl. Sci. **20**, 467 (1970)
- Konijn, J.: An improved parametrization of the optical potential for pionic atoms. In: Oset, E., Vicente Vacas, M.J., Garcia Rocio, C. (eds.) Pions in Nuclei, p. 303. World Scientific, Singapore (1992)
- Batty, C.J.: Light kaonic and antiprotonic atoms. Nucl. Phys. A **508**, 89C (1990)
- Backenstoss, G.: Antiprotonic atoms. Comtemp. Phys. **30**, 433 (1989)
- Korobov, V.I., Bakalov, D.: Fine and hyperfine structure of the (37, 35) state of the ${}^4\text{He}^+ p$ atom. J. Phys. B **34**, L519 (2001)
- Raghavan, P.: Table of nuclear moments. At. Data Nucl. Data Tables **42**, 189 (1989)
- Martin, M.J., Tuli, J.K. (eds.): Nuclear Data Sheets vol. 74–76. Academic Press, New York (1995). Each issue contains a guide to the most recent compilation for each atomic mass number
- Lederer, C.M., Shirley, V.S.: Table of Isotopes, 7th edn. Wiley, New York (1978)
- Brink, D.M., Satchler, G.R.: Angular Momentum, 2nd edn. Clarendon Press, Oxford (1968)
- Schwartz, C.: Theory of hyperfine structure. Phys. Rev. **97**, 380 (1955)
- Hughes, D.S., Eckart, C.: The effect of the motion of the nucleus on the spectra of Li I and Li II. Phys. Rev. **36**, 694 (1930)
- Drake, G.W.F., Yan, Z.-C.: Energies and relativistic corrections for the Rydberg states of helium: Variational results and asymptotic analysis. Phys. Rev. A **46**, 2378 (1992)

39. Stone, A.P.: Nuclear and relativistic effects in atomic spectra. Proc. Phys. Soc. **77**, 786 (1961)
40. Stone, A.P.: Nuclear and relativistic effects in atomic spectra: II. Proc. Phys. Soc. **81**, 868 (1963)
41. Zhao, P., Lawall, J.R., Pipkin, F.M.: High-precision isotope-shift measurement of 2^3S-2^3P transition in helium. Phys. Rev. Lett. **66**, 592 (1991)
42. Shiner, D., Dixon, R., Vedantham, V.: Three-nucleon charge radius: A precise laser determination using ^3He . Phys. Rev. Lett. **74**, 3553 (1995)
43. Marin, F., Minardi, F., Pavone, F.S., Drake, G.W.F.: Hyperfine structure of the 3^3P state of ^3He and isotope shift for the $2^3S-3^3P_0$ transition. Z. Phys. D **32**, 285 (1995)
44. Drake, G.W.F.: High-precision calculations for the Rydberg states of helium. In: Levin, F.S., Micha, D.A. (eds.) Long Range Casimir Forces: Theory and Recent Experiments on Atomic Systems, pp. 196–199. Plenum, New York (1993). For isotope shifts in Li+, see also Riis et al. (1994)
45. Pachucki, K., Yerokhin, V.A., Cancio-Pastor, P.: Quantum electrodynamic calculation of the hyperfine structure of ^3He . Phys. Rev. A **85**, 042517 (2012)
46. Villemoes, P., Wang, M., Arnesen, A., Weiler, C., Wännström, A.: Isotope shifts and hyperfine structure of optical transitions in $^{147-150,152,154}\text{Sm}$ II by fast-ion-beam–laser spectroscopy. Phys. Rev. A **51**, 2838 (1995)
47. Seltzer, E.C.: KX-Ray isotope shifts. Phys. Rev. **188**, 1916 (1969)
48. Fricke, G., Bernhardt, C., Heilig, K., Schaller, L.A., Schellenberg, L., Spera, E.B., Dejager, C.W.: Nuclear ground state charge radii from electromagnetic interactions. At. Data Nucl. Data Tables **60**, 177 (1995)
49. Aufmuth, P., Heilig, K., Steudel, A.: Changes in mean-square nuclear charge radii from optical isotope shifts. At. Data Nucl. Data Tables **37**, 455 (1987)
50. Blundell, S.A., Baird, P.E.G., Palmer, C.W.P., Stacey, D.N., Woodgate, G.K.: A reformulation of the theory of field isotope shift in atoms. J. Phys. B **20**, 3663 (1987)
51. King, W.H.: Comments on the article “Peculiarities of the isotope shift in the samarium spectrum”. J. Opt. Soc. Am. **53**, 638 (1963)
52. Pyykkö, P.: The nuclear quadrupole moments of the 20 first elements: High-precision calculations on atoms and small molecules. Z. Naturforsch. A **47**, 189 (1992)
53. Casten, R.F.: Nuclear Structure from a Simple Perspective. Oxford University Press, Oxford, pp 296–300 (1990)
54. Dankwort, W., Ferch, J., Gebauer, H.: Hexadecapole interaction in the atomic ground state of ^{165}Ho . Z. Phys. **267**, 229 (1974)
55. Becker, O., Enders, K., Werth, G., Dembczynski, J.: Hyperfine-structure measurements of the $^{151,153}\text{Eu}^+$ ground state. Phys. Rev. A **48**, 3546 (1993)
56. Castel, B., Towner, I.S.: Modern Theories of Nuclear Moments. Clarendon, Oxford (1990)
57. Yamazaki, T., Nomura, T., Nagamiya, S., Katou, T.: Anomalous orbital magnetism of proton deduced from the magnetic moment of the 11^- state of ^{210}Po . Phys. Rev. Lett. **25**, 547 (1970)
58. Pachucki, K.: Hyperfine splitting of 2^3S_1 state in He^3 . J. Phys. B **34**, 3357 (2001)
59. Pachucki, K.: Lithium hyperfine splitting. Phys. Rev. A **66**, 062501 (2002)
60. Jaccarino, V., King, J.G., Satten, R.A., Stroke, H.H.: Hyperfine structure of I^{127} . Nuclear magnetic octupole moment. Phys. Rev. **94**, 1798 (1954)
61. Kusch, P., Eck, T.G.: Hyperfine structure of In^{115} . Evidence of a nuclear octupole moment. Phys. Rev. **94**, 1799 (1954)
62. Mizushima, M.: Quantum Mechanics of Atomic Spectra and Atomic Structure. Benjamin, New York (1970). Sect. 9–10
63. Childs, W.J.: $M1$, $E2$, and $M3$ hyperfine structure and nuclear moment ratios for $^{151,153}\text{Eu}$. Phys. Rev. A **44**, 1523 (1991)
64. Bitter, F.: Nuclear magnetic moments and hyperfine structure of the rubidium isotopes. Phys. Rev. **76**, 150 (1949)
65. Bohr, A., Weisskopf, V.F.: The influence of nuclear structure on the hyperfine structure of heavy elements. Phys. Rev. **77**, 94 (1950)
66. Büttgenbach, S.: Magnetic hyperfine anomalies. Hyperfine Interact. **20**, 1 (1984)
67. Savard, G., Werth, G.: Precision nuclear measurements with ion traps. Ann. Rev. Nucl. Part. Sci. **50**, 119 (2000)
68. Sorensen, R.A.: Classical derivation of the magnetic hyperfine anomaly. Am. J. Phys. **35**, 1078 (1967)
69. Imura, H., Koizumi, M., Miyabe, M., Oba, M., Shibata, T., Shinohara, N., Ishida, Y., Horiguchi, T., Schuessler, H.A.: Nuclear moments and isotope shifts of ^{135}La , ^{137}La , and ^{138}La by collinear laser spectroscopy. Phys. Rev. C **68**, 054328 (2003)
70. Beiersdorfer, P., Crespo López-Urrutia, J.R., Utter, S.B., Träbert, E., Gustavsson, M.G.H., Forssén, C., Mårtensson-Pendrill, A.-M.: Hyperfine structure of heavy hydrogen-like ions. Nucl. Instrum. Methods. Phys. Res. B. **205**, 62 (2003)
71. Riis, E., Sinclair, A.G., Paulsen, O., Drake, G.W.F., Rowley, W.R.C., Levick, A.P.: Lamb shifts and hyperfine structure in $^6\text{Li}^+$ and $^7\text{Li}^+$: Theory and experiment. Phys. Rev. A **49**, 207 (1994)



Guy Emery Guy Emery was on the Brookhaven National Laboratory Staff, and taught physics at Indiana University and later Bowdoin College (Brunswick, ME). He was a visiting scientist at the Universities of Groningen and Osaka. His research has been in nuclear structure and reactions, the intersections of nuclear physics with atomic physics and particle physics, and in the history of physics.



Precision Oscillator Strength and Lifetime Measurements

18

Lorenzo J. Curtis

Contents

18.1	Introduction	261
18.2	Oscillator Strengths	262
18.2.1	Absorption and Dispersion Measurements	262
18.2.2	Emission Measurements	263
18.2.3	Combined Absorption, Emission and Lifetime Measurements	263
18.2.4	Branching Ratios in Highly Ionized Atoms	264
18.3	Lifetimes	264
18.3.1	The Hanle Effect	264
18.3.2	Time-Resolved Decay Measurements	265
18.3.3	Other Methods	266
18.3.4	Multiplexed Detection	267
	References	267

Abstract

The accuracy of oscillator strength and lifetime measurements has improved greatly in the past twenty years. Nevertheless, these high accuracies have been achieved for only a restricted number of lines belonging to a few elements and ionization stages [1]. Large numbers of precision measurements must still be made as improved experimental oscillator strengths are needed, both as tests of theoretical concepts, and for diagnostics and engineering applications.

Keywords

oscillator strength · decay curve · lifetime measurement · pulse electron beam · multiplex detection

18.1 Introduction

A spectral line arising from a radiative transition between atomic states i and k is characterized by its wavelength λ_{ik} , its intensity and its shape. In the limit of free atoms, the in-

tensity per atom is determined by the emission transition rate A_{ik} or absorption oscillator strength f_{ki} , and the shape by the natural width $\Gamma_i = \hbar/\tau_i$, where τ_i is the lifetime of the excited state. While classical spectroscopic methods provide precise wavelength measurements (1 part in 10^8 or better; Chap. 11), it has only recently been possible to measure oscillator strengths and lifetimes to better than a few percent, as discussed in this chapter. Examples of applications which require an accurate knowledge of these quantities are the interpretation of astrophysical data (Chap. 86), atmospheric physics (Chap. 88), combustion, the modeling and diagnosis of thermonuclear plasmas, nonlinear optics (Chap. 76), isotope separation (Chap. 17), and the development of new types of lasers (Chap. 75).

Precision measurements of oscillator strengths and lifetimes also provide stringent tests of atomic structure calculations. These quantities are very sensitive to the wave functions and the approximations used, particularly in cases where electron correlations (Sect. 24.2.1) and relativistic effects (Sect. 23.1) are significant. They provide experimental tests of fundamental theory; for example, of quantum electrodynamic corrections (Chap. 28), and of the nonconservation of parity predicted by the unified electro-weak theory (Sect. 32.1).

In applications where only modest precision is required, semi-empirical parameterizations involving quantum defects, charge screening and polarization allow a few precise measurements to be extrapolated along isoelectronic, homologous, isoionic and Rydberg sequences. Similar methods have been applied to the atomic energy levels themselves (Sect. 11.13). They allow one to produce a very large data base of moderate precision [2].

The spontaneous transition rate A_{ik} (Sect. 11.16.2) is the probability per unit time (s^{-1}) for an atom in any one of the g_i states of the energy level i to make a transition to any of the g_k states of the level k . The lifetime τ_i is then given by $1/\tau_i = \sum_k A_{ik}$. The branching fraction for the k th channel of the decay of level i is defined as $F_B = \tau_i A_{ik}$, and the branching ratio (Sect. 11.17) between two decay channels is

$R_B = A_{ik}/A_{ij}$. Emission and absorption rate constants differ by a factor of λ_{ik}^2 , and the absorption oscillator strength f_{ki} (Sect. 11.17) is defined by

$$g_k f_{ki} = C \lambda_{ik}^2 g_i A_{ik}, \quad (18.1)$$

where $C = (32\pi^3 \alpha a_0^2 \text{Ry})^{-1} = 1.49919 \times 10^{-14} \text{ nm}^{-2} \text{ s}$. Because of this relationship, the words transition rate and oscillator strength will be used almost interchangeably.

18.2 Oscillator Strengths

Oscillator strengths can be determined directly through absolute emission, absorption, or dispersion measurements, or through the combined measurement of branching ratios and lifetimes. Direct measurements compare different transitions at the same time, and require sample equilibrium, a knowledge of the absolute number density, and an absolute intensity measurement. These are in contrast to time-resolved lifetime measurements, which compare relative intensities from the same transition at different times, and require no absolute measurements. However, lifetime measurements yield oscillator strengths directly only in cases where a single decay transition channel exists, such as the lowest excited level in an atom or ion. Thus, combined measurements of lifetimes and branching ratios are often used where high precision values for oscillator strengths are required. Both absorption and dispersion measurements involve the number density of the lower level of the transition, whereas emission measurements involve that of the upper level.

18.2.1 Absorption and Dispersion Measurements

Absorption measurements involve placing a sample of atoms (for example, in a gas cell, an atomic beam, an arc, a shock tube, or within the vapor column in a furnace) between a continuous light source and a spectrometer. For an isolated spectral line, the absorption cross section for a beam of photons of frequency ν passing through the sample is

$$\sigma_{ik}(\nu) = \pi \alpha (\hbar/m) g(\nu) f_{ik}, \quad (18.2)$$

where $g(\nu)$ is the spectral distribution function per unit frequency normalized so that $\int_0^\infty g(\nu) d\nu = 1$. If there are N atoms per unit volume, the absorption coefficient is $k_\nu = N\sigma(\nu)$. The integrated intensity lost after passing through

a distance L of the sample is

$$\begin{aligned} \int_0^\infty \Delta I(\nu) d\nu &= I_0 \int_0^\infty (1 - \exp^{-\sigma_{ik}(\nu)NL}) d\nu \\ &\simeq I_0 \pi \alpha (\hbar/m) NL f_{ik}, \end{aligned} \quad (18.3)$$

where the second line applies if the sample is optically thin. Otherwise, the integral can be calculated directly, if $g(\nu)$ is known, to determine f_{ik} by the curve-of-growth method.

The Furnace Method

High precision absorption measurements have been achieved by *Blackwell* and co-workers [3], who have used the furnace method to study the astrophysically important neutral iron spectrum. These measurements have quoted accuracies of 0.5% on a relative scale, and 2.5% on an absolute scale. This accuracy was obtained through the use of a stable and isothermal furnace, low-noise spectral intensity recording techniques, and two identical high resolution spectrometers for the simultaneous recording of pairs of absorption lines. By selecting successive line pairs of a suitable oscillator strength ratio and adjusting the temperature and vapor pressure in the furnace, a large dynamic range of oscillator strengths could be covered. Recently, corroborative studies of the uncertainties quoted in these measurements have been undertaken, including tests that are coupled to other methods that use combinations of lifetime and branching ratio measurements [3].

The Hook Method

The absorption measurements described above determine the oscillator strength from the line intensity. An alternative absorptive approach is the anomalous dispersion or *hook* method, which determines the oscillator strength from the index of refraction at wavelengths near the edge of an absorption line [1]. The advantages of this method are its large dynamic range, its insensitivity to the line shape, and the fact that it does not saturate. The absorbing gas is placed in one arm of an interferometer and a compensator is placed in the other arm. This leads to the formation of oblique interference fringes with two characteristic hooks symmetric about the center of an absorption line. The oscillator strength is determined by the wavelength separation W between the hooks. Defining $K = \lambda_{ik} N_f$, where N_f is the number of fringes per unit wavelength, then

$$f_{ik} = \frac{\pi K W^2}{\lambda_{ik}^3 \alpha^2 a_0 NL}, \quad (18.4)$$

where a_0 is the Bohr radius.

Synchrotron Radiation

Storage ring synchrotron radiation facilities now provide a source of continuum radiation that can extend the wavelength range of absorption measurements. A technique [4] has been developed and applied that utilizes a hollow cathode discharge as an absorbing sample, synchrotron radiation as a continuum source, and a CCD array for vacuum ultraviolet (VUV) detection. Here relative oscillator strengths were obtained using two separate detection systems. However, VUV calibration standards are presently lacking (Sect. 18.2.4), and will be required to obtain independent tests (Sect. 18.2.3) of sets of branching fractions.

18.2.2 Emission Measurements

Emission methods use, for example, a hollow cathode, wall-stabilized arc, or shock tube to excite the source. Recent developments in the methods of Fourier transform spectrometry (FTS) [5, 6] offer several advantages over grating spectroscopy, as discussed next.

Fourier Transform Spectrometry

As opposed to the dispersive nature of a grating spectrograph, FTS uses interference effects from a Michelson interferometer. All radiation admitted to the spectrometer is thus incident on the detectors at all times, but different wavelengths are distinguished by their spatial modulation frequencies. The interferogram from all sinusoidal signals is sampled at a prescribed interval of path length, and compared with a laser of known frequency following the same optical path. The spectrum is recovered from the interferogram by means of a fast Fourier transform (Sect. 8.1.3). Thus, for an FTS instrument, the spectral range is determined by the sampling step size, whereas the resolution depends on the maximum path difference (this is in contrast to a grating spectrometer where the sampling step determines the resolution, and the scan length determines the spectral range).

The FTS method provides a number of attractive features in precision oscillator strength measurements. The axial symmetry and the replacement of the slit by a larger aperture can provide a throughput that is two orders of magnitude greater than that of a grating instrument of the same resolution. The precision and reproducibility are determined by the laser standard and the linearity of the wavenumber scale. The resolution can be increased as necessary to resolve a specific source line. The superior resolution allows blending and self-absorption to be more readily detected. The spectral range is limited only by detectors and filters. Recently, uv FTS instruments have been constructed that operate from the visible down to 175 nm. Since all wavelengths are observed at all times, errors from drifts in source conditions during scanning are reduced.

Hollow Cathode Lamps

Hollow cathode discharge lamps are used extensively for emission branching fraction measurements [5]. These lamps can generate an emission spectrum of essentially any element, and the relatively low collision rates result in line profiles that are narrow and primarily Doppler broadened. The narrow line width is a major advantage when studying line-rich spectra. The low collision rates also imply that the discharges are far from local thermodynamic equilibrium (LTE). However, this does not affect the determination of branching fractions, where only the relative strengths of lines from a common upper level are measured. These measurements can then be put on an absolute basis if lifetime measurements are available for all of the upper levels.

18.2.3 Combined Absorption, Emission and Lifetime Measurements

By combining measurements obtained in emission with those obtained in absorption (or dispersion) to obtain branching ratios, and then incorporating lifetime measurements, it is possible to use a scheme that requires no knowledge of level populations [1]. The scheme was originally proposed by Ladenburg in 1933, and its various modern implementations are known as *leap-frogging*, *linkage* and *bow ties*.

The principle of *leap-frogging* or *linkage* is illustrated in Fig. 18.1a. The decay of level 1 is unbranched, so the $1 \rightarrow 2$ transition rate is assumed known (kn) from a lifetime measurement. This is used to specify the $2 \rightarrow 3$ oscillator strength using relative absorption (ab) measurements for the $2 \rightarrow 1 : 2 \rightarrow 3$ oscillator strength ratio (and appropriate factors of the wavelengths and degeneracies). In a similar manner, this is subsequently combined with relative emission (em) measurements of the $3 \rightarrow 2 : 3 \rightarrow 4$ branching ratio to determine the $3 \rightarrow 4$ transition rate.

The principle of *bow ties* is illustrated in Fig. 18.1b. The two branching ratios for $1 \rightarrow 2 : 1 \rightarrow 4$ and for $3 \rightarrow 2 : 3 \rightarrow 4$

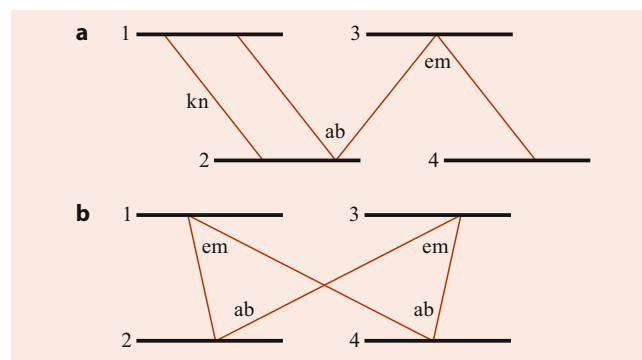


Fig. 18.1 Illustration of methods for the determination of ratios of oscillator strengths (ab = absorption, em = emission, kn = known)

are measured in emission (em). The two oscillator strength ratios for $2 \rightarrow 1 : 2 \rightarrow 3$ and for $4 \rightarrow 1 : 4 \rightarrow 3$ are measured in absorption (ab). After correction for wavelength and degeneracy factors between f and A values, these relationships are combined into a quantity known as the *bow tie ratio*, which would be unity for ideally accurate measurements. A significant deviation from unity can be used to trace the observations that are in error. Figure 18.1b is a *simple bow tie* connecting two upper and two lower levels with four transitions. Higher order sets of measurements can be similarly coupled; for example, a set of transitions between three lower levels and three upper levels can be coupled by nine simple bow ties.

In cases where both lifetime and complete branching ratio measurements exist for the same upper level, then the branching ratios can be normalized to branching fractions divided by the lifetime to obtain absolute transition probabilities.

18.2.4 Branching Ratios in Highly Ionized Atoms

In highly ionized atoms, many measurements of lifetimes in the 1–5% accuracy range have been made by ANDC (Sect. 18.3.2) analysis of beam–foil measurements. However, little work exists for the precision measurement of branching ratios in highly ionized atoms, where an intensity calibration of the detection equipment is particularly difficult. In beam-foil excitation, for example, Doppler broadening and Doppler shifts, polarization due to anisotropic excitation, and the short wavelength (≤ 200 nm) nature of the radiation are not well-suited for use with standard techniques for calibrating grating spectrometer and detection systems by the use of calibrated lamps. Calibrations have been carried out using synchrotron radiation, or through the use of previously known branching ratios.

One way in which lifetime measurements are used to determine branching ratios involves precision studies of the lifetimes of the individual fine structure components of a multiplet decay. If one fine structure level has a decay channel that is not available to the other levels (for example, a spin-changing transition or an autoionization mode made possible by a J -dependent intermediate coupling) then the transition rate of the extra channel can be determined by differential lifetime measurements.

The use of Si(Li) detectors in the measurement of very short wavelength radiation in highly ionized atoms also offers possibilities for branching ratio measurements. Since these devices can specify the photon energy from pulse height information without the need for a spectrometer, they can be calibrated for detection efficiency as a function of energy. This type of detection was recently used to determine the branching ratio of the magnetic dipole channel to the

two-photon decay channel in the $2s\ 2S_{\frac{1}{2}}$ state in one-electron krypton [7].

Although radiometric calibration standards are available for $\lambda > 280$ nm, technical challenges exist for their extension to shorter wavelengths. The urgent need for these standards and their desired characteristics have been discussed by Lawler et al. [4], and an operational prescription for combining sources of uncertainty in their specification has been presented by Sikström et al. [8]. A semi-empirical method for obtaining line intensity standards in the VUV has also been proposed [9, 10] that uses intermediate coupling (IC) amplitudes deduced from measured energy level data to obtain intensity ratios. This utilizes the observation that the ns^2np^2 and $ns^2np(n+1)s$ configurations in the Si, Ge and Sn isoelectronic sequences exhibit negligible configuration interaction, hence the intensity ratios within their transition arrays are accurately prescribed by the IC amplitudes. For the neutral atoms the transitions occur in the visible region, and measurements confirm the validity of the empirical values. Thus, isoelectronic extensions can yield VUV standards.

18.3 Lifetimes

The total transition rate summed over all decay channels can be measured either through frequency-resolved studies of the level width, or through time-resolved studies of the level lifetime. In order to determine the natural linewidth in a field-free spectroscopic measurement, either the lifetime must be very short, or the Doppler, pressure, and instrumental broadenings must be made very small. Line widths have been determined using Fabry–Perot spectrometry at very low temperatures and pressures, and in beam–foil studies of radiative transitions in which the lower level decays very rapidly via autoionization. The linewidth can also be determined through the use of the phase shift method. Here modulated excitation is applied to the source, thus producing similarly modulated emitted radiation, and the width can be specified from the phase shift between the two signals. Other methods involve resonance fluorescence techniques, where sub-Doppler widths are obtained because the width of the exciting radiation selects a subset of particle motions within the sample. Resonance fluorescence techniques that can be used to determine level widths include zero-field level crossing (the Hanle effect), high-field level crossing, and double optical resonance methods, but the Hanle effect is the most common.

18.3.1 The Hanle Effect

In its most commonly used form, the Hanle effect makes use of polarized resonance radiation to excite atoms in the presence of a known variable magnetic field. The mag-

netic substates of the sample are anisotropically excited, and the subsequent radiation possesses a preferred angular distribution. By applying the magnetic field in a direction perpendicular to the anisotropy, the angular distribution is made to precess, producing oscillations in the radiation observed at a fixed angle. At infinite precessional frequency the intensity would be proportional to the instantaneous average angular intensity, but at finite precessional frequency it depends upon the decay that has occurred during each quarter rotation. Measured as a function of magnetic field, the emitted intensity has a Lorentzian shape centered about zero field with a width that depends on the lifetime and g -factor of the level [2].

18.3.2 Time-Resolved Decay Measurements

The most direct method for the experimental determination of level lifetimes is through the time-resolved measurement of the free decay of the fluorescence radiation following a cutoff of the source of excitation. An important factor limiting the accuracy is the repopulation of the level of interest by cascade transitions from higher-lying levels. For this reason, decay curve measurements fall into two classes: those that involve selective excitation of the level of interest, thus eliminating cascading altogether; and those that use correlations between cascade connected decays to account for the effects of cascades.

Selective Excitation

Lifetime measurements accurate to within a few parts in 10^3 have been obtained through selective excitation produced when appropriately tuned laser light is incident on a gas cell or a thermal beam, or on a fast ion beam (Sect. 19.1). With a gas cell or thermal beam, the timing is obtained by a pulsed laser and delayed coincidence detection. With a fast ion beam, time-of-flight methods are used. In either case, after removal of the background, the decay curve of intensity versus time is a single exponential, and the lifetime is obtained from its semilogarithmic slope. Laser-excited time-of-flight studies were first carried out by observing the optical decay of the ion in flight following excitation using a laser beam which crossed the ion beam. In these studies, the laser light was tuned to the frequency of the desired absorption transition either through the use of a tunable dye laser, or by varying the angle of intersection to exploit the Doppler effect. Recent measurements have utilized diode laser excitation in this geometry [11]. A number of adaptations of this technique have been developed in which the laser and ion beams are made to be collinear, and are switched into and out of resonance within a segment of the beam by use of the Doppler effect [12]. The collinear geometry can provide a longer excitation region and less scattering of laser

Table 18.1 Measured np^2P_J lifetimes

Atom	n	J	τ (ns)
Li	2	1/2	27.20(20) ^a , 27.29(4) ^b
Na	3	1/2	16.38(8) ^c , 16.40(3) ^b , 16.30(2) ^d
	3	3/2	16.36(2) ^c , 16.25(2) ^d
Mg ⁺	3	1/2	3.854(30) ^d
	3	3/2	3.810(40) ^e
Ca ⁺	4	1/2	7.07(7) ^f , 7.098(20) ^g
	4	3/2	6.87(6) ^f , 6.924(19) ^g
Cu	4	1/2	7.27(6) ^h
	4	3/2	7.17(6) ^h
Sr ⁺	5	1/2	7.47(7) ⁱ
	5	3/2	6.69(7) ⁱ
Ag	5	1/2	7.408(32) ^j
	5	3/2	6.791(19) ^j
Cd ⁺	5	1/2	3.11(3) ^k
	5	3/2	2.77(6) ^k
Cs	6	3/2	30.55(27) ^l
Ba ⁺	6	1/2	7.92(8) ^l
	6	3/2	6.312(16) ^m

^a [26], ^b [27], ^c [28], ^d [29], ^e [30], ^f [31], ^g [32], ^h [33], ⁱ [34], ^j [35], ^k [36], ^l [11], ^m [37]

light into the detector than occurs in the crossed beam geometry. In one adaptation [13], excitation occurs within an electrostatic velocity switch, and the time resolution is obtained by physically moving the velocity switch. In another adaptation [12], the ion beam is accelerated with a spatially varying voltage ramp. The resonance region is moved relative to a fixed detector by time-sweeping either the laser tuning or the ramp voltage.

While these selective excitation methods totally eliminate the effects of cascade repopulation, they are generally limited to levels in neutral and singly ionized atoms that can be accessed from the ground state by strongly absorptive E1 transitions, and the selectivity itself is a limitation. Many very precise measurements have been made by these techniques, but they have primarily involved $\Delta n = 0$ resonance transitions in neutral alkali atoms and singly ionized alkali-like ions. A summary of these measurements is given in Table 18.1, and a comparison of these values with theoretical calculations is given in [14].

Advances have recently been made in the measurement of transition probabilities of long-lived metastable levels. Through a laser probing technique [15] using an ion storage ring, an extremely long lifetime (28 s) has been measured [16]. The metastable level is populated in the ion source and preserved in the storage ring until it is destructively probed at variable times after excitation. The laser light is collinearly merged with the beam and tuned to a transition that promotes the population of the metastable level to a higher unstable level. The fluorescence subsequently emitted by this unstable level gives a relative measure of the population of the metastable level. Thus, by varying the de-

lay time between the excitation and the laser probing, a decay curve of the population remaining is obtained.

Nonselective Excitation

Much more general access can be obtained by nonselective excitation methods, such as pulsed electron beam bombardment of a gas cell or gas jet, or in-flight excitation of a fast ion beam by a thin foil. Pulsed electron beam excitation can be achieved either through use of a suppressor grid, or by repetitive high frequency deflection of the beam across a slit so as to chop the beam. Particularly in the case of weak lines, the high frequency deflection technique offers the advantages of high current and sharp cutoff times. The high currents yield high light levels, so that high resolution spectroscopic methods can be used to eliminate the effects of line blending. Pulsed electron excitation methods are well suited to measurements in neutral and near neutral ions (although for very long lifetimes in ionized species, the decay curves can be distorted if particles escape from the viewing volume through the Coulomb explosion effect [17]). However, for highly ionized atoms, the only generally applicable method is thin foil excitation of a fast ion beam. Nonselective excitation techniques can also be applied to measurements such as the phase shift method [18] and the Hanle effect [19], in which case cascade repopulation also can become a serious problem. However, most of the attempts to eliminate or account for cascade effects have occurred in decay curve studies.

In beam-foil studies, the excitation is created in the dense solid environment of the foil, after which the ions emerge into a field free, collision free, high vacuum region downstream from the foil. A time-resolved decay curve is obtained by translating the foil upstream or downstream relative to the detection apparatus. The beam is a very tenuous plasma, which has both advantages and disadvantages. The low density avoids the effects of collisional de-excitation and radiation trapping, but also produces relatively low light levels. This requires fast optical systems with a corresponding reduction in wavelength dispersion, and care must be taken to avoid blending of these Doppler broadened lines. Methods have been developed by which grating monochromators can be refocused to a moving light source, thus utilizing the angular dependence of the Doppler effect to narrow and enhance the lines.

In these nonselective excitation methods, the decay curve involves a sum of many exponentials, one corresponding to the primary level, and one to each level that cascades (either directly or indirectly) into it. Decay exponentials do not comprise an orthogonal set of functions, and the representation of an infinite sum by a finite sum through curve fitting methods (Sect. 8.1.2) can lead to large errors. Fortunately, alternative methods to exponential curve fitting exist, which permit the accurate extraction of lifetimes to be made from correlated sets of nonselectively populated decay curves.

ANDC Method

Precision lifetime values have been extracted from cascade-affected decay curves by a technique known as the arbitrarily normalized decay curve (ANDC) method (Sect. 19.1.1, [20]), which exploits dynamical correlations among the cascade-related decay curves. These correlations arise from the rate equation that connects the population of a given level to those of the levels that cascade directly into it. The instantaneous population of each level n is, to within constant factors ξ_n involving the transition probabilities and detection efficiencies, proportional to the intensity of radiation $I_n(t)$ emitted in any convenient decay branch. In terms of these intensities, the population equation for the level n can be written in terms of its direct cascades from levels i as

$$\frac{dI_n}{dt}(t_p) = \sum_i \xi_i I_i(t_p) - I_n(t_p)/\tau_n. \quad (18.5)$$

Thus, if all decay curves are measured at the same discrete intervals of time t_p , the population equation provides a separate independent linear relationship among these measured decay curves for each value of t_p , with common constant coefficients given by the lifetime τ_n and the normalization parameters ξ_i . Although the sum over cascades is formally unbounded, the dominant effects of cascading from highly excited states are often accounted for by indirect cascading through the lower states, in which case the sum can be truncated after only a few terms. ANDC analysis consists of using this equation to relate the measured $I_k(t_p)$ (using numerical differentiation or integration) to determine τ_k and the ξ_i through a linear regression. If all significant direct cascades have been included, the goodness-of-fit will be uniform for all time subregions, indicating reliability. If important cascades have been omitted or blends are present, the fit will vary over time subregions, indicating a failure of the analysis. Very rugged algorithms have been developed [21] that permit accurate lifetimes to be extracted even in cases where statistical fluctuations are substantial, and studies of the propagation and correlation of errors have been made. Clearly the ANDC method is most easily applied to systems for which repopulation effects are dominated by a small number of cascade channels. Further applications are discussed in Sect. 19.1.1.

18.3.3 Other Methods

Coincidence measurements provide another method for elimination of cascade effects. While the low count rates and correspondingly high accidental rates make the application of these methods difficult for optical spectra, the use of Si(Li) detectors for the very short wavelength emission in very highly ionized systems offers new possibilities [22] for these measurements.

Another method of accounting for cascading involves the combined use of a laser and beam–foil excitation [23, 24]. The beam–foil excitation provides a source of ions in excited states, and a chopped laser is used to stimulate transitions between two excited states. By subtracting the decay curves obtained with laser on and with laser off, the cascade-free, laser-produced portion of the decay curve is obtained.

18.3.4 Multiplexed Detection

Recently, the detection efficiency and reliability of beam–foil measurements have been improved through the use of position sensitive detectors (PSD), which permits measurement of decay curves as a function both of wavelength and of time since excitation. The PSD is mounted at the exit focus of the analyzing monochromator, where it records all lines within a given wavelength interval simultaneously, including reference lines with the same Doppler shifts. Decay curves can be constructed by integrating over a line profile, and that profile can be examined for exponential content to eliminate blending. The time dependent backgrounds underlying the decay curves are directly available from the neighboring channels.

The use of multiplexed detection greatly enhances the data collection efficiency, and causes many possible systematic errors to cancel in differential measurements. Effects such as fluctuations in the beam current, degradation of the foil, divergence of the beam, etc., affect all decay curves in the same way.

The most accurate measurement [25] made by beam–foil excitation ($\pm 0.26\%$) used a type of multiplexed detection in which two spectrometers simultaneously viewed the decays of the 1P_1 and 3P_1 levels of the $1s3p$ configuration in neutral helium. The 1P_1 emission exhibited the desired multi-exponential decay curve (with only weak cascading), whereas the 3P_1 emission exhibited a zero field quantum beat pattern superimposed on its decay because of the anisotropic excitation of that level. The quantum beats provided an in-beam time base calibration which permitted this high precision.

References

- Huber, M.C.E., Sandeman, R.J.: The measurement of oscillator strengths. *Rep. Prog. Phys.* **49**, 397 (1986)
- Curtis, L.J.: *Atomic Structure and Lifetimes: A Conceptual Approach*. Cambridge Univ. Press, Cambridge (2003)
- Blackwell, D.E.: An appraisal of the accuracy of furnace gf measurements; their extension by use of a hollow cathode source. In: Hansen, J.E. (ed.) *Atomic Spectra and Oscillator Strengths for Astrophysics and Fusion Research*, p. 160. North-Holland, Amsterdam (1990)
- Lawler, J.E., Bergeson, S.D., Feldchak, J.A., Mullman, K.L.: VUV f-values of astrophysical interest from high sensitivity absorption spectroscopy on atomic ions. *Phys. Scr.* **T83**, 11 (1999)
- Lawler, J.E., Bergeson, S.D., Wamsley, R.C.: Advanced experimental techniques for measuring oscillator strengths of vacuum ultraviolet lines. *Phys. Scr.* **T47**, 29 (1993)
- Thorne, A., Litzn, U., Johansson, S.: *Spectrophysics: Principles and Applications*. Springer, Berlin, Heidelberg (1999)
- Cheng, S., Berry, H.G., Dunford, R.W., Gemmell, D.S., Kanter, E.P., Zabransky, B.J., Livingston, A.E., Curtis, L.J., Bailey, J., Nolen Jr., J.A.: Branching ratio for the $M1$ decay of the $2^2S_{1/2}$ state in one-electron krypton. *Phys. Rev. A* **47**, 903 (1993)
- Sikström, C.M., Nilsson, H., Litzén, U., Lundberg, H.: Uncertainty of oscillator strengths derived from lifetimes and branching fractions. *J. Quant. Spectrosc. Radiat. Transf.* **74**, 355 (2002)
- Curtis, L.J.: Use of intermediate coupling relationships to test measured branching fraction data. *J. Phys. B* **31**, L769 (1998)
- Curtis, L.J.: Intermediate coupling branching fractions for UV transitions in ions of the Si and Ge sequences. *J. Phys. B* **33**, L259 (2000)
- Tanner, C.E., Livingston, A.E., Rafac, R.J., Serpa, F.G., Kukla, K.W., Berry, H.G., Young, L., Kurtz, C.A.: Measurement of the $6p^2P_{3/2}$ state lifetime in atomic cesium. *Phys. Rev. Lett.* **69**, 2765 (1992)
- Jin, J., Church, D.A.: Collinear laser-beam-ion-beam measurement of the mean lifetime of the Ar II $4p^2F^{\circ}_{7/2}$ level. *Phys. Rev.* **47**, 132 (1993)
- Winter, H., Gaillard, M.L.: Lifetime measurement in $^{138}\text{Ba}^+$ using superimposed ion and laser beams. *Z. Phys. A* **281**, 311 (1977)
- Curtis, L.J.: Data-based methods for isoelectronic prediction of atomic lifetimes and energy levels. *Phys. Scr.* **48**, 599 (1993)
- Lidberg, J., Al-Kahlili, A., Norlin, L.O., Royen, P., Tordoir, X., Mannervik, S.: A technique for lifetime measurements of long-lived atomic states utilising laser excitation of stored ion beams. *Nucl. Instrum. Methods Phys. Res. B* **152**, 157 (1999)
- Hartman, H., Rostohar, D., Derkach, A., Lundin, P., Schef, P., Johansson, S., Lundberg, H., Mannervik, S., Norlin, L.-O., Royan, P.: The FERRUM project: an extremely long radiative lifetime in Ti II measured in an ion storage ring. *J. Phys. B* **36**, L197 (2003)
- Curtis, L.J., Erman, P.: Distortion effects in measurements of long optical lifetimes. *J. Opt. Soc. Am.* **67**, 1218 (1977)
- Curtis, L.J., Smith, W.H.: Radiative-lifetime and absolute-oscillator-strength studies for some resonance transitions of Si I, II, and III. *Phys. Rev. A* **9**, 1537 (1974)
- Dufay, M.: A survey of the cascade-induced alignment effects in beam-foil experiments. *Nucl. Instrum. Methods* **110**, 79 (1973)
- Curtis, L.J.: In: Bashkin, S. (ed.) *Beam–Foil Spectroscopy*, pp. 63–109. Springer, Berlin, Heidelberg (1976). Chap. 3
- Engström, L.: CANDY, a computer program to perform an ANDC analysis of cascade correlated decay curves. *Nucl. Instrum. Methods Phys. Res.* **202**, 369 (1982)
- Dunford, R.W., Berry, H.G., Cheng, S., Kanter, E.P., Kurtz, C., Zabransky, B.J., Livingston, A.E., Curtis, L.J.: Two-photon decay of the 2^1S_0 state in He-like bromine. *Phys. Rev. A* **48**, 1929 (1993)
- Harde, H., Guthöhrlein, G.: New method for cascade-free lifetime measurements. *Phys. Rev. A* **10**, 1488 (1974)
- Baudinet-Robinet, Y., Garnir, H.-P., Dumont, P.-D., Résimont, J.: Precision lifetime measurements of N II levels with the beam-foil-laser method. *Phys. Rev. A* **42**, 1080 (1990)
- Astner, G., Curtis, L.J., Liljeby, L., Mannervik, S., Martinson, I.: A high precision beam-foil meanlife measurement of the $1s\ 3p^1P$ level in He I. *Z. Phys.* **279**, 1 (1976)
- Carlsson, J., Sturesson, L.: Accurate time-resolved laser spectroscopy on lithium atoms. *Z. Phys. D* **14**, 281 (1989)
- Gaupp, A., Kuske, P., Andrä, H.J.: Accurate lifetime measurements of the lowest $^2P_{1/2}$ states in neutral lithium and sodium. *Phys. Rev. A* **26**, 3351 (1982)
- Carlsson, J.: Accurate time-resolved laser spectroscopy on sodium and bismuth atoms. *Z. Phys. D* **9**, 147 (1988)

29. Volz, U., Majerus, M., Liebel, H., Schmitt, A., Schmoranzner, H.: Precision lifetime measurements on NaI $3p^2P_{1/2}$ and $3p^2P_{3/2}$ by beam-gas-laser spectroscopy. *Phys. Rev. Lett.* **76**, 2862 (1996)
30. Ansbacher, W., Li, Y., Pinnington, E.H.: Precision lifetime measurement for the 3p levels of Mg II using frequency-doubled laser radiation to excite a fast ion beam. *Phys. Lett. A* **139**, 165 (1989)
31. Gosselin, R.N., Pinnington, E.H., Ansbacher, W.: Measurement of the lifetimes of the 4p levels in Ca II using laser excitation of a fast beam. *Nucl. Instrum. Methods Phys. Res.* **B31**, 305 (1988)
32. Jin, J., Church, D.A.: Precision lifetimes for the Ca^+ $4p^2P$ levels: experiment challenges theory at the 1% level. *Phys. Rev. Lett.* **70**, 3213 (1993)
33. Carlsson, J., Stuesson, L., Svanberg, S.: Accurate time-resolved laser spectroscopy on sputtered metal atoms. *Z. Phys. D* **11**, 287 (1989)
34. Kuske, P., Kirchner, N., Wittmann, W., Andrä, H.J., Kaiser, D.: Lifetime measurements by pulsed laser excitation of fast ion beams. *Phys. Lett. A* **64**, 377 (1978)
35. Carlsson, J., Jönsson, P., Stuesson, L.: Accurate time-resolved laser spectroscopy on silver atoms. *Z. Phys. D* **16**, 87 (1990)
36. Pinnington, E.H., van Hunen, J.J., Gosselin, R.N., Guo, B., Berends, R.W.: Beam-laser and cascade-corrected beam-foil measurements of the lifetimes of the 5p levels in singly-ionized cadmium. *Phys. Scr.* **49**, 331 (1994)
37. Andrä, H.J.: In: Sellin, I.A., Pegg, D.J. (eds.) *Beam-Foil Spectroscopy*, vol. 2, p. 835. Plenum, New York (1976)



Lorenzo J. Curtis Lorenzo J. Curtis was a Distinguished University Professor of Physics at the University of Toledo. He received his Ph.D. from the University of Michigan in 1963 and was awarded the degree Philosophiae Doctorem Honoris Causa by the University of Lund in 1999. His research involved time-resolved atomic spectroscopy and the structure of highly ionized atoms. He was the author of over 200 scientific articles and a textbook on atomic structure. He was an editor of *Physica Scripta* and a Member of the Editorial Board of *Physical Review A*. He passed away in 2020.



Spectroscopy of Ions Using Fast Beams and Ion Traps

19

Elmar Träbert  and Eric H. Pinnington

Contents

19.1	Spectroscopy Using Fast Ion Beams	269
19.1.1	Beam–Foil Spectroscopy	269
19.1.2	Beam–Gas Spectroscopy	270
19.1.3	Beam–Laser Spectroscopy	271
19.1.4	Other Techniques of Ion–Beam Spectroscopy	272
19.2	Spectroscopy Using Ion Traps	272
19.2.1	Electron Beam Ion Traps	273
19.2.2	Heavy-Ion Storage Rings	277
19.2.3	Conclusions	278
	References	279

Abstract

A knowledge of the spectra of ionized atoms is of importance in many fields. A wide variety of light sources are available for the study of such spectra. In recent years, techniques coming under the broad headings of fast ion beams and ion traps have been used extensively for such studies. This chapter will consider the advantages each technique has for particular applications.

Keywords

storage ring · dielectronic recombination · fast ion beam · merged beams · desired charge state

E. Träbert (✉)
Astronomical Institute, Ruhr University Bochum
Bochum, Germany
e-mail: traebert@astro.rub.de

E. H. Pinnington
Dept. of Physics, University of Alberta
Edmonton, Alberta, Canada
e-mail: pinning@phys.ualberta.ca

19.1 Spectroscopy Using Fast Ion Beams

A beam of ionized atoms has several advantages as a spectroscopic source. Unlike arcs, sparks, and high-temperature plasmas, the ions can be studied in an environment that is free of electric and magnetic fields and relatively free of interparticle collisions [1]. Standard accelerator techniques can be used to produce a well-collimated, mass-analyzed beam of ions having a low velocity spread. In principle, virtually any charge state of any element, isotopically pure if required, can be obtained. Finally, the well-defined velocity of the ions permits the study of processes evolving in time in terms of their spatial evolution along the beam. This is particularly important in the case of lifetime measurements.

19.1.1 Beam–Foil Spectroscopy

A beam of ions passing through a thin (50–200 nm) foil emerges in a range of ionization states, with the mean charge state increasing with the incident energy [2]. Thin foils made from a light element, usually carbon, are used to minimize particle scattering and energy straggling. Thus, a F^+ beam of 0.5 MeV that enters a carbon foil emerges with a mean charge of about $+2e$, while a Xe ion beam at 180 MeV emerges with a mean charge of about $+29e$ and a charge state distribution that may be some five to ten units wide. Inside the foil, the swift ions encounter a high (solid-state) electron density, frequent collisions, electron loss, and likely excitation to core and multiply excited levels. Upon leaving the foil, excitation stops, and the ions travel on in a low-electron density vacuum, while the remaining or recaptured electrons decay to lower states by electron or photon emission.

The beam–foil interaction is a highly nonselective excitation process, which is an advantage for spectroscopic studies but causes a problem of complexity for lifetime measurements. (Methods for tackling this problem are discussed

in Sect. 18.3.2.) A major disadvantage of the beam–foil light source is its low intensity; consequently, spectrometers equipped with position sensitive detectors, which permit the simultaneous recording of information over a certain spectral range, offer a greatly improved detection efficiency (Sects. 46.3, 46.4) compared to the earlier scanning monochromators.

The probability that more than one electron in a given ion will be collisionally excited or be captured in an excited state is high relative to other light sources, and hence the technique has been used extensively to study doubly and multiply excited states [3] (Sect. 68.1). The interaction also favors the production of high- L Rydberg states [4] (Chap. 15). At low incident ion energies, electron capture can give a downstream beam containing neutral and even negative ions. The first observation of photon emission between bound states in a negative ion was achieved using beam–foil excitation [5]. A more recent example of multiple excitation in a negative ion is the identification in lithium-like He^- of the $2p^3\ ^4S^o$ state in which all three electrons are excited [6, 7]. The observation of the same triply excited level in neutral Li has resulted in one of the most precise (40 ppm) wavelength measurements in beam–foil spectroscopy [8]. Multiple excitation of few-electron systems has since found new interest in X-ray laser experiments targeting atoms or small clusters.

An ion beam of reduced energy 0.5 MeV/amu travels at a speed of about 3% of the speed of light or about 1 cm/ns. The time resolution inherent in the geometry of the beam–foil source can also be used to aid in the identification of transitions from long-lived states, such as intercombination transitions [9] (Sect. 11.16). Here, the beam–foil spectrum is first recorded close to the foil and then far downstream (a few mm to a few cm); *far* in this context means that the short-lived states have had time to decay. The intercombination (or other long-lived) transitions are then easily identified by their relatively strong intensity in the (overall much weaker) downstream spectrum. This has been a decisive step in identifying laboratory lines with lines in the solar corona [10, 11]. A recent example of beam–foil spectroscopic analysis is given in [12].

One problem with using fast ions as a light source for precision wavelength measurements is the inevitable Doppler shift and broadening of the spectral lines. However, the latter can be largely removed by appropriately refocusing some spectrometers [13, 14]. Furthermore, since the Doppler width varies with the wavelength, and the linewidth of a given grating spectrometer used on a fast ion beam is usually dominated by spectrometer geometry, not by diffraction, Doppler broadening often becomes less important in measurements at shorter wavelengths, as in the UV or EUV. This is the primary range of emission from the more highly ionized atoms, and that is where beam–foil spectroscopy really comes into its own. For example, the leading terms omitted in calculations of the wavelengths of the $1s2s^3S - 1s2p\ ^3P^o$

transitions in He-like ions [15] scale as Z^4 . Hence, measurements made with higher- Z ions need not have as high a precision for a meaningful test of the calculation as would be required for a low- Z ion. The beam–foil measurement for the leading ($J = 1$ to $J = 2$) component in Ni^{26+} [16] has an uncertainty of 0.02%, which is about equal to that in the calculation. The two values agree well within this limit. (Naturally, measurements taken using the beam–laser techniques discussed in Sect. 19.1.3 yield results with a much higher precision, but such measurements are restricted to low- Z ions because of the excitation energy steps and transition wavelengths involved; the theoretical uncertainties in this case are also much smaller. An exception are hyperfine studies at high nuclear charge, see Sect. 19.2.)

In beam–foil lifetime measurements, the intensity of a given transition is studied as a function of the time that has elapsed since excitation, usually by stepping the foil upstream. Because of the nonselective nature of the excitation, the decay curve of a given atomic level of interest usually consists of a sum of exponential terms, one term corresponding to the primary level being studied and the other terms to higher-lying levels involved in repopulating that level. The analysis of such decay curves can be problematic. Several computer routines have been developed to tackle this problem, such as DISCRETE [17] and HOMER [18]. One useful trick here is to record the decay curve for each of the major transitions repopulating a given primary level and then include the lifetimes obtained for those transitions as fixed parameters in fitting the decay curves for that primary level. A more rigorous method to include the decay data from the repopulating transitions in the analysis of the primary lifetime is the ANDC (arbitrarily normalized decay curves) technique described in detail in Sect. 18.3.2. Whether the atomic lifetime measurement proceeds by such cascade measurements or is analyzed by cascade modeling, it is essential to understand the complexity of the individual decay scheme to obtain a reliable result and error estimate.

An additional problem may arise in the measurement of very short lifetimes, which tend to be associated with short-wavelength transitions for which no lenses are available to focus the beam at the spectrometer entrance slit. The observation region is then defined by the spectrometer aperture and extends for a finite length along the beam that can be comparable to, or even greater than, the decay length for that transition. Here, it is necessary to fit the decay curve including the vignettted region around the foil [19, 20]. Lifetimes in the picosecond regime have been successfully measured in this way.

19.1.2 Beam–Gas Spectroscopy

While the use of a gas target in place of a foil has the obvious advantage that it cannot break, the loss of a tightly

localized excitation region means that the fine time resolution of the beam–foil light source is largely lost. The beam–gas source, however, has two main advantages. First, the passage of a beam of fast, highly stripped ions through a neutral gas results in the production of recoil ions from the target gas (Sect. 69.2). If produced by collisions at large impact parameters, such recoil ions move very slowly relative to the beam ions, thus reducing the Doppler broadening problem mentioned earlier. Second, it is possible to study the details of the interaction between the gas and beam ions, such as charge-exchange (CX) reactions, as they occur, rather than merely observing their consequences. Such experiments have experienced a resurgence with the advent of the ECR ion source [21, 22]. A recent example of such work is given in [23].

The low recoil ion velocities largely point at right angles away from the primary ion beam trajectory, and by exploiting geometry, the Doppler effect in the observation may be reduced to the limit imposed by the thermal motion of the target gas atoms. Recoil ion spectroscopy is, therefore, a useful procedure for precision wavelength measurements for highly stripped ions, such as He-like Ar¹⁶⁺ recoil ions produced by a beam of 2 GeV U⁷⁰⁺ ions [24]. The energies and charge states of the recoil ions may be determined using standard time-of-flight techniques [25], and detecting the recoil ions in coincidence with their progenitor ions yields information on the dependence of the recoil energy on the details of the ionizing collision [26]. In later developments, the differentially pumped gas target has first been replaced by a supersonic jet target which reduces the thermal motion of the target particles, and then by a cold atom sample in an atom trap; replacing optical detection by position-sensitive fast-timing detectors for all collision products, the technique of COLTRIMS (cold target recoil ion momentum spectroscopy) can now be employed to study the momentum distribution of the collision partners (developed largely by the groups of H. Schmidt-Böcking (Frankfurt) and C. L. Cocke (Manhattan, Kansas)). Similar detection techniques have recently been applied to atomic targets under high-power short-pulse laser impact.

Measurements made on the projectile ions themselves also yield useful information about electron-capture processes. The strength of such a process is described in terms of its cross section (Sect. 67.1.2). Recent work has shifted from measurements of the total cross section for electron capture to more detailed studies of the individual capture channels [27]. Such studies provide much more stringent tests of theoretical models of ion–atom charge transfer processes. They often involve such techniques as spectroscopy of the optical radiation or of the Auger electrons (Sect. 26.1.1) emitted by the ions after electron exchange. This topic is covered in Chaps. 55, 68, and 69. A further example is the study by *Prior et al.* [28] of the angular distribution of

Auger electrons emitted by doubly excited states formed in hydrogen-like projectile ions with an energy of 40 keV, following double-electron capture from target helium atoms. They found that significant alignment of the magnetic substates of the projectile ions can result from electron capture. Such anisotropies in the Auger electron emission demonstrate the danger of using single-angle measurements to determine cross sections.

19.1.3 Beam–Laser Spectroscopy

As for the beam–foil source, excitation of a beam of fast ions by a transverse tuneable laser produces the localized excitation required for high temporal resolution. Now, however, the excitation is highly selective, permitting the population of just a single level. The laser-induced-fluorescence (LIF) signal as a function of the distance along the beam from the excitation region is, therefore, described by a single exponential decay, for which an exact analysis with rigorous error bounds is possible. The restriction to levels that can be accessed by electric dipole (E1) transitions from the ground, and metastable levels may be overcome by combining laser excitation with a nonselective mode of excitation, as in beam–gas–laser [29, 30] or beam–foil–laser [31] measurements. A discussion of precision lifetime measurements using laser excitation of a fast beam is given in Sect. 18.3.2. Here, the discussion will be limited to precision optical spectroscopy. Examples of precision beam–laser wavelength measurements may be found in [32, 33]. A further example is the measurement of the spin-forbidden $1s2s\ ^1S_0$ – $1s2p\ ^3P_1$ interval in N⁵⁺ [34], where the experimental value, 986.321(7) cm^{−1} is in agreement with the calculated value, 986.58(30) cm^{−1} [34]. An example of a similar measurement in a molecular ion is given in [35], while a recent study of the hyperfine structure in a rare-earth ion is given in [36].

A major aim in beam–laser spectroscopy is to minimize the width of the LIF signal. The instrumental linewidth of the laser itself can be reduced to below 1 kHz, so that the width of the LIF signal is usually dominated by the velocity spread of the ions and by the divergences of the ion and laser beams. The effects of beam divergence can be minimized by using a collinear geometry, in which the ion and laser beams are parallel. If the angle between the ion and laser beams is θ , the Doppler-shifted laser frequency, as measured in the ion's rest frame, is $f_L(1 - \beta \cos \theta)$, where f_L is the laser frequency, and $\beta = v/c$ and is much less than unity. Hence, the range in frequency resulting from a beam divergence $\Delta\theta$ is given by $f_L\beta \sin \theta \Delta\theta$, which tends to zero as θ tends to zero. One disadvantage of the collinear geometry is that, if the laser is brought into resonance with an atomic transition by adjusting the ion velocity and/or the laser frequency, the LIF signal

is produced over the entire overlap region between the ion and laser beams. The resonance can be restricted to a desired region by setting the ion velocity to be slightly off resonance. The velocity can then be adjusted locally for resonance with the laser by passing the ion beam through a Faraday cage electrode to which an adjustable voltage is applied [37, 38]. Here, the width of the resonance signal is usually dominated by the spread in the ion velocity, $c \Delta\beta$, usually arising in the ion source being used. The width resulting from a given $\Delta\beta$ can, therefore, be reduced by using a higher ion velocity. This is known as kinematic compression. In terms of the ion energy E , the range in the ion energy ΔE , and the ion mass M , the Doppler width of the LIF signal is given by $f_L \Delta E / (2Mc^2 E)^{1/2}$, and, thus, decreases as E is increased.

A more significant improvement in frequency resolution is made possible by including rf resonance in a laser double-resonance experiment. Here, the ions are brought into resonance with an off-resonance laser using two separate Faraday cage electrodes. The first resonance depletes the population in the ion state from which excitation occurs, thus weakening the second resonance signal. An rf field is then applied to the ions between the two electrodes. Tuning the frequency of this field over the region that corresponds to fine or hyperfine-structure intervals in the ion can then repopulate the state from which laser excitation occurs, thus reestablishing the second laser LIF resonance signal. The width of the resonance signal is now determined by the *transit-time broadening* that results from the finite time spent by the ions in the rf field. For example, in the experiments by Sen et al. [38] with a beam of $^{131}\text{Eu}^+$ ions at 1.35 keV, the width of the laser-rf double-resonance signal was 59 kHz, compared with a width of 45 MHz obtained using a single LIF resonance.

19.1.4 Other Techniques of Ion-Beam Spectroscopy

Ion beams find uses in many other applications, three of the main areas involving storage rings (discussed in Sect. 19.2.2), merged beams, and studies of the ion-surface interaction at grazing incidence. Merged beam experiments usually study recombination processes involving electrons and atomic or molecular ions (Sect. 58.1 regarding recombination processes). The advantage of using merged beams is that the time development of the processes may be studied spatially, while maintaining a low relative velocity between the ions and the electrons. This permits measurements at the low energies of importance in studies of Rydberg state formation and in some astrophysical applications. A very different type of experiment studies the ion-surface interaction using a well-collimated ion beam at grazing incidence on a clean, flat surface. Such experiments have revealed very

large atomic orientations [39]. This orientation can be passed on to the nuclei of the atoms via the hyperfine interaction, thus providing a source of oriented nuclei.

19.2 Spectroscopy Using Ion Traps

A basic purpose of ion traps is to confine ions to the field of view of detectors for time intervals that are much longer than the radiative lifetimes of long-lived atomic levels of possible interest. At thermal energies, the ion velocities are large enough to leave a typical detection zone within microseconds. Electrostatic (Kingdon), magnetic (Penning), and radiofrequency (Paul) traps have served for this task for decades (Chap. 79), with recent additions to the armory by electrostatic mirrors of various shapes [40, 41]. Two trap varieties of particular interest for spectroscopy, the electron beam ion trap and the heavy-ion storage ring, will be treated in Sects. 19.2.1 and 19.2.2, respectively.

Collisions with the neutral atoms and molecules of the residual gas cause charge exchange, and thus loss of the ion species. Therefore, an ultrahigh vacuum is of primary importance. Over the last four decades the figure of merit has moved from pressures of about 10^{-8} mbar to about 10^{-11} mbar. Further improvements can be expected from working with traps at liquid helium temperature; in fact, even ion traps as large as an ion storage ring at Aarhus (Sect. 19.2.1) have been cooled considerably to vary both the vacuum and the amount of blackbody radiation experienced by ions in weakly bound states. The new cryogenic storage ring CSR in Heidelberg has been designed for operation at a temperature of 10 K and lower, mainly in order to improve the vacuum to about 10^{-14} mbar for the benefit of longer storage times also for low-energy ions, as they dominate the interstellar medium.

The energy steps in multiply charged ions are regularly larger than what is available from lasers, at least for excitation from the ground state. Hence, single-ion trapping and laser spectroscopic investigation are rarely an option for these ions; many ions are needed to provide a sufficiently strong emission signal. The production of quantities of multiply charged ions used to be achieved by electron bombardment of a dilute gas inside the trap volume or by ablation from a surface. Evidently, this is detrimental to any subsequent measurements, since the residual gas is still present. Precision work like mass spectrometry that exploits the ion cyclotron motion of stored ions or detailed studies of the radiative processes (including the effects of the interrogating laser field) in ions nowadays employ a sequence of ion traps. In a first trap, the ions of interest are produced and possibly cooled by laser light or other mechanisms, and then, by applying electric fields, the ions of interest are moved to a second trap that works under better vacuum conditions or

that can be more finely tuned. In the same sense, a heavy-ion storage ring is usually being fed by an isotopically pure, charge-state selected ion beam. Any loss of ions, measured by whatever means, is thus hoped to be strictly proportional to the loss of the ion species of primary interest.

19.2.1 Electron Beam Ion Traps

Electron beam ion traps (EBIT) make use of the attractive potential of a high-density electron beam, as well as of the space charge compensation that is provided by the electron beam to any ion cloud already trapped. Most electron beam ion traps generate the high-current density electron beam by feeding the beam from an electron gun into a magnetic field that then compresses and guides the beam. In most cases, superconducting magnets with fields of 3 to 8 T are used, and current densities of the order of 10^4 A/cm² are reached. This high current density corresponds to an electron density of the order of 10^{11} /cm³. In the face of the high cost of liquid helium, a number of newer electron beam ion traps use high-temperature superconducting magnet coils or even permanent magnets. These devices are limited to lower magnetic field strengths and forfeit the ultimate benefit of deep cryocooling for extremely high vacuum; thus, they do not reach quite as high in maximum ion charge state. The low-density environment, roughly comparable to tokamak discharges, is one of the factors that renders the electron beam ion trap a very interesting device for laboratory astrophysics. The magnetic field helps to confine any ion cloud that is produced from the residual gas (or gas bled in) or from injected low charge ions. However, the ions could move away along the magnetic field lines, if they were not stopped by potential barriers provided by electrically charged drift tubes. Obviously, the basic design is the same as that of a Penning trap, with the permanent electron beam added. In fact, EBIT with the electron beam on has been said to operate in electronic trapping mode [42]; while the same device with the electron beam off (*magnetic trapping mode*) still works as a Penning trap. This option of producing an ion cloud with intense electron bombardment and then studying the ions without the electron beam present is the basis for a variety of experiments on charge exchange (CX) reactions and long-lived excited levels [43] (see below).

The first working electron beam ion trap, EBIT-I, has been set up at Livermore [44, 45]. The successful operation instigated an upgrade to SuperEBIT, the first such machine able to completely ionize all naturally occurring elements [46]. The EBIT operating principles have, for example, been described by *Currell* [47]. Based mostly on the Livermore design, more than a dozen high-charge state ion EBITs are now either running or under construction around the world, complemented by about as many of the low-charge state variety.

Ionization of ions trapped in the combination of electrical fields proceeds as long as the electron beam energy is high enough to overcome the ionization potential. Thus, the highest charge state can be preselected by the appropriate choice of the electron beam energy. The technical effort required to reach, for example, bare uranium in SuperEBIT is much smaller than in an ion accelerator. In both cases, the ionization is achieved by frequent energetic collisions of ions with electrons. In SuperEBIT, the ions are (practically) stationary, and the design energy of SuperEBIT, 250 keV, has been shown to be sufficient to remove even the last electron of uranium (or all but two from californium). At a heavy-ion accelerator, in contrast, the electrons are stationary (in a foil target), and the ions are fast. Consequently, an ion energy per nucleon that is higher by the proton/electron mass ratio is required—some 500 MeV/amu. Such energetic ion beams are only available in a few large accelerator laboratories, whereas an electron beam ion trap with its auxiliary equipment fits into an office-sized laboratory space. Of course, there are experiments that need the specific properties of either fast ion beams or stationary ions, so both types of devices have their specific merit.

The ions in an EBIT are not only stationary in the sense that they are localized in a cloud, and their motion constrained by the magnetic field. Moreover, their energy (temperature) can also be controlled by the height of the potential barriers. The voltages on the confining drift tubes are usually chosen to be few hundred volts. This makes for barrier potentials $+qeU$ (charge state q , elementary charge e , voltage U) that are higher for highly charged ions than for low-charge state ions. This benefits the confinement of highly charged ions both directly and indirectly; while light ions (residual gas or purposely bled in gases) may become fully ionized by the collisions with the electron beam and by charge exchange (which deepens the trap they experience), they still have a higher chance than heavier ions to evaporate from the trap and, thus, they cool the remaining ion cloud. Under typical conditions, the ion cloud may have a temperature of a few keV. This can be lowered by introducing a cooling gas and by lowering the potential barriers. With Cs⁴⁵⁺ in the trap, this has been demonstrated by reducing the (thermal) Doppler spread of X-ray emission lines until it was smaller than the natural linewidth of the emitter, thus yielding a measurement of femtosecond-level lifetimes from the line broadening seen in highly resolved X-ray spectra [48].

Another group of femtosecond lifetime levels are the $2s^2 2p^5 3d$ levels in the Ne-like ion Fe¹⁶⁺. The decays show up in the EUV spectra of terrestrial and astrophysical plasmas, and the line ratios persistently deviate from theoretical prediction. This has led to various hypotheses about distortions caused in the astrophysical environment. However, Livermore EBIT data have long since agreed with the astrophysical observations, practically invalidating the

speculations about environmental influences. However, the cleanest experiment on this problem so far used a classical fundamental atomic physics scheme. An ion cloud in the Heidelberg-built FLASH-EBIT was prepared to hold Fe^{16+} ions as the highest charge state, and the cloud was irradiated by light from the LCLS X-ray laser, scanning the wavelength across the photoexcitation resonance (near 800 eV photon energy). In order to extract the resonance fluorescence signal from the various noise contributions, the signal was gated to the subpicosecond pulse length of the X-ray laser, following the example of the first such experiment at the (EUV) FLASH facility [49]. (A control measurement lowered the electron beam energy in the ion trap so that no Fe^{16+} ions were produced.) The experiment confirmed the discrepancy between experimental and theoretically computed line ratios [50].

The other good atomic level lifetime measurement range of an EBIT reaches from a few microseconds (limited by practical switching issues) to many milliseconds. Under direct optical (X-ray, EUV, visible) observation of a spectral feature, the electron beam is used to produce an ion cloud with ions of a desired charge state. When the electron beam is stopped, all direct excitation and prompt emission ceases. Any later photon signal relates to delayed emission from long-lived levels or from excitation by charge transfer collisions (highly charged ions capturing electrons from the residual gas atoms). Charge exchange (CX) is an important ion loss mechanism, and the CX signal also serves as a monitor of the number of ions remaining in the trap. However, the CX can proceed via any of many intermediate levels, each of which provides only a weak signal, so that a wide-band photon detector is required for collecting sufficient statistics. Owing to the excellent vacuum in cryogenic EBITs, trapping times of many seconds, if not minutes, have been observed [43]. The ion loss rate is the major correction to the apparent decay time of the delayed photon signal. For atomic level lifetimes of a few milliseconds and less, this correction is small (a few percent or less). EBIT lifetime measurements that take this correction into account yield results that agree with those from heavy-ion storage rings [51] and that are, at uncertainties of 0.5% and less, remarkably consistent with theory in a case for which the theory can do very well (Fig. 19.1). This observation can be turned around and interpreted as a demonstration of the reliability of the experimental techniques that can then be applied to more complex cases in which theory evidently has problems (for examples, see [52–57]).

An example is the electric-dipole (E1) forbidden decays in the ground configuration of multielectron ions. The various levels of the ground configuration are easily excited in many plasmas, and the relative level population can serve for density diagnostics if the collision rate is comparable to or lower than the radiative decay rate by, for example, mag-

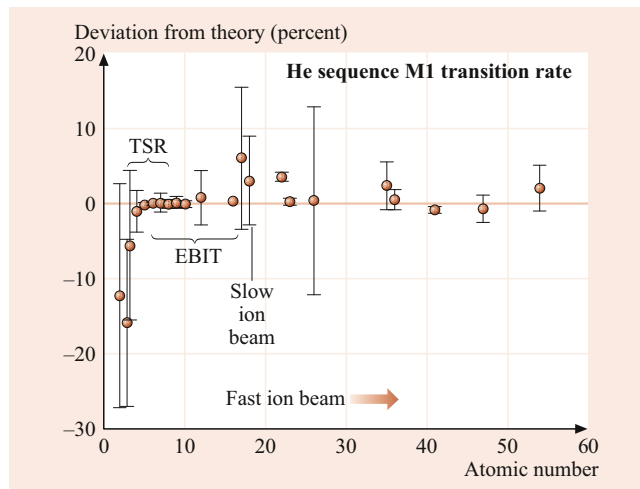


Fig. 19.1 The lifetime of the $1s2s\ ^3S_1$ level in the He isoelectronic sequence varies by 15 orders of magnitude from He (about 6000 s) to Xe^{52+} (a few picoseconds). The deviation of selected experimental results from calculations is shown, and the dominant experimental techniques for the various lifetime ranges indicated. The consistency of experimental results from a heavy-ion storage ring (TSR Heidelberg) and an electron beam ion trap (Livermore EBIT-II) with theory in the range up to $Z = 16$ is impressive (after [52], updated)

netic dipole (M1) transition. These transitions give rise to the coronal lines first seen in the solar corona during eclipses. Theoretically, the M1 transition rate is strictly proportional to a geometry factor (a matrix element derived by Racah algebra) and to the third power of the transition energy. Interestingly, there is a relatively large QED correction of 0.45% to this transition rate that is associated with the electron anomalous magnetic moment (EAMM). A radiative lifetime measurement of an accuracy better than 0.45% would thus be capable to test QED in a special case. Few atomic lifetime measurements (at a heavy-ion storage ring or EBIT) have returned such accurate results yet, and only one of these has concerned an M1 transition [54, 55]. Although the transition of interest in this case occurs in the simplest atomic system with such M1 transitions, the ground state of a boron-like ion, the calculated transition rates available in the literature scatter by much more than the assumed QED correction. In fact, at present, most of the predictions lie closer to the experimental finding without the QED correction. Consequently, although experimental data are available, this test of QED has to be postponed until classical quantum mechanics can treat such a few-electron atomic system with sufficiently high accuracy. Incidentally, the famous corona lines in astrophysics are not very well known in wavelength, probably because the astrophysical source (the solar corona) is easily visible only during eclipses and not very brightly, and because most laboratory light sources have too high a density to produce these E1-forbidden lines, which are easily outshone by the much brighter E1 transitions. Low-density EBIT to the rescue: the E1-forbidden lines have been used

to demonstrate the capabilities of optical spectroscopy at the Heidelberg EBIT [58] and also the feasibility of laser excitation of trapped ions [59]. The optical resolving power is so high that the Zeeman splitting in the 6 T field of the Heidelberg EBIT dominates the line profile.

An EBIT is an excellent light source for precision spectroscopy of highly charged ions because it not only gives access to all charge states of all elements but does so at low particle densities, at a relatively low source temperature (Doppler spread), and without any notable need for a Doppler correction of the wavelength scale (as with fast ion beams or rapidly expanding plasma plumes or solar ejections). Of particular interest to precision spectroscopy have been the ions with a single valence electron (Li, Na, Cu isoelectronic sequences) that are rather amenable to calculation. Such spectra of ions up to $Z = 60$ or 70 have been measured at low-density plasmas like the tokamak, and they have been found to agree well with theory. Higher charge states were then reached in laser-produced plasmas (Sect. 46.1.2), but the wavelength results seemed to deviate from the theoretical trend that had supported the tokamak results. There also were (very few) high-nuclear charge Z data from fast ion beams. Electron beam ion trap data have now confirmed that the trend of the tokamak data was correct and that theory [including second-order quantum electrodynamics (QED) contributions] provides a good description of the $n = 3$ (Na sequence) [60] and $n = 4$ levels (Cu sequence) [61] up to $Z = 92$, within the 40 ppm error margin of the EBIT results for the heaviest Cu-like ions. The agreement with theory for the Zn-like ions of the same elements used to be much poorer and has only recently made significant progress [62–64]. As the QED contributions in Cu-like and Zn-like ions are rather similar, this must be a problem of theory with the computational treatment of two (and more) valence electrons in the same shell.

The same situation is found with Na-like and Mg-like ions. While (mostly) EBIT measurements had established the isoelectronic trend of the resonance line wavelengths in Na-like ions up to uranium with an uncertainty on the order of 100 ppm quite a number of years ago, and basically in agreement with advanced theoretical computations, the much fewer data for Mg-like ions beyond Xe met a wide scatter of computational predictions. This unsatisfactory situation has only very recently been clarified by some better data and a few computations (see data and references in [65–67]), and the key transitions are now considered to be known to within 100 ppm. However, the same type of computation nowadays yields the resonance lines in Al-like ions (three electrons in the $n = 3$ valence shell) only to about 500 ppm reliability and progressively worse for more electrons. Again, the QED part of the computations that plays a major role at high Z is considered to be much better established than the quantum mechanical interaction of the electrons in the open

shells. The number of ($n = 2$) valence shell electrons is very restricted in Li-like and Be-like ions, and computations of these ions are competitive in accuracy with measurements. For this reason, some experiments actually address Li-like ions as stand-ins for H-like ions, which are more difficult to produce and may suffer from other obstacles, such as the line broadening of decays that involve $n = 2$ levels which in H-like ions can decay to $n = 1$. Here are two examples.

The dominant contributions of quantum electrodynamics (QED) to the binding energy of electrons scale with the fourth power of the nuclear charge Z , and, therefore, they are largest in the heaviest elements. The binding energy scales with Z^2 , and the fine structure splitting with Z^4 . Hence, measurements of the $n = 1$ level energy aim for uranium ($Z = 92$), while for the $n = 2$ levels, the QED contribution amounts to a fairly constant (Z -independent) fraction of the fine structure interval. The $n = 2$ Lamb shift amounts to roughly $1/8$ of the $n = 1$ level Lamb shift correction. Various experimental boundary conditions have to be considered in finding the optimum setting for a practical determination of the (QED) contributions. There also are theoretical considerations. The atomic systems purportedly under best theoretical control are H-like ions, with only one electron in total. However, the isotope $^{208}_{82}\text{Pb}$ has a doubly magic and, thus, rather spherical nucleus, which is beneficial for accurate calculations, whereas the uranium isotopes offer stronger fields and, thus, larger QED effects but with a nonspherical nucleus, the actual shape of which is less well established, causing some uncertainty in the accurate computation of the atomic structure. Nevertheless, uranium is a long-standing goal of experiments aiming at the ground state Lamb shift. H-like ions of uranium have been studied with fast ion beams (beam-foil/gas spectroscopy, see Sect. 19.1) at GSI Darmstadt and at the Livermore SuperEBIT. The resonance lines, $1s-2p$, with their energy of about 100 keV, fall into the hard-X-ray range, and the ground state Lamb shift of about 470 eV (of which roughly 60% and 40% are due to QED and finite nuclear size contributions, respectively) amounts to a small fraction of the transition energy. The lifetime broadening due to the short lifetime of the upper level is superimposed on the instrumental linewidth. At a fast ion beam, there also is the Doppler shift and Doppler broadening to correct for. At GSI, the highly charged ions were therefore produced as naked ions ($\text{U}92^+$) by ion-foil interaction at a high ion beam energy (for example, at 360 MeV/amu) and then decelerated by about a factor of 6 or 7 in an ion storage ring (which somewhat alleviates the Doppler correction problem). In this ring, some of the ions captured an electron from a gas jet target, so that the $n = 2$ levels might be populated and their X-ray decay be observed by a granular detector set. The X-ray spectrum was recorded in coincidence with (U^{91+}) ions, that is, after electron capture at the gas jet [68]. The year 2000 result for the ground state Lamb shift of 468(13) eV

was improved by a factor of 3 by replacing the gas jet target by free electrons from the electron cooler of the storage ring serving as the target a few years later [69]. The Livermore SuperEBIT experiment took a different route [70]. A high-resolution flat-field grazing incidence spectrograph recorded the $2s-2p_{1/2}$ transition of U^{89+} near 44 Å and determined a transition energy of 280.645 (15) eV. The result was close to earlier results obtained by Doppler-tuned spectroscopy of a fast ion beam [71] or by a measurement of dielectronic recombination in a heavy-ion storage ring combined with atomic structure calculations [72] but significantly more precise and more accurate than all the earlier studies. The SuperEBIT experimental result was then combined with theory values about the U^{89+} $2s-2p$ transition, as well as with theory values on U^{91+} , and a value for the U^{91+} $1s$ Lamb shift was determined that yielded a two-loop QED contribution of -1.27 ± 0.45 eV. This is the first time that any such two-loop contribution has ever been tested by experiment.

Hyperfine Structure

For decades, atomic spectroscopy has been employed to gain information on the nucleus via the hyperfine interaction of the nuclear spin with the unpaired electrons in the outer shells. However, only s electrons have a finite probability to be found inside the nucleus (rendering them most sensitive to the short-range nuclear fields). At the same time, the hyperfine splitting observable in atomic spectra grows with the third power of the nuclear charge and, thus, with Z^3 . Heavy elements have many electrons, and a detailed theoretical interpretation of hyperfine structure consequently requires a detailed understanding of an atomic system with many electrons. It would be highly advantageous to have only a single electron interacting with the nucleus, that is, an H-like ion. As discussed above, such ions can be produced at heavy-ion accelerators or in electron beam ion traps, and both have been employed in the quest for hyperfine measurements on one-electron heavy ions, mostly aiming at isotopes near the doubly magic nucleus $^{208}_{82}\text{Pb}$. The line of primary interest is from the transition between the hyperfine levels of the $1s$ ground state—the very transition that gives rise to the hydrogen 21 cm line used in radioastronomy. For heavy ions near Pb, the upper level has a millisecond-range lifetime. For two isotopes (of Bi and Pb), this transition has been induced by laser radiation in a heavy-ion storage ring [73], and for five isotopes (of Re, Ho, and Tl) emission spectroscopy at the SuperEBIT electron beam ion trap [74] was successful. Using the ion cloud (with its cross section largely determined by an electron beam diameter of about 70 μm) as a light source without a further entrance slit, a high-efficiency transmission grating spectrometer, and a position-sensitive detector, lines from two Tl isotopes were recorded simultaneously [74]. The differential effects of the two nuclei yielded additional information on the charge distribution in the nucleus, on top of the

magnetic moment distribution that makes up the dominant effect. These results are required for a better interpretation of parity nonconservation (PNC; Sect. 32.1) measurements of neutral Tl atoms, in which the nuclear magnetic moments have so far been treated only as a point dipole. The experimental data on the $1s$ hyperfine structure are in reasonable agreement with theoretical results based on various models. In order to clarify the validity of the model assumptions, the measurements have been extended to $n = 2$ levels, using Li-like ions for practical reasons. Moreover, a comparison of the hyperfine data for $n = 1$ and $n = 2$ levels of H- and Li-like ions, respectively, of the same isotope would enable a better differentiation of nuclear field and QED contributions to the result [75]. The most fundamental hyperfine interval in Li-like ions is between the sublevels of the $2s$ level, corresponding (for Bi^{80+}) to a transition in the infrared. While this transition was searched for (and not found in various attempts) in a laser resonance experiment on a fast ion beam at GSI Darmstadt, the Livermore SuperEBIT was employed in an indirect search, observing the $2s-2p_{1/2,3/2}$ transitions in the X-ray [76] and EUV [77] ranges, respectively. These transitions include the hyperfine intervals as part of the much larger transition energies. While less sensitive to the hyperfine structure, such measurements cover a much wider range of search. Both SuperEBIT measurements turned out results for the $2s_{1/2}$ hyperfine structure intervals that were compatible with prediction but not quite precise enough to distinguish between the individual calculations. Very recently, the laser resonance experiments at GSI Darmstadt succeeded on, both, H-like and Li-like ions of ^{209}Bi and yielded results with the full sensitivity of direct measurements [78, 79]. The much anticipated combination of hyperfine structure information on both ions indicates a significant discrepancy with theory [80].

One of the pertinent problems in astrophysics is the cataloguing of spectral lines in all spectral ranges, both for identifying spectral features and, thus, learning about the composition of a light source, and for modeling of the light source in order to understand its *operating conditions*. Even data bases that claim *practical completeness*, however, are found to be grossly incomplete in the EUV and soft-X-ray ranges that have been opened to high-resolution observations by the grating spectrometers on board the *Chandra*, *XMM-Newton*, and *Hinode* spacecrafts. Here, observations at electron beam ion traps fill in much of the needed data, at comparable quality. Moreover, an EBIT as a kind of analog computer does more than provide correct line positions; the spectra show line ratios from a light source with known electron energy (and the option of known temperature by simulating a Maxwellian energy distribution [81]) and particle density. This serves both as a check on collisional-radiative models and as an immediate data resource for astrophysics.

Most X-ray data from EBITs have been collected using solid state detectors [Si(Li), Ge] that offer high detection efficiency (large solid angle) and signal timing on the microsecond scale but feature poor spectral resolution. High-resolution instruments like crystal spectrometers are necessary to analyze spectra in any detail; equipped with position-sensitive detectors, such instruments do much better than scanning spectrometers in terms of data collection rate and calibration. However, they suffer from the low diffraction efficiency of the crystals. Recently, a new device, the microcalorimeter, has started to show its interesting properties. In these devices, small absorbers at mK-temperatures show a measurable temperature increase when absorbing an X-ray photon, and the signal is proportional to the deposited photon energy [82]. The linewidth of the best devices is below 10 eV (not as good as a crystal spectrometer but much better than a traditional solid state diode), the sensor pixels can be grouped in arrays to make for a larger area and for cross references among pixels (which helps with calibration and with the rejection of cosmic ray events), and the signal processing is fast enough to permit time resolution on the millisecond range. A spaceflight engineering spare has been used at the Livermore EBITs to study, for example, soft-X-rays of light elements as seen from CX near comets [83], or measure the (10 ms) time constant of the M3 decay in a Ni-like ion (Xe^{26+}). The hyperfine interaction with the nuclear spin can modify this electronic level lifetime, which was demonstrated by using isotope-separated isotopes ^{132}Xe and ^{129}Xe [84]. The results agreed with theoretical expectations [85].

High Multipole Order Radiation

Much of the above deals with the successive experimental exploration of the consequences of the multipole expansion of the electromagnetic radiation field in classical electrodynamics, which in the 1920s O. Laporte phrased into selection rules for transitions in the atom, and the corresponding multipole orders ascribed to transition types, such as (E1, M1, E2, M2), and so on. The nonexistence of electromagnetic monopole radiation follows the strict rule that $J = 0$ levels do not connect radiatively with other $J = 0$ levels. In spite of this, *Beiersdorfer* et al. recognized an X-ray line in the spectrum of the Ne-like ion Ar^{8+} that fits to the energy of the $3p^5 3s$ $J = 0$ level decaying to the $3p^6$ $J = 0$ ground state [86]. The line intensity grew with the magnetic field strength in the environment (tokamak plasma or EBIT) and suggested that the magnetic field plays a decisive role. Indeed, the distortion of the usual spherical symmetry of the atom/ion by the external field was seen as the clue to the process, and the transition mediated by a field-induced admixture of a $J = 1$ wave function component to the upper $J = 0$ level. Consequently, this line might serve as a high-magnetic field diagnostic, for example, in astrophys-

ical plasmas. A series of radiative lifetime measurements in an EBIT of the $3p^5 3s$ $J = 2, 0$ levels in Ne-like Fe^{16+} ions [87, 88] later yielded the M2 decay rate of the $J = 2$ level, the M1 decay rate (in the same configuration) of the $J = 0$ level, and the magnetic-field induced ground state transition rate of the latter level. The M2 rate result is much more precise than the scatter of various predictions, the measured M1 rate agrees well with computations, and the B-field induced rate is in reasonable agreement with theory [89].

Last, but not least, the well-defined and adjustable electron beam energy in an EBIT permits detailed studies of the interaction of fast electrons with highly charged ions. This includes, for example, the spectroscopy of dielectronic recombination (DR) resonances or the exploration of radiative recombination (RR) (Chap. 59). These processes can be investigated up to the highest ion charges, where relativistic and QED contributions (like the generalized Breit interaction) matter.

19.2.2 Heavy-Ion Storage Rings

With foil-excited ion beams and long level-lifetimes, decay curves spread out along the beam, and the signal from a given width of the field of view may drop to the detector background level. The decay lengths of microsecond lifetime levels are on the order of 10 m, and those of millisecond levels are tens of kilometers, which is clearly prohibitive in a linear arrangement. In such cases, it is advantageous to curve the beam line around on itself, forming a storage ring, in which the ions pass in front of the detector over and over again. Heavy-ion storage rings need excellent vacuum conditions (10^{-11} mbar and better) to reach storage times of seconds, minutes, or hours, depending on the electronic structure of the stored ions and on the ion beam energy. The dominant loss processes are electron capture and loss, small angle scattering, and large angle (inelastic) scattering as with any fast ion beams [90], but these are aggravated here by the much longer path lengths.

Storage rings (for example, TSR Heidelberg (now moved to an isotope separator at CERN), ASTRID Aarhus, CRYRING Stockholm (now in a new lease-of-life at GSI Darmstadt), ESR Darmstadt, and the new storage rings at the upcoming FAIR facility at the same compound), with magnetic dipoles and quadrupoles for beam transport and focusing, sort the stored particles by their momentum. The typical ion beam energies range from a few dozen keV total to hundreds of MeV per nucleon (ESR). Electrostatic storage rings (ELISA Aarhus, DESIREE Stockholm, CSR Heidelberg, and more under construction) only have electrical fields and select by particle energy, usually below about 100 keV (for a review, see [91]). They are more suitable for low-charge heavy ions and ion molecules, including

biomolecules, than the magnetic rings that can handle very fast particles. Magnetic storage rings usually have electron cooler sections in which a *cool* electron beam (with a low longitudinal velocity spread from kinematic compression) of almost the same velocity as the circulating ion beam is merged with the latter for a path of a few meters (and is then deflected out again). By scattering among electrons and ions, the momentum spread of the electrons (small) and ions (larger) equilibrates, leaving the ion beam with a narrower momentum distribution and, thus, cooled. Cooling, which typically takes a few seconds, improves the storage behavior of the ion beam and the energy resolution of, for example, dielectronic recombination (DR) studies (Chap. 59). For these, the same electron cooler is now tuned to provide electrons at a well-defined but different velocity. Thus, the electron cooler can serve as an electron target, without the complications of a foil target in beam–foil spectroscopy. The difference velocity can be chosen from a wide range, including zero. Extremely low energy collisions are being investigated for the study of DR and for the recombination of molecular radicals. When a beam of molecular ions is injected, storage is long enough to let some of the internal degrees of freedom relax, and then a beam of molecular ions that are closer to their ground state can be extracted.

A cooled ion beam, with its narrow velocity distribution, is also of interest for laser–ion interaction studies, offering higher resolution and better signals. Laser-assisted electron capture in the electron cooler, as well as laser spectroscopy on high-lying levels populated by DR, are possible. One of the problems with precision wavelength measurements involving fast ions is, as always, the accurate determination of the velocity, as a step towards determining Doppler corrections. At TSR Heidelberg, a beam of Li^+ ions was subjected to a laser beam from ahead, tuned to one of the $2s-2p$ transitions. A second laser beam from behind probed the position of the Lamb dip in the velocity distribution and, thus, assured that it would meet the same velocity group of the multi-MeV stored ions. Accurate off-line calibrations of the laser frequencies then permitted a test of the Doppler formula to a relative precision of 2.2×10^{-7} [92]. This research has since been extended to higher ion velocities at the ESR storage ring at GSI Darmstadt.

The Doppler shift determination in any observation of fast ions requires accurate angle measurements. These are nontrivial, because the detection efficiency of any finite size spectrometer or extended detector may be nonuniform as a function of position or angle. One technique calls for segmented (*granular*) X-ray detectors, the strips of which are calibrated individually [68]. Relativity changes the emission pattern seen in the laboratory rest frame to one that favors forward emission. This is beneficial for zero-degree spectroscopy, that is, an observation along the ion beam path. At ESR Darmstadt, bare ions captured an electron in the

electron cooler section, and the resulting X-rays were detected from straight ahead (behind the next dipole magnet that deflected the ion beam). This geometry maximizes the Doppler shift but minimizes the uncertainty relating to geometry. Also, after electron capture, the ion in the bending magnet section follows a trajectory that differs from that of the unperturbed ions. The ion can be detected and, in coincidence with the X-ray detector, make for a very clean and charge-specific spectrum. Similar coincidence measurements make it possible to use a low-pressure gas jet target in a high-energy ion storage ring, evaluating only coincidences of X-ray photons and charge-changing events [68]. Fast ions (energetic enough to achieve the desired charge state) can also be decelerated in a storage ring, which helps to do systematic checks of the Doppler effect and to work at lower Doppler shift [68].

As mentioned in Sect. 19.2.1, laser-resonance techniques have been used to find the ground-state hyperfine transition in two H-like heavy isotopes. In one of them, the lifetime was also measured by recording the fluorescence decay from the ion beam after switching off the laser [73]. For lower charge states, one can exploit the excitation that ions carry into the ring from their production in the ion source or from stripping processes in the injector accelerator [93]. Lifetimes from half a millisecond to several seconds have been measured this way by passive observation [52], with an accuracy of better than 0.2% in favorable cases. Other techniques use excitation by DR in the ring [94] or laser probing of the remaining metastable level population, so that fluorescence is emitted near a photomultiplier detector [95]. With a stored beam of negative ions, even blackbody radiation may be sufficient to photodetach the weakly bound last electron; the ensuing neutral atom is not deflected at the next bending section and leaves the ring to be detected. All in all, lifetime measurements at ion storage rings reach from 1 μs to about 1 min. The lower limit is related to the time the ions need to circulate in the storage ring, whereas the upper limit depends on the vacuum in the ring vessel and, thus, on ion loss processes associated with collisions of the beam ions with the residual gas. Cold vessels such as in the new cryogenic storage ring (CSR) will push this limit up. Such an extension of the measurement capability to atomic lifetimes on the order of many minutes is necessary for the study of E1-forbidden radiative processes in the low-charge state atomic and molecular ions of the interstellar medium.

19.2.3 Conclusions

In conclusion, beam–foil spectroscopy is very useful because of its inherent time resolution, and the efficient excitation at high and observation at low electron density. Atomic lifetime measurements are feasible over about four orders of magni-

tude, from a few picoseconds to many nanoseconds, and are achieved basically by virtue of geometry that is exploited by mechanical displacements. Because of the nonselective excitation, only a few beam–foil lifetime measurements have reached error bars smaller than 5%.

Heavy-ion storage rings pose the spectroscopic problem of large Doppler shifts, which with considerable effort can also be exploited for laser spectroscopy making use of the shift in wavelength between laboratory and moving ion rest frames. Practical atomic lifetime measurements have been done in the five orders of magnitude range from about 1 millisecond to some hundred seconds; this range will widen with better vacuum in cryogenic systems. A fair number of these lifetime measurements have reached uncertainties of less than 1%.

Electron beam ion traps yield access to the spectra of all elements and all charge states, they do not suffer from Doppler shift, and they grant options for high spectral resolution. They are a very economical tool to produce highly charged ions, but they are best for levels that are excited directly from the ground state. In terms of atomic lifetime measurements, femtosecond lifetimes can be measured spectroscopically via line broadening. Electronic lifetime measurements (with fast switching of the electron beam energy) work in the range from microseconds to seconds (six orders of magnitude), and possibly more in future clean traps.

Fig. 19.1 shows how the above three techniques have been applied to cover a very wide range of level lifetimes of a fundamental M1 transition along the isoelectronic sequence of two-electron spectra. The predicted Z^{10} dependence of this M1 transition rate is fully corroborated by experiment. However, further atomic structure insight requires even higher accuracy of the experiment. Some of the most precise atomic lifetime measurements ever achieved were done at EBITs, with uncertainties of a small fraction of 1%. Multitrap arrangements that separate ion production from measurement are coming into use in various laboratories. The combination of an EBIT for ion production at low particle density and a subsequent ion storage ring for lifetime measurements on a single ion species and charge state appear particularly promising in the quest for tests of the QED contribution to the M1 transition rate [57].

References

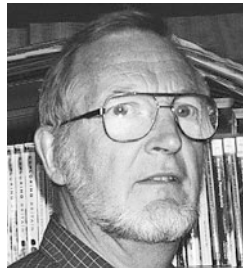
- Martinson, I.: Rep. Prog. Phys. **52**, 157 (1989)
- Shima, K., Mikumo, T., Tawara, H.: At. Data Nucl. Data Tables **34**, 357 (1986)
- Andersen, T., Mannervik, S.: Comments At. Mol. Phys. **16**, 185 (1985)
- Serpa, F.G., Livingston, A.E.: Phys. Rev. A **43**, 6447 (1991)
- Bunge, C.F.: Phys. Rev. Lett. **44**, 1450 (1980)
- Knystautas, E.J.: Phys. Rev. Lett. **69**, 2635 (1992)
- Träbert, E., Heckmann, P.H., Doerfert, J., Granzow, J.: J. Phys. B At. Mol. Opt. Phys. **25**, L353 (1992)
- Mannervik, S., Short, R.T., Sonnek, D., Träbert, E., Möller, G., Lodwig, V., Heckmann, P.H., Blanke, J.H., Brand, K.: Phys. Rev. A **39**, 3964 (1989)
- Träbert, E.: Phys. Scr. **48**, 699 (1993)
- Träbert, E., Hutton, R., Martinson, I.: Mon. Not. R. Astron. Soc. **227**, 27 (1987)
- Träbert, E.: Mon. Not. R. Astron. Soc. **297**, 399 (1998)
- Jupén, C., Bengtsson, P., Engström, L., Livingston, A.E.: Phys. Scr. **64**, 329 (2001)
- Stoner, J.O., Leavitt, J.A.: Opt. Acta **20**, 435 (1973)
- Bergkvist, K.-E.: A high-intensity method for beam-foil spectroscopy, with retained spatial resolution along the beam. In: Sellin, I.A., Pegg, D.J. (eds.) Beam Foil Spectroscopy, p. 719. Plenum, New York (1976)
- Drake, G.W.F.: Can. J. Phys. **66**, 586 (1988)
- Zacharias, A.S., Livingston, A.E., Lu, Y.N., Ward, R.F., Berry, H.G., Dunford, R.W.: Nucl. Instrum. Methods Phys. Res. B **31**, 41 (1988)
- Provencher, S.W.: J. Chem. Phys. **64**, 2772 (1976)
- Irwin, D.J.G., Livingston, A.E.: Comput. Phys. Commun. **7**, 95 (1974)
- Heckmann, P.H., Träbert, E., Winter, H., Hannebauer, F., Bukow, H.H., von Buttler, H.: Phys. Lett. A **57**, 126 (1976)
- Pinnington, E.H., Ansbacher, W., Kernahan, J.A., Ge, Z.-Q., Inamdar, A.S.: Nucl. Instrum. Methods Phys. Res. B **31**, 206 (1988)
- Geller, R.: App. Phys. Lett. **16**, 40 (1970)
- Lyneis, C.M., Antaya, T.A.: Rev. Sci. Instrum. **61**, 221 (1990)
- Smith, S.J., Lorenzo, J.A., Tayal, S.S., Chutjian, A.: Phys. Rev. A **68**, 062708 (2003)
- Laming, J.A., Silver, J.D.: Phys. Lett. A **123**, 395 (1987)
- Grandin, G.P., Hennecart, D., Husson, X., Lecler, D., Lesteven-Vaisse, I., Lisfi, D.: Europhys. Lett. **6**, 683 (1988)
- Levin, J.C., Short, R.T., O, C.-S., Cederquist, H., Elston, S.B., Gibbons, J.P., Sellin, I.A., Schmidt-Böcking, H.: Phys. Rev. A **36**, 1649 (1987)
- Barat, M.: Nucl. Instrum. Methods Phys. Res. B **9**, 364 (1985)
- Prior, M.H., Holt, R.A., Schneider, D., Randall, K.L., Hutton, R.: Phys. Rev. A **48**, 1964 (1993)
- Schulze-Hagenest, D., Harde, H., Brand, W., Demtröder, W.: Z. Phys. A **282**, 149 (1977)
- Schmoranzner, H., Volz, U.: Phys. Scr. T **47**, 42 (1993)
- Baudinet-Robinet, Y., Dumont, P.-D., Garnir, H.-P., El Himdy, A.: Phys. Rev. A **40**, 6321 (1989)
- Scholl, T.J., Cameron, R., Rosner, S.D., Zhang, L., Holt, R.A., Sansonetti, C.J., Gillaspay, J.D.: Phys. Rev. Lett. **71**, 2188 (1993)
- Dinneen, T.P., Berrah-Mansour, N., Berry, H.G., Young, L., Pardo, R.C.: Phys. Rev. Lett. **66**, 2859 (1991)
- Myers, E.G., Thompson, J.K., Gavathas, E.P., Clausen, N.R., Silver, J.D., Howie, D.J.H.: Phys. Rev. Lett. **75**, 3637 (1995)
- Scholl, T.J., Rosner, S.D., Holt, R.A.: Can. J. Phys. **76**, 39 (1998)
- Rivest, R.C., Izawa, M.R., Rosner, S.D., Scholl, T.J., Wu, G., Holt, R.A.: Can. J. Phys. **80**, 557 (2002)
- Gaillard, M.L., Pegg, D.J., Bingham, C.R., Carter, H.K., Mleko-daj, R.L., Cole, J.D.: Phys. Rev. A **26**, 1975 (1982)
- Sen, A., Childs, W.J., Goodman, L.S.: Nucl. Instrum. Methods Phys. Res. B **31**, 324 (1988)
- Andrá, H.J., Fröhling, R., Plöhn, H.J., Silver, J.D.: Phys. Rev. Lett. **37**, 1212 (1976)

40. Zajfman, D., Heber, O., Vejby-Christensen, L., Ben-Itzhak, I., Rappaport, M., Fishman, R., Dahan, M.: *Phys. Rev. A* **55**, 1577 (1997)
41. Schmidt, H.T., Cederquist, H., Jensen, J., Fardi, A.: *Nucl. Instrum. Methods Phys. Res. B* **173**, 523 (2001)
42. Beiersdorfer, P., Schweikhard, L., Crespo López-Urrutia, J., Widmann, K.: *Rev. Sci. Instrum.* **67**, 3818 (1996)
43. Schweikhard, L., Beiersdorfer, P., Träbert, E.: *AIP Conf. Proc.* **606**, 174 (2002)
44. Levine, M.A., Marrs, R.E., Bardsley, J.N., Beiersdorfer, P., Bennett, C.L., Chen, M.H., Cowan, T., Dietrich, D., Henderson, J.R., Knapp, D.A., Osterheld, A., Penetrante, B.M., Schneider, M.B., Scofield, J.H.: *Nucl. Instrum. Methods Phys. Res. B* **43**, 431 (1989)
45. Levine, M.A., Marrs, R.E., Henderson, J.R., Knapp, D.A., Schneider, M.B.: *Phys. Scr. T* **22**, 157 (1988)
46. Marrs, R.E., Elliott, S.R., Knapp, D.A.: *Phys. Rev. Lett.* **72**, 4082 (1994)
47. Currell, F.J.: The physics of electron beam ion traps. In: Gillaspy, J. (ed.) *Trapping Highly Charged Ions: Fundamentals and Applications*, p. 3. Nova Science, Commack (2001)
48. Beiersdorfer, P., Osterheld, A.L., Decaux, V., Widmann, K.: *Phys. Rev. Lett.* **71**, 2196 (1993)
49. Epp, S.W., Crespo López-Urrutia, J.R., Brenner, G., Mäckel, V., Mokler, P.H., Treusch, R., Kuhlmann, M., Yurkov, M.V., Feldhaus, J., Schneider, J.R., Wellhöfer, M., Martins, M., Wurth, W., Ullrich, J.: *Phys. Rev. Lett.* **98**, 183001 (2007)
50. Bernitt, S., Brown, G.V., Rudolph, J.K., Steinbrügge, R., Graf, A., Leutenegger, M., Epp, S.W., Eberle, S., Kubiček, K., Mäckel, V., Simon, M.C., Träbert, E., Magee, E.W., Beilmann, C., Hell, N., Schippers, S., Müller, A., Kahn, S.M., Surzhykov, A., Harman, Z., Keitel, C.H., Clementson, J., Porter, F.S., Schlotter, W., Turner, J.J., Ullrich, J., Beiersdorfer, P., Crespo López-Urrutia, J.R.: *Nature* **492**, 225 (2012)
51. Träbert, E., Beiersdorfer, P., Gwinner, G., Pinnington, E.H., Wolf, A.: *Phys. Rev. A* **66**, 052507 (2002)
52. Träbert, E.: *Can. J. Phys.* **80**, 1481 (2002)
53. Beiersdorfer, P., Träbert, E., Pinnington, E.H.: *Astrophys. J.* **587**, 836 (2003)
54. Lاپierre, A., Jentschura, U.D., Crespo López-Urrutia, J.R., Braun, J., Brenner, G., Bruhns, H., Fischer, D., González Martínez, A.J., Harman, Z., Johnson, W.R., Keitel, C.H., Mironov, V., Osborne, C.J., Sikler, G., Soria Orts, R., Shabaev, V., Tawara, H., Tupitsyn, I.I., Ullrich, J., Volotka, A.: *Phys. Rev. Lett.* **95**, 183001 (2005)
55. Lاپierre, A., Crespo López-Urrutia, J.R., Braun, J., Brenner, G., Bruhns, H., Fischer, D., González Martínez, A.J., Mironov, V., Osborne, C., Sikler, G., Soria Orts, R., Tawara, H., Ullrich, J., Shabaev, V.M., Tupitsyn, I.I., Volotka, A.: *Phys. Rev. A* **73**, 052507 (2005)
56. Brenner, G., Crespo López-Urrutia, J.R., Harman, Z., Mokler, P.H., Ullrich, J.: *Phys. Rev. A* **75**, 032504 (2007)
57. Träbert, E.: *J. Phys. B* **43**, 074034 (2005)
58. Draganić, I., Crespo López-Urrutia, J.R., DuBois, R., Fritzsche, S., Shabaev, V.M., Soria Orts, R., Tupitsyn, I.I., Zou, Y., Ullrich, J.: *Phys. Rev. Lett.* **91**, 183001 (2003)
59. Mäckel, V., Klawitter, R., Brenner, G., Crespo López-Urrutia, J.R., Ullrich, J.: *Phys. Rev. Lett.* **107**, 143002 (2011)
60. Beiersdorfer, P., Träbert, E., Chen, H., Chen, M.-H., May, M.J., Osterheld, A.L.: *Phys. Rev. A* **67**, 052103 (2003)
61. Träbert, E., Beiersdorfer, P., Chen, H.: *Phys. Rev. A* **70**, 032506 (2004)
62. Blundell, S.A.: *Can. J. Phys.* **87**, 55 (2009)
63. Chen, M.H., Cheng, K.T.: *J. Phys. B* **43**, 074019 (2010)
64. Träbert, E., Clementson, J., Beiersdorfer, P., Santana, J.A., Ishikawa, Y.: *Can. J. Phys.* **89**, 639 (2011)
65. Gillaspy, J.D., Osin, D., Ralchenko, Y., Reader, J., Blundell, S.A.: *Phys. Rev. A* **87**, 062503 (2013)
66. Träbert, E., Beiersdorfer, P., Hell, N., Brown, G.V.: *Phys. Rev. A* **92**, 022509 (2015)
67. Santana, J.A., Träbert, E.: *Phys. Rev. A* **91**, 022503 (2015)
68. Stöhlker, T., Mokler, P.H., Bosch, F., Dunford, R.W., Franzke, F., Klepper, O., Kozhuharov, C., Ludziejewski, T., Nolden, F., Reich, H., Rymuza, P., Stachura, Z., Steck, M., Swiat, P., Warczak, A.: *Phys. Rev. Lett.* **85**, 3109 (2000)
69. Gumberidze, A., Stöhlker, T., Banaś, D., Beckert, K., Beller, P., Beyer, H.F., Bosch, F., Hagmann, S., Kozhuharov, C., Liesen, D., Nolden, F., Ma, X., Mokler, P.H., Steck, M., Sierpowski, D., Tashenov, S.: *Phys. Rev. Lett.* **94**, 223001 (2005)
70. Beiersdorfer, P., Chen, H., Thorn, D.B., Träbert, E.: *Phys. Rev. Lett.* **95**, 233003 (2005)
71. Schweppe, J., Belkacem, A., Blumenfeld, L., Claytor, N., Feinberg, B., Gould, H., Kostroun, V.E., Levy, L., Misawa, S., Mowat, J.R., Prior, M.H.: *Phys. Rev. Lett.* **66**, 1434 (1991)
72. Brandau, C., Kozhuharov, C., Müller, A., Shi, W., Schippers, S., Bartsch, T., Böhm, S., Böhme, C., Hoffknecht, A., Knopp, H., Grün, N., Scheid, W., Steih, T., Bosch, F., Franzke, B., Mokler, P.H., Nolden, F., Steck, M., Stöhlker, T., Stachura, Z.: *Phys. Rev. Lett.* **91**, 073202 (2003)
73. Klafit, I., Borneis, S., Engel, T., Fricke, B., Grieser, R., Huber, G., Kühl, T., Marx, D., Neumann, R., Schröder, S., Seelig, P., Völker, L.: *Phys. Rev. Lett.* **73**, 2425 (1994)
74. Beiersdorfer, P., Utter, S.B., Wong, K.L., Crespo López-Urrutia, J.R., Britten, J.A., Chen, H., Harris, C.L., Thoe, R.S., Thorn, D.B., Träbert, E., Gustavsson, M.G.H., Forssén, C.: *Phys. Rev. A* **64**, 032506 (2001)
75. Yerokhin, V.A., Berseneva, E., Harman, Z., Tupitsyn, I.I., Keitel, C.H.: *Phys. Rev. A* **94**, 0232502 (2016)
76. Beiersdorfer, P., Osterheld, A.L., Scofield, J.H., Crespo López-Urrutia, J.R., Widmann, K.: *Phys. Rev. Lett.* **80**, 3022 (1998)
77. Beiersdorfer, P., Träbert, E., Brown, G.V., Chen, H., Clementson, J., Thorn, D.: In: *XXVth Int. Conf. on Photonic, Electronic and Atomic Collisions (ICPEAC) Freiburg (Germany)*. (2007). Abstract Mo179
78. Sánchez, R., Lochmann, M., Jöhren, R., Andelkovic, Z., Anielski, D., Botermann, B., Bussmann, M., Dax, A., Frömmgen, N., Geppert, C., Hammen, M., Hannen, V., Kühl, T., Litvinov, Y.A., López-Coto, R., Stöhlker, T., Thompson, R.C., Vollbrecht, J., Wen, W., Weinheimer, C., Will, E., Winters, D., Nörtershäuser, W.: *J. Phys. B At. Mol. Opt. Phys.* **50**, 085004 (2017)
79. Ullmann, J., Andelkovic, Z., Dax, A., Geithner, W., Geppert, C., Gorges, C., Hammen, M., Hannen, V., Kaufmann, S., König, K., Litvinov, Y., Lochmann, M., Maass, B., Meisner, J., Murböck, T., Sánchez, R., Schmidt, M., Schmidt, S., Steck, M., Stöhlker, T., Thompson, R.C., Vollbrecht, J., Weinheimer, C., Nörtershäuser, W.: *J. Phys. B At. Mol. Opt. Phys.* **48**, 144022 (2015)
80. Ullmann, J., Andelkovic, Z., Brandau, C., Dax, A., Geithner, W., Geppert, C., Gorges, C., Hammen, M., Hannen, V., Kaufmann, S., König, K., Litvinov, Y., Lochmann, M., Maass, B., Meisner, J., Murböck, T., Sánchez, R., Schmidt, M., Schmidt, S., Steck, M., Stöhlker, T., Thompson, R.C., Trageser, C., Vollbrecht, J., Weinheimer, C., Nörtershäuser, W.: *Nat. Commun.* **8**, 15484 (2017)
81. Savin, D.W., Beck, B., Beiersdorfer, P., Kahn, S.M., Brown, G.V., Gu, M.F., Liedahl, D.A., Scofield, J.H.: *Phys. Scr. T* **80**, 312 (1999)
82. Porter, F.S., Gygax, J., Kelley, R.L., Kilbourne, C.A., King, J.M., Beiersdorfer, P., Brown, G.V., Thorn, D.B., Kahn, S.: *Rev. Sci. Instrum.* **79**, 10E307 (2008)
83. Beiersdorfer, P., Boyce, K.R., Brown, G.V., Chen, H., Kahn, S.M., Kelley, R.L., May, M., Olson, R.L., Porter, F.S., Stahle, C.K., Tillotson, W.A.: *Science* **300**, 1558 (2003)

84. Träbert, E., Beiersdorfer, P., Brown, G.V.: Phys. Rev. Lett. **98**, 263001 (2007)
85. Yao, K., Andersson, M., Brage, T., Hutton, R., Jönsson, P., Zou, Y.: Phys. Rev. Lett. **97**, 183001 (2006)
86. Beiersdorfer, P., Scofield, J.H., Osterheld, A.L.: Phys. Rev. Lett. **90**, 235003 (2003)
87. Crespo López-Urrutia, J.R., Beiersdorfer, P.: Astrophys. J. **721**, 576 (2010)
88. Beiersdorfer, P., Crespo López-Urrutia, J.R., Träbert, E.: Astrophys. J. **817**, 67 (2016)
89. Li, J., Grumer, J., Li, W., Andersson, M., Brage, T., Hutton, R., Jönsson, P., Yang, Y., Zou, Y.: Phys. Rev. A **88**, 013416 (2013)
90. Dmitriev, I.S., Nikolaev, V.S., Teplova, Y.A.: Phys. Lett. **26A**, 122 (1968)
91. Andersen, L.H., Heber, O., Zajfman, D.: J. Phys. B **37**, R57 (2004)
92. Saathoff, G., Karpuk, S., Eisenbarth, U., Huber, G., Krohn, S., Reinhardt, S., Schwalm, D., Wolf, A., Gwinner, G.: Phys. Rev. Lett. **91**, 190403 (2003)
93. Doerfert, J., Träbert, E., Wolf, A., Schwalm, D., Uwira, O.: Phys. Rev. Lett. **78**, 4355 (1997)
94. Schmidt, H.T., Forck, P., Grieser, M., Habs, D., Kenntner, J., Miersch, G., Repnow, R., Schramm, U., Schüssler, T., Schwalm, D., Wolf, A.: Phys. Rev. Lett. **72**, 1616 (1994)
95. Mannervik, S.: Phys. Scr. T **105**, 67 (2003)



Elmar Träbert Elmar Träbert has pursued beam-foil spectroscopic measurements (spectra and ps/ns-lifetimes) in the EUV and X-ray ranges at Bochum, Oxford, GSI Darmstadt, and various other places. Since the 1990s, his work has expanded to ms/s-range atomic lifetime measurements at the TSR heavy-ion storage ring Heidelberg, and to electron beam ion traps (EBIT), mostly at Livermore.



Eric Pinnington Eric Pinnington obtained his PhD in Physics at Imperial College in 1962. Prior to joining the University of Alberta in 1965, he held an NRC Postdoctoral Fellowship at McMaster University in Hamilton, Ontario, and an Alexander von Humboldt Fellowship at the Max Planck Institute for Astrophysics in Munich. He was elected Fellow of the American Physical Society in 1995. He became Professor Emeritus of Physics in 1997.



Alan Gallagher

Contents

20.1	Collisional Line Shapes	283
20.1.1	Voigt Line Shape	284
20.1.2	Interaction Potentials	284
20.1.3	Classical Oscillator Approximation	284
20.1.4	Impact Approximation	285
20.1.5	Examples: Line Core	286
20.1.6	Δ and γ_c Characteristics	287
20.1.7	Quasistatic Approximation	288
20.1.8	Satellites	289
20.1.9	Bound States and Other Quantum Effects	289
20.1.10	Einstein A and B Coefficients	290
20.2	Radiation Trapping	290
20.2.1	Holstein–Biberman Theory	290
20.2.2	Additional Factors	292
20.2.3	Measurements	293
	References	294

Abstract

The shapes of collisionally broadened atomic lines is a topic almost as old as Fraunhofer's discovery of the existence of discrete lines. *Lorentz* provided the first quantitative theory in 1906 [1], and *Weisskopf* advanced this to the *impact theory* by 1933 [2]. *Holtzmark* [3], *Kuhn* [4] and *Margenau* [5] meanwhile developed the *quasistatic* or *statistical* theory which describes the line wing, and *Jablonski* put this on a quantum mechanical footing in the context of free–free molecular radiation [6, 7]. By the 1940s, satellite bands in the line wings, and a variety of high and low pressure line shapes and broadening rates had been measured. Initial confusion regarding the validity of the contrasting *impact* versus *static* approaches was largely resolved by unified treatments of the Fourier integral theory [8–13]. *Baranger* then provided a quantum basis for the impact theory, including level degenera-

cies [14]. Descriptions can be found in a variety of reviews and references therein, including [2, 5, 15–20]. The broadening of molecular lines involves the additional complication of rotationally nonadiabatic collisions; this was initially addressed by *Anderson* [12, 13] and later with great thoroughness by *van Kranendonk* [21]. This chapter and most of the above theories are concerned with neutral atomic gases, which is sometimes called *pressure broadening*. In plasmas, electron, ion, and neutral collisions all contribute to the line shapes and strengths; thus the emitted lines provide a powerful diagnostic of plasma conditions. Neither molecular nor plasma broadening will be covered here; the latter is reviewed in [17–20, 22], and in Chaps. 51 and 63.

Keywords

line shape · impact approximation · Doppler width · line core · Lorentzian line shape

20.1 Collisional Line Shapes

The neutral-gas theories described above generally used phenomenological or long range forms of the atomic and molecular interactions, and most measurements were not sufficiently detailed to test the validity of these parameterizations or the theoretical approximations. A great deal of the work since mid century has been directed towards obtaining more realistic and accurate descriptions of these interactions and of the full line shapes. In addition, many new types of observations have stimulated variations on the basic theories and descriptions. This includes topics such as collision-induced forbidden transitions, satellite shapes, spectral and polarization redistribution, orientation and alignment effects, Doppler-free spectroscopy and very low temperature collisions. Most of these topics are beyond the scope of this brief and basic description of neutral collisional line shapes.

A. Gallagher (✉)
Quantum Physics Division, University of Colorado
Boulder, CO, USA
e-mail: alang@jila.colorado.edu

20.1.1 Voigt Line Shape

An atomic (or molecular or ionic) line has an intrinsic Lorentzian shape that reflects the Fourier transform of the exponentially decaying spontaneous emission. For a spontaneous decay rate Γ , the fullwidth at half maximum (FWHM) is $\Delta\omega = \Gamma$. Due to the Maxwellian distribution of atomic velocities v in a thermal vapor, and the Doppler shift $\Delta\omega_D = v/\lambda$ where $\lambda = \lambda/(2\pi)$ and λ is the wavelength, the resonance frequencies of atoms in the laboratory frame have a Gaussian distribution. The Doppler width of this distribution is approximately $\omega_0 u/c$, where ω_0 is the resonant frequency and u is the mean thermal velocity. The full line shape is thus a convolution of the natural Lorentzian with the thermal Gaussian; a Voigt profile. In the presence of collisions, the line from each atom broadens, shifts and becomes asymmetric, and this is normally convoluted with the Gaussian velocity distribution to obtain the complete line shape. Collisions may also cause weak or dipole-forbidden transitions to become stronger as well as broader.

20.1.2 Interaction Potentials

Theories of collisional line shapes consider an ensemble average of collisional interactions. For atomic gases, the description of each individual collision or interaction generally starts with a molecular model for a pair of interacting atoms, since the Born–Oppenheimer approximation is appropriate for thermal atomic collisions (electron velocities \gg nuclear velocities) [23]. The radiative transition then occurs between adiabatic electronic molecular states that separate to the atomic states of the transition under consideration. The notation $V_u(R)$ denotes the electronic energy of the upper state, and $V_g(R)$ the lower state, where R is the internuclear separation, and the total atomic energies are E_1 and E_0 with $E_1 - E_0 = h\omega_0$ (Fig. 20.1). The next simplification is to assume that the atom-pair statistically branch into adiabatic motion along each of the molecular states associated with the initial atomic state, and radiation to each of the final states is summed independently, assuming they are also completely adiabatic. This ignores an inevitable nonadiabatic coupling between the states as their energy separation decreases to zero at large R , but as discussed below this has been shown to have a very minor effect on line broadening. The single-collision problem then reduces to calculating the spectrum of a molecular transition between each upper and lower pair of adiabatic states, for each initial state of internuclear motion and all possible final motions, and summing these weighted by the rate of initial collisional motions. However, such calculations are only necessary to elucidate particular quantum features, because the *classical oscillator approximation*, *impact approximation*, *quasistatic approximation*, and *classical*

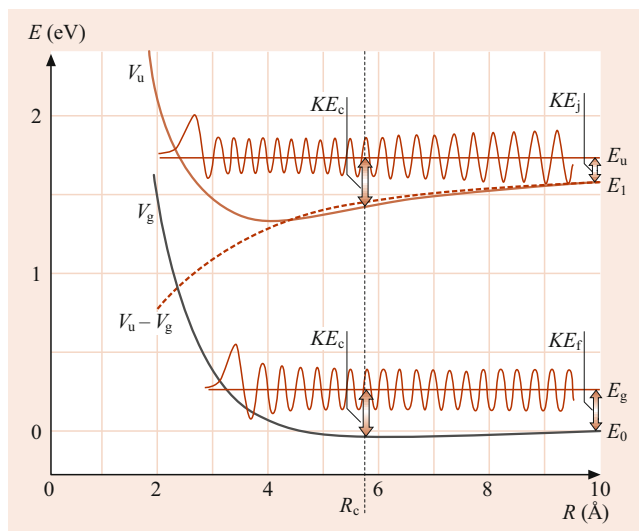


Fig. 20.1 Diagrammatic representation of a free–free molecular radiative transition and the classical Franck–Condon principle. Adiabatic potentials (V_u and V_g), the difference potential equal to the classical transition frequency (*dashed*), nuclear kinetic energies and wave functions $\Phi_u(R)$ and $\Phi_g(R)$ are indicated. The position R_c is the classical radiation position for the initial (E_u) and final (E_g) energies shown

Franck–Condon principle provide major conceptual and calculational simplifications. These are presented in the context of free–free transitions in the following sections.

20.1.3 Classical Oscillator Approximation

Consider a free–free molecular radiative transition of energy $\hbar\omega = E_u - E_g$ between upper (u) and lower (g) states of total energy E_u and E_g , as shown in Fig. 20.1. Each elastic scattering state is the product of an electronic adiabatic state $\phi(r, R)$ and a nuclear motion state $\Phi(R)$ of the molecule. The electronic states u and g have effective potentials

$$V_q^e = V_q + \frac{l(l+1)}{R^2}, \quad (20.1)$$

where $q = u$ or g . Examples of such $V(R)$ and $\Phi(R)$ for the case of $l = 0$ are shown in Fig. 20.1. The electric dipole radiation operator that couples these states is normally a weak perturbation that does not alter these potentials or wave functions. For definiteness assume the atom is initially in the upper state, and that an atom pair approach with kinetic energy \mathcal{T}_i and separate with \mathcal{T}_f , as indicated. The intensity I , or transition probability, is proportional to the squared matrix element of the dipole operator $er = e \sum_i r_i$ between initial and final states

$$\begin{aligned} I &\propto \left| \int d^3R \int d^3r \Phi_u(R)^* \phi_u(r, R)^* er \phi_g(r, R) \Phi_g(R) \right|^2 \\ &= \mu^2 \left| \int d^3R \Phi_u(R)^* \Phi_g(R) \right|^2, \end{aligned} \quad (20.2)$$

where the last factor is the Franck–Condon factor, μ is the dipole moment, here assumed to be the atomic value independent of R , and $d^3R = 4\pi R^2 dR$ for diatomics. The $\Phi(R)$ can be represented, in the WKB approximation, as

$$R\Phi_q = k_q^{-1/2} \exp \left[-i \int_0^\infty dR k_q(R) \right], \quad (20.3)$$

where

$$k_q = \frac{\left\{ 2M \left[E_q - V_q^e(R) \right] \right\}^{1/2}}{\hbar} \quad (20.4)$$

and M is the reduced mass of the atom pair ($\hbar^2 k^2 / (2M)$ is the kinetic energy in Fig. 20.1).

The integrand in the second line of Eq. (20.2) then contains $\exp[i \int d^3R (k_u - k_g)]$. If one multiplies $k_u - k_g$ by $(k_u + k_g) / (k_u + k_g)$, the exponent becomes

$$\frac{2M(\omega - \omega_c)}{\hbar(k_u + k_g)},$$

and if one further defines a variable $t(R)$ by $dt = dR/v(R)$ with $v(R) = \hbar(k_u + k_g)/2M$, the exponent becomes $i \int \omega_c(t') dt' - i\omega t$, where

$$\omega_c(R) = \frac{V_u(R) - V_g(R)}{\hbar} \quad (20.5)$$

and $R(t)$ is the classical trajectory in the average potential. Thus, the Franck–Condon factor reduces to the squared Fourier transform of $\exp[i \int^t \omega_c(t') dt']$, where $\hbar\omega_c(R) = V_u(R) - V_g(R)$ (Fig. 20.1). This is the *classical oscillator approximation* (COA), in which the atoms are considered to be a classical oscillator at $\omega_c(R)$ during the collisional interaction, and $R(t)$ is the classical orbit.

The \sqrt{k} in the denominator of the WKB wave function leads to $1/v(R)$ in the nuclear density at R , again corresponding to classical motion. This COA is used as the starting point in many line shape calculations. It is apparent that the COA breaks down when the initial- and final-state orbits are significantly different, or when the Born–Oppenheimer or WKB approximation is not valid. However, the COA is normally a very good approximation for thermal atomic vapors when $\hbar(\omega - \omega_0) \ll k_B T$, since most orbits are then straight lines within the R region that yields the observed radiation.

One further conceptual and mathematical simplification is to subtract ω_0 from $\omega_c(t')$ and from ω by defining $\Delta\omega_c = \omega_c - \omega_0$ and $\Delta\omega = \omega - \omega_0$. The Franck–Condon factor in Eq. (20.2) then becomes

$$I(\omega) = \left(\frac{4\mu^2 \omega^4}{3c^3} \right) \times \left| \int dt \exp \left[i \int^t \Delta\omega_c(t') dt' - i\Delta\omega t \right] \right|_{av}^2, \quad (20.6)$$

where the prefactors that yield the correct intensity are explained in [12, 13] (Sect. 11.6). The average is, in general, over a sequence of collisions leading to an integral over collision velocity and impact parameter, weighted by the rate of occurrence.

In the next section, the character of the broadened line core is obtained by the traditional method of evaluating Eq. (20.6) using the impact approximation.

20.1.4 Impact Approximation

Atomic collisions in thermal vapors typically occur in a time interval $\tau_c < 1$ ps, whereas the time between significant collisions is much longer at vapor pressures below a few atmospheres. Thus, one can consider the atom as radiating its unperturbed frequency ω_0 most of the time, but occasionally suffering a rapid, strong perturbation. If the duration of a collision is τ_c , then $\phi(t) = \int^t \Delta\omega_c(t') dt'$ in the exponent of Eq. (20.6) undergoes a net phase shift $\Delta\theta$ in a time τ_c , and is constant between collisions. If $\Delta\omega \ll 1/\tau_c$, then one can approximate this phase shift as instantaneous; this is the essential assumption of the *impact approximation*. When the factor $\exp[i\Delta\theta(b, v)]$, which then occurs in Eq. (20.6) is averaged over collision rates with velocity v and impact parameter b this leads to $(\gamma_c - i\delta)t$ in place of $\phi(t)$, where γ_c and δ are given by [15]

$$\gamma_c = \int_0^\infty n(v) v dv \int_0^\infty 2\pi b [1 - \cos \Delta\theta(b, v)] db,$$

$$\delta = \int_0^\infty n(v) v dv \int_0^\infty 2\pi b \sin \Delta\theta(b, v) db.$$

Including the spontaneous emission dipole decay rate $\exp(-\Gamma t/2)$, the Fourier integral produces the normalized Lorentzian line shape

$$I(\omega) = \frac{(\Gamma/2 + \gamma_c)}{\pi[(\Gamma/2 + \gamma_c)^2 + (\Delta\omega - \delta)^2]}. \quad (20.7)$$

The full line shape is then a Voigt profile with a Lorentzian-component half width $\Gamma + 2\gamma_c$ and a shift of δ from ω_0 . The shift can be understood as the perturbed oscillator frequency advancing relative to ω_0 by the average value of $\sin \Delta\theta$, or alternately as indicating the direction of the frequency shift of $V_u - V_g$. The Lorentz approximation corresponds to taking $1 - \cos \Delta\theta = 1$ or 0 , with the former representing a collision. This gives $\gamma = 1/\Delta t_c$, where Δt_c is the average time between strong collisions.

The b for which $\Delta\theta(b, \langle v \rangle) = 1$ is called the Weisskopf radius (R_W). The collisional line width $2\gamma_c$ can be thought of as

a collisional rate $n\langle v \rangle Q$, where $Q = \pi R_W^2$. The importance of R_W is that γ_c and δ result primarily from atomic interactions in the region $R \approx R_W$. Since the size of an electronic wave function increases with increasing excitation energy, $|\Delta V(R)| = |V(R) - V(\infty)|$ is normally larger for the upper state of a transition. (High Rydberg states can be an exception.) Since $\Delta\theta = 1$ for $b = R_W$ and $\Delta\theta \approx (\Delta V/\hbar)\tau_c$, then $\Delta V(R_W) \approx \hbar/\tau_c$. For a typical $\tau_c = 1$ ps this implies $\Delta V(R_W)/(hc) \approx 5 \text{ cm}^{-1}$, which is a relatively weak, long range interaction. Thus, reasonable approximations to the necessary $V(R)$ can often be obtained from atomic perturbation theory. Simple expressions for γ_c and δ are obtained for $V_i - V_f = A/R^n$ with $n > 2$ [24]. The case of $n = 3$ corresponds to the resonant interaction between identical atoms, while $n = 6$ corresponds to the van der Waals interaction, which holds at long range for foreign gas interactions. This result for one pair of adiabatic states must be averaged over all of the pairs that separate to each atomic state.

Higher order approximations obtain an asymmetric line, rather than a pure Lorentzian, due to the asymmetry of $\Delta V(R)$ [24]. In the line core this asymmetry appears as a multiplicative correction $1 + \Delta\omega/D$, where $|D| \approx 1/\tau_c$ [25], and with increasing detuning it increases until at $|\Delta\omega| > 1/\tau_c$ the static wing approaches the quasistatic limit described in Sect. 20.1.7. If $\Delta V(R)$ changes monotonically with decreasing R , only one side of the line has a static contribution and the other, antistatic side falls off exponentially at $|\Delta\omega| > \tau_c$ [11]. However, this situation is seldom observed, as more than one difference potential generally contributes and there is usually a static contribution on both sides of the line. Another factor that produces a small divergence from the Voigt profile is the velocity dependence of the shift and width. When combined with the higher velocities of atoms emitting or absorbing in the Doppler wing, this produces an asymmetry in the Doppler wings [26, 27].

20.1.5 Examples: Line Core

It is possible to deconvolve a Voigt line shape to separate the Doppler and Lorentzian components, and thereby deduce broadenings of considerably less than the Doppler width ([28] and references therein). However, the broadening is most easily observed at perturber densities where the collisional broadening exceeds the Doppler broadening. Such a pressure-dependent line shape is shown in Fig. 20.2, for a range of perturber density n_p such that the broadening exceeds the Doppler width and hyperfine structure, yet the line core is described by the impact theory [29]. In Fig. 20.2 the normalized line intensity has been divided by n_p ; as the line wings are proportional to n_p they are constant in such a plot, while the line center broadens and shifts with increasing n_p . For this case of fairly heavy atoms, $(2\pi c\tau_c)^{-1} = \Delta k_c$ corre-

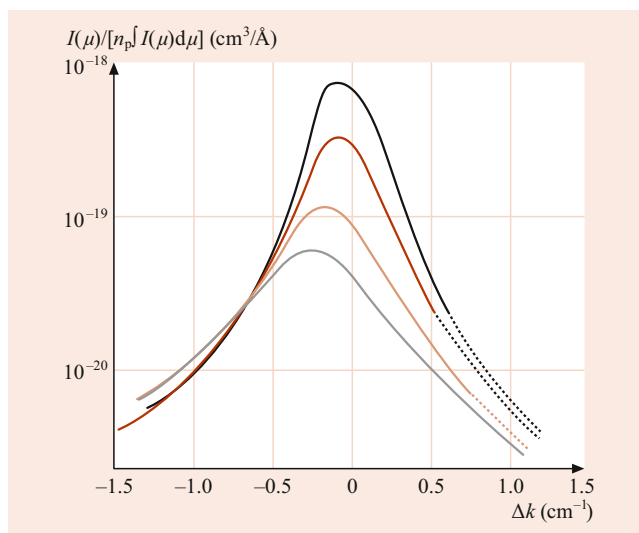


Fig. 20.2 Normalized line shape of the Rb $5P_{3/2}-5S_{1/2}$ transition broadened by Kr, for Kr densities of $4.5, 9, 18,$ and $27 \times 10^{18} \text{ cm}^{-3}$ (top to bottom). Hyperfine structure and instrumental resolution cause $\approx 0.3 \text{ cm}^{-1}$ of the broadening shown

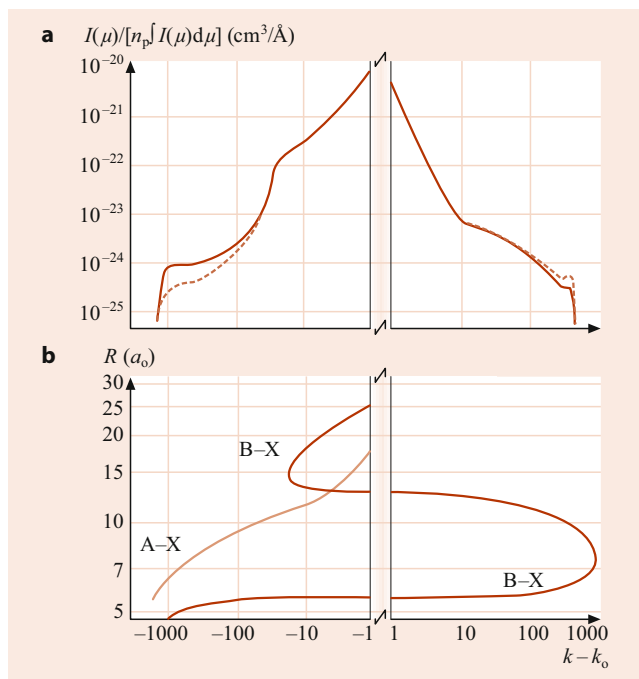


Fig. 20.3 Normalized intensity in the wings of the Rb $5P_{3/2}-5S_{1/2}$ transition broadened by Kr, in frequency units of $k = 1/\lambda$. The measured spectrum in (a) is from [29, 37, 39]. The *solid line* is at 310 K and the *dashed line* at 540 K. The difference potentials corresponding to the A, B and X states of Rb-Kr, taken from [36], are shown in (b)

sponds to $\approx 0.5 \text{ cm}^{-1}$, and the line becomes asymmetric and non-Lorentzian beyond $\approx 1 \text{ cm}^{-1}$ (Fig. 20.3a); the red wing intensity falls more slowly and the blue wing more rapidly than $(\Delta\omega)^{-2}$. This behavior is typical for most heavy perturbers, and is attributed to a long range attractive V_u which dominates $V_u - V_g$.

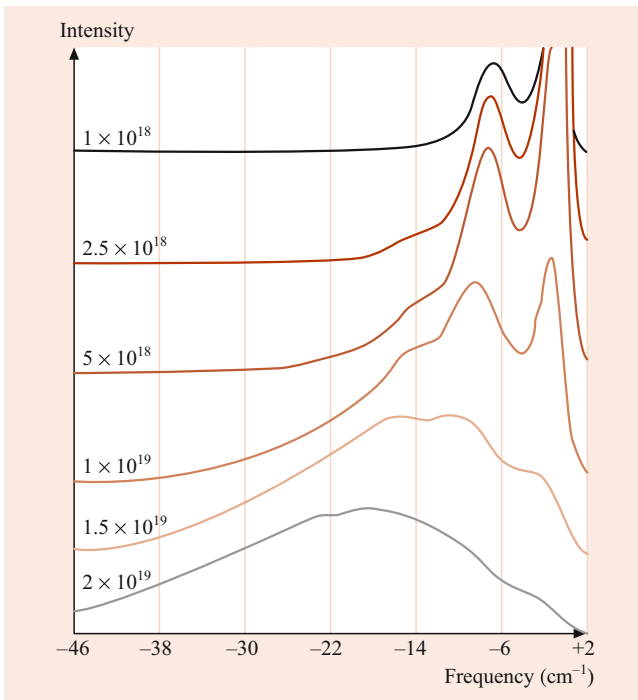


Fig. 20.4 Calculated line shapes of the Cs($^9P_{1/2}$ - $^6S_{1/2}$) line broadened by Xe at the densities indicated (from [16]). The assumed interaction is based on measured line shapes, but data corresponding to the calculated conditions are not available

For the lowest n_p shown in Fig. 20.2, a convolution with the Doppler, hyperfine and instrumental broadenings showed that the line is essentially a symmetric Lorentzian for $|\Delta k| < \Delta k_c$ [29]. However, at the highest density, the half-height point is beginning to fall outside of Δk_c ; the impact approximation is marginally valid for describing the half width of the line at this density. Most early experiments were done at more than 10 times this density [15]; most of the line-core was at $|\Delta k| > \Delta k_c$ and describable by the static theory (Sect. 20.1.7) rather than the impact approximation. The impact approximation was also not valid under these conditions because collisions overlap in time. These very broad lines are well represented by the multiple-perturber, static theories that assume scalarly additive perturber interactions [5, 8]. This transition between an impact and quasistatic line core, and to multiple perturber interactions, occurs at lower pressures for transitions to higher states, as the interactions have a longer range. In addition, nearby intensity peaks or satellites often occur, and strongly affect the line as pressure increases. An example calculation, based on an interpretation of measured spectra [16], is shown in Fig. 20.4. This shows how a line with a satellite feature progressively broadens and finally blends with the satellite as n_p increases.

With the advent of saturated-absorption (Doppler free) spectroscopy, collisional line broadening can be measured at much lower densities, where $2\gamma_c \ll \Delta\omega_D$. In principle, this can allow measurement of line broadenings and shifts,

although with a complication that affects the line shape; the same collisions that produce optical phase shifts also change the atomic velocity. These velocity changes have a minor effect outside the Doppler envelope where high pressure measurements are normally made, but they are quite important in saturated absorption line shapes. This affects primarily the low intensity wings of the line, so it does not prevent measuring the broadening and shift of the nearly Lorentzian core. Details can be found in [30] and references therein. Two-photon absorption yields Doppler free lines that are not affected by velocity changing collisions. This provides the most exacting test of line shapes. These narrow lines are precisely Lorentzian, with a broadening that reflects the upper state interaction since this is usually much stronger than that of the ground state. The technique has been used to measure the broadening of two photon transitions to many excited states [31, 32].

20.1.6 Δ and γ_c Characteristics

Since 1970, neutral broadening has generally been measured in the $|\Delta\omega| < 1/\tau_c$ region where the impact approximation and Eq. (20.7) is valid. Measurements through 1982 are tabulated in [16], and through 1992 in [33]. More recent measurements are tabulated in the NIST Reference Data bibliography, which is accessible (free) at the web site <http://physics.nist.gov/PhysRefData>. These involve primarily metal vapor resonance lines broadened by noble gases. For collisions with the heavier (more polarizable) gases, the sizes of these measured broadening rate coefficients generally fall within a factor of 10 range, and approximately fit the prediction of Eq. (20.7) with $\Delta V_u(R) - \Delta V_g(R) = C_6 R^{-6}$ [34] and C_6 given by a simple effective quantum number formula. This occurs because the potentials are fairly close to van der Waals for $R \geq R_W$ and the broadening is insensitive to details of the potentials at $R < R_W$ since $\cos \Delta\theta$ in Eq. (20.7) averages to ≈ 0 for the closer (strong) collisions. It also occurs because the full quantum solution for broadening by a van der Waals interaction, with Zeeman degeneracies, yields nearly the same result as the above single-level theory with an average C_6 [35].

For the heavy, more polarizable perturbers, the excited state interactions are attractive and red shifts occur, but the measured shifts have a very poor correlation with the van der Waals prediction. As b decreases and $\Delta\theta(b, v)$ increases, $\sin \Delta\theta$ oscillates and major cancellations occur in the average of $\sin \Delta\theta$ in Eq. (20.7). The shift is therefore only a fraction of the broadening and is very sensitive to the interaction throughout the region $R \approx R_W$. This often differs considerably from the van der Waals form, at the typical $\approx 5 \text{ cm}^{-1}$ interaction energy at R_W . The shape of the red wing just beyond $\Delta\omega_c$ also frequently fails to fit that expected for a van

der Waals interaction [29]. Thus, the often good agreement of γ_c with van der Waals numbers is not a reliable indicator of the actual $V(R)$ in the relevant R region, even for heavy noble gas perturbers.

For He and sometimes Ne perturbers, a repulsive interaction due to charge overlap normally dominates at $R \approx R_W$, causing a blue shift as well as a larger broadening than the van der Waals prediction.

20.1.7 Quasistatic Approximation

The impact approximation is valid for $|\Delta\omega| \ll 1/\tau_c$, where the $1/\tau_c$ is typically $1\text{--}10\text{ cm}^{-1}$. For larger $|\Delta\omega|$ the line shape becomes asymmetric, with higher intensity on the wing corresponding to the long-range $V_u(R) - V_g(R)$. At large detunings where $\Delta\omega \gg 1/\tau_c$ a major simplification occurs. The COA describes the interacting atom pair as an oscillator of frequency $\omega_c(R) = [V_u(R) - V_g(R)]/\hbar$ when at separation R . Since R is time dependent during the classical orbit, ω_c is as well and the Fourier spectrum is broadened relative to the simple distribution of $\omega_c(t)$ that occurs during the orbit. But if the motion is sufficiently slow, the intensity at ω reduces to the probability of finding the atom pair at the appropriate $R(\omega = \omega_c)$. The spectrum then reduces, at low pressure, to the probability distribution of pair separations R , subject to Eq. (20.5) between R and ω . This is the binary quasistatic, static, or statistical spectrum, which accurately describes most line wings for $|\Delta\omega| > 1/\tau_c$. When the pressure is large enough to yield a significant probability of one perturber at $R \leq R_c$, multiple-perturber interactions must also be considered as in [5].

This intuitive deduction of the statistical spectrum from the COA [4] can also be obtained more formally from Eq. (20.6) by expanding the exponent about the time during a collision when $\omega_c(t) = \omega$. Alternatively, it follows directly from Eq. (20.2) using WKB wave functions to evaluate free-free molecular Franck–Condon factors [6, 7]. This result is identical to the classical Franck–Condon principle (CFCP), originally established in the context of bound–bound molecular radiation.

The CFCP yields important insights for all molecular radiation. Again consider Eq. (20.2) with the substitution of the WKB wave functions ϕ_q , given below it. Examples of ϕ_u and ϕ_g are given in Fig. 20.1. For large detunings $\omega - \omega_0$, as shown in Fig. 20.1, the integrand on the right side oscillates rapidly everywhere except at the stationary phase point R_c , where $k_u = k_g$. As a consequence, the dominant contribution to the integral occurs at R_c and one can consider the transition to be localized at R_c . Since $k_u(R_c) = k_g(R_c)$, $\mathcal{T}_u(R_c) = \mathcal{T}_g(R_c) = \mathcal{T}_c$ also holds, and as can be seen in Fig. 20.1 it then follows that $\hbar\omega = V_u(R_c) - V_g(R_c)$. Thus, radiation at frequency ω occurs when the atoms are near

R_c , where the electronic state energies differ by $\hbar\omega$. Note that this holds for all initial kinetic energies and angular momenta, as long as the conditions for validity of the Born–Oppenheimer and WKB approximations hold for the initial and final nuclear motions. This is the CFCP, which is equivalent to the classical-oscillator model for radiation at large detunings from the atomic transition.

Another insight evident from Fig. 20.1 is that the photon energy associated with the frequency difference $\omega - \omega_c$ is supplied by nuclear kinetic energy $\hbar(\omega - \omega_0) = \mathcal{T}_i - \mathcal{T}_f$. This transformation of nuclear into electronic energy takes place as the nuclei move from large R to R_c on one $V(R)$ and back to large R on the other.

If an absorbing or emitting atom interacts as $V_i(R)$ with a density n_p of perturbers in a vapor of temperature T , the probability of a perturber at separation $R \rightarrow R + dR$ is $n_p 4\pi R^2 \exp[-V_i(R)/(k_B T)] dR$ if the interatomic motion is in equilibrium. Inverting Eq. (20.5) for $R(\omega)$ yields $dR = d\omega/(d\omega/dR)$, and this pair of relations yields the (single perturber) quasistatic (QS) spectrum

$$I(\omega) = N n_p \Gamma 4\pi R(\omega)^2 \times \exp\left[\frac{-V_i(\omega)}{k_B T}\right] \left/ \left[\frac{d\omega(R)}{dR} \right] \right., \quad (20.8)$$

where N is the radiator density and $I(\omega)$ the radiation per unit volume and frequency interval.

Figure 20.3a gives an example of far wing emission line shapes versus photon energy in units of cm^{-1} , for the Kr broadened Rb D2 line for which $\Delta k_c \approx 0.7\text{ cm}^{-1}$. These data are normalized by perturber density, so they are independent of perturber density for the density region of the experiment. The excited state produces two $V_u(R)$, called the A and B states, while the ground state produces one $V_g(R)$, called the X state. Each of these potentials has a single minimum at long range and is strongly repulsive at close range, but the well depths and positions are very different [36]. This causes the complex forms of $V_u(R) - V_g(R)$ that are shown in Fig. 20.3b. There I have plotted $\ln(R)$ vertically and $\ln(\Delta V(R)/(hc))$ horizontally, where ΔV refers to $V_A - V_X$ and $V_B - V_X$. The right side of Eq. (20.8) can also be written as the exponential and constant factors times $dR^3(\omega)/d\omega$. Since $\ln[R^3(\omega)] \propto \ln[R(\omega)]$, the static spectrum at $\Delta k = \Delta\omega/(2\pi c)$ is proportional to the slopes of the curves in Fig. 20.3b, divided by $|\Delta k|$ due to the $\ln(\Delta k)$ horizontal axis. One can see qualitatively that the overall spectrum follows such a relation to the lines in Fig. 20.3b; in fact in most spectral regions this relation is quantitatively accurate.

The temperature dependence in Fig. 20.3a corresponds to the exponential factors in Eq. (20.8) [37]. At large R , both $\Delta V(R)$ are attractive, and this causes a large intensity on the negative Δk (red) wing. However, once $|\Delta k|$ exceeds

$\approx 20 \text{ cm}^{-1}$, where $V_B - V_X$ reverses direction, the red wing intensity drops rapidly. This extremum in $\Delta V(R)$ causes a satellite at $\approx -20 \text{ cm}^{-1}$, although it is spread out by the finite collision speed and does not cause a distinct peak in the spectrum. Satellite features are discussed in more detail in the next paragraph. The antistatic blue wing drops rapidly for several decades, then suddenly flattens beyond $\approx 10 \text{ cm}^{-1}$ due to the positive portion of $V_B - V_X$ at small R . The remaining blue wing is the B–X band, and has a satellite at $\approx 350 \text{ cm}^{-1}$ as $V_B - V_X$ passes through another extremum. The theory predicts this at 800 cm^{-1} , but clearly represents all the basic aspects correctly. This satellite is also spread out by finite collision speed, but a definite intensity peak remains. The red wing beyond $\approx 50 \text{ cm}^{-1}$ is the A–X band. The feature near -1000 cm^{-1} is due to the exponential factor in Eq. (20.8), not an extremum in $\Delta V(R)$; the feature essentially disappears if the normalized intensity is extrapolated to infinite temperature.

20.1.8 Satellites

In regions of the wing where the intensity falls slowly with increasing frequency, motional broadening of the static spectrum is not noticeable and the static spectrum is a good approximation. However, if $\Delta V(R)$, or equivalently $\omega_c(R)$, has an extremum at some R_S , the denominator of Eq. (20.8) is zero at $\omega(R_S) = \omega_S$. This produces a local maximum, or satellite, in the far wing intensity, as seen in Fig. 20.3a at 350 cm^{-1} . If one expands $\omega(R)$ in a Taylor series about $R = R_S$ this produces in Eq. (20.8) a square root divergence of finite area, with no intensity beyond ω_S . The area under this feature is meaningful, but not its shape; the quasistatic assumption is clearly not valid for such sharp features. The more accurate satellite shape is obtained by returning to Eq. (20.2) and expanding $V_u(R)$, $V_g(R)$ and the WKB wave functions about R_S , or using Eq. (20.6) with $\omega_c(t)$ expanded about $t(R_S)$. Sando and Wormhoudt used the former method to obtain a universal satellite shape [38]. Szudy and Baylis improved the expansion to yield a smooth transition to the quasistatic spectrum at smaller detunings [34]. This result is nearly the same as Sando et al. in the spectral region of the satellite, but it more accurately connects to the adjacent static line wing. Intensity undulations between the satellite and the line occur in this calculation; these arise from alternating constructive and destructive interference between two contributions to the same frequency from $R > R_S$ and $R < R_S$. This can not be seen in the low resolution of Fig. 20.3a, but such undulations are seen near the 350 cm^{-1} satellite [39]. At antistatic detunings beyond ω_S , which are not quasistatically allowed, the calculated intensities decay exponentially. This is also observed experimentally [39] and is the same behavior predicted for the antistatic wing of a line [11].

At higher perturber densities and closer to the line core, corresponding to larger R interactions, the multiple perturber probability distribution must be included. If the interactions are additive, this leads to a secondary satellite at twice the detuning of the low pressure satellite, as seen in Fig. 20.4.

The wings of a collisionally broadened atomic line are molecular radiation. In the context of molecular bound state spectroscopy, a satellite is a *head of band heads*, corresponding to a frequency region where bound–bound band heads congregate. This occurs, of course, at the classical satellite frequency and when $V_u(R) - V_g(R)$ has an extremum [40].

An extremum in $\Delta V(R)$ is the most common cause of satellites, but similar looking features can occur for other reasons. Forbidden bands often appear in the wings of forbidden atomic transitions, due to an increase in the transition dipole moment $\mu(R)$ resulting from the collisional interaction. These are described, in the QS approximation, by Eq. (20.8) with Γ replaced by $\Gamma(R)$. If $\Gamma(R)$ increases rapidly with decreasing R , the intensity increases as ω moves into the far wing until the dR^3 and exponential factors cause a net decrease at small R . This leads to forbidden bands far from the atomic frequency, such as those in [41]. In some cases, a collision-induced feature also appears at the frequency of the forbidden transition. The shapes of such features, which also include radiative collisions, in which both atoms change state, are calculated and reviewed in [42].

A variety of related line shape phenomena has been investigated, including the relation between absorbed and emitted wavelengths (spectral redistribution), the dependence of fluorescence polarization on absorbed wavelength (polarization redistribution), and high power effects. Some references regarding these phenomena are [43–47].

20.1.9 Bound States and Other Quantum Effects

The validity of the QS spectrum requires the validity of the WKB approximation in the initial and final state, but it is not restricted to free–free molecular transitions. In fact, the equilibrium probability distribution in Eq. (20.8) must include bound states in an attractive $V_i(R)$. The QS spectrum describes the *average* behavior of bound–free and bound–bound molecular bands, as well as the free–free radiation implied by the above method of derivation. The quantum character is expressed in the discrete bound–bound lines that make up this average, and in *Condon oscillations*, where the intensity oscillates about the average $I_{QS}(\omega)$. The latter occur as oscillations in Franck–Condon factors in the bound–bound case, and as smooth oscillations in bound–free spectra and low resolution bound–bound spectra. An additional quantum feature occurs in regions of the spectrum dominated by classical turning points, usually at the far edge of a line wing where the intensity is dropping rapidly. There,

quantum tunneling past the edge of the classically allowed region spreads the spectrum. Yet another is the energy $h\omega_0/2$ of the ground vibrational state, which effectively adds to $k_B T$ in Eq. (20.8) for attractive V_1 . All of these quantum features become more pronounced as the reduced mass decreases; examples and details can be found in [40, 48–50].

20.1.10 Einstein A and B Coefficients

The relationship between absorption coefficient $B_{12}(\omega)$, stimulated emission coefficient $B_{21}(\omega)$ and spontaneous emission coefficient $A_{21}(\omega)$ are given by the Einstein relations; $A_{21}/B_{21} = 8\pi h\lambda^{-3}$ and $B_{21}/B_{12} = g_1/g_2$. These relations are most familiar for atomic lines, but if they are referred to the density of absorbers $dN_g/d\omega$ and emitters $dN_u/d\omega$ that emit or absorb at ω , then they also apply to the wings of lines, i.e.,

$$k(\omega) = B_{12}(\omega) \left(\frac{2\pi h}{\lambda} \right) \left(\frac{g_u}{g_g} \right) \frac{dN_g}{d\omega} \\ = \frac{1}{4} \lambda^2 A_{21}(\omega) \left(\frac{g_u}{g_g} \right) \frac{dN_g}{d\omega}, \quad (20.9)$$

$$g(\omega) = \frac{1}{4} \lambda^2 A_{21}(\omega) \frac{dN_u}{d\omega}, \quad (20.10)$$

$$I(\omega) = \hbar\omega A_{21}(\omega) \frac{dN_u}{d\omega}. \quad (20.11)$$

Here $k(\omega)$ is the absorption coefficient due to lower state atoms, $g(\omega)$ is the stimulated emission coefficient and $I(\omega)$ the spontaneous emission due to excited state population, and g_u and g_g are the statistical weights of the atomic states. For absorbing atoms of density N_g and perturber density n_p , the QS approximation with equilibrated internuclear motion sets

$$\frac{dN_g}{d\omega} = N_g n_p 4\pi R^2 \frac{dR}{d\omega} \exp\left(-\frac{V_g}{k_B T}\right), \quad (20.12)$$

and equivalently for a radiating atom density N_u with perturber interaction V_u . Normally most of the radiation, and $dN_g/d\omega$, is concentrated at the atomic line, so integrating over $d\omega$ near the line leads to the relations

$$\int_0^\infty k(\omega) d\omega = \frac{1}{2} \lambda^2 A_{21} N_g \left(\frac{g_u}{g_g} \right), \quad (20.13)$$

$$\int_0^\infty I(\omega) d\omega = A_{21} N_u \left(\frac{\hbar\omega}{2\pi} \right), \text{ etc.} \quad (20.14)$$

Note that

$$\frac{g(\omega)/N_u}{k(\omega)/N_g} \propto \exp\left(-\frac{\hbar\omega}{k_B T}\right); \quad (20.15)$$

if N_u/N_g is also in equilibrium at T , this yields the correct equilibrium relation between $k(\omega)$, $g(\omega)$, $I(\omega)$, and a black body spectrum. While these relations are much more general than the QS theory, the latter provides a helpful conceptual basis. The above expressions in terms of spontaneous emission thus cover all cases.

20.2 Radiation Trapping

Atoms and ions efficiently absorb their own resonance radiation, and their emission can be reabsorbed before escaping a vapor. Molecules are less efficient absorbers, since each electronic transition branches into multiple-line bands, but interesting effects result if such reabsorption occurs. This emission and reabsorption process is fundamental to the formation of stellar lines, where it is called *radiation transfer*, and to confined vapors and plasmas where it is also called *radiation diffusion* or *trapping*. Fraunhofer's observation of dark lines in the stellar spectrum result from this radiation transfer process. Highly sophisticated treatments of line formation in inhomogeneous and nonequilibrium plasmas containing many species [19, 20] also apply to laboratory plasmas, but the simplifications inherent in a one- or two-element, confined plasma with cylindrical or planar symmetry leads to easier treatments. This sections discusses only a uniform density and temperature, confined atomic vapor.

The fluorescent lamp in which 254 nm mercury radiation diffuses to the walls and excites a phosphor, provides a prime example of radiation trapping. Its improvement motivated the seminal *Biberman* [51, 52] and *Holstein* [53, 54] theories, continuing through modern theory and experiment that is particularly relevant to electrodeless and compact lamps. Dense clouds of cold, trapped atoms are also influenced by radiation trapping. Reference [55] provides an excellent overview of this topic, which we will not discuss here. The effect of radiation trapping on the *polarization* of fluorescent radiation played a major role in developing a correct understanding of the coherent response of atoms to radiation. This is reviewed in [44], and will not be covered here. *Molisch* and *Oehry* [56] have provided a detailed discussion of research on radiation transport up to 1998.

20.2.1 Holstein–Biberman Theory

An atom in a dense vapor may be excited by externally applied radiation plus the fluorescence from other excited atoms within the vapor, and it will decay by spontaneous emission (neglecting stimulated emission). This is expressed

by the Holstein–Biberman equation

$$\frac{dn(\mathbf{r}, t)}{dt} = S(\mathbf{r}, t) + \gamma \int_{\text{vol}} K(\mathbf{r} - \mathbf{r}') n(\mathbf{r}', t) d^3 \mathbf{r}' - \gamma n(\mathbf{r}, t), \quad (20.16)$$

where $n(\mathbf{r}, t)$ is the excited state density at position \mathbf{r} , $S(\mathbf{r}, t)$ is the excitation rate due to externally applied radiation, γ is the spontaneous emission rate, the kernel $K(\mathbf{r} - \mathbf{r}')$ is the probability of a reabsorption at \mathbf{r} due to fluorescence by an atom at \mathbf{r}' , and the integral is over the vapor filled volume [51–54]. Since $K(\mathbf{r}, \mathbf{r}')$ is assumed the same for all excited atoms, this contains an implicit assumption that all atoms emit the same fully redistributed spectrum. The solution of this linear integral equation, subject to boundary values at the vapor boundary, can be expressed as a sum over an orthogonal set of solutions $n(\mathbf{r}, t)_i = n(\mathbf{r})_i \exp(-g_i \gamma t)$ of the homogeneous equation

$$n(\mathbf{r}, t) = \sum_{i=1}^{\infty} a(t)_i n(\mathbf{r})_i, \quad (20.17)$$

where, if $S(\mathbf{r}, t) = S(\mathbf{r})f(t)$, then $a(t)_i = \bar{a}_i \int_{-\infty}^t f(t') \times \exp[-g_i \gamma (t - t')] dt'$ and $\bar{a}_i = \int S(\mathbf{r}) n(\mathbf{r})_i d^3 \mathbf{r}$. Here $n(\mathbf{r}, t)_i$ is the i th normal mode and $g_i \gamma$ is the decay rate of this mode, as it would decay without change in its shape $n(\mathbf{r})_i$ from a pulse of excitation.

Two shapes of vapor regions have been studied in detail: an infinitely long cylinder of radius R and the region between two infinite parallel plates with separation L . The first three symmetric modes of the latter slab geometry are shown with unit height in Fig. 20.5. A spatial integration over the normalized $i = 1$ or fundamental mode yields 1 and all others

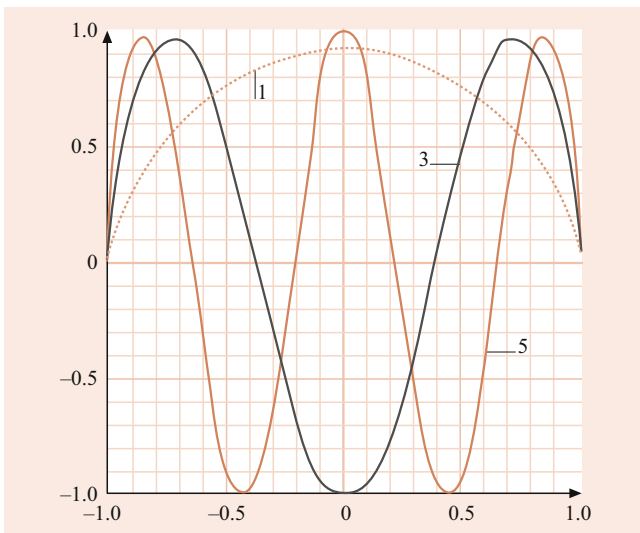


Fig. 20.5 The first three symmetric eigenfunctions ($j = 0, 2, 4$) of radiation trapping between slab windows, for a Doppler line profile, from [57–59]. The windows are at ± 1

integrate to zero, so $a(t)_1$ equals the total excited state population. g_1 is the escape probability; i.e., the probability of photon escape averaged over the fundamental mode distribution of emitters $n(\mathbf{r})_1$. Since $n(\mathbf{r}, t)$ must be everywhere positive, the negative contributions of the higher order modes only reduce the density in some regions. The g_i can vary from 0 to 1 and increase with increasing i , so that higher order modes die out faster after pulsed excitation. The ratios of decay rates is $g_1 : g_3 : g_5 = 1 : 3.7 : 6.4$ for the symmetric slab modes shown in Fig. 20.5. For steady state excitation, Eq. (20.17) yields $a(t)_i = \bar{a}_i / g_i \gamma$, so the lower order modes are more heavily weighted because they decay more slowly. The fundamental mode decay rate $g_1 \gamma$ is of primary interest in most situations, and we will now discuss its properties.

The kernel $K(x)$ is the probability of fluorescence transport over a distance x followed by reabsorption, averaged over the emitted frequency distribution. It is conceptually useful to express it in terms of the spectrally averaged transmission $T(x)$

$$K(x) = \frac{1}{4\pi x^2} \frac{dT(x)}{dx}, \quad (20.18)$$

$$T(x) = \int_0^{\infty} \mathcal{L}(\omega) \exp[-k(\omega)x] d\omega,$$

where $\mathcal{L}(\omega)$ is the emission line shape normalized to unit area, and $x = |\mathbf{r} - \mathbf{r}'|$. If one assumes that the fluorescence frequency of an atom does not depend on the frequency it absorbed (i.e., complete spectral redistribution), this leads to $k(\omega) = \kappa \mathcal{L}(\omega)$, where $\kappa = (\lambda^2 / 8\pi) (g_u / g_g) n \Gamma$ and g_u and g_g are statistical weights. This simplification applies under most conditions and will be used here; its range of validity and more accurate treatments are discussed below.

The transmission factor $\mathcal{L}(\omega)$ and the integrand of Eq. (20.18) are shown in Fig. 20.6, for a Gaussian line shape and several values of $k_0 x$, where k_0 is the line center absorption coefficient. At small $k_0 x$, the transmitted spectrum is similar to $\mathcal{L}(\omega)$; for these conditions $T(x) \simeq \exp(-k_{av} x)$, where $k_{av} \simeq 0.7 k_0$ is the average attenuation. For $k_0 x > 5$, the transmission is small except at the edges of the line. The transmitted radiation is then predominately in the ω region near ω_1 , defined by $k_0 x \mathcal{L}(\omega_1) = 1$. Since the integrand is sharply peaked near ω_1 , this leads to simple analytic forms for $T(x)$. In the large $k_0 x$ limit, $T(x) \simeq [k_0 x (\pi \ln k_0 x)^{1/2}]^{-1}$ in the Gaussian case, and $T(x) \simeq (\pi k_0 x)^{-1/2}$ for a Lorentzian line shape. These asymptotic forms of $T(x)$ are compared with the exact $T(x)$ in Fig. 20.7; $T(x)$ follows the asymptotic formulas for $k_0 x > 5$ and 10, respectively. $T(x)$ for several Voigt line shapes is also shown in Fig. 20.7; these follow the Gaussian $T(x)$ at smaller $k_0 x$, then rise above as ω_1 moves into the Lorentzian wing.

For radiative escape from a cell, transmission over distances near the cell dimension (R or L) is most important,

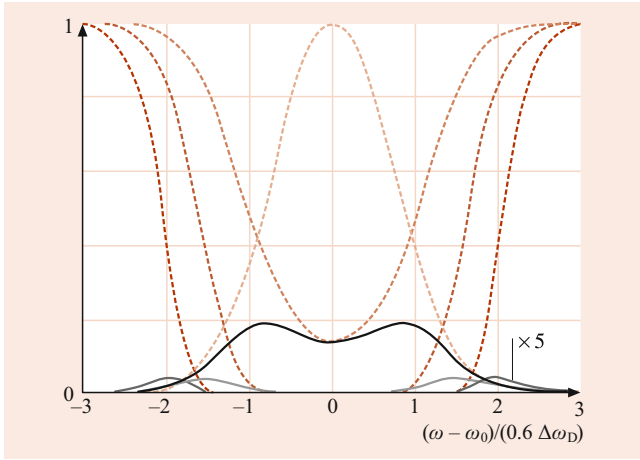


Fig. 20.6 Gaussian emission spectrum $\mathcal{L}(\omega)$ (short-dash line), transmissions $T(\omega)$ (long-dash lines), and transmitted intensities (solid lines) for $k_0 x = 2, 10,$ and 50

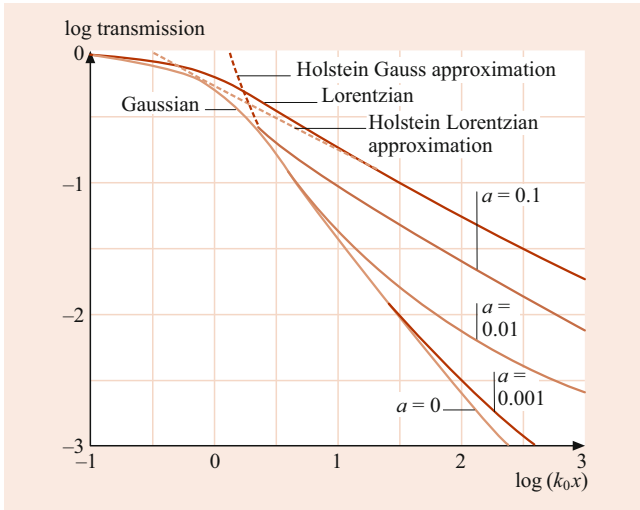


Fig. 20.7 Transmission $T(x)$ versus distance in units of $k_0 x$, for Voigt line shapes with the a parameters indicated, where $a = (\ln 2)^{1/2} \Delta\omega_{\text{Lor}}/\Delta\omega_{\text{Gauss}}$. The Gaussian limit corresponds to $a = 0$ and the Lorentzian limit to $a = 1$. The Holstein, large $k_0 x$, approximations are also indicated

since transport over this distance often escapes the vapor and transport over much smaller distances does not have much effect. The escape probability g_1 , averaged over the fundamental mode distribution, is close to $T(R)$ or $T(L/2)$, while the higher order modes are related to the same asymptotic forms of $T(x)$ at smaller distances. Thus, in the large $k_0 L$ slab case,

$$g_i = \frac{G_i}{k_0 L (\frac{1}{2} \ln k_0 L)^{1/2}} \quad \text{Gaussian line} \quad (20.19a)$$

$$g_i = \frac{G'_i}{(k_0 L)^{1/2}} \quad \text{Lorentzian line,} \quad (20.19b)$$

with $G_i = 1.03$ and $G'_i \simeq 0.65$. For an infinite cylinder, the same equations hold with $L/2 \rightarrow R$ and slightly larger G_i values. Exact G_i and G'_i values can be found in [57–59].

20.2.2 Additional Factors

As noted above, the line shape of a two-level atom in a thermal vapor is a Voigt shape; a convolution of a Lorentzian of width $\Gamma + 2\gamma_c$ with a Gaussian of width $\Delta\omega_D$. In most cases, $\Delta\omega_D \gg \Gamma$, so in the absence of a buffer gas the line shape is nearly Gaussian at low density (n). As a result, ω_1 is in the Gaussian region of the line at low density and g_1 behaves similarly to the Gaussian transmission in Fig. 20.7 with x replaced by the confinement dimension. k_0 is proportional to n , so from Eq. (20.19a) g_1 is approximately inversely proportional to n for $k_0 L > 5$. As n increases, ω_1 moves further into the wing of the line, and when ω_1 reaches the Lorentzian tail of the Voigt line profile a transition to Eq. (20.19b) occurs, where k_0 corresponds to a purely Lorentzian line. (That the core of the line does not have a Lorentzian shape does not matter, since the fraction of emission well into the Lorentzian wing is nearly the same as that of a pure Lorentzian line.)

In the absence of a collision, a two level atom reradiates in its rest frame the same frequency it absorbed. Thermal motion redistributes this coherent scattering frequency within the Doppler envelope when the emission and absorption are in different directions, but it does not transfer it into the natural Lorentzian wing outside the Doppler envelope. This leads to the property that an atomic vapor will scatter frequencies in the natural wing, but will not emit in this wing unless it absorbed there or is excited by or during a collision. With line broadening collisions, a fraction $\Gamma/(\Gamma + 2\gamma_c)$ of optical attenuation is coherently scattered and a fraction $2\gamma_c/(\Gamma + 2\gamma_c)$ is redistributed into *incoherent* emission with a Lorentzian spectrum of width $\Gamma + 2\gamma_c$ centered at $\omega_0 + \delta$ in the reference frame of the moving atom. This redistributed emission can escape in the Lorentzian wing of the Voigt line. In this radiation transport problem, the consequence is that Eq. (20.19b) with $k_0 = n(\lambda^2/2\pi)(\Gamma/\gamma_c)(g_u/g_g)$, corresponding to a Lorentzian with $\Gamma_{\text{Total}} = 2\gamma_c$ not $\Gamma + 2\gamma_c$, provides the best approximation to g_1 in the density region where ω_1 is in the Lorentzian wing of the line. Since $k_0 \propto n/\gamma_c$ and in the absence of a buffer gas $\gamma_c = k_c n$, where k_c is the rate coefficient for self broadening collisions, g_1 becomes independent of n . In fact, $k_c \propto \Gamma$ as well, so g_1 is also independent of Γ . For the case of a $J = 0$ ground state and a $J = 1$ excited state, $g_1 = 0.21(\lambda/L)^{1/2}$; the broadening coefficient for other cases can be found in [60]. If the broadening is due to a buffer gas, $\gamma_c = k_c n_B$ in Eq. (20.19b) yields

$$g_1 \propto \left(\frac{n_B}{n}\right)^{1/2}; \quad (20.20)$$

this has been studied in [61].

Post et al. have numerically evaluated g_1 for all values of $k_0 L$ for slab and cylinder geometries, by integrating the radiative escape probability $g(z)$ over the fundamental mode distribution $N(z)$, where z is the position between the windows [62]. To obtain $g(z)$ they integrate over the angular

distribution of the emission, using $T(x)$ from the exact line shape. Thus all features of the calculation correspond to the Holstein–Biberman theory for an isolated line without approximation. As will now be discussed real atomic vapors are generally not that simple.

Many atomic *lines* have multiple components due to hyperfine structure and isotope shifts; some components are isolated while others are separated by less than a Doppler line width and overlap. The absorption line shape then becomes a weighted sum over components, each with an equivalent Voigt shape. In a high density vapor or a plasma, collisions will usually distribute the excited state population between the isotopes and hyperfine states in proportion to their isotopic fraction and statistical weight. The emission line shape $\mathcal{L}(\omega)$ is then a similarly weighted distribution over components. Since radiation only escapes in the wings of a line component at high k_0L , overlapping components act almost as a single component. If the line has M isolated components, the right-hand side of Eqs. (20.19a) and (20.19b) become sums over the fraction f_j of the intensity in the j component times the escape probability for that component. The latter is obtained, for large k_0L , by replacing k_0 with $k_0 f_j$ in Eqs. (20.19a) and (20.19b). The net result, after summing over components, is an increase in g_1 by a factor of $\approx M$ in the Gaussian case and $\approx M^{1/2}$ in the Lorentzian. This approximation was obtained by Holstein in the context of the Hg 254 nm radiation under conditions appropriate to the fluorescent lamp [63]. Walsh made a more detailed study of these overlapping components [64], and the dependence of g_1 on the ratio of line separation to Doppler width is also given in [65].

20.2.3 Measurements

The overall behavior of g_1 versus n is shown in Fig. 20.8 for the Na($3P_{3/2}$) or D2 resonance line in pure Na vapor (i.e., the $3p^2P_{3/2} - 3s^2S_{1/2}$ transition) [65, 66]. In this type of experiment the fundamental mode decay rate is established by a combination of optimally exciting that spatial mode and of waiting until the fluorescence decay is exponential in time after termination of the excitation. A transition to approximately $1/n$ behavior, corresponding to Eq. (20.19a), is seen to occur at $k_0L/2 \approx 5$. At $k_0L/2 \approx 100$ the transition to n^0 behavior, corresponding to a self-broadened Lorentzian line in Eq. (20.19b), can be seen. The behavior at $k_0L < 5$ fits the Milne diffusion theory [67] as well as the Post et al. theory shown as a solid line; this is also similar to $T(L/2)$, as seen in Fig. 20.7. For $5 < k_0L/2 < 100$, the behavior is similar to Eq. (20.19a) (dashed line), but the Post et al. theory (solid line) is $\approx 20\%$ higher due to the inclusion of the Na hyperfine structure (hfs splitting \simeq Doppler width). For $k_0L/2 > 1000$,

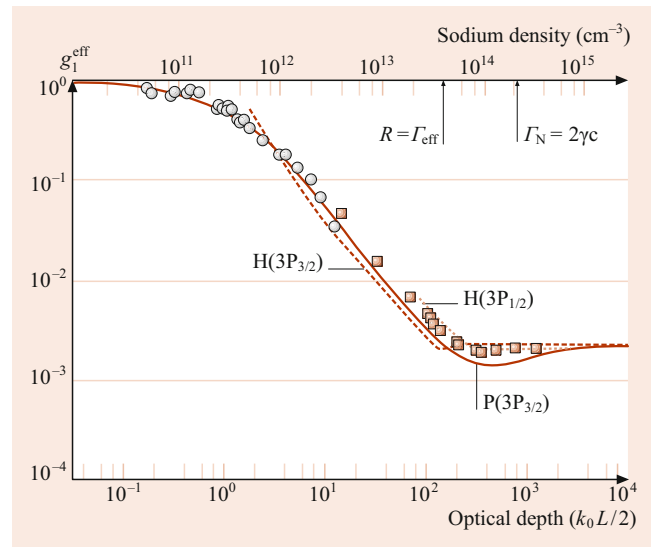


Fig. 20.8 Radiative escape probability g_1 for Na vapor excited to the $3P_{3/2}$ state, for a slab geometry. The Holstein (H) approximation for the $3P_{3/2}-3S_{1/2}$ (D2) line and the $3P_{1/2}-3S_{1/2}$ (D1) line are indicated as *dashed lines*. The Post-type (P) calculation of [80] for the D2 line is indicated as a *solid line*. *Solid squares* are data from [66], and *open circles* are data from [65]. The effective escape probability corresponds to the D2 line rate at low densities but a combination of D1 and D2 at high densities

the Post theory converges to the Holstein–Lorentzian-line result with $\Gamma_{\text{Total}} = 2\gamma_c$.

The experiment is complicated in the $50 < k_0L/2 < 500$ region by fine structure mixing [66]. The $3P_{3/2}$ state was excited, but at high densities, collisions populate the $3P_{1/2}$ state, which has a smaller g_1 than the $3P_{3/2}$ state (Fig. 20.8). At low densities, $g_1^{\text{eff}} = g_1(3P_{3/2})$, and at high densities these states are statistically populated and $g_1^{\text{eff}} = \frac{1}{3}g_1(3P_{1/2}) + \frac{2}{3}g_1(3P_{3/2})$. The transition density where the fine structure mixing rate R equals Γ_{eff} is indicated in Fig. 20.8. The theory is also complicated in this intermediate k_0L region by the necessity of including incomplete frequency redistribution [62]; this leads to the dip in g_1 near $k_0L \approx 500$. While the overall behavior of the data in Fig. 20.8 is consistent with the Post et al. theory, there is $\approx 30\%$ systematic discrepancy at $k_0L/2 = 10-100$ and the dip near 500 is not seen. Part of this difference probably results from the experimental geometry, which was between a slab and a cylinder of radius $R = L/2$; g_1 for the cylinder is 17% larger than the slab value used in Fig. 20.8.

The fundamental mode decay rate has also been measured for the Hg 254 nm [68] and 185 nm [62] lines, for the Ne resonance line [69] and for the Ar resonance line [70]. The Hg measurements are complicated by multiple isotopes and hyperfine structure, producing a mixture of partially overlapping and isolated lines combined with density-dependent uncertainties in excited state populations of the various isotopes. Serious efforts to model and measure these effects

have been made [62, 64, 68, 71]. The Ne and Ar measurements have similar complications, as will now be discussed.

In essence, g_1 behaves like the Gaussian $T(x = L/2)$ in Fig. 20.7 until n is large enough for ω_1 to approach the collision induced Lorentzian wing of the Voigt line. g_1 then decreases more slowly since the line wing does not fall off as rapidly as a Gaussian. With continued increase in n , ω_1 moves further into the Lorentzian wing, a broader spectral region escapes and g_1 reaches a minimum. Finally, when the entire escaping spectral region is Lorentzian, g_1 reaches the constant value described above. Independent and detailed treatments of this density region, including incomplete frequency redistribution, predict a dip in g_1 as seen in Fig. 20.8 [62, 70, 72, 73]. However, this has not been clearly confirmed experimentally. In Fig. 20.8 this dip occurs where fine structure mixing also occurs, and in addition the data are higher than the calculations throughout this n region. Post et al. [62] did observe such a dip for the Hg (149 nm) resonance line, but the data do not fit the calculation at other densities; hyperfine and isotopic structure within the line cause major complications. This long-standing issue has finally been clarified by *Menningen* and *Lawler* [74], who measured the decay of the Hg (185 nm) resonance line following laser excitation. They observed a clear dip in g_1 due to incomplete redistribution. They also carried out sophisticated Monte Carlo simulations, obtaining g_1 values that compared favorably with the measurements. By extending the simulations over a large range of a parameter space, they constructed an analytic formula for g_1 of a single-component line in cylindrical geometry [75]. This formula includes effects of incomplete frequency redistribution and varying ratios of Doppler broadening, radiative broadening and collisional broadening, so that it can be applied to any resonance line. *Payne* et al. [70] did not observe the predicted dip for the Ar resonance line; again a minor isotope with an isolated line occurs and could be very important at these high optical depths. *Phelps* [69] reported such a dip for the Ne 74.3 nm resonance line, but with rather large uncertainties due to the necessity of correcting for other collisional effects. Again there are isotopes with isolated lines that may have affected the data. Thus, experiments have verified the essential aspects of the above theories, but quantitative agreement in all aspects has not yet been achieved.

The fact that the escaping radiation is concentrated in the wings of the line, near the unity optical depth point ω_1 , is reflected in the emitted spectrum. Calculated examples are shown in [73]; the Gaussian case looks somewhat like the transmitted spectra in Fig. 20.6 for $x \approx L/4$. These spectra, and all results described so far, are calculated assuming no motion of the atoms. This is appropriate in the central region of the vapor, because the distance moved in an excited state lifetime ($L_v = v/\Gamma$) is much smaller than L . In fact, resonant collisions between excited and ground state

atoms further limits the distance an excited atom moves in one direction before transfer of excitation. However, near the window or wall of the container, atomic motion will cause wall collisions of excited atoms and loss of radiation. This loss will be primarily within the Doppler core of the line, since these frequencies can only escape if emitted near the vapor edge. This loss depends on the excited state density in the neighborhood of the wall, and can be significant if $L_v > 1/k_0$. The excited atom density near the wall must be self consistent with the radiation transport and wall quenching. This situation has been modeled and studied experimentally ([76] and references therein).

Additional aspects of radiation trapping, such as higher-order spatial modes and non-uniform absorber distributions, can be significant in lighting plasmas (and trapped atom clouds). Propagator function techniques have been developed for modeling radiation transport when the excitation has unusual temporal or spatial character [77, 78]. Non-uniform absorber spatial distributions can be particularly important at high power densities, and have been considered in [79].

References

1. Lorentz, H.A.: Proc. Amst. Akad. **8**, 591 (1906)
2. Weisskopf, V.: Phys. Z. **34**, 1 (1933)
3. Holtsmark, J.: Ann. Phys. (Leipzig) **58**, 577 (1919)
4. Kuhn, H.G.: Philos. Mag. **18**, 987 (1934)
5. Margenau, H., Watson, W.W.: Rev. Mod. Phys. **8**, 22 (1936)
6. Jablonski, A.: Z. Phys. **70**, 723 (1931)
7. Jablonski, A.: Acta Phys. Polon. **27**, 49 (1965)
8. Lindholm, E.: Ark. Mat. Astr. Fys. **32**, 1 (1945)
9. Foley, H.M.: Phys. Rev. **69**, 616 (1946)
10. Foley, H.M.: Phys. Rev. **73**, 259 (1948)
11. Holstein, T.: Phys. Rev. **79**, 744 (1950)
12. Anderson, P.W.: Phys. Rev. **76**, 647 (1949)
13. Anderson, P.W.: Phys. Rev. **86**, 809 (1952)
14. Baranger, M.: Phys. Rev. **112**, 855 (1958)
15. Chen, S.-Y., Takeo, M.: Rev. Mod. Phys. **29**, 20 (1957)
16. Allard, N., Kielkopf, J.: Rev. Mod. Phys. **54**, 1103 (1982)
17. Griem, H.: Plasma Spectroscopy. McGraw-Hill, New York (1964)
18. Griem, H.: Spectral Line Broadening by Plasmas. Academic Press, New York (1974)
19. Jeffries, J.: Spectral Line Formation. Blaisdell, Waltham (1968)
20. Mihalas, D.: Stellar Atmospheres. Freeman, San Francisco (1970)
21. van Kranendonk, J.: Can. J. Phys. **46**, 1173 (1968)
22. Cooper, J.: Rep. Prog. Phys. **29**, 35 (1966)
23. Simons, J.: Energetic Principles of Chemical Reactions. Jones Bartlett, Boston (1983)
24. Szudy, J., Baylis, W.E.: J. Quant. Spectrosc. Radiat. Trans. **17**, 681 (1977)
25. Walkup, R.E., Spielfiedel, A., Pritchard, D.E.: Phys. Rev. Lett. **45**, 986 (1980)
26. Ward, J., Cooper, J., Smith, E.W.: J. Quant. Spectrosc. Radiat. Trans. **14**, 555 (1974)
27. McCartan, D.G., Lwin, N.: J. Phys. B **10**, 17 (1977)
28. Stacey, D.N., Thompson, R.C.: Acta Phys. Polon. A **54**, 833 (1978)
29. Ottinger, C., Scheps, R., York, G.W., Gallagher, A.: Phys. Rev. A **11**, 1815 (1975)

30. O'Callaghan, M.J., Cooper, J.: *Phys. Rev. A* **39**, 6206 (1989)
31. Stoicheff, B.P., Weinberger, E.: *Phys. Rev. Lett.* **44**, 733 (1980)
32. Weber, K.H., Niemax, K.: *Z. Phys. A* **307**, 13 (1982)
33. Fuhr, J.R., Lesage, A.: *Bibliography of Atomic Line Shapes and Shifts*. NIST Special Publication 366. U.S. Government Printing Office, Washington (1993). Suppl. 4
34. Szudy, J., Baylis, W.E.: *J. Quant. Spectrosc. Radiat. Trans.* **15**, 641 (1975)
35. Stacey, D.N., Cooper, J.: *J. Quant. Spectrosc. Radiat. Trans.* **11**, 1271 (1971)
36. Pascale, J., Vandeplanque, J.: *J. Chem. Phys.* **60**, 2278 (1974)
37. Drummond, D., Gallagher, A.: *J. Chem. Phys.* **60**, 3426 (1974)
38. Sando, K.M., Wormhoudt, J.: *Phys. Rev. A* **7**, 1889 (1973)
39. Carrington, C.G., Gallagher, A.: *Phys. Rev. A* **10**, 1464 (1974)
40. Lam, L.K., Hessel, M.M., Gallagher, A.: *J. Chem. Phys.* **66**, 3550 (1977)
41. Tam, A., Moe, G., Park, W., Happer, W.: *Phys. Rev. Lett.* **35**, 85 (1975)
42. Holstein, T., Gallagher, A.: *Phys. Rev. A* **16**, 2413 (1977)
43. Carlston, J.L., Szoke, A.: *J. Phys. B* **9**, L231 (1976)
44. Omont, A.: *Prog. Quantum Electron.* **5**, 69 (1977)
45. Light, J., Szoke, A.: *Phys. Rev. A* **15**, 1029 (1977)
46. Burnett, K., Cooper, J., Ballagh, R.J., Smith, E.W.: *Phys. Rev. A* **22**, 2005 (1980)
47. Streater, A., Cooper, J., Sandle, W.J.: *J. Quant. Spectrosc. Radiat. Trans.* **37**, 151 (1987)
48. Tellinghausen, J.: *J. Mol. Spectrosc.* **103**, 455 (1984)
49. Mies, F.H.: *J. Chem. Phys.* **48**, 482 (1968)
50. Carrington, C.G., Drummond, D., Phelps, A.V., Gallagher, A.: *Chem. Phys. Lett.* **22**, 511 (1973)
51. Biberman, L.M.: *J. Exp. Theor. Phys. U. S. S. R.* **17**, 416 (1947)
52. Biberman, L.M.: *J. Exp. Theor. Phys. U. S. S. R.* **59**, 659 (1948)
53. Holstein, T.: *Phys. Rev.* **72**, 1212 (1947)
54. Holstein, T.: *Phys. Rev.* **83**, 1159 (1951)
55. Fioretti, A., Molisch, A.F., Müller, J.H., Verkerk, P., Allegrini, M.: *Opt. Commun.* **149**, 415 (1998)
56. Molisch, A.F., Oehry, B.P.: *Radiation Trapping in Atomic Vapours*. Clarendon, Oxford (1998)
57. van Trigt, C.: *Phys. Rev.* **181**, 97 (1969)
58. van Trigt, C.: *Phys. Rev. A* **4**, 1303 (1971)
59. van Trigt, C.: *Phys. Rev.* **13**, 726 (1976)
60. Carrington, C.G., Stacey, D.N., Cooper, J.: *J. Phys. B* **6**, 417 (1973)
61. Huennekens, J., Park, H.J., Colbert, T., McClain, S.C.: *Phys. Rev.* **35**, 2892 (1987)
62. Post, H.A., van de Weijer, P., Cremers, R.M.M.: *Phys. Rev. A* **33**, 2003 (1986)
63. Holstein, T.: *Phys. Rev.* **83**, 1159 (1951)
64. Walsh, P.J.: *Phys. Rev.* **116**, 511 (1959)
65. Colbert, T., Huennekens, J.: *Phys. Rev.* **41**, 6145 (1990)
66. Huennekens, J., Gallagher, A.: *Phys. Rev. A* **28**, 238 (1983)
67. Milne, E.: *J. Math. Soc. (London)* **1**, 40 (1926)
68. Holstein, T., Alpert, D., McCoubrey, A.O.: *Phys. Rev.* **85**, 985 (1952)
69. Phelps, A.V.: *Phys. Rev.* **114**, 1011 (1959)
70. Payne, M.G., Talmage, J.E., Hurst, G.S., Wagner, E.B.: *Phys. Rev. A* **9**, 1050 (1974)
71. Anderson, J.B., Maya, J., Grossman, M.W., Lagushenko, R., Weymouth, J.F.: *Phys. Rev. A* **3**, 2986 (1985)
72. Parker, G.J., Hitchon, W.N.G., Lawler, J.E.: *J. Phys. B* **26**, 4643 (1993)
73. van Trigt, C.: *Phys. Rev. A* **1**, 1298 (1970)
74. Menningen, K.L., Lawler, J.E.: *J. Appl. Phys.* **88**, 3190 (2000)
75. Lawler, J.E., Curry, J.J., Lister, G.G.: *J. Phys. D* **33**, 252 (2000)
76. Zajonc, A., Phelps, A.V.: *Phys. Rev. A* **23**, 2479 (1981)
77. Lawler, J.E., Parker, G.J., Hitchon, W.N.G.: *J. Quant. Spectrosc. Radiat. Trans.* **49**, 627 (1993)
78. Parker, G.J., Hitchon, W.N.G., Lawler, J.E.: *J. Phys. B* **26**, 4643 (1993)
79. Curry, J.J., Lawler, J.E., Lister, G.G.: *J. Appl. Phys.* **86**, 731 (1999)
80. Huennekens, J., Colbert, T.: *J. Quant. Spectrosc. Radiat. Trans.* **41**, 439 (1989)



Thomas-Fermi and Other Density-Functional Theories

21

John D. Morgan III

Contents

21.1	Introduction	297
21.2	Thomas–Fermi Theory and Its Extensions	298
21.2.1	Thomas–Fermi Theory	298
21.2.2	Thomas–Fermi–von Weizsäcker Theory	300
21.2.3	Thomas–Fermi–Dirac Theory	301
21.2.4	Thomas–Fermi–von Weizsäcker–Dirac Theory	301
21.2.5	Thomas–Fermi Theory with Different Spin Densities	301
21.3	Nonrelativistic Energies of Heavy Atoms	302
21.4	General Density Functional Theory	302
21.4.1	The Hohenberg–Kohn Theorem for the One-Electron Density	302
21.4.2	The Kohn–Sham Method for Including Exchange and Correlation Corrections	303
21.4.3	Density Functional Theory for Excited States	304
21.4.4	Locality of Density Functional Theory	304
21.4.5	Relativistic and Quantum Field Theoretic Density Functional Theory	304
21.5	Recent Developments	304
	References	306

Abstract

The key idea in Thomas–Fermi theory and its generalizations is the replacement of complicated terms in the kinetic energy and electron–electron repulsion energy contributions to the total energy by relatively simple functionals of the electron density ρ . This chapter first describes Thomas–Fermi theory and then its various generalizations that attempt to correct, with varying success, some of its deficiencies. It concludes with an overview of the Hohenberg–Kohn and Kohn–Sham density functional theories.

Keywords

density functional theory · neutral atom · external potential · electronic probability density · Scott correction

21.1 Introduction

In the early years of quantum physics, *Thomas* [1] and *Fermi* [2–5] independently invented a simplified theory, subsequently known as *Thomas–Fermi theory*, to describe nonrelativistically an atom or atomic ion with a large nuclear charge Z and a large number of electrons N . Many qualitative features of this model can be studied analytically, and the precise solution can be found by solving numerically a nonlinear ordinary differential equation. *Lenz* [6] demonstrated that this equation for the electrostatic potential could be derived from a variational expression for the energy as a functional of the electron density. Refinements to Thomas–Fermi theory include a term in the energy functional to account for electron exchange effects introduced by *Dirac* [7] and nonlocal gradient corrections to the kinetic energy introduced by *von Weizsäcker* [8].

Although the Hartree–Fock method or other more elaborate techniques for calculating electronic structure now provide much more accurate results (Chaps. 22–24), Thomas–Fermi theory provides quick estimates and global insight into the total energy and other properties of a heavy atom or ion. A rigorous analysis of Thomas–Fermi theory by *Lieb* and *Simon* [9, 10] showed that it is asymptotically exact in that it yields the correct leading asymptotic behavior, for both the total nonrelativistic energy and the electronic density, in the limit as both Z and N tend to infinity, with the ratio Z/N fixed. (In a real atom, of course, relativistic and other effects become increasingly important as Z increases.) However, Thomas–Fermi theory has the property that molecules do not bind, as first noted by *Sheldon* [11] and proved by

J. D. Morgan III (✉)
Dept. of Physics & Astronomy, University of Delaware
Newark, DE, USA
e-mail: jdmorgan@udel.edu

Teller [12]. That the interatomic potential energy curve for a homonuclear diatomic molecule is purely repulsive was demonstrated by Balázs [13].

This *no binding* property of clusters of atoms was used by Lieb and Thirring [14] to prove the *stability of matter*, in the sense that as the number of particles increases, the total nonrelativistic energy decreases only linearly rather than as a higher power of the number of particles, as it would if electrons were bosons rather than fermions. Lieb went on to explore the mathematical structure of the modifications of the Thomas–Fermi model when gradient terms (von Weizsäcker) and/or exchange (Dirac) terms are included [15, 16]. A review article by Spruch [17] explicates the linkage between long-developed physical intuition and the mathematically rigorous results obtained in the 1970s and 1980s. The older literature was reviewed by Gombás [18, 19] and by March [20].

An outgrowth of Thomas–Fermi theory is the general density functional theory initiated by Hohenberg and Kohn [21] and by Kohn and Sham [22], as discussed in Sect. 21.4.

21.2 Thomas–Fermi Theory and Its Extensions

21.2.1 Thomas–Fermi Theory

In a D -dimensional Euclidean space, the expectation value of the electronic kinetic energy operator in a quantum state ψ can be approximated by

$$\frac{\hbar^2}{m_e} 2\pi^2 \frac{D}{D+2} \left(\frac{D}{2\Omega_D} \right)^{2/D} \int \rho^{(D+2)/D}(\mathbf{r}) d^D r, \quad (21.1)$$

where

$$\Omega_D = \frac{D\pi^{D/2}}{\Gamma(1 + \frac{D}{2})} \quad (21.2)$$

is the surface area of a unit hypersphere in D dimensions [17, p. 176]. These expressions can easily be derived by considering the energy levels of a system of a large number of noninteracting fermions confined to a D -dimensional box. Specialization to the physically interesting case of $D = 3$ yields the well-known expression

$$\frac{\hbar^2}{m_e} 2\pi^2 \frac{3}{5} \left(\frac{3}{2\Omega_3} \right)^{2/3} \int \rho^{5/3}(\mathbf{r}) d\mathbf{r}, \quad (21.3)$$

where

$$\Omega_3 = \frac{3\pi^{3/2}}{\Gamma(1 + \frac{3}{2})} = 4\pi. \quad (21.4)$$

The electron–nucleus attraction energy in a three-dimensional space is given exactly by

$$\int \rho(\mathbf{r}) V(\mathbf{r}) d\mathbf{r}, \quad (21.5)$$

where $V(\mathbf{r})$ is the Coulomb potential due to a single nucleus [$V(\mathbf{r}) = -Z/r$] or several nuclei [$V(\mathbf{r}) = -\sum_i Z_i/|\mathbf{r} - \mathbf{R}_i|$]. The electron–electron Coulomb repulsion energy in a three-dimensional space is approximated by

$$U[\rho] = \frac{1}{2} \int \frac{\rho(\mathbf{r})\rho(\mathbf{r}')}{|\mathbf{r} - \mathbf{r}'|} d\mathbf{r} d\mathbf{r}', \quad (21.6)$$

which tends to overestimate the actual repulsion energy because it includes the self-energy of the densities of individual electrons. This is, however, a higher-order effect for a system with a large number of electrons concentrated in a small region of space. As was suggested by Fermi and Amaldi [23], this overestimation can be approximately corrected for an atom with N electrons by multiplying this term by the ratio of the number of ordered pairs of different electrons to the total number of ordered pairs

$$\frac{N(N-1)}{N^2} = 1 - \frac{1}{N}. \quad (21.7)$$

This is approximately correct for an atom, with many electrons concentrated close together, but it would still be an overestimate for a diffuse system, such as one composed of N electrons and N protons separated by large distances of $O(R)$, for which the ground-state electron–electron repulsion term should be proportional to $\frac{1}{2}N(N-1)/R$ rather than to N times a constant of $O(1)$. For this reason, the Fermi–Amaldi correction, which complicates the mathematical analysis without eliminating the unphysical overestimation of the electron–electron repulsion term, is not usually included. It is evident that the treatment of both the electronic kinetic energy term and the electron–electron repulsion energy term depends on the assumption that the number N of electrons (actually, the number of electrons *per atom*) is large. Hence, the Thomas–Fermi model is sometimes called the *statistical model* of an atom.

The three contributions to the total energy are now added together, and one seeks to minimize their sum, the Lenz functional [6]

$$E[\rho] = \frac{\hbar^2}{m_e} 2\pi^2 \frac{3}{5} \left(\frac{3}{2\Omega_3} \right)^{2/3} \int \rho^{5/3}(\mathbf{r}) d\mathbf{r} + \int \rho(\mathbf{r}) V(\mathbf{r}) d\mathbf{r} + \frac{1}{2} \int \frac{\rho(\mathbf{r})\rho(\mathbf{r}')}{|\mathbf{r} - \mathbf{r}'|} d\mathbf{r} d\mathbf{r}', \quad (21.8)$$

over all admissible densities ρ . The mathematical question now arises: what is an admissible density? The answer was provided by Lieb and Simon [9, 10]: a density for which both

$$\int \rho(\mathbf{r}) d\mathbf{r}, \quad (21.9)$$

the total number of electrons, and

$$\int \rho^{5/3}(\mathbf{r}) d\mathbf{r}, \quad (21.10)$$

which is proportional to the estimate of their kinetic energy, are finite, automatically yields finite values of the other terms in the expression for the energy. As Lieb and Simon proved, the minimization of this functional over all such densities yields a well-determined result.

Carrying out the variation of $E[\rho]$ with respect to ρ yields the Euler–Lagrange equation

$$0 = \frac{\hbar^2}{m_e} 2\pi^2 \left(\frac{3}{2\Omega_3} \right)^{2/3} \rho^{2/3}(\mathbf{r}) + V(\mathbf{r}) + \int \frac{\rho(\mathbf{r}')}{|\mathbf{r} - \mathbf{r}'|} d\mathbf{r}' . \quad (21.11)$$

The sum of the last two terms is, of course, the negative of the total electrostatic potential $\phi(\mathbf{r})$, so one sees that in Thomas–Fermi theory, the density is proportional to the 3/2-power of the potential. To simplify subsequent manipulations, let

$$\frac{\hbar^2}{m_e} 2\pi^2 \left(\frac{3}{2\Omega_3} \right)^{2/3} = \frac{\hbar^2}{2m_e} (3\pi^2)^{2/3} = \gamma_p , \quad (21.12)$$

so that

$$\gamma_p \rho^{2/3}(\mathbf{r}) = \phi(\mathbf{r}) . \quad (21.13)$$

By Poisson’s theorem,

$$-\nabla^2 \phi = 4\pi \left[\sum_i Z_i \delta^{(3)}(\mathbf{r} - \mathbf{R}_i) - \rho(\mathbf{r}) \right] , \quad (21.14)$$

and from Eq. (21.13) one has $\rho = \gamma_p^{-3/2} \phi^{3/2}$, so from the integral equation for the electronic density ρ , one obtains the differential equation

$$-\nabla^2 \phi = 4\pi \left[\sum_i Z_i \delta^{(3)}(\mathbf{r} - \mathbf{R}_i) - \gamma_p^{-3/2} \phi^{3/2} \right] , \quad (21.15)$$

for the potential ϕ . In the case of a single nucleus, the usual separation of variables in spherical polar coordinates yields for ϕ the ordinary differential equation

$$\frac{1}{r} \frac{d^2}{dr^2} (r\phi) = 4\pi \gamma_p^{-3/2} \phi^{3/2} , \quad (21.16)$$

whose similarity to Emden’s equation, which Eddington used to study the internal constitution of stars, was recognized by Milne [24]. The numerical solution of this equation with the appropriate boundary conditions at $r = 0$ and $r = \infty$ was discussed extensively by Baker [25], and accurate solutions tabulated by Tal and Levy [26]. The numerical solution determines that the total energy of a neutral atom is

$$E = -3.67874521\dots \gamma_p^{-1} Z^{7/3} \\ = -1.53749024\dots Z^{7/3} \text{Ry} . \quad (21.17)$$

Another possibility is to do the constrained minimization over all densities that obey

$$\int \rho(\mathbf{r}) d\mathbf{r} = \lambda , \quad (21.18)$$

where λ is the number of electrons, which for purposes of mathematical analysis is allowed to be nonintegral. One then introduces a Lagrange multiplier $-\mu$, the *chemical potential*, to correspond with this constraint, and thereby obtains the Euler–Lagrange equation

$$0 = \frac{\hbar^2}{m_e} 2\pi^2 \left(\frac{3}{2\Omega_3} \right)^{2/3} \rho^{2/3}(\mathbf{r}) + V(\mathbf{r}) + \int \frac{\rho(\mathbf{r}')}{|\mathbf{r} - \mathbf{r}'|} d\mathbf{r}' + \mu , \quad (21.19)$$

which holds wherever ρ is positive. As was shown by Lieb and Simon [9, 10], this procedure, too, is well defined. The analogue of Eq. (21.13), the relationship between the density and the electrostatic potential for the neutral atom, is now

$$\gamma_p \rho^{2/3}(\mathbf{r}) = [\phi(\mathbf{r}) - \mu]_+ , \quad (21.20)$$

where $[f]_+ = \max(f, 0)$. The corresponding differential equation for the potential ϕ is

$$-\nabla^2 \phi = 4\pi \left[\sum_i Z_i \delta^{(3)}(\mathbf{r} - \mathbf{R}_i) - \gamma_p^{-3/2} [\phi(\mathbf{r}) - \mu]_+^{3/2} \right] . \quad (21.21)$$

Lieb and Simon rigorously proved a large number of results concerning the solution of the Thomas–Fermi model. When $V(\mathbf{r})$ is a sum of Coulomb potentials arising from a set of nuclei of positive charges Z_i , with $\sum_i Z_i = Z$, then the energy $E(\lambda)$ is a continuous, monotonically decreasing function of λ for $0 \leq \lambda \leq Z$, and its derivative $dE/d\lambda$ is the chemical potential $-\mu(\lambda)$, which vanishes at $\lambda = Z$. For λ in this range, there is a unique minimizing density ρ , whereas for $\lambda > Z$ there is no unique minimizing ρ , since one can place arbitrarily large clumps of charge with arbitrarily low positive energies arbitrarily far away from the nuclei. In the atomic case, with a single nucleus, $\rho(\mathbf{r})$ is a spherically symmetric monotonically decreasing function of r .

Moreover, for an atom or atomic ion, the Thomas–Fermi density obeys the *virial theorem*

$$2\langle \mathcal{T} \rangle = -\langle V \rangle = -2E , \quad (21.22)$$

and for a neutral atom the electronic kinetic energy, electron–nucleus attraction energy, and electron–electron repulsion

energy terms in the expression for the total energy satisfy the ratios 3 : -7 : 1.

It is straightforward to examine the behavior of the Thomas–Fermi density ρ in the limit as either $r \rightarrow 0$ or $r \rightarrow \infty$. For large r , the electron density vanishes identically outside a sphere of finite radius for a positive ion. For a neutral atom, the ordinary differential equation (21.16) for the potential ϕ can be analyzed to show that

$$\phi(r) \simeq \gamma_p \left(\frac{3\gamma_p}{\pi} \right)^2 r^{-4}, \quad (21.23)$$

from which it follows that

$$\rho(r) \simeq \left(\frac{3\gamma_p}{\pi} \right)^3 r^{-6}, \quad (21.24)$$

independent of Z . This implies that as $Z \rightarrow \infty$, a neutral atom described by the Thomas–Fermi model has a finite size defined in terms of a radius within which all but a fixed amount of electronic probability density is located. For example, if one defines the size of an atom as that value of r_a for which

$$\int_{|r| \geq r_a} \rho(\mathbf{r}) d\mathbf{r} = \frac{1}{2}, \quad (21.25)$$

one finds that in the large- Z limit

$$r_a = \left(\frac{8\pi}{3} \right)^{1/3} \frac{3\gamma_p}{\pi}. \quad (21.26)$$

In atomic units, $\gamma_p = \frac{1}{2}(3\pi^2)^{2/3}$, and

$$r_a = (9\pi)^{2/3} a_0 \simeq 9.3 a_0, \quad (21.27)$$

which is about what one would expect for a *real* nonrelativistic atom with a large nuclear charge Z . On the other hand, the characteristic distance scale in Thomas–Fermi theory, defined as the *average* value of r , or in terms of a radius within which a fixed *fraction* of electronic probability density is located, is proportional to $Z^{-1/3}$, which shrinks to 0 as $Z \rightarrow \infty$. The resolution of this paradox is that outside the typical *core* scale of distance set by $Z^{-1/3}$, within which most of the electron density is located, there resides in the *mantle* region a fraction of electrons proportional to $Z^{2/3}/Z = Z^{-1/3}$, and almost all of these are concentrated within a sphere of radius of about $10 a_0$.

Moving deeper into the core and approaching the nucleus, the $-Z/r$ singularity in the electron–nucleus Coulomb potential dominates the smeared-out electron–electron potential, so one readily finds that

$$\rho(r) \simeq \left(\frac{Z}{\gamma_p r} \right)^{3/2}. \quad (21.28)$$

This singularity is integrable but unphysical, since it arises from the approximation of the local kinetic energy by $\rho^{5/3}$, which breaks down where ρ is rapidly varying on a length scale proportional to $1/Z$. In a *real* nonrelativistic heavy atom governed by the Schrödinger equation, the actual electron density at the nucleus is finite, being proportional to Z^3 . This unphysical singularity in the electron density in Thomas–Fermi theory can be eliminated by adding a gradient correction to the Thomas–Fermi kinetic energy term, as discussed in the following section.

21.2.2 Thomas–Fermi–von Weizsäcker Theory

The semiclassical approximation Eq. (21.3) for the quantum kinetic energy in terms of a power of the density is capable of improvement, particularly in regions of space where the density is rapidly varying. The incorporation of such corrections leads to a gradient expansion for the kinetic energy [27]. The leading correction is of the form

$$\frac{\hbar^2}{2m} \int |(\nabla \rho^{1/2})(\mathbf{r})|^2 d\mathbf{r}. \quad (21.29)$$

Addition of such a term to the Thomas–Fermi expression for the kinetic energy yields a theory that avoids many of the unphysical features of ordinary Thomas–Fermi theory at very short and moderately large distances. The more important points, as rigorously proved in Lieb’s review article [15, 16], are as follows. The leading features of the energy are unchanged; for large Z , the energy $E(Z)$ of a neutral atom or atomic ion is still proportional to $Z^{7/3}$, but now there enter higher-order corrections arising from the gradient terms of order $Z^{7/3}Z^{-1/3} = Z^2$ and higher powers of $Z^{-1/3}$. The maximum number of electrons that can be bound by an atom of nuclear charge Z is no longer exactly Z , but a slightly larger number; thus, Thomas–Fermi–von Weizsäcker theory allows for the formation of negatively charged atomic ions. It was further proven by *Benguria* and *Lieb* [28] that in the Thomas–Fermi–von Weizsäcker model a neutral atom can bind at most one extra electron, and that a neutral molecule can bind at most as many extra electrons as it has nuclei.

The effect on the electronic density ρ is more profound. While the general shape and properties of ρ in the *core* and *mantle* regions is unchanged, the fact that $\nabla \rho^{1/2}$ need not, and in general does not, vanish when ρ vanishes on some surface implies that for a positive ion ρ no longer vanishes outside of a sphere, as it does in the case of Thomas–Fermi theory, but instead extends over all space. For positive ions, neutral atoms, and negative ions alike, *differential inequality* techniques [29] can be used to show that $\rho(r)$ decays exponentially for large r , with the constant in the exponential proportional to $(\mu(\lambda))^{1/2}$. For small r , the gradient terms

dominate the energy expression, so one finds that the electronic density no longer diverges as $r \rightarrow 0$, but instead tends to a finite limit, with a first derivative that obeys a relation analogous to the Kato cusp condition [30]

The study of molecules within the Thomas–Fermi–von Weizsäcker model involves several subtleties and pitfalls, which can lead to physical absurdities. Since two neutral atoms with different nuclear charges will, in general, have different chemical potentials, a pair of such atoms placed a long distance apart will *spontaneously ionize*, with a small amount of electric charge being transferred from one to the other until the chemical potentials of the positively charged ion and the negatively charged ion become equal. The result is a long-range Coulomb attraction between them [31]. This phenomenon does *not* occur in the real world, since the amount of electric charge that can be transferred is quantized in units of $-e$, and it is empirically true that the smallest atomic ionization potential exceeds the largest atomic electron affinity. For two neutral atoms with the same nuclear charges, the situation is more subtle. Nonetheless, a careful analysis shows that in this case, too, although no spontaneous ionization occurs, there is a long-range attractive interaction between them arising from the overlap of the exponentially small tails of the electron clouds. Since electron correlation is not included in this model, it could not be expected to describe attractive van der Waals forces.

In summary, the Thomas–Fermi–von Weizsäcker model yields a more realistic picture of a single atom than does the Thomas–Fermi model. However, it does not provide a useful picture for understanding the interaction between atoms at large distances. These kinds of unphysical features provide a glimpse into the complicated nature of the universal density functional, which must include terms that rigorously suppress an unphysical feature like spontaneous ionization of a distant pair of heteronuclear atoms [32, 33]. It is evident from the mathematical properties of Thomas–Fermi–von Weizsäcker theory and related models that a density functional that fixes up the Thomas–Fermi expression simply by adding a few gradient terms and/or simple exchange terms and the like must still differ in important ways from the universal density functional, particularly for properties of extended systems.

21.2.3 Thomas–Fermi–Dirac Theory

The effect of the exchange of electrons can be approximated, following Dirac [7], by including in the Thomas–Fermi energy functional an expression of the form

$$-\frac{1}{4\pi^3}(3\pi^2)^{4/3} \int \rho^{4/3}(\mathbf{r})d\mathbf{r} . \quad (21.30)$$

Minimization of the resulting Thomas–Fermi–Dirac energy functional over all admissible densities ρ whose integral is λ yields a well-defined $E(\lambda)$, which has the correct behavior for $\lambda \leq Z$, and it has been shown that for an atom, the exchange correction to the energy is of order $Z^{5/3}$. However, this model exhibits unphysical behavior for $\lambda > Z$, because one can obtain a completely artificial lowering of the energy by placing many small clumps of electrons a large distance from the nucleus, for which the negative $\int \rho^{4/3}d\mathbf{r}$ term dominates the energy expression [15, 16]. At the conclusion of his original article, Dirac clearly stated that the correction he had derived, although giving a better approximation in the interior of an atom, gives a *meaningless result for the outside of the atom* [7]. It is, therefore, clear that any physically reasonable theory must somehow profoundly modify this correction in the region where the electronic density is very small.

21.2.4 Thomas–Fermi–von Weizsäcker–Dirac Theory

One can also include the Dirac exchange correction in the Thomas–Fermi–von Weizsäcker energy functional. In this case, however, the mathematical foundations of the theory are still incomplete ([15, 16, pp. 638–639]). Nonetheless, it is clear that this theory, too, suffers from the unphysical lowering of the energy by small clumps of electrons at large distances from the nucleus.

In summary, one can say that the inclusion of Dirac’s exchange correction in its most straightforward form leads to an improvement of energies for positive ions or neutral atoms but to unphysical behavior for systems where the charge of the electrons exceeds the nuclear charge, in line with Dirac’s own observations on the limitations of his correction [7]. Here, we again see a manifestation of how complicated the behavior of the true universal density functional must be.

21.2.5 Thomas–Fermi Theory with Different Spin Densities

As was remarked by Lieb and Simon [10], it is possible to consider a variant of Thomas–Fermi theory with a pair of spin densities ρ_α and ρ_β for the spin-up and spin-down electrons, with the two adding together to produce the total electronic density ρ . This theory was rigorously formulated and analyzed by Goldstein and Rieder [34]. Because the problem is nonlinear, the mathematical complications are substantial, and the theory is not a trivial extension of ordinary Thomas–Fermi theory. Goldstein and Rieder first considered the case where the total number of electrons of each type of spin is specified in advance [35]. There is no mathematical obstacle to constructing such a spin-

polarized Thomas–Fermi theory, but it does not yield the kind of spontaneous spin-polarization that one observes in the ground states of many real quantum mechanical atoms and molecules, which is not surprising in view of the fact that such spin-polarization in accord with Hund’s first rule arises from exchange and correlation effects not included in this simple functional. However, in the case where the electronic spins (but *not* their currents) are coupled to an external magnetic field, the ground state is naturally spin-polarized [34].

21.3 Nonrelativistic Energies of Heavy Atoms

Thomas–Fermi theory suggests that Eq. (21.17) provides the leading term in a power series expansion for the nonrelativistic energy of a neutral atom of the form

$$E(Z) = -(c_7 Z^{7/3} + c_6 Z^{6/3} + c_5 Z^{5/3} + \dots), \quad (21.31)$$

with $c_7 = 1.53749024\dots \text{Ry}$, $c_6 = -1 \text{ Ry}$, and $c_5 \simeq 0.5398 \text{ Ry}$. The c_6 term was first calculated by Scott [36] from the observation that it arises from the energy of the innermost electrons for which the electron–electron interaction can be neglected. The difference between the exact and Thomas–Fermi energies for this case of noninteracting electrons yields the correct c_6 [17, 37]. A mathematically nonrigorous but physically insightful justification of the Scott correction was provided in 1980 by Schwinger [38]. This result has now been rigorously proved, with upper and lower bounds coinciding [39–43].

The c_5 term is much more subtle, since it arises from a combination of effects from the exchange interaction and from the bulk motion of electrons in the Thomas–Fermi potential. A general analytic procedure devised by Schwinger [44] yields the above value, in good agreement with a much earlier estimate by March and Plaskett [45].

A numerical check of these results, based on a fit to Hartree–Fock calculations for Z up to 290 with correlation corrections, yielded the values [46] $c_5 = 0.55 \pm 0.02 \text{ Ry}$ and $c_4 \simeq 0$. It seems likely that, because of shell structure, the terms c_4 and beyond have an oscillatory dependence on Z [47]. The oscillatory structure and other refinements of Thomas–Fermi theory are considered in a series of papers by Englert and Schwinger [48–54] and a book by Englert [55].

Iantchenko, Lieb, and Siedentop [56] proved Lieb’s *strong Scott conjecture* that for small r , the rescaled density for the exact quantum system converges to the sum of the densities of the bound noninteracting hydrogenic orbitals; the properties of this function were explored by Heilman and Lieb [57]. Fefferman and Seco [58] rigorously proved the correctness of Schwinger’s procedure for calculating not just the $O(Z^{6/3})$ Scott correction but also the $O(Z^{5/3})$ exchange term. Their full proof includes a demonstration that the Hartree–Fock en-

ergy agrees with the exact quantum energy through $O(Z^{5/3})$, with an error of smaller order [59]. Numerous auxiliary theorems and lemmas are published in [60–63]. Progress toward obtaining higher-order oscillatory terms is described in [64–68]. The analytical evaluation of accurate approximations to the energy of a heavy atom, or at least of the contributions to that energy of all but the few outermost electronic orbitals, would be of particularly great value if it led to the construction of more accurate and better justified pseudopotentials [69–72] for describing the valence orbitals.

21.4 General Density Functional Theory

The literature on general density functional theory and its applications is enormous, so any bibliography must be selective. The reader interested in learning more could begin by consulting a number of review articles [73–79], collections of articles [80–82], conference proceedings [83–93], and the textbooks by Parr and Yang [94] and by Dreizler and Gross [95].

21.4.1 The Hohenberg–Kohn Theorem for the One-Electron Density

In 1964, Hohenberg and Kohn [21] argued that there exists a universal density functional $F[\rho]$, independent of the external potential $V(\mathbf{r})$, such that minimization of the sum

$$F[\rho] + \int \rho(\mathbf{r})V(\mathbf{r})d\mathbf{r}, \quad (21.32)$$

subject to the constraint

$$\int \rho(\mathbf{r})d\mathbf{r} = N \text{ (a positive integer)}, \quad (21.33)$$

yields the ground state energy of a quantum-mechanical N -electron system moving in this external potential. However, Hohenberg and Kohn’s theorem is like a mathematical *existence theorem*; no procedure exists to calculate this unknown universal functional explicitly, which surely is extremely complicated if it can be written down at all in closed form. (E. Bright Wilson, however, defined it, implicitly and whimsically, as follows: “Take the ground-state density and integrate it to find the total number of electrons. Find the cusps in the density to locate all nuclei, and then use the cusp condition – that the radial derivative of the density at the cusp is minus twice the nuclear charge density at each cusp – to determine the charges on each nucleus. Finally solve Schrödinger’s equation for the ground-state density or any other property that is desired” (paraphrased by B. I. Dunlap, in [89, p. 3], from J. W. D. Connolly).)

Moreover, Hohenberg and Kohn glossed over two problems: it is not clear *a priori* that every well-behaved ρ is derivable from a well-behaved properly antisymmetric many-electron wave function (the so-called *n*-representability problem, since *n* was used by Hohenberg and Kohn to represent the density of electrons), and it is also not clear *a priori* that every well-behaved density ρ can be derived from a quantum-mechanical many-electron wave function ψ , which is the properly antisymmetric ground-state wave function for a system of electrons moving in some external potential $V(\mathbf{r})$ (the so-called *v*-representability problem, since Hohenberg and Kohn used *v* in place of V).

The *n*-representability problem was solved by *Gilbert* [96] and by *Harriman* [97], who gave a prescription for starting from an arbitrary well-behaved ρ and from it constructing a many-electron wave function ψ that generated that ρ [33, 98]. The *v*-representability problem is much more formidable, as demonstrated by the discovery that there are well-behaved densities ρ that are *not* the ground-state densities for any fermionic system in an external potential V [98, 99]. Following *Percus*' definition of a universal kinetic energy functional for independent fermion systems [100], *Levy* [101] proposed to circumvent this *v*-representability problem by modifying the definition of $F[\rho]$ so that instead of being defined in terms of densities that might not be *v*-representable, it is defined as

$$F[\rho] = \min[\psi, (T + V)\psi], \quad (21.34)$$

with the minimum being taken over all properly antisymmetric normalized ψ 's that yield that ρ .

A great deal of effort has been devoted to trying to find approximate representations of the universal functional $F[\rho]$. One route is mathematical, and features a careful exploration of the abstract properties that $F[\rho]$ must have. Another route is numerical, and can be characterized as involving the guessing of some *ansatz* with a general resemblance to Thomas-Fermi-von Weizsäcker-Dirac theory, with some flexible parameters determined by least-squares fitting of the energies resulting from insertion of Hartree-Fock densities into the trial functional to theoretical Hartree-Fock energies, or the like. If, however, the basic *ansatz* exhibits unphysical features in the case of negatively charged ions or heteronuclear molecules, it is not likely that the optimization of parameters in that *ansatz* will get one closer to the true universal density functional. In the opinion of this writer, significant progress in density functional theory based solely upon the one-electron density is likely to require a major revolution in our mathematical understanding of this field, with a useful procedure made explicit for constructing progressively better approximations to the universal density functional, which, like π or other transcendental numbers, will probably never be written down exactly in closed form. Moreover, the numerical solution of the highly nonlinear Euler-Lagrange equations for

a very complicated density functional is likely to require large amounts of computer time, as well as problems with landing in local minima of the energy.

21.4.2 The Kohn-Sham Method for Including Exchange and Correlation Corrections

Density functional theory posed solely in terms of the one-electron density and based upon the Hohenberg-Kohn variational principle provides no general procedure for accurately calculating relatively small energy differences such as excitation energies, ionization potentials, electron affinities, or the binding energies of molecules. There is, however, a powerful method inspired by the Hohenberg-Kohn variational principle, which has been used with great success in the calculation of such quantities. This is the Kohn-Sham variational method [22].

The key idea in the Kohn-Sham variational method is to replace the nonlocal exchange term in the Hartree-Fock equations with an exchange-correlation potential, which, at least in principle, can be used to determine energies exactly. The oldest, simplest, and most common *ansatz* used for the exchange-correlation potential involves the local density approximation (LDA), in which one assumes that the exchange-correlation potential for the actual system under study has the same functional form as does the exchange-correlation potential for a uniform interacting gas of electrons. If the density is not too small or not too rapidly varying, the exchange part of this potential can be approximated by $\rho^{1/3}$, which appears in Dirac's first-order approximation for exchange energies, with a systematic procedure for deriving higher-order corrections in a gradient expansion. The correlation part of this potential is accurately known from *Ceperley* and *Alder*'s quantum Monte Carlo calculation of the properties of the uniform electron gas [102]. One, therefore, retains the important features of the quantum theory based on wave functions, with a determinantal approximation to ψ , while approximately including exchange and correlation effects through a simply computable effective potential. Higher corrections, which are important for quantitative accuracy, can be incorporated by taking account of the variation of ρ by means of a gradient expansion [27] involving $\nabla\rho$ and higher derivatives [95, Chap. 7], thus yielding a generalized gradient approximation (GGA) for the exchange-correlation potential.

The Kohn-Sham procedure has become the backbone for the vast majority of accurate calculations of the electronic structure of solids [78, 92]. In the 1990s, motivated by *Becke*'s work on constructing simple gradient-corrected exchange potentials [103–109], and incorporating the *Lee, Yang, and Parr* (LYP) expression for the correlation potential [110] derived from *Colle* and *Salvetti*'s correlation-energy formula [111–113], the Kohn-Sham method is find-

ing increasing application in efficiently estimating relatively small energy differences of relevance to chemistry [114–116] (However, Becke's gradient-corrected exchange potential does *not* have the correct $1/r$ behavior at large r , as was observed by several authors [117–119]). For definitive results, however, one must still resort to an *ab initio* theory that, at least in principle, converges toward the correct result.

The generation of improved generalized gradient approximations has recently become a growth industry, with increasingly many proposals of increasingly greater complexity [103, 110, 119–131]. Inevitably, some expressions work better for some properties than for others. It is found that usually most of the errors in the long-range tails of the exchange and correlation potentials tend to cancel each other, thus leading to better overall energies than one could reasonably expect [132]. Under these circumstances, it is important to have benchmarks for testing the accuracy of the various approximations. Such comparisons have been carried out for two important sets of two-electron systems [133–135]:

1. A pair of electrons moving in harmonic potential wells and coupled by the Coulomb repulsion, which yields an exactly solvable system.
2. Helium-like ions of variable nuclear charge Z , for which extremely accurate energies and wave functions are available, which take account of the behavior of the exact but unknown wave function in the vicinity of all two-particle coalescences and the three-particle coalescence.

The results indicate that the approximate exchange-correlation potentials differ quite considerably from the true exchange-correlation potentials, thus indicating the need for further analytical work in understanding how to design accurate exchange-correlation potentials and for devising tests of exchange-correlation potentials for larger atoms and for molecules.

Another important way of testing the validity of various approximate exchange and correlation potentials is checking whether they obey inequalities imposed by such general properties as scaling and the Hellmann–Feynman theorem. Such general tests were devised by *Levy* and his co-workers [136–145], who found that many of the commonly used approximate potentials violate general inequalities that must be obeyed by the exact potential. These abstract results are helpful in designing potentials that should be better approximations to the true potential.

21.4.3 Density Functional Theory for Excited States

The Hohenberg–Kohn theorem and the Kohn–Sham method were originally formulated in terms of the ground electronic state. These techniques can be extended to calculate

the ground state of a given symmetry [146], but that leaves unresolved the issue of using density functional theory to calculate the energies of excited states for a given symmetry. Using the Rayleigh–Ritz principle for ensembles, general abstract procedures for generalizing density functional theory to excited state calculations were formulated by *Theophilou* [147] and by several other workers [148–158]. Unfortunately, the errors typically seem to be much larger than for ground-state density functional theory.

21.4.4 Locality of Density Functional Theory

Although the locality of DFT was proved for a large class of functionals [159–161], this issue has come under dispute. The question that has been raised is whether there exists an exact Thomas–Fermi model for noninteracting electrons. If such an exact model does not exist, as it is a direct consequence of the Hohenberg–Kohn theorem, then DFT would be incomplete.

Nesbet [162–166] argued that such a theory would be inconsistent with the Pauli exclusion principle for atoms of more than two electrons (or for a two-electron atom where both electrons are in the same spin state). The contention is that if only the total electron density were normalized (which corresponds to only one Lagrange multiplier), as in the TF model, then no shell structure can exist; hence such a system would violate the exclusion principle.

A counterexample was constructed by *Lindgren* and *Salomonson* [167] showing that shell structure can, indeed, be generated through a single Lagrange multiplier. In addition, they verified numerically that a local Kohn–Sham potential can reproduce to high accuracy the many-body electron density and the $2s$ eigenvalue for the $1s2s^3S$ state of neutral helium.

21.4.5 Relativistic and Quantum Field Theoretic Density Functional Theory

At a formal level, one can discuss the development of density functional theory for a relativistic system of electrons. For an overview of this challenging subject, see the discussions by *Dreizler* and *Gross* [95, Chap. 8] and by *Dreizler* [168]. Much of the formalism carries over, but no good way of incorporating vacuum polarization corrections has yet been found.

21.5 Recent Developments

A recent article by *J.P. Solovej* [169] illustrates the good qualitative agreement of the Thomas–Fermi model's predictions of the sizes of atoms with Z from 1 to 50 with the empirical determinations of their radii in crystals by *W.L.*

Bragg [170] and J.C. Slater [171], and presents some new conjectures about asymptotic formulas for the upper and lower limits of the radii and ionization energies of atoms as $Z \rightarrow \infty$ (of course, ignoring relativistic effects).

Many of the important articles by Elliott Lieb and his numerous coworkers on Thomas–Fermi theory and its extensions and their applications to understanding atomic structure and the stability of bulk matter were conveniently reprinted in a single large volume in 2001 [172]. A more readily comprehensible overview of the main results of this large body of work, and of the mathematical theorems used to obtain them, was published by Lieb and Seiringer in 2010 [173].

Ever since the mid-1990s there has continued to be exponentially growing interest in applications of density functional theory of the Kohn–Sham variety to atoms and molecules, especially those of chemical relevance that are too large for accurate *ab initio* electronic structure calculations. The awarding of the 1998 Nobel Prize in Chemistry to Walter Kohn and John A. Pople recognized their individual contributions to this increasingly important field. Their Nobel lectures were published the following year in the *Reviews of Modern Physics* [174, 175].

In a review article published in 2012, Kieron Burke illustrated the exponential growth in the numbers of articles on density functional theory published each year and noted they would soon exceed 10,000 articles per year [176]. Since a comprehensive summary of the wide-ranging developments in density functional theory during the past two decades is not feasible within the limited space available for this supplementary section, I will briefly cite some of the most extensive surveys of various aspects of this field that have appeared since 1995.

Many aspects of density functional theory were reviewed in four consecutive volumes of *Topics in Current Chemistry* published in 1996 [177–180], and in 1999 an entire volume of *Advances in Quantum Chemistry* was devoted to density functional theory [181]. This has also been the subject of several textbooks [182–185] and conference proceedings [186–188]. The International Conferences on Density Functional Theory and Its Applications have been held in various European cities ever since 1995 in odd-numbered years. Recently, Burke [176] and Becke [189] and Yu, Li, and Truhlar [190] published review articles in the *Journal of Chemical Physics*.

An article by Perdew and coworkers provides qualitative explanations of many of the features and paradoxes of Kohn–Sham density functional theory [191]. Tension persists between the proponents of computational methods who seek primarily to develop density functionals with relatively few parameters that obey mathematically derived constraints in the never-ending quest to approach ever more closely the unattainable “Holy Grail” of the exact density functional

(e.g., [192]), and the developers and users of density functionals with few mathematical constraints and many adjustable parameters optimized for a class of molecules to generate predictions of the properties of similar molecules [193–195].

Within the context of Kohn–Sham density functional theory, Constantin, Snyder, Perdew, and Burke investigated the ionization potentials of neutral atoms and the behavior of the “ionization density”, defined as $[4q\pi r^2(\rho_{\text{atom}}(r) - \rho_{\text{ion}}(r))]$, where “ion” refers to the singly charged atomic ion with one electron removed, for Z up to 2938, corresponding to a noble gas atom with a filled outer shell with row number $n = 25$ [196]. Their results indicate that as Z increases, the periodic properties of atoms persist and tend to distinct limits as $Z \rightarrow \infty$, and that the averages of these periodic properties within a “shell” are close to the values given by Thomas–Fermi theory. These results are of mathematical interest, but of course, real atoms with such large nuclear charges do not exist, and even if they did, the effects of relativity and quantum electrodynamics would be profound not just on the orbitals in the “core” but also in the “mantle” and even in the outermost shell. Indeed, because the s-orbitals of atoms have appreciable probability density near the nucleus, there are significant relativistic effects on the physical and chemical properties of atoms already in the 6th period of the periodic table with atomic number Z running upward from 55 (cesium) [197, 198]. Both the unusual color of gold ($Z = 79$) and the unusually low melting point of mercury ($Z = 80$) are striking consequences of relativistic effects on the orbitals in the outermost shell of these atoms [199, 200]. See Chap. 23 for a review of the methodology for performing accurate relativistic calculations of the properties of atoms and atomic ions with large values of Z .

Recent attention has been paid to the use in density functional theory of the Lieb–Oxford lower bound to the indirect part of the Coulomb energy [201]

$$\langle \Psi V_{ee} \rangle \Psi - U[\rho_\Psi] \geq -C_D \int d^D r (\rho_\Psi(\mathbf{r}))^{(D+1)/D}, \quad (21.35)$$

where $\langle \Psi V_{ee} \rangle \Psi$ is the expectation value of the interelectronic interaction energy operator for an electronic wavefunction Ψ , and $U[\rho_\Psi]$ is the approximation to it with the corresponding one-electron density $\rho_\Psi(\mathbf{r})$ defined in Eq. (21.6), and C_D is a dimension-dependent constant ($D = 2$ or 3) for which upper and lower bounds have been derived with various improvements. (As of 2016 it had been established that $1.4119 \leq C_3 \leq 1.6358$.) Mirtschink, Seidl, and Gori-Giorgi demonstrated that this global lower bound obtained by integrating over all space cannot be converted into a local lower bound on the exchange–correlation potential $\epsilon_{xc}(\mathbf{r})$, which for large $|\mathbf{r}|$ decreases proportionally to $1/|\mathbf{r}|$, since such a lower bound would be violated in the outer regions of atoms or in the bond region of stretched molecules, where $\rho_\Psi(\mathbf{r})$ decreases exponentially with distance from the nuclei [202]. A further study

of densities $\rho_\psi(\mathbf{r})$, which challenge the Lieb–Oxford bound and thus provide lower bounds to C_3 , was published by *Seidl, Vuckovic, and Gori-Giorgi* [203]. Generalizations of the original Lieb–Oxford bound that include integrals involving the absolute value of the gradient of ρ and/or the gradient of fractional powers of ρ were constructed by *Benguria, Bley, and Loss* [204] and by *Lewin and Lieb* [205]. Clearly, there is ample room for further theoretical improvements in this area, both in tightening the lower and upper bounds for C_3 in the original Lieb–Oxford bound and in finding other bounds with more complicated functionals of ρ_ψ .

Developments in time-dependent density functional theory for chemical systems have been surveyed in several review articles and books [206–210]. A subtle point that was appreciated only recently is that the singularities in the electron–nucleus and electron–electron potential energies cause severe problems for the existence of Taylor series expansions in time [211, 212], which were used in the original Runge–Gross approach [213].

Acknowledgements I am grateful to Cyrus Umrigar and Michael P. Teter of Cornell University for generously providing sabbatical support in the spring of 1995. I should also like to thank them, as well as Elliott Lieb and Mel Levy, for helpful discussions. This work was supported by my National Science Foundation grant PHY-9215442.

References

1. Thomas, L.H.: Proc. Camb. Philos. Soc. **23**, 542 (1927)
2. Fermi, E.: Rend. Accad. Naz. Lincei **6**, 602 (1927)
3. Fermi, E.: Rend. Accad. Naz. Lincei **7**, 342 (1928)
4. Fermi, E.: Z. Phys. **48**, 73 (1928)
5. Fermi, E.: Z. Phys. **49**, 550 (1928)
6. Lenz, W.: Z. Phys. **77**, 713 (1932)
7. Dirac, P.A.M.: Proc. Camb. Philos. Soc. **26**, 376 (1930)
8. von Weizsäcker, C.F.: Z. Phys. **96**, 431 (1935)
9. Lieb, E.H., Simon, B.: Phys. Rev. Lett. **31**, 681 (1973)
10. Lieb, E.H., Simon, B.: Adv. Math. **23**, 22 (1977)
11. Sheldon, J.W.: Phys. Rev. **99**, 1291 (1955)
12. Teller, E.: Rev. Mod. Phys. **34**, 627 (1962)
13. Balázs, N.: Phys. Rev. **156**, 42 (1967)
14. Lieb, E.H., Thirring, W.: Phys. Rev. Lett. **35**, 687 (1975)
15. Lieb, E.H.: Rev. Mod. Phys. **53**, 603 (1981)
16. Lieb, E.H.: Rev. Mod. Phys. **54**, 311(E) (1982)
17. Spruch, L.: Rev. Mod. Phys. **63**, 151 (1991)
18. Gombás, P.: Die statistische Theorie des Atoms und ihre Anwendungen. Springer, Berlin, Heidelberg (1949)
19. Gombás, P.: In: Flüggé, S. (ed.) Atome II Handbuch der Physik, vol. 36, pp. 109–231. Springer, Berlin, Heidelberg (1956)
20. March, N.H.: Adv. Phys. **6**, 1 (1957)
21. Hohenberg, P., Kohn, W.: Phys. Rev. B **136**, 864 (1964)
22. Kohn, W., Sham, L.J.: Phys. Rev. A **140**, 1133 (1965)
23. Fermi, E., Amaldi, E.: Mem. Accad. Ital. **6**, 119 (1934)
24. Milne, E.A.: Proc. Camb. Philos. Soc. **23**, 794 (1927)
25. Baker, E.B.: Phys. Rev. **36**, 630 (1930)
26. Tal, Y., Levy, M.: Phys. Rev. A **23**, 408 (1981)
27. Hodges, C.H.: Can. J. Phys. **51**, 1428 (1973)
28. Benguria, R., Lieb, E.H.: J. Phys. B **18**, 1045 (1985)
29. Ahlrichs, R., Hoffmann-Ostenhof, T., Hoffmann-Ostenhof, M., Morgan III, J.D.: Phys. Rev. A **23**, 2107 (1981). and references therein
30. Kato, T.: Commun. Pure Appl. Math. **10**, 151 (1957)
31. Perdew, J.P., Parr, R.G., Levy, M., Balduz Jr., J.L.: Phys. Rev. Lett. **49**, 1691 (1982)
32. Levy, M., Perdew, J.P.: In: Dreizler, R.M., da Providência, J. (eds.) Density Functional Methods in Physics NATO ASI Series B, vol. 123, pp. 11–30. Plenum, New York (1985)
33. Lieb, E.H.: In: Dreizler, R.M., da Providência, J. (eds.) Density Functional Methods in Physics NATO ASI Series B, vol. 123, pp. 31–80. Plenum, New York (1985)
34. Goldstein, J.A., Rieder, G.R.: J. Math. Phys. **32**, 2907 (1991)
35. Goldstein, J.A., Rieder, G.R.: J. Math. Phys. **29**, 709 (1988)
36. Scott, J.M.C.: Philos. Mag. **43**, 859 (1952)
37. Lieb, E.H.: Rev. Mod. Phys. **48**, 553 (1976)
38. Schwinger, J.: Phys. Rev. A **22**, 1827 (1980)
39. Siedentop, H., Weikard, R.: Commun. Math. Phys. **112**, 471 (1987)
40. Siedentop, H., Weikard, R.: Invent. Math. **97**, 159 (1989)
41. Hughes, W.: Adv. Math. **79**, 213 (1990)
42. Bach, V.: Rep. Math. Phys. **28**, 213 (1989)
43. Ivrii, V.J., Sigal, I.M.: Ann. Math. **138**, 243 (1993)
44. Schwinger, J.: Phys. Rev. A **24**, 2353 (1981)
45. March, N.H., Plaskett, J.S.: Proc. R. Soc. A **235**, 419 (1956)
46. Shakeshaft, R., Spruch, L., Mann, J.: J. Phys. B **14**, L121 (1981)
47. Shakeshaft, R., Spruch, L.: Phys. Rev. A **23**, 2118 (1981)
48. Englert, B.-G., Schwinger, J.: Phys. Rev. A **26**, 2322 (1982)
49. Englert, B.-G., Schwinger, J.: Phys. Rev. A **29**, 2331 (1984)
50. Englert, B.-G., Schwinger, J.: Phys. Rev. A **29**, 2339 (1984)
51. Englert, B.-G., Schwinger, J.: Phys. Rev. A **29**, 2353 (1984)
52. Englert, B.-G., Schwinger, J.: Phys. Rev. A **32**, 28 (1985)
53. Englert, B.-G., Schwinger, J.: Phys. Rev. A **32**, 36 (1985)
54. Englert, B.-G., Schwinger, J.: Phys. Rev. A **32**, 47 (1985)
55. Englert, B.-G.: Semiclassical Theory of Atoms. Lecture Notes in Physics, vol. 300. Springer, Berlin, Heidelberg (1988)
56. Iantchenko, A., Lieb, E.H., Siedentop, H.: J. Reine Angew. Math. **472**, 177 (1996)
57. Heilman, O.J., Lieb, E.H.: Phys. Rev. A **52**, 3628 (1995)
58. Fefferman, C.L., Seco, L.A.: Bull. Am. Math. Soc. **23**, 525 (1990)
59. Fefferman, C., Seco, L.A.: Adv. Math. **107**, 1 (1994)
60. Fefferman, C., Seco, L.: Adv. Math. **95**, 145 (1992)
61. Fefferman, C., Seco, L.A.: Rev. Mat. Iberoam. **9**, 409 (1993)
62. Fefferman, C., Seco, L.: Adv. Math. **107**, 187 (1994)
63. Fefferman, C., Seco, L.: Adv. Math. **108**, 263 (1994)
64. Cordoba, A., Fefferman, C., Seco, L.: Proc. Natl. Acad. Sci. U. S. A. **91**, 5776 (1994)
65. Cordoba, A., Fefferman, C., Seco, L.A.: Rev. Mat. Iberoam. **11**, 165 (1995)
66. Fefferman, C., Seco, L.: Adv. Math. **111**, 88 (1995)
67. Fefferman, C., Seco, L.: Adv. Math. **119**, 26 (1996)
68. Fefferman, C.: Adv. Math. **124**, 100 (1996)
69. Heine, V.: Solid State Phys. **24**, 1 (1970)
70. Cohen, M.L., Heine, V.: Solid State Phys. **24**, 37 (1970)
71. Heine, V., Weaire, D.: Solid State Phys. **24**, 249 (1970)
72. Payne, M.C., Teter, M.P., Allan, D.C., Arias, T.A., Joannopoulos, J.D.: Rev. Mod. Phys. **64**, 1045 (1992)
73. Rajagopal, A.K.: Adv. Chem. Phys. **41**, 59 (1980)
74. Bamzai, A.S., Deb, B.M.: Rev. Mod. Phys. **53**, 95 (1981)
75. Bamzai, A.S., Deb, B.M.: Rev. Mod. Phys. **53**, 593(E) (1981)
76. Parr, R.G.: Ann. Rev. Phys. Chem. **34**, 631 (1983)
77. Callaway, J., March, N.H.: Solid State Phys. **38**, 135 (1984)
78. Jones, R.O., Gunnarsson, O.: Rev. Mod. Phys. **61**, 689 (1989)
79. Trickey, S.B.: In: Kryachko, E.S., Calais, J.L. (eds.) Conceptual Trends in Quantum Chemistry, vol. 1, pp. 87–100. Kluwer, Amsterdam (1994)

80. Lundqvist, S., March, N.H. (eds.): *Theory of the Inhomogeneous Electron Gas*. Plenum, New York (1983)
81. March, N.H., Deb, B.M. (eds.): *The Single-Particle Density in Physics and Chemistry*. Academic Press, New York (1987)
82. Trickey, S.B. (ed.): *Density Functional Theory of Many-Fermion Systems*. *Advances in Quantum Chemistry*, vol. 21. Academic Press, New York (1990)
83. Keller, J., Gázquez, J.L.: *Density Functional Theory*. *Lecture Notes in Physics*, vol. 187. Springer, Berlin, Heidelberg (1983)
84. Langreth, D., Suhl, H. (eds.): *Many-Body Phenomena at Surfaces*. Academic Press, New York (1984)
85. Dahl, J.P., Avery, J. (eds.): *Local Density Approximations in Quantum Chemistry and Solid State Physics*. Plenum, New York (1984)
86. Phariseau, P., Temmermann, W.M. (eds.): *The Electronic Structure of Complex Systems*. *NATO ASI Series B*, vol. 113. Plenum, New York (1984)
87. Dreizler, R.M., da Providência, J. (eds.): *Density Functional Methods in Physics*. *NATO ASI Series B*, vol. 123. Plenum, New York (1985)
88. Erdahl, R., Smith Jr., V.H. (eds.): *Density Matrices and Density Functionals*. Reidel, Dordrecht (1987)
89. Labanowski, J.K., Andzelm, J.W. (eds.): *Density Functional Methods in Chemistry*. Springer, New York (1991)
90. Grout, P.J., Lidiard, A.B.: *Philos. Mag.* **B 69**, 725 (1994)
91. Kryachko, E.S., Ludeña, E.V.: *Energy Density Functional Theory of Many-Electron Systems*. Kluwer, Dordrecht (1990)
92. Gross, E.K.U., Dreizler, R.M. (eds.): *Density Functional Theory*. *NATO ASI Series B*, vol. 337. Plenum, New York (1995)
93. Goursot, A., Mijoule, C., Russo, N.: *Theor. Chim. Acta* **91**, 111 (1995)
94. Parr, R.G., Yang, W.: *Density-Functional Theory of Atoms and Molecules*. Clarendon, Oxford (1989)
95. Dreizler, R.M., Gross, E.K.U.: *Density Functional Theory: An Approach to the Quantum Many-Body Problem*. Springer, Berlin, Heidelberg (1990)
96. Gilbert, T.L.: *Phys. Rev. B* **12**, 2111 (1975)
97. Harriman, J.E.: *Phys. Rev. A* **24**, 680 (1981)
98. Lieb, E.H.: In: Feshbach, H., Shimony, A. (eds.) *Physics as Natural Philosophy: Essays in Honor of Laszlo Tisza on his 75th Birthday*, pp. 111–149. MIT Press, Cambridge (1982). reprinted in Lieb, E.H.: *Int. J. Quantum Chem.* **24**, 243 (1983)
99. Levy, M.: *Phys. Rev. A* **26**, 1200 (1982)
100. Percus, J.K.: *Int. J. Quantum Chem.* **13**, 89 (1978)
101. Levy, M.: *Proc. Natl. Acad. Sci. U. S. A.* **76**, 6062 (1979)
102. Ceperley, D.M., Alder, B.J.: *Phys. Rev. Lett.* **45**, 566 (1980)
103. Becke, A.D.: *Phys. Rev. A* **38**, 3098 (1988)
104. Becke, A.D.: *Int. J. Quantum Chem. Symp.* **23**, 599 (1989)
105. Becke, A.D.: *J. Chem. Phys.* **96**, 2155 (1992)
106. Becke, A.D.: *J. Chem. Phys.* **97**, 9173 (1992)
107. Becke, A.D.: *J. Chem. Phys.* **98**, 5648 (1993)
108. Becke, A.D.: *J. Chem. Phys.* **98**, 1372 (1993)
109. Dickson, R.M., Becke, A.D.: *J. Chem. Phys.* **99**, 3898 (1993)
110. Lee, C., Yang, W., Parr, R.G.: *Phys. Rev. B* **37**, 785 (1988)
111. Colle, R., Salvetti, O.: *Theor. Chim. Acta* **37**, 329 (1975)
112. Colle, R., Salvetti, O.: *Theor. Chim. Acta* **53**, 55 (1979)
113. Colle, R., Salvetti, O.: *J. Chem. Phys.* **79**, 1404 (1983)
114. Johnson, B.G., Gill, P.M.W., Pople, J.A.: *J. Chem. Phys.* **98**, 5612 (1993)
115. Murray, C.W., Handy, N.C., Amos, R.D.: *J. Chem. Phys.* **98**, 7145 (1993)
116. Laming, G.J., Termath, V., Handy, N.C.: *J. Chem. Phys.* **99**, 8765 (1993)
117. Ortiz, G., Ballone, P.: *Phys. Rev. B* **43**, 6376 (1991)
118. Lee, C., Zhou, Z.: *Phys. Rev. A* **44**, 1536 (1991)
119. Engel, E., Chevary, J.A., Macdonald, L.D., Vosko, S.H.: *Z. Phys. D* **23**, 7 (1992)
120. Vosko, S.H., Wilk, L., Nusair, M.: *Can. J. Phys.* **58**, 1200 (1980)
121. Langreth, D.C., Mehl, M.J.: *Phys. Rev. Lett.* **47**, 446 (1981)
122. Langreth, D.C., Mehl, M.J.: *Phys. Rev. B* **28**, 1809 (1983)
123. Langreth, D.C., Mehl, M.J.: *Phys. Rev. B* **29**, 2310(E) (1984)
124. Perdew, J.P., Wang, Y.: *Phys. Rev. B* **33**, 8800 (1986)
125. Perdew, J.P.: *Phys. Rev. B* **33**, 8822 (1986)
126. Perdew, J.P.: *Phys. Rev. B* **34**, 7406(E) (1986)
127. DePristo, A.E., Kress, J.D.: *J. Chem. Phys.* **86**, 1425 (1987)
128. Wilson, L.C., Levy, M.: *Phys. Rev. B* **41**, 12930 (1990)
129. Perdew, J.P.: *Physica B* **172**, 1 (1991)
130. Perdew, J.P., Wang, Y.: *Phys. Rev. B* **45**, 13244 (1992)
131. Lacks, D.J., Gordon, R.G.: *Phys. Rev. A* **47**, 4681 (1993)
132. Perdew, J.P.: *Int. J. Quantum Chem. Symp.* **27**, 93 (1993)
133. Filippi, C., Umrigar, C.J., Taut, M.: *J. Chem. Phys.* **100**, 1290 (1994)
134. Umrigar, C.J., Gonze, X.: *Phys. Rev. A* **50**, 3827 (1994)
135. Umrigar, C.J.: In: Browne, D.A., Callaway, J., Drayer, J.P., Haymaker, R.W., Kalia, R.K., Tohline, J.E., Vashishta, P. (eds.) *Proc. of the Mardi Gras '93 Conference*, pp. 43–59. World Scientific, Singapore (1993)
136. Levy, M., Perdew, J.P.: *Phys. Rev. A* **32**, 2010 (1985)
137. Levy, M., Ou-Yang, H.: *Phys. Rev. A* **38**, 625 (1988)
138. Levy, M.: In: Trickey, S.B. (ed.) *Density Functional Theory of Many-Fermion Systems Advances in Quantum Chemistry*, vol. 21, pp. 69–95. Academic Press, New York (1990)
139. Levy, M.: In: Labanowski, J.K., Andzelm, J.W. (eds.) *Density Functional Methods in Chemistry*, pp. 175–193. Springer, New York (1991)
140. Görling, A., Levy, M.: *Phys. Rev. A* **45**, 1509 (1992)
141. Zhao, Q., Levy, M., Parr, R.G.: *Phys. Rev. A* **47**, 918 (1993)
142. Görling, A., Levy, M.: *Phys. Rev. B* **47**, 13105 (1993)
143. Levy, M., Perdew, J.P.: *Phys. Rev. B* **48**, 11638 (1993)
144. Görling, A., Levy, M.: *Phys. Rev. A* **50**, 196 (1994)
145. Levy, M., Görling, A.: *Philos. Mag. B* **69**, 763 (1994)
146. Gunnarson, O., Lundqvist, B.J.: *Phys. Rev. B* **13**, 4274 (1976)
147. Theophilou, A.K.: *J. Phys. C* **12**, 5419 (1979)
148. Hadjisavvas, N., Theophilou, A.: *Phys. Rev. A* **30**, 2183 (1984)
149. Hadjisavvas, N., Theophilou, A.K.: *Philos. Mag. B* **69**, 771 (1994)
150. Katriel, J.: *J. Phys. C* **13**, L375 (1980)
151. Theophilou, A.: *Phys. Rev. A* **32**, 720 (1985)
152. Kohn, W.: *Phys. Rev. A* **34**, 737 (1986)
153. Gross, E.K.U., Oliveira, L.N., Kohn, W.: *Phys. Rev. A* **37**, 2805 (1988)
154. Gross, E.K.U., Oliveira, L.N., Kohn, W.: *Phys. Rev. A* **37**, 2809 (1988)
155. Oliveira, L.N., Gross, E.K.U., Kohn, W.: *Phys. Rev. A* **37**, 2821 (1988). and earlier references therein
156. Englisch, H., Fieseler, H., Haufe, A.: *Phys. Rev. A* **37**, 4570 (1988)
157. Oliveira, L.N.: In: Trickey, S.B. (ed.) *Density Functional Theory of Many-Fermion Systems Advances in Quantum Chemistry*, vol. 21, pp. 135–154. Academic Press, New York (1990)
158. Oliveira, L.N., Gross, E.K.U., Kohn, W.: *Int. J. Quantum Chem. Symp.* **24**, 707 (1990)
159. Englisch, H., Englisch, R.: *Phys. Status Solidi (b)* **123**, 711 (1984)
160. Englisch, H., Englisch, R.: *Phys. Status Solidi (b)* **124**, 373 (1984)
161. van Leeuwen, R.: *Adv. Quantum Chem.* **43**, 25 (2003)
162. Nesbet, R.K.: *Phys. Rev. A* **58**, R12 (1998)
163. Nesbet, R.K.: *Phys. Rev. A* **65**, 010502(R) (2001)
164. Nesbet, R.K.: *Adv. Quantum Chem.* **43**, 1 (2003)
165. Nesbet, R.K.: arXiv:physics/0309120 (2003)
166. Nesbet, R.K.: arXiv:physics/0309121 (2003)
167. Lindgren, I., Salomonson, S.: *Phys. Rev. A* **70**, 032509 (2004)
168. Dreizler, R.M.: *Phys. Scr. T* **46**, 167 (1993)

169. Solovej, J.P.: *Mol. Phys.* **114**, 1036 (2016)
170. Bragg, W.L.: *Philos. Mag.* **40**, 169 (1920)
171. Slater, J.C.: *J. Chem. Phys.* **41**, 3199 (1964)
172. Thirring, W. (ed.): *The Stability of Matter: From Atoms to Stars – Selecta of Elliott H. Lieb*, 3rd edn. Springer, Berlin, Heidelberg (2001)
173. Lieb, E.H., Seiringer, R.: *The Stability of Matter in Quantum Mechanics*. Cambridge Univ. Press, Cambridge (2010)
174. Kohn, W.: *Rev. Mod. Phys.* **71**, 1253 (1999)
175. Pople, J.A.: *Rev. Mod. Phys.* **71**, 1267 (1999)
176. Burke, K.: *J. Chem. Phys.* **136**, 150901 (2012)
177. Nalewajski, R.F. (ed.): *Density Functional Theory I: Functionals and Effective Potentials*. Topics in Current Chemistry, vol. 180. Springer, New York (1996)
178. Nalewajski, R.F. (ed.): *Density Functional Theory II: Relativistic and Time Dependent Extensions*. Topics in Current Chemistry, vol. 181. Springer, New York (1996)
179. Nalewajski, R.F. (ed.): *Density Functional Theory III: Interpretation, Atoms, Molecules and Clusters*. Topics in Current Chemistry, vol. 182. Springer, New York (1996)
180. Nalewajski, R.F. (ed.): *Density Functional Theory IV: Theory of Chemical Reactivity*. Topics in Current Chemistry, vol. 183. Springer, New York (1996)
181. Seminario, J.M. (ed.): *Density Functional Theory*. Advances in Quantum Chemistry, vol. 33. Academic Press, New York (1999)
182. Koch, W., Holthausen, M.C.: *A Chemist's Guide to Density Functional Theory*. Wiley, New York (2001)
183. Fiolhais, C., Nogueira, F., Marques, M.: *A Primer in Density Functional Theory*. Lecture Notes in Physics, vol. 620. Springer, New York (2003)
184. Sholl, D., Steckel, J.A.: *Density Functional Theory: A Practical Introduction*. Wiley, Hoboken (2009)
185. Engel, E., Dreizler, R.M.: *Density Functional Theory: An Advanced Course*. Springer, Berlin, Heidelberg, New York (2011)
186. Laird, B.B., Ross, R.B., Ziegler, T.: *Chemical Applications of Density Functional Theory*. ACS Symposium Series, vol. 629. American Chemical Society, Washington (1996)
187. Dobson, J.F., Vignale, G., Das, M.P. (eds.): *Electronic Density Functional Theory: Recent Progress and New Directions*. Plenum, New York (1998)
188. Joubert, D. (ed.): *Density Functionals: Theory and Applications*. Springer, New York (1998)
189. Becke, A.D.: *J. Chem. Phys.* **140**, 18A301 (2014)
190. Yu, H.S., Li, S.L., Truhlar, D.G.: *J. Chem. Phys.* **145**, 130901 (2016)
191. Perdew, J.P., Ruzsinszky, A., Constantin, L.A., Sun, J., Csonka, G.I.: *J. Chem. Theory Comput.* **5**, 902 (2009)
192. Sun, J., Ruzsinszky, A., Perdew, J.P.: *Phys. Rev. Lett.* **115**, 036402 (2015)
193. Medvedev, M.G., Bushmarinov, I.S., Sun, J., Perdew, J.P., Lyssenko, K.A.: *Science* **355**, 49 (2017)
194. Medvedev, M.G., Bushmarinov, I.S., Sun, J., Perdew, J.P., Lyssenko, K.A.: *Science* **356**, 496c (2017)
195. Kepp, K.P.: *Science* **356**, 496 (2017)
196. Constantin, L.A., Snyder, J.C., Perdew, J.P., Burke, K.: *J. Chem. Phys.* **133**, 241103 (2010)
197. Pyykkö, P., Desclaux, J.-P.: *Acc. Chem. Res.* **12**, 276 (1979)
198. Thayer, J.S.: In: Barysz, M., Ishikawa, Y. (eds.) *Relativistic Methods for Chemists Challenges and Advances in Computational Chemistry and Physics*, vol. 10, pp. 63–97. Springer, Berlin, Heidelberg, New York (2010)
199. Norrby, L.J.: *J. Chem. Educ.* **68**, 110 (1991)
200. Pyykkö, P.: *Chem. Rev.* **88**, 563 (1988)
201. Lieb, E.H., Oxford, S.: *Int. J. Quantum Chem.* **19**, 427 (1981)
202. Mirtschink, A., Seidl, M., Gori-Giorgi, P.: *J. Chem. Theory Comput.* **8**, 3097 (2012)
203. Seidl, M., Vuckovic, S., Gori-Giorgi, P.: *Mol. Phys.* **114**, 1076 (2016)
204. Benguria, R.D., Bley, G.A., Loss, M.: *Int. J. Quantum Chem.* **112**, 1579 (2012)
205. Lewin, M., Lieb, E.H.: *Phys. Rev. A* **91**, 022507 (2015)
206. Marques, M.A.L., Gross, E.K.U.: *Annu. Rev. Phys. Chem.* **55**, 427 (2004)
207. Furche, F., Burke, K.: *Ann. Rep. Comput. Chem.* **1**, 19 (2004)
208. Maitra, N.T.: *J. Chem. Phys.* **144**, 220901 (2016)
209. Marques, M.A.L., Ullrich, C., Nogueira, F., Rubio, A., Burke, K., Gross, E.K.U. (eds.): *Time-Dependent Density Functional Theory*. Lecture Notes in Physics, vol. 706. (2006)
210. Marques, M.A.L., Maitra, N.T., Nogueira, F.M.S., Gross, E.K.U., Rubio, A. (eds.): *Fundamentals of Time-Dependent Density Functional Theory*. Lecture Notes in Physics, vol. 837. Springer, Berlin, Heidelberg, New York (2012)
211. Yang, Z.-H., Burke, K.: *Phys. Rev. A* **88**, 042514 (2013)
212. Fournais, S., Lampart, J., Lewin, M., Sørensen, T.Ø.: *Phys. Rev. A* **93**, 062510 (2016)
213. Runge, E., Gross, E.K.U.: *Phys. Rev. Lett.* **52**, 997 (1984)
214. Lieb, E.H.: *Int. J. Quantum Chem.* **24**, 243 (1983)



John D. Morgan III Dr Morgan, Associate Professor, obtained his BS from The George Washington University, his MSc in Theoretical Chemistry from Oxford University, and his PhD in Chemistry from Berkeley. He has served on the editorial boards of the *Journal of Mathematical Physics* and the *International Journal of Quantum Chemistry*. His interests include the application of sophisticated mathematical techniques to assist the accurate calculation of properties of atoms and molecules.



Atomic Structure: Variational Wave Functions and Properties

22

Charlotte Froese Fischer and Michel Godefroid

Contents

22.1	Nonrelativistic and Relativistic Hamiltonians	309
22.1.1	Schrödinger's Hamiltonian	310
22.1.2	Dirac–Coulomb(–Breit) Hamiltonian	310
22.1.3	Breit–Pauli Hamiltonian	310
22.2	Many-Electron Wave Functions	311
22.2.1	Nonrelativistic Orbitals and <i>LS</i> Configuration State Functions	311
22.2.2	Relativistic Dirac Orbitals and <i>jj</i> Configuration State Functions	312
22.3	Variational Principle	312
22.4	Hartree–Fock and Dirac–Hartree–Fock Methods	313
22.4.1	Diagonal Energy Parameters and Koopmans' Theorem	314
22.4.2	Hartree–Fock Operator	314
22.4.3	Brillouin's Theorem	315
22.4.4	The Dirac–Hartree–Fock Equations	315
22.4.5	Numerical Solution of Variational Equations	315
22.4.6	Properties of Hartree–Fock Solutions	317
22.5	Multiconfiguration (Dirac)-Hartree–Fock Method	318
22.5.1	<i>Z</i> -Dependent Theory	318
22.5.2	The MC(D)HF Approximation	319
22.5.3	Systematic Methods	320
22.5.4	Excited States	321
22.5.5	Autoionizing States	321
22.6	Configuration Interaction Methods	321
22.7	Atomic Properties	324
22.7.1	Transition Data—Allowed and Forbidden Lines	324
22.7.2	Electron Affinities	324
22.7.3	Metastable States and Autoionization	325
22.7.4	Nuclear Effects	326
22.8	Summary	328
	References	328

Abstract

This chapter describes variational methods for the determination of wave functions either in nonrelativistic (*LS*), quasi relativistic Breit–Pauli (*LSJ*), or Dirac (*jj*) theory. The emphasis is on Hartree–Fock and multiconfiguration Hartree–Fock theory with reference to similar Dirac theory. Although the underlying mathematics of the latter is technically different because of the properties of Dirac spinors, we draw parallels between the nonrelativistic and relativistic formulations that lay the foundation of, respectively, the Atomic Structure Package (ATSP) [1, 2] and the General Relativistic Atomic Structure Package (GRASP) [3, 4]. Some results from the application of these multiconfiguration methods are presented for a number of atomic properties. Although framed entirely in terms of nonrelativistic calculations, the present chapter reveals a pattern that can be, and actually is, explored in the review article of variational theory [5] as in the following Chap. 23 on *Relativistic Atomic Structure*.

Keywords

complete active space · configuration state functions · Hamiltonians · multiconfiguration wave functions · orbital rotation · quantum defect · Rydberg series · variational methods

22.1 Nonrelativistic and Relativistic Hamiltonians

A fully covariant relativistic many-body theory requires a field-theoretical approach, i.e., the use of quantum electrodynamics (QED) [6]. Although relativistic QED is the accepted theory describing the interaction of charged particles with the Maxwell field, it is too complicated to use for all but the simplest atomic structures. Almost all atomic structure calculations are, therefore, usually based on Hamil-

C. Froese Fischer (✉)
Dept. of Computer Science, University of British Columbia
Vancouver, Canada
e-mail: cff@cs.ubc.ca

M. Godefroid
Chemistry Department (SQUARES), Université libre de Bruxelles
(ULB)
Brussels, Belgium
e-mail: mrgodef@ulb.ac.be

tonian models. For a time-independent Hamiltonian, we may look for stationary solutions Ψ of the wave equation

$$(H - E)\Psi = 0, \quad (22.1)$$

where H is the Hamiltonian operator for the system and E the total energy. The operator H depends on the system (atomic, molecular, solid state, etc.) as well as the underlying quantum mechanical formalism (nonrelativistic, Dirac–Coulomb, or Dirac–Coulomb–Breit, etc.). All these Hamiltonians are of the form $T + V$, where T refers to the kinetic energy operator, and V approximates the electron–nucleus and electron–electron interactions.

22.1.1 Schrödinger’s Hamiltonian

Deriving V from the (point) Coulomb interactions of the classical potentials and describing the nucleus of charge Z as a point-charged nucleus of infinite mass, the nonrelativistic Schrödinger Hamiltonian of a N -electron atom is, in atomic units (see Chap. 1 for their definition),

$$H_{\text{nr}} = -\frac{1}{2} \sum_{i=1}^N \left(\nabla_i^2 + \frac{2Z}{r_i} \right) + \sum_{i<j} \frac{1}{r_{ij}}, \quad (22.2)$$

where r_i is the distance of electron i from the nucleus, and r_{ij} is the distance between electron i and electron j . The term $-Z/r$ represents the nuclear attraction and $1/r_{ij}$ the interelectron repulsion. The operator H_{nr} has both a discrete and continuous spectrum; for the former, the solution of Eq. (22.1), $\Psi(\mathbf{r}_1, \mathbf{r}_2, \dots, \mathbf{r}_N)$, has a probability interpretation and, consequently, must be square integrable.

22.1.2 Dirac–Coulomb(–Breit) Hamiltonian

Relativistic quantum mechanics [7] is required for a description of the atomic system when the electrons probe regions of spaces near the atomic nucleus. A good approximation for the relativistic Hamiltonian based on Dirac theory for a many-electron atomic system is the Dirac–Coulomb (DC) Hamiltonian [8, 9]

$$\begin{aligned} H_{\text{DC}} &= \sum_{i=1}^N h_{\text{D}}(i) + \sum_{j>i=1}^N \frac{1}{r_{ij}} \\ &= \sum_{i=1}^N [c\boldsymbol{\alpha}_i \cdot \mathbf{p}_i + V_{\text{nuc}}(r_i) + c^2(\beta_i - 1)] \\ &\quad + \sum_{j>i=1}^N \frac{1}{r_{ij}}, \end{aligned} \quad (22.3)$$

where h_{D} is the one-electron Dirac operator (shifted for the energy to coincide with nonrelativistic conventions), $\boldsymbol{\alpha}$ and β are usual 4×4 Dirac matrices, c is the speed of light ($c = 1/\alpha = 137.035\,999\,139(31)$ a. u.) according to the 2014 CODATA [10], and $\mathbf{p} = -i\nabla$ is the electron momentum operator. For each electron, β appearing in the relativistic single-electron Dirac kinetic energy is replaced by $\beta - 1$ to align the nonrelativistic rest energy of the electron, $E = 0$, and the relativistic one, $E = m_e c^2$. The nuclear potential $V_{\text{nuc}}(r)$ can be approximated as $-Z/r$, as it is in Eq. (22.2), but this point nuclear charge model ignores the fact that real nuclei often have nonspherical charge density distributions that have physical effects (isotope shifts, hyperfine structures, etc.). A spherical average density distribution $V_{\text{nuc}}(r)$ is, therefore, frequently included when modeling heavier atoms. A more realistic nuclear charge distribution can be a uniform nuclear charge distribution, a Fermi distribution, or other nuclear models deduced from nuclear scattering experiments (Chap. 23).

In Eq. (22.3), the electron–electron interaction is simply taken to be the static potential, while the full electron–electron interaction should be included to approach QED. The effective interaction of electrons depends of the choice of gauge potential. Their derivation in terms of the exchange of virtual photons leading to different gauge-dependent versions can be found in Chap. 23. In the Coulomb gauge, the low-frequency limit of the virtual exchanged photon between two electrons introduced in QED gives the Breit interaction

$$H_{\text{Breit}} = - \sum_{j>i=1}^N \frac{1}{2r_{ij}} \left[(\boldsymbol{\alpha}_i \cdot \boldsymbol{\alpha}_j) + \frac{(\boldsymbol{\alpha}_i \cdot \mathbf{r}_{ij})(\boldsymbol{\alpha}_j \cdot \mathbf{r}_{ij})}{r_{ij}^2} \right] \quad (22.4)$$

that approximates the magnetic interaction and retardation effects. The addition of Eqs. (22.3) and (22.4) defines the Dirac–Coulomb–Breit (DCB) Hamiltonian.

22.1.3 Breit–Pauli Hamiltonian

For small velocities ($v \ll c$), it is possible to derive the Breit–Pauli Hamiltonian

$$H_{\text{BP}} = H_{\text{nr}} + H_{\text{rel}}, \quad (22.5)$$

from the nonrelativistic limit of $H_{\text{DCB}} = H_{\text{DC}} + H_{\text{Breit}}$ [11, 12]; H_{rel} contains the relativistic corrections to the nonrelativistic Hamiltonian Eq. (22.2) up to the relative order $(\alpha Z)^2$ in energy [13] and may again be subdivided into nonfine structure (NF) and fine structure (F) contributions

$$H_{\text{rel}} = H_{\text{NF}} + H_{\text{F}}. \quad (22.6)$$

The NF contributions

$$H_{\text{NF}} = H_{\text{mass}} + H_{\text{Darwin}} + H_{\text{ssc}} + H_{\text{oo}} \quad (22.7)$$

shift nonrelativistic energy levels without splitting the levels. The mass-velocity term

$$H_{\text{mass}} = -\frac{\alpha^2}{8} \sum_i \nabla_i^4 \quad (22.8)$$

corrects for the variation of mass with velocity; the one- and two-body Darwin terms

$$H_{\text{Darwin}} = -\frac{\alpha^2 Z}{8} \sum_i \nabla_i^2 r_i^{-1} + \frac{\alpha^2}{4} \sum_{i<j} \nabla_i^2 r_{ij}^{-1} \quad (22.9)$$

are the corrections of the one-electron Dirac equation due to the retardation of the electromagnetic field produced by an electron; the spin–spin contact term

$$H_{\text{SSC}} = -\frac{8\pi\alpha^2}{3} \sum_{i<j} (\mathbf{s}_i \cdot \mathbf{s}_j) \delta(\mathbf{r}_{ij}) \quad (22.10)$$

accounts for the interaction of the spin magnetic moments of two electrons occupying the same space; the orbit–orbit interaction

$$H_{\text{OO}} = -\frac{\alpha^2}{2} \sum_{i<j} \left(\frac{\mathbf{p}_i \cdot \mathbf{p}_j}{r_{ij}} + \frac{\mathbf{r}_{ij}(\mathbf{r}_{ij} \cdot \mathbf{p}_i) \cdot \mathbf{p}_j}{r_{ij}^3} \right) \quad (22.11)$$

accounts for the interaction of two orbital moments.

The F contributions

$$H_F = H_{\text{so}} + H_{\text{soo}} + H_{\text{ss}}, \quad (22.12)$$

split the nonrelativistic energy levels into a series of closely-spaced fine structure levels. The nuclear spin–orbit interaction

$$H_{\text{so}} = \frac{\alpha^2 Z}{2} \sum_i \frac{1}{r_i^3} (\mathbf{l}_i \cdot \mathbf{s}_i) \quad (22.13)$$

represents the interaction of the spin and angular magnetic moments of an electron in the field of the nucleus. The spin–other–orbit term

$$H_{\text{soo}} = -\frac{\alpha^2}{2} \sum_{i \neq j} \left(\frac{\mathbf{r}_{ij}}{r_{ij}^3} \times \mathbf{p}_i \right) \cdot (\mathbf{s}_i + 2\mathbf{s}_j), \quad (22.14)$$

and the spin–spin term

$$H_{\text{ss}} = \alpha^2 \sum_{i<j} \frac{1}{r_{ij}^3} \left[\mathbf{s}_i \cdot \mathbf{s}_j - \frac{3}{r_{ij}^2} (\mathbf{s}_i \cdot \mathbf{r}_{ij})(\mathbf{s}_j \cdot \mathbf{r}_{ij}) \right], \quad (22.15)$$

arise from spin-dependent interactions with the other electrons in the system.

The Breit–Pauli approximation is usually only applied to light atoms but provides satisfactory results even up to $Z = 26$ – 30 for Na-like to Ar-like ions [14]. A finite nucleus correction can be readily estimated for small- Z nuclei from the value of the electron density calculated at the point-charge nucleus [15].

22.2 Many-Electron Wave Functions

The atomic wave function Ψ , an approximate solution of the wave equation (22.1) for a many-electron atomic system, is expanded in terms of configuration state functions (CSF) that can be expressed in terms of sums of Slater determinants built on one-electron orbitals [5].

22.2.1 Nonrelativistic Orbitals and LS Configuration State Functions

In the nonrelativistic approximation, the assignment of nl quantum numbers to electrons specifies a configuration, often written as $(n_1 l_1)^{q_1} (n_2 l_2)^{q_2} \dots (n_m l_m)^{q_m}$, where q_i is the occupation of subshell $(n_i l_i)$. Associated with each subshell are one-electron spin-orbitals

$$\phi(r, \theta, \varphi, \sigma) = \frac{1}{r} P_{nl}(r) Y_{lm_l}(\theta, \varphi) \chi_{m_s}(\sigma),$$

where $P_{nl}(r)$ is the radial function, $Y_{lm_l}(\theta, \varphi)$ a spherical harmonic, and $\chi_{m_s}(\sigma)$ a spinor. Each CSF is a linear combination of products of one-electron spin-orbitals, one for each electron in the system, such that the sum is an eigenfunction of the total angular momenta operators L^2 , L_z , and the total spin operators S^2 , S_z . It can be considered to be a product of radial factors, one for each electron, an angular and a spin factor obtained by vector coupling methods. It is also required to be antisymmetric with respect to the interchange of any pair of electron coordinates. Often, the specification of the configuration and the final LS quantum numbers are sufficient to define the configuration state, but this is not always the case. Additional information about the order of coupling or the seniority of a subshell of equivalent electrons may be needed. Let γ specify the configuration information and any additional information about coupling to uniquely specify the configuration state function denoted by $\Phi(\gamma LS)$. Using the building rules as detailed in [5], the most general form of a given CSF obtained by coupling the m subshell functions from left to right is

$$\begin{aligned} \Phi(\gamma L S M_L M_S) &\equiv |\gamma L S M_L M_S\rangle \\ &\equiv |(n_1 l_1)^{w_1} \alpha_1 \nu_1 L_1 S_1 (n_2 l_2)^{w_2} \alpha_2 \nu_2 L_2 S_2 L_{12} S_{12} \\ &\quad \cdot (n_3 l_3)^{w_3} \alpha_3 \nu_3 L_3 S_3 L_{123} S_{123} \dots \\ &\quad \cdot (n_m l_m)^{w_m} \alpha_m \nu_m L_m S_m L S M_L M_S\rangle, \end{aligned} \quad (22.16)$$

where the additional numbers α_i and ν_i uniquely specify the single-shell (i) state when there is more than one term with the same $L_i S_i$ value.

The wave function for a many-electron system is usually labeled in the same manner as a CSF and generally desig-

nates the largest component. Thus, in the LS approximation,

$$\Psi(\gamma LS) = \sum_{\alpha=1}^M c_{\alpha} \Phi(\gamma_{\alpha} LS). \quad (22.17)$$

However, cases are known where the configuration states are so highly mixed that no dominant component can be found. Then the assignment is made using other criteria. Clearly, no two states should have the same label.

In the LSJ scheme, the angular- and spin-momenta are coupled to form an eigenstate of the total momenta J^2 , J_z . The label often still includes an LS designation, as in $2p^2\ ^3P_2$, but only the subscript J is a good quantum number. Thus,

$$\Psi(\gamma LSJ) = \sum_{\alpha=1}^M c_{\alpha} \Phi(\gamma_{\alpha} L_{\alpha} S_{\alpha} J). \quad (22.18)$$

22.2.2 Relativistic Dirac Orbitals and jj Configuration State Functions

In the Dirac–Coulomb(–Breit) framework, the radial functions now are a pair of spinors, as in the solution of the hydrogenic equations where

$$\phi_{n\kappa m}(r, \theta, \varphi) = \frac{1}{r} \begin{pmatrix} P_{n\kappa}(r) \Omega_{\kappa m}(\theta, \varphi) \\ i Q_{n\kappa}(r) \Omega_{-\kappa m}(\theta, \varphi) \end{pmatrix}, \quad (22.19)$$

with

$$\kappa = \begin{cases} -(l+1) & \text{for } j = l + \frac{1}{2} \quad (\kappa \text{ negative}) \\ +l & \text{for } j = l - \frac{1}{2} \quad (\kappa \text{ positive}) \end{cases}; \quad (22.20)$$

$P_{n\kappa}(r)$ and $Q_{n\kappa}(r)$ are, respectively, the radial functions of the large and small components of the Dirac spinor. Note that in the nonrelativistic limit ($c \rightarrow \infty$), $P_{n\kappa} \rightarrow P_{nl}$ and $Q_{n\kappa}$ is order α in the Pauli approximation [11]. The relativistic configurations are written as $(n_1\kappa_1)^{q_1}(n_2\kappa_2)^{q_2} \dots (n_m\kappa_m)^{q_m}$, where q_i is the occupation of subshell $(n_i\kappa_i)$. The relativistic equivalent of Eq. (22.17) is

$$\Psi(\gamma J) = \sum_{\alpha=1}^M c_{\alpha} \Phi(\gamma_{\alpha} J). \quad (22.21)$$

where each relativistic CSF, written in jj coupling, has the following form

$$\begin{aligned} \Phi(\gamma JM_J) &\equiv |\gamma JM_J\rangle \\ &\equiv |(n_1\kappa_1)^{w_1} \alpha_1 \nu_1 J_1 (n_2\kappa_2)^{w_2} \alpha_2 \nu_2 J_2 J_{12} \\ &\quad \cdot (n_3\kappa_3)^{w_3} \alpha_3 \nu_3 J_3 J_{123} \dots \\ &\quad \cdot (n_m\kappa_m)^{w_m} \alpha_m \nu_m J_m JM_J\rangle. \end{aligned} \quad (22.22)$$

22.3 Variational Principle

In all cases, the angular functions for one-electron orbitals are known. What needs to be determined in the nonrelativistic or Breit–Pauli schemes are the radial functions, $P(nl; r)$ or, in the relativistic case, the radial functions $P(n\kappa; r)$ and $Q(n\kappa; r)$. What differs for the different approaches are the underlying Hamiltonians and their one-electron radial functions [5].

Variational theory shows the equivalence between solutions of the wave equation, $(H - E)\psi = 0$, and stationary solutions of an energy functional. For bound states where approximate solutions Ψ are restricted to a square integrable subspace, say $\tilde{\mathcal{H}}$, the best solutions are those for which the energy functional

$$\mathcal{E}(\Psi) = \frac{\langle \Psi | H | \Psi \rangle}{\langle \Psi | \Psi \rangle} \quad (22.23)$$

is stationary. The condition $\delta\mathcal{E}(\Psi) = 0$ for all allowed variations $\delta\Psi$ leads to

$$\langle \delta\Psi | H - E | \Psi \rangle = 0, \quad \forall \delta\Psi \in \tilde{\mathcal{H}}, \quad E = \mathcal{E}(\Psi). \quad (22.24)$$

Several results readily follow. The eigenvalues of H are bounded from below. Let $E_0 \leq E_1 \leq \dots$. Then,

$$E_0 \leq \mathcal{E}(\Psi), \quad \forall \Psi \in \tilde{\mathcal{H}}. \quad (22.25)$$

Consequently, for any approximate wave function, the computed energy is an upper bound to the exact lowest eigenvalue. By the Hylleraas–Undheim–MacDonald theorem (Sect. 12.3.1) the computed excited states are also upper bounds to the exact eigenvalues, provided that the correct number of states lies below.

The Rayleigh–Ritz variational methods work the same way for Dirac and Schrödinger equations at the one-electron level: in both schemes, the bound eigenvalues have a lower bound. The dominant electron–electron interaction giving positive energy contributions, one can extend this conclusion to many-electron systems, allowing us to set up the Hartree–Fock and Dirac–Hartree–Fock methods in the same way [8] (Chap. 23).

22.4 Hartree–Fock and Dirac–Hartree–Fock Methods

In the nonrelativistic Hartree–Fock (HF) approximation, the approximate wave function consists of only one configuration state function. The radial function of each spin–orbital is assumed to depend only on the nl quantum numbers. These are determined using the variational principle and the non-relativistic Schrödinger Hamiltonian.

The energy functional can be written as an energy expression for the matrix element $\langle \Phi(\gamma LS) | H | \Phi(\gamma LS) \rangle$. Racah algebra may be used to evaluate the spin–angular contributions, resulting in two types of radial integrals.

One-body Let \mathcal{L} be the differential operator

$$\mathcal{L} = \frac{d^2}{dr^2} + \frac{2Z}{r} - \frac{\ell(\ell+1)}{r^2}. \quad (22.26)$$

Then,

$$I(nl, n'l') = -\frac{1}{2} \int_0^\infty P(nl; r) \times \mathcal{L}P(n'l'; r) dr. \quad (22.27)$$

Two-body The other integrals arise from the multipole expansion of the two-electron Coulomb interaction

$$\frac{1}{r_{12}} = \sum_k \frac{r_{<}^k}{r_{>}^{k+1}} P^k(\cos \theta), \quad (22.28)$$

where θ is the angle between the vectors \mathbf{r}_1 and \mathbf{r}_2 , and $r_{<}$, $r_{>}$ are the lesser and greater of r_1, r_2 , respectively. In general, let a, b, c, d be four nl quantum numbers, two from the left (bra) and two from the right (ket) CSF. Then,

$$R^k(ab, cd) = \int_0^\infty \int_0^\infty P(a; r_1) P(b; r_2) \times \frac{r_{<}^k}{r_{>}^{k+1}} P(c; r_1) P(d; r_2) dr_1 dr_2, \quad (22.29)$$

which is called a Slater integral. It has the symmetries

$$R^k(ad, cb) \equiv R^k(cb, ad) \equiv R^k(cd, ab) \\ \equiv R^k(ab, cd).$$

In the Hartree–Fock approximation, the Slater integrals that occur depend on only two sets of quantum numbers. These special cases are denoted separately as

$$F^k(a, b) \equiv R^k(ab, ab) \quad \text{and} \\ G^k(a, b) \equiv R^k(ab, ba). \quad (22.30)$$

The former is the direct interaction between a pair of orbitals, whereas the latter arises from the exchange operator.

The energy expression may be written as

$$\mathcal{E}(\gamma LS) = \sum_i^m q_i \left[I(n_i l_i, n_i l_i) + \frac{q_i - 1}{2} \sum_{k=0}^{2l_i} f_k(i, i) F^k(n_i l_i, n_i l_i) \right] + \sum_{j < i} q_i q_j \left[\sum_{k=0}^{2 \min(l_i, l_j)} f_k(i, j) F^k(n_i l_i, n_j l_j) + \sum_{k=|l_i - l_j|}^{l_i + l_j} g_k(i, j) G^k(n_i l_i, n_j l_j) \right]. \quad (22.31)$$

In general, the coefficients $f_k(i, j)$ and $g_k(i, j)$ depend not only on the configuration, but also on the subshells coupling tree γ leading to the final LS symmetry. An extremely useful concept, introduced by Slater, is the *average energy of a configuration*, $\mathcal{E}(\text{av})$. This is a weighted average of all possible LS terms, where the weighting factor is the term degeneracy $g_{LS} = (2L + 1)(2S + 1)$. In this case, the coefficients have simple formulas that only depend on the angular orbital momenta involved in the interaction, i.e., on the configuration

$$f_k(i, i) = f_k^{av}(l_i, l_i) = 1, \quad k = 0, \\ = -\left(\frac{2l_i + 1}{4l_i + 1} \right) \begin{pmatrix} l_i & k & l_i \\ 0 & 0 & 0 \end{pmatrix}^2, \quad k > 0 \\ f_k(i, j) = f_k^{av}(l_i, l_j) = \delta_{k,0}, \quad i \neq j \\ g_k(i, j) = g_k^{av}(l_i, l_j) \\ = -\frac{1}{2} \begin{pmatrix} l_i & k & l_j \\ 0 & 0 & 0 \end{pmatrix}^2, \quad i \neq j. \quad (22.32)$$

In the more general case, expression Eq. (22.31) involving the number of interacting pairs, $q_i(q_i - 2)/2$ and $q_i q_j$ for equivalent and nonequivalent electrons respectively, still holds, but these coefficients may become shell dependent for a given angular momenta pair. The part of the expression that depends on $P(n_i l_i; r)$, for example, is the negative of the removal energy of the entire $(n_i l_i)^{q_i}$ subshell, say $-\bar{\mathcal{E}}[(n_i l_i)^{q_i}]$, a negative quantity. The stationary condition for a Hartree–Fock solution applies to this expression, but since the variations must be constrained in order to satisfy orthonormality assumptions, Lagrange multipliers λ_{ij} need to be introduced. The stationary condition applies to the functional

$$\mathcal{F}[P(n_i l_i)] = -\bar{\mathcal{E}}[(n_i l_i)^{q_i}] + \sum_j \delta_{i,j} \lambda_{ij} \langle P(n_i l_i) | P(n_j l_j) \rangle. \quad (22.33)$$

Applying the variational conditions to each of the integrals and dividing by $-q_i$, we get the equation

$$\left(\frac{d^2}{dr^2} + \frac{2}{r} [Z - Y(n_i l_i; r)] - \frac{l_i(l_i + 1)}{r^2} - \varepsilon_{ii} \right) P(n_i l_i; r) = \frac{2}{r} X(n_i l_i; r) + \sum_{j \neq i} \delta_{l_i, l_j} \varepsilon_{ij} P(n_j l_j; r), \quad (22.34)$$

where

$$\begin{aligned} Y(n_i l_i; r) &= (q_i - 1) \sum_k f_k(i, i) Y^k(n_i l_i n_i l_i; r) \\ &\quad + \sum_{j \neq i} q_j \sum_k f_k(i, j) Y^k(n_j l_j n_j l_j; r), \\ X(n_i l_i; r) &= \sum_{j \neq i} q_j \sum_k g_k(i, j) Y^k(n_i l_i n_j l_j; r) \\ &\quad \times P(n_j l_j; r), \end{aligned} \quad (22.35)$$

with

$$Y^k(ab; r) = r \int_0^\infty \frac{r^k}{r^{k+1}} P(a; s) P(b; s) ds. \quad (22.36)$$

The above is the standard derivation for Hartree–Fock differential equations. Numerical methods for their solution treat the exchange and Lagrange multiplier contributions as part of an inhomogeneous term [16] even though the equation is of eigenvalue type.

22.4.1 Diagonal Energy Parameters and Koopmans' Theorem

The diagonal (ε_{ii}) and off-diagonal (ε_{ij}) energy parameters are related to the Lagrange multipliers by $\varepsilon_{ii} = 2\lambda_{ii}/q_i$ and $\varepsilon_{ij} = \lambda_{ij}/q_i$. In fact,

$$\varepsilon_{ii} = \frac{2}{q_i} \bar{E}[(n_i l_i)^{q_i}] - (q_i - 1) \sum_k f_k(i, i) F^k(n_i l_i, n_i l_i), \quad (22.37)$$

where $\bar{E}[(n_i l_i)^{q_i}]$ is the Hartree–Fock value of the removal energy functional $\bar{E}[(n_i l_i)^{q_i}]$. In the special case where $q_i = 1$, ε_{ii} is twice the removal energy or ionization energy. This is often referred to as Koopmans' theorem.

22.4.2 Hartree–Fock Operator

By introducing an exchange operator, \bar{X} , Eq. (22.34) can be written as an eigenvalue problem. Applying the stationary

condition, the variation of each orbital a results in a system of m coupled eigenvalue equations where m is the number of orbitals. The equations are coupled by the orthogonality constraints. For a CSF (like $1s^2 2s$) with only two orbitals a, b , subject to orthogonality, the equations have the form [17]

$$\begin{bmatrix} H^a & 0 \\ 0 & H^b \end{bmatrix} \begin{bmatrix} P_a \\ P_b \end{bmatrix} = \begin{bmatrix} \varepsilon_{aa} & \varepsilon_{ab} \\ \varepsilon_{ba} & \varepsilon_{bb} \end{bmatrix} \begin{bmatrix} P_a \\ P_b \end{bmatrix}, \quad (22.38)$$

where H^a , for example, is the integro-differential operator

$$\begin{aligned} H^a &= q_a \left[-\frac{1}{2} \frac{d^2}{dr^2} - \frac{Z}{r} + \frac{l_a(l_a + 1)}{2r^2} \right] \\ &\quad + Y(a; r) + \bar{X}(a; r), \end{aligned} \quad (22.39)$$

and

$$\bar{X}(a; r) P_a(r) = \sum_{bk} g_{abk} \left(\frac{Y^k(ab; r)}{r} \right) P_b(r). \quad (22.40)$$

Contributions to the direct potential $Y(a; r)$ arise from the $F^k(ab)$ integrals in the energy functional, whereas contributions to the exchange potential $\bar{X}(a; r)$ arise from the $G^k(ab)$ terms. In other words, for the exchange contributions, the function $P_a(r)$ is part of an integrand, making the equation an integro-differential equation of eigenvalue type when $\varepsilon_{ab} = 0$.

In these equations, where the variation is *not* divided by an occupation number, the matrix (ε_{ab}) is called the energy matrix [16] and is symmetric since its elements are directly related to Lagrange multipliers ensuring orthonormality. Consequently,

$$\begin{aligned} \varepsilon_{aa} &= \langle P_a | H^a | P_a \rangle, & \varepsilon_{ab} &= \langle P_b | H^a | P_a \rangle, \\ \varepsilon_{ba} &= \langle P_a | H^b | P_b \rangle, & \varepsilon_{bb} &= \langle P_b | H^b | P_b \rangle. \end{aligned} \quad (22.41)$$

Equation (22.39) represents the conditions that a stationary solution must satisfy when single orbitals are perturbed. In Hartree's book [18] this was the only condition. In fact, the variational principle requires a solution be stationary for *all* allowed perturbations. The latter includes orthogonal transformations. The condition that a solution be stationary to such transformations leads to an implicit condition that a solution must satisfy and not a computational procedure.

Orthogonal transformations of orbitals are related to the "rotation" of orbitals in orbital space. In a two-dimensional space, such a transformation can be defined in terms of a single parameter $\epsilon \in [-1, 1]$ as in

$$\mathbf{O} = \begin{bmatrix} 1 & -\epsilon \\ \epsilon & 1 \end{bmatrix} / \sqrt{1 + \epsilon^2}, \quad (22.42)$$

where $1/\sqrt{1+\epsilon^2} = \cos(\theta)$ and θ represents the angle of rotation. The radial transformation $P^* = OP$ allows the effect of a rotation on the energy to be expanded in powers of ϵ , namely,

$$E(\epsilon) = E(0) + g\epsilon + g'\epsilon^2 + \text{higher-order terms},$$

where g represents the gradient of the energy with respect to rotation, and $E(0)$ is the energy before orbitals are rotated. Then the stationary condition

$$\frac{\partial E}{\partial \epsilon} = 0 = g + 2g'\epsilon \quad (22.43)$$

leads to $\epsilon = -g/(2g')$. When this condition is satisfied, rules for determining g and g' from the energy expression are given in [19]. When g and g' are both zero, a unique solution does not exist, as for $1s^2 2s^2$.

22.4.3 Brillouin's Theorem

The Hartree–Fock approximation has some special properties not possessed by other single configuration approximations. One such property is referred to as satisfying Brillouin's theorem.

Let $\Phi^{\text{HF}}(\gamma LS)$ be a Hartree–Fock configuration state function (CSF), where γ denotes the configuration and coupling scheme. With $\Phi^{\text{HF}}(\gamma LS)$ are associated the m Hartree–Fock radial functions $P^{\text{HF}}(n_1 l_1; r)$, $P^{\text{HF}}(n_2 l_2; r)$, ..., $P^{\text{HF}}(n_m l_m; r)$. To this set may be added virtual orbitals that maintain the necessary orthonormality conditions. Let one of the radial functions (nl) be replaced by another ($n'l$), either occupied or virtual, without any change in the coupling of the spin–angular factor. Let the resulting function be denoted by $F(nl \rightarrow n'l)$.

The perturbation of the Hartree–Fock radial function, $P(nl; r) \rightarrow P^{\text{HF}}(nl; r) + \epsilon P(n'l; r)$ induces a perturbation $\Phi^{\text{HF}}(\gamma LS) \rightarrow \Phi^{\text{HF}}(\gamma LS) + \epsilon F(nl \rightarrow n'l)$. But the Hartree–Fock energy is stationary with respect to such variations and so,

$$\langle \Phi^{\text{HF}}(\gamma LS) | H | F(nl \rightarrow n'l) \rangle = 0. \quad (22.44)$$

If the function $F(nl \rightarrow n'l)$ is a CSF for a configuration γ^* , or proportional to one, then Brillouin's theorem is said to hold between the two configuration states. It may happen that $F(nl \rightarrow n'l)$ is a linear combination of CSFs. An example is the $2p \rightarrow 3p$ replacement from $2p^3 {}^2P$, yielding a linear combination of $\{2p^2({}^1S)3p, 2p^2({}^3P)3p, 2p^2({}^1D)3p\}$, the linear combination being determined by coefficients of fractional parentage. Thus, Brillouin's theorem will not hold for any of the three individual configuration states in the above equation, only for a specific linear combination.

When perturbations are in the form of a rotation of orbitals it has the form $F(nl \rightarrow n'l, n'l \rightarrow -nl)$. For $1s^2 2s^2 {}^2S$, the simultaneous perturbations, $F(1s \rightarrow 2s, 2s \rightarrow -1s)$, lead to a linear combination of $\{1s 2s^2 {}^2S, 1s^3 {}^2S\}$. The CSF for the $1s^3 {}^2S$ is identically zero by antisymmetry, and so Brillouin's theorem holds for the lithium-like ground state. In the $1s 2s^3 {}^3S$ state, neither the $1s \rightarrow 2s$ nor the $2s \rightarrow 1s$ substitutions are allowed; in fact, it can be shown that for these states, Brillouin's theorem holds for all monoexcited configurations. The same is not true for $1s 2s^1 {}^1S$ where the simultaneous perturbations lead to the condition

$$\langle \Phi^{\text{HF}}(1s 2s^1 {}^1S) | H | [\Phi(1s^2) - \Phi(2s^2)] \rangle = 0. \quad (22.45)$$

Thus, Brillouin's theorem is not obeyed for either the $\Phi(1s^2)$ or $\Phi(2s^2)$ CSF in an HF calculation for $1s 2s$.

The importance of Brillouin's theorem lies in the fact that certain interactions have already been included to first order. This has the consequence that certain classes of diagrams can be omitted in many-body perturbation theory [20].

22.4.4 The Dirac–Hartree–Fock Equations

In jj -coupling, many subshells split into two subshells, so occupation numbers are different. For example, $2p^6 \rightarrow 2p_-^2 2p_+^4$, where $2p_- \equiv 2p_{j=1/2}$ and $2p_+ \equiv 2p_{j=3/2}$. Instead of one second-order differential equation, the Dirac–Hartree–Fock equations are a pair of first-order equations

$$\begin{aligned} q_a \begin{bmatrix} V(a; r) & -c \left[\frac{d}{dr} - \frac{\kappa_a}{r} \right] \\ c \left[\frac{d}{dr} + \frac{\kappa_a}{r} \right] & V(a; r) - 2c^2 \end{bmatrix} \begin{bmatrix} P_a(r) \\ Q_a(r) \end{bmatrix} \\ = \sum_b \epsilon_{ab} \delta_{\kappa_a \kappa_b} \begin{bmatrix} P_b(r) \\ Q_b(r) \end{bmatrix}, \end{aligned} \quad (22.46)$$

where $V(a; r) = (V_{\text{nuc}}(r) + Y(a; r) + \bar{X}(a; r))$. In this expression, $V_{\text{nuc}}(r)$ is the effective electron–nucleus potential at radius r that can take into account the finite size of the nuclear charge distribution, $Y(a; r)$ is the direct potential, and $\bar{X}(a; r)$ contains the exchange contributions in integro-differential form as described above in the HF method. For bound state solutions, the boundary conditions are $P_a(r) = 0$ at $r = 0$ and $r \rightarrow \infty$, as well as for $Q_a(r)$. A more detailed discussion is presented in Chap. 23.

22.4.5 Numerical Solution of Variational Equations

Numerical methods based on finite differences for the integro-differential equations [21] are implemented in both

ATSP [1, 2] and GRASP [3, 4] computer codes. Both methods perform outward and inward integration procedures with energy adjustments to match the joins. Because the equations are of eigenvalue type with many solutions, node counting is needed to control the convergence to a particular solution. Because of orbital rotation, node counting is an art since nodes with small amplitudes in the tail region may need to be ignored. Both codes rely on several methods to solve the equations in the event that the default method fails.

When radial functions (nonrelativistic or relativistic) are expressed as expansions over a B-spline basis, and the Galerkin method is used for determining the expansion coefficients, the equations can be solved using matrix eigenvalue methods. These have been implemented in a B-spline Hartree–Fock program, named SPHF for (B-)“Spline Hartree-Fock” [19].

Given a grid of strictly increasing knots, $t_i, i = 0, \dots, n_v, t_{i-1} < t_i$, where t_0 and t_{n_v} are knots of multiplicity k , the B-spline functions $B_i^k(r), i = 1, \dots, n_v$ form a basis for piecewise polynomial functions that are polynomials of degree $k - 1$ in each interval and whose derivatives up to order $k - 2$ are continuous at the interior knots. The number of basis elements is $n_s = n_v + k - 1$, where each basis function is nonzero over k adjacent intervals. Furthermore, only $B_1^k(r)$ is nonzero at $r = t_0$, and $B_{n_s}(r)$ is nonzero at $r = t_{n_v}$. For atoms, $t_0 = 0$, and the last grid point is referred to as R . Thus, the grid defines a sequence of subintervals over the range $[0, R]$. The spline basis is determined recursively as

$$B_i^k(r) = \frac{r - t_i}{t_{i+k-1} - t_i} B_i^{k-1}(r) + \frac{t_{i+k} - r}{t_{i+k} - t_{i+1}} B_{i+1}^{k-1}(r), \quad (22.47)$$

where

$$B_i^1 = \begin{cases} 1, & t_i \leq r \leq t_{i+1} \\ 0, & \text{otherwise} \end{cases}. \quad (22.48)$$

A radial function for orbital a , say $P(a; r)$, in this piecewise polynomial function space has associated with it a vector $a = (a_1, a_2, \dots, a_{n_s})$ of expansion coefficients so that

$$P(a; r) = \sum_{i=1}^{n_s} a_i B_i^k(r). \quad (22.49)$$

Note that as an argument, a simply denotes an orbital. For bound orbitals the boundary conditions are $a_1 = a_{n_s} = 0$, but for additional numerical stability we apply two boundary conditions at the end of the range (equivalent to $P(R) = P'(R) = 0$), namely $a_{n_s-1} = a_{n_s} = 0$. Additional boundary conditions could also be applied at the origin to enforce r^{l+1} behavior but has not been applied in this program. The L_2 norm in this function space is

$$|P(a; r)|^2 = a^t B a,$$

where $B = B(i, j)$ is the matrix of overlap integrals,

$$B(i, j) = \int B_i^k(r) B_j^k(r) dr.$$

It is a symmetric, positive definite, banded matrix of bandwidth $2k_s - 1$.

Given an energy expression for a Hartree–Fock wave function, assuming for the time being that there are no orthogonality constraints, and applying the variational principle to it [19], yields the generalized eigenvalue problem

$$(H^a - \varepsilon_{aa} B) a = 0, \quad (22.50)$$

where H^a and B are matrices of size $n_s \times n_s$ before boundary conditions are applied. When exchange terms are present, the matrix H^a is a full matrix. Thus, a is the m^{th} eigenvector of the generalized eigenvalue problem, where m depends on the nl quantum numbers and possible orthogonality constraints, with $m = 1$ being the lowest eigenvalue satisfying the orthogonality constraints.

When two orbitals, a and b , are constrained through orthogonality and both are varied, Lagrange multipliers $\varepsilon_{aa}, \varepsilon_{ab} = \varepsilon_{ba}, \varepsilon_{bb}$ must be introduced, and the equations for the pair become [17]

$$\begin{bmatrix} H^a & \\ & H^b \end{bmatrix} \begin{bmatrix} a \\ b \end{bmatrix} - \begin{bmatrix} \varepsilon_{aa} & \varepsilon_{ab} \\ \varepsilon_{ba} & \varepsilon_{bb} \end{bmatrix} \begin{bmatrix} B a \\ B b \end{bmatrix} = 0. \quad (22.51)$$

Projection operators may then be applied to eliminate the off-diagonal Lagrange multipliers so that each equation then becomes a generalized eigenvalue problem.

Since the matrix H^a depends on current estimates of orbitals, an iterative method of solution is needed. For singly occupied orbitals, the eigenvalue method is ideal, but for multiply occupied orbitals, the equations can be viewed as a system of nonlinear equations for which the Newton–Raphson method can yield quadratic convergence. The SCF process, in which orbitals are updated one at a time, has been implemented as follows:

```

For each orbital i = 1, nwf
  For each orbital j = 1, nwf
    call rotate (i, j), if needed
  compute H
  if qsum(i) = 1 or orbital estimates are not accurate,
    then apply projection operators, if necessary,
    and call HF-eigenvalue procedure
  else
    call HF-Newton-Raphson procedure

```

In the above, $qsum(i)$ is the occupation number of orbital i , and nwf is the number of one-electron wave functions

or radial functions. Results to machine accuracy can be obtained.

The DBSR [22] code uses spline methods for solving Dirac–Hartree–Fock equations. Technically, the Hartree–Fock method assumes a single CSF, but it is convenient to relax the definition in the relativistic case to the equivalent of a nonrelativistic Hartree–Fock calculation. For example, the $2p^3\ ^3P_{3/2}$ nonrelativistic CSF is a linear combination of $2p^3$, $2p^22p_-$, and $2p2p_-^2$, $J = 3/2$ CSFs in jj -coupling.

An advantage of the eigenvalue method is that, once the HF or DHF potential has been determined, the set of all eigenstates having the same boundary conditions at $r = R$ can be computed, where R defines the range of the desired bound state. This set of eigenstates defines a complete basis for perturbation theory based calculations (Chap. 24).

A feature of B-spline Galerkin methods is that the spectrum for the second-order Schrödinger radial equation and the pair of first-order equations are not the same. This can readily be confirmed by comparing results from $y'' = -\lambda^2 y$ and $y' = \lambda z$, $z' = -\lambda y$, where both y and z are expanded in a basis of B-splines of the order k . However, if z is expanded in a basis of order $k - 1$, and y is a function expanded in a basis of order k , then the equation $y' = -\lambda z$ can be solved exactly since both y' and z are in the same $k - 1$ function space. However, an error would be introduced when z is expanded in a basis of order k that the Galerkin method would minimize. The most important result is that expansions in a $(k, k - 1)$ basis reproduce an R -matrix boundary condition [23], which is important in R -matrix theory for continuum processes.

22.4.6 Properties of Hartree–Fock Solutions

Term dependence The radial distribution for a given nl orbital may depend significantly on the LS term. A well-known example is the $1s^22s2p$ configuration in Be, which may couple to form either a $^3P^\circ$ or $^1P^\circ$ term. The energy expression differs only in the exchange interaction, $\pm(1/3)G^1(2s, 2p)$, where the $+$ refers to $^1P^\circ$ and the $-$ to $^3P^\circ$. Clearly, the energies of these two terms differ. What is not quite as obvious is the extent to which the $P(2p; r)$ radial functions differ for the two states. The most affected orbital is the one that is least tightly bound, which, in this case, is the $2p$ orbital. Figure 22.1 shows the two radial functions. The $^1P^\circ$ $2p$ orbital is far more diffuse (not as localized) as the one for 3P . Such a change in an orbital is called LS term dependence.

Orbital collapse Another phenomenon, called *orbital collapse*, occurs when an orbital rapidly contracts as a function of the energy. This could be an LS -dependent effect, but it can also occur along an isoelectronic sequence. This effect

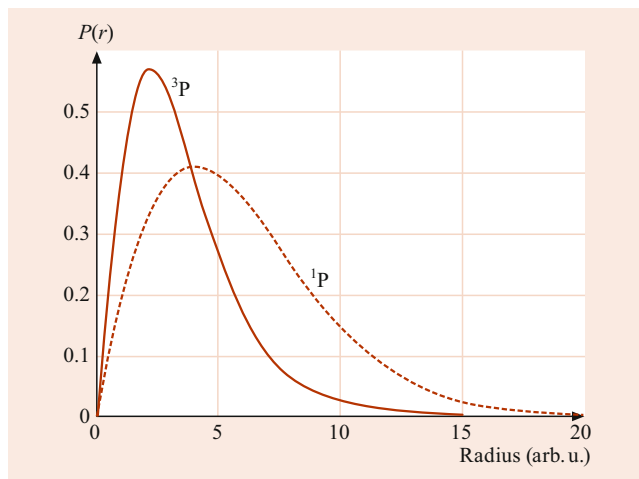


Fig. 22.1 A comparison of the $2p$ Hartree–Fock radial functions for the $1s2p\ ^1,^3P^\circ$ states of Be

is most noticeable in the high- l orbitals with large angular momenta. In hydrogen, the mean radius of an orbital is $\langle r \rangle = (1/2)[3n^2 - l(l + 1)]a_0$. Thus, the higher- l orbitals are more contracted; but in neutral systems, the high- l orbitals have a higher energy and are more diffuse. This is due, in part, to the $l(l + 1)/r^2$ angular momentum barrier that appears in the definition of the \mathcal{L} operator. In the Hartree model, it is possible for $V(r) + l(l + 1)/r^2$ to have two wells: an inner well and an outer shallow well [24]. As the lowest eigenfunction changes rapidly from the outer well to the inner well, as Z changes, orbital collapse is said to occur.

Quantum defects and Rydberg series Spectra of atoms often exhibit phenomena associated with a Rydberg series of states where one of the electrons is in an nl orbital, with n assuming a sequence of values. An example is the $1s^22snd\ ^3D$ series in Be, $n = 3, 4, 5, \dots$. For such a series, a useful concept is that of a quantum defect parameter δ . In hydrogen, the ionization energy (I_P) in atomic units is $1/(2n^2)$. In complex neutral systems, the effective charge would be the same at large r . As n increases, the mean radius becomes larger, and the probability of the electron being in the hydrogen-like potential increases. Thus, one could define an effective quantum number, $n^* = n - \delta$, such that

$$I_P(nl) = \frac{1/2}{(n - \delta)^2}. \quad (22.52)$$

For ionized systems, the equation must be modified to $I_P(nl) = (1/2)[(Z - N + 1)/(n - \delta)]^2$.

Often, this parameter is defined with respect to observed data, but it can also be used to evaluate Hartree–Fock energies, where $I_P = \varepsilon_{nl, nl}/2$, so that

$$\varepsilon_{nl, nl} = \left(\frac{Z - N + 1}{n - \delta} \right)^2.$$

Table 22.1 The effective quantum number and quantum defect parameters of the $2snd$ Rydberg series in Be

n	3D		1D	
	n^*	$\delta(nl)$	n^*	$\delta(nl)$
3	2.968	0.032	3.014	-0.014
4	3.960	0.040	4.012	-0.012
5	4.957	0.043	5.013	-0.013
6	5.955	0.045	6.013	-0.013

Table 22.1 shows the effective quantum number and quantum defect for the Hartree–Fock $2snd$ 3D and 1D orbitals in Be as a function of n . For the triplet spectrum, the quantum defect is positive, whereas for the singlet it is negative. This is the effect of exchange. Note that as n increases, the quantum defect becomes constant. This observation is often the basis for determining ionization potentials from observed data.

22.5 Multiconfiguration (Dirac)-Hartree–Fock Method

The Hartree–Fock method predicts many atomic properties remarkably well, but when analyzed carefully, systematic discrepancies can be observed. Consider the ionization potentials tabulated in Table 22.2 compared with the observed values. In these calculations, the energy of the ion was computed using the same radial functions as for the atom. Thus, no *relaxation* effects were included.

The observed data include other effects as well, such as relativistic effects, finite mass and volume of the nucleus, but these are small for light atoms. For these systems, the largest source of discrepancy arises from the fact that the Hartree–Fock solution is an independent particle approximation to the exact solution of Schrödinger’s equation. Neglected entirely is the notion of *correlation in the motion of the electrons*; each electron is assumed to move independently in a field determined by the other electrons. For this reason, the error in the energy was defined by Löwdin [25], to be the correlation energy, that is,

$$E^{\text{corr}} = E^{\text{exact}} - E^{\text{HF}}. \quad (22.53)$$

Table 22.2 Observed and Hartree–Fock ionization potentials for the ground states of neutral atoms, in eV (also Table 22.3)

Atom	Obs.	HF	Diff.
Li	5.39	5.34	0.05
Be	9.32	8.42	0.90
B	8.30	8.43	-0.13
C	11.26	11.79	-0.53
N	14.53	15.44	-0.91
O	13.62	14.45	-0.85
F	17.42	18.62	-1.20
Ne	21.56	23.14	-1.58

In this definition, E^{exact} is not the observed energy—it is the exact solution of Schrödinger’s equation, which itself is based on a number of assumptions.

22.5.1 Z -Dependent Theory

An indication of the important correlation corrections can be obtained from a perturbation theory study of the exact wave function. In the following section, we closely follow the approach taken by Layzer et al. [26] in the study of the Z -dependent structure of the total energy.

Let us introduce a new scaled length, $\rho = Zr$. Then, the Hamiltonian becomes

$$H = Z^2(H_0 + Z^{-1}V), \quad (22.54)$$

where

$$H_0 = -\frac{1}{2} \sum_i \left(\nabla_i^2 + \frac{2}{\rho} \right), \quad (22.55)$$

$$V = \sum_{i>j} \frac{1}{\rho_{ij}}, \quad (22.56)$$

and Schrödinger’s equation becomes

$$(H_0 + Z^{-1}V)\psi = (Z^{-2}E)\psi. \quad (22.57)$$

With $Z^{-1}V$ regarded as a perturbation, the expansions of ψ and E in the powers of Z^{-1} are

$$\psi = \psi_0 + Z^{-1}\psi_1 + Z^{-2}\psi_2 + \dots \quad (22.58)$$

in the ρ unit of length, and

$$E = Z^2(E_0 + Z^{-1}E_1 + Z^{-2}E_2 + Z^{-3}E_3 + \dots). \quad (22.59)$$

The zero-order equation is

$$H_0\psi_0 = E_0\psi_0. \quad (22.60)$$

The solutions of this equation are products of hydrogenic orbitals.

Let $|(nl)vLS\rangle$ be a configuration state function constructed by vector coupling methods from products of hydrogenic orbitals. Here, (nl) represents a set of N quantum numbers $(n_1l_1, n_2l_2, \dots, n_Nl_N)$ and v any additional quantum numbers, such as the coupling scheme or seniority needed to distinguish the different configuration states. Then,

$$H_0|(nl)vLS\rangle = E_0|(nl)vLS\rangle, \quad (22.61)$$

$$E_0 = -\frac{1}{2} \sum_i \frac{1}{n_i^2}. \quad (22.62)$$

Since E_0 is independent of the l_i , different configurations may have the same E_0 ; that is, E_0 is degenerate. According to first-order perturbation theory for degenerate states, ψ_0 then is a linear combination of the degenerate configuration state functions $|(nl')v'LS\rangle$ with the same set of principal quantum numbers n_i and parity π . The coefficients are components of an eigenvector of the interaction matrix $\langle (nl')v'LS|V|(nl)vLS\rangle$, and E_1 is the corresponding eigenvalue. This is the set of configurations referred to as the *complex* by Layzer [27] and denoted by the quantum numbers $(n)\pi LS$. The relativistic generalization of the non-relativistic Z -dependent theory of many-electron atoms was described by Layzer and Bahcall [28].

The zero-order wave function ψ_0 describes the many-electron system in a general way. It can be shown that the square of the expansion coefficients of ψ_0 over the degenerate set of configuration states can be interpreted as a probability that the many-electron system is in that configuration state, that ψ_1 is then a weighted linear combination of first-order corrections to each such configuration state. Let us now assume the nondegenerate case where $\psi_0 = \Phi(\gamma LS)$. The configurations interacting with γLS are of two types: those that differ by a single electron (single substitution S) and those that differ by two electrons (double substitution D). The former can be further subdivided into three categories:

- (i) Those that differ from γLS by one principal quantum number but retain the same spin–angular coupling. These configuration states are part of *radial correlation*.
- (ii) Those that differ by one principal quantum number but differ in their coupling. If the only change is the coupling of the spins, the configuration states are part of *spin polarization*.
- (iii) Those that differ in the angular momentum of one electron and are accompanied by a change in angular coupling of the configuration state and possibly also the spin coupling. The latter represent *orbital polarization*.

The sums over intermediate states involve infinite sums. In practice, the set of orbitals is finite. In the nondegenerate case, these orbitals can be divided into occupied orbitals and unoccupied, or virtual, orbitals, depending on whether or not they occur in the *reference configuration* that defines γLS . Single and double (SD) replacements of occupied orbitals by other occupied or virtual orbitals generate the set of configurations that interact with ψ_0 . Consider the $1s^2 2s$ ground state of Li and the $\{1s, 2s, 3s, 4s, 2p, 3p, 4p, 3d, 4d, 4f\}$ set of orbitals, which we will refer to as the $n = 4$ set. The $1s$ and $2s$ orbitals are occupied, and all the other orbitals are virtual orbitals, vl . The set of replacements can then be classified as described in Table 22.3.

The above discussion has considered only the Z -dependence of the wave function, but the notion can readily

Table 22.3 Classification of replacements from the $1s^2 2s$ ground state of Li. The $1s$ and $2s$ orbitals are occupied, and all the other orbitals are virtual orbitals, vl

Replacement	Configuration	Type of correlation
$1s \rightarrow 2s$	$1s2s^2$	Radial and spin polarization
$2s \rightarrow vs$	$1s^2 vs$	Radial
$1s \rightarrow vs$	$1svs(^1S)2s$	Radial
	$1svs(^3S)2s$	Spin polarization
$1s2s \rightarrow vlv'l$	$1svl v'l$	Core polarization
$1s^2 \rightarrow vlv'l$	$2svl v'l$	Core

be extended to other properties. For example, in transition studies, the dipole transition matrix element decreases as $1/Z$, whereas the transition energy increases linearly with Z for $\Delta n = 0$ transitions, and quadratically as Z^2 otherwise. A first-order theory for oscillator strengths (FOTOS) [29] is based on similar concepts.

22.5.2 The MC(D)HF Approximation

In the multiconfiguration Hartree–Fock (MCHF) method, the wave function is approximated by a linear combination of orthogonal configuration states so that

$$\Psi(\gamma LS) = \sum_i^M c_i \Phi(\gamma_i LS), \quad (22.63)$$

where

$$\sum_i^M c_i^2 = 1.$$

Then the energy expression becomes

$$\mathcal{E}[\Psi(\gamma LS)] = \sum_i^M \sum_j^M c_i c_j H_{ij}, \quad (22.64)$$

where

$$H_{ij} = \langle \Phi(\gamma_i LS) | H | \Phi(\gamma_j LS) \rangle. \quad (22.65)$$

Because $H_{ij} = H_{ji}$, the sum over i, j may be limited to the diagonals and the lower part of the matrix $\mathbf{H} = (H_{ij})$, called the *interaction matrix*. Let $\mathbf{c} = (c_i)$ be a column vector of the expansion coefficients, also called *mixing coefficients*. Then the energy of the system is

$$E = \mathbf{c}^T \mathbf{H} \mathbf{c}. \quad (22.66)$$

Let \mathbf{P} be the column vector of radial functions, $(P_a, P_b, \dots)^T$. Since the interaction matrix elements depend on the radial functions, it is clear that the energy functional depends on both \mathbf{P} and \mathbf{c} .

In deriving the MCHF equations, the energy needs to be expressed in terms of the radial functions and c . From the theory of angular momenta, it follows that

$$H_{ij} = \sum_{ab} q_{ab}^{ij} I(a, b) + \sum_{abcd;k} v_{abcd;k}^{ij} R^k(ab, cd), \quad (22.67)$$

where the sum over ab or $abcd$ covers the occupied orbitals of configuration states i and j .

Substituting into the energy expression Eq. (22.64) and interchanging the order of summation, we get

$$\mathcal{E}(\Psi) = \sum_{ab} q_{ab} I(a, b) + \sum_{abcd;k} v_{abcd;k} R^k(ab, cd), \quad (22.68)$$

where

$$q_{ab} = \sum_i \sum_j c_i c_j q_{ab}^{ij} \quad \text{and} \\ v_{abcd;k} = \sum_i \sum_j c_i c_j v_{abcd;k}^{ij}.$$

In this form, the energy is expressed as a list of integrals and their contribution to the energy, a form suitable for the derivation of the MCHF radial equations.

As in the derivation of the Hartree–Fock equations, the stationary principle must be applied to a functional that includes Lagrange multipliers for all the orthonormality constraints. Thus,

$$\mathcal{F}(\mathbf{P}, \mathbf{c}) = \mathcal{E}(\Psi) + \sum_{a < b} \delta_{\ell_a, \ell_b} \lambda_{ab} \langle a | b \rangle - E \sum_i c_i^2. \quad (22.69)$$

In deriving the stationary conditions with respect to variations in c_i , the most convenient form for $\mathcal{E}(\Psi)$ is Eq. (22.64), which leads to the secular equation

$$\mathbf{H} \mathbf{c} = E \mathbf{c}. \quad (22.70)$$

Thus, the Lagrange multiplier E is the total energy of the system.

The requirement of a stationary condition with respect to variations in the radial functions leads to a system of equations with exactly the same form as the Hartree–Fock equations except: (i) the occupation numbers q_{aa} are no longer integers but rather *expected* occupation numbers, and (ii) the operator $\tilde{X}(a; r)$ arises not only from the exchange of electrons within a configuration state but also from interactions between configuration states. Differential equation methods divide the variation of the energy functional by q_{aa} . Since the latter may approach zero, the associated diagonal energies become large, but this no longer implies a large binding energy [30, 31]. Computationally, methods such as

those used for eigenvalue methods that retain the symmetry of the energy matrix are preferred.

A solution of the MCHF problem requires the simultaneous solution of the secular equation and the variational radial equations. When the latter are assumed to be given, then only the secular problem needs to be solved, and the problem is called a *configuration interaction* (CI) problem. If any radial function is optimized, the calculation is called a *multiconfiguration Hartree–Fock* (MCHF) calculation. The iterative procedure for its solution is the MCHF-SCF method, the details of which can be found in [21].

The derivation of the MCDHF equations is very similar [5], using a configuration space spanned by relativistic CSFs and the DCB Hamiltonian for building the interaction matrix.

22.5.3 Systematic Methods

For MCHF calculations with only a few configuration states, the latter must be carefully chosen. According to first-order perturbation theory, the expansion coefficient is $c_i = \langle \Phi_i | H | \Phi_0 \rangle / (E_0 - E_i)$. Clearly, configurations near in energy to the state under investigation are candidates for a strong interaction, but it is also important to remember the numerator in this expression. Generally, the latter is large if the electrons in the two configurations occupy the same region of space. Thus, in the ground state of beryllium, the strongest mixing is with $2p^2\ ^1S$, even though the energy of the latter is far removed from the energy of $2s^2\ ^1S$. In highly ionized systems, the complex identifies the configurations that might interact strongly, but for neutral systems, there are many exceptions, particularly in atoms such as the transition metals where the 4s and 4p subshells may be filled before the 3d subshell.

For large-scale computation, it is desirable to define the configuration states systematically in terms of an active set (AS) of orbitals. Several notations are commonly used for this set. A very simple designation is *the $n = 4$ active set* in that all orbitals up to and including those with principal quantum number $n = 4$ are included. Another notation common in quantum chemistry is one where the number of orbitals of each symmetry is specified, as in 4s3p2d1f.

Closely associated with this set is the set of configuration states that can be generated. The latter is referred to as the complete active space (CAS). Often, the CAS is defined relative to a set of closed shells (or subshells) common to all configurations. For example, the complex for the $3s^2 3p^2\ ^3P$ ground state of Si, is a neon-like core, $1s^2 2s^2 2p^6$, coupled to the $\{N = 4, \pi = \text{even},\ ^3P\}$ CAS of the active set $\{3s, 3p, 3d\}$. If the AS is extended to $\{3s, 3p, 3d, 4s, 4p, 4d, 4f\}$, then all single, double, triple, quadruple (SDTQ) replacements from the outer four electrons are generated. Of course, the number

of CSF increases rapidly, both with the size of the active set and with the number of electrons N defining the CAS. The size of a CAS expansion in neon $\{N = 10, \pi = \text{even}, {}^1\text{S}\}$ grows from 4567 CSFs for the $3s2p1d$ AS to 3986026 CSFs for $4s3p2d1f$. For this reason, other models may be used, such as multireference singles and doubles (MR–SD) modeled on the results of Z -dependent perturbation theory. These multireference functions may be extended to include all important contributors to a wave function. Calculations in which correlation is restricted to a few outer electrons is called *valence correlation*.

A consequence of a CAS expansion is that the MCHF problem may be over determined: a rotation of radial functions of the same symmetry merely transforms the CSFs and the expansion coefficients. The wave function and energy do not change. When similar situations occur in Hartree–Fock theory, Koopmans’ theorem requires that the Lagrange multiplier associated with the rotation be set to zero. In MCHF calculations, the degree of freedom is usually used to eliminate a CSF or, more precisely, to determine that solution for which a specific CSF has a zero expansion coefficient. A generalized Brillouin’s theorem (GBT) then holds. In the case of the helium ground state (or any ns^2 pair function), applying GBT leads to the *natural orbital expansion* of the form $\{1s^2, 2s^2, 3s^2, \dots, 2p^2, 3p^2, \dots, 3d^2, \dots\}$ in which all CSF differ by two electrons. For other symmetries, such as $1s2p^3P^\circ$, a *reduced form* [32] can also be defined in which all CSF differ by two electrons, but now involves different sets of orthonormal radial functions for the different partial waves as in $\{1s2p_1, 2s3p_1, 3s4p_1, \dots, 2p_23d_1, 3p_24d_1, \dots\}$. Such expansions yield the fastest rate of convergence, but are difficult to apply in complex systems. For a history of Brillouin’s theorem and its use in solving multiconfiguration self-consistent field problems, see [33].

22.5.4 Excited States

For ground states or atomic states lowest in their symmetry, the variational procedure is a minimization procedure, and consequently any approximate energy is an upper bound. For all others, the energies are stationary. Such calculations may be difficult. One of the most difficult has been the HF calculation for $1s2s^1\text{S}$ and, once obtained, is disappointing since the energy is too low. Excited state calculations become minimization problems through the use of the Hylleraas–Undheim–MacDonald theorem (Sect. 12.3.1). Consider a CAS calculation over the active set $\{1s, 2s\}$ for which the CSFs are $\{1s^2, 1s2s, 2s^2\}$. In determining orbitals, we have a degree of freedom, so one CSF may be removed. Selecting $2s^2$ has the consequence that the eigenvalue for the $1s2s$ state to be determined is now the second eigenvalue, and, hence, an upper bound to the exact energy.

The description of excited states that are members of a Rydberg series is often challenging. The $3snl\ ^{1,3}\text{L}$ ($L = l$) series in magnesium is a good example. In the single Hartree–Fock approximation, the desired solution can be selected by counting the number of expecting nodes of the spectroscopic orbitals, as a starting point for further MCHF calculations. Rydberg series are often strongly perturbed by multiply-excited states whose relative position in the spectrum changes along the isoelectronic sequence and whose description may be more difficult. The description of the $3p3d$ perturber of the $3snf\ ^{1,3}\text{F}^\circ$ that is the fourth state of its symmetry for Al II ($Z = 13$) illustrates this [34]. In the MCHF approximation, the approximation $\{3s4f, 3p3d\}$ can, in principle, represent the interaction of $3p3d$ with the entire $3snf$ series, the variationally determined $4f$ orbital including the contribution from the entire nf series according to GBT. However, difficulties are encountered with the variational procedure in that part of the series ($4s4f$ to $3s6f$) interacts with $3p3d$ so as to raise the total energy whereas the remainder interacts so as to lower the energy. Some variationally equivalent representation has to be found to circumvent these problems [34, 35].

22.5.5 Autoionizing States

The MCHF variational method may be applied to core excited states imbedded in the continuum, provided that certain CSFs with filled shells are omitted. An example is $1s2s2p^2P^\circ$ of lithium. An MCHF calculation omitting $1s^2np$ configuration states represents the localized charge distribution of a state in the continuum. However, including $1s^22p$ and optimizing on the second eigenvalue would make the energy an upper bound. Otherwise a saddle-point variational method, as described in Chap. 26 is needed for such states.

22.6 Configuration Interaction Methods

Configuration interaction (CI) methods differ from variational methods like MC(D)HF in that the radial functions are assumed to be fixed, and, hence, known in advance. There are several situations where these methods can be used effectively.

MCHF with Breit–Pauli Since the Breit–Pauli operators are valid only as first-order perturbations, variational calculations for the Breit–Pauli Hamiltonian are not justified. Instead, MCHF calculations are performed to provide a basis for LSJ wave functions of Eq. (22.18). The expansion coefficients are obtained as a CI calculation. Usually, such expansions are a concatenation of the expansions of all the LS terms of a configuration and possibly some close lying

configurations. Most Breit–Pauli codes require a single orthonormal basis. An example is the ATSP code [2]. In order to have an orbital basis that simultaneously describes the correlation of all these LS terms from a systematic procedure, the MCHF derivation described earlier has been extended to derive systems of coupled equations for linear combinations of energy functionals, one for each LS term and eigenstate. With this extension, it has been possible to perform *spectrum* calculations in which all LSJ levels up to a certain point in the spectrum are included. This requires a balanced correlation approach, so that the energy differences with respect to the ground state are in good agreement with the observed excitation energy. Once wave functions have been obtained for each level, transition probabilities can be computed. With all E1 transitions between these levels and some E2/M1 transitions, the lifetimes of levels can be obtained [36].

Full-core methods The full-core plus correlation method (FCPC) [37] is a configuration interaction method. It is mostly used for an atomic system in which a well-defined *core* is present. For example, in a system such as the three-electron $1s^2nl$ or the four-electron $1s^2nl'n'l'$, the system has a $1s1s$ core. In this case, the wave function for an N -electron system is written as

$$\Psi(1, 2, 3, \dots, N) = \mathcal{A}\phi_{1s1s}(1, 2) \sum_i C_i \Phi_i(3, 4, \dots, N) + \mathcal{A} \sum_j D_j \psi_j(1, 2, 3, \dots, N),$$

where $\phi_{1s1s}(1, 2)$, the wave function of the core, is used as a single term, and \mathcal{A} denotes antisymmetrization. The relaxation of the core and other correlation effects are accounted for by the last term in this equation. The correlation effect of the $1s1s$ core is, in general, very strong, and it is difficult to fully account for this effect in a conventional N -electron wave function. If inaccurate results are obtained from such a wave function, it may be difficult to distinguish between errors coming from the core part or from the other parts. In the FCPC method, the correlation effect in $\phi_{1s1s}(1, 2)$ can be precalculated to a desired accuracy, such that ψ_j no longer contains the contribution from the unperturbed core. In physical processes such as ionization, optical transitions and others, the $1s1s$ core wave function in the final state does not change much from that of the initial state. Using the same $\phi_{1s1s}(1, 2)$ for the core may minimize possible errors due to the inaccuracy of the core wave function. The application of this method is not limited to systems with $1s1s$ cores. For example, for the lithium-like $1s2snp^4P^\circ$, for $n \geq 4$, the $1s2s^3S$ can also be considered as an appropriate *core*.

From a computational viewpoint, the FCPC wave function has the advantage that it reduces the matrix size of the secular equation substantially. This drastically reduces the memory

Table 22.4 Comparison of theoretical and experimental energies for Be $1s^22s^2^1S$ in hartrees. All theoretical values include some form of extrapolation

Reference	Method	$-E_{NR}$	$-E_{rel}$
[39]	FEM MCHF	14.66737	14.66967
[40]	MCHF	14.667315	
[38]	Full-core CI	14.6673492	14.6696774
[41]	Semiempirical	14.667353	
[42]	Experiment		14.6696759

and CPU time needed on a computer. This method has been quite successful in getting accurate results for four-electron systems, as shown in Table 22.4. See [38] for more details.

Slater type orbitals The essential characteristic of a radial function can be well represented by the expansion

$$P_{nl}(r) = \sum_j c_{jnl} \phi_{jnl}(r),$$

where

$$\phi_{jnl}(r) = \left(\frac{(2\xi_{jnl})^{2I_{jnl}+1}}{(2I_{jnl})} \right)^{1/2} r^{I_{jnl}} \exp(-\xi_{jnl}r)$$

is a *Slater type orbital* (STO). Optimized sets of parameters have been tabulated for many Hartree–Fock wave functions, and these may be used to represent the core [43]. Others may be added and selected orbitals *exponent optimized* (only the exponent is varied), so as to augment the basis. This method has been used effectively by Hibbert as implemented in the *Configuration Interaction Version 3* program [44].

Spline basis The analytic basis methods described in the previous section have some similarities with MCHF in that linear combinations of STOs first represent orbitals, which then define the CSFs. These bases result in extensive cancellation as shown by Hansen et al. [45]. An expansion in B-spline basis functions, $B_i^k(r)$, which are a basis for a piecewise polynomial subspace (Chap. 8), provide a more flexible basis with very little cancellation in this representation.

By solving a radial equation with a well-chosen potential using the spline Galerkin method that leads to a matrix eigenvalue problem, a complete set of orbitals for a piecewise polynomial space can be obtained. The resulting orthogonal orbital basis may then be used in CI calculations. Such methods were reviewed by Hansen et al. [45]. Methods that deal directly with the primitive B-spline basis have been applied to the study of Rydberg series [47], although orthogonality to target orbitals was still required. More recently, by using nonorthogonal theory, an R -matrix-CI method that leads to a generalized eigenvalue problem was developed. As in the

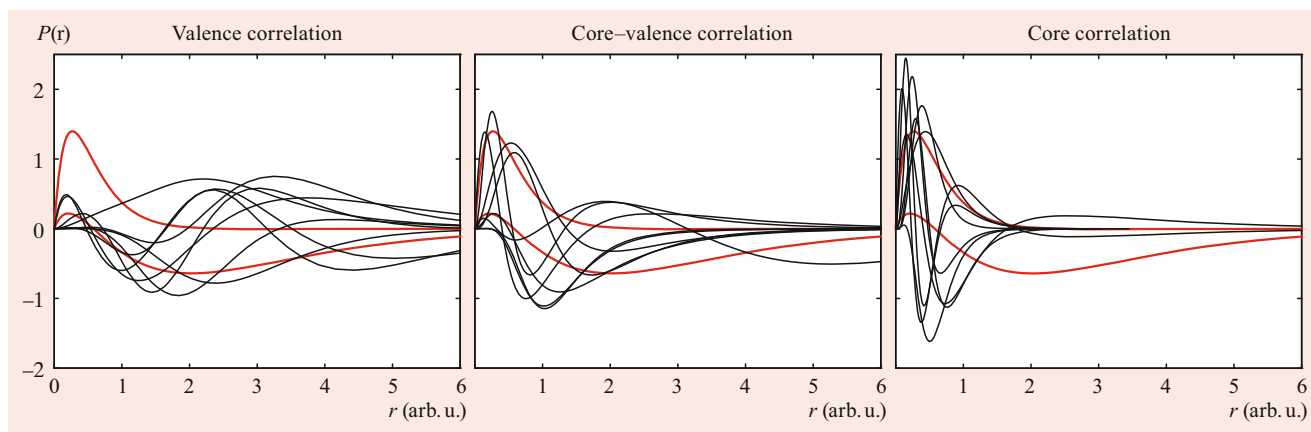


Fig. 22.2 Contraction of the correlation orbitals from valence, core-valence, and core-core correlation MCHF calculations of Be $1s^2 2s^2 \ ^1S$. The two thick red lines correspond to the spectroscopic 1s (no node) and 2s (one node) Hartree-Fock frozen orbitals. Other lines represent the radial distributions of the correlation orbitals of the $n = 4$ active set. Note the location of the maxima of the different types of orbitals (taken from [46])

close-coupling approximation, the wave function is expressed in terms of one or more *targets*, each coupled to a Rydberg orbital, and an arbitrary number of pseudo states. Each Rydberg orbital is expressed as a linear combination of B-splines, but there is no requirement of orthogonality of the Rydberg orbital to the orbitals defining the target function [48].

PCFI method The MCHF orbitals being optimized on a given energy functional lie in the region where their interaction with the reference orbitals is found to be the most favorable, as revealed for the beryllium ground state by the progressive radial collapse of correlation orbitals when going from a valence (VV) $\{1s^2 2s^2 \ ^1S, 1s^2 n l n' l\}$, a core-valence (CV) $\{1s^2 2s^2 \ ^1S, 1s 2s n l n' l\}$, to a core (CC) $\{1s^2 2s^2 \ ^1S, 2s^2 n l n' l\}$ SD-MCHF calculation [49]. This is illustrated in Fig. 22.2 [46] for the three separate $n = 4$ active set calculations of valence, core-valence, and core correlation. This observation allows us to target specific correlation components through the optimization of appropriate virtual orbitals by tailoring the CSFs expansions to the desired effect through the orbital occupation numbers. This strategy is exploited in the partition correlation function interaction (PCFI) approach [46] that combines preoptimized MCHF basis through a compact configuration interaction matrix that takes higher-order effects into account. The price to pay is the appearance of radial nonorthogonalities in the matrix elements coupling the different CSF subspaces, which can be still performed efficiently using radial orbital biorthonormal transformations followed by adequate eigenvector counter-transformations [50]. The advantages of such an approach can be measured by the results reported in Table 22.5 for the beryllium ground state comparing CAS-MCHF results based on a single orthonormal orbital set with PCFI results obtained by diagonalizing an (8×8) interaction matrix. In the latter approach, an $n = 3$ valence-CAS calculation on $1s^2 \{2s, 2p, 3s, 3p, 3d\}^2 \ ^1S$ is first performed to get a zero-

order multireference wave function. The resulting orbitals are kept frozen in three subsequent MCHF calculations targeting VV, CV, and CC correlation. Each of these three independent MCHF calculations provides a tailored set of correlation orbitals for a given active set n . The three PCFs are as such finally combined with the five CSFs of the multireference expansion in a (8×8) configuration interaction matrix. The results are promising when realizing the huge gain in computational time for the PCFI approach in comparison with the CAS-MCHF approach, with a resulting lower total energy for active sets $n \geq 5$. One should, however, be aware that the number of optimized orbitals is sensitively different: for $n = 5$, the numbers of radial functions are 15 and 33 in the CAS-MCHF and PCFI approach, respectively. By (partially) deconstraining the mixing coefficients within each PCF subspace, one converges to the correct limits and keeps the tremendous advantage of improved convergence rates that comes from the use of several orbital sets [51]. Reducing ultimately each PCF to a single CSF with its own orbital basis leads to a nonorthogonal configuration interaction approach. This approach has been successfully used to estimate the doublet-quartet energy separation of neutral boron with the spectroscopic accuracy [52].

Table 22.5 Comparison of CAS-MCHF and PCFI total energies (in hartrees) for the ground state of beryllium with increasing orbital active sets. NCSF corresponds to the size M of the CSF expansion Eq. (22.17)

Active set ($n \leq$)	CAS-MCHF		PCFI	
	NCSF	$-E_{\text{total}}$	NCSF	$-E_{\text{total}}$
4	460	14.661 403 17	229	14.660 679 48
5	2432	14.664 839 93	564	14.665 553 46
6	10 081	14.666 067 32	1110	14.666 582 83
7	34 641	14.666 541 14	1910	14.666 905 87
8	102 824	14.666 857 41	3009	14.667 047 86
9	271 733	14.667 012 75	4451	14.667 122 76
10	652 683	14.667 114 20	6280	14.667 168 08

22.7 Atomic Properties

The discussion so far has concentrated entirely on determining accurate wave functions based on expressions for the energy. Energy levels are a byproduct of such calculations, but once a wave function is known, a number of atomic properties can be evaluated [53].

22.7.1 Transition Data—Allowed and Forbidden Lines

The most fundamental quantity for the probability of a transition from an initial state i to a final state f is the reduced matrix element related to the line strength by

$$S^{1/2} = \langle \Psi_i || O || \Psi_f \rangle, \quad (22.71)$$

where O is the transition operator. In the case of the electric dipole transition, there are two frequently used forms: the length form $O = \sum_j \mathbf{r}_j$ and the velocity form, $O = \sum_j \nabla_j / E_{if}$, where $E_{if} = E_f - E_i$. For exact *nonrelativistic* wave functions, the two forms are equivalent, but for approximate wave functions, the matrix elements, in general, differ. Thus, the computation of the line strength and the oscillator strength, or f -value, where

$$f = \frac{(2/3)E_{if}S}{(2S_i + 1)(2L_i + 1)},$$

forms a critical test of the wave function in nonrelativistic theory and also the model describing a many-electron system. The same operators are often also used in Breit–Pauli calculations. In this case, the velocity form of the operator has neglected some terms of order $(\alpha Z)^2$, and the length value is preferred. When transition rates are computed for all transitions between a set of levels, their accuracy varies. The latter depends on both the transition energy and the line strength. Usually, the accuracy of the energy level structure can be evaluated by a comparison of computed wavelengths with observation, even if only for a few lines. For calculations where wave functions predict energy levels in good agreement with observation, the discrepancy between length and velocity transition rates serve as a good “indicators of accuracy”. For relativistic calculations, transition rates for intercombination lines are accompanied by extensive cancellation and have less accuracy [54, 55].

Some well-known discrepancies between theory and experiment existed for more than a decade for the resonance transitions of Li and Na. For the nonrelativistic 2s–2p transition in Li, a full-core CI [56] calculation produced f -values of (0.74704, 0.74704, 0.75378) for the length, velocity, and acceleration forms, respectively. When relativistic corrections were included, the value changed to

Table 22.6 Convergence of transition data for the $1s^22s^22p^2P^o \rightarrow 1s^22s2p^2^2D$ transition in boron with increasing active set

n	gf_l	gf_v	S_l	ΔE (cm ⁻¹)
3	0.6876	0.8156	2.5534	53 197
4	0.2456	0.2696	0.9959	48 720
5	0.2625	0.2695	1.0705	48 440
6	0.2891	0.2866	1.1868	48 125
7	0.2928	0.2900	1.2036	48 051
Expt. ^a	0.28(02)			47 857

^a [60]

0.74715, in agreement with a number of theories, tabulated to only four decimal places. A fast beam-laser experiment by *Gaupp* et al. [57], yielded a value of 0.7416 ± 0.0012 , but this value was revised in 1996 by a beam-gas-laser experiment in perfect agreement with theory [58]. In the case of the resonance transition in Na, when theory included correlation in the core as well as core-polarization and some relativistic effects, results were in agreement with an almost simultaneous cascade of new experimental values [59].

For MCHF calculations of transition data, an important consideration is that the matrix element is between two different states. For independently optimized wave functions, the orbitals of the initial and final states are not orthonormal, as assumed when Racah algebra techniques are used to evaluate the transition matrix element. Through the use of biorthogonal transformations, the orbitals and the coefficients of expansion of the wave functions of the initial and final state can be transformed efficiently so that standard Racah algebra techniques may be applied [50]. Table 22.6 shows the convergence of an MCHF calculation for the ground state of Boron from independently optimized wave functions.

Similar systematic strategies are used with relativistic expansions, demonstrating that large-scale calculations can give transition energies of spectroscopic accuracy, i.e., with an accuracy comparable to the one obtained from observations, as well as transition rates with estimated uncertainties of a few percent for a broad range of ions [61]. However, some surprising puzzles remain. A recent one is the theory-observation discrepancy in the 3C/3D f -value ratio in Fe XVII for which several large-scale MCHF+BP and MCDHF calculations are all in remarkable agreement, providing a theoretical ratio larger than observed by 36% [62, 63]. Nonlinear dynamical modeling with its nonequilibrium plasma effects was neglected in the analysis of experimental data and might explain some of the discrepancies [64].

22.7.2 Electron Affinities

By definition, the electron affinity is $A_e = E(A) - E(A^-)$. Thus, it is the energy difference between Hamiltonians dif-

fering by one electron. Correlation plays a very important role in the binding of the extra electron in the negative ion. For small systems such as Li, the electron affinity has been computed [65] to experimental accuracy [66] of (0.6176 ± 0.0002) eV. It has been known for a long time that the alkali metals have a positive electron affinity, but only recently has it been found, theoretically [67] and experimentally [68], that some of the alkaline earths may also be able to bind an extra electron. The d-electrons need to play a strong role, so Be and Mg, do not have a positive A_e , but according to the most recent experimental measurement, the electron affinity for Ca is 18 meV [69]. A calculation based on the spline methods and using a model potential with adjustable parameters to describe the core, obtained a value of 17.7 meV [70] in close agreement with experiment.

Atomic systems such as Ca are often thought of as two-electron systems and, indeed, for qualitative descriptions, many observations can be explained. A number of physical effects need to be considered when predicting such electron affinities:

- (i) Valence correlation is crucial for obtaining binding.
- (ii) Intershell correlation between the valence electrons and the core (core polarization) is also important. The first electron may polarize the core considerably, but this is reduced by the second electron since the two avoid each other dynamically and prefer to be on opposite sides of the core.
- (iii) Core rearrangement, which occurs because of the presence of one or more outer electrons and is particularly large if any of these penetrate the core. In the case of Ca^+ , the fixed-core Hartree–Fock energy of $3d^2D$ state is 300 meV higher if computed in the fixed potential of the Ca^{2+} ion compared with a fully variational calculation!
- (iv) Intracore exclusion effects due to the presence of an extra valence electron that reduces the correlation of the core.
- (v) Relativistic shift effects, which are present in observed levels and are particularly important for s-electrons.

Model potential methods attempt to capture all but valence correlation in a potential so that calculations for calcium, for example, can proceed as for a two-electron system. A review of various theoretical approaches, many of which include different effects, may be found in [71].

22.7.3 Metastable States and Autoionization

States above an ionization threshold may decay via a radiationless transition to a continuum. When the interaction with the continuum is spin-forbidden, the state is metastable. The

$nsnp^2^4P$ of negative ions, for example, decay through Breit–Pauli interactions with $nsnp^2$ doublets. The latter, in turn, interact with continuum states, thus opening a decay channel. Such metastable states may be treated as bound states.

The foundation for the theory of autoionization was laid down by *Fano* [72], where he developed a configuration interaction (CI) theory for autoionization. Let $\Psi_b(N; \gamma LS)$ be a normalized, multiconfiguration component of a discrete perturber for an N -electron system, in which all orbitals are bound orbitals, decaying exponentially for large r . Let Ψ_k be an asymptotically normalized continuum component of the wave function, also for an N -electron system, at energy E , of the form,

$$\Psi_k(N; E \gamma' LS) = |\Psi_b(N-1; \beta \tilde{L} \tilde{S}) \cdot \phi(kl) LS\rangle, \quad (22.72)$$

where $\Psi_b(N-1; \beta \tilde{L} \tilde{S})$ is a bound MCHF wave function for the $(N-1)$ -electron target system. Then, in the LS -coupling scheme, the width of the autoionizing state is given by the *Golden Rule*

$$\Gamma = 2\pi V_{E_0}^2, \quad (22.73)$$

where

$$V_{E_0} = \langle \Psi_b(N; \gamma LS) | H - E_0 | \Psi_k(N; E_0 \gamma' LS) \rangle. \quad (22.74)$$

A similar formula can be derived for the LSJ -scheme and the Breit–Pauli Hamiltonian. In the above equation, $E_0 = \langle \Psi_b(N; \gamma LS) | H | \Psi_b(N; \gamma LS) \rangle$. The energy of the core, or target, is $E_{\text{target}} = \langle \Psi_b(N-1; \beta \tilde{L} \tilde{S}) | H | \Psi_b(N-1; \beta \tilde{L} \tilde{S}) \rangle$, where H in the latter equation is the Hamiltonian for an $(N-1)$ -electron system.

The wave function for the continuum component is assumed to have only one unknown, namely $\phi(kl) = P_{kl}(r) |ls\rangle$, the one-particle continuum function, where $|ls\rangle$ is the known spin–angular part. The radial equation for $P_{kl}(r)$ has exactly the same form as Eq. (22.34), except that $\varepsilon_{nl, nl} = -k^2$, where $E_0 = E_{\text{target}} + k^2/2$. The radial function can be obtained iteratively using an SCF procedure from outward integration.

One of the more accurate calculations of a lifetime is that for $\text{He}^- 1s2s2p^4P_{5/2}^o$ by *Miecznik et al.* [73]. In this case, a lifetime of $345 \pm 10 \mu\text{s}$ was found and compared with the experimental value of $350 \pm 15 \mu\text{s}$ [74]. In this LSJ state, the $^4P^o$ interacts with the $1s^2kf^2F^o$. It was found that correlation in the target of the continuum orbital modified the lifetime. In calculations like these, it is always a question whether orthogonality conditions should be applied [as in projection operator formalism (Chap. 26)]. Some theorems relating to this question were published by *Brage et al.* [75].

The position and widths of autoionizing resonances can also be determined from the study of photoionization or photodetachment using a spline Galerkin method together with

inverse iteration. No boundary condition needs to be applied at the end of the range of integration, nor is there an inner and outer region. Resonance properties are obtained from a fitting of the cross section [76]. Nonorthogonal, spline-based R -matrix methods with an inner and outer region have also been developed, where there is no need for the *Buttle correction* and, at the same time, the nonorthogonality eliminates the need of certain pseudo states [77]. For an extensive review of the application of splines in atomic and molecular physics, see [78].

22.7.4 Nuclear Effects

Line isotope shifts The isotope shift observed in atomic transitions can be separated into a mass shift and a field shift. The mass shift is due to differences in the nuclear mass of the isotopes and is the dominant effect for light atoms. The volume shift arises from the finite volume of the nuclear charge distribution and is important for heavy atoms. From a physical point of view, the field shift is the more interesting, since it yields information about differences in the nuclear charge distribution between the isotopes.

The isotope shift in a transition is given as the difference between the shift for the upper and lower level. The individual shifts are often large, but cancel, and therefore it is necessary to calculate them very accurately in order to get a reliable value for the difference. The energy shifts are evaluated in first-order perturbation theory with wave functions obtained from the zero-order Schrödinger Hamiltonian, H_0 .

Mass shift Up to this point, the nuclear mass has been taken to be infinite. If instead it has a finite value M , an N -electron atom turns into an $(N + 1)$ -particle dynamical system. A transformation to center of mass \mathbf{R} plus relative coordinates $\mathbf{r}'_i = \mathbf{r}_i - \mathbf{r}_{\text{nuc}}$ yields the transformed Hamiltonian [79] (Chap. 12)

$$H = \frac{P^2}{2M_{\text{tot}}} + \sum_{i=1}^N \frac{p_i^2}{2\mu} + \sum_{i<j}^N \frac{\mathbf{p}'_i \cdot \mathbf{p}'_j}{M} + V(\mathbf{r}'_i), \quad (22.75)$$

where $M_{\text{tot}} = M + Nm_e$ is the total mass, and $\mu = Mm_e/(M + m_e)$ is the reduced mass. The first term is the kinetic energy of the center of mass, which can be omitted if \mathbf{R} is an ignorable coordinate. Introducing the scaled distances $\rho_i = \mathbf{r}'_i/a_\mu$, where $a_\mu = (m_e/\mu)a_0$ is the scaled Bohr radius, and assuming the potential as entirely Coulombic, H takes the form

$$H = -\frac{1}{2} \sum_{i=1}^N \nabla_{\rho_i}^2 - \frac{\mu}{M} \sum_{i<j}^N \nabla_{\rho_i} \cdot \nabla_{\rho_j} + V(\rho_i) \quad (22.76)$$

in units of e^2/a_μ . This can be written in the form $H = H_0 + H_{\text{MP}}$, where H_0 includes the first and last terms of Eq. (22.76), and

$$H_{\text{MP}} = -\frac{\mu}{M} \sum_{i<j}^N \nabla_{\rho_i} \cdot \nabla_{\rho_j} \frac{e^2}{a_\mu} \quad (22.77)$$

is the additional *mass polarization* term.

Equation (22.76) gives rise to two kinds of mass shifts. First, since H is identical to the infinite mass Hamiltonian, all its eigenvalues E_0 are multiplied by $a_0/a_\mu = \mu/m_e$, resulting in the *normal mass shift* (nms)

$$\Delta E_{\text{nms}} = -\frac{\mu}{M} E_0. \quad (22.78)$$

Second, if H_{MP} is treated as a first-order perturbation, then the resulting *specific mass shift* (sms) is

$$\Delta E_{\text{sms}} = \langle \Psi_0 | H_{\text{MP}} | \Psi_0 \rangle \frac{e^2}{a_\mu}, \quad (22.79)$$

where Ψ_0 is an eigenvector of H_0 . The specific mass shift parameter S_{sms} is defined by

$$S_{\text{sms}} = \langle \Psi_0 | -\sum_{i<j}^N \nabla_{\rho_i} \cdot \nabla_{\rho_j} | \Psi_0 \rangle. \quad (22.80)$$

Field shift The field shift of an atomic energy level is due to the extended nuclear charge distribution. The field inside the nucleus deviates from the Coulomb field of a point charge, and this is reflected in the calculated levels. For light atoms, the resulting energy correction to the level E_0 is expressed in terms of the nonrelativistic electron probability at the origin, $|\Psi(0)|^2$

$$E_{\text{fs}} = \frac{2\pi}{3} Z \langle r_N^2 \rangle |\Psi(0)|^2, \quad (22.81)$$

where $\langle r_N^2 \rangle$ is the mean square radius of the nucleus. For heavier atoms ($Z > 10$), it becomes necessary to include a relativistic correction factor. Numerical values of this correction factor can be found in [15].

Table 22.7 shows the convergence of an MCHF calculation for the specific mass shift parameter and the electron density at the nucleus of the ground state of boron II as the active set increases. The calculated $^{11}\text{B}-^{10}\text{B}$ isotope shift is 13.3 mÅ with an estimated uncertainty of 1%. The size of the isotope shift is similar to the limit of resolution of the Goddard High Resolution Spectrograph aboard the Hubble Space Telescope [80].

The above theoretical concepts apply to nonrelativistic systems. For relativistic ones, both the mass and field shifts need to be reformulated in the four-component relativistic formalism [81]. A recent example of useful application in nuclear physics can be found in [82].

Table 22.7 Specific mass shift parameter and electron density at the nucleus as a function of the active set

Active set	S_{sms} (arb. u.)	$ \psi(0) ^2$
HF	0.00000	72.629
2s 1p	-0.02017	72.452
3s 2p 1d	0.62518	72.490
4s 3p 2d 1f	0.62481	72.497
5s 4p 3d 2f 1g	0.60169	72.501
6s 5p 4d 3f 2g 1h	0.59803	72.503
7s 6p 5d 4f 3g 2h 1i	0.59709	72.504

Hyperfine structures The magnetic hyperfine structure (hfs) is due to an interaction between the magnetic field generated by the electrons and the nuclear magnetic dipole moment. The interaction couples the nuclear and electronic angular momenta to a total momentum $\mathbf{F} = \mathbf{I} + \mathbf{J}$, and the interaction energy can be written as the expectation value of a scalar product between an electronic and a nuclear tensor operator [83] (Chap. 17)

$$W_{M1}(J) = \langle \gamma_I \gamma_J I J F M_F | \mathbf{T}^{(1)} \mathbf{M}^{(1)} | \gamma_I \gamma_J I J F M_F \rangle. \quad (22.82)$$

The nuclear operator $\mathbf{M}^{(1)}$ is related to the scalar magnetic dipole moment, μ_I , according to

$$\langle \gamma_I I I | M_0^{(1)} | \gamma_I I I \rangle = \mu_I. \quad (22.83)$$

The magnetic dipole moments are known quantities, obtained with high accuracy from experiments. For a recent tabulation see [84].

The electronic operator is

$$\begin{aligned} \mathbf{T}^{(1)} = & \frac{\alpha^2}{2} \sum_{i=1}^N \left\{ 2I^{(1)}(i)r_i^{-3} \right. \\ & - g_s \sqrt{10} [C^{(2)}(i) \times s^{(1)}(i)]^{(1)} r_i^{-3} \\ & \left. + g_s \frac{8}{3} \pi \delta(\mathbf{r}_i) s^{(1)}(i) \right\}, \quad (22.84) \end{aligned}$$

where $g_s = 2.0023193$ is the electron spin g -factor, $\delta(\mathbf{r})$ the three-dimensional delta function, and $C_q^{(k)} = \sqrt{4\pi/(2k+1)} Y_{kq}$, with Y_{kq} being a normalized spherical harmonic. The first term of the electronic operator represents the magnetic field generated by the orbiting electric charges and is called the orbital term. The second term represents the field generated by the orbiting magnetic dipole moments, which are coupled to the spin of the electrons. This is the spin-dipole term. The last term represents the contact interaction between the nuclear magnetic dipole moment and the electron magnetic moment. It is called the Fermi contact term and contributes only for s-electrons.

By uncoupling I and J that constitute the components $\mathbf{F} = \mathbf{I} + \mathbf{J}$, the interaction energy can be rewritten as

$$\begin{aligned} W_{M1}(J) = & (-1)^{I+J-F} W(IJII; F1) \\ & \times \langle \gamma_J J | \mathbf{T}^{(1)} | \gamma_J J \rangle \langle \gamma_I I | \mathbf{M}^{(1)} | \gamma_I I \rangle, \quad (22.85) \end{aligned}$$

where $W(IJII; F1)$ is a W coefficient of Racah. When the magnetic dipole interaction constant

$$A_J = \frac{\mu_I}{I} \frac{1}{[J(J+1)(2J+1)]^{\frac{1}{2}}} \langle \gamma_J J | \mathbf{T}^{(1)} | \gamma_J J \rangle \quad (22.86)$$

is introduced, the energy is given by

$$W_{M1}(J) = \frac{1}{2} A_J C, \quad (22.87)$$

where $C = F(F+1) - J(J+1) - I(I+1)$. In theoretical studies, the A -factor is often given as a linear combination of the hyperfine parameters [85]

$$a_l = \langle \gamma_L S M_L M_S | \sum_i l_0^{(1)}(i) r_i^{-3} | \gamma_L S M_L M_S \rangle, \quad (22.88)$$

$$a_d = \langle \gamma_L S M_L M_S | \sum_i 2C_0^{(2)}(i) s_0^{(1)}(i) r_i^{-3} | \gamma_L S M_L M_S \rangle, \quad (22.89)$$

$$a_c = \langle \gamma_L S M_L M_S | \sum_i 2s_0^{(1)}(i) r_i^{-2} \delta(r_i) | \gamma_L S M_L M_S \rangle, \quad (22.90)$$

where $M_L = L$ and $M_S = S$. These parameters correspond to the orbital, spin-dipole, and Fermi contact term of the electronic operator.

The electric hyperfine structure is due to the interaction between the electric field gradient produced by the electrons and the nonspherical charge distribution of the nucleus. The interaction energy is

$$W_{E2}(J) = \langle \gamma_I \gamma_J I J F M_F | \mathbf{T}^{(2)} \mathbf{M}^{(2)} | \gamma_I \gamma_J I J F M_F \rangle, \quad (22.91)$$

where the nuclear operator $\mathbf{M}^{(2)}$ is related to the scalar electric quadrupole moment, Q , according to

$$\langle \gamma_I I I | M_0^{(2)} | \gamma_I I I \rangle = \frac{Q}{2}. \quad (22.92)$$

The electronic operator is

$$\mathbf{T}^{(2)} = - \sum_{i=1}^N C^{(2)}(i) r_i^{-3} \quad (22.93)$$

and represents the electric field gradient. By introducing the electric quadrupole interaction constant B ,

$$\begin{aligned} B_J = & 2Q \left(\frac{J(2J-1)}{(J+1)(2J+1)(2J+3)} \right)^{\frac{1}{2}} \\ & \times \langle \gamma_J J | \mathbf{T}^{(2)} | \gamma_J J \rangle, \quad (22.94) \end{aligned}$$

Table 22.8 MCHF hyperfine constants (in MHz) for the $1s^2 2s 2p^1 P^\circ$ state of B II

Active set	^{10}B		^{11}B	
	A_1	B_1	A_1	B_1
HF	60.06	8.338	179.36	4.001
2s 1p	60.22	8.360	179.83	4.011
3s 2p 1d	60.98	8.193	182.11	3.932
4s 3p 2d 1f	60.05	7.677	179.34	3.684
5s 4p 3d 2f 1g	60.48	7.764	180.62	3.725
6s 5p 4d 3f 2g 1h	60.85	8.052	181.71	3.864
7s 6p 5d 4f 3g 2h 1i	60.81	8.002	181.60	3.840

the interaction energy can be written as

$$W_{E2}(J) = B_J \frac{\frac{3}{4}C(C+1) - I(I+1)J(J+1)}{2I(2I-1)J(2J-1)}. \quad (22.95)$$

In many cases, the electric hyperfine interaction is weaker than the magnetic one and manifests itself as a small deviation from the Landé interval rule for the magnetic hfs.

Nuclear parameters can be extracted from observed hyperfine structures if the electronic part of the interaction can be calculated accurately. A recent illustration is the determination of the nuclear electric moment $Q(^{67}\text{Zn})$ from the theoretical estimation of the electric field gradient using elaborate correlation models for MC(D)HF calculations [86]. A tabulation of nuclear quadrupole moments is given in [87].

Table 22.8 shows the convergence of an MCHF active space calculation for two different isotopes for the $1s^2 2s 2p^1 P^\circ$ state of B II [80]. Some oscillations are observed since each new layer of orbitals may localize in different regions of space. Ab-initio studies of hyperfine structure parameters are definitely helpful for assessing the reliability of hyperfine constants extracted from observed spectra. A nice example is given by recent work reconciling theory with observation through the reinterpretation of saturation spectra of low lying states of $^{14,15}\text{N}$ [88]. Relativistic effects on hyperfine constants can be much more important than expected, even for light, a-priori nonrelativistic systems, such as neutral fluorine [89]. The inclusion in the Hamiltonian of the Breit–Pauli terms that mix terms having different LS -symmetries [Eq. (22.18)] can be crucial in some specific cases, as confirmed by fully relativistic MCDHF calculations [90].

Isotope shifts on electron affinities In neutral oxygen, it has been found that there is an “anomalous” isotope effect [91] corresponding to a larger electron affinity for the lightest isotope. In all systems considered in the second and third periods of the periodic table ($^{7,9,11}\text{Be}^-$, $^{13,13,14}\text{C}^-$, $^{16,17,18}\text{O}^-$, $^{28,30}\text{Si}^-$, $^{32,34}\text{S}^-$, $^{35,37}\text{Cl}^-$) chlorine is the only pair

for which the normal mass shift dominates the counteracting specific mass shift contribution and, therefore, has an isotope shift that can be qualified as “normal” [92]. The predictive value of MCHF calculations can be illustrated by the theoretical estimation of the IS on the carbon electron affinity, $E_a(^{13}\text{C}) - E_a(^{12}\text{C}) = -7.04 \text{ m}^{-1}$, which has been confirmed by the photodetachment microscopy measurements ($= -7.3(6) \text{ m}^{-1}$) [93].

22.8 Summary

More comprehensive treatments of atomic structure may be found in [8, 9, 24, 94]. Atomic structure packages are available in [1–4] for many of the calculations described in the present chapter. Reviews of the application of systematic procedures to the prediction of atomic properties are available in [49, 95–97]. As has been mentioned at different places, atomic structure methods and their implementation in ATSP and GRASP are very similar. Advanced nonrelativistic (MCHF) and relativistic (MCDHF) multiconfiguration methods for the calculation of energies and wave functions of complex atoms are considered in detail in [5]. An extension of this review paper focusing on the applications is in progress [98].

References

1. Froese Fischer, C.: *Comput. Phys. Commun.* **64**, 369 (1991)
2. Froese Fischer, C., Tachiev, G., Gaigalas, G., Godefroid, M.: *Comput. Phys. Commun.* **176**, 559 (2007)
3. Jönsson, P., He, X., Froese Fischer, C., Grant, I.P.: *Comput. Phys. Commun.* **177**, 597 (2007)
4. Froese Fischer, C., Gaigalas, G., Jönsson, P., Bieroń, J.: *Comput. Phys. Commun.* **237**, 184 (2019)
5. Froese Fischer, C., Godefroid, M., Brage, T., Jönsson, P., Gaigalas, G.: *J. Phys. B* **49**, 182004 (2016)
6. Lindgren, I.: *Relativistic Many-Body Theory: A New Field-Theoretical Approach*. Springer Series on Atomic, Optical, and Plasma Physics, vol. 63. Springer, Berlin (2011)
7. Berestetskii, V.B., Lifshitz, E.M., Pitaevskii, L.P.: *Relativistic Quantum Theory*. Pergamon, Oxford (1971)
8. Grant, I.P.: *Relativistic Quantum Theory of Atoms and Molecules. Theory and Computation*. Springer Series on Atomic, Optical, and Plasma Physics. Springer, New York (2007)
9. Johnson, W.R.: *Atomic Structure Theory*. Springer, Berlin, Heidelberg, New York (2007)
10. Mohr, P.J., Taylor, B.N., Newell, D.B.: *Rev. Mod. Phys.* **88**, 035009 (2016)
11. Armstrong Jr., L., Feneuille, S.: *Adv. At. Mol. Phys.* **10**, 1 (1974)
12. Akhiezer, A.I., Berestetskii, V.B.: *Quantum Electrodynamics*. Wiley (Interscience), New York (1965)
13. Glass, R., Hibbert, A.: *Comput. Phys. Commun.* **16**, 19 (1978)
14. Froese Fischer, C., Tachiev, G., Irimia, A.: *At. Data Nucl. Data Tables* **92**, 607 (2006)

15. King, W.H.: *Isotope Shifts in Atomic Spectra*. Plenum, New York (1984)
16. Froese Fischer, C.: *The Hartree-Fock Method for Atoms. A Numerical Approach*. Wiley, New York (1977)
17. Froese Fischer, C.: B-splines in variational atomic structure calculations. In: Arimondo, E., Berman, P.R., Lin, C.C. (eds.) *Advances in Atomic, Molecular, and Optical Physics*, Vol. 55, pp. 235–291. Academic Press, London (2008)
18. Hartree, D.R.: *The Calculation of Atomic Structures*. Wiley, New York (1957)
19. Froese Fischer, C.: *Comput. Phys. Commun.* **182**, 1315 (2011)
20. Lindgren, I., Morrison, J.: *Atomic Many-Body Theory*. Springer, Berlin, Heidelberg, New York (1982)
21. Froese Fischer, C.: *Comput. Phys. Rep.* **3**, 273 (1986)
22. Zatsarinny, O., Froese Fischer, C.: *Comput. Phys. Commun.* **202**, 287 (2016)
23. Froese Fischer, C., Zatsarinny, O.: *Comput. Phys. Commun.* **180**, 879 (2009)
24. Cowan, R.D.: *The Theory of Atomic Structure and Spectra*. Univ. California Press, Berkeley (1981)
25. Löwdin, P.-O.: *Phys. Rev.* **97**, 1509 (1955)
26. Layzer, D., Horák, Z., Lewis, M.N., Thompson, D.P.: *Ann. Phys. (N. Y.)* **29**, 101 (1964)
27. Layzer, D.: *Ann. Phys. (N. Y.)* **8**, 271 (1959)
28. Layzer, D., Bahcall, J.: *Ann. Phys.* **177**, 177 (1962)
29. Nicolaides, C.A., Beck, D.R.: *Chem. Phys. Lett.* **35**, 79 (1975)
30. Froese Fischer, C.: *Nucl. Instrum. Methods Phys. Res. B* **235**, 100 (2005)
31. Froese Fischer, C., Gaigalas, G., Ralchenko, Y.: *Comput. Phys. Commun.* **175**, 738 (2006)
32. Froese Fischer, C.: *J. Comput. Phys.* **13**, 502 (1973)
33. Godefroid, M.R., Liévin, J., Metz, J.-Y.: *Int. J. Quantum Chem.* **40**, 243 (1991)
34. Froese Fischer, C.: *J. Opt. Soc. Am.* **69**, 118 (1979)
35. Vaeck, N., Godefroid, M., Hansen, J.E.: *Phys. Rev. A* **38**, 2830 (1988)
36. Tachiev, G., Froese Fischer, C.: *J. Phys. B* **32**, 5805 (1999)
37. Chung, K.T.: In: Chang, T.N. (ed.) *Many-Body Theory of Atomic Structure and Photoionization*, p. 83. World Scientific, Singapore (1993)
38. Chung, K.T., Zhu, X.-W., Wang, Z.-W.: *Phys. Rev. A* **47**, 1740 (1993)
39. Mårtensson-Pendrill, A.-M., Alexander, S.A., Adamowicz, L., Oliphant, N., Olsen, J., Öster, P., Quiney, H.M., Salomonson, S., Sundholm, D.: *Phys. Rev. A* **43**, 3355 (1991)
40. Froese Fischer, C.: *J. Phys. B* **26**, 855 (1993)
41. Lindroth, E., Persson, H., Salomonson, S., Mårtensson-Pendrill, A.-M.: *Phys. Rev. A* **45**, 1493 (1992)
42. Kelly, R.L.: *J. Phys. Chem. Ref. Data* **16**(Suppl. 1), 1371 (1987)
43. Clementi, E., Roetti, C.: *At. Data Nucl. Data Tables* **14**, 177 (1974)
44. Hibbert, A.: *Comput. Phys. Commun.* **9**, 141 (1975)
45. Hansen, J.E., Bentley, M., van der Hart, H.W., Landtman, M., Lister, G.M.S., Shen, Y.-T., Vaeck, N.: *Phys. Scr.* **47**, 7 (1993)
46. Verdebout, S., Jönsson, P., Gaigalas, G., Godefroid, M., Froese Fischer, C.: *J. Phys. B* **43**, 074017 (2010)
47. Brage, T., Froese Fischer, C.: *Phys. Scr.* **49**, 651 (1994)
48. Zatsarinny, O., Froese Fischer, C.: *J. Phys. B* **35**, 4669 (2002)
49. Godefroid, M., Jönsson, P., Froese Fischer, C.: *Phys. Scr.* **78**, 33 (1998)
50. Olsen, J., Godefroid, M.R., Jönsson, P., Malmqvist, P.Å., Froese Fischer, C.: *Phys. Rev. E* **52**, 449 (1995)
51. Verdebout, S., Rynkun, P., Jönsson, P., Gaigalas, G., Froese Fischer, C., Godefroid, M.: *J. Phys. B* **46**, 085003 (2013)
52. Froese Fischer, C., Verdebout, S., Godefroid, M., Rynkun, P., Jönsson, P., Gaigalas, G.: *Phys. Rev. A* **88**, 062506 (2013)
53. Godefroid, M., Froese Fischer, C., Jönsson, P.: *J. Phys. B* **34**, 1079 (2001)
54. Froese Fischer, C.: *Phys. Scr.* **134**, 014019 (2009)
55. Ekman, J., Godefroid, M., Hartman, H.: *Atoms* **2**, 215 (2014)
56. Chung, K.T.: In: *Proceedings of the International Conference on Highly Charged Ions AIP Conference Proceedings*, vol. 274, AIP, New York (1993)
57. Gaupp, A., Kuske, P., Andriä, H.J.: *Phys. Rev. A* **26**, 3351 (1982)
58. Volz, U., Schmoranzler, H.: *Phys. Scr.* **65**, 48 (1996)
59. Jönsson, P., Ynnerman, A., Froese Fischer, C., Godefroid, M.R., Olsen, J.: *Phys. Rev. A* **53**, 4021 (1996)
60. O'Brian, T.R., Lawler, J.E.: *Astron. Astrophys.* **255**, 420 (1992)
61. Jönsson, P., Gaigalas, G., Rynkun, P., Radžiūtė, L., Ekman, J., Gustafsson, S., Hartman, H., Wang, K., Godefroid, M., Froese Fischer, C., Grant, I., Brage, T., Del Zanna, G.: *Atoms* **5**, 16 (2017)
62. Bernitt, S., Brown, G.V., Rudolph, J.K., Steinbrügge, R., Graf, A., Leutenegger, M., Epp, S.W., Eberle, S., Kubiček, K., Mäckel, V., Simon, M.C., Träbert, E., Magee, E.W., Beilmann, C., Hell, N., Schippers, S., Müller, A., Kahn, S.M., Surzhykov, A., Harman, Z., Keitel, C.H., Clementson, J., Porter, F.S., Schlotter, W., Turner, J.J., Ullrich, J., Beiersdorfer, P., Crespo López-Urrutia, J.R.: *Nature* **492**, 225 (2012)
63. Wang, K., Jönsson, P., Ekman, J., Brage, T., Chen C.Y., Froese Fischer, C., Gaigalas, G., Godefroid, M.: *Phys. Rev. Lett.* **119**, 189301 (2017)
64. Li, Y., Fogle, M., Loch, S.D., Ballance, C.P., Fontes, C.J.: *Can. J. Phys.* **95**, 869 (2017)
65. Froese Fischer, C.: *J. Phys. B* **26**, 855 (1993)
66. Dellwo, J., Liu, Y., Pegg, D.J., Alton, G.D.: *Phys. Rev. A* **45**, 1544 (1992)
67. Froese Fischer, C., Lagowski, J.B., Vosko, S.H.: *Phys. Rev. Lett.* **59**, 2263 (1987)
68. Pegg, D.J., Thompson, J.S., Compton, R.N., Alton, G.D.: *Phys. Rev. Lett.* **59**, 2267 (1989)
69. McLaughlin, K.W., Duquette, D.W.: *Phys. Rev. Lett.* **72**, 1176 (1994)
70. van der Hart, H.W., Laughlin, C., Hansen, J.E.: *Phys. Rev. Lett.* **71**, 1506 (1993)
71. Froese Fischer, C., Brage, T.: *Can. J. Phys.* **70**, 1283 (1992)
72. Fano, U.: *Phys. Rev.* **129**, 1866 (1961)
73. Miecznik, G., Brage, T., Froese Fischer, C.: *Phys. Rev. A* **47**, 3718 (1993)
74. Andersen, T., Andersen, L.H., Balling, P., Haugen, H.K., Hvelplund, P., Smith, W.W., Taulbjerg, K.: *Phys. Rev. A* **47**, 890 (1993)
75. Brage, T., Froese Fischer, C., Vaeck, N.: *J. Phys. B* **26**, 621 (1993)
76. Xi, J., Froese Fischer, C.: *Phys. Rev. A* **53**, 3169 (1996)
77. Zatsarinny, O., Froese Fischer, C.: *J. Phys. B* **35**, 4161 (2002)
78. Bachau, H., Cormier, E., Declewa, P., Hansen, J.E., Martin, F.: *Rep. Prog. Phys.* **64**, 1815 (2001)
79. Hughes, D.S., Eckart, C.: *Phys. Rev.* **36**, 694 (1930)
80. Jönsson, P., Johansson, S.G., Froese Fischer, C.: *Astrophys. J.* **429**, L45 (1994)
81. Ekman, J., Jönsson, P., Godefroid, M., Nazé, C., Gaigalas, G., Bieroń, J.: *Comput. Phys. Commun.* **235**, 433 (2019)
82. Bissell, M.L., Carette, T., Flanagan, K.T., Vingerhoets, P., Billowes, J., Blaum, K., Cheal, B., Fritzsche, S., Godefroid, M., Kowalska, M., Krämer, J., Neugart, R., Neyens, G., Nörtershäuser, W., Yordanov, D.T.: *Phys. Rev. C* **93**, 064318 (2016)
83. Lindgren, I., Rosén, A.: *Case Stud. At. Phys.* **4**, 93 (1974)
84. Stone, N.J.: *At. Data Nucl. Data Tables* **90**, 75 (2005)
85. Hibbert, A.: *Rep. Prog. Phys.* **38**, 1217 (1975)
86. Bieroń, J., Filippin, L., Gaigalas, G., Godefroid, M., Jönsson, P., Pyykkö, P.: *Phys. Rev. A* **97**, 062505 (2018)
87. Pyykkö, P.: *Mol. Phys.* **116**, 1328 (2018)

88. Carette, T., Nemouchi, M., Jönsson, P., Godefroid, M.: *Eur. Phys. J. D* **60**, 231 (2010)
89. Carette, T., Nemouchi, M., Jönsson, P., Godefroid, M.: *Phys. Rev. A* **88**, 042501 (2013)
90. Aourir, N., Nemouchi, M., Godefroid, M., Jönsson, P.: *Phys. Rev. A* **97**, 032506 (2018)
91. Godefroid, M.R., Froese Fischer, C.: *Phys. Rev. A* **60**, R2637 (1999)
92. Carette, T., Godefroid, M.: *J. Phys. B* **46**, 095003 (2013)
93. Bresteau, D., Drag, C., Blondel, C.: *Phys. Rev. A* **93**, 013414 (2016)
94. Sobel'man, I.I.: *Introduction to the Theory of Atomic Spectra*. Pergamon, Oxford (1972)
95. Froese Fischer, C., Jönsson, P.: *Comput. Phys. Commun.* **84**, 37 (1994)
96. Godefroid, M., Froese Fischer, C., Jönsson, P.: *Phys. Scr.* **65**, 70 (1996)
97. Froese Fischer, C., Brage, T., Jönsson, P.: *Computational Atomic Structure: An MCHF Approach*. IOP, Bristol (1997)
98. Froese Fischer, C., Godefroid, M., Brage, T., Jönsson, P., Gaigalas, G., Bieroń, J., Ekman, J.: *Advanced multiconfiguration methods for complex atoms: II. Atomic properties*. *J. Phys. B. in preparation*



Charlotte Froese Fischer Charlotte Froese Fischer is Professor Emerita of Computer Science at Vanderbilt University and an Affiliate Professor at the University of British Columbia. She is a Fellow of the Division of Atomic and Molecular Physics as well as the Royal Society of Canada. Her research interests are computational atomic structure theory for predicting atomic properties, particularly transition probabilities in complex spectra.



Michel Godefroid Michel Godefroid is Research Director Emeritus of the "Fonds National de la Recherche Scientifique" (F.R.S.-FNRS) and full Professor at Université libre de Bruxelles (Brussels, Belgium), teaching physical chemistry and atomic and molecular physics. His research is mainly focused on the development of original and efficient computational strategies for describing electron correlation and relativistic effects on atomic structures and properties.



Relativistic Atomic Structure

23

Ian Grant

Contents

23.1	Mathematical Basics	332	23.8	Many-Electron Atoms	356
23.1.1	Relativistic Notation: Minkowski Space-Time	332	23.8.1	Atomic States	356
23.1.2	Lorentz Transformations	332	23.8.2	Atomic Orbitals	356
23.1.3	Classification of Lorentz Transformations	332	23.8.3	Slater Determinants	356
23.1.4	Contravariant and Covariant Vectors	333	23.8.4	Configurational States	356
23.1.5	Poincaré Transformations	333	23.8.5	ASFs and CSF	357
23.2	Dirac's Equation	333	23.8.6	Matrix Construction	357
23.2.1	Characterization of Dirac States	334	23.8.7	Dirac–Hartree–Fock–Breit	357
23.2.2	The Charge-Current Four-Vector	334	23.8.8	Electron Correlation	359
23.3	QED: Relativistic Atomic and Molecular Structure	335	23.8.9	Electron Self-Energy and Vacuum Polarization	359
23.3.1	The QED Equations of Motion	335	23.8.10	Radiative Transitions	360
23.3.2	The Quantized Electron–Positron Field	335	23.9	GRASP – Information and Software	360
23.3.3	Quantized Electromagnetic Field	336	References		360
23.3.4	QED Perturbation Theory	336			
23.3.5	Propagators	338			
23.3.6	Effective Interaction of Electrons	339			
23.4	Many-Body Theory For Atoms	339			
23.4.1	Effective Hamiltonians	340			
23.4.2	Nonrelativistic Limit: Breit–Pauli Hamiltonian	340			
23.4.3	Perturbation Theory: Nondegenerate Case	340			
23.4.4	Perturbation Theory: Open-Shell Case	341			
23.4.5	Perturbation Theory: Algorithms	342			
23.5	Spherical Symmetry	342			
23.5.1	Eigenstates of Angular Momentum	342			
23.5.2	Dirac Hamiltonian in Spherical Coordinates	343			
23.5.3	Solutions Near the Nucleus	345			
23.5.4	Bound states: $r \rightarrow \infty$	346			
23.5.5	Hydrogenic Atoms	347			
23.5.6	The Free Electron Problem in Spherical Coordinates	348			
23.6	Numerical Methods for the Radial Dirac Equation	349			
23.6.1	Dirac's Equation on a Finite Domain	349			
23.6.2	Expansion Methods	349			
23.6.3	Finite Basis Set Formalism	350			
23.6.4	Physically Acceptable Basis Sets	350			
23.6.5	Basis Sets Defined on \mathbb{R}^3	352			
23.6.6	B-Splines	353			
23.7	Finite Differences	354			

Abstract

Relativistic quantum mechanics is required for the description of atoms and molecules whenever their orbital electrons probe regions of space with high potential energy near the atomic nuclei. Primary effects of a relativistic description include changes to spatial and momentum distributions, spin–orbit interactions, quantum electrodynamic corrections such as the Lamb shift, and vacuum polarization. Secondary effects in many-electron systems arise from shielding of the outer electrons by the distributions of electrons in penetrating orbitals; they change orbital binding energies and dimensions and so modify the order in which atomic shells are filled in the lower rows of the periodic table. All these mechanisms must be considered in any attempt to estimate observable quantities to spectroscopic accuracy.

Relativistic atomic and molecular structure theory can be regarded as a simplification of the fundamental description provided by quantum electrodynamics (QED). This treats the atom or molecule as an assembly of electrons and atomic nuclei interacting primarily by exchanging photons. This model is far too difficult and general for most purposes, and simplifications are required. The most important of these is the representation of the nuclei as classical charge distributions, or even as point particles.

I. Grant (✉)
Oxford Mathematical Institute, University of Oxford
Oxford, UK

Since the motion of the nuclei is usually slow relative to the electrons, it is often adequate to treat the nuclear motion nonrelativistically, or even to start from nuclei in fixed positions, correcting subsequently for nuclear motion.

The emphasis in this chapter is on relativistic methods for the calculation of atomic structure for general many-electron atoms based on an effective Hamiltonian derived from QED in the manner sketched in Sect. 23.2 below. An understanding of the Dirac equation, its solutions and their numerical approximation, is essential material for studying many-electron systems, just as the corresponding properties of the Schrödinger equation underpin Chap. 22. Indeed, recent software developments aimed to improve the performance of atomic structure calculations apply to relativistic as much as to nonrelativistic programs. We shall use atomic units throughout. Where it aids interpretation, we shall, however, insert factors of c , m_e and \hbar . In these units, the velocity of light, c , has the approximate numerical value $\alpha^{-1} = 137.035999139$ (31), as recommended in [1], where α is the fine structure constant.

Keywords

relativistic quantum mechanics · quantum electrodynamics · atomic structure theory · Dirac–Hartree–Fock · qed corrections · radiative transitions · Dirac equation · many-body theory

23.1 Mathematical Basics

23.1.1 Relativistic Notation: Minkowski Space-Time

An *event* in Minkowski space-time is defined by a *contravariant* four-vector $x = \{x^\mu\}$ ($\mu = 0, 1, 2, 3$), where $x^0 = ct$ is the time coordinate, and x^1, x^2, x^3 are Cartesian coordinates in three-space. We shall use the Einstein suffix convention, in which matched pairs of upper and lower Greek subscripts are assumed to be summed over all values 0, 1, 2, 3, whenever convenient. The metric of Minkowski space is defined by

$$g = (g_{\mu\nu}) = (g^{\mu\nu}) = \begin{pmatrix} 1 & 0 & 0 & 0 \\ 0 & -1 & 0 & 0 \\ 0 & 0 & -1 & 0 \\ 0 & 0 & 0 & -1 \end{pmatrix}, \quad (23.1)$$

where $g_{\mu\nu} = g^{\mu\nu}$ are called *metric coefficients*. *Covariant* four-vectors x_μ are related to contravariant four-vectors by

$$x_\mu = g_{\mu\nu} x^\nu \quad \text{and} \quad x^\nu = g^{\nu\mu} x_\mu.$$

The bilinear form

$$(x, y) = x_\nu y^\nu = x^\mu g_{\mu\nu} y^\nu = x^\mu y_\mu \quad (23.2)$$

is an *inner product* on Minkowski space, invariant under Lorentz transformations. See also Sect. 23.1.4.

23.1.2 Lorentz Transformations

Lorentz transformations are defined as linear mappings Λ such that

$$(\Lambda x, \Lambda y) = (x, y), \quad (23.3)$$

so that

$$g_{\mu\nu} = \Lambda^\rho{}_\mu g_{\rho\sigma} \Lambda^\sigma{}_\nu. \quad (23.4)$$

This furnishes 10 equations connecting the 16 components of Λ ; at most 6 components can be regarded as independent parameters. The (infinite) set of Λ matrices forms a regular matrix group (with respect to matrix multiplication) called the Lorentz group, \mathcal{L} , designated $O(3,1)$ [2, 3].

23.1.3 Classification of Lorentz Transformations

Rotations Lorentz transformations with matrices of the form

$$\Lambda = \begin{pmatrix} 1 & \mathbf{0}^\top \\ \mathbf{0} & \mathbf{R} \end{pmatrix}, \quad (23.5)$$

where $\mathbf{R} \in \text{SO}(3)$ is an orthogonal 3×3 matrix with determinant $+1$, and $\mathbf{0}$ is a null three-dimensional column vector, correspond to three-dimensional space rotations. They form a group isomorphic to $\text{SO}(3)$.

Boosts Lorentz transformations with matrices of the form

$$\Lambda = \begin{pmatrix} \gamma(v) & \gamma(v)\mathbf{v} \\ \gamma(v)\mathbf{v} & \mathbf{I}_3 + (\gamma(v) - 1)\mathbf{nn}^\top \end{pmatrix}, \quad (23.6)$$

with $\mathbf{v} = v\mathbf{n}$ a three-dimensional column vector, $|\mathbf{n}| = 1$, $v = |\mathbf{v}|$ and $\gamma(v) = (1 - v^2/c^2)^{-1/2}$, are called *boosts*. The matrix Λ describes an *active* transformation from an inertial frame in which a free classical particle is at rest to another inertial frame in which its velocity is \mathbf{v} .

Boosts form a submanifold of \mathcal{L} although they do not in general form a subgroup. However, the set of boosts in a fixed direction \mathbf{n} form a one-parameter subgroup.

Discrete transformations The matrices

$$P = \begin{pmatrix} 1 & \mathbf{0}^\top \\ \mathbf{0} & -\mathbf{I}_3 \end{pmatrix}, \quad T = \begin{pmatrix} -1 & \mathbf{0}^\top \\ \mathbf{0} & \mathbf{I}_3 \end{pmatrix} \quad (23.7)$$

with $PT = -\mathbf{I}_4$ are called *discrete* Lorentz transformations and form a subgroup of the Lorentz group along with the identity \mathbf{I}_4 . The matrix P performs *space* or *parity inversion*; the matrix T performs *time reversal*.

Infinitesimal Lorentz transformations The proper Lorentz transformations close to the identity are of particular importance; they have the form

$$\begin{aligned} \Lambda^\mu{}_\nu &= \delta^\mu{}_\nu + \epsilon \omega^\mu{}_\nu + \dots, \\ (\Lambda^{-1})^\mu{}_\nu &= \delta^\mu{}_\nu - \epsilon \omega^\mu{}_\nu + \dots, \end{aligned} \quad (23.8)$$

where $\omega^\mu{}_\nu = g^{\mu\rho}\omega_{\rho\nu}$, $\omega_{\mu\nu} = -\omega_{\nu\mu}$, and ϵ is infinitesimal. The *infinitesimal generators*, components $\omega_{\mu\nu}$, can be treated as quantum mechanical observables; see Sect. 23.2.1.

The Lorentz group The Lorentz group \mathcal{L} is a Lie group with a six-dimensional group manifold that has four connected components, namely

$$\mathcal{L}_+^\uparrow \equiv \{ \Lambda \in \mathcal{L} \mid \Lambda^0{}_0 \geq 1, \det \Lambda = +1 \}, \quad (23.9)$$

$$\mathcal{L}_-^\uparrow \equiv \{ \Lambda \in \mathcal{L} \mid \Lambda^0{}_0 \geq 1, \det \Lambda = -1 \} = P \mathcal{L}_+^\uparrow, \quad (23.10)$$

$$\mathcal{L}_+^\downarrow \equiv \{ \Lambda \in \mathcal{L} \mid \Lambda^0{}_0 \leq 1, \det \Lambda = -1 \} = T \mathcal{L}_+^\uparrow, \quad (23.11)$$

$$\mathcal{L}_-^\downarrow \equiv \{ \Lambda \in \mathcal{L} \mid \Lambda^0{}_0 \leq 1, \det \Lambda = +1 \} = PT \mathcal{L}_+^\uparrow. \quad (23.12)$$

The connected component \mathcal{L}_+^\uparrow containing the identity is a Lie subgroup of \mathcal{L} called the *proper Lorentz group*. All its group elements can be obtained from boosts and rotations. It is not simply connected because the subgroup of rotations is not simply connected. The group is also noncompact as the subset of boosts is homeomorphic to \mathcal{R}^3 .

These topological properties of \mathcal{L}_+^\uparrow are essential for understanding the properties of relativistic wave equations. In particular, the multiple connectedness forces the introduction of spinor representations and the appearance of half-integer angular momenta or spin.

23.1.4 Contravariant and Covariant Vectors

Contravariant four-vectors (such as events x) transform according to the rule

$$a^\mu \mapsto a^{\mu'} = \Lambda^{\mu'}{}_\nu a^\nu. \quad (23.13)$$

Covariant four-vectors can be formed by writing

$$a_\mu = g_{\mu\nu} a^\nu, \quad (23.14)$$

so that

$$a^\mu a_\mu = a^\mu g_{\mu\nu} a^\nu = (a, a) \quad (23.15)$$

is invariant with respect to Lorentz transformations. Similarly, we can construct a contravariant four-vector from

a covariant one by writing

$$a^\mu = g^{\mu\nu} a_\nu. \quad (23.16)$$

The transformation law for covariant vectors is, therefore,

$$a_\mu \mapsto a'_\mu = [\Lambda^{-1}]^\nu{}_\mu a_\nu. \quad (23.17)$$

The most important example of a covariant vector is the four-momentum operator

$$p_\mu = i \frac{\partial}{\partial x^\nu} \quad \mu = 0, 1, 2, 3. \quad (23.18)$$

From this, we derive the *contravariant* four-momentum operator with components p^μ by writing

$$\begin{aligned} p^\mu &= g^{\mu\nu} p_\nu \\ &= \left(i \frac{\partial}{\partial x^0}, -i \frac{\partial}{\partial x^1}, -i \frac{\partial}{\partial x^2}, -i \frac{\partial}{\partial x^3} \right), \end{aligned} \quad (23.19)$$

in agreement with nonrelativistic expressions.

23.1.5 Poincaré Transformations

More generally, a Poincaré transformation is obtained by combining Lorentz transformations and space-time translations:

$$\Pi(x) = \Lambda x + a. \quad (23.20)$$

The set of all Poincaré transformations, $\Pi = (a, \Lambda)$, with the composition law

$$(a_1, \Lambda_1)(a_2, \Lambda_2) = (a_1 + \Lambda_1 a_2, \Lambda_1 \Lambda_2), \quad (23.21)$$

also forms a group, \mathcal{P} .

Properties of the Lorentz and Poincaré groups will be introduced as needed. For a concise account of their properties, see [4]. For more details on relativistic quantum mechanics in general, see textbooks such as [4, 5].

23.2 Dirac's Equation

We present Dirac's equation for an electron in a classical electromagnetic field defined by the four-potential $A_\mu(x)$:

Covariant form

$$\{ \gamma^\mu [p_\mu - e A_\mu(x)] - m_e c \} \psi(x) = 0. \quad (23.22)$$

where

$$\gamma^\mu (\mu = 0, 1, 2, 3), \text{ are } 4 \times 4 \text{ matrices.}$$

$\psi(x)$ is a four-component spinor wave function.

Here, and elsewhere in this chapter, identity matrices are omitted when it is safe to do so.

Dirac gamma matrices

- Anticommutation relations:

$$\gamma^\mu \gamma^\nu + \gamma^\nu \gamma^\mu = 2g^{\mu\nu} .$$

- Standard representation:

$$\gamma^0 = \begin{pmatrix} 1 & 0 \\ 0 & -1 \end{pmatrix},$$

$$\gamma^i = \begin{pmatrix} 0 & \sigma^i \\ -\sigma^i & 0 \end{pmatrix}, \quad i = 1, 2, 3 ,$$

where σ_i ($i = 1, 2, 3$) are Pauli matrices [2–5].

Noncovariant form In the majority of atomic structure calculations, a frame of reference is chosen in which the nuclear center is taken to be fixed at the origin. In this case, it is convenient to write Dirac's equation in noncovariant form. Then, functions of

$$x = (x^0, \mathbf{x}) ,$$

where $x^0 = ct$, can be regarded as functions of the time t and the position three-vector \mathbf{x} , so that Eq. (23.22) is replaced by

$$i \frac{\partial}{\partial t} \psi(\mathbf{x}, t) = \hat{\mathbf{h}}_D \psi(\mathbf{x}, t) , \quad (23.23)$$

where the scalar and three-vector potentials are defined by

$$\phi(\mathbf{x}, t) = cA^0(\mathbf{x}, t) , \quad (23.24)$$

$$\mathbf{A}(\mathbf{x}, t) = [A^1(\mathbf{x}, t), A^2(\mathbf{x}, t), A^3(\mathbf{x}, t)] ,$$

and

$$\hat{\mathbf{h}}_D = c\boldsymbol{\alpha} \cdot [\mathbf{p} - e\mathbf{A}(\mathbf{x}, t)] + e\phi(\mathbf{x}, t) + \beta m_e c^2 \quad (23.25)$$

defines the Dirac Hamiltonian. The 4×4 matrices $\boldsymbol{\alpha}$, with Cartesian components $(\alpha^1, \alpha^2, \alpha^3)$, and β , have the standard representation

$$\beta = \gamma^0 = \begin{pmatrix} I_2 & 0 \\ 0 & -I_2 \end{pmatrix}, \quad (23.26)$$

$$\alpha^i = \gamma^0 \gamma^i = \begin{pmatrix} 0 & \sigma^i \\ \sigma^i & 0 \end{pmatrix}, \quad i = 1, 2, 3 . \quad (23.27)$$

23.2.1 Characterization of Dirac States

The solutions of Dirac's equation span representations of the Lorentz and Poincaré groups, whose infinitesimal generators can be identified with physical observables. The Lorentz group algebra has ten independent self-adjoint infinitesimal generators; these can be taken to be the components p^μ of the four-momentum (which generate displacements

in each of the four coordinate directions), the three generators, J_i , of rotations about each space-coordinate axis, and the pseudovector w_μ . The irreducible representations can be characterized by invariants

$$(p, p) = m_e^2 c^2 , \quad (23.28)$$

$$(w, w) = -m_e^2 c^2 s^2 = -\frac{3}{4} m_e^2 c^2 , \quad (23.29)$$

where p is the momentum four-vector and \mathbf{s} is a three-vector defined in terms of Pauli matrices by

$$s_i = \frac{1}{2} \sigma_i , \quad i = 1, 2, 3 ,$$

which can be interpreted as the electronic angular momentum (intrinsic spin) in its rest frame. For more details, see [4] and the original papers [6–9].

23.2.2 The Charge-Current Four-Vector

Dirac's equation (23.22) is covariant with respect to Lorentz Eq. (23.3) and Poincaré Eq. (23.20) transformations, provided that there exists a nonsingular 4×4 matrix $S(\Lambda)$ with the property

$$\psi'(x) = S(\Lambda) \psi[\Lambda^{-1}(x - a)] . \quad (23.30)$$

The matrices $S(\Lambda)$ are characterized by the equation

$$S^{-1}(\Lambda) \gamma^\lambda S(\Lambda) = \Lambda^\lambda{}_\mu \gamma^\mu . \quad (23.31)$$

The most important observable expression required in this chapter is the *charge-current four-vector*

$$j^\mu = ec \bar{\psi}(x) \gamma^\mu \psi(x) , \quad (23.32)$$

where the Dirac adjoint is defined by

$$\bar{\psi}(x) = \psi^\dagger(x) \gamma^0 , \quad (23.33)$$

and the dagger denotes spinor conjugation and transposition. Since

$$\begin{aligned} \bar{\psi}'(x) &= \bar{\psi}[\Lambda^{-1}(x - a)] \gamma^0 S(\Lambda)^\dagger \gamma^0 \\ &= \bar{\psi}[\Lambda^{-1}(x - a)] S^{-1}(\Lambda) , \end{aligned}$$

$j^\mu(x)$ transforms as a four-vector

$$j^\mu(x) = \Lambda^\mu{}_\nu j^\nu(x)$$

by virtue of Eq. (23.31). The component $j^0(x)$ can be interpreted as a multiple of the *charge density* $\rho(x)$,

$$j^0(x) = ec\rho(x) = ec \bar{\psi}(x) \gamma^0 \psi(x) = ec \psi^\dagger(x) \psi(x) \quad (23.34)$$

and the space-like components as the *current density*

$$j^i(x) = ec\bar{\psi}(x)\gamma^i\psi(x) = ec\psi^\dagger(x)\alpha^i\psi(x). \quad (23.35)$$

The charge–current density satisfies a continuity equation, which in noncovariant form reads

$$\frac{\partial\rho(x)}{\partial t} + \sum_{i=1}^3 \frac{\partial j^i(x)}{\partial x^i} = 0,$$

or, in covariant notation,

$$\partial_\mu j^\mu = 0. \quad (23.36)$$

This is readily proved by using the Dirac equation (23.22) and its Dirac adjoint. Equation (23.36) is clearly invariant under Poincaré transformations, and this yields the important property that *electric charge* is conserved in Dirac theory.

23.3 QED: Relativistic Atomic and Molecular Structure

23.3.1 The QED Equations of Motion

The conventional starting point [10–13] for deriving equations of motion in quantum electrodynamics (QED) is a Lagrangian density of the form

$$\mathcal{L}(x) = \mathcal{L}_{\text{em}}(x) + \mathcal{L}_e(x) + \mathcal{L}_{\text{int}}(x). \quad (23.37)$$

The first term is the Lagrangian density for the free electromagnetic field, $F^{\mu\nu}(x)$,

$$\mathcal{L}_{\text{em}}(x) = -\frac{1}{4}F^{\mu\nu}F_{\mu\nu}, \quad (23.38)$$

and the second term is the Lagrangian density for the electron–positron field in the presence of the external potential $A_{\text{ext}}^\mu(x)$,

$$\mathcal{L}_e(x) = \bar{\psi}(x)\{\gamma_\mu[p^\mu - eA_{\text{ext}}^\mu(x)] - m_e c\}\psi(x). \quad (23.39)$$

We assume that the electromagnetic fields are expressible in terms of the four-potentials by

$$F^{\mu\nu} = \partial^\mu A_{\text{tot}}^\nu - \partial^\nu A_{\text{tot}}^\mu,$$

where

$$A_{\text{tot}}^\mu(x) = A_{\text{ext}}^\mu(x) + A^\mu(x)$$

is the sum of a four-potential $A_{\text{ext}}^\mu(x)$ describing the fields generated by classical external charge–current distributions, and a quantized field $A^\mu(x)$, which through

$$\mathcal{L}_{\text{int}}(x) = -j_\mu(x)A^\mu(x), \quad (23.40)$$

accounts for the interaction between the uncoupled electrons and the radiation field. The field equations deduced from Eq. (23.37) are

$$\begin{aligned} \{\gamma_\mu[p^\mu - A_{\text{ext}}^\mu(x)] - m_e c\}\psi(x) &= \gamma_\mu A^\mu(x)\psi(x) \\ \partial_\mu F^{\mu\nu}(x) &= j^\nu(x) \end{aligned} \quad (23.41)$$

and clearly exhibit the coupling between the fields.

Quantum electrodynamics requires the solution of the system Eq. (23.41) when $A^\mu(x)$, $\psi(x)$ and its adjoint $\bar{\psi}(x)$ are quantized fields. This presentation is purely formal it ignores all questions of zero-point energies, normal ordering of operators, choice of gauge associated with the quantized photon field, or the need to include (infinite) counterterms to render the theory finite.

23.3.2 The Quantized Electron–Positron Field

Furry’s bound interaction picture of QED [10, 14] exploits the fact that a one-electron model is often a good starting point for a more accurate calculation of atomic or molecular properties. The electrons are described by a field operator

$$\psi(x) = \sum_{E_m > E_F} a_m \psi_m(x) + \sum_{E_n < E_F} b_n^\dagger \psi_n(x), \quad (23.42)$$

where $E_F \geq -mc^2$ is a *Fermi level* separating the states describing electrons (bound and continuum) from the positron states (lower continuum) in the chosen time-independent model potential $V(\mathbf{r})$. Equation (23.42) is written as if the spectrum were entirely discrete, as in finite matrix models; more generally, this must be replaced by integrals over the continuum states together with a sum over the bound states. We assume that the amplitudes $\psi_m(x)$ are orthonormal (which can be achieved, for example, by enclosing the system in a finite box). The operators a_m and a_m^\dagger , respectively, annihilate and create electrons, and b_n and b_n^\dagger perform the same role for vacancies in the *negative energy* states, which we interpret as antiparticles (positrons). These operators satisfy the *anticommutation* rules (Chap. 6.1.1)

$$\begin{aligned} [a_m, a_{m'}^\dagger]_+ &= \delta_{m,m'}, \\ [b_n, b_{n'}^\dagger]_+ &= \delta_{n,n'}, \end{aligned} \quad (23.43)$$

where $[a, b]_+ = ab + ba$. All other anticommutators vanish. The operator representing the number of electrons in state m is then

$$N_m = a_m^\dagger a_m, \quad (23.44)$$

having the eigenvalues 0 or 1; the states of a system of non-interacting electrons and positrons can, therefore, be labeled by listing the occupation numbers, 0 or 1 of the one-electron states participating.

We define the *vacuum state* as the (reference) state $|0\rangle$ in which $N_m = N_n = 0$ for all m, n , so that

$$a_m|0\rangle = b_n|0\rangle = 0. \quad (23.45)$$

The operator representing the total number of particles is given by

$$N = \int \psi^\dagger(x)\psi(x)d\mathbf{x} = \sum_{E_m > E_F} N_m + \sum_{E_n < E_F} (1 - N_n).$$

This is not quite satisfactory: N is infinite for the vacuum state, $N_m = N_n = 0 \forall m, n$, as are the total charge and energy of the vacuum.

These infinite *zero-point* values can be eliminated by introducing *normal ordered operators*. A product of annihilation and creation operators is in normal order if it is rearranged so that all annihilation operators are to the right of all creation operators. Such a product has a null value in the vacuum state. In performing the rearrangement, each anticommutator is treated as if it were zero. We denote normal ordering by placing the operators between colons. Thus, $: a_m^\dagger a_m := a_m^\dagger a_m$ whilst $: b_n b_n^\dagger := -b_n^\dagger b_n$. This means that if we *redefine* N by

$$N = \int : \psi^\dagger(x)\psi(x) : d\mathbf{x} = \sum_{E_m > E_F} N_m - \sum_{E_n < E_F} N_n, \quad (23.46)$$

then $\langle 0|N|0\rangle = 0$. The same trick eliminates the infinity from the total energy of the vacuum;

$$\begin{aligned} H_0 &= \int : \psi^\dagger(x)\hat{\mathbf{h}}_D\psi(x) : d\mathbf{x} \\ &= \sum_{E_m > E_F} N_m E_m - \sum_{E_n < E_F} N_n E_n, \end{aligned} \quad (23.47)$$

so that $\langle 0|H_0|0\rangle = 0$.

The current density operator is given by the commutator of two field variables

$$j^\mu(x) = -\frac{1}{2}ec[\bar{\psi}(x)\gamma^\mu, \psi(x)], \quad (23.48)$$

where the Dirac adjoint, $\bar{\psi}(x)$, is defined by Eq. (23.33). The definition Eq. (23.48) differs from Eq. (23.32) by expressing the total current as the difference between the electron (negatively charged) and positron (positively charged) currents. We can write

$$j^\mu(x) =: j^\mu(x) : + ec \text{Tr}[\gamma^\mu S_F(x, x)], \quad (23.49)$$

where $S_F(x, y)$ is the Feynman causal propagator, defined below. Since $\langle 0|: j^\mu(x) : |0\rangle = 0$, the last term in Eq. (23.49) is the *vacuum polarization current* due to the asymmetry

between positive and negative energy states induced by the external field. From this, the net charge of the system is

$$\begin{aligned} Q &= \frac{1}{c} \int j^0(x) d^3x \\ &= -e \left(\sum_{E_m > E_F} N_m - \sum_{E_n < E_F} N_n \right) + Q_{\text{vac}}; \end{aligned} \quad (23.50)$$

Q_{vac} is the total charge of the vacuum, which vanishes for free electrons but is finite in the presence of an external field (the phenomenon of *vacuum polarization*). Note that whilst Q is conserved for all processes, the total number of particles need not be; it is always possible to add virtual states incorporating electron–positron pairs without changing Q .

23.3.3 Quantized Electromagnetic Field

The four-potential of the quantized electromagnetic field can be expressed in terms of a spectral expansion over the field modes in, for example, plane waves

$$\begin{aligned} A_\mu(x) &= \int \frac{d^3k}{2(2\pi)^3 k_0} \sum_{\lambda=0}^3 \left[q^{(\lambda)}(k) \epsilon_\mu^{(\lambda)}(k) e^{-ik \cdot x} \right. \\ &\quad \left. + q^{(\lambda)\dagger}(k) \epsilon_\mu^{(\lambda)*}(k) e^{ik \cdot x} \right]. \end{aligned} \quad (23.51)$$

The vectors $\epsilon_\mu^{(\lambda)}(k)$ describe the polarization modes; there are four linearly independent vectors, which may be assumed real, for each k on the positive light cone. Two of these ($\lambda = 1, 2$) can be chosen perpendicular to the photon momentum \mathbf{k} (*transverse polarization*); one component ($\lambda = 3$) along \mathbf{k} (*longitudinal polarization*), and the final component ($\lambda = 0$) is time like (*scalar polarization*). The operators $q^{(\lambda)}(k)$ and $q^{(\lambda)\dagger}(k)$ describe, respectively, photon absorption and emission. They satisfy commutation relations

$$\begin{aligned} [q^{(\lambda)}(k), q^{(\lambda')\dagger}(k')] &= \delta_{\lambda, \lambda'} \delta_{k, k'}, \quad \lambda, \lambda' = 1, 2, 3, \\ [q^{(0)}(k), q^{(0)\dagger}(k')] &= -\delta_{k, k'}; \end{aligned} \quad (23.52)$$

all other commutators vanish. The photon vacuum state, $|0\rangle_\gamma$, is such that

$$q^{(\lambda)}(k)|0\rangle_\gamma = 0. \quad (23.53)$$

Further details may be found in the texts [10–13].

23.3.4 QED Perturbation Theory

The textbook perturbation theory of QED, see for example [10, 11, 13, 15] and other works, has been adapted for

applications to relativistic atomic and molecular structure and is also the source of methods of nonrelativistic many-body perturbation theory (MBPT). We offer a brief sketch emphasizing details not found in the standard texts.

The perturbation expansion The Lagrangian approach leads to an interaction Hamiltonian

$$H_1 = - \int j^\mu(x) A_\mu(x) \, dx . \quad (23.54)$$

In the interaction representation, this gives an equation of motion

$$i\hbar \partial_t |\Phi(t)\rangle = H_1(t) |\Phi(t)\rangle , \quad (23.55)$$

where $|\Phi(t)\rangle$ is the QED state vector, and

$$H_1(t) = \exp\left(\frac{iH_0 t}{\hbar}\right) H_1 \exp\left(\frac{-iH_0 t}{\hbar}\right) ,$$

where $H_0 = H_{\text{em}} + H_c$ is the Hamiltonian for the uncoupled photon and electron–positron fields. If $S(t, t')$ is the *time development* operator such that

$$|\Phi(t)\rangle = S(t, t') |\Phi(t')\rangle ,$$

then

$$i\hbar \partial_t S(t, t') = H_1(t) S(t, t') .$$

The equivalent integral equation, incorporating the initial condition $S(t, t) = 1$,

$$S(t, t_0) = 1 - \frac{i}{\hbar} \int_{t_0}^t H_1(t_1) S(t_1, t_0) dt_1 , \quad (23.56)$$

can be solved iteratively, giving

$$S(t, t_0) = 1 + \sum_{n=1}^{\infty} S^{(n)}(t, t_0) , \quad (23.57)$$

where

$$S^{(n)}(t, t_0) = \left(\frac{-i}{\hbar}\right)^n \int_{t_0}^t dt_1 \int_{t_0}^{t_1} dt_2 \cdots \int_{t_0}^{t_{n-1}} dt_n \\ \times H_1(t_1) H_1(t_2) \cdots H_1(t_n) .$$

This can be put into a more symmetric form by using *time-ordered* operators. Define the T -product of two operators by

$$T[A(t_1)B(t_2)] = \begin{cases} A(t_1)B(t_2) , & t_1 > t_2 \\ \pm B(t_2)A(t_1) , & t_2 > t_1 \end{cases} , \quad (23.58)$$

where the *positive* sign refers to the product of photon operators and the *negative* sign to electrons. Then,

$$S^{(n)}(t, t_0) = \frac{(-i/\hbar)^n}{n!} \int_{t_0}^t dt_1 \int_{t_0}^{t_1} dt_2 \cdots \int_{t_0}^{t_{n-1}} dt_n \\ \times T[H_1(t_1)H_1(t_2) \cdots H_1(t_n)] . \quad (23.59)$$

The operator $S(t, t')$ relates the state vector at time t to the state vector at some earlier time $t' < t$. Its matrix elements, therefore, give the transition amplitudes for different processes, for example the emission or absorption of radiation by a system or the outcome of scattering of a projectile from a target. The techniques for extracting cross sections and other observable quantities from the S -operator are described at length in the texts [10, 11, 13, 15].

Although the use of normal ordering means that the charge and mass of the reference state, the vacuum, is zero, it fails to remove other infinities due to the occurrence of divergent integrals. The method of extracting finite quantities from this theory involves *renormalization* of the charge and mass of the electron. We shall refer especially to [13, Chap. 8] for a detailed discussion. The most difficult technical problems are posed by *mass renormalization*. Formally, we modify the interaction Hamiltonian to read

$$j^\mu(x) A_\mu(x) - \delta M(x) ,$$

where $\delta M(x)$ is the *mass renormalization operator*

$$\delta M(x) = \frac{1}{2} \delta m [\bar{\psi}(x), \psi(x)] ,$$

where δm is infinite.

A further problem is that electrons in a many-electron atom or molecule move in a potential that is quite unlike that of the bare nucleus. It is, therefore, useful to introduce a local *mean field* potential, say $U(x)$, representing some sort of average interaction with the rest of the electron charge distribution, so that the zero-order orbitals satisfy

$$[c\boldsymbol{\alpha} \cdot \mathbf{p} + \beta c^2 + V_{\text{nuc}}(\mathbf{x}) + U(\mathbf{x}) - E_m] \psi_m(\mathbf{x}) = 0 . \quad (23.60)$$

With this starting point, the interaction Hamiltonian becomes

$$H_1(x) = H_1^{(1)}(x) + H_1^{(2)}(x) , \quad (23.61)$$

where

$$H_1^{(1)}(x) = -U(x), \quad H_1^{(2)}(x) = j^\mu(x) A_\mu(x) - \delta M(x) ,$$

and the electron current is defined in terms of the mean field orbitals of Eq. (23.60). The expression $H_1^{(2)}(x)$ is sometimes referred to as a *fluctuation potential*. The term $j^\mu(x) A_\mu(x)$ is proportional to the electron charge, e , which serves as an ordering parameter for perturbation expansions.

Effective interactions Although the S-matrix formalism provides in principle a complete computational scheme for many-electron systems, it is generally too cumbersome for practical use, and approximations are necessary. Usually, this is a matter of selecting a subset of dominant contributions to the perturbation series, depending on the application. We are faced with the evaluation of T -products of the form

$$T[\phi(t_1)\phi(t_2)\cdots\phi(t_n)],$$

which is done using Wick's theorem [13, p. 25].

In the simplest case,

$$T[\phi(t_1)\phi(t_2)] = :\phi(t_1)\phi(t_2): + \langle 0|T[\phi(t_1)\phi(t_2)]|0\rangle. \quad (23.62)$$

The vacuum expectation value is called a *contraction*. More generally, we have

$$\begin{aligned} T[\phi(t_1)\phi(t_2)\cdots\phi(t_n)] &= :\phi(t_1)\phi(t_2)\cdots\phi(t_n): \\ &+ \{\langle 0|T[\phi(t_1)\phi(t_2)]|0\rangle : \phi(t_3)\cdots\phi(t_n) : + \text{permutations}\} \\ &+ \{\langle 0|T[\phi(t_1)\phi(t_2)]|0\rangle \langle 0|T[\phi(t_3)\phi(t_4)]|0\rangle \\ &\quad \times : \phi(t_5)\cdots\phi(t_n) : + \text{permutations}\} \dots \end{aligned}$$

This result has the effect that a T -product with an odd number of factors vanishes. A rigorous statement can be found in all standard texts; each term in the expansion gives rise to a Feynman diagram that can be interpreted as the amplitude of a physical process. As an example, consider the simple but important case

$$S^{(2)} = \frac{(ie)^2}{2!} T[j^\mu(x)A_\mu(x) \cdot j^\nu(y)A_\nu(y)]. \quad (23.63)$$

One of the terms (there are others) found by using Wick's Theorem is

$$j^\mu(x)j^\nu(y)\langle 0|T[A_\mu(x)A_\nu(y)]|0\rangle.$$

We can see that this involves the contraction of two photon amplitudes

$$-\frac{1}{2}D_{F\mu\nu}(x-y) = \langle 0|T[A_\mu(x)A_\nu(y)]|0\rangle,$$

which plays the role of a *propagator* Eq. (23.69); it relates the photon amplitudes at two space-time points x, y . With the introduction of a spectral expansion for the electron current Eq. (23.48), the contribution to the energy of the system becomes

$$\frac{1}{2} \sum_{pqrs} : a_p^\dagger a_q^\dagger a_s a_r : \langle pq|V|rs\rangle, \quad (23.64)$$

which can be interpreted, in the familiar language of ordinary quantum mechanics, as the energy of two electrons due to the electron–electron interaction V , which is directly related to the photon propagator.

23.3.5 Propagators

Propagators relate field variables at different space-time points. Here we briefly define those most often needed in atomic and molecular physics.

Electrons Define Feynman's causal propagator for the electron–positron field by the contraction

$$S_F(x_2, x_1) = \langle 0|T[\psi(x_2)\bar{\psi}(x_1)]|0\rangle. \quad (23.65)$$

This has a spectral decomposition of the form

$$S_F(x_2, x_1) = \begin{cases} \sum_{E_m > E_F} \psi_m(x_2)\bar{\psi}_m(x_1) & t_1 > t_2, \\ -\sum_{E_n < E_F} \psi_n(x_2)\bar{\psi}_n(x_1) & t_1 < t_2, \end{cases} \quad (23.66)$$

which ensures that positive energy solutions are propagated forwards in time and negative energy solutions backwards in time in accordance with the antiparticle interpretation of the negative energy states. By noting that the stationary state solutions $\psi_m(x)$ have time dependence $\exp(-iE_m t)$, we can write Eq. (23.66) in the form

$$\begin{aligned} S_F(x_2, x_1) &= \frac{1}{2\pi i} \int_{-\infty}^{\infty} \sum_n \frac{\psi_n(\mathbf{x}_2)\bar{\psi}_n(\mathbf{x}_1)}{E_n - z(1 + i\delta)} e^{-iz(t_2 - t_1)} dz \\ &= \frac{1}{2\pi i} \int_{-\infty}^{\infty} G(\mathbf{x}_2, \mathbf{x}_1, z) \gamma^0 e^{-iz(t_2 - t_1)} dz, \end{aligned} \quad (23.67)$$

where δ is a small positive number, the sum over n includes *the whole spectrum*, and where the Green's function $G(\mathbf{x}_2, \mathbf{x}_1, z)$, in the specific case in which the potential of the external field $a^\mu(x)$ has only a scalar time-independent part, $V_{\text{nuc}}(\mathbf{x})$, satisfies

$$\begin{aligned} [c\boldsymbol{\alpha} \cdot \mathbf{p} + \beta c^2 + (V_{\text{nuc}}\mathbf{x}) - z]G(\mathbf{x}, \mathbf{y}, z) \\ = \delta^{(3)}(\mathbf{x}_2 - \mathbf{x}_1); \end{aligned} \quad (23.68)$$

$G(\mathbf{x}_2, \mathbf{x}_1, z)$ is a meromorphic function of the complex variable z with branch points at $z = \pm c^2$, and two cuts (c^2, ∞) and $(-\infty, -c^2)$ along the real axis. The poles lie on the segment $(-c^2, c^2)$ at the bound eigenvalues of the Dirac Hamiltonian for this potential.

Photons We construct the photon propagator $D_{F\mu\nu}(x_2 - x_1)$ in a similar manner:

$$-\frac{1}{2}D_{F\mu\nu}(x_2 - x_1) = \langle 0|T[A_\mu(x_2)A_\nu(x_1)]|0\rangle, \quad (23.69)$$

where μ_0 is the permeability of the vacuum. This has the integral representation

$$\begin{aligned} D_{F\mu\nu}(x_2 - x_1) &= g_{\mu\nu}D_F(x_2 - x_1) \\ &= -g_{\mu\nu} \frac{i}{(2\pi)^4} \int d^4q D(q^2), \end{aligned} \quad (23.70)$$

where

$$D(q^2) = \frac{1}{q^2 + i\delta},$$

and δ is a small positive number. This is not unique, as the four-potentials depend on the choice of gauge; for details, see [11, Sect. 77]. The various forms for the electron–electron interaction given below express such gauge choices.

23.3.6 Effective Interaction of Electrons

The expression Eq. (23.63) can be viewed in several ways: it is the interaction of the current density $j^\mu(x)$ at the space-time point x with the four-potential due to the current $j^\mu(y)$; the interaction of the current density $j^\mu(y)$ with the four-potential due to the current $j^\mu(x)$; or, as is commonly assumed in nonrelativistic atomic theory, the effective interaction between two charge density distributions, as represented by Eq. (23.64). In terms of the corresponding Feynman diagram, it can be thought of as the energy due to the exchange of a virtual photon.

The form of V depends on the choice of gauge potential, as follows.

Feynman gauge

$$\begin{aligned} & \langle pq|V|rs\rangle \\ &= \int \int \psi_p^\dagger(\mathbf{x})\psi_r(\mathbf{x})v_{sq}^F(\mathbf{x},\mathbf{y})\psi_q^\dagger(\mathbf{y})\psi_s(\mathbf{y})d^3x d^3y, \end{aligned} \quad (23.71)$$

where

$$v_{sq}^F(\mathbf{x},\mathbf{y}) = \frac{e^{i\omega_{sq}R}}{R}(1 - \boldsymbol{\alpha}_x \cdot \boldsymbol{\alpha}_y), \quad (23.72)$$

with

$$\mathbf{R} = \mathbf{x} - \mathbf{y}, \quad R = |\mathbf{R}|, \quad \omega_{sq} = \frac{E_s - E_q}{c}.$$

This interaction gives both a real and an imaginary contribution to the energy; only the former is usually taken into account in structure calculations. Since the orbital indices are dummy variables, it is usual to symmetrize the interaction kernel by writing

$$\bar{v}^F(\mathbf{x},\mathbf{y}) = \frac{1}{2} \left[v_{sq}^F(\mathbf{x},\mathbf{y}) + v_{rp}^F(\mathbf{x},\mathbf{y}) \right],$$

which places the orbitals on an equal footing.

Coulomb gauge Here, the Feynman propagator is replaced by that for the Coulomb gauge, giving

$$\begin{aligned} v_{sq}^T(\mathbf{x},\mathbf{y}) &= \frac{e^{i\omega_{sq}R}}{R} - \left[\boldsymbol{\alpha}_x \cdot \boldsymbol{\alpha}_y \frac{e^{i\omega_{sq}R}}{R} \right. \\ &\quad \left. + (\boldsymbol{\alpha}_x \cdot \nabla)(\boldsymbol{\alpha}_y \cdot \nabla) \frac{e^{i\omega_{sq}R} - 1}{\omega_{sq}^2 R} \right], \end{aligned} \quad (23.73)$$

in which the operator ∇ involves differentiation with respect to \mathbf{R} . Symmetrization is also used with this interaction.

Breit operator The *low-frequency limit*, $\omega_{rp} \rightarrow 0$, $\omega_{sq} \rightarrow 0$, is known as the Breit interaction:

$$\lim_{\omega_{rp}, \omega_{sq} \rightarrow 0} v_{sq}^T(\mathbf{x},\mathbf{y}) = \frac{1}{R} + v^B(\mathbf{R}), \quad (23.74)$$

where

$$v^B(\mathbf{R}) = -\frac{1}{2R} \left(\boldsymbol{\alpha}_x \cdot \boldsymbol{\alpha}_y + \frac{\boldsymbol{\alpha}_x \cdot \mathbf{R} \boldsymbol{\alpha}_y \cdot \mathbf{R}}{R^2} \right).$$

Gaunt operator This is a further approximation in which $v^B(\mathbf{R})$ is replaced by

$$v^G(\mathbf{R}) = -\frac{\boldsymbol{\alpha}_x \cdot \boldsymbol{\alpha}_y}{R}, \quad (23.75)$$

the residual part of the Breit interaction being neglected.

Comments The choice of gauge should not influence the predictions of QED for atomic and molecular structure when the perturbation series is summed to convergence, so that it should not matter if the unapproximated effective operators are taken in Feynman or Coulomb gauge. However, this need not be true at each order of perturbation. It has been shown that the results are equivalent, order by order, if the orbitals have been defined in a *local* potential, but not otherwise. There have also been suggestions that the Feynman operator introduces spurious terms in lower orders of perturbation that are canceled in higher orders [16]. For this reason, most structure calculations have used Coulomb gauge.

It is often argued, following *Bethe and Salpeter* [17, Sect. 38], that the Breit interaction should only be used in first-order perturbation theory. The reason is the approximation $\omega \rightarrow 0$. However, it takes into account the dominant magnetic interactions in self-consistent field calculations. The Coulomb gauge operator Eq. (23.73) has also been used in relativistic configuration interaction calculations but so far not in self-consistent calculations.

23.4 Many-Body Theory For Atoms

The development of a practical relativistic theory of atomic structure remains a challenging problem. Recently, there have been studies of the feasibility of merging the QED approach with many-body perturbation theory MBPT to perform *accurate* QED calculations on light elements [18, 19], but these remain unimplemented. Dzuba et al. [20] attempt to treat properties of superheavy elements (with atomic numbers $Z > 100$) using relativistic configuration interaction combined with perturbation theory, an approach that has features similar to those used in the GRASP2K programs [21] on which this chapter focuses.

GRASP2K is based on RMCDFH, a relativistic Dirac Hartree–Fock self-consistent field program using the Dirac–Coulomb Hamiltonian with a basis of trial atomic state functions (ASFs) that are linear combinations of configurational state functions (CSFs). As well as determining the coefficients of this linear combination, the program determines an orthonormal basis of Dirac four-component orbitals on which the CSFs are built. This constructs a multireference (MR) first approximation for the basic atomic states of interest, which can then be improved (electron correlation) by extending the MR CSF and orbital bases systematically, keeping the MR orbitals frozen. A relativistic configuration interaction (RCI) program incorporating the Breit interaction and approximations for QED corrections demonstrates how well the model converges. The general strategy is much the same as that used for the nonrelativistic models described in more detail in Chap. 22 [22].

23.4.1 Effective Hamiltonians

The models that are closest to QED are those in which the full electron–electron interaction is included, usually in Coulomb gauge. We define a Fock space Hamiltonian

$$H_{\text{DCB}} = H_0 + H_1 + H_2, \quad (23.76)$$

where, as in Eq. (23.47),

$$H_0 = \sum_{E_m > E_F} N_m E_m - \sum_{E_n < E_F} N_n E_n, \quad (23.77)$$

in which the states are those determined with respect to a mean-field central potential $U(\mathbf{x})$ as in Eq. (23.60)

$$[c\boldsymbol{\alpha} \cdot \mathbf{p} + \beta c^2 + V_{\text{nuc}}(\mathbf{x}) + U(\mathbf{x}) - E_m] \psi_m(\mathbf{x}) = 0,$$

and

$$H_1 = - \sum_{pq} : a_p^\dagger a_q : \langle p | U(\mathbf{x}) | q \rangle,$$

$$H_2 = \frac{1}{2} \sum_{pqrs} : a_p^\dagger a_q^\dagger a_r a_s : \langle pq | V | sr \rangle.$$

Here, the sums run only over states p with $E_p > E_F$; this means that states with $E_p < E_F$ are treated as inert.

The models are named according to the choice of V from Sect. 23.5.3.

Dirac–Coulomb–Breit models These incorporate the *full* Coulomb gauge operator Eq. (23.73) or the less accurate Breit operator Eq. (23.74). The fully retarded operator is usually taken in the symmetrized form. The Gaunt operator Eq. (23.75) is sometimes considered as an approximation to the Breit operator.

Dirac–Coulomb models Here, the electron–electron interaction is just the static $1/R$ potential. Note that although the equations are relativistic, the choices of electron–nucleus interaction all implicitly restrict these models to a frame in which the nuclei are fixed in space. The full electron–electron interaction is gauge invariant; however, it is common to start from the Dirac–Coulomb operator, in which case the gauge invariance is lost. Since radiative transition rates are sensitive to loss of gauge invariance [23], the choice of potential in Eq. (23.76) can make a big difference. Such choices may also affect the rate of convergence in correlation calculations in which the relativistic parts of the electron–electron interaction are treated as a second, independent, perturbation.

23.4.2 Nonrelativistic Limit: Breit–Pauli Hamiltonian

The nonrelativistic limit of the Dirac–Coulomb–Breit Hamiltonian is described in Chap. 22. The derivation is given in many texts, for example [11, 13, 17], and in principle involves the following steps:

1. Express the relativistic four-spinor in terms of nonrelativistic Pauli two-spinors of the form (Sect. 22.2)

$$\phi_{nlm_l m_s}(\mathbf{x}) = \text{const.} \frac{P_{nl}(r)}{r} Y_{lm_l}(\theta, \phi) \chi_{m_s}(\sigma), \quad (23.78)$$

where χ_{m_s} is a two-component eigenvector of the spin operator \mathbf{s} to lowest order in $1/c$.

2. Extract effective operators to order $1/c^2$.

Thus, the Breit–Pauli Hamiltonian is written as the sum of terms of Sect. 22.2, which can be correlated with specific parts of the parent relativistic operator:

1. One-body terms originate from the Dirac Hamiltonian: they are H_{mass} (Sect. 22.8), the one-body part of H_{Darwin} (Sect. 22.9) and the spin–orbit couplings H_{so} (Sect. 22.13) and H_{soo} (Sect. 22.14). The forms given in these equations assume that the electron interacts with a point-charge nucleus and only require the Coulomb part of the electron–electron interaction.
2. Two-body terms, including the two-body parts of H_{Darwin} (Sect. 22.9), the spin–spin contact term H_{ssc} (Sect. 22.10), the orbit–orbit term H_{oo} (Sect. 22.11), and the spin–spin term H_{ss} (Sect. 22.15) originate from the Breit interaction.

23.4.3 Perturbation Theory: Nondegenerate Case

We give a brief resumé of the Rayleigh–Schrödinger perturbation theory following *Lindgren* [24]. The material pre-

sented here supplements the general discussion of perturbation theory in Chap. 5. First consider the simplest case with a nondegenerate reference state Φ belonging to the Hilbert space \mathcal{H} satisfying

$$H_0|\Phi\rangle = E_0|\Phi\rangle, \quad (23.79)$$

which is a first approximation to the solution of the full problem

$$H|\Psi\rangle = E|\Psi\rangle, \quad H = H_0 + V. \quad (23.80)$$

Next, introduce a projection operator P such that

$$P = |\Phi\rangle\langle\Phi|, \quad P|\Phi\rangle = |\Phi\rangle,$$

and its complement $Q = 1 - P$, projecting onto the complementary subspace $\mathcal{H} \setminus \{\Phi\}$. With the *intermediate normalization*

$$\langle\Phi|\Psi\rangle = \langle\Phi|\Phi\rangle = 1,$$

it follows that

$$P|\Psi\rangle = |\Phi\rangle\langle\Phi|\Psi\rangle = |\Phi\rangle,$$

so that the perturbed wave function can be decomposed into two parts:

$$|\Psi\rangle = (P + Q)|\Psi\rangle = |\Phi\rangle + Q|\Psi\rangle.$$

Thus, with intermediate normalization,

$$E = \langle\Phi|H|\Psi\rangle = E_0 + \langle\Phi|V|\Psi\rangle.$$

We now use this decomposition to write Eq. (23.80) in the form

$$(E_0 - H_0)|\Psi\rangle = (V - \Delta E)|\Psi\rangle, \quad (23.81)$$

where $\Delta E = \langle\Phi|V|\Psi\rangle$. Thus,

$$(E_0 - H_0)Q|\Psi\rangle = Q(V - \Delta E)|\Psi\rangle. \quad (23.82)$$

Introduce the *resolvent operator*

$$R = \frac{Q}{E_0 - H_0}, \quad (23.83)$$

which is well-defined except on $\{\Phi\}$. Then the perturbation contribution to the wave function is

$$Q|\Psi\rangle = R(V - \Delta E)|\Psi\rangle = R(V|\Psi\rangle - |\Psi\rangle\langle\Phi|V|\Psi\rangle).$$

The *Rayleigh–Schrödinger* perturbation expansion can now be written

$$\begin{aligned} |\Psi\rangle &= |\Phi\rangle + |\Psi^{(1)}\rangle + |\Psi^{(2)}\rangle + \dots \\ E &= E_0 + E^{(1)} + E^{(2)} + \dots \end{aligned}$$

The contributions are ordered by the number of occurrences of V , the leading terms being

$$\begin{aligned} |\Psi^{(1)}\rangle &= RV|\Phi\rangle, \\ |\Psi^{(2)}\rangle &= (RVRV - R^2VPV)|\Phi\rangle, \end{aligned}$$

and so on. The corresponding contribution to the energy can then be found from

$$E^{(n)} = \langle\Phi|V|\Psi^{(n-1)}\rangle.$$

23.4.4 Perturbation Theory: Open-Shell Case

Consider now the case in which there are several unperturbed states, $|\Phi^{(a)}\rangle$, $a = 1, 2, \dots, d$, having the same energy E_0 , which span a d -dimensional linear subspace (the *model space*) $\mathcal{M} \subset \mathcal{H}$, so that

$$H_0|\Phi^{(a)}\rangle = E_0|\Phi^{(a)}\rangle, \quad a = 1, 2, \dots, d.$$

Let P be the projector onto \mathcal{M} and Q onto the orthogonal subspace \mathcal{M}^\perp .

The perturbed states $|\Psi^{(a)}\rangle$, $a = 1, 2, \dots, d$ are related to the unperturbed states by the *wave operator* Ω ,

$$|\Psi^{(a)}\rangle = \Omega|\Phi^{(a)}\rangle, \quad a = 1, 2, \dots, d.$$

The *effective Hamiltonian*, H_{eff} , is defined so that

$$H_{\text{eff}}|\Phi^{(a)}\rangle = E^{(a)}|\Phi^{(a)}\rangle,$$

and thus

$$\Omega H_{\text{eff}}|\Phi^{(a)}\rangle = E^{(a)}|\Psi^{(a)}\rangle = H\Omega|\Phi^{(a)}\rangle.$$

Thus, on the domain \mathcal{M} we can write an operator equation

$$\Omega H_{\text{eff}}P = H\Omega P, \quad (23.84)$$

known as the Bloch equation. We partition H_{eff} so that

$$H_{\text{eff}}P = (H_0 + V_{\text{eff}})P,$$

enabling a reformulation of Eq. (23.84) as the commutator equation

$$[\Omega, H_0]P = (V\Omega - \Omega V_{\text{eff}})P. \quad (23.85)$$

With the intermediate normalization convention of Sect. 23.4.3, this becomes

$$|\Psi^{(a)}\rangle = P|\Phi^{(a)}\rangle,$$

so that $P\Omega P = P$ and

$$H_{\text{eff}}P = PH\Omega P, \quad V_{\text{eff}}P = PV\Omega P.$$

Then Eq. (23.85) can be put in the final form

$$[\Omega, H_0]P = (V\Omega - \Omega PV\Omega)P. \quad (23.86)$$

The general Rayleigh–Schrödinger perturbation expansion can now be generated by expanding the wave operator order by order

$$\Omega = 1 + \Omega^{(1)} + \Omega^{(2)} + \dots,$$

and inserting into Eq. (23.86), resulting in a hierarchy of equations

$$\begin{aligned} [\Omega^{(1)}, H_0]P &= (V - PV)P = QVP, \\ [\Omega^{(2)}, H_0]P &= (QV\Omega^{(1)} - \Omega^{(1)}PV)P, \end{aligned}$$

and so on, with $H_{\text{eff}}^{(n)} = PV\Omega^{(n-1)}$.

23.4.5 Perturbation Theory: Algorithms

The techniques of QED perturbation theory of Sect. 23.3.4 can be utilized to give computable expressions for perturbation calculations order by order. They exploit the second quantized representation of operators of Sect. 23.4.1 along with the use of diagrams to express the contributions to the wave operator and the energy as sums over virtual states. The use of Wick’s theorem to reduce products of normally-ordered operators, and the *linked-diagram* or *linked-cluster* theorem are explained in *Lindgren’s* article [24] and Chap. 5. Further references and discussion of features that can exploit vector-processing and parallel-processing computer architectures may be found in [25].

The theory can also be recast so as to sum certain classes of terms to completion. This depends on the possibility of expressing the wave operator as a normally ordered exponential operator

$$\Omega = \{\exp S\} = 1 + \{S\} + \frac{1}{2!}\{S^2\} + \dots,$$

where the normally ordered operator S is known as the *cluster* operator. Expanding S order by order leads to the *coupled cluster expansion* (Chaps. 5 and 28).

23.5 Spherical Symmetry

A popular starting point for most calculations in atomic and molecular structure is the independent particle central field approximation. This assumes that the electrons move independently in a potential field of the form

$$\begin{aligned} A_0(x) &= \frac{1}{c}\phi(r), \quad r = |\mathbf{x}|; \\ A_i(x) &= 0, \quad i = 1, 2, 3. \end{aligned} \quad (23.87)$$

Clearly, $\phi(r)$ is left unchanged by any rotation about the origin, $r = 0$, but transforms as the component $A_0(x)$ of a four-vector under other types of Lorentz and Poincaré transformation such as boosts or translations. However, solutions in central potentials of this form have a simple form that is convenient for further calculation.

With this restriction on the four-potential, Dirac’s Hamiltonian becomes

$$\hat{\mathbf{h}}_D = \{c\boldsymbol{\alpha} \cdot \mathbf{p} + e\phi(r) + \beta m_e c^2\}. \quad (23.88)$$

Consider stationary solutions with energy E satisfying

$$\hat{\mathbf{h}}_D \psi_E(x) = E \psi_E(x).$$

Since $\hat{\mathbf{h}}_D$ is invariant with respect to rotation about $r = 0$, it commutes with the generators J_1, J_2, J_3 mentioned in Sect. 23.1.1, corresponding to components of the total angular momentum \mathbf{j} of the electron, usually decomposed into an orbital part \mathbf{l} and a spin part \mathbf{s} ,

$$\mathbf{j} = \mathbf{l} + \mathbf{s}, \quad (23.89)$$

where

$$\begin{aligned} l_j &= i\epsilon_{jkl}x_k\partial_l, \quad j = 1, 2, 3, \\ s_j &= \frac{1}{2}\epsilon_{jkl}\sigma_{kl}, \quad j = 1, 2, 3. \end{aligned}$$

23.5.1 Eigenstates of Angular Momentum

We can construct simultaneous eigenstates of the operators \mathbf{j}^2 and j_3 by using the product representation $\mathcal{D}^{(l)} \times \mathcal{D}^{(1/2)}$ of the rotation group $\text{SO}(3)$, which is reducible to the Clebsch–Gordan sum of two irreps

$$\mathcal{D}^{(l+1/2)} \oplus \mathcal{D}^{(l-1/2)}. \quad (23.90)$$

We construct a basis for each irrep from products of basis vectors for $\mathcal{D}^{(1/2)}$ and $\mathcal{D}^{(l)}$, respectively. $\mathcal{D}^{(1/2)}$ is a two-dimensional representation spanned by the simultaneous

eigenstates ϕ_σ of \mathbf{s}^2 and s_3

$$\mathbf{s}^2 \phi_\sigma = \frac{3}{4} \phi_\sigma, \quad s_3 \phi_\sigma = \sigma \phi_\sigma, \quad \sigma = \pm \frac{1}{2},$$

for which we can use two-rowed vectors

$$\phi_{1/2} = \begin{pmatrix} 1 \\ 0 \end{pmatrix}, \quad \phi_{-1/2} = \begin{pmatrix} 0 \\ 1 \end{pmatrix}.$$

The representation $\mathcal{D}^{(l)}$ is $(2l + 1)$ -dimensional; its basis vectors can be taken to be the spherical harmonics

$$\{Y_l^m(\theta, \varphi) \mid m = -l, -l + 1, \dots, l\},$$

so that

$$\begin{aligned} \mathbf{I}^2 Y_l^m(\theta, \varphi) &= l(l + 1) \hbar^2 Y_l^m(\theta, \varphi), \\ l_3 Y_l^m(\theta, \varphi) &= m \hbar Y_l^m(\theta, \varphi). \end{aligned}$$

We shall assume that spherical harmonics satisfy the standard relations

$$l_\pm Y_l^m(\theta, \varphi) = [l(l + 1) - m(m \pm 1)]^{1/2} \hbar Y_l^{m \pm 1}(\theta, \varphi),$$

where $l_\pm = l_1 \pm l_2$, so that

$$\begin{aligned} Y_l^m(\theta, \varphi) &= \left(\frac{2l + 1}{4\pi} \right)^{1/2} C_l^m(\theta, \varphi), \\ C_l^m(\theta, \varphi) &= (-1)^m \left(\frac{(l - m)!}{(l + m)!} \right)^{1/2} P_l^m(\theta) e^{im\varphi}, \quad \text{if } m \geq 0, \\ C_l^{-m}(\theta, \varphi) &= (-1)^m C_l^m(\theta, \varphi)^*. \end{aligned} \quad (23.91)$$

Basis functions for the representations \mathcal{D}^j with $j = l \pm \frac{1}{2}$ have the form

$$\begin{aligned} \chi_{j,m,a}(\theta, \varphi) \\ = \sum_\sigma \left\langle l, m - \sigma, \frac{1}{2}, \sigma \mid l, \frac{1}{2}, j, m \right\rangle Y_l^{m-\sigma}(\theta, \varphi) \phi_\sigma, \end{aligned} \quad (23.92)$$

where $\langle l, m - \sigma, \frac{1}{2}, \sigma \mid l, \frac{1}{2}, j, m \rangle$ is a Clebsch–Gordan coefficient with

$$\begin{aligned} l &= j - \frac{1}{2}a, \quad a = \pm 1, \\ m &= -j, -j + 1, \dots, j - 1, j. \end{aligned}$$

[The order of coupling is significant, and great confusion results from a mixing of conventions. Here, we couple in the order l, s, j . The same spin-angle functions are obtained if we use the order s, l, j but there is a phase difference $(-1)^{l-j+1/2} = (-1)^{(l-a)/2}$. You have been warned!]

Inserting explicit expressions for the Clebsch–Gordan coefficients gives

$$\begin{aligned} \chi_{j,m,-1}(\theta, \varphi) &= \begin{pmatrix} -\left(\frac{j+1-m}{2j+2} \right)^{1/2} Y_{j+1/2}^{m-1/2}(\theta, \varphi) \\ \left(\frac{j+1+m}{2j+2} \right)^{1/2} Y_{j+1/2}^{m+1/2}(\theta, \varphi) \end{pmatrix}, \\ \chi_{j,m,1}(\theta, \varphi) &= \begin{pmatrix} \left(\frac{j+m}{2j} \right)^{1/2} Y_{j-1/2}^{m-1/2}(\theta, \varphi) \\ \left(\frac{j-m}{2j} \right)^{1/2} Y_{j-1/2}^{m+1/2}(\theta, \varphi) \end{pmatrix}. \end{aligned} \quad (23.93)$$

The vectors Eq. (23.93) satisfy

$$\begin{aligned} \mathbf{j}^2 \chi_{j,m,a} &= j(j + 1) \chi_{j,m,a}, \quad \mathbf{s}^2 \chi_{j,m,a} = \frac{3}{4} \chi_{j,m,a}, \\ \mathbf{I}^2 \chi_{j,m,a} &= l(l + 1) \chi_{j,m,a}, \quad l = j - \frac{1}{2}a, \quad a = \pm 1. \end{aligned} \quad (23.94)$$

The parity of the angular part is given by $(-1)^l$, with the two possibilities distinguished by means of the operator

$$K' = -(\mathbf{j}^2 - \mathbf{I}^2 - \mathbf{s}^2 + 1) = -(2\mathbf{s} \cdot \mathbf{I} + 1), \quad (23.95)$$

so that

$$K' \chi_{j,m,a} = k' \chi_{j,m,a}, \quad k' = -\left(j + \frac{1}{2} \right) a, \quad a = \pm 1.$$

The basis vectors are orthonormal on the unit sphere with respect to the inner product

$$\begin{aligned} &(\chi_{j',m',a'} \mid \chi_{jma}) \\ &= \int \int \chi_{j',m',a'}^\dagger(\theta, \varphi) \chi_{j,m,a}(\theta, \varphi) \sin \theta \, d\theta \, d\varphi \\ &= \delta_{j',j} \delta_{m',m} \delta_{a',a}. \end{aligned} \quad (23.96)$$

23.5.2 Dirac Hamiltonian in Spherical Coordinates

Eigenstates of Dirac's Hamiltonian Eq. (23.88) in spherical coordinates with a spherically symmetric potential $V(r) = e\phi(r)$,

$$\hat{\mathbf{h}}_D \psi_E(\mathbf{r}) = E \psi_E(\mathbf{r}), \quad (23.97)$$

are also simultaneous eigenstates of \mathbf{j}^2 , of j_3 and of the operator

$$K = \begin{pmatrix} K' & 0 \\ 0 & -K' \end{pmatrix}, \quad (23.98)$$

where K' is defined in Eq. (23.95) above. Denote the corresponding eigenvalues by j, m and κ , where

$$\kappa = \pm \left(j + \frac{1}{2} \right). \quad (23.99)$$

Then the simultaneous eigenstates take the form

$$\psi_{E\kappa m}(\mathbf{r}) = \frac{1}{r} \begin{pmatrix} P_{E\kappa}(r)\chi_{\kappa,m}(\theta, \varphi) \\ iQ_{E\kappa}(r)\chi_{-\kappa,m}(\theta, \varphi) \end{pmatrix}, \quad (23.100)$$

where $\kappa = -(j + 1/2)a$ is the eigenvalue of K' , and the notation $\chi_{\kappa,m}$ replaces the notation $\chi_{j,m,a}$ used previously in Eq. (23.92). The factor i in the lower component ensures that, at least for bound states, the radial amplitudes $P_{E\kappa}(r)$, $Q_{E\kappa}(r)$ can be chosen to be real. This decomposition into radial and angular factors exploits the identity

$$\begin{aligned} \boldsymbol{\sigma} \cdot \mathbf{p} \left[\frac{F(r)}{r} \chi_{\kappa,m}(\theta, \varphi) \right] \\ = i\hbar \frac{1}{r} \left(\frac{dF}{dr} + \frac{\kappa F}{r} \right) \chi_{-\kappa,m}(\theta, \varphi) \end{aligned} \quad (23.101)$$

and gives, writing $\varepsilon = E - mc^2$, the radial equation

$$t_\kappa u_{E\kappa} = \varepsilon u_{E\kappa}, \quad u_{E\kappa} = \begin{pmatrix} P_{E\kappa}(r) \\ Q_{E\kappa}(r) \end{pmatrix}, \quad (23.102)$$

$$t_\kappa = cJ \frac{d}{dr} + \frac{W_\kappa(r)}{r},$$

$$J = -i\sigma^2 = \begin{pmatrix} 0 & -1 \\ 1 & 0 \end{pmatrix},$$

$$W_\kappa(r) = \begin{pmatrix} -Z(r) & c\kappa \\ c\kappa & -2mc^2r - Z(r) \end{pmatrix},$$

where the potential $\phi(r)$ of Eq. (23.87) has been expressed in terms of $\phi(r) = -Z(r)/r$.

This equation requires suitable boundary conditions, which are discussed in more detail in Sects. 23.5.3 and 23.5.4.

Angular density distributions It is a remarkable fact that the angular density distribution

$$A_{\kappa,m}(\theta, \varphi) = \chi_{\kappa,m}(\theta, \varphi)^\dagger \chi_{\kappa,m}(\theta, \varphi), \quad (23.103)$$

where $m = -j, -j + 1, \dots, j - 1, j$, is independent of the sign of κ ; the equivalence of

$$\begin{aligned} A_{j+1/2,m}(\theta, \varphi) &= \frac{1}{4\pi} \frac{(j-m)!}{(j+m)!} \\ &\times \left[(j-m+1)^2 \left| P_{j+1/2}^{m-1/2}(\mu) \right|^2 + \left| P_{j+1/2}^{m+1/2}(\mu) \right|^2 \right], \end{aligned}$$

and

$$\begin{aligned} A_{-(j+1/2),m}(\theta, \varphi) &= \frac{1}{4\pi} \frac{(j-m)!}{(j+m)!} \\ &\times \left[(j+m)^2 \left| P_{j-1/2}^{m-1/2}(\mu) \right|^2 + \left| P_{j-1/2}^{m+1/2}(\mu) \right|^2 \right], \end{aligned}$$

where $\mu = \cos \theta$ was demonstrated by *Hartree* [26].

Table 23.1 Relativistic angular density functions

$ \kappa $	$ m $	$4\pi A_{ \kappa ,m}(\theta, \varphi)$
1	$\frac{1}{2}$	1
2	$\frac{3}{2}$	$\frac{3}{2} \sin^2 \theta$
	$\frac{1}{2}$	$\frac{1}{2}(1 + 3 \cos^2 \theta)$
3	$\frac{5}{2}$	$\frac{15}{8} \sin^4 \theta$
	$\frac{3}{2}$	$\frac{3}{8} \sin^2 \theta (1 + 15 \cos^2 \theta)$
	$\frac{1}{2}$	$\frac{3}{4} (3 \cos^2 \theta - 1)^2 + 3 \sin^2 \theta \cos^2 \theta$

Table 23.2 Nonrelativistic angular density functions

l	$ m $	$4\pi A_{l,m}(\theta, \varphi)_{nr}$
0	0	1
1	1	$\frac{3}{2} \sin^2 \theta$
	0	$3 \cos^2 \theta$
2	2	$\frac{15}{8} \sin^4 \theta$
	1	$\frac{15}{2} \sin^2 \theta \cos^2 \theta$
	0	$\frac{5}{4} (3 \cos^2 \theta - 1)^2$

Angular densities for the lowest $|\kappa|$ values are given in Table 23.1. The corresponding nonrelativistic angular densities

$$\begin{aligned} A_{l,m}(\theta, \varphi)_{nr} &= \left| Y_l^m(\theta, \varphi) \right|^2 \\ &= \frac{2l+1}{4\pi} \frac{(l-m)!}{(l+m)!} \left| P_l^{|m|}(\mu) \right|^2 \end{aligned}$$

are listed in Table 23.2.

Radial density distributions The probability density distribution $\rho_{E\kappa m}(\mathbf{r})$ associated with the stationary state Eq. (23.100) is given by

$$\begin{aligned} \rho_{E,\kappa,m}(\mathbf{r}) \\ = \frac{1}{r^2} \left[|P_{E,\kappa}(r)|^2 A_{\kappa,m}(\theta, \varphi) + |Q_{E,\kappa}(r)|^2 A_{-\kappa,m}(\theta, \varphi) \right]. \end{aligned} \quad (23.104)$$

Since $A_{\kappa,m}$ does not depend on the sign of κ , the angular part can be factored so that

$$\rho_{E,\kappa,m}(\mathbf{r}) = \frac{D_{E,\kappa}(r)}{r^2} A_{|\kappa|,m}(\theta, \varphi),$$

where

$$D_{E,\kappa}(r) = |P_{E,\kappa}(r)|^2 + |Q_{E,\kappa}(r)|^2 \quad (23.105)$$

defines the *radial density* distribution.

Subshells in jj coupling The notion of a *subshell* depends on the observation that the set $\{\psi_{E,\kappa,m}, m = -j, \dots, j\}$ have a common radial density distribution. The simplest atomic

Table 23.3 Spectroscopic labels and angular quantum numbers

Label:	s	\bar{p}	p	\bar{d}	d	\bar{f}	f
$\kappa = -(j + \frac{1}{2})a$	-1	+1	-2	+2	-3	+3	-4
$j = l + \frac{1}{2}a$	$\frac{1}{2}$	$\frac{1}{2}$	$\frac{3}{2}$	$\frac{3}{2}$	$\frac{5}{2}$	$\frac{5}{2}$	$\frac{7}{2}$
a	1	-1	1	-1	1	-1	1
$l = j - \frac{1}{2}a$	0	1	1	2	2	3	3
$\bar{l} = j + \frac{1}{2}a$	1	0	2	1	3	2	4

model is one in which the electrons move independently in a mean field central potential. Since

$$\sum_{m=-j}^j \rho_{E,\kappa,m}(\mathbf{r}) = \frac{2j+1}{4\pi} \frac{D_{E,\kappa}(r)}{r^2}, \quad (23.106)$$

a state of $2j + 1$ independent electrons, with one in each member of the set $\{\psi_{E,\kappa,m}, m = -j, \dots, j\}$, has a spherically symmetric probability density. If E belongs to the point spectrum of the Hamiltonian, then Eq. (23.106) gives a distribution localized in r , and we refer to the states $\{E, \kappa, m\}, m = -j, \dots, j$ as belonging to the subshell $\{E, \kappa\}$.

The notations in use for Dirac central field states are set out in Table 23.3. Here, l is associated with the orbital angular quantum number of the upper pair of components and \bar{l} with the lower pair. Note the useful equivalence

$$\kappa(\kappa + 1) = l(l + 1).$$

Defining $\bar{\kappa} := -\kappa$ we have also $\bar{\kappa}(\bar{\kappa} + 1) = \bar{l}(\bar{l} + 1)$.

23.5.3 Solutions Near the Nucleus

Textbooks on quantum electrodynamics usually contain extensive discussions of the formalism associated with the Dirac equation but rarely go beyond the treatment of the hydrogen atom (Chap. 11). *Greiner's* textbook [5] is an honorable exception, with many worked examples. A more exhaustive list of problems in which exact solutions are known is contained in [27]; it is particularly rich in detail about equations of motion and Green's functions in external electromagnetic fields of various configurations, coherent states of relativistic particles, and charged particles in quantized plane wave fields. It also incorporates discussion of extensions of the Dirac equations due to Pauli, which include explicit interaction terms arising from anomalous magnetic or electric moments.

Atoms and molecules with more than one electron are not soluble analytically, so that numerical models are needed to make predictions. The solutions are sensitive to boundary conditions, on which we focus in this section. For large r , solutions of Eq. (23.102) can be found proportional

to $\exp(\pm\lambda r)$, where

$$\lambda = +\sqrt{c^2 - \frac{E^2}{c^2}}. \quad (23.107)$$

Thus, λ is *real* when $-c^2 \leq E \leq c^2$, and *pure imaginary* otherwise.

Singular point at $r = 0$ Singularities of the nuclear potential near $r = 0$ have a major influence on the nature of solutions of the Dirac equation. Suppose that the potential has the form

$$V(r) = -\frac{Z(r)}{r}, \quad (23.108)$$

so that $Z(r)$ is the effective charge seen by an electron at radius r from the nuclear center. The dependence of $Z(r)$ on r may reflect the finite size of the nuclear charge distribution, so far treated as a point, or the screening due to the environment. Assume that $Z(r)$ can be expanded in a power series of the form

$$Z(r) = Z_0 + Z_1 r + Z_2 r^2 + \dots \quad (23.109)$$

in a neighborhood of $r = 0$. This property characterizes a number of well-used models

1. *Point nucleus:* $Z_0 \neq 0; Z_n = 0, n > 0$.
2. *Uniform nuclear charge distribution:*

$$V(r) = \begin{cases} -\frac{3Z}{2a} \left(1 - \frac{r^2}{3a^2}\right), & 0 \leq r \leq a, \\ -\frac{Z}{r}, & r > a. \end{cases} \quad (23.110)$$

This gives the expansion $Z_0 = 0, Z_1 = -3Z/2a, Z_2 = 0, Z_3 = +Z/2a^3, Z_n = 0$ for $n > 3$ when $r \leq a$ and $Z_0 = Z; Z_n = 0$ when $r > a$.

3. *Fermi distribution:* The nuclear charge density has the form

$$\rho_{\text{nuc}}(r) = \frac{\rho_0}{1 + \exp[(r-a)/d]},$$

where ρ_0 is chosen so that the total charge on the nucleus is Z .

Other nuclear models, reflecting the density distributions deduced from nuclear scattering experiments, can be found in the literature.

Series Solutions near $r = 0$ Any solution for the radial amplitudes of Dirac's equation in a central potential with

$$u(r) = \begin{pmatrix} P(r) \\ Q(r) \end{pmatrix}, \quad (23.111)$$

with radial density

$$D(r) = P^2(r) + Q^2(r),$$

can be expanded in a power series near the singular point at $r = 0$ in the form

$$u(r) = r^\gamma (u_0 + u_1 r + u_2 r^2 + \dots), \quad (23.112)$$

where

$$u_k = \begin{pmatrix} p_k \\ q_k \end{pmatrix}, \quad k = 1, 2, \dots,$$

and γ, p_k, q_k are constants that depend on the nuclear potential model.

Point nuclear models For a Coulomb singularity, $Z_0 \neq 0$, the leading coefficients satisfy

$$\begin{aligned} -Z_0 p_0 + c(\kappa - \gamma)q_0 &= 0, \\ c(\kappa + \gamma)p_0 - Z_0 q_0 &= 0, \end{aligned} \quad (23.113)$$

so that

$$\begin{aligned} \gamma &= \pm \sqrt{\kappa^2 - \frac{Z_0^2}{c^2}}, \\ \frac{q_0}{p_0} &= \frac{Z_0}{c(\kappa - \gamma)} = \frac{c(\kappa + \gamma)}{Z_0}. \end{aligned} \quad (23.114)$$

Finite nuclear models Finite nuclear models, for which $Z_0 = 0$, have no singularity in the potential at $r = 0$. The indicial equation (23.114) reduces to $\gamma = \pm|\kappa|$, so that for $\kappa < 0$,

$$P(r) = p_0 r^{l+1} + O(r^{l+3}), \quad (23.115)$$

$$Q(r) = q_1 r^{l+2} + O(r^{l+4}), \quad (23.116)$$

with

$$\begin{aligned} \frac{q_1}{p_0} &= \frac{(E - mc^2 + Z_1)}{[c(2l + 3)]}, \\ q_0 &= p_1 = 0, \end{aligned}$$

and for $\kappa \geq 1$,

$$P(r) = p_1 r^{l+1} + O(r^{l+3}), \quad (23.117)$$

$$Q(r) = q_0 r^l + O(r^{l+2}), \quad (23.118)$$

$$\begin{aligned} \frac{p_1}{q_0} &= -\frac{(E - mc^2 + Z_1)}{[c(2l + 1)]}, \\ p_0 &= q_1 = 0. \end{aligned}$$

In both cases, the solutions consist of either purely *even* powers or purely *odd* powers of r , contrasting strongly with the point nucleus case, where both even and odd powers are present in the series expansion.

The nonrelativistic limit For a solution linked to a nonrelativistic state with orbital angular momentum l , one expects the nonrelativistic limit

$$P(r) = O(r^{l+1}), \quad c \rightarrow \infty.$$

The limiting behavior reveals some significant features.

Finite nuclear models The behavior is entirely regular:

$$P(r) = O(r^{l+1}), \quad Q(r) = O(c^{-1}) \rightarrow 0.$$

Point nuclear models Since

$$\gamma = |\kappa| - \frac{Z^2}{2c^2|\kappa|} + \dots,$$

Equation (23.114) shows that the leading coefficient p_0 vanishes in the limit so that,

$$P(r) \approx p_1 r^{l+1} [1 + O(r^2)], \quad \text{when } \kappa \geq 1, \quad l = \kappa. \quad (23.119)$$

All higher powers of *odd* relative order vanish in the limit for both components. The behavior in the case $\kappa < 0$ is entirely regular.

23.5.4 Bound states: $r \rightarrow \infty$

Square integrable solutions require $\int D_{E,\kappa}(r) dr$ to be finite; since the solutions are smooth, except possibly near the singular endpoints $r \rightarrow 0$ and $r \rightarrow \infty$, we focus on the behavior at the endpoints:

For *real* values of λ the condition

$$\int_R^\infty D_{E,\kappa}(r) dr < \infty, \quad 0 < R < \infty,$$

requires that $P_{E\kappa}(r), Q_{E\kappa}(r)$ are proportional to $\exp(-\lambda r)$ with $\lambda > 0$. This means that bound states can only exist

when E lies in the interval $-c^2 \leq E \leq c^2$. Outside this interval, solutions are necessarily of scattering type and so

$$\int_R^\infty D_{E,\kappa}(r) dr$$

diverges when $|E| > c^2$.

Near the origin, we require

$$\int_0^{R'} D_{E,\kappa}(r) dr < \infty, \quad R' > 0.$$

Since $D_{E,\kappa}(r) \approx r^{\pm 2\gamma}$ as $r \rightarrow 0$, this condition holds when $\pm\gamma > -\frac{1}{2}$. Only the solution with $\gamma > 0$ satisfies the condition when $|\gamma| > \frac{1}{2}$, or $Z < \alpha^{-1} \sqrt{\kappa^2 - 1/4}$, and the solution with $\gamma < 0$ must be disregarded. This corresponds to the *limit point case* of a second-order differential operator [28]. In the special case $|\kappa| = 1$ or $j = \frac{1}{2}$, this limits Z to be smaller than $c\sqrt{3}/2 \approx 118.6$. For $Z > c\sqrt{3}/2$, both solutions are square integrable near the origin (the *limit circle case*), and the differential operator is no longer essentially self-adjoint.

The Coulomb potential must have a finite expectation for any physically acceptable solution, so that we also require

$$\int_0^{R'} D_{E,\kappa}(r) \frac{dr}{r} < \infty, \quad R' > 0.$$

This is always satisfied by the solution with $\gamma > 0$ for all $|Z| < \alpha^{-1}|\kappa|$, but not by the solution with $\gamma < 0$. Imposing this condition restores essential self-adjointness (on a more restricted domain) for $118 < Z \leq 137$.

23.5.5 Hydrogenic Atoms

Hydrogenic solutions reveal dynamical effects of relativity in the absence of screening by orbital electrons. In this case, $Z_0 = Z$, $Z_n = 0$, $n > 0$. When $-c^2 < E < c^2$, we have bound states. The parameter λ , Eq. (23.107), can conveniently be written,

$$\lambda = \frac{Z}{N}, \quad (23.120)$$

so that rearranging Eq. (23.107) gives

$$E = +c^2 \sqrt{1 - \frac{Z^2}{N^2 c^2}}, \quad (23.121)$$

essentially equivalent to Sommerfeld's fine structure formula. In the formal nonrelativistic limit, $c \rightarrow \infty$, we have

$$E = c^2 - \frac{Z^2}{2N^2} + O\left(\frac{1}{c^2}\right),$$

so that N is closely related to the principal quantum number, n , appearing in the Rydberg formula.

Define the *inner quantum number*

$$n_r = -\gamma + \frac{NE}{c^2}, \quad n_r = 0, 1, 2, \dots$$

Substitute for E from Eq. (23.121) to get

$$\begin{aligned} N &= [(n_r + \gamma)^2 + \alpha^2 Z^2]^{1/2} \\ &= [n^2 - 2n_r(|\kappa| - \gamma)]^{1/2}, \end{aligned} \quad (23.122)$$

where $n = n_r + |\kappa|$ is the *principal quantum number*, the exact equivalent of the principal quantum number of the non-relativistic state to which the Dirac solution reduces in the limit $c \rightarrow \infty$. With this notation, the radial amplitudes for bound hydrogenic states are

$$\begin{aligned} P_{E\kappa}(r) &= \mathcal{N}_{E\kappa} \left(c + \frac{E}{c} \right)^{1/2} \rho^\gamma e^{-\rho/2} \\ &\quad \times [-n_r M(-n_r + 1, 2\gamma + 1; \rho) \\ &\quad + (N - \kappa) M(-n_r, 2\gamma + 1; \rho)] \end{aligned} \quad (23.123)$$

$$\begin{aligned} Q_{E\kappa}(r) &= \mathcal{N}_{E\kappa} \left(c - \frac{E}{c} \right)^{1/2} \rho^\gamma e^{-\rho/2} \\ &\quad \times [-n_r M(-n_r + 1, 2\gamma + 1; \rho) \\ &\quad - (N - \kappa) M(-n_r, 2\gamma + 1; \rho)], \end{aligned} \quad (23.124)$$

where $\rho = 2\lambda r$ and

$$\mathcal{N}_{E\kappa} = \left(\frac{\alpha Z}{2N^2(N - \kappa)} \cdot \frac{\Gamma(2\gamma + n_r + 1)}{n_r! [\Gamma(2\gamma + 1)]^2} \right)^{1/2}$$

is the normalization constant. For definitions of the confluent hypergeometric functions $M(a, b; c; z)$, see [29, Sect. 13.1].

Table 23.4 lists expectation values of simple powers of the radial variable $\rho = 2Zr/N$ from [30] and [31]. Simple algebra, using the inequalities $\gamma < |\kappa|$ and $N < n$, yields the inequality

$$\langle \rho^s \rangle_{n\kappa} < \langle \rho^s \rangle_{nl}, \quad s > 0;$$

the inequality is reversed for $s < 0$. In the same way, it is easy to deduce that relativistic hydrogenic eigenvalues lie below the nonrelativistic eigenvalues

$$\epsilon_{n\kappa} < \epsilon_{nl}.$$

Thus, in the absence of screening, Dirac orbitals both *contract* and are *stabilized* with respect to their nonrelativistic counterparts. The relativistic and nonrelativistic expectation values approach each other as the *relativistic coupling constant*, $Z/c = \alpha Z \rightarrow 0$. This formal *nonrelativistic limit* is approached as $\alpha \rightarrow 0$ or $c \rightarrow \infty$, in which the speed of light is regarded as infinite.

Table 23.4 Radial moments $\langle \rho^s \rangle$

s	Nonrelativistic	Relativistic
2	$2n^2[5n^2 + 1 - 3l(l + 1)]$	$2[N^2(5N^2 - 2\kappa^2)R^2(N) + N^2(1 - \gamma^2) - 3\kappa N^2 R(N)]$
1	$3n^2 - l(l + 1)$	$-\kappa + (3N^2 - \kappa^2)R(N)$
0	1	1
-1	$\frac{1}{2n^2}$	$\frac{n\gamma + (\kappa - \gamma) \kappa }{2\gamma N^3}$
-2	$\frac{1}{2n^3(2l + 1)}$	$\frac{\kappa^2 R(N)}{2\gamma^2 N^3(2\gamma - \text{sgn}\kappa)}$
-3	$\frac{1}{4n^3 l(l + 1)(2l + 1)}$	$\frac{N^2 + 2\gamma^2 \kappa^2 - 3N^2 \kappa R(N)}{4N^5 \gamma(\gamma^2 - 1)(4\gamma^2 - 1)}$

Note: $R(N) = \sqrt{1 - Z^2/N^2 c^2}$

23.5.6 The Free Electron Problem in Spherical Coordinates

The radial equation (23.102) for the free electron ($V(r) = 0$) gives a pair of first-order ordinary differential equations

$$\begin{aligned} (mc^2 - E)P_{E\kappa}(r) &= c \left(\frac{d}{dr} - \frac{\kappa}{r} \right) Q_{E\kappa}(r), \\ c \left(\frac{d}{dr} + \frac{\kappa}{r} \right) P_{E\kappa}(r) &= (mc^2 + E)Q_{E\kappa}(r), \end{aligned} \quad (23.125)$$

from which we deduce that

$$\begin{aligned} \frac{d^2 P_{E\kappa}(r)}{dr^2} + \left(p^2 - \frac{\kappa(\kappa + 1)}{r^2} \right) P_{E\kappa}(r) &= 0, \\ \frac{d^2 Q_{E\kappa}(r)}{dr^2} + \left(p^2 - \frac{\bar{\kappa}(\bar{\kappa} + 1)}{r^2} \right) Q_{E\kappa}(r) &= 0, \end{aligned} \quad (23.126)$$

where $p^2 = m^2 c^2 - E^2/c^2 = \mathbf{p} \cdot \mathbf{p}$ and the angular quantum numbers κ and $\bar{\kappa}$ are associated, respectively, with the upper and lower components. These are defining equations of Riccati–Bessel functions [29, Sect. 10.1.1] of orders l and \bar{l} , respectively, where

$$\kappa(\kappa + 1) = l(l + 1), \quad \bar{\kappa}(\bar{\kappa} + 1) = \bar{l}(\bar{l} + 1).$$

Thus, the solutions of Eq. (23.126) are functions of the variable $x = pr$ of the form

$$P_{E\kappa}(r) = Ax f_l(x), \quad Q_{E\kappa}(r) = Bx f_{\bar{l}}(x),$$

where the ratio of A and B is determined by Eq. (23.125), and where $f_l(x)$ is a spherical Bessel function of the first, second, or third kind [29, Sect. 10.1.1]. Thus,

$$\begin{aligned} P_{E\kappa}(r) &= \mathcal{N} \left(\frac{E + mc^2}{\pi E} \right)^{1/2} x f_l(x), \\ Q_{E\kappa}(r) &= \mathcal{N} \text{sgn}(\kappa) \left(\frac{E - mc^2}{\pi E} \right)^{1/2} x f_{\bar{l}}(x). \end{aligned} \quad (23.127)$$

Equations (23.125) require that Riccati–Bessel solutions of the same type be chosen for both components. The possibilities are:

Standing waves The two solutions of the same type are $f_l(x) = j_l(x)$, $f_l(x) = y_l(x)$. The $j_l(x)$ are bounded everywhere, including the singular points $x = 0$, $x \rightarrow \infty$ and have zeros of order l at $x = 0$. The $y_l(x)$ are bounded at infinity but have poles of order $l + 1$ at $x = 0$.

Progressive waves The spherical Hankel functions (functions of the third kind) are linear combinations

$$h_l^{(1)}(x) = j_l(x) + iy_l(x), \quad h_l^{(2)}(x) = j_l(x) - iy_l(x).$$

Recalling that p is real if and only if $|E| > mc^2$, we see that $h_l^{(1)}(x), h_l^{(2)}(x)$ are bounded as $x \rightarrow \infty$ and have poles of order $l + 1$ at $x = 0$. Notice that when $|E| < mc^2$, which does not occur for a free particle, p becomes pure imaginary, and no solution that is finite at both singular points exists.

The normalization constant \mathcal{N} can be determined by using the well-known result

$$\int_0^\infty j_l(pr) j_l(p'r) r^2 dr = \frac{\pi}{2p^2} \delta(p - p').$$

The choice $\mathcal{N} = 1$ ensures that

$$\int_0^\infty D_{E\kappa}(r) dr = \delta(p - p').$$

Noting that

$$\delta(E - E') = \left| \frac{dp}{dE} \right| \delta(p - p'),$$

and $dp/dE = c^2 p/E$ gives

$$\int_0^\infty D_{E\kappa}(r) dr = \delta(E - E'),$$

when $\mathcal{N} = (|E|/c^2 p)^{1/2}$.

23.6 Numerical Methods for the Radial Dirac Equation

The main drive for understanding methods of numerical approximation of Dirac's equation in atomic and molecular physics comes from their application to many-electron systems. Approximate wave functions for atomic or molecular states are usually constructed from products of one-electron orbitals, and their determination exploits knowledge gained from the treatment of one-electron problems. Whilst the numerical methods described in this section are strictly one-electron in character, the extension to many-electron problems is relatively straightforward.

23.6.1 Dirac's Equation on a Finite Domain

Physical observables are represented in quantum theory by self-adjoint operators on a suitable Hilbert space¹. In scattering calculations, for example using the R-matrix or CCC methods, it is usual to divide the region of interest into an inner and an outer part, with appropriate boundary conditions at the interface. As first pointed out by Bloch [33], it is essential to take account of the boundary conditions on a finite region if the Hamiltonian operator is to be self-adjoint. Bloch's analysis was for Schrödinger Hamiltonians, but the argument applies equally to the Dirac differential operator on a finite region $\mathcal{V} \in \mathbb{R}^3$. Then, since

$$\begin{aligned} (\phi, \hat{\mathbf{h}}_D \psi)_\mathcal{V} - (\hat{\mathbf{h}}_D \phi, \psi)_\mathcal{V} &= -ic \int_{\mathcal{V}} \nabla \cdot [\phi^\dagger \boldsymbol{\alpha} \psi] d\mathbf{r} \\ &= -ic \int_{\partial\mathcal{V}} [\phi^\dagger \boldsymbol{\alpha} \psi] \cdot \mathbf{n} dS \end{aligned}$$

does not vanish, where \mathbf{n} and dS are the outward normal and surface element on the region's smooth boundary $\partial\mathcal{V}$, the operator $\hat{\mathbf{h}}_D$, Eq. (23.25), on \mathcal{V} is not self-adjoint. Following Bloch [33], we can construct a *self-adjoint operator*, $\hat{\mathbf{H}}_D$ on \mathcal{V} as

$$\hat{\mathbf{H}}_D = \hat{\mathbf{h}}_D + \mathcal{L}, \quad (23.128)$$

where the radial parts are

$$\begin{aligned} t_\kappa &= cJ \frac{d}{dr} + \frac{W_\kappa(r)}{r}, \\ J &= -i\sigma^2 = \begin{pmatrix} 0 & -1 \\ 1 & 0 \end{pmatrix}, \\ W_\kappa(r) &= \begin{pmatrix} -Z(r) & c\kappa \\ c\kappa & -2mc^2r - Z(r) \end{pmatrix}, \end{aligned}$$

¹ For the mathematical definition of a self-adjoint Hermitian operator, see [32, p. 255].

and the Bloch operator is

$$\mathcal{L} = \delta(\mathbf{r} - \boldsymbol{\rho}) \frac{c}{2} [\mathcal{B} + i\boldsymbol{\alpha} \cdot \mathbf{n}],$$

where \mathcal{B} is a 4×4 symmetric matrix chosen so that $(\phi, \hat{\mathbf{H}}_D \psi)_\mathcal{V} - (\hat{\mathbf{H}}_D \phi, \psi)_\mathcal{V} = 0$, and $\boldsymbol{\rho}$ ranges over points on the boundary $\partial\mathcal{V}$ with normal \mathbf{n} .

In most practical applications, \mathcal{V} is the spherical shell bounded by radii R_1 and R_2 [34]. In this case, we need only consider the Dirac radial operator t_κ for symmetry κ , augmented by the Bloch operators [34, Eq. (35)]

$$l_R(r) = \frac{c}{2} \delta(r - R) \begin{pmatrix} \beta(R) & 1 \\ -1 & -\frac{1}{\beta(R)} \end{pmatrix}, \quad (23.129)$$

where $\beta(R) = -Q(R)/P(R)$ is the required ratio of the radial components on the spherical shell radius R . The radial Dirac operator

$$T_\kappa = t_\kappa + l_{R_1} - l_{R_2} \quad (23.130)$$

is then self-adjoint on the spherical shell $R_1 \leq r \leq R_2$.

Values of $\beta(R_1)$ as $R_1 \rightarrow 0$ can be derived from Sect. 23.5.2. For a *point charge nucleus* Z ,

$$\beta(R_1) = -\frac{(\kappa + \gamma)c}{Z}, \quad R_1 \rightarrow 0, \quad (23.131)$$

and for a finite size nucleus,

$$\beta(R_1) = \begin{cases} -\frac{(\epsilon + Z_1)R_1}{(2l + 3)c}, & \kappa < 0 \\ +\frac{(2l + 1)c}{(\epsilon + Z_1)R_1}, & \kappa > 0 \end{cases} \quad (23.132)$$

At the outer boundary, R_2 , a common choice assumes that the components are roughly nonrelativistic, so that we can use the Pauli approximation,

$$Q(r) \approx \frac{1}{2c} \left(\frac{dP}{dr} + \frac{\kappa P}{r} \right) \left[1 + O\left(\frac{1}{c^2}\right) \right], \quad (23.133)$$

$$\beta(R_2) = -\frac{(b + \kappa)}{2R_2c}, \quad (23.134)$$

where $b = (dP/dr)/P$ has a prescribed value, often taken to be zero.

23.6.2 Expansion Methods

The idea of expressing HF trial functions as a linear combination of analytic functions was first promoted by Hall [35] and Roothaan [36]. Kim [37, 38] was the first to adapt the method for DHF models, but with limited success [39, Sect. 9.3]. He used STO functions $\{r^\nu \exp(-\lambda_m r)\}$, $m = 1, \dots, N$ for both large and small components. In 1975, Kagawa [40, 41] tried integer powers instead of the noninteger

γ with similar results. In 1981, *Drake and Goldman* [42] used $\{r^{\nu+i} \exp(-\lambda r), i = 0, \dots, N-1\}$. This basis worked well for negative κ states in hydrogenic atoms but gave a single spurious eigenvalue for positive κ , which they just ignored. Various test calculations are included in their 1988 review [43, Sect. IV].

Quantum chemists began to explore relativistic molecular structure calculations with Gaussian type orbitals in the late 1970s, often with catastrophic results. This initiated heated controversy for many years. Quantum chemists were mostly unaware of the criteria set out in Sect. 23.6.4. In the Schrödinger case, the usual variational formulation is legitimized by the fact that the spectrum has a finite lower bound. The spectrum of the Dirac Hamiltonian is unbounded above and below, so that the apparent absence of a finite lower bound for the bound state spectrum was the most popular explanation for this *variational collapse*.

The two most popular remedies to be investigated were *kinetic balance* and *projection operators*. Kinetic balance, suggested by *Lee and McLean* [44], advocated augmenting a GTO basis, common to both large and small components, with additional functions to “balance the set kinetically”. This appeared to *fix up* the problem for the upper spectrum but introduced spurious states, mainly in the lower part of the spectrum, as well as increasing the size of the small component basis set. This approach violates many of the criteria for acceptable basis sets in Sect. 23.6.4 and has now been dropped.

Projection operators to select trial solutions of “positive energy” to get rid of the troublesome “negative energy” states were also suggested as a remedy. This is easy to do for free electrons, where the operators $\Lambda^\pm = (\hat{\mathbf{h}}_D \pm E)/2|E|$ select positive/negative energy solutions. There is no corresponding simple formula in the presence of a potential. The *negative energy sea* also depends upon the choice of potential; perturbing the potential (as long as it does not change the domain of the Hamiltonian) induces a unitary transformation on the basis, which inevitably mixes the unperturbed positive and negative energy states. A relativistic calculation on a hydrogenic atom in which the nuclear charge is perturbed gives incorrect answers if the negative energy contribution to the perturbation series is omitted [45]. This means disaster for “no-pair” formulations of the bound-state QED advocated in, for example [46], which aim to eliminate the negative energy sea from bound state calculations.

23.6.3 Finite Basis Set Formalism

Assume that each solution of the target problem is approximated as a linear combination

$$\psi_{\kappa m}(\mathbf{r}) = \frac{1}{r} \sum_j \begin{pmatrix} c_{\kappa j}^L f_{\kappa j}^L(r) \chi_{\kappa, m}(\theta, \varphi) \\ i c_{\kappa j}^S f_{\kappa j}^S(r) \chi_{-\kappa, m}(\theta, \varphi) \end{pmatrix}, \quad (23.135)$$

where $c_{\kappa j}^L, c_{\kappa j}^S$ $j = 1, \dots, N$, are arbitrary constants, and $f_{\kappa j}^L(r)$ and $f_{\kappa j}^S(r)$ are real, so that each term in the sum Eq. (23.135) has the same structure. This enables us to construct a *Rayleigh quotient*

$$W[\psi] = \frac{\langle \psi | \hat{\mathbf{h}}_D | \psi \rangle}{\langle \psi | \psi \rangle}, \quad (23.136)$$

where both $\langle \psi | \hat{\mathbf{h}}_D | \psi \rangle$ and $\langle \psi | \psi \rangle$ are quadratic expressions in the expansion coefficients c_j^L, c_j^S . By requiring that $W[\psi]$ shall be stationary with respect to arbitrary variations in the expansion coefficients, we arrive at the matrix eigenvalue equation

$$\mathbf{f}_\kappa \begin{pmatrix} \mathbf{c}^L \\ \mathbf{c}^S \end{pmatrix} = \epsilon \begin{pmatrix} \mathbf{S}_\kappa^{LL} & 0 \\ 0 & \mathbf{S}_\kappa^{SS} \end{pmatrix} \begin{pmatrix} \mathbf{c}^L \\ \mathbf{c}^S \end{pmatrix}, \quad (23.137)$$

where the matrix Hamiltonian is denoted by

$$\mathbf{f}_\kappa = \begin{pmatrix} \mathbf{V}_\kappa^{LL} & c \mathbf{\Pi}_\kappa^{LS} \\ c \mathbf{\Pi}_\kappa^{SL} & \mathbf{V}_\kappa^{SS} - 2mc^2 \mathbf{S}_\kappa^{SS} \end{pmatrix};$$

$\mathbf{c}^L, \mathbf{c}^S$ are N -vectors, and $\mathbf{V}_\kappa^{LL}, \mathbf{V}_\kappa^{SS}, \mathbf{S}_\kappa^{LL}, \mathbf{S}_\kappa^{SS}, \mathbf{\Pi}_\kappa^{LS}$ and $\mathbf{\Pi}_\kappa^{SL}$ are all finite $N \times N$ matrices. Using superscripts T to denote either of the letters L, S , the elements of the matrices are defined by

$$S_{\kappa ij}^{TT} = \int_0^\infty f_{i\kappa}^T(r) f_{j\kappa}^T(r) dr, \quad (23.138)$$

$$V_{\kappa ij}^{TT} = \int_0^\infty f_{i\kappa}^T(r) V(r) f_{j\kappa}^T(r) dr, \quad (23.139)$$

and

$$\Pi_{\kappa ij}^{LS} = \int_0^\infty f_{i\kappa}^L(r) \left(-\frac{d}{dr} + \frac{\kappa}{r} \right) f_{j\kappa}^S(r) dr, \quad (23.140)$$

$$\Pi_{\kappa ij}^{SL} = \int_0^\infty f_{i\kappa}^S(r) \left(\frac{d}{dr} + \frac{\kappa}{r} \right) f_{j\kappa}^L(r) dr. \quad (23.141)$$

If $f_{i\kappa}^L(r)$ and $f_{i\kappa}^S(r)$ vanish at both $r = 0$ and $r \rightarrow \infty$, then a simple integration by parts shows that $\mathbf{\Pi}_\kappa^{LS}$ and $\mathbf{\Pi}_\kappa^{SL}$ are Hermitian conjugate matrices.

23.6.4 Physically Acceptable Basis Sets

So far, we have not defined basis functions $f_{j\kappa}^L(r)$ and $f_{j\kappa}^S(r)$ with acceptable properties. We expect the generalized eigenproblem Eq. (23.137) to have a pure point spectrum with three pieces: N eigensolutions with $E < -mc^2$ ($\epsilon < -2mc^2$) representing the lower continuum; $N_b < N$ eigensolutions

in the gap $-mc^2 < E < mc^2$ corresponding to bound states ($-2mc^2 < \epsilon < 0$), and $N - N_b$ eigensolutions with $E > mc^2$ ($\epsilon > 0$) representing the upper continuum.

Physically acceptable bases are, in practice, confined to a box of radius R and have the following properties:

- A. They should exploit the Dirac central-field structure of Eq. (23.135) with the correct symmetry properties.
- B. Sect. 23.5.3 sets out boundary conditions to be satisfied by $f_{i\kappa}^L(r)$ and $f_{i\kappa}^S(r)$ near the nucleus. These are essential as the electromagnetic properties of the nucleus drive the electronic dynamics of the atom.
- C. Sect. 23.5.4 sets out boundary conditions as $r \rightarrow R$. Many suitable basis sets are square integrable on \mathbb{R}^3 and have negligible amplitudes on the boundary. Scattering calculations involve wave functions having a finite amplitude on $r = R$; see Sect. 23.6.1
- D. Acceptable spinor basis functions should satisfy the *kinetic matching* (Pauli) relation

$$\begin{aligned} i\hbar \frac{f_{i\kappa}^S(r)}{r} \chi_{-\kappa,m}(\theta, \varphi) \\ = \text{const.} \lim_{c \rightarrow \infty} \boldsymbol{\sigma} \cdot \mathbf{p} \frac{f_{i\kappa}^L(r)}{r} \chi_{\kappa,m}(\theta, \varphi). \end{aligned} \quad (23.142)$$

The nonrelativistic reduction of the Dirac equation to Schrödinger's equation [5, p. 97] depends upon the operator identity

$$\mathbf{p}^2 = (\boldsymbol{\sigma} \cdot \mathbf{p})(\boldsymbol{\sigma} \cdot \mathbf{p}).$$

In the relativistic basis set formalism, the matrix equivalent of this equation is

$$T_{lij} = \lim_{c \rightarrow \infty} \frac{1}{2} \sum_{k=1}^N \Pi_{\kappa ik}^{LS} \Pi_{\kappa kj}^{SL}. \quad (23.143)$$

The criterion Eq. (23.142) or, in terms of radial amplitudes Eq. (23.133), ensures that

$$\begin{aligned} T_{lij} = \frac{1}{2} \int_0^\infty f_{i\kappa}^L(r) \\ \times \left(-\frac{d^2}{dr^2} + \frac{l(l+1)}{r^2} \right) f_{j\kappa}^L(r) dr, \end{aligned}$$

the ij -element of the familiar nonrelativistic radial kinetic energy matrix T_l for orbital angular momentum l [47, 48].

Another way of viewing this result is to observe that for a general basis set, the sum over a finite set of intermediate states, k , in Eq. (23.143) is necessarily incomplete.

The Hermitian conjugacy property, $\Pi_{\kappa ij}^{LS} = \Pi_{\kappa ji}^{SL}$ ensures that the omitted terms give real and nonnegative contributions. Thus, other choices of basis set cause Eq. (23.143) to *underestimate* the nonrelativistic kinetic energy [47], resulting in spuriously large relativistic energy corrections.

- E. Basis functions in the domain of the Dirac operator must give finite expectation values for all observables; the meaning of this statement can be made precise in a functional analytic discussion such as in [4]. Some implications for the finite basis set approach are given in the author's paper [49], which discusses the convergence of expectation values of standard Dirac operators with trial functions constructed from acceptable basis functions. Here, the main importance is that a (possibly singular) multiplicative operator $V(r)$ (say, $-Z/r$) has *finite* $N \times N$ matrices $\mathbf{V}_{\kappa}^{LL}, \mathbf{V}_{\kappa}^{SS}$. In particular, both matrices must have a *lowest eigenvalue* $V_{\min}^{(N)}$, say. Consider now the quantity $(\psi | \hat{\mathbf{h}}_D(\lambda) | \psi)$, where

$$\hat{\mathbf{h}}_D(\lambda) = (c\boldsymbol{\alpha} \cdot \mathbf{p} + \beta m_e c^2) + \lambda V(r).$$

With $\lambda = 0$, we have a free Dirac particle with a two-branched continuous spectrum $E > mc^2$ and $E < -mc^2$. A negative definite $V(r)$ always has an expectation bounded below by $V_{\min}^{(N)}$; clearly we want

$$V_{\min}^{(N)} \geq V_{\min} > -2mc^2, \quad (23.144)$$

for all values of N . So, if we increase λ from 0 to 1, the eigenvalues of trial solutions corresponding to eigenvalues in the upper continuum at $\lambda = 0$ will be smoothly decreasing functions of λ bounded below by V_{\min} for all values of N . It follows that *the upper set of eigenvalues has a fixed lower bound* in the gap $(-mc^2, mc^2)$. If the basis set satisfies suitable completeness criteria in an appropriate Hilbert space as $N \rightarrow \infty$ (see [49, 50] for more details) and if Eq. (23.144) holds for all values of N , the sequence $\{E_{N+i}^{(N)}, i = 1, 2, \dots\}$ of approximate eigenvalues will converge to limiting values $\{E_i, i = 1, 2, \dots\}$ in $(-mc^2, mc^2)$. Thus, relativistic and nonrelativistic Rayleigh–Ritz approximations converge in the same way [48, 50].

The way in which relativistic solutions approach the nonrelativistic solutions in the limit $c \rightarrow \infty$ is easy to understand in the light of this picture. Using the same basis functions for the nonrelativistic trial function as the Dirac large component, we see that the energies have a common lower bound V_{\min} independent of c . The states of interest vary as $c \rightarrow \infty$ but without changing the character of the upper spectrum. The lower spectrum disappears to $-\infty$ leaving the familiar nonrelativistic picture.

23.6.5 Basis Sets Defined on \mathbb{R}^3

A. L-Spinors

L-spinors [50] are related to Dirac hydrogenic functions in much the same way as Sturmian functions [51, 52] are related to Schrödinger hydrogenic functions (Sect. 23.3). They are solutions of the differential equation system

$$\begin{bmatrix} 1 - \frac{(N_{n_r, \kappa} + n_r + \gamma)}{x} & -\frac{d}{dx} + \frac{\kappa}{x} \\ \frac{d}{dx} + \frac{\kappa}{x} & 1 + \frac{(N_{n_r, \kappa} - n_r - \gamma)}{x} \end{bmatrix} \times \begin{bmatrix} f_{n_r, \kappa}^L(x) \\ f_{n_r, \kappa}^S(x) \end{bmatrix} = 0, \quad (23.145)$$

where $x = 2\lambda r$ and $\lambda > 0$ is constant. This choice ensures that $f_{n_r, \kappa}^L(x)$ tends smoothly to the corresponding Coulomb Sturmian in the nonrelativistic limit $c \rightarrow \infty$ [50]. If $\lambda = Z/N_{n_r, \kappa}$, then $f_{n_r, \kappa}^L(x)$, $f_{n_r, \kappa}^S(x)$, respectively, coincide with the Dirac-Coulomb eigenfunctions $P_{n\kappa}(r)$ and $Q_{n\kappa}(r)$ having principal quantum number $n = n_r + |\kappa|$. The explicit form for L-spinors, in terms of Laguerre polynomials (Chap. 9.3.2), $L_{n_r}^{(2\gamma)}(x)$, is

$$f_{\kappa, n_r}^{(L)}(x) = \mathcal{N}_{n_r, \kappa} x^\gamma e^{-x/2} \times \left[-(1 - \delta_{n_r, 0}) L_{n_r-1}^{(2\gamma)}(x) + \frac{(N_{n_r, \kappa} - \kappa)}{(n_r + 2\gamma)} L_{n_r}^{(2\gamma)}(x) \right], \quad (23.146)$$

$$f_{\kappa, n_r}^{(S)}(x) = \mathcal{N}_{n_r, \kappa} x^\gamma e^{-x/2} \times \left[-(1 - \delta_{n_r, 0}) L_{n_r-1}^{(2\gamma)}(x) - \frac{(N_{n_r, \kappa} - \kappa)}{(n_r + 2\gamma)} L_{n_r}^{(2\gamma)}(x) \right], \quad (23.147)$$

where

$$\mathcal{N}_{n_r, \kappa} = \left(\frac{n_r! (2\gamma + n_r)}{2N_{n_r, \kappa} (N_{n_r, \kappa} - \kappa) \Gamma(2\gamma + n_r)} \right)^{1/2} \quad (23.148)$$

is chosen so that the diagonal elements g_{n_r, n_r}^κ of the Gram (or overlap) matrix are unity for both large and small components. Both Gram matrices are tridiagonal with nonzero off-diagonal elements

$$g_{n_r, (n_r+1)}^{(\kappa)} = g_{(n_r+1), n_r}^{(\kappa)} = \frac{\eta^T}{2} \left(\frac{(n_r + 1)(2\gamma + n_r + 1)(N_{n_r, \kappa} - \kappa)}{N_{n_r, \kappa} N_{(n_r+1), \kappa} (N_{(n_r+1), \kappa} - \kappa)} \right)^{1/2}, \quad (23.149)$$

where $T = L, S$, $\eta^L = -1$ and $\eta^S = +1$. This convention facilitates the construction of the blocks of the matrix Hamiltonian Eq. (23.137), which are banded when the operators are the powers r^n , $n > -1$. The properties of Laguerre polynomials ensure that the matrix of the Coulomb poten-

tial is diagonal. For a full discussion of L-spinor properties, orthogonality, completeness, and applications to hydrogenic atoms, see [50]. The paper demonstrates numerical convergence of expectation values of observables, sum rules, and perturbation expansions, including contributions from negative energy (positronic) states. L-spinor properties have also been exploited in the Relativistic Convergent Close-Coupling Method devised by Fursa, Bray, and Bostock for the calculation of cross sections of electron collisions with atoms and ions. For a detailed tutorial on the RCCC method with extensive references and applications involving two-electron and quasi two-electron targets, see Bostock [53]. L-spinors are also useful for studies of isolated atoms in strong electromagnetic fields (Chap. 14). The equivalent nonrelativistic Coulomb Sturmians have been used for a long time to study the Zeeman effect on high Rydberg levels, especially in the region where chaotic behavior is expected [54] (Chap. 16).

B. S-Spinors

S-spinors have the functional form of the *most nearly nodeless* L-spinors characterized by the minimal value of n_r and can be viewed as the relativistic analogues of Slater functions (STOs). When κ is negative, take $n_r = 0$, so that

$$f_{\kappa, 0}^{(L)}(x) = -f_{\kappa, 0}^{(S)}(x) = \mathcal{N}_{\kappa, 0} x^\gamma \exp\left(\frac{-x}{2}\right) \frac{N_{0, \kappa} - \kappa}{2\gamma} L_0^{(2\gamma)}(x).$$

When κ is positive, we must take $n_r = 1$, and then

$$f_{\kappa, 1}^{(L)}(x) = \mathcal{N}_{1, \kappa} x^\gamma e^{-x/2} \times \left[-L_0^{(2\gamma)}(x) + \frac{N_{1, \kappa} - \kappa}{1 + 2\gamma} L_1^{(2\gamma)}(x) \right],$$

$$f_{\kappa, 1}^{(S)}(x) = \mathcal{N}_{1, \kappa} x^\gamma e^{-x/2} \times \left[-L_0^{(2\gamma)}(x) - \frac{N_{1, \kappa} - \kappa}{1 + 2\gamma} L_1^{(2\gamma)}(x) \right].$$

These can be simplified by inserting the explicit expressions $L_0^{(2\gamma)}(x) = 1$, $L_1^{(2\gamma)}(x) = 2\gamma + 1 - x$. We define a *set of S-spinors* with exponents $\{\lambda_m, m = 1, 2, \dots, N\}$ by rewriting the above in the form

$$f_m^{(T)}(r) = (A^T + B^T r) r^\gamma e^{-\lambda_m r}, \quad (23.150)$$

where $T = L, S$,

$$\left. \begin{aligned} A^L &= A^S = 1, \quad B^L = B^S = 0 \quad \text{for } \kappa < 0, \\ A^L &= \frac{(\kappa + 1 - N_{1, \kappa})(2\gamma + 1)}{2(N_{1, \kappa} - \kappa)} \\ A^S &= \frac{(\kappa - 1 - N_{1, \kappa})(2\gamma + 1)}{2(N_{1, \kappa} - \kappa)} \\ B^L &= B^S = 1 \end{aligned} \right\} \quad \text{for } \kappa > 0, \quad (23.151)$$

and

$$\gamma = \sqrt{\frac{\kappa^2 - Z^2}{c^2}}, \quad N_{1,\kappa} = \sqrt{\kappa^2 + 2\gamma + 1}.$$

The choice of the set of positive real exponents $\{\lambda_m, m = 1, 2, \dots, N\}$, must be such as to optimize Rayleigh–Ritz convergence [49]. In particular, if *one* particular exponent is chosen to have the value $\lambda_m = Z/N_{n_r,\kappa}$, then the corresponding S-spinor is a true hydrogenic solution. Clearly, S-spinors inherit the desirable properties of L-spinors and, in particular, satisfy criteria A–D.

All elements of the matrix Hamiltonian of the Dirac hydrogenic problem can be expressed in terms of Euler’s integral for the gamma function [29, Sect. 6.1.1]:

$$\Gamma(z) = k^z \int_0^\infty t^{z-1} e^{-kt} dt, \quad (\Re z > 0, \Re k > 0)$$

and are, therefore, readily written down and evaluated. The effectiveness of this method depends upon the choice of exponent set; see Sect. D below. We refer to calculations using this scheme for many-electron systems in Sect. 23.8.

C. G-Spinors

The G-spinors are the relativistic analogues of nonrelativistic spherical Gaussians (SGTO), popular in quantum chemistry for studying the electronic structure of atoms and molecules. They satisfy the relativistic boundary conditions for a *finite size* nuclear charge density distribution at $r = 0$ and are, therefore, the most convenient for relativistic molecular electronic structure calculations. The matching requirement gives

$$f_m^{(S)}(r) = \text{const.} \left(\frac{d}{dr} + \frac{\kappa}{r} \right) f_m^{(L)}(r). \quad (23.152)$$

Thus, if

$$f_m^{(L)}(r) = \mathcal{N}_{l,m}^{(L)} r^{l+1} e^{-\lambda_m r^2},$$

then

$$f_m^{(S)}(r) = \mathcal{N}_{l,m}^{(S)} r^l [(\kappa + l + 1) - 2\lambda_m r^2] e^{-\lambda_m r^2}. \quad (23.153)$$

Note that the $\kappa + l + 1$ vanishes when $\kappa < 0$, so that the radial amplitude $r^{-1} f_m^{(S)}(r)$ is never singular, even in the s -state case when $\kappa = -1, l = 0$.

D. Exponent Sets for S- and G-Spinors

Quantum chemists are familiar with the use of nonrelativistic STO and GTO basis sets, and there are extensive collections of optimized exponents that permit economical calculations for the calculations of many atoms and molecules [59–62].

These sets are also a good starting point for relativistic calculations.

An effective alternative to optimization, especially for atoms, is to use geometrical sequences $\{\lambda_m\}$ of the form

$$\lambda_m = \alpha_N \beta_N^{m-1}, \quad m = 1, 2, \dots, N, \quad (23.154)$$

which depend upon just two parameters α_N, β_N . A convenient way to do this is to find a pair $\alpha_{N_0}, \beta_{N_0}$ for small N_0 , say $N_0 = 9$, in a cheap and simple nonrelativistic calculation and then to increase N systematically using relations such as

$$\frac{\alpha_N}{\alpha_{N_0}} = \left(\frac{\beta_N - 1}{\beta_{N_0} - 1} \right)^a, \quad \text{or} \quad \frac{\ln \beta_N}{\ln \beta_{N_0}} = \left(\frac{N_0}{N} \right)^b,$$

where a, b are positive constants. Experience shows that no linear dependence problems (caused by ill-conditioning of the \mathbf{S}^T matrices) are encountered when $\beta_N > 1.2$ for S-spinors, with N up to about 30 or $\beta_N > 1.5$ for G-spinors with N up to about 50.

23.6.6 B-Splines

The comprehensive review [58] of B-splines in atomic and molecular physics introduces it as “one of the most significant developments” of recent years. However, it barely mentions applications to relativistic calculations, beginning in the 1980s, which have much promise for future work in both atomic and molecular structures and collision processes.

Here, we discuss the use of B-splines as basis functions for relativistic atomic calculations in the spirit of Sect. 23.6.1. Although this leads to generalized eigenproblems similar to those of Sect. 23.6.3, expansion in a finite number of piecewise polynomial functions implies confinement to a finite interval $[R_1, R_2]$, so that we need to take proper account of the boundary conditions,

$$F(r) \approx \sum_i c_i B_i^k(r). \quad (23.155)$$

Full details of B-spline properties are given in the book by *de Boor* [59] and in [58, Sect. 2]. The basis functions $B_i^k(r)$ of order k are polynomials of degree $k - 1$ that are nonzero on an interval $t_i \leq r < t_{i+k}$. The coefficients c_i are chosen so that the approximation is continuous up to a certain order at each of the *knots*, t_i , separating adjacent intervals. The knots are often grouped in an increasing set of *breakpoints* $\xi_1, \xi_2, \dots, \xi_{l+1}$, such that $\xi_j = t_{\mu_{j-1}} = \dots = t_{\mu_{j-1} + \mu_j}$ of multiplicity μ_j . It is usual to choose $\mu_1 = \mu_{l+1} = k$ with $\mu_j = 1$ elsewhere [58, Sect. 2].

B-splines are defined recursively, starting with

$$B_i^1(r) = 1; \quad t_i \leq r < t_{i+1}, \quad B_i^1(r) = 0, \quad (23.156)$$

otherwise, followed by

$$B_i^k(r) = \frac{r - t_i}{t_{i+k-1} - t_i} B_i^{k-1}(r) + \frac{t_{i+k} - r}{t_{i+k} - t_{i+1}} B_{i+1}^{k-1}(r), \quad (23.157)$$

for $k = 2, 3, \dots$. In applying this to the Dirac Hamiltonian, it is clear that we are dealing with a finite interval $[R_0, R_1]$ so that we need to take care with what happens at the endpoints.

B-Splines on Finite Intervals

The analysis of the radial Dirac operator in Sect. 23.6.1 revealed that t_κ must be replaced by T_κ to take account of the boundary conditions at the ends of the interval, where

$$T_\kappa = t_\kappa + l_{R_2} - l_{R_1}. \quad (23.158)$$

is then self-adjoint on the spherical shell $R_1 \leq r \leq R_2$. The Bloch operators are defined by

$$l_R(r) = \frac{c}{2} \delta(r - R) \begin{pmatrix} \beta(R) & 1 \\ -1 & -\frac{1}{\beta(R)} \end{pmatrix}, \quad (23.159)$$

where $\beta(R) = -Q(R)/P(R)$ is the required ratio of the radial components on the spherical shell radius R ; suitable values at R_1 and R_2 are given in Sect. 23.6.1.

The Galerkin Equations

The set $\{B_i^k(r)\}$ can be assembled in a vector $\mathbf{B}^k(r)$, so that we approximate the radial components by

$$P(r) \approx \mathbf{B}^k(r)^\dagger \cdot \mathbf{p}, \quad Q(r) \approx \mathbf{B}^k(r)^\dagger \cdot \mathbf{q}, \quad (23.160)$$

where \mathbf{p}, \mathbf{q} are coefficient vectors. Using the notation of Eq. (23.137), the Galerkin equations are

$$\begin{pmatrix} \widehat{\mathbf{V}} & c\Pi \\ c\Pi^\dagger & \widehat{\mathbf{V}} - 2mc^2\mathbf{S} \end{pmatrix} \begin{pmatrix} \mathbf{p} \\ \mathbf{q} \end{pmatrix} = \varepsilon \begin{pmatrix} \mathbf{Sp} \\ \mathbf{Sq} \end{pmatrix}, \quad (23.161)$$

where the symmetric matrices $\mathbf{S}, \widehat{\mathbf{V}}$ have elements

$$S_{ij} = \int B_i^k(r) B_j^k(r) dr, \quad (23.162)$$

$$\widehat{V}_{ij} = V_{ij} + \delta_{iN} \delta_{jN} \beta(R_2) - \delta_{i1} \delta_{j1} \beta(R_1)$$

$$\text{with } V_{ij} = \int B_i^k(r) V(r) B_j^k(r) dr, \quad (23.163)$$

and

$$\Pi_{ij} = \int B_i^k(r) \left(-\frac{d}{dr} + \frac{\kappa}{r} \right) B_j^k(r) dr + \frac{1}{2} \left[B_i^k(s) B_j^k(s) \right]_{R_1}^{R_2} \quad (23.164)$$

$$\Pi_{ij}^\dagger = \int B_i^k(r) \left(+\frac{d}{dr} + \frac{\kappa}{r} \right) B_j^k(r) dr - \frac{1}{2} \left[B_i^k(s) B_j^k(s) \right]_{R_1}^{R_2}. \quad (23.165)$$

Integration by parts shows that $\Pi_{ij}^\dagger = \Pi_{ji}$, so that the matrix Hamiltonian

$$\mathbf{H} = \begin{pmatrix} \widehat{\mathbf{V}} & c\Pi \\ c\Pi^\dagger & \widehat{\mathbf{V}} - 2mc^2\mathbf{S} \end{pmatrix} \quad (23.166)$$

is real symmetric, as expected. Note that the integrands are nonzero when the product $B_i^k(r) B_j^k(r)$ is nonzero and that the Bloch operator contributes to all submatrices in \mathbf{H} .

Johnson et al. [60, 61], following earlier work on relativistic ion-ion collisions by Bottcher and Strayer [62], popularized the use of a basis of B-splines in relativistic atomic calculations. The method has mainly been of use in relativistic many-body calculations on the spectra of heavy ions. However, their method had important defects, notably the appearance of spurious and rapidly oscillating solutions with eigenvalues zero or distant from the bound states of interest. Although they discarded the spurious solutions in subsequent MBPT and QED calculations, the results cannot be regarded as a fully satisfactory representation of the physics. Subsequently, several investigations, for example by Shabaev et al. [63] and by Igarashi [64, 65], have used the ideas of kinetic balance in relativistic B-spline calculations, suggesting analogies with Sect. 23.6.4. The arguments of that section, designed for expansions in analytic radial basis functions defined on the whole of $0 \leq r \leq R$ are not applicable to piecewise polynomial expansions in B-splines.

More successfully, Fischer and Parpia explored the spline-Galerkin approach for the Dirac equation [66], and Fischer and Zatsarinny [67] more recently used a formulation similar to the one above but with B-splines of different orders k_p, k_q with $|k_q - k_p| = 1$. This scheme has now been applied successfully to R-matrix calculations of electron collisions with atoms [67–69]. Zatsarinny published the BSR computer package for R-matrix calculations [70] and also the DBSR_HF program [71] DHF calculations.

23.7 Finite Differences

The numerical approximation of eigensolutions of the first-order system of differential equations (23.102) can be achieved by more or less standard finite difference methods given in texts such as [72]. For states in either continuum, $E > mc^2$ or $E < -mc^2$, the calculation is completely specified as an *initial value problem* for a prescribed value of E starting from power series solutions in the neighborhood of $r = 0$. Solutions of this sort exist for all values of (complex) E except at the bound states in the gap $-mc^2 < E < mc^2$. Here, we focus on what is characterized as a *two-point boundary value problem* in which each eigenstate and its eigenvalue E are determined simultaneously.

Suppose that the radial coordinate r is expressed in terms of a smooth differentiable function $f(s)$ of a new independent variable s and let $\varepsilon_{n\kappa} = E_{n\kappa} - mc^2$ be the energy eigenvalue relative to the nonrelativistic zero of energy. Then Eq. (23.102), generalized by the addition of a two-vector $X(s)$ on the right-hand side, can be written

$$J \frac{du}{ds} + \frac{1}{c} \frac{dr}{ds} [r \varepsilon - W(s)] u(s) = X(s) \frac{dr}{ds}, \quad (23.167)$$

where

$$J = \begin{pmatrix} 0 & -1 \\ 1 & 0 \end{pmatrix},$$

$$W_\kappa(r) = \begin{pmatrix} -Z(r) & c\kappa \\ c\kappa & -2mc^2r - Z(r) \end{pmatrix},$$

with $Z(r) = -rV(r)$

$$u(s) = \begin{pmatrix} P_{n\kappa} \\ Q_{n\kappa} \end{pmatrix}.$$

When discretizing, we define s on a uniform grid so that

$$s_n = nh, \quad n = 0, 1, 2, \dots, N.$$

Common choices for the mapping $s \rightarrow r = f(s)$ are

$$r_n = r_0 e^{s_n},$$

$$A r_n + \log\left(1 + \frac{r_n}{r_0}\right) = s_n,$$

for suitable values of the parameters r_0 and h , and where A is a constant, chosen so that the spacing in r_n increases exponentially for small values of n and approaches a constant for large values of n . The exponentially increasing spacing is appropriate for tightly bound solutions, but a nearly linear spacing is advisable to ensure numerical stability in the tails of extended and continuum solutions.

The finite difference approach involves a marching process, in which $u(r_n)$ is constructed from values at nearby grid points. There are many such algorithms that generate oscillatory solutions in the interval from the origin to a radius close to the turning point for classical motion. Beyond this point, we want a bound state solution that is of negative exponential character and to suppress any parasitic increasing solution. It is usual, therefore, to employ a *double shooting* method, marching from both $s_0 = 0$ and $s_N = Nh$ along the grid towards an intermediate *join* point s_n , $n = J$, adjusting ϵ until the trial solutions have the right number of nodes and have left and right-limits where they meet that agree to a preset tolerance (commonly about one part in 10^8).

The *deferred correction* method [39, 73] allows the precision of the numerical approximation in a self-consistent field calculation to be improved as the iteration converges.

Consider the simplest implicit linear difference scheme for the first-order system

$$\frac{dy}{ds} = F[y(s), s],$$

based on the trapezoidal quadrature rule

$$z_{j+1} = z_j + \frac{h[F_{j+1} + F_j]}{2}, \quad (23.168)$$

which has a local truncation error $O(h^2)$. The precision with which the grid point estimates z_j approach $y(s_j)$ can be improved at greater cost per iterative cycle by adding higher-order difference terms to the right-hand side of Eq. (23.168). These can be estimated by evaluating the added terms using the result from the previous iteration. This leaves the numerical stability properties of the simple scheme Eq. (23.168) unchanged but increases the accuracy of successive estimates z_j .

To apply this to the Dirac system, write $f(s) = dr/ds$ and

$$A_j^\pm = J \mp \frac{h f(s_j) W(s_j)}{2c}.$$

In a further generalization that is used in MCDHF problems, we replace the electron-nucleus potential $Z(r)$ by the discretized vectors $U_j^{(v)}, X_j^{(v)}$, which may change from one iteration to the next. The first iteration is

$$A_{j+1}^{+(0)} U_{j+1}^{(1)} - A_j^{-(0)} U_j^{(1)}$$

$$+ \varepsilon^{(0)} \frac{h}{2c} [r_{j+1} f(s_{j+1}) U_{j+1}^{(1)} + r_j f(s_j) U_j^{(1)}]$$

$$= \frac{h}{2} [f(s_{j+1}) X_{j+1}^{(0)} + f(s_j) X_j^{(0)}], \quad (23.169)$$

and subsequent iterations have the form

$$A_{j+1}^{+(v)} U_{j+1}^{(v+1)} - A_j^{-(v)} U_j^{(v+1)}$$

$$+ \varepsilon^{(v)} \frac{h}{2c} [r_{j+1} f(s_{j+1}) U_{j+1}^{(v+1)} + r_j f(s_j) U_j^{(v+1)}]$$

$$= \frac{h}{2} [f(s_{j+1}) X_{j+1}^{(v)} + f(s_j) X_j^{(v)}]$$

$$+ \frac{1}{12} \delta^3 U_{j+1/2}^{(v)} + \dots, \quad (23.170)$$

where $\delta^3 U_{j+1/2}^{(v)}$ is the third-order difference correction using the result of the previous iteration [29, Sect. 25.1.2]. Higher-order difference corrections (at least to order 5) are included in modern codes to improve the accuracy and numerical stability of weakly bound solutions. This deferred correction algorithm can be shown to converge asymptotically to the required solution of the differential system with a local truncation error $O(h^{2p+2})$ when using central differences of order h^{2p+1} [74].

23.8 Many-Electron Atoms

The first attempt to formulate a numerical method to solve the DHF relativistic self-consistent field problem was published in 1935 by *Swirles* [75]. This predated both Racah’s essential contributions to the quantum theory of angular momentum in 1942 and 1943 and the computer age, without which this chapter could not have been written. The reformulation [76], exploiting both Racah algebra and finite difference methods, was followed by several implementations in the following decade [39, Sect. 10]. Whilst these early calculations showed promise, it was clear that MCDHF methods were the next step, leading to *Desclaux’s* code [77, 78] and the Oxford MCDHF code [79], a precursor of GRASP2K [21]. More details on the formulation and numerical methods of GRASP2K can be found in [39, 73] and [80, Chap. 5].

This development has been free of the controversy surrounding variational methods on which the numerical algorithms are based, in stark contrast to the heated debates over expansion methods. The essential reason is that the finite difference algorithms assume that the solutions are of bound state type; the kinetic energy is always positive, and the boundary conditions, especially at the nucleus, are those needed to ensure that the trial functions, expressed as numerical values on the radial grid, are similar to the nonrelativistic equivalents, so that the arguments of Sect. 23.6.4 apply in the same way.

So far, the twenty-first century has seen major improvements in the modeling of many-electron atoms and ions for both astrophysical and terrestrial applications. This has been fostered in part by access to increasingly powerful computer resources but also by a drive to improve the accuracy of atomic calculations, so that today it is possible to claim that results have “spectroscopic accuracy” in favorable situations [81]. The ability to work with matrices constructed from different orthonormal basis sets is a major technical advance. It makes it possible to start with a reference model that includes the most important CSFs for the states of interest, to study different types of electron correlation independently, and then to see how they interact. The search for efficient ways to improve the modeling of electron correlation continues [22, 82].

23.8.1 Atomic States

Relativistic atomic structure calculations assign a trial wave function, ASF (atomic state function), to each atomic state of interest. In programs such as GRASP2K, each ASF is a linear combination of CSFs (configuration state functions), each of which is an antisymmetrized product of N Dirac atomic orbitals (satisfying Pauli’s exclusion principle), with

given total angular momentum and parity. The construction of CSFs symmetrized in this way using Racah algebra as developed by Fano has been described in [73, Sect. 2]. Newer codes such as GRASP2K have used second quantization in both angular momentum and spin spaces [21, 83] to reformulate the construction, resulting in much faster execution.

23.8.2 Atomic Orbitals

Four-component Dirac central field orbitals with the structure of Eq. (23.100) are the building blocks needed for CSFs. Ideally, they should comprise an orthonormal set, mathematically complete in a suitable function space, so as to guarantee convergence as the set dimension increases. In practice, the sets are often far from complete, so that error estimation is difficult if not impossible. All the methods described in Sect. 23.6 have been used to generate numerical orbital bases.

23.8.3 Slater Determinants

An antisymmetric state of N independent electrons in configuration space can be constructed in the form

$$\begin{aligned} & \{ \alpha_1, \alpha_2, \dots, \alpha_N \} \\ & = \langle \mathbf{x}_1, \mathbf{x}_2, \dots, \mathbf{x}_n | a_{\alpha_1}^\dagger a_{\alpha_2}^\dagger \dots a_{\alpha_N}^\dagger | 0 \rangle \\ & = \frac{1}{N!} \begin{vmatrix} \psi_{\alpha_1}(\mathbf{x}_1) & \psi_{\alpha_2}(\mathbf{x}_1) & \dots & \psi_{\alpha_N}(\mathbf{x}_1) \\ \psi_{\alpha_1}(\mathbf{x}_2) & \psi_{\alpha_2}(\mathbf{x}_2) & \dots & \psi_{\alpha_N}(\mathbf{x}_2) \\ \dots & \dots & \dots & \dots \\ \psi_{\alpha_1}(\mathbf{x}_N) & \psi_{\alpha_2}(\mathbf{x}_N) & \dots & \psi_{\alpha_N}(\mathbf{x}_N) \end{vmatrix}, \end{aligned} \quad (23.171)$$

This *Slater determinant* is an antisymmetric eigenfunction of H_0 with energy eigenvalue $\sum_{n=1}^N E_{\alpha_n}$ and of the angular momentum projection $J_z = \sum j_{z,\alpha_n}$ corresponding to the eigenvalue $M = \sum m_{\alpha_n}$. Defining the parity of a Dirac electron orbital as that of its upper component, $(-1)^{l_{\alpha_n}}$, we see that this has parity $\prod_n (-1)^{l_{\alpha_n}}$. Eigenfunctions of \mathbf{J}^2 and \mathbf{J}_z are linear combinations of Slater determinants of the type of Eq. (23.171).

23.8.4 Configurational States

Configurational state functions (CSF) having specified total angular momentum J and parity Π are of the form

$$\begin{aligned} \phi(\gamma JM) & = \sum_{\{m_{\alpha_n}\}} \langle \gamma JM | m_{\alpha_1}, m_{\alpha_2}, \dots, m_{\alpha_N} \rangle \\ & \times \{ \alpha_1, \alpha_2, \dots, \alpha_N \}, \end{aligned} \quad (23.172)$$

where $\langle \gamma JM | m_{\alpha_1}, m_{\alpha_2}, \dots, m_{\alpha_N} \rangle$ is a generalized Clebsch–Gordon coefficient, and γ defines the angular momentum coupling scheme.

An *electron configuration* is an assignment of the N -electrons to an orbital set $\{\alpha_1, \alpha_2, \dots, \alpha_N\}$. If the configuration belongs to a single subshell, then the states share a common set of labels $\{n, \kappa\}$, where n is the principal quantum number. In jj -coupling, the N_α *subshell states* of equivalent electrons can, therefore, be labeled $\alpha^{N_\alpha}, \gamma_\alpha, J_\alpha$, where γ_α distinguishes degenerate states of the same J_α . For jj -coupling, such labels are needed only for $j \geq \frac{5}{2}$. The *seniority scheme*, [73, Sects. 2.3, 2.4], provides a complete classification for $j < \frac{9}{2}$. A list of states of configurations j^N , classified in terms of the *seniority number* v and of *total angular momentum* J , appears in Table 23.5. Rudzikas [84] presents an equivalent classification using quasispin, which is used in GRASP2K.

23.8.5 ASFs and CSF

Atomic state functions (ASF) are linear superpositions of CSFs, of the form

$$\Psi(\gamma \Pi J) = \sum_{\alpha=1}^N c_\alpha \phi(\gamma_\alpha J), \quad (23.173)$$

where c_α are a set of (normally) real coefficients, and we have dropped the common label M . They are obtained by diagonalizing the chosen Hamiltonian in a basis of CSFs $\{\phi(\gamma_\alpha J)\}$. The orbitals used to construct the CSFs can be generated along with the c_α in a multiconfigurational self-consistent field calculation, for example, using the RMCDHF program of GRASP2K [21].

23.8.6 Matrix Construction

A full presentation of the reduction of matrix elements between CSFs to computable form is beyond the scope of this chapter. There is an extensive literature [39, 73, 84]. Second quantization and diagrammatic methods of the quantum theory of angular momentum express matrix elements between atomic CSFs of all one and two-electron operators treated in this chapter to a linear combination of radial integrals. A full implementation within the jj -coupling seniority scheme is exploited in the GRASP2K programs [21, 83].

23.8.7 Dirac–Hartree–Fock–Breit

The construction of Dirac–Hartree–Fock–Breit models mirrors the nonrelativistic pattern described in Chap. 22; rela-

Table 23.5 j^N configurational states in the seniority scheme. The multiplicity of each unresolved degenerate state is indicated by a superscript

j	N	v	J
$\frac{1}{2}$	0, 2	0	0
	1	0	$\frac{1}{2}$
$\frac{3}{2}$	0, 4	0	0
	1, 3	1	$\frac{3}{2}$
	2	0	0
	2	2	2
$\frac{5}{2}$	0, 6	0	0
	1, 5	1	$\frac{5}{2}$
	2, 4	0	0
		2	2, 4
	3	1	$\frac{5}{2}$
		3	$\frac{3}{2}, \frac{9}{2}$
$\frac{7}{2}$	0, 8	0	0
	1, 7	1	
	2, 6	0	0
		2	2, 4, 6
	3, 5	1	$\frac{7}{2}$
		3	$\frac{3}{2}, \frac{5}{2}, \frac{9}{2}, \frac{11}{2}, \frac{15}{2}$
	4	0	0
		2	2, 4, 6
		4	2, 4, 5, 8
$\frac{9}{2}$	0, 10	0	0
	1, 9	1	$\frac{9}{2}$
	2, 8	0	0
		2	2, 4, 6, 8
	3, 7	1	$\frac{9}{2}$
		3	$\frac{3}{2}, \frac{5}{2}, \frac{7}{2}, \frac{9}{2}, \frac{11}{2}, \frac{13}{2}, \frac{15}{2}, \frac{17}{2}, \frac{21}{2}$
	4, 6	0	0
		2	2, 4, 6, 8
		4	0, 2, 3, 4 ² , 5, 6 ² , 7, 8, 9, 10, 12
	5	1	$\frac{9}{2}$
		3	$\frac{3}{2}, \frac{5}{2}, \frac{7}{2}, \frac{9}{2}, \frac{11}{2}, \frac{13}{2}, \frac{15}{2}, \frac{17}{2}, \frac{21}{2}$
	5	$\frac{3}{2}, \frac{5}{2}, \frac{7}{2}, \frac{9}{2}, \frac{11}{2}, \frac{13}{2}, \frac{15}{2}, \frac{17}{2}, \frac{19}{2}, \frac{25}{2}$	

tivistic counterparts of Koopmans’ theorem, fixed-core approximations, Brillouin’s theorem are easy to obtain. The fact that, for example, np orbitals (with $\kappa = -2, j = \frac{3}{2}$) and $n\bar{p}$ orbitals (with $\kappa = +1, j = \frac{1}{2}$) have different spatial distributions as a consequence of the dynamical and indirect effects of relativity, makes it essential to formulate the equations in terms of jj -coupling. Although relativistic ASF and CSF construction uses the same ideas as in nonrelativistic models, the details are different. For further insight, see [22, 30, 39].

There are several relativistic self-consistent field programs built on these lines. The program GRASP2K [21, 83] is the most recent development of [85–87]. The MCDFGME

program [88] is a development of [77, 78]. The flexible atomic code (FAC) is described in [89].

Finite matrix methods for atoms Here, we extend the equations of Sect. 23.4.2 to the many-body problem based on the effective Hamiltonian of Sect. 23.4.1. This leads to an energy functional of the form

$$E = E_0 + E_1, \quad (23.174)$$

where E_0 is the expected value of H_0 Eq. (23.76), and E_1 the expected value of H_1 for the finite basis many-body trial function. Simple variational arguments lead to matrix Dirac–Fock equations of the form

$$\mathbf{F}\mathbf{X} = \mathbf{E}\mathbf{S}\mathbf{X}. \quad (23.175)$$

In general, the Fock matrix \mathbf{F} is a sum of several matrices

$$\mathbf{F} = \mathbf{f} + \mathbf{g} + \mathbf{b}, \quad (23.176)$$

where, for each symmetry κ , \mathbf{f} can be partitioned into blocks

$$\mathbf{f}_{A\kappa} = \begin{pmatrix} \mathbf{V}_{\kappa}^{LL} & c\mathbf{\Pi}_{\kappa}^{LS} \\ c\mathbf{\Pi}_{\kappa}^{SL} & \mathbf{V}_{\kappa}^{SS} - 2mc^2\mathbf{S}_{\kappa}^{SS} \end{pmatrix}. \quad (23.177)$$

The matrix

$$\mathbf{g} = \begin{pmatrix} \mathbf{J}^{LL} - \mathbf{K}^{LL} & -\mathbf{K}^{LS} \\ -\mathbf{K}^{SL} & \mathbf{J}^{SS} - \mathbf{K}^{SS} \end{pmatrix} \quad (23.178)$$

is the matrix of the Coulomb repulsion part of the electron–electron interaction, and

$$\mathbf{b} = \begin{pmatrix} \mathbf{B}^{LL} & \mathbf{B}^{LS} \\ \mathbf{B}^{SL} & \mathbf{B}^{SS} \end{pmatrix} \quad (23.179)$$

is the matrix of the Breit interaction, modeling the magnetic interaction of electron currents.

Using superscripts T to label the L or S components and the notation \bar{T} to denote the complementary label: $\bar{T} = S$ when $T = L$ or $\bar{T} = L$ when $T = S$, then the direct Coulomb part \mathbf{J}_{κ}^{TT} has matrix elements

$$J_{\kappa pq}^{\text{TT}} = \sum_{\kappa'rs} (2j' + 1) \left(D_{\kappa'rs}^{\text{TT}} J_{\kappa pq, \kappa'rs}^{0, \text{TTTT}} + D_{\kappa'rs}^{\bar{\text{T}}\bar{\text{T}}} J_{\kappa pq, \kappa'rs}^{0, \text{TT}\bar{\text{T}}\bar{\text{T}}} \right), \quad (23.180)$$

whilst the exchange part $\mathbf{K}_{\kappa}^{\text{TT}'}$ has the form

$$K_{\kappa pq}^{\text{TT}'} = \sum_{\kappa'rs} \sum_{\nu} (2j' + 1) b_{\nu}(jj') D_{\kappa'rs}^{\text{TT}'} K_{\kappa pq, \kappa'rs}^{\nu, \text{TT}'\text{TT}'}, \quad (23.181)$$

where TT' denotes any combination of component matrix with elements

$$D_{\kappa pq}^{\text{TT}'} = c_{\kappa p}^{\text{T}*} c_{\kappa q}^{\text{T}'}, \quad (23.182)$$

where $c_{\kappa p}^{\text{T}}$ are the expansion coefficients. The Breit interaction matrices have a similar form

$$B_{\kappa pq}^{\text{TT}} = \sum_{\kappa'rs} \sum_{\nu} (2j' + 1) e_{\nu}(jj') D_{\kappa'rs}^{\bar{\text{T}}\bar{\text{T}}} K_{\kappa pq, \kappa'rs}^{\nu, \text{TT}\bar{\text{T}}\bar{\text{T}}}, \quad (23.183)$$

and

$$B_{\kappa pq}^{\bar{\text{T}}\bar{\text{T}}} = \sum_{\kappa'rs} \sum_{\nu} (2j' + 1) D_{\kappa'rs}^{\bar{\text{T}}\bar{\text{T}}} \times \left[d_{\nu}(\kappa\kappa') K_{\kappa pq, \kappa'rs}^{\nu, \bar{\text{T}}\bar{\text{T}}\bar{\text{T}}\bar{\text{T}}} + g_{\nu}(\kappa\kappa') M_{\kappa pq, \kappa'rs}^{\nu, \bar{\text{T}}\bar{\text{T}}\bar{\text{T}}\bar{\text{T}}} \right]. \quad (23.184)$$

The matrix elements are constructed from standard radial integrals

$$J_{\kappa pq, \kappa'rs}^{\nu, \text{TTT}'\text{T}'} = \int_0^{\infty} \int_0^{\infty} f_{\kappa p}^{\text{T}}(r_1) f_{\kappa q}^{\text{T}}(r_1) U_{\nu}(r_1, r_2) \times f_{\kappa'r}^{\text{T}'}(r_2) f_{\kappa's}^{\text{T}'}(r_2) dr_2 dr_1, \quad (23.185)$$

where

$$U_{\nu}(r_1, r_2) = \begin{cases} \frac{r_1^{\nu}}{r_2^{\nu+1}} & \text{for } r_1 < r_2, \\ \frac{r_2^{\nu}}{r_1^{\nu+1}} & \text{for } r_1 > r_2. \end{cases}$$

Similarly,

$$K_{\kappa pq, \kappa'rs}^{\nu, \text{TT}'\text{TT}'} = J_{\kappa p, \kappa'r, \kappa q, \kappa's}^{\nu, \text{TTT}'\text{T}'}, \quad (23.186)$$

and

$$M_{\kappa pq, \kappa'rs}^{\nu, \bar{\text{T}}\bar{\text{T}}\bar{\text{T}}\bar{\text{T}}} = \int_0^{\infty} \int_{r_1}^{\infty} f_{\kappa p}^{\text{T}}(r_1) f_{\kappa'r}^{\bar{\text{T}}}(r_1) U_{\nu}(r_1, r_2) \times f_{\kappa q}^{\bar{\text{T}}}(r_2) f_{\kappa's}^{\text{T}}(r_2) dr_2 dr_1. \quad (23.187)$$

Further details about the coefficients $b_{\nu}(jj')$, $e_{\nu}(jj')$, $d_{\nu}(\kappa\kappa')$, and $g_{\nu}(\kappa\kappa')$ may be found in [90].

This formalism has been implemented for closed shell atoms with both S-spinors and G-spinors [90]. The computation of radial integrals using S-spinors is discussed in [91, 92], and can be adapted with relative ease to G-spinor basis sets. Applications can be found in [90, 93–96], which deal with Dirac–Fock and Dirac–Fock–Breit calculations, many-body perturbation theory, and coupled-cluster schemes. Methods based on the approximation of radial functions with B-splines lead to similar matrix structures.

G-spinor basis sets provide the most promising technique for application to the electronic structure of molecules [97]. L-spinors underpin the RCCC (relativistic convergent close coupling) method for particle collision studies [53].

23.8.8 Electron Correlation

Methods of dealing with electron correlation for atoms have advanced greatly in the last few years; see Chap. 22 for a detailed account. The strategies being actively researched nonrelativistically are equally applicable to relativistic calculations. Codes such as GRASP2K [21, 83] are now able to use high-power multiprocessor systems, so that the user is able to employ trial ASFs composed of as many as 10^6 – 10^7 CSFs. The first step is to construct a *multireference wave function* (MR) using a RMCDHF model built with the most strongly interacting CSFs to represent the target states of interest, accounting for what is often termed *static correlation*. *Dynamic correlation* effects can then be modeled by the *active space* (AS) method; the orbital and CSF sets are expanded systematically, *layer by layer* [22, 82]. A new layer of correlation orbitals in the AS is constructed with a RMCDHF calculation keeping MR orbitals frozen. Single and double substitutions from the MR CSFs into this layer are then used to expand the CSF basis according to prescribed rules for a chosen correlation mechanism (valence-valence, core-valence or core-core). These independent calculations converge to partition correlation functions (PCF). Each PCF will have its own orbital set, so that PCF interactions require biorthogonal algorithms for their evaluation [98]. The full Hamiltonian matrix incorporating the PCFs can then be diagonalized in a relativistic configuration calculation (RCI).

This program structure has great flexibility; the layer-by-layer process allows the user to assess convergence in an unprecedented manner. The disadvantage is the explosive increase in problem dimensions. Current research focuses on the PCFI method (partition correlation function interaction) in which the results of separate PCF calculations are combined in a final RCI calculation of relatively small dimension. The final ASF are then available for calculating atomic properties: energy levels, splittings, radiative transitions, and other properties.

Many-body perturbation theory calculations and coupled-cluster calculations are not well suited to calculations with finite difference codes, because of the expense of calculating more than a limited orbital basis and all the matrix elements required. Calculations based on finite matrix methods enable this sort of calculation to be done more economically. Some justification for the use of finite matrix methods in relativistic many-body theory is given in [49].

23.8.9 Electron Self-Energy and Vacuum Polarization

The main programs, RMCDHF and RCI, of the GRASP2K package account for the major interactions between the atom's constituents. The RMCDHF program usually uses

the Dirac–Coulomb Hamiltonian, Sect. 23.4.1 to generate MR orbitals and correlation orbitals needed to populate the CSF sets. The configuration interaction program RCI adds the Breit interaction to the effective Hamiltonian, or the more complex complete transverse interaction if requested. In future, it should be possible to self-consistently treat the Breit operator, which captures the dominant magnetic interactions, in RMCDHF. This will slightly change the orbitals generated. The more complex transverse photon interaction, whose predictions vary little from those of the Breit interaction, can be handled perturbatively.

The next most important processes described by QED perturbation theory are the polarization of the vacuum by the nuclear charge distribution, and the electron self-energy, both of which are modeled as perturbations of the effective Hamiltonian in GRASP2K and other software. Here, it is the electron self-energy in a many-electron atom that is the most difficult to model, and most studies have relied on approximations adapting the results of elaborate calculations for one-electron atoms; see in particular Chap. 28 of this Handbook.

Vacuum polarization As shown by Eq. (23.49), the nuclear potential generates a current in the vacuum that is responsible for a short-range screening of the nuclear charge. This can be represented as a local perturbing potential that is easy to take into account in the RCI program [99–101].

Electron self-energy GRASP2K and similar programs model the electron self-energy correction as a diagonal contribution to the effective Hamiltonian matrix in the CSF basis of the form

$$H_{rr}^{\text{SE}} = \sum_A q_r(A) E_A^{\text{SE}}, \quad (23.188)$$

where $q_r(A)$ is the occupation number of subshell A in CSF r . No simple methods of direct evaluation of E_A^{SE} in a many-electron atom are currently available. Most programs use the expression

$$\frac{E_{n\kappa}^{\text{SE}}}{mc^2} = \frac{\alpha (\alpha Z)^4}{\pi n^3} F(\alpha Z), \quad (23.189)$$

for an electron in the $n\kappa$ subshell of a hydrogenic atom with atomic number Z ; $F(\alpha Z)$ is a smooth function of its argument, and *Mohr* [102] tabulated values for $1s, 2s, 2p_{1/2}, 2p_{3/2}$ states with point charge nuclei for $Z = 5, 10, 15, \dots, 110$. *Shabaev* et al. [103, Tables I–V] published results for a similar range of Z , with corrections for finite size nuclear charge distributions where appropriate, for $ns, np_{1/2}, np_{3/2}, nd_{3/2}$ and $nd_{5/2}$ states with $n \leq 5$.

A common approach is to interpolate to a value Z_{eff} for each orbital of the many-electron atom when calculating Eq. (23.188). Several prescriptions exist; GRASP2K

currently searches for the best overlap with a hydrogenic $n\kappa$ orbital to the corresponding spectroscopic MR orbital. *Shabaev et al.* [103] devised a more complex model operator approach, published as the QEDMOD program [104].

23.8.10 Radiative Transitions

The operator $j^\mu(x)A_\mu(x)$ that occurs in the interaction Hamiltonian Eq. (23.61) describes processes in which the number of photons present can increase or decrease by one. The Fock space operator may be written

$$H_{\text{int}} = \sum_{a,b} \sum_{\rho} \left[a_a^\dagger a_b q_\rho^\dagger M_{ab}^{(\rho)\dagger}(t) + a_a^\dagger a_b q_\rho M_{ab}^{(\rho)}(t) \right], \quad (23.190)$$

where the first set of terms in the sum represents emission of a photon in the mode labeled ρ and the second to absorption of a photon by the same initial state. The operators a_a and a_a^\dagger are *anticommuting* annihilation and creation operators of electrons, whilst q_ρ and q_ρ^\dagger are *commuting* annihilation and creation operators of photons. If ω denotes photon frequency, then

$$M_{ab}^{(\rho)\dagger}(t) = M_{ab}^{(\rho)} e^{i(E_a - E_b + \omega)t},$$

$$M_{ab}^{(\rho)}(t) = M_{ab}^{(\rho)} e^{i(E_a - E_b - \omega)t},$$

where

$$M_{ab}^{(\rho)} = \left(\frac{\omega}{\pi c} \right)^{1/2} \int \psi_a^\dagger(\mathbf{x}) [\Phi^{(\rho)}(\mathbf{x}) + c\boldsymbol{\alpha} \cdot \mathbf{A}^{(\rho)}(\mathbf{x})] \times \psi_b(\mathbf{x}) d^3x$$

is the transition amplitude. For a discussion of this expression, including the effect of gauge transformations on the computed amplitudes, the elimination of angular coordinates for atomic central field orbitals, and connection with the non-relativistic limit, see [13, 23, 73].

23.9 GRASP – Information and Software

Additions, updates and instructions on downloading and commissioning the GRASP programs will be found on the website <https://github.com/compas/grasp>. See also [106]

References

1. Tiesinga, E., Mohr, P., Newell, D., and Taylor, B. (Eds.): 2018 CODATA Recommended Values of the Fundamental Constants of Physics and Chemistry, Special Publication (NIST SP)–959 (2019)

2. Wybourne, B.G.: *Classical Groups for Physicists*. Wiley, New York (1974)
3. Elliott, J.P., Dawber, P.G.: *Symmetry in Physics*. Macmillan, Basingstoke, London (1979)
4. Thaller, B.: *The Dirac Equation*. Springer, Berlin, Heidelberg (1992)
5. Greiner, W.: *Relativistic Quantum Mechanics*. Springer, Berlin, Heidelberg (1990)
6. Foldy, L.L.: *Phys. Rev.* **102**, 568 (1956)
7. Shirokov, Y.M.: *Sov. Phys. JETP* **6**, 568 (1958)
8. Shirokov, Y.M.: *Sov. Phys. JETP* **6**, 919 (1958)
9. Shirokov, Y.M.: *Sov. Phys. JETP* **6**, 929 (1958)
10. Schweber, S.S.: *Introduction to Relativistic Quantum Field Theory*. Harper Row, New York (1964)
11. Berestetskii, V.B., Lifshitz, E.M., Pitaevskii, L.P.: *Relativistic Quantum Theory*. Pergamon, Oxford (1971)
12. Itzykson, C., Zuber, J.-B.: *Quantum Field Theory*. McGraw-Hill, New York (1980)
13. Labzowsky, L.N., Klimchitskaya, G.L., Dmitriev, Y.Y.: *Relativistic Effects in the Spectra of Atomic Systems*. Institute of Physics Publishing, Bristol (1993)
14. Furry, W.H.: *Phys. Rev.* **81**, 115 (1951)
15. Grant, I.P., Quiney, H.M.: *Adv. At. Mol. Phys.* **23**, 37 (1988)
16. Lindgren, I.: *J. Phys. B* **23**, 1085 (1990)
17. Bethe, H.A., Salpeter, E.E.: *Quantum Mechanics of One-, and Two-Electron Systems*. Springer, Berlin, Heidelberg (1957)
18. Lindgren, I., Salomonson, S., Åsén, B.: *Phys. Rep.* **389**, 164 (2004)
19. Lindgren, I.: *Relativistic Many-Body Theory: A New Field-Theoretical Approach*. Springer, Heidelberg (2007)
20. Lackenby, B.G.C., Dzuba, V.A., Flambaum, V.V.: *Phys. Rev. A* **98**, 022518 (2018). arXiv:1804-08244v1 [physics.atom-ph]
21. Jönsson, P., Gaigalas, G., Bieroń, J., Froese Fischer, C., Grant, I.P.: *Comput. Phys. Commun.* **184**, 2197 (2013)
22. Froese Fischer, C., Godefroid, M., Brage, T., Jönsson, P., Gaigalas, G.: *J. Phys. B* **49**, 182004 (2016)
23. Grant, I.P.: *J. Phys. B* **7**, 1458 (1974)
24. Lindgren, I.: In: Johnson, W.R., Mohr, P.J., Sucher, J. (eds.) *Relativistic, Quantum Electrodynamics, and Weak Interaction Effects in Atoms*, pp. 3–27. AIP, New York (1989)
25. Baker, D.J., Moncrieff, D., Wilson, S.: In: Evans, R.G., Wilson, S. (eds.) *Supercomputational Science*, pp. 201–209. Plenum Press, New York (1990)
26. Hartree, D.R.: *Math. Proc. Camb. Philos. Soc.* **25**, 225 (1929)
27. Bagrov, V.G., Gitman, D.M.: *Exact Solutions of Relativistic Wave Equations*. Kluwer Academic, Dordrecht (1990)
28. Coddington, E.A., Levinson, N.: *Theory of Ordinary Differential Equations*. McGraw-Hill, New York (1955)
29. Abramowitz, M., Stegun, I.A.: *Handbook of Mathematical Functions*. Dover, New York (1965)
30. Burke, V.M., Grant, I.P.: *Proc. Phys. Soc.* **90**, 297 (1967)
31. Kobus, J., Karwowski, J., Jaskolski, W.: *Phys. Rev. A* **20**, 3347 (1987)
32. Reed, M., Simon, B.: *Methods of Modern Mathematical Physics. I: Functional Analysis*. Academic Press, New York, San Francisco, London (1972)
33. Bloch, C.: *Nucl. Phys.* **4**, 503 (1957)
34. Grant, I.P.: *J. Phys. B* **41**, 055002 (2008)
35. Hall, G.G.: *Proc. R. Soc. A* **208**, 328 (1951)
36. Roothaan, C.C.J.: *Rev. Mod. Phys.* **23**, 69 (1951)
37. Kim, Y.-K.: *Phys. Rev.* **154**, 17 (1967)
38. Kim, Y.-K.: *Phys. Rev. A* **159**, 190 (1967)
39. Grant, I.P.: *Adv. Phys.* **19**, 747 (1970)
40. Kagawa, T.: *Phys. Rev. A* **12**, 2245 (1975)
41. Kagawa, T.: *Phys. Rev. A* **22**, 2340 (1980)

42. Drake, G.W.F., Goldman, S.P.: *Phys. Rev. A* **23**, 2093 (1981)
43. Drake, G.W.F., Goldman, S.P.: *Adv. At. Mol. Phys.* **25**, 393 (1988)
44. Lee, Y.S., McLean, A.D.: *J. Chem. Phys.* **76**, 735 (1982)
45. Quiney, H.M., Grant, I.P., Wilson, S.: *J. Phys. B* **18**, 2805 (1985)
46. Sucher, J.: In: Johnson, W.R., Mohr, P.J., Sucher, J. (eds.) *Relativistic, Quantum Electrodynamical, and Weak Interaction Effects in Atoms*, pp. 28–46. AIP, New York (1989)
47. Dyall, K.G., Grant, I.P., Wilson, S.: *J. Phys. B* **17**, 493 (1984)
48. Grant, I.P.: *J. Phys. B* **19**, 3187 (1986)
49. Grant, I.P.: In: Johnson, W.R., Mohr, P.J., Sucher, J. (eds.) *Relativistic, Quantum Electrodynamical, and Weak Interaction Effects in Atoms*, pp. 235–253. AIP, New York (1989)
50. Grant, I.P., Quiney, H.M.: *Phys. Rev. A* **62**, 022508 (2000)
51. Rotenberg, M.: *Ann. Phys.* **19**, 262 (1962)
52. Rotenberg, M.: *Adv. At. Mol. Phys.* **6**, 233 (1970)
53. Bostock, C.J.: *J. Phys. B* **44**, 083001 (2011)
54. Clark, C.W., Taylor, K.T.: *J. Phys. B* **15**, 1175 (1982)
55. Čarsky, P., Urban, M.: *Ab Initio Calculations. Methods and Applications in Chemistry*. Springer, Berlin, Heidelberg (1980)
56. Huzinaga, S., Andzelm, J., Klobukowski, M., Radzio-Andzelm, E., Sakai, Y., Tatewaki, H. (eds.): *Gaussian Basis Sets for Molecular Calculations*. Elsevier, Amsterdam (1984)
57. Poirier, R., Kari, R., Csizmadia, I.G.: *Handbook of Gaussian Basis Sets*. Elsevier, Amsterdam (1985)
58. Bachau, H., Cormier, E., Decleva, P., Hansen, J.E., Martin, F.: *Rep. Prog. Phys.* **64**, 1815 (2001)
59. de Boor, C.: *A Practical Guide to Splines*. New York, Springer (2001). revised edition
60. Johnson, W.R., Blundell, S.A., Sapirstein, J.: *Phys. Rev. A* **37**, 307 (1988)
61. Johnson, W.R., Blundell, S.A., Sapirstein, J.: *Phys. Rev. A* **40**, 2233 (1988)
62. Bottcher, C., Strayer, M.R.: In: *Atomic Theory Workshop on Relativistic and QED Effects in Heavy Atoms AIP Conference Proceedings*, vol. 136, pp. 268–298. AIP, New York (1985)
63. Shabaev, V.M., Tupitsyn, I.I., Yerokhin, V.A., Plunien, G., Soff, G.: *Phys. Rev. Lett.* **93**, 130405 (2004)
64. Igarashi, A.: *J. Phys. Soc. Japan* **75**, 114301 (2006)
65. Igarashi, A.: *J. Phys. Soc. Japan* **76**, 054301 (2007)
66. Fischer, C.F., Parpia, F.A.: *Phys. Lett. A* **179**, 198 (1993)
67. Fischer, C.F., Zatsarinny, O.: *Comput. Phys. Commun.* **180**, 879 (2009)
68. Zatsarinny, O., Barschat, K.: *Phys. Rev. A* **77**, 062701 (2008)
69. Zatsarinny, O., Barschat, K.: *Phys. Rev. A* **79**, 042713 (2008)
70. Zatsarinny, O.: *Comput. Phys. Commun.* **174**, 273 (2006)
71. Zatsarinny, O., Fischer, C.F.: *Comput. Phys. Commun.* **202**, 287 (2016)
72. Hall, G., Watt, J.M.: *Modern Numerical Methods for Ordinary Differential Equations*. Clarendon Press, Oxford (1976)
73. Grant, I.P.: *Methods in Computational Chemistry vol. 2*. Clarendon Press, Oxford (1976)
74. Grant, I.P.: *Phys. Scr.* **21**, 443 (1980)
75. Swirles, B.: *Proc. R. Soc. A* **152**, 625 (1935)
76. Grant, I.P.: *Proc. R. Soc. A* **262**, 555 (1961)
77. Desclaux, J.P.: *Comput. Phys. Commun.* **9**, 31 (1975)
78. Desclaux, J.P.: *Comput. Phys. Commun.* **13**, 71 (1977)
79. Grant, I.P., McKenzie, B.J., Norrington, P.H., Mayers, D.F., Pyper, N.C.: *Comput. Phys. Commun.* **21**, 207 (1980)
80. Grant, I.P.: *Relativistic Quantum Theory of Atoms and Molecules: Theory and Computation*. Springer, New York (2007)
81. Jönsson, P., Gaigalas, G., Rynkun, P., Radžiūtė, L., Ekman, J., Gustafsson, S., Hartman, H., Wang, K., Godefroid, M., Froese Fischer, C., Grant, I.P., Brage, T., del Zanna, G.: *Atoms* **5**, 16 (2017)
82. Bieroń, J., Froese Fischer, C., Fritzsche, S., Gaigalas, G., Grant, I.P., Indelicato, P., Jönsson, P., Pykkö, P.: *Phys. Scr.* **90**, 054011 (2015)
83. Jönsson, P., He, C., Froese Fischer, C., Grant, I.P.: *Comput. Phys. Commun.* **176**, 597 (2007)
84. Rudzikas, Z.B.: *Theoretical Atomic Spectroscopy*. Cambridge Univ. Press, Cambridge (1997)
85. Grant, I.P., McKenzie, B.J., Norrington, P.H., Mayers, D.F., Pyper, N.C.: *Comput. Phys. Commun.* **21**, 207 (1980)
86. Dyall, K.G., Grant, I.P., Johnson, C.T., Parpia, F.A., Plummer, E.P.: *Comput. Phys. Commun.* **55**, 425 (1989)
87. Parpia, F.A., Fischer, C.F., Grant, I.P.: *Comput. Phys. Commun.* **94**, 249 (1996)
88. Desclaux, J.P., Indelicato, P.: MCDPFGME code writeup (2005)
89. Gu, M.F.: *Can. J. Phys.* **86**, 675 (2008)
90. Quiney, H.M., Grant, I.P., Wilson, S.: *J. Phys. B* **20**, 1413 (1987)
91. Quiney, H.M.: In: Evans, R.G., Wilson, S. (eds.) *Supercomputational Science*, pp. 159–184. Plenum Press, New York (1990)
92. Quiney, H.M.: In: Evans, R.G., Wilson, S. (eds.) *Supercomputational Science*, pp. 185–200. Plenum Press, New York (1990)
93. Wilson, S.: In: Wilson, S. (ed.) *Methods in Computational Chemistry*, vol. 2, p. 73. Plenum Press, New York (1988)
94. Quiney, H.M.: In: Wilson, S. (ed.) *Methods in Computational Chemistry*, vol. 2, p. 227. Plenum Press, New York (1988)
95. Quiney, H.M., Grant, I.P., Wilson, S.: In: Kaldor, U. (ed.) *Many-Body Methods in Quantum Chemistry Lecture Notes in Chemistry*, vol. 52, pp. 307–344. Springer, Berlin, Heidelberg (1989)
96. Quiney, H.M., Grant, I.P., Wilson, S.: *J. Phys. B* **23**, L271 (1990)
97. De Santis, M., Belapassi, L., Tarantelli, F., Storchi, L.: *Rend. Lincei Sci. Fis. Nat.* **29**, 209 (2018)
98. Verdebout, S., Rynkun, P., Jönsson, P., Gaigalas, G., Froese Fischer, C., Godefroid, M.: *J. Phys. B* **46**, 085003 (2013)
99. Uehling, E.A.: *Phys. Rev.* **48**, 55 (1935)
100. Wichmann, E.H., Kroll, N.M.: *Phys. Rev.* **101**, 843 (1956)
101. Fullerton, L.W., Rinker, G.A.: *Phys. Rev. A* **13**, 1283 (1976)
102. Mohr, P.J.: *Phys. Rev. A* **46**, 4421 (1999)
103. Shabaev, V.M., Tupitsyn, I.I., Yerokhin, V.A.: *Phys. Rev. A* **88**, 021513 (2013)
104. Shabaev, V.M., Tupitsyn, I.I., Yerokhin, V.A.: *Comput. Phys. Commun.* **189**, 175 (2015)
105. Johnson, W.R., Mohr, P.J., Sucher, J. (eds.): *Relativistic, Quantum Electrodynamical, and Weak Interaction Effects in Atoms*. AIP, New York (1989)
106. Froese Fischer, C., Gaigalas, G., Jönsson, P., Bieroń, J.: *Comput. Phys. Commun.* **237**, 184 (2018)



Ian Grant Ian Grant is Emeritus Professor of Mathematical Physics, University of Oxford. An Oxford graduate, he is best known for over 250 papers and a book (2007) on relativistic quantum theory of atoms and molecules, arising from his work at UKAEA, Aldermaston, 1956–1964. He returned to Oxford as a full-time member of the academic staff until his retirement in 1998. He has also worked on radiative transfer problems in stellar and planetary atmospheres.



Many-Body Theory of Atomic Structure and Processes

24

Miron Y. Amusia 

Contents

24.1	Diagrammatic Technique	364
24.1.1	Basic Elements	364
24.1.2	Construction Principles for Diagrams	364
24.1.3	Correspondence Rules	365
24.1.4	Higher-Order Corrections and Summation of Sequences	367
24.2	Calculation of Atomic Properties	368
24.2.1	Electron Correlations in Ground State Properties	368
24.2.2	Characteristics of One-Particle States	369
24.2.3	Electron Scattering	371
24.2.4	Two-Electron and Two-Vacancy States	372
24.2.5	Electron–Vacancy States	373
24.2.6	Photoionization in RPAE and Beyond	374
24.2.7	Photon Emission and Bremsstrahlung	377
24.2.8	RPAE in the Magnetic Channel	378
24.2.9	Consideration of “Big Atoms”	379
24.3	Concluding Remarks	380
	References	381

Abstract

All atoms except hydrogen are many-body systems, in which the interelectron interaction plays an important or even decisive role. The aim of this chapter is to describe a consistent method for calculating the structure of atoms and the characteristics of different atomic processes by applying perturbation theory to take into account the interelectron interaction. This method involves drawing a characteristic diagram based on the structure or process. This is then used to create an analytical expression to the lowest order in the interelectron interaction. Higher-order corrections are subsequently generated.

This technique was invented almost 70 years ago for quantum electrodynamics by *Feynman* [1] and then modified and adjusted for multiparticle systems by a number of authors [2, 3]. Its application to atomic structure and atomic processes required further modifications, which were initiated in the 1960s [4, 5]. The corresponding technique was successfully applied to the calculation of a wide variety of characteristics and processes in hun-

dreds of papers, a number of review articles, and several books [6]. The increasing amount of experimental data available has led to improved accuracy of this technique, so that it can be applied to current problems considering not only atoms and ions, both positive and negative [6–9], but also molecules [10], clusters [11], and so-called “big atoms” [12] – fullerenes and endohedrals [13].

The elements of the diagrammatic technique, which form a convenient and simple *language*, are given together with the rules for creating *sentences* using basic *words*. A kind of *dictionary* helps to translate diagrammatic *sentences* into analytical expressions suitable for calculations.

Keywords

photoionization cross section · spectroscopic factor · giant resonance · diagrammatic technique · single vacancy · electron correlation

An essential part of the program is to learn how the simplest approximation can be formed and then consistently improved. It is important to understand the mechanisms and processes connected with and responsible for higher-order perturbation theory terms that describe the corrections to the simplest approximation.

When the diagrammatic technique of many-body theory is used, it is unnecessary to be restricted to a finite number of lowest-order terms in the interelectron interaction. On the contrary, some infinite sequences may be taken into account. The sum of all many-body diagrams is completely equivalent to the many-particle Schrödinger equation. Therefore, taking all of them into account is just as complicated as solving the corresponding equation. Compared with other approaches, the diagrammatic technique can easily uncover hidden approximations and transparently demonstrate possible sources of corrections.

24.1 Diagrammatic Technique

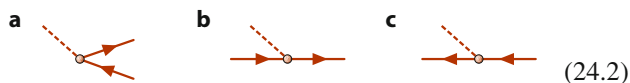
24.1.1 Basic Elements

Each physical atomic process (a process with participation of a molecule, cluster, fullerene, or endohedral) involves an electronic interaction with a projectile or external field, in general time dependent, or a mutual interelectron interaction. By convention, the ground state of the atom (if it is not degenerate) is regarded as the vacuum state. Then the simplest process in this target is excitation of an electron to an unoccupied level, leaving behind a vacancy. The basic elements of a diagram are



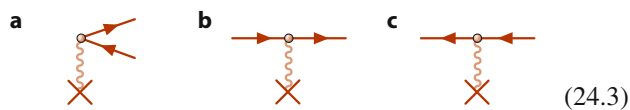
where (a) a line with an arrow directed to the right represents an electron excited to a vacant level, (b) a line with an arrow directed to the left represents a vacancy, (c) a wavy line with a cross represents the static Coulomb interaction, (d) a wavy line represents the interelectron Coulomb interaction, (e) a dashed line represents interaction with a time-dependent external field, usually electromagnetic, and (f) a dot represents the very act of interaction.

The elements Eq. (24.1a, b, e, f) in combination can describe the following real or virtual basic processes



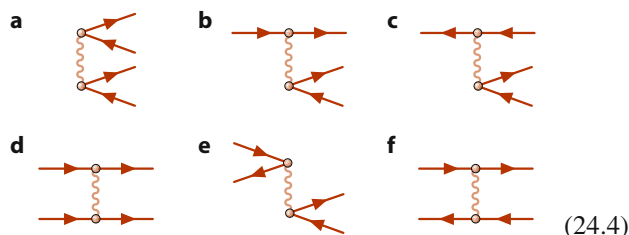
which represent (a) photon absorption by the vacuum with electron–vacancy pair creation, (b) electron excitation, and (c) vacancy excitation. Diagrams Eq. (24.2) depict processes as developing in time, shown increasing from left to right. A vacancy can be thought of as an antiparticle to the electron, moving backward in time. The time-reversal of processes Eq. (24.2) represent processes of photon emission due to annihilation of an electron–vacancy pair, vacancy transition, and electron inelastic scattering, respectively.

A static [for example, Coulomb Eq. (24.1c)] field can virtually create an electron–vacancy pair or affect the moving electron or vacancy, as shown in the following diagrams:



Just as for Eq. (24.2), diagrams Eq. (24.3) have their time-reversed counterparts.

Inclusion of interelectron interaction leads to a number of processes of which some examples are



Here, Eq. (24.4a) describes creation of two electron–vacancy pairs, Eq. (24.4b) represents the simplest picture of electron inelastic scattering, Eq. (24.4c) depicts vacancy decay with electron–vacancy pair creation, Eq. (24.4d) stands for electron–electron scattering, Eq. (24.4e) represents a process which can be called electron–vacancy annihilation and creation, while Eq. (24.4f) shows electron–vacancy scattering.

Just as for Eqs. (24.2) and (24.3), diagrams Eq. (24.5) have their time-reversed counterparts.

24.1.2 Construction Principles for Diagrams

The foundations of diagrammatic techniques are discussed in a number of books such as [14]. This chapter presents recipes for the construction and evaluation of diagrams corresponding to various atomic processes [15, 16].

The basic procedure is to connect the initial and final states of the system considered, drawn at the left and right-hand sides of the diagram, respectively, using appropriate elements from Eq. (24.1). In doing so, the following rules apply:

1. At each dot Eq. (24.1f), only three lines can meet: wavy (or dashed) and electron–vacancy.
2. A vacancy cannot be transformed into an electron or vice versa.
3. Electrons and vacancies can be created only pairwise from the vacuum.
4. Only linked diagrams are allowed, i.e., only those having no parts entirely disconnected from one another.

The simplest or initial approximation to a process is represented by a diagram that includes the lowest possible number of elements Eqs. (24.1)–(24.4). Higher-order corrections can be derived by including additional elements of interaction with the static field of the nucleus Eq. (24.1c) and between electrons and/or vacancies Eq. (24.1d).

As illustration of the method, consider the following three processes:

1. One-electron photoionization – the initial state is a photon while the simplest final state is an electron–vacancy pair.

They can be combined together giving the basic diagram Eq. (24.2a).

2. Elastic electron scattering – the initial and final states are single electrons. To describe the simplest scattering process, the interaction with the Coulomb field must be taken into account, leading to Eq. (24.3b). To account for inter-electron interaction, the simplest element



must be introduced. It is a modification of Eq. (24.4b) accounting for the interaction of an incoming electron with all target electrons individually, not altering their states. This is emphasized by the loop in which the same vacancy leaving the lower dot reenters it. The indistinguishability of all electrons as fermions is taken into account by permutation of the electron (vacancy) line ends, as illustrated in the following diagrams:

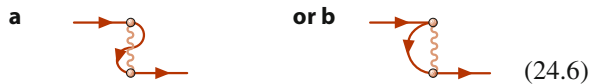
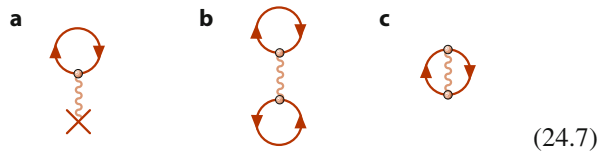


Diagram Eq. (24.6a) is obtained from Eq. (24.5) by permutation of the electron lines on one side of the interelectron interaction. Diagram (24.6b) is equivalent to Eq. (24.6a) but is simpler to draw.

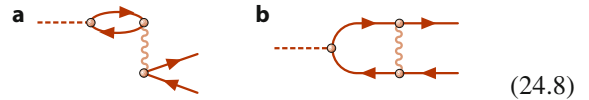
3. Inelastic electron scattering – the initial state is a single electron. For the final state, we choose one with two electrons and, therefore, a single vacancy. The simplest diagram in this case is given by Eq. (24.4b).

To illustrate the description of the ground state characteristics, consider the contributions to the ground state energy of an atom. If this state is not degenerate, its potential energy is given by vacuum diagrams that have no free lines in the initial or final states. The simplest vacuum diagrams are



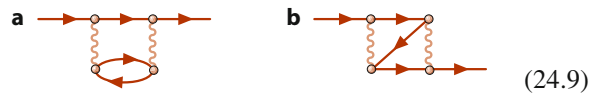
Higher-order corrections to all these diagrams can be obtained by adding elements such as a static external field Eq. (24.3) or interelectron interaction Eq. (24.4) without changing the initial and final states of the processes. The lowest-order processes are represented by Eqs. (24.2a), (24.5), (24.6), (24.4b), and (24.7). There are many corrections even in the next order of interaction, either with an external field or with electrons or vacancies. To illustrate, only one correction to each process will be presented:

1. Simple photoionization Eq. (24.2a) may be combined with Eqs. (24.4e) and (24.4f) to obtain

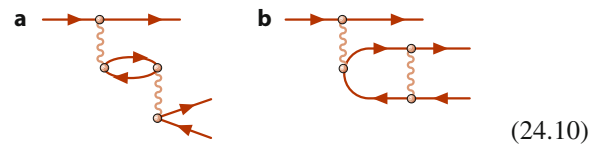


This describes the effect of the creation of another electron–vacancy pair, after annihilation of the first one formed by absorption of the initial photon.

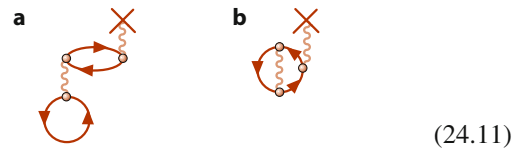
2. Simple elastic electron scattering Eq. (24.5) can be combined with an extra interaction term Eq. (24.4f) between the incoming electron and the vacancy of the loop Eqs. (24.5) and (24.6b), to obtain



3. Simple inelastic electron scattering Eq. (24.4b) can also be combined with Eqs. (24.4e) and (24.4f), accounting for the interaction of an electron and vacancy created in the lowest-order process, to obtain



4. The ground state energy terms Eqs. (24.7b) and (24.7c) can be combined with Eq. (24.7) and the element Eq. (24.3c) of the interaction between the vacancy in the Eqs. (24.7b) and (24.7c) loops to obtain



Higher-order corrections can be constructed step by step by introducing further elements of interaction. In some cases, classes of diagrams may be taken into account up to infinite order by solving closed systems of integral or differential equations.

24.1.3 Correspondence Rules

These rules describe how to obtain an analytical expression corresponding to a given diagram. One starts by choosing a zero-order approximation, which for atoms can be that of independent electrons moving in the Coulomb field of an atomic nucleus. For nonatomic objects, e.g., molecules or clusters, other approximations are chosen as zero-order. Objects with

a nondegenerate ground state correspond to the vacuum. For atoms, the vacuum is a state with all completely occupied or closed subshells. Electron (vacancy) states are characterized in this case by the quantum numbers n, ℓ, m_ℓ , and $\sigma = \pm 1/2$, with good accuracy, as vacuum can be treated an atom with a semifilled shell. Such an atom is considered as constructed from two different types of electrons, called *up* and *down* electrons and denoted by their spin directions \uparrow and \downarrow [16].

The first correspondence rule is to substitute a matrix element for each interaction

$$\begin{aligned} \text{Diagram (24.2)} &\rightarrow \langle p|W|q \rangle, \\ \text{Diagram (24.3)} &\rightarrow \langle p|U|q \rangle, \\ \text{Diagram (24.4)} &\rightarrow \langle pt|V|qs \rangle, \end{aligned} \quad (24.12)$$

where W is the interaction potential of an electron with the external time-dependent field, U is the interaction potential of an electron (vacancy) with an external static field, for example that of the nucleus, and V is the Coulomb interelectron interaction. Each of the letters p, q, t, s represents a full set of n, ℓ, m_ℓ, σ quantum numbers. Vacancy states are below (and include) the highest occupied energy level, called the Fermi level, so that $p \leq F$. Electron states are above the Fermi level so that $q > F$. Thus, diagram Eq. (24.2a) is represented by $\langle p|W|q \rangle$ with $p \leq F$ and $q > F$.

Apart from initial and final states, each diagram can have sections, i.e., intervals between successive interactions. For instance, Eqs. (24.9) and (24.10) each have one section. Each section is represented by an inverse energy denominator ε_d^{-1} . It includes the sum over all vacancy energies $\sum_{\text{vac}} \varepsilon_i$ minus the sum of the electron energies $\sum_{\text{el}} \varepsilon_n$ to which the entrance energy E of the diagram (e.g., $\hbar\omega$ for a time-dependent field) must be added:

$$\varepsilon_d^{-1} = \left(\sum_{\text{vac}} \varepsilon_i - \sum_{\text{el}} \varepsilon_n + E \right)^{-1}. \quad (24.13)$$

The second correspondence rule is to identify sections and write down their energy denominators. After attributing to each electron (vacancy) line a letter, denoting its state, the analytical expression for a diagram is given by

$$\begin{aligned} &\text{Analytical Expression} \\ &= (\text{the product of all interaction matrix elements}) \\ &\times (\text{all energy denominators})^{-1} \\ &\times (-1)^L \text{ summed over all intermediate electron} \\ &\quad \text{and vacancy states,} \end{aligned} \quad (24.14)$$

where L is equal to the sum of the total number of vacancy lines and closed vacancy or electron–vacancy loops.

Although electrons are fermions, the summation in Eq. (24.14) has no additional restrictions caused by the Pauli

principle. It runs over all electron ($> F$) and vacancy ($\leq F$) states, including those where two or more electrons (or vacancies) are in the same state. The correspondence rules Eqs. (24.12), (24.13), and (24.14) can be illustrated by giving as examples the analytical expressions of two diagrams Eqs. (24.8) and (24.9).

Attributing letters denoting electron and vacancy states, diagram Eq. (24.8) becomes

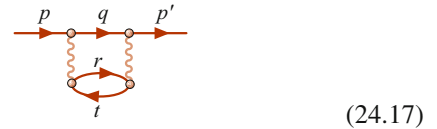


According to Eqs. (24.12)–(24.14), the analytical formula

$$A_{if}(\omega) = \sum_{r>F, t \leq F} \frac{\langle t|W|r \rangle \langle ri|V|tf \rangle}{\varepsilon_t - \varepsilon_r + \omega} (-1)^{2+1} \quad (24.16)$$

is obtained. The symbol \sum includes summation over discrete levels and integration over a continuous spectrum. In Eq. (24.16), the intermediate state is $r > F, t \leq F$, and the diagram has two vacancies (t and i) and one loop rt . Integration must be performed over those states r that belong to the continuum.

Assigning letters denoting states, Eq. (24.9) appears as



where $p, q, p', r > F$, while $t \leq F$. According to Eq. (24.14),

$$\Delta E = \sum_{r, q > F; t \leq F} \frac{\langle pt|V|qr \rangle \langle qr|V|p't \rangle}{\varepsilon_t - \varepsilon_q - \varepsilon_r + \varepsilon_p} (-1)^{1+1}, \quad (24.18)$$

where the intermediate states are $q, r > F$ and $t \leq F$. It has one vacancy and one electron–vacancy loop rt .

An intermediate state in a diagram can be real or virtual. It is real if the energy conservation law can be fulfilled, i.e., if for some values of the section energy the following relation holds

$$E = \sum_{\text{el}} \varepsilon_n - \sum_{\text{vac}} \varepsilon_i. \quad (24.19)$$

If Eq. (24.19) can be fulfilled, a prescription for avoiding the singularity in Eq. (24.13) is to substitute the expression ε_d^{-1} by for Q , where

$$Q = \lim_{\eta \rightarrow 0} \left(E - \sum_{\text{el}} \varepsilon_n + \sum_{\text{vac}} \varepsilon_i + i\eta \right)^{-1}$$

$$= P \left(E - \sum_{\text{el}} \varepsilon_n + \sum_{\text{vac}} \varepsilon_i \right)^{-1} - i\pi \delta \left(E - \sum_{\text{el}} \varepsilon_n + \sum_{\text{vac}} \varepsilon_i \right), \quad (24.20)$$

for ε_d^{-1} . Here, P denotes that the principal value is to be taken on integration over intermediate state energies. The result of Eq. (24.20) can thus be complex.

An intermediate state is virtual if the energy conservation law in Eq. (24.19) is violated for all values of the section energy. In general, the bigger the virtuality, i.e., the difference $E - \sum_{\text{el}} \varepsilon_n + \sum_{\text{vac}} \varepsilon_i$, the smaller the contribution to the amplitude of the process.

24.1.4 Higher-Order Corrections and Summation of Sequences

An important feature of the diagrammatic technique is the convenience in constructing higher-order corrections and in the summation of infinite sequences of diagrams. According to Eq. (24.13), each new interaction line leads to an additional interaction matrix element, an extra energy denominator, and summation over new intermediate states.

An important example of infinite summation is that of determining the one-electron states. The interaction with the nucleus in atoms Eq. (24.3b) (or nuclei in multiatomic objects, e.g., molecules) and with atomic (or e.g., molecular) electrons Eqs. (24.5) and (24.6) is not small and must be taken into account nonperturbatively; i.e., these elements must be iterated infinitely. To simplify the drawing, only the element Eq. (24.5) is repeated, leading to the diagrammatic equation:

$$= \text{[Diagrammatic Equation (24.21)]} \quad (24.21)$$

Indeed, everything in the infinite sum that is in front of the dashed line repeats the infinite sum itself, thus leading to a closed equation of the form

$$\langle \tilde{p} | = \langle p | + \sum_{q>F} \langle \tilde{p} i | V | q i \rangle \frac{1}{-\varepsilon_q + \varepsilon_p} \langle q |. \quad (24.22)$$

The two interactions leading to Eq. (24.21) can be permuted, so that interaction 1 can be after interaction 2. This leads to extension of the sum to include states with $q \leq F$. As a result, the summation in Eq. (24.22) must be performed over all states q .

Interaction with the nucleus (nuclei in multiatomic objects) and the other electrons also affects the occupied (or vacancy) states i in Eq. (24.21), and, therefore, the latter must be modified by inserting the elements Eqs. (24.3b), (24.5), and (24.6) into them. Here again, the vacancy line in Eqs. (24.5) and (24.6) must be modified by including the corrections Eqs. (24.3b), (24.5), (24.6), and so on. Finally, the diagrammatic equation

$$= \text{[Diagrammatic Equation (24.23)]} \quad (24.23)$$

is obtained. The doubled line for i emphasizes that the vacancy wave function is determined by an equation similar to Eq. (24.21). The corresponding analytical equation looks like Eq. (24.22), but includes also the Coulomb interaction with the nucleus and the exchange interaction with other atomic electrons. The summation over q in this equation is extended over all q , not only $q > F$. Multiplying the corresponding equation by $(\hat{H}_0 - \varepsilon_p)$ from the right (atomic units are used in this chapter: $e = m_e = \hbar = 1$), where $\hat{H}_0 = -\nabla^2/2$, and using the completeness of the functions $\sum_q |q\rangle \langle q| = \delta(\mathbf{r} - \mathbf{r}')$, results in the equation

$$\left[-\frac{\nabla^2}{2} - \frac{Z}{r} + \sum_{i \leq F} \int \frac{d\mathbf{r}'}{|\mathbf{r}' - \mathbf{r}|} |\phi_i(\mathbf{r}')|^2 - \varepsilon_p \right] \phi_p(\mathbf{r}) = \sum_{i \leq F} \int \frac{d\mathbf{r}'}{|\mathbf{r}' - \mathbf{r}|} \phi_i^*(\mathbf{r}') \phi_p(\mathbf{r}') \phi_i(\mathbf{r}), \quad (24.24)$$

for the electron wave function $\phi_p(\mathbf{r})$ in an atom; Z/r is the nucleus Z Coulomb potential. Here, $\phi_i(\mathbf{r})$ are wave functions determined by equations similar to Eq. (24.24). For multiatomic objects, instead of Z/r another potential $U(\mathbf{r})$ appears in these equations, called the Hartree-Fock (HF) equations.

HF includes a part of interelectron interaction matrix elements, namely those given by Eqs. (24.5) and (24.6). The rest is called the residual interaction, and its inclusion leads beyond the HF frame, accounting for correlations.

When a perturbative approach is used, it is essential to define the zero-order approximation. In this chapter, and very

often in the literature, the Hartree–Fock approximation is used in this role. To simplify the drawing of diagrams, from now on single (rather than double) lines will represent electrons (vacancies), whose wave functions are determined in the HF approximation by Eq. (24.24). Obviously, in this case, elements Eqs. (24.3a), (24.5), and (24.6) should not be added to any other diagrams.

The procedure used in deriving Eqs. (24.21) and (24.23) is, in fact, more general. Let us separate all diagrams describing elastic scattering that do not include a single one-electron or one-vacancy state as intermediate. Depicting their total contribution by a square, the precise one-particle state is determined by an infinite sequence of iterative diagrams that can be summed, similarly to Eq. (24.21), by

$$\begin{aligned}
 & \text{Diagram with square } \hat{a} = \text{Diagram 1} + \text{Diagram 2} + \text{Diagram 3} + \dots \\
 & = \text{Diagram 1} + \text{Diagram 2}
 \end{aligned}
 \quad (24.25)$$

Here, the single line stands for an HF state. Using the correspondence rule Eq. (24.14), an analytical equation similar to the Schrödinger equation can be derived with the operator $\hat{\Sigma}$ playing the role of an external potential. The essential difference is, however, that this *potential* in principle depends upon the energy and state of the particle. The same kind of iterative procedure leading to Eq. (24.21) or (24.23) will be used several times in this chapter.

Other zero-order approximations can be chosen. But then diagrams with corrections of the type Eq. (24.3a) must be included, with the external static field potential equal to the difference between the HF and the chosen one.

To calculate the numerical value of a given diagram or a sequence of diagrams one needs to know, according to the description given above, the matrix elements of external fields and interelectron interactions obtained with the help of one-electron HF wave functions. The required calculational procedures are described in [17] and [18].

24.2 Calculation of Atomic Properties

24.2.1 Electron Correlations in Ground State Properties

A major advantage of the diagrammatic technique in many-body theory is that it is usually unnecessary to know the total wave function of the atom or other considered object. On the contrary, only actively participating electrons or vacancies appear in a diagram. The HF zero-order approximation

for one-electron and one-vacancy wave functions is used in what follows. All atomic characteristics and cross sections for atomic processes calculated with HF form the one-electron approximation. Everything beyond the HF frame, i.e., caused by residual interaction, is called correlation corrections or correlations. They can be calculated using the many-body perturbation theory (MBPT) [4], random phase approximation (RPA) [19], and random phase approximation with exchange (RPAE) [15] or its generalized version GRPAE [15–17].

The simplest diagrammatic expression for the correlation energy is given by the two diagrams

$$\text{Diagram (a)} \quad \text{Diagram (b)} \quad (24.26)$$

The analytical expression $\Delta E_{\text{corr}}^{(2)}$ for Eq. (24.26a) is

$$\Delta E_{\text{corr}}^{(2)} = \sum_{k,n>F;i,j\leq F} \frac{\langle ij|V|kn\rangle\langle kn|V|ij\rangle}{\varepsilon_i + \varepsilon_j - \varepsilon_k - \varepsilon_n}. \quad (24.27)$$

The analytical expression for Eq. (24.26b) differs from Eq. (24.27) by the sign and an exchange matrix element $\langle kn|V|ji\rangle$ instead of a direct $\langle kn|V|ij\rangle$ one. As concrete calculations show, the contribution Eq. (24.26) overestimates the correlation energy by $\approx 10\%$.

Diagrams Eq. (24.26) can also be used to describe the interaction potential of two atoms, designated A and B. Let the ki states belong to A and nj to B. At large distances R between the atoms, the contribution of Eq. (24.26b) is exponentially small. Because the vacancies i and j are located inside atoms A and B, respectively, the interelectron potential $V = |\mathbf{r}_A - \mathbf{r}_B + \mathbf{R}|^{-1}$ at large distances $R \gg R_{A,B}$ ($R_{A,B}$ are atomic radii) can be expanded as a series in powers of R^{-1} . The first term giving a nonvanishing contribution to Eq. (24.27) is $V \simeq R^{-3}[(\mathbf{r}_A \cdot \mathbf{r}_B) - 3(\mathbf{r}_A \cdot \mathbf{n})(\mathbf{r}_B \cdot \mathbf{n})]$, \mathbf{n} being the unit vector in the direction of \mathbf{R} . Substituted into Eq. (24.27), this potential leads to the expression

$$U(R) = -\frac{C_6}{R^6}, \quad (24.28)$$

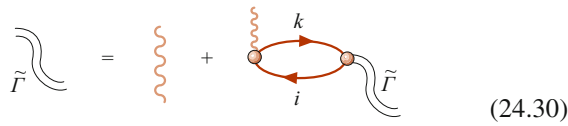
for the interatomic potential [20], where

$$C_6 \approx \sum_{k,n>F;i,j\leq F} \frac{|(i|\mathbf{r}|k)|^2|(j|\mathbf{r}|n)|^2}{(\varepsilon_i + \varepsilon_j - \varepsilon_k - \varepsilon_n)}. \quad (24.29)$$

Calculations [21] show that the inclusion of higher-order correlations is important for obtaining accurate values for ΔE_{corr}

and C_6 . However, to improve accuracy by taking into account the corrections to diagrams Eq. (24.26) requires considerable effort. Indeed, there are several types of corrections to Eq. (24.26) such as (i) screening of the Coulomb interelectron interaction by the electron–vacancy excitations, (ii) interaction between vacancies ij , (iii) interaction between electrons and vacancies $ki(nj)$ ($kj(ni)$), and (iv) interaction between electrons kn . Corrections to the HF field itself, which acts upon electrons k, n and vacancies i, j , are discussed in Sect. 24.2.3.

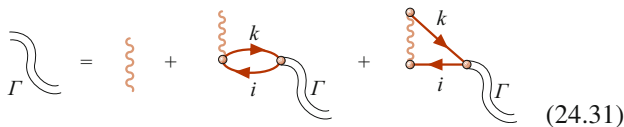
Screening of the Coulomb interelectron interaction is very important, and in many cases must be taken into account non-perturbatively. The simplest way to do this is to use RPA, which defines the effective interelectron interaction $\tilde{\Gamma}$ as a solution of an integral equation, shown diagrammatically by



$$\tilde{\Gamma} = V + V \tilde{\Gamma} \quad (24.30)$$

If V in Eq. (24.27) is replaced by $\tilde{\Gamma}$, an expression for ΔE_{corr} in RPA can be derived.

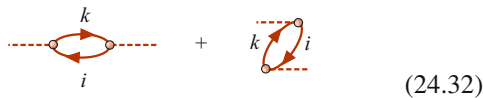
Exchange is very important in atoms and molecules, so diagram Eq. (24.30) can be modified to include this effect, thus leading to the effective interaction Γ in RPAE [15–17, 21]:



$$\Gamma = V + V \Gamma + V \Gamma \quad (24.31)$$

Replacing V in Eq. (24.27) by Γ gives a rather accurate expression for ΔE_{corr} in RPAE. Taking into account screening also affects the long-range interatomic interaction considerably by altering the constant C_6 in Eq. (24.28).

The ground state energy of an atom or molecule is modified by an external field. For a not too intense electromagnetic field, the simplest correction to the ground state energy is given by the diagrams



$$\quad + \quad \quad (24.32)$$

Considering a dipole external field, its interaction with the atomic electrons is given by $W = \sum_{i \leq F} \mathbf{E} \cdot \mathbf{r}_i$, \mathbf{E} being the strength of the field. The ground state energy shift is given by $\Delta E = -\alpha(\omega) E^2/2$, where $\alpha(\omega)$ is the dynamical dipole polarizability, and ω is the frequency of the field. According to Eq. (24.32), $\alpha(\omega)$ is determined by

$$\alpha(\omega) = \sum_{k>F; i \leq F} \frac{2|\langle i|z|k \rangle|^2 (\varepsilon_k - \varepsilon_i)}{(\varepsilon_k - \varepsilon_i)^2 - \omega^2}, \quad (24.33)$$

where z is a component of the vector \mathbf{r} .

RPAE corrections to $\alpha(\omega)$ are discussed in Sect. 24.2.5 in connection with the photoionization process.

Nondipole polarizabilities of other multipolarities can be obtained in the lowest order of interelectron interaction using Eq. (24.32) with a properly chosen interaction operator between the electromagnetic field and an electron, instead of $W = \sum_{i \leq F} \mathbf{E} \cdot \mathbf{r}_i$.

24.2.2 Characteristics of One-Particle States

A single vacancy or electron can propagate from one instant of interaction to another, as described to zero order by elements Eq. (24.1b) [or Eq. (24.1a)] with dots Eq. (24.1f) at the ends. For an atom, this line represents a HF one-particle state with a given angular momentum, spin, and total momentum. Accounting for virtual or real atomic excitations leads, for a vacancy, to a diagram similar to Eq. (24.25) but with oppositely directed arrows. Because the interaction with these excitations is usually much smaller than the energy distance between shells, in the sum over q only the term $q = i$, i being the considered vacancy state, need be taken into account. Interaction with the vacuum leaves the angular momentum, spin, and total momentum unaltered. It can, however, change the energy and lead to a finite lifetime for a vacancy state.

Analytically, the vacancy propagation in the HF approximation is described by the one-particle HF Green's function G^{HF} :

$$G_i^{\text{HF}}(E) = 1/(\varepsilon_i - E). \quad (24.34)$$

Solving Eq. (24.25) for a vacancy i with only Σ_{ii} terms included gives

$$G_i(E) = 1/[\varepsilon_i + \Sigma_{ii}(E) - E]. \quad (24.35)$$

The pole in $G(E)$, which determines the vacancy energy, is shifted from $E = \varepsilon_i$ to $E_i = \varepsilon_i + \Sigma_{ii}(E_i)$. The quantity $\Sigma_{ii}(E)$ is called the self-energy, and is, in general, a complex function of energy, its imaginary part determining the lifetime of the vacancy i . Near E_i , Eq. (24.35) can be written in the form

$$G_i(E) \approx F_i/[\varepsilon_i + \Sigma_{ii}(E_i) - E] = F_i/(E_i - E), \quad (24.36)$$

where

$$F_i = \left(1 - \frac{\partial \Sigma_{ii}(E)}{\partial E} \Big|_{E=E_i} \right)^{-1} \quad (24.37)$$

is called the *spectroscopic factor*. It characterizes the probability for more complicated configurations to be admixed into a single vacancy state i [15, 22].

An important problem is to calculate the self-energy part $\Sigma(E)$. The first nonzero contributions are

$$(24.38)$$

Specific calculations [16, 21] demonstrate that if the intermediate electron states n [in Eq. (24.38a)] and kn [in Eq. (24.38b)] are found in the field of vacancies jj' and $i'j$, the diagrams Eq. (24.38) are able to reproduce the values of the correlation energy shift with about 5% accuracy. For outer subshell vacancies, the contributions Eqs. (24.38a) and (24.38b) are almost equally important, to a large extent canceling each other. For example, Eq. (24.38a) shifts the outer 3p vacancy in Ar to lower binding energies by 0.1 Ry, while the contribution of Eq. (24.38b) is -0.074 Ry. The total value 0.026 Ry is small and close to the experimental one, which is 0.01 Ry. For inner vacancies, Eq. (24.38a) is dominant because the intermediate states in Eq. (24.38b) have large virtualities and are, therefore, small. The main contribution to the sum over j' comes from the term $j' = i' = i$, which gives for the energy shift of level i

$$\Delta\varepsilon_i = \Sigma_{ii}^{(2)}(\varepsilon_i) = \sum_{n>F; j \leq F} \frac{|\langle n|r^{-1}|j \rangle|^2}{\varepsilon_n - \varepsilon_j}. \quad (24.39)$$

The value of Eq. (24.39) is positive. Most important higher-order corrections will be included if V in Eq. (24.27) is replaced by Γ from Eq. (24.31).

The physical meaning of diagram Eq. (24.38a) is transparent: it accounts for configuration mixing of one vacancy i and two vacancies jj' – one-electron n states in the lowest order in the interelectron interaction. Diagram Eq. (24.38b) is not as transparent, and for $i = i'$, its intermediate state appears to violate the Pauli principle. However, as noted in connection with Eq. (24.14), the Pauli principle should not be considered as a restriction in constructing intermediate states.

Diagram Eq. (24.38a) and its exchange can have an imaginary part, which gives the probability of Auger decay $\gamma_i^{(A)}$, calculated to the lowest order in the interelectron interaction. For Eq. (24.38a), one has

$$\begin{aligned} \gamma_i^{(A)} &= \text{Im}[\Sigma_{ii}(E_i)] \\ &= 2\pi \sum_{j, j' \leq F; n > F} |\langle in|V|jj' \rangle|^2 \delta(\varepsilon_j + \varepsilon_{j'} - \varepsilon_n - \varepsilon_i). \end{aligned} \quad (24.40)$$

The width $\gamma_i^{(A)}$ is usually much smaller than $\text{Re}[\Sigma_{ii}(E_i)]$, but there are several exceptional cases with abnormally large Auger widths, among which the most impressive is the 4p-vacancy in Xe with its $\gamma_{4p} \approx 10$ eV.

Along with Auger, radiative decay of vacancies takes place. Its amplitude is presented by time reverse of Eq. (24.2b) diagram. The radiation width $\gamma_i^{(\nu)}$ in its HF approximation is given by equation

$$\gamma_i^{(\nu)HF} = \frac{1}{c^3} \sum_{i < j \leq F} \omega_{ji}^3 |\langle i|\mathbf{er}|j \rangle|^2, \quad (24.41)$$

where \mathbf{e} is the emitted photon polarization vector, $\omega_{ji} \equiv \varepsilon_j - \varepsilon_i$.

Higher-order corrections include those that are taken into account when V in Eq. (24.40) is replaced by Γ from Eq. (24.31). The others include jj' vacancy–vacancy interaction, the interaction between vacancies jj' and the electron n , and so on. As noted above, all of these can be obtained step by step by inserting the elements Eq. (24.4) into Eq. (24.38). To select the most important corrections, a physical idea and/or experience are necessary. For instance, if the energy transferred in the decay process $\Delta\varepsilon = \varepsilon_{j'} - \varepsilon_j$ is close to some threshold energies of atomic intermediate or outer shells, corrections that include virtual excitation of this shell must be taken into account.

The contribution to the spectroscopic factor from Eq. (24.38a) is given according to Eq. (24.37) by

$$F_i^{(2)} \equiv \left(1 + \sum_{j, j' \leq F; n > F} \frac{|\langle in|V|j'j \rangle|^2}{(\varepsilon_j + \varepsilon_{j'} - \varepsilon_n - \varepsilon_i)^2} \right)^{-1}. \quad (24.42)$$

Generally, for any Fermi particle, $F_i \leq 1$ [17] because there cannot be more than one particle in a given state. Note that the integrand in Eq. (24.42) is the lowest-order admixture of the $jj'n$ state to a pure one-vacancy state i . A small F value means strong mixing. For atoms, F_i is usually close to 1, but there are exceptions where F is small. For example, F_{5s} in Xe is about 0.33 [15].

The operator $\Sigma_{ij(n)}(\varepsilon)$ has nondiagonal matrix elements, which leads to admixture of other one-vacancy j or one-electron n states to the vacancy i . A measure of this admixture is given by the ratio $\Sigma_{ij(n)}(\varepsilon_i)/(\varepsilon_{j(n)} - \varepsilon_i)$.

In higher orders, decay processes more complex than those described by the imaginary part of Eq. (24.40) become possible. For example, this could be a two-electron Auger decay in which the transition energy is distributed between two outgoing electrons. An example of the lowest-order diagram for this process is

$$(24.43)$$

This is one of those diagrams that describe the mixing of a pure one-vacancy state with a quite complex configuration $jj_1j_2\varepsilon_1\varepsilon_2$.

24.2.3 Electron Scattering

Propagation of an electron in a discrete level or in a scattering state can be described in the same way as for a vacancy. The electron wave function is determined by Eq. (24.25). Using the correspondence rule Eq. (24.14), Eq. (24.25) can be expressed analytically in the form

$$\begin{aligned} & \left[-\frac{\nabla^2}{2} - \frac{Z}{r} + \sum_{i \leq F} \int \frac{d\mathbf{r}'}{|\mathbf{r}' - \mathbf{r}|} |\phi_i(\mathbf{r}')|^2 - \varepsilon \right] \psi_\varepsilon(\mathbf{r}) \\ &= \sum_{i \leq F} \int \frac{d\mathbf{r}'}{|\mathbf{r}' - \mathbf{r}|} \phi_i^*(\mathbf{r}') \psi_\varepsilon(\mathbf{r}') \phi_i(\mathbf{r}) \\ &+ \int \hat{\Sigma}(\mathbf{r}, \mathbf{r}', \varepsilon) \psi_\varepsilon(\mathbf{r}') d\mathbf{r}'. \end{aligned} \quad (24.44)$$

The terms with the Coulomb interelectron interaction $|\mathbf{r}' - \mathbf{r}|^{-1}$ determine the Hartree–Fock self-consistent potential. The last term in Eq. (24.44) represents the nonlocal energy dependent polarization interaction of the continuous spectrum electron with the target atom. For HF wave functions for molecular targets, one has to substitute the proper multinuclear Coulomb potential for $-Z/r$ in Eq. (24.44). Although Eq. (24.44) resembles the ordinary Schrödinger equation, because of the energy dependence of the self-energy part $\hat{\Sigma}(\mathbf{r}, \mathbf{r}', \varepsilon)$, it is not the same. Consequently, the wave function $\psi_\varepsilon(\mathbf{r})$, often called a Dyson orbital, must be normalized according to the condition

$$\langle \psi_{\varepsilon'} | \psi_\varepsilon \rangle = F_\varepsilon \delta(\varepsilon' - \varepsilon), \quad (24.45)$$

where

$$F_\varepsilon = \left[1 - \left(\varepsilon \left| \frac{\partial \hat{\Sigma}(\mathbf{r}, \mathbf{r}', E)}{\partial E} \right| \varepsilon \right) \Big|_{E=\varepsilon} \right]^{-1}. \quad (24.46)$$

The relation in Eq. (24.45) is different from that for ordinary wave functions by the factor $F_\varepsilon < 1$. In F_ε , the matrix element of the operator $\partial \hat{\Sigma}(\mathbf{r}, \mathbf{r}', E) / \partial E$ is calculated between states $\psi_\varepsilon(\mathbf{r})$. It is seen that F_ε is the same spectroscopic factor as determined by Eq. (24.37) but for a continuous spectrum or an excited electron state.

The object described by the wave function $\psi_\varepsilon(\mathbf{r})$ differs from an individual electron because it can be unstable, and its state is mixed with those of more complicated configurations, such as *two electrons* $k'k''$ – one vacancy j'' . This object is called a *quasi electron*.

Equation (24.44) also determines the energies of electrons in discrete levels that are shifted from their HF values. Con-

trary to the case of deep vacancies, it is impossible to predict the sign of the energy shift without detailed calculations.

For incoming electron energies ε higher than the target ionization threshold, the operator $\hat{\Sigma}(\mathbf{r}, \mathbf{r}', \varepsilon)$ acquires an imaginary part, thus becoming an optical potential for the projectile. The additional elastic scattering phase shifts from their HF values can be expressed via matrix elements of $\hat{\Sigma}(\mathbf{r}, \mathbf{r}', \varepsilon)$ between the wave functions $\phi_\varepsilon^*(\mathbf{r})$ and $\psi_\varepsilon(\mathbf{r})$; but to find numbers for these phase shifts, the self-energy part or polarization interaction $\hat{\Sigma}(\mathbf{r}, \mathbf{r}', \varepsilon)$ must be calculated. It appears that the second-order projectile–target interactions

$$\text{a} \quad \text{b} \quad + \text{exchange terms} \quad (24.47)$$

provide a reasonably good approximation [10, 16, 21].

The expression for $\hat{\Sigma}(\mathbf{r}, \mathbf{r}', \varepsilon)$ simplifies at distances far from the target. Only Eq. (24.47a) contributes in this region, while other terms are exponentially small. Expanding the Coulomb interelectron interactions in Eq. (24.47a) in powers of $r_1'/r_1 \ll 1$, $r_2'/r_2 \ll 1$ gives

$$\Sigma(\mathbf{r}, \mathbf{r}', \varepsilon) = -\delta(\mathbf{r} - \mathbf{r}') \frac{\alpha^{\text{HF}}(0)}{2r^4}, \quad r, r' \rightarrow \infty, \quad (24.48)$$

where $\alpha^{\text{HF}}(0)$ is the static ($\omega = 0$) dipole polarizability determined by Eq. (24.33).

Accounting for each additional interaction between the projectile and target increases the power of r in the denominator of Eq. (24.48). The interaction between target electrons is most important. By including this, the asymptotic expression in Eq. (24.48) is also modified, where instead of $\alpha^{\text{HF}}(0)$, the RPAE polarizability $\alpha^{\text{RPAE}}(0)$ appears. If the target–projectile interelectron interaction is taken into account to second order, as in Eq. (24.47), while all the rest is included exactly, the expression for $\hat{\Sigma}(\mathbf{r}, \mathbf{r}', \varepsilon)$ for $r, r' \rightarrow \infty$ is still given by Eq. (24.48) but with the exact static polarizability.

Many experimental results for low energy electron scattering by noble gases, alkalis, and alkaline earths agree well with the calculations of elastic scattering phase shifts obtained by solving Eq. (24.44) in which $\hat{\Sigma}(\mathbf{r}, \mathbf{r}', \varepsilon)$ is given by Eq. (24.47) with RPAE corrections taken into account. Total cross sections are reproduced with an accuracy as high as several percent, including the Ramsauer minimum region. This is illustrated in Fig. 24.1 for the $e^- + \text{Xe}$ case [16, 23]. This approximation is also reasonably good in describing the angular distributions. As the projectile energy ε increases, the contribution of Eq. (24.47) decreases rapidly.

The simplest amplitude of inelastic electron scattering is represented by the Eq. (24.4b) diagram. Higher-order correc-

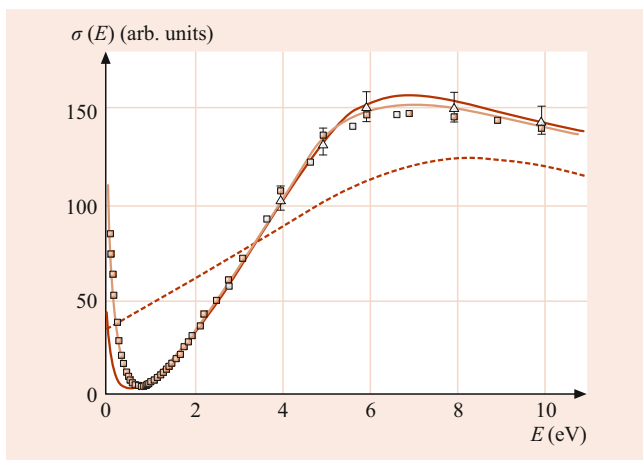


Fig. 24.1 Electron–Xe atom elastic scattering cross section [16]. *Dark solid line*: including polarization interaction; *dashed line*: HF; *light solid line*: experiment

tions to it include additional interaction between electrons and between electrons and the vacancy in the final state, as well as corrections to all electron (vacancy) HF lines, such as Eq. (24.38). If one considers inelastic scattering, the situation becomes more simple, and the process becomes similar to photoionization (Sect. 24.2.6), with the operator of photon–electron interaction being substituted by $\frac{1}{q^2} \cdot \exp^{i\vec{q} \cdot \vec{r}}$, where \vec{q} is the linear momentum transferred from the projectile to target in the collision process [20].

The approach presented here also applies to other incoming particles, such as, for instance, positrons e^+ . The exchange between e^+ and target electrons must be omitted by discarding Eq. (24.6) and all but Eq. (24.47a) terms in the polarization interaction $\hat{\Sigma}(\mathbf{r}, \mathbf{r}', \varepsilon)$. The incoming positron in its intermediate state k' [see Eq. (24.47a)] interacts strongly with the virtually excited electron k'' , forming a positronium-like object. Corresponding diagrams are obtained by inserting elements Eq. (24.4d) for the e^+e^- interaction into Eq. (24.47a). Summation of the infinite sequence of such diagrams corresponds to substituting the product $\phi_{k'}(\mathbf{r}_1)\phi_{k''}(\mathbf{r}_2)$ in the intermediate state of Eq. (24.47a) by the exact e^+e^- wave function in the field of a target with a vacancy j . Such a program is very complicated, and a crude simplification has proven to be satisfactory. Only the positronium (Ps) binding is taken into account by subtracting its binding energy in the denominator of Eq. (24.13). This is equivalent to adding the Ps ionization potential I_{Ps} to ε in Eq. (24.47) [24]. It enhances the polarization interaction and leads to an interesting qualitative feature: the possibility of alteration of the sign of the interaction Eq. (24.47). Indeed, instead of $\alpha(0)$, the corresponding polarization expression Eq. (24.47) for e^+ -atom collision includes $\alpha(I_{Ps})$. For alkalis, the binding energy is less than I_{Ps} , and for the energy region $\omega > I_{Ps}$, the polarizability in Eq. (24.33) is negative, while $\alpha(0) > 0$. This leads to a repulsive polarization inter-

action, rather than the usual attractive one. This difference affects the cross section qualitatively [25].

Another, more complicated, approximation substitutes $\phi_{k'}(\mathbf{r}_1)\phi_{k''}(\mathbf{r}_2)$ by the product of the precise Ps wave function $\psi_{Ps}(|\mathbf{r}_1 - \mathbf{r}_2|)$ and the wave function of the free motion of the Ps center of gravity [26].

According to the diagrams Eq. (24.23), Eq. (24.44) describes the target with an additional electron. If the target is a neutral atom, the solution of Eq. (24.44) with discrete energy values describes negative ion states, both ground and excited ones.

Again, as in Sect. 24.2.2, diagrams Eq. (24.47) with RPAE corrections form a reasonably good starting point for calculating the negative ion binding energies, even in cases when this binding is comparatively small, as in alkaline earth negative ions [27]. The inclusion of only the outer shell polarizability (j is a vacancy in the outer shell) leads to overbinding of the additional electron forming the negative ion. Only the inclusion of screening due to inner shell excitations yields good agreement with experiment. For instance, measurements of Ca^- affinity [28] give about 20 meV, while the calculations without inner shell excitations give about 50 meV [27]. Their inclusion must reduce the theoretical value considerably.

24.2.4 Two-Electron and Two-Vacancy States

One can construct a diagrammatic equation for the wave function of a two-electron or a two-vacancy state by separating all diagrams describing two-electron (two-vacancy) scattering that do not include these states as intermediate, and denoting their total contribution by a circle. Then the exact two-electron (vacancy) state is determined by the infinite sequence of diagrams

$$\begin{aligned}
 \text{Diagram} &= \text{Diagram 1} + \text{Diagram 2} + \text{Diagram 3} + \dots \\
 &= \text{Diagram 4} + \text{Diagram 5} + \text{Diagram 6} + \dots
 \end{aligned}
 \tag{24.49}$$

The analytic equation for two electrons in an atom or any multiatomic system, interacting with each other can be written in the form

$$\begin{aligned}
 &(\hat{H}_1^{\text{HF}} + \hat{\Sigma}_1 + \hat{H}_2^{\text{HF}} + \hat{\Sigma}_2 + \hat{Q}\hat{\Pi}_{12} - \varepsilon) \\
 &\times \psi_{12}(\mathbf{r}_1 \cdot \mathbf{r}_2) = 0.
 \end{aligned}
 \tag{24.50}$$

Here, $\hat{H}_{1(2)}^{\text{HF}}$ is the HF part of the one-particle Hamiltonian in Eq. (24.24), $\hat{\Pi}_{12}$ is the effective interelectron interaction, and \hat{Q} is the projection operator

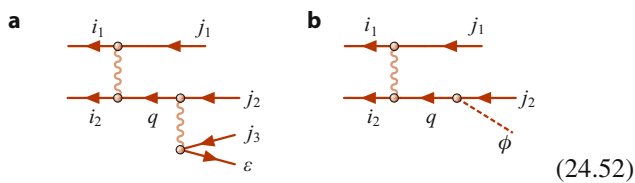
$$\hat{Q} \equiv (1 - n_1)(1 - n_2) - n_1 n_2 = 1 - n_1 - n_2, \quad (24.51)$$

with $n_{1(2)}$ being the Fermi step function, $n_{1(2)} = 1$ for $1(2) \leq F$, and $n_{1(2)} = 0$ for $1(2) > F$. The function $n_{1(2)}$ thus eliminates contributions of vacant states. The operator \hat{Q} takes into account the fact that propagation of two electrons (or, more precisely, quasi electrons due to the presence of $\hat{\Sigma}$) takes place in a system of other particles, which occupy all levels up to the Fermi level. The presence of \hat{Q} makes Eq. (24.50) essentially different from a simple two-electron Schrödinger equation: \hat{Q} requires that after each act of interaction described by $\hat{\Pi}_{12}$, both participants either remain electrons or become vacancies.

Diagrams Eq. (24.49) describe the states of two electrons outside the closed shell core, or electron scattering by an atom with one electron outside the closed shells. In general, $\hat{\Pi}_{12}$ is nonlocal, dependent upon ε , and can have an imaginary part. The lowest-order approximation to $\hat{\Pi}_{12}$ is $V = |\mathbf{r}_1 - \mathbf{r}_2|^{-1}$. Equation (24.50) must be solved in order to obtain, for example, the excitation spectrum of two electrons in atoms with two electrons outside closed subshells, such as Ca. Instead of V , the interaction Γ from Eq. (24.31) can be used, which would account for screening due to virtual excitation of inner shell electrons. For low-level two-electron excitations, the energy dependence of $\hat{\Pi}_{12}$ can be neglected.

The same type of equation can be obtained for two-vacancy states, describing their energies, decay widths, and structure due to configuration mixing with more complex states. For inner and intermediate shell vacancies in atoms, however, the corresponding corrections can be taken into account perturbatively, and the screening by outer shells is not essential. The admixture of outer shell excitation with inner vacancies is important, leading to so-called satellites of the main spectral lines.

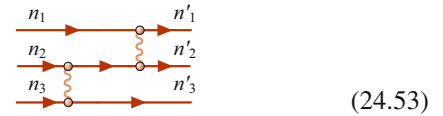
The interaction between vacancies leads to correlated two-vacancy decay processes in which the energy is carried away by a single electron or photon. Some diagrams exemplifying these processes in the lowest possible order of interaction are



Even in this order, there are several diagrams that together give the amplitude of the correlation Auger Eq. (24.52a) and

radiative Eq. (24.52b) decay rates. For inner shells, a specific feature of such processes is that the released energy is about twice that for a single vacancy decay. Of course, in these cases, the decay probability is relatively small. It is not, however, necessarily much smaller than that of individual vacancies if the energies of the intermediate and initial states are close to each other.

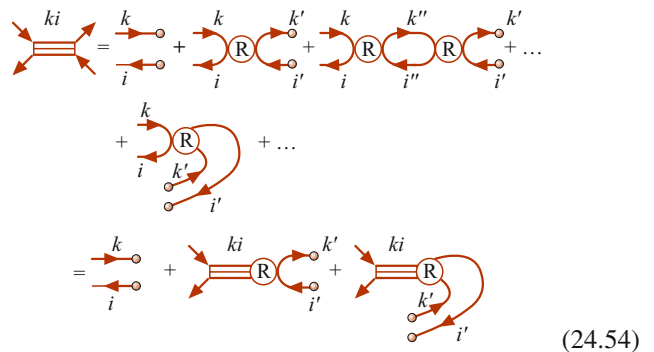
The presence of residual two-body forces leads to effective multiparticle interactions. The simplest diagram presenting a three-electron interaction is given by



The role of multiparticle interactions in the atomic structure is far from being clear. Diagrams similar to Eq. (24.53) are important if it is of interest to calculate the energy levels of atoms with three or more electrons (or vacancies) outside of closed shells. This is a very complicated calculation because even two electrons in the Coulomb field of the nucleus are a difficult three-body problem.

24.2.5 Electron–Vacancy States

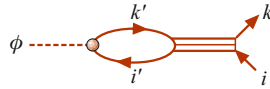
The one-electron–one-vacancy state is the simplest excitation of a closed shell system under the action of an external time-dependent field, represented by Eq. (24.2a). Beginning with the electrons and vacancies described in the HF approximation, the result of residual interactions leads to excitations of more complex states, including those with two or more electron–vacancy pairs. The interaction can also lead to a single electron–vacancy pair. Let us concentrate on the latter case and separate all diagrams describing electron–vacancy interaction that do not include these states as intermediate and denote them by a circle. Then the exact electron–vacancy state is determined by the infinite sequence of diagrams



Contrary to the electron–electron case in Sect. 24.2.4, the analytical expression corresponding to Eq. (24.54) cannot be

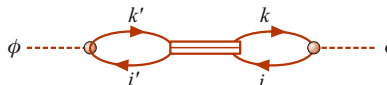
represented as a Schrödinger-type equation. Indeed, being symmetric under time reversal, Eq. (24.54) leads to an equation depending, unlike Eq. (24.50), upon the second power of the electron–vacancy energy ω . Note that R in Eq. (24.54) and \hat{T} in Eq. (24.49) are different.

It is necessary to solve Eq. (24.54) when calculating the photoabsorption amplitude, which can then be represented as



$$(24.55)$$

The amplitude for elastic photon scattering is also expressed via the exact electron–vacancy state, determined by (24.54) to be



$$(24.56)$$

The other case where it is necessary to solve Eq. (24.54) is the scattering of electrons, both elastic and inelastic, by atoms with a vacancy in their outer shell, such as halogens.

The simplest approximation to R is given by the Coulomb interaction to lowest order Eqs. (24.4e) and (24.4f). With such R , the sequence of diagrams Eq. (24.54) is the same as Eq. (24.31) and, thus, forms the RPAE, which is often used to describe photoionization and other atomic processes [15, 16]. Both terms Eqs. (24.4e) and (24.4f) contribute to the electron–vacancy in Eq. (24.54) only if the external field is spin independent, such as an ordinary photon. For a magnetic interaction, which is proportional to spin, the term Eq. (24.4e) does not contribute.

24.2.6 Photoionization in RPAE and Beyond

In RPAE, the photoionization amplitude $\langle k|D(\omega)|i\rangle$ is determined by solving an integral equation obtained from Eqs. (24.54) and (24.55) using the correspondence rule Eq. (24.14) [15, 16]

$$\begin{aligned} \langle k|D(\omega)|i\rangle &= \langle k|d|i\rangle \\ &+ \sum_{k'>F; i'\leq F} \left(\frac{\langle k'|D(\omega)|i'\rangle \langle ki'|V|ik' - k'i\rangle}{\omega - \varepsilon_{k'} + \varepsilon_{i'} + i\eta} \right. \\ &\quad \left. - \frac{\langle i'|D(\omega)|k'\rangle \langle kk'|V|ii' - i'i\rangle}{\omega + \varepsilon_{k'} - \varepsilon_{i'} - i\eta} \right), \end{aligned} \quad (24.57)$$

where d is the dipole operator describing the photon–electron interaction, and $V = |\mathbf{r}_1 - \mathbf{r}_2|^{-1}$. To obtain the RPAE photoionization cross section, the usual expression

in Eq. (24.19) must be multiplied by the square modulus of the ratio $\langle k|D(\omega)|i\rangle/\langle k|d|i\rangle$, with $\omega = \varepsilon_k + I_i$. The RPAE corrections described by the term in round brackets in Eq. (24.57) are very large for outer and intermediate electron shells. Through the sum over i' , if only terms with the same energies $\varepsilon_{i'} = \varepsilon_i$ are included, Eq. (24.57) accounts for intrashell correlations. By adding terms with $\varepsilon_{i'} \neq \varepsilon_i$, the effect of intershell correlations is taken into account.

One can obtain the radiative width in RPAE $\gamma_i^{(y)RPAE}$ from Eq. (24.41), substituting $\langle i|d|j\rangle$ by $\langle i|D(\omega_{ji})|j\rangle$.

For atoms, Eq. (24.57) has to be solved numerically but can be presented in a symbolical operator form that creates the possibility of qualitative analyses of its solutions

$$D(\omega) = d + D(\omega)\chi(\omega)U, \quad (24.58)$$

where U is a combination of the direct V_d and exchange V_e Coulomb interelectron potentials, $U = V_d - V_e$, $\chi(\omega) = \chi_1(\omega) + \chi_2(\omega)$, $\chi_1(\omega) = 1/(\omega - \omega' + i\eta)$, and $\chi_2(\omega) = -1/(\omega + \omega')$, with ω' being the excitation energy of the virtual electron–vacancy state. Thus, $\chi(\omega) = 2\omega'/(\omega^2 - \omega'^2 + i\eta)$. Using Γ from Eq. (24.31), one can present $D(\omega)$ as

$$D(\omega) = d + d\chi(\omega)\Gamma(\omega). \quad (24.59)$$

Equation (24.58) allows a rather simple, also symbolic, solution

$$D(\omega) = d/[1 - \chi(\omega)U]. \quad (24.60)$$

If the denominator in Eq. (24.60) has a solution Ω determined by the equation

$$1 - \chi(\Omega)U = 0, \quad (24.61)$$

at $\Omega > I$, where I is the atomic ionization potential, $\chi(\Omega) > 0$, then the cross section has a powerful maximum called a giant resonance with energy Ω .

A giant resonance is of collective nature in the sense that it appears to be due to coherent virtual excitation of all electrons of at least one considered multielectron subshell.

These intrashell correlations are most important for multielectron shells with large photoionization cross sections. Their inclusion leads to a quantitative description of the above-mentioned giant resonances – huge maxima in the photoionization cross sections. An example is the $4d^{10}$ photoionization cross section of Xe shown in Fig. 24.2 [16], where satisfactory agreement with experiment is demonstrated. In [16], one can find a number of examples of other Giant resonances.

It appears that all RPAE intrashell time-forward diagrams, such as that on the first line in Eq. (24.54), and the first term in brackets in Eq. (24.57) with $\varepsilon_{i'} = \varepsilon_i$, may be taken into account by the matrix element $\langle \tilde{k}|d|i\rangle$. This is the

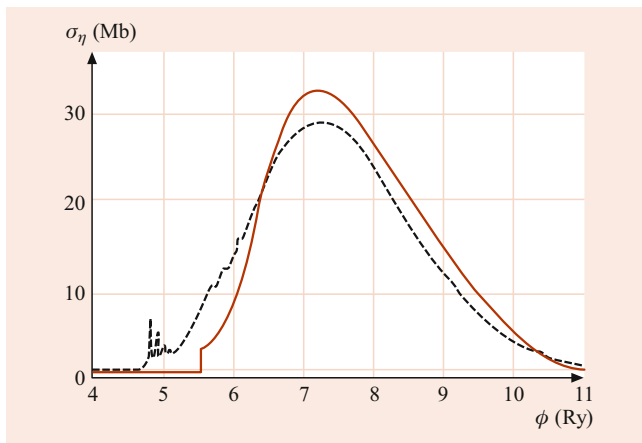


Fig. 24.2 Photoabsorption in the vicinity of the $4d^{10}$ subshell threshold in Xe [8]. Solid line: RPAE; dashed line: experiment

one-electron approximation but with the function $\tilde{\phi}_k(r)$ calculated in the term-dependent HF approximation [15–18]. Term-dependency means that only the total angular momentum and spin and their projections for the electron–vacancy pair are conserved, being equal to that of the incoming photon. The individual values for the electron and vacancy angular momentum and spin are not considered to be good quantum numbers. Thus, the term-dependent HF includes a large fraction of RPAE correlations.

RPAE allows the calculation of interference resonances. To describe them, let us consider a situation in which the direct HF amplitude d_s is small, while there are other electrons with large photoionization amplitude D_b , $D_b(\omega) \gg d_s$. Then, from Eq. (24.58) one has

$$\begin{aligned} D_s(\omega) &\approx d_s + D_b(\omega)\chi(\omega)U_{bs} \\ &\approx D_b(\omega)\chi(\omega)U_{bs} \gg d_s, \end{aligned} \quad (24.62)$$

if the intertransition interaction U_{bs} is not too small. The enhancement of the photoionization amplitude described by Eq. (24.62) manifests itself as a resonance in the partial cross section of s electrons photoionization. Very often, the term $D_b(\omega)\chi(\omega)U_{bs}$ and d_s are of opposite sign, so that the total amplitude acquires two minima, along with an extra maximum, thus forming a rather complicated structure in the partial cross section, which was named *interference* or *correlation* resonance.

Usually, these resonances are manifestations of intershell correlations. These are taken into account if the sum over i' in Eq. (24.57) includes terms with $\varepsilon_{i'} \neq \varepsilon_i$. An example is the $5s^2$ subshell in Xe, which is strongly affected by the outer $5p^6$ and inner $4d^{10}$ neighboring electrons. Due to this interaction, the $5s^2$ cross section is completely altered, as illustrated in Fig. 24.3 [15, 16]. The RPAE results predict a qualitative feature of the experimental data, namely the formation of a maximum and two minima in the cross section. The second

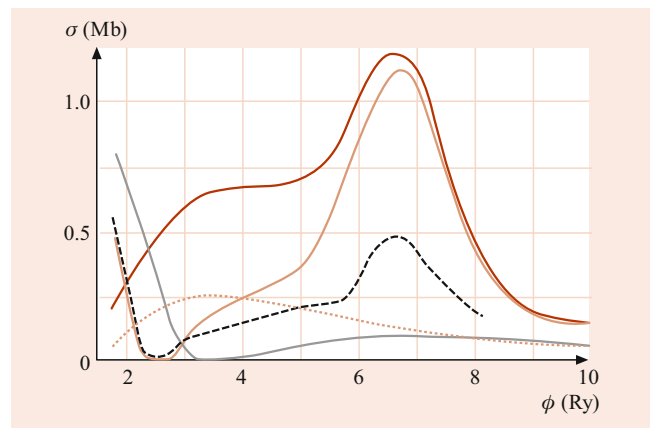


Fig. 24.3 Photoionization of $5s^2$ electrons in Xe [8]. light brown solid line: RPAE with effects of $5p^6$ and $4d^{10}$ included; dotted line: $5s^2$ electrons only; grey solid line: with effect of $5p^6$ electrons; dark brown solid line: with effect of $4d^{10}$ electrons; black dashed line: experiment

minimum is not seen in Fig. 24.3, since it lies at considerably higher ω .

RPAE is able to describe a number of other effects, such as *giant autoionization* resonance (decay of a powerful discrete excitation into a continuum, with which the excitation interacts strongly), *continuous spectrum autoionization* (modification of a broad continuous spectrum excitation due to its strong interaction with a narrow continuum that occurs in negative ions [27]), and *quadrupole giant resonances* [29].

Above we concentrated on dipole giant resonances. Quadrupole amplitudes in RPAE are determined by an equation similar to Eq. (24.58):

$$Q(\omega) = q + Q(\omega)\chi(\omega)U, \quad (24.63)$$

where q is the quadrupole amplitude in HF approximation.

Giant quadrupole resonance was found in excitations of $4d^6$ electrons in Xe [30]. Its direct observation in photoabsorption is almost impossible, since the corresponding cross section is very small due to the inclusion of the extra factor $\alpha^2 = 1/c^2 \approx 10^{-4}$ as compared to the dipole cross section. However, the quadrupole amplitude leads to noticeable corrections to the angular distributions of photoelectrons where their relative contribution is considerably bigger [16].

Note that the amplitude of electron elastic scattering on an atom with a vacancy is expressed in RPAE via Γ given by Eq. (24.31) [31].

For the inner or deep intermediate shells, RPAE proves to be insufficient. First, screening of the Coulomb interaction between the outgoing or virtually excited electron and the vacancy [see Eq. (24.4f)] must be taken into account. This can be done by replacing V with Γ from Eq. (24.31). The ionization potential (or the energy of the vacancy i) must also be corrected, which requires inclusion of at least the contribution from the first term of Eq. (24.38). It has been demon-

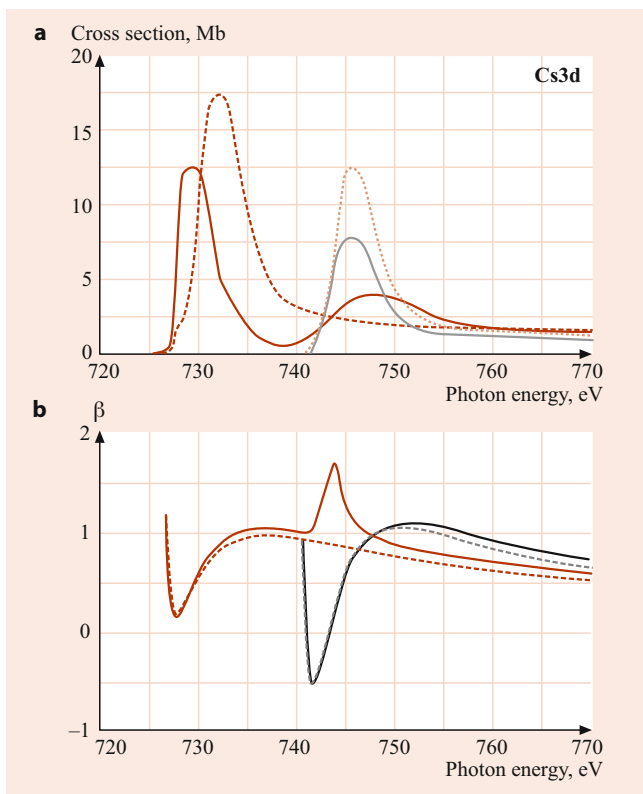


Fig. 24.4 Intradoublet resonance in $3d^{10}$ Cs. (a) Partial photoionization cross sections $\sigma_{5/2}$ (left peaks) and $\sigma_{3/2}$ (right peaks) [33]. Dashed curves represent the HF approximation. (b) Dipole angular anisotropy parameters $\beta_{5/2}$ and $\beta_{3/2}$. Solid red line: data for 5/2 with account of 3/2; dashed red line: data for 5/2 without account of 3/2; solid black line: data for 3/2 with account of 5/2; dashed black line: data for 3/2 without account of 5/2

strated [32] that the screening of the electron–vacancy interaction can be taken into account by calculating the wave function of the virtually excited or outgoing electron in the self-consistent HF field of an ion instead of that of a neutral atom. A method that uses only these one-particle wave functions in Eqs. (24.55) and (24.57) is called the generalized RPAE or GRPAE [16]. The use of this approximation improves the agreement with experiment near the intermediate shell thresholds considerably, decreasing the cross section value there and shifting its maximum to higher energies. GRPAE reveals *intradoublet resonances* that result from the interaction of electrons belonging to two components of the spin–orbit doublet, e.g., $3d_{3/2}$ and $3d_{5/2}$ in Xe, Cs, and Ba atoms [29, 33].

RPAE and GRPAE corrections do not only affect the cross sections but also the characteristics of the photoelectron angular distribution, i.e., dipole and nondipole angular anisotropy parameters [15, 21, 29]. As an example, Fig. 24.4a presents the partial cross sections [33], while Fig. 24.4b depicts the dipole anisotropy parameter β [29] for $3d_{5/2}$ and $3d_{3/2}$ electrons in Cs. The effect of intradoublet resonance – an additional maximum in the $3d_{5/2}$ cross section under the action of $3d_{3/2}$ electrons – can be seen clearly.

Figure 24.5 depicts the nondipole angular anisotropy parameter γ_{5s} for 5s electrons in Xe [34]. The parameter γ_{ns} (in Fig. 24.5, $n = 5$) is given by the simple formula [21]

$$\gamma_{ns}(\omega) = 6[|Q_{ns}(\omega)|/|D_{ns}(\omega)|] \cos(\Delta_q - \Delta_d), \quad (24.64)$$

where $Q_{ns}(D_{ns})$ are the RPAE (GRPAE) quadrupole (dipole) photoionization amplitudes, and $\Delta_q(\Delta_d)$ are their phases. Thus, $\gamma_{ns}(\omega)$ is sensitive to the presence of interference, dipole, and quadrupole resonances. The latter is presented by a small but noticeable maximum on the high energy slope of the huge maximum, caused by the presence of the giant dipole resonance. The variation of γ_{5s} near the 5s threshold is determined by the resonant behavior of $\cos(\Delta_q - \Delta_d)$, called *phase resonance* [29].

Close to inner shell thresholds, the Auger decay of a deep vacancy must be taken into account. Due to decay, the photoelectron instantly finds itself in the field of at least two vacancies instead of one, leading to considerable growth of the threshold cross section. Diagrammatically, the effect of decay may be described by

$$(24.65)$$

Here, the double line emphasizes that starting from the moment of decay; the photoelectron moves in the field $j_1 j_2$ of a double instead of a single i vacancy. For inner vacancies, this is a strong effect, which can lead even to recapture of the photoelectron into some of the discrete levels in the field of the double vacancy $j_1 j_2$. The instant change of the outgoing electron wave function due to rapid vacancy decay is called *postcollision*.

This effect in photoionization can be taken into account by the diagram Eq. (24.65) when the Auger electron is much faster than the photoelectron [35]. If their speed is of the same order, their mutual Coulomb repulsion must be accounted for, leading to additional alteration of energy and angular redistributions.

A photoelectron can excite or knock out another atomic electron. To lowest order in the residual interelectron interaction, this process can be represented by the diagrams Eqs. (24.66) and (24.67)

$$(24.66)$$

While the formation of an initial electron–vacancy ki_1 pair requires RPAE or GRPAE for its description, the sec-

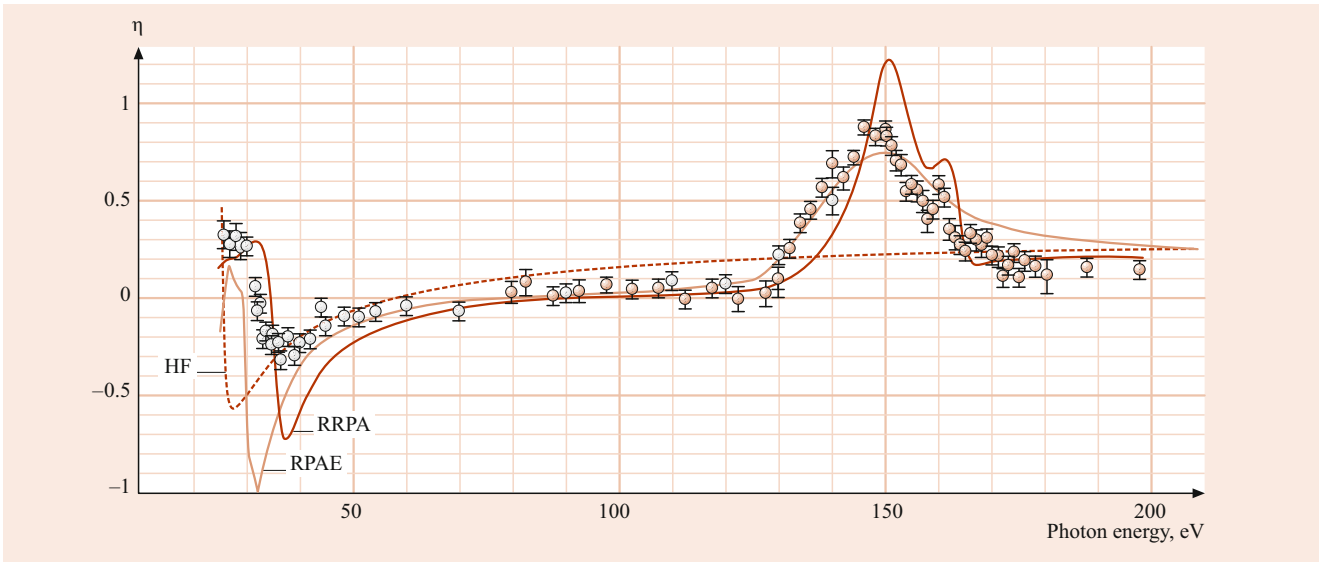
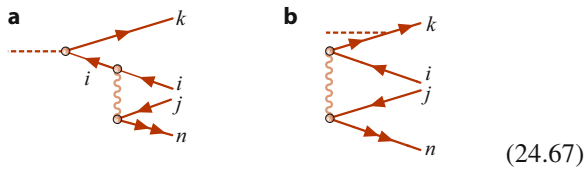


Fig. 24.5 Nondipole anisotropy parameter $\gamma_{5s}(\omega)$ of $5s^2$ electrons in Xe [34]

ond step of Eq. (24.66a) can be reproduced reasonably well by the lowest-order term in V . It appears that process Eq. (24.66a) has a high probability of not too fast photoelectrons, changing the cross section [36] considerably for ionization by creating a vacancy i_1 . Comparatively simple diagrams



describe the photoionization process in which a more complicated state is created in the ion than a single vacancy, e.g., a state with two vacancies and one electron. Here, the double arrow indicates that the electron is in a discrete level n .

If one considers cases when n also belongs to a continuous spectrum, the diagrams (Eqs. (24.65)–(24.67)) present in the lowest order the amplitude of two-electron–one-photon ionization. Usually, the contribution of this process to the total photon absorption cross section is small, but it contains very important information on the role of interelectron correlations in atoms.

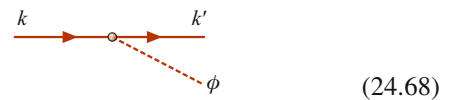
Diagrams (Eqs. (24.65)–(24.67)) present some corrections that mix electron–vacancy and two-electron–two-vacancy configurations. Each additional interaction line increases the number of possible physical processes considerably. With the growth of the number of particles actively participating in a process, the calculational difficulties increase enormously. However, this is not a shortcoming of the diagrammatic approach but a specific feature of more and more complex physical processes.

Most prominent are multielectron effects in photoionization of outer and intermediate subshells and close to the inner thresholds of intermediate and heavy atoms. However, even at very high, although nonrelativistic, energies, the role of correlations is important. For example, the ionization probability for a dipole satellite to a $l > 0$ level decreases with the photon energy; ω grows as $\approx \omega^{-7/2}$, which is much slower than for the main line itself: $\approx \omega^{-7/2-l}$. Correlations alter the asymptotic behavior of the cross section of all subshells with $l > 1$ that acquire a universal behavior $\approx \omega^{-9/2}$ instead of the HF value $\approx \omega^{-7/2-l}$ [37].

Note that inelastic scattering of any fast charge particle can be studied and described as mentioned above, similarly to photoionization if one substitutes the dipole operator d in Eq. (24.57) for $4\pi \exp(i\mathbf{q}\mathbf{r})/q^2$, where q is the momentum transferred from the projectile to the target [20]. Fast particle scattering as a tool to study a target’s structure has some advantages as compared to photoionization [38].

24.2.7 Photon Emission and Bremsstrahlung

The amplitude of photon emission in lowest order is given by the time-reversal of Eq. (24.2c):



This diagram represents ordinary Bremsstrahlung, i.e., a photon emission in the process of projectile deceleration in the field of the target. If the target has an internal structure like atoms, it can be really or virtually excited during the collision process. The simplest excitation means the creation of

an electron–vacancy pair. The annihilation of this pair results via the time-reversal of Eq. (24.2a) in photon emission. The process thus looks like

$$(24.69)$$

To obtain the total Bremsstrahlung amplitude, the terms in Eqs. (24.68) and (24.69) must be summed. The *polarization radiation* (PR) created by the mechanism Eq. (24.69) has a number of features that are different from the ordinary Bremsstrahlung (OB) represented by Eq. (24.68). The intensity is proportional to $1/M_p^2$ for OB, where M_p is the projectile mass, and the spectrum, at least for high ε_k , is proportional to $1/\omega$. On the other hand, the PR intensity is almost completely independent of M_p , and its frequency dependence is quite complex, being determined by the target polarizability $\alpha(\omega)$ [39]. PR is most important for frequencies ω of the order of and higher than the target's ionization potential. At sufficiently large distances and for neutral targets, PR starts to predominate over OB. Close to discrete excitations of the k' electron, the contribution Eq. (24.69) becomes resonantly enhanced.

Higher-order corrections are important in the PR amplitude. First, the Coulomb interaction V in Eq. (24.69) must be replaced by Γ from Eq. (24.31).

The analytical expression for the total Bremsstrahlung amplitude, including RPAE corrections to Eq. (24.69), is given by the expression

$$\begin{aligned} & \langle k|A(\omega)|k' \rangle \\ &= \langle k|d|k' \rangle + \sum_{k''>F; i \leq F} \langle ki|V|k'k'' \rangle \\ & \times \lim_{\eta \rightarrow +0} \frac{2(\varepsilon_{k''} - \varepsilon_i)}{\omega^2 - (\varepsilon_{k''} - \varepsilon_i)^2 + i\omega\eta} \langle i|D(\omega)|k'' \rangle. \end{aligned} \quad (24.70)$$

To derive the Bremsstrahlung spectrum, the usual general expression must be multiplied by the square modulus of the ratio $\langle k|A(\omega)|k' \rangle / \langle k|d|k' \rangle$. If the incoming electron is slow, corrections Eq. (24.47) also become important. The intermediate state in Eq. (24.47a) includes two electrons k' and k , and a vacancy i . The extent of the interaction between them could be considerable.

An important feature of PR is that it is nonzero even if the projectile is neutral but is able to polarize the target. For example, it leads to emission of continuous spectrum radiation in atom–atom collisions, whose intensity for frequencies of the order of the ionization potentials is close to that in electron–atom collisions.

The second and higher orders in the residual interaction involve processes that are more complicated than

Eq. (24.69), for instance those that include simultaneous photon emission and target excitation (ionization) [40, 41]. More general mechanisms of PR, other than those depicted in Eq. (24.69), are discussed in [42].

24.2.8 RPAE in the Magnetic Channel

Above, we considered the absorption and emission of pure electric photons that do not interact with the spin of electrons. So, the total spin of excitation is $S = 0$. Of interest is RPAE in the magnetic channel with $S = 1$. The respective channels do not mix if the spin of an electron (vacancy) in the system under consideration is a good quantum number. The $\text{RPAE}_{S=1}$ is obtained from Eq. (24.57) by the contribution of direct terms in the V matrix element only Eq. (24.4f) and discarding Eq. (24.4e). Thus, the $\text{RPAE}_{S=1}$ amplitude $\langle k|\mathbf{H}(\omega)|i \rangle$ is determined by the following equation

$$\begin{aligned} & \langle k|\mathbf{H}(\omega)|i \rangle \\ &= \langle k|\boldsymbol{\sigma}|i \rangle \\ & - \sum_{k'>F; i' \leq F} \left(\frac{\langle k'|\mathbf{H}(\omega)|i' \rangle \langle ki'|V|k'i \rangle}{\omega - \varepsilon_{k'} + \varepsilon_{i'} + i\eta} \right. \\ & \left. - \frac{\langle i'|\mathbf{H}(\omega)|k' \rangle \langle kk'|V|i'i \rangle}{\omega - \varepsilon_{k'} - \varepsilon_{i'} - i\eta} \right), \end{aligned} \quad (24.71)$$

where $\boldsymbol{\sigma}$ is the operator describing the interaction of an electron with the magnetic field. Just like Eq. (24.57), this equation can be presented in a symbolical operator form that creates the possibility of qualitative analyses of its solutions:

$$\mathbf{H}(\omega) = \vec{\boldsymbol{\sigma}} + \mathbf{H}(\omega)\chi(\omega)V_e, \quad (24.72)$$

where V_e is the exchange Coulomb interelectron potential Eq. (24.4f), $\chi(\omega) = \chi_1(\omega) + \chi_2(\omega)$, $\chi_1(\omega) = 1/(\omega - \omega' + i\eta)$, and $\chi_2(\omega) = 1/(\omega + \omega')$, with ω' being the excitation energy of the virtual electron–vacancy state in the $S = 1$ channel. Equation (24.72) allows a rather simple, also symbolic, solution

$$\mathbf{H}(\omega) = \vec{\boldsymbol{\sigma}} / [1 + \chi(\omega)V_e]. \quad (24.73)$$

Here, $\chi(\omega) = 2\omega'/(\omega^2 - \omega'^2)$. For $\omega < I_1$, where I_1 is the lowest possible excitation energy in the system under consideration, $\chi(\omega) < 0$, and according Eq. (24.73), the magnetic excitation enhances. If $[1 + \chi(0)V_e] < 0$, the system under consideration undergoes a phase transition, since $S = 1$ electron–vacancy pair creation proceeds without a supply of external energy. This is why open subshell systems have the maximum possible, compatible to the Pauli principle, spin, i.e., they obey the so-called Hund rule.

24.2.9 Consideration of “Big Atoms”

The theory presented can be applied to any many-body system. However, each object has some specific features. In the previous sections of this chapter, we concentrated on atoms. In addressing molecules, clusters, fullerenes, and endohedrals one can use two approaches. The first is “brutal force” or the first-principle approach. This approach employs the technique presented above where the action of all nuclei upon electrons is described by the potential $U(r)$

$$U(r) = - \sum_{\text{All nuclei } i} \frac{Z_i}{|r - \mathbf{R}_i|}, \quad (24.74)$$

where \mathbf{R}_i is the location of the i -th nucleus. One-electron wave functions must be calculated using the Eq. (24.74) expression for U instead of $-Z/r$, as in Eq. (24.57). Then all the techniques presented above can be applied directly. However, this is a difficult approach that requires solution of three-dimensional multicenter equations. For all but the simplest molecules, this approach is beyond the capabilities of modern computers. Simplifications are necessary to decrease the computational complexity for properties and processes in multiatomic formations.

However, the so-called “big atom” [12] or endohedral, which is a fullerene C_N stuffed by an atom A (denoted as $A@C_N$), permits essential simplification, making them only a little bit more complex than ordinary atoms. As one can read in a number of sources (e.g., [13]), a potential that acts upon an electron in an endohedral can be taken into account by adding to Eq. (24.57) $U_F(r)$, which is, e.g., a square well of depth U_0 , radius R_F , and width b . This allows one to describe *confinement resonances*, which are manifestations of resonances in reflection of the photoelectron wave by $U_F(r)$. This reflection strongly affects the encapsulated atom photoionization cross section. The Giant resonance of Xe 4d¹⁰ subshell, when Xe is caged in fullerene C_{60} , serves as an example. As a result the curve Fig. 24.2 is completely modified, as can be seen in Fig. 24.6 [43].

The fullerene electron shell is an object with a big polarizability [16]. This polarizability affects photon absorption in the polarizability maximum region. The treatment is essentially simplified in many cases, when, with good accuracy, one can consider $R_F \gg b$ and $R_F \gg r_a$, where r_a is the atom’s A radius. The effects of the static fullerene shell potential and its polarizability lead to *giant endohedral resonances*, prominent maxima in the inner atom photoionization cross section. This effect is illustrated by the cross section of the 5p subshell of endohedral Xe@ C_{60} depicted in Fig. 24.7 [44, 45].

The presence of a fullerene shell in $A@C_{60}$ opens up a number of new channels in endohedral processes as com-

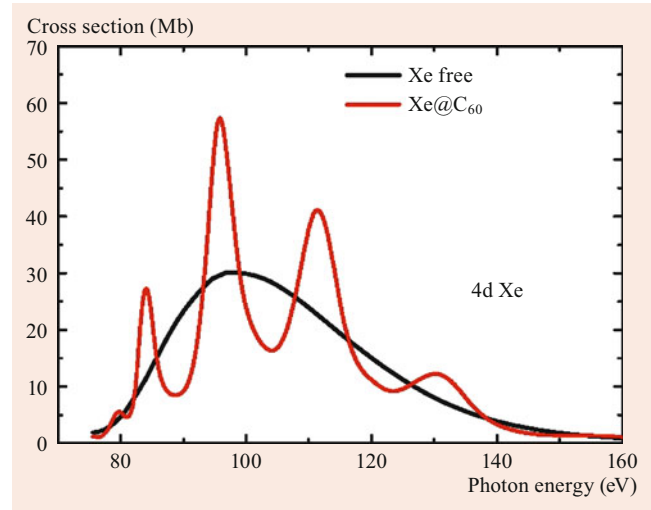


Fig. 24.6 Photoionization cross section of 4d-electrons for the Xe free atom and Xe@ C_{60} in RPAE

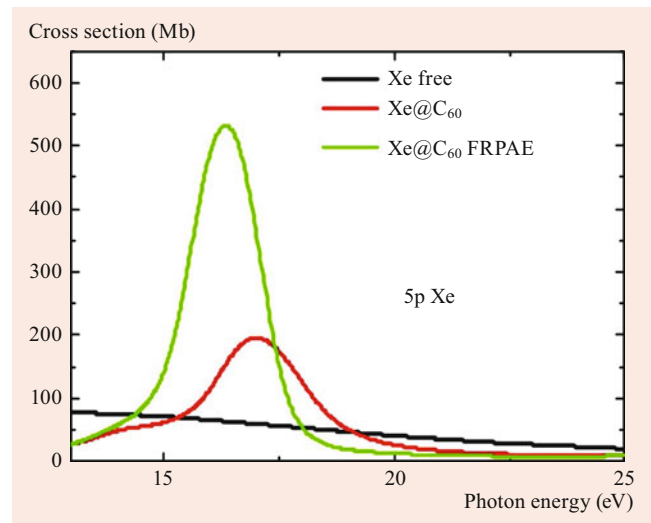


Fig. 24.7 Photoionization cross section of 5p-electrons for the Xe free atom in RPAE and Xe@ C_{60} in RPAE and with account of fullerene shell polarization – FRPAE

pared to the atomic ones, e.g., in multielectron ionization and vacancy decay. In both of these channels, the interaction between atomic and fullerenes’ electrons is important. For example, the subvalent vacancies in noble gases decay only radiatively, since the decay energy is smaller than the outer electrons’ ionization potential. The presence of fullerenes’ electrons opens the Auger decay channel for subvalent vacancy [16, 38],

$$\gamma_{if}^{(A)A@C_N} = \gamma^{(\gamma)A} \frac{3}{8\pi} \left(\frac{c}{\omega_{if}} \right)^4 \frac{\sigma_{C_N}(\omega_{if})}{R_F^6}, \quad (24.75)$$

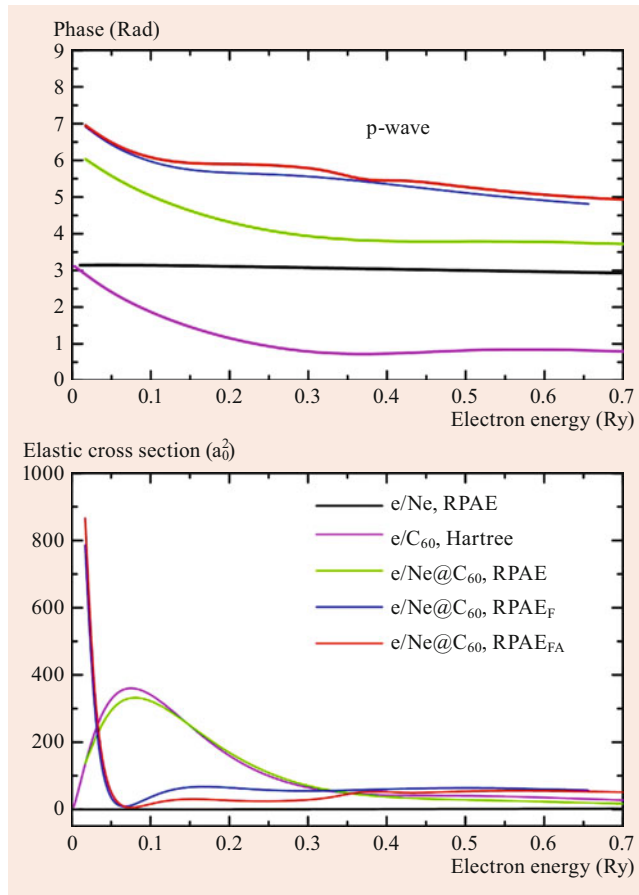


Fig. 24.8 Phases and cross sections of the p-wave contribution in electron collisions with $\text{Ne}@C_{60}$. Index F marks the inclusion of fullerenes' polarization potential, while FA denotes the mutual influence of Ne and C_{60} polarizations

where $\gamma_{if}^{(A)A@C_N}$ is the width of the noble gas endohedral subvalent i vacancy decay via electron transition $i \rightarrow j$ into the outer shell vacancy j , c is the speed of light, $\gamma^{(\gamma)A}$ is the pure atomic radiative decay probability, and $\sigma_{C_N}(\omega_{if})$ is the endohedrals photoionization cross section at frequency ω_{if} . The width in Eq. (24.75) increases by four to six orders of magnitude, as compared to $\gamma^{(\gamma)A}$.

The presence of A in $A@C_{60}$ strongly alters the low-energy $e^- + A@C_{60}$ cross section as compared to that of $e^- + C_{60}$, in spite of the fact that fullerene C_{60} is much bigger than the atom A . The quantum mechanical nature of this process is also reflected in a multitude of scattering resonances, maxima, and minima, including Ramsauer minimum in higher than $l = 0$ scattering waves, which is exemplified by Fig. 24.8 [46]. Of interest is the scattering $e^+ + A@C_{60}$ that differs from $e^- + A@C_{60}$ not only due to the lack of exchange but also due to effects of target polarization, which are different for $e^- + A@C_{60}$ and $e^+ + A@C_{60}$ processes [47].

24.3 Concluding Remarks

It is most convenient to apply diagrammatic techniques to closed shell objects whose ground state is nondegenerate. Degeneracy means that some of the energy denominators in Eq. (24.13) become zero with nonzero statistical weight. All such contributions must be summed to eliminate this degeneracy. This leads to strong mixing of some states. For example, the energy required for electron–vacancy transitions jn [see Eq. (24.38)] within an open shell is zero, thus leading to strong mixing of i and ijn states. If a pair with zero excitation energy has nonzero angular momentum, taking into account the mixing within such a pair destroys angular momentum as a characteristic of a one-vacancy state. This makes all calculations much more complicated, reflecting a specific feature of the degenerate physical system.

In using the diagrams and formulas presented above, it is essential that the interelectron and electron–nucleus interactions be purely potential. Inclusion of retardation and spin-dependence in the interparticle interaction makes the calculations much more complicated. These parts of the interaction appear as relativistic corrections. They are comparatively small in all but the heaviest atoms and can be taken into account perturbatively. Beyond lowest order, these additional interactions are strongly altered when virtual excitations of electron–vacancy pairs and the Coulomb interaction between them is taken into account. An example is given by the sequence of diagrams

The diagram shows a sequence of four terms representing different interaction paths. The first term is a simple scattering process with incoming momenta k_1 and k_2 and outgoing momenta k'_1 and k'_2 . The second term shows a loop interaction between the two particles. The third and fourth terms show more complex multi-loop interactions involving spin-dependent interactions (represented by heavy dashed lines) and electron–vacancy loops. The sequence is labeled (24.76).

where the heavy dashed line stands for the spin-dependent interelectron interaction. Note that here there are no electron–vacancy loops as in Eq. (24.38) because the Coulomb interaction is unable to affect the electron spin and thus to transfer spin excitations.

The same kind of diagrams describe the one-particle field acting upon an electron or vacancy due to the presence of spin–orbit interaction or weak interaction between electrons and the nucleus. For instance, the effective weak potential includes contributions from the sequence

The diagram shows a sequence of three terms representing interactions with a one-particle field. The first term is a simple scattering process with incoming momenta k_1 and k and outgoing momenta k' and k . The second and third terms show interactions with a field W_i (represented by a cross in a box) and include electron–vacancy loops. The sequence is labeled (24.77).

This is another example demonstrating how flexible and convenient the many-body approach is for considering different processes and interactions.

References

1. Feynman, R.P.: Quantum Electrodynamics. Benjamin, New York (1961)
2. Bethe, H.A., Goldstone, J.: Proc. R. Soc. Lond. A **238**, 551 (1957)
3. Mattuck, R.D.: A Guide to Feynman Diagrams in the Many-Body Problem, 2nd edn. Dover Books on Physics. (2012)
4. Kelly, H.P.: In: Brueckner, K.A. (ed.) Advances in Theoretical Physics, vol. 2, pp. 75–169. Academic Press, New York (1968)
5. Amusia, M.Y.: Many-Body Effects in Electron Atomic Shells. A. F. Ioffe Physical-Technical Institute Publications, Leningrad, pp 1–144 (1968). in Russian
6. Amusia, M.Y.: X-Ray and inner-shell processes. In: Johnson, R.L., Schmidt-Böking, H., Sonntag, B.F. (eds.) AIP Conf. Proc., vol. 389, pp. 415–430. AIP Press, Woodbury (1997)
7. Amusia, M.Y., Connerade, J.-P.: Rep. Prog. Phys. **63**, 41 (2000)
8. Amusia, M.Y.: Phys. Essays **13**, 444 (2000)
9. Amusia, M.Y.: In: Konjevich, N., Petrovich, Z.L., Malovich, G. (eds.) The Physics of Ionized Gases, pp. 19–40. Institute of Physics, Belgrade (2001)
10. Cherepkov, N.A., Semenov, S.K., Hikosaka, Y., Ito, K., Motoki, S., Yagishita, A.: Phys. Rev. Lett. **84**, 250 (2000)
11. Ipatov, A.N., Ivanov, V.K., Agap'ev, B.D., Ekaradt, W.: J. Phys. B At. Mol. Opt. Phys. **31**, 925 (1998)
12. Amusia, M.Y.: Chem. Phys. **414**, 168 (2013)
13. Dolmatov, V.K.: Photoionization of atoms encaged in spherical fullerenes. Adv. Quantum Chem. **58**, 13–68 (2009)
14. March, N.H., Young, W.H., Sampanthar, S.: The Many-Body Problem in Quantum Mechanics. Cambridge Univ. Press, Cambridge (1967)
15. Amusia, M.Y.: Atomic Photoeffect. Plenum Press, New York (1990)
16. Amusia, M.Y., Chernysheva, L.V., Yarzhevsky, V.G.: Handbook of Theoretical Atomic Physics, Data for Photon Absorption, Electron Scattering, Vacancies Decay. Springer, Berlin (2012)
17. Amusia, M.Y., Chernysheva, L.V.: Computation of Atomic Processes. Institute of Physics Publishing, Bristol-Philadelphia (1997)
18. Amusia, M.Y., Semenov, S.K., Chernysheva, L.V.: ATOM-M Algorithms and Programs for Investigation of Atomic and Molecular Processes. Nauka, Sankt-Peterburg (2016)
19. Pines, D.: The Many-Body Problem. Benjamin, New York (1961)
20. Landau, L.D., Lifshits, E.M.: Quantum Mechanics. Pergamon, Oxford, pp 319–322 (1965)
21. Amusia, M.Y., Cherepkov, N.A.: Case Stud. At. Phys. **5**, 47 (1975)
22. Migdal, A.B.: Theory of Finite Fermi-Systems and Applications to Atomic Nuclei. Interscience, New York (1967)
23. Johnson, W.R., Guet, C.: Phys. Rev. A **49**, 1041 (1994)
24. Amusia, M.Y., Cherepkov, N.A., Chernysheva, L.V.: JETP **124**, 1 (2003)
25. Zhou, S., Parikh, S.P., Kauppila, W.E., Kwan, C.K., Lin, D., Surodovich, A., Stein, T.S.: Phys. Rev. Lett. **73**, 236 (1994)
26. Gribakin, G.F., King, W.A.: Can. J. Phys. **74**, 449 (1996)
27. Ivanov, V.K.: J. Phys. B At. Mol. Opt. Phys. **32**, R67 (1999)
28. Walter, C.W., Peterson, J.R.: Phys. Rev. Lett. **68**, 2281 (1992)
29. Amusia, M.Y.: Radiat. Phys. Chem. **70**, 237 (2004)
30. Johnson, W., Cheng, K.: Phys. Rev. A **63**, 022504 (2001)
31. Amusia, M.Y., Sosnivker, V.A., Cherepkov, N.A., Chernysheva, L.V., Sheftel, S.I.: J. Tech. Phys. **60**, 1 (1990). in Russian
32. Amusia, M.Y.: In: Becker, U., Shirley, D. (eds.) Photoionization in VUV and Soft X-Ray Frequency Regions, pp. 1–46. Plenum, New York (1996)
33. Amusia, M.Y., Chernysheva, L.V., Manson, S.T., Msezane, A.Z., Radoevich, V.: Phys. Rev. Lett. **88**, 093002 (2002)
34. Hemmers, O., Guillemin, R., Kanter, E.P., Krassig, B., Lindle, D.W., Southworth, S.H., Wehlitz, R., Baker, J., Hudson, A., Lotrakul, M., Rolles, D., Stolte, W.C., Tran, I.C., Wolska, A., Yu, S.W., Amusia, M.Y., Cheng, K.T., Chernysheva, L.V., Johnson, W.R., Manson, S.T.: Phys. Rev. Lett. **91**, 053002 (2003)
35. Amusia, M.Y., Kuchiev, M.Y., Sheinerman, S.A.: J. Exp. Theor. Phys. **76**(2), 470 (1979)
36. Amusia, M.Y., Gribakin, G.F., Tsemekhaman, K.L., Tsemekhaman, V.L.: J. Phys. B **23**, 393 (1990)
37. Amusia, M.Y., Avdonina, N.B., Drukarev, E.G., Manson, S.T., Pratt, R.H.: Phys. Rev. Lett. **85**(22), 4703–4706 (2000)
38. Amusia, M.Y.: J. Electron Spectrosc. Relat. Phenomena **159**, 81 (2007)
39. Amusia, M.Y.: Phys. Rep. **162**, 249 (1988)
40. Tsitovich, V.N., Oiringel, I.M. (eds.): Polarizational Radiation of Particles and Atoms. Plenum, New York (1992)
41. Astapenko, V.: Polarization Bremsstrahlung on Atoms, Plasmas, Nanostructures and Solids. Springer, Heidelberg, New York, Dordrecht, London (2013)
42. Amusia, M.Y.: Radiat. Phys. Chem. **75**, 1232 (2006)
43. Amusia, M.Y., Baltenkov, A.S., Chernysheva, L.V., Felfi, Z., Msezane, A.Z.: J. Phys. B At. Mol. Opt. Phys. **38**, L169 (2005)
44. Amusia, M.Y., Baltenkov, A.S., Chernysheva, L.V.: JETP Lett. **87**, 230 (2008)
45. Amusia, M.Y., Baltenkov, A.S., Chernysheva, L.V.: JETP **134**(2), 221 (2008)
46. Dolmatov, V.K., Amusia, M.Y., Chernysheva, L.V.: Phys. Rev. A **95**, 012709 (2017)
47. Amusia, M.Y., Chernysheva, L.V.: JETP Lett. **106**, 1 (2017)



Miron Ya. Amusia Dr Miron Amusia was Professor of Physics (Emeritus) at Hebrew University of Jerusalem, Israel, and Principal Scientist of the Ioffe Physical-Technical Institute, St. Petersburg, Russia. His research interests included the many-body theory of atoms, nuclei, endohedrals, and condensed matter. He received the Humboldt Research Award, Konstantinov and Frenkel medals and awards, Ioffe award, Kapitsa and Semenov medals, and was a member of the Russian Academy of Natural Sciences.



Anthony F. Starace

Contents

25.1	General Considerations	383
25.1.1	The Interaction Hamiltonian	383
25.1.2	Alternative Forms for the Transition Matrix Element	384
25.1.3	Selection Rules for Electric Dipole Transitions	385
25.1.4	Boundary Conditions on the Final State Wave Function	385
25.1.5	Photoionization Cross Sections	386
25.2	An Independent Electron Model	386
25.2.1	Central Potential Model	386
25.2.2	High Energy Behavior	387
25.2.3	Near-Threshold Behavior	387
25.3	Particle–Hole Interaction Effects	388
25.3.1	Intrachannel Interactions	388
25.3.2	Virtual Double Excitations	389
25.3.3	Interchannel Interactions	389
25.3.4	Photoionization of Ar	389
25.4	Theoretical Methods for Photoionization	390
25.4.1	Computational Methods	390
25.4.2	Other Interaction Effects	390
25.5	Related Photoionization Processes	391
25.6	Applications to Other Processes	391
25.6.1	Applications to Two and Three-Photon Ionization Processes	392
25.6.2	Application to High-Order Harmonic Generation	392
25.7	Future Directions	392
	References	393

Abstract

This chapter outlines the theory of atomic photoionization and the dynamics of the photon–atom collision process. Those kinds of electron correlation that are most important in photoionization are emphasized, although many qualitative features can be understood within a central field model. The particle–hole type of electron correlations are discussed, as they are by far the most important for describing the single photoionization of atoms near ionization thresholds. Detailed reviews of atomic photoionization are presented in [1, 2] and [3]. Additional related aspects are well-described in two books [4, 5]. Also, reviews of experimental results for noble gas atom photoionization [6] and for metal atom photoionization [7] provide valuable information on the corresponding theoretical results. At the end of this chapter, some recent applications of the theory of atomic photoionization to few-photon ionization and to high-order harmonic generation are discussed.

toionization are presented in [1, 2] and [3]. Additional related aspects are well-described in two books [4, 5]. Also, reviews of experimental results for noble gas atom photoionization [6] and for metal atom photoionization [7] provide valuable information on the corresponding theoretical results. At the end of this chapter, some recent applications of the theory of atomic photoionization to few-photon ionization and to high-order harmonic generation are discussed.

Keywords

electric dipole transition · partial cross section · cross section minimum · resonance profile · independent particle model

25.1 General Considerations

25.1.1 The Interaction Hamiltonian

Consider an N -electron atom with nuclear charge Z . In the nonrelativistic approximation, it is described by the Hamiltonian

$$H = \sum_{i=1}^N \left(\frac{p_i^2}{2m} - \frac{Ze^2}{r_i} \right) + \sum_{i>j=1}^N \frac{e^2}{|\mathbf{r}_i - \mathbf{r}_j|}. \quad (25.1)$$

The one-electron terms in brackets describe the kinetic and potential energy of each electron in the Coulomb field of the nucleus; the second set of terms describes the repulsive electrostatic potential energy between electron pairs. The interaction of this atom with external electromagnetic radiation is described by the additional terms obtained upon replacing \mathbf{p}_i by $\mathbf{p}_i + (|e|/c)\mathbf{A}(\mathbf{r}_i, t)$, where $\mathbf{A}(\mathbf{r}_i, t)$ is the vector po-

tential for the radiation. The interaction Hamiltonian is, thus,

$$H_{\text{int}} = \sum_{i=1}^N \left\{ \frac{+|e|}{2mc} [\mathbf{p}_i \cdot \mathbf{A}(\mathbf{r}_i, t) + \mathbf{A}(\mathbf{r}_i, t) \cdot \mathbf{p}_i] + \frac{e^2}{2mc^2} |\mathbf{A}(\mathbf{r}_i, t)|^2 \right\}. \quad (25.2)$$

Under the most common circumstance of single-photon ionization of an outer-subshell electron, the interaction Hamiltonian in Eq. (25.2) may be simplified considerably. First, the third term in Eq. (25.2) may be dropped, as it introduces two-photon processes (since it is of second order in \mathbf{A}). In any case, it is small compared with single-photon processes since it is of second order in the coupling constant $|e|/c$. Second, we choose the Coulomb gauge for \mathbf{A} , which fixes the divergence of \mathbf{A} as $\nabla \cdot \mathbf{A} = 0$; \mathbf{A} thus describes a transverse radiation field. Furthermore, \mathbf{p} and \mathbf{A} now commute, and, hence, the first and second terms in Eq. (25.2) may be combined. Third, we introduce the following form for \mathbf{A}

$$\mathbf{A}(\mathbf{r}_i, t) = \left(\frac{2\pi c^2 \hbar}{\omega V} \right)^{\frac{1}{2}} \hat{\boldsymbol{\epsilon}} e^{i(\mathbf{k} \cdot \mathbf{r}_i - \omega t)}. \quad (25.3)$$

This classical expression for \mathbf{A} may be shown [8] to give photoabsorption transition rates that are in agreement with those obtained using the quantum theory of radiation. Here, \mathbf{k} and ω are the wave vector and angular frequency of the incident radiation, $\hat{\boldsymbol{\epsilon}}$ is its polarization unit vector, and V is the spatial volume. Fourth, the *electric dipole* (E1) approximation, in which $\exp[i(\mathbf{k} \cdot \mathbf{r}_i)]$ is replaced by unity, is usually appropriate. The radii r_i of the atomic electrons are usually of order 1 Å. Thus, for $\lambda \gg 100$ Å, $|\mathbf{k} \cdot \mathbf{r}_i| \ll 1$. Now $\lambda \gg 100$ Å corresponds to photon energies $\hbar\omega \ll 124$ eV. For outer atomic subshells, most of the photoabsorption occurs for much smaller photon energies, thus validating the use of the E1 approximation. (This approximation cannot be used uncritically, however. For example, photoionization of excited atoms (which have large radii), photoionization of inner subshells (which requires the use of short wavelength radiation), and calculation of differential cross sections or other measurable quantities that are sensitive to the overlap of electric dipole and higher multipole amplitudes all require that the validity of the electric dipole approximation be checked.) The use of all of the above conventions and approximations allows the reduction of H_{int} in Eq. (25.2) to the simplified form

$$H_{\text{int}} = \frac{+|e|}{mc} \left(\frac{2\pi c^2 \hbar}{\omega V} \right)^{\frac{1}{2}} \sum_{i=1}^N \hat{\boldsymbol{\epsilon}} \cdot \mathbf{p}_i \exp(-i\omega t); \quad (25.4)$$

H_{int} thus has the form of a harmonically time-dependent perturbation. According to time-dependent perturbation theory, the photoionization cross section is proportional to the absolute square of the matrix element of Eq. (25.4) between

the initial and final electronic states described by the atomic Hamiltonian in Eq. (25.1). Atomic units, in which $|e| = m = \hbar = 1$, are used in what follows.

25.1.2 Alternative Forms for the Transition Matrix Element

The matrix element of Eq. (25.4) is proportional to the matrix element of the momentum operator $\sum_i \mathbf{p}_i$. Alternative expressions for this matrix element may be obtained from the following operator equations involving commutators of the exact atomic Hamiltonian in Eq. (25.1)

$$\sum_{i=1}^N \mathbf{p}_i = -i \left[\sum_{i=1}^N \mathbf{r}_i, H \right], \quad (25.5)$$

$$\left[\sum_{i=1}^N \mathbf{p}_i, H \right] = -i \sum_{i=1}^N \frac{\mathbf{Z} \mathbf{r}_i}{r_i^3}. \quad (25.6)$$

Matrix elements of Eqs. (25.5) and (25.6) between eigenstates $\langle \psi_0 |$ and $|\psi_f \rangle$ of H having energies E_0 and E_f , respectively, give

$$\langle \psi_0 | \sum_{i=1}^N \mathbf{p}_i | \psi_f \rangle = -i\omega \langle \psi_0 | \sum_{i=1}^N \mathbf{r}_i | \psi_f \rangle, \quad (25.7)$$

$$\langle \psi_0 | \sum_{i=1}^N \mathbf{p}_i | \psi_f \rangle = \frac{-i}{\omega} \langle \psi_0 | \sum_{i=1}^N \frac{\mathbf{Z} \mathbf{r}_i}{r_i^3} | \psi_f \rangle, \quad (25.8)$$

where $\omega = E_f - E_0$. Matrix elements of $\sum_{i=1}^N \mathbf{p}_i$, $\sum_{i=1}^N \mathbf{r}_i$, and $\sum_{i=1}^N \mathbf{Z} \mathbf{r}_i / r_i^3$ are known as the *velocity*, *length*, and *acceleration* forms of the E1 matrix element. Equality of the matrix elements in Eqs. (25.7) and (25.8) does not hold when approximate eigenstates of H are used [9]. In such a case, qualitative considerations may help to determine which form is most reliable. For example, the length form tends to emphasize the large r part of the approximate wave functions, the acceleration form tends to emphasize the small r part of the wave functions, and the velocity form tends to emphasize intermediate values of r .

If instead of employing approximate eigenstates of the exact H , one employs exact eigenstates of an approximate N -electron Hamiltonian, then inequality of the matrix elements in Eqs. (25.7) and (25.8) is a measure of the nonlocality of the potential in the approximate Hamiltonian [10–12]. The exchange part of the Hartree–Fock potential is an example of such a nonlocal potential. Nonlocal potentials are also implicitly introduced in configuration interaction calculations employing a finite number of configurations [10–12]. One may eliminate the ambiguity of which form of the E1 transition operator to use by requiring that the Schrödinger equation be gauge invariant. Only the length form is consistent with such gauge invariance [10–12].

However, equality of the alternative forms of the transition operator does not necessarily imply high accuracy. For example, they are exactly equal when one uses an approximate local potential to describe the N -electron atom, as in a central potential model, even though the accuracy is often poor. The length and velocity forms are also exactly equal in the random phase approximation with exchange (RPAE) [1, 3], which generally gives accurate cross sections for single photoionization of closed shell atoms. No general prescription exists, however, for ensuring that the length and velocity matrix elements are equal at each level of approximation to the N -electron Hamiltonian. However, if all corrections of a given order in interelectron interaction are taken into account, length and velocity matrix elements are equal [3].

25.1.3 Selection Rules for Electric Dipole Transitions

If one ignores relativistic interactions, then a general atomic photoionization process may be described in LS -coupling as follows

$$\mathcal{A}(L, S, M_L, M_S, \pi_{\mathcal{A}}) + \gamma(\pi_{\gamma}, \ell_{\gamma}, m_{\gamma}) \longrightarrow \mathcal{A}^+(\bar{L}\bar{S}\pi_{\mathcal{A}^+})\varepsilon\ell(L', S', M_{L'}, M_{S'}) . \quad (25.9)$$

Here, the atom \mathcal{A} is ionized by the photon γ to produce a photoelectron with kinetic energy ε and orbital angular momentum ℓ . The photoelectron is coupled to the ion \mathcal{A}^+ with total orbital and spin angular momenta L' and S' . In the electric dipole approximation, the photon may be regarded as having odd parity, i.e., $\pi_{\gamma} = -1$, and unit angular momentum, i.e., $\ell_{\gamma} = 1$. This is obvious from Eqs. (25.7) and (25.8), where the E1 operator is seen to be a vector operator. The component m_{γ} of the photon in the E1 approximation is ± 1 for right or left circularly polarized light and 0 for linearly polarized light. (The z axis is taken as $\hat{\mathbf{k}}$ in the case of circularly polarized light and as $\hat{\mathbf{e}}$ in the case of linearly polarized light, where \mathbf{k} and $\hat{\mathbf{e}}$ are defined in Eq. (25.3).) Angular momentum and parity selection rules for the E1 transition in Eq. (25.9) imply the following relations between the initial and final state quantum numbers

$$L' = L \oplus 1 = \bar{L} \oplus \ell , \quad (25.10)$$

$$M_{L'} = M_L + m_{\gamma} = M_{\bar{L}} + m_{\ell} , \quad (25.11)$$

$$S' = S = \bar{S} \oplus \frac{1}{2} , \quad (25.12)$$

$$M_{S'} = M_S = M_{\bar{S}} + m_s , \quad (25.13)$$

$$\pi_{\mathcal{A}}\pi_{\mathcal{A}^+} = (-1)^{\ell+1} . \quad (25.14)$$

Equation (25.14) follows from the parity $(-1)^{\ell}$ of the photoelectron. The direct sum symbol \oplus denotes the vector addition of \mathbf{A} and \mathbf{B} , i.e., $\mathbf{A} \oplus \mathbf{B} = \mathbf{A} + \mathbf{B}, \mathbf{A} + \mathbf{B} - 1, \dots, |\mathbf{A} - \mathbf{B}|$.

In Eq. (25.9), the quantum numbers $\alpha \equiv \bar{L}, \bar{S}, \pi_{\mathcal{A}^+}, \ell, L', S', M_{L'}, M_{S'}$ (plus any other quantum numbers needed to specify the state of the ion \mathcal{A}^+ uniquely) define a final state *channel*. All final states that differ only in the photoelectron energy ε belong to the same channel. The quantum numbers $L', S', M_{L'}, M_{S'}$, and $\pi_{\text{tot}} = (-1)^{\ell} \pi_{\mathcal{A}^+}$ are the only good quantum numbers for the final states. Thus, the Hamiltonian Eq. (25.1) mixes final state channels having the same angular momentum and parity quantum numbers but differing quantum numbers for the ion and the photoelectron; i.e., differing $\bar{L}, \bar{S}, \pi_{\mathcal{A}^+}$, and ℓ but the same $L', S', M_{L'}, M_{S'}$ and $(-1)^{\ell} \pi_{\mathcal{A}^+}$.

25.1.4 Boundary Conditions on the Final State Wave Function

Photoionization calculations obtain final state wave functions satisfying the asymptotic boundary condition that the photoelectron is ionized in channel α . This boundary condition is expressed as

$$\begin{aligned} & \psi_{\alpha E}^{-}(\mathbf{r}_1 s_1, \dots, \mathbf{r}_N s_N) \\ & \xrightarrow{r_N \rightarrow \infty} \theta_{\alpha}(\mathbf{r}_1 s_1, \dots, \hat{\mathbf{r}}_N s_N) \frac{1}{i(2\pi k_{\alpha})^{\frac{1}{2}}} \frac{1}{r_N} e^{i\Delta_{\alpha}} \\ & - \sum_{\alpha'} \theta_{\alpha'}(\mathbf{r}_1 s_1, \dots, \hat{\mathbf{r}}_N s_N) \frac{1}{i(2\pi k_{\alpha'})^{\frac{1}{2}}} \frac{1}{r_N} e^{-i\Delta_{\alpha'}} S_{\alpha'\alpha}^{\dagger} , \end{aligned} \quad (25.15)$$

where the phase appropriate for a Coulomb field is

$$\Delta_{\alpha} \equiv k_{\alpha} r_N - \frac{1}{2} \pi \ell_{\alpha} + \frac{1}{k_{\alpha}} \log 2k_{\alpha} r_N + \sigma_{\ell_{\alpha}} . \quad (25.16)$$

The minus superscript on the wave function in Eq. (25.15) indicates an *incoming wave* normalization; i.e., asymptotically $\psi_{\alpha E}^{-}$ has outgoing spherical Coulomb waves only in channel α , while there are incoming spherical Coulomb waves in all channels; $S_{\alpha'\alpha}^{\dagger}$ is the Hermitian conjugate of the S -matrix of scattering theory, θ_{α} indicates the coupled wave function of the ion and the angular and spin parts of the photoelectron wave function, k_{α} is the photoelectron momentum in channel α and ℓ_{α} is its orbital angular momentum, and $\sigma_{\ell_{\alpha}}$ in Eq. (25.16) is the Coulomb phase shift.

While one calculates channel functions $\psi_{\alpha E}^{-}$, experimentally one measures photoelectrons that asymptotically have well-defined linear momenta \mathbf{k}_{α} and well-defined spin states $m_{\frac{1}{2}}$, and ions in well-defined states $\bar{\alpha} \equiv \bar{L}\bar{S}M_{\bar{L}}M_{\bar{S}}$. The wave function appropriate for this experimental situation is related to the channel functions by uncoupling the ionic and electronic orbital and spin angular momenta and projecting the photoelectron angular momentum states $\ell_{\alpha}, m_{\alpha}$ onto the direction $\hat{\mathbf{k}}_{\alpha}$ by means of the spherical harmonic $Y_{\ell_{\alpha} m_{\alpha}}^*(k_{\alpha})$.

This relation is [2]

$$\begin{aligned} & \psi_{\bar{\alpha}k_\alpha}^-(\mathbf{r}_1s_1, \dots, \mathbf{r}_Ns_N) \\ &= \sum_{\ell_\alpha m_\alpha} \frac{i^{\ell_\alpha} \exp(-i\sigma_{\ell_\alpha})}{k_\alpha^{\frac{1}{2}}} Y_{\ell_\alpha m_\alpha}^*(\hat{\mathbf{k}}_\alpha) \\ & \times \sum_{LM_L SM_S} \langle \bar{L}M_{\bar{L}} \ell_\alpha m_\alpha | LM_L \rangle \\ & \times \langle \bar{S}M_{\bar{S}} \frac{1}{2} m_{\frac{1}{2}} | SM_S \rangle \psi_{\bar{\alpha}E}^-(\mathbf{r}_1s_1, \dots, \mathbf{r}_Ns_N), \end{aligned} \quad (25.17)$$

where the coefficients in brackets are Clebsch–Gordan coefficients. This wave function is normalized to a delta function in momentum space, i.e.,

$$\int (\psi_{\bar{\alpha}k_\alpha}^-)^\dagger \psi_{\bar{\alpha}'k_{\alpha'}}^- d^3\mathbf{r} = \delta_{\bar{\alpha}\bar{\alpha}'} \delta(\mathbf{k}_\alpha - \mathbf{k}_{\alpha'}). \quad (25.18)$$

The factors $i^{\ell_\alpha} \exp(-i\sigma_{\ell_\alpha}) k_\alpha^{-\frac{1}{2}}$ ensure that for large r_N , Eq. (25.17) represents a Coulomb wave (with momentum \mathbf{k}_α) times the ionic wave function for the state $\bar{\alpha}$ plus a sum of terms representing incoming spherical waves. Thus, only the ionic term $\bar{\alpha}$ has an outgoing wave. One uses the wave function in Eq. (25.17) to calculate the angular distribution of photoelectrons.

25.1.5 Photoionization Cross Sections

If one writes H_{int} in Eq. (25.4) as $H_{\text{int}}(t) = H_{\text{int}}(0) e^{-i\omega t}$, then from first-order time-dependent perturbation theory, the transition rate for the transition from an initial state with energy E_0 and wave function ψ_0 to a final state with total energy E_f and wave function $\psi_{\bar{\alpha}k_\alpha}^-$ is

$$\begin{aligned} dW_{k_\alpha} &= 2\pi |\langle \psi_0 | H_{\text{int}}(0) | \psi_{\bar{\alpha}k_\alpha}^- \rangle|^2 \\ & \times \delta(E_f - E_0 - \omega) k_\alpha^2 dk_\alpha d\Omega(\hat{\mathbf{k}}_\alpha). \end{aligned} \quad (25.19)$$

The delta function expresses energy conservation, and the last factors on the right-hand side are the phase space factors for the photoelectron. Dividing the transition rate by the incident photon current density c/V , integrating over dk_α , and inserting $H_{\text{int}}(0)$, the differential photoionization cross section is

$$\frac{d\sigma_{\bar{\alpha}}}{d\Omega} = \frac{4\pi^2}{c} \frac{k_\alpha}{\omega} \left| \hat{\boldsymbol{\epsilon}} \cdot \langle \psi_0 | \sum_{i=1}^N \mathbf{p}_i | \psi_{\bar{\alpha}k_\alpha}^- \rangle \right|^2. \quad (25.20)$$

Implicit in Eqs. (25.19) and (25.20) is an average over initial magnetic quantum numbers $M_{L_0} M_{S_0}$ and a sum over final magnetic quantum numbers $M_{\bar{L}} M_{\bar{S}} m_{\frac{1}{2}}$. The length form of Eq. (25.20) is obtained by replacing each \mathbf{p}_i by $\omega \mathbf{r}_i$ Eq. (25.7).

Substitution of the final state wave function Eq. (25.17) in Eq. (25.20) permits one to carry out the numerous summations over magnetic quantum numbers and obtain the form

$$\frac{d\sigma_{\bar{\alpha}}}{d\Omega} = \frac{\sigma_{\bar{\alpha}}}{4\pi} [1 + \beta P_2(\cos \theta)] \quad (25.21)$$

for the differential cross section [13]. Here, $\sigma_{\bar{\alpha}}$ is the partial cross section for leaving the ion in the state $\bar{\alpha}$, β is the asymmetry parameter [23], $P_2(\cos \theta) = \frac{3}{2} \cos^2 \theta - \frac{1}{2}$, and θ indicates the direction of the outgoing photoelectron with respect to the polarization vector $\hat{\boldsymbol{\epsilon}}$ of the incident light. The form of Eq. (25.21) follows in the electric dipole approximation from general symmetry principles, provided that the target atom is unpolarized [15]. The partial cross section is given in terms of reduced E1 matrix elements [14] involving the channel functions in Eq. (25.15) by

$$\sigma_{\bar{\alpha}} = \frac{4\pi^2}{3c} \omega [L]^{-1} \sum_{\ell_\alpha L'} \left| \langle \psi_0 | \left\| \sum_{i=1}^N r_i \right\|^{[1]} | \psi_{\bar{\alpha}E}^- \rangle \right|^2. \quad (25.22)$$

The β parameter has a much more complicated expression involving interference between different reduced dipole amplitudes [16, 23]. Thus, measurement of β provides information on the relative phases of the alternative final state channel wave functions, whereas the partial cross section in Eq. (25.22) does not. From the requirement that the differential cross section in Eq. (25.21) be positive, one can see that $-1 \leq \beta \leq +2$.

25.2 An Independent Electron Model

The many-body wave functions ψ_0 and $\psi_{\bar{\alpha}E}^-$ are usually expressed in terms of a basis of independent electron wave functions. Key qualitative features of photoionization cross sections can often be interpreted in terms of the overlaps of initial and final state one-electron radial wave functions [2, 14]. The simplest independent electron representation of the atom, the central potential model, proves useful for this purpose.

25.2.1 Central Potential Model

In the central potential (CP) model, the exact H in Eq. (25.1) is approximated by a sum of single-particle terms describing the independent motion of each electron in a central potential $V(r)$

$$H_{\text{CP}} = \sum_{i=1}^N \left[\frac{p_i^2}{2m} + V(r_i) \right]. \quad (25.23)$$

The potential $V(r)$ must describe the nuclear attraction and the electron–electron repulsion as well as possible and must satisfy the boundary condition

$$V(r) \xrightarrow{r \rightarrow 0} -Z/r \quad \text{and} \quad V(r) \xrightarrow{r \rightarrow \infty} -1/r \quad (25.24)$$

in the case of a neutral atom; H_{CP} is separable in spherical coordinates and its eigenstates can be written as Slater determinants of one-electron orbitals of the form $r^{-1}P_{n\ell}Y_{\ell m}(\Omega)$ for bound orbitals and of the form $r^{-1}P_{\varepsilon\ell}(r)Y_{\ell m}(\Omega)$ for continuum orbitals. The one-electron radial wave functions satisfy

$$\frac{d^2P_{\varepsilon\ell}(r)}{dr^2} + 2\left[\varepsilon - V(r) - \frac{\ell(\ell+1)}{2r^2}\right]P_{\varepsilon\ell}(r) = 0, \quad (25.25)$$

subject to the boundary condition $P_{\varepsilon\ell}(0) = 0$, and similarly for the discrete orbitals $P_{n\ell}(r)$. *Hermann* and *Skillman* [17] have tabulated a widely used central potential for each element in the periodic table, as well as radial wave functions for each occupied orbital in the ground state of each element.

25.2.2 High Energy Behavior

The hydrogen atom cross section, which is nonzero at threshold and decreases monotonically with increasing photon energy, serves as a model for inner-shell photoionization cross sections in the X-ray photon energy range. A sharp onset at threshold followed by a monotonic decrease above threshold is precisely the behavior seen in X-ray photoabsorption measurements. A simple hydrogenic approximation at high energies may be justified theoretically as follows: (1) Since a free electron cannot absorb a photon (because of kinematical considerations), at high photon energies one expects the more strongly bound inner electrons to be preferentially ionized as compared with the outer electrons. (2) Since the $P_{n\ell}(r)$ for an inner electron is concentrated in a very small range of r , one expects the integrand of the radial dipole matrix element to be negligible except for those values of r where $P_{n\ell}(r)$ is greatest. (3) Thus, it is only necessary to approximate the atomic potential locally, e.g., by means of a screened Coulomb potential

$$V_{n\ell}(r) = -\left(\frac{Z - s_{n\ell}}{r}\right) + V_{n\ell}^o \quad (25.26)$$

appropriate for the $n\ell$ orbital. Here, $s_{n\ell}$ is the *inner-screening* parameter, which accounts for the screening of the nuclear charge by the other atomic electrons, and $V_{n\ell}^o$ is the *outer-screening* parameter, which accounts for the lowering of the

$n\ell$ electrons' binding energy due to repulsion between the outer electrons and the photoelectron as the latter leaves the atom. The potential in Eq. (25.26) predicts hydrogen-like photoionization cross sections for inner-shell electrons with onsets determined by the outer-screening parameters $V_{n\ell}^o$.

The use of more accurate atomic central potentials in place of the screened hydrogenic potential in Eq. (25.26) generally enables one to obtain photoionization cross sections below the keV photon energy region to within 10% of the experimental results [18]. For $\ell > 0$, subshells and photon energies in the keV region and above, the independent particle model becomes increasingly inadequate owing to coupling with nearby ns -subshells, which generally have larger partial cross sections at high photon energies [19]. For high, but still nonrelativistic, photon energies, i.e., $\omega \ll mc^2$, the energy dependence of the cross section for the $n\ell$ subshell within the independent particle model is [20]

$$\sigma_{n\ell} \approx \omega^{-\ell-\frac{7}{2}}. \quad (25.27)$$

However, when interchannel interactions are taken into account, the asymptotic energy dependence for subshells having $\ell > 0$ becomes independent of ℓ [21]

$$\sigma_{n\ell} \approx \omega^{-\frac{9}{2}} (\ell > 0). \quad (25.28)$$

This result stems from coupling of the $\ell > 0$ photoionization channels with nearby s -subshell channels.

25.2.3 Near-Threshold Behavior

For photons in the vacuum ultra violet (VUV) energy region, i.e., near the outer-subshell ionization thresholds, the photoionization cross sections for subshells with $\ell \geq 1$ frequently have distinctly nonhydrogenic behavior [22, 24]. The cross section, instead of decreasing monotonically as for hydrogen, rises above threshold to a maximum (the so-called *delayed maximum* above threshold). Then it decreases to a minimum (the *Cooper minimum* [25, 26]) and rises to a second maximum. Finally, the cross section decreases monotonically at high energies in accordance with hydrogenic behavior. Such nonhydrogenic behavior may be interpreted as due either to an effective potential barrier or to a zero in the radial dipole matrix element. We examine each of these effects in turn. The *delayed maximum* above outer subshell ionization thresholds of heavy atoms (i.e., $Z \gtrsim 18$) is due to an *effective potential barrier* seen by $\ell = 2$ and $\ell = 3$ photoelectrons in the region of the outer edge of the atom Eq. (25.25). This effective potential lowers the probability of photoelectron escape until the photoelectrons have enough excess energy to surmount the barrier. Such behavior is nonhydrogenic. Furthermore, in cases where an inner subshell with $\ell = 2$ or 3

is being filled as Z increases (as in the transition metals, the lanthanides and the actinides) there is a double well potential. This double well has profound effects on the $3p$ -subshell spectra of the transition metals, the $4d$ -subshell spectra of the lanthanides, and the $5d$ -subshell spectra of the actinides, as well as on atoms with Z just below those of these series of elements [27, 28]. The potential barrier effects on the photoionization cross sections of these elements are often referred to as “giant dipole resonances”. In fact, to describe the $4d$ subshell, interaction of at least all $4d$ electrons has to be taken into account. The many-electron nature of “giant dipole resonances” is presented in Chap. 24 (also [1]).

Cross section minima arise due to a change in sign of the radial dipole transition matrix element in a particular channel [29, 30]. Rules for predicting their occurrence were developed in [25, 26]. Studies of their occurrence in photoionization from excited states [31], in high Z atoms [32], and in relativistic approximation [33] have been carried out. A proof has been given [34] that such minima do not occur in atomic hydrogen spectra. For other elements, there are further rules on when and how many minima may occur [35–37].

Often within such minima, one can observe the effects of weak interactions that are otherwise obscured. Relativistic and weak correlation effects on the asymmetry parameter β for s -subshells is a notable example [38]. Wang et al. [39] also emphasized that near such minima in the E1 amplitudes, one cannot ignore the effects of quadrupole and higher corrections to the differential cross section. Central potential model calculations [39] show that quadrupole corrections can be as large as 10% of the E1 cross section at such cross section minima, even for low photon energies. Particularly strong is the role of quadrupole effects in the so-called nondipole angular anisotropy parameters (e.g., [40]).

25.3 Particle–Hole Interaction Effects

The experimental photoionization cross sections for the outer subshells of the noble gases have played a prominent role in the development of the theory of photoionization for two reasons. These were among the first elements studied by experimentalists with synchrotron radiation beginning in the 1960s. Also, their closed-shell, spherically symmetric ground states simplified the theoretical analysis of their cross sections. The cross sections near the ionization thresholds can be understood in terms of interactions between the photoelectron, the residual ion, and the photon field that are called, in many-body theory language, *particle–hole* interactions (Chap. 24). These may be described as interactions in which two electrons either excite or de-excite each other out of or into their initial subshell locations in the unexcited atom. To analyze the effects of these interactions on the cross section, it is con-

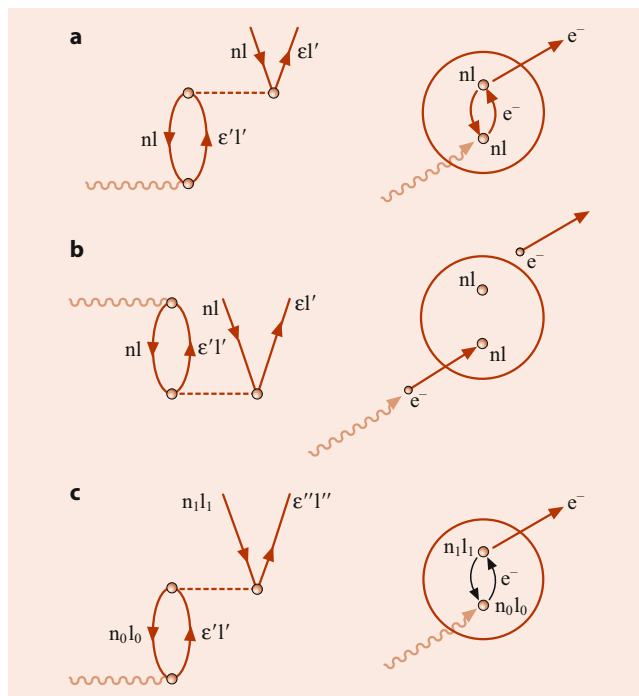


Fig. 25.1 MBPT diagrams (*left*) and scattering pictures (*right*) for three kinds of particle–hole interaction: (a) intrachannel scattering following photoabsorption; (b) photoabsorption by a virtual doubly excited state; (c) interchannel scattering following photoabsorption

venient to classify them into three categories: intrachannel, virtual double excitation, and interchannel. In many publications, however, another classification is used: intrasubshell and intersubshell correlations (Chap. 24). These alternative kinds of particle–hole interactions are illustrated in Fig. 25.1 using both many-body perturbation theory (MBPT) diagrams and more *physical* scattering pictures. We discuss each of these types of interaction in turn.

25.3.1 Intrachannel Interactions

The MBPT diagram for this interaction is shown on the left-hand side of Fig. 25.1a; on the right-hand side, a slightly more pictorial description of this interaction is shown. The wiggly line indicates a photon, which is absorbed by the atom in such a way that an electron is excited out of the nl subshell. During the escape of this excited electron, it collides or interacts with another electron from the same subshell in such a way that the second electron absorbs all the energy imparted to the atom by the photon; the first electron is de-excited back to its original location in the nl subshell. For closed-shell atoms, the photoionization process leads to a 1P_1 final state in which the intrachannel interaction is strongly repulsive. This interaction tends to broaden cross section maxima and push them to higher photon energies as compared with the results of central potential model calculations.

Intrachannel interaction effects are taken into account automatically when the correct Hartree–Fock (HF) basis set is employed, in which the photoelectron sees a net Coulomb field due to the residual ion and is coupled to the ion to form the appropriate total orbital L and spin S angular momenta [3]. Any other basis set requires explicit treatment of intrachannel interactions.

25.3.2 Virtual Double Excitations

The MBPT diagram for this type of interaction is shown on the left-hand side of Fig. 25.1b. Topologically, this diagram is the same as that on the left-hand side in Fig. 25.1a. In fact, the radial parts of the two matrix elements are identical; only the angular factors differ. A more pictorial description of this interaction is shown on the right-hand side of Fig. 25.1b. The ground state of the atom before photoabsorption is shown to have two electrons virtually excited out of the $n\ell$ subshell. In absorbing the photon, one of these electrons is de-excited to its original location in the $n\ell$ subshell, while the other electron is ionized. These virtual double excitations imply a more diffuse atom than in central-potential or HF models, with the effect that the overly repulsive intrachannel interactions are weakened, leading to cross sections for noble gas atoms that are in very good agreement with experiment with the exception that resonance features are not predicted. As an impressive example of strong intrachannel coupling serves the formation of so-called atomic giant resonance (Chap. 24, Fig. 24.2).

25.3.3 Interchannel Interactions

The interchannel interaction shown in Fig. 25.1c is important, particularly for s subshells. This interaction has the same form as the intrachannel interaction shown in Fig. 25.1a, except now when an electron is photoexcited out of the $n_0\ell_0$ subshell, it collides or interacts with an electron in a different subshell – the $n_1\ell_1$ subshell. This interaction causes the second electron to be ionized, and the first electron to fall back into its original location in the $n_0\ell_0$ subshell.

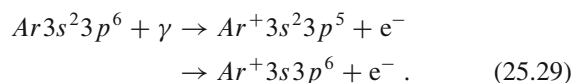
Interchannel interaction effects are usually very conspicuous features of photoionization cross sections. When the interacting channels have partial photoionization cross sections that differ greatly in magnitude, one finds that the calculated cross section for the weaker channel is completely dominated by its interaction with the stronger channel. A good example of interchannel (or intershell) interaction is the photoionization cross section of $5s$ subshell in Xe that is totally determined by $5s$ interaction with its many-electron neighboring $5p$ and $4d$ subshells (Chap. 24, Fig. 24.3). At the same time, it is often a safe approximation to ignore

the effect of weak channels on stronger channels. In addition, when the interacting channels have differing binding energies, their interchannel interactions lead to a resonance structure in the channel with lower binding energy (arising from its coupling to the Rydberg series in the channel with higher binding energy).

At high photon energies, s -subshell partial cross sections dominate over $\ell > 0$ subshell partial cross sections (Eqs. (25.27), (25.28)). Hence, interchannel interactions of $\ell > 0$ subshells with nearby s -subshells change independent particle model predictions significantly. In particular, as noted in Sect. 25.3.2, such interactions can drastically change the magnitudes of the $\ell > 0$ partial cross sections [19], as well as their asymptotic energy behavior [21].

25.3.4 Photoionization of Ar

An example of both the qualitative features exhibited by photoionization cross sections in the VUV energy region and of the ability of the theory to calculate photoionization cross reactions accurately is provided by photoionization of the $n = 3$ subshell of argon, i.e.,



First calculations of photoionization cross section of Ar $3p_6$ subshell with account of many-electron correlations was performed by *Amusia et al.* [41] in RPAE. Good agreement with experiment was achieved. Figure 25.2 shows the MBPT calculation of *Kelly and Simons* [42], which includes both intrachannel and interchannel interactions, as well as the effect of virtual double excitations. The cross section is in excellent agreement with experiment [43, 44], even to the extent of describing the resonance behavior due to discrete members of the $3s \rightarrow \epsilon p$ channel.

Figure 25.2 illustrates most of the features of photoionization cross sections described so far. First, the cross section rises to a delayed maximum just above the threshold because of the potential barrier seen by photoelectrons from the $3p$ subshell having $\ell = 2$. For photon energies in the range of 45–50 eV, the calculated cross section goes through a minimum because of a change in sign of the $3p \rightarrow \epsilon d$ radial dipole amplitude. The HFL and HFV calculations include the strongly repulsive intrachannel interactions in the 1P final-state channels and calculate the transition amplitude using the length (L) and velocity (V) form, respectively, for the electric dipole transition operator Eq. (25.7). With respect to the results of central potential model calculations, the HFL and HFV results have lower and broader maxima at higher energies. They also disagree with each other by a factor of 2! Inclusion of virtual double excitations results in length and

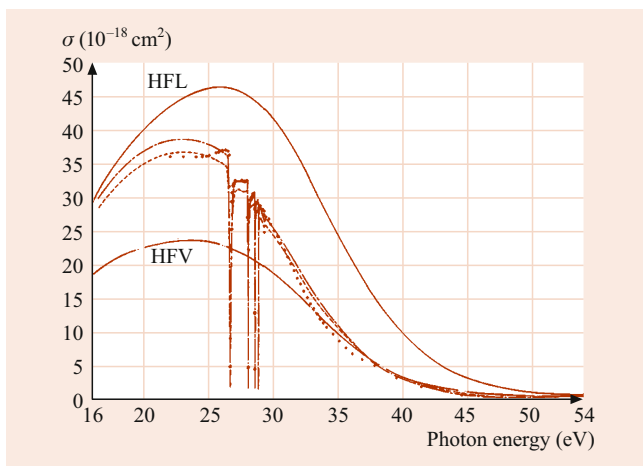


Fig. 25.2 Photoionization cross section for the 3p and 3s subshells of Ar. HFL and HFV indicate the length and velocity results obtained using HF orbitals calculated in a 1P_1 potential. Dot-dash and dashed lines represent the length and velocity results of the MBPT calculation of Kelly and Simons [42]. Only the four lowest $3s \rightarrow np$ resonances are shown; the series converges to the 3s threshold at 29.24 eV. Experimental results are those of Samson [43] above 37 eV and of Madden et al. [44] below 37 eV (after [42])

velocity results that agree to within 10% with each other and with experiment, except that the resonance structures are not reproduced. Finally, taking into account the interchannel interactions, one obtains the length and velocity form results shown in Fig. 25.2 by dash-dot and dashed curves, respectively. The agreement with experiment is excellent, and the observed resonances are well reproduced.

25.4 Theoretical Methods for Photoionization

25.4.1 Computational Methods

Most of the ab initio methods for the calculation of photoionization cross sections (e.g., the MBPT method [45], the close-coupling (CC) method [46], the R-matrix method [47, 48], the random phase approximation with exchange (RPAE) method [1, 3, 49], the relativistic RPAE method [50], the transition matrix method [51, 52], the multiconfiguration Hartree–Fock (MCHF) method [53–55], time-dependent multiconfiguration methods [56], etc.) have successfully calculated outer p -subshell photoionization cross sections of the noble gases by treating in their alternative ways the key interactions described above, i.e., the particle–hole interactions. In general, these methods all treat both intrachannel and interchannel interactions to infinite order and differ only in their treatment of ground state correlations. (The exception is MBPT, which often treats interchannel interactions between weak and strong channels only to first or second order.) These methods, therefore, stand in contrast to central potential model calculations, which do not treat any

of the particle–hole interactions, and single-channel term-dependent HF calculations, which treat only the intrachannel interactions. The key point is that selection of the interactions that are included in a particular calculation is more important than the method by which such interactions are handled.

Treatment of the photoionization of atoms other than the noble gases presents additional challenges for theory. For example, elements such as the alkaline earths, which have s^2 outer subshells, require careful treatment of electron pair excitations in both initial and final states. Open-shell atoms have many more ionization thresholds than do the noble gases. Treatment of the resultant rich resonance structures typically relies heavily on quantum defect theory [55] (Chap. 32). All the methods listed above can be used to treat elements other than the noble gases, but a method that has come to prominence because of the excellent results it obtains for both alkaline earth and open-shell atoms is the eigenchannel R-matrix method [57].

25.4.2 Other Interaction Effects

A number of interactions, not of the particle–hole type, lead to conspicuous effects in localized energy regions. When treating photoionization in such energy regions, one must be careful to choose a theoretical method that is appropriate. Among the interactions that may be important are the following:

Relativistic and spin-dependent interactions The fact that $j = \ell - \frac{1}{2}$ electrons are contracted more than $j = \ell + \frac{1}{2}$ electrons at small distances has an enormous effect on the location of cross section minima in heavy elements [18, 58]. It may explain the large differences observed in the profiles of a resonance decaying to final states that differ only in their fine structure quantum numbers [59]. Impressive effects in the photoionization cross section appear due to interaction not only between inner but also intermediate sublevels $\ell + \frac{1}{2}$ and $\ell - \frac{1}{2}$ [60].

Inner-shell vacancy rearrangement Inner-shell vacancies often result in a significant production of satellite structures in photoelectron spectra. Calculations for inner-subshell partial photoionization cross sections are often substantially larger than results of photoelectron measurements [61–63]. This difference is attributed to such satellite production that is often not treated in theoretical calculations, as well as to effect of inner-shell rearrangement, due to its ionization, upon the outgoing photoelectron [3, 49].

Polarization and relaxation effects Negative ion photodetachment cross sections often exhibit strong effects of core polarization near the threshold. These effects can be treated

semempirically, resulting in excellent agreement between theory and experiment [64]. Even for inner-shell photoionization cross sections of heavy elements, *ab initio* theories do not reproduce measurements near threshold without the inclusion of polarization and relaxation effects [65, 66].

An example The calculation of the energy dependence of the asymmetry parameter β for the $5s$ subshell of xenon requires the theoretical treatment of all of the above effects. In the absence of relativistic interactions, β for Xe $5s$ would have the energy-independent value of 2. Deviations of β from 2 are, therefore, an indication of the presence of these relativistic interactions. The greatest deviation of β from 2 occurs in the localized energy region where the partial photoionization cross section for the $5s$ subshell has a minimum. In this region, however, relativistic calculations show larger deviations from 2 than are observed experimentally. Inner-shell rearrangement and relaxation effects play an important role [67, 68] and must be included to achieve good agreement with experiment.

25.5 Related Photoionization Processes

One of the most intensively studied areas in atomic photoionization has been the *double photoionization of the helium atom*. Extensive sets of experimental measurements for the two electron angular distributions (i.e., the triply differential cross sections) have provided stringent tests for various theoretical models and their treatments of electron correlations. A number of excellent reviews of this field have been published recently [69–71].

Another intensively studied area has been the analysis and measurement of *nondipole effects in photoionization*, which were first observed in the X-ray region [72] but have been found to be significant even in the VUV photon energy region [73, 74]. In general, these effects stem from interference between electric quadrupole and the (usual) electric dipole transition amplitudes in differential cross sections (for a review, [75]). Besides asymmetries in the photoelectron angular distributions, nondipole effects also lead to new features for spin-resolved measurements [76, 77], and for the case of polarized atoms [78]. Nondipole effects have been predicted to be significant also in double photoionization of helium at relatively low photon energies [79]. In fact, the so-called “back-to-back” two-electron photoionization, predicted quite long ago [80] and experimentally observed recently [81], is entirely nondipole.

Finally, both experimental and theoretical *studies of ionic species* have flourished since the 1990s. In particular, photodetachment of negative ions near excited atomic thresholds provides an opportunity to study correlated, three-body Coulomb states unencumbered by Rydberg series. The ad-

vent of powerful computer workstations in the 1990s enabled theorists to carry out numerical calculations for such high, doubly excited states with spectroscopic accuracy. Following experiments for photodetachment of H^- with excitations of atomic levels in $H(n > 2)$, theorists developed propensity rules for identifying and characterizing the dominant photodetachment channels [82–84]. Experimental and theoretical [85–88] interest also focused on the negative alkali ions (e.g., Li^- and Na^-), which for low photon energies have outer electron detachment spectra grossly resembling that of H^- . However, the negative alkali spectra contain clear signatures of propensity-rule-forbidden states that become increasingly prominent as the atomic number increases (owing to the nonhydrogenic inner electron cores). A brief review of low-energy negative alkali photodetachment is given in [89]. Among the more general features brought to light by these studies is the mirroring of resonance profiles in alternative partial cross sections, which appears to be a very general phenomenon common to photodetachment and photoionization processes involving highly excited residual atoms or ions [90].

Recently, high-energy (K -shell) photodetachment of the negative ions Li^- and He^- (resulting in two-electron ionization) was studied both experimentally and theoretically [91, 92]. These studies represent the first results for inner-shell photodetachment. There is general agreement between theory and experiment well above the K edge, but the theoretical cross sections at the K edge are significantly higher than the experimental measurements. The latter discrepancy is now understood as arising from recapture of the low-energy detached electron following Auger decay of the inner-shell vacancy, which when taken into account theoretically has been shown to provide results that agree with experiment [93, 94]. Also, the first experimental data together with theoretical analyses were recently presented for photoionization of ground and metastable positive ions (O^+ and Sc^{++}) [95, 96]. With the advent of data for photoionization of positive ions it now becomes possible (using the principle of detailed balance) to make connections to data for electron–ion photo-recombination cross sections [96].

25.6 Applications to Other Processes

The detailed understanding of single-photon ionization processes in atoms described in this chapter have recently proved useful in interpreting more complex interactions of electromagnetic radiation with atoms. First, potential barrier effects, which are key features of single-photon ionization of the heavier rare gases, have been shown to also be key features of two and three-photon ionization processes in rare gases. Second, prominent features of the high-order harmonic generation (HHG) spectra of an atom have been

shown to stem from features of that atom's photoionization cross section. We discuss each of these two applications of the theory of atomic photoionization below.

25.6.1 Applications to Two and Three-Photon Ionization Processes

Potential barriers in the effective radial potential experienced by a photoexcited electron have been shown to result in dramatic, resonance-like effects in both two-photon ionization processes [97] and three-photon ionization processes [98] in rare gas atoms. In these two-photon and three-photon ionization processes, such potential barriers were found to affect not only the final state of the electron (as in ordinary photoionization), but also the intermediate-state electron wave packets corresponding to the absorption of one or two photons when the energy absorbed places the intermediate state wave packet in the energy vicinity of the effective potential barrier. These effects were illustrated for the generalized two and three-photon cross sections for ionization of Ar, Kr, and Xe within a single-active-electron, central-potential model [97, 98]. The results are relevant to experimental studies of nonlinear extreme ultraviolet and X-ray processes [99]. Numerous theoretical treatments of electron correlation effects relevant to few-photon ionization processes have been carried out (e.g., [100–103]). Interest in these theoretical treatments is likely to increase when experimental few-photon (nonlinear) ionization cross sections become available as a function of photon frequency.

25.6.2 Application to High-Order Harmonic Generation

The photoionization cross section of an atom has been found to have a direct connection to the high-order harmonic generation (HHG) spectrum of that atom, which is an unexpected relationship between linear and highly nonlinear interactions of an atom with electromagnetic radiation. The relation between the two processes may be understood by means of the quasi-classical interpretation of HHG as a three-step process [104–106] involving: (1) tunnel ionization of an electron in an atom by a strong low-frequency laser field; (2) propagation of the ionized electron in the (laser-dressed) continuum away from and back to the atomic ion by the oscillating laser field; and (3) recombination of the returning electron back to the atom ground state with emission of a harmonic photon. The approach that permits us to understand and describe atomic photoionization by a strong field, called “atomic antenna” was first suggested by *Kuchiev* [107]. It includes the above-mentioned steps (1) and (2). The three-step model suggests a phenomenological parametrization [108, 109] of

the HHG yield Y as the product of an electronic wave packet $W(E)$ (corresponding to the first two steps) and the field-free photorecombination cross section (PRCS) $\sigma(E)$

$$Y \propto W(E)\sigma(E), \quad E = E_\Omega - I_p, \quad (25.30)$$

where E is the energy of the recombining electron, E_Ω is the harmonic energy, and I_p is the target binding energy. This phenomenological parametrization has been confirmed by analysis of exactly solvable model systems [110–112]. The intensity of the harmonic radiation thus carries information on the PRCS of an electron whose momentum is directed along the linear polarization axis of the driving laser field.

Since the photorecombination process is the inverse to that for photoionization, the PRCS is directly related (through the principle of detailed balance) to the photoionization cross section for photon energy E_Ω . Thus, the form of the HHG spectrum replicates the shape of the photoionization cross section. Indeed, experimental and theoretical studies for the case of linearly polarized driving laser fields have shown that HHG spectra exhibit such key features of the corresponding photoionization cross sections as Cooper minima [110, 113] and potential barrier-induced (“giant dipole”) resonances [110, 114–116]. Extension of such studies to the case of two-dimensional driving laser waveforms has shown that this “HHG spectroscopy” can enable the extraction of not only photoionization cross sections but also the photoelectron angular distribution asymmetry parameters [117, 118].

25.7 Future Directions

A main new direction in photoionization is toward time-domain studies in the extreme ultraviolet (XUV) and X-ray regimes. First, advances in high-order harmonic generation have led to the production of isolated pulses of XUV light whose temporal width is measured in tens or hundreds of attoseconds [119]. The shortest such pulses have durations of only a few optical cycles so that (i) they have significant bandwidth, and (ii) the probability of photoionization depends on the phase of the electric field within the pulse envelope. Second, the construction of free-electron lasers (FELs) around the world has enabled studies of intense X-ray interactions with atoms (e.g., [120, 121]). Thus, inner-shell vacancy production and decay, satellite production, and multiple ionization phenomena are all being increasingly studied on timescales comparable to the durations of the FEL X-ray pulses, which are estimated to be on the order of tens of femtoseconds. Of essential importance are also studies of photoionization of fullerenes and endohedrals that represent ordinary atoms “stuffed” inside a fullerene shell, such as, e.g., C60 [122].

References

1. Amusia, M.Y., Cherepkov, N.A.: *Case Stud. At. Phys.* **5**, 47 (1975)
2. Starace, A.F.: In: Mehlhorn, W. (ed.) *Handbuch der Physik*, vol. XXXI, pp. 1–121. Springer, Berlin, Heidelberg (1982)
3. Amusia, M.Y.: *Atomic Photoeffect*. Plenum, New York (1990)
4. Chang, T.N. (ed.): *Many-Body Theory of Atomic Structure and Photoionization*. World Scientific, Singapore (1993)
5. Becker, U., Shirley, D.A.: *VUV and Soft X-Ray Photoionization Studies*. Plenum, New York (1994)
6. Schmidt, V.: *Rep. Prog. Phys.* **55**, 1483 (1992)
7. Sonntag, B., Zimmerman, P.: *Rep. Prog. Phys.* **55**, 911 (1992)
8. Sakurai, J.J.: *Advanced Quantum Mechanics*. Addison-Wesley, Reading, p 39 (1967)
9. Chandrasekhar, S.: *Astrophys. J.* **102**, 223 (1945)
10. Amusia, M.Y., Cherepkov, N.A., Chernysheva, L.V., Sheftel, S.I.: *Phys. Lett. A* **28**(11), 726 (1969)
11. Starace, A.F.: *Phys. Rev. A* **3**, 1242 (1971)
12. Starace, A.F.: *Phys. Rev. A* **8**, 1141 (1973)
13. Blatt, J.M., Biedenharn, L.C.: *Rev. Mod. Phys.* **24**, 258 (1952)
14. Starace, A.F.: In: Mehlhorn, W. (ed.) *Handbuch der Physik*, vol. XXXI, pp. 1–121. Springer, Berlin, Heidelberg (1982). Sect. 7
15. Yang, C.N.: *Phys. Rev.* **74**, 764 (1948)
16. Amusia, M.Y., Cherepkov, N.A., Chernysheva, L.V.: *Phys. Lett. A* **40**(1), 15 (1972)
17. Hermann, F., Skillman, S.: *Atomic Structure Calculations*. Prentice-Hall, Englewood Cliffs (1963)
18. Pratt, R.H., Ron, A., Tseng, H.K.: *Rev. Mod. Phys.* **45**, 273 (1973)
19. Dias, E.W.B., Chakraborty, H.S., Deshmukh, P.C., Manson, S.T., Hemmers, O., Glans, P., Hansen, D.L., Wang, H., Whitfield, S.B., Lindle, D.W., Wehlitz, R., Levin, J.C., Sellin, I.A., Perera, R.C.C.: *Phys. Rev. Lett.* **78**, 4553 (1997)
20. Bethe, H.A., Salpeter, E.E.: *Quantum Mechanics of One- and Two-Electron Atoms*. Springer, Berlin, Heidelberg (1957). Sects. 69–71
21. Amusia, M.Y., Avdonina, N.B., Drukarev, E.G., Manson, S.T., Pratt, R.H.: *Phys. Rev. Lett.* **85**, 4703 (2000)
22. Lukirskii, A.P., Britov, I.A., Zimkina, T.M.: *Opt. Spektrosk.* **17**, 438 (1964)
23. Lukirskii, A.P., Britov, I.A., Zimkina, T.M.: *Opt. Spectrosc. (USSR)* **17**, 234 (1964). English Transl.
24. Ederer, D.L.: *Phys. Rev. Lett.* **13**, 760–763 (1964)
25. Cooper, J.W.: *Phys. Rev.* **128**, 681 (1962)
26. Fano, U., Cooper, J.W.: *Rev. Mod. Phys.* **40**, 441 (1968)
27. Starace, A.F.: In: Mehlhorn, W. (ed.) *Handbuch der Physik*, vol. XXXI, pp. 50–55. Springer, Berlin, Heidelberg (1982)
28. Connerade, J.P., Estiva, J.M., Karnatak, R.C. (eds.): *Giant Resonances in Atoms, Molecules, and Solids*. Plenum, New York (1987). and references therein
29. Bates, D.R.: *Mon. Not. R. Astron. Soc.* **106**, 432 (1946)
30. Seaton, M.J.: *Proc. R. Soc. A* **208**, 418 (1951)
31. Msezane, A.Z., Manson, S.T.: *Phys. Rev. Lett.* **48**, 473 (1982)
32. Kim, Y.S., Pratt, R.H., Ron, A.: *Phys. Rev. A* **24**, 1626 (1981)
33. Kim, Y.S., Ron, A., Pratt, R.H., Tambe, B.R., Manson, S.T.: *Phys. Rev. Lett.* **46**, 1326 (1981)
34. Oh, S.D., Pratt, R.H.: *Phys. Rev. A* **34**, 2486 (1986)
35. Pratt, R.H., Yin, R.Y., Liang, X.: *Phys. Rev. A* **35**, 1450 (1987)
36. Yin, R.Y., Pratt, R.H.: *Phys. Rev. A* **35**, 1149 (1987)
37. Yin, R.Y., Pratt, R.H.: *Phys. Rev. A* **35**, 1154 (1987)
38. Manson, S.T., Starace, A.F.: *Rev. Mod. Phys.* **54**, 389 (1982)
39. Wang, M.S., Kim, Y.S., Pratt, R.H., Ron, A.: *Phys. Rev. A* **25**, 857 (1982)
40. Amusia, M.Y., Arifov, P.U., Baltenkov, A.S., Grinberg, A.A., Shapiro, S.G.: *Phys. Lett. A* **47**(1), 66 (1974)
41. Amusia, M.Y., Chernysheva, L.V., Cherepkov, N.A.: *Phys. Lett. A* **31**(10), 553 (1970)
42. Kelly, H.P., Simons, R.L.: *Phys. Rev. Lett.* **30**, 529 (1973)
43. Samson, J.A.R.: *Adv. At. Mol. Phys.* **2**, 177 (1966)
44. Madden, R.P., Ederer, D.L., Codling, K.: *Phys. Rev.* **177**, 136 (1969)
45. Kelly, H.P.: In: Wuilleumier, F.J. (ed.) *Photoionization and Other Probes of Many-Electron Interactions*, pp. 83–109. Plenum, New York (1976)
46. Burke, P.G., Seaton, M.J.: *Methods Comput. Phys.* **10**, 1 (1971)
47. Burke, P.G., Robb, W.D.: *Adv. At. Mol. Phys.* **11**, 143 (1975)
48. Burke, P.G., Robb, W.D.: In: Watel, G. (ed.) *Electronic and Atomic Collisions: Invited Papers and Progress Reports*, pp. 201–280. North Holland, Amsterdam (1978)
49. Amusia, M.Y., Chernysheva, L.V., Yarzhevsky, V.G.: *Handbook of Theoretical Atomic Physics: Data for Photon Absorption, Electron Scattering, Vacancies Decay*. Springer, Berlin, p 806 (2012)
50. Johnson, W.R., Lin, C.D., Cheng, K.T., Lee, C.M.: *Phys. Scr.* **21**, 409 (1980)
51. Chang, T.N., Fano, U.: *Phys. Rev. A* **13**, 263 (1976)
52. Chang, T.N., Fano, U.: *Phys. Rev. A* **13**, 282 (1976)
53. Swanson, J.R., Armstrong Jr., L.: *Phys. Rev. A* **15**, 661 (1977)
54. Swanson, J.R., Armstrong Jr., L.: *Phys. Rev. A* **16**, 1117 (1977)
55. Seaton, M.J.: *Rep. Prog. Phys.* **46**, 167 (1983)
56. Hochstuhl, D., Hinz, C.M., Bonitz, M.: *Eur. Phys. J. Spec. Top.* **223**, 177–336 (2014)
57. Greene, C.H.: In: Briggs, J.S., Kleinpoppen, H., Lutz, H.O. (eds.) *Fundamental Processes of Atomic Dynamics*, pp. 105–127. Plenum, New York (1988). and references therein
58. Lindle, D.W., Ferrett, T.A., Heiman, P.A., Shirley, D.A.: *Phys. Rev. A* **37**, 3808 (1988)
59. Krause, M., Cerrina, F., Fahlman, A., Carlson, T.A.: *Phys. Rev. Lett.* **51**, 2093 (1983)
60. Amusia, M.Y., Chernysheva, L.V., Manson, S.T., Msezane, A.Z., Radojevich, V.: *Phys. Rev. Lett.* **88**(9), 093002/1–4 (2002)
61. West, J.B., Woodruff, P.R., Codling, K., Houlgate, R.G.: *J. Phys. B* **9**, 407 (1976)
62. Adam, M.Y., Wuilleumier, F., Sandner, N., Schmidt, V., Wendin, G.: *J. Phys.* **39**, 129 (1978)
63. Becker, U., Prescher, T., Schmidt, E., Sonntag, B., Wetzell, H.-E.: *Phys. Rev. A* **33**, 3891 (1986)
64. Taylor, K.T., Norcross, D.W.: *Phys. Rev. A* **34**, 3878 (1986)
65. Amusia, M.Y.: In: Marrus, R., Prior, M., Shugart, H. (eds.) *Atomic Physics 5*, pp. 537–565. Plenum, New York (1977)
66. Jitschin, W., Werner, U., Materlik, G., Doolen, G.D.: *Phys. Rev. A* **35**, 5038 (1987)
67. Wendin, G., Starace, A.F.: *Phys. Rev. A* **28**, 3143 (1983)
68. Tulkki, J.: *Phys. Rev. Lett.* **62**, 2817 (1989)
69. Briggs, J.S., Schmidt, V.: *J. Phys. B* **33**, R1 (2000)
70. King, G.C., Avaldi, L.: *J. Phys. B* **33**, R215 (2000)
71. Berakdar, J., Klar, H.: *Phys. Rep.* **340**, 474 (2001)
72. Krässig, B., Jung, M., Gemmel, M.S., Kanter, E.P., LeBrun, T., Southworth, S.H., Young, L.: *Phys. Rev. Lett.* **75**, 4736 (1995)
73. Hemmers, O., Guillemin, R., Kanter, E.P., Krässig, B., Lindle, D.W., Southworth, S.H., Wehlitz, R., Baker, J., Hudson, A., Lotrakul, M., Rolles, D., Stolte, W.C., Tran, I.C., Wolska, A., Yu, S.W., Amusia, M.Y., Cheng, K.T., Chernysheva, L.V., Johnson, W.R., Manson, S.T.: *Phys. Rev. Lett.* **91**, 053002 (2003)
74. Kanter, E.P., Krässig, B., Southworth, S.H., Guillemin, R., Hemmers, O., Lindle, D.W., Wehlitz, R., Amusia, M.Y., Chernysheva, L.V., Martin, N.L.S.: *Phys. Rev. A* **68**, 012714 (2003)
75. Lindle, D.W., Hemmers, O.: *J. Electron Spectrosc. Relat. Phenom.* **100**, 297 (1999). Special Issue, October
76. Cherepkov, N.A., Semenov, S.K.: *J. Phys. B* **34**, L211 (2001)

77. Khalil, T., Schmidtke, B., Drescher, M., Müller, N., Heinzmann, U.: *Phys. Rev. Lett.* **89**, 053001 (2002)
78. Grum-Grzhimailo, A.N.: *J. Phys. B* **34**, L359 (2001)
79. Istomin, A.Y., Manakov, N.L., Meremianin, A.V., Starace, A.F.: *Phys. Rev. Lett.* **92**, 062002 (2004)
80. Gorshkov, V.G., Drukarev, E.G., Kazachkov, M.P.: *J. Phys. B* **8**(8), 1248–1266 (1975)
81. Schöffler, M.S., Stuck, C., Waitz, M., Trinter, F., Jahnke, T., Lenz, U., Jones, M., Belkacem, A., Landers, A.L., Pindzola, M.S., Cocke, C.L., Colgan, J., Kheifets, A., Bray, I., Schmidt-Böcking, H., Dörner, R., Weber, T.: *Phys. Rev. Lett.* **111**, 013003 (2013)
82. Sadeghpour, H.R., Greene, C.H.: *Phys. Rev. Lett.* **65**, 313 (1990)
83. Rost, J.M., Briggs, J.S., Feagin, J.M.: *Phys. Rev. Lett.* **66**, 1642 (1991)
84. Sadeghpour, H.R., Greene, C.H., Cavagnero, M.: *Phys. Rev. A* **45**, 1587 (1992)
85. Pan, C., Starace, A.F., Greene, C.H.: *J. Phys. B* **27**, L137 (1994)
86. Pan, C., Starace, A.F., Greene, C.H.: *Phys. Rev. A* **53**, 840 (1996)
87. Liu, C.N., Starace, A.F.: *Phys. Rev. A* **58**, 4997 (1998)
88. Liu, C.N., Starace, A.F.: *Phys. Rev. A* **59**, 3643 (1999)
89. Starace, A.F.: In: Aumayr, F., Winter, H. (eds.) *Novel Doubly Excited States Produced in Negative Ion Photodetachment*, pp. 107–116. World Scientific, Singapore (1998)
90. Liu, C.N., Starace, A.F.: *Phys. Rev. A* **59**, R1731 (1999)
91. Berrah, N., Bozek, J.D., Wills, A.A., Turri, G., Zhou, L.L., Manson, S.T., Akerman, G., Rude, B., Gibson, N.D., Walter, C.W., VoKy, L., Hibbert, A., Ferguson, S.M.: *Phys. Rev. Lett.* **87**, 253002 (2001)
92. Berrah, N., Bozek, J.D., Turri, G., Akerman, G., Rude, B., Zhou, H.L., Manson, S.T.: *Phys. Rev. Lett.* **88**, 093001 (2002)
93. Sanz-Vicario, J.L., Lindroth, E., Brandefelt, N.: *Phys. Rev. A* **66**, 052713 (2002)
94. Gorczyca, T.W., Zatsarinny, O., Zhou, H.L., Manson, S.T., Felfli, Z., Msezane, A.Z.: *Phys. Rev. A* **68**, 050703 (2003)
95. Covington, A.M., Aguilar, A., Covington, I.R., Gharaibeh, M., Shirley, C.A., Phaneuf, R.A., Alvarez, I., Cisneros, C., Hinojosa, G., Bozek, J.D., Dominguez, I., Sant'Anna, M.M., Schlachter, A.S., Berrah, N., Nahar, S.N., McLaughlin, B.M.: *Phys. Rev. Lett.* **87**, 243002 (2001)
96. Schippers, S., Müller, A., Ricz, S., Bannister, M.E., Dunn, G.H., Bozek, J., Schlachter, A.S., Hinojosa, G., Cisneros, C., Aguilar, A., Covington, A.M., Gharaibeh, M.F., Phaneuf, R.A.: *Phys. Rev. Lett.* **89**, 193002 (2002)
97. Pi, L.-W., Starace, A.F.: *Phys. Rev. A* **82**, 053414 (2010)
98. Pi, L.-W., Starace, A.F.: *Phys. Rev. A* **90**, 023403 (2014)
99. Bergues, B., Rivas, D.E., Weidman, M., Muschet, A.A., Helml, W., Guggenmos, A., Pervak, V., Kleineberg, U., Marcus, G., Kienberger, R., Charalambidis, D., Tzallas, P., Schröder, H., Krausz, F., Weisz, L.: *Optica* **5**, 237 (2018)
100. L'Huillier, A., Wendin, G.: *Phys. Rev. A* **36**, 4747 (1987)
101. L'Huillier, A., Wendin, G.: *Phys. Rev. A* **36**, 5632 (1987)
102. L'Huillier, A., Wendin, G.: *J. Phys. B* **20**, L37 (1987)
103. Karamatskou, A., Santra, R.: *Phys. Rev. A* **95**, 013415 (2017)
104. Corkum, P.B.: *Phys. Rev. Lett.* **71**, 1994 (1993)
105. Kulander, K.C., Schafer, K.J., Krause, J.L.: In: L'Huillier, A., Piraux, B., Rzazewski, K. (eds.) *Super-Intense Laser-Atom Physics* NATO Science Series B, vol. 316, pp. 95–110. Springer, New York (1993)
106. Corkum, P.B., Krausz, F.: *Nat. Phys.* **3**, 381 (2007)
107. Kuchiev, M.Y.: *JETP Lett.* **45**(7), 404 (1987)
108. Morishita, T., Le, A.T., Chen, Z., Lin, C.D.: *Phys. Rev. Lett.* **100**, 013903 (2008)
109. Le, A.T., Morishita, T., Lin, C.D.: *Phys. Rev. A* **78**, 023814 (2008)
110. Frolov, M.V., Manakov, N.L., Sarantseva, T.S., Emelin, M.Y., Ryabikin, M.Y., Starace, A.F.: *Phys. Rev. Lett.* **102**, 243901 (2009)
111. Frolov, M.V., Manakov, N.L., Sarantseva, T.S., Starace, A.F.: *Phys. Rev. A* **83**, 043416 (2011)
112. Okajima, Y., Tolstikhin, O.L., Morishita, T.: *Phys. Rev. A* **85**, 063406 (2012)
113. Wörner, H.J., Niikura, H., Bertrand, J.B., Corkum, P.B., Villeneuve, D.M.: *Phys. Rev. Lett.* **102**, 103901 (2009)
114. Frolov, M.V., Manakov, N.L., Starace, A.F.: *Phys. Rev. A* **82**, 023424 (2010)
115. Shiner, A.D., Schmidt, B.E., Trallero-Herrero, C., Wörner, H.J., Patchkovskii, S., Corkum, P.B., Kieffer, J.-C., Légaré, F., Villeneuve, D.M.: *Nat. Phys.* **7**, 464 (2011)
116. Pabst, S., Santra, R.: *Phys. Rev. Lett.* **111**, 233005 (2013)
117. Sarantseva, T.S., Frolov, M.V., Manakov, N.L., Ivanov, M.Y., Starace, A.F.: *J. Phys. B* **46**, 231001 (2013)
118. Frolov, M.V., Sarantseva, T.S., Manakov, N.L., Fulfer, K.D., Wilson, B.P., Troß, J., Ren, X., Poliakoff, E.D., Silaev, A.A., Vvedenskii, N.V., Starace, A.F., Trallero-Herrero, C.A.: *Phys. Rev. A* **93**, 031403 (2016)
119. Krausz, F., Ivanov, M.: *Rev. Mod. Phys.* **81**, 163 (2009)
120. Young, L., et al.: *Nature* **466**, 56 (2010)
121. Richter, M., Amusia, M.Y., Bobashev, S.V., Feigl, T., Jurani, P.N., Martins, M., Sorokin, A.A., Tiedtke, K.: *Phys. Rev. Lett.* **102**, 163002 (2009)
122. Amusia, M.Y.: *Chem. Phys.* **414**, 168–175 (2013)



Anthony F. Starace Dr Starace earned his PhD from the University of Chicago (1971) and became George Holmes University Professor of Physics at the University of Nebraska (2001). His primary research interests were the interaction of intense laser light with atoms, especially single and multiphoton detachment and ionization processes. He was a Fellow of the American Physical Society and the American Association for the Advancement of Science. He passed away in 2019.



Contents

26.1	Introduction	395
26.1.1	Auger Effect	395
26.1.2	Autoionization, Autodetachment, and Radiative Decay	395
26.1.3	Formation, Scattering, and Resonances	396
26.2	Projection Operator Formalism	396
26.2.1	Optical Potential	396
26.2.2	Expansion of V_{op} : The QHQ Problem	396
26.3	Forms of P and Q	396
26.3.1	The Feshbach Form	396
26.3.2	Reduction for the $N = 1$ Target	397
26.3.3	Alternative Projection and Projection-Like Operators	398
26.4	Width, Shift, and Shape Parameter	398
26.4.1	Width and Shift	398
26.4.2	Shape Parameter	398
26.4.3	Relation to Breit–Wigner Parameters	400
26.5	Other Computational Methods	400
26.5.1	Complex Rotation Method	400
26.5.2	Pseudopotential Method	402
26.5.3	Exact Bound States in Continuum	403
26.6	Related Topics	403
	References	404

Abstract

The phenomenon of autoionization, or more particularly the autoionization state itself, is treated for the most part in this chapter as a bound state. The process is rigorously a part of the scattering continuum, but, due mostly to the work of *Feshbach* [1], a rigorous formulation can be es-

tablished whereby the main element of the theory can be made into a bound state problem with the scattering elements built around it. The major constituent of both these features is accomplished with projection operators. A brief description of the above elements of the theory, centered around projection operators, is the aim of this chapter [2], although some additional methods are discussed in Sect. 26.5. Another class of resonances, shape resonances, is also briefly discussed, because one of the additional methods, complex rotation, reveals both Feshbach and shape resonances.

Keywords

projection operator · resonance parameter · Feshbach resonance · pseudopotential method · autoionization state

26.1 Introduction

26.1.1 Auger Effect

Autoionization falls within the general class of phenomena known as the Auger effect. In the Auger effect, an atomic system *seemingly* (Sect. 26.1.3) spontaneously decays into a partition of its constituent parts.

26.1.2 Autoionization, Autodetachment, and Radiative Decay

If the initial, composite system is neutral, or positively charged, and its constituent decay particles are an electron and the residual ion, then the process is called *autoionization*. If the original system is a negative ion, so that the residual heavy particle system is neutral, then the process is technically called *autodetachment*; for the most part, the physics and the mathematical treatment are the same.

A. K. Bhatia (✉)
Laboratory for Astronomy & Solar Physics, NASA Goddard Space Flight Center
Greenbelt, MD, USA
e-mail: anand.k.bhatia@nasa.gov

A. Temkin (✉)
Laboratory for Solar and Space Physics, NASA Goddard Space Flight Center
Greenbelt, MD, USA
e-mail: aarongladys@yahoo.com

It is also possible, before electron emission takes place, that the system will alternatively decay radiatively to an autoionization state of lower energy or a true bound state of the composite system. The latter process is called *radiative stabilization* (which is a basic part of dielectronic recombination (Chap. 59)).

26.1.3 Formation, Scattering, and Resonances

Autoionizing states are formed by scattering processes and photoabsorption. These are the inverses of the autoionization and photon emission processes by which they can decay. In the scattering process, formation of the autoionization state corresponds to a resonance in the scattering cross section (Chap. 49). Autoionization is the process that corresponds to the decay of the resonance. The decay of the resonance (autoionization) is then seen to be the last half of the resonant scattering process. Strictly speaking, therefore, the resonant or autoionization state, although it may be long lived, is not completely stationary, and that is the reason that the word *seemingly* was used to describe the Auger process. The compound system can also be formed by absorption of photons impinging on a bound state (usually the ground state) of the compound system, in which case the autoionization state shows up as a *line* in the absorption spectrum.

26.2 Projection Operator Formalism

In the energy domain where the Schrödinger equation (SE)

$$H\Psi = E\Psi \quad (26.1)$$

describes scattering, the wave function does not vanish at infinity, i.e.,

$$\lim_{r_i \rightarrow \infty} \Psi \neq 0, \quad (26.2)$$

where r_i is the radial coordinate of the i -th electron.

The basic idea of the projection operator formalism [1] is to define projection operators P and Q , which separate Ψ into scattering-like ($P\Psi$) and quadratically integrable ($Q\Psi$) parts

$$\Psi = P\Psi + Q\Psi. \quad (26.3)$$

Implicit in Eq. (26.3) are

$$\begin{aligned} \text{completeness} \quad & P + Q = 1, \\ \text{idempotency} \quad & P^2 = P, \quad Q^2 = Q, \\ \text{orthogonality} \quad & PQ = 0, \end{aligned} \quad (26.4)$$

and the asymptotic properties

$$\lim_{r_i \rightarrow \infty} \begin{cases} P\Psi = \lim_{r_i \rightarrow \infty} \Psi \\ Q\Psi = 0 \end{cases}. \quad (26.5)$$

26.2.1 Optical Potential

Straightforward manipulation of Eqs. (26.1) and (26.3) leads to an important relation between $Q\Psi$ and $P\Psi$

$$Q\Psi = (E - QHQ)^{-1} QHP\Psi. \quad (26.6)$$

From Eq. (26.6), a basic equation for $P\Psi$ (which, by virtue of Eq. (26.5), contains all the scattering information) emerges

$$(PHP + V_{\text{op}} - E)P\Psi = 0. \quad (26.7)$$

The most significant part of Eq. (26.7) is the optical potential V_{op} given by

$$V_{\text{op}} = PHQ(E - QHQ)^{-1} QHP; \quad (26.8)$$

V_{op} is a nonlocal potential; the most incisive way to give it meaning is to define the QHQ problem.

26.2.2 Expansion of V_{op} : The QHQ Problem

The following eigenvalue problem constitutes the heart of projection operator formalism

$$QHQ\Phi_n = \mathcal{E}_n\Phi_n. \quad (26.9)$$

For calculational purposes, it is best to recast Eq. (26.9) in the variational form

$$\delta \left(\frac{\langle \Phi QHQ\Phi \rangle}{\langle \Phi Q\Phi \rangle} \right) = 0. \quad (26.10)$$

This equation may yield a discrete plus a continuous spectrum in an energy domain where the SE has only a continuous spectrum. Moreover, if the Q operator is appropriately chosen, then the discrete eigenvalues \mathcal{E}_n are close to the desired class of many-body resonances, called variously Feshbach resonances, core-excited [3], or doubly excited states. In terms of these solutions, V_{op} has the expansion

$$V_{\text{op}} = \sum_n^{\wedge} PHQ|\Phi_n\rangle(E - \mathcal{E}_n)^{-1}\langle\Phi_n|QHP. \quad (26.11)$$

26.3 Forms of P and Q

26.3.1 The Feshbach Form

Projection operators are not unique. *Feshbach* [1] sketched a derivation of a *robust* projection operator for the general N -electron target system. Robust means that $Q\Phi$ is devoid

of open channels. The complete expression for P , including inelastic channels, was derived in [4]

$$P = \sum_{i=1}^{N+1} \left[\langle \psi(r^{(i)}) \rangle \cdot \langle \psi(r^{(i)}) \rangle + \sum_{\lambda_\alpha} \frac{v_\alpha(r_i) \cdot \psi(r^{(i)}) \langle v_\alpha(r_i) \cdot \psi(r^{(i)}) \rangle}{\lambda_\alpha - 1} \right], \quad (26.12)$$

where the prime on the second summation means that terms with $\lambda_\alpha = 1$ are to be omitted; r_i denotes the radial coordinate of electron i , and $r^{(i)}$ stands for the angular and spin coordinates of electron i plus all coordinates of the remaining N electrons. Thus, $r^{(i)}$ indicates the totality of all coordinates of the $(N + 1)$ electrons *except* the radial coordinate of the i -th electron r_i ; $\psi(r^{(i)})$ is the vector channel wave function in which the angular momentum and spin of the electron i are coupled to the target in state v ($v = 0, \dots, v_{\max}$). A component of a vector labels the inelastic channel, and dot products represent sums over channels. The Q operator is then made explicit by completeness: $Q = 1 - P$, Eq. (26.4).

The α -indexed quantities in Eq. (26.12) arise from exchange; they are the eigensolutions of the integral eigenvalue problem

$$v_\alpha(r_i) = \lambda_\alpha \langle \mathbf{K}(r_i|r_j) \cdot v_\alpha(r_j) \rangle_{r_j}. \quad (26.13)$$

Here, $\mathbf{K}(r_i|r_j)$ is a matrix with components

$$K_{\mu\nu}(r_i|r_j) \propto N \langle \psi_\mu(r^{(i)}) \psi_\nu(r^{(j)}) \rangle_{r^{(ij)}}, \quad (26.14)$$

and $r^{(ij)}$ indicates that all variables, except r_i and r_j , are integrated over. In the inelastic regime, therefore, the $[v_\alpha, \lambda_\alpha]$ are not associated with specific channels but rather with the totality of open channels. This means that every component of v_α is associated with all inelastic channels [4]. The v_α are orthogonal and can be normalized so that $\langle v_\alpha \cdot v_\beta \rangle = \delta_{\alpha\beta}$. The λ_α obey several sum rules [5], of which the most useful is

$$\sum_{\alpha=1}^{n_\lambda} (\lambda_\alpha)^{-1} = \sum_{v=0}^{v_{\max}} \langle K_{vv}(r|r) \rangle_r, \quad (26.15)$$

where n_λ is the number of eigenvalues of Eq. (26.13). The v_α can be accurately calculated by use of a variational principle [5]. A test of Eq. (26.15) for the lowest He⁻(²S) resonance, using Hylleraas functions to construct Q in the evaluation of QHQ , is shown in Table 26.1 [5], and results for the resonance position are compared in Table 26.2.

26.3.2 Reduction for the $N = 1$ Target

Explicit rigorous P and Q operators of the above type are only possible for $N = 1$ (i.e., hydrogenic) targets. In that case, spin can be easily eliminated by using spatially sym-

Table 26.1 Test of sum rule in Eq. (26.15) for the lowest He⁻(1s2s²2S) autodetachment state [5]. Projection operators are based on a 4 term Hylleraas ϕ_0 and the variational form of v_α given below. Values of other constants are given in [5]

$$\begin{aligned} \phi_0 &\propto (1 + C_1 r_1 + C_2 r_2 + C_{12} r_{12}) \exp(-\gamma_1 r_1 - \gamma_2 r_2) \\ &\quad + (1 \leftrightarrow 2) + (r_1 \leftrightarrow r_2), \\ v_\alpha &\propto (c_{11}^{(\alpha)} + c_{12}^{(\alpha)} r) \exp(-\gamma_1 r) + (c_{21}^{(\alpha)} + c_{22}^{(\alpha)} r) \exp(-\gamma_2 r), \end{aligned}$$

and the variational eigenvalues are [5]

$$\lambda_1 = 1.009453, \lambda_2 = 232.8540, \lambda_3 = 80.101.08, \lambda_4 = 4.817,341$$

Summation	Value (Ry ⁻¹)
$\sum_{\alpha=1}^4 (\lambda_\alpha)^{-1}$	0.9949425
$\langle K(r r) \rangle_r$	0.9949514

Table 26.2 Comparison of methods for calculating the energy of the lowest He⁻(1s2s²2S) autodetachment state. The QHQ results are denoted $(\hat{E} - E_0)_{\text{Quasi}}$ for the quasi-projection method and $(E - E_0)_{\text{Complete}}$ for the complete projection method [5]. The entries labeled *Other results* give the full resonant energy. Units are eV

Target	$(\hat{E} - E_0)_{\text{Quasi}}$	$(E - E_0)_{\text{Complete}}^a$
Closed shell	19.366	19.593
Open shell	19.385	19.666
1s1s' + 2p ²	19.388	19.615
4-term Hylleraas	19.381	19.496
10-term Hylleraas	19.379	19.504

Other results 19.402^b, 19.376^c, 19.367^d, 19.367 ± 0.007^e

^a Values obtained using $R_\infty = 13.605698$ eV and $E_0 = -79.0151$ eV [6]

^b Complex rotation method; *Junker and Huang* [7]

^c Hole-projection complex-rotation; *Davis and Chung* [8]

^d Hermitian-representation complex-rotation; [9]

^e Experiment; *Brunt et al.* [10]

metric or antisymmetric wave functions. In the elastic region, P and Q reduce to [12, 13]

$$P = P_1 + P_2 - P_1 P_2; \quad Q = 1 - P_1 - P_2 + P_1 P_2. \quad (26.16)$$

Here, the $P_i = \phi(r_i) \langle \phi(r_i) \rangle$ are purely spatial projectors. Forms for the inelastic continuum are easily generalized [11].

There have been many calculations of QHQ for two-electron systems ($N = 1$), starting with fundamental work of *O'Malley and Geltman* [11]. A small sample is given in Table 26.3. They are given for their historical importance, demonstrating for the first time the convergence of eigenvalues to well-defined values in the continuum. All eigenvalues

Table 26.3 Energies E_s of the He(2s2p¹P⁰) autoionization states below He⁺ ($n = 2$) threshold from the variational calculations of *O'Malley and Geltman* [11]. Units are Ry; N is the number of terms in the trial function

N	$s = 1$	$s = 2$	$s = 3$
9	-1.37708	-1.17892	-1.09716
15	-1.38044	-1.18312	-1.10432
20	-1.38216	-1.18348	-1.10828
25	-1.38316	-1.19000	-1.11188

(below the $n = 2$ threshold, in this case) correspond to resonances.

26.3.3 Alternative Projection and Projection-Like Operators

Two alternative methods based on the idea of projection are available: quasi projectors and hole projection operators. Quasi projectors [14] relax the condition of idempotency but still maintain a discrete spectrum, which is in a one-to-one correspondence with resonances, with a predeterminable number of exceptions [2]. Hole projection operators have proven to be a more practical and effective approach [15]. The method uses one-particle (say, hydrogenic) orbitals, $\phi_n(q; \mathbf{r})$, to build holes via projectors, $[1 - \sum_n \phi_n] \langle \phi_n |$, operating on the $(N + 1)$ -particle wave function. The Rayleigh–Ritz functional is minimized with respect to the linear parameters in Φ , but it is maximized with respect to q , the nonlinear parameter in all the ϕ_n . In a model case, this *minimax* procedure was shown [15] to optimize the eigenvalues to describe resonance energies; many calculations since then [16] have verified the minimax criteria in many-electron systems. More recently, the technique was combined with complex rotation, so as to enable calculation of other resonant quantities [17]. Remarkably accurate results have been obtained.

Finally, hole projectors are ideally suited for inner-shell vacancy states of many-electron systems if high accuracy is required [2]. Effectively, this amounts to a reliable method for optimizing parameters of a hole orbital to be used in an Auger transition integral for filling such a vacancy, although that method has apparently never been used (Chap. 66).

26.4 Width, Shift, and Shape Parameter

26.4.1 Width and Shift

Here, one requires $P\Psi$ as well as $Q\Psi$. The former is obtained from a *nonresonant continuum*, defined as the scattering solution of

$$[P\mathcal{H}P + V_s^{(\text{nr})} - E]P\Psi_s^{(\text{nr})} = 0, \quad (26.17)$$

where the nonresonant potential,

$$V_s^{(\text{nr})} = V_{\text{op}} - PHQ\Phi_s \langle E - \mathcal{E}_s \rangle^{-1} \langle \Phi_s QHP, \quad (26.18)$$

excludes the resonant state s from the optical potential. In terms of $P\Psi_s^{(\text{nr})}$, whose phase shift, η_0 , is smooth in the vicinity of $E \approx \mathcal{E}_s$, a solution of the complete problem, Eq. (26.7), can be constructed [11] with a phase shift $\eta_0 + \eta_r$,

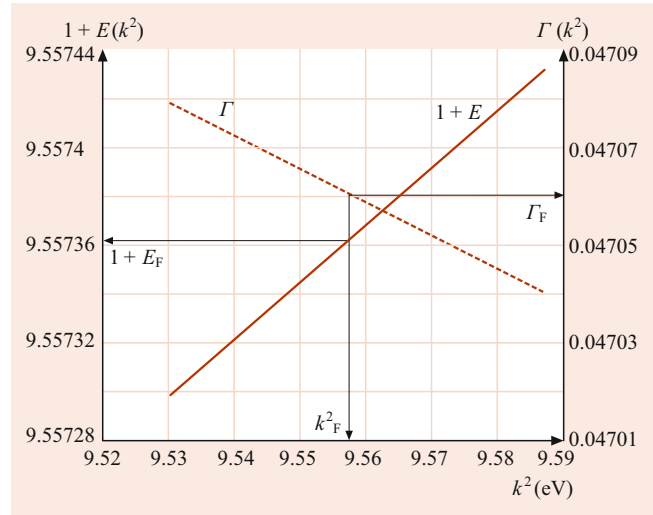


Fig. 26.1 Precision calculation of $\text{H}^- (1\text{S})$ resonance. *Solid curve*: $E + 1$ versus k^2 , where $E = \mathcal{E} + \Delta$, Eq. (26.20). k_F^2 is that value of k^2 at which $E + 1 = k^2$. *Dashed curve* is Γ versus k^2 from Eq. (26.21), and $\Gamma_F = \Gamma(k_F^2)$. Curves are from calculations of [18]; results are $E_F = 9.55735$ eV and $\Gamma_F = 0.0470605$ eV. Applying corrections, Eq. (26.31) finally gives $E_{\text{BW}} = E_F + O(10^{-6})$, $\Gamma_{\text{BW}} = 0.04717$ eV

where the additional phase shift

$$\eta_r = \arctan\left(\frac{\Gamma/2}{(\mathcal{E}_s + \Delta_s) - E}\right) \quad (26.19)$$

exhibits typical resonant behavior ($0 < \eta_r < \pi$). From Eq. (26.19), it is clear that the *true* position of the resonance is

$$E_s(E) = \mathcal{E}_s + \Delta_s(E). \quad (26.20)$$

The width Γ_s and shift Δ_s are given by [11]

$$\Gamma_s(E) = 2k |\langle \Psi_s^{(\text{nr})}(E) PHQ \Phi_s \rangle|^2, \quad (26.21)$$

$$\Delta_s(E) = \langle \Phi_s QHP G_P(E) PHQ \Phi_s \rangle, \quad (26.22)$$

where k is the scattering momentum (i.e., $k^2 = E - E_0$), and G_P is the Green's function associated with Eq. (26.17); G_P , whose asymptotic form is given in [2, 11], is the usual combination of regular and irregular solutions of Eq. (26.17).

Equation (26.20) is an implicit equation for the energy at which the resonance occurs. It can be solved graphically [18], and that energy defines the Feshbach resonant energy E_F , which differs (very slightly) from the Breit–Wigner energy (Sect. 26.4.3 and Fig. 26.1).

26.4.2 Shape Parameter

The shape of an isolated radiative transition between an autoionization state and some other state can be described by

Table 26.4 Comparison of high-precision calculations with the experiment for the resonance parameters of the He($1P^0$) resonances below the $n = 2$ threshold. For photoabsorption, the appropriate Rydberg constant is $R_M = R_\infty/(1 + m/M)$ [19]. The value used here is $R_M = 13.603833$ eV, and $E_0 = -79.0151$ eV [6]

Quantity	Units	Calculation ^a		Experiment	
		$s = 1$	$s = 2$	$s = 1$	$s = 2$
\mathcal{E}_s	Ry	-1.3857895	-1.194182		
Δ	eV	-0.00713	0.0006202		
$E_s - E_0$	eV	60.1444	62.7587	60.133 ± 0.015^b	62.756 ± 0.01^b
				60.151 ± 0.0103^c	
Γ	eV	0.0369 ^d	0.0001165	0.038 ± 0.004^b	
				0.038 ± 0.002^c	
q_s		-2.849 ^e	-4.606 ^e	-2.80 ± 0.25^b	
				-2.55 ± 0.16^c	

^a Bhatia and Temkin [19], except as noted; ^b Madden and Codling [20]; ^c Morgan and Ederer [21]; ^d Bhatia, Burke, and Temkin [22]; ^e Bhatia and Temkin [23]

Γ , E , and an additional parameter q_s , often called the shape parameter [24]. The ratio of transition probability (in, say, absorption from an initial state labeled i) through the resonant state to its nonresonant value, parametrized in its Fano form [24] on the left-hand side of Eq. (26.23), can be equated to its meaning in Feshbach terms on the right-hand side of Eq. (26.23)

$$\frac{(e_s + q_s)^2}{1 + e_s^2} = \frac{|\langle P\Psi + Q\Psi|T|i\rangle|^2}{|\langle P\Psi_s^{(nr)} + Q\Psi_s^{(nr)}|T|i\rangle|^2}, \quad (26.23)$$

where e_s is the scaled energy

$$e_s = (E - E_s)/(\Gamma_s/2), \quad (26.24)$$

and T is a radiative transition operator Eq. (26.25).

To analyze Eq. (26.23) in the Feshbach formalism, the key point [11] is to recognize that the bras on the right-hand side must include P , as well as Q parts of the respective wave functions, as is indicated in Eq. (26.23). That is because the T operator is a perturbation and not part of the dynamical problem. With T in length form

$$T \propto \sum_{j=1}^{N+1} z_j, \quad (26.25)$$

the right-hand side of Eq. (26.23) can be calculated by noting that $P\Psi_s$ and $P\Psi_s^{(nr)}$ can, in principle, be determined from Eqs. (26.7) and (26.17); $Q\Psi_s$ is then derived from $P\Psi_s$ using Eq. (26.6). However, $Q\Psi_s^{(nr)}$ excludes the s th term from the right-hand side of Eq. (26.6)

$$Q\Psi_s^{(nr)} = \sum_{n \neq s} \frac{\Phi_n \langle \Phi_n | QHP\Psi^{(nr)} \rangle}{E - \mathcal{E}_n}. \quad (26.26)$$

With use of these relations in the right-hand side of Eq. (26.23), an explicit formula for q_s was derived in [2];

it is given by

$$q_s = \frac{\langle \Phi_s | \tilde{Q} | T | i \rangle}{k \langle i | T | \Psi_s^{(nr)} \rangle \langle \Psi_s^{(nr)} | PHQ \Phi_s \rangle}, \quad (26.27)$$

where

$$\tilde{Q} = Q + QHPG_s + \sum_{n \neq s} \frac{QHPPG_s HQ | \Phi_n \rangle \langle \Phi_n |}{E - \mathcal{E}_n}. \quad (26.28)$$

Green's function G_s in Eq. (26.28) is the one associated with Eq. (26.17). It can be expanded in terms of the eigensolutions of Eq. (26.17), but its spectrum may have a discrete as well as continuous part, in which case,

$$G_s = \sum_{\nu}' \frac{P\Psi_{\nu}^{(nr)} \langle P\Psi_{\nu}^{(nr)} |}{E_s - E_{\nu}} + \frac{\wp}{\pi} \int \frac{P\Psi_s^{(nr)}(E') \langle P\Psi_s^{(nr)}(E') | \sqrt{E'} dE'}{E_s - E'}. \quad (26.29)$$

The sum over ν refers to the discrete part of the spectrum of Eq. (26.17) (if there is one), and \wp denotes a principal value integral over the continuum solutions. The latter are always assumed to be normalized as plane waves (not energy normalized) throughout this chapter.

Equation (26.27) is a nontrivial example of what can be done with the projection operator technique. Not only does it allow very accurate calculations ([17, 19] and footnote in Table 26.4), but it provides a theoretical incisiveness that far exceeds all previous resonance formalisms.

A formula for the resonant scattering cross section, which is of the same form as the left-hand side of Eq. (26.23), can be derived; however, in that case, the parameter corresponding to q_s is related to the nonresonant phase shift [25] and has no quantitative relationship to the above shape parameter (q_s).

26.4.3 Relation to Breit–Wigner Parameters

Inferring resonance parameters from experimental data is generally done by fitting to resonance formulae in which the resonance parameters are assumed to be energy independent. A phase shift, for example, would be inferred by assuming

$$\eta(E) = \delta_0(E) + \arctan\left(\frac{\Gamma_{\text{BW}}/2}{E_{\text{BW}} - E}\right). \quad (26.30)$$

The relation between the above Breit–Wigner parameters and those of the Feshbach theory was derived in lowest order by *Drachman* [26]

$$\begin{aligned} E_{\text{BW}} &= E_{\text{F}} - (1/4)\Gamma_{\text{F}}(d\Gamma_{\text{F}}/dE)_{E=E_{\text{F}}}, \\ \Gamma_{\text{BW}} &= \Gamma_{\text{F}}(1 + d\Delta_{\text{F}}/dE)_{E=E_{\text{F}}}, \\ \delta_0(E) &= \eta_0(E) - (1/2)d\Gamma_{\text{F}}/dE. \end{aligned} \quad (26.31)$$

So far these differences have been evaluated in only one precision calculation (for the lowest ^1S resonance in electron–hydrogen scattering) [18]. A précis is given in Fig. 26.1.

26.5 Other Computational Methods

We now briefly review two calculational methods used for basic applications in autoionization of few body systems: (a) complex rotation and (b) a pseudopotential method.

26.5.1 Complex Rotation Method

Complex rotation, which is based on a theorem of *Balslev* and *Combes* [27], has been extensively applied with great accuracy. Two additional basic systems to be mentioned here are H^- and Ps^- (Ps = positronium). In complex rotation, the particle distances are multiplied by a common phase factor

$$r_i \rightarrow r_i e^{i\theta}. \quad (26.32)$$

Under this replacement, the Hamiltonian undergoes the transformation

$$H \rightarrow T e^{-2i\theta} + V e^{-i\theta} \quad (26.33)$$

(only Coulomb interactions are assumed). A real variational wave function Φ is used (for the applications here, they are of Hylleraas form, multiplied by rotational harmonics of symmetric Euler angles of the desired angular momentum, parity, and spin [28]). The functional

$$[E] = \frac{\langle \Phi | H | \Phi \rangle}{\langle \Phi | \Phi \rangle} = \frac{\langle \Phi | T | \Phi \rangle e^{-2i\theta} + \langle \Phi | V | \Phi \rangle e^{-i\theta}}{\langle \Phi | \Phi \rangle} \quad (26.34)$$

is then evaluated. Minimization of Eq. (26.34) with respect to the linear parameters, for a given value of θ , is carried out in the usual way, but by virtue of the complex dependence on rotation angle, the matrix elements H_{ij} in the matrix eigenvalue equation

$$\det |H_{ij}(\theta) - E\Delta_{ij}| = 0 \quad (26.35)$$

are complex. Thus, the solution of Eq. (26.35) gives rise to complex eigenvalues $E_\lambda = E_\lambda(\theta)$. For a given λ , the optimum θ is the one for which $E_\lambda(\theta)$ is effectively stationary as a function of θ [29]. Note that no projection operators are used: the real part of E_λ corresponds to the Breit–Wigner (i.e., experimental) position of the resonance, and $\text{Im}(E_\lambda) = \Gamma_{\text{BW}}/2$, where Γ_{BW} corresponds to the Breit–Wigner width of the resonance. These parameters thus include the full Feshbach values plus corrections Eq. (26.31).

Using Hylleraas wave functions with up to 1230 terms in the complex rotation method, resonance parameters have been obtained for resonance states of H^- below the $n = 2$ and 3 thresholds of H , which compare very well with those obtained using the projection-operator, R-matrix, and close-coupling methods. Results for the $^1\text{D}^e$ states of H^- are given in Table 26.5. Similar calculations for Ps^- have been carried out [30]. The complex rotation method has been applied to the autoionization states of many different systems, including muonic systems [31], as well as to study the combined effect of electric field and spin–orbit interaction on resonance parameters [32].

The following are more recent very accurate results for Feshbach resonances using the complex-rotation method. They show that this method is a very powerful technique for uncovering not only Feshbach but also shape resonances, as well as exact bound states in the continuum.

Using Hylleraas type wave functions, *Lindroth* [35] calculated the resonance parameters for singlet and triplet S , P , D , and F states of He below $n = 2$ and 3 threshold of He^+ . Some of her results below $n = 2$ are given in Table 26.6.

Burgers et al. [36] also carried out a very extensive calculation (up to 24497 Sturmian functions) for parameters of resonance states of He below thresholds up to $n = 10$ of He^+ . They used perimetric coordinates introduced by *Coolidge* and *James* [37]. Their results for a few states below $n = 2$ are given in Table 26.6. The resonance parameters of some of the states obtained in these calculations are compared in Table 26.6 with those obtained by *Bhatia* and *Temkin* [19]. We use $R_\infty = 13.605826$ eV throughout.

Similar calculations have carried out by *Lindroth* [35] and *Burgers* et al. [36] to calculate resonance parameters for triplet states of He . Their results are given in Table 26.7 and compared with those obtained by *Bhatia* and *Temkin* [19].

Ho [38] has calculated resonances parameters in Ps^- below the $n = 2, 3, 4$, and 5 thresholds of Ps using Hylleraas

Table 26.5 Comparison of resonance parameters (in eV) obtained from different methods for calculating $^1D^e$ states in H^-

Threshold n	Complex-coordinate rotation [29]		R-matrix [33]		Feshbach projection [19] Eq. (26.31)	
	E	Γ	E	Γ	E_F	Γ_F
2	10.12436	0.00862	10.1252	0.00881	10.1244	0.010
3	11.81102	0.04512	11.81097 ^a	0.04449 ^a		

^a Close coupling (18-state), [34]

Table 26.6 Singlet autoionization states of He of S , P , D , and F angular momentum below the $n = 2$ threshold of He^+ . Results are in eV relative to the ground state energy of He = -5.8074475 Ry

State	Ref. [35]		Ref. [36]		Ref. [19]	
	E_{res}	Γ	E_{res}	Γ	E_{res}	Γ
S(1)	57.8481	1.24(−1)	57.8481	1.24(−1)	57.8435	1.25(−1)
S(2)	62.0915	5.88(−3)	62.0915	5.87(−3)	62.0911	6.67(−3)
S(3)	62.9633	3.70(−2)	62.9631	3.71(−2)		
S(4)	64.1007	2.07(−4)	64.1008	2.04(−3)		
P(1)	60.1538	3.74(−2)				
P(2)	62.7679	1.04(−5)				
P(3)	63.6653	8.19(−3)				
D(1)	59.9140	6.43(−2)			59.9146	7.29(−2)
F(1)	63.8234	3.48(−4)				

Table 26.7 Triplet autoionization states of He of S , P , D , and F angular momentum below the $n = 2$ threshold of He^+ . Results are in eV relative to the ground state energy of He = -5.8074475 Ry

State	Ref. [36]		Ref. [37]		Ref. [19]	
	E_{res}	Γ	E_{res}	Γ	E_{res}	Γ
S(1)	62.6179	1.81(−4)	62.6180	1.81(−4)	62.6173	4.21(−5)
S(2)	63.7834	56.97(−6)	63.7835	7.08(−6)	63.7831	7.09(−6)
P(1)	63.1053	2.24(−3)			63.1066	42.61(−3)
P(2)	63.2588	5.12(−5)			63.2595	4.88(−5)
P(3)	64.0803	4.35(−7)				
F(1)	63.6079	6.37(−4)				

type wave functions. Ps^- is similar to H^- except that the proton in H is replaced by a positron. But for Ps^- the mass polarization term in the Hamiltonian becomes important and must be included. Ps^- results are approximately close to half of the values in H^- . Ho's results for the singlet and triplet S states are given in Table 26.8. Note that there is more than one state below the n -th state of Ps. He used 364 Hylleraas terms for singlet states and 455 terms for triplet states in the wave functions, respectively. It is seen that in He and Ps^- systems, the singlet resonances have lower energies than the triplet resonances. The parameters for these resonances (not shown here) have also been calculated by Papp et al. [39] by solving Faddeev–Merkuriev integral equations for three-body Coulombic systems by using Coulomb–Sturmian separable expansion approach. They found several new resonances in addition to those calculated by Ho [38].

Ho and Bhatia [40] have calculated resonance parameters for the $^3P^e$ states of Ps^- below the thresholds $n = 2, 3, 4, 5$, and 6 of Ps. The results are given in Table 26.9. These states can autoionize to orthopositronium of odd parity and an electron with angular momentum equal to one.

Table 26.8 Singlet and triplet autoionization states of Ps^- . Results are in eV relative to the ground state energy of Ps = 0.5 Ry

n	1S		3S	
	E_{res}	Γ	E_{res}	Γ
2	4.7340	1.17(−3)	5.0742	1.36(−4)
	5.0709	2.72(−6)		
3	7.7646	2.04(−3)	6.0038	2.72(−4)
	5.9908	1.50(−3)		
4	6.2526	3.27(−3)	6.3383	2.72(−4)
	6.3267	4.08(−3)		
	6.3317	4.63(−3)		
5	6.4519	6.12(−3)		
	6.4723	1.91(−3)		

The autoionization states described above are compound states in which the incoming electron is, in fact, attached to an excited state of the target. These states are referred to as Feshbach resonances. However, there is another class of compound states that arise when an incoming electron is in effect caught in a potential barrier set up by the incoming electron interacting with the target atom or ion. These states are referred to as shape resonances. Shape resonances

Table 26.9 $^3P^e$ states of Ps^- . Results are in eV relative to the ground state energy of $Ps = 0.5 Ry$

n	E_{res}	Γ
3	5.9422	4.87(-3)
	6.0381	7.46(-4)
4	6.2888	4.10(-4)
	6.3527	2.45(-4)
5	6.4637	6.93(-4)
	6.5023	7.13(-4)
	6.5082	3.59(-4)
6	6.5635	1.44(-3)
	6.5867	1.58(-3)
	6.5879	1.55(-3)

Table 26.10 Odd parity $^{1,3}P$ states of Ps^- . Resonance positions are with respect to the ground state energy of $Ps = 0.5 Ry$

n	State	E_{res}	Γ
2	$^1P(1)$	5.08429	2.700(-5)
	$^3P(1)$	4.8075	3.478(-3)
	$^3P(2)$	5.08589	4.350(-4)
3	$^1P(1)$	5.94236	6.030(-3)
	$^1P(2)$	6.00787	4.100(-4)
	$^3P(1)$	5.85395	1.649(-3)
	$^3P(2)$	5.99738	1.118(-3)

occur above the energy necessary to excite the target. They are also allowed to decay by autoionization. Theoretically, the appearance of shape resonances is based on a theorem of *Balslev and Combes* [27].

Resonance parameters for odd parity $^{1,3}P$ states in Ps^- were calculated by *Bhatia and Ho* [42] using the complex-rotation method. Their results are given in Table 26.10. The lowest odd parity state was observed in Ps^- by using laser beams of 2285 and 2297 Å by *Michishio et al.* [43]. Their results for the energy and width agree with those given in Table 26.10 and also with the energy and width calculated by *Botero and Greene* [44].

26.5.2 Pseudopotential Method

The second method in this section is included for the reason that it represents a rather different idea for the calculation of autoionization rather than being a more elaborate application of methodologies that are already known, with results too numerous to be referenced here. The method, described as a pseudopotential approach, was introduced by *Martin et al.* [45]. An effective Hamiltonian H_{eff} is defined as

$$H_{eff} = H + MP, \quad (26.36)$$

where M is a scalar parameter (i.e., a number), which will be taken to be very large, multiplying the P operator,

Eq. (26.16). [Applications have thus far been restricted to one-electron targets and resonances below the $n = 3$ excited state.] In practice, one minimizes the expectation value of H_{eff} , i.e.,

$$\delta \left(\frac{\langle \Psi_v | H_{eff} | \Psi_v \rangle}{\langle \Psi_v | \Psi_v \rangle} \right) = 0, \quad (26.37)$$

using an arbitrary, quadratically integrable, variational function Ψ_v .

In order to understand the nature of the spectrum that arises from this variation, we imagine Ψ_v divided into its P and Q space components

$$\Psi_v = Q\Psi_v + P\Psi_v = \Psi_v^Q + \Psi_v^P. \quad (26.38)$$

The expectation value $\langle \Psi_v | H_{eff} | \Psi_v \rangle$ is written in matrix form as

$$\begin{aligned} & \langle \Psi_v | H_{eff} | \Psi_v \rangle \\ &= \left\langle \begin{pmatrix} \Psi_v^Q & \Psi_v^P \end{pmatrix} \begin{pmatrix} H_{QQ} & H_{QP} \\ H_{PQ} & H_{PP} + M \end{pmatrix} \begin{pmatrix} \Psi_v^Q \\ \Psi_v^P \end{pmatrix} \right\rangle. \end{aligned} \quad (26.39)$$

The eigenvalue problem resulting from Eq. (26.37) reduces to finding the eigenvalues of the determinant

$$\det \begin{pmatrix} \langle H_{QQ} \rangle - \lambda & \langle H_{QP} \rangle \\ \langle H_{PQ} \rangle & \langle H_{PP} \rangle + M - \lambda \end{pmatrix} = 0. \quad (26.40)$$

Note that only the bottom right-hand side component contains the term M . As a result, in the limit of large M , the eigenvalues, which can readily be solved for from Eq. (26.39), are

$$\lim_{M \rightarrow \text{large}} \lambda = \begin{cases} M + \langle H_{PP} \rangle \\ \langle H_{QQ} \rangle \end{cases}. \quad (26.41)$$

The lower eigenvalue is the desired Feshbach resonant energy $\mathcal{E}_F = \langle H_{QQ} \rangle$. The width is calculated from [with our normalization, Eq. (26.21)]

$$\Gamma = 2k |\langle \Psi_\lambda | H_{eff} | \chi_E \rangle|^2, \quad (26.42)$$

where χ_E is the solution of the exchange approximation

$$(H_{PP} - E)\chi_E = 0. \quad (26.43)$$

It is emphasized that this method only calculates the Feshbach energy; thus the shifts are not included. On the other hand, the method uses no projection operators in calculating the matrix elements of H , and only the matrix elements of P by itself occur. This is much easier than a standard QHQ calculation (Sect. 26.2.2).

In practice, the matrix in Eq. (26.39) will expand to an $N \times N$ matrix, where N is the number of linear parameters

Table 26.11 Resonance energies \mathcal{E}_F (Ry) and widths (eV) for 1P states of He below the $n = 2$ threshold (-1 Ry) of He^+

State	Martin et al. [45]		Lipsky and Conneely [46]		Bhatia and Temkin [19, 23]	
	Position	Width	Position	Width	Position	Width
1	-1.38400	0.0382	-1.37672	0.0341	-1.38579	0.0363
2	-1.19460	0.000146	-1.19312	0.000131	-1.19418	0.000106
3	-1.12752	0.000860	-1.12584	0.00727	-1.12772	0.0090

in Ψ_V , and (if one uses a Hylleraas form of Ψ_V , for example) the matrix in Eq. (26.39) will not overtly divide itself into the simple form of this heuristic exposition pictured in Eq. (26.39) or (26.40). Nevertheless, the conclusion holds; in detail, the eigenvalue spectrum will span a range of values with those below the threshold, appropriate to the P operator being used, corresponding to real resonances, and the largest eigenvalue will approach the value of M used in the specific calculation.

A sample of results for the $\text{He}(^1P)$ resonances below the $n = 2$ threshold of He^+ taken from [45], with some comparisons, is given in Table 26.11. Note that the value of \mathcal{E}_F of the second resonance in the Martin et al. [45] calculation is lower than the rigorous QHQ calculation [19]. It is believed that this may be due to the residual M dependence of H_{eff} .

26.5.3 Exact Bound States in Continuum

There is another class of “autoionization” states, which are states in the Coulomb limit: i.e., only Coulomb potentials in the Hamiltonian whose energy although in the continuum of the electron–atom scattering process are of symmetry different from a scattering state into which they might otherwise be allowed to decay. A prime example of such states is the $^3P^e$ state of H^- [47] whose energy (9.6669 eV) is lower than the $n = 2$ state of H (10.2044 eV). Such a state cannot decay by Coulomb forces to the ground state (1S) plus an outgoing electron; the outgoing electron would have to be a P-wave (to conserve angular momentum). However, in that case, the total parity of the electron plus the residual atom (singlet S) would be odd, whereas the parity of the initial system ($^3P^e$) is even! Such states have various consequences from a calculational point of view. (a) They can be calculated as ordinary bound states, e.g., using the Rayleigh-Ritz variational principle

$$\delta \left(\frac{\langle \Psi H \Psi \rangle}{\langle \Psi \Psi \rangle} \right) = 0. \quad (26.44)$$

Using an ansatz for Ψ with the correct quantum symmetry (in the $^3P^e$ case, such a function would be labeled $\Psi(2p3p^3P^e)$. (b) From the point of view of the projection operators’ formalism, such a state would correspond to a state with parameters for which $P = 0$ and $Q = 1$, and, thus, no projection operators are needed in doing the variational calculations. (c) From the point of view of complex rotation, one would

Table 26.12 $^3P^e$ shape resonances in Ps^- . Results are in eV relative to the ground state energy of $\text{Ps}^- = -0.5$ Ry

n	E (eV)	Γ (eV)
2	5.1103	7.35(−3)
4	6.3815	8.71(−4)
6	6.7842	5.44(−4)

find three things: first that the stationary value would occur at $\Theta = 0$; second that the $[E]$ from Eq. (26.34) would behave like an ordinary bound state, and third that the fact that $[E]$ is a real number (with no imaginary parts) implies that its width $\Gamma \propto \text{Im}[E] = 0$.

Ho and Bhatia [40] also calculated parameters for $^3P^e$ shape resonances of Ps^- above $n = 2, 4$, and 6. They are given in Table 26.12.

Accurate resonance parameters in two-electron systems H^- , He , and Li^+ have also been determined by using a hybrid theory of scattering [48] in which the short-range and the long-range correlations are included, and it is variationally correct. The complex rotation method has also been applied to calculate resonance parameters of the $^2\Pi_g$ shape resonance of N_2^- [49].

26.6 Related Topics

This chapter is necessarily of limited scope. Within the projection operator formalism, overlapping resonance theory [50] is discussed in Chap. 49.1.3.

Previous calculations [51] have shown that such effects, when present, can induce significant alteration of isolated resonance results. Other prominent items not included are stabilization methods [52] and hyperspherical coordinate methods [53, 54]. The latter methods have the appealing property of presenting energies as a function of the hyper-radius, $R = (\sum_i r_i^2)^{1/2}$, which look like potential energy curves of diatomic molecules as a function of the intermolecular separation, which is also usually denoted by R . The molecular structure analogy has also been used to uncover additional (approximate) symmetries with corresponding quantum labels [53, 54]. They thus have a global character not present in the foregoing methods. On a purely quantitative level, however, they are not generally as accurate as methods based on the projection operator or complex rotation formalism.

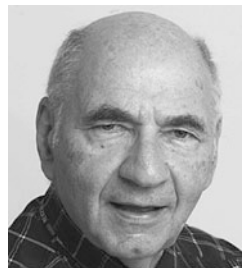
There are many other areas in which autoionization can play an important role, such as satellite line formation [55] and inner-shell ionization [56], to mention only a couple (Chap. 66 and [57]). In addition, significant application of the phenomena associated with autoionization to diagnostics of astrophysical [58] and fusion [59] plasmas, for example, shows that autoionization has considerable applied utility.

References

- Feshbach, H.: *Ann. Phys.* **19**, 287 (1962)
- Temkin, A., Bhatia, A.K.: In: Temkin, A. (ed.) *Autoionization, Recent Developments and Applications*. Plenum, New York (1985). pp. 1 ff, 35 ff
- Taylor, H.S.: *Adv. Chem. Phys.* **18**, 91 (1970)
- Temkin, A., Bhatia, A.K.: *Phys. Rev. A* **31**, 1259 (1985)
- Berk, A., Temkin, A.: *Phys. Rev. A* **32**, 3196 (1985)
- Pekeris, C.L.: *Phys. Rev.* **112**, 1649 (1958)
- Junker, B.R., Huang, C.L.: *Phys. Rev. A* **18**, 313 (1978)
- Davis, B.F., Chung, K.: *Phys. Rev. A* **29**(313), 2437 (1978)
- Bylicki, M.: *J. Phys. B* **24**, 413 (1991)
- Brunt, J., King, G., Read, F.: *J. Phys. B* **10**, 433 (1977)
- O'Malley, T.F., Geltman, S.: *Phys. Rev. A* **137**, 1344 (1965)
- Hahn, Y., O'Malley, T.F., Spruch, L.: *Phys. Rev.* **128**, 932 (1962)
- Hahn, Y.: *Ann. Phys.* **58**, 137 (1960)
- Temkin, A., Bhatia, A.K., Bardsley, J.N.: *Phys. Rev. A* **7**, 1633 (1972)
- Chung, K.T.: *Phys. Rev. A* **20**, 1743 (1979)
- Chung, K.T., Davis, B.F.: Hole-projection method for calculating Feshbach resonances and inner shell vacancies. In: Temkin, A. (ed.) *Autoionization, Recent Developments and Applications*, p. 73. Plenum, New York (1985)
- Chung, K.T., Davis, B.F.: *Phys. Rev. A* **26**, 3278 (1982)
- Ho, Y.-K., Bhatia, A.K., Temkin, A.: *Phys. Rev. A* **15**, 1432 (1977)
- Bhatia, A.K., Temkin, A.: *Phys. Rev. A* **11**, 2018 (1975)
- Madden, R.P., Codling, K.: *Astrophys. J.* **141**, 364 (1965)
- Morgan, H., Ederer, D.: *Phys. Rev. A* **29**, 1901 (1984)
- Bhatia, A.K., Burke, P.G., Temkin, A.: *Phys. Rev. A* **8**, 21 (1973)
- Bhatia, A.K., Temkin, A.: *Phys. Rev. A* **29**, 1895 (1984)
- Fano, U.: *Phys. Rev.* **124**, 1866 (1960)
- Smith, K.: *The Calculation of Atomic Collision Processes*. Wiley, New York, p 47 (1971)
- Drachman, R.J.: *Phys. Rev. A* **15**, 1432 (1977)
- Balslev, E.B., Combes, J.M.: *Comm. Math. Phys.* **22**, 280 (1971)
- Bhatia, A.K., Temkin, A.: *Rev. Mod. Phys.* **36**, 1050 (1964)
- Bhatia, A.K., Ho, Y.K.: *Phys. Rev. A* **41**, 504 (1990)
- Bhatia, A.K., Ho, Y.K.: *Phys. Rev. A* **42**, 1119 (1990)
- Hu, C.-Y., Bhatia, A.K.: *Muon Catalyzed Fusion* **5/6**(1990), 439 (1991)
- Ivanov, I.A., Ho, Y.K.: *Phys. Rev. A* **68**, 033410 (2003)
- Scholz, T., Scott, P., Burke, P.G.: *J. Phys. B* **21**, L139 (1988)
- Callaway, J.: *Phys. Rev. A* **26**, 199 (1982)
- Lindroth, E.: *Phys. Rev. A* **49**, 4473 (1994)
- Burgers, A., Wintgen, D., Rost, J.-M.: *J. Phys. B* **28**, 3163 (1995)
- Coolidge, A.S., James, H.M.: *Phys. Rev.* **51**, 855 (1937)
- Ho, Y.K.: *Phys. Lett.* **102A**, 348 (1984)
- Papp, Z., Darai, J., Nishimura, A., Hlousek, Z.T., Hu, C.Y., Yakovlev, S.L.: *Phys. Lett.* **304A**, 36 (2002)
- Ho, Y.K., Bhatia, A.K.: *Phys. Rev. A* **45**, 6268 (1992)
- Aguilar, J., Combes, J.M.: *Comm. Math. Phys.* **22**, 269 (1971)
- Bhatia, A.K., Ho, Y.K.: *Phys. Rev. A* **42**, 1119 (1990)
- Michishio, K., Kanai, K., Kuma, S., Azuna, T., Wada, K., Mochizuki, I., Hyodo, T., Yasuyuki, A., Nagashima, Y.: *Nat. Comm.* **7**, 11060 (2016)
- Botero, J., Greene, C.: *Phys. Rev. Lett.* **56**, 1366 (1986)
- Martin, F., M6, O., Riera, A., Yáñez, M.: *Europhys. Lett.* **4**, 799 (1987)
- Lipsky, L., Conneely, M.J.: *Phys. Rev. A* **14**, 2193 (1976)
- Bhatia, A.K.: *Phys. Rev.* **2**, 1667 (1970)
- Bhatia, A.K.: *Phys. Rev. A* **77**, 052707 (2008)
- Riss, U.V., Meyer, H.D.: *J. Phys. B* **26**, 4503 (1993)
- Feshbach, H.: *Ann. Phys.* **43**, 410 (1967)
- Griffin, D.C., Pindzola, M.S., Robicheaux, F., Gorczyca, T.W., Badnell, N.R.: *Phys. Rev. Lett.* **72**, 3491 (1994)
- Mandelstam, V.A., Ravuri, T.R., Taylor, H.S.: *J. Chem. Phys.* **101**, 8792 (1994)
- Lin, C.-D. (ed.): *Classifications and properties of doubly excited states of atoms*. In: Lin, C.-D. (ed.): *Review of Fundamental Processes and Applications of Atoms and Ions*. World Scientific, Singapore, p 24 (1993)
- Herrick, D.R., Sinanoglu, O.: *Phys. A* **11**, 97 (1975)
- Bely-Debau, F., Gabriel, A.H., Valonte, S.: *Mon. Not. R. Astron. Soc.* **186**, 305 (1979)
- Powell, C.J.: Inner shell ionization cross sections. In: Mark, T.D., Dunn, G.H. (eds.) *Electron Impact Ionization*. Springer, Berlin, Heidelberg (1985). Chap. 6
- Cowan, R.D.: *The Theory of Atomic Structure and Spectra*. Univ. of California Press, Berkeley (1981)
- Doschek, G.: Diagnostics of solar and astrophysical plasmas dependent on autoionization. In: Temkin, A., Bhatia, A.K. (eds.) *Autoionization, Recent Developments and Applications*, p. 171. Plenum, New York (1985)
- Finkenthal, M.: Atomic processes responsible for XUV emission. In: Kim, Y.-K., Elton, R.E. (eds.) *AIP Conference Proceedings # 206; Atomic Processes in Plasmas, 1990*, p. 95. American Institute of Physics, New York (1990)



Anand K. Bhatia Dr Bhatia received his PhD in Theoretical Physics from the University of Maryland in 1963. Since then he has been at Goddard Space Flight Center. He has published a large number of papers on various topics in atomic and astrophysics: scattering of electrons and positrons from atoms, muonic fusion, polarizabilities of two-electron systems, Lamb shift, Rydberg states, excitation of ions, etc. He is a Fellow of the American Physical Society.



Aaron Temkin Dr Temkin is a research physicist (emeritus) at NASA/GSFC He has specialized (primarily) in scattering problems of electrons from atoms and molecules, and associated processes (autoionization, in particular). He received his PhD degree from the Massachusetts Institute of Technology in 1956, and has been at his present institution since 1960.



Contents

27.1	Introduction	405
27.2	The Two-Point Green's Function	406
27.3	The Four-Point Green's Function	409
27.4	Radiative Transitions	410
27.5	Radiative Corrections	412
	References	414

Abstract

The discussion in this chapter is restricted to Green's function techniques as applied to problems in atomic physics, specifically to the calculation of higher order (correlation, Breit, as well as radiative) corrections to energy levels, and also of transition amplitudes for radiative transitions of atoms which are gauge invariant (GI) at every level of approximation.

Green's function techniques were first applied to many-electron atoms in 1971 as specific instances of the use of field theory techniques in many-particle problems [1, 2]. They initially provided alternative derivations of known approximations such as the Hartree–Fock (HF) approximation and random phase approximation (RPA). The starting point for the derivations was a nonrelativistic (NR) field-theoretical effective Hamiltonian for the system, which involved the nucleus–electron potential and only Coulomb interactions between electrons.

Keywords

field theory · Green's function · radiative transition · Dyson equation · Fourier transform · lepton charge · Coulomb exchange · Koopmans' theorem · MBPT calculation · radiative correction

27.1 Introduction

It subsequently became apparent that it was possible to formulate the problem more generally, with the full quantum electrodynamic (QED) Hamiltonian as a starting point [3, 4]. Thus, the theory contains both relativity, and virtual and real transverse photons, as well as the Coulomb interaction between the electrons. The relativistic (R) approximate equations, such as the Dirac–Fock (DF) and relativistic random phase approximation (RRPA) are the natural outcomes of the formalism, and the NR results can be viewed as approximations to these R cases. Moreover, the Green's function approach (GFA) now provides a means of carrying out programs involving systematic approximations of successively higher and higher accuracy. The GFA provides a framework which allows one to make corrections to results obtained in the DF approximation or in the coupled cluster approximation (CCA) and many-body perturbation theory (MBPT), including magnetic (Breit type) interactions [5, 6]. It ensures that there is neither double counting nor omission of contributions. For radiative transitions, the formalism allows for a systematic treatment of such effects which is gauge independent that at any given level of approximation [7–10]. (It should be noted that there is a subtle difference between gauge invariance and gauge independence. The first refers to the transition amplitude and the second to quantities which are directly observable experimentally.) Finally, the GFA is numerically implementable. Renormalization can be carried out for radiative corrections, resulting in finite and calculable expressions [11–13]. The integro-differential equations (i.e., the Dyson equations) needed to calculate energies or transition amplitudes in nontrivial approximations are also soluble [8, 9, 14].

In quantum field theory, Green's functions are defined in terms of vacuum expectation values of products of field operators. While this restriction can be relaxed, expecta-

tion values must still be taken for a nondegenerate state. As a practical matter, this requirement ultimately restricts one to consider atoms with electron numbers associated only with closed shells or subshells, and those with closed shells or subshells plus or minus one or two electrons. The corresponding Green's functions considered here are the two- and four-point functions for energy levels, and the three- and five-point functions for transition amplitudes (leading to oscillator strengths). The restriction in electron numbers is clearly not a severe one. It allows one to cover many atomic species.

Starting from relativistic QED, the electron field operator $\psi(\mathbf{r}, t)$ written in the Heisenberg picture, satisfies equal-time anticommutation relations

$$[\psi(\mathbf{r}, t), \psi(\mathbf{r}', t)] = [\psi^\dagger(\mathbf{r}, t), \psi^\dagger(\mathbf{r}', t)] = 0, \quad (27.1)$$

$$[\psi(\mathbf{r}, t), \psi^\dagger(\mathbf{r}', t)] = \delta^3(\mathbf{r} - \mathbf{r}'). \quad (27.2)$$

(Spinor labels are suppressed.)

The time-translation operator, acting on any Heisenberg operator $\mathcal{O}(\mathbf{r}, t) = \{\psi(\mathbf{r}, t), \psi^\dagger(\mathbf{r}, t), j_\mu(\mathbf{r}, t), \dots\}$, is

$$\mathcal{O}(\mathbf{r}, t) = e^{i\mathcal{H}t} \mathcal{O}(\mathbf{r}, 0) e^{-i\mathcal{H}t}, \quad (27.3)$$

where \mathcal{H} is the full QED Hamiltonian.

Notations and Definitions

For brevity, plainface numbers are used to denote both a coordinate and time, while boldface numbers denote a coordinate vector alone. For example,

$$\begin{aligned} 1 &\equiv (\mathbf{1}, t_1) \equiv (\mathbf{r}_1, t_1), \\ d^3\mathbf{1} &\equiv d^3\mathbf{r}_1, \\ d^4\mathbf{1} &\equiv d^3\mathbf{r}_1 dt_1. \end{aligned} \quad (27.4)$$

For radiative transitions, $\mathcal{M}_{fi}^{N'}(k_0)$ denotes the transition amplitude for the emission of a single photon of energy k_0 for an N' -electron atom from an initial energy $E_i^{N'}$ to a final energy $E_f^{N'}$, where

$$\mathcal{M}_{fi}^{N'}(k_0) \equiv (2\pi)^4 \delta(E_f^{N'} - E_i^{N'} - k_0) M_{fi}^{N'}(k_0). \quad (27.5)$$

The notation on the right-hand side of Eq. (27.5) is somewhat redundant, since k_0 is taken to be $k_0 = E_f^{N'} - E_i^{N'}$.

The current density operators at $t = 0$ are given respectively by

$$\begin{aligned} j_\mu(\mathbf{r}, 0) &= \begin{cases} \frac{1}{2} \int d^3\mathbf{1} d^3\mathbf{2} [\psi^\dagger(\mathbf{1}, 0), u_\mu^R(\mathbf{12}; \mathbf{r}) \psi(\mathbf{2}, 0)], & \text{for R} \\ \int d^3\mathbf{1} d^3\mathbf{2} \psi^\dagger(\mathbf{1}, 0) u_\mu^{NR}(\mathbf{12}; \mathbf{r}) \psi(\mathbf{2}, 0), & \text{for NR} \end{cases} \end{aligned} \quad (27.6)$$

with

$$\begin{aligned} u_\mu(\mathbf{12}; \mathbf{r}) &= \begin{cases} e\alpha_\mu \delta^3(\mathbf{1} - \mathbf{r}) \delta^3(\mathbf{2} - \mathbf{r}), & \text{for R} \\ e \left[1, \left(\frac{1}{2im} \right) (\nabla_2 - \nabla_1) \delta^3(\mathbf{1} - \mathbf{r}) \delta^3(\mathbf{2} - \mathbf{r}) \right], & \text{for NR} \end{cases} \end{aligned} \quad (27.7)$$

where $\alpha_\mu = (\boldsymbol{\alpha}, 1)$, and the components of $\boldsymbol{\alpha}$ are the usual Dirac matrices.

The corresponding charge operators are defined as

$$\mathcal{Q} = \begin{cases} \frac{1}{2} e \int d^3\mathbf{1} [\psi^\dagger(\mathbf{1}, 0), \psi(\mathbf{1}, 0)], & \text{for R} \\ e \int d^3\mathbf{1} \psi^\dagger(\mathbf{1}, 0) \psi(\mathbf{1}, 0), & \text{for NR} \end{cases}. \quad (27.8)$$

The transition amplitude for a photon of polarization four-vector $\epsilon^\mu(k)$, momentum \mathbf{k} , energy k_0 ($k_0 = |\mathbf{k}|$), and photon attachment point \mathbf{r} is

$$M_{fi}^{N'}(k_0) = \int d^3\mathbf{r} \frac{e^{i\mathbf{k}\cdot\mathbf{r}}}{\sqrt{2k_0}} M_{fi}^{N'}(\mathbf{r}; k_0). \quad (27.9)$$

In terms of the current density operator, $M_{fi}^{N'}(\mathbf{r}; k_0)$ can be written as

$$\begin{aligned} M_{fi}^{N'}(\mathbf{r}; k_0) &= \left\langle f^{N'} \left| \epsilon^\mu(k) j_\mu(\mathbf{r}, 0) \right| i^{N'} \right\rangle \\ &\equiv \left\langle f^{N'} \left| j^k(\mathbf{r}, 0) \right| i^{N'} \right\rangle, \end{aligned} \quad (27.10)$$

where $|i^{N'}\rangle$ is a state of leptonic charge number N' , with N' corresponding to an atom of N' electrons, with total energy $E_n^{N'}$. The term *lepton charge* is used to refer to the charge of electrons and positrons.

In the dipole approximation, $e^{i\mathbf{k}\cdot\mathbf{r}} \approx 1$, $\epsilon^\mu j_\mu$ contains the quantity

$$\epsilon^\mu(k) u_\mu(\mathbf{12}; \mathbf{r}) \equiv \lambda_k(\mathbf{r}) \delta(\mathbf{1} - \mathbf{r}) \delta(\mathbf{2} - \mathbf{r}), \quad (27.11)$$

where, in the radiation gauge,

$$\lambda_k(\mathbf{r}) = \begin{cases} e\boldsymbol{\epsilon}(k) \cdot \boldsymbol{\alpha}, & \text{velocity form} \\ ie k_0 \boldsymbol{\epsilon}(k) \cdot \mathbf{r}, & \text{length form} \end{cases}. \quad (27.12)$$

27.2 The Two-Point Green's Function

The two-point Green's function, or one-body propagator [3, 4], for a system of lepton charge Ne is defined as the expectation value of a time-ordered product

$$G^N(1, 1') \equiv -i \langle 0^N | T [\psi(1) \psi^\dagger(1')] | 0^N \rangle, \quad (27.13)$$

where $|^N_0\rangle$ is the ground state of leptonic charge number N , with N corresponding to an atom with electron number N in a filled shell or subshell ($N = 2, 4, 8, \dots$).

The relative time $(t_1 - t'_1)$ Fourier transform of Eq. (27.13) yields the spectral representation of $G^N(\mathbf{1}, \mathbf{1}')$:

$$G^N_\omega = \sum_j \frac{|u^j\rangle\langle u^j|}{\omega - \varepsilon^j + i\eta} + \sum_\zeta \frac{|v^\zeta\rangle\langle v^\zeta|}{\omega - \varepsilon^\zeta + i\eta}, \quad \eta = 0^+, \quad (27.14)$$

where

$$G^N_\omega(\mathbf{1}, \mathbf{1}') \equiv \langle \mathbf{1} | G^N_\omega | \mathbf{1}' \rangle, \quad u^j(\mathbf{r}) \equiv \langle \mathbf{r} | u^j \rangle, \quad \text{etc.}, \quad (27.15)$$

and where the symbol \sum denotes a summation over discrete and integration over continuous states. The two terms in Eq. (27.14) are obtained by counting each time-ordering separately in Eq. (27.13), introducing a complete set of intermediate states and using the time translation operator Eq. (27.3). The functions $u^j(\mathbf{r})$ and $v^\zeta(\mathbf{r})$ are defined by

$$u^j(\mathbf{r}) \equiv \langle ^N_0 | \psi(\mathbf{r}, 0) | ^{N+1}_j \rangle, \\ \langle ^N_0 | \psi(\mathbf{r}, t) | ^{N+1}_j \rangle = e^{i(E^N_0 - E^{N+1}_j)t} u^j(\mathbf{r}), \quad (27.16)$$

and

$$v^\zeta(\mathbf{r}) \equiv \langle ^{N-1}_\zeta | \psi(\mathbf{r}, 0) | ^N_0 \rangle, \\ \langle ^{N-1}_\zeta | \psi(\mathbf{r}, t) | ^N_0 \rangle = e^{i(E^{N-1}_\zeta - E^N_0)t} v^\zeta(\mathbf{r}). \quad (27.17)$$

Here, $|^N_0\rangle$ is the ground state of an atom of lepton charge number N (corresponding to a nondegenerate state – a closed shell or subshell) of energy E^N_0 , $|^{N+1}_j\rangle$ an atomic state of total energy E^{N+1}_j and leptonic charge number $N + 1$, and $|^{N-1}_\zeta\rangle$ is the state of energy E^{N-1}_ζ and leptonic charge number $N - 1$. These several states satisfy the eigenvalue equations

$$\mathcal{H} |^N_0\rangle = E^N_0 |^N_0\rangle, \\ \mathcal{H} |^{N+1}_j\rangle = E^{N+1}_j |^{N+1}_j\rangle, \\ \mathcal{H} |^{N-1}_\zeta\rangle = E^{N-1}_\zeta |^{N-1}_\zeta\rangle. \quad (27.18)$$

The energy parameters ε^j and ε^ζ are defined by

$$\varepsilon^j \equiv E^{N+1}_j - E^N_0, \quad (27.19)$$

$$\varepsilon^\zeta \equiv E^N_0 - E^{N-1}_\zeta. \quad (27.20)$$

Equations (27.19) and (27.20) are generalizations of Koopman's theorem [15] (see Sect. 22.4.1). In the DF approximation, the state $|^{N+1}_j\rangle$ can be thought of as N effective particles

(electrons) making up the core, plus one valence electron, with energy label j . The atom can also be an isoelectronic ion with nuclear charge number Z . In this (DF) approximation, the state $|^{N-1}_\zeta\rangle$ is one of two possible types. It can have N independent electrons making up the core, with one of the core electrons missing, or equivalently the N electron core with one electron-hole, with energy label ζ . There is a finite number N of such hole states, which shall be labeled a . There are no other states in the NR (HF) case. In the R (DF) case, the second group of states $|^{N-1}_\zeta\rangle$ can also describe an atom with a core of N electrons, plus one positron. Its continuum energy label, will be taken as $\zeta = \bar{\ell}$. This energy will appear with a negative sign in Eq. (27.14).

The second step in leading to an explicit $G^N(1, 1')$ is the generation of a Dyson equation which it satisfies. In both the DF and HF approximations, the Dyson equation can be obtained through a successive series of steps [11]. Working in the Coulomb gauge (see Chap. 28), begin with the Coulomb interaction between electrons and neglect the exchange of transverse virtual photons. The Dyson equation for the resulting two-point function is then expanded as a power series in the electron-electron (ee) interaction

$$V_{\text{ee}} \equiv V = \frac{\alpha}{|\mathbf{x} - \mathbf{y}|}, \quad (27.21)$$

resulting in an infinite set of Feynman diagrams ($\alpha = e^2/4\pi$ in rationalized mks units). As a next approximation, consider only diagrams involving single Coulomb exchanges and their iterates (*ladders*). That is, set aside for later consideration nonladder Feynman diagrams of two or more Coulomb photons and their iterates (e.g., two crossed Coulomb photon lines). A summation of the infinite set of these remaining terms generates an equation for a propagator labeled $G^N_{\omega, \text{Coul}}$, which contains Coulomb radiative corrections in its kernel. Finally, modify the kernel by isolating these radiative corrections (self energy and vacuum polarization) by constructing a spectral representation of G^N_{ω} which mimics that for the usual QED propagator, which is a vacuum (rather than an N -lepton ground state) expectation value. This requires shifting the poles corresponding to core energies of the atom from the upper to the lower complex ω plane. The shifting of poles is accomplished by means of the equation

$$\frac{1}{x - i\eta} - \frac{1}{x + i\eta} = 2\pi i \delta(x), \quad (27.22)$$

which, when used to shift the poles of core electrons in the ω plane, gives

$$G^N_{\omega, \text{Coul}} = 2\pi i \sum_{a=1}^N |v^a\rangle\langle v^a| \delta(\omega - \varepsilon^a) + G^N_{\omega}{}^{00}. \quad (27.23)$$

It is the first term on the right-hand side of this equation which occurs in the kernel of Eq. (27.24) below and generates the DF approximation.

Some of the terms set aside in the course of this sequence of approximations are reconsidered in Sect. 27.5 to obtain more accurate energy results. What remains at the end of this sequence is an approximation to G_ω^N of Eq. (27.14), designated as $G_{\omega,DF}^N$, and which satisfies the self-consistent Dyson equation

$$G_{\omega,DF}^N = g_\omega + g_\omega \Sigma_{DF}^N G_{\omega,DF}^N, \quad (27.24)$$

where Σ_{DF}^N is the kernel defined in Eq. (27.27). For the R (DF) case,

$$g_\omega^{-1} = \omega - h^R(\mathbf{r}), \quad h^R(\mathbf{r}) = \boldsymbol{\alpha} \cdot \mathbf{p} + m\beta - \frac{Z\alpha}{r}, \quad (27.25)$$

and the corresponding h^{NR} , used in the HF case, is

$$h^{NR}(\mathbf{r}) = \frac{\mathbf{p}^2}{2m} - \frac{Z\alpha}{r}. \quad (27.26)$$

The function g_ω in Eq. (27.25) is the R or NR Coulomb Green's function. It is the solution of the corresponding inhomogeneous c-number Schrödinger or Dirac equation. It is a single-particle equation which has had a long history of specific treatments (see Chap. 9 and [16–19]). It is the semi-classical limit of the two-point propagator we consider here when only the c-number nuclear Coulomb potential is kept and all other (q-number) interactions are turned off.

In the DF and HF approximations in Eq. (27.14), we replace ε^j by $e_j > 0$, $|u^j\rangle$ by $|j\rangle$ (the valence energies and states of an atom with $N + 1$ electrons and a frozen relaxed core of N electrons), ε^ξ by $e_a > 0$, $|u^\xi\rangle$ by $|a\rangle$, for the N discrete electron core states, and ε^ζ by $e_{\bar{\ell}} < 0$, $|u^\zeta\rangle$ by $|\bar{\ell}\rangle$, for the continuum of negative energy states (which do not appear in the HF approximation). The kernel Σ_{DF}^N contains *only* core states $|a\rangle$, in *both* the DF and HF approximations, and is given by the sum over states

$$\begin{aligned} \langle m | \Sigma_{DF}^N | n \rangle &= \alpha \sum_{a=1}^N \int d^3\mathbf{x} d^3\mathbf{y} \frac{1}{|\mathbf{x} - \mathbf{y}|} \langle m | \mathbf{x} \rangle \langle a | \mathbf{y} \rangle \\ &\quad \times (\langle \mathbf{x} | n \rangle \langle \mathbf{y} | a \rangle - \langle \mathbf{x} | a \rangle \langle \mathbf{y} | n \rangle) \\ &\equiv \sum_{a=1}^N [{}^m_a | V |^n_a] \\ &\equiv \sum_{a=1}^N [{}^m_a | V |^n_a] \end{aligned} \quad (27.27)$$

for arbitrary states m and n . The first term in brackets is the Hartree term and the second is the electron exchange term

in the DF (HF) approximation. The DF (HF) equation is the homogeneous equation corresponding to the inhomogeneous Eq. (27.24). Thus,

$$(e_n - h - \Sigma_{DF}^N) | n \rangle = 0, \quad \langle n | n' \rangle = \delta_{nn'}. \quad (27.28)$$

The states $|n\rangle$ (valence, core, and negative energy states) are orthonormal and complete. In the coordinate basis, Eq. (27.28) takes the more familiar form

$$[e_n - h(\mathbf{x})] \langle \mathbf{x} | n \rangle - \langle \mathbf{x} | \Sigma_{DF}^N | n \rangle = 0, \quad (27.29)$$

where

$$\begin{aligned} \langle \mathbf{x} | \Sigma_{DF}^N | n \rangle &= \not\int_m \sum_{a=1}^N \langle \mathbf{x} | m \rangle [{}^m_a | V |^n_a] \\ &\equiv \sum_{a=1}^N [{}^x_a | V |^n_a] \\ &\equiv \int V_{DF}(\mathbf{x}, \mathbf{y}) d^3\mathbf{y} \langle \mathbf{y} | n \rangle. \end{aligned} \quad (27.30)$$

One can also generate equations corresponding to higher approximations than DF using the same approach. For example, one can obtain a Brueckner equation [20],

$$[e_n - h - \Sigma_{DF}^N - \Sigma_B^N(e_n)] | n \rangle = 0, \quad (27.31)$$

and the states now satisfy the orthonormality condition

$$\begin{aligned} \lim_{\omega \rightarrow e_n} \int d^3\mathbf{x} d^3\mathbf{y} \langle n | \mathbf{x} \rangle \langle \mathbf{y} | n' \rangle \\ \times \left(\frac{\{(\omega - e_n) \delta^3(\mathbf{x} - \mathbf{y}) - \langle \mathbf{x} | \{ \Sigma_B^N(\omega) - \Sigma_B^N(e_n) \} | \mathbf{y} \rangle\}}{\omega - e_n} \right) \\ = \delta_{nn'}, \end{aligned} \quad (27.32)$$

where the energy-dependent kernel $\Sigma_B(e_n)$ arises from irreducible Feynman diagrams involving two Coulomb photons. The kernel is given by

$$\begin{aligned} \langle m | \Sigma_B^N(e_n) | n \rangle &= \not\int_{a,i,j} \frac{1/2}{e_n + e_a - e_i - e_j} [{}^m_a | V |^i_j] [{}^i_j | V |^n_a] \\ &\quad + \not\int_{a,b,i} \frac{1/2}{e_n + e_i - e_a - e_b} [{}^m_i | V |^a_b] [{}^a_b | V |^n_i]. \end{aligned} \quad (27.33)$$

$\not\int$ involves summations over core states (a, b), and summation and integration over valence states (i, j). In perturbation theory, the lowest order contribution of $\Sigma_B(e_n)$ is an ee correlation term.

27.3 The Four-Point Green's Function

The four-point Green's function [4, 8, 11], or two-body propagator, is defined as

$$G^N(12, 1'2') \equiv -\langle 0^N | T[\psi(1)\psi^\dagger(1')\psi(2)\psi^\dagger(2')] | 0^N \rangle. \quad (27.34)$$

In order to avoid unnecessary complication, only simple ladders of $V_{ee} \equiv V$ are considered. There are 4! possible time orderings. Of these, there are four groups of four with $t_1, t_{1'} > t_2, t_{2'}$, $t_1, t_{1'} < t_2, t_{2'}$, $t_1, t_2 > t_{1'}, t_{2'}$, and $t_1, t_2 < t_{1'}, t_{2'}$, corresponding to the particle-hole (PH/HP) and the two-particle/two-hole (2P/2H) cases for the first eight and last eight time orderings, respectively. For each of these cases, introduce a total time and relative time variable defined by

$$\begin{aligned} T &= \frac{1}{2}(t_1 + t_{1'}), & T' &= \frac{1}{2}(t_2 + t_{2'}), \\ t &= t_1 - t_{1'}, & t' &= t_2 - t_{2'}, \end{aligned} \quad (27.35)$$

for the first eight cases (PH/HP) and

$$\begin{aligned} T &= \frac{1}{2}(t_1 + t_2), & T' &= \frac{1}{2}(t_{1'} + t_{2'}), \\ t &= t_1 - t_2, & t' &= t_{1'} - t_{2'}, \end{aligned} \quad (27.36)$$

for the last eight cases (2P/2H). For a particular set of eight time orderings, a time translation with respect to the relevant c.m. time t or t' , followed by a separate Fourier transformation for each case with respect to $T - T'$ (with integration variable $d\Omega$), yields contributions with poles in the separately defined Ω -planes at

$$\omega_{(ia)} = E_{(ia)}^N - E_0^N, \quad \text{for PH} \quad (27.37a)$$

$$-\omega_{(ia)} = E_0^N - E_{(ia)}^N, \quad \text{for HP} \quad (27.37b)$$

$$\omega_{(ij)} = E_{(ij)}^{N+2} - E_0^N, \quad \text{for 2P} \quad (27.38a)$$

$$\omega_{(ab)} = E_0^N - E_{(ab)}^{N-2}, \quad \text{for 2H}. \quad (27.38b)$$

Equations (27.37a), (27.37b) parallel Eqs. (27.19) and (27.20) as generalizations of Koopmans' theorem. The spectral representation is of a form similar to Eq. (27.14), with wave functions corresponding to Eqs. (27.16) and (27.17) given by

$$\begin{aligned} \chi_{(ia)}(11') &\equiv \langle \mathbf{1} | \chi_{(ia)}(t) | \mathbf{1}' \rangle e^{-i\omega_{(ia)}T} \\ &= \langle 0^N | T[\psi(1)\psi^\dagger(1')] | 0^N \rangle_{(ia)} \end{aligned} \quad (27.39)$$

for the PH/HP case and

$$\begin{aligned} \varphi_{(ij)}(12) &\equiv \langle \mathbf{1}\mathbf{2} | \varphi_{(ij)}(t) \rangle e^{-i\omega_{(ij)}T} \\ &= \langle 0^N | T[\psi(1)\psi(2)] | 0^N \rangle_{(ij)}^{N+2}, \end{aligned} \quad (27.40)$$

$$\begin{aligned} \gamma_{(ab)}(1'2') &\equiv \langle \mathbf{1}'\mathbf{2}' | \gamma_{(ab)}(t') \rangle e^{-i\omega_{(ab)}T'} \\ &= \langle 0^N | T[\psi(1')\psi(2')] | 0^N \rangle_{(ab)}^{N-2}, \end{aligned} \quad (27.41)$$

for the 2P and 2H cases, respectively. The antisymmetry under exchange follows from the definitions Eqs. (27.40) and (27.41):

$$\zeta_{(\tau)}(12) = -\zeta_{(\tau)}(21), \quad \zeta_{(\tau)} = \varphi_{(ij)}, \gamma_{(ab)}, \quad (27.42)$$

where it is understood that the suppressed spinor indices are interchanged as well as the coordinate and time variables.

The three amplitudes defined above satisfy Bethe-Salpeter (BS) equations. The PH/HP case is the analog of the positronium atom and the 2P case is analogous to He. For the case of Coulomb ladder exchanges, to which we have restricted ourselves, these BS equations can be reduced to simpler ones, with the relative time set equal to zero (the Salpeter equation [21]). The corresponding BS wave functions in the DF (HF) basis (rather than the coordinate basis), are for PH/HP,

$$\langle m | \bar{\chi}_{(ia)} | n \rangle \equiv \int d^3\mathbf{1} d^3\mathbf{1}' \langle m | \mathbf{1} \rangle \langle \mathbf{1} | \chi_{(ia)}(0) | \mathbf{1}' \rangle \langle \mathbf{1}' | n \rangle, \quad (27.43)$$

with $m = k$ and $n = c$, or $m = c$ and $n = k$, and for 2P/2H,

$$\langle mn | \bar{\zeta}_{(\tau)} \rangle \equiv \int d^3\mathbf{1} d^3\mathbf{2} \langle m | \mathbf{1} \rangle \langle n | \mathbf{2} \rangle \langle \mathbf{1}\mathbf{2} | \zeta_{(\tau)}(0) \rangle, \quad (27.44)$$

where $\zeta_{(\tau)} = \varphi_{(ij)}, \gamma_{(ab)}$. The states $|i\rangle, |j\rangle, |a\rangle, |b\rangle, |m\rangle$, and $|n\rangle$ label one-particle DF (HF) eigenkets and e_i, e_j, e_a, e_b, e_m , and e_n , the corresponding eigenvalues.

In the PH/HP case, the BS equation is

$$\begin{aligned} &-(\omega_{(ia)} - e_k + e_c) \langle i | \bar{\chi}_{(ia)} | a \rangle \\ &= \sum_j^k \left\{ \left[\begin{matrix} k \\ b \end{matrix} \middle| V \right| \begin{matrix} j \\ c \end{matrix} \right] \langle j | \bar{\chi}_{(ia)} | b \rangle + \left[\begin{matrix} k \\ j \end{matrix} \middle| V \right| \begin{matrix} b \\ c \end{matrix} \right] \langle b | \bar{\chi}_{(ia)} | j \rangle \right\}, \\ &(\omega_{(ia)} - e_c + e_k) \langle a | \bar{\chi}_{(ia)} | i \rangle \\ &= \sum_{j,b}^c \left\{ \left[\begin{matrix} c \\ b \end{matrix} \middle| V \right| \begin{matrix} j \\ k \end{matrix} \right] \langle j | \bar{\chi}_{(ia)} | b \rangle + \left[\begin{matrix} c \\ j \end{matrix} \middle| V \right| \begin{matrix} b \\ k \end{matrix} \right] \langle b | \bar{\chi}_{(ia)} | j \rangle \right\}. \end{aligned} \quad (27.45)$$

In the 2P/2H case, the coupled pairs of BS equations are

$$\begin{aligned} &-(\omega_{(\tau)} - e_c - e_d) \langle cd | \bar{\zeta}_{(\tau)} \rangle = \sum_{m>n}^c \left[\begin{matrix} c \\ d \end{matrix} \middle| V \right| \begin{matrix} m \\ n \end{matrix} \right] \langle mn | \bar{\zeta}_{(\tau)} \rangle, \\ &(\omega_{(\tau)} - e_k - e_\ell) \langle k\ell | \bar{\zeta}_{(\tau)} \rangle = \sum_{m>n}^k \left[\begin{matrix} k \\ \ell \end{matrix} \middle| V \right| \begin{matrix} m \\ n \end{matrix} \right] \langle mn | \bar{\zeta}_{(\tau)} \rangle, \end{aligned} \quad (27.46)$$

with m and n in these equations labeling either both core, or both valence states.

The wave functions also satisfy the additional conditions:

$$\langle c | \bar{\chi}_{(ia)} | d \rangle = \langle k | \bar{\chi}_{(ia)} | \ell \rangle = 0, \quad \text{PH/HP (no 2P/2H terms)} \quad (27.47)$$

$$\langle ck | \bar{\varphi}_{(ij)} \rangle = \langle ck | \bar{\gamma}_{(ab)} \rangle = 0, \quad \text{2P/2H (no PH/HP terms)} \quad (27.48)$$

The single indices a, b, c, d refer to core and i, j, k, ℓ to valence DF (HF) states. The BS wave functions satisfy the orthonormality conditions

$$\begin{aligned} \sum_{k,c} (\langle k | \bar{\chi}_{(ia)} | c \rangle \langle c | \bar{\chi}_{(ia)'} | k \rangle + \langle c | \bar{\chi}_{(ia)} | k \rangle \langle k | \bar{\chi}_{(ia)'} | c \rangle) \\ = \delta_{(ia)(ia)'} , \end{aligned} \quad (27.49)$$

for the PH/HP case, and

$$\begin{aligned} \pm \left(\sum_{c>d} \langle \bar{\xi}_{(\tau)} | cd \rangle \langle cd | \bar{\xi}_{(\tau)'} \rangle - \sum_{k>\ell} \langle \bar{\xi}_{(\tau)} | k\ell \rangle \langle k\ell | \bar{\xi}_{(\tau)'} \rangle \right) \\ = \delta_{(\tau)(\tau)'} , \end{aligned} \quad (27.50)$$

where $+$ ($-$) corresponds to the 2H(2P) case and $(\tau) = (ab)$ or (ij) .

The PH/HP case in the GFA, involving Coulomb ladders for the ee interaction, is just the R and NR RPA [2]. The labels c, d should also refer to antiparticles, but the contributions of the integrals from these terms to Eqs. (27.45) and (27.46) are negligible.

27.4 Radiative Transitions

For the majority of applications, one begins with the function $\Gamma^N(12; 3)$, the reducible three-point vertex:

$$\Gamma^N(12; 3) = -\langle \bar{0}^N | T[\psi(1)j^k(3)\psi^\dagger(2)] | \bar{0}^N \rangle . \quad (27.51)$$

The usual strategy is followed. The spectral representation serves to identify the functions of ultimate interest. (Energies are not relevant in this case.) One then generates Dyson equations in the chosen approximation by summing an infinite series of perturbation terms.

There are $3!$ time orderings in Eq. (27.51). As with the four-point function, not all of them are subsequently useful. The two useful cases are $t_1 > t_3 > t_2$, and $t_2 > t_3 > t_1$. To obtain a spectral representation for these two cases, one first carries out a time translation of t_3 , using the operator $\exp(i\mathcal{H}t_3)$ of Eq. (27.3), so that $t_1 \rightarrow \tau_1 = t_1 - t_3$, $t_2 \rightarrow \tau_2 = t_2 - t_3$. One then introduces complete sets of intermediate states. The functions defined in connection with the two-point function in Eqs. (27.16) and (27.17) will now appear, as well as the radiative transition amplitude, defined in Eq. (27.10). If one next carries out a separate time translation of τ_1 and τ_2 and Fourier-transforms the resulting expressions, one obtains

(with $\mathbf{3}$ replaced by \mathbf{r})

$$\begin{aligned} \Gamma^N(\mathbf{r}; \omega_1 \omega_2) \\ = \sum_{j\ell} \frac{|u^j\rangle M_{j\ell}^{N+1}(\mathbf{r}) \langle u^\ell|}{(\omega_1 - \varepsilon_j + i\eta)(\omega_2 - \varepsilon_\ell + i\eta)} \\ + \sum_{\xi\chi} \frac{|v^\xi\rangle M_{\xi\chi}^{N-1}(\mathbf{r}) \langle v^\chi|}{(\omega_1 - \varepsilon_\xi - i\eta)(\omega_2 - \varepsilon_\chi - i\eta)} + \dots \end{aligned} \quad (27.52)$$

We next define the three-point irreducible electron vertex Λ^N from the reducible vertex Γ^N (the electron legs in Γ^N are missing in Λ^N) as

$$\begin{aligned} \langle \mathbf{1} | \Gamma^N(\mathbf{r}; \omega_1 \omega_2) | \mathbf{2} \rangle \\ \equiv \int \int d^3\mathbf{1}' d^3\mathbf{2}' \langle \mathbf{1} | G_{\omega_1}^N | \mathbf{1}' \rangle \langle \mathbf{1}' | \Lambda^N(\mathbf{r}; \omega_1 \omega_2) | \mathbf{2}' \rangle \\ \times \langle \mathbf{2}' | G_{\omega_2}^N | \mathbf{2} \rangle , \end{aligned} \quad (27.53)$$

and pick out the residues of the ω_1 and ω_2 poles at specific energies ε_m and ε_n . [$\Lambda^N(\mathbf{r}; \omega_1 \omega_2)$ has no such poles.] With the equivalent of the DF(HF) approximation to the Dyson equations in Eq. (27.57) below, the corresponding kets form an orthonormal set, and scalar products are calculated with respect to $\langle m |$ and $| n \rangle$. The second term on the right-hand side of Eq. (27.52) refers to hole states and is of less interest than the first term describing 1P–1P transitions. From the first term, the transition matrix element in terms of Λ^N is

$$M_{fi}^{N+1}(\mathbf{r}; k_0) = \langle f | \Lambda^N(\mathbf{r}; e_f e_i) | i \rangle . \quad (27.54)$$

Generation of a Dyson Equation

The approximation of only Coulomb ladder ee interactions in the two-point Green's function produces an infinite set of Feynman diagrams to which one end of a single transverse photon line is attached in all possible ways. A resummation of these diagrams generates the $G_{\omega, \text{Coul}}^N$ functions, which are approximated by the DF (HF) propagators written in their spectral form. The scalar products leading to Eq. (27.54) can then be taken.

A further simplification results because of the Coulomb ladder approximation, which is the same as in the four-point Green's function case: the relative time can be set equal to zero, which corresponds to integrating over the relative frequency, $\omega = \omega_1 - \omega_2$. With the total frequency defined as $\Omega = \frac{1}{2}(\omega_1 + \omega_2)$, and the definitions

$$\begin{aligned} \bar{\Lambda}^N(\mathbf{r}, \Omega) &= \frac{1}{2\pi} \int d\omega \Lambda^N\left(\mathbf{r}; \omega + \frac{1}{2}\Omega, \omega - \frac{1}{2}\Omega\right) , \\ \langle m | \bar{\Lambda}^N(\Omega) | n \rangle &= \int d^3\mathbf{r} \frac{e^{ik\cdot\mathbf{r}}}{\sqrt{2k_0}} \langle m | \bar{\Lambda}^N(\mathbf{r}, \Omega) | n \rangle , \\ \Omega_{mn} &= e_n - e_m = k_0 , \end{aligned} \quad (27.55)$$

with a relation similar to Eq. (27.55) for the quantity $\lambda_k(\mathbf{r})$ defined in Eq. (27.11), i.e.,

$$\langle m|\lambda(k_0)|n\rangle = \int d^3\mathbf{r} \frac{e^{i\mathbf{k}\cdot\mathbf{r}}}{\sqrt{2k_0}} \langle m|\lambda_k(\mathbf{r})|n\rangle, \quad (27.56)$$

the matrix elements in the DF (HF) basis are [14, 20]

$$\begin{aligned} & \langle m|\bar{\Lambda}^N(k_0)|n\rangle \\ &= \langle m|\lambda(k_0)|n\rangle \\ &+ \sum_{aj} \left\{ \frac{1}{e_a - e_j + k_0} \left[\begin{matrix} m \\ j \end{matrix} \middle| V \right| \begin{matrix} n \\ a \end{matrix} \right] \langle a|\bar{\Lambda}^N(k_0)|j\rangle \right. \\ &\left. + \frac{1}{e_a - e_j - k_0} \left[\begin{matrix} m \\ a \end{matrix} \middle| V \right| \begin{matrix} n \\ j \end{matrix} \right] \langle j|\bar{\Lambda}^N(k_0)|a\rangle \right\}. \quad (27.57) \end{aligned}$$

As discussed in Sect. 27.2, the label a should include not just hole states but also negative energy states, which have been neglected in Eq. (27.57). Note also that only PH or HP matrix elements appear on the right-hand side of Eq. (27.57). Therefore, a closed set of inhomogeneous linear algebraic equations for $\langle b|\bar{\Lambda}^N(k_0)|\ell\rangle$ and $\langle \ell|\bar{\Lambda}^N(k_0)|b\rangle$ results from setting $m = b$, $n = \ell$ or $m = \ell$, $n = b$, respectively, in Eq. (27.57). These equations can be solved numerically, and the resulting $\langle a|\bar{\Lambda}^N(k_0)|j\rangle$ and $\langle j|\bar{\Lambda}^N(k_0)|a\rangle$ substituted in Eq. (27.57) to obtain the final result

$$M_{\text{fi}}^{N+1}(k_0) \equiv \langle f|\bar{\Lambda}^N(k_0)|i\rangle. \quad (27.58)$$

An integro-differential equation form, which provides the option of choosing alternative numerical techniques [14], is obtained from Eq. (27.57), after some rearrangement and passage to a coordinate basis. Defining $m_{\text{fi}}(k_0)$ from $\lambda(k_0)$ in analogy with the definition of $M_{\text{fi}}^{N+1}(k_0)$ from $\bar{\Lambda}^N(k_0)$ in Eq. (27.58), one has

$$\begin{aligned} M_{\text{fi}}^{N+1}(k_0) &= m_{\text{fi}}(k_0) + \sum_a (\langle a|\lambda(k_0)|A^- \rangle \\ &+ \langle A^+|\lambda(k_0)|a\rangle), \quad (27.59) \end{aligned}$$

where

$$\begin{aligned} & [h(\mathbf{r}) \mp k_0 - e_a] \langle \mathbf{r}|A^\pm \rangle + \sum_a \left[\begin{matrix} r \\ a \end{matrix} \middle| V \right| \begin{matrix} A^\pm \\ a \end{matrix} \right] \\ &= - \sum_j \langle \mathbf{r}|j\rangle \langle j|[v_\pm + \mathcal{V}_\pm]|a\rangle, \quad (27.60) \end{aligned}$$

$$\langle j|v_+|a\rangle = \left[\begin{matrix} j \\ i \end{matrix} \middle| V \right| \begin{matrix} a \\ i \end{matrix} \right], \quad \langle j|v_-|a\rangle = \left[\begin{matrix} j \\ i \end{matrix} \middle| V \right| \begin{matrix} a \\ i \end{matrix} \right], \quad (27.61)$$

$$\langle j|\mathcal{V}_\pm|a\rangle = \sum_b \left\{ \left[\begin{matrix} j \\ b \end{matrix} \middle| V \right| \begin{matrix} a \\ B_\pm \end{matrix} \right] + \left[\begin{matrix} j \\ B_\mp \end{matrix} \middle| V \right| \begin{matrix} a \\ b \end{matrix} \right] \right\}. \quad (27.62)$$

The three-point Green's function, as can be seen from this summary, describes transition amplitudes for radiative transitions between two valence states of atoms with closed shells (subshells) plus one electron (the 1P case). In the Coulomb

ladder approximation, closely related to the DF equation, the photon vertex $\langle \mathbf{1}|\Lambda^N(\mathbf{r}; \omega_1\omega_2)|\mathbf{2}\rangle$ of Eq. (27.53), is nonlocal in space, rather than the local vertex $\langle \mathbf{1}|\lambda_k(\mathbf{r})|\mathbf{2}\rangle$ of Eq. (27.11) [as follows from the factor of $\delta^3(\mathbf{1}-\mathbf{r})\delta^3(\mathbf{2}-\mathbf{r})$]. The presence of these additional nonlocal contributions to $M_{\text{fi}}^{N+1}(k_0)$ is made apparent in Eq. (27.59). The $m_{\text{fi}}(k_0)$ term is the contribution of the local vertex. Of course, if one knew the *exact* $N+1$ electron wave functions and energies, only the local vertex would enter and a GI result would be obtained. However, the length and velocity versions of Eq. (27.12) are equal and GI even in the approximation just discussed [3, 7]. Gauge invariance is an *essential* constraint on radiative transition amplitudes. It has been proven for general gauges not only in the present approximation, but also in the ones discussed below [8, 10], all of them arising in the GFA. Since the effective potential in the DF (or HF) approximation is nonlocal, the effective current must also be nonlocal in order to maintain the GI.

The somewhat more complicated Dyson equation satisfied by the nonlocal vertex corresponding to the Brueckner approximation has also been generated [22], and put in a numerically implementable form.

An alternative approximation [3, 7] for transition matrix elements, proposed earlier [2] than the one just discussed, is based on the RPA [our PH/HP case, with wave function $\bar{\chi}_{(fa)}$ the solution of Eq. (27.45)]. Reference to Eqs. (27.6), (27.7), (27.10) and (27.11) gives immediately

$$M_{fa}^N(\mathbf{r}; \omega_{(fa)}) = -\lambda_k(\mathbf{r}) \langle \mathbf{r}|\bar{\chi}_{(fa)}|\mathbf{r}\rangle, \quad (27.63)$$

where $k_0 = k = \omega_{(fa)}$ and N corresponds to atoms with a closed shell or subshell of electrons.

Aside from being a different approximation to transition amplitudes than Eqs. (27.54), (27.63) covers a different set of cases than does Eq. (27.54), since the corresponding initial states i in Eq. (27.54) are restricted to core states a in Eq. (27.63). Thus, for example, the case $N=2$ in Eq. (27.54) can describe transitions between any two valence states of Li. The corresponding case for Eq. (27.63) is $N=4$, but only transitions to a higher level, originating in the 1s or 2s level of Li, can be described by the formalism.

Finally, we shall discuss radiative transitions [8] for 2P atoms (closed shell/subshell plus two valence electrons). The general case involves a five-point nonlocal vertex. However, in the ladder approximation, this reduces to transition matrix elements which contain combinations of DF, 2P BS wave functions, and three-point functions. The final expressions are

$$\begin{aligned} & M_{\text{fi}}^{N+2}(\mathbf{r}; k_0) \\ &= \langle \bar{\zeta}_{(fp)} | \left(\frac{\bar{\Lambda}^N(\mathbf{r}, k_0)}{k_0 - \Delta H} V - V \frac{\bar{\Lambda}^N(\mathbf{r}, k_0)}{k_0 - \Delta H} \right) | \bar{\zeta}_{(iq)} \rangle. \quad (27.64) \end{aligned}$$

The expressions appearing in this equation are, in more detail, in the DF basis:

$$\left\langle \begin{matrix} m \\ n \end{matrix} \middle| \frac{\bar{\Lambda}^N(\mathbf{r}, k_0)}{k_0 - \Delta H} \middle| \begin{matrix} q \\ s \end{matrix} \right\rangle \equiv \frac{\langle m | \bar{\Lambda}^N(\mathbf{r}, k_0) | q \rangle \delta_{ns}}{k_0 + e_q - e_m}, \quad (27.65)$$

where m, n, q, s label DF states (P or H), $|s^q\rangle \equiv |qs\rangle \equiv |q\rangle|s\rangle$; Eq. (27.65) serves to define ΔH , as a difference of two DF Hamiltonians, the argument \mathbf{r} of $\bar{\Lambda}$ refers to the electron which emits the photon, and

$$\langle {}^m_n | V | \bar{\xi}_{(\tau)} \rangle = \sum_{cd} \langle {}^m_n | V | c_d \rangle \langle c_d | \bar{\xi}_{(\tau)} \rangle + \sum_{k\ell} \langle {}^m_n | V | k_\ell \rangle \langle k_\ell | \bar{\xi}_{(\tau)} \rangle. \quad (27.66)$$

In Eq. (27.66) we used the fact that, in the DF basis, $|\bar{\xi}_{(\tau)}\rangle$ only has 2P or 2H components Eqs. (27.46), (27.48).

27.5 Radiative Corrections

This section summarizes radiative corrections for 1P/1H atoms, starting from the two-point Green's function. The Dyson equations are generated and solved perturbatively for the energy to order $\alpha^5 m$ (α^3 a.u.). The perturbation theory starts from the DF solution as the zero-order one.

As done for the three-point function in Sect. 27.4, the Dyson equation for radiative corrections involving a single transverse photon is generated by expanding the two-point propagator to all orders in the Coulomb ladder approximation, inserting a transverse virtual photon in all possible ways, and then resumming. The resulting integral equation [23] is quite complicated, containing even the three-point vertex in its inhomogeneous term, as well as a mass counter term to eliminate divergences. It is sufficient for the present purposes to expand these vertices through first order matrix elements of $V_{ee} \equiv V$, but to exclude matrix elements of type $\langle {}^m_n | V | a_n \rangle$ (where a is the label for core states), since these are already included in the DF approximation [see Eq. (27.27)].

Other radiative corrections are also generated, which include Coulomb photons. Two of these corrections, involving only such photons, have already been referred to in the text between Eqs. (27.21) and (27.23). Finally, to order $\alpha^5 m$, corrections involving two transverse photons must be included.

Systematic application of the pole-shifting process in Eq. (27.23) to the one- and two-transverse-photon and the Coulomb-photon expressions yields two types of terms: first, photon exchange (of one transverse photon or of two-photons of either kind, Coulomb or transverse) between core and valence states; and second, self-energy and vacuum polarization contributions. Among the photon exchange terms,

one can identify those contributions included in other approaches (at least for a few special cases, such as those arising from a single transverse photon interaction, and from two Coulomb interactions and Coulomb–Breit interactions with positive energy intermediate electron states). These are electron correlation terms which are included as part of a MBPT calculation [5], or one which involves consideration of an infinite subset of MBPT terms [6]. They need not be re-evaluated. The terms not covered by calculations of the type in [5, 6], which are of $O(m\alpha^5 c^2)$, involve retardation in Coulomb-transverse photon exchange, negative energy intermediate electron states for two Coulomb and Coulomb-transverse photon exchanges, two transverse photon exchange, self-energy and vacuum polarization terms, as well as anomalous magnetic moment corrections.

After lengthy calculation, one obtains final results in finite analytic form, which are numerically implementable. The results given below are obtained after further approximations. First, the remnants of the original integral equation are solved iteratively. Second, the self-energy terms are calculated in a joint expansion [24–26] in α and αZ , and are thus only valid for low Z in isoelectronic sequences. Finally, there are characteristic logarithmic terms generated by low virtual photon momenta in the self-energy contributions. A standard approach is to scale these with a factor of $(\alpha Z)^2$ to obtain Bethe log (BL) terms as constants independent of α , together with constant log (CL) terms of the form $\ln(\alpha Z)^2$. The BL terms are independent of Z for hydrogenic ions, and remain nearly so for other atoms. BL and CL terms are associated with both nuclear and ee Coulomb potentials. The ee CL terms arising from core and valence self-energy terms are canceled exactly by those coming from Coulomb and transverse photon exchange. Thus, the numerous and rather complicated corresponding ee BL terms, which also are *individually* small compared to their associated CL terms, should additionally almost cancel, and are therefore neglected.

One finally obtains (with all state labels denoting principal and orbital quantum numbers as well as spin indices: $n \equiv (n, \ell; m_s)$)

$$\Delta E(n, \ell) = Z |\langle \mathbf{0} | n \rangle|^2 F(n, \ell), \quad (27.67)$$

in a.u., where $\langle \mathbf{0} | n \rangle \equiv \langle \mathbf{0} | n, 0 \rangle$ is the s-state HF wave function at the origin of coordinates, and serves to define an effective (shielded) nuclear charge $Z_{n,\text{eff}}$:

$$\langle \mathbf{r} | n, \ell \rangle \equiv \Psi_{n,\ell}(\mathbf{r}), |\langle \mathbf{0} | n \rangle|^2 \equiv \frac{1}{\pi n^3} (Z_{n,\text{eff}} \alpha)^3. \quad (27.68)$$

(Just as in hydrogen, for which the final expressions for the radiative corrections require NR and not R wave functions and energies, so in this case we use HF (NR) and not DF (R) quantities.) $F(n, \ell)$ consists of a valence or hole contribution

$F_{v,h}$, a core term $F_{\text{core}}(n, \ell)$, and one due to photon exchange between electrons $F_{\text{ee}}(n, \ell)$:

$$F(n, \ell) = F_{v,h}(n, \ell) + F_{\text{core}}(n, \ell) + F_{\text{ee}}(n, \ell), \quad (27.69)$$

$$F_{v,h}(n, \ell) = \frac{4}{3} [N(Z)\delta_{\ell 0} + L(n\ell) + U_{v,h}^{\text{so}}(n\ell)], \quad (27.70)$$

$$F_{\text{core}}(n, \ell) = \frac{4}{3Z} [N(Z)\rho(n\ell) + L_{\text{core}}(n\ell) + U(n\ell) + U_{\text{core}}^{\text{so}}(n\ell)], \quad (27.71)$$

$$F_{\text{ee}}(n, \ell) = \frac{4}{3Z} [E(Z)K^C(n\ell) + K^L(n\ell)], \quad (27.72)$$

with $U_{v,h}^{\text{so}}(n\ell)$ and $U_{\text{core}}^{\text{so}}(n\ell)$ being the spin-orbit terms,

$$N(Z) = \ln \frac{1}{(Z\alpha)^2} + \frac{19}{30} + Z\alpha C_5, \quad (27.73)$$

$$C_5 = 3\pi \left(1 + \frac{11}{128} - \frac{1}{2} \ln 2 \right), \quad (27.74)$$

$$E(Z) = -\frac{7}{2} \ln \frac{1}{Z\alpha} + \frac{59}{20} - \frac{9}{8}\pi, \quad (27.75)$$

$$L(n\ell) = \frac{i/4\pi}{|\langle \mathbf{0} | n \rangle|^2} \langle n, \ell | \left[\mathbf{p} \cdot \mathcal{L}_B(n\ell) \frac{\mathbf{r}}{r^3} - \frac{\mathbf{r}}{r^3} \mathcal{L}_B(n\ell) \cdot \mathbf{p} \right] | n, \ell \rangle, \quad (27.76)$$

$$\mathcal{L}_B(n\ell) \equiv \ln \frac{Z^2}{2|e_n - H|}, \quad (27.77)$$

H the HF Hamiltonian, $e_n \equiv e(n\ell)$ the HF energy,

$$U_{v,h}^{\text{so}}(n\ell) = \frac{3/16\pi}{|\langle \mathbf{0} | n \rangle|^2} \langle n | \frac{1}{r^3} | n \rangle C_\ell, \quad (27.78)$$

where

$$C_\ell = \begin{cases} \ell & j = \ell + \frac{1}{2} \\ -(\ell + 1) & j = \ell - \frac{1}{2} \end{cases}, \quad (27.79)$$

$$\rho(n\ell) = \frac{i/4\pi}{|\langle \mathbf{0} | n \rangle|^2} \sum_a \sum_{jk} \left\{ \frac{(e_k - e_j)(e_a - 2e_k + e_j)}{e_a - e_j} \times \left[{}^n_a V | j \right] \langle j | \mathbf{r} | k \rangle \cdot \langle k | \mathbf{p} | a \rangle + \text{c.c.} \right\}, \quad (27.80)$$

$$L_{\text{core}}(n\ell) = \frac{i/4\pi}{|\langle \mathbf{0} | n \rangle|^2} \sum_a \sum_{jk} \left\{ \frac{(e_k - e_j)(e_a - 2e_k + e_j)}{e_a - e_j} \times \left[{}^n_a V | j \right] \ln \frac{Z^2}{2|e_a - e_k|} \langle j | \mathbf{r} | k \rangle \cdot \langle k | \mathbf{p} | a \rangle + \text{c.c.} \right\}, \quad (27.81)$$

$$U_{(1)}(n\ell) = \frac{1/2\pi}{|\langle \mathbf{0} | n \rangle|^2} \sum_a \left\{ \langle a | \mathbf{p}^2 | a \rangle \left[{}^n_a V | a \right] - \left[{}^n_{(a')} V | a \right] - \left(\left[{}^{(b')}_a V | a \right] + \text{c.c.} \right) \delta_{nb} \right\}, \quad (27.82)$$

$$U_{(2)}(n\ell) = \frac{i/2\pi}{|\langle \mathbf{0} | n \rangle|^2} \sum_a \sum_{k < q} \left\{ \frac{(2e_a - e_k - e_q)}{e_q - e_k} \left[{}^n_q V | k \right] \times \left(\ln \left| \frac{e_a - e_q}{e_a - e_k} \right| + 2 \right) \langle a | \mathbf{p} | q \rangle \cdot \langle k | \mathbf{p} | a \rangle + \text{c.c.} \right\}, \quad (27.83)$$

$$U_{\text{core}}^{\text{so}}(n\ell) = \frac{3/16\pi}{|\langle \mathbf{0} | n \rangle|^2} \sum_{aj} \left\{ \frac{\delta_{\ell a \ell_j}}{e_a - e_j} \left[{}^n_a V | j \right] \times \langle j | \frac{1}{r^3} | a \rangle C_\ell + \text{c.c.} \right\}, \quad (27.84)$$

$$K^C(n\ell) = \frac{1}{|\langle \mathbf{0} | n \rangle|^2} \sum_a \left[{}^n_a \delta^3(\mathbf{x} - \mathbf{y}) \right]_a, \quad (27.85)$$

$$K^L(n\ell) = \frac{7/2}{|\langle \mathbf{0} | n \rangle|^2} \sum_a \left[{}^n_a \frac{1}{4\pi} \nabla^2 \times \left(\frac{\ln(Z|\mathbf{x} - \mathbf{y}|) + \gamma}{|\mathbf{x} - \mathbf{y}|} \right) \right]_a, \quad (27.86)$$

where

$$U(n\ell) \equiv U_{(1)}(n\ell) + U_{(2)}(n\ell), \quad (27.87)$$

$$\langle \mathbf{r} | (a)' \rangle \equiv \frac{d}{dr} \langle \mathbf{r} | a \rangle, \quad (27.88)$$

and γ is the Euler–Mascheroni constant. As in Eq. (27.27), x refers to the top row and y to the bottom row in the two-row expression in Eq. (27.86).

$L(n\ell)$, which is associated with the valence electron and the nuclear Coulomb potential, has the form of a hydrogenic BL, except that it is calculated with HF wave functions and energies. $L_{\text{core}}(n\ell)$ comes from BL terms associated with core electrons.

The expressions appearing in Eqs. (27.80), (27.81), and (27.83) originate from the double commutator $[\mathbf{p} \cdot [\mathbf{p}, H]]$, which is then approximated by using the commutator $[\mathbf{r}, H] \approx i\mathbf{p}$. This is not an exact result because the ee exchange term in the HF potential is neglected. One thus obtains [13]

$$\langle m | [\mathbf{p} \cdot [\mathbf{p}, H]] | n \rangle \approx i(e_n - 2e_k + e_m)(e_k - e_n) \langle m | \mathbf{p} | k \rangle \cdot \langle k | \mathbf{r} | n \rangle. \quad (27.89)$$

A less accurate approximation is [12]

$$4\pi Z \delta^3(\mathbf{r}) \approx [\mathbf{p} \cdot [\mathbf{p}, H]]. \quad (27.90)$$

Using the left-hand side of this equation instead of the approximation Eq. (27.89) to the right-hand side would lead to only s-state a, j and p-state k contributions in Eq. (27.80) and alternative forms of Eqs. (27.81) and (27.83).

The major part of the contribution to the energy due to radiative corrections comes from $F_{v,h}(n, 0)$ (s-states), and

numerical tests indicate that the principal effect in this term comes from the renormalization of the electron density at the coordinate origin due to electron shielding. This reduction occurs because the shielded wave function is more spread out than the unshielded one. Thus, one can extend the above results semi-empirically to high Z (for which $F_{\text{core}}(n, \ell)$ and $F_{\text{ee}}(n, \ell)$ play a much smaller role because of their $1/Z$ dependence) by using the hydrogenic results [27] for high Z , i.e., replacing Z^4 for hydrogen by $Z(Z_{n,\text{eff}})^3$ for 1P/1H atoms (where $Z_{n,\text{eff}}$ is the shielded nuclear charge number, defined in Eq. (27.68), and Z is the unshielded nuclear charge number). The results obtained in this way are competitive with other evaluations of ΔE_n [28].

Finally, there is a correction to $F(n, \ell)$ for smaller Z when the integral equations for the self-energy and vacuum polarization contributions are solved more accurately than by iteration. These corrections play little role in s-state energies, but are somewhat more important in p-states for the hard core case (closed shells, $N = 2, 10$, etc.). They are expected to provide a much more significant contribution in the soft core case (closed *subshells*, $N = 4, 12$, etc.).

The correction is based on the simpler approximation given in Eq. (27.90) of the more accurate Eq. (27.89). It is given by

$$\delta F(n, \ell) = \frac{1}{Z \langle \mathbf{0} | n \rangle^2} \sum_a \sum_j^f \left\{ \frac{\left[\begin{smallmatrix} n \\ a \end{smallmatrix} | V \begin{smallmatrix} n \\ j \end{smallmatrix} \right]}{e_a - e_j} \left[\langle j | \mathcal{E} | a \rangle - Z \mathcal{F}_{\text{v,h}}^{(0)}(j | \mathbf{0} \rangle \langle \mathbf{0} | a \rangle \right] + \text{c.c.} \right\}, \quad (27.91)$$

where

$$\langle j | \mathcal{E} | a \rangle = Z \mathcal{F}_{\text{v,h}}^{(0)}(j | \mathbf{0} \rangle \langle \mathbf{0} | a \rangle + \sum_b \sum_k^f \left(\frac{\left[\begin{smallmatrix} j \\ b \end{smallmatrix} | V \begin{smallmatrix} a \\ k \end{smallmatrix} \right]}{e_b - e_k} \left[\langle k | \mathcal{E} | b \rangle + \text{c.c.} \right] \right), \quad (27.92)$$

$$\mathcal{F}_{\text{v,h}}^{(0)} = \frac{4}{3} \{ N(Z) + L \}. \quad (27.93)$$

The inhomogeneous term in Eq. (27.92) appears only for states $|j\rangle$ and $|a\rangle$ which are s-states. L in Eq. (27.93) is taken to be a constant, an approximation sufficient for the desired accuracy, and reflects the fact that $L(n, 0)$ for s-states is essentially constant as a function of radial quantum number,

and is approximately the same for hydrogen and the HF approximation.

In order to obtain the correction $\delta F(n, \ell)$ of Eq. (27.91), it is necessary first to solve the coupled inhomogeneous linear equations of Eq. (27.92). While the sum \sum_a over core states is always over a finite number of discrete states, the symbol \sum_j^f denotes an infinite sum over discrete bound valence states and an integral over the continuum of such states. Indeed, expressions of this type occur throughout the GFA. They can be dealt with by the use of finite basis techniques, for example the B-spline approach [29, 30].

References

1. Fetter, A.L., Walecka, J.D.: Quantum Theory of Many Particle Systems. McGraw-Hill, New York (1971)
2. Csanak, G., Taylor, H.S., Yaris, R.: Adv. Atom. Mol. Phys. **7**, 287 (1971)
3. Feldman, G., Fulton, T.: Ann. Phys. (N.Y.) **172**, 40 (1986)
4. Feldman, G., Fulton, T.: Ann. Phys. (N.Y.) **179**, 20 (1987)
5. Johnson, W.R., Blundell, S.A., Sapirstein, J.: Phys. Rev. A **37**, 2764 (1988)
6. Johnson, W.R., Blundell, S.A., Liu, Z.W., Sapirstein, J.: Phys. Rev. A **40**, 2233 (1989)
7. Feldman, G., Fulton, T.: Ann. Phys. (N.Y.) **152**, 376 (1984)
8. Liaw, S.-S., Feldman, G., Fulton, T.: Phys. Rev. A **38**, 5985 (1988)
9. Liaw, S.-S.: Phys. Rev. A **47**, 1726 (1993)
10. Liaw, S.-S., Chiou, F.-Y.: Phys. Rev. A **49**, 2435 (1994)
11. Feldman, G., Fulton, T.: Ann. Phys. (N.Y.) **201**, 193 (1990)
12. Feldman, G., Fulton, T., Ingham, J.: Ann. Phys. (N.Y.) **219**, 1 (1992)
13. Devoto, A., Feldman, G., Fulton, T.: Ann. Phys. (N.Y.) **232**, 88 (1994)
14. Fulton, T., Johnson, W.R.: Phys. Rev. A **34**(3), 1686 (1986)
15. Koopmans, T.H.: Physica **1**, 104 (1933)
16. Hostler, L.: J. Math. Phys. **5**, 1234 (1964)
17. Swainson, R.A., Drake, G.W.F.: J. Phys. A Math. Gen. **24**, 1801 (1991)
18. Schwinger, J.: J. Math. Phys. **5**, 1606 (1964)
19. Swainson, R.A., Drake, G.W.F.: J. Phys. A Math. Gen. **24**, 95 (1991)
20. Liaw, S.-S.: Phys. Rev. A **48**, 3555 (1993)
21. Salpeter, E.E.: Phys. Rev. **87**, 328 (1952)
22. Liaw, S.-S., Chiou, F.-Y.: Phys. Rev. A **49**(4), 2435 (1994)
23. Feldman, G., Fulton, T.: Ann. Phys. **201**(193), 6 (1990)
24. French, J.B., Weisskopf, V.F.: Phys. Rev. **75**, 1240 (1949)
25. Erickson, G.W., Yennie, D.R.: Ann. Phys. (N.Y.) **35**, 271 (1965)
26. Erickson, G.W., Yennie, D.R.: Ann. Phys. (N.Y.) **35**, 447 (1965)
27. Johnson, W.R., Soff, G.: Data Tables. At. Data Nucl. **33**, 405 (1985)
28. Cheng, K.T., Johnson, W.R., Sapirstein, J.: Phys. Rev. Lett. **66**, 2960 (1991)
29. de Boor, C.: A Practical Guide to Splines. Springer, Berlin, Heidelberg (1987)
30. Johnson, W.R., Sapirstein, J.: Phys. Rev. Lett. **57**, 1126 (1986)



Jonathan R. Sapirstein

Contents

28.1	Introduction	415
28.2	Basic QED Formalism	417
28.3	Perturbation Theory with Green Functions	420
28.4	Two-Particle Bound States	426
28.5	Many-Electron Bound States	428
28.6	Recoil Corrections at High Z	429
28.7	Concluding Remarks	430
	References	431

Abstract

Theoretical issues in bound state quantum electrodynamics are discussed with emphasis on a unified derivation of radiative and recoil corrections with the use of Green functions.

Keywords

effective field theory · vacuum polarization · Lamb shift · order perturbation theory · Feynman gauge

28.1 Introduction

Quantum electrodynamics (QED) is now understood to be a component of the Standard Model, the theory which describes the strong, weak, and electromagnetic interactions in the framework of quantum field theory (QFT). It was historically the first QFT, describing the interactions of electrons and photons, consistently incorporating quantum mechanics

and relativity. Many of the seminal papers on the subject are collected in [1]. Corrections to the lowest order predictions of the theory are proportional to powers of α , the fine structure constant. However, difficulties are encountered with ultraviolet divergent integrals when setting up perturbation theory in this small ($\approx 1/137$) parameter, and while the first papers on QED date from 1928, the difficulties were not overcome until 1947 [2]. Once the modern renormalized form of QED was established, work on the perturbation expansion in α could proceed, and efforts by many researchers that continue to the present day have led to theoretical predictions of unparalleled accuracy for a number of systems. The hydrogen atom in particular plays a central role in QED tests, and the breaking of the Dirac degeneracy between the $2s$ and $2p_{1/2}$ states, the Lamb shift, will be discussed in some detail below. Along with the Lamb shift, corrections to the Dirac equation's prediction $g = 2$, first explained by *Schwinger* [3], are of central importance in QED. As bound state issues are emphasized here, we note only that this anomalous magnetic moment of the electron was first detected in hydrogen hyperfine splitting and Zeeman effect experiments, and that its present status is discussed in Chap. 29 "Tests of Fundamental Physics" in this volume along with a number of other extraordinarily high-precision tests of the theory.

It is the purpose of this chapter to discuss how the theory is applied to bound state problems. While almost every textbook on QFT describes the basic structure of QED, the applications given are usually to calculate scattering cross sections, the evaluation of one-loop radiative corrections, and the implementation of the renormalization program. The free electron propagator, which has a relatively simple form in momentum space, is used in the one-loop calculations. However, most of the precision tests of QED involve electrons that are bound, generally in a hydrogen-like atom. Even for the anomalous magnetic moment of the electron, which is calculated in terms of free Feynman diagrams, the electron is, in fact, bound in the constant magnetic field of a Penning trap [4]. While most QED effects require the evaluation of loop diagrams, these bound state calculations have rela-

J. R. Sapirstein (✉)
Department of Physics, University of Notre Dame
Notre Dame, IN, USA
e-mail: jsapirst@nd.edu

tively unfamiliar features that will be concentrated on here. It is, of course, important to test free QED with scattering experiments at the highest possible energies. To a large degree these tests have now merged with tests of the Standard Model. Experiments, for example, on electron–positron annihilation into muon or tau pairs have to include both the photon and the Z boson in the intermediate state along with a unified treatment of radiative corrections [5].

The fact that QED is part of the Standard Model affects bound states in two notable ways. Because of the weak interactions, parity nonconserving transitions become possible through Z boson exchange, as discussed elsewhere in this volume. The strong interactions, which in principle describe the nucleus of the bound state in terms of QCD, cannot yet provide precise predictions for charge radii and other nuclear properties. This leads to limitations on predictions for atomic structure. In this case, if QED is understood well enough, and accurate experiments are available, atomic spectroscopy can be used to obtain information about nuclear properties. At the time of this writing a prominent example of this is the case of muonic hydrogen, where measurements imply a smaller proton size than had been expected [6].

The Lamb shift in hydrogen is smaller than the atomic unit of energy ($1 \text{ a.u.} = m_e c^2 \alpha^2$) by a factor α^3 , under one part per million (ppm). For almost all electromagnetically bound states such a tiny correction is negligible compared to the uncertainty in the energy when solving the many-electron Schrödinger equation, $H\psi = E\psi$, where

$$H \equiv \sum_i^N \left(\frac{\mathbf{p}_i^2}{2m} - \frac{Z\alpha\hbar c}{r_i} \right) + \sum_{i>j=1}^N \frac{\hbar c\alpha}{|\mathbf{r}_i - \mathbf{r}_j|} \quad (28.1)$$

$$\psi = \psi(\mathbf{r}_1, \mathbf{r}_2, \dots, \mathbf{r}_N).$$

Solving for a particular bound state energy E_v this way we refer to as the Hamiltonian approach. For a single electron bound to any positively charged nucleus (which will be referred to as hydrogen for simplicity in what follows) this uncertainty is not present, and QED corrections are easily identified. For many-electron atoms, however, the electron–electron interaction term usually makes it too difficult to solve for E_v with the accuracy required to see such corrections. The techniques used to deal with the many-body problem are rather different from those used for QED corrections. While attempts to create a unified approach have been made [7], the most advanced atomic QED calculations have been carried out for hydrogen [8, 9]. To study QED in atoms with more than one electron accurate solutions to the structure problem are required, which are available for few electron atoms, particularly helium, and certain highly charged ions, as will be discussed below.

The Coulomb potential of the nucleus in Eq. (28.1),

$$V_C(r) \equiv -\frac{Z\alpha\hbar c}{r}, \quad (28.2)$$

is responsible for the dominant physics of binding. It is, thus, very useful to incorporate it into bound state QED calculations, which we will do here when we introduce Furry picture QED [10]. This is an example of an external field approximation [11]. Such approximations are very good for an electron in a classical electric or magnetic field, as a single electron has essentially no effect on the charge distributions and currents that create the external field. In an atom, the success of the Schrödinger equation shows that even a single nucleus effectively creates an external field. In this case, the fact that the nucleus is a single particle leads to observable corrections to the external field approximation. They are called recoil corrections, and if the nucleus is taken to have mass m_N , begin in order m/m_N . They vanish in the limit of infinite nuclear mass, which is called the nonrecoil limit.

The first QED treatments of recoil corrections were by *Salpeter* [12, 13], using the equation he had earlier derived with *Bethe* [14]. They formed a field theoretic function of the total energy of hydrogen E that had a pole at $E = E_v$, with recoil corrections identified as the difference of E_v with its nonrecoil limit.

This approach can also be used to calculate nonrecoil corrections in bound state QED, and the central purpose of this chapter is to show how this technique allows a unified treatment of both types of QED correction. The treatment also leads to a rigorous justification of the external field approximation for hydrogen.

Three central objects in the following are the electron propagator for one electron, the electron–nucleus propagator, and the many-electron propagator. While the terms propagator and Green function are basically synonymous, it is convenient to designate propagators as functions of time, and Green functions as time Fourier transforms depending on an energy E . We will show that the latter have poles when $E = E_v$ and develop perturbation theory for QED using this behavior. While QED has a Hamiltonian, the analysis that will be described here is based on the Green functions of the theory, and the approach is fundamentally different from the Hamiltonian approach. While for most bound state problems the Hamiltonian approach suffices, there are situations in which an approach grounded in field theory is absolutely necessary.

This chapter is organized as follows. In the next section free QED is set up in Coulomb gauge, and photon and electron propagators introduced. The perturbation expansion in the interaction picture is described, and the connection with Feynman gauge, which is particularly useful for calculating loop corrections, is shown.

In the next section, the Green functions for the free and bound electrons are formed as time Fourier transforms of the propagators, and the field theory based analog of Rayleigh–Schrödinger perturbation theory developed. The formulas for the one-loop electron self-energy and vacuum polarization

are derived and analyzed, and a short discussion of the two-loop Lamb shift is given.

In the following section, the approach is extended to electron–nucleus scattering, with emphasis placed on the emergence of the bound electron propagator in the limit of infinite nuclear mass. The perturbation theory for recoil corrections is described.

We then turn to the generalization of the method to many-electron atoms, and mention some applications of QED to highly charged many-electron ions. In the final section an alternative to the Bethe–Salpeter approach to recoil corrections is given, and remarks about nonrelativistic QED (NRQED) [15] are made.

28.2 Basic QED Formalism

In the following, we work in SI units, keeping all factors of c , \hbar , and ϵ_0 . The photon momentum \mathbf{q} is understood to be \hbar times the associated wavenumber \mathbf{k} . The electron and proton charges are denoted q_e and q_p . The elementary charge e is understood to be positive, so $q_e = -e$ and $q_p = e$. In calculations, we will replace e^2 with $4\pi\hbar c\epsilon_0\alpha$. The charge and mass of the nucleus are $q_N = Ze$ and m_N . Before treating bound states, we set up QED for free electrons. The electron field will be understood to describe either an electron or positron state, and the vacuum is the state with zero electrons, positrons, and photons, indicated by

$$\begin{aligned} b_s(\mathbf{p})|0\rangle &= 0 \\ d_s(\mathbf{p})|0\rangle &= 0 \\ a_\lambda(\mathbf{q})|0\rangle &= 0. \end{aligned} \quad (28.3)$$

The destruction operators above have creation operator counterparts, and the only cases in which photon operators do not commute, or electron operators do not anticommute, are

$$\begin{aligned} [a_{\lambda_1}(\mathbf{q}_1), a_{\lambda_2}^\dagger(\mathbf{q}_2)] &= (2\pi)^3 \delta_{\lambda_1\lambda_2} \delta^3(\mathbf{q}_1 - \mathbf{q}_2) \\ \{b_{s_1}(\mathbf{p}_1), b_{s_2}^\dagger(\mathbf{p}_2)\} &= \{d_{s_1}(\mathbf{p}_1), d_{s_2}^\dagger(\mathbf{p}_2)\} \\ &= (2\pi)^3 \delta_{s_1s_2} \delta^3(\mathbf{p}_1 - \mathbf{p}_2). \end{aligned} \quad (28.4)$$

The electron field operator is given by

$$\begin{aligned} \psi(\mathbf{x}, t) &= \int \frac{d\mathbf{p}}{(2\pi)^3} \sqrt{\frac{mc^2}{E_p\hbar^3}} \sum_s \left[e^{-ip\cdot x/\hbar} b_s(\mathbf{p}) u(\mathbf{p}, s) \right. \\ &\quad \left. + e^{ip\cdot x/\hbar} d^\dagger(\mathbf{p}) v(\mathbf{p}, s) \right], \end{aligned} \quad (28.5)$$

with $p\cdot x = E_p t - \mathbf{p}\cdot\mathbf{x}$, $E_p = \sqrt{(mc^2)^2 + c^2\mathbf{p}^2}$; $u(\mathbf{p}, s)$ and $v(\mathbf{p}, s)$ are Dirac spinors that form the projection operators

$$\Lambda_+(\mathbf{p}) \equiv \sum_s u(\mathbf{p}, s) \bar{u}(\mathbf{p}, s) = \frac{E_p \gamma_0 - c\boldsymbol{\gamma}\cdot\mathbf{p} + mc^2}{2E_p}$$

$$\Lambda_-(\mathbf{p}) \equiv \sum_s v(\mathbf{p}, s) \bar{v}(\mathbf{p}, s) = \frac{E_p \gamma_0 + c\boldsymbol{\gamma}\cdot\mathbf{p} - mc^2}{2E_p}. \quad (28.6)$$

The noncovariant normalization $u^\dagger(\mathbf{p}, s)u(\mathbf{p}, s') = \delta_{ss'}$, $v^\dagger(\mathbf{p}, s)v(\mathbf{p}, s') = \delta_{ss'}$ is used.

The charge density and current in terms of the electron field operators are

$$\begin{aligned} \rho(\mathbf{x}, t) &= \psi^\dagger(\mathbf{x}, t)\psi(\mathbf{x}, t) \\ \mathbf{j}(\mathbf{x}, t) &= \psi^\dagger(\mathbf{x}, t)\boldsymbol{\alpha}\psi(\mathbf{x}, t). \end{aligned} \quad (28.7)$$

Normal ordering of the operators, in which destruction operators are moved to the right and creation to the left, is left implicit. The free electron Hamiltonian is

$$H_0(t) = \int d\mathbf{x} \bar{\psi}(\mathbf{x}, t) [-i\hbar c\boldsymbol{\alpha}\cdot\nabla + mc^2\beta] \psi(\mathbf{x}, t); \quad (28.8)$$

H_0 without t dependence indicated refers to the operator in square brackets.

Turning to the quantization of the electromagnetic field, as we use Coulomb gauge,

$$\nabla\cdot\mathbf{A}(\mathbf{x}, t) = 0. \quad (28.9)$$

This gives a constraint when quantizing $\mathbf{A}(\mathbf{x}, t)$, so that only the physical degrees of freedom of photons need be dealt with, and the field operator is

$$\begin{aligned} \mathbf{A}(\mathbf{x}, t) &= \sqrt{\frac{1}{\hbar c\epsilon_0}} \sum_{\lambda=1}^2 \int \frac{d\mathbf{q}}{(2\pi)^3 \sqrt{2|\mathbf{q}|}} \\ &\quad \times \left[a(\lambda, \mathbf{q}) \hat{\epsilon}_\lambda(\hat{\mathbf{q}}) e^{-iq\cdot x/\hbar} + a^\dagger(\lambda, \mathbf{q}) \hat{\epsilon}_\lambda(\hat{\mathbf{q}}) e^{iq\cdot x/\hbar} \right]. \end{aligned} \quad (28.10)$$

The scalar potential, which is not quantized, is fixed by

$$\nabla^2\phi(\mathbf{x}, t) = -\frac{\rho(\mathbf{x}, t)}{\epsilon_0}, \quad (28.11)$$

and the Hamiltonian describing the electrostatic energy is

$$\begin{aligned} H_C(t) &= \frac{e^2}{8\pi\epsilon_0} \int d\mathbf{x} \int d\mathbf{y} \\ &\quad \times \frac{\psi^\dagger(\mathbf{x}, t)\psi(\mathbf{x}, t)\psi^\dagger(\mathbf{y}, t)\psi(\mathbf{y}, t)}{|\mathbf{x} - \mathbf{y}|}. \end{aligned} \quad (28.12)$$

If the negative energy summation is removed from ψ , this Hamiltonian can be used to organize atomic many-body perturbation theory (MBPT) calculations [16]. Historically,

although QED was developed first, the power of the diagrammatic approach was later applied to many-electron atoms starting with the work of *Kelly* [17].

The remaining part of the interaction Hamiltonian comes from the minimal coupling replacement $c\boldsymbol{\alpha} \cdot \mathbf{p} \rightarrow c\boldsymbol{\alpha} \cdot (\mathbf{p} - q_e \mathbf{A}(\mathbf{x}, t))$,

$$H_T(t) = -q_e c \int d\mathbf{x} \mathbf{A}(\mathbf{x}, t) \cdot \psi^\dagger(\mathbf{x}, t) \boldsymbol{\alpha} \psi(\mathbf{x}, t), \quad (28.13)$$

where the subscript T stands for transverse.

The sum of $H_C(t)$ and $H_T(t)$ is the interaction Hamiltonian $H_I(t)$ and enters perturbation theory through its role in the time evolution operator $U(t_2, t_1)$. After transforming from the Schrödinger to the interaction picture through

$$|\psi_I(t)\rangle = e^{iH_0(t)t/\hbar} |\psi_S(t)\rangle, \quad (28.14)$$

it is given by

$$\begin{aligned} U(t_2, t_1) &= 1 + \frac{1}{i\hbar} \int_{t_1}^{t_2} dt H_I(t) + \left(\frac{1}{i\hbar}\right)^2 \int_{t_1}^{t_2} dt \\ &\quad \times \int_{t_1}^t dt' H_I(t) H_I(t') + \dots \\ &= 1 + \frac{1}{i\hbar} \int_{t_1}^{t_2} dt H_I(t) + \frac{1}{2!} \left(\frac{1}{i\hbar}\right)^2 \int_{t_1}^{t_2} dt \\ &\quad \times \int_{t_1}^t dt' T(H_I(t) H_I(t')) + \dots \\ &= T\left(e^{\frac{1}{i\hbar} \int_{t_1}^{t_2} dt H_I(t)}\right). \end{aligned} \quad (28.15)$$

Of particular importance is its value for $t_1 = -\infty, t_2 = \infty$, denoted S , and the matrix elements, the S -matrix,

$$\begin{aligned} S &\equiv U(\infty, -\infty) \\ S_{fi} &= \langle f | S | i \rangle. \end{aligned} \quad (28.16)$$

When one encounters the vacuum expectation value of a product of operators, a theorem due to Wick allows one to rearrange it in terms of creation and annihilation operators multiplying factors of the electron and photon propagators,

$$S_F(x, y) \equiv -i \langle 0 | T(\psi(x, t) \bar{\psi}(y, t')) | 0 \rangle \quad (28.17)$$

and

$$D^{ij}(x, y) \equiv -i \langle 0 | T(A^i(\mathbf{x}, t) A^j(\mathbf{y}, t')) | 0 \rangle. \quad (28.18)$$

Their form in momentum space is relatively simple,

$$S_F(x, y) = \frac{1}{\hbar^3} \int \frac{d^4 p}{(2\pi)^4} \frac{e^{-ip \cdot (x-y)/\hbar}}{p_0 \gamma_0 - \vec{\gamma} \cdot \vec{p} - mc + i\epsilon}, \quad (28.19)$$

$$D^{ij}(x, y) = \frac{1}{\epsilon_0 \hbar c} \int \frac{d^4 q}{(2\pi)^4} e^{-iq \cdot (x-y)/\hbar} \frac{\left(\delta_{ij} - \frac{q_i q_j}{q^2}\right)}{q_0^2 - \mathbf{q}^2 + i\epsilon}; \quad (28.20)$$

$D^{ij}(x, y)$ is called the transverse photon propagator.

The compact form for $S_F(x, y)$ given above can be expanded into a form that separates positive and negative energy states,

$$\frac{1}{\not{p} - mc + i\epsilon} = \frac{\Lambda_+(\mathbf{p})}{p_0 - E_p/c + i\epsilon} + \frac{\Lambda_-(\mathbf{p})}{p_0 + E_p/c - i\epsilon}, \quad (28.21)$$

which will be used later.

If one wants the S -matrix for electron–electron scattering, for example, one chooses

$$\begin{aligned} |i\rangle &= b^\dagger(\mathbf{p}_1, s_1) b^\dagger(\mathbf{p}_2, s_2) |0\rangle \\ \langle f| &= \langle 0 | b(\mathbf{p}_3, s_3) b(\mathbf{p}_4, s_4) \end{aligned} \quad (28.22)$$

(the states are properly antisymmetrized because the operators anticommute) and applies Wick's theorem. This procedure is greatly facilitated by a set of rules introduced by Feynman; they can be learned quickly, and correct QED matrix elements can be set up in an automatic way.

Unless the initial and final states are identical, the first contribution to S_{fi} comes from the term linear in H_C . Another term with the same number of factors q_e comes from the quadratic term with two H_T 's. The latter involves a transverse photon propagator between the electrons. It is convenient to introduce a corresponding Coulomb photon propagator in order to rewrite the H_C term so that it also arises from a quadratic term. This can be done by including with D^{ij} another propagator, D^{00} . If one generalizes D^{ij} to $D^{\mu\nu}$, with $D^{0i} = D^{i0} = 0$ and

$$\begin{aligned} D^{00}(x, y) &= \frac{1}{\epsilon_0 \hbar c} \int \frac{d^4 q}{(2\pi)^4} e^{-iq \cdot (x-y)/\hbar} \frac{1}{q^2} \\ &= \frac{\delta(t-t')}{4\pi\epsilon_0 |\mathbf{x}-\mathbf{y}| c^2}, \end{aligned} \quad (28.23)$$

one reproduces S_{fi} by using

$$H_I(t) = q_e c \int d\mathbf{x} A^\mu(\mathbf{x}, t) \bar{\psi}(\mathbf{x}, t) \gamma^\mu \psi(\mathbf{x}, t) \quad (28.24)$$

and using the photon propagator in Coulomb gauge described above.

This simpler form for $H_I(t)$ comes at the apparent cost of the more complicated photon propagator just described, but the photon propagator is always encountered in the form $A_\mu(q)D^{\mu\nu}B_\nu(q)$. If one requires $q^\mu A_\mu = 0$ and $q^\mu B_\mu = 0$, a short calculation shows

$$\begin{aligned} \frac{A_0 B_0}{q^2} + \frac{q^2 \mathbf{A} \cdot \mathbf{B} - \mathbf{A} \cdot \mathbf{q} \mathbf{B} \cdot \mathbf{q}}{q^2(q_0^2 - q^2)} &= -\frac{A_0 B_0 - \mathbf{A} \cdot \mathbf{B}}{q_0^2 - q^2} \\ &= -\frac{A_\mu B_\nu g^{\mu\nu}}{q^2}, \end{aligned} \quad (28.25)$$

where we will suppress the $i\varepsilon$ in the following for brevity. Because of this one can use the simpler Feynman gauge propagator

$$D_F^{\mu\nu}(x, y) = \frac{1}{\hbar c \varepsilon_0} \int \frac{d^4 q}{(2\pi)^4} e^{-iq \cdot (x-y)/\hbar} \frac{-g^{\mu\nu}}{q^2}. \quad (28.26)$$

The requirement that $A^\mu q_\mu = B^\mu q_\mu = 0$ can be shown to be satisfied as long as a gauge invariant set of diagrams are evaluated together. In the following, we will use both gauges: Coulomb gauge is useful for recoil calculations and Feynman gauge for calculations involving loops with ultraviolet divergences.

In cases when a fixed external electromagnetic potential is present, one would decompose

$$A^\mu(x) \rightarrow A_{\text{ext}}^\mu(x) + A^\mu(x), \quad (28.27)$$

quantizing only the second term. This is the external field approximation [11]. The part of H_I involving the external field can then be grouped with $H_0(t)$ so that, restricting our attention to external fields constant in time,

$$\begin{aligned} H_0(t) = \int d\mathbf{x} \psi^\dagger(\mathbf{x}, t) [-i\hbar c \boldsymbol{\alpha} \cdot \nabla - q_e c \boldsymbol{\alpha} \cdot \mathbf{A}_{\text{ext}}(\mathbf{x}) \\ + mc^2 \beta + V(\mathbf{x})] \psi(\mathbf{x}, t), \end{aligned} \quad (28.28)$$

with $q_e A_{\text{ext}}^0(\mathbf{x}) = V(\mathbf{x})$. If the removal of the quantized part of H_I is carried out in this case, the interaction picture is referred to as the Furry picture [10]. This form of QED is extremely useful, as it builds in the dominant physics of binding, although at the cost of a more complicated electron propagator.

In Furry picture QED, the photon propagator is unchanged, but the electron propagator now depends on both \mathbf{x} and \mathbf{y} rather than only on their difference. We distinguish the free electron propagator $S_F(x, y)$ from the bound propagator by including a suffix V , and define the related Green function through

$$S_F^V(x, y) = \int \frac{dE}{2\pi} e^{-iE(t-t')/\hbar} G(E, \mathbf{x}, \mathbf{y}) \gamma_0. \quad (28.29)$$

When $V(\mathbf{r})$ is the Coulomb potential, we call $S_F^V(x, y)$ the Coulomb propagator, and $G(E, \mathbf{x}, \mathbf{y})$ the Coulomb Green function. In general, the Green function satisfies

$$[E - (H_0 + V(\mathbf{x}))]G(E, \mathbf{x}, \mathbf{y}) = \delta^3(\mathbf{x} - \mathbf{y}). \quad (28.30)$$

All information about the energy eigenvalues and eigenfunctions is contained in $G(E, \mathbf{x}, \mathbf{y})$. This is most clearly seen when it is represented as a spectral decomposition,

$$G(E, \mathbf{x}, \mathbf{y}) = \sum_m \frac{\psi_m(\mathbf{x}) \psi_m^\dagger(\mathbf{y})}{E - \varepsilon_m(1 - i\delta)}. \quad (28.31)$$

In this form, one identifies the eigenvalues ε_m as the position of simple poles of E , with the eigenvectors associated with the residue of the pole. (If there is a continuous distribution of energies, the pole is replaced with a branch cut.)

To isolate a particular pole $m = v$, we form the projection

$$G_{vv}(E) \equiv \int d\mathbf{x} \int d\mathbf{y} \psi_v^\dagger(\mathbf{x}) G(E, \mathbf{x}, \mathbf{y}) \psi_v(\mathbf{y}), \quad (28.32)$$

which collapses the sum over m in the spectral decomposition, giving

$$G_{vv}(E) = \frac{1}{E - \varepsilon_v}. \quad (28.33)$$

The related identities

$$\begin{aligned} \int d\mathbf{x} \psi_v^\dagger(\mathbf{x}) G(E, \mathbf{x}, \mathbf{y}) &= \frac{1}{E - \varepsilon_v} \psi_v^\dagger(\mathbf{y}) \\ \int d\mathbf{y} G(E, \mathbf{x}, \mathbf{y}) \psi_v(\mathbf{y}) &= \frac{1}{E - \varepsilon_v} \psi_v(\mathbf{x}) \end{aligned} \quad (28.34)$$

will also be used.

For the free case, we denote the Green function as $G_0(E, \mathbf{x}, \mathbf{y})$. It satisfies Eq. (28.30) with $V = 0$, and a useful representation of it is

$$G_0(E, \mathbf{x}, \mathbf{y}) = \frac{1}{\hbar^3} \int \frac{d\mathbf{p}}{(2\pi)^3} \frac{e^{i\mathbf{p} \cdot (\mathbf{x}-\mathbf{y})/\hbar}}{E \gamma_0 - c \boldsymbol{\gamma} \cdot \mathbf{p} - mc^2 + i\varepsilon} \gamma_0. \quad (28.35)$$

The two functions are related by

$$\begin{aligned} G(E, \mathbf{x}, \mathbf{y}) &= G_0(E, \mathbf{x}, \mathbf{y}) \\ &+ \int d\mathbf{r} G_0(E, \mathbf{x}, \mathbf{r}) V(\mathbf{r}) G(E, \mathbf{r}, \mathbf{y}), \end{aligned} \quad (28.36)$$

which leads to the expansion

$$\begin{aligned}
 G(E, \mathbf{x}, \mathbf{y}) &= G_0(E, \mathbf{x}, \mathbf{y}) \\
 &+ \int d\mathbf{r}_1 G_0(E, \mathbf{x}, \mathbf{r}_1) V(\mathbf{r}_1) G_0(E, \mathbf{r}_1, \mathbf{y}) \\
 &+ \int d\mathbf{r}_1 \int d\mathbf{r}_2 G_0(E, \mathbf{x}, \mathbf{r}_1) V(\mathbf{r}_1) \\
 &\quad \times G_0(E, \mathbf{r}_1, \mathbf{r}_2) V(\mathbf{r}_2) G_0(E, \mathbf{r}_2, \mathbf{y}) + \dots
 \end{aligned} \tag{28.37}$$

A characteristic difficulty of the atomic bound state problem is that going to the next order in the expansion of $G(E, \mathbf{x}, \mathbf{y})$ does not always lead to additional powers of α . Each term is nominally of the same order, and in many cases, the series must be summed to all orders. However, the expansion remains very useful. One reason for this is that the ultraviolet divergences of QED are generally associated with the first and second terms of the expansion, and isolating them allows manipulations to simplify loop calculations. As those are carried out in momentum space, we will need the momentum space version of the expansion of Eq. (28.37),

$$\begin{aligned}
 G(E, \mathbf{p}, \mathbf{q}) \gamma_0 &= \hbar^3 \left[\frac{(2\pi)^3 \delta^3(\mathbf{p} - \mathbf{q})}{E\gamma_0 - c\boldsymbol{\gamma} \cdot \mathbf{p} - mc^2} \right. \\
 &+ \frac{1}{E\gamma_0 - c\boldsymbol{\gamma} \cdot \mathbf{p} - mc^2} \gamma_0 \frac{4\pi Z\alpha c}{|\mathbf{p} - \mathbf{q}|^2} \\
 &\times \frac{1}{E\gamma_0 - c\boldsymbol{\gamma} \cdot \mathbf{q} - mc^2} \\
 &+ \frac{1}{E\gamma_0 - c\boldsymbol{\gamma} \cdot \mathbf{p} - mc^2} \gamma_0 \int \frac{d\mathbf{k}}{(2\pi)^3} \\
 &\times \frac{4\pi Z\alpha c}{|\mathbf{p} - \mathbf{k}|^2} \frac{1}{E\gamma_0 - c\boldsymbol{\gamma} \cdot \mathbf{p} - mc^2} \\
 &\times \gamma_0 \frac{4\pi Z\alpha c}{|\mathbf{k} - \mathbf{q}|^2} \frac{1}{E\gamma_0 - c\boldsymbol{\gamma} \cdot \mathbf{q} - mc^2} + \dots \left. \right].
 \end{aligned} \tag{28.38}$$

An interesting feature of the Furry picture is the role of negative energy states for many electron atoms. For free electrons, the unitary transformation to the interaction picture is unambiguous, chosen to subtract H_I , and the spinors $u(\mathbf{p}, s)$ and $v(\mathbf{p}, s)$ that enter the electron field operator are also unique. For hydrogen, the solutions are solutions to the Dirac equation in a Coulomb field, which are also unambiguous. However, for many electron atoms, an extended Furry representation can be used in order to account for some portion of electron screening, and this can be done using any local potential $U(\mathbf{x})$. This extension involves introducing an additional interaction Hamiltonian,

$$H_I'(t) = - \int d\mathbf{x} U(\mathbf{x}) \psi^\dagger(\mathbf{x}, t) \psi(\mathbf{x}, t) \tag{28.39}$$

along with changing $V(\mathbf{x}) \rightarrow V(\mathbf{x}) + U(\mathbf{x})$ in Eq. (28.28), and will be used when we discuss many-electron calculations. The positive and negative energy solutions to the Dirac equation now depend on the choice of the screening potential. For the positive energy solutions, one then faces the same problem as in the Hamiltonian approach. Except for atoms with only a few electrons, the only practical way to even form a wave function is to assume that all electrons move in the same potential, so that a lowest order approximation of the wave function as a Slater determinant of occupied states can be formed. When the potential is modified to incorporate screening, a modification of the Furry picture leads to a replacement of the Coulomb potential with the screened potential, as will be discussed later. The associated negative energy states also depend on the potential, so that forming a general projection operator to remove them, a useful approximation in relativistic many body physics, is problematical.

28.3 Perturbation Theory with Green Functions

We now introduce the basic approach to calculating energy levels in QED, which is to form a function of an energy E that has poles at the eigenvalue E_v . We first generalize the lowest order electron propagator that we have been dealing with to its exact form. This is done by starting in Heisenberg representation, defining

$$S_2(x, y) = \langle 0 | T(\psi_H(x) \bar{\psi}_H(y)) | 0 \rangle, \tag{28.40}$$

sometimes referred to as the two-point function. We then define the associated Green function,

$$\begin{aligned}
 G_2(E, \mathbf{x}, \mathbf{y}) &= -\frac{i}{\hbar} \int dt e^{iEt/\hbar} \\
 &\times \langle 0 | T(\psi_H(\mathbf{x}, t) \bar{\psi}_H(\mathbf{y}, 0)) | 0 \rangle e^{-\varepsilon|t|/\hbar}.
 \end{aligned} \tag{28.41}$$

We have set $t' = 0$ and introduced a convergence factor with the understanding that the limit $\varepsilon \rightarrow 0$ is to be taken.

We next note that a positive energy state ψ_v that satisfies $H\psi_v = E_v\psi_v$ leads to a pole at $E = E_v$ once the integral over positive values of t is carried out. This is because for such values the operators are already time ordered, and a complete set of states can be inserted between them, so that

$$\begin{aligned}
 G_2(E, \mathbf{x}, \mathbf{y}) &= -\frac{i}{\hbar} \sum_m \int_0^\infty dt e^{-\varepsilon t/\hbar} e^{iEt/\hbar} \\
 &\times \langle 0 | \psi_H(\mathbf{x}, t) | m \rangle \langle m | \psi_H(\mathbf{y}, 0) | 0 \rangle
 \end{aligned}$$

$$= -\frac{i}{\hbar} \sum_m \int_0^\infty dt e^{it(E-E_m+i\epsilon)/\hbar} \times \langle 0 | \psi_H(\mathbf{x}, 0) | m \rangle \langle m | \bar{\psi}(y, 0) | 0 \rangle. \quad (28.42)$$

We have used

$$\psi_H(\mathbf{x}, t) = e^{iHt/\hbar} \psi_H(\mathbf{x}, 0) e^{-iHt/\hbar} \quad (28.43)$$

to remove the time dependence from the electron field operator. This makes it possible to carry out the t integration, so for a particular state v

$$G_2(E, \mathbf{x}, \mathbf{y}) \approx \frac{1}{E - E_v + i\epsilon}. \quad (28.44)$$

We now have a way of finding E_v through the analysis of $G_H(E, \mathbf{x}, \mathbf{y})$, an object that is well defined in field theory. Of course, determining E_v is tantamount to exactly solving QED, so in practice, some kind of perturbation expansion must be made. Going to interaction representation allows the expansion to be derived through expanding the time evolution operator. However, while Feynman diagrams can be used for the expansion, instead of generating S -matrix elements we will find modifications of the Green function involving double poles, and the energy shifts will be the factors multiplying them. An extremely thorough treatment of this approach is given by *Shabaev* in [18]. The basic idea follows by considering the second term in the Taylor expansion of

$$\frac{1}{E - \epsilon_v - \delta E_v} = \frac{1}{E - \epsilon_v} + \frac{\delta E_v}{(E - \epsilon_v)^2} + \dots \quad (28.45)$$

The third term in the expansion will give a term with a triple pole, and so on, but to generalize first-order Rayleigh–Schrödinger perturbation theory to field theory it suffices to find terms with double poles and identify the factor with δE_v . As emphasized by *Yennie* [19], this approach to QED perturbation theory allows one to examine a limited set of Feynman diagrams contributing to a Green function. To find the shift of a state $\psi_v(\mathbf{x})$ with energy ϵ_v , one projects out that state as described above Eq. (28.33), and reads off the energy shift from coefficients of $1/(E - \epsilon_v)^2$.

Transforming from the Heisenberg to the interaction representation is done by including a factor of $U(\infty, -\infty)$ in the two-point function and dividing by the vacuum expectation value,

$$S_2(x, y) = \frac{\langle 0 | T(U \psi(\mathbf{x}, t) \bar{\psi}(y, 0)) | 0 \rangle}{\langle 0 | U | 0 \rangle}. \quad (28.46)$$

The denominator term eliminates contributions involving disconnected diagrams. We have already shown in

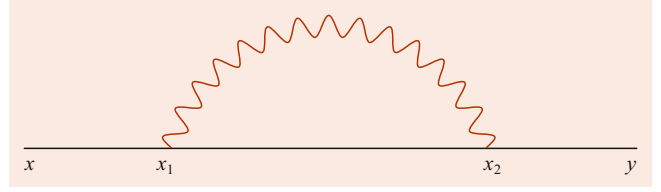


Fig. 28.1 The Green function for one-loop self-energy

Eq. (28.33) that in lowest order, the projected Green function has a pole at the Dirac energies ϵ_v . In particular, the $2s$ and $2p_{1/2}$ are degenerate. The experimental measurement of the energy difference of the state by *Lamb and Retherford* [20] was an important impetus for developing methods to calculate δE_v .

The first nonvanishing term in the Taylor expansion when using Feynman gauge is from second order, as one needs at least a pair of photon fields to combine into a propagator. The six electron fields contract into three propagators in two topologies, the self-energy (SE) and vacuum polarization (VP). We start with the self-energy, shown in Fig. 28.1.

$$G_{SE}(E) = -\frac{i}{\hbar} \int \frac{dE}{2\pi} e^{iEt/\hbar} \left(\frac{q_e c}{\hbar} \right)^2 \int dx_2 \int dx_1 \times S_F^V(x, x_1) \gamma_\mu S_F^V(x_1, x_2) \gamma_\nu S_F^V(x_2, y) \times D_F^{\mu\nu}(x_1, x_2). \quad (28.47)$$

The “outside” propagators $S_F^V(x, x_1)$ and $S_F^V(x_2, y)$ are next replaced with integrals over the variables E_1 and E_3 of $G(E_1, \mathbf{x}, \mathbf{x}_1)$ and $G(E_3, \mathbf{x}_2, \mathbf{y})$ using Eq. (28.29), and represented as spectral decompositions as in Eq. (28.31). The interior Green function is written as an integral over E_2 of $G(E_2, \mathbf{x}_2, \mathbf{x}_1)$ and left in that form. We collapse the sums as described earlier. The integral over t involves only $S(x, x_1)$, and carrying it out gives a delta function that puts $E_1 = E$. The remaining integrals over t_1 and t_2 force $E_3 = E$ and $E_2 = E - cq_0$, and we have a double pole term,

$$G_{SE}(E)_{vv} = -\frac{1}{(E - \epsilon_v)^2} \frac{ie^2 c}{\epsilon_0 \hbar} \int dx dy \times \int \frac{d^4 q}{(2\pi)^4} \frac{e^{iq \cdot (x-y)/\hbar}}{q^2 + i\delta} \bar{\psi}_v(\mathbf{x}) \gamma_\mu \times G(E - cq_0, \mathbf{x}, \mathbf{y}) \gamma_0 \gamma^\mu \psi_v(\mathbf{y}). \quad (28.48)$$

The factor multiplying the double pole is identified with the self-energy part of the one-loop Lamb shift,

$$E_{SE}^{(2)} = -4\pi i \alpha c^2 \int dx dy \int \frac{d^4 q}{(2\pi)^4} \frac{e^{iq \cdot (x-y)/\hbar}}{q^2 + i\delta} \times \bar{\psi}_v(\mathbf{x}) \gamma_\mu G(\epsilon_v - cq_0, \mathbf{x}, \mathbf{y}) \gamma_0 \gamma^\mu \psi_v(\mathbf{y}), \quad (28.49)$$

where we have replaced E with ϵ_v in the numerator of G .

Because the integral over q is ultraviolet infinite, $E_{SE}^{(2)}$ is not defined as it stands. If the d^4q integral were Euclidean, the radial part of the integral would go as $q^3 dq$: the denominator at large q goes as q^3 , so it is nominally linearly divergent. Before meaningful results can be calculated, two steps are needed: regularization and renormalization. Regularization involves making the integral a finite quantity, for example by cutting the q integral off at a large momentum Λ . Renormalization then involves showing that terms that diverge when Λ goes to infinity have the effect of changing quantities like the electron mass and charge. In a renormalizable theory such as QED, a limited number of renormalizations lead to finite results, with residual terms depending on the regularization vanishing in the limit.

An important breakthrough made in QED, which had basically been stalled for years by these infinities, was the realization they were present for both free and bound electrons. To show this, it is useful to present the self-energy term in momentum space,

$$E_{SE}^{(2)} = -\frac{4\pi i \alpha c^2}{\hbar^6} \int \frac{d^4q}{(2\pi)^4} \frac{1}{q^2} \int \frac{d\mathbf{p}_2}{(2\pi)^3} \int \frac{d\mathbf{p}_1}{(2\pi)^3} \times \bar{\psi}_v(\mathbf{p}_2) \gamma_\mu G(\varepsilon_v - cq_0, \mathbf{p}_2 - \mathbf{q}, \mathbf{p}_1 - \mathbf{q}) \times \gamma_0 \gamma^\mu \psi_v(\mathbf{p}_1) \quad (28.50)$$

and examine the first two terms in the expansion of the Green function given in Eq. (28.38).

Introducing a four-vector $p = (\varepsilon_v/c, \mathbf{p})$, the first term, the “zero potential” or OP term, can be written as

$$E_{0P}^{(2)} = \frac{1}{\hbar^3} \int \frac{d\mathbf{p}}{(2\pi)^3} \bar{\psi}_v(\mathbf{p}) \Sigma(p) \psi_v(\mathbf{p}), \quad (28.51)$$

where

$$\Sigma(p) = -4\pi i \alpha \int \frac{d^4q}{(2\pi)^4} \frac{1}{q^2} \gamma_\mu \times \frac{(\varepsilon_v - cq_0) \gamma_0 - c \boldsymbol{\gamma} \cdot (\mathbf{p} - \mathbf{q}) + mc^2}{(q - p)^2 - m^2 c^2} \gamma^\mu, \quad (28.52)$$

and the identity

$$\frac{1}{\not{p} - mc} = \frac{\not{p} + mc}{p^2 - m^2 c^2} \quad (28.53)$$

has been used. (If, instead, Eq. (28.21) is used for the electron propagator, it can be shown that there is a linear divergence present in the two parts that cancels.) We proceed by combining the denominators using

$$\frac{1}{AB} = \int_0^1 dx \frac{1}{(Ax + B(1-x))^2} \quad (28.54)$$

and find

$$\Sigma(p) = -4\pi i \alpha c \int \frac{d^4q}{(2\pi)^4} \int_0^1 dx \times \frac{\gamma_\mu (\boldsymbol{\gamma} \cdot (\mathbf{p} - \mathbf{q}) + mc) \gamma^\mu}{[(q - xp)^2 - xm^2 c^2 (1 - (1-x)p^2/(mc)^2)]^2}. \quad (28.55)$$

In this form, it is not hard to see that the divergence is logarithmic: the linear divergence, associated with the factor q , vanishes by symmetry after transforming $q \rightarrow q + xp$.

A powerful technique to regulate these infinities is dimensional regularization [21], where $d^4q \rightarrow dq_0 d^r q$, with $r = 3 - \varepsilon$. With ε small but nonzero, the integrals above can be done after transforming to a Euclidean form through $q_0 \rightarrow iq_4$. After defining a constant $C \equiv (4\pi)^{\varepsilon/2} \Gamma(1 + \varepsilon/2)$ and then expanding the result to order ε^0 , one has

$$\Sigma(p) = \frac{\alpha}{\pi} \left(\frac{3C}{2\varepsilon} + 1 \right) mc^2 - \frac{\alpha}{2\pi} \left(\frac{C}{\varepsilon} + 1 \right) (c \not{p} - mc^2) - \frac{\alpha}{4\pi} \int dx \ln(1 - (1-x)p^2/(mc)^2) \times [mc^2(1+x) - (1-x)(c \not{p} - mc^2)]. \quad (28.56)$$

For an on-shell free electron, only the first term survives and is termed the second-order electron self-mass, $\delta m^{(2)}$. It has the effect of shifting the electron mass from m to $m + \delta m^{(2)}$. This is to be identified with the observed mass of the electron, so if we use the observed mass in propagators, a renormalization counterterm must be included in the interaction Hamiltonian.

For a bound electron, the counterterm also removes the divergent self-mass term. The realization that a renormalization process that accounted for the changed meaning of the mass of free electrons would remove a divergence of bound electrons was a crucial step in establishing the modern form of QED. However, a divergence still remains for hydrogen. It is also removed by another renormalization, but because of an identity associated with current conservation, also directly cancels with a divergence from another part of the self-energy, the one-potential (1P) term.

The 1P term comes from the second term in Eq. (28.37), which is represented by the vertex diagram shown in Fig. 28.3. If we now define the two four-vectors $p_1 = (\varepsilon_v/c, \mathbf{p}_1)$ and $p_2 = (\varepsilon_v/c, \mathbf{p}_2)$, this part of the self-energy is

$$E_{1P}^{(2)} = \frac{1}{\hbar^3} \int \frac{d\mathbf{p}_2}{(2\pi)^3} \frac{d\mathbf{p}_1}{(2\pi)^3} \bar{\psi}_v(\mathbf{p}_2) \Gamma_0(p_2, p_1) \times \psi_v(\mathbf{p}_1) \frac{4\pi Z \alpha c}{|\mathbf{p}_2 - \mathbf{p}_1|^2}, \quad (28.57)$$

with

$$\Gamma_\rho(p_2, p_1) = -4\pi i \alpha \int \frac{d^4 q}{(2\pi)^4} \frac{1}{q^2} \gamma^\mu \frac{1}{\not{p}_1 - \not{q} - mc} \times \gamma_\rho \frac{1}{\not{p}_2 - \not{q} - mc} \gamma^\mu. \quad (28.58)$$

As with $\Sigma(p)$, $\Gamma_\rho(p_2, p_1)$, the one-loop vertex, is a standard one-loop expression that can be evaluated independently of the bound state problem. When it is sandwiched between on-shell electron wave functions, it can be expressed in terms of two form factors,

$$\Gamma_\rho(p_2, p_1) = \gamma_\rho F_1(q^2) + F_2(q^2) \frac{i\sigma^{\rho\nu} q_\nu}{2mc}, \quad (28.59)$$

where $q = p_2 - p_1$. Note that $q^2 = -|p_2 - p_1|^2$. While we will concentrate on $F_1(q^2)$, we note that $F_2(q^2)$ goes to $\alpha/2\pi$ when q is small compared to mc , which is the case for atomic momenta. This gives a contribution to the leading order Lamb shift, and in the case of the external field being a magnetic field gives the Schwinger correction [3].

The $F_1(q^2)$ has two divergences, the first being the same kind of ultraviolet divergence that dimensional regularization controls, and the second an infrared divergence. Although there is no infrared divergence in $E_{1P}^{(2)}$, the requirement of being on shell induces one in $F_1(q^2)$. For small values of q , one has

$$F_1(q^2) = \frac{\alpha}{2\pi} \left(\frac{C}{\varepsilon} + 1 \right) + \frac{\alpha}{3\pi} \frac{q^2}{(mc)^2} \left(\ln \frac{mc^2}{\varepsilon} - \frac{3}{8} \right), \quad (28.60)$$

where ε is a lower cutoff energy used to regulate the infrared divergence. The ultraviolet divergence can be seen to cancel with the 0P term after using the Dirac equation.

After noting the cancelation of the ultraviolet divergences, while the calculation of this term can be carried out numerically, one can immediately determine important properties of the energy shift by considering the form given above. In particular, the term of order q^2 in F_1 , when put into $E_{1P}^{(2)}$, leads to a factor of the wave function at the origin squared, as the p_1 and p_2 integrations are decoupled and can be carried out separately. Using the nonrelativistic form, this leads to a logarithmic term

$$E_{1P}^{(2)} \approx \frac{mc^2 \alpha (Z\alpha)^4}{\pi n^3} \frac{4}{3} \ln \frac{mc^2}{\varepsilon}. \quad (28.61)$$

The factor multiplying $4/3 \ln mc^2/\varepsilon$ characterizes the basic size of the Lamb shift. Compared to the scale of Bohr energies, $mc^2(Z\alpha)^2$, the effect is suppressed by a factor $\alpha(Z\alpha)^2$; while less than a ppm effect at low Z , it can be of order of a percent at high Z , as will be discussed later.

If the replacement $\varepsilon \rightarrow m(Z\alpha)^2$ is made, the cutoff form factor term gives, for s-states,

$$\Delta E = \frac{mc^2 \alpha (Z\alpha)^4}{\pi n^3} \frac{4}{3} \ln(Z\alpha)^{-2}, \quad (28.62)$$

the largest contribution, at 1334.801 MHz, to the Lamb shift in hydrogen. As the measurement is about 1057 MHz, the constant term is also important. It involves energies less than the cutoff and is sensitive to atomic structure. It receives contributions from each term in the expansion of the propagator we have been using, but the sum of the terms, the Bethe logarithm, can be numerically evaluated to high precision [22].

While the lowest order contribution to the self-energy, of order $mc^2 \alpha (Z\alpha)^4$, is understood, it is corrected by powers of $Z\alpha$ along with logarithms of $Z\alpha$, referred to as binding corrections. While the difficulty of the calculations increases as the power increases, they have been carried out to the high orders described elsewhere. However, for high Z this approach breaks down, and a numerical calculation is needed. For this reason, we now turn to a discussion of these calculations. We note, however, the useful constraint of requiring that the numerical methods, which work at any value of Z (although the numerical difficulty increases as Z gets small), agree with the power series expansion at low Z .

While the program began in 1955 [23, 23], numerical control to high accuracy was only relatively recently achieved. To set the calculations up, one first carries out the dq integration and does the Wick rotation $q_0 \rightarrow iu/c$ in Eq. (28.49). Both the Coulomb Green function and the photon Green function are expanded in partial waves. Using spherical symmetry allows the four angle integrations to be done, leaving a sum over partial waves of a three-dimensional integral. The main difficulty for the numerical approach is the fact the summation over partial waves extends to infinity. The most accurate values have been presented in [25], where acceleration techniques are used to extrapolate the sum to infinity, after which the radial and energy integrals are done. Highly accurate results have been presented for the $n = 1$ and $n = 2$ states for all Z in [26]. In this case, the integrations are carried out before the partial wave expansion, but subtraction techniques, to be discussed below, are used to make the partial wave expansion converge very rapidly, so that fewer than 20 terms are needed [27].

All numerical approaches involve subtractions, which are done in a number of ways. We have already examined the first and second terms in Eq. (28.37). The finite terms left over after the ultraviolet divergent terms have been canceled can be accurately evaluated, so if we add and subtract $E_{0P}^{(2)} + E_{1P}^{(2)}$ from the one-loop self-energy but express the subtracted part in coordinate space, we have an ultraviolet finite coordinate space term to deal with called the many-potential (MP) term. It is called this since only the second-order and higher

terms in Eq. (28.37) remain after the subtraction. This approach was suggested by *Blundell and Snyderman* [28] and has been used extensively.

This procedure involves subtracting, using a shorthand notation for the second term in Eq. (28.37), $G_0 V G_0$. Originally, however, *Mohr* [29] instead subtracted a term $G_0 \bar{V} G_0$, where, undoing the shorthand notation,

$$G_0 \bar{V} G_0 = \frac{V(x_2) + V(x_1)}{2} \times \int d\mathbf{w} G_0(E, \mathbf{x}_2, \mathbf{w}) G_0(E, \mathbf{w}, \mathbf{x}_1). \quad (28.63)$$

The integral over \mathbf{w} can be carried out using

$$\begin{aligned} & \int d\mathbf{w} G_0(E, \mathbf{x}_2, \mathbf{w}) G_0(E, \mathbf{w}, \mathbf{x}_1) \\ &= \int d\mathbf{w} \sum_m \frac{\psi_m(\mathbf{x}_2) \psi_m^\dagger(\mathbf{w})}{E - \varepsilon_m} \sum_n \frac{\psi_n(\mathbf{w}) \psi_n^\dagger(\mathbf{x}_1)}{E - \varepsilon_n} \\ &= \sum_m \frac{\psi_m(\mathbf{x}_2) \psi_m^\dagger(\mathbf{x}_1)}{(E - E_m)^2} \\ &= -\frac{d}{dE} G_0(E, \mathbf{x}_2, \mathbf{x}_1), \end{aligned} \quad (28.64)$$

and a much simpler function results. This allowed the first accurate calculations of the self-energy for a range of Z [29]. The argument just given for two Green functions applies to the product of any number of them, resulting in successively higher derivatives of a single Green function. This was used in [27] to form the subtractions mentioned above.

A set of corrections to the self-energy arise when it is perturbed that illustrate other aspects of the Green function perturbation theory expansion [30–32]. These corrections must be evaluated, for example, when dealing with radiative corrections to the Zeeman effect. For laboratory magnetic fields, the energy shift of a bound electron in an atom, E_Z , need be treated only in first order. However, to include the effect of the one-loop self-energy (which in the nonrelativistic case is dominated by the Schwinger correction), one must treat the diagrams of both figures (Figs. 28.2 and 28.3). (For Fig. 28.2, the Green functions are understood to be $G(z, \mathbf{x}, \mathbf{y})$ rather than $G_0(z, \mathbf{x}, \mathbf{y})$, and the vertical photon line as the magnetic field rather than the Coulomb field of the proton.) The latter diagrams have four electron propagators. We recall that for the one-loop self-energy, one of the three propagators was not decomposed, and the other two gave a double pole.

The same arguments apply to Fig. 28.2, and one leaves both interior propagators unexpanded. For the diagrams of Fig. 28.3, one encounters terms involving $\Sigma(p)$, but with argument E not replaced with ε_v , sandwiched with various states. Because only one propagator is left “as is”, there is a triple pole at $E = \varepsilon_v$. The triple pole itself gives no new

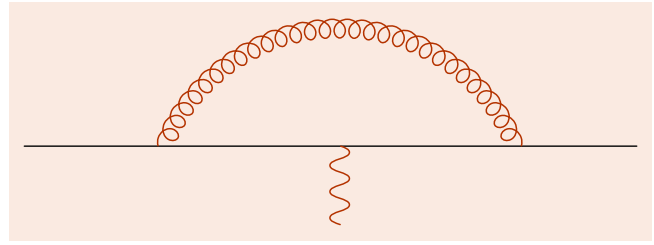


Fig. 28.2 $G_0 V G_0$ contribution



Fig. 28.3 Green functions leading to derivative and perturbed orbital terms

energy shift, but there are two ways a residual double pole can be generated. The first comes from expanding

$$\Sigma(E) = \Sigma(\varepsilon_v) + (E - \varepsilon_v) \Sigma'(\varepsilon_v) + \dots \quad (28.65)$$

and is called the derivative term. The second comes from restricting one of the “outside” propagators so that $m \neq v$, which again leads to a double pole. (The excluded term is associated with a cross term in the Taylor expansion of $1/(E - \Sigma_{vv} - E_Z)$.) This is referred to as a perturbed orbital term, since one can form a state $|\tilde{v}\rangle$ and show that the term is $\Sigma_{v\tilde{v}}(\varepsilon_v) + \Sigma_{\tilde{v}v}(\varepsilon_v)$. If written as

$$\Delta E_{PO} = \sum_{m \neq v} \left[\frac{\langle v | \Sigma | m \rangle \langle m | V | v \rangle}{\varepsilon_m - \varepsilon_v} + \frac{\langle v | V | m \rangle \langle m | \Sigma | v \rangle}{\varepsilon_m - \varepsilon_v} \right], \quad (28.66)$$

the close relation of the term to second-order Rayleigh–Schrödinger perturbation theory is seen.

The self-energy term discussed above has both the electron and the photon propagate from the same initial point to the same final point. Another term in which the photon propagates from x_1 to x_2 , but the electron propagates from x_2 to the same point is present, called the vacuum polarization term. The diagram representing it is shown in Fig. 28.4. If one expands the electron propagator using Eq. (28.37), only terms with odd powers of V contribute. The term linear in V gives the bulk of the effect and is called the Uehling term. The exact calculation was considered in [33], where it was shown that a partial wave expansion can be formed of the difference of the full VP with the Uehling term. The resulting Wichmann–Kroll terms are quite small. The fact that the basic expression for vacuum polarization involves $G(E, \mathbf{x}_2, \mathbf{x}_2)$, which is very singular, was analyzed in [34]

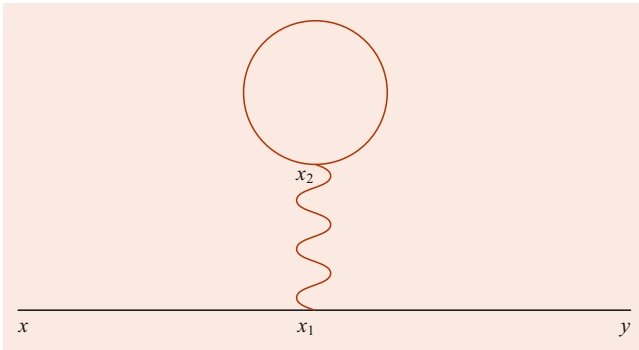


Fig. 28.4 Green function for vacuum polarization

using an alternative to dimensional regularization, Pauli–Villars regularization [35]. We present some details of the calculation, which illustrates charge renormalization.

Following the same steps as with the self-energy, we note that the energy of the photon line, cq_0 , is now forced to vanish, which allows the \mathbf{q} integration to be carried out, leading to a double pole with factor

$$E_{VP}^{(2)} = i\alpha\hbar c \int d\mathbf{x}_1 d\mathbf{x}_2 \frac{\bar{\psi}_v(\mathbf{x}_1)\gamma_0\gamma_\mu\psi_v(\mathbf{x}_1)}{|\mathbf{x}_1 - \mathbf{x}_2|} \times \int \frac{dz}{2\pi} \text{Tr}[\gamma^\mu G(z, \mathbf{x}_2, \mathbf{x}_2)\gamma_0]. \quad (28.67)$$

The $\mu = 0$ component of this then describes the Coulomb field of the charge density of the state v interacting with an electron looping from the point of interaction back to the same point.

Pauli and Villars [35] analyzed the ultraviolet infinities of one-loop vacuum polarization and showed that they could be regularized by introducing two similar expressions, but with the electron mass ($m \equiv M_0$) replaced by either M_1 or M_2 . If the two expressions are multiplied by the factors $(M_0^2 - M_2^2)/(M_2^2 - M_1^2)$ and $(M_1^2 - M_0^2)/(M_2^2 - M_1^2)$, respectively, and added to the original term, they showed the ultraviolet infinities were eliminated, and explicitly finite expressions could be analyzed. It is of interest to show how the calculation works for the case $M_1 = 20M_0$ and $M_2 = 30M_0$, even though they are understood to be taken to infinity after renormalization.

If one starts by considering the energy of a positive charge e in the Coulomb field of a fixed proton, one has $E_0(r) = \hbar c\alpha/r$. The effect of vacuum polarization on the energy breaks into two parts. One part is proportional to the lowest order energy,

$$E_1(r) = -\frac{2\alpha}{3\pi} \left[C_1 \ln \frac{M_1}{m} + C_2 \ln \frac{M_2}{m} \right] E_0(r) \equiv (Z_3 - 1)E_0(r). \quad (28.68)$$

For the Pauli–Villars masses chosen, $Z_3 = 1.004138$. Even though in the limit of infinite masses this so-called photon

renormalization constant is formally infinite, the smallness of α and the slow increase of the logarithm function make this formally infinite term close to 1 for the values chosen.

As with the electron mass renormalization, one must realize that this contribution is always present when two charges interact. If one could somehow suppress the effect of vacuum polarization, the effective elementary charge, which is called the bare charge e_0 , would be smaller. The effect of $E_1(r)$ is to renormalize e_0 to the observed charge e through $e = e_0\sqrt{Z_3}$. Alternatively, one can simply work with the observed charge and drop E_1 . In either case, the finite remainder is what of interest. The Uehling term is the term independent of C_1 and C_2 in

$$E_2(r) = -\frac{\alpha}{12\pi^2} E_0(r) \int_1^\infty dt \sqrt{t^2 - 1} \left(\frac{1}{t^2} + \frac{2}{t^4} \right) \times \left[e^{-2\frac{M_0 c}{\hbar} t r} + C_1 e^{-2\frac{M_1 c}{\hbar} t r} + C_2 e^{-2\frac{M_2 c}{\hbar} t r} \right]. \quad (28.69)$$

It plays a role in the Lamb shift, and by itself would act to make the $2s$ state more strongly bound than the $2p_{1/2}$ state. The other two terms are small and can be shown to vanish quadratically for large values of the masses M_1, M_2 .

Our using finite masses allows a central point about the renormalization program to be emphasized. As long as one works with renormalized quantities, finite calculations can be carried out. As shown in the example here, there is some dependence on the masses; however, there is little sensitivity to it, technically because of a quadratic falloff. A renormalizable theory in this picture should be thought of as insensitive to the high energy behavior: even if there is some new physics associated with the large momentum part of the loops, the predictions of a renormalizable theory like QED will change very little.

An important, relatively recent advance in exact calculations is in the two-loop Lamb shift. As with the one-loop case, both expansions in $Z\alpha$ and numerical treatments have been made. An example of a contribution is the overlapping loop diagram (Ov) shown in Fig. 28.5.

$$E_{SE}^{(4)}(\text{Ov}) = \alpha^2 c^4 \int \frac{d^4 q_1}{(2\pi)^4} \frac{d^4 q_2}{(2\pi)^4} \frac{1}{q_1^2} \frac{1}{q_2^2} \int d\mathbf{x} d\mathbf{z} d\mathbf{w} \times d\mathbf{y} \bar{\psi}_v(\mathbf{x})\gamma_\mu G(\varepsilon_v - cq_{10}, \mathbf{x}, \mathbf{z}) \times \gamma^\nu G(\varepsilon_v - cq_{10} - cq_{20}, \mathbf{z}, \mathbf{w}) \times \gamma^\mu G(\varepsilon_v - cq_{20}, \mathbf{w}, \mathbf{y})\gamma_\nu \psi_v(\mathbf{y}) e^{i\mathbf{q}\cdot(\mathbf{x}-\mathbf{y})/\hbar}. \quad (28.70)$$

A striking feature of the expansion in $Z\alpha$ was the discovery of a very large coefficient by Pachucki [36], who found

$$E_{SE}^{(4)} = \frac{mc^2\alpha^2(Z\alpha)^4}{\pi^2 n^3} [0.538941 - 21.55447(Z\alpha) + \dots] \quad (28.71)$$

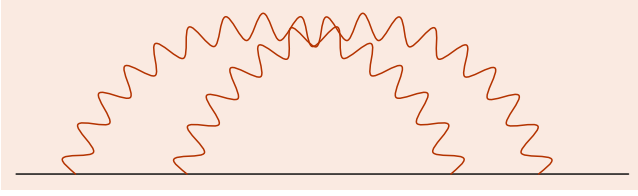


Fig. 28.5 Representative two-loop Lamb shift diagram

This emphasizes the need for the numerical approach for even moderate values of Z , as the above function changes sign by $Z = 4$. A recent discussion of the present status of two-loop calculations can be found in [37].

28.4 Two-Particle Bound States

We have so far dealt with hydrogen using the external field approximation, with the only role of the nucleus being the creation of a static Coulomb potential. We now will treat the nucleus dynamically, so that we must deal with two-particle bound states. To firstly justify the approximation, and secondly set up a perturbation theory to evaluate corrections to it, specifically recoil corrections, we now generalize $G_2(E, \mathbf{x}, \mathbf{y})$ from Eq. (28.41) to

$$\begin{aligned} G_4(E, \mathbf{x}_1, \mathbf{x}_2, \mathbf{y}_1, \mathbf{y}_2) &= -\frac{i}{\hbar} \int_{-\infty}^{\infty} dt e^{iEt/\hbar} \langle 0 | T(\psi_H(\mathbf{x}_1, t) \phi_H(\mathbf{x}_2, t) \\ &\quad \times \bar{\psi}_H(\mathbf{y}_1, 0) \bar{\phi}_H(\mathbf{y}_2, 0)) | 0 \rangle. \end{aligned} \quad (28.72)$$

Because the structure of the proton brings up issues not directly related to what we want to stress, it is convenient to treat it as a positive muon, so the field ϕ_H denotes that particle. No external field is now assumed, so the perturbation expansion will involve the free electron propagator, with mass denoted m_1 , and the free muon propagator, with mass denoted m_2 .

The argument given previously for $G_2(E, \mathbf{x}, \mathbf{y})$ showing that a pole is present carries through almost unchanged. The only difference is that to eliminate the time dependence from the product of the two operators one writes, after choosing $t > 0$ and inserting a complete set of states,

$$\begin{aligned} \langle 0 | \psi_H(\mathbf{x}_1, t) \phi_H(\mathbf{x}_2, t) | m \rangle &= \langle 0 | e^{iHt/\hbar} e^{-iHt/\hbar} \psi_H(\mathbf{x}_1, t) e^{iHt/\hbar} e^{-iHt/\hbar} \\ &\quad \times \phi_H(\mathbf{x}_2, t) e^{iHt/\hbar} e^{-iHt/\hbar} | m \rangle \\ &= \langle 0 | \psi_H(\mathbf{x}_1, 0) \phi_H(\mathbf{x}_2, 0) | m \rangle e^{-iE_m t/\hbar}. \end{aligned} \quad (28.73)$$

This argument can clearly be extended to a string of any number of operators, and the conclusion that a pole at $E = E_v$ is present is the same.

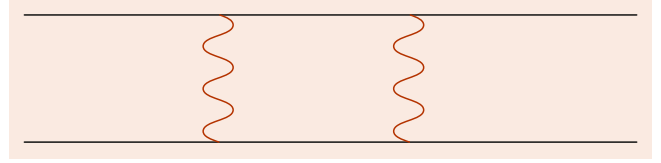


Fig. 28.6 Two-rung ladder diagram

We again begin by transforming to the interaction picture, but use Coulomb gauge rather than Feynman gauge. In lowest order,

$$\begin{aligned} \langle 0 | T(\psi(\mathbf{x}_1, t) \phi(\mathbf{x}_2, t) \bar{\psi}(\mathbf{y}_1, t') \bar{\phi}(\mathbf{y}_2, t')) | 0 \rangle \\ = -[S_F(\mathbf{x}_1, \mathbf{y}_1, t - t')]_1 [S_F(\mathbf{x}_2, \mathbf{y}_2, t - t')]_2, \end{aligned} \quad (28.74)$$

and we introduce a free propagator

$$\begin{aligned} S_0(\mathbf{x}_1, \mathbf{x}_2, \mathbf{y}_1, \mathbf{y}_2, t - t')_{ab,cd} \\ = [S_F(\mathbf{x}_1, \mathbf{y}_1, t - t')]_{ab} [S_F(\mathbf{x}_2, \mathbf{y}_2, t - t')]_{cd}. \end{aligned} \quad (28.75)$$

Binding is associated with an infinite summation of Coulomb photon exchanges described by the function, now taking $t' = 0$,

$$\begin{aligned} S_L(\mathbf{x}_1, \mathbf{x}_2, \mathbf{y}_1, \mathbf{y}_2, t)_{ab,cd} \\ = S_0(\mathbf{x}_1, \mathbf{x}_2, \mathbf{y}_1, \mathbf{y}_2, t)_{ab,cd} \\ + \int d\mathbf{w}_1 d\mathbf{w}_2 dt_w S_0(\mathbf{x}_1, \mathbf{x}_2, \mathbf{w}_1, \mathbf{w}_2, t - t_w)_{ae,cf} \\ \cdot \gamma_{0eg} \gamma_{0fh} \frac{\alpha}{|\mathbf{w}_1 - \mathbf{w}_2|} S_L(\mathbf{w}_1, \mathbf{w}_2, \mathbf{y}_1, \mathbf{y}_2, t_w)_{gb,hd}. \end{aligned} \quad (28.76)$$

Expanding this leads to a set of terms whose Feynman diagrams look like a ladder, with the Coulomb interaction forming the rungs. A two-rung ladder is shown in Fig. 28.6.

Before analyzing S_L , it is useful to form the Green function of S_0 and analyze it. It is

$$\begin{aligned} G_0(E, \mathbf{x}_1, \mathbf{x}_2, \mathbf{y}_1, \mathbf{y}_2) &= -\frac{i}{\hbar} \int_{-\infty}^{\infty} dt e^{iEt/\hbar} S_F^{(1)}(\mathbf{x}_1, t, \mathbf{y}_1, 0) S_F^{(2)}(\mathbf{x}_2, t, \mathbf{y}_2, 0) \\ &= -\frac{i}{\hbar} \int_{-\infty}^{\infty} dt \int \frac{dE_1}{2\pi} \int \frac{dE_2}{2\pi} e^{it(E-E_1-E_2)/\hbar} \\ &\quad \times [G_0(E_1, \mathbf{x}_1, \mathbf{y}_1) \gamma_0]_1 [G_0(E_2, \mathbf{x}_2, \mathbf{y}_2) \gamma_0]_2 \\ &= -i \int \frac{dE_1}{2\pi} [G_0(E_1, \mathbf{x}_1, \mathbf{y}_1) \gamma_0]_1 \\ &\quad \times [G_0(E - E_1, \mathbf{x}_2, \mathbf{y}_2) \gamma_0]_2. \end{aligned} \quad (28.77)$$

Using Eq. (28.35) and the decomposition given in Eq. (28.21) then gives

$$\begin{aligned}
G_0(E, \mathbf{x}_1, \mathbf{x}_2, \mathbf{y}_1, \mathbf{y}_2) &= -i \frac{1}{\hbar^6} \int \frac{dE_1}{2\pi} \int \frac{d\mathbf{p}_1}{(2\pi)^3} e^{i\mathbf{p}_1 \cdot (\mathbf{x}_1 - \mathbf{y}_1)/\hbar} \int \frac{d\mathbf{p}_2}{(2\pi)^3} \\
&\times e^{i\mathbf{p}_2 \cdot (\mathbf{x}_2 - \mathbf{y}_2)/\hbar} \left[\frac{\Lambda_+(\mathbf{p}_1)}{E_1 - E_{p_1} + i\delta} + \frac{\Lambda_-(\mathbf{p}_1)}{E_1 + E_{p_1} - i\delta} \right]_1 \\
&\times \left[\frac{\Lambda_+(\mathbf{p}_2)}{E - E_1 - E_{p_2} + i\delta} + \frac{\Lambda_-(\mathbf{p}_2)}{E - E_1 + E_{p_2} - i\delta} \right]_2. \quad (28.78)
\end{aligned}$$

Finally, using the Cauchy residue theorem to carry out the E_1 integration gives

$$\begin{aligned}
G_0(E, \mathbf{x}_1, \mathbf{x}_2, \mathbf{y}_1, \mathbf{y}_2) &= -\frac{1}{\hbar^6} \int \frac{d\mathbf{p}_1}{(2\pi)^3} e^{i\mathbf{p}_1 \cdot (\mathbf{x}_1 - \mathbf{y}_1)/\hbar} \\
&\times \int \frac{d\mathbf{p}_2}{(2\pi)^3} e^{i\mathbf{p}_2 \cdot (\mathbf{x}_2 - \mathbf{y}_2)/\hbar} \frac{[\Lambda_+(\mathbf{p}_1)]_1 [\Lambda_+(\mathbf{p}_2)]_2}{E - E_{p_1} - E_{p_2} + i\delta} \\
&- \frac{[\Lambda_-(\mathbf{p}_1)]_1 [\Lambda_-(\mathbf{p}_2)]_2}{E + E_{p_1} + E_{p_2} - i\delta}. \quad (28.79)
\end{aligned}$$

The early calculations of recoil effects used this relatively complicated Green function. However, one has the freedom to work with simpler expressions, as long as the difference between the Green functions is accounted for in perturbation theory. The term with two factors of Λ_{--} is small and can be dropped. We further note that one can avoid the need to use the Cauchy residue theorem by the following manipulation. The Λ_{++} part of the muon propagator in Eq. (28.78) has a denominator that can be rewritten as

$$\begin{aligned}
&\frac{1}{E - E_1 - E_{p_2} + i\delta} \\
&= \left[\frac{1}{E - E_1 - E_{p_2} + i\delta} - \frac{1}{E - E_1 - E_{p_2} - i\delta} \right] \\
&+ \frac{1}{E - E_1 - E_{p_2} - i\delta} \\
&= -2\pi i \delta(E_1 - (E - E_{p_2})) + \frac{1}{E - E_1 - E_{p_2} - i\delta}. \quad (28.80)
\end{aligned}$$

This motivates using an approximation to the muon propagator,

$$\begin{aligned}
&[G_0(E - E_1, \mathbf{x}_2, \mathbf{y}_2)\gamma_0]_2 \\
&\rightarrow -2\pi i \delta(E_1 - \tilde{E}) \delta^3(\mathbf{x}_2 - \mathbf{y}_2) \left[\frac{1 + \gamma_0}{2} \right]_2, \quad (28.81)
\end{aligned}$$

where $\tilde{E} \equiv E - m_2 c^2$. The term not involving the delta function has been dropped because it has a pole that is on

the same side of the axis as the pole associated with the electron's positive projector term and, thus, fails to vanish only for the electron's negative energy projector, which gives a small result. For purposes of illustration, we have further approximated $E_{p_2} = m_2 c^2$ and $\Lambda_{++} = \frac{1 + \gamma_0}{2}$, the $m_2 \rightarrow \infty$ limit, although for practical calculations, it is useful to retain some parts of the muon propagator. When this approximation is made in the ladder diagrams, the muon propagators essentially drop out of the calculation; the position variables are all forced to all be at the same place, which we choose as the origin. If one creates the Green function of S_L from Eq. (28.76), approximating the muon line as just described, it now effectively depends only on the electron variables, and one can show it satisfies

$$\begin{aligned}
G_L(E, \mathbf{x}_1, \mathbf{y}_1) &= G_0(E, \mathbf{x}, \mathbf{y}) \gamma_0 \\
&+ \int d\mathbf{w} G_0(E, \mathbf{x}, \mathbf{w}) \gamma_0 \frac{\alpha \hbar c}{|\mathbf{w}|} G_L(E, \mathbf{w}, \mathbf{y}). \quad (28.82)
\end{aligned}$$

The muon positive energy projector $[(1 + \gamma_0)/2]_2$ is understood as a common factor. Outside of that factor, this equation is identical to that satisfied by the Coulomb Green function, leading to the expansion previous given in Eq. (28.37) when V is a Coulomb potential. However, we know that this Green function has poles at the Dirac eigenvalues, so although we started with free propagators, we now have an function of E that has poles at the nonrecoil values and can now start building in the effect of recoil.

Once we have a Green function that has bound state poles that approximate the full Green function, recoil corrections can be found in the way we described previously. Since now we can represent this approximated Green function as a spectral representation of the form in Eq. (28.31), although with the wave functions ψ_m we now have a muon component multiplied in, the goal (which involves some fairly complicated manipulations that we will not show here) is to set up an equation of the form

$$G_4 = G_L + G_L \delta K G_4, \quad (28.83)$$

where δK is formed from both pure "kernels", diagrams that cannot be split in two by a cut through the electron and muon lines (unlike Fig. 28.6) and the effect of simplifying the Green function. Approximating G_4 with G_L on the right-hand side can be seen to give a double pole, with an energy shift equal to the matrix element of δK .

An example of this kind of calculation applied to positronium hyperfine splitting is given in [38, 39]. The heart of the calculation involves the treatment of kernels with three exchanged photons in Coulomb gauge. The calculation was originally done by *Pachucki* [40], and while quite different

in many details, requires the evaluation of the same set of diagrams.

An important generalization of the Bethe–Salpeter approach is having the two bound particles being electrons in helium and accounting for the nucleus by using the Furry picture. This program was carried out by *Araki* [41] and *Sucher* [42]. As with recoil calculations, the basic step is consideration of an infinite ladder of Coulomb exchanges. In place of free propagators between the rungs, one has Coulomb Green functions. By carrying out approximations valid in the nonrelativistic limit one can form a Green function with poles at the nonrelativistic energies known from solving Eq. (28.1) for two electrons. As stressed earlier, because these lowest order energies can be determined with an accuracy far exceeding the level at which QED corrections enter, the study of these corrections is quite advanced. However, the present state-of-the-art calculations are carried out in the framework of NRQED, and we defer the discussion of helium to the concluding remarks.

28.5 Many-Electron Bound States

The incorporation of QED effects in many-electron bound states is a problem of fundamental interest, although as emphasized earlier, it must be possible to solve the Schrödinger equation with high accuracy. As a matter of principle, though, we now wish to show that the use of Green functions allows a QED approach to the many-electron problem. It now has to describe both radiative corrections and the exchange of photons between different electrons consistently.

An active subfield of QED is the study of highly charged ions, generally with two or more electrons remaining after the others have been stripped from a high Z atom. Relativistic and QED effects are enhanced in these ions, and a QED treatment is needed. In highly charged ions, the dominant effect on electrons is their attraction to the nucleus, and it can be shown that electron–electron interactions have a factor $1/Z$ and can be treated in perturbation theory. This can lead to situations where one can, indeed, study the larger QED effects relatively free of structure uncertainty, and the study of the spectra of some of these ions now provides tests of QED in intense Coulomb fields.

A treatment of the QED alternative to the Green function approach described here is afforded through S -matrix techniques [43, 44]. In these calculations, an adiabatic factor ε plays a central role. It is used to “turn off” H_I at large positive and negative times. An example of how it works for the sodium isoelectronic sequence is given in [45]. Here, we show some of the features of the Green function approach. To be specific we work with lithium-like ions and consider

a six-point Green function. One starts with

$$G_6(E, \mathbf{x}_1, \mathbf{x}_2, \mathbf{x}_3, \mathbf{y}_1, \mathbf{y}_2, \mathbf{y}_3) = -\frac{i}{\hbar} \int_{-\infty}^{\infty} dt e^{iEt/\hbar} \langle 0 | T(\psi_H(\mathbf{x}_1, t) \psi_H(\mathbf{x}_2, t) \psi_H(\mathbf{x}_3, t) \times \bar{\psi}_H(\mathbf{y}_1, 0) \bar{\psi}_H(\mathbf{y}_2, 0) \bar{\psi}_H(\mathbf{y}_3, 0)) | 0 \rangle. \quad (28.84)$$

The formal treatment showing the presence of poles at $E = E_v$ is identical to the earlier discussion. To carry out calculations one uses the Furry or extended Furry picture, with either a Coulomb potential or some screened potential defining the states.

With many electrons present, these states are Slater determinants of occupied orbitals, and the starting point of QED calculations is the same as for MBPT calculations. The non-radiative QED terms, in fact, have a close relation to the MBPT expansion. For the example here, if considering the ground and first excited states, one would use

$$|V\rangle = b^\dagger_v b^\dagger_a b^\dagger_b |0\rangle, \quad (28.85)$$

with v being a $2s$, $2p_{1/2}$, or $2p_{3/2}$ state, and a and b the two spin states of the $1s$ state.

In lowest order, the energy should be the sum of the three energies of the populated states, in this case $\varepsilon_v + 2\varepsilon_a$. It actually takes a little work to show that the energies add, but the calculation is instructive. The lowest order Green function has three electron propagators, with associated integrals over E_1 , E_2 , and E_3 . The t integration then gives a delta function of $E - E_1 - E_2 - E_3$. Using it to eliminate E_3 , say, leaves an integral over E_1 and E_2 of the form

$$\int \frac{dE_1}{2\pi} \int \frac{dE_2}{2\pi} \frac{1}{E_1 - \varepsilon_a + i\delta} \frac{1}{E_2 - \varepsilon_b + i\delta} \times \frac{1}{E - E_1 - E_2 - \varepsilon_v + i\delta}. \quad (28.86)$$

Because the three states all have positive energy, the E_1 and E_2 integrations can be carried out with Cauchy’s residue theorem, giving the expected factor

$$\frac{1}{E - E_v - E_a - E_b}. \quad (28.87)$$

One can then proceed finding double poles to find the shift of the energy.

The self-energy and vacuum polarization terms enter in the same way as for hydrogen, with the other electrons as “spectators”. If the extended Furry picture is used, the Coulomb Green function cannot be used, and the Green function must be formed numerically. Unless the ion studied is

hydrogenic, one must account for the interaction between electrons. A perturbative treatment works well for highly charged ions that have a simple electronic structure, particularly ions with one valence electron and a filled core. In place of the helium treatment, where the Coulomb interaction between the electrons was treated to all orders, one calculates order by order, with diagrams roughly ordered by the number of photons present.

An example of how QED has been tested is provided by lithium-like bismuth. This is a case where QED calculations have been carried out [46, 47], and at the level of the one-loop Lamb shift, one can see that extra physics must be included. The accurate measurement required for QED effects to be studied was provided by measurements in the LLNL EBIT [48], where

$$E = 2788.139(39) \text{ eV} \quad (28.88)$$

was found for the $2p_{3/2} - 2s$ splitting.

Before including the Lamb shift, calculations not including it were carried out in a range of screening potentials. Despite starting off differently, inclusion of up to three-photon exchange diagrams led to a common answer of 2814.348 eV. As was mentioned above, the field theory treatment of photon exchange has an interesting relationship to MBPT. One photon exchange can be done in either Coulomb or Feynman gauge, with the latter being more convenient computationally. However, in Coulomb gauge, one can see that exchange of a Coulomb photon is exactly equivalent to first-order MBPT. Exchange of a transverse photon is again equivalent to the MBPT treatment of the Breit interaction, with retardation included. However, when two photons are exchanged between two electrons, one encounters diagrams of the form of Fig. 28.6, with the understanding that spectator electrons are present. When both photons are Coulomb photons, the same contour integral encountered in the recoil discussion arises. It is well defined, with the two positive energy projectors giving a standard second-order MBPT term, and the other part giving a small contribution. We stress this point because this is a case where the use of field theory automatically avoids a term that would arise if one included negative energy states in MBPT perturbation theory in a straightforward manner. In sums over states m and n , MBPT would appear to include terms with m positive and n negative energy, and those terms can have vanishing denominators. They do not occur in the field theory calculation because they have poles on the same side of the axis, and the contour integration can be chosen to avoid them, giving zero. The more complicated case of having two transverse photons is also of interest, having a history dating back to Breit's calculations of helium fine structure. The equation he used, named after him, suffers from problems similar to those just

discussed, in particular leading to a term apparently of the order of the fine structure that had to be artificially removed. The integration is more complicated in this case, but the end result is that the two transverse photon term that appeared to be of the order of fine structure is reduced by a factor of α . This aspect of QED in atomic physics is just as important as the Lamb shift, although it does not require renormalization.

Because of the high charge of this ion, radiative corrections are now a one percent effect. They are dominated by the one-loop Lamb shift, which has to be treated with the numerical methods described earlier. However, while it is of the correct size, different potentials give differing answers. This disparity is removed to a large extent by including a set of "screening" diagrams, similar to Figs. 28.2 and 28.3, but with the lower photon line connecting to another electron. After including these (along with the effect of the counterterm Eq. (28.39) on the self-energy if extended Furry picture is used), a unique answer of -26.308 eV is found, taking theory to 2788.040 eV. This differs only slightly from experiment and shows that QED works even in very intense Coulomb fields. However, the experiment has sufficient accuracy to show clearly that extra physics must be accounted for.

Two obvious sources of known physics can account for the remaining discrepancy, recoil corrections and the two-loop Lamb shift. Remarkably, even though the bismuth nucleus is quite heavy, sophisticated recoil corrections are needed before the actual two-loop Lamb shift can be treated. These will be described in Sect. 28.6. After their removal an effect expected to be dominated by the $2s$ two-loop Lamb shift remains. As with the one-loop Lamb shift, an expansion in $Z\alpha$ could not be expected to be reliable, and exact numerical calculations had to be carried out. The result is consistent with experiment. The present status of that large-scale effort is described in [37].

28.6 Recoil Corrections at High Z

The first recoil calculations were carried out in the context of the Bethe–Salpeter equation. They relied heavily on expanding in powers of $Z\alpha$. For highly charged ions, $Z\alpha$ is no longer a small parameter, so the calculation of recoil corrections in hydrogenic ions with high Z requires the consideration of an infinite set of kernels rather than just a few. The problem was treated by *Grotch* and *Pachucki* in [49], and Bethe–Salpeter type calculations were done in [50] and [51]. The combinatoric problems are considerable, but the simplicity of the final expressions that result suggests that a simpler approach is possible. Such an approach was, indeed, found by *Shabaev* [52], and we describe it here.

The simplest way to derive the leading effect of the finite mass of the nucleus can be found in the context of classi-

cal mechanics, where in a system with N_e light particles of mass m (the electrons) and a heavy particle of mass M (the nucleus), one considers the heavy particle's nonrelativistic kinetic energy,

$$T_N = \frac{\vec{P}_N^2}{2M}, \quad (28.89)$$

and evaluates it in the center of mass system. In that frame, one can eliminate T_N through

$$\vec{P}_N \rightarrow -\sum_{i=1}^{N_e} \vec{p}_i. \quad (28.90)$$

Adding this to the nonrelativistic kinetic energy of the electrons (the first term in Eq. (28.1)) gives a total kinetic energy

$$T_{\text{tot}} = \sum_{i=1}^{N_e} \frac{\vec{p}_i^2}{2m_r} + H_{\text{MP}}, \quad (28.91)$$

where $m_r = m/(1 + m/M)$ is the reduced mass, and

$$H_{\text{MP}} = \sum_{i \neq j} \frac{\vec{p}_i \cdot \vec{p}_j}{2M} \quad (28.92)$$

is the mass polarization Hamiltonian. When this classical argument is extended to nonrelativistic quantum mechanics, it incorporates recoil exactly. However, if one works in the approximation of keeping only m/M corrections, extending the classical argument described above to field theory allows recoil to be treated relativistically for both one and many-electron systems.

To generalize Eq. (28.90) to field theory, we first note that the electron momentum is now described as a single field operator,

$$\vec{p}_e = -i\hbar \int d^3x \psi^\dagger(x) \vec{\nabla} \psi(x). \quad (28.93)$$

We also must include the electromagnetic field with the nuclear momentum in the usual way, with Eq. (28.89) now becoming

$$T_N \rightarrow \frac{|\vec{P}_N + Ze\vec{A}(\vec{0}, t)|^2}{2M}. \quad (28.94)$$

The position of the nucleus is close to the origin, so \vec{A} is evaluated there. Now the operation of going to the center of mass frame replaces \vec{P}_N with the negative of Eq. (28.93),

$$\vec{P}_N \rightarrow -\vec{p}_e, \quad (28.95)$$

and we see that including the kinetic energy of the nucleus leads to three new interaction Hamiltonians, operators to be

added to \tilde{H}_I ,

$$H_R = H_R(CC) + H_R(CT) + H_R(TT), \quad (28.96)$$

with

$$H_R(CC) = -\frac{\hbar^2}{2M} \int d^3x \int d^3y \psi^\dagger(\vec{x}, t) \times \vec{\nabla}_x \psi(\vec{x}, t) \cdot \psi^\dagger(\vec{y}, t) \vec{\nabla}_y \psi(\vec{y}, t), \quad (28.97)$$

$$H_R(CT) = \frac{iZe\hbar}{M} \vec{A}(\vec{0}, t) \cdot \int d^3x \psi^\dagger(\vec{x}, t) \vec{\nabla}_x \psi(\vec{x}, t), \quad (28.98)$$

and

$$H_R(TT) = \frac{Z^2 e^2}{2M} \vec{A}(\vec{0}, t) \cdot \vec{A}(\vec{0}, t). \quad (28.99)$$

We note the similarity of $H_R(CC)$ with the Coulomb part of the QED Hamiltonian H_C , Eq. (28.12).

Treating the new interaction Hamiltonians then to first order will account for all m/M corrections to all order in $Z\alpha$. One can equally well extend the calculations to many-electron ions, although accounting for the electron–electron interaction requires including as many factors coming from the initial interaction Hamiltonian as are required for convergence.

28.7 Concluding Remarks

Precision QED is presently a quite active field, and we have touched on only a few topics. Conferences on the subject are frequent, with the biannual International Conference on Precision Atomic Physics being of note; the interested reader should be able to access the talks given at them through the internet. A particularly active field involves applications of NRQED, which has been developed to quite a high level by a number of researchers. In these recent works, dimensional regularization is used in conjunction with the Foldy–Wouthuysen transformation along with powerful numerical methods that allow treatment of Green functions involving more than one electron. Of particular note is the completion of the treatment of helium fine structure in [53] to order $mc^2\alpha^7$, which can be used to determine the fine structure constant. More recently, we note the very large-scale calculation of the properties of singlet helium in [54]. What we wish to emphasize in closing is that the basic framework of QED as the theory underpinning our understanding of all electromagnetically bound states is in some sense simple, despite the extreme complexity of present calculations. We have discussed the two basic propagators, that of the electron and the photon, and the interaction Hamiltonian $H_I(t)$ given

in Eq. (28.24), and an approach based on a Feynman diagram treatment of Green functions to calculate the energies of bound states. That is all that is needed to describe a vast array of systems, and when they are simple enough, agreement with experiment at the ppm level is routinely found from just a few basic assumptions.

Acknowledgements Donald Yennie was working on the basic idea of using the Green function approach of the Bethe–Salpeter equation for atoms with many electrons, in particular using a two-time formalism. His unpublished paper “Bethe–Salpeter Approach to Atomic Physics”, along with [19], shaped the treatment of QED given in this chapter.

References

- Schwinger, J.: Selected Papers on Quantum Electrodynamics. Dover, New York (1958)
- Schweber, S.: A very thorough treatment of the breakthrough is given in *QED and the Men who Made it*. Academic Press, London (2000)
- Schwinger, J.: Phys. Rev. **73**, 416 (1948)
- Brown, L.S., Gabrielse, G.: Rev. Mod. Phys. **58**, 233 (1986)
- Aaij, R., et al.: LHCb collaboration. JHEP **11**, 90 (2015)
- Anotognini, A., et al.: Science **339**(6118), 417 (2013)
- Lindgren, I., Holmberg, J., Salomonson, S.: Theor. Chem. Acc. **134**, 123 (2015)
- Eides, M.I., Grotch, H., Shelyto, V.A.: Theory of Light Hydrogenic Bound States. Springer Tracts in Mod. Phys., vol. 222. Springer, Berlin, Heidelberg, New York (2007)
- Eides, M.I., Grotch, H., Shelyto, V.A.: Theory of Light Hydrogenic Bound States. Phys. Rep. **342**(2-3), 63 (2001)
- Furry, W.: Phys. Rev. **81**, 115 (1951)
- Jauch, J.M., Rohrlich, F.: See the discussion in Chapters 14 and 15 of *The Theory of Photons and Electrons*. Addison-Wesley, Cambridge (1955)
- Salpeter, E.E.: Phys. Rev. **87**, 150 (1952)
- Salpeter, E.E., Newcomb, W.A.: Phys. Rev. **87**, 150 (1952)
- Salpeter, E.E., Bethe, H.A.: Phys. Rev. **84**, 1232 (1951)
- Caswell, W., Lepage, G.P.: Phys. Lett. B. **167**, 437 (1986)
- Blundell, S.A., Guo, D.S., Johnson, W.R., Sapirstein, J.: Data Tables. At. Data Nucl. **37**, 103 (1987)
- Kelly, H.P.: Phys. Rev. **131**, 684 (1963)
- Shabaev, V.M.: Phys. Rep. **356**, 119 (2002)
- Yennie, D.R.: AIP Conference Proceedings No. 189. American Institute of Physics, New York (1989). p. 393, and unpublished
- Lamb, W.E., Retherford, R.C.: Phys. Rev. **72**, 241 (1947)
- t’Hooft, G., Veltman, M.: Nucl. Phys. B. **44**, 189 (1972)
- Drake, G.W.F., Swainson, R.A.: Phys. Rev. A **41**, 1243 (1990)
- Brown, G.E., Mayers, D.F.: Proc. R. Soc. Lond. Ser. A **251**, 92 (1951)
- Desiderio, A.M., Johnson, W.R.: Phys. Rev. A **14**, 1943 (1976)
- Jentschura, U.D., Mohr, P.J., Soff, G.: Phys. Rev. A **63**, 042512 (2001)
- Yerokhin, V.A., Shabaev, V.M.: J. Phys. Chem. Ref. Data **44**, 0033103 (2015)
- Yerokhin, V.A., Pachucki, K., Shabaev, V.M.: Phys. Rev. A **72**, 042502 (2005)
- Blundell, S.A., Snyderman, N.: Phys. Rev. A **44**, R1427 (1991)
- Mohr, P.J.: Ann. Phys. (ny) **88**, 26 (1974)
- Blundell, S.A., Cheng, K.T., Sapirstein, J.: Phys. Rev. A **55**, 1857 (1997)
- Indelicato, P., Mohr, P.J.: Phys. Rev. A **63**, 052507 (2001)
- Indelicato, P., Mohr, P.J.: Phys. Rev. A **58**, 165 (1998)
- Wichmann, E.H., Kroll, N.M.: Phys. Rev. **101**, 843 (1956)
- Indelicato, P., Mohr, P., Sapirstein, J.: Phys. Rev. A **89**, 042021 (2014)
- Pauli, W., Villars: Rev. Mod. Phys. **21**, 434 (1949)
- Pachucki, K.: Phys. Rev. Lett. **72**, 3154 (1994)
- Yerokhin, V.A.: Phys. Rev. A **97**, 052509 (2018)
- Adkins, G.A., Sapirstein, J.: Phys. Rev. A **58**, 3552 (1998)
- Adkins, G.A., Sapirstein, J.: Phys. Rev. A **61**, 069902 (2000). (E)
- Pachucki, K.: Phys. Rev. A **56**, 297 (1997)
- Araki, H.: Prog. Theor. Phys. **17**, 619 (1957)
- Sucher, J.: PhD thesis. Columbia University, New York City (1957)
- Gell-Mann, M., Low, F.: Phys. Rev. **84**, 350 (1951)
- Sucher, J.: Phys. Rev. **107**, 1448 (1957)
- Sapirstein, J., Cheng, K.T.: Phys. Rev. A **91**, 062508 (2015)
- Sapirstein, J., Cheng, K.T.: Phys. Rev. A **64**, 022502 (2001)
- Yerokhin, V.A., Artemyev, A.N., Beier, T., Plunien, G., Shabaev, V.M., Soff, G.: Phys. Rev. A **60**, 3522 (1999)
- Beiersdorfer, P., Osterheld, A.L., Scofield, J.H., Crespo Lopez-Urrutia, J.R., Widmann, K.: Phys. Rev. Lett. **80**, 3022 (1998)
- Pachucki, K., Grotch, H.: Phys. Rev. **51**, 1854 (1995)
- Shabaev, V.M., Artemyev Beier Soff, A.N.T.G.: J. Phys. B **31**(8), L337 (1998)
- Adkins, G.S., Morrison, S., Sapirstein, J.: Phys. Rev. A **76**, 042508 (2007)
- Shabaev, V.M.: Phys. Rev. A **57**, 59 (1998)
- Pachucki, K., Yerokhin, V.A.: Phys. Rev. Lett. **104**, 070403 (2010)
- Pachucki, K., Patkos, V., Yerokhin, V.A.: Phys. Rev. A **95**, 012508 (2017)



Jonathan R. Sapirstein Dr Sapirstein earned his PhD from Stanford University in 1979. He did postdoctoral work at UCLA and Cornell and has been at the University of Notre Dame, Indiana, since 1984. His current research interests are parity nonconservation in atoms, QED effects in highly charged many-electron ions, and QED calculations in hydrogen, positronium, muonium, and helium. Dr Sapirstein is a Fellow of the American Physical Society.



Eite Tiesinga and Peter J. Mohr 

Contents

29.1	Introduction	433
29.2	Consistency of Fundamental Physics	434
29.3	Topics in This Review	436
29.4	Electron g-Factor Anomaly	437
29.5	Atom Recoil Experiments and Mass Spectrometry	438
29.6	Mass-Ratio Measurements Using the g-Factor of Hydrogen-Like Ions	438
29.6.1	Theory for the g -Factor of Hydrogen-Like Ions	439
29.7	Hydrogen Atom Energy levels	441
29.7.1	Theory for the Hydrogen Energy Levels	442
	References	446

Abstract

We describe recent developments in tests of quantum electrodynamics (QED), the theory of the interactions of matter with electromagnetic fields. The tests focus on consistency in the determination of parameters or constants within QED obtained via multiple independent means and, in particular, by comparisons of precision measurements with equivalently accurate theoretical calculations. The most precise tests rely on a combination of the spectroscopy of atomic hydrogen, g -factor measurements of a free electron as well as that of an electron bound in a hydrogen-like ion, and finally the mass determination of the ions through atom recoil experiments and mass spectrometry. These experiments determine the dimensionless

fine-structure constant and the mass of the electron to about ten significant digits, orders of magnitude better than any other description of nature. We also show that an international system of units (SI) based on fixed values of the Planck constant and the charge of the electron (in addition to the fixed value of the speed of light in vacuum) modifies the interpretation of some of these tests.

Keywords

fundamental constants · quantum electrodynamics · g -factors · proton radius puzzle · hydrogen energy levels

29.1 Introduction

Tests of the fundamental laws of nature are crucial for the foundations of our knowledge of physics. The most precise theory is quantum electrodynamics (QED), which describes charged particles interacting with electromagnetic fields. It is a well-verified theory with uncertainties of observables approaching a few parts in 10^{13} for the g -factor of the electron. Our ability to test the theory is still improving with no sign of a breakdown. For example, Fig. 29.1 shows that over the past 100 years the relative uncertainty of the dimensionless fine-structure constant α has seen an exponential improvement by eight orders of magnitude to a 2014 relative uncertainty of 2×10^{-10} . In some cases, the precision of the tests is now limited by our understanding of another fundamental theory, namely quantum chromodynamics (QCD). For example, nuclear-structure effects limit the comparison between theory and experiment for the hyperfine structure of hydrogen.

On May 20, 2019 the International System of Units (SI) [2] was redefined based on fixing the values of fundamental constants that appear naturally in the laws of physics. This continues a trend started in 1983 when the speed of light

E. Tiesinga (✉)
National Institute of Standards and Technology
Gaithersburg, MD, USA
e-mail: eite.tiesinga@nist.gov

P. J. Mohr
National Institute of Standards and Technology
Gaithersburg, MD, USA
e-mail: mohr@nist.gov

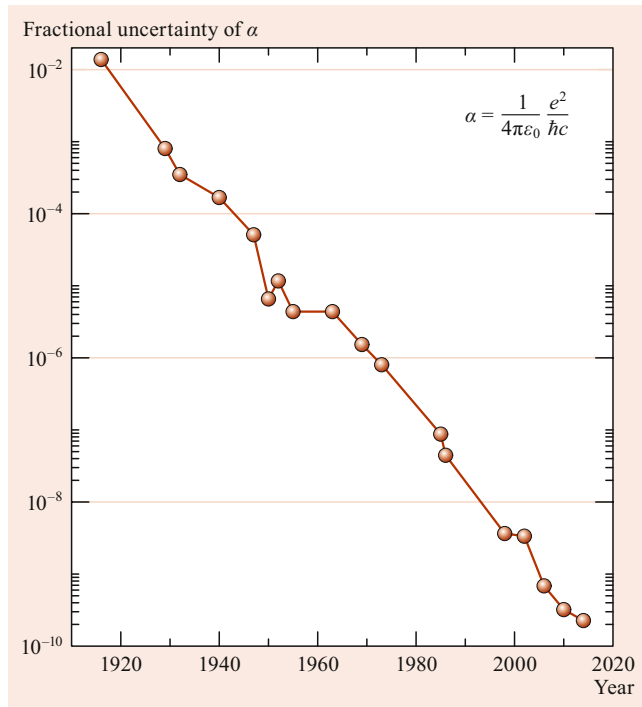


Fig. 29.1 Fractional uncertainty of the fine-structure constant α over the past 100 years, starting in 1916 with the introduction of α by A. Sommerfeld [1]

in vacuum, c , was fixed [3]. Now the reduced Planck constant \hbar , electron charge e , the Boltzmann constant k , and the Avogadro constant N_A have also been fixed. Although the laws of nature are independent of the definitions of the units, the transition to the revised SI does change our perspective on the tests.

This chapter reviews comparisons between theory and experiment that test our understanding of laws of nature. The focus is on quantitative tests of QED through measurements of hydrogen energy levels, the g -factors of the electron and hydrogen-like ions, and atom recoil energies from photon interactions. These measurements determine the fine-structure constant α , the electron mass m_e , and atomic masses, and demonstrate consistency of the theory. It is worth noting that the dimensionless constant $\alpha \equiv e^2/(4\pi\epsilon_0\hbar c)$ is much less than one, where ϵ_0 is the electric constant or permittivity of vacuum. Recent reviews that cover topics in this chapter are given in [4, 5]. Our values of inexactly-known fundamental constants are the 2014 CODATA recommended values [5], unless otherwise noted.

29.2 Consistency of Fundamental Physics

The most precise tests of quantum electrodynamics are intertwined with the determination of the fine-structure constant, electron mass, and masses of atoms. In fact, the measure-

ments are determinations of transition frequencies in hydrogen, spin-flip and cyclotron frequencies of the free and bound electron in a magnetic field, as well as atom recoil energies. They are compared to theoretical expressions for these observables, which, generally, are functions of fundamental constants.

For a hydrogen atom at rest, the energy of state i is

$$E_i = (m_p + m_e)c^2 - \frac{1}{2}m_e c^2 \alpha^2 \left\{ \frac{1}{n_i^2} + \dots \right\}, \quad (29.1)$$

where m_p is the mass of the proton, and n_i is the principal quantum number of state i . It will be convenient to use the Hartree energy $E_h = m_e c^2 \alpha^2$. The dots in this theoretical expression indicate corrections that are small compared to the leading term. Examples are contributions that are higher-order in α , of order of the electron–proton mass ratio m_e/m_p , and of order of the ratio of the root-mean-square (rms) proton charge radius to the Bohr radius r_p/a_0 . Equation (29.1) also sets the mass of the hydrogen atom in state i , that is, $m(\text{H}_i) = E_i/c^2$.

Many (angular) transition frequencies

$$\omega = \frac{E_j - E_i}{\hbar} \quad (29.2)$$

have been measured over the decades. They primarily determine the Hartree energy E_h (or equivalently the Rydberg constant R_∞ .) Often the experiments, such as those measuring the energy differences between two S states, involve two-photon transitions where ω is replaced by 2ω . A second class of transitions relevant for our purposes is that where the contribution from the Bohr energies, proportional to $1/n^2$, cancels. An example is the Lamb shift between the $2P_{1/2}$ and $2S_{1/2}$ states. In this case, the transition frequencies are proportional to a higher power in α than α^2 .

The frequency measurements provide a first example of the change in perspective introduced by the revised SI. In particular, in precise spectroscopy, photon frequencies ω are measured from which energy differences $\hbar\omega$ are inferred. In the SI in which \hbar is not exact, this inference leads to relatively inaccurate energies in units of joules. In the revised SI, there is no loss of accuracy in this conversion.

The second ingredient for our tests of QED is a measurement of the anomaly a_e of the g -factor of the free electron placed in a homogeneous magnetic field \vec{B} [6]. The electron undergoes cyclotron motion with angular frequency

$$\omega_c = 2 \frac{\mu_B}{\hbar} B \quad (29.3)$$

and spin-flip transitions with frequency

$$\omega_s = |g_e| \frac{\mu_B}{\hbar} B, \quad (29.4)$$

where $\mu_B = e\hbar/(2m_e)$ is the Bohr magneton, and the electron g -factor is $g_e = -2[1 + a_e(\alpha, \dots)]$. The anomaly is then extracted from a direct measurement of the difference of the spin-flip and cyclotron frequencies, $\omega_s - \omega_c$ and a measurement of ω_c . That is,

$$\left. \frac{\omega_s - \omega_c}{\omega_c} \right|_{\text{exp}} = a_e(\alpha, \dots) = \frac{1}{2} \frac{\alpha}{\pi} + \dots \quad (29.5)$$

The \dots indicate small corrections of higher order in α . Additional corrections are proportional to the mass ratio m_e/m_μ for vacuum polarization corrections from virtual muon loops, for example.

The hydrogen spectroscopy is, thus, a means to determine $m_e c^2 \alpha^2 / \hbar$ (or equivalently $m_e c \alpha^2$), while g -factor measurements of the free electron determine α . Together, the two experiments thus specify α and m_e . This, however, does not constitute a test of a fundamental theory. It only determines values of the constants. The required additional input is achieved with atom recoil measurements.

The recoil energy of a neutral atom X of mass $m(X)$ initially at rest after absorption of a photon from a laser beam with angular frequency ω_1 and subsequent (resonant) emission of a photon into a laser beam with a slightly-smaller frequency ω_2 propagating in the opposite direction is

$$E_{\text{rec}} = \hbar(\omega_1 - \omega_2) = \frac{(2\hbar k)^2}{2m(X)} + \dots, \quad (29.6)$$

where the average momentum of the photons is $\hbar k$, $k = \omega/c$ and $\omega = (\omega_1 + \omega_2)/2$. The \dots represent small corrections mainly due to the difference in momentum of the photons in the two laser beams. (In actual realizations, many photons are scattered from the atom in order to improve accuracy.)

Photon frequencies and their differences can be measured more accurately than any of the other parameters in Eq. (29.6). Thus, we restate this equation as

$$\left. \frac{\omega^2}{(\omega_1 - \omega_2)} \right|_{\text{exp}} = \frac{1}{2} \frac{m(X)c^2}{\hbar} + \dots \quad (29.7)$$

Hence, recoil measurements determine mass $m(X)$ in the revised SI as both c and \hbar are exactly defined. In the old SI, \hbar was not exact, and the experiment only measured $m(X)/\hbar$.

A measurement of atomic mass does not immediately help in testing fundamental theory. We can complete the story, illustrated in Fig. 29.2, by determining the atom-to-electron mass ratio $m(X)/m_e$ and, thus, find an independent value for the electron mass. To date this occurs in a two-step process. First, mass spectrometry of atomic ions [7, 8] measures mass ratios of low-charge-state ions of atoms X and Y . The mass ratio of the corresponding neutral atom is then accurately inferred by accounting for the appropriate number of electron masses and ionization energies.

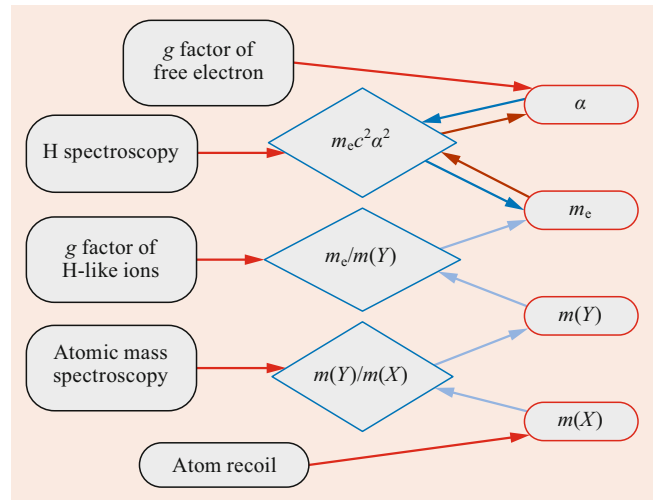


Fig. 29.2 Flow diagram for tests of QED based on the revised SI. Black boxes on the left-hand side correspond to the five precision experiments used to determine four fundamental constants in red boxes on the right-hand side. Arrows describe one-way connections from experiments to the constants. The constants are the fine-structure constant α , the electron mass m_e , and masses of various atoms, $m(X)$ and $m(Y)$. Most experiments only measure products or ratios of the fundamental constants shown as blue diamonds. For example, atomic mass spectrometry only determines ratios of atomic masses. The relations among α , m_e , and $m_e c^2 \alpha^2$ can be traversed in either direction

Second, g -factor measurements of the electron bound in a hydrogen-like ion Y^{q+} determine mass ratios $m(Y^{q+})/m_e$ through spin-flip and cyclotron frequency ratios of the ion in a magnetic field and the relationship

$$\left. \frac{\omega_s(Y^{q+})}{\omega_c(Y^{q+})} \right|_{\text{exp}} = -\frac{1}{2q} \frac{m(Y^{q+})}{m_e} g_Y(\alpha, \dots). \quad (29.8)$$

Here, $q = Z_Y - 1$, Z_Y is the charge number of the nucleus of the ion, and the theoretical (negative) g -factor g_Y can be calculated with sufficient accuracy. The ratio $m(Y)/m_e$ is then inferred as in mass spectrometry measurements. It may seem surprising that g_Y can be calculated accurately. The key is that $g_Y \approx -2$ to lowest order in Dirac theory, and, therefore, corrections need not be computed as accurately as for the anomaly of a free electron.

This indirect approach to obtain $m(X)/m_e$ is needed as recoil experiments use atoms for which hydrogen-like g -factor measurements are not available. Moreover, mass differences between ionization stages of an atom, including those due to the binding energy of the electrons, can only be accurately accounted for in small- Z_Y ions.

The change in units from the old to the revised SI is also reflected in our understanding of mass. Figure 29.3 shows the contributions to and uncertainties of the mass of the ground-state hydrogen atom, $m(\text{H})$, in the SI unit of mass (kg) and in the atomic mass unit (amu) $m_u = m(^{12}\text{C})/12$, one twelfth of the mass of a ^{12}C atom. Clearly, the mass of the proton

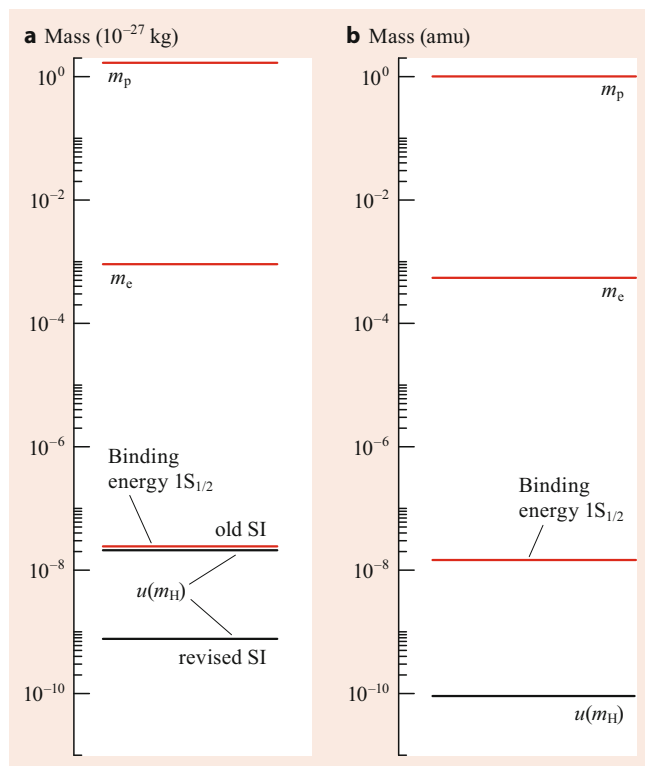


Fig. 29.3 Contributions to the mass of a $1S_{1/2}$ hydrogen atom, $m(\text{H})$, in kilograms (a) and atomic mass units (b) on a logarithmic scale. From top to bottom, the red lines in each panel correspond to the mass of the proton, electron, and the absolute value of the binding energy (divided by c^2), respectively. In (a), the black horizontal lines are the uncertainties of the hydrogen mass, $u(m_{\text{H}})$, in the old and revised SI. The black line in (b) shows $u(m_{\text{H}})$ in atomic mass units

is by far the largest contribution and, in fact, its uncertainty fully determines the uncertainty in both units of mass. Nevertheless, in units of m_{u} , the hydrogen mass is known with ten significant digits as it can be relatively easily compared to the mass of a carbon atom. This has not changed in the redefinition. We also observe that in the old SI, the uncertainty of $m(\text{H})$ in kg nearly coincides with the contribution from the binding energy. With the redefinition, the uncertainty of $m(\text{H})$ in kg has improved by more than an order of magnitude to 1 part in 10^9 and is mainly limited by our ability to measure the fine-structure constant. This follows from expressing the hydrogen mass in terms of the atomic mass unit and that of the electron, i.e.,

$$m(\text{H}) = \frac{m(\text{H})}{m_{\text{u}}} \frac{m_{\text{u}}}{m_{\text{e}}} m_{\text{e}} = A_{\text{r}}(\text{H}) \frac{1}{A_{\text{r}}(\text{e})} \left[\frac{E_{\text{h}}}{\hbar} \right] \frac{1}{\alpha^2} \frac{\hbar}{c^2},$$

where $A_{\text{r}}(X) \equiv m(X)/m_{\text{u}}$, and we used the definition of the Hartree energy to rewrite the dependence on the electron mass. The relative uncertainties in $A_{\text{r}}(\text{H})$, $A_{\text{r}}(\text{e})$, and E_{h} are currently smaller than that of α .

In summary, we have described five experiments that determine four quantities. This is an overdetermined data set and

checks for consistency. To date these checks are good to parts in 10^{10} and confirm the theory at this level. We stress, however, that the tests of fundamental theory are more wide ranging than suggested by the limited number of measurements. They include at least two implicit assumptions that are worth mentioning. The first is energy conservation and leads to the fact that the frequency of an emitted or absorbed photon equals the frequency difference of energy levels of the atom. A second assumption is that particles have a wave-like nature as well or, more precisely, that the momentum p of a massive particle or massless photon is inversely proportional to its reduced wavelength λ . In fact, $p = \hbar k$, where $k = 1/\lambda$ is the photon wavenumber. This relation combined with energy-momentum conservation underpins the atom recoil experiments.

29.3 Topics in This Review

The description of tests of QED in the previous section needs to be refined to include the role of small corrections and their parameters. For example, in hydrogen spectroscopy, the mass and charge radius of the proton must be considered. In g -factor measurements and hydrogen spectroscopy, virtual vacuum polarization loops containing the heavier muon and tau leptons, as well as quarks, lead to additional mass dependencies. The next sections summarize how these dependencies arise.

We only consider a subset of tests of QED. Some of the omitted topics are the spectroscopy of positronium, QED of highly-charged simple ions, Delbrück scattering of photons by nuclei, and helium fine structure. Positronium would suffer less from corrections due to hadronic effects. The theory, however, is more difficult due to the absence of a small parameter, such as the electron-to-proton mass ratio. Highly-charged ions are a means of studying strong field effects near their nucleus. Photon scattering by nuclei can create virtual lepton pairs in a domain beyond the Compton scattering process. The helium measurements are an independent means of determining the fine-structure constant. Some of these topics are covered in other chapters of this book. Although these topics may be considered equally important, our attention in this chapter is focused on the most precise tests of QED.

The remainder of this article has the following structure. Section 29.4 summarizes the required QED theory for the g -factor of the free electron and our ability to extract α . Section 29.5 then describes mass measurements by atom recoil experiments and mass-ratio measurements by atomic mass spectrometry for the heavier atoms. Mass-ratio determinations $m(Y)/m_{\text{e}}$ for light atoms are discussed in Sect. 29.6. The section also summarizes the theory of the electron g -factor in hydrogen-like ions. Combined, Sects. 29.5 and 29.6 lead to the most-accurate value for m_{e} . We finish with a discussion of QED theory for the hydrogen atom in Sect. 29.7.

29.4 Electron g -Factor Anomaly

The theoretical expression for the anomaly of the electron $a_e(\text{th})$ may be written as

$$a_e(\text{th}) = a_e(\text{QED}) + a_e(\text{weak}) + a_e(\text{had}) , \quad (29.9)$$

where the terms denoted by “QED”, “weak”, and “had” account for the purely quantum electrodynamic, predominantly electroweak, and predominantly hadronic (that is, strong interaction) contributions to a_e , respectively. The QED contribution may be written as

$$a_e(\text{QED}) = \sum_{n=1}^{\infty} C_e^{(2n)} \left(\frac{\alpha}{\pi}\right)^n , \quad (29.10)$$

where index n corresponds to contributions with n virtual photons. Here, $n > 5$ contributions can be neglected, and

$$C_e^{(2n)} = A_1^{(2n)} + A_2^{(2n)}(x_{e\mu}) + A_2^{(2n)}(x_{e\tau}) + \dots , \quad (29.11)$$

with coefficients $A_1^{(2n)}$ and functions $A_2^{(2n)}(x)$ evaluated at $x = x_{eX} \equiv m_e/m_X \ll 1$ for lepton $X = \mu$ or τ . For $n > 1$, the coefficients $A_1^{(2n)}$ include vacuum-polarization corrections with virtual electron/positron pairs, while $A_2^{(2n)}(x)$ are vacuum-polarization corrections due to heavier leptons. For $x \rightarrow 0$, we have $A_2^{(4)}(x) = x^2/45 + \mathcal{O}(x^4)$ and $A_2^{(6)}(x) = x^2(b_0 + b_1 \ln x) + \mathcal{O}(x^4)$ with $b_0 = 0.593274\dots$ and $b_1 = 23/135$ [9, 10]. The $\mathcal{O}(x^4)$ contributions are known and included in the calculations but not reproduced here. The functions $A_2^{(8)}(x)$ and $A_2^{(10)}(x)$ are also $\mathcal{O}(x^2)$ for small x but are not reproduced here [11, 12]. Currently, vacuum-polarization corrections for the free-electron anomaly that depend on two lepton mass ratios can be neglected. Table 29.1 lists the relevant coefficients as used in the 2014 CODATA adjustment. Uncertainties in parenthesis here and elsewhere are combined one-standard-deviation statistical and systematic uncertainties. Additional references to the

Table 29.1 Coefficients for the QED contributions to the electron anomaly. The coefficients $A_1^{(2n)}$ and functions $A_2^{(2n)}(x)$, evaluated at $x = x_{e\mu} \equiv m_e/m_\mu$ and $x_{e\tau} \equiv m_e/m_\tau$ for the muon and tau leptons, respectively, are listed with two significant digits for ease of comparison; summed values $C_e^{(2n)}$, based on the 2014 CODATA adjustment, are listed as accurately as needed for the tests described in this article. Missing values indicate that their contribution to the electron anomaly is negligible

n	$A_1^{(2n)}$	$A_2^{(2n)}(x_{e\mu})$	$A_2^{(2n)}(x_{e\tau})$	$C_e^{(2n)}$
1	1/2	0	0	0.5
2	-0.33	5.2×10^{-7}	1.8×10^{-9}	-0.32847844400...
3	1.2	-7.4×10^{-6}	-6.6×10^{-8}	1.181234017...
4	-1.9	9.2×10^{-4}	7.4×10^{-6}	-1.91206(84)
5	7.8	-3.8×10^{-3}		7.79(34)

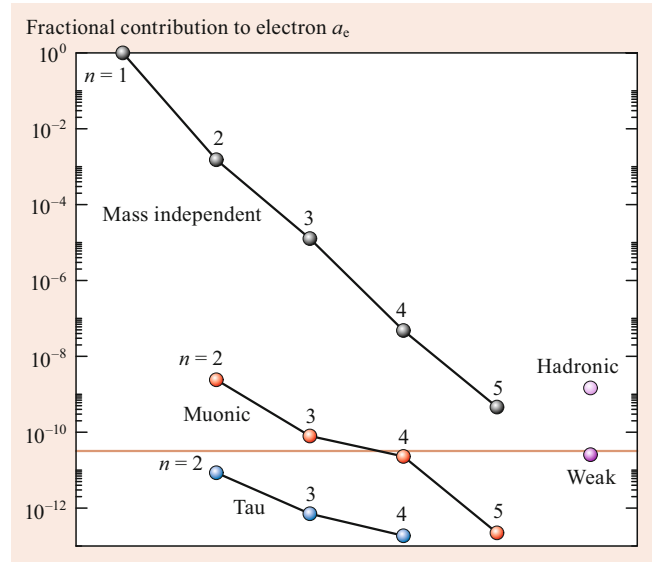


Fig. 29.4 Fractional absolute values of the contributions to the theoretical g -factor anomaly of the free electron. QED contributions are due to the mass-independent $A_1^{(2n)}$ (black markers), to the muon-dependent $A_2^{(2n)}(x_{e\mu})$ (red markers), and to the tau-dependent $A_2^{(2n)}(x_{e\tau})$ (blue markers) corrections, respectively. Contributions due to the weak and hadronic interactions are also shown. The horizontal orange line shows the relative uncertainty in the determination of $a_e(\text{th})$. The graph is based on the 2014 CODATA value for the fine-structure constant

original literature can be found in the paper on the adjustment. It is worth noting that since 2014 the coefficient $A_1^{(8)}$ has been evaluated virtually exactly in a tremendous effort described in [13], while $A_2^{(10)}$ has been updated, shifting its value [14].

The electroweak contribution is

$$a_e(\text{weak}) = 0.02973(23) \times 10^{-12} \quad (29.12)$$

and is calculated as discussed in the 1998 CODATA adjustment but with the 2014 values of the Fermi coupling constant $G_F/(\hbar c)^3$ and the weak mixing angle θ_W [15]. The total hadronic contribution is

$$a_e(\text{had}) = 1.734(15) \times 10^{-12} \quad (29.13)$$

and is a sum of multiple vacuum-polarization contributions.

Figure 29.4 shows a graphical representation of contributions to the electron anomaly. The QED corrections decrease roughly exponentially in size with order n for both mass-independent and dependent contributions. Contributions from virtual loops containing τ leptons are currently negligible. Weak and hadronic contributions are more important. The theoretical uncertainty of the anomaly (absent any uncertainty in the fine-structure constant) is dominated by two contributions: the mass-independent $n = 5$ QED correction and the hadronic contribution. In fact, it is given by

$$u[a_e(\text{th})] = 0.037 \times 10^{-12} = 0.32 \times 10^{-10} a_e \quad (29.14)$$

and is significantly smaller than the uncertainty of the most-accurate experimental value of $2.4 \times 10^{-10} a_e$ [6]. Consequently, the relative uncertainty of the fine-structure constant is essentially the same as the experimental relative uncertainty. That is, equating the theoretical expression of a_e (th) and the experimental value yields

$$\alpha^{-1}(a_e) = 137.035999160(33) \quad [2.4 \times 10^{-10}]. \quad (29.15)$$

The number in square brackets is the relative uncertainty of the fine-structure constant, $u_r(\alpha) = u(\alpha)/\alpha$.

29.5 Atom Recoil Experiments and Mass Spectrometry

Atom recoil experiments are performed with the heavier alkali-metal atoms, ^{87}Rb and ^{133}Cs . These atoms have easily accessible atomic transitions in the optical frequency domain, with excited states that only decay back to the ground state and can, thus, be brought to a near standstill by laser cooling techniques. For the 2014 CODATA adjustment, the most accurate measurement relied on the ^{87}Rb isotope [16] and gave

$$\frac{m(^{87}\text{Rb})}{\hbar} = 1,368,480,428.9(1.7) \text{ m}^{-2} \text{ s} \quad [1.2 \times 10^{-9}]. \quad (29.16)$$

In the revised SI with a fixed reduced Planck constant, this translates into an equally accurate measurement of $m(^{87}\text{Rb})$ in kg. A 2018 value for $m(^{133}\text{Cs})/\hbar$ for atomic cesium with a three times smaller relative uncertainty is reported in [17].

In mass spectrometry, the most accurate measurements compare the mass of two or more low-charge-state ions. Over the years, these measurements have been performed for most stable and unstable atoms in the periodic table. After accounting for the mass of the electrons and binding energies, mass data for neutral atoms were collated in [18, 19] in the atomic mass unit m_u . For ^{87}Rb and ^{28}Si , this 2012 database gives

$$A_r(^{87}\text{Rb}) = \frac{m(^{87}\text{Rb})}{m_u} = 86.9091805319(65) \quad [7.5 \times 10^{-11}], \quad (29.17)$$

and

$$A_r(^{28}\text{Si}) = 27.97692653465(44) \quad [1.6 \times 10^{-11}], \quad (29.18)$$

respectively, which have a much smaller relative uncertainty than that for masses determined by atom recoil measurements. The improved 2016 evaluation can be found in [7, 20].

In any case, from this recoil measurement, we calculate

$$m(^{12}\text{C}) = m(^{87}\text{Rb}) \times \frac{12}{A_r(^{87}\text{Rb})} \quad (29.19)$$

in kg in the revised SI to determine $m(^{12}\text{C})$ with a relative uncertainty of 1.2×10^{-9} through error propagation. Similarly, relationships can be used for the mass of ^{28}Si .

29.6 Mass-Ratio Measurements Using the g -Factor of Hydrogen-Like Ions

Measurements of the spin-flip and cyclotron frequencies of ground-state hydrogen-like atomic ions in a homogeneous magnetic field are currently the most accurate means to determine atom-to-electron mass ratios. This method relies on the ability of theorists to calculate the g -factor of the bound electron accurately. This approach is competitive as long as the trapped ion is relatively light. Accounting for the electron removal energies of ions becomes prohibitively hard for heavy atoms. Similarly, computing the g -factor within the framework of relativistic QED bound-state theory is more complex for heavier hydrogen-like ions as corrections with higher powers in $Z\alpha$ are more important. For nuclei with zero nuclear spin, the mass ratio follows from rearranging Eq. (29.8) to

$$\frac{m(Y^{q+})}{m_e} = -2q \frac{1}{g_Y(\alpha, \dots)} \frac{\omega_s(Y^{q+})}{\omega_c(Y^{q+})} \Big|_{\text{exp}} \quad (29.20)$$

and

$$\frac{m(Y)}{m_e} = \frac{m(Y^{q+})}{m_e} + q - \sum_{m=0}^{q-1} \frac{E_1(Y^{m+})}{m_e c^2}, \quad (29.21)$$

where $E_1(Y^{m+})$ is the positive ionization energy of ion Y^{m+} , and we recall that $q = Z_Y - 1$.

A broad program involving researchers from a number of European laboratories has measured spin-flip and cyclotron frequency ratios and calculated the g -factor for different ions, most notably $^{12}\text{C}^{5+}$ and $^{28}\text{Si}^{13+}$. The measurements themselves were performed at the Max-Planck Institut für Kernphysik (MPIK), Heidelberg, Germany. Recently reported values are [21, 22]

$$\frac{\omega_s(^{12}\text{C}^{5+})}{\omega_c(^{12}\text{C}^{5+})} = 4376.21050087(12) \quad [2.8 \times 10^{-11}], \quad (29.22)$$

and [23]

$$\frac{\omega_s(^{28}\text{Si}^{13+})}{\omega_c(^{28}\text{Si}^{13+})} = 3912.86606484(19) \quad [4.8 \times 10^{-11}]. \quad (29.23)$$

These two frequency ratios are correlated with a correlation coefficient $r = 0.347$ mainly due to image charge corrections [24]. The authors of [24] also slightly reassessed the values given in the original references. The reassessed values are quoted here.

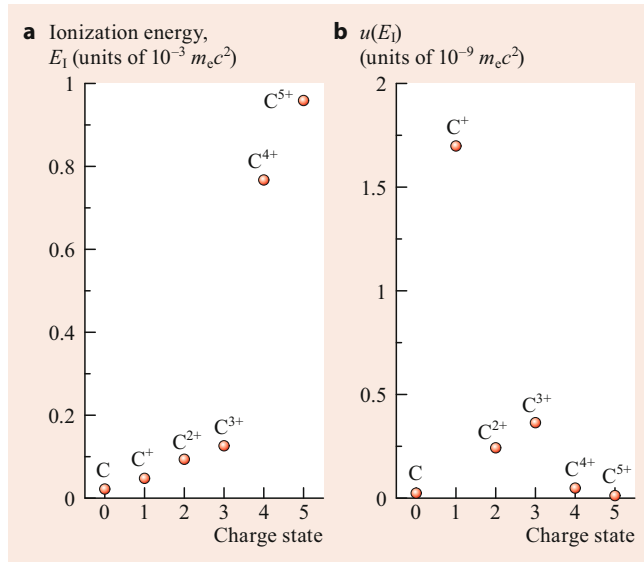


Fig. 29.5 Ionization energies (a) and their uncertainties (b) of the six charge states $^{12}\text{C}^{m+}$ of carbon-12 expressed in units of $m_e c^2$. Notice the large difference in scale between the two panels. In practice, ionization energies, E_I , are reported in units of hc . The unit conversion of the energies and their uncertainties is based on the identity $E/(m_e c^2) = \alpha^2/(2R_\infty) \times E/(hc)$, where R_∞ is the Rydberg constant, and we observe that $\alpha^2/(2R_\infty)$, with a relative uncertainty of 5×10^{-10} , does not increase the uncertainty of the E_I

The theoretical electron g -factors for $^{12}\text{C}^{5+}$ and $^{28}\text{Si}^{13+}$ have a relative uncertainty of 1.3×10^{-11} and 8.5×10^{-10} , respectively, as explained in the next section. Hence, the relative uncertainty for the mass ratio m_{Yq+}/m_e is 3.0×10^{-11} and 8.5×10^{-10} for these two ions, respectively. Next, we use Eq. (29.21) to determine the neutral atom to electron mass ratio. Figure 29.5 shows the ionization energies and their uncertainties for all charge states of ^{12}C in units of $m_e c^2$. We observe that, as expected, the ionization energy increases with charge state, but that, possibly surprisingly, the ionization energy with the largest uncertainty by far is that for the singly charged carbon ion. The ionization energies are added to give the electron removal energy $\Delta E_B = 1.0569819(18) \times 10^{-3} m_e c^2$ from ^{12}C to $^{12}\text{C}^{5+}$.

We combine the results of Sects. 29.5 and 29.6 to find the values

$$\frac{m(^{12}\text{C})}{m_e} = 21,874.66183428(66) \quad [3.0 \times 10^{-11}]$$

and

$$\begin{aligned} \frac{m_e}{\hbar} &= \frac{m_e}{m(^{12}\text{C})} \frac{m(^{12}\text{C})}{m(^{87}\text{Rb})} \frac{m(^{87}\text{Rb})}{\hbar} \\ &= 8.637992726(11) \times 10^3 \text{ m}^{-2} \text{ s} \quad [1.2 \times 10^{-9}]. \end{aligned} \quad (29.24)$$

We observe that the removal energy ΔE_B has a measurable effect on the mass of the carbon-12 atom but that the uncertainty of m_e/\hbar is currently limited by the atom recoil

experiment. An evaluation of m_e/\hbar based on ^{28}Si data gives a consistent value with only a slightly larger uncertainty. The two values can be combined to find more accurate values for $m(^{12}\text{C})/m_e$ and m_e/\hbar as long as the strong correlations between the uncertainties of the g -factor, as well as those of the frequency ratio ω_s/ω_c , are taken into account. With the 2018 atom recoil experiments with ^{133}Cs [17], the uncertainty of m_e/\hbar has improved by a factor of 3.

29.6.1 Theory for the g -Factor of Hydrogen-Like Ions

We summarize the contributions to the theoretical description of the electron g -factor of ground S -state hydrogen-like ions. The main contributions to the g -factor can be categorized as

$$g_Y = g_D + \Delta g_{\text{rad}} + \Delta g_{\text{rec}} + \Delta g_{\text{ns}} + \dots, \quad (29.25)$$

where g_D is the Dirac (relativistic) value, and Δg_{rad} , Δg_{rec} , and Δg_{ns} are due to radiative, recoil, and nuclear size corrections, respectively. Other corrections, indicated by the dots, are negligible at this time. Numerical results for the various contributions are summarized in Table 29.2 for $^{12}\text{C}^{5+}$ and Table 29.3 for $^{28}\text{Si}^{13+}$.

The Dirac value is known exactly [25] from the Dirac equation for an electron in the field of a fixed point charge of magnitude Ze , where, for clarity, we omit subscript Y on Z for the remainder of this section. Its value is

$$g_D = -\frac{2}{3} \left[1 + 2\sqrt{1 - (Z\alpha)^2} \right], \quad (29.26)$$

with an uncertainty that is solely due to the uncertainty in α . Radiative corrections may be written as

$$\Delta g_{\text{rad}} = -2 \sum_{n=1} C_e^{(2n)}(Z\alpha) \left(\frac{\alpha}{\pi} \right)^n, \quad (29.27)$$

where the functions $C_e^{(2n)}(x)$ are evaluated at $x = Z\alpha$, correspond to contributions with n virtual photons, and are slowly varying functions of x . They are related to the coefficients for the free electron $C_e^{(2n)}$, defined in Sect. 29.4, by

$$\lim_{x \rightarrow 0} C_e^{(2n)}(x) = C_e^{(2n)}. \quad (29.28)$$

The function $C_e^{(2)}(x)$ is computed as the sum of three contributions. The first contribution is a self-energy correction given by

$$\begin{aligned} C_{e,\text{SE}}^{(2)}(x) &= \frac{1}{2} \left\{ 1 + \frac{1}{6} x^2 + x^4 \left[\frac{32}{9} \ln(x^{-2}) + \frac{247}{216} \right. \right. \\ &\quad \left. \left. - \frac{8}{9} \ln k_0 - \frac{8}{3} \ln k_3 \right] + x^5 R_{\text{SE}}(x) \right\}, \end{aligned} \quad (29.29)$$

where $\ln k_0 = 2.984128556$ and $\ln k_3 = 3.272806545$. Values for the remainder function $R_{SE}(x)$ are based on extrapolations from numerical calculations at high Z . In particular, $R_{SE}(6\alpha) = 22.160(10)$ and $R_{SE}(14\alpha) = 20.999(2)$ based on the 2014 CODATA adjustment. In 2017, the values for $R_{SE}(x)$ were significantly improved [26].

The second and third contributions to $C_e^{(2)}(x)$ are two lowest-order vacuum-polarization corrections [27]. In the second “wave function” correction, the vacuum polarization loop modifies the interaction between the bound electron and the Coulomb field of the nucleus, and in the third “potential” correction, the loop modifies the interaction between the bound electron and the external magnetic field. The sum of the one-photon vacuum polarization contributions are

$$C_{e,VP}^{(2)}(6\alpha) = -0.000001832142(12), \quad (29.30)$$

and

$$C_{e,VP}^{(2)}(14\alpha) = -0.0000505452(11), \quad (29.31)$$

for $^{12}\text{C}^{5+}$ and $^{28}\text{Si}^{13+}$, respectively.

The $n = 2$ two-photon correction for the ground S -state is [28, 29]

$$\begin{aligned} C_e^{(4)}(x) &= \left(1 + \frac{x^2}{6}\right) C_e^{(4)} \\ &+ x^4 \left[\frac{14}{9} \ln(x^{-2}) + \frac{991,343}{155,520} - \frac{2}{9} \ln k_0 - \frac{4}{3} \ln k_3 \right. \\ &+ \left. \frac{679\pi^2}{12,960} - \frac{1441\pi^2}{720} \ln 2 + \frac{1441}{480} \zeta(3) \right] + \mathcal{O}(x^5) \\ &= \begin{cases} -0.3285778(23) & \text{for } x = 6\alpha \\ -0.32917(15) & \text{for } x = 14\alpha \end{cases}, \end{aligned} \quad (29.32)$$

where $\zeta(z)$ is the Riemann zeta function. The quoted uncertainty is an estimate of uncalculated higher-order contributions given by [28]

$$u[C_e^{(4)}(x)] = 2 |x^5 C_e^{(4)} R_{SE}(x)|. \quad (29.33)$$

Since the remainder function differs only by about one percent for carbon and silicon, the main Z (or x) dependence of the uncertainty is given by x^5 , and we assume that the uncertainty of the two-photon correction is completely correlated for the two ions. The authors of [30, 31] calculated some of the two-loop vacuum polarization diagrams of order x^5 and found them to be on the order of the uncertainty in Eq. (29.32). The authors of [32] computed an additional light-by-light contribution to $C_e^{(4)}(x)$, which shifts its value within its uncertainty. It is not included here.

The leading binding correction to $C_e^{(2n)}(x)$ is

$$C_e^{(2n)}(x) = \left(1 + \frac{x^2}{6} + \dots\right) C_e^{(2n)}, \quad (29.34)$$

for any n . This surprising result was derived in [33, 34], and for $n = 1$ and 2 it is evident from Eqs. (29.29) and (29.32). As the uncertainty due to uncalculated higher-order terms is negligible we use $C_e^{(2n)}(x) \rightarrow (1 + x^2/6)C_e^{(2n)}$ for the three, four, and five ($n = 3, 4,$ and 5) photon contributions with an uncertainty solely determined by the uncertainty of $C_e^{(2n)}$ in Table 29.1.

The corrections g_D and Δg_{rad} are based on the assumption that nuclei have an infinite mass. The recoil correction to the g -factor associated with a finite mass is

$$\Delta g_{\text{rec}} = \Delta g_{\text{rec}}^{(0)} + \Delta g_{\text{rec}}^{(2)}, \quad (29.35)$$

corresponding to terms that are zero-order and first-order in α/π , respectively. For $\Delta g_{\text{rec}}^{(0)}$, we have

$$\begin{aligned} \Delta g_{\text{rec}}^{(0)} &= \left\{ -(Z\alpha)^2 + \frac{(Z\alpha)^4}{3[1 + \sqrt{1 - (Z\alpha)^2}]^2} - (Z\alpha)^5 P(Z\alpha) \right\} \\ &\times \frac{m_e}{m_N} + (1 + Z)(Z\alpha)^2 \left(\frac{m_e}{m_N} \right)^2, \end{aligned} \quad (29.36)$$

where m_N is the mass of the nucleus. Mass ratios, based on the 2014 adjustment values of the constants, are $m_e/m(^{12}\text{C}^{6+}) = 0.0000457275\dots$ and $m_e/m(^{28}\text{Si}^{14+}) = 0.0000196136\dots$. The authors of [35] evaluated the function $P(x)$ numerically for a discrete set of $x < 1$, with the result $P(6\alpha) = 10.49395(1)$ for hydrogenic carbon. For silicon, we use the interpolated value $P(14\alpha) = 7.16223(1)$. For $\Delta g_{\text{rec}}^{(2)}$, we have

$$\Delta g_{\text{rec}}^{(2)} = \frac{\alpha}{\pi} \frac{(Z\alpha)^2}{3} \frac{m_e}{m_N}. \quad (29.37)$$

The uncertainty in $\Delta g_{\text{rec}}^{(2)}$ is negligible compared to that of $\Delta g_{\text{rad}}^{(2)}$.

Finally, the finite size of the nucleus leads to a small correction to the g -factor given by [36]

$$\Delta g_{\text{ns}} = -\frac{8}{3} (Z\alpha)^4 \left(\frac{r_N}{\lambda_C} \right)^2 + \dots, \quad (29.38)$$

where r_N is the nuclear rms charge radius, and $\lambda_C = \hbar/(m_e c)$ is the reduced Compton wavelength of the electron. The authors of [37] calculated additional corrections but gave numerical values for Δg_{ns} based on early r_N values. We incorporate their corrections using an $(r_N)^2$ scaling and the updated $r_N = 2.4703(22)$ fm and $r_N = 3.1223(24)$ fm for ^{12}C and ^{28}Si , respectively [38].

The theoretical value for the g -factor of the electron in hydrogen-like carbon 12 or silicon 28 is the sum of the individual contributions discussed above and summarized in Tables 29.2 and 29.3. For each contribution the tables also list the uncertainty. For both ions the uncertainty is dominated by

Table 29.2 Theoretical contributions and total value for the g -factor of hydrogenic carbon 12 based on the 2014 CODATA recommended values of the constants and corresponding theory. The total g -factor has a relative uncertainty of 1.3×10^{-11}

Contribution	Value	Source
Dirac g_D	$-1.9987213543921(6)$	Eq. (29.26)
$\Delta g_{SE}^{(2)}$	$-0.002323672435(4)$	Eq. (29.29)
$\Delta g_{VP}^{(2)}$	0.000000008511	Eq. (29.30)
$\Delta g^{(4)}$	$0.000003545677(25)$	Eq. (29.32)
$\Delta g^{(6)}$	-0.000000029618	Eq. (29.34)
$\Delta g^{(8)}$	0.000000000111	Eq. (29.34)
$\Delta g^{(10)}$	-0.000000000001	Eq. (29.34)
Δg_{rec}	-0.000000087629	Eq. (29.35)
Δg_{ns}	$-0.00000000408(1)$	Eq. (29.38)
$g(^{12}\text{C}^{5+})$	$-2.001041590183(26)$	

Table 29.3 Theoretical contributions and total value for the g -factor of hydrogenic silicon 28 based on the 2014 CODATA recommended values of the constants and corresponding theory. The total g -factor has a relative uncertainty of 8.5×10^{-10}

Contribution	Value	Source
Dirac g_D	$-1.993023571557(3)$	Eq. (29.26)
$\Delta g_{SE}^{(2)}$	$-0.00232891747(5)$	Eq. (29.29)
$\Delta g_{VP}^{(2)}$	$0.00000023481(1)$	Eq. (29.31)
$\Delta g^{(4)}$	$0.0000035521(17)$	Eq. (29.32)
$\Delta g^{(6)}$	-0.00000002966	Eq. (29.34)
$\Delta g^{(8)}$	0.00000000011	Eq. (29.34)
$\Delta g^{(10)}$	-0.00000000000	Eq. (29.34)
Δg_{rec}	-0.00000020588	Eq. (29.35)
Δg_{ns}	$-0.0000002053(3)$	Eq. (29.38)
$g(^{28}\text{Si}^{13+})$	$-1.9953489581(17)$	

that of the two-photon $n = 2$ correction $\Delta g^{(4)}$. The relative uncertainties of the $^{12}\text{C}^{5+}$ and $^{28}\text{Si}^{13+}$ values are 1.3×10^{-11} and 8.5×10^{-10} , respectively, sufficient for the purpose of determining competitive atom-to-electron mass ratios. Finally, the two g -factors have a correlation coefficient $r = 0.79$.

29.7 Hydrogen Atom Energy levels

Measurements of the hydrogen energy levels are currently the most precise way to determine the Hartree energy divided by the reduced Planck constant or, equivalently, the Rydberg constant. The measurements also help determine α and the proton charge radius. The eigenstates are labeled by $n\ell_j$, where $n = 1, 2, \dots$ is the principal quantum number, $\ell = 0, 1, \dots, n-1$ is the nonrelativistic angular momentum quantum number, and j is the total angular momentum quantum number. Their energies are denoted by $E(n\ell_j)$ and, following the usual convention, we use S, P, D, \dots to denote $\ell = 0, 1, 2, \dots$ states. Our discussion will omit hyperfine effects from coupling of the electron to the magnetic and other moments of the proton, as at 2014 accuracy levels they can easily be accounted for.

The world's best-known optical transition frequency is that for the $1S_{1/2}-2S_{1/2}$ Lyman-alpha line of hydrogen, which has been obtained by an experimental group in Garching, Germany [39, 40]. They quote

$$\omega_H(1S_{1/2}-2S_{1/2}) = 2\pi \times 2,466,061,413,187,035(10) \text{ rad/s} \quad [4.2 \times 10^{-15}]$$

or

$$\nu_H(1S_{1/2}-2S_{1/2}) = 2,466,061,413,187,035(10) \text{ Hz}$$

in 2011 and

$$\omega_H(1S_{1/2}-2S_{1/2}) = 2\pi \times 2,466,061,413,187,018(11) \text{ rad/s} \quad [4.4 \times 10^{-15}]$$

or

$$\nu_H(1S_{1/2}-2S_{1/2}) = 2,466,061,413,187,018(11) \text{ Hz}$$

in 2013. The two values are correlated with a correlation coefficient $r = 0.707$ [41].

The frequency of this Lyman-alpha line is known to almost 15 significant digits. The analytical, theoretical determination of this transition frequency, which in its simplest description by Bohr equals $3E_h/(8h)$, is equally impressive, although less accurate. It has 13 contributions ranging from the Dirac eigenvalue, QED corrections with one or more virtual photons and lepton-antilepton pairs, as well as nuclear size and recoil effects. Figure 29.6a gives a visual representation of the size and uncertainties of these contributions. We postpone the discussion of the name for and mathematical form of each of the corrections until Sect. 29.7.1. The sizes of the contributions vary by orders of magnitude, although size is not necessarily an indication of its uncertainty. The uncertainty of both the Dirac energy and the correction due to the proton charge radius are the largest at ≈ 10 kHz and reflect the uncertainty of constants E_h/\hbar and r_p , respectively. The largest theoretical uncertainties are in the two-photon and three-photon corrections and reflect uncomputed terms. (The individual uncertainties of the Dirac energy and correction due to the proton charge radius are large compared to that of the experimental $1S_{1/2}-2S_{1/2}$ transition frequency. As a result the uncertainties are highly correlated with a correlation coefficient very close to one.)

The $2P_{1/2}-2S_{1/2}$ transition, or Lamb shift, is equally important, because the Dirac or Bohr energies cancel, and the dominant contribution by far is the self-energy correction, a QED correction where the bound electron emits and absorbs a virtual photon. It is of order $\alpha^3 E_h$ as seen in Sect. 29.7.1. The energy contributions to this transition are shown in Fig. 29.6b, while the two best measurements of this transition frequency are

$$\nu_H(2P_{1/2}-2S_{1/2}) = 1,057,845.0(9.0) \text{ kHz} \quad [8.5 \times 10^{-6}]$$

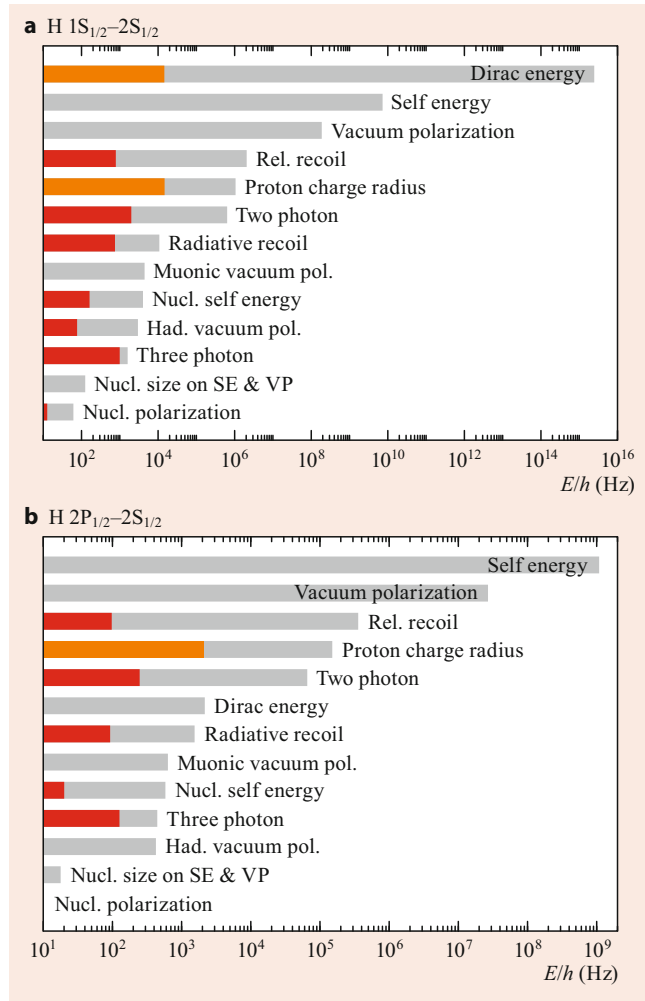


Fig. 29.6 Absolute value of the 13 contributions (gray bars) and their uncertainty (red and orange bars) to the hydrogen $1S_{1/2}-2S_{1/2}$ (a) and $2P_{1/2}-2S_{1/2}$ (b) transition frequencies on a logarithmic scale. The values are sorted by the size of the contribution. The label next to each contribution is defined in the text. The uncertainty of a contribution is either fully due to the uncertainty of constants within QED theory, here the Hartree frequency, E_h/\hbar , and proton charge radius (orange bars), or by the estimated value of missing or uncomputed terms (red bars). The two transition frequencies have been measured to 10 and 9 kHz, respectively

and

$$\nu_H(2P_{1/2}-2S_{1/2}) = 1,057,862(20) \text{ kHz} \quad [1.9 \times 10^{-5}],$$

from research groups at Harvard University [42] and the University of Sussex [43], respectively. The theoretical value for this transition from the 2014 CODATA least-squares adjustment is

$$\nu_H(2P_{1/2}-2S_{1/2}) = 1,057,843.7(2.1) \text{ kHz} \quad [2.0 \times 10^{-6}]$$

and is in agreement with the experiments. The largest contribution to the theoretical uncertainty is due to the uncertainty

in the proton charge radius, while uncertainties from uncomputed terms in the two-photon and three-photon corrections are much smaller than the experimental uncertainty.

In a naive least-squares adjustment that includes only these two transitions, the Lyman-alpha line and Lamb shift determine (relatively inaccurate) values for α and m_e . Data on other transitions and the measurements discussed in the previous sections significantly decrease their uncertainties, constrain the value for the proton charge radius, and check for consistency. Indeed, the focus has shifted to complementary transitions in H [44, 45] and measurements on and theory of muonic-hydrogen with the goal of resolving the discrepancies in the determination of the charge radius of the proton. In the 2014, CODATA adjustment muonic-hydrogen data was not included.

29.7.1 Theory for the Hydrogen Energy Levels

Theoretical values for hydrogen energy levels as for the bound-electron g -factor are determined by the Dirac eigenvalue, QED effects such as self-energy and vacuum polarization, and proton size and motion or recoil effects. Theoretical energies of different states are correlated. For example, for S-states, uncalculated contributions are primarily of the form of an unknown constant divided by n^3 . This is taken into account by using covariances between levels in addition to the uncertainties of the individual levels. Hence, we distinguish between components of uncertainty that are proportional to $1/n^3$ and those that are uncorrelated, where necessary. They are denoted by u_0 and u_n , respectively.

We now consider each of the contributions to the energy in turn, as well as explain how to combine the uncertainties of the contributions. Table 29.4 gives a list of the contributions, their size both in terms of fundamental constants, as well as order-of-magnitude numerical values for the $1S_{1/2}-2S_{1/2}$ transition.

Dirac Eigenvalue

The energy of an electron in a static Coulomb field with charge Ze with infinite mass is predominantly determined by the relativistic Dirac eigenvalue

$$E_D = f(n, \kappa) m_e c^2, \quad (29.39)$$

where

$$f(n, \kappa) = \left[1 + \frac{(Z\alpha)^2}{(n - \delta)^2} \right]^{-1/2}, \quad (29.40)$$

with defect $\delta = |\kappa| - \sqrt{\kappa^2 - (Z\alpha)^2}$ and κ is the angular momentum-parity quantum number ($\kappa = -1, 1, -2, 2, -3$ for $S_{1/2}, P_{1/2}, P_{3/2}, D_{3/2},$ and $D_{5/2}$ -states, respectively). States

Table 29.4 List of contributions and their main dependence on fundamental constants to the hydrogen transition frequencies ordered by appearance in the text. The first two columns give the section in Sec. 29.7.1 in which the contribution is described in detail and the name of the contribution, respectively. The fundamental-constant dependence of a contribution in the third column is given in terms of the Hartree energy $E_h = m_e c^2 \alpha^2$ and four dimensionless variables with values small compared to one: the fine-structure constant α , the proton charge radius divided by the reduced Compton wavelength r_p/λ_C , and the mass ratios m_e/m_μ and m_e/m_p . The last column gives the order of magnitude of each of the contributions in Hz for the $1S_{1/2}-2S_{1/2}$ transition

	Contribution	Scaling	Δ/h (Hz)
<i>a</i>	Dirac energy	E_h	10^{15}
<i>b</i>	Relativistic recoil	$(m_e/m_p)\alpha^3 E_h$	10^6
<i>c</i>	Nuclear polarizability	–	10^2
<i>d</i>	Self-energy	$\alpha^3 E_h$	10^{10}
<i>e</i>	Vacuum polarization	$\alpha^3 E_h$	10^8
<i>e</i>	Muon vacuum polarization	$(m_e/m_\mu)^2 \alpha^3 E_h$	10^4
<i>e</i>	Hadronic vacuum pol.	–	10^3
<i>f</i>	Two-photon	$\alpha^4 E_h$	10^6
<i>g</i>	Three-photon	$\alpha^5 E_h$	10^3
<i>h</i>	Nuclear size	$(r_p/\lambda_C)^2 \alpha^2 E_h$	10^6
<i>i</i>	Nucl. size on SE & VP	$(r_p/\lambda_C)^2 \alpha^4 E_h$	10^2
<i>j</i>	Radiative recoil	$(m_e/m_p)\alpha^4 E_h$	10^4
<i>k</i>	Nuclear self-energy	$(m_e/m_p)^2 \alpha^3 E_h$	10^3

with the same n and $j = |\kappa| - 1/2$ have degenerate eigenvalues. Finally, $\ell = |\kappa + 1/2| - 1/2$, and we retain the atomic number Z in the equations in order to classify the various contributions to the energies.

Corrections to the Dirac eigenvalue that approximately take into account the finite mass of the proton m_p are included in a more general expression for atomic energy levels. That is, we replace Eq. (29.39) by [46, 47]

$$E_M = M c^2 + \left\{ f(n, \kappa) - 1 - \frac{1}{2} [f(n, \kappa) - 1]^2 \frac{m_r}{M} + \frac{1}{2} \frac{1 - \delta_{\ell 0}}{\kappa(2\ell + 1)} \frac{(Z\alpha)^4 m_r^2}{n^3 m_p^2} + \dots \right\} m_r c^2, \quad (29.41)$$

where $M = m_e + m_p$ and $m_r = m_e m_p / (m_e + m_p)$ is the reduced mass. Note that in this equation, the energy of $nS_{1/2}$ -states differs from that of $nP_{1/2}$ -states.

Relativistic Recoil

The leading relativistic-recoil correction, to lowest order in $Z\alpha$ and all orders in m_e/m_p , is [47, 48]

$$E_S = \frac{m_r^3}{m_e^2 m_p} \frac{(Z\alpha)^5}{\pi n^3} m_e c^2 \times \left\{ \frac{1}{3} \delta_{\ell 0} \ln(Z\alpha)^{-2} - \frac{8}{3} \ln k_0(n, \ell) - \frac{1}{9} \delta_{\ell 0} - \frac{7}{3} a_n - \frac{2}{m_p^2 - m_e^2} \delta_{\ell 0} \left[m_p^2 \ln\left(\frac{m_e}{m_r}\right) - m_e^2 \ln\left(\frac{m_p}{m_r}\right) \right] \right\}, \quad (29.42)$$

Table 29.5 Values of the Bethe logarithms $\ln k_0(n, \ell)$. Missing entries correspond to states for which no experimental measurements are available

<i>n</i>	S	P	D
1	2.984128556		
2	2.811769893	−0.030016709	
3	2.767663612		
4	2.749811840	−0.041954895	−0.006740939
6	2.735664207		−0.008147204
8	2.730267261		−0.008785043
12			−0.009342954

where $a_n = -2 \ln(2/n) - 2 + 1/n - 2 \sum_{i=1}^n (1/i)$ for $\ell = 0$ and $a_n = 1/[\ell(\ell+1)(2\ell+1)]$ otherwise. Values for the Bethe logarithms $\ln k_0(n, \ell)$ are given in Table 29.5.

Additional contributions to lowest order in the mass ratio and of higher order in $Z\alpha$ are

$$E_R = \frac{m_e}{m_p} \frac{(Z\alpha)^6}{n^3} m_e c^2 [D_{60} + D_{72} Z\alpha \ln^2(Z\alpha)^{-2} + \dots], \quad (29.43)$$

where $D_{60} = 4 \ln 2 - 7/2$ for $\ell = 0$ and $D_{60} = 2[3 - \ell(\ell+1)/n^2]/[(2\ell-1)(2\ell+1)(2\ell+3)]$ otherwise. Finally, $D_{72} = -11/(60\pi) \delta_{\ell 0}$. Recently, the coefficients D_{71} and D_{70} have been computed [49, 50], where, in particular, the D_{71} was found to be surprisingly large. In [49], the nuclear-size correction to $E_S + E_R$ was also computed.

The uncertainty in the relativistic recoil correction $E_S + E_R$ is

$$[0.1\delta_{\ell 0} + 0.01(1 - \delta_{\ell 0})] E_R. \quad (29.44)$$

Covariances follow from the $1/n^3$ scaling of the uncertainty.

Nuclear Polarizability

For the energy correction due to the nuclear polarizability in hydrogen, we use

$$E_P(\text{H}) = -0.070(13) h \frac{\delta_{\ell 0}}{n^3} \text{kHz}. \quad (29.45)$$

The effect is neglected for states of higher ℓ .

Self-Energy

The one-photon self-energy of an electron bound to a stationary point nucleus is

$$E_{SE}^{(2)} = \frac{\alpha}{\pi} \frac{(Z\alpha)^4}{n^3} F(Z\alpha) m_e c^2, \quad (29.46)$$

where the function

$$F(x) = A_{41} \ln(x^{-2}) + A_{40} + A_{50} x + A_{62} x^2 \ln^2(x^{-2}) + A_{61} x^2 \ln(x^{-2}) + G_{SE}(x) x^2, \quad (29.47)$$

with $A_{41} = 4/3 \delta_{\ell 0}$, and $A_{40} = -(4/3) \ln k_0(n, \ell) + 10/9$ for $\ell = 0$ and $-(4/3) \ln k_0(n, \ell) - 1/[2\kappa(2\ell + 1)]$ otherwise. Next, $A_{50} = (139/32 - 2 \ln 2)\pi \delta_{\ell 0}$, $A_{62} = -\delta_{\ell 0}$, and

$$A_{61} = \left[4 \left(1 + \frac{1}{2} + \dots + \frac{1}{n} \right) + \frac{28}{3} \ln 2 - 4 \ln n - \frac{601}{180} - \frac{77}{45n^2} \right] \delta_{\ell 0} + \frac{n^2 - 1}{n^2} \left(\frac{2}{15} + \frac{1}{3} \delta_{j\frac{1}{2}} \right) \delta_{\ell 1}, \\ + \frac{[96n^2 - 32\ell(\ell + 1)](1 - \delta_{\ell 0})}{3n^2(2\ell - 1)(2\ell)(2\ell + 1)(2\ell + 2)(2\ell + 3)}.$$

Values for $G_{SE}(\alpha)$ in Eq. (29.47) are listed in Table 29.6. The uncertainty of the self-energy contribution is due to the uncertainty of $G_{SE}(\alpha)$ listed in the table and is taken to be type u_n . See [51] for details.

Following convention, $F(Z\alpha)$ is multiplied by the factor $(m_r/m_e)^3$, except the magnetic moment term $-1/[2\kappa(2\ell + 1)]$ in A_{40} , which is instead multiplied by the factor $(m_r/m_e)^2$, and the argument $(Z\alpha)^{-2}$ of the logarithms is replaced by $(m_e/m_r)(Z\alpha)^{-2}$.

Vacuum Polarization

The stationary point nucleus second-order vacuum-polarization level shift is

$$E_{VP}^{(2)} = \frac{\alpha}{\pi} \frac{(Z\alpha)^4}{n^3} H(Z\alpha) m_e c^2, \quad (29.48)$$

where $H(x) = H^{(1)}(x) + H^{(R)}(x)$ with

$$H^{(1)}(x) = V_{40} + V_{50}x + V_{61}x^2 \ln(x^{-2}) + G_{VP}^{(1)}(x)x^2,$$

with $V_{40} = -4/15 \delta_{\ell 0}$, $V_{50} = 5\pi/48 \delta_{\ell 0}$, and $V_{61} = -2/15 \delta_{\ell 0}$. Values of $G_{VP}^{(1)}(\alpha)$ are given in Table 29.7. Moreover, $H^{(R)}(x) = G_{VP}^{(R)}(x)x^2$ with

$$G_{VP}^{(R)}(x) = \frac{19}{45} - \frac{\pi^2}{27} + \left(\frac{1}{16} - \frac{31\pi^2}{2880} \right) \pi x + \dots, \quad (29.49)$$

for $\ell = 0$ and zero otherwise. Higher-order terms are negligible. We multiply Eq. (29.48) by $(m_r/m_e)^3$ and include a factor of (m_e/m_r) in the argument of the logarithm of the term proportional to V_{61} .

Vacuum polarization from $\mu^+\mu^-$ pairs is

$$E_{\mu VP}^{(2)} = \frac{\alpha}{\pi} \frac{(Z\alpha)^4}{n^3} \left[-\frac{4}{15} \delta_{\ell 0} \right] \left(\frac{m_e}{m_\mu} \right)^2 \left(\frac{m_r}{m_e} \right)^3 m_e c^2 + \dots, \quad (29.50)$$

while the hadronic vacuum polarization is given by

$$E_{had VP}^{(2)} = 0.671(15) E_{\mu VP}^{(2)}. \quad (29.51)$$

Uncertainties are of type u_0 . The muonic and hadronic vacuum-polarization contributions are negligible for higher- ℓ -states.

Two-Photon Corrections

The two-photon correction is

$$E^{(4)} = \left(\frac{\alpha}{\pi} \right)^2 \frac{(Z\alpha)^4}{n^3} m_e c^2 F^{(4)}(Z\alpha), \quad (29.52)$$

where

$$F^{(4)}(x) = B_{40} + B_{50}x + B_{63}x^2 \ln^3(x^{-2}) \\ + B_{62}x^2 \ln^2(x^{-2}) + B_{61}x^2 \ln(x^{-2}) + B_{60}x^2 \\ + B_{72}x^3 \ln^2(x^{-2}) + B_{71}x^3 \ln(x^{-2}) + \dots,$$

with

$$B_{40} = \left[\frac{3\pi^2}{2} \ln 2 - \frac{10\pi^2}{27} - \frac{2179}{648} - \frac{9}{4} \zeta(3) \right] \delta_{\ell 0} \\ + \left[\frac{\pi^2 \ln 2}{2} - \frac{\pi^2}{12} - \frac{197}{144} - \frac{3\zeta(3)}{4} \right] \frac{1 - \delta_{\ell 0}}{\kappa(2\ell + 1)},$$

$B_{50} = -21.55447(13) \delta_{\ell 0}$, $B_{63} = -8/27 \delta_{\ell 0}$, and

$$B_{62} = \frac{16}{9} \left[\frac{71}{60} - \ln 2 + \psi(n) + \gamma - \ln n - \frac{1}{n} + \frac{1}{4n^2} \right] \delta_{\ell 0} \\ + \frac{4}{27} \frac{n^2 - 1}{n^2} \delta_{\ell 1},$$

with Euler's constant γ and Psi function $\psi(z)$.

Values and uncertainties for B_{61} and B_{60} are listed in Tables 29.8 and 29.9, respectively. For the S-state values, the first number in parentheses for B_{60} is the state-dependent uncertainty $u_n(B_{60})$, while the second number in parentheses is the state-independent uncertainty $u_0(B_{60})$. It is worth noting that recently [32] computed an additional light-by-light correction to B_{61} for S-states. It only shifts this coefficient within its current uncertainty.

For S-states, the next term B_{72} is state independent, but its value is not known. The B_{71} coefficient is state dependent, although only the difference

$$\Delta B_{71}(nS) = B_{71}(nS) - B_{71}(1S) = \pi \left(\frac{427}{36} - \frac{16}{3} \ln 2 \right) \\ \times \left[\frac{3}{4} - \frac{1}{n} + \frac{1}{4n^2} + \psi(n) + \gamma - \ln n \right] + \dots$$

is known with a relative uncertainty $u_n(\Delta B_{71}) = 0.5 \Delta B_{71}$. For our calculations, we use $B_{71}(1S) = 0$.

As with the one-photon correction, the two-photon correction is multiplied by the reduced-mass factor $(m_r/m_e)^3$, except the magnetic moment term proportional to $1/[\kappa(2\ell + 1)]$ in B_{40} , which is multiplied by the factor $(m_r/m_e)^2$, and the argument $(Z\alpha)^{-2}$ of the logarithms is replaced by $(m_e/m_r)(Z\alpha)^{-2}$.

Table 29.6 Values of the function $G_{SE}(\alpha)$. Missing entries correspond to states for which no experimental measurements are available

n	$S_{1/2}$	$P_{1/2}$	$P_{3/2}$	$D_{3/2}$	$D_{5/2}$
1	-30.290240(20)				
2	-31.185150(90)	-0.97350(20)	-0.48650(20)		
3	-31.04770(90)				
4	-30.9120(40)	-1.1640(20)	-0.6090(20)		0.03163(22)
6	-30.711(47)				0.03417(26)
8	-30.606(47)			0.007940(90)	0.03484(22)
12				0.009130(90)	0.03512(22)

Table 29.7 Values of the function $G_{VP}^{(1)}(\alpha)$. No experimental data is available for missing entries. Zero values indicate that their contributions are negligibly small

n	$S_{1/2}$	$P_{1/2}$	$P_{3/2}$	$D_{3/2}$	$D_{5/2}$
1	-0.618724				
2	-0.808872	-0.064006	-0.014132		
3	-0.814530				
4	-0.806579	-0.080007	-0.017666		-0.000000
6	-0.791450				-0.000000
8	-0.781197			-0.000000	-0.000000
12				-0.000000	-0.000000

Table 29.8 Values of B_{61} used in the 2014 CODATA adjustment. Zero values indicate that their contributions are negligibly small

n	$S_{1/2}$	$P_{1/2}$	$P_{3/2}$	$D_{3/2}$	$D_{5/2}$
1	48.95859024(1)				
2	41.06216431(1)	0.157775547(1)	-0.092224453(1)		
3	38.904222(1)				
4	37.909514(1)	0.191192600(1)	-0.121307400(1)		0.0(0)
6	36.963391(1)				0.0(0)
8	36.504940(1)			0.0(0)	0.0(0)
12				0.0(0)	0.0(0)

Table 29.9 Values of B_{60} used in the 2014 CODATA adjustment. The uncertainties of B_{60} for S-states are explained in the text

n	$S_{1/2}$	$P_{1/2}$	$P_{3/2}$	$D_{3/2}$	$D_{5/2}$
1	-81.3(0.3)(19.7)				
2	-66.2(0.3)(19.7)	-1.6(3)	-1.7(3)		
3	-63.0(0.6)(19.7)				
4	-61.3(0.8)(19.7)	-2.1(3)	-2.2(3)		-0.005(2)
6	-59.3(0.8)(19.7)				-0.008(4)
8	-58.3(2.0)(19.7)			0.015(5)	-0.009(5)
12				0.014(7)	-0.010(7)

Three-Photon Corrections

The three-photon contribution in powers of $Z\alpha$ is

$$E^{(6)} = \left(\frac{\alpha}{\pi}\right)^3 \frac{(Z\alpha)^4}{n^3} m_e c^2 [C_{40} + C_{50}(Z\alpha) + C_{63}(Z\alpha)^2 \ln^3(Z\alpha)^{-2} + \dots]. \tag{29.53}$$

The leading term C_{40} is

$$C_{40} = \left[-\frac{568 a_4}{9} + \frac{85 \zeta(5)}{24} - \frac{121 \pi^2 \zeta(3)}{72} - \frac{84,071 \zeta(3)}{2304} - \frac{71 \ln^4 2}{27} - \frac{239 \pi^2 \ln^2 2}{135} + \frac{4787 \pi^2 \ln 2}{108} + \frac{1591 \pi^4}{3240} - \frac{252,251 \pi^2}{9720} + \frac{679,441}{93,312} \right] \delta_{\ell 0}$$

$$+ \left[-\frac{100 a_4}{3} + \frac{215 \zeta(5)}{24} - \frac{83 \pi^2 \zeta(3)}{72} - \frac{139 \zeta(3)}{18} - \frac{25 \ln^4 2}{18} + \frac{25 \pi^2 \ln^2 2}{18} + \frac{298 \pi^2 \ln 2}{9} + \frac{239 \pi^4}{2160} - \frac{17,101 \pi^2}{810} - \frac{28,259}{5184} \right] \frac{1 - \delta_{\ell 0}}{\kappa(2\ell + 1)},$$

where $a_4 = \sum_{n=1}^{\infty} 1/(2^n n^4) = 0.517479061\dots$ Only partial results for C_{50} have been obtained [52, 53]. We use $C_{50} = 0$ with uncertainty $u_0(C_{50}) = 30\delta_{\ell 0}$. Finally, we use $C_{63} = 0$ and $u_n(C_{63}) = 1$ for this unknown coefficient. Recently, *Karshenboim* and *Ivanov* [54] determined several of these coefficients. The dominant effect of the finite mass of the nucleus is taken into account by multiplying the term proportional to $\delta_{\ell 0}$ by the reduced-mass factor $(m_r/m_e)^3$ and the term proportional to $1/[\kappa(2\ell + 1)]$, the magnetic mo-

ment term, by the factor $(m_r/m_e)^2$. The contribution from four photons is expected to be negligible at the level of uncertainty of current interest.

Finite Nuclear Size

For S-states, the leading and next-order correction to the level shift due to the finite size of the nucleus is given by

$$E_{\text{NS}} = \mathcal{E}_{\text{NS}} \left\{ 1 - C_\eta \frac{m_r}{m_e} \frac{r_p}{\lambda_C} Z\alpha - \left[\ln \left(\frac{m_r}{m_e} \frac{r_p}{\lambda_C} \frac{Z\alpha}{n} \right) + \psi(n) + \gamma - \frac{(5n+9)(n-1)}{4n^2} - C_\theta \right] (Z\alpha)^2 \right\}, \quad (29.54)$$

where

$$\mathcal{E}_{\text{NS}} = \frac{2}{3} \left(\frac{m_r}{m_e} \right)^3 \frac{(Z\alpha)^2}{n^3} m_e c^2 \left(\frac{Z\alpha r_p}{\lambda_C} \right)^2. \quad (29.55)$$

The coefficients C_η and C_θ are constants that depend on the charge distribution in the nucleus with values $C_\eta = 1.7(1)$ and $C_\theta = 0.47(4)$ for hydrogen.

For the $P_{1/2}$ -states in hydrogen, the leading term is

$$E_{\text{NS}} = \mathcal{E}_{\text{NS}} \frac{(Z\alpha)^2 (n^2 - 1)}{4n^2}. \quad (29.56)$$

For $P_{3/2}$ -states and higher- ℓ -states, the nuclear-size contribution is negligible.

Nuclear-Size Correction to Self-Energy and Vacuum Polarization

For the lowest-order self-energy and vacuum polarization, the correction due to the finite size of the nucleus is

$$E_{\text{NSE}} = \left(4 \ln 2 - \frac{23}{4} \right) \alpha (Z\alpha) \mathcal{E}_{\text{NS}} \delta_{\ell 0}, \quad (29.57)$$

and

$$E_{\text{NVP}} = \frac{3}{4} \alpha (Z\alpha) \mathcal{E}_{\text{NS}} \delta_{\ell 0}, \quad (29.58)$$

respectively.

Radiative-Recoil Corrections

Corrections for radiative-recoil effects are

$$E_{\text{RR}} = \frac{m_r^3}{m_e^2 m_p} \frac{\alpha (Z\alpha)^5}{\pi^2 n^3} m_e c^2 \delta_{\ell 0} \times \left[6 \zeta(3) - 2 \pi^2 \ln 2 + \frac{35 \pi^2}{36} - \frac{448}{27} + \frac{2}{3} \pi (Z\alpha) \ln^2 (Z\alpha)^{-2} + d_{61} (Z\alpha) \ln (Z\alpha)^{-2} + \dots \right]. \quad (29.59)$$

The uncertainty is controlled by the unknown coefficient d_{61} inside the square brackets. We use $d_{61} = 0$, $u_0(d_{61}) = 10$, and $u_n(d_{61}) = 1$. Corrections for higher- ℓ -states are negligible.

Nucleus Self-Energy

The nucleus self-energy correction for S-states of hydrogen is

$$E_{\text{SEN}} = \frac{4Z^2 \alpha (Z\alpha)^4 m_r^3}{3\pi n^3 m_p^2} c^2 \times \left[\ln \left(\frac{m_p}{m_r (Z\alpha)^2} \right) \delta_{\ell 0} - \ln k_0(n, \ell) \right], \quad (29.60)$$

with an uncertainty u_0 given by Eq. (29.60), with the factor in the square brackets replaced by 0.5. For higher- ℓ -states, the correction is negligible.

Total energy and uncertainty: the energy $E(n\ell_j)$ of a level is the sum of the contributions listed above. Uncertainties in the energy due to the fundamental constants, i.e., α , $m_e c^2$, etc., are taken into account through a least-squares adjustment. Uncertainties in the theory, i.e., from estimates of missing and uncomputed terms in the contributions, are taken into account with an energy correction $\delta(n\ell_j)$, with an uncertainty that is the rms sum of the uncertainties of the individual contributions

$$u^2[\delta(n\ell_j)] = \sum_i [u_{0i}^2(n\ell_j) + u_{ni}^2(n\ell_j)], \quad (29.61)$$

where $u_{0i}(n\ell_j)$ and $u_{ni}(n\ell_j)$ are the components of uncertainty u_0 and u_n of contribution i . Covariances of the δ s are

$$u[\delta(n_1\ell_j), \delta(n_2\ell_j)] = \sum_i u_{0i}(n_2\ell_j) u_{0i}(n_1\ell_j). \quad (29.62)$$

The corrections $\delta(n\ell_j)$, their uncertainties, and covariances are input data in the least-squares adjustment. A value for $\delta(n\ell_j)$ returned by the adjustment that lies outside its uncertainty indicates either an underestimate of the value of uncomputed terms in the contributions or a role for unexpected physics beyond QED. No such discrepancies have been found.

Acknowledgments The authors gratefully acknowledge helpful conversations with David Newell.

References

1. Sommerfeld, A.: Ann. Phys. **356**, 1 (1916)
2. International Bureau of Weights and Measures (BIPM). <https://www.bipm.org/en/about-us/>
3. Newell, D.B.: Phys. Today **67**, 35 (2014)
4. Eides, M.I., Grotch, H., Shelyuto, V.A.: Phys Rep **342**, 63 (2001)
5. Mohr, P.J., Newell, D.B., Taylor, B.N.: Rev. Mod. Phys. **88**, 035009 (2016)
6. Hanneke, D., Fogwell, S., Gabrielse, G.: Phys. Rev. Lett. **100**, 120801 (2008)
7. Wang, M., Audi, G., Kondev, F.G., Huang, W.J., Naimi, S., Xu, X.: Chin. Phys. C(41), 030003 (2017)

8. Feng, X.J., Zhang, J.T., Moldover, M.R., Yang, I., Plimner, M.D., Lin, H.: *Metrologia* **54**, 339 (2017)
9. Laporta, S., Remiddi, E.: *Phys. Lett. B.* **301**, 440 (1993)
10. Laporta, S.: *Nuovo Cimento* **106**, 675 (1993)
11. Kurz, A., Liu, T., Marquard, P., Steinhauser, M.: *Nucl. Phys. B.* **879**, 1 (2014)
12. Aoyama, T., Hayakawa, M., Kinoshita, T., Nio, M.: *Phys. Rev. D* **91**, 033006 (2015)
13. Laporta, S.: *Phys. Lett. B.* **772**, 232 (2017)
14. Aoyama, T., Kinoshita, T., Nio, M.: *Phys. Rev. D* **97**, 036001 (2018)
15. Particle Data Group: *Chin. Phys. C* **38**, 090001 (2014)
16. Bouchendira, R., Cladé, P., Guellati-Khélifa, S., Nez, F., Biraben Phys, F.: *Rev. Lett.* **106**, 080801 (2011)
17. Parker, R.H., Yu, C., Zhong, W., Estey, B., Müller, H.: *Science* **360**, 191 (2018)
18. Audi, G., Wang, M., Wapstra, A.H., Kondev, F.G., MacCormick, M., Xu, X., Pfeiffer, B.: *Chin. Phys. C* **36**, 1287 (2012)
19. Wang, M., Audi, G., Wapstra, A.H., Kondev, F.G., MacCormick, M., Xu, X., Pfeiffer, B.: *Chin. Phys. C* **36**, 1603 (2012)
20. Huang, W.J., Audi, G., Wang, M., Kondev, F.G., Naimi, S., Xu, X.: *Chin. Phys. C* **41**, 030002 (2017)
21. Sturm, S., Köhler, F., Zatorski, J., Wagner, A., Harman, Z., Werth, G., Quint, W., Keitel, C.H., Blaum, K.: *Nature* **506**, 467 (2014)
22. Köhler, F., Sturm, S., Kracke, A., Werth, G., Quint, W., Blaum, K.J.: *Phys. B* **48**, 144032 (2015)
23. Sturm, S., Wagner, A., Kretzschmar, M., Quint, W., Werth, G., Blaum, K.: *Phys. Rev. A* **87**, 030501 (2013)
24. Sturm, S., Wagner, A., Kretzschmar, M., Quint, W., Werth, G., Blaum, K. (2015), private communication.
25. Breit, G.: *Nature* **122**, 649 (1928)
26. Yerokhin, V.A., Harman, Z.: *Phys. Rev. A* **95**, 060501 (2017)
27. Beier, T., Lindgren, I., Persson, H., Salomonson, S., Sunnergren, P., Häffner, H., Hermanspahn, N.: *Phys. Rev. A* **62**, 032510 (2000)
28. Pachucki, K., Czarnecki, A., Jentschura, U.D., Yerokhin, V.A.: *Phys. Rev. A* **72**, 022108 (2005)
29. Jentschura, U.D., Czarnecki, A., Pachucki, K., Yerokhin, V.A.: *Int. J. Mass. Spectrom.* **251**, 102 (2006)
30. Jentschura, U.D.: *Phys. Rev. A* **79**, 044501 (2009)
31. Yerokhin, V.A., Harman, Z.: *Phys. Rev. A* **88**, 042502 (2013)
32. Czarnecki, A., Szafron, R.: *Phys. Rev. A* **94**, 060501 (2016)
33. Eides, M.I., Grotch, H.: *Ann. Phys.* **260**, 191 (1997)
34. Czarnecki, A., Melnikov, K., Yelkhovskiy, A.: *Phys. Rev. A* **63**, 012509 (2001)
35. Shabaev, V.M., Yerokhin, V.A.: *Phys. Rev. Lett.* **88**, 091801 (2002)
36. Karshenboim, S.G.: *Phys. Lett. A.* **266**, 380 (2000)
37. Glazov, D.A., Shabaev, V.M.: *Phys. Lett. A.* **297**, 408 (2002)
38. Angeli, I.: *Data Tables. At. Data. Nucl.* **87**, 185 (2004)
39. Parthey, C.G., Matveev, A., Alnis, J., Bernhardt, B., Beyer, A., Holzwarth, R., Maistrou, A., Pohl, R., Predehl, K., Udem, T.: *Phys. Rev. Lett.* **107**, 203001 (2011)
40. Matveev, A., Parthey, C.G., Predehl, K., Alnis, J., Beyer, A., Holzwarth, R., Udem, T., Wilken, T., Kolachevsky, N., Abgrall, M.: *Phys. Rev. Lett.* **110**, 230801 (2013)
41. T. Udem (2014), private communication.
42. Lundeen, S.R., Pipkin, F.M.: *Metrologia* **22**, 9 (1986)
43. Newton, G., Andrews, D.A., Unsworth, P.J.: *Philos. Trans. R. Soc. Lond. Ser. A* **290**, 373 (1979)
44. Beyer, A., Maisenbacher, L., Matveev, A., Pohl, R., Khabarova, K., Grinin, A., Lamour, T., Yost, D.C., Hänsch, T.W., Kolachevsky, N.: *Science* **358**, 79 (2017)
45. Fleurbaey, H., Galtier, S., Thomas, S., Bonnaud, M., Julien, L., Biraben, F., Nez, F., Abgrall, M., Guéna, J.: *arXiv*, 1801:0881 (2018)
46. Barker, W.A., Glover, F.N.: *Phys. Rev.* **99**, 317 (1955)
47. Sapirstein, J.R., Yennie, D.R.: chap. 12. In: Kinoshita, T. (ed.) in *Quantum Electrodynamics*, pp. 560–672. World Scientific, Singapore (1990)
48. Erickson, G.W.: *J. Phys. Chem. Ref. Data* **6**, 831 (1977)
49. Yerokhin, V.A., Shabaev, V.M.: *Phys. Rev. Lett.* **115**, 233002 (2015)
50. Yerokhin, V.A., Shabaev, V.: *Phys. Rev. A* **93**, 062514 (2016)
51. Mohr, P.J., Taylor, B.N., Newell, D.B.: *Rev. Mod. Phys.* **84**, 1527 (2012)
52. Eides, M.I., Shelyuto, V.A.: *Phys. Rev. A* **70**, 022506 (2004)
53. Eides, M.I., Shelyuto, V.A.: *Can. J. Phys.* **85**, 509 (2007)
54. Karshenboim, S.G., Ivanov, V.G.: *Phys. Rev. A* **98**, 022522 (2018)



Eite Tiesinga Dr Eite Tiesinga received his PhD from Eindhoven University of Technology in The Netherlands in 1993. He works at the National Institute of Standards and Technology and the University of Maryland in the US. His research focuses on developing clocks and sensors using laser-cooled atoms. He maintains a web-based database of fundamental constants, an initiative by the Committee on Data of the International Science Council (CODATA).



Peter Mohr Peter Mohr received his PhD from the University of California at Berkeley (1973) and spent some years at the Lawrence Berkeley Laboratory (1973–1978), Yale University (1978–1985), the National Science Foundation (1985–1987), and the National Bureau of Standards/National Institute of Standards and Technology (from 1987). He held the Chair of the CODATA Task Group on Fundamental Constants (1999–2006) and was Chair of the Precision Measurement and Fundamental Constants Topical Group of the American Physical Society (2000–2001).



Atomic Clocks and Constraints on Variations of Fundamental Constants

30

Savely G. Karshenboim, Victor Flambaum , and Ekkehard Peik

Contents

30.1	Atomic Clocks and Frequency Standards	450
30.1.1	Caesium Atomic Fountain	450
30.1.2	Trapped Ions	451
30.1.3	Laser-Cooled Neutral Atoms	452
30.1.4	Two-Photon Transitions and Doppler-Free Spectroscopy	452
30.1.5	Optical Frequency Measurements	453
30.1.6	Limitations on Frequency Variations	453
30.2	Atomic Spectra and Their Dependence on the Fundamental Constants	454
30.2.1	The Spectrum of Hydrogen and Nonrelativistic Atoms	454
30.2.2	Hyperfine Structure and the Schmidt Model	454
30.2.3	Atomic Spectra: Relativistic Corrections	454
30.3	Laboratory Constraints on Temporal Variations of Fundamental Constants	455
30.3.1	Constraints from Absolute and Relative Optical Measurements	456
30.3.2	Constraints from Microwave Clocks	457
30.3.3	A Model-Independent Constraint on the Variation of the Electron-to-Proton Mass Ratio from Molecular Spectroscopy	457
30.3.4	Other Model-Dependent Constraints	457
30.4	Summary	458
	References	458

Abstract

Fundamental constants play an important role in modern physics, being landmarks that designate different areas. We call them constants, however, as long as we only consider minor variations with the cosmological time/space scale, their constancy is an experimental fact rather than a basic theoretical principle. Modern theories unifying gravity with electromagnetic, weak, and strong interactions, or even the developing quantum gravity itself, often suggest such variations.

Many parameters that we call *fundamental constants*, such as the electron charge and mass (Chap. 1 and [1]), are actually not truly fundamental constants but effective parameters that are affected by renormalization or the presence of matter [2, 3]. Living in a changing universe we cannot expect that matter will affect these parameters the same way during any given cosmological epoch. An example is the inflationary model of the universe, which states that in a very early epoch, the universe experienced a phase transition, which, in particular, changed a vacuum average of the so-called Higgs field, which determines the electron mass. The latter was zero before this transition and reached a value close or equal to the present value after the transition.

The problem of variations of constants has many facets, and here we discuss aspects related to atomic clocks and precision frequency measurements. Other related topics may be found in [4, 5].

Keywords

relativistic corrections · frequency standards · fundamental constants · atomic clocks · optical clocks

Laboratory searches for a possible time variation of fundamental physical constants currently consist of two important parts: (i) one has to measure a certain physical quantity at two different moments of time that are separated by at least a few

S. G. Karshenboim (✉)
Faculty of Physics, Ludwig-Maximilians-University
Munich, Germany
e-mail: savely.karshenboim@mpq.mpg.de

V. Flambaum (✉)
Dept. of Physics, University of New South Wales
Sydney, Australia
e-mail: v.flambaum@unsw.edu.au

E. Peik
Physikalisch-Technische Bundesanstalt
Braunschweig, Germany
e-mail: ekkehard.peik@ptb.de

years; (ii) one has to be able to interpret the result in terms of fundamental constants. The latter is a strong requirement for a cross comparison of different results.

The measurements that may be performed the most accurately are frequency measurements, and thus, frequency standards or atomic clocks will be involved in most of the laboratory searches.

With the introduction of laser cooling, ion trapping, frequency comb technology, atomic interferometry, and quantum entanglement, frequency metrology has shown great progress in the past two decades and will continue to do so for some time. The constraints on the variations of the fundamental constants obtained in this manner for the present epoch are now more stringent than those from other methods (astrophysics, geochemistry), when these are extrapolated under the assumption of a linear drift in time. Laboratory experiments on frequency comparisons allow for checks of reproducibility, a very clear interpretation of the final results, and a transparent evaluation procedure, making them less susceptible to systematic errors.

The most advanced atomic clocks are discussed in Sect. 30.1. They are realized with many-electron atoms, and their frequency cannot be interpreted in terms of fundamental constants. However, a much simpler problem needs to be solved: to interpret their variation in terms of fundamental constants. This idea is discussed in Sect. 30.2. The current laboratory constraints on the variations of the fundamental constants are summarized in Sect. 30.3.

30.1 Atomic Clocks and Frequency Standards

Frequency standards are important tools for precision measurements and serve various purposes that, in turn, have different requirements that must be satisfied. In particular, it is not necessary for a practical frequency standard to reproduce a frequency that is related to a certain atomic transition, although it may be expressed in terms of it. A well-known example is the hydrogen maser, where the frequency is affected by the wall shifts, which may vary with time [6]. For the study of time variations of fundamental constants, it is necessary to use standards similar to a primary caesium clock. In this case, any deviation of its frequency from the unperturbed atomic transition frequency should be known (within a known uncertainty) because this is a necessary requirement for being a *primary* standard.

From the point of view of fundamental physics, the hydrogen maser is an artefact quite similar, in a sense, to the prototype of the kilogram held at the Bureau International des Poids et Mesures (BIPM) in Paris. Both artefacts are somehow related to fundamental constants (e.g., the mass of the prototype can be expressed in terms of the nucleon masses and their number), but they also have a kind of resid-

ual classical-physics flexibility, which allows their properties to change. In contrast, standards similar to the caesium clock have a frequency (or other property) that is determined by a certain natural constant, which is not flexible, being of pure quantum origin. It may change only if the fundamental constants are changing.

In Sect. 30.3, the results obtained with the most advanced microwave and optical frequency standards are discussed. The former include the ones based on caesium and rubidium fountains, while the latter deal with precision spectroscopy with atomic beams using two-photon excitation, with laser-cooled ions in traps and atoms in optical lattices.

30.1.1 Caesium Atomic Fountain

Caesium clocks are the most accurate primary standards for time and frequency [7]. The hyperfine splitting frequency between the $F = 3$ and $F = 4$ levels of the $^2S_{1/2}$ ground state of the ^{133}Cs atom at 9.192 GHz has been used for the definition of the SI second since 1967. In a so-called caesium fountain [8] (Fig. 30.1), a dilute cloud of laser cooled caesium atoms at a temperature of about $1\ \mu\text{K}$ is launched upwards to initiate a free parabolic flight with an apogee at about 1 m above the cooling zone. A microwave cavity is mounted near the lower endpoints of the parabola and is traversed by the atoms twice – once during ascent and once during descent – so that Ramsey’s method of interrogation with separated oscillatory fields [6] can be realized. The total interrogation

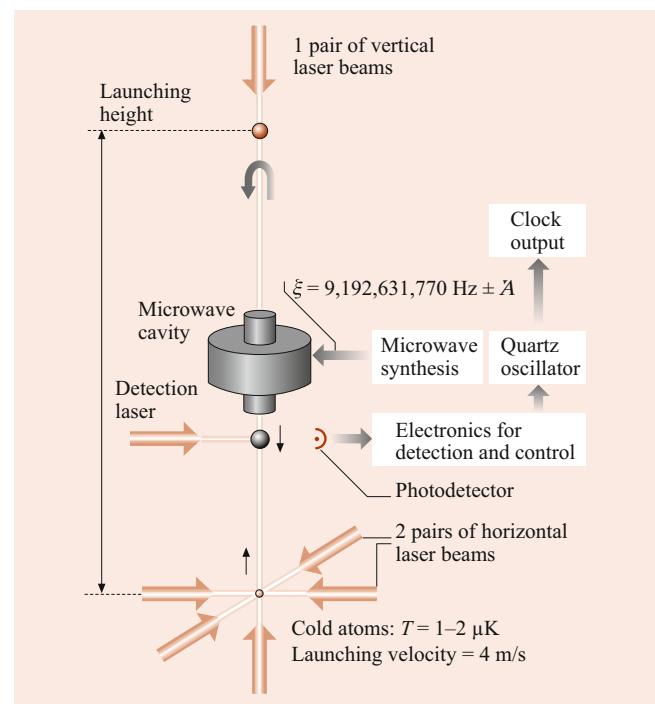


Fig. 30.1 Schematic of an atomic fountain clock

time being on the order of 0.5 s, a resonance linewidth of 1 Hz is achieved, about a factor of 100 narrower than in devices using a thermal atomic beam from an oven. Selection and detection of the hyperfine state is performed via optical pumping and laser-induced resonance fluorescence. In a carefully controlled setup, a relative uncertainty in the low 1×10^{-16} range can be reached in the realization of the resonance frequency of the unperturbed Cs atom. The averaging time that is required to reach this level of uncertainty is in the range of 10^4 to 10^5 s. One limiting effect that contributes to the systematic uncertainty of the caesium fountain is the frequency shift due to cold collisions between the atoms. In this respect, a fountain frequency standard based on the ground state hyperfine frequency of the ^{87}Rb atom at about 6.835 GHz is more favorable, since its collisional shift is lower by more than a factor of 50 for the same atomic density. While the caesium frequency is fixed by definition in the SI system, the ^{87}Rb frequency has been measured repeatedly and is one of the recommended secondary realizations of the second [9]. While a number of optical frequency standards have been evaluated with lower uncertainty, the realization of the caesium standards remains the base of international time and frequency measurements. A number of them, realized independently in numerous national metrological laboratories, are regularly compared via satellite time and frequency transfer to a fractional uncertainty of a few 10^{-16} . At such a level of accuracy, the effects of general relativity should be carefully taken into account. From the gravitational potential of the Earth, a correction of 1×10^{-16} will appear due to a displacement of the clocks by 1 m in the vertical direction.

30.1.2 Trapped Ions

An alternative to interrogating atoms in free flight, and a possibility to obtain practically unlimited interaction time, is to store them in a trap. Ions are well suited because charged particles can be trapped in radio frequency ion traps (Paul traps [10], Chap. 79) that provide confinement around a field-free saddle point of an electric quadrupole potential. This ensures that the internal level structure is only minimally perturbed by the trap. Combined with laser cooling it is possible to reach the Lamb–Dicke regime, i.e., localization within a volume whose extension is smaller than the wavelength of the spectroscopic transition, leading to an elimination of the linear Doppler shift. A single ion, trapped in an ultrahigh vacuum is highly isolated from external perturbations, permitting excellent control of systematic frequency shifts [11]. The use of the much higher optical reference frequency allows one to obtain a stability that is superior to microwave frequency standards, although only a single ion is used to obtain the steering signal for the reference oscillator.

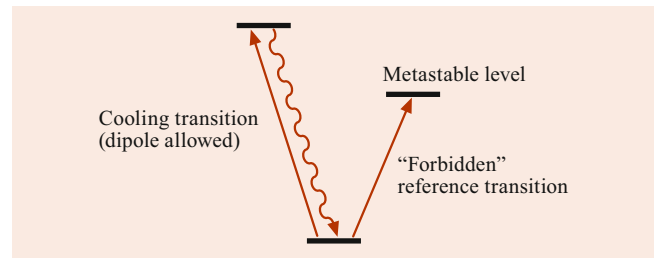


Fig. 30.2 Double-resonance scheme applied in single-ion-trap frequency standards

A number of possible optical reference transitions with natural linewidths of the order of 1 Hz or below are available in different ions. Most ions of interest possess a level scheme where two transitions, a dipole-allowed transition and a forbidden reference transition of the optical clock, can be driven with two lasers from the ground state (Fig. 30.2). The dipole transition is used for laser cooling and for the optical detection of the ion via its resonance fluorescence. If the clock laser excites the ion to the metastable upper level of the reference transition, the fluorescence is interrupted, and every single excitation of the reference transition can thus be detected with unit efficiency as a dark period in the fluorescence signal.

Different types of forbidden reference transitions are investigated [12]: ions with a single valence electron and $s_{1/2}$ ground state possess metastable d levels that couple to the ground state via electric quadrupole (E2) radiation. This level scheme is found in Ca^+ , Sr^+ , Yb^+ [13] and Hg^+ [14, 15]. In Yb^+ , the lowest excited level is an f state, coupled to the ground state only by an electric octupole (E3) transition [16]. In ions with two valence electrons, like Al^+ and In^+ , the total electronic angular momentum couples to 0 in the $^1\text{S}_0$ ground and $^3\text{P}_0$ lowest excited state. The vanishing angular momentum and high intrinsic symmetry of these states makes them less susceptible to level shifts induced by external fields. Hyperfine coupling with a nuclear spin mixes the P_0 and P_1 levels and induces a weak electric dipole transition between $^3\text{P}_0$ and $^1\text{S}_0$.

The absolute transition frequencies of several trapped ion optical frequency standards have been measured with an uncertainty that is essentially limited by the Cs reference (Table 30.1). Frequency standards based on $^{27}\text{Al}^+$ and $^{171}\text{Yb}^+$ have been evaluated with relative systematic uncertainties in the 10^{-18} range [12]. A distinctive feature of the Al^+ system is that it does not rely on direct laser cooling of the ion, because Al^+ does not possess a cooling transition at a technically convenient wavelength. Instead, the ion is cooled sympathetically via the Coulomb interaction by a laser-cooled ion of Be^+ or Ca^+ in the same trap. The two ions form a quasi molecule with joint motional degrees of freedom. Laser excitation of motional sidebands is used to transfer information about the internal state of the Al^+ ion

to a joint motional mode and onwards to an internal state of the coolant ion, where it can be read out via fluorescence detection. Such quantum logic protocols make it possible to perform precision spectroscopy on ions that cannot be directly laser cooled.

The double resonance technique with the observation of dark periods in the fluorescence signal can also be employed if the reference transition is in the microwave domain, and a number of accurate measurements of hyperfine structure intervals in trapped ions have been performed. In particular, the HFS interval in $^{171}\text{Yb}^+$ has been measured several times [17–19] and can be used to obtain constraints on temporal variations.

30.1.3 Laser-Cooled Neutral Atoms

Optical frequency standards have been developed with laser-cooled neutral atoms, most notably of the alkaline-earth elements that possess narrow intercombination transitions and the $J = 0 \rightarrow 0$ transitions discussed for ions above. The atoms are collected and cooled in a magneto-optical trap. They may then be released and interrogated as free atoms by a sequence of laser pulses to realize a frequency-sensitive Ramsey–Bordé atom interferometer [20]. Of these systems, the one based on the $^1\text{S}_0 \rightarrow ^3\text{P}_1$ intercombination line of ^{40}Ca at 657 nm has reached the lowest relative uncertainty so far (about 2×10^{-14}) [21, 22]. Limiting factors in the un-

certainty of these standards are the residual linear Doppler effect and phase front curvature of the laser beams that excite the ballistically expanding atom cloud. For an optical frequency standard of high precision, it is, therefore, necessary to confine the atoms in an optical lattice, i.e., in the array of interference maxima produced by several intersecting, red-detuned laser beams [23, 24]. The wavelength of the trapping laser can be chosen such that the light shift it produces in the ground and excited state of the reference transition are equal, and, therefore, it does not induce a shift of the reference frequency (Fig. 30.3). Such a so-called “magic” wavelength can be estimated with reasonable accuracy theoretically and later on verified experimentally. This approach is presently applied to the very narrow (mHz natural linewidth) $^1\text{S}_0 \rightarrow ^3\text{P}_0$ transitions in neutral strontium, ytterbium, and mercury [12]. As in the case of trapped ions, absolute transition frequencies of several so-called lattice clocks with neutral atoms have been measured with an uncertainty that is essentially limited by the Cs reference (Table 30.1), and systems based on Sr and Yb have been evaluated with relative systematic uncertainties in the 10^{-18} range.

30.1.4 Two-Photon Transitions and Doppler-Free Spectroscopy

The linear Doppler shift of an absorption resonance can also be avoided if a two-photon excitation is induced by two counterpropagating laser beams. A prominent example that has been studied with high precision is the two-photon excitation of the $1s \rightarrow 2s$ transition in atomic hydrogen. The precise measurement of this frequency is of importance for the determination of the Rydberg constant and as a test of quantum electrodynamics (QED). Hydrogen atoms are cooled by collisions in a cryogenic nozzle and interact with a standing laser wave of 243 nm wavelength inside a resonator. Since the atoms are not as cold as in laser-cooled samples, a correction for the second-order Doppler effect is performed. The laser excitation is interrupted periodically, and the excited atoms are detected in a time-resolved manner so that their velocity can be examined. The experiments on absolute frequency measurement were carried out at the Max-Planck-Institut für Quantenoptik, which is not a national metrological institute and does not possess its own primary caesium standard. The problem of the lack of such a standard was resolved by use of a transportable caesium fountain [25] from the Observatoire de Paris and comparing their hydrogen transition frequency with the caesium reference at PTB via a 920 km fiber link [26]. An accuracy of about 4×10^{-15} has been obtained.

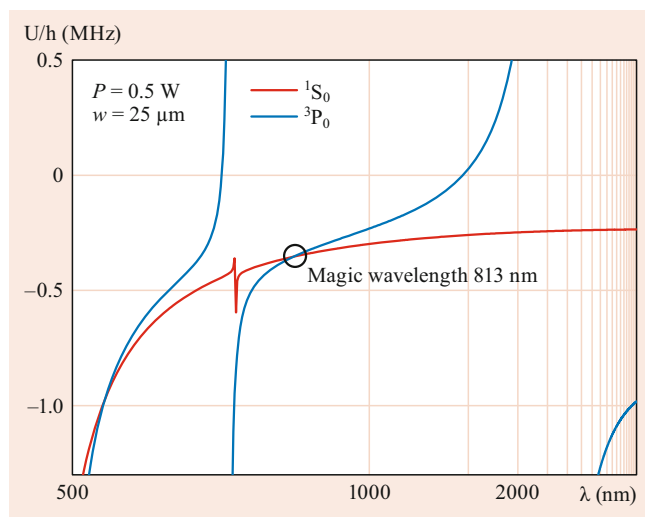


Fig. 30.3 Light shift of the $^1\text{S}_0$ ground state and $^3\text{P}_0$ first excited state of Sr as a function of wavelength. At the ‘magic’ wavelength of 813 nm both levels are shifted equally. Sr atoms in an optical lattice at this wavelength do not show a frequency shift for the $^1\text{S}_0 \rightarrow ^3\text{P}_0$ transition. Equivalent conditions can be found for reference transitions in other atoms

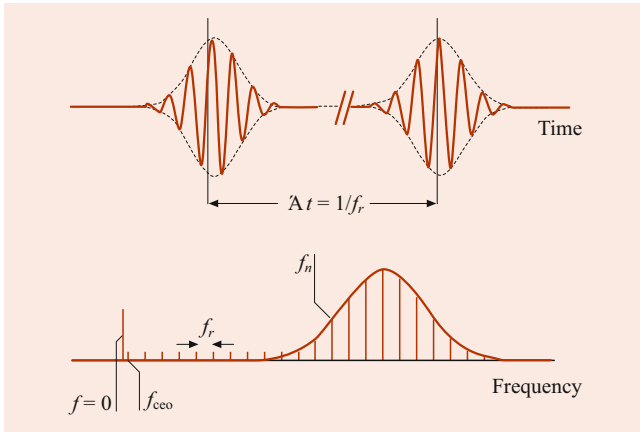


Fig. 30.4 Frequency comb generated from femtosecond laser pulses

30.1.5 Optical Frequency Measurements

An essential tool for the measurement of optical frequencies with respect to a Cs clock in the microwave range is the so-called femtosecond laser frequency comb generator [27]. Briefly, a mode-locked femtosecond laser produces, in the frequency domain, a comb of equally spaced optical frequencies f_n (Fig. 30.4) that can be written as $f_n = n f_r + f_{\text{ceo}}$ (with $f_{\text{ceo}} < f_r$), where f_r is the pulse repetition rate of the laser, the mode number n is a large integer (of order 10^5), and f_{ceo} (carrier-envelope-offset) is a shift of the whole comb that is produced by group velocity dispersion in the laser. The repetition rate f_r can easily be measured with a fast photodiode. In order to determine f_{ceo} , the comb is broadened in a non-linear medium, so that it covers at least one octave. Now, the second harmonic of mode n from the *red* wing of the spectrum, at frequency $2(n f_r + f_{\text{ceo}})$, can be mixed with mode $2n$ from the *blue* wing, at frequency $2n f_r + f_{\text{ceo}}$, and f_{ceo} is obtained as a difference frequency. In this way, the precise relation between the two microwave frequencies f_r and f_{ceo} , and the numerous optical frequencies f_n , is known. The setup can now be used for an absolute optical frequency measurement by referencing f_r and f_{ceo} to a microwave standard and recording the beat note between the optical frequency f_o to be measured and the closest comb frequency f_n . Vice versa, the setup may work as an optical clockwork, for example, by adjusting f_{ceo} to zero and by stabilizing one comb line f_n to f_o , so that f_r is now an exact subharmonic to order n of f_o . The precision of these transfer schemes has been investigated and was found to be so high that it will not limit the performance of optical clocks for the foreseeable future.

Since the most precise optical frequency standards are now more stable and reproducible than primary caesium clocks, it is important to be able to measure the ratio of two

Table 30.1 Accurately measured atomic transition frequencies and their fractional uncertainty ([9, 12] and references therein). These transitions have been used in evaluations of temporal variation of fundamental constants

Atom, transition	f (GHz)	u_r (10^{-15})	Ref.
H, Opt	2,466,061	14	[25, 26]
Al ⁺ , Opt	1,121,015	0.6	
Sr, Opt	429,228	0.4	
Rb, HFS	6.835	0.3	
Yb ⁺ , Opt E2	688,359	0.5	
Yb ⁺ , Opt E3	642,121	0.4	
Yb ⁺ , HFS	12.642	73	
Hg ⁺ , Opt	1,064,721	9	[14, 15]

optical transition frequencies without the use of a microwave reference. A frequency comb generator can be configured for this task, for example by referencing the optical beat notes and f_{ceo} to f_r . In this way, the dimensionless optical frequency ratio $f_1/f_2 = (n_1 + f_{o1}/f_r + f_{\text{ceo}}/f_r)/(n_2 + f_{o2}/f_r + f_{\text{ceo}}/f_r)$ can be measured to an accuracy that is only limited by the optical frequency standards. A number of such measurements have been performed. They will provide essential consistency checks for the developing system of optical frequency standards and build the basis for the most stringent laboratory tests for changes of the fine structure constant.

30.1.6 Limitations on Frequency Variations

A variety of frequency standards described above have been successfully developed and their accuracy has been improved dramatically. This progress, as a consequence, has led to certain constraints on the possible variations of the fundamental constants. Considering frequency variations, one has to have in mind that not only the numerical value but also the unit may vary. For this reason, one needs to deal with dimensionless quantities, which are unit independent. During the last decade, a number of transition frequencies were measured in the corresponding SI unit, the hertz (Table 30.1). These-dimensional results are actually related to dimensionless quantities since a frequency measurement in SI is a measurement with respect to the caesium hyperfine interval

$$\{f\} = 9,192,631,770 \frac{f}{f_{\text{HFS}}(\text{Cs})}, \quad (30.1)$$

where $\{f\}$ stands for the numerical value of the frequency f . (Most absolute frequency measurements have been realized as a direct comparison with a primary caesium standard.) In Sect. 30.3, in order to simplify notation, this symbol for the numerical value is dropped.

30.2 Atomic Spectra and Their Dependence on the Fundamental Constants

30.2.1 The Spectrum of Hydrogen and Nonrelativistic Atoms

The hydrogen atom is the simplest atom, and one can easily calculate the leading contribution to different kinds of transitions in its spectrum, such as the gross, fine, and hyperfine structure. The scaling behavior of these contributions with the values of the Rydberg constant R_∞ , the fine structure constant α , and the magnetic moments of proton and Bohr magneton is clear. The results for some typical hydrogenic transitions are

$$\begin{aligned} f(2p \rightarrow 1s) &\simeq \frac{3}{4} c R_\infty, \\ f(2p_{3/2} - 2p_{1/2}) &\simeq \frac{1}{16} \alpha^2 c R_\infty, \\ f_{\text{HFS}}(1s) &\simeq \frac{16}{3} \alpha^2 \frac{\mu_p}{\mu_B} c R_\infty. \end{aligned} \quad (30.2)$$

In the nonrelativistic approximation, the basic frequencies and the fine and hyperfine structure intervals of all atomic spectra have a similar dependence on the fundamental constants in Eq. (30.2)

$$\begin{aligned} f_{\text{gross structure}} &\propto c R_\infty, \\ f_{\text{fine structure}} &\propto \alpha^2 c R_\infty, \\ f_{\text{HFS}} &\propto \alpha^2 \frac{\mu}{\mu_B} c R_\infty, \end{aligned} \quad (30.3)$$

where μ stands for the nuclear magnetic moment. The presence of a few electrons and a nuclear charge of $Z \neq 1$ makes theory more complicated and introduces certain multiplicative numbers but involves no new parameters. The importance of this scaling for a search for the variations of the atomic constants was first pointed out in [28] and was applied to astrophysical data.

Similar results may be presented for molecular transitions (electronic, vibrational, rotational, and hyperfine) [29]

$$\begin{aligned} f_{\text{electronic}} &\propto c R_\infty, \\ f_{\text{vibrational}} &\propto (m_e/M)^{1/2} c R_\infty, \\ f_{\text{rotational}} &\propto (m_e/M) c R_\infty. \end{aligned} \quad (30.4)$$

Up to now, no laboratory measurement with molecules has been performed at a level of accuracy that is competitive with atomic transitions (e.g., Sect. 30.3.3). However, they have widely been used in a search for variations of constants in astrophysical observations (e.g., [30]).

Table 30.2 Magnetic moments and relativistic corrections for atoms involved in microwave standards. The relativistic sensitivity κ is defined in Sec. 30.2.3. Here, μ is an actual value of the nuclear magnetic moment, μ_N is the nuclear magneton, and μ_S stands for the Schmidt value of the nuclear magnetic moment; the nucleon g factors are $g_p/2 \simeq 2.79$ and $g_n/2 \simeq -1.91$

Z	Atom	μ/μ_N	μ_S/μ_N	μ/μ_S	κ
37	^{87}Rb	2.75	$g_p/2 + 1$	0.74	0.34
55	^{133}Cs	2.58	$7/18(10 - g_p)$	1.50	0.83
70	$^{171}\text{Yb}^+$	0.49	$-g_n/6$	0.77	1.5

30.2.2 Hyperfine Structure and the Schmidt Model

The atomic hyperfine structure

$$f_{\text{NR}}(\text{HFS}) = \text{const.} \alpha^2 \frac{\mu}{\mu_B} c R_\infty \quad (30.5)$$

involves nuclear magnetic moments μ , which are different for different nuclei; thus, a comparison of the constraints on the variations of nuclear magnetic moments has a reduced value. To compare them, one may apply the Schmidt model [2, 3, 31], which predicts all the magnetic moments of nuclei with an odd number of nucleons (odd value of atomic number A) in terms of the proton and neutron g -factors, g_p , and g_n , respectively, and the nuclear magneton only. Unfortunately, the uncertainty of the calculation within the Schmidt model is quite high (usually from 10 to 50%). The Schmidt model, being a kind of *ab initio* model, only allows for improvements that, unfortunately, involve more effective phenomenological parameters. This would not really improve the situation but return us to the case where there are too many possibly varying independent parameters. A comparison of the Schmidt values to the actual data is presented for caesium, rubidium, and ytterbium in Table 30.2. The measurements of the hyperfine intervals in those atoms supply us with the constraints on the variation of the nuclear magnetic moments.

30.2.3 Atomic Spectra: Relativistic Corrections

A theory based on the leading nonrelativistic approximation may not be accurate enough. Any atomic frequency can be presented as

$$f = f_{\text{NR}} F_{\text{rel}}(\alpha), \quad (30.6)$$

where the first (nonrelativistic) factor is determined by a scaling similar to the hydrogenic transitions in Eq. (30.3). The second factor stands for relativistic corrections that vanish at $\alpha = 0$; and thus, $F_{\text{rel}}(0) = 1$.

The importance of relativistic corrections for the hyperfine structure was first emphasized in [32]. Relativistic

many-body calculations for various transitions were performed in [33–38]. A typical accuracy is about 10%. Some results are summarized in Tables 30.2 and 30.3, where we list the relative sensitivity of the relativistic factors F_{rel} to changes in α ,

$$\kappa = \frac{\partial \ln F_{\text{rel}}}{\partial \ln \alpha}. \quad (30.7)$$

Note that the relativistic corrections in heavy atoms are proportional to $(Z\alpha)^2$ because of the singularity of relativistic operators. Due to this, the corrections rapidly increase with the nuclear charge Z .

The signs and magnitudes of κ are explained by a simple estimate of the relativistic correction. For example, an approximate expression for the relativistic correction factor for the hyperfine structure (Casimir factor) of an s -wave electron in an alkali-like atom is [32]

$$F_{\text{rel}}(\alpha) = \frac{1}{\sqrt{1 - (Z\alpha)^2}} \frac{1}{1 - (4/3)(Z\alpha)^2}.$$

The related integral for the matrix element of the hyperfine interaction rapidly converges in a vicinity of the nucleus, on the distance about a_B/Z , where a_B is the Bohr radius. The wave function of a valence electron at such distance is proportional to the Coulomb wave function with zero energy since the energy of valence electron is negligible there, and nuclear charge is not screened. That allows one to perform an analytical calculation.

A similar rough estimation for the energy levels may be performed for the gross structure

$$E = -\frac{(Z_a\alpha)^2 mc^2}{2n_*^2} \left(1 + \frac{(Z\alpha)^2}{n_*} \frac{1}{j + 1/2} \right). \quad (30.8)$$

Here, j is the electron angular momentum, n_* is the effective value of the principle quantum number (which determines the nonrelativistic energy of the electron), and Z_a is the charge *seen* by the valence electron – it is 1 for neutral atoms, 2 for singly charged ions, etc. This equation tells us that κ , for the excitation of the electron from the orbital j to the orbital j' , has a different sign for $j > j'$ and $j < j'$. The difference of sign between the sensitivities of the ytterbium and mercury transitions in Table 30.3 reflects the fact that in Yb^+ , a 6s-electron is excited to the empty 5d-shell, while in Hg^+ , a hole is created in the filled 5d-shell if the electron is excited to the 6s-shell.

Usually, the sensitivity is roughly of order of unity (Table 30.3). However, it may happen that it is greatly enhanced. One can rewrite the definition in Eq. (30.7) as

$$\kappa = \frac{\partial \ln(f/f_{\text{NR}})}{\partial \ln \alpha} = -\frac{\partial \ln f_{\text{NR}}}{\partial \ln \alpha} + \frac{1}{f} \frac{\partial f}{\partial \ln \alpha}. \quad (30.9)$$

Table 30.3 The frequencies of different transitions in neutral atoms and ions, applied or tried for precision spectroscopy, and their sensitivity to variations in α due to relativistic corrections

Atom, transition	κ
H, 1s – 2s	0.00
^{40}Ca , $^1\text{S}_0 - ^3\text{P}_1$	0.02
^{87}Sr , $^1\text{S}_0 - ^3\text{P}_0$	0.06
^{88}Sr , $^1\text{S}_0 - ^3\text{P}_0$	0.06
^{111}Cd , $^1\text{S}_0 - ^3\text{P}_0$	0.23
^{171}Yb , $^1\text{S}_0 - ^3\text{P}_0$	0.31
^{174}Yb , $^1\text{S}_0 - ^3\text{P}_0$	0.31
^{199}Hg , $^1\text{S}_0 - ^3\text{P}_0$	0.81
$^{27}\text{Al}^+$, $^1\text{S}_0 - ^3\text{P}_0$	0.01
$^{40}\text{Ca}^+$, $\text{S}_{1/2} - \text{D}_{5/2}$	0.15
$^{88}\text{Sr}^+$, $\text{S}_{1/2} - \text{D}_{5/2}$	0.43
$^{115}\text{In}^+$, $^1\text{S}_0 - ^3\text{P}_0$	0.18
$^{171}\text{Yb}^+$, $^2\text{S}_{1/2} - ^2\text{D}_{3/2}$	1.0
$^{171}\text{Yb}^+$, $\text{S}_{1/2} - \text{F}_{7/2}$	–6.0
$^{199}\text{Hg}^+$, $^2\text{S}_{1/2} - ^2\text{D}_{5/2}$	–2.9

The first term here is a standard one, while the second term may be enhanced if the frequency f is very small. In other words, if a certain frequency is a difference between two transitions that have different nonrelativistic quantum numbers (which means that the value of f_{NR} is not small) and has a [very] small value ($f \ll f_{\text{NR}}$), it may be enhanced. A small eventual value of the frequency means that there is an accidental cancelation between the nonrelativistic contribution and the relativistic correction, which depends differently on α . An example of such a transition is the one between two nearly degenerate states $4f^{10}5d6s$ and $4f^95d^26s$ in atomic dysprosium. The presence of a strong enhancement $\kappa \simeq 5.7 \times 10^8$ there was pointed out in [38]. The dysprosium transition was studied in [39, 40].

30.3 Laboratory Constraints on Temporal Variations of Fundamental Constants

Logarithmic derivatives in Eq. (30.7) appear since we are looking for a variation of the constants in relative units. In other words, we are interested in a determination of, e.g., $\Delta\alpha/\alpha\Delta t$, while the input data of interest are related to $\Delta f/f\Delta t$. Their relation takes the form

$$\frac{\partial \ln f}{\partial t} = \frac{\partial \ln f_{\text{NR}}}{\partial t} + \kappa \frac{\partial \ln \alpha}{\partial t}. \quad (30.10)$$

If one compares transitions of the same type – gross structure, fine structure – the first term cancels.

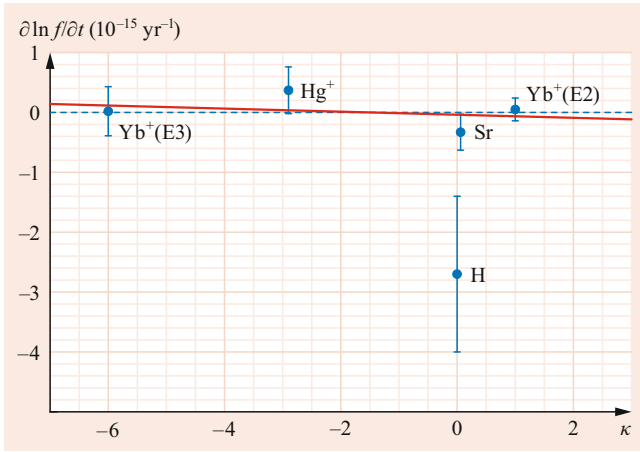


Fig. 30.5 Frequency variations versus their sensitivity κ following Eq. (30.11)

30.3.1 Constraints from Absolute and Relative Optical Measurements

Absolute frequency measurements offer the possibility to compare a number of optical transitions with frequencies f_{NR} , which scale as cR_{∞} , with the caesium hyperfine structure. One can rewrite Eq. (30.10) as

$$\frac{\partial \ln f_{\text{opt}}}{\partial t} = \frac{\partial \ln cR_{\infty}}{\partial t} + \kappa \frac{\partial \ln \alpha}{\partial t}, \quad (30.11)$$

where dimensional quantities, such as frequency and the Rydberg constant, are stated in SI units in Eq. (30.1). This equation may be used in different ways. For example, in Fig. 30.5, we plot experimental data for $\partial \ln f_{\text{opt}}/\partial t$ as a function of the sensitivity κ and derive a model-independent constraint on the variation of the fine structure constant and the numerical value of the Rydberg frequency cR_{∞} in the SI unit of hertz. The latter is of great metrological importance, being related to a common drift of optical clocks with respect to a caesium clock, i.e., to the definition of the SI second. The SI definition of the meter is impractical and so, in practice, the optical wavelengths of reference lines calibrated against the caesium standard are used to determine the SI meter [9].

Equation (30.11) allows us a simple graphic interpretation (Fig. 30.5). The data around $\kappa = 0$ are those, whose frequencies are well described by nonrelativistic formulas and have a low sensitivity to α variation.

A direct comparison of two optical frequencies allows us a model-independent constraint on a variation of the fine structure constant α , which for relative optical measurements is given by

$$\frac{d \ln(f_1/f_2)}{dt} = \frac{(\kappa_1 - \kappa_2)d \ln \alpha}{dt}. \quad (30.12)$$

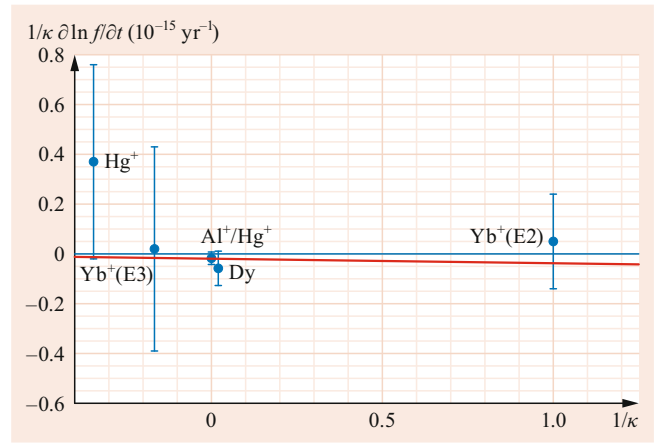


Fig. 30.6 Frequency variations versus their sensitivity κ following Eq. (30.14): value of $\partial \ln f_{\text{opt}}/\partial t/\kappa$ as function of $1/\kappa$

Progress with relative optical frequency measurements [14, 15], comparing the transitions in a mercury ion and an ion of aluminum, delivers the constraints on α variation

$$\frac{\partial \ln \alpha}{\partial t} = (-1.7 \pm 2.5) \times 10^{-17} \text{yr}^{-1}. \quad (30.13)$$

This relative-measurement result, which contributes the dominant constraint on the α variation, cannot be presented in such a plot as in Fig. 30.5 since the disappearance of the cR_{∞} term makes the result equivalent to the result for an infinite value of the overall sensitivity in the terms of Eq. (30.11).

There is an alternative equation,

$$\frac{1}{\kappa} \frac{\partial \ln f_{\text{opt}}}{\partial t} = \frac{1}{\kappa} \frac{\partial \ln cR_{\infty}}{\partial t} + \frac{\partial \ln \alpha}{\partial t}, \quad (30.14)$$

which can be applied for a graphic presentation. In Fig. 30.6, the intercept at $1/\kappa = 0$ is the α constraint, while the slope reflects the variation of cR_{∞} .

To plot all the data we have to use a two-dimensional plot (see below). The constraints on the variations of α and cR_{∞} are correlated, and the standard uncertainty ellipse, defined as

$$\sum_i \frac{1}{u_i^2} \left(\frac{\partial \ln f_i}{\partial t} - \frac{\partial \ln R_{\infty}}{\partial t} - \kappa_i \frac{\partial \ln \alpha}{\partial t} \right)^2 = 1 + \chi_{\text{min}}^2,$$

is presented in Fig. 30.7. Here, we sum over all available data: $\partial(\ln f_i)/\partial t$ is the central value of the observed drift rate, u_i its 1σ uncertainty, and χ_{min}^2 the minimized χ^2 of the fit. The results of the fit are presented in Table 30.4.

The progress in the constraint on the time variation of the fine structure constant and of the numerical value of the Rydberg constant is summarized in Table 30.5.

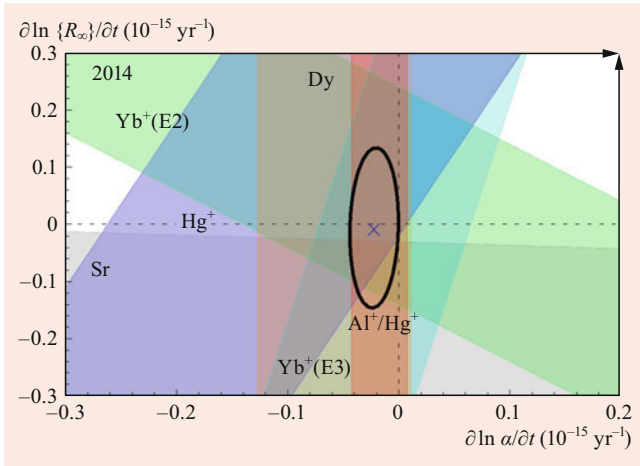


Fig. 30.7 Constraints on the time variations of the fine structure constant α and the numerical value of the Rydberg constant (from [41])

Table 30.4 Model-independent laboratory constraints on the possible time variations of natural constants [41, 42]

X	$\partial \ln X / \partial t$
α	$-0.022(22) \times 10^{-15} \text{ yr}^{-1}$
$\{cR_\infty\}$	$-0.01(14) \times 10^{-15} \text{ yr}^{-1}$
$\mu_{\text{Cs}}/\mu_{\text{B}}$	$0.07(16) \times 10^{-15} \text{ yr}^{-1}$
$\mu_{\text{Rb}}/\mu_{\text{Cs}}$	$-0.15(9) \times 10^{-15} \text{ yr}^{-1}$
$\mu_{\text{Yb}}/\mu_{\text{Cs}}$	$(3 \pm 3) \times 10^{-14} \text{ yr}^{-1}$

Table 30.5 Progress in constraining a possible time variation of the fundamental constants: the results of 2004 (following [43, 44]), 2008 (following [45]), and of 2014 using data summarized in [42] but following [43, 44] (see [41] for details). Here, ρ is the correlation coefficient $\rho(\partial \ln \alpha / \partial t, \partial \ln \{R_\infty\} / \partial t)$

Year	$\partial \ln \alpha / \partial t$ (10^{-15} yr^{-1})	$\partial \ln \{R_\infty\} / \partial t$ (10^{-15} yr^{-1})	ρ
2004	$-0.4(2.0)$	$-1.5(3.2)$	0.13
2008	$-0.018(23)$	$0.20(37)$	0.17
2014	$-0.022(22)$	$-0.01(14)$	0.08

The numerical value of the Rydberg constant, from the point of view of fundamental physics, can be expressed in terms of the caesium hyperfine interval in atomic units, and its variation may be expressed in terms of the variations of α and $\mu_{\text{Cs}}/\mu_{\text{B}}$. A constraint for the latter is presented in Table 30.4. Because of that, there is also an alternative parameterization applied for the 2D constraint. It is based on the relation

$$\frac{\partial \ln cR_\infty}{\partial t} = \frac{\partial \ln(\mu_{\text{Cs}}/\mu_{\text{e}})}{\partial t} + (\kappa + 2.83) \frac{\partial \ln \alpha}{\partial t}. \quad (30.15)$$

To compare the results of two equivalent evaluations one has to remember the correlations in the results for the fitting parameters (Table 30.5). The correlation is unimportant for the central values but affects the uncertainty of the outcome.

We have also to mention a ‘nonclock’ constraint on the α variation obtained from the study of the dysprosium atom on a determination of the splitting between the $4f^{10}5d\ 6s$ and $4f^95d^2\ 6s$ states. The most recent Dy constraint is [40]

$$\frac{\partial \ln(\alpha)}{\partial t} = (-0.6 \pm 0.7) \times 10^{-16} \text{ yr}^{-1}.$$

30.3.2 Constraints from Microwave Clocks

A model-independent comparison of different HFS transitions is not simple because their nonrelativistic contributions f_{NR} are not the same but involve different magnetic moments. Applying Eq. (30.15) to experimental data, one can obtain constraints on the relative variations of the magnetic moments of Rb, Cs, and Yb (Table 30.4).

30.3.3 A Model-Independent Constraint on the Variation of the Electron-to-Proton Mass Ratio from Molecular Spectroscopy

Vibrational and rotational spectroscopy of molecules provide direct access to transition frequencies that depend on the electronic to nuclear mass ratio. Precision measurements have been performed with two-photon Ramsey spectroscopy of a rovibrational transition in a supersonic beam of SF_6 . A relative uncertainty of 2.8×10^{-14} has been obtained for the transition frequency at 28.4 THz, and from a sequence of measurements against a primary Cs clock spanning about 2 years, a limit on the temporal variation of the proton to electron mass ratio has been derived [46]

$$\frac{\partial \ln(m_{\text{p}}/m_{\text{e}})}{\partial t} = (-3.8 \pm 5.6) \times 10^{-14} \text{ yr}^{-1}.$$

This result makes use of the more stringent limit on a variation of the Cs magnetic moment, obtaining essentially a model-independent constraint on a change of $m_{\text{p}}/m_{\text{e}}$.

30.3.4 Other Model-Dependent Constraints

In order to gain information on constants more fundamental than the nuclear magnetic moments, any further evaluation of the experimental data should consider the model. Here, we apply the Schmidt model, which is far from perfect. It is an *ab initio* model, but its accuracy for any individual case is unclear. The model-dependent constraints obtained by exploiting the Schmidt model are summarized in Table 30.6.

The nucleon g factors, in turn, depend on a dimensionless fundamental constant $m_{\text{q}}/\Lambda_{\text{QCD}}$, where m_{q} is the quark mass, and Λ_{QCD} is the quantum chromodynamic (QCD) scale. A study of this dependence may supply us with deep

Table 30.6 Model-dependent laboratory constraints on possible time variations of fundamental constants. The uncertainties here do not include uncertainties from the application of the Schmidt model

X	$\partial \ln X / \partial t$
m_e/m_p	$-0.02(16) \times 10^{-15} \text{ yr}^{-1}$
μ_p/μ_e	$-0.08(16) \times 10^{-15} \text{ yr}^{-1}$
g_p	$-0.07(5) \times 10^{-15} \text{ yr}^{-1}$
g_n	$(3 \pm 3) \times 10^{-14} \text{ yr}^{-1}$

insight into the possible variations of the more fundamental properties of Nature (see [33, 34] for details). This approach is promising, but its accuracy needs to be better understood. Following the model suggested in [47, 48], the constraint on the variation of the proton-to-electron mass ratio reads [42]

$$\frac{\partial \ln(m_p/m_e)}{\partial t} = (-0.5 \pm 1.6) \times 10^{-16} \text{ yr}^{-1}.$$

30.4 Summary

The results collected in Tables 30.4 and 30.6 are competitive with or even more sensitive than data from other searches and have a more reliable interpretation. The results from astrophysical searches and the study of the samarium resonance from Oklo data (e.g., [4, 5]) possess sensitivity over extended time scales; however, they are more difficult to interpret. We have, for example, not assumed any hierarchy in variation rates or that some constants stay fixed while others vary, as it is done in the study of the position of the Oklo resonance. The evaluation presented here is transparent, and any particular calculation or measurement can be checked. In contrast, the astrophysical data show significant results only after an intensive statistical evaluation.

The laboratory searches involving atomic clocks have definitely shown progress, and a further increase in the accuracy of these clocks can be expected, as well as an increase in the number of different kinds of frequency standards (e.g., optical Sr, Sr⁺, Yb, Yb⁺, Hg standards are being tried). Systems of enhanced sensitivity have been identified, for example in highly charged ions [49], and experiments for their study are under development. An optical clock based on a nuclear transition in Th-229 is also under consideration [50, 51]. Such a clock would offer different sensitivity to systematic effects, as well as to variations of different fundamental constants [52].

Laboratory searches are not necessarily limited to experiments with metrological accuracy. An example of a high-sensitivity search with a relatively low accuracy is the study of the dysprosium atom for a determination of the splitting between the 4f¹⁰5d 6s and 4f⁹5d²6s states, which offers a great sensitivity value of $\kappa \simeq 5.7 \times 10^8$ [38].

Variations of constants on the cosmological time scale can be expected, but the magnitude, as well as other details, are

unclear. Because of a broad range of options there is a need for the development of as many different searches as possible, and the laboratory search for variations is an attractive opportunity to open up a way that could lead to new physics.

Precision frequency measurements with or without the use of clocks are the most accurate among the other measurements. They are used not only to constrain the variation of the values of the constants but also on some other possible effects of new physics, ranging from the violation of Lorentz invariance to modified fundamental theories, opening a window of opportunities for new physics [49].

Acknowledgements The authors are very grateful to their colleagues and to participants of the ACFC-2003, 2007, 2011, and 2015 meetings for useful and stimulating discussions. The work of SGK was in part supported by DFG (under grant # KA 4645/1-1). The authors are grateful to V.A. Dzuba and, V.G. Ivanov for useful and stimulating discussions.

References

- Mohr, P.J., Newell, D.B., Taylor, B.N.: Rev. Mod. Phys. **88**, 035009 (2016)
- Karshenboim, S.G.: Time and space variation of fundamental constants: motivation and laboratory search. In: Bigi, I.I., Faessler, M. (eds.) Time and Matter, p. 26. World Scientific, New Jersey, London, Singapore, Shanghai, Taipei, Chennai (2006)
- Karshenboim, S.G.: Gen. Rel. Grav. **38**, 159 (2006)
- Karshenboim, S.G., Peik, E. (eds.): Astrophysics, Clocks and Fundamental Constants. Lect. Notes in Phys., vol. 648. Springer, Berlin, Heidelberg (2004)
- S. G. Karshenboim, E. Peik (Eds.) Atomic Clocks and Fundamental Constants, Eur. Phys. J. Special Topics **163** (2008). Special issue
- Ramsey, N.F.: Rev. Mod. Phys. **62**, 541 (1990)
- Bauch, A., Telle, H.R.: Rep. Prog. Phys. **65**, 789 (2002)
- Wynands, R., Weyers, S.: Metrologia **42**, 64 (2005)
- Riehle, F., Gill, P., Arias, F., Robertsson, L.: Metrologia **55**, 188 (2018)
- Paul, W.: Rev. Mod. Phys. **62**, 531 (1990)
- Dehmelt, H.: IEEE Trans. Instrum. Meas. **31**, 83 (1982)
- Ludlow, A.D., Ye, M.M.B.J., Peik, E., Schmidt, P.O.: Rev. Mod. Phys. **87**, 637 (2015)
- Stenger, J., Tamm, C., Haverkamp, N., Weyers, S., Telle, H.R.: Opt. Lett. **26**, 1589 (2001)
- Udem, T., Diddams, S.A., Vogel, K.R., Oates, C.W., Curtis, E.A., Lee, W.D., Itano, W.M., Drullinger, R.E., Bergquist, J.C., Hollberg, L.: Phys. Rev. Lett. **86**, 4996 (2001)
- Bize, S., Diddams, S.A., Tanaka, U., Tanner, C.E., Oskay, W.H., Drullinger, R.E., Parker, T.E., Heavner, T.P., Jefferts, S.R., Hollberg, L., Itano, W.M., Wineland, D.J., Bergquist, J.C.: Phys. Rev. Lett. **90**, 150802 (2003)
- Huntemann, N., Okhapkin, M.V., Lipphardt, B., Tamm, C., Peik, E.: Phys. Rev. Lett. **108**, 090801 (2012)
- Fisk, P.T.H., Sellars, M.J., Lawn, M.A., Coles, C.: IEEE Trans. UFFC **44**, 344 (1997)
- Fisk, P.T.: Rep. Prog. Phys. **60**, 761 (1997)
- Warrington, R.B., Fisk, P.T.H., Wouters, M.J., Lawn, M.A.: Proceedings of the 6th Symposium Frequency Standards and Metrology. World Scientific, Singapore, p 297 (2002)
- Bordé, C.J.: Phys. Lett. A. **140**, 10 (1989)

21. Wilpers, G., Binnewies, T., Degenhardt, C., Sterr, U., Helmcke, J., Riehle, F.: *Phys. Rev. Lett.* **89**, 230801 (2002)
22. Riehle, F., Degenhardt, C., Lisdat, C., Wilpers, G., Schnatz, H., Binnewies, T., Stoehr, H., Sterr, U.: An optical frequency standard with cold and ultra-cold calcium atoms. In: Karshenboim, S.G., Peik, E. (eds.) *Astrophysics, Clocks and Fundamental Constants Lect. Notes in Phys.*, vol. 648, p. 229. Springer, Berlin, Heidelberg (2004)
23. Katori, H., Takamoto, M., Pal'chikov, V.G., Ovsiannikov, V.D.: *Phys. Rev. Lett.* **91**, 173005 (2003)
24. Jun Ye, Kimble, H.J., Katori, H.: *Science* **320**, 1734 (2008)
25. Parthey, C.G., Matveev, A., Alnis, J., Bernhardt, B., Beyer, A., Holzwarth, R., Maistrou, A., Pohl, R., Predehl, K., Udem, T., Wilken, T., Kolachevsky, N., Abgrall, M., Rovera, D., Salomon, C., Laurent, P., Hänsch, T.W.: *Phys. Rev. Lett.* **107**, 203001 (2011)
26. Matveev, A., Parthey, C.G., Predehl, K., Alnis, J., Beyer, A., Holzwarth, R., Udem, T., Wilken, T., Kolachevsky, N., Abgrall, M., Rovera, D., Salomon, C., Laurent, P., Grosche, G., Terra, O., Legero, T., Schnatz, H., Weyers, S., Altschul, B., Hänsch, T.W.: *Phys. Rev. Lett.* **110**, 230801 (2013)
27. Udem, T., Reichert, J., Holzwarth, R., Diddams, S., Jones, D., Ye, J., Cundiff, S.: T. W. H. nsch, J. Hall: A new type of frequency chain and its application to fundamental frequency metrology. In: Karshenboim, S.G., Pavone, F.S., Bassani, F., Inguscio, M., Hänsch, T.W. (eds.) *The Hydrogen Atom: Precision Physics of Simple Atomic Systems Lect. Notes in Phys.*, vol. 570, p. 229. Springer, Berlin, Heidelberg (2001)
28. Savedoff, M.P.: *Nature* **178**, 688 (1956)
29. Thompson, R.I.: *Astrophys. Lett.* **16**, 3 (1975)
30. Varshalovich, D.A., Ivanchik, A.V., Orlov, A.V., Potekhin, A.Y., Petitjean, P.: Current status of the problem of cosmological variability of fundamental physical constants. In: Karshenboim, S.G., Smirnov, V.B. (eds.) *Precision Physics of Simple Atomic Systems Lect. Notes in Phys.*, vol. 627, p. 199. Springer, Berlin, Heidelberg (2003)
31. Karshenboim, S.G.: *Can. J. Phys.* **78**, 639 (2000)
32. Prestage, J.D., Tjoelker, R.L., Maleki, L.: *Phys. Rev. Lett.* **74**, 3511 (1995)
33. Flambaum, V.V.: Limits on temporal variation of fine structure constant, quark masses and strong interaction from atomic clock experiments. In: Hannaford, P., Sidorov, A., Bachor, H., Baldwin, K. (eds.) *Laser Spectroscopy*, p. 49. World Scientific, New Jersey, London, Singapore, Shanghai, Taipei, Chennai (2004)
34. Flambaum, V.V., Leinweber, L.B., Thomas, A.W., Young, R.D.: *Phys. Rev.* **69**, 115006 (2004)
35. Dzuba, V.A., Flambaum, V.V., Webb, J.K.: *Phys. Rev. Lett.* **82**, 888 (1999)
36. Dzuba, V.A., Flambaum, V.V., Webb, J.K.: *Phys. Rev. A* **59**, 230 (1999)
37. Dzuba, V.A., Flambaum, V.V.: *Phys. Rev. A* **61**, 034502 (2001)
38. Dzuba, V.A., Flambaum, V.V., Marchenko, M.V.: *Phys. Rev. A* **68**, 022506 (2003)
39. Cingöz, A., Lapierre, A., Nguyen, A.-T., Leefer, N., Budker, D., Lamoreaux, S.K., Torgerson, J.R.: *Phys. Rev. Lett.* **98**, 040801 (2007)
40. Leefer, N., Weber, C.T.M., Cing z, A., Torgerson, J.R., Budker, D.: *Phys. Rev. Lett.* **111**, 060801 (2013)
41. Karshenboim, S.G., Ivanov, V.G.: *Appl. Phys. B.* **123**, 18 (2017)
42. Huntemann, N., Lipphardt, B., Tamm, C., Gerginov, V., Weyers, S., Peik, E.: *Phys. Rev. Lett.* **113**, 210802 (2014)
43. Peik, E., Lipphardt, B., Schnatz, H., Schneider, T., Tamm, Chr., Karshenboim, S.G.: *Phys. Rev. Lett.* **93**, 170801 (2004)
44. Karshenboim, S.G., Flambaum, V.V., Peik, E.: In: Drake, G.W.F. (ed.) *Springer Handbook of Atomic, Molecular and Optical*

- Physics*, p. 455. Springer, NY (2005). (That is the same chapter but in the previous edition of the Handbook.)
45. Karshenboim, S.G., Peik, E.: *Eur. Phys. J. Special Top.* **163**, 1 (2008)
46. Shelkownikov, A., Butcher, R.J., Chardonnet, C., Amy-Klein, A.: *Phys. Rev. Lett.* **100**, 150801 (2008)
47. Flambaum, V.V., Tedesco, A.F.: *Phys. Rev. C* **73**, 055501 (2006)
48. Dinh, T.H., Dunning, A., Dzuba, V.A., Flambaum, V.V.: *Phys. Rev. A* **79**, 054102 (2009)
49. Safronova, M.S., Budker, D., DeMille, D., Kimball, D.F.J., Derevianko, A., Clark, C.W.: *Rev. Mod. Phys.* **90**, 025008 (2018)
50. Peik, E., Tamm, C.: *Europhys. Lett.* **61**, 181 (2003)
51. Peik, E., Okhapkin, M.: *C. R. Phys.* **16**, 516 (2015)
52. Berengut, J.C., Dzuba, V.A., Flambaum, V.V., Porsev, S.G.: *Phys. Rev. Lett.* **102**, 210801 (2009)



Savely G. Karshenboim Dr Savely G. Karshenboim graduated in 1983 from St. Petersburg (then Leningrad) State University, from where he also received his PhD (1992) and DSc (1999). He was with D.I. Mendeleev Institute for Metrology, Max-Planck-Institut für Quantenoptik (Garching), and Pulkovo Observatory. He is currently with Ludwig-Maximilians-Universität München. His scientific interests include precision physics of simple atoms, quantum electrodynamics, determination of fundamental constants, and the search for their variations.



Victor Flambaum Dr Victor Flambaum is a Professor of Physics and holds a Chair of Theoretical Physics. PhD, DSc from the Institute of Nuclear Physics, Novosibirsk, Russia. He has about 400 publications in atomic, nuclear, particle, solid state, statistical physics, general relativity and astrophysics including works on violation of fundamental symmetries (parity, time reversal, Lorentz), test of unification theories, temporal and spatial variation of fundamental constants from Big Bang to present, many-body theory and high precision atomic calculations, as well as statistical theory of finite chaotic Fermi systems and enhancement of weak interactions.



Ekkehard Peik Dr Ekkehard Peik is Head of the Time and Frequency Department at PTB in Braunschweig. His research interests are in the fields of optical clocks with laser-cooled and trapped ions, precision laser spectroscopy, the low-energy nuclear isomer of Th-229, the metrology of time and frequency, and tests of fundamental physics with atomic clocks.



Searches for New Particles Including Dark Matter with Atomic, Molecular, and Optical Systems

31

Victor Flambaum and Yevgeny Stadnik

Contents

31.1	Nongravitational Interactions of Spinless Bosons . . .	462
31.2	New Forces	462
31.2.1	Macroscopic-Scale Experiments	463
31.2.2	Atomic-Scale Experiments	463
31.3	Laboratory Sources	464
31.4	Astrophysical Sources	465
31.5	Cosmological Sources	466
31.5.1	Haloscope Experiments	466
31.5.2	Spin-Precession Experiments	466
31.5.3	Time-Varying Physical Constants	467
	References	467

scales. The nature of these effects depends on the specific particles and their nongravitational interactions. In this chapter, we give a brief overview of how atomic, molecular, and optical systems can be used to search for new particles. To illustrate the basic principles behind these methods, we focus on the simplest class of particles, namely new spinless bosons.

Keywords

dark matter · astrophysics · axion · fundamental constants · electric dipole moment · clock spectroscopy · laser · cavity · interferometry · magnetometry

Abstract

The “standard model” of physics has been successful in explaining most physical processes and phenomena that we see around us. However, despite the great success of the standard model, there remain a number of unresolved puzzles within the model, as well as questions about the self-consistency of the framework. Additionally, various independent astrophysical and cosmological observations contradicting the predictions of the standard model have been accumulating over the course of the past century. Many of these puzzles and unexpected observations can be elegantly explained by postulating the existence of at least one new particle or field outside of the present standard model.

New particles can manifest their effects in many settings, ranging from effects on subatomic to galactic length

The “standard model” of particle physics at present provides the most fundamental framework for understanding the basic building blocks of matter and describing various known interactions between these building blocks. The standard model does incredibly well in describing physical processes and phenomena that take place over a very broad range of energies and length scales, from explaining the binding of the constituents of atoms to understanding the formation and evolution of stars.

However, numerous astrophysical and cosmological observations that cannot be explained by the standard model have been accumulating over the course of the past century. Observations of stellar orbits about the galactic center from as early as the 1930s indicate the presence of a nonbaryonic matter component that is traditionally termed “dark matter” (this nonbaryonic matter component does not appreciably emit or absorb electromagnetic radiation) [1]. Further astrophysical evidence for dark matter comes from measurements of angular fluctuations in the cosmic microwave background spectrum [2] and the need for nonbaryonic matter to explain the observed structure formation in our universe [1]. Additionally, distance and redshift measurements of supernovae show that the expansion of the universe is accelerating, indicating that the universe is being pushed apart by a repulsive

V. Flambaum (✉)
Dept. of Physics, University of New South Wales
Sydney, Australia
e-mail: v.flambaum@unsw.edu.au

Y. Stadnik
School of Physics, The University of Sydney
Sydney, Australia
e-mail: yevgenystadnik@gmail.com

force associated with a “dark energy” component [3]. These dark components (which are naturally explained by postulating the existence of at least one new particle or field) overwhelmingly dominate the observed matter-energy content of our universe, with ordinary baryonic matter making up only a small fraction of the total content [2].

Another profound mystery is the observed predominance of matter over antimatter in our universe—the problem of baryogenesis. The standard model contains the necessary ingredients to produce ever slightly more matter than antimatter; however, the observed predominance of matter over antimatter in our universe is much larger than can be accommodated within the standard model [4]. One of the key ingredients for baryogenesis is CP violation, which is the violation of the product of the charge parity ($C =$ exchange of particles and antiparticles) and parity ($P =$ inversion of spatial coordinates) symmetries. Additional sources of CP violation necessary to explain baryogenesis may come from new particles possessing CP -violating interactions with ordinary matter. Intriguingly, practically no CP violation has been observed in strong processes in the standard model (compared with the relatively large amount of CP violation in weak processes). This puzzling observation—termed the “strong CP problem”—is most elegantly explained by postulating the existence of a new low-mass feebly-interacting spinless boson called the axion [5].

In order to corroborate or refute models that claim to explain the above problems and observations via putative new particles, one needs experimental probes for such particles. New particles may arise in several different settings:

- (1) As mediators of new interactions between particles or bodies (Sect. 31.2)
- (2) Produced in laboratories or colliders (Sect. 31.3)
- (3) Produced in stars and astrophysical processes (Sect. 31.4)
- (4) Constitute the observed dark matter or dark energy (Sect. 31.5).

Atomic, molecular, and optical systems lie at the heart of some of the highest precision measurements currently available. Optical clocks, which measure transition frequencies in atoms and ions, have demonstrated a fractional precision at the level $\approx 10^{-18}$ [6, 7]. Optical magnetometers, which measure magnetic fields using atoms, have demonstrated a magnetic field sensitivity at the level $\approx 10^{-15}$ T Hz $^{-1/2}$ [8]. Laser interferometers (which have directly detected gravitational waves) have demonstrated an equivalent sensitivity to length fluctuations at the level $\approx 10^{-23}$ Hz $^{-1/2}$ [9].

Can these extraordinary levels of precision and sensitivity be leveraged to search for new particles? The answer to this question is in the affirmative. Indeed, new particles arising in all types of settings described above can be sought for with experiments using atomic, molecular, and optical systems. In this chapter, we present a brief overview of how this can

be done, focusing mainly on new spinless bosons (which are the simplest possibility from the theoretical point of view) to help illustrate the basic principles behind the methods. We begin by presenting the simplest possible nongravitational interactions of spinless bosons with ordinary matter (Sect. 31.1). We then explain how atomic, molecular, and optical systems can be used to search for spinless bosons possessing nongravitational interactions in a broad variety of settings (Sects. 31.2–31.5). Unless explicitly stated otherwise, we adopt the natural units $\hbar = c = 1$ in this chapter.

31.1 Nongravitational Interactions of Spinless Bosons

The possible nongravitational interactions of spinless bosons can be broadly distinguished on the basis of the parity symmetry (behavior under the inversion of spatial coordinates). The most relevant scalar-type (even-parity) interactions of a spinless boson ϕ with ordinary matter are:

$$\mathcal{L}_{\text{scalar}}^{\text{lin.}} = \frac{g_{\gamma}^s}{4} \phi F_{\mu\nu} F^{\mu\nu} - \phi \sum_{\psi} g_{\psi}^s \bar{\psi} \psi, \quad (31.1)$$

$$\mathcal{L}_{\text{scalar}}^{\text{quad.}} = \frac{h_{\gamma}^s}{4} \phi^2 F_{\mu\nu} F^{\mu\nu} - \phi^2 \sum_{\psi} h_{\psi}^s \bar{\psi} \psi, \quad (31.2)$$

where the first term represents the interaction of the spinless boson with the electromagnetic field tensor F , and the second term represents the interaction of the spinless boson with a fermion field ψ , with $\bar{\psi} = \psi^{\dagger} \gamma^0$ the Dirac adjoint. Here, $g_{\gamma,\psi}^s$ and $h_{\gamma,\psi}^s$ are parameters that determine the relevant nongravitational interaction strengths.

The most relevant pseudoscalar-type (odd-parity) interactions of a spinless boson ϕ with ordinary matter are:

$$\begin{aligned} \mathcal{L}_{\text{pseudoscalar}} = & \frac{g_{\gamma}^p}{4} \phi F_{\mu\nu} \tilde{F}^{\mu\nu} + \frac{g_{\mathcal{G}}^p}{4} \phi G_{\mu\nu} \tilde{G}^{\mu\nu} \\ & - i \phi \sum_{\psi} g_{\psi}^p \bar{\psi} \gamma_5 \psi, \end{aligned} \quad (31.3)$$

where the first term represents the interaction of the spinless boson with the electromagnetic field tensor F , with \tilde{F} the dual field tensor, the second term represents the interaction of the spinless boson with the gluonic field tensor G , and the third term represents the interaction of the spinless boson with a fermion field ψ . Here, $g_{\gamma,g,\psi}^p$ are parameters that determine the relevant nongravitational interaction strengths.

31.2 New Forces

In the presence of the nongravitational interactions in Eqs. (31.1)–(31.3), new forces can be mediated between particles or bodies via the exchange of spinless boson(s). The

simplest possibility involves the exchange of a single boson between two fermions in the presence of the linear-in- ϕ interactions in the last terms of Eqs. (31.1) and (31.3). In this case, there are three distinct potentials that arise from the permutation of the two vertex types. In the nonrelativistic limit, these potentials take the following form [10, 11]:

$$V_{ss}(\mathbf{r}) = -g_1^s g_2^s \frac{e^{-m_\phi r}}{4\pi r}, \quad (31.4)$$

$$V_{ps}(\mathbf{r}) = +g_1^p g_2^s \boldsymbol{\sigma}_1 \cdot \hat{\mathbf{r}} \left(\frac{1}{r^2} + \frac{m_\phi}{r} \right) \frac{e^{-m_\phi r}}{8\pi m_1}, \quad (31.5)$$

$$V_{pp}(\mathbf{r}) = -\frac{g_1^p g_2^p}{4} \left\{ \boldsymbol{\sigma}_1 \cdot \boldsymbol{\sigma}_2 \left[\frac{1}{r^3} + \frac{m_\phi}{r^2} + \frac{4\pi}{3} \delta(\mathbf{r}) \right] - (\boldsymbol{\sigma}_1 \cdot \hat{\mathbf{r}})(\boldsymbol{\sigma}_2 \cdot \hat{\mathbf{r}}) \left[\frac{3}{r^3} + \frac{3m_\phi}{r^2} + \frac{m_\phi^2}{r} \right] \right\} \times \frac{e^{-m_\phi r}}{4\pi m_1 m_2}. \quad (31.6)$$

Here, m_ϕ is the mass of the exchanged boson, $\boldsymbol{\sigma}_1$ and $\boldsymbol{\sigma}_2$ denote the Pauli spin matrix vectors of the two fermions, $\hat{\mathbf{r}}$ is the unit vector directed from fermion 2 to fermion 1, and r is the distance between the two fermions. In Eq. (31.5), the cross term (obtained by permuting the particle indices $1 \leftrightarrow 2$) is implicit.

Other relatively common potentials include the potential mediated by the exchange of a single boson between two bodies with nonzero electromagnetic energies in the presence of the linear-in- ϕ interaction in the first term of Eq. (31.1) [12], the potential mediated by the exchange of a pair of bosons between two fermions in the presence of the quadratic-in- ϕ interactions in the last term of Eq. (31.2) [13], and the potential mediated by the exchange of a pair of fermions (including neutrinos) between two particles [14]. In the limit when the mass of the exchanged particles is small, these potentials scale as $V(r) \propto 1/r$, $V(r) \propto 1/r^3$ and $V(r) \propto 1/r^5$, respectively.

31.2.1 Macroscopic-Scale Experiments

When the condition $m_\phi \ll 1/r$ is satisfied, the potentials in Eqs. (31.4)–(31.6) can be treated as long-range (since the exponential terms reduce to $e^{-m_\phi r} \approx 1$ when $m_\phi r \ll 1$). Experiments performed on macroscopic length scales provide an excellent way of probing these new interactions. These types of experiments employ a massive body, such as the Sun, Earth, Moon, or a massive object in the laboratory, which functions as the source of new bosons. In order to detect effects associated with the anomalous interactions mediated by these bosons, a high-precision detector is required. Various methods can be used to search for new spin-independent forces in macroscopic-scale experiments:

- (1) Torsion pendula to search for anomalous torques [17–20]
- (2) Atom interferometers to search for anomalous accelerations [21, 24]
- (3) Atomic clocks and other spectroscopy-based measurements to search for anomalous frequency shifts [12, 25, 26].

The first two types of methods involve measurements of vector quantities, namely differences of torques and accelerations, respectively, of two different test bodies, while the third method involves measuring a scalar quantity, namely the difference in the ratio of two transition frequencies at two different distances from a massive body. We mention that lunar laser ranging measurements can also be used to search for spin-independent anomalous interactions [27].

Various methods can be used to search for new spin-dependent forces in macroscopic-scale experiments:

- (4) Torsion pendula to search for anomalous torques [28, 29]
- (5) Magnetometers to search for anomalous spin-precession effects [30–38].

Current limits from macroscopic-scale experiments on several types of nongravitational interactions of spinless bosons are shown in Figs. 31.1–31.3.

31.2.2 Atomic-Scale Experiments

Compared with the macroscopic-scale experiments discussed in Sect. 31.2.1, the condition $m_\phi \ll 1/r$ holds up to much larger boson masses when a boson is exchanged between the constituents of an atom or molecule. This is because the interparticle separations between the constituents of atomic systems are much smaller than the length scales in macroscopic-scale experiments. Thus, phenomena originating on atomic and subatomic length scales are generally much more sensitive to bosons with larger masses. Various atomic-scale phenomena can be used to search for new forces:

- (1) Comparison of measured and predicted spectra of atoms, molecules and ions to search for new parity-conserving forces [14, 40, 44–49]
- (2) Comparison of measured and predicted parity-violating observables in atoms and molecules to search for new parity-violating forces [50]
- (3) Measurements of permanent electric dipole moments in atoms and molecules to search for new parity and time-reversal-invariance-violating forces [39, 51].

There is an important difference between atomic-scale and macroscopic-scale experiments in the regime of a large boson mass, $m_\phi \gg 1/r$. Macroscopic-scale experiments lose

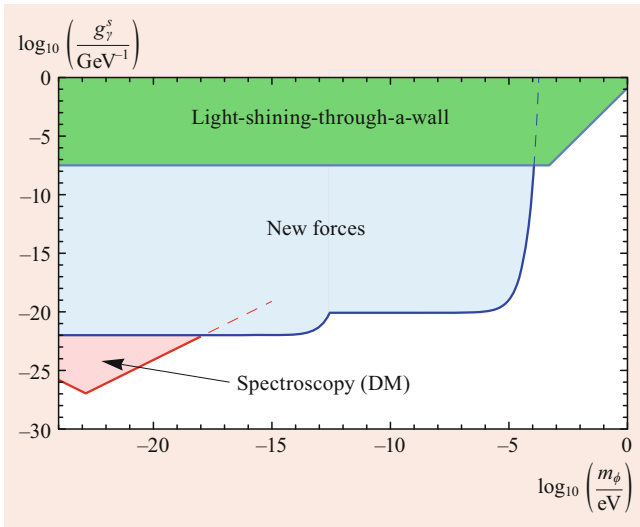


Fig. 31.1 Limits on the linear scalar interaction of a spinless boson ϕ with the photon, as defined in the first term of Eq. (31.1). The region in *green* corresponds to constraints from light-shining-through-a-wall experiments [15, 16]. The region in *blue* corresponds to constraints from macroscopic-scale experiments that search for new forces [12, 17–21]. The region in *red* corresponds to constraints from atomic spectroscopy measurements that search for the effects of a relic coherently oscillating field $\phi = \phi_0 \cos(m_\phi t)$, which saturates the local cold dark matter (DM) content [22, 23]

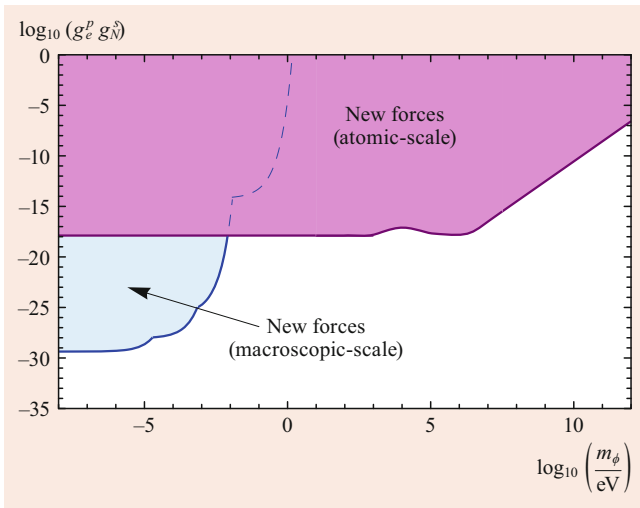


Fig. 31.2 Limits on the P, T -violating scalar-pseudoscalar nucleon-electron interaction mediated by a spinless boson ϕ , as given in Eq. (31.5) (which arises from the last terms of Eqs. (31.1) and (31.3)). The region in *blue* corresponds to constraints from macroscopic-scale experiments that search for new forces [28–30, 37, 38]. The region in *magenta* corresponds to constraints from atomic and molecular electric dipole moment experiments [39]

sensitivity to new forces exponentially quickly when the boson mass becomes large, because the interaction becomes contact-like, and so the very heavy boson cannot propagate between the source body and detector. In atomic-scale phe-

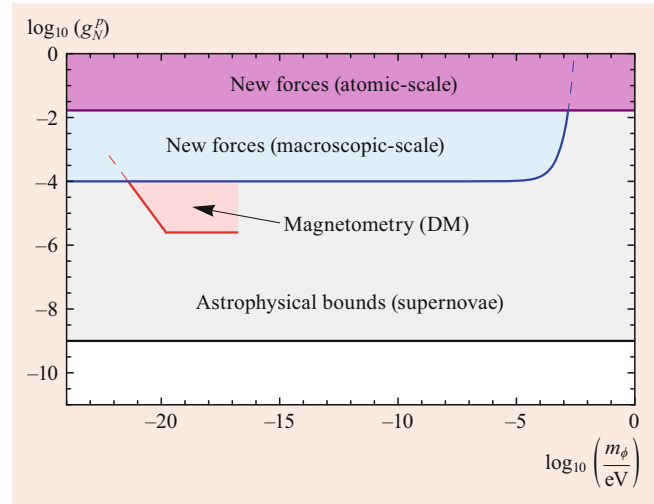


Fig. 31.3 Limits on the linear pseudoscalar interaction of a spinless boson ϕ with nucleons, as defined in the last term of Eq. (31.3). The region in *blue* corresponds to constraints from a macroscopic-scale experiment that searches for new forces [31]. The region in *magenta* corresponds to constraints from molecular hydrogen spectroscopy measurements and comparison with theory [40]. The region in *red* corresponds to constraints from magnetometry measurements that search for the effects of a relic coherently oscillating field $\phi = \phi_0 \cos(m_\phi t)$, which saturates the local cold dark matter (DM) content [41]. The region in *light gray* corresponds to astrophysical constraints pertaining to supernova energy-loss bounds [42, 43]

nomena, however, there is always a finite probability for two constituent particles to be located very close to each other, and so these types of experiments lose sensitivity to new forces much more slowly (at a power-law rate) when the boson mass becomes large. Current limits from atomic-scale experiments on several types of nongravitational interactions of spinless bosons are shown in Figs. 31.2 and 31.3.

31.3 Laboratory Sources

In the presence of the nongravitational interactions in the first terms of Eqs. (31.1) and (31.3), spinless bosons may interconvert with photons. Several different types of methods can be used to exploit this possible interconversion:

(1) “Light-shining-through-a-wall” experiments [15, 16, 52, 53]. The basic idea here is to shine a powerful laser into a region of strong magnetic field. Some of the laser photons will convert into spinless bosons (provided that the energy of these photons is not less than the rest-mass energy of the spinless boson), which then pass through a wall that is impenetrable to photons (but not to the spinless bosons). A second strong magnetic field is applied on the other side of this wall in order to reconvert some of the transmitted spinless bosons back into photons for detection. In principle, it is not necessary for all of the incident laser photons to be blocked by the

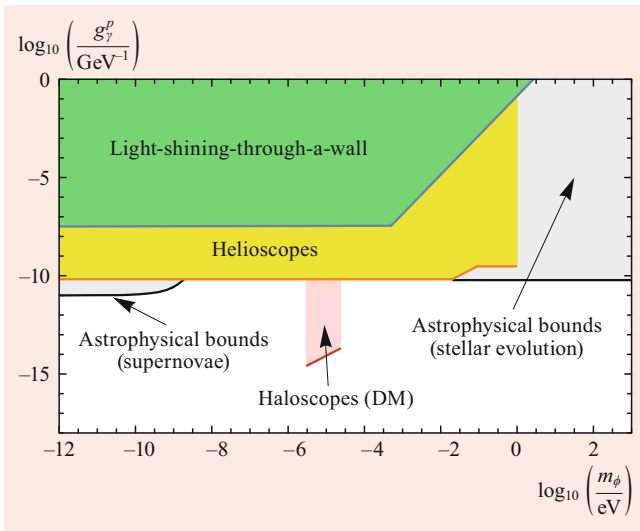


Fig. 31.4 Limits on the linear pseudoscalar interaction of a spinless boson ϕ with the photon, as defined in the first term of Eq. (31.3). The region in *green* corresponds to constraints from “light-shining-through-a-wall” experiments [15, 16]. The region in *yellow* corresponds to constraints from helioscope experiments that search for bosons emitted from the Sun [59, 60]. The region in *red* corresponds to constraints from haloscope experiments that search for the conversion of galactic dark matter (DM) bosons into photons [61, 62]. The regions in *light gray* correspond to astrophysical constraints pertaining to stellar evolution and supernova energy-loss bounds [42, 43]

wall. A tiny fraction of incident photons can be transmitted through the wall, so that an atomic or molecular transition can be resonantly induced involving the interference of photon and spinless-boson-induced amplitudes (assuming there exists a nongravitational interaction between the spinless boson and electron) [54].

(2) Experiments to search for vacuum birefringence and dichroism [55–58]. The basic idea in these types of experiments is to shine a polarized laser into a region of strong magnetic field. Vacuum birefringence involves different indices of refraction for light polarized parallel and perpendicular to an applied magnetic field and is caused by virtual spinless bosons. Dichroism involves different absorptivities for light of different polarizations in an applied magnetic field and is caused by the production of real spinless bosons.

Although electric fields could also be used in these experiments, in practice it is much easier to generate a stronger magnetic field (in terms of the equivalent electromagnetic energy density) in the laboratory. An advantage of producing spinless bosons in the laboratory is that the energies of these bosons are fixed by energy conservation, so resonance techniques can be applied without having to scan over an *a priori* unknown range of boson energies. Current limits from laboratory source experiments on several types of nongravitational interactions of spinless bosons are shown in Figs. 31.1 and 31.4.

31.4 Astrophysical Sources

In the presence of the nongravitational interactions in Eqs. (31.1)–(31.3), spinless bosons can be produced and subsequently emitted from the hot interiors of active stars (such as the Sun) and dead stars (such as white dwarfs), as well as in supernovae explosions. Excessive emission of spinless bosons from astrophysical sources would contradict observations and corresponding standard-model calculations, providing strong constraints on possible nongravitational interactions of spinless bosons (Figs. 31.3–31.6) [42, 43]. If spinless bosons are emitted from the nearest star (the Sun), then it also becomes feasible to search for these particles in terrestrial experiments.

Spinless bosons emitted from the Sun can be detected using helioscope experiments, which seek to exploit the interconversion of spinless bosons with photons in a strong applied magnetic field [59, 60, 63–65]. Helioscope experiments are somewhat similar to the “light-shining-through-a-wall” experiments discussed in Sect. 31.3, except that the source of spinless bosons in helioscope experiments is provided by nature. The nature of the spinless boson sources in these two types of experiments is very different, however. In a “light-shining-through-a-wall” experiment, the energy of the spinless bosons depends on the frequency of the laser source used and can, thus, be altered. Additionally, since lasers

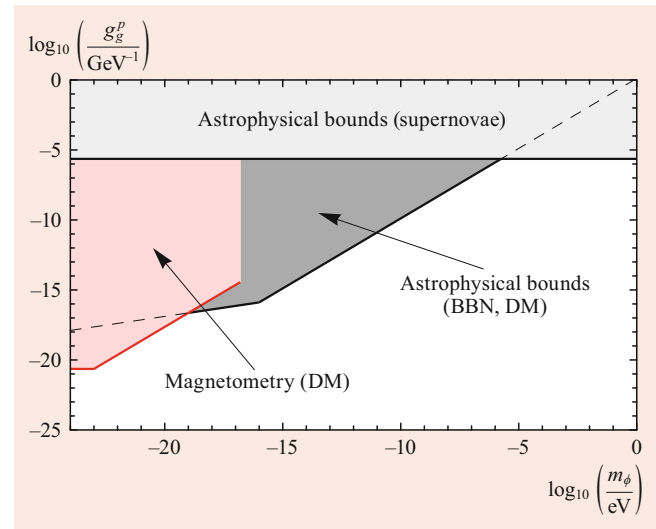


Fig. 31.5 Limits on the linear pseudoscalar interaction of a spinless boson ϕ with gluons, as defined in the second term of Eq. (31.3). The region in *red* corresponds to constraints from magnetometry measurements that search for the effects of a relic coherently oscillating field $\phi = \phi_0 \cos(m_\phi t)$, which saturates the local cold dark matter (DM) content [41]. The region in *light gray* corresponds to astrophysical constraints pertaining to supernova energy-loss bounds [77]. The region in *dark gray* corresponds to astrophysical constraints pertaining to big bang nucleosynthesis (BBN) measurements, assuming that spinless bosons saturate the DM content [78–80]

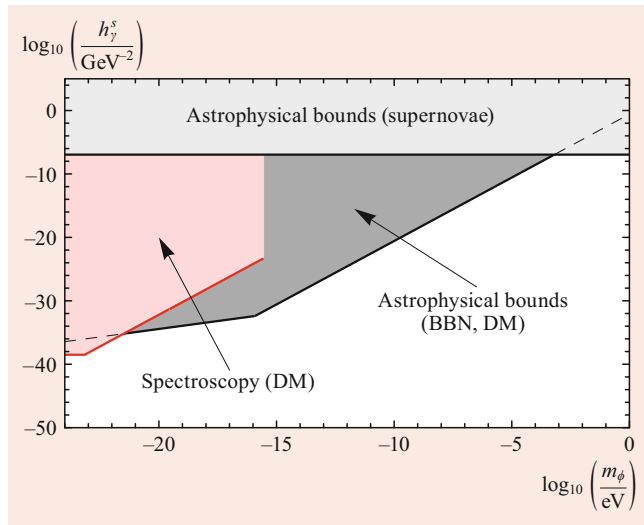


Fig. 31.6 Limits on the quadratic scalar interaction of a spinless boson ϕ with the photon, as defined in the first term of Eq. (31.2). The region in *red* corresponds to constraints from atomic spectroscopy measurements that search for the effects of a relic coherently oscillating field $\phi = \phi_0 \cos(m_\phi t)$, which saturates the local cold dark matter (DM) content [79, 90]. The region in *light gray* corresponds to astrophysical constraints pertaining to supernova energy-loss bounds [13]. The region in *dark gray* corresponds to astrophysical constraints pertaining to big bang nucleosynthesis (BBN) measurements, assuming that spinless bosons saturate the DM content [79]

are practically monochromatic sources of light, the resulting energy spectrum of spinless bosons is likewise sharply peaked in these types of laboratory experiments. On the other hand, in a helioscope experiment, the energies of the spinless bosons are determined by the core temperature of the Sun (≈ 1 keV), and the energy spectrum of the bosons is relatively broad. Current limits from solar source experiments on one type of nongravitational interaction of a spinless boson are shown in Fig. 31.4.

31.5 Cosmological Sources

Low-mass (sub-eV) spinless bosons can be produced efficiently via nonthermal production mechanisms (which impart practically no kinetic energy to the bosons), such as “vacuum misalignment” in the early universe [66], and subsequently form a coherently oscillating classical field: $\phi = \phi_0 \cos(\omega t)$, with the angular frequency of oscillation given by $\omega \approx m_\phi c^2 / \hbar$, where m_ϕ is the boson mass, c is the speed of light, and \hbar is the reduced Planck constant. The classical nature of this field arises due to the large number of low-mass bosons per reduced de Broglie volume. The oscillating bosonic field carries the energy density $\rho_\phi \approx m_\phi^2 \phi_0^2 / 2$, which may saturate the local cold dark matter (DM) energy density $\rho_{\text{DM}}^{\text{local}} \approx 0.4 \text{ GeV}/\text{cm}^3$ [67]. If these bosons comprise all of the DM, then the requirement that the boson de

Broglie wavelength does not exceed the DM halo size of the smallest dwarf galaxies gives the lower boson mass bound $m_\phi \gtrsim 10^{-22} \text{ eV}$.

A variety of atomic, molecular, and optical experiments can be used to search for oscillating DM fields. The specific detection methods crucially depend on the particular nongravitational interactions between the bosonic DM and ordinary matter that are probed. In this section, we give a brief overview of the main types of detection methods for oscillating bosonic fields. We note that similar detection strategies can also be implemented to search for bosonic fields that form “clump-like” DM, except in this case, a network of detectors is required to unambiguously confirm the passage of such DM clumps [68–72]. Additionally, spinless bosonic fields with certain self-interactions are conjectured in “chameleonic” models of dark energy [73] and may be sought for with atom interferometry techniques [74, 75].

31.5.1 Haloscope Experiments

In the presence of the nongravitational interaction in the first term of Eq. (31.3), spinless bosons may interconvert with photons. Spinless bosons that make up (part of) the galactic DM can be detected using haloscope experiments, which aim to convert galactic DM bosons into photons in the presence of a strong applied magnetic field inside a microwave cavity [61–63, 76]. Haloscope experiments are examples of “resonance-type” experiments, since the resonant frequency of a cavity mode must match the boson’s energy, $h\nu_{\text{mode}} \approx m_\phi c^2$. Although resonance-type experiments are sensitive to very feeble nongravitational interactions, the drawback of these types of experiments is that the boson mass (and hence energy) are not known *a priori*, meaning that these types of experiments have to scan over a very large range of frequencies in order to find a narrow resonance. Indeed, galactic bosonic DM in the vicinity of the Solar System is expected to have a root-mean-square velocity of $v_{\text{rms}} \approx 300 \text{ km/s}$, giving the oscillating galactic bosonic field the finite coherence time: $\tau_{\text{coh}} \approx 2\pi / m_\phi v_{\text{rms}}^2 \approx 2\pi \times 10^6 / m_\phi$, which is equivalent to a relative width of $\Delta\omega / \omega \approx 10^{-6}$. Current limits from haloscope experiments on one type of nongravitational interaction of a spinless boson are shown in Fig. 31.4.

31.5.2 Spin-Precession Experiments

In the presence of the nongravitational interactions in the last two terms of Eq. (31.3), bosonic DM fields can induce a number of time-varying spin-dependent effects. In particular, the second term in Eq. (31.3) gives rise to time-varying electric dipole moments of nucleons [81] and atoms and molecules [82], with the angular frequency of oscilla-

tion governed by the boson mass. The last term in Eq. (31.3) gives rise to anomalous time-varying spin-precession effects due to the motion of Earth through an apparent time-varying *pseudo*-magnetic field [77, 82, 83]. Various types of methods can be used to search for time-varying spin-dependent effects:

- (1) Atomic magnetometers and ultracold neutrons to search for time-varying anomalous spin-precession effects [41, 80, 82, 83]
- (2) Torsion pendula to search for time-varying anomalous torques [80, 82, 83]
- (3) Nuclear-magnetic-resonance techniques to search for the resonant build-up of transverse magnetization [77, 84, 85]
- (4) Resonant conversion of galactic DM bosons into photons in a magnetized material [86–89].

In the case of time-varying electric dipole moments, which can be sought for with methods (1) and (3), it is necessary to apply an electric field in the experiment. In the case of methods (1)–(3), the observables scale only to the first power of the underlying interaction constant. This is a particularly attractive feature of these types of methods, compared with the methods discussed in Sects. 31.2–31.5.1, where the observables scale either to the second or fourth power in a small interaction constant. Current limits from spin-precession experiments on several types of nongravitational interactions of spinless bosons are shown in Figs. 31.3 and 31.5.

31.5.3 Time-Varying Physical Constants

In the presence of the nongravitational interactions in Eqs. (31.1) and (31.2), bosonic DM fields can induce “apparent” variations in the physical constants [70, 79, 91]. One particularly powerful class of measurements to search for these apparent oscillations in the physical constants involve high-precision comparisons of atomic and molecular transition frequencies [22, 23, 70, 79, 90, 91], which were previously used to search for “slow temporal drifts” in the physical constants [92], Chap. 30. The basic idea of clock-comparison experiments is to compare two transition frequencies with different sensitivities to variations in the physical constants. For example, in the atomic units $\hbar = e = m_e = 1$, an atomic optical transition frequency scales as $\omega_{\text{opt}} \propto F_{\text{rel}}^{\text{opt}}(Z\alpha)$, while an atomic hyperfine transition frequency scales as $\omega_{\text{hf}} \propto [\alpha^2 F_{\text{rel}}^{\text{hf}}(Z\alpha)](m_e/m_N)\mu$, where F_{rel} are relativistic factors (which generally increase rapidly with the nuclear charge Z), and μ is the nuclear magnetic dipole moment. A summary of calculated sensitivity coefficients for various atomic, molecular, and nuclear transitions can be found in [92], Chap. 30.

Instead of comparing two transition frequencies, it is also possible to compare a transition frequency against a reference frequency determined by the length of an optical cavity or an interferometer arm, or to compare two (different) cavities or arms [70, 93, 94]. In this case, the reference frequency scales roughly as $\omega_{\text{ref}} \propto 1/L \propto 1/a_B$ if the solid length is allowed to vary freely, while the reference frequency is practically independent of the physical constants for a “fixed” length where fluctuations in the arm length are deliberately shielded. The sensitivity coefficients for laser/maser interferometry experiments depend on the specific configuration and mode of operation and were calculated in [70, 93, 94]. Like some of the methods discussed in Sect. 31.5.2 to search for time-varying spin-dependent effects, the observables in the types of experiments discussed in this section also have the attractive feature of scaling to the first power of the underlying interaction constant. Current limits on several types of nongravitational interactions of spinless bosons from experiments that search for apparent oscillations in the physical constants are shown in Figs. 31.1 and 31.6.

References

1. Bertone, G., Hooper, D., Silk, J.: *Phys. Rep.* **405**, 279 (2005)
2. Ade, P.A.R., et al.: *Astron. Astrophys.* **594**, A13 (2016). Planck Collaboration
3. Frieman, J.A., Turner, M.S., Huterer, D.: *Ann. Rev. Astron. Astrophys.* **46**, 385 (2008)
4. Riotto, A., Trodden, M.: *Ann. Rev. Nucl. Part. Sci.* **49**, 35 (1999)
5. Kim, J.E., Carosi, G.: *Rev. Mod. Phys.* **82**, 557 (2010)
6. Derevianko, A., Katori, H.: *Rev. Mod. Phys.* **83**, 331 (2011)
7. Ludlow, A.D., Boyd, M.M., Ye, J., Peik, E., Schmidt, P.O.: *Rev. Mod. Phys.* **87**, 637 (2015)
8. Budker, D., Romalis, M.V.: *Nat. Phys.* **3**, 227 (2007)
9. Abbott, B.P., et al.: *Phys. Rev. Lett.* **116**, 061102 (2016). LIGO Scientific Collaboration and Virgo Collaboration
10. Moody, J.E., Wilczek, F.: *Phys. Rev. D* **30**, 130 (1984)
11. Fadeev, P., Stadnik, Y.V., Ficek, F., Kozlov, M.G., Flambaum, V.V., Budker, D.: *Phys. Rev. A* **99**, 022113 (2019)
12. Leefer, N., Gerhardus, A., Budker, D., Flambaum, V.V., Stadnik, Y.V.: *Phys. Rev. Lett.* **117**, 271601 (2016)
13. Olive, K.A., Pospelov, M.: *Phys. Rev. D* **77**, 043524 (2008)
14. Stadnik, Y.V.: *Phys. Rev. Lett.* **120**, 223202 (2018)
15. Ehret, K., et al.: *Phys. Lett. B* **689**, 149 (2010). ALPS Collaboration
16. Ballou, R., et al.: *Phys. Rev. D* **92**, 092002 (2015). OSQAR Collaboration
17. Braginsky, V., Panov, V.: *Sov. Phys. JETP* **34**, 463 (1972). *Zh. Eksp. Teor. Fiz.* **61**, 873 (1971)
18. Smith, G.L., Hoyle, C.D., Gundlach, J.H., Adelberger, E.G., Heckel, B.R., Swanson, H.E.: *Phys. Rev. D* **61**, 022001 (1999)
19. Schlamminger, S., Choi, K.-Y., Wagner, T.A., Gundlach, J.H., Adelberger, E.G.: *Phys. Rev. Lett.* **100**, 041101 (2008)
20. Adelberger, E., Gundlach, J., Heckel, B., Hoedl, S., Schlamminger, S.: *Prog. Part. Nucl. Phys.* **62**, 102 (2009)
21. Zhou, L., et al.: *Phys. Rev. Lett.* **115**, 013004 (2015)
22. Van Tilburg, K., Leefer, N., Bougas, L., Budker, D.: *Phys. Rev. Lett.* **115**, 011802 (2015)

23. Hees, A., Guena, J., Abgrall, M., Bize, S., Wolf, P.: *Phys. Rev. Lett.* **117**, 061301 (2016)
24. Tino, G., Kasevich, M.: *Proceedings of the International School of Physics “Enrico Fermi”*. In: *Atom Interferometry*. (Ios Press Inc, Netherlands) (2014)
25. Blatt, S., et al.: *Phys. Rev. Lett.* **100**, 140801 (2008)
26. Guena, J., et al.: *Phys. Rev. Lett.* **109**, 080801 (2012)
27. Williams, J.G., Turyshv, S.G., Boggs, D.H.: *Phys. Rev. Lett.* **93**, 261101 (2004)
28. Hoedl, S.A., Fleischer, F., Adelberger, E.G., Heckel, B.R.: *Phys. Rev. Lett.* **106**, 041801 (2011)
29. Terrano, W.A., Adelberger, E.G., Lee, J.G., Heckel, B.R.: *Phys. Rev. Lett.* **115**, 201801 (2015)
30. Youdin, A.N., Krause Jr., D., Jagannathan, K., Hunter, L.R., Lamoreaux, S.K.: *Phys. Rev. Lett.* **77**, 2170 (1996)
31. Vasilakis, G., Brown, J.M., Kornack, T.W., Romalis, M.V.: *Phys. Rev. Lett.* **103**, 261801 (2009)
32. Serebrov, A.: *Phys. Lett. B* **680**, 423 (2009)
33. Petukhov, A.K., Pignol, G., Jullien, D., Andersen, K.H.: *Phys. Rev. Lett.* **105**, 170401 (2010)
34. Tullney, K., et al.: *Phys. Rev. Lett.* **111**, 100801 (2013)
35. Bulatowicz, M., et al.: *Phys. Rev. Lett.* **111**, 102001 (2013)
36. Afach, S., et al.: *Phys. Lett. B* **745**, 58 (2015)
37. Crescini, N., Braggio, C., Carugno, G., Falferi, P., Ortolan, A., Ruoso, G.: *Phys. Lett. B* **773**, 677 (2017)
38. Rong, X., et al.: *Nat. Commun* **9**, 739 (2018)
39. Stadnik, Y.V., Dzuba, V.A., Flambaum, V.V.: *Phys. Rev. Lett.* **120**, 013202 (2018)
40. Ramsey, N.F.: *Physica* **96A**, 285 (1979)
41. Abel, C., et al.: *Phys. Rev. X* **7**, 041034 (2017)
42. Raffelt, G.G.: *Annu. Rev. Nucl. Part. Sci.* **49**, 163 (1999)
43. Raffelt, G.G.: In: Kuster, M., Raffelt, G., Beltran, B. (eds.) *Axions: Theory, Cosmology, and Experimental Searches*, pp. 51–71. Springer, Berlin (2008)
44. Karshenboim, S.G.: *Phys. Rev. Lett.* **104**, 220406 (2010)
45. Karshenboim, S.G., Flambaum, V.V.: *Phys. Rev. A* **84**, 064502 (2011)
46. Ledbetter, M.P., Romalis, M.V., Kimball, D.F.J.: *Phys. Rev. Lett.* **110**, 040402 (2013)
47. Ficek, F., Jackson Kimball, D.F., Kozlov, M.G., Leefler, N., Pustelny, S., Budker, D.: *Phys. Rev. A* **95**, 032505 (2017)
48. Delaunay, C., Frugiuele, C., Fuchs, E., Soreq, Y.: *Phys. Rev. D* **96**, 115002 (2017)
49. Ficek, F., et al.: *Phys. Rev. Lett.* **120**, 183002 (2018)
50. Dzuba, V.A., Flambaum, V.V., Stadnik, Y.V.: *Phys. Rev. Lett.* **119**, 223201 (2017)
51. Dzuba, V.A., Flambaum, V.V., Samsonov, I.B., Stadnik, Y.V.: *Phys. Rev. D* **98**, 035048 (2018)
52. Okun', L.B.: *Sov. Phys. JETP* **56**, 502 (1982). *Zh. Eksp. Teor. Fiz.* **83**, 892 (1982)
53. Chou, A.S., et al.: *Phys. Rev. Lett.* **100**, 080402 (2008)
54. Tran Tan, H.B., Flambaum, V.V., Samsonov, I.B., Stadnik, Y.V., Budker, D.: *Phys. Dark Universe* **24**, 100272 (2019)
55. Maiani, L., Petronzio, R., Zavattini, E.: *Phys. Lett. B* **175**, 359 (1986)
56. Valle, F.D., et al.: *Eur. Phys. J. C* **76**, 24 (2016). PVLAS Collaboration
57. Chen, S.J., Mei, H.H., Ni, W.T.: *Mod. Phys. Lett. A* **22**, 2815 (2007)
58. Battesti, R., et al.: *Eur. Phys. J. D* **46**, 323 (2008). BMV Collaboration
59. Inoue, Y., Akimoto, Y., Ohta, R., Mizumoto, T., Yamamoto, A., Minowa, M.: *Phys. Lett. B* **668**, 93 (2008)
60. CAST Collaboration: CAST Collaboration. *Nat. Phys.* **13**, 584 (2017)
61. Brubaker, B.M., et al.: *Phys. Rev. Lett.* **118**, 061302 (2017)
62. Du, N., et al.: *Phys. Rev. Lett.* **120**, 151301 (2018). ADMX Collaboration
63. Sikivie, P.: *Phys. Rev. Lett.* **51**, 1415 (1983)
64. Avignone, F.T., et al.: *Phys. Rev. Lett.* **81**, 5068 (1998). SOLAX Collaboration
65. Irastorza, I., et al.: *J. Cosmol. Astropart. Phys.* **06**, 013 (2011)
66. Marsh, D.J.E.: *Phys. Rep.* **643**, 1 (2016)
67. Catena, R., Ullio, P.: *J. Cosmol. Astropart. Phys.* **08**, 004 (2010)
68. Stadnik, Y.V., Flambaum, V.V.: *Phys. Rev. Lett.* **113**, 151301 (2014)
69. Derevianko, A., Pospelov, M.: *Nat. Phys.* **10**, 933 (2014)
70. Stadnik, Y.V., Flambaum, V.V.: *Phys. Rev. Lett.* **114**, 161301 (2015)
71. Wcislo, P., et al.: *Nat. Astron.* **1**, 0009 (2016)
72. Roberts, B.M., et al.: *Nat. Comm.* **8**, 1195 (2017)
73. Khoury, J., Weltman, A.: *Phys. Rev. Lett.* **93**, 171104 (2004)
74. Burrage, C., Copeland, E.J., Hinds, E.A.: *J. Cosmol. Astropart. Phys.* **03**, 042 (2015)
75. Hamilton, P., Jaffe, M., Haslinger, P., Simmons, Q., Mueller, H., Khoury, J.: *Science* **349**, 849 (2015)
76. McAllister, B.T., et al.: *Phys. Dark Universe* **18**, 67 (2017)
77. Graham, P.W., Rajendran, S.: *Phys. Rev. D* **88**, 035023 (2013)
78. Blum, K., D’Agnolo, R.T., Lisanti, M., Safdi, B.R.: *Phys. Lett. B* **737**, 30 (2014)
79. Stadnik, Y.V., Flambaum, V.V.: *Phys. Rev. Lett.* **115**, 201301 (2015)
80. Stadnik, Y.V.: *Manifestations of Dark Matter and Variations of the Fundamental Constants of Nature in Atoms and Astrophysical Phenomena*. Springer, Cham, Switzerland (2017)
81. Graham, P.W., Rajendran, S.: *Phys. Rev. D* **84**, 055013 (2011)
82. Stadnik, Y.V., Flambaum, V.V.: *Phys. Rev. D* **89**, 043522 (2014)
83. Flambaum, V.V.: *Proceedings of the 9th Patras Workshop on Axions, WIMPs and WISPs* (2013). http://axion-wimp2013.desy.de/e201031/index_eng.html. Mainz, Germany
84. Budker, D., Graham, P.W., Ledbetter, M., Rajendran, S., Sushkov, A.O.: *Phys. Rev. X* **4**, 021030 (2014)
85. Garcon, A., et al.: *Quantum Sci. Technol.* **3**, 014008 (2018)
86. Krauss, L. M., Moody, J., Wilczek, F., Morris, D. E.: Preprint HUTP-85/A006 (1985)
87. Barbieri, R., Cerdonio, M., Fiorentini, G., Vitale, S.: *Phys. Lett. B* **226**, 357 (1989)
88. Kakhizde, A.I., Kolokolov, I.V.: *Sov. Phys. JETP* **72**, 598 (1991)
89. Barbieri, R., et al.: *Phys. Dark Universe* **15**, 135 (2017)
90. Stadnik, Y.V., Flambaum, V.V.: *Phys. Rev. A* **94**, 022111 (2016)
91. Arvanitaki, A., Huang, J., Van Tilburg, K.: *Phys. Rev. D* **91**, 015015 (2015)
92. Flambaum, V.V., Dzuba, V.A.: *Can. J. Phys.* **87**, 25 (2009)
93. Stadnik, Y.V., Flambaum, V.V.: *Phys. Rev. A* **93**, 063630 (2016)
94. Grote, H., Stadnik, Y.V.: *Phys. Rev. Res.* **1**, 033187 (2019)



Victor Flambaum Professor Victor Flambaum received his PhD and DSc from the Institute of Nuclear Physics, Novosibirsk, Russia. He has about 400 publications in atomic, nuclear, particle, solid state, statistical physics, general relativity and astrophysics, including works on the violation of fundamental symmetries, tests of unification theories, temporal and spatial variation of fundamental constants from the Big Bang to the present, many-body theory, and high-precision atomic calculations.



Yevgeny Stadnik Dr Yevgeny Stadnik completed his PhD at the University of New South Wales, Australia. He was a Humboldt Research Fellow at the Johannes Gutenberg University of Mainz, Germany, and a Kavli Fellow and Assistant Professor at Kavli IPMU within the University of Tokyo, Japan. Yevgeny is currently a DECRA Fellow at the University of Sydney, Australia. His research interests include the manifestations and phenomenology of dark matter in low-energy atomic and astrophysical phenomena.



Marianna S. Safronova

Contents

32.1	Parity Nonconserving Effects in Atoms	471
32.1.1	Nuclear-Spin-Independent PNC Effects	472
32.1.2	Nuclear-Spin-Dependent PNC Effects	472
32.1.3	PNC in Cesium and Implications for Particle and Hadronic Physics	473
32.1.4	Current PNC Experiments	474
32.2	Electric Dipole Moments and Related Phenomena	475
32.2.1	Experiments with Paramagnetic Systems	475
32.2.2	Experiments with Diamagnetic Systems	476
32.2.3	Impact on Particle Physics	477
32.3	Tests of the CPT Symmetry	477
32.4	Lorentz Symmetry Tests	478
32.4.1	Electron–Photon Sector of SME	478
32.4.2	Proton and Neutron Sectors of SME	480
32.5	AMO Tests of General Relativity	481
32.5.1	Tests of the Einstein Equivalence Principle	481
32.5.2	Other AMO Tests of Gravity	481
32.5.3	Detection of Gravitational Waves	482
	References	482

Abstract

While the Standard Model (SM) of particle physics has been very successful in describing as well as predicting numerous phenomena, it provides no insight into the nature of dark matter and dark energy. Moreover, SM is not consistent with the present observable Universe, which has a glaring imbalance of matter and antimatter. Despite decades of effort, all attempts to unify gravity with other fundamental interactions remain unsuccessful.

The advances in atomic, molecular, and optical (AMO) precision measurements, coupled with improved theoretical description, enabled new tests of fundamental physics. Revolutionary developments led to the extraordinary precision now reached by atomic clocks, other spectroscopy

measurements, atomic magnetometers, laser and atom interferometers, and other precision AMO experiments. These advances bring forth a question: Do our current laws of fundamental physics hold at the level of experimental precision?

Modern physics is based on a number of cornerstone principles such as Lorentz invariance, universality of free fall, local position invariance, constancy of fundamental constants, etc. However, in many theories beyond the Standard Model (BSM), these principles no longer hold, and discovery of their violation will be a first glimpse into the nature of BSM physics. AMO studies aimed to search for new physics beyond SM and to test the fundamental physics postulates are the subject of this chapter. This entire topic was recently reviewed in detail in [1]. In this chapter, we briefly discuss AMO studies in parity nonconservation, time-reversal violation including electric dipole moments, tests of the *CPT* theorem, tests of general relativity, and the search of the violation of local Lorentz invariance. The tests of quantum electrodynamics (QED), constraints on variations of fundamental constants, and searches for new particles, including dark matter, are discussed in other chapters.

Keywords

parity violation · anapole moment · electric dipole moments · CPT symmetry · Lorentz symmetry · tests of general relativity · gravitational waves · Einstein equivalence principle

32.1 Parity Nonconserving Effects in Atoms

Under the parity transformation P , the position vector \mathbf{r} transforms to $-\mathbf{r}$, which corresponds to mirror reflection and 180° rotation. Until 1957, the invariance of the laws of

M. S. Safronova (✉)
Dept. of Physics & Astronomy, University of Delaware
Newark, DE, USA
e-mail: msafrono@udel.edu

physics under the process of parity inversion was assumed to hold. The concept of this invariance has its origin in atomic physics, where Laporte introduced it to explain certain aspects of the iron spectrum. The underlying theory of atomic structure, quantum electrodynamics, is an example of a theory that has this invariance. In 1956, it was suggested by *Lee* and *Yang* [2] that weak interaction processes are not invariant under parity inversion, and the parity violation in nuclear β -decay was discovered by *Wu* et al. [3].

Zeldovich [4] discussed a possibility of observing parity nonconservation (PNC) in atoms but estimated the effect to be too small to be observed. The parity violation in atoms leads to a nonzero amplitude for atomic transitions otherwise forbidden by the parity selection rule, such as the $6s-7s$ transition in cesium. In 1974, the *Bouchiats* [5] showed that these effects in heavy atoms with a nuclear charge Z were enhanced by approximately a factor of Z^3 .

In 1978, the first P -violating signal in an atom was observed in bismuth [6]. Parity violation was observed in other atoms, including lead [7], thallium [8, 9], cesium [10, 11], and ytterbium [12, 13]. Atomic parity violation has been discussed in detail in a number of reviews, most recently in [1, 14, 15]. The goals of high-precision atomic PNC studies are to search for new physics beyond the Standard Model by accurate determination of the weak charge and to probe hadronic parity violation.

In the Standard Model, atomic PNC arises from weak interactions mediated by a Z boson. The contact contribution to the SM Hamiltonian density is given by [16]

$$H_{\text{PV}} = \frac{G_{\text{F}}}{\sqrt{2}} \sum_q \left(C_q^{(1)} \bar{e} \gamma_\mu \gamma_5 e \bar{q} \gamma^\mu q + C_q^{(2)} \bar{e} \gamma_\mu e \bar{q} \gamma^\mu \gamma_5 q \right), \quad (32.1)$$

where q and e are field operators for quarks and electrons, respectively, sum q is over all quark flavors, γ_μ are Dirac matrices, and γ_5 is the Dirac matrix associated with pseudo scalars. The Fermi constant $G_{\text{F}} = 2.22 \times 10^{-14}$ a.u. quantifies the strength of the weak interactions. In Eq. (32.1), the first term describes a coupling of the electron axial-vector current to the quark vector current, $V_q A_e$, parameterized by the constant $C_q^{(1)}$. The second term describes a coupling of the electron vector current to the quark axial-vector current, $A_q V_e$. The $V_q A_e$ term dominates, because all the quarks contribute coherently. The $A_q V_e$ term contributes to the PNC effects that depend on nuclear spin.

For the description of the atomic PNC, it is convenient to combine $C_q^{(i)}$ ($i = 1, 2$) quantities into the corresponding constants for protons and neutrons [17]

$$\begin{aligned} C_p^{(1)} &= 2C_u^{(1)} + C_d^{(1)} = \frac{1}{2}(1 - 4 \sin^2 \theta_{\text{W}}), \\ C_n^{(1)} &= C_u^{(1)} + 2C_d^{(1)} = -\frac{1}{2}, \\ C_p^{(2)} &= -C_n^{(2)} = g_A C_p^{(1)}, \end{aligned}$$

where u and d refer to up and down quarks, θ_{W} is the weak mixing angle, and $g_A \approx 1.26$. We use a nucleon subscript N in expressions for the nucleon vector V_N or axial-vector A_N currents below. Substituting the value of the weak mixing angle, $\sin^2 \theta_{\text{W}} = 0.23122(4)$ [18] (M_Z value) into the equation above shows that atomic PNC is dominated by the neutron contribution.

Other contributions to atomic PNC are discussed in the next sections.

32.1.1 Nuclear-Spin-Independent PNC Effects

Because the nucleon current $V_N A_e$ in the first term of Eq. (32.1) is of vector nature, one can introduce a conserved charge, the nuclear *weak charge* Q_{W}

$$Q_{\text{W}} = 2ZC_p^{(1)} + 2NC_n^{(1)} = Z(1 - 4 \sin^2 \theta_{\text{W}}) - N. \quad (32.2)$$

Here, Z is the number of protons and N the number of neutrons. This is the lowest-order $Q_{\text{W}} \approx -N$ value, which is modified by SM radiative corrections at a level of a few percent [16, 18].

Assuming that the nucleon motion is nonrelativistic and averaging over nucleon distribution, the $V_N A_e$ contribution to H_{PV} reduces to the effective electron-sector weak Hamiltonian,

$$H_{\text{W}} = \frac{G_{\text{F}}}{\sqrt{8}} Q_{\text{W}} \rho(r) \gamma_5, \quad (32.3)$$

where $\rho(r)$ is a nuclear density. The expression above neglects the difference between the proton and the neutron distribution. It is accounted for by a so-called ‘‘neutron skin’’ correction. The neutron skin is defined as the difference between the root-mean-square radii of neutron and proton distributions [19]. It is small, 0.2% for the Cs $6s-7s$ PNC amplitude, increasing for heavier atoms [20].

Due to the smallness of the G_{F} , the matrix elements of the H_{W} are exceptionally small. For example, PNC matrix element in Cs is $\approx 10^{-11}$ a.u., while allowed electric-dipole matrix elements are typically on the order of an atomic unit (ea_0 , where e is the electric charge, and a_0 is the Bohr radius). The PNC interaction due to the exchange of Z between two atomic electrons is much smaller than the electron-nucleon Z exchange. The correction due to weak $e-e$ processes in Cs is only 0.03% [20], significantly below both experimental and theoretical uncertainties.

32.1.2 Nuclear-Spin-Dependent PNC Effects

The nuclear spin-dependent PNC effects, contributing in open-shell atoms with nuclear spin $I \neq 0$, are described by

the effective interactions in the electron sector [1]

$$H_{\text{NSD}} = \frac{G_{\text{F}}}{\sqrt{2}}(\eta_{\text{axial}} + \eta_{\text{NAM}} + \eta_{\text{hf}})(\boldsymbol{\alpha} \cdot \mathbf{I})\rho(r), \quad (32.4)$$

where $\boldsymbol{\alpha}$ is the velocity operator ($\alpha_i = \gamma_0 \gamma^i$) for atomic electrons. The first term is associated with the $A_N V_e$ term of H_{PV} given by Eq. (32.1). The second term arises from the anapole moment contribution, which generally dominates for heavy atoms. It is described in more detail below. The third term describes a combined effect of the hyperfine interactions and the Z-boson exchange interaction from the $V_N A_e$ term of H_{PV} . The corresponding parameter η_{hf} was calculated for transitions of experimental interest by *Johnson, Safronova, and Safronova* [21]. Another nuclear spin-dependent PNC effect was pointed out and evaluated for cases of experimental interest in [22]: nuclei with spin $I \leq 1$ have a weak quadrupole moment leading to a tensor weak interaction that mixes states of opposite parity for atomic levels with total angular momentum difference $\Delta J \leq 2$.

Nonzero nuclear multipolar electric (EJ) and magnetic (MJ) moments, such as charge ($E0$), magnetic dipole moment ($M1$), electric quadrupole moment ($E2$), etc., are all even under the parity transformation and T -reversal. Weak interactions inside the nucleus result in additional parity-odd nuclear moments. The nuclear anapole moment \mathbf{a} is such a leading parity-odd, time-reversal even nuclear moment [23]. For a current density distribution $\mathbf{J}(r)$, the anapole moment is given by

$$\mathbf{a} = -\pi \int d^3r r^2 \mathbf{J}(r). \quad (32.5)$$

The electromagnetic coupling of atomic electrons to the nuclear anapole moment is given by $\boldsymbol{\alpha} \cdot \mathbf{A}$, where $\mathbf{A} = \mathbf{a}\delta(\mathbf{r})$ is the corresponding vector potential. Just as in the case of the nuclear magnetic moment, \mathbf{a} is proportional to the nuclear spin. The anapole moment is related to the parameter η_{NAM} of Eq. (32.4) by

$$\mathbf{a} = \frac{G_{\text{F}}}{|e|\sqrt{2}} \eta_{\text{NAM}} \mathbf{I}. \quad (32.6)$$

The nonzero nuclear anapole moment was observed for the first time in the Cs PNC experiment [11], providing insight into hadronic weak interactions, as discussed in Sect. 32.1.3.

32.1.3 PNC in Cesium and Implications for Particle and Hadronic Physics

The most accurate PNC measurement was carried out in Cs [11]. Cs has a single electron outside a closed xenon-like core with 54 electrons. This is the simplest electronic

structure among all atoms for which the PNC effects were measured, allowing for accurate theoretical calculations of the PNC amplitude, required for the analysis of the experiment. In the text below, we omit the core electrons in the electronic level designations and only list the state of the valence electron.

The PNC transition in cesium that has been studied is $6s \rightarrow 7s$, which is forbidden by parity selection rules, i.e., the electric-dipole matrix element $\langle 7s|D|6s\rangle = 0$. This transition becomes weakly allowed due to PNC effects, which mixes the $6s$ and the $7s$ states with the opposite parity np states. The ^{133}Cs nucleus has 78 neutrons and 55 protons, its nuclear spin is $I = 7/2$. The total angular momentum of atomic ns $J = 1/2$ states is then $F = 3$ or $F = 4$. Both of the transitions,

$$6s(F=4) \rightarrow 7s(F=3)$$

and

$$6s(F=3) \rightarrow 7s(F=4),$$

have been measured, allowing the isolation of PNC effects that depend on the spin of the nucleus. The Boulder experiment [11] used the Stark interference method, applying the external electric field \mathbf{E} to provide an additional admixture of the np states. This induces an electric-dipole transition with a transition amplitude proportional to \mathbf{E} and a vector transition polarizability β (which is determined separately). The $6s$ – $7s$ transition is then excited with a 540 nm elliptically polarized laser light to get a nonzero interference between the Stark-induced amplitude and the parity-violating amplitude E_{PV} . The ratio of the two amplitudes is measured, using reversals of the electric fields, changes in magnetic substates, and in laser polarization to further isolate the PNC effect. The final results for both $6s$ – $7s$ transitions were reported to be

$$\text{Im} \frac{E_{\text{PV}}^{\text{exp}}}{\beta} = \begin{cases} -1.6349(80) & F=4 \rightarrow 3 \\ -1.5576(77) & F=3 \rightarrow 4 \end{cases} \quad (32.7)$$

in units of mV/cm.

Nuclear spin-independent part

The *average* of these values, combined with the value of β , gives *spin-independent* PNC amplitude, accurate to 0.35%. The value of the weak charge can be extracted from this averaged value using

$$E_{\text{PV}}^{\text{exp}} = k_{\text{PV}} Q_{\text{W}}, \quad (32.8)$$

where k_{PV} is the theoretical value of the PNC amplitude in terms of Q_{W} . Such a calculation in Cs with a subpercent accuracy was an extremely formidable task. The major

theoretical effort involved a very accurate treatment of the many-body Coulomb correlations, requiring both implementation of the coupled-cluster method and the fourth-order many-body perturbation theory, accomplished in [20, 24]. Their k_{PV} value, calculated with 0.27% uncertainty is the result of the most accurate and complicated PNC computation in heavy atoms accomplished to date. In addition, the small corrections due to the Breit interaction, radiative QED effects, and the neutron skin had to be calculated at this level of accuracy, which required the work of several groups. These calculations are reviewed by *Derevianko* and *Porsev* [14]. The resulting value of the weak charge

$$Q_w(^{133}\text{Cs}) = -73.16(29)[20], \quad (32.9)$$

where the first error is experimental and the second theoretical [20, 24], in agreement with the SM value [18]. Recent reevaluation of small Coulomb correlation corrections, contributions of the core, and highly excited states [25], raised the theoretical uncertainty to 0.5%, slightly shifting the value of k_{PV} but maintaining agreement with the SM. Theoretical effort to resolve the issue of the accuracy of the highly excited terms is currently in progress.

The Cs experiment, combined with theoretical calculations, provides the most accurate low-energy test of the SM electroweak sector. In combination with particle physics experiments, atomic PNC demonstrated the 3% “running” (i.e., dependence on the four-momentum transfer Q) of the electroweak interactions across five orders of energy values. This result is illustrated in Fig. 32.1 from [1] (adapted from [26]), which shows the Cs atomic parity violation (APV) result together with values from particle physics experiments.

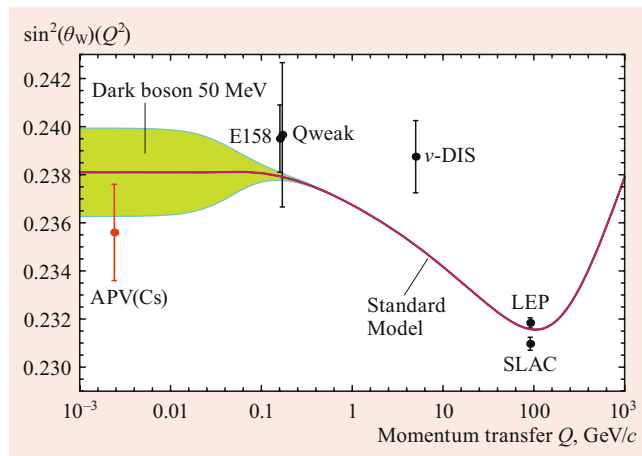
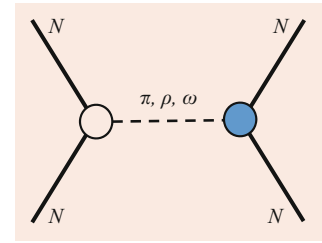


Fig. 32.1 Running of the weak mixing angle with momentum transfer Q . The solid red curve is the SM prediction. The Cs APV result is supplemented with data from particle physics experiments: E158, Møller [electron–electron] scattering; Q-weak, PNC electron–proton scattering, ν -DIS, deep inelastic scattering; LEP and SLAC results. The colored area comes from one of the “new physics” scenarios [26]: a dark boson of mass 50 MeV. From [1] (adapted from [26])

Fig. 32.2 Illustration of the nucleon–nucleon interaction, mediated by a meson exchange



Atomic PNC studies are sensitive to extra Z bosons, setting limits on such particles with TeV masses, with limits only recently improved at the Large Hadron Collider [18]. APV is also uniquely sensitive to some “dark forces” [26], with the limits on the 50 MeV dark boson shown in Fig. 32.1. The AMO searches for new particles, including dark matter, are further discussed in Chap. 31.

Nuclear spin-dependent part

Next, we discuss the analysis of the Cs result in terms of the spin-dependent PNC effects. The *difference* of the values for two transitions in Eq. (32.7), $0.077(11)$ mV/cm, combined with the value of β , gives the *spin-dependent* PNC amplitude, accurate to 15%. To extract the value of the anapole moment, the theoretical calculation of the nuclear spin-dependent amplitude E_{PV}^{NSD} is needed, just as in the case of the spin-independent part, only using the H_{NSD} Hamiltonian (32.4), along with the calculations of η_{axial} and η_{hf} ; E_{PV}^{NSD} was calculated in [27] using the linearized coupled-cluster approach with 1% uncertainty, much exceeding the experimental accuracy.

The nuclear anapole moment arises due to nucleon–nucleon interaction, mediated by a meson (π , ω , ρ) exchange illustrated in Fig. 32.2, where one of the nucleon–meson vertexes is strong and another is weak and P -violating. Therefore, the experimental PNC result combined with the theoretical value of the spin-dependent PNC amplitude can be used to probe weak hadronic interactions. Such an analysis, carried out in [28], yielded the values of the weak meson–nucleon couplings in disagreement with other constraints. More recent limits on the values of the weak meson–nucleon couplings are given in [29], but the discrepancy remains unsolved, complicated by the difficulty in the required nuclear calculation [28]. More experiments, including anapole moment measurements in other atoms or molecules are required to solve this long-standing puzzle.

32.1.4 Current PNC Experiments

The Yb PNC experiment (ongoing in Mainz, Germany) recently reported the measurements of atomic parity violation, made on a chain of ytterbium isotopes with mass numbers $A = 170, 172, 174$, and 176 [13]. The PNC effect in

Yb is approximately 100 times larger than that of Cs. The advantage of the experiment with several isotopes is the potential of carrying out the analysis without the need for high-precision calculations, not currently feasible for the Yb PNC amplitude. Experiments with Dy, which has nearly-degenerate states of opposite parity, are being carried out by the same group. While PNC in Dy was not previously observed [30], it should be within the sensitivity of the new experiment.

An experiment to remeasure PNC in the $6s-7s$ transition of Cs is underway in Purdue, using new two-pathway coherent control technique [31]. An Fr PNC experiment is being pursued at TRIUMF in Vancouver [32], which is complicated by the requirement that it be performed at a facility capable of producing needed radioactive isotopes. Measurements in a chain of Fr isotopes are planned, with the main goal of measuring nuclear anapole moments. The TRIUMF collaboration plans to measure PNC in both optical $7s-8s$ and ground state hyperfine transitions. Experiments to measure spin-dependent PNC effects in molecules are underway at Yale [33].

32.2 Electric Dipole Moments and Related Phenomena

In this section, we continue with the discussion of the P -violating effects but consider phenomena that are also odd under the time reversal (T). Such searches probe the energy scales well above 1 TeV in particle theory models such as supersymmetry, considered to be natural extensions of the SM. Thus, the AMO studies of P, T -violating effects are of particular significance for particle physics. Numerous detailed reviews of this topic are available in the literature (e.g. [1, 34, 35] and references therein). Here, we discuss the most recent results.

The combined symmetry of charge conjugation C , parity transformation P , and time reversal T , i.e., CPT , is preserved in quantum field theory. Therefore, the violation of T implies the violation of CP . Tests of CPT invariance are discussed in Sect. 32.3. The question of CP -violation is directly related to the problem of baryon asymmetry, observed dominance of matter over the antimatter in our Universe. CP violation is required to generate baryon asymmetry [36], but CP violation in the Standard Model is by far too small to account for it. Therefore, there must be other sources of CP violation leading to the effects already well within the precision of the experiments described in this chapter. As a result, AMO searches for CP -violating effects have a particularly high potential of discovering new physics.

A permanent electric dipole moment (EDM) of a particle, d , along its spin s violates both P and T . The Hamiltonian describing the EDM interaction with an electric field E is

given by

$$H_{\text{EDM}} = -d \cdot E. \quad (32.10)$$

While it would seem that EDMs of electrons and nucleons will simply lead to observable effects (i.e., shifts in energy levels) in atoms and molecules, this issue turns out to be more complicated. According to Schiff's theorem [37], there is no energy shift resulting from constituent particles' EDMs when an E -field is applied to a neutral system, assuming nonrelativistic point particles in an electrostatic potential. This means that the other parts of the atomic system rearrange to completely screen the external E -field felt by the charged particle, otherwise it will experience a net acceleration. A number of effects (finite nuclear size, relativistic effects, magnetic interactions, and others) allow to evade the Schiff's theorem leading to potentially observable experimental signals.

In atoms and molecules, P, T -violating effects arise from EDMs of electrons, protons, and neutrons, P, T -violating electron–nucleon interactions and P, T -violating nucleon–nucleon interactions. Different atoms and molecules have various sensitivities to these effects, but one may divide them into two groups: paramagnetic (with unpaired electron spins) and diamagnetic (with closed electron shells but nonzero nuclear spin). The first group is the most sensitive to the electron EDM (eEDM) and one type of electron–nucleus interaction. The second is the most sensitive to EDMs of nucleons, purely hadronic (nucleon–nucleon) interactions, and other types of electron–nucleon interactions.

32.2.1 Experiments with Paramagnetic Systems

The relativistic motion of a bound electron in a heavy atom can lead to energy shifts due to eEDM that are larger than a shift for the free electron, i.e., EDM effects are enhanced in some atoms and molecules. For example, the EDM of a Tl atom is

$$d(^{205}\text{Tl}) = K d_e \approx 573 d_e,$$

where K is the enhancement factor calculated theoretically using a hybrid approach that combines configuration interaction and a linearized coupled cluster method [38] with a 3% accuracy. This enhancement makes measurement of EDM in heavy atoms and molecules containing heavy atoms particularly attractive. Measurement of the EDM of ^{205}Tl atom [39] placed the bound on the electron EDM $d_e < 1.6 \times 10^{-27} e \text{ cm}$. This limit was improved by the YbF molecular experiment to $d_e < 1.05 \times 10^{-27} e \text{ cm}$ [40]. The current best limit on eEDM comes from the ACME experiment with ThO molecules [41]; $d_e < 8.7 \times 10^{-29} e \text{ cm}$ with 90% confidence.

The valence electrons in some molecules, such as ThO, can experience exceptionally large intramolecular effective electric field E_{eff} , on the order of 100 GV/cm. If an electron has an EDM, such enormous field (which can not be achieved in the lab) leads to an enhanced energy shift $-d_e E_{\text{eff}}$, making these molecules particularly attractive for EDM searches. Unlike atoms, the ThO molecule can also be fully polarized applying an ≈ 100 V/cm external electric field. For the Ω -doublet $H^3\Delta_1$ electronic state in ThO, the effective field was calculated to be ≈ 80 GV/cm, with an uncertainty of about 10–20% ([42, 43] and references therein). The use of the Ω -doublet states is particularly advantageous as they provide for “internal comagnetometry”, which allows for the reversal of the EDM interaction without changing any lab fields, minimizing the systematic effects. The $H^3\Delta_1$ state has an additional advantage of the unusually small magnetic moment, which reduces the systematic effect due to spurious magnetic fields.

To measure d_e , ACME performed a spin precession measurement on pulses of $^{232}\text{Th}^{16}\text{O}$ molecules from a cryogenic buffer gas beam source, which has the advantages of a low internal temperature, high flux, and low forward velocity in comparison with conventional molecular beam sources.

Besides the electron EDM, ThO is also sensitive to the pseudoscalar electron–scalar nucleon T -violating interaction, quantified by the coupling C_S . This effect would lead to an additional frequency shift, $-W_S C_S$, where W_S is calculated theoretically [42, 43]. The electron EDM limit above assumes $C_S = 0$. Setting $d_e = 0$ yields $C_S < 6 \times 10^{-9}$ [41].

In 2017, an electron EDM result from a new experiment at JILA with HfF^+ molecular ions was reported [44]. *Cairncross* et al. used a rotating electric field ($E \approx 20$ V/cm) to trap and fully polarize Ω -doublet levels of a metastable $^3\Delta_1$ state. Combining the experimental result with the calculated value $E_{\text{eff}} \approx 23$ GV/cm [45, 46], this experiment gives $d_e < 13 \times 10^{-29}$ e cm at a 90% confidence level or $C_S < 14 \times 10^{-9}$. A combination of ThO and HfF^+ values may be used to improve the constraints further due to different relative sensitivities of the two experiments to d_e and C_S .

Improvements in ACME [47], HfF^+ , and YbF experiments are underway, and significant improvements in accuracy are expected. *Kozryev* and *Hutzler* [48] recently proposed using polyatomic paramagnetic molecules, which can be laser cooled and have a level structure favorable for electron EDM measurements.

32.2.2 Experiments with Diamagnetic Systems

The Hg EDM search at the University of Washington [49, 50] is the most sensitive EDM experiment with a diamagnetic system. Because ^{199}Hg has a closed-shell 1S_0 electronic ground state and nuclear spin $I = 1/2$, the EDM must point

along the nuclear spin axis. The nuclear spins are polarized by optical pumping with a resonant laser beam. When spin-polarized ^{199}Hg atoms are immersed in electric and magnetic fields, the Larmor frequency is given by

$$h\nu_L = 2|\mu B \pm dE|, \quad (32.11)$$

where μ and d are magnetic and electric dipole moments, and \pm sign denotes parallel (antiparallel) fields. The $d \neq 0$ EDM experimental signature would be a Larmor frequency change correlated with the electric field when \mathbf{E} is reversed relative to \mathbf{B} . Hg atoms are contained in four nominally identical high-density vapor cells. The inner cells have strong, equal, and opposite \mathbf{E} fields along the \mathbf{B} -field axis, while the outer cells have $\mathbf{E} = 0$ to cancel fluctuations not only in the average value of \mathbf{B} but also in its first-order gradient. With 252 daily runs, the experiment was sensitive to the PT -violating energy shift of $\Delta E/h < 20$ pHz. The final result for the Hg EDM was [49]

$$d_{\text{Hg}} = (2.20 \pm 2.75_{\text{stat}} \pm 1.48_{\text{sys}}) \times 10^{-30} e \text{ cm},$$

with a 95% confidence limit of

$$d_{\text{Hg}} < 7.4 \times 10^{-30} e \text{ cm}.$$

Theoretical interpretation of this limit in terms of the Schiff moment \mathbf{S}_{Hg} , which is the leading-order P , T -violating nuclear moment not completely screened by the electron cloud, gives

$$|\mathbf{S}_{\text{Hg}}| < 3 \times 10^{-13} e \text{ fm}^3,$$

where results of several theoretical calculations were averaged to provide

$$d_{\text{Hg}} = -2.4 \times 10^{-4} \mathbf{S}_{\text{Hg}}/\text{fm}^2.$$

Further limits on neutron EDM and proton EDM were derived from the corresponding contributions to \mathbf{S}_{Hg} in a random-phase approximation calculation with core polarization [51]

$$d_{\text{Hg}} = (1.9 d_n + 0.2 d_p) \text{ fm}^2.$$

The resulting limits are $d_n < 1.6 \times 10^{-26}$ e cm and $d_p < 2.0 \times 10^{-25}$ e cm, where the other terms were assumed to be zero, and 30% uncertainty was assigned to the d_p contribution. The ^{199}Hg experiment also set the best limits on the combined chromo-EDM of the up and down quarks, the observable QCD θ -parameter, $\bar{\theta}_{\text{QCD}} < 1.5 \times 10^{-10}$, and hadronic T -odd, P -odd couplings, pseudoscalar-scalar and tensor-tensor semileptonic couplings.

Other experiments with diamagnetic systems were carried out with ^{129}Xe [52], ^{225}Ra atoms [53] and ^{205}TlF molecules [54]. The groups at Yale, Columbia, and the University of Massachusetts are constructing a new experiment (CeN-TREX) to measure the Schiff moment of ^{205}Tl using a cryogenic beam of TlF molecules. A review of other new EDM experiments is given in [1].

32.2.3 Impact on Particle Physics

Calculations of the size of the relevant T , P -violating parameters were made for a wide range of theoretical models, in particular those that include supersymmetry (SUSY) that is broken near the electroweak scale. Attractive features of such theories include predictions of superpartner particles with mass $M_{\text{SUSY}} \approx M_Z \approx 0.1 \text{ TeV}$ that provide potential dark matter candidates, a solution to the problem of the stabilization of the Higgs mass against radiative corrections, extra sources of CP -violation to resolve the matter-antimatter asymmetry, etc. These theories predict EDMs that are already well within the experimental reach and improving EDM sensitivity by 1–2 orders of magnitude will either yield a discovery or conclusively rule out many SUSY models. Even in the scenarios when primary contribution to EDMs comes from the two-loop diagrams, the electron EDM and quark chromo-EDM limits correspond to lower bounds of $\approx 2\text{--}4 \text{ TeV}$ on the masses of the lighter SUSY particles, if $\delta_{\text{SUSY}} \approx 1$ [1, 55]. For these types of SUSY particles, this is well beyond the direct reach of the Large Hadron Collider [18]. EDM experiments also set limits on models with extra scalar fields, analogous to the Higgs boson [34], also exceeding LHC bounds.

32.3 Tests of the CPT Symmetry

Current laws of physics are believed to be invariant under the CPT transformation. However, CPT symmetry breaking may arise in physics beyond the Standard Model, such as string theories [56]. The CPT invariance ensures the same masses and magnetic moments of particles and corresponding antiparticles [57, 58]. Therefore, comparisons of particle/antiparticle properties test CPT symmetry. Such experiments were recently reviewed in [1, 59–61]. We only provide a brief summary of the most recent results of the CPT tests with antihydrogen ($\bar{\text{H}}$), antiprotons \bar{p} , and antiprotonic helium $\bar{p}\text{He}^+$. Antihydrogen experiments at CERN aimed at CPT and gravity tests include ATRAP, ALPHA, ASACUSA, AEGIS, and GBAR.

Recently, the ALPHA experiment performed a laser-spectroscopic measurement of the $1S\text{--}2S$ transition fre-

quency of antihydrogen using two-photon laser excitation with 243 nm light [62], which was a long-standing goal of the antihydrogen experiments. A comparison of this result with the $1S\text{--}2S$ frequency in hydrogen provided a test of with CPT invariance at a relative precision of 2×10^{-10} . In 2017, an observation of the hyperfine spectrum of antihydrogen was reported [63], finding a ground-state hyperfine splitting in $\bar{\text{H}}$ to be $1420.4 \pm 0.5 \text{ MHz}$. This result is consistent with a corresponding value in atomic hydrogen at the level of four parts in 10^4 .

ALPHA collaboration reported an experimental limit on the charge Qe of antihydrogen, in which e is the elementary charge, to be $|Q| < 0.71$ parts per billion (one standard deviation) [64]. This measurement constrained the relative difference between the positron and elementary charge at a level of about one part per billion (ppb), assuming charge superposition and using the best measured value of the antiproton charge [18].

Another focus of the antihydrogen experiments (GBAR, AEGIS, and ALPHA) is testing whether antimatter is affected by gravity in the same way as matter. Weakness of the gravitational interaction requires such direct laboratory tests to be conducted with neutral particles, making antihydrogen the best available system. These tests are complicated by the need for increased production of cold antihydrogen, requiring new cooling techniques [65, 66].

The goal of the Baryon Antibaryon Symmetry Experiment (BASE) is precise comparisons of the fundamental properties of antiprotons and protons for tests of CPT [67]. This experiment carries out measurements with single trapped particles.

In 2017, BASE collaboration reported a parts-per-billion measurement of the antiproton magnetic moment [68] using an advanced cryogenic multi-Penning trap system. This experiment used a particle with an effective temperature of 300 K for magnetic field measurements and a cold particle at 0.12 K for spin transition spectroscopy, reporting the value of $\mu_{\bar{p}} = 2.792\,847\,3441(42)\mu_N$, where μ_N is the nuclear magnetic moment (at the 68% confidence level). A measurement of the proton magnetic moment at the 0.3 ppb level was reported by the same team [69]. A comparison of the $\mu_{\bar{p}}$ with the new proton value $\mu_p = 2.792\,847\,344\,62(82)\mu_N$ constrains CPT -violating effects. In the future, BASE collaboration proposes to use quantum-logic technologies to further advance the CPT tests. They plan to sympathetically cool and probe the (anti)proton using a coupling to an atomic “qubit” ion trapped in its vicinity via the Coulomb interaction. This technique has a potential to enable the proton and antiproton magnetic moment measurements at the parts per trillion level [69].

The BASE collaboration also compared the charge-to-mass proton and antiproton ratios using high-precision cy-

clotron frequency comparisons carried out in a Penning-trap system, establishing a limit [70]

$$\frac{(q/m)_{\bar{p}}}{(q/m)_p} - 1 = 1(69) \times 10^{-12}.$$

Single-photon spectroscopy of antiprotonic helium, $\bar{p}\text{He}^+$, which consists of an α -particle, an electron, and an antiproton, was performed in [71]. Combining their experimental result with the high-precision calculations of the relevant transition frequencies [72], yielded a value of $m_{\bar{p}}/m_e = 1836.152\,673\,4(15)$ [71]. This value agrees with the CODATA proton to electron mass ratio [73] at a level of 0.8 ppb. A recent review of “magnetometry” CPT tests, which do not require antimatter is given in [74].

A number of very recent CPT tests described above mark a turning point from proof-of-principle experiments to high-precision metrology and CPT comparisons, with prospects for significant improvements in a near future.

32.4 Lorentz Symmetry Tests

Local Lorentz invariance (LLI) is the cornerstone of modern physics: the outcome of any local nongravitational experiment is independent of the orientation and the velocity of the (freely falling) apparatus. In the SM field theory, the Lorentz invariance and the CPT invariance, discussed in Sect. 32.3, are closely related. However, one may be violated but not the other in some BSM frameworks, which is a subject of recent debates (e.g. [75] and references therein).

Current LLI tests span almost all fields of physics as separate violations of LLI are possible for all particles. The resulting limits and references are compiled in the *Data Tables for Lorentz and CPT Violation* [76]. A scaling argument is used to provide some guidance to the Lorentz symmetry violation (LV) searches: one may expect the LV effects to be suppressed by some power of the ratio R between the electroweak scale and the natural (Planck) energy scale for strings: $R = m_{\text{ew}}/M_{\text{Pl}} = 2 \times 10^{-17}$ [56] or electron mass to Planck scale 4×10^{-23} [77]. The LV tests in the electron sector are just at the $R = 1$ boundary, while some limits for other particles have already surpassed it. This presents a particular attraction of the LV tests: any verified positive signal will be an unambiguous sign of the new physics.

Lorentz violation tests are analyzed in the context of an effective field theory known as the Standard Model extension (SME) [78]. The AMO LV tests include experiments with atomic clocks [79], other precision spectroscopy measurements [80], magnetometers [81, 82], rotating optical and microwave resonators [83–85], quantum-information trapped-ion technologies [86], and quartz oscillators [87]. In this section, we highlight the most recent AMO results; a detailed review is given in [1].

In minimal SME, a general expression for the quadratic Hermitian Lagrangian density in the presence of Lorentz violation describing a single spin-1/2 Dirac fermion of mass m is given by [88]

$$\mathcal{L} = \frac{1}{2} i c \bar{\psi} \Gamma_\nu \overleftrightarrow{\partial}^\nu \psi - M c^2 \bar{\psi} \psi, \quad (32.12)$$

where ψ is a four-component Dirac spinor,

$$f \overleftrightarrow{\partial}^\nu g = f \partial^\nu g - g \partial^\nu f, \quad (32.13)$$

$$M = m + a_\mu \gamma^\mu + b_\mu \gamma_5 \gamma^\mu + \frac{1}{2} H_{\mu\nu} \sigma^{\mu\nu},$$

and

$$\Gamma_\nu = \gamma_\nu + c_{\mu\nu} \gamma_\nu + d_{\mu\nu} \gamma_5 \gamma_\nu + e_\nu + i \gamma_5 f_\nu + \frac{1}{2} g_{\lambda\mu\nu} \sigma_{\lambda\mu}. \quad (32.14)$$

The first terms in the expressions for M and Γ_ν are from the SM Lagrangian. The coefficients in Eq. (32.13) have dimensions of mass, while the coefficients in Eq. (32.14) are dimensionless. Lorentz violation is parameterized by the coefficients b_μ , $c_{\mu\nu}$, $d_{\mu\nu}$, e_μ , f_μ , $g_{\lambda\mu\nu}$, and $H_{\mu\nu}$. The field operators in Eqs. (32.13), (32.14) containing the coefficients $c_{\mu\nu}$, $d_{\mu\nu}$, and $H_{\mu\nu}$ are even under CPT , and the remaining ones are odd under CPT . Therefore, the results of the CPT experiments discussed in Sect. 32.3 can also be parameterized by SME. AMO experiments may be interpreted as Lorentz-invariance tests for the photon, electron, proton and neutron, and their combinations, with photon contributions appearing in all atomic experiments.

32.4.1 Electron–Photon Sector of SME

Atomic LV experiments in the electron–photon sector [80, 86] use the different sensitivities of various energy levels to the hypothetical Lorentz violation. The quantization axis is set by the direction of the magnetic field, and the energy difference of two atomic levels with different LV sensitivities is monitored during the Earth’s rotation and motion around the Sun. No additional rotation of the experiment is required. The resulting data are combined with the theoretical calculations of the relevant LV-violating matrix elements and are analyzed to extract the SME coefficients. The SME coefficients are frame-dependent but have unique values in the specified frame. Generally, one uses the Sun centered celestial-equatorial frame (SCCEF) for the analysis of the experiments [89], indicated by the coordinate indexes T , X , Y , and Z . The experiment below set limits on the coefficient of the $c_{\mu\nu}$ tensor, which has nine components that need to be experimentally determined: parity-even c_{TT} and c_{JK}

and parity-odd c_{TJ} , where $J, K = X, Y, Z$. The elements c_{JK} describe the rotational effects and have a leading order time-modulation period related to the sidereal day (12-h and 24-h modulation), while the c_{TJ} and c_{TT} describe the boost effects of the laboratory frame and have a leading order time-modulation period related to the sidereal year. Therefore, the terms c_{TJ} are suppressed in comparison to c_{JK} by a ratio of the Earth's orbital velocity to the speed of light $\beta_{\oplus} \approx 10^{-4}$. The c_{TT} term is suppressed by $\beta_{\oplus}^2 \approx 10^{-8}$.

The LV effect on the bound electronic states is described by the Hamiltonian [80, 88]

$$\delta H = -\left(C_0^{(0)} - \frac{2U}{3c^2}c_{00}\right)\frac{\mathbf{p}^2}{2m_e} - \frac{1}{6m_e}C_0^{(2)}T_0^{(2)}, \quad (32.15)$$

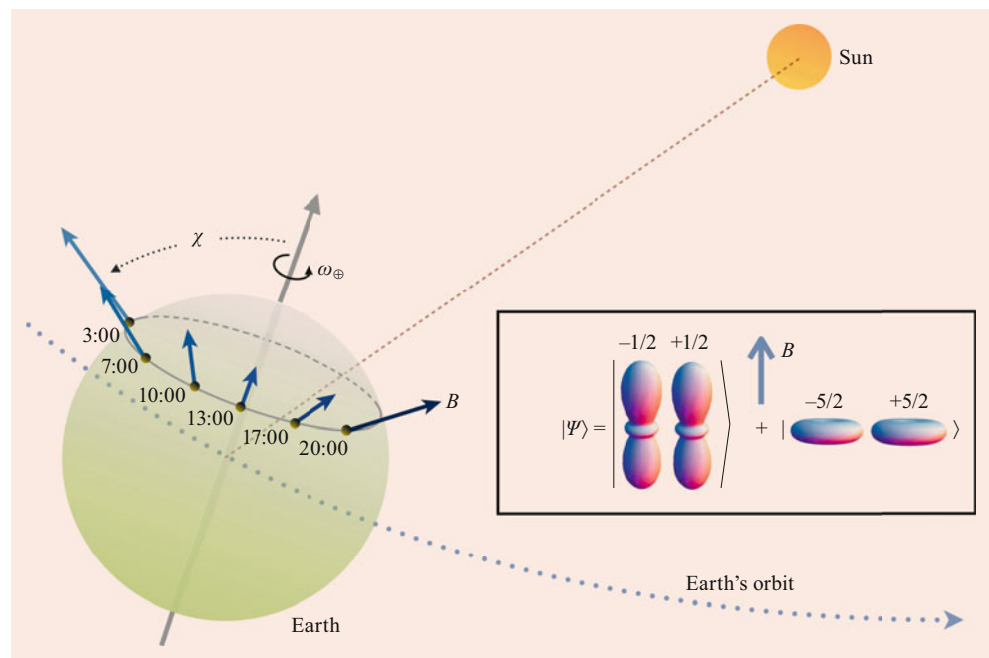
where \mathbf{p} is the momentum of a bound electron, and $T_0^{(2)} = \mathbf{p}^2 - 3p_z^2$ in nonrelativistic approximation. Interpretation of the LV experiments requires theoretical calculations of the expectation values of these operators for the states of interest. The second term in the parentheses gives the leading order gravitational redshift anomaly in terms of the Newtonian potential U . The parameters $C_0^{(0)}$ and $C_0^{(2)}$ are elements of the $c_{\mu\nu}$ tensor in the laboratory frame defined by Eq. (32.14)

$$C_0^{(0)} = c_{00} + (2/3)c_{jj}, \quad (32.16)$$

$$C_0^{(2)} = c_{jj} + (2/3)c_{33}, \quad (32.17)$$

where $j = 1, 2, 3$. The other $C_i^{(2)}$ components do not contribute to the energy shift of bound states.

Fig. 32.3 Rotation of the quantization axis of the experiment with respect to the Sun as the Earth rotates. A magnetic field (B) is applied vertically in the laboratory frame to define the eigenstates of the system. As the Earth rotates with an angular frequency given by $\omega_{\oplus} = 2\pi/(23.93 \text{ h})$, the orientation of the magnetic field and, consequently, that of the electron wave packet (as shown in the inset in terms of probability envelopes) changes with respect to the Sun's rest frame. The angle χ is the colatitude of the experiment. From [86]



The formalism above also applies to the LV violation in the nuclei, but the expectation values of the \mathbf{p}^2 and $T_0^{(2)}$ operators for the nuclear states determine the sensitivity.

Here, we describe LV tests with Dy [80] and Ca^+ [86], performed using very different techniques. Both experiments only involve isotopes with zero nuclear spin making them insensitive to nuclear LV effects.

Dy has two opposite parity states with leading configurations $[\text{Xe}]4f^{10}5d6s$ $J = 10$ (state A) and $[\text{Xe}]4f^95d^26s$ $J = 10$ (state B) that are nearly degenerate. The $\Delta E = E_A - E_B$ energy difference is highly sensitive to the LV effects and can be measured directly by driving an electric-dipole transition between the states A and B with a radio-frequency (rf) field. The sign of the frequency shift is opposite for ^{162}Dy and ^{164}Dy allowing to reduce systematic effects. Repeated frequency measurements over the span of 2 years allowed to constrain eight of the nine elements of the $c_{\mu\nu}$ tensor, limiting Lorentz violation for electrons at the level of 10^{-17} for the c_{JK} components and improving bounds on gravitational redshift anomalies for electrons [90] by two orders of magnitude, to 10^{-8} .

In the $^{40}\text{Ca}^+$ trapped ion experiment, the LV-dependent energy difference of the two Zeeman substates of the $^2D_{5/2}$ manifold was monitored for 23 h [86]. A pair of $^{40}\text{Ca}^+$ ions was trapped in a linear Paul trap, with an applied static magnetic field pointed up defining the quantization axis (i.e., a z axis of the lab frame). The direction of this magnetic field changes with respect to the Sun as the Earth rotates resulting in a rotation of the experiment as illustrated in Fig. 32.3.

Using the theoretical calculation of the matrix elements of the $T_0^{(2)}$ operator for the ${}^2D_{5/2}$ atomic state, the energy difference $\Delta E = E_{m_J=5/2} - E_{m_J=1/2}$ of these two Zeeman levels induced by Lorentz violation is given by

$$\frac{\Delta E}{h} = [-4.45(9) \times 10^{15} \text{ Hz}] \times C_0^{(2)}. \quad (32.18)$$

This experiment was not sensitive to the scalar $C_0^{(0)}$ coefficient of Eq. (32.15).

The main problem of such LV experiments is the effect of the magnetic field noise, which causes frequency shifts. The Ca^+ experiment used quantum-information inspired techniques to create a decoherence-free two-ion product state, shown in Fig. 32.3, that is insensitive to magnetic field fluctuations to first order.

Pruttivarasin et al. [86] noted that electron and photon sector Lorentz violation can not be separated in the LV experiments involving atomic energy levels as LV violation in the photon sector affects the Coulomb potential. Therefore, the experimental results may be interpreted in terms of either photon or electron LV violation described via $c'_{\mu\nu} = c_{\mu\nu} + k_{\mu\nu}/2$, where two terms refer to the electron and photon LV, respectively. The Ca^+ experiment improved the limits to the c'_{JK} coefficients of the LV-violation in the electron–photon sector by a factor of 100.

The LV tests with Yb^+ octupole clock state, $4f^{13}6s^2 F_{7/2}$, and highly-charged ions proposed in [91, 92] promise another five orders of magnitude improvements in LV tests in the electron sector. *Harabati* et al. [93] proposed measuring transition energies of rare-earth ions doped in crystalline lattices, which can be highly sensitive to the electron SME parameters.

LLI tests in the photon sector were carried out with rotating optical and microwave resonators [83–85].

32.4.2 Proton and Neutron Sectors of SME

Wolf et al. [79] used a cold Cs atomic clock, which is also the primary frequency standard defining the second, to test nucleon LLI. The Cs atomic clock operates on the

$$|F = 3, m_F = 0\rangle \leftrightarrow |F = 4, m_F = 0\rangle \quad (32.19)$$

hyperfine transition at 9.2 GHz, where $\mathbf{F} = \mathbf{J} + \mathbf{I}$ is the total angular momentum, and m_F is a corresponding magnetic quantum number. This transition is insensitive to either Lorentz violation or first-order magnetic field effects. To test Lorentz symmetry, a combination of the clock transition above and two other transitions, which are LV sensitive,

was monitored

$$|F = 3, m_F = 3\rangle \leftrightarrow |F = 4, m_F = 3\rangle, \quad (32.20)$$

$$|F = 3, m_F = -3\rangle \leftrightarrow |F = 4, m_F = -3\rangle. \quad (32.21)$$

To suppress the magnetic field fluctuations to the first order, they used a combined observable

$$\nu_c = \nu_{+3} + \nu_{-3} - 2\nu_0, \quad (32.22)$$

where ν_0 , ν_{+3} , and ν_{-3} are frequencies of (32.19), (32.20), and (32.21) transitions.

The combined observable is not sensitive to the Lorentz-violating tensor component from the electron sector but is sensitive to the nuclear (mostly proton) LV violation since the ${}^{133}\text{Cs}$ nucleus has one unpaired proton. The Cs clock experiment set the limits for SME parameters for the proton at the 10^{-21} – 10^{-25} level. Recent reanalysis of the Cs experiment [94] placed improved bounds on the LV for the proton and neutron.

Some of the most stringent clock-comparison tests of LLI [81, 95] were carried out using the self-compensating spin-exchange relaxation-free (SERF) comagnetometry scheme.

The experiment of [95] was performed with K and ${}^3\text{He}$ coupled via spin-exchange collisions with the magnetic field along the z -direction tuned to the compensation point where the K- ${}^3\text{He}$ SERF comagnetometer is insensitive to magnetic fields but highly sensitive to anomalous interactions that do not scale with the magnetic moments. The orientation of the apparatus was alternated between North–South or East–West every 22 s over the course of many days to test the LV effects. The results of this experiment probed neutron couplings to SME background fields (b_μ) at energy scales $\approx 10^{-25}$ eV [95]. Recent work [96] analyzed the Coulomb interactions between the constituent particles of atoms and nuclei, and used comagnetometer experiments [81] to establish that the speed of light is isotropic to a part in 10^{28} .

A related experiment [81] used a ${}^{21}\text{Ne}$ -Rb-K SERF comagnetometer with an order of magnitude better shot-noise-limited sensitivity to LLI violations. Moreover, this experiment probed tensor anisotropies in addition to the vector ones since the nuclear spin of ${}^{21}\text{Ne}$ is $I = 3/2$. To further control the gyro-compass effect, a version of this experiment is being carried out at the South Pole for further improvement of precision.

A different scheme was used by [82] to test LV in the neutron sector with ${}^3\text{He}$ and ${}^{129}\text{Xe}$ atoms. We note a following discussion in the literature [97, 98] regarding this experiment. A novel approach to LLI tests in the matter sector was proposed and demonstrated by *Goryachev* et al. [99] using quartz bulk acoustic-wave oscillators.

32.5 AMO Tests of General Relativity

32.5.1 Tests of the Einstein Equivalence Principle

According to the weak equivalence principle (WEP) the trajectory of a freely falling body is independent of its internal structure and composition. All bodies in a common gravitational field fall with the same acceleration, which is referred to as the universality of free fall (UFF). The equivalence principle implies that all forms of matter-energy respond to gravity in the same way, which may not be the case for most theories aimed at unifying all four fundamental interactions, such as string theories [100]. Therefore, WEP may be violated at small but measurable levels [101]. General tests of gravity including the EEP tests are reviewed in [100]. A review of the WEP tests and future proposals, including torsion-balance experiments, free-fall experiments, and measurement of relative motions of celestial bodies (for example, lunar laser ranging) is given in [102]. We briefly review best classical WEP limits before discussing quantum-based AMO tests of the WEP.

If the WEP is violated, the gravitational mass of a body, m_g , is not equal to its inertial mass, m_1 , and the acceleration a of a body in a gravitational field g is given by

$$a = \frac{m_g}{m_1} g .$$

The violation of the WEP is generally quantified by the Eötvös ratio η

$$\eta = 2 \left| \frac{a_1 - a_2}{a_1 + a_2} \right| , \quad (32.23)$$

where a_1 , a_2 are the accelerations of the two falling bodies, which differ in their composition. The strictest WEP laboratory Earth-based constraints (at a 10^{-13} level) is from the “Eöt-Wash” torsion-balance experiments, which compare differential accelerations of beryllium-aluminum and beryllium-titanium test-body pairs [103, 104]. The lunar laser-ranging experiments provided similar limits [105, 106]. A significant improvement in probing WEP is expected to come from space-based missions. MicroSCOPE is an ongoing Centre National d’Études Spatiales (CNES)/European Space Agency (ESA) gravity-research minisatellite mission [107]. Its first results have already yielded improved limits

$$\eta = (-1 \pm 27) \times 10^{-15}$$

at a 2σ confidence level.

Recent progress in control of the ultracold atoms started the field of the weak-equivalence tests with quantum matter using atom interferometers (AI) to directly compare the

phase shifts of two different types of matter waves without the use of classical gravimeters [108, 109]. The sensitivity of atom interferometers to WEP violations increases linearly with the momentum difference between the two matter waves and quadratically with the time of free fall. Therefore, increasing either of these parameters improves the sensitivity of the AI WEP tests, with an ultimate goal of the space-based tests.

A proof-of-principle AI quantum tests of the universality of free fall were performed at the 10^{-8} – 10^{-9} level [110, 111]. A scheme to compensate the effects of gravity gradients that pose a major challenge for high-precision tests of the WEP with atom interferometry was proposed recently [112]. Implementation of this scheme by *Overstreet* et al. [113] demonstrated that one can bring down the systematic effects due to the gravity gradients in WEP tests to one part in 10^{14} , making future AI tests eventually competitive with tests employing macroscopic masses. *Hartwig* et al. [114] proposed a long baseline (with over 10 m of free fall) AI test of WEP with Rb and Yb, estimated to reach 7×10^{-13} accuracy in the Eötvös ratio.

We note that using quantum matter for gravity tests provides the opportunity to perform qualitatively different (from the classical) WEP tests using “test masses” with a definite spin for a search of the spin-gravity coupling effects. An experiment to study the possible influence of entanglement between two test masses on the universality of free fall was proposed [115].

A number of quantum WEP tests in microgravity are being pursued with the promise of greatly increased precision of the current quantum WEP tests. In 2017, the QUANTUS collaboration [116] conducted the successful MAIUS 1 (matter-wave interferometry in microgravity) experiment aboard a sounding rocket at an altitude of up to 243 km above the Earth’s surface, conducting ≈ 100 discrete matter-wave experiments during the 6-min experimental phase of this flight.

32.5.2 Other AMO Tests of Gravity

Tests of gravity with antimatter were briefly discussed in Sect. 32.3. A number of AMO gravity tests are related to searches for exotic forces. Atomic spectroscopy was used to search for Yukawa-type fifth-forces [117] by studying the behavior of atomic transition frequencies at varying distances away from massive bodies. A search for subgravitational forces on atoms from a miniature source mass was carried out in [118].

An intriguing possibility was proposed in [119]: a realization of the gravitational Aharonov–Bohm effect by

measuring phase shifts with an atom interferometer due to a gravitational potential U in the absence of a gravitational force.

Asenbaum et al. [120] measured a phase shift in an atom interferometer due to spacetime curvature across its wave function. In this experiment, interfering atomic wave packets were separated by a macroscopic (up to 16 cm) distance to study the interplay of recoil effects and gravitational curvature from a nearby Pb source mass.

32.5.3 Detection of Gravitational Waves

In 2015, the Advanced LIGO detected the gravitational waves (GW) for the first time [121], starting the field of gravitational-wave astronomy. However, the detection capability of such terrestrial detectors is limited to GWs with frequencies above ≈ 10 Hz by seismic and Newtonian noise [122]. The detection of the gravitational waves at lower frequencies will significantly increase the number and mass range of potentially observed GW sources, allow for longer observation of the inspiralling binary stars before the merger, and may improve the chances of detecting relic GWs from the early evolution of the Universe [123]. This is the goal of space-based laser interferometry detectors such as the Laser Interferometer Space Antenna (LISA) [124] and TianQin [125].

Rapid progress of matter-wave interferometry and atomic clocks opens other approaches to gravitational wave detection, with a number of proposals for both terrestrial and space-based detectors ([126–129] and references therein).

The Matter wave-laser based Interferometer Gravitation Antenna (MIGA) is a hybrid atom-laser detector in the 100 mHz–1 Hz frequency range [126]. MIGA will employ several atom interferometers simultaneously interrogated by the resonant mode of an optical cavity, with a cavity length of 200 m. It is the first very long baseline atom interferometry instrument, now under construction, to be located in dedicated tunnels, 500 m underground in France.

Hogan and Kasevich [127] proposed a space-based GW detector with light-pulse AIs separated by a long baseline (over 100 000 km), capable of detecting GWs in the 0.1-mHz to 1-Hz frequency band, requiring only two satellites and potentially exceeding the sensitivity of proposed the LISA detector. AI GW detector that can operate in a resonant detection mode and can switch between the broadband and narrowband detection modes to increase sensitivity was proposed in [128]. Geiger [130] reviewed the perspective of using AI for GW detection in the mHz to about 10 Hz frequency band. Kolkowitz et al. [129] proposed to use atomic optical lattice clocks (rather than atom interferometers) for a sensitive, narrowband GW space-based detector in a two-satellite configuration.

Mid-band Atomic Gravitational Wave Interferometric Sensor (MAGIS) collaboration assessed the technical feasibility of a satellite mission based on precision atomic sensors (involving both AI and atomic clocks) with laser-cooled atomic Sr [131]. MAGIS is expected to be sensitive to GWs of the 0.03 to 3 Hz observation band, intermediate between the LISA and advanced LIGO ranges, and also suited for performing dark matter searches.

References

1. Safronova, M.S., Budker, D., DeMille, D., Kimball, D.F.J., Derevianko, A., Clark, C.W.: Rev. Mod. Phys. **90**, 025008 (2018)
2. Lee, T.D., Yang, C.N.: Phys. Rev. **104**, 254 (1956)
3. Wu, C.S., Ambler, E., Hayward, R.W., Hoppes, D.D., Hudson, R.P.: Phys. Rev. **105**, 1413 (1957)
4. Zeldovich, Y.B.: Sov. Phys. JETP **9**, 682 (1959)
5. Bouchiat, M.A., Bouchiat, C.: J. Phys. **35**, 899 (1974)
6. Barkov, L.M., Zolotarev, M.S.: Pis'ma Zh. Eksp. Teor. Fiz **28**, 544 (1978). JETP Lett. **28**, 503 (1978)
7. Phipp, S.J., Edwards, N.H., Baird, P.E.G., Nakayama, S.: J. Phys. B **29**, 1861 (1996)
8. Edwards, N.H., Phipp, S.J., Baird, P.E.G., Nakayama, S.: Phys. Rev. Lett. **74**, 2654 (1995)
9. Vetter, P.A., Meekhof, D.M., Majumder, P., Lamoreaux, S.K., Fortson, E.N.: Phys. Rev. Lett. **74**, 2658 (1995)
10. Lintz, M., Guena, J., Bouchiat, M.A.: Eur. Phys. J. A **32**, 525 (2007)
11. Wood, C.S., et al.: Science **275**, 1759 (1997)
12. Tsigutkin, K., Dounas-Frazer, D., Family, A., Stalnaker, J.E., Yashchuk, V.V., Budker, D.: Phys. Rev. Lett. **103**, 071601 (2009)
13. Antypas, D., Fabricant, A., Stalnaker, J.E., Tsigutkin, K., Budker, D.: Nat. Phys. **15**, 120 (2019)
14. Derevianko, A., Porsev, S.G.: Eur. Phys. J. A **32**, 517 (2007)
15. Roberts, B., Dzuba, V., Flambaum, V.: Ann. Rev. Nucl. Part. Sci. **65**, 63 (2015)
16. Langacker, P.: Precision Tests of the Standard Electroweak Model. World Scientific, Singapore, p 170 (1995)
17. Marciano, W.J., Sanda, A.I.: Phys. Rev. D **17**, 3055 (1978)
18. M.T., et al.: Phys. Rev. D **98**, 030001 (2018). Particle Data Group
19. Brown, B.A., Derevianko, A., Flambaum, V.V.: Phys. Rev. C **79**, 035501 (2009)
20. Porsev, S.G., Beloy, K., Derevianko, A.: Phys. Rev. D **82**, 36008 (2010)
21. Johnson, W., Safronova, M., Safronova, U.: Phys. Rev. A **67**, 062106 (2003)
22. Flambaum, V.V., Dzuba, V.A., Harabati, C.: Phys. Rev. A **96**, 012516 (2017)
23. Zel'dovich, Y.B.: Sov. Phys. JETP **6**, 1184 (1958)
24. Porsev, S.G., Beloy, K., Derevianko, A.: Phys. Rev. Lett. **102**, 181601 (2009)
25. Dzuba, V.A., Berengut, J.C., Flambaum, V.V., Roberts, B.: Phys. Rev. Lett. **109**, 203003 (2012)
26. Davoudiasl, H., Lee, H.S., Marciano, W.J.: Phys. Rev. D **89**, 095006 (2014)
27. Safronova, M.S., Pal, R., Jiang, D., Kozlov, M.G., Johnson, W.R., Safronova, U.I.: Nucl. Phys. A. **827**, 411 (2009)
28. Haxton, W.C., Wieman, C.E.: Annu. Rev. Nucl. Part. Sci. **51**, 261 (2001)
29. Haxton, W.C., Holstein, B.R.: Prog. Part. Nucl. Phys. **71**, 185 (2013)

30. Nguyen, A.T., Budker, D., DeMille, D., Zolotov, M.: *Phys. Rev. A* **56**, 3453 (1997)
31. Antypas, D., Elliott, D.S.: *Can. J. Chem.* **92**, 144 (2014)
32. Aubin, S., et al.: *Hyperfine Interact* **214**, 163 (2013)
33. Altuntas, E., Ammon, J., Cahn, S.B., DeMille, D.: *Phys. Rev. Lett.* **120**, 142501 (2018)
34. Engel, J., Ramsey-Musolf, M.J., van Kolck, U.: *Prog. Part. Nucl. Phys.* **71**, 21 (2013)
35. Chupp, T., Fierlinger, P., Ramsey-Musolf, M., Singh, J.: *Rev. Mod. Phys.* **91**, 015001 (2019)
36. Sakharov, A.D.: *Jetp Lett.* **5**, 24 (1967)
37. Schiff, L.I.: *Phys. Rev.* **132**, 2194 (1963)
38. Porsev, S.G., Safronova, M.S., Kozlov, M.G.: *Phys. Rev. Lett.* **108**(17), 173001 (2012)
39. Regan, B., Commins, E., Schmidt, C., DeMille, D.: *Phys. Rev. Lett.* **88**, 18 (2002)
40. Hudson, J.J., Kara, D.M., Smallman, I.J., Sauer, B.E., Tarbutt, M.R., Hinds, E.A.: *Nature* **473**, 493 (2011)
41. Baron, J., Campbell, W.C., DeMille, D., Doyle, J.M., Gabrielse, G., Gurevich, Y.V., Hess, P.W., Hutzler, N.R., Kirilov, E., Kozryyev, I.: *Science* **343**, 269 (2014)
42. Skripnikov, L.V.: *J Chem Phys* **145**(21), 214301 (2016)
43. Denis, M., Fleig, T.: *J Chem Phys* **145**, 214307 (2016)
44. Cairncross, W.B., Gresh, D.N., Grau, M., Cossel, K.C., Roussy, T.S., Ni, Y., Zhou, Y., Ye, J., Cornell, E.A.: *Phys. Rev. Lett.* **119**, 153001 (2017)
45. Skripnikov, L.V.: *J Chem Phys* **147**, 021101 (2017)
46. Fleig, T.: *Phys. Rev. A* **96**, 040502 (2017)
47. Panda, C.D., O'Leary, B.R., West, A.D., Baron, J., Hess, P.W., Hoffman, C., Kirilov, E., Overstreet, C.B., West, E.P., DeMille, D., Doyle, J.M., Gabrielse, G.: *Phys. Rev. A* **93**(5), 52110 (2016)
48. Kozryyev, I., Hutzler, N.R.: *Phys. Rev. Lett.* **119**, 133002 (2017)
49. Graner, B., Chen, Y., Lindahl, E.G., Heckel, B.R.: *Phys. Rev. Lett.* **116**, 161601 (2016)
50. Swallows, M.D., Loftus, T.H., Griffith, W.C., Heckel, B.R., Fortson, E.N., Romalis, M.V.: *Phys. Rev. A* **87**(1), 012102 (2013)
51. Dmitriev, V.F., Sen'kov, R.A.: *Phys. Rev. Lett.* **91**(21), 212303 (2003)
52. Rosenberry, M., Chupp, T.: *Phys. Rev. Lett.* **86**, 22 (2001)
53. Bishof, M., Parker, R.H., Bailey, K.G., Greene, J.P., Holt, R.J., Kalita, M.R., Korsch, W., Lemke, N.D., Lu, Z.-T., Mueller, P., O'Connor, T.P., Singh, J.T., Dietrich, M.R.: *Phys. Rev. C* **94**, 025501 (2016)
54. Cho, D., Sangster, K., Hinds, E.: *Phys. Rev. A* **44**, 2783 (1991)
55. Giudice, G.F., Romanino, A.: *Phys. Lett. B.* **634**, 307 (2006)
56. Kostelecký, V.A., Potting, R.: *Phys. Rev. D* **51**, 3923 (1995)
57. Lüders, G., Zumino, B.: *Phys. Rev.* **106**, 385 (1957)
58. Bluhm, R., Kostelecký, V.A., Russell, N.: *Phys. Rev. Lett.* **79**, 1432 (1997)
59. Yamazaki, Y., Ulmer, S.: *Ann. Phys.* **525**, 493 (2013)
60. Gabrielse, G., Hoogerheide, S.F., Dorr, J., Novitski, E.: *Fundamental physics in particle traps*. In: Quint, W., Vogel, M. (eds.) *Springer Tracts in Modern Physics*, vol. 256, p. 1. Springer, Berlin, Heidelberg (2014)
61. Kellerbauer, A.: *Eur. Rev.* **23**, 45 (2015)
62. Ahmadi, M., et al.: *Nature* **541**, 506 (2017)
63. Ahmadi, M., et al.: *Nature* **548**, 66 (2017)
64. Ahmadi, M., et al.: *Nature* **529**, 373 (2016)
65. Pérez, P., et al.: *Hyperfine Interact* **233**, 21 (2015)
66. Aghion, S., et al.: *Nat. Commun.* **5**, 4538 (2014)
67. Smorra, C., et al.: *Euro. Phys. J. Spec. Top.* **224**, 3055 (2015)
68. Smorra, C., et al.: *Nature* **550**, 371 (2017)
69. Schneider, G., et al.: *Science* **358**, 1081 (2017)
70. Ulmer, S., et al.: *Nature* **524**, 196 (2015)
71. Hori, M., et al.: *Science* **354**, 610 (2016)
72. Korobov, V.I., Hilico, L., Karr, J.-P.: *Hyperfine Interact* **233**, 75–82 (2015)
73. Mohr, P.J., Newell, D.B., Taylor, B.N.: *Rev. Mod. Phys.* **88**, 035009 (2016)
74. Kimball, D.F.J., Lamoreaux, S.K., Chupp, T.E.: *Tests of fundamental physics with optical magnetometers*. In: Budker, D., Kimball, D.F.J. (eds.) *Optical Magnetometry*, p. 339. Cambridge University, Cambridge, UK (2013)
75. Kostelecký, V.A., Vargas, A.J.: *Phys. Rev. D* **92**, 056002 (2015)
76. Kostelecký, V. A., Russell, N.: arXiv:0801.0287v15 (2022)
77. Liberati, S., Maccione, L.: *Annu. Rev. Nucl. Part. Sci.* **59**, 245 (2009)
78. Colladay, D., Kostelecký, V.A.: *Phys. Rev. D* **58**, 116002 (1998)
79. Wolf, P., Chapelet, F., Bize, S., Clairon, A.: *Phys. Rev. Lett.* **96**, 060801 (2006)
80. Hohensee, M.A., Leefer, N., Budker, D., Harabati, C., Dzuba, V.A., Flambaum, V.V.: *Phys. Rev. Lett.* **111**, 050401 (2013)
81. Smiciklas, M., Brown, J.M., Cheuk, L.W., Smullin, S.J., Romalis, M.V.: *Phys. Rev. Lett.* **107**, 171604 (2011)
82. Allmendinger, F., et al.: *Phys. Rev. Lett.* **112**, 110801 (2014)
83. Eisele, C., Nevsky, A.Y., Schiller, S.: *Phys. Rev. Lett.* **103**, 090401 (2009)
84. Nagel, M., et al.: *Nat. Commun.* **6**, 8174 (2015)
85. Chen, Q., Magoulakis, E., Schiller, S.: *Phys. Rev. D* **93**, 022003 (2016)
86. Pruttivarasin, T., Ramm, M., Porsev, S.G., Tupitsyn, I.I., Safronova, M.S., Hohensee, M.A., Häffner, H.: *Nature* **517**, 592 (2015)
87. Lo, A., et al.: *Phys. Rev. X* **6**, 011018 (2016)
88. Kostelecký, V.A., Lane, C.D.: *Phys. Rev. D* **60**, 116010 (1999)
89. Kostelecký, V.A., Mewes, M.: *Phys. Rev. D* **66**, 056005 (2002)
90. Hohensee, M.A., Chu, S., Peters, A., Müller, H.: *Phys. Rev. Lett.* **106**, 151102 (2011)
91. Dzuba, V.A., Flambaum, V.V., Safronova, M.S., Porsev, S.G., Pruttivarasin, T., Hohensee, M.A., Häffner, H.: *Nature Phys* **12**, 465–468 (2016)
92. Shaniv, R., Ozeri, R., Safronova, M.S., Porsev, S.G., Dzuba, V.A., Flambaum, V.V., Häffner, H.: *Phys. Rev. Lett.* **120**, 103202 (2018)
93. Harabati, C., Dzuba, V.A., Flambaum, V.V., Hohensee, M.A.: *Phys. Rev. A* **92**, 040101 (2015)
94. Pihan-Le Bars, H., et al.: *Phys. Rev. D* **95**, 075026 (2017)
95. Brown, J.M., Smullin, S.J., Kornack, T.W., Romalis, M.V.: *Phys. Rev. Lett.* **105**, 151604 (2010)
96. Flambaum, V.V., Romalis, M.V.: *Phys. Rev. Lett.* **118**, 142501 (2017)
97. Romalis, M.V., Sheng, D., Saam, B., Walker, T.G.: *Phys. Rev. Lett.* **113**, 188901 (2014)
98. Allmendinger, F., et al.: *Phys. Rev. Lett.* **113**, 188902 (2014)
99. Goryachev, M., Kuang, Z., Ivanov, E.N., Haslinger, P., Muller, H., Tobar, M.E.: *IEEE Trans. Ultrason., Ferroelect., Freq. Contr.* **65**, 991 (2018)
100. Will, C.M.: *Living Rev. Relativ.* **17**, 4 (2014)
101. Damour, T.: *Class. Quantum Gravity* **29**, 184001 (2012)
102. Sondag, A., Dittus, H.: *Adv. Space Res.* **58**, 644 (2016)
103. Schlamminger, S., Choi, K.-Y., Wagner, T.A., Gundlach, J.H., Adelberger, E.G.: *Phys. Rev. Lett.* **100**, 041101 (2008)
104. Wagner, T.A., Schlamminger, S., Gundlach, J.H., Adelberger, E.G.: *Class. Quantum Gravity* **29**, 184002 (2012)
105. Williams, J.G., Turyshev, S.G., Boggs, D.H.: *Phys. Rev. Lett.* **93**, 261101 (2004)
106. Williams, J.G., Turyshev, S.G., Boggs, D.H.: *Class. Quantum Gravity* **29**, 184004 (2012)
107. Bergé, J., Touboul, P., Rodrigues, M.: *J. Phys. Conf. Ser.* **610**, 012009 (2015). for the MICROSCOPE team

108. Hogan, J.M., Johnson, D.M.S., Kasevich, M.A.: In: Arimondo, E., Ertmer, W., Schleich, W.P., Rasel, E.M. (eds.) *Atom Optics and Space Physics*, p. 411. IOS, Amsterdam, Oxford, Tokyo, Washington D.C. (2009)
109. Kleinert, S., Kajari, E., Roura, A., Schleich, W.P.: *Phys. Rep.* **605**, 1 (2015)
110. Zhou, L., et al.: *Phys. Rev. Lett.* **115**, 013004 (2015)
111. Rosi, G., et al.: *Nat. Commun.* **8**, 15529 (2017)
112. Roura, A.: *Phys. Rev. Lett.* **118**, 160401 (2017)
113. Overstreet, C., Asenbaum, P., Kovachy, T., Notermans, R., Hogan, J.M., Kasevich, M.A.: *Phys. Rev. Lett.* **120**, 183604 (2018)
114. Hartwig, J., et al.: *New J. Phys.* **17**, 035011 (2015)
115. Geiger, R., Trupke, M.: *Phys. Rev. Lett.* **120**, 043602 (2018)
116. Seidel, S.T., et al.: *European Rocket and Balloon: Programmes and Related research. Esa Special Publ.* **730**, 309 (2015)
117. Leefer, N., Gerhardus, A., Budker, D., Flambaum, V., Stadnik, Y.: *Phys. Rev. Lett.* **117**, 271601 (2016)
118. Jaffe, M., et al.: *Nat. Phys.* **13**, 938–942 (2017)
119. Hohensee, M.A., Estey, B., Hamilton, P., Zeilinger, A., Müller, H.: *Phys. Rev. Lett.* **108**, 230404 (2012)
120. Asenbaum, P., Overstreet, C., Kovachy, T., Brown, D.D., Hogan, J.M., Kasevich, M.A.: *Phys. Rev. Lett.* **118**, 183602 (2017)
121. Abbott, B.P., et al.: *Phys. Rev. Lett.* **116**, 061102 (2016). LIGO Scientific Collaboration, V Collaboration
122. Saulson, P.R.: *Phys. Rev. D* **30**, 732 (1984)
123. Dimopoulos, S., Graham, P.W., Hogan, J.M., Kasevich, M.A., Rajendran, S.: *Phys. Rev. D* **78**, 122002 (2008)
124. Danzmann, K., et al.: *Assessment Study Report. ESA/SRE* **3**, 2 (2011)
125. Hu, X.-C., et al.: *Class. Quantum Gravity* **35**, 095008 (2018)
126. Canuel, B., et al.: *Sci. Rep.* **8**, 14064 (2018)
127. Hogan, J.M., Kasevich, M.A.: *Phys. Rev. A* **94**, 033632 (2016)
128. Graham, P.W., Hogan, J.M., Kasevich, M.A., Rajendran, S.: *Phys. Rev. D* **94**, 104022 (2016)
129. Kolkowitz, S., Pikovski, I., Langellier, N., Lukin, M.D., Walsworth, R.L., Ye, J.: *Phys. Rev. D* **94**, 124043 (2016)
130. Geiger, R.: In: Augar, G., Plagnol, E. (eds.): *An Overview of Gravitational Waves: Theory, Sources and Detection*, pp. 285–313. World Scientific, New Jersey (2017)
131. Graham, P. W., Hogan, J. M., Kasevich, M. A., Rajendran, S., Romani, R. W.: *arXiv:1711.02225* (2017)



Marianna Safronova Marianna Safronova is Professor of Physics at the University of Delaware. Her research interests include the study of fundamental symmetries and the search for physics beyond the standard model of elementary particles and fundamental interactions, the development of high-precision methodologies for calculating atomic properties and exploring their applications, atomic clocks, ultracold atoms and quantum information, long-range interactions, superheavy atoms, highly-charged ions, atomic anions, and other topics.

Part C
Molecules

Part C begins with a discussion of molecular structure from a theoretical/computational perspective using the Born–Oppenheimer approximation as the point of departure. The key role that symmetry considerations play in organizing and simplifying our knowledge of molecular dynamics and spectra is described. The theory of radiative transition probabilities, which determine the intensities of spectral lines, for the rotationally resolved spectra of certain model molecular systems is summarized. The ways in which molecular photodissociation is studied in the gas phase are outlined. The results presented are particularly relevant to the investigation of combustion and atmospheric reactions. Modern experimental techniques allow the detailed motions of the atomic constituents of a molecule to be resolved as

a function of time. A brief description of the basic ideas behind these techniques is given, with an emphasis on gas phase molecules in collision-free conditions. The semiclassical and quantal approaches to nonreactive scattering are outlined. Various quantitative approaches toward a description of the rates of gas phase chemical reactions are presented and then evaluated for their reliability and range of application. Ionic reactions in the gas phase are also considered. Clusters, which are important in many atmospheric and industrial processes, are arranged into six general categories, and then the physics and chemistry common to each category is described. The most important spectroscopic techniques used to study the properties of molecules are presented in detail.



David R. Yarkony

Contents

33.1	Concepts	488
33.1.1	Nonadiabatic Ansatz: Born–Oppenheimer Approximation	488
33.1.2	Born–Oppenheimer Potential Energy Surfaces and Their Topology	489
33.1.3	Classification of Interstate Couplings: Adiabatic and Diabatic Bases	489
33.1.4	Surfaces of Intersection of Potential Energy Surfaces	490
33.2	Characterization of Potential Energy Surfaces	490
33.2.1	The Self-Consistent Field (SCF) Method	491
33.2.2	Electron Correlation: Wave Function Based Methods	491
33.2.3	Electron Correlation: Density Functional Theory	494
33.2.4	Weakly Interacting Systems	495
33.3	Intersurface Interactions: Perturbations	495
33.3.1	Derivative Couplings	496
33.3.2	Breit–Pauli Interactions	497
33.3.3	Surfaces of Intersection	498
33.4	Nuclear Motion	499
33.4.1	General Considerations	499
33.4.2	Rotational–Vibrational Structure	500
33.4.3	Coupling of Electronic and Rotational Angular Momentum in Weakly Interacting	500
33.4.4	Reaction Path	501
33.5	Reaction Mechanisms: A Spin-Forbidden Chemical Reaction	502
33.6	Recent Developments	504
	References	504

Abstract

Molecular structure is a reflection of the Born–Oppenheimer separation of electronic and nuclear motion, which is in turn a consequence of the large difference between the electron and nuclear masses. One consequence of

this separation is the concept of a potential energy surface for nuclear motion created by the faster moving electrons. Corollaries include equilibrium structures, transition states, and reaction paths which are the foundation of the description of molecular structure and reactivity. However the Born–Oppenheimer approximation is not uniformly applicable and its breakdown results in perturbations in molecular spectra, radiationless decay, and nonadiabatic chemical reactions.

There are many issues that can be addressed in a discussion of molecular structure, including the structure and bonding of individual classes of molecules, computational and/or experimental techniques used to determine or infer molecular structure, the accuracy of those methods, etc. In an effort to provide a broad view of the essential aspects of molecular structure, this Chapter considers issues in molecular structure from a theoretical/computational perspective using the Born–Oppenheimer approximation as the point of origin. Rather than providing a compendium of results, this chapter will explain how issues in molecular structure are investigated and how the questions that can be addressed reflect the available methodology. Even with these restrictions the scope of this topic remains enormous and precludes a detailed presentation of any one issue. Thus the abbreviated discussions in this work are supplemented by ample references to the literature.

Several aspects of potential energy surfaces and their relation to molecular structure will be considered: (i) the electronic structure techniques used to determine a single point on a potential energy surface, and the interactions that couple the electronic states in question, (ii) the local properties of potential energy surfaces, in particular equilibrium structures and rovibrational levels that provide the link to experimental inferences concerning molecular structure, (iii) global chemistry deduced from potential energy surfaces including reaction mechanisms and reaction paths and (iv) phenomena resulting from the nonadiabatic interactions that couple potential energy surfaces.

D. R. Yarkony (✉)
Dept. of Chemistry, The Johns Hopkins University
Baltimore, MD, USA
e-mail: yarkony@jhu.edu

Keywords

wave function · potential energy surface · reaction path
· configuration interaction · conical intersection · Born–Oppenheimer approximation

33.1 Concepts**33.1.1 Nonadiabatic Ansatz:
Born–Oppenheimer Approximation****Basic Quantities**

The total Hamiltonian for electronic and nuclear motion in the space fixed coordinate frame, in atomic units, is

$$H^{\text{eN}}(\mathbf{r}, \mathbf{R}) = \sum_{\alpha=1}^N \frac{-1}{2M_{\alpha}} \nabla_{\alpha}^2 + H^{\text{e}}(\mathbf{r}; \mathbf{R}) \\ \equiv T^{\text{nuc}} + H^{\text{e}}(\mathbf{r}; \mathbf{R}), \quad (33.1)$$

where \mathbf{R} denotes the $3N$ nuclear coordinates, with $\mathbf{R} = (\mathbf{R}_1, \mathbf{R}_2, \dots, \mathbf{R}_N)$, $\mathbf{R}_i = (X_i, Y_i, Z_i)$, \mathbf{r} denotes the $3M$ electronic coordinates using similar conventions, T^{nuc} is the nuclear kinetic energy operator and $H^{\text{e}}(\mathbf{r}, \mathbf{R})$ is the total electronic Hamiltonian taken as

$$H^{\text{e}}(\mathbf{r}; \mathbf{R}) = H^0(\mathbf{r}; \mathbf{R}) + H^{\text{rel}}(\mathbf{r}; \mathbf{R}). \quad (33.2)$$

Here $H^0(\mathbf{r}; \mathbf{R})$ is the nonrelativistic Born–Oppenheimer Hamiltonian

$$H^0(\mathbf{r}; \mathbf{R}) = -\frac{1}{2} \sum_{i=1}^M \nabla_i^2 - \sum_{K,i} \frac{Z_K}{|\mathbf{R}_K - \mathbf{r}_i|} \\ + \frac{1}{2} \sum_{i \neq j}^M \frac{1}{|\mathbf{r}_i - \mathbf{r}_j|} + \frac{1}{2} \sum_{K \neq L}^N \frac{Z_K Z_L}{|\mathbf{R}_K - \mathbf{R}_L|}, \quad (33.3)$$

and $H^{\text{rel}}(\mathbf{r}; \mathbf{R})$ is the relativistic contribution to the electronic Hamiltonian, for light atoms conventionally treated within the Breit–Pauli approximation [1] and discussed further in Sect. 33.3.2. Note that in Eq. (33.3) the nuclear kinetic energy is absent, so that only the \mathbf{r}_i are dynamical variables in Eqs. (33.2) and (33.3). Using the Born–Huang approach [2] to the Born–Oppenheimer approximation, the total wave function $\Psi_L^{\text{eN}}(\mathbf{r}, \mathbf{R})$ is expanded in a basis of electronic states, $\Psi_I^{\text{e}}(\mathbf{r}; \mathbf{R})$. The total wave function for the system thus has the form

$$\Psi_L^{\text{eN}}(\mathbf{r}, \mathbf{R}) = \sum_I \Psi_I^{\text{e}}(\mathbf{r}; \mathbf{R}) \beta_I^L(\mathbf{R}). \quad (33.4)$$

Equation (33.4) is valid for any complete set of electronic states depending parametrically on nuclear coordinates. The parametrical dependence of $\Psi_I^{\text{e}}(\mathbf{r}; \mathbf{R})$ on \mathbf{R} , denoted by the semicolon, reflects the fact that the \mathbf{R} are not dynamical variables in Eqs. (33.2) and (33.3). As a practical matter it is necessary to make a particular choice of $\Psi_I^{\text{e}}(\mathbf{r}; \mathbf{R})$ in order to limit the size of the expansion in electronic states. An adiabatic electronic state is an eigenfunction of $H^{\text{e}}(\mathbf{r}; \mathbf{R})$ for fixed \mathbf{R} . A particularly useful choice of adiabatic state, denoted by $\Psi_I^0(\mathbf{r}; \mathbf{R})$, employs $H^0(\mathbf{r}; \mathbf{R})$ rather than the full $H^{\text{e}}(\mathbf{r}, \mathbf{R})$. These electronic wave functions satisfy

$$H^0(\mathbf{r}; \mathbf{R}) \Psi_I^0(\mathbf{r}; \mathbf{R}) = E_I^0(\mathbf{R}) \Psi_I^0(\mathbf{r}; \mathbf{R}). \quad (33.5)$$

The $\Psi_I^0(\mathbf{r}; \mathbf{R})$ are determined up to a geometry dependent phase. This phase is usually chosen such that the $\Psi_I^0(\mathbf{r}; \mathbf{R})$ are real. This assumption is acceptable except in the situation where there is a conical intersection on the potential energy surface in question. In that case, the real-valued $\Psi_I^0(\mathbf{r}; \mathbf{R})$ changes sign when a closed loop surrounding the conical intersection point is traversed, that is, $\Psi_I^0(\mathbf{r}; \mathbf{R})$ is not single-valued [3]. This geometric or *Berry* [4] phase condition has consequences in such phenomena as the dynamic Jahn–Teller effect [5, 6] but will not be addressed in detail in this review.

As a consequence of the parametric dependence of $\Psi_I^0(\mathbf{r}; \mathbf{R})$ on \mathbf{R} , $E_I^0(\mathbf{R})$ becomes a function of \mathbf{R} and is referred to as the nonrelativistic Born–Oppenheimer potential energy surface for reasons discussed below. Approaches based on Eq. (33.5) are most appropriate for molecular systems with only light atoms. However with the use of pseudopotential techniques [7], formally equivalent approaches can be developed for heavier systems (Sect. 33.3.2).

Inserting Eq. (33.4) into the time independent Schrödinger equation $[H^{\text{eN}}(\mathbf{r}; \mathbf{R}) - E] \Psi^{\text{eN}}(\mathbf{r}; \mathbf{R}) = 0$ and taking the inner product with the electronic basis state $\Psi_I^0(\mathbf{r}; \mathbf{R})$ gives the following system of coupled equations for the rovibronic functions $\beta_I^L(\mathbf{R})$ [8, 9]:

$$[T^{\text{nuc}} + E_I^0(\mathbf{R}) - E] \beta_I(\mathbf{R}) \\ = - \sum_J \left(\tilde{K}^{IJ}(\mathbf{R}) + H_{IJ}^{\text{BP}}(\mathbf{R}) \right. \\ \left. - \sum_{\alpha=1}^N \left\{ \frac{1}{2M_{\alpha}} [f_{\alpha}^{IJ}(\mathbf{R}) \cdot \nabla_{\alpha} + \nabla_{\alpha} \cdot f_{\alpha}^{IJ}(\mathbf{R})] \right\} \right) \beta_J(\mathbf{R}), \quad (33.6)$$

where the state label L on β_I^L has been suppressed, and

$$f_{\alpha}^{IJ}(\mathbf{R}) \equiv [f_{X_{\alpha}}^{IJ}(\mathbf{R}), f_{Y_{\alpha}}^{IJ}(\mathbf{R}), f_{Z_{\alpha}}^{IJ}(\mathbf{R})], \quad (33.7)$$

$$\tilde{K}^{JI}(\mathbf{R}) = \sum_{W,\alpha} \frac{1}{2M_{\alpha}} \tilde{k}_{W_{\alpha} W_{\alpha}}^{JI}(\mathbf{R}), \quad (33.8)$$

$$f_{W_\alpha}^{JJ}(\mathbf{R}) = \left\langle \Psi_J^0(\mathbf{r}; \mathbf{R}) \left| \frac{\partial}{\partial W_\alpha} \Psi_I^0(\mathbf{r}; \mathbf{R}) \right. \right\rangle_{\mathbf{r}}, \quad (33.9)$$

$$\tilde{k}_{W_\alpha W_\beta}^{JJ} = \left\langle \frac{\partial}{\partial W_\alpha} \Psi_J^0(\mathbf{r}; \mathbf{R}) \left| \frac{\partial}{\partial W_\beta} \Psi_I^0(\mathbf{r}; \mathbf{R}) \right. \right\rangle_{\mathbf{r}}, \quad (33.10)$$

with $W = X, Y, Z, \alpha = 1 \cdots N$. The subscript \mathbf{r} on the matrix elements in Eqs. (33.9)–(33.10) denotes integration over all electronic coordinates and the final ∇_α in Eq. (33.6) acts on both $f_\alpha^{IJ}(\mathbf{R})$ and $\beta_J(\mathbf{R})$. While this representation may not be optimal for a treatment of the nuclear dynamics, since it employs a space fixed frame representation, it is adequate for the present development as it clearly displays the origins of the Born–Oppenheimer approximation and its breakdown.

Modifications to the Nonrelativistic Born–Oppenheimer Potential Energy Surface

When the interstate couplings on the right-hand side of Eq. (33.6) can be neglected, the nuclear motion is governed by the effective potential given by $V^I(\mathbf{R}) \equiv E_I^c(\mathbf{R}) + \tilde{K}^{II}(\mathbf{R}) \equiv E_I^0(\mathbf{R}) + H_{II}^{\text{BP}}(\mathbf{R}) + \tilde{K}^{II}(\mathbf{R})$ and the Born–Oppenheimer approximation is valid. Here it is assumed that $f_\alpha^{II}(\mathbf{R}) = 0$, a sufficient condition for which is that the $\Psi_I^0(\mathbf{r}; \mathbf{R})$ are chosen real-valued [see discussion following Eq. (33.5)]. $E_I^0(\mathbf{R})$ is generally the principal \mathbf{R} -dependent contribution to $V^I(\mathbf{R})$. $H_{II}^{\text{BP}}(\mathbf{R})$ is referred to as the relativistic contribution to the nonrelativistic Born–Oppenheimer potential energy surface and is discussed further in Sect. 33.3.2. The contribution $\tilde{K}^{II}(\mathbf{R})$ is referred to as the adiabatic correction. Unlike $E_I^0(\mathbf{R})$ and $H_{II}^{\text{BP}}(\mathbf{R})$, which are independent of mass, $\tilde{K}^{II}(\mathbf{R})$ is mass dependent Eqs. (33.8) and (33.10). It has been computed from first principles [10–12] and inferred from experiments [13, 14] principally for diatomic systems.

33.1.2 Born–Oppenheimer Potential Energy Surfaces and Their Topology

$E_I^0(\mathbf{R})$ is the main focus of this chapter. There have been several recent reviews of ground state ($I = 1$) potential energy surfaces [15, 16].

Equilibrium structures (stable or metastable species) represent local minima on $E_I^0(\mathbf{R})$, that is $g_{W_\alpha}^I(\mathbf{R}) \equiv \partial E_I^0(\mathbf{R}) / \partial W_\alpha = 0$ for all W_α at $\mathbf{R} = \mathbf{R}^e$. There may be several equilibrium structures for a given set of nuclei; for example the atoms H, C and N form stable molecules HCN and HNC. Saddle points or transition states, extrema on $E_I^0(\mathbf{R})$ with one negative eigenvalue of the Hessian matrix $\mathbf{F}^I(\mathbf{R})$, whose elements are defined by $F_{W_\alpha W_\beta}^I(\mathbf{R}) \equiv \partial^2 E_I^0(\mathbf{R}) / \partial W_\alpha \partial W_\beta$, represent mountain passes separating the various equilibrium structures and the asymptotes – values of \mathbf{R} corresponding to isolated molecular fragments. This situation is illustrated in Fig. 33.1.

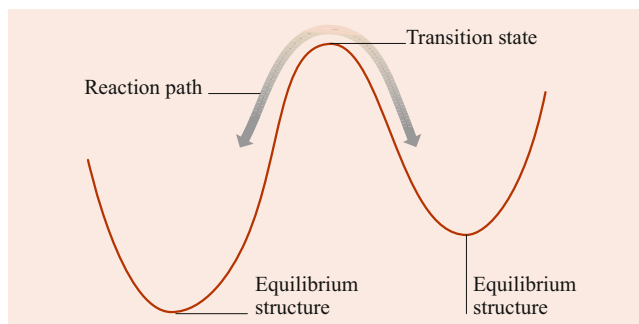


Fig. 33.1 Schematic representation of a transition state and reaction path connecting two minima

Reaction paths [17] connect the asymptotes, minima, and saddle points. They can best be defined as the steepest descent paths from a transition state structure down to local minima [17], although methods for walking uphill (shallowest ascent path) [18] also exist. Unlike equilibrium structures and saddle points which are independent of the choice of coordinate system used to represent \mathbf{R} , the reaction path is coordinate system dependent. The intrinsic reaction coordinate [17], the reaction coordinate in mass weighted cartesian coordinates $\mathbf{R}_i \rightarrow \mathbf{R}_i M_i$, is most frequently used (Sect. 33.4.4)

These features of the potential energy surfaces and their determination will be discussed further below. Their determination consists of two parts: (i) the level of treatment, i.e., the electronic structure technique used to determine $E_I^0(\mathbf{R})$ and (ii) the characterization of the features of $E_I^0(\mathbf{R})$, i.e., minima, saddle points, and reaction paths [19, 20] at the level of treatment chosen. In this chapter, only fully ab initio levels of treatment are considered [21, 22].

33.1.3 Classification of Interstate Couplings: Adiabatic and Diabatic Bases

Intersurface couplings, shown on the right-hand side of Eq. (33.6), result in the breakdown of the single potential energy surface Born–Oppenheimer approximation. Within the Born–Huang ansatz such a nonadiabatic process is interpreted in terms of motion on more than one Born–Oppenheimer potential energy surface [8]. From Eq. (33.6), it is seen that there are three types of matrix elements coupling the electronic states, $\tilde{K}^{IJ}(\mathbf{R})$, $H^{\text{BP}IJ}(\mathbf{R})$ and $f^{IJ}(\mathbf{R})$. Two of these couplings, $\tilde{K}^{IJ}(\mathbf{R})$ and $f^{IJ}(\mathbf{R})$ arise from the nuclear kinetic energy operator T^{nuc} , while the third coupling arises from the Breit–Pauli interaction H^{BP} . This classification of the intersurface interactions is a consequence of the choice of the adiabatic electronic states through Eq. (33.5). Other choices of $\Psi_I^0(\mathbf{r}; \mathbf{R})$, most notably the diabatic electronic states [23–27], are possible.

In the adiabatic state basis, $H^0(\mathbf{r}; \mathbf{R})$ is diagonal and in the absence of relativistic effects, intersurface couplings

originate exclusively from the derivative coupling terms in Eqs. (33.9) and (33.10). The diabatic basis seeks to *transfer* the intersurface coupling from these derivative operators to a potential term analogous in form to $H_{IJ}^{\text{BP}}(\mathbf{R})$. The diabatic basis, $\Psi_I^{0-d}(\mathbf{r}; \mathbf{R})$, is a unitary transformation of the adiabatic electronic basis, defined such that [24]

$$f_{R_\alpha}^{JJ,d} \equiv \left\langle \Psi_I^{0-d}(\mathbf{r}; \mathbf{R}) \left| \frac{\partial}{\partial R_\alpha} \Psi_I^{0-d}(\mathbf{r}; \mathbf{R}) \right. \right\rangle_r = 0, \quad (33.11)$$

where R_α is an internal coordinate. For polyatomic systems ($N > 2$), rigorous diabatic bases do not exist [27] and approximate diabatic bases are sought [27–30]. A discussion of this issue can be found in [31].

33.1.4 Surfaces of Intersection of Potential Energy Surfaces

The intersurface couplings are most effective in promoting a nonadiabatic process when $|V^I(\mathbf{R}) - V^J(\mathbf{R})|$ is small for some J on the right-hand side of Eq. (33.6), so that

$$\begin{aligned} E_I^e(\mathbf{R}) + \tilde{K}^{II}(\mathbf{R}) - [E_J^e(\mathbf{R}) + \tilde{K}^{JJ}(\mathbf{R})] \\ \equiv \Delta E_{IJ}^0(\mathbf{R}) + \Delta E_{IJ}^{\text{BP}}(\mathbf{R}) + \Delta K_{IJ}(\mathbf{R}) \end{aligned} \quad (33.12)$$

is small. Here

$$\Delta E_{IJ}^0(\mathbf{R}) \equiv E_I^0(\mathbf{R}) - E_J^0(\mathbf{R}), \quad (33.13)$$

$$\Delta K_{IJ}(\mathbf{R}) \equiv \tilde{K}^{II}(\mathbf{R}) - \tilde{K}^{JJ}(\mathbf{R}), \quad (33.14)$$

$$\Delta E_{IJ}^{\text{BP}}(\mathbf{R}) \equiv H_{II}^{\text{BP}}(\mathbf{R}) - H_{JJ}^{\text{BP}}(\mathbf{R}). \quad (33.15)$$

Since in general $\Delta K_{IJ}(\mathbf{R})$ is quite small, and for the low atomic number systems considered here H_{II}^{BP} is itself small, we are led to consider regions of nuclear coordinate space for which the magnitude of $\Delta E_{IJ}^0(\mathbf{R})$ is small, referred to as avoided intersections when $\Delta E_{IJ}^0(\mathbf{R}) \neq 0$ and as conical and Renner-type [32] intersections when $\Delta E_{IJ}^0(\mathbf{R}) = 0$. The set of \mathbf{R} for which $\Delta E_{IJ}^0(\mathbf{R}) = 0$, the noncrossing rule, was first discussed in 1929 by *von Neumann* and *Wigner* [33]. The rule states that for diatomic systems, crossings between two potential energy curves of the same symmetry are not possible (actually, are extremely rare), whereas for polyatomic systems, potential energy surface intersections are allowed. Mathematically the noncrossing rule is expressed in terms of the dimensions of a surface, the surface of intersection, on which a set of conditions can be satisfied [3, 34]. For electronic states of the same symmetry (neglecting electron spin degeneracy), the dimension of the surface of conical intersection is $K - 2$, where K is the number of internal nuclear degrees of freedom. For states of different spin symmetry, the dimension of the surface of intersection is $K - 1$.

33.2 Characterization of Potential Energy Surfaces

This section is concerned with the determination of the approximate solution of Eq. (33.5). For this purpose it is frequently convenient to re-express $H^0(\mathbf{r}; \mathbf{R})$ in second quantized [35] form as

$$H^0(\mathbf{r}; \mathbf{R}) = \sum_{i,j} h_{ij} a_i^\dagger a_j + \frac{1}{2} \sum_{i,j,k,l} (il|jk) a_i^\dagger a_j^\dagger a_k a_l, \quad (33.16)$$

where h_{ij} and $(il|jk)$ are standard abbreviations [36] for the one electron (kinetic energy and nuclear–electron attraction) and two electron (electron–electron repulsion) integrals respectively, and a_i^\dagger and a_i are the fermion creation and destruction operators. The integrals and the creation and destruction operators are defined in terms of a basis of one electron functions, usually molecular spin-orbitals $\phi_i \gamma_i$, $\gamma_i = \alpha$ or β . Thus

$$\begin{aligned} h_{ij}(\mathbf{R}) = \langle \phi_i(\mathbf{r}_k) \gamma_i | -\frac{1}{2} \nabla_k^2 \\ - \sum_K \frac{Z_K}{|\mathbf{R}_K - \mathbf{r}_k|} | \phi_j(\mathbf{r}_k) \gamma_j \rangle_{\mathbf{r}_k} \end{aligned} \quad (33.17)$$

$$\begin{aligned} (ij|kl) = \left\langle \phi_i(\mathbf{r}_m) \gamma_i \phi_j(\mathbf{r}_m) \gamma_j \left| \frac{1}{|\mathbf{r}_m - \mathbf{r}_n|} \right. \right. \\ \left. \left. \times \left| \phi_k(\mathbf{r}_n) \gamma_k \phi_l(\mathbf{r}_n) \gamma_l \right. \right\rangle_{\mathbf{r}_m, \mathbf{r}_n}. \end{aligned} \quad (33.18)$$

Equation (33.18) is referred to as the Mulliken notation [37] for a two-electron integral. It differs from the frequently used [36] bra-ket representation $\langle ij|kl \rangle = \langle ik|jl \rangle$. The molecular orbitals $\phi_i(\mathbf{r}_j; \mathbf{R})$ are in turn expanded in terms of a basis set of atom-centered functions [38], $\chi(\mathbf{r}_j; \mathbf{R})$, with $\phi_i(\mathbf{r}_j; \mathbf{R}) = \sum_{P=1}^L \chi_P(\mathbf{r}_j; \mathbf{R}) T_{P,i}(\mathbf{R})$. Note that here we have distinguished between a spin-orbital $\phi_i(\mathbf{r}_j; \mathbf{R}) \gamma_i$ and a molecular orbital $\phi_i(\mathbf{r}_j; \mathbf{R})$, but we will follow the usual convention of allowing the functions in Eqs. (33.17) and (33.18) to be molecular orbitals or spin-orbitals with the use being clear from the context.

Since $H^0(\mathbf{r}; \mathbf{R})$ is independent of electron spin, it can also be written in terms of the \tilde{E}_{pq} , spin-averaged excitation operators [39], where $\tilde{E}_{pq} = \sum_\gamma a_{p\gamma}^\dagger a_{q\gamma}$, p, q label orbitals and $\gamma = \alpha, \beta$ so that

$$H^0(\mathbf{r}; \mathbf{R}) = \sum_{i,j} h_{ij} \tilde{E}_{ij} + \frac{1}{2} \sum_{i,j,k,l} (ij|kl) \tilde{E}_{ij} \tilde{E}_{kl} - \delta_{jk} \tilde{E}_{il}. \quad (33.19)$$

The \tilde{E}_{pq} satisfy $[\tilde{E}_{ij}, \tilde{E}_{kl}] = \tilde{E}_{il} \delta_{jk} - \tilde{E}_{kj} \delta_{il}$ as a consequence of the commutation relations for the a_i^\dagger and a_i and are generators of the unitary group [40], (Chap. 4). This observation

allows the powerful machinery of the unitary group to be applied to the evaluation of $E_I^0(\mathbf{R})$ [41] (Sect. 33.1.2).

The determination of $E_I^0(\mathbf{R})$ involves two steps; (i) the determination of the molecular orbitals $\phi_i(\mathbf{r}_j; \mathbf{R})$, and (ii) sometimes simultaneously, the determination of the approximate wave function $\Psi_I^0(\mathbf{r}; \mathbf{R})$.

Wave functions discussed in this section are constructed from functions that are antisymmetrized products of spin-orbitals $\phi_i(\mathbf{r}_j; \mathbf{R})\gamma_i$

$$\Psi_I^0(\mathbf{r}; \mathbf{R}) = \mathcal{A} \prod_{i=1}^M \phi_i(\mathbf{r}_j; \mathbf{R})\gamma_i, \quad (33.20)$$

where $\gamma_i = \alpha$ or β . The antisymmetrizer \mathcal{A} is required to take into account the Fermi statistics of the electrons. The wave function in Eq. (33.20) is referred to as a Slater determinant and is an eigenfunction of M_z , the z -component of total electron spin. A linear combination of Slater determinants that is also an eigenfunction of S^2 is referred to as a configuration state function (CSF) [42]. Equation (33.20) corresponds to a particular distribution of electrons in the orbitals $\phi_i(\mathbf{r}_j; \mathbf{R})$. This distribution is referred to as an electron configuration.

In principle, it is possible to learn everything about the topology of a potential energy surface from the pointwise evaluation of $E_I^0(\mathbf{R})$. In practice however, the determination of topological features, including location of equilibrium structures, saddle points and reaction paths, characterization of quadratic and anharmonic force fields [43], and even the evaluation of derivative couplings [44], has benefitted immensely from techniques in which the energy gradient $\mathbf{g}^I(\mathbf{R})$ or higher derivatives are determined directly from knowledge of the wave function at the \mathbf{R} in question. These analytic derivative techniques, i.e., techniques that do not use divided difference differentiation, have been actively developed since their first introduction [45].

The techniques most commonly used to calculate $E_I^0(\mathbf{R})$ and its derivatives are described below.

33.2.1 The Self-Consistent Field (SCF) Method

The SCF Energy

In this most basic treatment, the electronic wave function $\Psi_I^{0-\text{SCF}}$ is taken as a single Slater determinant or a single CSF. The spin-orbitals are determined to give an extremum of the energy functional $\langle \Psi_I^{0-\text{SCF}}(\mathbf{r}; \mathbf{R}) | H^0(\mathbf{r}; \mathbf{R}) | \Psi_I^{0-\text{SCF}}(\mathbf{r}; \mathbf{R}) \rangle_r$. This gives rise to the self-consistent field conditions. For restricted closed shell wave functions [46], defined by the conditions

$$\Psi_I^{0-\text{RSCF}}(\mathbf{r}; \mathbf{R}) = \mathcal{A} \prod_{i=1}^L \phi_{2i}(\mathbf{r}_{2i}; \mathbf{R})\alpha\phi_{2i+1}(\mathbf{r}_{2i+1}; \mathbf{R})\beta \quad (33.21)$$

with $\phi_{2i}(\mathbf{r}_j; \mathbf{R}) = \phi_{2i-1}(\mathbf{r}_j; \mathbf{R})$, $i = 1, \dots, L$ and $2L = M$, the SCF equations are

$$\varepsilon_{ri} = h_{ri} + \sum_{j \in \{j_{\text{occ}}\}} 2(ir|jj) - (ij|rj) = 0 \quad (33.22)$$

for ϕ_i , ϕ_r occupied and virtual orbitals, respectively. Here, occupied orbitals j_{occ} are those occurring in the orbital product in Eq. (33.21), and the remainder of the orbitals are referred to as virtual orbitals. The solution to Eq. (33.22) is referred to as the canonical SCF solution, provided the orbitals satisfy the SCF equations

$$F\phi_i = \lambda_i\phi_i, \quad (33.23)$$

where the Fock operator F is defined by $F_{ri} = \varepsilon_{ri}$ and $\lambda_i = \varepsilon_{ii}$. The corresponding electronic energy is $E_I^0(\mathbf{R}) \equiv E_I^{0-\text{SCF}}(\mathbf{R}) = \sum_{j \in \{j_{\text{occ}}\}} (\varepsilon_{jj} + h_{jj})$.

SCF Energy Derivatives

The derivative of $E_I^{0-\text{SCF}}(\mathbf{R})$ can be expanded through third order using analytic gradient techniques [47, 48], and through fourth order using divided differences and more recently using analytic derivative techniques [43]. The ability to evaluate the energy derivatives or force field through fourth order is important in the determination of vibrational properties of molecules, as discussed in Sect. 33.4.2.

Direct SCF

The range of molecular systems accessible to treatment at the SCF level has been expanded considerably by the introduction of the direct SCF methods [49]. In this method, none of the two-electron integrals in the χ basis ($pq|rs$) are stored during the iterative solution of Eqs. (33.22) and (33.23). Since the number of such integrals grows as $L^4/8$, direct SCF procedures avoid the L^4 -storage bottleneck, enabling SCF wave functions to be determined for systems with more than 100 atoms and basis sets with more than 1000 functions. (If all the $L^4/8$ integrals were stored on disk this basis would require ≈ 1000 gigabytes).

33.2.2 Electron Correlation: Wave Function Based Methods

Wave functions more accurate than SCF wave functions are obtained by including the effects of electron correlation. The correlation energy is defined as $E_I^{\text{corr}}(\mathbf{R}) \equiv E_I^0(\mathbf{R}) - E_I^{0-\text{SCF}}(\mathbf{R})$. Methods for the determination of $E_I^{\text{corr}}(\mathbf{R})$ are commonly classified as single reference or multireference methods. In single reference methods, an SCF wave function $\Psi_I^{0-\text{SCF}}(\mathbf{r}; \mathbf{R})$ given by Eq. (33.20) is improved. In multireference methods, the starting point is the space spanned by

a set of terms like Eq. (33.20). This space is referred to as the reference space and the functions in the space as the reference configurations. Sometimes the molecular orbitals $\phi(\mathbf{r}_i; \mathbf{R})$ for the reference space are the SCF orbitals of a single reference configuration calculation, but more often the $\phi(\mathbf{r}_i; \mathbf{R})$ are chosen to satisfy multiconfigurational self-consistent field (MCSCF) equations [50–53].

Single Reference Methods

Second Order Møller–Plesset Perturbation Theory (MP2)

In this approach [54], the solutions of the SCF equations are used to determine $E_I^0(\mathbf{R})$ to second order as

$$E_I^{0\text{-MP2}}(\mathbf{R}) = E_I^{0\text{-SCF}}(\mathbf{R}) - \frac{1}{4} \sum_{a,b,i,j} \frac{(ab||ij)^2}{\lambda_a + \lambda_b - \lambda_i - \lambda_j}, \quad (33.24)$$

where i, j denote occupied orbitals, a, b denote virtual orbitals, and

$$(ab||ij) = (ai|bj) - (aj|bi) = \langle ab|ij \rangle - \langle ab|ji \rangle.$$

Both gradients of $E_I^{0\text{-MP2}}(\mathbf{R})$ and direct implementations of MP2 [37, 55] are currently available. Higher order perturbation theories, also in common use, are discussed in the context of coupled cluster methods which are considered next.

Coupled Cluster Method

Perhaps the most reliable method currently available for characterizing near equilibrium properties of moderately sized molecules is the coupled cluster approach [56–60] (Chap. 5). In this approach, the exact wave function is written as a unitary transformation of a reference wave function $\Phi_0(\mathbf{r}; \mathbf{R})$ [usually, but not necessarily, the SCF wave function $\Phi_0(\mathbf{r}; \mathbf{R}) = \Psi_I^{0\text{-SCF}}(\mathbf{r}; \mathbf{R})$],

$$\Psi_I^{0\text{-CC}} = \exp(T)\Phi_0. \quad (33.25)$$

where T is an excitation operator defined as

$$T = \sum_p T_p; \quad (33.26)$$

with

$$T_p = \frac{1}{p!^2} \sum_{i,j,k,\dots,a,b,c} t_{ijk\dots}^{abc\dots} a_a^\dagger a_b^\dagger a_c^\dagger a_i a_j a_k, \quad (33.27)$$

where i, j, k denote occupied orbitals in Φ_0 and a, b, c denote virtual orbitals. Thus

$$\Psi_I^{0\text{-CC}} = \Phi_0 + \sum_{i,a} t_i^a \Phi_i^a + \frac{1}{4} \sum_{i,j,a,b} t_{ij}^{ab} \Phi_{ij}^{ab} + \dots, \quad (33.28)$$

where Φ_i^a, Φ_{ij}^{ab} are single and double excitations from Φ_0 , and it is the amplitudes t that must be determined. Wave functions of the form in Eqs. (33.25)–(33.28) have the important property referred to as size consistency [60] or size extensivity [59]. Consider N noninteracting helium atoms. The electronic wave function for the i th helium atom in the natural orbital basis [61] can be written as $\Psi_i = [1 + T_2(i)]\phi_0(i)$, so that the N atom electronic wave function becomes

$$\Psi = \prod_i \Psi_i = \prod_i [1 + T_2(i)]\Phi_0 = \left[\exp \sum_i T_2(i) \right] \Phi_0 = \exp(T_2)\Phi_0 \quad (33.29)$$

Thus this exponential type of solution scales properly with the number of particles.

To obtain the amplitudes t , define $H_N = H^0 - \langle \Phi_0 | H^0 | \Phi_0 \rangle, E_I^{0\text{-CC}} = \Delta E_I^{0\text{-CC}} + \langle \Phi_0 | H^0 | \Phi_0 \rangle \equiv \Delta E_I^{0\text{-CC}} + E_I^{0-0}, P = |\Phi_0\rangle\langle\Phi_0|$ and $Q = 1 - P$. Then, inserting Eqs. (33.25)–(33.28) into Eq. (33.5) gives the energy Eq. (33.30) and amplitude Eq. (33.31) equations, which define the coupled cluster approach:

$$\Delta E_I^{0\text{-CC}} = \langle \Phi_0 | \tilde{H}_N | \Phi_0 \rangle, \quad (33.30)$$

$$\langle \Phi_{ijk\dots}^{abc\dots} | \tilde{H}_N | \Phi_0 \rangle = 0 \text{ for all } \Phi_{ijk\dots}^{abc\dots}, \quad (33.31)$$

where

$$\begin{aligned} \tilde{H}_N &= \exp(-T)H_N \exp(T) \\ &= -E_I^{0-0} + \exp(-T)H^0 \exp(T). \end{aligned} \quad (33.32)$$

To appreciate the nature of these equations, consider the approximation $T = T_2$ constructed from SCF orbitals [36, 59], referred to as the coupled cluster doubles (CCD) level. At this level the energy equation becomes

$$\begin{aligned} E_I^{0\text{-CCD}} &= \langle \Phi_0 | \exp(-T_2)H^0 \exp(T_2) | \Phi_0 \rangle \\ &= \langle \Phi_0 | H^0 T_2 | \Phi_0 \rangle + E_I^{0-0} \\ &= E_I^{0-0} + \frac{1}{4} \sum_{i,j,r,s} \Phi_0 H^0 a_i^\dagger a_s^\dagger a_i a_j \Phi_0 t_{ij}^{rs} \\ &= E_I^{0-0} + \frac{1}{4} \sum_{i,j,r,s} (rs||ij) t_{ij}^{rs} \end{aligned} \quad (33.33)$$

for i, j occupied and r, s virtual orbitals. The amplitude equations become

$$\begin{aligned} &\langle \Phi_{ij}^{rs} | \exp(-T_2)H^0 \exp(T_2) | \Phi_0 \rangle \\ &= \langle \Phi_{ij}^{rs} | \left(1 - T_2 + \frac{1}{2} T_2^2 \right) H^0 \left(1 + T_2 + \frac{1}{2} T_2^2 \right) | \Phi_0 \rangle \\ &= 0 \end{aligned} \quad (33.34)$$

which reduces (after considerable commutator algebra) [36] to

$$\begin{aligned}
 & (\lambda_r + \lambda_s - \lambda_i - \lambda_j)t_{ij}^{rs} \\
 &= -(rs||ij) - \sum_{p>q} (rs||pq)t_{ij}^{pq} - \sum_{k>l} (kl||ij)t_{kl}^{rs} \\
 &+ \sum_{k,p} [(ks||jp)t_{ik}^{rp} - (kr||jp)t_{ik}^{sp} \\
 &- (ks||ip)t_{jk}^{rp} + (kr||ip)t_{jk}^{sp}] \\
 &- \sum_{k>l;p>q} (kl||pq) \left[t_{ij}^{pq} t_{kl}^{rs} - 2(t_{ij}^{rp} t_{kl}^{sq} + t_{ij}^{sq} t_{kl}^{rp}) \right. \\
 &\left. - 2(t_{ik}^{rs} t_{jl}^{pq} + t_{ik}^{pq} t_{jl}^{rs}) + 4(t_{ik}^{rp} t_{jl}^{sq} + t_{ik}^{sq} t_{jl}^{rp}) \right]. \quad (33.35)
 \end{aligned}$$

The solution to Eq. (33.35) is obtained iteratively. The first iteration gives $t_{ij}^{rs} = -(rs||ij)/(\lambda_r + \lambda_s - \lambda_i - \lambda_j)$, which when inserted into Eq. (33.33) gives Eq. (33.24), i.e., the MP2 result. If the quadratic terms in Eq. (33.35) are neglected, then the second iteration gives the third order Møller–Plesset (MP3) result [36]. The result of iterating Eq. (33.35) to convergence gives the CCD result.

Of the levels of coupled cluster treatments in current use, those including T_1 , T_2 , T_3 , and T_4 in Eq. (33.25) provide the most reliable results [62–66].

Multireference Methods

Single reference methods provide probably the most powerful tools for treating near-equilibrium properties of ground electronic state systems. In other instances, such as the study of electronically excited states, determination of global potential energy surfaces and for systems with multiple open shells such as diradicals, multireference techniques are found to be extremely useful. In the multireference techniques discussed below, the wave function is written as

$$\Psi_I^{0-\text{MRF}}(\mathbf{r}; \mathbf{R}) = \sum_{\alpha} c_{\alpha}^I \psi_{\alpha}(\mathbf{r}; \mathbf{R}) \quad (33.36)$$

where $\psi_{\alpha}(\mathbf{r}; \mathbf{R})$ is a CSF. This expansion is usually referred to as a configuration interaction (CI) expansion, and the coefficients $c^I(\mathbf{R})$ are referred to as CI coefficients [42]. Since Eq. (33.36) does not involve the exponential ansatz, it is not automatically size extensive. In the description of these wave functions, it is useful to generalize the notion of occupied and virtual orbitals to inactive, active, and virtual orbitals, where, referring to the CSF's defining the reference space, inactive orbitals are fully occupied in all CSFs, virtual orbitals are not occupied in any CSF and the active orbitals are (partially) occupied in at least one CSF.

Most multireference techniques begin with the determination of a multiconfigurational self-consistent field (MCSCF) wave function or state averaged MCSCF(SA-MCSCF) wave

function [50–53, 67]. This approach is capable of describing the internal or static correlation energy, the part of the correlation energy that leads to sizeable separation of two electrons in a pair, and near-degeneracy effects. A particularly robust type of MCSCF wave function, the complete active space (CAS) [68–70] wave function, includes in Eq. (33.36) all CSFs arising from the distribution of the available electrons among the active orbitals. Note that a CAS wave function is size consistent.

The remaining part of the correlation energy, the dynamic correlation, describes the two-electron cusp, i.e., the regions of space for which two electrons experience the singularity in the Coulomb potential. Empirically, it has been shown [71] that wave functions capable of providing chemically accurate descriptions of the dynamic correlation can be obtained by augmenting the MCSCF or reference wave function with all CSFs that differ by at most two molecular orbitals, double excitations Eq. (33.28) from those of the reference space. Such wave functions are generally referred to as multireference single and double excitation configuration interaction (MR-SDCI) wave functions. First (second) order wave functions [72] include all single (single and double) excitations relative to a CAS reference space.

Multiconfigurational Self-Consistent Field (MCSCF)

Theory

In the MCSCF approximation, a wave function $\Psi_I^{0-\text{MCSCF}}(\mathbf{r}; \mathbf{R}) = \sum_{\alpha} c_{\alpha}^I \psi_{\alpha}(\mathbf{r}; \mathbf{R})$ of the form in Eq. (33.36) is to be determined. In this procedure, both the molecular orbitals $\phi(\mathbf{r}; \mathbf{R})$ and $c^I(\mathbf{R})$ are determined from the requirement that

$$\begin{aligned}
 E_I^{0-\text{MCSCF}} \\
 = \langle \Psi_I^{0-\text{MCSCF}}(\mathbf{r}; \mathbf{R}) | H^0 | \Psi_I^{0-\text{MCSCF}}(\mathbf{r}; \mathbf{R}) \rangle_r, \quad (33.37)
 \end{aligned}$$

be a minimum. In a popular variant, the state averaged MCSCF (SA-MCSCF) [50–53] procedure, the average energy functional

$$\begin{aligned}
 E^{0-\text{SA-MCSCF}} = \sum_{I=2}^K w_I \langle \Psi_I^{0-\text{MCSCF}}(\mathbf{r}; \mathbf{R}) | H^0 | \\
 \times \Psi_I^{0-\text{MCSCF}}(\mathbf{r}; \mathbf{R}) \rangle_r, \quad (33.38)
 \end{aligned}$$

where the weight vector $\mathbf{w} = (w_1, w_2, \dots, w_K)$ has only positive elements, is minimized. This procedure should be compared with the multireference CI approach described below in which a predetermined set of molecular orbitals is used.

The optimum molecular orbitals and CI coefficients can be written as unitary transformations of an initial set of such quantities, i.e.,

$$\Psi_I^{0-\text{MCSCF}} = \exp(\gamma) \exp(\Delta) \Phi_I^0, \quad (33.39)$$

where

$$\boldsymbol{\gamma} = \sum_{i,s} \gamma_{s,i} a_s^\dagger a_i, \quad \Delta = \sum_{n,l} \Delta_{l,n} |\Phi_l^0\rangle \langle \Phi_n^0|, \quad (33.40)$$

and $\boldsymbol{\gamma}$, Δ are general anti-Hermitian matrices. Since $m_{i,j} = -m_{j,i} \equiv m_{ij}$ for $\mathbf{m} = \boldsymbol{\gamma}$, Δ , the upper triangle of \mathbf{m} forms a vector $\vec{\mathbf{m}}$ that enumerates the independent parameters of \mathbf{m} . The MCSCF or SA-MCSCF equations can be succinctly formulated by inserting Eq. (33.39) into Eq. (33.37) or Eq. (33.38), expanding the commutators to second order and requiring $\partial E / \partial m_{ij} = 0$ [36]. The result provides a system of Newton–Raphson equations that can be solved iteratively for the $\boldsymbol{\gamma}$, Δ [52, 53, 67, 73].

Multireference Configuration Interaction Theory: The MR-SDCI Method

In multireference configuration interaction theory, the wave function is again of the form $\Psi_I^{0-\text{MRCI}}(\mathbf{r}; \mathbf{R}) = \sum_{\alpha} c_{\alpha}^I(\mathbf{R}) \psi_{\alpha}(\mathbf{r}; \mathbf{R})$, but now CSFs involving the large space of virtual orbitals are included. In this approach the CI coefficients are found for a predetermined set of molecular orbitals. The CSF expansions at the MR-SDCI level become quite large (1–10 million CSFs is routine), and even larger expansions are tractable using specialized methods. The c^I satisfy the usual matrix equation

$$(\mathbf{H}^0 - E_I^0) \mathbf{c}^I = 0, \quad (33.41)$$

where

$$\begin{aligned} H_{\alpha\beta}^0 &= \langle \psi_{\alpha} | H^0 | \psi_{\beta} \rangle \\ &= \sum_{i,j} A_{ij}^{\alpha\beta} h_{ij} + \sum_{i,j,k,l} A_{ijkl}^{\alpha\beta} (ij|kl). \end{aligned} \quad (33.42)$$

It is the computationally elegant solution of Eq. (33.41) for large expansions that is the essence of modern MR-SDCI methods.

Because of the large dimension of the CSF space, it is not possible (or even desirable) to find all the solutions of Eq. (33.41). The few lowest eigenstates and eigenvalues can be found [74] using an iterative direct CI procedure [75] in which a subspace is generated sequentially from the residual defined at the k th iteration by

$$\sigma_{\mu}^{(k)} = \sum_{\nu} (H_{\mu\nu}^0 - E^{(k-1)} \delta_{\mu\nu}) c_{\nu}^{(k-1)}, \quad (33.43)$$

where for simplicity of notation, the state index I is suppressed. The computationally demanding step in this procedure is the efficient evaluation of the $A_{ijkl}^{\alpha\beta} = \langle \psi_{\alpha} | \tilde{E}_{ij} \tilde{E}_{kl} - \delta_{jk} \tilde{E}_{il} | \psi_{\beta} \rangle$. Key to the efficiency of this evaluation is the factorization formally achieved by

$$\langle \psi_{\alpha} | \tilde{E}_{ij} \tilde{E}_{kl} | \psi_{\beta} \rangle = \sum_m \langle \psi_{\alpha} | \tilde{E}_{ij} | \psi_m \rangle \langle \psi_m | \tilde{E}_{kl} | \psi_{\beta} \rangle. \quad (33.44)$$

Using unitary group techniques, this apparently intractable summation can be used to express the $A_{ijkl}^{\mu\nu}$ as a simple finite product [76].

Contracted CI and Complete Active Space Perturbation Theory (CASPT2)

The direct approach outlined above makes treatment of large MR-SDCI expansions possible. However, as the size of the reference space grows, the CSF space in the MR-SDCI expansion may become intractably large, particularly if the full second-order wave function is used. To avoid this bottleneck, the reference CSFs may be selected from the active space, and perturbation theory may be used to select CSFs involving orbitals in the virtual space [42]. The use of selection procedures complicates the implementation of *direct* techniques although recently progress in selected direct CI procedures has been reported [77–79]. Alternatively, new techniques have been developed that avoid this selection procedure. In these approaches, the MCSCF wave function itself is used as the reference wave function for CI or perturbation theory techniques. The use of a reference wave function rather than a reference space considerably reduces the size of the CSF space to be handled. In this approach, one of the principal computational complications is that the excited functions are not necessarily mutually orthogonal. Two computational procedures currently in wide use, known as contracted CI [80–83] and CASPT2 [84, 85], are based on this approach.

The CASPT2 method is a computationally efficient variant of second order perturbation theory in which the reference wave function is a CAS-MCSCF wave function and thus may itself contain tens of thousands of CSFs. In this case the full multireference CI problem would be intractable owing to the large space of double excitations. A similar approach is adopted in the contracted CI method, in that the excitations are defined in terms of a general MCSCF reference wave function $\Psi_I^{0-\text{MRF}}$ rather than the reference space as in the MR-SDCI methods described above.

33.2.3 Electron Correlation: Density Functional Theory

The approaches in Sect. 33.1.1 and 33.1.2 can be referred to as wave function based approaches in the sense that determination of $E_I^0(\mathbf{R})$ is accompanied by the determination of the corresponding electronic wave function $\Psi_I^0(\mathbf{r}; \mathbf{R})$. An alternative approach is known as density functional theory (DFT) [86]. The ultimate goal of DFT is the determination of total densities and energies without the determination of wave functions, as in the Thomas–Fermi approximation. DFT is based on the Hohenberg–Kohn Theorem [87], which states that the total electronic density can be considered

to be the independent variable in a multi-electron theory (Chap. 21). Computationally viable approaches exploit the Kohn and Sham formulation [88], which introduces molecular orbitals as an intermediate device.

The essential features of the Kohn–Sham (KS) theory [86] are as follows [89]. Assume that the real N -electron system for a particular arrangement of the nuclei \mathbf{R} has a total electron density $\rho(\mathbf{r}; \mathbf{R})$. Consider a system of N independent noninteracting electrons subject to a one-body potential V_0 with total density $\rho^0(\mathbf{r}; \mathbf{R})$ such that $\rho(\mathbf{r}; \mathbf{R}) = \rho^0(\mathbf{r}; \mathbf{R})$. The corresponding independent particle orbitals, the Kohn–Sham orbitals $\phi_i^{\text{KS}}(\mathbf{r}_j; \mathbf{R})$, satisfy a Hartree–Fock-like equation

$$\left(-\frac{1}{2}\nabla^2 + V_0 - \varepsilon_i\right)\phi_i^{\text{KS}} = 0 \quad (33.45)$$

with

$$\rho^0(\mathbf{r}; \mathbf{R}) = \sum_i |\phi_i^{\text{KS}}|^2. \quad (33.46)$$

The relation between the energy of the ideal system and that of the true system $E^{0\text{-DFT}}(\mathbf{R})$ is obtained from the adiabatic connection formula [89].

In order to determine $E^{0\text{-DFT}}(\mathbf{R})$, functions ϕ_i^{KS} are required, which in turn means that V_0 , the Kohn–Sham noninteracting one-body potential, must be determined. V_0 is written as Eq. (33.3)

$$V_0 = V_{e\text{-N}} + V_{\text{Coul}} + V_{\text{xc}} \quad (33.47)$$

where V_{Coul} is the Coulomb interaction corresponding to the electron density, $V_{e\text{-N}}$ is the electron–nuclear attraction interaction and V_{xc} is the exchange–correlation density. The effect of Eq. (33.47) is to isolate from V_0 the straightforward contributions V_{Coul} and $V_{e\text{-N}}$, and transfers our ignorance to the remaining portion V_{xc} . Although, by the Hohenberg–Kohn theorem V_{xc} must exist, its determination remains the challenge of modern density functional theory, which currently uses approximate functional forms. These approximate treatments of V_{xc} are quite useful in practice, and for large systems, DFT offers a promising alternative to wave function based methods.

Through Eq. (33.45), the KS approach is formally similar to SCF theory, although the Kohn–Sham theory is in principle exact. This formal similarity is exploited in the evaluation of the derivative $E^{0\text{-DFT}}(\mathbf{R})$ [90].

33.2.4 Weakly Interacting Systems

When attempting to describe weak chemical interactions such as van der Waals or dispersion forces, the techniques

outlined in Sect. 33.2.2 must be modified somewhat. These modifications arise from the finiteness, and hence incompleteness, of the basis (the set χ) used to describe the molecular orbitals. Assume that the interaction of two molecules A and B is to be determined. Consider the description of molecule A as the distance between A and B decreases from infinity. The atom centered basis functions on molecule B augment those on molecule A , lowering its energy, independent of any physical interaction. This computational artifact serves to overestimate the interaction energy, and is known as the basis set superposition error [91, 92]. In chemically bonded systems where interaction energies are large, it is of negligible importance. However in weakly bonded systems for which the interaction energies may be on the order of 10 to 100 cm^{-1} , the basis set superposition error can be significant.

The basis set superposition error can be reduced by the counterpoise correction [93, 94]. In this approach, the interaction energy is evaluated directly as

$$E_I^{0\text{-int}}(\mathbf{R}) = E_I^0(\mathbf{R}) - [E_I^{0\text{-}A}(\mathbf{R}) + E_I^{0\text{-}B}(\mathbf{R})], \quad (33.48)$$

where $E_I^{0\text{-}A}(\mathbf{R})$ and $E_I^{0\text{-}B}(\mathbf{R})$, the energies of A and B respectively, are evaluated in the full basis.

33.3 Intersurface Interactions: Perturbations

The existence of interstate interactions can lead to *unexpected* shifts in spectral lines as well as predissociation of the states themselves [95]. These situations are illustrated in Fig. 33.2a,b which present the 1, 2, 3 $^3\Pi_g$ potential energy curves for Al_2 and the corresponding derivative couplings $f^{IJ}(\mathbf{R})$ respectively. The derivative couplings were evaluated using the method described in Sect. 33.3.1. In this molecule, derivative couplings between the 2, 3 $^3\Pi_g$ states are responsible for the perturbations in the vibrational levels of the bound 2, 3 $^3\Pi_g$ states. Derivative couplings of these states with the 1 $^3\Pi_g$ state causes predissociation of all levels in the 2, 3 $^3\Pi_g$ manifold [96].

Sect. 33.1 describes two classes of interstate matrix elements that can lead to these nonadiabatic phenomena, the derivative coupling matrix elements in Eqs. (33.7)–(33.10) and H_{IJ}^{rel} , which is usually treated for low Z systems within the Breit–Pauli approximation. An illustration of a nonadiabatic process induced by H^{rel} is provided in Sect. 33.5. A key issue in the treatment of the electronic structure aspects of these phenomena is the reliable evaluation of the interstate matrix elements. The interstate interactions are usually of most interest in regions of nuclear coordinate space far removed from the equilibrium nuclear configuration. Thus it is desirable to evaluate these interactions using multireference CI wave functions which (Sect. 33.1) are well suited

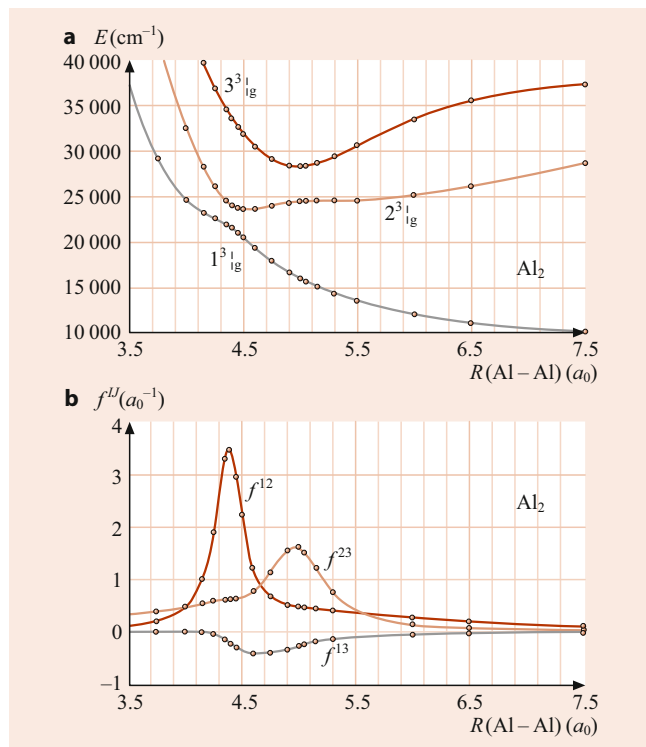


Fig. 33.2 (a) Adiabatic potential energy curves for the 1, 2, 3³Π_g states of Al₂ from [96]. (b) Derivative couplings $F^{IJ}(\mathbf{R})$ for $(I, J) = 1, 3^3\Pi_g$ and $2, 3^3\Pi_g$ from [96]

for use in these regions of coordinate space. The evaluation of nonadiabatic interactions, based on SA-MCSCF/CI wave functions, is discussed below.

33.3.1 Derivative Couplings

From Eqs. (33.9)–(33.11), two classes of matrix elements are required, $\tilde{k}_{W_\alpha W_\beta}^{II}(\mathbf{R})$ and $f_{W_\alpha}^{II}(\mathbf{R})$. In fact, techniques to evaluate both of these exist [44]. However, it is common to approximate $\tilde{k}_{W_\alpha W_\beta}^{II}(\mathbf{R})$ by

$$\begin{aligned} \tilde{k}_{W_\alpha W_\beta}^{II}(\mathbf{R}) &= \sum_M \left\langle \frac{\partial}{\partial W_\alpha} \Psi_J^0(\mathbf{r}; \mathbf{R}) \middle| \Psi_M^0(\mathbf{r}; \mathbf{R}) \right\rangle_r \\ &\quad \times \left\langle \Psi_M^0(\mathbf{r}; \mathbf{R}) \middle| \frac{\partial}{\partial W_\beta} \Psi_I^0(\mathbf{r}; \mathbf{R}) \right\rangle_r \\ &= \sum_M f_{W_\alpha}^{MJ} f_{W_\beta}^{MI}. \end{aligned} \quad (33.49)$$

with the (in principle infinite) summation over states truncated to reflect only the states explicitly treated in the nonadiabatic dynamics. Thus it is sufficient to discuss the determination of $f_{W_\alpha}^{II}(\mathbf{R})$.

The use of analytic derivative theory [97, 98] greatly improves the computational efficiency of evaluating $f_{W_\alpha}^{II}(\mathbf{R})$

relative to the earlier divided difference techniques [99]. The key ideas are given below. In this presentation, the standard, real-valued normalization is used. Additional contributions owing to the geometric phase, if required, must be evaluated separately as they do not follow from the electronic Schrödinger equation at a single point [100].

Differentiation of the $\Psi_J^0(\mathbf{r}; \mathbf{R})$ defined in Eq. (33.36) gives:

$$\begin{aligned} \frac{\partial}{\partial W_\alpha} \Psi_I^0(\mathbf{r}; \mathbf{R}) &= \sum_\lambda \left\{ \left[\frac{\partial}{\partial W_\alpha} c_\lambda^I(\mathbf{R}) \right] \psi_\lambda(\mathbf{r}; \mathbf{R}) \right. \\ &\quad \left. + c_\lambda^I(\mathbf{R}) \left[\frac{\partial}{\partial W_\alpha} \psi_\lambda(\mathbf{r}; \mathbf{R}) \right] \right\}. \end{aligned} \quad (33.50)$$

Thus $f_{W_\alpha}^{II}(\mathbf{R})$, consists of two terms

$$f_{W_\alpha}^{II}(\mathbf{R}) = {}^{\text{CI}} f_{W_\alpha}^{II}(\mathbf{R}) + {}^{\text{CSF}} f_{W_\alpha}^{II}(\mathbf{R}), \quad (33.51)$$

where the CI contribution is given by

$${}^{\text{CI}} f_{W_\alpha}^{II}(\mathbf{R}) = \sum_\lambda c_\lambda^J(\mathbf{R}) \left[\frac{\partial}{\partial W_\alpha} c_\lambda^I(\mathbf{R}) \right], \quad (33.52)$$

and the CSF contribution has the form

$$\begin{aligned} {}^{\text{CSF}} f_{W_\alpha}^{II}(\mathbf{R}) &= \sum_{\lambda, \mu} c_\lambda^J(\mathbf{R}) \left\langle \psi_\lambda(\mathbf{r}; \mathbf{R}) \middle| \frac{\partial}{\partial W_\alpha} \psi_\mu^I(\mathbf{r}; \mathbf{R}) \right\rangle_r c_\mu^I(\mathbf{R}). \end{aligned} \quad (33.53)$$

Evaluation of ${}^{\text{CSF}} f_{W_\alpha}^{II}(\mathbf{R})$ is straightforward using analytical derivative techniques [101], so that the remainder of the discussion focusses on ${}^{\text{CI}} f_{W_\alpha}^{II}(\mathbf{R})$. From Eq. (33.52), it would appear that the derivative of the CI coefficients $\partial/\partial W_\alpha c_\lambda^I(\mathbf{R}) \equiv V_{W_\alpha, \lambda}^I(\mathbf{R})$ would be required to evaluate ${}^{\text{CI}} f_{W_\alpha}^{II}(\mathbf{R})$. This is quite costly and is in fact not necessary, since only the projection onto the state $\Psi_J^0(\mathbf{r}; \mathbf{R})$ is required. Equation (33.52) for ${}^{\text{CI}} f_{W_\alpha}^{II}(\mathbf{R})$ can be recast in a form similar to that of $\mathbf{g}^I(\mathbf{R})$. This transformation of Eq. (33.52) enables the explicit determination of $V_{W_\alpha}^I(\mathbf{R})$ to be avoided, and is the key to the efficient use of analytic gradient techniques in the evaluation of $\mathbf{f}^{II}(\mathbf{R})$.

Differentiating Eq. (33.41) with respect to W_α gives

$$\begin{aligned} [\mathbf{H}^0 - E_I^0(\mathbf{R})] V_{W_\alpha}^I(\mathbf{R}) &= - \left\{ \frac{\partial}{\partial W_\alpha} [\mathbf{H}^0 - E_I^0(\mathbf{R})] \right\} \mathbf{c}^I(\mathbf{R}). \end{aligned} \quad (33.54)$$

Taking the inner product of Eq. (33.54) with $\mathbf{c}^J(\mathbf{R})$ gives

$${}^{\text{CI}} f_{W_\alpha}^{II}(\mathbf{R}) \equiv \mathbf{c}^J(\mathbf{R})^\dagger V_{W_\alpha}^I(\mathbf{R}) \quad (33.55)$$

$$= \Delta E_{IJ}^0(\mathbf{R})^{-1} \mathbf{c}^J(\mathbf{R})^\dagger \frac{\partial \mathbf{H}^0(\mathbf{R})}{\partial W_\alpha} \mathbf{c}^I(\mathbf{R}) \quad (33.56)$$

$$\equiv \Delta E_{IJ}^0(\mathbf{R})^{-1} h_{W_\alpha}^{II}(\mathbf{R}). \quad (33.57)$$

Observe that Eq. (33.56) and Eq. (33.57) are not the Hellmann–Feynman theorem [101, 102] (Chap. 55), to which they bear a formal resemblance, since it is not the Hamiltonian operator $H^0(\mathbf{r}; \mathbf{R})$ but rather the Hamiltonian matrix $\mathbf{H}^0(\mathbf{R})$ that is being differentiated. Since the energy gradient has the form [44]

$$\frac{\partial}{\partial W_\alpha} E_I^0(\mathbf{R}) = \mathbf{c}^I(\mathbf{R})^\dagger \frac{\partial \mathbf{H}^0(\mathbf{R})}{\partial W_\alpha} \mathbf{c}^I(\mathbf{R}), \quad (33.58)$$

its relation to $\text{CI}f_{W_\alpha}^{JI}(\mathbf{R})$ is clear. This identification is the key step in the evaluation of $\text{CI}f_{W_\alpha}^{JI}(\mathbf{R})$ using analytic gradient techniques [97, 98].

33.3.2 Breit–Pauli Interactions

For light systems, it is possible to introduce relativistic effects using the Breit–Pauli approximation [1], in which the four component Dirac description of a single electron is replaced by a two component (α, β) description. The $H^e(\mathbf{r}; \mathbf{R})$ becomes [1, 103]

$$H^e(\mathbf{r}; \mathbf{R}) = H^0(\mathbf{r}; \mathbf{R}) + H^{\text{rel}}(\mathbf{r}; \mathbf{R}), \quad (33.59)$$

where, in parallel with Eqs. (33.4)–(33.13) for the atomic case, the relativistic correction $H^{\text{rel}} = \sum_{k=1}^3 H^k(\mathbf{r}; \mathbf{R})$ can be divided into spin-dependent (SD) and spin-independent (SI) parts, plus an external field interaction term H^{ext} . These are given by

$$H^1 = H^{\text{SD}} \equiv H^{\text{so}} + H^{\text{soo}} + H^{\text{ss}}, \quad (33.60)$$

$$H^2 = H^{\text{SI}} \equiv H^{\text{mass}} + H^{\text{D}} + H^{\text{ssc}} + H^{\text{oo}}, \quad (33.61)$$

$$H^3 = H^{\text{ext}}, \quad (33.62)$$

where, in atomic units,

$$H^{\text{so}} = \frac{\alpha^2}{2} \sum_{K,i} \frac{Z_K(\mathbf{r}_i - \mathbf{R}_K) \times \mathbf{p}_i \cdot \mathbf{s}_i}{|\mathbf{r}_i - \mathbf{R}_K|^3}, \quad (33.63)$$

$$H^{\text{soo}} = -\frac{\alpha^2}{2} \sum_{i \neq j} \frac{\mathbf{r}_{ij} \times \mathbf{p}_i \cdot (\mathbf{s}_i + 2\mathbf{s}_j)}{|\mathbf{r}_{ij}|^3}, \quad (33.64)$$

$$H^{\text{ss}} = \alpha^2 \sum_{i < j} \left[\frac{\mathbf{s}_i \cdot \mathbf{s}_j}{|\mathbf{r}_{ij}|^3} - \frac{3(\mathbf{r}_{ij} \cdot \mathbf{s}_i)(\mathbf{r}_{ij} \cdot \mathbf{s}_j)}{|\mathbf{r}_{ij}|^5} \right], \quad (33.65)$$

$$H^{\text{mass}} = -\frac{\alpha^2}{8} \sum_i p_i^4, \quad (33.66)$$

$$H^{\text{D}} = -\frac{\alpha^2}{8} \left[\sum_{K,i} Z_K \nabla_i^2 |\mathbf{r}_i - \mathbf{R}_K|^{-1} - \sum_{i \neq j} \nabla_i^2 |\mathbf{r}_{ij}|^{-1} \right], \quad (33.67)$$

$$H^{\text{ssc}} = -\frac{8\pi\alpha^2}{3} \sum_{i < j} (\mathbf{s}_i \cdot \mathbf{s}_j) \delta(\mathbf{r}_{ij}), \quad (33.68)$$

$$H^{\text{oo}} = -\frac{\alpha^2}{4} \left(\sum_{j \neq i} \frac{\mathbf{p}_i \cdot \mathbf{p}_j}{|\mathbf{r}_{ij}|} - \frac{\mathbf{r}_{ij} \cdot [\mathbf{r}_{ij} \cdot \mathbf{p}_j] \mathbf{p}_i}{|\mathbf{r}_{ij}|^3} \right), \quad (33.69)$$

$$H^{\text{ext}} = \frac{\alpha^2}{2} \sum_i \mathbf{E}(\mathbf{r}_i) \times \mathbf{p}_i \cdot \mathbf{s}_i + \frac{i\alpha^2}{4} \sum_i \mathbf{E}(\mathbf{r}_i) \cdot \mathbf{p}_i + 2\mu \sum_i \mathcal{H}(\mathbf{r}_i) \cdot \mathbf{s}_i, \quad (33.70)$$

$\mathbf{E}(\mathbf{r})$ and $\mathcal{H}(\mathbf{r})$ are electric and magnetic fields, and $\mu = e\hbar/(2m_e)$ is the Bohr magneton. The physical significance of these terms is discussed in Chap. 22.1. One of the most important consequences of these relativistic effects is that total electron spin is no longer a good quantum number as it is in $H^0(\mathbf{r}; \mathbf{R})$. The term H^{SD} couple states corresponding to distinct eigenvalues of S^2 and lead to the nonadiabatic effects that are the subject of this section.

The Breit–Pauli approximation is most useful for light atoms, but the approximation breaks down when Z becomes large [104–106]. One of the principal effects omitted in a treatment which includes only H^{SD} is the relativistic contraction of the molecular orbitals [107] due to the mass-velocity operator (H^{mass}), an effect whose importance increases with Z . Several approaches exist which attempt to correct this situation while retaining the spirit and simplifications of the Breit–Pauli approximation. The first of these is the relativistic effective core potential (ECP) approximation [108–111]. In this approach, the results of an atomic Dirac–Fock calculation [112] are used to replace innermost or core electrons of a given atom with (i) an effective one electron potential that modifies the electron–nuclear attraction term in H^0 and (ii) an effective one electron spin-orbit operator, so that

$$H^e(\mathbf{r}; \mathbf{R}) \rightarrow H^{e-\text{ECP}}(\mathbf{r}; \mathbf{R}) = H^{0-\text{ECP}}(\mathbf{r}; \mathbf{R}) + H^{\text{so}-\text{ECP}}(\mathbf{r}; \mathbf{R}). \quad (33.71)$$

The formal similarity between $H^{e-\text{ECP}}$ and $H^e(\mathbf{r}; \mathbf{R})$ results in a similar phenomenological interpretation of relativistically induced nonadiabatic processes. Applications of this approach have been reviewed [107, 113].

A second approach includes all electrons explicitly, and uses H^{SD} as defined above. The relativistic contraction of the core electrons is included by using a variational one-component spin-free approximation [114, 115] to the no-pair Hamiltonian [116] at the orbital optimization stage. The variational nature of the approximation provides advantages over the use of the H^{mass} term. Applications of this approach to the spectra of CuH and NiH have been reported [117, 118].

In order to evaluate $H_{IJ}^{\text{SD}}(\mathbf{R})$, it is necessary to specify the molecular orbitals to be used to construct the $\Psi_I^0(\mathbf{r}; \mathbf{R})$. The choice of molecular orbitals is dictated by the following considerations. Matrix elements of H^{SD} between different states

are required. The molecular orbitals appropriate for one state may not be appropriate for the description of the second state. Two approaches are available to handle this situation. In one approach, distinct sets of (mutually nonorthogonal) molecular orbitals are used to describe each state [119]. This permits a more compact description of the spaces in question. However in this case one is required to evaluate the matrix element of a two electron operator H^{soo} and/or H^{ss} in a nonorthogonal molecular orbital basis, an imposing computational task. This significantly limits the size of the CSF space which is tractable. The alternative approach is to use a common orthonormal basis balanced between the two spaces in question, and to use larger CSF spaces [120–122]. The use of a common orthonormal basis decreases significantly the computational effort required to evaluate the matrix elements. A symbolic matrix element method [123] has been applied to H^{SD} , as described in the review [124].

33.3.3 Surfaces of Intersection

The preceding subsections have considered what must be calculated in order to characterize an electronically nonadiabatic process. As noted in Sect. 33.1, it is also necessary to consider where in nuclear coordinate space electronic nonadiabaticity is important. Nonadiabatic processes are important in regions of close approach of the potential energy surfaces with regions of surface intersections being of pre-eminent interest. Until recently, these surfaces of intersection were determined by indirect methods, i.e., the potential energy surfaces were characterized, and then the surface of intersection was determined. This made the determination of these surfaces of intersection a computationally daunting task. However, computational advances have made it possible to determine these surfaces of intersection directly, i.e., without prior determination of the individual potential energy surfaces. This point is discussed next.

A point on the surface of conical intersection of two states of the same symmetry, subject to a set of geometric equality constraints of the form $C_i(\mathbf{R}) = 0$, $i = 1, \dots, m$, is determined from the Newton–Raphson equations [125]

$$-\begin{pmatrix} \mathbf{Q}^{IJ}(\mathbf{R}, \boldsymbol{\xi}, \boldsymbol{\lambda}) & \mathbf{g}^{IJ}(\mathbf{R}) & \mathbf{h}^{IJ}(\mathbf{R}) & \mathbf{k}(\mathbf{R}) \\ \mathbf{g}^{IJ}(\mathbf{R})^\dagger & 0 & 0 & \mathbf{0} \\ \mathbf{h}^{IJ}(\mathbf{R})^\dagger & 0 & 0 & \mathbf{0} \\ \mathbf{k}(\mathbf{R})^\dagger & \mathbf{0}^\dagger & \mathbf{0}^\dagger & \mathbf{0} \end{pmatrix} \begin{pmatrix} \delta \mathbf{R} \\ \delta \xi_1 \\ \delta \xi_2 \\ \delta \boldsymbol{\lambda} \end{pmatrix} = \begin{pmatrix} \mathbf{g}^I(\mathbf{R}) + \xi_1 \mathbf{g}^{IJ}(\mathbf{R}) + \xi_2 \mathbf{h}^{IJ}(\mathbf{R}) + \sum_{i=1}^m \lambda_i \mathbf{k}^i(\mathbf{R}) \\ \Delta E_{IJ}(\mathbf{R}) \\ 0 \\ \mathbf{C}(\mathbf{R}) \end{pmatrix} \quad (33.72)$$

where $\delta \mathbf{R} = \mathbf{R}' - \mathbf{R}$, $\delta \boldsymbol{\lambda} = \boldsymbol{\lambda}' - \boldsymbol{\lambda}$, $\delta \boldsymbol{\xi} = \boldsymbol{\xi}' - \boldsymbol{\xi}$, $\mathbf{g}_\alpha^{IJ}(\mathbf{R}) \equiv \partial \Delta E_{IJ}(\mathbf{R}) / \partial R_\alpha$, $\mathbf{k}_\alpha^i(\mathbf{R}) \equiv \partial C_i(\mathbf{R}) / \partial R_\alpha$, $\mathbf{h}_\alpha^{IJ}(\mathbf{R}) \equiv \mathbf{c}^{I\dagger}(\mathbf{R}) \mathbf{H}^0(\mathbf{R}) / \partial R_\alpha \mathbf{c}^J(\mathbf{R})$, $\boldsymbol{\xi}$ and $\boldsymbol{\lambda}$ are Lagrange multipliers, and $\mathbf{Q}^{IJ}(\mathbf{R}, \boldsymbol{\xi}, \boldsymbol{\lambda})$ is a matrix of second derivatives [125]. For two states of different symmetry, the analogue of Eq. (33.72) is used with the terms related to ξ_2 omitted [126]. The excellent performance of this algorithm has been documented [125, 127].

Equations (33.72) can be motivated as follows. \mathbf{R}^c is sought so that $E_I^0(\mathbf{R})$ is minimized subject to the constraints $E_I^0(\mathbf{R}) = E_J^0(\mathbf{R})$ and $\mathbf{C}(\mathbf{R}) = 0$. The key is to impose the first of these constraints, noting that at each step in the Newton–Raphson procedure, $\mathbf{c}^I(\mathbf{R})$ and $\mathbf{c}^J(\mathbf{R})$ are eigenvectors. Equation (33.72) are the Newton–Raphson equations corresponding to the Lagrangian function [128]

$$L_{IJ}(\mathbf{R}, \boldsymbol{\xi}, \boldsymbol{\lambda}) = E_I(\mathbf{R}) + \xi_1 \Delta E_{IJ}(\mathbf{R}) + \xi_2 H_{IJ}(\mathbf{R}) + \sum_{k=1}^M \lambda_k C_k(\mathbf{R}), \quad (33.73)$$

provided that the gradient of $H_{IJ}^0(\mathbf{R})$ is interpreted as a change in $\mathbf{H}^0(\mathbf{R})$ within the subspace spanned by $\mathbf{c}^I(\mathbf{R})$ and $\mathbf{c}^J(\mathbf{R})$. This can be derived from quasidegenerate perturbation theory and understood as follows. Assume for convenience that $m = 0$, i.e., there are no geometrical constraints.

Consider an \mathbf{R} for which Eq. (33.72) is not satisfied. The 2×2 matrix $\mathbf{H}(\mathbf{R})$ with matrix elements $H_{KL}(\mathbf{R})$, $K, L \in \{I, J\}$ becomes at $\mathbf{R} + \delta \mathbf{R}$

$$\mathbf{H}_{IJ}(\mathbf{R} + \delta \mathbf{R}) = \mathbf{c}^{I\dagger}(\mathbf{R}) \left(\mathbf{H}(\mathbf{R}) + \sum_\alpha \frac{\partial \mathbf{H}(\mathbf{R})}{\partial R_\alpha} \delta R_\alpha \right) \mathbf{c}^J(\mathbf{R}), \quad (33.74)$$

$\mathbf{H}(\mathbf{R})$ is diagonal but nondegenerate at \mathbf{R} , i.e.,

$$\mathbf{H}(\mathbf{R}) = \begin{pmatrix} E_I^0(\mathbf{R}) - E_J^0(\mathbf{R}) & 0 \\ 0 & 0 \end{pmatrix}. \quad (33.75)$$

From Eq. (33.74) at $\mathbf{R}^c = \mathbf{R} + \delta \mathbf{R}$, $\mathbf{H}(\mathbf{R}^c)$ becomes, to first order, ignoring an irrelevant uniform shift of the diagonal elements,

$$\mathbf{H}(\mathbf{R}^c) = \begin{pmatrix} \Delta E_{IJ}(\mathbf{R}) + \mathbf{g}^{IJ\dagger} \cdot \delta \mathbf{R} & \mathbf{h}^{IJ\dagger} \cdot \delta \mathbf{R} \\ \mathbf{h}^{IJ\dagger} \cdot \delta \mathbf{R} & 0 \end{pmatrix}. \quad (33.76)$$

Thus Eq. (33.72) is seen to be the requirement that $\mathbf{H}(\mathbf{R}^c)$ has degenerate eigenvalues, with eigenvectors $\mathbf{c}^I(\mathbf{R})$ and $\mathbf{c}^J(\mathbf{R})$. When Eq. (33.72) have been solved, $\mathbf{H}_{IJ}(\mathbf{R}^c)$ is diagonal and degenerate, $E_I(\mathbf{R}^c)$ has been minimized, and $\mathbf{g}^I(\mathbf{R}^c) = 0$, except along directions contained in the two

dimensional subspace spanned by $\mathbf{g}^{IJ}(\mathbf{R}^c)$ and $\mathbf{h}^{IJ}(\mathbf{R}^c)$. From Eq. (33.76), it is these two directions which lift the degeneracy of $\mathbf{H}(\mathbf{R}^c)$. Equation (33.72) is also relevant to the reaction path in a nonadiabatic process as discussed in Sect. 33.4. A discussion of these points from an alternative perspective has been presented by Radazos et al. [129].

A solution to Eq. (33.72) is referred to as a conical intersection, although rigorously degenerate states cannot be obtained from a numerical procedure. If required, the existence of a conical intersection can be rigorously established by showing that the adiabatic wave functions undergo a change of sign when transported around a closed loop containing \mathbf{R}^c in the plane defined by $\mathbf{g}^{IJ}(\mathbf{R}^c)$ and $\mathbf{h}^{IJ}(\mathbf{R}^c)$. This is the geometric or Berry phase criterion [130, 131]. It has been explicitly demonstrated for a conical intersection in O_3 by Ruedenberg and coworkers [132].

33.4 Nuclear Motion

33.4.1 General Considerations

The determination of the rovibrational spectrum of polyatomic systems from first principles is a problem of primary importance since it allows the determination of molecular forces and structure from spectral data. In the adiabatic case, the solution of Eq. (33.6)

$$[T^{\text{nuc}}(\mathbf{R}) + E_I^0(\mathbf{Q}) - E_K] \beta_K(\mathbf{R}) = 0 \quad (33.77)$$

is sought, where \mathbf{Q} denotes a set of internal nuclear coordinates. The reliability of the solution of Eq. (33.77) reflects the accuracy of the Born–Oppenheimer potential energy surface $E_I^0(\mathbf{Q})$ appearing in that equation. The methods for determining $E_I^0(\mathbf{Q})$ were discussed in Sect. 33.2. Conversely, the determination of the E_K from spectroscopic measurements can be used to infer information concerning $E_I^0(\mathbf{Q})$. In either case, the accurate solution of Eq. (33.77) is requisite and this section is concerned with its solution.

The operator in Eq. (33.77) has a continuous spectrum since T^{nuc} includes translations of the nuclear center of mass (cm). An operator with a discrete spectrum is obtained by replacing the Hamiltonian in Eq. (33.77) with one in which the translation of the nuclear c.m. has been eliminated by transforming to the c.m. frame. In the center of mass frame, Eq. (33.77) has the general form [133]

$$[T^{\text{vr}}(\boldsymbol{\Omega}, \mathbf{Q}) + T^{\text{vib}}(\mathbf{Q}) + E_I^0(\mathbf{Q}) - E_K] \beta(\boldsymbol{\Omega}, \mathbf{Q}) = 0, \quad (33.78)$$

where $\boldsymbol{\Omega}$ are three rotational coordinates and T^{vr} and T^{vib} are the rotational and vibrational kinetic energy operators. In $T^{\text{vr}}(\boldsymbol{\Omega}, \mathbf{Q})$ all the complexity associated with the coupling of nuclear and electronic angular momentum is buried. The

determination of the appropriate form for Eq. (33.78) is by no means straightforward [134, 135], and treatment of the effects of multiple angular momentum is a complex problem in angular momentum algebra.

In diatomic systems, the vibrational problem involves only one internal coordinate and is straightforward. Angular momentum coupling is usually treated using Hund's case (a), (b), etc., or an intermediate case approach [95] with Van Vleck's reversed angular momentum commutation relations being helpful in analyzing the coupled angular momentum problem [134].

Polyatomic systems introduce new complications, since in addition to the increased dimensionality of the vibrational problem, internal and rotational coordinates interconvert for colinear arrangements of the nuclei; this is particularly relevant in triatomic systems. In addition, since the $C_{\infty v}$ point group has doubly degenerate representations at collinear geometries, electronic state degeneracies may arise (the Renner–Teller effect) [32, 136, 137], further complicating the analysis. Techniques associated with the description of triatomic systems involving coupled angular momentum and electronic degeneracy are illustrated in Sect. 33.4.3.

More generally, Eq. (33.78) can be rewritten as

$$[T^{\text{vr}}(\boldsymbol{\Omega}, \mathbf{Q}^e) + T^{\text{vib}}(\mathbf{Q}) + E_I^{\text{sep}}(\mathbf{Q}) - E_K] \beta(\mathbf{R}) = -\Delta T^{\text{vr}}(\boldsymbol{\Omega}, \mathbf{Q}) \beta(\mathbf{R}) - \Delta E_I^0(\mathbf{Q}), \quad (33.79)$$

where

$$\Delta T^{\text{vr}}(\boldsymbol{\Omega}, \mathbf{Q}) \equiv T^{\text{vr}}(\boldsymbol{\Omega}, \mathbf{Q}) - T^{\text{vr}}(\boldsymbol{\Omega}, \mathbf{Q}^e), \quad (33.80)$$

$$\Delta E_I^0(\mathbf{Q}) \equiv E_I^0(\mathbf{Q}) - E_I^{\text{sep}}(\mathbf{Q}), \quad (33.81)$$

\mathbf{Q}^e is an equilibrium structure, and $E_I^{\text{sep}}(\mathbf{Q})$ is a separable function of the normal coordinates. In this case, the solution to the left-hand side of Eq. (33.79) can be factorized into a rotational part and a vibrational part [138] according to

$$\psi_I^J = \sum_K k_K^J D_{K0}^J(\theta, \chi) \prod_i \alpha_i(Q_i) \quad (33.82)$$

where D_{K0}^J is a symmetric top wave function [139], and $\alpha_i(Q_i)$ is a pure vibrational wave function, e.g., harmonic oscillator function, for the i th internal normal coordinate. It is in this approximation that the notion of a molecule rotating and vibrating about a fixed molecular structure is achieved. In this case, E_K is just the sum of the pure rotational and vibrational energies. These rigid rotator–vibrator solutions then form the basis for the inclusion of the effects of the right-hand side using, for example, perturbation theory [140]. They can also be used as a basis for a nonperturbative treatment (Sect. 33.4.2).

The classic treatments of Eq. (33.77) [141–144] have been periodically revisited [134, 145]. In these investigations, the contributions of electronic angular momentum to

this Hamiltonian were frequently suppressed [144] so that these treatments are appropriate to totally symmetric electronic states. *Van Vleck* [134] has shown how the effects of electronic angular momentum can be incorporated into these treatments.

For nonlinear polyatomic systems, the Hamiltonian in Eq. (33.78) can be transformed to the Eckart or body fixed frame in which the reference axis is a body fixed axis oriented along the principal moments of inertia [146], although other choices of the body fixed axes are possible [147]. The principal moments of inertia represent the eigenvectors of the inertial tensor matrix I_{ij} , $i, j = x, y, z$, where [144]

$$I_{xx} = \sum_i M_i (\mathbf{R}_i^e \cdot \mathbf{R}_i^e - X_i^e X_i^e), \quad (33.83)$$

$$I_{xy} = - \sum_i M_i (X_i^e Y_i^e), \quad (33.84)$$

and cyclic permutations, and \mathbf{R}^e denotes an equilibrium structure. The Hamiltonian determined by this procedure is referred to as the Watson Hamiltonian [145], and is widely used in discussing the rovibrational spectrum of nonlinear polyatomic molecules in singlet electronic states. Treatments of the Watson Hamiltonian are mentioned in Sect. 33.4.2. For linear molecules, an alternative treatment is required since there is one fewer overall rotational coordinate and one more internal coordinate [138].

33.4.2 Rotational-Vibrational Structure

Various approaches to the solution of Eq. (33.79) exist. The principal issues, which are interrelated, are (i) the range of nuclear configurations over which $E_l^0(\mathbf{Q})$ is known, (ii) the coordinate system used to express the internal coordinates, and (iii) particularly in larger systems, the number of modes or internal coordinates retained in the calculations (Sect. 33.4.3). With regard to point (i), two approaches are currently in use. The force field method uses a power series expansion of $E_l^0(\mathbf{Q})$ about $E_l^0(\mathbf{Q}^e)$, that is (using the Einstein summation convention)

$$E_l^0(\mathbf{Q}) = E_l^0(\mathbf{Q}^e) + \frac{1}{2} \frac{\partial^2 E_l^0(\mathbf{Q}^e)}{\partial Q_i \partial Q_j} \Delta Q_i \Delta Q_j + \frac{1}{6} \frac{\partial^3 E_l^0(\mathbf{Q}^e)}{\partial Q_i \partial Q_j \partial Q_k} \Delta Q_i \Delta Q_j \Delta Q_k \quad (33.85)$$

together with perturbation theory to determine spectroscopic constants. In this approach, the force fields [the partial derivatives in Eq. (33.85)] are usually evaluated directly with the aid of analytic gradient techniques (Sect. 33.2). Since the expansion of $E_l^0(\mathbf{Q})$ is truncated, the results are not independent of the coordinate system used. For example,

significant differences in the description of Fermi-resonance parameters [148, 149] in rectilinear and curvilinear coordinates [150] have been reported.

Alternatively, $E_l^0(\mathbf{Q})$ can be represented by a grid of points around \mathbf{Q}^e . In the most reliable calculations reported to date, $E_l^0(\mathbf{Q})$ is determined using the coupled cluster techniques discussed in Sect. 33.2. Then Eq. (33.79) can be solved in a basis analogous to ψ_l^J in Eq. (33.82). This approach is frequently referred to as the vibrational CI problem [151]. The reliability of the results depends to a considerable extent on the basis functions and coordinate system used to describe the problem. Considerable success has been reported for a technique in which the Watson Hamiltonian and harmonic oscillator functions are used to solve Eq. (33.79) [151, 152].

33.4.3 Coupling of Electronic and Rotational Angular Momentum in Weakly Interacting

An understanding of the molecular structure of the weakly bound compounds of noble gas atoms and diatomic molecules provides important insights into the nature of chemical bonding. The inference of structural data from spectroscopic observations is an important aspect of this problem. In this subsection, a theoretical framework for understanding the spectroscopy of these systems is outlined as an illustration of the methods used to treat coupling of electronic and nuclear angular momentum in weakly interacting triatomic molecular systems. Detailed discussion of this class of problems can be found in [153–155].

As an example, consider the rovibronic structure of a noble gas-diatom complex Rg-AB , in either its $^1\Sigma^+$ or $^1\Pi$ states (which may be closely spaced). Note that degeneracy of the $^1\Pi$ state will only persist for collinear geometries of the triatom system. The rovibrational wave functions can be expanded in a product basis of functions describing (i) the rovibronic structure of AB and (ii) the relative motion (vibrational and end-over-end rotation) of Rg and AB . Since total angular momentum J and its space fixed projections M are good quantum numbers, the rovibronic wave function can be expanded as

$$\Psi^{JM} = \frac{1}{R} \sum_{vj\Omega l \varepsilon} C_{j\Omega l \varepsilon}^{JM}(R) |\psi_{\text{Rg}}\rangle |v_{Ij}\rangle |Ij \Omega \varepsilon, l; JM\rangle, \quad (33.86)$$

where ψ_{Rg} is the ground state wave function for the noble gas atom, l denotes the angular momentum associated with the end-over-end motion, and v, j, ε and I denote respectively the vibrational, angular momentum (electronic + rotational), e/f symmetry index and state label of the electronic state

of the AB molecule in Hund's case (a) basis. The angular momentum coupling algebra noted above is reflected in the definition of $|Ij\Omega\varepsilon, l; JM\rangle$, which is

$$|Ij\Omega\varepsilon, l; JM\rangle = \sum_{m_j m_l} \langle j m_j l m_l | JM \rangle Y_{lm_l}(\theta, \phi) \psi_{Ij m_j \Omega \varepsilon}(\beta, \alpha), \quad (33.87)$$

where θ, ϕ and β, α are the polar and azimuthal angles for the line connecting the noble gas atom to the center of mass of the diatom and the diatom axis, respectively, and $\langle \dots | \dots \rangle$ is a Clebsch–Gordan coefficient [156] (Chap. 2). The $\psi_{Ij m_j \Omega \varepsilon}$ are defined in turn by [95]

$$\begin{aligned} \psi_{Ij m_j \Omega \varepsilon} &= \left(\frac{2J+1}{8\pi} \right)^{1/2} \\ &\times [D_{m_j, \Omega}^j(\alpha, \beta, 0)^* |I^{2S+1}\Lambda^+(\Sigma)\rangle \\ &+ \varepsilon D_{m_j, -\Omega}^j(\alpha, \beta, 0)^* |I^{2S+1}\Lambda^-(-\Sigma)\rangle] \end{aligned} \quad (33.88)$$

or

$$\psi_{Ij m_j \Omega \varepsilon} = \left(\frac{2J+1}{4\pi} \right)^{1/2} D_{m_j, 0}^j(\alpha, \beta, 0)^* |I^{2S+1}\Lambda(\Sigma)\rangle \quad (33.89)$$

when $\Lambda = \Sigma = 0$, where the electronic state has term symbol $I^{2S+1}\Lambda$ with $\Omega = \Lambda + \Sigma$.

The $C^{JM}(\mathbf{R})$ satisfy the usual close coupled equations [157, 158] Chap. 49.1.1

$$\left[\left(\frac{-1}{2\mu} \frac{d^2}{dR^2} + \frac{l(l+1)}{2\mu R^2} \right) \mathbf{I} - \frac{\mathbf{k}^2}{2\mu} + V(r) \right] C^{JM}(r) = 0, \quad (33.90)$$

where $l(l+1)$ and $\mathbf{k}^2/2\mu$ designate the diagonal matrices of orbital angular momentum and asymptotic net scattering energy of individual channels. $V(R)$ represents the matrix elements of $H^e(\mathbf{r}; \mathbf{R})$ in the vibronic basis defined in Eqs. (33.86)–(33.89). It is built from terms of the form

$$\begin{aligned} &\langle Y_{lm} D_{m_j \Omega}^{j*} v_{Ij} | \langle \psi_{Rg} I^{2S+1}\Lambda | H^e(\mathbf{r}; \mathbf{R}) \\ &\times | \psi_{Rg} I^{2S'+1}\Lambda' \rangle_r | v_{I'j'} Y_{l'm'} D_{m'_j \Omega'}^{j'*} \rangle \\ &\equiv \langle Y_{lm} D_{m_j \Omega}^{j*} v_{Ij} | H_{II'}^e(R, \tilde{\beta}, r) | Y_{l'm'} D_{m'_j \Omega'}^{j'*} v_{I'j'} \rangle. \end{aligned} \quad (33.91)$$

The angle $\tilde{\beta}$ is the polar angle of the diatom with respect to the atom-diatom axis. The angular integrations on the right-hand side of Eq. (33.91) are accomplished by expanding the angular dependence of $H_{II'}^e$ in d -matrices and using angular momentum coupling algebra [158]. $H_{II'}^e$ gives the interaction potential of the ground state noble gas atom and the

$I^{2S+1}\Lambda$ state of AB . It represents the potential coupling in the diabatic basis $\psi_{Rg} | I^{2S+1}\Lambda \rangle$. These matrix elements are derived from the corresponding adiabatic potential energy surfaces, determined using the techniques of Sect. 33.2. Since the van der Waals interaction is weak, the counterpoised method discussed in Sect. 33.2.4 should be used. When only one electronic state of a given symmetry is involved (point group C_s in the case of a triatom), the adiabatic and diabatic potentials are taken as equal. This is the case if, for example, only the $^1\Pi$ state of AB is considered. When more than one electronic state of a given symmetry is involved, for example, when both $^1\Pi$ and $^1\Sigma^+$ electronic states of AB are included, the adiabatic potentials are used to determine the diabatic state potentials using an approximate adiabatic \rightarrow diabatic state transformation [159, 160].

The solution to Eq. (33.90) can be obtained by either variational methods or by direct integration [153]. Results for Ar-OH [161], Ar-BH [155], and Ar-CH [162], based on potential energy surfaces determined from multireference contracted CI wave functions, are encouraging. In these studies, the r -dependence of the potential energy surfaces was neglected.

33.4.4 Reaction Path

The rovibrational spectrum reflects the molecular structure in the vicinity of an equilibrium structure of the molecule. However a chemical reaction samples a much broader range of molecular structures. The evolution of molecular structure can be characterized by the reaction path, which represents a minimum energy path along the potential energy surface connecting the reactants and products. The reaction path Hamiltonian [163, 164] enables dynamical aspects of a chemical reaction to be inferred from a characterization of the reaction path.

The reaction path $\mathbf{R}(s)$ on potential energy surface $E_I^0(\mathbf{R})$ is the curve in mass weighted Cartesian coordinates given parametrically in terms of the arc length s and is defined as that solution to the differential equation

$$\frac{d\mathbf{R}}{ds} = \mathbf{g}^I / \sqrt{\mathbf{g}^{I\dagger} \mathbf{g}^I} \equiv \mathbf{R}'(s) \quad (33.92)$$

which approaches the saddle point from below [17, 165], where the arc length is given by

$$ds^2 = \sum_{i=1}^N dR_i^2. \quad (33.93)$$

At each point s , $\mathbf{R}(s)$ represents the molecular structure in terms of $3N$ mass weighted Cartesian coordinates. (In this subsection, the notation suppresses the difference between Cartesian and mass weighted Cartesian coordinates.)

The reaction path can be obtained by integrating Eq. (33.92). Integration begins at the saddle point along the direction of the single negative eigenvalue of \mathbf{F}^I , which is related to the reaction path curvature $d\mathbf{R}^2/ds^2$, by

$$\frac{d\mathbf{R}^2}{ds^2} \equiv \frac{d\mathbf{R}'}{ds} = \frac{[\mathbf{F}^I \mathbf{R}' - (\mathbf{R}'^\dagger \mathbf{F}^I \mathbf{R}') \mathbf{R}']}{\sqrt{\mathbf{g}^{I\dagger} \mathbf{g}^I}}. \quad (33.94)$$

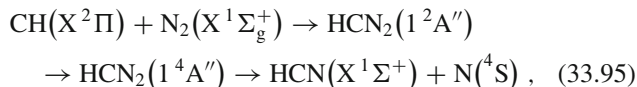
Thus integration of Eq. (33.92) gives the steepest descent path from the saddle point. This integration requires, in principle, only knowledge of the energy gradient, $\mathbf{g}^I(\mathbf{R})$, which is readily available using analytic gradient techniques (see Sect. 33.2). This approach works quite well when the reaction path is used only to investigate the topology of a potential energy surface. However if quantities such as the curvature are desired, procedures that follow the reaction path more closely are required. Such procedures require higher derivatives of the energy, as fully discussed in [165].

In a nonadiabatic process, the reaction path necessarily involves more than one potential energy surface. In the case of nonadiabatic reactions involving avoided intersections, the reaction path is difficult to define since the propensity for an intersurface transition spreads out over a range of nuclear coordinates. However, for nonadiabatic reactions that proceed through a surface of intersection of two potential energy surfaces, the reaction path passes through the minimum energy point on the surface of intersection of the two potential energy surfaces [166]. An example of such a process is provided in Sect. 33.5. The minimum energy point on the surface of intersection satisfies Eq. (33.72) with no geometric constraints. For a spin-forbidden reaction, the solution of Eq. (33.72) yields $\mathbf{g}^I \mathbf{R} + \xi_1 \mathbf{g}^{IJ}(\mathbf{R}) = 0$, so that $\mathbf{g}^I(\mathbf{R}) = \xi_1/(1 + \xi_1) \mathbf{g}^J(\mathbf{R})$, i.e., the gradients on the two surfaces are either parallel or anti-parallel depending on the value of ξ_1 . The relationship between the gradients in the vicinity of an intersection of two states of the same symmetry is not as simple. The wave functions are not differentiable at a point of intersection. In the vicinity of the point of intersection, the condition $\mathbf{g}^I(\mathbf{R}) + \xi_1 \mathbf{g}^{IJ}(\mathbf{R}) + \xi_2 \mathbf{h}^{IJ}(\mathbf{R}) \approx 0$ holds, so that $\mathbf{g}^I(\mathbf{R})$ and $\mathbf{g}^J(\mathbf{R})$ will not be simply related. Finally, note that the adiabatic correction, defined in Sect. 33.1, is large (and positive) in the vicinity of the conical intersection, so that the nuclear wave function exhibits a node at this point.

33.5 Reaction Mechanisms: A Spin-Forbidden Chemical Reaction

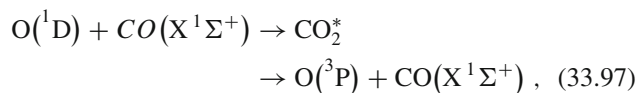
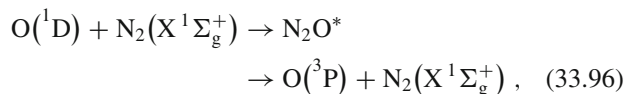
This section presents an example to illustrate how the ideas outlined in the preceding sections can be used to obtain a mechanistic description of a chemical reaction which could

not be deduced on intuitive grounds. Considered here is the ground state reaction



which is of considerable importance in the chemistry of planetary atmospheres [167, 168] and hydrocarbon flames, having been suggested as the initial step in the production of prompt or Fenimore NO [168–171]. However, because the reaction is spin-forbidden, its importance has been questioned.

The reaction will be interpreted in terms of the intermediate complex model [172, 173]. In this model, the reaction can occur despite a small probability for intersystem crossing by repeatedly traversing the $2A''$ – $4A''$ surface of intersection. The repeated traversals result from a local minimum on the $2A''$ potential energy surface. This mechanism is operative for the spin-forbidden oxygen quenching reactions [172, 173]



which are important in the chemistry of the atmosphere.

To demonstrate the feasibility of reaction Eq. (33.95) as an intermediate complex assisted chemical reaction it is necessary to (i) determine the energetically relevant portion of the doublet-quartet surface of intersection, (ii) determine the spin-orbit interaction coupling the doublet and quartet surfaces, (iii) characterize a local minimum on the doublet surface from which the surface of intersection is accessible, (iv) characterize a path from the reactant channel to this region, and (v) determine the exit channel path on the quartet surface. The results of electronic structure calculations at the MR-CI level, addressing these points [174–178] are summarized below.

Local Extrema on the $2A''$ – $4A''$ Surface of Intersection

Points in the $2A''$ – $4A''$ surface of intersection were determined from the solution to Eq. (33.72) [126, 174]. The minimum energy point on the surface of intersection, labelled $C_{\text{mex}}^{C_{2v}}$, has approximate C_{2v} symmetry, and is shown in Fig. 33.3. It is the region of this crossing point that must be accessed from the doublet surface.

The Spin-Orbit Interaction

In the double group corresponding to C_s symmetry, the $4A''$ and $2A''$ wave functions each carry degenerate ir-

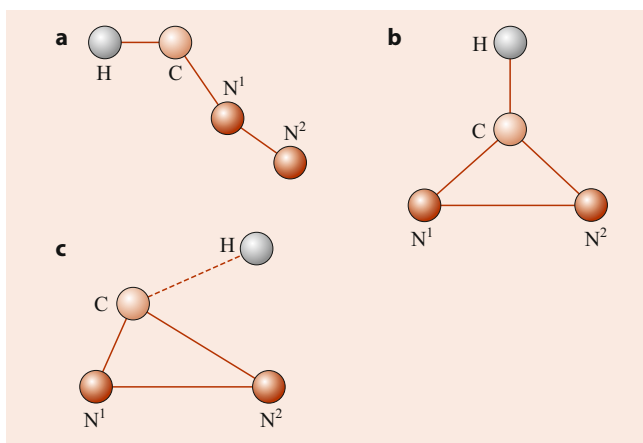


Fig. 33.3 Key bond distances in Å for (a) $R_{\min}^{\text{dative}}(\text{CH}) = 1.082$, $R_{\min}^{\text{dative}}(\text{CN}^1) = 1.340$, $R_{\min}^{\text{dative}}(\text{N}^1\text{N}^2) = 1.143$; (b) $R_{\min}^{\text{C}_{2v}}(\text{CH}) = 1.071$, $R_{\min}^{\text{C}_{2v}}(\text{CN}^1) = 1.311$; $R_{\min}^{\text{C}_{2v}}(\text{N}^1\text{N}^2) = 1.735$; $R_{\text{mex}}^{\text{C}_{2v}}(\text{CH}) = 1.076$, $R_{\text{mex}}^{\text{C}_{2v}}(\text{CN}^1) = 1.3$, $R_{\text{mex}}^{\text{C}_{2v}}(\text{N}^1\text{N}^2) = 2.221$; (c) $R_{\text{TS}}^c(\text{CH}) = 1.093$, $R_{\text{TS}}^c(\text{CN}^1) = 1.515$, $R_{\text{TS}}^c(\text{N}^1\text{N}^2) = 1.214$. The notation is as defined in Sect. 33.5. The dashed line in structure (c) indicates that H is out of the plane of the paper. (a), (b) after [124], (c) after [177]

reducible representations, Kramer's doublets [179]. The following pairs of nonrelativistic zeroth-order wave functions can be used to span these degenerate representations (i) $\Psi^0[2A''(\frac{1}{2})]$, $\Psi^0[2A''(-\frac{1}{2})]$, (ii) $i\Psi^0[4A''(\frac{1}{2})]$, $i\Psi^0[4A''(-\frac{1}{2})]$, and (iii) $i\Psi^0[4A''(\frac{3}{2})]$, $i\Psi^0[4A''(-\frac{3}{2})]$, where the M_s value has been given parenthetically. In this case, all nonvanishing matrix elements connecting the components of the $4A''$ and $2A''$ states can be expressed in terms of the single real-valued matrix element [139]

$$H^{\text{so}}(4A'', 2A'') \equiv \langle i\Psi^0[4A''(\frac{3}{2})] | H^{\text{so}} | \Psi^0[2A''(\frac{1}{2})] \rangle, \quad (33.98)$$

which was found to be $\approx 12.5 \text{ cm}^{-1}$ [126, 174] in the vicinity of the minimum energy crossing point determined above.

Local Extrema on the $2A''$ Potential Energy Surface

Two local minima on the $2A''$ potential energy surface have been found [174–176]. The local minimum configuration labeled C_{\min}^{dative} pictured in Fig. 33.3 represents a datively bonded structure in which N_2 donates a pair of electrons to the empty $\text{CH}(1\pi)$ orbital. This can be thought of as a reactant channel structure, since the N–N and C–H bond lengths are similar to those in the isolated molecules. This point on the $2A''$ potential energy surface is stable by 20.2 kcal/mol relative to the doublet asymptote in the reactant channel. The second minimum on the $2A''$ potential energy surface is also pictured in Fig. 33.3 and is seen to have C_{2v} symmetry. This configuration point, denoted $C_{\min}^{\text{C}_{2v}}$, is stable by 22.3 kcal/mol relative to the doublet asymptote in the reactant channel.

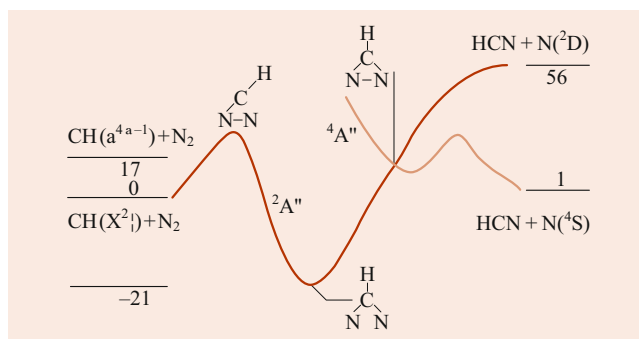


Fig. 33.4 Reaction path for $\text{CH}(X^2\Pi) + \text{N}_2(X^1\Sigma_g^+) \rightarrow \text{HCN}(X^1\Sigma^+) + \text{N}(^4\text{S})$ after [177]. Energy scale, which is approximate, is in kcal/mol

Note that $C_{\min}^{\text{C}_{2v}}$ and $C_{\text{mex}}^{\text{C}_{2v}}$ differ only in the length of the N–N bond.

Reaction Path

From the above data it might appear that both the $C_{\min}^{\text{C}_{2v}}$ and C_{\min}^{dative} structures are involved in the mechanism of reaction Eq. (33.95). However, the energy of the transition state connecting these two minima is quite large [176], so that the reaction path avoids C_{\min}^{dative} [177]. The true reaction path involves $C_{\min}^{\text{C}_{2v}}$, $C_{\text{mex}}^{\text{C}_{2v}}$, and a reactant channel transition state C_{TS}^c that connects $C_{\min}^{\text{C}_{2v}}$ and the reactant channel species $\text{CH} + \text{N}_2$. C_{TS}^c is also pictured in Fig. 33.3. It involves the nonplanar cis-approach of HC to N_2 [177]. The total reaction path is presented in Fig. 33.4 [178]. Note that following intersystem crossing, the system encounters a final transition state before proceeding to the spin-forbidden products.

From this qualitative analysis, a bimodal picture of the reaction of ground state CH with N_2 emerges. $\text{CH}(^2\Pi)$ can be removed by either (i) forming a complex C_{\min}^{dative} which is stabilized by a third body collision or (ii) forming the spin-forbidden products with the reaction mechanism indicated in Fig. 33.4. This mechanism has been deduced entirely from the computational results cited above. The key computational findings responsible for this mechanism are (i) the existence and geometrical relationship between $C_{\min}^{\text{C}_{2v}}$ and $C_{\text{mex}}^{\text{C}_{2v}}$, (ii) the large barrier separating C_{\min}^{dative} and $C_{\min}^{\text{C}_{2v}}$, and (iii) the entrance channel path across C_{TS}^c to $C_{\min}^{\text{C}_{2v}}$.

Since there is apparently no or little barrier to forming C_{\min}^{dative} [176], at low temperatures CH will be removed exclusively by this process at a rate with a small or negative temperature dependence, indicating a barrierless reaction. At higher temperatures, the rate constant is expected to exhibit a more usual Arrhenius type behavior as the spin-forbidden channel can be accessed [180]. These expectations are consistent with previous low temperature measurements [168, 181] and high temperature shock tube results [171, 182, 183]. The above reaction path for the spin-forbidden reaction has been used in a two internal coordinate model for reaction Eq. (33.95) [180] that also supports the proposed description of this reaction.

33.6 Recent Developments

Added by Mark M. Cassar

If the motion of nuclei within a molecule causes more than one Born–Oppenheimer potential energy surface to intersect, then nonadiabatic transitions become an essential process in molecular dynamics. These transitions are at the heart of many biological processes, such as light harvesting by plants [184, 185], which depends on electronic excitation transfer, and a host of processes in the upper atmosphere. In recent years, it has become apparent that conical intersections (see Sect. 33.3.3 for a definition) of two states of the same symmetry are a fundamental element of electronically nonadiabatic phenomena [186]. As an example, conical intersections can facilitate transitions from upper to lower electronic states. Transitions of this nature provide efficient pathways to lower electronic states, and are thus amenable to experimental study (e.g., through dissociation products of photoexcitation [187]).

Although points of conical intersection, which are not individual but form seams, can be located in a straightforward manner, finding points of minimum energy has proved more difficult. This difficulty has been attributed to the erratic behavior of the parameters used in the search algorithm. This seemingly intrinsic problem which would preclude extrapolation – a consequence of the singular nature of the intersection itself – has been avoided through the use of extrapolatable functions [188]. This recent work introduces functions that vary smoothly (i.e., are well-behaved) as one moves along the intersection seam, and hence allow the use of extrapolation techniques.

The study of conical intersections has also been extended to include three-state intersections and first-order relativistic effects. Accidental conical intersections (i.e., those not required by symmetry arguments) of three states of the same symmetry, which may provide an efficient mechanism for radiationless decay, have been shown to exist [189]. Spin-orbit effects are essential for the proper description of the nuclear dynamics in molecules containing an odd number of electrons [190]. The topography of conical intersections changes in this case, requiring the development of new algorithms [191].

References

1. Bethe, H.A., Salpeter, E.E.: *Quantum Mechanics of One and Two Electron Atoms*. Plenum/Rosetta, New York (1977)
2. Born, M., Huang, K.: *Dynamical Theory of Crystal Lattices*. Oxford University Press, Oxford (1954)
3. Herzberg, G., Longuet-Higgins, H.C.: *Disc. Faraday Soc.* **35**, 77 (1963)
4. Berry, M.V.: *Proc. R. Soc. Lond.* **45**(1984), A392

5. Longuet-Higgins, H.C.: *Adv. Spectrosc.* **2**, 429 (1961)
6. Gerber, W.H., Schumacher, E.: *J. Chem. Phys.* **69**, 1692 (1978)
7. Kahn, L.R., Baybutt, P., Truhlar, D.G.: *J. Chem. Phys.* **65**, 3826 (1976)
8. Tully, J.C.: In: Miller, W.H. (ed.) *Modern Theoretical Chemistry*, vol. 2, p. 217. Plenum, New York (1976)
9. Garrett, B.C., Truhlar, D.G.: *Theoretical Chemistry Advances and Perspectives*. Academic Press, New York (1981)
10. Bishop, D.M., Cheung, L.M.: *J. Chem. Phys.* **78**, 1396 (1983)
11. Bishop, D.M., Cheung, L.M.: *J. Chem. Phys.* **80**, 4341 (1984)
12. Jensen, J.O., Yarkony, D.R.: *J. Chem. Phys.* **89**, 3853 (1988)
13. Vidal, C.R., Stwalley, W.C.: *J. Chem. Phys.* **77**, 883 (1982)
14. Chen, Y.C., Harding, D.R., Stwalley, W.C., Vidal, C.R.: *J. Chem. Phys.* **85**, 2436 (1986)
15. Murrell, J.N., Carter, S., Farantos, S.C., Huxley, P., Varandas, A.J.C.: *Molecular Potential Energy Surfaces*. Wiley, New York (1984)
16. Truhlar, D.G., Steckler, R., Gordon, M.S.: *Chem. Rev.* **87**, 217 (1987)
17. Fukui, K.: *Acc. Chem. Res.* **14**, 363 (1981)
18. Cerjan, C.J., Miller, W.H.: *J. Chem. Phys.* **75**, 2800 (1981)
19. Schlegel, H.B.: *Adv. Chem. Phys.* **67**, 249 (1987)
20. Schlegel, H.B.: In: Yarkony, D.R. (ed.) *Modern Electronic Structure Theory, Part 1*. World Scientific, Singapore (1995)
21. Schaefer, H.F. (ed.): *Modern Theoretical Chemistry*. Plenum, New York (1976)
22. Yarkony, D.R. (ed.): *Modern Electronic Structure Theory*. World Scientific, Singapore (1995)
23. McLachlan, A.D.: *Mol. Phys.* **4**, 417 (1961)
24. Smith, F.T.: *Phys. Rev.* **179**, 111 (1969)
25. Lichten, W.: *Phys. Rev.* **131**, 339 (1963)
26. Lichten, W.: *Phys. Rev.* **164**, 131 (1967)
27. Mead, C.A., Truhlar, D.G.: *J. Chem. Phys.* **77**, 6090 (1982)
28. Baer, M.: *Chem Phys Lett* **35**, 112 (1975)
29. Baer, M.: *Chem Phys* **15**, 49 (1976)
30. Pacher, T., Mead, C.A., Cederbaum, L.S., Koppel, H.: *J. Chem. Phys.* **91**, 7057 (1989)
31. Sidis, V.: In: Baer, M., Ng, C.Y. (eds.) *State-Selected and State-to-State Ion-Molecule Reaction Dynamics Part 2, Theory*, 82 edn., p. 73. Wiley, New York (1992)
32. Renner, R.: *Z. Phys* **92**, 172 (1934)
33. von Neumann, J., Wigner, E.: *Z. Phys.* **30**, 467 (1929)
34. Mead, C.A.: *J. Chem. Phys.* **70**, 2276 (1979)
35. Szabo, A., Ostlund, N.S.: *Modern Quantum Chemistry: Introduction to Advanced Electronic Structure Theory*. McMillan, New York (1982)
36. Jensen, P.J., Simons, J.: *Second Quantization Based Methods in Quantum Chemistry*. Academic Press, New York (1981)
37. Almlöf, J.: In: Yarkony, D.R. (ed.) *Modern Electronic Structure Theory, Part 1*, p. 1. World Scientific, Singapore (1995)
38. Dunning, T.H., Hay, P.J.: In: Schaefer, H.F. (ed.) *Modern Theoretical Chemistry*, vol. 3, Plenum, New York (1976)
39. Roos, B.O., Linse, P., Siegbahn, P.E.M., Blomberg, M.R.A.: *Chem Phys* **66**, 197 (1982)
40. Moshinsky, M.: *Group Theory and the Many Body Problem*. Gordon and Breach, New York (1968)
41. Hinze, J.: *The Unitary Group*, Lecture Notes in Chem. Springer, Berlin, Heidelberg, p 22 (1979)
42. Shavitt, I.: In: Schaefer, H.F. (ed.) *Modern Theoretical Chemistry*, vol. 3, p. 189. Plenum, New York (1976)
43. Yamaguchi, Y., Osamura, Y., Goddard, J.D., Schaefer, H.F.: *A New Dimension to Quantum Chemistry: Analytic Derivative Methods in ab initio Molecular Electronic Structure Theory*. Oxford University Press, Oxford (1994)

44. Lengsfeld, B.H., Yarkony, D.R.: In: Baer, M., Ng, C. (eds.) *State-Selected and State to State Ion-Molecule Reaction Dynamics: Part 2, Theory*, vol. 82, Wiley, New York (1992)
45. Pulay, P.: *Mol. Phys.* **17**, 197 (1969)
46. Roothaan, C.C.J.: *Rev. Mod. Phys.* **23**, 69 (1951)
47. Gaw, J.F., Yamaguchi, Y., Schaefer, H.F.: *J. Chem. Phys.* **81**, 6395 (1984)
48. Gaw, J.F., Yamaguchi, Y., Schaefer, H.F., Handy, N.C.: *J. Chem. Phys.* **85**, 5132 (1986)
49. Almlf, J.: *J. Comput. Chem.* **3**, 385 (1982)
50. Docken, K., Hinze, J.: *J. Chem. Phys.* **57**, 4928 (1972)
51. Hinze, J.: *J. Chem. Phys.* **59**, 6424 (1973)
52. Werner, H., Meyer, W.: *J. Chem. Phys.* **74**, 5794 (1981)
53. Lengsfeld, B.H.: *J. Chem. Phys.* **77**, 4073 (1982)
54. Iler, C.M., Plesset, M.S.: *Phys. Rev.* **46**, 618 (1934)
55. Almlf, J.: *Chem Phys Lett* **181**, 319 (1991)
56. Cizek, J.: *J. Chem. Phys.* **45**, 4256 (1966)
57. Cizek, J.: *Adv. Chem. Phys.* **14**, 35 (1969)
58. Paldus, J., Cizek, J.: In: Smith, D., McRae, W.B. (eds.) *Energy Structure and Reactivity*, p. 35. Wiley, New York (1973)
59. Bartlett, R.J., Purvis III, G.D.: *Int. J. Quantum Chem. Symp.* **14**, 561 (1978)
60. Pople, J.A., Krishnan, R., Schlegel, H.B., Binkley, J.S.: *Int. J. Quantum Chem.* **14**, 545 (1978)
61. Löwdin, P.O.: *Phys. Rev.* **97**, 1474 (1955)
62. Bartlett, R.J., Watts, J.D., Kucharski, S.A., Noga, J.: *Chem Phys Lett* **165**, 513 (1990)
63. Kucharski, S.A., Bartlett, R.J.: *Chem Phys Lett* **158**, 550 (1989)
64. Raghavachari, K., Trucks, G.W., Pople, J.A., Head-Gordon, M.: *Chem. Phys. Lett.* **157**, 479 (1989)
65. Watts, J.D., Gauss, J., Bartlett, R.J.: *J. Chem. Phys.* **98**, 8718 (1993)
66. Bartlett, R.J.: In: Yarkony, D.R. (ed.) *Modern Electronic Structure Theory*, p. 2. World Scientific, Singapore (1995)
67. Diffenderfer, R.N., Yarkony, D.R.: *J. Chem. Phys.* **86**, 5098 (1982)
68. Roos, B.O., Taylor, P.R., Siegbahn, P.E.M.: *Chem Phys* **48**, 157 (1980)
69. Roos, B.O.: *Int. J. Quantum Chem. Symp.* **14**, 175 (1980)
70. Siegbahn, P., Heiberg, A., Roos, B., Levy, B.: *Phys. Scr.* **21**, 323 (1980)
71. Bauschlicher, C.W., Langhoff, S.R., Taylor, P.R.: *Adv. Chem. Phys.* **77**, 103 (1990)
72. Silverstone, H.J., Sinanoglu, O.: *J. Chem. Phys.* **44**, 1899 (1966)
73. Dalgaard, E., Rognesen, P.J.: *J. Chem. Phys.* **69**, 3833 (1978)
74. Davidson, E.R.: *J. Comput Phys* **17**, 87 (1975)
75. Roos, B.O.: *Chem Phys Lett* **15**, 153 (1972)
76. Siegbahn, P.E.M.: *J. Chem. Phys.* **72**, 1647 (1980)
77. Harrison, R.J.: *J. Chem. Phys.* **94**, 5021 (1991)
78. Caballol, R., Malrieu, J.P.: *Chem Phys Lett* **188**, 543 (1992)
79. Povill, A., Rubio, J., Illas, F.: *Theo. Chim. Acta* **82**, 229 (1992)
80. Knowles, P.J., Werner, H.: *Chem Phys Lett* **115**, 259 (1985)
81. Knowles, P.J., Werner, H.: *Chem Phys Lett* **145**, 514 (1988)
82. Werner, H., Knowles, P.J.: *J. Chem. Phys.* **82**, 5053 (1985)
83. Werner, H., Knowles, P.J.: *J. Chem. Phys.* **89**, 5803 (1988)
84. Andersson, K., Malmqvist, P.Å., Roos, B.O., Sadlej, A.J., Wolinski, K.: *J. Phys. Chem.* **94**, 5483 (1990)
85. Andersson, K., Malmqvist, P.Å., Roos, B.O.: *J. Chem. Phys.* **96**, 1218 (1992)
86. Parr, R.G., Yang, W.: *Density-Functional Theory of Atoms and Molecules*. Oxford, New York (1989)
87. Hohenberg, P., Kohn, W.: *Phys. Rev. B* **136**, 864 (1964)
88. Kohn, W., Sham, L.J.: *Phys. Rev. A* **140**, 1133 (1965)
89. Becke, A.D.: In: Yarkony, D.R. (ed.) *Modern Electronic Structure Theory, Part 2*. World Scientific, Singapore (1995)
90. Pula, P.: In: Yarkony, D.R. (ed.) *Modern Electronic Structure Theory, Part 2*. World Scientific, Singapore (1995)
91. Liu, B., McLean, A.D.: *J. Chem. Phys.* **59**, 4557 (1973)
92. Liu, B., McLean, A.D.: *J. Chem. Phys.* **91**, 2348 (1989)
93. Boys, S.F., Bernardi, F.: *Mol. Phys.* **19**, 553 (1970)
94. Gutowski, M., van Lenthe, J., van Duijneveldt, J.C.G.M., van Duijneveldt, F.B.: *J. Chem. Phys.* **98**, 4728 (1993)
95. Lefebvre-Brion, H., Field, R.W.: *Perturbations in the Spectra of Diatomic Molecules*. Academic Press, New York (1986)
96. Han, S., Hettema, H., Yarkony, D.R.: *J. Chem. Phys.* **102**, 1955 (1995)
97. Lengsfeld, B.H., Saxe, P., Yarkony, D.R.: *J. Chem. Phys.* **81**, 4549 (1984)
98. Saxe, P., Lengsfeld, B.H., Yarkony, D.R.: *Chem Phys Lett* **113**, 159 (1985)
99. Buenker, R.J., Hirsch, G., Peyerimhoff, S.D., Bruna, P.J., Romelt, J., Bettendorff, M., Petrongolo, C.: In: Carbo, R. (ed.) *Current Aspects of Quantum Chemistry 1981*, vol. 21, p. 81. Elsevier, New York (1982)
100. Mead, C.A.: *J. Chem. Phys.* **78**, 807 (1993)
101. Hellmann, J.: *Einführung in die Quantenchemie*. Deuticke, Leipzig (1937)
102. Feynman, R.P.: *Phys. Rev.* **56**, 340 (1939)
103. Langhoff, S.R., Kern, C.W.: In: Schaefer, H.F. (ed.) *Modern Theoretical Chemistry*, vol. 4, p. 381. Plenum, New York (1977)
104. Blume, M., Watson, R.E.: *Proc. R. Soc. Lond. A* **270**, 127 (1962)
105. Blume, M., Watson, R.E.: *Proc. R. Soc. Lond. A* **271**, 565 (1963)
106. Fraga, S., Saxena, K.M.S., Lo, B.W.N.: *At. Data* **3**, 323 (1971)
107. Ermler, W.C., Ross, R.B., Christiansen, P.A.: *Advances in Quantum Chemistry* vol. 19. Academic Press, New York, p. 139 (1988)
108. Ermler, W.C., Lee, Y.S., Christiansen, P.A., Pitzer, K.S.: *Chem Phys Lett* **81**, 70 (1981)
109. Lee, Y.S., Ermler, W.C., Pitzer, K.S.: *J. Chem. Phys.* **67**, 5861 (1977)
110. Pitzer, R.M., Winter, N.W.: *J. Chem. Phys.* **92**, 3061 (1988)
111. Stevens, W.J., Krauss, M.: *J. Chem. Phys.* **76**, 3834 (1982)
112. Desclaux, J.P.: *Comp. Phys. Comm.* **9**, 31 (1975)
113. Balasubramanian, K.: *J. Phys. Chem.* **93**, 6585 (1989)
114. Hess, B.A.: *Phys. Rev. A* **33**, 3742 (1986)
115. Hess, B.A., Chandra, P.: *Phys. Scr.* **36**, 412 (1987)
116. Sucher, J.: *Phys. Rev. A* **22**, 348 (1980)
117. Marian, C.M.: *J. Chem. Phys.* **93**, 1176 (1990)
118. Marian, C.M.: *J. Chem. Phys.* **94**, 5574 (1991)
119. Furlani, T.R., King, H.F.: *J. Chem. Phys.* **82**, 5577 (1985)
120. Hess, B.A., Buenker, R.J., Marian, C.M., Peyerimhoff, S.D.: *Chem Phys* **71**, 79 (1982)
121. Yarkony, D.R.: *J. Chem. Phys.* **84**, 2075 (1986)
122. Jensen, J.O., Yarkony, D.R.: *Chem Phys Lett* **141**, 391 (1987)
123. Liu, B., Yoshimine, M.: *J. Chem. Phys.* **74**, 612 (1981)
124. Yarkony, D.R.: *Int. Rev. Phys. Chem.* **11**, 195 (1992)
125. Manaa, M.R., Yarkony, D.R.: *J. Chem. Phys.* **99**, 5251 (1993)
126. Yarkony, D.R.: *J. Chem. Phys.* **97**, 4407 (1993)
127. Yarkony, D.R.: *J. Chem. Phys.* **100**, 3639 (1994)
128. Fletcher, R.: *Practical Methods of Optimization* vol. 2. Wiley, New York (1981)
129. Radzios, I.N., Robb, M.A., Bernardi, M.A., Olivucci, M.: *Chem Phys Lett* **197**, 217 (1992)
130. Herzberg, G., Longuet-Higgins, H.C.: *Disc. Faraday Soc.* **35**, 77 (1963)
131. Berry, M.V.: *Proc. R. Soc. Lond. A* **392**, 45 (1984)
132. Xantheas, S., Elbert, S.T., Ruedenberg, K.: *J. Chem. Phys.* **93**, 7519 (1990)
133. Tennyson, J., Miller, S., Sutcliffe, B.T.: *J. Chem. Soc. Faraday Trans.* **84**, 1295 (1988)

134. Van Vleck, J.H.: *Rev. Mod. Phys.* **23**, 213 (1951)
135. Mizushima, M.: *The Theory of Rotating Diatomic Molecules*. Wiley, New York (1975)
136. Lee, T.J., Fox, D.J., Schaefer, H.F., Pitzer, R.M.: *J. Chem. Phys.* **81**, 356 (1984)
137. Dixon, R.N.: *Mol. Phys.* **54**, 333 (1985)
138. Whitehead, R.J., Handy, N.C.: *J. Mol. Spec.* **55**, 356 (1975)
139. Rose, M.E.: *Elementary Theory of Angular Momentum*. Wiley, New York (1957)
140. Mills, I.M.: In: Rao, K.N., Mathews, C.W. (eds.) *Molecular Spectroscopy: Modern Research*, p. 115. Academic Press, New York (1970)
141. Eckart, C.: *Phys. Rev.* **47**, 552 (1935)
142. Wilson Jr., E.B., Howard, J.B.: *J. Chem. Phys.* **4**, 260 (1936)
143. Darling, B.T., Dennison, D.M.: *Phys. Rev.* **57**, 128 (1940)
144. Wilson, E.B., Decius, J.C., Cross, P.C.: *Molecular Vibrations*. McGraw-Hill, New York (1955)
145. Watson, J.K.G.: *Mol. Phys.* **15**, 479 (1968)
146. Zare, R.N.: *Angular Momentum*. Wiley, New York (1988)
147. Sutcliffe, B.T., Tennyson, J.: *Mol. Phys.* **58**, 1053 (1986)
148. Segall, J., Zare, R.N., Dubal, H.R., Lewerenz, M., Quack, M.: *J. Chem. Phys.* **86**, 634 (1987)
149. Green, W.H., Lawrence, W.D., Moore, C.B.: *J. Chem. Phys.* **86**, 6000 (1987)
150. Amos, R.D., Gaw, J.G., Handy, N.C., Carter, S.: *J. Chem. Soc. Faraday Trans.* **84**, 1247 (1988)
151. Botschwina, P.: *Chem Phys* **68**, 41 (1982)
152. Botschwina, P.: *J. Chem. Soc. Faraday Trans.* **84**, 1263 (1988)
153. Hutson, J.M.: In: Bowman, J.M., Ratner, M.A. (eds.) *Advances in Molecular Vibrations and Collision Dynamics*, vol. 1A, JAI Press, Greenwich (1991)
154. Dubernet, M.L., Flower, D., Hutson, J.M.: *J. Chem. Phys.* **94**, 7602 (1991)
155. Alexander, M.H., Gregurick, S., Dagdigian, P.J.: *J. Chem. Phys.* **101**, 2887 (1994)
156. Brink, D.M., Satchler, G.R.: *Angular Momentum*. Clarendon, Oxford (1968)
157. Arthurs, A., Dalgarno, A.: *Proc. Roy. Soc. Lond. A* **256**, 540 (1960)
158. Alexander, M.: *Chem Phys* **92**, 337 (1985)
159. Werner, H., Follmeg, B., Alexander, M.H.: *J. Chem. Phys.* **89**, 3139 (1988)
160. Werner, H., Follmeg, B., Alexander, M.H., Lemoine, D.: *J. Chem. Phys.* **91**, 5425 (1989)
161. Chakravarty, C., Clary, D.: *J. Chem. Phys.* **94**, 4149 (1991)
162. Alexander, M.H., Gregurick, S., Dagdigian, P.J., Lemire, G.W., McQuaid, M.J., Sausa, R.C.: *J. Chem. Phys.* **101**, 4547 (1994)
163. Miller, W.H.: In: Clary, D.C. (ed.) *The Theory of Chemical Reaction Dynamics*. Reidel, Dordrecht (1986)
164. Miller, W.H., Handy, N., Adams, J.: *J. Chem. Phys.* **72**, 99 (1980)
165. Page, M., McIver, J.W.: *J. Chem. Phys.* **88**, 922 (1988)
166. Kato, S., Jaffe, R.L., Komornicki, A., Morokuma, K.: *J. Chem. Phys.* **78**, 4567 (1983)
167. Strobel, D.F.: *Planet. Space. Sci.* **30**, 839 (1982)
168. Berman, M.R., Lin, M.C.: *J. Phys. Chem.* **87**, 3933 (1983)
169. Fenimore, C.P.: 13th International Symposium on Combustion. The Combustion Institute, Pittsburgh, p 373 (1971)
170. Blauwens, J., Smets, B., Peeters, J.: 16th International Symposium on Combustion. The Combustion Institute, Pittsburgh, p 1055 (1977)
171. Dean, A.J., Hanson, R.K., Bowman, C.T.: 23rd International Symposium on Combustion. The Combustion Institute, Pittsburgh, p 259 (1990)
172. Tully, J.C.: *J. Chem. Phys.* **61**, 61 (1974)
173. Zahr, G.E., Preston, R.K., Miller, W.H.: *J. Chem. Phys.* **62**, 1127 (1975)
174. Manaa, M.R., Yarkony, D.R.: *J. Chem. Phys.* **95**, 1808 (1991)
175. Manaa, M.R., Yarkony, D.R.: *Chem Phys Lett* **188**, 352 (1992)
176. Martin, J.M.L., Taylor, P.R.: *Chem Phys Lett* **209**, 143 (1993)
177. Walch, S.P.: *Chem Phys Lett* **208**, 214 (1993)
178. Seideman, T., Walch, S.P.: *J. Chem. Phys.* **101**, 3656 (1994)
179. Tinkham, M.: *Group Theory and Quantum Mechanics*. McGraw-Hill, New York (1964)
180. Seideman, T.: *J. Chem. Phys.* **101**, 3662 (1994)
181. Becker, K.H., Engelhardt, B., Geiger, H., Kurtenbach, R., Schrey, G., Wissen, P.: *Chem Phys Lett* **154**, 342 (1992)
182. Lindackers, D., Burmeister, M., Roth, P.: 23rd International Symposium on Combustion. Combustion Institute, Pittsburgh, p 251 (1990)
183. Lindackers, D., Burmeister, M., Roth, P.: *Combust Flame* **81**, 251 (1990)
184. Hu, X., Schulten, K.: *Phys. Tod.* **50**, 28 (1997)
185. Weber, W., Helms, V., Mc Mammon, A., Langhoff, P.W.: *Proc. Natl. Acad. Sci. U.S.A.* **96**, 6177 (1999)
186. Yarkony, D.R.: *J. Phys. Chem. A.* **105**, 6277 (2001)
187. Yarkony, D.R.: *J Chem Phys* **121**, 628 (2004)
188. Yarkony, D.R.: *J. Phys. Chem. A.* **108**, 3200 (2004)
189. Matsika, S., Yarkony, D.R.: *J Chem Phys* **117**, 6907 (2002)
190. Matsika, S., Yarkony, D.R.: *J. Phys. Chem. B.* **106**, 8108 (2002)
191. Matsika, S., Yarkony, D.R.: *J Chem Phys* **115**, 5066 (2001)



William G. Harter and Tyle C. Reimer

Contents

34.1	Dynamics and Spectra of Molecular Rotors	507
34.1.1	Rigid Rotors	508
34.1.2	Molecular States Inside and Out	508
34.1.3	Rigid Asymmetric Rotor Eigensolutions and Dynamics	509
34.2	Rotational Energy Surfaces and Semiclassical Rotational Dynamics	511
34.3	Symmetry of Molecular Rotors	513
34.3.1	Asymmetric Rotor Symmetry Analysis	513
34.4	Tetrahedral-Octahedral Rotational Dynamics and Spectra	514
34.4.1	Semirigid Octahedral Rotors and Centrifugal Tensor Hamiltonians	515
34.4.2	Octahedral and Tetrahedral Rotational Energy Surfaces	515
34.4.3	Octahedral and Tetrahedral Rotational Fine Structure	515
34.4.4	Octahedral Superfine Structure	517
34.5	High-Resolution Rovibrational Structure	518
34.5.1	Tetrahedral Nuclear Hyperfine Structure	518
34.5.2	Superhyperfine Structure and Spontaneous Symmetry Breaking	520
34.5.3	Large Spherical Top Molecules: Cubic-Octahedral Symmetry Effects	521
34.5.4	Icosahedral Spherical Top Molecules: Extreme Spin Symmetry Effects	523
34.5.5	$^{12}\text{C}_{60}$ versus $^{13}\text{C}_{60}$: a World of Difference in Spin- $\frac{1}{2}$ Hyperfine Spectroscopy	525
34.6	Composite Rotors and Multiple RES	528
34.6.1	3-D-Rotor and 2-D-Oscillator Analogy	529
34.6.2	Gyro-Rotors and 2-D-Local Mode Analogy	530
34.6.3	Multiple Gyro-Rotor RES and Rotational Energy Eigensurfaces (REES)	531
34.6.4	Multi-Quantum CF_4 Rovibrational Polyads and REES Visualization	533
References	534

W. G. Harter (✉)
Dept. of Physics, University of Arkansas
Fayetteville, AR, USA
e-mail: wharter@uark.edu

T. C. Reimer
University of Arkansas
Fayetteville, AR, USA
e-mail: tcreimer@cox.net

Abstract

Molecules are aggregates of two or more nuclei bound by at least one electron. The nuclei of most stable molecules can be imagined to be points in a more or less rigid body whose relative positions are constrained by an electronic bonding potential. This potential depends strongly upon the electronic state, as described in Chap. 33. Most of this discussion is about stable molecules in their electronic ground state. The high/symmetry molecules CF_4 and SF_6 are discussed in Sect. 34.5 and compared to C_{60} or “Buckyball”, a recently discovered case of the highest 3-D symmetry. Section 34.6 introduced molecules with excited or “loose”= parts.

Keywords

angular momentum · rigid rotor · body frame · tunneling rate · molecular rotation

34.1 Dynamics and Spectra of Molecular Rotors

Motions that stretch or compress the bonds are called *vibrational* motions and give rise to spectral resonances in the infrared region of the spectrum. Typical fundamental vibrational quanta (ν_0) lie between 80 cm^{-1} (the lowest GeBr_4 mode) and 3020 cm^{-1} (the highest CH_4 mode). (A 1000 cm^{-1} wave has a wavelength of $10\text{ }\mu\text{m}$ and a frequency defined by the speed of light: 29.9792458 THz .) Vibrational amplitudes are usually tiny since zero-point motions or vibrations involving one or two quanta ($\nu = 0, 1, 2, \dots$) are constrained by the steep bonding potential to less than a few percent of the bond lengths, but high overtones may lead to dissociation, i.e., molecular breakup.

The overall rotation of molecules in free space is unconstrained and gives rise to far-infrared or microwave

pure rotational transitions or sidebands on top of vibrational spectra. Typical rotational quanta ($2B$) lie between 0.18 cm^{-1} (5.4 GHz) for SF_6 and 10.6 cm^{-1} for CH_4 . Individual molecules are free to rotate or translate as a whole while undergoing tiny but usually rapid vibrations. Vibrating molecules may be thought of as tumbling collections of masses held together by “springs” (the electronic vibrational potential or force field) and are called semirigid rotors. The coupling of rotational and vibrational motion is called rovibrational coupling and includes centrifugal and Coriolis coupling, which will be introduced in Sect. 34.6.

This discussion of molecular dynamics and spectra mainly involves the molecular rotation and properties of rotationally excited molecules, particularly those with high rotational quantum number $J = 10\text{--}200$. However, the discussion also applies to molecules in excited vibrational states, and even certain cases of molecules in excited electronic states. The analysis of vibronic (vibrational-electronic), rovibrational (rotation-vibration), or rovibronic (all three) types of excitation can be very complicated [1–5] and is beyond the scope of this chapter, but these problems can also benefit from the elementary considerations to be introduced here.

34.1.1 Rigid Rotors

As a first approximation, and for the purposes of discussing basic molecular dynamics and spectra, one may ignore vibrations and model stable molecules as “stick-and-ball” structures or rigid rotors. Then the Hamiltonian has just three terms

$$H = AJ_x^2 + BJ_y^2 + CJ_z^2. \quad (34.1)$$

Here, $\{J_x, J_y, J_z\}$ are rotational angular momentum operators, and the rotational constants are half the inverses of the principal moments of inertia I_α of the body

$$A = \frac{1}{2I_x}, \quad B = \frac{1}{2I_y}, \quad C = \frac{1}{2I_z}. \quad (34.2)$$

This simple form follows if the J -coordinate system is assumed fixed to the rotor’s body and aligned to its principal axes, an elementary body, or Eckart frame.

Many molecules, and particularly all diatomic molecules, have two of the three rotational constants equal, say, $A = B$. Such rotors are called symmetric tops, and their Hamiltonian involves the usual total angular momentum squared $\mathbf{J} \cdot \mathbf{J}$ with one other body z -axial component J_z , in the form

$$\begin{aligned} H &= BJ_x^2 + BJ_y^2 + CJ_z^2 \\ &= BJ_x^2 + BJ_y^2 + BJ_z^2 + (C - B)J_z^2 \\ &= B\mathbf{J} \cdot \mathbf{J} + (C - B)J_z^2. \end{aligned} \quad (34.3)$$

This gives a simple formula for the symmetric top rotational energy levels in terms of the quantum numbers J for the total angular momentum and K for the body z -component

$$E(J, K) = BJ(J + 1) + (C - B)K^2. \quad (34.4)$$

However, this eigenvalue formula may be a little too simple, since it hides the structure of the eigenstates or eigenfunctions. Indeed, the full Schrödinger angular differential equation based upon the Hamiltonian in Eq. (34.1) is more lengthy. Note that H is written in a rotating body $\bar{x}, \bar{y}, \bar{z}$ coordinate frame moving relative to a star-fixed or laboratory frame.

34.1.2 Molecular States Inside and Out

Rotor angular momentum eigenfunctions can be expressed as continuous linear combinations of rotor angular position states $|\alpha\beta\gamma\rangle$ defined by Euler angles of the lab azimuth α , the polar angle β of body \bar{z} -axis, and the body azimuth, “gauge twist”, γ . The eigenfunctions are

$$\begin{aligned} \left| \begin{matrix} J \\ MK \end{matrix} \right\rangle &= \frac{\sqrt{2J + 1}}{8\pi^2} \int_0^{2\pi} d\alpha \int_0^\pi \sin\beta d\beta \\ &\quad \times \int_0^{2\pi} d\gamma D_{MK}^J{}^*(\alpha\beta\gamma) |\alpha\beta\gamma\rangle. \end{aligned} \quad (34.5)$$

Here, the rotor wave functions $D_{MK}^J{}^*$ are just the conjugates of the Wigner rotation matrices described in Sect. 34.3.1, and row and column indices M and K , respectively, are the lab and body z -components of angular momentum [6, 7]. It may surprise atomic physicists that polyatomic molecular angular momentum states have two kinds of polar quantum numbers. In addition to the usual lab component of momentum M associated with the lab coordinate α (usually α and β are labeled ϑ and φ), there is a body component K associated with the Euler coordinate γ , the body azimuthal angle of the lab z -axis relative to the body \bar{z} -axis.

The physics of atomic or diatomic angular momentum states has no internal or “body” structure, so the quantum number K is always zero. Unless one sets $K = 0$, the energy formula in Eq. (34.4) blows up for a point particle because z -inertia for a point is zero, and C is infinite. Also, the dimension of the angular momentum state multiplet of a given J is larger than the usual $(2J + 1)$ found in atomic or diatomic molecular physics. In polyatomic rotors, the number of states for each J is $(2J + 1)^2$, since both quantum numbers M and K range between $-J$ and $+J$. Also surprising, and this is a more pleasant surprise, is that the molecular rotor wave functions contain, as a special ($K = 0$) case, all

the usual atomic spherical harmonics Y_m^ℓ complete with correct normalization and phase, since

$$\sqrt{4\pi}Y_m^\ell(\vartheta, \varphi) = D_{m0}^{\ell*}(\varphi, \vartheta) \sqrt{2\ell + 1}. \quad (34.6)$$

This is part of a powerful symmetry principle: group representations are quantum wave functions, and symmetry analysis is an extension of Fourier analysis of plane e^{ikx} waves for cyclic C_n group translations as in Fourier's original work and holds for any group of symmetry operations. The usual Fourier coefficients are replaced by the D functions in the rotational Fourier transforms embodied by Eq. (34.5).

Molecular rotational analysis displays another important but little known aspect of symmetry analysis in general. For every group of symmetry operations, such as the external lab-based rotations familiar to atomic physics, there is an independent dual group of internal or body-based operations. The external symmetry of the environment or laboratory is independent of the internal symmetry of the molecular body, and all the operations of one commute with all those of the other. The molecular rotation group is thus written as an outer product $R(3)_{\text{LAB}} \otimes R(3)_{\text{BODY}}$ of the external and internal parts, and the degeneracy associated with this group's representations for a single J is $(2J + 1)^2$ as mentioned above. It is a special \otimes -product, however, since the J -number is shared.

The inversion or parity operator $\mathbf{I}(\mathbf{r} \rightarrow -\mathbf{r})$ can be defined to be the same for both lab and body frames. Including \mathbf{I} with the rotational group $R(3)$ gives the orthogonal group $O(3) = R(3) \otimes \{\mathbf{1}, \mathbf{I}\}$. If parity is conserved (e.g., no weak neutral currents), the fundamental molecular orthogonal group is $O(3)_{\text{LAB}} \otimes O(3)_{\text{BODY}}$.

How this symmetry breaks down and which levels split depends upon both the perturbative laboratory environment and

the internal molecular structure. A spherical top Hamiltonian is Eq. (34.1) with $A = B = C$. This has a full $O(3)_{\text{BODY}}$ (spherical) symmetry since it is just $B\mathbf{J} \cdot \mathbf{J}$. Given that the rotor is in an $O(3)_{\text{LAB}}$ laboratory (empty space), the original symmetry $O(3)_{\text{LAB}} \otimes O(3)_{\text{BODY}}$ remains intact, and the $(2J + 1)^2$ degeneracy is to be expected. However, a symmetric rotor in a lab vacuum has its internal symmetry broken down to $O(2)_{\text{BODY}}$ if $A = B \neq C$, and the energies given by Eq. (34.4) consist of internal quantum singlets for $K = 0$ and $\pm K$ doublets for $K \neq 0$. But each of these levels still has a lab degeneracy of $(2J + 1)$ if $O(3)_{\text{LAB}}$ is still in effect. So the $(2J + 1)^2$ level degeneracies are each split into multiplets of degeneracy $(2J + 1)$ and $2(2J + 1)$ for $K = 0$ and $K \neq 0$, respectively. The resulting levels are often labeled $\Sigma, \Pi, \Delta, \Phi, \Gamma, \dots$ in a somewhat inappropriate analogy with the atomic s, p, d, f, g, \dots labels of Bohr model electronic orbitals.

Only by perturbing the lab environment can one reduce the $O(3)_{\text{LAB}}$ symmetry and split the M degeneracies. For example, a uniform electric field would reduce the $O(3)_{\text{LAB}}$ to an $O(2)_{\text{LAB}}$, giving Stark splittings that consist of external quantum singlets for $M = 0$ and $\pm M$ doublets for $M \neq 0$. A uniform magnetic field would reduce the $O(3)_{\text{LAB}}$ to an $R(2)_{\text{LAB}}$, giving Zeeman splittings into external quantum singlets for each M . The analogy between atomic external field splitting and internal molecular rotational structure splitting is sometimes a useful one and will be used later.

34.1.3 Rigid Asymmetric Rotor Eigensolutions and Dynamics

The general case for the rigid rotor Hamiltonian in Eq. (34.1) has three unequal principal moments of inertia ($A \neq B \neq C$).

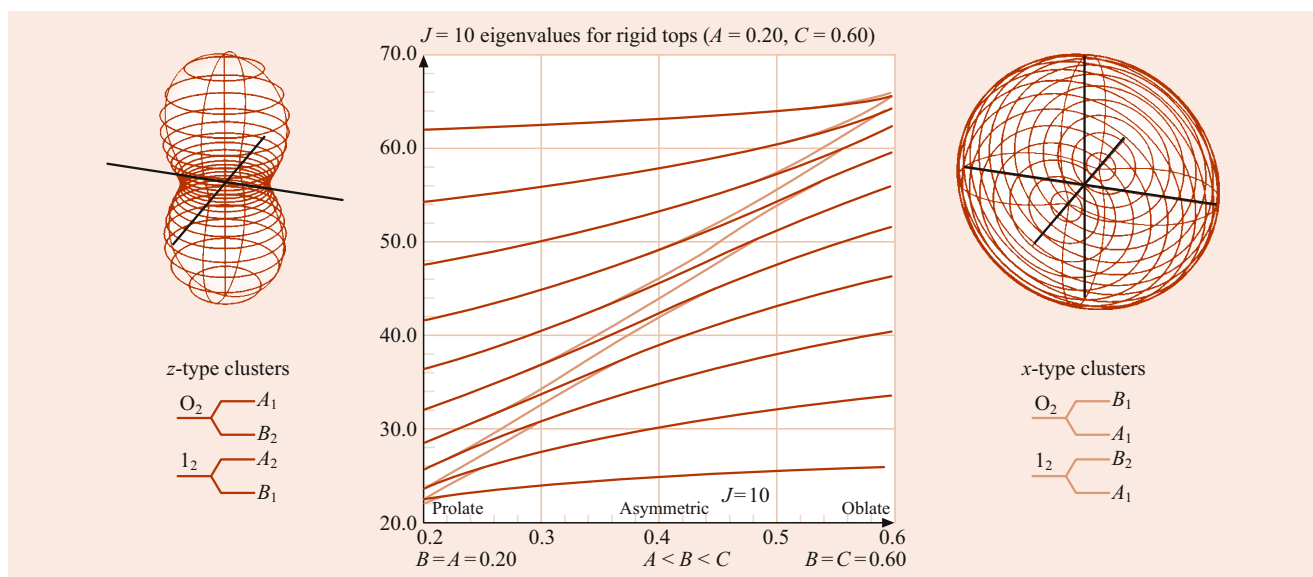


Fig. 34.1 $J = 10$ eigenvalue plot for symmetric rigid rotors ($A = 0.2, C = 0.6 \text{ cm}^{-1}, A < B < C$). Prolate and oblate RE surfaces are shown

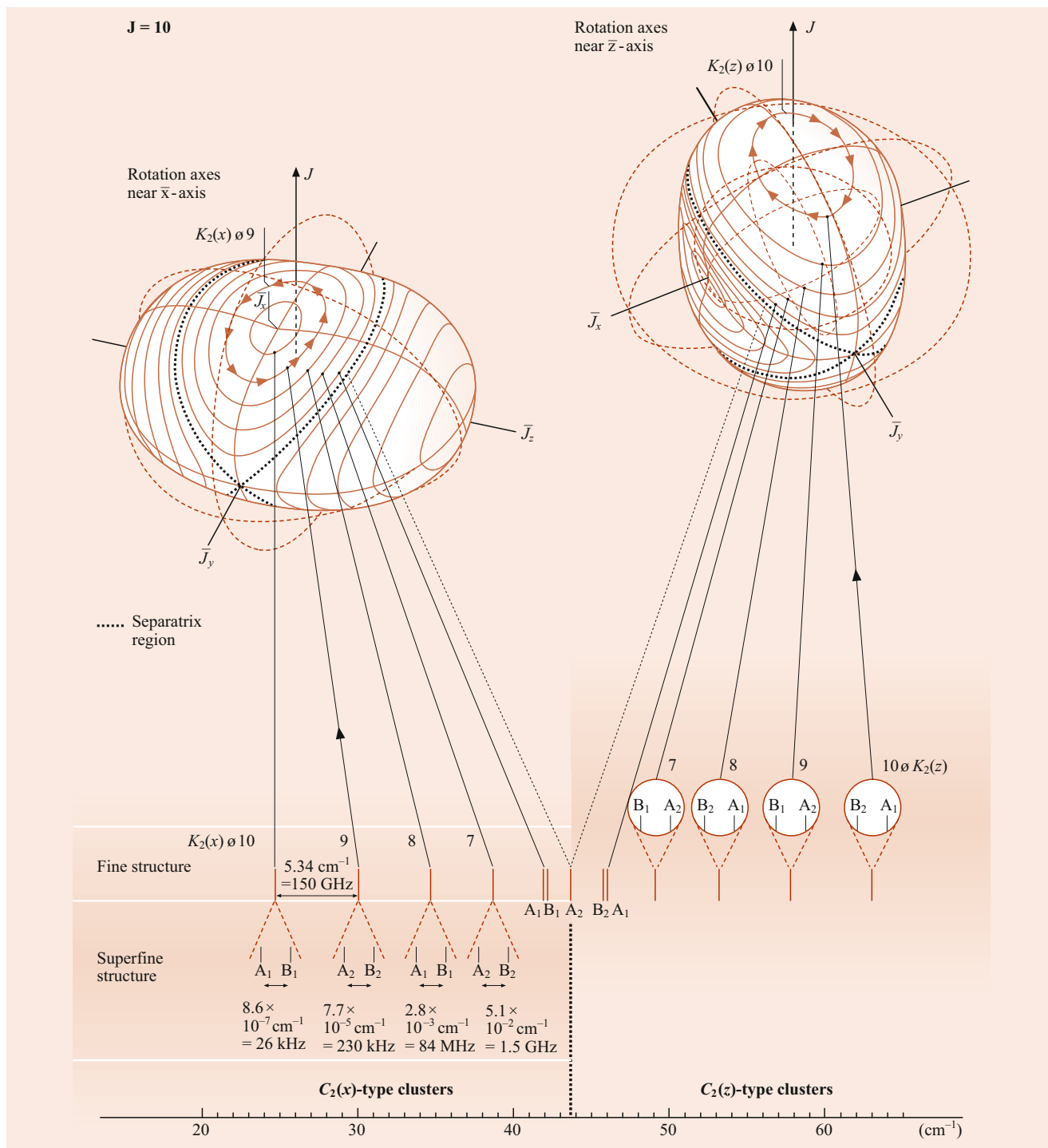


Fig. 34.2 $J = 10$ rotational energy surface and related level spectrum for an asymmetric rigid rotator ($A = 0.2$, $B = 0.4$, $C = 0.6 \text{ cm}^{-1}$)

This is called the rigid asymmetric top Hamiltonian and provides a first approximation for modeling the rotation of low-symmetry molecules, such as H_2O . Also, a number of properties of its eigensolutions are shared by more complicated systems. The dynamics of an asymmetric top is quite remarkable, as demonstrated by tossing a tennis racquet in

the air, flat side up. The corresponding quantum behavior of such a molecule is also nontrivial.

Given the total angular momentum J , one may construct a $(2J + 1)$ -dimensional matrix representation of H using standard matrix elements of the angular momentum operators J_x , J_y , and J_z , as given in Chap. 2. The H matrix

connects states with $(2J + 1)$ -different body quantum numbers K ($-J \leq K \leq J$), but the matrix is independent of the lab quantum numbers M , so there are $(2J + 1)$ identical H matrices; one for each value of the lab quantum number M .

A plot of the 21 eigenvalues of Eq. (34.1) for $J = 10$ is shown in Fig. 34.1. Here, the constants are set to $A = 0.2 \text{ cm}^{-1}$ and $C = 0.6 \text{ cm}^{-1}$, while B is varied between $B = A$, which corresponds to a prolate symmetric top (an elongated cylindrical object) and $B = C$, which corresponds to an oblate symmetric top (a flattened cylindrical object or discus). For all B -values between those of A and C , the object is asymmetric.

The left-hand end ($A = B = 0.2 \text{ cm}^{-1}$, $C = 0.6 \text{ cm}^{-1}$) of the plot in Fig. 34.1 corresponds to a prolate symmetric top. The symmetric top level spectrum is given by Eq. (34.4). It consists of a lowest singlet state corresponding to $K = 0$ and an ascending quadratic ladder of doublets corresponding to $K = \pm 1, \pm 2, \dots, \pm J$. The right-hand end ($A = 0.2 \text{ cm}^{-1}$, $B = C = 0.6 \text{ cm}^{-1}$) of the plot corresponds to an oblate symmetric top with a descending quadratic ladder of levels, the $K = 0$ level being highest. Also, the internal K -axis of quantization switches from the body \bar{z} -axis for ($A = B = 0.2 \text{ cm}^{-1}$, $C = 0.6 \text{ cm}^{-1}$) to the body x -axis for ($A = 0.2 \text{ cm}^{-1}$, $B = C = 0.6 \text{ cm}^{-1}$). The lab M -degeneracy is invisible here but exists nevertheless.

For intermediate values of B , one has an asymmetric top level structure and, strictly speaking, no single axis of quantization. As a result, the eigenlevel spectrum is quite different. A detailed display of asymmetric top levels for the case ($A = 0.2 \text{ cm}^{-1}$, $B = 0.4 \text{ cm}^{-1}$, $C = 0.6 \text{ cm}^{-1}$) is given at the bottom of Fig. 34.2. They are shown to correspond to the semiclassical orbits discussed in Sect. 34.2. This example is the most asymmetric top, since parameter B has a value midway between the symmetric top limits of $B = A$ and $B = C$.

The twenty-one $J = 10$ asymmetric top levels are arranged into roughly ten asymmetry doublets and one singlet that resemble the symmetric top levels, except that the doublets are split by varying amounts, and the singlet is isolated from the other levels in the middle of the band instead of being crowded at the top or bottom. The doublet splittings are magnified in circles drawn next to the levels, and these indicate that the splitting decreases quasi exponentially with each doublet's separation from the central singlet.

An asymmetric doublet splitting is also called a superfine structure and can be viewed as the result of a dynamic tunneling process in a semiclassical model of rotation [8–10]. Such a model clarifies the classical-quantum correspondence for polyatomic rovibrational dynamics in general. It can also help to derive simple approximations for eigenvalues and eigenvectors.

34.2 Rotational Energy Surfaces and Semiclassical Rotational Dynamics

A semiclassical model of molecular rotation can be based upon what is called a rotational energy surface (RES) [7–14]. Examples of RES for an asymmetric top are shown in the previous Fig. 34.2 and for prolate and oblate symmetric tops in Fig. 34.1. Each surface is a radial plot of the classical energy derived from the Hamiltonian in Eq. (34.1) as a function of the polar direction of the classical angular momentum \mathbf{J} -vector in the “body” frame. The magnitude $|\mathbf{J}|$ of \mathbf{J} is fixed for each surface. Note that the \mathbf{J} -vector in the “lab” frame is a classical constant of the motion if there are no external perturbations. However, \mathbf{J} may gyrate considerably in the moving body frame, but its magnitude $|\mathbf{J}|$ stays the same in all frames for free rotation.

The RES differs from what is called a CE or constant energy surface, which is obtained by simply plotting $E = H = \text{const}$ in \mathbf{J} -space using Eq. (34.1). A rigid rotor CE surface is an ellipsoid covering a range of $|\mathbf{J}|$ -values at a single energy. A RES, on the other hand, is a spherical harmonic plot at a single $|\mathbf{J}|$ -value for a range of energies, so it is better for spectroscopic studies of fine structure, since one value of the rotational quantum number J corresponds to a multiplet of energy levels or transitions. The RES also shows loci of high and low energy rotations. Also, it has roughly the same shape as the body it represents, i.e., an RES is long in directions that its molecule is long (but vice versa for CE surfaces).

For a freely rotating molecule, the laboratory components of the classical total angular momentum \mathbf{J} are constant. If one chooses to let \mathbf{J} define the lab z -axis, then the direction of the \mathbf{J} -vector in the body frame is given by polar and body azimuthal coordinates β and γ , which are the second and third Euler angles, respectively. (It is conventional to use the negatives $-\beta$ and $-\gamma$ as polar coordinates, but this will not be necessary here.) Then the body components of the \mathbf{J} -vector are written

$$\begin{aligned} J_x &= |\mathbf{J}| \sin \beta \cos \gamma, & J_y &= |\mathbf{J}| \sin \beta \sin \gamma, \\ J_z &= |\mathbf{J}| \cos \beta. \end{aligned} \quad (34.7)$$

Here, the magnitude of the quantum value $|\mathbf{J}| = \sqrt{J(J+1)} \cong J + \frac{1}{2}$.

Substituting this into the Hamiltonian in Eq. (34.1) gives an expression for the general rigid rotor RES radius in polar coordinates

$$\begin{aligned} E(\beta, \gamma) &= \langle H \rangle \\ &= J(J+1) \\ &\quad \times [\sin^2 \beta (A \cos^2 \gamma + B \sin^2 \gamma) + C \cos^2 \beta]. \end{aligned} \quad (34.8)$$

The prolate symmetric top ($A = B < C$) expression is independent of azimuthal angle γ ,

$$E(\beta) = \langle H \rangle = J(J+1)[B + (C-B)\cos^2\beta]. \quad (34.9)$$

The three-dimensional plots of these expressions are shown in Figs. 34.1 and 34.2.

The RES has topography lines of constant energy ($E = \text{const}$) that are the intersection of the RES (constant $|J|$) with spheres of constant energy. The topography lines are allowed classical paths of the angular momentum J -vector in the body frame, since these paths conserve both energy and momentum.

The trajectories in these figures are special ones. They are the quantizing trajectories for total angular momentum $J = 10$. For the prolate symmetric top, the quantizing trajectories have integral values for the body z -component K of angular momentum. Using a Dirac vector model, angular momentum vectors trace out a cone of altitude K and slant height $|J| = \sqrt{J(J+1)}$. Quantizing polar angles are given by

$$\begin{aligned} \Theta_K^J &= \cos^{-1} \frac{K}{\sqrt{J(J+1)}} \\ (K &= J, J-1, \dots, -J). \end{aligned} \quad (34.10)$$

These are the latitude angles of the paths on the RES in Fig. 34.1 for $K = 10, 9, 8, \dots, -10$. (For the oblate RES, the angles are relative to the x -axis.) If $\beta = (\Theta_K^J)$ is substituted into the symmetric top RES in Eq. (34.9), the result is

$$E(\Theta_K^J) = J(J+1)B + (C-B)K^2, \quad (34.11)$$

which is precisely the symmetric top eigenvalue in Eq. (34.4). The quantizing paths are circles lying at the intersections of the Dirac angular momentum cones and the RES. Angle (Θ_K^J) is a measure of the angular momentum uncertainty ΔJ_x or ΔJ_y transverse to the z -axis of quantization. Clearly, $K = \pm J$ states have minimum uncertainty.

For the asymmetric top, the classical paths (which conserve both $|J|$ and E) fall into one of two types. First, there are those pairs of equal-energy orbits that go around the hills on the plus or minus end of the body z -axis and correspond to the $\pm K$ pairs of levels in the upper half of the level spectrum drawn in Fig. 34.2. Then there are the pairs of levels belonging to the equal-energy orbits in either of the two valleys surrounding the body x -axis, associated with the pairs of levels in the lower half of the level spectrum. Different eigensolutions occupy different geography.

The upper pairs of paths are seen to be distorted versions of the prolate top orbits seen on the left-hand side of Fig. 34.1, while the lower pairs are distorted versions of the oblate top orbits seen on the right-hand side of Fig. 34.1. The distortion makes J_z deviate from a constant K -value and corresponds to K -mixing in the quantum states. This also shows that one needs to consider more than one axis of quan-

tization; the prolate-like paths are based on the z -axis, while the oblate-like paths belong to the body x -axis.

The two types of orbits, x and y , are separated by a so-called separatrix curve crossing containing saddle points on either side of the body y -axis. In the example shown in Fig. 34.2, the separatrix is associated with a single level that separates the upper and lower energy doublets. The doublets that are closer to the separatrix level are split more than those farther away. Apart from the splitting, the energy levels can be obtained by generalized Bohr quantization of the classical paths on the RES. The quantization condition is,

$$\oint J_z d\gamma = K \oint J_z d\gamma = K, \quad (34.12a)$$

where

$$J_z = \sqrt{\frac{J(J+1)(C\cos^2\gamma + B\sin^2\gamma) - E}{(C\cos^2\gamma + B\sin^2\gamma) - A}} \quad (34.12b)$$

follows from Eqs. (34.7) and (34.8). The resulting E_K -values are obtained by iteration.

The doublet or superfine splitting is a quantum effect that may be associated with tunneling between orbits that would have had equal energies E_K in the purely classical or semiclassical model. Approximate tunneling rates are integrals over the saddle point between each pair of equal-energy quantizing paths. The K -th rate, or amplitude, is

$$S_K = \nu_K e^{-P_K}, \quad (34.13)$$

where

$$\begin{aligned} P_K &= i \int_{\gamma^-}^{\gamma^+} d\gamma \\ &\times \sqrt{\frac{J(J+1)(C\cos^2\gamma + B\sin^2\gamma) - E_K}{(C\cos^2\gamma + B\sin^2\gamma) - A}} \end{aligned} \quad (34.14)$$

is the saddle path integral between the points of closest approach, γ^+ and γ^- , and ν_K is the classical precession frequency or quantum level spacing around energy level E_K . Since there are two tunneling paths, amplitude S_K is doubled in a tunneling Hamiltonian matrix for the K -th semiclassical doublet of z and $-z = \bar{z}$ paths,

$$\langle H \rangle_K = \begin{pmatrix} E_K & 2S_K \\ 2S_K & E_K \end{pmatrix} \begin{pmatrix} |z\rangle \\ |\bar{z}\rangle \end{pmatrix}. \quad (34.15)$$

The resulting tunneling energy eigensolutions are given in Table 34.1.

Table 34.1 Tunneling energy eigensolutions

Eigenvectors	$ z\rangle$	$ \bar{z}\rangle$	Eigenvalues
$ A\rangle$	1	1	$E^A(K) = E_K + 2S_K$
$ B\rangle$	1	-1	$E^B(K) = E_K - 2S_K$

A - or B -states correspond to symmetric and antisymmetric combinations of waves localized on the two semiclassical paths. Rotational symmetry is considered in Sect. 34.3.

The total doublet splitting is $4S_K$ and decreases exponentially with the saddle point integral in Eq. (34.14). Superfine A – B splittings in Fig. 34.2 range from several GHz near the separatrix to only 26 kHz for the highest- K doublets at the band edges.

Meanwhile, the typical interdoublet level spacing or classical precessional frequency is about 150 GHz for the $J = 10$ levels shown in Fig. 34.2. This K -level spacing is called rotational fine structure splitting and is present in the symmetric top case, as well. (Superfine splitting of the symmetric top doublets is exactly zero, since they have $O(2)_{\text{BODY}}$ symmetry if $A = B$ or $B = C$ and tunneling amplitudes cancel.)

Classical precession of \mathbf{J} in the body frame follows a “left-hand” rule quite like what meteorologists use to determine Northern Hemisphere cyclonic rotation. A left “thumbs-down” or “low” has anticlockwise precession, as does an oblate rotor valley, but a prolate RES “high” supports clockwise motion just like a weather “high”.

Finally, consider the spacing between adjacent J -levels, which is called rotational structure, in a spectrum. This spacing is

$$E(J, K) - E(J - 1, K) = 2BJ, \quad (34.16)$$

according to the symmetric top energy formulas in Eq. (34.4). For this example, $2BJ$ is about 10 cm^{-1} or 300 GHz. It corresponds to the actual rotation frequency of the body. It is the only kind of rotational dynamics or spectrum that is possible for a simple diatomic rotor. However, a diatomic molecule may have internal electronic or nuclear spin rotation which gives an additional fine structure, as discussed later [1, 6, 15].

To summarize, polyatomic molecules can be expected to exhibit all three types of rotational motion and spectra. Noted above were three types of motion (from faster to slower): *rotational*, *precessional*, and *precessional tunneling*. These were related to three kinds of spectral structure (from coarser to finer spectra): *rotational* structure, *fine* structure, and *superfine structure*, respectively. Again, this neglects internal rotational and spin effects that can have abnormally strong rotational resonance coupling due to the superfine structure [9, 16]. Examples of this are discussed further along in this chapter.

34.3 Symmetry of Molecular Rotors

Molecular rotational symmetry is most easily introduced using examples of rigid rotors. Molecular rotor structures may have more or less internal molecular symmetry depending on how their nuclei are positioned relative to one another in the

body frame. A molecule’s rotational symmetry is described by one of the elementary rotational point symmetry groups. These are the n -fold axial cyclic groups C_n and polygonal dihedral groups D_n ($n = 1, 2, \dots$), the tetrahedral group T , the cubic-octahedral group O , or the icosahedral group Y . All other point groups, such as C_{nv} , T_d , and O_h , are one of these in combination with the inversion operation $\mathbf{I}(\mathbf{r} \rightarrow -\mathbf{r})$. Each of these groups consists of operations that leave at least one point (origin) of a structure fixed while mapping identical atoms or nuclei into each other in such a way that the structure ends up looking the same as it did before the operation. The point groups map onto subgroups of the nuclear permutation groups [17].

In other words, molecular symmetry is based upon one of the most fundamental (and mysterious!) properties of atomic physics: the absolute identity of all atoms or, more precisely, nuclei of a given atomic number Z and mass number A . It is the identity of the so-called “elementary” electronic and nucleonic constituent particles that underlies the symmetry.

A quite mysterious axiom of modern physics is the Pauli principle that states: *All half-integer spin particles are antisymmetrized with every other one of their kind in the universe.* The Pauli–Fermi antisymmetry and related Bose–Einstein symmetrization principle determine much of molecular symmetry and dynamics just as the Pauli exclusion principle is fundamental to atomic and molecular electronic structure.

34.3.1 Asymmetric Rotor Symmetry Analysis

For an asymmetric rigid rotor, any rotation that interchanges x -, y -, or z -axes of the body cannot possibly be a symmetry, since all three axes are assumed to have different inertial constants. This restricts one to consider only 180° rotations about the body axes, and these are the elements of the rotor groups C_2 and D_2 .

The two symmetry types for C_2 are even (denoted A or 0_2) and odd (denoted B or 1_2) with respect to a 180° rotation. For D_2 , which is just $C_2 \otimes C_2$, the four symmetry types are even-even (denoted A_1), even-odd (denoted A_2), odd-even (denoted B_1), and odd-odd (denoted B_2) with respect to 180° rotations about the y and x -axes, respectively. (The z -symmetry is determined by a product of the other two since $\mathbf{R}_z = \mathbf{R}_x \mathbf{R}_y$.) This is summarized in the character Tables 34.2 and 34.3.

The rotational energy surface for the rigid rotor shown in Fig. 34.2 is invariant under 180° rotations about each of the three body axes. Therefore, its Hamiltonian symmetry is

Table 34.2 Character table for symmetry group C_2

C_2	1	\mathbf{R}
A	1	1
B	1	–1

Table 34.3 Character table for symmetry group D_2

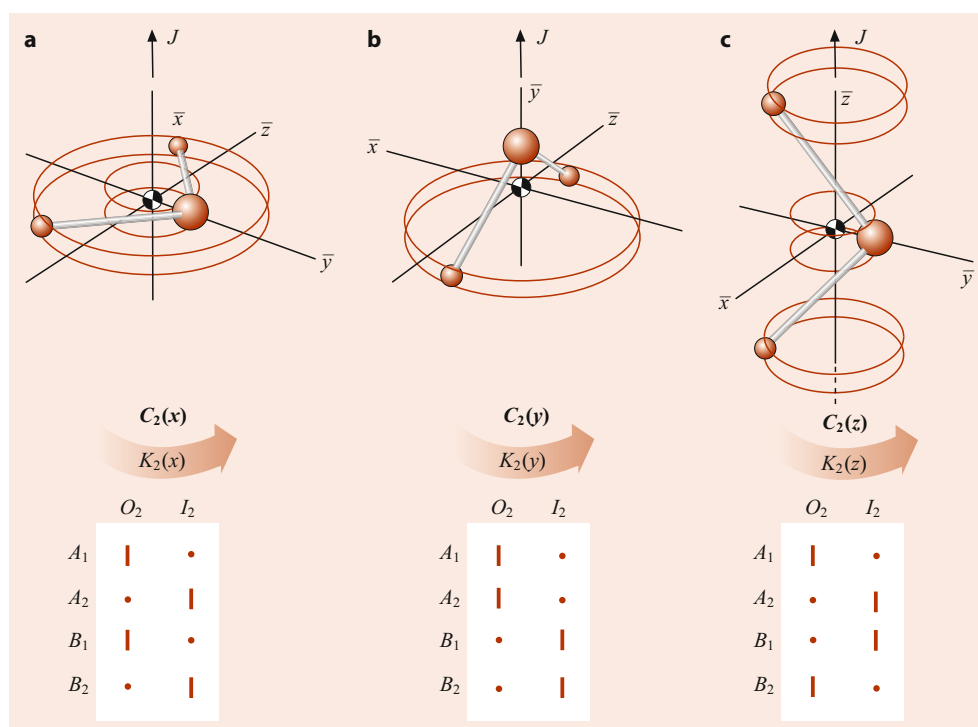
D_2	1	R_x	R_y	R_z
A_1	1	1	1	1
A_2	1	-1	1	-1
B_1	1	1	-1	-1
B_2	1	-1	-1	1

D_2 , and its quantum eigenlevels must correspond to one of the four types listed under D_2 in Table 34.3. The D_2 symmetry labels are called rotational (or, in general, rovibronic) species of the molecular state. The species label the symmetry of a quantum wave function associated with a pair of C_2 symmetric semiclassical paths.

The classical J -paths come in D_2 symmetric pairs, but each individual classical J -path on the rigid rotor RES has a C_2 symmetry that is a subgroup of D_2 . Each path in the valley around the x -axis is invariant under just the 180° rotation around the x -axis. This is $C_2(x)$ symmetry. The other member of its pair that goes around the negative x -axis also has this local $C_2(x)$ symmetry. The combined pair of paths has the full D_2 symmetry, but classical mechanics does not permit occupation of two separate paths. Such co-occupation is a completely quantum effect.

Similarly, each individual J -path on the hill around the z -axis is invariant under just the 180° rotation around the z -axis, so it has $C_2(z)$ symmetry as does the equivalent path around the negative z -axis. Only the separatrix has the full D_2 symmetry, since its pairs are linked up on the y -axis to form the boundary between the x and z paths. No J -paths encircle the unstable y -axis since it is a saddle point.

Fig. 34.3 Tables of correlations between D_2 symmetry species and the even (O_2) and odd (I_2) symmetric species of subgroups (a) $C_2(x)$, (b) $C_2(y)$, and (c) $C_2(z)$



Each classical J -path near the x or z -axes belongs to a particular K -value through semiclassical quantization conditions in Eqs. (34.12a) and (34.12b). Depending upon whether the K -value is even (denoted by O_2) or odd (denoted by I_2), the corresponding K -doublet will be correlated with a pair of D_2 species as shown in the columns of the correlation tables in Fig. 34.3. These three correlation tables give the axial 180° rotational symmetry of each D_2 species for rotation near each body axis x , y , and z , respectively, but only the stable rotation axes x and z support stable path doublets for this Hamiltonian in Eq. (34.1).

For example, consider $K = 10$ paths, which lie lowest in the x -axis valleys. Since $K = 10$ is even (O_2), it is correlated with an A_1 and B_1 superfine doublet (see the O_2 column of the $C_2(x)$ table). On the high end near the z -axis hilltop, $K = 10$ gives rise to an A_1 and B_2 doublet (see the O_2 column of the $C_2(z)$ table). All the doublets in Fig. 34.2 may be assigned in this way.

34.4 Tetrahedral-Octahedral Rotational Dynamics and Spectra

The highest symmetry rigid rotor is the *spherical top* for which the three inertial constants are equal ($A = B = C$). As was previously mentioned the spherical top Hamiltonian

$$H = B \mathbf{J} \cdot \mathbf{J}$$

has full $R(3)_{\text{LAB}} \otimes R(3)_{\text{BODY}}$ symmetry. Inversion parity symmetry is $O(3)_{\text{LAB}} \otimes O(3)_{\text{BODY}}$. In any case, the J -levels

are $(2J + 1)^2$ -fold degenerate. The resulting $BJ(J + 1)$ energy expression is the first approximation for molecules that have regular polyhedral symmetry of, for example, a tetrahedron (CF_4), cube (C_6H_6), octahedron (SF_6), dodecahedron or icosahedron ($\text{C}_{20}\text{H}_{20}$, $\text{B}_{12}\text{H}_{12}$, or C_{60}) [18, 19] discussed in later sections. Rigid regular polyhedra have isotropic or equal inertial constants and rotate just like they were perfectly spherical distributions of mass.

No molecule can really have spherical $O(3)_{\text{BODY}}$ symmetry since even molecules of the highest symmetry are made of a finite number of nuclear mass points. Evidence of octahedral or tetrahedral symmetry shows up in fine structure splittings analogous to those for asymmetric tops. However, spherical top fine structure is due to symmetry breaking caused by anisotropic or tensor rotational distortion, and so they are called semirigid rotors.

34.4.1 Semirigid Octahedral Rotors and Centrifugal Tensor Hamiltonians

The lowest-order tensor centrifugal distortion perturbation has the same form for both tetrahedral and octahedral molecules. It is simply a sum of fourth powers of angular momentum operators given in the third term of

$$H = B|J|^2 + D|J|^4 + 10t_{044} \times \left[J_x^4 + J_y^4 + J_z^4 - (3/5)J^4 \right]. \quad (34.17)$$

The first two terms are the scalar rotor energy and the scalar centrifugal energy. The tensor term includes the scalar $(3/5)J^4$ to preserve the center of gravity of the tensor level splitting. *Hecht* [20] first used this type of semirigid rotor Hamiltonian in the study of methane (CH_4) spectra.

The scalar terms do not reduce the symmetry or split the levels, but the tensor (t_{044}) term breaks the molecular symmetry from $O(3)_{\text{LAB}} \otimes O(3)_{\text{BODY}}$ to a lower symmetry subgroup $O(3)_{\text{LAB}} \otimes T_d_{\text{BODY}}$, or $O(3)_{\text{LAB}} \otimes O_h_{\text{BODY}}$ and splits the $(2J + 1)^2$ -fold degeneracy into intricate fine structure patterns that are analogous to cubic crystal field splitting of atomic orbitals. The first calculations of the tensor spectrum were done by direct numerical diagonalization [20–23]. As a result, many subtle symmetry properties were missed. Semiclassical analysis [24], described in the following sections, exposes these properties.

34.4.2 Octahedral and Tetrahedral Rotational Energy Surfaces

By substituting in Eq. (34.7) and plotting the energy as a function of body polar angles β and γ one obtains a rotational energy (RE) surface, two views of which are shown

in Fig. 34.4. Here, the tensor term is exaggerated in order to exhibit the topography clearly. (In $(n = 0)$ SF_6 , the t_{044} coefficient is only about 5.44 Hz, while the rotational constant is $B = 0.09 \text{ cm}^{-1}$. The t_{244} coefficient of $(n = 1)$ SF_6 is much greater.)

A positive tensor coefficient ($t_{044} > 0$) gives an octahedral-shaped RES, as shown in Fig. 34.4. This is appropriate for octahedral molecules since they are the least susceptible to distortion by rotations around the x , y , and z -axes containing the strong radial bonds. Thus, rotational energy is highest for a \mathbf{J} -vector near one of six body axes $(\pm 1, 0, 0)$, $(0, \pm 1, 0)$, or $(0, 0, \pm 1)$, i.e., one of the six RES hills in Fig. 34.4.

However, if the \mathbf{J} -vector is set in any of the eight interaxial directions $(\pm 1, \pm 1, \pm 1)$, the centrifugal force will bend the weaker angular bonds more easily, raise the molecular inertia, and lower the rotational energy to that of one of the eight valleys on the RES in Fig. 34.4.

A negative tensor coefficient ($t_{044} < 0$) gives a cubic shaped RES. Usually, this is appropriate for cubic and tetrahedral molecules since they are most susceptible to distortion by rotations around the x , y , and z -axes that lie between the strong radial bonds on the cubic diagonals. Instead of six hills and eight valleys, one finds six valleys and eight hills on the cubic RES. Both freon CF_4 and cubane C_8H_8 are examples of this type of topology.

It should be noted that a semirigid tetrahedral rotor may have the same form of rotational Hamiltonian and RES as a cubic rotor. The four tetrahedral atomic sites are in the same directions as four of the eight cubic sites. The other four cubic sites form an inverted tetrahedron of the same shape.

If only tetrahedral symmetry was required, the Hamiltonian might have third-order terms like $J_x J_y J_z$. However, such terms do not have the time-reversal symmetry that makes energy the same for \mathbf{J} and $-\mathbf{J}$, so that rotational sense does not matter. So simple rotor RES have inversion symmetry even if their molecules do not. Compound rotors containing spins or other rotors may have “lopsided” pairs of RES as shown in Sect. 34.6.

34.4.3 Octahedral and Tetrahedral Rotational Fine Structure

An example of rotational fine structure for angular momentum quantum number $J = 30$ is shown in Fig. 34.4. The levels consist mainly of clusters of levels belonging to the octahedral symmetry species A_1 , A_2 , E , T_1 , or T_2 . The characters of these species are the following Table 34.4. (The tetrahedral T_d group has a similar table where T_1 and T_2 are often labeled F_1 and F_2 .)

The first column gives the dimension or degeneracy of each species: A_1 and A_2 are singlets, E is a doublet, and T_1 and T_2 are triplets. These species form two clusters (A_1, T_1, T_2, A_2)

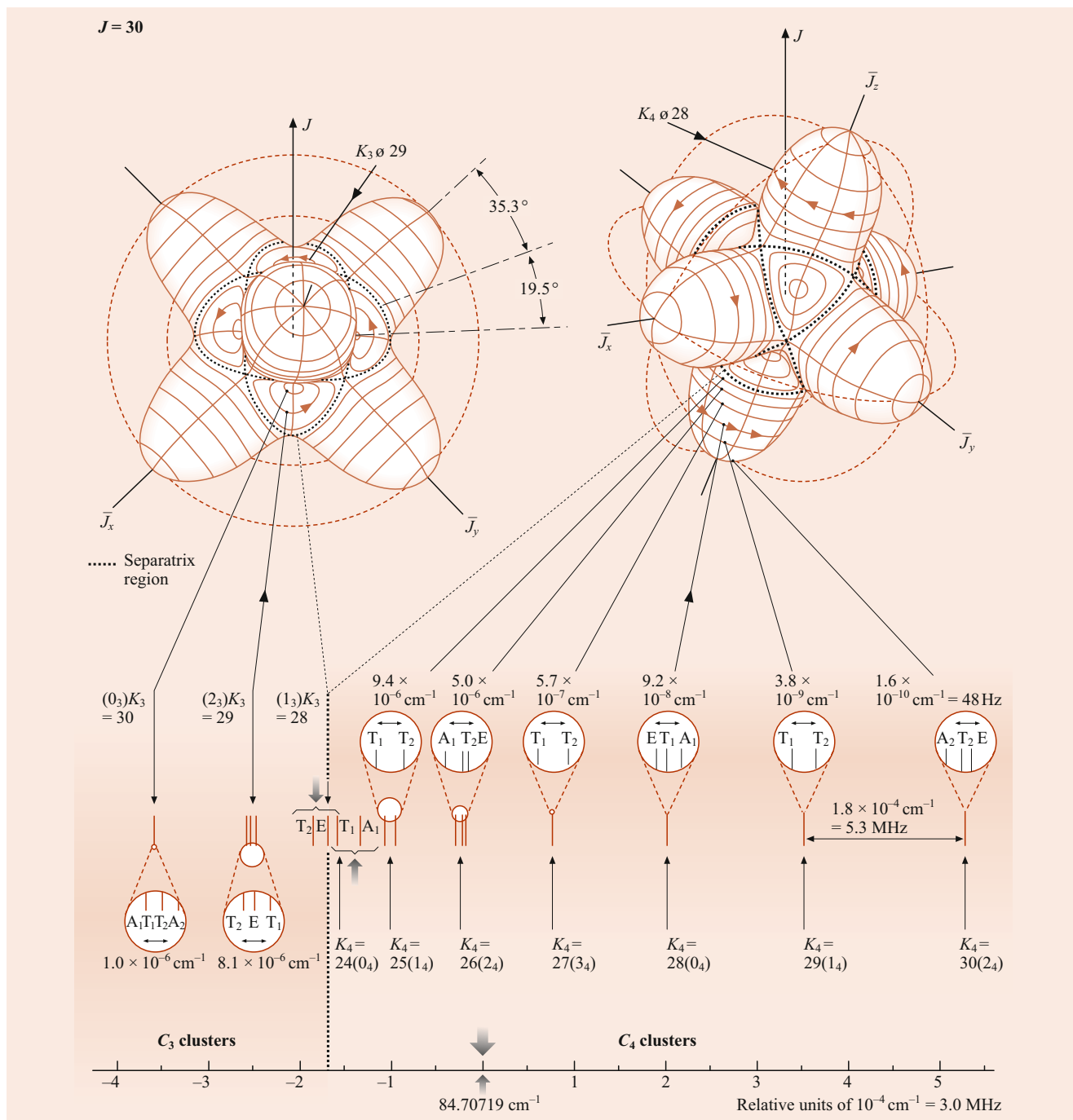


Fig. 34.4 $J = 10$ rotational energy surface related level spectrum for a semirigid octahedral or tetrahedral rotor

Table 34.4 Character table for symmetry group O

O	0°	120°	180°	90°	180°
A_1	1	1	1	1	1
A_2	1	1	1	-1	-1
E	2	-1	2	0	0
T_1	3	0	-1	1	-1
T_2	3	0	-1	-1	1

and (T_2, E, T_1) on the low end of the spectrum and six clusters (T_1, T_2) , (A_2, T_2, E) , (T_1, T_2) , (E, T_1, A_1) , (T_1, T_2) , and (A_2, T_2, E) on the upper part of the spectrum. (Right-hand side of Fig. 34.4.) Note that the total dimension or (near) degeneracy for each of the two lower clusters is eight: $(1 + 3 + 3 + 1)$ and $(3 + 2 + 3)$, while the upper clusters each have a sixfold (near) degeneracy: $(3 + 3)$, $(1 + 3 + 2)$, etc.

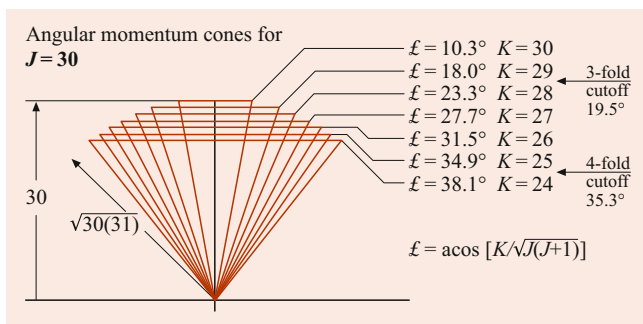


Fig. 34.5 $J = 30$ angular momentum cone half angles and octahedral cutoffs

Each of the two lower eightfold clusters can be associated with a semiclassical quantizing path in an RES valley as shown in Fig. 34.4. The eightfold dimension or (near) degeneracy occurs because each quantizing path is repeated eight times; once in each of the eight identical valleys. Similarly, the sixfold cluster dimension $((3 + 3), (1 + 3 + 2), \dots \text{etc.})$ occurs because there are six identical hills, and each quantizing path is repeated six times around the surface.

The majority of the paths lie on the hills because the hills are bigger than the valleys. The hills subtend a half angle of 35.3° to the separatrix, while the valleys only have 19.5° . To estimate the number of paths or clusters in hills or valleys, one may calculate the angular momentum cone angles for $J = 30$ using Eq. (34.10). The results are displayed in Fig. 34.5. The result is consistent with the spectrum

in Fig. 34.4. Only the two highest K -values of $K = 30$ and 29 have cones small enough to fit in the valleys, while the six states of $K = 30, 29, 28, 27, 26,$ and 25 can fit onto the hills.

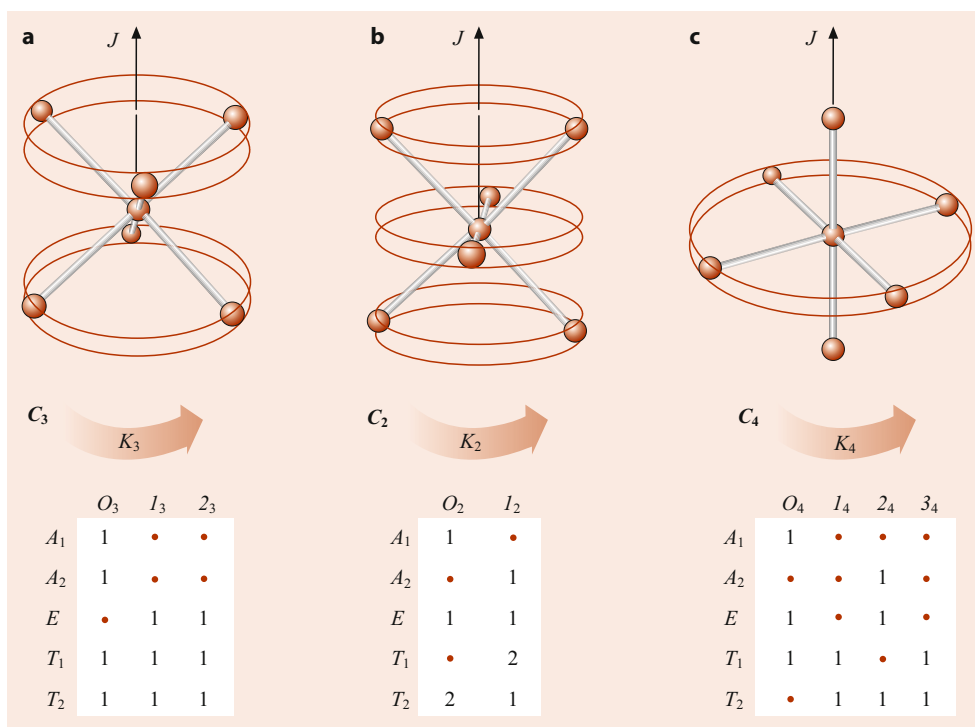
The angular momentum cone formula also provides an estimate for each level cluster energy. The estimates become more accurate as K increases (approaching J) so the uncertainty angle decreases. Higher- K paths are more nearly circular and, therefore, more nearly correspond to symmetric top quantum states of pure K . The paths on octahedral RES are more nearly circular for a given K than are those on the asymmetric top RES, and so one can better approximate octahedral rotor states with those of a symmetric top.

34.4.4 Octahedral Superfine Structure

The octahedral RES has many more local hills and valleys and corresponding types of semiclassical paths than are found on the rigid asymmetric top RES. The tunneling between multiple paths gives an octahedral superfine structure that is more complicated than the asymmetric top doublets. Still, the same symmetry correlations and tunneling mechanics apply.

First, the octahedral symmetry must be correlated with the local symmetry of the paths on the hills and in the valleys. The hill paths have a C_4 symmetry, while the valley paths have a local C_3 symmetry. This is seen most clearly for the low- K paths near the separatrix that are less circular. The C_3

Fig. 34.6 Tables of correlations between 0 symmetry species and the cyclic axial symmetry species (K_p means $K \bmod p$) of subgroups (a) C_3 , (b) C_2 , and (c) C_4



and C_4 correlations are given in Fig. 34.6 with corresponding sketches of molecular rotation for each type of path.

To find the octahedral species associated with a $K_3 = 30$ path in a C_3 valley one notes that 30 is 0 modulo 3. Hence, the desired species are found in the 0_3 column of the C_3 correlation table. One finds (A_1, A_2, T_1, T_2) , and this is what appears (not necessarily in that order) on the extreme lower left-hand side of Fig. 34.4. Similarly, the species (A_2, E, T_2) for a $K_4 = 30$ path on top of a C_4 hill are found in the 2_4 column of the C_4 correlation table since 30 is 2 modulo 4, and these appear on the other side of Fig. 34.4. Similarly, clusters (T_1, T_2) for $K_4 = 29$ and (A_1, E, T_1) for $K_4 = 28$ follow.

A multiple path tunneling calculation analogous to the one for rigid rotors can be applied to approximate octahedral superfine splittings. Consider the cluster (A_1, E, T_1) for $K_4 = 28$, for example. One may label six C_4 -symmetric paths located on octahedral vertices on opposite sides of the $\pm x$ -, $\pm y$ -, and $\pm z$ -axes as on the right-hand side of matrix H in Eq. (34.18), which is the tunneling matrix between the six paths

$$\langle H \rangle_{K_4=28} = \begin{pmatrix} H & 0 & S & S & S & S \\ 0 & H & S & S & S & S \\ S & S & H & 0 & S & S \\ S & S & 0 & H & S & S \\ S & S & S & S & H & 0 \\ S & S & S & S & 0 & H \end{pmatrix} \begin{matrix} |x\rangle \\ |\bar{x}\rangle \\ |y\rangle \\ |\bar{y}\rangle \\ |z\rangle \\ |\bar{z}\rangle \end{matrix} \quad (34.18)$$

Here, the tunneling amplitude S is assumed between nearest neighbor octahedral vertices but is assumed to be zero between antipodal vertices. The eigenvectors and eigenvalues for this matrix are given in Table 34.5. K -cone polar uncertainty angles for $J = 30$ are listed in Fig. 34.5.

This predicts that the triplet (T_1) level should fall between the singlet (A_1) and the doublet (E) levels, and the singlet-triplet spacing ($4S$) should be twice the splitting ($-2S$) between the triplet and doublet. This 2:1 ratio is observed in the (E, T_1, A_1) and (A_2, T_2, E) clusters, which can be resolved and in numerical calculation as well [20–23].

The tunneling amplitudes can be calculated by a separatrix path integral analogous to the asymmetric top formula in Eq. (34.13) [10, 11]. As shown in Fig. 34.4, the tunneling rates or superfine splittings near the separatrix are ≈ 1 MHz, which is only slightly slower than the classical precessional

frequency. However, as K approaches J on the hilltops, the tunneling rate slows quasi exponentially to ≈ 3 mHz, that is by a factor of about 10^{-9} .

34.5 High-Resolution Rovibrational Structure

A display of spectral hierarchy for higher and higher resolution is shown in Fig. 34.7 for the 630 cm^{-1} or $16\text{ }\mu\text{m}$ bands of CF_4 [18, 19, 24, 25]. This summarizes the possible rovibrational spectral structures and places them in a larger context. The ν_4 resonance in part (a) corresponds to a dipole active $n_4 = 0 \rightarrow 1$ vibrational transition and is just one of many vibrational structures to study. The $P(54)$ sideband resonance in part (b) corresponds to a $(J = 54) \rightarrow (J - 1)$ rotational transition, and is just one of hundreds of rotational structures to study within the ν_4 bands.

Each band is like a Russian doll; it contains structure within structure within structure down to the resolution of few tens of Hz. Examples of rotational fine and superfine structures described in Sect. 34.4 are shown in Fig. 34.7c,d, but even more resolution is needed to see the hyperfine structure in Fig. 34.7e [26]. Such extreme resolution was reached with a CO_2 saturation absorption spectrometer [27, 28]. The $10\text{ }\mu\text{m}$ bands of SF_6 and SiF_4 have been studied in this manner, the latter being similar to CF_4 [26].

34.5.1 Tetrahedral Nuclear Hyperfine Structure

High-resolution spectral studies of SiF_4 showed unanticipated effects involving the four fluorine nuclear spin and magnetic moments giving rise to associated hyperfine states. First, and this was well known, the Pauli principle restricts the nuclear spin multiplicity associated with each of the rotational symmetry species in much the same way that atomic $L - S$ coupled states ^{2S+1}L have certain spin multiplicities $(2S + 1)$ allowed for a given orbital L species involving two or more equivalent electrons. Secondly, and this was not so well known, since superfine splittings can easily be tiny, different spin species can end up close enough that hyperfine interactions, however small, can cause strongly resonant mixing of the normally inviolate species. Finally, one gets to witness a pure and simple form of spontaneous symmetry breaking in which otherwise equivalent nuclei fall into different subsets due to quantum rotor dynamics.

Connecting nuclear spin to rotational species is done by correlating the full permutation symmetry (S_n for XY_n molecules) with the full molecular rotation and parity symmetry [$O(3)_{\text{LAB}} \otimes T_{d\text{BODY}}$ for CF_4 molecules or $O(3)_{\text{LAB}} \otimes O_{h\text{BODY}}$ and for SF_6]. For four spin-1/2 nuclei, the Pauli principle allows a total spin of $I = 2$ having multiplicity of five ($2I + 1 = 5$) for (J^+, A_2) or (J^-, A_1) species, but ex-

Table 34.5 $H_{K=28}$ matrix solutions

Eigenvector	$ x\rangle$	$ \bar{x}\rangle$	$ y\rangle$	$ \bar{y}\rangle$	$ z\rangle$	$ \bar{z}\rangle$	Eigenvalue
$\sqrt{6} A_1\rangle =$	1	1	1	1	1	1	$E^{A_1} = H + 4S$
$\sqrt{12} E, 1\rangle =$	2	2	-1	-1	-1	-1	$E^E = H - 2S$
$2 E, 2\rangle =$	0	0	1	1	-1	-1	
$\sqrt{2} T_1, 1\rangle =$	1	-1	0	0	0	0	$E^{T_1} = H$
$\sqrt{2} T_1, 2\rangle =$	0	0	1	-1	0	0	
$\sqrt{2} T_1, 3\rangle =$	0	0	0	0	1	-1	

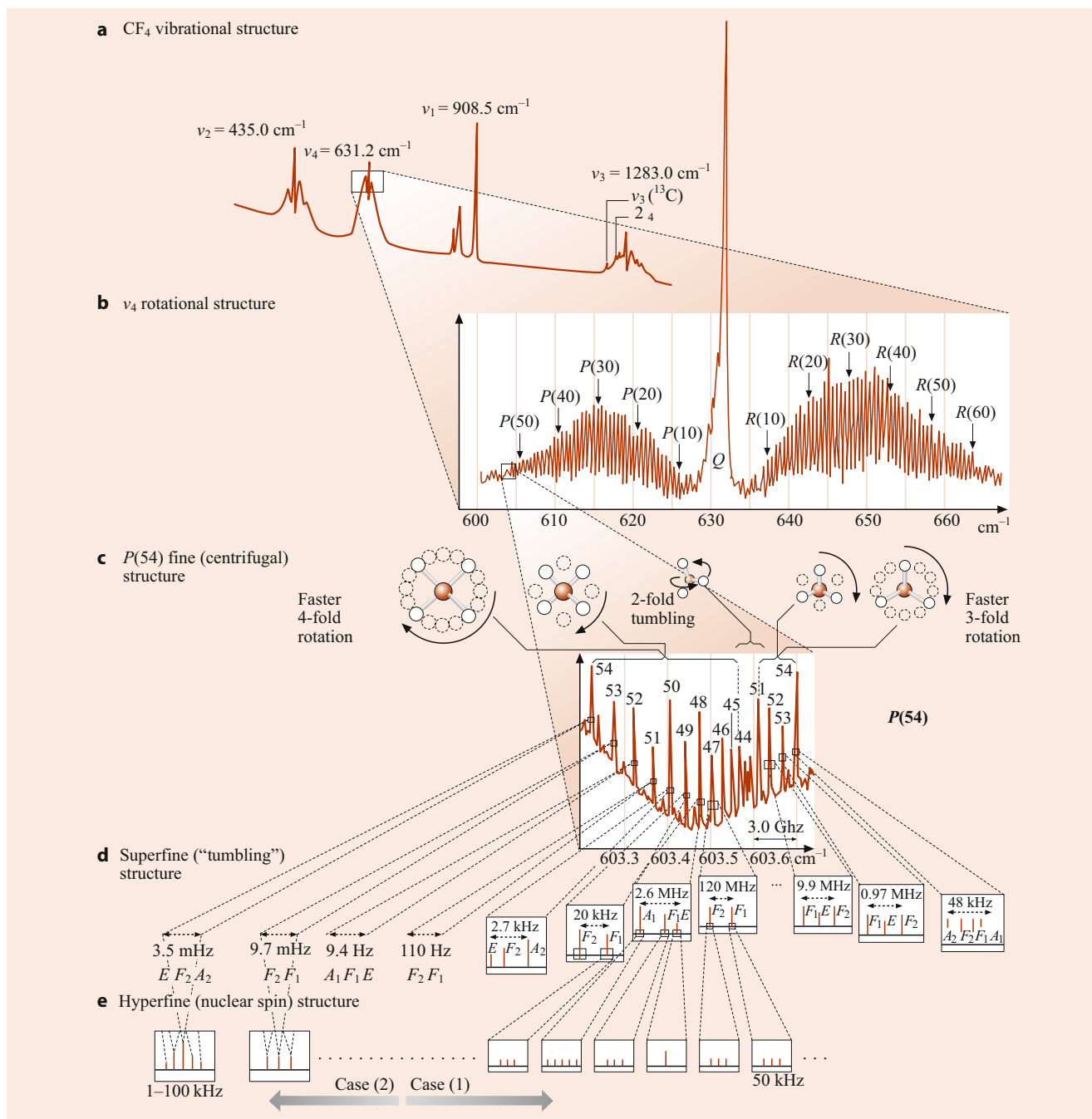


Fig. 34.7 Rovibrational structure in the 630 cm^{-1} or $16 \mu\text{m}$ bands of CF_4 [16]. (a) Vibrational resonances and band profiles. (Raman spectra from [29]). (b) Rotational P , Q , and R band structure corresponding to $J \rightarrow J - 1$, $J \rightarrow J + 1$ transitions. (FTIR spectra from [34]). (c) P(54) rotational fine structure due to rotation–vibration coupling and angular momentum precessional motion. (Laser diode spectra from [35]). (d) Superfine structure due to precessional tunneling [26]. (e) Hyperfine structure due to nuclear spin precession [26]

cludes (J^-, A_2) or (J^+, A_1) species altogether. Pauli allowed spin for (J^+, T_1) or (J^-, T_2) species is $I = 1$ with a multiplicity of three, but there are no allowed (J^+, T_2) or (J^-, T_1) species. Finally, both (J^+, E) and (J^-, E) belong to singlet spin $I = 0$ and are singlet partners to an inversion doublet. (None of the other species can have both + and – parity.)

The E inversion doublet is analogous to the doublet in NH_3 that is responsible for the ammonia maser. However, NH_3 inversion is not feasible in CF_4 or SiF_4 , and so the splitting of the E doublet in these molecules is due to hyperfine resonance [29] and analyzed by unitary symmetry [9, 16] given below and in later sections.

The Pauli analysis gives the number of hyperfine lines that each species would exhibit if it were isolated and resolved, as shown in the center of Fig. 34.7e. The rotational singlets A_1 and A_2 give five lines each, the rotational triplets T_1 and T_2 are spin triplets, and the rotational doublet E is a spin singlet but an inversion doublet. If the hyperfine structure of a given species A_1 , A_2 , T_1 , T_2 , or E is not resolved, then their line heights are proportional to their total spin weights of 5, 5, 3, 3, and 2, respectively.

If the unresolved species are clustered, then the total spin weights of each will add to give a characteristic cluster line height. The line heights of the C_4 clusters (T_1 , T_2), (A_2 , T_2 , E), (T_1 , T_2), (E , T_1 , A_1) are 6, 10, 6, 10, respectively. The line heights of the C_3 clusters (A_1 , T_1 , T_2 , A_2), (T_1 , E , T_2), (T_1 , E , T_2) are 16, 8, 8, respectively. This is roughly what is seen in the $P(54)$ spectrum in Fig. 34.7c.

34.5.2 Superhyperfine Structure and Spontaneous Symmetry Breaking

Superfine cluster splittings ($2S$, $4S$, etc.) are proportional to the J -precessional tunneling or “tumbling” rates between equivalent C_3 or C_4 symmetry axes that decrease with increasing K_3 or K_4 . At some point the superfine splittings decrease to less than the hyperfine splittings that are meanwhile actually increasing with K . The resulting collision of superfine and hyperfine structure has been called superhyperfine structure or Case 2 clusters. The following is a rough sketch of the phenomenology of this very complex spectra, using the results of Pfister [26].

As long as the tunneling rates are a megahertz or more, the nuclear spins will tend to average over spherical top motion. The spins couple into states of good total nuclear spin I , which, in turn, couple weakly with the overall angular momentum and with well-defined rovibrational species A_1 , A_2 , T_1 , T_2 , or E as described above. The resulting coupling is called Case 1. It is analogous to LS -coupling in atoms.

Stick figures for two examples of spectra observed by Pfister [26] are shown in Fig. 34.8a,b. The first Case 1 cluster, shown in Fig. 34.8a, is a C_4 type (0_4) cluster (A_1 , T_1 , E), which was solved in Table 34.6. The other Case 1 cluster, shown in Fig. 34.8b, is a C_3 type ($\pm 1_3$) cluster (T_1 , E , T_2) (recall C_3 correlations in Fig. 34.3). They are similar to the corresponding sketches shown in Fig. 34.7e. One notable difference is that the inversion doublet shows little or no splitting in the (A_1 , T_1 , E) cluster but does split in the (T_1 , E , T_2) cluster.

When the tunneling rates fall below 10 or 20 kHz, the angular momentum could remain near a particular C_3 or C_4 symmetry axis for a time that is longer than the nuclear spin precession rates. Spin precession rates and the corre-

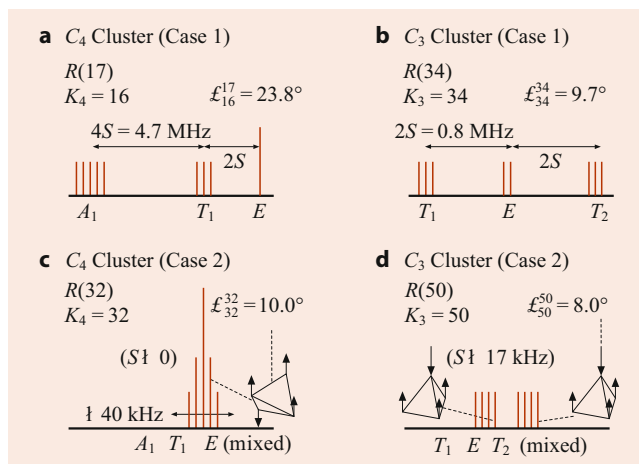


Fig. 34.8 Stick sketches for the example of superfine and hyperfine spectral structure found by Pfister [26]; (a, b) Case 1 clusters (high tunneling amplitude S); (c, d) Case 2 clusters (low tunneling amplitude S)

Table 34.6 Hyperfine spin states

$I_z = 2$	$I_z = 1$	$I_z = 0$	$I_z = -1$	$I_z = -2$
		$\begin{array}{c} \uparrow \uparrow \\ \downarrow \downarrow \end{array}$		
		$\begin{array}{c} \uparrow\downarrow \uparrow\downarrow\rangle \\ \downarrow\uparrow \downarrow\uparrow\rangle \end{array}$		
	$ \uparrow\downarrow \uparrow\uparrow\rangle$	$ \downarrow\downarrow \uparrow\uparrow\rangle$	$ \downarrow\downarrow \uparrow\downarrow\rangle$	
$ \uparrow\uparrow \uparrow\uparrow\rangle$	$ \uparrow\uparrow \uparrow\downarrow\rangle$	$ \uparrow\uparrow \downarrow\downarrow\rangle$	$ \uparrow\downarrow \downarrow\downarrow\rangle$	$ \downarrow\downarrow \downarrow\downarrow\rangle$

sponding hyperfine splittings are on the order of 50 kHz, and increasing with K . Hence, there would be plenty of time for each of the nuclear spins to align or antialign with the C_3 or C_4 symmetry axes of rotation. The resulting coupling is called Case 2 coupling, and the resulting spectrum resembles that of an NMR scan of the nuclei with the magnetic field provided by the molecule itself through its own body frame rotation.

If SiF_4 rotates uniformly about one C_4 symmetry axis, then all four F nuclei occupy equivalent positions that are the same distance on average from the rotation axis and experience the same local magnetic fields. The molecule is like a paired diatomic F_2 - F_2 rotor with each one symmetrized or antisymmetrized so as to make the whole state symmetric. Table 34.6 shows the spin-1/2 base states listed horizontally by total projection I_z of nuclear spins on the C_4 axis. Horizontal arrays ($\uparrow\downarrow$) of spins denote symmetric states, while vertical arrays ($\uparrow\downarrow$) denote antisymmetric spin states.

The hyperfine energy is approximately proportional to the projection I_z . The resulting spectrum is a (1, 2, 4, 2, 1)-degenerate pyramid of equally spaced lines as shown in Fig. 34.8c. Four spin-1/2 states without symmetry restrictions would give the standard binomial (1, 4, 6, 4, 1)-degeneracy seen in NMR spectra.

If the molecule settles upon C_3 symmetry axes of rotation, the situation is markedly different. The four nuclei no

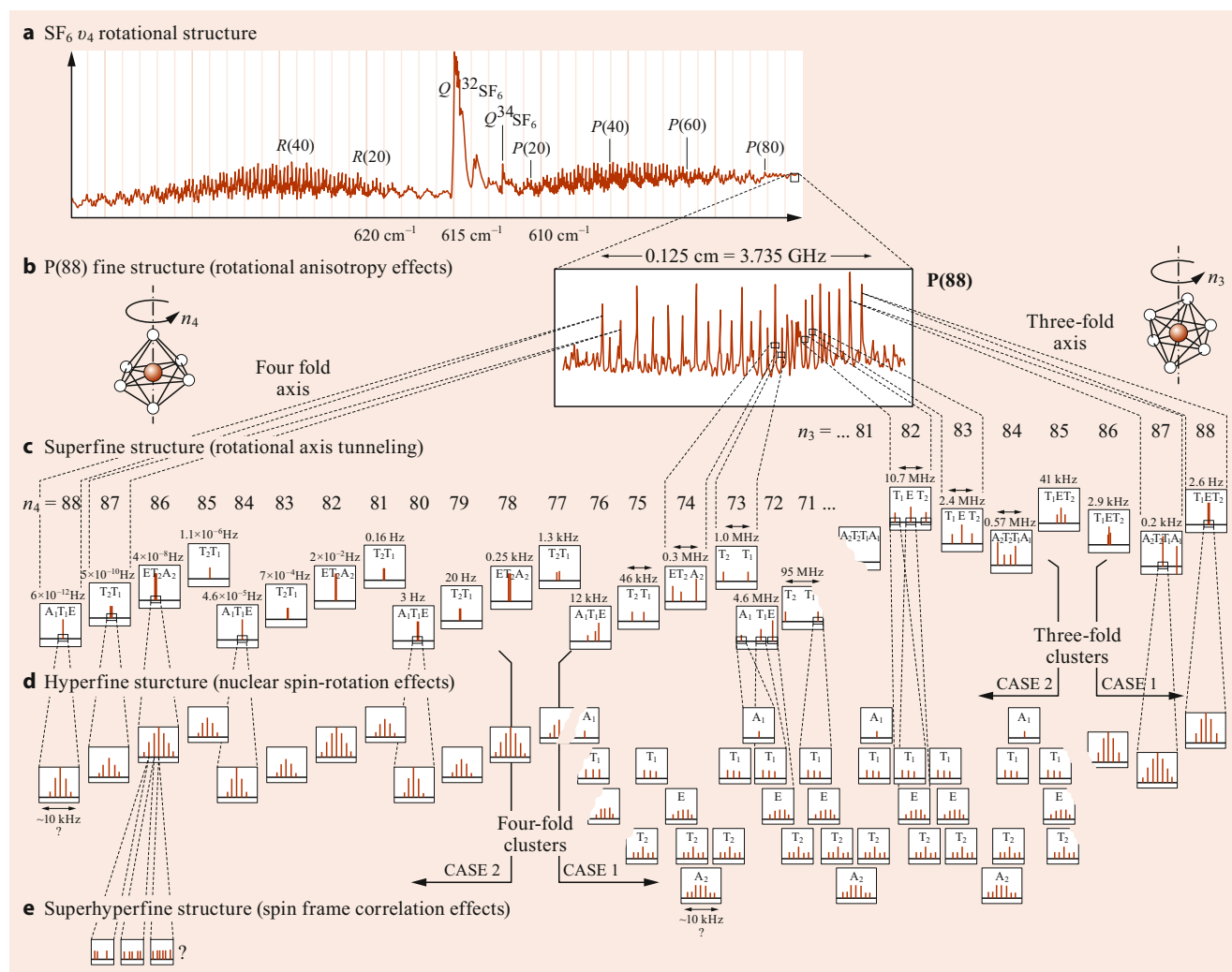


Fig. 34.9 SF₆ 16 μm ν₄ P(88) spectral clusters for C₄-axis rotation on the left and C₃-axis on the right

longer occupy equivalent positions. One nucleus sits on the rotation axis, while the other three nuclei occupy equivalent positions that are off the axis. The off-axis nuclei experience a different local magnetic field than the single on-axis nucleus (Fig. 34.8d). From the spectrum, it appears that the spin-up to spin-down energy difference is much greater for the lone on-axis nucleus than it is for the three equatorial nuclei. The spin states for the three equatorial nuclei form an energy quartet of spin states. The lone on-axis nucleus has an energy doublet with a large splitting, so together the four nuclei give a doublet of quartets as shown in Fig. 34.8d.

If the off-axis nuclei had experienced the greatest splitting, then the spectrum could have been a quartet of doublets instead of a doublet of quartets. Such affects also appear in the superhyperfine structure of SF₆ analyzed below. For either of these molecules, it is remarkable how different the rovibrational “chemical shifts” can become for equivalent symmetry sites. The result is a microscopic example of spontaneous symmetry breaking.

34.5.3 Large Spherical Top Molecules: Cubic-Octahedral Symmetry Effects

The most common high-symmetry molecules belong to either the tetrahedral T_d or cubic-octahedral O or O_h groups. The T_d group of order 24 matches order ${}^{\circ}S_4 = 4!$ of CF₄ nuclear permutation. O_h symmetry is more complicated. The octahedral O_h molecule SF₆ has F-spin-1/2 permutation symmetry S_6 of order $6! = 720$, 15 times larger than O_h . This allows O_h species to be correlated with a supercluster of S_6 symmetries that define nuclear spin hyperfine multiplets just as each C₄ or C₃ subgroup species correlate in Fig. 34.6 with a cluster of O_h symmetries.

Bordé et al. [27, 28, 30] first resolved hyperfine structure in 10 μm ν₃ bands of SF₆. Figure 34.9 displays 16 μm ν₄ bands [31] with focus on P(88) fine structures in Fig. 34.9b that contain superfine clusters in Fig. 34.9c, which in turn have hyperfine (Fig. 34.9d) and superhyperfine structure (Fig. 34.9e). Like SF₄ spectra in Fig. 34.7, SF₆ ν₄P(N)-

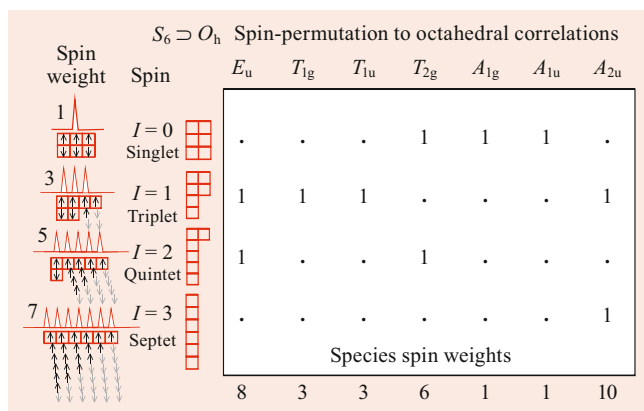


Fig. 34.10 SF_6 states of nuclear spin $I = 0-3$ correlated with O_h symmetry species listed on top

cluster bands avoid $P(N \pm 1)$ neighbours, while SF_6 $\nu_3P(N)$ -bands are crowded together by having lower scalar Coriolis splitting factors ($\xi_3 < \xi_4$) or greater tensor cluster splitting factors ($\tau_3 > \tau_4$) [29, 32, 33].

In either case, asymmetry correlation is done in Fig. 34.10 between O_h subgroup species $\{A_g, \dots, T_{2u}\}$ and supergroup S_6 species labeled by six-box spin-1/2 Young tableaux of 1 or 2 rows. Pauli-Fermi antisymmetry matches each spin tableau to its conjugate spatial tableau of 1 or 2 columns. Each matched pair belongs to a total nuclear spin of $I = 0$ (singlet state), $I = 1$ (triplet), $I = 2$ (quintet), or $I = 3$ (septet). This is correlated with one or more of the seven allowed O_h subgroup species $\{E_u, T_{1g}, T_{1u}, T_{2g}, A_{1g}, A_{1u}, A_{2u}\}$, and three species E_g, T_{2u} and A_{2g} are forbidden. They would be allowed if the F-spin were greater than 1/2. If the F-spin is less, i.e., zero, then only A_{1g} is allowed.

Case 1 hyperfine SF_6 spectra are sketched in the center and lower right-hand side boxes of Fig. 34.9d,e, as was done for CF_4 in Fig. 34.7d,e. Case 1 has greater superfine cluster splitting between O_h species than spin multiplet splitting within them as seen by comparing these boxes to Fig. 34.10.

The lowest A_2 boxes hold an ($I = 1$) triplet and ($I = 3$) septet for spin weight 10 below A_{2u} in Fig. 34.10. Above that lie T_{2g} boxes with an ($I = 0$) singlet and ($I = 2$) quintet (weight 6), E_u with an ($I = 1$) triplet and ($I = 2$) quintet (weight 8), T_{1g} or T_{1u} triplet boxes, and finally A_{1g} or A_{1u} singlets.

To form an SF_6 molecule requires considerable spontaneous symmetry breaking to make six F atoms, free to undergo (at the very least) $6!$ permutations and settle into O symmetry around a sulfur atom that has only 24 permutations. (A full $O_h \subset S_6$ correlation valid for any Fermi or Bose XY_6 octahedral molecule is given in [32]) Thus, SF_6 spectra in Fig. 34.9 involves a more severe symmetry downfall than that of CF_4 in Fig. 34.7.

This kind of downfall amounts to a breakdown of Herzberg's rule concerning rovibronic spin species [2, 3]:

transitions between species are very strictly forbidden since the nuclear moments are so very slight. In other words, if subkilohertz interactions are negligible between states separated by MHz or GHz, then resonant mixing of different species is unlikely.

However, it was only found later how symmetric molecules have tight level clusters that force subkilohertz near-degeneracy such as 6×10^{-12} Hz for the A_1T_1E cluster $n_4 = 88$ in Fig. 34.9c. Here, the exponential die-off of intracluster tunneling causes Case 2 superhyperfine mixing of species in the range from $n_4 = 88$ down to about $n_4 = 78$ where subkilohertz splitting begins. Also, on the right-hand side of Fig. 34.9c, the C_3 clusters labeled by $n_3 = 88$ and 87 may also fall into Case 2.

When O_h species levels such as the A_2T_2E cluster $n_4 = 86 = 2 \pmod{4}$ in Fig. 34.9c are crushed together, the corresponding energies and states mix and reorganize as shown in Fig. 34.11. With $O \subset S_6$ symmetry of Case 1, all 6 O -axes $\{x\bar{x}y\bar{y}z\bar{z}\}$ are equivalent. The three cluster levels are labeled by O_h symmetry species A_{2u} (lowest J -tunneling energy: $H - 4S$), T_g (middle: H), E_u (highest: $H + 2S$), and the six-box S_6 tableaux correlated by Fig. 34.10 columns A_{2u}, T_{2g} , and E_u . The columns match each O_h to one or two spin multiplets. A_{2u} is the winner with the highest hyperfine weight of 10: ($I = 3$)-septet + ($I = 1$)-triplet that gives a Bordé A_{2u} spectra like the one shown in the lower right-hand side of Fig. 34.11. (Note that the Bordé spectral curve is a derivative of the seven peaks. Ideally, seven zeroes of that curve precisely locate septet peaks.) The middle Case 1 T_{2g} has the lowest spin weight of 6: ($I = 2$)-quintet + ($I = 0$)-singlet with an easily read Bordé spectrum of 5 peaks and central peak doubled. The top E_u has a spin weight of 8: ($I = 2$)-quintet + ($I = 1$)-triplet with a more confusing Bordé spectrum, possibly due to onset of Case 2 mixing that happens if ATE splitting S is approaching that of hyperfine multiplets.

When the 6-axis J -tunneling rate S goes to zero, the SF_6 becomes stuck to rotating on single-axis pair $\{z\bar{z}\}$. So four F-atoms rotate around the equator, while the other two take up a more sedate residence at North (z) and South ($-\bar{z}$) poles. Such restrictions of freedom or symmetry breaking is indicated symbolically by literally breaking the six-box tableaux of S_6 into four-box and two-box pairs labeling subgroups of $S_4 \otimes S_2$ or $D_4 \otimes C_2$. Each orbit tableau is Fermi-matched to a conjugate spin tableau (Fig. 34.10) as shown in Case 2 level side of Fig. 34.11.

The whirling four-box nuclei enjoy greater spin-rotation coupling than their sedate two-box cohorts. To flip one of their four spins from \downarrow to \uparrow takes more energy than to flip a two-box spin. (The Bordé spectra in Fig. 34.11 indicate about four times more.) So raising $\downarrow\downarrow\downarrow\downarrow$ to $\uparrow\uparrow\uparrow\uparrow$ costs the entire width of superhyperfine pattern, while raising $\downarrow\downarrow$ to $\uparrow\uparrow$ costs only a triplet width. The scalar paired two-box spins $\uparrow\downarrow$ and four-box spins $\uparrow\uparrow\downarrow\downarrow$ are invariants.

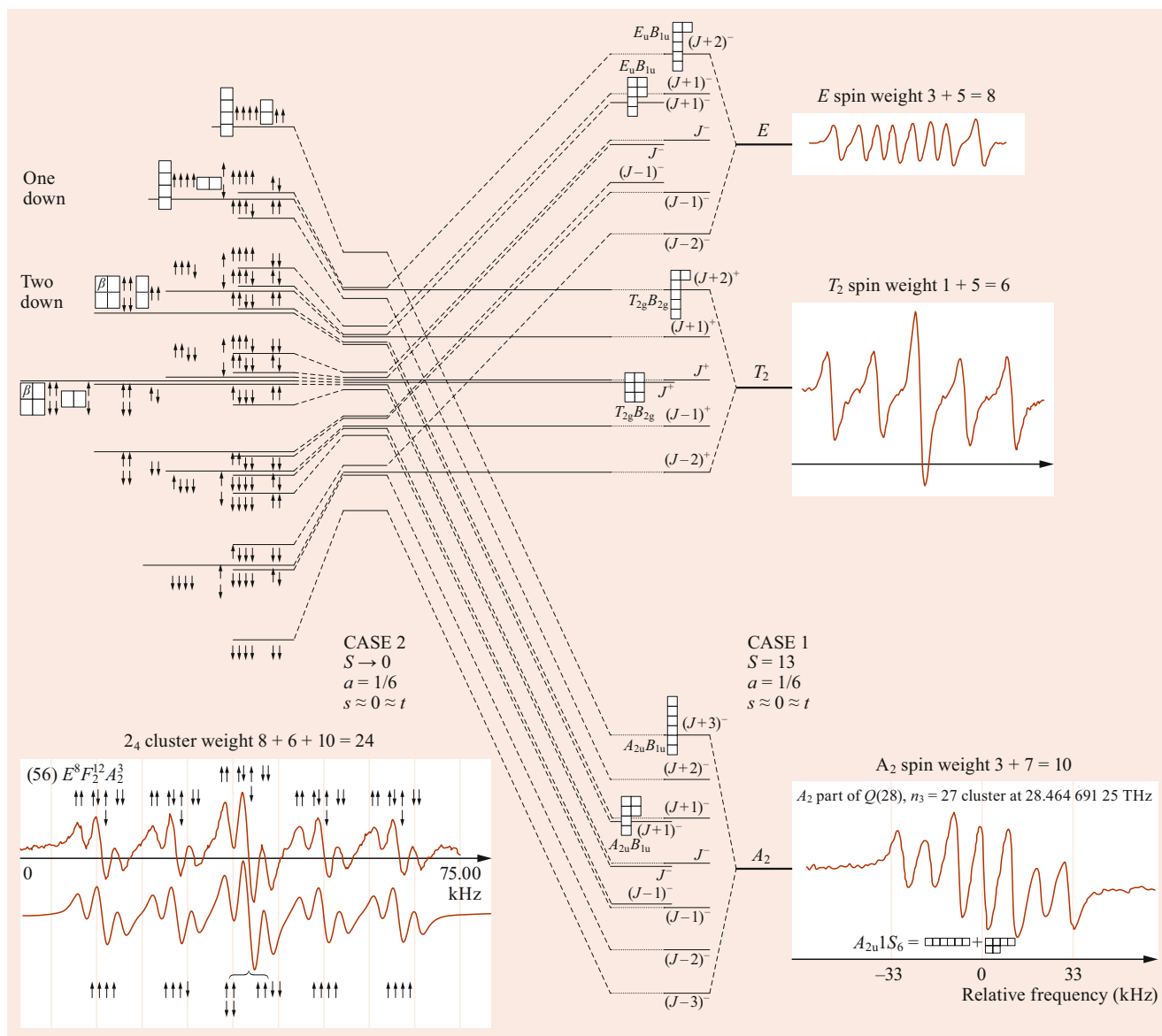


Fig. 34.11 Case 1 $S_6 \supset O\{A_1 T_2 E\}$ levels mix to become Case 2 $C_{4v} \otimes C_{2h}$ superhyperfine levels [9, 33]

34.5.4 Icosahedral Spherical Top Molecules: Extreme Spin Symmetry Effects

Until the recent discovery of fullerenes and the structure of virus capsids, molecules with the highest icosahedral symmetry were thought to be rare or nonexistent in nature [34, 35]. With the discovery of Buckminsterfullerenes (Buckyballs) C_{60} with molecular point symmetry Y_h or I_h , one expects extreme dynamical symmetry effects. It helps to compare Y_h -symmetric C_{60} to the O_h -symmetric SF_6 first by their symmetry-allowed rotation Hamiltonians of lowest rank [36–38]

an extreme example of symmetry breaking effects, consider the Buckminsterfullerene or Buckyball molecule C_{60} , which has the highest possible molecular point symmetry

Y_h . A semiclassical approach to rotational symmetry and dynamics is useful here since the rotational quantum constant is so small for the fullerenes (for C_{60} $2B = 0.0056 \text{ cm}^{-1}$ or 168 MHz) [36–40].

$$\begin{aligned} \mathbf{H}_{SF_6}^{\text{Rot}} = & B_{SF_6} \mathbf{J}^2 \\ & + t_{044} \left[\sqrt{\frac{7}{12}} \mathbf{T}_0^{(4)} + \sqrt{\frac{5}{24}} (\mathbf{T}_{+4}^{(4)} + \mathbf{T}_{-4}^{(4)}) \right] + \dots \end{aligned} \quad (34.19a)$$

$$\begin{aligned} \mathbf{H}_{C_{60}}^{\text{Rot}} = & B_{C_{60}} \mathbf{J}^2 \\ & + t_{066} \left[\sqrt{\frac{11}{25}} \mathbf{T}_0^{(6)} + \sqrt{\frac{7}{25}} (\mathbf{T}_{+5}^{(6)} + \mathbf{T}_{-5}^{(6)}) \right] + \dots \end{aligned} \quad (34.19b)$$

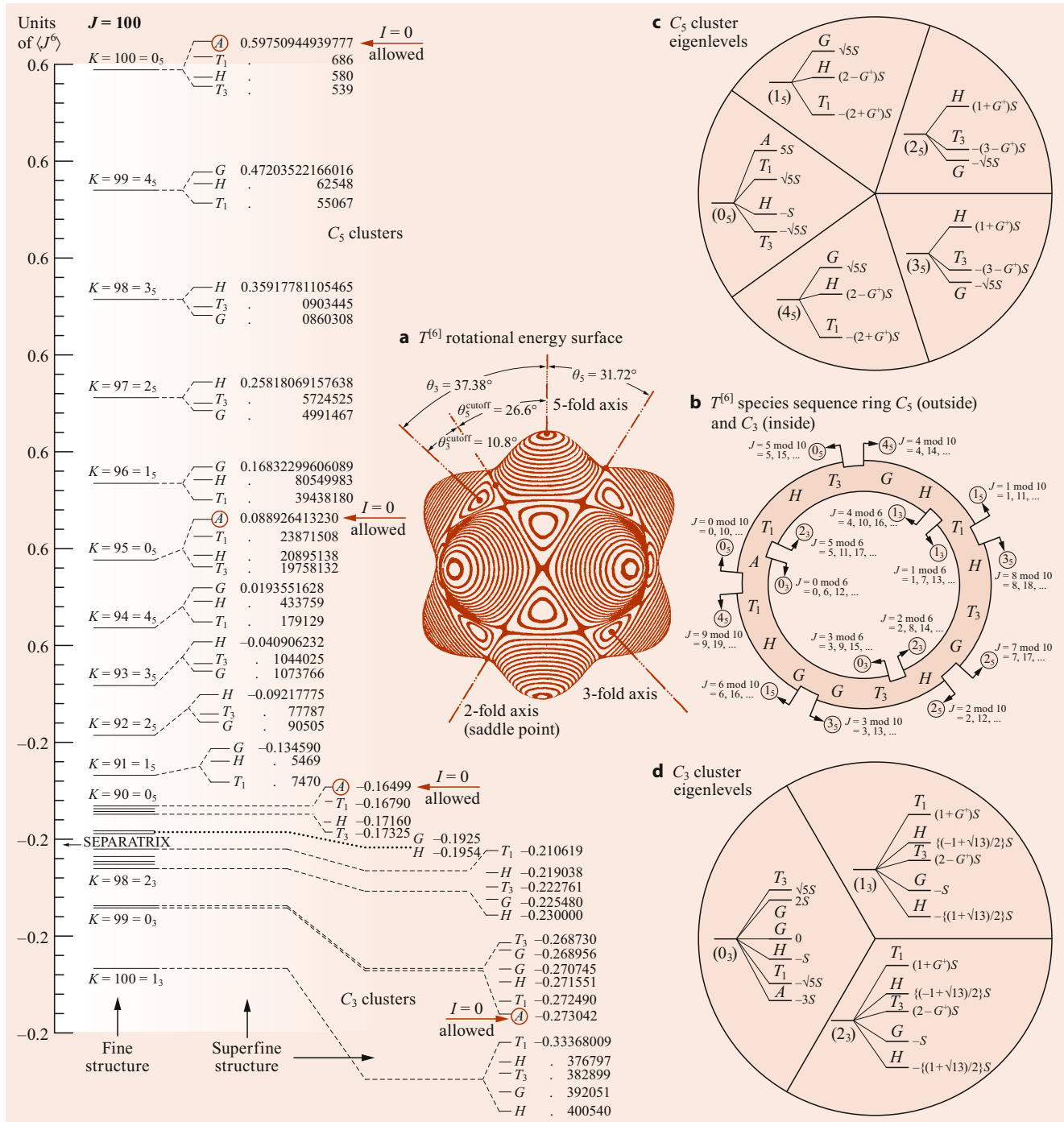


Fig. 34.12 $J = 100$ Y_h -symmetry sublevels. $^{12}\text{C}_{60}$ allows only the 4 A-species. $^{13}\text{C}_{60}$ allows all. (a) $T^{[6]}$ RES of 26.6° C_5 hills or 10.8° C_3 valleys hold (b, c) many C_5 levels, and (d) few C_3 levels

Both have large rotor inertia I and a small rotor constant $B = \frac{1}{2I}$. (For C_{60} : $2B = 0.0056 \text{ cm}^{-1}$ or 168 MHz . For SF_6 : $2B = 0.091 \text{ cm}^{-1}$) [39, 40]. Both use Wigner–Eckart form for tensor matrix elements,

$$\langle J' | \mathbf{T}_q^{(k)} | J \rangle = C_{qKK'}^{JJ'} (J || k || J); \quad (34.19c)$$

$J = 30$ eigenvalues of $\mathbf{H}_{\text{SF}_6}^{\text{Rot}}$ in Fig. 34.4 are to be compared to $J = 100$ -values of $\mathbf{H}_{\text{C}_{60}}^{\text{Rot}}$ in Fig. 34.12. Six C_4 hills of $\mathbf{H}_{\text{SF}_6}^{\text{Rot}}$ RES (rotational energy surface) compare to 12 C_5 hills on $\mathbf{H}_{\text{C}_{60}}^{\text{Rot}}$ RES, and 8 C_3 valleys of $\mathbf{H}_{\text{SF}_6}^{\text{Rot}}$ RES compare to 20 C_3 valleys on $\mathbf{H}_{\text{C}_{60}}^{\text{Rot}}$ RES. The C_3 cut-off angle $\theta_3^{\text{cut-off}} = 10.8^\circ$ for $\mathbf{H}_{\text{C}_{60}}^{\text{Rot}}$ is half of 19.5° for $\mathbf{H}_{\text{SF}_6}^{\text{Rot}}$. So the huge $J = 100$ man-

ifold has room for only two C_3 clusters. A first comparison of SF_6 and $^{13}C_{60}$ assumes fluorine, and ^{13}C nuclei causes no hyperfine splitting. (Here, we ignore Fig. 34.11 and assume that C_{60} rotates slowly with ^{13}C magnetic moments too weak to observe.) Just as order is maintained in a sequence of SF_6 species between C_3 valleys and C_4 hills in Fig. 34.4, so also is the order of $^{13}C_{60}$ symmetry species maintained as C_3 valley clusters morph into C_5 hill clusters on either side of the separatrix in Fig. 34.12b.

While SF_6 or $^{13}C_{60}$ level sequence is maintained, their intra and intercluster level *spacing* is not. The C_3 valley intra-cluster level *spacing* in Fig. 34.12c is quite different from the C_5 hill intracluster level *spacing* in Fig. 34.12d, and similarly for SF_6 cluster level eigenvalues in Table 34.5. Intracluster (superfine)eigenvalues have a quasi exponential tunneling “sneak” factor S , which was first defined for the asymmetric rotor by Eq. (34.13). It depends on local angular momentum m_n of each C_n cluster and J -momentum cone polar angle $\Theta_{m_n}^J$ as diagrammed in Fig. 34.5.

$$\Theta_{m_n}^J = \arccos \frac{m_n}{\sqrt{J(J+1)}}. \quad (34.20)$$

Asymmetric-rotor eigenvalues in Table 34.1 and CF_4 or SF_6 eigenvalues in Table 34.5 have numerical rationality and contrast with the rationality of C_{60} Golden ratios ($G^+ = (1 + \sqrt{5})/2$ and $\sqrt{13}$) of superfine eigenvalues in Fig. 34.12c,d. Rational frequencies give Poincaré periodicity, while irrational ones give quasi periodicity.

However, the discussion of the similarity of SF_6 and $^{13}C_{60}$ ends when the hyperfine structure of the latter overwhelms that of the former. This is revealed in the following section.

34.5.5 $^{12}C_{60}$ versus $^{13}C_{60}$: a World of Difference in Spin- $\frac{1}{2}$ Hyperfine Spectroscopy

SF_6 has one stable F-isotope. C_{60} chooses from two stable C isotopes: $^{12}C_{60}$ (spin 0) of 98.9% abundance or $^{13}C_{60}$ (spin- $\frac{1}{2}$) at 1.1%. ^{12}C spectroscopy is simpler than that of ^{13}C . (The ^{14}C spin-0 isotope is even trickier, with its 5707-year half-life β -decay into ^{14}N .) It helps to compare purely bosonic $^{12}C_{60}$ with purely fermionic $^{13}C_{60}$. In between are many mixed $^{12}C_n^{13}C_{60-n}$ isotopomers. The first $^{12}C_{59}^{13}C$ is 33% likely and is an extreme example of isotopic symmetry breaking [41]. A *single extra neutron* reduces the very highest 3-D point symmetry Y_h (120 operators) down to a lowly C_h (one planar reflection) [42, 43].

After comparing levels of SF_6 and $^{13}C_{60}$ above one should also compare SF_6 ($J = 30$) levels in Fig. 34.4 to *allowed* $^{12}C_{60}$ ($J = 100$) levels in Fig. 34.12. Only *four* of its 201 levels are Bose-allowed A -species: $K = n_5 = 100$, $K = n_5 =$

95, $K = n_5 = 90$, and finally $K = n_5 = 99$, in the second to lowest cluster in the C_3 valley. The upper three are $K = 0 \pmod{5} = 0_5$ waves orbiting C_5 hills. $K = n_3 = 99$ is the only 0-mod-3 wave in the tiny C_3 valley of the RES and, thus, the valley’s only $^{12}C_{60}$ -allowed level in Fig. 34.12.

Clearly, $^{12}C_{60}$ has a very sparse fine structure. This helps spectroscopists to assign lines and determine $^{12}C_{60}$ constants that will approximate those of $^{13}C_{60}$. (If $^{12}C_{60}$ has molecular weight of 720 atomic units, then $^{13}C_{60}$ weights in around 780.) Recently (as this article was being written), the very first J -resolved $^{12}C_{60}$ spectra was observed in its 8.4 μm_2 bands by Jun Ye’s group at JILA [44] that pioneered direct frequency comb spectroscopy. In this work, they used cavity-enhanced comb spectroscopy along with buffer gas cooling. [45, 46] This followed 27 years of failed attempts by other labs around the world. Now it suggests that a “Mt. Everest” of molecular spectroscopy, namely the $^{13}C_{60}$ spin-monster, might be attainable.

There is both good and bad news concerning this. The good news: Fermi-symmetric $^{13}C_{60}$ has only ten times as many rotating spin- $\frac{1}{2}$ nuclei as SF_6 . The bad news is that the factor-of-10 lies in exponents!

So, $^{13}C_{60}$ has about 2^{60} hyperfine states or about 1.15×10^{18} spin states distributed among its ten species [32], as listed in Fig. 34.13. That is in contrast to Bose-symmetric $^{12}C_{60}$, which has only a handful of A -states in each J -multiplet. Yet a single neutron entering $^{12}C_{60}$ to form $^{12}C_{59}^{13}C$ causes many of the excluded levels to arise under lower C_h symmetry labels.

SF_6 spin weights $\{8, 3, 3, 6, 1, 1, 10\}$ in $O_h \subset S_6$ correlation of Fig. 34.10 fit a sum identity of O_h irrep dimension

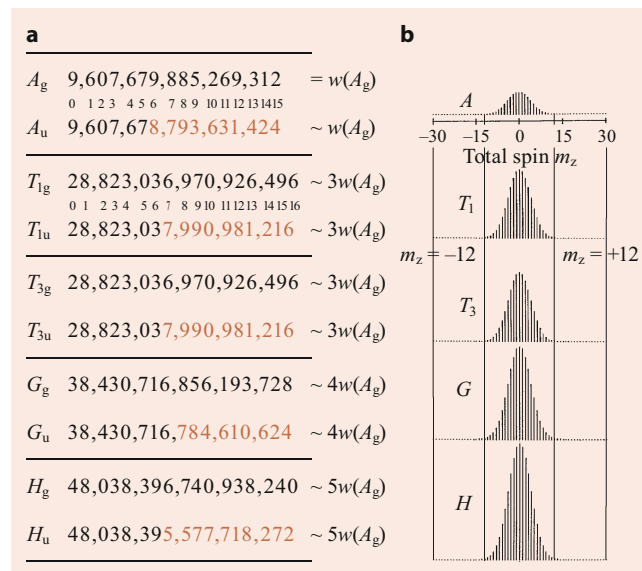


Fig. 34.13 (a) Total spin weights and (b) m_z -distributions for $Y_h \subset S_{60}$ symmetry species

(ℓ^μ) times each of its spin weights. This equals its total spin dimension $2^6 = 64$.

$$\begin{aligned}
 & 8\ell^{E_u} + 3\ell^{T_{1u}} + 3\ell^{T_{1g}} + 6\ell^{T_{2g}} + 1\ell^{A_{1g}} + 1\ell^{A_{1u}} + 10\ell^{A_{2u}} \\
 &= 16 + 9 + 9 + 18 + 1 + 1 + 10 \\
 &= 64 = 2^6.
 \end{aligned}
 \tag{34.21}$$

A similar identity uses products of $U(2)$ spin- $\frac{1}{2}$ dimensions $(2S + 1)$ with irreps of group S_6 whose tableaux match $U(2)$ tableaux that belong to each total spin $S = 3, 2, 1, 0$ made by six spin- $\frac{1}{2}$ nuclei.

$$\begin{aligned}
 2^6 &= \ell_{U(2)} + \ell_{S_6} + \ell_{U(2)} + \ell_{S_6} \\
 &+ \ell_{U(2)} + \ell_{S_6} + \ell_{U(2)} + \ell_{S_6} \\
 &= (2S + 1 = 7) \cdot 1 + (2S + 1 = 5) \cdot 5 \\
 &+ (2S + 1 = 3) \cdot 9 + (2S + 1 = 1) \cdot 5.
 \end{aligned}
 \tag{34.22}$$

Tableau hook-length formulas give the irrep dimension for S_n and for $U(m)$ ([15, p. 65]).

$$\begin{aligned}
 \ell_{S_{15}} &= \frac{15!}{\text{hooklength product:}} \begin{array}{|c|c|c|c|c|} \hline 8 & 7 & 5 & 3 & 1 \\ \hline 7 & 5 & 3 & 1 & \\ \hline 5 & 3 & 1 & & \\ \hline 2 & 1 & & & \\ \hline \end{array} \tag{34.23a}
 \end{aligned}$$

$$\begin{aligned}
 \ell_{U_5} &= \frac{\text{integer product:}}{\text{hooklength product:}} \begin{array}{|c|c|c|c|c|} \hline 5 & 6 & 7 & 8 & 9 \\ \hline 4 & 5 & 6 & 7 & \\ \hline 3 & 4 & 5 & & \\ \hline 2 & 3 & & & \\ \hline \end{array} \begin{array}{|c|c|c|c|c|} \hline 8 & 7 & 5 & 3 & 1 \\ \hline 7 & 5 & 3 & 1 & \\ \hline 5 & 3 & 1 & & \\ \hline 2 & 1 & & & \\ \hline \end{array} \tag{34.23b}
 \end{aligned}$$

The *hook length* h of a tableau box is the number n_r of boxes to its right plus the number n_b below it plus one for itself, that is, $h = n_r + n_b + 1$. The numerator for S_n formula in Eq. (34.23a) is $n!$ (here $n = 15$). The denominator has exactly n -boxes with one hook length for each particle. The same denominator applies to $U(m)$ irrep dimension and Eq. (34.23b) for an n -particle- m -state system (here $m = 5$), but the numerator fills the same tableau frame with a matrix whose corner diagonal is (m, m, m, \dots) , and $\pm 1^{\text{st}}$ off-diagonals are $\pm(m \pm 1, m \pm 1, m \pm 1, \dots)$, $\pm 2^{\text{nd}}$ off-diagonals are $\pm(m \pm 2, m \pm 2, m \pm 2, \dots)$, etc.

The Eqs. (34.23a) and (34.23b) fractions always yield a positive integer if the desired representation exists and

zero otherwise; $U(2)$ fractions ($m = 2$) derive factors $\ell_{S_6}^{[\mu]} = \{1, 5, 9, 5\}$ in Eq. (34.21).

$$\begin{aligned}
 \ell_{S_6}^{[\mu]} &= \{1, 5, 9, 5\} \\
 &= \left\{ \ell_{O_h}^{A_{2u}}, \ell_{O_h}^{E_u} + \ell_{O_h}^{T_{2g}}, \ell_{O_h}^{A_{2u}} + \ell_{O_h}^{E_u} + \ell_{O_h}^{T_{1g}} + \ell_{O_h}^{T_{1u}}, \right. \\
 &\quad \left. \ell_{O_h}^{A_{2g}} + \ell_{O_h}^{A_{1u}} + \ell_{O_h}^{T_{2g}} \right\}.
 \end{aligned}
 \tag{34.24}$$

This is consistent with Eqs. (34.22), (34.23a), and (34.23b), and the $O_h \subset S_6$ correlation table in Fig. 34.10, if we recall that each Fermi spin tableau has to be the *transpose* of its rotor tableau in order to make the Fermi-Dirac-Pauli distribution a totally antisymmetric spin-rotor state. The hook-length formulae structure in Eqs. (34.23a) and (34.23b) shows that a tableau has the same dimensions as its transpose for both S_n and $U(m)$.

As powerful as tableau formulae are, they do not quite prepare us for the huge tableau dimensions and correlations associated with $^{13}C_{60}$ and its permutation symmetry S_{60} containing its icosahedral symmetry subgroup $Y_h \subset S_{60}$. The analogous spin weights in Fig. 34.13 for a $Y_h \subset S_{60}$ correlation are truly enormous numbers when compared to the analogous $O_h \subset S_6$ numbers in Fig. 34.10. Most C_{60} spin states have no Y or Y_h symmetry. Applying all 60 Y operators to a typical state generally gives 60 orthogonal spin states spanning 60-by-60 *regular representation* and reducing to $1A \oplus 3T_1 \oplus 3T_3 \oplus 4G \oplus 5H$ that obeys its group order sum relation.

$$\begin{aligned}
 \circ Y &= (\ell^A)^2 + (\ell^{T_1})^2 + (\ell^{T_3})^2 + (\ell^G)^2 + (\ell^H)^2 \\
 &= 1^2 + 3^2 + 3^2 + 4^2 + 5^2 = 60.
 \end{aligned}
 \tag{34.25}$$

So Y_h species weights in Fig. 34.13 are (to one part in 10^6) proportional to the irrep dimension. Thus, the approximate weight ratios are $(A : T_1 : T_3 : G : H) = (1 : 3 : 3 : 4 : 5)$ with relatively tiny ratio variations between odd (u) and even (g) parity species. However, as Fig. 34.13 shows, the arithmetic variations are in the billions! This is in contrast to SF_6 , where the u and g ratios of O_h species differ markedly and even leave the three species A_{2g} , E_g , and T_{2u} with *zero* weight.

Plots of species weight versus spin z -component ($-30 \leq m_z \leq 30$) are shown in Fig. 34.13b. The height of each vertical line is proportional to the number of a given species $A, T_1, T_3, G,$ or H that have the m_z -value that line represents. Each species has its tallest line at $m_z = 0$ and then falls quasi exponentially on either side. They become too small to plot for m_z -values outside the interval $(-12 \leq m_z \leq +12)$ and thereafter are just lines of dots. The dots for scalar icosahedral A-species at extreme values of $m_z = +30$ or $m_z = -30$ are lines of height $\ell^{[60,0]} = 1$ for the S_{60} tableaux below.

The S_{60} dimension $\ell^{[30,30]}$ for this zero-spin tableau is given by applying Eq. (34.23a)

$$\begin{aligned} \ell^{[30,30]} &= \frac{60 \cdot 59 \cdot 58 \cdot 57 \cdots 2 \cdot 1}{31 \cdot 30 \cdot 29 \cdot 28 \cdots 3 \cdot 2} = \frac{60!}{(31!)(30!)} \\ &= 3.8149865020923 \cdot 10^{15}. \end{aligned} \quad (34.28)$$

That number of zero- m_z states is apportioned by ratios 1 : 3 : 3 : 4 : 5 ($\pm 0.0001\%$) to species A , T_1 , T_3 , G , and H , respectively (the exact ratio calculation is tricky and required an erratum [42, 43]). If ever the resulting panoply of $^{13}\text{C}_{60}$ superhyperfine spectra is observed, it will dwarf that of SF_6 in Figs. 34.9 and 34.10. A plot comparing $J = 100$ superfine levels of $^{13}\text{C}_{60}$ to those of $^{12}\text{C}_{60}$ in Fig. 34.12 only begins to relate to SF_6 levels in Fig. 34.4. An attempt to relate spectra of $^{13}\text{C}_{60}$ to $^{12}\text{C}_{60}$ is sketched by Fig. 34.14 as a highly speculative P(50) prognostication where only two A-singlet $^{12}\text{C}_{60}$ lines exist while $^{13}\text{C}_{60}$ has seven large clusters. The $(K = 50)0_5(AT_1HT_3)$ cluster is a Case 1 guess for superfine structure of astronomical numbers of hyperfine lines. The resolution assignment of such super-hyper-spectra will require a wealth of future technology and theory.

34.6 Composite Rotors and Multiple RES

So far, the discussion has focused on Hamiltonians and involved functions of even multipolarity, i.e., constant ($k = 0$), quadratic or quadrupole ($k = 2$), quartic or hexadecapole ($k = 4$), while ignoring functions that are linear-dipole ($k = 1$) or cubic-octupole ($k = 3$), for reasons of time-reversal symmetry. However, for composite “rotor-rotors” any multipolarity is possible, and the dipole is of primary utility.

A composite rotor is one composed of two or more objects with more or less independent angular momenta. This could be a molecule with attached methyl (CH_3) “gyro” or “pinwheel” subrotors, a system of considerable biological interest. It could be a molecule with a vibration or “phonon” excitation that couples strongly to rotation. Also, any nuclear or electronic spin with significant coupling may be regarded as an elementary subrotor. The classical analogy is a spacecraft with gyro(s) on board.

A rotor-rotor Hamiltonian has the following general interaction form

$$H_{\text{rotor } R+S} = H_{\text{rotor } R} + H_{\text{rotor } S} + V_{RS}. \quad (34.29)$$

A useful approximation assumes that the rotor_S gyro is fastened to the frame of rotor_R so the interaction V_{RS} becomes a constraint, does no work, and is thus assumed to be

zero. An asymmetric top with body-fixed spin is the following modified version of Eq. (34.1)

$$\begin{aligned} H_{R+S(\text{Body-fixed})} &= AR_x^2 + BR_y^2 + CR_z^2 + H_{\text{rotor } S} \\ &+ (\approx 0). \end{aligned} \quad (34.30a)$$

The system total angular momentum is a conserved vector $\mathbf{J} = \mathbf{R} + \mathbf{S}$ in the lab frame and a conserved magnitude $|\mathbf{J}|$ in the rotor-R body frame. So we use $\mathbf{R} = \mathbf{J} - \mathbf{S}$ in place of \mathbf{R} ,

$$\begin{aligned} H_{R,S(\text{fixed})} &= A(\mathbf{J}_x - \mathbf{S}_x)^2 + B(\mathbf{J}_y - \mathbf{S}_y)^2 \\ &+ C(\mathbf{J}_z - \mathbf{S}_z)^2 + H_{\text{rotor } S} \\ &= A\mathbf{J}_x^2 + B\mathbf{J}_y^2 + C\mathbf{J}_z^2 - 2A\mathbf{J}_x\mathbf{S}_x \\ &- 2B\mathbf{J}_y\mathbf{S}_y - 2C\mathbf{J}_z\mathbf{S}_z + H'_{\text{rotor } S}. \end{aligned} \quad (34.30b)$$

Gyro-spin components S_a are treated at first as constant classical parameters S_a ,

$$\begin{aligned} H_{R,S(\text{fixed})} &= \text{const } 1 - 2AS_x\mathbf{J}_x - 2BS_y\mathbf{J}_y - 2CS_z\mathbf{J}_z \\ &+ A\mathbf{J}_x^2 + B\mathbf{J}_y^2 + C\mathbf{J}_z^2 \\ &= M_0T_0^0 + \sum_d D_dT_d^1 + \sum_q Q_qT_q^2. \end{aligned} \quad (34.30c)$$

This is a simple Hamiltonian *multipole tensor operator expansion* having here just a monopole T_0^0 term, three dipole T_a^1 terms, and two quadrupole T_q^2 terms shown in Fig. 34.15.

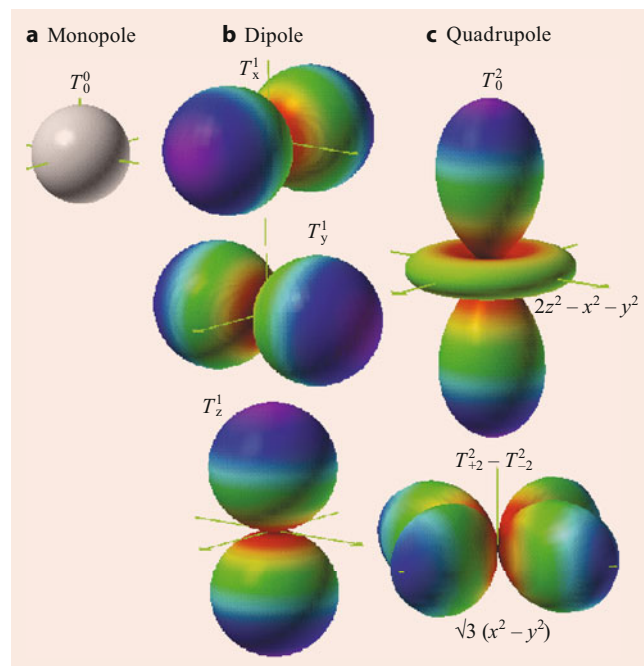


Fig. 34.15 The six lowest-order RES components needed to describe rigid gyro rotors

Each is a radial plot of a spherical harmonic function $Y_q^k(\varphi, \vartheta)$ representing a tensor operator T_q^k

$$T_0^0 = \frac{J_x^2 + J_y^2 + J_z^2}{3} \quad (34.31a)$$

$$T_x^1 = J_x = \frac{T_{+1}^1 + T_{-1}^1}{\sqrt{2}}$$

$$T_y^1 = J_y = \frac{T_{+1}^1 - T_{-1}^1}{i\sqrt{2}}$$

$$T_z^1 = J_z = T_0^1 \quad (34.31b)$$

$$T_{zz}^2 = \frac{2J_z^2 - J_x^2 - J_y^2}{2} = T_0^2$$

$$T_{x^2-y^2}^2 = J_x^2 - J_y^2 = \frac{2(T_2^2 - T_{-2}^2)}{\sqrt{6}}. \quad (34.31c)$$

The constant coefficients or *moments* indicate the strength of each multipole symmetry,

$$M_0 = A + B + C + 3H'_{\text{rotor } S} \quad (34.32a)$$

$$D_x = -2AS_x,$$

$$D_y = -2BS_y,$$

$$D_z = -2CS_z \quad (34.32b)$$

$$Q_{zz} = (2C - A - B)/6$$

$$Q_{x^2-y^2} = (A - B)/2, \quad (34.32c)$$

The scalar monopole RES in Eq. (34.32a) is a sphere, while vector dipole RES in Eq. (34.32b) are bispheres pointing along Cartesian axes, and the RES in Eq. (34.32c) resemble quadrupole antenna patterns. Also, Fig. 34.15a–c plots the six s, p, and d Bohr–Schrödinger orbitals that are analogs for the six octahedral J -tunneling states listed in Table 34.5.

The asymmetric and symmetric rotor Hamiltonians in Eqs. (34.1) and (34.2) are combinations of a monopole in Eq. (34.31a), which by itself makes a spherical rotor, and varying amounts of the two quadrupole terms in Eq. (34.31c) to give the rigid rotor RES pictured previously in Figs. 34.1 and 34.2. Both Q coefficients in Eq. (34.32c) are zero for a spherical top ($A = B = C$), but only one is zero for a symmetric top ($A = B$).

Combining monopole in Eq. (34.31a) with dipole terms in Eq. (34.31b) gives a gyro-rotor Hamiltonian in Eq. (34.30b) for a spherical rotor ($A = B = C$) that has the following form

$$H = \text{const} + BJ^2 - g\mu S \cdot J \quad (34.33)$$

(where: $-g\mu = 2A = 2B = 2C$);

H resembles a dipole potential $-m \cdot B$ for a magnetic moment $m = gJ$ that precesses clockwise around a lab-fixed magnetic field $B = \mu S$. (The PE is least for J along S .)

Here, the Hamiltonian in Eq. (34.33) is a simple example of Coriolis rotational energy. It is least for J along S , where

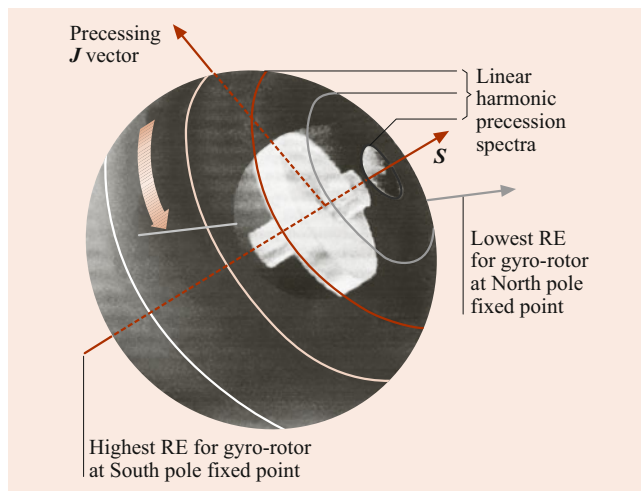


Fig. 34.16 The spherical gyro-rotor RES is a cardioid of revolution around gyro spin S

$|R| = |J - S|$ is least, and rotor kinetic energy BR^2 is least. (Magnitudes $|J|$ and $|S|$ are constant here.) The spherical rotor-gyro RES in Fig. 34.16 is minimum along the body-axis $+S$ and maximum along $-S$, where BR^2 is greatest.

As is the case for the rigid solid rotors in Figs. 34.1 and 34.2, the RES energy topography lines determine the precession J -paths in the body frame, wherein gyro- S is fixed in Fig. 34.16. The left-hand rule gives J -precession sense in the body S -frame, i.e., all J precess *anti*-clockwise relative to the “low” on the $+S$ -axis, or clockwise relative to the “high” on the $-S$ -axis. In the lab, S precess clockwise around a fixed J .

Gyro-RES differ from solid rotor RES, which have two opposite “high” and/or two opposite “lows” separated by saddle fixed points where the precessional flow direction reverses, as can be seen in Fig. 34.2. The gyro-RES in Fig. 34.16 has no saddle fixed points and only one “high” and one direction of flow with the same harmonic precession frequency for all J -vectors between the high $+S$ and low $-S$ -axes. This is because the spectrum of the gyro-rotor Hamiltonian in Eq. (34.33) is *harmonic* or *linear* in the momentum quanta K ,

$$\langle \frac{J}{K} | H | \frac{J}{K} \rangle = \text{const.} + BJ(J+1) - 2BK. \quad (34.34)$$

In contrast, even the symmetric rigid rotor spectrum in Eq. (34.4) is *quadratic* in K . Other rotors shown in Figs. 34.2 and 34.4 have levels that are quite nonlinear.

34.6.1 3-D-Rotor and 2-D-Oscillator Analogy

Linear levels belong to harmonic *oscillators*, not rotors, but the gyro-rotor’s linear spectrum highlights a 160-year-old analogy of 3-D rotor motion to 2-D vibration. *Stokes* [47]

described 2-D electric vibration or *optical polarization*, by a 3-D vector that became known as the Stokes vector \mathbf{S} and labeled appropriately by the letter \mathbf{S} . (Now we say \mathbf{S} labels “spin”.) Stokes’ spin uses *Hamilton quaternions* [48, 49] re-done 80 years later as *Pauli spinor* σ_μ components [50] of a general 2-D Hermitian operator H ,

$$H = \begin{pmatrix} A & B - iC \\ B + iC & D \end{pmatrix} \\ = \frac{A+D}{2}\sigma_0 + \frac{A-D}{2}\sigma_A + B\sigma_B + C\sigma_C, \quad (34.35)$$

where

$$\sigma_0 = \begin{pmatrix} 1 & 0 \\ 0 & 1 \end{pmatrix}, \quad \sigma_A = \begin{pmatrix} 1 & 0 \\ 0 & -1 \end{pmatrix}, \\ \sigma_B = \begin{pmatrix} 0 & 1 \\ 1 & 0 \end{pmatrix}, \quad \sigma_C = \begin{pmatrix} 0 & -i \\ i & 0 \end{pmatrix}.$$

Our labels A (“asymmetric-diagonal”), B (“bilateral-balanced”), and C (“circular-Coriolis”) are mnemonic alternatives to Pauli’s z , x , and y , respectively. The 2-D Hamiltonian has the $\mathbf{S} \cdot \mathbf{J}$ form of the Coriolis coupling in Eq. (34.33).

$$H = S_0\mathbf{1} + S_A J_A + S_B J_B + S_C J_C \\ = S_0 J_0 + \vec{S} \cdot \mathbf{J}, \quad (34.36)$$

where

$$J_0 = \mathbf{1}, \quad J_A = \frac{\sigma_A}{2}, \quad J_B = \frac{\sigma_B}{2}, \quad J_C = \frac{\sigma_C}{2},$$

and

$$S_0 = (A+D)/2, \quad S_A = (A-D), \quad S_B = 2B, \\ S_C = 2C.$$

The 2-D–3-D analogy is helped by using elementary oscillator ladder $a^\dagger a$ operators in Eq. (34.37),

$$\mathbf{J}_0 = N = a_1^\dagger a_1 + a_2^\dagger a_2, \quad \mathbf{J}_A = \frac{1}{2}(a_1^\dagger a_1 - a_2^\dagger a_2), \\ \mathbf{J}_B = \frac{1}{2}(a_1^\dagger a_2 + a_2^\dagger a_1), \quad \mathbf{J}_C = \frac{-i}{2}(a_1^\dagger a_2 - a_2^\dagger a_1), \quad (34.37)$$

where

$$a_1^\dagger a_1 = \begin{pmatrix} 1 & 0 \\ 0 & 0 \end{pmatrix}, \quad a_1^\dagger a_2 = \begin{pmatrix} 0 & 1 \\ 0 & 0 \end{pmatrix}, \\ a_2^\dagger a_1 = \begin{pmatrix} 0 & 0 \\ 1 & 0 \end{pmatrix}, \quad a_2^\dagger a_2 = \begin{pmatrix} 0 & 0 \\ 0 & 1 \end{pmatrix}.$$

This is a Jordan–Schwinger map of 2-D oscillation to 3-D rotation [51–53].

This easily gives Schwinger’s 3-D angular momentum raising-lowering operators $\mathbf{J}_+ = \mathbf{J}_B + i\mathbf{J}_C = a_1^\dagger a_2$ and $\mathbf{J}_- = \mathbf{J}_B - i\mathbf{J}_C = a_2^\dagger a_1$, where two dimensions 1 and 2 are spin-up ($+\hbar/2$) and spin-down ($-\hbar/2$) instead of the x - and y -polarized states envisioned by Stokes.

The angular 3-D ladder operation is replaced by a simpler 2-D oscillator operation

$$\mathbf{J}_+ |n_1 n_2\rangle = a_1^\dagger a_2 |n_1 n_2\rangle \\ = \sqrt{n_1 + 1} \sqrt{n_2} |n_1 + 1, n_2 - 1\rangle, \\ \mathbf{J}_- |n_1 n_2\rangle = a_2^\dagger a_1 |n_1 n_2\rangle \\ = \sqrt{n_1} \sqrt{n_2 + 1} |n_1 - 1, n_2 + 1\rangle. \quad (34.38)$$

2-D oscillator states are labeled by the *total* number $N = (n_1 + n_2)$ of quanta and the *net* quantum population $\Delta N = (n_1 - n_2)$. 3-D angular momentum states $|J_K^J\rangle$ are similarly labeled by the total momentum $J = N/2 = (n_1 + n_2)/2$ and z -component $K = \Delta N/2 = (n_1 - n_2)/2$, just half (or $\hbar/2$) of N and ΔN ,

$$|n_1, n_2\rangle = \frac{(a_1^\dagger)^{n_1} (a_2^\dagger)^{n_2}}{\sqrt{n_1! n_2!}} |0, 0\rangle = \\ |J_K^J\rangle = \frac{(a_1^\dagger)^{J+K} (a_2^\dagger)^{J-K}}{\sqrt{(J+K)!(J-K)!}} |0, 0\rangle, \quad (34.39)$$

where

$$n_1 = J + K, \quad n_2 = J - K.$$

From this, *Schwinger* [52] rederived the Wigner matrices $D_{MK}^J(\alpha\beta\gamma)$ appearing in Eqs. (34.5) and (34.6) and the Clebsch–Gordan $C_{qKK'}^{kJJ'}$ coefficient or Wigner–Eckart tensor relation. This helps clarify RES approximation such as Eqs. (34.10) and (34.11) that use (J, K) -cone levels on RES,

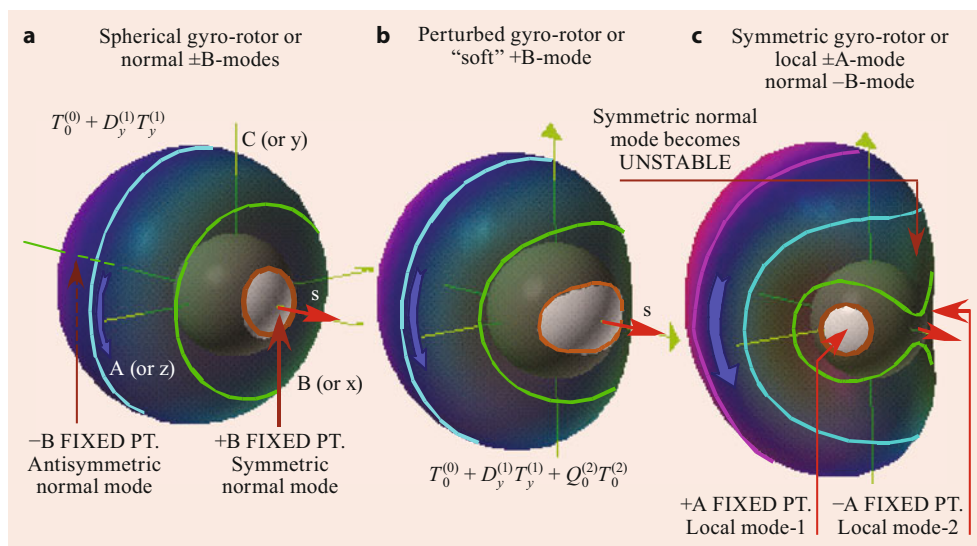
$$\left\langle \begin{matrix} J' \\ K' \end{matrix} \middle| T_q^k \middle| \begin{matrix} J \\ K \end{matrix} \right\rangle = C_{qKK'}^{kJJ'} \langle J' || k || J \rangle \\ \approx C_{0KK}^{kJJ} \langle J || k || J \rangle \approx D_{JK}^J(\Theta_K^J).$$

34.6.2 Gyro-Rotors and 2-D-Local Mode Analogy

The 2-D–3-D analogy provides insight into NMR spin [54], laser quasi spin (Rabi-rotation) [55], rovibrational dynamics [56, 57], and the local mode formation [58, 59]. It also has computational value. Part of this involves relating single 2-D-oscillator (Stokes model) to a model of two 1-D oscillators with coordinates $x_1 = x$ and $x_2 = y$.

Two identical side-by-side oscillators have bilateral or B -symmetry, and a H_B Hamiltonian commutes with both σ_B ($a + 45^\circ$ mirror reflection of axes $\pm x \rightleftharpoons \pm y$) and with $-\sigma_B$ ($a - 45^\circ$ mirror reflection of axes $\mp x \rightleftharpoons \pm y$) both of which

Fig. 34.17 A spherical gyro-rotor becomes an asymmetric gyro-rotor by adding T_0^2



interchange oscillators. This means that to first order the Hamiltonian is $H_B = 2B\sigma_B$, i.e., a gyro-rotor T_x^1 with S along the B -axis, as shown in Fig. 34.17. (Added T_0^0 affects eigenvalues but not states.)

Eigenvectors of H_B are the symmetric and antisymmetric normal modes that belong to the fixed points on the S -vector or $\pm B$ -axes of the Stokes space. If instead, the S -vector lies on the A -axis, the Hamiltonian is an asymmetric diagonal $H_A = 2A\sigma_A$ matrix. From Eq. (34.35), we can see that the operator σ_A reflects y into $-y$ but leaves x alone, so eigenvectors of H_A are localized on the x -oscillator or the y -oscillator, but not both. Such motions are local modes but are not modes of H_B , which does not commute with H_A .

Hamiltonian H_B precesses a J vector from the $+A$ -axis (local x -mode) around to the $-C$ -axis to the $-A$ (local y -mode), then to the $+C$ -axis, and then home to $+A$. The J -path is the largest equator of Fig. 34.17a. The $\pm C$ -axes are what Stokes would label circular polarization chirality, right and left, respectively. In a B -beat, $\pm C$ belong to resonant transitions where one vibrator's phase is 90° ahead and pumping up the other.

Simple mode beat transfer dynamics is disrupted by adding anharmonic T_0^2 or $T_{\pm 2}^2$ terms to existing B -symmetry terms T_x^1 and T_0^0 , as shown in Fig. 34.17b,c.

In molecular rotation theory, the T_0^2 terms along with T_0^0 make the initial unperturbed Hamiltonian in Eq. (34.3) of a symmetric top, and gyro terms T_q^1 are viewed as perturbations. For vibration theory, the latter make up a normal-mode Hamiltonian, and the former T_0^2 term is viewed as an anharmonic perturbation.

The effect of T_0^2 , seen in Fig. 34.17c, is to replace the stable fixed point $+B$ (representing the (+)-normal mode) by a saddle point as B bifurcates (splits) into a pair of fixed points that head toward the $\pm A$ -axes. So one normal mode dies and begets two stable local modes, wherein one mass

may keep its energy without losing it to the other through the usual B -beating process. (The A -modes become anharmonically detuned.)

Pairs of classical modes that each localize energy on one side of an RES in Fig. 34.17 are analogous to asymmetric top $\pm K$ -precession pairs in Fig. 34.2. However, one must consider more than the classical aspects of RES pictures. Quantum-tunneling Hamiltonians such as Eq. (34.15) give a superfine doublet for each trajectory pair with (\pm)-combination eigenstates (Table 34.1), and they occupy both paths just as each gyro-spin doublet would have J both up and down the A -axis in a quantum picture.

34.6.3 Multiple Gyro-Rotor RES and Rotational Energy Eigensurfaces (REES)

Just as quantum rotor theory allows J to occupy multiple paths, so also may J occupy multiple RES. In this way gyro-rotors differ from the analogous J precession around a lab-fixed B field or around the body-fixed S of a classical gyro. By allowing the S to be a quantum entity, the possibility arises for distribution over multiple RES [60, 61]. A simple quantum theory of S allows both $+S$ and $-S$ at once. The RES for each is plotted one on top of the other, as in Fig. 34.18a, while component RES are shown in Fig. 34.18b for $+S$ and in Fig. 34.18c for $-S$. An energy sphere is shown intersecting an RES pair for an asymmetric gyro-rotor. If the spin S is set to zero, the pair of RES collapse to a rigid asymmetric top RES shown in Fig. 34.2 having angular inversion (time-reversal $J \rightarrow -J$) and reflection symmetry. The composite RES in Fig. 34.18a has inversion symmetry but lacks reflection symmetry. Its parts in Fig. 34.18b,c have neither symmetry due to their body-fixed gyro-spins $\pm S$.

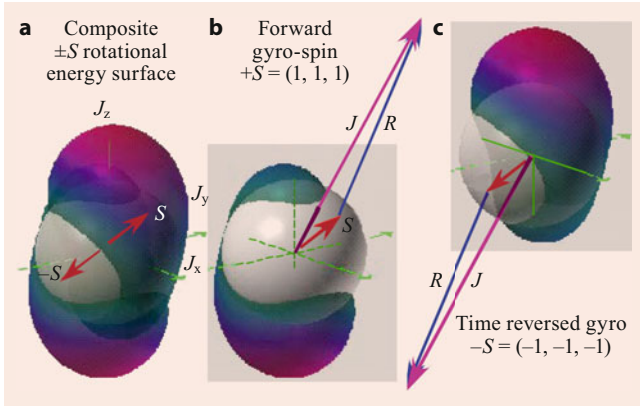


Fig. 34.18 Asymmetric gyro-rotor RES (classical body-fixed spin case); (a) composite $\pm S$; (b) forward spin $\pm S$; (c) reversed spin $-S$

Gyro-rotor Hamiltonians in Eq. (34.40) allow tunneling or mixing of multiple RES. A two-state spin- $1/2$ gyro-spin model has a 2-by-2 Hamiltonian matrix and two-base RES.

$$H_{\text{gyro}} = M_0 \mathbf{J} \cdot \mathbf{J} + D_x S_x J_x + D_y S_y J_y + D_z S_z J_z + Q_{xx} J_x^2 + Q_{yy} J_y^2 + Q_{zz} J_z^2, \quad (34.40)$$

As in Eq. (34.7), \mathbf{J} is approximated by classical vector components in the body frame.

$$J_x = |J| \sin \beta \cos \gamma, \quad J_y = |J| \sin \beta \sin \gamma, \quad J_z = |J| \cos \beta. \quad (34.41a)$$

However, the gyro-spin S uses its quantum representation $S = |S|\sigma/2 = \sqrt{3}\sigma/2$ from Eq. (34.34)

$$\begin{aligned} \langle H_{\text{gyro}} \rangle &= M_0 J^2 + Q_{xx} J_x^2 + Q_{yy} J_y^2 + Q_{zz} J_z^2 \\ &\quad + D_x |S| \|\sigma_x J_x + D_y |S| \|\sigma_y J_y + D_z |S| \|\sigma_z J_z \\ &= \begin{pmatrix} h(J) + D_z |S| \|J_z & |S| \|(D_x J_x - iD_y J_y) \\ |S| \|(D_x J_x + iD_y J_y) & h(J) - D_z |S| \|J_z \end{pmatrix} \\ &= \begin{pmatrix} h(J) + d_z \cos \beta & (d_x \cos \gamma - id_y \sin \gamma) \\ & \times \sin \beta \\ (d_x \cos \gamma + id_y \sin \gamma) & h(J) - d_z \cos \beta \\ & \times \sin \beta \end{pmatrix}, \end{aligned} \quad (34.41b)$$

where

$$h(J) = M_0 J^2 + Q_{xx} J_x^2 + Q_{yy} J_y^2 + Q_{zz} J_z^2,$$

and

$$d_\mu = D_\mu |S| |J|. \quad (34.41c)$$

The semiclassical H_{gyro} makes spin expectation in $\langle S \rangle$ to precess around an angular velocity crank vector Ω with the

following \mathbf{J} -dependent body frame components

$$\Omega_x = d_x \sin \beta \cos \gamma, \quad \Omega_y = d_y \sin \beta \sin \gamma, \quad \Omega_z = d_z \cos \beta. \quad (34.41d)$$

The quantum REES shown in Fig. 34.19 results from substituting quantum spin $S = \frac{1}{2}\sigma$ matrices $\frac{1}{2}\sigma_x$, $\frac{1}{2}\sigma_y$, or $\frac{1}{2}\sigma_z$ for each algebraic Hamiltonian factor S_x , S_y , S_z of Eq. (34.40) to make a matrix Hamiltonian in Eq. (34.41a)–(34.41d) that is then diagonalized. The resulting pair of eigenvalues are plotted to make a pair of REES functions of polar body frame angles β and γ . In comparing the classical composite RES in Fig. 34.18a or Fig. 34.20 with the quantum REES in Fig. 34.19 one may note that they have similar shapes in regions where classical $\pm J$ -surfaces of Fig. 34.20 are well

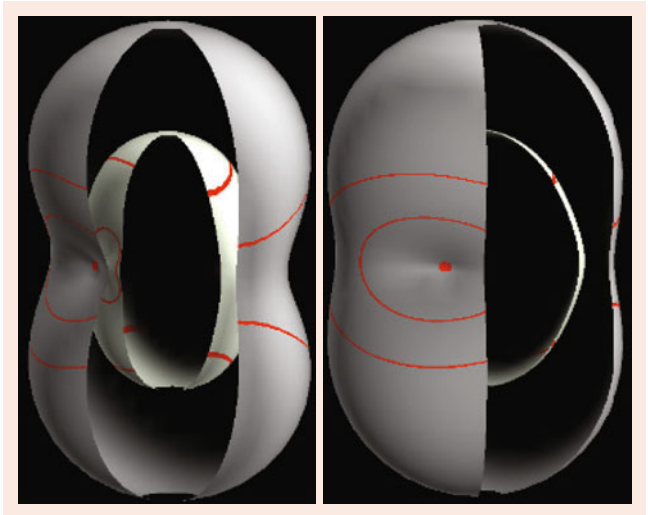


Fig. 34.19 Quantum gyro-rotor REES views based on eigenvalues of Eqs. (34.41a)–(34.41d) with $S = \sigma/2$

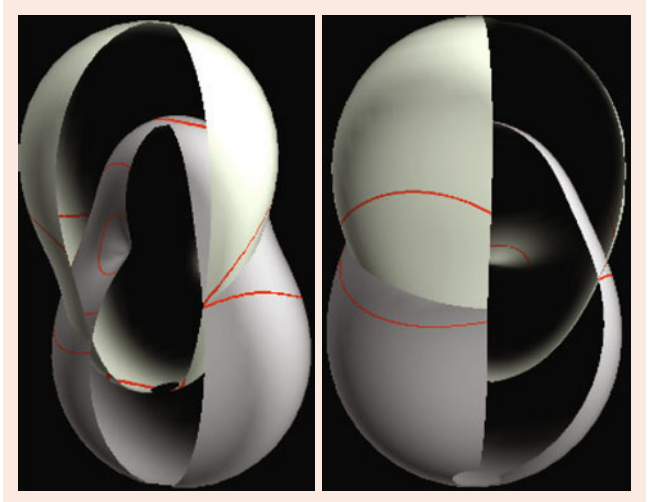


Fig. 34.20 Classical gyro-rotor c-RES views of Fig. 34.18a based on Eq. (34.40)

separated. Wherever the classical RES cross the quantum REES differ most differently due to their intersurface resonance.

Each REES resembles a wrapped symmetric top RES that is most perturbed at points where the two classical RES cross the RES pair intersection along the horizontal x -axis (in figure plane) becomes an REES avoided crossing. The RES pair intersection along the y -axis (out of figure plane) becomes an REES *diabolical* point so-named after a toy top called a diabolo. A current term for such a dual-cone singularity is *Dirac point*.

Near-crossing RES are the rotational equivalent of near-crossing vibrational-potential (VES) employed in treatments of Jahn–Teller effects [62, 63]. The classical, semiclassical, and quantum theory for such loosely bound or fluxional systems is a rapidly growing subfield of atomic, molecular, and optical physics.

34.6.4 Multi-Quantum CF_4 Rovibrational Polyads and REES Visualization

Molecular quantum data comes first in the form of spectral line frequencies that are correlated with theory derived from Hamiltonian energy operator eigenvalues or differences thereof. Second comes a much larger dataset that includes spectral transition rates and intensities that are correlated with eigenvector matrices or density operators. As more AMOP phenomena become available researchers are trying to understand this deluge of data and find ways to visualize it. Section 34.4 provides a theory for level clustering of octahedral and tetrahedral molecules and shows a way to visualize underlying eigenstates using rotational energy surfaces (RES).

A possibility for visualizing ever more complex spectral phenomena involves rovibronic energy eigenvalue surfaces (REES) introduced in Sect. 34.6.3. An example involves the $\text{CF}_4\nu_3/2\nu_4$ rovibrational polyad. It begins with a plot versus the total angular momentum $J = 0$ –70 in Fig. 34.21 of level cluster bands found in this polyad as calculated by Boudon et al. [64, 65].

The plot uses squares (\square) as boundary points containing C_4 -level clusters such as are shown in Fig. 34.4 (right) and C_4 in Fig. 34.6c. Triangular points (\triangle) mark bands of C_3 -clusters shown in Fig. 34.4 (left) and C_3 -correlated in Fig. 34.6a.

Figure 34.21 also has C_2 -cluster regions marked by diamond (\diamond) points where C_2 -correlated species in Fig. 34.6 (centre) might appear. These are rare in O_h or T_d as the RES have saddle points at the C_2 -axes as in Fig. 34.4 so they are unstable. The asymmetric rotor in Fig. 34.2 is a prime example of an RES with unstable $C_2 \pm y$ -saddle points.

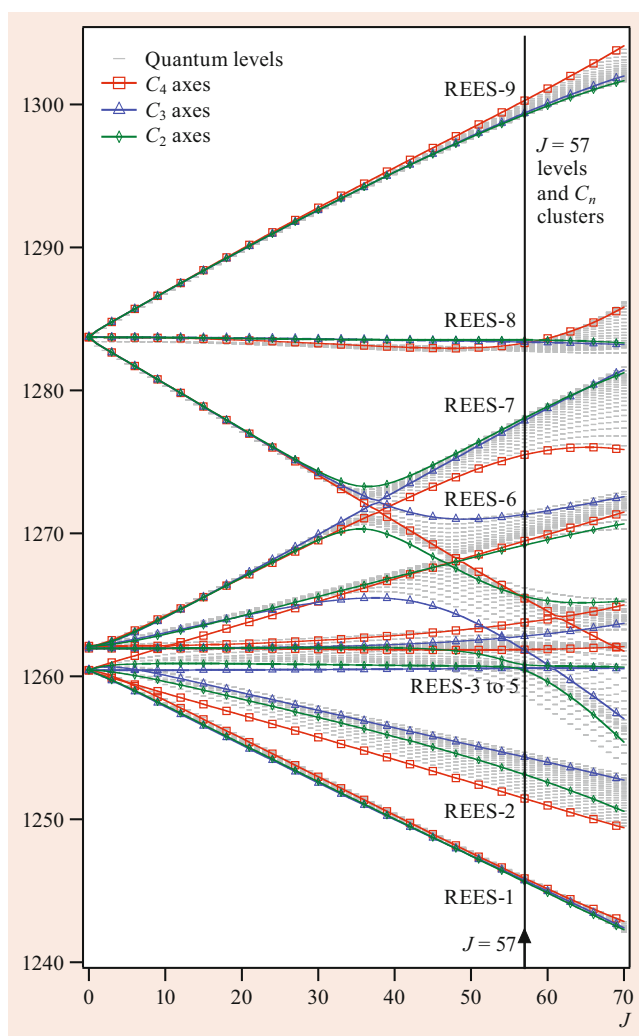


Fig. 34.21 CF_4 Molecular rovibrational level clusters for $\nu_3/2\nu_4$ polyad $J = 0$ to $J = 70$. Adapted from Boudon [64]. Energy units are 1 kayser (1 cm^{-1})

However, overtone and combination resonances give rise to the larger clusters that have lower local symmetry of C_2 and C_1 (no symmetry). The $\nu_3/2\nu_4$ REES for ($J = 57$)-states has five of its nine shells showing in Fig. 34.22 [66].

The innermost and lowest REES shell is nearly spherical at the scale of Fig. 34.22 and corresponds to the lowest cluster levels in Fig. 34.21 that come up if expanded, and would reveal usual ordering C_3 -below- C_4 separated by C_2 saddle as in Fig. 34.4. The shell above that has a cubic (as opposed to octahedral) shape with inverted ordering C_4 -below- C_3 clearly shown by levels in the next-to-lowest $J = 57$ cluster bunch in Fig. 34.21.

The three highest REES shells shown in Fig. 34.22 involve a level-cluster mashup in the middle of Fig. 34.21. A pair of shells form diabolical points on C_2 -axes and avoided-crossing pairs of orbits on both C_3 - and C_4 -axes. Above that

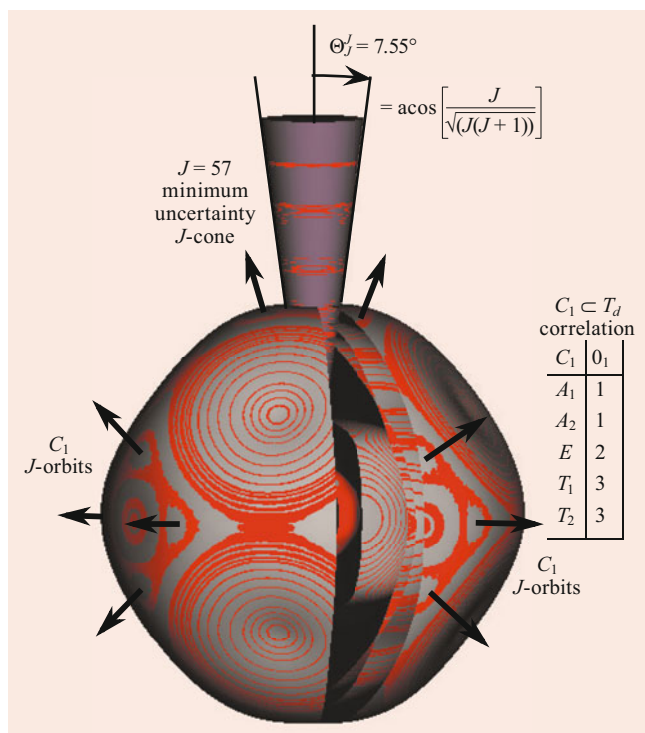


Fig. 34.22 CF_4 Molecular ($J = 57$) REES-1-to-5 for $\nu_3/2\nu_4$ polyad levels plotted in Fig. 34.21 (adapted from [66])

is an extraordinary REES shell with 24 C_1 orbits indicated by arrows emerging from their groups. This fifth shell also supports many C_3 orbits, a few C_4 orbits, and a bizarre saddle shape on the C_2 -axes.

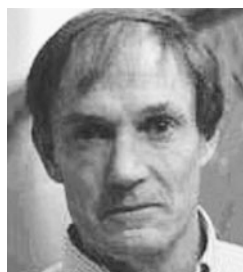
The 24-cluster of C_1 orbits belongs to species correlation $O_1 \uparrow O = A_1 \oplus A_2 \oplus E \oplus T_1 \oplus T_2$ of a regular representation of the isomorphic groups $S_4 \approx T_d \approx O$ that now uses the identity subgroup $C_1 = \{1\}$. The relevant C_1 , C_2 , C_3 , and C_4 correlation tables are matched to corresponding cluster orbits in Fig. 34.22, while each of the 24 C_1 orbits lack rotational symmetry, they each do maintain a local reflection symmetry $C_v = \{1, \sigma_v\}$. At much higher J one should expect to find O_h clusters of 48 species levels, indeed, a majority of them in analogy to the majority of regular S_{60} spin states of unit S_1 symmetry in the correlation table of Fig. 34.13.

References

- Herzberg, G.: Spectra of Diatomic Molecules. Molecular Spectra and Structure, vol. I. Van-Norstrand-Reinhold, New York (1950)
- Herzberg, G.: Infrared and Raman Spectra of Polyatomic Molecules. Molecular Spectra and Structure, vol. II. Van-Norstrand-Reinhold, New York (1945)
- Herzberg, G.: Electronic Structure of Polyatomic Molecules. Molecular Spectra and Structure, vol. III. Van-Norstrand-Reinhold, New York (1966)

- Wilson, F.B., Decius, V.C., Cross, P.C.: Molecular Vibrations. McGraw-Hill, New York (1955)
- Papoušek, D., Aliev, M.R.: Molecular Vibrational-Rotational Spectra, Studies Phys. Theor. Chem. 17. Elsevier, Amsterdam (1982)
- Zare, R.N.: Angular Momentum: Understanding Spatial Aspects in Chemistry and Physics. Wiley, New York (1988)
- Harter, W.G.: Principles of Symmetry, Dynamics, and Spectroscopy. Wiley, New York (1993)
- Harter, W.G., Patterson, C.W.: J. Math. Phys. **20**, 1453 (1979)
- Harter, W.G.: Phys. Rev. A **24**, 192 (1981)
- Harter, W.G., Patterson, C.W.: J. Chem. Phys. **80**, 4241 (1984)
- Harter, W.G.: Comp. Phys. Rep. **8**, 319 (1988)
- Sadovskii, D.A., Zhilinskii, B.I.: Mol. Phys. **65**, 109 (1988)
- Sadovskii, D.A., Zhilinskii, B.I.: Phys. Rev. A **47**, 2653 (1993)
- Pavlichenkov, I.M.: Phys. Rep. **226**, 173 (1993)
- Harter, W.G., Patterson, C.W., daPaixao, F.J.: Rev. Mod. Phys. **50**, 37 (1978)
- Harter, W.G., Patterson, C.W.: Phys. Rev. A **19**, 2277 (1979)
- Bunker, P.R.: Molecular Symmetry and Spectroscopy. Academic Press, New York (1979)
- Stein, A., Rabinowitz, P., Kalder, A.: Exxon Labs (1977)
- McDowell, R.S., Galbraith, H.W., Reisfield, M.J., Aldridge, J.P.: Los Alamos T-12. In: Hall, J., Carlsten, J. (eds.) Laser Spectroscopy, vol. III, p. 102. Springer, Berlin (1977)
- Hecht, K.T.: J. Mol. Spectrosc. **5**, 355 (1960)
- Lea, K.R., Leask, M.J.M., Wolf, W.P.: J. Phys. Chem. Solids **23**, 1381 (1962)
- Dorney, A.J., Watson, J.K.G.: J. Mol. Spectrosc. **42**, 1 (1972)
- Fox, K., Galbraith, H.W., Krohn, B.J., Louck, J.D.: Phys. Rev. A **15**, 1363 (1977)
- Harter, W.G., Patterson, C.W.: J. Chem. Phys. **66**, 4872 (1977)
- Monostari, B., Weber, A.: J. Chem. Phys. **33**, 1867 (1960)
- Pfister, O.: Etude experimentale et theorique des interactions hyperfines dans la bande de vibration ν_3 de la molecule $^{28}SiF_4$. Univ. Paris-Nord, Paris (1993). Dissertation,
- Borde, J., Borde, C., Salomon, C., Van Lerberghe, A., Ouhayoun, M., Cantrell, C.: In: Walther, H., Rothe, K. (eds.) Laser Spectroscopy, vol. IV, p. 142. Springer, Berlin (1979)
- Borde, J., Borde, C.: J. Mol. Spectrosc. **78**, 353 (1979)
- Butcher, R.J., Chardonnet, C., Borde, C.: Phys. Rev. Lett. **70**, 2698 (1993)
- Borde, C., Ouhayoun, M., VanLerberghe, A., Salomon, C., Avriplier, S., Cantrell, C., Borde, J.: Phys. Rev. Lett. **45**, 14 (1980)
- Kim, K., Person, W., Seitz, D., Krohn, B.: J. Mol. Spectrosc. **76**, 322 (1979)
- Harter, W.G.: Phys. Rev. A **24**, 192 (1981)
- Borde, J., Borde, C.: Chem. Phys. **71**, 417 (1982)
- Kroto, H.W., Heath, J.R., O'Brian, S.C., Curl, R.F., Smalley, R.E.: Nature **318**, 162 (1985)
- Kratschmer, W., Lamb, W.D., Fostiropoulos, K., Huffman, D.R.: Nature **347**, 354 (1990)
- Harter, W.G., Weeks, D.E.: Chem. Phys. Lett. **132**, 387 (1986)
- Weeks, D.E., Harter, W.G.: Chem. Phys. Lett. **144**, 366 (1988)
- Harter, W.G., Weeks, D.E.: J. Chem. Phys. **90**, 4744 (1989)
- Weeks, D.E., Harter, W.G.: Chem. Phys. Lett. **176**, 209 (1991)
- Harter, W.G., Reimer, T.C.: J. Chem. Phys. **94**, 5426 (1991)
- Reimer, T.C., Harter, W.G.: J. Chem. Phys. **106**, 1326 (1997)
- Harter, W.G., Reimer, T.C.: Chem. Phys. Lett. **194**, 230 (1992)
- Harter, W.G., Reimer, T.C.: Chem. Phys. Lett. **198**, 429 (1992). erratum
- Changala, P.B., Weichman, M.L., Lee, K.F., Fermann, M.E., Ye, J.: Science **363**, 49–54 (2019)
- Spaun, B., Changala, P., Patterson, D., Bjork, B., Heckl, O., Doyle, J., Ye, J.: Nature **533**, 517 (2016)

46. Bjork, B., Bui, T., Heckl, O., Changala, P., Spaum, B., Heu, P., Follman, D., Deutsch, C., Cole, G., Aspemeyer, M., Okumura, M., Ye, J.: *Science* **354**, 444 (2016)
47. Stokes, G.: *Proc. R. Soc. Lond.* **11**, 547 (1862)
48. Hamilton, W.R.: *Proc. R. Ir. Acad.* **II**, 424 (1844)
49. Hamilton, W.R.: *Philos. Mag.* **25**, 489 (1844)
50. Pauli, W.: *Z. Phys.* **37**, 601 (1927)
51. Jordan, P.: *Z. Phys.* **94**, 531 (1935)
52. Schwinger, J.: In: Biedenharn, L.C., van Dam, H. (eds.) *Quantum Theory of Angular Momentum*, p. 229. Academic Press, New York (1965)
53. Biedenharn, L.C., Louck, J.D.: *Angular Momentum in Quantum Physics*. In: Rota, G.C. (ed.) *Encyclopedia of Mathematics*, vol. 8, p. 212. Addison Wesley, Reading (1981)
54. Rabi, I.I., Ramsey, N.F., Schwinger, J.: *Rev. Mod. Phys.* **26**, 167 (1954)
55. Feynman, R.P., Vernon, F.I., Helwarth, R.W.: *J. Appl. Phys.* **28**, 49 (1957)
56. Harter, W.G., dos Santos, N.: *Am. J. Phys.* **46**, 251 (1978)
57. Lehmann, K.K.: *J. Chem. Phys.* **79**, 1098 (1983)
58. Harter, W.G.: *J. Chem. Phys.* **85**, 5560 (1986)
59. Li, Z., Xiao, L., Kellman, M.E.: *J. Chem. Phys.* **92**, 2251 (1990)
60. Harter, W.G.: *Phys. Rep.* **8**(319), 378–385 (1988)
61. Ortigoso, J., Kleiner, I., Hougen, J.T.: *J. Chem. Phys.* **110**, 11688 (1999)
62. Jahn, H.A., Teller, E.: *Proc. R. Soc. Lond.* **A161**, 220 (1937)
63. Jahn, H.A., Teller, E.: *Proc. R. Soc. Lond.* **A164**, 117 (1938)
64. Boudon, V., Mitchell, J., Domanskaya, A., Maul, C., Georges, R., Benidar, A., Harter, W.G.: *Mol. Phys.* **58**, 391–400 (2012)
65. Carlos, M., Gruson, O., Richard, C., Boudon, V., Rotger, M., Thomas, X., Maul, C., Sydow, C., Domanskaya, A., Georges, R., Soulard, P., Piralí, O., Goubet, M., Asselin, P., Huet, T.R.: *J. Quant. Spectrosc. Radiat. Transf.* **201**, 2273 (2017)
66. Harter, W.G., Mitchell, J.C.: *Int. J. Mol. Phys.* **14**, 796 (2013)



William G. Harter Professor Harter's research centers on the theory of spectroscopy and what it reveals about quantum phenomena and symmetry principles of structure and dynamics. Current study focuses on how wave mechanics of light relates to matter waves and their relativistic symmetry ranging from intrinsic frames of floppy molecules to manifold dynamics of astrophysical objects. A strong educational effort is being developed to make modern theory more accessible.



Radiative Transition Probabilities

35

David L. Huestis

Contents

35.1	Overview	537
35.1.1	Intensity Versus Line-Position Spectroscopy	537
35.2	Molecular Wave Functions in the Rotating Frame	538
35.2.1	Symmetries of the Exact Wave Function	538
35.2.2	Rotation Matrices	539
35.2.3	Transformation of Ordinary Objects into the Rotating Frame	539
35.3	The Energy–Intensity Model	539
35.3.1	States, Levels, and Components	539
35.3.2	The Basis Set and Matrix Hamiltonian	540
35.3.3	Fitting Experimental Energies	541
35.3.4	The Transition Moment Matrix	541
35.3.5	Fitting Experimental Intensities	542
35.4	Selection Rules	542
35.4.1	Symmetry Types	542
35.4.2	Rotational Branches and Parity	542
35.4.3	Nuclear Spin, Spatial Symmetry, and Statistics	543
35.4.4	Electron Orbital and Spin Angular Momenta	544
35.5	Absorption Cross Sections and Radiative Lifetimes	545
35.5.1	Radiation Relations	545
35.5.2	Transition Moments	545
35.6	Vibrational Band Strengths	546
35.6.1	Franck–Condon Factors	546
35.6.2	Vibrational Transitions	547
35.7	Rotational Branch Strengths	547
35.7.1	Branch Structure and Transition Type	547
35.7.2	Hönl–London Factors	548
35.7.3	Sum Rules	548
35.7.4	Hund’s Cases	549
35.7.5	Symmetric Tops	550
35.7.6	Asymmetric Tops	550
35.8	Forbidden Transitions	551
35.8.1	Spin-Changing Transitions	551
35.8.2	Orbitally-Forbidden Transitions	551
35.9	Recent Developments	552
	References	552

Abstract

This chapter summarizes the theory of radiative transition probabilities or intensities for rotationally-resolved (high-resolution) molecular spectra. A combined treatment of diatomic, linear, symmetric-top, and asymmetric-top molecules is based on angular momentum relations. Generality and symmetry relations are emphasized. The *energy-intensity* model is founded in a rotating-frame basis-set expansion of the wave functions, Hamiltonians, and transition operators. The intensities of the various rotational branches are calculated from a small number of transition-moment matrix elements, whose relative values can be assumed from the supposed nature of the transition, or inferred by fitting experimental intensities.

Keywords

wave function · angular momentum · diatomic molecule · transition moment · transition matrix element

35.1 Overview

35.1.1 Intensity Versus Line-Position Spectroscopy

The fact that atoms and molecules absorb and emit radiation with propensities that vary with wavelength is the origin of the field called spectroscopy. The relatively sharp intensity maxima are interpreted as corresponding to transitions between discrete states or energy levels. The frequencies or energies of these transitions are used as the primary source of information about the internal structure of the atom or molecule. Line positions can be measured with very high precision (1 ppm or better). Excellent calibration standards have been developed. The quality of these experimental data has attracted extensive analytical and theoretical effort.

D. L. Huestis (✉)
Molecular Physics Laboratory, SRI International
Menlo Park, CA, USA

Sophisticated parametrized models have been developed in which the smallest shifts from the expected line positions can be used to identify perturbations or other subtle effects.

For molecules, knowledge of the strengths of these transitions is far less well developed. One reason is that quantitative experimental data on rotationally-resolved absorption cross sections and emission intensities are much rarer and the experiments themselves are much more difficult to calibrate. Few measurements claim a precision better than 1% and agreement within 10% of measurements in different laboratories is typically viewed as good. This situation is undesirable because most applications of molecular spectroscopy are in fact measurements of intensity. In many cases the strengths of absorptions or emissions are used to infer gas composition, temperature, time evolution, or other environmental conditions. In other examples the actual absorption and emission is the primary interest. Among the most important of these are atmospheric absorption of solar radiation and the greenhouse effect.

35.2 Molecular Wave Functions in the Rotating Frame

35.2.1 Symmetries of the Exact Wave Function

The exact total wave function for any isolated molecule with well-defined energy and total angular momentum can be expressed in a basis-set expansion over configurations with well-defined internal quantum numbers,

$$\Phi_{\text{exact}} = \Phi_{\text{trans}} \sum_{\alpha\beta\gamma\delta\epsilon} C_{\alpha\beta\gamma\delta\epsilon} \Phi_{\text{rot}}^{\alpha} \Phi_{\text{vib}}^{\beta} \Phi_{\text{elec}}^{\gamma} \Phi_{\text{espin}}^{\delta} \Phi_{\text{nsin}}^{\epsilon} \quad (35.1)$$

In principle, the coefficients $C_{\alpha\beta\gamma\delta\epsilon}$ can be found only by diagonalizing the exact Hamiltonian. In practice one attempts to find a sufficiently good approximation, containing only a few terms, with coefficients chosen by diagonalizing an approximate or model Hamiltonian. This is the basis of the energy–intensity model developed in Sect. 35.3. As discussed by *Longuet-Higgins* [1] and *Bunker* [2], there are only six true symmetries of the exact Hamiltonian of an isolated molecule:

1. translation of the center of mass;
2. permutation of electrons;
3. permutation of identical nuclei;
4. time reversal or momentum reversal;
5. inversion of all particles through the center of mass;
6. rotation about space-fixed axes.

Of these, only the symmetries numbered 5 and 6 give quantum numbers (parity and the total angular momentum F) that are both rigorous and useful spectroscopic labels of the states of the molecule. The other symmetries are convenient for simplifying the description of the molecular wave function, for the evaluation of relations between matrix elements, and for classification of molecular states according to approximate symmetries.

The first symmetry, translation of the center of mass, allows the choice of a coordinate system referenced to the center of mass, and suppression of the portion of the wave function describing motion through space (as long as the molecule does not dissociate).

Symmetry number 2, exchange of electrons, does not directly provide any labels or quantum numbers, since the Fermi–Dirac statistics of electrons require that all wave functions must be antisymmetric. However, it provides considerable information about the probable electronic states since it controls whether molecular orbitals can be doubly or only singly occupied. For most (low- Z) molecules, each state will have a nearly well-defined value of electron spin: singlet or triplet for example. Admixture of other spin values usually can be treated as a perturbation. These points will be elaborated in Sects. 35.4.4 and 35.7.4.

Permutation of identical nuclei, symmetry number 3, also gives an identical quantum number to all the states of the molecule (± 1 depending on the character of the permutation and on whether nuclei with integral or half-integral spin are being permuted). It supplies little direct information about the energy separations between the states of the molecule. On the other hand, many molecules have identical nuclei in geometrically or dynamically equivalent positions. The existence of spatial symmetry, for nonplanar molecules, is really the same thing as permutational symmetry. Consequently, nuclear permutation, combined with inversion (symmetry number 5), is the basis for naming the states according to the approximate spatial symmetry group of the molecular frame and vibrational motion. These concepts will be explored in Sect. 35.4.3.

Symmetry number 4, time reversal, is both subtle and simple. In the absence of external magnetic fields the Hamiltonian for a molecule will contain only even combinations of angular momentum operators, e.g., $F_{\alpha}F_{\beta}$, $F_{\alpha}L_{\beta}$, or $F_{\alpha}S_{\beta}$. Thus changing the signs of all the angular momenta should result in an equivalent wave function. This will require that matrix elements retain the same absolute value when the angular quantum numbers are reversed, leading in general to complex conjugation [3].

Spatial inversion, symmetry number 5, is always an allowed operation for any molecule, even if it appears to lack internal inversion symmetry. This operation can be considered as a symmetry of the spherically-symmetric laboratory

in which the molecule resides. If the molecule is linear, triatomic, rigid with a plane of symmetry, or is nonrigid with accessible vibrational or tunneling modes that correspond to plane reflections, inversion symmetry divides the states of the molecule into two classes, called parities. Perturbations can occur only between states of the same parity. For optical transitions, the change in parity of the states must match the parity of the operator. Otherwise, reflection of the molecule in a plane will interchange inconvertible optical isomers. Such optical isomers are energetically degenerate, so in all cases, inversion through the center of mass remains a valid symmetry of the rotating molecule. However, the separation of the states into two kinds does not provide any selection rules. The two parity classes are perfectly degenerate, thus there is always an allowed level with the correct parity either for perturbations or for optical transitions.

35.2.2 Rotation Matrices

The final symmetry, rotation about the center of mass, restricts the discussion to states with well-defined laboratory angular momentum, and to re-expression of the exact wave function by changing variables from *laboratory* coordinates to *body-fixed* or internal coordinates, and introducing the Euler angles relating these two coordinate systems,

$$\Phi_{\text{exact}}^{F,M_F}(\text{lab}) = \sum_{K_F} \Phi_{\text{rot}}^{F,M_F K_F}(\text{Euler angles}) \times \Phi_{\text{vesn}}^{(F,K_F)}(\text{internal, spins}). \quad (35.2)$$

Here F is the total angular momentum of the molecule, including vibrational, mechanical-rotation, electron-orbital, electron-spin, and nuclear-spin contributions. M_F and K_F are the projections of F in the laboratory and body-fixed frames, respectively. In the majority of cases, the magnitude of nuclear hyperfine interactions is sufficiently small that its influence can be ignored when analyzing wave functions and computing energies. Thus the quantum numbers J , M_J , and K_J , or just J , M , and K can be used.

Explanation is postponed of how the body-fixed frame is to be selected, but for any choice, the wave function for rotation of the entire molecule can be expressed using a rotation matrix [4, 5]

$$\Phi_{\text{rot}}^{F,M_F K_F}(\text{Euler angles}) = \left(\frac{(2F+1)}{8\pi^2} \right)^{1/2} D_{M_F K_F}^{*F}(\phi, \theta, \chi). \quad (35.3)$$

For diatomics, Zare [5] suggests multiplying by $(2\pi)^{1/2}$ and setting $\chi = 0$. The internal wave function for the vibrational, electronic, electron-spin, and nuclear-spin degrees of free-

dom (thus the label (vesn)) can be thought of as the partial summation

$$\Phi_{\text{vesn}}^{(F,K_F)}(\text{internal, spins}) = \sum_{\beta\gamma\delta\epsilon} C_{(FK_F)\beta\gamma\delta\epsilon} \Phi_{\text{vib}}^\beta \Phi_{\text{elec}}^\gamma \Phi_{\text{espin}}^\delta \Phi_{\text{nsin}}^\epsilon, \quad (35.4)$$

expressed in the internal or rotated coordinate system. Note that the FK_F designation is only a parametric label. The rotational wave function has been absorbed into the rotation matrix.

35.2.3 Transformation of Ordinary Objects into the Rotating Frame

The assumption of rotational symmetry allows re-expression of matrix elements between total wave functions as a sum of matrix elements between internal wave functions. For example, the tensor operator $T^{(L)}$ belonging to the L representation of the rotation group, can be written in the rotating frame as [5–8]

$$T_p^{(L)}(\text{lab}) = \sum_q D_{pq}^{*L}(\phi\theta\chi) T_q^{(L)}(\text{body}), \quad (35.5)$$

and can be used to evaluate matrix elements that might represent radiative transitions

$$\begin{aligned} & \langle \psi^{F',M_F'+p} | T_p^{(L)}(\text{lab}) | \Phi^{F'',M_F''} \rangle \\ &= \left(\frac{(2F''+1)}{(2F'+1)} \right)^{1/2} \langle F''M_F'', Lp | F'M_F''+p \rangle \\ & \times \sum_{qK_F''} \langle F''K_F'', Lq | F'K_F''+q \rangle \\ & \times \langle \psi_{\text{vesn}}^{(F',K_F'+q)} | T_q^{(L)}(\text{body}) | \Phi_{\text{vesn}}^{(F'',K_F'')} \rangle, \end{aligned} \quad (35.6)$$

where $\langle F''M_F'', Lp | F'M_F''+p \rangle$ and $\langle F''K_F'', Lq | F'K_F''+q \rangle$ are Clebsch–Gordan coefficients that vanish if $|F'-F''| > L$, $|M_F''+p| > F'$, or $|K_F''+q| > F'$.

This transformation forms the basis for the derivation of rotational branch strengths (Sect. 35.7.2) and for the description of electron motions that are weakly coupled to the molecular frame (Sect. 35.7.4).

35.3 The Energy–Intensity Model

35.3.1 States, Levels, and Components

The previous section introduced the concept of representing the wave function of a molecule as a product of five simpler wave functions:

$$\psi \approx \psi_{\text{elec}} \psi_{\text{vib}} \psi_{\text{rot}} \psi_{\text{espin}} \psi_{\text{nsin}}. \quad (35.7)$$

This construction yields a similar separation of the Hamiltonian,

$$H \approx H_{\text{elec}} + H_{\text{vib}} + H_{\text{rot-fs}} + H_{\text{hf}}, \quad (35.8)$$

and representations of the energies as sums of contributions,

$$E \approx T_e + G_v + F_c(J), \quad (35.9)$$

and absorption or emission transition strengths as products,

$$I \approx I_{\text{elec}} I_{\text{vib}} I_{\text{rot-fs}} I_{\text{hf}}. \quad (35.10)$$

Whatever theoretical arguments might favor such a separation, the real impetus is the empirical observation that most molecular absorption and emission spectra exhibit recognizable patterns arising from the dissimilar magnitudes of the energies associated with these five degrees of freedom. Separation of the wave function and the Hamiltonian into these four or five contributions facilitates the assignment of molecular spectra, in addition to suggesting models with parameters that can be adjusted to quantitatively represent the observed spectra.

Most states of molecules are dominated by a single set of electronic and vibrational quantum numbers. Electronic states are often well separated. With each electronic state is associated a potential energy surface, the energy at the minimum being labeled T_e . Motion of nuclei within this potential generates various levels corresponding to different vibrational quantum numbers, following regular patterns or progressions in energy, summarized by a small number of parameters called vibrational frequencies. The quantity G_v represents the energy of the vibrational level above the potential minimum. For each vibrational level, a progression of rotational levels is expected. For linear molecules in electronic states without electronic angular momentum (i.e., $^1\Sigma$ states) the rotational energies are also reproduced by a few rotational constants.

For more complicated molecules and electronic states, i.e., most cases, there are multiple energetically distinct levels with the same value of J (in addition to the $2J + 1$ orientational degeneracy of each level). These multiple levels all share the same nominal quantum numbers (additional analysis may subdivide them into parity or permutational symmetry types). These sublevels are called *components* with energies expressed by the notation $F_c(J)$. The quantity N_c , the number of components expected, reflects the assignment of the nature of the vibronic state. For linear molecules there is a limited number of components corresponding to the various orientations of electron spin and orbital angular momentum. For example, a $^2\Pi$ electronic state will have four components for each value of J (except for $J = 1/2$, where there are only two components). For nonlinear molecules the number of components increases with J , proportional to $2J + 1$, corresponding to various possible projections of the total angular momentum onto the tumbling molecular frame.

The conclusion of this analysis is that a basis set be chosen, over which a model rotational and fine-structure Hamiltonian can be expressed. The wave functions then become vectors of numbers. A priori, only the form of the matrix elements and their dependence on J and body-frame projection (K or Ω) are known. Little is known in advance about how strong the interactions are in any given molecule. Thus one tends to write the Hamiltonian with parameters that are to be determined by fitting the observed energy levels.

Similarly, the choice of the basis sets for the upper and lower states specifies the overall form of the matrix of transition moments between the basis functions. The transition can be chosen to be of a simple standard form, for example, parallel or perpendicular, with only one unknown parameter representing the overall strength of the transition. Alternatively, the transition matrix elements can be considered to be independently adjustable, within the symmetry restrictions that are required (time reversal) or assumed (spatial symmetry).

35.3.2 The Basis Set and Matrix Hamiltonian

For linear molecules it is convenient to choose a basis set labeled by the projections of orbital and spin angular momenta in the body-frame coordinate system, represented symbolically by

$$|\Lambda\Sigma; JM\Omega\rangle = \left(\frac{(2J+1)}{8\pi^2}\right)^{1/2} D_{M\Omega}^{*J} |\Lambda\Sigma\rangle, \quad (35.11)$$

where $\Omega = \Lambda + \Sigma$. This is called the Hund's case (a) basis set, which is an accurate representation in a single term if the body-frame angular momenta are nearly conserved. This is true if the spin-orbit interaction is larger than the separation between rotational levels. Under all circumstances, this basis set facilitates construction of the matrix Hamiltonian and representation of sources of transition probability [9].

One parametrization for the spin-rotation Hamiltonian is provided by *Brown et al.* [10–12]:

$$\begin{aligned} H_{\text{spin-rot}} = & T_e + G_v + B_v N^2 - D_v N^4 \\ & + \frac{1}{2} [A_v + A_{D_v} N^2, L_z S_z]_+ \\ & + (\gamma_v + \gamma_{D_v} N^2) N \cdot S \\ & + \frac{1}{3} [\lambda_v + \lambda_{D_v} N^2, 3S_z^2 - S^2]_+ \\ & + \eta_v L_z S_z \left[S_z^2 - \frac{1}{5} (3S^2 - 1) \right] \\ & - \frac{1}{4} [o_v + o_{D_v} N^2, \Lambda_+^2 S_-^2 + \Lambda_-^2 S_+^2]_+ \\ & + \frac{1}{4} [p_v + p_{D_v} N^2, \Lambda_+^2 S_- N_- + \Lambda_-^2 S_+ N_+]_+ \\ & + \frac{1}{4} [q_v + q_{D_v} N^2, \Lambda_+^2 N_-^2 + \Lambda_-^2 N_+^2]_+, \end{aligned} \quad (35.12)$$

where $[x, y]_+$ is the anticommutator ($xy + yx$), and $N = J - S$. Zare et al. [13] provide an alternative parametrization, with different interpretations of the *spectroscopic constants* (B, D, A, γ, λ , etc.) because they multiply different symbolic operators. One significant difference is that Zare et al. use the *mechanical angular momentum* $R = J - L - S$ as the expansion operator, rather than N , which might be called the *spinless angular momentum*. These differences mean that care must be taken in attempting to construct simulated spectra from published constants. In spite of much discussion in the literature, there is little theoretical foundation for preferring one parametrization over another, as long as the observed levels are accurately fit. In a number of cases naive assumptions about the origin of certain types of interactions have been overturned. For example, the spin-spin interaction, represented by the constant λ , is often dominated by level shifts due to off-diagonal spin-orbit perturbations [14].

For polyatomic molecules, a suitable basis set for expansion can be chosen to have a similar form [8, 15, 16]

$$|l\Lambda\Sigma; JMK\rangle = \left(\frac{(2J+1)}{8\pi^2}\right)^{1/2} D_{MK}^{*J} |l\Lambda\Sigma\rangle, \quad (35.13)$$

where Λ and Σ represent the projections of the electron-orbital (L) and spin (S) angular momenta, and l represents the projection of the vibrational angular momentum (p for degenerate vibrational modes). This is the symmetric top basis set. Generalizing the work of Watson [17, 18], the parametrized Hamiltonian might be written in a form such as

$$\begin{aligned} H_{\text{rot}} = \sum h_{\xi\eta\theta l}^{\alpha\beta\gamma\delta\epsilon} & \left\{ (J^2)^\alpha (J_z)^{2\beta} (J_+^{2\gamma} + J_-^{2\gamma}) \right. \\ & \times (\mathbf{J} \cdot \mathbf{p})^\delta (\mathbf{J} \cdot \mathbf{L})^\epsilon (\mathbf{J} \cdot \mathbf{S})^\zeta \\ & \left. \times (\mathbf{p} \cdot \mathbf{L})^\eta (\mathbf{p} \cdot \mathbf{S})^\theta (\mathbf{L} \cdot \mathbf{S})^l \right\}, \end{aligned} \quad (35.14)$$

where the $\{\}$ indicates that an appropriately symmetric combination be constructed with anticommutators.

For both linear and nonlinear molecules, it is convenient to use the Wang transformation [19] to combine basis functions with opposite sense of rotation: for diatomics

$$\frac{1}{\sqrt{2}} [|l\Lambda, \Sigma; J, M, \Omega\rangle \pm |l\Lambda, -\Sigma; J, M, -\Omega\rangle]; \quad (35.15)$$

and for polyatomics

$$\frac{1}{\sqrt{2}} [|l, \Lambda, \Sigma; J, M, K\rangle \pm |l, -\Lambda, -\Sigma; J, M, -K\rangle]. \quad (35.16)$$

For diatomic molecules, these combinations can be assigned the parity $\pm(-1)^{J+S+s}$, where $s = 1$ for Σ^- states, and 0 otherwise [13, 20]. For symmetric top molecules, each term

is to be accompanied by the appropriate hidden nuclear-spin basis function [8, 21].

For asymmetric top molecules, the Wang transformation divides the basis functions into four symmetry classes E^\pm and O^\pm according to the combining sign and whether K is even or odd. The eigenstates are often labeled by two projection quantum numbers called K_{-1} and K_1 . Assuming that $A \geq B \geq C$, the asymmetry parameter

$$\kappa = \frac{(2B - A - C)}{(A - C)} \quad (35.17)$$

ranges from -1 for a prolate symmetric top ($B = C$) to 1 for an oblate symmetric top ($B = A$). A, B , and C are the rotational constants, or reciprocals of the moments of inertia, about the three principal top axes. Each asymmetric top level can be correlated with specific symmetric top levels (i.e., K -values) in the two limits. The prolate limiting K -value is called K_{-1} and the oblate limit is called K_1 (i.e., $\kappa = \pm 1$). Note that the symmetric-top principal axes rotate by 90° during this correlation. The eigenstates are given additional symmetry names (ee, eo, oe, oo) according to whether K_{-1} and K_1 are even or odd. Papousek and Aliiev [18] discuss the relations between the (E^\pm, O^\pm) and (ee, eo, oe, oo) labeling schemes.

35.3.3 Fitting Experimental Energies

Having chosen a basis set and model Hamiltonian for both the upper and lower levels, the observed transition energies can be used to infer the numerical values of the constants that best fit the spectrum. The following quotation provides a good description of the process:

The calculational procedure logically divides into three steps: (1) The matrix elements of the upper and lower state Hamiltonians are calculated for each J value using initial values of the adjustable molecular constants; (2) both Hamiltonians are numerically diagonalized and the resulting sets of eigenvalues are used to construct a set of calculated line positions; and (3) from a least-squares fit of the calculated to the observed line positions, an improved set of molecular constants is generated. This nonlinear least-squares procedure is repeated until a satisfactory set of molecular constants is obtained.

This quotation is taken from the article by Zare et al. [13] in which they describe the basis for the LINFIT computer program, one of the first to accomplish direct extraction of constants from diatomic spectral line positions based on numerically diagonalized Hamiltonians.

35.3.4 The Transition Moment Matrix

Diagonalization of the model Hamiltonians for the upper and lower states yields vector wave functions that can be used for calculating matrix elements, especially those needed to eval-

uate radiative transition probabilities. The wave functions for diatomic molecules have the form

$$\begin{aligned}\psi'_{J'M'\Omega'} &= \sum_{\Lambda'\Sigma'} b_{\Lambda'\Sigma'}^{J'\Omega'} |\Lambda'\Sigma'; J'M'\Omega'\rangle, \\ \Phi''_{J''M''\Omega''} &= \sum_{\Lambda''\Sigma''} a_{\Lambda''\Sigma''}^{J''\Omega''} |\Lambda''\Sigma''; J''M''\Omega''\rangle.\end{aligned}\quad (35.18)$$

Section 35.2.3 expresses matrix elements of laboratory-frame operators in terms of matrix elements in the rotating body-fixed frame. Terms of the form

$$\mu_{K'K''} = \langle \psi^{(J'K')} | T_q^{(L)}(\text{body}) | \Phi^{(J''K'')} \rangle \theta(-q) \quad (35.19)$$

need to be evaluated. These terms are multiplied by zero if $K' \neq K'' + q$. In the diatomic basis set these become

$$\mu_{\Lambda'\Sigma'\Lambda''\Sigma''} = \langle \Lambda'\Sigma' | T_q^{(L)}(\text{body}) | \Lambda''\Sigma'' \rangle \theta(-q), \quad (35.20)$$

where $\theta(-q)$ is a phase factor described in Sect. 35.7.2. Only a few of these matrix elements are independent and nonzero. For electric dipole transitions ($L = 1$), time-reversal and inversion-symmetry can be used to establish the relation

$$\mu_{-\Omega' - \Omega''} = \eta(-1)^{\Omega' - \Omega''} \mu_{\Omega' \Omega''}. \quad (35.21)$$

The sign of $\eta = \pm 1$ is determined by the overall character of the electronic transition, and is related to the classification of levels into e - and f -parity types and to the determination of which components are involved in the rotational branches (P , Q , and R). These concepts are elaborated in Sect. 35.4.

35.3.5 Fitting Experimental Intensities

For allowed transitions in linear molecules and symmetric tops, only one independent parameter is normally expected in the transition moment matrix. Thus no additional information is available from fitting the experimental rotational branch strengths (assuming the energy–intensity model is adequate). In diatomic molecules, the intensities of different vibrational bands can be used to infer the internuclear-distance dependence of the electronic transition moment (for example, see *Luque and Crosley* [22]).

For forbidden transitions and allowed transitions in asymmetric tops, more than one independent parameter is expected. The intensity of a single given rotational line can be expressed in the form

$$I^{\text{line}} = \left| \sum_{K'K''} \mu_{K'K''} Z_{K'K''}(\text{line}) \right|^2, \quad (35.22)$$

where $Z_{K'K''}(\text{line})$ can be calculated in advance from the energies (wave functions) and quantum numbers alone, using the formulas in Sect. 35.7.2. Nonlinear least-squares fitting can be used to derive the best intensity parameters [23–26], analysis of which can help characterize the nature of the transition, and identify the sources of transition probability.

35.4 Selection Rules

35.4.1 Symmetry Types

Selection rules are guidelines for identifying which transitions are expected to be strong and which are expected to be weak. These rules are based on classifying rovibronic levels into labeled symmetry types. Some symmetry distinctions are effectively exact: such as total angular momentum F , or laboratory-inversion parity. Others are approximate, derived from estimates that certain matrix elements are expected to be much larger than others. The most important of these are based on electron spin (for light molecules) and geometrical point-group symmetry (for relatively rigid polyatomics). In actual fact, no transition is completely forbidden. The multipole nature of electromagnetic radiation (electric-dipole, magnetic-dipole, electric-quadrupole, etc.) implies that any change in angular momentum or parity is possible in principle. Practical interest emphasizes identification of the origin of the strongest source of transition probability, and estimation of the strengths of the weak transitions relative to the stronger ones. The result is a collection of *propensity rules* using *selection rules* as tools of estimation.

Basis functions for expansion of the wave functions for the upper and lower states were chosen in Sect. 35.3.2. The first step in the symmetry classification of rovibronic levels consists of identifying various linear combinations of basis functions that block-diagonalize the exact or approximate Hamiltonians. Symmetry-type names are then assigned to these linear combinations based on the value of F or J and knowledge of the symmetry properties of the underlying vibrational and electronic states. Thus each eigenfunction or rovibronic level consists of an expansion over only one of the kinds of linear combination, and the level can be assigned a specific symmetry type.

Similarly, the basis-set expansion leads to a matrix representation of the possible transitions. Spin- and spatial-symmetry arguments establish relationships between these transition matrix elements, and provide estimates of which are much smaller than the others. Each combination of upper- and lower-state symmetry types results in a specific pattern of rotational branches. The most important patterns are ΔJ even (Q -branches) or odd (P - and R -branches), and intensity alternation for consecutive values of J (nuclear spin statistics).

35.4.2 Rotational Branches and Parity

The symmetry of time or momentum reversal implies that changing the signs of all the angular momenta should result in an equivalent wave function. For example, the phase con-

vention

$$\begin{aligned} & \Phi_{\text{vesn}}^{(F,-K_F)} \text{ (internal, spins)} \\ & = (-1)^{-F+K_F} \Phi_{\text{vesn}}^{*(F,K_F)} \text{ (internal, -spins)} \end{aligned} \quad (35.23)$$

can be chosen to establish that the relative phases of matrix elements of the Hamiltonian can be taken as

$$\begin{aligned} & \left\langle D_{M_F-K_F}^{*F} \Phi_{\text{vesn}}^{(F,-K_F)} \middle| H \middle| D_{M_F-K_F}^{*F} \Phi_{\text{vesn}}^{(F,-K_F)} \right\rangle \\ & = \left\langle D_{M_F K_F}^{*F} \Phi_{\text{vesn}}^{(F,K_F)} \middle| H \middle| D_{M_F K_F}^{*F} \Phi_{\text{vesn}}^{(F,K_F)} \right\rangle^* . \end{aligned} \quad (35.24)$$

The formula for matrix elements of optical transition operators can also be reanalyzed,

$$\begin{aligned} & \langle \psi^{F',M_F'+p} | T_p^{(L)} \text{ (lab)} | \Phi^{F'',M_F''} \rangle \\ & = \left[\frac{(2F''+1)}{(2F'+1)} \right]^{1/2} \langle F'' M_F'', Lp | F' M_F' + p \rangle \\ & \times \frac{1}{2} \sum_{qK''} \langle F'' K_F'', Lq | F' K_F' + q \rangle \\ & \times \left\{ \left\langle \psi_{\text{vesn}}^{(F',K_F'+q)} \middle| T_q^{(L)} \text{ (body)} \middle| \Phi_{\text{vesn}}^{(F'',K_F'')} \right\rangle \right. \\ & \quad + (-1)^{F'+L-F''} \\ & \quad \left. \times \left\langle \psi_{\text{vesn}}^{(F',-K_F'-q)} \middle| T_{-q}^{(L)} \text{ (body)} \middle| \Phi_{\text{vesn}}^{(F'',-K_F'')} \right\rangle \right\} , \end{aligned} \quad (35.25)$$

to establish that all contributions are purely real or purely imaginary [27]. Since such transition matrix elements will be used as absolute squares, they can be treated as if they were purely real.

Parity classification of molecular states according to inversion through the center of mass is important for establishing which transitions are electric-dipole allowed and which states can perturb each other. As discussed by Larsson [4], such classification is not without subtlety and opportunity for confusion. Inversion of the laboratory spatial coordinates (i_{sp} , also called E^* [2]) is equivalent to a reflection σ of the molecule-fixed electronic and nuclear coordinates in an arbitrary plane followed by rotation of the molecular frame by 180° about an axis through the origin and perpendicular to the reflection plane (if F is half-integral special care must be taken about the sense of rotation). It follows that

$$\begin{aligned} & i_{\text{sp}} \Phi_{\text{exact}}^{F,M_F} \text{ (lab)} \\ & = E^* \Phi_{\text{exact}}^{F,M_F} \text{ (lab)} \\ & = \eta(-1)^{F-\gamma} \Phi_{\text{exact}}^{F,M_F} \text{ (lab)} \\ & = \left[\frac{(2F+1)}{8\pi^2} \right]^{1/2} \\ & \times \sum_{K_F} (-1)^{F-K_F} D_{M_F-K_F}^{*F} \sigma_{xz} \Phi_{\text{vesn}}^{(F,K_F)} \end{aligned} \quad (35.26)$$

and

$$\sigma_{xz} \Phi_{\text{vesn}}^{(F,K_F)} = \eta(-1)^{K_F-\gamma} \Phi_{\text{vesn}}^{(F,-K_F)} , \quad (35.27)$$

where $\gamma = 0$ or $1/2$ for integral or half-integral F , respectively, and η is the parity label for the state, having values of ± 1 . In linear molecules, levels with $\eta = +1$ are called e -levels while those with $\eta = -1$ are called f -levels [28, 29].

Inversion symmetry can be combined with time reversal to establish that all matrix elements of the Hamiltonian can be taken to be real [27]. The wave function can also be expressed in the form of the Wang transformation [19], uniting the $\pm K_F$ components,

$$\begin{aligned} \Phi_{\text{exact}}^{F,M_F} \text{ (lab)} & = \left(\frac{(2F+1)}{8\pi^2} \right)^{1/2} \\ & \times \sum_{K_F \geq 0} [D_{M_F K_F}^{*F} \Phi_{\text{vesn}}^{(F,K_F)} \eta(-1)^{-K_F+\gamma} D_{M_F -K_F}^{*F} \sigma_{xz} \Phi_{\text{vesn}}^{(F,K_F)}] \\ & \times [2(1 + \delta_{K_F 0})]^{-1/2} . \end{aligned} \quad (35.28)$$

If the molecule is rigid and has a plane of symmetry, or is nonrigid with accessible vibrational or tunneling modes that correspond to plane reflections, inversion symmetry divides the states of the molecule into two classes, according to the sign of η . Perturbations can occur only for $\Delta F = 0$ and $\eta' \eta'' = +1$. For optical transitions, the change in parity of the states must match the parity of the operator. Odd operators (e.g., electric-dipole) require $\eta' \eta'' (-1)^{\Delta F} = -1$. Even operators (e.g., magnetic-dipole and electric-quadrupole) require $\eta' \eta'' (-1)^{\Delta F} = +1$.

35.4.3 Nuclear Spin, Spatial Symmetry, and Statistics

For most molecules, the coupling of nuclear spin with the electron-spin, electron-orbital, and frame-rotational angular momenta is sufficiently weak that treatment of the energetics of hyperfine interactions can be postponed. The first-order effect of nuclear spin is that rovibronic wave functions for molecules containing identical nuclei must be combined with appropriate nuclear spin wave functions in order to obtain the necessary Fermi–Dirac or Bose–Einstein nuclear permutation symmetry. For many molecules, there exist combinations of nuclear permutations that correspond to combinations of frame rotations, laboratory inversions, and feasible vibrational motions (the rotational wave function makes a contribution because renumbering the nuclei requires a reanalysis of the Euler angles). For rigid molecules, these permutations (possibly including inversion) can be used to generate the point symmetry group of the molecule. For

fluxional molecules, with multiple energetically equivalent nuclear configurations, a rather large *molecular symmetry group* can result, one that may not correspond to any ordinary point group [1, 2].

In the discussion immediately following, consider the case of N occurrences of one kind of nucleus, the others being unique (e.g., PD_3). The treatment can easily be extended to the case of multiple kinds of identical nuclei (e.g., C_2H_6). The exact wave function can be rearranged into a sum over products of the form

$$\Phi_{\text{exact}} = \sum_{a,b} \Phi_{\text{rves}}^{(a)} \Phi_{\text{nspin}}^{(b)}, \quad (35.29)$$

where $\Phi_{\text{rves}}^{(a)}$ is a rovibronic wave function belonging to the $\Gamma(a)$ representation of the symmetric group S_N of permutations over N objects, and $\Phi_{\text{nspin}}^{(b)}$ is a nuclear spin wave function, belonging to the $\Gamma(b)$ representation of S_N . In order to obtain the correct permutation symmetries for the overall wave function, the only terms that can appear in this sum are those for which the direct product $\Gamma(a) \otimes \Gamma(b)$ contains the symmetric or antisymmetric representation, for bosons or fermions, respectively.

Assumption of negligible hyperfine interactions allows evaluation of matrix elements of the form

$$\begin{aligned} & \langle \Phi_{\text{rves}}^{(c)} \Phi_{\text{nspin}}^{(d)} | H | \Phi_{\text{rves}}^{(a)} \Phi_{\text{nspin}}^{(b)} \rangle \\ &= \langle \Phi_{\text{rves}}^{(c)} | H | \Phi_{\text{rves}}^{(a)} \rangle \langle \Phi_{\text{nspin}}^{(d)} | \Phi_{\text{nspin}}^{(b)} \rangle, \end{aligned} \quad (35.30)$$

which vanishes unless $\Gamma(a) = \Gamma(c)$ and $\Gamma(b) = \Gamma(d)$. Thus the nearly-exact wave function can be written as a sum over products where the rovibronic and nuclear-spin factors correspond to basis functions from single known representations:

$$\Phi_{\text{exact}} \approx \sum_{a,b} \Phi_{\text{rves}}^{(a)} \Phi_{\text{nspin}}^{(b)}, \quad (35.31)$$

with $\Gamma(a) = \Gamma_{\text{rves}}$ and $\Gamma(b) = \Gamma_{\text{nspin}}$. This divides the states of the molecule into a number of noninteracting symmetry classes, labeled by the representations of the symmetric group. In the absence of hyperfine interactions, optical transitions are possible only within a certain symmetry class.

Thus the existence of spatial or dynamical symmetry implies that each rovibronic wave function transforms according to a particular representation of a subgroup of the permutation-inversion group (called CNPI by *Bunker* [2]). Each representation includes only specific values of nuclear spin, corresponding to the permutational properties of the nuclear spin wave functions. The most important effect of this analysis is to assign statistical weights or relative intensities to the different symmetry types. For example, the symmetry group for NH_3 is D_{3h} (including umbrella inversion), with representations A'_1 , A'_2 , A''_1 , A''_2 , E' , and E'' . The A'_1 and A'_1

representations must be combined with the (nonexistent) antisymmetric spin function, yielding a statistical weight of 0. Similarly, A'_2 and A''_2 combine with the symmetric $I = 3/2$ spin function, with a statistical weight of 4 (i.e., $2I + 1$). E' and E'' combine with the nonsymmetric $I = 1/2$ spin functions, with a statistical weight of 2. This material is discussed from various viewpoints in numerous articles and text books, of which only a few can be cited here [1, 2, 8, 18, 21, 30–36]. See Chap. 34 for additional details and examples.

Although this analysis appears rather complicated, the selection rules that result are actually the same, at least in simple cases, as the ones that are derivable from simpler ideas. For example, for a ${}^1\Sigma_g^+$ lower state, even J levels are permutation symmetric and have parity $+1$, while odd J levels are permutation antisymmetric and have parity -1 . For a ${}^1\Sigma_u^+$ upper state, even J levels are permutation antisymmetric and have parity $+1$, while odd J levels are permutation symmetric and have parity -1 . Both the parity selection rule and permutation-symmetry selection rule independently require that $\Delta J = \pm 1$ for electric-dipole transitions. Similarly, that the permanent dipole moment of a symmetric-top molecule must lie along the body-fixed axis replicates the $\Delta K = 0$ selection rule for pure-rotation transitions provided by permutational symmetry arguments. This means that when simulating absorption and emission spectra, the nuclear-spin wave function can usually be ignored. The intensity alternation imposed by spin-statistics can be represented by multiplying each wave function by the appropriate factor, for example, 0 or $[(2I + 1)/(2i + 1)^N]^{1/2}$, where I is the total nuclear spin, and i is the spin of one of the N equivalent nuclei.

Group theory remains vital for understanding the relative strengths of vibrational transitions in polyatomics (see *Cotton* [37], for example, and Sect. 35.6.2) and becomes very interesting as interaction between vibration and rotation increases. For the purposes of this discussion, the most important issue is identification of which transition-moment matrix elements $\mu_{K'K''}$ vanish and which are related by symmetry.

35.4.4 Electron Orbital and Spin Angular Momenta

For all molecules, the strongest transitions tend to be those that conserve electron spin. The zero-order transition-moment matrix is diagonal both in total spin and in spin-projection onto the body-frame axis. In the $|\Lambda\Sigma\rangle$ basis set for linear molecules this is expressed by

$$\mu_{\Lambda'\Sigma'\Lambda''\Sigma''} = \mu_{\Lambda'\Lambda''} \delta_{\Sigma'\Sigma''}. \quad (35.32)$$

The transition-moment tensor operator $T_q^{(L)}$ (body) can connect basis functions that differ in Λ by at most L . Allowed

electric-dipole transitions thus satisfy

$$\mu_{\Lambda'\Lambda''} = 0, \quad \text{for } |\Lambda' - \Lambda''| > 1. \quad (35.33)$$

In the usual case that the upper and lower states each consist of only a single value of $|\Lambda|$, there is only one independent, nonzero, matrix element $\mu_{|\Lambda'|,|\Lambda''|}$ with

$$\mu_{-|\Lambda'|,-|\Lambda''|} = \eta(-1)^{|\Lambda'|-|\Lambda''|} \mu_{|\Lambda'|,|\Lambda''|}. \quad (35.34)$$

See Sect. 35.8 for a discussion of spin-forbidden and orbitally-forbidden transitions. Similar arguments and phase relationships can be developed for polyatomic molecules with nonzero electron spin or degenerate vibrational or electronic states.

35.5 Absorption Cross Sections and Radiative Lifetimes

35.5.1 Radiation Relations

Among the most important radiation relations is the connection between the absorption cross section and the rate of spontaneous emission. *Einstein* [38] introduced his A and B coefficients to describe the rates of absorption and emission of radiation of a collection of two-level atoms or molecules in equilibrium with a radiation field at the same temperature. The discussion here follows that of *Condon and Shortley* [39], *Penner* [40], *Thorne* [41], and *Steinfeld* [42] (with corrections). Also see Chaps. 11, 18, 72 of this Handbook. The number of absorption events per unit volume per unit time is written as

$$N_l B_{lu} \rho(\nu). \quad (35.35)$$

While the rate of emission is

$$N_u B_{ul} \rho(\nu) + N_u A_{ul}. \quad (35.36)$$

In thermal equilibrium, the radiative energy density is given by the Planck blackbody law

$$\rho(\nu) = \left(\frac{8\pi h \nu^3}{c^3} \right) (e^{h\nu/kT} - 1)^{-1}, \quad (35.37)$$

and the ground and excited state densities satisfy a Boltzmann relationship,

$$\frac{N_u}{N_l} = \left(\frac{g_u}{g_l} \right) e^{-h\nu/kT}, \quad (35.38)$$

where g_u and g_l are the degeneracies of the upper and lower states. The requirement that the rates of absorption and emission must be equal leads to the relations

$$A_{ul} = \left(\frac{8\pi h \nu^3}{c^3} \right) B_{ul} = \left(\frac{8\pi h \nu^3}{c^3} \right) \left(\frac{g_l}{g_u} \right) B_{lu}. \quad (35.39)$$

Numerical values of the B coefficients can be derived from the optical absorption cross section, and thus

$$\begin{aligned} A_{ul} &= \left(\frac{8\pi \nu^2}{c^2} \right) \left(\frac{g_l}{g_u} \right) \int \sigma_{\text{abs}}(\nu) d\nu \\ &= \left(\frac{8\pi \nu^2}{c^2} \right) \int \sigma_{\text{se}}(\nu) d\nu. \end{aligned} \quad (35.40)$$

Finally, the expression for the absorption oscillator strength is

$$\begin{aligned} f_{\text{abs}} &= (4\pi\epsilon_0) \left(\frac{mc^3}{8\pi^2 \nu^2 e^2} \right) \left(\frac{g_u}{g_l} \right) A_{ul} \\ &= (4\pi\epsilon_0) \left(\frac{mc}{\pi e^2} \right) \int \sigma_{\text{abs}}(\nu) d\nu. \end{aligned} \quad (35.41)$$

The emission oscillator strength is simply related to that for absorption: $f_{\text{em}} = -(g_l/g_u) f_{\text{abs}}$. The oscillator strength offers considerable advantages as a means of reporting and comparing the strengths of radiative transitions. It is dimensionless, obeys the simple sum rule (for electric-dipole transitions)

$$\sum_u f_{ul} = \text{number of electrons}, \quad (35.42)$$

and is directly derivable from an experimental absorption cross section even before the assignment of the upper level has been determined (i.e., before its degeneracy is known).

35.5.2 Transition Moments

In many cases, the intention is to construct model quantum mechanical wave functions for the two states involved in the transition under study. In addition, ab initio electronic wave functions and matrix elements may be available (see Chap. 33). Quantum mechanics suggests the following expression for the Einstein A coefficient (see Sect. 12.6.1)

$$A_{ul} = \left(\frac{64\pi^4 \nu^3}{3hc^3} \right) \left(\frac{1}{4\pi\epsilon_0} \right) \left(\frac{1}{g_u} \right) \sum_{u',l'',p} |\langle \psi_{u'} | e r_p | \psi_{l''} \rangle|^2. \quad (35.43)$$

The summation is over all three optical polarization directions p (i.e., r_p runs over x , y , and z in the lab frame), all degenerate components l'' of the lower state (i.e., g_l of them), and all degenerate components u' of the upper state (i.e., g_u of them). This triple sum is also called the *line strength* S_{ul} . Division by the upper-level degeneracy corrects for the fact that the transitions should be averaged rather than summed over the initial levels.

In practice, choosing the appropriate degeneracy to divide by is a question of some ambiguity. For atoms, it is sufficient to understand how the individual matrix elements and

the line strength were calculated. For example, *Bethe* and *Salpeter* [43] use a degeneracy of $(2L + 1)$ for Schrödinger wave functions for the hydrogen atom, and $(2J + 1)$ for Dirac wave functions.

For molecules with internal angular momentum, i.e., everything other than $^1\Sigma$ states of linear molecules, the situation is much more complicated. For electric-dipole allowed transitions in light molecules, ab initio transition moments are calculated in a body-fixed coordinate system, ignoring spin, and not summed over anything.

For diatomic molecules, following the work of *Whiting* et al. [44, 45], the transition probability from a single upper-state component ($J'c'$) to a single lower-state component ($J''c''$) is written as

$$A_{J'c'J''c''} = \left(\frac{64\pi^4\nu^3}{3hc^3} \right) \left(\frac{1}{4\pi\epsilon_0} \right) \times \left(\frac{1}{2J'+1} \right) q_{v'v''} |R_e|^2 S_{J'J''}^{c'c''}. \quad (35.44)$$

In this formula $q_{v'v''} |R_e|^2$ represents the rotationless contribution to the transition moment, symbolically represented as a product of a vibrational overlap ($q_{v'v''}$, i.e., a Franck–Condon factor) and an electronic-only component $|R_e|^2$ (Sect. 35.6.1). All of the rotational complexity is absorbed into the rotational-branch strength factor $S_{J'J''}^{c'c''}$ (Sects. 35.7.2 and 35.7.3). The issue to be addressed here is how to divide numerical factors between $|R_e|^2$ and $S_{J'J''}^{c'c''}$. One approach is to construct an estimate for the rotationless transition probability

$$A_{v'v''} = \left(\frac{1}{N'_c} \right) \sum_{c'J''c''} A_{J'c'J''c''}, \quad (35.45)$$

where N'_c is the number of internal spin-orbit components of the upper state. *Whiting* et al. suggest that $S_{J'J''}^{c'c''}$ be normalized such that for spin-allowed transitions

$$\sum_{c'J''c''} S_{J'J''}^{c'c''} = (2 - \delta_{0,\Lambda'}\delta_{0,\Lambda''})(2S + 1)(2J' + 1). \quad (35.46)$$

The first factor is 1 for Σ – Σ transitions, and 2 for all others. The final factor is replaced by $(2J'' + 1)$ if the sum is over J' instead of J'' . For spin-forbidden transitions the following is a plausible extension of this sum rule,

$$\sum_{c'J''c''} S_{J'J''}^{c'c''} = \max(N'_c, N''_c)(2J' + 1). \quad (35.47)$$

Section 35.7.3 provides a corresponding sum rule for polyatomic molecules. This normalization yields

$$A_{v'v''} = \left(\frac{64\pi^4\nu^3}{3hc^3} \right) \left(\frac{1}{4\pi\epsilon_0} \right) \left(\frac{\max(N'_c, N''_c)}{N'_c} \right) q_{v'v''} |R_e|^2 \quad (35.48)$$

and for spin-allowed transitions, the simple spin-free expressions for the electronic transition moments

$$|R_e|^2 = |\langle \Lambda | e_z | \Lambda \rangle|^2 \quad (35.49)$$

for parallel transitions and

$$|R_e|^2 = \left| \langle \Lambda + 1 | e \frac{1}{\sqrt{2}}(x + iy) | \Lambda \rangle \right|^2 \quad (35.50)$$

for perpendicular transitions.

35.6 Vibrational Band Strengths

35.6.1 Franck–Condon Factors

The Born–Oppenheimer separation of electron and nuclear motion suggests that during an optical transition between different electronic states the nuclei should change neither their position nor momentum. This concept was developed from semiclassical arguments by *Franck* [46] and justified quantum mechanically by *Condon* [47]. Following *Herzberg* [48] and *Steinfeld* [42] the vibronic transition moment can be written as

$$\begin{aligned} \mu_{v'v''} &= \langle \psi'_e \psi'_{v'} | \mu | \psi''_e \psi''_{v''} \rangle, \\ &= \int dR \psi'_{v'}(R) \psi''_{v''}(R) \\ &\quad \times \int dr \psi'_e(r, R) \psi''_e(r, R) \mu(r, R), \\ &= \int dR \psi'_{v'}(R) \psi''_{v''}(R) \mu(R). \end{aligned} \quad (35.51)$$

If the R -dependence of $\mu(R)$ is sufficiently weak, it can be factored out to obtain

$$\mu_{v'v''} = R_e \int dR \psi'_{v'}(R) \psi''_{v''}(R), \quad (35.52)$$

where R_e is called the electronic transition moment. The transition probability is proportional to the square of the above, which is usually written as

$$I \approx q_{v'v''} R_e^2, \quad (35.53)$$

where

$$q_{v'v''} = \left| \int dR \psi'_{v'}(R) \psi''_{v''}(R) \right|^2, \quad (35.54)$$

the square of the overlap between initial and final vibrational wave functions, is called the Franck–Condon factor.

The Franck–Condon factors satisfy the sum rule

$$\sum_{v'} q_{v'v''} = \sum_{v''} q_{v'v''} = 1 \quad (35.55)$$

provided the summations include the continuum vibrational wave functions above the dissociation limits. The Franck–Condon approach also can be used to calculate intensities and cross sections for bound–free [49] and free–free [50] emission and absorption.

In some cases the variation of $\mu(R)$ is significant. Calculation of the effect on the intensities can usually be handled by the *r*-centroid method in which the expression

$$\bar{r}_{v'v''} = \frac{\langle \psi'_{v'} | R | \psi''_{v''} \rangle}{\langle \psi'_{v'} | \psi''_{v''} \rangle} \quad (35.56)$$

is used to calculate an effective internuclear distance for the transition. The transition strength is then proportional to $q_{v'v''} |\mu(\bar{r}_{v'v''})|^2$. An advantage of this formulation is that the vibrational overlaps can be calculated from energy information only, before the transition moment function is known and before the transition strengths are investigated experimentally. The quantitative accuracy of the *r*-centroid method for transition moments that are not linear in the internuclear distance, has been addressed by a considerable literature, which has been summarized by *McCallum* [51].

A second complication arises from the fact that the vibrational wave functions themselves depend parametrically on the rotational angular momentum. Calculation of rotationally-dependent Franck–Condon factors is described by *Dwivedi* et al. [52] who also discuss the *r*-centroid method.

35.6.2 Vibrational Transitions

Vibrational transitions derive their strength from the variation of the *permanent* dipole moment of the molecule as a function of geometry or internuclear coordinates. As described by several authors [31, 32, 34, 53] one can expand the dipole moment as a power series in the internal-Cartesian or normal-mode coordinates

$$M_{xyz}(Q) = M_{xyz}^0 + \sum_i \left(\frac{\partial M_{xyz}}{\partial Q_i} \right) Q_i + \dots \quad (35.57)$$

and calculate intensities from a formula like

$$I \approx \left| \langle \psi_{v'_1} \psi_{v'_2} \dots | M(Q) | \psi_{v''_1} \psi_{v''_2} \dots \rangle \right|^2. \quad (35.58)$$

For homonuclear diatomic molecules, the dipole moment vanishes identically, so there is no rovibrational spectrum. The dipole moment for heteronuclear diatomics is often close to linear in the internuclear distance. The harmonic oscillator model suggests that transitions with $\Delta v = \pm 1$ are the strongest, with intensities approximated by

$$I_{v+1,v} \approx \left| \frac{dM}{dR} \right|^2 (v+1). \quad (35.59)$$

Overtone bands, i.e., with $|\Delta v| > 1$, are observed, as dramatically illustrated by the $\Delta v = 4, 5$ emissions from the OH radical observed from the Earth's night sky [54].

For polyatomic molecules, overtone and combination bands are often quite strong. The presence or absence of which is used to establish the symmetries of the vibrational modes. In general, it is difficult to construct quantitative vibrational intensity formulas with only a few parameters that can be inferred experimentally.

35.7 Rotational Branch Strengths

35.7.1 Branch Structure and Transition Type

The overall rotational structure of a molecular transition is determined by the relative values and phases of the body-frame transition-moment matrix elements, the relative values and phases of coefficients in the expansion of the upper-state and lower-state component wave functions over the angular-momentum-projection basis functions, the energy separations between the components, and the relative values and phases of the vector-coupling coefficients. In simple cases, each lower component might be connected to only a single upper component (Hund's case (b) or symmetric tops), or $\Delta J = \pm 1$ (*P*- and *R*-branches) may dominate over $\Delta J = 0$ (*Q*-branches).

For diatomic molecules, symmetry arguments are used to divide the components into the two parity classes *e* and *f*. For electric dipole transitions, the selection rules from Sect. 35.4.2 imply that

$$\begin{aligned} (N'_e N''_e + N'_f N''_f) & \quad P\text{- and } R\text{-branches} \\ (N'_e N''_f + N'_f N''_e) & \quad Q\text{-branches} \end{aligned} \quad (35.60)$$

are expected, where N_e and N_f indicate the number of components of each parity class (N_e and N_f differ by no more than one). Rotational branches are labeled with the notation $\Delta^R \Delta J_{c'c''}$, using symbols *P* for -1 , *Q* for 0 , and *R* for $+1$. ΔR indicates the *apparent* change in mechanical rotational angular momentum (i.e., energy) (see Hund's case (b) in Sect. 35.7.4) and ΔJ indicates the *actual* change (i.e., quantum mechanical). The labels *c'c''* indicate the components involved. Thus a ${}^P Q_{21}$ branch is expected to be *red shaded* ($\Delta R = -1$) with $\Delta J = 0$ involving the second component of the upper state and the first (lowest) component of the lower state. The notation ${}^P Q_{21}(J)$ (or sometimes ${}^P Q_{21}(R = N)$ for Σ lower states) identifies an individual rotational line and specifies the rotational quantum number of the lower state involved in the transition. If the upper- and lower-state component numbers are the same, one of them may be dropped. Thus P_{22} is sometimes written as P_2 .

For symmetric top molecules, the rotational branches are labeled ΔJ_K (e.g., P_1). For asymmetric tops, the branches are labeled by $\Delta J_{\Delta K_{-1}, \Delta K_1}$, where K_{-1} and K_1 are the prolate- and oblate-limit angular momenta projections (described in Sect. 35.3.2).

The transition dipole moment commonly lies parallel or perpendicular to the body-frame axis. In the former case, $\mu_{K'K''}$ vanishes for $K' \neq K''$, and in the latter for $K' = K''$. Thus parallel bands correspond to $\Delta K = 0$ transitions, while perpendicular bands have $\Delta K = \pm 1$. As enforced by the vector-coupling coefficients or Hönl–London factors described below, for low values of K (e.g., diatomics), $\Delta K = 0$ implies strong $\Delta J = \pm 1$ (P and R) branches and weak $\Delta J = 0$ (Q) branches. On the other hand, $\Delta K = \pm 1$ leads to Q -branches that are approximately twice as strong as either the P - or R -branches.

35.7.2 Hönl–London Factors

The matrix model Hamiltonians for the upper and lower states have been diagonalized, yielding the wave functions

$$\psi_{c'}^{J'M'} = \sum_{K'} b_{J'c'}^{K'} \left(\frac{(2J'+1)}{8\pi^2} \right)^{1/2} D_{M'K'}^{*J'}(\text{lab}) \chi_{K'}(\text{body}) \quad (35.61)$$

and

$$\Phi_{c''}^{J''M''} = \sum_{K''} a_{J''c''}^{K''} \left(\frac{(2J''+1)}{8\pi^2} \right)^{1/2} D_{M''K''}^{*J''}(\text{lab}) \xi_{K''}(\text{body}). \quad (35.62)$$

In these expressions, the designations K' and K'' are slightly symbolic. They represent the body-frame projection of the total angular momentum and also a running index over basis functions. For complicated cases, more than one basis function can have a given value of K .

Following Sect. 35.2.3, the rotational branch strength is then written as

$$\begin{aligned} S_{J',J''}^{c',c''} &= \sum_{pM'M''} |\langle \psi_{c'}^{J'M'} | T_p^{(L)}(\text{lab}) | \Phi_{c''}^{J''M''} \rangle|^2 \\ &= (2J''+1) \left| \sum_{q'K'K''} b_{J'c'}^{*K'} a_{J''c''}^{K''} \langle \chi_{K'} | T_q^{(L)}(\text{body}) | \xi_{K''} \rangle \right. \\ &\quad \left. \times \langle J''K'', Lq | J'K' \rangle \right|^2 \end{aligned} \quad (35.63)$$

or

$$S_{J',J''}^{c',c''} = \left| \sum_{K'K''} b_{J'c'}^{*K'} a_{J''c''}^{K''} \mu_{K'K''} \zeta(J', K', J'', K'') \right|^2, \quad (35.64)$$

where

$$\mu_{K'K''} = \langle \chi_{K'} | T_q^{(L)}(\text{body}) | \xi_{K''} \rangle \theta(K'' - K') \quad (35.65)$$

is the body-frame transition-moment matrix introduced in Sect. 35.3.4, with relative values that are hypothesized based on interpretation of the nature of the transition, calculated from ab initio wave functions, or inferred by fitting the observed rotational branch strengths. The Clebsch–Gordan expression

$$\begin{aligned} \zeta(J', K', J'', K'') &= (2J''+1)^{1/2} \langle J''K'', LK' - K'' | J'K' \rangle \\ &\quad \times \theta(K'' - K') \theta(J' - J'') \end{aligned} \quad (35.66)$$

represents the transformation of the radiation field from the laboratory-frame to the body-frame, also related to the *direction cosines* used by many authors. The additional phase factors

$$\theta(k) = \text{sgn}(k) = \begin{cases} +1 & k \geq 0 \\ -1 & k < 0 \end{cases} \quad (35.67)$$

have been included here to make the signs and symmetry relations of $\mu_{K'K''}$ and $\zeta(J', K', J'', K'')$ agree with those already in use [9, 44, 55, 56]. They are related to the choice of the leading signs when T_+ and T_- are expressed as $\pm(T_x + iT_y)$ and $\pm(T_x - iT_y)$. Their inclusion has no effect for spin-allowed transitions with only one source of transition probability, e.g., purely parallel or perpendicular.

In the usual case of electric-dipole (or magnetic-dipole) radiation (i.e., $L = 1$), ζ^2 is the well-known Hönl–London factor [57]. $\zeta(J', K', J'', K'')$ is a real, signed quantity: negative for $\Delta J \Delta K > 0$; or $\Delta J = \Delta K = 0$ and $K < 0$; otherwise positive [9].

Setting $L = 2$ provides intensity formulas for electric-quadrupole [58], Raman [59], and two-photon [60, 61] transitions. Additional Rayleigh-like terms can appear for $K' = K'' \neq 0$. Halpern et al. [61] also give formulas for three-photon transitions in diatomics, expressed in terms of Clebsch–Gordan coefficients with $L = 3$ and $L = 1$ (for $|\Delta\Omega| \leq 1$).

35.7.3 Sum Rules

The orthonormality relations for component eigenvectors

$$\sum_{c'} b_{J'c'}^{*K'} b_{J'c'}^K = \delta_{K',K}, \quad (35.68)$$

$$\sum_{c''} a_{J''c''}^{*K''} a_{J''c''}^K = \delta_{K'',K} \quad (35.69)$$

can be used to construct the sum rule

$$\sum_{c'c''} S_{J'J''}^{c'c''} = \sum_{K'K''} |\mu_{K'K''} \zeta(J', K', J'', K'')|^2. \quad (35.70)$$

Finally, the orthonormality relations of the Clebsch–Gordan coefficients result in

$$\sum_{J'c'c''} S_{J'J''}^{c'c''} = (2J'' + 1) \sum_{K'K''} |\mu_{K'K''}|^2, \quad (35.71)$$

$$\sum_{J''c'c''} S_{J'J''}^{c'c''} = (2J' + 1) \sum_{K'K''} |\mu_{K'K''}|^2. \quad (35.72)$$

As discussed in Sect. 35.5.2, it is convenient to have the $\mu_{K'K''}$ matrix elements consist of numbers that represent the nature of the transition but not its strength, the latter being expressed by the *vibrational* ($q_{v'v''}$) and *electronic* (R_e) contributions. Following Sect. 35.5.2, for diatomic molecules, the *orientational* part $\mu_{K'K''}$ is taken to have a fixed sum rule

$$\sum_{K'K''} |\mu_{K'K''}|^2 = \max(N'_c, N''_c), \quad (35.73)$$

where N'_c is the number of components (K' values, or basis functions) for the upper state, and N''_c is the number of components in the lower state. For polyatomic molecules, the sum rule can be written as

$$(2J + 1)^2 (\mu_a^2 + \mu_b^2 + \mu_c^2) \max(N'_c, N''_c), \quad (35.74)$$

where

$$\mu_a^2 + \mu_b^2 + \mu_c^2 = |\mu_+|^2 + |\mu_-|^2 + |\mu_0|^2 = 1 \quad (35.75)$$

and N'_c and N''_c are the numbers of spin-electronic-vibrational components in the upper and lower states, respectively. Also see *Whiting* et al. [44, 45] and *Brown* et al. [7].

35.7.4 Hund's Cases

In diatomic molecules, several limiting cases are useful as short-hand or first-approximation concepts for classification of energy levels and rotational branch strengths. These are called the *Hund's cases* [62–64]. They are distinguished by the extent to which the electron orbital and spin angular momenta are rigidly attached to the tumbling molecular frame, i.e., whether Λ , Σ , and S are good quantum numbers. Hund's cases are discussed in many journal articles and in every textbook dealing with the rotational structure of diatomic spectra. An appealing recent description is provided by *Nikitin* and *Zare* [65].

In most works, the emphasis has been on finding a favorable zero-order approximation for perturbation expansion

of energy levels. The advance of precision measurement of transition energies and the availability of sophisticated parametrical matrix models and fast computers on which to realize them, has reduced the importance of Hund's cases for actual computations. In particular, the need to derive and implement numerous explicit energy and intensity formulas leads to unfortunate transcription errors. Nevertheless, they remain of value for qualitative and pedagogical understanding, especially for estimates of the relative intensities of rotational branches.

Hund's case (a) describes the situation in which Λ and Σ are separately well-defined. This is a common case in which the separation between electronic states, i.e., different values of $|\Lambda|$, is larger than the spin-orbit interaction, which in turn, is larger than the separation between rotational levels. At low J , there are $(2S + 1)$ pairs of nearly-degenerate energy levels separated from each other by the spin orbit constant: $E \approx A\Lambda\Sigma + BJ(J + 1)$. The wave functions are of the form

$$\begin{aligned} \psi_{\Omega\pm}^{JM} &= \frac{1}{\sqrt{2}} \left(\frac{(2J + 1)}{8\pi^2} \right)^{1/2} \\ &\times [D_{M\Lambda+\Sigma}^{*J} |\Lambda, \Sigma\rangle \pm D_{M-\Lambda-\Sigma}^{*J} |-\Lambda, -\Sigma\rangle] \\ &= \frac{1}{\sqrt{2}} [|\Lambda, \Sigma; J, M, \Omega\rangle \\ &\pm |-\Lambda, -\Sigma; J, M, -\Omega\rangle], \end{aligned} \quad (35.76)$$

with only two nonzero expansion coefficients a_{Jc}^K . If both the upper and lower states are well described by Hund's case (a), then each lower component is optically connected only to the upper components with the same value of $|\Sigma|$. Then

$$S_{J'J''}^{\Omega'\Omega''} = (2J'' + 1) | \langle J''\Omega'', 1\Omega' - \Omega | J'\Omega' \rangle |^2, \quad (35.77)$$

with $\Omega'' = \Lambda'' + \Sigma$ and $\Omega' = \Lambda' + \Sigma$.

Hund's case (b) indicates that Λ is well-defined, but spin-orbit coupling is weak. The components correspond to well-defined values of $N = J - S$, ranging from $|J - S|$ to $(J + S)$, with energies approximated by $E \approx BN(N + 1)$, and wave functions of the form

$$\begin{aligned} \psi_{N\pm}^{JM} &= \sum_{\Sigma} (-1)^{S+\Sigma} \langle J - \Omega, S\Sigma | N - \Lambda \rangle \\ &\times \frac{1}{\sqrt{2}} [|\Lambda, \Sigma; J, M, \Omega\rangle \\ &\pm |-\Lambda, -\Sigma; J, M, -\Omega\rangle]. \end{aligned} \quad (35.78)$$

This equation is derivable from *Mizushima's* equation (2-3-26) [14] and *Zare's* equations (2.8), (2.26), and (3.105) [5], using the lab-to-body transformation

$$|SM_S\rangle (\text{lab}) = \sum_{\Sigma} D_{M_S\Sigma}^{*S} (\phi\theta\chi) |S\Sigma\rangle (\text{body}). \quad (35.79)$$

It disagrees with Judd's problem 9.1 [66] by a phase factor $(-1)^{J+2S+\Sigma-N}$ but agrees with Mizushima's expansion of a $^3\Pi$ state [14, p. 287] if the Clebsch–Gordan coefficients are taken from Condon and Shortley [39, p. 76].

If both the upper and lower states are well described by Hund's case (b), these wave functions can be substituted into the general rotational-branch strength equations above. Following Edmonds [67, (6.2.8) and (6.2.13), and Table 5] yields the square of a product of Clebsch–Gordan and Racah coefficients

$$S_{J'J''}^{N'N''} = (2J'' + 1)(2J' + 1)(2N'' + 1) \times \left| \langle N'' \Lambda'', 1 \Lambda' - \Lambda'' | N' \Lambda' \rangle \times W(N', J'', N'', J'; S, 1) \right|^2. \quad (35.80)$$

The Clebsch–Gordan coefficient enforces the case (b) selection rule $\Delta N = 0, \pm 1$, while the Racah coefficient provides the $\Delta J = \Delta N$ propensity rule, which becomes more precise as N increases. A similar propensity rule, $\Delta F = \Delta J$, is common for transitions between hyperfine components (see also Femenias [68]).

Hund's case (c) corresponds to the situation in which spin-orbit coupling is so strong that each level described by the projection Ω actually consists of multiple values of $|\Lambda|$ (e.g., mixing of Σ and Π states) or multiple values of S (e.g., mixing of singlet and triplet spins). This limiting case is formally similar to Hund's case (a), but no assumptions can be made about the relative magnitudes of transition-moment matrix elements $\mu_{\Omega'\Omega''}$. Any of which can be nonzero for $|\Delta\Omega| \leq 1$, for example

$$S_{J'J''}^{\Omega'+\Omega''\pm} = \frac{1}{4} \left| \mu_{\Omega'\Omega''} \zeta(J', \Omega', J'', \Omega'') \pm \mu_{\Omega'-\Omega''} \zeta(J', \Omega', J'', -\Omega'') + \mu_{-\Omega'\Omega''} \zeta(J', -\Omega', J'', \Omega'') \pm \mu_{-\Omega'-\Omega''} \zeta(J', -\Omega', J'', -\Omega'') \right|^2. \quad (35.81)$$

The symmetry (sign) relations between $\mu_{\Omega'\Omega''} \zeta(J', \Omega', J'', \Omega'')$ and $\mu_{-\Omega'-\Omega''} \zeta(J', -\Omega', J'', -\Omega'')$ determine whether this transition occurs only for $\Delta J = \pm 1$ (P - and R -branches) or only for $\Delta J = 0$ (Q -branches).

The interest and complexity of Hund's case (c) were exemplified by a seminal work by Kopp and Hougen [69], who considered $\Omega' = 1/2, \Omega'' = 1/2$ transitions, under the assumption that both states could consist of arbitrary mixtures of $^2\Sigma_{1/2}$ and $^2\Pi_{1/2}$ character. Each of the six rotational branches shows constructive or destructive interference of parallel ($\Delta\Omega = 0$) and perpendicular ($\Delta\Omega = \pm 1$) contributions. Hund's case (c) also describes spin-orbit mixing collisions [70] or dissociation to specific spin-orbit limits [71–73].

Hund's case (d) arises in the investigation of Rydberg series [74], in which the separation between Σ and Π from the same orbital configuration approach each other as the prin-

cipal quantum number (n) increases. Spin-orbit coupling between these projections also diminishes. The eigenfunction components correspond to well-defined values of $\mathbf{R} = \mathbf{J} - \mathbf{L}$, ranging from $|J - L|$ to $(J + L)$, with energies approximated by $E \approx BR(R + 1)$, and wave functions of the form

$$\psi_{RL}^{JM} = \sum_{\Lambda} (-1)^{L+\Lambda} \langle J - \Lambda, L \Lambda | R 0 \rangle | L \Lambda; J M \Lambda \rangle. \quad (35.82)$$

Carroll [74] used intensity formulas provided by Kovacs [58] to analyze, by spectral simulation, the $4p-15p$ ($^1\Sigma_u^+$ and $^1\Pi_u$) Rydberg states of N_2 excited from the ground $X^1\Sigma_g^+$. Three strong Q -form branches survive, corresponding to $R' = J''$, two arising from $\Pi \leftarrow \Sigma$ and one from $\Sigma \leftarrow \Sigma$ case (a) branches. The remaining O -form ($R' = J'' - 2$) and S -form ($R' = J'' + 2$) branches fade rapidly as n increases. With the phase conventions used here, this situation corresponds to body-frame transition matrix elements satisfying

$$\mu_{00} = \mu_{-10} = -\mu_{10}. \quad (35.83)$$

In the opposite case, corresponding to a parity change of the parent-ion core [73], two of the Q -form branches are extinguished, while one Q -form, one O -form, and one S -form branch remain. The transition matrix elements would satisfy

$$\mu_{00} = 0, \quad \mu_{-10} = \mu_{10}. \quad (35.84)$$

Hund's case (d) polyatomics are also known [8].

Hund's case (e) would correspond to a situation in which L and S are strongly coupled to each other, but neither is strongly coupled to the internuclear axis. No examples are known for bound states of molecules.

35.7.5 Symmetric Tops

For transitions between nondegenerate vibronic states, the transition moment must lie along the principal top axis, leading to the selection rule $\Delta K = 0$. Otherwise, Hougen's convenient quantum number [33] $G = \Lambda + l - K$, provides the selection rule $\Delta G = 0, \pm n$ (for an n -fold major symmetry axis) (Sects. 35.3.2, 35.4.3, and Chap. 34). Transitions with $\Delta G = \pm n$ are much weaker than those with $\Delta G = 0$ and are not calculable from a simple formula. Branch intensities can be calculated with the Hönl–London formulas of Sect. 35.7.2.

35.7.6 Asymmetric Tops

In general, no assumptions can be made about the orientation of the transition moment. The vector representations (μ_x, μ_y, μ_z) , (μ_a, μ_b, μ_c) , and $(\mu_0, \mu_{+1}, \mu_{-1})$ can have any

combination of independent nonzero values. It is common that one of the (μ_a, μ_b, μ_c) values is significantly larger than the others, especially for planar molecules with a two-fold symmetry axis. In this case one obtains a type *A*, *B*, or *C* band, if μ_a, μ_b, μ_c dominates, respectively [31, 75]. The tradition of analytic calculation of line strengths from explicit representations of wave functions and transition moments leads to formulas of considerable complexity, with somewhat restrictive assumptions [35, 36, 76]. In the more general notation of Sect. 35.7.2, the rotational line strength can be written as

$$S_{J'J''}^{\tau'\tau''} = \left| \sum_{K'K''} b_{J'\tau'}^{*K'} a_{J''\tau''}^{K''} (\mu_0 \delta_{K'K''} + \mu_+ \delta_{K'K''+1} + \mu_- \delta_{K'K''-1}) \zeta(J', K', J'', K'') \right|^2, \quad (35.85)$$

where

$$\begin{aligned} \mu_0 &= \mu_c, & |\mu_+| &= |\mu_-|, \\ |\mu_+|^2 + |\mu_-|^2 &= \mu_a^2 + \mu_b^2. \end{aligned} \quad (35.86)$$

Papousek and Aliev [18] and Zare [5] follow the present formulation, but with somewhat less generality with respect to wave function expansion coefficients or transition moment components.

35.8 Forbidden Transitions

35.8.1 Spin-Changing Transitions

The formalism presented above permits simulation of any allowed transition or forbidden transitions mediated by spin-orbit or spin-spin perturbations, or any perturbation that is diagonal in Ω . For spin-allowed transitions, the transition moment matrix is taken to be diagonal in and independent of the spin projection, so that

$$\mu_{\Lambda'\Sigma'\Lambda''\Sigma''} = \mu_{\Lambda'\Lambda''} \delta_{\Sigma'\Sigma''}. \quad (35.87)$$

For forbidden transitions, or complicated Hund's case (c) mixings, the transition moment matrix elements can be considered as independent variable parameters, limited only by the symmetry constraint

$$\mu_{-\Omega'-\Omega''} = \eta(-1)^{\Omega'-\Omega''} \mu_{\Omega'\Omega''}, \quad (35.88)$$

and the fact that terms with $|\Delta\Omega| > 1$ will be multiplied by zero. Alternatively, a specific set of candidate perturbers can be selected, and the Λ - and Σ -dependence of their contributions to the transition-moment matrix evaluated explicitly.

For example, first-order spin-orbit mixing would lead to terms of the form

$$\begin{aligned} \mu_{\Lambda'\Sigma'\Lambda''\Sigma''}^{S'S''} &= \sum_{\Lambda} \left[\mu_{\Lambda'\Sigma'\Lambda\Sigma'}^{S'S'} \frac{\langle S'\Lambda\Sigma' | H_{SO} | S''\Lambda''\Sigma'' \rangle}{\Delta E''} \right. \\ &\quad \left. + \left(\frac{\langle S'\Lambda'\Sigma' | H_{SO} | S''\Lambda\Sigma'' \rangle}{\Delta E'} \right) \mu_{\Lambda\Sigma''\Lambda''\Sigma''}^{S''S''} \right]. \end{aligned} \quad (35.89)$$

However, care must be taken in reducing these matrix elements using the Wigner–Eckart theorem, for example, following *Lefebvre-Brion* and *Field* [55], in order to satisfy the $\Delta\Omega = 0$ requirement for matrix elements of the rotationless Hamiltonian.

35.8.2 Orbitally-Forbidden Transitions

Even if the upper and lower states share the same value of electron spin, the transition may still be forbidden. The change in orbital angular momentum may be too large, $|\Delta\Lambda| > 1$, or a change in reflection parity, $\Sigma^- \rightarrow \Sigma^+$, may cause the zero-order transition matrix elements to vanish. Spin-orbit mixing with other $^{2S+1}\Lambda$ states, as described above, is usually the largest source of transition probability. In addition, terms in the Hamiltonian of the form $\mathbf{J} \cdot \mathbf{L}$ lead to contributions to the transition strength that increase with J , and that may mix-in higher values of Ω than were present in the zero-order $\Lambda\Sigma$ basis set for the upper and lower states. This situation can be represented by generalizing the formula from Sect. 35.7.2, following *Huestis* et al. [23],

$$S_{J'J''}^{c'e''} = \left| \sum_{K'K''} b_{J'c'}^{*K'} a_{J''e''}^{K''} \sum_{i=-1}^1 \mu_{K'K''}^{(i)} \zeta^{(i)}(J', K', J'', K'') \right|^2, \quad (35.90)$$

where $\mu_{K'K''}^{(0)}$ is the rotationless contribution ($\mu_{K'K''}$ from Sect. 35.7.2) and $\mu_{K'K''}^{(\pm 1)}$ are the new rotation-assisted terms. The new reflection-symmetry rule is

$$\mu_{-K'-K''}^{(i)} = \eta(-1)^{K'-K''+i} \mu_{K'K''}^{(-i)}. \quad (35.91)$$

The revised square-root Hönl–London factors are

$$\zeta^{(0)}(J', K', J'', K'') = \zeta(J', K', J'', K'') \quad (35.92)$$

(from Sect. 35.7.2) and

$$\begin{aligned} &\zeta^{(\pm 1)}(J', K', J'', K'') \\ &= \frac{1}{2} \{ [J'(J'+1) - K'(K' \mp 1)]^{1/2} \\ &\quad \times \zeta(J', K' \mp 1, J'', K'') \\ &\quad + [J''(J''+1) - K''(K'' \pm 1)]^{1/2} \\ &\quad \times \zeta(J', K', J'', K'' \pm 1) \}. \end{aligned} \quad (35.93)$$

As in Sect. 35.7.2 the symbols K' and K'' represent $\Lambda'\Sigma'$ and $\Lambda''\Sigma''$ when used as labels, and Ω' and Ω'' when used as numbers (a distinction that is relevant only when $S \geq |\Lambda|$ and $\Lambda \neq 0$). This formulation is more symmetric than that proposed by Huestis et al. [23], in that it explicitly allows for either the upper or lower state to be mixed by rotation (of significance only for low J and $\Delta\Lambda > 1$).

35.9 Recent Developments

Added by Mark M. Cassar. Astronomical sky spectra are important for an understanding of processes both in Earth's and other terrestrial environments. These spectra are the background spectra obtained through the slit of a spectrometer while excluding the object of primary interest to the astronomer—the star, galaxy, etc. The sky spectrum is subsequently subtracted from the object spectrum so that the final product contains no emissions from extraneous sources—nightglow, zodiacal light, and the light of other stellar objects. This operation then leaves the astronomer with purer astronomical spectra, which can then be compared to theoretical transition probability calculations to identify emission sources. This procedure has recently been used to identify the atomic oxygen green line in the Venus night airglow [77], which relied on an understanding of molecular oxygen emissions. In addition, interpretation of the intensities of molecular oxygen emissions also furthers the understanding of the elementary processes occurring in the Earth's atmosphere [78].

Two recent studies have focused on the radiative properties of the CaN and $^{39}\text{K}^{85}\text{Rb}$ molecules. In the former study, the radiative transition probabilities and lifetimes for the $A^4\Pi - X^4\Sigma^-$ and $B^4\Sigma^- - X^4\Sigma^-$ band systems were calculated [79]. These results will in turn facilitate future spectroscopic studies of CaN showing the essential interplay between theory and experiment, which is required for a deeper understanding of these processes. (Radiative properties are sensitive to electronic coupling schemes and to configuration interaction, and thus present an important testing ground for theoretical models [80, 81].) The second study provides quantitative estimates for the radiative cooling of heteronuclear translationally ultracold molecules [82, 83]. By calculating the radiative transition probabilities for $^{39}\text{K}^{85}\text{Rb}$, which lead to the radiative lifetime through the total Einstein A coefficient, it has been shown that under appropriate laboratory conditions such a cooling process is not relevant [84].

Acknowledgements This work was supported by the NSF Atmospheric Chemistry Program, the NASA Stratospheric Chemistry Section, and the NASA Space Physics Division.

References

1. Longuet-Higgins, H.C.: Mol. Phys. **6**, 445 (1963)
2. Bunker, P.R.: Molecular Symmetry and Spectroscopy. Academic Press, New York (1979)
3. Wigner, E.P.: Group Theory. Academic Press, New York (1959)
4. Larsson, M.: Phys. Scr. **23**, 835 (1981)
5. Zare, R.N.: Angular Momentum. Wiley, New York (1988)
6. Chang, E.S., Fano, U.: Phys. Rev. A **6**, 173 (1972)
7. Brown, J.M., Howard, B.J., Kerr, C.M.L.: J. Mol. Spectrosc. **60**, 433 (1976)
8. Helm, H., Lembo, L.J., Cosby, P.C., Huestis, D.L.: Photoionization and dissociation of the triatomic hydrogen molecule. In: Ehlötzky, F. (ed.) Fundamentals of Laser Interactions II. Springer, Berlin, Heidelberg (1989)
9. Hougen, J.T.: The Calculation of Rotational Energy Levels and Rotational Line Intensities in Diatomic Molecules. NBS Monograph, vol. 115. U.S. Government Printing Office, Washington, DC (1970)
10. Brown, J.M., Colbourn, E.A., Watson, J.K.G., Wayne, F.D.: J. Mol. Spectrosc. **74**, 294 (1979)
11. Brown, J.M., Merer, A.J.: J. Mol. Spectrosc. **74**, 488 (1979)
12. Brown, J.M., Milton, D.J., Watson, J.K.G., Zare, R.N., Albritton, D.L., Horani, M., Rostas, J.: J. Mol. Spectrosc. **90**, 139 (1981)
13. Zare, R.N., Schmeltekopf, A.L., Harrop, W.J., Albritton, D.L.: J. Mol. Spectrosc. **46**, 37 (1973)
14. Mizushima, M.: The Theory of Rotating Diatomic Molecules. Wiley, New York (1975)
15. Herzberg, G.: Molecular Spectra and Molecular Structure III. Electronic Spectra and Electronic Structure of Polyatomic Molecules. Van Nostrand, New York (1966)
16. Lembo, L.J., Helm, H., Huestis, D.L.: J. Chem. Phys. **90**, 5299 (1989)
17. Watson, J.K.G.: Aspects of quartic and sextic centrifugal effects on rotational energy levels. In: Durig, J. (ed.) Vibrational Spectra and Structure, vol. 6, Elsevier, Amsterdam (1977)
18. Papousek, D., Aliev, M.R.: Molecular Vibrational-Rotational Spectra. Elsevier, Amsterdam (1982)
19. Wang, S.C.: Phys. Rev. **34**, 243 (1929)
20. Helm, H., Cosby, P.C., Saxon, R.P., Huestis, D.L.: J. Chem. Phys. **76**, 2516 (1982)
21. Townes, C.H., Schawlow, A.L.: Microwave Spectroscopy. McGraw-Hill, New York, p 1975 (1955). (reprinted, Dover, New York)
22. Luque, J., Crosley, D.R.: J. Quant. Spectrosc. Radiat. Transf. **53**, 189 (1995)
23. Huestis, D.L., Copeland, R.A., Knutsen, K., Slanger, T.G., Jongma, R.T., Boogaarts, M.G.H., Meijer, G.: Can. J. Phys. **72**, 1109 (1994)
24. Slanger, T.G., Huestis, D.L.: J. Chem. Phys. **78**, 2274 (1983)
25. Kerr, C.M.L., Watson, J.K.G.: Can. J. Phys. **64**, 36 (1986)
26. Dyer, M.J., Faris, G.W., Cosby, P.C., Huestis, D.L., Slanger, T.G.: Chem. Phys. **171**, 237 (1993)
27. Di Lauro, C., Lattanzi, F., Graner, G.: Mol. Phys. **71**, 1285 (1990)
28. Kronig, R.L.: Band Spectra and Molecular Structure. Cambridge Univ. Press, London (1930)
29. Brown, J.M., Hougen, J.T., Huber, K.-P., Johns, J.W.C., Kopp, I., Lefebvre-Brion, H., Merer, A.J., Ramsey, D.A., Rostas, J., Zare, R.N.: J. Mol. Spectrosc. **55**, 500 (1975)
30. Wilson Jr., E.B.: J. Chem. Phys. **3**, 276 (1935)
31. Herzberg, G.: Molecular Spectra and Molecular Structure II. Infrared and Raman Spectra of Polyatomic Molecules. Van Nostrand, New York (1945)

32. Wilson Jr., E.B., Decius, J.C., Cross, P.C.: *Molecular Vibrations*. McGraw-Hill, New York (1955)
33. Hougen, J.T.: *J. Chem. Phys.* **37**, 1433 (1962)
34. Allen, H.C., Cross, P.C.: *Molecular Vib-Rotors*. Wiley, New York (1963)
35. Wollrab, J.E.: *Rotational Spectra and Molecular Structure*. Academic Press, New York (1967)
36. Kroto, H.W.: *Molecular Rotation Spectra*. Wiley, London (1975). reprinted, Dover, New York 1992
37. Cotton, F.A.: *Chemical Applications of Group Theory*, 2nd edn. Wiley, New York (1971)
38. Einstein, A.: *Phys. Z.* **18**, 121 (1917)
39. Condon, E.U., Shortley, G.H.: *The Theory of Atomic Spectra*. Cambridge Univ. Press, London (1935). reprinted 1967
40. Penner, S.S.: *Quantitative Molecular Spectroscopy and Gas Emissivities*. Addison-Wesley, Reading (1995)
41. Thorne, A.P.: *Spectrophysics*. Chapman Hall, London (1974)
42. Steinfeld, J.I.: *Molecules and Radiation*. MIT Press, Cambridge (1978)
43. Bethe, H.A., Salpeter, E.E.: *Quantum Mechanics of One- and Two-Electron Atoms*. Springer, Berlin, Heidelberg (1957)
44. Whiting, E.E., Nicholls, R.W.: *Astrophys. J. Suppl. Ser.* **235**, 27 (1974)
45. Whiting, E.E., Schadee, A., Tatum, J.B., Hougen, J.T., Nicholls, R.W.: *J. Mol. Spectrosc.* **80**, 249 (1980)
46. Franck, J.: *Trans. Faraday Soc.* **21**, 536 (1925)
47. Condon, E.U.: *Phys. Rev.* **32**, 858 (1928)
48. Herzberg, G.: *Molecular Spectra and Molecular Structure I. Spectra of Diatomic Molecules*. Van Nostrand, New York (1950)
49. Winans, J.G., Stueckelberg, E.C.G.: *Proc. Nat. Acad. Sci.* **14**, 867 (1928)
50. Hedges, R.E.M., Drummond, D.L., Gallagher, A.: *Phys. Rev. A* **6**, 1519 (1972)
51. McCallum, J.C.: *J. Quant. Spectrosc. Radiat. Transf.* **21**, 563 (1979)
52. Dwivedi, P.H., Branch, D., Huffaker, J.H., Bell, R.A.: *Astrophys. J. Suppl.* **36**, 573 (1978)
53. King, G.W.: *Spectroscopy and Molecular Structure*. Holt, Rinehart and Winston, New York (1964)
54. Meinel, A.B.: *Astrophys. J.* **111**, 555 (1950)
55. Lefebvre-Brion, H., Field, R.W.: *Perturbations in the Spectra of Diatomic Molecules*. Academic Press, New York (1986)
56. Huestis, D.L.: *DIATOM Spectral Simulation Computer Program, Version 7.0*. SRI International, Menlo Park (1994)
57. Hönl, H., London, F.: *Z. Phys.* **33**, 803 (1925)
58. Kovacs, I.: *Rotational Structure in the Spectra of Diatomic Molecules*. Elsevier, New York (1969)
59. Weber, A.: High resolution Raman studies of gases. In: Anderson, A. (ed.) *The Raman Effect*, vol. 2, Dekker, New York (1973)
60. Chen, K., Yeung, E.S.: *J. Chem. Phys.* **69**, 43 (1978)
61. Halpern, J.B., Zacharias, H., Wallenstein, R.: *J. Mol. Spectrosc.* **79**, 1 (1980)
62. Hund, F.: *Z. Phys.* **36**, 657 (1926)
63. Hund, F.: *Z. Phys.* **40**, 742 (1927)
64. Hund, F.: *Z. Phys.* **42**, 93 (1927)
65. Nikitin, E.E., Zare, R.N.: *Mol. Phys.* **82**, 85 (1994)
66. Judd, B.R.: *Angular Momentum Theory for Diatomic Molecules*. Academic Press, New York (1975)
67. Edmonds, A.R.: *Angular Momentum in Quantum Mechanics*, 2nd edn. Princeton Univ. Press, Princeton (1960). reprinted with corrections 1974
68. Femenias, J.L.: *Phys. Rev. A* **15**, 1625 (1977)
69. Kopp, I., Hougen, J.T.: *Can. J. Phys.* **45**, 2581 (1967)
70. Hickman, A.P., Huestis, D.L., Saxon, R.P.: *J. Chem. Phys.* **96**, 2099 (1992)
71. Helm, H., Cosby, P.C., Huestis, D.L.: *J. Chem. Phys.* **73**, 2629 (1980)
72. Helm, H., Cosby, P.C., Huestis, D.L.: *Phys. Rev. A* **30**, 851 (1984)
73. Cosby, P.C., Huestis, D.L.: *J. Chem. Phys.* **97**, 6108 (1992)
74. Carroll, P.K.: *J. Chem. Phys.* **58**, 3597 (1973)
75. Nielsen, H.H.: *Phys. Rev.* **38**, 1432 (1931)
76. Cross, P.C., Hainer, R.M., King, G.W.: *J. Chem. Phys.* **12**, 210 (1944)
77. Slinger, T.G., Crosby, P.C., Huestis, D.L., Bida, T.A.: *Science* **291**, 463 (2001)
78. Slinger, T.G., Copeland, R.A.: *Chem. Rev.* **103**, 4731 (2003)
79. Peligrini, M., Roberto-Neto, O., Machado, F.B.C.: *Chem. Phys. Lett.* **375**, 9 (2003)
80. Biémont, E., Garnir, H.P., Palmeri, P., Quinet, P., Li, Z.S., Zhang, Z.O., Svanberg, S.: *Phys. Rev. A* **64**, 022503 (2001)
81. Xu, H.L., Persson, A., Svanberg, S., Blagoev, K., Malcheva, G., Pentchev, V., Biémont, E., Campos, J., Ortiz, M., Mayo, R.: *Phys. Rev. A* **70**, 042508 (1970)
82. Stwalley, W.C., Wang, H.: *J. Mol. Spectrosc.* **195**, 194 (1999)
83. Bahns, J.T., Gould, P.L., Stwalley, W.C.: *Adv. At. Mol. Opt. Phys.* **42**, 171 (2000)
84. Zemke, W.T., Stwalley, W.C.: *J. Chem. Phys.* **120**, 88 (2004)



David L. Huestis David L. Huestis received his PhD in Chemistry from the California Institute of Technology in 1973. He is a Fellow of the American Physical Society. His research activities include a wide range of experimental and theoretical investigations of fundamental kinetic and optical processes involving atoms, small molecules, liquids, and solids. Two major application areas have been chemical kinetics and optical physics of high-power visible and ultraviolet gas lasers and the optical emissions of terrestrial and planetary atmospheres.



Abigail J. Dobbyn, David H. Mordaunt, and Reinhard Schinke

Contents

36.1	Observables	557
36.1.1	Scalar Properties	557
36.1.2	Vector Correlations	557
36.2	Experimental Techniques	558
36.3	Theoretical Techniques	559
36.4	Concepts in Dissociation	561
36.4.1	Direct Dissociation	561
36.4.2	Vibrational Predissociation	561
36.4.3	Electronic Predissociation	562
36.5	Recent Developments	562
36.6	Summary	563
	References	564

Abstract

Molecular photodissociation is the photoinitiated fragmentation of a bound molecule [1]. The purpose of this chapter is to outline the ways in which molecular photodissociation is studied in the gas phase [2]. The results are particularly relevant to the investigation of the species involved in combustion and atmospheric reactions [3].

Keywords

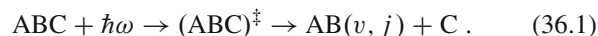
potential energy surface · absorption cross section · exit channel · partial cross section · vector correlation · wavepacket · autocorrelation function

A. J. Dobbyn · D. H. Mordaunt
Göttingen, Germany

R. Schinke (✉)
Max-Planck-Institute for Dynamics and Self-Organization
Göttingen, Germany
e-mail: rschink@wdg.de

Introduction

Conceptually, the photodissociation process can be divided into three stages. During the first stage, the molecule absorbs a photon and is promoted to an excited state. This is generally an excited electronic state but can be a highly excited vibrational state in the ground electronic state. In the second stage, the transient complex evolves through a series of *transition states*, until finally, in the third stage, the molecule enters the *exit channel* and dissociates into the products. Schematically, this might be represented, for a triatomic molecule ABC (Fig. 36.1), as



In the case of the triatomic molecule represented here, the dissociation involves the transformation of one of the vibrational modes to a translational, or dissociative, mode, another vibrational mode (the bending) to rotational motion of the products (j), whilst the third vibrational mode is preserved (v).

When the molecule is promoted to an electronic state that has a purely repulsive potential energy surface (PES), it undergoes very rapid dissociation, often in less than one vibrational period. This is called *direct dissociation*. However, the dissociation of the transient complex can be delayed, taking place over many vibrational periods. This is called *indirect dissociation*, or predissociation, and has been divided into three different categories [4], although as with the division between direct and indirect, this is sometimes somewhat arbitrary.

Vibrational predissociation (Herzberg Type II)

In this case, the transient complex is on a vibrationally adiabatic potential energy surface (this is an effective potential for the molecule when it is in a particular vibrational state v), which is not dissociative or which has a barrier to dissociation. Therefore, to dissociate it must either tunnel through the barrier, which is the only possibility for $v = 0$, or undergo

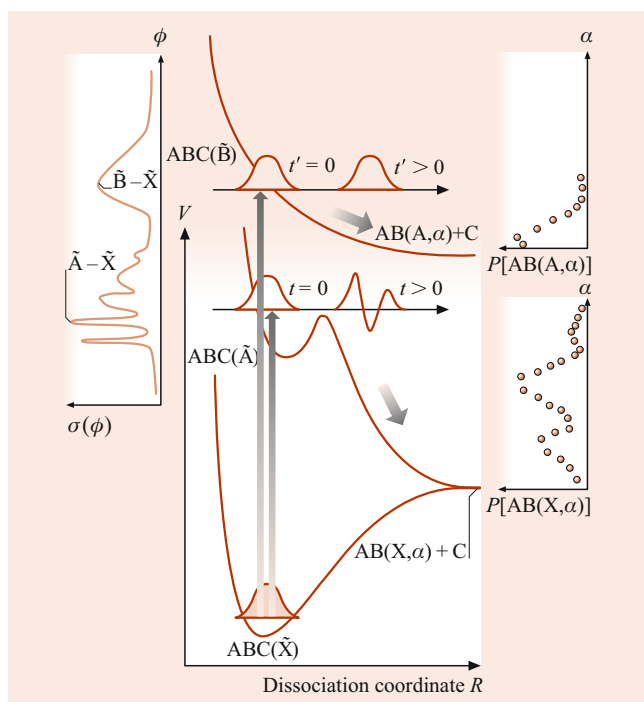


Fig. 36.1 UV photodissociation of a triatomic molecule ABC into products AB(α) and C, illustrating the total absorption cross section $\sigma(\omega)$, evolution of the molecular wave packet, and asymptotic product state distributions $P(\alpha)$, for direct and indirect dissociations on B and \tilde{A} state PESs, respectively

a nonadiabatic transition to a lower vibrational state, thereby transferring energy from a vibrational degree of freedom to the dissociative mode. This process of energy exchange is commonly called the intramolecular redistribution of vibrational energy (IVR).

Rotational predissociation (Herzberg Type III)

In this case, the transient complex is on a nondissociative rotationally adiabatic potential energy surface. Therefore, in a similar manner to vibrational predissociation, if it is to dissociate it must undergo a nonadiabatic transition to a lower rotational state, thereby transferring energy from rotation to the dissociative mode.

Electronic predissociation (Herzberg Type I)

In this case, the PES of the electronic state of the transient complex is not dissociative at the given energy, and in order to dissociate the molecule must undergo a nonadiabatic transition to a second dissociative electronic state. This involves the coupling of nuclear and electronic motion and, therefore, leads to a breakdown of the Born–Oppenheimer (BO) approximation. There are two main types of electronic predissociation. In the first case, there is only a very small coupling, and no actual crossing, between two different electronic states, and the transition between the two is driven by the very high density of vibrational states on

the second electronic state. This is called internal conversion for spin-allowed processes and intersystem crossing for spin-forbidden processes. In the second case, the transition between the electronic states is driven by strong coupling. This coupling can be vibronic (vibrational-electronic) in nature, e.g., for the Renner–Teller and Jahn–Teller effects, or purely electronic, as in the case of a *conical intersection*.

Selection rules

Two sets of selection rules apply to photodissociation. The first set governs the allowed states to which the molecule can be promoted by the photon. These selection rules are simply those for bound-state spectroscopy (Sect. 35.4). Note in particular the selection rule $\Delta J = 0, \pm 1$. This has important practical implications since it means that a molecule that is initially rotationally cold remains so after absorption of a photon. Thus, those observables that are averaged over J will have a clear structure experimentally and will be easier to calculate theoretically. This is in contrast to scattering experiments, which in general involve a summation over many J states (Chap. 38).

The second set of selection rules governs the dissociation process. The transient complex, or prepared (p) state will undergo transitions to a final (f) vibrational, rotational, or electronic state in order to dissociate; these transitions have their own set of selection rules. As for all selection rules, these are determined on the basis of symmetry. For a total wave function Ψ and a perturbation function W , which consists of the coupling terms or neglected terms in the Hamiltonian, $\int \Psi_p^* W \Psi_f d\tau$ must be nonzero for a transition to take place. As W forms a part of the Hamiltonian, it is totally symmetric, and therefore the integral is nonzero only if the prepared and final state irreducible representations are equal, $\Gamma_p = \Gamma_f$. If there is a transition to an excited electronic state, the point groups of the initial and final states are often not the same, in which case the point group formed by the joint elements of symmetry is used, or, in the case where there is no stable geometry for one of the states, the symmetry of the potential is used. These selection rules are given in Table 52.1 for a diatomic molecule.

If the motion can be separated into vibrational, rotational, and electronic parts, so that $\Psi = \Psi^v \Psi^r \Psi^e$ and $W = W^v + W^r + W^e$, it is then possible to derive three separate selection rules: $\Gamma_p^r = \Gamma_f^r$ for the rotational motion, i.e., conservation of internal angular momentum; $\Gamma_p^e = \Gamma_f^e$ for the electronic motion; and $\Gamma_p^v = \Gamma_f^v$ for the vibrational motion. Since the final vibrational state is in the continuum, in practice, all vibrational species (Γ_f^v) are available at a given energy, so that the vibrational selection rule is not significantly restrictive. This separation is not possible in the case of electronic predissociation occurring through the Renner–Teller or Jahn–Teller effect, where it is necessary to consider the vibronic species of the initial and final states.

36.1 Observables

Fundamental to any study of photodissociation is the measurement or calculation of the characteristic properties, or observables, of the reaction, from which the underlying dynamics of the fragmentation process can be inferred.

36.1.1 Scalar Properties

The absorption cross section $\sigma(\omega)$ is a measure of the capacity of the molecule to absorb photons with frequency ω . It is analogous to the line intensity in bound-state spectroscopy. Assuming that the light–matter interaction is weak (Chap. 72), and that the light pulse is on for a long time, the absorption cross section is given by

$$\sigma(\omega) \propto \omega_{\text{fi}} |\langle \Psi_{\text{f}} | \mathbf{E} \cdot \hat{\boldsymbol{\mu}} | \Psi_{\text{i}} \rangle|^2, \quad (36.2)$$

where Ψ_{i} and Ψ_{f} represent the initial and final states, whose energies differ by $\hbar\omega_{\text{fi}}$; \mathbf{E} is a unit vector in the direction of the polarization of the electric field, and $\hat{\boldsymbol{\mu}}$ is the electric dipole operator of the molecule. Assuming the Born–Oppenheimer separation of electronic and nuclear motion, Eq. (36.2) can be rewritten as

$$\sigma(\omega) \propto \omega_{\text{fi}} |\langle \Psi_{\text{f}}^{\text{rv}} | \mu_{\text{fi}} | \Psi_{\text{i}}^{\text{rv}} \rangle|^2, \quad (36.3)$$

where the electronic transition dipole moment μ_{fi} equals $\langle \Psi_{\text{f}}^{\text{e}} | \mathbf{E} \cdot \hat{\boldsymbol{\mu}} | \Psi_{\text{i}}^{\text{e}} \rangle$, and is, in general, dependent on the internal coordinates of the molecule. The superscripts (r, v) will be dropped from now on, and Ψ will refer to the wave function for the internal coordinates of the molecule.

The absorption cross section reflects not only the nature of the transient complex but also its evolution through the transition states. For direct dissociation the absorption cross section is usually very broad and structureless. In contrast, the absorption cross section for predissociation is structured, containing lines that are normally Lorentzian in shape, and whose widths Γ are related to the lifetime of the transient complex at that energy by $\tau = \hbar/\Gamma$.

The partial photodissociation cross sections $\sigma(\omega, \alpha)$ are a measure of the capacity of the molecule to absorb photons with frequency ω and to yield products in quantum state α . They are defined by

$$\sigma(\omega, \alpha) \propto \omega_{\text{fi}} |\langle \Psi_{\text{f}}^{\alpha} | \mu_{\text{fi}} | \Psi_{\text{i}} \rangle|^2, \quad (36.4)$$

where Ψ_{f}^{α} is the final wave function for the products in the quantum state α . The partial cross sections for direct dissociation are broad and featureless. For predissociation, similar structures are seen in the partial cross sections as in the absorption cross section. The absorption or total cross section

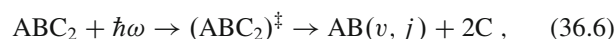
is given by the sum of the partial cross sections over all final product states

$$\sigma(\omega) = \sum_{\alpha} \sigma(\omega, \alpha). \quad (36.5)$$

The rotational and vibrational product distributions $P(\omega, \alpha)$ provide information about the amount of product formed by a photon with frequency ω in a particular rotational or vibrational state α . These are related to the partial cross sections by $P(\omega, \alpha) = \sigma(\omega, \alpha)/\sigma(\omega)$. The rotational and vibrational product distributions reflect the nature of the transient complex as it enters the exit channel, as well as the dynamics in the exit channel.

The branching ratios for different chemical species produced in photodissociation are defined as the fraction of the total number of parent molecules that produce the particular species of interest. In Eq. (36.1), the molecule ABC is dissociated into AB + C. It might equally well have dissociated to A + BC, or indeed A + B + C. It is clear then that there may be several different reaction schemes, or channels, for the photodissociation of one particular molecule. Thus, the branching ratio for forming AB is the yield of this first channel divided by the total dissociation yield into all possible channels. Further, it would sometimes be possible to produce AB, or any of the other chemical species, in various electronic, vibrational, or/and rotational quantum states. In this case, the branching ratio for forming AB(α) is the yield of AB in the specific quantum state α divided by the total yield of AB; however, this describes the branching into only this particular reaction channel.

For the reaction scheme represented in Eq. (36.1), the quantum yields of the products AB and C are the same. However, for example, in the reaction



the quantum yield of C is twice that for AB. In general, the quantum yield of a particular product fragment for one reaction channel is the ratio of the number of fragments formed to the number of photons absorbed. However, it is again possible for a molecule to dissociate into various different reaction channels. In such a case, to obtain the overall quantum yield for a particular product, the quantum yield for each reaction channel must be summed over all the available reaction channels, taking into account the branching ratios for the channels.

36.1.2 Vector Correlations

Photodissociation is by its very nature an anisotropic process, as can be seen from Eq. (36.2). The operator $\hat{\boldsymbol{\mu}}$ defines a specific axis in the molecular body-fixed frame of reference. At

the instant of photoexcitation, $\hat{\mu}$ is preferentially aligned parallel to the polarization of the electric field \mathbf{E} in the *external laboratory space-fixed* frame of reference. Hence, \mathbf{E} defines a specific axis, and thus cylindrical symmetry in the body-fixed frame. If fragmentation occurs on a timescale that is short compared with overall rotation of the excited complex, this correlation persists between the body-fixed frame and the space-fixed frame, and a wealth of information can be obtained. However, rotation of the transient complex prior to fragmentation serves to degrade this symmetry in the external body-fixed frame.

Three vectors fully describe the photodissociation process for both the parent molecule and the products: (i) $\hat{\mu}$ in the body-fixed frame (and hence \mathbf{E} , in the space-fixed frame, at the instant of photoexcitation); (ii) \mathbf{v} , the recoil velocity of the products; and (iii) \mathbf{j} , the rotational angular momenta of the fragments. Vector correlations can exist between all of these vectors [5].

The most commonly observed is the angular distribution of the photofragments $I(\theta, \alpha)$, i.e., the relation

$$I(\theta, \alpha) \propto \frac{1}{4\pi} \left[1 + \beta(\alpha) P_2(\cos \theta) \right] \quad (36.7)$$

between \mathbf{v} and \mathbf{E} ; $P_2(x)$ is the second-order Legendre polynomial, and θ is the angle between \mathbf{v} and \mathbf{E} . The *anisotropy parameter* $\beta(\alpha)$ ranges between -1 for a perpendicular transition and $+2$ for a parallel transition. Thus, measuring the angular distribution of the fragments provides information about the type of electronic transition and, hence, the electronic symmetry of the excited state [6]. If the alignment between the body-fixed and space-fixed frames is destroyed, the angular distribution becomes *isotropic* and $\beta(\alpha) = 0$. The anisotropy parameter depends on the product channel α .

A second vector correlation concerns the direction of \mathbf{j} with respect to \mathbf{E} . Fragmentation generates rotational motion in the nuclear plane; for a perpendicular transition, this is perpendicular to the plane containing the atoms, leading to the projection of \mathbf{j} being preferentially aligned parallel to $\hat{\mu}$, and thus \mathbf{E} in the space-fixed frame. For a parallel transition, the opposite would be true, i.e., \mathbf{j} would be aligned in the plane perpendicular to $\hat{\mu}$. The alignment of \mathbf{j} leads to polarized emission/absorption depending on whether molecules are created in an electronically excited/ground state. Therefore, the orientation of the product polarization with respect to the original photolysis polarization \mathbf{E} also yields information about the symmetry of the electronic states involved in dissociation.

The final association in this series is independent of the space-fixed frame, since \mathbf{v} and \mathbf{j} are both defined in the body-fixed frame. Unlike the two previous correlations, a long lifetime does not destroy the alignment, as it is not established until the bond breaks, and the two fragments recoil. For a tetratomic (or larger) molecule there are, in principle,

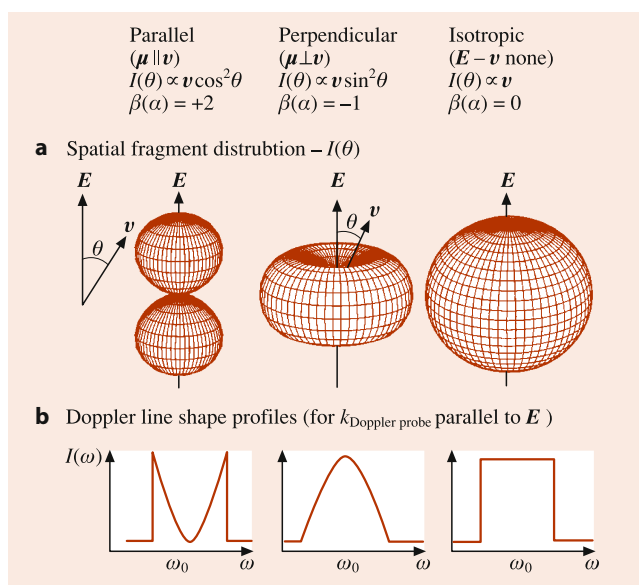


Fig. 36.2 Spatial recoil anisotropies and Doppler line shape profiles for parallel and perpendicular transitions compared with an isotropic distribution

two possible sources of product rotational excitation: bending motion in a plane of the molecule producing fragments with \mathbf{v} perpendicular to \mathbf{j} or torsional motion leading to fragment rotation out of the plane. A prime example of this is the distinction between frisbee and propeller-type motion of the two OH fragments in the dissociation of hydrogen peroxide [7, 8]. Measurement of only the scalar properties *cannot* discriminate between these two possibilities, highlighting the additional information that can be gained about the bond rupture and the exit channel dynamics by the study of vector correlations (Fig. 36.2).

36.2 Experimental Techniques

Early photochemical experiments used broad white-light continuum sources and large diffractometers [4]. However, it has been the development of lasers in combination with molecular-beam techniques that has dramatically increased the understanding of photodissociation processes. The ever-increasing spectral and time resolutions of lasers, in addition to the power and range of wavelengths available, have made it possible to excite molecules selectively and with high efficiency. This has enabled state-specific preparation of the parent molecule, the study of time evolution, as well as the measurement of the scalar and vector properties of the asymptotic products [9].

Specification of the initial state

A room-temperature sample of a gas will have a Boltzmann distribution over rotational states. Molecular beam

techniques provide an improved specification of the initial angular momenta in the parent molecule by isentropically cooling its internal rotational energy [10]. Full quantum state specification can be achieved by various two-photon excitation schemes, e.g., stimulated emission pump (SEP) spectroscopy and vibrationally mediated dissociation. SEP is commonly used to study dissociation on the ground state PES; the molecules are excited to a stable upper electronic state, stimulated emission back to the ground state prepares a *single* quasi-bound state. Vibrationally mediated dissociation provides information about both ground and upper electronic states; the molecules are excited to a stable intermediate vibrational level on the ground state, and further excitation promotes this fully defined wave function to an upper dissociative electronic state [11].

Detailed measurement of the absorption cross section

UV and VUV electronic spectroscopy has proven to be a very powerful tool for examining the interaction of a photon with a parent molecule. Absorption cross sections are typically measured by scanning the frequency domain and monitoring either the intensity of radiation absorbed or the flux of product molecules produced. State-specific detection of the product flux yields the partial cross section $\sigma(\omega, \alpha)$. Explicit measurement of $\sigma(\omega)$ is a direct application of the Beer-Lambert law (Sect. 73.2) and, thus, depends on the length of the optical cavity; cavity ring-down spectroscopy with multiple passes through a cell provides an effective cell length of several tens of kilometers.

Evolution of the transient complex

The evolution of the molecular wave packet can be probed by time-resolved spectroscopy, as discussed in Chap. 37 and [12]. Real-time analysis of the molecular wave packet provides a direct insight into the forces acting during molecular photodissociation. This type of time-resolved spectroscopy and the energy-resolved spectroscopy described above are mutually exclusive due to the time-energy uncertainty principle (Sect. 84.3.1).

Asymptotic properties

The vast majority of photodissociation studies determine asymptotic properties of the dissociation process, measuring either internal energy, recoil velocity, or angular distributions of the dissociation products. The product state distributions are usually explicitly probed by laser-induced fluorescence (LIF), resonance-enhanced multiphoton ionization (REMPI) spectroscopy, or coherent Raman scattering with the relative populations of the products obtained via line intensities.

The distribution and anisotropy of the recoil velocities are measured using Doppler spectroscopy or time-of-flight (TOF) techniques [13]. Doppler spectroscopy uses the Doppler-broadening of lines in the LIF or REMPI ex-

citation spectra (Sect. 73.6); the profile of the line shape also depends on the recoil anisotropy of the probed species (Fig. 36.2). However, many important molecular fragments are not amenable to spectroscopic detection. Thus, though lacking the ultimate state specificity of spectroscopy, TOF techniques by virtue of their general applicability provide an appealing alternative route to determine the product state distributions. In TOF techniques, the time is recorded for photofragments to recoil a known distance from the interaction region to a detector. Due to total energy and momentum conservation, the translational energy distribution of a fragment state specifically detected directly implies the internal energy distribution of the other partner product. In less favorable cases where this is not possible, *coincidence* detection schemes are employed to define the partition between translational and internal energies. Rotation of the detection axis with respect to the polarization of the photolysis laser yields the recoil anisotropy. Advances in spatially resolved detection schemes are now providing an improved measure of vector correlations. Mass spectrometry can be used to measure branching ratios and quantum yields, which can also be obtained from the techniques described above.

36.3 Theoretical Techniques

The calculation of the observables of photodissociation can be carried out using quantum mechanics either in the time-independent or the time-dependent frame, as well as using classical mechanics [1]. Theoretical studies have contributed greatly to the understanding of photodissociation processes, as they provide the ability not only to calculate the observables, but also, through the knowledge of the wave function, to view the dissociation dynamics directly. This has enabled the inference of the underlying dynamics from the observables of the reaction to be more precisely established.

Due to computer limitations, the majority of quantum mechanical studies currently only treat three degrees of freedom fully, and, thus, have mainly concentrated on triatomic molecules. Jacobi coordinates are usually used, with the appropriate set for the dissociation of ABC into AB and C as follows: R , denoting the distance between the atom C and the center of mass of the AB fragment; r , denoting the internal vibration coordinate of AB; and γ , denoting the bending angle between R and r .

The initial state Ψ_i is generally taken to be a single bound state. It is obtained either by the solution of the Schrödinger equation at a particular energy (Sect. 33.4) or simply by taking a product of three Gaussians in the three coordinates, with the parameters of the Gaussians being determined from spectroscopic information on the ground state.

Further, to calculate the observables it is also necessary to have information about μ_{fi} . However, this is often assumed

to be a constant, i.e., independent of the internal coordinates of the molecule. The *Franck–Condon principle* assumes that the nuclear geometry changes after the electronic transition and not during it. Therefore, a molecule, with a particular geometry, will, when promoted by the photon to the excited electronic state, be centered around the same geometry, which is thus referred to as the Franck–Condon region or point.

To carry out any dynamical calculations it is necessary to have PESs for the electronic states involved. These are usually obtained from ab-initio calculations, which are described in Chap. 33. The accuracy of the PES surface largely determines the accuracy of the results obtained, as the PES essentially determines the dynamics of the fragmentation process.

In the *time-independent* approach, a solution of the time-independent Schrödinger equation

$$(\hat{H} - E)\Psi^\alpha = 0, \quad (36.8)$$

is sought for a specific total energy E subject to appropriate boundary conditions at infinite product separation. There are many different approaches to solving this problem, but they can be broadly separated into two groups: scattering methods and \mathcal{L}^2 methods. The scattering methods involve the solution of the coupled channel equations described in Chap. 38. These can be solved directly to yield the wave functions, which can then be used to calculate the observables, or they can be solved indirectly to provide similar information. The use of \mathcal{L}^2 methods, which attempt to expand Ψ in a finite basis set, is not directly applicable since the wave functions are in the continuum and spread out to infinite distances in the R coordinate. Thus, various modifications have been intro-

duced in order to take this into account. The most important of these use variational principles [14], such as that due to *Kohn* [15]. In the Kohn variational principle, the wave function in the inner or interaction region is expanded in a finite \mathcal{L}^2 basis. However, in the outer region, the wave function is expanded in an energy-dependent basis of outgoing and incoming waves, which are approximate solutions of the coupled channel equations. Other methods which can sometimes be used to indirectly extract information about the observables are stabilization [16] and complex scaling [17].

In the *time-dependent* approach [18], one solves the time-dependent Schrödinger equation

$$i\hbar \frac{\partial}{\partial t} \Phi(t) = \hat{H} \Phi(t) \quad (36.9)$$

for the wave packet $\Phi(t)$ with initial condition $\Phi(0) = \Psi_i$, i.e., it is assumed that the molecule is *vertically* promoted by an infinitely short pulse to the electronic state under consideration. The wave packet is a coherent superposition of stationary wave functions Ψ^α (Chap. 37), and since it comprises many of the stationary states, it contains all the information necessary to characterize the dissociation (Fig. 36.3).

The total absorption cross section is given by

$$\sigma(\omega) \propto \int_{-\infty}^{+\infty} dt S(t) e^{-i\omega t}, \quad (36.10)$$

where the autocorrelation function $S(t)$ is defined as

$$S(t) = \langle \Phi(0) | \Phi(t) \rangle. \quad (36.11)$$

The autocorrelation function reflects the motion of the wave packet, and is, therefore, a convenient means for visualizing

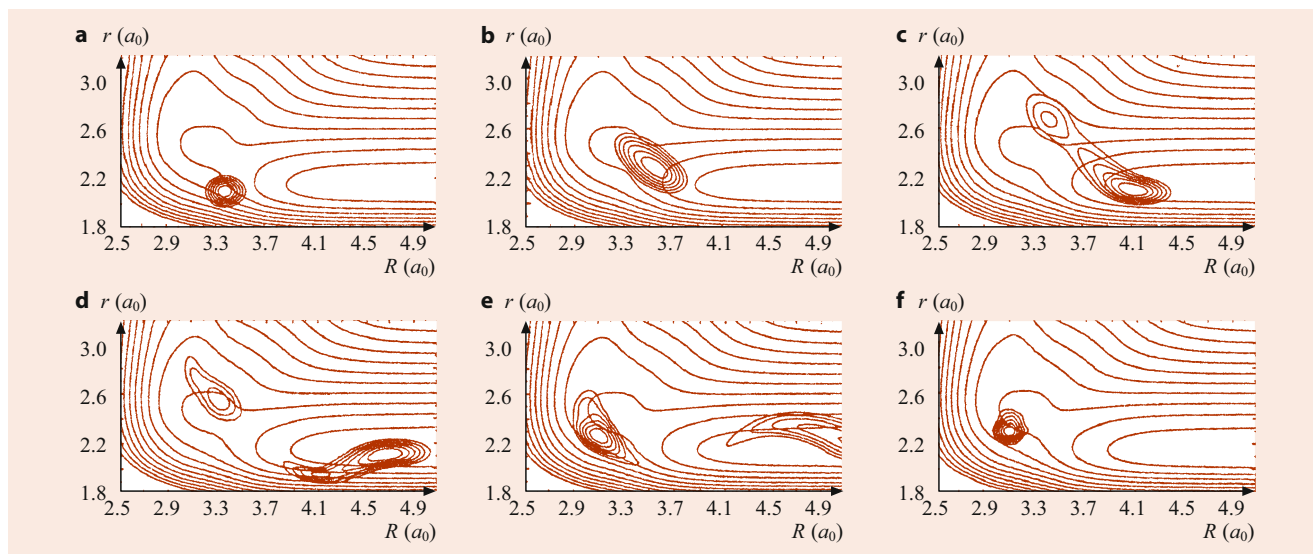


Fig. 36.3 Time evolution of a wave packet in the dissociation of FNO in the S_1 state

the molecular dynamics. The individual partial cross sections can be obtained in the limit $t \rightarrow \infty$ by projection of the wave packet onto the stationary wave functions of the products, i.e., plane waves in the dissociation coordinate and vibrational-rotational wave functions for the free products.

36.4 Concepts in Dissociation

There has been substantial experimental and theoretical work to elucidate the processes involved in photodissociation from knowledge of the observables, and much progress has been made. In this section, an attempt is made to present some of the simpler ideas which have emerged [1].

36.4.1 Direct Dissociation

Direct dissociation is the very fast rupture of a bond after a molecule has been promoted to an electronic state that has a purely repulsive PES. A very clear picture of this process can be obtained from wave packet calculations; the wave packet that is placed on the repulsive surface moves directly down the PES and into the exit channel. The autocorrelation function decays from one to zero in a short time and does not show any recurrences, i.e., oscillations in the autocorrelation function. The absorption cross section $\sigma(\omega)$, which is the Fourier transform of the autocorrelation function in Eq. (36.10), is, therefore, a very broad Gaussian with no structure. The breadth of $\sigma(\omega)$ is inversely proportional to the width of the autocorrelation function and, using simple classical pictures, can be taken to be approximately proportional to the steepness of the potential at the Franck–Condon point. The partial cross sections have a similar structure to the total cross section, although they have differing intensities and are shifted relative to each other on the energy scale.

The product distributions can be predicted using simple classical pictures. These methods can be divided into two groups, depending on the extent of the excitation/de-excitation, or coupling, in the exit channel. If there is very little excitation/de-excitation in the exit channel, the rotational and vibrational product distributions are best described using Franck–Condon mapping. Another model that gives good results for the rotational distributions is the impact parameter, or impulsive, model. If excitation/de-excitation in the exit channel is not negligible, the product distributions are best described using the *reflection principle*. This relates the distribution of the initial wave packet in γ to the final rotational distributions through the classical excitation function. Similarly, the distribution of the initial wave packet in space is related to the final vibrational distributions through another classical excitation function.

Even for a purely repulsive PES, the potential may be very flat in the Franck–Condon region, so that the molecule may be able to undergo one internal vibration before it dissociates. In this case, there is a diffuse structure in $\sigma(\omega)$, associated with recurrences in the autocorrelation function. The spacing of the structures in $\sigma(\omega)$ are related to the period of the internal vibrations by $\Delta E = 2\pi\hbar/T$. Diffuse structures in $\sigma(\omega)$ have also been linked to unstable periodic orbits.

36.4.2 Vibrational Predissociation

Vibrational predissociation is dissociation delayed due to the trapping of the energy of the molecule in modes orthogonal to the dissociation coordinate. It can be explained very clearly in the time-independent picture as resonances (sometimes known as Feshbach resonances), which are simply extensions of the bound states into the continuum; $\sigma(\omega)$ in this case consists of a series of Lorentzian lines, whose width is inversely proportional to the lifetime of the resonance. In the case where the internal modes of the molecule are not strongly coupled to each other or to the dissociation mode, these resonance states can often be assigned, with the number of quanta in each mode being specified. In this case, the lines in $\sigma(\omega)$ form a series of progressions. The widths of these lines, and thus the lifetimes of the resonance states, often show trends relating the lifetimes to the assignment. This is called *mode specificity*. In the case when the system is strongly mixed, it is not possible to make an assignment of the resonances, and the lifetimes show strong fluctuations. This is called *statistical state specificity* [19].

The resonances can also be seen in the time-dependent picture, where the autocorrelation function shows many recurrences with periods T , depending on the fundamental frequencies of the internal modes $\omega = 2\pi/T$ (Chap. 37).

The partial cross sections for vibrational predissociation also consist of Lorentzian lines, with positions and widths exactly as for the total cross sections but with differing intensities. The partial widths, which describe the rate of dissociation into each product channel, are given by

$$\Gamma_{\alpha} = \Gamma \frac{\sigma(\omega, \alpha)}{\sigma_{\text{tot}}(\omega)}. \quad (36.12)$$

In the weak coupling case, simple pictures can be used to describe the product distributions. The rotational product distributions can be explained using, again, the reflection principle; but in this case, instead of considering the distribution of the initial wave function in γ , the distribution of the wave function at the transition state is used. The vibrational product distributions can often be well described by examining vibrationally adiabatic curves.

In the case when the modes are strongly coupled, the simple models break down. It is then sometimes possible

to use statistical models to describe both the rates and the product distributions. One example of these unimolecular-statistical theories is the Ramsperger–Rice–Karplus–Marcus (RRKM) theory, which is widely used for the description of unimolecular dissociations [20]. Another example is phase space theory (PST) [21, 22], which is often used to calculate the product distributions for reactions that have no barrier. The quantum mechanical results fluctuate about these average values. These fluctuations, which can be considered as being independent of the system and can be described well by the predications of random matrix theory [23].

36.4.3 Electronic Predissociation

Nonadiabatic transitions between two or more electronic states are a common phenomenon in photodissociation [24] as well as in other chemical reactions (Chap. 52). Such transitions can result in the production of both electronically excited and ground state fragments.

Adiabatic molecular PESs can vary in complex fashions. Many of these contortions arise from avoided and real crossings of the surfaces, and in all such cases, the physical and chemical understanding is greatly facilitated by expressing the adiabats in terms of the diabatic states (Chap. 33). The electronic diabatic states are chosen to simplify the structure of the electronic wave functions by incorporating the off-diagonal or coupling elements as a pure potential energy term, rather than as a kinetic term, or a mixture of both.

Under these conditions, the BO approximation is inadequate since there is coupling between the different adiabatic states, and the electronic and nuclear motion cannot be separated. Therefore, the solution of the time-dependent Schrödinger equation (Sect. 36.3) requires the set of coupled equations

$$i\hbar \frac{\partial}{\partial t} \begin{pmatrix} \Psi_1 \\ \Psi_2 \end{pmatrix} = \begin{pmatrix} V_{11} + T_{11} & V_{12} \\ V_{12} & V_{22} + T_{22} \end{pmatrix} \begin{pmatrix} \Psi_1 \\ \Psi_2 \end{pmatrix} \quad (36.13)$$

to be propagated, where the coupling between the diabatic surfaces is in the potential (V) and not the kinetic (T) terms. The wave packet evolves on both diabatic (or adiabatic) surfaces and shows a complicated motion in moving between the two surfaces. The coupling between the nuclear and electronic motion can be thought of as resulting in the nuclear motion forcing the transfer of a valence electron to another molecular orbital. Since the efficiency of this transfer is greatest when the orbitals are degenerate, the crossings of the wave packet between the PESs are generally localized around their degeneracies. Finally, the wave packet moves out on the adiabatic surfaces towards the products, with which they are correlated.

36.5 Recent Developments

In recent years, the field of photodissociation has seen a number of intriguing applications and comparisons between detailed experimental data and high-quality ab-initio calculations. These applications have become feasible mainly because of the possibility to construct accurate potential energy surfaces from first-principle electronic structure calculations. Cases in which the fragmentation proceeds via two or several electronic states have been especially concentrated on [25]. In these cases, the Born–Oppenheimer approximation is not valid, and the coupling between electronic and nuclear degrees of freedom is essential (Sect. 36.4.3). A nice example is the photodissociation of water in the second absorption band. Since water has only ten electrons, highly accurate potential energy surfaces have been calculated theoretically, and these have been used in extensive dynamics calculations – including motion on three potential energy surfaces [26]. The agreement between the calculated and the measured absorption cross section at room temperature is outstanding [27]. From the elaborate analysis of product state distributions (rotational, vibrational, and electronic), many details about the coupled motion on several potential energy surfaces have been learned [28, 29]. The electronic density of water is small, and therefore the photodissociation can be treated on a nearly exact level. For other triatomic molecules, with more electrons and a higher density of electronic states, this is generally not feasible. An important example is ozone, which plays a vital role in the atmosphere. The electronic structure of O_3 is illustrated in Fig. 36.4, where many spin-allowed as well as spin-forbidden fragmentation pathways are seen [30]. The photodissociation of ozone in the UV range has been the target of many experimental studies [31]. The interpretation of the many experimental results on the basis of realistic potential energy surfaces is a great challenge for theoretical chemistry.

Photodissociation studies are particularly rewarding if the lifetime in the excited electronic state is long because then the absorption spectrum shows well-resolved lines (resonances), the widths of which are inversely related to the state-specific lifetimes [32]. A typical situation is the excitation of a particular vibrational-rotational state in a bound electronic state, which can decay only via coupling to a dissociative electronic state. The lifetime then reflects the coupling of this state to the continuum of the dissociative state (predissociation). An example is the photodissociation of HCO [33, 34]; in this case, the upper and the lower state are coupled by Renner–Teller coupling. A similar example is the photodissociation of HNO. For this molecule, the lower state has a deep potential well that supports long-lived states in its own continuum. The mixing between the quasi-bound states of the upper state with the resonance states of the lower state leads to interest-

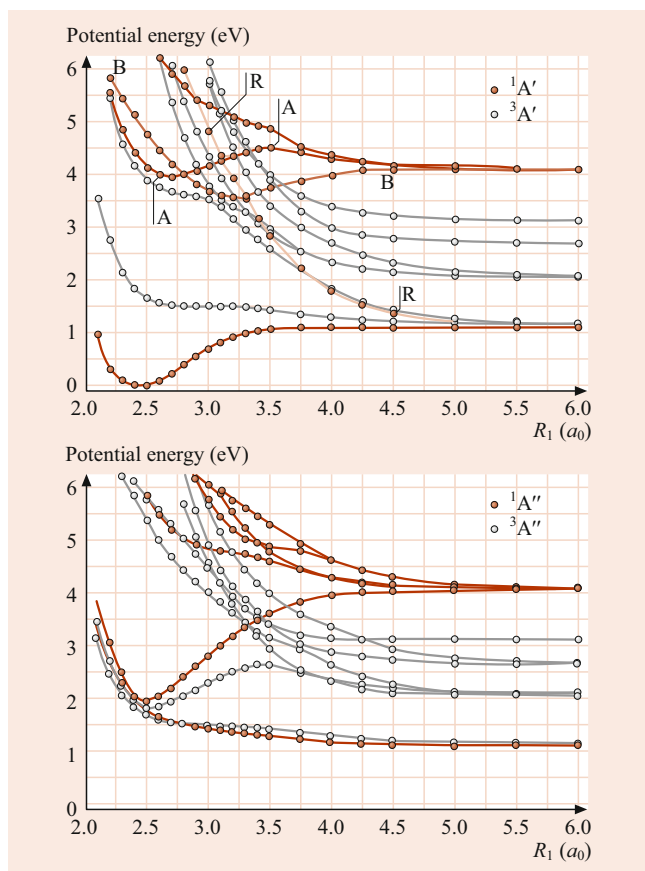


Fig. 36.4 Electronic structure of ozone. Shown are cuts through the potential energy surfaces for the singlet and triplet states. After [30]

ing behavior in the lifetime as a function of the rotational quantum number [35] (resonance between resonances).

Resonances are also prominent features of ground state potential energy surfaces; they are the continuation of the true bound states into the continuum (Sect. 36.4.2). Since resonances determine the kinetics of chemical reactions, they are usually studied in the framework of *unimolecular dissociations* or *unimolecular reactions* [36]. On the other hand, these resonance states can be excited by photons, and therefore it is meaningful to discuss them also in the context of photodissociation. In the past few years, numerical methods have been developed to efficiently calculate the resonance parameters [37–39]; see [36] for a comprehensive overview. Several triatomic molecules with dramatically different intramolecular dynamics have been investigated. The main observation is a strong fluctuation in the resonance lifetimes over several orders of magnitude, even for molecules whose classical dynamics is chaotic, such as NO_2 [40]. Figure 36.5 shows the results for $\text{HOCl} \rightarrow \text{HO} + \text{Cl}$ [41, 42]. The large fluctuations of the lifetimes (or dissociation rates) are believed to affect the fall-off behavior of recombination rate coefficients [43].

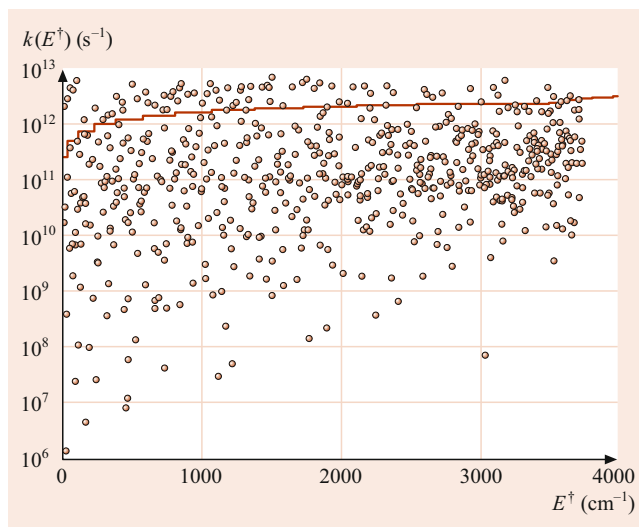


Fig. 36.5 Overview of the calculated dissociation rates of HOCl as a function of the excess energy. The solid line is the prediction of a statistical model. After [42]

The concept of first calculating a potential energy surface as function of all coordinates and then performing dynamics calculations is suitable only for triatomics. For molecules with more than four atoms, it is not applicable, simply because of the rapidly increasing number of degrees of freedom. For larger molecules, *direct dynamics* simulations, in which the methodology of classical trajectory simulations is coupled directly to electronic structure calculations, are the method of choice [44, 45]. In these simulations, the derivatives of the potential, which are required for the numerical integration of the equations of motion, are obtained directly from electronic structure theory without the need for an analytic potential energy surface. An important application of direct dynamics is the study of post-transition state intramolecular and unimolecular dynamics. When the dissociation proceeds through a transition state, it may be sufficient to start trajectories at the transition state and to follow them into the product channels [46, 47]

36.6 Summary

Photodissociation of polyatomic molecules is an ideal field for studying the details of molecular dynamics. The primary goal of the experimental and theoretical approaches (Sects. 36.2 and 36.3) is to understand the connection between the observables (Sect. 36.1) and the underlying chemical dynamics (Sect. 36.4). Once this connection has been established, it is possible to have a detailed understanding of the dissociation dynamics, transition state geometries, and the PESs that ultimately govern the molecular chemical reactivity. The interplay between powerful experimental and

theoretical techniques has enabled this goal to be realized for many photodissociation reactions.

References

- Schinke, R.: *Photodissociation Dynamics*. Cambridge University Press, Cambridge (1993)
- Okabe, H.: *Photochemistry of Small Molecules*. Wiley, New York (1978)
- Wayne, R.P.: *Chemistry of Atmospheres*, 2nd edn. Oxford University Press, New York (1991)
- Herzberg, G.: *Molecular Spectra and Molecular Structure III, Electronic Spectra and Electronic Structure of Polyatomic Molecules*. Van Nostrand, New York (1967)
- Hall, G.E., Houston, P.L.: *Ann. Rev. Phys. Chem.* **40**, 375 (1989)
- Zare, R.N.: *Angular Momentum*. Wiley, New York (1988)
- Grunewald, A.U., Gericke, K.-H., Comes, F.J.: *J. Chem. Phys.* **87**, 5709 (1987)
- Grunewald, A.U., Gericke, K.-H., Comes, F.J.: *J. Chem. Phys.* **89**, 345 (1988)
- Ashfold, M.N.R., Baggott, J.E. (eds.): *Molecular Photodissociation Dynamics*. Royal Society of Chemistry, London (1987)
- Scoles, G. (ed.): *Atomic and Molecular Beams Methods*. Oxford University Press, New York (1988)
- Crim, F.F.: *Ann. Rev. Phys. Chem.* **44**, 397 (1993)
- Manz, J., Wöste, L. (eds.): *Femtosecond Chemistry*. VCH, Weinheim (1995)
- Ashfold, M.N.R., Lambert, I.R., Mordaunt, D.H., Morley, G.P., Western, C.M.: *J. Phys. Chem.* **96**, 2938 (1992)
- Nesbet, R.K.: *Variational Methods in Electron-Atom Scattering Theory*. Plenum, New York (1980)
- Zhang, J.Z.H., Miller, W.H.: *J. Phys. Chem.* **92**, 1811 (1990)
- Lefebvre, R.: *J. Phys. Chem.* **89**, 4201 (1985)
- Reinhardt, W.P.: *Ann. Rev. Phys. Chem.* **33**, 223 (1982)
- Kosloff, R.: *J. Phys. Chem.* **92**, 2087 (1988)
- Hase, W.L., Cho, S., Lu, D., Swamy, K.N.: *Chem Phys* **139**, 1 (1989)
- Robinson, P.J., Holbrook, K.A.: *Unimolecular Reactions*. Wiley, London (1972)
- Pechukas, P., Light, J.C.: *J Chem Phys* **42**, 3285 (1965)
- Pechukas, P., Light, J.C., Rankin, C.: *J Chem Phys* **44**, 794 (1966)
- Brody, T.A., Flores, J., French, J.B., Mello, P.A., Pandey, A., Wong, S.S.M.: *Rev. Mod. Phys.* **53**, 385 (1981)
- Dixon, R.N.: *Chem. Soc. Rev.* **23**, 375 (1994)
- Schinke, R.: Quantum mechanical studies of photodissociation dynamics using accurate global potential energy surfaces. In: Domcke, W., Yarkony, D.R., Köppel, H. (eds.) *Conical Intersections*. World Scientific, Singapore (2004)
- van Harrevelt, R., van Hemert, M.C.: *J Chem Phys* **112**, 5777 (2000)
- Cheng, B.-M., Chung, C.-Y., Bahou, M., Lee, Y.-P., Lee, L.C., van Harrevelt, R., van Hemert, M.C.: *J. Chem. Phys.* **120**, 224 (2004)
- Fillion, J.H., van Harrevelt, R., Ruiz, J., Castillejo, M., Zanganeh, A.H., Lemaire, J.L., van Hemert, M.C., Rostas, F.: *J. Phys. Chem. A* **105**, 11414 (2001)
- Harich, S.A., Yang, X.F., Yang, X., van Harrevelt, R., van Hemert, M.C.: *Phys. Rev. Lett.* **87**, 263001 (2001)
- Zhu, H., Qu, Z.-W., Tashiro, M., Schinke, R.: *Chem Phys Lett* **384**, 45 (2004)
- Matsumi, Y., Kawasaki, M.: *Chem. Rev.* **103**, 4767 (2003)
- Schinke, R., Keller, H.-M., Stumpf, M., Dobbyn, A.J.: *J. Phys. B* **28**, 3081 (1995)
- Neyer, D.W., Houston, P.L.: The HCO potential energy surface; probes using molecular scattering and photodissociation. In: Liu, K., Wagner, A. (eds.) *The Chemical Dynamics and Kinetics of Small Radicals*. World Scientific, Singapore (1994)
- Weiß, J., Schinke, R., Mandelshtam, V.A.: *J Chem Phys* **113**, 4588 (2000)
- Weiß, J., Schinke, R.: *J Chem Phys* **115**, 3173 (2001)
- Grebenschikov, S.Y., Schinke, R., Hase, W.L.: State-specific dynamics of unimolecular dissociation. In: Green, N. (ed.) *Unimolecular Kinetics*. Elsevier, Amsterdam (2003)
- Moiseyev, N.: *Phys Rep* **302**, 211 (1998)
- Mandelshtam, V.A., Taylor, H.S.: *J Chem Phys* **102**, 7390 (1995)
- Mandelshtam, V.A., Taylor, H.S.: *J Chem Phys* **106**, 5085 (1997)
- Delon, A., Reiche, F., Abel, B., Grebenshchikov, S.Yu., Schinke, R.: *J. Phys. Chem. A* **104**, 10374 (2000)
- Skokov, S., Bowman, J.M.: *J Chem Phys* **110**, 9789 (1999)
- Hauschildt, J., Weiß, J., Beck, C., Grebenshchikov, S. Yu., Düren, R., Schinke, R., Koput, J.: *Chem. Phys. Lett.* **300**, 569 (1999)
- Hippler, H., Krasteva, N., Striebel, F.: *Phys. Chem. Chem. Phys.* **6**, 3383 (2004)
- Sun, L., Hase, W.L.: Born-Oppenheimer direct dynamics classical trajectory simulations. In: Lipkowitz, K.B., Larter, R., Cundari, T.R. (eds.) *Review in Computational Chemistry*, vol. 19, Wiley-VCH, Hoboken, NJ (2003)
- Hase, W.L., Song, K., Gordon, M.S.: *Comp. Sci. Eng.* **5**, 36 (2003)
- Bolton, K., Schlegel, H.B., Hase, W.L., Song, K.: *Phys. Chem. Chem. Phys.* **1**, 999 (1999)
- Chen, W., Hase, W.L., Schlegel, H.B.: *Chem Phys Lett* **228**, 436 (1994)



Reinhard Schinke Dr Reinhard Schinke received his PhD from the Physics department of the University of Kaiserslautern in 1976. His main areas of research are molecular dynamics, in particular energy transfer in atomic collisions, chemical reactions, photodissociation, and recombination processes. He retired in 2015.



Volker Engel  and Patrick Nuernberger 

Contents

37.1	Introduction	565
37.2	The Principle of Time-Resolved Spectroscopy	566
37.3	Pump-Probe Scheme	568
37.4	Transient Absorption in the Liquid Phase	568
37.5	Further Implementations	570
37.5.1	Coherent Two-Dimensional Spectroscopy	570
37.5.2	Ultrafast Dynamics Studied with X-Ray and Electron Pulses	570
37.5.3	Dynamics and Control	571
	References	572

Abstract

The interaction of molecules with ultrashort laser pulses results in the preparation of nonstationary quantum states and may trigger photophysical and photochemical processes. As a result, measurements of molecular observables explicitly depend on time, thus reflecting the underlying dynamics. This chapter presents a theoretical description of a so-called pump-probe scheme that involves the preparation and detection of the molecular motion. As a particular example, the experimental realization of transient absorption spectroscopy is described. Utilizing this technique, a photochemical reaction proceeding differently in dependence on the solvent environment is discussed, illustrating the versatility of pump-probe measurements for investigating the dynamics of chemical reactions in real time. Further topical experimental

developments in the ultrafast spectroscopy of molecular systems are outlined. These recent approaches comprise coherent two-dimensional spectroscopy, X-ray and electron diffraction, and also the possibility of quantum control with shaped laser pulses.

Keywords

ultrashort pulse · wave packet dynamics · transient absorption · coherent 2-D spectroscopy

37.1 Introduction

Time-resolved experiments have been performed on a multitude of molecular systems. Applications of spectroscopic techniques that work in the time domain range from the detection of simple vibrational motion of a diatomic molecule to the direct determination of relaxation times in polyatomic molecules in a liquid environment, or the recording of isomerization processes in biomolecules. The underlying principles of these experiments are more or less the same. Here, we summarize the basic ideas of transient spectroscopy. First, the quantum-mechanical description of a so-called “pump-probe” scheme is given, where two time-delayed interactions prepare and detect molecular dynamics (Sect. 37.2). This is followed in Sect. 37.3 by a summary of experimental realizations of the pump-probe scheme. To further illustrate the latter, an example of transient absorption measurements in the liquid phase is presented in Sect. 37.4. Finally, more recent developments and additional aspects are outlined in Sect. 37.5.

There exists an extensive amount of literature on the topic of time-resolved molecular dynamics. To follow the developments over the years and keep track of the evolution of the exciting field and its latest innovations, it is instructive to consult the book series related to the biennial “International Conference on Ultrafast Phenomena” [1–11].

V. Engel (✉)

Institute of Physical and Theoretical Chemistry, Universität Würzburg
Würzburg, Germany
e-mail: volker.engel@uni-wuerzburg.de

P. Nuernberger

Institute of Physical and Theoretical Chemistry, Universität
Regensburg
Regensburg, Germany
e-mail: patrick.nuernberger@ur.de

37.2 The Principle of Time-Resolved Spectroscopy

We exemplarily look at the phenomenon of wave packets and discuss how to coherently induce and subsequently observe them with ultrashort laser pulses. Regard a molecule with Hamiltonian \hat{H}_0 so that the time-independent Schrödinger equation reads

$$\hat{H}_0 |\psi_n\rangle = E_n |\psi_n\rangle. \quad (37.1)$$

Here, $|\psi_n\rangle$ are the eigenstates with eigenenergies E_n . The time-dependent Schrödinger equation for a general state $|\psi(t)\rangle$ is

$$i\hbar \frac{\partial}{\partial t} |\psi(t)\rangle = \hat{H}_0 |\psi(t)\rangle. \quad (37.2)$$

If the state at the initial time $t = 0$ is an eigenstate, i.e., $|\psi(0)\rangle = |\psi_n\rangle$, the time-evolution simply reads

$$|\psi_n(t)\rangle = e^{-\frac{i}{\hbar} E_n t} |\psi_n\rangle, \quad (37.3)$$

and the expectation value of an operator \hat{A} is time-independent

$$\begin{aligned} \langle \hat{A} \rangle(t) &= \langle \psi_n(t) | \hat{A} | \psi_n(t) \rangle = \langle \psi_n(0) | \hat{A} | \psi_n(0) \rangle \\ &= \langle \hat{A} \rangle(0). \end{aligned} \quad (37.4)$$

This means that if a measurement of an observable A with associated operator \hat{A} is performed on a molecule in an eigenstate, then the result of the measurement does not depend on time.

Assume now that the state of the molecule at time $t = 0$ is a superposition of eigenstates so that

$$|\psi\rangle = \sum_n c_n |\psi_n\rangle, \quad (37.5)$$

with coefficients c_n . Such superposition states are called wave packets, and their time dependence is given by

$$|\psi(t)\rangle = \sum_n c_n e^{-\frac{i}{\hbar} E_n t} |\psi_n\rangle. \quad (37.6)$$

Taking the expectation value of \hat{A} with respect to this state, we find that it now depends on time

$$\langle \hat{A} \rangle(t) = \sum_m \sum_n c_m^* c_n e^{i \Delta_{mn} t} \langle \psi_m | \hat{A} | \psi_n \rangle, \quad (37.7)$$

with $\Delta_{mn} = (E_m - E_n)/\hbar$. The time-dependence is contained in the phase factors that result in characteristic oscillations with frequencies determined by the energy differences between the molecular eigenenergies.

The obvious principle evolving from the above considerations is that a time-dependent experiment may reflect the induced dynamics, if we prepare the system in a superposition state. This is possible if it is subject to a time-dependent perturbation which, as we here are concerned with spectroscopic measurements, is a laser field. The time-dependent Schrödinger equation is then

$$i\hbar \frac{\partial}{\partial t} |\psi(t)\rangle = \left(\hat{H}_0 + \hat{W}_1(t) \right) |\psi(t)\rangle, \quad (37.8)$$

with the molecule–field interaction $\hat{W}_1(t)$, which starts at the reference time $t = 0$. Writing the state vector as

$$|\psi(t)\rangle = \sum_n b_n(t) e^{-\frac{i}{\hbar} E_n t} |\psi_n\rangle, \quad (37.9)$$

with time-dependent coefficients $b_n(t)$, the Schrödinger equation can, by projection, be transformed to a coupled system of linear differential equations for the coefficients, which reads

$$i\hbar \frac{\partial}{\partial t} b_m(t) = \sum_n b_n(t) e^{i \Delta_{mn} t} \langle \psi_m | \hat{W}_1(t) | \psi_n \rangle. \quad (37.10)$$

In order to find conditions for the preparation of wave packets, we regard the situation where the time-dependent interaction results in photon absorption. Inserting the explicit form of the electric dipole interaction we have

$$\hat{W}_1(t) = -\frac{1}{2} \hat{\mu} f_1(t) e^{-i\omega_1 t}, \quad (37.11)$$

where $\hat{\mu}$ is the projection of the dipole operator on the polarization vector of the electric field, ω_1 the frequency of the laser pulse (commonly referred to as the *pump pulse*), and $f_1(t)$ is an envelope function. Then Eq. (37.10) takes the form

$$i\hbar \frac{\partial}{\partial t} b_m(t) = -\frac{1}{2} \sum_n \langle \psi_m | \hat{\mu} | \psi_n \rangle b_n(t) f_1(t) e^{i(\Delta_{mn} - \omega_1)t}. \quad (37.12)$$

The coefficients $b_m(t)$ become time-independent when the interaction is over ($b_m(t) = \bar{b}_m$), and we have

$$\bar{b}_m = b_m(0) + \frac{1}{i\hbar} \sum_n \langle \psi_m | \hat{\mu} | \psi_n \rangle I_{mn}(1), \quad (37.13)$$

with the integrals

$$I_{mn}(1) = -\frac{1}{2} \int_0^\infty dt b_n(t) f_1(t) e^{i(\Delta_{mn} - \omega_1)t}, \quad (37.14)$$

where the argument (1) refers to the properties of the pump pulse. In general, several of the coefficients will be nonzero

so that, after the interaction, the state vector is a wave packet

$$|\psi(t)\rangle = \sum_n \bar{b}_n e^{-\frac{i}{\hbar} E_n t} |\psi_n\rangle. \quad (37.15)$$

The characteristic timescales for the molecular motion are determined by the energy differences

$$T_{mn} = \left| \frac{2\pi}{\Delta_{mn}} \right|, \quad (37.16)$$

where the longest oscillation period T_{\max} is obtained for the smallest energy separation between two eigenstates. If the pulse duration T_{p1} is longer than T_{\max} , and the excitation of the molecule is resonant with a single transition, i.e., $\Delta_{m_r n_r} - \omega_1 = 0$, then, due to the oscillating phase factors, only one integral $I_{mn}(1)$ is nonzero. This means that, for longer interaction times, a single eigenstate rather than a linear combination of states is excited. Thus, the condition for the preparation of wave packets is that the pulse duration is smaller than, or in the order of, the longest characteristic timescale for the molecular motion, i.e., $T_{p,1} < T_{\max}$. Typical, oscillation periods for the vibrational motion of molecules are in the femtosecond range, so that time-resolved experiments need ultrashort pulses in the femtosecond regime. The same applies to the fastest photochemical reactions, which, for direct dissociations, take place on the sub-100-fs timescale. On the other hand, rotational periods are in the order of picoseconds (and longer), so they can be resolved with ps laser pulses.

Having prepared a wave packet with the pump interaction at the reference time $t = 0$, the question is how to detect its motion. This is realized in perturbing the system, at a defined delay time T , with another laser pulse (the *probe pulse*). Restricting the discussion to a second photon absorption, the interaction energy is as in Eq. (37.11), but the pulse envelope $f_2(t)$ starts at the delay time, and the frequency ω_2 may be different. The wave packet at time T is now written as

$$|\psi(t')\rangle = \sum_n d_n(t') e^{-\frac{i}{\hbar} E_n(t'+T)} |\psi_n\rangle, \quad (37.17)$$

where $d_n(0) = \bar{b}_n$, and the new time variable starts at $t' = 0$. Following the same procedure as above, one arrives at the coupled equations

$$i\hbar \frac{\partial}{\partial t'} d_m(t') = -\frac{1}{2} \sum_n \langle \psi_m | \hat{\mu} | \psi_n \rangle \times d_n(t') f_2(t') e^{i(\Delta_{mn} - \omega_2)t'} e^{i\Delta_{mn}T}. \quad (37.18)$$

We may integrate this equation and regard times after the interaction when the coefficients become time-independent,

so that

$$\bar{d}_m = d_m(0) + \frac{1}{i\hbar} \sum_n \langle \psi_m | \hat{\mu} | \psi_n \rangle I_{mn}(2) e^{i\Delta_{mn}T}, \quad (37.19)$$

where

$$I_{mn}(2) = -\frac{1}{2} \int_0^\infty dt' d_n(t') f_2(t') e^{i(\Delta_{mn} - \omega_2)t'}. \quad (37.20)$$

Regarding the quantity $I_{mn}(2)$ we see again that for a pulse being substantially longer than the oscillations times T_{mn} , the probe laser couples only levels that are in resonance with its frequency ω_2 .

If we now regard the wave packet after the two laser interactions [Eq. (37.17) with $d_n(t') = \bar{d}_n$], the expectation value of an operator \hat{A} depends not only on the propagation time t' but also on the delay time between the pump pulse and the probe pulse. This scheme is readily extended to experiments that involve more than two interactions. For example, in a third-order photon echo experiment, three pulses are delayed to each other. Then the expectation value of the dipole operator, which is the third-order polarization, depends on two delay times τ , T and on the propagation (or detection) time t' .

As described in the previous sections, the preparation of wave packets and the detection of their motion are essential to time-resolved spectroscopy [12–14]. If regarded in coordinate space, the probability density of a wave packet changes as a function of time. As an example, we regard a one-dimensional, coupled electron-nuclear motion. The employed model of this reduced dimensionality dynamics is such that the nuclear motion can be described with the Born–Oppenheimer approximation [15]. Then, the nuclear probability density moves in a bound-state potential, and the electronic density follows the nuclear dynamics. This is illustrated in the left-hand panels of Fig. 37.1. The densities move towards larger distances R , and upon reflection at the outer potential wall, the motion is reversed. The right-hand panels illustrate another case where the bound-state potential curve exhibits a potential barrier at $R = 0$, and the mean energy of the electron-nuclear wave packet is in the order of the barrier height. Then, a splitting occurs where the densities are partly reflected at the barrier.

One-dimensional wave packet motion has been studied extensively using pump-probe fluorescence [16, 17]. Later, other techniques like pump-probe ionization [18, 19] or time-resolved CARS spectroscopy [20] were applied. A beautiful example is the detection of vibrational motion in the Na₂ molecule via time-resolved photoelectron spectroscopy. Following theoretical studies [21, 22], it was documented that the time-dependent probability density of nuclear wave packets can be directly mapped onto the energy dependence of the photoelectron spectra [23–25].

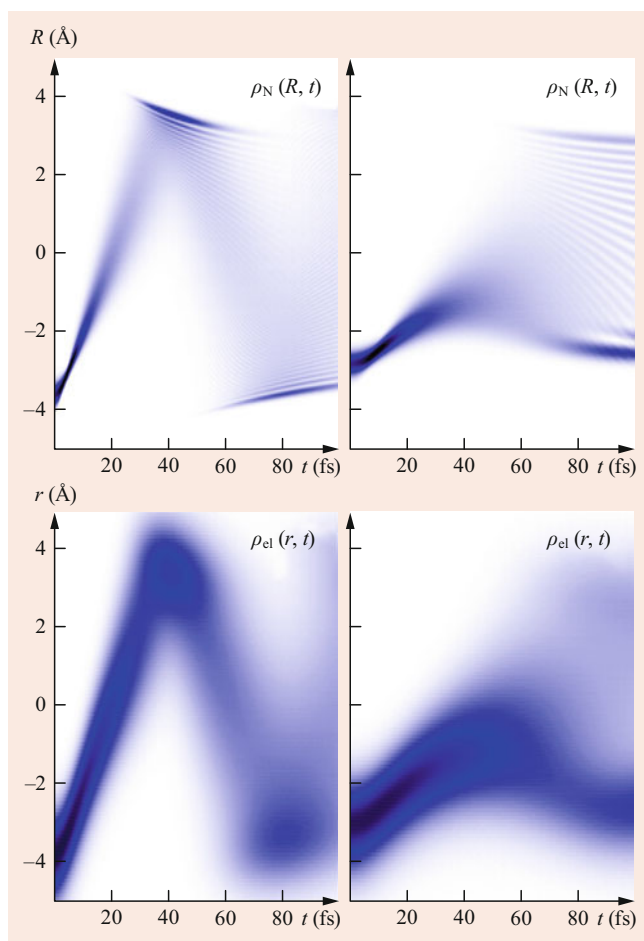


Fig. 37.1 Wave packet bound-state motion. From the solution of the time-dependent Schrödinger equation for a simplified one-dimensional electron-nuclear motion, the nuclear ($\rho_N(R, t)$) and electronic ($\rho_{el}(r, t)$) probability densities are obtained. The motion proceeds adiabatically, so that the electronic density follows the nuclear geometry changes. *Left-hand panels:* the nuclear wave packet moves in a bound-state potential outward until it is reflected at a potential wall. The electronic density adapts adiabatically to the nuclear motion. *Right-hand panels:* the nuclear density is partly reflected at a potential barrier, and the same applies to the electronic density. The data was originally discussed in [15]

37.3 Pump-Probe Scheme

The pump-probe scheme outlined above can be realized in various ways. In the majority of experiments on ultrafast dynamics, the time resolution is obtained by employing two laser pulses: the first one (termed pump pulse) interacts with the sample and starts the process to be studied, whereas after a well-defined, adjustable delay time T , a second laser pulse (called probe pulse) interacts and thereby monitors the time evolution induced by the pump pulse [26–28]. In order to detect signals as a function of T , different detection schemes have been realized and depend on the sample that is investigated. Nonoptical detection may record the amount

of ions or electrons generated by the probe pulse, e.g., from a molecular beam, a liquid microjet, a surface, or its adsorbate in a vacuum chamber system; optical detection may comprise the emission intensity from a higher-lying state reached by the probe pulse (laser-induced fluorescence) or the degree of attenuation of the probe pulse (transient absorption).

Generally, the signal detected reflects the temporal evolution of the system as induced by the pump pulse. In the case of wave packet dynamics, an oscillatory behavior can be detected, because the wave packet's spatial distribution varies with time (Fig. 37.1), and properties like the ionization cross section or the absorption coefficient are, thereby, transiently modulated. Beyond coherent effects, many processes can cause signal changes on an ultrafast timescale, among them relaxation and solvation, or actual reactions originating from the state reached by the pump pulse, e.g., photodissociation, energy or charge transfer, photoisomerization, rearrangement and other geometrical changes, intersystem crossing and quenching, and very often a combination of several of these processes.

There are also ultrafast techniques that do not incorporate two laser pulses interacting with the sample. In fluorescence upconversion as well as in fluorescence Kerr gating, the emitted light from a sample excited by the pump pulse is strobed by a second laser pulse (often called the gate pulse) in a nonlinear process. Since the delay time between the pump (and thus the fluorescence) and the gate pulse is again adjustable in a well-defined fashion, the temporal emission profile is obtained. Great advances have also been achieved by an ultrashort pump pulse in combination with streak cameras or time-correlated single-photon counting, yet the best time resolution can be achieved in the nonlinear approaches with very short laser pulses [27].

In the past decades, laser sources have been perpetually improved. In the visible spectral domain, pulse durations of 20 fs are routinely employed; soft X-rays even allow the generation of attosecond pulses. The accessible spectral range has been continuously extended as well, so that pump-induced dynamics can be performed or probed with pulses from the far-infrared [29] or from the X-ray regime (Sect. 37.5.2), and basically all spectral regions in between.

37.4 Transient Absorption in the Liquid Phase

Chemical reaction dynamics in solution can be elucidated with ultrafast transient absorption spectroscopy in a unique fashion. A schematic experimental implementation is shown in Fig. 37.2a. The spectrally resolved intensity of the probe beam is measured as a function of the pump-probe delay T . To separate the transient from stationary absorption signals, the difference in optical density is determined from two

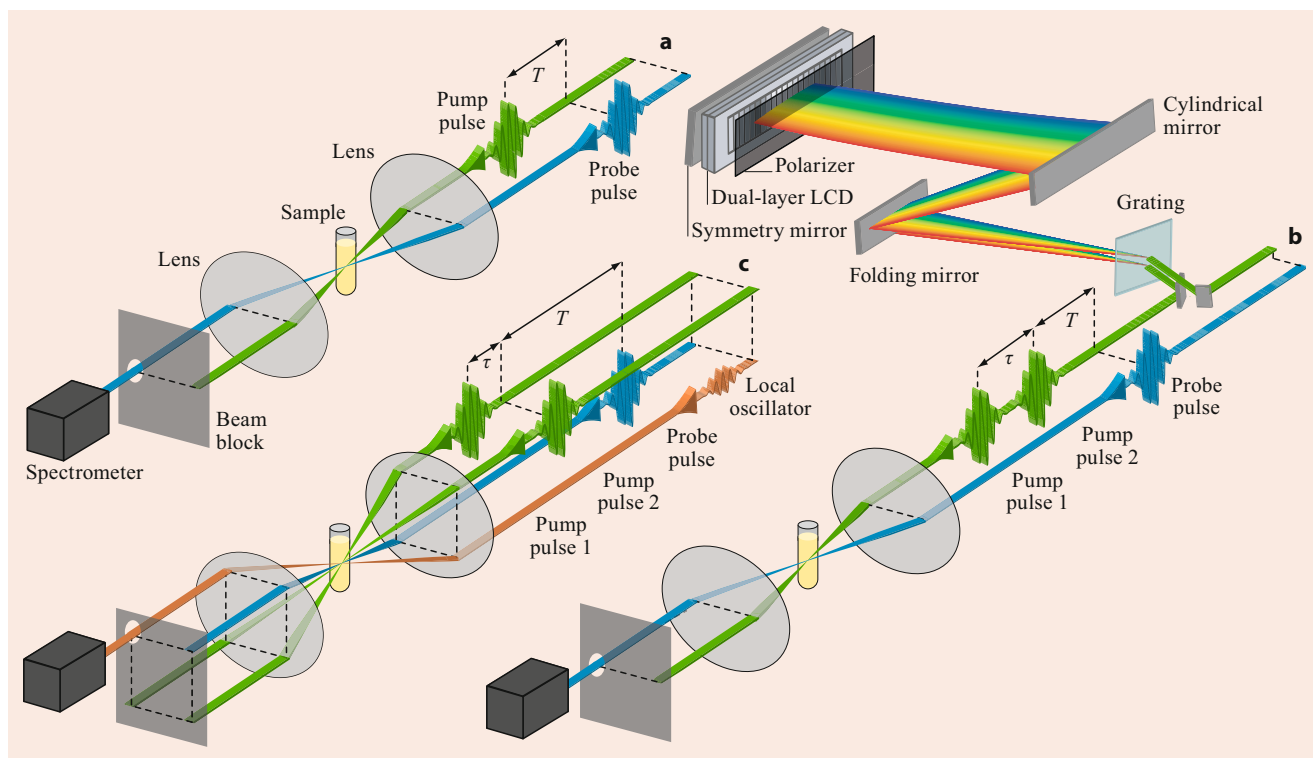


Fig. 37.2 Three ultrafast liquid-phase spectroscopy approaches (plotted with lenses and a minimal amount of optics for simplicity). **a** Transient absorption: a spectrometer determines the probe spectrum for different values of the pump-probe delay T . **b** Coherent 2-D spectroscopy in pump-probe geometry. The spectrometer measures the probe spectrum for each combination of pump-probe delay T and the delay τ of a phase-stable pump-pulse pair, here generated by a liquid-crystal display (LCD) pulse shaper in a folded zero-dispersion compressor setup. Subsequent Fourier transformation with respect to τ yields 2-D spectra for each value of T . **c** Coherent 2-D spectroscopy in boxcars geometry: the phase-stable pump pulses and the probe pulse traverse the sample from different directions, a local oscillator heterodynes the signal field emitted. Thus, the spectrometer measures the interference of the signal field and the local oscillator for each combination of T and τ

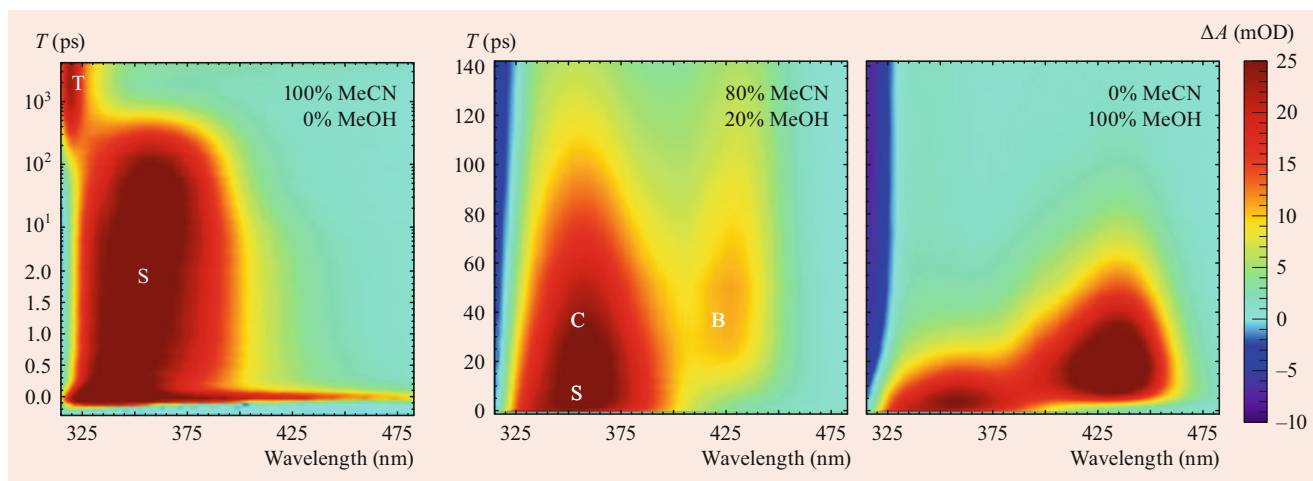


Fig. 37.3 Transient absorption maps of Ph_2CN_2 in binary solvent mixtures of MeCN and MeOH. Note the logarithmic ordinate for T values beyond 2 ps in the left panel. The data was originally discussed in [30], and graphs are adapted therefrom

measurements, one with and one without the pump pulse, respectively

$$\Delta OD(\lambda_{\text{probe}}, T) = -\log_{10} \left[\frac{I_{\text{pumped}}(\lambda_{\text{probe}}, T)}{I_{\text{unpumped}}(\lambda_{\text{probe}})} \right]; \quad (37.21)$$

ΔOD is positive if the probe encounters absorbing species that were not there in the absence of the pump pulse, i.e., excited reactants or products, whereas it is negative for stimulated emission from excited species or in case of the ground-state bleach caused by a reduced number of reactants in the ground state.

As an example, the photodynamics of Ph_2CN_2 (diphenyldiazomethane) in different solvent environments are shown in Fig. 37.3. Upon excitation at $T = 0$ with a pump pulse centered at 285 nm, N_2 is photolyzed off, and a reactive carbene $^1\text{Ph}_2\text{C}$ is formed, which is initially in a singlet configuration. The singlet absorption is observed around 355 nm (labeled **S** in Fig. 37.3). In the aprotic solvent MeCN (acetonitrile), $^1\text{Ph}_2\text{C}$ (**S**) will turn into a triplet $^3\text{Ph}_2\text{C}$ (**T**) within several hundred ps. In the presence of the protic solvent MeOH (methanol), a benzhydryl cation Ph_2CH^+ (**B**) or a hydrogen-bonded complex $^1\text{Ph}_2\text{C} \cdots \text{HOME}$ (**C**) can be formed, depending on whether or not the close-by MeOH molecule is part of a hydrogen-bond network with other MeOH molecules, respectively. Both **B** and **C** react on to an ether that does not absorb in the covered spectral range. As can be seen in Fig. 37.3, the signal of the benzhydryl cation **B** is the most pronounced and decays the most rapidly in the absence of MeCN. Thus, these exemplary data sets emphasize that transient absorption is a powerful tool to reveal the different reaction pathways and the characteristic time scales of chemical reactions in solution.

37.5 Further Implementations

The arsenal of ultrafast experimental techniques is increasing at an incredible speed. Besides extending to new spectral regions and lower pulse durations, the nonlinearity of the light–matter interaction and also the number of laser pulses employed are adapted to unravel previously unexplored photophysical and photochemical aspects. In the following, a few of these recent developments are outlined.

37.5.1 Coherent Two-Dimensional Spectroscopy

While in a transient absorption experiment, molecules are excited with a wavenumber $\tilde{\nu}_{\text{pump}}$ and probed with $\tilde{\nu}_{\text{probe}}$ (note that often frequency or wavenumber rather than wavelength is used for data presentation) after a delay time T , a transient absorption map as in Fig. 37.3 is a representation of the system response as a function of the latter two quantities only. To gain information on the role of the pump wavenumber, the spectral position of the pump pulse can be tuned, and each time a transient absorption map is recorded (Fig. 37.4a). However, the spectral bandwidth of the pump pulse limits the spectral resolution along $\tilde{\nu}_{\text{pump}}$. This can be overcome by splitting the pump pulse into a phase-stable pulse pair whose delay τ is scanned (e.g. by a pulse shaper as in Fig. 37.2b), a subsequent Fourier transform of the detected signal with respect to τ yields the dependence on $\tilde{\nu}_{\text{pump}}$. Hence, for each delay time T , which can be varied as well to capture the full dynamics, the information is spread along two frequency

axes (Fig. 37.4b), thereby allowing in an intuitive way the identification of couplings, transfer processes, or generally how a pumped species interacts with or turns into a probed one. This technique of coherent two-dimensional (2-D) spectroscopy [31–37] can be understood as an optical analogue of recording frequency-correlation spectra in 2-D nuclear magnetic resonance.

Many different implementations of 2-D spectroscopy exist, all with pros and cons, the most versatile but possibly also experimentally most challenging being the boxcars geometry (Fig. 37.2c), where the three pulses all come from different directions, and the desired signal from the sample is emitted in yet another direction. With the help of an adequate local oscillator, that is a further pulse that together with the signal field impinges upon the detector, the signal field can be fully retrieved in both amplitude and phase, and thus the system's response to the interacting fields is fully accessible.

2-D spectroscopy is successfully applied in many spectral ranges, from THz [38] to ultraviolet [39–43]. In 2-D infrared spectroscopy, vibrations are labeled by the pump event, and subsequent processes (coupling between vibrational modes, spectral diffusion, relaxation, chemical exchange, ...) are monitored, making it a versatile tool for assessing molecular structure and associated dynamics [34, 35, 44]. 2-D electronic spectroscopy correlates electronic transitions and has proven to be particularly powerful for unraveling electronic couplings and exciton dynamics in light-harvesting systems [45, 46] and has opened the door to tackle the pressing question as to which extent coherent phenomena affect functionality in chemical or biological systems [46].

37.5.2 Ultrafast Dynamics Studied with X-Ray and Electron Pulses

In recent years, ultrashort pulses have been extended into the X-ray regime [47–52]. Laboratory-based sources often rely on a laser-induced plasma or a high-harmonic-generation (HHG) process. In the latter, photons at odd multiples of the initial laser frequency are generated in a strong-field nonlinear effect up to a spectral cutoff region, so that the radiation comprises coherent soft X-rays, which even allow the formation of attosecond pulses. Pump-probe schemes involving these soft X-rays opened a new way for unraveling nuclear and electron dynamics in atoms but also in molecules, both for gas-phase samples and in the condensed phase, providing insight into processes like charge transfer, ring opening, and photofragmentation [51–53]. Many of these experiments make use of a high photon-energy pump pulse in order to prepare core-excited states such that the following dynamics could be detected with a time-delayed optical probe pulse. In a second scenario, a visible or UV pump pulse initiates a chemical reaction that is followed by a time-delayed

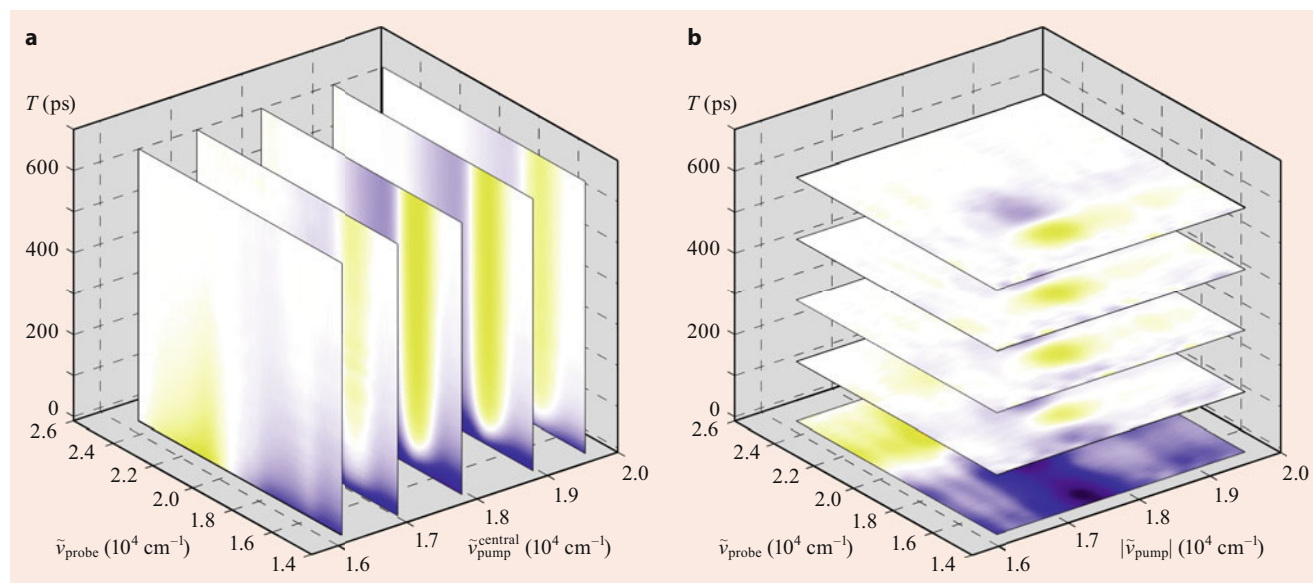


Fig. 37.4 Ultrafast spectroscopy data for the molecule 6-nitro-1', 3', 3'-trimethylspiro[2*H*-1-benzopyran-2, 2'-indoline] (6-nitro-BIPS). By transient absorption with different central pump wavenumbers $\tilde{\nu}_{\text{pump}}^{\text{central}}$ (a), the dynamics can be investigated in a 3-D space with dimensions representing the central pump wavenumber, the pump-probe delay time T , and the probe wavenumber. 2-D spectroscopy (b) measurements can span the same 3-D space but without the disadvantage of a spectral blurring along the pump wavenumber axis as present in transient absorption as a consequence of the pump pulse's spectral width. The graphs are adapted from [37]

X-ray pulse, which is then able to selectively excite core levels of the atoms involved in the process and thereby track the transient changes due to structural dynamics. This requires femtosecond hard X-ray pulses, as are available from storage rings with electron-bunch slicing and more recently from X-ray free-electron lasers (XFELs) delivering high-intensity hard X-ray pulses with durations of a few fs. Hard X-ray pulses have helped to elucidate structural changes after photoexcitation, e.g., in iron complexes that exhibit rapid spin-crossover processes: for $[\text{Fe}^{\text{II}}(\text{bpy})_3]^{2+}$, absorption changes near the K-edge of Fe disclose bond lengthening after spin-crossover [48], resonant inelastic X-ray scattering applied to $\text{Fe}(\text{CO})_5$ in an ethanol jet can separate triplet and ligation reaction channels on sub-ps time scales after photolysis of one CO [54].

These soft and hard X-ray approaches provide insight into structural dynamics not accessible in a similar fashion with ultrafast techniques in more conventional spectral regimes. A further example is the ring-opening reaction of 1,3-cyclohexadiene to 1,3,5-hexatriene, which has been extensively studied both with ultrafast spectroscopy and dynamics simulations (as e.g., summarized in [55]). The reaction dynamics could also be investigated by X-ray core ionization from an XFEL [56], the temporal evolution of the valence electronic structure was explored by soft X-rays near the carbon K-edge generated by HHG [57], while fs X-ray scattering in combination with calculated reaction trajectories provide real-space images of transient structures in this electrocyclic reaction [58].

The latter study is an example of a time-resolved X-ray diffraction experiment, an area that strongly benefits from recent advances in XFELs [49, 50]. Instead of using electromagnetic waves, a complementary approach with pulses of electrons (ultrafast electron diffraction) has been developed, with high sensitivity and spatiotemporal resolution so that structural dynamics are followed in real time [59, 60]. These powerful techniques provide an auspicious perspective for resolving structural dynamics with unprecedented possibilities, probing changes in molecular geometry rather than in energy.

37.5.3 Dynamics and Control

As has been discussed throughout this chapter, molecular motion can be traced with the help of time-resolved spectroscopy. It is also possible to go one step ahead and use laser pulses to control molecular motion. For a long time, the field of "quantum control" has been dominated by theoretical work, see the textbooks [25, 61, 62]. However, the technical advances in laser technology have led to experimental realizations of proposed theoretical schemes. Employing sophisticated devices to modify the amplitude, phase, and/or polarization state of the laser pulses in a well-defined way [63], e.g., pulse shapers [64] as in Fig. 37.2b, the outcome of a chemical reaction can be influenced by specifically tailored light pulses. For the determination of the latter, feedback algorithms can be employed [65]. The range of photochemical reactions for which such an approach

was demonstrated spans from molecular dimers in the gas phase via reactions on surfaces, organic molecules in solution, processes in solids, to large biological systems relevant in photosynthesis. It is worthwhile taking a look at one of the reviews [66–70] summarizing the accomplishments with quantum control approaches.

References

1. Conference proceedings *Ultrafast Phenomena*, vol. X: Springer Ser. Chem. Phys. **62** (1996)
2. Conference proceedings *Ultrafast Phenomena*, vol. XI: Springer Ser. Chem. Phys. **63** (1998)
3. Conference proceedings *Ultrafast Phenomena*, vol. XII: Springer Ser. Chem. Phys. **66** (2001)
4. Conference proceedings *Ultrafast Phenomena*, vol. XIII: Springer Ser. Chem. Phys. **71** (2003)
5. Conference proceedings *Ultrafast Phenomena*, vol. XIV: Springer Ser. Chem. Phys. **79** (2005)
6. Conference proceedings *Ultrafast Phenomena*, vol. XV: Springer Ser. Chem. Phys. **88** (2007)
7. Conference proceedings *Ultrafast Phenomena*, vol. XVI: Springer Ser. Chem. Phys. **92** (2009)
8. Conference proceedings *Ultrafast Phenomena*, vol. XVII: Oxford University Press, New York (2011)
9. Conference proceedings *Ultrafast Phenomena*, vol. XVIII: EPJ Web Conf. **41** (2013)
10. Conference proceedings *Ultrafast Phenomena*, vol. XIX: Springer Proc. Phys. **162** (2015)
11. Conference proceedings *Ultrafast Phenomena*, vol. XX: OSA Technical Digest (online) <https://www.osapublishing.org/conference.cfm?meetingid=29&yr=2016>
12. Garraway, B.M., Suominen, K.-A.: Rep. Prog. Phys. **58**, 365 (1995)
13. Yeazell, J., Uzer, T. (eds.): The Physics and Chemistry of Wave Packets. Wiley, New York (2000)
14. Manz, J.: Molecular wavepacket dynamics: theory for experiments 1926–1966. In: Sundström, V., Forsén, S., Eberg, U., Hjalmarsson, H. (eds.) *Femtochemistry and Femtobiology: Ultrafast Reaction Dynamics at Atomic-Scale Resolution*, pp. 80–319. Imperial College Press, London (1996)
15. Schaupp, T., Albert, J., Engel, V.: Eur. Phys. J. B **91**, 97 (2018)
16. Rose, T.S., Rosker, M.J., Zewail, A.H.: J. Chem. Phys. **88**, 6672 (1988)
17. Bowman, R.M., Dantus, M., Zewail, A.H.: Chem. Phys. Lett. **161**, 297 (1989)
18. Baumert, T., Gerber, G.: Adv. Atom. Mol. Phys. **35**, 163 (1995)
19. Fischer, I., Villeneuve, D.M., Vrakking, M.J.J., Stolow, A.: J. Chem. Phys. **102**, 5566 (1995)
20. Materny, A., et al.: Appl. Phys. B **71**, 299 (2000)
21. Seel, M., Domcke, W.: J. Chem. Phys. **95**, 7806 (1991)
22. Meier, C., Engel, V.: Chem. Phys. Lett. **212**, 691 (1993)
23. Assion, A., et al.: Phys. Rev. A **54**, R4605 (1996)
24. Wollenhaupt, M., Engel, V., Baumert, T.: Annu. Rev. Phys. Chem. **56**, 25 (2005)
25. Tannor, D.J.: Introduction to Quantum Mechanics: A Time-Dependent Perspective. University Science Books, Sausalito (2007)
26. Fleming, G.R.: Chemical Applications of Ultrafast Spectroscopy. Oxford University Press, New York (1986)
27. Simon, J.D.: Ultrafast Dynamics of Chemical Systems. Springer Science & Business Media, Dordrecht (1994)
28. Mukamel, S.: Principles of Nonlinear Optical Spectroscopy. Oxford University Press, New York (1995)
29. Schmittenmaier, C.A.: Chem. Rev. **104**, 1759 (2004)
30. Knorr, J., et al.: Nat. Comm. **7**, 12968 (2016)
31. Mukamel, S.: Annu. Rev. Phys. Chem. **51**, 691 (2000)
32. Jonas, D.M.: Annu. Rev. Phys. Chem. **54**, 425 (2003)
33. Cho, M.: Two-Dimensional Optical Spectroscopy. CRC Press, Boca Raton (2009)
34. Fayer, M.: Annu. Rev. Phys. Chem. **60**, 21 (2009)
35. Hamm, P., Zanni, M.: Concepts and Methods of 2D Infrared Spectroscopy. Cambridge University Press, New York (2011)
36. Fuller, F.D., Ogilvie, J.P.: Annu. Rev. Phys. Chem. **66**, 667 (2015)
37. Nuernberger, P., Ruetzel, S., Brixner, T.: Angew. Chem. Int. Ed. **54**, 11368 (2015)
38. Woerner, M., et al.: New J. Phys. **15**, 025039 (2013)
39. Tseng, C., Matsika, S., Weinacht, T.C.: Opt. Express **17**, 18788 (2009)
40. Selig, U., et al.: Opt. Lett. **35**, 4178 (2010)
41. West, B.A., Moran, A.M.: J. Phys. Chem. Lett. **3**, 2575 (2012)
42. Krebs, N., Pugliesi, I., Hauer, J., Riedle, E.: New J. Phys. **15**, 085016 (2013)
43. Consani, C., Auböck, G., van Mourik, F., Chergui, M.: Science **339**, 1586 (2013)
44. Kraack, J.P.: Top. Curr. Chem. **375**, 86 (2017)
45. Brixner, T., et al.: Nature **434**, 625 (2005)
46. Scholes, G.D., et al.: Nature **543**, 647 (2017)
47. Pfeifer, T., Spielmann, C., Gerber, G.: Rep. Prog. Phys. **69**, 443 (2006)
48. Bressler, C., Chergui, M.: Annu. Rev. Phys. Chem. **61**, 263 (2010)
49. Schoenlein, R.W., Boutet, S., Miniti, M.P., Dunne, A.M.: Appl. Sci. **7**, 850 (2017)
50. Barty, A., Küpper, J., Chapman, H.N.: Annu. Rev. Phys. Chem. **64**, 415 (2013)
51. Krausz, F., Ivanov, M.: Rev. Mod. Phys. **81**, 163 (2009)
52. Kraus, P.M., et al.: Nat. Rev. Chem. **2**, 82 (2018)
53. Ramasesha, K., Leone, S.R., Neumark, D.M.: Annu. Rev. Phys. Chem. **67**, 41 (2016)
54. Wernet, P., et al.: Nature **520**, 78 (2015)
55. Deb, S., Weber, P.M.: Annu. Rev. Phys. Chem. **62**, 19 (2011)
56. Petrović, V.S., et al.: Phys. Rev. Lett. **108**, 253006 (2012)
57. Attar, A.R., et al.: Science **356**, 54 (2017)
58. Miniti, M.P., et al.: Phys. Rev. Lett. **114**, 255501 (2015)
59. Zewail, A.H.: Annu. Rev. Phys. Chem. **57**, 65 (2006)
60. Miller, R.J.D.: Annu. Rev. Phys. Chem. **65**, 583 (2014)
61. Rice, S.A., Zhao, M.: Optical Control of Molecular Dynamics. Wiley, New York (2000)
62. Shapiro, M., Brumer, P.: Principles of the Quantum Control of Molecular Processes. Wiley, New York (2003)
63. Wollenhaupt, M., Assion, A., Baumert, T.: Femtosecond laser pulses: linear properties, manipulation, generation and measurement. In: Träger, F. (ed.) Springer Handbook of Lasers and Optics, pp. 937–983. Springer, New York (2007)
64. Weiner, A.M.: Opt. Commun. **284**, 3669 (2011)
65. Judson, R.S., Rabitz, H.: Phys. Rev. Lett. **68**, 1500 (1992)
66. Brixner, T., Gerber, G.: ChemPhysChem **4**, 418 (2003)
67. Dantus, M., Lozovoy, V.V.: Chem. Rev. **104**, 1813 (2004)
68. Nuernberger, P., Vogt, G., Brixner, T., Gerber, G.: Phys. Chem. Chem. Phys. **9**, 2470 (2007)
69. Brif, C., Chakrabarti, R., Rabitz, H.: New J. Phys. **12**, 075008 (2010)
70. Glaser, S.J., et al.: Eur. Phys. J. D **69**, 279 (2015)



Volker Engel Volker Engel studied Physics at the University of Göttingen, where he also received his Doctorate in 1986. Afterwards he worked at UC Santa Barbara and the University of Freiburg. In 1994, he was appointed as Professor of Theoretical Chemistry at the University of Würzburg. The focus of his research is on time-dependent quantum mechanics and spectroscopy.



Patrick Nuernberger Patrick Nuernberger received his Doctorate in Physics from the University of Würzburg in 2007. He further worked at SUNY Stony Brook, Ecole Polytechnique, and Ruhr-University Bochum. Since 2019, he has held the Chair of Physical Chemistry at the University of Regensburg. His research focuses on investigating femtosecond dynamics and photochemical reactions with advanced ultrafast spectroscopic methods and quantum control approaches.



Alexandre Faure , Francois Lique , and David R. Flower

Contents

38.1	Definitions	575
38.2	Quantal Method	576
38.3	Symmetries and Conservation Laws	577
38.4	Coordinate Systems	577
38.5	Scattering Equations	578
38.6	Matrix Elements	578
38.6.1	Interaction Potential	578
38.6.2	Centrifugal Potential	579
38.7	Semi and Quasi-Classical Methods	579
38.8	Example: CO–H₂	579
38.9	New Directions	580
	References	580

Abstract

The basic formulations of nonreactive scattering are presented in the sections to follow. The quantal approach to this problem is outlined. Specific symmetries, and their closely related conservation laws, which reduce the complexity of computation, are discussed, along with the usual coordinate systems used to express the necessary scattering equations. The derivation of the matrix elements needed for a given calculation is provided in

A. Faure (✉)
 Institute of Planetology and Astrophysics of Grenoble (IPAG),
 University of Grenoble Alpes (CNRS)
 Grenoble, France
 e-mail: alexandre.faure@univ-grenoble-alpes.fr

F. Lique
 CNRS, IPR (Institut de Physique de Rennes), Université de Rennes 1
 Rennes, France
 e-mail: francois.lique@univ-rennes1.fr

D. R. Flower
 Dept. of Physics, University of Durham
 Durham, UK
 e-mail: david.flower@durham.ac.uk

the case of a diatom-diatom collision. Semiclassical and quasi-classical methods are also briefly introduced. The chapter ends with a comparison between theory and experiment for the benchmark CO–H₂ system and an outline of future directions in the field.

Keywords

classical trajectory · relative collision · Coriolis coupling · centrifugal potential · Wigner coefficient · quasi-classical and semi-classical scattering · Feshbach resonances

38.1 Definitions

The cross section σ for a transition from state i to f is defined classically as

$$\sigma(i \rightarrow f) = 2\pi \int_0^{\infty} P_b(i \rightarrow f) b db, \quad (38.1)$$

where P_b is the transition probability for impact parameter b (Fig. 38.1). The impact parameter is related to the relative angular momentum quantum number, ℓ , by

$$\begin{aligned} 2\mu E b^2 &= \ell(\ell + 1) \\ &= k^2 b^2, \end{aligned} \quad (38.2)$$

where k is the wave number at relative collision energy E , and μ is the reduced mass; atomic units ($e = m_e = \hbar = 1$) are used throughout. Differentiating Eq. (38.2) and setting $d\ell = 1$ in the quantal limit,

$$bdb = \frac{2\ell + 1}{2k^2},$$

whence the quantum mechanical equivalent of Eq. (38.1) may be obtained

$$\sigma(i \rightarrow f) = \frac{\pi}{k_i^2} \sum_{\ell} (2\ell + 1) P_{\ell}(i \rightarrow f), \quad (38.3)$$

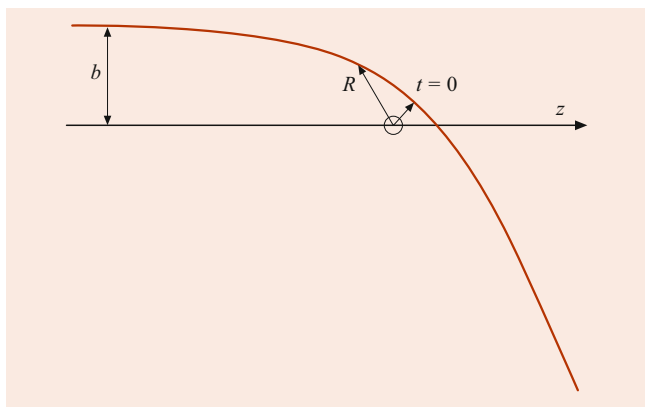


Fig. 38.1 Classical scattering by a fixed scattering center. The trajectory is symmetric about the point of closest approach, which is the time origin

k_i being the wave number in the initial state. If the initial state is degenerate, and ω_i is the degeneracy, then

$$P_{\ell}(i \rightarrow f) = \frac{1}{\omega_i} |T_{\ell}(i, f)|^2, \quad (38.4)$$

where T_{ℓ} is an element of the transmission matrix \mathbf{T} , which contains all the information on the scattering event. The scattering matrix \mathbf{S} is related to the \mathbf{T} matrix by

$$\mathbf{S} = \mathbf{1} - \mathbf{T} \quad (38.5)$$

and thence to the reactance matrix \mathbf{K} through

$$\mathbf{S} = \frac{\mathbf{1} + i\mathbf{K}}{\mathbf{1} - i\mathbf{K}}. \quad (38.6)$$

The elements of the \mathbf{K} matrix are real. Conservation of the incident flux of particles requires that

$$\sum_f |S(i, f)|^2 = 1. \quad (38.7)$$

Microreversibility (time-reversal symmetry) implies that the \mathbf{S} matrix is symmetric,

$$S(i, f) = S(f, i),$$

and hence

$$\sigma(i \rightarrow f) k_i^2 \omega_i = \sigma(f \rightarrow i) k_f^2 \omega_f. \quad (38.8)$$

The thermally averaged (Maxwellian) rate coefficient for a transition from state i to f is

$$\langle \sigma v \rangle_{i \rightarrow f} = \left(\frac{8k_B T}{\pi \mu} \right)^{\frac{1}{2}} \int_0^{\infty} x_i \sigma(i \rightarrow f) e^{-x_i} dx_i, \quad (38.9)$$

where $x_i = \mu v_i^2 / 2k_B T$, v_i being the relative collision velocity; k_B is Boltzmann's constant, and $(8k_B T / \pi \mu)^{\frac{1}{2}}$ may be identified with the mean thermal velocity at temperature T . From Eqs. (38.8) and (38.9),

$$\langle \sigma v \rangle_{i \rightarrow f} \omega_i \exp \frac{-\varepsilon_i}{k_B T} = \langle \sigma v \rangle_{f \rightarrow i} \omega_f \exp \frac{-\varepsilon_f}{k_B T}, \quad (38.10)$$

where $\varepsilon_i, \varepsilon_f$ denote the energies of the states i, f with respect to the reference level. Equation (38.10) relates the rate coefficients of forwards and reverse transitions to their relative degeneracies and excitation energies.

38.2 Quantal Method

The usual approach to nonreactive scattering [1] is based on the Born–Oppenheimer (BO) approximation. This approximation postulates that electrons adapt adiabatically to the motion of the much heavier nuclei. The BO approximation allows us to describe inelastic collisions as the motion of nuclei on the interaction potential V , which is a known function of the nuclear coordinates. The total Hamiltonian may then be written as

$$H = -\frac{1}{2\mu} \nabla_R^2 + h_1(\mathbf{x}_1) + h_2(\mathbf{x}_2) + V(\mathbf{R}, \mathbf{x}_1, \mathbf{x}_2), \quad (38.11)$$

where \mathbf{R} is the intermolecular distance, the first term represents the relative kinetic energy of the target and projectile, and h_1, h_2 are functions of the intramolecular nuclear coordinates $\mathbf{x}_1, \mathbf{x}_2$. In the time-independent scheme, the eigenfunctions ψ_1, ψ_2 of h_1, h_2 describe the internal motions of the colliding partners and form a basis for expanding the total wave function Ψ of the system

$$\Psi(\mathbf{R}, \mathbf{x}_1, \mathbf{x}_2) = \sum_{\alpha_1 \alpha_2 \ell m} \frac{F(\alpha_1 \alpha_2 \ell m | R)}{R} \times Y_{\ell m}(\Theta, \Phi) \psi_1(\alpha_1 | \mathbf{x}_1) \psi_2(\alpha_2 | \mathbf{x}_2). \quad (38.12)$$

In Eq. (38.12), α_1, α_2 denote the sets of quantum numbers required to specify the states of the isolated molecules, and $Y_{\ell m}(\Theta, \Phi)$ is a spherical harmonic function of the angular coordinates of the intermolecular vector \mathbf{R} ; $F(\alpha_1 \alpha_2 \ell m | R)$ are R -dependent expansion coefficients, which are solutions of the (time-independent) Schrödinger equation

$$(H - E)\Psi = 0, \quad (38.13)$$

where E is the total energy. These solutions may be arranged as the columns of a square matrix, $\mathbf{F}(R)$, in which each

column is labeled by a different initial scattering state. The radial functions must satisfy the physical boundary conditions,

$$\begin{aligned} \mathbf{F}(R) &\rightarrow \mathbf{0} && \text{as } R \rightarrow 0 \\ \mathbf{F}(R) &\rightarrow \mathbf{J}(R)\mathbf{A} - \mathbf{N}(R)\mathbf{B} && \text{as } R \rightarrow \infty, \end{aligned}$$

where \mathbf{J} and \mathbf{N} are diagonal matrices whose nonvanishing elements are given by

$$J_{ii} = k_i^{\frac{1}{2}} R j_\ell(k_i R), \quad (38.14)$$

$$N_{ii} = k_i^{\frac{1}{2}} R n_\ell(k_i R), \quad (38.15)$$

and j_ℓ, n_ℓ are spherical Bessel functions of the first and second kinds; k_i is the wave number in channel i (a given set of values of the quantum numbers $\alpha_1 \alpha_2 \ell m$). The reactance matrix,

$$\mathbf{K} = \mathbf{B}\mathbf{A}^{-1}, \quad (38.16)$$

yields the state-to-state cross sections. We note that the quantum scattering equations can also be solved in a time-dependent scheme by propagation of a wave packet. In contrast to the time-independent approach, the wave-packet method is not adapted to cold and ultracold collisions due to difficulties in damping outgoing waves with long de Broglie wavelengths.

38.3 Symmetries and Conservation Laws

The expansion of the total wave function, Eq. (38.12), does not explicitly incorporate the invariance of the Hamiltonian under an arbitrary rotation in space or reflection in the coordinate origin. The Hamiltonian commutes with \mathbf{J}^2 , where \mathbf{J} is the total angular momentum, and any component of \mathbf{J} , J_x , J_y , or J_z , although these components do not commute amongst themselves. Eigenfunctions of H may, therefore, be chosen to be simultaneous eigenfunctions of \mathbf{J}^2 and (conventionally) J_z , with eigenvalues $J(J+1)$ and M . If \mathbf{j}_1 and \mathbf{j}_2 are the angular momenta of the isolated collision partners, then

$$\mathbf{j}_{12} = \mathbf{j}_1 + \mathbf{j}_2$$

is their resultant, and

$$\mathbf{J} = \mathbf{j}_{12} + \boldsymbol{\ell},$$

where $\boldsymbol{\ell}$ denotes the relative angular momentum of the two molecules. The coupling of the angular momenta to the multipolar expansion of the electromagnetic field (i.e., the interaction potential) gives rise to collisional selection rules.

The parity operator, P , reflects the coordinates in the origin. Because two successive operations with P restore

the original values of the coordinates, the corresponding eigenvalue p satisfies the equation $p^2 = 1$ or $p = \pm 1$. For electromagnetic interactions, the commutation of P and H implies conservation of the parity of the system.

If one takes advantage of the conservation laws associated with these symmetries of the system, substantial savings in computing time can be made: only one value of the total angular momentum and of the parity need to be considered simultaneously, i.e., J and the parity are conserved during the collision.

38.4 Coordinate Systems

The natural choice of coordinate system in which to express the interaction potential, $V(\mathbf{R}, \mathbf{x}_1, \mathbf{x}_2)$, is a body-fixed (BF) system in which the z -axis coincides with the direction of the intermolecular vector $\mathbf{R} = (R, \Theta, \Phi)$. A rotation of the space-fixed (SF) coordinate system through the Euler angles $(\Phi, \Theta, 0)$ generates such a BF frame. The intramolecular coordinates $\mathbf{x}_1, \mathbf{x}_2$ must then be expressed relative to the BF frame, as must the Laplacian operator ∇_R^2 , which appears in the expression for the total Hamiltonian, Eq. (38.11). The latter may be written as

$$\begin{aligned} \nabla_R^2 &= \frac{1}{R} \frac{\partial^2}{\partial R^2} R - \frac{\ell^2}{R^2} \\ &= \frac{1}{R} \frac{\partial^2}{\partial R^2} R - \frac{(\mathbf{J} - \mathbf{j}_{12})^2}{R^2}, \end{aligned} \quad (38.17)$$

which are the forms suitable for calculations in SF and BF coordinates, respectively.

A unitary transformation relates the normalized eigenfunctions of a given parity in SF and BF coordinates. In Dirac notation,

$$\begin{aligned} |j_{12} \ell JM\rangle_{\text{SF}} \\ = \sum_{\bar{\Omega}} |j_{12} \bar{\Omega} \varepsilon JM\rangle_{\text{BF}} \langle j_{12} \bar{\Omega} \varepsilon JM | j_{12} \ell JM \rangle, \end{aligned} \quad (38.18)$$

where $\bar{\Omega} = |\Omega|$ and Ω is the projection of \mathbf{J} on the BF z -axis. As the projection of $\boldsymbol{\ell}$ on the intermolecular axis is zero, Ω is also the projection of \mathbf{j}_{12} on the BF z -axis. The absolute value of Ω appears in the transformation because $|j_{12} \pm \Omega JM\rangle$ are *not* eigenfunctions of the parity operator P , whereas the linear combinations

$$|j_{12} \bar{\Omega} \varepsilon JM\rangle = \frac{|j_{12} \Omega JM\rangle + \varepsilon |j_{12} - \Omega JM\rangle}{[2(1 + \delta_{\bar{\Omega}0})]^{\frac{1}{2}}}$$

($\varepsilon = \pm 1$) are eigenfunctions of P . The factor $[2(1 + \delta_{\bar{\Omega}0})]^{\frac{1}{2}}$ ensures the correct normalization of these functions. The elements of the matrix that performs the unitary transformation

in Eq. (38.18) are

$$\begin{aligned} & \langle j_{12} \bar{\Omega} \varepsilon JM | j_{12} \ell JM \rangle \\ &= \left[\frac{2(2\ell + 1)}{(1 + \delta_{\bar{\Omega}0}) (2J + 1)} \right]^{\frac{1}{2}} C_{\bar{\Omega}0\bar{\Omega}}^{j_{12}\ell J}, \end{aligned} \quad (38.19)$$

where $C_{\bar{\Omega}0\bar{\Omega}}^{j_{12}\ell J}$ is a Clebsch–Gordan coefficient.

38.5 Scattering Equations

Schrödinger's equation for the scattering system may be reduced to a set of coupled, ordinary, second-order differential equations for the radial functions $F(R)$. Expressed in matrix form, these coupled-channel or close-coupling equations become

$$\left[\mathbf{1} \frac{d^2}{dR^2} + \mathbf{W}(R) \right] \mathbf{F}(R) = 0. \quad (38.20)$$

There exists a set of equations in Eq. (38.20) for each value of the total angular momentum J and parity p (Sect. 38.3). The matrix \mathbf{W} may be written as

$$\mathbf{W}(R) = \mathbf{k}^2 - 2\mu \mathbf{V}_{\text{eff}}, \quad (38.21)$$

where \mathbf{k}^2 is a diagonal matrix whose nonvanishing elements are

$$k_{\alpha_1 \alpha_2}^2 = 2\mu(E - \varepsilon_{\alpha_1} - \varepsilon_{\alpha_2}); \quad (38.22)$$

$k_{\alpha_1 \alpha_2}$ is the wave number at infinite separation ($R \rightarrow \infty$) when the collision partners are in eigenstates α_1, α_2 with eigenenergies $\varepsilon_{\alpha_1}, \varepsilon_{\alpha_2}$; \mathbf{V}_{eff} is the matrix of the effective potential,

$$V_{\text{eff}} = V(\mathbf{R}, \mathbf{x}_1, \mathbf{x}_2) + \frac{\ell^2}{2\mu R^2}, \quad (38.23)$$

in which V is the interaction potential, and $\ell^2/(2\mu R^2)$ may be identified with the centrifugal potential. There exist standard computer codes for solving equations of the form in Eq. (38.20) [2–4].

38.6 Matrix Elements

38.6.1 Interaction Potential

The interaction potential is usually expressed and computed in BF coordinates. For the purposes of the analysis, it is convenient to derive a multipolar expansion of the potential from

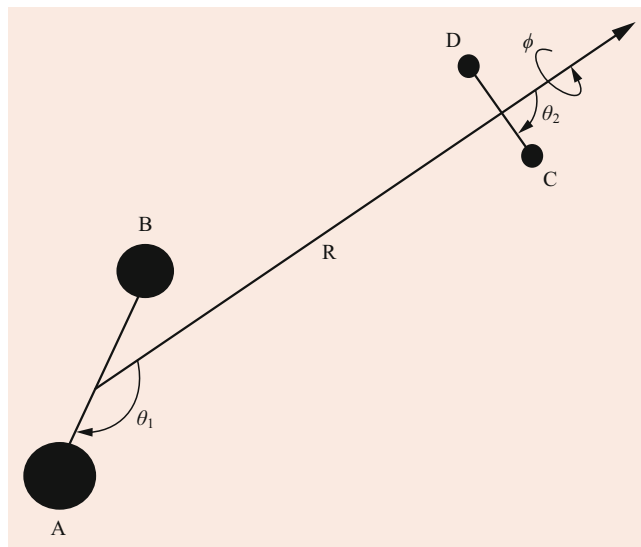


Fig. 38.2 The body-fixed Jacobi coordinates system for the scattering of two rigid rotors

a least-squares fit to the original data points. If the collision calculations are being done in the BF frame, the potential matrix elements may be evaluated directly. However, if the SF frame is to be used, the potential expansion must first be transformed into SF form.

Consider the interaction between two rigid rotors. This example serves as a paradigm. The geometry of the collisional complex is characterized by three angles θ_1 , θ_2 , and ϕ , and the distance R between the centers of mass of the two colliding partners (Fig. 38.2). The polar angles of the two rigid rotor with respect to \mathbf{R} are denoted θ_1 and θ_2 , respectively, while ϕ denotes the dihedral angle. In the BF frame, the potential can be expanded as

$$V(R, \theta_1, \theta_2, \phi) = \sum_{l_1, l_2; \mu} v_{l_1, l_2; \mu}(R) s_{l_1, l_2; \mu}(\theta_1, \theta_2, \phi). \quad (38.24)$$

The basis functions $s_{l_1, l_2; \mu}(\theta_1, \theta_2, \phi)$ are products of associated Legendre functions P_{lm}

$$\begin{aligned} s_{l_1, l_2; \mu}(\theta_1, \theta_2, \phi) &= \left(\frac{2\mu + 1}{4\pi} \right)^{1/2} \\ &\times \left\{ \langle l_1 0 l_2 0 | l_1 l_2 \mu 0 \rangle P_{l_1 0}(\theta_1) P_{l_2 0}(\theta_2) \right. \\ &+ \sum_m (-)^m 2 \langle l_1 m l_2 - m | l_1 l_2 \mu 0 \rangle \\ &\left. \times P_{l_1 m}(\theta_1) P_{l_2 m}(\theta_2) \cos(m\phi) \right\}, \end{aligned} \quad (38.25)$$

where $\langle \dots | \dots \rangle$ is a Clebsch–Gordan coefficient.

The P_{lm} functions are related to spherical harmonics. Here, l_1, l_2 are associated to the rotational motion of the two collision partners.

The matrix elements of the potential are

$$\begin{aligned} & \langle j_1 j_2 j_{12} l J M | V(R, \theta_1, \theta_2, \phi,) | j_1' j_2' j_{12}' l' J M \rangle \\ &= (4\pi)^{-3/2} \sum_{l_1, l_2, \mu} v_{l_1, l_2; \mu}(R) (-1)^{j_1 + j_2 + j_{12}' + J} \\ & \quad \times [(2j_1 + 1)(2j_2 + 1)(2j_1' + 1)(2j_2' + 1) \\ & \quad \times (2j_{12} + 1)(2j_{12}' + 1)(2l + 1)(2l' + 1) \\ & \quad \times (2l_1 + 1)(2l_2 + 1)]^{1/2} (2\mu + 1) \begin{pmatrix} l' & l & \mu \\ 0 & 0 & 0 \end{pmatrix} \\ & \quad \times \begin{pmatrix} j_1' & j_1 & l_1 \\ 0 & 0 & 0 \end{pmatrix} \begin{pmatrix} j_2' & j_2 & l_2 \\ 0 & 0 & 0 \end{pmatrix} \\ & \quad \times \begin{Bmatrix} l' & l & \mu \\ j_{12} & j_{12}' & J \end{Bmatrix} \begin{Bmatrix} j_{12}' & j_2' & j_1' \\ j_{12} & j_2 & j_1 \\ \mu & l_2 & l_1 \end{Bmatrix}, \quad (38.26) \end{aligned}$$

where $\begin{pmatrix} \dots \\ \dots \\ \dots \end{pmatrix}$ is a Wigner $3j$ -coefficient, $\begin{Bmatrix} \dots \\ \dots \\ \dots \end{Bmatrix}$ a $6j$ -coefficient, and $\left\{ \begin{matrix} \dots \\ \dots \\ \dots \end{matrix} \right\}$ a $9j$ -coefficient.

The close-coupling method has been applied to rigid symmetric and asymmetric tops colliding with a spherical atom and/or a rigid rotor and to open-shell systems. The main difference resides in the computation of the matrix elements of the potential, and we refer the reader to references [5–10].

38.6.2 Centrifugal Potential

When evaluated in the SF frame, the matrix of the centrifugal potential is diagonal, with nonvanishing elements $\ell(\ell + 1)/(2\mu R^2)$. In the BF frame, the diagonal elements are (see Eq. (38.17))

$$\begin{aligned} & \langle j_{12} \bar{\Omega} \varepsilon J M | (\mathbf{J} - \mathbf{j}_{12})^2 / 2\mu R^2 | j_{12} \bar{\Omega} \varepsilon J M \rangle \\ &= [J(J + 1) + j_{12}(j_{12} + 1) - 2\bar{\Omega}^2] / (2\mu R^2), \quad (38.27) \end{aligned}$$

and, in addition, there are off-diagonal elements

$$\begin{aligned} & \langle j_{12} \bar{\Omega} \varepsilon J M | (\mathbf{J} - \mathbf{j}_{12})^2 / 2\mu R^2 | j_{12} \bar{\Omega} \pm 1 \varepsilon J M \rangle \\ &= -\{(1 + \delta_{\bar{\Omega}0})(1 + \delta_{\bar{\Omega} \pm 1, 0}) \\ & \quad \times [J(J + 1) - \bar{\Omega}(\bar{\Omega} \pm 1)] \\ & \quad \times [j_{12}(j_{12} + 1) - \bar{\Omega}(\bar{\Omega} \pm 1)]\}^{1/2} / (2\mu R^2). \quad (38.28) \end{aligned}$$

The matrix elements in Eq. (38.28), which are off-diagonal in $\bar{\Omega}$, are associated with the rotation in space of the BF coordinate system (Coriolis coupling). In the *coupled states* approximation [11, 12], the off-diagonal elements in Eq. (38.28) are neglected, and the diagonal elements in

Eq. (38.27) are often replaced by their SF equivalent form $\ell(\ell + 1)/(2\mu R^2)$. The matrix of the interaction potential, on the other hand, continues to be evaluated in BF coordinates. The net effect of these approximations is to ignore the rotation of the BF frame in the course of the collision, and the associated dynamical terms.

38.7 Semi and Quasi-Classical Methods

The above quantal method is the most accurate approach, but it is also computationally very expensive if the density of energy levels of both the target and the projectile is large. Besides decoupling approximations such as the coupled-states approach, semiclassical and quasi-classical approximations offer useful alternatives. The former consists in solving the time-dependent Schrödinger equation

$$i\hbar \frac{\partial \Psi}{\partial t} = H \Psi, \quad (38.29)$$

while in the latter, the classical Hamilton equations of motion are integrated

$$\frac{dq}{dt} = \frac{\partial H}{\partial p}, \quad (38.30)$$

$$\frac{dp}{dt} = -\frac{\partial H}{\partial q}, \quad (38.31)$$

where q are the coordinates and p the conjugate momenta. Their common feature is that at least one degree of freedom in the collision system is treated classically. Difficulties in the application of semiclassical theories have precluded their being employed routinely. In contrast, quasi-classical methods have been widely employed in both reactive and nonreactive scattering studies. In the quasi-classical trajectory (QCT) approach, batches of trajectories are sampled with random (Monte Carlo) initial conditions and analyzed through statistical methods. State-resolved cross sections are extracted by use of the correspondence principle combined with bin histogram methods. QCT methods are very efficient, but, of course, they ignore purely quantum effects such as interferences, tunneling, and resonances [13].

38.8 Example: CO–H₂

An important result of quantal theory for nonreactive scattering is the prediction of a rich resonance structure at low collisional energy. Two different types of scattering resonances can occur, shape or Feshbach. A shape (or orbiting) resonance corresponds to a quasi bound state that is confined behind a centrifugal barrier and correlates with the initial or final monomer levels of the colliding partners. A Feshbach resonance corresponds to a quasi bound state that corre-

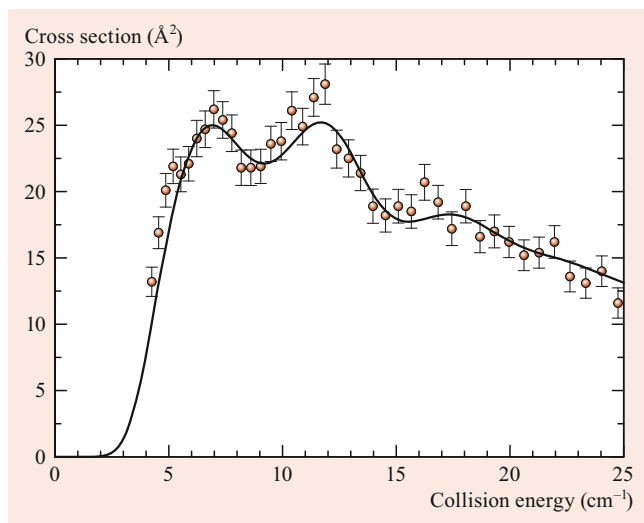


Fig. 38.3 Cross section for the CO rotational excitation $j = 0 \rightarrow 1$ induced by *normal*-H₂ as function of collision energy. The experimental data (circles) are compared to theory (full line)

lates with an energetically inaccessible or “closed” monomer level. Both types of resonances are predicted to occur at collision energies lower than the well depth of the interaction potential. Observing these resonances experimentally remained elusive until recent crossed molecular beam experiments [14, 15]. Such experimental data are presented in Fig. 38.3 for the CO excitation $j = 0 \rightarrow 1$ by *normal*-H₂. The measured resonance structures are in good quantitative agreement with the close-coupling calculations presented in [16], suggesting that theory and experiment have converged for this benchmark system.

38.9 New Directions

An important application field of nonreactive scattering studies is astrophysics. Indeed, since collisions compete with radiative processes in altering the populations of energy levels, the estimation of molecular abundances in the interstellar medium from spectral line data requires collisional rate coefficients with the most abundant collision partners, i.e., He, H and H₂, and free electrons [17]. Hence, one of the major challenge for the coming years is the study of vibrational excitation of interstellar polyatomics since important molecules such as HCN, C₂H₂, or CH₄ have been observed in vibrationally excited levels in various astrophysical environments, such as stellar envelopes and protoplanetary disks. Analysis of their emission spectra requires collisional data, and the development of new methods to deal with vibrational excitation will have to be considered.

Special attention will have to be given also to complex organic molecules with more than five atoms. There is only very little data for these species despite the fact that they are the object of many investigations using ground-based and space telescopes. For such heavy molecules with small rotational and vibrational constants, the main limitation is the computing resources, and approximate methods will have to be employed.

Another important application field is cold chemistry. Novel experimental techniques allow the formation of molecules cooled down to very low temperatures ($T < 1$ K). These cold molecules allow new insights into molecular interaction dynamics. In particular, purely quantum effects are expected to dominate collisional processes at these low temperatures, and it will be essential to have accurate quantum theoretical results to support the new experiments.

References

- Bernstein, R.B.: Atom–Molecule Collision Theory. Plenum, New York (1979)
- Hutson, J.M., Le Sueur, C.R.: *Comp. Phys. Commun.* **241**, 9 (2019)
- Flower, D.R., Bourhis, G., Launay, J.-M.: *Comput. Phys. Comm.* **131**, 187 (2000)
- Alexander, M. H., Manolopoulos, D. E., Werner, H.-J., Follmeg, B., Ma, Q., Dagdigian, P. J., with contributions by Vohralik, P. F., Lemoine, D., Corey, G., Gordon, R., Johnson, B., Orlikowski, T., Berning, A., Degli-Esposti, A., Rist, C., Pouilly, B., van der Sanden, G., Yang, M., de Weerd, F., Gregurick, S., Klos, J., Lique, F.: HIBRIDON is a package of programs for the time-independent quantum treatment of inelastic collisions and photodissociation, More information and/or a copy of the code can be obtained from the website <http://www2.chem.umd.edu/groups/alexander/hibridon/hib43>
- Green, S.: *J. Chem. Phys.* **64**, 3463 (1976)
- Garrison, B.J., Lester, W.A., Miller, W.H.: *J. Chem. Phys.* **65**, 2193 (1976)
- Alexander, M.H.: *J. Chem. Phys.* **76**, 3637 (1982)
- Corey, G.C., Alexander, M.H.: *J. Chem. Phys.* **83**, 5060 (1985)
- Rist, C., Alexander, M.H., Valiron, P.: *J. Chem. Phys.* **98**, 4662 (1993)
- Phillips, T.R., Maluendes, S., Green, S.: *J. Chem. Phys.* **102**, 6024 (1995)
- McGuire, P., Kouri, D.J.: *J. Chem. Phys.* **60**, 2488 (1974)
- Pack, R.T.: *J. Chem. Phys.* **60**, 633 (1974)
- Faure, A., Lique, F., Wiesenfeld, L.: *Mon. Not. Roy. Astron. Soc.* **460**, 2103 (2016)
- Chefdeville, S., Stoecklin, T., Bergeat, A., Hickson, K.M., Naulin, C., Costes, M.: *Phys. Rev. Lett.* **109**, 023201 (2012)
- Chefdeville, S., Stoecklin, T., Naulin, C., Jankowski, P., Szalewicz, K., Faure, A., Costes, M., Bergeat, A.: *Astrophys. J.* **799**, L9 (2015)
- Faure, A., Jankowski, P., Stoecklin, T., Szalewicz, K.: *Sci. Rep.* **6**, 28449 (2016)
- Roueff, E., Lique, F.: *Chem. Rev.* **113**, 8906 (2013)



Alexandre Faure Alexandre Faure received his PhD from the University Joseph Fourier at Grenoble (France) in 1999. He worked at University College London in the UK and at the Laboratoire d'Astrophysique de Grenoble. His research focuses on computational molecular physics and is mainly concerned with processes of astrophysical relevance.



David R. Flower David R. Flower is Emeritus Professor of Physics at the University of Durham (UK). He was awarded his PhD by the University of London in 1969. After working at the Observatoire de Paris (Meudon, France) and at the ETH (Zuerich, Switzerland), he joined the Physics Department of the University of Durham in 1978. He has been Professor of Physics since 1994. His research interests are in atomic and molecular physics related to astrophysics.



François Lique François Lique received his PhD from Sorbonne University in Paris (France) in 2006. He worked at the University of Maryland in USA and at the University of Le Havre Normandy (France). He is now full professor at the University Rennes 1 (France). His research mainly focuses on the modeling of physical and chemical processes of astrophysical interest.



Eric Herbst

Contents

39.1	Introduction	583
39.2	Normal Bimolecular Reactions	585
39.2.1	Capture Theories	585
39.2.2	Phase Space Theories	587
39.2.3	Short-Range Barriers	588
39.2.4	Complexes Followed by Barriers	589
39.2.5	The Role of Tunneling	590
39.3	Association Reactions	591
39.3.1	Radiative Stabilization	591
39.3.2	Complex Formation and Dissociation	592
39.3.3	Competition with Exoergic Channels	593
39.4	Concluding Remarks	593
	References	594

Abstract

The rates of gas phase chemical processes can generally be described by rate laws in which the rate of formation of products or disappearance of reactants is related to the product of the concentrations of reactants raised to various powers [1]. Rate laws are deterministic expressions that are usually accurate even though they are used to represent a stochastic reality. Rate equations may fail in the limit of small numbers of reacting particles, where both fluctuations and discrete aspects are important. Exceptions to the reliability of rate equations have been found recently in a variety of fields including surface chemistry on small particles [2]. Moreover, both Monte Carlo and master equation methods can be used in their place, given sufficient computing power [3–6].

Keywords

rate coefficient · transition state theory · microscopic reversibility · phase space theory · tunneling correction

39.1 Introduction

As an example of a rate law, consider the rate of disappearance of reactant A in a gas mixture containing species A , B , and C . The rate law for this disappearance can be expressed by the equation

$$\frac{d[A]}{dt} = -k[A]^a[B]^b[C]^c, \quad (39.1)$$

where the symbols $[]$ refer to concentration, and the rate coefficient k is dependent on temperature, and possibly other parameters such as the total gas density. The above law is not the most general that can be envisaged. For example, if species A reacts via more than one set of processes, more than one negative term on the right-hand side of the equation will be needed. In addition, if the reverse reaction to form A from products is appreciable, a positive term must also be included. At equilibrium, the rate of change of reactant must be zero.

The relation above does not necessarily refer to one chemical reaction, but to a succession of elementary reactions known collectively as a mechanism. The most elementary reaction is a simple bimolecular process with a second order rate law of the type

$$\frac{d[C]}{dt} = -\frac{d[A]}{dt} = k[A][B], \quad (39.2)$$

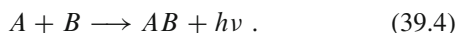
where two species A and B collide to form products, one of which can be labeled C . In this law, the rate coefficient k is related simply to the reaction cross section σ via the equation

$$k = \sigma v, \quad (39.3)$$

E. Herbst (✉)
Dept. of Chemistry and Dept. of Astronomy, University of Virginia
Charlottesville, VA, USA
e-mail: eh2ef@virginia.edu

where v is the relative velocity of reactants. The rate coefficient in a bimolecular process has units of volume per time, typically $\text{cm}^3 \text{s}^{-1}$. In a thermal system, the rate coefficient $k(T)$ is averaged over all degrees of freedom of the reactants, both internal and translational. The most specific rate coefficient is termed a state-to-state coefficient and refers to a process in which reactant A in quantum state a reacts with reactant B in quantum state b at a specific translational energy \mathcal{T} to form products in specific states separating with a specific translational energy [7].

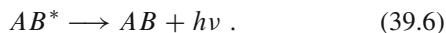
Although normal bimolecular processes produce more than one product, it is also possible for the two reactants A and B to stick together if sufficient energy is released in the form of a photon



Such a process is called radiative association [8], and has mainly been studied for ion-molecule systems, i.e., reactions in which one of the two reactants is an ion. The process of radiative association is normally thought to occur in two steps. The first step produces a collision complex AB^* , which is a molecule existing in a transitory fashion above its dissociation limit



Once formed, the complex, which is often thought of as an ergodic entity retaining memory only of its total energy and angular momentum, can either redissociate into reactants, or emit a photon of sufficient energy to stabilize itself



Since redissociation of the complex is generally more rapid than radiative emission, radiative association rate coefficients are normally small. Emission of one infrared photon is sufficient to achieve stabilization, but stabilization of a complex via electronic emission may be a more rapid mechanism if suitable electronic states exist [8, 9]. The lifetime of the complex against redissociation into reactants is a strong direct function of the binding energy of the species and the number of atoms it possesses.

In addition to bimolecular processes, two other types of reactions often referred to as elementary are unimolecular and termolecular reactions. Although complex reaction mechanisms are sometimes divided into unimolecular and termolecular steps, these are not strictly elementary because they can be subdivided into a series of bimolecular steps. In a unimolecular reaction [10, 11], a molecule A is destroyed at sufficiently high gas density by a process that has the seemingly simple first order rate law

$$\frac{d[A]}{dt} = -k[A] . \quad (39.7)$$

At low pressures, on the other hand, the rate law is second order. A simplified series of events, called the Lindemann mechanism, explains these limiting cases by invoking the activation of species A by strong inelastic collisions with bath gas M to form an activated complex A^* which can either be deactivated by inelastic collisions or spontaneously decompose, since it possesses sufficient energy to do so. The steps are written as



where the spontaneous destruction of A^* can be thought of as a truly elementary unimolecular reaction, akin to spontaneous emission of radiation. Studies of spontaneous dissociation occupy an important place in gas phase reaction theory, and are discussed in Sects. 39.2.2 and 39.2.4 in the context of dissociation of intermediate complexes. If the rate coefficients for the forward and reverse processes in Eq. (39.8) are labeled k_1 and k_{-1} respectively, and the rate-coefficient for spontaneous dissociation of A^* into products is labeled $k_2(\text{s}^{-1})$, application of the steady-state principle to the concentration of the activated complex, namely,

$$\frac{d[A^*]}{dt} = k_1[A][M] - k_{-1}[A^*][M] - k_2[A^*] \approx 0 \quad (39.10)$$

leads to the rate law

$$-\frac{d[A]}{dt} = k'[A][M] , \quad (39.11)$$

where

$$k' = \frac{k_1 k_2}{k_{-1}[M] + k_2} . \quad (39.12)$$

At low pressures, $k_{-1}[M] \ll k_2$ and $k' \approx k_1$ so that a second order rate law prevails. At high pressures, $k_{-1}[M] \gg k_2$ and $k' \approx k_1 k_2 / k_{-1}[M]$ so that the rate law becomes first order

$$-\frac{d[A]}{dt} \approx \frac{k_1}{k_{-1}} k_2 [A] . \quad (39.13)$$

Since both the activation and deactivation of complexes occur stepwise, rather than in single strong collisions, reality is far more complex than the Lindemann mechanism [12], and, at the highest degree of detail, master equation treatments are needed, especially for intermediate pressures [13].

In a termolecular reaction, which is actually the inverse of a unimolecular process [13], two species B and C collide to form a collision complex A^* , which can be regarded as the activated complex of stable species A . The collision complex can be stabilized by subsequent strong collisions with other species



or can redissociate into reactants. If the complex formation step occurs with a bimolecular rate coefficient k_{-2} , and k_{-1} and k_2 refer to complex stabilization and dissociation as in the unimolecular case, the rate law for the termolecular process can be written

$$\frac{d[A]}{dt} = k'[B][C][M], \quad (39.15)$$

where

$$k' = \frac{k_{-2}k_{-1}}{k_{-1}[M] + k_2}. \quad (39.16)$$

At low pressures, $k' \approx k_{-2}k_{-1}/k_2$ and the rate law is third order. At high pressures, when every activated complex is deactivated, the rate law becomes second order since $k' \approx k_{-2}/[M]$. Actually, at very low pressures radiative stabilization of the complex dominates and the rate law once again becomes second order. As in the unimolecular case, the complex does not really undergo strong inelastic collisions, so that reality is once again more complex than pictured here [13]. For detailed theories of thermal reactions, there is the additional problem in Eqs. (39.12) and (39.16) of deciding when thermalization of the partial rate coefficients should be undertaken. In reality, the partial rate coefficients refer to reactions with specific amounts of energy and angular momentum, and should not be thermally averaged before incorporation into the equations for k' .

39.2 Normal Bimolecular Reactions

The rates of elementary (bimolecular) chemical reactions are governed by Born–Oppenheimer potential surfaces, which contain electronic energies and nuclear-nuclear repulsions. Reactions can be classified as exoergic or endoergic depending upon whether the 0 K energies of the products lie below or above those of the reactants, respectively. In the simplest types of exoergic chemical reactions, the potential energy flows downhill from reactants to products, or flows downhill from reactants to a global minimum (the reaction complex) after which it flows uphill to products. More commonly, the morphology of the potential surface is such that after some long-range attraction, the potential rises as old chemical bonds are broken before falling as new bonds are formed. Generally, there is a minimum energy pathway through the region of large potential referred to as the reaction coordinate. The system is said to traverse a transition state barrier, which refers to the configuration of atoms at which a potential saddle point occurs. The height of this transition state barrier is related to the activation energy barrier E_a in the classical Arrhenius rate law

$$k(T) = A(T) \exp \frac{-E_a}{k_B T}, \quad (39.17)$$

for rate coefficients of bimolecular reactions which contain short-range barriers [1]. In the Arrhenius expression, k_B is the Boltzmann constant, and the pre-exponential factor $A(T)$ can be related to the form of the long-range potential, or to an equilibrium coefficient between the transition state and reactants (see the discussion of activated complex theory in Sect. 39.2.3). Although fits of experimental data over short temperature ranges often assume the pre-exponential factor to be totally independent of temperature, theories show that this is not strictly true in most instances. A more serious problem with the expression undoubtedly occurs at low temperatures since tunneling will clearly lead to deviations.

Although, in principle, it is possible to calculate reaction cross sections and rate coefficients via the quantum theory of scattering, in practice few systems have been studied by this technique given the immense computational effort required [14, 15]. Another set of approaches, which has been used to study a large variety of systems, is known as classical molecular dynamics (see Chap. 62). In these approaches, the atoms move classically on the quantum mechanically generated Born–Oppenheimer potential surfaces. For many reactions, however, neither technique is applicable, and a variety of simpler approaches has been developed, using capture and statistical approximations; these approaches will be emphasized here. Indeed, the use of an ergodic complex in our preliminary discussion of association and unimolecular reactions above presages the use of statistical approximations. An excellent high-level review article on many of the topics covered here has been written by Troe [16].

39.2.1 Capture Theories

For reactions that do not possess a potential energy barrier at short-range, it is tempting to apply long-range capture theories between structureless particles to calculate the reaction rate coefficient. Such theories assume that (a) all hard collisions lead to reaction, and (b) hard collisions occur for all partial waves up to a maximum impact parameter b_{\max} or relative angular momentum quantum number L_{\max} . This is normally defined so that the reactant translational energy \mathcal{T}_{AB} is just sufficient to overcome a centrifugal barrier. The centrifugal barrier produces a long-range maximum in the effective potential energy function V_{eff} given by the relation

$$V_{\text{eff}}(r, b) = V(r) + \mathcal{T}_{AB} b^2 / r^2, \quad (39.18)$$

where r is the separation between reactants and $\mathcal{T}_{AB} b^2 / r^2$ is the angular kinetic energy. If the reactants overcome the centrifugal barrier, they will spiral in towards each other in the absence of short-range repulsive forces. The approach has had its most notable success for exoergic reactions between ions and nonpolar neutral molecules [17]. The long-range po-

tential in this situation is simply (in cgs-esu units)

$$V(r) = -e^2\alpha_d/2r^4, \quad (39.19)$$

where α_d is the polarizability of the neutral reactant. This potential leads to the Langevin rate coefficient

$$k = v\pi b_{\max}^2 = 2\pi e \left(\frac{\alpha_d}{\mu} \right)^{1/2}, \quad (39.20)$$

where μ is the reduced mass of the reactants. The theory leads to a temperature-independent rate coefficient with magnitude $\approx 10^{-9} \text{ cm}^3 \text{ s}^{-1}$. Numerous experiments from above room temperature to below 30 K confirm its validity for the majority of ion–molecule reactions, which appear rarely to possess potential energy surfaces with short-range barriers [18, 19].

An analogous central force potential for structureless neutral–neutral reactants is the van der Waals or Lennard–Jones attraction

$$V(r) = \frac{-C_6}{r^6}, \quad (39.21)$$

where C_6 can be defined simply in terms of the ionization potentials and polarizabilities of the reactants [20, 21]. The rate coefficient obtained using a capture theory with this long-range potential is given, after translational thermal averaging, by the equation [21]

$$k(T) = 8.56 C_6^{1/3} \mu^{-1/2} (k_B T)^{1/6}, \quad (39.22)$$

where all quantities are in cgs units. Equation (39.22) leads to estimates for the rate coefficient at room temperature in the range $\approx 10^{-10}$ – $10^{-9} \text{ cm}^3 \text{ s}^{-1}$. Unlike the situation for ion–molecule reactions, this estimate has not received much attention mainly because most neutral–neutral reactions involve activation energy. Even for those systems without activation energy, the approximation appears to lead to rate coefficients that are too large by at least a factor of a few [21]. In place of the result of Eq. (39.22), kineticists often use the simple hard-sphere model with atomic dimensions for the reaction cross section. The hard-sphere model leads to a temperature dependence of $T^{1/2}$, which is in disagreement with a whole series of new experiments on fast neutral–neutral reactions down to temperatures near 10 K [22].

Both long-range potentials considered above are isotropic in nature. A variety of capture theories [23, 24] have been developed which take angular degrees of freedom into account. For ion–molecule systems in which the neutral species has a permanent dipole moment μ_d , the long-range potential becomes

$$V(r, \theta) = -\frac{e^2\alpha_d}{2r^4} - \frac{e\mu_d \cos \theta}{r^2}, \quad (39.23)$$

where θ is the angle between the radius vector from the charged species to the center-of-mass of the dipolar species and the dipole vector. Adiabatic effective (centrifugal) potential energy curves can be defined at any given fixed intermolecular separation r by diagonalizing angular kinetic energy and potential energy matrices using a suitable basis set. If an atomic ion is reacting with a linear neutral, a suitable basis set would consist of spherical harmonics for the rotation of the linear molecule (angular momentum j) as well as rotation matrices for the relative motion (angular momentum L) between the species. The eigenvalues of a matrix with fixed total angular momentum J then correspond to the effective radial potential energy functions V_{eff} at each r . The L, j labeling of the potential curves can be ascertained by starting the calculation at sufficiently large r so that L and j are reasonably good quantum numbers. Additional approximations, such as the centrifugal sudden approximation, can be made to facilitate the calculation [25]. Making the adiabatic assumption that transitions between these potentials are not allowed at long range, one obtains an adiabatic capture rate coefficient for each initial value of j and translational (radial kinetic) energy \mathcal{T}_{AB} from the criterion

$$V_{\text{eff}}(j, L_{\max}, R) = \mathcal{T}_{AB}, \quad (39.24)$$

where R is the separation corresponding to the maximum effective potential. Unlike the Langevin approach, the rate coefficients thermalized over translation for each j show an inverse dependence on temperature, with the $j = 0$ state showing the most severe dependence since the dipole is essentially *locked* for this state. Thermal averaging over j typically leads to rate coefficients with an inverse dependence on temperature between $T^{-1/2}$ and T^{-1} [26]. Rate coefficients as large as $10^{-7} \text{ cm}^3 \text{ s}^{-1}$ can be obtained as the temperature approaches 10 K. Although most ion–dipole reactions seem to obey capture theory models at low temperature, there are exceptions.

An alternative approach to ion–dipole reactions using the classical concept of adiabatic invariants has been developed [27]. In addition, variants to the capture theory discussed here have been formulated. A statistical adiabatic approach has been developed [23], in which adiabatic effective potential maxima are not used to define capture cross sections, but to define rate coefficients via the activated complex (transition state) theory discussed in Sect. 39.2.3, which posits thermal equilibrium between reactants and the species existing at the potential maxima. One advantage of this simplification is that it permits the adiabatic treatment to be more easily extended to complex geometries, especially if perturbation approximations are utilized. Other approaches involve the variational principle; an upper bound to the capture rate coefficient can be determined within the transition state, or bottleneck approach, which defines the

transition state through minimization of the number of available vibrational/rotational states at the bottleneck [28] (see Sect. 39.2.3).

Nonspherical capture theories have also been used [29, 30] to study rapid neutral–neutral reactions. The role of atomic fine structure at low temperatures is an especially interesting application; reactions involving atomic C and O with a variety of reactants have been studied. Use of an electrostatic potential shows that the reactivity of C or O atoms in their 3P_0 states with dipolar species is minimal. This is particularly important for atomic carbon since at low temperatures it lies primarily in its ground 3P_0 state. The choice of an electrostatic potential has been disputed [21] because experimental results for C–hydrocarbon reactions at room temperature are best understood if the long-range potential is dispersive (Lennard–Jones) in character rather than electrostatic.

Reactions between radicals in $^2\Pi$ states (e.g. OH) and $^2\Sigma$ states (e.g. CN) and stable molecules have also been considered, especially at low temperature, with long range potentials that contain both electrostatic and dispersion terms. The results can be compared with new low temperature experimental results on the CN–O₂ reaction, but the temperature dependence is not matched by theory if the dispersion term is included [30, 31]. In general, even the most recent capture theories are not as reliable as those for ion–molecule systems [32]. Rapid neutral–neutral reactions can also be treated by transition state theories (see below) [33] or, rarely, by detailed quantum mechanical means [34].

The last five years have witnessed a burgeoning interest in rapid neutral–neutral reactions at low temperature studied with the so-called CRESU technique (an acronym for Cinétique de Réaction en Ecoulement Supersonique Uniforme) [22, 35–37]. The new data should provoke new attempts at theoretical understanding.

39.2.2 Phase Space Theories

Capture theories tell us neither the products of reaction, if several sets of exoergic products are available, nor the distributions of quantum states of the products. The simplest approach to these questions for reactions with barrierless potentials is to make a statistical approximation – all detailed outcomes being equally probable as long as energy and angular momentum are conserved. Such a result requires strong coupling at short range. The most prominent treatment along these lines is referred to as phase space theory [38]. In this theory, the cross section σ for a reaction between two species A and B with angular momentum quantum numbers J_A and J_B and in specific vibrational-electronic states colliding with asymptotic translational kinetic energy \mathcal{T}_{AB} to form products C and D in specific vibrational-electronic states with angu-

lar momentum quantum numbers J_C and J_D is

$$\begin{aligned} \sigma(J_A, J_B \rightarrow J_C, J_D) &= \frac{\pi \hbar^2}{2\mu \mathcal{T}_{AB}} \sum_{L_i, J} (2L_i + 1) \\ &\times P(J_A, J_B, L_i \rightarrow J) P'(J \rightarrow J_C, J_D), \end{aligned} \quad (39.25)$$

where J is the total angular momentum of the combined system, L_i is the initial relative angular momentum of reactants, P is the probability that the angular momenta of the reactants add vectorially to form J , P' is the probability that the combined system with angular momentum J dissociates into the particular final state of C and D , μ is the reduced mass of reactants, and the summation is over the allowable ranges of initial relative angular momentum and total angular momentum quantum numbers. P' is equal to the sum over the final relative angular momentum L_f , of angular momentum allowed ($J \rightarrow L_f, J_C, J_D$) combinations leading to the specific product state divided by the sum of like combinations for all energetically accessible product and reactant states. The ranges of initial and final relative angular momenta are given by appropriate capture models (e.g. Langevin, ion–dipole, Lennard–Jones) as well as angular momentum triangular rules. This procedure involves the implicit assumption that strong coupling does not occur at long range; rather, adiabatic effective potentials can be assumed for initial and final states. The state-to-state rate coefficient is simply the cross section multiplied by the relative velocity of the two reactants. Summation over all product states, as well as thermal averaging over the reactant state distributions and the translational energy distribution, can all be undertaken. Strategies for summing/integrating over rotational/vibrational degrees of freedom have been given [39]. As can be seen by writing out the expression for P' , the phase space formula for the state-to-state cross section in Eq. (39.25) obeys microscopic reversibility

$$\begin{aligned} 2\mu \mathcal{T}_{AB} \sigma(J_A, J_B \rightarrow J_C, J_D) &= 2\mu' \mathcal{T}'_{AB} \sigma(J_A, J_B \leftarrow J_C, J_D), \end{aligned} \quad (39.26)$$

where the reduced mass and asymptotic translational energy of the products are denoted by primes. Thus, thermalization of the forward and backward rates leads to detailed balancing.

As a detailed theory for prediction of reaction products and their state distributions, phase space theory and its variants have had mixed success. It is true that the theory correctly predicts that exoergic reactions occurring on barrierless potential surfaces proceed on every strong collision. It is also true, however, that the theory is generally not useful in predicting the branching ratios among several sets of exoergic products because potential surfaces do not

often show barrierless pathways for more than one set of products. When applied to product state distributions, the theory yields statistical results, so that population inversions in nondegenerate degrees of freedom (such as the vibrations of a diatomic molecule) are not replicated. With respect to more thermalized entities, such as total cross sections versus collision energy for endoergic reactions [40], the theory can be quite successful, especially when the potential surface involves a deep minimum or intermediate complex. In this instance, the strong coupling hypothesis comes closest to actuality. A deep well is also associated with a high density of vibrational states in the quasicontinuum above the dissociation limit of the molecular structure defined by the potential minimum [1, 41, 42]. Such a high density renders direct (specific) dynamical processes less likely.

A useful variant of phase space theory if complex lifetimes are needed [43] (see Sects. 39.2.4 and 39.3) is based on a unimolecular decay theory of *Klots* [44]. The reaction is considered to proceed via a capture cross section to form the intermediate complex, which then can dissociate into all available reactant and product states consistent with conservation of energy and angular momentum. The complex dissociation rate k_{uni} into a specific state can be obtained via the principle of microscopic reversibility in terms of the capture cross section from that state, obtained with $P' = 1$ in Eq. (39.25), to form the complex. In particular, if a complex with total angular momentum J can dissociate into one state of reactants A and B separating with translational energy \mathcal{T}_{AB} , then

$$k_{\text{uni}} = \rho_{\text{vib}}^{-1} g(J)^{-1} g(J_A) g(J_B) 2\mu \mathcal{T}_{AB} \sigma(J_A, J_B \rightarrow J), \quad (39.27)$$

where ρ_{vib} is the density of complex vibrational states obtained via a variety of prescriptions [1, 41, 42], and g is the rotational degeneracy. A cross section analogous to that in Eq. (39.25) can be formulated in terms of capture to form the complex multiplied by the complex dissociation rate into a particular state divided by the total (summed) dissociation rate. Note that the dissociation rate of the complex is proportional to ρ_{vib}^{-1} . Since ρ_{vib} is a strong function of the well depth, long-lived complexes are associated with large well depths (>1 eV). The *Klots* form for k_{uni} is especially useful for ion–molecule systems, where the cross section for complex formation can be assumed to be Langevin or ion–dipole. The concept of a long-range potential is less useful for most neutral–neutral systems, so that unimolecular rate coefficients for unstable entities are normally obtained quite differently in terms of ρ_{vib} at the transition state (Sect. 39.2.4).

For smaller reaction systems, especially those involving ions, it is quite common for the electronic states of reactants to correlate with more than one potential surface of the com-

bined system, although typically only one surface leads to energetically accessible products. In such instances, it is normal to assume statistical partitioning, although fine structure effects can complicate this picture. A generalization of phase space theory to account for multiple potential surfaces has been proposed for the $\text{C}^+ + \text{H}_2$ reaction [45].

Phase space theory has been used to predict product branching ratios for dissociative recombination reactions between polyatomic positive ions and electrons [46]; its success here has been limited at best.

39.2.3 Short-Range Barriers

Most reactions involving neutral molecules, as well as a minority of ion–molecule reactions, possess potential surfaces with short-range barriers. The experimental rate coefficients of these systems over selected temperature ranges are normally fit to the Arrhenius expression in Eq. (39.17).

The simplest theoretical method of taking short-range potential barriers into account is the line-of-centers approach, which resembles the capture theories previously discussed [7]. In this crude approximation, it is assumed that structureless reactants colliding with impact parameter b along a repulsive potential must reach some minimum distance, d , for reaction to occur. If the potential energy in the absence of angular momentum at d is E_0 , this condition implies that the asymptotic translational energy of reactants \mathcal{T}_{AB} must exceed the sum of E_0 and the centrifugal energy $\mathcal{T}_{AB} b^2/d^2$, which in turn yields a maximum impact parameter b_{max} . Thermal averaging of the rate coefficient $k = v \pi b_{\text{max}}^2$ over a Maxwell–Boltzmann distribution then yields

$$k(T) = \pi d^2 \left(\frac{8k_B T}{\pi \mu} \right)^{1/2} \exp \frac{-E_0}{k_B T}, \quad (39.28)$$

which bears some resemblance to the Arrhenius expression if one equates the parameter E_0 with the activation energy. Assuming $T = 300$ K, $\mu = 10$ u, and $d = 1$ Å, the pre-exponential factor is $2.5 \times 10^{-11} \text{ cm}^3 \text{ s}^{-1}$, which lies in a typical range.

The simple line-of-centers approach reduces the problem to that of structureless particles. The standard method of including all degrees of freedom is to use canonical ensemble statistical mechanics and to imagine that the transition state is in equilibrium with reactants. In the transition state, one of the vibrational degrees of freedom of a normal polyatomic molecule is replaced by a degree of freedom (the reaction coordinate) along which the potential is a maximum (with a corresponding imaginary frequency of vibration). The reaction coordinate is treated as a separable translation, so that the reaction rate coefficient can be envisaged as the equilibrium coefficient between transition state (minus one

coordinate) and reactants multiplied by the (average) speed of the transition state structure over the saddle point in the potential energy surface. The canonical result for $k(T)$ is given by [1, 7]

$$k(T) = \frac{k_B T}{h} \frac{q_{AB^\ddagger}}{q_A q_B} \exp \frac{-E_0}{k_B T} \quad (39.29)$$

for reactants A and B , where E_0 is the energy difference between the transition state and the reactants referred to zero-point levels, the \ddagger refers to the transition state, and the q are partition functions per unit volume. The partition functions can be factored into products representing electronic, vibrational, rotational, and translational degrees of freedom [47]. This formulation for $k(T)$ is known as the activated complex theory (ACT); a more appropriate name would be transition state theory since the term activated complex is also used to refer to an unstable state of a molecule in a deep potential well. The rate coefficient can also be written in terms of the thermodynamic parameters ΔH^\ddagger and ΔS^\ddagger [1].

Both the size and temperature dependence of the pre-exponential factor depend critically on the characteristics of transition state and reactants. Originally, ACT theory was used mainly to fit transition state characteristics to rate data. Increasingly accurate ab initio calculations of potential surfaces now allow purely theoretical determinations of $k(T)$ [48].

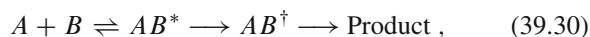
In addition to the assumption of a separable reaction coordinate that can be treated as a translation, several other assumptions have gone into the derivation of the ACT rate coefficient. First, molecules at the saddle point configuration (the transition state) have been arbitrarily chosen to be in equilibrium with reactants. More recently, the transition state assumption has been generalized to refer to that portion of the potential surface in which the reaction flux or number of states is a minimum [49], whether or not this occurs at a well-defined saddle point. Loose transition states can thus be defined even if there is no barrier along the reaction coordinate [50]. The procedure can be undertaken for transition states as a function of temperature, energy, or, in its most detailed version, energy and angular momentum. The variational theorem shows rate coefficients determined in this way to be upper bounds to the true rate coefficients, the more detailed procedures leading to the better bounds [23, 49, 50]. Secondly, the implicit assumption is made that translation along the reaction coordinate at the transition state structure invariably leads to products. Sometimes a transmission coefficient κ is used as an unknown factor in the expression for $k(T)$ to account for the possibility that translation leads back to reactants instead. Thirdly, the assumption is made that two-body collisions can lead to canonical statistical equilibrium. This assumption becomes worse as temperature declines, because at low temperatures

the long-range centrifugal constraints on angular momentum become more significant [8]. The influence of the long-range potential on ACT is contained in the statistical adiabatic theory discussed earlier [23]. Here loose transition states are defined as the maxima of effective adiabatic potential curves, and Eq. (39.29) must be modified since, as in detailed variational transition state theory, the transition states are themselves dependent on energy and angular momentum. A related problem is how to treat angular momentum constraints at low temperatures for potential surfaces which also contain a large short-range barrier or tight transition state. One approach is discussed in Sect. 39.2.4.

Rate coefficients derived from ACT do not indicate what the reaction products or sets of products might be. This information can be obtained from ab initio studies of the potential surface if different transition states lead to different products.

39.2.4 Complexes Followed by Barriers

Since long-range forces are always attractive, it makes sense to consider theories in which attraction and repulsion occur sequentially. For ion–molecule systems, this is especially important because many potential surfaces are monotonically attractive from long range to formation of a deep minimum at short range, but possess transition state barriers in their exit channels which are not large enough to prevent reaction but which affect the reaction dynamics. In addition, there are ion–molecule systems with potential surfaces closer to the norm for neutral–neutral species; in these systems there is only a weak long-range minimum followed by a short-range transition state barrier with energy above that of reactants. For the former type and, more arguably, for the latter type of potential surface, one can assume that the reaction proceeds through initial formation of an ergodic complex, followed by dissociation of the complex back into reactants or over the transition state barrier. If the reactants are labeled A and B , the complex AB^* , and the transition state AB^\ddagger , the mechanism is



which leads to the steady-state rate law

$$\frac{d[A]}{dt} = -k[A][B] , \quad (39.31)$$

$$k = \frac{k_{cf}}{k_{cd} + k_{cd'}} , \quad (39.32)$$

where k_{cf} , k_{cd} , and $k_{cd'}$ are the rate coefficients for complex formation, redissociation into reactants, and dissociation into products over the transition state, respectively. One statistical approach to such systems is to use a capture theory for complex formation, to use the Klots formulation of complex redissociation into reactants, and to use a different theory for

the unimolecular dissociation of the complex into products. Transition state theories of unimolecular complex decay have been studied for many years [1]. The current version is called RRKM theory, after the four authors Rice, Ramsperger, Kassel, and Marcus [10–13]. This theory builds upon the earlier RRK approach, in which random intramolecular vibrational energy transfer leads to large amounts of energy in the bond to be broken. An alternative hypothesis, in which amplitudes of well-defined normal modes add up to extend the bond to be broken past a certain amount, is now discredited [51]. In the RRKM approach, which is perfectly analogous to ACT theory, an equilibrium is envisaged between the activated complex and transition state species. The main use of the theory is in thermal unimolecular decay where it explains complex activation, deactivation, and random unimolecular dissociation as a function of gas density. At high density in a thermal environment, an equilibrium among complex, activated complex, and transition state leads to a thermal unimolecular decay rate in Eq. (39.13)

$$k_{\text{RRKM}}(T) = \frac{k_{\text{B}}T}{h} \frac{q_{\text{AB}^\ddagger}}{q_{\text{AB}}} \exp \frac{-E_0}{k_{\text{B}}T}, \quad (39.33)$$

which is perfectly analogous to the ACT result. At lower pressures, the activated complex is not in thermal equilibrium with the stable complex and the details of complex activation and deactivation are important [12, 13].

In the microcanonical formulation of RRKM theory, the dissociation rate coefficient k_{RRKM} as a function of (activated) complex total energy E and angular momentum J is given by

$$k_{\text{RRKM}}(E, J) = \frac{N^\ddagger[E - E_0 - E_{\text{rot}}(J)]}{h\rho^*[E - E_{\text{rot}}(J)]}, \quad (39.34)$$

where N^\ddagger refers to the total number of vibrational states of the transition state from its minimum allowable saddle point energy E_0 through E , and ρ^* refers to the density of vibrational states of the complex at energy E . For both the transition state and the complex, the available vibrational energy is the total available energy minus the rotational energy $E_{\text{rot}}(J)$, which is a function of the angular momentum. The energy not used for vibration and rotation in the transition state is considered to belong to the separable reaction coordinate. The most common expressions for the number and density of vibrational states are the semiclassical empirical values [1, 41, 42]; direct counting schemes also exist [52]. Both empirical and direct counting refer to states representing a bath of harmonic oscillators; anharmonic effects are rarely treated.

A theory of reaction rates for the mechanism in Eq. (39.30) incorporating a capture theory, and the Klots and RRKM unimolecular decays has been applied successfully to a variety of ion–molecule reactions in competition with asso-

ciation channels for which the reaction proceeds via a deep well and an exit channel barrier (see Sect. 39.3.3) [53–55]. Some authors prefer to use RRKM theory to describe redissociation of the complex into reactants [13, 56] by means of a loose transition state [57], which can be defined via a variety of variational and other methods [50]. Some recent work on unimolecular decay of polyatomic ions and neutrals following excitation indicates the superiority of the variational RRKM approach to unimolecular decay [58], especially if there is a significant amount of energy. Both the Klots and RRKM approaches to complex redissociation have problems associated with them: the Klots expression obeys microscopic reversibility but requires both a capture cross section and the assumption that the phase space formulation of the probability of individual quantum states is accurate; the RRKM expression does not obviously obey microscopic reversibility and, unless a variational calculation is performed, can create a somewhat artificial transition state.

Reaction mechanisms with more than one potential barrier can also be treated via a combination of ACT, capture, and unimolecular approaches [59, 60].

39.2.5 The Role of Tunneling

The role of tunneling in bimolecular and unimolecular reactions grows in importance as the temperature is lowered and hopping over potential barriers becomes more difficult. A simple one-dimensional correction for tunneling in the ACT expression for bimolecular rate coefficients, obtained by *Wigner* [1, 61], appears to be reasonable if the tunneling mechanism is not dominant. This correction $\Gamma > 1$ is simply the quantum correction to the partition function for the reaction coordinate

$$\Gamma \approx 1 - \frac{(h\nu_i)^2}{24(k_{\text{B}}T)^2} + \dots, \quad (39.35)$$

where ν_i is the (imaginary) harmonic frequency at the saddle point. Improved corrections have also been developed [62, 63] and, for the $H + H_2$ reaction, tested versus accurate quantum calculations [64]. At very low temperatures, such as those found in the interstellar medium, tunneling corrections are likely to be very large and to require proper multidimensional treatments.

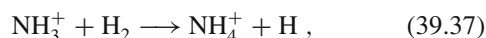
A one-dimensional tunneling correction to the RRKM expression for the microcanonical unimolecular decay rate coefficient also exists [65]. The effective potential representing the reaction coordinate at the saddle point is assumed to be an Eckart barrier. The probability of tunneling for each vibrational state of the transition state is computed, and this probability takes the place of simply counting the state in the standard formula for k_{RRKM} . In particular, $N^\ddagger(E - E_0 - E_{\text{rot}})$

in the equation for $k_{\text{RRKM}}(E, J)$ is replaced by

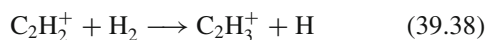
$$N_{\text{QM}}^{\ddagger}(E - E_0 - E_{\text{rot}}) = \sum_n P(E - E_0 - E_{\text{rot}} - \epsilon_n), \quad (39.36)$$

where ϵ_n is the vibrational energy of state n of the transition state with respect to its zero point energy, and the sum is over all states n for which the energy in the reaction coordinate (the energy in parentheses on the right-hand-side) is negative, but not so negative that the classical energy in the reaction coordinate lies below the minimum of the complex potential well. In general, only a few vibrational states of the transition state need be considered for the tunneling correction.

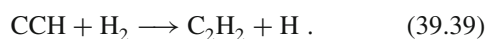
This tunneling correction has been incorporated into statistical theories for the rate of reactions that proceed via complexes and transition state barriers [60]. It has been used recently in a calculation of the slow ion–molecule reaction



which successfully reproduces the observation that, despite initially decreasing as the temperature is reduced below 300 K, the reaction rate coefficient begins to increase as the temperature is decreased below 100 K [66]. The parameters for the calculation were obtained from an ab initio calculation of the potential surface, which shows the system to proceed through a weakly-bound long-range complex before encountering a transition state with a rather small barrier of ≈ 0.25 eV. Although the dynamical theory is not quantitative (presumably because of the one-dimensional tunneling approximation), it does reproduce the isotope effects seen when the reactants $\text{NH}_3^+ + \text{D}_2$ and $\text{ND}_3^+ + \text{H}_2$ are used, definitively showing that tunneling is the cause. The actual increase in rate at very low temperature comes from the fact that the tunneling rate is less dependent on temperature than the dissociation rate of the complex into reactants. Similar calculations have been performed for the analogous ion–molecule reaction



to explain a similar observation, although in this latter instance there is still a controversy concerning whether or not the reaction is truly exoergic [67]. It is interesting to speculate on whether similar effects can be detected for analogous neutral radical– H_2 reactants with moderate activation energy barriers, such as



This system possesses a transition state of rather moderate energy [48], but the only long-range complex is presumably the very weakly-bound van der Waals structure. Unlike the ion–molecule case, there are very few experimental studies of low temperature neutral–neutral reactions. Studies of pressure broadening at very low temperatures do reveal, however, the strong influence of the van der Waals bond [68].

39.3 Association Reactions

Association reactions have been studied for both ion–molecule and neutral–neutral systems. For the ion–molecule case, association processes can be investigated in great detail at low densities near or in the radiative association regime because ions can be stored in low pressure traps. Review articles [69, 70] describe such experiments for small and large ions, respectively. The results of many higher pressure studies of termolecular ion–molecule association, especially those undertaken in the SIFT apparatus, are also available [71]. In general, below the high pressure limit, the rate of association reactions without activation energy is known to increase with (a) an increase in the size of the reactants, (b) an increase in the bond energy of the product species, and (c) a decrease in temperature. These trends are all reproduced by statistical theories in which association proceeds by the formation of a complex followed by radiative and/or collisional stabilization [8]. More limited data for termolecular neutral–neutral reactions, with and without short-range potential barriers, have also been reviewed [72]. Although radiative stabilization can proceed via a single photon, collisional stabilization proceeds most probably in a stepwise fashion rather than in a single strong collision. The most detailed statistical theories incorporating multistep collisional stabilization use master equation techniques; in general it is preferable to solve the inverse problem of unimolecular dissociation via detailed RRKM theory and then invoke detailed balance [13, 56]. Such theories are more successful than strong collision approaches, especially in considering the dependence of ternary association rates on pressure. This dependence can be especially difficult to treat when association competes with an exoergic channel which does not necessarily dominate because of a barrier in the exit channel.

39.3.1 Radiative Stabilization

The problem of radiative association in the absence of competitive exoergic channels is in principle much more simple. In addition to the rates of complex formation and dissociation, one needs only the rate of stabilization via spontaneous emission. If the complex abundance is at steady state, the rate law for radiative association of species A and B is simply

$$\frac{d[A]}{dt} = -k_{\text{ra}}[A][B], \quad (39.40)$$

$$k_{\text{ra}} = \frac{k_{\text{cf}}}{k_{\text{cd}} + k_{\text{rad}}} k_{\text{rad}}, \quad (39.41)$$

where k_{ra} represents the rate coefficient for radiative association and k_{rad} refers to the rate coefficient for radiative stabilization. If ternary association is considered in addition,

the rate coefficient for radiative association is the low pressure limit of a more complex rate expression.

Radiative stabilization, which is normally considered to proceed via emission of a single infrared photon, has been studied in some detail [73–75]. If the unstable complex is imagined to be a collection of harmonic oscillators, each vibrational state i , which is best regarded as a Feshbach resonance, can be expressed as a set of occupation numbers $n_1^i, n_2^i, \dots, [n^i]$ for the assorted modes. If it is further assumed that upon formation, the complex has a probability P_i of being formed in state i , the rate of single-photon vibrational emission k_{rad} (s^{-1}) is then given by

$$k_{\text{rad}} = \sum_{i,j} P_i A_{i \rightarrow j} = \sum_{[n^i],[n^j]} P_{[n^i]} A_{[n^i] \rightarrow [n^j]}, \quad (39.42)$$

where the sum is over initial states i and final states j , and A is the Einstein coefficient for spontaneous emission. With some algebraic manipulation and the assumption that dipole selection rules apply, the result simplifies to

$$k_{\text{rad}} = \sum_{k=1}^s \sum_{n_k} P_{n_k}^k n_k A_{1 \rightarrow 0}^k, \quad (39.43)$$

where the index k refers to each of the s normal modes, the index n_k to the occupation number of mode k , and the Einstein A coefficient, which here refers to the fundamental transition of mode k , can be expressed in terms of the absorption intensity (see Chap. 11). The probability $P_{n_k}^k$ that mode k is excited to state n_k is given by the statistical formula

$$P_{n_k}^k = \frac{\rho'_{\text{vib}}(E_{\text{vib}} - n_k h\nu_k)}{\rho_{\text{vib}}(E_{\text{vib}})}, \quad (39.44)$$

where ρ_{vib} is the vibrational density of states and ρ'_{vib} is the reduced density of states when n_k quanta are assigned to mode k . The role of overtone and combination contributions to the radiative emission rate has also been investigated [74], as have a canonical approximation to the microcanonical formulation discussed here [75] and the small additional effect of stabilization by sequential emission [73]. With the use of the classical approximation to the standard vibrational density of state functions [41, 42], Eq. (39.43) for k_{rad} reduces to a linear function of the vibrational energy

$$k_{\text{rad}} = \frac{E_{\text{vib}}}{s} \sum_{k=1}^s \frac{A_{1 \rightarrow 0}^k}{h\nu_k}. \quad (39.45)$$

The constant of proportionality between k_{rad} and E_{vib} depends strongly on the fundamental intensities; many of these can be obtained from infrared absorption spectra, although there is normally insufficient information for all of the active modes in polyatomic molecules, especially ions. Reasonable

estimates, as well as limited experimental data, show that k_{rad} varies between 10 and 1000 s^{-1} for vibrational energies up to a few eV [69, 70, 73–75]. The radiative stabilization rate typically decreases slightly with increasing molecular size due to the inclusion of infrared inactive modes of vibration. There also appears to be a distinction between ions and neutral species, with rates for ions apparently faster.

Since spontaneous emission rates between electronic states are often far more rapid than infrared vibrational rates, the possibility that radiative stabilization can proceed via electronic emission has been examined [9]. The well-studied association between C^+ and H_2 appears to proceed via electronic relaxation, with a radiative stabilization rate one to two orders of magnitude larger than would be the case for vibrational emission. Whether or not the association between CH_3^+ and H_2 proceeds via an electronically excited complex has been debated for some time; the answer is apparently negative [69].

39.3.2 Complex Formation and Dissociation

The formation and dissociation of the complex can be studied with a variety of statistical approximations other than what is discussed in this section. In particular, complex dissociation has been treated by a thermal RRKM approach [70, 75], an energy but not angular momentum specific RRKM approach [73], variational transition state theory, statistical adiabatic theory, and flexible transition state theory [72]. We first consider a simple thermal approximation for systems without activation energy incorporating microscopic reversibility [8]. In the limit that the complex redissociation into reactants is much more rapid than radiative stabilization, the rate coefficient k_{ra} for radiative association in the thermal model is

$$k_{\text{ra}} = K(T)k_{\text{rad}}, \quad (39.46)$$

where $K(T)$ is the ratio between k_{cf} and k_{cd} in a canonical ensemble, and the radiative stabilization rate has been assumed to be independent of temperature. The equilibrium coefficient $K(T)$ between complex and reactants can be rewritten in terms of partition functions in the standard way [47]. However, the partition function of the complex is best calculated via the equation

$$q_{AB^*} = \int_0^\infty \rho_{\text{vr}}(E + D_0) \exp \frac{-E}{k_{\text{B}}T} dE, \\ \approx \rho_{\text{vr}}(D_0)k_{\text{B}}T, \quad D_0 \gg k_{\text{B}}T, \quad (39.47)$$

where ρ_{vr} is the density of vibrational-rotational states [41, 42], E is the energy of reactants, and D_0 is the bond energy of the complex. One immediate prediction of this approach

(deriving mainly from the rotational partition functions of the reactants) is that k_{ra} possesses a strong inverse dependence on temperature since

$$K(T) \propto T^{-(r_A+r_B+1)/2}, \quad (39.48)$$

where r refers to the number of rotational degrees of freedom (two for a linear molecule and three for a nonlinear one). It also predicts a strong dependence on well depth and size of the complex since the density of complex states is a strong function of both these parameters. Although the thermal model agrees with the strong inverse temperature dependence of the coefficients for both radiative and, more commonly, ternary ion–molecule association [8, 71] (in which case, the thermal model with strong collisions replaces k_{rad} with a collisional rate coefficient), the absolute rate coefficients calculated tend to range up to an order of magnitude too high. Given the large range of values exhibited by radiative association rate coefficients (10^{-20} – 10^{-9} cm³ s⁻¹), this might not seem too large a problem. It has been shown, however, that the thermal model is deficient, especially at low temperatures because thermal equilibrium cannot be achieved by two-body collisions [8]. A revised approach, called the modified thermal theory, replaces the rovibrational density of complex states in the thermal model with a vibrational density of states coupled with sums over the allowable ranges of complex angular momentum achievable from the specific capture model assumed [8]. The result is a somewhat lessened inverse temperature dependence and somewhat smaller rate coefficients, especially at low temperatures. Both modifications result in better agreement with experiment [8].

The modified thermal approach considers structureless reactants; full consideration of the internal states of the reactants is achieved via the Klots version of phase space theory, in which k_{cf} and k_{cd} in Eq. (39.41) are the capture and unimolecular rates discussed in Sect. 39.2.2. The phase space treatment reduces to the modified thermal treatment for small reactant angular momentum if the possibility of saturation [$k_{\text{cd}}(E, J) < k_{\text{rad}}$] may be ignored. Both conditions are normally met. The phase space approach has also been used for ion–molecule ternary association reactions, but here is coupled with the strong collision hypothesis and must be regarded as inferior to the more detailed RRKM calculations with master equation treatments for collisional stabilization [13, 56].

39.3.3 Competition with Exoergic Channels

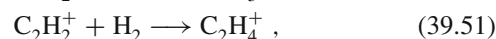
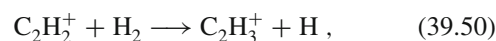
There have been numerous reactions reported (especially ion–molecule reactions) in which exoergic reaction channels compete with association channels, both radiative (at low pressure) and ternary (at higher pressures). One view

of such competition is that it occurs via a sequential mechanism in which the reactants form a long-lived collision complex which either redissociates, dissociates into exoergic products, or is stabilized [53, 54]. The rate coefficient for competitive radiative association is then given by the steady-state expression

$$k_{\text{ra}} = \frac{k_{\text{cf}}}{k_{\text{cd}} + k_{\text{cd}'} + k_{\text{rad}}} k_{\text{rad}}, \quad (39.49)$$

where $k_{\text{cd}'}$ refers to complex dissociation into products. The additional and normally large $k_{\text{cd}'}$ term in the denominator means that the thermal and modified thermal theories cannot, in general, be used. The phase space treatment for this mechanism [53, 54, 76, 77] shows that association cannot compete with exoergic channels unless there is a significant barrier in the exit channel which considerably slows the dissociation rate of the complex into products, especially for partial waves of high angular momentum. Such barriers tend to be large enough to slow dissociation down, but not large enough to require tunneling. Although the results of phase space calculations are in good agreement with experiment for a variety of competitive systems [69, 76], they are once again inferior to RRKM calculations with master equation collisional deactivation when the competition involves collisional stabilization of the complex [13, 53, 54, 56].

Another mechanism exists for competition between association and normal exoergic channels [69]. Ab initio studies show that there is a parallel type of competition in which the product and association channels occur on different portions of the potential surface, with a branching at long range in the entrance channel. For example, the competing reactions [69, 78]



occur via distinct pathways. The former reaction is a possibly endoergic direct process in which the molecular hydrogen attacks perpendicularly, leading to the cyclic form of the C_2H_3^+ ion, whereas the association reaction occurs via the deep well of the ethylene ion. The competition in the analogous $\text{C}_3\text{H}^+ + \text{H}_2$ system is not currently well understood, with both parallel and series mechanisms suggested [69, 79].

39.4 Concluding Remarks

While the study of chemical reaction dynamics and kinetics is a relatively mature area of investigation, many challenges remain. A central one is the development of an efficient, fully quantum mechanical method for evaluating $k(T)$ that can be applied to a range of systems [80]. A second set of

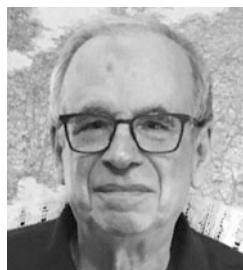
challenges comes in the intrinsically non-adiabatic nature of chemical reactions. As a system moves from reactants to products, there is a dramatic change in the electronic wave function. In fact the very existence of a transition state reflects the avoided crossing of two potential energy surfaces. There is experimental and theoretical evidence that the fact that the dynamics takes place on multiple potential surfaces has a large effect on the gas-phase state-to-state dynamics, and eventually the rate coefficients. Finally, as the evaluation of the electronic structure of atoms and molecules becomes more easily accomplished through the use of sophisticated computer packages, researchers will be able to ask more detailed questions about the relationships between the topology of potential surfaces and the corresponding rate coefficients than was possible as recently as ten years ago [81].

Acknowledgements E.H. wishes to acknowledge funding from the National Science Foundation (US) for his research in astrochemistry via grant AST-1906489.

References

- Johnston, H.S.: Gas Phase Reaction Rate Theory. Ronald, New York (1966)
- Stantcheva, T., Shematovich, V.I., Herbst, E.: *Astron. Astrophys.* **391**, 1069 (2002)
- Gillespie, D.T.: *J. Comp. Phys.* **22**, 403 (1976)
- Charnley, S.B.: *Astrophys. J.* **509**, L121 (1998)
- Biham, O., Furman, I., Pirronello, V., Vidali, G.: *Astrophys. J.* **553**, 595 (2001)
- Green, N.J.B., Toniazzo, T., Pilling, M.J., Ruffle, D.P., Bell, N., Hartquist, T.W.: *Astron. Astrophys.* **375**, 1111 (2001)
- Levine, R.D., Bernstein, R.B.: *Molecular Reaction Dynamics*. Oxford University Press, New York (1974)
- Bates, D.R., Herbst, E.: In: Millar, T.J., Williams, D.A. (eds.) *Rate Coefficients in Astrochemistry*, p. 17. Kluwer, Dordrecht (1988)
- Herbst, E., Bates, D.R.: *Astrophys. J.* **329**, 410 (1988)
- Robinson, P.J., Holbrook, K.A.: *Unimolecular Reactions*. Wiley, New York (1972)
- Forst, W.: *Theory of Unimolecular Reactions*. Academic Press, New York (1973)
- Troe, J.: *J. Phys. Chem.* **83**, 114 (1979)
- Gilbert, R.G., Smith, S.C.: *Theory of Unimolecular and Recombination Reactions*. Blackwell, Oxford (1990)
- Jakubetz, W., Sokolovski, D., Connor, J.N.L., Schatz, G.C.: *J. Chem. Phys.* **97**, 6451 (1992)
- Auerbach, S.M., Miller, W.H.: *J. Chem. Phys.* **98**, 6917 (1993)
- Troe, J.: *Part. Adv. Chem. Phys.* **LXXXII**(2), 485 (1992)
- Su, T., Bowers, M.T.: In: Bowers, M.T. (ed.) *Gas Phase Ion Chemistry*, vol. 1, p. 83. Academic Press, New York (1979)
- Rowe, B.R.: In: Millar, T.J., Williams, D.A. (eds.) *Rate Coefficients in Astrochemistry*, p. 135. Kluwer, Dordrecht (1988)
- Anicich, V.G., Huntress, W.T.: *Astrophys. J. Suppl.* **62**, 553 (1986)
- Hirschfelder, J.O., Curtiss, C.F., Bird, R.B.: *Molecular Theory of Gases and Liquids*. Wiley, New York (1954)
- Clary, D.C., Halder, N., Husain, D., Kabir, M.: *Astrophys. J.* **422**, 416 (1994)
- Herbst, E.: Cold chemistry and beyond: the astrochemical context. In: Rowe, B.R., Canosa, A., Heard, D.E. (eds.) *Uniform Supersonic Flows in Chemical Physics*. World Scientific, London, UK, in press
- Smith, S.C., Troe, J.: *J. Chem. Phys.* **97**, 8820 (1992)
- Clary, D.C.: In: Millar, T.J., Williams, D.A. (eds.) *Rate Coefficients in Astrochemistry*, p. 1. Kluwer, Dordrecht (1988)
- Clary, D.C.: *J. Chem. Phys.* **91**, 1718 (1987)
- Adams, N.G., Smith, D., Clary, D.C.: *Astrophys. J.* **196**, L31 (1985)
- Bates, D.R., Morgan, W.L.: *J. Chem. Phys.* **87**, 2611 (1987)
- Smith, S.C., McEwan, M.J., Gilbert, R.G.: *J. Phys. Chem.* **93**, 8142 (1989)
- Graff, M.M.: *Astrophys. J.* **339**, 239 (1989)
- Clary, D.C., Stoecklin, T.S., Wickham, A.G.: *J. Chem. Soc. Faraday Trans.* **89**, 2185 (1993)
- Rowe, B.R., Canosa, A., Sims, I.R.: *J. Chem. Soc. Faraday Trans.* **89**, 2193 (1993)
- Dashevskaya, E.I., Maergoiz, A.I., Troe, J., Litvin, I., Nikitin, E.E.: *J. Chem. Phys.* **118**, 7313 (2003)
- Georgievskii, Y., Klippenstein, S.J.: *J. Chem. Phys.* **118**, 5442 (2003)
- Clary, D.C., Buonomo, E., Sims, I.R., Smith, I.W.M., Geppert, W.D., Naulin, C., Costes, M., Cartechini, L., Casavecchia, P.: *J. Phys. Chem.* **A106**, 5541 (2002)
- Chastaing, D., James, P.L., Sims, I.R., Smith, I.W.M.: *J. Chem. Soc. Faraday Discuss.* **109**, 165 (1998)
- Rowe, B.R., Rebrion-Rowe, C., Canosa, A.: In: Minh, Y.C., van Dishoeck, E.F. (eds.) *Astrochemistry: from Molecular Clouds to Planetary Systems*, p. 237. Sheridan Books, Chelsea (2000)
- Chastaing, D., Le Picard, S.D., Sims, I.R., Smith, I.W.M.: *Astron. Astrophys.* **365**, 241 (2001)
- Light, J.C.: *Disc. Faraday Soc.* **44**, 14 (1967)
- Chesnavich, W.J., Bowers, M.T.: In: Bowers, M.T. (ed.) *Gas Phase Ion Chemistry*, p. 119. Academic Press, New York (1979)
- Gerlich, D.: *J. Chem. Phys.* **90**, 3574 (1989)
- Whitten, G.Z., Rabinovitch, B.S.: *J. Chem. Phys.* **38**, 2466 (1963)
- Whitten, G.Z., Rabinovitch, B.S.: *J. Chem. Phys.* **41**, 1883 (1964)
- Bass, L.M., Chesnavich, W.J., Bowers, M.T.: *J. Am. Chem. Soc.* **101**, 5493 (1979)
- Klots, C.E.: *J. Phys. Chem.* **75**, 1526 (1971)
- Herbst, E., Knudson, S.K.: *Chem. Phys.* **55**, 293 (1981)
- Galloway, E.T., Herbst, E.: *Astrophys. J.* **376**, 531 (1991)
- Hill, T.L.: *An Introduction to Statistical Thermodynamics*. Addison-Wesley, Reading (1960)
- Harding, L.B., Schatz, G.C., Chiles, R.A.: *J. Chem. Phys.* **76**, 5172 (1982)
- Truhlar, D.G., Garrett, B.C.: *Acc. Chem. Res.* **13**, 440 (1980)
- Hase, W.L., Wardlaw, D.M.: In: Ashfold, M.N.R., Baggott, J.E. (eds.) *Bimolecular Collisions*, p. 171. Royal Society of Chemistry, London (1989)
- Slater, N.B.: *Theory of Unimolecular Reactions*. Cornell Univ. Press, Ithaca (1959)
- Stein, S.E., Rabinovitch, B.S.: *J. Chem. Phys.* **58**, 2438 (1973)
- Bass, L.M., Cates, R.D., Jarrold, M.F., Kirchner, N.J., Bowers, M.T.: *J. Am. Chem. Soc.* **105**, 7024 (1983)
- Herbst, E.: *J. Chem. Phys.* **82**, 4017 (1985)
- Wlodek, S., Bohme, D.K., Herbst, E.: *Mon. Not. R. Astron. Soc.* **242**, 674 (1990)
- Smith, S.C., Wilson, P.F., Sudkeaw, P., MacLagan, R.G.Á.Ř., McEwan, M.J., Anicich, V.G., Huntress, W.T.: *J. Chem. Phys.* **98**, 1944 (1993)
- Smith, S.C.: *J. Chem. Phys.* **97**, 2406 (1993)
- Klippenstein, S.J., Faulk, J.D., Dunbar, R.C.: *J. Chem. Phys.* **98**, 243 (1993)
- Chen, Y., Rauk, A., Tschuikow-Roux, E.: *J. Phys. Chem.* **95**, 9900 (1991)

60. Frost, M.J., Sharkey, P., Smith, I.W.M.: *J. Phys. Chem.* **97**, 12254 (1993)
61. Wigner, E.P.: *Z. Phys. Chem.* **B19**, 203 (1932)
62. Truong, T.N., Truhlar, D.G.: *J. Chem. Phys.* **93**, 1761 (1990)
63. Truong, T.N., Truhlar, D.G.: *J. Chem. Phys.* **97**, 8820 (1993)
64. Takayanagi, T., Masaki, N., Nakamura, K., Okamoto, M., Sato, S., Schatz, G.C.: *J. Chem. Phys.* **86**, 6133 (1987)
65. Miller, W.H.: *J. Am. Chem. Soc.* **101**, 6810 (1979)
66. Herbst, E., DeFrees, D.J., Talbi, D., Pauzat, F., Koch, W., McLean, A.D.: *J. Chem. Phys.* **94**, 7842 (1991)
67. Smith, D., Glosik, J., Skalsky, V., Spanel, P., Lindinger, W.: *Int. J. Mass Spectrom. Ion Proc.* **129**, 145 (1993)
68. Flatin, D.C., Holton, J.J., Beaky, M.M., Goyette, T.M., DeLucia, F.C.: *J. Mol. Spectrosc.* **164**, 425 (1994)
69. Gerlich, D., Horning, S.: *Chem. Rev.* **92**, 1509 (1992)
70. Dunbar, R.C.: In: Ng, C.Y., Baer, T., Powis, I. (eds.) *Unimolecular and Bimolecular Ion-Molecule Reaction Dynamics*, p. 270. Wiley, New York (1994)
71. Adams, N.G., Smith, D.: In: Fonijn, A., Clyne, M.A.A. (eds.) *Reactions of Small Transient Species: Kinetics and Energetics*, p. 311. Academic Press, New York (1983)
72. Davies, J.W., Pilling, M.J.: In: Ashfold, M.N.R., Baggott, J.E. (eds.) *Bimolecular Collisions*, p. 105. Royal Society of Chemistry, London (1989)
73. Barker, J.R.: *J. Phys. Chem.* **96**, 7361 (1992)
74. Herbst, E.: *Chem. Phys.* **65**, 185 (1982)
75. Dunbar, R.C.: *Int. J. Mass Spectrom. Ion Proc.* **100**, 423 (1990)
76. Herbst, E., McEwan, M.J.: *Astron. Astrophys.* **229**, 201 (1990)
77. Herbst, E., Dunbar, R.C.: *Mon. Not. R. Astron. Soc.* **253**, 341 (1991)
78. Maluendes, S.A., McLean, A.D., Herbst, E.: *Chem. Phys. Lett.* **217**, 571 (1994)
79. Maluendes, S.A., McLean, A.D., Yamashita, K., Herbst, E.: *J. Chem. Phys.* **99**, 2812 (1993)
80. Miller, W.H.: *Acc. Chem. Res.* **26**, 174 (1993)
81. Klippenstein, S.K., Harding, L.B.: *J. Phys. Chem. A.* **103**, 9388 (1999)



Eric Herbst Dr. Eric Herbst is Commonwealth Professor of Chemistry and Astronomy at the University of Virginia. Herbst is a Fellow of the American Physical Society and the Royal Society of Chemistry (UK), where he won the Centenary Prize. His major work is in the field of astrochemistry, in which he studies how chemistry can deepen our understanding of the universe.



Nigel G. Adams

Contents

40.1	Overview	597
40.2	Reaction Energetics	598
40.3	Chemical Kinetics	599
40.4	Reaction Processes	600
40.4.1	Binary Ion–Neutral Reactions	600
40.4.2	Ternary Ion–Molecule Reactions	603
40.5	Electron Attachment	604
40.6	Recombination	604
40.6.1	Electron–Ion Recombination	604
40.6.2	Ion–Ion Recombination (Mutual Neutralization)	605
	References	606

Abstract

Ionic reactions in the gas phase is a broad field encompassing a multitude of interactions between ions (both positively and negatively charged), electrons and neutrals. These can be as simple as the transfer of an electron between molecules, or can be complex with considerable bond breaking, reforming and rearrangement. Reactions of the general type



illustrating this diversity, are given in Table 40.1. The reaction process can be considered as consisting of three parts: (a) the initial interaction, in which the colliding particles, $A^{+\cdot-}$ and $B^{-\cdot n}$ are drawn together by an attractive potential, (b) the reaction intermediate and transition state, in which reactants are transformed into products and (c) the weakening interaction as the product particles separate. Interactions can also occur where only elastic scattering is involved but these are considered elsewhere.

Keywords

rate coefficient · proton affinity · intermediate complex · electron attachment · dissociative recombination

40.1 Overview

Part (a) of the interaction is readily studied theoretically by classical mechanics in terms of reactant particle motions controlled by the interaction potential $u(r)$ between the particles, where r is the interparticle separation. For ion–neutral interactions, this can take the form (i) of an attractive ion-polarization or induced dipole potential [1] $u(r) = -\alpha_d q^2 / 2r^4$, where α_d is the polarizability of the neutral and q is the charge on the ion; anisotropy in the polarizability can also be taken into account [2], (ii) of an ion-permanent dipole potential [3] with $u(r) = -q\mu_D \cos \theta / r^2$, where μ_D is the permanent dipole of the neutral and θ is the angle that the dipole makes with r , and (iii) of an ion-quadrupole potential [4] with $u(r) = -Qq(3 \cos^2 \theta - 1) / 2r^3$, where Q is the quadrupole moment and θ is the angle the quadrupole axis makes with r . Such capture theories are considered in Chap. 39. Other interaction potentials can be considered, but these are of lesser significance. Coulombic interaction potentials $u(r) = -q_1 q_2 / r$, where q_1 and q_2 are the charges on the interacting particles, are appropriate for positive ion–negative ion recombination (more correctly termed mutual neutralization) and electron–ion recombination. For processes involving electrons, i.e., electron attachment and electron–ion recombination, the wave nature of the electron also has to be considered [5, 6].

In addition to providing a means of bringing the reactant particles together, the attractive interaction potential has another function. In part (b) of the reaction mechanism, where considerable rearrangement of the atoms in the colliding species may occur (i.e., in the intermediate complex and transition state), there may be barriers to reaction. Here, the kinetic energy gained from the interaction potential is available in the intermediate complex for overcoming such energy barriers (very much less interaction energy is available in neutral–neutral reactions and the effects of energy barriers are very much more evident [7]). Of course, this energy has to be reconverted to potential energy as the product particles separate, and is therefore not available to drive the overall

Table 40.1 Examples illustrating the range of ionic reactions that can occur in the gas phase

Reaction Process	Reaction Type
Ar ⁺ + O ₂ → O ₂ ⁺ + Ar O ₂ ⁻ + NO ₂ → NO ₂ ⁻ + O ₂	Nondissociative charge transfer/charge exchange
He ⁺ + O ₂ → O ⁺ + O + He	Dissociative charge transfer
C ₆₀ ³⁺ + Corannulene → Corannulene ²⁺ + C ₆₀ ⁺	Multiple charge transfer
O ⁺ + N ₂ → NO ⁺ + N	Ion/atom interchange or atom abstraction
O ⁻ + CH ₄ → OH ⁻ + CH ₃	Atom abstraction
H ₃ O ⁺ + HCN → H ₂ CN ⁺ + H ₂ O OH ⁻ + HCN → CN ⁻ + H ₂ O	Proton transfer
OH ⁻ + H → H ₂ O + e ⁻	Associative detachment
C ⁺ + C ₂ H ₂ → C ₃ H ⁺ + H	Atom insertion
CH ₃ ⁺ + H ₂ + M → CH ₅ ⁺ + M Cl ⁻ + BCl ₃ + M → BCl ₄ ⁻ + M	Ternary collisional association
He ₂ ⁺ + e ⁻ → He ₂ (2He) + hν	Radiative electron–ion recombination
HCO ⁺ + e ⁻ → H + CO	Dissociative electron–ion recombination
NO ⁺ + NO ₂ ⁻ → NO + NO ₂	Ion–ion recombination (mutual neutralization)
e ⁻ + CCl ₄ → Cl ⁻ + CCl ₃	Dissociative electron attachment
e ⁻ + C ₇ F ₁₄ → C ₇ F ₁₄ ⁻	Nondissociative electron attachment
e ⁻ + O ₂ + M → O ₂ ⁻ + M	Ternary collisionally stabilized attachment
¹³ C ⁺ + ¹² CO ⇌ ¹² C ⁺ + ¹³ CO OD ⁻ + NH ₃ ⇌ OH ⁻ + NH ₂ D	Isotope exchange

reaction. However, the amount of energy returned may differ from that initially converted to kinetic energy since the polarizability/dipole moment of the product neutral(s) may differ from those of the reactant neutrals. Generally, the final part (c) of the interaction has little influence on the magnitude of the reaction rate coefficient or on the product distribution once the products have significantly separated (i.e., beyond the range at which processes such as long range electron transfer can occur). Thus, to a major degree, part (b) of the mechanism and the reaction energetics determine the products of the reaction. Theories which address this part of the interaction are also discussed in Chap. 39 and these have met with mixed success. Thus, at present, experimental measurements are providing a more definitive understanding of reactions and their mechanisms.

Also, the situation is not in general clear as to the form of the thermodynamic energy that governs whether a reaction will proceed spontaneously, i.e., whether it is controlled by the enthalpy change ΔH in the reaction or by the Gibbs' free energy change $\Delta G = \Delta H - T\Delta S$, where ΔS is the entropy change in the reaction [8]. This is discussed in more detail in Sect. 40.2.

Rate coefficients and product distributions for these reaction processes are important in all ionized media where molecular species exist, such as interstellar gas clouds [9], planetary atmospheres [10] (including that of the Earth [11, 12]), comets (Chap. 87), the space shuttle environment [13], laser plasmas [14], plasmas used to etch semiconductors [15], hydrocarbon flames [16], etc.

40.2 Reaction Energetics

The availability of sufficient energy is a primary consideration for determining whether a reaction can proceed spontaneously. Criteria for determining whether energy is given out or absorbed in a reaction are (i) exo- or endoergicity, ΔE representing the internal energy change involved in a single interaction, (ii) exo- or endothermicity for an ensemble of particles in thermal equilibrium as defined by the enthalpy change per mole, ΔH , in the reaction and (iii) exergonic or endergonic as defined by the Gibbs' free energy change, ΔG [17]. ΔE is related to ΔH at temperature T by

$$\Delta H_T \approx -N\Delta E_T, \quad (40.2)$$

where N is Avogadro's number. ΔE is usually deduced from bond energies [18–20], ionization potentials [21], electron affinities [22, 23], proton affinities [22, 24, 25], gas phase basicities [22, 24–26], etc. ΔH_T^0 is determined from the heats of formation $H_{f,T}^0$ by [27]

$$\Delta H_T^0 = \sum_{\text{products}} H_{f,T}^0 - \sum_{\text{reactants}} H_{f,T}^0, \quad (40.3)$$

where the superscript 0 refers to the standard state [17] of the reactants and products [for example, see Eq. (40.1)]. ΔG_T^0 is determined from ΔH_T^0 and the entropy change ΔS_T^0 by

$$\Delta G_T^0 = \Delta H_T^0 - T\Delta S_T^0, \quad (40.4)$$

where

$$\Delta S_T^0 = \sum_{\text{products}} S_T^0 - \sum_{\text{reactants}} S_T^0, \quad (40.5)$$

and the S_T^0 are the standard entropies [17]. In cases where all of the $H_{i,T}^0$ and S_T^0 are not available, they can often be deduced by constructing other reactions involving the species of interest and other species for which the required thermodynamic information is known ([17] discusses the details of ways in which this can be achieved). Alternatively, the magnitude of a thermodynamic parameter can be calculated using equilibrium statistical thermodynamics, if the energies of all of the occupied molecular energy levels are known [28]. For studies where all reacting particles of a given type have the same energy, such as in beam/beam interactions where cross sections $\sigma(E)$ are measured, then ΔE is most appropriate. Alternatively, for reactions involving an ensemble of particles in thermal equilibrium at a temperature T , such as those studied in high pressure mass spectrometer ion sources or afterglows where rate coefficients $k(T)$ are measured, ΔH and ΔG are more appropriate. (The terms *rate coefficient* and *rate constant* are used interchangeably in the literature.) $\sigma(E)$ and $k(T)$ are directly related via

$$k(T) = \int_0^{\infty} v(E) f(E) \sigma(E) dE, \quad (40.6)$$

where $v(E)$ is the relative speed of the reactants and $f(E)$ is the Maxwell–Boltzmann energy distribution. Whether ΔH or ΔG is more important for determining reaction spontaneity depends on the degree of interaction of the reacting systems with the surroundings during the course of the whole reaction process. For example, if the reactions occur at low pressure such that the reaction time is much less than the collision time with the background gas, there will be no interactions with the surroundings, and the only energy available in the reactions will be ΔH . Here, ΔS can only determine the probability that the intermediate complex dissociates forward to products or back to reactants. At the other extreme, if the reactions are conducted at high pressure such that the reaction species are always in thermal equilibrium with the surroundings (the limiting case of this is reaction in solution), then the additional energy $T\Delta S$ is available, and ΔG determines whether the reactions are spontaneous. Obviously, for intermediate pressures, there is a varying degree of contact with the surroundings, and which of ΔH and ΔG is most applicable is more obscure. The definition of surrounding is also somewhat loose, since in the present context it represents anything that can provide a source of energy during the reaction (for example, vibrational modes of the

reacting species that are not involved in the interaction and which could be cooled as the reaction proceeds). Usually, the $T\Delta S$ term is not sufficiently large that ΔH and ΔG have different signs so that confusion about the spontaneity of reactions often does not arise. Recently, however, reactions have been discovered which appear to proceed spontaneously even though ΔH is positive, and there has been considerable discussion of this [8].

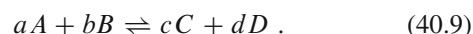
Eventually, all reaction processes will reach equilibrium as defined by

$$\Delta G = -RT \ln K, \quad (40.7)$$

where

$$K = \frac{p_C^c p_D^d}{p_A^a p_B^b} \quad (40.8)$$

is the equilibrium constant for the reaction



The subscripts to the pressures p denote the components A to D , and the superscripts represent the stoichiometries [17, 28]. The equilibrium constant K also equals k_f/k_r , the ratio of the forward to reverse rate coefficients, obtained for thermalized particles at temperature T . Thus, from measurements of k or the equilibrium constant at a series of temperatures, ΔH and ΔS of the reaction can be separately obtained.

40.3 Chemical Kinetics

The rate coefficient k for the reaction process



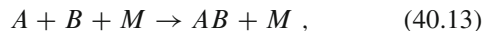
is defined by the rate equation [29]

$$\frac{d[A]}{dt} = \frac{d[B]}{dt} = -k[A][B], \quad (40.11)$$

where the square parentheses represent the concentrations of the enclosed species, and the units of k are typically $\text{cm}^3 \text{molec}^{-1} \text{s}^{-1}$ (often molec^{-1} is not written explicitly in the units). These k are deduced from the time variation of specific concentrations of thermalized reactants under a variety of conditions. For ion–neutral reactions, with A being the positive or negative ion species, the situation can usually be achieved in the laboratory where $[B] \gg [A]$, i.e., a pseudo first-order reaction. Simple integration yields

$$[A]_t = [A]_0 \exp(-k [B]_0 t), \quad (40.12)$$

where the subscript 0 indicates that this concentration is time invariant. Similar circumstances apply to binary electron attachment reactions, where $[A] = [e]$, the electron number density (the symbol β is often used here in place of k). If the reaction proceeds by association that is stabilized by collision with a third body M then



and the solution is

$$[A]_t = [A]_0 \exp(-k [B]_0 [M]_0 t), \quad (40.14)$$

with k now having units of $\text{cm}^6 \text{molec}^{-2} \text{s}^{-1}$. Note that situations exist where binary and ternary reactions can occur simultaneously.

If $[B] \gg [A]$, the solution of Eq. (40.11) is different. For the special case $[B] = [A]$, integration yields

$$\frac{1}{[A]_t} - \frac{1}{[A]_0} = kt, \quad (40.15)$$

and similarly for $[B]$. This situation is usually achieved in the laboratory for the determination of k for electron–ion and ion–ion recombination (the symbols α_e and α_i respectively are often used to replace k here). In many applications where several processes contribute to changes in $[A]$ and $[B]$, and where the simple limits are not applicable, the situation has to be analyzed numerically.

40.4 Reaction Processes

Recently, a nine volume series, concerned with all aspects of mass spectrometry, is being published of which Volume 1 deals with theoretical and experimental aspects of ionic reactions in great detail [30]. The reader is recommended to first consult the present chapter to get an overview of the reaction processes, and to go to this other text if more detail is required.

The wide variety of possible reaction processes is listed in Table 40.1 by specific examples. However, the reaction mechanisms illustrated are completely general. Magnitudes of the rate coefficients for binary interactions between charged and neutral particles, vary from $10^{-7} \text{cm}^3 \text{s}^{-1}$ for electron attachment [31, 32] to 10^{-8} or $10^{-9} \text{cm}^3 \text{s}^{-1}$ for unit efficiency ion–molecule reactions [33–36]. The efficiency is defined as the ratio of the measured k to the theoretical collisional value, i.e., that determined using the appropriate interaction potential. Ion–molecule reactions involving molecules with large permanent dipoles (for example, HCN at 2.98 D and HCl at 1.08 D [37]), can have $k > 10^{-7} \text{cm}^3 \text{s}^{-1}$ at low T [37–39] due to locking of the dipole along the

line joining the reactant species, thereby maximizing the strength of the interaction. Rate coefficients can be much smaller (by orders of magnitude) than these upper limits if the efficiency of part (b) of the mechanism is small. The part of the mechanism after collision occurs is treated by transition state theory in terms of the partition function of the transition state; where the transition state is, and its partition function, relates to the number of ways that the available energy can be distributed in the transition state [40]. More details of the theories are given in Chap. 39 and [41].

For dissociative electron–ion recombination, the upper limits on k are generally much larger as a consequence of the long range Coulombic interaction potential, varying from $\approx 10^{-7} \text{cm}^3 \text{s}^{-1}$ for diatomic ions to $> 10^{-6} \text{cm}^3 \text{s}^{-1}$ for more polyatomic species [42–45]. For ion–ion recombination, the rate coefficients are about an order of magnitude smaller than these values because of the larger mass of the negative ion relative to the electron, and thus the smaller interaction velocity (the σ of the two processes are, in fact, similar) [46]. Electron–ion recombinations that are radiatively stabilized generally have a small k , as small as $\approx 10^{-12} \text{cm}^3 \text{s}^{-1}$ [47], because of the large magnitude of the radiative lifetime of the reaction intermediate compared with the time for autoionization. For most reaction types, experimental rate coefficients are available at room temperature, and for some, the temperature and/or energy dependencies have also been determined [31, 32, 43, 44, 46, 48]. Generally, only the ion products are identified using mass spectrometry, and the product neutrals are not determined (unless the energetics allow only one neutral product), and the states of excitation of the products are not identified.

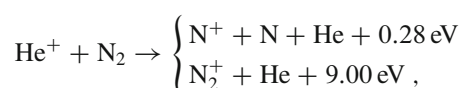
For ternary processes involving association, k varies from totally saturated at the binary collision limit to very small ($\approx 10^{-32} \text{cm}^6 \text{s}^{-1}$) for ion–neutral reactions [33, 34] and similarly for electron attachment [49]. Little is known about collision stabilized recombination [50]. Each type of reaction process has its own characteristic behavior and dependence on temperature. Rate coefficients, temperature dependencies, and product distributions (where available) have been tabulated for ion–neutral reactions [33, 34, 51] and electron attachment [31, 32]. Less data are available for electron–ion and ion–ion recombination, so no attempts have been made to compile these. Data are available in [6, 42–44, 46].

40.4.1 Binary Ion–Neutral Reactions

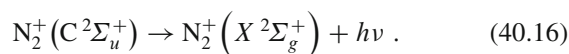
Over the years, these reaction processes have been reviewed several times, but from different perspectives. Most recently, studies of positive ion–molecules in flow tubes [52] and negative ion–molecule reactions from an organic mechanistic viewpoint [53] have been discussed.

Charge Transfer and Charge Exchange

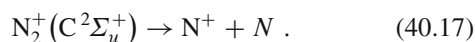
These processes involve the exchange of an electron which can occur at relatively large interparticle separations (i.e., up to $\approx 6 \text{ \AA}$ [54]). Thus, in principle, k values can be larger than the collisional limiting value. Such reactions are, in general, relatively fast, although there are some notable exceptions (for example, $\text{He}^+ + \text{H}_2$, $k = 1 \times 10^{-13} \text{ cm}^3 \text{ s}^{-1}$; $\text{Ne}^+ + \text{H}_2$, $k < 2 \times 10^{-14}$ and $\text{Ne}^+ + \text{N}_2$, $k = 1.1 \times 10^{-13}$ [33]). Attempts have been made to relate the efficiency of charge transfer to the Franck–Condon overlap between the neutral reactant and the product ion, with mixed success [55]. More energy is generally available in the positive ion reactions than the negative ion reactions since ionization potentials are much larger than electron affinities, and thus more dissociative products would be expected, as is usually observed. The reaction



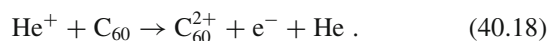
is particularly interesting and has been studied in considerable detail. The product distribution slightly favors N^+ (60%) rather than N_2^+ [56], with the N^+ channel becoming even more important with increasing vibrational temperature of the N_2 [57]. Spectroscopic emission studies [58] have shown that a significant fraction ($\geq 5\%$) of the reactions proceed by charge transfer into the N_2^+ ($\text{C}^2\Sigma_g^+$) state followed by the radiative decay



This channel competes with the predissociation



A new mechanism has recently been observed in which charge transfer occurs in parallel with chemi-ionization (or, equivalently, electron detachment)



Such a process is, of course, only energetically possible for high recombination energy ions like He^+ and Ne^+ [59]. Also, multiply charged C_{60} (C_{60}^{3+}) has been seen to undergo two electron transfer with Corannulene and some Polycyclic Aromatic Hydrocarbons (PAH's), generally in parallel with a whole series of other reaction channels [60].

Proton Transfer

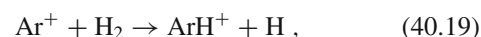
Where proton transfer is significantly exoergic, as determined by the difference in the proton affinities of the reactant and product neutrals, reaction usually proceeds at the collisional rate [61]. If the reaction is close to thermoneutral, then the amount of phase space available when the intermediate

complex dissociates to products is similar to that available when it dissociates back to the reactants, and the k approximates to one-half the collisional value. For proton transfer reactions which are not highly exo- or endoergic, k_f and k_r can be measured and thus ΔG determined (using Eq. (40.7)). If ΔS can be determined in some way, or if k_f/k_r can be determined as a function of T , then ΔH can be deduced and used to obtain the proton affinity difference (ΔS can also be determined in the latter case). This has been used to construct proton affinity scales [24, 25]. Care is required in such studies to ensure that no vibrational excitation remains in the reactant ion due to its formation, and that the identities (i.e., isomeric forms) of the reactant and product ions are known (e.g. whether the ion is HCO^+ or the higher energy form COH^+ [62]).

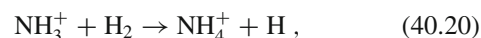
Often the individual reaction processes do not occur in isolation. For example, in the reactions of CH_4^+ with COS , H_2S , NH_3 , H_2CO and CH_3OH , both charge transfer and proton transfer are energetically possible, and both channels are observed. Here, the least exoergic channel is favored in all cases [63]. Proton transfer also occurs in negative ion reactions, for example those of OH^- and NH_2^- giving H_2O and NH_3 respectively (e.g. see Table 40.1), and these types of reactions are production sources for many negative ions [53, 64].

Ion–Atom Interchange and Atom Abstraction

In many simple cases, these two processes are the same, for example



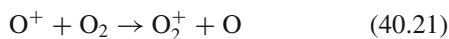
but not so for the more complicated molecules (e.g., $\text{O}^- + \text{CH}_4$; see Table 40.1). Such reactions, when exoergic, usually occur close to the collisional rate although somewhat slower. Series of such reactions with H_2 occur in the interstellar medium and are responsible for producing the hydrogenation in many of the species observed there, for example, in CH_3^+ production from CH^+ , NH_4^+ from NH^+ and H_3O^+ from OH^+ (see Chap. 86). The reaction,



is particularly interesting. At temperatures greater than 300 K, the reaction shows an activation energy barrier of 2 kcal mol^{-1} . The rate coefficient k decreases with decreasing T , reaching a minimum of $2 \times 10^{-13} \text{ cm}^3 \text{ s}^{-1}$ at 80 K and then increases at lower T due to tunneling through the barrier [48]. This behavior occurs because, at the higher temperatures, the lifetime of the intermediate complex is not sufficient for significant tunneling to occur, but there is sufficient energy in the reacting species to overcome the barrier. At lower temperatures, there is not sufficient energy available

to overcome the barrier, but the lifetime of the intermediate complex becomes long enough for significant tunneling to occur [65]. This explanation has been substantiated by the isotopic studies of the reactions $\text{NH}_3^+ + \text{D}_2$, and $\text{ND}_3^+ + \text{H}_2$ and D_2 [66].

For some reactions, isotopic labeling has been used to identify the reaction mechanism. For example, the reaction



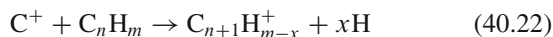
has been shown to be predominantly charge transfer, rather than ion–atom interchange, by labeling the ion as $^{18}\text{O}^+$ [67, 68].

Associative Detachment

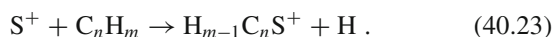
For negative ions, an additional process is possible for which there is no equivalent positive ion analog (although there is the related process of chemi-ionization, i.e., $AB + C \rightarrow ABC^+ + e^-$). In this process, the negative ion and the neutral associate, and the association is stabilized by the ejection of the electron (see Table 40.1). Such reactions can only occur when the electron detachment energy is less than the energy of the bond that is produced. Therefore, these reactions usually involve radical species which produce stable molecules. k values are usually an appreciable fraction of the collisional values [69, 70]. Infrared emissions have been detected from a series of these reactions [71], for example O^- with CO and F^- , Cl^- and CN^- with H , and show that the reactions populate the highest vibrational levels that are energetically accessible.

Other Binary Ion–Molecule Reaction Channels

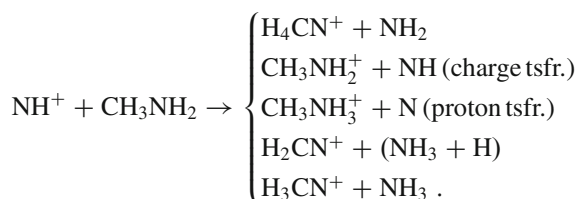
As reactant species become more polyatomic, there is a greater variety of reaction processes that can occur, and these often occur in parallel. The processes that occur are too numerous to list so a few examples will have to suffice. Reactions that occur in isolation are insertion reactions of the type [72]



and



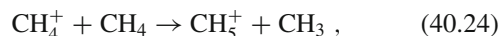
Multiple channels are very evident in reactions of ions produced from species with large ionization potentials and small proton affinities, for example, NH^+ [73],



In addition to charge and proton transfer, other channels requiring more rearrangement are evident.

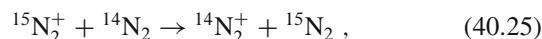
Isotopically Labeled Reactants

A great deal can be learned about reaction mechanisms in significantly exoergic ion–neutral reactions by isotopic labeling. Some such reactions have been mentioned above, but a particularly graphic example is the reaction

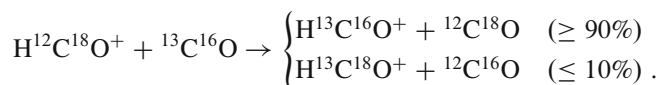


which was assumed to be either proton transfer and/or H-atom abstraction, depending on the interaction energy. By studying the reaction with both the ion and the neutral reactants separately deuterated, the reaction was shown to be much more complex, with the product ions being CH_4D^+ (10%), CH_3D_2^+ (22%), CH_2D_3^+ (43%) and CHD_4^+ (25%) for the reaction of CH_4^+ with CD_4 [74]. The reaction clearly proceeds via a long-lived intermediate in which there is a large degree of isotope mixing before unimolecular decomposition to products.

A further class of isotopic reactions are those for which the exoergicity is provided only by the different zero point energies of the reactants and products. Many such reactions have been studied. Examples of the various types are: (i) The symmetrical charge transfer

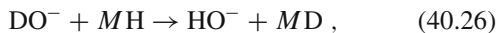


which proceeds in both directions at more than half the collisional rate. This implies that the reaction proceeds via long-range charge transfer, a conclusion substantiated by the fact that no mixed product $^{14}\text{N}^{15}\text{N}^+$ is produced [67]. (ii) Proton transfer reactions exemplified by $^{14}\text{N}_2\text{H}^+ + ^{15}\text{N}_2$ and $\text{H}^{12}\text{CO}^+ + ^{13}\text{CO}$, which are both exoergic by about 1 meV [48]. Some isotopic scrambling has been observed in the latter reaction by using the double isotopic substitution [75],



Other examples where considerable isotope scrambling occurs are H/D exchange in the reaction systems $\text{H}_3^+ + \text{H}_2$, $\text{CH}_3^+ + \text{H}_2$, $\text{H}_3\text{O}^+ + \text{H}_2\text{O}$, $\text{CH}_5^+ + \text{CH}_4$, etc. [48]. Such scrambling reactions are believed to proceed via proton bound dimer intermediates (e.g., $\text{H}_2\text{O} \cdots \text{H}^+ \cdots \text{D}_2\text{O}$). (iii) Isotope exchange reactions such as $^{13}\text{C}^+ + ^{12}\text{CO} \rightarrow ^{12}\text{C}^+ + ^{13}\text{CO}$ have also been studied. For this reaction, both k_f and k_r increase with decreasing T due to an increase in the intermediate complex lifetime; k_r decreases at lower T due to the endoergicity in this reaction direction [74].

Isotope exchange is also observed to occur with negative ions, viz.



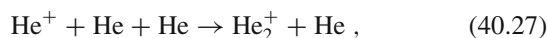
and is a common process. Particularly significant is the comparison where MH is H_2 and NH_3 . These species have very similar gas phase acidities, and thus the exoergicities of the reactions are similar. However, NH_3 has a larger polarizability than H_2 and, in addition, has a permanent dipole moment. The observation that the k for the NH_3 reaction is a factor of ten larger than that for the H_2 reaction is explained as being due to the stronger interaction potential which makes more energy available in the intermediate complex and facilitates H/D exchange [64].

Temperature Dependencies of Binary Reactions

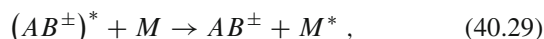
When the k values at room temperature are close to the collisional value, appreciably exoergic reactions generally exhibit little temperature dependence. For slower reactions, a significant inverse temperature dependence is observed, being $\approx T^{-1/2}$ for several reactions. This behavior is rationalized as a decreasing lifetime of the intermediate complex with increasing temperature, thus allowing less time for reaction [48].

40.4.2 Ternary Ion–Molecule Reactions

In cases where binary channels are not energetically possible, association reactions can still occur, both for positive and negative ions. The reactions can be as simple as



to associations more complex than those listed in Table 40.1. Rate coefficients k_3 at room temperature vary from $1 \times 10^{-31} \text{ cm}^6 \text{ s}^{-1}$ for reactions such as Eq. (40.27) to in excess of $1 \times 10^{-25} \text{ cm}^6 \text{ s}^{-1}$, this upper limit being due to experimental constraints rather than the reaction itself. The mechanism usually postulated is

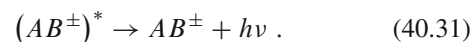


where M stabilizes the excited intermediate, $(AB^\pm)^*$ by removing energy in the collision. For this type of reaction, there is a considerable dependence of k on T . Statistical theory predicts (see Chap. 39),

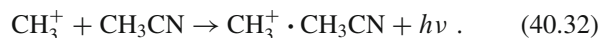
$$k_3 \propto T^{-(\ell/2+\delta)} , \quad (40.30)$$

where ℓ is the number of rotational degrees of freedom in the separated reactants, and δ is a parameter attributed to the temperature variation of the collision efficiency of the stabilizing third body M . Experimentally, many association reactions exhibit such power law dependencies of the k_3 [48, 51] with δ being small (≈ 0.2 or 0.3) for a helium third body. Also, some evidence exists for a contribution of vibrational degrees of freedom to the temperature coefficient in cases where the vibrational levels in the reactant neutral are closely spaced [76].

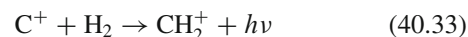
For complex reactant species, lifetimes of intermediate complexes become very long so that, in the higher pressure experiments (see below), all intermediate complexes are stabilized, and thus the reaction is independent of the pressure of M . This form of *saturation* can be eliminated in many cases by using low pressure experiments, so that the time between collisions is long, and normal ternary kinetics in Eq. (40.14) are restored. Under these conditions, sometimes there is still a pressure independent component to the k which is postulated as being due to radiative stabilization of the intermediate, viz.



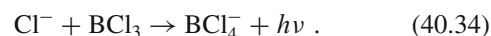
An example of this is the reaction [77]



The stabilizing photon is often considered to be in the infrared due to a vibrational transition within the ground electronic state (with a radiative lifetime of $\approx 10^{-2}$ to 10^{-3} s). Note that only a photon with $h\nu > 3/2k_B T$ is required for the complex (although still vibrationally excited) to be stable against unimolecular dissociation. However, there are cases where it is believed that an electronically excited state is accessed [78, 79]. Examples are

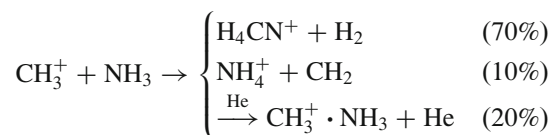


and



As yet, radiative association has not been observed directly (i.e., by the detection of the emitted photon), however, the kinetic evidence is strong for the existence of this process.

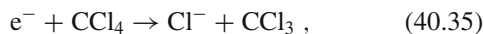
For the more rapid collisional associations, competition with binary channels is possible, for example



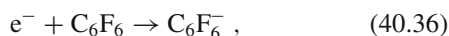
where the percentages refer to product abundances at a He pressure of 0.2 Torr [80].

40.5 Electron Attachment

These reactions have generally been studied by different techniques from those used to examine ion–neutral reactions and also by different workers [31, 32]. Analogous to the ion–neutral situation, there are dissociative processes,



and nondissociative processes,



the former being stabilized by dissociation, and the latter occurring because of the long lifetime of the intermediate against autodetachment with eventual collisional stabilization (cf. saturation in ion–neutral association reactions; Sect. 40.4.2). Measured rate coefficients vary in the range 1×10^{-7} to the smallest measurable value of $\approx 1 \times 10^{-12} \text{ cm}^3 \text{ s}^{-1}$ [31, 32]. The upper limit on k for this process is determined, from a consideration of the electron de Broglie wavelength $\lambda = \lambda/2\pi$, to be $\approx 5 \times 10^{-7} (300/T)^{1/2} \text{ cm}^3 \text{ s}^{-1}$ [81], or, more rigorously,

$$k(E) = \sum_i (\sigma/\pi\lambda^2)_i / [h\rho(E)], \quad (40.37)$$

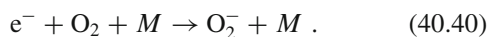
where $\rho(E)$ is the density of states and

$$\sigma/\pi\lambda^2 \approx 1 - \exp[-(4\gamma^2\mathcal{T})^{1/2}], \quad (40.38)$$

with $\gamma^2 R_\infty = (2\mu/m)^2 \alpha_d/a_0^3$ [5]; σ is the collision cross section, \mathcal{T} the kinetic energy, α_d the polarizability, a_0 the Bohr radius, μ the reduced mass, and i represents the available product channels. Where k is less than the upper limit value, this is usually due to activation energy barriers, and k shows Arrhenius behavior

$$k(T) = k_0 \exp \frac{-\Delta E}{k_B T}, \quad (40.39)$$

where k_B is the Boltzmann constant, with the barrier height ΔE being in the range 0 to $\approx 300 \text{ meV}$ [32]. If the attachment is nondissociative, and the lifetime of the intermediate complex against autoionization is small compared with the collision time (as occurs for less complex species), the reaction exhibits normal ternary behavior, for example,



Some interesting mechanisms have been identified for attachment. Different product ions have been observed in experiments conducted at very different pressures, for example, in the reaction



at high pressures ($\approx 1 \text{ Torr}$), the products, as indicated, were observed with an association channel [see Eq. (40.42)] being detected [82]. This association channel was not seen in low pressure experiments [83]. Such behavior is explained in terms of the relative magnitudes of the autodetachment lifetime and the time between collisions. When the former time is larger, the association product will dominate, whereas if the converse is true, dissociation products dominate. Thus, the different product distributions, rather than indicating discrepancies, yield information about the autodetachment lifetime.

In attachments to the Br-containing compounds, CF_2Br_2 , CFBr_3 , and $\text{CF}_2\text{BrCF}_2\text{Br}$ and $\text{CH}_2\text{BrCH}_2\text{Br}$, in which the Br atoms are on different carbon atoms, up to a 20% Br_2^- product is observed [84]. This shows that atoms in product molecules can come from spatially separated parts of the reactant molecule. Thus, considerable distortion and rearrangement must occur in the intermediate complex.

40.6 Recombination

This process has been much less studied than ion–neutral reactions with only ≈ 100 reactions being studied [44] compared to about 10,000 in the former case [33]. Also, relatively little information is available concerning the products since these are neutral and very much more difficult to detect than ions.

40.6.1 Electron–Ion Recombination

Electron–ion recombination can proceed by series of mechanisms, which have been discussed in detail recently [85], and these are included in Table 40.1. In brief, these are radiative recombination, where the neutralized ion (excited into the continuum) is stabilized by radiation emission, dielectronic recombination, which is similar to radiative recombination, except that there is a double electron excitation into the continuum, collisionally stabilized recombination, where the intermediate is stabilized by collisions with electrons or a heavy third body (combined collisional radiative recombination is also possible), and dissociative recombination. Dissociative recombination can obviously only occur when the recombining ion is molecular, however, when it occurs it is usually several orders of magnitude faster than the other recombination processes. Thus, only dissociative recombination will be discussed here.

Rate coefficients for dissociative electron–ion recombination at room temperature vary from $> 1 \times 10^{-6}$ for polyatomic ions to $\approx 1 \times 10^{-7} \text{ cm}^3 \text{ s}^{-1}$ for diatomic ions [42, 43]. For large k , there is little temperature dependence, temperature dependencies being more marked for the slower reactions.

Two mechanisms were initially proposed: (i) the direct mechanism [86] where the neutralized ion undergoes a radiationless transition to a repulsive potential curve on which dissociation to products occurs, and (ii) the indirect mechanism [87] where the neutralized ion initially transfers to a Rydberg state and then undergoes a radiationless transition to the repulsive curve. For the former process, the theoretical temperature dependence is $T_e^{-0.5}$, while it is $T_v^{-1} T_T^{-1.5}$ for the latter, where the subscripts T and e refer to the thermal ion vibrational and electron temperatures respectively [6]. There is no reason why these two processes cannot occur in parallel, although it is not straightforward to determine the relative contributions [87]. Fortunately, both processes are automatically included in multichannel quantum defect theory (MQDT) [88]. Experimental T -dependencies for reactions which are not close to the collisional limit have power law dependencies in the range ≈ 0.7 to 1.5 [43, 89, 90], i.e., between the theoretical predictions. In cases where there is detailed temperature data, e.g., for some hydrocarbon ions (CH_5^+ , C_2H_3^+ , C_2H_5^+ , C_3H_7^+ , C_6H_7^+) [89, 90], the dependence changes from the lower dependence at low temperature to the higher dependence at higher temperature.

Less is known about the products. Detailed theory carried out for the diatomic ions O_2^+ , NO^+ and N_2^+ , and to a large degree HCO^+ , are in general agreement with experiment [91, 92]. For the more polyatomic ions, the theory is not yet sufficiently quantitative [93, 94] and reliance is placed on experiment. H-atom contributions to the product distributions for ten ions (N_2H^+ , HCO^+ , HCO_2^+ , N_2OH^+ , OCSH^+ , H_2CN^+ , H_3O^+ , H_3S^+ , NH_4^+ and CH_5^+) vary from $\approx 20\%$ for OCSH^+ to 120% for CH_5^+ [95]. OH is a substantial product (30 to 65%) in the above reactions where it is energetically possible [96] (i.e., excluding HCO^+), except in the case of OCSH^+ , perhaps indicating that the proton is exclusively on the S-atom rather than the O-atom (i.e., in the lowest energy form [97, 98]). More complete product distributions are now being obtained, initially using flowing afterglows (O_2H^+ , HCO_2^+ , H_2O^+ , H_3O^+) [99], but more recently using storage rings (including H_3^+ , CH_2^+ , H_2O^+ , NH_2^+ , H_3O^+ , CH_3^+ , NH_4^+ , CH_5^+) [100]. These studies are showing that fragmentation to give three products is a common, indeed dominant, mechanism [101]. Dissociative recombination has recently been reviewed by [102].

Electron-ion recombination is an energetic process and electronically excited states can also be populated. Vibrational population distributions for these states can readily be determined if Einstein A coefficients are known for the observed transitions ($I \propto A[*]$, where I is the photon intensity, and $[*]$ is the number density of the excited state). The N_2 ($\text{B}^3\Pi_g$) state and the CO ($\text{a}^3\Pi_r$) state vibrational population produced in the recombinations of N_2H^+ , HCO^+ , HCO_2^+ and CO_2^+ have been determined [103, 104]. Possible

mechanisms [105] have been suggested for this vibrational excitation: (i) the impulsive force on the molecular fragments as the neutralized ion rapidly dissociates, and (ii) the Franck-Condon overlap between the wave functions of the molecular products (in various vibrational states) and the wave function of this particular fragment in the neutralized ion before it dissociates. Theory underestimates the populations of the higher levels, but does predict the small observed oscillation in the occupancy of the various vibrational levels in the CO ($\text{a}^3\Pi_r$) state generated in the recombination of HCO^+ [106].

The theories of recombination discussed above assume favorable potential curve crossings, however, it has been shown both experimentally [107, 108] and theoretically [109] that such are not necessary when quantum tunneling can occur. Experimental evidence has been obtained in the recombinations of N_2H^+ and N_2D^+ where the populations of the $\nu' = 6$ vibrational level of the N_2 electronically excited ($\text{B}^3\Pi_g$) state is greatly enhanced (≈ 6 at 100 K) for N_2H^+ over N_2D^+ . This level is resonant with the $\nu = 0$ vibrational level of the recombining ion, making tunneling more facile; and H atom tunneling is further enhanced because of the smaller mass [108].

40.6.2 Ion-Ion Recombination (Mutual Neutralization)

Less information is available on this process than on electron-ion recombination; a detailed review has recently been published [110]. k values vary from about 4×10^{-8} to $1 \times 10^{-7} \text{ cm}^3 \text{ s}^{-1}$ at room temperature [44, 46] with power law temperature dependencies of ≈ 0.4 for the only two systems that have been studied as a function of T ($\text{NO}^+ + \text{NO}_2^-$ and $\text{NH}_4^+ + \text{Cl}^-$) [46]. This is consistent with theory [111] in which the Landau-Zener approximation is used to determine the probability of a crossing between the Coulombic ion-ion attractive potential and the potentials of the neutral products. This transition occurs by an electron transfer (the optimum distance for such a transfer when a favorable crossing exists is about 10 \AA). Theory gives that

$$k \approx 2(v^2 Q) \left(\frac{\mu}{2\pi k_B T} \right)^{1/2}, \quad (40.43)$$

where Q is the cross section

$$Q = \pi R_c^2 [1 + (R_c E)^{-1}]. \quad (40.44)$$

R_c is the crossing distance, E is the interaction energy and v is the relative velocity at the crossing point [111]. Once neutralized by electron transfer, the products continue undeflected with the velocity gained from the Coulombic field. Photon emission has been detected from a series of excited state products. Following the early detection [112] of

NO ($A^2\Sigma^+$) emissions from $\text{NO}^+ + \text{NO}_2^-$, a variety of NO emissions have been detected from NO^+ recombinations with molecular (SF_6^- , C_6F_6^- , and $\text{C}_6\text{F}_5\text{CH}_3^-$) and atomic (Cl^- and I^-) negative ions [113, 114] and He_2 emissions from He_2^+ recombinations with C_6F_6^- and $\text{C}_6\text{F}_5\text{Cl}^-$ [113]. These emissions were interpreted in terms of long-range electron transfer [112], however, in the recombination of Kr^+ and Xe^+ with SF_6^- , KrF , and XeF , excimer emissions have been seen [113], suggesting an intimate encounter in these cases. Also, few data are available on the effects of pressure. For the reactions $\text{SF}_3^+ + \text{SF}_5^-$ and $\text{NO}^+ + \text{NO}_2^-$, k increases by about a factor of 4 between 1 and 8 Torr [46, 50].

References

1. Gioumousis, G., Stevenson, D.P.: *J. Chem. Phys.* **29**, 294 (1958)
2. Bass, L., Su, T., Bowers, M.T.: *Int. J. Mass Spectrom. Ion. Phys.* **28**, 389 (1978)
3. Su, T., Bowers, M.T.: Classical ion–molecule collision theory. In: Bowers, M.T. (ed.) *Gas Phase Ion Chemistry*, vol. 1, p. 83. Academic Press, New York (1979)
4. Su, T., Bowers, M.T.: *Int. J. Mass Spectrom. Ion Phys.* **25**, 1 (1975)
5. Klots, C.E.: *Chem. Phys. Lett.* **38**, 61 (1976)
6. Bardsley, J.N., Biondi, M.A.: *Adv. At. Mol. Phys.* **6**, 1 (1970)
7. Smith, I.W.M.: Experimental measurements of the rate constants for neutral–neutral reactions. In: Millar, T.J., Williams, D.A. (eds.) *Rate Coefficients in Astrochemistry*, p. 103. Kluwer, Dordrecht (1988)
8. Henschman, M.J.: Entropy driven reactions: Summary of the panel discussion. In: Ausloos, P., Lias, S.G. (eds.) *Structure/Reactivity and Thermochemistry*, p. 381. Reidel, Dordrecht (1987)
9. Dalgarno, A.: *J. Chem. Soc. Farad. Trans.* **89**, 2111 (1993)
10. Atreya, S.K.: *Atmospheres and Ionospheres of the Outer Planets and their Satellites*. Springer, Berlin, Heidelberg (1986)
11. Ferguson, E.E., Fehsenfeld, F.C., Albritton, D.L.: Ion chemistry of the Earth's atmosphere. In: Bowers, M.T. (ed.) *Gas Phase Ion Chemistry*, vol. 1, p. 45. Academic Press, New York (1979)
12. Smith, D., Adams, N.G.: *Top. Curr. Chem.* **89**, 1 (1980)
13. Murad, E., Lai, S.: *J. Geophys. Res.* **91**, 13745 (1986)
14. McDaniel, E.W., Nighan, W.L.: *Applied Atomic Collision Physics*. Academic Press, New York (1982)
15. Turban, G.: *Pure. Appl. Chem.* **56**, 215 (1984)
16. Williams, S., et al.: *J. Phys. Chem. A* **104**, 10336 (2000)
17. Klotz, I.M., Rosenberg, R.M.: *Chemical Thermodynamics*. Krieger, Malabar (1991)
18. West, R.C. (ed.): *CRC Handbook of Chemistry and Physics*, 69th edn. CRC, Boca Raton (1988)
19. Huber, K.P., Herzberg, G.: *Constants of Diatomic Molecules. Molecular Spectra and Molecular Structure*, vol. IV. Van Nostrand, New York (1979)
20. Herzberg, G.: *Electronic Spectra and Electronic Structure of Polyatomic Molecules. Molecular Spectra and Molecular Structure*, vol. III. Van Nostrand, New Jersey (1967)
21. Rosenstock, H.M., Draxl, K., Steiner, B.W., Herron, J.T.: *J. Phys. Chem. Ref. Data* **6**, 11 (1977)
22. NIST Positive and Negative Ion Energetics Database, Standard Reference Data Program (Gaithersburg, Maryland, 1990)
23. Janousek, B.K., Brauman, J.I.: Electron affinities. In: Bowers, M.T. (ed.) *Gas Phase Ion Chemistry*, vol. 2, p. 53. Academic Press, New York (1979)
24. Lias, S.G., Liebman, J.F., Levin, R.D.: *J. Phys. Chem. Ref. Data* **13**, 695 (1984)
25. Lias, S.G., Bartmess, J.E., Liebman, J.F., Holmes, J.L., Levin, R.D., Mallard, W.G.: *J. Phys. Chem. Ref. Data* **17**, 1-861 (1988)
26. Bartmess, J.E., McIver, R.T.: The gas phase acidity scale. In: Bowers, M.T. (ed.) *Gas Phase Ion Chemistry*, vol. 2, p. 87. Academic Press, New York (1979)
27. Chase, M.W.: NIST-JANAF Thermochemical Tables, *J. Phys. Chem. Ref. Data* **25**, 1069-1111 (1998)
28. McQuarrie, D.A.: *Statistical Mechanics*. Harper-Collins, New York (1976)
29. Steinfeld, J.I., Francisco, J.S., Hase, W.L.: *Chemical Kinetics and Dynamics*. Prentice-Hall, Englewood, p 1 (1989)
30. Armentrout, P.B.: *The Encyclopedia of Mass Spectrometry* vol. 1. Elsevier, Amsterdam (2003)
31. Christophorou, L.G., McCorkle, D.L., Christodoulides, A.A.: Electron attachment processes. In: Christophorou, L.G. (ed.) *Electron-Molecule Interactions and their Applications*, vol. 1, p. 477. Academic Press, Orlando (1984)
32. Smith, D., Adams, N.G.: Studies of plasma reaction processes using a flowing afterglow/langmuir probe apparatus. In: Lindinger, W., Mark, T.D., Howorka, F. (eds.) *Swarms of Ions and Electrons in Gases*, p. 284. Springer, Vienna (1984)
33. Ikezoe, Y., Matsuoka, S., Takebe, M., Viggiano, A.A.: *Gas Phase Ion-Molecule Reaction Rate Constants through 1986*. Maruzen, Tokyo (1987)
34. Anicich, V.G.: *J. Phys. Chem. Ref. Data* **22**, 1469 (1993)
35. Anicich, V.: *Astrophys. J.* **84**, 215 (1993)
36. Anicich, V.: An Index of the Literature for Bimolecular Gas Phase Cation-Molecule Reaction Kinetics. JPL Publication 03-19. JPL, Pasadena, California (2003)
37. Clary, D.C., Smith, D., Adams, N.G.: *Chem. Phys. Lett.* **119**, 320 (1985)
38. Clary, D.C.: *Mol. Phys.* **54**, 605 (1985)
39. Adams, N.G., Smith, D., Clary, D.C.: *Ap. J.* **296**, L31 (1985)
40. McQuarrie, D.A.: *Statistical Mechanics*. Harper & Row, New York (1976)
41. Ridge, D.R.: Ion–molecule collision theory. In: Armentrout, P.B. (ed.) *The Encyclopedia of Mass Spectrometry*, vol. 1, p. 1. Elsevier, Amsterdam (2003)
42. Johnsen, R.: *Int. J. Mass Spectrom. Ion Proc.* **81**, 67 (1987)
43. Adams, N.G., Smith, D.: Laboratory studies of dissociative recombination and mutual neutralization and their relevance to interstellar chemistry. In: Millar, T.J., Williams, D.A. (eds.) *Rate Coefficients in Astrochemistry*, p. 173. Kluwer, Dordrecht (1988)
44. Mitchell, J.B.A.: *Phys. Rep.* **186**, 216 (1990)
45. Mitchell, J.B.A., Rebrion-Rowe, C.: *Int. Rev. Phys. Chem.* **16**, 201 (1997)
46. Smith, D., Adams, N.G.: Studies of ion–ion recombination using flowing afterglow plasmas. In: Brouillard, F., McGowan, J.W. (eds.) *Physics of Ion-Ion and Electron-Ion Collisions*, p. 501. Plenum, New York (1983)
47. Bates, D.R., Dalgarno, A.: Electronic recombination. In: Bates, D.R. (ed.) *Atomic and Molecular Processes*, p. 245. Academic Press, London (1962)
48. Adams, N.G., Smith, D.: Ion–molecule reactions at low temperatures. In: Fontijn, A. (ed.) *Reactions of Small Transient Species*, p. 311. Academic Press, London (1983)
49. Massey, H.W.S.: *Negative Ions*. Cambridge University Press, Cambridge (1976)
50. Smith, D., Adams, N.G.: *Geophys. Res. Lett.* **9**, 1085 (1982)
51. Meot-Ner, M.: Temperature and pressure effects in the kinetics ion–molecule reactions. In: Bowers, M.T. (ed.) *Gas Phase Ion Chemistry*, vol. 1, p. 198. Academic Press, New York (1979)
52. Bohme, D.K.: *Int. J. Mass. Spectrom.* **200**, 97 (2000)

53. DePuy, C.H.: *Int. J. Mass. Spectrom.* **200**, 79 (2000)
54. Smith, D., Adams, N.G., Alge, E., Villinger, H., Lindinger, W.: *J. Phys. B* **13**, 2787 (1980)
55. Lauderslager, J.B., Huntress, W.T., Bowers, M.T.: *J. Chem. Phys.* **61**, 4600 (1974)
56. Adams, N.G., Smith, D.: *J. Phys. B* **9**, 1439 (1976)
57. Schmeltekopf, A.L., Ferguson, E.E., Fehsenfeld, F.C.: *J. Chem. Phys.* **48**, 2966 (1968)
58. Inn, E.C.: *Planet. Space. Sci.* **15**, 19 (1967)
59. Javahery, G., Petrie, S., Wang, J., Bohme, D.K.: *Chem. Phys. Lett.* **195**, 7 (1992)
60. Javahery, G., et al.: *Org. Mass Spectrom.* **20**, 1005 (1993)
61. Bohme, D.K.: The kinetics and energetics of proton transfer. In: Ausloos, P. (ed.) *Interactions between Ions and Molecules*, p. 489. Plenum, New York (1975)
62. McEwan, M.J.: Flow tube studies of small isomeric ions. In: Adams, N.G., Babcock, L.M. (eds.) *Advances in Gas Phase Ion Chemistry*, vol. 1, p. 1. JAI Press, Greenwich (1992)
63. Adams, N.G., Smith, D.: *Chem. Phys. Lett.* **54**, 530 (1978)
64. DePuy, C.H.: SIFT-drift studies of anions. In: Almoester Ferreira, M.A. (ed.) *Ionic Processes in the Gas Phase*, p. 227. Reidel, Dordrecht (1984)
65. Barlow, S.E., Dunn, G.H.: *Int. J. Mass Spectrom. Ion Proc.* **80**, 227 (1987)
66. Adams, N.G., Smith, D.: *Int. J. Mass Spectrom. Ion Proc.* **61**, 133 (1984)
67. Fehsenfeld, F.C., Albritton, D.L., Bush, D.L., Fournier, P.G., Govers, T.R., Fourier, J.: *J. Chem. Phys.* **61**, 2150 (1974)
68. Dotan, I.: *Chem. Phys. Lett.* **75**, 509 (1980)
69. Fehsenfeld, F.C.: Associative detachment. In: Ausloos, P. (ed.) *Interactions between Ions and Molecules*, p. 387. Plenum, New York (1975)
70. Viggiano, A.A., Paulson, J.F.: Reactions of negative ions. In: Lindinger, W., Mark, T.D., Howorka, F. (eds.) *Swarms of Ions and Electrons in Gases*, p. 218. Springer, Vienna (1984)
71. Bierbaum, V.M., Ellison, G.B., Leone, S.R.: Flowing afterglow studies of ion reaction dynamics using infrared chemiluminescence and laser-induced fluorescence. In: Bowers, M.T. (ed.) *Gas Phase Ion Chemistry*, vol. 3, p. 1. Academic Press, New York (1984)
72. Smith, D., Adams, N.G., Ferguson, E.E.: Interstellar ion chemistry: Laboratory studies. In: Hartquist, T.W. (ed.) *Molecular Astrophysics*, p. 181. Cambridge University Press, Cambridge (1990)
73. Adams, N.G., Smith, D., Paulson, J.F.: *J. Chem. Phys.* **72**, 288 (1980)
74. Smith, D., Adams, N.G.: Isotope exchange in ion-molecule reactions. In: Almoester Ferreira, M.A. (ed.) *Ionic Processes in the Gas Phase*, p. 41. Reidel, Dordrecht (1984)
75. Smith, D., Adams, N.G.: *Ap. J.* **242**, 424 (1980)
76. Viggiano, A.A., Paulson, J.F.: *J. Phys. Chem.* **95**, 10719 (1991)
77. Herbst, E., McEwan, M.J.: *Astron. Astrophys.* **229**, 201 (1990)
78. Herbst, E., Schubert, J.G., Certain, P.R.: *Ap. J.* **213**, 696 (1977)
79. Herd, C.R., Babcock, L.M.: *J. Phys. Chem.* **93**, 245 (1989)
80. Smith, D., Adams, N.G.: *Chem. Phys. Lett.* **54**, 535 (1978)
81. Warman, J.M., Sauer, M.C.: *Int. J. Radiat. Chem.* **3**, 273 (1971)
82. Herd, C.R., Adams, N.G., Smith, D.: *Int. J. Mass Spectrom. Ion Proc.* **87**, 331 (1989)
83. Naff, W.T., Compton, R.N., Cooper, C.D.: *J. Chem. Phys.* **54**, 212 (1971)
84. Smith, D., Herd, C.R., Adams, N.G., Paulson, J.F.: *Int. J. Mass Spectrom. Ion Proc.* **96**, 341 (1990)
85. Adams, N.G., Babcock, L.M., McLain, J.L.: Electron-ion recombination. In: Armentrout, P.B. (ed.) *The Encyclopedia of Mass Spectrometry*, vol. 1, p. 542. Elsevier, Amsterdam (2003)
86. Bates, D.R.: *Phys. Rev.* **78**, 492 (1950)
87. Bardsley, J.N.: *J. Phys. B* **1**, 349 (1968)
88. Giusti, A.: *J. Phys. B* **13**, 3867 (1980)
89. McLain, J.L., Poterya, V., Molek, C.D., Adams, N.G., Babcock, L.M.: *J. Phys. Chem. A* **108**, 6704 (2004)
90. Ehlerding, A., et al.: *J. Phys. Chem. A* **107**, 2179 (2003)
91. Guberman, S.L.: Electron-ion continuum-continuum mixing in dissociative recombination. In: Rowe, B.R., Mitchell, J.B.A., Canosa, A. (eds.) *Dissociative Recombination: Theory, Experiment and Applications*, p. 47. Plenum, New York (1993)
92. Talbi, D., Ellinger, Y.: A theoretical study of the HCO⁺ and HCS⁺ electronic dissociative recombinations. In: Rowe, B.R., Mitchell, J.B.A., Canosa, A. (eds.) *Dissociative Recombination: Theory, Experiment and Applications*, p. 59. Plenum, New York (1993)
93. Bates, D.R.: *Ap. J.* **344**, 531 (1989)
94. Galloway, E.T., Herbst, E.: *Ap. J.* **376**, 531 (1991)
95. Adams, N.G., Herd, C.R., Geoghegan, M., Smith, D., Canosa, A., Rowe, B.R., Queffelec, J.L., Morlais, M.: *J. Chem. Phys.* **94**, 4852 (1991)
96. Herd, C.R., Adams, N.G., Smith, D.: *Ap. J.* **349**, 388 (1990)
97. Jasien, P.G., Stevens, W.J.: *J. Chem. Phys.* **83**, 2984 (1985)
98. Scarlett, M., Taylor, P.R.: *Chem. Phys.* **101**, 17 (1986)
99. Adams, N.G.: *Adv. Gas-ph. Ion Chem.* **1**, 272 (1992)
100. Larsson, M.: Dissociative electron-ion recombination studies using ion synchrotrons. In: Ng, C.-Y. (ed.) *Photoionization and Photodetachment*, vol. II, p. 693. World Scientific, Singapore (2000)
101. Datz, S.: *J. Phys. Chem. A* **105**, 2369 (2001)
102. Adams, N.G., Poterya, V., Babcock, L.M.: *Mass Spectrom. Revs* (2005). (in press)
103. Adams, N.G., Babcock, L.M.: *J. Phys. Chem.* **98**, 4564 (1994)
104. Skrzypkowski, M., Gougousi, T., Golde, M.F.: Spectroscopic emissions from the recombination. In: Larsson, M., Mitchell, J.B.A., Schneider, I.F. (eds.) *Dissociative Recombination: Theory, Experiment and Applications*, vol. IV, p. 200. World Scientific, Singapore (2000). of N₂O⁺, N₂OH⁺/HN₂O⁺, CO₂⁺, CO₂H⁺, HCO⁺/COH⁺, H₂O⁺, NO₂⁺, HNO⁺ and LIF measurements of the H atom yield from H₃⁺
105. Bates, D.R.: *Mon. Not. R. Astron. Soc.* **263**, 369 (1993)
106. Adams, N.G., Babcock, L.M.: *Ap. J.* **434**, 184 (1994)
107. Butler, J.M., Babcock, L.M., Adams, N.G.: *Mol. Phys.* **91**, 81 (1997)
108. Poterya, V., McLain, J.L., Adams, N.G., Babcock, L.M.: *J. Phys. Chem. A* **32**, 7181-7186 (2005)
109. Bates, D.R.: *Adv. Atom. Mol. Opt. Phys.* **34**, 427 (1994)
110. Adams, N.G., Babcock, L.M., Molek, C.D.: Ion-ion recombination. In: Armentrout, P.B. (ed.) *The Encyclopedia of Mass Spectrometry*, vol. 1, p. 555. Elsevier, Amsterdam (2003)
111. Olsen, R.E.: *J. Chem. Phys.* **56**, 2979 (1972)
112. Smith, D., Adams, N.G., Church, M.J.: *J. Phys. B* **11**, 4041 (1978)
113. Tsuji, M.: *Adv. Gas-ph. Ion Chem.* **4**, 137 (2001)
114. Spanel, P., Smith, D.: *Chem. Phys. Lett.* **258**, 477 (1996)



Mary L. Mandich

Contents

41.1	Introduction	609
41.2	Metal Clusters	610
41.2.1	Geometric Structures	610
41.2.2	Electronic and Magnetic Properties	610
41.2.3	Chemical Properties	612
41.2.4	Stable Metal Cluster Molecules and Metallo-carbohedrenes	612
41.3	Carbon Clusters	613
41.3.1	Small Carbon Clusters	613
41.3.2	Fullerenes	614
41.3.3	Giant Carbon Clusters: Tubes, Capsules, Onions, Russian Dolls, Papier Mâché	615
41.4	Ionic Clusters	615
41.4.1	Geometric Structures	615
41.4.2	Electronic and Chemical Properties	616
41.5	Semiconductor Clusters	616
41.5.1	Silicon and Germanium Clusters	616
41.5.2	Group III–V and Group II–VI Semiconductor Clusters	617
41.6	Noble Gas Clusters	618
41.6.1	Geometric Structures	618
41.6.2	Electronic Properties	618
41.6.3	Doped Noble Gas Clusters	619
41.6.4	Helium Clusters	619
41.7	Molecular Clusters	620
41.7.1	Geometric Structures and Phase Dynamics	620
41.7.2	Electronic Properties: Charge Solvation	621
41.8	Recent Developments	621
	References	622

Abstract

Clusters are small aggregates of atoms or molecules which are transitional forms of matter between atoms or molecules and their corresponding bulk forms. Just as this definition spans an incredibly broad range of clus-

ters from, say, He_2 to Na_{10000} , so do the properties of these clusters span a broad range. This chapter attempts to bring order to this diverse cluster kingdom by first sorting them into six general categories. Within each category, the physics and chemistry of the more or less similar cluster species are described. Particular emphasis is placed on the unique properties of clusters owing to their finite size and finite lattice.

This chapter summarizes one of the youngest topics in this volume. Much of what is known is highly qualitative and has not yet been assembled into overarching tables or equations. Thus, this review is best regarded as a progress report on the current knowledge in this rapidly advancing field. Many of the concepts and the language used to discuss clusters are derived from condensed matter physics. The nature of these clusters impels such descriptions.

Keywords

metal cluster · excess electron · carbon cluster · molecular cluster · fullerene cage

41.1 Introduction

Clusters discussed in this chapter are isolated species composed primarily of a single type of atom or molecule. Most of these clusters are highly reactive and can only be made and studied under rarified conditions such as in a molecular beam. In keeping with the definition of clusters given above, this chapter will not attempt to cover the truly vast literature on atomic and molecular dimers and trimers. A great many of these species have been thoroughly characterized, however they are better described as molecules rather than *tiny clusters*. Stabilized clusters in the form of Zintl ions, colloids, and nanoparticles have also been made. While it is impossible to resist mentioning these clusters throughout this chapter, they are more appropriate to condensed matter physics. Finally, experimental and theoretical techniques for

M. L. Mandich (✉)
NOKIA Corp. (retired)
Martinsville, NJ, USA
e-mail: mstgrwld@aol.com

forming and studying clusters will not be covered; excellent reviews of these methods are available elsewhere [1–6].

41.2 Metal Clusters

Clusters of a wide variety of refractory and nonrefractory metals have been made and studied. These include clusters of alkali metals, transition metals, coinage metals, main group metals, and lanthanides. Clusters of alkali metals, particularly sodium, are the most well studied and understood. The emerging picture of alkali clusters is that they behave much like quasifree electron metal spheres. Thus, approximations such as the jellium model used for describing bulk metals explain a large number of alkali metal properties quite well [2]. Other metallic clusters, such as some main group metal and noble metal clusters, can also be understood within the jellium model. Nonetheless, there are examples of metallic clusters which deviate significantly from these simple models, particularly among the transition metal clusters.

41.2.1 Geometric Structures

The ground state geometry is known accurately for only a handful of small metal clusters. Examples include lithium and sodium clusters containing up to nine atoms, where electronic spectra are compared with accurate *ab initio* quantum chemical calculations to deduce their structures [5–7]. Such an approach is not a general one, either experimentally or theoretically. As the size and/or atomic valency of the metal cluster increases, the number of possible ground state structures grows enormously. Interpretation of experimental spectra requires theoretical guidance, which means that each one of these structures must be calculated using an accurate electronic structure calculational method. Thorough theoretical investigation is only practical with current computational tools for clusters containing up to about thirteen atoms. Methods such as molecular dynamics combined with density functional calculations have been used to speed up the process of finding and comparing various isomers [4, 8]. Such approaches are still restricted by available computational power to clusters with relatively few atoms and valence electrons per atom. Metal clusters of atoms with higher valency, e.g., mid-row transition metals, have proved to be quite difficult to treat accurately [9]. The large electron correlation problems inherent in these clusters must be treated semi-empirically, leading to large uncertainties in the relative energies between isomers of different spin and geometry.

Despite these difficulties, approximate geometries are known for many metal clusters. For cluster sizes greater than, roughly, several tens of atoms, there is strong experimental evidence that spherical close packed geometries, particularly

the Mackay filled icosahedra, predominate the geometric structures [7, 10, 11] (The Mackay filled icosahedra contain concentric closed icosahedral shells of atoms plus one central atom. These structures are pentagonally symmetric and occur every n atoms by $n = 13, 55, \dots, 1/3(2n + 1)(5n^2 + 5n + 3)$ [4]). These geometries have been deduced by a variety of means. For example, abundance mass spectra of metal clusters up to sizes containing thousands of atoms show intensity enhancements, termed *magic numbers*, at each cluster size which corresponds to a complete Mackay icosahedron. Saturation coverages of transition metal clusters with various reagents can be explained in terms of covering the icosahedral faces of these clusters. The persistence of icosahedral structures to large cluster sizes raises the question about where the crossover to the metallic packing occurs. For example, a spherical piece of an fcc metal would have cuboctohedral symmetry rather than noncrystalline icosahedral symmetry. Ultrafine metal particles containing 10^4 to 10^5 atoms typically have bulk crystalline geometries [12]. Little theoretical or experimental data currently exist to resolve the question of when the bulk crystalline structure emerges [10]. The point of crossover must involve kinetic as well as energetic factors. Although icosahedral packing is seen in beam experiments on metal clusters containing hundreds to thousands of atoms, high resolution electron microscopy experiments on supported metal particles in this size range show fluctuating structures that can rapidly evolve between icosahedral, cuboctohedral, and other crystalline arrangements, depending on cluster temperature [13].

41.2.2 Electronic and Magnetic Properties

A number of electronic properties have been measured for metallic clusters, particularly alkali metal and noble metal clusters. These include ionization potentials, electronic affinities, polarizabilities, and photoabsorption cross sections.

The spherical jellium approximation is generally a good model for these properties in clusters of alkali and noble metals [2, 7]. This model treats the valence electrons of the cluster as a delocalized sea of electrons smeared over a uniform spherical background of ionic cores. The energy levels of such a jellium sphere can be calculated by confining the jellium electrons to a three dimensional potential. A suitable form of this potential yields level spacings that are given by principal and angular momentum quantum numbers (n) and (l). There are no restrictions on l for a given n , and the degeneracy of a given l level is $2(2l + 1)$. The levels order as 1s, 1p, 1d, 2s, 1f, 2p, 1g, 2d, 3s, \dots . The electron configuration of a cluster is given by filling successive energy levels (termed shells) with the available valence electrons. Special stability occurs for those clusters with a closed shell config-

uration. This stabilization can be seen in the experimental measurements of the dependences of total binding energies, ionization potentials, electron affinities, and polarizabilities on cluster size [2, 7, 10, 11, 13, 14]. The potential used to calculate the energy levels within the jellium model has been formulated to include elliptical distortions of open shell clusters [7]. This refinement has been successful in describing the fine structures of these trends. Despite the usefulness of the jellium model, it is not applicable for very small or very large clusters. In many smaller clusters containing up to a few tens of atoms, electron-ionic lattice interactions cannot be neglected, and the spherical approximation is poor. For these clusters, accurate quantum chemical calculations must be used to determine the electronic structure. Alternatively, for clusters larger than roughly 500 to 3000 atoms (depending on which clusters and the cluster temperature), the level spacings become increasingly continuous, blurring the shell structure. When this occurs, other effects are seen to dominate the trends in cluster stability, particularly the stability arising from completing a geometric shell of atoms on the cluster [7, 10, 11, 15, 16].

The convergence of cluster electronic structure to bulk metal electronic structure has been seen in the evolution of metal cluster ionization potentials (I_P) and electron affinities (A_e) as a function of cluster size. A good approximation for the overall trend in the I_P as a function of cluster size (N is the number of atoms) is given by the electrostatic model for the work function of a classical conducting sphere [2]

$$I_{P,N} = W_B + A \frac{e^2}{R_N}, \quad (41.1)$$

where W_B is the work function of the bulk metal, e is the electron charge, and R is the cluster radius, which is often set proportional to $N^{1/3}$. A is a constant which is found experimentally to have values of about 0.3 to 0.5; the theoretically derived value for A depends on the model used [2, 11]. A similar form of Eq. (41.1), where A is replaced by $(A - 1)$, describes the A_e of a negatively charged cluster. Experimentally, the I_P and A_e of alkali metal, noble metal, and some main group metal clusters behave as described by Eq. (41.1) with shell structure superimposed on the overall trend [2, 6, 14]. Equation (41.1) predicts a smooth convergence of the work function to the bulk value with increasing cluster size. This has been seen experimentally, such as in copper cluster valence and inner shell A_e which extrapolate smoothly to the corresponding bulk values [17]. In mercury clusters, the transition to bulk metallic behavior occurs more abruptly and clusters with less than ≈ 17 atoms appear to behave as nonmetals [18]. Transition metal clusters often deviate strongly from the trend in Eq. (41.1) [10].

Electronic spectra are available for a number of metal clusters including alkali, noble metal, transition metal, and aluminum clusters [7, 10, 11]. Small alkali clusters exhibit

rich spectra in the visible. Many of these spectra have been assigned using accurate electronic structure calculations as described above. Visible spectra of larger alkali metal clusters and other metal clusters are typified by giant resonances with cross sections reaching values as large as 2000 \AA^2 [6, 7]. In the absence of detailed electronic structure information, these spectra have been assigned using comparisons with bulk metal spectra. In particular, the giant resonances are assigned to collective excitations of the cluster valence electrons, in an analogy to bulk metal plasmon resonances. Theoretical treatments of these giant resonances for clusters have been derived from classical treatments of conducting spheres driven by an external electromagnetic field [7, 10]. While the blue shift of the resonance frequency with increasing cluster size is well predicted by the classical models, other details are less well described, such as the magnitude of the shift and the width of the resonance. Clusters which are known to be nonspherical from other measurements exhibit multiple resonance peaks; these have yet to be quantitatively described by theory. Transition metal clusters also show evidence of collective excitations; however, the magnitudes of these absorptions are 2 to 5 times larger than predicted by classical models [19]. An intriguing *non sequitur* occurs when the classical models are extended down to describe the resonances of small alkali clusters. This is illustrated by the example of Na_8 , which exhibits a large single resonance in the photoabsorption spectrum. At first glance, the classical jellium model does fine: it predicts a spherical closed shell cluster which should exhibit a single resonance. Yet, a more thorough examination of the time dependence of this feature has revealed that it consists of four overlapping absorptions [10, 20]. These multiple absorptions clearly must arise from one-electron excitations, not a collective all-electron excitation [5]. Further work is needed to weave together the two disparate pictures of collective versus one electron excitations in metal clusters.

Inner shell electrons of some metal clusters have been probed spectroscopically. Whereas excitations of the delocalized valence electrons primarily reflect the entire cluster environment, excitations of the localized inner shell electrons reflect the atomic environment. In mercury clusters, excitation of the 5d core electrons reveals a transition from insulating clusters at small sizes to more metal-like clusters with increasing s-p hybridization typical of bulk mercury [21]. Inner core electron spectra of copper and antimony clusters also reveal details regarding the evolution of the cluster lattice structure as a function of size [11, 17]. Such valuable information can be obtained from inner shell electron spectra of metal clusters that more experiments are warranted.

Magnetic moments have been measured and described theoretically for a range of transition metal, rare earth, and Group III metal clusters [5, 7, 10, 22–24]. Examples of clusters which exhibit a positive magnetic moment include

cobalt, iron, nickel, gadolinium, and terbium clusters. Clusters of metals such as vanadium, palladium, chromium, and aluminum are observed to be diamagnetic. The effective moment per atom, μ , in magnetic clusters is greater than in the bulk because of the lower average coordination number in clusters [24]. As the cluster size increases, the surface to volume atom ratio decreases and μ converges to the bulk value. The size of these magnetic clusters is smaller than the critical domain size for bulk ferromagnetism, thus they are best described as paramagnetic with a single moment given by $N\mu$, where N is the number of atoms in the cluster. Stern–Gerlach deflection data have been obtained to measure μ . A critical parameter in interpreting these data is the so-called blocking temperature T_B , the temperature at which the cluster moment unlocks from the cluster axes and orients thermally in an external field. For clusters with temperatures $T > T_B$, the observed effective moment μ_{eff} for paramagnetic clusters is given by [24]

$$\mu_{\text{eff}} = \mu \left[\coth \left(\frac{N\mu H}{k_B T} \right) - \frac{k_B T}{N\mu H} \right], \quad (41.2)$$

where k_B is the Boltzmann constant, and H is the magnetic field strength. Medium size iron and cobalt clusters behave well according to this classically derived expression. Deviations from this model are observed in internally cold clusters and rare earth clusters which can be explained by partial and complete locking of the magnetic moment to the cluster lattice. Also, in very large clusters, $N\mu$ becomes sufficiently large that alignment overwhelms thermal statistical behavior.

41.2.3 Chemical Properties

The chemistry of both charged and neutral metal clusters has been studied, particularly for clusters of transition metals and Group III metals [6, 7, 25, 26]. Both chemisorption and physisorption are seen, depending on the type of metal cluster and reagent. In many cases, the observed chemistry is quite similar to that observed for the corresponding bulk metal. For example, platinum clusters dehydrogenate hydrocarbons, hydrogen chemisorbs on transition metal clusters with the exception of coinage metal clusters, and oxygen reacts readily with aluminum and iron clusters.

Chemisorption reactions of metal clusters have been seen with a wide variety of reagents. Products, reaction rates, and activation barriers have been measured as a function of cluster size. With a few notable exceptions, such as the reactions of hydrogen with nickel and aluminum clusters, none of these reactions are understood at the microscopic level [10, 11]. Macroscopically, some correlations have been seen between reaction rates and other measured cluster properties. For example, some cluster reactions show evidence

that the shell structure affects reaction rates, with open shell clusters having much higher reaction rate and lower activation barriers than clusters with closed shells. In other cases, the pattern of cluster reaction rates with cluster size correlates with the cluster I_p 's. These correlations have been used to infer the essential cluster-reagent interaction which governs the reactivity for a given set of clusters with a given reagent. For example, open shell clusters and clusters with low I_p 's favor reactions which involve electron donation from the cluster to the reagent at a critical point along the reaction coordinate. Such generalities must be made with caution, however, since they do not hold up well over a broad range of cluster sizes, compositions, and reagents. Even a single cluster size can exhibit complex reactivity: isomers with different reactivity have been observed for niobium clusters and, in some cases, these isomers have been interconverted by annealing. Of course, complexity is to be expected, given the richness and diversity of chemistry that is known to occur for different metal systems in various electronic and geometric environments.

Geometric structures of transition metal clusters have been studied using physisorption reactions. Weakly bound adsorbates such as hydrogen, water, and ammonia show strong saturation behavior in their uptake by metal clusters [10, 11, 27, 28]. Trends in the saturation coverage with cluster size yield information about the type of binding site and total number of binding sites for a given cluster size. Additional information regarding the nature of the adsorbate site is often available from studies of the corresponding physisorption on bulk metal surfaces. This knowledge is used to sort through possible cluster structures and deduce which geometries exhibit the correct number and type of adsorbate binding sites. For example, saturation coverages of iron, cobalt, and nickel clusters correlate with icosahedrally packed geometries over a wide range of sizes. Adsorbate binding energies have also been determined in some cases [27, 28].

41.2.4 Stable Metal Cluster Molecules and Metallocarbohedrenes

Thus far, this section has focussed entirely on the properties of metal clusters isolated in the gas phase. This discussion would not be complete, however, without mentioning that a number of metal cluster molecules have been made which are sufficiently stable that they can be made in quantity and bottled [7, 10, 11, 29, 30]! Also, recently a new class of metal–carbon clusters has been discovered, termed metallocarbohedrenes, that are believed to be sufficiently stable and abundant that they can be made in bulk. The brief overview of these isolatable clusters given below is not meant to be complete but is intended to introduce the large and impressive body of work in this field. Interested readers

are encouraged to consult the reviews cited and references therein.

Metal cluster molecules consist of a metal cluster core surrounded by a stabilizing ligand shell. A large number of such metal cluster molecules has been made, including some with metal cores as large as 300 platinum or 561 palladium atoms. In many cases, crystals of single size clusters have been made with an exactly known number of metal atoms in the core. The availability of macroscopic samples of these clusters has made it possible to measure a number of their properties. Exact structures are known for many metal cluster molecules from X-ray crystallography. Electronic and magnetic properties have been determined which reveal the development of metallic behavior within the metal core. The ligand shell is found to interact strongly with the metal atoms on the surface of the metal core. This outer shell of metal atoms does not behave as a surface of metal atoms with free valence electrons such as is found on the surface of a bulk metal. Undoubtedly, such strong interactions between surface metal atoms and coordinating ligands are necessary to make a cluster which is sufficiently stable to be isolated and crystallized without coalescing. The core of atoms inside the outer metal shell of atoms does not appear to be greatly perturbed by the coordinating ligands. Studies of the electronic and magnetic properties of the core show the onset of metallic properties as a function of particle size and atomic packing.

A distinct class of transition metal-carbon clusters has been recently found which have been termed metal-carbohedrenes [31]. Within this class, the clusters M_8C_{12} ($M = \text{Ti, V, and Zr}$) are particularly abundant and stable. Extensive electronic structure calculations show that the structure of M_8C_{12} is metallic and should be viewed as a distorted M_8 cube where each face is decorated with a C_2 dimer [32]. This structure differs greatly from the corresponding bulk metal carbides, which have cubic rock salt crystalline forms. Furthermore, the metal carbide cluster formation conditions can be adjusted to yield cubic fragments of the bulk. The related metal nitride clusters are only observed to form cubic structures. Theoretical calculations on the metalcarbohedrene and cubic forms of these metal carbides and nitrides show that they are comparable in energy for the carbides, but that the cubic structures are much more stable in the metal nitride clusters [33]. Despite their apparent stability, none of the metalcarbohedrenes has yet been isolated and purified.

41.3 Carbon Clusters

The discovery of the especially stable, spherical cluster of sixty carbon atoms, named buckminsterfullerene, has ignited an intense research effort in carbon clusters [7, 8, 10, 11, 34–39]. The family of pure carbon clusters that have been made

extends from the dimer all the way up to tubular shaped clusters containing thousands of atoms. Several of these clusters, most notably C_{60} and C_{70} , have been isolated as a single size in macroscopic quantities [40]. The fascinating properties of bulk materials made of pure and doped C_{60} and C_{70} are outside the scope of this review [8, 10, 11, 37, 39, 41].

Carbon clusters can be roughly grouped into three distinct classes. The first consists primarily of small carbon clusters which have linear or ring geometries. Hollow spheres (termed fullerenes) appear at about 28 carbon atoms and persist up to at least several hundred atoms. Very large carbon clusters containing hundreds to thousands of atoms assume various forms, including onion-like structures of concentric spheres and hollow tubes.

41.3.1 Small Carbon Clusters

Theoretical and experimental studies have found that rings and linear chains are the most stable configurations for small carbon clusters. Below about ten atoms, linear cumulenes are the most stable structures for odd numbered carbon clusters and ionic carbon clusters [13, 26, 42, 43]. For the even numbered neutral carbon clusters, C_4 , C_6 , and C_8 , however, cyclic and linear geometries are nearly isoenergetic [7, 11, 13, 42]. Various theoretical and experimental studies have yielded conflicting results as to which geometry is more stable for each of these three clusters [7, 42, 44]. Much of the controversy over the experimental evidence probably arises because the two structures are so close in energy that either isomer or both may be present, depending on the preparation conditions. By way of proof, direct experimental data have been found for coexisting linear and cyclic isomers of C_{7-9}^+ and C_{11} [26, 44]. Also, some experimental probes are not equally sensitive to the signature from a linear versus a cyclic geometry.

At ten carbon atoms, a distinct transition occurs from linear to cyclic structures [26, 43, 44]. Starting at this size, the additional bonding stabilization accrued by joining the two ends of the linear chain overcomes the strain energy resulting from ring closure. Stable monocyclic ring structures are observed for carbon clusters over a surprisingly wide range of sizes, even persisting into the size range where three dimensional fullerenes appear. Bicyclic rings, higher order polycyclic rings, and graphitic fragments also occur in this size range but many of these configurations appear to be metastable [43, 45].

A_e 's and I_P 's have been measured for these small carbon clusters. Dramatic effects appear in the size dependence of the A_e 's as a result of the changeover from linear to ring structures [44]. A_e 's of the chain structures are noticeably higher than for ring structures for carbon clusters containing similar numbers of atoms. Distinct odd-even alternations in

the A_e 's are also seen, plus there is evidence for aromatic stabilization according to the $4n + 2$ rule. No break in the I_p 's is seen across the structural transition, but the trend in the I_p 's also follows the $4n + 2$ rule expected for aromaticity.

Chemical reactions have been observed for both neutral and charged small carbon clusters, particularly for the cations [7, 26, 43]. In general, the linear cationic clusters, containing fewer than ten atoms, react readily with a variety of reagents and exhibit reactivity typical of carbenes. The ring shaped cationic clusters with ten or more atoms are much less reactive, and often show no detectable reaction with reagents that react efficiently with the smaller carbon clusters. It is this differential reactivity which has revealed the presence of co-existing linear and cyclic isomers. Evidence for polyacetylene versus cumulene structure in the small linear chains can also be seen in the cluster reaction patterns.

41.3.2 Fullerenes

Fullerenes make up a class of carbon clusters with closed hollow carbon atom cage morphologies. The term *fullerene* was inspired by the geodesic domes of architect R. Buckminster Fuller, and has come into widespread usage despite its non-standard nomenclature. The fullerene cage network is composed of interlocking rings of sp^2 hybridized carbon atoms, where every carbon atom is bonded to three other carbon atoms. Five and six member rings predominate in the cages. Highly strained four and smaller membered rings are unfavorable. Seven and higher membered rings usually can readily rearrange within the network to form five and six membered rings. Delocalization of the π electrons over the cage contributes significantly to the stabilization of the fullerenes.

Assuming at least five-membered rings, the smallest possible fullerene is C_{20} , consisting of twelve pentagons. However, the observed fullerenes all contain about 30 atoms or more. Larger fullerenes are formed by joining together pentagons, hexagons, and heptagons, with the pentagons providing the curvature necessary to close the cage. In fullerene structures composed entirely of pentagons, hexagons, and heptagons, it can be rigorously shown from Euler's theorem that, $N_5 = N_7 + 12$, where N_5 is the number of pentagons and N_7 the number of heptagons. By far the most abundant fullerene that is seen is C_{60} . There are 1812 possible isomers for C_{60} but only one forms in great abundance [37], which has each of its 12 pentagons isolated and surrounded by its 20 hexagons. The resulting molecule, resembling a soccer ball, belongs to the highest point symmetry group I_h , where all the carbon atoms are equivalent [34–37]. The *isolated pentagon rule* arises out of minimizing strain and maximizing resonance energy and is a powerful tool for predicting the most stable fullerene isomers [37]. Besides C_{60} , a number of other fullerenes have been seen, most notably C_{70} which

is the next larger fullerene that can be constructed using the isolated pentagon rule. The largest proven fullerene structure contains 84 carbon atoms. It is possible to construct increasingly larger fullerene cages containing hundreds of carbon atoms. Such giant fullerenes have yet to be conclusively verified in experiments, however evidence for their existence has been seen in bulk samples containing fullerene mixtures and in gas phase abundances of carbon clusters [36, 37, 39].

A number of the fullerenes has been made and purified as a single size in macroscopic quantities [37, 39, 40]. This has enabled their geometries to be determined quite accurately using a wide variety of spectroscopic and theoretical techniques. Even structures of fullerenes such as C_{76} , C_{78} , and C_{84} which occur as isomeric mixtures have been elucidated. The electronic structures of many of these fullerenes have been calculated and compared with experiment [37, 38].

Yet to be resolved is the issue of how these low entropy fullerene structures can form so efficiently in carbon vapor. One proposal is that cup-like prefullerenes form first which add new carbon moieties to close the cage. Other suggestions include coalescence of small carbon rings such as C_6 or C_{10} , or stacking of intermediate size rings on a small *seed* ring such as C_{10} , or folding up of large defective graphitic fragments to form closed hollow spheroids [8, 10, 36, 37]. Some intriguing insights into this open question are provided by experiments on nonfullerene metastable forms of carbon clusters in the fullerene size regime [43]. These species can be made in the gas phase and are found to have bicyclic, graphitic, and other polycyclic ring shapes which are not in the form of partial fullerene cages. Upon annealing, some of these ring forms are seen to convert into the fullerenes, which suggests that they are important intermediates for forming the fullerene cage. Similar polycyclic ring shapes are observed during the initial *melting* of fullerenes in molecular dynamics simulations [46].

Since the fullerenes are hollow, much attention has focussed on putting something inside. A wide variety of noble gas atoms and metal atoms has been successfully loaded into fullerenes, forming a family of so-called *endohedral* complexes [36, 37, 39, 47–51]. Noble gas atoms encapsulated in fullerenes appear to assume central positions within the cage and do not perturb the overall electronic structure of the fullerene [11, 47, 52]. Endohedral complexes where the encapsulated species is a metal atom, called *metallofullerenes*, encompass a wide range of metals (M) and fullerene sizes from $U@C_{28}$ to $Sc_3@C_{82}$ (@ denotes that the metal atom is inside the fullerene). Separation and purification of a macroscopic amount has been achieved for several of these [48, 49, 51]. Theoretical and experimental data indicate that the endohedral metallofullerenes have considerable charge transfer from metal atom(s) to the fullerene cage [37, 47, 48, 51, 52]. This interaction affects the oxidation states of the metal atom(s) and the cage and, in some

cases, causes the metal atom(s) to locate off-center. It is yet to be generally understood why, within the range of known fullerene sizes, only some form endohedral complexes, particularly C_{28} , C_{60} , C_{70} , C_{74} , C_{80} , C_{82} , and C_{84} . The $M@C_{28}$ endohedral complex is especially intriguing because it appears that C_{28} itself does not form as an empty fullerene.

The unsaturated surfaces of fullerenes undergo a broad range of chemical reactions. The availability of macroscopic samples of fullerenes, especially C_{60} and C_{70} , has enabled the preparation of numerous fullerene derivatives. With their high electron affinities, fullerenes readily form a wide variety of charge transfer compounds. These include the so-called *exohedral* complexes, where metal atoms are attached to the outside of the cage. Particularly stable exohedral metal-fullerene clusters have been observed which have one alkaline earth atom decorating each ring of the cage [53]. The unsaturated double bonds of the fullerenes can be functionalized with reagents such as halogens, aromatics, and alcohols [37, 39]. Some of the bulk forms of these complexes and derivatives exhibit amazing properties such as superconductivity at temperatures as high as 33 K seen in C_{60} films doped with alkali or alkaline earth metals [51]. References [37, 39, 51] contain recent reviews.

41.3.3 Giant Carbon Clusters: Tubes, Capsules, Onions, Russian Dolls, Papier Mâché

Giant clusters of pure carbon have been found which have tubular, capsular, and spherical shapes [8, 10, 37, 51, 54]. These clusters occur both as single entities and with multiple concentric layers. The basic structure consists of a spiralled or rolled graphitic sheet made up of hexagonal rings of sp^2 hybridized carbon atoms. Just as in the fullerenes, pentagonal rings provide the curvature required to form a ball or to cap the ends of tube shapes. Negative curvature has also been seen which is believed to result from heptagonal rings. Carbon tubes and capsules are formed prolifically in the same carbon arcs which produce fullerenes. Typical diameters range from about 5 to 100 nm, depending on the inner diameter and number of layers, and lengths of up to several microns are seen. For concentric or spiralled structures, the average interlayer spacing is 3.4 to 3.5 Å which is slightly larger than in crystalline graphite. Although tubes and capsules are the most commonly seen morphologies, these are observed to convert to layered spherical *onion* structures under intense irradiation [8]. This suggests that collapsed onion structures are more stable. Currently, there exists some debate over whether the multilayer tubes or capsules consist of layers of complete shells within shells, such as in a *Russian doll*, or whether these layers are so highly defective that the overall structures are best described as *papier-mâché* consisting of numerous overlying graphitic fragments [54].

Little experimental detail is available on the electronic or mechanical properties of these tubes. Theoretical calculations have been performed on the electronic properties of perfect tubes constructed in various ways [37, 51]. Numerous configurations of tubes are possible, depending on the tube diameter and the overall screw axis formed by the rows of carbon hexagons wound around the tube waist. The geometrical arrangement strongly affects the electronic properties of a tube. Appropriate choices of diameter and tilt angle of the screw axis yield tubes which are metallic or semiconducting. Tubes and capsules with perfect lattice arrangements are calculated to be extremely stiff, forming the strongest carbon fibers known. Almost no data exist on the chemical properties of carbon tubes, capsules, and onions. While they are stable enough to isolate in air, reaction occurs with O_2 and CO_2 at high temperatures which destroy the tubes [51]. Finally, as for the fullerenes, tubes, capsules, and onions have a hollow cavity which can be filled. These *nanocapsules* have been successfully loaded with lead and gold atoms, as well as crystalline metal carbide particles [51].

41.4 Ionic Clusters

A growing body of experimental and theoretical evidence on alkali halide and alkaline earth oxide clusters shows that these tiny clusters of ionic materials are ionically bound. Most of these clusters have highly ordered crystal structures even at very small sizes. Thus, these clusters offer excellent systems for studying electron localization on finite-sized crystalline lattices.

41.4.1 Geometric Structures

Most ionic clusters of alkali halides and alkaline earth oxides assume the cubic rock salt lattice typical of bulk sodium chloride [6, 7, 10, 13, 55]. This lattice is favored not only for clusters of rock salt cubic solids such as NaCl and NaF, but also for other clusters such as Cs_xI_y where the bulk form has the cesium chloride cubic crystal structure. Exceptions occur when the cluster size is smaller than, roughly, a unit cube, or when the cluster anions and cations differ greatly in ionic radius, such as in lithium bromide clusters (even though solid LiBr has the NaCl crystal structure) [10]. The bulk rock salt lattice is retained even for clusters where the number of anions and cations are unequal, as long as the deviation from stoichiometry is not too great. In clusters with a large excess of alkali atoms, the extra metal atoms segregate to a face of the cluster and form a metallic overlayer [55].

Maximization of ionic interactions and minimization of surface energy leads to cuboid crystal morphologies for these clusters which have as many (1 0 0) faces as possible. Partic-

ularly stable clusters occur for sizes where the cuboid lattice is completely filled and has nearly equal numbers of ions on all sides [55]. Excess electrons or holes also play a crucial role in the stability of ionic clusters. For example, while the $[\text{Na}_{14}\text{Cl}_{13}]^+$ cluster forms a particularly stable cube (with 9 atoms on each square face and one atom in the center), its counterpart $[\text{Na}_{13}\text{Cl}_{14}]^+$ does not because it has fewer holes than the available electrons; however, the anion $[\text{Na}_{13}\text{Cl}_{14}]^-$ does form a particularly stable cube [11, 55].

41.4.2 Electronic and Chemical Properties

The I_p 's, A_e 's, photoabsorption spectra and photoabsorption cross sections have all been measured for ionic clusters, particularly alkali halide $[\text{M}_j\text{X}_k]$ clusters. Understanding the role of the coulombic interactions, particularly excess electrons, in these clusters is key to understanding the trends in their electronic properties with cluster size, composition, and overall charge. Excess electrons are known to localize in at least four distinct ways: at anion vacancies, in weakly bound surface states, on specific alkali metal ions, or in cation-anion pair dipole fields [11, 55, 56].

First, there is a large class of ionic clusters which contain equal numbers of electrons and holes, such as clusters in the series $[\text{M}_{j+1}\text{X}_j]^+$. I_p and A_e of clusters within this class reflect the overall stability associated with forming the *perfect* filled cuboid lattices described in Sect. 41.4.1. Such *perfect* clusters do not chemisorb polar molecules, whereas the *imperfect* clusters readily do [55]. The lowest energy absorptions for clusters in this class result from charge transfer excitations, just as in perfect ionic solids. Spectra obtained for $[\text{Cs}_{j+1}\text{I}_j]^+$ clusters show large cross sections for absorption, consistent with charge transfer, and features which converge towards the bulk for the perfectly cubic cluster, $[\text{Cs}_{14}\text{I}_{13}]^+$ [57].

Other ionic clusters do not contain equal numbers of electrons and holes; clusters with excess electrons have been the most studied. One such class consists of clusters with at least one anionic vacancy and one or more excess electrons. In this class, e.g., $[\text{Na}_{14}\text{Cl}_{12}]^+$, the excess electron localizes at the lattice site of the missing anion. This is conceptually similar to an *F*-center in an ionic bulk crystal. Enhanced stabilization is observed for those size clusters within this class where the excess electron sitting at an anionic site yields a filled cuboid lattice. Nonetheless, because the localized electron has a large zero-point energy, its binding energy is much less than an anion at the same site. This is reflected in both the first and second I_p 's, as well as the A_e 's of this class of clusters [55]. Just as for *F*-centers in ionic crystals, clusters with an excess electron localized on an anionic vacancy have strong optical absorptions at energies well below the charge transfer bands [55].

The next class of ionic clusters with excess electrons consists of perfect cuboid ionic clusters which contain one or more excess electrons, but do not have a defect binding site such as an anionic vacancy or an excess metal atom. In these clusters, e.g., $\text{Na}_{14}\text{Cl}_{13}$, the electron is quite weakly bound in a surface state which primarily involves the surface metal cations. These clusters have particularly low electron binding energies; for example, the I_p of $\approx 1.9\text{eV}$ determined for $\text{Na}_{14}\text{F}_{13}$ is the lowest I_p measured for any compound [55].

In the other two known classes of ionic clusters with excess electrons, the extra electrons have been calculated to localize on a metal cation or in a dipole potential well [58]. Some evidence for these forms of localization has been seen in photoabsorption, I_p 's and A_e 's [10, 11, 55]. For example, the photoelectron spectra of some $[\text{Na}_{j+1}\text{Cl}_j]^-$ clusters show that the two excess electrons are singlet-coupled, and localized either at an anion vacancy, or at a single Na site so that they behave as a Na^- anion loosely bound to a neutral $[\text{Na}_j\text{Cl}_j]$ cluster. The spectral behavior of other clusters within this same series, however, suggests they have the two excess electrons in a triplet coupled state, forming the analog of a bipolaron in a solid [10].

41.5 Semiconductor Clusters

Semiconductor clusters make up a class of clusters where, by analogy with bulk semiconductors, covalent forces are expected to dominate electronic and geometric structure. Silicon clusters are by far the most studied of the semiconductor clusters. Some information is available on germanium clusters and compound clusters made of Groups III and V atoms or Groups II and IV atoms. Also, there are the well known stable molecules of bulk semiconductors such as the P_4 tetrahedron and various sulfur rings; these have been reviewed in detail elsewhere [3]. Clusters of other possible semiconductors have been made, but little data beyond their nascent distributions are available [3]. There is also a growing body of data on silicon, III–V, and, especially II–VI semiconductor clusters in the nanometer size regime where bulk samples of stabilized forms of these clusters have been made and isolated. The crystalline and electronic structure properties, particularly quantum confinement effects, are reviewed in [10, 11, 59–61].

41.5.1 Silicon and Germanium Clusters

The geometries of small silicon clusters depart radically from microcrystalline fragments of the bulk silicon diamond lattice. The structures of silicon clusters containing up to about 13 atoms have been studied extensively both experimentally and theoretically [62]. These structures are more compact

and, starting at Si_7 which has a pentagonal bipyramidal structure, have higher coordination than silicon in the bulk lattice. Multiple isomers of similar energy also appear starting at about Si_{10} . For example, the tetracapped trigonal prism and the symmetric tetracapped octahedron structures of Si_{10} are nearly isoenergetic; microcrystalline fragments such as the adamantane form of Si_{10} are much higher in energy. The geometric structures of larger silicon clusters are less well known. The gross shapes of clusters containing up to about 60 silicon atoms have been found experimentally to undergo a transition between Si_{20} and Si_{30} from increasingly elongated structures to more spherical structures [26]. In the transition region, both prolate and oblate isomers are observed for a single cluster size. Multiple isomers over a wide range of silicon cluster sizes have been repeatedly observed in various experiments; it appears that somewhat different sets of isomers can be produced depending on the cluster formation conditions [26]. Elucidating the ground state structures of these larger clusters theoretically is, in general, an intractable problem and requires simplifying approaches. Use of semiempirical quantum mechanical techniques or silicon interaction potentials derived from bulk silicon, however, has led to unsatisfactory results, which suggests that the silicon atoms in silicon clusters are strongly reconstructed away from the usual sp^3 silicon atom environment [63, 64]. Some consensus has recently emerged that larger silicon clusters consist of internal silicon atoms strongly interconnected to a surrounding cage that has been described as a buckled fullerene [63, 65, 66]. Such a silicon cage must not be construed as a true fullerene, however, since silicon does not form the strong double bonds which stabilize the interconnected carbon rings of the fullerenes. Within this scenario, the shape change is believed to occur at the point where the cage begins to contain one or more internal atoms which provide the additional bonding needed to stabilize a spherical geometry.

I_p 's and A_e 's, cohesive energies, and photoabsorption spectra have been measured for silicon clusters containing up to several hundred atoms. Silicon cluster I_p 's start near the Si atom I_p , fall abruptly between 20 and 22 silicon atoms where the shape change has been observed, and then slowly converge towards the bulk work function. This convergence is apparently quite gradual since little change is seen between Si_{100} and Si_{200} [67]. A_e 's are only known for silicon clusters up to ≈ 15 atoms and reflect the large structural changes which occur in this small size regime [3]. Indication of a structural shape change is not observed in either the trends in the cohesive energies or the electronic spectra for silicon clusters. The cohesive energies increase smoothly with increasing size and exceed the cohesive energy of bulk silicon by 10–20% [68]. Silicon clusters exhibit strong sharp absorption spectra in the near UV. A common set of absorption features appears at $\approx \text{Si}_{15}$ and persists up to at least Si_{70} [69]. This suggests that the strong absorptions arise from

localized Si–Si bond excitations, and that these obscure the delocalized excitations which are more sensitive to silicon cluster structure. The most unusual aspect of these spectra is that the common signature for these minute clusters which are strongly reconstructed from the bulk is, nonetheless, strikingly similar to the spectrum of bulk diamond-lattice crystalline silicon.

Silicon cluster ions are observed to react with a variety of reagents [3, 26, 68]. For example, silicon clusters chemisorb small organic molecules such as ethylene, and inorganic molecules such as O_2 , NH_3 , and XeF_2 . Some of these reactions are sufficiently exothermic that they cause cluster fragmentation, or loss of small neutral fragments. The chemistry of silicon clusters often bears a close relationship to that known for bulk silicon surfaces; however, the clusters are often much less reactive by as much as several orders of magnitude. Silicon cluster reactions reveal the presence of numerous isomers which differ in their reaction rate for a given reagent. Isomerization has been induced by adding sufficient thermal energy to some clusters; the resulting more stable cluster form may or may not be more reactive than the higher energy isomer. This is particularly well illustrated in reactions of oblate versus prolate isomers where the more reactive isomer varies depending on cluster size [26]. In general, differential chemistry is not a useful predictor of cluster geometry *per se*, and appears to correlate more readily with other factors such as the number and type of dangling bonds available for reaction.

Much less is known about germanium clusters. The most stable structures that have been calculated for germanium clusters are quite similar to those for silicon clusters, although the overall binding energies are lower for germanium clusters [3, 7]. Available data such as A_e 's and photoelectron spectra for germanium clusters also underscore their similarities to silicon clusters in general [3]. The chemistry of germanium clusters has not been reported.

41.5.2 Group III–V and Group II–VI Semiconductor Clusters

Geometric structures have been calculated for some of the smaller III–V and II–VI clusters, particularly aluminum phosphide, gallium arsenide, and magnesium sulfide clusters [3, 11, 70–72]. As for silicon clusters, these clusters differ significantly from microcrystalline fragments snipped from their corresponding bulk crystalline forms. Electronegativity differences between the two constituent atoms play a major role in determining and stabilizing these structures. This is manifested in several ways. The bonding arrangements in the most stable structures have, in general, alternating electropositive and electronegative atoms. In those clusters such as III–V clusters where electronegativity dif-

ferences are smaller, covalent interactions predominate ionic interactions and the energetics of the various geometric structures are similar to those of the covalent silicon clusters. In II–VI clusters, electronegativity differences are much larger, and these clusters have structures more comparable to those seen in ionic clusters where ionic interactions are maximized.

Some data are available on the electronic structures of III–V clusters. A strong even–odd alternation occurs in both the I_p 's and A_e 's of gallium arsenide clusters where those clusters having a total even number of atoms have higher I_p 's and lower A_e 's than neighboring odd-numbered clusters [3, 73]. This has been explained by electronic structure calculations which find that, in general, the odd clusters are triplets while the even clusters of gallium arsenide are singlets [70–72]. Electronic absorption spectra have also been recorded for indium phosphide clusters which exhibit strong differences with cluster size and stoichiometry [74]. These spectra are also consistent with odd-numbered In_xP_y clusters having open-shell configurations, and even-numbered In_xP_y clusters having closed-shell singlet ground states, even for clusters which are considerably off-stoichiometry. A strikingly similar strong continuum-like absorption appears in the blue end of spectra for the even-numbered In_xP_y clusters. The onset of these absorptions lies close to the bulk indium phosphide band gap. The overall spectral behavior, however, is quantitatively similar to the absorptions seen in semiconductor glasses.

Little is known about the chemical properties of these clusters, with gallium arsenide clusters being the only ones studied. Hydrogen chloride is observed ubiquitously to etch $[\text{Ga}_x\text{As}_y]^-$; however, multiple isomers are seen with differing degrees of reactivity [3]. Chemisorption of ammonia on $[\text{Ga}_x\text{As}_y]^+$ has also been seen with the highest rates of reactivity occurring for the stoichiometric ($x = y$) clusters [75].

41.6 Noble Gas Clusters

Clusters have been made of all of the stable noble gases including helium. As a general class, these clusters are the most weakly bound of all clusters, and are held together only by van der Waals forces. These interactions are well understood theoretically, and thus noble gas clusters are excellent model systems for studying a variety of structural and electronic effects at finite sizes. Helium clusters behave much as quantum liquids, and are treated separately in the discussion below.

41.6.1 Geometric Structures

The overall evolution of noble gas cluster structures as a function of size is well established [4, 6, 11, 76, 77]. Icosahedral packing dominates at small cluster sizes. This packing involves polyicosahedral structures for the small cluster

sizes, and different noble gas clusters exhibit somewhat different preferred arrangements. Starting at 100 to 250 atoms (depending on which noble gas), formation of closed-shell Mackay icosahedra dominates the structures [78]. Finally, at somewhere in the range 600 to 6000 atoms, the structures cross over to the close-packed fcc arrangement of the noble gas solids.

The increased coordination characteristic of the Mackay icosahedra explains why this morphology is adopted at small cluster sizes. With the addition of each successive icosahedral shell however, this five-fold symmetric packing becomes increasingly strained as a result of both atom–atom radial compression and tangential dilation. At some size, icosahedral structures are no longer more stable than fcc structures, and the noble gas clusters undergo a phase change. Currently, the critical size required for fcc packing is a matter of some dispute. Experimental evidence for this transformation at ≈ 600 atoms comes from electron diffraction data [76]. The spectral signatures of molecules doped in noble gas clusters suggest however, that this transition occurs at ≈ 2000 atoms [77]. Theoretical studies find a range of critical sizes, depending on the treatment used, but typically favor an even larger size regime [4, 11, 13, 77].

Knowledge of accurate pair-wise interaction potentials for noble gases has enabled extensive simulations of the physical properties of noble gas clusters [4, 6, 7, 79–81]. Phenomena such as specific heat, bond length and coordination number fluctuations, phase equilibria, dynamical freezing and melting, isomerization, and solvation have been explored using various molecular dynamics simulations. Numerous effects peculiar to the finite sizes and proliferation of isomers in small noble gas clusters are observed. For example, the melting temperature decreases significantly with an overall decrease in cluster size. Internal diffusion rates depend strongly on cluster size and the stability of certain favored structures such as the complete Mackay icosahedra. A well-studied finite size effect is the dependence of the mean energy per particle in a cluster versus the particle temperature (the so-called *caloric curve*) in the region where the particle is observed to *melt*. Unlike in the bulk, calculations find hysteresis in the melting transition of small noble gas clusters where solid-like and liquid-like forms are observed to coexist. Such coexistence is quite size-dependent. It becomes more pronounced when the clusters are rapidly heated or cooled, and appears to be a finite time averaging effect [4, 6, 7].

41.6.2 Electronic Properties

The fragility of noble gas clusters has hampered measurements of their I_p 's and A_e 's. Extensive fragmentation is known to accompany ionization, making it difficult to establish the size of the ionized parent cluster. Nonetheless,

I_p 's have been measured for cluster sizes containing up to several tens of atoms [82]. Measured I_p 's agree with theoretical predictions which are based on the assumption that the ionizing state within the cluster is a dimer, trimer, or higher n -mer cationic core [6, 82]. Absorption profiles of noble gas cations provide supporting evidence for the delocalization of the positive charge over a n -mer unit within the cluster, although consensus has yet to be reached on the size of this cationic cluster within the cluster [6, 11].

Several distinct types of electronic excitations are observed in absorption spectra of neutral noble gas clusters [6, 7, 11, 83]. Clusters containing less than ≈ 30 atoms exhibit broad absorptions near the atomic resonance lines. These absorptions are molecular-like, but have not been described in detail above the dimer. In addition, broad continuum absorptions assigned to Rydberg excitations are observed at these small sizes. Bulk-like excitations corresponding to surface and bulk excitons in solid noble gases emerge for clusters larger than ≈ 50 atoms. The profiles of these excitonic absorptions indicate that they arise from delocalized excitations analogous to Wannier excitons in bulk solids. These cluster exciton absorptions are blue-shifted relative to the bulk as a result of quantum confinement of the exciton within the small cluster. Another type of excitonic excitation has also been reported which appears to be a localized excitonic state whose character is sensitive to the cluster structure. Relaxation of cluster excited states is accompanied by extensive fragmentation [7]. Details of the relaxation processes differ according to noble gas, cluster size and cluster structure. Again, these differences can be traced to finite size effects in these noble gas clusters [4].

41.6.3 Doped Noble Gas Clusters

Various chromophores have been added to noble gas clusters as a microscopic variation of matrix isolation [3, 4, 7, 10, 11, 77, 84]. A wide range of chromophores have been studied including other noble gas atoms, metal atoms, small polyatomic molecules such as SF₆, CH₃F, and HCl, and a variety of organic molecules such as benzene, carbazole, and naphthalene. Comparisons of the electronic and vibrational spectra of these guest molecules with their spectra in noble gas liquids or solid matrices have revealed information such as noble gas cluster structure, solvation effects, and solute diffusion.

A crucial issue in understanding the spectral signatures of doped noble gas clusters is the location of the solute in or on the noble gas cluster. Chromophores well-embedded in a noble gas cluster behave as molecules surrounded by a dielectric medium, which is most correctly viewed as both imperfect and finite sized [4, 7, 84, 85]. The evolution of the spectral changes with cluster size reflect the interplay of re-

pulsive forces and collective dielectric effects as the cluster builds the solvent shell around the solute core. Both theoretical and experimental data illustrate this evolution and show how, once the first few solvent shells are established, the spectrum converges asymptotically to the matrix isolation value. For smaller clusters, the effects of too few or incomplete solvation shells appear as shifts and/or broadening of the spectral lines relative to the bulk [3, 4]. Differential solvation of the ground and excited states causes spectral shifts which are typically to lower energy since the excited state is usually more stabilized than is the ground state. Spectral broadening results from multiple isomers. Broadened electronic spectra have also been explained as a signature of cluster melting, although this interpretation has been questioned [3, 4, 84, 85]. Some infrared spectra of solute molecules have also yielded information on the nature of the solute binding site, revealing that the solvating noble gas cluster undergoes an icosahedral to fcc phase transition in a critical size regime [77].

Not all dopant species are found well-solvated, or *wetted* in the cluster interior. Both electronic and infrared dopant spectra indicate the existence of chromophores bound to the cluster surface. In some cases, the chromophore is ubiquitously *nonwetting*, such as for SF₆-Xe_{*n*} and SiF₄-Ar_{*n*}, and resides exclusively on the cluster surface [77]. In other systems, e.g., carbazole-Ar_{*n*} and CF₃Cl-Ar_{*n*}, both wetting and nonwetting are observed [7, 77, 84]. Systems such as these have enabled measurements of solute diffusion rates into or out of the cluster. Finally, wetting-nonwetting transitions have been observed which depend on cluster size and/or cluster temperature [7, 84]. Understanding this wide variety of behavior requires modeling cluster solute-solvent structures (in both ground and excited states in order to interpret electronic spectra) as a function of size and temperature. To date, most of the theoretical simulations have focussed on smaller clusters at a given temperature [4, 7, 77, 84, 85]. Nonetheless, theoretical models have provided qualitative and quantitative explanations for some of the observed spectral shifts, and have shown that the propensity for wetting/nonwetting can be related to the degree to which maximum possible coordination within the solvent is attainable.

41.6.4 Helium Clusters

Quantum effects play a dominant role in helium clusters since they consist of very weakly interacting small mass particles. Statistical effects are also expected since ³He is a fermion and ⁴He is a boson. Overall, helium clusters are believed to be in fluid-like or superfluid-like states with highly fluctuating structures [86].

Neutral helium clusters have been made experimentally in sizes ranging from the dimer up to 10⁶ atoms [4, 11, 77]. The

diatomic He_2 , has just been detected recently and is found to have a binding energy of only $\approx 10^{-7}$ eV with an average internuclear distance of $\approx 55 \text{ \AA}$ [87, 88]. Evidence for magic numbers in the helium cluster abundances is seen; however, the sizes of these especially stable clusters differ substantially from what is seen in the other noble gas clusters [4]. Helium cluster structures have been theoretically investigated using fully quantum mechanical treatments [4, 86]. These studies find that $^4\text{He}_n$ clusters should be bound at all sizes, but that a minimum number of atoms, ≈ 30 , are required for $^3\text{He}_n$ clusters to be stable. The latter prediction has not yet been verified experimentally, owing to the expense of ^3He , and the difficulties of ascertaining the true size of helium clusters since they easily boil off atoms upon ionization. Calculations reveal that the packing of helium clusters is highly delocalized with no evidence of icosahedral morphology. The structures derived have been found to be extremely sensitive to temperature and total angular momentum. Cluster binding energies and densities increase smoothly and monotonically with increasing size, approaching bulk behavior at about 300 atoms. Thus, helium clusters do not exhibit any especially stable sizes (magic numbers) such as the heavier noble gases do. In short, helium clusters behave as liquid-like quantum fluids, and may even be superfluid-like at the temperatures required to stabilize them in beam experiments. Based on these calculations, it appears that the magic numbers observed experimentally in abundance spectra pertain to the more strongly bound ionized helium clusters, rather than the neutral clusters which are the subject of this discussion.

Electronic absorption spectra have recently been recorded for clusters containing $\approx 50\text{--}10^6$ helium atoms [89]. Broad strong absorption bands are observed which do not behave like the Wannier exciton bands seen for the heavier noble gas clusters, nor are they well-described by the Frenkel excitonic model. Note that although the Wannier and Frenkel exciton models were originally developed for solids with translational symmetry, they are also good descriptions for excitations in liquid noble gases [4]. At this writing, the helium cluster electronic spectra cannot be compared with absorption spectra of liquid or solid helium because these latter spectra have not yet been measured! With this limitation and a current lack of sufficient theoretical guidance, the helium cluster spectra have not yet been thoroughly interpreted. Theoretical calculations are available which describe the collective excitations in helium clusters on the electronic ground state surface [86]. Spectra in this energy regime have not yet been recorded.

Experimentally, it has been quite easy to dope helium clusters with various atomic and molecular species such as other noble gas atoms, oxygen, and SF_6 [4, 11, 77]. Electrons, however, are not well-solvated and negatively charged helium clusters only appear for sizes containing more than $10^5\text{--}10^6$ atoms [11]. Impurity species provide a spectro-

scopic probe for studying the properties of the solvating helium cluster. Infrared spectra of helium clusters doped with SF_6 show that the impurity molecule resides on the cluster surface, in contradiction of theoretical calculations which predict that it should be found inside a helium cluster. Understanding this discrepancy has stimulated further theoretical investigations that reveal the dramatic structural effects which can occur when angular momentum is added to these very fragile clusters during dopant pick-up [90].

41.7 Molecular Clusters

Molecular clusters are in many ways similar to noble gas clusters. Both are weakly bound, and the interactions between the particles which make up the cluster can usually be described to a good approximation as the sum of pairwise interactions. The molecule constituency adds complexity, however, which is reflected in the diversity seen amongst these clusters. Molecular clusters provide model systems for studying solvation, including electron solvation, nucleation, and phase transitions at finite sizes. Furthermore, properties which are often difficult to study in the bulk, such as phase transition dynamics, are much more amenable to study in molecular clusters.

Numerous molecular clusters have been made and studied. By far the most work has focussed on the smaller molecular clusters such as molecular dimers, trimers and tetramers. A number of outstanding reviews are available on this subset of molecular clusters [3, 4, 6, 76, 91, 92].

41.7.1 Geometric Structures and Phase Dynamics

In contrast to noble gas clusters, molecular clusters typically assume bulk phase structures at relatively small sizes. Thus, the range of condensed phases of molecular solids is reflected in the variety of packing structures found in molecular clusters. At one extreme are clusters of small nearly-spherical molecules such as CH_4 and N_2 which form clusters closely connected to noble gas clusters [76]. Small clusters of these molecules are packed in polyicosahedral arrangements at small sizes, and cross over to fcc structures at sizes containing several thousand atoms. At another extreme are clusters such as water clusters where stronger hydrogen bonding forces lead to the formation of crystalline networks such as in a diamond cubic phase [76]. Some molecular clusters appear to be liquid-like with thermal motion wiping out any persistent periodic order. The liquid-like structure observed in clusters of molecules such as benzene and various hydrocarbons may freeze into a crystalline or amorphous state at sufficiently low temperatures.

Some molecular clusters have been found to exhibit a panoply of phases, depending on size and temperature. For example, not only do clusters of TeF_6 assemble into the bulk body-centered cubic and orthorhombic phases, they can also be made in other phases including two trigonal forms, a rhombohedral phase, and two monoclinic phases [93, 94]. Similarly complex phase formation has been found in other clusters of other hexafluoride molecules such as SF_6 , SeF_6 , MoF_6 , and WF_6 .

Phase transitions in molecular clusters have been examined both experimentally and theoretically using molecular dynamics. Transition temperatures are found to depend on cluster size, and span a much broader range than in the corresponding bulk phase transitions. Large rates for nucleation and phase changes are seen in molecular clusters. Once the critical nucleus, which initiates the phase change, forms in the interior of the cluster, the remainder of the cluster transforms to the new phase extremely rapidly. Critical nucleus sizes depend on the cluster size and are typically quite small, e.g., for TeF_6 clusters, they contain only a few dozen molecules for clusters consisting of a few hundred molecules [10, 93, 94]. A key finding is that phase transitions in molecular clusters appear to violate *Ostwald's step rule*, which states that equilibrium systems must pass through all intermediate-energy stable phases during a transition from a higher energy to a lower energy phase [10]. This non-compliance apparently occurs because of the speed at which molecular clusters undergo phase transitions: intermediate phases simply do not have time to form.

41.7.2 Electronic Properties: Charge Solvation

I_p 's, A_e 's, and some spectral data are available for larger molecular clusters. Nearly all of the spectra measured pertain to clusters containing less than ten molecules [3, 4, 6, 76, 91, 92]. Precise molecular orientations within many of these clusters have been derived from detailed analyses of these spectra. Such information has not yet emerged from the few spectra that have been measured for larger molecular clusters [3, 6]. Alternatively, measurements of electronic properties of larger clusters have generally targeted a different issue: solvation of excess positive or negative charge in a restricted bulk-like system.

Charged molecular clusters provide model systems for studying the mechanism of charge stabilization within the confines of a finite system. Excess positive charge appears to be highly localized in molecular clusters, residing on a small unit containing at most a few monomers. This positive core is surrounded and stabilized by overlying shells of molecules. For example, $(\text{CO}_2)_n^+$ clusters behave as the dimer cation $(\text{CO}_2)_2^+$, surrounded by the remaining CO_2 molecules [4]. Positively charged solutes such as alkali cations have also

been introduced to study solvation of positive charge within molecular clusters [10]. For those dopants which have much lower ionization potentials than the solvating molecules, the positive charge remains strongly localized on the impurity. The cluster molecules are observed to build up solvation shells around this central impurity. The first few solvation shells are strongly affected by the positive charge, which has a decreasing influence with each successive layer. The structure of such a cluster reflects the accommodation between the geometry of the molecules influenced by the central positive charge, and those in the outer solvation layers where intermolecular forces predominate [10, 95]. Evidence for intracluster reactions in positively charged clusters has also been seen, such as proton transfer in cationic water or ammonia clusters [3, 11].

Whereas virtually every molecular cluster containing as little as two molecules exists stably as a positive ion, the same cannot be said for the negative cluster ions. Measurements of the minimum number of molecules required within the cluster to support an additional electron show that, while the dimeric $(\text{HCl})_2^-$, $(\text{SO}_2)_2^-$, and $(\text{H}_2\text{O})_2^-$ clusters are stable, ≈ 35 or ≈ 41 molecule-clusters of ND_3 or NH_3 , respectively, are required to stabilize an electron [4]. Spectroscopic studies show evidence for internal and external solvation of the excess electron in these anionic clusters.

Charge solvation in water clusters has been examined in some detail. Of particular interest is the $(\text{H}_2\text{O})_{20}$ cluster which, from experimental and theoretical data, appears to form an especially stable, well-defined clathrate cage. The interior of this cage is large enough that it can and does hold various cations such as NH_4^+ , H_3O^+ , and alkali ions [10]. This cage is not observed to surround negative ions or electrons, which instead, reside on the surface [10]. This is a general result for excess negative charge in water clusters in this size regime where excess charge can be external to the cluster. Excess electrons in water clusters are found on the cluster surface for small cluster sizes up to 60 to 70 water molecules. Above this size, the electron resides in the cluster interior, and behaves analogously to hydrated electrons in bulk water [4, 7].

41.8 Recent Developments

Added by Mark M. Cassar. Experimental and theoretical work on clusters has continued to be an active and rapidly growing area of research over the past decade. This section provides a non-exhaustive snapshot of some recent work in the vast field of cluster science.

The original focus on the scalable properties of clusters (concerning a smooth transition from small particles to bulk matter) has now extended to include important non-scalable properties. These properties, particularly at the nanoscale

level, have enormous potential for technological application [96–98]. Studies aimed at understanding the underlying atomic structure of noble-metal clusters and nanoparticles, which is the first step toward their controlled use in future nanotechnologies, e.g., catalysis, labeling, or photonics, have been carried out [99]. Ab initio all-electron molecular-orbital calculations for small ($n = 7–11$) and medium ($n = 12–20$) silicon clusters Si_n have been performed in order to study their structure and relative stability [100, 101]; such calculations are important in determining the scalability of present day semiconductor technology.

Other interesting work has been done on the electron transfer properties of metal clusters that could act as conducting bridges between molecular wires [102]; and in the role that tetramanganese clusters play in one of the active photosynthesis sites (photosystem II) in green plants, and in certain bacteria and algae [103].

The reader is referred to various reviews that can be found in the literature: for time-resolved photoelectron spectroscopy (TRPES) of clusters, which allows the dynamics along the entire reaction coordinate to be followed, see [104]; for ultrafast dynamics in cluster systems and atomic clusters, see [105, 106]; for small carbon clusters, important in the chemistry of carbon stars, comets, interstellar molecular clouds, and hydrocarbon flames, see [107]; for the relation between electronic structure, atomic structure and magnetism of clusters of transition elements, see [97].

References

- Special issue on gas phase clusters, *Chem. Rev.* **86**, 375 (1986)
- deHeer, W.A., Knight, W.D., Chou, M.Y., Cohen, M.L.: Electronic shell structure and metal clusters. In: Ehrenreich, H., Turnbull, D. (eds.) *Solid State Physics*, vol. 40, Academic Press, New York (1987)
- Bernstein, E.R. (ed.): *Atomic and Molecular Clusters*. Elsevier, New York (1990)
- Scoles, G. (ed.): *The Chemical Physics of Atomic and Molecular Clusters*. North-Holland, New York (1990)
- Bonacic-Koutecky, V., Fantucci, P., Koutecky, J.: Special issue on gas phase clusters. *Chem. Rev.* **91**, 1035 (1991)
- Haberland, H. (ed.): *Clusters of Atoms and Molecules*. Springer, Berlin (1994)
- Echt, O., Recknagel, E. (eds.): Proceedings of the 5th international meeting on small particles and inorganic clusters. *Z. Phys. D*, vol. 19–20. (1991)
- Kumar, V., Martin, T.P., Tosatti, E. (eds.): *Clusters and Fullerenes*. World Scientific, River Edge (1993)
- Morse, M.D.: *Chem. Rev.* **86**, 1049 (1986)
- Berry, R.S., Castleman, A., Jellinek, J. (eds.): Proceedings of the 6th international meeting on small particles and inorganic clusters. *Z. Phys. D*, vol. 26–26S. (1993)
- Jena, P., Khanna, S.N., Rao, B.K. (eds.): *Physics and Chemistry of Finite Systems: From Clusters to Crystals* vol. 1 & 2. Kluwer, Netherlands (1992)
- Granqvist, C.G., Buhrman, R.A.: *J. Appl. Phys.* **47**, 2200 (1976)
- Chapon, C., Gillet, M.F., Henry, C.R. (eds.): Proceedings of the 4th international meeting on small particles and inorganic clusters. *Z. Phys. D*, vol. 12. (1989)
- Duncan, M.A. (ed.): *Advances in Metal and Semiconductor Clusters* vol. 2. JAI, Greenwich (1994)
- Bjørnholm, S., Borggreen, J., Echt, O., Hansen, K., Pedersen, J., Rasmussen, H.D.: *Phys. Rev. Lett.* **65**, 1627 (1990)
- Martin, T.P., Bergmann, T., Gohlich, H., Lange, T.: *Chem. Phys. Lett.* **172**, 209 (1990)
- Cheshnovsky, O., Taylor, K.J., Conceicao, J., Smalley, R.E.: *Phys. Rev. Lett.* **64**, 1785 (1990)
- Rademann, K.: *Ber. Bunsenges. Phys. Chem.* **93**, 653 (1989)
- Knickelbein, M.B., Menezes, W.J.C.: *Phys. Rev. Lett.* **69**, 1046 (1992)
- Baumert, T., Rottgermann, C., Rothenfusser, C., Thalweiser, R., Weiss, V., Gerber, G.: *Phys. Rev. Lett.* **69**, 1512 (1992)
- Bréchnignac, C., Broyer, M., Cahuzac, P., Delacretaz, G., Labastie, P., Wolf, J.P., Wöste, L.: *Phys. Rev. Lett.* **60**, 275 (1988)
- Bucher, J.P., Douglass, D.C., Bloomfield, L.A.: *Phys. Rev. Lett.* **66**, 3052 (1991)
- Billas, I.M.L., Becker, J.A., Chatelain, A., deHeer, W.A.: *Phys. Rev. Lett.* **71**, 4067 (1993)
- Khanna, S.N., Linderoth, S.: *Phys. Rev. Lett.* **67**, 742 (1991)
- Cox, D.M., Reichmann, K.C., Trevor, D.J., Kaldor, A.: *J. Chem. Phys.* **88**, 111 (1988). and references therein
- Parent, D.C., Anderson, S.L.: *Chem. Rev.* **92**, 1541 (1992)
- Parks, E.K., Klots, T.D., Winter, B.J., Riley, S.J.: *J. Chem. Phys.* **99**, 5831 (1993)
- Parks, E.K., Riley, S.J.: *J. Chem. Phys.* **99**, 5898 (1993)
- Schmid, T.: *Chem. Rev.* **922**, 1709 (1992)
- de Jongh, L.J., Brom, H.B., van Ruitenbeek, J.M., Thiel, R.C., Schmid, G., Longoni, G., Ceriotti, A., Benfield, R.E., Zaroni, R.: Physical and chemical properties of high nuclearity metal-cluster compounds: Model systems for small metal particles. In: Pacchioni, G., Bragusa, P.S., Parmigiani, F. (eds.) *Cluster Models for Surface and Bulk Phenomena*. Plenum, New York (1992)
- Buo, B.C., Kerns, K.P., Castleman, A.W.: *Science* **255**, 1411 (1992)
- Chen, H., Feyereisen, M., Long, X.P., Fitzgerald, G.: *Phys. Rev. Lett.* **71**, 1732 (1993)
- Reddy, B.V., Khanna, S.N.: *Chem. Phys. Lett.* **209**, 104 (1993)
- Kroto, H.W., Heath, J.R., O'Brien, S.C., Curl, R.F., Smalley, R.E.: *Nature* **318**, 162 (1985)
- Creasy, W.R.: *Fuller. Sci. Tech.* **1**, 23 (1993)
- Kroto, H.W., Allaf, A.W., Balm, S.P.: *Chem. Rev.* **91**, 1213 (1991)
- Billups, W.E., Ciufolini, M.A. (eds.): *Buckminsterfullerenes*. VCH, New York (1993)
- Cioslowski, J.: *Electronic Structure Calculations on Fullerenes and Their Derivatives*. Topics in Physical Chemistry. Oxford University Press, Oxford (1995)
- McLafferty, F. (ed.): Special issue on Buckminsterfullerenes. *Acc. Chem. Res.*, vol. 25. (1992)
- Kratschmer, W., Lamb, L.D., Fostiropoulos, K., Huffman, D.R.: *Nature* **347**, 354 (1990)
- Hebard, A.F., Rosseinsky, M.J., Haddon, R.C., Murphy, D.W., Glarum, S.H., Palstra, T.T.M., Ramirez, A.P., Kortan, A.R.: *Nature* **350**, 600 (1991)
- Heath, J.R., Saykally, R.J.: In: Reynolds, P.J. (ed.) *On Clusters and Clustering*, p. 7. North-Holland, Amsterdam (1993)
- von Helden, G., Hsu, M.-T., Gotts, N., Bowers, M.T.: *J. Phys. Chem.* **97**, 8182 (1993)
- Weltner, W., Van Zee, R.J.: *Chem. Rev.* **89**, 1713 (1989)
- McElvany, S.W., Ross, M.M., Bohme, D.K. (eds.): Special issue on fullerenes, carbon, and metal-carbon clusters. *Int. J. Mass Spectrom. Ion Processes*, vol. 138. (1994)

46. Kim, S.G., Tomanek, D.: *Phys. Rev. Lett.* **72**, 2418 (1994)
47. Bethune, D.S., Johnson, R.D., Salem, R.J., de Vries, M.S., Yan- noni, C.S.: *Nature* **366**, 123 (1993)
48. Wang, X.-D., Hazhizume, T., Xue, Q., Shinohara, H., Saito, Y., Nishina, Y., Sakurai, T.: *Jpn. J. Appl. Phys.* **32**, L147 (1993)
49. Hino, S., Takahashi, H., Iwasaki, K., Matsumoto, K., Miyazaki, T., Hasegawa, S., Kikuchi, K., Achiba, Y.: *Phys. Rev. Lett.* **71**, 4261 (1993)
50. Saunders, M., Jimenez-Vazquez, H.A., Cross, R.J., Mroczkowski, S., Gross, M.L., Giblin, D.E., Poreda, R.J.: *J. Am. Chem. Soc.* **116**, 2193 (1994)
51. Ehrenreich, H., Spaepen, F. (eds.): *Fullerenes in Solid State Physics* vol. 48. Academic Press, New York (1994)
52. Cioslowski, J.: Ab initio electronic structure calculations on en- dohedral complexes of the C₆₀ cluster. In: Davies, J.E.D. (ed.) *Spectroscopic and Computational Studies of Supramolecular Sys- tems*, vol. 40, Kluwer, Netherlands (1992)
53. Zimmermann, U., Malinowski, N., Naher, U., Frank, S., Martin, T.P.: *Phys. Rev. Lett.* **72**, 3542 (1994)
54. Zhou, O., Fleming, R.M., Murphy, D.W., Chen, C.H., Haddon, R.C., Ramirez, A.P., Glarum, S.H.: *Science* **263**, 1744 (1994)
55. Whetten, R.L.: *Acc. Chem. Res.* **26**, 49 (1993)
56. Barnett, R.N., Landman, U., Scharf, D., Jortner, J.: *Acc. Chem. Res.* **22**, 350 (1989)
57. Li, X., Whetten, R.L.: *J. Chem. Phys.* **98**, 6170 (1993)
58. Rajagopal, G., Barnett, R.N., Landman, U.: *Phys. Rev. Lett.* **67**, 727 (1991)
59. Steigerwald, M.L., Brus, L.E.: *Acc. Chem. Res.* **23**, 183 (1990)
60. Wang, Y.: *Acc. Chem. Res.* **24**, 133 (1991)
61. Brus, L.: *Adv. Mater.* **5**, 286 (1993)
62. Raghavachari, K., Curtiss, L.A.: Accurate theoretical studies of small elemental clusters. In: Langhoff, R.S. (ed.) *Quantum Me- chanical Electronic Structure Calculations with Chemical Accu- racy*. Kluwer, Netherlands (1994)
63. Raghavachari, K.: *Phase Transit.* **24–26**, 61 (1990)
64. Bingelli, N., Martins, J.L., Chelikowsky, J.R.: *Phys. Rev. Lett.* **68**, 2956 (1992)
65. Kaxiras, E., Jackson, K.: *Phys. Rev. Lett.* **71**, 727 (1993)
66. Röthlisberger, U., Andreoni, W., Parrinello, M.: *Phys. Rev. Lett.* **72**, 665 (1994)
67. Fuke, K., Tsukamoto, K., Misaizu, F., Sanekata, M.: *J. Chem. Phys.* **99**, 7807 (1993)
68. Jarrold, M.F.: *Science* **252**, 1085 (1991)
69. Rinnen, K.-D., Mandich, M.L.: *Phys. Rev. Lett.* **69**, 1823 (1992)
70. Al-Laham, M.A., Raghavachari, K.: *J. Chem. Phys.* **98**, 8770 (1993)
71. Lou, L., Nordlander, P., Smalley, R.E.: *J. Chem. Phys.* **97**, 1858 (1992)
72. Graves, R.M., Scuseria, G.E.: *J. Chem. Phys.* **95**, 6602 (1991)
73. Jin, C., Taylor, K.J., Conceicao, J., Smalley, R.E.: *Chem. Phys. Lett.* **175**, 17 (1990)
74. Rinnen, K.-D., Kolenbrander, K.D., DeSantolo, A.M., Mandich, M.L.: *J. Chem. Phys.* **96**, 4088 (1992)
75. Wang, L., Chibante, L.P.F., Tittel, F.K., Curl, R.F., Smalley, R.E.: *Chem. Phys. Lett.* **172**, 335 (1990)
76. Special issue on gas phase clusters, *Chem. Rev.* **86** (1986)
77. Goyal, S., Schutt, D.L., Scoles, G.: *Acc. Chem. Res.* **26**, 123 (1993)
78. Miehle, W., Kandler, O., Leisner, T.: *J. Chem. Phys.* **91**, 5940 (1989)
79. Wales, D.J.: *Mol. Phys.* **78**, 151 (1993)
80. Berry, R.S.: *Chem. Rev.* **93**, 2379 (1993)
81. Matsuoka, H., Hirokawa, T., Matsui, M., Doyama, M.: *Phys. Rev. Lett.* **69**, 297 (1992)
82. Kamke, W., de Vries, J., Krauss, J., Kaiser, E., Kamke, B., Hertel, I.V.: *Z. Phys. D* **14**, 339 (1989)
83. Wormer, J., Joppien, M., Zimmerer, G., Moller, T.: *Phys. Rev. Lett.* **67**, 2053 (1991)
84. Leutwyler, S., Bosiger, J.: *Chem. Rev.* **90**, 189 (1990)
85. Adams, J.E., Stratt, R.M.: *J. Chem. Phys.* **99**, 789 (1993)
86. Whaley, K.B.: *Int. Rev. Phys. Chem.* **13**, 41 (1994)
87. Luo, F., McBane, G.C., Kim, G., Giese, C.F., Gentry, W.R.: *J. Chem. Phys.* **98**, 3564 (1993)
88. Anderson, J.A., Traynor, C.A., Boghosian, B.M.: *J. Chem. Phys.* **99**, 345 (1993)
89. Joppien, M., Karbach, R., Moller, T.: *Phys. Rev. Lett.* **71**, 2654 (1993)
90. McMahon, M.A., Barnett, R.N., Whaley, K.B.: *J. Chem. Phys.* **99**, 8816 (1993)
91. Bieske, E.J., Maier, J.P.: *Chem. Rev.* **93**, 2603 (1993)
92. McIlroy, A., Nesbitt, D.J.: *Adv. Mol. Vib. Collis. Dyn. A* **1**, 109 (1991)
93. Xu, S., Bartell, L.S.: *J. Phys. Chem.* **97**, 13544 (1993)
94. Xu, S., Bartell, L.S.: *J. Phys. Chem.* **97**, 13550 (1993)
95. Selegue, T.J., Moe, N., Draves, J.A., Lisy, J.M.: *J. Chem. Phys.* **96**, 7268 (1992)
96. Jortner, J.: *Faraday Discuss.* **108**, 1 (1997)
97. Alonso, J.A.: *Chem. Rev.* **100**, 637 (2000)
98. Meloni, G., Ferguson, M.J., Sheehan, S., Neumark, D.M.: *Chem. Phys. Lett.* **399**, 389 (2004)
99. Häkkinen, H., Moseler, M., Kostkos, O., Morgner, N., Hoffmann, M., v. Issendorff, B.: *Phys. Rev. Lett.* **93**, 093401 (2004)
100. Zhu, X.L., Zeng, X.C.: *J. Chem. Phys.* **118**, 3558 (2003)
101. Zhu, X.L., Zeng, X.C., Lei, Y.A., Pan, B.: *J. Chem. Phys.* **120**, 8985 (2004)
102. Yip, J.H.K., Wu, J., Wong, K.-Y., Ho, K.P., Pun, C.S., Vittal, J.J.: *J. Chin. Chem. Soc.* **51**, 1245 (2004)
103. Mukhopadhyay, S., Mandal, S.K., Bhaduri, S., Armstrong, W.H.: *Chem. Rev.* **104**, 2981 (2004)
104. Neumark, D.M.: *Annu. Rev. Phys. Chem.* **52**, 255 (2001)
105. Dermota, T.E., Zhong, Q., Castleman Jr., A.W.: *Chem. Rev.* **104**, 1862 (2004)
106. Bonacic-Kontecy, V., Mitric, R.: *Chem. Rev.* **104**, 1861 (2004)
107. Van Orden, A., Saykelly, R.J.: *Chem. Rev.* **98**, 2313 (1998)



Mary L. Mandich Mary Mandich is retired from NOKIA Corp. where she was a Technical Manager at Bell Laboratories and Distinguished Member of Technical Staff in the High Speed Optical Products Division. She obtained her Ph.D. degree in Physical Chemistry at Columbia University. She holds 9 US Patents and has authored 2 book chapters and 55+ scientific publications in chemistry, physics, and materials science.



Infrared Spectroscopy

42

Henry Buijs

Contents

42.1	Introduction	626
42.2	Historical Evolution of Infrared Spectroscopy Practice	626
42.3	Quantitative Analysis by Infrared Spectroscopy	627
42.4	Molecular Spectroscopy	627
42.5	Remote Sensing	628
42.6	The Evolution of Fourier Transform Infrared Spectroscopy (FTIR)	628
42.7	Laser-Based Infrared Spectroscopy	629
42.8	Intensities of Infrared Radiation	629
42.9	Sources for IR Spectroscopy	630
42.10	Relationship Between Source Spectrometer Sample and Detector	630
42.11	Simplified Principle of FTIR Spectroscopy	630
42.11.1	Interferogram Generation: The Michelson Interferometer	630
42.11.2	Description of Wavefront Interference with Time Delay	631
42.11.3	Operation of Spectrum Determination	631
42.11.4	Optical Aspects of FTIR Technology	632
42.12	The Scanning Michelson Interferometer	633
42.13	Infrared Spectroscopy Application Activity 2020	634
42.13.1	Analytical Chemistry Laboratories	634
42.13.2	Biomedical and Pharmaceutical Laboratories	635
42.13.3	Forensic Investigation	635
42.13.4	Infrared Spectroscopy in Quality Assurance Laboratories	636
42.13.5	Process Monitoring by Infrared Spectroscopy	636
42.13.6	Environmental Monitoring	637
42.13.7	Remote Sensing	637
42.14	Conclusion	638
	References	639

Abstract

Coblentz determined the relation between infrared spectra and molecular identity. Infrared spectroscopy became a tool for chemical analysis widely used in analytical chemistry laboratories. Prism or grating “dispersive” spectrometers fulfill this function well. Molecular spectroscopy was first practiced in the visible and UV range using large high-resolution spectrographs to record the fine spectral lines of vapor phase molecules. Extension to the infrared region was impeded by the lack of sensitivity of single-element infrared detectors and the challenge of making ever larger spectrometers to achieve high resolution. Dispersive spectrometers were superseded by “interferometric” spectrometers that possessed a much larger optical throughput and, when combined with the Fourier technique, permitted multiplexing the entire spectrum efficiently on a single detector enabling extending high-resolution molecular spectroscopy to the infrared region. As Fourier transform spectroscopy technology matured, measurement accuracy and reproducibility were also enabled. Quantitative infrared spectroscopy has opened a wide range of new applications in industry, environmental monitoring, and monitoring of atmospheric variations in relation to weather forecasting. Space probes use Fourier transform spectrometers to determine the chemical nature of planetary atmospheres and surfaces and even the measurement of the cosmic background radiation remnant. Low-cost Fourier transform spectrometers have also replaced dispersive spectrometers in analytical chemistry laboratories. Given its importance in a wide range of applications, a detailed description of the technique is provided.

Keywords

infrared · spectrometer · FTIR · chemical identification · molecular structure determination · quantitative analysis · reproducibility · remote sensing · transmission · absorption · emission

H. Buijs (✉)
FTS Consulting
Québec, Québec, Canada
e-mail: hlbuijs@gmail.com

42.1 Introduction

Infrared spectroscopy consists of the measurement of interactions of waves of the infrared (IR) part of the electromagnetic spectrum with matter. The IR spectrum starts just beyond the red part of the visible spectrum at a wavelength of approximately $\lambda = 700$ nm extending to 2500 nm and is usually called near-IR, from $\lambda = 2500$ to 25,000 nm or $\lambda = 2.5$ to 25 μm called mid-IR, and from $\lambda = 25$ to 1000 μm called far-IR. For the mid-IR ($\sigma = 4000$ to 400 cm^{-1}) and far-IR regions ($\sigma = 400$ to 10 cm^{-1}), it is common practice to use frequency σ expressed in number of wavelengths per cm (wavenumbers, cm^{-1}) instead of wavelengths.

The interactions observed in the mid-IR region principally involve energies associated with molecular structure change. Harmonic overtones, as well as combinations of mid-IR frequencies, are expressed in the near-IR region and can also be associated with the same molecular structure change as can be observed in the mid-IR but appear less obvious. Interactions observed in the far-IR involve molecular structure change having low energy. These are predominantly changes in molecular rotation energy.

The most common IR analysis of a sample is by IR absorption spectroscopy. Samples may consist of solid or liquid samples, called condensed phase samples and gas phase samples. IR absorption spectroscopy involves transmitting a beam of intense IR radiation through the sample and observing the distribution of wavenumbers absorbed by molecules when compared to a spectrum measured without the sample. Condensed phase samples generally absorb strongly in the mid-IR region, requiring a path length through the sample of only a fraction of a mm. In the near-IR, these samples absorb at least an order of magnitude less, permitting path lengths through a sample of up to a cm. Gas phase samples absorb much less due to their lower density compared with condensed phase samples and may require a path length of several meters in the mid-IR. Molecules in a sample may also be studied by IR emission spectroscopy simply by observing specific wavenumbers being emitted by virtue of their nonzero absolute temperature. Finally, radiation reflected from a smooth surface of a solid sample also provides information about the molecular structure of the material by virtue of the anomalous dispersion associated with absorption bands.

Historically, infrared spectroscopy started out as a *qualitative* method for identifying different molecular species present in a sample, as is also done by various titration methods used by chemists. Today, infrared spectroscopy has been extended to include accurate quantitative determination of molecular concentrations. This has enabled applications such as quality assurance and process control in chemical manufacturing and applications where multiple different spectrometers are required to provide quantitatively reproducible measurements. The evolution from qualitative to

increasingly accurate quantitative infrared analysis will be described. Molecular spectroscopy research covers spectral analysis at high spectral resolution covering the UV to the far-infrared. Infrared spectroscopy plays a key role in remote sensing. Satellite-based thermal infrared emission and near-infrared reflected solar spectroscopy is an essential part of weather forecasting, pollution monitoring, and climate change research related to Earth's atmosphere. Infrared remote sensing is also used extensively in conjunction with interplanetary space probes, as well as astronomy.

42.2 Historical Evolution of Infrared Spectroscopy Practice

After the discovery of infrared radiation by *Herschel* in 1800 [1, 2], it was not until the late nineteenth century that *William Coblentz* [3] obtained infrared spectra of many substances using both glass and salt prisms, reaching as far as $\lambda = 15$ μm in the mid-infrared. By studying the correlations amongst spectra of different substances Coblentz derived a number of important properties of infrared spectra, such as conservation of the unique spectral band positions and shapes of a given substance in mixtures of a sample. The unique correlation between the infrared spectral signatures and the molecular species being measured even in complex mixtures permitted Coblentz to establish infrared spectroscopy as a tool for identifying molecular structure for a variety of chemical species. These observations led to the concept of functional groups in infrared spectroscopy that permits us to elucidate a wide range of molecular structures from infrared and Raman spectra [4]. A great diversity of unique spectral signatures is found in the region from 400 to 2000 cm^{-1} and is commonly known as the "fingerprint" region.

It was not until the 1940s that infrared spectroscopy became a widely used tool for chemical analysis. This was driven by the need for chemical analysis in support of the development and manufacture of synthetic chemical products such as rubber and aviation fuels. Several thousand spectrometers were produced for this purpose. More widespread use of infrared spectrometers was enabled by the introduction of the Perkin Elmer model 137 "Infracord" [5] in 1956, a double-beam spectrometer that traced the sample *transmittance* directly on paper in real time. This quickly became a popular analytical tool for the chemistry laboratory displacing tedious titration methods for general chemical identification.

Prisms made from various infrared transparent materials and diffraction gratings angularly disperse incident radiation as a function of the wavelength. Intensities at these wavelengths can be measured sequentially by scanning the dispersed radiation past a narrow slit. Gratings mostly re-

placed prisms for infrared spectroscopy starting in the 1950s, following improvements in the uniformity of groove spacing, as well as the technique of replicating gratings from masters, thereby greatly reducing cost. Today, the use of spectrometers consisting of a grating and a linear detector array covering the full dispersed spectrum simultaneously is common for the UV and visible regions, as well as the near-infrared down to about 1700 nm (5880 cm^{-1}). These are simple, easy to use spectrometers for which economical and performant detector arrays are available. Extension to the mid and far-IR of this combination has been impeded by the cost and complexity of linear detector arrays for these regions, which require operation at low temperature to achieve optimal sensitivity. With two-dimensional imaging detector arrays, a line with many fields of view along the length of a slit can be measured simultaneously, where the spectra are dispersed along the columns of the 2-D array perpendicular to the rows of fields of view. Scanning the slit across an extended field of view and repeatedly recording two-dimensional data arrays builds up a hyperspectral image.

Gratings have several significant advantages over prisms. Groove spacing provides flexibility in resolution and spectral region selection, gratings with blazed grooves improve optical efficiency for selected spectral regions, and concave gratings minimize the need for additional focusing optics. A limitation of gratings is that multiple different wavelengths are diffracted at the same angle, presenting multiple orders to a detector. Therefore, gratings require order selection filtering to avoid superposition of orders of different spectral regions.

Starting in the 1950s infrared spectroscopy was being developed for use beyond the chemistry laboratory in three distinct areas. One area was the development of quantitative methods of chemical analysis, another was the development of high-resolution IR molecular spectroscopy, and, finally, a variety of remote-sensing applications.

42.3 Quantitative Analysis by Infrared Spectroscopy

Least squares comparison of a measured infrared spectrum with a reconstruction of spectral signatures for each of the components in a sample is impractical for condensed phase samples. Spectral features of a condensed phase sample compared with the spectral features of the same sample in the vapor phase shows a strong broadening due to intermolecular interactions of close neighbor molecules. Vapor phase spectral features typically have a width $< 0.1\text{ cm}^{-1}$ at atmospheric pressure, whereas in the condensed phase, these features often have widths of $> 4\text{ cm}^{-1}$. In a mixture of different molecules, these intermolecular interactions vary somewhat from the homogeneous case, thus slightly distort-

ing band shapes in a mixture with respect to pure component band shapes. Infrared spectroscopic determination of accurate molecular concentration for condensed phase samples, therefore, requires the acquisition of infrared spectra of prepared standard mixtures representative of the range of sample variations to be analyzed. These standards are used in a principal component analysis. Since the set of standard mixtures used for the principal component modeling may not permit exact reconstruction of the measured spectrum, a chemometric technique of "partial least squares" is employed [6, 7]. It permits controlling overrepresentation of a measured spectrum by the reconstructed spectrum. This technique was first employed in the determination of concentrations of protein and moisture in wheat via near-IR diffuse reflection to establish its commercial value [8].

It was soon realized that measurements of spectra employing different spectrometers presented significant errors. As a result, the prepared standards measured with different spectrometers expanded the number of standard spectra used as inputs for the principal component analysis. Improvement of grating spectrometers with respect to reproducibility such as to minimize the need for standard samples to be measured with multiple different spectrometers met with limited success. Small variations in slit geometry as well as scanning mechanisms prevented the achievement of adequate reproducible measurements. Improved reproducibility for spectrometers used at different sites was one of the driving forces for the development of Fourier transform spectroscopy.

42.4 Molecular Spectroscopy

Molecular spectroscopy dates back to the 1920s, following the elegant description of molecular dynamics via quantum mechanics. It is carried out mainly using samples in the vapor phase where intermolecular interaction is minimized such that spectra consist of narrow spectral features. Resolving many different spectral features and determining precise wavelengths of these features is key to determining the detailed energy states of a molecule and, thereby, its structure [9]. An early study was carried out using large high-resolution monochromators and photographic recording of spectra. Extension to the infrared was enabled by the availability of sensitive infrared detectors operating at low temperatures starting in the 1950s. To achieve high resolution, large gratings are required to minimize dispersion by diffraction and projection of a greatly expanded spectral dispersion at a narrow slit requiring long focal length optics. Scanning all the wavelengths of a highly dispersed spectrum is time consuming using a single infrared detector and is much less efficient than photographic recording of the full spectrum. This was another driving force behind the development of Fourier transform spectroscopy [10].

42.5 Remote Sensing

Measuring infrared spectra of remotely located targets is highly variable and is dependent on the temperature and emissivity of the targets. Spectrometers used for remote sensing require the best achievable sensitivity. Over time, Fourier transform spectrometers have become the spectrometers of choice for remote sensing not only for their favorable sensitivity but also for the flexibility of operating parameters, such as spectral resolution, spectral range, and measurement speed. Atmospheric remote sensing from satellites has become an essential tool for weather prediction by providing vertical distribution profiles of temperature and moisture, which are the most important thermodynamic drivers of weather. The technique is also used to determine the detailed composition of the atmosphere and its variations over time and geographic location.

42.6 The Evolution of Fourier Transform Infrared Spectroscopy (FTIR)

Infrared detectors represent an important aspect of infrared spectroscopy. Pyroelectric bolometric mid-infrared detectors operating at ambient temperature are widely used for chemistry laboratory infrared analysis. Using a pyroelectric detector with a scanning grating spectrometer, spectral measurements are time consuming, and the spectra are of modest quality. A Fourier transform spectrometer records an encoded signal for all wavelengths simultaneously on a single detector. The Fourier transform type spectrometer using a pyroelectric detector permits significant enhancement of measurement speed and quality.

A semiconductor made from a small bandgap material can, in principle, provide broadband detection like a bolometer; however, thermal noise currents increase rapidly at smaller bandgaps, requiring operation at ever lower temperature. A proliferation of different bandgap infrared detectors are available, permitting optimization of sensitivity and degrees of cooling for targeted spectral regions.

The demand for measurement speed, spectral resolution, reproducibility, and sensitivity are driven by a proliferation of applications of infrared spectroscopy. An alternative to the dispersive spectrometer was sought. In the 1960s, the Fourier transform spectrometer was seen as a strong candidate but required much technological development.

Fourier transform spectroscopy was pioneered early in the twentieth century by *Albert A. Michelson* [11] as an alternative use of the two-beam interferometer he had invented for the purpose of determining the inhomogeneity of the velocity of light. However, due to a lack of tools to measure and process data he relied on visual observation of “visibility curves” that permitted him to characterize some aspect

of spectra. *Lord Rayleigh* [12] pointed out to Michelson that the relation between the observed visibility curves of the interferometer and their spectra is the Fourier transformation. Observing all wavelengths simultaneously with a Michelson interferometer, like recording the complete spectrum with photographic film, was not realized until 1949 by the work of *P. Fellgett* [13, 14]. Fellgett computed the Fourier transform of a limited set of measurements laboriously by hand. As digital computers started their exponential growth in capacity and computation speed, year over year Fourier transform spectroscopy became increasingly accessible. In the 1960s, Fourier transform spectroscopy became usable but required access to a large computing center. Early implementations of the scanning Michelson interferometer were sensitive to perturbations and required a skilled operator to maintain the alignment of the scanning mirror. The high cost and complexity of operating an early version of an FTIR limited its use to research centers. Nevertheless, the great increase in sensitivity and measurement speed provided access to measurement problems not available with dispersive spectrometers. As an example, *Buijs* and *Gush* [15] described the high-resolution measurement of the electric field induced absorption spectrum of hydrogen with a homemade Fourier transform spectrometer. In 1965, the interferometer scanning mirror positions were determined using a Hg¹⁹⁸ lamp as monochromatic metrology source, since lasers were not yet available. Furthermore, the computation of the Fourier transform of the interferograms containing about 4000 numerical data points typically took up to 20 min on a large mainframe IBM 7094 computer. In the late 1960s, *Cooly* and *Tukey* [16, 17] presented a method of factoring the Fourier transform calculation making use of symmetries in the trigonometric matrix and, thereby, greatly reducing the number of calculations required; this is commonly called the fast Fourier transform or FFT. The same calculation as above on the same computer was realized in about 10 s. As well, in the late 1960s, lasers became available. The He-Ne laser permitted scan control of the moving mirror with much higher precision than the Hg¹⁹⁸ lamp and over much longer mirror displacements. It is seen that over a period of 20 years Fourier transform spectroscopy progress depended greatly on new technological developments.

By 1984 the introduction of the personal computer (PC) and advances in interferometer design permitted the realization of a low-cost versatile and easy to use Fourier transform spectrometer. The efficiency of measuring all wavelengths simultaneously called the multiplex advantage as described by *Fellgett* [13, 14] and the greater light throughput by elimination of the narrow slit as described by *Jacquinot* [18] allowed infrared spectra to be measured much more rapidly and with much greater signal-to-noise ratio. This development led to a rapid replacement of dispersive spectrometers in chemistry laboratories by FTIR, particularly for the mid-IR and the far-

IR. In the near-IR, the intensity of illumination sources, such as the tungsten lamp, and the availability of high sensitivity of InGaAs, PbS, and other room-temperature semiconductor detectors allowed both near-IR grating spectrometers and FT-NIR to flourish.

The availability of linear array detectors in the visible and UV that have intrinsic noise lower than photon statistics noise permit dispersive spectrometers to perform more favorably than FT spectrometers. Both techniques measure all spectral elements simultaneously; however, the array detector of a dispersive spectrometer localizes excess photon noise due to intense spectral features at certain elements of the detector array and avoids adding this noise to the lower photon noise of weaker spectral features at other elements of the detector array. The FT spectrometer, however, accumulates the photon noise of all spectral features on a single detector. This is particularly disadvantageous for FT spectrometers when measuring wide spectral intervals. UV and visible dispersive spectrometers with an array detector that has intrinsic noise lower than the source photon statistics noise can, therefore, measure weak spectral features with lower noise than strong features, effectively increasing the dynamic range of intensity measurement, which the FT spectrometer does not permit.

With the maturing of FTIR technology, a great diversity of infrared spectroscopy applications has been enabled. With FTIR, spectral resolution and spectral range can be varied freely. Current scanning Michelson interferometers are constructed to maintain the precise alignment required either using “cube corner” retroreflectors instead of flat mirrors or servo-controlled dynamic alignment applied to flat mirrors. This advanced control of interferometer alignment has opened the possibility to operate FTIRs in hostile environments of vibration and temperature with minimal effect on performance. It has also permitted scanning the mirror distances as large as several meters to offer spectral resolution that far exceeds that of dispersive spectrometers.

In the vapor phase at pressures well below atmospheric, spectral lines of specific energy transitions may be very narrow. Here the line width is limited by doppler shifts due to thermal motion of the molecules and is dependent on temperature and is linearly proportional to the molecular weight and frequency. As pressure is increased line width increases due to random collisions of molecules that are density dependent. At room temperature and low density in the mid-IR, spectral linewidths may be $< 0.002 \text{ cm}^{-1}$. FT spectrometers where the scanning mirror can be translated through several meters are also capable of resolution down to $< 0.002 \text{ cm}^{-1}$, which is far higher than any dispersive spectrometer, while still maintaining sufficient optical efficiency due to the Jacquinot advantage. These spectrometers are capable of covering the full infrared range and have enabled efficient extension of molecular spectroscopy to the infrared beyond photographic recording.

42.7 Laser-Based Infrared Spectroscopy

In the quest for the study of ever finer detail in infrared spectra, the use of tunable lasers has permitted still higher resolution and with significantly higher precision. Using cavity-enhanced absorption spectroscopy such as cavity ring-down or integrated cavity-enhanced spectroscopy, faint spectral lines can be observed with great clarity. Today, much research on molecular structure by infrared spectroscopy is performed using tunable laser spectroscopy. As well, cavity-enhanced absorption spectroscopy is used to measure ultralow concentrations of components in a gas mixture for the purpose of environmental monitoring and contamination assessments. Current tunable lasers have a limited spectral range capability requiring multiple lasers to cover a wide spectral range.

Given its versatility for infrared spectroscopy applications it is useful to describe the common practice and elements of infrared Fourier transform (FTIR) spectroscopy.

42.8 Intensities of Infrared Radiation

For strong interactions of electromagnetic waves with matter, the emitted and absorbed intensities are governed by Planck's radiation law in addition to the emissivity and absorptivity of the material. Planck's radiation law for thermal radiation from an ideal black body is

$$P_{bb}(\sigma T)d\sigma = \frac{C_1\sigma^3 d\sigma}{\exp\left(\frac{h\sigma}{K_b T}\right) + 1}, \quad (42.1)$$

where σ is the frequency in cm^{-1} , h is Planck's constant, K_b is the Boltzmann constant, T is the temperature of the black-body in K, and C_1 is a proportionality constant. Depending on the definition of C_1 , $P_{bb}(\sigma T)$ may represent a radiation density per unit spectral interval cm^{-1} in a cavity at temperature T in ergs/cm^3 , or an energy flux emitted from a surface in $\text{W}/(\text{cm}^2\text{-steradians})$. At frequencies that are low compared with $h/K_b T$, the energy distribution increases with σ^2 and is approximately proportional to T at a given σ . At high frequency, the energy distribution falls off exponentially. In the near-IR, a high temperature is required to emit radiation. Room-temperature objects emit the most strongly in the 500 to 1800 cm^{-1} region and emit negligible energy above 3000 cm^{-1} . Materials cooled to liquid nitrogen temperature (77 K) only emit below 100 cm^{-1} , while materials cooled to liquid He temperature (4.2 K) emit below 20 cm^{-1} . In contrast to visible spectroscopy, IR absorption spectroscopy is complicated by emission of IR radiation from the sample and the surrounding environment.

42.9 Sources for IR Spectroscopy

A silicon carbide element electrically heated to 1400 K provides a strong continuum of IR radiation over a major part of the IR spectrum. It is commonly used as a source of radiation for IR absorption spectroscopy. For near-IR spectroscopy, a tungsten filament lamp operated at 2800 K provides a strong continuum all the way up to the visible part of the spectrum; it is not useful below 3000 cm^{-1} because of absorption by the glass or quartz envelope. Various electrically heated ceramic elements, such as the Nernst glower and high-temperature carbon rods, have been devised to achieve higher intensity.

42.10 Relationship Between Source Spectrometer Sample and Detector

Since a sample at room temperature emits IR radiation in the mid-IR, it is important to distinguish between the transmitted radiation used in the determination of its absorption spectrum and its emission spectrum. By employing an intense IR beam, the effect of emission is minimized. A further distinction is achieved by encoding the IR beam before it impinges on the sample. With classical grating or prism spectrometers, the source radiation is chopped by means of a mechanical chopper before it passes through the sample. The IR detector is provided with a means of synchronously decoding the chopped signal, thereby eliminating the emitted spectrum. Often, the chopper is arranged such that it alternately switches between an empty reference beam and the sample. The logarithm of the ratio of the demodulated sample and reference spectra provides the absorption spectrum directly.

In Fourier transform infrared (FTIR) spectroscopy, a scanning Michelson interferometer provides the encoding function directly, and no chopper is required. The interferometer is commonly placed before the sample so that it does not encode the thermally emitted radiation of the sample.

If it is not convenient to place the sample after the scanning Michelson interferometer, the absorption spectrum of a sample placed in front of the interferometer can be deduced by subtracting the separately recorded emission spectrum from the combined transmission plus emission spectrum. Infrared emission and reflection spectroscopy form the basis for remote sensing. Solid and gaseous (cloud) objects may be identified and quantified by direct observation of their IR spectra at a distance. Gaseous clouds reflect poorly, providing only transmitted or emitted IR radiation. Their emission spectrum is contrasted directly with the spectrum of the scene or object beyond the cloud. With a background at lower temperature than the gas cloud, the gas spectrum appears in emission, while with a warmer background, the gas spectrum appears in absorption. Only a few solid materials transmit IR radiation

over a substantial thickness. Remote sensing of solid objects, therefore, relates to surface emission and (diffuse) reflection of IR radiation from the surrounding environment.

42.11 Simplified Principle of FTIR Spectroscopy

In FTIR spectroscopy, the spectrum of a beam of incident IR radiation is obtained by first generating and recording an interferogram with a scanning Michelson interferometer. Subsequently, the interferogram is inverted into the spectrum by means of a cosine Fourier transform.

42.11.1 Interferogram Generation: The Michelson Interferometer

The scanning Michelson interferometer shown in Fig. 42.1 consists of a beamsplitter, which is a substrate with a dielectric coating such that 50% of an incident beam is reflected, and the remaining 50% is transmitted, and two plane mirrors (M_1 and M_2), one or both of which are translated along the direction of the beam. After splitting, the two equal amplitude wavefronts are propagated along different optical paths. The mirrors at the end of each path return the wavefronts to the beamsplitter, which then acts as a wavefront combiner. Because of their common coherent origin, the wavefronts interfere with one another when they combine. The state of interference is varied by scanning one or both of the mirrors such that there is a variable time delay between the two separated beams. The resulting intensity variation of the combined output beam as a function of relative time delay is the interferogram.

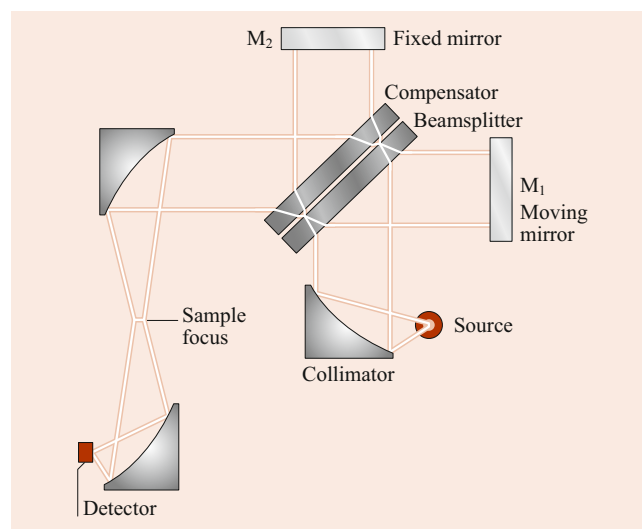


Fig. 42.1 The Michelson interferometer

42.11.2 Description of Wavefront Interference with Time Delay

The intensity $I_0(\vartheta)$ at frequency ϑ of a plane wave in space is given by the expectation value of its electric field vector $E(\vartheta, t) = E(\vartheta)e^{-i2\pi\vartheta t}$

$$I_0(\vartheta) = \langle E(\vartheta, t) | E(\vartheta, t) \rangle = E(\vartheta)^2. \quad (42.2)$$

The intensity at the output of the interferometer due to an incident intensity $I_0(\vartheta)$ is given by $I(\vartheta, \delta)$, where δ is the time delay between the two wavefronts, which have propagated along different paths. Further,

$$\begin{aligned} I(\vartheta, \delta) &= \langle E(\vartheta, t) + E(\vartheta, t + \delta) | E(\vartheta, t) + E(\vartheta, t + \delta) \rangle \\ &= \frac{1}{2} I_0(\vartheta) [1 + \cos(2\pi\vartheta\delta)]. \end{aligned} \quad (42.3)$$

As can be seen, the output intensity of a single frequency source at the output of an ideal scanning Michelson interferometer fluctuates sinusoidally between zero and the input intensity $I_0(\nu)$ as the time delay δ between the separated wavefronts is varied by means of scanning one of the mirrors.

The quantity δ is related to mirror displacement x with respect to equal distance of the mirrors from the beamsplitter by

$$\delta = 2 \frac{x}{c} \cos \theta, \quad (42.4)$$

where θ is the angle between of the wavefront and the optical axis of the spectrometer, and the optical axis is the normal to each mirror M1 and M2. From this, Eq. (42.3) becomes

$$I(\nu, x(\theta)) = \frac{1}{2} I_0(\nu) \left\{ 1 + \cos \left[2\pi\nu \left(2 \frac{x}{c} \cos \theta \right) \right] \right\} \quad (42.5)$$

or, using $\sigma = \frac{\nu}{c}$,

$$I(\sigma, x(\theta)) = \frac{1}{2} I_0(\sigma) \{ 1 + \cos[2\pi\sigma(2x \cos \theta)] \}. \quad (42.6)$$

Thus, the output intensity fluctuates at spatial frequency σ by $2x \cos \theta$ as a function of the mirror displacement x . The incident intensity generally consists of a distribution of intensities over many frequencies $S(\nu)d\nu$ with integrated intensity

$$I_0 = \int S(\nu) d\nu. \quad (42.7)$$

The intensity fluctuations for all frequencies in the incident beam is given by

$$I_0(\delta) = 1/2 \int S(\nu) [1 + \cos(2\pi\nu\delta)] d\nu. \quad (42.8)$$

The second term on the right-hand side of Eq. (42.8) has the form of the cosine Fourier transform of the spectrum. By rearrangement of Eq. (42.8), it is given by

$$\frac{1}{2} \int [S(\nu) \cos 2\pi\nu\delta] d\nu = I_0(\delta) - \frac{1}{2} I_0. \quad (42.9)$$

The constant term I_0 provides no useful information about the spectrum. The inverse cosine Fourier transform of $2I_0(\delta)$ results in the spectrum $S(\nu)$ according to

$$S(\nu) = 2 \int I_0(\delta) \cos(2\pi\nu\delta) d\delta, \quad (42.10)$$

$$S(\sigma) = 2 \int I_0(\delta) \cos(2\pi\sigma\delta) d\delta. \quad (42.11)$$

Some early FTIR spectrometers were arranged with the same dual beam for direct determination of the transmittance of a sample as was done for dispersive spectrometers. It was quickly determined that the reproducibility of two spectra recorded sequentially using a single optical path was significantly more precise than the reproducibility for two separate optical beams. The manipulation of the numerical representations of the sequentially measured sample and reference spectra became negligible using a digital computer.

Contrary to classical spectrometers, where the spectrum is sequentially scanned, there is no segregation of frequencies of the input intensity. All frequencies in the source are modulated simultaneously by the scanning Michelson interferometer into a single interferogram signal. It contributes to a large advantage in sensitivity compared with dispersive spectrometers and is referred to as the Fellgett or multiplex advantage.

The reciprocal of the sampling interval Δx of optical path difference determines the extent of the numerically computed spectrum. A higher density of sampling permits a wider spectral range to be determined

$$\sigma_{\max} = \frac{1}{2\Delta x}. \quad (42.12)$$

Beyond σ_{\max} , the spectrum repeats in reverse order, and beyond $2\sigma_{\max}$, the spectrum repeats as is. This is called spectral aliasing and results from the incomplete knowledge of the full interferogram function between the discrete numeric representation.

To ensure that the numeric representation of the interferogram describes the continuous function uniquely, it is important to band limit the interferogram information to the range 0 to σ_{\max} by means of optical and electrical filtering.

Conversely, the higher the density of sampling in the spectral domain, the longer the interferogram needs to be. For a wavenumber interval $\Delta\sigma$, the interferogram length is

$$x_{\max} = \frac{1}{2\Delta\sigma}. \quad (42.13)$$

42.11.3 Operation of Spectrum Determination

The interferogram signal is detected by an IR detector that converts the intensity variations $I_0(x)$ as a function of different mirror positions x into an electrical signal. Continuous

determination of the inverse cosine Fourier transform of the evolving interferogram requires continuous multiplication of the signal by cosine functions with all the different frequencies of the spectrum and integrating these products. It is, however, far more practical to capture the interferogram signal in numerical form, using an analog to digital converter, store the digitized data in computer memory, and compute the Fourier transform numerically after the mirror displacement range has been covered.

A particularly convenient and accurate way to establish the sampling locations of the interferogram is the use of a single-frequency laser directed coaxially with the source radiation through the scanning Michelson interferometer. The intensity of the laser at the output of the interferometer is a pure cosine wave with one cycle per change in mirror movement of one half wavelength of the laser light, typically about 400 nm. It has long been the practice to digitize the interferogram signal at the precise mirror positions provided by the laser signal. However, as in digital audio recording, the currently highest fidelity of numerical representation of an analog signal is obtained with $\Delta\Sigma$ analog to digital (ADC) technology, which can represent a precisely linear signal dynamic range up to 2^{24} to 1. However, these ADCs can only operate at a constant measurement rate.

When applying a constant rate of digitizing to an interferogram signal the optical path different intervals measured depend on the velocity of scanning of the mirror of the interferometer. Since this is a mechanical displacement it is subject to velocity variations due to perturbations resulting from shocks and vibrations. The parallel monochromatic laser light passing through the interferometer (metrology signal) being a pure sinusoidal function of the optical path difference can provide path difference information at the same time that the infrared signal is digitized. By employing high-density “uniform time” sampling of an interferogram, intensities at a “uniform mirror displacement” can be accurately computed by interpolation based on the measured timing of the metrology signal information [19]. This approach has become a key feature in obtaining highly accurate and reproducible spectra, even in the presence of scan velocity perturbations. Errors in the spacing of measured interferogram data points along the path difference axis have the same effect as errors in the spacing of grooves of a diffraction grating; it leads to ghost features in the spectra. Residual sampling errors in modern FTIRs may be as low as subnanometers even in the presence of significant scan velocity variations.

By the above-described approach, the numerical representation of the interferogram is determined at uniform intervals of mirror displacement Δx . The computed spectrum is then determined at uniform intervals of spatial frequency $\Delta\sigma$ by the discrete cosine Fourier transform

$$S(j\Delta\sigma) = \sum_n 2I_0(n\Delta x) \cos(2\pi jn\Delta\sigma\Delta x). \quad (42.14)$$

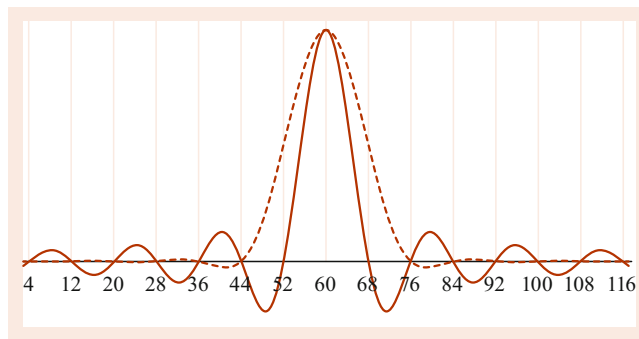


Fig. 42.2 The *solid curve* is the ILS (interpolated), and the *dashed curve* is ILS (interpolated) for an apodized interferogram. The *vertical grid lines* are locations where the output of the Fourier transform computation occur

From the orthogonality property of the discrete cosine Fourier transform, unique linearly independent information can occur only at spectral intervals equal to or greater than the sampling interval $\Delta\sigma$. Hence, the sampling interval in the spectrum is related to the achievable resolution. The full width at half maximum of the representation of a single frequency in the spectrum is $1.2\Delta\sigma$. This factor applies for the case where a single cosine wave interferogram has been abruptly truncated at the end of the mirror scan. The lineshape function for this case is quite oscillatory due to the abrupt termination of the interferogram signal at the end of the scan, known as the *Gibbs* phenomenon [20]. This is not always satisfactory, and frequently the interferogram is modified by a “windowing” or “apodization” function to make the lineshape more localized and monotonic. Apodization always results in an increase in the full width at half maximum. Figure 42.2 illustrates this.

42.11.4 Optical Aspects of FTIR Technology

The description of wavefront interference developed in Sect. 42.11.2 applies to interference of plane wave fronts only. A plane wave of IR radiation is obtained at the output of a collimator optics having an IR point source at its focus. In practice, a point source has insignificant intensity. A finite size source, which may be represented by a distribution of point sources in the focal plane of a collimator, provides a distribution of plane wavefronts with different angles of propagation through the scanning Michelson interferometer.

As shown in Eq. (42.4), this distribution of angles results in a distribution of modulation frequencies as a function of mirror displacement x of the output intensity for a given IR wavenumber. This is illustrated in Fig. 42.3, which shows, for a single-frequency IR source, the distribution of output intensity modulation frequencies for an ideal point source a on the optical axis, a circularly symmetric distribution of uniform intensity centered on the optical axis b, and, finally,

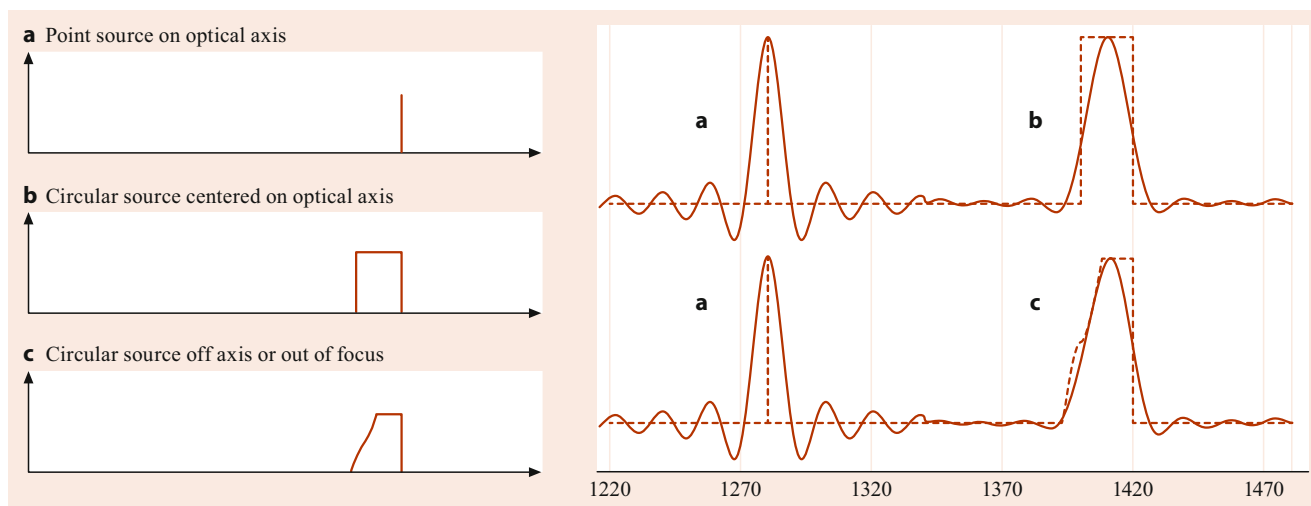


Fig. 42.3 *left*: distribution of interferogram modulation frequencies for a single optical frequency; *right*: the observed instrumental line shape functions (ILS) obtained from Fourier transformation of a finite data set representing the frequency distributions shown on the *left*

a circularly symmetric distribution positioned slightly off the axis of the collimator c [21].

As a result of illuminating the scanning Michelson interferometer with a finite size source, a single IR frequency is observed having a distribution of modulation frequencies in its interferogram signal. This distribution limits the ability to resolve two closely spaced IR frequencies and determines the *optical* resolution limit of the FTIR; the larger the extent of the source, the more restricted the resolution becomes. The ratio $\sigma/\Delta\sigma$ is the resolving power R of the scanning Michelson interferometer and, based on Eq. (42.4), is given by

$$R = \frac{1}{(1 - \cos \theta_m)}, \quad (42.15)$$

where θ_m is the maximum off-axis angle of illumination. For small θ_m , $\cos \theta_m \approx 1 - \frac{1}{2}\theta^2$, so that

$$R \approx \frac{2}{\theta^2}. \quad (42.16)$$

From Eq. (42.13), a resolution limit is also imposed by the maximum length of the interferogram recorded. The interferogram length-dependent resolution is constant for all spectral regions, while the optical resolution is proportional to the spectral frequency. Both resolution limits combine to give the overall resolution of an FTIR. At low resolution, the available throughput is so high that the optical resolution is often negligible compared with the length resolution. At high resolution, the throughput is at a premium, and the optical resolution is often closely matched to the length resolution at the frequency of interest.

To ensure a symmetrical frequency distribution, the area integrated illumination must increase as $\sin \theta$, which is approximately linear for small angles, up to its maximum θ_m ,

as shown with the centered circular illumination in Fig. 42.3. Any deviation from this, such as off-axis positioning of the circle, noncircular shapes, or a poorly focused centered symmetrical circle, will result in a gradual roll-off of the distribution on the low-frequency side only [21]. This results in an asymmetric spectral lineshape.

For a collimator of given focal length and for a given resolving power, it is easily shown that the area of the source, or the stop that delineates it, is much larger than the slit area for classical grating spectrometers. This is particularly the case at high resolving powers. The stop that delineates the source extent for a scanning Michelson interferometer is often referred to as the Jacquinot stop or the field of view stop.

42.12 The Scanning Michelson Interferometer

Optical throughput is not only determined by the area of the field of view stop but also the solid angle subtended by the rays traversing this area. The solid angle Ω of rays traversing a Jacquinot stop positioned in the focal plane of an input collimator is given by the ratio of the interferometer beam area divided by the square of the focal length of the collimator.

For a given collimator focal length, the area of the Jacquinot stop is inversely proportional to the resolving power. To maintain equal throughput, the area of the interferometer optics should be increased as the resolving power is increased to offset the decrease in the Jacquinot stop area.

It is common to construct interferometers with 2.5 cm diameter optics for resolving powers up to 5,000, 5.0 cm diameter optics for resolving powers up to 40,000, and 7.5 cm diameter optics for resolving powers up to 1,000,000.

In order to obtain a uniform state of interference across the entire beam of the interferometer, the beamsplitter substrate

and the two mirrors must be flat to within a small fraction of the wavelength used. Also, these elements must be oriented correctly so that the optical path difference error across the beam is less than a small fraction of the wavelength.

Figure 42.1 shows two substrates at the beamsplitter position. One of the substrates supports the beamsplitting coating, while the companion substrate of precisely the same thickness acts as a compensating element to insure identical optical paths through the two arms of the interferometer. To avoid secondary interference effects, both beamsplitter and compensator substrates are normally wedged. The direction of the wedges of the two substrates must be aligned again to insure symmetry in both arms of the interferometer.

The maintenance of a close angular alignment tolerance of the two mirrors with respect to the beamsplitter in a stable manner over time and while scanning one of the mirrors has been a significant challenge of interferometer design and has also been the greatest weakness of FTIR.

In early FTIR models, alignment was maintained by means of a stable mechanical structure and often using a highly precise linear air bearing for the scanning mirror. Satisfactory operation required a stable environment and frequent alignment tuning and could be achieved for mirror displacements of only several centimeters, thus limiting the maximum resolution.

Different techniques have been developed to overcome this weakness of FTIR. The two most prominent are: (1) dynamic alignment of the interferometer, where optical alignment is servo-controlled using the reference laser not only for mirror displacement control but also for mirror orientation control, and (2) the use of cube corner mirrors in place of the flat mirrors in the interferometer. Dynamic alignment has the advantage of retaining simplicity in the optical design of the interferometer. On the other hand, it is more complex electronically. Cube corner mirrors have the property of always reflecting light 180° to incident light independent of orientation. Cube corners always ensure wavefront parallelism at the point of recombination of the two beams in the interferometer. Cube corners lack a defined optical axis. In a cube corner interferometer, the optical axis is defined by the direction in which the wavefronts undergo zero shear.

The scanning Michelson interferometer is normally provided with a drive mechanism to displace one of the mirrors precisely parallel to its initial position and at uniform velocity. The uniform velocity translates the mirror displacement-dependent intensities into time-dependent intensities. This facilitates signal processing electronics. In some measurement scenarios, however, where the sample spectrum may vary with time, it is undesirable to deal with the multifrequency time-varying intensities of the interferogram signal. In this case, it is preferable to scan the moving mirror in a stepwise mode, where the mirror is momentarily stationary

at the time of signal measurement and then advanced rapidly to the next position. The mirror scan velocity v can also be varied, so that electrical signals can have different frequencies for the same optical frequencies

$$f = \frac{\sigma}{2v} . \quad (42.17)$$

The scan velocity is normally selected to provide the most favorable frequency regime for the detector and electronics used and for the mechanical capabilities of the mirror drive. Typically, the velocity range is from 0.05 to 4 cm s^{-1} , putting the frequencies in the audio range. At these velocities, the measurement scan may be completed in a shorter time than is desired for signal averaging purposes. In this case, it is common to repeat the scan a number of times and add the results together; this is called coadding of scans.

As stated earlier, in FTIR there is no segregation of frequencies of the input intensity. All frequencies of the spectrum are transmitted through the interferometer simultaneously. In the commonly encountered case where the field of view is small, so that the interferogram length determines the resolution and lineshape, the lineshape closely matches the same analytical function for all spectral components. Along with the absence of dispersion in the interferometer providing a highly linear frequency scale that is calibrated at a single frequency FTIR provides a high degree of reproducibility.

This is frequently used to reconstruct observed spectra based on predetermined spectral parameters for molecules present in the sample. By least squares fitting several attributes of the sample can be determined.

42.13 Infrared Spectroscopy Application Activity 2020

Infrared spectroscopy using FTIR has become a mature activity with many thousands of simple benchtop units produced. Due to innovative design and efficient manufacturing these FT spectrometers cost much less than the early pioneering versions. Below is a description of some of the areas of use of infrared spectroscopy using FTIR. The laboratory applications are routine, while applications outside the laboratory are more specialized, particularly some of the remote-sensing applications.

42.13.1 Analytical Chemistry Laboratories

The traditional analytical chemistry laboratory is routinely equipped with an FTIR that covers the spectral range from about 400 to about 5000 cm^{-1} . It is used mostly for the

analysis of liquid samples in transmittance and solids (in powder form) by diffuse reflectance. Condensed phase samples (liquids and solids) show spectral features that are mostly $> 4 \text{ cm}^{-1}$ wide and are rarely narrower than 2 cm^{-1} . Hence, the full width at half maximum intensity (FWHM), spectral resolution selected is mostly 4 cm^{-1} . To avoid the need for spectral filtering, the numerically computed spectra typically cover the range from 0 to about 8000 cm^{-1} or higher.

The absorptivity of most condensed phase samples is high, particularly in the 400 to 2000 cm^{-1} fingerprint region. A short pathlength is, therefore, selected to avoid regions of zero transmittance. An efficient sampling method is to place a drop of liquid sample or a small amount of powder on the surface of an IR transparent crystal with a high index of refraction through which IR radiation is propagated via total internal reflection. The presence of the sample permits penetration of an evanescent wave several μm into the sample and, thereby, produces a transmittance spectrum corresponding to a path length of typically up to about $10 \mu\text{m}$; this is called attenuated total internal reflection (ATR) spectroscopy.

The measured spectra are typically used for the semiquantitative determination of molecular concentration. However, since the frequency axis in FTIR is calibrated via the scan control metrology laser, the precision (repeatability) is exceptionally high. In the numerical format, the method of spectral subtraction can bring to light subtle differences between comparable samples typically due to small amounts of contaminants mixed in the samples. Moreover, the scaled spectral subtraction is a powerful method of concentration determination.

42.13.2 Biomedical and Pharmaceutical Laboratories

Medical formulations may consist of mixtures of complex molecular compounds. Infrared spectroscopy is one of the many analysis techniques employed for the determination of accuracy of formulation. It is found that the efficacy of a formulation may not only depend on a particular molecular formulation but also on the “chirality” of the formulation. In stereo chemistry, chirality provides the distinction between two enantiomers of otherwise identical molecules. Enantiomers are the right-hand and left-hand versions of otherwise identical molecules; a “spiral spring” may be coiled in two different ways, right-hand and left-hand, without affecting its spring property. Determination of the chirality of a sample by infrared spectroscopy consists of measuring the difference in absorption of right and left circular polarized radiation. Since this difference in absorption is typically five orders of magnitude weaker than the normal absorption

spectrum it is challenging to measure chirality. A Fourier transform spectrometer provided with a means of rapidly switching between right and left circular polarization, such as using a photoelastic modulator, permits demodulation of the difference absorption of the two circular polarizations [22].

42.13.3 Forensic Investigation

Due to the capability of mid-IR spectroscopy to relate a large number of different substances to their unique infrared spectra, IR spectroscopy is an indispensable tool in forensic laboratories. The emphasis here is to analyze samples in many forms and frequently in exceedingly small amounts. The analysis of liquids by transmission is a small subset of the variety of samples that may occur. Many of the samples to be investigated may not be transparent or just have a surface contaminant that is of interest. Both specular and diffuse reflection are, therefore, often employed. In forensic investigation, sometimes extremely small amounts of sample may be of particular interest. Many microsampling accessories are available, amongst which the IR microscope is the most powerful. The IR microscope permits focusing the modulated IR beam onto spots as small as $10 \mu\text{m}$ and analysis of 50 to $100 \mu\text{m}$ areas is routine. To be sure the focusing down to an area of less than $100 \mu\text{m}$ utilizes only a small fraction of the available intensity of the FTIR. IR microscopes are normally provided with dedicated liquid nitrogen cooled Hg-Cd-Te semiconductor detectors. Increasingly available mid-IR, Hg-Cd-Te imaging detector arrays with high image frame rates are being used in conjunction with IR microscopes. These provide the capability of examining microscopic samples with inhomogeneous composition distribution.

A common property of infrared detectors is that their noise level is proportional to the square root of their area. Hence, a single pixel detector of a detector array with small area will have significantly lower noise than a larger single detector module. This permits recording a 2-D array of spectra of a microsample with low noise, where individual pixels may cover an area as small as a few μm .

A complementary method used in forensic investigation and other applications is Raman spectroscopy. Spectra like mid-IR spectra of a sample are obtained via inelastic scattering of laser illumination from their surface. Raman spectroscopy is more tolerant to sample shape irregularity and texture and does not require contact. For some samples, fluorescence induced by the laser illumination can interfere with the Raman spectrum.

Identifying the chemical makeup of samples from their measured mid-IR or Raman spectra is achieved using search algorithms applied to digital IR libraries of IR and Raman spectra. As many as 225,000 infrared spectra are available

for searching. Because of small variations in sample accessories, instrument calibrations, and contaminants in the sample, the spectral identification is presented as a probable identification with a confidence index. Several probable identification candidates are returned with a decreasing confidence index.

42.13.4 Infrared Spectroscopy in Quality Assurance Laboratories

A quality assurance laboratory evaluates conformity to the required specification of manufactured products or the concentration of essential components in products such as wheat, milk, medicinal formulations, and industrial chemical formulations. The demands of the QA laboratory are quite different from those of the analytical chemistry laboratory. The measurement accuracy (the agreement with a production standard) needs to be in line with the specifications of uniformity of the product.

Increasingly, the manufacture of FTIR spectrometers includes a specification of reproducibility in addition to repeatability and low noise of the measured spectra. This means that the FTIR spectrometer, including the sampling arrangement, must conform to a limit of sameness of frequency scale calibration, sameness of instrumental lineshape function, FWHM, and sameness of the transmittance of a standard sample.

Mid-IR sampling requires a short optical path through samples to avoid excessive absorption. Typically, the path length is below 50 μm and may be as low as a few μm . For quantitative concentration determinations, the path length is a required parameter. Therefore, the near-IR is preferred because, here, the harmonics and combinations of the mid-IR bands absorb much less strongly than the fundamental bands in the mid-IR and can be measured with longer path-length liquid cells that can have quite accurate path-length values. The determination of concentrations is done by means of chemometric models, such as partial least squares, which uses a set of standard samples to build a model. In order to insure accurate reproducibility of spectra, FTIR spectrometers are tested with a “golden standard” sample for which the spectrum can be rendered reproducible. Often, a sample, such as toluene with 99.99% purity at constant temperature, is used. This has led to the ability of deploying spectrometers at different measurement sites while maintaining identical measurement results. In these applications, FTIR, due to its laser-controlled scanning, provides significantly more accurate measurements than a dispersive grating spectrometer. The above is an example of applying FTIR at short wavelengths in the near-IR. Due to the brightness of near-IR light sources, the constraint of photon statistics noise in FTIR is not present.

42.13.5 Process Monitoring by Infrared Spectroscopy

Continuous process monitoring of parameters such as temperature and pressure are common. In some processes, it is valuable to continuously monitor the product composition as well. Like methods used in quality assurance laboratories, process monitoring most frequently uses quantitative near-IR spectroscopy. An illustrative example is the blending of gasoline in refineries.

There are several challenges in the blending of gasoline related to performance, as indicated by octane number, as well as insuring low viscosity in cold weather conditions and low evaporation in hot weather, and, finally, to conform to environmental restrictions. All these factors complicate the formulation, allowing only a limited number of different solvents to be used for blending. Figure 42.4 shows a near-infrared spectrum of gasoline identifying the bands attributed to different types of hydrocarbons.

In the range of permitted gasoline blends, the near-IR spectra such as shown in Fig. 42.4 vary by only a few percent in absorbance. To continuously monitor the blending process and report the required parameters requires highly accurate and stable spectroscopy; the overlay of spectra of the same sample measured with 14 different analyzers is shown in Fig. 42.4. The reporting of (nonspectroscopic) quality parameters is derived from chemometric models with many combinations of different known standard samples. Application of FT-NIR to this requirement has been shown to be exceptionally stable over time, as well as highly reproducible for different analyzers. The latter is significant because it avoids the costly and extensive recalibration of analyzers.

Table 42.1 shows a typical performance summary achieved with a process FT-NIR that continuously monitors the blending process. It is used to control and adjust the blending process in real time.

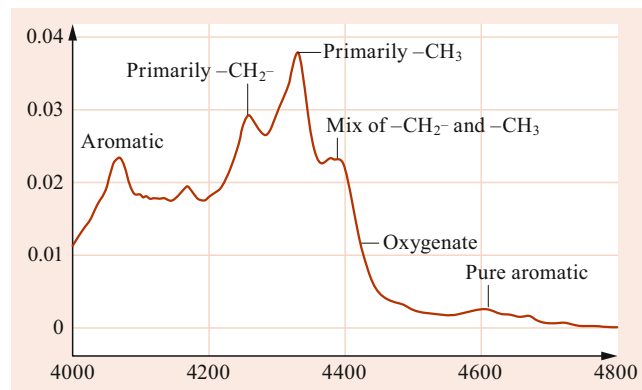


Fig. 42.4 Near-IR absorbance spectra of gasoline identifying bands of different hydrocarbons

Table 42.1 Summary of reproducibility, accuracy, and precision of measured components

Gasoline property data				FTNIR transportability	
Measurement	Units	NIR		ASTM	On-line to on-line North American refinery blender
		Typical	Range		
		Std. dev.		Std. dev.	Absolute difference
RON	Octane number	0.30	0.2–0.4	0.21	0.05
MON	Octane number	0.30	0.2–0.4	0.32	0.05
Total aromatics	%	1.50		1.20	0.11
Total olefins	%	1.00		1.80	0.05
RVP	psi	0.15	0.1–0.2	0.15	0.09
E200	%	1.50		1.19	0.03
E300	%	1.00		0.54	0.10
IBP	°F	3.70		4.60	0.41
10%	°F	6.00		3.25	0.21
30%	°F	2.90		2.80	0.95
50%	°F	4.80		2.80	0.06
70%	°F	4.20		2.80	0.51
90%	°F	4.90		1.60	0.75
FBP	°F	6.70		5.70	1.05

42.13.6 Environmental Monitoring

Infrared spectroscopy is used extensively for the continuous monitoring of emission gases from a variety of industrial and utility smokestacks. The purpose is to comply with environmental regulations. Combustion processes produce large concentrations of carbon dioxide, as well as moisture. It is common to precipitate moisture from a gas sample prior to IR measurement. This permits the employment of simple, low-cost nondispersive IR analyzers (discrete narrowband filter-based analyzers). Particularly challenging is the monitoring of smokestacks that may emit water soluble gases such as HCl and HF. With a sample without precipitation of moisture, the infrared spectrum shows much interference by strong moisture bands covering large spectral regions. FTIR spectroscopy has been particularly effective in such applications because interference is minimized by choosing a spectral resolution that permits separating spectral features of the different components.

42.13.7 Remote Sensing

In remote sensing, spectral information about remote objects is obtained by their thermal emission. At ambient temperature, the radiation emitted is the strongest in the 500 to 1800 cm^{-1} region and is, therefore, widely used.

Satellite-based remote sensing of Earth's atmosphere is of particular interest to support weather prediction and to determine levels of pollution. Satellite-based thermal infrared measurements routinely provide input data for weather prediction and climate change models. Thermal emission from a gas depends on the opacity (absorbance) of the gas. Oxygen and nitrogen, which make up most of Earth's atmosphere,

have virtually no opacity. Thermally emitted radiance by Earth's atmosphere is dependent on small amounts of gases such as carbon dioxide, ozone, water vapor, and other minor constituents present in the atmosphere that have infrared absorption bands.

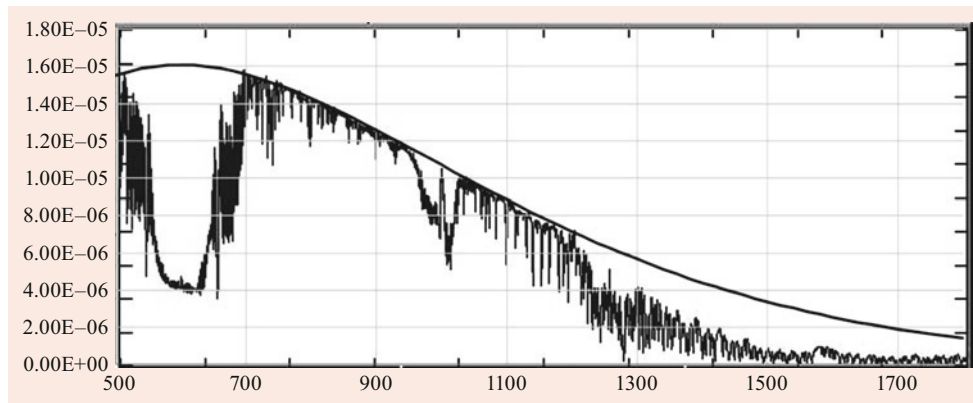
The major thermodynamic drivers that affect Earth's weather the most are temperature and water vapor variations. Meteorologists working with large computer simulations of local and extended weather patterns count on hourly updates of accurately measured three-dimensional maps (geographic and altitude resolved) atmospheric temperature, and water vapor distribution. In addition, the knowledge of detailed maps of surface emissivity and temperature, as well as albedo for solar reflection, are important drivers of weather.

In Fig. 42.5 the reduced radiance near 650 cm^{-1} is due to thermal emission to space by carbon dioxide in the upper atmosphere where it is much colder than 305 K. Likewise some reduced radiance near 1000 cm^{-1} is due to colder ozone and beyond 1300 cm^{-1} due to cold water vapor.

It can be seen that if Earth had no atmosphere, it would radiate more radiance to space (smooth curve), keeping Earth at a lower temperature than in the presence of our atmosphere; this is a clear demonstration of the greenhouse effect.

Temperature as a function of altitude can be derived from these spectra by realizing that the concentration of carbon dioxide is known and is uniformly mixed through the atmosphere. Having different band intensities provides the information to retrieve temperature as a function of altitude. The recent introduction of sophisticated new satellite-based Fourier transform spectrometer sounders has greatly improved the accuracy and detail in the vertical profiles of both temperature and moisture [23]. These new sounders have demanding requirements of spectral reproducibility, sensitivity, and speed of measurement. In order to map the entire globe

Fig. 42.5 A typical, clear sky, radiance in $\text{W}/\text{cm}^2\text{-sr}\text{-cm}^{-1}$ in the thermal infrared observed from space. The *smooth line* is a Planck curve for a high-emissivity surface at 305 K



more than once per day they typically produce over 400,000 spectra/day.

Exploration of the Solar System by interplanetary probes was started by sending probes to the moon in order to determine the suitability of landing there. Mars has been extensively surveyed both on the surface and in its atmosphere. Besides visual images, infrared spectroscopy has been used to determine surface and atmospheric composition. One of the more recent probes is the Cassini–Huygens probe [24] to investigate Saturn and some of its moons. Saturn being almost 10 times further from the Sun as our Earth it receives much less heat from the Sun. Infrared spectroscopy of this probe is primarily centered on far-infrared thermal emission.

A spectacular feat of infrared spectroscopy has been the measurement of the remnant of cosmic background radiation. Expected to be a Planck-type blackbody radiation at only an estimated 2.7 K, its spectrum occurs in the range 0 to about 20 cm^{-1} and has a peak near 5 cm^{-1} . Both the NASA COBE satellite mission [25] and the COBRA suborbital rocket experiment [26] used Fourier transform spectrometers. Since almost any part of the spectrometer might have a comparable temperature to the source of interest, the COBRA FTIR consisted of a precisely balanced dual-input and dual-output interferometer. The experiment measured the difference spectrum between the space view at one input against a calibrated blackbody at the second input. Adjusting the temperature of the blackbody to achieve a null interferogram provided a precise value for the temperature. Spectral analysis of the residual null interferogram confirmed that the structure of the spectrum closely matched the Planck blackbody curve at 2.736 K.

42.14 Conclusion

Infrared spectroscopy is widely used to identify the chemical nature of a range of different substances in a variety of measurement settings. A compact low-cost FTIR spectrome-

ter is a required tool for the chemistry laboratory. Expanding on this, today, the power of identifying the chemical nature of substances is incorporated into compact handheld FTIR and Raman spectrometers that permit noncontact “point and measure” for the determination of the molecular nature of chemicals. The sampling approach may be diffuse reflection and laser Raman scattering or on a small area point contact by means of attenuated total internal reflection (ATR).

Due to continual improvement in operation stability, FTIR has become well known for its precise repeatability, including outstanding stability over time. The repeatability of FTIR is attributable to the highly precise measurement of the interferometer scan distance using a wavelength stabilized single-mode laser. The instrumental lineshape function (ILS) is determined by the precision of the scan distance measurement and not by any geometric factors in the instrument. This fundamental difference in the aspect of measurement precision has led to the development not only of high accuracy spectral measurements but additionally to excellent reproducibility amongst FTIRs. These developments have led to a reputation of FTIR as an accurate quantitative analysis tool. Increasingly, FTIR is being deployed for quality assurance in chemical manufacturing. An example is the determination of the hydroxyl value in a variety of surfactants. Here, easy-to-operate FTIR has replaced a laborious skill-demanding and costly titration method.

These features have been quite useful in molecular spectroscopy research as well. This permits accurate reproducibility of the frequency scale from instrument to instrument. The instrumental lineshape function when defined by the field of view stop (sometimes called the Jacquinot stop) can be expressed by an analytical function and is invariant over a defined frequency range. This is a key factor in achieving precisely reproducible spectral response with different instruments. Finally, a reason for the diversity of applications enabled with FTIR is its ease of adaptability to various needs for spectral resolution as well as scan velocities and spectral ranges.

References

- Herschel, W.: Experiments on the refrangibility of the invisible rays of the Sun. *Phil. Trans. R. Soc. Lond.* **90**, 284–292 (1800)
- Holden, E.S.: *Sir William Herschel His Life and Works* (2009).
- Coblentz, W.W.: *Investigations of Infra-Red Spectra*. Carnegie Institution of Washington, Washington, DC (1905)
- Lin-Vien, D., Colthup, N.B., Fateley, W.G., Grasselli, J.G.: *The Handbook of Infrared and Raman Characteristic Frequencies of Organic Molecules*. Academic Press, San Diego (1991).
- PerkinElmer: *60 Years of Innovation in Infrared Spectroscopy*. PerkinElmer, Shelton (2005).
- Hirschfeld, T., Callis, J.B., Kowalski, B.R.: Chemical sensing in process analysis. *Science* **226**(4672), 312–318 (1984)
- Martens, H., Naes, T.: *Multivariate Calibration*. Wiley, New York (1989).
- Williams, P.C.: *Cereal Chem.* **52**, 561–576 (1975)
- Herzberg, G.: *Molecular Spectra and Molecular Structure: I. Spectra of Diatomic Molecules*. Krieger, Malabar (1989)
- Connes, J., Connes, P., Delouis, H., Guelachvili, G., Maillard, J.P., Michel, G.: *Nouv. Rev. Opt. Appl.* **1**(1), 3 (1970)
- Michelson, A.A.: *Philos. Mag.* **34**, 280 (1892)
- Rayleigh, J.W.S.: *Philos. Mag.* **34**, 407 (1892)
- Fellgett, P.B.: *J. Phys. Radium* **19**(187), 237 (1958)
- Fellgett, P.: Multichannel Spectroscopy (extended abstract). Ohio State University International Symposium on Molecular Spectroscopy, II (1952)
- Buijs, H., Gush, H.: High resolution Fourier transform spectroscopy. *J. Phys. Coll.* **28**(C2), 105–108 (1967). (archive, *Journal de Physique*)
- Cooly, J.W., Tukey, J.W.: *Math. Comp.* **19**, 296 (1965)
- Forman, M.L., Steel, W.H., Vanasse, G.A.: *J. Opt. Soc. Am.* **56**, 59 (1966)
- Jacquinet, P.: *J. Opt. Soc. Am.* **44**, 761 (1954)
- Brault, J.W.: New approach to high-precision Fourier transform spectrometer design. *Appl. Opt.* **35**(16), 2891–2896 (1996). <https://doi.org/10.1364/AO.35.002891>
- Gibbs, J.W.: Fourier's series. *Nature* **59**(1522), 200 (1898)
- Saarinen, P., Kauppinnen, J.: *Appl. Opt.* **31**, 2353 (1992)
- Nafie, L.: *Vibrational Optical Activity: Principles and Applications*. Wiley, Chichester (2011)
- Strow, L., Motteler, H., Tobin, D., Revercomb, H., Hannon, S., Buijs, H., Predina, J., Suwinski, L., Glumb, R.: Spectral calibration and validation of the cross-track infrared sounder on the Suomi NPP satellite. *J. Geophys. Res. Atmos.* **118**, 12486–12496 (2013).
- Jennings, D.E., et al.: Composite infrared spectrometer (CIRS) on Cassini. *Appl. Opt.* **56**(18), 5274–5294 (2017).
- Boggess, N.W., et al.: The COBE mission: Its design and performance two years after launch. *Astrophys. J.* **397**, 420–429 (1992).
- Gush, H.P., Wishnow, E.H., Halpern, H.: *Phys. Rev. Lett.* **65**(5), 537–540 (1990)



Henry Buijs Henry Buijs founded Bomem Inc. in 1973 to commercialize Fourier transform spectrometers for a wide range of applications. In 1962 he helped Dr Herbert Gush build and operate a Fourier transform spectrometer for the study of airglow from a balloon platform. He received his PhD from the University of British Columbia in 1970. Bomem Inc became a leader in high performance FT spectrometers for a very wide range of applications.



Laser Spectroscopy in the Submillimeter and Far-Infrared Regions

43

Kenneth Evenson and John M. Brown

Contents

43.1	Introduction	641
43.2	Experimental Techniques Using Coherent SM-FIR Radiation	642
43.2.1	Tunable FIR Spectroscopy with CO ₂ Laser Difference Generation in a MIM Diode	642
43.2.2	Laser Magnetic Resonance	644
43.2.3	TuFIR and LMR Detectors	645
43.3	Submillimeter and FIR Astronomy	645
43.4	Upper Atmospheric Studies	646
	References	646

Abstract

Recent technical developments in sub-millimeter and far-infrared laser spectroscopy are described. This includes new laser sources, both side-band and difference-frequency generation. An experiment which uses fixed-frequency far-infrared lasers to study open-shell molecules (free radicals) is described; the technique is known as laser magnetic resonance (LMR). Sub-millimeter and far-infrared laser spectroscopies are finding expensive use in the detection and monitoring of molecules in astrophysical sources and in the earth's atmosphere.

Keywords

waveguide laser · absorb water vapor · polyatomic species · fine structure · transition laser · magnetic resonance

43.1 Introduction

Research in the submillimeter and far-infrared (SM-FIR) regions of the electromagnetic spectrum (1000 to 150 μm , 0.3 to 2.0 THz; and 150 to 20 μm , 2.0 to 15 THz, respectively) had been relatively inactive until about 30 years ago. Three

events were responsible for enhanced activity in this part of the electromagnetic spectrum: the discovery of far-infrared (FIR) lasers [1], the development of background-limited detectors [2], and the invention of the FIR Fourier transform (FT) spectrometer [3]. Following these developments major discoveries have taken place in laboratory spectroscopic studies [4, 5], in astronomical observations [6], and in spectroscopic studies of our upper atmosphere [7].

Rotational transition frequencies of light molecules (such as hydrides) lie in this region, and the associated electric dipole transitions are especially strong at these frequencies. In fact they are 10,000 times stronger than at microwave frequencies because they are 100 times typical microwave frequencies and their peak absorptivities depend approximately on the square of the frequency. Fine structure transitions of atoms and molecules also lie in this region; however, they are much weaker, magnetic dipole transitions. The observation of fine structure spectra is very important in determining atomic concentrations in astronomical and atmospheric sources and for determining the local physical conditions. Bending frequencies of larger molecules also lie in this region, but their transitions are not as strong as rotational transitions (typically a factor of 10^3 weaker).

Spectral accuracy has been increased by several orders of magnitude with the extension of direct frequency measurement metrology into the SM-FIR region [8]. Transitions whose frequencies have been measured (including absorptions and laser emissions) are useful wavelength calibration sources ($\lambda_{\text{vac}} = c/\nu$) for FT spectrometers. FIR spectra of a series of rotational transitions have been measured in CO [9], HCl [10], HF [11], and CH₃OH [12] to be used for FT calibration standards. These lines are ten to a hundred times more accurately measured than can be realized in present state-of-the-art Fourier transform spectrometers; thus, they are excellent calibration standards. High-accuracy and high-resolution spectroscopy has permitted the spectroscopic assignment of the SM-FIR lasing transitions themselves [13] resulting in a much better understanding of the lasing process.

Astronomical spectroscopy in this region [6] may be in emission or absorption and is performed using either interferometric [14] (wavelength-based), or heterodyne (frequency-based) [15] techniques to resolve the individual spectral features.

Most high resolution spectra of our upper atmosphere have been taken with FT spectrometers flown above the heavily absorbing water vapor region in the lower atmosphere. Emission lines are generally observed in these spectrometers [7].

43.2 Experimental Techniques Using Coherent SM-FIR Radiation

The earliest sources of coherent SM radiation came from harmonics of klystron radiation generated in point-contact semiconductor diodes [16]. Spectroscopically useful powers up to about one terahertz are produced. This technique is being replaced by electronic oscillators which oscillate to over one terahertz [17]. The group at Cologne University, Germany [18] has been particularly successful with this approach. Spectroscopy above this frequency generally is performed with either lasers or FT spectrometers (see Chap. 42).

Laser techniques use either tunable radiation synthesized from the radiation of other lasers, or fixed-frequency SM-FIR laser radiation and tuning of the transition frequency of the species by an electric or magnetic field. Spectroscopy with tunable far-infrared radiation is called TuFIR spectroscopy. Spectroscopy with fixed frequency lasers is called either laser electric resonance (LER) or laser magnetic resonance (LMR). LMR is applicable only to paramagnetic species and is noteworthy for its extreme sensitivity. LMR spectroscopy has been more widely applied than LER, and is discussed in this chapter.

Tunable SM-FIR radiation has been generated either by adding microwave sidebands to radiation from a SM-FIR laser [19] or by using a pair of higher frequency lasers and generating the frequency difference [20]. The sideband technique was first reported by *Dymanus* [19] and uses a Schottky diode as the mixing element. It has been used up to 4.25 THz and produces a few microwatts of radiation [21]. Groups at Berkley, California [22] and Cologne, Germany [23] have developed this technique to good effect. The CO₂ laser frequency-difference technique with difference generation in the metal-insulator-metal (MIM) diode covers the FIR region out to over 6 THz and produces about 0.1 μW. This technique uses fluorescence-stabilized CO₂ lasers whose frequencies have been directly measured, and it is about two orders of magnitude more accurate than the sideband technique. However, it is somewhat less sensitive because of the decreased power available. There are several review articles on the laser

sideband technique [21, 24], and only the laser difference technique is described here.

43.2.1 Tunable FIR Spectroscopy with CO₂ Laser Difference Generation in a MIM Diode

There are two different ways of generating FIR radiation using a pair of CO₂ lasers and the MIM diode. One is by second-order generation, in which tunability is achieved by using a tunable waveguide CO₂ laser as one of the CO₂ lasers; it is operated at about 8 kPa (60 Torr) and is tunable by about ±120 MHz. The second technique uses third-order generation, in which tunable microwave sidebands are added to the difference frequency of the two CO₂ lasers. The complete spectrometer which can be operated in either second or third order is shown in Fig. 43.1.

The FIR frequencies generated are

$$\text{second-order: } \nu_{\text{fir}} = |\nu_{1,\text{CO}_2} - \nu_{\text{W,CO}_2}| \quad (43.1a)$$

$$\text{third-order: } \nu_{\text{fir}} = |\nu_{1,\text{CO}_2} - \nu_{\text{W,CO}_2}| \pm \nu_{\text{mw}} \quad (43.1b)$$

where ν_{fir} is the tunable FIR radiation, ν_{1,CO_2} and $\nu_{\text{W,CO}_2}$ are the CO₂ laser frequencies, and ν_{mw} is the microwave frequency.

Different MIM diodes are used for the two different orders: in second-order, a tungsten whisker contacts a nickel base and the normal oxide layer on nickel serves as the insulating barrier; in third-order, a cobalt base with its natural cobalt oxide layer is substituted for the nickel base. The third-order cobalt diodes produce about one third as much FIR radiation in each sideband as there is in the second-order difference; hence third-order generation is not quite as sensitive as second-order. The much larger tunability, however, makes it considerably easier to use.

The common isotope of CO₂ is used in both the waveguide laser and in laser 2; in laser 1, one of four isotopic species is used. Ninety percent of all frequencies from 0.3 to 4.5 THz can be synthesized; the coverage decreases between 4.5 and 6.3 THz. Ninety megahertz acoustooptic modulators (AOMs) are used in the output beams of the two CO₂ lasers which irradiate the MIM diode; they increase the frequency coverage by an additional 180 MHz and isolate the CO₂ lasers from the MIM diode. This isolation decreases amplitude noise in the generated FIR radiation, caused by the feedback to the CO₂ laser from the MIM diode, by an order of magnitude; hence, the spectrometer sensitivity increases by an order of magnitude.

The radiations from laser 1 and the waveguide laser are focused on the MIM diode. Laser 2 serves as a frequency reference for the waveguide laser; the two lasers beat with each other in the HgCdTe detector and a servosystem offset-locks the waveguide laser to laser 2. Lasers 1 and 2 are frequency

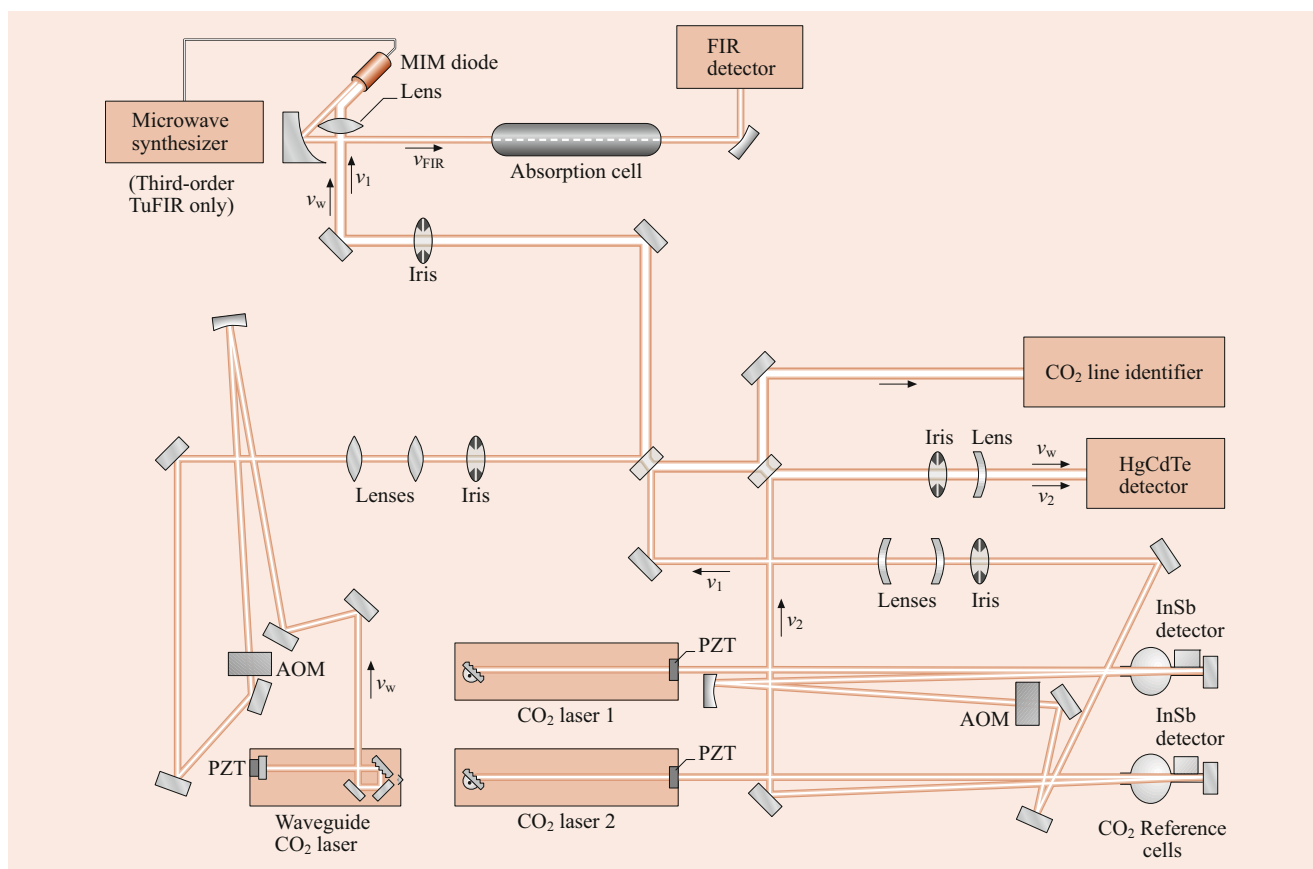


Fig. 43.1 Tunable far-infrared (TuFIR) spectrometer for second- or third-order operation using CO₂ laser difference-frequency generation in the MIM diode

modulated using piezoelectric drivers on the end mirrors, and they are servoed to the line center of 4.3 μm saturated fluorescence signals obtained from the external low-pressure CO₂ reference cells. In both second and third order, the CO₂ reference lasers are stabilized to line center with an uncertainty of 10 kHz. The overall uncertainty in the FIR frequency due to two lasers is thus $\sqrt{2} \times 10$ or 14 kHz. This number was determined experimentally in a measurement of the rotational frequencies of CO out to $J = 38$ (4.3 THz), with the analysis of the data set determining the molecular constants [9].

The CO₂ radiation is focused by a 25 mm focal length lens onto the conically sharpened tip of the 25 μm diameter tungsten whisker. The FIR radiation is emitted from the 0.1 to 3 mm long whisker in a conical long-wire antenna pattern. Then it is collimated to a polarized beam by a corner reflector [25] and a 30 mm focal length off-axis segment of a parabolic mirror.

The largest uncertainty in the measurement of a transition frequency comes from finding the centers of the Doppler broadened lines. This is about 0.05 of the line width for lines observed with a signal-to-noise ratio of 50 or better and corresponds to about 0.05 to 0.5 MHz. A linefitting program [26] improves the line center determinations by nearly

an order of magnitude. The FIR radiation is frequency modulated due to a 0.5 to 6 MHz frequency modulation of CO₂ laser 1; this modulation is at a rate of 1 kHz. The FIR detector and lock-in amplifier detect at this modulation rate; hence the derivatives of the absorptions are recorded.

Absorption cells from 0.5 to 3.5 m in length with diameters ranging from 19 to 30 mm have been used in the spectrometer. The cells have either glass, copper, or Teflon walls and have polyethylene or polypropylene windows at each end. These long absorption cells lend themselves naturally to electrical discharges for the study of molecular ions. A measurement of the HCO⁺ line at 1 THz exhibited a signal-to-noise ratio of 100 : 1 using a 1 s time constant; this is the same signal-to-noise ratio that was obtained using the laser sideband technique.

The instrumental resolution of the spectrometer is limited by the combined frequency fluctuation from each CO₂ laser (about 15 kHz). This is less than any Doppler-limited line width and, therefore, does not limit the resolution. The entire data system is computerized to facilitate the data recording and optimize the data handling.

Improvements in this TuFIR technique may come from either better diodes or detection schemes. The nonlinearity

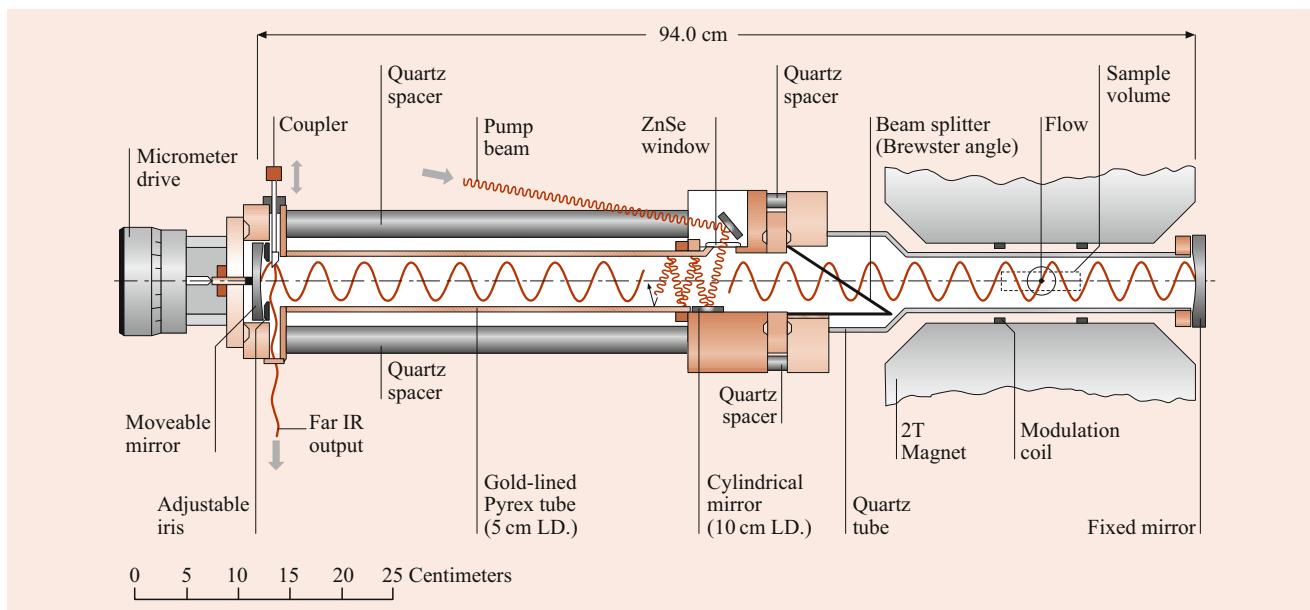


Fig. 43.2 40 μm to 1000 μm Far-infrared laser magnetic resonance (LMR) spectrometer using an optically pumped FIR laser

of the MIM diode is extremely small, and conversion efficiencies could be much larger if a more efficient diode is discovered. Differential detection (which requires more sensitive detectors) could also significantly improve the sensitivity and permit the detection of weaker lines.

43.2.2 Laser Magnetic Resonance

Laser magnetic resonance (LMR) is performed by magnetically tuning the transition frequencies of paramagnetic species into coincidence with the fixed frequency radiation from a laser. LMR is a type of Zeeman spectroscopy [27], and its chief forte is its extreme sensitivity. Approximately one hundred species have been observed in the SM-FIR region. These include atoms, diatomics (especially hydrides), polyatomics, ions, metastables, metastable ions [28], and many *first observations* of free radicals. These observations are summarized in several review articles on LMR [29–31].

The FIR LMR spectrometer at NIST, Boulder is shown in Fig. 43.2. This spectrometer has an intracavity paramagnetic sample in a variable magnetic field which is labeled *sample volume* in the figure. A regular 38 cm EPR magnet with a 7.5 cm air gap is used. The laser cavity is divided into two parts by a Brewster angle polypropylene beam splitter about 12 μm thick. A CO_2 laser optically pumps the FIR laser gas. This pump beam makes many nearly perpendicular passes reflected by the walls of the gold-lined Pyrex tube. A 45° coupler serves to couple out the FIR radiation from the cavity to the helium-cooled detector. Mirrors each with an 89 cm radius of curvature are used in the nearly confocal geometry of the 94 cm cavity. One of the gold-coated end

mirrors is moved with a micrometer to tune the cavity to resonance and also to determine the oscillating wavelength by moving the end mirror several half-wavelengths. The beam splitter is rotatable so that the polarization of the laser can be varied with respect to the magnetic field. Quartz spacers are used to minimize the thermal expansion of the cavity. This LMR spectrometer oscillates at wavelengths between 40 and 1000 μm . The technology of FIR lasers has been reviewed by Douglas [32].

The LMR technique requires a close coincidence (typically within 20 GHz) between the absorption line and the frequency of the laser. Zero field frequencies which are 100 times more accurate than those obtained from optical spectra are obtained from the analysis of the Zeeman spectra observed (i.e. using the laser frequency and the magnetic field values). The accuracy is within 1 or 2 MHz and has permitted the far infrared astronomical observation of many of these species.

Atomic FIR LMR spectra are due to fine structure transitions and are magnetic dipole transitions; hence, they are several orders of magnitude weaker than electric dipole rotational spectra of molecules. The production of a sufficient atomic number density can be difficult; however, *atomic flames* have been very effective sources, and the high sensitivity of LMR has been the most successful spectroscopic technique for measuring these transitions. The atoms O, C, metastable Mg, S, Si, Fe, Al, N^+ , C^+ , P^+ , Fe^+ , and F^+ have been measured by FIR LMR. Atomic Zeeman spectra are relatively simple to analyze, and fine structure frequencies accurate to within 1 MHz can be determined.

In a FIR LMR spectrometer the sample is inside the laser cavity; hence, sub-Doppler line widths can be observed by

operating the sample at low pressure and observing saturation dips in the signals. This has permitted the resolution of proton hyperfine structure in a number of hydrides. The observation of the resolved hyperfine structure is useful in the identification of the species involved and also yields accurate values of the hyperfine splittings.

Rotational spectra of most hydrides lie in this spectral region and many of the hydrides, such as OH, CH, SH, and NH have been observed. Others, such as CaH, MnH, TiH, and ZnH are excellent candidates for LMR studies. Ions are much more difficult because of their low concentrations; however, the use of a special microwave discharge operating in the magnetic field has proved to be an extremely productive source of ions for LMR studies [28].

The spectra of a number of polyatomic species has been observed by LMR: for example, NO₂, HO₂, HCO, PH₂, CH₂, NH₂, AsH₂, HO₂, HS₂, CH₃O, and CCH. The spectra of these polyatomic species are more difficult to analyze, resulting in a somewhat less accurate prediction of the zero-field frequencies. Spectra of the extremely elusive CH₂ and CD₂ radicals have finally yielded to analysis with the simultaneous observation of FIR LMR spectra [33] and IR LMR spectra [34]. The data yield rotational constants which predict the ground state rotational transition frequencies and permit the determination of the singlet–triplet splitting in that molecule [35].

In the last ten years, there has been an experimental push to higher frequencies in FIR spectroscopy. In the LMR spectrometer (shown in Fig. 43.2), this has been achieved principally by reducing the internal diameter of the gold-lined tube in the pumping region to 19 mm so as to increase the overlap between the laser gain medium and the FIR radiation field in the laser cavity. As a result, many new laser lines have been discovered; the system operates down to below 40 μm. This has enabled molecules with larger fine-structure intervals to be studied (e.g., FO and HF⁺ [36, 37]) and has also led to the first detection of vibration-rotation transitions in molecules with low-frequency bending vibrations (CCN, HCCN, FeH₂) [38–40].

The sensitivity of TuFIR is only about 1% of that of laser magnetic resonance, but it is difficult to compare the two because the sample can be very large in the TuFIR spectrometer and is limited to about 2 cm³ in the LMR spectrometer.

43.2.3 TuFIR and LMR Detectors

Four different detectors have been used in the TuFIR and LMR spectrometers: (1) an InSb 4 K, liquid ⁴He-cooled, hot-electron bolometer, operating from 0.3 to 0.6 THz with a noise equivalent power (NEP) of about 10⁻¹³ W/√Hz; (2) a gallium doped germanium bolometer, cooled to the lambda

point of liquid-helium, operating from 0.6 to 8.5 THz with an NEP of about 10⁻¹³ W/√Hz; (3) a similar, but liquid ³He-cooled bolometer, with a NEP two orders of magnitude smaller; and (4) an unstressed Ge:Ga photoconductor, cooled to 4 K, with an NEP of 10⁻¹⁴ W/√Hz, operating from 2.5 to 8.5 THz. The optimization of detector systems for this new technique has been responsible for a significant improvement in sensitivity of these spectrometers.

43.3 Submillimeter and FIR Astronomy

Submillimeter astronomy is reviewed in [6]. Many atomic species (both neutrals and ions) and more than 100 molecules have been detected in interstellar space; many were first observed in the submillimeter and FIR region. In the microwave and submillimeter region, radio (heterodyne) techniques are employed in the receivers. At higher frequencies, interferometric techniques are used [14]; however, heterodyne techniques recently have been employed at these higher frequencies and have resulted in the detection of CO [41] and OH [42] at 2.5 THz and a search for the IR band of methylene [43] at 30 THz. Submillimeter radio astronomy observatories (at high altitudes above much of the water vapor absorptions in our atmosphere) use laboratory determined frequencies. For example, the Kuiper Airborne Observatory and the submillimeter and FIR telescopes on Mauna Kea, Hawaii require frequencies accurate to about 1 MHz in their heterodyne receivers. For heterodyne detection, fixed frequency FIR gas lasers generally serve as local oscillators, and the frequencies of these lasers must be known.

The discovery and direct frequency measurement of FIR laser lines has continued apace since the last major review of this topic was published in 1986 [44]. Almost 1000 lines were listed in that publication; the present number is at least twice this. Two main factors have fuelled this progress. First, the design of CO₂ lasers has continued to develop so that now a single laser can produce 275 individual transitions from the regular, hot [45], and sequence [46] bands of CO₂ with power levels from 2 to 30 W. Secondly, many new, short-wavelength laser lines have been discovered in a cavity specially designed to promote them. As a result, many high frequency lines have now been characterized, several in the range of 26 to 45 μm. The main lasing molecules used in this work are CH₃OH [47–50] and hydrazine, N₂H₄ [51].

Recent observations of FIR transitions in molecules in the interstellar medium have been made from satellite-based platforms such as the Infrared Space Observatory (ISO) [52] using Fourier Transform methods. Attention has been paid to the measurement of less abundant isotopic forms, such as ¹⁸OH and ¹⁷OH, because of the information that they provide about star formation processes.

There are four main goals of laboratory SM-FIR spectroscopy which serve the needs of the SM-FIR radio astronomy field:

1. To provide accurate frequencies of SM-FIR species for their detection,
2. To find new far infrared active species,
3. To measure the frequencies of FIR species which can be used to calibrate Fourier transform spectrometers, and
4. To measure frequencies of far-infrared lasers for use as local oscillators in radio astronomy receivers (and to be used in the analysis of laboratory LMR data).

43.4 Upper Atmospheric Studies

A very impressive set of SM-FIR spectra of our upper atmosphere has been observed using balloon-borne FT spectrometers flown at altitudes where the lines are narrow and the spectrometer is above the *black*, heavily absorbing water vapor transitions [7]. A number of very important species with strong SM-FIR spectra have been observed. They include: O₂, H₂O, NO, ClO, OH, HO₂, O₃, and O. Numerous lines have not yet been identified. It is difficult to calibrate these instruments absolutely because the spectra come from the species emitting at temperatures of about 200 K, and from an indeterminate path length. The high sensitivity of LMR might provide an alternate way of measuring the paramagnetic species in our upper atmosphere by flying an LMR spectrometer to high altitudes. A light-weight solenoid magnet could be used to increase the path length. Absolute concentrations of the paramagnetic species such as OH, HO₂, NO, and O could be obtained.

Acknowledgements We have benefitted invaluable from the help and collaboration of I. G. Nolt of NASA, Langley for his assistance with the detector technology, and of Kelly Chance for his line shape fitting program and his assistance with our studies of upper atmospheric species.

References

1. Crocker, A., Gebbie, H.A., Kimmitt, M.F., Mathias, L.E.S.: *Nature* **201**, 250 (1964)
2. Haller, E.E.: *Infrared Phys. Technol.* **35**, 127–146 (1994)
3. Strong, J., Vanasse, G.: *J. Opt. Soc. Amer.* **49**, 884 (1959)
4. Evenson, K.M., Broida, H.P., Wells, J.S., Mahler, R.J.: *Phys. Rev. Lett.* **21**, 1038 (1968)
5. Zuidberg, B.F.J., Dymanus, A.: *Appl. Phys. Lett.* **32**, 367 (1978)
6. Phillips, T.G.: *Techniques of submillimeter astronomy*. In: Burton, W.B. (ed.) *Millimetre and Submillimetre Astronomy*, p. 1. Kluwer, Dordrecht (1988)
7. Traub, W.A., Chance, K.V., Johnson, D.G., Jucks, K.W.: *Proc. Soc. Photo-Opt. Instrum. Eng.* **1491**, 298 (1991)
8. Jennings, D.A., Evenson, K.M., Knight, D.J.E.: *Proc. IEEE* **74**, 168 (1986)
9. Varberg, T.D., Evenson, K.M.: *IEEE Trans. Instrum. Meas.* **42**, 412 (1993)
10. Nolt, I.G., Radostitz, J.V., DiLorenzo, G., Evenson, K.M., Jennings, D.A., Leopold, K.R., Vanek, M.D., Zink, L.R., Hinz, A., Chance, K.V.: *J. Mol. Spectrosc.* **125**, 274–287 (1987)
11. Jennings, D.A., Evenson, K.M., Zink, L.R., Demuyneck, C., Destombes, J.L., Lemoine, B.: *J. Mol. Spectrosc.* **122**, 477 (1987)
12. Matsushima, F., Evenson, K.M., Zink, L.R.: *J. Mol. Spectrosc.* **164**, 517 (1994)
13. Xu, L.-H., Lees, R.M., Evenson, K.M., Chou, C.-C., Shy, J.-T., Vasconcellos, E.C.C.: *Can. J. Phys.* **72**, 1155 (1994)
14. Storey, J.W.V., Watson, D.M., Townes, C.H.: *Int. J. Infrared Millimeter Waves* **1**, 15 (1980)
15. Röser, H.-P.: *Infrared Phys.* **32**, 385 (1991)
16. Helminger, P., Messer, J.K., DeLucia, F.C.: *Appl. Phys. Lett.* **42**, 309 (1983)
17. Belov, S.P., Gershstein, L.I., Krupnov, A.F., Maslovsky, A.V., Spirko, V., Papousek, D.: *J. Mol. Spectrosc.* **84**, 288 (1980)
18. Winnewisser, G.: *Vib. Spectrosc.* **8**, 241 (1995)
19. Zuidberg, B.F.J., Dymanus, A.: *Appl. Phys. Lett.* **32**, 367 (1978)
20. Evenson, K.M., Jennings, D.A., Petersen, F.R.: *Appl. Phys. Lett.* **44**, 576 (1984)
21. Verhoeve, P., Zwart, E., Versluis, M., Drabbels, M., ter Meulen, J.J., Meerts, W.L., Dymanus, A.: *Rev. Sci. Instrum.* **61**, 1612 (1990)
22. Cohen, R.C., Busarow, K.L., Laughlin, K.B., Blake, G.A., Havenith, M., Lee, Y.T., Saykally, R.J.: *J. Chem. Phys.* **89**, 4494 (1988)
23. Lewen, F., Michael, E., Gendriesch, R., Stutzki, J., Winnewisser, G.: *J. Molec. Spectrosc.* **183**, 207 (1997)
24. Blake, G.A., Laughlin, K.B., Cohen, R.C., Busarow, K.L., Gwo, D.-H., Schmuttenmaer, C.A., Steyert, D.W., Saykally, R.J.: *Rev. Sci. Instrum.* **62**, 1693–1701 (1991)
25. Grossman, E.N.: *Infrared Phys.* **29**, 875 (1989)
26. Chance, K.V., Jennings, D.A., Evenson, K.M., Vanek, M.D., Nolt, I.G., Radostitz, J.V., Park, K.: *J. Mol. Spectrosc.* **146**, 375 (1991)
27. Wells, J.S., Evenson, K.M.: *Rev. Sci. Instrum.* **41**, 226 (1970)
28. Varberg, T.D., Evenson, K.M., Brown, J.M.: *J. Chem. Phys.* **100**, 2487 (1994)
29. Evenson, K.M.: *Faraday Discuss.* **71**, 7 (1981)
30. Russell, D.K.: *Laser magnetic resonance spectroscopy*. In: Symons, M. (ed.) *Specialist Periodical Reports Electron Spin Resonance*, vol. 16, p. 64. The Royal Society of Chemistry, London (1990)
31. Chichinin, A.I.: *Magnetic Resonance: Laser Magnetic Resonance*. In: Linton, J., Tranter, G., Holmes, J. (eds.) *Encyclopedia of Spectroscopy and Spectrometry*, pp. 1133–1140. Academic Press, London (2000)
32. Douglas, N.G.: *Millimetre and Submillimetre Wavelength Lasers*. Springer, Berlin, Heidelberg (1990)
33. Sears, T.J., Bunker, P.R., McKellar, A.R.W., Evenson, K.M., Jennings, D.A., Brown, J.M.: *J. Chem. Phys.* **77**, 5348 (1982)
34. Sears, T.J., Bunker, P.R., McKellar, A.R.W.: *J. Chem. Phys.* **75**, 4731 (1981)
35. McKellar, A.R.W., Bunker, P.R., Sears, T.J., Evenson, K.M., Saykally, R.J., Langhoff, S.R.: *J. Chem. Phys.* **79**, 5251 (1983)
36. Tamassia, F., Brown, J.M., Evenson, K.M.: *J. Chem. Phys.* **110**, 7273 (1999)
37. Allen, M.D., Evenson, K.M., Brown, J.M.: *J. Mol. Spectrosc.* **227**, 13 (2004)
38. Allen, M.D., Evenson, K.M., Gillett, D.A., Brown, J.M.: *J. Mol. Spectrosc.* **201**, 18 (2000)
39. Allen, M.D., Evenson, K.M., Brown, J.M.: *J. Mol. Spectrosc.* **209**, 143 (2001)

40. Körsgen, H., Evenson, K.M., Brown, J.M.: *J. Chem. Phys.* **107**, 1025 (1997)
41. Boreiko, R.T., Betz, A.L.: *Astrophys. J.* **346**, L97 (1989)
42. Betz, A.L., Boreiko, R.T.: *Astrophys. J.* **346**, L101 (1989)
43. Goldhaber, D.M., Betz, A.L., Ottusch, J.J.: *Astrophys. J.* **314**, 356 (1987)
44. Inguscio, M., Moruzzi, G., Evenson, K.M., Jennings, D.A.: *J. Appl. Phys.* **60**, R161 (1986). Table 5
45. Maki, A.G., Chou, C.-C., Evenson, K.M., Zink, L.R., Shy, J.-T.: *J. Mol. Spectrosc.* **167**, 211 (1994)
46. Chou, C.-C., Maki, A.G., Tochitsky, S.J., Shy, J.-T., Evenson, K.M., Zink, L.R.: *J. Mol. Spectrosc.* **172**, 233 (1995)
47. Zerbetto, S.C., Vasconcellos, E.C.C.: *Int. J. Infrared Millimeter Waves* **15**, 889 (1994)
48. Pereira, D., Telles, E.M., Strumia, F.: *Int. J. Infrared Millimeter Waves* **15**, 1 (1994)
49. Zerbetto, S.C., Zink, L.R., Evenson, K.M., Vasconcellos, E.C.C.: *Int. J. Infrared Millimeter Waves* **17**, 1049 (1996)
50. Telles, E.M., Odashima, H., Zink, L.R., Evenson, K.M.: *J. Mol. Spectrosc.* **195**, 360 (1999)
51. Vasconcellos, E.C.C., Zerbetto, S.C., Zink, L.R., Evenson, K.M.: *J. Opt. Soc. Am. B.* **15**, 1839 (1998)
52. Ceccarelli, C., Baluteau, J.-P., Walmsley, M., Swinyard, B.M., Caux, E., Sidher, S.D., Cox, P., Gry, C., Kessler, M., Prusti, T.: *Astron. Astrophys.* **383**, 603 (2002)



John M. Brown Professor Brown obtained his Ph.D. degree from the University of Cambridge in 1966. Before moving to Oxford in 1983, he was a Lecturer in the Department of Chemistry at Southampton University. He was a high-resolution, gas-phase spectroscopist with a special interest in free radical species. In addition to experimental studies at all wavelengths, he was interested in the development of theoretical models to describe the experimental results. He was elected a Fellow of the Royal Society in 2003. He passed away in 2009 soon after his retirement.



Paul Engelking

Contents

44.1	Laser Basics	649
44.1.1	Stimulated Emission	649
44.1.2	Laser Configurations	649
44.1.3	Gain	650
44.1.4	Laser Light	650
44.2	Laser Designs	651
44.2.1	Cavities	651
44.2.2	Pumping	652
44.3	Interaction of Laser Light with Matter	652
44.3.1	Linear Absorption	652
44.3.2	Multiphoton Absorption	654
44.3.3	Level Shifts	654
44.3.4	Hole Burning	654
44.3.5	Nonlinear Optics	655
44.3.6	Raman Scattering	655
44.4	Recent Developments	656
	References	656

Abstract

As a primary research tool, the laser plays a fundamental role in the spectroscopic study of atomic and molecular systems. This Chapter describes the basic operating principles, configurations, and characteristic parameters of lasers. Laser designs are discussed and then the details of the interaction of the laser light with matter delineated. The reader is also referred to other chapters in the book for further information on laser principles and types of lasers.

Keywords

optical parametric oscillator · gain medium · integrated cross section · frequency comb · hole burning

P. Engelking (✉)
Dept. of Chemistry and Chemical Physics Institute, University of Oregon
Eugene, OR, USA

44.1 Laser Basics

44.1.1 Stimulated Emission

A cross section σ_{21} for absorption of radiation by a lower state 1 engenders a balancing cross section σ_{12} for emission stimulated by radiation interacting with an upper state 2. Detailed balance relates these two cross sections according to

$$g_2\sigma_{12} = g_1\sigma_{21}, \quad (44.1)$$

where g_1 and g_2 are the statistical degeneracies of their respective states [1].

For a collection of emitting and absorbing states with densities n_2 and n_1 , amplification may occur when $n_2\sigma_{12} > n_1\sigma_{21}$, which leads to a requirement for an *inversion* of the state populations

$$n_2/n_1 > g_2/g_1. \quad (44.2)$$

The rate of spontaneous emission at frequency ν can be modeled itself by stimulated emission induced by a noise source of the magnitude of the density of states $\rho(\nu)$

$$\gamma_{12}(\nu) = \sigma_{12}(\nu)\rho(\nu)/c = \sigma_{12}(\nu)8\pi\lambda^{-2}. \quad (44.3)$$

44.1.2 Laser Configurations

A practical laser combines a population inversion with a means for controlling the radiation.

The basic laser source is the laser oscillator, an amplifier possessing positive feedback. The usual form is simply a piece of active gain medium placed inside a resonant optical cavity (Fig. 44.1). Tunability is produced if the resonant cavity is frequency selective and adjustable (Fig. 44.2). Many laser sources use an amplifier after the oscillator.

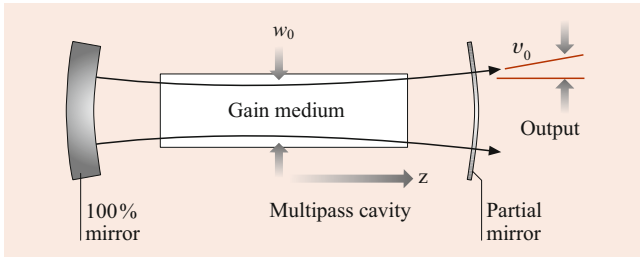


Fig. 44.1 Simple laser oscillator and beam parameters. Distances z are generally measured from the minimum beam waist w_0 . The beam appears with a far-field divergence angle θ_0

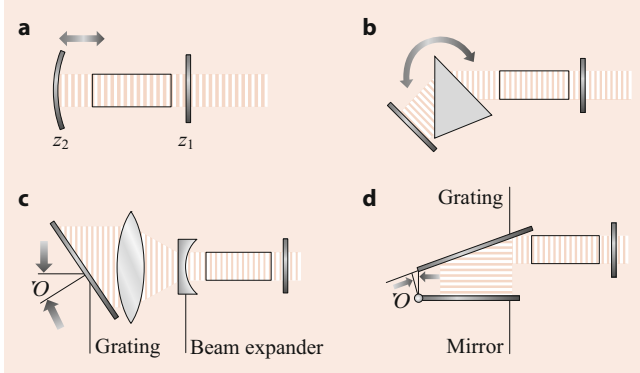


Fig. 44.2 Tunable laser oscillator geometries. **a** Fabry-Perot: tuning is usually done by changing the cavity length, although changing the index of refraction by changing the temperature or current is common with solid state laser diodes. **b** Littrow prism line selector: typical of atomic ion lasers capable of multiple line output. **c** Littrow grating tuning: common in pulsed dye lasers with high gain (> 10) per pass. Telescope increases resolution by filling, and reducing angular divergence at the grating. **d** Grazing incidence, mirror tuned, grating mount

44.1.3 Gain

The fundamental gain per pass is given by

$$G = J/J_0 = \exp[(\kappa - \mu)L], \quad (44.4)$$

where J/J_0 is the ratio of light output to input, κ is the gain coefficient, μ is the nonradiative loss rate, and L is the path length. The gain coefficient

$$\kappa = n^* \sigma_{12} \quad (44.5)$$

depends upon the net inversion n^* ,

$$n^* = n_2 - (g_1/g_2)n_1. \quad (44.6)$$

If λ is the wavelength of radiation, F_{12} is the emission line shape function normalized over frequency ν , τ_2 is the lifetime of the transition, and f_{12} is the branching ratio for the upper state to undergo this transition, then the stimulated

emission cross section is

$$\sigma_{12} = \frac{\lambda^2 f_{12} F_{12}(\nu)}{8\pi \tau_2}. \quad (44.7)$$

For a Lorentzian lifetime-broadened line, the cross section for stimulated emission at the line center becomes

$$\sigma_{12} = \frac{\lambda^2 f_{12}}{4\pi^2 \Gamma_{12} \tau_2}, \quad (44.8)$$

where Γ_{12} is the full width at half maximum of the line.

44.1.4 Laser Light

Lasers are inherently bright sources of radiation: the radiation field within a practical laser must be high enough for stimulated emission to compete with spontaneous emission. The effective source of spontaneous fluctuations approximates that of the density of states. In terms of the beam parameters photon flux J per solid angle Ω , and frequency ν , this is

$$\frac{d^2 J}{d\Omega d\nu} = \frac{2\nu^2}{\epsilon_r c^2}. \quad (44.9)$$

Beam *quality* is given by the product of the angular divergence times the beam width. Highest beam quality is associated with diffraction limited light emitted from a Gaussian spot. For circular laser beams traveling in the z -direction, this corresponds to a solution of the electromagnetic wave equation

$$u(r, \phi, z) = \psi(r, z) \exp(-ikz), \quad (44.10)$$

where u is a polarization component of the field. For high values of $k = 2\pi/\lambda$, corresponding to short wavelength, the adiabatic radial solution is also Gaussian

$$\psi(r, z) = \exp\{-i[P + kr^2/(2q)]\}, \quad (44.11)$$

where the complex phase shift P , beam parameter q , and beam radius w are functions of z

$$P(z) = -i \ln \left[1 - i \frac{\lambda z}{\pi w_0^2} \right] \\ = -i \ln \sqrt{1 + \left[\frac{\lambda z}{\pi w_0^2} \right]^2} - \tan^{-1} \left[\frac{\lambda z}{\pi w_0^2} \right], \quad (44.12)$$

$$q(z) = i\pi w_0^2/\lambda + z, \quad (44.13)$$

$$w^2(z) = w_0^2 \left[1 + \left(\frac{\lambda z}{\pi w_0^2} \right)^2 \right]. \quad (44.14)$$

Here, w_0 is the beam waist parameter, the minimum width of the Gaussian beam at a focused spot. For Gaussian beams, the product of the minimum beam waist and beam divergence angle θ_0 is given by

$$\theta_0 w_0 = \lambda / \pi . \quad (44.15)$$

The beam waist and divergence follow optical imaging according to paraxial ray theory.

Higher order circular modes with p radial nodes and l angular node planes are specified by multiplying Eqs. (44.11) and (44.12) by angular and radial factors to obtain

$$\psi_{pl}(r, \phi, z) = \left(\sqrt{2}r/w \right)^l L_p^l(2r^2/w^2) e^{il\phi} \psi(r, z) , \quad (44.16)$$

$$P_{pl}(z) = (2p + l + 1)P(z) . \quad (44.17)$$

Here, the functions $L_p^l(x)$ are the Laguerre polynomials as defined in Sect. 9.4.2. The radial phase shifts produce a wave front curvature of effective radius

$$R = z + [(2p + l + 1)/2 + w_0^2\pi/\lambda^2]w_0^2\pi/z . \quad (44.18)$$

Modes with the same values of $2p + l$ have identical axial and radial phase shifts. The two polarization components of the electromagnetic field double the degeneracies of all modes considered here. Often these degeneracies are split in practice by optical inhomogeneities of the medium through which they pass. More details can be found in the summary of *Kogelnick and Li* [2], or in the texts by *Verdeyen* [3] or *Svelto* [4].

Some applications require knowledge of the electric field in addition to the flux density J . For purely sinusoidal single mode beams, the rms field is

$$\langle E \rangle = \left(\frac{h\nu J}{c\epsilon_0} \right)^{1/2} . \quad (44.19)$$

Nonlinear effects are often expressed in terms of powers of the field by

$$\langle E^n \rangle = 2^{(n-1)/2} \langle E \rangle^n \quad (44.20)$$

for single mode and multimode radiation of random frequency spacings. For m equally spaced modes, this is increased by $m!/(m-n)!$.

44.2 Laser Designs

44.2.1 Cavities

The simple Fabry–Perot cavity consists of two spherical mirrors facing one another. The surfaces are chosen to be constant phase surfaces for the desired modes in Eq. (44.18).

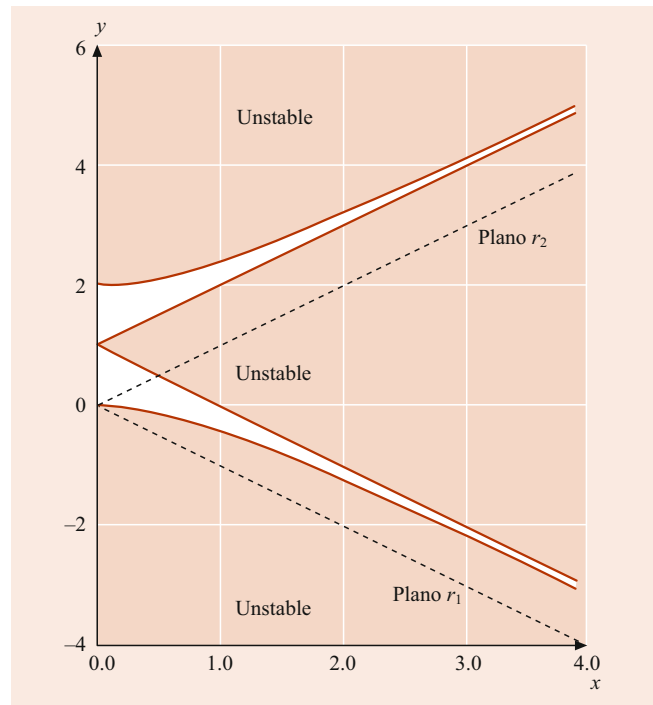


Fig. 44.3 Stability parameters for simple two-mirror laser cavities of length L and mirror radii of curvature R_1 and R_2 . Here, $x = \frac{1}{2}(L/R_1 - L/R_2)$ is the mean curvature difference of the two mirrors; $y = \frac{1}{2}(L/R_1 + L/R_2)$ is the mean curvature of the two mirrors. Cavities with parameters in the unshaded region are stable

Stability criteria are shown in Fig. 44.3. A cavity is stable when initial angles θ and displacements r of paraxial rays transform during a round trip into θ' and r' satisfying

$$-2 < \frac{\partial\theta'}{\partial\theta} + \frac{\partial r'}{\partial r} < 2 . \quad (44.21)$$

At frequencies for which the round-trip phase change per passage

$$\begin{aligned} \delta(\nu) &= 2\pi(z_2 - z_1)\nu/c + 2[P_{pl}(z_2) - P_{pl}(z_1)] \\ &\approx 2\pi(z_2 - z_1)/\lambda + \pi(2p + l + 1) \end{aligned} \quad (44.22)$$

is an integer multiple of 2π , the phases from different passages interfere constructively, giving longitudinal modes. (Here $P_{pl}(z_i)$ gives the additional phase shift for higher transverse modes at mirrors $i = 1, 2$.)

For a particular radial mode structure in an empty Fabry–Perot cavity, the ratio of the maximum cavity decay time for these standing waves to the minimum cavity decay time for frequencies between longitudinal modes is

$$(1 + r)^2/(1 - r)^2 . \quad (44.23)$$

Here r is the reflectivity of the end mirrors; for cavities with mirrors having different reflectivities, one may use the square

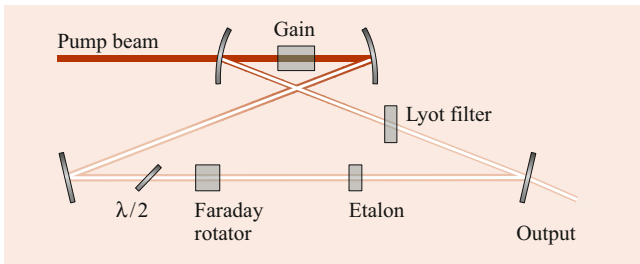


Fig. 44.4 Ring laser. The Faraday rotator and half-wave plate permit circulation of the cavity fields in only one direction

root of the product of their reflectivities. A simple Fabry–Perot cavity may be tuned by changing the cavity length or by changing the index of refraction of the cavity material. Since both of these may be properties of temperature, temperature tuning may be possible. The index of refraction of a material may also be sensitive to the intensity of excitation. Diode lasers consisting of a semiconductor die with polished, reflecting faces are often tuned by changing temperature and pumping current.

For lasers with a dispersive optical element within the cavity, highest selectivity is obtained when the light has low angular divergence and impinges upon the dispersive element as nearly plane waves. A beam expander may reduce the angular spread while simultaneously increasing the beam width. For a grating used as a mirror in a Littrow mount, the dispersion equation is

$$\Delta\lambda = (d/n) \cos\phi \Delta\phi, \quad (44.24)$$

where n is the diffraction order, d is the distance between lines, and ϕ is the angle of incidence off normal.

Cavities with prisms or gratings can be conveniently tuned by rotating the angle of the dispersive element. For a grating used as a mirror in a Littrow mount, the grating equation is

$$\lambda = (2d/n) \sin\phi. \quad (44.25)$$

Often, more than one longitudinal cavity mode operates within the selected frequency band, and tuning consists of *hopping* from mode to mode, rather than smoothly sweeping a single line across a band of frequencies. Smooth frequency tuning can be achieved, for example, in a design by *Wallenstein* and *Hänsch* [5], in which the grating and Fabry–Perot cavity are placed together inside a chamber. The whole laser is then tuned by changing the index of refraction of the gas inside by varying its pressure.

The current trend with pulsed lasers is to use a very lossy, short oscillator cavity in which the longitudinal modes are nearly absent, making up for the cavity losses with a very high gain lasing medium. The front, output mirror of such a cavity may actually be *antireflection* coated, with a reflectivity of only a percent or less.

Low gain, continuous wave (cw) lasers often use a combination of cavity length tuning along with dispersive element rotation, such as a prism or Lyot filter. Often, lasing on a traveling wave in a ring configuration is used to avoid longitudinal modes, as illustrated in Fig. 44.4. Some commonly used gain media are listed in Tables 44.1 and 44.2.

44.2.2 Pumping

Many methods, including electrical discharges and flash-lamps, have been used to pump the gain media of lasers. Generally, the best pump is another laser.

Two notable pump lasers have dominated the field of tunable, visible lasers: pulsed neodymium YAG, frequency doubled to ≈ 503 nm, and cw Ar II ion at 514.5 nm. Both are extremely effective at exciting the highly efficient rhodamine class dyes in the red–yellow portion of the visible spectrum. The typical pump beam of a Nd/YAG laser enters the amplifying dye cell transversely along one of the faces of the cell. The typical cw pump beam enters the dye almost collinearly with the laser axis.

By temporarily *spoiling* the Q by making the laser cavity lossy, lasing can be held off until the gain medium stores a greater energy density than the minimum required for lasing. Rapidly switching off the loss mechanism releases this energy in one giant pulse. An electronic optical shutter, such as a Pockels cell, or a saturable dye inside the laser cavity, designed to photobleach from the spontaneous emission just before the laser reaches threshold, are commonly used.

Periodically spoiling the laser gain or the cavity Q at the period of a round trip produces intense, short pulses. Viewed from the frequency domain, the phases of individual longitudinal modes are *locked* together to produce a light packet circulating at the frequency of the reciprocal of the mode spacing. Extremely short pulses (< 1 ps) can be produced by mode locking. Practically, mode locking can be achieved by using a thin, saturable absorber near one of the cavity mirrors [6], or by acoustically modulating an optical element in the cavity – even an end mirror itself. One of the best ways of mode locking is to pump a short lifetime gain medium, such as a dye, with mode locked laser light, such as from a mode locked argon ion laser [7].

44.3 Interaction of Laser Light with Matter

44.3.1 Linear Absorption

The absorption cross section σ_{fi} for transition to the final state $|f\rangle$, when integrated over frequency ν , is given theoretically by the leading first-order perturbation of the initial

Table 44.1 Fixed frequency lasers

Laser	Wavelength (nm)	Excitation method
ArCl	≈170 (band)	Pulsed, gas discharge
ArF	≈193	Pulsed, gas discharge
KrCl	≈222	Pulsed, gas discharge
KrF	≈248	Pulsed, gas discharge
XeBr	≈282	Pulsed, gas discharge
XeCl	≈308	Pulsed, gas discharge
XeF	≈351, 353	Pulsed, gas discharge
N ₂	≈337.1 (other bands)	Pulsed (1–10 ns), gas discharge
Ar ⁺	488.0, 514.5 (454.4, 457.9, 465.8, 472.7, 476.5, 501.7, 528.7)	cw, gas discharge
Ar ⁺²	351.1, 363.8	cw, gas discharge, high magnetic field
Kr ⁺	568.2, 647.1, (476.2, 520.8, 530.9)	cw, gas discharge
Kr ⁺²	350.7, 356.4, 406.7	cw, gas discharge, high magnetic field
Ne/He	632.8, 1152.3, 3390 (others)	cw, gas discharge
Cr ⁺³ -Ruby	694.3	Pulsed, flashlamp
Nd ⁺³ -YAG	≈1065, ≈1300	Pulsed: flashlamp; cw: lamp, LED or laser diode
Nd ⁺³ -glass(various)	≈920, ≈1060, ≈1370	Pulsed, flashlamp
Yb ⁺³ -glass	≈1060	Pulsed, flashlamp
Er ⁺³ -glass(various)	≈1540, ≈1536, ≈1543, ≈1550	Pulsed: flashlamp; cw: lamp, LED or laser diode
Xe	3507	cw gas discharge
CO ₂	≈10 600 (lines)	cw: gas discharge or gas dynamic
Molecular vibration and rotation	1 × 10 ⁵ –3 × 10 ⁶ (numerous lines)	IR laser (CO ₂ , CO, ...)

Table 44.2 Approximate tuning ranges for tunable lasers

Laser	Wavelengths (nm)	Notes
Dye solution	<330 – >1200 [≈10 each dye]	Pulsed: laser, flashlamp; cw: laser
Alexandrite	700–820	Pulsed: lamp, laser; cw: laser
Ti ⁺³ /Sapphire	680–1100	Pulsed: laser, lamp; cw: laser
GaAs	840–900	pn junction
InGaAlP/GaAs	630–700 [1–10]	pn junction
GaAsP	550–880	pn junction
AlGaAs, AlGaAs/GaAs	≈820 [1–20], 720–880	pn junction, temp. & current tuning
InP	≈900	pn junction, temp. & current tuning
GaInAs	906–3100	pn junction, temp. & current tuning
InGaAlAs/GaAs	800–1100	pn junction, temp. & current tuning
InPAs	900–4000 [1–50]	pn junction, temp. & current tuning
InGaAsP/InP	1200–1650	pn junction, temp. & current tuning
InAs	≈3100	pn junction, temp. & current tuning
InSb	≈5200	pn junction, temp. & current tuning
PbS	≈4300	pn junction, temp. & current tuning
PbTe	≈6500	pn junction, temp. & current tuning
PbSe	≈8500	pn junction, temp. & current tuning
PbSnSeTe “Lead Salt Diode”	4500–15,000 [1–50]	pn junction, temp. & current tuning
Color Centers: (F ²⁺)/LiF	800–1040	cw: laser, Ar, Kr
/NaF	900–1050	cw: laser, Ar, Kr
/KCl:Ti	1400–1700	cw: laser, Ar, Kr, Nd/YAG
/KF	1300–1400	cw: laser, Ar, Kr, Nd/YAG
/NaCl	1400–1600	cw: laser, Ar, Kr, Nd/YAG
/KCl	1600–1700	cw: laser, Ar, Kr, Nd/YAG
/KBr	1700–1900	cw: laser, Ar, Kr, Nd/YAG
/KCl:Li	2500–2900	cw: laser, Ar, Kr, Nd/YAG
/KCl:Na	1600–1950	cw: laser, Ar, Kr, Nd/YAG

state $|i\rangle$ in the electric dipole approximation

$$\int \sigma_{fi}(v) dv = 4\pi^2 \alpha \bar{v} \left| \langle f | \sum_e \mathbf{r}_e \cdot \hat{\boldsymbol{\epsilon}} | i \rangle \right|^2, \quad (44.26)$$

where the sum is over all charges e at distances r_e , $\hat{\boldsymbol{\epsilon}}$ is a unit polarization vector, and \bar{v} is the averaged transition energy. Averaged over orientations and summed over possible final states, each electron contributes to the total integrated absorption cross section one electron oscillator, $\pi r_0 c \approx 0.03 \text{ cm}^2 \text{ s}^{-1}$; here, r_0 is the classical electron radius. Electronic absorption bands typically contain an oscillator strength $f = 0.01\text{--}0.5$ of an *electron oscillator*, while weaker vibrational transitions have $f = 10^{-6}\text{--}10^{-4}$ in each band.

For narrow lines with radiation of broader band width $\Delta\nu$ at flux density J , the linear absorption rate constant can be usefully estimated as $(\pi r_0 c) f J / \Delta\nu$.

44.3.2 Multiphoton Absorption

Second-order perturbation theory gives the theoretical two-photon contribution to the absorption. An absorption cross section $\sigma^{(2)} J_1$ for a photon of frequency ν_2 is induced by an off-resonance monochromatic field of frequency ν_1 and photon flux density J_1 . When integrated over the frequency of the second photon, the second-order cross section can be related to the dipole matrix elements

$$\int \sigma_{fi}^{(2)}(\nu_1, \nu_2) J_1 d\nu_2 = \frac{4\pi^2 \alpha^2}{\nu_1 \bar{\nu}_2} J_1 \times \left| \sum_m \frac{\nu_{fm} \nu_{mi} \langle r_{fm} \rangle \langle r_{mi} \rangle}{\nu_{mi} - \nu_1} \right|^2, \quad (44.27)$$

where

$$\begin{aligned} \langle r_{fm} \rangle &= \langle f | \sum_e \mathbf{r}_e \cdot \hat{\boldsymbol{\epsilon}}_2 | m \rangle, \\ \langle r_{mi} \rangle &= \langle m | \sum_e \mathbf{r}_e \cdot \hat{\boldsymbol{\epsilon}}_1 | i \rangle, \end{aligned} \quad (44.28)$$

and the sum is taken over intermediate states $|m\rangle$ having frequencies ν_{mi} and ν_{fm} for transitions to the initial and final states. The energy for the overall transition comes from two photons; hence the two-photon resonance condition $\nu_{fi} = \nu_1 + \nu_2$. A special case often occurs when only one radiation frequency is used: then $\nu_1 = \nu_2$, and two-photon resonance is achieved when the energy of the transition corresponds to twice the frequency of the radiation field.

This integrated, induced cross section is roughly of the order $\alpha(\pi r_0 c)^2 J_1 / (\nu_1 \bar{\nu}_2)$. Two-photon absorption becomes

comparable to the one-photon absorption with off-resonance fields on the order of

$$J_1 \approx \frac{\nu_1 \nu_2}{\alpha \pi c r_0}, \quad (44.29)$$

or about $10^{21} \text{ photons s}^{-1} \text{ cm}^{-2}$ ($10^{17} \text{ W m}^{-2} \text{ s}^{-1}$ for typical green light).

Typical dipole-allowed molecular multiphoton absorption cross sections are $\approx 10^{-58} \text{ m}^4 \text{ s}$ for two photons and $10^{-94} \text{ m}^6 \text{ s}^2$ for three photons.

Multiphoton absorption was one of the first effects explored with lasers. Two-photon absorption was first reported for inorganic crystals containing europium ions [8]. Blue and ultraviolet fluorescence appeared in the interaction of red ruby laser light with organic compounds [9–12]. Others observed two-photon absorption directly [13, 14]. Selection rules for multiphoton absorption are summarized by *McClain* [15]; recent work is reviewed by *Ashfold* and *Howe* [16].

Highly excited states may subsequently ionize in the intense fields in a multiphoton ionization (MPI) process. The ionization signal is often detected in a proportional ionization cell. A low pressure cell containing the vapor of a transition metal organometallic, such as iron carbonyl or ferrocene which photodissociates to give the metal atom, may be used for wavelength calibration by MPI.

44.3.3 Level Shifts

High radiation power causes resonant frequencies to shift, responding to the ac Stark effect [17, 18]. Even moderate fields, tuned near resonance, interact strongly with an atom or small molecule, which undergoes rapid excitation and stimulated emission at the characteristic power dependent Rabi frequency,

$$\nu_{\text{Rabi}} = \frac{2\pi g_1}{g_1 + g_2} \sigma_{21} J. \quad (44.30)$$

Fluorescence from such an interacting system has a characteristic *head and shoulders* spectrum best understood as radiation at the fundamental frequency amplitude modulated at the Rabi frequency [19].

44.3.4 Hole Burning

Radiation at a particular frequency generally moves population out of states that absorb that radiation. Molecules that interact resonantly with the radiation may also spontaneously emit at different frequencies, thereby ending in nonabsorbing states. This optical pumping effect can make resonance

features in an absorption spectrum disappear at high power levels [20]. Depletion may appear as a *hole* in the absorption spectrum [21]. Recently, interest has shifted to permanent *hole burning* as a method of information storage in materials.

Hole burning is the basis for Doppler-free Lamb-dip spectroscopy, in which only absorbing atoms or molecules having little or no velocity component along the axis of two counterpropagating beams are temporarily depleted [22]. This technique is commonly used for laser frequency stabilization, such as with the iodine-locked He–Ne laser.

44.3.5 Nonlinear Optics

Multiplying

Nonlinear susceptibility of an optical medium can generate radiation at frequencies which are multiples of the frequency of laser radiation passing through. Phenomenologically, the second order polarization

$$P_{2\nu} = \epsilon_0 \chi^{[2]} E_\nu^2 \quad (44.31)$$

is given in terms of the second order nonlinear susceptibility $\chi^{[2]}$, a third rank tensor, and the electric field at the fundamental frequency (see Chap. 76). This nonlinear susceptibility can range from 0.5–5 pm/V for typical materials used for frequency doubling. Typical materials and their use are reviewed by *Bordui* and *Fejer* [23].

For a nonlinear process occurring over a length l in a cylindrical region with Gaussian waist w_0 with polarization P_0 on axis, the far field flux is given by

$$J(R, \theta) = \frac{\pi^4 \nu^3 n^3 w_0^4 P_0^2}{4hc^3 \epsilon_0 R^2} \left(\frac{\sin^2[(k_0 - k \cos \theta)l/2]}{(k_0 - k \cos \theta)^2} \right) \times \exp[-k^2 w_0^2 \sin^2(\theta)/2]. \quad (44.32)$$

Here, n is the index of refraction and k the propagation constant for the induced radiation, while k_0 is that for the induced polarization, the vector sum of those of the original radiation. When phase matched, $k_0 - k \cos \theta = 0$, and the term in the brackets maximizes to $(l/2)^2$.

The greatest difficulty is in selecting materials which can be phase matched such that the relative phases of the fundamental and overtone radiation propagate together through the material; otherwise radiation at the higher frequency generated at different places inside the material destructively interfere. Phase matching is usually achieved by either angle tuning of a birefringent crystal, or by temperature tuning.

Only materials without a center of inversion in their crystal structures have a second order nonlinear susceptibility. All materials, including gases, will have a third order nonlinear susceptibility $\chi^{[3]}$. This can be used to generate

third harmonics, especially in the vacuum ultraviolet (VUV), where doubling materials are not available [24, 25].

Mixing

The same materials that permit frequency doubling and tripling also allow 3-wave and 4-wave frequency mixing. The frequency matching conditions are, respectively,

$$\begin{aligned} \nu_1 \pm \nu_2 &= \nu_3, \\ \nu_1 \pm \nu_2 \pm \nu_3 &= \nu_4. \end{aligned} \quad (44.33)$$

Tunable UV radiation may be generated by adding the frequencies of a fixed and tunable visible outputs. Tunable IR has been obtained by differencing fixed and tunable visible lasers. Mixing of radiation from an Ar ion laser with that from a tuned R6G dye laser in lithium iodate to produce tunable 2200–4600 nm radiation is noteworthy.

Optical Parametric Oscillator

It is possible to reverse 3-wave mixing, generating two frequencies whose sum is that of the input radiation. In parametric generation, the output frequencies are given by the phase match conditions. Both the desired frequency and the secondary *idler* frequency must be allowed to build up in the nonlinear medium. The idler radiation is not present initially, but results from the frequency mixing process itself. The process has many of the characteristics of a laser oscillator, including that of a gain threshold. This makes tuning of an optical parametric oscillator similar to that of a laser, but with more degrees of freedom: now oscillation at two frequencies must be attained simultaneously, along with the correct *phase matching* of the nonlinear material [26].

44.3.6 Raman Scattering

It is possible to have one or more of the fields in a mixing process belong to just polarization, rather than radiation. The frequency additive case of multiphoton absorption has already been considered; the frequency subtractive case is Raman scattering.

Incoherent Raman Scattering

Radiation at a higher frequency can excite a lower frequency vibration or rotation within a material, with appearance of radiation at the frequency of the incident radiation minus that of the absorption. The integrated cross section for this effect is given by Eq. (44.27). However, in this case the cross section is for *emission* of the second photon. The rate of spontaneous Raman emission is obtained by multiplying Eq. (44.27) by the spectral flux density of the zero-point field, $8\pi \nu^2 / \epsilon_1 c$. Typical vibrational Raman cross sections for

transparent molecules are about $10^{-34} \text{ m}^2 \text{ sr}^{-1}$ in the blue-green (488 nm) [27].

Alternatively, energy can be extracted from an excited state, with the inelastically scattered photon departing with the sum of the incident frequency and that of the deexcitation. The term *anti-Stokes* distinguishes it from the more usual *Stokes* type of Raman scattering.

Coherent Raman Emission

The integrated cross section for emission stimulated at the Raman frequency is given directly by Eq. (44.27).

A fourth-order mixing process that is less susceptible to saturation involves coherent anti-Stokes Raman scattering (CARS). Two beams excite the material: the difference of their frequencies corresponds to an excitation of the material. Stimulated Raman scattering excites the material, which then deexcites through an anti-Stokes process, giving rise to a third, higher frequency radiation field. The phase is determinate, and the radiation leaves the region of scattering as a beam [28].

If the incident radiation induces a Raman process over a sufficiently long path, the stimulated Raman process can be used for gain at both the Stokes and anti-Stokes frequencies. Since spontaneous Raman processes are proportional to the integrated cross section, while gain in the stimulated Raman process is proportional to the peak cross section, simple materials with sharp, simple line spectra are most suitable for Raman gain media. While Raman lasers have been produced using vibrational excitation of organic liquids, currently the most important technical application is for Raman shifting the output of lasers, tunable or otherwise, to frequencies which otherwise would be inaccessible. The high pressure H_2 Raman shifter produces, at low powers, beams consisting almost entirely of well separated, sharp lines shifted by 4160 cm^{-1} from the pump beam; at high powers, a series of Stokes and anti-Stokes bands appear, each separated by 4160 cm^{-1} from each other.

44.4 Recent Developments

One of the most exciting advancements in the past decade in laser physics has been the generation of optical frequency combs; and, more specifically, their applicability in the domain of high-resolution laser spectroscopy. Basically, through a superposition process of many continuous wave modes, a short train of frequency spikes may be produced from a mode-locked laser [29] (see also Sect. 30.1.5). These spikes are equally spaced and are referred to as a frequency comb. The frequency ω_n of the n -th cavity mode may be expressed as

$$\omega_n = n\omega_r + \omega', \quad (44.34)$$

where ω_r is characteristic of the laser and ω' is a frequency offset due to the difference between the phase and group velocity of the superposed waves.

The microwave frequencies ω_r and ω' are determined through the use of nonlinear optics. Once these two parameters are determined, any unknown optical frequency ω_o may be measured by recording the beat frequency between it and the closest comb frequency. This technique gives experimenters a high-precision method for the spectroscopic determination of such fundamental quantities as the fine structure constant, the Rydberg constant, and the Lamb shift [30, 31].

Acknowledgment Text and references updated by Mark M. Cassar.

References

1. Einstein, A.: Phys. Z. **18**, 121 (1917)
2. Kogelnik, H., Li, T.: Proc. IEEE **54**, 1312 (1966)
3. Verdeyen, J.T.: Laser Electronics, 3rd edn. Prentice Hall, Englewood Cliffs (1994)
4. Svelto, O.: Principles of Lasers. Plenum, New York (1976)
5. Wallenstein, R., Hänsch, T.W.: Opt. Commun. **14**, 353 (1975)
6. Ippen, E.P., Shank, C.V., Dienes, A.: Appl. Phys. Lett. **21**, 348 (1972)
7. Jain, R.K., Ausschnitt, C.P.: Opt. Lett. **2**, 117 (1978)
8. Kaiser, W., Garrett, C.G.B.: Phys. Rev. Lett. **7**, 229 (1961)
9. Peticolas, W.L., Goldsborough, J.P., Rieckhoff, K.E.: Phys. Rev. Lett. **10**, 4345 (1963)
10. Peticolas, W.L., Reickhoff, K.E.: J. Chem. Phys. **39**, 1347 (1963)
11. Singh, S., Stoicheff, B.P.: J. Chem. Phys. **38**, 2032 (1963)
12. Weisz, S.Z., Zahlen, A.B., Gilreath, J., Jarnagin, R.C., Silver, M.: J. Chem. Phys. **41**, 3491 (1964)
13. Hopfield, J.J., Warlock, J.M., Park, K.: Phys. Rev. Lett. **11**, 414 (1963)
14. Staginnus, B., Frölich, D., Caps, T.: Rev. Sci. Instrum. **39**, 1129 (1968)
15. McClain, W.M.: Acc. Chem. Res. **7**, 129 (1974)
16. Ashfold, M.N., Howe, J.D.: Annu. Rev. Phys. Chem. **45**, 57 (1994)
17. Carmichael, H.J., Walls, D.F.: J. Phys. B **9**, 1199 (1976)
18. Li, L.-P., Yang, B.-X., Johnson, P.M.: J. Opt. Soc. Am. **2**, 748 (1985)
19. Mallow, B.R.: Phys. Rev. **188**, 1969 (1969)
20. Rothberg, L.J., Gerrity, D.P., Vaida, V.: J. Chem. Phys. **75**, 4403 (1981)
21. Völker, S.: Annu. Rev. Phys. Chem. **40**, 499 (1989)
22. Bennett Jr., W.R.: Phys. Rev. **126**, 580 (1962)
23. Bordui, P.F., Fejer, M.M.: Annu. Rev. Mater. Sci. **23**, 321 (1993)
24. Kung, A.: Opt. Lett. **8**, 24 (1983)
25. Bokor, J., Bucksbaum, P., Freeman, R.: Opt. Lett. **8**, 217 (1983)
26. Falk, J., Yarborough, J.M., Ammann, E.O.: IEEE J. Quantum Elec. **7**, 359 (1971)
27. Penney, C.M., St. Peters, R.L., Lapp, M.: J. Opt. Soc. Am. **64**, 712 (1974)
28. Regnier, P.R., Taran, J.P.: Appl. Phys. Lett. **23**, 240 (1973)
29. Udem, T., Holzwarth, R., Zimmerman, M., Goble, C., Hänsch, T.: Top. Appl. Phys. **95**, 295 (2004)
30. Hensley, J.M.: A precision measurement of the fine structure constant. Ph.D. Thesis. University, Stanford, Stanford (2001)
31. de Beauvoir, B., Schwob, C., Acef, O., Jozefowski, L., Hilico, L., Nez, F., Julien, L., Clairon, A.: Eur. Phys. J. D **12**, 61 (2000)



Spectroscopic Techniques: Cavity-Enhanced Methods

45

Barbara Paldus and Alexander A. Kachanov

Contents

45.1	Limitations of Traditional Absorption Spectrometers	657
45.2	Cavity Ring-Down Spectroscopy	658
45.2.1	Pulsed Cavity Ring-Down Spectroscopy	659
45.2.2	Continuous-Wave Cavity Ring-Down Spectroscopy (CW-CRDS)	659
45.3	Cavity-Enhanced Spectroscopy	660
45.3.1	Cavity-Enhanced Transmission Spectroscopy (CETS)	661
45.3.2	Locked Cavity-Enhanced Transmission Spectroscopy (L-CETS)	662
45.4	Extensions to Solids and Liquids	663
45.4.1	Evanescence-Wave Cavity Ring-Down Spectroscopy (EW-CRDS)	663
45.4.2	Cavity Ring-Down of Condensed Media for Analytical Chemistry	663
45.4.3	Cavity Ring-Down Spectroscopy Using Waveguides	663
	References	664

Abstract

Cavity-enhanced spectroscopy (CES) methodology provides a much higher degree of sensitivity than that available from conventional absorption spectrometers. The aim of this chapter is to present the fundamentals of the method and the various modifications and extensions that have been developed. In order to set the stage, the limitations of traditional absorption spectrometers are discussed first, followed by a description of cavity ring-down spectroscopy (CRDS), the most popular CES embodiment. A few other well-known CES approaches are also de-

scribed in detail. The chapter concludes with a discussion of recent work on extending CRDS to the study of liquids and solids.

Keywords

cavity ring-down spectroscopy · tunable diode laser absorption spectroscopy · cavity · effective path length · integrated cavity output spectroscopy

45.1 Limitations of Traditional Absorption Spectrometers

An absorption spectrometer measures the difference in intensity between the incident light intensity I_0 and the transmitted light intensity $I(x, \lambda)$. Beer's law relates the absorbed light to the sample absorption $\alpha(\lambda)$

$$I(x, \lambda) = I_0 e^{-\alpha(\lambda)x}, \quad (45.1)$$

where λ is the wavelength, and x is the path length. Absorption is related to concentration C through the extinction coefficient $\varepsilon(\lambda)$, namely $\alpha(\lambda) = C\varepsilon(\lambda)$. Typically, a spectral feature, called an absorption peak, of the target species is measured in order to obtain its concentration. The performance of a spectrometer has two figures of merit: sensitivity and selectivity.

Sensitivity is the smallest detectable change in 1 cm of path length that a spectrometer can measure during 1 s. If many measurements can be made within a second, averaging may be used to further improve (by a factor of the square root of the number of measurements or the square root of the data acquisition rate) the achievable sensitivity. Sensitivity has units of $\text{cm}^{-1} \text{Hz}^{-1/2}$. Sensitivity can also be quantified using the minimum detectable absorption loss (MDAL), i.e., the normalized standard deviation of the smallest detectable change in absorption (units of cm^{-1}). Equation (45.1) shows

B. Paldus (✉)
Skymoon Ventures
Palo Alto, CA, USA
e-mail: bpaldus@gmail.com

A. A. Kachanov
Picarro, Inc.
Sunnyvale, CA, USA
e-mail: akachanov@picarro.com

that the sensitivity of a spectrometer depends not only on the light path's length through the sample but also on the intensity noise of the light source.

Selectivity is the ability of a spectrometer to distinguish between two different species absorbing at similar wavelengths. The instrument must be able to resolve the different spectral lines. Thus, selectivity depends on spectral resolution, which has units of frequency (MHz), wavelength (nm), or wavenumbers (cm^{-1}).

Traditional spectrometers, such as nondispersive infrared (NDIR) and Fourier transform infrared (FTIR), use incoherent thermal light sources. For both techniques, the physical length of their sample chamber limits their sensitivity. Some devices try to fold the light path several times through the sample chamber in order to improve sensitivity, but this approach encounters physical size and mechanical stability limitations. Typical MDAL are in the 10^{-5} cm^{-1} range. These instruments, therefore, rely on measuring the strongest absorption transitions available, which are found in the mid-infrared range (3 to $12 \mu\text{m}$). Often, however, the strongest transitions overlap with features of other species found in the sample mixture. The instrument's performance becomes a sensitivity–selectivity tradeoff.

Laser-based optical detection methods, called tunable diode laser absorption spectroscopy (TDLAS), circumvent some of these problems by exploiting the coherent nature of laser light. A tunable continuous-wave laser source brings two benefits:

- A narrow linewidth, which allows high spectral resolution scans to be performed.
- Low spatial beam divergence, which allows it to be folded hundreds, if not thousands, of times.

By transmitting laser light with a small beam size over long distances, multipass cells can be designed to achieve up to a kilometer of path length enhancement. Multipass cell laser spectroscopy systems have demonstrated MDAL down to 10^{-9} cm^{-1} . However, such instruments still remain limited by laser intensity fluctuations and interference fringes. Moreover, standard multipass techniques do not provide an absolute optical loss measurement.

45.2 Cavity Ring-Down Spectroscopy

Cavity ring-down spectroscopy (CRDS) is a more recently developed TDLAS approach that replaces a multipass cell with a stable optical resonator, called the ring-down cavity (RDC). CRDS is based on the principle of measuring the rate of decay of light intensity inside the RDC. The transmitted wave decays exponentially in time. The decay rate is proportional to the total optical losses inside the RDC.

In a typical CRDS setup, light from a laser is first injected into the RDC, and is then interrupted. The circulating light inside the RDC is both scattered and transmitted by the mirrors on every round-trip and can be monitored using a photodetector placed behind one of the cavity mirrors. The decay constant, also called the ring-down time τ , is then measured as a function of the laser wavelength to obtain a spectrum of the cavity optical losses. Detailed mathematical treatments of CRDS can be found in [1]. A simple derivation is presented here.

For a given wavelength λ , the transmitted light $I(t, \lambda)$ from the RDC is given by

$$I(t, \lambda) = I_0 e^{-\frac{t}{\tau(\lambda)}}, \quad (45.2)$$

where I_0 is the transmitted light at the time the light source is shut off, and $\tau(\lambda)$ is the ring-down time constant. The total optical loss inside the cavity is $L(\lambda) = [c\tau(\lambda)]^{-1}l_{\pi}$, where c is the speed of light. The total optical loss comprises the empty cavity optical loss and the sample optical loss. CRDS provides an absolute measurement of these optical losses. The empty cavity (round-trip) optical loss $L_{\text{empty}}(\lambda)$ comprises the scattering and transmission losses of the mirrors. In general, better mirrors provide lower empty cavity losses and higher sensitivity. The sample (round-trip) optical loss is $A(\lambda) = \alpha(\lambda)l_{\pi}$, where l_{π} is the cavity round-trip length and is simply the difference between total cavity losses and empty cavity losses, namely $A(\lambda) = L(\lambda) - L_{\text{empty}}(\lambda)$. Once the absorption spectrum $\alpha(\lambda)$ of the sample has been measured, the sample concentration can be readily computed using the absorption cross section and lineshape parameters.

The MDAL for a CRDS system is defined by

$$\alpha_{\min} = \frac{1}{l_{\text{eff}}} \left(\frac{\Delta\tau}{\tau} \right), \quad (45.3)$$

where $(\Delta\tau/\tau)$ is called the shot-to-shot noise of the system. The effective path length of a CRDS measurement is $l_{\text{eff}} = c\tau$. For typical RDC mirrors with a reflectivity of 99.995% and scattering losses of less than 0.0005%, the path length enhancement can exceed 20,000. For a 20 cm long sample cell, the effective path length is 8 km, which exceeds the best performance of multipass spectroscopy by a factor of 3, based on the effective path length alone. A good CRDS system can achieve a shot-to-shot variation of 0.03%, leading to an MDAL of $4 \times 10^{-10} \text{ cm}^{-1}$. Note also that the CRDS measurement is not dependent on either the initial intensity of the light inside the cavity, provided that the signal has a sufficient signal-to-noise ratio at the detector, or on the physical sample path length like traditional absorption spectroscopy. Moreover, CRDS can use laser sources with narrow linewidths and achieve high spectral resolution.

CRDS can resolve all three limitations of absorption spectroscopy, namely sensitivity, selectivity, and dependence on

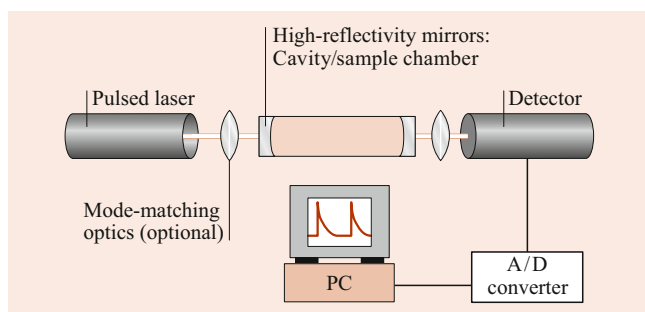


Fig. 45.1 Typical P-CRDS setup

the intensity noise of the light source [1]. CRDS has been implemented using many different approaches. This chapter will discuss several commonly used variations on the CRDS technique.

45.2.1 Pulsed Cavity Ring-Down Spectroscopy

Early implementations of CRDS used pulsed laser sources (P-CRDS) [2]. A typical P-CRDS setup is shown in Fig. 45.1. Today, CRDS has been implemented in the broadest possible range of wavelengths, from the UV (216 nm) to the mid-infrared (10 μm). Because of its experimental simplicity, P-CRDS has become a widespread tool for chemists and spectroscopists, finding applications in the measurement of predissociation dynamics, photolysis products, radiative lifetimes, aerosols or soot detection, temporal imaging, overtone vibrational spectroscopy, and kinetic studies. Typical P-CRDS sensitivity is $1 \times 10^{-9} \text{ cm}^{-1} \text{ Hz}^{-1/2}$.

P-CRDS methods have also been combined with other detection methodologies. Variations on P-CRDS include:

- Fourier-transform (FT) P-CRDS [3], where an RDC is excited with a broadband source, and time-resolved FT scans of the RDC output waveform are taken. Inversion of the interferogram then produces time-dependent ring-down waveforms at all resolved frequencies within the source wavelength range.
- Polarization P-CRDS [4], where the spectral splitting induced by the magnetic field is observed from the difference of the ring-down spectra of the two orthogonal polarizations.
- Pulse-stacked P-CRDS [5], where the length of the RDC is set so that pulses from a very high repetition rate pulsed source coherently add together, which increases the effective cavity light throughput to yield improved detection of the ring-down waveform.

The spectral resolution and sensitivity of P-CRDS are, however, limited by the use of short-pulse lasers. The effects of pulsed laser bandwidth on spectral resolution of P-CRDS

have been studied extensively and have led to system designs where only a single longitudinal and transverse mode of the RDC is excited [6]. However, single-mode P-CRDS is difficult to implement experimentally and still has limited sensitivity because the laser pulse is substantially attenuated by the RDC mirrors at the cavity output. The requirement for both improving CRDS sensitivity by reducing the variability in the measurement of the decay constant from shot to shot with single-mode excitation and improving the light transmission through the cavity to increase the signal-to-noise ratio of the decay waveform on the detector, provided the catalyst to implement continuous wave (CW) lasers in CRDS.

45.2.2 Continuous-Wave Cavity Ring-Down Spectroscopy (CW-CRDS)

CW lasers have narrow linewidths (< 50 MHz) and can be tuned in small spectral increments (< 50 MHz) to achieve high spectral resolution with excellent wavelength reproducibility. Moreover, owing to their narrow linewidths, they are better suited for efficient coupling into a single mode of a high finesse RDC, thereby reducing shot-to-shot variations in the measured ring-down decay constant. Furthermore, they can be directly modulated, thereby allowing higher data repetition rates, which, in turn, leads to improved sensitivity.

The first efforts in CW-CRDS involved optically locking a laser diode to a high-finesse cavity, but the performance was limited because the laser diode would drift and lock to different RDC modes. The use of sufficient optical isolation and an external optical switch resolved this issue. The most common approach used today is to sweep a RDC mode through the emission profile of a diode laser and shut the laser off with an acousto-optic modulator (AOM) (Fig. 45.2) when sufficient light is injected into the cavity [7]. Numerous variations on this approach exist. For example, CW-CRDS can be implemented by rapidly sweeping the cavity mode into and out of resonance with the laser. The simplest approach is to sweep the laser wavelength into and out of resonance with a cavity mode and directly modulate the laser source current [8]. The most popular CW lasers used today are distributed feedback (DFB) diode lasers.

In most CW-CRDS embodiments, the ring-down cavities are linear, i.e., consist of two mirrors. Ring resonators (e.g., triangular or bow-tie cavities) can also be used. Ring cavities provide the benefits of minimizing optical feedback and eliminating the need for extensive isolation or frequency shifting of the laser source. Moreover, ring resonators break the frequency degeneracy between cavity modes with orthogonal polarizations, effectively creating two coupled resonators with high and low finesse, respectively. The low-finesse cavity can be used to lock the laser

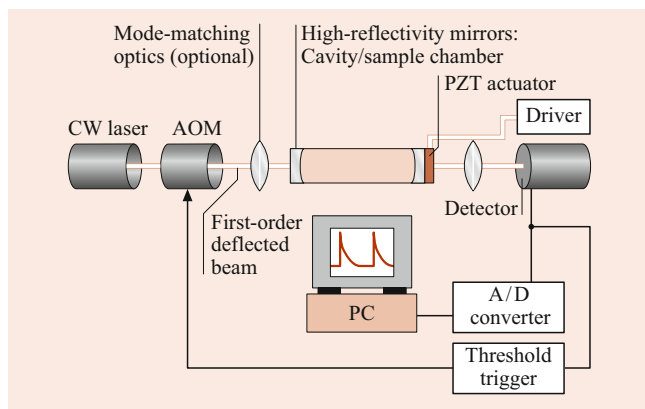


Fig. 45.2 Typical CW-CRDS setup

to single-cavity mode, while the high finesse cavity can be used for CRDS. The AOM acts as both a frequency-shifter and an on-off switch. This method was used to demonstrate the highest CRDS sensitivity achieved to date, namely $1.0 \times 10^{-12} \text{ cm}^{-1} \text{ Hz}^{-1/2}$ [9].

Prism-based, rather than mirror-based, cavities have also been used [10]. Such cavities comprise two prisms whose intracavity facing angles are at Brewster's angle, and whose extracavity facing angles are such that total internal reflection occurs and results in unit reflectivity. One of the prisms has a curved facet to create a stable optical resonator. The purpose of this design is to extend operation over a much broader range of wavelengths than can be achieved using dielectric coatings. Currently, high-reflectivity mirrors are limited in bandwidth to about $\pm 15\%$ of their center wavelength.

CW-CRDS has been applied over a wide range of wavelengths. It has been used for medical breath analysis, trace gas detection in environmental and process control applications, and isotopic analysis. In the near-infrared, CW-CRDS systems achieve sensitivities of $10^{-11} \text{ cm}^{-1} \text{ Hz}^{-1/2}$ and a concentration measurement repeatability of 1 part in 5000. Similar performance in the mid-infrared ($3 \mu\text{m}$) resulted in the detection of parts-per-trillion ethylene concentrations [11].

Extensions of the basic CW-CRDS technique have also been developed:

- Phase-shifted CW-CRDS [12]: the phase shift accrued by a sinusoidally modulated CW laser is measured for both an empty RDC and one with a sample. The concentration is deduced from these two measurements.
- Heterodyne CW-CRDS [13]: enhances the power in the ring-down decay waveform by mixing with a local oscillator. For example, the local oscillator can be the orthogonal polarization used to lock the laser to the RDC or can be the reflected signal from the RDC when laser is frequency shifted (by the local oscillator frequency) off resonance from the RDC mode. Heterodyne CRDS can approach the shot-noise limit.

- V-cavity CW-CRDS [14]: a three-mirror V-shaped RDC is exploited to achieve consistent repetitive optical locking of a DFB diode laser to a single cavity mode, thereby significantly enhancing light throughput.

CW-CRDS is now maturing to a level of robustness and reliability such that it can be commercially deployed in industrial applications, where the sensitivity requirements can no longer be met by FTIR, NDIR, or gas chromatography.

45.3 Cavity-Enhanced Spectroscopy

Most CRDS systems capture the ring-down waveform using a digital oscilloscope. The Levenberg–Marquardt (LM) method produces the optimal fit, so that LM methods have become the de-facto *gold standard* in CRDS [15]. However, the LM algorithm can require multiple iterations, thereby limiting the data acquisition times to several hundred Hz. Fast-fitting algorithms that closely approximate the LM fit but allow data acquisition rates up to 10 kHz have recently gained widespread deployment [16]. Today, the data acquisition rates are no longer limited by the back-end numerical fit. Rather, the speed of CRDS systems is limited by the speed of laser modulation itself.

Cavity-enhanced spectroscopy (CES) was developed in an effort to simplify CRDS and eliminate the requirement for the digitization of a time-domain signal and laser modulation. CES has many different implementations. All CES methods are based on the principle that the buildup of intracavity power, and hence cavity throughput, depends on intracavity losses, which include absorption by a sample. CES involves measuring the steady-state transmission through a cavity as a function of wavelength in order to determine changes in the integrated transmitted intensity caused by the absorbing species.

For a cavity with two mirrors of intensity reflectivity, R , and length, L , the effective steady-state path length is $L_{\text{eff}} = L/(1 - R)$. If an absorbing gas is present, the reflectivity will be reduced by the Beer–Lambert factor $e^{-\alpha L}$ namely $R' = R e^{-\alpha L}$, so that one can effectively relate the ratio R'/R to the Beer–Lambert ratio I/I_0 for a single pass. The steady-state transmitted laser intensity for such a cavity is given by $I = I_L C_p T [2(1 - R)]^{-1}$, where T is the intensity transmissivity, I_L is the laser intensity, and C_p is the coupling efficiency in the cavity mode. Thus, for an absorbing gas, the change in transmitted intensity at a given wavelength is

$$\Delta I/I = GA(1 + GA)^{-1}, \quad (45.4)$$

where $A = 1 - e^{-\alpha L}$ and $G = R/(1 - R)$ so that for $\alpha L \ll 1$, $(\Delta I/I) \approx GA \approx G\alpha L$. This latter relation has been interpreted as a linear response in absorption loss, multiplied by

an effective cavity *gain* of $R/(1 - R)$, i.e., the absorbance is measured over the effective length of the cavity, which corresponds to the number of cavity passes occurring within the cavity ring-down time constant. Note that the transmitted power level will be attenuated by the mirror transmissivity, T , so that these methods are limited by laser power and detector sensitivity.

Because CES techniques measure transmitted light intensity, they are no longer immune to laser intensity noise. Furthermore, when the absorbance becomes comparable to the cavity loss, the sensitivity improvement of CES saturates, as the sample absorption begins to dominate the effective number of cavity passes. Note that in this case, the effective path length becomes a function of the sample concentration, which underlines another limitation of CES: this technique is not independent of the cavity length and, hence, depends on cavity alignment. Moreover, CES systems are not self-calibrated to the species extinction coefficient, and therefore require calibration against a known sample concentration, or against the absolute cavity loss, often measured using CRDS. Finally, it should be noted that the rate of data collection in CES is limited by the RDC time constant, because the cavity acts like a single-pole, low-pass filter with a 3 dB frequency of $(2\pi\tau)^{-1}$, which can range from 5 to 50 kHz. Unlike CRDS, CES does not require fast digitization of the decay waveform followed by a nonlinear fit, so that the data acquisition hardware can be a much slower, less expensive A/D converter, and spectral data can be acquired almost instantaneously.

Five distinguishable variants of CES have been developed and are discussed. The first three methods, called cavity-enhanced transmission spectroscopy (CETS), find their origins in CRDS. These methods are cavity-enhanced absorption spectroscopy (CEAS) [17], integrated cavity output spectroscopy (ICOS) [18], and off-axis ICOS [19]. For these three approaches, the laser intensity is no longer interrupted to observe a *ring-down event*, although the path-length enhancing properties of the RDC remain. More sensitive CES methods involve locking the laser to the cavity mode resonance. These will be referred to as locked cavity-enhanced transmission spectroscopy and have two variations: locked cavity-enhanced transmission spectroscopy (L-CETS) [20] and noise-immune, cavity-enhanced optical heterodyne molecular spectroscopy (NICE-OHMS) [21].

45.3.1 Cavity-Enhanced Transmission Spectroscopy (CETS)

CETS has been implemented using several variations, all of which are based on measuring the time-integrated transmission through a high-finesse RDC as a function of the wavelength. As stated earlier, the transmitted light provides

an effectively enhanced path length to any sample absorption inside the cavity. In all CETS approaches, the transmitted light intensity is a small fraction [about $(1 - R)$] of the incident intensity, which reduces the signal to noise on detection, so that averaging is required. All CETS approaches are also dependent on laser intensity noise and sample path length.

The tradeoff in using a high-finesse cavity is that in steady state, its transmission is a nonuniform function of the wavelength and consists of a series of sharp cavity mode peaks, namely the transverse and longitudinal modes. This transmission pattern repeats itself periodically in every free spectral range (FSR). The density of the mode spacing is a function of the cavity design: the round-trip length and the mirror radius of curvature. The quality of mode matching between the laser and the RDC determines the number of modes into which light can couple efficiently.

CEAS is the simplest CETS approach: the laser, coupled through an RDC, is tuned in wavelength over the absorption feature of interest, and the integrated cavity transmission is measured as a function of the wavelength [17]. The cavity length is free-running (neither modulated nor locked to the laser). In order to minimize the nonuniformity of the cavity transmission, CEAS exploits cavity geometries such that the inherent mode structure is as dense as possible. No mode matching is employed, so that laser light is coupled into as many modes as possible. The laser is scanned multiple times over the cavity modes in order to time average over the unstabilized cavity length. Extensive averaging can be required to achieve reasonable performance. The residual mode structure of the cavity can be significant and produces intensity modulation in the spectrum. Typically, the laser linewidth is larger than the individual cavity mode resonances, so that the output can be very noisy. CEAS does appear to have mechanical stability advantages, in that a cavity length change or deformation is, in fact, desirable to randomize the excited modes over wavelength. Typical sensitivities of CEAS range from 5×10^{-7} to $10^{-9} \text{ cm}^{-1} \text{ Hz}^{-1/2}$.

ICOS tries to achieve uniform transmission through the RDC by systematically disrupting the cavity mode resonances in order to recover the frequency-averaged response of the cavity as a function of the wavelength [18]. RDC length modulation was implemented by either moving one of the cavity mirrors using a piezo-electric transducer (PZT) or by slightly modulating the angle of injection in the cavity using a PZT-driven mirror mount. When the laser is scanned over the desired wavelength range with only the RDC modulation sweeping the modes (5 to 10 free spectral ranges), the resulting absorption spectra show an intensity modulation of about 10%. This intensity modulation results from a periodic nonuniformity in the mirror movement at the turning points of the PZT modulation, where the increased overlap time between the cavity mode and laser produces a higher

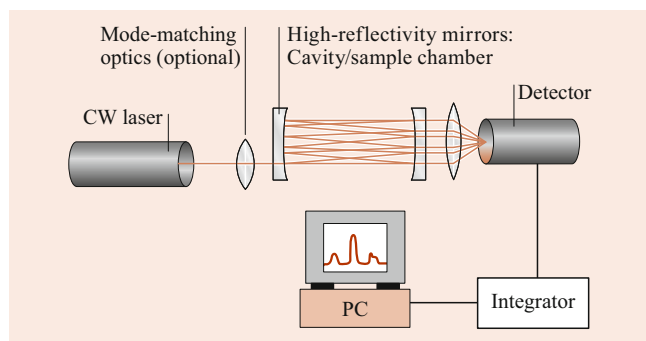


Fig. 45.3 Typical off-axis ICOS setup

transmitted light intensity. In order to eliminate this intensity modulation, the laser wavelength is frequency modulated simultaneously. The typical sensitivity of the ICOS approach is about $2 \times 10^{-7} \text{ cm}^{-1} \text{ Hz}^{-1/2}$.

A third approach, called off-axis ICOS, resolves the cavity transmission uniformity problem of CEAS and eliminates the need for modulation of ICOS. In off-axis ICOS, shown in Fig. 45.3, the RDC is aligned so as to generate a set of spatially separated reflections within the cavity that eventually satisfy the reentrant condition [19]. Furthermore, the mirrors are slightly astigmatized, which results in Lissajous spot patterns on the mirrors. The combination of this alignment and slight astigmatism significantly reduces the RDC mode degeneracy. As a result, the cavity mode spacing can become smaller than the cavity mode width and the cavity transmission appears to become largely frequency independent, or *white*. Thus, the RDC provides path length enhancement without introducing intensity noise in the transmitted spectrum. However, increasing the number of spots on the mirrors usually requires larger mirrors (e.g., 2 inches for off-axis ICOS versus 0.5 inches for CRDS), which in turn results in a larger cavity (sample) volume. In cases of low sample flow, sample chamber filling times can limit the measurement time. Moreover, the system is now dependent on the mechanical stability of the cavity and the laser to cavity alignment. The best off-axis ICOS sensitivity achieved to date is $3 \times 10^{-11} \text{ cm}^{-1} \text{ Hz}^{-1/2}$ and is comparable to CW-CRDS.

45.3.2 Locked Cavity-Enhanced Transmission Spectroscopy (L-CETS)

An alternative approach (L-CETS) achieves higher sensitivity by locking the laser frequency to a single cavity resonance and then scanning the cavity over the absorption feature of interest [20]. In this case, the cavity throughput becomes uniform across the entire spectral scan, and the cavity transmission increases to the maximum theoretical value, leading to better signal to noise at the detector than CETS ap-

proaches. Laser wavelength jitter at high frequencies, which cannot be compensated by the locking control loops, will lead to increased noise in the spectral scans. In order to lock the laser and cavity together robustly, the laser linewidth typically cannot exceed the cavity mode resonance linewidth, so that for a high-finesse sample cavity, the laser choice can be limited. Sensitivities of $10^{-11} \text{ cm}^{-1} \text{ Hz}^{-1/2}$ have been demonstrated using L-CETS.

The NICE-OHMS technique was developed to overcome the dependence of L-CETS on laser wavelength jitter [21]. NICE-OHMS combines the benefits of frequency modulation (FM) spectroscopy with the path length enhancements of a high-finesse optical resonator. The technique is called *noise immune*, because it does not depend on the quality of the laser and cavity lock. Effectively, it is immune to laser frequency noise, although residual amplitude modulation can reduce the performance. NICE-OHMS sensitivity depends on the laser power transmitted, the efficiency and bandwidth of the photodetector, and the FM modulation index. NICE-OHMS has exploited cavities with a finesse of 100,000 to achieve sensitivities of $1 \times 10^{-14} \text{ cm}^{-1} \text{ Hz}^{-1/2}$. NICE-OHMS holds the world record in detection sensitivity of all cavity-enhanced techniques.

In a NICE-OHMS experiment, phase modulation of the laser produces sidebands that are set to equal the free spectral range of the high-finesse resonator. Because the sidebands are transmitted by the cavity in the same manner as the carrier, any small wavelength fluctuations in the laser or small optical phase shifts of the transmitted carrier that contribute to noise in the transmitted intensity will appear identically in the sidebands. After demodulation, this noise will cancel out. Thus, the transmitted carrier and sidebands are an accurate representation of the carrier and sidebands impinging on the input mirror of the cavity. The carrier laser frequency is locked to the peak of the optical cavity mode and tracks this mode if the cavity length is changed in order to produce a spectral scan. The sidebands are detected and demodulated as in conventional FM spectroscopy. The key to NICE-OHMS is that the noise level can approach the intrinsic shot noise of the laser at the FSR frequency (namely hundreds of MHz).

If there is no sample in the cavity, the transmitted sidebands will cancel after demodulation because they have opposite phases. No signal will be observed. If there is a sample in the cavity, the sidebands will experience different transmission amplitudes, so that demodulation will produce a signal proportional to the difference in absorption between the sideband frequencies. In addition, the absorption feature produces a phase shift that pulls the carrier cavity mode frequency, so that the sidebands become detuned from the mode peak and acquire a phase shift on transmission. This sideband phase shift contributes to the demodulated signal.

45.4 Extensions to Solids and Liquids

Thus far, the discussion of cavity-enhanced techniques has addressed traditional optical resonators formed using high-reflectivity dielectric mirrors that encompass gas samples. Extensions of cavity-enhanced methods to liquid and solid media has required additional innovation, specifically in the optical cavities used.

45.4.1 Evanescent-Wave Cavity Ring-Down Spectroscopy (EW-CRDS)

Evanescent-wave CRDS (EW-CRDS) exploits the fact that total internal reflection allows probing the surface layer of a sample in contact with a prism. The simplest configuration places a Brewster prism inside a linear ring-down cavity. The prism folds the cavity beam path by 90 degrees, thereby producing one point in the prism with a total internal reflection [22]. The evanescent wave produced by this internal reflection can be used to probe liquid or solid samples. Another possible embodiment is a ring cavity with its optical path inside a multifaceted polygon, where at each facet, total internal reflection occurs [23]. Light is coupled into and out of the polygon by photon tunneling – which effectively controls the overall finesse of the cavity. The absorbing sample material can then be placed on any one or more of the polygon facets, and its detection is done using the polygon's evanescent waves.

45.4.2 Cavity Ring-Down of Condensed Media for Analytical Chemistry

More direct approaches to measuring liquid samples involved confining the liquid samples within a more traditional RDC. The most direct method involves placing a liquid directly into the cavity, but this approach results in very limited sensitivity. By placing a Brewster cell filled with liquid sample in an RDC, the sensitivity of the P-CRDS can be slightly improved. By matching the Brewster angles to the refractive indices of the adjacent media (the outside angle matches the air-filled RDC, while the inner angle matches the index of the liquid), the sensitivity can be improved dramatically [24]. The peak-to-peak baseline noise level of such a P-CRDS system was 1.0×10^{-5} absorbance units (AU), rivaling the best available commercial ultraviolet-visible (UV-VIS) direct absorption detectors. The performance remained limited by the excitation of multiple cavity modes. A CW-CRDS system using the same angle-matched Brewster cell [25] improved the peak-to-peak baseline noise by a factor of 50 to 2×10^{-7} AU. This CRDS detector outperformed the best commercially available UV-VIS detector by a factor of 30, again

illustrating the potential for CRDS to replace standard absorption spectroscopy techniques.

Similar inroads into liquid measurement have been made using CEAS with incoherent broadband sources such as Xenon lamps or more practically solid-state light-emitting diodes (LEDs). Given that most liquid solutions have broad and fairly featureless absorption spectra, the integrated intensity measurement is an easier approach than measuring very short ring-down times. Unfortunately for the incoherent broadband sources used, matching the Brewster angle for all wavelengths is not possible, so a 0-degree geometry that overlaps the back reflection with the excitation beam was adopted. In this approach, the reflectivity of the cavity is balanced between extending the mirror reflectivity spectral range for broadband spectra, maximizing the cavity enhancement factor, and maintaining a detectable cavity output signal [26]. Interestingly, the lower limit for detection obtained with this approach was only five times worse than that obtained with the elaborate laser-based, pulsed CRDS setup [27]. Target applications for liquid CRDS focused mainly on improving the sensitivity of liquid chromatography absorption detection.

Solid samples have also been placed inside linear CRDS cavities for characterization. Mostly, P-CRDS are used. Examples of applications include characterization of C-60 films, thin-film coatings, and silicon wafers.

45.4.3 Cavity Ring-Down Spectroscopy Using Waveguides

The typical setup of fiber loop cavity ring-down leverages optical components developed for DWDM telecommunications, so that the laser, fiber loop with Bragg gratings, and detector are all coupled together with fiber splices or telecommunications fiber connectors, leading to a robust and relatively straightforward system assembly. The cavity can be either a linear one with two Bragg gratings at either end, or a fiber loop with a very low loss coupler to extract the detector signal.

Fiber cavities are attractive because they can extend the use of CRDS into harsh environments, can probe liquids as well as gases, and can be used to measure bending loss [28] (when applied to the fiber loop), pressure [29] (when applied to the fiber loop), and temperature [30] (via physical changes in a fiber Bragg grating inserted into the fiber loop). The high-reflectivity mirrors on each end of the fiber can be either dielectrically coated, as in a traditional ring-down cavity design, or can consist of fiber Bragg gratings. Fiber-based CRDS has also been applied to detection in liquid media via a fiber loop cavity wherein a liquid sample replaced the index matching fluid in the gap between fibers at the connector splice [31]. This approach produced a hundredfold enhancement over linear detection.

The most recent and interesting application of waveguide-based CRDS is the detection of analytes delivered using a microcapillary to a gap in the loop. The dimensions of the flow channel govern the choice of waveguide: the cross section of the detection region and the flow channel need to be similar in size in order to not build up pressure in the flow channel or build up a large “dead volume”. The emerging field of absorption detection in microfluidics using CRDS still remains largely unexplored, although attempts have begun [32].

It is anticipated that CRDS will eventually reach sensitivities for liquid and thin film samples that are comparable to those achieved in gases. CRDS is also expected to find commercial applications in high-performance liquid chromatography, thin film characterization, and biological detection. Combination techniques of CRDS and fluorescence, or CRDS and Raman spectroscopy, may also be on the not-so-distant horizon, where CRDS provides the quantification, while the complementary technique provides identification [33].

Overall, the CRDS field has expanded rapidly in the last decade from an average of 16 papers published per year between 1985 and 1995, 240 papers published per year between 1995 and 2005, to 913 papers published per year between 1995 and 2015. Most recently, the number of annual published papers exceeded 1,000 in 2012 and exceeded 1,500 in 2018, showing the wide applicability of the methodology in fields ranging from atmospheric chemistry, medical breath analysis, thin film growth and process monitoring in solid-state physics, combustion and plasma studies, molecular transient studies in astrophysics, and analytical chemistry [34].

Acknowledgements We have benefited invaluable from the collaboration with our co-workers at Picarro, and would like to extend our gratitude to Prof. Richard N. Zare and Dr. Marc Levenson for their unwavering support in helping make CRDS a commercial reality over the past two decades. We would also like to express our appreciation to all of our scientific collaborators worldwide, both industrial and academic, for their friendship, openness, and help over the years. Barb would like to dedicate this chapter to her father, Prof. Josef Paldus, who has been an inspiration to her throughout her career, and with whom it is an honor to share a publication in the same book.

References

1. Busch, K.W. (ed.): *Cavity Ringdown Spectroscopy: An Ultratrace Absorption Measurement Technique*. ACS Symp. Ser., vol. 720. Oxford University Press, Washington (1997)

2. O’Keefe, A., Deacon, D.A.G.: *Rev. Sci. Instrum.* **59**, 2544 (1988)
3. Engeln, R., Meijer, G.: *Rev. Sci. Instrum.* **67**, 2708 (1996)
4. Engeln, R., Bierden, G., van den Berg, E., Meijer, G.: *J. Chem. Phys.* **107**, 4458 (1997)
5. Crosson, E.R., Haar, P., Marcus, G.A., Schwettman, H.A., Paldus, B.A., Spence, T.G., Zare, R.N.: *Rev. Sci. Instrum.* **70**, 4 (1999)
6. van Zee, R.D., Hodges, J.T., Looney, J.P.: *Appl. Opt.* **38**, 3951 (1999)
7. Romanini, D., Kachanov, A.A., Sadeghi, N., Stoeckel, F.: *Chem. Phys. Lett.* **270**, 538 (1997)
8. Paldus, B. A., Zare, R. N.: U.S. Patent #6466322
9. Spence, T.G., Harb, C.C., Paldus, B.A., Zare, R.N., Willke, B., Byer, R.L.: *Rev. Sci. Instrum.* **71**, 347 (2000)
10. Lehmann, K. K., Rabinowitz, P.: U.S. Patent #5973864
11. Kuhnemann, F., Muller, F., von Basun, B., Halmer, D., Popp, A., Schiller, S., Hering, P., Murtz, M.: *SPIE Proc* **5337**, paper 18. SPIE, Bellingham (2004)
12. Engeln, R., Von Helden, G., Berden, G., Meijer, G.: *Chem. Phys. Lett.* **262**, 105 (1996)
13. Levenson, M.D., Paldus, B.A., Spence, T.G., Harb, C.C., Harris, J.S., Zare, R.N.: *Chem. Phys. Lett.* **290**, 335 (1998)
14. Romanini, D., Kachanov, A.A., Morville, J., Chenevier, M.: *EOS/SPIE International Symp. on Ind. Lasers Inspection Environments*, **3821**, 94. SPIE, Bellingham (1999)
15. Naus, H., van Stokkum, I.H.M., Hogervorst, W., Ubachs, W.: *Appl. Opt.* **40**, 4416 (2001)
16. Halmer, D., von Basun, G., Hering, P., Murtz, M.: *Rev. Sci. Instrum.* **75**, 2187 (2004)
17. Engeln, R., Berden, G., van den Berg, E., Meijer, G.: *J. Chem. Phys.* **107**, 4458 (1997)
18. O’Keefe, A., Scherer, J.J., Paul, J.B.: *Chem. Phys. Lett.* **307**, 343 (1999)
19. Paul, J.B., Lapson, L., Anderson, J.G.: *Appl. Opt.* **40**, 4904 (2001)
20. Gianfrani, L., Fox, R.W., Hollberg, L.: *J. Opt. Soc. Am. B.* **16**, 2247 (1999)
21. Ye, J., Ma, L.S., Hall, J.L.: *J. Opt. Soc. Am. B.* **15**, 6 (1998)
22. Pipino, A.C.R., Hudgens, J.W., Huie, R.E.: *Rev. Sci. Instrum.* **68**, 2978 (1997)
23. Pipino, A.C.R.: *Phys. Rev. Lett.* **83**, 3093 (1999)
24. Snyder, K., Zare, R.N.: *Anal. Chem.* **75**, 3086 (2003)
25. Snyder, K., Zare, R.N., Kachanov, A.A., Paldus, B.A.: *Anal. Chem.* **77**, 1177 (2005)
26. Islam, M., Seetohul, L., Ali, Z.: *Appl. Spectrosc.* **61**, 649 (2007)
27. van der Sneppen, L., Wiskerke, A., Ariese, F., Gooijer, C., Ubachs, W.: *Anal. Chim. Acta* **558**, 2 (2006)
28. von Lerber, T., Sigrist, M.W.: *Appl. Opt.* **41**, 3567 (2002) and EP00121314.9
29. Wang, C.J., Scherrer, S.T.: *Appl. Opt.* **43**, 6458 (2004)
30. Wang, C.J., Mbi, A.: *Meas. Sci. Technol.* **17**, 1741 (2006)
31. Brown, R.S., Kozin, I., Tong, Z., Oleschuk, R.D., Loock, H.P.: *J. Chem. Phys.* **117**, 10444 (2002)
32. Loock, H.P.: *Trends Anal. Chem.* **25**, 655 (2006)
33. Richmann, B.A., Kachanov, A.A., Paldus, B.A., Strawa, A.W.: *Opt. Express* **13**, 3376 (2005)
34. Berden, G., Engeln, R.: *Cavity Ring-Down Spectroscopy Techniques and Applications*. Wiley, Chichester (2009)



Barbara Paldus Dr Barbara Paldus received her PhD in Electrical Engineering from Stanford University. She is a partner at Sekhmet Ventures and CEO at Codex Labs. Previously, she was CEO at Finesse Solutions and CTO at Picarro, which she founded in 2005 and 1998, respectively. She holds over 45 patents and has received numerous research awards, most recently the Adolph Lomb Prize (2001) by the OSA for her work in cavity ringdown spectroscopy.



Alexander A. Kachanov Alexander Kachanov received his MSc in Physics from Moscow Institute of Physics and Technology in 1976 and his PhD in Physics from the Institute of Spectroscopy of the Russian Academy of Sciences in 1987. In 2001, he joined Picarro, Inc., where his research interests focus on ultrasensitive gas detection and the development of novel laser sources.



Glenn Stark, Nelson de Oliveira , and Peter L. Smith 

Contents

46.1	Light Sources	668
46.1.1	Synchrotron Radiation	668
46.1.2	Laser-Produced Plasmas	670
46.1.3	Arcs, Sparks, and Discharges	670
46.1.4	Supercontinuum Radiation	670
46.2	VUV Lasers	671
46.2.1	Primary Lasers	671
46.2.2	Nonlinear Techniques	671
46.3	Spectrometers	673
46.3.1	Grating Spectrometers	673
46.3.2	Fourier Transform Spectrometers	674
46.4	Detectors	675
46.4.1	Photomultiplier Tubes	675
46.4.2	Microchannel Plates	675
46.4.3	Silicon Photodiodes	675
46.4.4	Charge-Coupled Devices	676
46.5	Optical Materials	676
46.5.1	Windows	676
46.5.2	Capillaries	676
46.5.3	Thin Films	676
46.5.4	Coatings	677
46.5.5	Interference Filters and Multilayer Coatings	677
46.5.6	Polarizers	677
References	677

Abstract

The design of UV spectroscopic experiments and apparatus must conform to the constraints associated with producing, dispersing, and detecting UV (ultraviolet) photons. In this chapter, we review the instrumentation available for UV spectroscopy, concentrating on the VUV (vacuum ultraviolet), where special instrumentation is necessary.

An inclusive review of vacuum ultraviolet techniques can be found in *Vacuum Ultraviolet Spectroscopy I & II* (1998), edited by Samson and Ederer [1]. There are many comprehensive reviews of VUV light sources, spectrometers, and detectors, which are referenced in the appropriate sections of this chapter.

Keywords

synchrotron radiation · harmonic generation · grazing incidence · silicon photodiode · dark count rate

The ultraviolet (UV) spectral region extends from the short wavelength side of the visible, about 400 nm, to the long wavelength side of the X-ray region at approximately 10 nm. Ultraviolet photon energies range from about 3 to 120 eV. Because laboratory air at standard temperature and pressure does not transmit below about 200 nm, the UV region is conventionally subdivided into the near ultraviolet, wavelengths $\lambda > 200$ nm, and the vacuum ultraviolet (VUV), $\lambda < 200$ nm.

Further subdivisions are widespread but not uniformly adopted. The term middle ultraviolet (MUV) is sometimes used to designate the 200–300 nm wavelength region, with the term near UV used only for 300–400 nm.

VUV wavelengths are often divided into the far ultraviolet (FUV), 100–200 nm, and the extreme ultraviolet (EUV), 10–100 nm. In this review, we will simply refer to the UV (10–400 nm), the near UV (200–400 nm), and the VUV (10–200 nm).

G. Stark (✉)
Dept. of Physics, Wellesley College
Wellesley, MA, USA
e-mail: gstark@wellesley.edu

N. de Oliveira
Ligne DESIRS, Synchrotron Soleil
Gif-sur-Yvette Cedex, France
e-mail: nelson.de.oliveira@synchrotron-soleil.fr

P. L. Smith
retired
Cathedral City, CA, USA
e-mail: plsmith44@gmail.com

The absorption of UV radiation by atoms and molecules involves transitions to highly excited discrete and continuum levels. The relevant atomic and molecular physics of highly excited states is discussed in Chaps. 15, 25, 26, and 65. Ultraviolet absorption initiates many important photochemical reactions; applications in astrophysics, aeronomy, and combustion are reviewed in Chaps. 86 and 88. The experimental techniques used at ultraviolet wavelengths include high-resolution spectroscopic measurements of wavelengths and line shapes (Chap. 11), absolute photoabsorption oscillator strength and radiative lifetime measurements (Chap. 18), fluorescence spectroscopy, and energy, angle, and spin-resolved photoelectron spectroscopy (Chap. 65).

46.1 Light Sources

46.1.1 Synchrotron Radiation

Synchrotron radiation (SR) facilities provide intense continuum radiation in the infrared, visible, UV, and soft X-ray spectral regions. The radiation is emitted by relativistic electrons (or positrons) accelerated by the Lorentz force of a magnetic field. In addition to its continuum nature, synchrotron radiation is characterized by high degrees of collimation and polarization. Advances in specialized magnet designs, e.g., wigglers and undulators, which dramatically increase spectral brightness at selectable wavelengths, have stimulated continuing growth in synchrotron-radiation-based spectroscopic research. References [2–12] present general reviews on the nature of synchrotron radiation and on specific SR-based experimental techniques.

SR facilities use either a linear accelerator, a microtron, or a synchrotron to accelerate electrons or positrons to relativistic energies (0.1–10 GeV). The particles are then injected into a storage ring, where a series of bending magnets steers them in a closed orbit. The particles in the storage ring radiate energy, which is replaced by radio-frequency accelerating cavities that are part of the ring. These accelerating systems produce well-defined, regularly spaced bunches of stored particles, so that radiation from SR facilities is characterized by subnanosecond pulses with an interbunch spacing of a few nanoseconds, leading to repetition rates of several hundred MHz. Some beamline experiments require a lower repetition rate, for example the study of the dynamics of photo-induced processes through pump-probe experiments. In modern facilities, this class of experiments is accommodated via so-called “temporal modes” with 1–10 MHz repetition rates and 20–100 ps pulse widths.

Typical storage ring currents are on the order of 100 mA to 1 A. The current decreases continuously because of collisions with residual gas molecules and electron–electron (or positron–positron) scattering. During operation, some facili-

ties are able to periodically inject a small number of electrons into the storage ring, resulting in a quasi-constant total current ($\delta I/I$ of a few percent). Typically, injections occur every 2–5 min. In addition to the advantage of producing an almost constant photon flux at the experimental level, this mode also results in better machine and beamline stability. Storage ring pressures must be in the 10^{-10} Torr range in order to reduce collisions to acceptable levels; such pressure requirements can restrict the types of measurements performed at SR facilities.

The spectral properties of synchrotron radiation can be derived from Larmor’s formula for an accelerating relativistic charged particle [3, 13–17]. The total power P radiated by a beam of current I and energy E in a bending magnet field B is

$$P = 0.0265 E^3 I B \quad [\text{kW}], \quad (46.1)$$

where, throughout this chapter, I is in mA, E is in GeV, and B is in T. For example, a 300 mA beam of 1 GeV electrons radiates at a rate of about 8 kW when traversing the field of a typical 1.0 T bending magnet. One-half of the total power is radiated above the critical wavelength, λ_c , where

$$\lambda_c = \frac{1.9}{BE^2} \quad [\text{nm}]. \quad (46.2)$$

For the example just considered, $\lambda_c = 1.9$ nm.

The power radiated by, and the flux from, synchrotron radiation sources is often expressed per fractional (or percent) bandwidth. For example, the flux, in units of photons $(\text{cm}^2 \text{s})^{-1}$, at 10 nm (124 eV) per 1% bandwidth is the flux in a 0.1 nm band centered at 10 nm, which is the same as that in a 1.24 eV energy band. The radiated power per fractional bandwidth peaks at $\lambda \approx 0.75\lambda_c$.

The flux per fractional bandwidth reaches a broad maximum at $\lambda \approx 3.3\lambda_c$ and decreases slowly at longer wavelengths, with a limiting behavior that is proportional to $\lambda^{-1/3}$ for $\lambda \gg \lambda_c$. Thus, although the photon flux typically peaks in the soft X-ray region, a high flux is also present throughout the VUV wavelength range. Below λ_c , the flux drops rapidly, with little usable radiation at wavelengths below about $0.1\lambda_c$.

The angular distribution of the radiated light is sharply peaked in the instantaneous direction of the beam of radiating particles. Practically all the radiation is emitted into an opening half-angle θ that at $\lambda = \lambda_c$ is equal to $1/\gamma$, where $\gamma = E/mc^2$; i.e.,

$$\theta = \frac{1}{\gamma} = \frac{5.11 \times 10^{-4}}{E} \quad [\text{rad}]. \quad (46.3)$$

Radiation from beams with energies of a few GeV has a divergence somewhat less than 1 mrad at λ_c . The divergence

increases at longer wavelengths, with

$$\theta = \frac{1}{\gamma} \left(\frac{\lambda}{\lambda_C} \right)^{\frac{1}{3}} \quad [\text{rad}]. \quad (46.4)$$

Radiation from bending magnets maintains this narrow divergence only in the vertical plane; in the orbital plane, the radiation is emitted in an opening angle equal to the bending angle of the magnet (typically a few 10s of mrad). Typical beam cross sections are 0.01 to 1 mm². Thus, the extremely high spectral brightness, i.e., photon flux per unit solid angle and % bandwidth, of synchrotron sources reflects both the very low divergence of the radiation and the small source size. A typical brightness associated with bending magnet radiation is on the order of 10¹² photons (s mm² mrad² 0.1% bandwidth)⁻¹. At the time of this review, some facilities are undertaking a significant machine technical upgrade to “diffraction limited storage rings” (DLSRs). In these “fourth-generation” synchrotron light sources, a low emittance should be achievable in both the horizontal and vertical planes, leading to a typical improvement in brightness of one to three orders of magnitude. DLSRs will be especially beneficial for soft and hard X-ray beamlines [18].

The pulsed nature of the radiation at synchrotron facilities is ideal for subnanosecond time-resolved spectroscopies [19–23].

Electron bunch lengths l_b are typically a few centimeters; radiation is, thus, observed from each bunch for a time interval given by $l_b/c \leq 100$ ps. The time for one full orbit is determined by the size of the storage ring and varies from about 20 ns at the smallest rings to 500–1000 ns at the larger rings. In modern facilities, the geometry and number of bunches stored are quite flexible and can be adapted to a variety of experiments that require particular temporal structures [24].

Third-generation synchrotron facilities incorporate straight sections between bending magnets to accommodate insertion devices such as wigglers and undulators. These are linear arrays of magnets with alternating polarities that cause the beam trajectory to oscillate, although no net displacement of the beam occurs. The oscillations produce synchrotron radiation that is characterized by extremely high brightness and that can be spectrally tailored to individual experiments [3, 12, 16, 25, 26].

Wigglers and undulators are distinguished by the value of their deflection parameter K , which is a measure of the maximum bending angle of the stored particle beam in units of θ , the angular divergence of the emitted radiation. The deflection parameter K is determined by the peak strength of the alternating magnetic field B_0 and its spatial period x_B by

$$K = 0.934 B_0 x_B, \quad (46.5)$$

with x_B in cm.

In the wiggler regime, $K \gg 1$; i.e., the angle at which the magnets deflect the electron beam is large compared with θ . The resulting spectrum resembles that from a bending magnet but is brighter by a factor of N_m of magnet periods (usually 10–100). Wigglers are generally used as wavelength shifters; magnetic fields larger than those available in conventional bending magnets decrease the critical wavelength of the spectral distribution and shift the overall spectrum to shorter wavelengths.

In the undulator regime, $K \approx 1$; i.e., the angle at which the electrons are deflected is on the order of θ , and radiation from individual oscillations adds coherently at certain resonant wavelengths, producing a gain of N_m^2 in brilliance. Undulator radiation is characterized by sharp peaks at a fundamental wavelength λ_1 and its odd harmonics; λ_1 is determined by the beam energy and x_B

$$\lambda_1 \approx \frac{0.1 x_B}{2\gamma^2} = 1.3 x_B E^{-2} \quad [\text{nm}], \quad (46.6)$$

where x_B is in cm. For example, the fundamental wavelength is 6.5 nm for a 1 GeV beam traversing an undulator with a spatial period of 5 cm. The fractional bandwidth of the peaks in an undulator spectrum is $\approx 1/N_m$. Unlike the radiation from a bending magnet, the angular divergence of undulator radiation is sharply peaked both vertically and in the orbital plane; the brightness of undulator radiation is $\approx 10^{18}$ to 10^{19} photons (s mm² mrad² 0.1% bandwidth)⁻¹, about six orders of magnitude greater than bending magnet radiation. The wavelength of the fundamental is tunable; the strength of the peak magnetic field is altered via changes in the size of the gaps between the poles of the magnets or by changes in the strength of the magnetic fields.

Typically, experiments require a single undulator harmonic interacting with the sample and, thus, a system to filter out higher harmonics at the experimental end-station is used. In the UV, materials that have a limited transmission in the VUV can be used for this purpose: MgF₂, LiF, CaF₂, or fused silica. At higher energies, windowless gas filters, with continuous flows of noble gases, remove the undulator harmonics falling above the atomic ionization energy. Xenon, krypton, argon, and neon are used to remove harmonics at wavelengths below 102.2, 88.6, 78.7, and 57.5 nm, respectively [27, 28].

Synchrotron radiation has well-characterized polarization properties. Within the orbital plane, the radiation is completely linearly polarized with the electric field vector in the orbital plane; above and below the orbital plane, the radiation is elliptically polarized, with the degree of polarization dependent on both wavelength and viewing angle.

Undulator designs incorporating either crossed planar magnets or a helical array of magnets can produce circularly polarized light [29, 30]. Considerable progress has been

made on undulator-based beamline designs that offer high flux, stability, and tunability, as well as a controlled and tailored level of elliptical polarization. The undulator can provide any orientation of the electrical field vector over the spectral range covered by a beamline. However, the state of polarization is rarely conserved throughout a beamline due to chromatic phase shifts introduced by the reflection of the beam off mirrors. In order to determine precisely the polarization state at the sample and to compensate for beamline phase shifts, purely reflective UV-VUV polarimeters have been developed [31, 32], providing almost perfectly circularly polarized light over the entire VUV region [33].

Synchrotron-based circular dichroism studies, which take advantage of the broad polarization options afforded by modern undulator designs, reveal essential structural information on biomolecules in solution and can be seen as complementary to conventional high-resolution biomolecular x-ray crystallography [34, 35]. In the UV and near VUV regions, photoelastic modulators are robust optical devices that can be used to convert linearly polarized incident light to right or left circularly polarized light; this technique is used routinely and has been employed, for example, in CD measurements on thin films [36, 37] and biomolecules in aqueous solution [38]. Photoelectron circular dichroism (PECD) has been exploited at synchrotron facilities and provides a much stronger CD signal on gas phase chiral targets than conventional absorption techniques. PECD is a very sensitive technique for both the study of photoionization dynamics and molecular structure; a review can be found in [39].

46.1.2 Laser-Produced Plasmas

When the output of a high-power pulsed laser is focused onto a solid target, a short-lived, high-temperature ($T \approx 50$ to 100 eV), high-density ($n_e \approx 10^{21} \text{ cm}^{-3}$) plasma is created. The radiation from certain target materials, particularly the rare earths ($57 \leq Z \leq 71$) and neighboring metals in the periodic table, produces a strong VUV quasi continuum that is essentially free of discrete lines [40, 41]. The continua are the most intense in the 4–30 nm region but often extend to about 180 nm. A review of laser-produced plasmas and their applications in the VUV can be found in [42].

The primary mechanisms responsible for the continua are recombination radiation (ionization stages up to ≈ 16 are attained) and bremsstrahlung. The absence of discrete features in rare earth plasmas is thought to be caused by the extreme complexity of rare earth atomic energy level structures; individual emission lines are blended into an apparent continuum [43]. The necessary peak laser powers, which are in the range of 10^{10} to $10^{12} \text{ W cm}^{-2}$, are easily achieved with commercially available Q -switched lasers. The continuum pulse duration is comparable to the duration of the laser

pulse. The target material is often a cylindrical rod that is rotated to present a fresh surface for each laser shot. References [44–48] present and discuss the spectral characteristics of several laser-produced plasma sources. Atomic photoabsorption techniques based on laser-produced plasma sources are described in [43, 49, 50].

46.1.3 Arcs, Sparks, and Discharges

Several laboratory sources of VUV line and continuum radiation are based on gas discharges, high-pressure arcs, and low-pressure and vacuum sparks. While these well-established radiation sources are not as intense as synchrotron radiation and laser-produced plasmas, the traditional sources have the advantages of being portable and inexpensive. Reviews can be found in [51, 52].

Direct current discharges (approximately 100–500 mA) through 1–2 Torr of H_2 or D_2 generate continuum radiation from about 165 to 350 nm [53]. The continuum is produced by transitions from the bound $1s\sigma 2s\sigma a^3 \sum_g^+$ state to the repulsive $1s\sigma 2p\sigma b^3 \sum_u^+$ state [54]; the very steep potential curve of the lower state results in the extended nature of the continuum. The photon flux per unit wavelength from such lamps peaks at about 185 nm; below 165 nm the many-line spectra of H_2 or D_2 begin to dominate. A commercially available electrodeless xenon discharge source, heated by a CW laser, produces broadband light from 170 nm into the infrared.

Hollow cathode discharges [55], which are easy and inexpensive to construct and operate, are the most common line-emission sources used in UV spectroscopy. Low-power (approximately 5 W) lamps designed to produce spectra of about 70 elements are commercially available for spectrochemical and atomic absorption spectroscopy. Line widths are narrow, so blends are minimized. Most manufacturers can provide lamps with transmissive windows for use at VUV wavelengths.

High-current, differentially pumped hollow cathode sources, which have been developed for use as radiometric standards in the 40–125 nm wavelength range [56], can also be used as line sources. At shorter wavelengths, e.g., 5–40 nm, the Penning discharge has proved to be a useful source of line radiation [52, 57]. Electron-beam excitation sources [52] produce stable and reproducible line emission spectra and find use as VUV calibration standards [55, 58]. Electron-beam ion trap (EBIT) sources [59, 60] generate VUV and X-ray spectra of highly ionized atomic species.

46.1.4 Supercontinuum Radiation

Continua extending throughout the near UV wavelength range to below 200 nm can be produced by focusing

femtosecond laser pulses in liquids, noble gases, and glasses. This supercontinuum generation allows for time-resolved, subpicosecond spectroscopy of photochemical reactions [61]. The supercontinuum arises from a number of competing nonlinear processes [62–64]. Access to the UV was demonstrated in the 1990s both by focusing 308 nm laser pulses in water [65] and by focusing 248 nm laser pulses in high pressure (10–40 atm) cells of Ne, Ar, and Kr [66]. The continuum produced using H₂O is particularly broad, extending from 200 to 600 nm. More recently, supercontinuum radiation has been demonstrated down to 120 nm with He-filled and Ne-filled hollow-core photonic crystal fibers [67].

46.2 VUV Lasers

Advances in recent decades in laser technologies have led to an impressive increase in spectroscopically useful VUV laser sources (Chap. 75). Early reviews can be found in [68, 69]. The following summary of VUV lasers does not cover the rapidly developing fields of X-ray and soft X-ray lasers [70, 71] or the development of free electron lasers ([72, 73] and references therein, also in Chap. 75).

46.2.1 Primary Lasers

Pulsed lasing at VUV wavelengths is achieved in a number of media, including the molecular gases H₂, CO, and F₂, excimer systems (Ar₂, Kr₂, Xe₂, ArF, KrF, XeF, XeCl), and Auger-pumped noble gases (Xe, Kr) [74]. The fundamental barrier to producing stimulated emission in the VUV is the ν^3 dependence of the spontaneous emission rate, which necessitates very high pump powers to create and maintain population inversions. Existing VUV primary lasers have generally not been widely used in spectroscopic applications because of either a lack of tunability or unacceptably broad line widths.

Pulsed lasing in CO, H₂ and F₂ occurs between rovibronic levels of a high-lying electronic state and excited vibrational levels of the ground electronic state. The lasing output consists of discrete lines and is not tunable. The CO and H₂ outputs [75, 76] span relatively broad regions (181–197 and 110–164 nm, respectively), while the F₂ laser output consists of two or three closely spaced lines at 157 nm [77]. Pulse energies are in the 1–100 μ J range for CO and H₂ lasers. Commercially available F₂ lasers offer pulse energies of about 50 mJ at 50 Hz repetition rates.

Noble-gas and noble-gas-halide excimer lasers operate via bound-upper-level to continuum-lower-level transitions. (Reviews of excimer laser technologies can be found in [78, 79].) The resulting gain profiles are broad, and the outputs are typically tunable over about 2 nm. ArF excimer sys-

tems (193 nm) are pumped by high-pressure gas discharges; lasers with pulse energies of \approx 20 to 40 mJ are commercially available; Xe₂ (173 nm), Kr₂ (146 nm), and Ar₂ (126 nm) lasers [80–82] produce comparable pulse energies but require electron beam excitation. Auger-pumped lasers achieve a population inversion through the ejection of an inner-shell electron from a neutral atom to produce a highly excited singly ionized species, followed by Auger decay to excited states of the doubly ionized species. The soft X-ray (approximately 100 eV) pump photons often originate from a laser-produced plasma. The lasing output is not tunable. Lasing in Xe (108.9 nm) and Kr (90.7 nm) [83, 84] has been achieved with output pulses in the range of a few μ J.

46.2.2 Nonlinear Techniques

In the past 40 years, developments in the techniques of nonlinear optics have extended the range of tunable, pulsed coherent radiation to VUV wavelengths. Nonlinear frequency conversion techniques, such as stimulated anti-Stokes Raman scattering, harmonic generation, sum-frequency and difference-frequency mixing (Chaps. 75 and 76), and high-harmonic generation (appears in Chap. 75) can produce narrow-bandwidth radiation spanning the entire VUV. The generated VUV radiation has the spectral and spatial characteristics of the input laser radiation. Pulses of 10^{10} to 10^{12} photons are commonly generated with bandwidths on the order of 0.1 cm^{-1} . Many reviews are available on this subject [74, 85–91]. A comprehensive review of precision laser spectroscopies in the extreme ultraviolet can be found in [92]. The standard nonlinear techniques for producing tunable coherent radiation with $\lambda < 200 \text{ nm}$ are summarized below.

Second harmonic generation in nonlinear optical crystals is a well-established method for generating tunable laser light in the near UV. At the shortest wavelengths, second harmonic generation in β -barium borate (BBO) produces usable outputs down to approximately 205 nm, below which the phase matching requirement between the fundamental and the second harmonic cannot be met. Sum-frequency mixing ($\omega = \omega_1 + \omega_2$) in BBO [93, 94], where ω_1 is typically the Nd:YAG fundamental (1064 nm), and ω_2 is tunable UV light, extends the useful range of BBO to approximately 190 nm, where the crystal begins to exhibit strong absorption.

Stimulated anti-Stokes Raman scattering of UV laser light in molecular gases (e.g., H₂, N₂, CH₄) is used to generate coherent radiation down to about 120 nm, although low conversion efficiencies often restrict the usable output to $\lambda > 160 \text{ nm}$. The scattering is a four-wave mixing process resulting in a series of output frequencies shifted from the pump laser frequency by multiples of the vibrational splitting of the ground electronic state of the gas [95]. Because

high anti-Stokes orders are not efficiently generated, H₂, with its large ground state vibrational splitting of 4155 cm⁻¹, is often the gas of choice. The experimental requirements are relatively minimal; a tunable visible or UV source (e.g., a frequency-doubled dye laser) and a high-pressure gas cell (about 2–10 atm of H₂ in a 1 m cell). Conversion efficiencies are a few percent for the first few anti-Stokes orders in H₂ with pump laser energies of about 10–50 mJ [96]; efficiencies then drop continuously, reaching about 10⁻⁵ to 10⁻⁶ for the highest orders ($n = 9$ to 13) reported. Stokes seeding techniques [97] have been shown to increase efficiencies for the highest anti-Stokes orders by as much as a factor of 100.

Third harmonic generation ($\omega = 3\omega_1$), sum-frequency mixing ($\omega = 2\omega_1 + \omega_2$), and difference-frequency mixing ($\omega = 2\omega_1 - \omega_2$) in appropriate noble gases and metal vapors are broadly applicable methods for producing tunable VUV light. These processes result from the presence of the third-order nonlinear term in the expansion of the induced macroscopic polarization of the gas as a power series in the electric field (Chap. 76). (The second-order term, which is responsible for frequency doubling in crystals, is zero for isotropic media such as gases.) The power generated in third-order effects is proportional to

$$N^2 |\chi^{(3)}|^2 P_1^2 P_2 F, \quad (46.7)$$

where N is the number density of the gas, $\chi^{(3)}$ is the third-order nonlinear susceptibility, P_1 and P_2 are the input laser powers at ω_1 and ω_2 , and the factor F describes the phase matching between the generated VUV light and the induced polarization [98, 99]. For third harmonic generation, $P_1^2 P_2$ is replaced by P_1^3 .

A critical constraint in third-order frequency conversion is the phase matching requirement; a comprehensive treatment is presented in [100]. The factor F is a function of the product $b\Delta k$, where b is the confocal beam parameter of the focused input radiation, and Δk is the phase mismatch between the generated VUV light and the input radiation

$$\Delta k = k - (2k_1 + k_2), \quad (46.8)$$

where k_i is the wave vector of the radiation with frequency ω_i . In the standard case of tight focusing ($b \ll L$, where L is the linear dimension of the gas cell) for sum-frequency mixing and third harmonic generation processes, F is nonzero only for $\Delta k < 0$. Therefore, these techniques are applicable only in spectral regions where the gas exhibits negative dispersion. In contrast, for difference-frequency mixing, the factor F is nonzero in regions of both positive and negative dispersion, and wider tuning ranges are generally possible.

Conversion efficiencies for sum-frequency and difference-frequency mixing schemes are usually in the range of 10⁻⁷ to 10⁻⁴ with input peak laser powers of 1–10 MW.

Resonant enhancement of $\chi^{(3)}$, achieved by tuning the input radiation to transition frequencies in the gas, dramatically increases conversion efficiencies (by factors of about 10⁴) and allows for much lower (≈ 1 kW) input laser powers. Most commonly, one of the incident frequencies is tuned to an allowed two-photon transition, with the second input frequency providing subsequent tunability in the VUV; resonant methods, therefore, require two tunable inputs.

Metal vapors (e.g., Mg, Zn, Hg) are negatively dispersive over fairly broad regions of the VUV between 85 and 200 nm and are consequently used for sum-frequency mixing and third harmonic generation. Conversion efficiencies are further enhanced in these vapors by three-photon resonances ($2\omega_1 + \omega_2$) with the ionization continuum or broad autoionizing features [85]. One experimental drawback is the complexity associated with generating the metal vapors in ovens or heat pipes.

Noble gases are generally less suited for sum frequency mixing because they exhibit negative dispersion over fairly limited spectral ranges in the VUV. However, they do provide an experimentally simple medium for difference-frequency mixing schemes. In particular, Xe, Kr, and Ar (as well as H₂) have been used in resonant and nonresonant difference-frequency mixing schemes to produce tunable radiation over the 100–200 nm region [101–107]. The noble gases are also used for sum-frequency mixing and third harmonic generation. Kr, Ar, and Ne are used for the generation of tunable radiation down to 65 nm [101, 108–111]. Below the LiF transmission cutoff (105 nm), the gases are introduced as pulsed jets. In [112], a narrowband tunable extreme ultraviolet laser system based on resonance-enhanced four-wave mixing in Kr, is described, and in [113, 114], an ultranarrow bandwidth (0.008 cm⁻¹) system, utilizing resonance-enhanced sum-frequency mixing in rare gases, capable of producing coherent radiation between 62 and 124 nm is described. A representative summary of third-order frequency conversion schemes is presented in Table 46.1.

Most third-order frequency conversion designs use nano-second-pulsed lasers as primary sources. With the higher intensities ($> 10^{13}$ W/cm²) that are associated with picosecond and femtosecond pulsed lasers, higher-order frequency conversion is readily achieved. These conversion techniques have been used to generate both fixed frequency and tunable coherent radiation shortward of 70 nm. Tunable radiation at 58 nm was produced through fifth harmonic generation in C₂H₂ using the frequency-doubled output of a dye laser [124, 125]; a high repetition rate (up to 500 kHz) fiber-amplifier based system with harmonics down to 30 nm is reported by [90]. A picosecond tunable system with continuous tunability over the 40–100 nm region with sub-cm⁻¹ resolution has been developed using high-order harmonic generation in Ar and Kr [126]. Frequency combs, first up-converted into the VUV in 2005 [127, 128], allow for ultra-high precision

Table 46.1 Representative third-order frequency conversion schemes for generation of tunable coherent VUV light

Medium	λ (nm)	Process	Reference
Sr	165–200	res. diff. mixing	[115]
	178–196	res. sum mixing	[116]
Mg	121–174	res. sum mixing	[85]
Zn	106–140	res. sum mixing	[117]
Hg	142–182	nonres. tripling	[98]
	117–122	res. sum mixing	[118]
	104–108	res. sum mixing	[119]
	85–125	res. sum mixing	[102]
Xe	160–206	nonres. diff. mixing	[120]
	140–147	nonres. tripling	[121]
	113–119	nonres. sum mixing	[102]
Kr	117–150	res. diff. mixing	[122]
	110–116	nonres. sum mixing	[102]
	120–124	nonres. tripling	[123]
	127–180	res. diff. mixing	[101]
	72–83	res. sum mixing	[101]
Ar	102–124	res. diff. mixing	[105]
	97–105	nonres. tripling	[108]
Ne	72–74	nonres. tripling	[109]

spectroscopies and metrology in the VUV [129, 130]; the relevant techniques are reviewed in [92].

46.3 Spectrometers

46.3.1 Grating Spectrometers

The design and characteristics of VUV grating spectrometers and monochromators are reviewed by many authors [131–135]. Two basic types of spectrometer are used in the VUV: normal incidence instruments for $200 \text{ nm} > \lambda > 30 \text{ nm}$ and grazing incidence instruments for $50 \text{ nm} > \lambda > 2 \text{ nm}$. The particulars of these two types are largely dictated by the low reflectivities of both metal and dielectric surfaces in the VUV.

Concave gratings are used almost exclusively in VUV spectrometers. Such gratings provide both dispersion and focusing, thus eliminating the need for additional mirrors and their associated reflection losses. Most VUV spectrometers make use of the focusing properties of the Rowland circle, which is tangent to the grating at its center, lies in a plane perpendicular to the grating grooves, and has a diameter equal to the radius of the curvature of the grating [136]. A source on a horizontal Rowland circle is focused horizontally by the grating to a location also on the circle. The dispersion introduced by the grating results in a focused, diffracted spectrum lying on the Rowland circle. Almost all normal incidence and grazing incidence VUV instruments are designed with the entrance and exit slits lying on, or nearly on, the Rowland circle.

The image formed by a concave grating is not stigmatic, i.e., the vertical focus does not coincide with the horizontal focus. Hence, a point source is imaged into a vertical line on the Rowland circle [133, 137]. Astigmatism is particularly severe at grazing incidence angles, resulting in both loss of signal (the image of the entrance slit being larger in extent than the exit slit) and loss of resolution (the image of the entrance slit is curved in the dispersion direction). Aspherical concave gratings (e.g., toroidal gratings) reduce the astigmatism associated with conventional spherical gratings ([137] and references in [138]). The most important advances in concave grating production are the use of interference techniques to produce holographic gratings [138, 139] and the development of variable line spacing gratings [140, 141]. Interference techniques eliminate the periodic irregularities in conventionally ruled gratings that lead to spectroscopic “ghosts”, reduce the level of scattered light by significant amounts, allow for very high groove densities (e.g., 4800 mm^{-1}), and can be relatively easily applied to aspheric surfaces. Mechanically ruled variable line spacing gratings correct for spherical aberrations and allow for relatively simple focusing and scanning designs in EUV spectrometers and monochromators [141].

Normal incidence grating designs are appropriate for wavelengths greater than about 30–40 nm. The most common types include the Eagle, Wadsworth, and Seya–Namioka designs [131, 133, 134]. Eagle mounts, with entrance and exit slits on the Rowland circle and approximately equal angles of incidence and reflection ($< 10^\circ$), can be either in-plane or off-plane. Photoelectric resolving powers $\lambda/\delta\lambda$ of 2×10^5 were achieved in the 100 nm region with 6.65 m Eagle mount instruments [142–144], although most of these large instruments have now been decommissioned. In the Wadsworth mount, the light source is at a large distance from the grating, and no entrance slit is required. This design is appropriate for collimated light sources such as synchrotron radiation. It has the advantages of high throughput and minimal astigmatism [132]. The Seya–Namioka mount is a Rowland circle instrument in which the angle subtended by the fixed entrance and exit slits relative to the center of the grating is approximately 70° . The spectrometer remains in good focus for small grating rotations, resulting in a simple scanning mechanism and, thus, an inexpensive design. Seya–Namioka instruments provide high throughput at moderate spectral resolutions (typically 0.02–0.05 nm) [132].

The normal incidence reflectance of all standard metal coatings is no greater than a few percent for $\lambda < 30 \text{ nm}$ [133]; in this wavelength region, grazing incidence instruments take advantage of the total reflection of photons at extreme grazing angles. There is a sharp reflectance cutoff at photon energies above a characteristic energy that typically limits the use of grazing incidence optics to $\lambda > 1 \text{ nm}$. Grazing

incidence designs, tailored to the constraints of synchrotron radiation facilities, are described in [3, 132, 135].

Astigmatism becomes severe at grazing angles; interferometrically produced aspherical gratings and mechanically ruled variable line spacing gratings are used to reduce this aberration [139, 141]. The resolving power of a grazing incidence instrument is generally lower than that of a comparably sized normal incidence instrument, in large part because of the decreased effective width of the grating at grazing incidence.

A number of nonstandard instrument designs are reported in the literature, often for use in VUV astronomy and aeronomy applications. These novel designs take advantage of the properties of conical diffraction [145–147] and dual-grating crossed dispersion or echelle mounts [148, 149] to reduce the effects of aberrations. Reference [131] reviews many specialized VUV spectrometer designs.

46.3.2 Fourier Transform Spectrometers

Fourier transform spectroscopy (FTS) is a well-established technique for high-resolution emission and absorption spectroscopy at infrared and visible wavelengths (Chap. 42). An interferometric signal is recorded as a function of an optical path difference made possible, for example, by the displacement of a Michelson interferometer mirror. FTS can be understood as a transfer of optical frequencies into the audio range via the beating interferometric signal as a scan is recorded; the low-frequency interferogram is suitable for time-resolved photodetection. The technique has been extended into the near UV and VUV regions, where FTS is characterized by the large optical throughput, high spectral resolution, and accurate linear wavenumber scale available at longer wavelengths [150]. However, the multiplex advantage of FTS is not realized at UV wavelengths because the signal-to-noise ratio is photon-noise limited rather than detector limited. Moreover, the required stabilities, both for the light source and the interferometer optics, make the extension of this technique quite challenging at short wavelengths. A review of interferometric techniques in the VUV can be found in [151].

A scanning Michelson interferometer with a fused silica beamsplitter has achieved a resolving power of 1.8×10^6 at wavelengths down to 178 nm [150]. The same interferometer design, with a MgF_2 beamsplitter, has achieved a resolving power of 8.5×10^5 at wavelengths down to 150 nm [152]. This spectral resolution is significantly better than that realized by the best VUV grating instruments [153]. At shorter wavelengths, FTS based on wave amplitude division interferometers is fundamentally limited by the transmission of VUV materials such as MgF_2 (≈ 115 nm) or LiF (≈ 105 nm). The manufacture of VUV beamsplitters becomes extremely

challenging due to both the strong absorption of these materials and the high optical quality required for a strong interferometric signal. Membrane-based beamsplitters have been proposed, but, up to now, these are mainly adapted to laser-based applications [154].

A Fourier transform spectrometer based on an all-reflecting wave-front-division interferometer has been developed to operate over a large spectral range, allowing the extension of FTS into the far VUV region [155]. Two roof-shaped reflectors split and reflect the incident light following a design similar to the standard Fresnel bimirror interferometer. The displacement of one reflector's position is controlled and measured by a separate He-Ne stabilized laser interferometer. The instrument has been coupled to a UV-VUV undulator-based synchrotron beamline, allowing Fourier transform absorption spectroscopy in the range 300–40 nm [156]. A raw line width of 0.13 cm^{-1} was measured on the Rydberg series of Kr near 88 nm, corresponding to a resolving power greater than 10^6 [155]. In contrast to wave amplitude division interferometers, wavefront division interferometers require a certain degree of spatial coherence, and thus, this technique is not well adapted to low brilliance sources.

Diffraction gratings can be used as division-of-amplitude beamsplitters to create all-reflecting interference spectrometers for VUV-XUV wavelengths; this idea has been applied to a Mach-Zender interferometer configuration [157, 158].

In parallel with the development of tunable laser-based laboratory sources in the UV-VUV range, original designs that can be related to FTS have been proposed for spectroscopy applications. When a VUV laser pulse created via high harmonic generation is split by a pair of mirrors, and one of the mirrors is translated to create a time delay between the resulting two pulses, the far field profile of the recombined pulses displays an interference pattern that can be exploited as a source diagnostic [159, 160]. Another method produces pulse pairs in the infrared that emerge as phase-locked harmonics in the VUV. Precise control of the pulse delay can be generated by a conventional Michelson interferometer [161, 162] or a movable wedge prism system [163]. This latter design has been applied to the measurement of the spatially resolved absorption of an inhomogeneous thin film in the VUV but with a rather limited spectral resolution [164].

Frequency comb sources operating in the infrared have been coupled to Fourier transform spectrometers, revealing a remarkable potential for unprecedented sensitivity and spectral resolution [165]. In recent years, an innovative approach combining two phase-locked frequency combs (dual comb spectroscopy) has led to high resolution FTS without any moving components [166–168]; a review presenting the advances and the application offered by frequency comb sources in the field of molecular and atomic spectroscopy can be found in [169]. This technique could possibly be implemented in the VUV by coupling a double comb to

harmonic generation based on femtosecond enhancement cavities [170].

46.4 Detectors

There is a wide variety of photon detectors with useful response and sensitivity at VUV wavelengths. With the exception of those involving the photoionization of gases, VUV detectors are based on the same underlying principles as their counterparts in the visible and infrared regions – the common detection schemes are initiated by surface photoemission or electron–hole pair creation in semiconducting materials. The details of the design of VUV detectors, and the constraints on their use, are often determined by the low levels of transmission of VUV light through suitable window and semiconducting materials. Nevertheless, VUV detectors with single-photon counting sensitivities and/or imaging capabilities are widely available. Reviews of VUV detectors can be found in [1, 171–175]. References [176–178] review the operating characteristics and calibration of VUV detector standards. More general summaries of photon detector technologies are presented in [179, 180]. Below, we summarize and compare the most common VUV detection schemes, including the use of photomultiplier tubes, multichannel plate detectors, silicon photodiodes, and charge-coupled devices.

46.4.1 Photomultiplier Tubes

Photomultiplier tubes (PMTs) [181] are used through the VUV for single-photon-counting, nonimaging, applications. Dark count rates are low (about 1 s^{-1}) for solar-blind tubes with 1 cm^2 photocathodes; pulse rise times are about 1–10 ns ([182] for a general review of amplifying detectors in the VUV). In the 105–200 nm region, useful PMT window materials are fused silica, MgF_2 , and LiF ; sapphire is also used in environments where ionizing radiation, which causes sapphire to fluoresce, is not present. In the windowless region of the VUV wavelength range ($2\text{ nm} \leq \lambda \leq 105\text{ nm}$), two options are available: the PMT may be operated bare, i.e., without a window, or a fluorescent coating can be deposited on the window to down-convert the VUV light to longer wavelengths.

Peak quantum efficiencies for VUV photomultiplier tubes are about 15–20%. Some of the most useful coatings for photocathodes in the VUV are CsI, KBr, and other alkali halides. These materials combine high VUV quantum efficiencies with a solar-blind response – their relatively high photoelectric work functions result in long wavelength cutoffs between 150 and 300 nm. Solar-blind PMTs have low dark count rates and minimal response to stray ambient light.

Bare PMTs, although used in some applications, are constrained by the degradation of many photocathode and dynode

surfaces upon exposure to air and humidity. Metal surfaces such as tungsten and aluminum/ Al_2O_3 [172] must be used rather than the higher efficiency alkali halide coated surfaces. Sodium salicylate is the most commonly used VUV-visible conversion phosphor; others include lithium, terphenyl, and coronene [183, 184]. The conversion efficiency of sodium salicylate (peak fluorescence about 430 nm) is relatively constant for VUV light from 30 to 200 nm.

The review by *Krizan* [185] discusses recent advances in fast single-photon detection, including multianode PMTs and hybrid PMT-microchannel-plate designs.

46.4.2 Microchannel Plates

The microchannel plate (MCP) detector is a photo-emissive array detector that combines the single-photon counting sensitivity of a PMT with high-resolution imaging capability. See [186, 187] for recent reviews; other general references include [171–173, 182, 188]. An MCP consists of an array of semiconducting glass channels with diameters of about 10–25 μm and length-to-diameter ratios of about 50:1. Electrons ejected from the front surface of an MCP via the photoelectric effect are accelerated through the channels; repeated collisions with the channel walls result in an amplification of the charge by about 10^6 . The exiting charge clouds are detected by a variety of position-sensing anode structures.

Bare MCPs have quantum efficiencies of about 10% for $\lambda \leq 100\text{ nm}$ and a long wavelength cutoff of about 120 nm. Alkali halide coatings increase the quantum efficiency to about 20% and extend MCP sensitivities toward longer wavelengths. Feedback instabilities produced by positive ions created in the channels during the electron cloud amplification are minimized through two common channel geometries: the chevron configuration, where two or more straight-channel MCPs oriented at different angles are cascaded [189], or a configuration with one set of curved channels [190].

Readout schemes for determining the position of individual detected photons rely on either direct detection of the resulting electron cloud or conversion of the electron cloud into visible photons via a phosphor to produce an optical image [182]. Direct detection schemes include centroid-detecting anodes, such as the wedge and strip design [191] and cross strip anodes [192]. Other designs are described in [193, 194].

46.4.3 Silicon Photodiodes

Broad use of silicon photodiodes at VUV wavelengths has traditionally been limited by the strong absorption of VUV photons in the outer SiO_2 passivation layer that covers the p–n junction of these devices. Standard silicon detectors are

sensitive throughout the infrared and visible regions and also in the soft X-ray ($\lambda < 2$ nm) and X-ray regions. Significant improvements in silicon photodiode sensitivities in the VUV are realized by thinning the SiO₂ passivation region to thicknesses of about 5–10 nm. Reference [195] reviews VUV semiconductor photodiode designs.

There has been active development of non-silicon-based photodiodes as VUV detectors, e.g., wide bandgap materials such as GaN, e.g., [196, 197], and significant work on a variety of innovative semiconductor designs based on nanofabrication techniques – see [175, 198] for recent reviews. The development of photodiodes with appreciable VUV sensitivity and good temporal stability has led to their use as radiometric transfer standards [199]. Because silicon photodiodes respond strongly to radiation throughout the visible, IR, and X-ray regions, a method for rejection of stray light is essential for their effective use in the VUV. Reference [200] reports on the use of thin-film filters, deposited on the photodiode surface, to restrict the bandpass of the radiation impinging on the diode to selected VUV wavelengths. Wide bandgap semiconductors reject visible light with their natural solar-blind response [199].

46.4.4 Charge-Coupled Devices

CCDs are widely used for low light level imaging applications throughout the visible and near-IR regions. In the VUV, charge-coupled devices suffer from strong absorption both by surface gate structures and by the inactive passivation layer [182]. Two approaches are employed to overcome these limitations: the CCD front surface is overcoated with a photon down-converting phosphor [201] or a thinned and surface-treated CCD is back-illuminated with VUV light [202, 203]. Such techniques have resulted in CCD VUV quantum efficiencies that rival those of photoemissive devices such as microchannel plates. Recent CCD designs with multilayer antireflection coatings based on molecular beam epitaxial doping technologies [204, 205] achieve quantum efficiencies above 60% in the spectral region centered around 200 nm.

46.5 Optical Materials

The design of VUV instrumentation is dictated in large part by the constraints of VUV optical materials. Transmission through bulk materials is limited to $\lambda > 105$ nm, the short wavelength transmission limit of LiF. Normal incidence reflectance from metal surfaces and coatings decreases dramatically at short wavelengths; polarizers and narrow-band interference filters are relatively difficult to produce because of the lack of materials with suitable optical con-

stants. Below, we briefly summarize the properties and uses of VUV optical materials. Comprehensive discussions can be found in [1, 206].

46.5.1 Windows

Few bulk materials transmit light below 200 nm; none transmit light from about 2 to 105 nm. In the 105–200 nm wavelength region, the most common window materials are synthetic fused quartz or suprasil (with a short wavelength transmission cutoff of about 160 nm), sapphire (145 nm), CaF₂ (125 nm), MgF₂ (112 nm), and LiF (105 nm). Compilations of the transmission characteristics of these and other materials are presented in [133, 207, 208]. Single crystal windows with dimensions up to 10 cm can be obtained for most of these materials. Sapphire fluoresces when struck by ionizing radiation and is, therefore, not suitable for certain environments.

46.5.2 Capillaries

In the windowless region, 2–105 nm, it is standard practice to use differentially pumped slits or circular apertures to isolate different pressure regions, e.g., to isolate an absorption cell from a vacuum spectrometer. This technique has the drawback of requiring large pumping capacities and limiting optical throughputs. Thin films (see below) can be used below 105 nm as windows, but they provide limited transmission in narrow bandpasses and cannot support large pressure differentials. Differentially pumped MCP capillary arrays can serve as an alternative window in the VUV; see, for example, [209]. The capillaries are typically ≈ 3 mm in length and have diameters of 10–100 μ m. Measured optical transmissions are in the 20–50% range throughout the VUV; tradeoffs must be considered between optical throughput and gas conductance. One significant limitation to an MCP window is its small angular aperture.

46.5.3 Thin Films

Below 105 nm, thin (about 10–200 nm) metallic films are used as transmission filters with bandpasses of approximately 10–50 nm. Details of filter properties are given in [208, 210]. Reference [211] describes composite metallic filters (e.g., Al/Ti/C, Ti/Sb/Al), developed for the Extreme Ultraviolet Explorer satellite, with transmission bandpasses of about 10–20 nm and high rejection at wavelengths of strong VUV geocoronal lines. The stability of metallic thin films under intense EUV irradiation is discussed in [212].

46.5.4 Coatings

Above 120 nm, the principal broadband reflector for VUV wavelengths is Al with a thin protective overcoat of MgF₂, having a normal incidence reflectance of ≈ 80 to 85% [213]. The normal incidence reflectivities of all materials drop dramatically below about 100 nm. A compilation of coating reflectivities at normal and grazing incidence is presented in [214]. Materials with the highest reflectivities include Os, Pt, Au, and Ir, with reflectivities of 15–30% from 30 to 110 nm [215]. Reference [216] reports grazing incidence reflection coefficients for Rh, Os, Pt, and Au from 5 to 30 nm; Rh has the highest reflectivity in this region.

46.5.5 Interference Filters and Multilayer Coatings

The development of interference filters for VUV wavelengths has been limited by the availability of coating materials with both high transmission and appreciable range of refractive differentials [217]. Multilayer dielectric reflectors, thus, require many layers to compensate for the small reflectivities at the material interfaces. The theory of multilayer reflecting optics and optic designs are reviewed in [218]. A variety of multilayer coatings with high narrowband reflectivities have been developed, references include [219–226]. Metal-dielectric bandpass filters with reflectivities as high as 90% in the ultraviolet are described in [227].

Normal incidence optics with multilayer reflection coatings can also be used in the nominally grazing incidence spectral region below 30 nm [228–230]. References [231–236] describe normal incidence gratings coated with Mo/Si multilayers. The performances of other multilayer coatings are described in [237–240].

46.5.6 Polarizers

The production and detection of linearly polarized light in the VUV is discussed in [133, 241]. Above about 112 nm, transmission polarizers, based on the birefringence of MgF₂, are often employed [242]. Reference [243] describes multilayer transmissive and reflective polarizing coatings for the hydrogen Lyman-alpha line. Reflection polarizers are usually used below 112 nm (e.g., [244]); [245] describe transmission multilayer polarizers for the 55–90 eV region. An analysis of double-reflection circular polarizers is given in [246], and multilayer transmission quarter wave plates for the generation of circular polarization are described in [247].

References

1. Samson, J.A.R., Ederer, D.L. (eds.): *Vacuum Ultraviolet Spectroscopy I & II*. Academic Press, San Diego (1998)
2. Brown, G.S., Moncton, D.E. (eds.): *Handbook on Synchrotron Radiation* vol. 3. North Holland, Amsterdam (1991)
3. Margaritondo, G.: *Introduction to Synchrotron Radiation*. Oxford Univ. Press, New York (1988)
4. Marr, G.V. (ed.): *Handbook on Synchrotron Radiation* vol. 2. North Holland, Amsterdam (1987)
5. Schmidt, V.: *Rep. Prog. Phys.* **55**, 1483 (1992)
6. Winick, H.: *Synchrotron radiation*. In: *Physics of Particle Accelerators*, p. 2138. AIP, New York (1989)
7. Winick, H.: *Synchrotron Radiation Sources: A Primer*. World Scientific, Singapore (1994)
8. Hulbert, S.L., Williams, G.P.: *Synchrotron radiation sources*. In: Samson, J.A.R., Ederer, D.L. (eds.) *Vacuum Ultraviolet Spectroscopy I*, p. 1. Academic Press, San Diego (1998)
9. Winick, H.: *J. Synchrotron Radiat.* **5**, 168 (1998)
10. Wiedemann, H.: *Synchrotron Radiation*. Springer, Berlin, Heidelberg (2003)
11. Bordovitsyn, V.A. (ed.): *Synchrotron Radiation Theory and its Development*. World Scientific, Singapore (1999)
12. Ciocci, F., Dattoli, G., Torre, A., Renieri, A.: *Insertion Devices for Synchrotron Radiation and Free Electron Lasers*. World Scientific, Singapore (2000)
13. Koch, E.-E., Eastman, D.E., Farge, Y.: *Synchrotron radiation – A powerful tool in science*. In: Koch, E.-E. (ed.) *Handbook on Synchrotron Radiation*, vol. 1, p. 1. North Holland, Amsterdam (1983)
14. Krinsky, S., Perlman, M.L., Watson, R.E.: *Characteristics of synchrotron radiation and its sources*. In: Koch, E.-E. (ed.) *Handbook on Synchrotron Radiation*, vol. 1, p. 65. North Holland, Amsterdam (1983)
15. Munro, I.H., Marr, G.V.: *Synchrotron radiation sources*. In: Marr, G.V. (ed.) *Handbook on Synchrotron Radiation*, vol. 2, p. 1. North Holland, Amsterdam (1987)
16. Wille, K.: *Rep. Prog. Phys.* **54**, 1005 (1991)
17. Winick, H.: *Properties of synchrotron radiation*. In: Winick, H., Doniach, S. (eds.) *Synchrotron Radiation Research*, p. 11. Plenum, New York (1980)
18. Hettel, R.: *J. Synchrotron Radiat.* **21**, 843 (2014)
19. Möller, T., Zimmerer, G.: *Phys. Scr.* **1987**, 177 (1987)
20. Munro, I.H., Schwentner, N.: *Nucl. Instrum. Methods* **208**, 819 (1983)
21. Rehn, V.: *Nucl. Instrum. Methods* **177**, 193 (1980)
22. Craseman, B.: *Can. J. Phys.* **76**, 251 (1998)
23. Lindle, D.W., Hemmers, O.A.: *J. Alloys Compd.* **328**, 27 (2001)
24. Couprie, M.-E., Nadolski, L.S., Nagaoka, R., Brunelle, P., Loulergue, A., Tordeux, M.A., Lamarre, J.F., Nadjai, A.: *Synchrotron Radiat. News* **26**, 14 (2013)
25. Brown, G.S., Lavender, W.: *Synchrotron-radiation spectra*. In: Brown, G.S., Moncton, D.E. (eds.) *Handbook on Synchrotron Radiation*, vol. 3, p. 37. North Holland, Amsterdam (1991)
26. Elleaume, P.: *Rev. Sci. Instrum.* **63**, 321 (1992)
27. Mercier, B., Compin, M., Prevost, C., Bellec, G., Thissen, R., Duituit, O., Nahon, L.: *J. Vac. Sci. Technol. A* **18**, 2533 (2000)
28. Suits, A.G., Heimann, P., Yang, X., Evans, M., Hsu, C.-W., Lu, K., Lee, Y.T., Kung, A.H.: *Rev. Sci. Instrum.* **66**, 4841 (1995)
29. Nahon, L., Corlier, M., Peupardin, P., Marteau, F., Marcouillé, O., Brunelle, P., Alcaraz, C., Thiry, P.: *Nucl. Instrum. Methods Phys. Res. A* **396**, 237 (1997)

30. Onuki, H., Elleaume, P.: *Undulators, Wigglers and Their Applications*. Taylor & Francis, New York (2003)
31. Koide, T., Shidara, T., Yuri, M., Kandaka, N., Yamaguchi, K., Fukutani, H.: *Nucl. Instrum. Methods Phys. Res. A* **308**, 635 (1991)
32. Nahon, L., Alcaraz, C.: *Appl. Opt.* **43**, 1024 (2004)
33. Nahon, L., de Oliveira, N., Garcia, G.A., Gil, J.-F., Pilette, B., Marcouillé, O., Lagarde, B., Polack, F.: *J. Synchrotron Radiat.* **19**, 508 (2012)
34. Réfrégiers, M., Wien, F., Ta, H.-P., Premvardhan, L., Bac, S., Jamme, F., Rouam, V., Lagarde, B., Polack, F., Giorgetta, J.-L., Ricaud, J.-P., Bordessoule, M., Giuliani, A.: *J. Synchrotron Radiat.* **19**, 831 (2012)
35. Wallace, B.A.: *Q. Rev. Biophys.* **42**, 317 (2009)
36. Meinert, C., Bredehöft, J.H., Filippi, J.-J., Baraud, Y., Nahon, L., Wien, F., Jones, N.C., Hoffmann, S.V., Meierhenrich, U.J.: *Angew. Chem. Int. Ed.* **51**, 4484 (2012)
37. Miles, A.J., Janes, R.W., Brown, A., Clarke, D.T., Sutherland, J.C., Tao, Y., Wallace, B.A., Hoffmann, S.V.: *J. Synchrotron Radiat.* **15**, 420 (2008)
38. Matsuo, K., Fukuyama, T., Yonehara, R., Namatame, H., Taniguchi, M., Gekko, K.: *J. Electron Spectrosc. Relat. Phenom.* **1023**, 144 (2005)
39. Nahon, L., Garcia, G.A., Powis, I.: *J. Electron Spectrosc. Relat. Phenom.* **204**, 322 (2015)
40. Carroll, P.K., Kennedy, E.T., O'Sullivan, G.: *Opt. Lett.* **2**, 72 (1978)
41. Carroll, P.K., Kennedy, E.T., O'Sullivan, G.: *Appl. Opt.* **19**, 1454 (1980)
42. Richardson, M.: *Laser-produced plasmas*. In: Samson, J.A., Ederer, D.L. (eds.) *Vacuum Ultraviolet Spectroscopy I*, p. 83. Academic Press, San Diego (1998)
43. O'Sullivan, G., Cummings, A., Dong, C.Z., Dunne, P., Hayden, P., Morris, O., Sokell, E., O'Reilly, F., Su, M.G., White, J.: *J. Phys. Conf. Ser.* **163**, 012003 (2009)
44. Gohil, P., Kaufman, V., McIlrath, T.J.: *Appl. Opt.* **25**, 2039 (1986)
45. Orth, F.B., Ueda, K., McIlrath, T.J., Ginter, M.L.: *Appl. Opt.* **25**, 2215 (1986)
46. Eidmann, K., Kishimoto, T.: *Appl. Phys. Lett.* **49**, 377 (1986)
47. Meighan, O., Gray, A., Mosnier, J.P., Whitty, W., Costello, J.T., Lewis, C.L.S., MacPhee, A., Allott, R., Turcu, I.C.E., Lamb, A.: *Appl. Phys. Lett.* **70**, 1497 (1997)
48. Giulietti, D., Gizzi, L.A.: *Riv. Nuovo Cim.* **21**, 1 (1998)
49. Su, M.G., Dong, C.Z., Murphy, N., O'Sullivan, G., Hayden, P., White, J.: *Phys. Rev. A* **78**, 043401 (2008)
50. Gaynor, L., Murphy, N., Dunne, P., O'Sullivan, G.: *J. Phys. B* **41**, 245002 (2008)
51. Roberts, J.R.: *Glow discharges and wall-stabilized arcs*. In: Samson, J.A., Ederer, D.L. (eds.) *Vacuum Ultraviolet Spectroscopy I*, p. 37. Academic Press, San Diego (1998)
52. Kühne, M.: *Hollow cathodes and Penning discharges*. In: Samson, J.A., Ederer, D.L. (eds.) *Vacuum Ultraviolet Spectroscopy I*, p. 65. Academic Press, San Diego (1998)
53. Thorne, A.P., Litzen, U., Johansson, S.: *Spectro-Physics: Principles and Applications*. Springer, Berlin (1999)
54. Huber, K.P., Herzberg, G.: *Constants of Diatomic Molecules*. Van Nostrand, New York (1979)
55. Kühne, M.: *Radiometric characterization of VUV sources*. In: Samson, J.A., Ederer, D.L. (eds.) *Vacuum Ultraviolet Spectroscopy I*, p. 119. Academic Press, San Diego (1998)
56. Hollandt, J., Kühne, M., Wende, B.: *Appl. Opt.* **33**, 68 (1994)
57. Heise, C., Hollandt, J., Kling, R., Kock, M., Kühne, M.: *Appl. Opt.* **33**, 5111 (1994)
58. Risle, J.S., Westerveld, W.B.: *Appl. Opt.* **28**, 389 (1989)
59. Beiersdorfer, P.: *Annu. Rev. Astron. Astrophys.* **41**, 343 (2003)
60. Micke, P., Kühn, S., Buchauer, L., Harries, J.R., Bücking, T.M., Blaum, K., Cieluch, A., Egl, A., Hollain, D., Kraemer, S., Pfeifer, T., Schmidt, P.O., Schüssler, R.X., Schweiger, C., Stöhlker, T., Sturm, S., Wolf, R.N., Bernitt, S., Crespo López-Urritia, J.R.: *Rev. Sci. Instrum.* **89**, 063109 (2018)
61. Glowina, J.H., Misewich, J.A., Sorokin, P.P.: *Utilization of UV and IR supercontinua in gas-phase subpicosecond kinetic spectroscopy*. In: Alfano, R.R. (ed.) *The Supercontinuum Laser Source*, p. 337. Springer, New York (1989)
62. Alfano, R.R. (ed.): *The Supercontinuum Laser Source*, 3rd edn. Springer, New York (2016)
63. Corkum, P.B., Rolland, C.: *Self-focusing and continuum generation in gases*. In: Alfano, R.R. (ed.) *The Supercontinuum Laser Source*, 3rd edn., p. 281. Springer, New York (2016)
64. Shen, Y.R., Yang, G.: *Theory of self-phase modulation and spectral broadening*. In: Alfano, R.R. (ed.) *The Supercontinuum Laser Source*, 3rd edn., p. 1. Springer, New York (2016)
65. Rodriguez, G., Roberts, J.P., Taylor, A.J.: *Opt. Lett.* **19**, 1146 (1994)
66. Gosnell, T.R., Taylor, A.J., Greene, D.P.: *Opt. Lett.* **15**, 130 (1990)
67. Ermolov, A., Mak, K.F., Frosz, M.H., Travers, J.C., Russell, P. St J.: *Phys. Rev. A* **92**, 033821 (2015)
68. Jaeglé, P.: *Vacuum ultraviolet lasers*. In: Samson, J.A.R., Ederer, D.L. (eds.) *Vacuum Ultraviolet Spectroscopy I*, p. 101. Academic Press, San Diego (1998)
69. Misra, P., Dubinskii, M.A.: *Ultraviolet Spectroscopy and UV Lasers*. Marcel Dekker, New York (2002)
70. Rohringer, N., Ryan, D., London, R.A., Purvis, M., Albert, F., Dunn, J., Bozek, J.D., Bostedt, C., Graf, A., Hill, R., Hau-Riege, S.P., Rocha, J.J.: *Nature* **481**, 488 (2012)
71. Kawachi, T., Bulanov, S.V., Daido, H., Kato, Y. (eds.): *X-ray Lasers 2016 – Proceedings of the 15th International Conference on X-ray Lasers*. Springer Proceedings in Physics, vol. 202. Springer, Cham (2018)
72. Ayvazyan, V., Baboi, N., Bohnet, I., Brinkmann, R., Castellano, M., Castro, P., Catani, L., Choroba, S., Cianchi, A., Dohlus, M., Edwards, H.T., Faatz, B., Fateev, A.A., Feldhaus, J., Flöttmann, K., Gamp, A., Garvey, T., Genz, H., Gerth, C., Gretchko, V., Grigoryan, B., Hahn, U., Hessler, C., Honkavaara, K., Hüning, M., Ischebeck, R., Jablonka, M., Kamps, T., Körfer, M., Krasilnikov, M., Krzywinski, J., Liepe, M., Liero, A., Limberg, T., Loos, H., Luong, M., Magne, C., Menzel, J., Michelato, P., Minty, M., Müller, U.-C., Nölle, D., Novokhatski, A., Pagani, C., Peters, F., Pflüger, J., Piot, P., Plucinski, L., Rehlich, K., Reyzl, I., Richter, A., Rossbach, J., Saldin, E.L., Sandner, W., Schlarb, H., Schmidt, G., Schmäser, P., Schneider, J.R., Schneidmiller, E.A., Schreiber, H.-J., Schreiber, S., Sertore, D., Setzer, S., Simrock, S., Sobierajski, R., Sonntag, B., Steeg, B., Stephan, F., Sytchev, K.P., Tiedtke, K., Tonutti, M., Treusch, R., Trines, D., Türke, D., Verzilov, V., Wanzenberg, R., Weiland, T., Weise, H., Wendt, M., Will, I., Wolff, S., Wittenburg, K., Yurkov, M.V., Zapfe, K.: *Phys. Rev. Lett.* **88**, 104802 (2002)
73. McNeil, B.W.J., Thompson, N.R.: *Nat. Photonics* **4**, 814 (2010)
74. Hooker, S.M., Webb, C.E.: *Prog. Quantum Electron.* **18**, 227 (1994)
75. Dreyfus, R.W., Hodgson, R.T.: *Phys. Rev. A* **9**, 2635 (1974)
76. Hodgson, R.T.: *J. Chem. Phys.* **55**, 5378 (1971)
77. Sansonetti, C.J., Reader, J., Vogler, K.: *Appl. Opt.* **40**, 1974 (2001)
78. Eden, J.G.: *IEEE J. Sel. Top. Quantum Electron.* **6**, 1051 (2000)
79. Ewing, J.J.: *IEEE J. Sel. Top. Quantum Electron.* **6**, 1061 (2000)
80. Hoff, P.W., Swingle, J.C., Rhodes, C.K.: *Appl. Phys. Lett.* **23**, 245 (1973)
81. Hughes, W.M., Shannon, J., Hunter, R.: *Appl. Phys. Lett.* **24**, 488 (1974)
82. Hutchinson, M.H.R.: *Appl. Opt.* **19**, 3883 (1980)

83. Kapteyn, H.C., Lee, R.W., Falcone, R.W.: *Phys. Rev. Lett.* **57**, 2939 (1986)
84. Kapteyn, H.C., Falcone, R.W.: *Phys. Rev. A* **37**, 2033 (1988)
85. Stoicheff, B.P.: Laser spectroscopy in the far-ultraviolet region. In: Hänsch, T.W., Inguscio, M. (eds.) *Frontiers in Laser Spectroscopy*, p. 105. North Holland, Amsterdam (1994)
86. Wallace, S.C.: Nonlinear optics and laser spectroscopy in the vacuum ultraviolet. In: McGlynn, S.P., Findley, G.L., Huebner, R.H. (eds.) *Photophysics and Photochemistry in the Vacuum Ultraviolet*, p. 105. Reidel, Dordrecht (1985)
87. Döbele, H.F.: *Plasma Sources Sci. Technol.* **4**, 224 (1995)
88. Lipson, R.H., Dimov, S.S., Wang, P., Shi, Y.J., Mao, D.M., Hu, X.K., Vanstone, J.: *Instrum. Sci. Technol.* **28**, 85 (2000)
89. Eden, J.G.: *Prog. Quantum Electron.* **28**, 197 (2004)
90. Hädrich, S., Rothhardt, J., Krebs, M., Tavella, F., Willner, A., Limpert, J., Tünnermann, A.: *Opt. Express* **18**, 20242 (2010)
91. Ubachs, W., Salumbides, E.J., Eikema, K.S.E., de Oliveira, N., Nahon, L.: *J. Electron Spectrosc. Relat. Phenom.* **196**, 159 (2014)
92. Eikema, K.S.E., Ubachs, W.: Precision laser spectroscopy in the extreme ultraviolet. In: Quack, M., Merkt, F. (eds.) *Handbook of High-Resolution Spectroscopy*, p. 1373. Wiley, Chichester (2011)
93. Mückenheim, W., Lokai, P., Burghardt, B., Basting, D.: *Appl. Phys. B* **45**, 259 (1988)
94. Bhar, G.C., Chatterjee, U., Rudra, A.M., Kumbhakar, P.: *Quantum Electron.* **29**, 800 (1999)
95. Shen, Y.R.: *The Principles of Nonlinear Optics*. Wiley, New York (1984)
96. Huo, Y., Shimizu, K., Yagi, T.: *J. Appl. Phys.* **72**, 3258 (1992)
97. Goehlich, A., Czarnetzki, U., Döbele, H.F.: *Appl. Opt.* **37**, 8453 (1998)
98. Hilbig, R., Hilber, G., Lago, A., Wolff, B., Wallenstein, R.: *Comments At. Mol. Phys.* **18**, 157 (1986)
99. Jamroz, W., Stoicheff, B.P.: *Prog. Opt.* **20**, 327 (1983)
100. Bjorklund, G.J.: *IEEE J. Quantum Electron.* **11**, 289 (1975)
101. Hilber, G., Lago, A., Wallenstein, R.: *J. Opt. Soc. Am. B* **4**, 1753 (1987)
102. Hilbig, R., Wallenstein, R.: *Appl. Opt.* **21**, 913 (1982)
103. Wellegehausen, B., Welling, H., Momma, C., Feuerhake, M., Mas-savi, K., Eichmann, H.: *Opt. Quantum Electron.* **28**, 267 (1996)
104. Melikechi, N., Gangopadhyay, S., Eyler, E.E.: *Appl. Opt.* **36**, 7776 (1997)
105. Nazarkin, A., Korn, G., Kittlemann, O., Ringling, J., Hertel, I.V.: *Phys. Rev. A* **56**, 671 (1997)
106. Faris, G.W., Meyer, S.A., Dyer, M.J., Banks, M.J.: *J. Opt. Soc. Am. B* **17**, 1856 (2000)
107. Wittmann, M., Wick, M.T., Steinkellner, O., Stert, V., Farmanara, P., Radloff, W., Korn, G., Hertel, I.V.: *Opt. Commun.* **173**, 323 (2000)
108. Hilbig, R., Wallenstein, R.: *Opt. Commun.* **44**, 283 (1983)
109. Hilbig, R., Lago, A., Wallenstein, R.: *Opt. Commun.* **49**, 297 (1984)
110. Cromwell, E., Trickl, T., Lee, Y.T., Kung, A.H.: *Rev. Sci. Instrum.* **60**, 2888 (1989)
111. Palm, H., Merkt, F.: *Appl. Phys. Lett.* **73**, 157 (1998)
112. Hannemann, S., Hollenstein, U., van Duijn, E.-J., Ubachs, W.: *Opt. Lett.* **30**, 1494 (2005)
113. Hollenstein, U., Palm, H., Merkt, F.: *Rev. Sci. Instrum.* **71**, 4023 (2000)
114. Rupper, P., Merkt, F.: *Rev. Sci. Instrum.* **75**, 613 (2004)
115. Yamanouchi, K., Tsuchiya, S.: *J. Phys. B* **28**, 133 (1995)
116. Hodgson, R.T., Sorokin, P.P., Wynne, J.J.: *Phys. Rev. Lett.* **32**, 343 (1974)
117. Jamroz, W., LaRocque, P.E., Stoicheff, B.P.: *Opt. Lett.* **7**, 148 (1982)
118. Mahon, R., Tomkins, F.S.: *IEEE J. Quantum Electron.* **18**, 913 (1982)
119. Kwon, C.H., Kim, H.L., Kim, M.S.: *Rev. Sci. Instrum.* **74**, 2939 (2003)
120. Herman, P.R., Stoicheff, B.P.: *Opt. Lett.* **10**, 502 (1985)
121. Hilbig, R., Wallenstein, R.: *IEEE J. Quantum Electron.* **17**, 1566 (1981)
122. Strauss, C.E.M., Funk, D.J.: *Opt. Lett.* **16**, 1192 (1991)
123. Cotter, D.: *Opt. Commun.* **31**, 397 (1979)
124. Eikema, K.S.E., Ubachs, W., Vassen, W., Hogervorst, W.: *Phys. Rev. Lett.* **71**, 1690 (1993)
125. Eikema, K.S.E., Ubachs, W., Vassen, W., Hogervorst, W.: *Phys. Rev. A* **55**, 1866 (1997)
126. Brandi, F., Neshev, D., Ubachs, W.: *Phys. Rev. Lett.* **91**, 163901 (2003)
127. Gohle, C., Udem, T., Herrmann, M., Rauschenberger, J., Hol-warth, R., Schluessler, H.A., Krausz, F., Hänsch, T.W.: *Nature* **436**, 234 (2005)
128. Jones, R.J., Moll, K.D., Thorpe, M.J., Ye, J.: *Phys. Rev. Lett.* **94**, 193201 (2005)
129. Zinkstok, R.T., Witte, S., Ubachs, W., Hogervorst, W., Eikema, K.S.E.: *Phys. Rev. A* **73**, 061801 (2006)
130. Kandula, D.Z., Gohle, C., Pinkert, T.J., Ubachs, W., Eikema, K.S.E.: *Phys. Rev. A* **84**, 062512 (2011)
131. Hunter, W.R.: Diffraction gratings and mountings for the vacuum ultraviolet spectral region. In: Vanasse, G. (ed.) *Spectrometric Techniques*, vol. IV, p. 63. Academic Press, New York (1985)
132. Johnson, R.L.: Grating monochromators and optics for the VUV and soft x-ray region. In: Koch, E.E. (ed.) *Handbook of Synchrotron Radiation*, vol. 1, p. 173. North-Holland, Amsterdam (1983)
133. Samson, J.A.R.: Far ultraviolet region. In: Williams, D. (ed.) *Methods of Experimental Physics*, vol. 13, p. 204. Academic Press, New York (1976)
134. Koike, M.: Normal incidence monochromators. In: Samson, J.A.R., Ederer, D.L. (eds.) *Vacuum Ultraviolet Spectroscopy II*, p. 1. Academic Press, San Diego (1998)
135. Padmore, H.A., Howells, M.R., McKinney, W.R.: Grazing incidence monochromators. In: Samson, J.A.R., Ederer, D.L. (eds.) *Vacuum Ultraviolet Spectroscopy II*, p. 21. Academic Press, San Diego (1998)
136. Palmer, E.W., Hutley, M.C., Franks, A., Verrill, J.F., Gale, B.: *Rep. Prog. Phys.* **38**, 975 (1975)
137. Underwood, J.H.: Imaging properties and aberrations of spherical optics and non-spherical optics. In: Samson, J.A.R., Ederer, D.L. (eds.) *Vacuum Ultraviolet Spectroscopy I*, p. 145. Academic Press, San Diego (1998)
138. Hutley, M.C.: *Diffraction Gratings*. Academic Press, New York (1982)
139. Namioka, T.: Diffraction gratings. In: Samson, J.A.R., Ederer, D.L. (eds.) *Vacuum Ultraviolet Spectroscopy I*, p. 347. Academic Press, San Diego (1998)
140. Hettrick, M.C.: *Appl. Opt.* **24**, 1251 (1985)
141. Underwood, J.H.: Spectrographs and monochromators using varied line spacing gratings. In: Samson, J.A.R., Ederer, D.L. (eds.) *Vacuum Ultraviolet Spectroscopy II*, p. 55. Academic Press, San Diego (1998)
142. Ito, K., Namioka, T., Morioka, Y., Sasaki, T., Noda, H., Goto, K., Katayama, T., Koike, M.: *Appl. Opt.* **25**, 837 (1986)
143. Ito, K., Namioka, T.: *Rev. Sci. Instrum.* **60**, 1573 (1989)
144. Yoshino, K., Freeman, D.E., Parkinson, W.H.: *Appl. Opt.* **19**, 66 (1980)
145. Cash, W.C.: *Appl. Opt.* **21**, 710 (1982)
146. Neviere, M., Maystre, D., Hunter, W.R.: *J. Opt. Soc. Am.* **68**, 1106 (1978)

147. Lemaire, P.: *Appl. Opt.* **30**, 1294 (1991)
148. Cash, W.C.: *Appl. Opt.* **22**, 3971 (1983)
149. Hettrick, M.C., Bowyer, S.: *Appl. Opt.* **22**, 3921 (1983)
150. Thorne, A.P., Harris, C.J., Wynne-Jones, I., Learner, R.C.M., Cox, G.: *J. Phys. E* **20**, 54 (1987)
151. Thorne, A.P., Howells, M.R.: Interferometric spectrometers. In: Samson, J.A.R., Ederer, D.L. (eds.) *Vacuum Ultraviolet Spectroscopy II*, p. 73. Academic Press, San Diego (1998)
152. Thorne, A.P., Cox, G., Smith, P.L., Parkinson, W.H.: *Proc. SPIE* **2282**, 58 (1994)
153. Nahon, L., Alcaraz, C., Marlats, J.-L., Lagarde, B., Polack, F., Thissen, R., Lepère, D., Ito, K.: *Rev. Sci. Instrum.* **72**, 1320 (2001)
154. Hilbert, V., Rödel, C., Brenner, G., Döppner, T., Dusterer, S., Dziarzhytski, S., Fletcher, L., Förster, E., Glenzer, S.H., Harmand, M., Hartley, N.J., Kazak, L., Komar, D., Laarmann, T., Lee, H.J., Ma, T., Nakatsutsumi, M., Przystawik, A., Redlin, H., Skruszewicz, S., Sperling, P., Tiggesbäumker, J., Toleikis, S., Zastrau, U.: *Appl. Phys. Lett.* **105**, 101102 (2014)
155. de Oliveira, N., Roudjane, M., Joyeux, D., Phalippou, D., Rodier, J.C., Nahon, L.: *Nat. Photonics* **5**, 149 (2011)
156. de Oliveira, N., Joyeux, D., Roudjane, M., Gil, J.-F., Pilette, B., Archer, L., Ito, K., Nahon, L.: *J. Synchrotron Radiat.* **23**, 887 (2016)
157. Howells, M.R., Frank, K., Hussain, Z., Moler, E.J., Reich, T., Möller, D., Shirley, D.A.: *Nucl. Instrum. Methods Phys. Res. A* **347**, 182 (1994)
158. Agåker, M., Andersson, J., Englund, C.-J., Olsson, A., Ström, M., Nordgren, J.: *Nucl. Instrum. Methods Phys. Res. A* **601**, 213 (2009)
159. Klisnick, A., Guilbaud, O., Ros, D., Cassou, K., Kazamias, S., Jamelot, G., Lagron, J.-C., Joyeux, D., Phalippou, D., Lechantre, Y., Edwards, M., Mistry, P., Tallents, G.J.: *J. Quantum Spectrosc. Radiat. Trans.* **99**, 370 (2006)
160. Nabekawa, Y., Shimizu, T., Furukawa, Y., Takahashi, E.J., Midorikawa, K.: *Phys. Rev. Lett.* **102**, 213904 (2009)
161. Corsi, C., Liontos, I., Cavalieri, S., Bellini, M., Venturi, G., Eramo, R.: *Opt. Express* **23**, 4106 (2015)
162. Kovačev, M., Fomichev, S., Priori, E., Mairesse, Y., Merdji, H., Monchicourt, P., Breger, P., Norin, J., Persson, A., L'Huillier, A., Wahlström, C.-G., Carré, B., Salières, P.: *Phys. Rev. Lett.* **95**, 223903 (2005)
163. Meng, Y., Zhang, C., Marceau, C., Naumov, A.Y., Corkum, P.B., Villeneuve, D.M.: *Opt. Express* **23**, 28960 (2015)
164. Jansen, G.S.M., Rudolf, D., Freisem, L., Eikema, K.S.E., Witte, S.: *Optica* **3**, 1122 (2016)
165. Mandon, J., Guelachvili, G., Picqué, N.: *Nat. Photonics* **3**, 99 (2009)
166. Bernhardt, B., Ozawa, A., Jacquet, P., Jacquy, M., Kobayashi, Y., Udem, T., Holzwarth, R., Guelachvili, G., Hänsch, T.W., Picqué, N.: *Nat. Photonics* **4**, 55 (2010)
167. Schiller, S.: *Opt. Lett.* **27**, 766 (2002)
168. Ycas, G., Giorgetta, F.R., Baumann, E., Coddington, I., Herman, D., Diddams, S.A., Newbury, N.R.: *Nat. Photonics* **12**, 202 (2018)
169. Picque, N., Hansch, T.W.: *Nat. Photonics* **13**, 146 (2019)
170. Lee, J., Carlson, D.R., Jones, R.J.: *Opt. Express* **19**, 23315 (2011)
171. Siegmund, O.H.W., Gummin, M.A., Stock, J., Marsh, D.: Microchannel plate imaging detectors for the ultraviolet. In: Guyenne, T.D., Hunt, J. (eds.) *Photon Detectors for Space Instrumentation*, p. 356. ESA, Paris (1992)
172. Timothy, J.G., Madden, R.P.: Photon detectors for the ultraviolet and x-ray region. In: Koch, E.-E. (ed.) *Handbook on Synchrotron Radiation*, vol. 1, p. 315. North-Holland, Amsterdam (1983)
173. Timothy, J.G.: Photon-counting detector systems: Current status and future prospects. In: Morgan, B.L. (ed.) *Photoelectronic Imaging Devices*, p. 85. IOP, Bristol (1991)
174. Shaw, G.A., Siegel, A.M., Model, J., Geboff, A., Soloviev, S., Vert, A., Sandvik, P.: *Proc. SPIE* **7320**, 88 (2009)
175. Sang, L., Liao, M., Masatomo, S.: *Sensors* **13**, 10482 (2013)
176. Shaw, P.S., Larason, T.C., Gupta, R., Lykke, K.R.: *Rev. Sci. Instrum.* **73**, 1625 (2002)
177. Gottwald, A., Kroth, U., Richter, M., Schoppe, H., Ulm, G.: *Meas. Sci. Technol.* **21**, 125101 (2010)
178. Thornagel, R., Fliegau, R., Klein, R., Kroth, S., Paustein, W., Richter, M.: *Rev. Sci. Instrum.* **86**, 013106 (2015)
179. Rieke, G.: *Detection of Light*. Univ. Cambridge, Cambridge (2003)
180. Carruthers, G.R.: Ultraviolet and x-ray detectors. In: Waynant, R.W., Ediger, M.N. (eds.) *Electro-Optics Handbook*, 2nd edn. McGraw-Hill, New York (2000). Chap. 15
181. Polyakov, S.V.: Photomultiplier tubes. In: Migdall, Polyakov, S.V., Fan, J., Bienfang, J.C. (eds.) *Single Photon Generation and Detection Experimental Methods in the Physical Sciences*, vol. 45, Academic Press, San Diego (2013). Chap. 3
182. Siegmund, O.H.W.: Photodiode detectors. In: Samson, J.A.R., Ederer, D.L. (eds.) *Vacuum Ultraviolet Spectroscopy II*, p. 139. Academic Press, San Diego (1998)
183. Samson, J.A.R., Haddad, G.N.: *J. Opt. Soc. Am.* **64**, 1346 (1974)
184. McKinsey, D.N., Brome, C.R., Butterworth, J.S., Golub, R., Habicht, K., Huffman, P.R., Lamoreaux, S.K., Mattoni, C.E.H., Doyle, J.M.: *Nucl. Instrum. Methods Phys. Res. B* **132**, 351 (1997)
185. Krizan, P.: *J. Instrum.* **9**, C10010 (2014)
186. Siegmund, O.H.W., Vallerger, J.V., Tremsin, A.S., McPhate, J., Michalet, X., Colyer, R.A., Weiss, S.: *Proc. SPIE* **8033**, 245 (2011)
187. Timothy, J.G.: Microchannel plates for photon detection and imaging in space. In: Huber, M.C.E., Pauluhn, A., Culhane, J.L., Timothy, J.G., Wilhelm, K., Zehnder, A. (eds.) *Observing Photons in Space*. Springer, New York (2013)
188. Siegmund, O.H.W., Tremsin, A.S., Vallerger, J.V.: *Nucl. Instrum. Methods A* **510**, 185 (2003)
189. Wiza, J.L.: *Nucl. Instrum. Methods* **162**, 587 (1979)
190. Timothy, J.G.: *Rev. Sci. Instrum.* **52**, 1131 (1981)
191. Martin, C., Jelinsky, P., Lampton, M., Malina, R.F.: *Rev. Sci. Instrum.* **52**, 1067 (1981)
192. Siegmund, O.H.W., Tremsin, A.S., Vallerger, J.V., Hull, J.: *IEEE Trans. Nucl. Sci.* **48**, 430 (2001)
193. Vickers, J.S., Chakrabarti, S.: *Rev. Sci. Instrum.* **70**, 2912 (1999)
194. Lapington, J.S., Rees, K.: *Nucl. Instrum. Methods A* **477**, 273 (2002)
195. Rzeghi, M., Rogalski, A.: *J. Appl. Phys.* **79**, 7433 (1996)
196. Monroy, E., Omnès, F., Calle, F.: *Semicond. Sci. Technol.* **18**, R33 (2003)
197. Velazquez, R., Aldalbahi, A., Rivera, M., Feng, P.: *AIP Advances* **6**, 085117 (2016)
198. Chen, H.Y., Liu, K.W., Hu, L.F., Al-Ghamdi, A.A., Fang, X.S.: *Mater. Today* **18**, 493 (2015)
199. Vest, R.E., Hertog, B., Chow, P.: *Metrologia* **40**, S141 (2003)
200. Canfield, L.R., Vest, R., Woods, T.N., Korde, R.: *Proc. SPIE* **2282**, 31 (1994)
201. Morrissey, P.F., McCandliss, S.R., Feldman, P.D., Friedman, S.D.: *Appl. Opt.* **33**, 2534 (1994)
202. Janesick, J., Campbell, D., Elliot, T., Daud, T.: *Opt. Eng.* **26**, 853 (1987)
203. Morrissey, P.F., McCandliss, S.R., Feldman, P.D.: *Appl. Opt.* **34**, 4640 (1995)
204. Nikzad, S., Hoenk, M.E., Greer, F., Jaquot, B., Monacos, S., Jones, T.J., Blacksberg, J., Hamden, E., Schiminovich, D., Martin, C.: *Appl. Opt.* **51**, 365 (2012)
205. Hamden, E.T., Jewell, A.D., Shapiro, C.A., Cheng, S.R., Goodsall, T.M., Hennessy, J., Hoenk, M.E., Jones, T., Gordon, S., Ong, H.R.,

- Schiminovich, D., Martin, D.C., Nikzad, S.: *J. Astron. Telesc. Instrum. Syst.* **2**, 036003 (2016)
206. Rife, J.C.: Optical materials – UV, VUV. In: Waynant, R.W., Ediger, M.N. (eds.) *Electro-Optics Handbook*, 2nd edn. McGraw-Hill, New York (2000). Chap. 10
207. Palik, E.D.: *Handbook of Optical Constants of Solids*. Academic Press, New York (1985)
208. Hunter, W.R.: Windows and filters. In: Samson, J.A.R., Ederer, D.L. (eds.) *Vacuum Ultraviolet Spectroscopy I Experimental Methods in the Physical Sciences*, vol. 31, p. 305. Academic Press, San Diego (1998)
209. Chatterton, J.D., Upadhyaya, G.S., Shohet, J.L., Lauer, J.L., Bathke, R.D., Kukkad, K.: *J. Appl. Phys.* **100**, 043306 (2006)
210. Powell, F.R., Vedder, P.W., Lindblom, J.F., Powell, S.F.: *Opt. Eng.* **26**, 614 (1990)
211. Vedder, P.W., Vallerga, J.V., Siegmund, O.H.W., Gibson, J., Hull, J.: *Proc. SPIE* **1159**, 392 (1989)
212. Tarrío, C., Berg, R.F., Lucatorto, T.B., Lairson, B., Lopez, H., Ayers, T.: *Rev. Sci. Instrum.* **86**, 116103 (2015)
213. Larruquert, J.I., Keski-Kuha, R.A.M.: *Opt. Commun.* **215**, 93 (2003)
214. Hunter, W.R.: Reflectance spectra of single materials. In: Samson, J.A.R., Ederer, D.L. (eds.) *Vacuum Ultraviolet Spectroscopy I*, p. 205. Academic Press, San Diego (1998)
215. Flint, B.K.: *Adv. Space Res.* **2**, 135 (1983)
216. Hettrick, M.C., Flint, S.A., Edelstein, J.: *Appl. Opt.* **24**, 3682 (1985)
217. Zukic, M., Torr, D.G., Spann, J.F., Torr, M.R.: *Appl. Opt.* **29**, 4284 (1990)
218. Spiller, E.: Reflecting optics: Multilayers. In: Samson, J.A.R., Ederer, D.L. (eds.) *Vacuum Ultraviolet Spectroscopy I*, p. 271. Academic Press, San Diego (1998)
219. Zukic, M., Torr, D.G., Spann, J.F., Torr, M.R.: *Appl. Opt.* **29**, 4293 (1990)
220. Zukic, M., Torr, D.G.: *Appl. Opt.* **31**, 1588 (1992)
221. Larruquert, J.I., Keski-Kuha, R.A.M.: *Appl. Opt.* **38**, 1231 (1999)
222. Larruquert, J.I., Keski-Kuha, R.A.M.: *Appl. Opt.* **40**, 1126 (2001)
223. Windt, D.L., Seely, J.F., Kjørnattanawanich, B., Uspenskii, Y.A.: *Opt. Lett.* **30**, 3186 (2005)
224. Vidal-Dasilva, M., Fernández-Perea, M., Méndez, J.A., Aznárez, J.A., Larruquert, J.I.: *Opt. Express* **17**, 22773 (2009)
225. Hamden, E.T., Greer, F., Hoenk, M.E., Blacksborg, J., Dickie, M.R., Nikzad, S., Martin, C., Schiminovich, D.: *Appl. Opt.* **50**, 4180 (2011)
226. Kjørnattanawanich, B., Windt, D.L., Seely, J.F., Uspenskii, Y.A.: *Appl. Opt.* **45**, 1765 (2006)
227. Hennessy, J., Jewell, A.D., Hoenk, M.E., Nikzad, S.: *Appl. Opt.* **54**, 3507 (2015)
228. Barbee, T.W., Mrowka, S., Hettrick, M.C.: *Appl. Opt.* **24**, 883 (1985)
229. Bixler, J.V., Barbee, T.W., Dietrich, D.D.: *Proc. Soc. Photo-Opt. Instrum. Eng.* **1160**, 648 (1989)
230. Naulleau, P.P., Liddle, J.A., Anderson, E.H., Gullikson, E.M., Mirkarimi, P., Salmassi, F., Spiller, E.: *Opt. Commun.* **229**, 109 (2004)
231. Seely, J.F., Brown, C.M.: *Appl. Opt.* **32**, 6288 (1993)
232. Slaughter, J.M., Schulze, D.W., Hills, C.R., Mirone, A., Stalia, R., Watts, R.N., Tarrío, C., Lucatorto, T.B., Krumrey, M., Mueller, T.B., Falco, C.M.: *J. Appl. Phys.* **76**, 2144 (1994)
233. Stearns, D.G., Rosen, R.S., Vernon, S.P.: *Appl. Opt.* **32**, 6952 (1993)
234. Toyoda, M., Miyata, N., Yanagihara, M., Watanabe, M.: *Jpn. J. Appl. Phys.* **37**, 2066 (1998)
235. Montcalm, C., Grabner, R.F., Hudyma, R.M., Schmidt, M.A., Spiller, E., Walton, C.C., Wedowski, M., Folta, J.A.: *Appl. Opt.* **41**, 3262 (2002)
236. Spiller, E., Baker, S.L., Mirkarimi, P.B., Sperry, V., Gullikson, E.M., Stearns, D.G.: *Appl. Opt.* **42**, 4049 (2003)
237. Thomas, R.J., Keski-Kuha, R.A.M., Neupert, W.M., Condor, C.E., Gunn, J.S.: *Appl. Opt.* **30**, 2245 (1991)
238. Grigonis, M., Knystautas, E.J.: *Appl. Opt.* **36**, 2839 (1997)
239. Hotta, Y., Furudate, M., Yamamoto, M., Watanabe, M.: *Surf. Rev. Lett.* **9**, 571 (2002)
240. Seely, J.F., Uspenskii, Y.A., Pershin, Y.P., Kondratenko, V.V., Vinogradov, A.V.: *Appl. Opt.* **41**, 1846 (2002)
241. Hunter, W.R.: Polarization. In: Samson, J.A.R., Ederer, D.L. (eds.) *Vacuum Ultraviolet Spectroscopy I*, p. 227. Academic Press, San Diego (1998)
242. Winter, H., Ortjohann, H.W.: *Rev. Sci. Instrum.* **58**, 359 (1987)
243. Larruquert, J.I., Malvezzi, A.M., Giglia, A., Aznarez, J.A., Rodriguez-de, L.M., Mendez, J.A., Miotti, P., Frassetto, F., Massonne, G., Nannarone, S., Crescenzo, G., Capobianco, G., Fineschi, S.: *J. Opt.* **16**, 125713 (2014)
244. Hatano, T., Kondo, Y., Saito, K., Ejima, T., Watanabe, M., Takahashi, M.: *Surf. Rev. Lett.* **9**, 587 (2002)
245. Hu, W.B., Hatano, T., Yamamoto, M., Watanabe, M.: *J. Synchrotron Radiat.* **5**, 732 (1998)
246. Westerveld, W.B., Becker, K., Zetner, P.W., Orr, J.J., McConkey, J.W.: *Appl. Opt.* **24**, 2256 (1985)
247. Schmidt, J., Guggenmos, A., Hofstetter, M., Chew, S.H., Kleineberg, U.: *Opt. Express* **23**, 33564 (2015)



Glenn Stark Professor Stark's research interest is in the field of experimental molecular spectroscopy. His laboratory programs emphasize molecular transitions of interest to the astrophysics and aeronomy communities, primarily involving the measurement and interpretation of high-resolution absorption spectra of vacuum ultraviolet and extreme ultraviolet transitions. Related activities include Fourier transform spectroscopy of diatomic molecules and laser spectroscopies of diatomics.



Nelson de Oliveira Nelson de Oliveira received a PhD in Optics and Photonics from the Université Pierre et Marie Curie (Paris) in 2001. His main scientific interest is the development of instrumentation and sample environments for spectroscopy applications, designed to operate in the VUV spectral range. He is currently working at the Synchrotron Soleil facility as a beamline scientist on the DESIRS beamline.



Peter Smith Peter Smith (PhD Physics Caltech 1972) retired in 2009 after 36 years at the Harvard-Smithsonian Center for Astrophysics, performing measurements of atomic and molecular parameters at ultraviolet wavelengths for analyses of astronomical spectra, designing/calibrating instruments for ultraviolet spectral radiometric measurements of the Sun from satellites, and helping manage instrument development for the SDO satellite. He failed at retirement and spent 2013–2016 helping manage development of an instrument for the Parker Solar Probe.

Part D
Scattering Theory

Part D collects together the topics and approaches used in scattering theory. A handy compendium of equations, formulae, and expressions for the classical, quantal, and semiclassical approaches to elastic scattering is given; reactive systems and model potentials are also considered. The dependence of scattering processes on the angular orientation of the reactants and products is discussed through the analysis of scattering experiments, which probe atomic collision theories at a fundamental level. The detailed quantum mechanical techniques available to perform accurate calculations of scattering cross sections from first principles are presented. The theory of elastic, inelastic, and ionizing collisions of electrons with atoms and atomic ions is covered and then extended to include collisions with molecules. The powerful methods of quantum defect theory are discussed and applied to low-energy scattering processes, including multichannel processes. The standard scattering theory for electrons is extended to include positron collisions with atomic and molecular systems. Slow collisions of atoms or molecules within the adiabatic approximation are discussed; important deviations from this model are presented in some detail for the low energy case. Applications to collision processes involving Rydberg atoms in ultracold gases are particularly highlighted. The main methods in the theoretical treatment of ion-atom and atom-atom collisions are summarized with a focus on intermediate and high collision velocities. The molecular structure and collision dynamics

involved in ion-atom charge exchange reactions is studied. Both the perturbative and variational capture theories of the continuum distorted wave model are presented. The Wannier theory for threshold ionization is then developed. Studies of the energy and angular distribution of electrons ejected by the impact of high-velocity atomic or ionic projectiles on atomic targets are overviewed. A useful collection of formulae, expressions, and specific equations that cover the various approaches to electron-ion and ion-ion recombination processes is given. A basic theoretical formulation of dielectronic recombination is described, and its importance in the interpretation of plasma spectral emission is presented. Many of the equations used to study theoretically the collisional properties of both charged and neutral particles with atoms and molecules in Rydberg states are collected together; the primary approximations considered are the impulse approximation, the binary encounter approximation, and the Born approximation. The Thomas mass-transfer process is considered from both a classical and a quantal perspective. Additional features of this process are also discussed. The theoretical background, region of validity, and applications of the classical trajectory Monte Carlo method are then delineated. One-photon processes are discussed, and aspects of line broadening directly related to collisions between an emitting, or absorbing, atom and an electron, a neutral atom, or an atomic ion are considered.



Classical, Quantal, and Semiclassical Propagators and Applications to Elastic Scattering

47

Jan-Michael Rost

Contents

47.1	What Is Semiclassics?	685	47.8	Coulomb Elastic Scattering	705
47.2	Quantum, Classical, and Semiclassical Propagators	686	47.8.1	Quantum Phase Shift, Rutherford and Mott Scattering	705
47.2.1	The Quantum Propagator as a Feynman Path Integral	686	47.8.2	Classical Coulomb Scattering	706
47.2.2	The Classical Propagator	687	47.8.3	Semiclassical Coulomb Scattering	706
47.2.3	The Semiclassical Propagator	687	47.8.4	Born Approximation for Coulomb Scattering	706
47.3	Advantages and Disadvantages of Semiclassics	689	47.9	Results for Model Potentials	707
47.4	Applications to Elastic Scattering	689	47.9.1	Classical Deflection Functions and Cross Sections	707
47.4.1	Central Field	689	47.9.2	Amplitudes and Cross Sections in Born Approximation	710
47.4.2	Center-of-Mass to Laboratory Coordinate Conversion	689	References		711
47.5	Quantal Elastic Scattering	690			
47.5.1	Scattering Amplitude from the Propagator	690			
47.5.2	Partial Wave Expansion	690			
47.5.3	Phase Shift and Cross Sections	691			
47.5.4	Identical Particles: Symmetry Oscillations	692			
47.5.5	Low-Energy $E \rightarrow 0$ Scattering	693			
47.5.6	Nonspherical Potentials	695			
47.5.7	Reactive Systems	695			
47.6	Classical Elastic Scattering	696			
47.6.1	Elastic Scattering Cross Section	696			
47.6.2	Deflection Functions	696			
47.6.3	Glory and Rainbow Scattering	697			
47.6.4	Orbiting and Spiraling Collisions	698			
47.6.5	Deflection Function and Time Delay from Action	698			
47.6.6	Approximate Actions	698			
47.7	Semiclassical Elastic Scattering	698			
47.7.1	Semiclassical Amplitudes and Cross Sections	698			
47.7.2	Diffraction and Glory Amplitudes	700			
47.7.3	Small-Angle (Diffraction) Scattering	701			
47.7.4	Small-Angle (Glory) Scattering	701			
47.7.5	Oscillations in Elastic Scattering	702			
47.7.6	Scattering Amplitude in Poisson Sum Representation	702			
47.7.7	Semiclassical Phase Shifts	702			
47.7.8	Semiclassical Amplitudes: Integral Representation	704			

Abstract

Semiclassical methods predate even full quantum mechanics starting with Bohr's atom model. Semiclassical propagators have been developed continuously in chemical physics ever since Miller's seminal classical S-matrix. Semiclassics was revived with the success of periodic orbit quantization and chaotic dynamics entering the quantum domain. Today, semiclassical and even classical concepts are accepted to describe microscopic phenomena, from protein folding over plasma physics all the way to atoms in strong laser fields. Thereby, semiclassical approximations are used for computation as well as for physical insight. Explicit formulae are given for elastic scattering, always covering quantum, classical, and semiclassical expressions.

Keywords

elastic scattering · integral cross section · transport cross section · deflection function · quasi-bound state · semiclassical propagator · quantum propagator

47.1 What Is Semiclassics?

Broadly speaking, semiclassics is asymptotic quantum theory taking \hbar as a small parameter and is, therefore, an approximation between full quantum mechanics and clas-

J.-M. Rost (✉)
Max Planck Institute for the Physics of Complex Systems
Dresden, Germany
e-mail: rost@pks.mpg.de

sical mechanics. The latter has always played an important role for molecular dynamics to describe molecular reactions and spectra. More recently, it has been widely applied also in electronic problems, most prominently when bound electrons move under the influence of intense laser pulses and are eventually ionized. Hence, we will briefly provide the quantum (finite \hbar) and the classical propagator ($\hbar = 0$) before introducing the standard semiclassical propagator ($\hbar \ll 1$).

What does a reader expect from a *Handbook of AMO Physics* chapter in the age of limitless internet access? If one is only vaguely familiar with a topic, e.g., semiclassics, one does not know how things are related and what may matter – my intention is to provide a guideline for this situation and some recipes. Newcomers may also not know which are the relevant methods, mechanisms and therefore key words, suitable to access additional resources from the internet. For this reason, we will put such phrases that are important in the context of semiclassics in italics in the following. Clearly, even for providing an overview (not a review!) the topics covered by *semiclassics* are by far too many. Hence, we do restrict ourselves to a subjective selection relevant for elastic scattering. The methods introduced are influenced by few-body physics, although most concepts are not restricted in the number of degrees of freedom (DoF). For the same reason, only nonrelativistic real-time propagation will be addressed, while imaginary time propagation describing thermal ensembles will not be covered, although it is treatable semiclassically as well. Furthermore, we will not touch semiclassical approximations to second quantization or many-body techniques even though there has been interesting progress.

There are, of course, excellent monographs about semiclassics; a recent one being [1] with a time-dependent phase space perspective and intuitive arguments, written by Eric Heller, who has been deeply involved in chemical and atomic physics as well as in chaotic dynamics and billiards. A bit older and maybe easier to approach is the monograph [2], which is based on Matthias Brack's research interest and provides an additional aspect related to nuclear and cluster physics. A real treat (and not so difficult to read) is Martin Gutzwiller's book [3], and a more mathematical account but well approachable for physicists is provided by Alfredo Ozorio Almeida in [4]. An original project lead by Predrag Cvitanovic is the online "chaos book", with part V being relevant for semiclassics [5]. Out of the many reviews, we would like to point out two "classic" ones, namely that about elastic scattering by Berry and Mount [6], and arguably the foundation for the useful application of semiclassical propagators for quantum dynamics, Bill Miller's review of his own work on the "classical S-matrix", which is, in fact, semiclassical [7]. Directly relevant in particular for the first sections of this chapter is [8].

47.2 Quantum, Classical, and Semiclassical Propagators

47.2.1 The Quantum Propagator as a Feynman Path Integral

The most general mathematical object describing evolution in the time domain is the propagator,

$$K(q, q', t) \equiv \langle q | e^{-\frac{iHt}{\hbar}} | q' \rangle = \int \mathcal{D}[q_t] e^{\frac{iS[q_t]}{\hbar}}, \quad (47.1)$$

where for simplicity we restrict ourselves to time-independent Hamiltonians H . Semiclassically, any time-dependent Hamiltonian can be turned by a formal extension of phase space into a time-independent one. Formulated as a Feynman path integral, the propagator contains *all* paths q_t leading from q' to q in time t , where q is a state (often position or momentum) for an arbitrary number of degrees of freedom F , and the action S is the integral over the classical Lagrangian while the paths themselves are not classical in general [9]. Arguably, the path integral is not a very transparent expression. Moreover, it is difficult to compute. This is one motivation to resort to a semiclassical approximation to be introduced in Sect. 47.2.3.

Analytical quantum propagators exist for a few problems only. The commonly known ones are those for the free particle of mass m and initial and final spatial coordinates \mathbf{x}' and \mathbf{x} , respectively,

$$K_0^{(F)}(\mathbf{x}, \mathbf{x}', t) = \left(\frac{m}{2\pi i \hbar t} \right)^{\frac{F}{2}} \exp \left[\frac{-m(\mathbf{x} - \mathbf{x}')^2}{2i \hbar t} \right] \quad (47.2a)$$

and the harmonic oscillator with frequency ω

$$K_{\text{HO}}^{(F)}(\mathbf{x}, \mathbf{x}', t) = \left(\frac{m\omega}{2\pi i \hbar \sin \omega t} \right)^{F/2} \times \exp \left[- \left(\frac{m\omega((\mathbf{x}^2 + \mathbf{x}'^2) \cos \omega t - 2\mathbf{x}\mathbf{x}')}{2i \hbar \sin \omega t} \right) \right]. \quad (47.2b)$$

The corresponding propagators in momentum space read

$$K_0^{(F)}(\mathbf{p}, \mathbf{p}', t) = \delta(\mathbf{p} - \mathbf{p}') \exp \left[- \frac{i t \mathbf{p}^2}{2m \hbar} \right] \quad (47.2c)$$

and for the harmonic oscillator

$$K_{\text{HO}}^{(F)}(\mathbf{p}, \mathbf{p}', t) = \left(\frac{1}{2\pi i \hbar m \omega \sin \omega t} \right)^{F/2} \times \exp \left[- \left(\frac{(\mathbf{p}^2 + \mathbf{p}'^2) \cos \omega t - 2\mathbf{p}\mathbf{p}'}{2i \hbar m \omega \sin \omega t} \right) \right], \quad (47.2d)$$

where the latter is easily obtained from Eq. (47.2b) through the equivalence $x \leftrightarrow p/(m\omega)$.

Since propagation in each degree of freedom for both problems is independent, the propagator for F degrees of freedom is simply the product, e.g., in coordinate space

$$K_F(\mathbf{x}, \mathbf{x}', t) = \prod_{j=1}^F K_1(x_j, x'_j, t). \quad (47.2e)$$

This also implies, of course, that N particles in d dimensions are simply described by $F = 2Nd$ DoF.

There are other scarce analytical results, mostly quite involved and requiring an algebraic computer manipulation tool to handle them, such as, e.g., for the Coulomb interaction [10].

47.2.2 The Classical Propagator

Classically, densities (not amplitudes) and corresponding observables of a system are evolved in time. The quantum expression that answers the question “What is the probability of finding a system after time t at q given that it was initially at q' ” is answered by the probability density $\mathcal{P}(q, q', t) = |K(q, q', t)|^2$. Classically, it has the intuitive form of a *correlation function* over phase space,

$$\mathcal{P}_{\text{cl}}(q, q', t) = \frac{1}{\Gamma} \int dq' dp' \delta(q - q_t) \delta(q' - q_0), \quad (47.3)$$

where $q_t = q(t)$ is a variable evolving under the system dynamics, and Γ is a normalization constant. The phase space integral can, in principle, be taken at any time; here, we carry it out with the conjugate phase space variables at time $t = 0$, since then the integration over q' is trivial. For the integral over p' , one has to find those initial momenta p'_j that fulfil the remaining δ -function and the integral reduces to the sum over trajectories

$$\mathcal{P}_{\text{cl}}(q, q', t) = \sum_j \mathcal{P}_j \quad (47.4a)$$

$$\mathcal{P}_j = \frac{1}{\Gamma} \left| \left[\frac{\partial q_t(p', q')}{\partial p'} \right] \right|_{q_t(p'_j, q')=q}^{-1}, \quad (47.4b)$$

where each trajectory contributes the weight equation (47.4b). Here, and in the following, $[M] = \det M$ if M is a matrix. This expression holds again in arbitrary dimensions, i.e., q and p can be vectors, and the absolute value of the determinant from $\partial q/\partial p'$, the *Jacobi matrix*, measures the phase space volume around the trajectory j . The function $q = q_t(p', q')$, and generally a set of final variables γ as a function of the initial variables γ' , is called a *deflection*

function. The quite transparent interpretation of the classical probability density equation (47.3) is with the help of Eqs. (47.4a) and (47.4b) a sum over individual probability densities for all classical trajectories that connect q and q' in time t . To obtain the normalization Γ we ask “What is the probability of finding the system at time $t = 0$ with a momentum p' in the neighborhood $\Delta p'$, if it is located within $\Delta q'$ of q' ?” We know that the system is in this neighborhood for sure, and since the phase space integral in Eq. (47.3) is trivially fulfilled, we get

$$1 = \mathcal{P}(p', q') \Delta p' \Delta q' = \frac{1}{\Gamma} \Delta p' \Delta q', \quad (47.5a)$$

which means $\Gamma = \Delta p' \Delta q'$, the phase space volume the system occupies initially (or more precisely at the time, the integration $dp' dq'$ is performed). We can ask the same question quantum mechanically: “What is the probability of finding momentum $|p'\rangle$ for a system in state $|q'\rangle$?” Since there is nothing to propagate, the answer is

$$|K(p', q', 0)|^2 = |\langle p' | q' \rangle|^2 = \left| \frac{e^{ip'q'/\hbar}}{(2\pi\hbar)^{\frac{F}{2}}} \right|^2 = \frac{1}{(2\pi\hbar)^F}, \quad (47.5b)$$

for F degrees of freedom. A comparison with Eq. (47.5a) reveals that the classical normalization compatible with the quantum result is $\Gamma_F = (2\pi\hbar)^F$, for F DoF. Obviously, this is a reasonable normalization, and if one wants to describe microscopic systems classically, it must be emphasized that this is a judicial choice. By no means does the classical propagator Eq. (47.3) contain an \hbar -dependence per se.

47.2.3 The Semiclassical Propagator

Essentially an asymptotic expansion of the Feynman path integral Eq. (47.1) to first order in \hbar , the *semiclassical propagator* is more subtle to formulate. The decisive step is the reduction of paths. It is justified by the argument of stationary phase: the phase $S[q_t]/\hbar$ varies substantially for $\hbar \ll 1$ for different paths connecting q and q' , rendering their added contribution marginal. The surviving paths have an action that is stationary under variation of the paths, $\delta S[q_t]/\delta q_t = 0$. Since this stationarity condition defines the classical equations of motion, the surviving paths are exactly the trajectories following Newtonian dynamics. Hence, the stationary phase argument for small \hbar reduces the path integral to a sum over the trajectories.

The van Vleck–Gutzwiller (VG) propagator reads

$$K_{\text{sc}}(q, q', t) = \sum_j \mathcal{P}_j^{\frac{1}{2}} \exp\left(-\frac{iv_j \pi}{2} + \frac{iS_j(q, q', t)}{\hbar}\right), \quad (47.6)$$

where \mathcal{P}_j is the classical probability density from Eq. (47.4b) with the normalization $\Gamma = (2\pi\hbar)^F$ for F degrees of freedom, as derived in Eqs. (47.5a) and (47.5b). At a first glance, the semiclassical propagator has the simple and intuitive form of a sum over classical trajectories whose weights are now complex amplitudes formed by the square root of the classical probability and multiplied by a phase factor given by the classical action of the trajectory, as originally suggested already in 1928 by *van Vleck* [11]. The truth is more complicated, as the semiclassical propagator retains a memory about the topology of the paths contributing between q and q' . At certain points in time, the trajectory bundle around traj. j may not span the full local phase space volume $|\partial q(t)/\partial p'_j|$ due to a *focal point* or a *caustic*. Propagating the trajectory across such a point where the determinant is singular may change the sign of $[\partial q(t)/\partial p'_j]$. This is formally encoded in the *Maslov phase* ν_j counting the number of sign changes of the eigenvalues of the Jacobi matrix in time along trajectory j , as pointed out by *Gutzwiller* only in 1967 [12].

Two features make the van Vleck–Gutzwiller propagator difficult to compute. To determine ν_j is cumbersome and, also, to find the initial momenta p' that allow a trajectory to start at q' and end at q in time t requires numerically expensive root searches. An alternative formulation in phase space is particular suitable for numerical propagation.

The Hermann Kluk propagator is given [13] as an integral over the initial conditions (p_0, q_0) of the trajectories (q_t, p_t) , propagated under a classical Hamiltonian H ,

$$K_\gamma(q, q', t) = \frac{1}{(2\pi\hbar)^F} \iint d^F q_0 d^F p_0 R_\gamma(p_t, q_t) \times \exp\left(\frac{i}{\hbar} S(p_t, q_t)\right) f_\gamma(q, q_t, p_t) f_\gamma^*(q', q_0, p_0). \quad (47.7)$$

Each trajectory is the center of a Gaussian

$$f_\gamma(q, q', p') = \exp\left(-\frac{\gamma^2}{2}(q - q')^2 + \frac{i}{\hbar} p'(q - q')\right). \quad (47.8)$$

The action $S = \int(p\dot{q} - H) dt$ accumulated along the trajectory enters Eq. (47.7) as well as the probability density of each trajectory $R_\gamma(p_t, q_t)$, which contains all four blocks

$$M_{xy}(t, 0) = \frac{\partial x_t}{\partial y_0}, \quad (47.9)$$

$\in \mathbb{R}^F \times \mathbb{R}^F$ of the *monodromy matrix*

$$\begin{pmatrix} \delta q_t \\ \delta p_t \end{pmatrix} = \begin{pmatrix} M_{qq} & M_{qp} \\ M_{pq} & M_{pp} \end{pmatrix} \begin{pmatrix} \delta q_0 \\ \delta p_0 \end{pmatrix}. \quad (47.10)$$

The actual form of the probability density depends on a width parameter γ , which determines the admixture of the different blocks M_{xy} in the determinant

$$R_\gamma(p_t, q_t) = \left[\frac{1}{2} \left(M_{qq} + M_{pp} - i\gamma^2 \hbar M_{qp} - \frac{1}{i\gamma^2 \hbar} M_{pq} \right) \right]^{\frac{1}{2}}. \quad (47.11)$$

Although this semiclassical propagator is not uniquely defined through its dependence on a suitable chosen parameter γ , it is exactly the feature that provides approximate global *uniformization* since at a *caustic*, R_γ always remains finite, which is an important advantage over other forms. Secondly, as was already pointed out, one does not have to keep track of *Maslov indices*. Instead, one has to make R_γ continuous as the radicant crosses the branch cut. Finally, the root search has been circumvented. All semiclassical propagators with this property use the *initial value representation* (IVR), i.e., the integral is over phase space coordinates at a single point in time (typically the initial time) only.

By taking $\gamma \rightarrow \infty$ or $\gamma \rightarrow 0$, one obtains the semiclassical IVR propagators in position or momentum space, respectively.

Expressions take a particularly simple and appealing form if the propagator Eq. (47.7) is used in conjunction with wavefunctions that contain the Gaussians with the same width γ . The correlation function $c(t) = \langle \Psi | \exp(-iH/\hbar) | \Psi \rangle$ probing the spectrum of H is a general example.

The semiclassical correlation function c_{sc} using Eq. (47.7) with a normalized Gaussian $\Psi = (\gamma^2/\pi)^{3/4} f_\gamma(q, q', p')$ reads

$$c_{sc}(t) = \langle \Psi | K_\gamma(t) | \Psi \rangle = \frac{1}{(2\pi\hbar)^F} \iint d^F q_0 d^F p_0 R(p_t, q_t) \times \exp\left(\frac{i}{\hbar} S(p_t, q_t)\right) \times g_\gamma(q_0, p_0, q', p') g_\gamma^*(q_t, p_t, q', p'), \quad (47.12)$$

where

$$g_\gamma(q, p, q', p') = \exp\left(-\frac{\gamma^2}{4}(q - q')^2 - \frac{1}{4\gamma^2 \hbar^2}(p - p')^2 + \frac{i}{2\hbar}(p + p')(q - q')\right). \quad (47.14)$$

The integral in Eq. (47.12) is again over phase space representing the initial conditions (q_0, p_0) of the trajectories (q_t, p_t) and is calculated in practice by *Monte Carlo integration*. The number of sampling points (trajectories to be run)

to achieve convergence depends on the initial wave packet Ψ and the part of the spectrum of H covered by it through the parameters (γ, p', q') .

Analytical semiclassical propagators. For interactions up to quadratic order (constant, linear, and harmonic potentials) $\langle V'(x) \rangle = V'(\langle x \rangle)$ holds, and, therefore, the quantum system observables can, indeed, be described with classical trajectories. This is a consequence of the *Ehrenfest theorem*, which casts quantum observables into a form similar to *Hamilton's equations*

$$m \frac{d\langle x \rangle}{dt} = \langle p \rangle, \quad \frac{d\langle p \rangle}{dt} = -\langle V'(x) \rangle. \quad (47.15)$$

Hence, the quantum propagators for the free particle and the harmonic oscillator in arbitrary dimensions Eqs. (47.2a)–(47.2e) are identical to the corresponding semiclassical propagators.

47.3 Advantages and Disadvantages of Semiclassics

Advantages of Semiclassics:

- Relies on classical mechanics only but describes quantum interference
- Reveals dominant structure of a quantum problem (via *stationary phase*)
- Is exact for interactions up to quadratic order (Ehrenfest theorem)
- Excellent approximation if dynamics evolves through many degrees of freedom
- Formally offers a quantum formulation (complex amplitudes) and can, therefore, be seamlessly blended in approximation containing other quantum parts
- Offers many possibilities for additional approximations
- Is straightforward to compute.

Disadvantages of Semiclassics:

- “Hard” quantum properties, such as *tunnelling*, *diffraction* and *entanglement*, are not described.
- While straightforward to code, the numerical effort may be exponential due to the nonlinearity of classical mechanics.
- Instabilities and serious errors can occur at *caustics*, when two stationary phase points (trajectories) coalesce. *Uniformization* (higher-order correction) is then necessary, which is tedious and often does not yield an improvement worth the effort.

In particular, fragmentation into several particles is ideally suited for classical and semiclassical treatments since one can follow the particle trajectories numerically to their asymptotic momenta and simply bin them into finite intervals to arrive at a cross section. Analytical expressions that also give an idea about the singularities one encounters in classical and semiclassical scattering can be best exemplified with elastic scattering. A more exhaustive account of elastic scattering is given in previous editions of the Handbook.

47.4 Applications to Elastic Scattering

Elastic scattering is governed by the Hamiltonian $H = \mathbf{p}^2/(2m) + V(\mathbf{r})$ in the center-of-mass frame for the relative motion of two collision partners with reduced mass m .

47.4.1 Central Field

For a conservative (real) potential $V(r)$ depending only on the distance r from the scattering center O , the total energy $E > 0$ and orbital the angular momentum L are conserved. Due to the different mathematical structures classical and quantum theory take advantage of this effect in quite different ways. Classically, the deflection function mapping the impact parameter b to the scattering angle θ in the scattering plane characterizes elastic scattering. Quantum mechanically, the phase shift for each angular momentum component is relevant, as it describes the change of the corresponding partial wave due to scattering. Alternatively, initial (vectorial) momentum \mathbf{p}' is converted into final momentum \mathbf{p} through scattering, and the ensuing scalar product $\mathbf{p}' \cdot \mathbf{p} = 2mE \cos \theta$ encloses the scattering angle θ . This description can be applied in quantum and classical mechanics.

47.4.2 Center-of-Mass to Laboratory Coordinate Conversion

Let ψ_1, ψ_2 be the angles for scattering and recoil, respectively, of the projectile by a target initially at rest in the lab frame. Then,

$$\begin{aligned} \sigma_1(\psi_1) d\Omega_1 &= \sigma_2(\psi_2) d\Omega_2 \\ &= \sigma_{\text{cm}}^{(1,2)}(\theta) d\Omega_{\text{cm}}, \quad 0 \leq \theta \leq \pi; \\ \sigma_{\text{cm}}^{(2)}(\theta, \phi) &= \sigma_{\text{cm}}^{(1)}(\pi - \theta, \phi + \pi). \end{aligned} \quad (47.16)$$

(A) Elastic scattering of two bodies with masses m_1 and m_2 without conversion of translational kinetic energy into

internal energy: (1) + (2) \rightarrow (1) + (2).

$$\begin{aligned}\sigma_1(\psi_1) &= \sigma_{\text{cm}}(\theta) \frac{(1 + 2x \cos \theta + x^2)^{3/2}}{|1 + x \cos \theta|}; \\ \sigma_2(\psi_2) &= \sigma_{\text{cm}}(\theta) \left| 4 \sin \frac{1}{2} \theta \right|; \\ \psi_2 &= \frac{1}{2}(\pi - \theta), \quad 0 \leq \psi_2 \leq \frac{1}{2}\pi; \\ \tan \psi_1 &= \frac{\sin \theta}{(x + \cos \theta)}, \quad x = m_1/m_2. \quad (47.17)\end{aligned}$$

$m_1 > m_2$: As $0 \leq \theta \leq \theta_c = \cos^{-1}(-m_2/m_1)$,
 $0 \leq \psi_1 \rightarrow \psi_1^{\text{max}} = \sin^{-1}(m_2/m_1) < \frac{1}{2}\pi$.

As $\theta_c \leq \theta \rightarrow \pi$, $\psi_1^{\text{max}} \leq \psi_1 \rightarrow 0$;
 θ is a double-valued function of ψ ;

$m_1 = m_2$: $\sigma_1(\psi_1) = (4 \cos \psi_1) \sigma_{\text{cm}}(\theta = 2\psi_1)$,
 $0 \leq \psi_1 \leq \frac{1}{2}\pi$, $\psi_1 + \psi_2 = \frac{1}{2}\pi$;
 no backscattering;

$m_1 \ll m_2$: $\sigma_1(\psi_1) = \sigma_{\text{cm}}(\theta = \psi_1)$;
 lab and cm frames identical.

(B) Two-body elastic scattering process with conversion of translational kinetic energy into internal energy: (1) + (2) \rightarrow (3) + (4). For conversion of internal energy ε_i so that kinetic energy of relative motion (in the cm frame) increases from E_i to $E_f = E_i + \varepsilon_i$. For $j = 3, 4$,

$$\begin{aligned}\sigma_j(\psi_j) &= \sigma_{\text{cm}}(\theta) \frac{[1 + 2x_j \cos \theta + x_j^2]^{3/2}}{|1 + x_j \cos \theta|}, \\ x_3 &= \left(\frac{m_1 m_3 E_i}{m_2 m_4 E_f} \right)^{1/2}, \\ x_4 &= - \left(\frac{m_1 m_4 E_i}{m_2 m_3 E_f} \right)^{1/2}, \\ \tan \psi_3 &= \frac{\sin \theta}{(x_3 + \cos \theta)}, \quad \tan \psi_4 = \frac{\sin \theta}{(|x_4| - \cos \theta)}. \quad (47.18)\end{aligned}$$

47.5 Quantal Elastic Scattering

Throughout this section we use reduced energy k^2 and potential $U(r)$,

$$\begin{aligned}k^2 &= (2m/\hbar^2)E, \\ U(r) &= (2m/\hbar^2)V(r).\end{aligned}$$

The basic quantity in quantal elastic scattering is the differential cross section

$$\frac{d\sigma}{d\Omega} = |f(\theta)|^2 \quad (47.19)$$

in terms of the complex *scattering amplitude* $f(E, \theta)$ contained in the wavefunction

$$\Psi(\mathbf{r}) \rightarrow \exp(ikz) + \frac{1}{r} f(\theta) \exp(ikr) \quad (47.20)$$

as $r \rightarrow \infty$.

47.5.1 Scattering Amplitude from the Propagator

The scattering amplitude from incident momentum \mathbf{p}' to scattered momentum \mathbf{p} can be expressed with the *S-matrix* through the relation

$$\langle \mathbf{p} | S - 1 | \mathbf{p}' \rangle = -\frac{m}{2\pi i \hbar} \delta(E - E') f(\mathbf{p}, \mathbf{p}'). \quad (47.21a)$$

Using the definition of the S-matrix in terms of the propagator K_0 for free motion Eq. (47.2c),

$$S = \lim_{t \rightarrow \infty} K_0^\dagger(t) K(2t) K_0^\dagger(t), \quad (47.21b)$$

and the representation

$$\begin{aligned}\delta(E - E') &= \frac{m}{p} \delta(p - p') \\ &= \frac{m}{p} \lim_{t \rightarrow \infty} \left(\frac{t}{2\pi i \hbar m} \right)^{1/2} \exp\left(\frac{i(p - p')^2 t}{2m\hbar} \right)\end{aligned} \quad (47.21c)$$

of the δ -function we get [8]

$$\begin{aligned}f(\mathbf{p}, \mathbf{p}') &= \frac{p}{m} \lim_{t \rightarrow \infty} ((2\pi i \hbar m)^3 / t)^{1/2} \\ &\times \langle \mathbf{p} | K_0^\dagger(t) K(2t) K_0^\dagger(t) - 1 | \mathbf{p}' \rangle, \quad (47.21d)\end{aligned}$$

which is a representation for the scattering amplitude that can be used for the semiclassical formulation in conjunction with the propagators given in Sect. 47.2.3. For the direct quantum calculation, one normally makes use of the conserved angular momentum for partial waves. Using all constants of motion an S-matrix element between initial and final variables can be written as

$$\langle E, \ell, m | S | E', \ell', m' \rangle = S_\ell(E) \delta(E - E') \delta_{\ell\ell'} \delta_{mm'}. \quad (47.22)$$

Since the S-matrix is unitary, $S_\ell = \exp(2i\eta_\ell)$ can be expressed through a phase η_ℓ . Why this is called phase shift and how it is most conveniently determined will become clear through partial wave expansion.

47.5.2 Partial Wave Expansion

Due to the spherical symmetry, angular momentum ℓ is conserved, and the wavefunction $\Psi(\mathbf{r})$ as well as the scattering

amplitude $f(\theta)$ can be expanded into partial waves for each ℓ with the coefficients formulated in terms of phase shifts $\eta_\ell(E)$

$$\Psi(\mathbf{r}) = \frac{1}{kr} \sum_{\ell=0}^{\infty} A_\ell v_\ell(kr) P_\ell(\cos \theta), \quad (47.23a)$$

$$A_\ell = i^\ell (2\ell + 1) \exp(i\eta_\ell). \quad (47.23b)$$

The phase shift η_ℓ is obtained from the asymptotic solution of the radial Schrödinger equation

$$\frac{d^2 v_\ell}{dr^2} + \left(k^2 - \frac{2mV(r)}{\hbar^2} - \frac{\ell(\ell+1)}{r^2} \right) v_\ell(r) = 0, \quad (47.24)$$

where v_ℓ is normalized so that

$$\begin{aligned} v_\ell(r) &\stackrel{r \geq r_0}{=} \cos \eta_\ell F_\ell(kr) + \sin \eta_\ell G_\ell(kr) \\ &\rightarrow \sin\left(kr - \frac{1}{2}\ell\pi + \eta_\ell\right) \text{ as } r \rightarrow \infty. \end{aligned} \quad (47.25)$$

Hence, $v_\ell(r)$ is expressed in terms of the regular and irregular solution of the free radial Schrödinger equation ($V = 0$) containing the spherical Bessel j_ℓ and Neumann n_ℓ functions, respectively,

$$\begin{aligned} F_\ell(kr) &= (kr)j_\ell(kr) \\ &\rightarrow \begin{cases} (kr)^{\ell+1}/(2\ell+1)!!, & r \rightarrow 0 \\ \sin\left(kr - \frac{1}{2}\ell\pi\right), & r \rightarrow \infty, \end{cases} \end{aligned} \quad (47.26)$$

$$\begin{aligned} G_\ell(kr) &= -(kr)n_\ell(kr) \\ &\rightarrow \begin{cases} (2\ell-1)!!/(kr)^\ell, & r \rightarrow 0 \\ \cos\left(kr - \frac{1}{2}\ell\pi\right), & r \rightarrow \infty. \end{cases} \end{aligned} \quad (47.27)$$

The standard asymptotic scattering solution Eq. (47.25) contains the effect of scattering through the phase shift η_ℓ in the regular standing wave. By changing the normalization of A_ℓ one can express this effect in many different ways. The most common ones are to add to the regular standing wave either an irregular standing wave of real amplitude K_ℓ in Eq. (47.30) or, a spherical outgoing wave of amplitude T_ℓ in Eq. (47.31). Another possibility is to convert in Eq. (47.32) the incoming spherical wave of unit amplitude to an outgoing spherical wave of amplitude S_ℓ . The different amplitudes are related as

$$S_\ell(k) = \exp(2i\eta_\ell), \quad (47.28a)$$

$$T_\ell(k) = \sin \eta_\ell \exp(i\eta_\ell), \quad (47.28b)$$

$$K_\ell(k) = \tan \eta_\ell. \quad (47.28c)$$

The different asymptotic forms and normalizations for v_ℓ read

$$\begin{aligned} \text{(a)} \quad A_\ell &= i^\ell (2\ell + 1) \exp i\eta_\ell, \\ v_\ell(r) &\rightarrow \sin\left(kr - \frac{1}{2}\ell\pi + \eta_\ell\right); \end{aligned} \quad (47.29)$$

$$\begin{aligned} \text{(b)} \quad A_\ell &= i^\ell (2\ell + 1) \cos \eta_\ell, \\ v_\ell(r) &\rightarrow \sin\left(kr - \frac{1}{2}\ell\pi\right) + K_\ell \cos\left(kr - \frac{1}{2}\ell\pi\right); \end{aligned} \quad (47.30)$$

$$\begin{aligned} \text{(c)} \quad A_\ell &= i^\ell (2\ell + 1), \\ v_\ell(r) &\rightarrow \sin\left(kr - \frac{1}{2}\ell\pi\right) + T_\ell e^{i(kr - \ell\pi/2)}; \end{aligned} \quad (47.31)$$

$$\begin{aligned} \text{(d)} \quad A_\ell &= \frac{1}{2} i^{\ell+1} (2\ell + 1), \\ v_\ell(r) &\rightarrow e^{-i(kr - \ell\pi/2)} - S_\ell e^{i(kr - \ell\pi/2)}. \end{aligned} \quad (47.32)$$

47.5.3 Phase Shift and Cross Sections

The scattering amplitude in terms of partial waves ℓ reads

$$\begin{aligned} f(\theta) &= \frac{1}{2ik} \sum_{\ell=0}^{\infty} (2\ell + 1) [\exp(2i\eta_\ell) - 1] P_\ell(\cos \theta) \\ &= \sum_{\ell=0}^{\infty} f_\ell(\theta). \end{aligned} \quad (47.33a)$$

The phase shifts η_ℓ can be determined from the numerical solution of the radial Schrödinger equation Eq. (47.24).

The differential cross section (DCS) can be reexpanded in Legendre polynomials $P_\ell(\cos \theta)$,

$$\frac{d\sigma(E, \theta)}{d\Omega} = \frac{1}{k^2} \sum_{L=0}^{\infty} a_L(E) P_L(\cos \theta), \quad (47.34a)$$

$$\begin{aligned} a_L &= \sum_{\ell=0}^{\infty} \sum_{\ell'=|\ell-L|}^{\ell+L} (2\ell + 1)(2\ell' + 1) \\ &\quad \times (\ell\ell'00 | \ell\ell'L0)^2 \\ &\quad \times \sin \eta_\ell \sin \eta_{\ell'} \cos(\eta_\ell - \eta_{\ell'}), \end{aligned} \quad (47.34b)$$

where $(\ell\ell'mm' | \ell\ell'LM)$ are Clebsch–Gordan coefficients.

The integral cross section simplifies considerably since integration over the angle reveals the orthogonality of the partial waves,

$$\sigma(E) = 2\pi \int_0^\pi |f(\theta)|^2 d(\cos \theta) = \sum_{\ell=0}^{\infty} \sigma_\ell(E), \quad (47.35a)$$

with the partial cross sections

$$\sigma_\ell(E) = \frac{4\pi}{k^2} \sum_{\ell=0}^{\infty} (2\ell + 1) \sin^2 \eta_\ell . \quad (47.35b)$$

Optical theorem

$$\sigma(E) = (4\pi/k) \text{Im}[f(0)] . \quad (47.36)$$

S, P wave ($\ell = 0, 1$) net contribution

$$\frac{d\sigma}{d\Omega} = \frac{1}{k^2} \left\{ \sin^2 \eta_0 + [6 \sin \eta_0 \sin \eta_1 \cos(\eta_1 - \eta_0)] \right. \\ \left. \times \cos \theta + 9 \sin^2 \eta_1 \cos^2 \theta \right\} , \quad (47.37)$$

$$\sigma(E) = \frac{4\pi}{k^2} (\sin^2 \eta_0 + 3 \sin^2 \eta_1) . \quad (47.38)$$

For pure S -wave scattering, the DCS is isotropic. For pure P -wave scattering, the DCS is symmetric about $\theta = \pi/2$, where it vanishes; the DCS rises to equal maxima at $\theta = 0, \pi$. For combined S and P -wave scattering, the DCS is asymmetric with forward-backward asymmetry.

Collision integrals. Averages of $\sigma^{(n)}(E)$ over a Maxwellian distribution at temperature T are

$$\Omega^{(n,s)}(T) = [(s+1)!(kT)^{s+2}]^{-1} \int_0^{\infty} \sigma^{(n)}(E) \\ \times \exp(-E/kT) E^{s+1} dE . \quad (47.39)$$

Normalization factors are chosen so that the above expressions for $\sigma^{(n)}$ and $\Omega^{(n,s)}$ reduce to πd^2 for classical rigid spheres of diameter d .

Mobility. The mobility K of ions of charge e in a gas of density N is given by the Chapman–Enskog formula

$$K = \frac{3e}{8N} \left(\frac{\pi}{2MkT} \right)^{1/2} [\Omega^{(1,1)}(T)]^{-1} . \quad (47.40)$$

47.5.4 Identical Particles: Symmetry Oscillations

Colliding particles, each with spin s , in a total spin S_t resolved state in the range $(0 \rightarrow 2s)$ Particle interchange: $\Psi(\mathbf{r}) = (-1)^{S_t} \Psi(-\mathbf{r})$

$$I_{A,S}(\theta) = \frac{1}{2} |f(\theta) \mp f(\pi - \theta)|^2 , \quad (47.41a)$$

$$\Psi_{A,S}(\mathbf{r}) \rightarrow [\exp(ikZ) \mp \exp(-ikZ)] \\ + \frac{1}{R} [f(\theta) \mp f(\pi - \theta)] \exp(ikr) , \quad (47.41b)$$

$$I_{A,S}(\theta) = \frac{1}{4k^2} \left| \sum_{\ell=0}^{\infty} \omega_\ell (2\ell + 1) [\exp 2i\eta_\ell - 1] P_\ell(\cos \theta) \right|^2 , \quad (47.41c)$$

$$\sigma_{A,S}(E) = \frac{4\pi}{k^2} \sum_{\ell=0}^{\infty} \omega_\ell (2\ell + 1) \sin^2 \eta_\ell , \quad (47.41d)$$

where A and S denote antisymmetric and symmetric wavefunctions (with respect to particle interchange) for collisions of identical particles with odd and even total spin S_t

$$\text{A: } S_t \text{ odd } \quad \omega_\ell = 0 \ (\ell \text{ even}) ; \quad \omega_\ell = 2 \ (\ell \text{ odd}) ;$$

$$\text{S: } S_t \text{ even } \quad \omega_\ell = 2 \ (\ell \text{ even}) ; \quad \omega_\ell = 0 \ (\ell \text{ odd}) .$$

Spin states S_t unresolved S/A combination

$$I(\theta) = g_A I_A(\theta) + g_S I_S(\theta) , \quad (47.42a)$$

$$\sigma(E) = g_A \sigma_A(E) + g_S \sigma_S(E) , \quad (47.42b)$$

where g_A and g_S are the fractions of states with odd and even total spins $S_t = 0, 1, 2, \dots, 2s$. For fermions (F) with half integer spin s and bosons (B) with integral spin s ,

$$\text{F: } g_A = (s+1)/(2s+1) , \quad g_S = s/(2s+1) ,$$

$$\text{B: } g_A = s/(2s+1) , \quad g_S = (s+1)/(2s+1) ,$$

so that Eqs. (47.42a) and (47.42b) have the alternative forms

$$I(\text{F}) = |f(\theta)|^2 + |f(\pi - \theta)|^2 - \mathcal{I} , \quad (47.43a)$$

$$\sigma(\text{F}) = \frac{1}{2} [\sigma_S + \sigma_A] - \frac{1}{2} [\sigma_S - \sigma_A] / (2s+1) , \quad (47.43b)$$

$$I(\text{B}) = |f(\theta)|^2 + |f(\pi - \theta)|^2 + \mathcal{I} , \quad (47.43c)$$

$$\sigma(\text{B}) = \frac{1}{2} [\sigma_S + \sigma_A] + \frac{1}{2} [\sigma_S - \sigma_A] / (2s+1) , \quad (47.43d)$$

where the interference term is

$$\mathcal{I} = \left(\frac{2}{2s+1} \right) \text{Re}[f(\theta) f^*(\pi - \theta)] . \quad (47.43e)$$

Example: for fermions with spin $1/2$,

$$\sigma(E) = \frac{2\pi}{k^2} \left[\sum_{\ell=\text{even}}^{\infty} (2\ell + 1) \sin^2 \eta_\ell \right. \\ \left. + 3 \sum_{\ell=\text{odd}}^{\infty} (2\ell + 1) \sin^2 \eta_\ell \right] . \quad (47.44)$$

Symmetry oscillations originate from the interference between unscattered incident particles in the forward ($\theta = 0$) direction and backward scattered particles ($\theta = \pi, \ell = 0$). Symmetry oscillations are sensitive to the repulsive wall of the interaction.

Singlet–triplet spin flip cross section

$$\sigma_{\text{ST}}(E) = \frac{\pi}{k^2} \sum_{\ell=0}^{\infty} (2\ell + 1) \sin^2(\eta_{\ell}^{\text{s}} - \eta_{\ell}^{\text{t}}), \quad (47.45)$$

where $\eta_{\ell}^{\text{S,T}}$ are the phase shifts for individual scattering by the singlet and triplet potentials, respectively.

47.5.5 Low-Energy $E \rightarrow 0$ Scattering

Blatt–Jackson effective range formula For short-range potentials,

$$k \cot \eta_0 = -\frac{1}{a_s} + \frac{1}{2} r_e k^2 + \mathcal{O}(k^4) \quad (47.46a)$$

with effective range

$$r_e = 2 \int_0^{\infty} [u_0^2(r) - v_0^2(r)] dr, \quad (47.46b)$$

where $u_0 = \sin(kr + \eta_0)/\sin \eta_0$ is the $k = 0$ limit of the potential-free $\ell = 0$ radial wavefunction and normalized so that $u_0(r)$ goes to unity as $k \rightarrow 0$. The potential distorted $\ell = 0$ radial function v_0 is normalized at large r to $u_0(r)$. The effective range is a measure of the distance over which v_0 differs from u_0 . The outside factor of 2 in Eq. (47.46b) is chosen such that $r_e = a$ for a square well of range a .

The elastic cross section for $k \rightarrow 0$ can be expressed as

$$\begin{aligned} \sigma(k \rightarrow 0) &= \frac{4\pi}{k^2} \sin^2 \eta_0 \\ &= 4\pi a_s^2 \left(\left(1 - \frac{1}{2} k^2 a_s r_e\right)^2 + k^2 a_s^2 \right)^{-1} \end{aligned} \quad (47.47a)$$

$$\rightarrow 4\pi a_s^2 [1 + a_s k^2 (r_e - a_s)], \quad (47.47b)$$

with the

scattering length

$$a_s = -\lim_{k \rightarrow 0} f(\theta). \quad (47.47c)$$

Relation with Bound Levels

Levinson's theorem A radial potential $V(r)$ can support n_{ℓ} bound states of angular momentum ℓ and energy E_n , such that

$$\lim_{k \rightarrow 0} \eta_0(k) = \begin{cases} n_0 \pi, & E_n < 0 \\ (n_0 + \frac{1}{2}) \pi, & E_{n+1} = 0, \end{cases} \quad (47.48a)$$

$$\lim_{k \rightarrow 0} \eta_{\ell}(k) = n_{\ell} \pi, \quad \ell > 0. \quad (47.48b)$$

If an $\ell = 0$ bound level of energy $E_n = -\hbar^2 k_n^2/2m$ is sufficiently close to the dissociation limit, the effective range and scattering lengths, r_e and a_s , respectively, are related by

$$-\frac{1}{a_s} = -k_n + \frac{1}{2} r_e k_n^2 + \dots \quad (47.49)$$

Wigner causality condition If η_{ℓ} provides the dominant contribution to $f(\theta)$, then

$$\frac{\partial \eta_{\ell}(k)}{\partial k} \geq -a_s, \quad (47.50)$$

where a_s is the scattering length ($\ell = 0$) and is a measure of the range of the interaction.

Effective range formulae The Blatt–Jackson formula must be modified [14–16] for long-range interactions as follows.

(1) Coulomb tail: $V(r) \approx Z_1 Z_2 e^2/r$

$$\begin{aligned} 2(K/a_0) &= -(1/a_s) + \frac{1}{2} r_e k^2 \\ K &= \frac{\pi \cot \eta_0}{e^{2\pi\alpha} - 1} - \ln \beta - 0.5772 \\ &\quad + \beta^2 \sum_{n=1}^{\infty} [n(n^2 + \beta^2)]^{-1}, \end{aligned} \quad (47.51)$$

where $\beta = Z_1 Z_2 e^2/\hbar v = Z_1 Z_2/(ka_0)$ and $\alpha = Z_1 Z_2 e^2/(2Er_e)$.

(2) Polarization: $V(r) = -\alpha_d e^2/2r^4$,

$$\begin{aligned} \tan \eta_0 &= -a_s k - \frac{\pi}{3} C_4 k^2 - \frac{4}{3} C_4 a_s k^3 \ln(ka_0) \\ &\quad + D k^3 + F k^4, \end{aligned} \quad (47.52a)$$

$$\tan \eta_1 = \frac{\pi}{15} C_4 k^2 - a_s^{(1)} k^3, \quad (47.52b)$$

$$\begin{aligned} \tan \eta_{\ell} &= \frac{\pi C_4 k^2}{(2\ell + 3)(2\ell + 1)(2\ell - 1)} \\ &\quad + \mathcal{O}(k^{2\ell+1}), \end{aligned} \quad (47.52c)$$

for $\ell > 1$, where

$$C_4 = \frac{2m}{\hbar^2} \left(\frac{\alpha_d e^2}{2} \right) = \left(\frac{\alpha_d}{a_0} \right) \left(\frac{m}{m_e} \right).$$

Example: $e^- - \text{Ar}$ low energy collisions. The values

$$\begin{aligned} a_s &= -1.459 a_0; & D &= 68.93 a_0^3 \\ a_s^{(1)} &= 8.69 a_0^3; & F &= -97 a_0^4 \end{aligned}$$

allow for an accurate fit to measurements [17].

(3) Van der Waals: $V(r) = -C/r^6$

$$\begin{aligned} k \cot \eta_0 &= -\frac{1}{a_s} + \frac{1}{2} r_e k^2 - \frac{\pi}{15 a_s^2} \left(\frac{2mC}{\hbar^2} \right) k^3 \\ &\quad - \frac{4}{15 a_s} \left(\frac{2mC}{\hbar^2} \right) k^4 \ln(ka_0) + \mathcal{O}(k^4). \end{aligned} \quad (47.53)$$

e-Atom collisions with polarization attraction As $k \rightarrow 0$, the differential cross section is

$$\frac{d\sigma}{d\Omega} = a_s^2 \left[1 + \frac{C_4}{a_s} k \sin \frac{\theta}{2} + \frac{8}{3} C_4 k^2 \ln(ka_0) + \dots \right], \quad (47.54)$$

and the elastic and diffusion cross sections are

$$\sigma(k \rightarrow 0) = 4\pi a_s^2 \left[1 + \frac{2\pi C_4 k}{3a_s} + \frac{8}{3} C_4 k^2 \ln(ka_0) + \dots \right], \quad (47.55)$$

$$\sigma_d(k \rightarrow 0) = 4\pi a_s^2 \left[1 + \frac{4\pi C_4 k}{5a_s} + \frac{8}{3} C_4 k^2 \ln(ka_0) + \dots \right]. \quad (47.56)$$

For e⁻-noble gas collisions, the scattering lengths are

	He	Ne	Ar	Kr	Xe
$a_s(a_0)$	1.19	0.24	-1.459	-3.7	-6.5

For atoms with $a_s < 0$, a Ramsauer–Townsend minimum appears in both σ and σ_d at low energies, provided that scattering from higher partial waves can be neglected, because from Eq. (47.52a), $\eta_0 \simeq 0$ at $k = -3a_s/\pi C_4$.

Semiclassical scattering lengths. In the limit $E \rightarrow 0$, the semiclassical phase shift tends to

$$\eta_0^{\text{SC}} = \left(\frac{2m}{\hbar^2} \right)^{1/2} \int_{r_m}^{\infty} |V(r)|^{1/2} dr, \quad (47.57)$$

where r_m is the turning point. Equation (47.57) can be used to calculate some scattering lengths analytically and estimate the number of bound states in the potential [16]:

(a) Hard-core + well

$$V(r) = \begin{cases} \infty, & r < r_0 \\ -V_0, & r_0 \leq r < r_1 \\ 0, & r_1 < r, \end{cases}$$

$$a_s = [1 - \tan \eta_0^{\text{SC}}/(k_0 r_1)] r_1, \quad (47.58a)$$

$$\eta_0^{\text{SC}} = k_0(r_1 - r_m), \quad k_0^2 = 2mV_0/\hbar^2. \quad (47.58b)$$

The phase-averaged scattering length is $\langle a_s \rangle = r_1$.

(b) Hard-core + power law ($n > 2$)

$$V(r) = \begin{cases} \infty, & r < r_0 \\ \pm C/r^n, & r > r_0. \end{cases} \quad (47.59)$$

Repulsion (+): with $\gamma^2 = 2mC/\hbar^2$,

$$a_s^{(+)} = \left(\frac{\gamma}{n-2} \right)^{2/(n-2)} \Gamma\left(\frac{n-3}{n-2}\right) / \Gamma\left(\frac{n-1}{n-2}\right). \quad (47.60)$$

Attraction (-): with $\theta_n = \pi/(n-2)$,

$$a_s^{(-)} = a_s^{(+)} [1 - \tan \theta_n \tan(\eta_0^{\text{SC}} - \frac{1}{2}\theta_n)] \cos \theta_n, \quad (47.61)$$

$$\eta_0^{\text{SC}} = \gamma \int_{r_m}^{\infty} r^{-n/2} dr = \frac{2\gamma r_0^{1-n/2}}{n-2}, \quad (47.62)$$

$$\langle a_s^{(-)} \rangle = a_s^{(+)} \cos \theta_n. \quad (47.63)$$

Number of bound states

$$N_b = \text{int} \left\{ \frac{1}{\pi} \left[\eta_0^{\text{SC}} - \frac{1}{2}(n-1)\theta_n \right] \right\} + 1, \quad (47.64)$$

where $\text{int}(x)$ denotes the largest integer of the real argument x . For integer x , $a_s^{(-)}$ is infinite, and a new bound state appears at zero energy.

Born approximation for phase shifts

$$\tan \eta_\ell^{\text{B}}(k) = -k \int_0^{\infty} U(r) [j_\ell(kr)]^2 r^2 dr. \quad (47.65)$$

For $\lambda = (\ell + 1/2) \gg ka$, substitute

$$\langle k^2 r^2 [j_\ell(kr)]^2 \rangle = \frac{1}{2} (1 - \lambda^2/k^2 r^2)^{-1/2}. \quad (47.66)$$

Born S-wave phase shift

$$\tan \eta_0^{\text{B}}(k) = -\frac{1}{k} \int_0^{\infty} U(r) \sin^2(kr) dr. \quad (47.67)$$

Examples: (i) $U = U_0 \frac{e^{-\alpha r}}{r}$, (ii) $U = \frac{U_0}{(r^2 + r_0^2)^2}$;

$$(i) \tan \eta_0^{\text{B}} = -\frac{U_0}{4k} \ln(1 + 4k^2/\alpha^2), \quad (47.68)$$

$$(ii) \tan \eta_0^{\text{B}} = -\frac{\pi U_0}{4k r_0^3} [1 - (1 + 2kr_0)e^{-2kr_0}]. \quad (47.69)$$

Born phase shifts (large ℓ) For $\ell \gg ka$,

$$\tan \eta_\ell^{\text{B}} = -\frac{k^{2\ell+1}}{[(2\ell+1)!!]^2} \int_0^{\infty} U(r) r^{2\ell+2} dr, \quad (47.70)$$

valid only for finite range interactions $U(r > a) = 0$.

Example: $U = -U_0, r \leq a$ and $U = 0, r > a$.

$$\tan \eta_\ell^{\text{B}}(\ell \gg ka) = U_0 a^2 \frac{(ka)^{2\ell+1}}{[(2\ell+1)!!]^2 (2\ell+3)}. \quad (47.71)$$

For $\ell \gg ka$, $\eta_{\ell+1}/\eta_\ell \approx (ka/2\ell)^2$.

47.5.6 Nonspherical Potentials

The plane wave scattering states are

$$\phi_{\mathbf{k}}(\mathbf{r}) = \exp(i\mathbf{k} \cdot \mathbf{r}) = \phi_{\mathbf{k}}^*(\mathbf{r}), \quad (47.72)$$

and the full scattering solutions have the form

$$\Psi_{\mathbf{k}}^{(\pm)}(\mathbf{r}) \approx \phi_{\mathbf{k}}(\mathbf{r}) + \frac{f(\mathbf{k}, \mathbf{k}')}{r} \exp(\pm ikr), \quad (47.73a)$$

where the scattering amplitude is

$$f(\mathbf{k}, \mathbf{k}') = -\frac{1}{4\pi} \langle \phi_{\mathbf{k}'}(\mathbf{r}) | U(\mathbf{r}) | \Psi_{\mathbf{k}}^{(+)}(\mathbf{r}) \rangle. \quad (47.73b)$$

Close to analytical solutions can typically only be obtained in the following.

Born approximation: Set $\Psi_{\mathbf{k}}^+ = \phi_{\mathbf{k}}$ in Eq. (47.73b). Then

$$f_{\text{B}}(K) = -\frac{1}{4\pi} \int U(\mathbf{r}) \exp(i\mathbf{K} \cdot \mathbf{r}) d\mathbf{r}, \quad (47.74)$$

with momentum transfer $\mathbf{K} = \mathbf{k} - \mathbf{k}'$, and $K = 2k \sin \frac{1}{2}\theta$. For a symmetric potential,

$$f_{\text{B}}(K) = -\int \frac{\sin kr}{kr} U(r) r^2 dr \quad (47.75)$$

is consistent with Eq. (47.65) since

$$\frac{\sin kr}{kr} = \sum_{\ell=0}^{\infty} (2\ell + 1) [j_{\ell}(kr)]^2 P_{\ell}(\cos \theta). \quad (47.76)$$

The static e^- -atom scattering potential and Born scattering amplitude are

$$V(r) = -\frac{Ze^2}{r} + e^2 \int \frac{|\psi(\mathbf{r}')|^2 d\mathbf{r}'}{|\mathbf{r} - \mathbf{r}'|}, \quad (47.77)$$

$$f_{\text{B}}(K) = \frac{2me^2}{\hbar^2} \frac{[Z - F(K)]}{K^2}, \quad (47.78)$$

where the *elastic form factor* is

$$F(K) = \int |\psi(\mathbf{r})|^2 \exp(i\mathbf{K} \cdot \mathbf{r}) d\mathbf{r}. \quad (47.79)$$

For a pure Coulomb field, $F(K) = 0$, and $\sigma_{\text{B}}(\theta, E) = |f_{\text{B}}(K)|^2$ reduces to Eq. (47.177e).

47.5.7 Reactive Systems

All nonelastic processes (e.g., inelastic scattering and rearrangement collisions/chemical reactions) can be viewed as a net absorption from the incident beam current vector \mathbf{J} and modeled by a complex optical potential

$$V(r) = V_{\text{r}}(r) + iV_{\text{i}}(r). \quad (47.80)$$

The continuity equation is then

$$\nabla \cdot \mathbf{J} = -\frac{2}{\hbar} V_{\text{i}}(r) |\Psi(\mathbf{r})|^2, \quad (47.81)$$

so that particle absorption implies $V_{\text{i}} > 0$ and particle creation $V_{\text{i}} < 0$. Since particle conservation implies $|S_{\ell}|^2 = 1$, the phase shift

$$\delta_{\ell}(k) = \eta_{\ell}(k) + i\gamma_{\ell}(k) \quad (47.82a)$$

is also complex. Then

$$S_{\ell} = A_{\ell}(k) \exp(2i\eta_{\ell}), \quad (47.82b)$$

where the absorption (inelasticity) factor is

$$A_{\ell} = \exp(-2\gamma_{\ell}) \leq 1. \quad (47.82c)$$

The elastic, absorption, and total cross sections read

$$f_{\text{el}}(\theta) = \frac{1}{2ik} \sum_{\ell=0}^{\infty} (2\ell + 1) (A_{\ell} e^{2i\eta_{\ell}} - 1) P_{\ell}(\cos \theta), \quad (47.83a)$$

$$\sigma_{\text{el}}(k) = \frac{\pi}{k^2} \sum_{\ell=0}^{\infty} (2\ell + 1) |A_{\ell} e^{2i\eta_{\ell}} - 1|^2, \quad (47.83b)$$

$$\sigma_{\text{abs}}(k) = \frac{\pi}{k^2} \sum_{\ell=0}^{\infty} (2\ell + 1) (1 - A_{\ell}^2), \quad (47.83c)$$

$$\sigma_{\text{tot}}(k) = \sigma_{\text{el}}(k) + \sigma_{\text{abs}}(k). \quad (47.83d)$$

Upper limits to the partial cross sections are

$$\sigma_{\ell}^{\text{el}} \leq \frac{4\pi}{k^2} (2\ell + 1), \quad \sigma_{\ell}^{\text{abs}} \leq \frac{\pi}{k^2} (2\ell + 1), \quad (47.84a)$$

$$\sigma_{\ell}^{\text{tot}} \leq \frac{4\pi}{k^2} (2\ell + 1) = \frac{4\pi}{k} \text{Im}[f_{\ell}^{\text{el}}(\theta = 0)]. \quad (47.84b)$$

For pure elastic scattering with no absorption, $A_{\ell} = 1$. All nonelastic processes ($0 \leq A_{\ell} < 1$) are always accompanied by elastic scattering, even in the ($A_{\ell} = 0$) limit of full absorption.

Eikonal formulae for forward reactive scattering

$$f_{\text{el}}(\theta) = -ik \int_0^{\infty} (e^{2i\delta} - 1) J_0(2kb \sin \frac{1}{2}\theta) b db, \quad (47.85a)$$

$$\sigma_{\text{el}}(k) = 2\pi \int_0^{\infty} |(1 - e^{-2\gamma} e^{2i\eta})|^2 b db, \quad (47.85b)$$

$$\sigma_{\text{abs}}(k) = 2\pi \int_0^{\infty} (1 - e^{-4\gamma}) b db, \quad (47.85c)$$

$$\sigma_{\text{tot}}(k) = 4\pi \int_0^{\infty} (1 - e^{-2\gamma} \cos 2\eta) b db, \quad (47.85d)$$

where the phase shift function $\delta = \eta + i\gamma$ at impact parameter b can be either the Jeffrey–Born phase

$$\delta_{\text{JB}}(b) = -\frac{m}{k\hbar^2} \int_b^{\infty} \frac{V(r) dr}{(1 - b^2/r^2)^{1/2}}, \quad (47.86)$$

where $kb = \lambda = (\ell + 1/2)$, or the eikonal phase

$$\delta_{\text{E}}(b) = -\frac{m}{2k\hbar^2} \int_{-\infty}^{\infty} V(b, Z) dZ. \quad (47.87)$$

Fraunhofer diffraction by a black sphere For a complex spherical well V

$$V = \begin{cases} V_r + iV_i, & R < a \\ 0, & R > a. \end{cases} \quad (47.88)$$

The eikonal phase function Eq. (47.87) is

$$\delta(b) = \begin{cases} mV/(k\hbar^2)(a^2 - b^2)^{1/2}, & 0 \leq b \leq a \\ 0 & b > a. \end{cases} \quad (47.89)$$

The absorption factor is

$$A(b)^2 \equiv e^{-4\gamma} = \exp[-2(a^2 - b^2)^{1/2}/\lambda], \quad (47.90)$$

where $\lambda = k\hbar^2/(2mV_i)$ is the mean free path towards absorption. For strong absorption, $\lambda \ll a$, so that

$$f_{\text{el}}(\theta) = ik \int_0^a J_0\left(2kb \sin \frac{1}{2}\theta\right) b db, \quad (47.91)$$

$$\frac{d\sigma_{\text{el}}}{d\Omega} = (ka)^2 \left(\frac{J_1(2ka \sin \frac{1}{2}\theta)}{2ka \sin \frac{1}{2}\theta} \right)^2 a^2, \quad (47.92)$$

which has a diffraction-shaped peak of width $\approx \theta \leq (ka)^{-1}$ about the forward direction, and

$$\sigma_{\text{tot}} = \frac{4\pi}{k} \text{Im}[f_{\text{el}}(\theta = 0)] = 2\pi a^2 \quad (47.93)$$

is composed of πa^2 for classical absorption and πa^2 for edge diffraction or shadow (nonclassical) elastic scattering. This result also holds for the perfectly reflecting sphere (πa^2 for classical elastic scattering and πa^2 for edge diffraction).

47.6 Classical Elastic Scattering

Conservation of energy $E > 0$ and orbital angular momentum L for a central field $V(r)$ imply classically that the relative motion with reduced mass m takes place in the plane perpendicular to the angular momentum vector $\mathbf{L} = \mathbf{b} \times \mathbf{p}'$, where the impact parameter \mathbf{b} and the initial momentum \mathbf{p}' with $|\mathbf{p}'| = p_a = (2mE)^{1/2}$, normally taken perpendicularly, define this plane. Hence, classically, elastic scattering reduces for central potentials to the analysis of a one-dimensional deflection function Θ , mapping the initial impact parameter b into the final scattering angle θ in the scattering plane. This can be surprisingly complicated if trajectories exist that circle the scattering center several times before exiting with θ , corresponding to a nonmonotonic deflection function.

47.6.1 Elastic Scattering Cross Section

The differential cross section $\frac{d\sigma}{d\Omega}$ asks which area of initial conditions, typically parameterized by the impact parameter $d\sigma = b db$, is scattered into the solid angle $d\Omega = d \cos \theta d\phi$.

With the general formulation Eq. (47.4a) of classical propagators and Eqs. (47.96a) and (47.96b) the classical differential cross section for elastic scattering from a central potential reads

$$\begin{aligned} \frac{d\sigma}{d\Omega} &= 2\pi \int db b \delta(\cos \Theta(b, E) - \cos \theta) \\ &= \frac{2\pi}{|\sin \theta|} \sum_j b_j \left| \frac{d\Theta}{db} \right|_{\cos \Theta(b_j) = \cos \theta}^{-1}, \end{aligned} \quad (47.94)$$

where the sum runs over all trajectories j connecting an impact parameter b_i with a scattering angle θ . If $\cos \Theta(b)$ is monotonic, Eq. (47.94) simplifies to $\frac{d\sigma}{d\Omega} = b db / d(\cos \theta)$.

47.6.2 Deflection Functions

The deflection function $\Theta(E, b)$, $(-\infty \leq \Theta < \pi)$ can be expressed through $\Theta(E, b) = \pi - 2\psi(r \rightarrow \infty; E, b)$ with the

angle ψ between initial (or final) momentum vector and the line that connects the scattering center with the point r_m of closest approach of the scattering trajectory, defined through radial momentum $p(r_m) = 0$. We define

$$\begin{aligned} p(r) &= [p_a^2 - 2mV(r) - L^2/r^2]^{\frac{1}{2}} \\ &= [p_a^2 - 2mV(r) - b^2E/r^2]^{\frac{1}{2}}, \\ &= [p_a^2 - 2mV_{\text{eff}}(r)]^{1/2}, \end{aligned} \quad (47.95)$$

with $p_a = \sqrt{2mE}$. Then we can write

$$\begin{aligned} \Theta(E, L) &= \pi - 2\psi(r \rightarrow \infty; E, L) \\ &= \pi + 2 \frac{\partial}{\partial L} \int_{r_m}^{\infty} p(r) dr, \end{aligned} \quad (47.96a)$$

$$\begin{aligned} \Theta(E, b) &= \pi - 2\psi(r \rightarrow \infty; E, b) \\ &= \pi + \frac{2}{p_a} \frac{\partial}{\partial b} \int_{r_m}^{\infty} p(r) dr. \end{aligned} \quad (47.96b)$$

Small-angle scattering With $V(r_m)/E \ll 1$, $b \approx r_m$

$$\begin{aligned} \Theta(E, b) &= \left(\frac{r_m}{E}\right) \int_{r_m}^{\infty} \frac{[V(r_m) - V(r)]r dr}{(r^2 - r_m^2)^{3/2}} \\ &= \frac{1}{E} \int_0^1 \frac{[V(r_m) - V(r_m/x)]dx}{(1 - x^2)^{3/2}}, \end{aligned} \quad (47.97a)$$

$$= \frac{1}{E} \int_0^1 \frac{[V(r_m) - V(r_m/x)]dx}{(1 - x^2)^{3/2}}, \quad (47.97b)$$

where $x = r_m/r$. Other forms are

$$\Theta(E, b) = -\frac{1}{E} \frac{\partial}{\partial b} \int_b^{\infty} \frac{V(r) dr}{(1 - b^2/r^2)^{1/2}} \quad (47.97c)$$

$$= -\frac{b}{E} \int_b^{\infty} \left(\frac{dV}{dr}\right) \frac{dr}{(r^2 - b^2)^{1/2}} \quad (47.97d)$$

$$= -\frac{1}{2E} \frac{\partial}{\partial b} \int_{-\infty}^{\infty} V(b, z) dz. \quad (47.97e)$$

Straight-line paths With $r^2 = b^2 + v^2t^2$, Eq. (47.96b) yields the impulse-momentum result

$$\Theta(E, b) = \frac{1}{mv} \int_{-\infty}^{\infty} F_{\perp}(t) dt = \frac{\Delta p_{\perp}}{p_a}, \quad (47.98)$$

where Δp_{\perp} is the momentum transferred perpendicular to the incident direction, and $F_{\perp} = -(\partial V/\partial r)(b/r)$ is the impulsive force causing scattering. Special cases are:

Head-on collisions ($b = 0$):	$\Theta(E, 0) = \pi$.
Overall repulsion:	$0 < \Theta \leq \pi$.
Overall attraction:	$-\infty \leq \Theta \leq 0$.
Forward glory:	$\Theta = -2n\pi$.
Backward glory:	$\Theta = -(2n - 1)\pi$,
	$n = 0, 1, 2, \dots$
Rainbow scattering:	$(d\Theta/db) = 0$ at $\Theta_r < 0$.
Deflection range:	$\Theta_r \leq \Theta \leq \pi$.
Orbiting collisions:	cf. Eq. (47.100).
Diffraction scattering:	$\Theta \rightarrow 0$ as $b \rightarrow \infty$.

The scattered particle may wind or spiral many times around ($\Theta \rightarrow -\infty$) the scattering center. The experimentally observed quantity is the scattering angle θ ($0 \leq \theta \leq \pi$), which is associated with various deflections

$$\begin{aligned} \Theta_i &= +\theta, -\theta, -2\pi \pm \theta, -4\pi \pm \theta, \dots \\ &\quad (i = 1, 2, \dots, n) \end{aligned}$$

resulting from n different impact parameters b_i ; see Eq. (47.94).

Small-angle diffraction scattering The small-angle scattering regime is defined by the conditions $V(r_m)/E \ll 1$, $b \geq r_m$, where $\theta = |\Theta|$. The main contribution to $d\sigma/d\Omega$ for small-angle scattering arises from the asymptotic branch of the deflection function Θ at large impact parameters b and is primarily determined by the long-range (attractive) part of the potential $V(r)$ (Sect. 47.7.3).

Large-angle scattering The main contribution to $d\sigma/d\Omega$ for large-angle scattering arises from the positive branch of Θ at small b and is mainly determined by the repulsive part of the potential.

47.6.3 Glory and Rainbow Scattering

Glory The deflection function Θ passes through $-2n\pi$ (forward glory) or $-(2n + 1)\pi$ (backward glory) at finite impact parameters b_g . Since $\sin \theta = \sin \Theta = 0$, the prefactor $1/|\sin \theta|$ in the cross section Eq. (47.94) diverges.

Rainbow The deflection function Θ passes through a minimum at b_r , so that

$$\Theta(b) = \Theta(b_r) + \omega_r(b - b_r)^2, \quad (47.99a)$$

$$\omega_r = \frac{1}{2} \frac{d^2\Theta}{db^2} \Big|_{b_r} > 0. \quad (47.99b)$$

The classical cross section diverges as

$$\frac{d\sigma}{d\Omega} = \frac{b_r}{2 \sin \theta} [\omega_r(\theta_r - \theta)]^{-\frac{1}{2}}, \quad \theta < \theta_r \quad (47.99c)$$

and is augmented by the contribution from the positive branch of $\Theta(b)$.

47.6.4 Orbiting and Spiraling Collisions

If strong enough, attractive interactions $V(r)$ can bind particles with $E > 0$ held inside the maximum of the effective potential $V_{\text{eff}}(r) = V(r) + b^2 E/r^2$. The trajectory that touches this maximum at r_o does not move radially and defines an orbiting resonance through the conditions

$$\left. \frac{dV_{\text{eff}}}{dr} \right|_{r=r_o} = 0 \quad \text{and} \quad p_{b_o, E}(r_o) = 0 \quad (47.100)$$

which determine r_o and b_o . The corresponding total cross section is

$$\sigma_{\text{orb}}(E) = \pi b_o^2. \quad (47.101)$$

For $b < b_o$, the particle spirals inwards.

47.6.5 Deflection Function and Time Delay from Action

Relevant is the change in action of a classical path from incoming momentum p' to final momentum p due to interaction with the potential $V(r)$ relative to the free path for a given L or b . In spherical momentum coordinates (p, L) , the action reduces to radial momenta integrals only, since L is conserved

$$\begin{aligned} S(E, L) &= - \int_{p'}^p (\mathbf{r} - \mathbf{r}_o) d\mathbf{p}'' \\ &= -2 \int_0^{p_a} (r(p) - r_o(p)) dp \quad (47.102a) \end{aligned}$$

$$= 2 \int_{r_m}^{\infty} p(r) dr - 2 \int_{b(E, L)}^{\infty} p_0(r) dr. \quad (47.102b)$$

The boundary terms are the same with $r(p)$ and without potential $r_o(p)$, and, therefore, Eq. (47.102b) holds. The deflection angle Θ is conjugate to L . Hence, the deflection function is given by

$$\Theta(E, L) = \left. \frac{\partial S(E, L)}{\partial L} \right|_E = \pi - 2L \int_{r_m}^{\infty} \frac{dr}{p(r)r^2} \quad (47.103a)$$

in agreement with Eqs. (47.96a), (47.96b) since $2L \int_b^{\infty} (p_0(r)r^2)^{-1} dr = \pi$. Similarly, the time delay τ , conjugate to E , is given by

$$\tau(E, L) = \left. \frac{\partial S(E, L)}{\partial E} \right|_L. \quad (47.103b)$$

47.6.6 Approximate Actions

Jeffrey–Born phase function For small V/E and $b \approx r_m$, we get the action S_{JB} , better known as the Jeffrey–Born phase, $\eta_{JB} = S_{JB}/\hbar$,

$$S_{JB}(E, b) = - \frac{m}{p_a} \int_b^{\infty} \frac{V(r) dr}{(1 - b^2/r^2)^{1/2}}. \quad (47.104)$$

Eikonal action For small V/E and a linear trajectory $r^2 = b^2 + z^2$, the action reduces to

$$S_{\text{Eiko}}(E, \mathbf{b}) = - \frac{m}{p_a} \int_{-\infty}^{\infty} V(\mathbf{b}, z) dz. \quad (47.105)$$

Applying Eq. (47.103a) to these actions one gets the corresponding deflection functions Eqs. (47.97a)–(47.97e).

47.7 Semiclassical Elastic Scattering

Semiclassical elastic scattering is conceptually quite involved since the scattering angle is defined over a finite range $\theta \in [0, \pi]$, while classically action and its conjugate, the deflection angle, are accumulated along a collision path without limits. Hence, several deflections differing by $\Delta\theta = 2n\pi$ contribute to differential scattering Eq. (47.94). Moreover, as a constitutive element for the construction of the scattering amplitude from the semiclassical propagator, we need the action in a “mixed representation”, that is, mapping $(p', L') \rightarrow (p, \Theta)$ and not in full momentum representation $(p', L') \rightarrow (p, L)$ as defined in $S(E, L)$ of Eqs. (47.102a) and (47.2e). The change of variables is achieved with a Legendre transformation

$$S^C(\Theta) = S(E, L) - L\Theta(E, L). \quad (47.106)$$

Decomposition into partial waves for constant angular momentum quantum number ℓ (Sect. 47.5.3) and the description of elastic scattering with resulting phase shifts η_ℓ is a powerful technique. Its semiclassical formulation requires quantizing the classical angular momentum such that the classical L is replaced for semiclassical partial waves by

$$L/\hbar \rightarrow \lambda = \ell + \frac{1}{2}, \quad (47.107)$$

which is a consequence of the Langer modification taking into account that the radial coordinate is only positive.

47.7.1 Semiclassical Amplitudes and Cross Sections

With the structure of the semiclassical propagator Eq. (47.6) and the classical cross section Eq. (47.94), the semiclassical

scattering amplitude is a sum over contributions from trajectories j starting with different impact parameters b_j , or equivalently, angular momenta λ_j ,

$$f(\theta) = \sum_{j=1}^N f_j(\theta), \quad (47.108)$$

where each classical path $b_j = b_j(\theta)$ or SP-point $\lambda_j = \lambda_j(\theta)$ contributes $f_j(\theta)$ to the amplitude

$$f_j(\theta) = -i\alpha_j \beta_j \sigma_j^{1/2}(\theta) \exp[iS_j^C(\theta)/\hbar] \quad (47.109)$$

$$\Theta'_j = (d\Theta/d\lambda)_j, \quad (47.110)$$

$$\alpha_j = e^{\pm i\pi/4}; \quad (+), \Theta'_j > 0; \quad (-), \Theta'_j < 0; \quad (47.111a)$$

$$\beta_j = e^{\pm i\pi/4}; \quad (+), \Theta_j > 0; \quad (-), \Theta_j < 0. \quad (47.111b)$$

The classical cross section for each trajectory [Eq. (47.94)] is

$$\sigma_j(\theta) = b_j \left| \frac{d \cos \Theta}{db} \right|_{\cos \Theta(b_j) = \cos \theta}^{-1} = \frac{1}{k^2} \frac{\lambda_j}{\sin \theta |\Theta'_j|}, \quad (47.112)$$

with $kb = (\ell + 1/2) = \lambda$; N classical deflections Θ_j provide the same θ

$$\Theta_j = \Theta(\lambda_j) = \theta, -\theta, -2\pi \pm \theta, -4\pi \pm \theta, \dots \quad (47.113)$$

resulting in the phases $s(\Theta) \equiv S^C(E, L; \Theta)/\hbar$

$$s_j = 2\eta(\lambda_j) - \lambda_j \Theta(\lambda_j) \quad (47.114a)$$

$$= 2\eta(\lambda_j) - \lambda_j \theta, \quad 0 \leq \theta \leq \pi \quad (47.114b)$$

$$= 2\eta(\lambda_j) + \lambda_j \theta - m\pi, \quad \theta < 0, \quad (47.114c)$$

where $m = 0, 1, 2, \dots$ is the number of times the ray has traversed the backward direction during its attractive windings about the scattering center.

A. Amplitude addition: for three well-separated regions of stationary phase $\lambda_1 < \lambda_2 < \lambda_3$. A scattering angle θ in the range $0 < \theta < \theta_r$ (rainbow angle) typically results from deflections Θ_j at three impact parameters b (or λ): $\theta = \{\Theta(b_1), -\Theta(b_2), -\Theta(b_3)\} \equiv \{\Theta_j\}$. Scattering in the range $\theta_r \leq \theta < \pi$ results from one deflection at b_1 ; b_1 is in the positive branch (inner repulsion), and $b_{2,3}$ are in the negative branch (outer attraction) of the deflection function $\Theta(b)$, such that $b_1 < b_2 < b_3$. Thus,

$$f(\theta) = \sum_{j=1}^3 f_j(\theta) = \sum_{j=1}^3 [\sigma_j(\theta)]^{1/2} \exp(is_j), \quad (47.115)$$

where the overall phases of each f_j are

$$s_1 = 2\eta(\lambda_1) - \lambda_1 \theta - \pi/2, \quad (47.116a)$$

$$s_2 = 2\eta(\lambda_2) + \lambda_2 \theta - \pi, \quad (47.116b)$$

$$s_3 = 2\eta(\lambda_3) + \lambda_3 \theta - \pi/2, \quad (47.116c)$$

which are appropriate, respectively, to deflections $\Theta_1 = \theta$ at λ_1 , $\Theta_2 = -\theta$ at λ_2 and $\Theta_3 = -\theta$ at λ_3 , within the range $-\pi \leq \Theta \leq \pi$.

The elastic differential cross section

$$\begin{aligned} \sigma(\theta) &= \sum_{j=1}^3 \sigma_j(\theta) + 2 \sum_{i<j}^3 [\sigma_i(\theta) \sigma_j(\theta)]^{1/2} \cos(s_i - s_j) \\ &\equiv \sigma_c(\theta) + \Delta\sigma(\theta) \end{aligned} \quad (47.117)$$

exhibits interference effects. The first term σ_c is the classical background DCS with no oscillations. The second term $\Delta\sigma$ provides the oscillatory structure that originates from interference between classical actions associated with the different trajectories resulting in a given θ . The part of $s_i - s_j$ most rapidly varying with θ is the angular action changes $(\lambda_1 + \lambda_2)\theta$, $(\lambda_1 + \lambda_3)\theta$, and $(\lambda_2 - \lambda_3)\theta$. Interference oscillations between the action phases s_1 and s_2 or between s_1 and s_3 then have angular separations

$$\Delta\theta_{1;(2,3)} = \frac{2\pi n}{(\lambda_1 + \lambda_{2,3})}, \quad (47.118)$$

which are much smaller than the separation

$$\Delta\theta_{2;3} = \frac{2\pi n}{(\lambda_2 - \lambda_3)}, \quad (47.119)$$

for interference between phases s_2 and s_3 . The oscillatory structure in $\Delta\sigma(\theta)$ is, therefore, composed of supernumerary rainbow oscillations with large angular separations $\Delta\theta_{2;3}$ from s_2 and s_3 interference, with superimposed rapid oscillations with smaller separation $\Delta\theta_{1;(2,3)}$ from interference between s_1 and s_2 or s_1 and s_3 .

For deflections $\Theta_j = \theta, -\theta, -2\pi \mp \theta, -4\pi \mp \theta, \dots$, then the Δ^+ -branch of Eq. (47.158a) provides additional contributions to Eq. (47.115) with phases

$$s_{2m}^{\pm} = 2\eta(\lambda_{2m}) \pm \lambda_{2m} \theta - 2m\pi - \pi, \quad (47.120a)$$

$$s_{3m}^{\pm} = 2\eta(\lambda_{3m}) \pm \lambda_{3m} \theta - 2m\pi - \pi/2, \quad (47.120b)$$

for $m = 1, 2, 3, \dots$

B. Uniform Airy result: for two regions of stationary phase that can coalesce. The combined contribution

$f_{23}(\theta)$ from the λ_2 and λ_3 attractive regions in Δ^+ branch is

$$f_{23}(\theta) = \sigma_2^{1/2} e^{is_2} F_{23} + \sigma_3^{1/2} e^{is_3} F_{23}^*, \quad (47.121a)$$

$$F_{23} = (A + iB) e^{-is_{23}/2}, \quad (47.121b)$$

$$s_{23} = s_2 - s_3 = 2(\eta_2 - \eta_3) + (\lambda_2 - \lambda_3)\theta - \frac{1}{2}\pi, \quad (47.121c)$$

$$A(z) = \pi^{1/2} z^{1/4} \text{Ai}(-z), \quad (47.121d)$$

$$B(z) = \pi^{1/2} z^{-1/4} \text{Ai}'(-z), \quad (47.121e)$$

$$\frac{4}{3}|z|^{3/2} = s_{23} + \frac{1}{2}\pi. \quad (47.121f)$$

The amplitude f_{23} tends to the primitive result $f_2(\theta) + f_3(\theta)$ in the limit of well-separated regions ($z \gg 1$), when $F_{23} \rightarrow 1$. An equivalent form of Eq. (47.121a) is

$$f_{23}(\theta) = \left[A(\sigma_2^{1/2} + \sigma_3^{1/2}) + iB(\sigma_2^{1/2} - \sigma_3^{1/2}) \right] \times \exp(i\bar{s}), \quad (47.122)$$

where the mean phase $\bar{s} = \frac{1}{2}(s_2 + s_3)$. This form is useful for analysis of caustic regions at $\theta \approx \theta_r$, where $z \rightarrow 0$.

C. Transitional result: neighborhood of caustic or rainbow at $(\theta_r, b_r, \lambda_r)$. In the vicinity of rainbow angle $\theta \approx \theta_r$,

$$\Theta' = \frac{\partial \Theta}{\partial \lambda} = [2(\theta_r - \theta)\Theta''(\lambda_r)]^{1/2} \quad (47.123)$$

$$z = (\theta_r - \theta)[2/\Theta''(\lambda_r)]^{1/3} > 0 \quad (47.124)$$

$$s_r = \frac{1}{2}(s_1 + s_2) = 2\eta(\lambda_r) + \lambda_r \theta_r - \frac{3}{4}\pi. \quad (47.125)$$

The scattering amplitude

$$f_{23}(\theta_r) = \left(\frac{2\pi\lambda_r}{k^2 \sin \theta_r} \right)^{\frac{1}{2}} \left(\frac{2}{\Theta''(\lambda_r)} \right)^{\frac{1}{3}} \text{Ai}(-z) e^{is_r} \quad (47.126)$$

is finite at the rainbow angle θ_r . In Eq. (47.122), the $(\theta_r - \theta)^{-1/4}$ divergence in $|\Theta'_\ell|^{1/2}$ of Eq. (47.123) arising in the constructive interference term $(\sigma_2^{1/2} + \sigma_3^{1/2})$ is exactly balanced by the $z^{1/4}$ term of $A(z)$. Also, $(\sigma_2^{1/2} - \sigma_3^{1/2}) \rightarrow 0$ in Eq. (47.122) more rapidly than $z^{-1/4}$ in $B(z)$, so that Eq. (47.122) at θ_r is finite and reproduces Eq. (47.126).

The uniform semiclassical DCS

$$\frac{d\sigma}{d\Omega} = \left| \sigma_1^{\frac{1}{2}} e^{is_1} + \sigma_2^{\frac{1}{2}} F_{23} e^{is_2} + \sigma_3^{\frac{1}{2}} F_{23}^* e^{is_3} \right|^2 \quad (47.127)$$

contains, in addition to the s_i/s_j interference oscillations in the primitive result Eq. (47.117), the θ -variation of the Airy function $|\text{Ai}(z)|^2$, which has a principal finite (rainbow) maximum at $\theta \leq \theta_r$, the classical rainbow angle, and subsidiary maxima (supernumary rainbows) at smaller angles. The DCS decreases exponentially as θ increases past θ_r into the classical forbidden region and tends to $\sigma_1(\theta)$ at larger angles. For $\theta_r < \theta < \pi$,

$$f(\theta) = \sigma_1^{1/2}(\theta) \exp(is_1). \quad (47.128)$$

47.7.2 Diffraction and Glory Amplitudes

Diffraction

Diffraction arises from the outer (attractive) part of the potential. Many contributions arise from the attractive Δ^+ branch appropriate for negative Θ at large b where η is small. Here, Θ and Θ' tend to zero.

Glory

The deflection function Θ passes through zero at a finite λ_g . A confluence of the two maxima of each phase shift from the positive and negative branches of $\Theta(b)$ occurs at $b_1 = b_2 = b_g = \lambda_g/k$; η_g is maximum for $\Theta = 0$. In general, $\Theta(b_m) = -2m\pi$ (forward glory); $\Theta(b_m) = -(2m-1)\pi$ (backward glory); $m = 0, 1, 2, \dots$. There is only a forward glory at $\Theta = 0$ when the deflection at the rainbow is $|\Theta_r| < 2\pi$. In contrast to diffraction, the glory contribution can be calculated by the *stationary phase approximation*.

Transitional results for forward and backward glories

Forward glories Contributions arise from $\Theta = \pm\theta, -2\pi \pm \theta, \dots, -2m\pi \pm \theta$ as $\theta \rightarrow 0$. The stationary phase points λ_m are located at

$$\Theta(\lambda_m) = \Theta_m = -2m\pi; \quad m \geq 0. \quad (47.129)$$

The phase function in the neighborhood of a glory is

$$\eta(\lambda) = \eta_m - m\pi(\lambda - \lambda_m) + \frac{1}{4}\Theta'_m(\lambda - \lambda_m)^2. \quad (47.130)$$

The $m = 0$ term provides zero deflection Θ due to a net balance of attractive and repulsive scattering for a finite impact parameter b_g or λ_g , where $\eta(\lambda)$ attains its maximum value η_m . The glories at θ are due to a confluence of the two contributions from the deflections $\Theta_m = -2m\pi \pm \theta$ at the stationary phase points $\lambda_{mn} = \lambda_{m1}$ and λ_{m2} . SP integration of Eq. (47.161a) with Eq. (47.130) yields the forward glory amplitude

$$f_{FG} = \frac{1}{k} \sum_{n=1}^2 \sum_{m=0}^{\infty} \lambda_{mn} \left(\frac{2\pi}{|\Theta'_m|} \right)^{1/2} J_0(\lambda_{mn}\theta) e^{is_{mn}^{(g)}}, \quad (47.131)$$

$$s_{mn}^{(g)} = 2\eta(\lambda_{mn}) + m\pi(\lambda_{mn} - 1) - \frac{3}{4}\pi. \quad (47.132)$$

Backward glories Contributions arising from $\Theta = -\pi \pm \alpha, -3\pi \pm \alpha, \dots, -(2m-1)\pi \pm \alpha$ coalesce as $\alpha \equiv \pi - \theta \rightarrow 0$. The phase function near a backward glory is

$$\eta(\lambda) = \eta(\lambda_m) + \frac{1}{2}\Theta_m(\lambda - \lambda_m) + \frac{1}{4}\Theta'_m(\lambda - \lambda_m)^2. \quad (47.133)$$

The $m = 0$ term provides the normal backward amplitude due to head-on ($b = 0$) repulsive collisions; $m > 0$ terms provide contributions from attractive collisions for which there are two points λ_{mn} of stationary phase for each m in $\Theta_m = -(2m - 1)\pi \pm \alpha$.

The backward glory amplitude at $\theta = \pi - \alpha$ is

$$f_{\text{BG}} = \frac{1}{k} \sum_{n=1}^2 \sum_{m=0}^{\infty} \lambda_{mn} \left(\frac{2\pi}{|\Theta'_{mn}|} \right)^{1/2} J_0(\lambda_{mn}\alpha) e^{i s_{mn}^{(\text{g})}}, \quad (47.134)$$

$$s_{mn}^{(\text{g})} = 2\eta(\lambda_{mn}) + \pi(2m - 1) \left(\lambda_{mn} - \frac{1}{2} \right) - \frac{3}{4}\pi. \quad (47.135)$$

In contrast to the Bessel amplitudes (below), these transitional formulae do not uniformly connect with the primitive semiclassical results for $(f_1 + f_2)$ away from the critical glory angles.

Uniform Bessel amplitude for glory scattering The combined contributions from $\Theta_1 = -N\pi + \theta$ and $\Theta_2 = -N\pi - \theta$, where $N = 2m$, for forward and $N = 2m - 1$ for backward scattering, yield [6]

$$f_{\text{G}}(\theta) = \frac{\alpha_j}{2i} e^{-iN\pi/2} (\pi s_{21})^{1/2} \exp[i\bar{s}(\theta)] \times \left[(\sigma_1^{1/2} + \sigma_2^{1/2}) J_0\left(\frac{1}{2}s_{21}\right) - i(\sigma_1^{1/2} - \sigma_2^{1/2}) J_1\left(\frac{1}{2}s_{21}\right) \right], \quad (47.136)$$

where $s_{21}(\theta) = s_2 - s_1$ is the difference of the collision phases Eq. (47.114a),

$$s_i(\theta) = 2\eta(\lambda_i) - \lambda_i \Theta_i, \quad i = 1, 2, \quad (47.137)$$

with mean

$$\bar{s}_{21}(\theta) = \frac{1}{2}(s_2 + s_1), \quad (47.138)$$

and

$$\alpha_j = e^{\pm i\pi/4}; \quad (+), \Theta'_j > 0; \quad (-), \Theta'_j < 0, \quad (47.139)$$

and the ordinary Bessel functions $J_n(z)$ satisfy the relationships $J_1(z) = -J'_0(z)$, $J_1(-z) = -J_1(z)$. This formula, valid for both forward ($\theta \approx 0$) and backward ($\theta \approx \pi$) glories, does uniformly connect the primitive result for $(f_1 + f_2)$, valid when $s_{21} \gg 1$ and to the transitional results Eqs. (47.131) and (47.134), valid only in the vicinity of the glories.

47.7.3 Small-Angle (Diffraction) Scattering

Diffraction originates from scattering in the forward direction by the long-range attractive tail of $V(r)$, where Θ , Θ' and $\eta \rightarrow 0$. The cross section is formed from many contributions with small action $S(\lambda) = \hbar\eta(\lambda)$ at a large angular momentum λ . A representation of the scattering amplitude as an integral over $\eta(\lambda)$ avoids the classical singularity; see Sect. 47.7.8.

47.7.4 Small-Angle (Glory) Scattering

Amplitude and cross section The other contribution to forward scattering is the forward glory, which originates from the combined null effect of attraction and repulsion at a specified glory impact parameter $b_g = \lambda_g/k$, where $\eta(\lambda)$ attains a maximum value of η_g . The $m = 0$ term of Eq. (47.131) yields

$$f_{\text{G}}(\theta) = \sigma_{\text{G}}^{1/2}(\theta) \exp[iS_{\text{G}}(E)], \quad (47.140a)$$

$$\sigma_{\text{G}}(\theta) = \frac{\lambda_g^2}{k^2} \left(\frac{2\pi}{|\Theta'_g|} \right) J_0^2(\lambda_g\theta), \quad (47.140b)$$

$$S_{\text{G}}(E) = 2\eta_g(E) - \frac{3}{4}\pi, \quad (47.140c)$$

where $J_0^2(x) \approx 1 - \frac{1}{4}x^2 + \dots$. The classical divergence is recovered by averaging Eq. (47.140b) over several oscillations with $\langle J_0^2(x) \rangle = (\pi x)^{-1}$.

Diffraction-glory oscillations

$$\sigma(E) = \frac{4\pi}{k} \text{Im}[f_{\text{D}}(0) + f_{\text{G}}(0)] \quad (47.141a)$$

$$= \sigma_{\text{D}}(E) + \Delta\sigma_{\text{G}}(E), \quad (47.141b)$$

where the diffraction cross section is Eq. (47.171), and where

$$\Delta\sigma_{\text{G}}(E) = \frac{4\pi}{k^2} \lambda_g \left(\frac{2\pi}{|\Theta'_g|} \right)^{1/2} \sin\left(2\eta_g(E) - \frac{3}{4}\pi\right) \quad (47.142)$$

oscillates with E .

For sufficiently deep attractive wells, the phase shift η_g successively decreases with increasing E through a series of multiples of $\pi/2$. Writing $\eta_g(E) = \pi(N - 3/8)$, maxima appear at $N = 1, 2, \dots$, and minima at $N = 3/2, 5/2, 7/2, \dots$. The glories are indexed by N in order of appearance, starting at high energies. $\eta_g(E \rightarrow 0)$ is related to the number n of bound states by Levinson's theorem: $\eta_0(E \rightarrow 0) = (n + 1/2)\pi$. Diffraction-glory oscillations also occur in the DCS at a frequency governed entirely by the energy variation of $\eta_g(E)$ and n of Eq. (47.175).

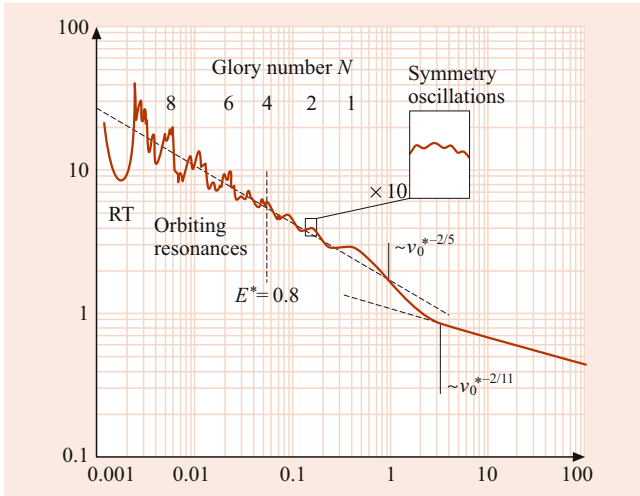


Fig. 47.1 All the various oscillatory effects for elastic scattering by a Lennard–Jones (12,6) potential of well depth ϵ and equilibrium distance R_e . Ordinate $\sigma^* = \sigma/(2\pi R_e^2)$, abscissa $v^* = \hbar v/(\epsilon R_e)$

47.7.5 Oscillations in Elastic Scattering

Figure 47.1 is an illustration [18, Chap. 1, p. 47] of all the various oscillatory structure and effects – Ramsauer–Townsend minimum (Sect. 47.5.5), orbiting resonances Eq. (47.204), diffraction-glory oscillations Eq. (47.141b), and symmetry oscillations Eq. (47.41d) – for elastic scattering by a Lennard–Jones (12, 6) potential. Note the shift of velocity dependence from $v^{-2/5}$ at low v to $v^{-2/11}$ at high v ; $\sigma = 2\pi r_e^2$ is the averaged cross section $2\pi b_0^2$ in Eq. (47.168) at $b_0 = r_e$. The region $\sigma^* > 1$ probes the attractive part of the potential at low speeds, and $\sigma^* < 1$ probes the repulsive part at high speeds. The four distinct types of structure originate from the nonrandom behavior of $\sin^2 \eta$ in Eq. (47.166). Orbiting trajectories exist for $E < 0.8\epsilon$ (Sect. 47.9).

47.7.6 Scattering Amplitude in Poisson Sum Representation

With the help of the (exact) Poisson sum formula one can convert a sum over discrete variables into an integral of a continuous variable. This allows one to directly derive from the quantum partial wave expansion Eq. (47.33a) semiclassical expressions for the phase shift in terms of classical paths. The Poisson sum formula reads for $\lambda = \ell + \frac{1}{2}$ [Eq. (47.107)]

$$\sum_{\ell=0}^{\infty} F\left(\ell + \frac{1}{2}\right) = \sum_{m=-\infty}^{\infty} (-1)^m \int_0^{\infty} F(\lambda) e^{i2m\pi\lambda} d\lambda. \quad (47.143)$$

When applied to Eq. (47.33a),

$$f(\theta) = (ik)^{-1} \sum_{m=-\infty}^{\infty} (-1)^m \int_0^{\infty} \lambda (e^{2i\eta(\lambda)} - 1) \times P_{\lambda-\frac{1}{2}}(\cos \theta) e^{i2m\pi\lambda} d\lambda, \quad (47.144)$$

where $\eta(\lambda)$ and $P_{\lambda-1/2} \equiv P(\lambda, \theta)$ are now phase functions and Legendre functions of the continuous variable λ , being interpolated from discrete to continuous ℓ . This infinite-sum-of-integrals representation for $f(\theta)$ is, in principle, exact. The particular merit of the Poisson sum in the present context is that the index m labels the classical paths that have encircled the (attractive) scattering center m times, and that the terms with $m < 0$ have no regions of stationary phase (SP). For deflections Θ in the range $-\pi < \Theta < \pi$, the only SP contribution is the $m = 0$ term.

47.7.7 Semiclassical Phase Shifts

Semiclassical analysis ([6] and references therein) involves reducing Eq. (47.144) by the three approximations represented by cases A to C below. Since the integrands can oscillate very rapidly over large regions of λ , the main contributions to the integrals arise from points λ_i of the stationary phase of each integrand. The amplitude can then be evaluated by the method of stationary phase, the basis of semiclassical analysis.

A. Legendre Function Asymptotic Expansions

Main range: $\sin \theta > \lambda^{-1}$, θ not within λ^{-1} of zero or π .

$$P_\ell(\cos \theta) = (2/(\pi \lambda \sin \theta))^{1/2} \cos(\lambda\theta - \pi/4). \quad (47.145)$$

Forward formula: θ within λ^{-1} of zero.

$$P_\ell(\cos \theta) = [\theta/\sin \theta]^{1/2} J_0(\lambda\theta), \quad (47.146a)$$

$$J_0(\lambda\theta) = \frac{1}{\pi} \int_0^\pi e^{-i\lambda\theta \cos \phi} d\phi. \quad (47.146b)$$

Backward formula: θ within λ^{-1} of π .

$$P_\ell(\cos \theta) = \left(\frac{\pi - \theta}{\sin \theta}\right)^{1/2} \times J_0[\lambda(\pi - \theta)] e^{-i\pi(\lambda-1/2)}. \quad (47.147)$$

Equations (47.145)–(47.147) are useful for analysis of caustics (rainbows), diffraction, and forward and backward glories, respectively. Also, a useful identity is

$$\sum_{\ell=0}^{\infty} (2\ell + 1) P_\ell(\cos \theta) = \begin{cases} 4\delta(1 - \cos \theta), & \theta > 0 \\ 0 & \theta = 0, \end{cases}$$

where $\delta(x)$ is the Dirac delta function.

B. JWKB Phase Shift Functions

$$\eta(\lambda) = \int_{r_m}^{\infty} k_{\lambda}(r) dr - \int_{\lambda/k}^{\infty} \left(k^2 - \frac{\lambda^2}{r^2}\right)^{1/2} dr \quad (47.148a)$$

$$= \lim_{r \rightarrow \infty} \left[\int_{r_m}^{\infty} k_{\ell}(r') dr' - kr \right] + \frac{1}{2}\lambda\pi, \quad (47.148b)$$

with local wavenumber

$$k_{\lambda}^2(r) = k^2 - U(r) - \lambda^2/r^2. \quad (47.149)$$

The wavenumber is related to the impact parameter b and to Eqs. (47.102a) and (47.2e) through $\eta = S(E, \lambda\hbar)/\hbar$ and the Langer modification Eq. (47.107)

$$b = \frac{\sqrt{\ell(\ell+1)}}{k} = \frac{\ell+1/2}{k} = \frac{\lambda}{k}. \quad (47.150)$$

We note a useful identity. As $r \rightarrow \infty$,

$$\sin \left[\int_{\frac{\lambda}{k}}^r \left(k^2 - \frac{\lambda^2}{r^2}\right)^{1/2} dr + \frac{\pi}{4} \right] \rightarrow \sin \left(kr - \frac{1}{2}\ell\pi \right). \quad (47.151)$$

JWKB phase functions are valid when variation of the potential over the local wavenumber $k_{\lambda}^{-1}(r)$ is a small fraction of the available kinetic energy $E - V(r)$. Many wavelengths can then be accommodated within a range Δr for a characteristic potential change ΔV . The classical method is valid when $(1/k)(dV/dr) \ll (E - V)$.

Phase-deflection function relation

$$\Theta(\lambda) = 2 \frac{\partial \eta(\lambda)}{\partial \lambda}. \quad (47.152)$$

C. Stationary Phase Approximations (SPA) to Generic Integrals

$$A^{\pm}(\theta) = \int_{-\infty}^{\infty} g(\theta; \lambda) \exp[\pm i\gamma(\theta; \lambda)] d\lambda, \quad (47.153)$$

for parametric θ . In cases where the phase function γ has two stationary points, a phase minimum γ_1 at λ_1 , and a phase maximum γ_2 at λ_2 , then $\gamma'_i = 0$, $\gamma''_1 > 0$, $\gamma''_2 < 0$, where $\gamma'_i = (d\gamma/d\lambda)$ at λ_i and $\gamma''_i = (d^2\gamma/d\lambda^2)$ for $i = 1, 2$. Since g is real, $A^- = (A^+)^*$, $g_i(\theta) = g(\theta, \lambda_i)$.

Uniform Airy result

$$A^+(\theta) = a_1(\theta) e^{i(\gamma_1 + \pi/4)} F^*(\gamma_{21}) + a_2(\theta) e^{i(\gamma_2 - \pi/4)} F(\gamma_{21}), \quad (47.154a)$$

$$a_i(\theta) = [2\pi/|\gamma''_i|]^{1/2} g_i(\theta), \quad i = 1, 2, \quad (47.154b)$$

$$\gamma_{21}(\theta) = \gamma_2 - \gamma_1 \equiv \frac{4}{3}|z(\theta)|^{3/2} > 0, \quad (47.154c)$$

$$F[\gamma_{21}(\theta)] = [z^{1/4} \text{Ai}(-z) + iz^{-1/4} \text{Ai}'(-z)] \sqrt{\pi} \times e^{-i(\gamma_{21}/2 - \pi/4)}, \quad (47.154d)$$

where Ai and Ai' are the Airy function and its derivative.

This result holds for all separations $(\lambda_2 - \lambda_1)$ in the location of stationary phases including a caustic (or rainbow), which is a point of inflection in γ , i.e. $\gamma_1 = \gamma_2$, $\gamma'_i = 0 = \gamma''_i$. An equivalent expression is [6]

$$A^+(\theta) = [(a_1 + a_2)z^{1/4} \text{Ai}(-z) - i(a_1 - a_2)z^{-1/4} \text{Ai}'(-z)] \sqrt{\pi} e^{i\bar{\gamma}}, \quad (47.155)$$

where the mean phase is $\bar{\gamma} = \frac{1}{2}(\gamma_1 + \gamma_2)$. The first form of Eq. (47.154a) is useful for analysis of widely separated regions of stationary phase when $\gamma_{21} \gg 0$ and $F \rightarrow 1$. The equivalent second form Eq. (47.155) is valuable in the neighborhood of caustics or rainbows when the stationary phase regions coalesce as $a_1 \rightarrow a_2$.

Primitive result

For widely separated regions λ_1 and λ_2 , $F \rightarrow 1$ and

$$A^{\pm}(\epsilon) = [a_1(\epsilon) \mp ia_2(\epsilon) e^{\pm i\gamma_{21}}] e^{\pm i(\gamma_1 + \pi/4)}, \quad (47.156a)$$

$$A^{\pm}(\epsilon) = a_1(\epsilon) \exp\left[\pm i\left(\gamma_1 + \frac{\pi}{4}\right)\right] + a_2(\epsilon) \exp\left[\pm i\left(\gamma_2 - \frac{\pi}{4}\right)\right]. \quad (47.156b)$$

Note that the minimum phase γ_1 is increased by $\pi/4$, and the maximum phase γ_2 is reduced by $\pi/4$.

Transitional Airy result

In the neighborhood of a caustic or rainbow where $\gamma'' = 0$, at the inflection point $\lambda_1 = \lambda_2 = \lambda_r$, and then

$$A^{\pm}(\theta) = 2\pi \left| \frac{2}{\gamma'''(\lambda_r)} \right|^{1/3} g(\theta; \lambda_r) \text{Ai}(-z) e^{\pm i\gamma(\theta; \lambda_r)} \quad (47.157a)$$

$$z = \frac{2}{|\gamma'''(\lambda_r)|^{1/3} \gamma'(\theta; \lambda_r)}. \quad (47.157b)$$

Only over a very small angular range does this result agree in practice with the uniform result Eq. (47.154a), which

uniformly connects Eqs. (47.156a) and (47.157a). These stationary-phase formulae are not only applicable to integrals involving (λ, θ) but also to (t, E) and (R, p) combinations, which occur in the method of variation of constants and in Franck–Condon overlaps of vibrational wavefunctions, respectively.

47.7.8 Semiclassical Amplitudes: Integral Representation

A. Off-Axis Scattering: $\sin \theta > \lambda^{-1}$

Except in the forward and backward directions, Eq. (47.144) with Eq. (47.145) reduces to

$$f(\theta) = -\frac{1}{k(2\pi \sin \theta)^{1/2}} \sum_{m=-\infty}^{\infty} (-1)^m \times \int_0^{\infty} d\lambda \lambda^{1/2} \times \left(e^{i\Delta^+(\lambda, m)} - e^{i\Delta^-(\lambda, m)} \right), \quad (47.158a)$$

$$\Delta^\pm(\lambda; m) = 2\eta(\lambda) + 2m\pi\lambda \pm \lambda\theta \pm \pi/4 \equiv S^C \pm \pi/4, \quad (47.158b)$$

where S^C is the classical action Eq. (47.106) divided by \hbar .

The stationary phase condition $d\Delta^\pm/d\lambda = 0$ yields the deflection function Θ to the scattering angle θ relation

$$\Theta(\lambda_i) = \mp\theta - 2m\pi, \quad (47.159)$$

where λ_i are points of stationary phase (SP). Since $\pi \geq \Theta \geq -\infty$, integrals with $m < 0$ have no SPs and vanish under the SPA. For cases involving no orbiting (where $\Theta \rightarrow -\infty$) and when $\pi > \Theta > -\pi$, integrals with $m > 0$ also vanish under SPA, so that the only remaining contribution from $m = 0$ to Eq. (47.158b) is

$$f(\theta) = -\frac{1}{k(2\pi \sin \theta)^{1/2}} \times \int_0^{\infty} \lambda^{1/2} \left[e^{i\Delta^+(\lambda)} - e^{i\Delta^-(\lambda)} \right] d\lambda, \quad (47.160a)$$

$$\Delta^\pm(\lambda) = 2\eta(\lambda) \pm \lambda\theta \pm \pi/4. \quad (47.160b)$$

The attractive branch Δ^+ contributes only negative deflections, and the repulsive branch Δ^- contributes only positive deflections and has one SP point at λ_1 where Δ^- is maximum.

Rainbow angle θ_r : $(\Delta^+)''_{\lambda_r} = 0$, so that $\Theta'(\lambda_r) = 0$, where $\Theta(\lambda_r) < 0$ has reached its most negative value.

$$\begin{aligned} \theta < \theta_r: & \quad \Delta^+ \text{ has two SP points } \lambda_{2,3}; \\ & \quad \text{a maximum at } \lambda_2 \text{ and} \\ & \quad \text{a minimum at } \lambda_3. \end{aligned}$$

$$\begin{aligned} \theta = \theta_r: & \quad \lambda_2 = \lambda_3: \text{ SP's coalesce.} \\ \theta > \theta_r: & \quad \text{no classical attractive scattering.} \\ & \quad \Delta^+ \text{ has no SP points.} \end{aligned}$$

B. Forward Amplitude: $\sin \theta \approx \theta < \lambda^{-1}$

$$f(\theta) = \frac{1}{ik} \left(\frac{\theta}{\sin \theta} \right)^{1/2} \sum_{m=-\infty}^{\infty} e^{-im\pi} \int_0^{\infty} \lambda J_0(\lambda\theta) \times (e^{2i\eta(\lambda)} - 1) e^{2im\pi\lambda} d\lambda. \quad (47.161a)$$

Stationary phase points: $\gamma'(\lambda_m) = 0$.

$$\Theta(\lambda_m) = 2 \left(\frac{\partial \eta}{\partial \lambda} \right) = -2m\pi. \quad (47.161b)$$

Terms with $m < 0$, therefore, make no SP contribution to $f(\theta)$ since $\Theta \leq \pi$. The $m = 0$ term provides diffraction due to $\Theta \rightarrow 0$, $\Theta' \rightarrow 0$ at long range and a forward glory due to $\Theta \rightarrow 0$ at a finite λ_g and nonzero Θ'_g .

C. Backward Amplitude: $\theta \approx \pi - \Theta(\lambda^{-1})$

$$f(\theta) = \frac{1}{k} \left(\frac{\pi - \theta}{\sin \theta} \right)^{1/2} \times \sum_{m=-\infty}^{\infty} e^{im\pi} \int_0^{\infty} \lambda J_0[\lambda(\pi - \theta)] \times e^{i[2\eta(\lambda) + (2m-1)\pi\lambda]} d\lambda. \quad (47.162a)$$

Stationary phase points

$$\Theta(\lambda_m) = 2 \left(\frac{\partial \eta}{\partial \lambda} \right) = -(2m-1)\pi. \quad (47.162b)$$

There are no SPs for $m < 0$. The $m = 0$ term provides a normal backward amplitude due to repulsive collisions ($\Theta = \pi$), and $m > 0$ terms are due to attractive half-windings.

D. Eikonal Amplitude

The $m = 0$ term of Eq. (47.161a) gives

$$f_E(\theta) = \frac{1}{ik} \int_0^{\infty} \lambda (e^{2i\eta(\lambda)} - 1) J_0(\lambda\theta) d\lambda \quad (47.163a)$$

$$= -ik \int_0^{\infty} (e^{2i\eta(b)} - 1) J_0(kb\theta) b db, \quad (47.163b)$$

and for potentials with cylindrical symmetry, $kb\theta$ can be replaced by $2kb \sin \frac{1}{2}\theta = \mathbf{k} \cdot \mathbf{b}$, and

$$f_E(\theta) = -\frac{ik}{2\pi} \int (e^{2i\eta(b)} - 1) J_0(\mathbf{k} \cdot \mathbf{b}) d\mathbf{b}. \quad (47.164)$$

From the optical theorem,

$$\sigma_E(E) = 8\pi \int_0^\infty \sin^2 \eta(b, E) b db . \quad (47.165)$$

E. Small-Angle Diffraction Corrected Scattering

In small-angle scattering θ , θ' , and $\eta \rightarrow 0$, where diffraction occurs due to scattering in the forward direction by the long-range attractive tail of $V(r)$. The main contributions to Eq. (47.163a) arise from a large number of small $\eta(\lambda)$ at large λ . The Jeffrey–Born phase function Eq. (47.104) can, therefore, be used in Eq. (47.163b) for $f(\theta)$ and in Eqs. (47.166) and (47.168), respectively, for $\sigma(E)$. A finite forward diffraction peak as $\theta \rightarrow 0$ is obtained for $f(\theta)$ in contrast to the classical infinite result. With Eq. (47.165) one gets the Landau–Lifshitz cross section

$$\sigma_{LL}(E) = 8\pi \int_0^\infty [\sin^2 \eta_{JB}(E, b)] b db . \quad (47.166)$$

The Massey–Mohr cross section is

$$\eta(E, b_0) = \frac{1}{2}, \quad \langle \sin^2 \eta(E, b < b_0) \rangle = \frac{1}{2}, \quad (47.167)$$

$$\sigma_{MM}(E) = 2\pi b_0^2 + 8\pi \int_{b_0}^\infty \eta_{JB}^2(E, b) b db . \quad (47.168)$$

An example

For $V(r) = -C/r^n$, the Landau–Lifshitz (LL) and Massey–Mohr (MM) cross sections are [Eq. (47.207a)]

$$\sigma_{LL}(E) = \pi \left(\frac{2CF(n)}{(n-1)\hbar v} \right)^{2/(n-1)} \times \pi \left[\sin\left(\frac{\pi}{n-1}\right) \Gamma\left(\frac{2}{n-1}\right) \right]^{-1}, \quad (47.169)$$

$$\sigma_{MM}(E) = \pi \left(\frac{2CF(n)}{(n-1)\hbar v} \right)^{2/(n-1)} \left(\frac{2n-3}{n-2} \right), \quad (47.170)$$

where $F(n) = \sqrt{\pi} \Gamma(\frac{1}{2}n + \frac{1}{2}) / \Gamma(\frac{1}{2}n)$, and v is the relative speed. Both σ_{LL} and σ_{MM} have the general form

$$\sigma_D(E) = \gamma \left(\frac{C}{\hbar v} \right)^{2/(n-1)}. \quad (47.171)$$

Ion–atom collisions

For $n = 4$ attraction at low energy, $\sigma_D \approx v^{-2/3}$, $\gamma_{LL} = 11.373$, and $\gamma_{MM} = 10.613$. For $n = 12$ repulsion at high energy, $\sigma_D \approx v^{-2/11}$, $\gamma_{LL} = 6.584$, and $\gamma_{MM} = 6.296$.

Atom–atom collisions

For $n = 6$ (attraction), $\sigma_D \approx v^{-2/5}$, $\gamma_{LL} = 8.083$, and $\gamma_{MM} = 7.547$ Fig. 47.1. Exact numerical calculations favor σ_{LL} over σ_{MM} ([19, pp. 1325] for details).

Differential cross section

$$\frac{d\sigma}{d\Omega} = f_i^2(\theta) + f_r^2(\theta), \quad (47.172a)$$

$$f_i = \frac{2}{k} \int_0^\infty \lambda \sin^2 \eta(\lambda) \left(1 - \frac{1}{4} \lambda^2 \theta^2 \right) d\lambda \quad (47.172b)$$

$$= \frac{k\sigma_D(E)}{4\pi} \left[1 - \left(\frac{k^2\sigma_D}{16\pi} \right) g_1(n)\theta^2 \right], \quad (47.172c)$$

$$f_r = \frac{1}{k} \int_0^\infty \lambda \sin 2\eta(\lambda) \left(1 - \frac{1}{4} \lambda^2 \theta^2 \right) d\lambda \quad (47.172d)$$

$$= \frac{k\sigma_D(E)}{4\pi} \left[1 - \left(\frac{k^2\sigma_D}{16\pi} \right) g_2(n)\theta^2 \right] \tan\left(\frac{\pi}{n-1}\right), \quad (47.172e)$$

where σ_D is given by Eq. (47.171), and

$$g_j(n) = \pi^{-1} \tan\left(\frac{j\pi}{n-1}\right) \frac{\{\Gamma[2/(n-1)]\}^2}{\Gamma[4/(n-1)]}. \quad (47.173)$$

The optical theorem Eq. (47.36) is satisfied, and

$$f_D(\theta \approx 0) = \sigma_D^{1/2}(E) e^{iS_D(n)}, \quad (47.174)$$

where the (energy-independent) phase is

$$S_D(n) = \frac{\pi(n-3)}{2(n-1)}. \quad (47.175)$$

47.8 Coulomb Elastic Scattering

The Coulomb potential has the remarkable property that the quantum cross section (Rutherford cross section) agrees with the classical and semiclassical result, as well as with the Born approximation. Furthermore, the s-wave phase shift is semiclassically also correct, hence also the Mott cross section containing interferences due to identical particles is semiclassically correct. We will often use the abbreviations

$$\begin{aligned} C &= Z_1 Z_2 e^2, \\ \beta &= C/\hbar v = Z_1 Z_2 / (ka_0), \\ r_c(E) &= Z_1 Z_2 e^2 / (2E) = \beta / (2k). \end{aligned} \quad (47.176)$$

47.8.1 Quantum Phase Shift, Rutherford and Mott Scattering

Direct solution of Eq. (47.24) yields

$$v_\ell \approx \sin(kr - \frac{1}{2}\ell\pi + \eta_\ell^c - \beta \ln 2kr). \quad (47.177a)$$

Coulomb phase shift

$$\eta_\ell^c = \arg \Gamma(\ell + 1 + i\beta) = \text{Im}[\ln \Gamma(\ell + 1 + i\beta)]. \quad (47.177b)$$

Coulomb **S**-matrix element

$$S_\ell^c = \exp(2i\eta_\ell^c) = \frac{\Gamma(\ell + 1 + i\beta)}{\Gamma(\ell + 1 - i\beta)}. \quad (47.177c)$$

Coulomb scattering amplitude

$$f^c(\theta) = -\frac{\beta \exp[2i\eta_\ell^c - i\beta \ln(\sin^2 \frac{1}{2}\theta)]}{2k \sin^2 \frac{1}{2}\theta}. \quad (47.177d)$$

Rutherford cross section

$$\frac{d\sigma^c}{d\Omega} = \frac{Z_1^2 Z_2^2 e^4}{16E^2} \frac{1}{\sin^4 \frac{1}{2}\theta} = r_c(E)^2 \csc^4 \frac{1}{2}\theta, \quad (47.177e)$$

which is the Coulomb differential cross section.

Mott formula for elastic scattering of two indistinguishable charged particles. From Eqs. (47.43a) and (47.43c), one gets the positive (+, symmetric solutions, e.g., spin-zero bosons as for ${}^4\text{He}$ - ${}^4\text{He}$) or negative (-, antisymmetric solutions, e.g., spin- $\frac{1}{2}$ fermions as for H^+ - H^+ , e^\pm - e^\pm)

$$\begin{aligned} \frac{d\sigma^c}{d\Omega} = r_c(E)^2 & \left(\csc^4 \frac{1}{2}\theta + \sec^4 \frac{1}{2}\theta \right. \\ & \left. \pm 2 \csc^2 \frac{1}{2}\theta \sec^2 \frac{1}{2}\theta \cos \gamma \right), \end{aligned} \quad (47.178)$$

where $\gamma = 2\beta \ln(\tan \frac{1}{2}\theta)$.

47.8.2 Classical Coulomb Scattering

There is only a single trajectory, or in other words, the deflection function is monotonic. Hence,

$$\theta(b, E) = |\Theta| = 2 \csc^{-1} \left[1 + \frac{b^2}{r_c(E)^2} \right]^{1/2}, \quad (47.179a)$$

$$b(\theta, E) = r_c(E) \cot \frac{1}{2}\theta, \quad (47.179b)$$

and according to Eq. (47.94) and in agreement with Eq. (47.177e), we get

$$\frac{d\sigma^c}{d\Omega} = \frac{bdb}{d(\cos \theta)} = \frac{r_c(E)^2}{4} \csc^4 \frac{1}{2}\theta. \quad (47.179c)$$

47.8.3 Semiclassical Coulomb Scattering

Since the monotony of the deflection function Eq. (47.179a) allows only for a single trajectory contributing to the cross section, the semiclassical Coulomb cross section between distinguishable particles reduces to the Rutherford cross section Eq. (47.179c).

For semiclassical Mott scattering, we also need the classical action in the scattering amplitude defined with the semiclassical propagator

$$f(\mathbf{p}, \mathbf{p}') = \sum_j \left(\frac{d\sigma_j}{d\Omega} \right)^{1/2} e^{iS_j^c(\mathbf{p}, \mathbf{p}')/\hbar - i\nu_j \pi/2} \quad (47.180)$$

to determine

$$\begin{aligned} \frac{d\sigma}{d\Omega} &= \frac{1}{2} |f(\mathbf{p}, \mathbf{p}') \pm f(\mathbf{p}, -\mathbf{p}')|^2 \\ &= \frac{1}{2} |f(\theta) \pm f(\pi - \theta)|^2, \end{aligned} \quad (47.181)$$

where the sum of the scattering amplitudes refers to bosons and the difference to fermions, while $\mathbf{p} \neq \mathbf{p}'$ denote final and initial momentum, respectively, and $\theta = \arccos[\mathbf{p} \cdot \mathbf{p}' / (pp')]$. The action between any two momenta \mathbf{p}, \mathbf{p}' that are connected by a classical trajectory of energy E under Coulomb interaction, is given by [3, p. 182],

$$\Delta\Phi(\mathbf{p}, \mathbf{p}', E) = -p_a r_c \ln \frac{\sqrt{1+\Delta} + 1}{\sqrt{1+\Delta} - 1} \quad (47.182)$$

$$\Delta = \frac{(p^2 - p_a^2)(p'^2 - p_a^2)}{p_a^2 |\mathbf{p} - \mathbf{p}'|^2}. \quad (47.183)$$

We need the action only in the asymptotic regime outside the range of the potential, $p, p' \rightarrow p_a$, where for all nonzero scattering angles ($\mathbf{p} \neq \mathbf{p}'$), $\Delta \ll 1$. Then [8]

$$S^C(\mathbf{p}, \mathbf{p}') = \lim_{p, p' \rightarrow p_a} \Delta\Phi(\mathbf{p}, \mathbf{p}', E) \quad (47.184)$$

$$= 2(\sigma_0 - p_a r_c \ln[\sin \Theta/2]), \quad (47.185)$$

with

$$\sigma_0 = \frac{p_a r_c}{2} \ln \left[\frac{(p^2 - p_a^2)(p'^2 - p_a^2)}{p_a^4} \right], \quad (47.186)$$

where $p_a = (2mE)^{1/2}$ is the asymptotic momentum, and m the reduced mass of the two colliding particles. The constant $\sigma_0/\hbar = \delta_0$ is the semiclassical phase shift for zero angular momentum, not dependent on the scattering angle θ .

47.8.4 Born Approximation for Coulomb Scattering

The scattering amplitude for Coulomb scattering reads accordingly [see Eq. (47.75)]

$$f_B^c(\mathbf{p}, \mathbf{p}') = \frac{r_c(E)}{2} \frac{1}{\sin^2(\theta/2)}, \quad (47.187)$$

which gives the correct cross section for Rutherford scattering but not for Mott scattering since it lacks the relevant phase for the latter in contrast to the full quantum or semiclassical scattering amplitude.

47.9 Results for Model Potentials

Exact results for various quantities in classical, quantal, and semiclassical elastic scattering are obtained for the model potentials (a)–(s) in Table 47.1.

47.9.1 Classical Deflection Functions and Cross Sections

(a) Hard sphere

$$\theta(b; E) = \Theta = \begin{cases} \pi - 2 \sin^{-1}(b/a), & b \leq a; \\ 0, & b > a. \end{cases} \quad (47.188a)$$

$$b(\theta) = a \cos \frac{\theta}{2}, \quad (47.188b)$$

$$\sigma(\theta) = \frac{d\sigma}{d\Omega} = \frac{1}{4}a^2; \quad \text{isotropic}, \quad (47.188c)$$

$$\sigma = \pi a^2 \quad (\text{geometric cross section}); \quad (47.188d)$$

θ , $\sigma(\theta)$, and σ are all independent of the energy E .

(b) Potential barrier For $E < V_0$, classical scattering is the same as for hard sphere reflection as given by

Eqs. (47.188a)–(47.188d). For $E > V_0$ and $\theta = \Theta$, define $n^2 = 1 - V_0/E$, $b_0 = na$. Then

$$\theta(b) = \begin{cases} 2[\sin^{-1}(b/na) - \sin^{-1}(b/a)] & 0 \leq b \leq b_0 \\ \pi - 2 \sin^{-1}(b/a), & b_0 \leq b \leq a, \end{cases} \quad (47.189a)$$

and $\theta_{\max} = 2 \cos^{-1} n$. For a given θ , the two impact parameters that contribute are

$$b_1(\theta) = \frac{an \sin \frac{1}{2}\theta}{(1 - 2n \cos \frac{1}{2}\theta + n^2)^{1/2}}, \quad 0 < b_1 \leq b_0 \quad (47.189b)$$

$$b_2(\theta) = a \cos \frac{1}{2}\theta, \quad b_0 < b_2 \leq a. \quad (47.189c)$$

For $0 \leq \theta \leq \theta_{\max}$,

$$\frac{d\sigma}{d\Omega} = \frac{1}{4}a^2 + \frac{a^2 n^2 (n \cos \frac{1}{2}\theta - 1)(n - \cos \frac{1}{2}\theta)}{4 \cos \frac{1}{2}\theta (n^2 + 1 - 2 \cos \frac{1}{2}\theta)^2}, \quad (47.189d)$$

and $d\sigma/d\Omega = 0$ for $\theta_{\max} \leq \theta \leq \pi$. Finally,

$$\sigma = \int_{\theta=0}^{\theta_{\max}} \left(\frac{d\sigma}{d\Omega} \right) d\Omega = \pi a^2. \quad (47.189e)$$

Table 47.1 Model interaction potentials

	Potential	$V(r)$
(a)	Hard sphere	$\infty, r \leq a; 0, r > a$
(b)	Barrier	$V_0, r \leq a; 0, r > a$
(c)	Well	$-V_0, r \leq a; 0, r > a$
(d)	Coulomb (\pm)	$\pm C/r$
(e)	Finite-range Coulomb	$-C/r + C/r_s, r \leq r_s; 0, r > r_s$
(f)	Pure dipole	$\pm \alpha/r^2$
(g)	Finite-range dipole	$\pm \alpha \left(\frac{1}{r^2} - \frac{1}{a^2} \right), r \leq a; 0, r > a$
(h)	Dipole + hard sphere	$\pm \alpha/r^2, r \leq a; 0, r > a$
(i)	Power law attractive	$-C/r^n, (n > 2)$
(j)	Fixed dipole + polarization	$-\frac{De \cos \theta_d}{r^2} - \frac{\alpha_d e^2}{2r^4}$
(k)	Fixed dipole + Coulomb	$-\frac{De \cos \theta_d}{r^2} + \frac{e^2}{r}$
(l)	Lennard–Jones ($n, 6$)	$\frac{\epsilon n}{n-6} \left[\frac{6}{n} \left(\frac{r_e}{r} \right)^n - \left(\frac{r_e}{r} \right)^6 \right]$
(m)	Polarization ($n, 4$)	$\frac{\epsilon n}{n-4} \left[\frac{4}{n} \left(\frac{r_e}{r} \right)^n - \left(\frac{r_e}{r} \right)^4 \right]$
(n)	Multiple-term power law	$\frac{C_m}{r^m} - \frac{C_n}{r^n} = V_m(r) - V_n(r)$
(o)	Exponential	$V_0 \exp(-\alpha r)$
(p)	Screened Coulomb	$V_0 \exp(-\alpha r)/r$
(q)	Morse	$\epsilon [e^{2\beta(r_e-r)} - 2e^{\beta(r_e-r)}]$
(r)	Gaussian	$V_0 \exp(-\alpha^2 r^2)$
(s)	Polarization finite	$-V_0/(r^2 + r_0^2)^2$

(c) Potential well The results are similar to those for potential barrier case above, except that there is only a single scattering trajectory with $\theta = -\Theta$, and $n = (1 + V_0/E)^{1/2}$ is the effective index of refraction for the equivalent problem in geometrical optics. Refraction occurs on entering and exiting the well. Then

$$\theta(b) = -2[\sin^{-1}(b/na) - \sin^{-1}(b/a)], \quad (47.190a)$$

$$\theta(b = a) = \theta_{\max} = 2 \cos^{-1}(1/n), \quad (47.190b)$$

$$b(\theta) = \frac{-an \sin \frac{1}{2}\theta}{(1 - 2n \cos \frac{1}{2}\theta + n^2)^{1/2}}, \quad (47.190c)$$

$$\frac{d\sigma}{d\Omega} = \frac{a^2 n^2 (n \cos \frac{1}{2}\theta - 1)(n - \cos \frac{1}{2}\theta)}{4 \cos^2 \frac{1}{2}\theta (n^2 + 1 - 2n \cos \frac{1}{2}\theta)^2}, \quad (47.190d)$$

$$\sigma = \pi a^2. \quad (47.190e)$$

(d) Rutherford or Coulomb The cross section for pure Coulomb scattering is discussed in Sect. 47.8.2.

(e) Finite-range Coulomb

$$r_c(E) = \frac{Z_1 Z_2 e^2}{2E}, \quad \alpha(E) = r_c(E)/r_s, \\ \frac{d\sigma}{d\Omega} = \frac{r_c^2}{4} \left(\frac{1 + \alpha}{\alpha^2 + (1 + 2\alpha) \sin^2 \frac{1}{2}\theta} \right)^2. \quad (47.191)$$

(f) Pure dipole $r_0^2(E) = \alpha/E$.

Repulsion (+): $\Theta > 0$, $\Theta = \theta$,

$$b^2(\Theta) = r_0^2 \left[\left(\frac{1}{\Theta} + \frac{1}{2\pi - \Theta} \right) \frac{\pi}{2} - 1 \right], \quad (47.192a)$$

$$\frac{d\sigma}{d\Omega} = \frac{\pi r_0^2}{4 \sin \theta} \left| \frac{1}{\theta^2} - \frac{1}{(2\pi - \theta)^2} \right|. \quad (47.192b)$$

Attraction (-): $\Theta < 0$.

$$b^2(\Theta) = r_0^2 \left[\left(\frac{1}{|\Theta|} - \frac{1}{|\Theta| + 2\pi} \right) \frac{\pi}{2} + 1 \right]. \quad (47.193a)$$

There is an infinite number of (negative) deflections $\Theta = \Theta_n^\pm$ associated with a given scattering angle θ

$$|\Theta_n^+| = 2\pi n + \theta, \quad n = 0, 1, 2, \dots, \quad (47.193b)$$

$$|\Theta_n^-| = 2\pi n - \theta, \quad n = 1, 2, 3, \dots \quad (47.193c)$$

The infinite sum over contributions from $b_n^\pm = b(\Theta_n^\pm)$ for the attractive dipole yields

$$\frac{d\sigma}{d\Omega} = \frac{\pi r_0^2}{4 \sin \theta} \left| \frac{1}{\theta^2} + \frac{1}{(2\pi - \theta)^2} \right|. \quad (47.193d)$$

(g) Finite Range Dipole Scattering $r_0^2 = \alpha/E$, $(r^\pm)^2 = b^2 \pm r_0^2$, $(b_0^\pm)^2 = a^2 \pm r_0^2$.

Repulsion (+): for $b \leq a$,

$$\Theta(b) = \frac{\pi(r_m^+ - b)}{r_m^+} + \frac{2b}{r_m^+} \sin^{-1} \left(\frac{r_m^+}{b_0^+} \right) \\ - 2 \sin^{-1} \left(\frac{b}{a} \right), \\ \Theta(0) = \pi, \quad \Theta(b \geq a) = 0, \quad \sigma = \pi a^2. \quad (47.194a)$$

Attraction (-): for $b > r_0$,

$$\Theta(b) = \frac{\pi(r_m^- - b)}{r_m^-} + \frac{2b}{r_m^-} \sin^{-1} \left(\frac{r_m^-}{b_0^-} \right) \\ - 2 \sin^{-1} \left(\frac{b}{a} \right), \quad (47.194b)$$

$$\Theta(r_0) \rightarrow \infty, \quad \Theta(b \geq a) = 0, \quad \sigma = \pi a^2. \quad (47.194c)$$

(h) Dipole plus hard sphere scattering $r_0^2 = \alpha/E$, $(r_m^\pm)^2 = b^2 \pm r_0^2$, $(b_0^\pm)^2 = a^2 \pm r_0^2$.

Repulsion (+): for $0 \leq b \leq b_0$,

$$\Theta(b) = \frac{\pi(r_m^+ - b)}{r_m^+} + \frac{2b}{r_m^+} \sin^{-1} \left(\frac{r_m^+}{a} \right) \\ - 2 \sin^{-1} \left(\frac{b}{a} \right), \quad (47.195a)$$

$$b_0 \leq b \leq a; \quad \Theta(b) = \pi - 2 \sin^{-1}(b/a), \quad (47.195b)$$

$$\Theta(0) = \pi, \quad \Theta(b \geq a) = 0, \quad \sigma = \pi a^2. \quad (47.195c)$$

Attraction (-): for $b > r_0$,

$$\Theta(b) = \frac{\pi(r_m^- - b)}{r_m^-} + \frac{2b}{r_m^-} \sin^{-1} \left(\frac{r_m^-}{a} \right) \\ - 2 \sin^{-1} \left(\frac{b}{a} \right),$$

$$\Theta(b) = \Theta_{\min} \text{ at } b = a,$$

$$\Theta(0) = \pi, \quad \Theta(b \geq a) = 0, \quad \sigma = \pi a^2. \quad (47.196)$$

Orbiting or Spiraling Collisions

From Sect. 47.6.5, the parameters are

Orbiting radius: r_0 .

Focusing factor: $F = [1 - V(r_0)/E]$.

Orbiting cross section: $\sigma_{\text{orb}} = \pi r_0^2 F$.

(i) Attractive power law potentials

$$V_{\text{eff}}(r_0) = \left(1 - \frac{1}{2}n\right)V(r_0), \quad n > 2,$$

$$r_0(E) = \left(\frac{(n-2)C}{2E}\right)^{1/n}, \quad F = \left(\frac{n}{(n-2)}\right), \quad (47.197a)$$

$$\sigma_{\text{orb}}(E) = \pi \left(\frac{n}{(n-2)}\right) \left(\frac{(n-2)C}{2E}\right)^{2/n}. \quad (47.197b)$$

For the case $n = 4$ with $V(r) = -\alpha_d e^2/2r^4$, this gives the Langevin cross section

$$\sigma_L(E) = 2\pi r_0^2 = 2\pi \left(\frac{\alpha_d e^2}{2E}\right)^{1/2} \quad (47.198)$$

for orbiting collisions, and the Langevin rate

$$k_L = v\sigma_L(E) = 2\pi(\alpha_d e^2/M)^{1/2}, \quad (47.199)$$

which is independent of E .

The case $n = 6$ with $V(r) = -C/r^6$ is the van der Waals potential for which

$$\sigma_{\text{orb}}(E) = \frac{3}{2}\pi r_0^2 = \frac{3}{2}\pi(2C/E)^{1/3}. \quad (47.200)$$

(j) Fixed dipole plus polarization potential

$$r_0^2(E) = \left(\frac{\alpha_d e^2}{2E}\right)^{1/2}, \quad (47.201a)$$

$$\sigma_{\text{orb}}(E) = 2\pi \left(\frac{\alpha_d e^2}{2E}\right)^{1/2} + \left(\frac{\pi D e \cos \theta_d}{E}\right). \quad (47.201b)$$

For a locked-in dipole, the orientation angle is $\theta_d = 0$, and $\sigma_{\text{orb}}(E) > 0$, for all θ_d , when $E > E_c = (D^2/2\alpha_d)$.

Averaging over all θ_d from 0 to $\theta_{\text{max}} = [\frac{1}{2}\pi + \sin^{-1}(2Er_0^2/De)]$, which satisfies $\sigma_{\text{orb}}(E) > 0$, for all E , then

$$\langle \sigma_{\text{orb}}(E) \rangle_{\theta_d} = \pi \left[\left(\frac{\alpha_d e^2}{2E}\right)^{1/2} + \left(\frac{\alpha_d e^2}{2E_c}\right)^{1/2} \right] + \frac{\pi D e}{4E} \left(1 - \frac{E}{E_c}\right) \quad (47.202a)$$

$$\rightarrow \sigma_L(E) \text{ as } E \rightarrow E_c. \quad (47.202b)$$

(k) Fixed dipole plus Coulomb repulsion

$$r_0^2(E) = e^2/2E. \quad (47.203a)$$

For all E and fixed rotations in the range $0 \leq \theta_d \leq \theta_{\text{max}} = \cos^{-1}(e^2/2De)$,

$$\sigma_{\text{orb}}(E) = (\pi D e \cos \theta_d)/E - \pi r_0^2(E). \quad (47.203b)$$

(l) Lennard–Jones ($n, 6$) For the following two interactions, there are two roots of $E = V_{\text{eff}}(r_0) = V(r_0) + \frac{1}{2}r_0 V'(r_0)$. They correspond to stable and unstable circular orbits [with different angular momenta associated with the minimum and maxima of the different $V_{\text{eff}}(R)$]. Analytical expressions can only be derived for the orbiting cross section at the critical energy E_{max} , above which no orbiting can occur.

For the Lennard–Jones ($n, 6$) potential, orbiting occurs for $E < E_{\text{max}} = 2\epsilon[4/(n-2)]^{6/(n-6)}$. The orbiting radius at E_{max} is

$$r_0(E_{\text{max}}) = r_e[(n-2)/4]^{1/(n-6)}.$$

The orbiting cross section at $E_{\text{max}} = 2\epsilon(r_e/r_0)^6$ is

$$\sigma_{\text{orb}}(E_{\text{max}}) = \pi b_0^2(E_{\text{max}}) = \frac{3}{2}\pi r_0^2 \left(\frac{n}{n-2}\right). \\ n = 12: E_{\text{max}} = 4\epsilon/5, \quad r_0 = 1.165r_e, \\ \sigma_{\text{orb}} = 2.4\pi r_e^2. \quad (47.204)$$

(m) Polarization ($n, 4$) As discussed for case (l),

$$E_{\text{max}} = \epsilon \left(\frac{2}{n-2}\right)^{4/(n-4)}, \quad (47.205a)$$

$$r_0(E_{\text{max}}) = r_e \left(\frac{n-2}{2}\right)^{1/(n-4)}, \quad (47.205b)$$

$$\sigma_{\text{orb}}(E_{\text{max}}) = 2\pi r_0^2 \frac{n}{(n-2)}, \quad (47.205c)$$

$$n = 12: E_{\text{max}} = \epsilon/\sqrt{5}; \\ r_0 = 1.22r_e; \sigma_{\text{orb}} = 3.6\pi r_e^2.$$

Small-Angle Scattering

For the power law potential $V(r) = -C/r^n$, Eqs. (47.96a) and (47.96b) can be expanded in powers of $V(r)/E$ to obtain analytic expressions for Θ and η_{JB} . The general form is

$$\Theta(b) = \sum_{j=1}^{\infty} \left(\frac{V(b)}{E}\right)^j F_j(n) = \frac{2}{k} \frac{\partial \eta}{\partial b}, \quad (47.206a)$$

$$F_j(n) = \frac{\pi^{1/2} \Gamma(\frac{1}{2}jn + \frac{1}{2})}{\Gamma(j+1) \Gamma(\frac{1}{2}jn - j + 1)}. \quad (47.206b)$$

The leading $j = 1$ terms equivalent to Eq. (47.97d) are $F_1(n) \equiv F(n)$, as defined following Eq. (47.169). Then to first order in V/E ,

$$\eta_{\text{JB}} = -\left(\frac{k}{2E}\right) \left(\frac{CF(n)}{n-1}\right) b^{1-n}, \quad (47.207a)$$

$$\frac{d\sigma}{d\Omega} = I_c(\theta) = \left(\frac{CF(n)}{E\theta}\right)^{2/n} \frac{1}{n\theta \sin \theta}. \quad (47.207b)$$

From a log–log plot of $\sin \theta(d\sigma/d\Omega)$ versus E , C and n can both be determined.

The integral cross sections for scattering by $\theta \geq \theta_0$ is

$$\begin{aligned}\sigma(E) &= 2\pi \int_{\theta_0}^{\pi} I_c(\theta) d(\cos \theta) = 2\pi \int_0^{b_{\max}} b db \\ &= \pi \left(\frac{CF(n)}{E\theta_0} \right)^{2/n},\end{aligned}\quad (47.208)$$

where θ_0 is the smallest measured scattering angle corresponding to a trajectory with impact parameter $b_{\max} = [CF(n)/E\theta_0]^{1/n}$. A plot of $\ln \sigma(E)$ versus $\ln E$ is a straight line with slope $(-2/n)$.

The Landau–Lifshitz cross section Eq. (47.169) and the Massey–Mohr cross section Eq. (47.170) follow from use of the JB phases Eq. (47.207a).

(n) Multiple-term power-law potentials

$$\Theta(E, b) = \frac{1}{E} [V_m(b)F(m) - V_n(b)F(n)]. \quad (47.209)$$

For example, a Lennard–Jones ($n, 6$) potential Table 47.1 has the following features

$$\begin{aligned}\text{Forward glory: } \Theta &= 0 \quad \text{when } b_g = \alpha_n^{1/(n-6)} r_e, \\ &\quad \text{where } \alpha_n = 6F(n)/[nF(6)].\end{aligned}$$

$$\text{Rainbow: } d\Theta/db = 0 \text{ at } b_r = (n\alpha_n/6)^{1/(n-6)} r_e.$$

$$\Theta_r = -F(n)(E/E)(r_e/b_r)^n, \quad (47.210a)$$

$$\omega_r = \frac{1}{2} (d^2\Theta_r/db^2)_r = \frac{3n}{b_r^2} |\Theta(b_r)|. \quad (47.210b)$$

(o) Exponential potential

$$\begin{aligned}\eta_{\text{JB}}(E, b) &= -\frac{1}{2} kb \frac{V_0}{E} K_1(\alpha b) \\ &\xrightarrow{\text{large } b} -\frac{1}{2} kb \frac{V(b)}{E} \left(\frac{\pi b}{2\alpha} \right)^{1/2}.\end{aligned}\quad (47.211)$$

(p) Screened Coulomb potential

$$\begin{aligned}\Theta(E, b) &= \alpha(V_0/E) K_1(\alpha b) \\ &\xrightarrow{\text{large } b} \left(\frac{1}{2} \pi \alpha b \right)^{1/2} V(b)/E,\end{aligned}\quad (47.212a)$$

$$\begin{aligned}\eta_{\text{JB}}(E, b) &= -\frac{k}{2E} V_0 K_0(\alpha b) \\ &\xrightarrow{\text{large } b} -\frac{k}{2E} V(b) \left(\frac{\pi b}{2\alpha} \right)^{1/2}.\end{aligned}\quad (47.212b)$$

(q) Morse potential

$$\begin{aligned}\Theta(E, b) &= (2\beta b) \left(\frac{\epsilon}{E} \right) \\ &\quad \times [e^{2\beta r_e} K_0(2\beta b) - e^{\beta r_e} K_0(\beta b)] \\ &\xrightarrow{\text{large } b} (\pi\beta b)^{1/2} \left(\frac{\epsilon}{E} \right) [e^{2\beta(r_e-b)} - \sqrt{2} e^{\beta(r_e-b)}], \\ b_r &= r_e + (2\beta)^{-1} \ln 2, \\ \Theta_r &= -(\pi\beta b_r)^{1/2} (\epsilon/2E), \\ \omega_r &= \beta^2 |\Theta_r| r_e^2.\end{aligned}\quad (47.213)$$

Large-Angle Scattering

For power law potentials $V(r) = C/r^n$,

$$\Theta(b) = \pi - \sum_{j=1}^n \left(\frac{E}{V(b)} \right)^{(2j-1)/n} G_j(n), \quad (47.214a)$$

$$G_j(n) = \frac{(-1)^{j-1}}{\Gamma(j)\Gamma(k)} \left(\frac{2\pi^{1/2}}{n} \right) \Gamma\left(\frac{2j-1}{n} \right), \quad (47.214b)$$

with $k = [(2j-1)/n] - j - \frac{1}{2}$. For the $j = 1$ term,

$$\Theta(b) = \pi - \left(\frac{E}{C} \right)^{1/n} G_1(n) b, \quad (47.214c)$$

$$I_c(\theta) = \frac{d\sigma}{d\Omega} = \left(\frac{C}{E} \right)^{2/n} G_1^{-2}(n), \quad (47.214d)$$

which is isotropic. Including both $j = 1$ and 2 terms provides a good approximation to the entire repulsive branch of the deflection function Θ . Series Eq. (47.214a) for large angles and Eq. (47.206a) for small angles eventually diverge for impact parameters $b < b_c$ and $b > b_c$, respectively, where

$$b_c = n^{1/2} \left(\frac{C}{2E} \right)^{1/n} \frac{|n-2|^{1/n}}{|n-2|^{1/2}}. \quad (47.214e)$$

47.9.2 Amplitudes and Cross Sections in Born Approximation

$$k^2 = 2mE/\hbar^2, \quad K = 2k \sin \frac{1}{2}\theta,$$

$$U_0 = 2mV_0/\hbar^2, \quad U_0/k^2 = V_0/E,$$

in the general expression Eq. (47.75) for the first Born approximation.

(a) Exponential $V(r) = V_0 \exp(-\alpha r)$

$$f_{\text{B}}(\theta) = -\frac{2\alpha U_0}{(\alpha^2 + K^2)^2}, \quad (47.215a)$$

$$\begin{aligned}\sigma_{\text{B}}(E) &= \frac{16\pi}{3} U_0^2 \frac{3\alpha^4 + 12\alpha^2 k^2 + 16k^4}{\alpha^4(\alpha^2 + 4k^2)^3}, \\ &\xrightarrow{E \rightarrow \infty} \frac{4}{3} \pi \left(\frac{V_0}{E} \right) \left(\frac{U_0}{\alpha^4} \right).\end{aligned}\quad (47.215b)$$

(b) **Gaussian** $V(r) = V_0 \exp(-\alpha^2 r^2)$

$$f_B(\theta) = -\left(\frac{\pi^{1/2} U_0}{4\alpha^2}\right) \exp(-K^2/4\alpha^2), \quad (47.216a)$$

$$\sigma_B(E) = \left(\frac{\pi^2 U_0}{8\alpha^4}\right) \left(\frac{V_0}{E}\right) [1 - \exp(-2k^2/\alpha^2)]. \quad (47.216b)$$

(c) **Spherical well** $V(r) = V_0$ for $r < a$, $V(r) = 0$ otherwise

$$f_B(\theta) = -\frac{U_0}{K^3} (\sin Ka - Ka \cos Ka), \quad (47.217a)$$

$$\sigma_B(E) = \frac{\pi V_0}{2E} (U_0 a^4) [1 - (ka)^{-2} + (ka)^{-3} \sin 2ka - (ka)^{-4} \sin^2 2ka]. \quad (47.217b)$$

(d) **Screened Coulomb** $V(r) = V_0 \exp(-\alpha r)/r$, $V_0 = Z_1 Z_2 e^2$, $U_0 = 2Z_1 Z_2 / a_0$

$$f_B(\theta) = -\frac{U_0}{\alpha^2 + K^2}, \quad (47.218a)$$

$$\sigma_B(E) = \frac{4\pi U_0^2}{\alpha^2(\alpha^2 + 4k^2)} \rightarrow \pi \left(\frac{V_0}{E}\right) \left(\frac{U_0}{\alpha^2}\right). \quad (47.218b)$$

When $\alpha \rightarrow 0$, then $f_B(\theta) = -U_0/K^2$.

(e) **e⁻-atom**

$$V(r) = -Ne^2[Z/a_0 + 1/r] \exp(-2Zr/a_0), \quad (47.219a)$$

H(1s): N = 1, Z = 1; He(1s²): N = 2; Z = 27/16.

$$f_B(\theta) = \frac{2N}{a_0} \left(\frac{2\alpha^2 + K^2}{(\alpha^2 + K^2)^2} \right), \quad \alpha = 2Z/a_0, \quad (47.219b)$$

$$\sigma_B(E) = \frac{\pi a_0^2 N^2 (12Z^4 + 18Z^2 k^2 a_0^2 + 7k^4 a_0^4)}{3Z^2 (Z^2 + k^2 a_0^2)^3}. \quad (47.219c)$$

Also, f_B decomposes Eq. (47.78) as

$$f_B(K) = f_B^{eZ}(K) + f_B^{ee}(K)F(K), \quad (47.219d)$$

where f_B^{ij} are two-body Coulomb amplitudes for (i, j) scattering, and $F(K)$ is the elastic form factor Eq. (47.79).

(f) **Dipole** $V(r) = V_0/r^2$.

$$f_B(\theta) = \pi U_0 / 2K. \quad (47.220)$$

(g) **Polarization** $V(r) = V_0(r^2 + r_0^2)^{-2}$

$$f_B(\theta) = -\frac{\pi U_0}{4 r_0} \exp(-Kr_0), \quad (47.221a)$$

$$\sigma_B(E) = \frac{\pi^3 U_0 V_0}{32r_0^4 E} [1 - (1 + 4kr_0) \exp(-4kr_0)]. \quad (47.221b)$$

References

1. Heller, E.J.: The Semiclassical Way to Dynamics and Spectroscopy. Princeton University Press, Oxford (2018)
2. Brack, M., Bhaduri, R.: Semiclassical Physics. Addison-Wesley, Reading, Mass. (1997)
3. Gutzwiller, M.C.: Chaos in classical and quantum mechanics. Interdisciplinary Applied Mathematics. Springer, Berlin (1990)
4. Ozorio de Almeida, A.M.: Hamiltonian Systems: Chaos and Quantization. Cambridge University Press, Cambridge (1988)
5. Cvitanović, P., Artuso, R., Mainieri, R., Tanner, G., Vattay, G.: Chaos: Classical and Quantum. ChaosBook.org, Niels Bohr Institute, Copenhagen (2016)
6. Berry, M.V., Mount, K.E.: Semiclassical approximations in wave mechanics. Rep. Prog. Phys. **35**(1), 315 (1972)
7. Miller, W.H.: The Classical S-Matrix in Molecular Collisions vol. 30., pp 77–136 (1975)
8. Rost, J.M.: Semiclassical S-matrix theory for atomic fragmentation. Phys. Rep. **297**, 271–344 (1998)
9. Kleinert, H.: Path Integrals in Quantum Mechanics Statistics and Polymer Physics. World Scientific, Singapore (1995)
10. Blinder, S.M.: Analytic form for the nonrelativistic Coulomb propagator. Phys. Rev. A **43**, 13–16 (1991)
11. Van Vleck, J.H.: The Correspondence Principle in the Statistical Interpretation of Quantum Mechanics. Proc. Natl. Acad. Sci. U.S.A. **14**(2), 178–188 (1928)
12. Gutzwiller, M.C.: Phase-Integral Approximation in Momentum Space and the Bound States of an Atom. J. Math. Phys. **8**(10), 1979–2000 (1967)
13. Herman, M.F., Kluk, E.: A semiclassical justification for the use of non-spreading wavepackets in dynamics calculations. Chem. Phys. **91**(1), 27–34 (1984)
14. O'Malley, T.F., Spruch, L., Rosenberg, L.: Modification of Effective-Range Theory in the Presence of a Long-Range Potential. J. Math. Phys. **2**(4), 491–498 (1961)
15. O'Malley, T.F.: Extrapolation of electron-rare gas atom cross sections to zero energy. Phys. Rev. **130**, 1020–1029 (1963)
16. Gribakin, G.F., Flambaum, V.V.: Calculation of the scattering length in atomic collisions using the semiclassical approximation. Phys. Rev. A **48**, 546–553 (1993)
17. Petović, Z.L., O'Malley, T.F., Crompton, R.W.: J. Phys. B **28**, 3309 (1995)
18. McDaniel, M.W., Mitchell, J.B.A., Rudd, M.A.: Atomic Collisions: Heavy Particle Projectiles. Wiley, New York (1993)
19. Massey, H.S.W., Burhop, E.H.S., Gilbody, H.B. (eds.): Electronic and Ionic Impact Phenomena. Clarendon, Oxford (1974)



Jan-Michael Rost Jan-Michael Rost studied physics and philosophy in Munich and Freiburg. He received his PhD (1990) and spent postdoctoral years at the University of Washington, Seattle, and at Harvard University (1990–1993). He has been Director at the Max Planck Institute for the Physics of Complex Systems, Dresden, since 1999 and Professor of Quantum Dynamics at TU Dresden since 2000. His theoretical work includes ultrafast and ultracold highly excited quantum dynamics from atoms to nanosystems.



Orientation and Alignment in Atomic and Molecular Collisions

48

Nils Andersen

Contents

48.1	Introduction	713
48.2	Collisions Involving Unpolarized Beams	714
48.2.1	The Fully Coherent Case	714
48.2.2	The Incoherent Case with Conservation of Atomic Reflection Symmetry	717
48.2.3	The Incoherent Case Without Conservation of Atomic Reflection Symmetry	717
48.3	Collisions Involving Spin-Polarized Beams	718
48.3.1	The Fully Coherent Case	718
48.3.2	The Incoherent Case with Conservation of Atomic Reflection Symmetry	718
48.3.3	The Incoherent Case Without Conservation of Atomic Reflection Symmetry	720
48.4	Example	721
48.4.1	The First Born Approximation	721
48.5	Further Developments	722
48.5.1	S → D Excitation	722
48.5.2	P → P Excitation	722
48.5.3	Relativistic Effects in S → P Excitation	722
48.6	Summary	722
	References	722

Abstract

This chapter deals with the concepts of orientation and alignment in atomic and molecular physics. The terms refer to parameters related to the shape and dynamics of an excited atomic or molecular level, as it is manifested in a nonstatistical population of the magnetic sublevels. To take full advantages of the possibilities of this approach, one utilizes *third generation experiments*, i.e., scattering experiments that exploit the planar scattering symmetry, contrary to an angular differential cross section determination (a *second generation experiment*) having

cylindrical symmetry, or a total cross section measurement (a *first generation experiment*) integrating over all scattering angles. In this way, one is often able to probe atomic collision theories at a more fundamental level, and in favorable cases approach a *perfect scattering experiment* in which the complex quantal scattering amplitudes are completely determined. This term was coined by *Bederson* [1] and has since served as an ideal towards which scattering experiments attempt to strive.

Keywords

density matrix · differential cross section · coherence analysis · reflection symmetry · Stokes vector · polarization · orientation · alignment

48.1 Introduction

The study of anisotropies has a long history in atomic physics, with light polarization, or Stokes parameter analysis, as a prominent example. A pioneering review by *Fano* and *Macek* [2] laid the mathematical and conceptual foundation for most of the later work. Advances in coincidence techniques, laser preparation methods, and the development of efficient sources for polarized electrons [3] have boosted the field further. Parallel developments of powerful computational codes have enabled a matching theoretical effort. In this way, detailed insights into the collision dynamics have been obtained, such as the locking radius model for low-energy atomic collisions, propensity rules for orientation in fast electronic and atomic collisions, and spin effects in polarized electron-heavy atom scattering. Presentations of these developments are contained in [4] and Chaps. 39, 53, 55, 67, 68, and 70. A comprehensive and critical review of the literature and the mathematical formalism was initiated by the National Institute of Standards and Technology (NIST) [5–7].

N. Andersen (✉)
The Niels Bohr Institute, University of Copenhagen
Copenhagen, Denmark
e-mail: noa@science.ku.dk

Space limitations allow only presentation of the formalism for the simplest case of excitation. Recent developments in the description of processes involving polarized beams are included. The presentation is restricted to atomic outer-shell excitation. Other reviews describe excitation of inner shells [8] and molecular levels [9]. Related material on density matrices is contained in Chap. 7 [10].

48.2 Collisions Involving Unpolarized Beams

48.2.1 The Fully Coherent Case

Consider first the simplest nontrivial case of $S \rightarrow P$ excitation. A general property of an atomic collision is that the total reflection symmetry with respect to the scattering plane of the total wave function describing the system is conserved. In simple cases, such as electron impact excitation of He singlet states, or atom excitation by fast, heavy particle impact, the projectile acts as a structureless particle, with only the target atom changing its quantum state. In this case, the reflection symmetry of the target wave function alone is conserved.

Figure 48.1 shows the angular parts of the simplest $|lm\rangle$ -states with $l = 0, 1, 2$. The arrows indicate how the two families of states with positive or negative reflection symmetry may couple internally. Thus, in an $S \rightarrow P$ transition, an atom initially in an S-state may be excited to the (p_{+1}, p_{-1}) subspace, while the p_0 -state is not accessible. A characteristic feature of the corresponding electron charge cloud is that it has *zero height*, i.e., zero electron density in the direction perpendicular to the scattering plane. Furthermore, the expectation value of the orbital angular momentum has a nonvanishing component in this direction only.

The resulting electron charge cloud may, thus, have a shape as shown in Fig. 48.2a. We shall now discuss the parametrization of the wave function of this state and analyze the connection between the wave function and the corresponding photon radiation pattern emitted when the state decays back to the initial S-state, using the properties of electric dipole radiation.

Basic Definitions and Coordinate Frames

The coordinate frames that are of particular use in describing the wave function are as follows. The *collision frame*, (x^c, y^c, z^c) , is defined by $\hat{z}^c \parallel \mathbf{k}_{\text{in}}$ and $\hat{y}^c \parallel \mathbf{k}_{\text{in}} \times \mathbf{k}_{\text{out}}$. The *natural frame*, (x^n, y^n, z^n) , is defined by $\hat{x}^n \parallel \mathbf{k}_{\text{in}}$ and $\hat{z}^n \parallel \mathbf{k}_{\text{in}} \times \mathbf{k}_{\text{out}}$. Finally, the *atomic frame* is identical to the natural frame, except that it is rotated by an angle γ around $z^n = z^a$ such that x^a is parallel to the major symmetry axis of the P-state charge cloud, as shown in Fig. 48.2. Most scattering calculations use the collision coordinate system as the reference frame, while mathematical analysis is of-

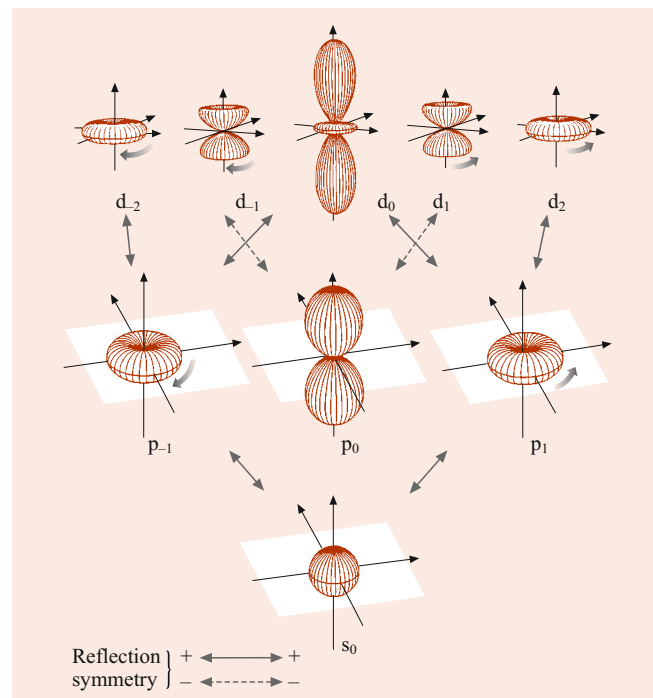


Fig. 48.1 Reflection symmetry of the simplest spherical harmonics, corresponding to S, P, and D-states

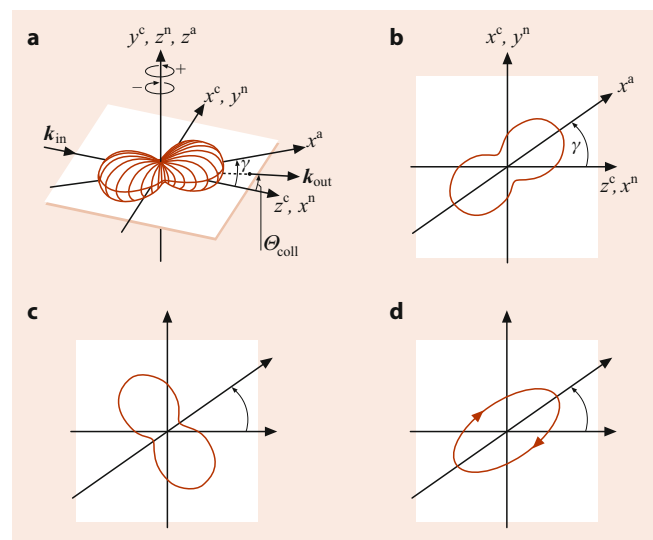


Fig. 48.2 **a** Shows the shape, or the angular part, of a P-state with positive reflection symmetry with respect to the scattering plane. Some relevant coordinate frames are also indicated; **b** shows a cut of this shape in the scattering plane. **c** is the angular distribution of photons emitted in the scattering plane; **d** is the polarization ellipse for light emitted in the direction perpendicular to the plane, as observed from above

ten most conveniently performed in the natural frame, where the algebra is particularly simple. Many expressions are even simpler in the atomic frame, but it has the disadvantage that the angle γ varies with collision parameters, such as impact velocity, impact parameter, etc.

The expansion of the P-state wave function in the three coordinate systems is

$$|\Psi\rangle = a_{+1}^c |p_{+1}^c\rangle + a_0^c |p_0^c\rangle + a_{-1}^c |p_{-1}^c\rangle \quad (48.1)$$

$$= a_{+1}^n |p_{+1}^n\rangle + a_{-1}^n |p_{-1}^n\rangle \quad (48.2)$$

$$= a_{+1}^a |p_{+1}^a\rangle + a_{-1}^a |p_{-1}^a\rangle . \quad (48.3)$$

Conservation of reflection symmetry in the scattering plane implies

$$a_{+1}^c = -a_{-1}^c , \quad (48.4)$$

$$a_0^n = 0 , \quad (48.5)$$

$$a_0^a = 0 . \quad (48.6)$$

The normalization condition implies

$$\begin{aligned} |a_0^c|^2 + 2|a_{+1}^c|^2 &= |a_{+1}^n|^2 + |a_{-1}^n|^2 \\ &= |a_{+1}^a|^2 + |a_{-1}^a|^2 \\ &= 1 . \end{aligned} \quad (48.7)$$

Finally, the a_m coefficients are related to the scattering amplitudes f_m and the differential cross section $\sigma(\theta)$ by

$$a_m = f_m(k_{\text{out}}/k_{\text{in}})^{\frac{1}{2}} \sigma(\theta)^{-\frac{1}{2}} \quad (48.8)$$

$$\sigma(\theta) = (k_{\text{out}}/k_{\text{in}}) \left(|f_0^c|^2 + 2|f_{+1}^c|^2 \right), \text{ etc.} \quad (48.9)$$

Except for an arbitrary phase factor, the pure state in Eq. (48.1) may thus be characterized by two dimensionless parameters. Traditionally, they have been chosen as (λ, χ) defined as [11]

$$\lambda = \frac{|a_0^c|^2}{|a_0^c|^2 + 2|a_{+1}^c|^2} , \quad (48.10)$$

$$\chi = \arg(a_{+1}^c a_0^{c*}) . \quad (48.11)$$

An alternative parametrization (L_{\perp}, γ) is given by [5]

$$L_{\perp} = \frac{|a_{+1}^n|^2 - |a_{-1}^n|^2}{|a_{+1}^n|^2 + |a_{-1}^n|^2} , \quad (48.12)$$

$$\begin{aligned} \gamma &= \frac{1}{2} \arg(a_{-1}^n a_{+1}^{n*}) \pm \frac{\pi}{2} , \\ &= -\frac{1}{2} (\delta \pm \pi) , \end{aligned} \quad (48.13)$$

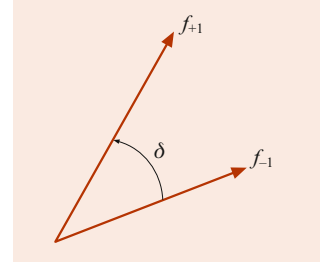
with the notation of Fig. 48.3. Referring to the natural coordinate frame, the expectation value of the electronic orbital angular momentum is, thus,

$$\langle \Psi | L | \Psi \rangle = (0, 0, L_{\perp}) . \quad (48.14)$$

Coherence Analysis: Stokes Parameters

We now discuss the information obtainable from a polarization analysis of the emitted light. In the notation of classical

Fig. 48.3 Fully coherent $S \rightarrow P$ excitation may be described by two independent scattering amplitudes, characterized by their relative size and phase



optics (e.g., *Born and Wolf* [12]) the components of the Stokes vector (P_1, P_2, P_3) measured in the direction $+y^c$ ($+z^n$) perpendicular to the scattering plane and defined by

$$IP_1 = I(0^\circ) - I(90^\circ) , \quad (48.15)$$

$$IP_2 = I(45^\circ) - I(135^\circ) , \quad (48.16)$$

$$IP_3 = I(\text{RHC}) - I(\text{LHC}) , \quad (48.17)$$

with

$$\begin{aligned} I &= I(0^\circ) + I(90^\circ) \\ &= I(45^\circ) + I(135^\circ) \\ &= I(\text{RHC}) + I(\text{LHC}) , \end{aligned} \quad (48.18)$$

are given by

$$P_1 = 2\lambda - 1 , \quad (48.19)$$

$$P_2 = -2\sqrt{\lambda(1-\lambda)} \cos \chi , \quad (48.20)$$

$$P_3 = 2\sqrt{\lambda(1-\lambda)} \sin \chi , \quad (48.21)$$

or, alternatively,

$$P_1 = P_l \cos 2\gamma , \quad (48.22)$$

$$P_2 = P_l \sin 2\gamma , \quad (48.23)$$

$$P_3 = -L_{\perp} , \quad (48.24)$$

with

$$P_l = \sqrt{P_1^2 + P_2^2} . \quad (48.25)$$

Here, $I(\theta)$ is the intensity transmitted through an ideal linear polarizer with the transmission direction tilted by an angle θ with respect to the z^c or x^n -direction. Similarly, RHC (LHC) (right (left) hand circularly polarized light) refers to photons with negative (positive) helicity. Inspection of Eqs. (48.19) to (48.25) shows that determination of the Stokes vector in the direction perpendicular to the collision plane determines the wave function in Eq. (48.1) completely. A determination of the Stokes vector, thus, constitutes a *perfect scattering experiment*.

The Stokes vector (P_1, P_2, P_3) is a unit vector characterizing the state $|\Psi\rangle$, and it may be represented by a point on the Poincaré sphere; see Fig. 48.4.

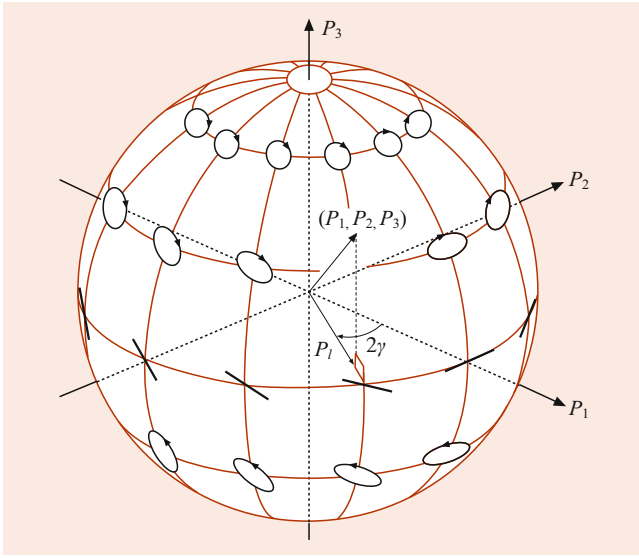


Fig. 48.4 The Poincaré sphere. The Stokes vector for a pure state $|\Psi\rangle$ corresponds to a characteristic polarization ellipse, represented by a point on the unit sphere. Generally, the light is elliptically polarized, with the sense of rotation indicated by the arrows on the selected ellipses drawn. Special cases are the north and south poles, where the polarization is purely circular, and the equator, where it is purely linear, with the direction indicated by the orientation of the lines

Correlation Analysis

Another experimental approach is to map the angular distribution of the photons emitted in the subsequent $S \rightarrow P$ decay. For this purpose, we first note that the angular part $\Upsilon(\theta, \phi)$ of the electron probability density $\langle \Psi | \Psi \rangle$ corresponding to the wave function in Eq. (48.1) may be written as

$$\Upsilon(\theta, \phi) = \frac{1}{2} [1 + P_l \cos 2(\phi - \gamma)] \sin^2 \theta. \quad (48.26)$$

Figure 48.2b shows a cut of this charge cloud in the scattering plane,

$$\Upsilon\left(\frac{1}{2}\pi, \phi\right) = \frac{1}{2} [1 + P_l \cos 2(\phi - \gamma)]. \quad (48.27)$$

The relative length, l , and width, w of the charge cloud are given by

$$l = \frac{1}{2}(1 + P_l), \quad (48.28)$$

$$w = \frac{1}{2}(1 - P_l). \quad (48.29)$$

The degree of linear polarization P_l is, thus, a measure of the shape of the charge cloud, since

$$P_l = \frac{l - w}{l + w}. \quad (48.30)$$

According to the properties of electric dipole radiation, the pattern $I(\phi)$ in the scattering plane is

$$I(\phi) = \frac{1}{2} [1 - P_l \cos 2(\phi - \gamma)]. \quad (48.31)$$

A mapping of the radiation pattern in the collision plane determines γ and P_l , and thereby the absolute value of the angular momentum by

$$|L_\perp| = \sqrt{1 - P_l^2}. \quad (48.32)$$

However, the sign of L_\perp cannot be determined by correlation analysis, and accordingly this approach does not qualify for classification as a *perfect scattering experiment*.

Density Matrix Representation

Recalling that $\rho_{mn} = a_m a_n^*$, the density matrices in the various basis sets introduced above are

$$\rho^c = \frac{1}{\sqrt{8}} \begin{pmatrix} \frac{1}{\sqrt{2}}(1 - P_1) & -P_2 + iP_3 & -\frac{1}{\sqrt{2}}(1 - P_1) \\ -P_2 - iP_3 & \sqrt{2}(1 - P_1) & P_2 + iP_3 \\ -\frac{1}{\sqrt{2}}(1 - P_1) & P_2 - iP_3 & \frac{1}{\sqrt{2}}(1 - P_1) \end{pmatrix}, \quad (48.33)$$

$$\rho^n = \frac{1}{2} \begin{pmatrix} 1 + L_\perp & 0 & -P_l e^{-2i\gamma} \\ 0 & 0 & 0 \\ -P_l e^{2i\gamma} & 0 & 1 - L_\perp \end{pmatrix}, \quad (48.34)$$

$$\rho^a = \frac{1}{2} \begin{pmatrix} 1 + L_\perp & 0 & -P_l \\ 0 & 0 & 0 \\ -P_l & 0 & 1 - L_\perp \end{pmatrix}. \quad (48.35)$$

The density matrices illustrate the algebraic simplifications obtained using the natural coordinate frame. In the following, this frame will be used unless otherwise stated, and we therefore suppress the superscript n below.

Postcollisional Depolarization Due to Fine Structure and Hyperfine Structure Effects

After the collision, the isolated atom evolves under the influence of internal forces, such as fine structure and hyperfine structure, until the optical decay. While typical collision times are of the order 10^{-15} s, the light emission occurs after a time interval of 10^{-9} s. This is long compared with the Larmor precession time of the electron spin ($\approx 10^{-12}$ s), and one can, thus, assume that the atom has completely relaxed into, e.g., its ${}^2P_{1/2}$ and ${}^2P_{3/2}$ -states before the photon emission. For the simplest nontrivial case of electron spin $S = \frac{1}{2}$, the Stokes vector $\mathbf{P}(S)$ of the subsequent ${}^2P \rightarrow {}^2S$ transition

is modified to become

$$P_{1,2}\left(\frac{1}{2}\right) = \frac{3}{7}P_{1,2}(0), \quad (48.36)$$

$$P_3\left(\frac{1}{2}\right) = P_3(0), \quad (48.37)$$

and the Stokes vector is, thus, no longer a unit vector. In general, the Stokes vector components are reduced by depolarization factors c_i (a table of c_i coefficients for the most common values of electron and nuclear spin is given in Appendix B of [5])

$$P_i(S) = c_i P_i(0). \quad (48.38)$$

This suggests introduction of *reduced polarizations*

$$\bar{P}_i = P_i(S)/c_i. \quad (48.39)$$

The *reduced* Stokes vector $(\bar{P}_1, \bar{P}_2, \bar{P}_3)$ is again a unit vector, and the formalism developed above for the spinless case can then be applied. We shall assume that this correction has been made, and the *bar* will be dropped.

48.2.2 The Incoherent Case with Conservation of Atomic Reflection Symmetry

The picture outlined above has to be modified in cases where the experiment sums over several, in principle distinguishable, channels, each of which, however, conserves reflection symmetry. Prototype examples are electron impact excitation of hydrogen or light alkali atoms. Here, the excitation process is described by singlet and triplet scattering amplitudes, respectively, and we have the possibility of direct and exchange scattering. This doubles the number of scattering amplitudes from two to four. The experimental results are, thus, an incoherent sum over these channels (singlet and triplet), the unraveling of which would require the application of spin-polarized beams; see Sect. 48.3. The atomic P-state can no longer be described as a single pure state, Eq. (48.1), but as a mixed state (Chap. 7). The expressions in Eqs. (48.33) to (48.35) for the density matrix are unchanged, but the matrix elements are now sums of the contributions from the individual channels (we shall discuss its decomposition below); P_l and L_\perp are now independent quantities, and the (reduced) Stokes vector \mathbf{P} is generally no longer a unit vector. The degree of polarization P may thus be less than 1, i.e.,

$$P^2 = P_1^2 + P_2^2 + P_3^2 = P_l^2 + L_\perp^2 \leq 1. \quad (48.40)$$

For electron impact excitation, deviation of the parameter P from unity may, thus, serve as a measure of the effect of electron exchange. Accordingly, we have three independent observables, e.g., (L_\perp, γ, P_l) . This set of variables is

frame independent. A photon correlation experiment in the scattering plane may extract the (γ, P_l) pair, while coherence analysis in the z -direction provides the complete set. An alternative set of (frame-dependent) parameters used in particular for hydrogen is (λ, R, I) , with

$$\lambda = \frac{1}{2}(1 + P_1), \quad (48.41)$$

$$R = -\frac{1}{\sqrt{8}}P_2, \quad (48.42)$$

$$I = \frac{1}{\sqrt{8}}P_3. \quad (48.43)$$

48.2.3 The Incoherent Case Without Conservation of Atomic Reflection Symmetry

In the general case, the assumption of positive reflection symmetry with respect to the scattering plane for the wave function of the excited atom cannot be maintained. For example, for electron impact excitation of a P-state of a heavy atom, spin-orbit effects may be so strong that they flip the electron spin, thereby allowing population of the $|p_0^n\rangle$ -state. Thus, the total number of scattering amplitudes is now six. Typical examples are mercury or the heavy noble gases. The total angular momentum of the excited state is $J = 1$, the fine structure being completely resolved in these cases. Strictly speaking, the density matrix elements no longer describe the electronic charge cloud, but rather the excited state ($J = 1$) distribution. Similarly, L_\perp should be replaced by J_\perp , but, for simplicity, we keep the notation. This state radiates as a set of classical oscillators, completely analogous to the 1P_1 -state described above, so we shall maintain our previous notation, simply replacing the term charge cloud density by oscillator density. The main difference from the cases considered above is that the density now displays a height; see Fig. 48.5.

Blum, da Paixão, and collaborators, [13, 14], were the first to formulate a parametrization of the general case. Here, we shall use the expression for the density matrix in the natural frame as the starting point and decompose it into the two terms with positive and negative reflection symmetry, respectively,

$$\rho^n = (1 - h) \frac{1}{2} \begin{pmatrix} 1 - P_3 & 0 & -P_l^+ e^{-2i\gamma} \\ 0 & 0 & 0 \\ -P_l^+ e^{2i\gamma} & 0 & 1 + P_3 \end{pmatrix} + h \begin{pmatrix} 0 & 0 & 0 \\ 0 & 1 & 0 \\ 0 & 0 & 0 \end{pmatrix}, \quad (48.44)$$

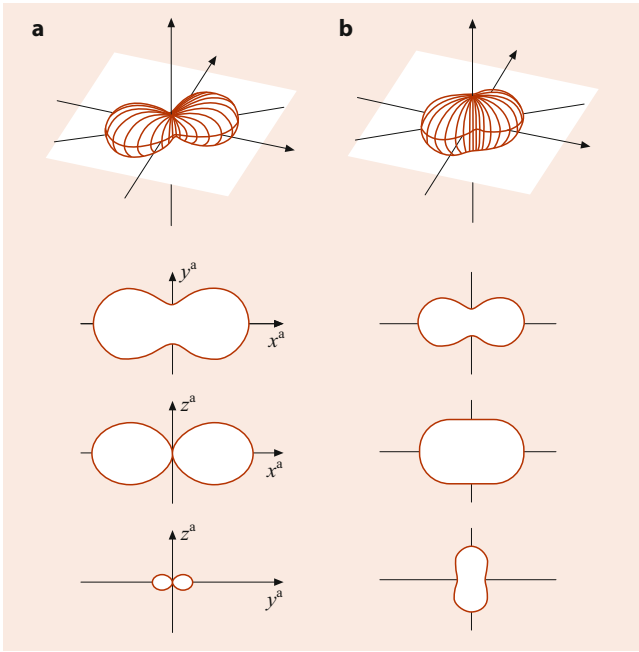


Fig. 48.5 The top row shows classical oscillator densities for height parameters $h = 0$ and $h = 1/3$, respectively. The alignment angle is $\gamma = 35^\circ$ and $P_l^+ = 0.6$ in both cases. Cuts along the symmetry axes are shown in the other rows

where the linear polarization P_l^+ is labeled with a + referring to the positive reflection symmetry. Similarly, we define

$$L_\perp^+ \equiv -P_3, \quad (48.45)$$

$$P^{+2} \equiv P_1^2 + P_2^2 + P_3^2 \leq 1. \quad (48.46)$$

The shape of the density is now characterized by the three parameters

$$l = (1 - h) \frac{1}{2}(1 + P_l), \quad (48.47)$$

$$w = (1 - h) \frac{1}{2}(1 - P_l), \quad (48.48)$$

$$h = \rho_{00}, \quad (48.49)$$

with $l + w + h = 1$. There are, thus, four independent observables, chosen as $(L_\perp^+, \gamma, P_l^+, h)$. Again, this set of variables is frame independent. Determination of the height parameter evidently requires observation from a direction other than the z^n -direction. Traditionally, the Stokes parameter $(P_4, 0, 0)$ is measured from the y^n -direction to obtain

$$h = \frac{(1 + P_l)(1 - P_4)}{4 - (1 - P_l)(1 - P_4)}. \quad (48.50)$$

Thus, all four parameters may be obtained from analysis of the light coherence, but two directions of observation are necessary. Similarly, photon correlation analysis in two planes is required to extract (γ, P_l^+, h) ; see, e.g., [5] for a discussion.

The various cases with unpolarized beams discussed in this section are summarized in Table 48.1.

Table 48.1 Summary of cases of increasing complexity and the orientation and alignment parameters necessary for unpolarized beams; N_p is the number of independent parameters, and N_d is the number of observation directions required

Variable	Sect. 48.2.1	Sect. 48.2.2	Sect. 48.2.3
Forces	Coulomb	+exchange	+spin-orbit
Representation	Wave func.	ρ_{mn}	ρ_{mn}
Refl. symmetry	+	+	+, -
Ang. mom.	L_\perp	L_\perp	L_\perp^+
Align. angle	γ	γ	γ
Linear pol.	P_l	P_l	P_l^+
Degree of pol.	$P = 1$	$P \leq 1$	$P^+ \leq 1$
Height	$h = 0$	$h = 0$	$h \geq 0$
N_p	2	3	4
N_d	1	1	2

48.3 Collisions Involving Spin-Polarized Beams

In this section, we discuss the additional information that can be gained by the application of a polarized beam compared with an unpolarized beam. Collisions with polarized electron beams are discussed in particular, but most of the ideas presented are easily generalized to beams of atoms in polarized, or otherwise prepared, states. We shall keep the order of increasing complexity introduced in the previous section.

48.3.1 The Fully Coherent Case

As can be seen in Sect. 48.2.2, a simple example of a fully coherent excitation process is $\text{He } 1^1\text{S} \rightarrow n^1\text{P}$ excitation, for which complete information can be obtained from experiments using unpolarized beams. Consequently, in this case, the application of polarized electrons will add nothing new. Also, the polarization of the scattered electron can be trivially predicted, since no change is possible in the scattering process.

48.3.2 The Incoherent Case with Conservation of Atomic Reflection Symmetry

The targets of interest here are hydrogen or light alkali atoms with an electron spin $S = \frac{1}{2}$. Since we now have the possibility of triplet (t) and singlet (s) scattering, this doubles the number of scattering amplitudes from two to four (recall that $f_0 = 0$); see Fig. 48.6.

The amplitudes of interest are

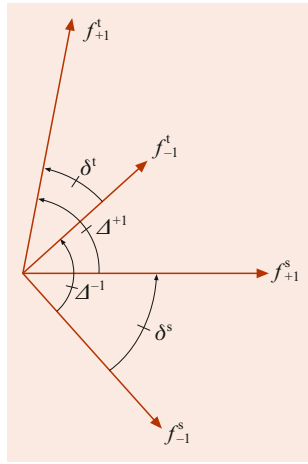
$$f_{+1}^t = \alpha_+ e^{i\phi_+}, \quad (48.51)$$

$$f_{-1}^t = \alpha_- e^{i\phi_-}, \quad (48.52)$$

$$f_{+1}^s = \beta_+ e^{i\psi_+}, \quad (48.53)$$

$$f_{-1}^s = \beta_- e^{i\psi_-}. \quad (48.54)$$

Fig. 48.6 For ${}^2S \rightarrow {}^2P$ electron impact excitation of hydrogen or light alkali atoms, four scattering amplitudes come into play



Neglecting an overall phase, seven independent parameters are needed to characterize the amplitudes completely. Traditionally, one is chosen as the differential cross section σ_u corresponding to unpolarized particles. Six additional dimensionless parameters may be defined: three to characterize the relative lengths of the four vectors, and three to define their relative phase angles.

The density matrix is parametrized, in analogy to the unpolarized beam case, according to [15]

$$\rho^t = \sigma^t \frac{1}{2} \begin{pmatrix} 1 + L_{\perp}^t & 0 & -P_l^t e^{-2i\gamma^t} \\ 0 & 0 & 0 \\ -P_l^t e^{2i\gamma^t} & 0 & 1 - L_{\perp}^t \end{pmatrix}, \quad (48.55)$$

$$\rho^s = \sigma^s \frac{1}{2} \begin{pmatrix} 1 + L_{\perp}^s & 0 & -P_l^s e^{-2i\gamma^s} \\ 0 & 0 & 0 \\ -P_l^s e^{2i\gamma^s} & 0 & 1 - L_{\perp}^s \end{pmatrix}, \quad (48.56)$$

where

$$\sigma^t = \alpha_+^2 + \alpha_-^2, \quad (48.57)$$

$$\sigma^s = \beta_+^2 + \beta_-^2, \quad (48.58)$$

$$L_{\perp}^t = \frac{1}{\sigma^t} (\alpha_+^2 - \alpha_-^2), \quad (48.59)$$

$$L_{\perp}^s = \frac{1}{\sigma^s} (\beta_+^2 - \beta_-^2), \quad (48.60)$$

$$P_l^t e^{2i\gamma^t} = P_1^t + iP_2^t = -\frac{2\alpha_+\alpha_-}{\sigma^t} e^{-i\delta^t}, \quad (48.61)$$

$$P_l^s e^{2i\gamma^s} = P_1^s + iP_2^s = -\frac{2\beta_+\beta_-}{\sigma^s} e^{-i\delta^s}. \quad (48.62)$$

In the case of an unpolarized beam, the total density matrix becomes the weighted sum of the two matrices ρ^s and ρ^t , i.e.,

$$\rho_u = \sigma_u \frac{1}{2} \begin{pmatrix} 1 + L_{\perp} & 0 & -P_l e^{-2i\gamma} \\ 0 & 0 & 0 \\ -P_l e^{2i\gamma} & 0 & 1 - L_{\perp} \end{pmatrix}$$

$$= 3w^t \sigma_u \frac{1}{2} \begin{pmatrix} 1 + L_{\perp}^t & 0 & -P_l^t e^{-2i\gamma^t} \\ 0 & 0 & 0 \\ -P_l^t e^{2i\gamma^t} & 0 & 1 - L_{\perp}^t \end{pmatrix} + w^s \sigma_u \frac{1}{2} \begin{pmatrix} 1 + L_{\perp}^s & 0 & -P_l^s e^{-2i\gamma^s} \\ 0 & 0 & 0 \\ -P_l^s e^{2i\gamma^s} & 0 & 1 - L_{\perp}^s \end{pmatrix}, \quad (48.63)$$

where

$$w^t = \frac{\sigma^t}{\sigma^s + 3\sigma^t} = \frac{\sigma^t}{4\sigma_u}, \quad (48.64)$$

$$w^s = \frac{\sigma^s}{\sigma^s + 3\sigma^t} = \frac{\sigma^s}{4\sigma_u} = 1 - 3w^t, \quad (48.65)$$

$$\sigma_u = (3w^t + w^s)\sigma_u = \frac{3}{4}\sigma^t + \frac{1}{4}\sigma^s. \quad (48.66)$$

The six parameters σ_u , w^t , L_{\perp}^t , L_{\perp}^s , γ^t , and γ^s have now been introduced, leaving one parameter still to be chosen. Inspection of Fig. 48.6 suggests, for example, the angle Δ^+ . The fourth angle, Δ^- , is then fixed through the relation

$$\Delta^+ - \Delta^- = \delta^t - \delta^s = 2(\gamma^s - \gamma^t). \quad (48.67)$$

The following set of six dimensionless parameters is thus complete

$$w^t, L_{\perp}^t, L_{\perp}^s, \gamma^t, \gamma^s, \Delta^+. \quad (48.68)$$

Detailed recipes for the extraction of the parameters from coherence experiments are somewhat complicated, and we refer to discussions in the literature [7, 15, 16]. Using spin-polarized electrons and spin-polarized targets, all parameters may be determined, except for information about singlet-triplet phase differences, such as Δ^+ .

The reduced Stokes vector \mathbf{P} of the unpolarized beam experiment is given by the singlet and triplet (unit) Stokes vectors $\mathbf{P}^{s,t}$ as

$$\mathbf{P} = 3w^t \mathbf{P}^t + w^s \mathbf{P}^s, \quad (48.69)$$

from which the set of parameters (L_{\perp}, γ, P_l) for the unpolarized beam experiment may be evaluated from

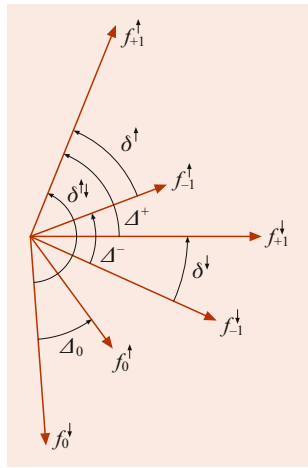
$$L_{\perp} = 3w^t L_{\perp}^t + w^s L_{\perp}^s, \quad (48.70)$$

$$P_l e^{2i\gamma} = 3w^t P_l^t e^{2i\gamma^t} + w^s P_l^s e^{2i\gamma^s}. \quad (48.71)$$

Since, in general, $L_{\perp}^t \neq L_{\perp}^s$ and $\gamma^t \neq \gamma^s$, this causes the (reduced) degree of polarization P to be smaller than unity.

To summarize this section, Stokes parameter analysis may provide five dimensionless parameters, the relative phase between the two f_{+1}^t and f_{-1}^t amplitudes and the relative phase between the two f_{+1}^s and f_{-1}^s amplitudes, as well as the relative sizes of all four amplitudes. However, none of the relative phases between any triplet and singlet amplitude can be

Fig. 48.7 For $J = 0 \rightarrow J = 1$, electron impact excitation of heavy atoms six scattering amplitudes come into play since spin-flip may occur



determined, and coherence analysis alone is, thus, not able to provide a *perfect scattering experiment*. The missing phase may be extracted from the so-called STU parameters of the scattered electron, ([16, 17] and Chap. 7).

48.3.3 The Incoherent Case Without Conservation of Atomic Reflection Symmetry

The results of coherence analysis of a $J = 0^e \rightarrow J = 1^o$ transition will now be discussed. We only analyze the photon polarization in the exit channel, not the electron spin parameters. There are six independent scattering amplitudes for a $J = 0 \rightarrow J = 1$ transition (Fig. 48.7), thereby requiring the determination of one absolute differential cross section, five relative magnitudes, and another five relative phases of the scattering amplitudes.

This large number of independent parameters leads to considerable complications. Nevertheless, the natural coordinate system enables disentangling of the scattering amplitudes and generalization of the parametrization of the density matrix for the case of unpolarized beams in a straightforward way [7, 18–20]. The nonvanishing amplitudes $f^n(M_f, m_f, m_i)$ in the natural frame (Fig. 48.7) for a $J = 0 \rightarrow J = 1$ transition are

$$f^n\left(1, \frac{1}{2}, \frac{1}{2}\right) \equiv f_{+1}^{\uparrow} = \alpha_+ e^{i\phi_+}, \quad (48.72)$$

$$f^n\left(1, -\frac{1}{2}, -\frac{1}{2}\right) \equiv f_{+1}^{\downarrow} = \beta_+ e^{i\psi_+}, \quad (48.73)$$

$$f^n\left(-1, \frac{1}{2}, \frac{1}{2}\right) \equiv f_{-1}^{\uparrow} = \alpha_- e^{i\phi_-}, \quad (48.74)$$

$$f^n\left(-1, -\frac{1}{2}, -\frac{1}{2}\right) \equiv f_{-1}^{\downarrow} = \beta_- e^{i\psi_-}, \quad (48.75)$$

$$f^n\left(0, \frac{1}{2}, -\frac{1}{2}\right) \equiv f_0^{\downarrow} = \beta_0 e^{i\psi_0}, \quad (48.76)$$

$$f^n\left(0, -\frac{1}{2}, \frac{1}{2}\right) \equiv f_0^{\uparrow} = \alpha_0 e^{i\phi_0}, \quad (48.77)$$

where we have omitted $J_i = M_i = 0$ and $J_f = 1$. Equations (48.72)–(48.75) represent noflip amplitudes that leave the projectile spin unchanged, while Eqs. (48.76) and (48.77) describe the cases where the electron spin is flipped.

We first assume a polarization perpendicular to the scattering plane, i.e., along the z -direction. In Eq. (48.44), the density matrix for heavy atoms such as Xe or Hg was decomposed into a pair of matrices with one having positive reflection symmetry with respect to the scattering plane, and the other one having negative reflection symmetry, respectively. The extension of this decomposition to the case of polarized electron beams is a pair of density matrices, one for spin-up electron impact excitation and one for spin-down excitation, where *up* and *down* correspond to the initial spin component orientation with respect to the scattering plane. Hence,

$$\begin{aligned} \rho_u &= \sigma_u \left[(1-h) \frac{1}{2} \begin{pmatrix} 1 + L_{\perp}^+ & 0 & -P_l^+ e^{-2i\gamma} \\ 0 & 0 & 0 \\ -P_l^+ e^{2i\gamma} & 0 & 1 - L_{\perp}^+ \end{pmatrix} \right. \\ &\quad \left. + h \begin{pmatrix} 0 & 0 & 0 \\ 0 & 1 & 0 \\ 0 & 0 & 0 \end{pmatrix} \right] \\ &= w^{\uparrow} \rho^{\uparrow} + w^{\downarrow} \rho^{\downarrow} \\ &= w^{\uparrow} \sigma_u \left[(1-h^{\uparrow}) \frac{1}{2} \right. \\ &\quad \times \begin{pmatrix} 1 + L_{\perp}^{+\uparrow} & 0 & -P_l^{+\uparrow} e^{-2i\gamma^{\uparrow}} \\ 0 & 0 & 0 \\ -P_l^{+\uparrow} e^{2i\gamma^{\uparrow}} & 0 & 1 - L_{\perp}^{+\uparrow} \end{pmatrix} \\ &\quad \left. + h^{\uparrow} \begin{pmatrix} 0 & 0 & 0 \\ 0 & 1 & 0 \\ 0 & 0 & 0 \end{pmatrix} \right] \\ &\quad + w^{\downarrow} \sigma_u \left[(1-h^{\downarrow}) \frac{1}{2} \right. \\ &\quad \times \begin{pmatrix} 1 + L_{\perp}^{+\downarrow} & 0 & -P_l^{+\downarrow} e^{-2i\gamma^{\downarrow}} \\ 0 & 0 & 0 \\ -P_l^{+\downarrow} e^{2i\gamma^{\downarrow}} & 0 & 1 - L_{\perp}^{+\downarrow} \end{pmatrix} \\ &\quad \left. + h^{\downarrow} \begin{pmatrix} 0 & 0 & 0 \\ 0 & 1 & 0 \\ 0 & 0 & 0 \end{pmatrix} \right]. \quad (48.78) \end{aligned}$$

Here, we have defined

$$L_{\perp}^{+\uparrow} = \frac{\alpha_+^2 - \alpha_-^2}{\alpha_+^2 + \alpha_-^2} = -P_3^{\uparrow}, \quad (48.79)$$

$$L_{\perp}^{+\downarrow} = \frac{\beta_+^2 - \beta_-^2}{\beta_+^2 + \beta_-^2} = -P_3^{\downarrow}, \quad (48.80)$$

$$P_l^{+\uparrow} e^{2i\gamma^{\uparrow}} = P_1^{\uparrow} + iP_2^{\uparrow} = -\frac{2\alpha_+\alpha_- e^{i(\phi_- - \phi_+)}}{\alpha_+^2 + \alpha_-^2}, \quad (48.81)$$

$$P_l^{+\downarrow} e^{2i\gamma^{\downarrow}} = P_1^{\downarrow} + iP_2^{\downarrow} = -\frac{2\beta_+\beta_- e^{i(\psi_- - \psi_+)}}{\beta_+^2 + \beta_-^2}, \quad (48.82)$$

$$\sigma^{\uparrow} = \alpha_+^2 + \alpha_-^2 + \alpha_0^2, \quad (48.83)$$

$$\sigma^{\downarrow} = \beta_+^2 + \beta_-^2 + \beta_0^2, \quad (48.84)$$

$$\begin{aligned} \sigma_u &= \frac{1}{2} (\alpha_+^2 + \alpha_-^2 + \alpha_0^2 + \beta_+^2 + \beta_-^2 + \beta_0^2) \\ &= \frac{1}{2} (\sigma^{\uparrow} + \sigma^{\downarrow}), \end{aligned} \quad (48.85)$$

$$h^{\uparrow} = \alpha_0^2 / \sigma^{\uparrow}, \quad (48.86)$$

$$h^{\downarrow} = \beta_0^2 / \sigma^{\downarrow}, \quad (48.87)$$

$$w^{\uparrow} = \sigma^{\uparrow} / (2\sigma_u), \quad (48.88)$$

$$w^{\downarrow} = \sigma^{\downarrow} / (2\sigma_u) = 1 - w^{\uparrow}. \quad (48.89)$$

From these definitions it follows that

$$\begin{aligned} (1-h)L_{\perp}^+ &= w^{\uparrow} (1-h^{\uparrow}) L_{\perp}^{+\uparrow} \\ &\quad + w^{\downarrow} (1-h^{\downarrow}) L_{\perp}^{+\downarrow}, \end{aligned} \quad (48.90)$$

$$\begin{aligned} (1-h)P_l^+ e^{2i\gamma} &= w^{\uparrow} (1-h^{\uparrow}) P_l^{+\uparrow} e^{2i\gamma^{\uparrow}} \\ &\quad + w^{\downarrow} (1-h^{\downarrow}) P_l^{+\downarrow} e^{2i\gamma^{\downarrow}}, \end{aligned} \quad (48.91)$$

$$\begin{aligned} h &= w^{\uparrow} h^{\uparrow} + w^{\downarrow} h^{\downarrow} \\ &= (\alpha_0^2 + \beta_0^2) / (2\sigma_u), \end{aligned} \quad (48.92)$$

$$P_l^{+\uparrow 2} + L_{\perp}^{+\uparrow 2} = P_l^{+\downarrow 2} + P_3^{\uparrow 2} = 1, \quad (48.93)$$

$$P_l^{+\downarrow 2} + L_{\perp}^{+\downarrow 2} = P_l^{+\downarrow 2} + P_3^{\downarrow 2} = 1. \quad (48.94)$$

Extraction of these parameters is facilitated by the introduction of *generalized Stokes parameters* [18]. In this way, $L_{\perp}^{+\uparrow}$, $L_{\perp}^{+\downarrow}$, γ^{\uparrow} , γ^{\downarrow} may be determined. If, in addition, h is known, e.g., by polarization analysis in the y -direction, the following set of seven dimensionless independent parameters can be derived from the generalized Stokes parameters in the z -direction

$$L_{\perp}^{+\uparrow}, L_{\perp}^{+\downarrow}, h^{\uparrow}, h^{\downarrow}, w^{\uparrow}; \gamma^{\uparrow}, \gamma^{\downarrow}. \quad (48.95)$$

This leaves three relative phases unknown. In the notation of Fig. 48.7, we can see from inspection that

$$\Delta^+ - \Delta^- = \delta^{\uparrow} - \delta^{\downarrow} = 2(\gamma^{\downarrow} - \gamma^{\uparrow}), \quad (48.96)$$

Table 48.2 Summary of cases of increasing complexity for spin-polarized beams. The number of independent dimensionless parameters N_p is listed, along with N_{OA} , the number determined from orientation and alignment only; N_d is the number of observation directions required

Variable	Sect. 48.3.1	Sect. 48.3.2	Sect. 48.3.3
Forces	Coulomb	+exchange	+spin-orbit
Representation	Wave func.	ρ_{mn}^{ts}	$\rho_{mn}^{\uparrow,\downarrow}$
Refl. symmetry	+	+	+, -
N_p	2	6	10
N_{OA}	2	5	9
N_d	1	1	2

in analogy to Eq. (48.67). A convenient choice for the remaining phase angles is $(\Delta^+, \Delta^0, \delta^{\uparrow,\downarrow})$, with

$$\delta^{\uparrow,\downarrow} \equiv \phi_+ - \psi_0. \quad (48.97)$$

A complete set of dimensionless independent parameters is then given by

$$(w^{\uparrow}, L_{\perp}^{+\uparrow}, L_{\perp}^{+\downarrow}, h^{\uparrow}, h^{\downarrow}, \gamma^{\uparrow}, \gamma^{\downarrow}, \Delta^+, \Delta^0, \delta^{\uparrow,\downarrow}). \quad (48.98)$$

Information about the remaining three phase angles may be obtained in experiments with *in-plane* spin polarization. Further analysis shows that the generalized Stokes parameters in the y (or x)-direction with in-plane spin polarization P_y or P_x provides two additional phases. None of the relative phases Δ^+ between f_{+1}^{\uparrow} and f_{+1}^{\downarrow} , etc., enter. Determination of the final remaining angle requires determination of generalized STU parameters, describing the electron spin in the exit channel.

Table 48.2 summarizes the various cases with polarized beams discussed in this section.

48.4 Example

48.4.1 The First Born Approximation

As a simple, illustrative example, consider the predictions of the first Born approximation (FBA). Here, $S \rightarrow P$ excitation by electron impact is described as creation of a pure p -orbital along the direction of the linear momentum transfer $\Delta\mathbf{k} = \mathbf{k}_{in} - \mathbf{k}_{out}$, along which there is axial symmetry. Evidently,

$$L_{\perp}^{FBA} = 0, \quad (48.99)$$

and, consequently,

$$P_l^{FBA} = 1. \quad (48.100)$$

The alignment angle is found from simple geometrical considerations; see Fig. 48.8. Denoting the incident energy by E

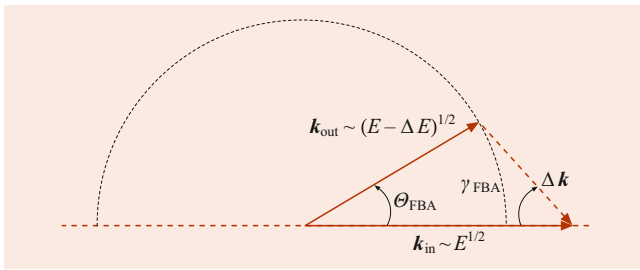


Fig. 48.8 Diagram for evaluation of the alignment angle γ in the first Born approximation

and the energy loss by ΔE , the relation between the projectile scattering angle Θ_{col} and the alignment angle γ is directly read from the figure,

$$\tan \gamma^{\text{FBA}} = \frac{\sin \Theta_{\text{col}}}{\cos \Theta_{\text{col}} - x}, \quad (48.101)$$

where $x = [E/(E - \Delta E)]^{1/2}$. For $\Delta E > 0$, γ^{FBA} is always negative, with its minimum value when $\Delta \mathbf{k} \perp \mathbf{k}_{\text{out}}$. Any theoretical effort beyond the FBA involves serious computations.

48.5 Further Developments

48.5.1 S \rightarrow D Excitation

The generalization of the formalism of Sect. 48.3.2 to the case of S \rightarrow D excitation involves the introduction of three scattering amplitudes, corresponding to a complete parameter set of one cross section, two relative amplitude sizes, and two relative phases. Analysis shows that a full coherence analysis of the light emitted in the subsequent D \rightarrow P optical decay is not sufficient for a complete experiment, instead two solutions are obtained. A triple coincidence experiment may resolve the ambiguity [21].

48.5.2 P \rightarrow P Excitation

By proper optical preparation of the atomic target, collision studies involving specific excited states may be performed as a function of the scattering angle. For collision-induced P \rightarrow P transitions, a systematic preparation of specific initial P-states, combined with Stokes parameter analysis of the radiation pattern from the final P-state, may lead to a complete scattering experiment. The corresponding complete set of nine parameters describes the process in terms of five independent scattering amplitudes. In addition to the charge cloud shape and orientation parameters, three Euler angles are needed to describe the atomic reference frame of the charge cloud with respect to the laboratory frame [22].

48.5.3 Relativistic Effects in S \rightarrow P Excitation

It has been discussed to what extent relativistic effects can be studied for excitation of the two fine structure components of the resonance transitions of heavy alkali atoms, such as Rb or Cs. For electron-impact excitation, standard Stokes parameter analysis turns out to be extremely insensitive to the inclusion of relativistic effects in the numerical treatment, which explains the success of nonrelativistic theories. If spin-polarized electrons are used, either in the incident channel through measurement of spin asymmetries or in the final channels by performing a time-reversed generalized Stokes parameter experiment with a laser-prepared target and a spin-polarized electron beam, distinct relativistic effects, typically at the 5% level, may be revealed [23].

48.6 Summary

A selection of fundamental formulas describing orientation and alignment in atomic collisions is given, with emphasis on the simplest case, S \rightarrow P excitation. A tutorial introduction to the field with a series of examples and applications may be found in a recent textbook [20]. Other examples and discussions of perfect scattering experiments may be found in [24].

References

1. Bederson, B.: *Comments At. Mol. Phys.* **1**, 41 and 65 (1969)
2. Fano, U., Macek, J.H.: *Rev. Mod. Phys.* **45**, 553 (1973)
3. Kessler, J.: *Polarized Electrons*. Springer, Berlin, Heidelberg (1985)
4. Hertel, I.V., Schmidt, H., Bähring, A., Meyer, E.: *Rep. Prog. Phys.* **48**, 375 (1985)
5. Andersen, N., Gallagher, J.W., Hertel, I.V.: *Phys. Rep.* **165**, 1 (1988)
6. Andersen, N., Broad, J.T., Campbell, E.E.B., Gallagher, J.W., Hertel, I.V.: *Phys. Rep.* **278**, 107 (1997)
7. Andersen, N., Bartschat, K., Broad, J.T., Hertel, I.V.: *Phys. Rep.* **279**, 251 (1997)
8. Wille, U., Hippler, R.: *Phys. Rep.* **132**, 129 (1986)
9. Greene, C.H., Zare, R.N.: *Ann. Rev. Phys. Chem.* **33**, 119 (1982)
10. Blum, K.: *Density Matrix Theory and Applications*. Plenum, New York (1981)
11. Macek, J., Jaecks, D.H.: *Phys. Rev. A* **4**, 2288 (1971)
12. Born, M., Wolf, E.: *Principles of Optics*. Pergamon, New York (1970)
13. Blum, K., da Paixão, F.T., Csanak, G.: *J. Phys. B* **13**, L257 (1980)
14. da Paixão, F.T., Padial, N.T., Csanak, G., Blum, K.: *Phys. Rev. Lett.* **45**, 1164 (1980)
15. Hertel, I.V., Kelley, M.H., McClelland, J.J.: *Z. Phys. D* **6**, 163 (1987)
16. Andersen, N., Bartschat, K.: *Comments At. Mol. Phys.* **29**, 157 (1993)
17. Bartschat, K.: *Phys. Rep.* **180**, 1 (1989)
18. Andersen, N., Bartschat, K.: *J. Phys. B* **27**, 3189 (1994)

19. Andersen, N., Bartschat, K.: corrigendum. *J. Phys. B* **29**, 1149 (1996)
20. Andersen, N., Bartschat, K.: *Polarization, Alignment, and Orientation in Atomic Collisions*, 2nd edn. Springer, Cham (2017)
21. Andersen, N., Bartschat, K.: *J. Phys. B* **30**, 5071 (1997)
22. Sidky, E.Y., Grego, S., Dowek, D., Andersen, N.: *J. Phys. B* **35**, 2005 (2002)
23. Andersen, N., Bartschat, K.: *J. Phys.* **35**, 4507 (2002)
24. Kleinpoppen, H., Lohmann, B., Grum-Grzhimailo, A.N.: *Perfect/Complete Scattering Experiments*. Springer, Berlin, Heidelberg (2013)
25. Muktavat, K., Srivastava, R., Stauffer, A.D.: *J. Phys. B* **36**, 2341 (2003)



Nils Andersen Nils Andersen is Professor of Physics at the Niels Bohr Institute of the University of Copenhagen. His main activities include experimental and theoretical studies of atomic collisions involving optically prepared states. Recent research interests include cold and ultracold collisions.



Electron–Atom, Electron–Ion, and Electron–Molecule Collisions

49

Klaus Bartschat , Jonathan Tennyson , and Philip Burke

Contents

49.1	Electron–Atom and Electron–Ion Collisions	725
49.1.1	Low-Energy Elastic Scattering and Excitation	725
49.1.2	Relativistic Effects for Heavy Atoms and Ions	728
49.1.3	Multichannel Resonance Theory	729
49.1.4	Solution of the Coupled Integro-Differential Equations and Excitation	731
49.1.5	Intermediate and High-Energy Elastic Scattering	735
49.1.6	Ionization	737
49.2	Electron–Molecule Collisions	741
49.2.1	Laboratory Frame Representation	741
49.2.2	Molecular Frame Representation	742
49.2.3	Inclusion of the Nuclear Motion	742
49.2.4	Electron Collisions with Polyatomic Molecules	744
49.3	Electron–Atom Collisions in a Laser Field	744
49.3.1	Potential Scattering	744
49.3.2	Scattering by Complex Atoms and Ions	746
References	747

Abstract

This chapter summarizes the theory of electron collisions with atoms, ions, and molecules. Section 49.1 discusses elastic, inelastic, and ionizing collisions with atoms and atomic ions from close to threshold to high energies where the Born series becomes applicable. Section 49.2 extends the theory to treat electron collisions with molecules. Finally, the theory of electron–atom collisions in intense laser fields is discussed in Sect. 49.3. This chapter will not present detailed comparisons of theoretical predictions with experiment. Such comparisons are given in many books and review articles, such as [1–6]. The need

for proper uncertainty quantification in such calculations has recently been emphasized [7].

Keywords

electron collisions · scattering amplitudes and cross sections · potential scattering · born series · resonance theory · collisions in laser fields · optical-potential method · coupled-channel methods · close-coupling expansion

49.1 Electron–Atom and Electron–Ion Collisions

49.1.1 Low-Energy Elastic Scattering and Excitation

In this section, we consider the process

$$e^- + A_i \rightarrow e^- + A_j, \quad (49.1)$$

where A_i and A_j are bound states of the target atom or ion and where the speed of the incident or scattered electron is of the same order or less than that of the target electrons actively involved in the collision.

We assume initially that all relativistic effects can be neglected, which restricts the treatment to low- Z atoms and ions. The time-independent Schrödinger equation (TISE) describing the scattering of an electron by a target atom or ion containing N electrons and nuclear charge Z is

$$H_{N+1}\Psi = E\Psi, \quad (49.2)$$

where E is the total energy of the system. The $(N + 1)$ -electron nonrelativistic Hamiltonian H_{N+1} is given in atomic units by

$$H_{N+1} = \sum_{i=1}^{N+1} \left(-\frac{1}{2} \nabla_i^2 - \frac{Z}{r_i} \right) + \sum_{i>j=1}^{N+1} \frac{1}{r_{ij}}, \quad (49.3)$$

K. Bartschat (✉)
Dept. of Physics & Astronomy, Drake University
Des Moines, IA, USA
e-mail: klaus.bartschat@drake.edu

J. Tennyson
Dept. of Physics & Astronomy, University College London
London, UK
e-mail: j.tennyson@ucl.ac.uk

where $r_{ij} = |\mathbf{r}_i - \mathbf{r}_j|$, and \mathbf{r}_i and \mathbf{r}_j are the vector coordinates of electrons i and j relative to the origin of coordinates taken to be the target nucleus, which is assumed to have infinite mass.

The target eigenstates Φ_i and the corresponding eigenenergies w_i satisfy the equation

$$\langle \Phi_i | H_N | \Phi_j \rangle = w_i \delta_{ij}, \quad (49.4)$$

where H_N is defined by Eq. (49.3) with $N + 1$ replaced by N . The calculation of accurate target states is discussed in Chap. 22. The solution of Eq. (49.2), corresponding to the process Eq. (49.1), has the asymptotic form

$$\Psi_i \underset{r \rightarrow \infty}{\approx} \Phi_i \chi_{\frac{1}{2}m_i} e^{ik_i z} + \sum_j \Phi_j \chi_{\frac{1}{2}m_j} f_{ji}(\theta, \phi) e^{ik_j r}. \quad (49.5)$$

In Eq. (49.5), $\chi_{\frac{1}{2}m_i}$ and $\chi_{\frac{1}{2}m_j}$ are the spin eigenfunctions of the incident and scattered electrons, where the direction of spin quantization is usually taken to be the incident beam direction, and $f_{ji}(\theta, \phi)$ is the scattering amplitude. The spherical polar coordinates of the scattered electron are denoted by r, θ , and ϕ . The wave numbers k_i and k_j are related to the total energy of the system by

$$E = w_i + \frac{1}{2}k_i^2 = w_j + \frac{1}{2}k_j^2. \quad (49.6)$$

The outgoing-wave term in Eq. (49.5) contains contributions from all target states that are energetically allowed; i.e., for which $k_j^2 \geq 0$. If the energy is above the ionization threshold, this includes target continuum states. For an atomic ion, a logarithmic phase factor is also needed (see Eq. (49.16)).

The differential cross section for a transition from an initial state $|i\rangle = |\mathbf{k}_i, \Phi_i, \chi_{\frac{1}{2}m_i}\rangle$ to a final state $|j\rangle = |\mathbf{k}_j, \Phi_j, \chi_{\frac{1}{2}m_j}\rangle$ is given by

$$\frac{d\sigma_{ji}}{d\Omega} = \frac{k_j}{k_i} |f_{ji}(\theta, \phi)|^2, \quad (49.7)$$

and the total cross section is obtained by averaging over initial spin states, summing over final spin states, and integrating over all scattering angles.

In order to solve the Schrödinger equation to obtain the scattering amplitude and cross section at low energies, we make a partial-wave expansion of the total wave function

$$\begin{aligned} \Psi_j^\Gamma(\mathbf{X}_{N+1}) &= \mathcal{A} \sum_{i=1}^n \overline{\Phi}_i^\Gamma(\mathbf{x}_1, \dots, \mathbf{x}_N; \hat{\mathbf{r}}_{N+1} \sigma_{N+1}) \frac{F_{ij}^\Gamma(r_{N+1})}{r_{N+1}} \\ &+ \sum_{i=1}^m \chi_i^\Gamma(\mathbf{x}_1, \dots, \mathbf{x}_{N+1}) b_{ij}^\Gamma, \end{aligned} \quad (49.8)$$

where $\mathbf{X}_{N+1} \equiv \mathbf{x}_1, \mathbf{x}_2, \dots, \mathbf{x}_{N+1}$ represents the space and spin coordinates of all $N + 1$ electrons, $\mathbf{x}_i \equiv \mathbf{r}_i \sigma_i$ represents the space and spin coordinates of the i -th electron, and \mathcal{A} is the operator that antisymmetrizes the first summation with respect to exchange of all pairs of electrons in accordance with the Pauli exclusion principle. The channel functions $\overline{\Phi}_i^\Gamma$, assumed to be n in number, are obtained by coupling the orbital and spin angular momenta of the target states Φ_i with those of the scattered electron to form eigenstates of the total orbital and spin angular momenta L and S , their z components M_L and M_S , and the parity π , where

$$\Gamma \equiv LM_L SM_S \pi \quad (49.9)$$

is conserved in the collision. The square-integrable correlation functions χ_i^Γ allow for additional correlation effects not included in the first expansion in Eq. (49.8), which goes over a limited number of target eigenstates and possibly pseudo-states.

By substituting Eq. (49.8) into the Schrödinger equation (49.2), projecting onto the channel functions $\overline{\Phi}_i^\Gamma$ and the square-integrable functions χ_i^Γ , and eliminating the coefficients b_{ij}^Γ , we obtain n coupled integro-differential equations satisfied by the reduced radial functions F_{ij}^Γ representing the motion of the scattered electron

$$\begin{aligned} \left(\frac{d^2}{dr^2} - \frac{\ell_i(\ell_i + 1)}{r^2} + \frac{2(Z - N)}{r} + k_i^2 \right) F_{ij}^\Gamma(r) &= 2 \sum_{\ell} \left\{ V_{i\ell}^\Gamma(r) F_{\ell j}^\Gamma(r) \right. \\ &+ \left. \int_0^\infty [K_{i\ell}^\Gamma(r, r') + X_{i\ell}^\Gamma(r, r')] F_{\ell j}^\Gamma(r') dr' \right\}. \end{aligned} \quad (49.10)$$

Here, ℓ_i is the orbital angular momentum of the scattered electron, while $V_{i\ell}^\Gamma$, $W_{i\ell}^\Gamma$, and $X_{i\ell}^\Gamma$ are the local direct, nonlocal exchange, and nonlocal correlation potentials, respectively. If the correlation potential, which arises from the χ_i^Γ terms in Eq. (49.8), is not included, Eqs. (49.10) are called the *close-coupling equations*.

The direct potential can be written as

$$\begin{aligned} V_{ij}^\Gamma(r_{N+1}) &= \left\langle \overline{\Phi}_i^\Gamma(\mathbf{x}_1, \dots, \mathbf{x}_N; \hat{\mathbf{r}}_{N+1} \sigma_{N+1}) \right| \\ &\times \sum_{i=1}^N \frac{1}{r_{iN+1}} - \frac{N}{r_{N+1}} \\ &\times \left| \overline{\Phi}_j^\Gamma(\mathbf{x}_1, \dots, \mathbf{x}_N; \hat{\mathbf{r}}_{N+1} \sigma_{N+1}) \right\rangle, \end{aligned} \quad (49.11)$$

where the integral is taken over all electron space and spin coordinates, except for the radial coordinate of the $(N + 1)$ -th

electron. This potential has the asymptotic form

$$V_{ij}^{\Gamma}(r) = \sum_{\lambda=1}^{\lambda_{\max}} a_{ij}^{\lambda} r^{-\lambda-1} \quad \text{for } r \geq a, \quad (49.12)$$

where a is the range beyond which the orbitals in the target states Φ_i included in the first expansion in Eq. (49.8) are negligible. The $\lambda = 1$ term in Eq. (49.12) gives rise, in second order, to the long-range attractive polarization potential

$$V(r) \xrightarrow{r \rightarrow \infty} -\frac{1}{2} \frac{\alpha}{r^4} \quad (49.13)$$

seen by an electron incident on an atom. For an S -state atom in a state Φ_0 , the dipole polarizability α is given by

$$\alpha = 2 \sum_j \frac{|\langle \Phi_0 | (\frac{4\pi}{3})^{1/2} \sum_{i=1}^N r_i Y_{10}(\hat{r}_i) | \Phi_j \rangle|^2}{w_j - w_0}. \quad (49.14)$$

These long-range potentials have a profound influence on low-energy scattering.

The exchange and correlation potentials, unlike the direct potential, are both nonlocal, and the exchange potential vanishes exponentially for large r . Explicit expressions for these potentials are too complicated to write down, except in the case of e–H scattering, for which the direct and exchange potentials were first given by *Percival* and *Seaton* [8]. In practice, they are evaluated by general computer programs.

The scattering amplitude and cross section can be obtained by solving Eq. (49.10) for all relevant conserved quantum numbers Γ subject to the \mathbf{K} -matrix asymptotic boundary conditions

$$\begin{aligned} F_{ij}^{\Gamma} &\underset{r \rightarrow \infty}{\approx} k_i^{-1/2} \left(\sin \theta_i \delta_{ij} + \cos \theta_i K_{ij}^{\Gamma} \right) \\ &\quad \text{for open channels } (k_i^2 \geq 0); \\ F_{ij}^{\Gamma} &\underset{r \rightarrow \infty}{\approx} 0 \\ &\quad \text{for closed channels } (k_i^2 < 0). \end{aligned} \quad (49.15)$$

Here,

$$\theta_i = k_i r - \frac{1}{2} \ell_i \pi + \frac{z}{k_i} \ln(2k_i r) + \sigma_i, \quad (49.16)$$

with $z = Z - N$ and $\sigma_i = \arg \Gamma(\ell_i + 1 - iz/k_i)$. The \mathbf{S} -matrix and \mathbf{T} -matrix are related to the \mathbf{K} -matrix defined by Eq. (49.15) through the matrix equations

$$\mathbf{S}^{\Gamma} = \frac{\mathbf{I} + i\mathbf{K}^{\Gamma}}{\mathbf{I} - i\mathbf{K}^{\Gamma}}, \quad \mathbf{T}^{\Gamma} = \mathbf{S}^{\Gamma} - \mathbf{I} = \frac{2i\mathbf{K}^{\Gamma}}{\mathbf{I} - i\mathbf{K}^{\Gamma}}. \quad (49.17)$$

The dimensions of the matrices in these equations are $n_a \times n_a$, where n_a is the number of open channels at the energy under consideration for the given Γ . The hermiticity and time-reversal invariance of the Hamiltonian ensures that \mathbf{K}^{Γ} is real and symmetric, while \mathbf{S}^{Γ} is unitary and symmetric.

The scattering amplitude defined by Eq. (49.5) can be expressed in terms of the \mathbf{T} -matrix elements. For a neutral target,

$$\begin{aligned} f_{ji}(\theta, \phi) &= i \left(\frac{\pi}{k_i k_j} \right)^{1/2} \sum_{\substack{LS\pi \\ \ell_i \ell_j}} i^{\ell_i - \ell_j} (2\ell_i + 1)^{1/2} \\ &\quad \times (L_i M_{L_i} \ell_i 0 | L M_L) \\ &\quad \times \left(S_i M_{S_i} \frac{1}{2} m_i | S M_S \right) \\ &\quad \times (L_j M_{L_j} \ell_j m_{\ell_j} | L M_L) \\ &\quad \times \left(S_j M_{S_j} \frac{1}{2} m_j | S M_S \right) T_{ji}^{\Gamma} Y_{\ell_j m_{\ell_j}}(\theta, \phi) \end{aligned} \quad (49.18)$$

describes a transition from an initial state $\alpha_i L_i S_i M_{L_i} M_{S_i} m_i$ to a final state $\alpha_j L_j S_j M_{L_j} M_{S_j} m_j$, where α_i and α_j represent any additional quantum numbers required to completely define the initial and final states, and $(j_1 m_1 j_2 m_2 | J M)$ is a Clebsch–Gordan coefficient. The corresponding total cross section, obtained by averaging over the initial magnetic quantum numbers, summing over the final magnetic quantum numbers, and integrating over all scattering angles, is

$$\sigma_{\text{tot}}(i \rightarrow j) = \frac{\pi}{k_i^2} \sum_{\substack{LS\pi \\ \ell_i \ell_j}} \frac{(2L+1)(2S+1)}{2(2L_i+1)(2S_i+1)} \left| T_{ji}^{\Gamma} \right|^2. \quad (49.19)$$

It describes a transition from an initial target state $\alpha_i L_i S_i$ to a final target state $\alpha_j L_j S_j$. In applications, it is also useful to define a collision strength by

$$\Omega(i, j) = k_i^2 (2L_i + 1)(2S_i + 1) \sigma_{\text{tot}}(i \rightarrow j), \quad (49.20)$$

which is dimensionless and symmetric with respect to interchange of the initial and final states denoted by i and j . For scattering by an ion, the above expression for $f_{ji}(\theta, \phi)$ is modified by the inclusion of the Coulomb scattering amplitude when the initial and final states are identical.

For incident electron energies insufficient to excite the atom or ion, only elastic scattering is possible, and the above expressions simplify. Consider low-energy elastic electron scattering by a neutral atom in a 1S ground state. Then the expression for the scattering amplitude Eq. (49.18) reduces to

$$f(\theta) = \frac{1}{2ik} \sum_{\ell=0}^{\infty} (2\ell+1) (e^{2i\delta_{\ell}} - 1) P_{\ell}(\cos \theta), \quad (49.21)$$

where ℓ ($= L = \ell_i = \ell_j$) is the angular momentum of the scattered electron, k is its wave number, and the phase shift δ_ℓ can be expressed in terms of the \mathbf{K} -matrix, which now has only one element, since $n_a = 1$, given by

$$\tan \delta_\ell = K_{11}^\Gamma. \quad (49.22)$$

The corresponding expression for the total cross section is then

$$\sigma_{\text{tot}} = \frac{4\pi}{k^2} \sum_{\ell=0}^{\infty} (2\ell + 1) \sin^2 \delta_\ell. \quad (49.23)$$

The momentum-transfer cross section is defined as

$$\begin{aligned} \sigma_{\text{D}} &= 2\pi \int_0^\pi |f(\theta)|^2 (1 - \cos \theta) \sin \theta d\theta \\ &= \frac{4\pi}{k^2} \sum_{\ell=0}^{\infty} (\ell + 1) \sin^2(\delta_{\ell+1} - \delta_\ell). \end{aligned} \quad (49.24)$$

This cross section is important when considering the diffusion of electrons through gases.

At low incident electron energies, the behavior of the phase shift for an atom in an S-state is dominated by the long-range polarization potential Eq. (49.13). *O'Malley* et al. [9] showed that for s -wave scattering $k \cot \delta_0$ satisfies the effective-range expansion

$$\begin{aligned} k \cot \delta_0 &= -\frac{1}{a_s} + \frac{\pi\alpha}{3a_s^2} k \\ &\quad + \frac{2\alpha}{3a_s} k^2 \ln\left(\frac{\alpha k^2}{16}\right) + O(k^2), \end{aligned} \quad (49.25)$$

where a_s is the scattering length, while for $\ell \geq 1$

$$k^2 \cot \delta_\ell = \frac{8(\ell + \frac{3}{2})(\ell + \frac{1}{2})(\ell - \frac{1}{2})}{\pi\alpha} + \dots \quad (49.26)$$

Higher-order terms, which extend the energy range of usefulness of the expansion, were derived by Ali and Fraser [10].

Close to threshold, therefore, the total elastic cross section has the form

$$\sigma_{\text{tot}} = 4\pi a_s^2 + \frac{8}{3}\pi^2 \alpha a_s k + \dots \quad (49.27)$$

When an electron is elastically scattered by a positive or negative ion, these formulae for the low-energy behavior of the phase shift are modified. For scattering by a positive ion, *Seaton* [11] showed that

$$\frac{\cot \delta_\ell(k)}{1 - e^{2\pi\eta}} = \cot[\pi\mu(k^2)], \quad (49.28)$$

where $\eta = -z/k$, and $\mu(k^2)$ is the analytic continuation of the quantum defects of the electron-ion bound states to positive energies. This quantum-defect theory enables spectroscopic observations of bound-state energies to be extrapolated to positive energies to yield electron-ion scattering phase shifts. For a negative ion, where the Coulomb potential is repulsive, the phase shift behaves as

$$\delta_\ell \xrightarrow[k \rightarrow 0]{} \exp\left(2\pi \frac{z}{k}\right). \quad (49.29)$$

This vanishes rapidly as k tends to zero, since z is now negative. A discussion of quantum-defect theory is given in Chap. 50.

49.1.2 Relativistic Effects for Heavy Atoms and Ions

As the nuclear charge Z of the target increases, relativistic effects become important even for low-energy scattering. There are two ways in which relativistic effects play a role. First, there is a direct effect corresponding to the relativistic distortion of the wave function describing the scattered electron by the strong nuclear Coulomb potential. Second, there is an indirect effect caused by the change in the charge distribution of the target due to the use of relativistic wave functions discussed in Chap. 23. We will concentrate on the direct effect in this section.

For atoms and ions with small Z , the \mathbf{K} -matrices can first be calculated in LS -coupling while neglecting relativistic effects. The \mathbf{K} -matrices are then recoupled to yield transitions between fine-structure levels. We introduce the pair-coupling scheme

$$\mathbf{L}_i + \mathbf{S}_i = \mathbf{J}_i, \quad \mathbf{J}_i + \boldsymbol{\ell}_i = \mathbf{K}_i, \quad \mathbf{K}_i + \mathbf{s} = \mathbf{J}, \quad (49.30)$$

where \mathbf{J}_i is the total angular momentum of the target, $\boldsymbol{\ell}_i$ is the orbital angular momentum of the scattered electron, \mathbf{s} is its spin, and \mathbf{J} is the total electronic angular momentum, which together with the parity π is conserved in the collision. The transition from LS - to $J\ell K$ -coupling involves the recoupling coefficient

$$\begin{aligned} &\left\langle [(L_i S_i) J_i, \ell_i] K_i, \frac{1}{2}; J M_J \middle| (L_i \ell_i) L, \left(S_i \frac{1}{2}\right) S; J M_J \right\rangle \\ &= [(2J_i + 1)(2L + 1)(2K_i + 1)(2S + 1)]^{\frac{1}{2}} \\ &\quad \times W(L \ell_i S_i J_i; L_i K_i) W(L J S_i \frac{1}{2}; S K_i), \end{aligned} \quad (49.31)$$

where $W(\dots)$ is a Wigner 6- j -symbol. The corresponding \mathbf{K} -matrix elements transform as

$$K_{ij}^{J\pi} = \sum_{LS} \left\langle \left[(L_i S_i) J_i, \ell_i \right] K_i, \frac{1}{2}; JM_J \right\rangle \left\langle (L_i \ell_i) L, \left(S_i \frac{1}{2} \right) S; JM_J \right\rangle \times K_{ij}^F \times \left\langle (L_j \ell_j) L, \left(S_j \frac{1}{2} \right) S; JM_J \right\rangle \left\langle (L_j S_j) J_j, \ell_j \right\rangle K_j, \frac{1}{2}; JM_J \right\rangle. \quad (49.32)$$

This transformation was implemented in a computer program by *Saraph* [12, 13].

For intermediate- Z atoms and ions, relativistic effects can be included by adding terms from the Breit–Pauli Hamiltonian to the nonrelativistic Hamiltonian (*Jones* [14], *Scott and Burke* [15]). We write

$$H_{N+1}^{\text{BP}} = H_{N+1}^{\text{nr}} + H_{N+1}^{\text{rel}}, \quad (49.33)$$

where H_{N+1}^{nr} is defined by Eq. (49.3) and H_{N+1}^{rel} consists of one and two-body relativistic terms. The one-body terms are (Sect. 22.1)

$$H_{N+1}^{\text{mass}} = -\frac{1}{8}\alpha^2 \sum_{i=1}^{N+1} \nabla_i^4 \quad (\text{mass-correction term});$$

$$H_{N+1}^{\text{D1}} = -\frac{1}{8}\alpha^2 Z \sum_{i=1}^{N+1} \nabla_i^2 \left(\frac{1}{r_i} \right) \quad (\text{Darwin term});$$

$$H_{N+1}^{\text{so}} = \frac{1}{2}\alpha^2 \sum_{i=1}^{N+1} \frac{1}{r_i} \frac{\partial V}{\partial r_i} (\boldsymbol{\ell}_i \cdot \mathbf{s}_i) \quad (\text{spin-orbit term}).$$

The two-body terms are less important and are usually not included in collision calculations.

The modified Schrödinger equation defined by Eq. (49.2), with H_{N+1} replaced by H_{N+1}^{BP} , is solved by adopting an expansion similar in form to Eq. (49.8) but now using the pair-coupling scheme in the definition of the channel functions and square-integrable functions. We then obtain coupled integro-differential equations similar in form to Eq. (49.10), from which the \mathbf{K} -matrix, \mathbf{S} -matrix, and \mathbf{T} -matrix can be obtained. The corresponding total cross section in the pair-coupling scheme analogous to Eq. (49.19) is

$$\sigma_{\text{tot}}(i \rightarrow j) = \frac{\pi}{2k_i^2(2J_i + 1)} \sum_{K_i K_j \ell_i \ell_j}^{J\pi} (2J + 1) \left| T_{ji}^{J\pi} \right|^2. \quad (49.34)$$

It describes a transition from an initial target state $\alpha_i J_i$ to a final target state $\alpha_j J_j$. The corresponding collision strength is

$$\Omega(i, j) = k_i^2 (2J_i + 1) \sigma_{\text{tot}}(i \rightarrow j). \quad (49.35)$$

For high- Z atoms and ions, the Dirac Hamiltonian [16, 17]

$$H_{N+1}^{\text{D}} = \sum_{i=1}^{N+1} \left(c\boldsymbol{\alpha} \cdot \mathbf{p}_i + \boldsymbol{\beta}' c^2 - \frac{Z}{r_i} \right) + \sum_{i>j=1}^{N+1} \frac{1}{r_{ij}} \quad (49.36)$$

must be used instead of Eq. (49.3), where $\boldsymbol{\beta}' = \boldsymbol{\beta} - \mathbf{1}$ with $\boldsymbol{\alpha}$ and $\boldsymbol{\beta}$ being the usual Dirac matrices. The expansion of the total wave functions for a particular $JM_J\pi$ takes the general form of Eq. (49.8). However, now the bound orbitals in the target and the correlation functions, as well as the orbitals representing the scattered electron, are represented by Dirac orbitals. These are defined in terms of large and small components $P(r)$ and $Q(r)$ by

$$\phi(\mathbf{r}, \sigma) = \frac{1}{r} \begin{pmatrix} P_a(r) \chi_{\kappa m}(\hat{\mathbf{r}}, \sigma) \\ Q_a(r) \chi_{-\kappa m}(\hat{\mathbf{r}}, \sigma) \end{pmatrix}, \quad (49.37)$$

for the bound orbitals and

$$F(\mathbf{r}, \sigma) = \frac{1}{r} \begin{pmatrix} P_c(r) \chi_{\kappa m}(\hat{\mathbf{r}}, \sigma) \\ Q_c(r) \chi_{-\kappa m}(\hat{\mathbf{r}}, \sigma) \end{pmatrix}, \quad (49.38)$$

for the continuum orbitals. Here, $a = n\kappa m$, $c = k\kappa m$, and the spherical spinor is

$$\chi_{\kappa m}(\hat{\mathbf{r}}, \sigma) = \sum_{m_\ell m_i} \left(\ell m_\ell \frac{1}{2} m_i \mid j m \right) Y_{\ell m_\ell}(\theta, \phi) \chi_{\frac{1}{2} m_i}(\sigma), \quad (49.39)$$

where $\kappa = j + \frac{1}{2}$ when $\ell = j + \frac{1}{2}$, and $\kappa = -j - \frac{1}{2}$ when $\ell = j - \frac{1}{2}$.

One can derive coupled integro-differential equations for the functions $P_c(r)$ and $Q_c(r)$ in a similar way to the derivation of Eq. (49.10), except that these are now coupled first-order equations instead of coupled second-order equations. The \mathbf{K} -matrix, and hence the \mathbf{S} -matrix and \mathbf{T} -matrix, can be obtained from the asymptotic form of these equations. The total cross section in the jj -coupling scheme is again given by Eq. (49.34), and the corresponding collision strength is given by Eq. (49.35).

49.1.3 Multichannel Resonance Theory

General resonance theories have been developed by *Fano* [18, 19], *Feshbach* [20, 21], and *Brenig and Haag* [22].

They are also discussed in Chap. 26. Here, we will limit our discussion to the effect that resonances have on electron collision cross sections.

Following Feshbach, we introduce the projection operators P and Q , where P projects onto a finite set of low-energy channels in Eq. (49.8), and Q projects onto the orthogonal space. We limit our consideration to the space corresponding to a particular set of conserved quantum numbers Γ . In this space, we have

$$P^2 = P, \quad Q^2 = Q, \quad P + Q = 1. \quad (49.40)$$

The Schrödinger equation (49.2) can then be written as

$$P(H - E)(P + Q)\Psi = 0 \quad (49.41)$$

and

$$Q(H - E)(P + Q)\Psi = 0, \quad (49.42)$$

where we have omitted the subscript $N + 1$ on H and the superscript Γ on Ψ . After solving Eq. (49.42) for $Q\Psi$ and substituting into Eq. (49.41), we find

$$P\left(H - PHQ \frac{1}{Q(H - E)Q} QHP - E\right)P\Psi = 0, \quad (49.43)$$

where the term

$$V_{\text{opt}} = -PHQ \frac{1}{Q(H - E)Q} QHP, \quad (49.44)$$

called the *optical potential*, allows for propagation in the Q -space channels.

We now introduce the eigenfunctions ϕ_i and eigenvalues ε_i of the operator QHQ by

$$QHQ\phi_i = \varepsilon_i\phi_i. \quad (49.45)$$

It follows that the discrete eigenvalues ε_i each give rise to poles in V_{opt} at ε_i . If the energy E is in the neighborhood of an isolated pole or bound state ε_i , we can rewrite Eq. (49.43) as

$$\begin{aligned} & \left(PHP - \sum_{j \neq i} PHQ \frac{|\phi_j\rangle\langle\phi_j|}{\varepsilon_j - E} QHP - E \right) P\Psi \\ & = PHQ \frac{|\phi_i\rangle\langle\phi_i|}{\varepsilon_i - E} QHP\Psi, \end{aligned} \quad (49.46)$$

where the rapidly varying part of the optical potential has been separated and put on the right-hand side of Eq. (49.46). This equation can be solved by introducing Green's function G_0 and the solutions ψ_{0j} of the operator on the left-hand

side of Eq. (49.46). We find that the pole term on the right-hand side of this equation gives rise to a Feshbach resonance, whose position is

$$E_i = \varepsilon_i + \Delta_i - \frac{1}{2}i\Gamma_i = E_{i,r} - \frac{1}{2}i\Gamma_i, \quad (49.47)$$

where the resonance shift is

$$\Delta_i = \langle\phi_i|QHPG_0PHQ|\phi_i\rangle, \quad (49.48)$$

and the resonance width is

$$\Gamma_i = 2\pi \sum_j |\langle\phi_i|QHPP|\psi_{0j}\rangle|^2. \quad (49.49)$$

The summation in this equation is taken over all continuum states corresponding to the operator on the left-hand side of Eq. (49.46), and these states are normalized to a δ -function in energy.

In the neighborhood of the resonance energy $E_{i,r}$, the \mathcal{S} -matrix is rapidly varying with the form

$$\mathcal{S} = \mathcal{S}_0^{\frac{1}{2}} \left(\mathbf{I} - i\Gamma \frac{\boldsymbol{\gamma}_i \times \boldsymbol{\gamma}_i}{E - E_{i,r} + \frac{1}{2}i\Gamma_i} \right) \mathcal{S}_0^{\frac{1}{2}}, \quad (49.50)$$

where \mathcal{S}_0 is the slowly varying nonresonant or background \mathcal{S} -matrix corresponding to ψ_0 , and the partial widths $\boldsymbol{\gamma}_i$ are defined by

$$\langle\phi_i|QHPP|\psi_0\rangle = \Gamma_i^{\frac{1}{2}} \boldsymbol{\gamma}_i \cdot \mathcal{S}_0^{\frac{1}{2}}, \quad (49.51)$$

where $\boldsymbol{\gamma}_i \cdot \boldsymbol{\gamma}_i = 1$. A corresponding resonant expression can be derived for the \mathbf{K} -matrix (Burke [23]).

Let us now diagonalize the \mathcal{S} -matrix according to

$$\mathcal{S} = \mathbf{A} \exp(2i\boldsymbol{\Delta}) \mathbf{A}^T, \quad (49.52)$$

where \mathbf{A} is an orthogonal matrix, while $\boldsymbol{\Delta}$ is a diagonal matrix whose diagonal elements, δ_i , $i = 1, \dots, n_a$, are called the eigenphases. If we define the eigenphase sum δ_{sum} by

$$\delta_{\text{sum}} = \sum_{i=1}^{n_a} \delta_i, \quad (49.53)$$

we can show from Eq. (49.50) that in the neighborhood of the resonance the eigenphase sum follows a Breit–Wigner form

$$\delta_{\text{sum}}(E) = \delta_{0,\text{sum}}(E) + \tan^{-1} \left(\frac{\frac{1}{2}\Gamma_i}{E_{i,r} - E} \right), \quad (49.54)$$

where $\delta_{0,\text{sum}}$ is the slowly varying background eigenphase sum obtained by replacing \mathcal{S} by \mathcal{S}_0 in Eqs. (49.52) and

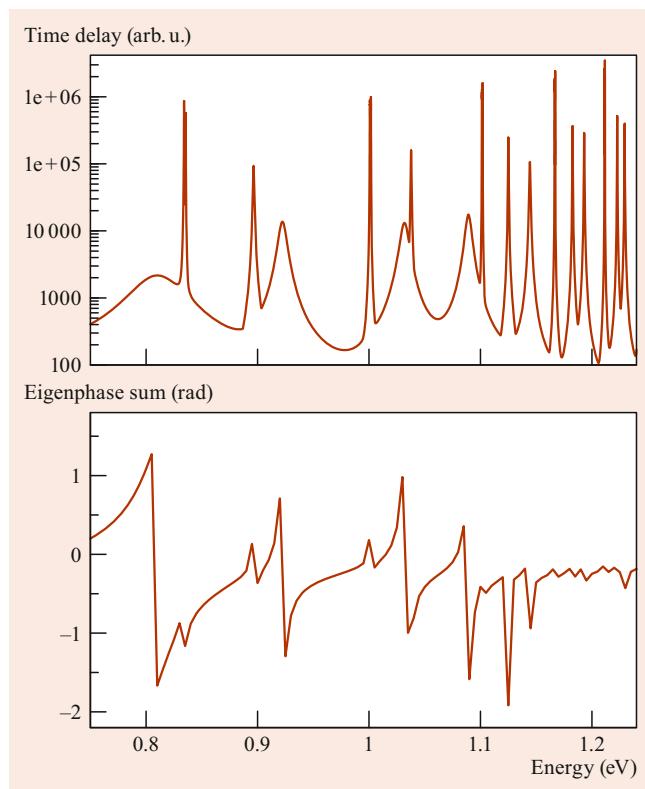


Fig. 49.1 Comparison of the longest time delay (*upper panel*) with the eigenphase sum, given modulo π (*lower panel*), at the same energy for a series of resonances found in $e\text{-N}_2^+$ scattering. Note that with higher energy resolution, some of the time delay peaks can be split to reveal multiple resonances. Adapted from *Little and Tennyson* [25] with thanks to Sergei Yurchenko

(49.53). It follows from Eq. (49.54) that the eigenphase sum increases by π radians in the neighborhood of the resonance energy. If there are m resonances, which may be overlapping, Eq. (49.54) generalizes to

$$\delta_{\text{sum}}(E) = \delta_{0,\text{sum}}(E) + \sum_{i=1}^m \tan^{-1} \left(\frac{\frac{1}{2}\Gamma_i}{E_{i,r} - E} \right). \quad (49.55)$$

This result has proven to be useful in analyzing closely spaced resonances to obtain the individual resonance positions and widths.

However, overlapping resonances can be difficult to fit using a Breit–Wigner form. An alternative approach, due originally to *Smith* [24], is based on the classical concept of time delay during a collision. Quantum-mechanically, the time delay in a collision can be represented in terms of the S -matrix and the time operator as

$$Q = -i\hbar S^* \frac{S}{E}. \quad (49.56)$$

The time delays are obtained by diagonalizing Q with resonances manifesting themselves as the longest time delay or largest eigenvalue. The corresponding eigenvector gives the

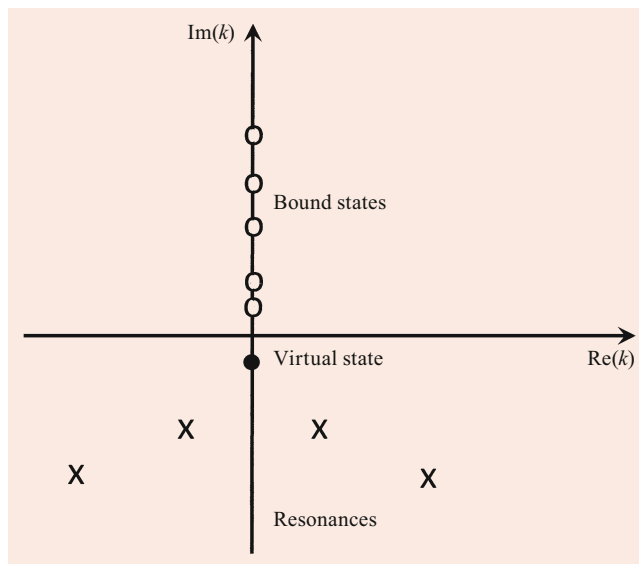


Fig. 49.2 Structure of the S -matrix as a function of complex wave-number, k . The features indicated correspond to poles of different physical meaning

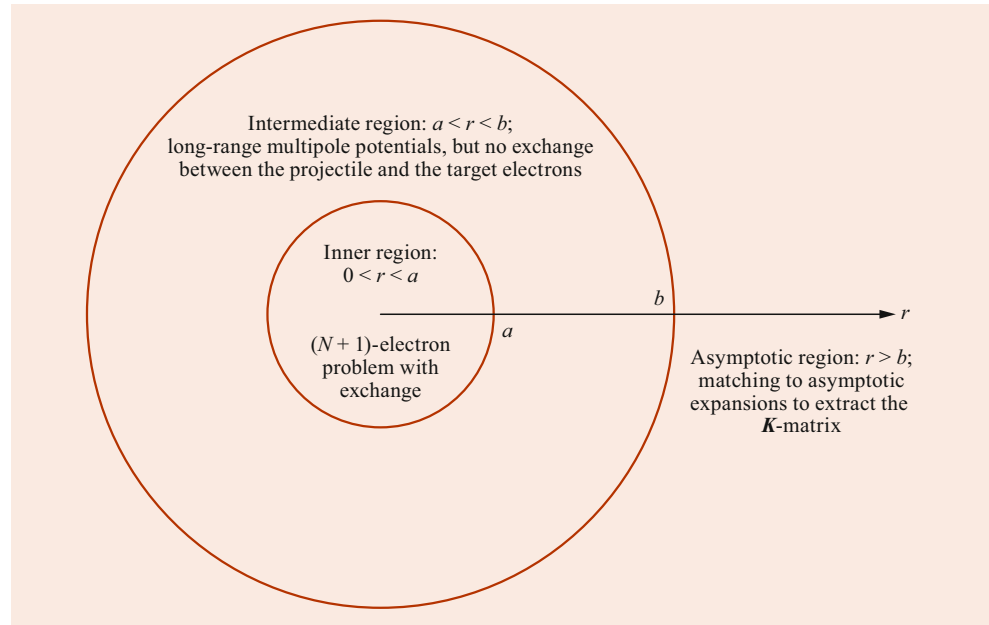
relative partial width associated with each channel. In this formulation, resonances have a Lorentzian shape as a function of energy.

Figure 49.1 compares the structure of the eigenphase sum (plotted modulo π) with that of the longest time delay for a series of resonances; in both cases, the positions of the resonances are readily apparent.

Analysis of the S -matrix as function of complex k also yields information of bound states, virtual states, and resonances. Figure 49.2 illustrates the location of these various features. Bound states are located as poles on the positive imaginary axis, as here $\frac{1}{2}k^2$ is negative. Virtual states, which can lead to pronounced features in low-energy scattering [26], form poles on the negative imaginary axis. Resonances give poles that are symmetrically placed on either side of the negative imaginary axis. Under these circumstances, the energy is complex; see Eq. (49.47). It is possible to characterize resonances by searching the S -matrix as a function of complex k [27], but in practice this is rarely done.

49.1.4 Solution of the Coupled Integro-Differential Equations

This section considers methods that have been developed for solving the coupled integro-differential equations (49.10). These equations arise in low-energy electron–atom and electron–ion collisions. Section 49.2.2 shows that similar equations also arise in low-energy electron–molecule collisions in the fixed-nuclei approximation. Thus, the methods discussed in this section are also applicable to electron–molecule collisions.

Fig. 49.3 The R -matrix method

R-Matrix Method

This method was first introduced in nuclear physics [28–30] in a study of resonance reactions. It has since been applied to a wide range of atomic, molecular, and optical processes, as reviewed in [31]. A comprehensive overview of the method and its many applications can be found in [32]. The review [3] presents a particular focus on electron–molecule problems. Figure 49.3 gives a schematic overview of the method.

The method starts by partitioning configuration space into two regions by a sphere of radius a , chosen so that the direct potential has achieved its asymptotic form given by Eq. (49.12) and the exchange and correlation potentials are negligible for $r \geq a$. The objective is then to calculate the R -matrix with elements $R_{ij}^{\Gamma}(E)$, which is defined by

$$F_{ij}^{\Gamma}(a) = \sum_{\ell=1}^n R_{i\ell}^{\Gamma}(E) \left(a \frac{dF_{\ell j}^{\Gamma}}{dr} - b_{\ell} F_{\ell j}^{\Gamma} \right)_{r=a}, \quad (49.57)$$

by solving Eq. (49.10) in the internal region.

The collision problem is solved for $r \leq a$ by expanding the wave function, in analogy with Eq. (49.8), in the form

$$\begin{aligned} \Psi_k^{\Gamma}(\mathbf{X}_{N+1}) &= \mathcal{A} \sum_{ij} \bar{\Phi}_i^{\Gamma}(\mathbf{x}_1, \dots, \mathbf{x}_N; \hat{\mathbf{r}}_{N+1} \sigma_{N+1}) \\ &\quad \times r_{N+1}^{-1} u_j(r_{N+1}) a_{ijk}^{\Gamma} \\ &\quad + \sum_i \chi_i^{\Gamma}(\mathbf{x}_1, \dots, \mathbf{x}_{N+1}) b_{ik}^{\Gamma}, \end{aligned} \quad (49.58)$$

where the u_j are radial basis functions defined over the range $0 \leq r \leq a$. For radial basis functions u_j satisfying arbitrary boundary conditions at $r = a$, the Hamiltonian H_{N+1} defined

by Eq. (49.3) is not Hermitian in the internal region due to the kinetic energy operators. It can, however, be made Hermitian by adding the Bloch operator [33]

$$L_b = \sum_{i=1}^n |\bar{\Phi}_i^{\Gamma}\rangle \frac{1}{2} \delta(r-a) \left(\frac{d}{dr} - \frac{b_i - 1}{r} \right) \langle \bar{\Phi}_i^{\Gamma}| \quad (49.59)$$

to H_{N+1} , where b_i is an arbitrary parameter. The Schrödinger equation (49.2) then becomes

$$(H_{N+1} + L_b - E) \Psi^{\Gamma} = L_b \Psi^{\Gamma}, \quad (49.60)$$

which can be formally solved as

$$\Psi^{\Gamma} = (H_{N+1} + L_b - E)^{-1} L_b \Psi^{\Gamma}. \quad (49.61)$$

We now expand the Green's function $(H_{N+1} + L_b - E)^{-1}$ in terms of the basis Ψ_k^{Γ} , where the coefficients a_{ijk}^{Γ} and b_{ik}^{Γ} in Eq. (49.58) are chosen to diagonalize $H_{N+1} + L_b$ according to

$$\langle \Psi_k^{\Gamma} | H_{N+1} + L_b | \Psi_{k'}^{\Gamma} \rangle = E_k^{\Gamma} \delta_{kk'}. \quad (49.62)$$

Equation (49.61) can then be written as

$$|\Psi^{\Gamma}\rangle = \sum_k \frac{|\Psi_k^{\Gamma}\rangle \langle \Psi_k^{\Gamma}|}{E_k^{\Gamma} - E} L_b |\Psi^{\Gamma}\rangle. \quad (49.63)$$

Finally, we project this equation onto the channel functions $\bar{\Phi}_i^{\Gamma}$ and evaluate it at $r = a$. Assuming that Ψ^{Γ} is given by Eq. (49.8), we retrieve Eq. (49.57), where the R -matrix elements are calculated from the expansion

$$R_{ij}^{\Gamma}(E) = \frac{1}{2a} \sum_k \frac{w_{ik}^{\Gamma} w_{jk}^{\Gamma}}{E_k^{\Gamma} - E}. \quad (49.64)$$

Here, we have introduced the surface amplitudes

$$w_{ik}^\Gamma = \sum_j u_j(a) a_{ijk}^\Gamma. \quad (49.65)$$

The main part of the calculation involves setting up and diagonalizing the matrix given by Eq. (49.62). This has to be carried out only *once* to determine the \mathbf{R} -matrix for *all* energies E , thereby making the method extremely efficient if results for many energies are required, e.g., for a detailed tracing of resonance structures.

In the external region $r \geq a$, Eq. (49.10) reduces to ordinary differential equations coupled by the potential $V_{ij}^\Gamma(r)$, which has achieved its asymptotic form Eq. (49.12). These equations can be integrated outwards from $r = a$ for each energy of interest, subject to the boundary conditions Eq. (49.57), to yield the \mathbf{K} -matrix given by Eq. (49.15), and hence the \mathbf{S} -matrix and collision cross sections. In practice, this is usually done by propagating the \mathbf{R} -matrix rather than integrating the coupled differential equations to some large but finite radius (b in Fig. 49.3) and then using an asymptotic expansion to find the \mathbf{K} -matrix [34].

There are many numerical implementations of the \mathbf{R} -matrix method in atomic and molecular physics. For electron collisions with atoms and ions, a general computer code [35] was published and continues to be updated and maintained [36]. Similarly, there are a number of general molecular implementations [37, 38]. In particular, the UK molecular \mathbf{R} -matrix codes have been routinely updated and published over time. The current implementation, known as UKRMol [39], is obtainable via the open-access CCPForge program repository and can be run through the Quantemol-N expert system [40, 41].

An important feature of the standard implementation of the \mathbf{R} -matrix method is the use of orthogonal one-electron orbitals for all physical and pseudo states in the expansion of the N -electron target and the $(N + 1)$ -continuum states. Using orthogonal orbitals has numerical advantages in setting up the Hamiltonian matrix in the internal region, but it is not required from first principles – only multielectron target states of the same symmetry must be orthogonal for a Hermitian operator. A disadvantage associated with the use of orthogonal one-electron orbitals is the limitation that such orbitals impose on the flexibility of generating a small configuration-interaction description with term-dependent, individually optimized orbitals for each state of interest. The \mathbf{R} -matrix with pseudo-states (RMPS) method (see Sect. 49.1.5) alleviates some of these problems, but others remain, particularly for complex targets with several open shells.

A very successful method to overcome these problems is the B -spline \mathbf{R} -matrix implementation developed by *Zat-*

sariny and coworkers. First introduced for a photoionization problem [42], it has since been applied in numerous structure and collision calculations, both for photon and electron impacts. The basic idea is to expand all one-electron orbitals into B -splines and then use the excellent numerical properties of this basis. Since neighboring B -splines have (limited) nonvanishing overlaps, it is necessary to handle the nonorthogonality of this basis. While the extension to nonorthogonal orbital sets expanded in the basis further increases the complexity, there are great benefits associated with the additional flexibility. A general BSR computer program using this approach in the nonrelativistic LS -coupling scheme as well as the semirelativistic Breit–Pauli approach was published [43], and later the method was extended to the full relativistic coupling scheme [44]. A comprehensive review of the BSR approach and its many applications can be found in [45]; the approach has recently been extended to molecules [46, 47].

Kohn Variational Method

The application of variational methods in electron–atom collision theory was reviewed by *Nesbet* [48]. An \mathbf{S} -matrix or complex Kohn version of this approach was developed [49], which eliminated singularities present in earlier \mathbf{K} -matrix versions of the theory. This method continues to be particularly important in electron–molecule collision calculations [50].

The approach starts from the basic expansion given by Eq. (49.8), where the reduced radial functions are chosen to satisfy the \mathbf{T} -matrix asymptotic boundary conditions

$$F_{ij}^\Gamma \underset{r \rightarrow \infty}{\approx} k_i^{-\frac{1}{2}} \left(\sin \theta_i \delta_{ij} + (2i)^{-1} e^{i\theta_i} T_{ij}^\Gamma \right), \quad (49.66)$$

which follow by taking linear combinations of the n_a solutions defined by Eq. (49.15) and using Eq. (49.17). We then define the integral

$$\mathbf{I}^\Gamma = -\frac{1}{2} \int_0^\infty (\mathbf{F}^\Gamma)^T \mathbf{L} \mathbf{F}^\Gamma dr, \quad (49.67)$$

where \mathbf{L} is the integro-differential operator given by Eq. (49.10) with all terms taken onto the left-hand side of the equation.

Now consider variations of the integral \mathbf{I}^Γ resulting from arbitrary variations $\delta \mathbf{F}^\Gamma$ of the functions \mathbf{F}^Γ about the exact solution of Eq. (49.10), where these solutions satisfy the boundary conditions Eq. (49.66), while the variations satisfy the boundary condition

$$\delta \mathbf{F}^\Gamma \underset{r \rightarrow \infty}{\approx} (2i)^{-1} \mathbf{k}^{-\frac{1}{2}} e^{i\theta} \delta \mathbf{T}^\Gamma. \quad (49.68)$$

The corresponding variation in \mathbf{I}^Γ to first order is

$$\delta \mathbf{I}^\Gamma = -\frac{1}{2} \int_0^\infty \left[(\delta \mathbf{F}^\Gamma)^T \mathbf{L} \mathbf{F}^\Gamma + (\mathbf{F}^\Gamma)^T \mathbf{L} \delta \mathbf{F}^\Gamma \right] dr, \quad (49.69)$$

which, after some manipulation, yields

$$\delta \mathbf{I}^\Gamma = (4i)^{-1} \delta \mathbf{T}^\Gamma. \quad (49.70)$$

It follows that the functional

$$[\mathbf{T}^\Gamma] = \mathbf{T}^\Gamma - 4i \mathbf{I}^\Gamma \quad (49.71)$$

is stationary for small variations about the exact solution. This is the complex Kohn variational principle.

This variational principle can be used to solve Eq. (49.10) by representing the reduced radial functions F_{ij}^Γ by the expansion

$$F_{ij}^\Gamma(r) = w_{1i}^\Gamma(r) \delta_{ij} + (2i)^{-1} w_{2i}^\Gamma(r) T_{ij}^\Gamma + \sum_k \phi_k^\Gamma(r) c_{ijk}^\Gamma, \quad (49.72)$$

where w_{1i}^Γ and w_{2i}^Γ are zero at the origin and have the asymptotic forms

$$w_{1i}^\Gamma(r) \underset{r \rightarrow \infty}{\approx} k_i^{-\frac{1}{2}} \sin \theta_i, \quad (49.73)$$

$$w_{2i}^\Gamma(r) \underset{r \rightarrow \infty}{\approx} k_i^{-\frac{1}{2}} \exp i \theta_i, \quad (49.74)$$

while the ϕ_k^Γ are square-integrable basis functions. The coefficients c_{ijk}^Γ and the \mathbf{T} -matrix elements T_{ij}^Γ can be determined as variational parameters in the variational principle Eq. (49.71).

Schwinger Variational Method

This method was used to calculate electron–molecule collision cross sections by *McKoy* and coworkers [51]. It starts from the Lippmann–Schwinger integral equation, which corresponds to the integro-differential equations Eq. (49.10), together with the \mathbf{K} -matrix or \mathbf{T} -matrix boundary conditions defined by Eqs. (49.15) or (49.66), respectively. The \mathbf{T} -matrix form of the Lippmann–Schwinger integral equation is

$$F_{ij}^\Gamma(r) = w_{1i}^\Gamma(r) \delta_{ij} + \sum_{k\ell} \int_0^\infty \int_0^\infty G_{ik}^{\Gamma(+)}(r, r') \times U_{k\ell}^\Gamma(r', r'') F_{\ell j}^\Gamma(r'') dr' dr'', \quad (49.75)$$

where $U_{k\ell}^\Gamma$ represents the sum of the potential terms $2(V_{k\ell}^\Gamma + K_{k\ell}^\Gamma + X_{k\ell}^\Gamma)$ in Eq. (49.10), and the multichannel outgoing-

wave Green's function $G_{ik}^{\Gamma(+)}$ is defined, assuming that all channels are open, by

$$G_{ij}^{\Gamma(+)}(r, r') = \begin{cases} -w_{1i}^\Gamma(r) w_{2i}^\Gamma(r') \delta_{ij}, & r < r'; \\ -w_{2i}^\Gamma(r) w_{1i}^\Gamma(r') \delta_{ij}, & r \geq r'. \end{cases} \quad (49.76)$$

Here, w_{1i}^Γ and w_{2i}^Γ are solutions of the Coulomb equation

$$\left(\frac{d^2}{dr^2} - \frac{\ell_i(\ell_i + 1)}{r^2} + \frac{2(Z - N)}{r} + k_i^2 \right) w_i(r) = 0 \quad (49.77)$$

that satisfy the asymptotic boundary conditions Eqs. (49.73) and (49.74), respectively.

An integral expression for the \mathbf{T} -matrix can be obtained by comparing Eqs. (49.66) and (49.75). This gives

$$T_{ij}^\Gamma = -2i \sum_k \int_0^\infty \int_0^\infty w_{1i}^\Gamma(r) U_{ik}^\Gamma(r, r') F_{kj}^\Gamma(r') dr dr', \quad (49.78)$$

or, rewriting this equation using Dirac bracket notation,

$$\mathbf{T} = -2i \langle \mathbf{w}_1 | \mathbf{U} | \mathbf{F}^{(+)} \rangle, \quad (49.79)$$

where the plus sign indicates that $\mathbf{F}^{(+)}$ satisfies the outgoing-wave boundary condition Eq. (49.66). For convenience of notation, we have suppressed the superscript Γ . In a similar way, the Lippmann–Schwinger equation corresponding to the ingoing-wave boundary condition,

$$F_{ij}^\Gamma \underset{r \rightarrow \infty}{\approx} k_i^{-\frac{1}{2}} \left(\sin \theta_i \delta_{ij} - (2i)^{-1} e^{-i\theta_i} T_{ij}^{\Gamma*} \right), \quad (49.80)$$

can be introduced. From that follows the integral expression

$$\mathbf{T} = -2i \langle \mathbf{F}^{(-)} | \mathbf{U} | \mathbf{w}_1 \rangle, \quad (49.81)$$

where $\mathbf{F}^{(-)}$ satisfies the ingoing-wave boundary condition Eq. (49.80). A further integral expression for the \mathbf{T} -matrix is obtained by substituting for \mathbf{w}_1 in Eq. (49.81) from Eq. (49.75), giving

$$\mathbf{T} = -2i \langle \mathbf{F}^{(-)} | \mathbf{U} - \mathbf{U} \mathbf{G}^{(+)} \mathbf{U} | \mathbf{F}^{(+)} \rangle. \quad (49.82)$$

Hence, a combination of Eqs. (49.79), (49.81), and (49.82) yields the functional

$$[\mathbf{T}] = -2i \langle \mathbf{w}_1 | \mathbf{U} | \mathbf{F}^{(+)} \rangle \times \left(\langle \mathbf{F}^{(-)} | \mathbf{U} - \mathbf{U} \mathbf{G}^{(+)} \mathbf{U} | \mathbf{F}^{(+)} \rangle \right)^{-1} \times \langle \mathbf{F}^{(-)} | \mathbf{U} | \mathbf{w}_1 \rangle. \quad (49.83)$$

This functional is stationary for small variations of $\mathbf{F}^{(+)}$ and $\mathbf{F}^{(-)}$ about the exact solution of Eq. (49.10) satisfying the boundary conditions Eqs. (49.66) and (49.80), respectively. It forms the basis for numerical calculations.

Linear Algebraic Equations Method

In this method, the integro-differential equations Eq. (49.10) are reduced directly to a set of linear algebraic (LA) equations [52]. Alternatively, Eq. (49.10) are first converted to integral form, given by Eq. (49.75), which are then reduced to a set of linear algebraic equations [53].

A direct approach [52] has been widely used for electron–atom and electron–ion collisions. As in the \mathbf{R} -matrix method, configuration space is first divided into two regions. A mesh of N points is used to span the internal region $r \leq a$, where

$$r_1 = 0; \quad r_{k-1} < r_k, \quad k = 1, \dots, N; \quad r_N = a. \quad (49.84)$$

In addition, two further mesh points r_{N+1} and r_{N+2} are introduced to enable the solution in the internal region to be matched to the solution in the external region $r \geq a$. In the external region, Eq. (49.10) reduces to coupled differential equations that can be solved by one of the same methods as adopted in the \mathbf{R} -matrix approach.

The n functions $F_{ij}^f(r)$, $i = 1, \dots, n$, in Eq. (49.10) are represented by their values at the mesh points r_k . Using a finite difference representation of the differential and integral operators, Eq. (49.10) reduces to a set of linear algebraic equations for the unknown values $F_{ij}^f(r_k)$ in the internal region. These equations can be solved using standard methods for each linearly independent solution $j = 1, \dots, n_a$ defined by the asymptotic boundary conditions Eq. (49.15).

49.1.5 Intermediate and High-Energy Elastic Scattering and Excitation

For electron–atom and electron–ion collisions at electron impact energies greater than the ionization threshold of the target, an infinite number of channels is open. Consequently, they cannot all be included explicitly in the expansion of the total wave function. Several approaches have been developed to treat collisions at these energies, such as extensions of low-energy methods based on expansion Eq. (49.8) to intermediate energies, the development of optical potentials that account for the loss of flux into the infinity of open channels in some average way, and extensions of the Born approximation to lower energies by including higher-order terms in the Born series.

Pseudostate Methods

In this approach, expansion Eq. (49.8) is extended by including a set of suitably chosen square-integrable pseudostates Φ_i^p that are orthogonal to the eigenstates Φ_i retained in expansion Eq. (49.8). These pseudostates are usually defined by diagonalizing the target Hamiltonian H_N in

a square-integrable basis. This yields an equation analogous to Eq. (49.4), viz.,

$$\langle \Phi_i^p | H_N | \Phi_j^p \rangle = \omega_i^p \delta_{ij}, \quad (49.85)$$

where the energies ω_i^p lie just below the ionization threshold or in the continuum. The pseudostates Φ_i^p , thus, represent in an average way the high-lying Rydberg states and the continuum states of the target, rather than just the low-lying target bound states as in Eq. (49.4). This enables the loss of flux into the continuum states to be represented, thereby enabling accurate excitation cross sections to be calculated at intermediate energies. In addition, by calculating the amplitudes for exciting these pseudostates, accurate ionization cross sections can be determined, as discussed in Sect. 49.1.6.

A proposal to include pseudostates in expansion Eq. (49.8) for e–H scattering was first made by *Burke and Schey* [54]. A modification of this expansion to include polarized pseudostates, which accounted for the long-range dipole and quadrupole polarizability in e–H scattering, was proposed by *Damburg and Karule* [55]. Later detailed e–H scattering calculations that included pseudostates were carried out by a number of authors [56–59]. The considerable success showed the validity of this approach.

The \mathbf{R} -matrix method, discussed in Sect. 49.1.4, was also extended to include pseudostates. This resulted in the intermediate-energy \mathbf{R} -matrix (IERM) method [60–63] and the \mathbf{R} -matrix with the pseudostates (RMPS) method [64–68], with the latter approach being applicable to multielectron atoms, ions, and molecules. Both of these approaches have enabled excitation and ionization cross sections to be accurately calculated above the ionization threshold.

Methods were also developed in which the pseudostates are represented by Sturmian functions. An expansion of this type was first proposed by *Rotenberg* [69]. A major development along these lines is the convergent close-coupling (CCC) method developed by *Bray, Stelbovics, Fursa*, and coworkers, which has been applied with considerable success for both electron impact excitation and ionization of few-electron systems. Comprehensive reviews of the method and references to numerous applications can be found in [70, 71]. The method has also been extended to molecules [72].

As an example of the CCC method, we consider e–H scattering. In this case, the radial functions of the target states are expanded in the complete Laguerre basis

$$\xi_{k\ell}(r) = \left(\frac{\lambda_\ell(k-1)!}{(2\ell+1+k)!} \right)^{1/2} \times (\lambda_\ell r)^{\ell+1} \exp\left(-\frac{\lambda_\ell r}{2}\right) L_{k-1}^{2\ell+2}(\lambda_\ell r), \quad (49.86)$$

where $L_{k-1}^{2\ell+2}(\lambda_\ell r)$ are associated Laguerre polynomials, and k ranges from 1 to the basis size N_ℓ , which depends on the

angular momentum ℓ . The target states $\Phi_{i\ell}$ are expanded for each angular momentum as

$$\Phi_{i\ell} = \sum_{k=1}^{N_\ell} \xi_{k\ell}(r) c_{ki\ell}, \quad i = 1, \dots, N_\ell, \quad (49.87)$$

where the coefficients $c_{ki\ell}$ are obtained by diagonalizing the target Hamiltonian H_1 according to

$$\langle \Phi_{i\ell} | H_1 | \Phi_{j\ell} \rangle = w_{i\ell} \delta_{ij}. \quad (49.88)$$

The states $\Phi_{i\ell}$ corresponding to the lower energies $w_{i\ell}$ provide an accurate representation of the low-lying bound eigenstates of the target for each ℓ , while the states corresponding to the higher energies correspond to pseudostates representing the high-lying Rydberg states and the continuum. As N_ℓ is increased for fixed range parameter λ_ℓ in Eq. (49.87), more bound target eigenstates are accurately represented, while at the same time the states corresponding to the higher energies provide a denser and more accurate representation of the continuum.

The scattering amplitude is written in the close-coupling approximation as

$$\begin{aligned} & \langle \psi_f | H_2 - E | \Psi_i^{S+} \rangle \\ & \simeq \langle \psi_f | I(H_2 - E) [1 + (-1)^S P] I | \Psi_i^{S+} \rangle, \end{aligned} \quad (49.89)$$

where P is the space exchange operator, which ensures that the total wave function has the correct symmetry for each total spin S , I is the projection operator onto the target states $\Phi_{i\ell}$ retained in the calculation, and $\langle \psi_f |$ is an eigenstate of the asymptotic Hamiltonian. The scattering amplitude is obtained by solving the close-coupling equations in momentum space [71].

Optical Potential Methods

The optical potential method [73] is, in principle, also capable of including the effect of all excited and continuum states. Adopting Feshbach projection operators P and Q as in Eq. (49.40), an optical potential V_{opt} is defined by Eq. (49.44), where now P projects onto those low-energy channels that can be treated exactly, for example by solving Eq. (49.10), and Q allows for the remaining infinity of coupled channels, including the continuum.

At sufficiently high energies, it is appropriate to make a perturbation expansion of V_{opt} , where the second-order term is given by

$$V^{(2)} = P V Q \frac{1}{E - \mathcal{T}_e - H_N + i\epsilon} Q V P. \quad (49.90)$$

Here, V is the electron–atom (ion) interaction potential, \mathcal{T}_e the kinetic energy operator of the scattered electron, and

H_N the target Hamiltonian. *Byron* and *Joachain* [74] converted the lowest-order terms of perturbation theory into an ab initio local complex potential for the elastic scattering of electrons and positrons from a number of atoms.

The optical potential calculated in second order was also used by *Bransden* et al. [75, 76] to describe e–H collisions, while *McCarthy* [77] studied an optical-potential approximation that goes beyond second order and also makes allowance for exchange. This method is called the coupled-channels optical (CCO) model. Finally, *Callaway* and *Oza* [78] constructed an optical potential using a set of pseudostates to evaluate the sum over intermediate states and obtained encouraging results for elastic scattering and excitation of the $n = 2$ states in e–H collisions.

Born Series Methods

In the high-energy domain, which can usually be assumed to extend from several times the ionization threshold of the target upwards, methods based on the Born series often give reliable results. Ignoring electron exchange for the moment, the Born series for the direct scattering amplitude can be written as [79, 80]

$$f = \sum_{n=1}^{\infty} f_{n,B}, \quad (49.91)$$

where the n -th Born term $f_{n,B}$ contains the interaction V between the scattered electron and the target atom or ion n times, and Green's function

$$G_0^{(+)} = (H_N + \mathcal{T}_e - E - i\epsilon)^{-1} \quad (49.92)$$

$(n - 1)$ times, where \mathcal{T}_e and H_N are defined following Eq. (49.90).

It is important to consistently retain all terms in the Born series with similar energy and momentum-transfer $\Delta = |\mathbf{k}_i - \mathbf{k}_f|$ dependencies. For elastic scattering, the scattering amplitude converges to the first Born approximation for all Δ , but at lower energies it is necessary to include $\text{Re}(f_{3,B})$, as well as the second Born terms, to obtain the cross section correct to k^{-2} . In the forward direction, convergence to the first Born approximation is slow because of the contribution from $\text{Im}(f_{2,B})$ that, from the optical theorem, corresponds to loss of flux into all open channels.

For inelastic scattering, the first Born approximation does not give the correct high-energy limit for large Δ . Instead, this comes from $\text{Im}(f_{2,B})$. Physically, this can be understood by noting that inelastic scattering at large angles involves two collisions: a collision of the incident electron with the nucleus to give the large scattering angle, followed or preceded by an inelastic collision with the bound electrons to give excitation [81–83]. Again, in the forward direction, it is necessary to retain $\text{Re}(f_{3,B})$ to obtain the cross section correct to k^{-2} .

Since the third Born term is difficult to evaluate, *Byron and Joachain* [84] suggested that, to third order, the scattering amplitude should be calculated using the eikonal Born series (EBS) approximation

$$f_{\text{EBS}} = f_{1,\text{B}} + f_{2,\text{B}} + f_{3,\text{G}} + g_{\text{och}}, \quad (49.93)$$

where $f_{3,\text{G}}$ is the third-order term in the expansion of the Glauber amplitude [85] in powers of V , which can be more easily calculated than $f_{3,\text{B}}$, and g_{och} is the *Ochkur* electron exchange amplitude [86]. The EBS method has been very successful when perturbation theory converges rapidly; namely, at high energies, at small and intermediate scattering angles, and for light atoms. The Born approximation is also routinely used to top up low-energy scattering from dipolar systems for which a large number of partial waves need to be taken into account [87].

Distorted-Wave Methods

The distorted-wave Born approximation (DWBA) is characterized by a separation of the interaction into two parts, one that is treated exactly while the other is treated in first order. The usual approach is based on the integral expressions for the T -matrix given by Eq. (49.79) or Eq. (49.81). The distorted-wave approximation is obtained by replacing the exact solution of Eq. (49.10), denoted by $F^{(+)}$ and $F^{(-)}$ in Eqs. (49.79) and (49.81), respectively, by approximate solutions that are usually obtained by omitting all channels except the final or initial channels of interest. In addition, the potential interaction U is often approximated by just the direct term in Eq. (49.10).

This method becomes more accurate at intermediate energies, as $Z - N$ increases, and as the angular momentum of the scattered electron becomes large. However, it generally gives poor results at low energies, where the coupling between the channels in Eq. (49.10) is strong, and resonances are often important. It has proven to be a very useful way of calculating electron–ion total and differential cross sections at intermediate and high energies well removed from threshold. Some examples can be found in [88].

A thorough introduction to the DWBA method for atomic and ionic targets can be found in [89]. Calculations using this and the closely related first-order many-body theory (FOMBT), which differs from the DWBA by the choice of distortion potentials, can be performed using the Los Alamos Atomic Collision Codes [90].

49.1.6 Ionization

This section discusses processes in which electrons are ejected from the target during the collision, giving rise to ionization. The main focus is single ionization, i.e., (e,2e)

processes of the general form

$$e^-(E_i) + A_i \rightarrow A_j^+ + e^-(E_A) + e^-(E_B). \quad (49.94)$$

Here, E_i , E_A , and E_B are the incident, scattered, and ejected electron energies, respectively. They are related through the energy conservation condition

$$E_i = E_A + E_B + \varepsilon, \quad (49.95)$$

where ε is the binding energy of the ejected atomic electron. The threshold behavior of the ionization cross section leading to the Wannier threshold law is treated in Chap. 56.

The scattering amplitude for the direct ionization process is [91]

$$f_i(\mathbf{k}_A, \mathbf{k}_B) = -(2\pi)^{\frac{1}{2}} e^{i\chi(\mathbf{k}_A, \mathbf{k}_B)} \left\langle (H_{N+1} - E)\Phi \left| \Psi_i^{(+)} \right. \right\rangle, \quad (49.96)$$

where $\Psi_i^{(+)}$ is an exact solution of Eq. (49.2) satisfying plane-wave plus outgoing-wave boundary conditions given by Eq. (49.5), while Φ is a solution of the equation

$$(H_{N+1} - V - E)\Phi = 0 \quad (49.97)$$

satisfying ingoing-wave boundary conditions. Also, \mathbf{k}_A and \mathbf{k}_B are the momenta of the two outgoing electrons, defined in terms of E_A and E_B by

$$\frac{1}{2}k_A^2 = E_A, \quad \frac{1}{2}k_B^2 = E_B. \quad (49.98)$$

In practice, the potential V is chosen so that Φ has a simple form. Thus, for electron scattering by H-like ions with nuclear charge Z , V is often chosen as

$$V = -\frac{Z - Z_A}{r_1} - \frac{Z - Z_B}{r_2} + \frac{1}{r_{12}}, \quad (49.99)$$

so that

$$\Phi(\mathbf{r}_1, \mathbf{r}_2) = \Psi_C^{(-)}(Z_A, \mathbf{k}_A, \mathbf{r}_1)\Psi_C^{(-)}(Z_B, \mathbf{k}_B, \mathbf{r}_2), \quad (49.100)$$

where the $\Psi_C^{(-)}$ are Coulomb wave functions satisfying ingoing-wave boundary conditions, while Z_A and Z_B are the effective charges seen by the two electrons. In order for the scattering amplitude not to contain a divergent phase factor, Z_A and Z_B must satisfy

$$\frac{Z_A}{k_A} + \frac{Z_B}{k_B} = \frac{Z}{k_A} + \frac{Z}{k_B} - \frac{1}{|\mathbf{k}_A - \mathbf{k}_B|}. \quad (49.101)$$

The phase factor in Eq. (49.96) is then given by

$$\chi(\mathbf{k}_A, \mathbf{k}_B) = \frac{Z_A}{k_A} \ln \frac{k_A^2}{k_A^2 + k_B^2} + \frac{Z_B}{k_B} \ln \frac{k_B^2}{k_A^2 + k_B^2}. \quad (49.102)$$

The exchange ionization amplitude $g_i(\mathbf{k}_A, \mathbf{k}_B)$ can be obtained from the *Peterkop* theorem [92]

$$g_i(\mathbf{k}_A, \mathbf{k}_B) = f_i(\mathbf{k}_B, \mathbf{k}_A). \quad (49.103)$$

This result follows from the fact that the amplitudes $f_i(\mathbf{k}_B, \mathbf{k}_A)$ and $g_i(\mathbf{k}_A, \mathbf{k}_B)$ describe the same physical process, where the electron at \mathbf{r}_{N+1} has momentum \mathbf{k}_A , while the electron at \mathbf{r}_N has momentum \mathbf{k}_B . In practice, the Peterkop theorem is not fulfilled if approximate wave functions are used to calculate the ionization amplitude. For this reason, a relative phase $\tau_i(\mathbf{k}_A, \mathbf{k}_B)$ between these two amplitudes is sometimes introduced by

$$g_i(\mathbf{k}_A, \mathbf{k}_B) = e^{i\tau_i(\mathbf{k}_A, \mathbf{k}_B)} f_i(\mathbf{k}_B, \mathbf{k}_A). \quad (49.104)$$

This adds an element of arbitrariness into the calculation, since different choices of this phase lead to different cross sections [93].

The ionization cross sections can be obtained directly from the scattering amplitudes. For random electron spin orientations, the triple-differential cross section (TDCS) for ionization of a target with one active electron from an initial state denoted by $|i\rangle$ is given by

$$\frac{d^3\sigma_i}{d\Omega_A d\Omega_B dE} = \frac{k_A k_B}{k_i} \left(\frac{1}{4} |f_i + g_i|^2 + \frac{3}{4} |f_i - g_i|^2 \right). \quad (49.105)$$

By integrating the TDCS with respect to $d\Omega_A$, $d\Omega_B$, or dE , we can form three different double-differential cross sections, as well as three different single-differential cross sections. Finally, the total ionization cross section is obtained by integrating Eq. (49.105) over all outgoing electron scattering angles and energies. The result is

$$\sigma_i = \frac{1}{k_i} \int_0^{E/2} dE k_A k_B \int d\Omega_A \times \int d\Omega_B \left[\frac{1}{4} |f_i + g_i|^2 + \frac{3}{4} |f_i - g_i|^2 \right], \quad (49.106)$$

where the upper limit of integration over the energy variable is $E/2$, because the two outgoing electrons are indistinguishable.

We conclude this general discussion of the theory of electron impact ionization by mentioning an integral representation for the ionization amplitude [94] that is free from

the ambiguity and divergence problems associated with earlier work [91, 92, 95, 96]. Another important aspect of this development is the fact that its form is suitable for practical calculations.

Next, we consider several approaches that have been used to obtain accurate ionization cross sections. As for electron impact excitation, we commence with low-energy methods and conclude with plane-wave Born and distorted-wave methods.

Pseudostate Methods

An important development was the realization that accurate ionization cross sections, especially close to threshold, can be obtained by representing the ionization continuum by suitably chosen square-integrable pseudostates. As was already discussed when we considered pseudostate approaches in Sect. 49.1.5, several methods, including the intermediate energy \mathbf{R} -matrix method [60–63], the \mathbf{R} -matrix with pseudostates method [64–67] (both in the standard form with orthogonal one-electron orbitals and in the B -spline framework [45]), and the convergent close-coupling method [70, 71] have been used to obtain accurate ionization cross sections.

The essential point is the description of the process in two steps. First, the electron-impact *excitation* problem for both the physical and the pseudostates needs to be treated. In a second step, excitation of the positive-energy pseudostates is (re)interpreted as ionization. To a very good approximation, the total angle-integrated ionization cross section can be obtained directly as the sum of the excitation cross sections for all the pseudostates above the ionization threshold.

A significant challenge, however, concerns the procedure of extracting the information from the wave function obtained for the atom left in an excited pseudostate. In the CCC approach, this is done by first projecting the \mathbf{T} -matrix elements for a pseudostate of given energy E_f to that of a proper continuum state with the *same* energy. In order to obtain results for the desired energy of the ejected electron, it is then necessary to interpolate the \mathbf{T} -matrix elements to this energy. This procedure works well for cases where only one final ionic state of the residual ion is possible, such as in electron impact ionization of atomic hydrogen, where a bare proton is left, or helium if the residual ion is left in $\text{He}^+(1s)$. Some peculiarities occur, however, such as a step function at equal energy sharing, and these have to be dealt with appropriately. Details can be found in [70, 71].

For the BSR approach [45, 97], it was suggested to obtain the scattering amplitudes for the excitation of all energy-accessible atomic pseudostates $\Phi^p(nl n' l', LS)$ and then generate a weighted sum with the weights given by the overlap factors between the true continuum states and the corresponding pseudostates. In this case, it is important to generate the continuum states with the same close-coupling

expansion that is employed to produce the pseudostates. Although this interpolation recipe does not have a formal origin [98], due to the fact that the individual pseudostates and the continuum state of interest have *different* energies, the above scheme has been very successful. In fact, it is applicable to general targets, as well as to cases such as simultaneous ionization plus excitation [45, 97, 99].

Time-Dependent Close-Coupling Method

Electron impact excitation and ionization amplitudes and cross sections can also be determined by solving the time-dependent Schrödinger equation (TDSE) directly [100–103]. In the case of electron scattering by atomic hydrogen or by an atom or atomic ion with one electron outside a closed inert shell, the total wave function can be expanded for each conserved $LS\pi$ symmetry as

$$\Psi^\Gamma(\mathbf{r}_1, \mathbf{r}_2, t) = \sum_{\ell_1 \ell_2} (r_1 r_2)^{-1} P_{\ell_1 \ell_2}^{LS}(r_1, r_2, t) \mathcal{Y}_{\ell_1 \ell_2}^{LM_L}(\hat{\mathbf{r}}_1, \hat{\mathbf{r}}_2), \quad (49.107)$$

where Γ is defined by Eq. (49.9), and the coupled spherical harmonics $\mathcal{Y}_{\ell_1 \ell_2}^{LM_L}$ are defined by

$$\begin{aligned} \mathcal{Y}_{\ell_1 \ell_2}^{LM_L}(\hat{\mathbf{r}}_1, \hat{\mathbf{r}}_2) &= \sum_{m_1 m_2} (\ell_1 m_1 \ell_2 m_2 | \ell_1 \ell_2 LM_L) \\ &\times Y_{\ell_1 m_1}(\theta_1, \phi_1) Y_{\ell_2 m_2}(\theta_2, \phi_2). \end{aligned} \quad (49.108)$$

Substituting Eq. (49.107) into the TDSE and projecting onto the coupled spherical harmonics $\mathcal{Y}_{\ell_1 \ell_2}^{LM_L}$ yields the coupled differential equations

$$\begin{aligned} i \frac{\partial P_{\ell_1 \ell_2}^{LS}(r_1, r_2, t)}{\partial t} &= T_{\ell_1 \ell_2}(r_1, r_2) P_{\ell_1 \ell_2}^{LS}(r_1, r_2, t) \\ &+ \sum_{\ell'_1 \ell'_2} V_{\ell_1 \ell_2 \ell'_1 \ell'_2}^L(r_1, r_2, t) P_{\ell'_1 \ell'_2}^{LS}(r_1, r_2, t), \end{aligned} \quad (49.109)$$

where

$$T_{\ell_1 \ell_2}(r_1, r_2) = -\frac{1}{2} \frac{\partial^2}{\partial r_1^2} - \frac{1}{2} \frac{\partial^2}{\partial r_2^2} + V_{\ell_1}(r_1) + V_{\ell_2}(r_2). \quad (49.110)$$

In this equation, V_ℓ is an ℓ -dependent pseudo potential representing the interaction of the valence or scattered electrons with the closed-shell core, and $V_{\ell_1 \ell_2 \ell'_1 \ell'_2}^L$ are the radial coupling potentials obtained by taking the matrix elements of the r_{12}^{-1} interaction between the valence and scattered electrons.

Equations (49.109) are solved on a two-dimensional grid using an explicit time propagator, which can be readily implemented on parallel computers. Commencing at time $t = 0$ with a wave function that is constructed as the appropriately

symmetrized product of an incoming radial wave packet for one electron and the stationary bound initial state for the other electron, the time-dependent equations (49.109) are integrated forward in time. Electron impact excitation and ionization amplitudes, and subsequently the cross section, are determined by projecting the time-evolved radial wave function $P_{\ell_1 \ell_2}^{LS}(r_1, r_2, t)$ onto a complete set of target states. A review of the method is given in [104].

Exterior Complex Scaling Method

In this approach, developed by *Rescigno* et al. [105–107], the time-independent Schrödinger equation for three charged particles is solved numerically on a two-dimensional grid without explicitly imposing asymptotic boundary conditions for three-body breakup. In the case of e–H scattering, the total wave function is partitioned into the sum of an appropriately symmetrized unperturbed wave function $\psi_{k_i}^\Gamma$ describing a free electron with momentum k_i incident on the target ground state and a scattered wave function Ψ_{sc}^Γ , which is expanded in the form

$$\Psi_{sc}^\Gamma(\mathbf{r}_1, \mathbf{r}_2) = \sum_{L \ell_1 \ell_2} r_1^{-1} r_2^{-1} \psi_{\ell_1 \ell_2}^{LS}(r_1, r_2) \mathcal{Y}_{\ell_1 \ell_2}^{L0}(\hat{\mathbf{r}}_1, \hat{\mathbf{r}}_2). \quad (49.111)$$

Since the z -axis is defined to lie along the incident beam direction, M_L in the coupled spherical harmonics defined by Eq. (49.108) is zero. Also, since parity is conserved, the summation in Eq. (49.111) is limited to terms for which $L + \ell_1 + \ell_2$ is even.

Substituting the expression for the total wave function into the Schrödinger equation yields the following set of coupled two-dimensional equations for the radial functions $\psi_{\ell_1 \ell_2}^{LS}$ for each L and S

$$\begin{aligned} [E - H_{\ell_1}(r_1) - H_{\ell_2}(r_2)] \psi_{\ell_1 \ell_2}^{LS}(r_1, r_2) \\ - \sum_{\ell'_1 \ell'_2} V_{\ell_1 \ell_2 \ell'_1 \ell'_2}^L(r_1, r_2) \psi_{\ell'_1 \ell'_2}^{LS}(r_1, r_2) = \chi_{\ell_1 \ell_2}^{LS}(r_1, r_2). \end{aligned} \quad (49.112)$$

In this equation, $H_\ell(r)$ is the radial hydrogenic Hamiltonian

$$H_\ell(r) = -\frac{1}{2} \frac{d^2}{dr^2} + \frac{\ell(\ell+1)}{2r^2} - \frac{1}{r}, \quad (49.113)$$

$V_{\ell_1 \ell_2 \ell'_1 \ell'_2}^L$, as in Eq. (49.109), are the radial coupling potentials obtained by taking the matrix elements of the electron–electron interaction r_{12}^{-1} , and the inhomogeneous term $\chi_{\ell_1 \ell_2}^{LS}(r_1, r_2)$ arises from the partial-wave expansion of the incident wave term.

The coupled differential equations (49.112) are solved on a two-dimensional grid using exterior complex scaling (ECS) boundary conditions, which avoids imposing detailed

asymptotic boundary conditions. The ECS transformation is taken as a mapping $r \rightarrow z(r)$ of all radial coordinates to a contour

$$z(r) \equiv \begin{cases} r, & r \leq R_0 \\ R_0 + (r - R_0)e^{i\eta} & r > R_0 \end{cases}, \quad (49.114)$$

which is real for $r \leq R_0$ but rotated into the upper half of the complex plane for $r > R_0$. This transformation has the desirable property that any outgoing wave evaluated on this contour dies exponentially as the coordinate becomes large. Thus, the ECS procedure transforms any outgoing wave into a function that falls off exponentially outside R_0 but is equal to the infinite-range wave over the finite region of space where the coordinates are real. Producing meaningful ionization cross sections at energies several eV above the ionization threshold requires R_0 to be at least $100 a_0$. The grid must extend beyond R_0 far enough to allow the complex scaled radial function to decay effectively to zero at the edge of the grid, thus requiring grids that extend an additional $25 a_0$ beyond R_0 . It should be checked that the final results do not depend significantly on the choice of R_0 . A detailed discussion of this method is given by *McCurdy et al.* [107].

Born and Distorted-Wave Methods

The integral expression Eq. (49.96) for the direct ionization amplitude provides a starting point for the calculation of cross sections at higher energies. Both the Born series methods and distorted-wave methods, which were described in Sect. 49.1.5 when we considered intermediate and high-energy elastic scattering and excitation, have been used to obtain ionization amplitudes.

An important development of the distorted wave method was made by *Jones and Madison* [108–110]. Their continuum distorted-wave with eikonal initial state (CDW-EIS) commences from the two-potential expression for the transition amplitude given by *Gell-Mann and Goldberger* [111]

$$T_{fi} = \langle \chi_f^- | W_f^+ | \Psi_i^+ \rangle + \langle \chi_f^- | V_i - W_f^+ | \beta_i \rangle. \quad (49.115)$$

In the first term of this equation, Ψ_i^+ is the exact scattering wave function developed from the initial state satisfying outgoing-wave boundary conditions, χ_f^- is a distorted wave corresponding to the final state satisfying incoming-wave boundary conditions, and the corresponding perturbation W_f^+ is the adjoint of the operator W_f and operates to the left. In the second term, β_i is the unperturbed initial state, which in the case of e–H scattering is

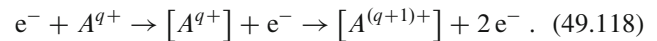
$$\beta_i = (2\pi)^{-3/2} \exp(i\mathbf{k}_0 \mathbf{r}_1) \psi_i(\mathbf{r}_2). \quad (49.116)$$

In this case, V_i is the initial-state interaction potential given by

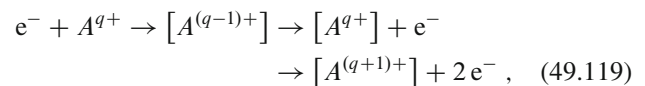
$$V_i = -\frac{1}{r_1} + \frac{1}{r_{12}}. \quad (49.117)$$

An eikonal approximation is made for the initial-state wave function Ψ_i^+ in Eq. (49.115), while the final state χ_f^- is represented by a CDW wave function [112]. In this way, distortion effects are included in both the initial-state and final-state wave functions. Results obtained with the CDW-EIS approximation were compared with ECS calculations for electron impact ionization of atomic hydrogen at 54.4 eV [113] and equal energy sharing between the outgoing electrons. The TDCSs from the two calculations were found to be in very good agreement. More information about this and related approaches, in particular the extension to molecular targets, can be found in [114].

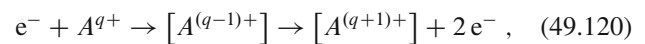
A further development of the distorted-wave method for ionization was made for situations when the incident electron is fast and interacts weakly with the target atom or ion, while the ejected electron is slow and interacts strongly with the residual ion [115, 116]. In this case, Eq. (49.96) is applicable, where the ionizing electron is represented by plane waves or distorted waves, while the initial target state and the ejected-electron–residual-ion interaction are both represented by the close-coupling expansion Eq. (49.8). This hybrid approximation is particularly useful when the ejected electron can be captured into an autoionizing state of the target atom or ion, which then decays giving rise to the excitation-autoionization (EA) process



In this equation, the bracket indicates a resonance state, while q is the charge on the atom A . This process, together with the related resonant excitation double autoionization (REDA) process



and the resonant excitation auto-double ionization (READI) process



have attracted considerable experimental and theoretical interest [117–121]. While the EA process can be accurately treated using a distorted-wave method if the incident electron is fast, both the REDA and READI processes involve capture of the incident electron into a resonant state, and hence a strong-coupling approach is required.

An Example and Conclusions

We conclude this section by mentioning a comparison between theory and experiment for electron impact ionization of hydrogen at 17.6 eV [122]. At this energy, which is only 4 eV above the ionization threshold, strong coupling effects between the incident and ejected electrons as well as the residual proton are important. Consequently, Born series and distorted-wave methods are not applicable. This comparison thus provides a stringent test of theoretical predictions. In the above work [122], TDCS data for coplanar outgoing electrons both having 2 eV energy were compared with ECS and CCC results. The two calculations show excellent overall agreement both with the shape and the magnitude of the experiment for a wide range of scattering angles.

More recently, a similar benchmark study was performed for electron impact ionization of $\text{He}(1s^2)^1S$ leaving the residual ion in its $\text{He}^+(1s)^2S$ ground state [123]. Excellent agreement between experiment and CCC, TDCC, and BSR predictions was obtained.

It is clear that a detailed theoretical understanding of electron impact ionization of simple targets, most notably H and He, has now been obtained over a wide range of energies and angles. Although further work is required to predict accurate cross sections involving highly excited states of interest in plasma physics and astrophysical applications, for example in astrophysical H II regions [124], methods have been developed that should enable these cross sections to be accurately determined.

Good progress has also been made in the study of electron impact ionization of multielectron atoms and ions such as Ne and Ar [125, 126]. Problems still remain both due to the need to obtain accurate target states, which also applies to elastic scattering and excitation, and due to fundamental difficulties in carrying out accurate calculations for REDA and READI processes defined by Eqs. (49.119) and (49.120), respectively. In the latter case, major theoretical difficulties arise in the accurate treatment of resonance states, which decay with the emission of more than one electron.

49.2 Electron–Molecule Collisions

Electron–molecule collision calculations are now routinely performed for a wide variety of reasons. These include precision calculations such as those achieved for the e–H₂ problem by *Zammit, Bray*, and coworkers [72], modeling complex systems, and the provision of data for problems not easily amenable to experimental studies.

49.2.1 Laboratory Frame Representation

The processes that occur in electron collisions with molecules are more diverse than those that occur in electron collisions with atoms and atomic ions because of the possibility of exciting degrees of freedom associated with the motion of the nuclei. In addition, the multicenter and non-spherical nature of the electron–molecule interaction complicates the solution of the collision problem considerably by reducing its symmetry and by introducing multicenter integrals that are more difficult to evaluate than those occurring for atoms and ions.

We first consider the derivation of the equations describing the collision in the laboratory frame of reference discussed by *Arthurs and Dalgarno* [127]. The Schrödinger equation describing the electron–molecule system is

$$(H_m + \mathcal{T}_e + V)\Psi = E\Psi, \quad (49.121)$$

where H_m is the molecular Hamiltonian, \mathcal{T}_e is the kinetic energy operator of the scattered electron, and V is the electron–molecule interaction potential

$$V(\mathbf{R}, \mathbf{r}_m, \mathbf{r}) = \sum_i \frac{1}{|\mathbf{r} - \mathbf{r}_i|} - \sum_i \frac{Z_i}{|\mathbf{r} - \mathbf{R}_i|}. \quad (49.122)$$

Here, \mathbf{R} represents the coordinates \mathbf{R}_i of all the nuclei, \mathbf{r}_m represents the coordinates \mathbf{r}_i of the electrons in the target molecule, and \mathbf{r} represents the coordinates of the scattering electron. The total energy E in Eq. (49.121) refers to the frame of reference where the center of mass of the entire system is at rest.

As in the case of electron–atom and electron–ion collisions, we introduce target eigenstates, and possibly pseudostates Φ_i , by the equation

$$\langle \Phi_i | H_m | \Phi_j \rangle = w_i \delta_{ij}, \quad (49.123)$$

and then expand the total wave function Ψ , in analogy with Eq. (49.8), in the form

$$\Psi_j = \mathcal{A} \sum_i \Phi_i(\mathbf{R}, \mathbf{r}_m) \mathcal{F}_{ij}(\mathbf{r}) + \sum_i \chi_i(\mathbf{R}, \mathbf{r}_m, \mathbf{r}) b_{ij}. \quad (49.124)$$

Here, the spin variables have been suppressed for simplicity of notation, and we have not carried out a partial-wave decomposition of the wave function \mathcal{F}_{ij} representing the scattered electron. The subscripts i and j now represent the

rotational and vibrational states of the molecule as well as its electronic states.

Coupled equations for the functions \mathcal{F}_{ij} can be obtained by substituting expansion Eq. (49.124) into Eq. (49.121) and projecting onto the target states Φ_i and the square-integrable functions χ_j . After eliminating the coefficients b_{ij} , the coupled integro-differential equations

$$(\nabla^2 + k_i^2)F_{ij}(r) = 2 \sum_{\ell} (V_{i\ell} + W_{i\ell} + X_{i\ell})F_{\ell j}(r) \quad (49.125)$$

are obtained, where $k_i^2 = 2(E - w_i)$, and $V_{i\ell}$, $W_{i\ell}$, and $X_{i\ell}$ are the direct, nonlocal exchange, and nonlocal correlation potentials. By expanding F_{ij} in partial waves, a set of coupled radial integro-differential equations result, analogous to Eq. (49.10) for atoms and ions.

The scattering amplitude and cross section for a transition from an initial state $|i\rangle = |k_i, \Phi_i, \chi_{\frac{1}{2}m_i}\rangle$ to a final state $|j\rangle = |k_j, \Phi_j, \chi_{\frac{1}{2}m_j}\rangle$ is given by Eq. (49.7), where now the subscripts i and j refer collectively to the rovibrational and electronic states of the molecule.

49.2.2 Molecular Frame Representation

The theory described in the previous section is completely general and has been the basis of a number of early calculations for simple diatomic molecules such as H_2 . However, major computational difficulties arise because of the very large number of rovibrational channels that need to be retained in expansion Eq. (49.124) for all but the simplest low-energy calculations.

This difficulty can be overcome by making a Born–Oppenheimer separation of the electronic and nuclear motion. The electronic motion is first determined with the nuclei held fixed. This is referred to as the fixed-nuclei approximation (FNA). The molecular rotational and vibrational motion is then included in a second step of the calculation. This procedure owes its validity to the large ratio of the nuclear mass to the electronic mass. It can be adopted when the collision time is much shorter than the periods of molecular rotation and vibration. Thus, it is expected to be valid when the scattered electron energy is not close to a threshold, or when the energy does not coincide with that of a narrow resonance. In these cases, further developments described below are needed to obtain reliable cross sections.

In order to formulate the collision process in this representation, we adopt a frame of reference that is rigidly attached to the molecule. The FNA then starts from the Schrödinger equation

$$(H_{\text{el}} + \mathcal{T}_e + V)\psi = E\psi, \quad (49.126)$$

where H_{el} is the electronic part of the target Hamiltonian obtained by assuming that the target nuclei have fixed coordinates denoted collectively by \mathbf{R} . It follows that H_{el} is related to H_m in Eq. (49.121) by

$$H_m = H_{\text{el}} + \mathcal{T}_R, \quad (49.127)$$

where \mathcal{T}_R is the kinetic energy operator for the rotational and vibrational motion of the nuclei. The remaining quantities \mathcal{T}_e and V are the same as in Eq. (49.121).

The solution of Eq. (49.126) proceeds in an analogous way to the solution of Eq. (49.2) for electron collisions with atoms and ions. We adopt an expansion similar to Eq. (49.8), where we now expand the function representing the motion of the scattered electron in terms of symmetry-adapted angular functions that transform as an appropriate irreducible representation (IRR) of the molecular point group (*Burke et al. [128]*). Substituting this expansion into Eq. (49.126), and projecting onto the corresponding channel functions and onto the square-integrable functions, yields a set of coupled integro-differential equations with the form given by Eq. (49.10), where now the channel indices i , j , and ℓ represent the component of the IRR, as well as the electronic state of the target, and where Γ represents the conserved quantum numbers that include the IRR and the total spin.

The final step is to solve these coupled integro-differential equations for each set of nuclear coordinates \mathbf{R} of importance in the collision, using one of the methods discussed in Sect. 49.1.4. This yields the \mathbf{K} -matrices, \mathbf{S} -matrices, and cross sections for fixed \mathbf{R} . For scattering calculations where only the ground electronic state has been included in the expansion, a number of approaches have been developed that replace the nonlocal exchange and correlation potentials by local potentials [129]. These approaches have proven particularly important in describing electronically elastic collisions of electrons with polyatomic molecules.

49.2.3 Inclusion of the Nuclear Motion

This section discusses how observables involving the nuclear motion, such as rotational and vibrational excitation cross sections, as well as dissociative attachment cross sections, can be obtained from the solutions of the fixed-nuclei equations.

The most widely used approach is the adiabatic-nuclei approximation [130–132]. In the case of diatomic molecules in a $^1\Sigma$ state, the scattering amplitude for a transition between electronic, vibrational, and rotational states represented by $i v j m_j$ and $i' v' j' m'_j$ is given by

$$\begin{aligned} & f_{i'v'j'm'_j, i v j m_j}(\hat{\mathbf{k}} \cdot \hat{\mathbf{r}}) \\ &= \langle \chi_{i'v'}(R) Y_{j'm'_j}(\hat{\mathbf{R}}) | f_{i'i}(\hat{\mathbf{k}} \cdot \hat{\mathbf{r}}; \mathbf{R}) | \chi_{iv}(R) Y_{j m_j}(\hat{\mathbf{R}}) \rangle, \end{aligned} \quad (49.128)$$

where $f_{i'j'}(\hat{\mathbf{k}} \cdot \hat{\mathbf{r}}; \mathbf{R})$ is the fixed-nuclei scattering amplitude, which depends parametrically on the nuclear coordinates \mathbf{R} , while χ_{iv} and Y_{jm_j} are the molecular vibrational and rotational eigenfunctions, respectively. This approximation is valid provided that the collision time is short compared with the vibration and/or rotation times, and it is widely used in such situations.

The cross section is usually averaged over the degenerate sublevels m_j and summed over m'_j , giving the cross section for the transition ivj to $i'v'j'$. This leads to the relation

$$\frac{d\sigma_{i'v'j',ivj}}{d\Omega} = \sum_{j_i=|j-j'|}^{j+j'} [(j0j_i0 | j'0)]^2 \frac{d\sigma_{i'v'j_i,iv0}}{d\Omega}, \quad (49.129)$$

provided that the small differences in the wave numbers for the different rotational channels can be neglected. A similar relation holds for symmetric top molecules such as NH_3 . For spherical-top molecules such as CH_4 , the equivalent relation is [133, 134]

$$\frac{d\sigma_{i'v'j',ivj}}{d\Omega} = \frac{2j'+1}{2j+1} \sum_{j_i=|j-j'|}^{j+j'} \frac{1}{2j_i+1} \frac{d\sigma_{i'v'j_i,iv0}}{d\Omega}. \quad (49.130)$$

The sum in Eq. (49.129) or Eq. (49.130) over the final rotational state j' is independent of the initial state j . Also, if the cross section is multiplied by the transition energy and then summed over j' , the result, which is for the mean energy loss by the incident electron, is still independent of j .

A general code, POLYDCS [135], is available. It uses a frame-transformation to include the effects of rotational motion in FNA scattering calculations. This approach has proved very successful and is the main source of rotational excitation cross sections, as the very small excitation energies for this process means that they largely defy experimental measurement. POLYDCS can also implement a Born correction for scattering off dipole systems, since this has to be performed simultaneously with a treatment of rotational motion that acts to dampen the long-range effects of the dipole.

The adiabatic-nuclei approximation breaks down close to threshold or in the neighborhood of narrow resonances [136]. A straightforward way of including nonadiabatic effects that arise in vibrational excitation is to retain the vibrational terms in the Hamiltonian, but still to treat the rotational motion adiabatically. Hence, instead of Eq. (49.126), the equation

$$(H_{\text{el}} + \mathcal{T}_{\text{vib}} + \mathcal{T}_e + V)\tilde{\psi} = E\tilde{\psi} \quad (49.131)$$

is solved, where \mathcal{T}_{vib} is the kinetic energy operator for the nuclear vibrational motion, and where the other quantities have the same meaning as in Eq. (49.126). Adopting

a frame of reference in which the molecule has fixed spatial orientation and separating out the angular variables of the scattered electron, coupled integro-differential equations coupling the target vibrational states as well the electronic states can be obtained. This approach has been adopted with success [137, 138], but it is computationally demanding, since the number of coupled channels can become very large.

Vibrational excitation and dissociative attachment are particularly important in resonance regions when the scattered electron spends an appreciable time in the neighborhood of the molecule. As a result, several approaches have been developed to describe these processes based on electron–molecule resonance theories (e.g., [139–143]). The basic idea is that a series of fixed-nuclei resonance states $\psi_n^{(r)}$ are introduced for a range of values of R , either by imposing Siegert outgoing-wave boundary conditions [144] or by introducing Feshbach projection operators [20, 21]. The amplitude for a transition from an initial electronic-vibrational state iv to a final state $i'v'$ is then given by

$$T_{i'v',iv} = \sum_n \langle \chi_{i'v'}(R') \zeta_{ni'}(R') | G_n^{(r)}(R', R) \times | \zeta_{ni}(R) \chi_{iv}(R) \rangle, \quad (49.132)$$

where χ_{iv} are the vibrational eigenfunctions, ζ_{ni} are the *entry amplitudes* from the initial or final electronic states into the resonance states $\psi_n^{(r)}$, and $G_n^{(r)}$ are the Green's functions that describe the propagation in the intermediate resonance states $\psi_n^{(r)}$. Dissociative attachment can be described by a straightforward extension of this theory.

The fixed-nuclei \mathbf{R} -matrix method was also extended to treat vibrational excitation and dissociative attachment [145]. A generalized \mathbf{R} -matrix is introduced by an equation that, in analogy with Eq. (49.132), is written as

$$R_{i'v',iv} = \frac{1}{2a} \sum_k \langle \chi_{i'v'}(R') w_{ik}^\Gamma(R') | G_k^{RM}(R', R) \times | w_{ik}^\Gamma(R) \chi_{iv}(R) \rangle, \quad (49.133)$$

where the surface amplitudes $w_{ik}^\Gamma(R)$ are defined by Eq. (49.65), and Green's function G_k^{RM} now describes the propagation in the intermediate \mathbf{R} -matrix states defined by Eq. (49.62). Once the generalized \mathbf{R} -matrix has been determined, the final step in the calculation is to solve the collision problem in the external region that, for diatomic molecules, is defined by the condition that the scattered electron coordinate r is greater than some given radius a , and the internuclear coordinate R is greater than some given radius A .

Electron collisions with CO_2 molecules are important technologically and provide a benchmark problem for the theoretical treatment of vibrational excitation in polyatomic molecules. Such collisions were calculated in the FNA using an electron–polyatomic molecular scattering program

based on the complex Kohn variational method [146]. At low energies, the cross section is dominated by a virtual state at threshold and a ${}^2\Pi_u$ shape resonance at 3.8 eV. As the molecule bends from its ground-state linear configuration, the shape resonance splits into nondegenerate 2A_1 and 2B_1 configurations. The fixed-nuclei complex resonance energy surfaces are parametrized, and motion on these surfaces is computed using a generalization of the boomerang model [147]. The results reproduce the oscillations resulting from the interference between the nuclear and electronic motion that were seen experimentally by *Allan* [148, 149]. Cross sections for excitations between excited states, which are important for plasma studies but not amenable to experimental investigation, are also available [150].

Another approach that includes nonadiabatic effects is the energy-modified adiabatic approximation introduced by *Nesbet* [151]. In this approach, the S -matrix elements connecting the vibrational states are defined by

$$S_{i'v',iv} = \langle \chi_{i'v'} | S_{i'i}(E - H_i; R) | \chi_{iv} \rangle, \quad (49.134)$$

where $S_{i'i}(E - H_i; R)$ are the elements of the S -matrix calculated in the FNA at the internuclear separation R for an energy defined by the operator $H_i = E_i(R) + \mathcal{T}_{\text{vib}}$. This has the effect of including the internal energy of the target into the S -matrix elements, thus giving the correct threshold energies.

Finally, we mention an off-shell T -matrix approach for including nonadiabatic effects discussed first by *Shugard* and *Hazi* [152]. This approach can also extend the range of validity of the adiabatic-nuclei approximation while retaining much of its inherent simplicity. It was applied with success to low-energy vibrational excitation of H_2 and CH_4 [153].

49.2.4 Electron Collisions with Polyatomic Molecules

Computer programs based on the ab initio methods described in Sect. 49.1.4 have been developed and used to calculate cross sections for electron collisions with polyatomic molecules of importance in many applications.

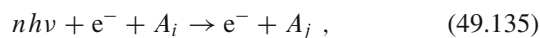
Data are provided for a variety of topics. Examples include technological plasmas where it has been argued that calculations provide the only viable means of providing complete datasets for the entire range of systems [154]. This is particularly true for open-shell species or radicals for which experimental data are almost entirely nonexistent. An example of this sort is the work of *Hamilton* and coworkers, who generated a complete dataset of electron collision cross sections for the NF_x $x = 1, 2, 3$ species [155], which was subsequently used as the input for detailed plasma models of these species [156, 157].

Similarly, input is used for atmospheric reentry plasma [158], fusion plasmas [47], and astrophysics. Astrophysically, electron collisions are important for dissociative recombination, which is a major destroyer of molecular ions in the interstellar medium [159], formation of molecular anions [160], and rotational excitation [161]. The cross sections were placed in databases [162, 163] and assembled into sets to address specific problems [161].

The observation by *Boudaïffa* et al. [164] that the DNA strand breaks, which result from damage by all types of radiation, were substantially caused by collisions with low-energy (sub 10 eV) electrons has led to the creation of a new and very active field of electron collision studies. The interest in characterizing the resonances supported by DNA fragments and DNA itself has led to electron-collision calculations with essentially all the theoretical methods described above and, of course, parallel experimental activity. These studies have been extensively reviewed [165–168]. Similar studies have also been performed on smaller biomolecules that constitute biofuels [168, 169].

49.3 Electron–Atom Collisions in a Laser Field

Electron–atom collisions in the presence of an intense laser field have recently attracted considerable attention because of the importance of these processes in applications such as laser–plasma interactions, and also because of their fundamental interest for atomic collision theory. This section summarizes the basic theory, commencing with the scattering of electrons by a potential in the presence of a laser field. The discussion is then generalized to the scattering of electrons by complex atoms and ions, where *dressing* of the atomic eigenstates by the laser field must be considered, and where simultaneous electron–photon excitation (SEPE) processes, defined by



can occur. Early reviews of some aspects of this subject were given by *Mason* [170], *Newell* [171], and *Mittleman* [172].

49.3.1 Potential Scattering

We adopt a semiclassical description of the collision process, in which the electrons and the target atom are described by the nonrelativistic Schrödinger equation, while the laser field is described classically. This is valid for most high-intensity fields of current interest, where a typical coherence volume of the field contains a very large number of photons [172].

The time-dependent Schrödinger equation describing an electron scattered by a potential $V(\mathbf{r})$ in the presence of an

external electromagnetic (laser) field is

$$\begin{aligned} i\frac{\partial}{\partial t}\Psi(\mathbf{r}, t) = & \left[-\frac{1}{2}\nabla^2 - \frac{i}{c}\mathbf{A}(\mathbf{r}, t) \cdot \nabla \right. \\ & \left. + \frac{1}{2c^2}\mathbf{A}^2(\mathbf{r}, t) + V(\mathbf{r}) \right] \Psi(\mathbf{r}, t), \end{aligned} \quad (49.136)$$

in the Coulomb gauge, such that the vector potential satisfies $\nabla \cdot \mathbf{A} = 0$. We also assume that the laser field is monochromatic, monomode, linearly polarized, and spatially homogeneous (i.e., its wavelength is large compared with the range of the potential, or, more generally, with the size of the atom). Hence we can write

$$\mathbf{A}(\mathbf{r}, t) = \mathbf{A}(t) = \hat{\mathbf{e}}A_0 \cos \omega t, \quad (49.137)$$

where $\hat{\mathbf{e}}$ is a unit vector along the field polarization direction, and ω is the angular frequency. The \mathbf{A}^2 term in Eq. (49.136) can be removed by the unitary transformation

$$\Psi(\mathbf{r}, t) = \exp\left(-\frac{i}{2c^2} \int^t \mathbf{A}^2(t') dt'\right) \Psi_V(\mathbf{r}, t), \quad (49.138)$$

where Ψ_V satisfies the Schrödinger equation in the velocity gauge given by

$$\begin{aligned} i\frac{\partial}{\partial t}\Psi_V(\mathbf{r}, t) = & \left[-\frac{1}{2}\nabla^2 - \frac{i}{c}\mathbf{A}(t) \cdot \nabla + V(\mathbf{r}) \right] \\ & \times \Psi_V(\mathbf{r}, t). \end{aligned} \quad (49.139)$$

The corresponding equation for the free electron with $V = 0$ is readily solved to give the Volkov wave function [173]

$$\chi_k(\mathbf{r}, t) = (2\pi)^{-\frac{3}{2}} \exp[i(\mathbf{k} \cdot \mathbf{r} - \mathbf{k} \cdot \boldsymbol{\alpha}_0 \sin \omega t - Et)], \quad (49.140)$$

where \mathbf{k} is the wave vector and $E = \frac{1}{2}k^2$ the kinetic energy. The quantity $\boldsymbol{\alpha}(t)$ is defined by

$$\boldsymbol{\alpha}(t) = \frac{1}{c} \int^t \mathbf{A}(t') dt' = \boldsymbol{\alpha}_0 \sin \omega t, \quad (49.141)$$

where $\boldsymbol{\alpha}_0 = \mathcal{E}_0/\omega^2$ with \mathcal{E}_0 being the electric field strength.

To solve Eq. (49.139), we introduce the causal Green's function $G_0^{(+)}(\mathbf{r}, t; \mathbf{r}', t')$ satisfying the equation

$$\begin{aligned} \left(i\frac{\partial}{\partial t} + \frac{1}{2}\nabla^2 + \frac{i}{c}\mathbf{A}(t) \cdot \nabla \right) G_0^{(+)}(\mathbf{r}, t; \mathbf{r}', t') \\ = \delta(\mathbf{r} - \mathbf{r}')\delta(t - t'). \end{aligned} \quad (49.142)$$

This Green's function is given by

$$\begin{aligned} G_0^{(+)}(\mathbf{r}, t; \mathbf{r}', t') \\ = -i\theta(t - t') \int \chi_k(\mathbf{r}, t)\chi_k^*(\mathbf{r}', t') d\mathbf{k}, \end{aligned} \quad (49.143)$$

where $\theta(x) = 1$ for $x > 0$ and $\theta(x) = 0$ for $x < 0$. The corresponding causal outgoing-wave solution of Eq. (49.139) is

$$\begin{aligned} \Psi_k^{(+)}(\mathbf{r}, t) = \chi_k(\mathbf{r}, t) + \int_{-\infty}^t dt' \int d\mathbf{r}' G_0^{(+)}(\mathbf{r}, t; \mathbf{r}', t') \\ \times V(\mathbf{r}')\Psi_k^{(+)}(\mathbf{r}', t'), \end{aligned} \quad (49.144)$$

and the S -matrix element for a transition $\mathbf{k}_i \rightarrow \mathbf{k}_f$ in the presence of the laser field is given by

$$S_{k_f, k_i} = -i\langle \chi_{k_f} | V | \Psi_{k_i}^{(+)} \rangle, \quad (49.145)$$

where an integration is carried out over all space and time in this matrix element. The time integration in Eq. (49.145) can be performed using the relation

$$\exp(ix \sin u) = \sum_{n=-\infty}^{\infty} J_n(x) \exp(inu), \quad (49.146)$$

where $J_n(x)$ is an ordinary Bessel function of order n . Then

$$S_{k_f, k_i} = -2\pi i \sum_{n=-\infty}^{\infty} \delta(E_{k_f} - E_{k_i} - n\omega) T_{k_f, k_i}^n, \quad (49.147)$$

where the δ -function ensures energy conservation, and n is the number of photons absorbed or emitted. The differential cross section for the scattering process $\mathbf{k}_i \rightarrow \mathbf{k}_f$ with exchange of n photons can then be defined in terms of the T -matrix elements T_{k_f, k_i}^n by

$$\frac{d\sigma_n}{d\Omega} = (2\pi)^4 \frac{k_f}{k_i} |T_{k_f, k_i}^n|^2. \quad (49.148)$$

There are two limiting cases in which considerable simplification in this expression occurs. First, at high energies or for weak potentials, the first Born approximation can be used to describe scattering by the potential $V(\mathbf{r})$. In this case, Eq. (49.148) reduces to

$$\frac{d\sigma_n^{1,B}}{d\Omega} = (2\pi)^4 \frac{k_f}{k_i} J_n^2(\boldsymbol{\Delta} \cdot \boldsymbol{\alpha}_0) |\mathcal{V}(\boldsymbol{\Delta})|^2, \quad (49.149)$$

where $\boldsymbol{\Delta} = \mathbf{k}_i - \mathbf{k}_f$ is the momentum-transfer vector and

$$\mathcal{V}(\boldsymbol{\Delta}) = (2\pi)^{-3} \int \exp(i\boldsymbol{\Delta} \cdot \mathbf{r}) V(\mathbf{r}) d\mathbf{r}. \quad (49.150)$$

It follows immediately that

$$\frac{d\sigma_n^{1,B}}{d\Omega} = J_n^2(\mathbf{A} \cdot \boldsymbol{\alpha}_0) \frac{d\sigma^{1,B}}{d\Omega}, \quad (49.151)$$

where $d\sigma^{1,B}/d\Omega$ is the field-free first Born differential cross section. Using the sum rule

$$\sum_{n=-\infty}^{\infty} J_n^2(x) = 1, \quad (49.152)$$

Eq. (49.151) yields

$$\sum_{n=-\infty}^{\infty} \frac{d\sigma_n^{1,B}}{d\Omega} = \frac{d\sigma^{1,B}}{d\Omega}. \quad (49.153)$$

The second limiting case is the low-frequency (soft-photon) limit, where the laser photon energy ω is small compared with the electron energy E_{k_i} . In this limit, the T -matrix element is given by [174]

$$T_{k_f, k_i}^n = J_n(\mathbf{A} \cdot \boldsymbol{\alpha}_0) \langle \chi_{k_f} | \mathcal{T}(E_{k_i}) | \chi_{k_i} \rangle + O(\omega^2), \quad (49.154)$$

where \mathbf{k}'_i and \mathbf{k}'_f are the shifted wave vectors

$$\mathbf{k}'_i = \mathbf{k}_i + \frac{n\omega}{\mathbf{A} \cdot \boldsymbol{\alpha}_0} \boldsymbol{\alpha}_0, \quad \mathbf{k}'_f = \mathbf{k}_f + \frac{n\omega}{\mathbf{A} \cdot \boldsymbol{\alpha}_0} \boldsymbol{\alpha}_0, \quad (49.155)$$

and $\mathcal{T}(E_{k_i})$ is the transition operator in the absence of the laser, corresponding to the energy $E_{k_i} = k_i^2/2$. The angle-differential cross section for the transfer of n photons is

$$\frac{d\sigma_n}{d\Omega} = \frac{k_f}{k_i} J_n^2(\mathbf{A} \cdot \boldsymbol{\alpha}_0) \frac{d\sigma}{d\Omega}(\mathbf{k}'_f, \mathbf{k}'_i) + O(\omega^2), \quad (49.156)$$

where $d\sigma(\mathbf{k}'_f, \mathbf{k}'_i)/d\Omega$ refers to the transition $\mathbf{k}'_i \rightarrow \mathbf{k}'_f$ in the absence of the laser. If the frequency is small enough to neglect the n -dependence of \mathbf{k}'_i and \mathbf{k}'_f , using the sum rule Eq. (49.152) brings Eq. (49.156) to

$$\sum_{n=-\infty}^{\infty} \frac{d\sigma_n}{d\Omega} = \frac{d\sigma}{d\Omega}, \quad (49.157)$$

where $d\sigma/d\Omega$ is the field-free differential cross section. The Kroll–Watson result Eq. (49.156) has been found to be surprisingly accurate, even for cases where $\omega/E_{k_i} \approx 0.5$ [175, 176]. A nonrigorous extension of the Kroll–Watson result to inelastic processes was considered by a number of authors and was found to give qualitative agreement with experiments on helium [177].

49.3.2 Scattering by Complex Atoms and Ions

The time-dependent Schrödinger equation describing an electron scattered by an N -electron atom or ion in the

presence of a laser field can be written in analogy with Eq. (49.136) as

$$\begin{aligned} & i \frac{\partial}{\partial t} \Psi(\mathbf{X}_{N+1}, t) \\ &= \left[H_{N+1} - \frac{i}{c} \sum_{i=1}^{N+1} \mathbf{A}(\mathbf{r}_i, t) \cdot \nabla_i \right. \\ & \quad \left. + \frac{1}{2c^2} \sum_{i=1}^{N+1} \mathbf{A}^2(\mathbf{r}_i, t) \right] \Psi(\mathbf{X}_{N+1}, t), \end{aligned} \quad (49.158)$$

where H_{N+1} is the $(N+1)$ -electron Hamiltonian defined by Eq. (49.3), and \mathbf{X}_{N+1} represents the space and spin coordinates of all $N+1$ electrons defined as in Eq. (49.8).

With the same assumptions made in the reduction of Eqs. (49.136)–(49.139), Eq. (49.152) can be rewritten in the velocity gauge form as

$$\begin{aligned} & i \frac{\partial}{\partial t} \Psi_V(\mathbf{X}_{N+1}, t) \\ &= \left(H_{N+1} + \frac{1}{c} \mathbf{A}(t) \cdot \mathbf{P}_{N+1} \right) \Psi_V(\mathbf{X}_{N+1}, t), \end{aligned} \quad (49.159)$$

where

$$\mathbf{P}_{N+1} = \sum_{i=1}^{N+1} -i\nabla_i \quad (49.160)$$

is the total linear-momentum operator.

The solution of Eq. (49.159) for e–H scattering in a strong laser field at high electron impact energies was considered by Francken and Joachain [178]. They discussed the use of the Born series and the eikonal Born series (EBS) approximations, given by Eq. (49.93), to describe the electron–atom collision and included the dressed wave function of the atomic hydrogen target to first order in the field strength \mathcal{E}_0 . Important effects related to the dressing of the target are the appearance in the cross sections of asymmetries between the absorption and emission of a given number of laser photons, as well as the appearance of new resonance structures in the cross sections.

Early detailed studies of low-energy electron–atom and electron–ion collisions in laser fields include the pioneering work on e–H⁺ collisions by Dimou and Faisal [179]. Collins and Csanak [180] found important resonance effects caused by the field coupling bound states to the continuum, and multichannel quantum defect theory was applied by Zoller and coworkers [181, 182] to study the behavior of Rydberg states in laser fields.

We conclude this section by briefly describing the R -matrix-Floquet method [183] for treating electron collisions with complex atoms and ions in a laser field, based on the R -matrix method discussed in Sect. 49.1.4. In this approach, configuration space is divided into internal and external regions, as in the field-free case. In the internal region,

a further gauge transformation of the field is made to the length gauge, so that the time-dependent Schrödinger equation (49.159) becomes

$$i \frac{\partial}{\partial t} \Psi_L(\mathbf{X}_{N+1}, t) = [H_{N+1} + \mathcal{E}(t) \cdot \mathbf{R}_{N+1}] \Psi_L(\mathbf{X}_{N+1}, t), \quad (49.161)$$

where $\mathbf{R}_{N+1} = \sum_{i=1}^{N+1} \mathbf{r}_i$, and we assume that the electric field $\mathcal{E}(t)$ is given by

$$\mathcal{E}(t) = -\frac{1}{c} \frac{d}{dt} \mathbf{A}(t) = \hat{\epsilon} \mathcal{E}_0 \cos \omega t. \quad (49.162)$$

In order to solve Eq. (49.161), we introduce the Floquet–Fourier expansion [184, 185]

$$\Psi_L(\mathbf{X}_{N+1}, t) = e^{-iEt} \sum_{n=-\infty}^{\infty} e^{-in\omega t} \Psi_n^L(\mathbf{X}_{N+1}). \quad (49.163)$$

Substituting this equation into Eq. (49.161), using Eq. (49.162), and equating the coefficients of $\exp[-i(E + n\omega)t]$ to zero gives

$$(H_{N+1} - E - n\omega) \Psi_n^L + D_{N+1} (\Psi_{n-1}^L + \Psi_{n+1}^L) = 0, \quad (49.164)$$

where we have introduced the operator

$$D_{N+1} = \frac{1}{2} \mathcal{E}_0 \hat{\epsilon} \cdot \mathbf{R}_{N+1}. \quad (49.165)$$

The functions Ψ_n^L can be regarded as the components of a vector Ψ^L in photon space. Equation (49.164) is then written in this space as

$$(\mathbf{H}_F - E\mathbf{I}) \Psi^L = 0, \quad (49.166)$$

where the Floquet Hamiltonian \mathbf{H}_F is an infinite tridiagonal matrix.

In order to solve Eq. (49.166) in the internal region, the components Ψ_n^L are expanded in a basis that, in analogy with Eq. (49.58), has the form

$$\begin{aligned} \Psi_{kn}^L(\mathbf{X}_{N+1}) &= \mathcal{A} \sum_{\Gamma ij} \bar{\Phi}_i^\Gamma(\mathbf{x}_1, \dots, \mathbf{x}_N; \hat{\mathbf{r}}_{N+1} \sigma_{N+1}) r_{N+1}^{-1} \\ &\times u_j(r_{N+1}) a_{ijkn}^\Gamma \\ &+ \sum_{\Gamma i} \chi_i^\Gamma(\mathbf{x}_1, \dots, \mathbf{x}_{N+1}) b_{ikn}^\Gamma, \end{aligned} \quad (49.167)$$

where the summation over Γ is required since the total orbital angular momentum L and the total parity π in Eq. (49.9) are no longer conserved. The coefficients a_{ijkn}^Γ and b_{ikn}^Γ are again

determined by diagonalizing $\mathbf{H}_F + \mathbf{L}_b$, where \mathbf{L}_b is an appropriate Bloch operator.

In the external region, the wave function describing the scattered electron is transformed to the velocity gauge, and the corresponding coupled equations are integrated outwards from the internal region boundary for each energy of interest [186]. After a further transformation to the acceleration frame (or Kramers–Henneberger frame [187]), the wave function can be fitted to an asymptotic form to yield the \mathbf{K} -matrix, \mathbf{S} -matrix, and collision cross sections. This approach has been used to calculate laser-assisted electron scattering by H and He atoms [188, 189], and a detailed discussion of the theory is given [190].

Following the rapid development of advanced light sources based, for example, on high-harmonic generation and free-electron lasers, as well as the appearance of intense few-cycle infrared lasers, much effort is currently being devoted to further improving the general description and the accompanying computer programs. Rather than using the Floquet approach for multicycle pulses as described above, it is again necessary to solve the TDSE directly by propagating an initial state under the influence of the laser field and extracting the physically meaningful information using appropriate projection techniques. More information can be found, for example, in [191–196], as well as references therein. In particular, the time-dependent \mathbf{R} -matrix method, originally formulated by *Burke* and *Burke* [197], is now finding practical implementation [198] for atoms and molecules in intense laser fields.

References

1. Burke, P.G., Joachain, C.J. (eds.): Photon and Electron Collisions with Atoms and Molecules. Plenum, New York (1997)
2. Brunger, M.J., Buckman, S.J.: Phys. Rep. **357**, 215 (2002)
3. Tennyson, J.: Phys. Rep. **491**, 29 (2010)
4. Bartschat, K.: J. Phys. D **44**, 334004 (2013)
5. Bartschat, K., Tennyson, J., Zatsariny, O.: Plasma Process. Polym. **49**, 1600093 (2017)
6. Bartschat, K.: J. Phys. B **51**, 132001 (2018)
7. Chung, H.K., Braams, B.J., Bartschat, K., Császár, A.G., Drake, G.W.F., Kirchner, T., Kokouline, V., Tennyson, J.: J. Phys. D **49**, 363002 (2016)
8. Percival, I.C., Seaton, M.J.: Proc. Camb. Philos. Soc. **53**, 654 (1957)
9. O'Malley, T.F., Spruch, L., Rosenberg, L.: J. Math. Phys. **2**, 491 (1961)
10. Ali, M.K., Fraser, P.A.: J. Phys. B **10**, 3091 (1977)
11. Seaton, M.J.: Rep. Prog. Phys. **46**, 167 (1983)
12. Saraph, H.E.: Comput. Phys. Commun. **3**, 256 (1972)
13. Saraph, H.E.: Comput. Phys. Commun. **15**, 247 (1978)
14. Jones, M.: Philos. Trans. R. Soc. A **277**, 587 (1975)
15. Scott, N.S., Burke, P.G.: J. Phys. B **13**, 4299 (1980)
16. Chang, J.J.: J. Phys. B **8**, 2327 (1975)
17. Norrington, P.H., Grant, I.P.: J. Phys. B **14**, L261 (1981)
18. Fano, U.: Phys. Rev. **124**, 1866 (1961)
19. Fano, U.: Rep. Prog. Phys. **46**, 97 (1983)

20. Feshbach, H.: *Ann. Phys.* **5**, 357 (1958)
21. Feshbach, H.: *Ann. Phys.* **19**, 287 (1962)
22. Brenig, W., Haag, R.: *Fortschr. Phys.* **7**, 183 (1959)
23. Burke, P.G.: *Adv. At. Mol. Phys.* **4**, 173 (1968)
24. Smith, F.T.: *Phys. Rev.* **118**, 349 (1960)
25. Little, D.A., Tennyson, J.: *J. Phys. B* **47**, 105204 (2014)
26. Morgan, L.A.: *Phys. Rev. Lett.* **80**, 1873 (1998)
27. Noble, C.J., Dörr, M., Burke, P.G.: *J. Phys. B* **26**, 2983 (1993)
28. Wigner, E.P.: *Phys. Rev.* **70**, 15 (1946)
29. Wigner, E.P.: *Phys. Rev.* **70**, 606 (1946)
30. Wigner, E.P., Eisenbud, L.: *Phys. Rev.* **72**, 29 (1947)
31. Burke, P.G., Berrington, K.A.: *Atomic and Molecular Processes: An R-Matrix Approach*. IOP, Bristol (1993)
32. Burke, P.G.: *R-Matrix Theory of Atomic Collisions*. Springer, Heidelberg (2011)
33. Bloch, C.: *Nucl. Phys.* **4**, 503 (1957)
34. Gailitis, M.: *J. Phys. B* **9**, 843 (1976)
35. Berrington, K.A., Eissner, W., Norrington, P.H.: *Comput. Phys. Commun.* **92**, 290 (1995)
36. Department of Physics at the University of Strathclyde: *Theoretical Atomic Collisions*. <http://amdpp.phys.strath.ac.uk/tamoc/>
37. Sarpal, B.K., Pflugst, K., Nestmann, B.M., Peyerimhoff, S.D.: *J. Phys. B* **29**, 857 (1996)
38. Morgan, L.A., Gillan, C.J., Tennyson, J., Chen, X.: *J. Phys. B* **30**, 4087 (1997)
39. Carr, J.M., Galitsatos, P.G., Gorfinkiel, J.D., Harvey, A.G., Lysaght, M.A., Madden, D., Masin, Z., Plummer, M., Tennyson, J.: *Eur. Phys. J. D* **66**, 58 (2012)
40. Tennyson, J., Brown, D.B., Munro, J.J., Rozum, I., Varambhia, H.N., Vinci, N.: *J. Phys. Conf. Ser.* **86**, 012001 (2007)
41. Quantemol Ltd: *Quantemol-N* (2021). <http://www.quantemol.com/products/quantemol-n/>
42. Zatsarinny, O., Fischer, C.F.: *J. Phys. B* **33**, 313 (2000)
43. Zatsarinny, O.: *Comput. Phys. Commun.* **174**, 273 (2006)
44. Zatsarinny, O., Bartschat, K.: *Phys. Rev. A* **77**, 062701 (2008)
45. Zatsarinny, O., Bartschat, K.: *J. Phys. B* **46**, 112001 (2013)
46. Marante, C., Klinker, M., Corral, I., Gonzalez-Vazquez, J., Argenti, L., Martin, F.: *J. Chem. Theory. Comput.* **13**, 499 (2017)
47. Darby-Lewis, D., Masin, Z., Tennyson, J.: *J. Phys. B* **50**, 175201 (2017)
48. Nesbet, R.K.: *Variational Methods in Electron-Atom Scattering Theory*. Plenum, New York (1980)
49. Miller, W.H.: *Comments At. Mol. Phys.* **22**, 115 (1988)
50. Schneider, B.I., Rescigno, T.N.: *Phys. Rev. A* **37**, 3749 (1988)
51. Takatsuka, K., McKoy, V.: *Phys. Rev. A* **24**, 2743 (1981)
52. Seaton, M.J.: *J. Phys. B* **7**, 1817 (1974)
53. Schneider, B.I., Collins, L.A.: *Comput. Phys. Rep.* **10**, 49 (1989)
54. Burke, P.G., Schey, H.M.: *Phys. Rev.* **126**, 147 (1962)
55. Damburg, R., Karule, E.: *Proc. Phys. Soc.* **90**, 637 (1967)
56. Burke, P.G., Webb, T.G.: *J. Phys. B* **3**, L131 (1970)
57. Callaway, J., Wooten, J.W.: *Phys. Lett. A* **45**, 85 (1973)
58. Callaway, J., Wooten, J.W.: *Phys. Rev. A* **9**, 1924 (1974)
59. Callaway, J., Wooten, J.W.: *Phys. Rev. A* **11**, 1118 (1975)
60. Burke, P.G., Noble, C.J., Scott, M.P.: *Proc. R. Soc. A* **410**, 289 (1987)
61. Scholz, T.T., Walters, H.R.J., Burke, P.G., Scott, M.P.: *J. Phys. B* **24**, 2097 (1991)
62. Dunseath, K.M., LeDourneuf, M., Terezo-Dunseath, M., Launay, J.-M.: *Phys. Rev. A* **54**, 561 (1996)
63. Scott, M.P., Stitt, T., Scott, N.S., Burke, P.G.: *J. Phys. B* **35**, L323 (2002)
64. Bartschat, K., Hudson, E.T., Scott, M.P., Burke, P.G., Burke, V.M.: *J. Phys. B* **29**, 115 (1996)
65. Bartschat, K., Bray, I.: *Phys. Rev. A* **54**, R1002 (1996)
66. Bartschat, K.: *J. Phys. B* **32**, L355 (1999)
67. Mitnik, D.M., Griffin, D.C., Balance, C.P., Badnell, N.R.: *J. Phys. B* **36**, 717 (2003)
68. Gorfinkiel, J.D., Tennyson, J.: *J. Phys. B* **37**, L343 (2004)
69. Rotenberg, M.: *Ann. Phys.* **19**, 262 (1962)
70. Bray, I., Fursa, D.V., Kheifets, A.S., Stelbovics, A.T.: *J. Phys. B* **35**, R117 (2002)
71. Bray, I., Fursa, D.V., Kadyrov, A.S., Stelbovics, A.T., Kheifets, A.S., Mukhamedzhanov, A.M.: *Phys. Rep.* **520**, 135 (2012)
72. Zammit, M.C., Fursa, D.V., Savage, J.S., Bray, I.: *J. Phys. B* **50**, 123001 (2017)
73. Mittleman, M.H., Watson, K.M.: *Phys. Rev.* **113**, 198 (1959)
74. Byron Jr., F.W., Joachain, C.J.: *J. Phys. B* **14**, 2429 (1981)
75. Bransden, B.H., Coleman, J.P.: *J. Phys. B* **5**, 537 (1972)
76. Bransden, B.H., Scott, T., Shingal, R., Raychoudhury, R.K.: *J. Phys. B* **15**, 4605 (1982)
77. McCarthy, I.E.: *Comments At. Mol. Phys.* **24**, 343 (1990)
78. Callaway, J., Oza, D.H.: *Phys. Rev. A* **32**, 2628 (1985)
79. Walters, H.R.J.: *Phys. Rep.* **116**, 1 (1984)
80. Joachain, C.J.: In: Gianturco, F.A. (ed.) *Collision Theory for Atoms and Molecules*, p. 59. Plenum, New York (1989)
81. Eitel, W., Kessler, J.: *Phys. Rev. Lett.* **24**, 1472 (1970)
82. Madison, D.H., Shelton, W.N.: *Phys. Rev. A* **7**, 514 (1973)
83. Bartschat, K., Blum, K.: *J. Phys. B* **15**, 2724 (1982)
84. Byron Jr., F.W., Joachain, C.J.: *Phys. Lett. C* **44**, 233 (1977)
85. Glauber, R.J.: In: Brittin, W.E. (ed.) *Lectures in Theoretical Physics*, vol. 1, p. 315. Interscience, New York (1959)
86. Ochkur, V.I.: *Sov. Phys. JETP* **18**, 503 (1964)
87. Norcross, D.W., Padiyal, N.T.: *Phys. Rev.* **25**, 226 (1982)
88. Madison, D.H., Bartschat, K.: *J. Phys. B* **20**, 5839 (1987)
89. Madison, D.H., Bartschat, K.: In: Bartschat, K. (ed.) *Computational Atomic Physics*, p. 65. Springer, Heidelberg (1996)
90. Los Alamos National Laboratory. <http://aphysics2.lanl.gov/tempweb/lanl/>
91. Rudge, M.R.H., Seaton, M.J.: *Proc. R. Soc. A* **283**, 262 (1965)
92. Peterkop, R.K.: *Proc. Phys. Soc.* **77**, 1220 (1961)
93. Rudge, M.R.H.: *Rev. Mod. Phys.* **40**, 564 (1968)
94. Kadyrov, A.S., Mukhamedzhanov, A.M., Stelbovics, A.T., Bray, I.: *Phys. Rev. Lett.* **91**, 253202 (2003)
95. Peterkop, R.K.: *Opt. Spektrosk.* **13**, 153 (1962). Translation in *Opt. Spectrosc.* **13**, 87 (1962)
96. Peterkop, R.K.: *Theory of Ionization of Atoms by Electron Impact*. Colorado Associated University Press, Boulder (1977)
97. Zatsarinny, O., Bartschat, K.: *Phys. Rev. Lett.* **107**, 023203 (2011)
98. Bray, I., Guilfoile, C.J., Kadyrov, A.S., Fursa, D.V., Stelbovics, A.T.: *Phys. Rev. A* **90**, 022710 (2014)
99. Zatsarinny, O., Bartschat, K.: *Phys. Rev. A* **93**, 012712 (2016)
100. Pindzola, M.S., Schultz, D.R.: *Phys. Rev. A* **53**, 1525 (1996)
101. Pindzola, M.S., Robicheaux, F.J.: *Phys. Rev. A* **54**, 2142 (1996)
102. Pindzola, M.S., Robicheaux, F.J.: *Phys. Rev. A* **61**, 052707 (2000)
103. Colgan, J., Pindzola, M.S., Robicheaux, F.J., Griffin, D.C., Baertschy, M.: *Phys. Rev. A* **65**, 042721 (2002)
104. Pindzola, M.S., Robicheaux, F., Loch, S.D., Berengut, J.C., Topcu, T., Colgan, J., Foster, M., Griffin, D.C., Ballance, C.P., Schultz, D.R.: *J. Phys. B* **40**, R39 (2007)
105. Rescigno, T.N., Baertschy, M., Isaacs, W.A., McCurdy, C.W.: *Science* **286**, 2474 (1999)
106. Baertschy, M., Rescigno, T.N., Isaacs, W.A., Lin, X., McCurdy, C.W.: *Phys. Rev. A* **63**, 022712 (2001)
107. McCurdy, C.W., Baertschy, M., Rescigno, T.N.: *J. Phys. B* **37**, R137 (2004)
108. Jones, S., Madison, D.H.: *Phys. Rev. Lett.* **81**, 2886 (1998)
109. Jones, S., Madison, D.H.: *Phys. Rev. A* **62**, 042701 (2000)
110. Jones, S., Madison, D.H.: *Phys. Rev. A* **65**, 052727 (2002)
111. Gell-Mann, M., Goldberger, M.L.: *Phys. Rev.* **91**, 398 (1953)
112. Crothers, D.S.F., McCann, J.F.: *J. Phys. B* **16**, 3229 (1983)

113. Jones, S., Madison, D.H., Baertschy, M.: *Phys. Rev. A* **67**, 012703 (2003)
114. Madison, D.H., Al-Hagan, O.: *J. At. Mol. Opt. Phys.* **2010**, 367180 (2010)
115. Jackubowicz, H., Moores, D.L.: *J. Phys. B* **14**, 3733 (1981)
116. Bartschat, K., Burke, P.G.: *J. Phys. B* **20**, 3191 (1987)
117. Müller, G.: In: Dalgarno, A., Freund, R.S., Koch, P.M., Lubell, M.S., Lucatarto, T.B. (eds.) *The Physics of Electronic and Atomic Collisions*, p. 418. AIP, New York (1990)
118. Rösel, T., Röder, J., Frost, L., Jung, K., Ehrhardt, H., Jones, S., Madison, D.H.: *Phys. Rev. A* **46**, 2539 (1992)
119. LaGattata, K.J., Hahn, Y.: *Phys. Rev. A* **24**, 2273 (1981)
120. Moores, D.L., Reed, K.J.: *Adv. At. Mol. Opt. Phys.* **34**, 301 (1994)
121. Scott, M.P., Teng, H., Burke, P.G.: *J. Phys. B* **33**, L63 (2000)
122. Röder, J., Baertschy, M., Bray, I.: *Phys. Rev. A* **67**, 010702 (2003)
123. Ren, X., Senftleben, A., Pflüger, T., Bartschat, K., Zatsarinny, O., Berakdar, J., Colgan, J., Pindzola, M.S., Bray, I., Fursa, D.V., Dorn, A.: *Phys. Rev. A* **92**, 052707 (2015)
124. Osterbrock, D.E.: *Astrophysics of Gaseous Nebulae and Active Galactic Nuclei*. University Science Books, Sausalito (1989)
125. Pflüger, T., Zatsarinny, O., Bartschat, K., Senftleben, A., Ren, X., Ullrich, J., Dorn, A.: *Phys. Rev. Lett.* **110**, 153202 (2013)
126. Ren, X., Amami, A., Zatsarinny, O., Pflüger, T., Weyland, M., Dorn, A., Madison, D.H., Bartschat, K.: *Phys. Rev. A* **93**, 062704 (2016)
127. Arthurs, A.M., Dalgarno, A.: *Proc. R. Soc. A* **256**, 540 (1960)
128. Burke, P.G., Chandra, N., Gianturco, F.A.: *J. Phys. B* **5**, 2212 (1972)
129. Curik, R., Gianturco, F.A., Sanna, N.: *Int. J. Quantum Chem.* **84**, 565 (2001)
130. Drozdov, S.I.: *Sov. Phys. JETP* **1**, 591 (1955)
131. Drozdov, S.I.: *Sov. Phys. JETP* **3**, 759 (1956)
132. Chase, D.M.: *Phys. Rev.* **104**, 838 (1956)
133. Shimamura, I.: *Chem. Phys. Lett.* **73**, 328 (1980)
134. Shimamura, I.: *J. Phys. B* **15**, 93 (1982)
135. Sanna, N., Gianturco, F.A.: *Comput. Phys. Commun.* **114**, 142 (1998)
136. Morrison, M.A.: *Adv. At. Mol. Phys.* **24**, 51 (1987)
137. Chandra, N., Temkin, A.: *Phys. Rev. A* **13**, 188 (1976)
138. Chandra, N., Temkin, A.: *Phys. Rev. A* **14**, 507 (1976)
139. Bardsley, J.N.: *J. Phys. B* **1**, 365 (1968)
140. Herzenberg, A., Mandl, F.: *Proc. R. Soc. A* **270**, 48 (1962)
141. Herzenberg, A.: In: Shimamura, I., Takayanagi, K. (eds.) *Electron Molecule Collisions*, p. 351. Plenum, New York (1984)
142. Bardsley, J.N.: *J. Phys. B* **1**, 349 (1968)
143. Domcke, W.: *Phys. Rep.* **208**, 97 (1991)
144. Siegert, A.F.J.: *Phys. Rev.* **56**, 750 (1939)
145. Schneider, B.I., Le Dourneuf, M., Burke, P.G.: *J. Phys. B* **22**, L365 (1979)
146. McCurdy, C.W., Isaacs, W.A., Meyer, H.-D., Rescigno, T.N.: *Phys. Rev. A* **67**, 042708 (2003)
147. Birtwistle, D.T., Herzenberg, A.: *J. Phys. B* **4**, 53 (1971)
148. Allan, M.: *Phys. Rev. Lett.* **87**, 033201 (2001)
149. Allan, M.: *J. Phys. B* **35**, L387 (2002)
150. Laporta, V., Tennyson, J., Celiberto, R.: *Plasma Sources Sci. Technol.* **25**, 06LT02 (2016)
151. Nesbet, R.K.: *Phys. Rev. A* **19**, 551 (1979)
152. Shugard, M., Hazi, A.U.: *Phys. Rev. A* **12**, 1895 (1975)
153. Rescigno, T.N.: In: Ehrhardt, H., Morgan, L.A. (eds.) *Electron Collisions with Molecules, Clusters and Surfaces*, p. 1. Plenum, New York (1994)
154. Bartschat, K., Kushner, M.K.: *Proc. Natl. Acad. Sci. U. S. A.* **113**, 7026 (2016)
155. Hamilton, J.R., Tennyson, J., Huang, S., Kushner, M.J.: *Plasma Sources Sci. Technol.* **26**, 065010 (2017)
156. Huang, S., Volynets, V., Hamilton, J.R., Lee, S., Song, I.-C., Lu, S., Tennyson, J., Kushner, M.J.: *J. Vac. Sci. Technol. A* **35**, 031302 (2017)
157. Huang, S., Volynets, V., Hamilton, J.R., Nam, S.K., Song, I.-C., Lu, S., Tennyson, J., Kushner, M.J.: *J. Vac. Sci. Technol. A* **36**, 021305 (2018)
158. Celiberto, R., Armenise, I., Cacciatore, M., Capitelli, M., Esposito, F., Gamallo, P., Janev, R.K., Laganà, A., Laporta, V., Laricchiuta, A., Lombardi, A., Rutigliano, M., Sayós, R., Tennyson, J., Wadehra, J.M.: *Plasma Sources Sci. Technol.* **25**, 033004 (2016)
159. Larsson, M., Orel, A.E.: *Dissociative Recombination of Molecular Ions*. Cambridge University Press, Cambridge (2008)
160. Herbst, E., Osamura, Y.: *Astrophys. J.* **679**, 1670 (2008)
161. Faure, A., Tennyson, J.: *Mon. Notices R. Astron. Soc.* **325**, 443 (2001)
162. Dubernet, M.-L., Alexander, M.H., Ba, Y.A., Balakrishnan, N., Balança, C., Ceccarelli, C., Cernicharo, J., Daniel, F., Dayou, F., Doronin, M., Dumouchel, F., Faure, A., Feautrier, N., Flower, D.R., Grosjean, A., Halvick, P., Klos, J., Lique, F., McBane, G.C., Marinakis, S., Moreau, N., Moszynski, R., Neufeld, D.A., Roueff, E., Schilke, P., Spielfiedel, A., Stancil, P.C., Stoecklin, T., Tennyson, J., Yang, B., Vasserot, A.-M., Wiesenfeld, L.: *Astron. Astrophys.* **553**, A50 (2013)
163. Wakelam, V., Loison, J.-C., Herbst, E., Pavone, B., Bergeat, A., Béroff, K., Chabot, M., Faure, A., Galli, D., Geppert, W.D., Gerlich, D., Gratier, P., Harada, N., Hickson, K.M., Honvault, P., Klippenstein, S.J., Le Picard, S.D., Nyman, G., Ruaud, M., Schlemmer, S., Sims, I.R., Talbi, D., Tennyson, J., Wester, R.: *Astrophys. J. Suppl.* **217**, 20 (2015)
164. Boudaïffa, B., Cloutier, P., Hunting, D., Huels, M.A., Sanche, L.: *Science* **287**, 1658 (2000)
165. Baccarelli, I., Bald, I., Gianturco, F.A., Illenberger, E., Kopyra, J.: *Phys. Rep.* **588**, 1 (2011)
166. Blanco, F., et al.: *Eur. Phys. J. D* **67**, 190 (2013)
167. Gorfinkiel, J.D., Ptasincka, S.: *J. Phys. B* **50**, 182001 (2017)
168. Brunger, M.J.: *Int. Rev. Phys. Chem.* **36**, 333 (2017)
169. Ridenti, M.A., et al.: *Eur. Phys. J. D* **70**, 161 (2016)
170. Mason, N.J.: *Rep. Prog. Phys.* **56**, 1275 (1993)
171. Newell, W.R.: *Comments At. Mol. Phys.* **28**, 59 (1992)
172. Mittleman, M.H.: *Introduction to the Theory of Laser-Atom Interactions*, 2nd edn. Plenum, New York (1993)
173. Joachain, C.J.: In: Ehlotzky, F. (ed.) *Fundamentals of Laser Interactions*. Springer, Berlin, Heidelberg (1985)
174. Kroll, N.M., Watson, K.M.: *Phys. Rev.* **8**, 804 (1973)
175. Shakeshaft, R.: *Phys. Rev. A* **28**, 667 (1983)
176. Shakeshaft, R.: *Phys. Rev. A* **29**, 383 (1984)
177. Geltman, S., Maquet, A.: *J. Phys. B* **22**, L419 (1989)
178. Francken, P., Joachain, C.J.: *J. Opt. Soc. Am.* **7**, 554 (1990)
179. Dimou, L., Faisal, F.H.M.: *Phys. Rev. Lett.* **59**, 872 (1987)
180. Collins, L.A., Csanak, G.: *Phys. Rev.* **44**, 5343 (1991)
181. Giusti-Suzor, A., Zoller, P.: *Phys. Rev. A* **36**, 5178 (1987)
182. Marte, P., Zoller, P.: *Phys. Rev. A* **43**, 1512 (1991)
183. Burke, P.G., Francken, P., Joachain, C.J.: *J. Phys. B* **24**, 761 (1991)
184. Shirley, J.H.: *Phys. Rev.* **138**, 979 (1965)
185. Potvliege, R.M., Shakeshaft, R.: In: Gavril, M. (ed.) *Atoms in Intense Laser Fields*, p. 373. Academic Press, San Diego, London (1993)
186. Dörr, M., Terao-Dunseath, M., Purvis, J., Noble, C.J., Burke, P.G., Joachain, C.J.: *J. Phys. B* **25**, 2809 (1992)
187. Henneberger, W.C.: *Phys. Rev. Lett.* **21**, 838 (1968)
188. Charlo, D., Tereo-Dunseath, M., Dunseath, K.M., Launay, J.-M.: *J. Phys. B* **31**, L539 (1998)
189. Tereo-Dunseath, M., Dunseath, K.M., Charlo, D., Hibbert, A., Allen, R.J.: *J. Phys. B* **34**, L263 (2001)
190. Tereo-Dunseath, M., Dunseath, K.M.: *J. Phys. B* **35**, 125 (2002)

191. Guan, X., Zatsarinny, O., Bartschat, K., Schneider, B.I., Feist, J., Noble, C.J.: *Phys. Rev. A* **76**, 053411 (2007)
192. Lysaght, M.A., van der Hart, H.W., Burke, P.G.: *Phys. Rev. A* **79**, 053411 (2009)
193. Guan, X., Zatsarinny, O., Noble, C.J., Bartschat, K., Schneider, B.I.: *J. Phys. B* **42**, 134015 (2009)
194. Moore, L.R., Lysaght, M.A., Nikolopoulos, L.A.A., Parker, J.S., van der Hart, H.W., Taylor, K.T.: *J. Mod. Opt.* **58**, 1132 (2011)
195. Yip, F.L., Rescigno, T.N., McCurdy, C.W., Martin, F.: *Phys. Rev. Lett.* **110**, 173001 (2013)
196. Yip, F.L., Palacios, A., Martin, F., Rescigno, T.N., McCurdy, C.W.: *Phys. Rev. A* **92**, 053404 (2015)
197. Burke, P.G., Burke, V.M.: *J. Phys. B* **30**, L383 (1997)
198. Lysaght, M.A., Moore, L.R., Nikolopoulos, L.A.A., Parker, J.S., van der Hart, H.W., Taylor, K.T.: In: Bandrauk, A.D., Ivanov, M. (eds.) *Quantum Dynamic Imaging: Theoretical and Numerical Methods*, p. 107. Springer, New York (2011)



Klaus Bartschat Klaus Bartschat is the Levitt Distinguished Professor of Physics at Drake University. His research focuses on the general theory and computational treatment of electron and photon collisions with atoms and ions, including the direct solution of the time-dependent Schrödinger equation for ultrashort intense laser-matter interactions and the use of the R-matrix (close-coupling) method for electron collisions with complex targets. He is a Fellow of the American Physical Society and was rewarded the Will Allis Prize in 2016.



Jonathan Tennyson Jonathan Tennyson received a PhD from the University of Sussex and after working at the University of Nijmegen and Daresbury Laboratory he moved to UCL. He works on problems involving electron collisions and spectroscopy of molecules with applications to areas including astrophysics and plasma physics. He was elected a Fellow of the Royal Society (London) in 2009.



Phil Burke Phil Burke was Professor of Mathematical Physics at the Queen's University of Belfast (1967–1998). He made significant contributions to the theory of atomic, molecular, and optical physics and played a leading role in developing the theory of resonances in atomic and molecular processes. He received the Guthrie Medal and Prize (1994), the David Bates Prize (2000), and the Will Allis Prize (2012). He was a Fellow of the Royal Society. He passed away in 2019.



Chris H. Greene

Contents

50.1	Overview	751
50.2	Conceptual Foundation of QDT	751
50.2.1	Single-Channel Nonrelativistic Quantum Defect Theory	752
50.2.2	Multichannel QDT	753
50.2.3	Molecular Ionization Channels Treated by the Rovibrational Frame Transformation	756
50.2.4	Ultracold Atom–Atom Collisions in MQDT	757
	References	759

Abstract

This chapter summarizes a collection of theoretical techniques collected under the umbrella term “quantum defect theory” (QDT). The simplest and earliest formulations of QDT date back to contributions from Hartree, Ham, and Seaton. This theory was formalized into a comprehensive description of electron collisions with atomic ions by *Seaton*, connecting Rydberg state properties to the behavior of scattering states near ionization thresholds, reviewed comprehensively in [1].

Keywords

multichannel quantum defect theory · frame transformations · smooth reaction matrix · complex resonance · Rydberg states · Fano–Feshbach resonance · autoionization · ultracold collisions

50.1 Overview

Following the initial formulation in the 1960s, the QDT theoretical framework was subsequently generalized to treat atomic and molecular photoabsorption processes involving

C. H. Greene (✉)
Dept. of Physics & Astronomy, Purdue University
West Lafayette, IN, USA
e-mail: chgreene@purdue.edu

Rydberg and/or valence electron excitations by *Fano*, *Jungen*, and their collaborators [2–5]. Further generalizations later showed that the ideas of quantum defect theory can be generalized to non-Coulombic long-range Hamiltonians, such as the attractive or repulsive C_4/r^4 long range potential relevant to negative ion photodetachment and ion–atom collisions, or charge-dipole long-range potentials C_2/r^2 relevant in some atomic or negative ion photoabsorption resonances [6–8]. In the modern realm of ultracold atomic collisions occurring at nanokelvin to millikelvin energies, the development of QDT for dipole–dipole interaction potentials C_3/r^3 , or for van der Waals $-C_6/r^6$, has been vital in contributing to advances relating to the behavior and control of degenerate quantum gases [9–13].

50.2 Conceptual Foundation of QDT

The key point of this simplest single-channel form of QDT emerges from the observation that, to an excellent approximation, an electron experiences a simple attractive Coulomb plus centrifugal potential energy, when moved sufficiently far ($r > r_0$) from any atomic ion. That is, if the ion consists of N_c electrons and a nucleus of charge Z , then the long-range potential energy experienced by an electron at $r > r_0$ equals $V(r) \rightarrow -\frac{Z-N_c}{r}$, where r_0 is the Bohr radius. The most common case, historically, is a Rydberg state of a neutral atom, in which case $N_c = Z - 1$; thus the large- r potential energy of the outermost Rydberg electron approaches $-1/r$ at distances beyond a few Bohr radii. The most important initial aspect of any QDT treatment for a long-range Coulomb potential, or any other long-range potential such as C_n/r^n , $n \geq 2$, is to define two linearly independent solutions $f_{\ell\ell}(r)$, $g_{\ell\ell}(r)$ of the radial Schrödinger equation, which have a smooth energy dependence at any finite radius, even for energies crossing a breakup threshold. The resulting characterization of observables in terms of smoothly varying “almost constant” quantities produces a dramatic simplification in the theoretical description, because the observables

such as energy levels, decay widths, and photoabsorption cross sections vary extremely rapidly with energy in the vicinity of ionization thresholds. The mathematical formulation starts from developing a thorough understanding of alternative solutions of the long-range radial Schrödinger equation for a two-body system of reduced mass m , energy ε , orbital angular momentum quantum number ℓ , namely

$$y''_{\varepsilon\ell}(r) + 2m\left(\varepsilon - \frac{C_N}{r^N}\right)y(r) - \frac{\ell(\ell+1)}{r^2}y(r) = 0. \quad (50.1)$$

Solutions $y(r)$ that are both regular at the origin (i.e., $y(0) = 0$) and have an energy-normalized amplitude $\sqrt{\frac{2m}{\pi k}}$ of a real sinusoidal function asymptotically are typically denoted as $f_{\varepsilon\ell}(r)$. In this context, we say that a function $y_{\varepsilon\ell}(r)$ is “energy normalized” in the usual sense, namely that $\int_0^\infty y_{\varepsilon\ell}(r)y_{\varepsilon'\ell}(r)dr = \delta(\varepsilon - \varepsilon')$. An irregular (at $r = 0$) energy-normalized function $g_{\varepsilon\ell}(r)$ is then defined to lag $f_{\varepsilon\ell}(r)$ by $\frac{\pi}{2}$ at large r , and with equal asymptotic amplitude, whereby an energy-normalized eigenfunction of the radial Schrödinger equation with a potential that becomes Coulombic asymptotically ($N = 1$), can simply be written in terms of the non-Coulomb part of the scattering phase shift $\delta_\ell(\varepsilon)$ as

$$y_{\varepsilon\ell}(r) = f_{\varepsilon\ell}(r) \cos \delta_\ell(\varepsilon) - g_{\varepsilon\ell}(r) \sin \delta_\ell(\varepsilon), \quad r > r_0. \quad (50.2)$$

As is discussed at length by *Seaton* [1], these energy normalized solutions (f, g) can be analytically continued rather smoothly to negative energies, by setting $k \rightarrow i\kappa \equiv i/v$, and they are convenient to work with in the sense of quantum defect theory, whereby asymptotic large- r boundary conditions are normally not imposed initially; instead, they are imposed only at the end when observables are computed. In addition to the fact that they are regular or irregular, respectively, at $r = 0$, additional key properties are their asymptotic expansions at positive and negative energies, namely for a unit attractive Coulomb potential,

$$f_{\varepsilon\ell}(r) \rightarrow \begin{cases} \sqrt{\frac{2m}{\pi k}} \sin\left(kr + \frac{1}{k} \ln 2kr - \frac{\ell\pi}{2} + \sigma_\ell(k)\right), & \varepsilon > 0 \\ \sqrt{\frac{m}{\pi\kappa}} [D^{-1}r^{-\nu} e^{\kappa r} \sin \gamma - Dr^\nu e^{-\kappa r} \cos \gamma], & \varepsilon < 0 \end{cases} \quad (50.3)$$

$$g_{\varepsilon\ell}(r) \rightarrow \begin{cases} -\sqrt{\frac{2m}{\pi k}} \cos\left(kr + \frac{1}{k} \ln 2kr - \frac{\ell\pi}{2} + \sigma_\ell(k)\right), & \varepsilon > 0 \\ -\sqrt{\frac{m}{\pi\kappa}} [D^{-1}r^{-\nu} e^{\kappa r} \cos \gamma + Dr^\nu e^{-\kappa r} \sin \gamma], & \varepsilon < 0 \end{cases}, \quad (50.4)$$

where $\sigma_\ell(k) \equiv \arg \Gamma(\ell + 1 - i/k)$, $\gamma \equiv \pi(\nu - \ell)$, $D \equiv \pi^{1/2}(2/\nu)^\nu [\Gamma(\nu - \ell)\Gamma(\nu + \ell + 1)]^{-1/2}$.

50.2.1 Single-Channel Nonrelativistic Quantum Defect Theory

The simplest scenario where QDT is useful is a simple radial potential energy function $V(r)$, which tends asymptotically to an attractive Coulomb potential $-\frac{Z}{r}$. For definiteness in the present discussion, imagine that $V(r) = -\frac{1}{r}$, exactly (to high accuracy), for all $r \geq r_0$. While for many problems this is not strictly satisfied for any finite value of r_0 , it is adequate for most applications to identify a finite r_0 , in practice. This is a reasonable description of the valence electron properties for any atom consisting of an electron that moves outside of a closed-shell ionic core. For this problem, solutions of the radial Schrödinger equation would normally be determined numerically at $r < r_0$, but regardless of the nature of that numerical solution, it will match smoothly in function and derivative to the outer region solution, namely:

$$y_{\varepsilon\ell}(r) \rightarrow f_{\varepsilon\ell}(r) \cos \pi\mu_\ell(\varepsilon) - g_{\varepsilon\ell}(r) \sin \pi\mu_\ell(\varepsilon), \quad r \geq r_0. \quad (50.5)$$

This equation applies both at positive energies where the solution describes scattering or photoionization solutions, and at negative energies where it will represent bound states. Here, $\mu_\ell(\varepsilon)$ is an r -independent constant that corresponds at negative energies to the *quantum defect* of traditional Rydberg state spectroscopy (as we show immediately below). At positive energies, on the other hand, $\pi\mu_\ell(\varepsilon)$ corresponds to the ordinary non-Coulomb part of the scattering phase shift $\delta_\ell(\varepsilon)$. We regard these as synonymous, since *Seaton* [1] has proved that they are equal at the ionization threshold $\varepsilon = 0$. The Rydberg formula is readily derived because the phase-shifted radial solution at an arbitrary negative energy, as written in Eq. (50.5), diverges exponentially at $r \rightarrow \infty$. This divergence occurs unless $\sin \pi(\nu - \ell + \mu_\ell(\varepsilon)) = 0$, which cancels the growing exponential term, i.e., unless $\nu + \mu_\ell(\varepsilon) = n$, an integer, in which case the allowed energies where $y_{\varepsilon\ell}(r)$ is regular at both the origin and at ∞ are quantized to obey

$$\varepsilon_{n\ell} = -\frac{1}{2(n - \mu_\ell)^2}, \quad (50.6)$$

in reduced Hartree energy units. The Hartree energy unit is defined by $E_H = \frac{e^2}{4\pi\varepsilon_0 a_B}$, with the reduced mass scaled value of the generalized Bohr radius given by $a_B = 4\pi\varepsilon_0 \hbar^2 / me^2$. The standard atomic units are defined for an electron in the field of an infinite mass nucleus, where $m = m_e$, and these values are $E_H = 4.359744650(54) \times 10^{-18} \text{ J} = 27.21138602(17) \text{ eV}$, and $a_B = 5.2917721067(12) \times 10^{-11} \text{ m}$. It is often adequate when working at modest levels of precision to use the bare electron mass Hartree energy unit, i.e., with $m = m_e$ in the formula

for the Bohr radius. For high-precision studies, however, the above Rydberg formula of energy levels becomes more precise if the reduced mass of the electron-(atomic-ion) system is used in the formula for the Bohr radius, rather than the bare electron mass. This single-channel quantum defect has a number of simple and desirable properties. One of the most important is that $\mu_\ell(\varepsilon)$ can be expanded into a sum over powers of the energy ε , $\mu_\ell(\varepsilon) \simeq \mu_\ell(0) + \varepsilon\mu'_\ell(0) + \dots$, and for many applications, only the energy-independent constant first term is needed. For an accurate parametrization of the low ℓ experimentally measured Rb Rydberg state energy levels using quantum defect formulas of this type, see [14].

50.2.2 Multichannel QDT

While the single-channel QDT gives a convenient way to relate simple quantities like scattering phase shifts and photoionization matrix elements to discrete state quantum defects and oscillator strengths, the power of the multichannel quantum defect theory (MQDT) yields even more extensive and powerful methods for analyzing complex spectral and collisional phenomena. In this section, the MQDT is described briefly, with a few examples that illustrate the capabilities of this theoretical framework.

An electron in the field of an atomic or molecular ion with many relevant energy levels can reside in a number of alternative channels, i , which collects the set of all the quantum numbers of the combined system of the outermost electron and the ion; typically, this set includes the spin and orbital angular momentum quantum numbers of the Rydberg electron and those of the residual ionic core in an energy eigenstate with energy E_i . For any time-independent quantum calculation performed on a system at total energy E , one can partition all of the fragmentation channels of the system into two groups. The first group is the set of *open channels* for the symmetry being treated, which have summed internal energy levels E_i of the fragmenting constituents that lie below the total energy E at which the calculation is being performed. These channels are energetically open in the sense that it is possible for the system to escape to infinity in them, with positive kinetic energy $E - E_i > 0$, even at infinite separation. All other channels of the system, for which $E - E_i < 0$, are denoted as *closed channels* because there is insufficient energy available for the system to escape to infinity in those channels. Because the energy is too low for the system to fragment in any closed two-body fragmentation channel with threshold energy E_i , its wavefunction component in channel i must decay asymptotically, roughly as $\exp[-\sqrt{2m_i(E - E_i)}r]$. While the total number of closed channels is usually infinite, it can be safely truncated to a finite number, provided that the energy range of interest is not too high. The set of retained closed channels has a further di-

vision into strongly closed and weakly closed channels. In the weakly closed channels, the radial kinetic energy of fragmentation is still positive or at least not too negative at the reaction boundary r_0 , the distance beyond which energy and angular momentum exchanges are negligible. An example illustrates the relevance of the division of channels into open, weakly closed, and strongly closed. Consider the $^1S^e$ states of the neutral helium atom at energy slightly below the energy of the $\text{He}^+(2s, 2p)$ levels. The lone $^1S^e$ channel that is open in this energy range is denoted in QDT as $1s\epsilon s$, whereas there are two weakly closed channels of this symmetry, $2s\epsilon s$ and $2p\epsilon p$. Here, ϵ stands for the outermost electron energy at infinity; $\epsilon_i \equiv E - E_i$, which is slightly negative in the weakly closed channels. The strongly closed channels in this energy range near the $n = 2$ ionization thresholds are all those that are higher, namely, $3s\epsilon s, 3p\epsilon p, \dots 4f\epsilon f$, etc. The use of ϵ in this notation is meant to signify that in quantum defect theory, the energy ϵ of the outermost electron can be either positive or slightly negative. In the i -th channel, the outermost electron has asymptotic kinetic energy $\varepsilon_i \equiv E - E_i$. A key point to keep in mind is that for a system with N open or weakly closed channels at a given total energy E , one expects there to be N linearly independent solutions to the multichannel Schrödinger equation that are well behaved at the origin. One can obtain a set of these N linearly independent solutions in various alternative ways. Popular and effective methods to accomplish this include the Kohn or Schwinger variational principles, while one of the most widely used is a variant of the R -matrix theory. Regardless of the method chosen, the set of N independent solutions can be represented at large electron distances, where the interaction potential is purely Coulombic, as a linear combination of Coulomb functions in every channel. That is, the β -th independent solution of the Schrödinger equation for some specified symmetry and one energy E can be written in the following form, for $r > r_0$,

$$\Psi_\beta = \mathcal{A} \sum_{i=1}^N \Phi_i(\Omega) [f_i(r)I_{i\beta} - g_i(r)J_{i\beta}]. \quad (50.7)$$

Here, \mathcal{A} represents an antisymmetrization operator, $\Phi_i(\Omega)$ is a channel eigenfunction of all spatial and spin degrees of freedom except the radial coordinate of the outermost electron. Note that the constant, energy-dependent matrices $I_{i\beta}$ and $J_{i\beta}$ determined by numerical solution of the Schrödinger equation inside $r < r_0$ are not unique, because right-multiplication by any nonsingular matrix gives an equivalent set of linearly independent solutions. One quite common way to standardize those solutions is to right-multiply by $(I^{-1})_{\beta i'}$, which gives the reaction matrix solutions, whose form at $r > r_0$ is

$$\Psi_{i'}^{(K)} = \mathcal{A} \sum_{i=1}^N \Phi_i(\Omega) [f_i(r)\delta_{ii'} - g_i(r)K_{ii'}]. \quad (50.8)$$

For a time-reversal invariant system with a hermitian Hamiltonian, the reaction matrix K is real and symmetric, which leads to a unitary, symmetric scattering matrix,

$$S = \frac{1 + iK}{1 - iK}. \quad (50.9)$$

For electric dipole photoabsorption processes from an initial state Ψ^{init} to the final states described by the MQDT solutions $\Psi_{i'}^{(K)}$, the cross sections will depend on reduced dipole matrix elements, $d_{i'}^K = \langle \Psi_{i'}^{(K)} || r^{(1)} || \Psi^{\text{init}} \rangle$, which are also normally smooth functions of energy except for isolated poles. (In cases where the poles are problematic or inconvenient to deal with, an alternative formulation of the MQDT equations in terms of nonsingular eigenchannel quantum defects μ_β of the K -matrix, its orthonormal eigenvectors $U_{i\beta}$, and reduced eigenchannel dipole elements d_β , whose physical interpretation was stressed by *Ugo Fano*, [15] can be convenient to work with instead of $\{K, d^K\}$ directly. See, for instance, Eqs. 23–32 of [4].) Everything written above in this paragraph should look familiar to the reader conversant with ordinary scattering theory, but, in fact, there is a fundamental difference with quantum defect theory. In ordinary scattering theory, the sum over channels i would only include the energetically open channels, but in quantum defect theory, this sum is extended to include (weakly) closed channels as well.

The inclusion of closed channels ($i \in Q$) has important mathematical and physical implications. Most importantly, one recalls that (f_i, g_i) are exponentially divergent at $r \rightarrow \infty$, which would seem initially undesirable. However, this exponential growth will be eliminated later in the calculation of observables, as will be demonstrated shortly. Nevertheless, one sometimes refers to this intermediate quantity, the MQDT S -matrix, as the “unphysical” or “single-pass” S -matrix. The reason for introducing this intermediate quantity is because it normally has far less energy dependence than the physical scattering matrix in the open channel subspace, which we denote as S^{phys} . This will be demonstrated with an example later, but first we show the rest of the steps needed to calculate scattering or photoabsorption observables using this smooth information in K or S . The asymptotic forms of the MQDT solutions $\Psi_{i'}^{(K)}$, at an energy E where the channel space includes both open ($\varepsilon_i > 0, i \in Q$) and closed ($\varepsilon_i < 0, i \in P$) channels, can be written in a partitioned matrix notation as follows

$$\begin{bmatrix} \Psi_{i \in P}^{(K)} \\ \Psi_{i \in Q}^{(K)} \end{bmatrix}_{i'} \xrightarrow{r \rightarrow \infty} \begin{bmatrix} \sqrt{\frac{2m}{\pi k_i}} \left[\sin\left(k_i r + \frac{1}{k_i} \ln r + \eta_i\right) \delta_{ii'} \right. \\ \left. + \cos\left(k_i r + \frac{1}{k_i} \ln r + \eta_i\right) K_{ii'} \right] \\ \sqrt{\frac{m}{\pi k_i}} D_i^{-1} r^{-\nu_i} e^{\kappa_i r} \left[\sin \pi(\nu_i - \ell_i) \delta_{ii'} \right. \\ \left. + \cos \pi(\nu_i - \ell_i) K_{ii'} \right] + \mathcal{O}(r^{\nu_i} e^{-\kappa_i r}) \end{bmatrix}, \quad (50.10)$$

where $\eta_i = \frac{1}{k_i} \ln 2k_i - \frac{\ell_i \pi}{2} + \sigma_{\ell_i}(k_i)$. This last expression shows the unphysical exponential divergence of the “energy-smooth” K -matrix solutions at $r \rightarrow \infty$. But since the exponentially growing terms are explicitly displayed, it is simple to analytically find the $N \times N_o$ -matrix of constants needed to right-multiply the radial solution matrix to obtain the “physical” K -matrix or S -matrix solutions,

$$\Psi_j^{(\text{phys})} = \sum_{i'} \Psi_{i'}^{(K)} B_{i',j}.$$

Specifically, with a line or two of algebra, we can see that if we write $B = \begin{pmatrix} B_{PP} \\ B_{QP} \end{pmatrix}$, then to have a physical K -matrix solution in the open channels only, with exponential decay in the closed channels asymptotically, we require $B_{PP} = 1_{PP}$, and $(B_{QP})_{i',j} = -(\tan \gamma + K_{QQ})^{-1} K_{QP}$, where $\gamma = \pi(\nu - \ell)$ is the diagonal matrix of negative energy phase parameters. Thus, we have algebraically enforced the required exponential decay in the closed channels, giving the (smaller) $N_o \times N_o$ physical reaction matrix

$$K^{\text{phys}} = K_{PP} - K_{PQ}(\tan \gamma + K_{QQ})^{-1} K_{QP}, \quad (50.11)$$

one of the most fundamental equations of MQDT. In particular, the inverted matrix in the second term, which becomes nearly singular at closed channel resonances, displays the expected resonance structure explicitly from the infinite number of Rydberg resonances that are attached to closed-channel thresholds. Moreover, if we denote

$$d^{K,\text{phys}} = d_P^K - d_Q^K(\tan \gamma + K_{QQ})^{-1} K_{QP} \quad (50.12)$$

as the vector of reduced dipole matrix elements connecting an unpolarized initial state of total angular momentum J_0 to the final states of angular momentum J described by this K^{phys} -matrix, then the total photoionization cross section at frequency ω is given in atomic units by

$$\sigma^{\text{tot}} = \frac{4\pi^2 \omega \alpha}{3(2J_0 + 1)} d^{K,\text{phys}} \cdot (1 + K^{\text{phys}} \cdot K^{\text{phys}})^{-1} \cdot d^{K,\text{phys}}. \quad (50.13)$$

The simplest nontrivial example of MQDT is a two-channel system with two ionization thresholds at energies E_1, E_2 . For such a system, there are three energy ranges of interest, (i) $E < E_1 < E_2$, where both channels are closed, and only discrete bound states exist; (ii) $E_1 < E < E_2$ where one channel is open and one is closed, and all states have a mixed continuum and bound state character (autoionization region, or Fano–Feshbach resonance region); and (iii) $E_1 < E_2 < E$ where both channels are open, and there are only scattering processes such as $1 \rightarrow 2$. In the discrete region (i), there exists only a set of discrete energy levels for which the wavefunction decays exponentially as $r \rightarrow \infty$ in both channels. The allowed energies are determined by a bound state quantization condition that enforces the exponential decay, and reads

$$\det(\tan \gamma + K) = 0. \quad (50.14)$$

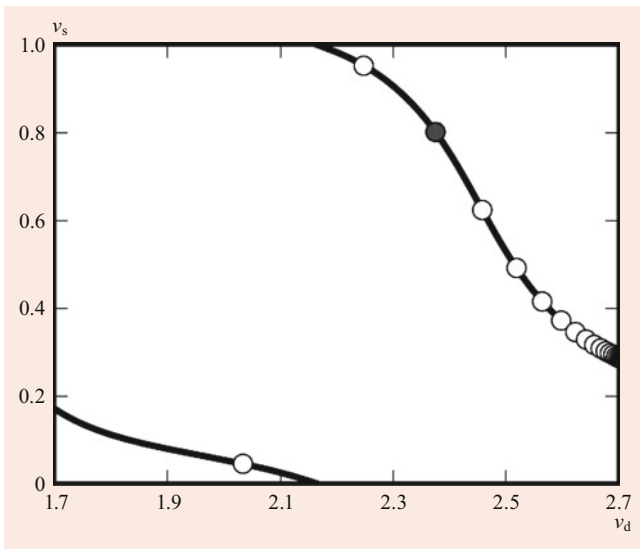


Fig. 50.1 Lu-Fano plot of the $1P^o$ bound levels of Sr, associated with the mixing of the $5snp$ and $4dnp$ channels. Taken from Vaillant et al. [17]

In general, these roots must be found by a numerical search, and it must be remembered that there is a constraint relating the effective quantum numbers ν_1 and ν_2 , namely $E = E_1 - \frac{1}{2\nu_1^2} = E_2 - \frac{1}{2\nu_2^2}$. The roots of the determinantal equation obey a double periodicity in ν_1 and ν_2 modulo an integer, which is strictly obeyed in the limit that the reaction matrix is energy independent. This double periodicity is emphasized in a popular representation of bound state energy levels for systems with two closed channel thresholds, which has come to be called the “Lu-Fano plot” [16]. The basic idea is to plot ν_1 or $\mu_1 \pmod{1}$ in the most weakly closed channel as a function of ν_2 , and then one sees that all levels fall on a single universal curve in this diagram, defined by the roots of the determinantal Eq. (50.14). To find any specific level one must enforce also the constraint equation relating ν_1 and ν_2 through energy conservation. Fig. 50.1 shows an example of a Lu-Fano plot for bound $1P^o$ energy levels of atomic Sr lying below the $5s$ ionization threshold.

In the autoionization region (ii), there is one channel (#2) that is energetically closed and one channel (#1) that is open. As an example of the type of spectrum you can expect in this region of a two-channel problem, consider the following K -matrix (dimensionless) and reduced dipole matrix elements (in a.u.).

The following model problem illustrates the value of having the multichannel Rydberg structure “built-in” to the theoretical description. Consider a system with three ionization thresholds at energies $E_i = \{0, 0.10, 0.105\}$ a.u., and an energy-independent 3×3 K -matrix. That symmetric K -matrix is defined by six independent real numbers, which

have been chosen arbitrarily for this illustrative example to equal

$$K = \begin{pmatrix} 1.4 & 1.0 & 0.5 \\ 1.0 & 0.9 & 1.4 \\ 0.5 & 1.4 & 3.8 \end{pmatrix}. \quad (50.15)$$

The atomic photoionization spectrum is determined by this K -matrix, plus three independent electric dipole matrix elements, chosen for this model to equal $\{d_1^K, d_2^K, d_3^K\} = \{3.0, 4.0, 5.0\}$. Thus, in the notation of Eq. 50.13, we would say that in this energy range, where channel 1 is open and channels 2 and 3 are weakly closed, the lone channel belonging to the P subspace is channel 1, while channels 2 and 3 belong to the Q subspace. Hence, at energies just below the threshold E_2 , there is only a single open channel (#1) with a complicated energy-dependent elastic scattering (physical) phase shift determined analytically, using Eq. 50.11 above, to be

$$\tan \delta \equiv K_{11}^{\text{phys}} = K_{11} - \frac{K_{13}K_{31}}{K_{33} + T_3} - \frac{\left(K_{12} - \frac{K_{12}K_{32}}{K_{33} + T_3}\right)^2}{K_{22} + T_2 - \frac{K_{23}K_{32}}{K_{33} + T_3}}, \quad (50.16)$$

where $T_i \equiv \tan(\pi\nu_i)$.

In the absence of channel interactions, a multichannel Rydberg spectrum would show a separate Rydberg series converging to every ionization threshold. But when short-range channel interactions are taken into account, as they are via the MQDT K -matrix, a complicated series of interacting resonances that mutually perturb each other in their energy eigenvalues and autoionization linewidths. In the absence of channel 3, one would observe a simple regular Rydberg series of levels converging to the threshold E_2 , with autoionization linewidths decreasing with the principal quantum number n in proportion to $(n - \mu_2)^{-3}$. But the presence of an interacting Rydberg series attached to threshold E_3 produces qualitative modifications of the spectrum and phenomena such as Fano linewidth “q-reversal” and “near-zero-width” states. One of the latter is clearly apparent in the model photoabsorption spectrum shown in Fig. 50.2 that is blown up near the complex resonance that modifies the Rydberg series all the way from about $\nu_2 \approx 25$ to $\nu_2 \approx 45$.

Semi-Empirical MQDT Versus Ab Initio MQDT

Historically, some of the early uses of MQDT were focused on developing models that could concisely characterize energy levels, autoionization widths, and bound and continuum oscillator strengths. When the number of channels N is not too large, say, less than five or six, for a given overall symmetry (total angular momentum, parity, etc.), then it is often possible to simply perform a least squares fit and determine an optimized $N \times N$ K -matrix and a set of N electric dipole

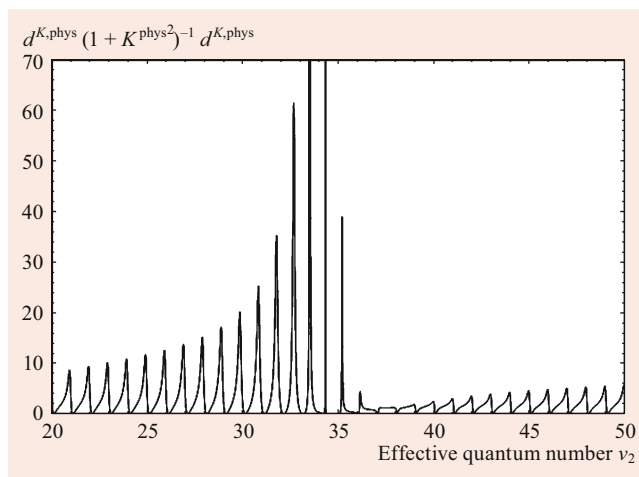


Fig. 50.2 Example photoabsorption spectrum for the three-channel model in the vicinity of a complex resonance, in the energy range below the second ionization threshold. This spectrum can be readily recomputed by the reader, for instance, by implementing Eqs. 50.12 and 50.13 with $\gamma = \pi \nu_i$ a 2 by 2 diagonal matrix in the closed-channel subspace $i = 2, 3$. Recall that the effective quantum number ν_i is defined only in the closed channels, where it equals $\nu_i = [2(E_i - E)]^{-1/2}$

matrix elements connecting the K -matrix states to an initial state whose photoabsorption is of interest. This would involve fitting $N(N + 1)/2 + N$ constants, if no theoretical input is used to reduce the number of parameters, and if their energy dependence is negligible over the energy range being fitted. Many early studies were carried out that determined these short-range MQDT parameters by fitting, as in [18], which gave fitted reaction matrices and dipole matrix elements that any experimentalist or theorist could use to accurately describe complex multichannel Rydberg spectra, e.g., for the rare gas atoms or for the alkaline earth metal atoms [19]. Other fits were carried out for the spectra of atomic silicon in a similar manner [20, 21] and, more recently, for several different symmetries of atomic strontium, by [17]. Armed with these fitted K -matrices and the experimentally known ionization thresholds, this allows immediate calculation of an infinite number of spectral levels, autoionizing resonance positions and widths, and spectral lineshapes.

When the number of channels grows much larger than about five or six, however, the fitted K -matrices become far more difficult to determine from any manageable data set, and moreover, the fits tend to be nonunique. For multichannel atomic Rydberg spectra, it is then advantageous to directly compute the smooth MQDT information through *nearly ab initio* computations, followed by small empirical adjustments if extremely high accuracy is required in any particular application. For instance, to describe the photoionization of the atomic barium ground state at energies up to the 6p threshold, this involves determination of a 13×13 reaction matrix and 13 dipole amplitudes, which amounts to

a total of 104 parameters. Various methods for computing the MQDT parameters from first principles have been developed and applied over the years, including the Fano–Lee iterative eigenchannel R-matrix theory, reformulated as a noniterative variational R-matrix treatment by a few different groups, as was reviewed in [22] with applications to atoms in several different columns of the periodic table. Another successful treatment used the relativistic random phase approximation to compute the MQDT K -matrices needed to describe Rydberg spectra in each of the rare gas atoms from Ne to Xe; that approach was developed by Johnson and coworkers, who in [23] tabulated the MQDT information needed to describe $J^\pi = 1^-$ Rydberg bound and autoionizing states to near-spectroscopic accuracy.

50.2.3 Molecular Ionization Channels Treated by the Rovibrational Frame Transformation

The starting point of any multichannel quantum defect calculation usually starts with a decision about which fragmentation channels are to be treated among the “open or weakly closed” set. Usually, all other channels are declared to be “strongly closed” in the energy range being studied, meaning that the enlarged or “unphysical” reaction matrix would have a dimension equal to the number of open or weakly closed channels for the specified symmetry being considered. For singly excited Rydberg states of a molecule such as H_2 , the ionization channels $|i\rangle$ (ignoring fine and hyperfine structure) would be characterized by rovibrational eigenstates $|v_i(N_i^+ \ell)JM\rangle$ of the molecular ion H_2^+ coupled to the quantum numbers of the angular (ℓ) and spin degrees of freedom of the outermost electron. We focus here on the spatial wavefunction of the singlet ungerade channels (omitting the singlet spinor common to all following expressions), which are predominantly p -waves ($\ell = 1$), and for a specific total angular momentum (J) and projection (M). The ionization threshold for channel $|i\rangle$ occurs at an energy E_i . Owing to the small rotational and vibrational spacings, the set of ionization thresholds E_i in a molecule are comparatively dense compared to simple atoms. Consequently, most MQDT treatments in molecules have a rather large number of channels in the reaction matrix K discussed above, e.g., 20–100 channels is not uncommon for diatomic molecules, and for polyatomics such as H_3 , the dimension of K is usually at least an order of magnitude larger. The structure of the reaction matrix K can then be represented as $K_{ii'} = \langle v_i(N_i^+ \ell)JM | \hat{K} | v_{i'}(N_{i'}^+ \ell)JM \rangle$, and once $K_{ii'}$ are known, and once the set of transition dipole matrix elements $d_{i'g}$ connecting these final states to the molecular ground state are known, the standard formulas of MQDT presented

above describe the ground state photoabsorption spectra over a wide range of energies.

Determination of this rather large amount of information contained in $K_{i'g}$ and $d_{i'g}$ might seem a daunting challenge, however, as there are at least dozens of interacting channels, and those channel interactions are known to be quite strong for low ℓ . In an exact theory, determination of $\{K_{i'g}, d_{i'g}\}$ would require solution of a large system of coupled equations, which has been formulated in principle as a “rovibrational close coupling theory” but rarely implemented in practice. Instead, the frame transformation approximation devised by Fano, Jungen, and their collaborators permits an effective and simple solution. This approximation is based on the Born–Oppenheimer separation of the electronic and nuclear motions. The idea is that the short-range electron reaction operator K should be very nearly diagonal in a representation with a fixed angular momentum projection on the internuclear axis (Λ) and with a fixed value of the internuclear distance (R). In physical terms, the conservation of R in a short-range collision follows because the electron zips in and out of the short-range reaction volume so fast that the nuclei do not have time to move appreciably. This approximation identifies the structure of the reaction matrix in the $|R, \ell \Lambda\rangle$ representation as $\langle R, \ell \Lambda | \hat{K} | R', \ell \Lambda' \rangle \simeq \delta(R - R') \delta_{\Lambda \Lambda'} \tan \pi \mu_{\ell \Lambda}(R)$. Here, $\mu_{\ell \Lambda}(R)$ is the body-frame quantum defect function that can be extracted from accurate potential curves $U_{n\ell \Lambda}(R)$ of neutral Rydberg states computed in *ab initio* quantum chemistry, and from the ionic potential curve $U^+(R)$, through the Rydberg formula at each R , i.e., in a.u.,

$$U_{n\ell \Lambda}(R) - U^+(R) \equiv -\frac{1}{2[n - \mu_{\ell \Lambda}(R)]^2}. \quad (50.17)$$

As written here, the weak n -dependence of the fixed-nuclei quantum defect function has been neglected, although in more sophisticated versions of this rovibrational frame transformation theory, it can also be incorporated into the theory. The main upshot is that the spectroscopy and scattering observables can be determined to an excellent approximation by now solving the MQDT equations on an arbitrarily fine energy mesh, using this reaction matrix computed by simple quadrature,

$$K_{i'g} = \sum_{\Lambda} \int dR \langle v_i(N_i^+ \ell) JM | R, \ell \Lambda \rangle \times \tan \pi \mu_{\ell \Lambda}(R) \langle R, \ell \Lambda | v_{i'}(N_{i'}^+ \ell) JM \rangle, \quad (50.18)$$

using the well-known transformation between the two representations, namely the eigenchannel ($|R, \ell \Lambda\rangle$, in Hund’s case b), and the fragmentation channel ($|v_i(N_i^+ \ell) JM\rangle$, in Hund’s case d)

$$\langle v(N^+ \ell) JM | R, \ell \Lambda \rangle = \chi_v^{(N^+)}(R) \langle N^+ | \Lambda \rangle^{(\ell J)}. \quad (50.19)$$

(A more robust singularity-free version of Eq. (50.18) that avoids divergences of the tangent functions can be formulated instead in terms of the $\sin \pi \mu_{\ell \Lambda}(R)$ and $\cos \pi \mu_{\ell \Lambda}(R)$ matrix elements.) Here, $\chi_v^{(N^+)}(R)$ is an ionic vibrational wavefunction, while the angular frame transformation coefficient relating Hund’s case d to b is known to be given in terms of a Clebsch–Gordan coefficient, e.g., in H_2 ,

$$\langle N^+ | \Lambda \rangle^{(\ell J)} = (-1)^{J+\Lambda-N^+} \sqrt{2 - \delta_{\Lambda,0}} \langle (\ell J) N^+ 0 | \ell - \Lambda, J \Lambda \rangle. \quad (50.20)$$

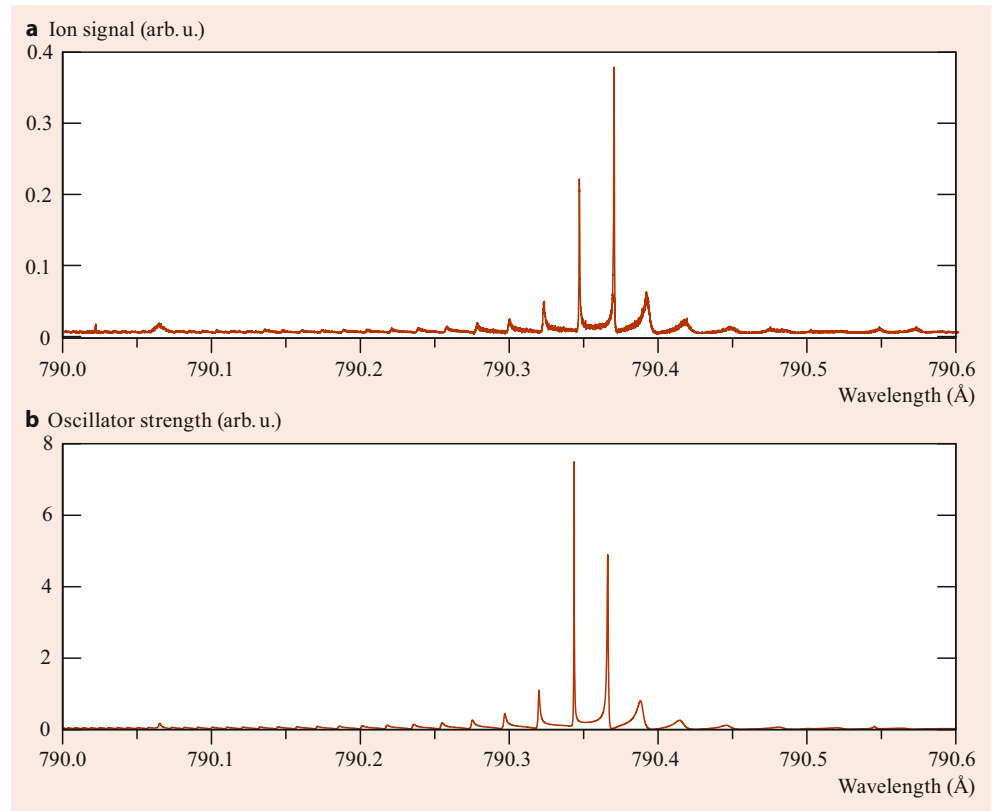
Examples of the power of this method, and the simplicity of the implementation, can be found in [24, 25]. In Fig. 50.3 shown here, the HD photoionization spectrum is plotted in a narrow energy range that is dominated by three-channel physics, and the qualitative resemblance to the three-channel model spectrum above is readily apparent. The ability of the rovibrational frame transformation theory, in combination with MQDT, to describe a complex experimental photoabsorption spectrum is also evident in Fig. 50.3. In addition to solving problems of molecular photoabsorption, in the presence of autoionization and predissociation, this basic formulation has been adopted to treat scattering processes, such as rotational and vibrational excitation of molecules, as well as dissociative recombination. Extensions of these methods to include the effects of hyperfine coupling have also been implemented by *Jungen, Merkt*, and coworkers, [26–28], although this involves more complexity in the angular momentum algebra, as one might expect.

Length limitations do not permit a discussion of a key extension to frame transformation theory, namely the idea of the *local* frame transformation that is needed when a change of coordinates is required. This issue arises, for instance, for the theoretical description of electric field effects on photoabsorption spectra. A mostly analytical theory, originally formulated by *Fano and Harmin*, was later improved by *Giannakeas et al.* [30–33]. The theory involves a spherical-to-parabolic coordinate transformation of the short-range spherical reaction matrix of MQDT, and using related information it can obtain sub-MHz accuracy on Stark-shifted levels of multichannel atoms and molecules.

50.2.4 Ultracold Atom–Atom Collisions in MQDT

One of the most exciting developments in ultracold physics in recent decades has been the demonstration of controllable atom–atom scattering lengths and many-body interactions via magnetic (and other) Fano–Feshbach resonances. [34] Quantum defect theory has been generalized to effectively describe atom–atom van der Waals and many other different types of long-range interactions [6–8, 10, 35] going

Fig. 50.3 Photoionization spectrum of the HD molecule in its ground rovibrational state, in the energy range that exhibits a complex resonance. Shown are both the experimental measurement of [29] and the result of a rovibrational frame transformation theory calculation with no adjustable parameters



far beyond the original scope [1], which was limited to Coulombic long-range potentials. One of the most fruitful generalizations has been to treat ultracold collisions in the sub-mK range of temperatures, which can give a convenient parameterization of field-dependent S -wave scattering lengths $a(B) \equiv -\lim_{k \rightarrow 0} \frac{\tan \delta_{\ell=0}}{k}$ and P -wave scattering volumes $\mathcal{V}(B) \equiv -\lim_{k \rightarrow 0} \frac{\tan \delta_{\ell=1}}{k^3}$. In ultracold physics, e.g., relevant to Bose–Einstein condensation (BEC) and degenerate Fermi gases (DFG), it is particularly crucial to accurately describe the field-dependent Fano–Feshbach resonances, and this can be treated compactly using generalized MQDT [9, 10, 13, 35].

When quantum defect theory is generalized to handle a non-Coulombic long-range potential $v^{LR}(r)$, a first key step is to identify a pair of independent solutions $\{f_{\ell}^0(\varepsilon, r), g_{\ell}^0(\varepsilon, r)\}$ to the radial Schrödinger equation of that potential, which are analytic functions of the energy ε near the potential asymptote ($\varepsilon = 0$). These need not be {regular, irregular}, respectively. Analyticity in ε is usually achieved by choosing them to be energy independent in the small r limit. These issues, and other details such as the modifications of the usual Wigner threshold laws in the presence of long-range power law potentials, are discussed in [10]. Figure 50.4 gives one simple example of the power of MQDT in the context of ultracold atom–atom collisions, specifically for $^{85}\text{Rb} - ^{85}\text{Rb}$ s -wave collisions in the $f = 2, m_f = -2$ state. In the range of energies and magnetic fields shown, the

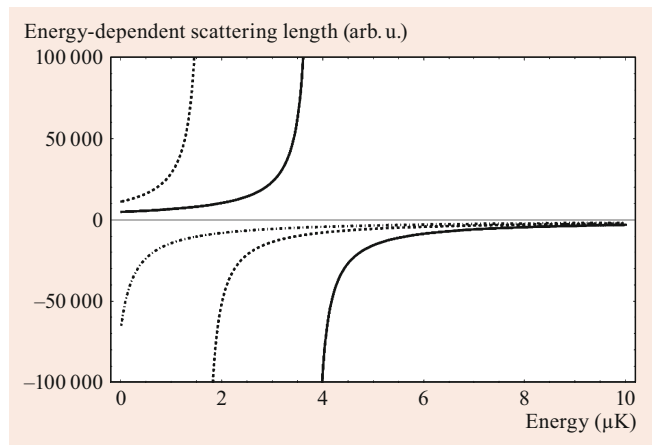


Fig. 50.4 The S -wave scattering length between two ^{85}Rb atoms, each in their $f = 2, m_f = -2$ state, is shown as a function of energy for three different magnetic fields, close to the broad Fano–Feshbach resonance at $B_{\text{res}} = 155\text{G}$. These curves are all computed using multi-channel quantum defect theory (MQDT), with a field-independent and energy-independent reaction matrix that was obtained using the methods described in [9]

physics can be described accurately using a 5 by 5 reaction matrix K that is independent of energy and field strength. The reaction matrix in this case was determined by solving the five coupled radial Schrödinger equations with a finite-element R-matrix method. Note that over the energy range shown, there is only one energetically open collision chan-

nel, and for this symmetry there are four closed channels, which are responsible for the Fano–Feshbach resonance apparent in Fig. 50.4.

References

- Seaton, M.J.: Quantum defect theory. *Rep. Prog. Phys.* **46**, 167–257 (1983)
- Fano, U.: Quantum defect theory of l uncoupling in H_2 as an example of channel-interaction treatment. *Phys. Rev. A* **2**, 353–365 (1970)
- Jungen, C., Dill, D.: Calculation of rotational-vibrational preionization in H_2 by multichannel quantum defect theory. *J. Chem. Phys.* **73**, 3338–3345 (1980)
- Greene, C.H., Jungen, C.: Molecular applications of quantum defect theory. *Adv. At. Mol. Phys.* **21**, 51–121 (1985)
- Gallagher, T.F.: *Rydberg Atoms*. Cambridge Monographs on Atomic. Cambridge University Press, Cambridge (2005)
- Greene, C.H., Fano, U., Strinati, G.: General form of the quantum-defect theory. *Phys. Rev. A* **19**, 1485–1509 (1979)
- Greene, C.H., Rau, A.R.P., Fano, U.: General form of the quantum-defect theory. II. *Phys. Rev. A* **26**, 2441 (1982)
- Watanabe, S., Greene, C.H.: Atomic polarizability in negative-ion photodetachment. *Phys. Rev. A* **22**, 158–169 (1980)
- Burke, J.P., Greene, C.H., Bohn, J.L.: Multichannel cold collisions: simple dependences on energy and magnetic field. *Phys. Rev. Lett.* **81**, 3355 (1998)
- Ruzic, B.P., Greene, C.H., Bohn, J.L.: Quantum defect theory for high-partial-wave cold collisions. *Phys. Rev. A* **87**, 032706 (2013)
- Mies, F.H., Raoult, M.: Analysis of threshold effects in ultracold atomic collisions. *Phys. Rev. A* **62**, 012708 (2000)
- Gao, B.: Quantum-defect theory of atomic collisions and molecular vibration spectra. *Phys. Rev. A* **58**, 4222–4225 (1998)
- Gao, B.: Solutions of the Schrödinger equation for an attractive $1/r^6$ potential. *Phys. Rev. A* **58**, 1728–1734 (1998)
- Li, W.H., Mourachko, I., Noel, M.W., Gallagher, T.F.: Millimeter-wave spectroscopy of cold Rb Rydberg atoms in a magneto-optical trap: Quantum defects of the ns, np, and nd series. *Phys. Rev. A* **67**, 052502 (2003)
- Fano, U.: Unified treatment of perturbed series, continuous spectra, and collisions. *J. Opt. Soc. Am.* **65**(9), 979–987 (1975)
- Lu, K.T., Fano, U.: Graphic analysis of perturbed Rydberg series. *Phys. Rev. A* **2**(1), 81 (1970)
- Vaillant, C.L., Jones, M.P.A., Potvliege, R.M.: Multichannel quantum defect theory of strontium bound Rydberg states. *J. Phys. B* **47**, 199601 (2014)
- Aymar, M.: Rydberg series of alkaline-earth atoms Ca through Ba – the interplay of laser spectroscopy and multichannel quantum defect analysis. *Phys. Rep.* **110**, 163–200 (1984)
- Gounand, F., Gallagher, T.F., Sandner, W., Safinya, K.A., Kachru, R.: Interaction between two Rydberg series of autoionizing levels in barium. *Phys. Rev. A* **27**, 1925–1938 (1983)
- Ginter, D.S., Ginter, M.L.: Transitions to and 3-limit, 4-channel representations for the m_{mp}^3 , $\text{mpnd } J=3^{\circ}$ levels in Si-I and Sn-I. *J. Chem. Phys.* **85**, 6536–6543 (1986)
- Eiles, M.T., Greene, C.H.: Ultracold long-range Rydberg molecules with complex multichannel spectra. *Phys. Rev. Lett.* **115**, 193201 (2015)
- Aymar, M., Greene, C.H., Luc-Koenig, E.: Multichannel Rydberg spectroscopy of complex atoms. *Rev. Mod. Phys.* **68**, 1015 (1996)
- Johnson, W.R., Cheng, K.T., Huang, K.N., LeDourneuf, M.: Analysis of Beutler-Fano autoionizing resonances in the rare-gas atoms using the relativistic quantum-defect theory. *Phys. Rev. A* **22**, 989–997 (1980)
- Greene, C.H., Jungen, C.: Molecular applications of quantum defect theory. *Adv. At. Mol. Phys.* **21**, 51–121 (1985)
- Child, M.S.: *Theory of Molecular Rydberg States*. Cambridge University Press, Cambridge (2011)
- Osterwalder, A., Wuest, A., Merkt, F., Jungen, C.: High-resolution millimeter wave spectroscopy and multichannel quantum defect theory of the hyperfine structure in high Rydberg states of molecular hydrogen H_2 . *J. Chem. Phys.* **121**, 11810–11838 (2004)
- Liu, J., Sprecher, D., Jungen, C., Ubachs, W., Merkt, F.: Determination of the ionization and dissociation energies of the deuterium molecule (D_2). *J. Chem. Phys.* **132**, 154301 (2010)
- Cheng, C.-F., Hussels, J., Niu, M., Bethlem, H.L., Eikema, K.S.E., Salumbides, E.J., Ubachs, W., Beyer, M., Holsch, N., Agner, J.A., Merkt, F., Tao, L.-G., Hu, S.-M., Jungen, C.: Dissociation energy of the hydrogen molecule at 10^{-9} accuracy. *Phys. Rev. Lett.* **121**, 013001 (2018)
- Greetham, G.M., Hollenstein, U., Seiler, R., Ubachs, W., Merkt, F.: High-resolution VUV photoionization spectroscopy of HD between the $X^2\Sigma_g^+ \nu^+ = 0$ and $\nu^+ = 1$ thresholds. *Phys. Chem. Chem. Phys.* **5**(12), 2528–2534 (2003)
- Fano, U.: Stark-effect of non-hydrogenic Rydberg spectra. *Phys. Rev. A* **24**, 619–622 (1981)
- Harmin, D.A.: Theory of the Stark-effect. *Phys. Rev. A* **26**, 2656–2681 (1982)
- Robicheaux, F., Giannakeas, P., Greene, C.H.: Schwinger-variational-principle theory of collisions in the presence of multiple potentials. *Phys. Rev. A* **92**, 022711 (2015)
- Giannakeas, P., Greene, C.H., Robicheaux, F.: Generalized local-frame-transformation theory for excited species in external fields. *Phys. Rev. A* **94**, 013419 (2016)
- Chin, C., Grimm, R., Julienne, P., Tiesinga, E.: Feshbach resonances in ultracold gases. *Rev. Mod. Phys.* **82**(2), 1225–1286 (2010)
- Gao, B., Tiesinga, E., Williams, C.J., Julienne, P.S.: Multichannel quantum-defect theory for slow atomic collisions. *Phys. Rev. A* **72**, 042719 (2005)



Chris H. Greene Chris H. Greene earned his PhD in 1980 from the University of Chicago following undergraduate work in Nebraska. After postdoctoral work at Stanford, he held faculty positions in physics departments at Louisiana State University and the University of Colorado, and is currently at Purdue University. His research is in atomic and molecular and few-body theoretical physics.



Joshua R. Machacek , Robert P. McEachran, and Allan D. Stauffer

Contents

51.1	Scattering Channels	761
51.1.1	Positronium Formation	762
51.1.2	Annihilation	762
51.2	Theoretical Methods	763
51.3	Particular Applications	765
51.3.1	Atomic Hydrogen	765
51.3.2	Noble Gases	765
51.3.3	Other Atoms	766
51.3.4	Molecular Hydrogen	766
51.3.5	Water	767
51.3.6	Other Molecules	767
51.4	Binding of Positrons to Atoms	768
51.5	Positronium Scattering	768
51.6	Antihydrogen	768
51.7	Reviews	768
	References	769

Abstract

The positron is the antiparticle of the electron, having the same mass but opposite charge. Positrons undergo collisions with atomic and molecular systems in much the same way as electrons do. Thus, the standard scattering theory for electrons can also be applied to positron scatter-

ing. However, there are a number of important differences from electron scattering, which we outline below.

Since the positron is a distinct particle from the atomic electrons, it cannot undergo an exchange process with the bound electrons during a collision, as is possible with electrons. Thus, the nonlocal exchange terms that arise in the description of electron scattering are not present for positrons. This leads to a simplification of the scattering equations from those for electrons. However, there are scattering channels available with positron scattering that do not exist with electrons. These are dealt with in Sect. 51.1.

Historically, beams of low-energy positrons were difficult to obtain and, consequently, there is considerably less experimental data available for positrons than for electrons. This was particularly true for quantities that required large incident positron fluxes, such as differential scattering cross sections and coincidence parameters. The recent development of cold trap-based positron beams with high resolution and high brightness by the San Diego group [1] has enabled significant progress in experimental positron scattering, which is discussed in Sect. 51.3.

Throughout this chapter we will employ atomic units unless otherwise noted.

Keywords

positron differential · elastic · excitation · ionization · positronium formation · total cross sections

51.1 Scattering Channels

Positrons colliding with atomic and molecular systems have the same scattering channels available as for electrons, viz., elastic, excitation, ionization, and for molecules, dissociation. However, two channels exist for positrons that do not exist for electrons, viz., positronium formation and annihilation.

J. R. Machacek (✉)
Research School of Physics, Australian National University
Canberra, ACT, Australia
e-mail: joshua.machacek@anu.edu.au

R. P. McEachran
Research School of Physics, Australian National University
Canberra, Australia
e-mail: robert.mceachran@anu.edu.au

A. D. Stauffer
Dept. of Physics & Astronomy, York University
Toronto, ON, Canada
e-mail: stauffer@yorku.ca

51.1.1 Positronium Formation

Positronium, a bound state of an electron–positron pair (Chap. 28), can be formed during the collision of a positron with an atomic or molecular target. The positronium *atom* (Ps) can escape to infinity leaving the target in an ionized state with a positive charge of 1. Thus, this process can be difficult to distinguish experimentally from direct ionization, where both the incident positron and the ionized electron are asymptotically free particles. The positronium atom can exist in its ground state or in any one of an infinite number of excited states after the collision. These states form two series; a singlet series ($S = 0$) referred to as parapositronium (*p*-Ps) and a triplet series ($S = 1$) referred to as orthopositronium (*o*-Ps). The level structure of both these series is, to order α^2 , where α is the fine-structure constant, identical to that of hydrogen, but with each level having half the energy of the corresponding hydrogenic state.

Positronium formation is a rearrangement channel, and thus, is a two-center problem. Because positronium is a light particle, having a reduced mass one-half that of an electron, the semiclassical type of approximations used in ion–atom collisions (Chap. 53) are not applicable here. We will discuss various theoretical approaches to this process in Sect. 51.2 and give references to experimental results in Sect. 51.3.

Positronium formation in the ground state has a threshold that is 1/4 of a Hartree (6.80285 eV) below the ionization threshold of the target. This means that it is normally the lowest inelastic channel in positron scattering from neutral atoms. For atoms with a small ionization potential, such as the alkalis, this channel is always open. The energy range between the positronium threshold and the first excited state of the atom is known as the Ore gap. In this range, positronium formation is the only possible inelastic process.

51.1.2 Annihilation

Annihilation is a process in which an electron–positron pair is converted into two or more photons. It can occur either directly with a bound atomic electron or after positronium formation has taken place. The direct annihilation cross section for a positron of momentum k colliding with an atomic or molecular target can be written as [2]

$$\sigma_a = \frac{\alpha^3 Z_{\text{eff}}}{k} (\pi a_0^2), \quad (51.1)$$

where Z_{eff} can be thought of as the effective number of electrons in the target with which the positron can annihilate. If $\Psi(\mathbf{r}_1, \mathbf{r}_2, \dots, \mathbf{r}_N, \mathbf{x})$ is the wave function for the system of a positron, with coordinate \mathbf{x} , colliding with an N -electron

target, then

$$Z_{\text{eff}} = \sum_{i=1}^N \int d\mathbf{r}_1 d\mathbf{r}_2 \dots d\mathbf{r}_N |\Psi(\mathbf{r}_1, \mathbf{r}_2, \dots, \mathbf{r}_N; \mathbf{r}_i)|^2. \quad (51.2)$$

While this formula can be naively derived by assuming that the positron can only annihilate with an electron if it is at the identical location, it actually follows from a quantum electrodynamical treatment of the process [3]. If the wave function Ψ is approximated by the product of the undistorted target wave function times a positron scattering function $F(\mathbf{x})$, then

$$Z_{\text{eff}} = \int d\mathbf{r} \rho(\mathbf{r}) |F(\mathbf{r})|^2, \quad (51.3)$$

where ρ is the electron number density of the target. Thus, in the Born approximation, where F is taken as a plane wave, Z_{eff} simply becomes the total number of electrons Z in the target. However, a pronounced enhancement of the annihilation rate in the vicinity of the Ps formation threshold due to virtual Ps formation was predicted [4, 5]. Subsequently, the Born approximation was shown to be grossly inadequate by the San Diego group, who found annihilation rates (Z_{eff}) at room temperature that are an order of magnitude larger for some atoms and even up to five orders of magnitude larger in large hydrocarbon molecules. Furthermore, there is evidence that only the outer shell of electrons takes part in the annihilation process. Two mechanisms have been proposed in order to explain these large values for Z_{eff} . One involves the enhancement of the direct annihilation process below the Ps formation threshold due to the attractive nature of the positron–electron interaction, which increases the overlap of positron and electron densities in the atom or molecule. The second mechanism is referred to as resonant annihilation, which occurs after the positron has been captured into a Feshbach resonance, where the positron is bound to a vibrationally excited molecule. A summary of the above results can be found in the review article by *Gribakin et al.* [6].

When a positron annihilates with an atomic electron, the most likely result is two 511 keV photons, if the positron–electron pair are in a singlet spin state (parapositronium). In the center-of-mass frame of the pair, the photons are emitted in opposite directions to conserve momentum. However, in the laboratory frame, the bound electron has a momentum distribution which is reflected in the photon directions not being exactly 180 degrees apart. This slight angular deviation, called the angular correlation, can be measured and gives information about the momentum distribution of the bound electrons. This quantity is given by [3]

$$S(\mathbf{q}) = \sum_{i=1}^N \int d\mathbf{r}_1 \dots d\mathbf{r}_{i-1} d\mathbf{r}_{i+1} \dots d\mathbf{r}_N \times \int d\mathbf{r}_i d\mathbf{x} e^{i\mathbf{q} \cdot \mathbf{x}} |\Psi(\mathbf{r}_1, \mathbf{r}_2, \dots, \mathbf{r}_N; \mathbf{x}) \delta(\mathbf{r}_i - \mathbf{x})|^2, \quad (51.4)$$

where \mathbf{q} is the resultant momentum of the annihilating pair. In evaluating this quantity, the positron is assumed to be thermalized in the gas before undergoing annihilation. Experimentally, only one component of \mathbf{q} is measured, so that $S(\mathbf{q})$ is integrated over the other two components of the momentum to obtain the measured quantity. The spin triplet component of an electron–positron pair (ortho-positronium) can only decay with the emission of three or more photons that do not have well-defined energies. This is a much less probable process than the two-photon decay from the singlet component.

51.2 Theoretical Methods

The basic theoretical approaches to the calculation of positron scattering from atoms and molecules were originally developed for electron scattering and later applied to the positron case. Thus, we emphasize here only the differences that arise between the electron and positron cases, both in the theoretical formulations, and in later sections, in the nature of the results.

The lowest-order interaction between a free positron and an atomic or molecular target is the repulsive static potential of the target

$$V_s = \langle \psi_0 | V | \psi_0 \rangle, \quad (51.5)$$

where ψ_0 is the unperturbed target wave function, and V is the electrostatic interaction potential between the positron and the target. Since this interaction has the opposite sign from that for electron scattering, the static potential also has the opposite sign in these two cases. On the other hand, the next higher-order of interaction is polarization, which arises from the distortion of the atom by the incident particle. If we represent this distortion of the target to first order by the wave function ψ_1 , as in the polarized-orbital approximation, for example, then the polarization interaction can be represented by the potential

$$V_p = \langle \psi_0 | V | \psi_1 \rangle. \quad (51.6)$$

This potential is attractive for both positron and electron scattering and has an asymptotic form with leading term $-\alpha_d/2r^4$, where α_d is the static dipole polarizability (Sect. 24.2.3) of the target. Thus, the static and polarization potentials for positron scattering from ground state systems are of opposite sign and tend to cancel one another. This leads to very different behavior from the electron case where they are of the same sign. In particular, the elastic scattering cross sections for positron scattering from an atom are much smaller than for electron scattering, and the phase shifts (Sect. 49.1.1) have very different magnitudes and dependencies on energy. This is illustrated for the case of scattering from helium in Fig. 51.1, where the results of the highly ac-

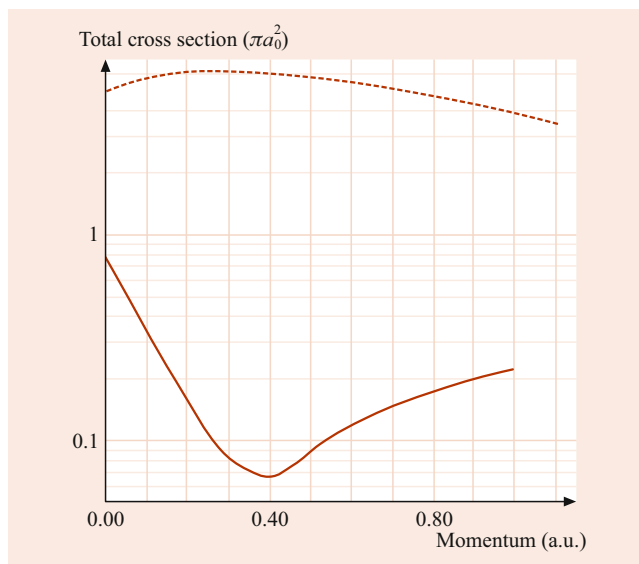


Fig. 51.1 Total elastic cross sections for electron (*dashed line*) and positron (*solid line*) from helium atoms [8, 10, 11]. The higher-order phase shifts were calculated from effective range theory (Sect. 49.1.1)

curate variational calculations for scattering by electrons and positrons are shown. There is a corresponding difference in sign between the electron and positron s -wave phase shifts for very small values of the incident momentum. In fact, the positron phase shift goes through zero, which leads to the Ramsauer minimum in the positron total cross section, as shown in Fig. 51.1. The large difference in magnitudes between the electron and positron s and p -wave phase shifts leads to the large difference in the total elastic cross sections, as shown [7–9].

Higher-order terms in the interaction potential may also give important contributions to scattering cross sections. For a detailed discussion, see the article by *Drachman and Temkin* [12].

A simple potential scattering calculation using the sum of the static and polarization potentials, but without the exchange terms that are present for the electron case, can be applied to elastic scattering calculations for closed shell systems (Sects. 51.3.1, 51.3.2). The potentials defined above can also be used in a distorted-wave approximation (Chap. 49), which can be applied to excitation and ionization by positron impact. Once again, the complicated exchange terms that arise in electron scattering are absent here [13].

For positrons with high enough incident energies (≈ 1 keV), the first Born approximation will become valid (Chap. 49). Since the first Born approximation is independent of the sign of the charge of the incident particles, this indicates that as the incident energy increases, the corresponding cross sections for electron and positron scattering will eventually merge. From flux conservation arguments, this means that the positronium formation cross section will rapidly decrease as the incident energy increases. In

fact, from experimental measurements, the total cross sections (summed over all possible channels) for electron and positron scattering appear to merge at a much lower energy than the cross sections for individual channels [14]. More elaborate calculations for high energy scattering have been carried out in the eikonal-Born series [15] (Chap. 49). These approximations allow for both polarization and absorption (i.e., inelastic processes) and yield good agreement with elastic experimental measurements of differential cross sections at energies above 100 eV. A detailed analysis [9, 15] of the various contributions to the scattering indicates that absorption effects due to the various open inelastic channels play a much more important role here than for electron scattering.

A more elaborate treatment of positron scattering is based on the close-coupling approximation (Chap. 49), where the wave function for the total system of positron plus target is expanded using a basis set comprised of the wave functions of the target. Once again, there are no exchange terms involving the positron and, in principle, a complete expansion including the continuum states of the target would include the possibility of positronium formation. However, such an expansion is not practicable if one wants to calculate explicit cross sections for positronium formation. Even in cases where such cross sections are not required, the considerable effect that the positronium formation channels can have on the other scattering cross sections is best included by a close-coupling expansion that includes terms representing positronium states plus the residual target ion. There is a problem of double counting of states in such an expansion but, in practice, this does not appear to be a problem if the number of states in the expansion is not large. Also, in many cases, additional pseudo states have to be included in the expansion in order to correctly represent the long-range polarization interaction.

A close-coupling expansion including positronium states is a two-center problem, i.e., it includes the centers of mass of both the target and the positronium states. This means that one is faced with a problem of considerable computational complexity [16–21].

Another way to take into account the effects of open inelastic channels without the complications of a full close-coupling approach is to use optical potentials. These are often based on a close-coupling formalism [9, 22] and lead to a complex potential, the real part of which represents distortions of the target (such as polarization), while the imaginary part allows for absorption (i.e., flux into open channels not explicitly represented). Such an approach was developed by *Chen et al.* [23] and applied to the noble gases [24]. Recently, a simple approach based upon an optical potential model, yielded good results for the positronium formation cross section in the noble gases [25].

Bray and Stelbovics [26] applied the convergent close-coupling (CCC) method to the scattering of positrons from

atoms. This method includes contributions from the continuum states of the target and sufficient terms in the expansion are included to ensure numerical convergence. Positronium states have been included via pseudostates for positron scattering with helium [27]. A single-center adiabatic-nuclei version has been used for positron scattering with molecular hydrogen [28].

The variational method (Chap. 49) uses an analytic form of trial wave function to represent the total system. The parameters of this analytic function are determined as part of the method. Given a trial wave function with sufficient flexibility and a large enough number of parameters, essentially exact results can be obtained in the elastic energy range and the Ore gap. Because the complexity of the trial function increases as the square of the number of electrons in the target, only positron scattering from hydrogen, helium and lithium, and the hydrogen molecule have been treated by this method to date [10, 29, 30].

Many-body theory has been applied to positron scattering from the noble gases below the positronium formation threshold. Of particular importance is the ability of many-body theory to account for positron–atom and electron–positron correlations, which have a large influence on both the scattering dynamics and the annihilation rate. Many-body theory has produced very good agreement with the most recent experimental results for elastic differential scattering [31].

In the case of direct ionization, there appears to be quite distinct threshold behavior of the cross sections for electron and positron collisions. For electrons, the Wannier threshold law (Sect. 56.3.1) has an exponent of 1.127, while a similar analysis for positrons [32] yields an exponent of 2.651. However, the existence of the positronium formation channel leaves in question whether this analysis will give the dominant term at the threshold. For a fuller discussion, see [33] and references therein. An experimental investigation of the threshold ionization of helium [34] obtained a value 2.2. This was followed by a theoretical investigation that considered anharmonic corrections to the Wannier threshold law to explain the experimental results [35]. A recent measurement within 2 eV of the ionization threshold obtained a value of 1.1 [36].

There has been an investigation [37] of the behavior of the elastic cross sections at the positronium formation threshold, which predicts the occurrence of a Wigner cusp for the noble gases using R-matrix methods. A comprehensive set of measurements using a high-resolution trap-based beams of the elastic scattering cross section about the positronium formation threshold revealed a family of Wigner cusps in the noble gases [38]. Subsequent measurements of the elastic scattering cross section about the positronium formation threshold in molecules that are isoelectronic with helium and neon, and did not show a Wigner cusp [39].

51.3 Particular Applications

51.3.1 Atomic Hydrogen

Because of the difficulty of taking measurements in atomic hydrogen, the available experimental data has so far been restricted to total cross sections, as well as to total ionization and positronium formation cross sections. Essentially exact variational calculations have been carried out in the elastic energy regime and the Ore gap [10]. These calculations are used to benchmark many-body theory [40].

Ionization cross sections have been measured by both the Bielefeld and London groups ([41, 42] and references therein) and have been calculated in a number of approximations [24, 26, 43–45]. However, disagreements between the experimental measurements mean that there is at present no reliable way of assessing the various theoretical approximations used. More elaborate calculations with asymptotically correct wave functions have been used to determine triple differential cross sections for ionization [46, 47]. However, the task of integrating these to produce total cross sections is a formidable one.

The total positron–hydrogen cross section has also been measured by the Detroit group [48] and is in quite good agreement with calculations based upon the coupled-pseudostate [45] and the convergent close-coupling [49] methods, except at very low energies where the experimental uncertainties are the greatest.

In order to determine reliable positronium formation cross sections, the explicit positronium states have to be included. Several such calculations have been carried out [17–20]. These indicate the necessity of explicitly including positronium formation channels in the expansion of the total wave function in order to obtain accurate results, even for elastic scattering. The most recent calculations [45, 49, 50] are in quite good agreement with various experiments [41, 51] over the majority of the energy range.

As is the case for electron scattering, positron cross sections exhibit resonances (Sect. 49.1.3). These have been extensively studied by *Ho* [52], who used variational and complex rotation methods.

51.3.2 Noble Gases

Because the noble gases are convenient experimental targets, a good deal of effort has gone into calculations for these targets, particularly for elastic scattering, ionization, and Ps formation. In the purely elastic energy range, i.e., for energies below the positronium formation threshold, the simple potential scattering approach using the static and polarization potentials defined above yields quite good results. Since the long-range behavior of the sum of the potentials

is attractive, the scattering phase shifts for positrons must be positive for sufficiently low energies. However, as its incident energy increases, the positron probes the repulsive inner part of the potential, and the phase shifts become negative. This behavior leads to the well-known Ramsauer minimum in the integral elastic cross sections (Chap. 49). The Ramsauer minimum has been observed in helium and neon ([53, 54] and references therein). In the case of argon, no minimum is observed given a sufficiently high-quality beam [55]. In general, this differs from electron scattering, where some low-energy phase shifts can be negative (modulo π) because of the existence of bound orbitals of the same symmetry.

Another difference between positron and electron scattering is exhibited by the differential cross sections (Chap. 49). For electrons, the shape of the cross section is determined by a few dominant phase shifts, whereas for positrons, many phase shifts contribute to the final shape [56]. Because of this behavior, the differential cross sections for positron scattering have much less overall structure than for electron scattering. However, the differential cross sections for positrons for many of the noble gases have a single minimum at relatively small angles, both below and above the first inelastic channel [57, 58]. The earlier results have been reviewed by *Kaupilla et al.* [59]. At intermediate energies, the simple potential scattering approximation is no longer sufficient, and the inelastic channels have to be taken into account via, for example, the use of an optical potential [9, 15, 23, 60] or convergent close-coupling method ([61] and references therein). Furthermore, in the inelastic scattering regime, the existence of open channels has a much more marked effect on the shape of the differential cross sections for positron scattering than that for electrons [57].

Absolute elastic differential cross sections were measured for argon, krypton, and xenon at low energies using a magnetized beam of cold positrons [58, 61, 62]. Magnetized beam measurements generally do not distinguish between forward and backward scattered positrons (or electrons). In this case, the reported elastic cross section is folded about 90 degrees. As with electrostatic beams, a portion of the angular scatter is indistinguishable from the incident beam, which plays an important role in the comparison of experiment and theory [55]. These results are in general agreement with a variety of different theoretical predictions [63–65]. A method that allows the scattering phase shifts to be extracted from the folded elastic differential scattering cross section was developed recently [66].

There is relatively little experimental data for the excitation of the noble gases. Some experimental work has been carried out for the lighter noble gases, helium, neon, and argon ([67] and references therein), and there is satisfactory agreement between these measurements and close-coupling [68], as well as distorted-wave [69] calculations.

The first state-resolved absolute excitation cross sections for the $4s [1/2]_1^0$ and $4s [3/2]_1^0$ states of argon and the $6s [3/2]_1^0$ state of xenon have been measured by the San Diego group [6, 70]. Relativistic distorted-wave calculations are in satisfactory agreement with the experiment for argon [71] but less so for xenon [72]. Excitation of the $n = 2$ states of helium was measured by the ANU group [73]. Convergent close-coupling calculations are in good agreement for both the 2^1S and 2^1P states [27].

The total ionization and positronium cross sections have been measured extensively for all of the noble gases. In general, there is good agreement amongst the various experiments for the ionization cross section but much less so for the positronium formation cross section, with a recent exception [25]. A summary of the experimental work on the ionization and positronium cross sections for neon, argon, krypton, and xenon can be found in the article by Marler et al. ([74] and references therein). A summary of the corresponding theoretical work can be found in [24, 25].

Both double and triple-differential ionization cross sections have been measured for helium [75] and argon [76, 77]. Distorted wave Born (DWBA) and three-continuum approximation (3C model) have also been applied to these systems ([78, 79] and references therein).

The formation of excited-state positronium has been measured for positron scattering from helium, argon, and xenon and has been compared to a number of theoretical results [80].

There exist some measurements of Z_{eff} and angular correlation parameters for these gases [81], mainly at room temperature, and calculations for them have been made in the polarized-orbital approximation [82]. Measurements have been made at various temperatures and are in relatively good agreement with early calculations [83].

The combination of available gas-phase scattering cross sections for energies between 0 and 10 keV has been used to model a single track of a positron through argon [84].

51.3.3 Other Atoms

In the case of positron scattering from the alkali atoms, the positronium formation channel is always open, and the simple potential scattering approach does not yield reliable results. The Detroit group has measured the total cross section, as well as the upper and lower bounds to the positronium formation cross section for sodium, potassium, and rubidium [48]. Although early close-coupling calculations of the elastic and excitation cross sections [85–87] were in surprisingly good agreement with the experimental total cross section, these calculations did not include the positronium formation channel. Subsequently, much more sophisticated calculations were carried out by the Belfast group using the

coupled-pseudo-state method, which included both eigenstates of the target, as well as positronium [45, 88–90]. These calculations also showed the increasing importance of positronium formation in excited states for the alkalis: potassium, rubidium, and caesium. The overall agreement between experimental results and those from the coupled-pseudo-state method are quite good for both potassium and rubidium; however, for sodium, the experimental positronium formation cross section is significantly above these theoretical calculations. A summary of the experimental work on the alkalis can be found in [48], while a corresponding summary of theoretical work is given in [45].

Substantial resonance features have been found in these positron–alkali atom cross sections using close-coupling calculations [91, 92]. More recently, various theoretical methods have been applied to the positron–lithium system ([93, 94] and references therein).

The positronium formation threshold for magnesium is very low, only 0.844 eV, and hence, the elastic and positronium formation cross sections will dominate in the low-energy region. Upper and lower bounds to the Ps formation cross section in magnesium have been determined [48, 95] and are in agreement with both close-coupling calculations [96] and the results of many-body theory [97].

51.3.4 Molecular Hydrogen

By its fundamental nature, molecular hydrogen has attracted considerable attention both experimentally and theoretically. The total elastic cross section has been measured by the Detroit group [51], the London group [98], and the ANU group [99]. There have been several theoretical calculations of this cross section by a variety of methods: Kohn variational [100], R -matrix [101], distributed positron model [102], a Schwinger multichannel method [101–103], and convergent close-coupling calculations by the Curtin group [104].

Calculations have shown the elastic cross section is strongly influenced by the positronium formation channel near the threshold. However, a recent measurement did not show any feature in the integral elastic cross section about the positronium formation threshold [39].

The vibrational ($0 \rightarrow 1$) excitation cross section of molecular hydrogen has been measured between 0.55 and 4 eV and is in quite good agreement with theoretical calculations [105] (and reference therein). The San Diego group has also measured the electronic excitation of the $B^1\Sigma$ state from the threshold to 30 eV [70]. Their data are in reasonable agreement with the Schwinger multichannel calculation of Lino et al. [106]. The measured positron excitation cross section appears to be larger than that measured for electron excitation.

The ionization cross section has been determined over a wide range of energies by a number of different groups ([107–111] and references therein). Since all of the above measurements are relative, they must be normalized to one another at particular energies. Theoretical calculations are in satisfactory agreement with the measurements ([112] and references therein).

Electron capture to the continuum has been observed in triple-differential ionization measurements [113]. Reasonable agreement has been found between available experimental measurements and the distorted-wave Born approximation (with the Ward–Macek approximation; [79] and references therein).

The positronium formation cross section has also been measured by a number of different groups and has been compared to the first Born approximation and a coupled-channels calculation, see [99] and reference therein.

Differential elastic cross sections have been measured by the ANU group and compared to a number of calculations [99]. The shape of these measurements are in good agreement with the complex model potential calculation [114]. More recently, a single-center adiabatic-nuclei convergent close-coupling method [104] showed good agreement between experiment and theory for the differential elastic cross section below the positronium formation threshold.

Rotational excitation cross sections have been calculated using the Schwinger multichannel method with fixed nuclei and the adiabatic rotational approximation ([115] and references therein). Recent progress in cryogenic positron traps by the San Diego group [116] will enable an experimental investigation of the rotational excitation of molecular hydrogen.

51.3.5 Water

From a biological perspective, water is fundamental, and it was recently studied experimentally and theoretically. The total scattering cross has been measured by the ANU group and compared to previous measurements and calculations ([117] and references therein). The ionization cross section has been measured by the London group [118]. The total elastic cross section and total inelastic cross section less positronium formation have been measured by the ANU group [119]. These measurements were compared to R-matrix and the independent atom model (IAM) methods ([119] and references therein).

Differential ionization cross sections have been measured by the London group [120]. Triple-differential ionization has been calculated using a second-order distorted-wave Born approximation [121].

51.3.6 Other Molecules

For diatomic and triatomic molecules, most of the experimental and theoretical work has been carried out for CO, CO₂, O₂, and N₂. Total cross sections for O₂, N₂, and CO₂ have been measured from the threshold to several hundred eV ([98] and references therein). Recently, the independent atom model (IAM) was compared to measurements for C₂, N₂, and O₂ [122] (and references therein). A spherical complex optical potential was used to determine the total scattering cross section for positron scattering from a number of simple molecules [123].

Relative differential cross sections have been measured for CO, CO₂, O₂, N₂, as well as N₂O, on both sides of the positronium formation threshold [124]. At low energies, the gases N₂, O₂, and CO exhibit a minimum in the DCS at small angles, as with the heavier noble gases. This minimum gradually disappears as the energy increases.

Vibrational excitation cross sections for CO and CO₂ have been measured [105] and are in excellent agreement with the theoretical calculations of [125] for CO, and in satisfactory agreement with theory [126] for CO₂. Electron excitation of the $a^1\Pi$ and $a^1\Sigma$ states of N₂ have been measured from threshold to 20 eV [70]. Interestingly, the positron cross section near the threshold is approximately double that for electrons.

Impact ionization, positronium formation, and electronic excitation have been measured for N₂, CO, and O₂ [127]. Additionally, positronium formation has been measured for CO₂ [128].

For small polyatomic molecules, the majority of experimental and theoretical work was carried out for CH₄. This includes the total cross section and quasi-elastic (summed over vibration–rotational levels) differential cross sections [129]. At low energies, there is a minimum in these DCS at small angles, as for the heavier noble gases which, in turn, also disappears at higher energies [59]. The positronium formation cross section has also been measured [130].

Recently, a large number of total scattering cross section measurements of organic compounds were studied experimentally by the Trento group ([131] and references therein). This work has been extended to purine nucleobasis and other biologically relevant molecules [132] (and references therein). Additionally, a comparison of the total scattering cross section from chiral enantiomers was also made [133].

Positronium formation has been measured for methanol and ethanol [134]. Total and elastic differential scattering, and positronium formation cross sections for a number of biologically relevant molecules have been measured by the ANU group ([135, 136] and references therein). In these cases, the scattering cross sections are summed over rotational and vibrational states. Nucleobases that are solid at

room temperature require a vacuum oven to produce vapor of the molecules. In these cases, relative cross sections were determined experimentally, and IAM calculations set the absolute scale at 150 eV.

51.4 Binding of Positrons to Atoms

There have been many recent investigations of the possible binding of positrons to a variety of atoms. As was mentioned in Sect. 48.1.2, such binding could greatly enhance the annihilation cross section and help explain the large measured values of Z_{eff} for both atoms and molecules. It has been shown theoretically that a positron will bind to a large number of one-electron and two-electron atomic systems ([137] and references therein). For one-electron systems, where the ionization potential is less than 6.80285 eV, the dominant configuration is a polarized positronium (Ps) cluster moving in the field of the residual positive ion, while for two-electron systems, with an ionization potential greater than 6.80285 eV, the dominant configuration involves a positron orbiting a polarized neutral atom [138]. So far, there is no experimental evidence for these positronic atoms [139]. However, a significant amount of theoretical work has shown that many atoms can bind a positron ([140] and references therein).

Enhancement of the annihilation rate (Z_{eff}) is observed in polyatomic molecules. The mechanism has been identified as vibrational Feshbach resonances mediating positron binding to molecules ([6] and references therein). In the case of linear alcohols, the binding energy depends linearly upon the molecular polarizability [141].

51.5 Positronium Scattering

There has been interest in positronium (Ps) scattering from atomic and molecular targets for a considerable time; see the work of *Fraser* and coworkers [142] and reference therein, but only recently has this field seen much activity. This is a two-center problem with the Ps *atom* being a light particle, so semiclassical methods are not applicable. There was some theoretical work by *Drachman* and *Houston* [143, 144], and recently there has been close-coupling calculations for simple target systems [145]. This problem has also been studied by a pseudo-potential method ([146] and references therein). The long-range interactions in positron–hydrogen scattering have recently been investigated [147]. The London group has measured the total cross sections for positronium scattering from the noble gases and small molecules (H_2 , N_2 , O_2 , H_2O , CO_2 , SF_6). Unexpectedly, the total cross sections for positronium scattering have been found to be very similar to scattering by

electron of the same velocity [148]. This has been explained in part by the polarization of the incident Ps [149].

The formation of the positronium negative ion, Ps^- , has been observed [150], and resonance structure has also been observed in the photodetachment of Ps^- [151, 152].

The formation of molecular positronium (Ps_2) has been observed [153] using intense positron pulses at a metal surface. The scattering of positronium atoms by positronium atoms has been investigated theoretically [154, 155] with an investigation of exciton-like nature of positronium [156].

The positronium atom is a boson, and, thus, there is fundamental interest in the creation of a Bose–Einstein condensate of an antimatter–matter composite boson. A unique feature of a Ps-BEC is the possibility of stimulated annihilation or the creation of a gamma-ray laser [157, 158]. More detailed theoretical treatments have appeared more recently [159–161].

51.6 Antihydrogen

Positron and positronium scattering play an important role in efforts to form antihydrogen, the bound state of an antiproton and a positron. This antimatter atom is an ideal system to test CPT. In the past decade, antihydrogen has been trapped [162] with the first spectroscopic measurements made recently [163]. In addition, the formation of an antihydrogen beam has been postulated [164]. Excited-state positronium has been found to be extremely useful in the formation of antihydrogen using detailed CCC calculations [165].

51.7 Reviews

For a number of years, a Positron Workshop has been held as a satellite of the International Conference on the Physics of Electronic and Atomic Collisions. The Proceedings [166–182] give an excellent summary of the state of positron scattering research, both experimental and theoretical, and applications to astro and biophysics.

There are several review articles on positron scattering in gases, including the early historical development [183], more comprehensive articles [2, 184–186], as well as more recent reviews [131, 187–191]. There are a number of reviews of the various antihydrogen efforts [192–195] with a special issue on antihydrogen and positronium [196]. A review on positronium laser physics [197] discusses the future for positron physics.

The book [198] discusses various aspects of both experimental and theoretical positron physics.

References

1. Danielson, J.R., Dubin, D.H.E., Greaves, R.G., Surko, C.M.: *Rev. Mod. Phys.* **87**, 247 (2015)
2. Fraser, P.A.: *Adv. At. Mol. Phys.* **4**, 63 (1968)
3. Ferrell, R.: *Rev. Mod. Phys.* **28**, 308 (1956)
4. Humberston, J.W., Van Reeth, P.: *Nucl. Instrum. Methods B* **143**, 127 (1998)
5. Laricchia, G., Wilkin, C.: *Nucl. Instrum. Methods B* **143**, 135 (1998)
6. Gribakin, G.F., Young, J.A., Surko, C.M.: *Rev. Mod. Phys.* **82**, 2557 (2010)
7. McEachran, R.P., Stauffer, A.D.: *J. Phys. B* **10**, 663 (1977)
8. Nesbet, R.K.: *Phys. Rev. A* **20**, 58 (1979)
9. Bartschat, K., McEachran, R.P., Stauffer, A.D.: *J. Phys. B* **21**, 2789 (1988)
10. Armour, E.A.G., Humberston, J.W.: *Phys. Rep.* **204**, 165 (1991)
11. Humberston, J.W., Campeanu, R.I.: *J. Phys. B* **13**, 4907 (1980)
12. Drachman, R.J., Temkin, A.: In: McDaniel, E.W., McDowell, M.R.C. (eds.) *Case Studies in Atomic Collision Physics II*. North-Holland, Amsterdam (1972). Chap. 6
13. Parcell, L.A., McEachran, R.P., Stauffer, A.D.: *Nucl. Instrum. Methods B* **192**, 180 (2002)
14. Kauppila, W.E., Stein, T.S.: *Can. J. Phys.* **60**, 471 (1982)
15. Joachain, C.J., Potvliege, R.M.: *Phys. Rev. A* **35**, 4873 (1987)
16. Hewitt, R.N., Noble, C.J., Bransden, B.H.: *J. Phys. B* **26**, 3661 (1993)
17. Higgins, K., Burke, P.G.: *J. Phys. B* **26**, 4269 (1993)
18. Mitroy, J.: *J. Phys. B* **26**, 4861 (1993)
19. Sarkar, N.K., Ghosh, A.S.: *J. Phys. B* **27**, 759 (1994)
20. Liu, G., Gien, T.T.: *Phys. Rev. A* **46**, 3918 (1992)
21. Campbell, C.P., McAlinden, M.T., Kernoghan, A.A., Walters, H.R.J.: *Nucl. Instrum. Methods B* **143**, 41 (1998)
22. McCarthy, I.E., Ratnavelu, K., Zhou, Y.: *J. Phys. B* **26**, 2733 (1993)
23. Chen, S., McEachran, R.P., Stauffer, A.D.: *J. Phys. B* **41**, 25201 (2008)
24. McEachran, R.P., Stauffer, A.D.: *J. Phys. B* **43**, 215209 (2010)
25. McEachran, R.P., Stauffer, A.D.: *J. Phys. B* **46**, 075203 (2013)
26. Bray, I., Stelbovics, A.: *Phys. Rev. A* **49**, R2224 (1994)
27. Utamuratov, R., Kadyrov, A.S., Fursa, D.V., Bray, I.: *J. Phys. B* **43**, 31001 (2010)
28. Zammit, M.C., Fursa, D.V., Savage, J.S., Bray, I., Chiari, L., Zecca, A., Brunger, M.J.: *Phys. Rev. A* **95**, 022707 (2017)
29. Humberston, J.W.: *J. Phys. B* **25**, L491 (1992)
30. Van Reeth, P., Humberston, J.W.: *J. Phys. B* **32**, 3651 (1999)
31. Green, D.G., Ludlow, J.A., Gribakin, G.F.: *Phys. Rev. A – At. Mol. Opt. Phys.* **90**, 032712 (2014)
32. Klar, H.: *J. Phys. B* **14**, 4165 (1981)
33. Kuo, T.-Y., Sun, H.-L., Huang, K.-N.: *Phys. Rev. A* **67**, 012705 (2003)
34. Ashley, P., Moxom, J., Laricchia, G.: *Phys. Rev. Lett.* **77**, 1250 (1996)
35. Ihra, W., Macek, J.H., Mahony, P.F.O.: *Phys. Rev. Lett.* **78**, 4027 (1997)
36. Babij, T.J., Machacek, J.R., Murtagh, D.J., Buckman, S.J., Sullivan, J.P.: *Phys. Rev. Lett.* **120**, 113401 (2018)
37. Meyerhof, W.E., Laricchia, G.: *J. Phys. B. At. Mol. Opt. Phys.* **30**, 2221 (1997)
38. Jones, A.C.L., Caradonna, P., Makochekanwa, C., Slaughter, D.S., McEachran, R.P., Machacek, J.R., Sullivan, J.P., Buckman, S.J.: *Phys. Rev. Lett.* **105**, 073201 (2010)
39. Machacek, J.R., Buckman, S.J., Sullivan, J.P.: *Phys. Rev. A* **90**, 042703 (2014)
40. Gribakin, G.F., Ludlow, J.: *Phys. Rev. A* **70**, 032720 (2004)
41. Weber, M., Hofmann, A., Raith, W., Sperber, W.: *Hyperfine Interact.* **89**, 221 (1994)
42. Jones, G.O., Charlton, M., Slevin, J., Laricchia, G., Kovar, A., Poulsen, M.R., Chormaic, S.N.: *J. Phys. B* **26**, L483 (1993)
43. Acacia, P., Campeanu, R.I., Horbatsch, M., McEachran, R.P., Stauffer, A.D.: *Phys. Lett. A* **179**, 205 (1993)
44. Hsu, S.-W., Kuo, T.-Y., Chen, C.J., Huan, K.-N.: *Phys. Lett.* **167A**, 277 (1992)
45. Kernoghan, A.A., Robinson, D.J.R., McAlinden, M.T., Walters, H.R.J.: *J. Phys. B* **29**, 2089 (1996)
46. Brauner, M., Briggs, J.S., Klar, H.: *J. Phys. B* **22**, 2265 (1989)
47. Jetzke, S., Faisal, F.H.M.: *J. Phys. B* **25**, 1543 (1992)
48. Stein, T.S., Jiang, J., Kauppila, W.E., Kwan, C.K., Li, H., Surduvovich, A., Zhou, S.: *Can. J. Phys.* **74**, 313 (1996)
49. Kadyrov, A.S., Bray, I.: *Phys. Rev. A* **66**, 012710 (2002)
50. Mitroy, J.: *J. Phys. B* **29**, L263 (1996)
51. Zhou, S., Li, H., Kauppila, W.E., Kwan, C.K., Stein, T.S.: *Phys. Rev. A* **55**, 361 (1997)
52. Ho, Y.K.: *Hyperfine Interact.* **73**, 109 (1992)
53. Sullivan, J.P., Makochekanwa, C., Jones, A., Caradonna, P., Buckman, S.J.: *J. Phys. B* **41**, 81001 (2008)
54. Jones, A.C.L., Makochekanwa, C., Caradonna, P., Slaughter, D.S., Machacek, J.R., McEachran, R.P., Sullivan, J.P., Buckman, S.J., Stauffer, A.D., Bray, I., Fursa, D.V.: *Phys. Rev. A* **83**, 32701 (2011)
55. Sullivan, J.P., Makochekanwa, C., Jones, A., Caradonna, P., Slaughter, D.S., Machacek, J., McEachran, R.P., Mueller, D.W., Buckman, S.J.: *J. Phys. B* **44**, 35201 (2011)
56. McEachran, R.P., Stauffer, A.D.: In: Kauppila, W.E., Stein, T.S., Wadehra, J.M. (eds.) *Positron (Electron)-Gas Scattering*, p. 122. World Scientific, Singapore (1986)
57. Kauppila, W.E., Stein, T.S.: *Hyperfine Interact.* **40**, 87 (1990)
58. Makochekanwa, C., Machacek, J., Jones, A., Caradonna, P., Slaughter, D., McEachran, R., Sullivan, J., Buckman, S., Bellm, S., Lohmann, B., Fursa, D., Bray, I., Mueller, D.W., Stauffer, A.D., Hoshino, M.: *Phys. Rev. A* **83**, 32721 (2011)
59. Kauppila, W.E., Kwan, C.K., Przybyla, D., Smith, S.J., Stein, T.S.: *Can. J. Phys.* **74**, 474 (1996)
60. Jain, A.: *Phys. Rev. A* **41**, 2437 (1990)
61. Machacek, J.R., Makochekanwa, C., Jones, A.C.L., Caradonna, P., Slaughter, D.S., McEachran, R.P., Sullivan, J.P., Buckman, S.J., Bellm, S., Lohmann, B., Fursa, D.V., Bray, I., Mueller, D.W., Stauffer, A.D.: *New J. Phys.* **13**, 125004 (2011)
62. Buckman, S.J., Boadle, R.A., Babij, T.J., Machacek, J.R., McEachran, R.P., Sullivan, J.P.: *Phys. Rev. A* **93**, 22712 (2016)
63. McEachran, R.P., Ryman, A.G., Stauffer, A.D.: *J. Phys. B* **12**, 1031 (1979)
64. McEachran, R.P., Stauffer, A.D., Campbell, L.E.M.: *J. Phys. B* **13**, 1281 (1980)
65. Dzuba, V.A., Flambaum, V.V., Gribakin, G.F., King, W.A.: *J. Phys. B* **29**, 3151 (1996)
66. Machacek, J.R., McEachran, R.P.: *J. Phys. B. At. Mol. Opt. Phys.* **51**, 065007 (2018)
67. Mori, S., Sueoka, O.: *J. Phys. B* **27**, 4349 (1994)
68. Hewitt, R.N., Noble, C.J., Bransden, B.H.: *J. Phys. B* **25**, 2683 (1992)
69. Parcell, L.A., McEachran, R.P., Stauffer, A.D.: *Nucl. Instrum. Methods B* **177**, 113 (2000)
70. Sullivan, J.P., Marler, J.P., Gilbert, S.J., Buckman, S.J., Surko, C.M.: *Phys. Rev. Lett.* **87**, 073201 (2001)
71. McEachran, R.P., Stauffer, A.D.: *Phys. Rev. A* **65**, 034703 (2002)
72. Parcell, L.A., McEachran, R.P., Stauffer, A.D.: *Nucl. Instrum. Methods B* **192**, 180–184 (2002)
73. Caradonna, P., Sullivan, J.P., Jones, A., Makochekanwa, C., Slaughter, D.S., Mueller, D.W., Buckman, S.J.: *Phys. Rev. A* **80**, 60701 (2009)

74. Marler, J.P., Sullivan, J.P., Surko, C.M.: *Phys. Rev. A* **71**, 22701 (2005)
75. Arcidiacono, C., Kover, A., Laricchia, G.: *Phys. Rev. Lett.* **95**, 223202 (2005)
76. Schmitt, A., Cerny, U., Moller, H., Raith, W., Weber, M.: *Phys. Rev. A* **49**, R5 (1994)
77. DuBois, R.D., Gavin, J., deLucio, O.G.: *J. Phys. Conf. Ser.* **488**, 072004 (2014)
78. Campeanu, R.I., Alam, M.: *Eur. Phys. J. D* **66**, 19 (2012)
79. Campeanu, R.I., Zohouri Haghian, N.: *Eur. Phys. J. D* **66**, 323 (2012)
80. Murtagh, D., Cooke, D., Laricchia, G.: *Phys. Rev. Lett.* **102**, 133202 (2009)
81. Iwata, K., Gribakin, G.F., Greaves, R.G., Kurz, C., Surko, C.M.: *Phys. Rev. A* **61**, 022719 (2000)
82. Schrader, D.M., Svetic, R.E.: *Can. J. Phys.* **60**, 517 (1982)
83. Kurz, C., Greaves, R., Surko, C.: *Phys. Rev. Lett.* **77**, 2929 (1996)
84. McEachran, R.P., Sullivan, J.P., Buckman, S.J., Brunger, M.J., Fuss, M.C., Muñoz, A., Blanco, F., White, R.D., Petrović, Z.L., Limão-Vieira, P., García, G.: *J. Phys. B* **45**, 45207 (2012)
85. Ward, S.J., Horbatsch, M., McEachran, R.P., Stauffer, A.D.: *J. Phys. B* **22**, 1845 (1989)
86. McEachran, R.P., Horbatsch, M., Stauffer, A.D.: *J. Phys. B* **24**, 2853 (1991)
87. McAlinden, M.T., Kernoghan, A.A., Walters, H.R.J.: *Hyperfine Interact.* **89**, 161 (1994)
88. McAlinden, M.T., Kernoghan, A.A., Walters, H.R.J.: *J. Phys. B* **29**, 555 (1996)
89. Kernoghan, A.A., McAlinden, M.T., Walters, H.R.J.: *J. Phys. B* **29**, 3971 (1996)
90. McAlinden, M.T., Kernoghan, A.A., Walters, H.R.J.: *J. Phys. B* **30**, 1543 (1997)
91. Ward, S.J., Horbatsch, M., McEachran, R.P., Stauffer, A.D.: *J. Phys. B* **22**, 3763 (1989)
92. Liu, F., Cheng, Y., Zhou, Y., Jiao, L.: *Phys. Rev. A* **83**, 032718 (2011)
93. Yamashita, T., Kino, Y.: *Eur. Phys. J. D* **70**, 190 (2016)
94. Umair, M., Jonsell, S.: *Phys. Rev. A* **93**, 52707 (2016)
95. Surdutovich, E., Harte, M., Kauppila, W.E., Kwan, C.K., Zhou, S.: *Phys. Rev. A* **68**, 022709 (2003)
96. Hewitt, R.N., Noble, C.J., Bransden, B.H.: *Can. J. Phys.* **74**, 559 (1996)
97. Gribakin, G.F., King, W.A.: *Can. J. Phys.* **74**, 449 (1996)
98. Charlton, M., Griffith, T.C., Heyland, G.R., Wright, G.L.: *J. Phys. B* **16**, 323 (1983)
99. Machacek, J.R., Anderson, E.K., Makochekanwa, C., Buckman, S.J., Sullivan, J.P.: *Phys. Rev. A* **88**, 42715 (2013)
100. Armour, E.A.G., Baker, D.J., Plummer, M.: *J. Phys. B* **23**, 3057 (1990)
101. Danby, G., Tennyson, J.: *J. Phys. B* **23**, 2471S (1990)
102. Gibson, T.L.: *J. Phys. B* **25**, 1321 (1992)
103. Germano, J.S.E., Lima, M.A.P.: *Phys. Rev. A* **47**, 3976 (1993)
104. Zammit, M.C., Fursa, D.V., Savage, J.S., Bray, I., Chiari, L., Zecca, A., Brunger, M.J.: *Phys. Rev. A* **95**, 22707 (2017)
105. Sullivan, J.P., Gilbert, S.J., Surko, C.M.: *Phys. Rev. Lett.* **86**, 1494 (2001)
106. Lino, J.L.S., Germano, J.S.E., Lima, M.A.P.: *J. Phys. B* **27**, 1881 (1994)
107. Fromme, D., Kruse, G., Raith, W., Sinapius, G.: *J. Phys. B* **21**, L261 (1988)
108. Knudsen, H., Brun-Nielsen, L., Charlton, M., Poulsen, P.M.: *J. Phys. B* **23**, 3955 (1990)
109. Moxom, J., Ashley, P., Laricchia, G.: *Can. J. Phys.* **74**, 367 (1996)
110. Ashley, P., Moxom, J., Laricchia, G.: *Phys. Rev. Lett.* **77**, 1250 (1996)
111. Jacobsen, F.M., Frandsen, N.P., Knudsen, H., Mikkelsen, U., Schrader, D.M.: *J. Phys. B* **28**, 4675 (1995)
112. Campeanu, R.I., Chis, V., Nagy, L., Stauffer, A.D.: *Phys. Lett. A* **310**, 445 (2003)
113. Kover, A., Laricchia, G.: *Phys. Rev. Lett.* **80**, 5309 (1998)
114. Reid, D.D., Klann, W.B., Wadehra, J.M.: *Phys. Rev. A* **70**, 062714 (2004)
115. Zanin, G.L., Tenfen, W., Arretche, F.: *Eur. Phys. J. D* **70**, 179 (2016)
116. Natisin, M.R., Danielson, J.D., Surko, C.M.: *Appl. Phys. Lett.* **108**, 24102 (2016)
117. Makochekanwa, C., Bankovic, A., Tattersall, W., Jones, A., Caradonna, P., Slaughter, D., Nixon, K., Brunger, M.J., Petrovic, Z., Sullivan, J.P., Buckman, S.J.: *New J. Phys.* **11**, 103036 (2009)
118. Arcidiacono, C., Beale, J., Pešić, Z.D., Kövér, Á., Laricchia, G.: *J. Phys. B* **42**, 065205 (2009)
119. Tattersall, W., Chiari, L., Machacek, J.R., Anderson, E., White, R.D., Brunger, M.J., Buckman, S.J., Garcia, G., Blanco, F., Sullivan, J.P.: *J. Chem. Phys.* **140**, 44320 (2014)
120. Kover, A., Murtagh, D.J., Williams, A.I., Laricchia, G.: *J. Phys. Conf. Ser.* **199**, 12020 (2010)
121. Singh, P., Purohit, G., Champion, C., Patidar, V.: *Phys. Rev. A* **89**, 032714 (2014)
122. Singh, S., Dutta, S., Naghma, R., Antony, B.: *J. Phys. Chem. A* **120**, 5685 (2016)
123. Singh, S., Dutta, S., Naghma, R., Antony, B.: *J. Phys. B. At. Mol. Opt. Phys.* **50**(13), 135202 (2017)
124. Przybyla, D., Addo-Asah, W., Kauppila, W., Kwan, C., Stein, T.: *Phys. Rev. A* **60**, 359 (1999)
125. Gianturco, F.A., Mukherjee, T., Paoletti, P.: *Phys. Rev. A* **56**, 3638 (1997)
126. Kimura, M., Takekawa, M., Itikawa, Y., Takaki, H., Sueoka, O.: *Phys. Rev. Lett.* **80**, 3936 (1998)
127. Marler, J.P., Surko, C.M.: *Phys. Rev. A* **72**, 062713 (2005)
128. Cooke, D.A., Murtagh, D.J., Laricchia, G.: *J. Phys. Conf. Ser.* **199**, 012006 (2010)
129. Przybyla, D.A., Kauppila, W.E., Kwan, C.K., Smith, S.J., Stein, T.S.: *Phys. Rev. A* **55**, 4244 (1997)
130. Kauppila, W.E., Stein, T.S., Miller, E.G., Surdutovich, F.: *Nucl. Instrum. Methods B* **221**, 48 (2004)
131. DuBois, R.D.: *J. Phys. B* **49**, 112002 (2016)
132. Chiari, L., Zecca, A., Blanco, F., García, G., Brunger, M.J.: *Phys. Rev. A* **91**, 012711 (2015)
133. Chiari, L., Zecca, A., Girardi, S., Defant, A., Wang, F., Ma, X.G., Perkins, M.V., Brunger, M.J.: *Phys. Rev. A* **85**, 052711 (2012)
134. Coleman, P.G., Culver, N.J., Dowler, B.M.W.M.: *Phys. Rev. A* **87**, 012712 (2013)
135. Palihawadana, P., Boadle, R., Chiari, L., Anderson, E.K., Machacek, J.R., Brunger, M.J., Buckman, S.J., Sullivan, J.P.: *Phys. Rev. A* **88**, 12717 (2013)
136. Anderson, E.K., Boadle, R.A., Machacek, J.R., Chiari, L., Makochekanwa, C., Buckman, S.J., Brunger, M.J., Garcia, G., Blanco, F., Inglfsson, O., Sullivan, J.P.: *J. Chem. Phys.* **141**, 34306 (2014)
137. Mitroy, J., Bromley, M.W.J., Ryzhikh, G.G.: *J. Phys. B* **35**, R81 (2002)
138. Mitroy, J.: *Phys. Rev. A* **66**, 010501R (2002)
139. Machacek, J.R., Boadle, R., Buckman, S.J., Sullivan, J.P.: *Phys. Rev. A* **86**, 064702 (2012)
140. Harabati, C., Dzuba, V.A., Flambaum, V.V.: *Phys. Rev. A* **89**, 22517 (2014)
141. Jones, A.C.L., Danielson, J.R., Gosselin, J.J., Natisin, M.R., Surko, C.M.: *New J. Phys.* **14**, 15006 (2012)
142. Hara, S., Fraser, P.A.: *J. Phys. B At. Mol. Phys.* **8**, 18 (1975)
143. Drachman, R.J., Houston, S.K.: *Phys. Rev. A* **12**, 885 (1975)
144. Drachman, R.J., Houston, S.K.: *Phys. Rev. A* **14**, 894 (1976)

145. Walters, H.R.J.: *Science* **330**, 762 (2010)
146. Fabrikant, I.I., Wilde, R.S.: *Phys. Rev. A* **97**, 52707 (2018)
147. Meredith, D.G., Fraser, P.A.: *J. Phys. B. At. Mol. Opt. Phys.* **51**, 055201 (2018)
148. Brawley, S.J., Armitage, S., Beale, J., Leslie, D.E., Williams, A.I., Laricchia, G.: *Science* **330**, 789 (2010)
149. Fabrikant, I.I., Gribakin, G.F.: *Phys. Rev. Lett.* **112**, 052717 (2014)
150. Mills, A.P.: *Phys. Rev. Lett.* **46**, 717–720 (1981)
151. Michishio, K., Tachibana, T., Terabe, H., Igarashi, A., Wada, K., Kuga, T., Yagishita, A., Hyodo, T., Nagashima, Y.: *Phys. Rev. Lett.* **106**, 153401 (2011)
152. Michishio, K., Kanai, T., Kuma, S., Azuma, T., Wada, K., Mochizuki, I., Hyodo, T., Yagishita, A., Nagashima, Y.: *Nat. Commun.* **7**, 11060 (2016)
153. Cassidy, D.B., Deng, S.H.M., Mills, A.P.: *Phys. Rev. A* **76**, 062511 (2007)
154. Oda, K., Miyakawa, T., Yabu, H., Suzuki, T.: *J. Phys. Soc. Japan* **70**, 1549–1555 (2001)
155. Ivanov, I.A., Mitrov, J., Varga, K.: *Phys. Rev. A* **65**, 022704 (2002)
156. Shumway, J., Ceperley, D.M.: *Phys. Rev. B* **63**, 165209 (2001)
157. Platzman, P.M., Mills, A.: *Phys. B Condens. Matter* **165–166**, 491–492 (1990)
158. Mills, A.P.: *Nucl. Instrum. Methods Phys. Res. B* **192**, 107–116 (2002)
159. Adhikari, S.K.: *Phys. Lett. A* **294**, 308–313 (2002)
160. Avetissian, H.K., Avetissian, A.K., Mkrtchian, G.F.: *Phys. Rev. Lett.* **113**, 023904 (2014)
161. Wang, Y.-H., Anderson, B.M., Clark, C.W.: *Phys. Rev. A* **89**, 43624 (2014)
162. Andresen, G.B., Ashkezari, M.D., Baquero-Ruiz, M., Bertsche, W., Bowe, P.D., Butler, E., Cesar, C.L., Chapman, S., Charlton, M., Deller, A., Eriksson, S., Fajans, J., Friesen, T., Fujiwara, M.C., Gill, D.R., Gutierrez, A., Hangst, J.S., Hardy, W.N., Hayden, M.E., Humphries, A.J., Hydomako, R., Jenkins, M.J., Jonsell, S., Jørgensen, L.V., Kurchaninov, L., Madsen, N., Menary, S., Nolan, P., Olchanski, K., Olin, A., Povilus, A., Pusa, P., Robicheaux, F., Sarid, E., Seif el Nasr, S., Silveira, D.M., So, C., Storey, J.W., Thompson, R.I., van der Werf, D.P., Wurtele, J.S., Yamazaki, Y.: *Nature* **468**, 673 (2010)
163. Ahmadi, M., Alves, B.X.R., Baker, C.J., Bertsche, W., Capra, A., Carruth, C., Cesar, C.L., Charlton, M., Cohen, S., Collister, R., Eriksson, S., Evans, A., Evetts, N., Fajans, J., Friesen, T., Fujiwara, M.C., Gill, D.R., Hangst, J.S., Hardy, W.N., Hayden, M.E., Isaac, C.A., Johnson, M.A., Jones, J.M., Jones, S.A., Jonsell, S., Khramov, A., Knapp, P., Kurchaninov, L., Madsen, N., Maxwell, D., McKenna, J.T.K., Menary, S., Momose, T., Munich, J.J., Olchanski, K., Olin, A., Pusa, P., Rasmussen, C., Robicheaux, F., Sacramento, R.L., Sameed, M., Sarid, E., Silveira, D.M., Stutter, G., So, C., Tharp, T.D., Thompson, R.I., Van Der Werf, D.P., Wurtele, J.S.: *Nature* **557**, 71–75 (2018)
164. Yamazaki, Y., Doser, M., Perez, P.: *Antihydrogen Beams*. IOP (2018)
165. Kadyrov, A.S., Bray, I., Charlton, M., Fabrikant, I.I.: *Nat. Commun.* **8**, 1544 (2017)
166. Darewych, J.W., Humberston, J.W., McEachran, R.P., Paul, D.A.L., Stauffer, A.D.: *Can. J. Phys.* **60**, 461–617 (1981)
167. Humberston, J.W., McDowell, M.R.C. (eds.): *Positron Scattering in Gases*. Plenum, New York (1984)
168. Kauppila, W.E., Stein, T.S., Wadehra, J.M. (eds.): *Positron (Electron)-Gas Scattering*. World Scientific, Singapore (1986)
169. Humberston, J.W., Armour, E.A.G. (eds.): *Atomic Physics with Positrons*. Plenum, New York (1987)
170. Drachman, R.J. (ed.): *Annihilation in Gases and Galaxies*. NASA Conference Publication, Washington, p 3058 (1990)
171. Parcell, L.A.: *Positron interaction with gases*, *Hyperfine Interact.* **73**, 1–232 (1992)
172. Raith, W., McEachran, R.P.: *Positron interactions with atoms, molecules and clusters*, *Hyperfine Interact.* **89**, 1–496 (1994)
173. McEachran, R.P., Stauffer, A.D.: *Proceedings of the 1995 positron workshop*, *Can. J. Phys.* **74**, 313–563 (1996)
174. Andersen, H.H., Armour, E.A.G., Humberston, J.W., Laricchia, G.A.: *Proceedings of the 1997 positron workshop*, *Nucl. Instrum. Methods B* **143**, 1–232 (1998)
175. Hara, S., Hyodo, T., Nagashima, Y., Rehn, L.: *Proceedings of the 1998 positron workshop*, *Nucl. Instrum. Methods B* **171**, 1–250 (2000)
176. Holzscheiter, M.H.: *Proceedings of the 2001 positron workshop*, *Nucl. Instrum. Methods B* **192**, 1–237 (2002)
177. Uggerhoj, U., Ichioka, T., Knudsen, H.: *Proceedings of the 2003 positron workshop*, *Nucl. Instrum. Methods B* **221**, 1–242 (2004)
178. Bromley, M.W.J., Lima, M.A.P., Laricchia, G.: *Phys. Scripta* **74**, C37 (2006)
179. Campeanu, R.I., Darewych, J.W., Stauffer, A.D.: *J. Phys. Conf. Ser.* **199**, 011001 (2010)
180. Limão-Vieira, P., Campeanu, R., Hoshino, M., Ingólfsson, O., Mason, N., Nagashima, Y., Tanuma, H.: *Eur. Phys. J. D* **68**, 263 (2014). <https://doi.org/10.1140/epjd/e2014-50564-9>
181. Limão-Vieira, P., García, G., Krishnakumar, E., Sullivan, J., Tanuma, H., Petrović, Z.: *Advances in positron and electron scattering*, *Eur. Phys. J. D* **78**, 202 (2016)
182. Brunger, M., Cassidy, D., Dujko, S., Marić, D., Marler, J., Sullivan, J., Fedor, J.: *Low-Energy Positron and Positronium Physics and Electron-Molecule Collisions and Swarms (POSMOL 2019)*, *Eur. Phys. J. D* **73** (2019), https://link.springer.com/journal/10053/topicalCollection/AC_5b7ff5fe1f55bcb1f7c744e7cc97e0b28
183. Massey, H.S.W.: *Can. J. Phys.* **60**, 461 (1982)
184. Kauppila, W.E., Stein, T.S.: *Adv. At. Mol. Opt. Phys.* **26**, 1 (1990)
185. Bransden, B.H.: In: McDaniel, E.W., McDowell, M.R.C. (eds.) *Case Studies in Atomic Collision Physics I*. Wiley, New York (1969). Chap. 4
186. Stein, T.S., Kauppila, W.E.: *Adv. At. Mol. Opt. Phys.* **18**, 53 (1982)
187. Buckman, S.J.: In: Surko, C.M., Gianturco, F.A. (eds.) *New Directions in Antimatter in Chemistry and Physics*, p. 391. Kluwer, Amsterdam (2001)
188. Surko, C.M., Gribakin, G.F., Buckman, S.J.: *J. Phys. B* **38**, R57 (2005)
189. Chiari, L., Zecca, A.: *Eur. Phys. J. D* **68**, 297 (2014)
190. Brunger, M.J., Buckman, S.J., Ratnavelu, K.: *J. Phys. Chem. Ref. Data* **46**, 023102 (2017)
191. Ratnavelu, K., Brunger, M.J., Buckman, S.J.: *J. Phys. Chem. Ref. Data* **48**, 023102 (2019)
192. Charlton, M., van der Werf, D.P.: *Sci. Prog.* **98**, 34–62 (2015)
193. Bertsche, W.A., Butler, E., Charlton, M., Madsen, N.: *J. Phys. B. At. Mol. Opt. Phys.* **48**, 232001 (2015)
194. Malbrunot, C., Amsler, C., Arguedas Cuendis, S., Breuker, H., Dupre, P., Fleck, M., Higaki, H., Kanai, Y., Kolbinger, B., Kuroda, N., Leali, M., Mäckel, V., Mascagna, V., Massiczek, O., Matsuda, Y., Nagata, Y., Simon, M.C., Spitzer, H., Tajima, M., Ulmer, S., Venturelli, L., Widmann, E., Wiesinger, M., Yamazaki, Y., Zmeskal, J.: *Philos. Trans. R. Soc. A Math. Phys. Eng. Sci.* **376**, 20170273 (2018)
195. Jonsell, S., Charlton, M.: *New J. Phys.* **20**, 043049 (2018)
196. Charlton, M., Mills, A.P., Yamazaki, Y.: *J. Phys. B. At. Mol. Opt. Phys.* **50**, 140201 (2017)
197. Cassidy, D.B.: *Eur. Phys. J. D* **72**, 53 (2018)
198. Charlton, M., Humberston, J.W.: *Positron Physics*. Cambridge University Press, Cambridge (2000)



Josh R. Machacek Josh Machacek received his PhD from the Australian National University. He was a postdoctoral scholar at JPL before returning to the ANU. He is a recipient of a DECRA Fellowship from the Australian Research Council and a US National Research Council Fellowship at the Air Force Institute of Technology. He is currently focused on quantum mechanically complete experiments involving positrons.



Allan D. Stauffer Allan Stauffer has published numerous papers in the field of electron and positron scattering from atoms and simple molecules. In collaboration with numerous colleagues, he has been involved with extensive scattering calculations and developed methods to carry out these investigations and has worked closely with groups involved in measuring these processes.



Robert P. McEachran Professor McEachran received his PhD from the University of Western Ontario, Canada. He spent 2 years at the University College London (England) before joining York University in Toronto in 1964. In 1997, he accepted an Adjunct Professorship at the Australian National University. His current research interests are the theoretical treatment of electron/positron scattering from heavy atoms within a relativistic framework.



Adiabatic and Diabatic Collision Processes at Low Energies

52

Evgeny Nikitin and Alexander Kandratsenka

Contents

52.1	Basic Definitions	773
52.1.1	Slow Quasi-Classical Collisions	773
52.1.2	Adiabatic and Diabatic Electronic States	774
52.1.3	Nonadiabatic Transitions: The Massey Parameter	774
52.2	Two-State Approximation	775
52.2.1	Relation Between Adiabatic and Diabatic Basis Functions	775
52.2.2	Coupled Equations and Transition Probabilities in the Common Trajectory Approximation	775
52.2.3	Selection Rules for Nonadiabatic Coupling	777
52.3	Single-Passage Transition Probabilities in Common Trajectory Approximation	778
52.3.1	Transitions Between Noncrossing Adiabatic Potential Energy Curves	778
52.3.2	Transitions Between Crossing Adiabatic Potential Curves	779
52.4	Double-Passage Transition Probabilities	780
52.4.1	Transition Probabilities in the Classically-Allowed and Classically-Forbidden WKB Regimes: Interference and Tunneling	780
52.4.2	Nonadiabatic Transitions near Turning Points	781
52.5	Multiple-Passage Transition Probabilities	782
52.5.1	Multiple Passage in Atomic Collisions	782
52.5.2	Surface Hopping	782
	References	783

Abstract

Adiabatic and diabatic electronic states of a system of atoms are defined and their properties are described. Nonadiabatic interaction for slow quasi-classical motion

E. Nikitin (✉)
Dept. of Physics, Technion – Israel Institute of Technology
Haifa, Israel
e-mail: nikitin@technion.ac.il

A. Kandratsenka (✉)
Dynamics at Surfaces, Max-Planck-Institute for Multidisciplinary Sciences
Göttingen, Germany
e-mail: akandra@mpinat.mpg.de

of atoms is discussed within the two-state approximation. Analytical formulae for nonadiabatic transition probabilities are presented for particular models with reference to single and double-passage of coupling regions. The generalization for multiple passages is described.

Keywords

potential energy surface · potential energy curve · Coriolis coupling · nonadiabatic transition · nonadiabatic coupling

52.1 Basic Definitions

52.1.1 Slow Quasi-Classical Collisions

Slow collisions of atoms or molecules (neutral or charged) are defined as collisions for which the velocity of the relative motion of colliding particles v is substantially lower than the velocity of valence electrons v_e

$$\frac{v}{v_e} \ll 1. \quad (52.1)$$

If v_e is estimated as $v_e \approx 1 \text{ a.u.} \approx 10^8 \text{ cm/s}$, then Eq. (52.1) is fulfilled for medium-mass nuclei ($\approx 10 \text{ amu}$) up to several keV.

Quasi-classical collisions are those for which the de Broglie wavelength λ_{dB} for relative motion is substantially smaller than the range parameter a of the interaction potential (the WKB (Wentzel–Kramers–Brillouin) condition [1–4])

$$\lambda_{dB} \ll a. \quad (52.2)$$

The two conditions in Eqs. (52.1) and (52.2) define the energy range within which collisions are slow and quasi classical. For medium-mass nuclei, this energy range covers collision energies above room temperature and below hundreds of eV. The parameter a should not be confused with

another important parameter, L_0 , which characterizes the extent of the interaction region. For instance, for the exchange interaction between two atoms, L_0 corresponds to the distance of closest approach of the colliding particles, while a is the range of the exponential decrease of the interaction. Typically, L_0 noticeably exceeds a .

52.1.2 Adiabatic and Diabatic Electronic States

Let r refer to a set of electronic coordinates in a body-fixed frame related to the nuclear framework of a colliding system and let \mathcal{R} refer to a set of nuclear coordinates determining the relative position of nuclei in this system. A configuration of electrons and nuclei in a frame fixed in space is completely determined by r , \mathcal{R} , and the set of Euler angles Ω , which relate the body-fixed frame to the space-fixed frame. With the total Hamiltonian of the system $\mathcal{H}(r, \mathcal{R}, \Omega)$, the stationary state wave function satisfies the equation

$$\mathcal{H}(r, \mathcal{R}, \Omega)\Psi_E(r, \mathcal{R}, \Omega) = E\Psi_E(r, \mathcal{R}, \Omega). \quad (52.3)$$

The electronic adiabatic Hamiltonian $H(r; \mathcal{R})$ is defined to be the part of $\mathcal{H}(r, \mathcal{R}, \Omega)$ in which the kinetic energy of the nuclei and certain weak interactions are ignored. Typically, $H(r; \mathcal{R})$ includes the electron–electron and electron–nuclear electrostatic interaction and, possibly, the spin–orbit interaction. The adiabatic electronic functions $\psi_n(r; \mathcal{R})$ are defined as eigenfunctions of $H(r; \mathcal{R})$ at a fixed nuclear configuration \mathcal{R} with set of electronic coordinates r

$$H(r; \mathcal{R})\psi_n(r; \mathcal{R}) = U_n(\mathcal{R})\psi_n(r; \mathcal{R}). \quad (52.4)$$

The eigenvalues $U_n(\mathcal{R})$ are called adiabatic potential energy surfaces (adiabatic PES). In the case of a diatom, the set \mathcal{R} collapses into a single coordinate, the internuclear distance R , and the PES become potential energy curves PEC, $U_n(R)$. The functions $\psi_n(r; \mathcal{R})$ depend explicitly on \mathcal{R} and implicitly on the Euler angles Ω . The significance of the adiabatic PES is related to the fact that in the limit of very low velocities, a system of nuclei will move across a single PES. In this approximation, called the adiabatic approximation, the function $U_n(\mathcal{R})$ plays the part of the potential energy, which drives the motion of the nuclei [1–4].

An electronic diabatic Hamiltonian is defined formally as a part of H , i.e., $H_0 = H + \Delta H$. The partitioning of H into H_0 and ΔH is dictated by the requirement that the eigenfunctions of H_0 , called diabatic electronic functions ϕ_n , depend weakly on the configuration \mathcal{R} . The physical meaning of this weak dependence is different for different problems. A perfect diabatic basis set $\phi_n(r)$ is \mathcal{R} independent; for practical purposes, one can use a diabatic set that is considered \mathcal{R} independent within a certain region of the configuration space \mathcal{R} .

Two basis sets ψ_n and ϕ_n generate the matrices

$$\begin{aligned} \langle \phi_m | H | \phi_n \rangle &= H_{mn}, \\ \langle \phi_m | \mathcal{H} | \phi_n \rangle &= H_{mn} + D_{mn}, \\ \langle \psi_m | \mathcal{H} | \psi_n \rangle &= U_n(\mathcal{R})\delta_{mn} + \mathcal{D}_{mn}. \end{aligned} \quad (52.5)$$

The eigenvalues of the matrix H_{mn} are U_n ; D_{mn} and \mathcal{D}_{mn} are the matrices of interactions ignored in the passage from the Hamiltonian \mathcal{H} to H . All the above matrices are, in principle, of infinite order. For low-energy collisions, the use of finite matrices of moderate dimension will usually suffice.

Diabatic PES are defined as the diagonal elements H_{nn} . The significance of the diabatic PES is that for velocities that are high [but still satisfy Eq. (52.1)] the system moves preferentially across diabatic PES, provided that the off-diagonal elements H_{mn} are small enough.

An adiabatic function $\psi_n(r; \mathcal{R})$ can be constructed as a linear combination of the diabatic functions $\phi_m(r)$ as

$$\psi_n(r; \mathcal{R}) = \sum_m C_{nm}(\mathcal{R})\phi_m(r). \quad (52.6)$$

52.1.3 Nonadiabatic Transitions: The Massey Parameter

Deviations from the adiabatic approximation manifest themselves in transitions between different PES, which are induced by the dynamic coupling matrix \mathcal{D} . At low energies, the transitions usually occur in localized regions of nonadiabatic coupling (NAR). In these regions, the motion of nuclei in different electronic states is coupled, and, in general, it cannot be interpreted as being driven by a single potential [3, 5–7].

An important simplifying feature of slow adiabatic collisions is that, typically, the distance between different NAR is substantially larger than the extents of each NAR. This makes it possible to formulate simple models for the coupling in isolated NAR, and, subsequently, to incorporate the solution for nonadiabatic coupling into the overall dynamics of the system.

For a system of s nuclear degrees of freedom, there are the following possibilities for the behavior of PES within NAR:

- (i) If two s -dimensional PES correspond to electronic states of different symmetry, they can cross along an $(s - 1)$ -dimensional line. For a system of two atoms, $s = 1$, and so two potential curves of different symmetry can cross at a point.
- (ii) If two s -dimensional PES correspond to electronic states of the same symmetry, they can cross along an $(s - 2)$ -dimensional line. For a system of two atoms, $s = 1$, and so two potential curves of different symmetry cannot cross.

- (iii) If two s -dimensional PES correspond to electronic states of the same symmetry in the presence of spin–orbit coupling, they can cross along an $(s - 3)$ -dimensional line.

Statement (ii) applied to a two-atom system is known as the Wigner–Witmer noncrossing rule. In applications to a system with $s > 1$, it is frequently discussed in terms of the conical intersection [8].

The efficiency of the nonadiabatic coupling between two adiabatic electronic states is determined according to the adiabatic principle of mechanics (both classical and quantum), by the value of the Massey (M) parameter ζ^M , which represents the product of the electronic transition frequency ω_{el} and the time τ_{nuc} that characterizes the rate of change of electronic function due to the nuclear motion. Putting $\omega_{el} \approx \Delta U(\mathcal{R})/\hbar$ and $\tau_{nuc} = \Delta L/v(\mathcal{R})$, we get

$$\zeta^M(\mathcal{R}) = \omega_{el}\tau_{nuc} = \Delta U(\mathcal{R})\Delta L/\hbar v(\mathcal{R}), \quad (52.7)$$

where ΔU is the spacing between any two adiabatic PES, and ΔL is a certain range that depends on the type of coupling. The nonadiabatic coupling is inefficient at those configurations \mathcal{R} where $\zeta^M(\mathcal{R}) \gg 1$. If $\zeta^M(\mathcal{R})$ is less than or of the order of unity, the nonadiabatic coupling is efficient, and a change in adiabatic dynamics of nuclear motion is very substantial.

The following relations usually hold for the parameters $\Delta L, a, L_0$ for slow collisions

$$\Delta L \ll a \ll L_0. \quad (52.8)$$

When the nonadiabatic coupling is taken into account, the total (electronic and nuclear) wave function, Ψ_E , can be represented as a series expansion in ψ_n or ϕ_n (the Euler angles Ω are suppressed for brevity)

$$\begin{aligned} \Psi_E(r, \mathcal{R}) &= \sum_n \psi_n(r; \mathcal{R})\chi_{nE}(\mathcal{R}) \\ &= \sum_n \phi_n(r)\kappa_{nE}(\mathcal{R}). \end{aligned} \quad (52.9)$$

Here, $\chi_{nE}(\mathcal{R})$ and $\kappa_{nE}(\mathcal{R})$ are the functions that have to be found as solutions to the coupled equations formulated in the adiabatic or diabatic electronic basis, respectively [3, 5–7, 9]. In general, different contributions to the first sum in Eq. (52.9) can be associated with nonadiabatic transition probabilities between different electronic states.

A practical means of calculating functions $\chi_{nE}(\mathcal{R})$ [or $\kappa_{nE}(\mathcal{R})$] consists of expanding them over certain basis functions $\mathcal{E}_{nv}(\mathcal{R}')$, where \mathcal{R}' denotes all coordinates \mathcal{R} save a single coordinate R . Writing

$$\chi_{nE}(\mathcal{R}) = \sum_v \mathcal{E}_{nv}(\mathcal{R}')\xi_{nvE}(\mathcal{R}), \quad (52.10)$$

one arrives at a set of coupled second-order equations for the unknown functions $\xi_{nvE}(\mathcal{R})$ (the scattering equations). In the adiabatic approximation, the total wave function is represented by a single term in the first sum of Eq. (52.9)

$$\Psi_E(r, \mathcal{R}) = \psi_n(r; \mathcal{R})\chi_{nE}(\mathcal{R}). \quad (52.11)$$

52.2 Two-State Approximation

52.2.1 Relation Between Adiabatic and Diabatic Basis Functions

In the two-state approximation, two adiabatic functions $\psi_k(r; \mathcal{R})$ are assumed to be expressed as a linear combination of two diabatic functions $\phi_k(r)$ via a rotation angle θ

$$\begin{aligned} \psi_1(r; \mathcal{R}) &= \cos \theta(\mathcal{R})\phi_1(r) + \sin \theta(\mathcal{R})\phi_2(r), \\ \psi_2(r; \mathcal{R}) &= -\sin \theta(\mathcal{R})\phi_1(r) + \cos \theta(\mathcal{R})\phi_2(r). \end{aligned} \quad (52.12)$$

The rotation angle, $\theta(\mathcal{R})$, is expressed via the diagonal and off-diagonal matrix elements of the adiabatic Hamiltonian H in the diabatic basis ϕ_1, ϕ_2

$$\tan 2\theta(\mathcal{R}) = \frac{2H_{12}(\mathcal{R})}{H_{11}(\mathcal{R}) - H_{22}(\mathcal{R})}. \quad (52.13)$$

The eigenvalues of H are

$$\begin{aligned} U_{1,2} &= \bar{U} \pm \Delta U, \\ \bar{U} &= (H_{11} + H_{22})/2 = \bar{H}, \\ \Delta U &= \frac{1}{2}\sqrt{(\Delta H)^2 + 4H_{12}^2}, \\ \Delta H &= H_{11} - H_{22}, \end{aligned} \quad (52.14)$$

implying

$$\begin{aligned} \Delta H &= \Delta U \cos 2\theta, \\ H_{12} &= (1/2)\Delta U \sin 2\theta. \end{aligned} \quad (52.15)$$

52.2.2 Coupled Equations and Transition Probabilities in the Common Trajectory Approximation

A two-state nonadiabatic wave function $\Psi(r, \mathcal{R})$ can be written as an expansion into either adiabatic or diabatic electronic wave functions

$$\begin{aligned} \Psi(r; \mathcal{R}) &= \psi_1(r; \mathcal{R})\alpha_1(\mathcal{R}) + \psi_2(r; \mathcal{R})\alpha_2(\mathcal{R}), \\ \Psi(r; \mathcal{R}) &= \phi_1(r)\beta_1(\mathcal{R}) + \phi_2(r)\beta_2(\mathcal{R}), \end{aligned} \quad (52.16)$$

in which the nuclear wave functions satisfy two coupled s -dimensional Schrödinger equations [1–3].

In the common trajectory (CT) approximation, the motion of the nuclei is described by the classical trajectory, i.e., by a one-dimensional manifold $Q(t)$ embedded in the s -dimensional manifold \mathcal{R} . A section of PES along this one-dimensional manifold determines a set of effective PEC. In the case of atomic collisions, Q coincides with the interatomic distance R , and the effective PEC are just ordinary PEC. A definition of a CT, or an effective potential that drives it, represents a challenging task which is not discussed here (e.g., references in the collection of notes [10, 11]).

A CT counterpart of Eq. (52.16) is

$$\begin{aligned}\Psi(r, t) &= \psi_1[r; Q(t)]a_1(t) + \psi_2[r; Q(t)]a_2(t), \\ \Psi(r; t) &= \phi_1(r)b_1(t) + \phi_2(r)b_2(t).\end{aligned}\quad (52.17)$$

The expansion coefficients $a_k(t)$ satisfy the set of equations

$$\begin{aligned}i\hbar \frac{da_1}{dt} &= U_1(Q)a_1 + i\dot{Q}g(Q)a_2, \\ i\hbar \frac{da_2}{dt} &= -i\dot{Q}g(Q)a_1 + U_2(Q)a_2.\end{aligned}\quad (52.18)$$

Here, the dynamical coupling function (defined in the adiabatic basis)

$$g(Q) = \langle \psi_1 | \frac{\partial}{\partial Q} | \psi_2 \rangle = -\langle \psi_2 | \frac{\partial}{\partial Q} | \psi_1 \rangle = \frac{d\theta}{dQ}, \quad (52.19)$$

arises from the action of the operator $i\hbar \partial / \partial t$ on the adiabatic functions and is expressed in terms of the angle $\theta(Q)$ (defined in the diabatic basis by Eq. (52.13)).

For low energies, function $g(Q)$ is localized near the NAR center, and Eqs. (52.18) decouple away from the NAR center. This property of coupled equations may be lost if they are formulated in the diabatic basis. The diabatic expansion coefficients $b_k(t)$ satisfy the set of equations

$$\begin{aligned}i\hbar \frac{db_1}{dt} &= H_{11}(Q)b_1 + H_{12}(Q)b_2, \\ i\hbar \frac{db_2}{dt} &= H_{21}(Q)b_1 + H_{22}(Q)b_2.\end{aligned}\quad (52.20)$$

Clearly, for a system of two atoms, $Q \equiv R$.

Solutions to Eqs. (52.18) and (52.20) are equivalent, provided that the initial conditions are matched, and the transition probability is properly defined with account taken for the coupling of the diabatic states away from the NAR center. It is customary to identify the center of the NAR with a value of $Q = Q_p$, which corresponds to the real part of the complex-valued coordinate Q_c at which two adiabatic PES cross and which possesses the smallest imaginary part [1].

The crossing conditions in the adiabatic and diabatic representations are

$$\begin{aligned}\Delta U(Q_c) &= 0, \\ [\Delta H(Q_c)]^2 + 4H_{12}^2(Q_c) &= 0.\end{aligned}\quad (52.21)$$

Since Q represents a one-dimensional manifold, the crossing condition Eq. (52.21) is satisfied for complex values of $Q = Q_c$, unless $H_{12} = 0$. Then, by definition, the location of the NAR center is identified with $Q_p = \text{Re } Q_c$. A characteristic width of an isolated NAR is determined by the width ΔQ_p of a peaked (at $\Delta Q = Q_p$) function $g(Q)$. Normally, ΔQ_p is about $\text{Im } Q_c$ [3]. A more general discussion of the crossing in the complex coordinate plane is given in the context of the hidden crossing [10].

For low energies, the Eq. (52.20) along a particular CT are partitioned into sets of adiabatic evolution and the sets of nonadiabatic transformation of the amplitudes. The spatial (or temporal) extension of the former is normally much larger compared to the latter, such that nonadiabatic transformation of the amplitudes can be described by Eq. (52.18) applied to an isolated NAR. Since the characteristic width of a NAR is small on the scale of the whole CT, the part of CT that is essential in describing the nonadiabatic transformation of $a_k(t)$ can be simplified in order to make Eq. (52.18) more easily handled. This simplification (to be called the local common trajectory, LCT) is a crux of the analytical solution for model cases of nonadiabatic coupling (Sect. 52.3) within an isolated NAR.

With the given functions $U_1(Q)$, $U_2(Q)$, $g(Q)$ (or $H_{11}(Q)$, $H_{22}(Q)$, and $H_{12}(Q)$), the Eq. (52.18) are completely defined by setting the LCT with $Q = Q_{\text{LCT}}(t)$. Equation (52.18) decouple on both sides of the NAR, say, at $t < t^{(-)}$ and $t > t^{(+)}$. At these values of t , the two-state function $\Psi(r, t)$ evolves adiabatically, and this behavior can be singled out by transformation ($t^{(-)} < t_p < t^{(+)}$)

$$a_k(t) = \bar{a}_k(t) \exp \left[-\frac{i}{\hbar} \int_{t_p}^t U_k[Q_{\text{LCT}}(t)] dt \right]. \quad (52.22)$$

The amplitudes $\bar{a}_k(t)$, which become time-independent outside NAR, satisfy equations

$$\begin{aligned}\frac{d\bar{a}_1}{dt} &= \bar{a}_2 \dot{Q}_{\text{LCT}} g(Q_{\text{LCT}}) \exp \left[\frac{i}{\hbar} \int_{t_p}^t \Delta U[Q_{\text{LCT}}(t)] dt \right], \\ \frac{d\bar{a}_2}{dt} &= -\bar{a}_1 \dot{Q}_{\text{LCT}} g(Q_{\text{LCT}}) \\ &\times \exp \left[-\frac{i}{\hbar} \int_{t_p}^t \Delta U[Q_{\text{LCT}}(t)] dt \right].\end{aligned}\quad (52.23)$$

Thus, the amplitudes $\bar{a}_k(t)$ are determined by two functions, $\Delta U(Q)$ and $g(Q)$, that evolve along a chosen LCT. These two functions are related to the two diabatic basis functions $H_{12}(Q)$ and $\Delta H(Q)$ by Eq. (52.14). It follows from Eq. (52.23) that \bar{a}_1 and \bar{a}_2 become time independent outside NAR. This property of the amplitudes in the adiabatic basis is lost for their counterparts in the diabatic basis.

A solution of the equations of the nonadiabatic coupling across an isolated maximum of $g(Q)$ within the time interval $t^{(-)} \leq t \leq t^{(+)}$ (LCT interval $Q_{\text{LCT}}^{(-)} \leq Q_{\text{LCT}} \leq Q_{\text{LCT}}^{(+)}$, accordingly) gives the single-passage (or one-way) matrix of the nonadiabatic evolution, $\mathcal{N}_{n,m}^{+,-}$, which connects the amplitudes $\{a_1^{(-)}, a_2^{(-)} \rightarrow a_1^{(+)}, a_2^{(+)}\}$ on both sides of NAR. In particular, the probability P_{12} of the nonadiabatic transition $1 \rightarrow 2$ and the probability $1 - P_{12}$ of the nonadiabatic survival $1 \rightarrow 1$ are

$$P_{12} = |\mathcal{N}_{2,1}^{+,-}|^2 \quad \text{and} \quad 1 - P_{12} = |\mathcal{N}_{1,1}^{+,-}|^2. \quad (52.24)$$

The efficiency of nonadiabatic coupling in crossing an isolated NAR can be estimated by the Landau formula for transition probability in the near-adiabatic limit when $P_{12} \ll 1$

$$P_{12} = \exp \left[-\frac{2}{\hbar} \left| \text{Im} \int_{t_r}^{t_c} \Delta U[Q_{\text{LCT}}(t)] dt \right| \right], \quad (52.25)$$

where t_c is a root of the equation $Q_{\text{LCT}}(t_c) = Q_c$, and t_r is any real-valued time. The single-passage transition probabilities are discussed in Sect. 52.3.

Once passage matrices $\mathcal{N}_{n,m}^{+,-}$ are known, they can be incorporated into the general scheme of nonadiabatic dynamics. In particular, the transition probabilities for the double passage of the same NAR are discussed in Sect. 52.4, and the nonadiabatic dynamics with multiple transitions is described in Sect. 52.5.

Table 52.1 Selection rules for the coupling between diabatic and adiabatic states of a diatomic quasi molecule ($w = g, u; \sigma = +, -$)

Interaction	$^{2S+1}A_w^{(\sigma)}$ nomenclature	$\Omega_w^{(\sigma)}$ nomenclature
Configuration interaction	$\Delta\Lambda = 0, \Delta S = 0$	$\Delta\Omega = 0$
(electrostatic)	$g \not\rightleftharpoons u, + \not\rightleftharpoons -$	$g \not\rightleftharpoons u, + \not\rightleftharpoons -$
Spin-orbit interaction	$\Delta\Lambda = 0, \pm 1, \Delta S = 0, \pm 1$	$\Delta\Omega = 0$
	$g \not\rightleftharpoons u, + \rightleftharpoons -$	$g \not\rightleftharpoons u, + \not\rightleftharpoons -$
Radial motion	$\Delta\Lambda = 0, \Delta S = 0$	$\Delta\Omega = 0$
	$g \not\rightleftharpoons u, + \not\rightleftharpoons -$	$g \not\rightleftharpoons u, + \not\rightleftharpoons -$
Rotational motion	$\Delta\Lambda = \pm 1, \Delta S = 0$	$\Delta\Omega = \pm 1$
	$g \not\rightleftharpoons u, + \not\rightleftharpoons -$	$g \not\rightleftharpoons u, + \not\rightleftharpoons -$
Hyperfine interaction	$\Delta\Lambda = 0, \pm 1, \Delta S = 0, \pm 1$	$\Delta\Omega = 0, \pm 1$
	$g \rightleftharpoons u, + \rightleftharpoons -$	$g \rightleftharpoons u, + \rightleftharpoons -$

52.2.3 Selection Rules for Nonadiabatic Coupling

In the general case, the coupling between adiabatic states or diabatic states is controlled by certain selection rules. The most detailed selection rules exist for a system of two colliding atoms, since this system possesses a high symmetry ($C_{\infty v}$ or, for identical atoms, $D_{\infty h}$ point symmetry in the adiabatic approximation). In the adiabatic representation, the coupling is due to the elements of the matrix \mathcal{D} . They fall into two different categories: those proportional to the radial nuclear velocity (coupling by radial motion or radial coupling) and those proportional to the angular velocity of rotation of the molecular axis (coupling by rotational motion or Coriolis coupling). Besides, \mathcal{D} includes the spin-orbit and other weak interactions if they are not included in the adiabatic Hamiltonian.

In a diabatic representation, the coupling is due to the parts of the interaction potential neglected in the definition of the diabatic Hamiltonian H_0 . In typical cases, these parts (besides the nuclear motion) are: the electrostatic interaction between different electronic states constructed as certain electronic configurations (H_0 corresponds to a self-consistent field Hamiltonian); spin-orbit interaction (H_0 corresponds to a nonrelativistic Hamiltonian); hyperfine interaction (H_0 ignores the magnetic interaction of electronic and nuclear spins); as well as the electrostatic interaction between electrons and quadrupole moments of nuclei. Different definitions of the adiabatic electronic states (i.e., different Hund coupling cases [1]) of a system of two atoms are discussed in [11]; the respective selection rules are summarized in [12]. The selection rules for the above interactions in this case are listed in Table 52.1 for two conventional nomenclatures for molecular states: Hund's case (a), $^{2S+1}A_w^{(\sigma)}$, and Hund's case (c), $\Omega_w^{(\sigma)}$.

For molecular systems with more than two nuclei, the selection rules cannot be put in a detailed form since, in general, the symmetry of the system is quite low. For the important case of three atoms, a general configuration is planar (C_s symmetry); particular configurations correspond to an isosceles triangle if two atoms are identical (C_{2v} symmetry),

Table 52.2 Selection rules for dynamic coupling between adiabatic states of a system of three atoms

C_s		A'		A''	
	C_{2v}	A_1	B_1	A_2	B_2
A'	A_1	z	y, R_x	R_z	R_y
	B_1	y, R_x	z	R_y	R_z
A''	A_2	R_z	R_y	z	y, R_x
	B_2	R_y	R_z	y, R_x	z

to an equilateral triangle for three identical atoms (D_{3h} symmetry), or to a linear configuration. For the last case, the selection rules are the same as for a system of two atoms. The selection rules for the dynamic coupling between adiabatic states classified according to the irreducible representations of the C_s and C_{2v} groups are listed in Table 52.2. In Table 52.2, z and y refer to two modes of the relative nuclear motion in the system plane, R_z and R_y refer to two rotations about principal axes of inertia lying in the system plane, and R_x refers to a rotation about the principal axis of inertia perpendicular to the system plane. In-plane motion of nuclei couples the state of the same reflection symmetry; rotation of the system plane couples the state of the different reflection symmetry. The spin-orbit interaction, if included in matrices D_{mn} and D_{mn} , couples the states of different reflection symmetry. For a more detailed discussion see [12].

52.3 Single-Passage Transition Probabilities in Common Trajectory Approximation

52.3.1 Transitions Between Noncrossing Adiabatic Potential Energy Curves

Single-passage transition probabilities between noncrossing adiabatic potential curves for different models can be classified by either diabatic or adiabatic Hamiltonians using the common trajectory with the NAR region. The following discussion refers to the cases of one-dimensional motion, when the transition probability can be expressed analytically. Here, a quite general model corresponds to exponential diabatic potentials and coupling (Nikitin (N) model [13]), with residual dynamical coupling neglected. It is formulated as

$$\begin{aligned} \Delta H^N(Q) &= -\Delta E [1 - \cos 2\vartheta e^{-\alpha(Q-Q_p)}], \\ H_{12}^N(Q) &= (\Delta E/2) \sin 2\vartheta e^{-\alpha(Q-Q_p)}. \end{aligned} \quad (52.26)$$

Here, ϑ is a parameter that defines the interplay between the off-diagonal element $H_{12}^N(Q)$ and the difference in the diagonal elements $\Delta H^N(Q)$. In addition, Eq. (52.26) includes asymptotic spacing ΔE of diabatic PEC (for $\alpha(Q-Q_p) \gg 1$) and characteristic scale $1/\alpha$ of the exponential interaction. The meaning of the characteristic coordinate Q_p is revealed,

when one passes to the adiabatic basis with the spacing $\Delta U(Q)$ and dynamical coupling $g(Q)$

$$\begin{aligned} \Delta U(Q) &= \Delta E \sqrt{1 - 2 \cos 2\vartheta e^{-\alpha(Q-Q_p)} + e^{-2\alpha(Q-Q_p)}}, \\ g(Q) &= \frac{\alpha}{2} \frac{\sin 2\vartheta e^{-\alpha(Q-Q_p)}}{1 - 2 \cos 2\vartheta e^{-\alpha(Q-Q_p)} + e^{-2\alpha(Q-Q_p)}}. \end{aligned} \quad (52.27)$$

As ϑ changes from very small values to $\pi/2$, the spacing of adiabatic PEC changes from the narrow avoided crossing to the wide one and ultimately displays strong divergence. The adiabatic PEC cross at

$$Q_c = Q_p \pm 2i\vartheta/\alpha. \quad (52.28)$$

This expression defines Q_p as the center of NAR, $Q_p = \text{Re } Q_c$, while the characteristic range of NAR is $\Delta Q_p = \text{Im } Q_c = 2\vartheta/\alpha$. The adiabatic states become uncoupled outside the NAR, while diabatic states remain coupled on the asymptotic side of NAR.

For this model, adiabatic wave functions coincide with diabatic functions before entering the coupling region (in the limit $\alpha(Q-Q_p) \gg 1$), but after exiting the coupling region (in the limit $\alpha(Q-Q_p) \ll -1$) they are ϑ -dependent linear combinations of the diabatic functions.

The definition of the exponential model within the LCT concept is completed once one specifies the LCT that crosses the NAR. It is taken to be a segment of a rectilinear trajectory,

$$Q(t) - Q_p = v_p(t - t_p), \quad (52.29)$$

where $v_p = \dot{Q}(t)|_{t=t_p}$ is additional parameter of the model, and t_p is the time corresponding to the center of NAR.

The solution of coupled equations yields the transition probability between adiabatic states

$$P_{12}^N = \frac{\sinh(\zeta \cos^2 \vartheta)}{\sinh \zeta} e^{-\zeta \sin^2 \vartheta}, \quad (52.30)$$

where $\zeta = \pi \Delta E / (\hbar \alpha v_p)$ is the asymptotic Massey parameter. Its value at the center of NAR is $\zeta_p = \zeta \sin^2 \vartheta$.

Special cases of the exponential model correspond to the linearly crossing diabatic potentials with the constant coupling (Landau-Zener (LZ) model [14–16]), parallel diabatic potentials with the exponential coupling (Demkov (D) model [17]), and the asymptotically degenerate diabatic potentials (resonance (R) model [13]).

The LZ model [14–16] is obtained from the exponential model by retaining Eq. (52.27) terms linear in ϑ and $\alpha(Q-Q_p)$ (i.e., for $\vartheta \ll 1$, $\zeta \gg 1$)

$$\begin{aligned} \Delta H^{LZ}(Q) &= \Delta E \alpha(Q-Q_p) \equiv \Delta F \alpha(Q-Q_p), \\ H_{12}^{LZ} &= \Delta E \vartheta \equiv V. \end{aligned} \quad (52.31)$$

Here, the right-hand-side corresponds to the standard parameterization of the LZ model, where $\Delta F = \Delta E \alpha$ denotes the difference in slopes of the diabatic crossing PEC at Q_p , and V is a constant. The pattern of the adiabatic PEC, with $\Delta U(Q_p)$ calculated from Eq. (52.31) as

$$\Delta U(Q) = \left| \sqrt{\Delta F^2 (Q - Q_p)^2 + 4V^2} \right|, \quad (52.32)$$

corresponds to an avoided crossing (or pseudo crossing). For this model, adiabatic wave functions coincide with diabatic functions on one side of the NAR, but on the other side, the former interchange with the latter accompanied by a sign reversal.

When $\vartheta \ll 1$ and $\zeta \gg 1$, Eq. (52.30) yields the LZ transition probability

$$P_{12}^{LZ} = \exp(-2\pi\zeta\vartheta^2) = \exp(-2\pi V^2/\Delta F v_p). \quad (52.33)$$

Remarkable properties of the Landau–Zener model are:

- (i) Expression Eq. (52.33) for the probability P_{12}^{LZ} is valid for arbitrary values of the exponent and not only for the large ones. In the latter case, the probability is very low, so that the system moves preferentially along a noncrossing adiabatic PEC.
- (ii) In the weak-coupling case (small value of the exponent in Eq. (52.33) termed narrow avoided crossing), the system moves preferentially along a crossing diabatic PES. The survival probability for a motion along the adiabatic PEC is then very low, $1 - P_{12}^{LZ} = 2\pi V^2/(\Delta F v_p)$.

The D model [17] is obtained from Eq. (52.27) by setting $\vartheta = \pi/4$

$$\begin{aligned} \Delta H^D(Q) &= \Delta E, \\ H_{12}^D(Q) &= (\Delta E/2) \exp[-\alpha(Q - Q_p)]. \end{aligned} \quad (52.34)$$

The transition probability in this case is

$$P_{12}^D = \frac{\exp(-\zeta)}{1 + \exp(-\zeta)}. \quad (52.35)$$

For this model, the adiabatic wave functions coincide with the diabatic functions on the one side of NAR, but on the other side, the former are expressed through the linear combinations of the latter with equal weights.

The R model is defined by the condition $\Delta E = 0$, i.e., $\zeta = 0$. For arbitrary ϑ , this case corresponds to the so-called accidental resonance (AR), and for $\vartheta = \pi/4$, it corresponds to the symmetric resonance (SR). In these two cases, the transition probabilities read

$$\begin{aligned} P_{12}^{AR} &= P_{12}^N|_{\zeta=0} = \cos^2 \vartheta, \\ P_{12}^{SR} &= P_{12}^N|_{\zeta=0, \vartheta=\pi/4} = 1/2. \end{aligned} \quad (52.36)$$

52.3.2 Transitions Between Crossing Adiabatic Potential Curves

The nomenclature of the adiabatic PEC within and outside a NAR differs for noncrossing and crossing adiabatic PES. For the former case, the assignment of the asymptotic states can be done according to their energies (e.g., $U_1(Q) > U_2(Q)$), while for the latter case, the inequality sign is reversed as a system passes the NAR. When applying the model for the noncrossing adiabatic PEC to the crossing PEC, one should take into account this reversal of the nomenclature. Then the transition probability P_{12} between the crossing adiabatic PEC can be recovered from the survival probability for the noncrossing adiabatic PEC with the proper modification of parameters.

A particular case of the linear crossing (LC) adiabatic potentials and the constant dynamical coupling corresponds to the Hamiltonian

$$\begin{aligned} \Delta U^{LC}(Q) &= \Delta F \alpha (Q - Q_c), \\ D_{12}^{LC} &= D = \text{const}. \end{aligned} \quad (52.37)$$

This Hamiltonian can be mapped onto the LZ Hamiltonian Eq. (52.31) by replacing the velocity v_p at the NAR center with the velocity v_c at the crossing point Q_c . Taking into account the reversal of the LZ nomenclature for the adiabatic and diabatic functions in crossing the NAR, the nonadiabatic transition probability for the LC P_{12}^{LC} is related to P_{12}^{LZ} as

$$\begin{aligned} P_{12}^{LC} &= 1 - P_{12}^{LZ}(V, v_p)|_{V \rightarrow D, v_p \rightarrow v_c} \\ &= 1 - \exp[-2\pi D^2/(\hbar \Delta F v_c)]. \end{aligned} \quad (52.38)$$

The matrix element D is often related to the Coriolis coupling between the adiabatic electronic states of different spatial symmetry. With D being proportional to the angular velocity of rotation of the molecular frame at the crossing point Q_c , this coupling is normally weak, and in this limit Eq. (52.38) reads

$$P_{12}^{LC} \approx 2\pi D^2/(\hbar \Delta F v_c). \quad (52.39)$$

With $P_{12}^{LC} \ll 1$, the system moves preferentially along the crossing PEC. However, sometimes the adiabatic PES are defined with the spin–orbit interaction neglected. In this case, the adiabatic electronic states are associated with different values of the electronic spin, and then the spin–orbit interaction is included into the coupling matrix element D . Then the approximation in Eq. (52.39) may not be valid, and one should use the general relation in Eq. (52.38) with the quantity D^2 in the exponent accounting for the contributions due to the dynamical (Coriolis) and static (spin–orbit) couplings.

52.4 Double-Passage Transition Probabilities

52.4.1 Transition Probabilities in the Classically-Allowed and Classically-Forbidden WKB Regimes: Interference and Tunneling

If a system traverses several NAR, its dynamics can be characterized by successive matching of the different \mathcal{N} matrices by the intermediate matrices of the adiabatic evolution. The latter have a simple expression when the system motion satisfies the standard WKB condition. In the case of an atomic collision, the set \mathcal{R} shrinks into a single coordinate, R , and $v_p = \sqrt{2(E - U_p)/\mu}$ is expressed through the radial energy, E , of the relative motion of the atoms having the reduced mass, μ , and the potential energy, $U_p = \bar{U}(R)|_{R=R_p}$. If there is only one NAR over the whole range of R , the colliding system traverses it twice, as the atoms approach and then recede, and there are two different paths between the center of the NAR, R_p , and the turning points, R_{t1} and R_{t2} , on the adiabatic potential curves, $U_1(R)$ and $U_2(R)$. The double-passage nonadiabatic event $1 \rightarrow 2$ consists of: (i) the single-passage transition $1 \rightarrow 2$, the adiabatic evolution $R_p \rightarrow R_{t2} \rightarrow R_p$ in the state $|2\rangle$, the single-passage survival $2 \rightarrow 2$; (ii) the single-passage survival $1 \rightarrow 1$, the adiabatic evolution $R_p \rightarrow R_{t1} \rightarrow R_p$ in state $|1\rangle$, and the single-passage transition $1 \rightarrow 2$. Accordingly, the double-passage nonadiabatic amplitude $\mathcal{A}_{12}^{\text{WKB}}$ for the transition $1 \rightarrow 2$ reads

$$\begin{aligned} \mathcal{A}_{12}^{\text{WKB}} &= \sqrt{P_{12}} \exp(2i\phi_2 + 2i\Delta\phi_{12}) \sqrt{P_{22}} \\ &+ \sqrt{P_{11}} \exp(2i\phi_1 + 2i\Delta\phi_{21}) \sqrt{P_{12}}, \end{aligned} \quad (52.40)$$

where $P_{22} = P_{11} = 1 - P_{12}$ are the survival probabilities, $2\phi_1$ and $2\phi_2$ are the WKB phases accumulated during the adiabatic motion of a diatom from the center of NAR to the turning points and back, and $2\Delta\phi_{12}$ and $2\Delta\phi_{21}$ are the so-called dynamical phases that originate from nonadiabatic dynamics in crossing the NAR. Then the double-passage transition probability, $\mathcal{P}_{12}^{\text{WKB}} = |\mathcal{A}_{12}^{\text{WKB}}|^2$, assumes the form

$$\begin{aligned} \mathcal{P}_{12}^{\text{WKB}}(E)|_{E>U_p} &= \\ 4P_{12}(1 - P_{12}) \sin^2(\Phi_{12}^{\text{WKB}} + \Delta\Phi_{12}). \end{aligned} \quad (52.41)$$

Here,

$$\begin{aligned} \hbar\Phi_{12}^{\text{WKB}}(E) &= \hbar(\phi_1 - \phi_2) \\ &= \int_{R_p}^{R_{t1}} p_1(R) dR - \int_{R_p}^{R_{t2}} p_2(R) dR, \\ \Delta\Phi_{12} &= \Delta\phi_{12} - \Delta\phi_{21}, \end{aligned} \quad (52.42)$$

where p_k are the classical moments for motion across adiabatic potentials $U_k(R)$. Equation (52.41) was first derived by Stückelberg [18] for an avoided crossing situation under assumption $\Delta\Phi_{12} = 0$.

If the single-passage transition probability is calculated in the LCT approximation, Eq. (52.41) represents a combination of LCT and WKB approximations. A further simplification of this expression corresponds to the replacement of the WKB phase, Φ_{12}^{WKB} , with its CT counterpart,

$$\Phi_{12}^{\text{CT}} = \frac{1}{\hbar} \int_{t_p}^{t_t} \Delta U(R(t)) dt, \quad (52.43)$$

where $\Delta U(R) = U_1(R) - U_2(R)$, $R(t)$ is a CT, and, t_p and t_t are the time moments corresponding to the NAR center and the turning points for the motion in the field of the CT potential, $U^{\text{CT}}(R)$, respectively. An ambiguity in the definition of $U^{\text{CT}}(R)$ shows up in the approximation for \mathcal{P}_{12} resulting from the passage $\Phi_{12}^{\text{WKB}} \rightarrow \Phi_{12}^{\text{LC}}$.

When P_{12} in Eq. (52.41) is considered within the LZ or D models, the respective expressions are called Landau–Zener–Stückelberg (LZS) probability and Rosen–Zener–Demkov probability (although the interference phase was calculated in Eq. [19] for a special case of time-dependent coupling). Analytical expressions for the dynamical phases for the models discussed in Sect. 52.3 are also available [3, 6].

A particular example of the LZS probability corresponds to the narrow avoided crossing between the adiabatic potentials (or to the weak coupling between the crossing diabatic curves). Here, one replaces the adiabatic potentials in Eq. (52.42) by their diabatic counterparts that define the phase, $\Phi_{12}^{\text{WKB-D}}$, with $\Delta\Phi_{12} = \pi/4$ [3]. Then Eq. (52.41), in the weak-coupling limit and with the LZS parameterization assumes the form derived by Landau (L) [14]

$$\begin{aligned} \mathcal{P}_{12}^{\text{L}}(E)|_{E>U_p} &= \frac{8\pi V^2}{\hbar\Delta F} \left[\frac{\mu}{2(E - U_p)} \right]^{1/2} \\ &\times \sin^2(\Phi_{12}^{\text{WKB-D}}(E) + \pi/4), \end{aligned} \quad (52.44)$$

which is valid for $\mathcal{P}_{12}^{\text{L}}(E)|_{E>U_p} \ll 1$. The unphysical divergence in Eq. (52.44) at $E \rightarrow U_p$ is due to the use of the WKB approximation, when turning points are close to the crossing point. For a correct expression in that case, see Sect. 52.4.2.

In many applications, one can use the mean transition probability $\langle \mathcal{P}_{12} \rangle$, which is obtained from \mathcal{P}_{12} , by averaging over several oscillations,

$$\langle \mathcal{P}_{12} \rangle = 2P_{12}(1 - P_{12}), \quad (52.45)$$

such that the double-passage transition probability $\langle \mathcal{P}_{12} \rangle$ is expressed only in terms of the single-passage transition probability, P_{12} . Equation (52.45) is a simple example of the

surface-hopping approximation [9], when one calculates the total transition probability as a results of two independent hop/survival events at the first and the second crossings of NAR: hop $1 \rightarrow 2$, (survival $2 \rightarrow 2$) + (survival $1 \rightarrow 1$), hop $2 \rightarrow 1$ (Sect. 52.5.2).

The main condition of applicability of Eqs. (52.40)–(52.45) is $\Phi_{12}^{\text{WKB}} \gg 1$, i.e., the energy, E , is well above the mean adiabatic potential at the NAR center, U_p . In this case, the NAR region is classically accessible, and the single-passage probabilities depend on the local kinetic energy $E - U_p$ at the NAR center. With decreasing collision energy, the condition $\Phi_{12}^{\text{WKB}} \gg 1$ for the WKB interference eventually breaks down, implying also the inapplicability of the LCT approximation for the single-passage transition probability. When the energy, E , drops well below U_p , one can again use the WKB approximation for the description of tunneling nonadiabatic transitions [1, 3]. Then the system reaches NAR by motion in the classically forbidden range of R , and this motion is characterized by the imaginary-value quantity $\Phi_{12}^{\text{WKB}}|_{E < U_p}$, which is obtained from the real-valued quantity, $\Phi_{12}^{\text{WKB}}|_{E > U_p}$, by the analytical continuation into the complex energy plane from the classically accessible to the classically forbidden WKB motion. Under the condition $|\text{Im} \Phi_{12}^{\text{WKB}}(E)|_{E < U_p} \gg 1$, the transition probability, $\mathcal{P}_{12}^{\text{WKB}}(E)|_{E < U_p}$, which is a classically forbidden counterpart of $\mathcal{P}_{12}^{\text{WKB}}(E)|_{E > U_p}$ in Eq. (52.41), is proportional to a small exponential factor

$$\mathcal{P}_{12}^{\text{WKB}}(E)|_{E < U_p} \propto \exp[-2|\text{Im} \Phi_{12}^{\text{WKB}}(E)|]. \quad (52.46)$$

The pre-exponential factor for Eq. (52.46) can be calculated either by specifying the integration contour for calculating the WKB transition amplitude or by the analytical continuation of Eq. (52.44) from the classically accessible to the classically forbidden WKB regions. In particular, the tunneling weak-coupling probability, $\mathcal{P}_{12}^{\text{L}}(E)|_{E < U_p}$, which is a counterpart of $\mathcal{P}_{12}^{\text{L}}(E)|_{E > U_p}$ in Eq. (52.44), reads

$$\mathcal{P}_{12}^{\text{L}}(E)|_{E < U_p} = \frac{2\pi V^2}{\hbar \Delta F} \left[\frac{2\mu}{E - U_p} \right]^{1/2} \times \exp[-2|\text{Im} \Phi_{12}^{\text{WKB-D}}(E)|]. \quad (52.47)$$

Another practically important example of the nonadiabatic transition that occurs in the deep tunneling region corresponds to the Landau–Teller [20] model of the vibrational relaxation of a diatomic molecule in a collision with atoms. The probability, P^{LT} , of the transition with the energy release, ΔE (which is induced by the relative motion in a field of a repulsive exponential potential of the range $1/\alpha$) is proportional to a small exponential factor with the expo-

nent that is different in the CT and WKB approximations

$$\begin{aligned} P^{\text{LT-CT}} &\propto \exp\left[-2\pi \Delta E \sqrt{\mu/2}/(\hbar \alpha \sqrt{E})\right], \\ P^{\text{LT-WKB}} &\propto \exp\left[-2\pi \frac{\sqrt{2\mu}(\sqrt{E + \Delta E} - \sqrt{E})}{\hbar \alpha}\right], \end{aligned} \quad (52.48)$$

where E is the initial collision energy. Since the LT-CT exponent in Eq. (52.48) is the first term of the expansion of the LT-WKB exponent in powers of the ratio $\Delta E/E$, the former provides a good approximation to the latter for $\Delta E/E \ll 1$.

52.4.2 Nonadiabatic Transitions near Turning Points

The effect of the turning points onto the double-passage probability shows itself in Eq. (52.41) through the phase Φ_{12}^{WKB} , assumed to be large enough. With E approaching U_p , the turning points become closer to the NAR center. In this situation, one can use a model of linearly crossing (LC) diabatic PEC.

In the CT approach, one keeps the LZ Hamiltonian Eq. (52.31) but introduces a CT that explicitly describes the incoming and outgoing motion within the NAR. For the case when the slopes, $-F_1$ and $-F_2$, of the diabatic potentials at R_c are of the same sign, the CT can be defined as the decelerated and accelerated motion in the field of the effective force \bar{F}

$$R(t) - R_p = \bar{F}t^2/(2\mu) - (E - U_p)/\bar{F}, \quad (52.49)$$

where \bar{F} is assumed to be a certain mean of F_1 and F_2 . For $E > U_p$, the trajectory $R(t)$ reaches the center of NAR twice at $t_p = \pm \sqrt{2\mu(E - U_p)}/\bar{F}$. For $E < U_p$, t_p is imaginary, and the center of NAR is classically inaccessible; then the trajectory $R(t)$ reaches the NAR center through the classically forbidden range of potentials. It turns out that when $\bar{F} = \sqrt{F_1 F_2}$, the semiclassical problem defined by the LZ Hamiltonian Eq. (52.31) and the CT Eq. (52.49) becomes equivalent to the quantum problem with the Hamiltonian Eq. (52.31) supplemented by the mean potential $\bar{U}(R) = U_p - (F_1 + F_2)(R - R_p)$ [3].

In the weak-coupling limit, the expression for the LC transition probability, $\mathcal{P}_{12}^{\text{LC}} \ll 1$, reads

$$\begin{aligned} \mathcal{P}_{12}^{\text{LC}}(E) &= 4\pi^2 V^2 \left(\frac{2\mu}{\hbar^2 \bar{F} \Delta F} \right)^{2/3} \\ &\times \text{Ai}^2 \left[(U_p - E) \left(\frac{2\mu \Delta F^2}{\hbar^2 \bar{F}^4} \right)^{1/3} \right], \end{aligned} \quad (52.50)$$

where A_i is the Airy function, and the difference $U_p - E$ can be of either sign.

The large absolute values of the argument of the Airy function correspond to the cases when the turning points are far from the NAR center; then Eq. (52.50) passes into the WKB expressions Eqs. (52.44) and (52.47), where the phases refer to the linear potentials

$$\mathcal{P}_{12}^{\text{LC}}(E) = \begin{cases} \mathcal{P}_{12}^{\text{LC}}(E)|_{E > U_p}, & \Phi_{12}^{\text{WKB-D}} \rightarrow \Phi_{12}^{\text{WKB-DL}} \gg 1, \\ \mathcal{P}_{12}^{\text{LC}}(E)|_{E < U_p}, & |\Phi_{12}^{\text{WKB-D}}| \rightarrow |\Phi_{12}^{\text{WKB-DL}}| \gg 1. \end{cases} \quad (52.51)$$

Here, the phase $\Phi_{12}^{\text{WKB-DL}}$, which is real for $E > U_p$ and imaginary for $E < U_p$, is

$$\Phi_{12}^{\text{WKB-DL}}(E) = \frac{2}{3}(E - U_p)^{3/2} \sqrt{\frac{2\mu}{\hbar^2} \frac{\Delta F}{F^2}}. \quad (52.52)$$

In the intermediate cases, when the Airy function cannot be approximated by its asymptotic expressions, Eq. (52.51) describes the situation when the center of NAR is close to the turning points. A further discussion on the transitions near turning points can be found in [3]. A review of different two-state models for single and double-passage nonadiabatic transitions is presented in [21].

52.5 Multiple-Passage Transition Probabilities

52.5.1 Multiple Passage in Atomic Collisions

In the case of atomic collisions, there is only one nuclear coordinate R . If there exist several NAR on the R -axis, those that are classically accessible (for given total energy, E , and total angular momentum, J) can be traversed several times. In the semiclassical approximation [22], the multiple-passage transition amplitude, A_{if} , for a given transition between initial state, i , and final state, f , can be calculated as a sum of transition amplitudes $A_{if}^{\mathcal{L}}$, over all possible classical paths, \mathcal{L} , which connect these states and which run along a one-dimensional manifold R

$$A_{if} = \sum_{\mathcal{L}} A_{if}^{\mathcal{L}}, \quad (52.53)$$

where each $A_{if}^{\mathcal{L}}$ can be expressed through the probability, $\mathcal{P}_{if}^{\mathcal{L}}$, and the phase, $\Phi_{if}^{\mathcal{L}}$, by [23]

$$A_{if}^{\mathcal{L}} = [\mathcal{P}_{if}^{\mathcal{L}}]^{1/2} \exp(i\Phi_{if}^{\mathcal{L}}). \quad (52.54)$$

The net transition probability is then

$$\begin{aligned} \mathcal{P}_{if} &= |A_{if}|^2 \\ &= \sum_{\mathcal{L}} \mathcal{P}_{if}^{\mathcal{L}} + \sum'_{\mathcal{L}, \mathcal{L}'} [\mathcal{P}_{if}^{\mathcal{L}} \mathcal{P}_{if}^{\mathcal{L}'}]^{1/2} \cos(\Phi_{if}^{\mathcal{L}} - \Phi_{if}^{\mathcal{L}'}). \end{aligned} \quad (52.55)$$

The first sum runs over all different paths and the second (primed) over all different pairs of paths. The primed sum usually yields a contribution to the transition probability, which oscillates rapidly with a change of the parameters entering into \mathcal{P}_{if} (i.e., E and J) and represents a multiple-passage counterpart to the Stückelberg oscillations.

If the Stückelberg oscillations are neglected, \mathcal{P}_{if} is equivalent to a mean transition probability $\langle \mathcal{P}_{if} \rangle$

$$\langle \mathcal{P}_{if} \rangle = \sum_{\mathcal{L}} \mathcal{P}_{if}^{\mathcal{L}}. \quad (52.56)$$

For one NAR, there are two equivalent paths, and $\mathcal{P}_{if}^{(1)} = \mathcal{P}_{if}^{(2)} = P_{if}(1 - P_{if})$. Then Eq. (52.56) yields Eq. (52.45).

52.5.2 Surface Hopping

For molecular collisions, Eqs. (52.53) and (52.54) apply as well. However, the manifold of \mathcal{R} to which a trajectory $\mathcal{Q}(t)$ belongs now comprises $3N - 5$ (for a linear arrangement of nuclei) or $3N - 6$ (for a nonlinear arrangement) degrees of freedom, where N is the number of atoms in the system. The approximation Eq. (52.56) is called, in the context of inelastic molecular collisions, the surface-hopping approximation [5, 24]. Each time a trajectory reaches a NAR, it bifurcates, and the system makes a hop from one PES to another with a certain probability. Keeping track of all the bifurcations and associated probabilities, one calculates $\mathcal{P}_{if}^{\mathcal{L}}$ along a path \mathcal{L} made up of different portions of trajectories running across different PES. Because of the complicated sequence of nonadiabatic events leading from the initial state to the final state, each $\mathcal{P}_{if}^{\mathcal{L}}$ is a complicated function of different single-passage transition probabilities, P_{nm} , and survival probabilities, $1 - P_{nm}$. Even if all P_{nm} are known in analytical form, the calculation of $\langle \mathcal{P}_{if} \rangle$ requires numerical computations to keep track of individual nonadiabatic events [24].

In order to formulate the approach implementing the surface-hopping approximation, often referred to as molecular dynamics with electronic transitions, it is convenient to rewrite Eqs. (52.18) for the time evolution of the wave function expansion coefficients in the more general density matrix notation. The diagonal density matrix elements in the adiabatic representation, $\rho_{11} = a_1 a_1^*$ and $\rho_{22} = a_2 a_2^*$, determining the electronic state populations then satisfy the following equations

$$\frac{d\rho_{22}}{dt} = -\frac{d\rho_{11}}{dt} = \dot{Q}g(\mathcal{Q})(\rho_{12} + \rho_{21}), \quad (52.57)$$

and the coherence defined by $\rho_{12} = a_1 a_2^*$ satisfies

$$\frac{d\rho_{12}}{dt} = i\hbar^{-1} \Delta U(\mathcal{Q})\rho_{12} + \dot{Q}g(\mathcal{Q})(\rho_{11} - \rho_{22}). \quad (52.58)$$

Equation (52.57) shows that it is the dynamical coupling function $g(Q)$ that promotes the changes in the electronic state populations, i.e., the electronic transitions. Due to these transitions the trajectory bifurcates, and the surface-hopping approach can be considered a procedure for selection of the proper branch for the system to evolve. The most popular version of that approach, fewest-switches surface hopping (FSSH) [25], proposed by *J. C. Tully* is considered here. Its key feature is the algorithm maintaining the statistical distribution of electronic state populations in agreement with those obtained by numerically integrating the system of differential equations (52.57) and (52.58). Let the system be at time t on a trajectory Q_1 corresponding to the state 1 with population $\rho_{11}(t)$. According to Eq. (52.57) the nonadiabatic coupling $g(Q)$ induces the electronic transitions in a small time interval δt , leading to the change of the state 1 population, $\delta\rho_1 = \rho_{11}(t + \delta t) - \rho_{11}(t)$. If $\delta\rho_1 \geq 0$, i.e., there is a gain in the state 1 population, then the probability of the switch is set to zero, and the system remains on the trajectory $Q_1(t)$. If, in contrast, $\delta\rho_1 < 0$, there exists a nonzero probability P_{12} for the trajectory to switch to the trajectory branch Q_2 corresponding to the state 2

$$P_{12}(t, \delta t) = -\frac{\delta\rho_1}{\rho_{11}(t)} \approx \frac{\lambda(t)\delta t}{\rho_{11}(t)}, \quad (52.59)$$

where $\lambda(t)$ denotes the right-hand side of Eq. (52.57). The decision to switch from state 1 to state 2 is made when the switch probability P_{12} is larger than a random number between 0 and 1 generated from the uniform distribution.

The FSSH algorithm automatically incorporates a number of important properties: (i) as P_{12} is proportional to dynamic coupling $g(Q)$, the transitions between electronic states can occur at any location and time, not only in the NAR specified by some predefined conditions like was done in Sect. 52.2.2 or in the earlier version of surface hopping, which makes the method applicable to any number of passages through NAR; (ii) for the large number of trajectories, their fraction located on the state i branch approaches $\rho_{ii}(t)$ at any t , thus reproducing the electronic state populations; (iii) the electronic coherences are propagated properly with Eq. (52.58) enabling the reproducing of quantum interference effects; (iv) the generalization for any number of coupled electronic states is straightforward, and FSSH was recently implemented to study the nonadiabatic dynamics of an open-shell molecule at a metal surface [26].

At the same time, surface hopping is not free from some *ad hoc* adjustments, which can limit its validity. For example, when a switch between state 1 and state 2 PES occurs, the velocities of classical degrees of freedom have to be rescaled to preserve the total energy, which leads to discontinuities in the classical trajectory, $Q(t)$, defined on the many-dimensional manifold, \mathcal{R} . Moreover, the amount of classical kinetic energy is not always sufficient to fill the gap between electronic

states (classically forbidden transitions). In that case, the switch is rejected (a so-called “frustrated hop”), which introduces artificial distortions in the state populations.

The manifold \mathcal{R} can be reduced in size if one treats other degrees of freedom, besides electronic ones, on the same footing. In this way one introduces adiabatic vibronic (vibrational + electronic) states and adiabatic vibronic PES, and considers nonadiabatic transitions between them [27]. In the vibronic representation, the formal theory remains the same; however its implementation is more difficult since there are many more possibilities for trajectory branching. Finally, under certain conditions, one can use a fully adiabatic description of all degrees of freedom, save one – the intermolecular distance R . This approach provides a basis for the statistical adiabatic channel model (SACM) of unimolecular reactions [28] where the receding fragments are scattered adiabatically in the exit channels after leaving the region of a statistical complex.

For a recent review of the theory of molecular nonadiabatic dynamics, see [7] and papers in [9], as well as the recent book [29].

References

1. Landau, L.D., Lifshitz, E.M.: Quantum Mechanics. Pergamon, Oxford (1977)
2. Bernstein, R.B. (ed.): Atom-Molecule Collision Theory: A Guide for the Experimentalist. Plenum, New York (1979)
3. Nikitin, E.E., Unamskii, S. Ya : Theory of Slow Atomic Collisions. Springer, Berlin, Heidelberg (1984)
4. Child, M.S.: Semiclassical Mechanics with Molecular Applications. Clarendon, Oxford (1994)
5. Tully, J.C.: Nonadiabatic dynamics. In: Thompson, D.L. (ed.) Modern Methods for Multidimensional Dynamics Computations in Chemistry, p. 34. World Scientific, Singapore (1998)
6. Nakamura, H.: Nonadiabatic Transition: Concepts, Basic Theories and Applications. World Scientific, Singapore (2012)
7. Lagana, A., Lendvai, G. (eds.): Theory of Chemical Reaction Dynamics. Kluwer, Dordrecht (2004)
8. Domke, W., Yarkony, D.R., Koeppe, H. (eds.) Conical intersections, Electronic structure, Dynamics and Spectroscopy. In: Advanced Series in Physical Chemistry, vol. 15. (2014)
9. Jasper, A.W., Kendrick, B.K., Mead, C.A., Truhlar, D.G.: Non-Born–Oppenheimer chemistry: Potential surfaces, couplings, and dynamics. In: Yang, X., Lui, K. (eds.) Modern Trends in Chemical Reaction Dynamics: Experiment and Theory (Part I), p. 329. World Scientific, Singapore (2004)
10. Shalashilin, D.V., de Miranda, M.P., Koeppe, H. (eds.): Multidimensional Quantum Mechanics with Trajectories. Collaborative Computational Project on Molecular Quantum Dynamics, Daresbury, UK (2009)
11. Nikitin, E.E., Zare, R.N.: Mol. Phys. **82**, 85 (1994)
12. Schwenke, D.W.: J. Chem. Phys. **142**, 144107 (2015)
13. Nikitin, E.E.: Discuss. Faraday Soc. **33**, 14 (1962)
14. Landau, L.D.: Phys. Z. Sowjetunion **1**, 88 (1932)
15. Landau, L.D.: Phys. Z. Sowjetunion **2**, 46 (1932)
16. Zener, C.: Proc. Roy. Soc. **137**, 396 (1932)
17. Demkov, Y.N.: Sov. Phys. JETP **18**, 138 (1964)
18. Stückelberg, E.C.G.: Helv. Phys. Acta **5**, 369 (1932)

19. Rosen, N., Zener, C.: *Phys. Rev.* **40**, 502 (1932)
20. Landau, L.D., Teller, E.: *Phys. Z. Sowjetunion* **10**, 34 (1936)
21. Nikitin, E.E.: *Annu. Rev. Phys. Chem.* **50**, 1 (1999)
22. Miller, W.H.: *Adv. Chem. Phys.* **30**, 77 (1975)
23. O'Rourke, S.F.C., Nesbitt, B.S., Crothers, D.S.F.: *Adv. Chem. Phys.* **103**, 217 (1998)
24. Chapman, S.: *Adv. Chem. Phys.* **82**, 423 (1992)
25. Tully, J.C.: *J. Chem. Phys.* **93**, 1061 (1990)
26. Shenvi, N., Roy, S., Tully, J.C.: *Science* **326**, 829 (2009)
27. Sidis, V.: *Adv. At. Opt. Phys.* **26**, 161 (1990)
28. Quack, M., Troe, J.: Statistical adiabatic channel models. In: Schleyer, P.R., Allinger, N.L., Clark, T., Gasteiger, J., Kollman, P.A., Schaefer III, H.F., Schreiner, P.R. (eds.) *Encyclopedia of Computational Chemistry*, vol. 4, p. 2708. Wiley, Chichester (1998)
29. Takatsuka, K., Yonehara, T., Hanasaki, K., Arasaki, Y.: *Chemical Theory beyond the Born-Oppenheimer Paradigm: Nonadiabatic Electronic and Nuclear Dynamics in Chemical Reactions*. World Scientific, Singapore (2014)



Evgeny Nikitin Evgeny Nikitin received his PhD (1958) from the Institute of Chemical Physics in Moscow. He worked there and at the Physical Technical Institute until 1994. Since then he has been working at the Israel Institute of Technology in Haifa and, as an invited Professor, at the Max Planck Institute for Biophysical Chemistry in Göttingen. His scientific interests are the theory of the quantum molecular dynamics and nonadiabatic effects in molecular collisions.



Alexander Kandratsenka Alexander Kandratsenka received his PhD from the Belarusian State Technological University in 2001. He worked at the Institute of Physical Chemistry, University of Göttingen, Germany, in the Department of Chemistry, Yale University, USA, and at the Max Planck Institute for Biophysical Chemistry in Göttingen, Germany. His research is focused on the nonadiabatic effects in (di)atomic scattering from metals.



Tom Kirchner , A. Lewis Ford, and John F. Reading

Contents

53.1	Introduction	785
53.2	General Considerations and Formulation of the Problem	785
53.3	Approximate Versus Full Many-Electron Treatments	787
53.4	Computational Techniques	789
53.4.1	Coupled-Channel Methods	789
53.4.2	Numerical Grid Methods	790
53.5	Description of the Ionization Continuum	791
	References	793

Abstract

This chapter summarizes the principal features of theoretical treatments of intermediate-energy ion–atom and atom–atom collisions. Here, intermediate means that the relative velocity between the projectile and target is on the order of, or larger than, the orbital speed of the active electron(s) but not large enough for relativistic effects to play a significant role. In this range, the semiclassical approximation in which the scattering problem is described by a time-dependent Schrödinger equation for the electronic motion in the field of classically moving nuclei is usually appropriate. The main goal of this chapter is to introduce the basic concepts, terminology, and methods to discuss ion–atom and atom–atom collisions in this framework.

T. Kirchner (✉)
Dept. of Physics & Astronomy, York University
Toronto, ON, Canada
e-mail: tomk@yorku.ca

A. L. Ford
Dept. of Physics, Texas A&M University
College Station, TX, USA
e-mail: ford@physics.tamu.edu

J. F. Reading
Dept. of Physics, Texas A&M University
College Station, TX, USA
e-mail: reading@physics.tamu.edu

Keywords

heavy particle scattering · double ionization · independent particle model · electron correlations · time-dependent Schrödinger equation

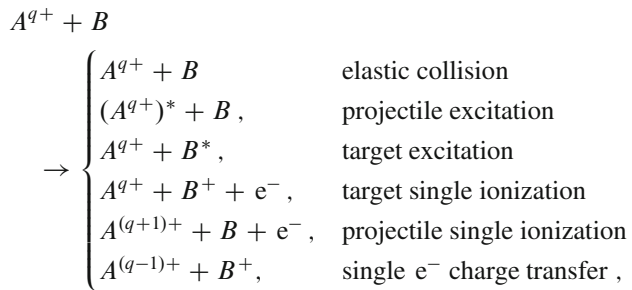
53.1 Introduction

Ion–atom and atom–atom collisions are the subject of several chapters in this Handbook. The wide range of experimentally accessible impact energies, the variety of processes that can occur, and the long and rich history of the field translate into a large number of theoretical approaches and computational methods that are in use to describe the physics at play. The emphasis of the present chapter is on general approaches to deal with this problem. There are several review articles and monographs, e.g., [1–4], which provide comprehensive and in-depth accounts of the many methods and techniques that have been developed and applied over the years.

53.2 General Considerations and Formulation of the Problem

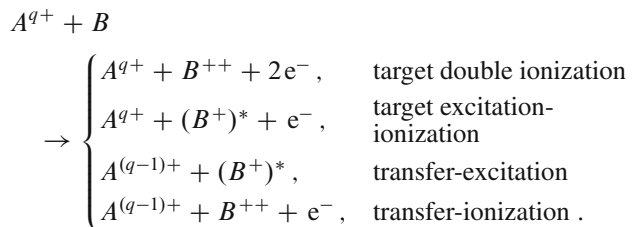
The collisions considered in this chapter involve a projectile ion or atom A and a target atom B . The collision kinematics can be described in the laboratory frame, where B is assumed to be initially at rest, and the collision energy is the kinetic energy of A when it is far from B prior to the collision, or in the center of mass frame. The primary quantities of interest are the cross sections for producing various final states of the system for given initial states of the target and projectile.

A few examples for a projectile with charge q in the initial state are



where A^* and B^* denote excited states. Variants of the above list would involve initially excited projectile and/or target species or the special case of a neutral projectile ($q = 0$).

For a multielectron collision system, combinations of the above processes may occur. A few representative examples are



One class of collision problems that has received much theoretical attention involves an initially bare projectile ion and a neutral target atom with one or several electrons in the initial (ground) state. Obviously, this represents a simpler problem than that of a collision system in which electrons are bound to both the target and the projectile initially. The simplest scenario is a bare ion colliding with the one-electron hydrogen atom. In this case, the single-electron processes target excitation, and target ionization and e^- charge transfer are the only inelastic collision channels that can occur. Figure 53.1 shows total cross sections for these channels for the p-H system as functions of the collision energy E_p ; $E_p = 25$ keV corresponds to a velocity of one atomic unit, i.e., the (average) orbital speed associated with the kinetic energy of the H(1s) electron and $E_p = 100$ keV to two atomic units of velocity. The three cross sections shown in Fig. 53.1 are of comparable magnitude in this energy interval. This illustrates a competition of collisional processes, or in more technical terms, the occurrence of coupled-channel dynamics, which calls for a nonperturbative solution of the scattering problem.

For the cross sections and the impact energy interval of Fig. 53.1, the semiclassical approximation (SCA), in which the motion of the nuclei is described classically and only the electron is described in terms of quantum-mechanical wave functions, is essentially exact [3, 5]. At $E_p \geq 10$ keV

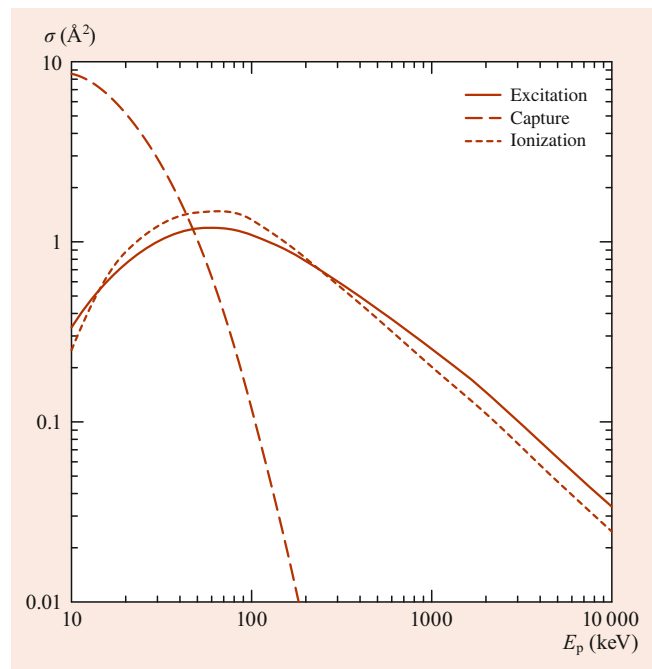


Fig. 53.1 Total cross sections for target excitation, e^- charge transfer (capture), and target ionization in p-H collisions as functions of impact energy. Curves correspond to theoretical results obtained from the two-center basis generator method [11, 12]

the projectile can be safely assumed to follow a straight-line path with constant speed v . At somewhat lower energies the deflection and change in speed of the projectile due to the projectile–target interaction are often incorporated. One can determine curved trajectories by considering the nonadiabatic coupling of the electronic and nuclear motions [6, 7], or one can use predetermined Coulomb trajectories due to the nucleus–nucleus interaction [8, 9] or trajectories corresponding to model potentials that account for electronic screening effects in addition [10]. For a bare positive ion projectile, such as the proton in p-H collisions, the Coulomb trajectory effects increase the distance of the closest approach for a given impact parameter b and reduce the projectile speed v in the interaction region.

In the SCA, the vector $\mathbf{R}(b, t)$ that locates the projectile relative to the target nucleus is a function of the impact parameter b and time t . The specific functional dependence is determined by the trajectory being used. For a straight-line, constant velocity v path, $\mathbf{R} = \mathbf{b} + \mathbf{v}t$. For the case of a bare projectile ion and a one-electron target, the time-dependent projectile–target interaction is given by

$$V(\mathbf{r}, b, t) = \frac{-Z_P e^2}{4\pi\epsilon_0 |\mathbf{r} - \mathbf{R}(b, t)|} + \frac{Z_P Z_T e^2}{4\pi\epsilon_0 R(b, t)}, \quad (53.1)$$

where Z_P and Z_T are the projectile and target nuclear charge numbers, e is the elementary charge, ϵ_0 the electric permittivity of the vacuum, and \mathbf{r} the position vector of the electron

relative to the target nucleus, which is chosen here as the origin of the (inertial) reference frame.

Using atomic units characterized by $\hbar = m_e = e = 4\pi\epsilon_0 = 1$ from here on, the full Hamiltonian for the one-electron ion–atom collision problem reads

$$\hat{H}(t) = -\frac{1}{2}\nabla^2 - \frac{Z_T}{|\mathbf{r}|} + V(\mathbf{r}, b, t), \quad (53.2)$$

and the time-dependent Schrödinger equation (TDSE)

$$(\hat{H}(t) - i\partial_t)\psi(\mathbf{r}, t) = 0 \quad (53.3)$$

has to be solved subject to the initial condition $\psi(\mathbf{r}, t = t_i) = \phi_i(\mathbf{r})$, where ϕ_i denotes, e.g., the hydrogen ground state. Exploiting cylindrical symmetry, the total cross section for a transition from the initial state ϕ_i to a final state ϕ_f is given by

$$\sigma_{i \rightarrow f} = 2\pi \int_0^\infty b |a_{fi}(b)|^2 db, \quad (53.4)$$

where $a_{fi} = \langle \phi_f | \psi(t_f) \rangle$ is the electronic transition amplitude for the process of interest taken at a final time t_f , which formally should approach infinity and in practice has to be large enough to ensure that when it is varied the transition probability does not change appreciably. As a consequence of the unitarity of the TDSE one has $\sum_f |a_{fi}|^2 = 1$, if the sum over the final states is complete.

It is noteworthy that the nuclear repulsion term in Eq. (53.1) does not involve the electronic coordinates and can be eliminated by a phase transformation. It thus makes no contribution to total cross sections for anything other than elastic scattering for which the total cross section does depend on the phase information in the amplitude

$$\sigma_{\text{elastic}} = 2\pi \int_0^\infty b |a_{f=i}(b) - 1|^2 db. \quad (53.5)$$

One might think that the framework of the SCA precludes the calculation of cross sections differential in the scattering angle Θ of the projectile. However, this is not the case. If the collision energy is high, and the projectile is scattered primarily by the static potential of the target, a classical treatment of the scattering can be used to relate b to Θ . Even when straight-line, constant speed projectile paths are used to calculate the transition probabilities, differential cross sections can be extracted by relating b to Θ . At lower energies, where the de Broglie wavelength of the projectile is not small compared with the range of the interaction, eikonal methods can be used to convert impact parameter dependent transition amplitudes to differential cross sections (e.g., [3, 13, 14] and references therein). These methods establish a two-dimensional Fourier-transform-like relation

between $a_{fi}(b)$ and the T -matrix of stationary scattering theory. Given that they involve *amplitudes* the calculated differential cross sections are sensitive to phase information and, as a consequence, to the nuclear repulsion term in Eq. (53.1).

53.3 Approximate Versus Full Many-Electron Treatments

In the semiclassical impact parameter method, as described in Sect. 53.2, for a one-electron collision system one has to calculate a single-particle wave function and from it single-electron transition amplitudes. For an N -electron collision problem, the situation is, in general, much more complicated since the Hamiltonian involves one-particle and two-particle terms

$$\hat{H}(t) = \sum_{i=1}^N \left(-\frac{1}{2}\nabla_i^2 - \frac{Z_T}{|\mathbf{r}_i|} + V(\mathbf{r}_i, b, t) \right) + \sum_{i < j}^N \frac{1}{|\mathbf{r}_i - \mathbf{r}_j|}. \quad (53.6)$$

The latter introduce electron correlations and prevent the TDSE from being separable.

However, a full account of the correlated many-electron problem is not always necessary. Consider a collision system in which a bare ion interacts with an alkali atom such as lithium. In such a case, it is often reasonable to assume that the inner-shell electrons are frozen to their initial state and merely provide an effective potential in which the active valence electron moves. This scenario corresponds to a single-particle Hamiltonian like the one in Eq. (53.2) with the electron–target Coulomb potential replaced by an effective atomic ground-state potential. Formally, one can derive this single active electron approximation by averaging the two-particle Hamiltonian Eq. (53.6) over the coordinates of the passive electrons [14, 15].

In the independent particle model (IPM), the two-particle electron–electron terms in Eq. (53.6) are approximated by effective one-body operators. The many-electron collision problem then reduces to a set of single-electron problems which, depending on the level of approximation used, may be coupled or uncoupled. An example of the former is the time-dependent Hartree–Fock (TDHF) method, which involves nonlinear single-particle equations and a nonlocal (Fock) exchange operator [16–18]. An example of the latter is an IPM, in which single-active-electron-model ground-state potentials are used, and the problems associated with the nonlocality of the Fock exchange term and the nonlinearity of the TDHF equations are avoided [14]. In either case, the solution of the single-particle equations at each impact parameter and energy gives single-electron transition amplitudes a_{fi} , which, when combined in an appropriate way, yield cross sections for multielectron transitions [19, 20].

The most sophisticated method of combining the single-particle solutions starts with the assumption that the initial and final many-electron states are represented by single Slater determinants. Transition probabilities for multielectron processes can then be written as combinations of determinants of reduced density matrices [21]. The determinantal structure of these expressions reflects the antisymmetry of the problem and has often been associated with so-called Pauli correlations [22]. If the Pauli correlations are neglected and the final-state analysis is based on simple product states instead of Slater determinants, the multielectron transition probabilities simplify to multinomial combinations of single-electron probabilities [23–25].

The effective single-particle character of the IPM equations is a consequence of an approximation, the replacement of the two-particle electron–electron interactions in Eq. (53.6) by one-body operators. By contrast, the Kohn–Sham scheme of time-dependent density functional theory (TDDFT) asserts that one can map the interacting many-body problem to a set of effective single-particle equations *exactly* [26, 27]. This seemingly contradictory statement is based on the insight that the electron density determines the state of a many-body system. More precisely, one can show (provided that certain conditions are met) that the solution Ψ of the TDSE for the Hamiltonian Eq. (53.6) is a unique functional of the density n , i.e., $\Psi = \Psi[n](t)$ and that n can be calculated from orbitals

$$n(\mathbf{r}, t) = \sum_{i=1}^N |\psi_i(\mathbf{r}, t)|^2, \quad (53.7)$$

which solve single-particle equations of the form

$$i \partial_t \psi_i(\mathbf{r}, t) = \left(-\frac{1}{2} \nabla^2 + v_{\text{TDKS}}[n](\mathbf{r}, t) \right) \psi_i(\mathbf{r}, t) \\ i = 1, \dots, N. \quad (53.8)$$

The effective potential v_{TDKS} in Eq. (53.8) is called the time-dependent Kohn–Sham (TDKS) potential and is itself a unique functional of the density. The problem is that the exact form of this functional is not known and has to be approximated in practical calculations. One usually starts by decomposing v_{TDKS} into different pieces associated with the external Coulomb interactions and with electronic screening, exchange, and correlation effects and then introduces different levels of approximation or models for the electronic pieces. In particular, the correlation portion is often neglected, which amounts to an IPM-like (“exchange-only”) treatment. For a two-electron spin-singlet system such as a bare-ion helium-atom collision problem exchange can be treated exactly without added difficulty [28, 29] or can be approximated in various ways [30, 31]. For more complex problems the Krieger–Li–Iafraite approximation [32] can be used to construct an almost exact exchange potential [33].

Similarly to the TDKS potential, most multielectron probabilities of interest in an ion–atom or atom–atom collision problem have to be approximated. These probabilities are readily expressed in terms of integrals that involve the many-electron wave function at an asymptotic time after the collision. Hence, they are functionals of n because $\Psi(t_f)$ is, but their exact functional form is normally not known because the exact $\Psi[n](t_f)$ is not available.

Some progress has been made in recent years in developing and implementing approximate density functionals that improve on IPM predictions for certain collision processes [34]. This parallels successes in the application of TDDFT to the somewhat related problem of the excitation and ionization of atoms (and molecules) by strong laser fields (Chap. 78). However, there is room for further improvement, and it remains to be seen whether the TDDFT approach will be capable of explaining well-known signatures of correlated electron dynamics in collisions.

A famous example of the latter is an observed factor-of-2 difference in the total double-ionization cross section of helium in the MeV/amu collision energy region, when the impacting projectile is either a proton ($Z_p = +1$) or an antiproton ($Z_p = -1$). The IPM fails to produce this difference, which can be qualitatively understood using arguments based on perturbation theory and by differentiating between externally and internally induced two-electron processes [35, 36].

In an externally induced two-electron process, the projectile interacts with both electrons and induces the transition of each. In the internal process, energy is transferred to just one electron; this energy is then shared with the other electron through the internal action of the correlating electron–electron force. At sufficiently high energies, the external reaction has an amplitude proportional to Z_p^2 . To lowest order, the reaction proceeds through two consecutive first-order Born collisions, perhaps more correctly described as a two-particle second-order Born collision. This is called the two-step two (TS2) mechanism. The internal reaction amplitude, again at sufficiently high energies, is proportional to Z_p , as a first-order Born reaction initiates the process. The sharing of energy with the second electron can be thought of in two ways. If the first electron is ejected without interacting with the second, there is a change in the screening that can be thought of as being responsible for shaking the second electron off. The main role of the electron–electron force here is to introduce correlation into the initial ground-state wave function. A second way for both electrons to be ionized is for the first electron to strike the second on the way out. This has been variously called interception or two-step one (TS1) [23, 37–39]. The role of the electron–electron force here is to introduce correlation into the final two-electron wave function.

At asymptotic energies the first Born term eventually dominates, and the internal correlated mechanism is solely responsible for double ionization. At lower energies, the ex-

ternal and internal amplitudes are of the same order, and thus they interfere. The interference produces terms in the transition probability that are proportional to odd powers of Z_P , and therefore leads to a cross section that changes when the sign of the projectile charge changes. This phenomenon has been observed for proton versus antiproton impact-induced double ionization [40].

Accounting for electron correlations directly by solving the nonseparable TDSE involving the Hamiltonian Eq. (53.6) is computationally costly. In coupled-channel calculations (Sect. 53.4), this brute-force approach becomes intractable if the number of electrons exceeds two or three, and more than a few coupled channels are important, which is usually the case at intermediate collision energies. Some full two-electron calculations have been carried out nevertheless [41–46], especially for antiproton-impact collisions ([40, 47] and references therein). In low-energy collisions where molecular basis expansions are appropriate, it is more likely that only a few channels are important, i.e., those involved in potential curve crossings or near crossings, and full electron calculations are more feasible (Chap. 55).

Some alternatives to full electron quantum calculations have been developed. In the nonperturbative regime they include the independent event model [48], classical dynamics calculations (Chap. 62), the frozen-correlation approximation (FCA) [49], and the forced impulse method (FIM) [38, 39]. The FCA distinguishes between static and dynamic correlation and takes into account the former, but neglects the latter. The FIM uses similar ideas of static and dynamic correlation and divides the collision time into short sequential segments such that an impulse approximation becomes valid. The system is allowed to collapse back into a fully correlated eigenstate at the end of each segment, but the electrons propagate independently during each segment. Provided that the number of segments is large enough, the FIM solution should be equivalent to the full electron solution.

Similarly to full electron approaches, the vast majority of calculations that use one of these alternative methods were carried out for two-electron systems. The most promising first-principles approach to deal with collision systems that involve more than two electrons is probably TDDFT. A recent work has addressed the three-electron He^+-He system, in which an active projectile electron has to be taken into account in addition to two active target electrons [33]. This approach holds promise to be extended to atom–atom collisions, which always involve (active) electrons on both centers. TDDFT methods have also been used to study low to intermediate energy ion collisions from (small) molecules [50–52]. This problem has attracted considerable attention in recent years but is, of course, even harder to address in terms of full electron approaches or one of the alternative methods described above than ion–atom or atom–atom collisions.

53.4 Computational Techniques

There is a wide variety of techniques used for computing cross sections for ion–atom and atom–atom collisions. One class uses approximate analytical methods. The expressions and the wave functions that enter into them may be sufficiently complicated that they must be evaluated on a computer, but they can be written down as closed-form expressions. One important example is the first Born approximation (FBA), in which the projectile–target interaction is treated in first order. Hence, the FBA is the most accurate for weak interactions, for example for small projectile charge and large collision energy (e.g., [5] and Chap. 57).

Higher-order Born calculations should extend the range of applicability of the FBA but are difficult to implement and, in practice, usually restricted to second order [53]. Distorted-wave methods are viable alternatives within the framework of perturbation theory; particularly variants of the continuum distorted-wave (CDW) model (Chap. 56) have been widely and successfully applied to ion–atom collision problems. Other approximate methods that lead to simple analytic expressions include the Glauber approximation [54–56] and the binary encounter approximation (BEA, Chap. 60).

A difficulty with these methods is that they normally do not admit to a sequence of successive improvements; there is no procedure for systematically driving them to convergence. This is to be contrasted with methods that solve the semiclassical TDSE, or even the full quantum-mechanical scattering problem, fully nonperturbatively. This class of largely numerical methods does allow for systematic convergence studies and, given the ever increasing availability of computational resources, highly accurate solutions.

53.4.1 Coupled-Channel Methods

The standard approach to solving the semiclassical TDSE nonperturbatively is to expand the electronic wave function in some basis set [2, 3, 57]. This procedure is called the coupled-channel or close-coupling method. It is convenient to diagonalize the target and projectile systems in the chosen basis to produce matrix eigenfunctions for the target and projectile. Putting this expansion into the TDSE leads to a set of coupled first-order equations for the time-dependent expansion coefficients. This set of equations is solved subject to the boundary condition that long before the collision, the expansion coefficient for the initial state wave function is unity and all other coefficients are zero. Then a long time after the collision, the expansion coefficients give the amplitudes for transitions into those states.

Several types of expansions are used. The notation appropriate to a single-electron problem will be used for simplicity in the following. In the single-centered expansion [58, 59],

the wave function is expanded in a set of target centered basis functions. Diagonalization of the target Hamiltonian in this basis yields a set of target eigenfunctions $\phi_j^T(\mathbf{r})$ and energies E_j . The expansion of the time-dependent wave function for the collision system is then

$$\psi_i(\mathbf{r}, b, t) = \sum_j a_{ji}(b, t) e^{-i(E_j - E_i)t} \phi_j^T(\mathbf{r}). \quad (53.9)$$

If the electron is initially in the target state i , the initial boundary condition is $a_{ji}(b, t_i \rightarrow -\infty) = \delta_{ji}$. At times long after the collision, the expansion coefficients, $a_{ji}(b, t_f \rightarrow +\infty)$, give the amplitudes for transitions from target state i to j . Ionization probabilities and the description of the ionization continuum will be discussed in Sect. 53.5. It suffices to say here that some of the $\phi_j(\mathbf{r})$ represent ionized states and account for transitions that leave the electron no longer in a target bound state.

This single-centered expansion is the natural approach to describing a collision system that involves antiproton projectiles that do not support bound electron states [40, 60]. It can also be used for positively charged projectile ions, although it does not directly allow for calculation of charge transfer amplitudes. However, it has been shown that if the number of angular momenta included in the set of $\phi_j(\mathbf{r})$ is large enough, the basis can accurately describe electron loss from the target bound states, i.e., the sum of electron capture and ionization events, even in cases where the charge transfer probability is large [59].

In a two-centered expansion [2, 61–65], the time-dependent wave function for the collision system is expanded in two sets of functions: a set of eigenfunctions centered on the target $\phi_j^T(\mathbf{r})$ and a set of projectile centered eigenfunctions $\phi_k^P(\mathbf{r} - \mathbf{R})$

$$\begin{aligned} \psi_i(\mathbf{r}, b, t) = & \sum_j a_{ji}^T(b, t) \exp[-i(E_j - E_i)t] \phi_j^T(\mathbf{r}) \\ & + \sum_k a_{ki}^P(b, t) \exp[-i(E_k - E_i)t] \\ & \times \exp[i\mathbf{p} \cdot \mathbf{r}] \phi_k^P(\mathbf{r} - \mathbf{R}). \end{aligned} \quad (53.10)$$

Here, $\exp[i\mathbf{p} \cdot \mathbf{r}]$ is an electron translation factor that accounts for the momentum \mathbf{p} that the electron has relative to the target when it moves with the projectile. The energies E_k also contain the kinetic energy in the target frame that the electron has when it moves with the projectile. The problem of electron translation factors when a two-centered molecular basis is used instead of the atomic basis has been extensively addressed [2, 3, 66].

The coefficients $a_{ji}^T(b, t_f \rightarrow +\infty)$ and $a_{ki}^P(b, t_f \rightarrow +\infty)$ are the amplitudes for transitions into target and projectile states. The two-centered expansion allows for charge transfer amplitudes to be calculated directly and is capable of an accurate description of the electron flux loss from the target

due to charge transfer, but the computational difficulty is significantly greater than in a single-centered expansion. One reason is that the projectile and target basis states are not orthogonal, and computational linear dependence can arise when both centers are close during the collision. This problem is most apparent in a symmetric collision system such as p-H, where the projectile-centered basis states will become nearly identical to the target-centered states at small internuclear distances [67, 68]. Very high numerical precision in the solution of the coupled-channel equations is required to deal with this situation.

There are other basis methods. To account for flux loss from the target region due to charge transfer, while retaining the computational efficiency of the single-centered expansion, a hybrid method called the one-and-a-half centered expansion was developed and applied to several collision problems with good success some time ago [69, 70]. Calculations have also been done with a triple-centered expansion [71, 72], in which bound atomic states are centered on each nucleus and on a third center (the center of charge) in order to simulate the molecular character of slow collisions. The orbitals on this third center represent the united-atom character of the wave function. These and other expansion techniques proposed and applied before the early 1990s are described in some detail in [3]. A somewhat more recent approach that is in active use is the basis generator method (BGM). In the BGM, a single-centered [73] or a two-centered [11] basis of bound states is augmented by pseudo states that are constructed by operating with a regularized potential operator on target states or on target and projectile states. At low impact energies these BGM pseudo states play a role that is similar to the center-of-charge states in a triple-center expansion. They also overlap with the continuum and, when orthogonalized to the bound states of both centers, allow for a description of ionization events.

53.4.2 Numerical Grid Methods

In grid-based approaches, the electronic wave function is represented on a spatial lattice and time-evolved fully numerically. A variety of methods can be used to this end, e.g., finite difference and Fourier collocation techniques [74–78]. The latter are based on splitting the time-evolution operator \hat{U} for a small time step into factors associated with kinetic (T) and potential (W) energy terms according to

$$\begin{aligned} \hat{U}(t + \Delta t, t) \approx & \exp[-i\hat{H}(t)\Delta t] \approx \exp[-iT\Delta t/2] \\ & \times \exp[-iW(t)\Delta t] \exp[-iT\Delta t/2] \end{aligned} \quad (53.11)$$

and switching back and forth between coordinate and momentum space using a fast Fourier transform algorithm when

applying \hat{U} to the wave function. The benefit of switching between representations is that each propagation step involves multiplicative operators only, either in coordinate space ($W(t) = W(\mathbf{r}, t)$) or in momentum space ($T = \mathbf{p}^2/2$).

In most lattice methods, the Coulomb singularities are avoided by using soft-core potentials and the wave function is prevented from being reflected at the boundaries of the numerical box by using mask functions or (complex) absorbing potentials. The bound-state contributions of the wave function at the final time are extracted by projection techniques to calculate charge transfer and target excitation probabilities. An appealing feature of lattice solutions is that they provide a direct view of the unbound part of the wave function, i.e., they appear to be well suited to describe differential ionization patterns.

There are also methods that one can view as hybrids of basis-expansion and lattice techniques; if one expands the electronic wave function into spherical harmonics, one obtains a set of coupled partial differential equations for time-dependent radial functions $R_{lm}(r, t)$ that can be solved by grid-based or other numerical techniques [47, 79]. A somewhat similar method to address the semiclassical scattering problem in momentum space is described in [80].

53.5 Description of the Ionization Continuum

In ion–atom and atom–atom collision calculations, the description of the ionization continuum presents particular difficulties. For hydrogenic systems, the exact continuum wave functions are known analytically, and these may be used in analytic approximations such as the FBA. For non-hydrogenic systems, screened hydrogenic wave functions or numerical wave functions computed from some local effective potential, such as the Hartree–Fock–Slater approximation, can be used [81, 82]. However, for coupled-channel calculations that involve expansion of the system wave function in terms of a discrete set of functions some discretization of the continuum must be performed.

A simple procedure for generating a discrete representation of the continuum is to diagonalize the target (or projectile) Hamiltonian in a finite basis of square integrable basis functions. Some commonly used basis functions are Sturmian [65], Gaussian [46, 68], Laguerre [83–85], or Slater-type orbitals [86]. The diagonalization produces a set of discrete matrix eigenvalues and eigenvectors. For a one-electron or effective one-electron system, the exact energy spectrum of the Hamiltonian consists of an infinite set of discrete bound states and an ionization continuum, and the interpretation of the matrix eigenvectors is straightforward. Those whose eigenvalues are below the first ionization threshold represent bound states. Let us assume that there are M such vectors. By the Hylleraas–Undheim theorem, their

eigenvalues are upper bounds to the first M exact energies (Sect. 12.3.1). The matrix eigenvectors with positive eigenvalues are usually called pseudo states and provide a discrete representation of the ionization continuum [87], similarly to the BGM pseudo states mentioned in Sect. 53.4.1. In contrast to the latter, they are related to the true continuum states in a direct way. Each positive energy pseudo state is accurately proportional to the exact continuum wave function at the pseudo-state energy for radial distances r out to the range of the basis. The proportionality constant gives the energy width of the pseudo state – the energy region of the continuum represented by that pseudo state [88, 89]. These widths are approximately equal to the energy spacing between pseudo states. The pseudo states represent the continuum in the sense that the total ionization cross section is equal to the sum of the continuum pseudo-state cross sections. For example, the total p-H ionization cross section shown in Fig. 53.1 has been obtained by summing up the BGM pseudo-state continuum contributions.

Driven by experimental advances, the description of differential ionization patterns has become a major objective of ion–atom collision calculations. Cross sections differential in the ionized electron’s energy [90, 91], cross sections differential in the electron’s emission angle, and cross sections differential in both energy and angle have been extracted from discretized continuum [83, 84] and numerical lattice [75] calculations. Ejected electron momentum distributions have also been studied [75, 80, 92–94]. It is even possible to extract triply differential cross sections, i.e., cross sections that are differential in the electron energy, electron emission angle, and in the projectile scattering angle Θ from semiclassical coupled-channel calculations [83, 84]. The eikonal methods mentioned in Sect. 53.2 are used in those works to convert impact parameter-dependent to Θ -dependent ionization amplitudes [95]. Alternatively, a close-coupling approach to the fully quantum-mechanical scattering problem has been developed to calculate total [85, 96] and differential [97] scattering cross sections.

Coupled-channel calculations have also been carried out with wave packets constructed at discrete energies from the exact continuum wave functions [98, 99]. This method has the advantage that the density of the continuum discretization can be made arbitrarily high, thereby improving the accuracy of calculated differential cross sections and allowing for the observation of features that are difficult to resolve in standard pseudo-state calculations [99].

Figure 53.2 shows a comparison of triply differential ionization cross sections in antiproton–hydrogen collisions obtained by using different methods. The geometry is chosen such that the momenta of all three particles in the final state are in the same plane. The electron ejection energy and the momentum transfer vector (whose transverse component determines Θ) are fixed, and the electron ejection angle is

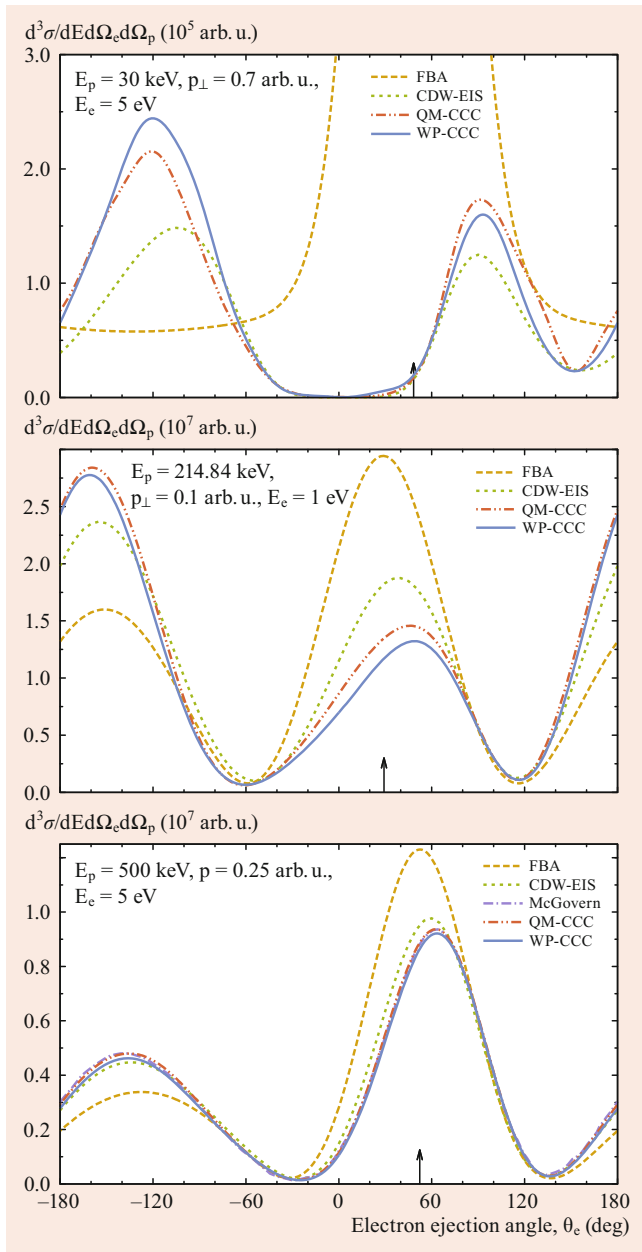


Fig. 53.2 Triply differential cross sections for antiproton-impact ionization of ground-state atomic hydrogen at various impact energies E_p , electron ejection energies E_e , and (perpendicular) momentum transfers $p_{(\perp)}$ plotted as functions of the electron ejection angle. Arrows indicate the direction of the momentum transfer vector. CDW-EIS: continuum distorted-wave eikonal initial-state [100], McGovern: coupled pseudo state [83], QM-CCC: quantum-mechanical convergent close-coupling [97], FBA and WP-CCC: first Born and wave-packet convergent close-coupling [99] calculations. After [99] by permission

measured with respect to the direction of the incident antiproton. All theories predict the familiar two-lobe structure of this cross section except for the FBA at $E_p = 30$ keV. This is a clear indication that first-order perturbation theory is not valid at such a relatively low impact energy. The continuum distorted-wave eikonal initial-state (CDW-EIS,

Chap. 56) model fares much better and qualitatively agrees with the fully nonperturbative calculations, which are either based on the SCA [83, 99] or a fully quantum-mechanical close-coupling method [97]. At $E_p = 500$ keV the level of agreement of all those calculations is very good with only the FBA deviating by more than a few percent from the other theories. At the lower impact energies the wave packet approach is deemed to be the most accurate one [99].

The coupled-channel calculations shown in Fig. 53.2 are based on single-centered expansions. Two-centered variants have also been developed in order to deal with differential ionization in p-H collisions at intermediate impact energy [101, 102]. It was noted that an ambiguity appears to arise in this case and that one had two choices to compute differential ionization cross sections: either by adding the scattering amplitude corresponding to the positive-energy target states to that corresponding to the projectile-centered states coherently or by adding them incoherently [101]. The ambiguity is related to the nonorthogonality problem of two-centered expansions discussed in Sect. 53.4.1. However, if the final-state analysis is carried out at a truly asymptotic distance where the target- and projectile-centered states do not overlap, formal arguments favor the coherent version.

As mentioned above, lattice methods give access to differential ionization patterns in a direct fashion. Once the bound-state parts of the wave function have been properly subtracted, the time evolution of the continuum wave packet can be monitored either in coordinate space or in momentum space. In recent work, scaled coordinates and a transformation of the wave function that removes a diverging phase factor have been employed to follow the density and current density distributions to truly asymptotic distances [103]. This has been key to the discovery of vortices in atomic collision systems and the investigation of their role in transferring angular momentum from nuclear to electronic motions [104].

Analyzing the continuum content of two-electron or multi-electron wave functions is more complex than for one-electron systems. The energy spectrum of a two-electron atom consists of an infinite set of bound states, an infinite set of overlapping single ionization continua that correspond to different residual ion states, and overlapping the higher energy part of these single-ionization continua, a double-ionization continuum where both electrons are unbound. The exact wave function for two electrons in the continuum of an ion is not known, but there are a number of approximate forms [105–107].

The interpretation of two-electron pseudo states is also complicated. For energies below the second single-ionization threshold, the energy of a pseudo state clearly identifies whether it represents a bound state or an ionized state. However, in the energy region where there are overlapping continua there are ambiguities. For example, a pseudo state with energy above the double-ionization threshold can rep-

resent a doubly ionized state, a singly ionized state of the same total energy, or some admixture of the two. A method to solve this pseudo-state interpretation problem was proposed some time ago [38, 39], but subsequent work suggested that the question is not completely settled [86]. In a number of calculations (for antiproton-impact ionization of helium), the more pragmatic approach to use uncorrelated product states to project out single and double-ionization transition amplitudes was followed [108–110]. This proved to be successful in practice but can be criticized on fundamental grounds since these simple product states do not diagonalize the two-electron Hamiltonian. A clustering analysis to sort pseudo-continuum states into singly and doubly ionized states based on a set of ad-hoc criteria was proposed in [111].

To conclude this chapter, all theory described here assumes (implicitly or explicitly) that the projectile momentum is sharp, i.e., that the impinging particles can be described by momentum-space wave packets with negligible spread. Recent work suggests that the conditions for this assumption to be correct are not always met in highly differential experiments. The consequence then is that the degree of coherence of the projectiles need to be considered in theoretical calculations to explain those measurements [112]. This topic is discussed in Chap. 69.

Acknowledgment One of us (T.K.) has been supported by the Natural Sciences and Engineering Research Council of Canada under Grant No. RGPIN-2019-06305. This chapter is based on a previous version written by A.L.F and J.F.R. for the first edition of the Handbook. It is hoped that the clear presentation of the subject matter in that original work shines through the substantial modifications and additions made.

References

- Briggs, J.S., Macek, J.H.: *Adv. At. Mol. Opt. Phys.* **28**, 1 (1991)
- Fritsch, W., Lin, C.D.: *Phys. Rep.* **202**, 1 (1991)
- Bransden, B.H., McDowell, M.R.C.: *Charge Exchange and the Theory of Ion-Atom Collisions*. Clarendon Press, Oxford (1992)
- Belkić, D.: *Quantum Theory of High-Energy Ion-Atom Collisions*. CRC Press, Boca Raton (2008)
- Hansteen, J.M.: *Phys. Scr.* **42**, 299 (1990)
- Deumens, E., Diz, A., Longo, R., Öhrn, Y.: *Rev. Mod. Phys.* **66**, 917 (1994)
- Cabrera-Trujillo, R.: *Plasma Sources Sci. Technol.* **19**, 034006 (2010)
- Swafford, G.L., Reading, J.F., Ford, A.L., Fitchard, E.: *Phys. Rev. A* **16**, 1329 (1977)
- Fritsch, W.: *J. Phys. B* **15**, L389 (1982)
- Jakob, A., Rösel, F., Trautmann, D., Bauer, G.: *Z. Phys. A* **309**, 13 (1982)
- Zapukhlyak, M., Kirchner, T., Lüdde, H.J., Knoop, S., Morgenstern, R., Hoekstra, R.: *J. Phys. B* **38**, 2353 (2005)
- Lüdde, H.J.: *Private communication* (2018)
- Gayet, R., Salin, A.: *Nucl. Instrum. Methods B* **56/57**, 82 (1991)
- Zapukhlyak, M., Kirchner, T., Hasan, A., Tooke, B., Schulz, M.: *Phys. Rev. A* **77**, 012720 (2008)
- Fainstein, P.D., Ponce, V.H., Rivarola, R.D.: *J. Phys. B* **21**, 287 (1988)
- Kulander, K.C., Sandhya Devi, K.R., Koonin, S.E.: *Phys. Rev. A* **25**, 2968 (1982)
- Stich, W., Lüdde, H.J., Dreizler, R.M.: *J. Phys. B* **18**, 1195 (1985)
- Gramlich, K., Grün, N., Scheid, W.: *J. Phys. B* **19**, 1457 (1986)
- Reinhardt, J., Müller, B., Greiner, W., Soff, G.: *Phys. Rev. Lett.* **43**, 1307 (1979)
- Reading, J.F., Ford, A.L.: *Phys. Rev.* **21**, 124 (1980)
- Lüdde, H.J., Dreizler, R.M.: *J. Phys. B* **18**, 107 (1985)
- Becker, R.L., Ford, A.L., Reading, J.F.: *Phys. Rev. A* **29**, 3111 (1984)
- McGuire, J.H.: *Adv. At. Mol. Opt. Phys.* **29**, 217 (1991)
- Sayasov, Y.S.: *J. Phys. B* **26**, 1197 (1993)
- Horbatsch, M.: *Phys. Rev. A* **49**, 4556 (1994)
- Marques, M.A.L., Maitra, N.T., Nogueira, F.M.S., Gross, E.K.U., Rubio, A. (eds.): *Fundamentals of Time-Dependent Density Functional Theory*. Springer, Berlin (2012)
- Ullrich, C.A.: *Time-Dependent Density-Functional Theory: Concepts and Applications*. Oxford University Press, Oxford (2012)
- Keim, M., Achenbach, A., Lüdde, H.J., Kirchner, T.: *Phys. Rev. A* **67**, 062711 (2003)
- Keim, M., Achenbach, A., Lüdde, H.J., Kirchner, T.: *Nucl. Instrum. Methods B* **233**, 240 (2005)
- Tong, X.-M., Watanabe, T., Kato, D., Ohtani, S.: *Phys. Rev. A* **66**, 032709 (2002)
- Anton, J., Fricke, B., Ma, X., Zhu, X.L., Li, B., Liu, H.P.: *Phys. Lett. A* **369**, 85 (2007)
- Krieger, J.B., Li, Y., Iafate, G.J.: *Phys. Rev. A* **45**, 101 (1992)
- Baxter, M., Kirchner, T., Engel, E.: *Phys. Rev. A* **96**, 032708 (2017)
- Baxter, M., Kirchner, T.: *Phys. Rev. A* **93**, 012502 (2016)
- Reading, J.F., Ford, A.L.: *Comments At. Mol. Phys.* **23**, 301 (1990)
- McGuire, J.H.: *Electron Correlation Dynamics in Atomic Collisions*. Cambridge University Press, Cambridge (1997)
- McGuire, J.H.: *Phys. Rev. Lett.* **49**, 1153 (1982)
- Reading, J.F., Ford, A.L.: *J. Phys. B* **20**, 3747 (1987)
- Bronk, T., Reading, J.F., Ford, A.L.: *J. Phys. B* **31**, 2477 (1998)
- Kirchner, T., Knudsen, H.: *J. Phys. B* **44**, 122001 (2011)
- Errea, L.F., Méndez, L., Riera, A.: *Phys. Rev. A* **27**, 3357 (1983)
- Martin, F., Riera, A., Yanez, M.: *Phys. Rev. A* **34**, 4675 (1986)
- Fritsch, W., Lin, C.D.: *Phys. Rev. A* **41**, 4776 (1990)
- Moribayashi, K., Hino, K., Matsuzawa, M., Kimura, M.: *Phys. Rev. A* **44**, 7234 (1991)
- Slim, H.A., Bransden, B.H., Flower, D.R.: *J. Phys. B* **26**, L159 (1993)
- Gao, J.W., Wu, Y., Sisourat, N., Wang, J.G., Dubois, A.: *Phys. Rev. A* **96**, 052703 (2017)
- Borbély, S., Feist, J., Tórkési, K., Nagele, S., Nagy, L., Burgdörfer, J.: *Phys. Rev. A* **90**, 052706 (2014)
- Marshall, D.P., LeSech, C., Crothers, D.S.F.: *J. Phys. B* **26**, L219 (1993)
- Diaz, C., Martin, F., Salin, A.: *J. Phys. B* **33**, 4373 (2000)
- Hong, X., Wang, F., Wu, Y., Gou, B., Wang, J.: *Phys. Rev. A* **93**, 062706 (2016)
- Quashie, E.E., Saha, B.C., Andrade, X., Correa, A.A.: *Phys. Rev. A* **95**, 042517 (2017)
- Covington, C., Hartig, K., Russakoff, A., Kulpins, R., Varga, K.: *Phys. Rev. A* **95**, 052701 (2017)
- Bransden, B.H., Dewangan, D.P.: *J. Phys. B* **12**, 1377 (1979)
- Glauber, R.: *Lectures in Theoretical Physics vol. 2*. Interscience, New York (1958)
- Franco, V., Thomas, B.K.: *Phys. Rev. A* **4**, 945 (1971)
- Binstock, J., Reading, J.F.: *Phys. Rev. A* **11**, 1205 (1975)

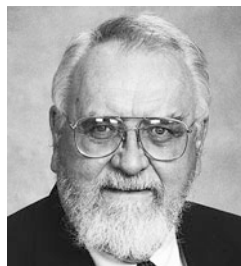
57. Winter, T.G.: *Adv. At. Mol. Opt. Phys.* **52**, 391 (2005)
58. Reinhold, C.O., Olson, R.E., Fritsch, W.: *Phys. Rev. A* **41**, 4837 (1990)
59. Ford, A.L., Reading, J.F., Hall, K.A.: *J. Phys. B* **26**(4537), 4553 (1993)
60. Martir, M.H., Ford, A.L., Reading, J.F., Becker, R.L.: *J. Phys. B* **15**, 1729 (1982)
61. Shakeshaft, R.: *Phys. Rev. A* **18**, 1930 (1978)
62. Fritsch, W., Lin, C.D.: *Phys. Rev. A* **27**, 3361 (1983)
63. Ermolaev, A.M.: *J. Phys. B* **23**, L45 (1990)
64. Slim, H.A.: *J. Phys. B* **26**, L743 (1993)
65. Winter, T.G.: *Phys. Rev. A* **87**, 032704 (2013)
66. Errea, L.F., Harel, C., Jouin, H., Méndez, L., Pons, B., Riera, A.: *J. Phys. B* **27**, 3603 (1994)
67. Kuang, J., Lin, C.D.: *J. Phys. B* **29**, 1207 (1996)
68. Toshima, N.: *Phys. Rev. A* **59**, 1981 (1999)
69. Reading, J.F., Ford, A.L., Becker, R.L.: *J. Phys. B* **14**, 1995 (1981)
70. Reading, J.F., Ford, A.L., Becker, R.L.: *J. Phys. B* **15**(625), 3257 (1982)
71. Antal, M.J., Anderson, D.G.M., McElroy, M.B.: *J. Phys. B* **8**, 1513 (1975)
72. Winter, T.G., Lin, C.D.: *Phys. Rev. A* **29**, 567 (1984)
73. Kroneisen, O.J., Lüdde, H.J., Kirchner, T., Dreizler, R.M.: *J. Phys. A* **32**, 2141 (1999)
74. Kolakowska, A., Pindzola, M.S., Robicheaux, F., Schultz, D.R., Wells, J.C.: *Phys. Rev. A* **58**, 2872 (1998)
75. Chassid, M., Horbatsch, M.: *Phys. Rev. A* **66**, 012714 (2002)
76. Minami, T., Pindzola, M.S., Lee, T.-G., Schultz, D.R.: *J. Phys. B* **39**, 2877 (2006)
77. Pindzola, M.S., Schultz, D.R.: *Phys. Rev. A* **77**, 014701 (2008)
78. Jorge, A., Suárez, J., Illescas, C., Errea, L.F., Méndez, L.: *Phys. Rev. A* **94**, 032707 (2016)
79. Pindzola, M.S., Colgan, J., Robicheaux, F., Lee, T.-G., Ciappina, M.F., Foster, M., Ludlow, J.A., Abdel-Naby, S.A.: *Adv. At. Mol. Opt. Phys.* **65**, 291 (2016)
80. Sidky, E.Y., Lin, C.D.: *J. Phys. B* **31**, 2949 (1998)
81. Choi, B.H.: *Phys. Rev. A* **11**, 2004 (1975)
82. Gulyás, L., Fainstein, P.D., Salin, A.: *J. Phys. B* **28**, 245 (1995)
83. McGovern, M., Assafrao, D., Mohallem, J.R., Whelan, C.T., Walters, H.R.J.: *Phys. Rev. A* **79**, 042707 (2009)
84. McGovern, M., Assafrao, D., Mohallem, J.R., Whelan, C.T., Walters, H.R.J.: *Phys. Rev. A* **81**, 032708 (2010)
85. Bray, I., Abdurakhmanov, I.B., Bailey, J.J., Bray, A.W., Fursa, D.V., Kadyrov, A.S., Rawlins, C.M., Savage, J.S., Stelbovics, A.T., Zammit, M.C.: *J. Phys. B* **50**, 202001 (2017)
86. Diaz, C., Martin, F., Salin, A.: *J. Phys. B* **35**, 2555 (2002)
87. Ford, A.L., Fitchard, E., Reading, J.F.: *Phys. Rev. A* **16**, 133 (1977)
88. Reading, J.F., Ford, A.L., Swafford, G.L., Fitchard, A.: *Phys. Rev. A* **20**, 130 (1979)
89. Becker, R.L., Ford, A.L., Reading, J.F.: *J. Phys. B* **13**, 4059 (1980)
90. Mukoyama, T., Lin, C.D., Fritsch, W.: *Phys. Rev. A* **32**, 2490 (1985)
91. Fu, J., Fitzpatrick, M.J., Reading, J.F., Garet, R.: *J. Phys. B* **34**, 15 (2001)
92. Pons, B.: *Phys. Rev. Lett.* **84**, 4569 (2000)
93. Pons, B.: *Phys. Rev. A* **63**, 012704 (2001)
94. Pons, B.: *Phys. Rev. A* **64**, 019904 (2001). erratum
95. Gulyás, L., Igarashi, A., Fainstein, P.D., Kirchner, T.: *J. Phys. B* **41**, 025202 (2008)
96. Abdurakhmanov, I.B., Kadyrov, A.S., Avazbaev, S.K., Bray, I.: *J. Phys. B* **49**, 115203 (2016)
97. Abdurakhmanov, I.B., Kadyrov, A.S., Bray, I., Stelbovics, A.T.: *J. Phys. B* **44**, 165203 (2011)
98. Mehler, G., Greiner, W., Soff, G.: *J. Phys. B* **20**, 2787 (1987)
99. Abdurakhmanov, I.B., Kadyrov, A.S., Bray, I.: *Phys. Rev. A* **94**, 022703 (2016)
100. Voitkiv, A.B., Ullrich, J.: *Phys. Rev. A* **67**, 062703 (2003)
101. Walters, H.R.J., Whelan, C.T.: *Phys. Rev. A* **92**, 062712 (2015)
102. Abdurakhmanov, I.B., Bailey, J.J., Kadyrov, A.S., Bray, I.: *Phys. Rev. A* **97**, 032707 (2018)
103. Lee, T.-G., Ovchinnikov, S.Y., Sternberg, J., Chupryna, V., Schultz, D.R., Macek, J.H.: *Phys. Rev. A* **050701**(R), 76 (2007)
104. Macek, J.H., Sternberg, J.B., Ovchinnikov, S.Y., Lee, T.-G., Schultz, D.R.: *Phys. Rev. Lett.* **102**, 143201 (2009)
105. Brauner, M., Briggs, J.S., Klar, H.: *J. Phys. B* **22**, 2265 (1989)
106. Briggs, J.S.: *Phys. Rev. A* **41**, 539 (1990)
107. Dal Cappello, C., Le Rouzo, H.: *Phys. Rev. A* **43**, 1395 (1991)
108. Barna, I.F., Grün, N., Scheid, W.: *Eur. Phys. J. D* **25**, 239 (2003)
109. Foster, M., Colgan, J., Pindzola, M.S.: *Phys. Rev. Lett.* **100**, 033201 (2008)
110. Guan, X., Bartschat, K.: *Phys. Rev. Lett.* **103**, 213201 (2009)
111. Gao, J.W., Miteva, T., Wu, Y., Wang, J.G., Dubois, A., Sisourat, N.: *Phys. Rev. A* **103**(3), L30803 (2021)
112. Schulz, M.: *Adv. At. Mol. Opt. Phys.* **66**, 508 (2017)



Tom Kirchner Tom Kirchner is a Professor of Physics at York University, Toronto, Canada. He received his PhD from Goethe University Frankfurt in 1999 and joined the York faculty in 2009 after postdoctoral stints at York and the Max Planck Institute for Nuclear Physics, and a junior professorship at TU Clausthal (Germany). His research is concerned with the quantum dynamics of multi-particle Coulomb systems, in particular atomic and molecular scattering processes. He is a Fellow of the American Physical Society.



A. Lewis Ford Dr Ford's research interests lie in theoretical atomic and molecular physics: inner-shell excitation, ionization, charge transfer, and electronic properties of diatomic molecules. He joined the Texas A&M faculty in 1973. After receiving his BA degree from Rice University, he completed his PhD at the University of Texas at Austin in 1972 and did post-doctoral work at Harvard. Professor Ford is a member of the American Physical Society, Division of Electron, Atomic, and Optical Physics.



John F. Reading Professor Reading earned his PhD from the University of Birmingham, UK in 1964. His current research interests are in theoretical calculations of cross sections for excitation and ionization following fast ion-atom collisions, the role of Pauli correlation in inner-shell vacancy production, and the role of dynamic electronic correlation, the latter especially in comparison of proton and antiproton-induced single and double ionization of helium.



Hossein Sadeghpour 

Contents

54.1	Zero/Short-Range Neutral Collisions	796
54.2	Low-Energy Phase Shift and Zero-Energy Scattering Length	797
54.3	Ultralong-Range Rydberg Molecules: Fermi’s Idea Redux	798
54.4	Fermi Extended: Do Elastic Collisions Result in Inelastic Chemical Reactions?	798
54.5	Ion-Pair Molecules	799
54.6	Few-Body Short-Range Scattering	800
54.6.1	Additivity of Binary Interactions	800
54.6.2	Three-Body Effective Interactions	800
54.7	Collective Quantum Many-Body Effects	800
54.7.1	Bose and Fermi Polarons	800
54.7.2	Linear Response Absorption	801
	References	802

Keywords

Rydberg spectral line broadening · Fermi pseudopotential · Rydberg molecules · Rydberg polarons · Pauli-induced rotational blockade

Abstract

Rydberg excitations have had a substantial impact on the development of atomic and molecular physics. Advances in cooling and trapping of atoms and molecules have allowed for precise interrogation of quantum processes in such atomic systems with Rydberg excitation as a probe. In this chapter, the reader is familiarized with extension of Rydberg spectral line broadening concepts to quantum collision of Rydberg electrons with atoms and molecules and how the Rydberg spectra reveal molecular oligomeric formation and the emergence of ozonic and fermionic polaron features. It is shown that with fermions as the gas particles, the Pauli exclusion principle suppresses molecular formation.

Much of the information gleaned from the quantum world comes to us via scattering of particles over a wide range of energies. At large collisional energies, compared with typical energies in the target particles, perturbative methods are employed with efficiency and efficacy to probe weak coupling. At the other end of the energy scale, strong coupling emerges at low energies. This new physics is consequential.

In 1934, *Edoardo Amaldi* and *Emilio Segre* performed absorption spectroscopy of sodium ($3s-np$) Rydberg lines in high-pressure nitrogen and hydrogen chambers [1]. They observed two unexpected results: (1) that the highly excited sodium lines survived in the N_2 and H_2 mixtures, and (2) that the lines in the presence of H_2 gas were blue shifted (“violet”). We will return to the first discovery as it becomes relevant to studies of Rydberg excitations in high-density quantum gases. The second crucial discovery became the foundation for Enrico Fermi’s exploration of what effectively is the birth of low-energy quantum physics.

When a free charge (or weakly bound electron) is immersed in a gas, it interacts with the nearby atoms or molecules, and if the neighboring gas species do not possess a permanent electric dipole moment, then the interaction of the charge with the surrounding ground-state atoms is, in the first-order perturbation theory, via the polarization potential

$$W(q_i) = - \sum_i \frac{e^2 \alpha}{2q_i^4}, \quad (54.1)$$

where α is the polarizability of the ground state particles, and q_i is the charge position from the i -th perturber core.

H. Sadeghpour (✉)
 Institute for Theoretical Atomic Molecular and Optical Physics
 (ITAMP), Harvard University
 Cambridge, MA, USA
 e-mail: hsadeghpour@cfa.harvard.edu, hrs@cfa.harvard.edu

The shift of the Rydberg lines due to dielectric screening is obtained in cm^{-1} as in [2, Eq. 23],

$$\Delta_\epsilon \approx 2.6 \left(\frac{4\pi}{3} \right)^{4/3} \left[\frac{(\epsilon - 1)}{16\pi^2 \hbar c} \right] e^2 \rho^{1/3}, \quad (54.2)$$

where ϵ is the dielectric constant, normalized to vacuum permittivity, and ρ is the gas density.

The immediate observation is that all spectral lines shift to the red. For the Na Rydberg excitation in H_2 , this was clearly not true. The flaw that Fermi discovered in this argument was to note that the quasi-bound Rydberg electrons scatter from the perturber atoms or molecules.

In the low-energy scattering of a Rydberg electron from perturber particles, the wave function will be slowly varying, except near the perturbers. To circumvent this fast oscillation, Fermi wrote down another wave function, $\bar{\psi}$, as the mean value of ψ around the perturbers, whose extent was to be small compared with the electron de Broglie wavelength but still have a volume large enough to contain a sizable number of perturber atoms.

This wave function, regular at the origin, can be written as

$$u(r) = r\psi(r) = (r - a_S(0))\bar{\psi}. \quad (54.3)$$

The parameter $a_S(0)$ is of dimension length called the scattering length and is the intercept at zero momentum ($k = 0$) of $k \cot \delta_S(k)$, i.e., $a_S(0) = -\lim_{k \rightarrow 0} \frac{1}{k} \tan(\delta_S(k))$, of the s-wave phase shift, $\delta_S(k)$.

The spectral energy shift in the long-wavelength limit becomes [2], in units of cm^{-1} ,

$$\Delta_a = \frac{\hbar a_S(0)\rho}{m_e c}, \quad (54.4)$$

with m_e the mass of the electron. When $a_S(0) > 0$, the spectral line shift can be to the blue if $\Delta_a > \Delta_\epsilon$, but when $a_S(0) < 0$, the shift is always to the red.

This description of spectral line broadening and shift, where the interaction is described as a zero-range interaction [2]

$$V_S(\mathbf{r} - \mathbf{R}) = 2\pi a_S(k)\delta(\mathbf{r} - \mathbf{R}), \quad (54.5)$$

is able to account for the peculiar line shifts in the experiment of *Amaldi and Segre* [1]. In the above expression, \mathbf{R} refers to the interparticle separation between the Rydberg core and the perturber atom. The concept of the pseudopotential, as in Eq. (54.5) is familiar and crucial in chemistry, condensed matter, and surface physics, where effective Hamiltonians need to be constructed for structure calculations of many-body systems [3].

Schwinger [4, Sects. 2 and 3] showed that the phase shift in triplet neutron-proton scattering can be written as

$$k \cot \delta = -\gamma + \frac{1}{2}(\gamma^2 + k^2)r_0 + \mathcal{O}(k^4 r_0^2), \quad (54.6)$$

where γ is related to the deuteron binding energy as $(\hbar^2 \gamma^2 / M)$, r_0 is the effective range of the nuclear forces, and the scattering length is $\frac{1}{a} = \gamma(1 - \frac{1}{2}\gamma r_0)$. This is the first proof that experiments can determine the effective range of the interaction. In deuteron triplet scattering, the scattering length is positive and a bound state forms, whereas in the singlet channel, the scattering length is negative and binding fails.

Bethe [5] first wrote down the fundamental expression of low-energy scattering,

$$k \cot \delta = -\frac{1}{a} + \frac{1}{2}k^2 r_0. \quad (54.7)$$

The scattering cross section, $\sigma = \frac{4\pi}{k^2} \left[\frac{1}{1 + \cot^2 \delta} \right]$ reaches unitarity when $k^2 = \frac{2}{ar_0}$. When the effective range term is small, at very low temperatures, the unitarity is achieved at $|a| \rightarrow \infty$. At zero energy, the cross section becomes $\sigma = 4\pi a^2$. When the atoms are indistinguishable, such as in a Bose-Einstein condensate, the cross section is $\sigma = 8\pi a^2$.

54.1 Zero/Short-Range Neutral Collisions

While many of the early applications of the zero-range scattering were in nuclear and condensed matter physics, the advent of low-temperature atomic traps in the last few decades has shifted the focus of research and application to cold and ultracold atomic and molecular collisions [6].

At low temperatures, the collision between two spherically symmetric ground state atoms, say alkali metal atoms, is mediated by the interaction at large separations, where in the lowest order of active perturbation, the interaction is

$$V(R) = \frac{C_6}{R^6} + \frac{C_8}{R^8} + \frac{C_{10}}{R^{10}} + \dots \quad (54.8)$$

where the successively shorter-range terms contain the van der Waals (vdW) coefficients, dictating the interatomic interaction [7]. Much of the work on the modification to the zero-range effective range theory due to short-range interactions (polarization, vdW, etc.) was done by *Spruch* [8], *Fabrikant* [9], and *Gao* [10–12].

In a quantum gas, the de Broglie wavelength $\lambda_{\text{dB}} = \left[\frac{2\pi\hbar^2}{mk_B T} \right]^{3/2} \sim 100 \mu\text{m}$ is larger than any interaction length, $R_{\text{vdW}} = \left[\frac{2\mu C_p}{\hbar^2} \right]^{1/p-2} \sim 10 \text{nm}$. In the above, m stands for the single particle mass, μ is the reduced binary mass, T is temperature, and R_{vdW} is the van der Waals length. For a polynomial in $1/R$ interaction of order p - the most common of all vdW interactions is with $p = 6$. In such circumstances, the interaction among the gas particles is no longer a product of pair interactions, and the wave function for the gas particles

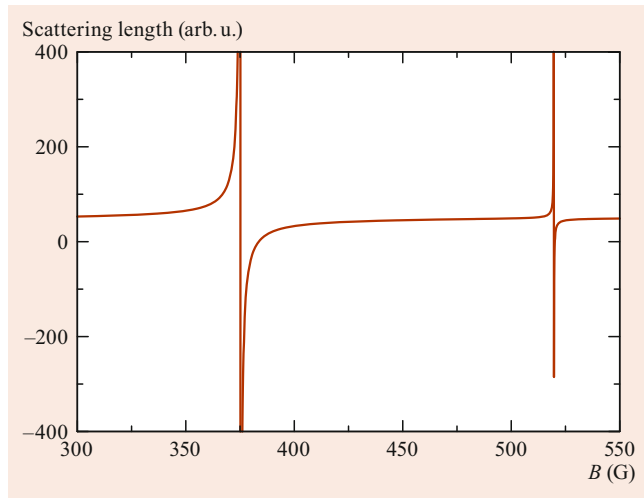


Fig. 54.1 Magnetically tuned Fano–Feshbach resonances in the collision of two atoms. A broad and a narrow resonance, a consequence of interacting potential curves correlating to different atomic hyperfine levels, are shown

in a cold trap obeys the Gross–Pitaevski (GP) equation

$$\left[-\frac{\hbar^2}{2m} \nabla^2 + V_{\text{trap}} + N U_0 |\Psi|^2 \right] \Psi = \mu \Psi, \quad (54.9)$$

where the trap potential is usually approximated as a harmonic well, $U_0 = \frac{4\pi\hbar^2 a}{m}$ is the strength the two-body short-range interaction between any pairs of N particles of mass m , and μ is the chemical potential, the energy needed to add one particle to the gas. The strength of the interaction is determined by the zero-momentum s-wave scattering length (a), whose sign also determines the stability of the trapped gas. For $a > 0$, as more atoms are added to the gas, the energy goes up, and so goes the density, until the critical value for condensation in the limit of noninteracting particles, i.e., $\rho\lambda_{\text{dB}}^3 \geq 2.612$ [13] is reached. Conversely, for $a < 0$, the aggregate energy decreases as more particles are added, leading to instability and the eventual collapse of the many-body state. The GP or the nonlinear Schrödinger equation (NLSE) has a quadratic nonlinearity, typical of quantum N -body Hamiltonians.

It is important to recognize that the nonlinear term in Eq. (54.9) is precisely that of the Fermi pseudopotential (Eq. (54.5)); the additional factor of 2 in Eq. (54.9) accounts for the indistinguishability of bosons.

The short-range pair interaction can be engineered nearly at will. A large body of literature now exists on how to tailor the scattering length between two atoms to a desired accuracy. All such techniques depend on engineering a form of resonant interaction [14, 15]. The workhorse method is via magnetic tuning of the pair interaction, the so-called magnetic Fano–Feshbach resonance, in which magnetic fields are used to couple atoms in different Zeeman sublevels. When

the coupling of two atomic Zeeman manifolds are different, rovibrational levels in one Born–Oppenheimer (BO) potential energy form in the continuum of the other manifold BO potential energy and, therefore, appear as resonances. One one side of this resonance, the scattering length is positive, leading to positive infinity, and on the other side, the scattering length becomes progressively negative; see Fig. 54.1. The crossover is the unitarity limit for strong interactions.

54.2 Low-Energy Phase Shift and Zero-Energy Scattering Length

Large spin-exchange cross sections for electrons scattering from alkali metal atoms [16] imply large differences between singlet ($S = 0$) and triplet ($S = 1$) $L = 0$ scattering phase shifts. The elastic phase shifts were calculated with coupled channel solutions [17], relativistic R-matrix with inclusion of fine structure splitting for heavier alkali metal atoms [18–21], and the pseudopotential method for electron interaction with the perturber atom [22].

The behavior of the $L = 0$ phase shift is markedly different at low momentum. The singlet phase shift has a negative slope resulting in a positive scattering length, i.e., positive electron affinity for the 1S_0 scattering, while the triplet scattering length is large and negative. This trend is observed for all alkali metal atoms. For electron scattering from heavy alkali-metal atoms, inner shell electron–electron repulsion

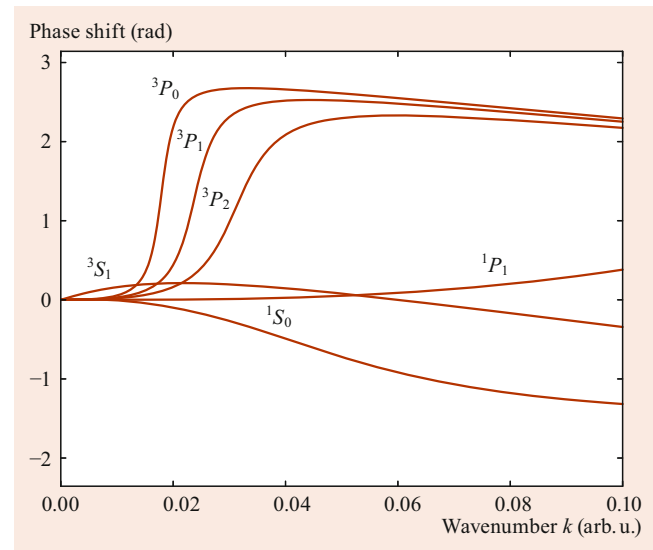


Fig. 54.2 The e^- –Cs(6s) scattering phase shifts as a function of the electron momentum for different scattering partial waves. The $^S L_J = ^1 P_1$ phase shift is from Thumm [23]. The $^{1,3}S_0$ and $^3 P_{J=0,1,2}$ resonant phase shifts are obtained by matching at short distances to observed scattering resonance positions and widths [7, 24]. The $^3 S_1$ phase shift has a positive slope near $k = 0$, which extrapolates to a scattering length of $a_S(0) = -16.5 a_0$ in Eq. (54.10). Reprinted by permission from [25]

pushes the $L = 1, S = 1$ bound states into the continuum, resulting in resonant 3P_J scattering states. These scattering resonances, e.g., Fig. 54.2, have been calculated and observed [18, 24]. The negative 3S scattering length allows for the formation of Rydberg molecule states in ultracold magneto-optical traps (MOT), e.g., Eq. (54.5), and the 3P_J resonances hugely distort the BO potential energy curves, e.g., Fig. 54.4, and affect the dynamics of molecular formation and fragmentation into neutral and ionic species.

54.3 Ultralong-Range Rydberg Molecules: Fermi's Idea Redux

The Fermi pseudopotential (Eq. (54.5)) made a debut in quantum electron collision physics in 2000, when Greene and coworkers realized that this widely used formalism for Rydberg line broadening and shift can be utilized to calculate realistic BO potential energy curves, albeit at large separations between atoms [26].

When one atom, say an alkali-metal atom, for simplicity as well as practicality because most ultracold species are of this variety, is excited into a Rydberg state, $\phi(\mathbf{r})$, where \mathbf{r} specify the radial degrees of freedom for the Rydberg electron, its excitation spectrum will be influenced, as Fermi formulated [2], by the surrounding atoms, which are at separation \mathbf{R} and are assumed to be in their ground state. The form of the BO potential energy is then

$$\begin{aligned} U_{\text{BO}}(R) &= E_{nl} - 2\pi a_S(0) |\langle \phi(\mathbf{r}) | \delta(\mathbf{r} - \mathbf{R}) | \phi(\mathbf{r}) \rangle| \\ &= E_{nl} - 2\pi a_S(0) |\phi_{nlm}(R)|^2. \end{aligned} \quad (54.10)$$

In this expression, the Rydberg states are at energies E_{nl} and have eigenwave functions ϕ_{nlm} . When a bath atom is at a distance near the minima in the potential wells, e.g., the red and green balls in Fig. 54.3, and provided that the Rydberg electron scattering from the atom has a negative scattering length, it may bind inside the Rydberg orbit and form a diatomic molecule at large separations R .

The original Fermi expression for spectral shift in Eq. (54.4) has a linear dependence on the atom number density. The Rydberg molecular shift in Eq. (54.10) offers a reinterpretation of density as the quantum mechanical electron probability density, i.e., the modulus of the wave function squared at the position of the perturber atom.

Equation 54.10 indicates that $U_{\text{BO}}(R)$ will oscillate with R because the Rydberg wave function oscillates, see Fig. 54.3. When $a_S(0)$ is negative, the potentials will possess localized wells at extremely large separations and scale with n^2 . These wells may support bound vibrational levels. The undulations in the BO potential energy curves are not unique to the Fermi model and have been confirmed with detailed quantum chemical calculations of ground atom and Rydberg atom interactions; e.g., [27].

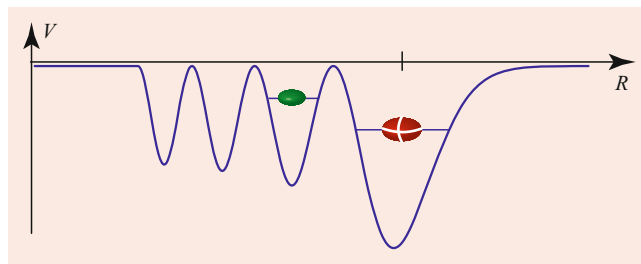


Fig. 54.3 BO potentials resulting from s -wave zero energy scattering of a Rydberg electron from a ground polarizable atom, as a function of internuclear separation. This illustrates the two most salient features of an ultracold, ultralong-range Rydberg molecule: the oscillatory behavior of the potential energy curve and the vibrational binding of the interaction

Given the energy resolution of discrete vibrational bound states of the Rydberg molecules, much below 1 cm^{-1} , ensures that they could only be found in conditions of ultracold atomic traps. However, the influence of Rydberg quasi-molecular interactions on the Rydberg satellite lines of alkali metal atoms was already proposed by *Niemax* in 1972 [28]. Subsequent measurements and interpretations of the spectral features in the wings of Rydberg lines showed strong correlation with the minima of the BO potential energy curves, as illustrated in Fig. 54.3 [29].

Nearly a decade after their prediction, ultralong-range Rydberg molecules were realized in an ultracold rubidium gas, where a fraction of atoms were excited into $\text{Rb}(ns)$ states [30]. A two-color excitation process was used to photoassociate $^3\Sigma$ Rydberg molecules. Several vibrational bound states were observed as peaks to the red of the atomic Rydberg $\text{Rb}(35s\text{--}37s)$ lines. Subsequent measurements observed ultralong-range Rydberg molecules in other species and in different initial atomic angular momentum states [31–38].

54.4 Fermi Extended: Do Elastic Collisions Result in Inelastic Chemical Reactions?

The natural extension of the Fermi pseudopotential to higher-order partial wave scattering, e.g., P-wave scattering, was done by *Omont* [39], more than 40 years after Fermi. *Omont*'s insight was that for low n excitations, when the electron kinetic energy $\text{KE} = E + e^2/R$, varies as a function of the perturber position R , a proper account of the electron-neutral interaction would have to include the energy dependence of the S-wave scattering length, $a_S(k) = -\tan(\delta_S(k))/k$, where $k = \sqrt{2 \text{KE}}$ is the electron momentum in atomic units.

The P-wave electron–atom interaction has the form [39],

$$V_P(\mathbf{r}) = 6\pi a_P^3(k) \delta(\mathbf{r}) \overleftarrow{\nabla} \cdot \overrightarrow{\nabla}, \quad (54.11)$$

where $a_P^3(k) = -\tan(\delta_P(k))/k^3$ is the energy-dependent P-wave scattering volume, with $\delta_P(k)$ the energy-dependent

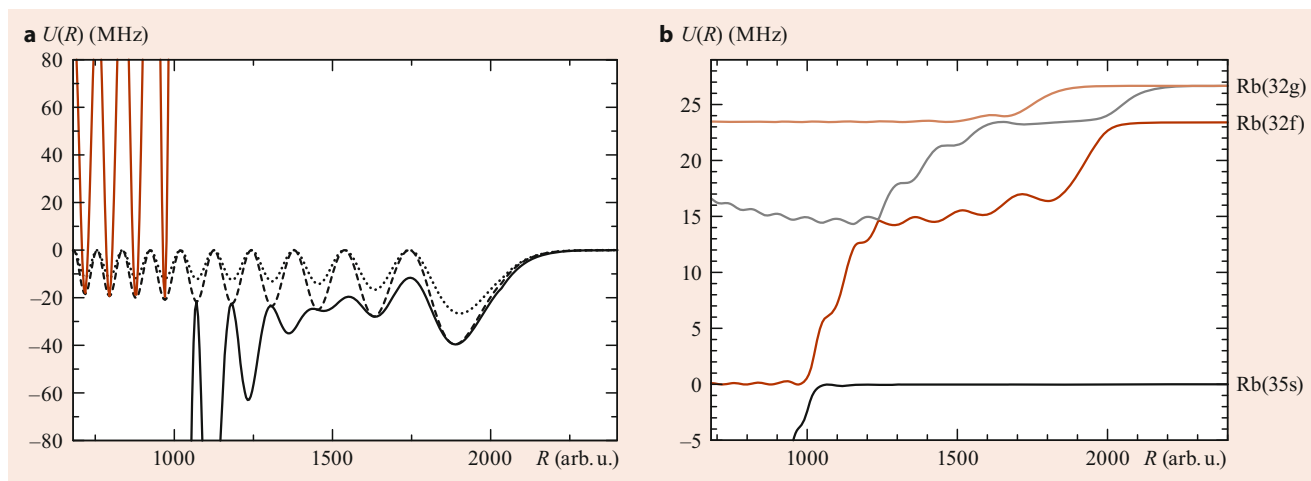


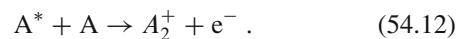
Fig. 54.4 BO potentials resulting from P-wave and P-wave zero energy scattering of a Rydberg electron from a ground polarizable atom as a function of internuclear separation. In **a**, the S-wave scattering curves at different levels of approximation, with just the Rb(35s) wave function (*dot-dashed line*), diagonalization in a manifold of s states (*dashed line*), including P-wave scattering (Eq. (54.11)) (*solid line*). In **b**, avoided crossings due to S-wave and P-wave resonant interactions occur. The effect of P-wave resonances is evident on the BO potential energy curves as they crash through several Rb(n l) atomic energies. Reprinted with permission from [40]

P-wave scattering phase shift. The arrows over the ∇ operators indicate the direction in which the operator acts. In the above expression, when $\delta_p(k) = \pi/2$, i.e., at resonant energy of a metastable state of an electron interacting with a neutral perturber, the P-wave contact interaction diverges. This is precisely what happens for the triple ($S = 1$) scattering of an electron with unit angular momentum from a heavy alkali-metal atom (Na, K, Rb, Cs). For e^-A interaction, where A is any of these atoms, the $L = 1, S = 1$ scattering contains a low-energy P-wave resonance [19, 41]; see also Fig. 54.4b.

An immediate observation from Fig. 54.4 is the imprint of the resonant P-wave scattering on the BO potential energy curves. The potential energy curves correlating to ground and excited atomic states crash through a manifold of Rydberg states due to interaction at and near the position of P-wave scattering resonances, mixing different l states and forming large numbers of avoided crossings within the same molecular symmetry. The influence of P-wave resonances, in different J quantum numbers, with the BO potential curves, has consequences for the lifetime of vibrational levels. In particular, excited levels can tunnel through the barriers, therefore inducing shorter lifetimes [42]. Change in kinetic energy of the Rydberg atoms, as they undergo l -changing collisions can be measured [43]. The threshold ionization field directly exploits the angular momentum change of the Rydberg atom, and the rate of l -changing collisions is obtained by monitoring the Landau–Zener probabilities through the manifold of crossings in Fig. 54.4b. Throughout, L refers to the electron scattering angular momentum, while l refers to the Rydberg orbital angular momentum.

As the collisions proceed to shorter distances, neutral atom–ion interaction, where the electronic distributions be-

tween the Rydberg atom and the ground neutral perturber overlap, dominates, leading to associative ionization



Indeed, through primarily elastic electron scattering collision with a neutral perturber at extreme low kinetic energy, it becomes possible to induce novel chemical reactions such as the above. The n -dependent branching ratio for production of the molecular ion, $P_{\text{Rb}_2^+}(n) = N_{\text{Rb}_2^+} / [N_{\text{Rb}_2^+} + N_{\text{Rb}^+}]$ can also be measured through the l -changing and short-range collisions [43, 44]. The high branching ratio, which depends on the density of the ultracold perturber atoms, at intermediate principal quantum numbers, is likely the result of l -changing collisions.

54.5 Ion-Pair Molecules

Electron hopping from one atomic center to another, induced in avoided crossings between the covalent potential energy curves correlating to Rydberg–neutral ground state atoms and the anion–cation potential energy curve of the same symmetry, leads to formation of long-range ion-pair molecules. These molecules are bound by ion-pair interaction: both have an infinite number of bound rovibrational states that obey the Rydberg formula with a heavy mass and large permanent electric dipole moments [25, 45].

The ion-pair molecules can be produced by excitation into Rydberg butterfly molecular states [37, 41] and transitioning into most Franck–Condon (FC) favorable ion-pair vibrational states [46].

54.6 Few-Body Short-Range Scattering

54.6.1 Additivity of Binary Interactions

The form of Eq. (54.10) suggests that for an isotropic Rydberg excitation, i.e., $l = 0$ state excitation, the BO potential energy is additive in the number of perturber interactions with the Rydberg atom,

$$U_{\text{BO}}(R) = \sum_k^N U_{\text{BO}}(R_k), \quad (54.13)$$

where the index k runs over the N number of perturber atoms, and R_k denotes the location of each perturber from the Rydberg core. The molecular binding energy of an oligomer is then combinatorially obtained from dimer energies. A series of theoretical and experimental efforts on Rb and Sr atoms [43, 47–49] identified and observed successive formation of oligomeric s-orbital angular momentum molecules (trimers, tetramers, pentamers, ...) whose energies are combinatorially determined from the dimer energies, see Fig. 54.5.

54.6.2 Three-Body Effective Interactions

The great additivity feature that facilitates oligomeric molecule formation is interrupted when Rydberg excitations are instead made to states with nonzero angular momenta, e.g., Rb(np , nd) states. Spectral Rydberg molecule lines in excitation in a Cs ultracold gas to Cs(nd) states were recently

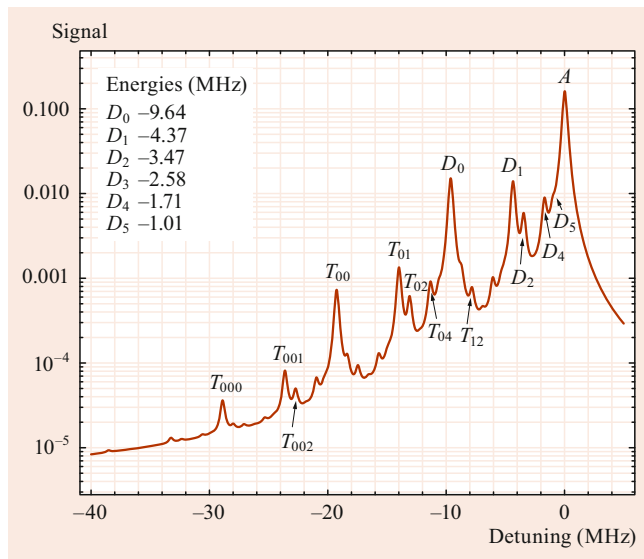


Fig. 54.5 The Rydberg absorption spectrum $A(\omega)$ for excitation in a Sr Bose gas. The peak at zero detuning is the atomic Rydberg line and D_j peaks refer to the formation of Rydberg dimers in ground and excited vibrational levels, T_{ij} trimer, T_{ijk} tetramer levels. Courtesy of Richard Schmidt

observed [50]. A number of red-detuned spectral features could not be ascribed to any two-body dimer (or three-body additive trimer) interactions.

A three-body effective Hamiltonian [50],

$$U_{\pm}(R, \theta) = U_{\text{dim}}(R) \left[1 \pm \left(-\frac{1}{2} + \frac{3}{2} \cos^2 \theta \right) \right], \quad (54.14)$$

where $U_{\text{dim}}(R)$ is the diatomic molecular energy, and θ is the angular degree of freedom between the internuclear distances from the Rydberg core to the perturber atoms, was able to in the first order describe the presence of nonadditive Rydberg trimers. In this scenario, each perturber atom sits in the different lobes of the Cs(nd) electron density. The effective three-body Hamiltonians, which here arises from the intrinsic anisotropy of the initial Rydberg excitation, are in vogue for simulations of various quantum many-body and quantum information systems, including quantum loop models and adiabatic quantum computing.

A natural question now arises: would this Lego-like molecular stack continue unabated with the addition of successive bath atoms inside a Rydberg orbit, or would some new and manifestly quantum behavior emerge?

54.7 Collective Quantum Many-Body Effects

54.7.1 Bose and Fermi Polarons

When the number of atoms inside the Rydberg orbit increases, either with increasing gas density or increasing the principal quantum number, the Rydberg spectral lines broaden and for extreme excitations approach the classical broadening [51], producing a density-dependent broadening, $\Delta = \frac{2\pi\hbar^2 a_s}{m} \int |\Psi(R)|^2 \rho(R) dR = \frac{2\pi\hbar^2 a_s}{m} \bar{\rho}$, where $\rho(R)$ is the local density and $\bar{\rho}$ the weighted average density.

Can quantum behavior, including quantum statistics and many-body effects, ever become evident in these spectra? The short answer is yes.

In the second quantization notation, the Hamiltonian for an impurity with mass M at position and momentum $\hat{\mathbf{R}}, \hat{\mathbf{p}}$, interacting with gas bosons is

$$\hat{H} = \frac{\hat{\mathbf{p}}^2}{2M} + \sum_{\mathbf{k}} \epsilon_{\mathbf{k}} a_{\mathbf{k}}^{\dagger} a_{\mathbf{k}} + \frac{1}{\mathcal{V}} \sum_{\mathbf{k}\mathbf{q}} V(\mathbf{q}) e^{-i\mathbf{q}\hat{\mathbf{R}}} a_{\mathbf{k}+\mathbf{q}}^{\dagger} a_{\mathbf{k}}, \quad (54.15)$$

where \mathcal{V} is the quantization volume, and $a_{\mathbf{k}}$ ($a_{\mathbf{k}}^{\dagger}$) are the annihilation (creation) operators for the bosons with dispersion $\epsilon_{\mathbf{k}} = \frac{\hbar^2 \mathbf{k}^2}{2m}$ [48, 52]. The last term contains the Rydberg impurity-boson interaction, the Fermi pseudopotential, in

the momentum-representation, i.e., $V(\mathbf{q})$ in Eq. (54.5). The widely used Fröhlich Hamiltonian is obtained by employing the Bogoliubov approximation and keeping interactions linear in the bosonic field operators [53]. The Fröhlich Hamiltonian cannot account for particle–particle scattering and the formation of bound states correctly. By including all impurity–boson interaction terms, an extended Fröhlich Hamiltonian [52] which accounts for the formation of dimers, trimers, and higher order oligomers can be obtained.

54.7.2 Linear Response Absorption

The polaron dynamics can be probed by absorption spectroscopy. In the ground state, a bosonic atom contact interaction with the surrounding Bosons is negligible compared to the Rydberg excited interaction $V(\mathbf{q})$ with the gas Bosons. In the linear response, the absorption amplitude at frequency ν is written in Fermi’s Golden rule,

$$\mathcal{A}(\nu) = 2\pi \sum_{if} w_i \left| \langle f | \hat{V}_L | i \rangle \right|^2 \times \delta(\nu - (E_i - E_f)). \quad (54.16)$$

In the above expression, all initial and final states of impurity and bath Bosons satisfy the eigen equations, $\hat{H}_0 |i\rangle = E_i |i\rangle$ and $\hat{H} |f\rangle = E_f |f\rangle$. Formally, the initial state of the impurity plus gas bosons is written at zero temperature as, $|i\rangle = |\text{BEC}\rangle \otimes |\mathbf{p} = 0\rangle_I \otimes |g\rangle_I$. The notation indicates that the Bose–Einstein condensate (BEC) atoms and the Rydberg impurity (I) are initially at zero momentum ($\mathbf{p} = 0$) in ground electronic state. At finite temperatures, the weights of the initial states are obtained from the initial density matrix, $\rho = e^{-\beta H_0} / Z$, with β the inverse temperature and Z the partition function. The laser operator $\hat{V}_L = |e\rangle\langle g| + \text{h.c.}$ connects the ground state to an excited state.

The absorption spectrum can be obtained in a way that formally encapsulates the non-equilibrium evolution of the system after a quantum quench at $t = 0$ by excitation of a Rydberg impurity,

$$\mathcal{A}(\nu) = 2 \text{Re} \int_0^\infty dt e^{i\nu t} S(t). \quad (54.17)$$

The many-body overlap, also called Loschmidt echo, is

$$S(t) = \text{tr}[e^{i\hat{H}_0 t} e^{-i\hat{H} t} \hat{\rho}], \quad (54.18)$$

where $\hat{\rho}$ represents the density matrix of the initial state; \hat{H}_0 is the Hamiltonian without the excitation. At $T = 0$, this density matrix is simply written as $\hat{\rho} = |\Psi_0\rangle\langle\Psi_0|$, where $|\Psi_0\rangle$ is the Fock state of the macroscopic occupation of bosons, $|\Psi_0\rangle = \frac{1}{\sqrt{N!}} (a_0^\dagger)^N |\text{vac}\rangle$, with N the particle number [48].

The Rydberg spectrum exhibiting the oligomeric molecule formation can be obtained from the Fourier transform of the above equation,

$$A(\omega) = 2 \text{Re} \int_0^\infty dt e^{i\omega t} S(t). \quad (54.19)$$

The full description of solving the overlap integral, known also as the Loschmidt echo, is given in [52]. The Loschmidt echo bears resemblance to the autocorrelation function in wave packet dynamics but for the application of interacting and noninteracting Hamiltonians.

An spectrum obtained from a Rydberg excitation in a Sr BEC (Sr(5s38s) excitation) is shown in Fig. 54.5, illustrating in intricate detail the formation of ground and excited vibrational dimers (D_i), trimers (T_{ik}), tetramers (T_{ijk}), pentamers (P_{ijklm}), . . . levels. At still higher quantum excitation and higher gas density, where the average number of gas atoms that fit into a Rydberg orbit approaches macroscopic numbers, a new phenomenon emerges, the so-called Bose polaron [48, 52]. Such Rydberg Bose polarons are characterized by localized states with discrete negative energies, which are bound to the Rydberg impurity. They can be contrasted to the usual Bose polarons in condensed matter systems that are dressed by the continuum phonon modes. The broad spectral tails, which match the Gaussian profile expected of polarons, progressively narrow with increasing local density, and have an n^{-3} analytical scaling with the Rydberg principal quantum number [49, 52].

In a degenerate Fermi gas, a Rydberg excitation leads to the formation of dimer Rydberg molecules, as with excitations in a Bose gas. However, fermions obey the Dirac–Fermi statistics, and unlike bosons, which can macroscopically occupy one quantum state, say the ground rovibrational state in the outer well in Fig. 54.3, spin-polarized fermions will occupy successively excited rotational levels, up to the Fermi energy. In addition, the nonlocal correlations in the fermionic wave function ensure that molecular reactivity beyond dimer formation is suppressed, i.e., formation of fermionic trimers, tetramers, etc., is greatly inhibited. This is termed Pauli-enforced rotational blockade [54]. In the high-density limit, the Fermi Rydberg polarons form, but their spectral width is narrowed due to Fermi compression [54].

The interaction of a Rydberg atom with a ground state atom is at the core of atomic physics. At extreme low kinetic energies, this interaction takes a deceptively simple form, e.g., the Fermi contact interaction, which allows for unique binding mechanisms, few-body and nonperturbative many-body states, and correlations. New vistas into several topical condensed matter problems, the Kondo singlet, the Bose polaron, and the central spin problems, are opening, aided by the low-energy electron scattering in quantum gases [55].

Just as magnetic tuning of the atom–atom scattering length [15] has tremendously advanced tailoring of interactions at will, it may become possible to also control the electron–atom scattering length in the near future.

Acknowledgments H.R.S. acknowledges support through an NSF grant to ITAMP at Harvard University and the Smithsonian Astrophysical Observatory.

References

- Amaldi, E., Segre, E.: Effetto della pressione sui termini elevati degli alcalini. *Il Nuovo Cimento* (1924–1942) **11**(3), 145–156 (1934)
- Fermi, E.: Sopra lo spostamento per pressione delle righe elevate delle serie spettrali. *Il Nuovo Cimento* (1924–1942) **11**(3), 157–166 (1934)
- Cohen, M.L.: The Fermi atomic pseudopotential. *Am. J. Phys.* **52**(8), 695–703 (1984)
- Blatt, J.M., Jackson, J.D.: On the Interpretation of Neutron-Proton Scattering Data by the Schwinger Variational Method. *Phys. Rev.* **76**, 18–37 (1949)
- Bethe, H.A.: Theory of the Effective Range in Nuclear Scattering. *Phys. Rev.* **76**, 38–50 (1949)
- Weiner, J., Vanderlei, S.: Experiments and theory in cold and ultracold collisions. *Rev. Mod. Phys.* **71**, 1–85 (1999)
- Marinescu, M., Sadeghpour, H.R., Dalgarno, A.: Dispersion coefficients for alkali-metal dimers. *Phys. Rev. A* **49**, 982–988 (1994)
- Spruch, L., O'Malley, T.F., Rosenberg, L.: Modification of Effective-Range Theory in the Presence of a Long-Range Potential. *Phys. Rev. Lett.* **5**, 375–377 (1960)
- Ilya I Fabrikant: Long-range effects in electron scattering by polar molecules. *J. Phys. B: At. Mol. Opt. Phys.* **49**(22), 222005 (2016)
- Gao, B.: Quantum-defect theory of atomic collisions and molecular vibration spectra. *Phys. Rev. A* **58**, 4222–4225 (1998)
- Gao, B.: Universal properties of Bose systems with van der Waals interaction. *J. Phys. B: At. Mol. Opt. Phys.* **37**(11), L227–L233 (2004)
- Gao, B.: Quantum-defect theory for $-1/r^4$ -type interactions. *Phys. Rev. A* **88**, 022701 (2013)
- Lee, T.D., Yang, C.N.: Low-Temperature Behavior of a Dilute Bose System of Hard Spheres. I. Equilibrium Properties. *Phys. Rev.* **112**, 1419–1429 (1958)
- Chin, C., Grimm, R., Julienne, P., Tiesinga, E.: Feshbach resonances in ultracold gases. *Rev. Mod. Phys.* **82**, 1225–1286 (2010)
- Jones, K.M., Tiesinga, E., Lett, P.D., Julienne, P.S.: Ultracold photoassociation spectroscopy: Long-range molecules and atomic scattering. *Rev. Mod. Phys.* **78**, 483–535 (2006)
- Balling, L.C.: Sodium-Electron Spin-Exchange Collisions. *Phys. Rev.* **151**, 1–6 (1966)
- Norcross, D.W.: Low energy elastic scattering of electrons by Li and Na. *J. Phys. B: At. Mol. Phys.* **4**(11), 1458–1475 (1971)
- Bahrim, C., Thumm, U.: Low-lying $^3P^o$ and $^3S^e$ states of Rb^- , Cs^- , and Fr^- . *Phys. Rev. A* **61**, 022722 (2000)
- Bahrim, C., Thumm, U., Fabrikant, I.I.: 3S_e and 1S_e scattering lengths for $e^- + \text{Rb}$, Cs and Fr collisions. *J. Phys. B* **34**(6), L195 (2001)
- Bahrim, C., Thumm, U.: Angle-differential and momentum-transfer cross sections for $e^- + \text{Rb}$, Cs , and Fr collisions at low energies: $^3F^o$ shape resonances in Rb^- , Cs^- , and Fr^- ions. *Phys. Rev. A* **64**, 022716 (2001)
- Bahrim, C., Thumm, U., Fabrikant, I.I.: Negative-ion resonances in cross sections for slow-electron–heavy-alkali-metal-atom scattering. *Phys. Rev. A* **63**, 042710 (2001)
- Khuskivadze, A.A., Chibisov, M.I., Fabrikant, I.I.: Adiabatic energy levels and electric dipole moments of Rydberg states of Rb_2 and Cs_2 dimers. *Phys. Rev. A* **66**, 042709 (2002)
- Uwe Thumm: (private communication)
- Scheer, M., Thøgersen, J., Bilodeau, R.C., Brodie, C.A., Haugen, H.K., Andersen, H.H., Kristensen, P., Andersen, T.: Experimental Evidence that the $6s6p^3P_J$ States of Cs^- Are Shape Resonances. *Phys. Rev. Lett.* **80**, 684–687 (1998)
- Markson, S., Rittenhouse, S.T., Schmidt, R., Shaffer, J.P., Sadeghpour, H.R.: Theory of Ultralong-Range Rydberg Molecule Formation Incorporating Spin-Dependent Relativistic Effects: $\text{Cs}(6s)\text{-Cs}(np)$ as Case Study. *Chemphyschem* **17**(22), 3683–3691 (2016)
- Greene, C.H., Dickinson, A.S., Sadeghpour, H.R.: Creation of Polar and Nonpolar Ultra-Long-Range Rydberg Molecules. *Phys. Rev. Lett.* **85**, 2458–2461 (2000)
- Yiannopoulou, A., Jeung, G.-H., Park, S.J., Lee, H.S., Lee, Y.S.: Undulations of the potential-energy curves for highly excited electronic states in diatomic molecules related to the atomic orbital undulations. *Phys. Rev. A* **59**, 1178–1186 (1999)
- Niemax, K.: Satellites of CsI lines. *Phys. Lett. A* **38**(3), 141–142 (1972)
- Greene, C.H., Hamilton, E.L., Crowell, H., Vadla, C., Niemax, K.: Experimental Verification of Minima in Excited Long-Range Rydberg States of Rb_2 . *Phys. Rev. Lett.* **97**, 233002 (2006)
- Bendkowsky, V., Butscher, B., Nipper, J., Shaffer, J.P., Löw, R., Pfau, T.: Observation of ultralong-range Rydberg molecules. *Nature* **458**(7241), 1005–1008 (2009)
- Tallant, J., Rittenhouse, S.T., Booth, D., Sadeghpour, H.R., Shaffer, J.P.: Observation of Blueshifted Ultralong-Range Cs_2 Rydberg Molecules. *Phys. Rev. Lett.* **109**, 173202 (2012)
- Booth, D., Rittenhouse, S.T., Yang, J., Sadeghpour, H.R., Shaffer, J.P.: Production of trilobite Rydberg molecule dimers with kilodebye permanent electric dipole moments. *Science* **348**(6230), 99–102 (2015)
- Bellos, M.A., Carollo, R., Banerjee, J., Eyler, E.E., Gould, P.L., Stwalley, W.C.: Excitation of Weakly Bound Molecules to Trilobite Rydberg States. *Phys. Rev. Lett.* **111**, 053001 (2013)
- Anderson, D.A., Miller, S.A., Raitchel, G.: Photoassociation of Long-Range nD Rydberg Molecules. *Phys. Rev. Lett.* **112**, 163201 (2014)
- Krupp, A.T., Gaj, A., Balewski, J.B., Ilzhöfer, P., Hofferberth, S., Löw, R., Pfau, T., Kurz, M., Schmelcher, P.: Alignment of D -State Rydberg Molecules. *Phys. Rev. Lett.* **112**, 143008 (2014)
- Saßmannshausen, H., Merkt, F., Deiglmayr, J.: Experimental Characterization of Singlet Scattering Channels in Long-Range Rydberg Molecules. *Phys. Rev. Lett.* **114**, 133201 (2015)
- Niederprüm, T., Thomas, O., Eichert, T., Lippe, C., Pérez-Ríos, J., Greene, C.H., Ott, H.: Observation of pendular butterfly Rydberg molecules. *Nat Commun* **7**, 12820 (2016)
- DeSalvo, B.J., Aman, J.A., Dunning, F.B., Killian, T.C., Sadeghpour, H.R., Yoshida, S., Burgdörfer, J.: Ultra-long-range Rydberg molecules in a divalent atomic system. *Phys. Rev. A* **92**, 031403 (2015)
- Omont, A.: On the theory of collisions of atoms in Rydberg states with neutral particles. *J. De Phys.* **38**(11), 1343–1359 (1977)
- Sadeghpour, H.R., Rittenhouse, S.T.: How do ultralong-range homonuclear Rydberg molecules get their permanent dipole moments? *Mol. Phys.* **111**(12–13), 1902–1907 (2013)

41. Hamilton, E.L., Greene, C.H., Sadeghpour, H.R.: Shape-resonance-induced long-range molecular Rydberg states. *J. Phys. B* **35**(10), L199 (2002)
42. Butscher, B., Bendkowsky, V., Nipper, J., Balewski, J.B., Kukota, L., Löw, R., Pfau, T., Li, W., Pohl, T., Rost, J.M.: Lifetimes of ultralong-range Rydberg molecules in vibrational ground and excited states. *J. Phys. B* **44**(18), 184004 (2011)
43. Schlagmüller, M., Liebisch, T.C., Nguyen, H., Lothead, G., Engel, F., Böttcher, F., Westphal, K.M., Kleinbach, K.S., Löw, R., Hofferberth, S., Pfau, T., Pérez-Ríos, J., Greene, C.H.: Probing an Electron Scattering Resonance using Rydberg Molecules within a Dense and Ultracold Gas. *Phys. Rev. Lett.* **116**, 053001 (2016)
44. Schlagmüller, M., Liebisch, T.C., Engel, F., Kleinbach, K.S., Böttcher, F., Hermann, U., Westphal, K.M., Gaj, A., Löw, R., Hofferberth, S., Pfau, T., Pérez-Ríos, J., Greene, C.H.: Ultracold Chemical Reactions of a Single Rydberg Atom in a Dense Gas. *Phys. Rev. X* **6**, 031020 (2016)
45. Kirrander, A., Rittenhouse, S.T., Ascoli, M., Eyler, E.E., Gould, P.L., Sadeghpour, H.R.: Approach to form long-range ion-pair molecules in an ultracold Rb gas. *Phys. Rev. A* **87**, 031402 (2013)
46. Hummel, F., Schmelcher, P., Ott, H., Sadeghpour, H.R.: An ultracold heavy Rydberg system formed from ultra-long-range molecules bound in a stairwell potential. *New J. Phys.* **22**(6), 063060 (2020)
47. Bendkowsky, V., Butscher, B., Nipper, J., Balewski, J.B., Shaffer, J.P., Löw, R., Pfau, T., Li, W., Stanojevic, J., Pohl, T., Rost, J.M.: Rydberg trimers and excited dimers bound by internal quantum reflection. *Phys. Rev. Lett.* **105**, 163201 (2010)
48. Schmidt, R., Sadeghpour, H.R., Demler, E.: Mesoscopic Rydberg Impurity in an Atomic Quantum Gas. *Phys. Rev. Lett.* **116**, 105302 (2016)
49. Camargo, F., Schmidt, R., Whalen, J.D., Ding, R., Woehl, G., Yoshida, S., Burgdörfer, J., Dunning, F.B., Sadeghpour, H.R., Demler, E., Killian, T.C.: Creation of Rydberg Polarons in a Bose Gas. *Phys. Rev. Lett.* **120**, 083401 (2018)
50. Fey, C., Yang, J., Rittenhouse, S.T., Munkes, F., Baluktian, M., Schmelcher, P., Sadeghpour, H.R., Shaffer, J.P.: Effective Three-Body Interactions in Cs(6s)—Cs(nd) Rydberg Trimers. *Phys. Rev. Lett.* **122**, 103001 (2019)
51. Gaj, A., Krupp, A.T., Balewski, J.B., Löw, R., Hofferberth, S., Pfau, T.: From molecular spectra to a density shift in dense Rydberg gases. *Nat Commun* **5**, 4546 (2014)
52. Schmidt, R., Whalen, J.D., Ding, R., Camargo, F., Woehl, G., Yoshida, S., Burgdörfer, J., Dunning, F.B., Demler, E., Sadeghpour, H.R., Killian, T.C.: Theory of excitation of Rydberg polarons in an atomic quantum gas. *Phys. Rev. A* **97**, 022707 (2018)
53. Tempere, J., Casteels, W., Oberthaler, M.K., Knoop, S., Timmermans, E., Devreese, J.T.: Feynman path-integral treatment of the BEC-impurity polaron. *Phys. Rev. B* **80**, 184504 (2009)
54. John Sous, H. R. Sadeghpour, T. C. Killian, Eugene Demler, Richard Schmidt: Rydberg impurity in a Fermi gas: Quantum statistics and rotational blockade, arXiv e-prints, arXiv:1907.07685 (Jul 2019)
55. Ashida, Y., Shi, T., Schmidt, R., Sadeghpour, H.R., Cirac, J.I., Demler, E.: Quantum Rydberg Central Spin Model. *Phys. Rev. Lett.* **123**, 183001 (2019)




Hossein Sadeghpour Hossein Sadeghpour is currently Director of the Institute for Theoretical Atomic and Molecular Physics (ITAMP) at Harvard University in Cambridge, MA. His current research focus is on quantum many-body processes involving Rydberg impurities and Rydberg interactions, mitigating surface noise effects in cold ion traps, and cluster formation in atmospheric haze and exoplanetary systems.



Ion–Atom Charge Transfer Reactions at Low Energies

55

Bernard Zygelman , Phillip C. Stancil, Muriel Gargaud, and Ronald McCarroll

Contents

55.1	Classical and Semiclassical Treatments	806
55.1.1	Over the Barrier Models	806
55.1.2	Langevin Orbiting	806
55.1.3	Landau–Zener–Rosen Theories	807
55.2	The Molecular Orbital Approach	808
55.2.1	A Gauge Theoretic Framework for the PSS Equations	809
55.3	Cold and Ultracold Charge Exchange and Association	810
55.4	New Developments and Future Prospects	811
	References	811

Keywords

Landau–Zener–Rosen · Langevin orbiting · molecular-orbital-close-coupling (MOCC) · radiative charge transfer · radiative association · gauge potentials · adiabatic approximation · PSS approximations · diabatic picture

Abstract

In this chapter, we review the over-the-barrier, Langevin-orbiting, Landau–Zener–Rosen, and molecular orbital close-coupling (MOCC), models used in calculations for low-energy ion–atom charge transfer reactions in which both the incident and exit configurations include at least one positively charged ion. We summarize theoretical descriptions for both radiative and nonradiative charge transfer processes.

Introduction

Consider a positively charged ion that slowly approaches a neutral atom. As the distance of approach R becomes comparable to the size of the atom, a tug of war ensues and, at a critical value of R , there is a finite probability that one, or more, electrons escape from the atom and attach to the interloper. In other words, a charge transfer reaction has occurred. We distinguish two classes: endoergic and exothermic reactions. In the first, the binding energy of the electron on the ion is less than that of the atom. Energy conservation requires that a portion of the kinetic energy of the approaching ion supplies the extra energy. However, for slow approaches in which an ion kinetic energy surplus is not available, charge transfer can only occur if the final electron binding energy is greater than or equal to its binding energy on the atom. If it is equal, the reaction is called resonant charge transfer; if not, a reaction proceeds either with the emission of a photon, radiation-less charge transfer, or both. The latter belong to the exothermic class of reactions. If radiation is emitted, we call the reaction radiative charge transfer/association and, if not, direct charge transfer.

Charge exchange reactions play an essential role in a diverse range of environments. They are an efficient generator of X-rays in astrophysical processes, and fuel X-ray sources in cometary and planetary atmospheres, the heliosphere, stars, and the interstellar medium [1]. Spectroscopy of atomic spectral lines, arising from ion–atom collisions, is a valuable diagnostic probe of those environments [2].

B. Zygelman (✉)
Dept. of Physics & Astronomy, University of Nevada, Las Vegas
Las Vegas, NV, USA
e-mail: bernard@physics.unlv.edu

P. C. Stancil (✉)
Dept. of Physics & Astronomy, The University of Georgia
Athens, GA, USA
e-mail: pstancil@uga.edu

M. Gargaud
Observatoire Aquitain des Sciences de l'Univers
Floirac, France
e-mail: gargaud@obs.u-bordeaux1.fr

R. McCarroll
Laboratoire de Chimie Physique, Université Pierre et Marie Curie
Paris, France
e-mail: mccarrol@ccr.jussieu.fr

Charge transfer reaction rates are essential ingredients for the accurate modeling of low-temperature edge plasmas in laboratory fusion devices [3]. The latter enables diagnostic capabilities in studies of the physical evolution and life cycle of laboratory plasmas.

We use atomic units throughout the discussion.

55.1 Classical and Semiclassical Treatments

55.1.1 Over the Barrier Models

The classical “over the barrier” model (COB) [4, 5] offers a simple qualitative understanding of the charge transfer mechanism when the kinetic energy of the collision partners can be ignored. Figure 55.1 provides a plot of the function

$$V(x) = -q/x - 1/|R - x|, \quad (55.1)$$

where x is the distance of a bound electron from the projectile; R is the distance between the two positive charges, and q is the charge of the ion. At its local maximum, the potential has the value

$$V_{\max} = -(\sqrt{q} + 1)^2/R, \quad (55.2)$$

and the electron attaches to the projectile if its binding energy, perturbed by the electron–ion Coulomb energy $-1/2 - q/R$, becomes greater than V_{\max} . Also, assuming that the binding energy of the electron at the projectile site is given by $E_n = -q^2/2n^2$, where n denotes a principal quantum number, energy conservation requires that

$$-1/2 - q/R = E_n - 1/R. \quad (55.3)$$

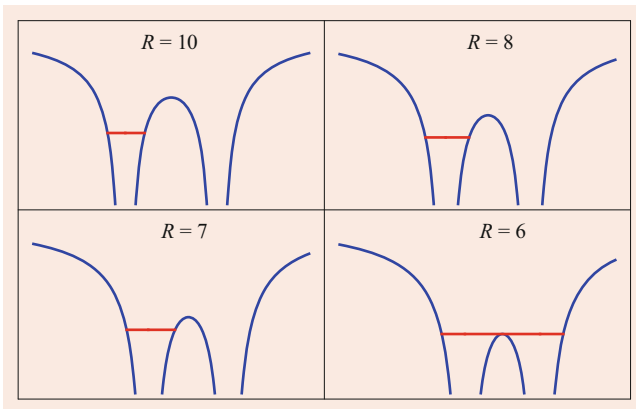


Fig. 55.1 Plot of potential (55.1) as function of the ion–electron distance x . Panels from upper left to lower right illustrate how the bound state energy of the electron, shown by the solid red line, varies as a function of the internuclear distance R . The charge transfer is precipitated when that energy surmounts the local barrier as shown in the right-most lower panel

Together these relations predict [5]

$$R_n = \frac{2(q-1)}{q^2/n^2 - 1}, \quad (55.4)$$

for the largest value of the internuclear distance in which an electron is transferred to the projectile with binding energy E_n . Assuming a transfer probability of 1/2, for projectile impact parameters $\leq R_n$, the COB model predicts a total charge transfer cross section [5]

$$\sigma_{CT} = \frac{\pi}{2} R_{n^*}^2, \quad (55.5)$$

where n^* is the value of n in Eq. (55.4) in which the equality holds. Comparison of prediction in Eq. (55.5) with experimental data for collisions of ions with charges $q = 3, 4, 5$ shows a fair qualitative agreement in the collision energy range $1 < k^2 < 6$ keV/amu [5]. In this notation, the relative kinetic energy of the approaching fragments is given by $E = k^2/2\mu$, where μ is the reduced mass of the system.

55.1.2 Langevin Orbiting

At very low collision energies, on the order of $k^2 < 0.1$ keV/amu, the COB picture fails in predicting the correct $1/v$, where v is the relative velocity of the collision partners, behavior observed in experimental studies [6]. That behavior was first predicted in a classical orbiting theory, the Langevin model [7], after P. Langevin who pioneered the study of ionized gases. In the Langevin picture, the approach of the ion induces, via polarization of the electron cloud, an energy shift of the ground state s-wave electron given by [8]

$$\Delta E = -\frac{1}{2}\alpha|\mathbf{E}|^2. \quad (55.6)$$

Here, α is called the polarizability of the atom [9] and $|\mathbf{E}| = q/R^2$ is the magnitude of the electric field impressed on the electron by the projectile. The collision partners follow a trajectory governed by this mutual attractive force or potential

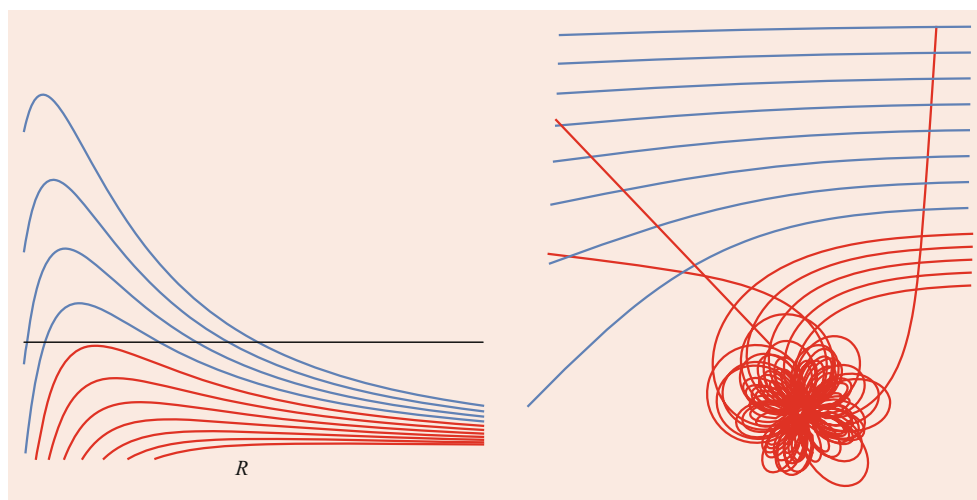
$$V_{\text{pol}} = -\frac{C_4}{R^4} \quad C_4 = \frac{\alpha}{2}q^2, \quad (55.7)$$

in addition to a centripetal effect described by an effective potential

$$V_L = \frac{L(L+1)}{2\mu R^2}; \quad (55.8)$$

$L = \mu v b$ is an angular momentum and b is an impact parameter. For a given b , the effective potential, the sum of Eqs. (55.7) and (55.8) possesses a local maximum $V_{\max}(b)$ at

Fig. 55.2 Trajectories displaying Langevin orbiting. The panel on left is a plot of the effective potential, as a function of R , for various impact parameters. The red lines correspond to impact parameters below the critical value b_c , obtained by equating $V_{\max}(b)$ with the total kinetic energy shown by the solid black line. The panel on the right illustrates classical trajectories for the corresponding impact parameters



a critical value R_c . The first panel in Fig. 55.2 depicts the effective potentials for various values of b as a function of the internuclear distance. The location and values for V_{\max} depend on the impact parameter. At a given collision energy E , all impact parameters in which $V_{\max} > E$ beget the trajectories shown in blue on the right panel of Fig. 55.2. For values of b in which $E < V_{\max}$, the collision partners overcome the repulsive barrier and engage in orbiting before returning to their asymptotic trajectories. The latter are shown in red in the second panel of that figure. Orbiting provides ample opportunity for the electron, being in close proximity to the ion, to “jump ship” and precipitate a charge transfer reaction. Solving for the impact parameter b_c for which that equality is satisfied, gives

$$b_c = \frac{1}{\sqrt{v}} \left(\frac{8C_4}{\mu} \right)^{1/4}. \quad (55.9)$$

Assuming a 100% charge transfer probability for all impact parameters $< b_c$,

$$\begin{aligned} \sigma_{CT} &= 2\pi \int_0^{b_c} db b \\ &= \pi b_c^2 = \frac{\pi}{v} \sqrt{\frac{8C_4}{\mu}} = \frac{2\pi q}{v} \sqrt{\frac{\alpha}{\mu}}. \end{aligned} \quad (55.10)$$

55.1.3 Landau–Zener–Rosen Theories

Classical descriptions invoke gross simplifying assumptions and lack quantum features observed in the laboratory. In a more nuanced analysis, for the case where the collisions partners approach slowly, it is convenient to assume adiabatic evolution. In that description, for a given nuclear separation, electrons equilibrate to an energy eigenstate of the electronic

Hamiltonian

$$\begin{aligned} H(\mathbf{R}_j, \mathbf{r}_i) &= - \sum_i \frac{1}{2} \nabla_i^2 \\ &\quad - \sum_i \sum_{j=1,2} \frac{q_j}{|\mathbf{R}_j - \mathbf{r}_i|} + \sum_{i < k} \frac{1}{|\mathbf{r}_i - \mathbf{r}_k|}. \end{aligned} \quad (55.11)$$

Here, \mathbf{R}_j are coordinates for the nuclei of charge q_j , and \mathbf{r}_i are the electronic coordinates. Factoring out the center of mass, and ignoring small isotopic couplings, the eigenstates of Eq. (55.11) are typically written in the form $\phi_n(\mathbf{r}, \mathbf{R})$, where \mathbf{r} is a collective coordinate for the electrons and \mathbf{R} a parameter that denotes the vector joining the two nuclei. The energy eigenstates $E_n(R)$ corresponding to these eigenstates are functions of the distance $R \equiv |\mathbf{R}|$. In an ion–atom collision scenario it is useful to focus on the pair of eigenstates whose asymptotic limits describe the pre and postcollision ion–atom configurations. For example, in the collision of a projectile A^{q+} on a neutral atom B in its ($1s$) ground state, we invoke the correlation rule

$$\begin{aligned} \phi_2(\mathbf{r}, \mathbf{R}) &\rightarrow A^{q+} + B(1s) \\ \phi_1(\mathbf{r}, \mathbf{R}) &\rightarrow A^{(q-1)+} + B^+. \end{aligned} \quad (55.12)$$

In Eq. (55.12), the arrow suggests that eigenstates ϕ_i approach, as $R \rightarrow \infty$, direct product eigenstates of the separated ion/atom configurations as shown in Fig. 55.3, which illustrates the electronic energy eigenvalues $E_n(R)$ for the states itemized in Eq. (55.12). Note that at a critical value of the internuclear distance R_c , the pair of curves share an avoided crossing, i.e., the energy defect $\Delta E = E_2(R) - E_1(R)$ has a local minimum at R_c . In a semiclassical description, the system evolves adiabatically on the potential surface that correlates asymptotically to the initial ion–atom configuration. As it reaches R_c , for a given impact parameter,

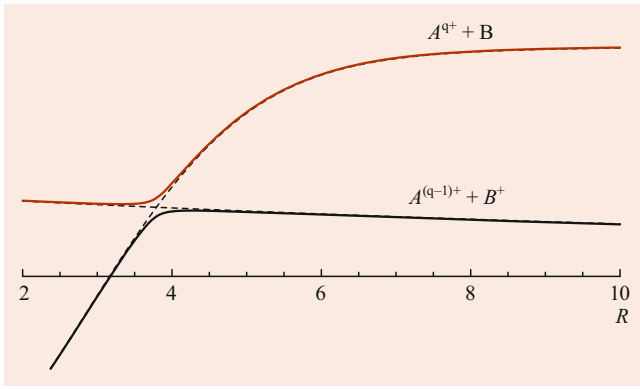


Fig. 55.3 An avoided crossing among Born–Oppenheimer energies. The *dashed lines* correspond to the diabatic couplings $V_{11}(R)$, $V_{22}(R)$ defined in Eq. (55.14)

there is a finite probability [4]

$$P(b) = \exp(-2\pi \Gamma)$$

$$\Gamma = \frac{V_{12}^2(R_c)}{|V'_{11}(R_c) - V'_{22}(R_c)| v_c} \quad (55.13)$$

of a transition to the neighboring electronic state. In Eq. (55.12) v_c , is the relative velocity of the collision partners at the crossing distance R_c , and $V_{11}(R)$, $V_{22}(R)$ are the, so-called, diabatic energy curves shown by the dashed lines in Fig. 55.3. They are related to the eigenvalues $E_1(R)$, $E_2(R)$ via

$$V_{11}(R) = E_1(R) \cos^2(\Omega(R)) + E_2(R) \sin^2(\Omega(R)) ,$$

$$V_{22}(R) = E_1(R) \sin^2(\Omega(R)) + E_2(R) \cos^2(\Omega(R)) , \quad (55.14)$$

where

$$\Omega(R) = -i \int^R A(R') dR' ,$$

$$A(R) \equiv i \langle \phi_1 | d/dR | \phi_2 \rangle , \quad (55.15)$$

and the $\langle | \rangle$ notation implies integration over all electronic coordinates. The diabatic coupling matrix element is

$$V_{12} = \frac{E_2(R) - E_1(R)}{2} \sin(2\Omega(R)) . \quad (55.16)$$

Summing the transition probabilities over all impact parameters one obtains [4] an expression for the total charge transfer cross section

$$\sigma_{CT} = 4\pi \int_0^{R_c} P(b)(1 - P(b)) b db . \quad (55.17)$$

In deriving expression in Eq. (55.17) we allowed for the possibility that the system traverses the crossing distance R_c twice. Once during the initial approach and again in the exit channel.

The Landau–Zener model provides fair estimates of charge transfer cross sections in the collision of ion projectiles C^{3+} , O^{2+} , O^{3+} , Ne^{3+} with atomic hydrogen at low energies [10]. Those estimates arrive at the correct order of magnitude, when compared to the results of more accurate fully quantal methods [2, 10].

Not all direct charge transfer reactions are precipitated by an avoided crossing. For example, in the $He^+ + Ne$ [11] collision system, the coupling term $A(R)$ is not localized near a crossing. Instead, its influence persists over a wide range of internuclear distances in which the pair of potential surfaces has a nearly constant energy defect. In that case, the Rosen–Zener–Demkov [12, 13] model is relevant. In that theory, one assumes that the diabatic coupling has the form $V_{12}(R) = V_0 \exp(-\lambda R)$, and a transition occurs at R_c , for which, $V_{12}(R_c) = 1/2 \Delta E(R_c)$, where ΔE is the energy defect between the two potential surfaces. An expression for the cross sections of the latter is given by

$$\sigma_{CT} = 2\pi \int_0^{R_c} b P(b) db$$

$$P(b) = \frac{1}{2} \operatorname{sech}^2 \left(\frac{\pi \Delta E(R_c)}{2 \lambda v(b)} \right) . \quad (55.18)$$

In the collision energy range $27.2 \text{ eV} < E < 8.2 \text{ keV}$, the predictions based on this model are in good agreement with the results of a fully quantal calculation [11], as well as with laboratory measurements [14].

55.2 The Molecular Orbital Approach

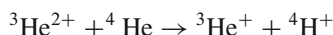
In the molecular orbital close-coupling (MOCC) approach, the total system amplitude is expressed as a sum of electronic eigenstates, whose expansion coefficients describe the motion of the nuclear coordinate \mathbf{R} . There are two versions of this theory. In the first, the nuclear motion is treated classically, but the electronic degrees of freedom are treated quantum mechanically. This approach, the method of perturbed stationary states (PSS), was first advocated by Massey and Smith in 1932 [15]. A quantum version of the PSS method was developed by David Bates and co-workers in the 1950s. But it was not until the 1980s, with the advent and availability of powerful supercomputers and vector machines, that the fully quantum MOCC calculations [10, 16, 17] became commonplace.

The quantum mechanical theory of resonant charge transfer [18] offers a compelling example of the predictive power

of the MOCC approach. In it, the charge cross section is given by the expression

$$\sigma_{CT} = \frac{\pi}{k^2} \sum_l (2l+1) \sin^2(\delta_1(l) - \delta_2(l)), \quad (55.19)$$

where $\delta_i(l)$ is the phase shift of the l -th partial wave of the scattering amplitude that evolves on the molecular potential surface that correlates to the i -th fragment. This expression is sensitive to the values of the adiabatic molecular potentials and is a stringent test of the molecular orbital paradigm. The results of laboratory measurements [19] for the near resonant charge transfer reaction



rate coefficients corresponding to collision energies below 1 eV, compare favorably with the results of calculations using the molecular elastic scattering expression (55.19).

55.2.1 A Gauge Theoretic Framework for the PSS Equations

In a fully quantal description of the PSS equations, the total (excluding the center of mass motion) system amplitude by an MOCC expansion

$$\psi(\mathbf{R}, \mathbf{r}) = \sum_n^N \phi_n(\mathbf{R}, \mathbf{r}) F_n(\mathbf{R}). \quad (55.20)$$

Here, $F_n(\mathbf{R})$ are quantal amplitudes that predict the probability for the system to occupy the n -th electronic states at \mathbf{R} . The index N is arbitrary but typically includes all states (channels) that are energetically open, i.e., if E is the collision energy, $E_N \leq E$. Of course, an unrestricted sum provides an exact description as the adiabatic states ϕ_n are complete for all \mathbf{R} , i.e.,

$$\sum_n \phi_n^\dagger(\mathbf{R}, \mathbf{r}) \phi_n(\mathbf{R}, \mathbf{r}') = \delta(\mathbf{r} - \mathbf{r}').$$

In practice, an exact description is not feasible. However, with a finite but sufficiently large value of N , the PSS equations are believed to provide an accurate description. Inserting the above expansion into the eigenvalue equation $(H - E)\psi = 0$, and projecting the latter onto the adiabatic basis vectors $|\phi_n\rangle$, we arrive at a set of coupled second-order partial differential equations

$$\begin{aligned} \nabla^2 F_i - 2i \sum_j^N (\nabla F_j) \cdot \mathbf{A}_{ij} - \sum_j^N B_{ij} F_j \\ - 2\mu \sum_j^N V_{ij} F_j + 2\mu E F_i = 0, \end{aligned} \quad (55.21)$$

where ∇ the nuclear gradient operator, and

$$\begin{aligned} \mathbf{A}_{ij}(\mathbf{R}) &\equiv i \langle \phi_i | \nabla | \phi_j \rangle \\ B_{ij}(\mathbf{R}) &\equiv -\langle \phi_i | \nabla \cdot \nabla | \phi_j \rangle \\ V_{ij}(R) &= \delta_{ij} E_j(R). \end{aligned} \quad (55.22)$$

Equation (55.21) is the quantal expression of the PSS equations and a starting point for all modern computational efforts; \mathbf{A}_{ij} are nonadiabatic matrix elements, B_{ij} constitute the Born-Huang-Dalgarno adiabatic corrections, and V_{ij} is the Born-Oppenheimer energy matrix of the system. With relation [11]

$$B_{ij} = \sum_k \mathbf{A}_{ik} \cdot \mathbf{A}_{kj} + i \nabla \cdot \mathbf{A}_{ij},$$

it is useful [11, 20] to rearrange Eq. (55.22) into the matrix form

$$-\frac{1}{2\mu} (\nabla - i\mathbf{A})^2 \underline{\mathbf{F}}(\mathbf{R}) + (\underline{\mathbf{V}}(\mathbf{R}) - E) \underline{\mathbf{F}}(\mathbf{R}) = 0, \quad (55.23)$$

where $\underline{\mathbf{F}}(\mathbf{R})$ is a column matrix whose entries are the amplitudes $F_i(\mathbf{R})$, and \mathbf{A} is an $N \times N$ matrix whose entries are the components defined in Eq. (55.22). The components of the scalar $N \times N$ matrix are given by [11]

$$\underline{\mathbf{V}}_{ij}(\mathbf{R}) = \delta_{ij} E_i(R) + \sum_{k \neq i,j} \mathbf{A}_{ik} \cdot \mathbf{A}_{kj}. \quad (55.24)$$

In the form of Eq. (55.23), the PSS equations manifest as a non-Abelian gauge theory [20, 21]. That is, the multichannel amplitude $\underline{\mathbf{F}}(\mathbf{R})$ is minimally coupled to vector \mathbf{A} and scalar $\underline{\mathbf{V}}$ gauge potentials, so that under the transformation $\underline{\mathbf{F}}(\mathbf{R}) \rightarrow \underline{\mathbf{U}}(\mathbf{R}) \underline{\mathbf{F}}(\mathbf{R})$, where $\underline{\mathbf{U}}$ is a unitary $N \times N$ matrix, the gauge potentials transform covariantly, i.e.,

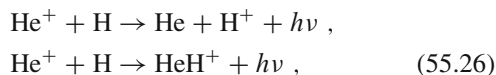
$$\begin{aligned} \mathbf{A}(\mathbf{R}) &\rightarrow U^{-1} \mathbf{A}(\mathbf{R}) U + i U^{-1} \nabla U \\ \underline{\mathbf{V}}(\mathbf{R}) &\rightarrow U^{-1} \underline{\mathbf{V}}(\mathbf{R}) U - i U^{-1} \partial U \partial t. \end{aligned} \quad (55.25)$$

There are several advantages in expressing the PSS equations as a gauge theory [20, 21]. Not least is the recognition [20, 22, 23] of the fact that once an adiabatic truncation of channel states is imposed, one cannot, in general, “transform away” the diagonal components of the vector gauge potential \mathbf{A} . The latter fact leads to the phenomenon of geometric magnetism [20, 24], also known as artificial or synthetic magnetism [25–27]. The standard PSS approach, in which the eigenfunctions of Hamiltonian Eq. (55.11) are employed has been modified to accommodate so-called translation factors [28]. The latter was first introduced into the classical version of the PSS paradigm [15] in order to allow for “traveling” orbitals. In the quantum version, translation factors

modify the nonadiabatic coupling matrix \mathbf{A} appearing in Eq. (55.23). They have been introduced in order to correct perceived anomalies, including fictitious origin-dependent and long-range couplings, in the standard MOCC expansion. However, other efforts [29–31] have argued for the fidelity of the standard PSS expansion.

55.3 Cold and Ultracold Charge Exchange and Association

In a study [17] of the direct charge transfer reaction $\text{He}^+ + \text{H} \rightarrow \text{He} + \text{H}^+$ at low collision energies, it was found that the competing processes



corresponding to radiative charge transfer and association, respectively, dominate direct charge transfer. At a collision energy of about 8 eV/amu the radiative and direct charge transfer cross sections are comparable. However, at lower collision energies the former exhibit Langevin behavior, whereas the latter cross sections are decreasing. Theories of radiative charge transfer [17, 32] exploit the fact that the coupling of radiation with matter is weak, thus allowing for a perturbative analysis. In the past decade or so, there has been renewed interest in understanding charge transfer at ultralow collision energies [33–35]. The development of hybrid ion traps [36, 37] has allowed researchers to explore this novel and uncharted energy regime. At ultralow collision energies, the speed associated with the approach of collision partners is typically on the order of a few mm or cm per second. In this regime, it is convenient to express the collision energy in terms of an effective temperature, so that $\mu v^2/2$ is proportional to $k_B T$, where k_B is the Boltzmann constant, and T is a temperature in units of Kelvin. At temperatures on the order of mK, centripetal repulsion prevents close ion–atom encounters, and so only a few partial waves contribute to the total cross section. In that limit, Langevin behavior, which requires the participation of many partial waves, is no longer effective. Instead, s-wave scattering dominates, and dynamics is dictated by Wigner threshold [8] behavior. For example, the s-wave cross section for association to a molecular ion, following charge transfer in an approach of an ion with a neutral atom, is given by the expression [35]

$$\sigma = \sum_n \frac{16\mu\pi\omega_n^3}{3c^3k} \left| \int_0^{R_0} dR \phi(R) D(R) \phi_{J=1}^n(R) \right|^2, \quad (55.27)$$

In Eq. (55.27), c is the speed of light, k the wavenumber corresponding to the kinetic energy of the initial approach, $\phi_{J=1}^n$

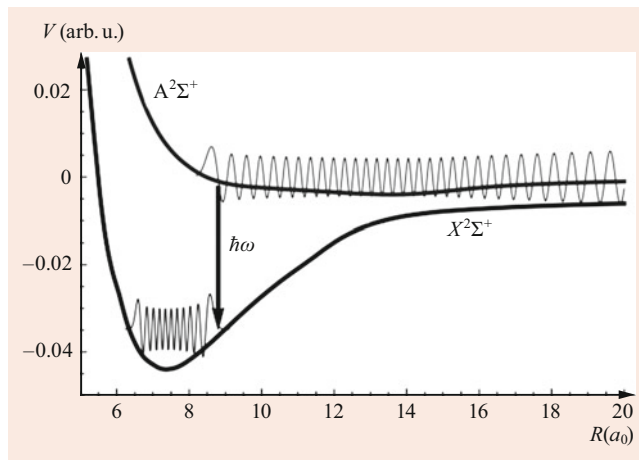
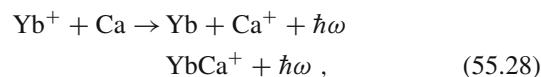


Fig. 55.4 Radiative association into the rovibrational levels in the $X^2\Sigma^+$ electronic state of the YbCa^+ ion, following initial approach in the $\text{Yb}^+ + \text{Ca}$ channel. A similar description (not shown) allows radiative decay in the continuum states of the YbCa^+ ion and corresponds to radiative charge transfer into the $\text{Yb} + \text{Ca}^+$ exit channel

are the $J = 1, n$, rovibrational states of the molecular ion, ω_n is the angular frequency of the photon emitted into the n -th rovibrational state, and $D(R)$ is a coupling element proportional to the transition dipole moment between the molecular states; $\phi(R)$ is the radial s-wave elastic scattering wavefunction normalized so that $d\phi(R)/dR|_{R_0} = 1$, and where R_0 is a sufficiently large internuclear distance in which $\phi(R)$ exhibits asymptotic behavior. In a study [35] of the radiative processes (see Fig. 55.4)



it was found that Langevin behavior persists to temperatures as low as a few micro-Kelvin. Below this threshold, s-wave scattering becomes more important. Figure 55.5 presents plots of the thermal average $\langle v\sigma \rangle$, or the rate constant, for the reaction in Eq. (55.28). Figure 55.5 shows a dramatic transition from Langevin behavior, in which the rate tends to a constant value, for temperatures above $\approx 10^{-6}$ K, to a rapid, isotope-dependent, variation in the rate. At ultralow temperatures, the rate again assumes a constant value, as predicted by expression Eq. (55.27), in which σ is a product of a constant with the $1/k$ kinematic factor. The large isotope dependence is explained by appealing to Wigner theory. In the latter, the s-wave S-matrix is expressed as the ratio of the Jost functions [38] for amplitude $\phi(R)$. If the system possesses a bound state near the zero-collision energy threshold, the denominator of that ratio exhibits a zero in the complex k -plane. That zero begets a singularity in the ratio of Jost functions and leads to a large enhancement factor [38]. In other words, the amplitude for $\phi(R)$ near its overlap with $\phi_{J=1}^n$ is large and leads to an enhanced value for the integral

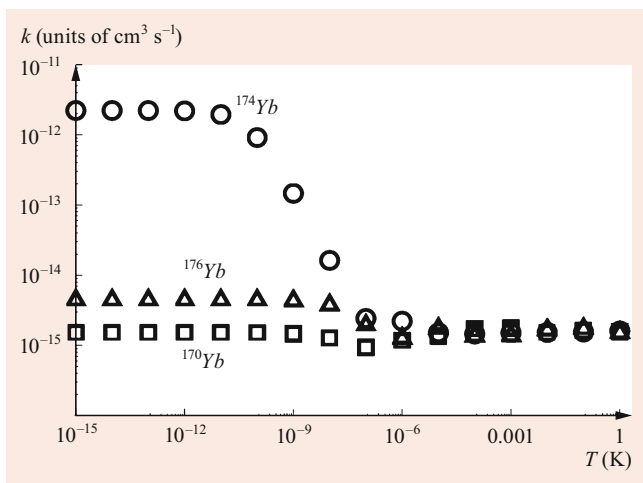


Fig. 55.5 Isotopic dependence of radiative association into the YbCa^+ molecular ion

in Eq. (55.27). As different isotopes possess bound states of differing energy defects from the zero energy threshold, the isotopic dependence of σ follows. A similar analysis holds for the radiative charge transfer reaction, although these reaction rates [35] are only a small fraction of the radiative association rates.

Other methods, such as the impression of external fields, pioneered in laboratory studies of ultracold neutral gases, can also be employed to adjust the energy defect of a bound state, or Feshbach-like resonances, in ion–atom systems. According to expression (55.27), this offers the possibility for external control of ion–atom reactions.

55.4 New Developments and Future Prospects

Even at the low collision energies of several milli-electron volts, corresponding to near room temperature, a typical charge transfer reaction involves the participation of hundreds of partial waves. Although quantum effects are important in this energy regime, it is still useful to adopt classical, or semiclassical, models to describe the latter. In order to flesh out quantum features, the de-Broglie wavelength corresponding to the ion–atom relative motion should be on the order of the distance of the closest approach for the colliding partners. In the related discipline of atom–atom collisions, this has been achieved due to laboratory advances in trapping and laser cooling of atoms. It has allowed researchers unprecedented access in investigations of collision phenomena in which quantum mechanics plays the leading role.

Several efforts, in the past decade or so, have been directed to probing ion–atom interactions where classical Langevin behavior breaks down and quantum effects dominate. Although there has been tremendous progress, using sympathetic cooling techniques, to reach the milli-Kelvin

regime [36, 37], access to nano-Kelvin temperatures has been hindered due to the strong coupling of the ion’s charge with the trapping potential. A novel, recent advance [39] promises to achieve the ultralow temperatures that are necessary to allow the conditions in which only a few partial waves participate in a charge transfer reaction. The ability to study partial wave-dependent charge transfer will provide stringent tests on theories that are based on the MOCC paradigm. In particular, such studies could assess the fidelity of theories that require the application of electronic translation factors.

References

- Dennerl, K.: Charge transfer reactions. *Space Sci. Rev.* **157**(1), 57–91 (2010)
- Dalgarno, A.: Charge transfer processes in astrophysical plasmas. *Nucl. Instruments Methods Phys. Res. B* **9**(4), 655–657 (1985)
- Janev, R.K.: *Atomic and Molecular Processes in Fusion Edge Plasmas*. Springer US, New York (2013)
- Bransden, B.H., McDowell, M.R.C.: *Charge Exchange and the Theory of Ion–Atom Collisions*. Oxford University Press, Oxford (1992)
- Ryufuku, H., Sasaki, K., Watanabe, T.: Oscillatory behavior of charge transfer cross sections as a function of the charge of projectiles in low-energy collisions. *Phys. Rev. A* **21**, 745–750 (1980)
- Havener, C.C., Huq, M.S., Krause, H.F., Schulz, P.A., Phaneuf, R.A.: Merged-beams measurements of electron-capture cross sections for $\text{O}^{5+} + \text{H}$ at electron-volt energies. *Phys. Rev. A* **39**, 1725–1740 (1989)
- Vogt, E., Wannier, G.H.: Scattering of ions by polarization forces. *Phys. Rev.* **95**, 1190 (1954)
- Sakurai, J.J., Napolitano, J.: *Modern Quantum Mechanics*, 2nd edn. Cambridge University Press, Cambridge (2017)
- Miller, T.M., Bederson, B.: Electric dipole polarizability measurements. In: Bates, D., Bederson, B. (eds.) *Advances in Atomic and Molecular Physics*, vol. 25, pp. 37–60. Academic Press, Boston (1989)
- Heil, T.G., Butler, S.E., Dalgarno, A.: Charge transfer of multiply charged ions at thermal energies. *Phys. Rev. A* **23**, 1100–1109 (1981)
- Zygelman, B., Dalgarno, A.: Direct charge transfer of He^+ in neon. *Phys. Rev. A* **33**, 3853–3858 (1986)
- Rosen, N., Zener, C.: Double Stern–Gerlach experiment and related collision phenomena. *Phys. Rev.* **40**, 502–507 (1932)
- Nikitin, E.E., Umanskii, S.Y.: *Theory of Slow Atomic Collisions*. Springer, Berlin (1984)
- Martinez, H., Cisneros, C., de Urquijo, J., Alvarez, I.: Absolute cross-section measurements of the direct charge transfer of He^+ in neon in the energy range 0.5–5 keV. *Phys. Rev. A* **38**, 5914–5916 (1988)
- Mott, N.F., Massey, H.S.W.: *The Theory of Atomic Collisions*, 3rd edn. Clarendon, Oxford, p 493 (1965)
- Gargaud, M., Hanssen, J., McCarroll, R., Valiron, P.: Charge exchange with multiply charged ions at low energies: application to the N^{3+}/H and C^{4+}/H systems. *J. Phys. B* **14**(13), 2259 (1981)
- Zygelman, B., Dalgarno, A., Kimura, M., Lane, N.F.: Radiative and nonradiative charge transfer in $\text{He}^+ + \text{H}$ collisions at low energy. *Phys. Rev. A* **40**, 2340–2345 (1989)
- Dalgarno, A., Yadav, H.N.: Electron Capture II: Resonance Capture from Hydrogen Atoms by Slow Protons. *Proc. Phys. Soc. A* **66**, 173–177 (1953)

19. Kyriakides, C., Clarke, B.S., O'Donnell, W.M., Zygelman, B., Kwong, V.H.S.: Resonant charge transfer of ${}^3\text{He}^{2+}$ with ${}^4\text{He}(1s^2)$ at energies below 1 eV. *J. Phys. B* **45**, 235701 (2012)
20. Zygelman, B.: Appearance of Gauge potentials in atomic collision physics. *Phys. Lett. A* **125**, 476 (1987)
21. Jackiw, R.: Berry's phase-topological ideas from atomic molecular and optical physics. *Comments At. Mol. Phys.* **21**, 71 (1988)
22. Mead, C.A., Truhlar, G.D.: On the determination of Born-Oppenheimer nuclear motion wave functions including complications due to conical intersections and identical nuclei. *J. Chem. Phys.* **70**(5), 2284–2296 (1979)
23. Moody, J., Shapere, A., Wilczek, F.: Realizations of magnetic-monopole gauge fields: Diatoms and spin precession. *Phys. Rev. Lett.* **56**(9), 893–896 (1986)
24. Berry, M.V.: The quantum phase, five years after. In: Shapere, A., Wilczek, F. (eds.) *Geometric Phases in Physics*, p. 1. World Scientific, Singapore (1989)
25. Dalibard, J., Gerbier, F., Juzeliūnas, G., Öhberg, P.: Colloquium: Artificial gauge potentials for neutral atoms. *Rev. Mod. Phys.* **83**, 1523–1543 (2011)
26. Goldman, N., Juzeliūnas, G., Öhberg, P., Spielman, I.B.: Light-induced gauge fields for ultracold atoms. *Rep. Prog. Phys.* **77**(12), 126401 (2014)
27. Zygelman, B.: Geometric gauge potentials and forces in low-dimensional scattering systems. *Phys. Rev. A* **86**(4), 042704 (2012)
28. Kimura, M., Lane, N.F.: The low-energy, heavy-particle collisions: A close coupling treatment. *Adv. At. Mol. Opt. Phys.* **26**, 80 (1989)
29. Matveenko, A.V., Ponomarev, L.N.: Method of Perturbed Stationary States. *Sov. J. Nucl. Phys.* **16**, 347 (1973)
30. Zygelman, B., Cooper, D.L., Ford, M.J., Dalgarno, A., Gerratt, J., Raimondi, M.: Charge transfer of N^{4+} with atomic hydrogen. *Phys. Rev. A* **46**(7), 3846–3854 (1992)
31. Zygelman, B.: Incorporating Electron Translation Effects, in Ion-Atom Collisions, Without Electron Translation Factors, Proceedings of XX ICPEAC Conference (Contributed Papers). Austria, Vienna (1997)
32. Cooper, D.L., Kirby, K., Dalgarno, A.: Radiative charge transfer and radiative association of helium ions with neon atoms. *Can. J. Phys.* **62**(12), 1622–1628 (1984)
33. Côté, R., Dalgarno, A.: Ultracold atom-ion collisions. *Phys. Rev. A* **62**(1), 012709 (2000)
34. Idziaszek, Z., Calarco, T., Julienne, P.S., Simoni, A.: Quantum theory of ultracold atom-ion collisions. *Phys. Rev. A* **79**, 010702 (2009)
35. Zygelman, B., Lucic, Z., Hudson, E.R.: Cold ion-atom chemistry driven by spontaneous radiative relaxation: a case study for the formation of the YbCa^+ molecular ion. *J. Phys. B* **47**(1), 015301 (2014)
36. Schmid, S., Härter, A., Denschlag, J.H.: Dynamics of a cold trapped ion in a Bose-Einstein condensate. *Phys. Rev. Lett.* **105**, 133202 (2010)
37. Hall, F.H.J., Eberle, P., Hegi, G., Raoult, M., Aymar, M., Dulieu, O., Willitsch, S.: Ion-neutral chemistry at ultralow energies: Dynamics of reactive collisions between laser-cooled Ca^+ ions and Rb atoms in an ion-atom hybrid trap. *Mol. Phys.* **111**, 2020–2032 (2013)
38. Schiff, L.I.: *Quantum Mechanics*, 3rd edn. McGraw-Hill, New York (1968)
39. Kleinbach, K.S., Engel, F., Dieterle, T., Löw, R., Pfau, T., Meinert, F.: Ionic impurity in a Bose-Einstein condensate at submicrokelvin temperatures. *Phys. Rev. Lett.* **120**, 193401 (2018)



Bernard Zygelman Bernard Zygelman is Professor of Physics at UNLV. He was a visiting scientist at the MIT Harvard Center for Ultra-Cold Atoms, the Smithsonian Institution, and the Institute for Theoretical Physics at Santa Barbara. His interests cover applications of AMO physics, including quantum information science.



Muriel Gargaud Muriel Gargaud is an astrophysicist at the “Observatoire Aquitain des Sciences de l’Univers” in Bordeaux, France. She studied the physicochemistry of the interstellar medium for 20 years. Her current research is on astrobiology. Astrobiology is an interdisciplinary research field (astronomy, geology, chemistry, biology) looking for the origins of life, its evolution, and its development on Earth but also in and beyond the Solar System.



Ronald McCarroll Ronald McCarroll is Professor of Physics at the Université Pierre et Marie Curie in Paris. He obtained his PhD in Theoretical Physics at Queen’s University, Belfast. He has worked in the field of atomic and molecular photodynamics. He is the author of more than 130 papers in refereed journals and has contributed more than 20 specialized reviews to books and other specialized publications.



Continuum Distorted Wave and Wannier Methods 56

Roberto D. Rivarola , Omar A. Fojón, Marcelo Ciappina , and Derrick Crothers

Contents

56.1	Introduction	813
56.2	Continuum Distorted Wave Method	814
56.2.1	Perturbation Theory	814
56.2.2	Relativistic Continuum Distorted Waves	816
56.2.3	Variational CDW	816
56.2.4	Ionization	817
56.2.5	Ionization of Molecular Targets	819
56.3	Wannier Method	822
56.3.1	The Wannier Threshold Law	822
56.3.2	Peterkop's Semiclassical Theory	822
56.3.3	The Quantal Semiclassical Approximation	823
	References	827

Abstract

The continuum distorted wave model has been extensively applied to charge transfer and ionization processes. We present both the perturbative and variational capture theories as well as highlighting the suitability of this model in describing the continuum final states in both heavy and light particle ionization for both atomic and molecular targets. Particular emphasis will be put in the application of distorted wave theories to the description of recent complete experiments. We then develop the Wannier theory for threshold ionization and further theoretical work

R. D. Rivarola (✉)
Instituto de Física Rosario, CONICET – UNR
Rosario, Argentina
e-mail: rivarola@ifir-conicet.gov.ar

O. A. Fojón
Instituto de Física Rosario
Rosario, Argentina
e-mail: fojon@ifir-conicet.gov.ar

M. Ciappina (✉)
Physics Program, Guangdong Technion – Israel Institute of
Technology
Shantou, Guangdong, China
e-mail: marcelo.ciappina@gtit.edu.cn

that led to the modern quantal semiclassical approximation. This very successful theory has provided the first absolute cross sections that are in good agreement with experiment. The present work is based on the previous one conceived by *Crothers* et al. [1]. Only a few minor modifications in the text have been introduced, and a complete subsection has been added in order to take into account the state of art of the subject.

Keywords

total cross section · semiclassical theory · triple differential cross section · bound-state wave function · classical turning point

56.1 Introduction

The development here presented includes third-order continuum distorted wave double scattering $1s-1s$ transitions (Sect. 56.2.1), relativistic continuum distorted waves (Sect. 56.2.2), a theory on magnetically quantized continuum distorted waves [2, 3] (Sect. 56.2.4), and single ionization of molecular targets (Sect. 56.2.5). A theory for low energies (below 80 keV) is also reported in which the target is considered as a one-electron atom, and the interactions between this active electron and the remaining target electrons are treated by a model potential including both short and long-range effects. In the final channel, the usual product of two continuum distorted wave functions, each associated with a distinct electron–nucleus interaction, is used [4].

In addition, Sect. 56.3 on the Wannier method reports the major progress made over the last years. These major advances include (a) the development of below-threshold semiclassical theory for the study of doubly excited states [5–8] (b) a more accurate variant of the semiclassical quantum-mechanical treatment of *Crothers* [9].

56.2 Continuum Distorted Wave Method

56.2.1 Perturbation Theory

Continuum distorted wave theory (CDW) is one of the most advanced and complete perturbative theories of heavy-particle collisions formulated to date. It was originally introduced by *Cheshire* [10] to model the process of charge transfer during the collision of an atom/ion with an ion (specifically, the resonant process of $p + \text{H}(1s) \rightarrow \text{H}(1s) + p$). These types of three-body collisions are made amenable to the perturbative approach when the ratio of the projectile impact velocity v to the electron initial bound-state mean velocity v_b satisfies

$$\frac{v}{v_b} \gtrsim 3. \quad (56.1)$$

The criterion for nonrelativistic collisions, in which electron capture is a dominant process, is that both v and v_b are small compared with the speed of light c . The theoretical description of collisions that involve the disturbance of a bound electron of mass m_e by the field of a fast moving heavy particle of mass M can be greatly simplified by exploiting the fact that, since the ratio m_e/M is so small, the heavy particle follows a straight-line trajectory throughout the collision.

This allows the parametrization of the internuclear vector \mathbf{R} in terms of an impact parameter \mathbf{b} , such that

$$\mathbf{R} = \mathbf{b} + \mathbf{v}t. \quad (56.2)$$

This impact parameter picture (IPP) of the collision is equivalent to the full quantal or wave treatment when the eikonal criterion for small angle scattering is satisfied [11].

It has become standard to work in a generalized nonorthogonal coordinate system in which the vectors \mathbf{r}_T (\mathbf{r}_P) from the target (projectile) to the electron are treated, along with \mathbf{R} , as independent variables [12]. Working in the frame centered on the target nucleus and using atomic units, the Lagrangian is given by

$$\begin{aligned} H - i \frac{d}{dt} \Big|_{\mathbf{r}_T} &= -\frac{1}{2} \nabla_{\mathbf{r}_T}^2 + V_T(\mathbf{r}_T) - i \frac{\partial}{\partial t} - \frac{1}{2} \nabla_{\mathbf{r}_P}^2 \\ &+ V_P(\mathbf{r}_P) + i\mathbf{v} \cdot \nabla_{\mathbf{r}_P} \\ &+ V_{TP}(\mathbf{R}) - \nabla_{\mathbf{r}_P} \cdot \nabla_{\mathbf{r}_T}, \end{aligned} \quad (56.3)$$

where $d/dt|_{\mathbf{r}_T}$ refers to differentiation with respect to t , keeping \mathbf{r}_T fixed, and where

$$V_T = -\frac{Z_T}{r_T}, \quad V_P = -\frac{Z_P}{r_P}, \quad V_{TP} = \frac{Z_T Z_P}{R}. \quad (56.4)$$

Since these potentials are pure Coulomb potentials, they continue to affect the relevant wave functions even at infinity. These long-range Coulomb boundary conditions are defined in Eqs. (56.10) and (56.11). The $+i\mathbf{v} \cdot \nabla_{\mathbf{r}_P}$ term gives rise to

the Bates–McCarroll electron translation factors, which are required to satisfy Galilean invariance.

The Lagrangian above has been written in such a way as to highlight the three two-body decompositions exploited in CDW, with the $-\nabla_{\mathbf{r}_P} \cdot \nabla_{\mathbf{r}_T}$ term, the so-called nonorthogonal kinetic energy, coupling the systems. The essence of CDW is to treat the bound electron as simultaneously being in the continuum of the other heavy particle.

The initial wave function can be written as

$$\xi_i^\pm = D_{-v}^\pm(\mathbf{r}_P) \Phi_i(\mathbf{r}_T, t) C(\mathbf{R}, t), \quad (56.5)$$

where D_{-v}^\pm is the distortion from the projectile, and C is a function that accounts for the internuclear potential, V_{TP} . The bound state $\Phi_i = \phi_i(\mathbf{r}_T) \exp(-i\epsilon_i t)$, where $\phi_i(\mathbf{r}_T)$ is the initial eigenstate, and ϵ_i is the initial eigenenergy.

In this form, the action of the Lagrangian can be split into three separate differential equations plus a residual interaction. This gives the following solutions: for the distortion D ,

$$\begin{aligned} D_{-v}^+ &= N(\zeta_P)_1 F_1(i\zeta_P; 1; i\mathbf{v} \cdot \mathbf{r}_P + ivr_P), \\ D_{-v}^- &= (D_{-v}^+)^*, \end{aligned} \quad (56.6)$$

with

$$N(\zeta) = \exp(\pi\zeta/2) \Gamma(1 - i\zeta), \quad \zeta_{T,P} = Z_{T,P}/v; \quad (56.7)$$

and for the internuclear function C ,

$$C(\mathbf{R}, t) = \exp\left[i \frac{Z_P Z_T}{v} \ln(vR - v^2 t) \right]. \quad (56.8)$$

Similarly, it can be shown that

$$\begin{aligned} \xi_f^\pm &= D_v^\pm(\mathbf{r}_T) \Phi_f(\mathbf{r}_P, t) C^*(\mathbf{R}, -t) \\ &\times \exp\left(i\mathbf{v} \cdot \mathbf{r}_T - i \frac{v^2}{2} t \right), \end{aligned} \quad (56.9)$$

where $i\mathbf{v} \cdot \mathbf{r}_T - i \frac{v^2}{2} t$ results from the Galilean transformation to the target frame. The superscripts plus and minus refer to outgoing and incoming Coulomb boundary conditions, respectively. These are determined by the asymptotic form of the wave functions

$$\begin{aligned} \lim_{t \rightarrow -\infty} \xi_i^+ &\approx \Phi_i(\mathbf{r}_T, t) \\ &\times \exp\left[i \frac{Z_P(Z_T - 1)}{v} \ln(vR - v^2 t) \right], \end{aligned} \quad (56.10)$$

and

$$\begin{aligned} \lim_{t \rightarrow +\infty} \xi_f^- &\approx \Phi_f(\mathbf{r}_P, t) \exp\left(i\mathbf{v} \cdot \mathbf{r}_T - i \frac{v^2}{2} t \right) \\ &\times \exp\left[-i \frac{Z_T(Z_P - 1)}{v} \ln(vR + v^2 t) \right]. \end{aligned} \quad (56.11)$$

Of course, ξ_i^+ and ξ_f^- are not exact solutions of the three-body Schrödinger equation; in fact,

$$\left(H - i\frac{d}{dt_{r_T}}\right)\xi_i^+ = W_i\xi_i^+ = -\nabla_{r_P}D_v^+ \cdot \nabla_{r_T}\Phi_i, \quad (56.12)$$

and

$$\begin{aligned} \left(H - i\frac{d}{dt_{r_T}}\right)\xi_f^- &= W_f\xi_f^- \\ &= -e^{i\mathbf{v}\cdot\mathbf{r}_T - i\frac{v^2}{2}t} \nabla_{r_T}D_v^- \cdot \nabla_{r_P}\phi_f. \end{aligned} \quad (56.13)$$

The CDW transition amplitude is written as

$$A_{if} = -i \int_{-\infty}^{+\infty} dt \langle \xi_f^- | T_{\text{CDW}} | \xi_i^+ \rangle. \quad (56.14)$$

A perturbative expansion via the distorted wave Lippmann–Schwinger equation can be made for T_{CDW} , either in the post form

$$T_{\text{CDW}}^+ = W_f^\dagger(1 + G_V W_i) + T_{\text{CDW}}^+ G_i V G_V W_i, \quad (56.15)$$

or in the prior form

$$T_{\text{CDW}}^- = (1 + W_f^\dagger G_V) W_i + W_f^\dagger G_V V G_f T_{\text{CDW}}^-, \quad (56.16)$$

where the Green functions are given by

$$G_{i,f} = \left(i\frac{d}{dt_{r_T}} - H + W_{i,f} + i\epsilon\right)^{-1}, \quad (56.17)$$

$$G_V = \left(i\frac{d}{dt_{r_T}} - H + V + i\epsilon\right)^{-1}, \quad (56.18)$$

and V is any potential which ensures that the kernels of the integral equations for T_{CDW} are continuous [13].

By taking the first term in the expansions in Eqs. (56.15) and (56.16), we get the post and prior forms of the CDW1 amplitude as used by Cheshire. When calculating these amplitudes, the separable nature of the CDW wave function is best exploited by using Fourier transforms to move to the time-independent wave picture. A similar transformation is not suitable in the coupled channel approach discussed in Sect. 56.2.3.

Crothers [13], working in the wave treatment, has calculated the second-order CDW2 amplitude using various approximations for the Green functions and showed that the CDW perturbation series converged very well to first order in most parts of the differential cross section. This is in contrast to the standard Born or Brinkman–Kramers approximations, which do not start to converge until expanded to second order. CDW1 is the only first-order perturbation theory, apart from asymmetric hybrid models derived from it, that produces the Thomas peak. Unfortunately, due to

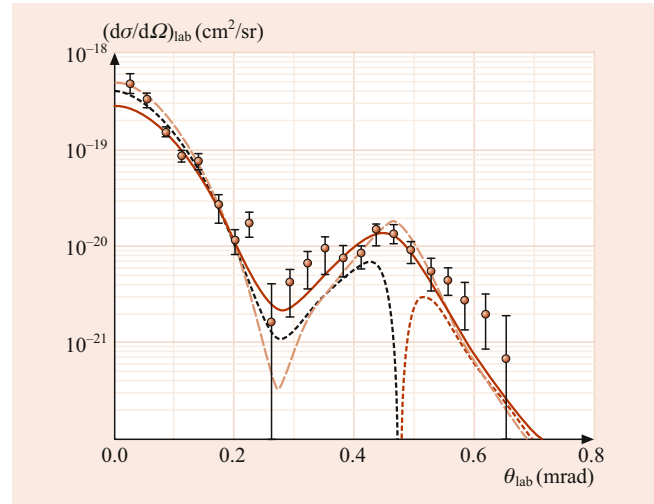


Fig. 56.1 Differential cross sections for electron capture in the collision $\text{H}^+ + \text{H}(1s) \rightarrow \text{H}(1s) + \text{H}^+$ as a function of laboratory scattering angle (θ_{lab}) for impact energy of 5 MeV: *solid line* TCDW, folded over the experimental resolution of Vogt et al. [15]. *Unfolded theoretical results: dashed line* TCDW; *dotted line* CDW1. *Experimental data; circles*, Vogt et al. [15]

the cancellation of the leading order terms, which are associated with the interference of contributions coming from two different mechanisms, corresponding to the intermediate excitation of the electron to a target continuum and to the intermediate capture to a projectile continuum state, CDW1 has an extreme dip at the Thomas angle [14]. This is illustrated in Fig. 56.1, which also includes both folded and unfolded versions of the asymmetric target CDW (TCDW) theory discussed below, as well as experimental data [15].

Further work in this area has included the development of the Thomas double-scattering electron capture at asymptotically high velocity within the third-order continuum distorted wave perturbation theory for 1s–1s transitions in proton hydrogen collisions. It has been shown [16] that at the critical proton scattering angles, namely the forward peak, Thomas double encounter peak, small angles, and the interference minimum, the CDW series has converged at second order. Moreover, it is proven that the third-order correction makes no contribution to the velocity-dependent v^{-11} and v^{-12} behavior of the Thomas double-scattering total cross section at the leading angles. In contrast, it may be seen in [16] that the Oppenheimer–Brinkman–Kramers (OBK) traveling atomic orbital theory (which, in general, suffers from a common phase factor that embraces intermediate elastic divergences [17] in the first and higher-order terms) does not converge at second order. It remains an open question as to whether fourth-order terms or higher in the OBK approximation contribute to various differential cross sections. It is concluded that the CDW model gives a superior description of the Thomas double-scattering mechanism when compared with the OBK model.

Anomalously large cross sections are obtained at low energies if the CDW wave function is not normalized at all times throughout the collision [12]. This is best demonstrated by the presence of the $N(\zeta)$ terms in

$$\lim_{t \rightarrow +\infty} \xi_i^+ = N(\zeta_P) \Phi_i(\mathbf{r}_T, t) \times \exp \left[i \frac{Z_P Z_T}{v} \ln(vR - v^2 t) \right] \quad (56.19)$$

and

$$\lim_{t \rightarrow -\infty} \xi_f^- = N^*(\zeta_T) \Phi_f(\mathbf{r}_P, t) \exp \left(i \mathbf{v} \cdot \mathbf{r}_T - i \frac{v^2 t}{2} \right) \times \exp \left[-i \frac{Z_T Z_P}{v} \ln(vR + v^2 t) \right]. \quad (56.20)$$

Using

$$\lim_{v \rightarrow 0} |N(Z/v)|^2 \approx \frac{2\pi Z}{v} \quad (56.21)$$

it is clear that the problem gets worse as v decreases. It can be corrected by defining

$$\hat{\xi}_{i,f}^\pm = \xi_{i,f}^\pm \left\langle \xi_{i,f}^\pm \left| \xi_{i,f}^\pm \right. \right\rangle^{-1/2}. \quad (56.22)$$

Simpler distorted wave models can be generated through further approximations. Two of the most popular are target CDW [$D_{-v}(\mathbf{r}_P) \rightarrow 1$] and projectile CDW [$D_v(\mathbf{r}_T) \rightarrow 1$]. These approximations are justified when $Z_T > Z_P$ and $Z_P > Z_T$, respectively, and are particularly simple to calculate when the simple Born-like residual interaction is used rather than the full CDW form.

The asymptotic forms of the CDW wave functions can be used throughout the collision, ensuring normalization, and this leads to the continuum distorted wave-eikonal initial state [18] or symmetric eikonal [19] models, which are among the most successful ones to describe experimental data.

56.2.2 Relativistic Continuum Distorted Waves

The CDW model can be naturally extended to the two-center time-dependent Dirac equation, so that a Lorentz invariant theory is obtained. When the electron orbital velocity αZc , or the collision velocity v , approaches the speed of light c , the kinematics are modified by time dilation. In addition, the particle interactions change because of retardation and the fact that spin-orbit effects are now important. Moreover, vacuum interactions such as radiative emissions and electron-positron pair production begin to play a role. A comprehensive account of atomic processes in relativistic heavy-particle collisions can be found in the books [11, 20, 21]. At high collision energies, $\gamma \equiv (1 - v^2/c^2)^{-1/2} \gg 1$, and high-charge states of the ions, the Dirac sea of negative energy states

becomes energetically accessible and strongly coupled. The process of electron capture, for example, may be mediated by spin-flip transitions [22], or spontaneous X-ray emission (radiative electron capture) [23] and even electron capture via pair production [24–27]. Although the importance of vacuum processes diminishes with energy, these mechanisms dominate in the extreme relativistic regime. Indeed, the last of these processes was used to produce antihydrogen in the laboratory [28] at GeV amu⁻¹ energies.

At relativistic energies, the principal inelastic process is collisional ionization [20, 21]. The extensions of the distorted wave theory to accommodate Lorentz invariance was developed by Rivarola and Deco [29, 30] and Crothers and coworkers [22] over the basis of previous works on the Born series [31] and impulse approximation [32]. In practical applications to electron capture cross sections, the symmetric semirelativistic CDW theory of Glass et al. [22] was found to be in very good agreement with experiments in the GeV amu⁻¹ energy range with charges $Z_{P,T} \approx 6-80$. For nonradiative electron capture, it was found that second-order retardation dominates at extreme relativistic velocities so that $\sigma \approx \gamma^{-1} (\ln \gamma)^2$ [33]. However, the momentum transfer kinematics for this process is unfavorable, and a more efficient mechanism based on electron-positron pair production with capture of the created electron is more strongly coupled. Theoretical estimates of this process using relativistic CDW [34] compared with experiments [35] are in very good agreement.

The same model has been applied to estimate yields of antihydrogen following antiproton impact with neutral high- Z atoms [28] following experiments at CERN and Fermilab. The virtual photon model of Baur [35] gives cross sections that agree well with the limited data [28]. However, these estimates are roughly ten times larger than the relativistic CDW results [20] and one hundred times the first Born estimate [36]. It appears that additional studies, both experimental and theoretical, would be worthwhile in order to understand this process more fully.

56.2.3 Variational CDW

As the ratio of v/v_b decreases, perturbation theory starts to fail. This is due to the effective interaction time between the projectile and target atoms being long enough for strong three-body coupling. In this environment, variational methods have proved successful. This procedure ensures both gauge invariance and unitarity – two fundamental attributes that perturbation theory usually cannot guarantee. Continuing in the IPP, we use the Sil variational principle, which gives

$$\delta \int_{-\infty}^{+\infty} dt \langle \Psi | H - i \frac{d}{dt} | \Psi \rangle = 0. \quad (56.23)$$

In the two-state CDW approximation, we may assume

$$\Psi_{\text{CDW}} = c_0(t)\xi_i^+ + c_1(t)\xi_f^-, \quad (56.24)$$

subject to the boundary conditions $c_0(-\infty) = 1$ and $c_1(-\infty) = 0$. Variation of c_0^* and c_1^* gives the standard coupled equations

$$iN_{00}\dot{c}_0 + iN_{01}\dot{c}_1 = H_{00}c_0 + H_{01}c_1, \quad (56.25)$$

$$iN_{10}\dot{c}_0 + iN_{11}\dot{c}_1 = H_{10}c_0 + H_{11}c_1, \quad (56.26)$$

where

$$\begin{aligned} N_{00} &= \left\langle \xi_i^+ \left| \xi_i^+ \right. \right\rangle, \\ N_{11} &= \left\langle \xi_f^- \left| \xi_f^- \right. \right\rangle, \\ N_{01} &= \left\langle \xi_i^+ \left| \xi_f^- \right. \right\rangle = N_{10}^*, \end{aligned} \quad (56.27)$$

and

$$\begin{aligned} H_{00} &= \left\langle \xi_i^+ \left| H - i \frac{d}{dt} \right| \xi_i^+ \right\rangle, \\ H_{01} &= \left\langle \xi_i^+ \left| H - i \frac{d}{dt} \right| \xi_f^- \right\rangle, \\ H_{10} &= \left\langle \xi_f^- \left| H - i \frac{d}{dt} \right| \xi_i^+ \right\rangle, \\ H_{11} &= \left\langle \xi_f^- \left| H - i \frac{d}{dt} \right| \xi_f^- \right\rangle. \end{aligned} \quad (56.28)$$

Equations (56.25) and (56.26) can clearly be written as a matrix equation,

$$iN\dot{c} = Hc, \quad (56.29)$$

which is then easily generalized for larger expansions of Ψ . By using an orthogonalized basis set of normalized functions in the manner of *Löwdin* [37, 38], the N matrix reduces to the unit matrix. This will be understood when considering expansions for Ψ from now on.

Another interesting, but potentially ruinous, result of the asymptotic forms in Eqs. (56.19) and (56.20) is their failure to obey the correct long-range Coulomb boundary conditions; compare this with their expressions at the opposite time extreme in Eqs. (56.10) and (56.11). This has no consequence until second-order VCDW is calculated in which divergent integrals arise as a direct result of this feature of the wave functions. These terms are analogous to the well-known intermediate elastic divergences that occur in Born-type expansions, which do not have the correct Coulomb phases.

A novel way to avoid this problem [39, 40] is to split the time plane into two parts, allowing the well-behaved set $\{\xi^+\}$ to be used exclusively for $t \leq 0$, while the set $\{\xi^-\}$ forms the basis for $t \geq 0$. This phase integral halfway house VCDW is based on the factorization of the scattering matrix S into a product of two Møller matrices,

$$S = \Omega_-^\dagger \Omega_+, \quad (56.30)$$

where Ω_-^\dagger represents the propagation of the initial state from $t = -\infty$ to $t = 0_-$, while Ω_+ represents the propagation of the final state from $t = +\infty$ to $t = 0_+$.

The total wave function is similarly split into two expansions over an orthogonal basis ψ , with

$$\Psi^- = c^- \psi^+, \quad t < 0, \quad (56.31)$$

$$\Psi^+ = c^+ \psi^-, \quad t > 0, \quad (56.32)$$

where the superscripts on the Ψ correspond to the respective heavy-particle motion. This, in turn, divides the coupled equations into two sets

$$i\dot{c}^- = H^{++}c^-, \quad t < 0, \quad (56.33)$$

$$i\dot{c}^+ = H^{--}c^+, \quad t > 0, \quad (56.34)$$

where

$$H^{\pm\pm} = \langle \Psi^\pm | H - i \frac{d}{dt} | \Psi^\pm \rangle. \quad (56.35)$$

The coefficients c^\pm then have to be matched over a local discontinuity in the total wave function at $t = 0$, such that $c^+(0) = c^-(0)$. Halfway house VCDW has all the appealing attributes of a variational theory but, by explicitly satisfying the long-range Coulomb boundary conditions, it is divergence free.

56.2.4 Ionization

CDW, by treating the Coulomb interactions to such a high degree, has obvious attractions for modeling the ionization process. Single ionization of an electron from an atom by a high-energy projectile is a perturbative process, and the Born approximation will match experimental total cross sections rather well. However, CDW-like representations of the initial and final states generate better results at lower energies, as well as producing features in the differential cross sections that are beyond the reach of the first Born approximation.

In full CDW ionization theory, the initial state is given by the usual charge transfer wave function ξ_i in Eq. (56.5), while the final state takes the form

$$\begin{aligned} \xi_f^- &= (2\pi)^{-2/3} \exp\left(i\mathbf{k} \cdot \mathbf{r}_T - i\frac{k^2}{2}t\right) \\ &\times \exp\left[-i\frac{Z_T Z_P}{v} \ln(vR + \mathbf{v} \cdot \mathbf{R})\right] \\ &\times N^*(Z_T/k) {}_1F_1(-iZ_T/k; 1; -i\mathbf{k} \cdot \mathbf{r}_T - ikr_T) \\ &\times N^*(Z_P/p) {}_1F_1(-iZ_P/p; 1; -i\mathbf{p} \cdot \mathbf{r}_P - ipr_P), \end{aligned} \quad (56.36)$$

where \mathbf{k} ($\mathbf{p} = \mathbf{k} - \mathbf{v}$) is the momentum of the electron relative to the target (projectile) nucleus.

CDW ionization theories presented prior to 1982 produced spuriously large results due to the unnormalized initial state. Since the matrix element $\langle \xi_i^+ | \xi_i^+ \rangle$ is computationally expensive to calculate as a function of \mathbf{b} and t , a very successful alternative is to take the initial state as an eikonal distorted state [41], thus ensuring normalization. The initial state in this CDW-EIS theory is thus taken to be

$$\xi_i^{\text{EIS}} = \hat{D}_{-v}^+(\mathbf{r}_P)\Phi_i(\mathbf{r}_T, t)C(\mathbf{R}, t), \quad (56.37)$$

where now

$$\hat{D}_{-v}^+(\mathbf{r}_P) = \exp\left[-i\frac{Z_P}{v}\ln(vr_P + \mathbf{v} \cdot \mathbf{r}_P)\right]. \quad (56.38)$$

The final state remains as in Eq. (56.36).

The CDW final state is most effective when differential cross sections are studied. The most interesting features are in the forward $\theta = 0$ ejection angle; i.e., the soft collision peak ($k \simeq 0$), the electron capture to the continuum peak ECC ($k \simeq v$) and the binary encounter peak ($k \simeq 2v$). CDW theories are especially suited to the description of the ECC peak that, theoretically, results from the presence of the $N(Z_P/p)$ factor in the wave function. This peak can be analyzed in detail via a multipole expansion, and much theoretical work has been centered on the dipole parameter β . A negative β is strongly suggested by both experiment and physical intuition. CDW, CDW-EIS, and halfway house VCDW all predict different values for β , with the last theory being the only one that gives the high energy limit, in which it remains negative [42].

Magnetically quantized continuum distorted wave theory also has been considered [2] in the description of ionization in ion-atom collisions. This generalizes the CDW-EIS theory of Crothers and McCann [3] to incorporate the azimuthal angle dependence of each CDW in the final state wave function. This is accomplished by the analytic continuation of hydrogenic-like wave functions from below to above threshold, using parabolic coordinates and quantum numbers, including magnetic quantum numbers, thus providing a more complete set of states. The continuation applies to excitation, charge transfer, ionization, and double and hybrid events for both light and heavy-particle collisions. It has successfully been applied to the calculation of double differential cross sections for the single ionization of the hydrogen atom and for a hydrogen molecule by a proton for electrons ejected in the forward direction at a collision energy of 50 keV and 100 keV, respectively.

It is well known that the CDW-EIS models are the best suited to the intermediate and high-energy regions. Recent results for proton-argon total ionization cross sections [43] highlight large discrepancies between CDW-EIS theory and experiment for energies below 80 keV. This problem has been addressed in [4]. Here, following the theory of [44], the authors in [4] use a Born initial state wave function. In the final channel, the usual product of two continuum distorted

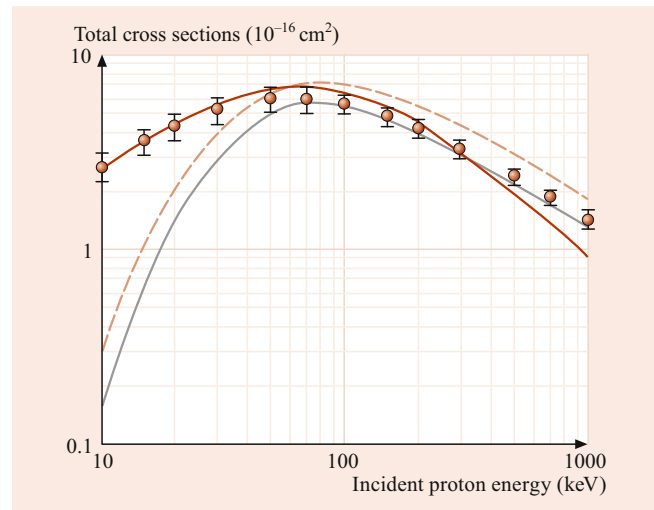


Fig. 56.2 Total ionization cross section for the proton-impact single ionization of Ar: *solid line* theoretical results of [4], *dashed line* theoretical results of OPM [43], and *dotted line* HFS [43]. Experimental data: *circles*, Rudd et al. [45]

wave functions, each associated with a distinct electron-nucleus interaction, is used. In their treatment, the target is considered as a one-electron atom, and the interactions between this active electron and remaining target electrons are treated by a model potential including both short and long-range effects. The success of this new theory for low energies is shown in Fig. 56.2. Here it is clear that the calculation in [4] gives good agreement for the total cross sections in the energy range 10–300 keV with the measurements of Rudd et al. [45].

Double ionization in general remains an extremely difficult area for theoretical models based on perturbative expansions – even those with explicit distortions built in. In this process, the explicit correlation between the electrons in the target atom is vitally important. However, one example where CDW theory can overcome these problems is in the bound-state wave function of *Pluvinage* [46]. This very successful treatment, which also includes a variationally determined parameter, is just the CDW analogy in bound-state theory, although this appeared well before Cheshire’s paper on scattering. The Pluvinage wave function for the ground state of a two-electron atom is given by

$$\begin{aligned} \phi = c(\kappa) & \left(\frac{Z_T^3}{\pi}\right) \exp[-Z_T(r_1 + r_2) + i\kappa r_{12}] \\ & \times {}_1F_1\left(1 + \frac{1}{2i\kappa}; 2; 2i\kappa r_{12}\right), \end{aligned} \quad (56.39)$$

where $r_{1,2}$ are the distances of the two electrons from the target nucleus, and r_{12} is the interelectron separation. The constant κ is variationally determined to be 0.41, giving the normalization constant $c = (0.36405)^{1/2}$.

An analogous wave function for two electrons in the target continuum was derived [12] and implemented later in a successful CDW treatment of ionization by electrons and positrons [47]. This BBK theory, so named in deference to the authors, demonstrates the high resolution CDW final states obtained, right down to triply differential cross sections (TDCS). However, this model suffers from the low-energy normalization problems associated with CDW and is also unable to describe the threshold effects that are in the domain of Wannier theory.

56.2.5 Ionization of Molecular Targets

The CDW-EIS model can be extended to treat single ionization of simple molecular targets by fast bare ions. Fast heavy ions in our framework implies that the projectile velocity is much larger, but still within the nonrelativistic range, than the typical electron velocity of bound electrons. At these high collision energies, for which the collision time is smaller than the relaxation one, corresponding to those electrons that remain bound to the molecule acting as spectators, the so-called passive electrons, we can assume in an acceptable approximation that they stay frozen in their respective molecular orbitals during the collision process. Additionally, we could also consider that the collision time is also shorter than the vibrational and rotational molecular times. In this way, the orientation of the molecule remains fixed in the space until the direct interaction of the projectile with the target ends. Specifically, for the projectile velocities we use and considering small molecules, the collision time τ is within the sub-fs to the -as domain ($1 \text{ fs} = 10^{-15} \text{ s}$, $1 \text{ as} = 10^{-18} \text{ s}$), while the typical vibration and rotational frequencies are in the range of $10^{13} \sim 10^{14} \text{ Hz}$ and $10^{10} \sim 10^{12} \text{ Hz}$, respectively (e.g., [48]).

An interesting set of phenomena can be related with the single ionization of simple molecules: the coherent superposition of quantum objects emitted from spatially separated positions. This process is often cited as the molecular double-slit scenario [49] in which a homonuclear diatomic molecule such as molecular hydrogen [50] or nitrogen [51] is ionized by irradiation with light or by impact of charged particles such as electrons or heavy ions. For decades particular attention has been paid to these phenomena due to their intrinsic importance in areas such as astrophysics and biology (see, e.g., the present book for more details). For the first time in 1966, *Howard Cohen* and *Ugo Fano*, in theoretical studies of photoionization of N_2 and O_2 molecules, recognized the existence of interference effects for these reactions [52]. They showed that an oscillating pattern appeared in the partial photoionization cross sections (PCS) when a two-center electron wave function was employed to model the coherent electron emission from both atomic center. Electrons can be emit-

ted coherently from both of the atoms in these molecules, in such a way that the electron waves could be either in phase or out of phase. In this way, these systems should exhibit an interference behavior equivalent to that seen in macroscopic double-slit experiments. Nevertheless, the first experimental confirmation for these interference phenomena appeared three decades later, in 2001, in the single ionization of H_2 molecules by impact of Kr^{34+} projectiles. Starting from this seminal work by *Stolterfoht* et al. [50], about coherent electron emission from H_2 molecules by impact of highly charged ions impact, there has been a true deluge of papers in the field (e.g., [53] and references therein).

Let us focus our interest here on the single ionization of diatomic molecules by impact of heavy ion projectiles. They possess a charge Z_p and incoming velocity v , and the beam is directed along the z -axis. In this way, we designate the $x-z$ plane as the scattering plane. The momentum transfer \mathbf{q} is defined as $\mathbf{q} = \mathbf{K}_i - \mathbf{K}_f$, where \mathbf{K}_i (\mathbf{K}_f) is the initial (final) momentum of the incident (scattered) particle, whereas \mathbf{k} is the momentum of the ionized electron, represented in usual spherical coordinates by the polar θ_e and azimuthal ϕ_e angles, respectively. Finally, the polar angle θ_ρ sets the orientation of the internuclear axis ρ with respect to the z -axis, and ϕ_ρ is the azimuthal angle, i.e., the angle of the internuclear axis with respect to the x -axis.

In the final channel of the reaction, we use the two-effective center (TEC) approximation introduced by *Wang* et al. [54] (also *Corchs* et al. [55]). This model was applied to the study of electron capture by impact of bare ions on homonuclear and heteronuclear molecules. Later, the TEC approximation was employed by *Galassi* et al. [56, 57] to describe single ionization of H_2 molecules by the impact of fast bare ions. In this approximation, the scattering matrix for the active electron can be written as

$$\begin{aligned} \tilde{T}_{fi}(\boldsymbol{\eta}, \boldsymbol{\rho}) = & \tilde{T}_{fi}^{(1)}(\boldsymbol{\eta}) \exp(i(1-\mu)\mathbf{q} \cdot \boldsymbol{\rho}) \\ & + \tilde{T}_{fi}^{(2)}(\boldsymbol{\eta}) \exp(-i\mu\mathbf{q} \cdot \boldsymbol{\rho}), \end{aligned} \quad (56.40)$$

where the atomic centers are displaced from the center of mass of the target by $(1-\mu)\boldsymbol{\rho}$ for the center 1 and $\mu\boldsymbol{\rho}$ for the center 2, $\mu \approx M_1/(M_1 + M_2)$ being the reduced mass, with M_1 and M_2 the masses of both centers, and $\tilde{T}_{fi}^{(1)}$ and $\tilde{T}_{fi}^{(2)}$ the corresponding effective atomic scattering matrix elements. In (56.40), $\boldsymbol{\eta}$ is the transversal component of \mathbf{q} , i.e., $\boldsymbol{\eta} \cdot \mathbf{v} = 0$.

For the case of homonuclear molecules, it is possible to demonstrate that

$$|\tilde{T}_{fi}(\boldsymbol{\eta}, \boldsymbol{\rho})|^2 = \{1 + \cos[(\mathbf{k} - \mathbf{q}) \cdot \boldsymbol{\rho}]\} |\tilde{T}_{fi}^{\text{eff}}(\boldsymbol{\eta})|^2, \quad (56.41)$$

with $\tilde{T}_{fi}^{\text{eff}}(\boldsymbol{\eta}) = \tilde{T}_{fi}^{(1)}(\boldsymbol{\eta}) = \tilde{T}_{fi}^{(2)}(\boldsymbol{\eta})$, an *effective* one-center scattering T -matrix element. The oscillatory factor in (56.41) is the signature of interference patterns coming from the electron emission of each of the two effective centers.

In the case of randomly oriented molecules, (56.41) should be averaged over all molecular orientations, so that

$$|\tilde{T}_{fi}(\boldsymbol{\eta}, \boldsymbol{\rho})|^2 = 4\pi \left[1 + \frac{\sin(|\mathbf{k} - \mathbf{q}|\rho)}{|\mathbf{k} - \mathbf{q}|\rho} \right] |\tilde{T}_{fi}^{\text{eff}}(\boldsymbol{\eta})|^2. \quad (56.42)$$

Furthermore, doubly differential cross sections (DDCS) as a function of the final energy and solid angle subtended by the ejected electron, averaged over all molecular orientations, can be obtained using (56.41) and (56.42)

$$\begin{aligned} \frac{d^2\sigma}{dE_k d\Omega_k} &= N_e (2\pi)^4 \frac{4\pi k}{v^2} \\ &\times \int d\boldsymbol{\eta} \left[1 + \frac{\sin(|\mathbf{k} - \mathbf{q}|\rho)}{|\mathbf{k} - \mathbf{q}|\rho} \right] |\tilde{T}_{fi}^{\text{eff}}(\boldsymbol{\eta})|^2 \\ &= S_{\text{dir}}(E_k, \Omega_k) + S_{\text{int}}(E_k, \Omega_k), \end{aligned} \quad (56.43)$$

with $S_{\text{dir}}(E_k, \Omega_k)$ being the contribution to the DDCS given by the effective atomic center and $S_{\text{int}}(E_k, \Omega_k)$ the interference contribution that corresponds to considering only the oscillatory part of the integrand in (56.43). The relevant physical quantity to observe interference patterns for oriented (fixed) molecules is the product $(\mathbf{k} - \mathbf{q}) \cdot \boldsymbol{\rho}$. On the other hand, for randomly oriented species, $|\mathbf{k} - \mathbf{q}|\rho$ is the factor that dominates the interference picture. Moreover, in order to get DDCS we should sum up over all the transverse momentum transfer values so that, depending on the molecular orientation, the interference traces may be washed out.

In Fig. 56.3, contributions to the ratio between DDCS for molecular H_2 and twice the atomic H is shown for the case of impact of $60 \text{ MeV amu}^{-1} \text{ Kr}^{34+}$ projectiles on H_2 targets. The direct $S_{\text{dir}}(E_k, \Omega_k)$ and interference $S_{\text{int}}(E_k, \Omega_k)$ terms are considered for the $\theta_e = 20^\circ$ emission angle. This ratio could be expected to be close to unity at the high impact energy considered. However, some differences are observed due to the different binding energies of H_2 and H, the corresponding effective charges Z_{eff} , and the normalization of the respective bound-state wave functions. While $S_{\text{dir}}(E_k, \Omega_k)$ increases monotonically, $S_{\text{int}}(E_k, \Omega_k)$ presents a damped oscillatory behavior as a function of the ejected electron velocity, demonstrating that interference patterns arise from coherent electron emission from the molecular centers.

Further experimental investigations, proving the existence of coherent electron emission, have been carried out. For instance, single ionization of H_2 molecules by impact of $68 \text{ MeV amu}^{-1} \text{ Kr}^{33+}$ [58] and 1, 3, and 5 MeV H^+ [59, 60] projectiles have been presented. Additionally, Misra et al. [61] measured DDCS for the cases of $1.5 \text{ MeV amu}^{-1} \text{ F}^{9+}$ and $1.0 \text{ MeV amu}^{-1} \text{ C}^{6+}$ ions impinging on atomic H and molecular H_2 targets. Cross section ratios were, thus, obtained by dividing both experimental results and compared with fully theoretical CDW-EIS calculations employing the model introduced by Galassi et al. [56]. Once again, the presence of interference patterns due to coherent electron emission from

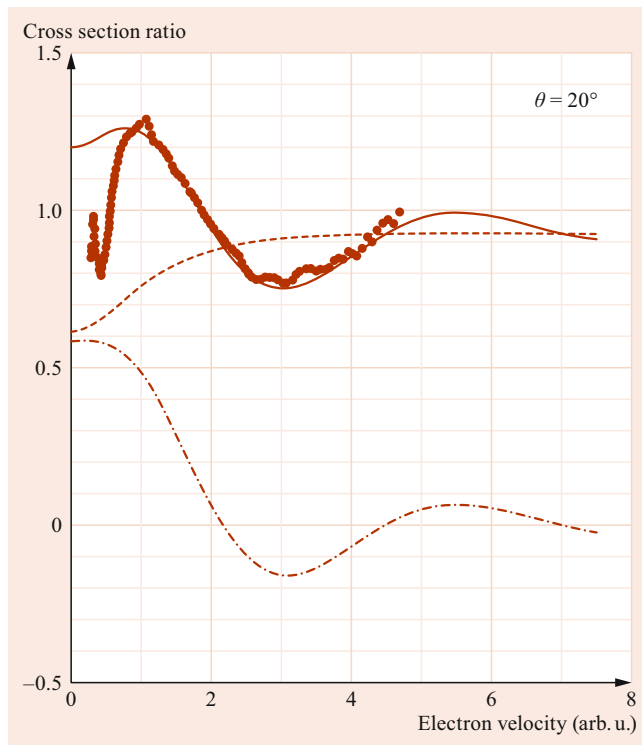


Fig. 56.3 Experimental-to-theoretical cross section ratios for the single ionization of H_2 molecules by $60 \text{ MeV amu}^{-1} \text{ Kr}^{34+}$ projectiles. The electron emission angle is $\theta_e = 20^\circ$. Solid circles: experiment from [50]. Theory: solid line, CDW-EIS calculation; dashed line, contribution from $S_{\text{dir}}(E_k, \Omega_k)$; dot-dashed line, contribution from $S_{\text{int}}(E_k, \Omega_k)$ [56]

the molecular centers was found, confirming the previous results.

Other distorted wave-based methods have been applied to single ionization of H_2 molecules by ion impact at intermediate energies. For instance, the molecular version of the three-body distorted wave-eikonal initial state (3DW-EIS), named M3DW-EIS, was introduced by Chowdhury et al. [62] to calculate triply differential cross sections (TDCS) and DDCS for single ionization of H_2 by 75-keV proton impact. For the initial state, the 3DW-EIS method uses a Hartree-Fock wave function for the bound electron and an eikonal wave for the heavy ion projectile. For the final state, a distorted wave is used for the ejected electron, a Coulomb wave is used for the projectile in the field of a point charge, and the Coulomb distortion between the projectile and the ejected electron is also included. The asymptotic Coulomb interactions between the projectile and target are contained in the eikonal approximation for the initial state. Given the two-center nature of the hydrogen molecule, the projectile can scatter from either center, which leads to the possibility of observing interference effects, and this feature is, indeed, captured by M3DW-EIS.

Let us extend our analysis now to the case of diatomic molecules formed by a few electron orbitals. In order to

model its initial fundamental state the corresponding wave functions are written as linear combinations of Slater-type orbitals (STO) centered on each one of the nuclei of the molecule, and both the exponents and the weight coefficients are variationally optimized by employing the quantum chemistry program Gaussian [63]. In turn, each STO is written as a combination of Gaussian-type orbitals by employing a minimal STO-6G basis set. The equilibrium distance ρ and each of the orbital energies ε_i are then calculated with a higher precision by means of the larger HF/6-311 G* basis set.

The scattering matrix element $T_{fi,MO}(\boldsymbol{\eta}, \boldsymbol{\rho})$ per electron corresponding to a definite molecular orbital may be expressed as a linear combination of effective one-center scattering matrix elements $T_{hj,MO}^{\text{eff}}(\boldsymbol{\eta}, \boldsymbol{\rho})$ associated with a basis of STO centered on the h -target nucleus, given by

$$T_{h,MO}^{\text{eff}}(\boldsymbol{\eta}, \boldsymbol{\rho}) = \sum_j \omega_{h,j} T_{hj,MO}^{\text{eff}}(\boldsymbol{\eta}, \boldsymbol{\rho}), \quad (56.44)$$

where $h = 1, 2$ indicates the nucleus of the molecules in which the STO is centered, and the subscript j denotes the corresponding quantum numbers nlm . The coefficients $\omega_{h,j}$ are determined by means of the above-mentioned program Gaussian [63].

The case of 1 MeV protons impacting on N_2 molecules was studied by *Tachino et al.* [64]. They considered two different orientations of the internuclear axis, i.e., parallel and perpendicular to the incident projectile velocity, and electrons emitted with an energy of 100 eV. The structures present in the TDCS for parallel orientation give evidence of the presence of interference patterns. At variance, these patterns are washed out for perpendicular orientation due to the contribution of different transverse momentum transfers, in this way erasing the signatures of the coherent electron emission. It must be remarked that the phase of the structures for parallel orientation is shifted with respect to the others, depending on the orbital considered. Consequently, it has, indeed, been verified that the TDCS for the complete molecule do not present oscillations coming from interference effects. This also explains the suppression of primary electron interferences in the experimental results by *Baran et al.* [65, 66], where DDCS were measured for impact of N_2 molecules by protons. These authors suggest that the delocalization of several molecular orbitals could be responsible for the suppression mentioned. Moreover, a similar behavior for impact of H^+ and $\text{O}^{5+,8+}$ projectile beams on O_2 targets was observed [67, 68].

Further experiments confirmed the theoretical predictions showing the absence of interference effects on single ionization DDCS of O_2 [69, 70] and N_2 [71] by fast bare carbon ions. In all these cases, the DDCS ratios for ionization of the molecular target and twice the corresponding atomic compounds were considered.

The CDW-EIS model was also able to describe successfully experimental differential and total cross sections for ionization of water vapor. Two different representations for the ground state molecular orbitals of the target were used [72]. One of them was the the complete neglect of differential overlap (CNDO) approximation, originally implemented by *Pople* [73–75], where the molecular orbitals for the valence electrons were described by means of a linear combination of atomic orbitals (LCAO), and the basis set employed was a minimal one formed by Slater-type functions (STF) with fixed characteristic exponents. Moreover, all inner shells were considered as a part of an unpolarized core. However, some complications appear to compute DDCS due to the fact that all the crossed terms between different atomic orbitals should be evaluated. To make the computations easier, *Senger* [76, 77] introduced a usually applied method in which all the overlapping integrals are disregarded, thus reducing the final DDCS for any MO to a weighted sum of atomic DDCS, for each of the atomic components of the molecule. The other one is a monocentric approach developed by *R. Moccia* [78–80], where the ground state orbitals of molecules of the type XH_n are constructed through a linear combination of STF described with reference to a common origin. In the mentioned molecules, this origin is placed at the location of the nucleus of the heaviest atom labeled X, i.e., where the electronic density is concentrated. Moreover, wave functions are obtained for fixed-in-space molecules. In order to compare with most experiments where the molecular target is randomly oriented, an average over all possible molecular orientations is required.

To circumvent the complexities of using numerical three-center molecular continuum wave functions, an additional assumption is introduced: the active electron-residual target potential in the final channel is accounted for through an effective Coulomb one with an effective charge chosen in close relation with the binding energy of the molecular orbital from which ionization is produced.

The prior version of the CDW-EIS approximation exhibited a very good accord with the available experimental DDCS as a function of the angular distribution of ejected electrons, corresponding to fixed final electron energies, for impact of fast H^+ , He^{2+} , C^{6+} , and O^{8+} ([72] and references therein). The results were quite insensitive to the theoretical descriptions of the initial state. Moreover, this theoretical model was also applied with success not only to describe the above-mentioned DDCS but also to electron energy spectra for fixed angle emission, as well as for single differential cross sections [81–83].

In addition, it should be noted that a molecular version of the CDW-EIS within a three-body description – active electron, residual target, and projectile – labeled CDW-EIS MO, was employed. In this version, the molecular orbitals were obtained through a contraction of Gaussian-type func-

tions, using the STO-3G basis set, based on an HF approach, and the associated orbital energies were determined. The target molecular continuum wave functions were approximated by means of a spherical averaged potential created by the nuclei and the residual electrons, where effective nuclear potentials are used. It was again shown that the results for both single-electron ionization and single-electron capture by proton impact were quite insensitive to the description of the initial state, by comparing DDCS with the ones obtained with the CNDO model.

Finally, the CDW and CDW-EIS approximations were also employed to investigate single-electron capture and single-electron ionization DDCS, SDSCS- and TCS of larger molecules like the nucleobases, namely adenine, cytosine, thymine, and guanine, and the sugar phosphate backbone composing the double-stranded deoxyribonucleic acid (DNA) as well as uracil [84, 85]. A similar description to that employed by *Tachino et al.* [72] for DNA and uracil total-energy calculations for all targets were performed in the gas phase with the Gaussian 09 software at the RHF/3-21G level of theory. The equilibrium geometries of the nucleobases were obtained without symmetry constraints [63]. The results were compared with the scarce experimental data that was available in those days. Those results stimulated the development of further experiments, which were successfully compared with CDW-EIS calculations [86–88].

56.3 Wannier Method

56.3.1 The Wannier Threshold Law

In 1953, *Wannier* [89] deduced the relationship between the cross section at the threshold of a reaction and the excess-of-threshold energy of the incident particle for a three-body ionization problem, where the final state consists of a residual unit positive charge and two electrons, with each body moving in the continuum of the other two. This extended the earlier two-body threshold law derived by *Wigner* [90] to three bodies (Sect. 64.2.2).

For final states with $L = 0$, *Wannier* employed hyperspherical coordinates $(\rho, \alpha, \theta_{12})$, where

$$\begin{aligned} \rho^2 &= r_1^2 + r_2^2, \quad \alpha = \tan^{-1}\left(\frac{r_2}{r_1}\right), \\ \theta_{12} &= \cos^{-1}(\hat{\mathbf{r}}_1 \cdot \hat{\mathbf{r}}_2). \end{aligned} \quad (56.45)$$

Here, we assume that the residual ion is infinitely massive and at rest with respect to the two electrons. By converting the two-electron problem to the case of motion of a single point in six-dimensional space, we can take the hyperradius ρ as the *size* of the hypersphere, α as the radial correlation of the electrons, and θ_{12} as their angular correlation. This allows

the Schrödinger equation for the final state to be written (in a.u.) as

$$\begin{aligned} \left(h_0 - \frac{l^2(\hat{\mathbf{r}}_1)}{\rho^2 \cos^2 \alpha} - \frac{l^2(\hat{\mathbf{r}}_2)}{\rho^2 \sin^2 \alpha} + 2E \right. \\ \left. + \frac{2Z(\alpha, \theta_{12})}{\rho} \right) \Psi(\mathbf{r}_1, \mathbf{r}_2) = 0, \end{aligned} \quad (56.46)$$

where

$$\begin{aligned} h_0 &= \frac{1}{\rho^5} \frac{\partial}{\partial \rho} \left(\rho^5 \frac{\partial}{\partial \rho} \right) + \frac{1}{\rho^2 \sin^2 \alpha \cos^2 \alpha} \frac{\partial}{\partial \alpha} \\ &\times \left(\sin^2 \alpha \cos^2 \alpha \frac{\partial}{\partial \alpha} \right), \end{aligned} \quad (56.47)$$

and

$$Z(\alpha, \theta_{12}) = \frac{1}{\cos \alpha} + \frac{1}{\sin \alpha} - \frac{1}{(1 - \cos \theta_{12} \sin 2\alpha)^{\frac{1}{2}}} \quad (56.48)$$

is the potential surface on which the particle is moving [91].

The most likely configuration of the electrons leading to double escape at threshold corresponds to the region $\mathbf{r}_1 = -\mathbf{r}_2$, i.e., the two electrons escape in opposite directions from the reaction zone, corresponding to the saddle point of the potential surface $Z(\alpha, \theta_{12})$ and defined as the Wannier ridge. Also, dynamic screening between the two electrons means there would be equal partitioning of the energy available for the two particles, and so they would have equal but opposite velocities on escape. In hyperspherical coordinates, the most important region for double escape is, therefore, $\alpha = \pi/4$, and $\theta_{12} = \pi$.

The main conclusion of *Wannier's* theory is that the total cross section for electron impact single ionization scales as

$$\sigma = kE^{m_{12}}, \quad (56.49)$$

where E is the excess-of-threshold energy,

$$m_{12} = -\frac{1}{4} + \frac{1}{4} \left(\frac{100Z - 9}{4Z - 1} \right)^{\frac{1}{2}}, \quad (56.50)$$

and Z the residual charge; m_{12} is 1.127 for a unit residual charge, with $m_{12} \rightarrow 1$ as $Z \rightarrow \infty$.

56.3.2 Peterkop's Semiclassical Theory

The Wannier threshold law has been verified both semiclassically [92] and quantum mechanically [93]. *Peterkop* [92]

adopted a semiclassical JWKB approach to the problem by using the three-dimensional WKB ansatz

$$\Psi_0 = P^{\frac{1}{2}} \exp\left(\frac{iS}{\hbar}\right), \quad (56.51)$$

for the final-state wave function, where S and P are, respectively, the solutions of the Hamilton–Jacobi equation,

$$(\nabla_1 S)^2 + (\nabla_2 S)^2 = 2(E - V), \quad (56.52)$$

and the continuity equation,

$$\nabla_1(P \nabla_1 S) + \nabla_2(P \nabla_2 S) = 0. \quad (56.53)$$

In hyperspherical coordinates, these equations become

$$\begin{aligned} & \left(\frac{\partial S}{\partial \rho}\right)^2 + \frac{1}{\rho^2} \left(\frac{\partial S}{\partial \alpha}\right)^2 + \frac{4}{\rho^2 \sin^2 2\alpha} \left(\frac{\partial S}{\partial \theta_{12}}\right)^2 \\ & = 2E + \frac{2Z}{\rho}, \end{aligned} \quad (56.54)$$

and

$$\begin{aligned} & D_0 \left(P \frac{\partial S}{\partial \rho} \right) + \frac{1}{\rho^2} \\ & \times \left[D_1 \left(P \frac{\partial S}{\partial \alpha} \right) + D_2 \left(\frac{\partial S}{\partial \theta_{12}} \right) \right] = 0, \end{aligned} \quad (56.55)$$

where

$$D_0 f = \frac{1}{\rho^5} \frac{\partial}{\partial \rho} (\rho^5 f), \quad (56.56)$$

$$D_1 f = \frac{1}{\sin^2 2\alpha} \frac{\partial}{\partial \alpha} (f \sin^2 2\alpha), \quad (56.57)$$

$$D_2 f = \frac{4}{\sin^2 2\alpha} \frac{1}{\sin \theta_{12}} \frac{\partial}{\partial \theta_{12}} (f \sin \theta_{12}). \quad (56.58)$$

Following Wannier's hypothesis, solutions of these equations are found in the region $\alpha = \pi/4$, $\theta_{12} = \pi$. Taking the Taylor expansion for $Z(\alpha, \theta_{12})$ as

$$Z(\alpha, \theta_{12}) = Z_0 + \frac{1}{2} Z_1 (\Delta\alpha)^2 + \frac{1}{8} Z_2 (\Delta\theta_{12})^2 + \dots, \quad (56.59)$$

where $\Delta\alpha = \alpha - \pi/4$ and $\Delta\theta_{12} = \theta_{12} - \pi$, it follows from Eq. (56.48) that

$$Z_0 = \frac{3}{\sqrt{2}}, \quad Z_1 = \frac{11}{\sqrt{2}}, \quad Z_2 = -\frac{1}{\sqrt{2}}. \quad (56.60)$$

Similarly, taking the solution of Eq. (56.54) in the form

$$S = S_0(\rho) + \frac{1}{2} S_1(\rho) (\Delta\alpha)^2 + \frac{1}{8} S_2(\rho) (\Delta\theta_{12})^2 + \dots \quad (56.61)$$

gives

$$\frac{dS_0}{d\rho} = \omega, \quad (56.62)$$

$$\omega \frac{dS_i}{d\rho} + \frac{S_i^2}{\rho^2} = \frac{Z_i}{\rho}, \quad i = 1, 2, \quad (56.63)$$

where $\omega = (2E + 2Z_0/\rho)^{\frac{1}{2}}$. The solutions are

$$S_0 = \rho\omega + \frac{Z_0}{\chi} \ln \frac{\rho(\chi + \omega)^2}{2Z_0}, \quad (56.64)$$

$$S_i = \rho^2 \omega \frac{1}{u_i} \frac{du_i}{d\rho}, \quad i = 1, 2, \quad (56.65)$$

where $\chi = (2E)^{\frac{1}{2}}$, and

$$u_i = C_{i1} u_{i1} + C_{i2} u_{i2}, \quad (56.66)$$

$$u_{ij} = \rho^{m_{ij}} {}_2F_1 \left(m_{ij}, m_{ij} + 1; 2m_{ij} + \frac{3}{2}; \frac{-E\rho}{Z_0} \right), \quad (56.67)$$

$$m_{i1} = -\frac{1}{4} - \frac{1}{2} \mu_i, \quad m_{i2} = -\frac{1}{4} + \frac{1}{2} \mu_i, \quad (56.68)$$

$$\mu_i = \frac{1}{2} \left(1 + \frac{8Z_i}{Z_0} \right)^{\frac{1}{2}}, \quad (56.69)$$

where, for $i = 2$, the principal branch is understood.

Expanding P in the same form as S , and restricting the solution to finding P_0 , gives

$$P_0 = \frac{C}{\rho^5 \omega u_1 u_2^2}, \quad (56.70)$$

where $C \approx C_{12} E^{1-m_{12}}$. By solving these equations, Peterkop extracted the Wannier cross section behavior by matching the exact wave function with an approximate one for which the energy dependence is known at some arbitrarily finite value r_0 of ρ , giving the total cross section as

$$\sigma_{\text{tot}} \approx E^{1.127}, \quad (56.71)$$

as required. However, neither this method of Peterkop nor the quantum mechanical approach of [93] were able to deduce the constant of proportionality.

56.3.3 The Quantal Semiclassical Approximation

As can be seen from the form of Eq. (56.70) for P_0 , u_2 vanishes in the double limit $\rho \rightarrow +\infty$, $E \rightarrow 0$, and so, the semiclassical theory breaks down at every configuration of importance. To avoid this problem, Crothers [9] adopted a change of the dependent variable to obtain a uniform

JWKB approximation. Taking $\alpha = \pi/4$, (i.e., $\Delta\alpha = 0$) as the natural barrier, he set the final-state wave function as

$$\psi^{-*} = \frac{x |\sin(\alpha - \pi/4)|^{1/2}}{\rho^{5/2} \sin \alpha \cos \alpha (\sin \theta_{12})^{1/2}}, \quad (56.72)$$

so that

$$\left[\frac{\partial^2}{\partial \rho^2} + \frac{1}{\rho^2 \sin |\Delta\alpha|} \frac{\partial}{\partial \alpha} \left(\sin |\Delta\alpha| \frac{\partial}{\partial \alpha} \right) + \frac{1}{\rho^2 \sin^2 \alpha \cos^2 \alpha} \frac{\partial^2}{\partial \theta_{12}^2} + 2E + \frac{2Z}{\rho} + \frac{(\frac{1}{4} + \frac{1}{4} \csc^2 \Delta\theta_{12})}{\rho^2 \sin^2 \alpha \cos^2 \alpha} - \frac{\csc^2 |\Delta\alpha|}{4\rho^2} \right] x = 0, \quad (56.73)$$

where $|\Delta\alpha|$ and θ_{12} are, respectively, the polar and azimuthal angles. Near $\theta_{12} = \pi$ and $\alpha = \pi/4$ (i.e., at $\Delta\theta_{12} = \Delta\alpha = 0$), the term $(4\rho^2)^{-1}$ is negligible compared with $\csc^2 \theta_{12}/(4\rho^2)$. Also, the θ_{12} pseudopotential is clearly attractive, while the α potential is repulsive, and both potentials are large just at the region of importance, i.e., at $\Delta\alpha = 0 = \Delta\theta_{12}$.

Again, following the method of Peterkop, the final state wave function is written in the form of Eqs. (56.51), (56.54), and (56.55), where now the action perturbation expression S must be generalized to

$$S = s_0 \ln |\Delta\alpha| + s_1 \ln(\Delta\theta_{12}) + S_0(\rho) + \frac{1}{2} S_1(\rho)(\Delta\alpha)^2 + \frac{1}{8} S_2(\rho)(\Delta\theta_{12})^2 + \dots, \quad (56.74)$$

where the extra logarithmic phases indicate long-range Coulomb potentials. By applying the Kohn variational principle perturbatively and invoking Jeffreys' [94] connection formula on the Wannier ridge with $\rho = 0$ as the classical turning point, the final state wave function is [9]

$$\begin{aligned} \psi_f^{-*} = & \frac{c^{1/2} E^{m_{12}/2} \rho^{m_{12}/2 + 1/4} r (2Z_0)^{1/4} (-\chi/2\pi)^{1/2}}{(2Z_0/\rho)^{1/4} \rho^{5/2} \sin \alpha \cos \alpha} \\ & \times \delta(\hat{\mathbf{k}}_1 - \hat{\mathbf{r}}_1) \delta(\hat{\mathbf{k}}_2 - \hat{\mathbf{r}}_2) \\ & \times \exp\left[4i(8Z_0\rho)^{-1/2}(\Delta\theta_{12})^{-2}\right] \\ & \times \left\{ \exp\left[-i(8Z_0\rho)^{1/2} - \frac{1}{2}i(\Delta\alpha)^2\right] \right. \\ & \quad \times (2Z_0\rho)^{1/2} m_{12} - \frac{1}{8}i(\Delta\theta_{12})^2 \\ & \quad \left. \times (2Z_0\rho)^{1/2} m_{21} - \frac{1}{4}i\pi \right] - \text{c.c.} \left. \right\}, \quad (56.75) \end{aligned}$$

where $\chi = 2\pi \text{Im}(m_{21})$.

Taking the total cross section for distinguishable particles as

$$\begin{aligned} \sigma = & \frac{\pi^2 a_0^2}{k_0} \iint d\hat{\mathbf{k}}_1 d\hat{\mathbf{k}}_2 \frac{\pi Z_2 \tanh \chi}{(2E)^{1/2}} \left| f(\hat{\mathbf{k}}_1, \hat{\mathbf{k}}_2) \right|^2 \\ & \times \exp\left[\frac{-Z_2}{4(2E)^{1/2}} (\Delta\theta_{12})^2 \pi \tanh \chi \right], \quad (56.76) \end{aligned}$$

where f is the scattering amplitude, then the corresponding TDCS is

$$\begin{aligned} & \frac{d^3\sigma}{d\hat{\mathbf{k}}_1 d\hat{\mathbf{k}}_2 d(\frac{1}{2}k_1^2)} \\ & = \frac{2\pi^2 a_0^2}{k_0} \frac{d}{dE} \frac{\pi Z_2 \tanh \chi}{(2E)^{1/2}} \\ & \quad \times \exp\left[\frac{-Z_2}{4(2E)^{1/2}} (\Theta_{12} - R\pi)^2 \pi \tanh \chi \right] \\ & \quad \times \left| f(\hat{\mathbf{k}}_1, \hat{\mathbf{k}}_2) \right|^2. \quad (56.77) \end{aligned}$$

Assuming that the contribution from triplet states is negligible, $|f|^2$ can be written as

$$\frac{1}{4} \left| f(\hat{\mathbf{k}}_1, \hat{\mathbf{k}}_2) + f(\hat{\mathbf{k}}_2, \hat{\mathbf{k}}_1) \right|^2, \quad (56.78)$$

where $f(\hat{\mathbf{k}}_1, \hat{\mathbf{k}}_2)$ (and by permutation $f(\hat{\mathbf{k}}_2, \hat{\mathbf{k}}_1)$, hereafter referred to as f and g , respectively) is given by

$$\begin{aligned} f \simeq & \frac{2i}{\pi} \int d\mathbf{r}_1 d\mathbf{r}_2 d\mathbf{r}_3 \Psi_f^{-*} \phi_f(2, \mathbf{r}_3) \\ & \times (H - E) \exp(i\mathbf{k}_0 \cdot \mathbf{r}_1) \psi_i(\mathbf{r}_2, \mathbf{r}_3). \quad (56.79) \end{aligned}$$

As a test of the above formulation for the process $e^- + \text{He} \rightarrow \text{He}^+ + 2e^-$ near the ionization threshold, Crothers [9] used an independent-electron open-shell wave function for the initial bound-state helium target, written as

$$\psi_i(\mathbf{r}_2, \mathbf{r}_3) = \frac{\phi(\mathbf{r}_2, z_0)\phi(\mathbf{r}_3, \beta) + \phi(\mathbf{r}_3, z_0)\phi(\mathbf{r}_2, \beta)}{[2(1 + S)]^{1/2}}, \quad (56.80)$$

where

$$\phi(\mathbf{r}, z_0) = z_0^{3/2} \pi^{-1/2} \exp(-z_0 r), \quad (56.81)$$

$$\begin{aligned} S = & \left[\int \phi(\mathbf{r}, z_0)\phi(\mathbf{r}, \beta) d\mathbf{r} \right]^2 \\ & = \left(\frac{4z_0\beta}{(z_0 + \beta)^2} \right)^3, \quad (56.82) \end{aligned}$$

and z_0 and β take the physical values $z_0 = 1.8072^{1/2}$, and $\beta = 2$. The total singlet cross section was found to be (in atomic units)

$$\sigma = 2.37 E^{m_{12}} a_0^2, \quad (56.83)$$

in line with Wannier's threshold law and with experiments [95], while the corresponding absolute TDCS were expressed as

$$\frac{d^3\sigma}{d\hat{k}_1 d\hat{k}_2 d(\frac{1}{2}k_1^2)} = \frac{70cz_0^2 2^{1/2} \chi \tanh \chi}{\pi R_\infty Z_0^{1/2} m_{12}} |f + g|^2 \times \left[\frac{d}{dE} E^{m_{12}-1/2} \exp\left(\frac{-Z_2(\Theta_{12} - \pi)^2 \pi \tanh \chi}{4(2E)^{1/2}}\right) \right] \quad (56.84)$$

in units of $10^{-19} \text{ cm}^2 \text{ sr}^{-2} \text{ eV}^{-1}$, where

$$c = \frac{\Gamma(m_{12} + 3/2)\Gamma(m_{12} + 1)}{2\pi Z_0^{m_{12}} \Gamma(2m_{12} + 3/2)}, \quad (56.85)$$

and where f (and similarly g for Θ_2) is given by

$$f = \int_0^\infty d\rho \rho^{3/2+m_{21}/2+1/4} \sum_{L=0}^{L_{\max}} i^L (2L+1) j_L\left(\frac{\rho z_0}{2^{1/2}}\right) \times P_L(\cos \Theta_1) \exp\left\{\frac{1}{8} \times \text{Im}[m_{21}(\Theta_{12}-\pi)^2 (2Z_0\rho)^{1/2}]\right\} \times 2 \cos\left\{(8Z_0\rho)^{1/2} + \frac{1}{8}\right\} \times \text{Re}[m_{21}(\Theta_{12}-\pi)^2 (2Z_0\rho)^{1/2}]\right\} \times r(\rho, \Theta_{12}) \quad (56.86)$$

with

$$(1+S)^{1/2} r(\rho, \Theta_{12}) = \exp\left(-\frac{\rho z_0}{2^{1/2}}\right) \left(2^{1/2} z_0 - \frac{1}{(1-\cos \Theta_{12})^{1/2}}\right) + \exp(-2^{1/2}\rho) \left[\frac{64(2)^{1/2}(z_0-1)}{(z_0+2)^3} + \frac{32}{(z_0+2)^3} [2(2)^{1/2} + (z_0+2)\rho] \exp\left(\frac{-\rho(z_0+2)}{2^{1/2}}\right)\right]. \quad (56.87)$$

These results have been found to compare favorably with both the relative experimental results of [96] and the absolute experimental results of [97]. The Crothers quantal semiclassical approximation has been successfully applied to other threshold (e, 2e) and (photon, 2e) collisions, namely two-electron photodetachment from H^- [98], $\text{He}(^4\text{P}_{5/2}^0)$ [99], and K^- [100]. Further investigations of the TDCS for helium at threshold have been since then carried out. The $^3\text{P}^0$ triplet contribution to the TDCS was studied in [101], where small

but notable improvements in the comparison with experimental results [96] and [97] were achieved for most configurations of the angles θ_1 and θ_2 . The inclusion of contributions from $^3\text{D}^{e,0}$ or $^3\text{F}^0$ to the absolute TDCS were found to be negligible in comparison with the effect of the $^3\text{P}^0$ [102], although the admittedly non-Wannier effective-charge investigation of $\theta_{12} = \pi$ by Pan and Starace [103] suggests that $^3\text{F}^0$ may be important at $\theta_1 = \pi/6$ or $5\pi/6$, in line with the experiment of Rösler et al. [97]. Another aspect that is thought to contribute to the TDCS is explicit correlation in the initial bound-state wave function for the helium target, in which the interelectronic distance r_{23} is explicitly contained. Absolute singlet TDCS have been obtained [104], using a helium ground state wave function developed by Le Sech [105]. Again, excellent agreement with the singlet results of [9] has been achieved, and, in most configurations, notable improvements with the corresponding experimental data are obtained, as shown in Fig. 56.4 for scattering angle $\theta_1 = 60^\circ$ (a) and 90° (b), indicating that electron correlation should also be considered if a full picture of threshold ionization is to be achieved.

Several significant new developments and contributions to the Wannier theory have also been presented. One notable achievement has been the analytical continuation of the uniform semiclassical wave function [9] to below the energy threshold to calculate the complex eigenenergies for doubly excited states of helium using a complex Bohr–Sommerfeld quantization rule with at least one complex transition point [5, 6]. The real parts of the eigenvalues were found to be in good agreement with the experimental results of Buckman et al. [106, 107] for the resonance positions, while the imaginary parts give the explicit widths of the resonances from which the intensities have been estimated. The theory in [5] was initially considered for the inaugural case of $L = 0$. Further investigation [6–8] extended the theory to include resonant states for $L = 1$ and $L = 2$. In the case of $L = 1$, an irrational quantum number was obtained, and attosecond lifetimes were obtained. Excellent results were obtained for the resonance positions, lifetimes, intensities, and scaling rules in comparison with the experimental data [106]. This success persuaded Deb and Crothers [108] to revisit the problem of quantal near-threshold ionization of He by electron impact. In particular, they reexamined the problem of above threshold ionization of He by electron impact by retaining the term $2L(L+1)/\rho^2$ in the hyperspherical equation

$$\left(\frac{1}{\rho^5} \frac{\partial}{\partial \rho} \rho^5 \frac{\partial}{\partial \rho} + \frac{1}{\rho^2 \sin^2 2\alpha} \frac{\partial}{\partial \alpha} \sin^2 2\alpha \frac{\partial}{\partial \alpha} + \frac{4}{\rho^2 \sin \theta_{12}} \frac{\partial}{\partial \theta_{12}} \sin \theta_{12} \frac{\partial}{\partial \theta_{12}} + 2E + \frac{2\zeta(\alpha, \theta_{12}) 2L(L+1)}{\rho^2}\right) \Psi = 0. \quad (56.88)$$

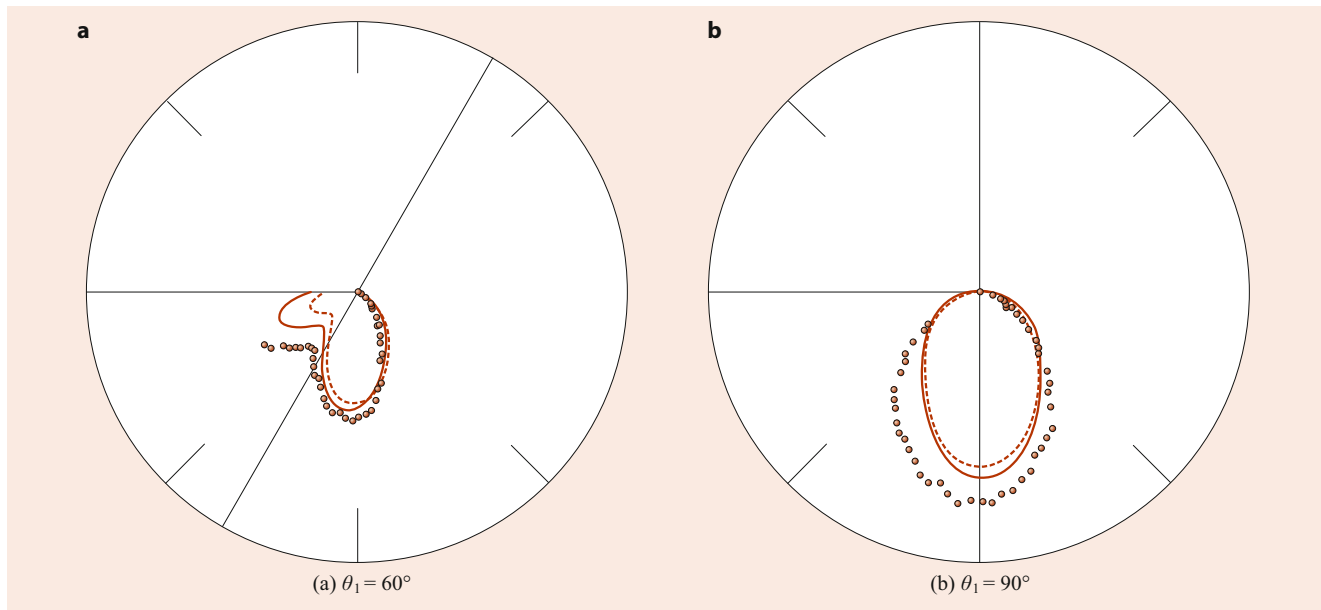


Fig. 56.4 Helium triply differential ionization cross section for coplanar geometry, $E_1 = E_2 = 1$ eV and $E = 2$ eV, calculated (full curve) TDCS of Copeland and Crothers [104] in polar coordinates, with polar coordinates as θ_2 , for scattering angles $\theta_1 = 60^\circ$ (a) and $\theta_1 = 90^\circ$ (b), in comparison with absolute experimental (circles) data of Rösel et al. [97], and theoretical results (broken curve) of Crothers [9]. The radius of each circle is $1.0 \times 10^{-19} \text{ cm}^2 \text{ sr}^{-2} \text{ eV}^{-1}$

Following the procedure of Crothers [9], they obtained

$$\begin{aligned} \Psi_f^{-*} = & \frac{c^{1/2} E^{m_{12}/2} u_1^{1/2}}{\tilde{\omega}^{1/2} \rho^{5/2} \sin \alpha \cos \alpha} \delta(\hat{\mathbf{k}}_1 - \hat{\mathbf{r}}_1) \\ & \times \delta(\hat{\mathbf{k}}_2 - \hat{\mathbf{r}}_2) \exp[4i(8Z_0\rho)^{-1/2}(\Delta\theta_{12})^{-2}] \\ & \times \exp\left\{-i\left[S_0 + \frac{1}{2}S_1(\Delta\alpha)^2\right.\right. \\ & \left.\left.+ \frac{1}{8}S_2(\Delta\theta_{12})^2 + \frac{\pi}{4}\right] - \text{conjugate}\right\}, \end{aligned} \quad (56.89)$$

where the classical action variables are given by

$$S_0 = \int_0^\rho d\tilde{\rho} \tilde{\omega}, \quad (56.90)$$

$$S_i = \rho^2 \omega (\ln u_i)', \quad i = 1, 2, \quad (56.91)$$

with

$$\tilde{\omega} = [\omega^2 - \omega(\ln u_2 - i \ln u_1)']^{1/2}, \quad (56.92)$$

$$\omega^2 = 2E + 2Z_0/\rho - 2L(L+1)/\rho^2. \quad (56.93)$$

The primes in Eqs. (56.91) and (56.92) denote derivatives with respect to ρ and $\tilde{\rho}$, respectively. It is to be noted here that the original work used the approximated form of ω by dropping the L -dependent term in Eq. (56.93). The inclusion

of this angular momentum term moves the classical turning point from the origin to ρ_+ , where

$$\rho_+ = \frac{-Z_0 + \sqrt{Z_0^2 + 4EL(L+1)}}{2E}. \quad (56.94)$$

As a result, the lower limit of ρ integration will be replaced by ρ_+ . The classical action variables S_1 and S_2 are now evaluated without introducing the limit $E\rho \rightarrow 0$. Using the final state wave function in Eq. (56.89) we first calculated the direct ionization amplitude. The exchange ionization amplitudes for the two indistinguishable atomic electrons were then obtained by interchanging the angles θ_1 and θ_2 in the direct amplitude. Singlet and triplet contributions are then accounted for in the usual ratio of 1 : 3.

Equation (56.89) is a more accurate variant of Eq. (56.75) used in the original theory of Crothers [9]. Using this refinement of the wave function, all partial wave contributions for singlets and triplets are accounted for up to $L = 6$ for the case of He by electron impact at an excess of 2 eV above threshold. It was found that within the coplanar geometry, both the symmetric and asymmetric triple differential cross sections, peaking at and near the Wannier ridge, are greatly improved when compared with experiment [109]. However, far away from the Wannier ridge, the TDCS tend to show qualitative differences from measurement [109].

The improved theory [108] has also been successfully applied to the calculation of total cross sections of positron impact ionization of helium for energies 0.5–10 eV above

threshold [110]. Excellent agreement with available experimental data [111] was obtained for the absolute theoretical calculation of positron impact ionization [110].

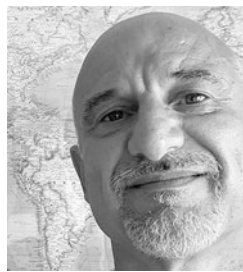
References

- Crothers, D.S.F., et al.: In: Drake, G.W.F. (ed.) Springer Handbooks of Atomic, Molecular, and Optical Physics, p. 775. Springer, Heidelberg (2006)
- Crothers, D.S.F., McSherry, D.M., O'Rourke, S.F.C., Shah, M.B., McGrath, C., Gilbody, H.B.: Phys. Rev. Lett. **88**, 053201 (2002)
- O'Rourke, S.F.C., McSherry, D.M., Crothers, D.S.F.: J. Phys. B **36**, 314 (2003)
- Bhattacharya, S., Das, R., Deb, N.C., Roy, K., Crothers, D.S.F.: Phys. Rev. A **68**, 052702 (2003)
- Loughan, A.M., Crothers, D.S.F.: Phys. Rev. Lett. **79**, 4966 (1997)
- Loughan, A.M.: Adv. Chem. Phys. **114**, 312 (2000)
- Loughan, A.M., Crothers, D.S.F.: J. Phys. B **31**, 2153 (1998)
- Crothers, D.S.F., Loughan, A.M.: Philos. Trans. R. Soc. Lond. A **357**, 1391 (1999)
- Crothers, D.S.F.: J. Phys. B **19**, 463 (1986)
- Cheshire, I.M.: Proc. Phys. Soc. **84**, 89 (1964)
- Bransden, B.H., McDowell, M.R.C.: Charge Exchange and the Theory of Ion-Atom Collisions. Clarendon, Oxford (1992)
- Crothers, D.S.F.: J. Phys. B **15**, 2061 (1982)
- Crothers, D.S.F.: J. Phys. B **18**, 2893 (1985)
- Rivarola, R.D., Miraglia, J.E.: J. Phys. B **15**, 2221 (1982)
- Vogt, H., Schuch, R., Justiniano, E., Schultz, M., Schwab, W.: Phys. Rev. Lett. **57**, 2256 (1986)
- O'Rourke, S.F.C., Crothers, D.S.F.: J. Phys. B **29**, 1969 (1996)
- Dewangan, D.P., Eichler, J.: J. Phys. B **18**, L65 (1985)
- Martinez, A.E., Deco, G.R., Rivarola, R.D.: Nucl. Instrum. Meth. Phys. Res. B **34**, 32 (1988)
- Maidagan, J.M., Rivarola, R.D.: J. Phys. B **17**, 2477 (1984)
- Crothers, D.S.F.: Relativistic Heavy-Particle Collision Theory. Kluwer Academic Plenum, New York (2000)
- Eichler, J., Meyerhof, W.E.: Relativistic Atomic Collisions. Academic Press, San Diego (1995)
- Glass, J.T., McCann, J.F., Crothers, D.S.F.: J. Phys. B **27**, 3445 (1994)
- Glass, J.T., McCann, J.F., Crothers, D.S.F.: Proc. R. Soc. Lond. A **453**, 387 (1997)
- Becker, U.: J. Phys. B **20**, 6563 (1987)
- Bertulani, C.A., Baur, G.: Phys. Rev. D **58**, 4005 (1998)
- Deco, G.R., Rivarola, R.D.: J. Phys. B **21**, 1229 (1988)
- Deco, G.R., Rivarola, R.D.: J. Phys. B **22**, 1043 (1989)
- Baur, G., et al.: Phys. Lett. B. **368**, 251 (1996)
- Deco, G.R., Rivarola, R.D.: J. Phys. B **19**, 1759 (1986)
- Deco, G.R., Fojón, O., Maidagan, J., Rivarola, R.D.: Phys. Rev. A **47**, 3769 (1993)
- Humphries, W.J., Moiseiwitsch, B.L.: J. Phys. B **17**, 2655 (1984)
- Jakubassa-Amundsen, D.H., Amundsen, P.A.: Z. Phys. A **298**, 13 (1980)
- McCann, J.F., Glass, J.T., Crothers, D.S.F.: J. Phys. B **29**, 6155 (1996)
- Lee, R.J.S., Mullan, J.V., McCann, J.F., Crothers, D.S.F.: Phys. Rev. A **63**, 062712 (2001)
- Baur, G.: Phys. Lett. B. **311**, 343 (1993)
- Eichler, J.: Phys. Rev. Lett. **75**, 3653 (1995)
- Löwdin, P.O.: Ark. Nat. Astron. Phys. **35A**, 918 (1947)
- Löwdin, P.O.: J. Chem. Phys. **18**, 365 (1950)
- Crothers, D.S.F.: Nucl. Instrum. Methods B **27**, 555 (1987)
- Crothers, D.S.F., Dub, L.J.: Adv. At. Mol. Phys. **30**, 287 (1993)
- Crothers, D.S.F., McCann, J.F.: J. Phys. B **16**, 3229 (1983)
- Crothers, D.S.F., O'Rourke, S.F.C.: J. Phys. B **25**, 2351 (1992)
- Kirchner, T., Gulyas, L., Ludde, H.J., Henne, A., Engel, E., Dreizler, R.M.: Phys. Rev. Lett. **79**, 1658 (1997)
- Sahoo, S., Das, R., Sil, N.C., Mukherjee, S.C., Roy, K.: Phys. Rev. A **62**, 022716 (2000)
- Rudd, M.E., Kim, Y.K., Madison, D.H., Gallagher, J.W.: Rev. Mod. Phys. **57**, 965 (1985)
- Pluvinae, P.: Ann. Phys. N. Y. **5**, 145 (1950)
- Brauner, M., Briggs, J.S., Klar, H.: J. Phys. B **22**, 2265 (1989)
- Bransden, B.H., Joachain, C.J.: Physics of Atoms and Molecules. Longman Group, London (1983)
- Becker, U.: Nature **474**, 586 (2011)
- Stolterfoht, N., Sulik, B., Hoffmann, V., Skogvall, B., Chesnel, J.Y., Rangama, J., Frémont, F., Hennecart, D., Cassimi, A., Husson, X., Landers, A.L., Tanis, J.A., Galassi, M.E., Rivarola, R.D.: Phys. Rev. Lett. **87**, 023201 (2001)
- Rolles, D., et al.: Nature **437**, 711 (2005)
- Cohen, H.D., Fano, U.: Phys. Rev. **150**, 30 (1966)
- Ciappina, M.F., Fojón, O., Rivarola, R.D.: J. Phys. B **47**, 042001 (2014)
- Wang, Y.D., McGuire, J.H., Rivarola, R.D.: Phys. Rev. A **40**, 3673 (1989)
- Corchs, S.E., Rivarola, R.D., McGuire, J.H.: Phys. Rev. A **47**, 3937 (1993)
- Galassi, M.E., Rivarola, R.D., Fainstein, P.D., Stolterfoht, N.: Phys. Rev. A **66**, 052705 (2002)
- Galassi, M.E., Rivarola, R.D., Fainstein, P.D.: Phys. Rev. A **70**, 032721 (2004)
- Stolterfoht, N., et al.: Phys. Rev. A **030702(R)**, 67 (2003)
- Hossain, S., et al.: Nucl. Instr. Meth. Phys. Res. B **205**, 484 (2003)
- Hossain, S., Landers, A.L., Stolterfoht, N., Tanis, J.A.: Phys. Rev. A **010701(R)**, 72 (2005)
- Misra, D., Khadane, U., Singh, Y.P., Tribedi, L.C., Fainstein, P.D., Richard, P.: Phys. Rev. Lett. **92**, 153201 (2004)
- Chowdhury, U., Schulz, M., Madison, D.H.: Phys. Rev. A **83**, 032712 (2011)
- Frisch, M.J., et al.: Gaussian 09 Revision A.02. Gaussian Inc, Wallingford, CT (2009)
- Tachino, C.A., Martin, F., Rivarola, R.D.: J. Phys. B **45**, 025201 (2012)
- Baran, J.L., Das, S., Járαι-Szábo, F., Nagy, L., Tanis, J.A.: J. Phys. Conf. Ser. **58**, 215 (2007)
- Baran, J.L., Das, S., Járαι-Szábo, F., Póra, K., Nagy, L., Tanis, J.A.: Phys. Rev. A **78**, 012710 (2008)
- Winkworth, M., et al.: Nucl. Instr. Meth. Phys. Res. B **267**, 373 (2009)
- Winkworth, M., et al.: J. Phys. Conf. Ser. **163**, 012044 (2009)
- Nandi, S., et al.: Phys. Rev. A **85**, 062705 (2012)
- Nandi, S., et al.: J. Phys. B **45**, 215207 (2012)
- Nandi, S., et al.: Eur. Phys. J. D **69**, 192 (2015)
- Tachino, C.A., Monti, J.M., Fojón, O.A., Champion, C., Rivarola, R.D.: J. Phys. B **47**, 035203 (2014)
- Pople, J., Santry, D., Segal, G.: J. Chem. Phys. **43**, 129 (1965)
- Pople, J., Segal, G.: J. Chem. Phys. **43**, 136 (1965)
- Pople, J., Segal, G.: J. Chem. Phys. **44**, 3289 (1966)
- Senger, B., Wittendorp-Rechenmann, E., Rechenmann, R.V.: Nucl. Instrum. Methods Phys. Res. **194**, 437 (1982)
- Senger, B., Rechenmann, R.V.: Nucl. Instrum. Methods. Phys. Res. B **2**, 204 (1984)
- Moccia, R.: J. Chem. Phys. **40**, 2164 (1964)
- Moccia, R.: J. Chem. Phys. **40**, 2176 (1964)
- Moccia, R.: J. Chem. Phys. **40**, 2186 (1964)

81. Ohsawa, D., Tawara, H., Soga, F., Galassi, M.E., Rivarola, R.D.: Phys. Scr. **T156**, 014939 (2013)
82. Nandi, S., Biswas, S., Khan, A., Monti, J.M., Tachino, C.A., Rivarola, R.D., Misra, D., Tribedi, L.C.: Phys. Rev. A **87**, 052710 (2013)
83. Bhattacharjee, S., Biswas, S., Bagdia, C., Roychowdhury, M., Nandi, S., Misra, D., Monti, J.M., Tachino, C.A., Rivarola, R.D., Champion, C., Tribedi, L.C.: J. Phys. B **49**, 065202 (2016)
84. Galassi, M.E., Champion, C., Weck, P.F., Rivarola, R.D., Fojón, O., Hanssen, J.: Phys. Med. Biol. **57**, 2081 (2012)
85. Champion, C., Weck, P.F., Lekadir, H., Galassi, M.E., Fojón, O.A., Abufager, P., Rivarola, R.D., Hanssen, J.: Phys. Med. Biol. **57**, 3039 (2012)
86. Agnihotri, A.N., Nandi, S., Kasthurirangan, S., Kumar, A., Galassi, M.E., Rivarola, R.D., Champion, C., Tribedi, L.C.: Phys. Rev. A **87**, 032716 (2013)
87. Agnihotri, A.N., Kasthurirangan, S., Nandi, S., Kumar, A., Champion, C., Lekadir, H., Hanssen, J., Weck, P.F., Galassi, M.E., Rivarola, R.D., Fojón, O., Tribedi, L.C.: J. Phys. B **46**, 185201 (2013)
88. Itho, A., Iriki, Y., Imai, M., Champion, C., Rivarola, R.D.: Phys. Rev. A **88**, 052711 (2013)
89. Wannier, G.H.: Phys. Rev. **90**, 817 (1953)
90. Wigner, E.P.: Phys. Rev. **73**, 1002 (1948)
91. Rudge, M.R.H., Seaton, M.J.: Proc. R. Soc. A **283**, 262 (1965)
92. Peterkop, R.K.: J. Phys. B **4**, 513 (1971)
93. Rau, A.R.P.: Phys. Rev. A **4**, 207 (1971)
94. Jeffreys, H.: Proc. Lond. Math. Soc. **23**, 428 (1923)
95. Cvejanović, S., Read, F.H.: J. Phys. B **7**, 1841 (1974)
96. Selles, P., Huetz, A., Mazeau, J.: J. Phys. B **20**, 5195 (1987)
97. Rösel, T., Röder, J., Frost, L., Jung, K., Ehrhardt, H.: J. Phys. B **25**, 3859 (1992)
98. McCann, J.F., Crothers, D.S.F.: J. Phys. B **19**, L399 (1986)
99. Crothers, D.S.F., Lennon, D.J.: J. Phys. B **21**, L409 (1988)
100. Carruthers, D.R.J., Crothers, D.S.F.: J. Phys. B **24**, L199 (1991)
101. Carruthers, D.R.J., Crothers, D.S.F.: Z. Phys. D **23**, 365 (1992)
102. Carruthers, D.R.J.: Ph. D. Thesis. Queen's University Belfast, Belfast (1993)
103. Pan, C., Starace, A.F.: Phys. Rev. A **45**, 4588 (1992)
104. Copeland, F.B.M., Crothers, D.S.F.: J. Phys. B **27**, 2039 (1994)
105. Siebbeles, L.D.A., Marshall, D.P., Le Sech, C.: J. Phys. B **26**, L321 (1993)
106. Buckman, S.J., Hammond, P., Read, F.H., King, G.C.: J. Phys. B **16**, 4039 (1983)
107. Buckman, S.J., Newman, D.S.: J. Phys. B **20**, L711 (1987)
108. Deb, N.C., Crothers, D.S.F.: J. Phys. B **33**, L623 (2000)
109. Rösel, T., Röder, J., Frost, L., Jung, K., Ehrhardt, H., Jones, S., Madison, D.H.: Phys. Rev. A **46**, 2539 (1992)
110. Deb, N.C., Crothers, D.S.F.: J. Phys. B **35**, L85 (2002)
111. Ashley, P., Moxom, J., Laricchia, G.: Phys. Rev. Lett. **77**, 1250 (1996)



Roberto D. Rivarola Roberto D. Rivarola born in Rosario, Argentina. He received his PhD from the Université de Bordeaux I (France) in 1984. He has been Full Professor of Physics at the Universidad Nacional de Rosario since 1990 and is Superior Researcher at the National Research Council (CONICET). At present, he is Vice President of CONICET and Chair of Commission on Atomic, Molecular and Optical Physics of IUPAP.



Omar A. Fojón Omar A. Fojón received his PhD from the National University of Rosario (UNR) in Argentina in 1994. He has held several postdoctoral positions at universities in France and in Spain. At present, he is Researcher at the National Research Council of Argentina and Professor at the UNR. His areas of interest include attosecond science and atomic collisions.



Marcelo Ciappina M. Ciappina received his PhD from the Balseiro Institute at Argentina in 2005 and a Research Professor degree from the Czech Academy of Sciences in 2019. His academic training includes postdoctoral stays at renowned institutions in Germany, Singapore, USA, Spain and Czechia. At present, he is Associate Professor at the Guangdong Technion – Israel Institute of Technology (GTIIT), Shantou, China. His areas of interest include attosecond science and atomic collisions.



Derrick Crothers Derrick Crothers is Professor of Theoretical Physics (Personal Chair). He research interests lie in atomic, molecular, optical, and condensed matter physics. The topics include heavy-particle collisions, threshold phenomena, dielectrics, and ferromagnetism. He was awarded an Honorary Professorship in Physics by St Petersburg State University in 2003. He passed away on January 15, 2021.



Basic Atomic Processes in High-Energy Ion–Atom Collisions

57

Alexander Voitkiv

Contents

57.1	Introduction	829
57.2	Atomic Ionization and Projectile-Electron Loss	830
57.2.1	Atomic Ionization in Collisions with a Bare Nucleus	832
57.2.2	Projectile-Electron Loss	834
57.3	Electron Transfer Processes	836
57.3.1	Nonradiative Electron Capture	836
57.3.2	Radiative Electron Capture	839
57.4	Electron–Positron Pair Production	840
57.4.1	Free Pair Production	841
57.4.2	Bound–Free Pair Production	842
57.4.3	Bound–Bound Pair Production	843
57.4.4	More Advanced Theoretical Methods	844
	References	844

Abstract

This chapter gives an overview of basic atomic physics processes occurring in a high-energy collision of an ion with an atom. These processes include ionization of the atom, electron loss from the ion, nonradiative and radiative electron transfer from the atom to the ion, as well as electron–positron pair production. Atomic units ($e = m_e = \hbar = 1$, where e is the elementary charge, m_e is the electron mass, and \hbar Planck’s constant) are used throughout unless otherwise stated.

Keywords

ionization · electron transfer · projectile-electron loss · electron–positron pair production · born approximation · doubly differential cross section · target electron · total ionization cross section · binary encounter

57.1 Introduction

In a collision between an ion (projectile) and a neutral atom (target), a multitude of atomic physics processes may occur. Their strength, importance, and even their very existence essentially depend on the colliding species and the impact velocity (energy). They range from relatively simple processes, in which a minimum possible number of “active” electrons (leptons) participate and which can be termed *basic*, to very complex ones involving many “active” electrons (leptons). In this chapter, we shall deal with basic atomic processes occurring in high-energy ion–atom collisions.

The definition “high-energy” means that the impact velocity v greatly exceeds the typical orbiting velocities v_0 of outer-shell atomic electrons: $v \gg v_0$, where $v_0 \simeq e^2/\hbar$. Thus, in terms of the impact velocity, the high-energy collisions refer to the interval $v_0 \ll v < c$, where $c = v_0/\alpha$ is the speed of light in vacuum ($\alpha = e^2/\hbar c \approx 1/137$ is the fine-structure constant). In terms of the impact energy, the lower boundary of the range of high-energy collisions can, somewhat arbitrarily, be defined as $\simeq 1$ MeV/u (corresponding to $v \simeq 6v_0$), whereas its upper boundary is formally infinite.

Three basic atomic physics processes can occur in collisions between a bare projectile nucleus and a target atom. (i) An atomic electron can be ejected (or excited) due to the interaction with the projectile. (ii) An atomic electron can be transferred to the projectile forming a bound state of the corresponding projectile ion. The transfer can proceed without or with emission of radiation and is called nonradiative or radiative electron capture, respectively. (iii) In relativistic collisions, electron–positron pair production becomes possible.

If initially the projectile has an electron, then in a collision with an atom it can be ejected (lost) or excited. In the rest frame of the projectile this can be viewed as “ionization” or excitation of the ion by the incident atom. In addition to the nucleus, the atom has electrons, which also interact with the electron of the ion. As a result, the physics of “ionization” of the ion by the impact of a neutral atom will, in general, differ

A. Voitkiv (✉)
The Institute of Theoretical Physics I, Heinrich-Heine University
Düsseldorf
Düsseldorf, Germany
e-mail: alexander.voitkiv@tp1.uni-duesseldorf.de

very substantially from that of atomic ionization in collisions with a bare nucleus. Thus, in collisions of partially stripped ions with neutral atoms, a new process – (iv) projectile electron loss (or excitation) – becomes possible.

In ion–atom collisions nuclear processes may also take place. However, compared to atomic processes, they are normally characterized by much smaller cross sections. Therefore, the nuclei of the colliding particles will be regarded as structureless point-like charges that cannot be excited or broken in the collision.

A theoretical consideration of processes (i)–(iv) exploits a huge difference between masses of electrons and nuclei. Because of this the nuclei move in the collision practically undeflected and can be regarded as the source of an *external field* in which the electrons move undergoing transitions. In the *semiclassical* (or *impact parameter*) approximation only the electrons are treated as quantum particles, whereas the nuclei are supposed to move along classical trajectories (e.g. [1, Chap. 4]). One often chooses a reference frame in which one of the nuclei is at rest and takes its position as the origin. The other nucleus moves in this frame along a straight-line trajectory $\mathbf{R}(t) = \mathbf{b} + \mathbf{v}t$, where \mathbf{b} is the impact parameter, \mathbf{v} the particle (collision) velocity, and t the time.

Using the semiclassical approximation one obtains the semiclassical transition amplitude $a_{fi}(\mathbf{b})$. The transition amplitude $S_{fi}(\mathbf{q}_\perp)$, obtained using a fully quantum treatment, is related to $a_{fi}(\mathbf{b})$ by the Fourier transformation

$$S_{fi}(\mathbf{q}_\perp) = \frac{1}{2\pi} \int d^2\mathbf{b} a_{fi}(\mathbf{b}) \exp(i\mathbf{q}_\perp \cdot \mathbf{b}), \quad (57.1)$$

where \mathbf{q}_\perp is the transverse part ($\mathbf{q}_\perp \cdot \mathbf{v} = 0$) of the momentum transfer in the collision.

57.2 Atomic Ionization and Projectile-Electron Loss

Let us consider collisions of two atomic particles, which we denote by labels 1 and 2 (see for an illustration Fig. 57.1). At the moment, we do not specify whether particle 1 (2) is the ion (the atom) or the atom (the ion). Since we are interested in electronic transitions caused by the collision we shall suppose that at least one of the particles changes its internal state. Let this be particle 1.

The transition amplitude $a_{fi}(\mathbf{b})$ can be written as ([2, Chap. 5])

$$a_{fi}(\mathbf{b}) = \left(-\frac{i}{c^2} \int d^4x J_{1\mu}(x) A_2^\mu(x) \right)_{fi}. \quad (57.2)$$

Here, $J_{1\mu}(x)$ ($\mu = 0, 1, 2, 3$) is the electromagnetic four-current of particle 1 at a space-time point x , and $A_2^\mu(x)$

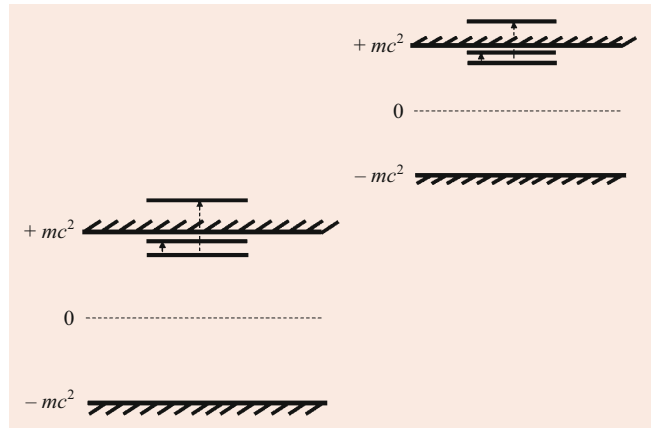


Fig. 57.1 Collision of an ion carrying (initially) electron(s) with an atom. Simultaneous electron transitions in both colliding species are possible

is the four-potential of the electromagnetic field created by particle 2 at the same point x . The summation over repeated Greek indices is implied.

The simplest consideration of the collisions is based on first-order perturbation theory in the interaction between the particles – *the (first) Born approximation* – which is valid provided that the colliding particles represent comparatively weak perturbations for each other. The latter is (overall) the case provided

$$\frac{Z}{v} \ll 1 \left(\frac{Ze^2}{\hbar v} \ll 1 \right), \quad (57.3)$$

where $Z = \max\{Z_1, Z_2\}$, and Z_1 and Z_2 are the atomic numbers of particles 1 and 2, respectively.

The condition Eq. (57.3) also means that the overlap in *the phase space* between the electrons of particles 1 and 2 will, in general, be quite small, and these two groups of electrons can be regarded as distinguishable.

In the Born approximation, the initial and final states of the particles are approximated by their unperturbed states, which are used to determine the four-current and the four-potential in Eq. (57.2). The amplitude Eq. (57.2) can be calculated by evaluating the current $J_{1\mu}$ of particle 1 in the reference frame K_1 (where its nucleus rests) and the potential A_2^μ of particle 2 in the reference frame K_2 (where its nucleus is at rest). Then this potential is transformed to the frame K_1 , where it is combined with $J_{1\mu}(x)$ in the amplitude Eq. (57.2). The result is (for its detailed derivation see [2, Chap. 5] and references therein)

$$\begin{aligned} a_{fi}(\mathbf{b}) &\equiv a_{0 \rightarrow n}^{0 \rightarrow m}(\mathbf{b}) \\ &= \frac{-i}{\pi v \gamma} \int d^2\mathbf{q}_\perp \exp(-i\mathbf{q}_\perp \cdot \mathbf{b}) \\ &\quad \times \frac{F_{1\mu}(n0; \mathbf{q}_1) \Lambda_v^\mu F_2^\nu(m0; -\mathbf{q}_2)}{-q_\lambda q^\lambda - i\zeta}. \end{aligned} \quad (57.4)$$

In Eq. (57.4) $\gamma = 1/\sqrt{1-v^2/c^2}$ is the collisional Lorentz factor, $\zeta \rightarrow +0$ gives the prescription to handle a (possible) singularity, the integration runs over the two-dimensional vector \mathbf{q}_\perp ($\mathbf{q}_\perp \cdot \mathbf{v} = 0, 0 \leq q_\perp < \infty$),

$$\begin{aligned} \mathbf{q}_1 &= (\mathbf{q}_\perp, q_{1\min}) \\ q_{1\min} &= \frac{\varepsilon_n - \varepsilon_0}{v} + \frac{\varepsilon_m - \varepsilon_0}{v\gamma}, \end{aligned} \quad (57.5)$$

and

$$\begin{aligned} \mathbf{q}_2 &= (\mathbf{q}_\perp, q_{2\min}), \\ q_{2\min} &= \frac{\varepsilon_m - \varepsilon_0}{v} + \frac{\varepsilon_n - \varepsilon_0}{v\gamma}. \end{aligned} \quad (57.6)$$

The four quantities,

$$\begin{aligned} F_{1_0}(n0; \mathbf{k}) &= - \int d^3\mathbf{r} \psi_n^\dagger \exp(i\mathbf{k} \cdot \mathbf{r}) \psi_0, \\ F_{1_l}(n0; \mathbf{k}) &= \int d^3\mathbf{r} \psi_n^\dagger \exp(i\mathbf{k} \cdot \mathbf{r}) \alpha_l \psi_0 \quad (l = 1, 2, 3), \end{aligned} \quad (57.7)$$

are the *inelastic* ($n \neq 0$) *form factors* of particle 1, where $\psi_0 = \psi_0(\mathbf{r})$ ($\psi_n = \psi_n(\mathbf{r})$) is the initial (final) state of the electron of particle 1 in the frame K_1 with an energy ε_0 (ε_n), α_l are the Dirac matrices, and \mathbf{r} is the electron coordinate (for simplicity, we assume that particle 1 has only one electron). Further, $\Lambda_{\mu\nu}$ is the Lorentz transformation matrix [3] from the frame K_2 to the frame K_1 , and F_{2_μ} are the form factors of particle 2 (given in K_2)

$$\begin{aligned} F_{2_0}(m0; \mathbf{k}) &= Z_2 \delta_{m0} - \int \prod_{i=1}^{N_2} d^3\xi_i u_m^\dagger \sum_{i=1}^{N_2} \exp(i\mathbf{k} \cdot \xi_i) u_0; \\ F_{2_l}(m0; \mathbf{k}) &= \int \prod_{i=1}^{N_2} d^3\xi_i u_m^\dagger \sum_{i=1}^{N_2} \alpha_{l(i)} \exp(i\mathbf{k} \cdot \xi_i) u_0, \end{aligned} \quad (57.8)$$

where N_2 is the number of the electrons of particle 2, $\alpha_{l(i)}$ are the Dirac matrices for the i -th electron, $u_0 = u_0(\xi_1, \dots, \xi_{N_2})$ ($u_m = u_m(\xi_1, \dots, \xi_{N_2})$) is the initial (final) electron state of particle 2 in the frame K_2 , ε_0 (ε_m) is its energy, and ξ_i is the coordinate of the i -th electron.

Using Eqs. (57.1) and (57.4) one can derive the quantum transition amplitude $S_{\text{fi}}(\mathbf{q}_\perp)$:

$$S_{\text{fi}}(\mathbf{q}_\perp) = - \frac{2i}{v\gamma} \frac{F_{1_\mu}(n0; \mathbf{q}_1) \Lambda_\nu^\mu F_{2_\nu}^v(m0; -\mathbf{q}_2)}{-q_\lambda q^\lambda - i\zeta}. \quad (57.9)$$

The quantity \mathbf{q}_1 (\mathbf{q}_2) has a physical meaning of the momentum transferred in the collision to particle 1 (2) in the frame K_1 (K_2). Further, $q_\lambda q^\lambda = (\varepsilon_n - \varepsilon_0)^2/c^2 - \mathbf{q}_1^2 \equiv (\varepsilon_m -$

$\varepsilon_0)^2/c^2 - \mathbf{q}_1^2$ is the square of the four-momentum of the (virtual) photon, which transmits the interaction between particles 1 and 2. Its explicit form is given by

$$\begin{aligned} -q_\lambda q^\lambda &= q_\perp^2 + \frac{(\varepsilon_n - \varepsilon_0 + \varepsilon_m - \varepsilon_0)^2}{v^2 \gamma^2} \\ &+ 2(\gamma - 1) \frac{(\varepsilon_n - \varepsilon_0)(\varepsilon_m - \varepsilon_0)}{v^2 \gamma^2}. \end{aligned} \quad (57.10)$$

If the photon is an on-mass-shell, $q_\mu q^\mu = 0$, the singularity appears in the amplitude Eq. (57.9) (and in the integrand of Eq. (57.4)). However, if $(\varepsilon_n - \varepsilon_0)(\varepsilon_m - \varepsilon_0) \geq 0$, then $q_\mu q^\mu = 0$ only provided that q_\perp , $(\varepsilon_m - \varepsilon_0)$ and $(\varepsilon_n - \varepsilon_0)$ are all equal to zero meaning the absence of any collision. Therefore, if $(\varepsilon_n - \varepsilon_0)(\varepsilon_m - \varepsilon_0) \geq 0$, then the restrictions imposed by the energy-momentum conservation in the collision do not permit the electromagnetic interaction between the particles to be transmitted by an on-mass-shell photon. In what follows, we assume that $(\varepsilon_n - \varepsilon_0)(\varepsilon_m - \varepsilon_0) \geq 0$, and the term $i\zeta$ in the amplitudes may be omitted.

The nonzero elements of the matrix Λ_ν^μ are [3]: $\Lambda_0^0 = \Lambda_3^3 = \gamma$, $\Lambda_1^1 = \Lambda_2^2 = 1$, and $\Lambda_3^0 = \Lambda_0^3 = (v/c)\gamma$. Hence, the explicit form of the form-factor coupling in Eqs. (57.4) and (57.9) reads

$$\begin{aligned} F_{1_\mu} \gamma^{-1} \Lambda_\nu^\mu F_2^v &= \left(F_{1_0} + \frac{v}{c} F_{1_3} \right) \left(F_2^0 + \frac{v}{c} F_2^3 \right) \\ &+ \frac{F_{1_3} F_2^3}{\gamma^2} + \frac{F_{1_1} F_2^1 + F_{1_2} F_2^2}{\gamma}. \end{aligned} \quad (57.11)$$

Taking into account Eqs. (57.10) and (57.11) we see that the form of the amplitudes Eqs. (57.4) and (57.9) is remarkably symmetric with respect to the quantities of the colliding particles.

For a collision in which particle 1 and particle 2 undergo transitions $\psi_0 \rightarrow \psi_n$ and $u_0 \rightarrow u_m$, respectively, the cross section differential in the transverse momentum transfer is given by

$$\frac{d^2\sigma_{0 \rightarrow n}^{0 \rightarrow m}}{d\mathbf{q}_\perp^2} = |S_{\text{fi}}(\mathbf{q}_\perp)|^2. \quad (57.12)$$

The total cross section can be expressed in two equivalent forms

$$\begin{aligned} \sigma_{0 \rightarrow n}^{0 \rightarrow m} &= \int d^2\mathbf{q}_\perp |S_{\text{fi}}(\mathbf{q}_\perp)|^2 \\ &= \int d^2\mathbf{b} |a_{\text{fi}}(\mathbf{b})|^2. \end{aligned} \quad (57.13)$$

The nonrelativistic limit. The amplitudes Eqs. (57.4) and (57.9) are obtained by using a fully relativistic treatment and can describe relativistic effects caused by high collision velocity and large values of the orbiting electron velocities

inside particles 1 and 2. The nonrelativistic limit of these amplitudes is obtained by setting $c \rightarrow \infty$, which yields

$$a_{0 \rightarrow n}^{0 \rightarrow m}(\mathbf{b}) = \frac{-i}{\pi v} \int d^2 \mathbf{q}_\perp \exp(-i \mathbf{q}_\perp \cdot \mathbf{b}) \times \frac{F_{1_0}(n0; \mathbf{q}) F_{2_0}(m0; -\mathbf{q})}{q^2}, \quad (57.14)$$

and

$$S_{0 \rightarrow n}^{0 \rightarrow m}(\mathbf{q}_\perp) = \frac{-2i}{v} \frac{F_{1_0}(n0; \mathbf{q}) F_{2_0}(m0; -\mathbf{q})}{q^2}, \quad (57.15)$$

where

$$\mathbf{q} = \left(\mathbf{q}_\perp, \frac{\varepsilon_n - \varepsilon_0 + \varepsilon_m - \varepsilon_0}{v} \right), \quad (57.16)$$

and the form factors F_{1_0} and F_{2_0} of the particles have to be evaluated with the nonrelativistic (Schrödinger) wave functions of the electrons. The application of the nonrelativistic Born approximation to atomic ionization and projectile-electron loss has a long history ([1, 4, 5] and references therein).

57.2.1 Atomic Ionization in Collisions with a Bare Nucleus

Let us now consider ionization of an atom (particle 1), assuming for simplicity that it has just one “active” electron, by collisions with a bare projectile nucleus (particle 2). The form factors of particle 2 are given by $F_{2_0} = Z_2$ and $F_{2_1} = F_{2_2} = F_{2_3} = 0$ (Eq. (57.8)), and $\varepsilon_m - \varepsilon_0 = 0$. Therefore, the form-factor coupling Eq. (57.11) reduces to $Z_2(F_{1_0} + (v/c)F_{1_3}) = -Z_2 \langle \psi_n | \exp(i \mathbf{q} \cdot \mathbf{r}) (1 - (v/c)\alpha_3) | \psi_0 \rangle$, and in the rest frame of the atom the quantum transition amplitude is given by

$$S_{\text{fi}}(\mathbf{q}_\perp) = \frac{2iZ_2 \langle \psi_p | \exp(i \mathbf{q} \cdot \mathbf{r}) (1 - \frac{v}{c}\alpha_3) | \psi_0 \rangle}{v \left(q_\perp^2 + \frac{(\varepsilon_p - \varepsilon_0)^2}{v^2 \gamma^2} \right)}. \quad (57.17)$$

Here, ψ_0 is the initial state of the atom with energy ε_0 , ψ_p describes the emitted electron with an asymptotic momentum \mathbf{p} , and energy ε_p (bound and continuum states in a Coulomb potential are considered in details in [6] and [7–9] for nonrelativistic and relativistic electrons, respectively), and

$$\mathbf{q} = \left(\mathbf{q}_\perp, \frac{\varepsilon_p - \varepsilon_0}{v} \right) \quad (57.18)$$

is the momentum transferred to the atom in its rest frame.

The semiclassical transition amplitude reads (e.g. [2, p. 189])

$$a_{\text{fi}}(\mathbf{b}) = \frac{2iZ_2}{v} \langle \psi_p | \exp(iq_z z) \left(1 - \frac{v}{c}\alpha_3 \right) \times K_0 \left(\frac{\omega_{n0}}{v\gamma} |\mathbf{r}_\perp - \mathbf{b}| \right) | \psi_0 \rangle, \quad (57.19)$$

where $q_z = (\varepsilon_p - \varepsilon_0)/v$, $\omega_{p0} = \varepsilon_p - \varepsilon_0$, and K_0 is a modified Bessel function [10].

Assuming that the electron continuum states ψ_p are normalized as $\langle \psi_{p'} | \psi_p \rangle = \delta^{(3)}(\mathbf{p}' - \mathbf{p})$ the ionization cross section differential in the momentum \mathbf{p} of the emitted electron in the rest frame of the atom is given by

$$\frac{d\sigma}{d^3 \mathbf{p}} = \int d^2 \mathbf{q}_\perp |S_{\text{fi}}(\mathbf{q}_\perp)|^2 = \frac{4Z_2^2}{v^2} \times \int d^2 \mathbf{q}_\perp \frac{|\langle \psi_p | \exp(i \mathbf{q} \cdot \mathbf{r}) (1 - \frac{v}{c}\alpha_3) | \psi_0 \rangle|^2}{\left(q_\perp^2 + \frac{\omega_{p0}^2}{v^2 \gamma^2} \right)^2}. \quad (57.20)$$

Since $d^3 \mathbf{p} = p^2 d p d\Omega_p = (p \varepsilon_p / c^2) d\varepsilon_p d\Omega_p$, where Ω_p is the solid angle for the emitted electron, the cross section Eq. (57.20) can be converted into the cross section $(d\sigma)/(d\varepsilon_p d\Omega_p)$ differential in the electron emission energy and emission angles. This cross section can be recalculated to any other inertial reference frame K' by using the transformation formula (see e.g. [11])

$$\frac{d\sigma'}{d\varepsilon_p' d\Omega_p'} = \frac{p'}{p} \frac{d\sigma}{d\varepsilon_p d\Omega_p}, \quad (57.21)$$

where the primed quantities refer to K' .

The Born approximation is “overall” valid if $Z_2/v \ll 1$. However, in the case of ionization an additional precaution is necessary. Let an unbound electron move in a Coulomb field of a nucleus with an atomic number Z . The influence of the field on the electron can be characterized by the Sommerfeld parameter $\eta_e = Z/v_e$, where v_e is the electron velocity relative to the nucleus. An electron emitted in ion–atom collision moves in the presence of two fields whose influence is characterized by $\eta_{1,e} = Z_1/v_e$ and $\eta_{2,e} = Z_2/|\mathbf{v}_e - \mathbf{v}|$, where \mathbf{v}_e and $\mathbf{v}_e - \mathbf{v}$ are the velocities of the emitted electron with respect to the atomic residue and the ionic projectile, respectively (for simplicity, here we neglect relativistic effects). It is obvious that the condition $Z_2/v \ll 1$ does not necessarily lead to $\eta_{1,e} \gg \eta_{2,e}$ and, hence, does not guarantee that the field of the atomic residue dominates the motion of the emitted electron.

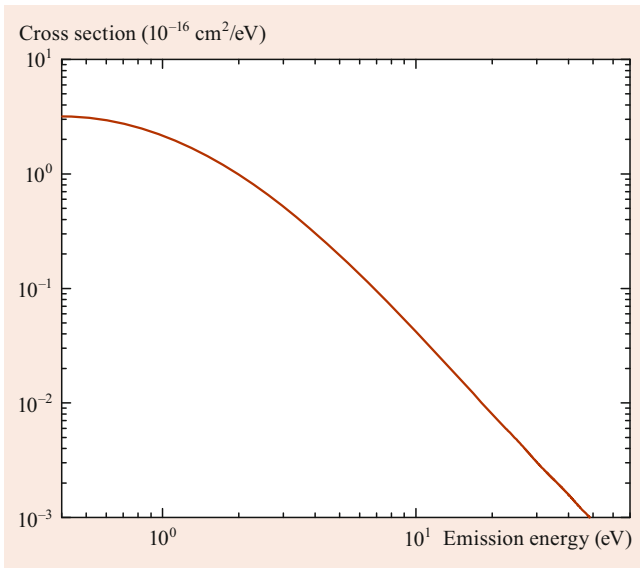


Fig. 57.2 The energy spectrum of soft electrons emitted in single ionization of He by 1 MeV p^+

In particular, if the emitted electron has a velocity close to that of the projectile, then the field of the latter strongly affects the electron motion invalidating the Born approximation. Such electrons, which correspond to *electron capture to the projectile continuum*, are observed in experiments ([12] and references therein) and can be described by continuum-distorted-wave models and two-center coupled-channel methods.

Provided that $Z_2/v \ll 1$, the Born approximation is applicable to the emission of electrons with velocities v_e substantially smaller than v . In collisions where the impact velocity v greatly exceeds the typical orbiting velocity v_0 of the electron in its initial state ($v_0 \simeq Z_1$), electrons emitted with velocities $v_e \ll v$ constitute the *soft-electron peak*. This peak consists of electrons with kinetic energies in the range $(0, E_{\max})$, where E_{\max} is of the order of the binding energy of the electron in its initial state and contributes most to the total ionization cross section. The energy distribution of these electrons decreases very rapidly with an increase in the emission energy (Fig. 57.2).

One more prominent emission feature is represented by *binary-encounter electrons*. They originate in collisions with vanishingly small momentum transfers to the atomic nucleus, from the *Bethe ridge* (e.g. [13]) and have kinetic energies ranging from 0 up to $2c^2(\gamma^2 - 1)$.

Expressions (Eqs. (57.17)–(57.20)) take into account relativistic effects related to the collision velocity and the velocities of the electron in its initial and final states. They are successfully applied to calculate electron emission from the *K*-shell of very heavy atoms by high-energy collisions

with protons and other light nuclei where both types of the relativistic effects are of importance.

However, the fully relativistic description of ionization is not always necessary, even if $v \rightarrow c$. For instance, in soft-electron emission from light atoms, the motion of the electrons in the initial and final states is nonrelativistic (in the rest frame of the atom), and the description can be simplified by replacing in Eqs. (57.17), (57.19), and (57.20)

$$\begin{aligned} \alpha_3 \exp(i\mathbf{q} \cdot \mathbf{r}) &\rightarrow \frac{1}{2c} (\hat{p}_z \exp(i\mathbf{q} \cdot \mathbf{r}) + \exp(i\mathbf{q} \cdot \mathbf{r}) \hat{p}_z) \\ \alpha_3 \exp(iq_z z) &\rightarrow \frac{1}{2c} (\hat{p}_z \exp(iq_z z) + \exp(iq_z z) \hat{p}_z) \\ \psi_0(\psi_p) &\rightarrow \varphi_0(\varphi_p), \end{aligned} \quad (57.22)$$

where φ_0 and φ_p are the corresponding nonrelativistic (Schrödinger) wave functions, and $\hat{p}_z = \hat{\mathbf{p}} \cdot \mathbf{v}/v$ ($\hat{\mathbf{p}}$ is the electron momentum operator). The resulting expressions describe only relativistic effects dependent on the collision velocity v .

If not only the motion of the electron is nonrelativistic but also $v \ll c$, then a further simplification is obtained by setting $c \rightarrow \infty$, which results in the fully nonrelativistic description of the collision.

The total cross section for ionization is obtained by integrating the cross section $d\sigma/d^3\mathbf{p}$ over the momenta of the emitted electrons. If for the overwhelming majority of ionization events the minimum momentum transfer $q_{\min} = (\varepsilon_p - \varepsilon_0)/v \approx Z_1^2/v$ is much smaller than the typical orbiting momentum of the electron in its initial state $\approx Z_1$ (which is the case provided that $Z_1/v \ll 1$), then one can derive a simple expression for the total cross section [4]

$$\sigma_t = a \frac{Z_2^2}{v^2} \left(\ln(bv\gamma) - \frac{v^2}{2c^2} \right), \quad (57.23)$$

where $a \approx Z_1^{-2}$ and $b \approx Z_1^{-1}$ are the quantities dependent on the properties of the target. As an estimate, Eq. (57.23) can also be used when the condition $Z_1/v \ll 1$ ($Z_1/c \ll 1$) is not fulfilled, but the impact energy is so high that $\gamma \gg 1$ [14].

At $v \rightarrow c$, the cross section Eq. (57.23) grows with an increase in the impact energy. The growth is caused by the Lorentz contraction, owing to which the range of the field produced by a point-like charge is reduced by a factor of γ in the direction along its velocity and is increased by the same factor in the plane perpendicular to it. As a result, when the impact energy increases, there appear contributions to the cross section given by larger and larger impact parameters. At $\gamma \rightarrow \infty$, the cross section Eq. (57.23) diverges. This divergence is, however, rather formal since all calculable quantities remain finite due to the target density effect (e.g. [15]) and/or the finite sizes of the target and projectile beam.

Beyond the Born approximation

As has already been stressed, the application of the Born approximation is restricted by the condition $Z_2/v \ll 1$. Moreover, even if it is fulfilled, this approximation may still break down when applied to the emission of fast electrons. Therefore, we now very briefly consider a few more advanced treatments for ionization.

- *Coupled-channel methods.* The wave function satisfying the equation

$$i \frac{\partial \psi(t)}{\partial t} = \hat{H}(t) \psi(t), \quad (57.24)$$

where $\hat{H} = \hat{H}_0 + \hat{V}$ is the full Hamiltonian, \hat{H}_0 is the Hamiltonian for the free (noninteracting) atom, and $\hat{V}(t)$ is the interaction with the projectile ion, can be expanded into a complete set of the eigenstates of \hat{H}_0 . By inserting this expansion into Eq. (57.24) we obtain a set of coupled equations for the expansion coefficients. Then this set is reduced to a tractable number of equations by taking into account only the “most essential” eigenstates of \hat{H}_0 . The remaining equations are solved rigorously (numerically).

- *Distorted-wave models.* In a distorted-wave approach, the full Hamiltonian is also split into two parts. However, one now tries to include as much of the ion–atom interaction as possible already into the definition of the initial and final states treating the remaining part of the Hamiltonian as a perturbation. Since this perturbation is weaker than the ion–atom interaction \hat{V} , a distorted-wave series has a better convergence, and it often suffices to consider just its first term.

Distorted-wave models for the ionization of atoms in non-relativistic collisions with bare nuclei are considered in Chap. 56 of this Handbook. For relativistic collisions they were reviewed in [16, Chap. 6] (see also [2, Chap. 6]).

- *The light-cone approximation.* Let us suppose that the projectile ion moves with such high energy that its velocity (the collision velocity) is almost equal to the speed of light. Then, by assuming that the projectile velocity is equal to the speed of light it is possible [17] to derive an exact expression for the transition amplitude in the impact parameter space, which reads

$$a_{fi}^{LC}(\mathbf{b}) = \langle \psi_p | \exp \frac{i\omega_{n0}z}{c} (1 - \alpha_3) \exp(iG_0) | \psi_0 \rangle, \quad (57.25)$$

where $G_0 = (2Z_2/c) \ln(|\mathbf{r}_\perp - \mathbf{b}|/b)$. Unlike the Born amplitude Eq. (57.19), the amplitude Eq. (57.25) contains the projectile’s charge Z_2 in the exponent, reflecting the fact that the interaction with the projectile is taken into account to all orders of perturbation theory. By comparing Eq. (57.25) with Eq. (57.19) we see that the exact and

Born amplitudes will, in general, differ even at $\gamma \rightarrow \infty$.

There exists an intimate link between the light-cone approximation and some of the distorted-wave models, which at $\gamma \rightarrow \infty$ yield the transition amplitude in the form of Eq. (57.25) [18].

- *Numerical solutions on a lattice.* Yet another nonperturbative – and fully numerical – treatment is the direct numerical solution of the time-dependent Dirac (or Schrödinger) equation on a lattice in position or momentum space (e.g. [19, Chap. 7], [2, Chap. 6] and references therein).
- *Classical trajectory Monte Carlo calculations.* This method is based on a purely classical description of ion–atom collisions. It is reviewed in Chap. 62 of this Handbook.

Basic Collision Dynamics

Most detailed and basic information about the collision dynamics is contained in the fully differential cross section (given by $|S_{fi}(\mathbf{q}_\perp)|^2$). The advent of reaction microscopes has enabled us to accurately measure such cross sections for the ionization of simple atoms (He, Li) by fast ions. In order to describe the experimental results, theory has to properly treat the behavior of the electron in the simultaneous presence of the fields of the atomic core and the projectile ion and address the role of the interaction between the projectile ion and the target nucleus. All this is missing in the Born approximation but can be successfully implemented within distorted-wave models and coupled-channel methods. Moreover, there are some indications that the coherence properties of the projectile should be also taken into account [20].

57.2.2 Projectile-Electron Loss

Let us consider collisions of a projectile ion with a target atom assuming that the ion carries initially one electron and focusing on its transitions. Now particle 1 is the ion ($n \neq 0$), particle 2 is the atom, and we can again apply Eq. (57.4) and/or Eq. (57.9).

For collisions of very simple atomic systems (like a hydrogen-like projectile ion on an atomic hydrogen) the cross sections can be calculated relatively easily for any particular reaction channel (e.g., for mutual ionization in which both the ion and the atom lose electron(s)). However, in collision experiments with a focus on transitions in the projectile ion, the final state of the target is often not observed, and one then has to deal with the cross section

$$\sigma_{0 \rightarrow n} = \sum_m \sigma_{0 \rightarrow n}^{0 \rightarrow m}, \quad (57.26)$$

where the sum runs over all possible final states of the target, including its continuum. In the case of atoms with more than one electron, rigorous calculations become infeasible,

and one has to use some simplifications [2]. The first of these consists of reducing the relativistic form-factor coupling according to

$$\frac{F_{1\mu} A_\nu^\mu F_2^\nu}{\gamma} \rightarrow F_2^0 \left(F_{1_0} + \frac{v}{c} F_{1_3} \right) = -Z_{2,\text{eff}}^{0 \rightarrow m} \times \langle \psi_n | \exp(i\mathbf{q} \cdot \mathbf{r}) \left(1 - \frac{v}{c} \alpha_3 \right) | \psi_0 \rangle, \quad (57.27)$$

where the quantity

$$Z_{2,\text{eff}}^{0 \rightarrow m} = F_2^0 = Z_2 \delta_{m0} - \langle u_m | \sum_{j=1}^{Z_2} \exp(i\mathbf{q}_2 \cdot \boldsymbol{\xi}_j) | u_0 \rangle \quad (57.28)$$

is the effective charge of the atom “seen” by the electron of the ion. This charge depends on the momentum transfer in the collision and also on the initial and final states of the atom.

It is customary to split the cross section Eq. (57.26) into two parts and discuss them separately.

Elastic Target Mode. Screening

One part represents the contribution to the cross section Eq. (57.26) from collisions in which the target remains in its initial internal state ($m = 0$). In this collision mode, the effective atomic charge

$$Z_{2,\text{eff}}^{0 \rightarrow 0}(\mathbf{q}_0) = Z_2 - \int d^3\xi \rho_{\text{el}}(\boldsymbol{\xi}) \exp(i\mathbf{q}_0 \cdot \boldsymbol{\xi}), \quad (57.29)$$

where $\mathbf{q}_0 = (-\mathbf{q}_\perp; -(\varepsilon_n - \varepsilon_0)/v\gamma)$ is the momentum transferred to the atom (in its rest frame), can be cast into a convenient form by using a parametrization

$$\rho_{\text{el}}(\boldsymbol{\xi}) = \frac{Z_2}{4\pi\xi} \sum_{j=1}^3 A_j \kappa_j^2 \exp(-\kappa_j \xi) \quad (57.30)$$

for the electron charge density $\rho_{\text{el}}(\boldsymbol{\xi})$ in the atomic ground state. The parameters A_j and κ_j ($j = 1, 2, 3$, $\sum_j^3 A_j = 1$) are tabulated in [21, 22]. This yields

$$Z_{2,\text{eff}}^{0 \rightarrow 0}(\mathbf{q}_0) = Z_2 q_0^2 \sum_{j=1}^3 \frac{A_j}{\kappa_j^2 + q_0^2}. \quad (57.31)$$

The effective atomic charge Eq. (57.31) varies between 0 (at $q_0 \rightarrow 0$) and Z_2 (at $q_0 \gg \kappa_j$). Such behavior is not related to a particular form used to parametrize the electron density and actually already follows from the analysis of Eq. (57.28) showing that the effective atomic charge vanishes in collisions in which the momentum transfer to the atom is much smaller than the typical momenta of the atomic electrons,

increases monotonously with the increase in q_0 and reaches a plateau ($Z_{2,\text{eff}}^{0 \rightarrow 0} = Z_2$) in collisions where the momentum transfer to the atom is large on the atomic scale. Thus, the effect of the target electrons in collisions where the target remains in its initial internal state is to partially or even fully *screen* the atomic nucleus that reduces the force acting on the electron of the ion compared to that in collisions with bare nucleus Z_2 .

With the effective charge in the form Eq. (57.31), the expressions for the amplitude and the cross sections are simplified substantially. In particular, the cross section for the electron-loss differential in the momentum of the emitted electron is given by an expression similar to Eq. (57.20), in which the constant charge Z_2 should be replaced by $Z_{2,\text{eff}}^{0 \rightarrow 0}(\mathbf{q}_0)$ from Eq. (57.31).

The projectile-target collision mode, in which the target does not change its internal state (while the projectile does), is often called the *elastic mode*, implying that it is elastic only for the target.

Inelastic Target Mode. Antiscreening

The remaining part of the cross section Eq. (57.26) describes collisions in which not only the electron of the ion but also the atomic electrons are “active” in the collision. This collision mode is called *doubly inelastic* or simply *inelastic*.

According to the Born approximation, the inelastic mode is not influenced by the interaction between the electron of the projectile and the nucleus of the target, and the projectile electron undergoes a transition solely due to its interaction with the target electrons ([2, 5, 23]).

The contributions from collisions in which the target changes its initial internal state increase the total cross section for electron loss. This action of the target electrons is exactly opposite to their effect in the elastic mode and is called *antiscreening*.

The relative role of the antiscreening mode is maximal for collisions with hydrogen decreasing with the increase in the atomic number Z_2 . In particular, in collisions with large momentum transfers, the contributions of the screening and antiscreening mode scale approximately as $\approx Z_2^2$ and $\approx Z_2$, respectively (Eq. (57.32)).

Beyond the Born Approximation

If the condition Eq. (57.3) is violated, the Born approximation becomes invalid, and more sophisticated theoretical methods have to be used.

In collisions of very highly charged projectiles with heavy atoms occurring at not too high impact energies only the impact parameters, which are quite small on the scale of a neutral atom, contribute noticeably to the loss process ([2, Chap. 6] and references therein). In such collisions, the field of the atomic nucleus becomes too strong to be described within the Born approximation, but the role of the atomic

electrons is of minor importance. Therefore, the problem of projectile-electron loss in collisions with a neutral atom can be reduced to the problem of “ionization” in a three-body system (the electron, the nuclei of the ion and atom) and then treated by using, for instance, *three-body distorted-wave models* ([2, Chap. 6], [16, Chap. 6], Chap. 56 of the present Handbook and references therein) or coupled-channel methods ([19, Chap. 2, 7, 8] and references therein).

For collisions with heavy atoms at noticeably higher impact energies, where the role of larger impact parameters increases and the screening effect of the atomic electrons can no longer be neglected [2], a *symmetric eikonal model*, in which the effect of the strong field of the neutral atom on the electron of the projectile is described by eikonal distortion factors, can be used [18]. In the limit $\gamma \rightarrow \infty$, this model goes over into the light-cone approximation and is expected to yield good results also for finite but large γ .

A different kind of *symmetric eikonal model* was developed for projectile-electron loss in nonrelativistic and relativistic collisions with very light atoms like hydrogen and helium ([2, Chap. 6] and references therein). In such collisions, the role of the atomic electrons is comparable to that of the atomic nucleus. In collisions with highly charged ions, the motion of the atomic electrons is influenced by the field of the ion, which may, in turn, affect their interaction with the electron of the ion. The model takes this influence into account by introducing eikonal distortion factors for the initial and final state of the target atom. Surprisingly, the model shows noticeable deviations from the predictions of the Born approximation even when the parameter Z_1/v is as small as 0.1. With its increase, the model itself eventually becomes invalid when the motion of the atomic electrons in the collision is already governed mainly by the field of the ion.

An electron in a highly charged ion is very tightly bound and, in order to remove it from the ion, the momentum transfers in the collision have to be sufficiently large. In particular, it may happen that the momentum transfers to the atom (Eq. (57.6)) will be much larger than the typical orbiting momenta of all atomic electrons. Then the motion of the atomic electrons in the collision is governed by the field of the ion, and the cross section for electron loss from (or excitation of) the ion is given by [24, 25]

$$\sigma = Z_2^2 \sigma_p + Z_2 \sigma_e, \quad (57.32)$$

where Z_2 is the atomic number of the atom, and σ_p and σ_e are the cross sections for electron loss in collisions with equivelocity incident protons and electrons, respectively (σ_e should be averaged over the atomic Compton profile, if necessary). In calculating σ_e it is of crucial importance to take into account the effect of the field of the highly charged ion on the incident and scattered electrons as well as on the emitted electron. Equation (57.32) was applied to excita-

tion of 212.9 MeV/u $U^{91+}(1s)$ in collisions with hydrogen, and a very good agreement with experiment was found [26]. Equation (57.32) was also applied to electron loss from $U^{91+}(1s)$ in collisions with hydrogen and helium [25]. However, available experimental data is not sufficiently accurate to test the theory.

Projectile-electron loss in nonrelativistic collisions with many-electron atoms was also considered by using *coupled-channel methods* (for the elastic mode only) and the *sudden approximation* ([2, Chap. 3] and references therein).

57.3 Electron Transfer Processes

In this section, we consider electron transfer processes in the basic situation when a bare ion Z_i collides with an atomic system consisting of one (“active”) electron and a nucleus Z_a .

57.3.1 Nonradiative Electron Capture

A starting point in our discussion of nonradiative capture will be the following two expressions for the transition amplitude,

$$\begin{aligned} a_{fi}^{(+)}(\mathbf{b}) &= -i \int_{-\infty}^{+\infty} dt \left\langle \left(\hat{H} - i \frac{\partial}{\partial t} \right) \chi_f(t) \middle| \psi_i^{(+)}(t) \right\rangle, \\ a_{fi}^{(-)}(\mathbf{b}) &= -i \int_{-\infty}^{+\infty} dt \left\langle \psi_f^{(-)}(t) \middle| \left(\hat{H} - i \frac{\partial}{\partial t} \right) \varphi_i(t) \right\rangle, \end{aligned} \quad (57.33)$$

where $a_{fi}^{(+)}$ and $a_{fi}^{(-)}$ represent the *post* and *prior* forms, respectively, of the amplitude. In Eq. (57.33), $\varphi_i(t)$ and $\chi_f(t)$ are the initial and final exact asymptotic states of the electron, respectively, and $\psi_i^{(+)}(t)$ and $\psi_f^{(-)}(t)$ are solutions of the full (two-center) Dirac equation

$$i \frac{\partial \psi^{(\pm)}(t)}{\partial t} = \hat{H} \psi^{(\pm)}(t), \quad (57.34)$$

with the “in” ($\psi_i^{(+)}$) and “out” ($\psi_f^{(-)}$) boundary conditions. The two-center Hamiltonian reads

$$\begin{aligned} \hat{H} &= c \boldsymbol{\alpha} \cdot \hat{\mathbf{p}} + \beta c^2 - [\Phi_a(\mathbf{r}, t) - \boldsymbol{\alpha} \cdot \mathbf{A}_a(\mathbf{r}, t)] \\ &\quad - [\Phi_i(\mathbf{r}, t) - \boldsymbol{\alpha} \cdot \mathbf{A}_i(\mathbf{r}, t)], \end{aligned} \quad (57.35)$$

where $\boldsymbol{\alpha} = (\alpha_1, \alpha_2, \alpha_3)$, β are the Dirac matrices, and (Φ_i, \mathbf{A}_i) and (Φ_a, \mathbf{A}_a) are two sets of the scalar and vector potentials, which describe the fields of the atomic and ionic nuclei, respectively.

These potentials are normally taken as follows. The field of that nucleus, which is chosen to be at rest, is fully described by its scalar potential. The field of the moving

nucleus is described in a gauge where its vector and scalar potentials are related by $\mathbf{A} = (\mathbf{v}/c)\Phi$. In the rest frame of the ion, *which is used throughout this section* and where the coordinate of the atomic nucleus is given by $\mathbf{R} = \mathbf{b} + \mathbf{v}t$ with $\mathbf{b} = (b_x, b_y, 0)$ and $\mathbf{v} = (0, 0, v)$, these potentials read

$$\begin{aligned}\Phi_a(\mathbf{r}, t) &= \frac{-\gamma Z_a}{s}, & A_a(\mathbf{r}, t) &= \frac{\mathbf{v}}{c}\Phi_a(\mathbf{r}, t), \\ \Phi_i(\mathbf{r}) &= \frac{-Z_i}{r}, & A_i(\mathbf{r}, t) &= 0,\end{aligned}\quad (57.36)$$

where $\mathbf{s} = (x - b_x, y - b_y, \gamma(z - vt))$, and $\mathbf{r} = (x, y, z)$ are the coordinates of the electrons with respect to the nuclei of the atom and ion, respectively (the atom is supposed to move along the z -axis).

The post and prior amplitudes Eq. (57.33) employing exact solutions of Eq. (57.34) are identical. However, such solutions are not known, and the amplitudes are evaluated using approximations for $\psi^{(\pm)}$. Then they will, in general, differ (the so-called *post–prior discrepancy*).

The nonrelativistic limit. If the collision velocity and the orbiting velocities of the electron in its initial and final bound states are all much less than the speed of light, then a nonrelativistic treatment of capture suffices. It is based on the Schrödinger equation with the two-center nonrelativistic Hamiltonian

$$\hat{H} = \frac{\hat{\mathbf{p}}^2}{2m} - \frac{Z_a e^2}{s} - \frac{Z_i e^2}{r}, \quad (57.37)$$

where $\mathbf{s} = (x - b_x, y - b_y, (z - vt))$.

Born Approximation

The simplest approach to capture – which is often called the Born approximation – consists of the following steps. In the post form, the state $\psi_i^{(+)}$ is replaced by the undistorted initial atomic state $\phi_a(t)$, and the state $\chi_f(t)$ is taken as the undistorted final state $\zeta_f(t)$ of the electron in the ion that leads to the residual interaction $(\hat{H} - i(\partial/\partial t))\zeta_f(t) = -(\gamma Z_a/s)(1 - (v/c)\alpha_3)\zeta_f(t)$. In the prior form, the approximations are similar: $\psi_f^{(-)} \rightarrow \zeta_f(t)$, $\varphi_i(t) \rightarrow \phi_a(t)$, and the residual interaction is $-Z_i/r$. Although the Born amplitudes are not exact, this approximation is free of post–prior discrepancy:

$$\begin{aligned}a_{\text{fi}}^{(BA,+)}(\mathbf{b}) &= -i \int_{-\infty}^{+\infty} dt \left\langle \left(\hat{H} - i \frac{\partial}{\partial t} \right) \zeta_f(t) \middle| \phi_a(t) \right\rangle, \\ &\equiv -i \int_{-\infty}^{+\infty} dt \left\langle \zeta_f(t) \middle| \left(\hat{H} - i \frac{\partial}{\partial t} \right) \phi_a(t) \right\rangle \\ &= a_{\text{fi}}^{(BA,-)}(\mathbf{b}),\end{aligned}\quad (57.38)$$

where in the transition from the first to the last expression in Eq. (57.38), we took into account that the Hamiltonian \hat{H} is hermitian, and the states $\phi_i(t)$ and $\zeta_f(t)$ at $t \rightarrow \pm\infty$ have a zero overlap in space.

States of a moving atom. Let $\phi'_a(\mathbf{r}', t') = \phi'_0(\mathbf{r}') \times \exp(-i\epsilon_i t')$ be the initial electron state in the atom given in the atomic rest frame, where \mathbf{r}' and t' are the electron coordinates and time in this frame. This state can be transformed to the rest frame of the ion according to (e.g. [27, Chap. 3, 6])

$$\begin{aligned}\phi_a(\mathbf{r}, t) &= \sqrt{\frac{1+\gamma}{2}} \left(I + \frac{v}{c} \frac{\gamma}{\gamma+1} \alpha_3 \right) \\ &\times \phi'_0(x - b_x, y - b_y, \gamma(z - vt)) \\ &\times \exp\left[-i\epsilon_i \gamma \left(t - \frac{v}{c^2} z \right)\right],\end{aligned}\quad (57.39)$$

where I is a unit 4×4 matrix, $\mathbf{r} = (x, y, z)$, and t are the electron coordinates and time in the rest frame of the ion ($x' = x - b_x$, $y' = y - b_y$, $z' = \gamma(z - vt)$, $t' = \gamma(t - vz/c^2)$).

In the nonrelativistic limit ($c \rightarrow \infty$), the state of an electron bound in the moving atom reads

$$\begin{aligned}\phi_a(\mathbf{r}, t) &= \phi'_0(x - b_x, y - b_y, z - vt) \exp(-i\epsilon_i t) \\ &\times \exp\left(imvz - i \frac{mv^2}{2} t \right),\end{aligned}\quad (57.40)$$

where $\exp[i(mvz - mv^2/2t)]$ is the *electron translational factor* (first obtained in [28]), and ϕ_a and ϕ'_0 are understood as the corresponding Schrödinger states.

The Born amplitudes for electron capture were evaluated for nonrelativistic and relativistic collisions ([16, Chap. 2] and [19, Chap. 9], as well as references therein). One of the main results obtained for the nonrelativistic domain is that at asymptotically high impact energies (where the collision velocity greatly exceeds the typical orbiting velocities of the electron in its initial and final bound states), the capture is dominated by the $1s \rightarrow 1s$ transition, and the cross section possesses a strong dependence on the impact energy E (the collision velocity v)

$$\sigma \approx \frac{Z_i^5 Z_a^5}{E^6} \approx \frac{Z_i^5 Z_a^5}{v^{12}}, \quad (57.41)$$

which is related to a very rapidly vanishing overlap between the initial and final states of the electron in the momentum space with the increase in the collision energy/velocity. In the relativistic domain, the dependence of the Born cross section on the impact energy becomes much steeper and at $\gamma \gg 1$, where the capture is dominated by the $1s \rightarrow 1s$ transition, is given by

$$\sigma \approx \frac{Z_i^5 Z_a^5}{E} \approx \frac{Z_i^5 Z_a^5}{\gamma}. \quad (57.42)$$

Because of the Lorentz contraction of the electron wave function in the position space along the collision velocity, the electron wave function in the momentum space becomes broader along this direction. This relativistic effect gives rise to a less steeper decrease in the overlap between the initial and final electron states in the momentum space, which, in turn, leads to a much slower decrease of the cross section with an increase in the impact energy than the nonrelativistic treatment suggests.

Electron transfer in high-energy collisions is characterized by the change in electron momentum much larger than the typical orbiting momenta of the electron in its initial and final bound states, and the $Z_{a,i}^5$ -dependences in Eq. (57.41) and Eq. (57.42) reflect the crucial role played in capture by the high-momentum components of these states.

Boundary-Corrected Born Approximation

Being strongly gauge-dependent the Born approximation is not very accurate even at asymptotically high impact energies. Better results for capture are yielded by the boundary-corrected Born approximation in which the initial and final states of the electron (considered in the rest frame of the ion) are taken as

$$\begin{aligned}\tilde{\phi}_a(t) &= \exp\left(-i\frac{Z_i}{v}\ln(R-vt)\right)\phi_a(t), \\ \tilde{\zeta}_f(t) &= \exp\left(i\frac{Z_a}{v}\ln(R'+vt')\right)\zeta_f(t),\end{aligned}\quad (57.43)$$

where

$$\begin{aligned}R &= \sqrt{b^2 + v^2t^2}, \\ R' &= \sqrt{b^2 + v^2t'^2}\end{aligned}\quad (57.44)$$

and t (t') is the time in the rest frame of the ion (atom) (e.g. [19, Chap. 9]). Compared to the Born approximation, the difference is that within its boundary-corrected version the account is taken of the long-range Coulomb field of the ion in the initial state and of the field of the atomic residue in the final state by solving the wave equations for these states, assuming asymptotically large distances between the nuclei (e.g. [19], Sect. 7.4). The residual interactions in the post and prior forms are given, respectively, by

$$\begin{aligned}\left(\hat{H} - i\frac{\partial}{\partial t}\right)\tilde{\zeta}_f(t) &= -\gamma Z_a f(s, R') \mathcal{E} \tilde{\zeta}_f(t), \\ \left(\hat{H} - i\frac{\partial}{\partial t}\right)\tilde{\phi}_a(t) &= -Z_i f(r, R) \tilde{\phi}_a(t),\end{aligned}\quad (57.45)$$

where $f(a, b) = 1/a - 1/b$ and $\mathcal{E} = (1 - v\alpha_3/c)$.

Impulse Approximation

Suppose that the momentum transferred to the electron in the collision is much larger than the typical momentum of

this electron in its bound state. Then one can neglect the action of the corresponding binding force during the collision to a good approximation. This is the physical essence of the impulse approximation.

In applications of the impulse approximation to nonradiative capture, it is assumed that the electron motion during the collision is driven mainly by the field of one of the nuclei, whereas the role of the other nucleus is to produce the electron momentum distribution in the initial (or final) bound state and to serve as the perturbation resulting in electron transfer. Such an approach is not symmetric with respect to the treatment of the nuclei and is, therefore, best suited to when the charges of the nuclei substantially differ.

Let a highly charged bare nucleus capture an electron from a light atom. In the impulse approximation, the transition amplitude in the rest frame of the ion is given by

$$a_{fi}^{(+)}(\mathbf{b}) = -i \int_{-\infty}^{+\infty} dt \langle \chi_f | \hat{W}_a | \psi_i^{(+)} \rangle. \quad (57.46)$$

Here, $\hat{W}_a = -(\gamma Z_a/s)(1 - (v/c)\alpha_3)$ is the interaction between the electron and the nucleus of the atom, $\chi_f(t)$ is the undistorted final bound state of the electron in the ion, and the initial state can be approximated [29] by

$$\begin{aligned}\psi_i^{(+)}(\mathbf{r}, t) &= \frac{\exp(-i\epsilon_a t/\gamma)}{\gamma} \int d^3\mathbf{p} \exp(-i\mathbf{p} \cdot \mathbf{R}) \\ &\times C_a \left(\mathbf{p}_\perp, -\frac{v\epsilon_a}{c^2} + \frac{p_z}{\gamma} \right) \chi_p^{(+)}(\mathbf{r}),\end{aligned}\quad (57.47)$$

where ϵ_a is the electron energy in the initial atomic state, $\chi_p^{(+)}(\mathbf{r})$ is the Coulomb continuum “in” state of the electron in the field of the highly charged nucleus with momentum $\mathbf{p} = (\mathbf{p}_\perp, p_z)$, and

$$C_a(\mathbf{k}) = \frac{1}{(2\pi)^{3/2}} \int d^3\mathbf{r}' \phi_0'(\mathbf{r}') \exp(-i\mathbf{k} \cdot \mathbf{r}') \quad (57.48)$$

is the Fourier transform of the initial (nonrelativistic) atomic state. According to Eqs. (57.47) and (57.48) the initial state of the electron is represented by a superposition of continuum states of the electron in the field of the ionic nucleus, where the coefficients in this superposition are related to the momentum decomposition of the initial atomic state.

The impulse approximation is expected to yield good results provided that the change in the momentum of the electron in the capture process greatly exceeds its typical orbiting momentum in the lighter of the colliding nuclei.

Various models for electron capture in nonrelativistic collisions based on the impulse approximation have been used for a long time ([1, 30, 31] and references therein). The impulse approximation was introduced to nonradiative capture in relativistic collisions in [32]. Its discussion from the perspective of distorted-wave models can be found in [16].

Other Distorted-Wave Models

Other very frequently used distorted-wave models for nonradiative electron capture include the asymmetric and symmetric eikonal approximations [19] and continuum-distorted-wave models [16].

Two-Center Coupled-Channel Methods

Coupled-channel methods for electron capture in ion–atom collisions are similar to those for atomic excitation or ionization. However, unlike ionization, in the case of capture, the wave function of the electron is always expanded simultaneously into two sets of eigenstates referring to the initial and final channel Hamiltonians [19].

We conclude this section with two remarks. First, in nonradiative electron transfer occurring in high-energy collisions ($Z_a/v \ll 1$ or $\gamma \gg 1$), the electron is captured mainly from the K -shell of the atom. In multielectron atoms, the presence of a vacancy in the K -shell leads to a multitude of atomic reactions driven by the interaction of the remaining atomic electrons with the radiation field and with each other, which results in emission of photons and electrons.

Second, an interesting peculiarity of nonradiative electron transfer in nonrelativistic collisions is that at asymptotically high impact energies this process is dominated by the *Thomas capture mechanism*. According to this mechanism, electron capture proceeds via a binary collision of the projectile ion with one of (quasi free) atomic electrons and a consequent re-scattering of this electron on the atomic nucleus, after which it moves with a vector velocity equal to that of the projectile ion. This mechanism is considered in Chap. 61 of this Handbook.

57.3.2 Radiative Electron Capture

In the process of radiative capture, the interaction of the electron with the radiation field plays a crucial role, and the electron transfer proceeds with emission of a photon. The interaction with the radiation field is also responsible for radiative recombination of an electron with an ion – a process that, under certain conditions, is very closely related to radiative electron capture.

We shall describe the radiation field by using a gauge in which the scalar potential is set to zero and the vector potential \hat{A} is transverse, $\nabla \cdot \hat{A} = 0$, and reads

$$\hat{A} = \sum_{\mathbf{k}, \lambda} \sqrt{\frac{2\pi c^2}{V\omega_k}} \mathbf{e}_{\mathbf{k}, \lambda} \times \{ \hat{a}_{\mathbf{k}, \lambda} \exp[i(\mathbf{k} \cdot \mathbf{r} - \omega_k t)] + \hat{a}_{\mathbf{k}, \lambda}^+ \exp[-i(\mathbf{k} \cdot \mathbf{r} - \omega_k t)] \}. \quad (57.49)$$

Here, $\hat{a}_{\mathbf{k}, \lambda}$ and $\hat{a}_{\mathbf{k}, \lambda}^+$ are the annihilation and creation operators, respectively, for a photon with momentum \mathbf{k} ($\hbar\mathbf{k}$), unit

polarization vectors $\mathbf{e}_{\mathbf{k}, \lambda}$ ($\lambda = 1, 2$, $\mathbf{e}_{\mathbf{k}, \lambda} \cdot \mathbf{k} = 0$, $\mathbf{e}_{\mathbf{k}, \lambda} \cdot \mathbf{e}_{\mathbf{k}, \lambda'} = \delta_{\lambda \lambda'}$) and frequency $\omega_k = c k$, V is the normalization volume for the radiation field, and the sum in Eq. (57.49) runs over all possible modes of the field.

The transition amplitude, calculated in the first-order perturbation theory in the interaction with the radiation field, is given by

$$a_{\text{fi}}(\mathbf{b}) = -i \int_{-\infty}^{+\infty} dt \langle \psi_f^{(-)}; \mathbf{k} \lambda | \hat{W} | \psi_i^{(+)}; 0 \rangle, \quad (57.50)$$

where

$$\hat{W} = -e\boldsymbol{\alpha} \cdot \hat{A} \quad (57.51)$$

is the interaction of the electron with the radiation field, $|\psi_i^{(+)}; 0\rangle$ and $|\psi_f^{(-)}; \mathbf{k} \lambda\rangle$ represent the initial and final states, respectively, of the quantum (sub)system involving the electron and the radiation field. The latter is initially in the vacuum state, $|0\rangle$, undergoing a transition into a state $|\mathbf{k} \lambda\rangle$ with one photon having momentum \mathbf{k} and polarization λ . Inserting Eqs. (57.49) and (57.51) into Eq. (57.50) we obtain

$$a_{\text{fi}}(\mathbf{b}) = -i \sqrt{\frac{2\pi c^2}{V\omega_k}} \int_{-\infty}^{+\infty} dt \langle \psi_f^{(-)} | \boldsymbol{\alpha} \cdot \mathbf{e}_{\mathbf{k}, \lambda} \times \exp[-i(\mathbf{k} \cdot \mathbf{r} - \omega_k t)] | \psi_i^{(+)} \rangle. \quad (57.52)$$

The nonrelativistic limit. Suppose that the collision velocity and the initial and final orbiting velocities of the electron are all much less than the speed of light. Then the electron can be treated using the Schrödinger equation with the nonrelativistic Hamiltonian Eq. (57.37), and the interaction with the radiation field reads

$$\hat{W} = -\frac{e}{mc} \hat{A} \cdot \hat{\mathbf{p}}. \quad (57.53)$$

In the treatment of radiative capture, which is of first order in the interaction with the radiation field but otherwise exact, the states $\psi_i^{(+)}(t)$ and $\psi_f^{(-)}(t)$ would have to be solutions of Eq. (57.34) with the two-center Hamiltonian Eq. (57.35) (or of the corresponding Schrödinger equation with the Hamiltonian Eq. (57.37)). Since such solutions are not known, in practice, the transition amplitude Eq. (57.50) is evaluated by using various approximations.

Born Approximation

The simplest approach to radiative capture – the Born approximation – consists of replacing the state $\psi_i^{(+)}(t)$ by the undistorted initial atomic state $\phi_a(t)$ and the state $\psi_f^{(-)}(t)$ by the undistorted final bound state $\zeta_f(t)$. The Born approximation is covariant under the transformation of a reference frame. Moreover, when the gauge Eq. (57.49) is employed, the Born approximation yields reasonable results provided

that $Z_{a(i)} \ll v$ and the basic consideration is given in the rest frame of the ion. The differential cross sections obtained in this frame can be recalculated to the laboratory frame similarly as is done for electron emission (see Eq. (57.21)).

At asymptotically high impact energies in the nonrelativistic domain ($Z_{a(i)} \ll v \ll c$), the Born approximation predicts that radiative capture proceeds mainly into the 1s-state of the ion, yielding for the total cross section

$$\sigma_{\text{rec}} \approx N_a \frac{Z_i^5}{E^{2.5}} \approx N_a \frac{Z_i^5}{v^5}, \quad (57.54)$$

where N_a is the number of the electrons in the atom, Z_i is the charge of the ion, and E is the impact energy. The cross section Eq. (57.54) strongly depends on the charge of the ion but is independent of the charge of the atomic nucleus, suggesting that the latter is just a *spectator* in this process and, thus, pointing to the connection between radiative capture in ion–atom collisions and radiation recombination of a free electron with an ion. Comparing Eq. (57.54) with Eq. (57.41) we see that, owing to a much weaker dependence on the impact energy, radiative capture can become more probable than nonradiative capture in collisions with light atoms, provided that the impact energy is high enough. For instance, in collisions of protons with atomic hydrogen, radiative capture becomes the dominant channel for electron transfer at impact energies $E \gtrsim 10$ MeV.

At high impact energies in the relativistic domain ($\gamma \gg 1$), the Born approximation predicts that

$$\sigma \approx N_a \frac{Z_i^5}{E} \approx N_a \frac{Z_i^5}{\gamma}, \quad (57.55)$$

with the capture also mainly proceeding into the 1s state of the ion.

In the Born approximation, the initial and final states of the electron are states of the different channel Hamiltonians. This does not affect its Lorentz (or Galilean) covariance but leads to a strong gauge-dependence of the calculated cross sections. Reference-frame and gauge transformations can become so intimately interrelated that gauge dependence is sometimes incorrectly interpreted as the lack of covariance under the transformation of a reference frame (for an in-depth discussion of this point see part A4 of [2] and references therein).

Impulse Approximation

The impulse approximation for radiative capture is formulated similarly as for nonradiative transfer. Since it is the interaction with the radiation field that leads to the electron transition, the “minor” nucleus now plays an even lesser role restricted to merely producing the initial momentum distribution of the electron. The impulse approximation is well suited for asymmetric collisions in which the electron is transferred from a light atom to a highly charged ion. Moreover, since in

radiative capture the symmetry between the initial and final states is already broken by the emitted photon, the impulse approximation can also be applied to more symmetric collisions.

The impulse approximation enables one to establish a close relation between radiative electron capture in ion–atom collisions and radiative recombination of a free electron with an ion. Therefore, in practice, the cross sections for radiative capture are often calculated by averaging the corresponding cross sections for radiative recombination over the Compton profile of the atomic electron(s) [33].

Continuum-Distorted-Wave Model

Theoretical models for radiative capture in which, unlike the impulse approximation, the nuclei of the ion and atom are considered on equal footing are also of great interest. One of these is the continuum-distorted-wave model. This was considered in detail for radiative capture in relativistic collisions in [16]. Some merits of this model in nonrelativistic collisions are discussed in part A4 of [2].

57.4 Electron–Positron Pair Production

Electron–positron pair production is one of the most fascinating predictions of quantum electrodynamics. In this process, the presence of electromagnetic fields makes the “empty space” (vacuum) unstable, resulting in the conversion of “energy into matter”. In general, one can speak about two qualitatively different limiting regimes of this process.

In one of them, an external electric field is almost time independent (on the time scale of the pair production process) but is so strong that it can provide an energy of the order of the electron rest energy mc^2 on a distance of the order of the electron Compton wave length $\lambda_C = \hbar/mc$. The strength E_{cr} of such a field, which is called *critical*, can be estimated according to $e E_{\text{cr}} \lambda_C = mc^2$, which results in $E_{\text{cr}} = m^2 c^3 / (\hbar e)$. The critical field is $\alpha^{-3} = (\hbar c/e^2)^3 \approx 2.57 \times 10^6$ times larger than the typical electric field $E_0 = m^2 e^5 / \hbar^4$ acting on the electron in the ground state of atomic hydrogen. This regime of pair production can, for instance, be encountered in comparatively slow collisions of two very heavy bare nuclei; when these nuclei closely approach each other their combined electric field may become close to the critical value.

In the other limiting regime of pair production, the fields may be not that strong but vary so rapidly in time that their characteristic frequencies multiplied by \hbar are larger than $2mc^2$. Possible realizations of this regime include a conversion of a high-energy photon into a pair in the field of a heavy nucleus and pair production in relativistic ion–atom (ion–ion) collisions. In the rest of this section, we shall discuss the latter in some detail.

A rigorous treatment of electron–positron pair production is possible within quantum electrodynamics. However,

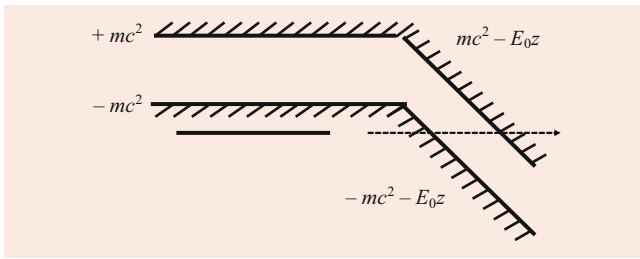
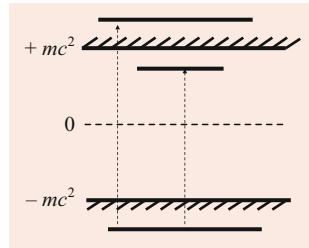


Fig. 57.3 Pair production in a strong constant electric field can be viewed as electron tunneling from the “negative-energy” to the “positive-energy” continuum

Fig. 57.4 Free and bound–free pair production in a rapidly time-varying electromagnetic field



very often, accurate results for this process can already be obtained using *relativistic quantum mechanics* (RQM) and the *Dirac sea* picture. Like *relativistic classical mechanics* (RCM), RQM predicts the existence of states with positive and negative total energies. However, in contrast to RCM, RQM also predicts the possibility of transitions between these states. In order to avoid electron transitions into negative-energy states (which would make even the ground states of atoms unstable due to spontaneous decay into the negative-energy states) P. Dirac assumed that under normal conditions all electron states with negative total energies are already occupied (*the Dirac “sea”*). Then, as a consequence of the Pauli exclusion principle, no more electrons can be added into the negative-energy continuum. In this picture, pair production is viewed as a transition of an electron from a state with a negative total energy to a state with a positive total energy. The absence of a negative-energy electron – a hole in the Dirac sea – is interpreted as a positron.

In Figs. 57.3 and 57.4 the Dirac sea picture is used to illustrate pair production in a strong constant electric field and a rapidly time-varying electromagnetic field, respectively.

Pair production in relativistic collisions can be subdivided into free, bound–free, and bound–bound pair production, which possess different dependences on the impact energy and the charges of the colliding particles.

57.4.1 Free Pair Production

In this process, the ion–atom (or ion–ion) collision results in the creation of free electrons and positrons. It was studied in much detail in a vast number of theoretical and experimental

papers (e.g., [34] for a review). Two theoretical methods are frequently used to describe this process.

In the first (and simplest) method, the lepton states are approximated by Dirac plane waves, and the interaction with the colliding heavy particles is treated within the second order of perturbation theory (see Fig. 57.5). The corresponding amplitude reads

$$a_{\text{fi}} = a_{\text{fi}}^{(\alpha)} + a_{\text{fi}}^{(\beta)}, \quad (57.56)$$

where

$$\begin{aligned} a_{\text{fi}}^{(\alpha)} &= - \sum_{p, \pm} \int_{-\infty}^{+\infty} dt \langle \varphi_{p_f}(t) | \hat{W}_1(t) | \varphi_p(t) \rangle \\ &\quad \times \int_{-\infty}^t dt' \langle \varphi_p(t') | \hat{W}_2(t') | \varphi_{p_i}(t') \rangle \\ a_{\text{fi}}^{(\beta)} &= - \sum_{p, \pm} \int_{-\infty}^{+\infty} dt \langle \varphi_{p_f}(t) | \hat{W}_2(t) | \varphi_p(t) \rangle \\ &\quad \times \int_{-\infty}^t dt' \langle \varphi_p(t') | \hat{W}_1(t') | \varphi_{p_i}(t') \rangle. \end{aligned} \quad (57.57)$$

Here, $\varphi_{p_i}(t)$ ($\varphi_{p_f}(t)$) refers to the initial (final) state of a free electron with momentum \mathbf{p}_i (\mathbf{p}_f) and total energy $\varepsilon_i = -\sqrt{p_i^2 c^2 + m^2 c^4}$ ($\varepsilon_f = +\sqrt{p_f^2 c^2 + m^2 c^4}$). (The created electron and positron have momenta and energies given by $\mathbf{p}_e = \mathbf{p}_f$, $\varepsilon_e = \varepsilon_f$ and $\mathbf{p}_p = -\mathbf{p}_i$, $\varepsilon_p = -\varepsilon_i$, respectively.) The sum in Eq. (57.57) runs over all intermediate plane-wave states with positive and negative total energies, and \hat{W}_1 (\hat{W}_2) denotes the interaction with the first (second) nucleus.

Within this method, pair production can be also viewed as a conversion of two virtual photons representing the fields of the colliding particles into an electron–positron pair. In extreme relativistic collisions, virtual photons closely resemble real photons, and one may relate pair production in collisions to photo pair production (the Weizsäcker–Williams approximation; e.g., [3, 35]).

At high impact energies ($\gamma \gg 1$), the total cross section for pair production in nucleus–nucleus collisions can be well approximated by

$$\sigma_{\text{ff}} = \frac{28}{27\pi} \lambda_C^2 (\alpha Z_1)^2 (\alpha Z_2)^2 \ln^3 \left(\frac{\gamma}{4} \right), \quad (57.58)$$

where Z_1 and Z_2 are the atomic numbers of the colliding nuclei.

In the second method, the interaction between the lepton field and one of the heavy particles is taken into account exactly, by describing electron states with negative and positive total energies by the corresponding solutions of the Dirac equation in the field of this heavy particle. The action of the other heavy particle is accounted for by using first-

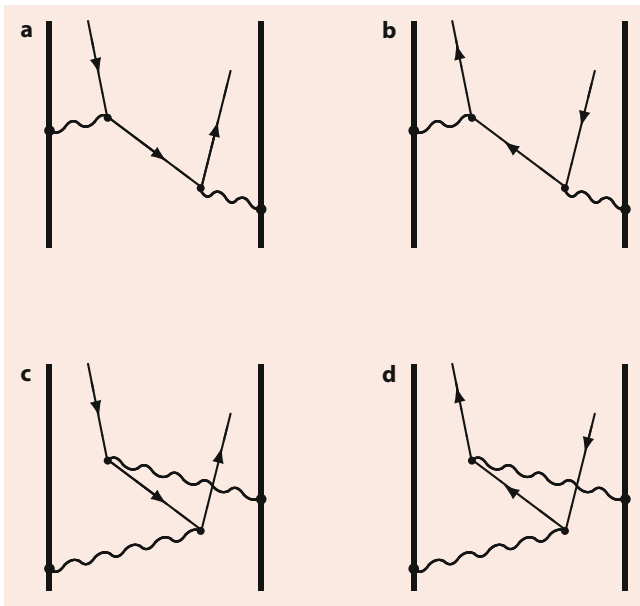


Fig. 57.5 Free pair production according to the second Born approximation. The nuclei and the leptons are indicated by *bold* and *thin solid lines*, respectively. *Wavy lines* show virtual photons representing the fields of the nuclei

order perturbation theory. Thus, pair production is regarded as a transition between negative-energy and positive-energy states in the field of one heavy particle induced by a single interaction with the field of the other (Fig. 57.4). Such a treatment is well suited for pair production in asymmetric collisions where the atomic numbers of the colliding particles differ substantially. At very high impact energies ($\gamma \rightarrow \infty$), it can also be applied to (more) symmetric collisions by performing two calculations: in one of them the initial and final states are states in the field of particle 1, whereas particle 2 represents the perturbation; in the other the roles of these particles are interchanged.

It is not difficult to realize that in the second method, the description of pair production in ion–atom (or ion–ion) collisions is actually given by the formalism discussed in Sect. 57.2. Indeed, in order to adapt it for pair production, we just need to replace bound–bound (or bound–positive-energy-continuum) electron transitions in one of the colliding particles (say particle 1) by transitions between its negative- and positive-energy states.

57.4.2 Bound–Free Pair Production

Unlike free pair production, in bound–free pair production, the electron is created in a bound state. In collisions between two bare nuclei, the created electron can be bound by either nucleus, whereas in ion(nucleus)–atom collisions, the electron will be most likely created in a bound state of the ion. Bound–free pair production can be regarded as *electron*

capture from vacuum. The capture mainly proceeds into the ground state of the ion.

This process can be viewed as a collision-induced transition of a negative-energy electron into a bound state (Fig. 57.4). In its simplest treatment, the interaction with that heavy particle, which binds the created electron, is taken into account exactly, whereas the action of the other heavy particle is described by using the first-order perturbation theory. Such a description is obviously equivalent to the second of the two methods discussed in Sect. 57.4.1, and the formalism presented in Sect. 57.2 can again be used. It is adapted to bound–free pair production by replacing bound–bound (or bound–positive-energy-continuum) electron transitions in one of the colliding particles (say particle 1) by transitions between its negative-energy continuum and a bound state.

Suppose, for instance, that electron–positron pair production occurring in the field of a bare nucleus (particle 1) is induced by collisions with another bare nucleus (particle 2). Then in the rest frame of particle 1, the corresponding quantum transition amplitude reads

$$S_{fi}(\mathbf{q}_\perp) = \frac{2iZ_2}{v} \frac{\langle \psi_f | \exp(i\mathbf{q} \cdot \mathbf{r}) (1 - \frac{v}{c}\alpha_3) | \psi_i \rangle}{\mathbf{q}_\perp^2 + \frac{(\varepsilon_f - \varepsilon_i)^2}{v^2\gamma^2}}. \quad (57.59)$$

Here, $\psi_i \equiv \psi_p$ is the state of a negative-energy electron with momentum $-\mathbf{p}$ and energy $\varepsilon_i = -\varepsilon_p \leq -mc^2$ (the created positron has momentum \mathbf{p} and energy $\varepsilon_p \geq mc^2$), $\psi_f = \psi_b$ is the bound state of the created electron with an energy $\varepsilon_f = \varepsilon_b$, and

$$\mathbf{q} = \left(\mathbf{q}_\perp, \frac{\varepsilon_f - \varepsilon_i}{v} \right) = \left(\mathbf{q}_\perp, \frac{\varepsilon_b + \varepsilon_p}{v} \right) \quad (57.60)$$

is the momentum transferred to particle 1 in its rest frame.

If particle 2 is a neutral atom, its electrons will influence pair production via the screening and antiscreening effects, and this can also be taken into account by using the formalism discussed in Sect. 57.2. Since the momentum transfers characteristic for pair production are very large, the screening effect of atomic electrons may remain modest even in extreme relativistic collisions (Fig. 57.6).

At high impact energies ($\gamma \gg 1$), the total cross section for bound–free pair production in collisions between two bare nuclei with the atomic numbers Z_1 and Z_2 can be approximated by

$$\sigma_{bf} \simeq a_1 \lambda_C^2 (\alpha Z_1)^5 (\alpha Z_2)^2 \ln(a_2 \gamma). \quad (57.61)$$

Here, the created electron forms a bound state with the nucleus Z_1 , and the parameters a_1 and a_2 depend on Z_1 . The cross section Eq. (57.61) increases with increasing impact energy. The increase, however, is weaker than in the case of free pair production (Eq. (57.58)). In Eq. (57.61), the dependence on Z_2 is similar to that for free pair production, but

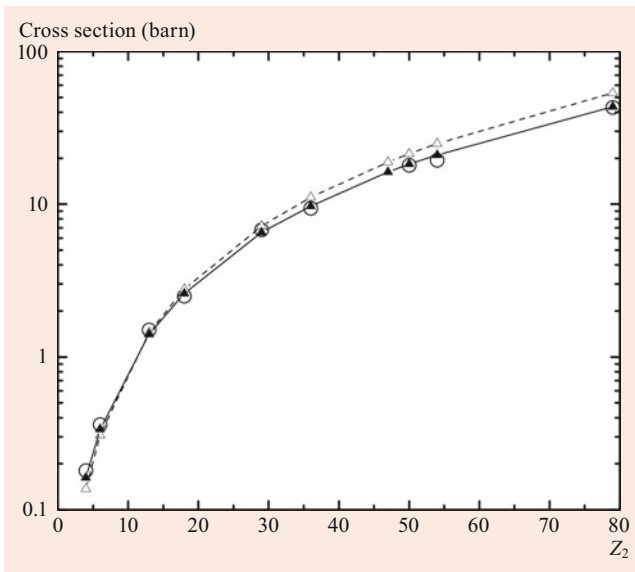


Fig. 57.6 Total cross section for bound–free pair production in collisions of 160 GeV/u Pb^{82+} nuclei with gas and solid-state targets as a function of the target atomic number. Circles represent experimental data for Be, C, Al, Cu, Ar, Kr, Sn, Xe, and Au targets [36–38]. Solid triangles connected by a solid curve and open triangles connected by dash curve are calculations for collisions with atoms of Be, C, Al, Ar, Cu, Kr, Ag, Sn, Xe, and Au and with the corresponding bare nuclei. The curves are just to guide the eye

the dependence on Z_1 is much steeper because the nucleus Z_1 accommodates the created electron.

Unlike electron transfer, in which the initial and final electron states belong to the different colliding particles, in bound–free pair production at high collision energies, the transition occurs between states of the same particle. However, similarly to electron transfer, pair production is characterized by large momentum transfers ($\simeq 2mc > Z_1$) due to large energies ($\simeq 2mc^2$) imparted to the vacuum. Because of this, the Z_1 -dependence in Eq. (57.61) is similar to the charge dependence of the capture cross sections (compare Eq. (57.61) with Eqs. (57.42) and (57.55)). At the same time, since bound–free pair production in high-energy collisions is essentially a single-center process, the increase in the impact energy just makes bound–free pair production more probable due to the increase of the range of the impact parameters contributing to this process. This is very similar to what takes place in ionization by high-energy charged particles, which is also essentially a single-center process (but characterized by much smaller momentum transfers). As a result, the dependences of the cross sections for bound–free pair production and ionization on the impact energy are similar (compare Eq. (57.61) with Eq. (57.23)).

If bound–free pair production occurs in collisions between a bare nucleus and a neutral atom, then at sufficiently high impact energies, the total cross section for this process “saturates” becoming independent of the impact energy ([2,

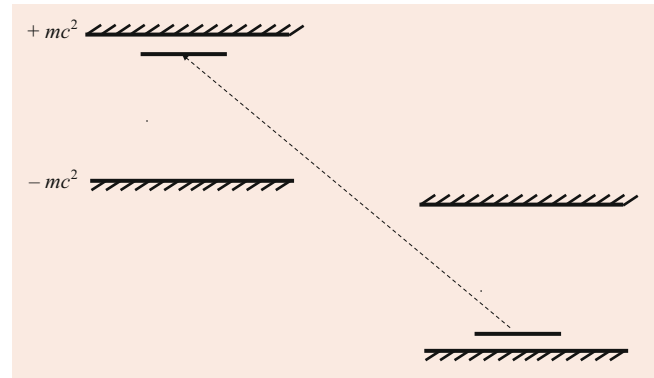


Fig. 57.7 Bound–bound pair production in relativistic collisions of a nucleus and an antinucleus

Chap. 8]). This is caused by the presence of atomic electrons that makes the field of the atom short ranged.

With an increase in the impact energy, the cross section for bound–free pair production increases (or saturates), whereas the cross sections for nonradiative and radiative electron transfer decrease. Therefore, in ion–atom collisions at high impact energies ($\gamma \gg 1$), bound–free pair production represents the main mechanism for the ion to change its charge.

57.4.3 Bound–Bound Pair Production

When the colliding nuclei possess charges of different signs, yet another pair production process becomes possible, in which not only the electron but also the positron is created in a bound state. This process is called bound–bound pair production [39] and, in the simplest picture, can be viewed as collision-induced electron transition between two bound states (Fig. 57.7). The initial bound state is formed by a negative-energy electron and the antinucleus, whereas the final bound state consists of a positive-energy electron and the nucleus. This picture suggests that bound–bound pair production has an important similarity with nonradiative electron capture (nonradiative capture is discussed in Sect. 57.3.2).

The cross section σ_{bb} for bound–bound pair production nonmonotonously depends on the impact energy (Fig. 57.8). The reasons for this are discussed in [39], where it is also shown that at $\gamma \gg 1$

$$\sigma_{bb} \approx \lambda_C^2 \frac{(\alpha Z_1)^5 (\alpha |Z_2|)^5}{\gamma}, \quad (57.62)$$

where the atomic numbers $Z_1 > 0$ and $Z_2 < 0$ refer to the nucleus and the antinucleus, respectively. The dependencies of the cross section Eq. (57.62) on Z_1 , $|Z_2|$ and γ turn out to be similar to those on Z_1 , Z_2 and γ for nonradiative electron transfer (see Eq. (57.42)) and have basically the same origin. In particular, the γ^{-1} -dependence of the cross section Eq. (57.62) reflects the decrease in the momentum overlap

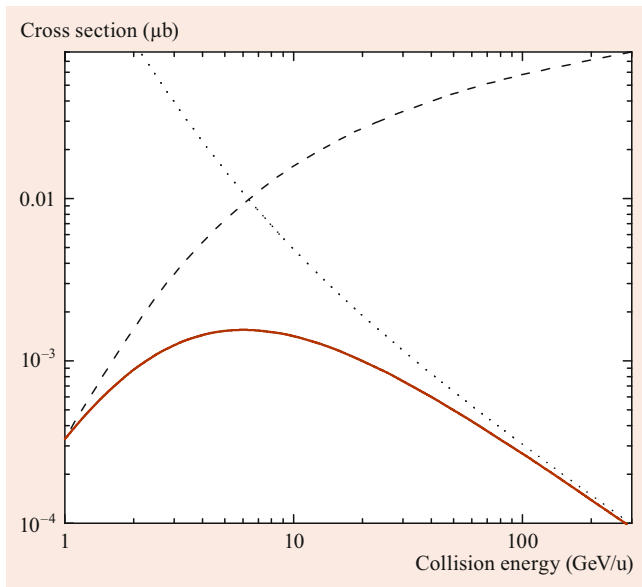


Fig. 57.8 Formation of antihydrogen via bound–bound, $p^- + U^{92+} \rightarrow \bar{H}(1s) + U^{91+}(1s)$ (solid curve), and bound–free, $p^- + U^{92+} \rightarrow \bar{H}(1s) + U^{92+} + e^-$ (dashed curve), pair production. For more information, the dotted curve displays the cross section for nonradiative capture, $H(1s) + U^{92+} \rightarrow p^+ + U^{91+}(1s)$, multiplied by 2

between the initial and final states with an increase in the impact energy.

57.4.4 More Advanced Theoretical Methods

In addition to the simplest theoretical methods, discussed in the previous sections, also more sophisticated models for pair production have been developed. In particular, they include one and two-center coupled-channel methods [19], direct numerical solutions of the time-dependent Dirac equation on a lattice [19], continuum-distorted-wave models [16], various eikonal approximations including the symmetric eikonal model [18], and the light-cone approximation [17].

References

1. McDowell, M.R.C., Coleman, J.P.: Introduction to the Theory of Ion-Atom Collisions. North-Holland, Amsterdam, London (1970)
2. Voitkiv, A.B., Ullrich, J.: Relativistic Collisions of Structured Atomic Particles. Springer, Berlin (2008)
3. Jackson, J.D.: Classical Electrodynamics, 3rd ed., Wiley, New York (1999)
4. Inokuti, M.: Rev. Mod. Phys. **43**, 297 (1971)
5. McGuire, J.H.: Electron Correlation Dynamics in Atomic Collisions. Cambridge University Press, Cambridge (1997)
6. Landau, L.D., Lifshitz, E.M.: Quantum Mechanics. Pergamon, Oxford (1977)
7. Bethe, H.A., Salpeter, E.E.: Quantum Mechanics of One- and Two-Electron Atoms. Academic Press, New York (1957)
8. Rose, M.E.: Relativistic Electron Theory. Wiley, New York (1975)

9. Berestetskii, V.B., Lifshitz, E.M., Pitaevskii, L.P.: Quantum Electrodynamics. Pergamon, Oxford (1982)
10. Abramowitz, M., Stegun, I.: Handbook of Mathematical Functions. Dover, New York (1965)
11. Dedrick, K.G.: Rev. Mod. Phys. **34**, 429 (1962)
12. Hillenbrand, P.-M., Hagmann, S., Jakobassa-Amundsen, D.H., Monti, J.M.: Phys. Rev. A **91**, 022705 (2015)
13. In Chapter 53 of Springer Handbook of Atomic, Molecular and Optical Physics (2005).
14. Anholt, R.: Phys. Rev. A **19**, 1004 (1979)
15. Landau, L.D., Pitaevskii, L.P., Lifshitz, E.M.: Electrodynamics of Continuous Media. Elsevier/Butterworth-Heinemann, Amsterdam, Boston (2008)
16. Crothers, D.S.F.: Relativistic Heavy-Particle Collision Theory. Kluwer Academic/Plenum, London (2000)
17. Baltz, A.J.: Phys. Rev. Lett. **78**, 1231 (1997)
18. Voitkiv, A.B., Najjari, B., Shevelko, V.P.: Phys. Rev. A **82**, 022707 (2010)
19. Eichler, J.: Lectures On Ion-Atom Collisions: From Nonrelativistic To Relativistic Velocities. Elsevier, Amsterdam (2005)
20. Schulz, M.: Adv. At. Mol. Opt. Phys. **66**, 508 (2017)
21. Moliere, G.: Naturforschung **2A**, 133 (1947)
22. Salvat, F., Martinez, J.D., Mayol, R., Parellada, J.: Phys. Rev. A **36**, 467 (1987)
23. Stolterfoht, N., DuBois, R.D., Rivarola, R.D.: Electron Emission in Heavy Ion-Atom Collisions. Springer, Berlin, Heidelberg (1997)
24. Voitkiv, A.B., Najjari, B.: Phys. Rev. A **85**, 052712 (2012)
25. Lyaschenko, K.N., Andreev, O.Y., Voitkiv, A.B.: J. Phys. B **51**, 055204 (2018)
26. Gumberidze, A., Thorn, D.B., Fontes, C.J., Najjari, B.: Phys. Rev. Lett. **110**, 213201 (2013)
27. Greiner, W.: Relativistic Quantum Mechanics, 3rd edn. Springer, Berlin, Heidelberg, New York (2000)
28. Bates, D.R., McCarroll, R.: Prog. Roy. Soc. Lond. A **245**, 175 (1958)
29. Najjari, B., Voitkiv, A.B., Artemyev, A., Surzhykov, A.: Phys. Rev. A **80**, 012701 (2009)
30. Dewangan, D.P., Eichler, J.: Phys. Rep. **247**, 59 (1994)
31. Dz. Belkic: Dz. Belkic. J. Comp. Meth. Sci. Tech. **1**, 1 (2001)
32. Jakobassa-Amundsen, D.H., Amundsen, P.A.: Z. Phys. A **298**, 13 (1980)
33. Eichler, J., Stöhlker, T.: Phys. Rep. **439**, 1 (2007)
34. Baur, G., Hencken, K., Trautmann, D.: Phys. Rep. **453**, 1 (2007)
35. Bertulani, C.A., Baur, G.: Phys. Rep. **163**, 299 (1988)
36. Krause, H.F., Vane, C.R., Datz, S.: Phys. Rev. Lett. **80**, 1190 (1998)
37. Krause, H.F., Vane, C.R., Datz, S.: Phys. Rev. A **63**, 032711 (2001)
38. Vane, C.R., Krause, H.F.: Nim B **261**, 244 (2007)
39. Voitkiv, A.B., Najjari, B., Di-Piazza, A.: New J. Phys. **12**, 063011 (2010)



Alexander Voitkiv received his PhD from the State University (Tashkent, USSR, 1989) and the degree of Doctor of Physical-Mathematical Sciences from the Lebedev Physics Institute (Moscow, Russia, 2010). He worked at the Institute of Electronics (Tashkent) and is currently at the Heinrich-Heine-University (Düsseldorf, Germany). His research focuses on the interactions of ions, electrons, and photons with atoms and molecules.



Electron–Ion, Ion–Ion, and Neutral–Neutral Recombination Processes

58

Edmund J. Mansky II and M. Raymond Flannery

Contents

58.1	Recombination Processes	846	58.9	One-Way Microscopic Equilibrium Current, Flux, and Pair Distributions	861
58.1.1	Electron–Ion Recombination	846	58.10	Microscopic Methods for Termolecular Ion–Ion Recombination	862
58.1.2	Positive–Ion Negative–Ion Recombination	846	58.10.1	Time-Dependent Method: Low Gas Density	862
58.1.3	Balances	846	58.10.2	Time-Independent Methods: Low Gas Density	863
58.1.4	Neutral–Neutral Recombination	847	58.10.3	Recombination at Higher Gas Densities	864
58.1.5	N-Body Recombination	848	58.10.4	Master Equations	865
58.2	Collisional-Radiative Recombination	849	58.10.5	Recombination Rate	865
58.2.1	Saha and Boltzmann Distributions	849	58.11	Radiative Recombination	866
58.2.2	Quasi-Steady State Distributions	850	58.11.1	Detailed Balance and Recombination-Ionization Cross Sections	867
58.2.3	Ionization and Recombination Coefficients	850	58.11.2	Kramers Cross Sections, Rates, Electron Energy-Loss Rates, and Radiated Power for Hydrogenic Systems	867
58.2.4	Working Rate Formulae	850	58.11.3	Basic Formulae for Quantal Cross Sections	869
58.2.5	Computer Codes	850	58.11.4	Bound-Free Oscillator Strengths	871
58.3	Macroscopic Methods	850	58.11.5	Radiative Recombination Rate	871
58.3.1	Resonant Capture-Stabilization Model: Dissociative and Dielectronic Recombination	850	58.11.6	Gaunt Factor, Cross Sections, and Rates for Hydrogenic Systems	872
58.3.2	Reactive Sphere Model: Three-Body Electron–Ion and Ion–Ion Recombination	851	58.11.7	Exact Universal Rate Scaling Law and Results for Hydrogenic Systems	873
58.3.3	Working Formulae for Three-Body Collisional Recombination at Low Density	853	58.12	Useful Quantities	873
58.3.4	Recombination Influenced by Diffusional Drift at High Gas Densities	853	References		873
58.4	Zero-Range Methods	855			
58.5	Hyperspherical Methods	856			
58.5.1	Three-Body Recombination Rate (Identical Particles)	856			
58.5.2	N-Body Recombination Rate (Identical Particles)	857			
58.6	Field-Assisted Methods	857			
58.7	Dissociative Recombination	857			
58.7.1	Curve-Crossing Mechanisms	857			
58.7.2	Quantal Cross Section	858			
58.7.3	Noncrossing Mechanism	860			
58.8	Mutual Neutralization	860			
58.8.1	Landau–Zener Probability for Single Crossing at R_X	860			
58.8.2	Cross Section and Rate Coefficient for Mutual Neutralization	861			

Abstract

This chapter collects together the formulae, expressions, and specific equations that cover various aspects, approximations, and approaches to electron–ion, ion–ion and neutral–neutral recombination processes. The primary focus is on recombination processes in the gas phase, both at thermal energies and in ultracold regimes.

Recombination processes are ubiquitous in nature. These reactions occur in a wide variety of applications and are an important formation or loss mechanism of atoms and molecules. To illustrate the types of problems where recombination is important, we enumerate six broad areas in which recombination processes occur: (a) collisional-radiative recombination processes, involving hydrogen

E. J. Mansky II (✉)
Eikonol Research Institute
Bend, OR, USA
e-mail: mansky@mindspring.com

and helium, which are important in understanding the cosmic microwave background in cosmology [1–3]; (b) radio recombination lines involving electrons and ions, which are central to understanding the observed spectra from interstellar clouds and planetary nebulae [4, 5]; (c) recombination processes, involving electrons and holes are important in semiconductors [6, 7]; (d) electron–ion and ion–ion recombination processes, which are important in understanding the properties of plasmas, whether they are in the upper atmosphere, the solar corona, or industrial reactors on earth [8–10]; (e) atom–molecule recombination involving oxygen, which are important mechanism for forming ozone [11]; and, finally, (f) three-body recombination processes, involving neutral bosons, which are an important loss mechanism in ultracold Rydberg atom collisions, leading to the depletion of the Bose Einstein condensate (BEC) [12–14].

Keywords

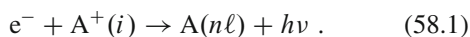
radiative recombination · mutual neutralization · dielectronic recombination · dissociative recombination · vibrational wave function

58.1 Recombination Processes

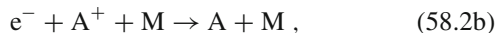
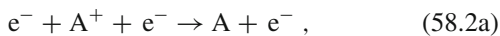
58.1.1 Electron–Ion Recombination

This proceeds via the following four processes:

(a) Radiative recombination (RR)

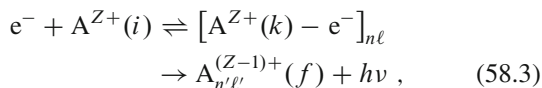


(b) Three-body collisional-radiative recombination

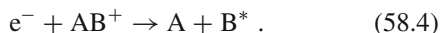


where the third body can be an electron or a neutral gas.

(c) Dielectronic recombination (DLR)



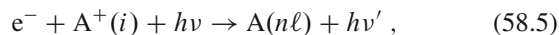
(d) Dissociative recombination (DR)



Electron recombination with bare ions can proceed only via (a) and (b), while (c) and (d) provide additional pathways for ions with at least one electron initially or for molecular ions AB^+ . Electron radiative capture denotes the combined effect of RR and DLR.

Field-assisted:

Electron–ion recombination can also occur by application of a laser field,

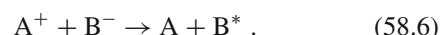


leading to high-order harmonic generation (HHG).

58.1.2 Positive–Ion Negative–Ion Recombination

This proceeds via the following three processes:

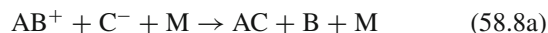
(e) Mutual neutralization



(f) Three-body (termolecular) recombination



(g) Tidal recombination



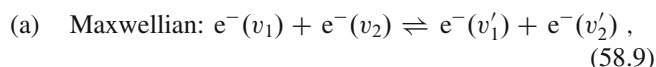
where M is some third species (atomic, molecular, or ionic). Although (e) always occurs when no gas M is present, it is greatly enhanced by coupling to (f). The dependence of the rate $\hat{\alpha}$ on density N of background gas M is different for all three cases, (e)–(g).

Processes (a), (c), (d), and (e) are elementary processes in that microscopic detailed balance (proper balance) exists with their true inverses, i.e., with photoionization (both with and without autoionization) as in (c) and (a), associative ionization and ion-pair formation as in (d) and (e), respectively. Processes (b), (f), and (g) in general involve a complex sequence of elementary energy-changing mechanisms as collisional and radiative cascade and their overall rates are determined by an input–output continuity equation involving microscopic continuum–bound and bound–bound collisional and radiative rates.

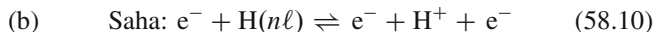
58.1.3 Balances

Proper Balances

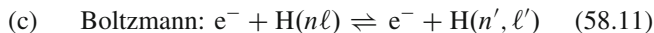
Proper balances are detailed microscopic balances between forward and reverse mechanisms that are direct inverses of one another, as in



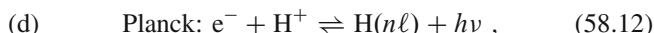
where the kinetic energy of the particles is redistributed;



between direct ionization from and direct recombination into a given level $n\ell$;



between excitation and deexcitation among bound levels;



which involves interaction between radiation and atoms in photoionization/recombination to a given level $n\ell$.

Improper Balances

Improper balances maintain constant densities via production and destruction mechanisms that are not pure inverses of each other. They are associated with flux activity on a macroscopic level as in the transport of particles into the system for recombination and net production and transport of particles (i.e. e^- , A^+) for ionization. Improper balances can then exist between dissimilar elementary production–depletion processes as in (a) coronal balance between electron-excitation into and radiative decay out of level n . (b) Radiative balance between radiative capture into and radiative cascade out of level n . (c) Excitation saturation balance between upward collisional excitations $n-1 \rightarrow n \rightarrow n+1$ between adjacent levels. (d) Deexcitation saturation balance between downward collisional de-excitations $n+1 \rightarrow n \rightarrow n-1$ into and out of level n .

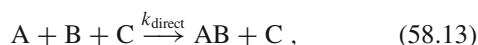
58.1.4 Neutral–Neutral Recombination

Neutral–neutral reactions, leading to recombination or dissociation, generally proceed via resonances involving transitions among molecular electronic states. At thermal energies, these reactions are studied via transition state theory, reaction rate theory, and a wide range of semiclassical techniques. See Chap. 37 of this Handbook and [15–19] for a general introduction to this vast literature in chemical physics and chemistry.

Distinguishable Particles [3]

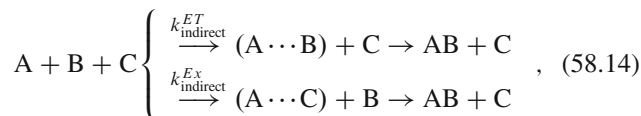
When one or more reactants in the process are distinguishable, the thermal reactions proceed via two broad pathways, *direct* and *indirect*:

Direct pathway



where k_{direct} is the reaction rate (cm^3/s) for the formation of molecule AB and reactant C.

Indirect pathways



where $(A \cdots B)$ indicates an intermediate collision complex formed between atoms A and B, and k_{indirect}^{ET} , k_{indirect}^{Ex} are the reaction rates (cm^3/sec) for the transfer and exchange reactions in Eq. (58.14) (upper/lower), respectively. Prediction of rates k , in both the direct and indirect pathways, depends upon detailed knowledge of the molecular potential energy surfaces, curve-crossings, and tunneling probabilities for specific reactants.

LTE effective rate equation

For systems in local thermodynamic equilibrium (LTE), the effective rate equations are

$$\frac{1}{[C]} \frac{d}{dt} [AB] = k_r [A][B] - k_d [AB], \quad (58.15)$$

where the square brackets indicate the number density of the enclosed species, and k_r denotes the rate constant for three-body recombination, while k_d the rate constant for collision-induced dissociation

$$k_r = \sum_{b,u} k_{u \rightarrow b} \frac{[AB(u)]}{[A][B]}, \quad (58.16a)$$

$$k_d = \sum_{b,u} k_{b \rightarrow u} \frac{[AB(b)]}{[AB]}, \quad (58.16b)$$

with b and u representing bound and unbound states of the indicated collision complex, respectively. The state-to-state rate coefficients are defined by

$$k_{i \rightarrow j} = \left(\frac{8k_B T}{\pi \mu} \right)^{1/2} (k_B T)^{-2} \int_0^\infty \sigma_{i \rightarrow j}(E_T) \times \exp(-E_T/k_B T) E_T dE_T, \quad (58.17)$$

where μ is the reduced mass, $E_T = E - E_i$ is the translational energy of the i -th state of the atom, and σ is the cross section for the indicated transition $i \rightarrow j$.

NLTE effective rate equations

For systems not in local thermodynamic equilibrium (NLTE) the effective rate equations are

$$\begin{aligned} 6 \frac{d}{dt} [AB(b)] = & [C] \sum_u (k_{u \rightarrow b} [AB(u)] - k_{b \rightarrow u} [AB(b)]) \\ & + [C] \sum_{b'} (k_{b' \rightarrow b} [AB(b')] - k_{b \rightarrow b'} [AB(b)]), \end{aligned} \quad (58.18a)$$

$$\begin{aligned} \frac{d}{dt}[\text{AB}(u)] = & [\text{C}] \sum_b (k_{b \rightarrow u}[\text{AB}(b)] - k_{u \rightarrow b}[\text{AB}(u)]) \\ & + [\text{C}] \sum_{u'} (k_{u' \rightarrow u}[\text{AB}(u')] - k_{u \rightarrow u'}[\text{AB}(u)]) \\ & + k_{f \rightarrow u}^{\text{elastic}}[\text{A}][\text{B}] - \frac{[\text{AB}(u)]}{\tau_u}, \end{aligned} \quad (58.18b)$$

where τ_u is the lifetime of the unbound state u , and $k_{f \rightarrow u}^{\text{elastic}}$ is the elastic two-body rate constant.

Identical Particles

At thermal energies, reactions involving identical particles proceed as detailed above. In ultracold regimes, collisions involving identical bosons proceed via Fano–Feshbach or Föster resonances [20–22]. These resonances can be exploited by varying the applied magnetic or electric fields used in traps to create and control Bose–Einstein condensates (BEC).

At thermal and higher energies, the rate-limiting step [23] is generally either collisional or radiative capture into high-lying Rydberg states ($n \gg 1$), followed by radiative decay into lower lying states via n and n, ℓ mixing collisions. In contrast, at ultracold regimes, the rate-limiting step is collisional ℓ mixing, wherein rapid collisional capture into very high-lying Rydberg states ($n > 200$) is followed by slow collisional-radiative decay. The result is a cloud of Rydberg atoms that has condensed into a long-lived macroscopic BEC, which can be controlled via the applied fields used in the trap.

For three identical particles, this proceeds as



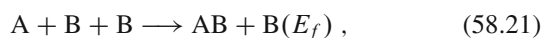
Time-dependent equation

$$\frac{dn_A}{dt} = \begin{cases} -3\alpha n_A^3 & \text{before onset of BEC} \\ -\frac{1}{2}\alpha n_A^3 & \text{at BEC} \end{cases}, \quad (58.20)$$

where α is the recombination rate coefficient (number of dimers $\text{cm}^{-3} \text{s}^{-1}$), and n_A is the number density of atoms A. At the onset of BEC in ultracold traps, the recombination rate is reduced by the factor $1/3!$ because of the symmetry of the macroscopic quantum state the atoms A are then in. See Sect. 58.4 for explicit closed-form expressions for α .

Heteronuclear Mixtures

For heteronuclear mixtures of particles, this proceeds as



for distinct atoms A and B.

At thermal energies this is analyzed as above using either LTE or NLTE formulations involving the relevant molecular potential surfaces. At ultracold regimes [24] the mixtures are

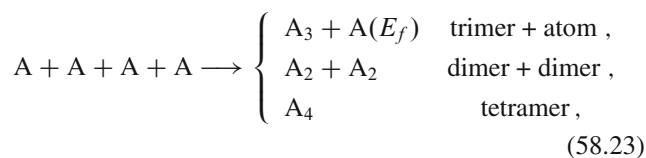
composed of heavy and light bosons, or bosons and fermions, or of a boson together with heavy and light fermions, and are analyzed using zero-range methods. See Table 1 of [25] for details on the various cases where the Efimov effect occurs in such systems and Sect. 58.4 for explicit expressions for α . For details on the Efimov effect, see Sects. 58.4 and 60.6 in this Handbook and [25, 26].

Time-dependent equation

$$\frac{dn_A}{dt} = -\alpha n_A n_B^2. \quad (58.22)$$

58.1.5 N-Body Recombination [27]

This proceeds, for four identical particles, as



and has been observed [28] in an ultracold sample of Cs atoms at 30 nK. See Fig. 58.1 for an illustration of the allowed regimes for the various reactant branches in (58.23) as a function of energy and inverse scattering length.

The general problem of N-body recombination is challenging both experimentally and theoretically. Samples involving alkali atoms at ultracold temperatures currently provide the best conditions for observing N-body recombination. At present, the hyperspherical method of solving the N-body Schrödinger equation has been used most extensively on the problem. See Sect. 58.5 for closed-form expressions for N-body recombination rates α .

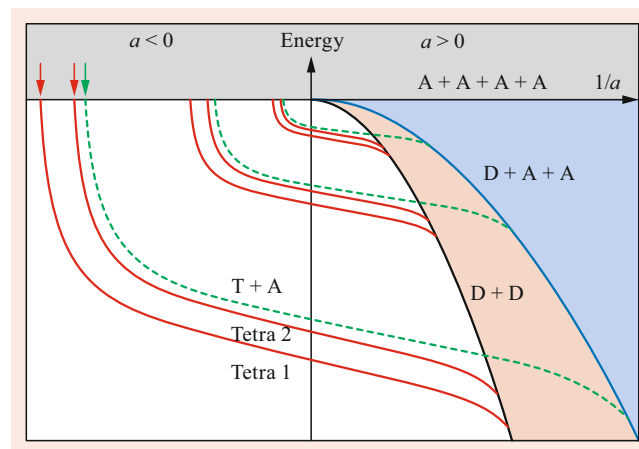


Fig. 58.1 Illustration of allowed regions for 4 bosons ($\text{A}+\text{A}+\text{A}+\text{A}$), Dimers + 2 bosons ($\text{D}+\text{A}+\text{A}$), 2 Dimers ($\text{D}+\text{D}$) and Trimers + bosons ($\text{T}+\text{A}$). See [28] for details

58.2 Collisional-Radiative Recombination

Radiative recombination

Process Eq. (58.1) involves a free-bound electronic transition with radiation spread over the recombination continuum. It is the inverse of photoionization without autoionization and favors high-energy gaps with transitions to low $n \approx 1, 2, 3$ and low angular momentum states $\ell \approx 0, 1, 2$ at higher electron energies.

Three-body electron–ion recombination

Processes Eq. (58.2a,b) favor free-bound collisional transitions to high levels n , within a few $k_B T$ of the ionization limit of $A(n)$ and collisional transitions across small energy gaps. Recombination becomes stabilized by collisional-radiative cascade through the lower-bound levels of A . Collisions of the $e^- - A^+$ pair with third bodies become more important for higher levels of n , and radiative emission is important down to and among the lower levels of n . In optically thin plasmas this radiation is lost, while in optically thick plasmas it may be reabsorbed. At low electron densities, radiative recombination dominates with predominant transitions taking place to the ground level. For process Eq. (58.2a) at high electron densities, three-body collisions into high Rydberg levels dominate, followed by cascade, which is collision dominated at low electron temperatures T_e and radiation dominated at high T_e . For process Eq. (58.2b) at low gas densities N , the recombination is collisionally radiatively controlled while, at high N , it eventually becomes controlled by the rate of diffusional drift Eq. (58.73) through the gas M .

Collisional-radiative recombination [29]

Here, the cascade collisions and radiation are coupled via the continuity equation. The population n_i of an individual excited level i of energy E_i is determined by the rate equations

$$\frac{dn_i}{dt} = \frac{\partial n_i}{\partial t} + \nabla \cdot (n_i \mathbf{v}_i) \quad (58.24)$$

$$= \sum_{i \neq f} [n_f v_{fi} - n_i v_{if}] = P_i - n_i D_i, \quad (58.25)$$

which involve temporal and spatial relaxation in Eq. (58.24) and collisional-radiative production rates P_i and destruction frequencies D_i of the elementary processes included in Eq. (58.25). The total collisional and radiative transition frequency between levels i and f is v_{if} and the f -sum is taken over all discrete and continuous (c) states of the recombining species. The transition frequency v_{if} includes all contributing elementary processes that directly link states i and f , e.g., collisional excitation and deexcitation, ionization ($i \rightarrow c$) and recombination ($c \rightarrow i$) by electrons and heavy particles, radiative recombination ($c \rightarrow i$), radiative decay ($i \rightarrow f$), possibly radiative absorption for optically thick plasmas, autoionization, and dielectronic recombination.

Production rates and processes

The production rate for a level i is

$$P_i = \sum_{f \neq i} n_e n_f K_{fi}^c + n_e^2 N^+ k_{ci}^R + \sum_{f > i} n_f (A_{fi} + B_{fi} \rho_\nu) + n_e N^+ (\hat{\alpha}_i^{RR} + \beta_i \rho_\nu), \quad (58.26)$$

where the terms in the above order represent (1) collisional excitation and deexcitation by $e^- - A(f)$ collisions, (2) three-body $e^- - A^+$ collisional recombination into level i , (3) spontaneous and stimulated radiative cascade, and (4) spontaneous and stimulated radiative recombination.

Destruction rates and processes

The destruction rate for a level i is

$$n_i D_i = n_e n_i \sum_{f \neq i} K_{if}^c + n_e n_i S_i + n_i \sum_{f < i} (A_{if} + B_{if} \rho_\nu) + n_i \sum_{f > i} B_{if} \rho_\nu + n_i B_{ic} \rho_\nu, \quad (58.27)$$

where the terms in the above order represent (1) collisional destruction, (2) collisional ionization, (3) spontaneous and stimulated emission, (4) photoexcitation, and (5) photoionization.

58.2.1 Saha and Boltzmann Distributions

Collisions of $A(n)$ with third bodies such as e^- and M are more rapid than radiative decay above a certain excited level n^* . Since each collision process is accompanied by its exact inverse the principle of detailed balance determines the population of levels $i > n^*$.

Saha Distribution

This connects equilibrium densities \tilde{n}_i , \tilde{n}_e , and \tilde{N}^+ of bound levels i , of free electrons at temperature T_e , and of ions by

$$\frac{\tilde{n}_i}{\tilde{n}_e \tilde{N}^+} = \left(\frac{g(i)}{g_e g_A^+} \right) \frac{h^3}{(2\pi m_e k T_e)^{3/2}} \exp(I_i / k_B T_e), \quad (58.28)$$

where the electronic statistical weights of the free electron, the ion of charge $Z + 1$, and the recombined $e^- - A^+$ species of net charge Z and ionization potential I_i are $g_e = 2$, g_A^+ , and $g(i)$, respectively. Since $n_i \leq \tilde{n}_i$ for all i , then the Saha–Boltzmann distributions imply that $n_1 \gg n_i$ and $n_e \gg n_i$ for $i \neq 1, 2$, where $i = 1$ is the ground state.

Boltzmann Distribution

This connects the equilibrium populations of bound levels i of energy E_i by

$$\tilde{n}_i/\tilde{n}_j = [g(i)/g(j)] \exp[-(E_i - E_j)/k_B T_e]. \quad (58.29)$$

58.2.2 Quasi-Steady State Distributions

The reciprocal lifetime of level i is the sum of radiative and collisional components, and this lifetime is, therefore, shorter than the pure radiative lifetime $\tau_R \approx 10^{-7} Z^{-4}$ s. The lifetime τ_1 for the ground level is collisionally controlled and depends on n_e , and, generally, is within the range of 10^2 and 10^4 s for most laboratory plasmas and the solar atmosphere. The excited level lifetimes τ_i are then much shorter than τ_1 . The (spatial) diffusion or plasma decay (recombination) time is then much longer than τ_i , and the total number of recombined species is much smaller than the ground-state population n_1 . The recombination proceeds on a timescale much longer than the time for population/destruction of the excited levels. The condition for quasi-steady state, or QSS-condition, $dn_i/dt = 0$ for the bound levels $i \neq 1$, therefore, holds. The QSS distributions n_i , therefore, satisfy $P_i = n_i D_i$.

58.2.3 Ionization and Recombination Coefficients

Under QSS, the continuity Eq. (58.25) then reduces to a finite set of simultaneous equations $P_i = n_i D_i$. This gives a matrix equation that is solved numerically for $n_i (i \neq 1) \leq \tilde{n}_i$ in terms of n_1 and n_e . The net ground-state population frequency per unit volume ($\text{cm}^{-3} \text{s}^{-1}$) can then be expressed as

$$\frac{dn_1}{dt} = n_e N^+ \hat{\alpha}_{\text{CR}} - n_e n_1 S_{\text{CR}}, \quad (58.30)$$

where $\hat{\alpha}_{\text{CR}}$ and S_{CR} , respectively, are the overall rate coefficients for recombination and ionization via the collisional-radiative sequence. The determined $\hat{\alpha}_{\text{CR}}$ equals the direct ($c \rightarrow 1$) recombination to the ground level supplemented by the net collisional-radiative cascade from that portion of bound-state population that originated from the continuum. The determined S_{CR} equals direct depletion (excitation and ionization) of the ground state reduced by the deexcitation collisional radiative cascade from that portion of the bound levels accessed originally from the ground level. At low n_e , $\hat{\alpha}_{\text{CR}}$ and S_{CR} reduce, respectively, to the radiative recombination coefficient summed over all levels and to the collisional ionization coefficient for the ground level.

C, \mathcal{E} , and S Blocks of Energy Levels

For the recombination processes in Eqs. (58.2a), (58.2b), and (58.7), which involve a sequence of elementary reactions,

the $e^- - A^+$ or $A^+ - B^-$ continuum levels and the ground $A(n=1)$ or the lowest vibrational levels of AB are, therefore, treated as two large particle reservoirs of reactants and products. These two reservoirs act as reactant and sink blocks C and S, which are, respectively, drained and filled at the same rate via a conduit of highly excited levels, which comprise an intermediate block of levels \mathcal{E} . This C draining and S filling proceeds, via block \mathcal{E} , on a timescale large compared with the short time for a small amount from the reservoirs to be redistributed within block \mathcal{E} . This forms the basis of QSS.

58.2.4 Working Rate Formulae

For electron-atomic-ion collisional-radiative recombination Eq. (58.2a), detailed QSS calculations can be fitted by the rate [30]

$$\hat{\alpha}_{\text{CR}} = (3.8 \times 10^{-9} T_e^{-4.5} n_e + 1.55 \times 10^{-10} T_e^{-0.63} + 6 \times 10^{-9} T_e^{-2.18} n_e^{0.37}) \text{ cm}^3 \text{ s}^{-1}, \quad (58.31)$$

which agrees with experiment for a Lyman α optically thick plasma with n_e and T_e in the range $10^9 \text{ cm}^{-3} \leq n_e \leq 10^{13} \text{ cm}^{-3}$ and $2.5 \text{ K} \leq T_e \leq 4000 \text{ K}$. The first term is the pure collisional rate Eq. (58.61), the second term is the radiative cascade contribution, and the third term arises from collisional-radiative coupling.

For ($e^- - \text{He}_2^+$), recombination in a high-pressure (5–100 Torr) helium afterglow, the rate for Eq. (58.2b) is [31]

$$\hat{\alpha}_{\text{CR}} = [(4 \pm 0.5) \times 10^{-20} n_e] (T_e/293)^{-(4 \pm 0.5)} + [(5 \pm 1) \times 10^{-27} n(\text{He}) + (2.5 \pm 2.5) \times 10^{-10}] \times (T_e/293)^{-(1 \pm 1)} \text{ cm}^3/\text{s}. \quad (58.32)$$

The first two terms are in accord with the purely collisional rates Eqs. (58.61) and (58.64b), respectively.

58.2.5 Computer Codes

A large number of computer codes for solving the collisional-radiative equations in astrophysical plasmas and fusion plasmas are available. See Table 58.1 for details.

58.3 Macroscopic Methods

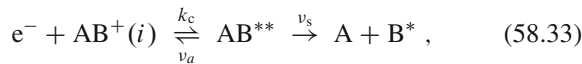
58.3.1 Resonant Capture-Stabilization Model: Dissociative and Dielectronic Recombination

The electron is captured dielectronically, Eq. (58.53), into an energy-resonant long-lived intermediate collision complex of

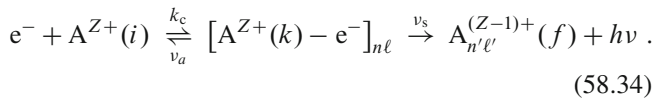
Table 58.1 Recombination computer codes

Name	Description	Reference/Link
ACQD	Radiative recombination of hydrogenic ions	CPC 1 (1969) 31
AAID	COLLRAD	CPC 12 (1976) 205
ADNT	CRModel	CPC 135 (2001) 135
AATR	COLRAD	CPC 44 (1987) 157
AEMA	RATIP	CPC 183 (2012) 1525
ABUV	TRIP 1	CPC 16 (1978) 129
RICO	Machine-learning recombination code for BBN	ApJSS 181 (2009) 627
RECFAST	BBN code	AA 475 (2007) 109
HYREC	Primordial hydrogen and helium recombination code	Phys. Rev. D 83 (2011) 043513
LASER	Los Alamos suite of relativistic atomic physics codes	[61] & http://aphysics2.lanl.gov/tempweb

superexcited states d , which can autoionize or be stabilized irreversibly into the final product channel f either by molecular fragmentation



as in direct dissociative recombination (DR), or by emission of radiation as in dielectronic recombination (DLR)



Production Rate of Superexcited States d

$$\frac{dn_d^*}{dt} = n_e N^+ k_c(d) - n_d^* [\nu_A(d) + \nu_S(d)]; \quad (58.35)$$

$$\nu_A(d) = \sum_{i'} \nu_a(d \rightarrow i'), \quad (58.36a)$$

$$\nu_S(d) = \sum_{f'} \nu_s(d \rightarrow f'). \quad (58.36b)$$

Steady-State Distribution

For a steady-state distribution, the capture volume is

$$\frac{n_d^*}{n_e N^+} = \frac{k_c(d)}{\nu_A(d) + \nu_S(d)}. \quad (58.37)$$

Recombination Rate and Stabilization Probability

The recombination rate to channel f is

$$\hat{\alpha}_f = \sum_d \left(\frac{k_c(d) \nu_s(d \rightarrow f)}{\nu_A(d) + \nu_S(d)} \right), \quad (58.38a)$$

and the rate to all product channels is

$$\hat{\alpha} = \sum_d \frac{k_c(d) \nu_S(d)}{\nu_A(d) + \nu_S(d)}. \quad (58.38b)$$

In the above, the quantities

$$P_f^S(d) = \nu_s(d \rightarrow f) / [\nu_A(d) + \nu_S(d)], \quad (58.39)$$

$$P^S(d) = \nu_S(d) / [\nu_A(d) + \nu_S(d)], \quad (58.40)$$

represent the corresponding stabilization probabilities.

Macroscopic Detailed Balance and Saha Distribution

$$K_{di}(T) = \frac{\tilde{n}_d^*}{\tilde{n}_e \tilde{N}^+} = \frac{k_c(d)}{\nu_a(d \rightarrow i)} = k_c(d) \tau_a(d \rightarrow i) \quad (58.41a)$$

$$= \frac{h^3}{(2\pi m_e k_B T)^{3/2}} \left(\frac{\omega(d)}{2\omega^+} \right) \exp(-E_{di}^* / k_B T), \quad (58.41b)$$

where E_{di}^* is the energy of superexcited neutral levels AB^{**} above that for ion level $AB^+(i)$, and ω are the corresponding statistical weights.

Alternative Rate Formula

$$\hat{\alpha}_f = \sum_d K_{di} \left(\frac{\nu_a(d \rightarrow i) \nu_s(d \rightarrow f)}{\nu_A(d) + \nu_S(d)} \right). \quad (58.42)$$

Normalized Excited-State Distributions

$$\rho_d = n_d^* / \tilde{n}_d^* = \frac{\nu_a(d \rightarrow i)}{[\nu_A(d) + \nu_S(d)]}, \quad (58.43)$$

$$\hat{\alpha} = \sum_d k_c(d) P^S(d) = \sum_d K_{di} \rho_d \nu_S(d) \quad (58.44a)$$

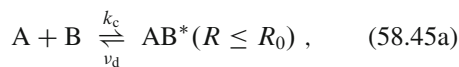
$$= \sum_d k_c(d) [\rho_d \nu_S(d) \tau_a(d \rightarrow i)]. \quad (58.44b)$$

Although equivalent, Eqs. (58.38a) and (58.42) are normally invoked for Eqs. (58.33) and (58.34), respectively, since $P^S \leq 1$ for DR, so that $\hat{\alpha}_{\text{DR}} \rightarrow k_c$; and $\nu_A \gg \nu_S$ for DLR with $n \ll 50$ so that $\hat{\alpha} \rightarrow K_{di} \nu_s$. For $n \gg 50$, $\nu_S \gg \nu_A$ and $\hat{\alpha} \rightarrow k_c$. The above results Eqs. (58.38a) and (58.42) can also be derived from microscopic Breit–Wigner scattering theory for isolated (nonoverlapping) resonances.

58.3.2 Reactive Sphere Model: Three-Body Electron–Ion and Ion–Ion Recombination

Since the Coulomb attraction cannot support quasi-bound levels, three body electron–ion and ion–ion recombination

do not, in general, proceed via time-delayed resonances but rather by reactive (energy-reducing) collisions with the third body M. This is particularly effective for A–B separations $R \leq R_0$, as in the sequence



In contrast to Eqs. (58.33) and (58.34), where the stabilization is irreversible, the forward step in Eq. (58.45b) is reversible. The sequence Eqs. (58.45a) and (58.45b) represents a closed system where thermodynamic equilibrium is eventually established.

Steady-State Distribution of AB^* Complex

$$n^* = \left(\frac{k_c}{\nu_s + \nu_d} \right) n_A(t) n_B(t) + \left(\frac{\nu_{-s}}{\nu_s + \nu_d} \right) n_s(t). \quad (58.46)$$

Saha and Boltzmann balances

$$\begin{aligned} \text{Saha:} \quad & \tilde{n}_A \tilde{n}_B k_c = \tilde{n}^* \nu_d, \\ \text{Boltzmann:} \quad & \tilde{n}_s \nu_{-s} = \tilde{n}^* \nu_s; \end{aligned} \quad (58.47)$$

\tilde{n}^* is in Saha balance with reactant block C and in Boltzmann balance with product block S .

Normalized Distributions

$$\rho^* = \frac{n^*}{\tilde{n}^*} = P^D \gamma_c(t) + P^S \gamma_s(t), \quad (58.48a)$$

$$\gamma_c(t) = \frac{n_A(t) n_B(t)}{\tilde{n}_A \tilde{n}_B}, \quad \gamma_s(t) = \frac{n_s(t)}{\tilde{n}_s}. \quad (58.48b)$$

Stabilization and Dissociation Probabilities

$$P^S = \frac{\nu_s}{(\nu_s + \nu_d)}, \quad P^D = \frac{\nu_d}{(\nu_s + \nu_d)}. \quad (58.49)$$

Time-Dependent Equations

$$\frac{dn_c}{dt} = -k_c P^S \tilde{n}_A \tilde{n}_B [\gamma_c(t) - \gamma_s(t)], \quad (58.50a)$$

$$\frac{dn_s}{dt} = -\nu_{-s} P^D \tilde{n}_s [\gamma_s(t) - \gamma_c(t)], \quad (58.50b)$$

$$\frac{dn_c}{dt} = -\hat{\alpha}_3 n_A(t) n_B(t) + k_d n_s(t), \quad (58.51)$$

where the recombination rate coefficient (cm^3/s) and dissociation frequency are, respectively,

$$\hat{\alpha}_3 = k_c P^S = \frac{k_c \nu_s}{(\nu_s + \nu_d)}, \quad (58.52)$$

$$k_d = \nu_{-s} P^D = \frac{\nu_{-s} \nu_d}{(\nu_s + \nu_d)}, \quad (58.53)$$

which also satisfy the macroscopic detailed balance relation

$$\hat{\alpha}_3 \tilde{n}_A \tilde{n}_B = k_d \tilde{n}_s. \quad (58.54)$$

Time-Independent Treatment

The rate $\hat{\alpha}_3$ given by the time-dependent treatment can also be deduced by viewing the recombination process as a source block C kept fully filled with dissociated species A and B maintained at equilibrium concentrations \tilde{n}_A, \tilde{n}_B (i.e., $\gamma_c = 1$) and draining at the rate $\hat{\alpha}_3 \tilde{n}_A \tilde{n}_B$ through a steady-state intermediate block \mathcal{E} of excited levels into a fully absorbing sink block S of fully associated species AB kept fully depleted with $\gamma_s = 0$, so that there is no backward redissociation from block S . The frequency k_d is deduced as if the reverse scenario, $\gamma_s = 1$ and $\gamma_c = 0$, holds. This picture uncouples $\hat{\alpha}$ and k_d and allows each coefficient to be calculated independently. Both dissociation (or ionization) and association (recombination) occur within block \mathcal{E} .

If $\gamma_c = 1$ and $\gamma_s = 0$, then

$$\rho^* = n^*/\tilde{n}^* = \nu_d/(\nu_s + \nu_d), \quad (58.55a)$$

$$K = \tilde{n}^*/\tilde{n}_A \tilde{n}_B = k_c/\nu_d = k_c \tau_d, \quad (58.55b)$$

$$P^S = \nu_s/(\nu_s + \nu_d) = \rho^* \nu_s \tau_s, \quad (58.55c)$$

and the recombination coefficient is

$$\hat{\alpha} = k_c P^S = k_c (\rho^* \nu_s \tau_d) = K \rho^* \nu_s. \quad (58.56)$$

Microscopic Generalization

From Eq. (58.206), the microscopic generalizations of rate in Eq. (58.52) and probability in Eq. (58.55c) are, respectively,

$$\hat{\alpha} = \bar{\nu} \int_0^\infty \varepsilon e^{-\varepsilon} d\varepsilon \int_0^{b_0} 2\pi b db P^S(\varepsilon, b; R_0), \quad (58.57a)$$

$$P^S(\varepsilon, b; R_0) = \oint_{R_i}^{R_0} \rho_i(R) v_i^b(R) dt \equiv \langle \rho \nu_s \rangle \tau_d, \quad (58.57b)$$

where $\rho_i(R) = n(\varepsilon, b; R)/\tilde{n}(\varepsilon, b; R)$; $v_i^{(b)}$ is the frequency Eq. (58.203a) of (A–B)–M continuum-bound collisional transitions at fixed A–B separation R , R_i is the pericenter of the orbit, ($i \equiv \varepsilon, b$), and

$$b_0^2 = R_0^2 [1 - V(R_0)/E], \quad \varepsilon = E/k_B T, \quad (58.57c)$$

$$\hat{\alpha} \equiv k_c \langle P^S \rangle_{\varepsilon, b}, \quad \bar{\nu} = (8k_B T/\pi M_{AB})^{1/2}, \quad (58.57d)$$

$$k_c = \{ \pi R_0^2 [1 - V(R_0)/k_B T] \bar{\nu} \}, \quad (58.57e)$$

where M_{AB} is the reduced mass of A and B.

Low Gas Densities

Here $\rho_i(R) = 1$ for $E > 0$,

$$P^S(\varepsilon, b; R_0) = \oint_{R_i}^{R_0} v(t) dt = \oint_{R_i}^{R_0} ds/\lambda_i; \quad (58.58)$$

$\lambda_i = (N\sigma)^{-1}$ is the microscopic path length towards the (A–B)–M reactive collision with frequency $\nu = N\nu\sigma$. For λ_i

constant, the rate in Eq. (58.57a) reduces at low N to

$$\hat{\alpha} = (v\sigma_0 N) \int_0^{R_0} \left(1 - \frac{V(R)}{k_B T}\right) 4\pi R^2 dR, \quad (58.59)$$

which is linear in the gas density N .

58.3.3 Working Formulae for Three-Body Collisional Recombination at Low Density

For three-body ion-ion collisional recombination of the form $A^+ + B^- + M$ in a gas at low density N , set $V(R) = -e^2/R$. Then Eq. (58.59) yields

$$\hat{\alpha}^c(T) = \left(\frac{8k_B T}{\pi M_{AB}}\right)^{1/2} \frac{4}{3} \pi R_0^3 \left(1 + \frac{3R_e}{2R_0}\right) (\sigma_0 N), \quad (58.60)$$

where $R_e = e^2/k_B T$, and the trapping radius R_0 , determined by the classical variational method, is $0.41R_e$, in agreement with detailed calculation. The special cases are the following.

(a) $e^- + A^+ + e^-$

Here, $\sigma_0 = \frac{1}{9}\pi R_e^2$ for ($e^- - e^-$) collisions for scattering angles $\theta \geq \pi/2$, so that

$$\hat{\alpha}_{ee}^c(T) = 2.7 \times 10^{-20} \left(\frac{300}{T}\right)^{4.5} n_e \text{ cm}^3 \text{ s}^{-1} \quad (58.61)$$

in agreement with *Mansbach* and *Keck* [32].

(b) $A^+ + B^- + M$

Here, $\sigma_0 \bar{v} \approx 10^{-9} \text{ cm}^3 \text{ s}^{-1}$, which is independent of T for polarization attraction. Then

$$\hat{\alpha}_3(T) = 2 \times 10^{-25} \left(\frac{300}{T}\right)^{2.5} N \text{ cm}^3 \text{ s}^{-1}. \quad (58.62)$$

(c) $e^- + A^+ + M$

Only a small fraction $\delta = 2m/M$ of the electron's energy is lost upon ($e^- - M$) collision, so that Eq. (58.57a) for constant λ is modified to

$$\hat{\alpha}_{eM} = \sigma_0 N \int_0^{R_0} 4\pi R^2 dR \int_0^{E_m} \tilde{n}(R, E) v dE \quad (58.63a)$$

$$= \bar{v}_e \sigma_0 N \int_0^{R_0} 4\pi R^2 dR \int_0^{\varepsilon_m} \left(1 - \frac{V(R)}{E}\right) \varepsilon e^{-\varepsilon} d\varepsilon, \quad (58.63b)$$

where $\varepsilon = E/k_B T$, and $E_m = \delta e^2/R = \varepsilon_m k_B T$ is the maximum energy for collisional trapping. Hence,

$$\hat{\alpha}_{eM}(T_e) = 4\pi \delta \left(\frac{8k_B T_e}{\pi m_e}\right)^{1/2} R_e^2 R_0 [\sigma_0 N] \quad (58.64a)$$

$$\approx \frac{10^{-26}}{M} \left(\frac{300}{T}\right)^{2.5} N \text{ cm}^3 \text{ s}^{-1}, \quad (58.64b)$$

where the mass M of the gas atom is now in a.m.u. This result agrees with the energy diffusion result of *Pitaevskii* [33] when R_0 is taken as the Thomson radius $R_T = \frac{2}{3}R_e$.

58.3.4 Recombination Influenced by Diffusional Drift at High Gas Densities

Diffusional-Drift Current

The drift current of A^+ towards B^- in a gas under an $A^+ - B^-$ attractive potential $V(R)$ is

$$\mathbf{J}(R) = -D \nabla n(R) - \left[\frac{K}{e} \nabla V(R)\right] n(R) \quad (58.65a)$$

$$= -\left(D \tilde{N}_A \tilde{N}_B e^{-V(R)/k_B T} \frac{\partial \rho}{\partial R}\right) \hat{\mathbf{R}}. \quad (58.65b)$$

Relative Diffusion and Mobility Coefficients

$$D = D_A + D_B,$$

$$K = K_A + K_B, \quad De = K(k_B T), \quad (58.66)$$

where the D_i and K_i are, respectively, the diffusion and mobility coefficients of species i in gas M .

Normalized Ion-Pair R -Distribution

$$\rho(R) = \frac{n(R)}{\tilde{N}_A \tilde{N}_B \exp[-V(R)/k_B T]}. \quad (58.67)$$

Continuity Equations for Currents and Rates

$$\frac{\partial n}{\partial t} + \nabla \cdot \mathbf{J} = 0, \quad R \geq R_0, \quad (58.68a)$$

$$\hat{\alpha}_{RN}(R_0) \rho(R_0) = \hat{\alpha} \rho(\infty). \quad (58.68b)$$

The rate of reaction for ion pairs with separations $R \leq R_0$ is $\alpha_{RN}(R_0)$. This is the recombination rate that would be obtained for a thermodynamic equilibrium distribution of ion pairs with $R \geq R_0$, i.e., for $\rho(R \geq R_0) = 1$.

Steady-State Rate of Recombination

$$\hat{\alpha} \tilde{N}_A \tilde{N}_B = \int_{R_0}^{\infty} \left(\frac{\partial n}{\partial t}\right) d\mathbf{R} = -4\pi R_0^2 J(R_0). \quad (58.69)$$

Steady-State Solution

$$\rho(R) = \rho(\infty) \left(1 - \frac{\hat{\alpha}}{\hat{\alpha}_{TR}(R)}\right), \quad R \geq R_0 \quad (58.70a)$$

$$\rho(R_0) = \rho(\infty) [\hat{\alpha}/\hat{\alpha}_{RN}(R_0)]. \quad (58.70b)$$

Recombination Rate

$$\hat{\alpha} = \frac{\hat{\alpha}_{\text{RN}}(R_0)\hat{\alpha}_{\text{TR}}(R_0)}{\hat{\alpha}_{\text{RN}}(R_0) + \hat{\alpha}_{\text{TR}}(R_0)} \quad (58.71a)$$

$$\rightarrow \begin{cases} \hat{\alpha}_{\text{RN}}, & N \rightarrow 0 \\ \hat{\alpha}_{\text{TR}}, & N \rightarrow \infty. \end{cases} \quad (58.71b)$$

Diffusional-Drift Transport Rate

$$\hat{\alpha}_{\text{TR}}(R_0) = 4\pi D \left(\int_{R_0}^{\infty} \frac{e^{V(R)/k_B T}}{R^2} dR \right)^{-1}. \quad (58.72)$$

With $V(R) = -e^2/R$,

$$\hat{\alpha}_{\text{TR}}(R_0) = 4\pi K e [1 - \exp(-R_e/R_0)]^{-1}, \quad (58.73)$$

where $R_e = e^2/k_B T$ provides a natural unit of length.

Langevin Rate

For $R_0 \ll R_e$, the transport rate

$$\hat{\alpha}_{\text{TR}} \rightarrow \hat{\alpha}_L = 4\pi K e \quad (58.74)$$

tends to the Langevin rate which varies as N^{-1} .

Reaction Rate

When R_0 is large enough that R_0 -pairs are in (E, L^2) equilibrium Eq. (58.206),

$$\hat{\alpha}_{\text{RN}}(R_0) = \bar{v} \int_0^{\infty} \varepsilon e^{-\varepsilon} d\varepsilon \int_0^{b_0} 2\pi b db P^S(\varepsilon, b; R_0) \quad (58.75a)$$

$$\equiv \bar{v} \int_0^{\infty} \varepsilon e^{-\varepsilon} d\varepsilon [\pi b_0^2 P^S(\varepsilon; R_0)] \quad (58.75b)$$

$$\equiv \bar{v} \pi b_{\text{max}}^2 P^S(R_0), \quad (58.75c)$$

where

$$b_{\text{max}}^2 = R_0^2 \left(1 - \frac{V(R_0)}{k_B T} \right), \quad (58.76)$$

and b_0 and ε are given by Eq. (58.57c) and \bar{v} by Eq. (58.57d).

The probability P^S and its averages over b and (b, E) for reaction between pairs with $R \leq R_0$ is determined in Eq. (58.75a–58.75c) from solutions of coupled master equations; P^S increases linearly with N initially and tends to unity at high N . The recombination rate in Eq. (58.71a) with Eq. (58.75a) and Eq. (58.73), therefore, increases linearly with N initially, reaches a maximum when $\hat{\alpha}_{\text{TR}} \approx \hat{\alpha}_{\text{RN}}$, and then decreases eventually as N^{-1} , in accord with Eq. (58.74).

Reaction Probability

The classical absorption solution of Eq. (58.196) is

$$P^S(E, b; R_0) = 1 - \exp\left(-\oint_{R_i}^{R_0} \frac{ds_i}{\lambda_i}\right). \quad (58.77)$$

With the binary decomposition $\lambda_i^{-1} = \lambda_{iA}^{-1} + \lambda_{iB}^{-1}$,

$$P^S = P_A + P_B - P_A P_B. \quad (58.78)$$

Exact b^2 -Averaged Probability

With $V_c = -e^2/R$ for the A^+B^- interaction in Eq. (58.75b), and at low gas densities N ,

$$P_{A,B}(E, R_0) = \frac{4R_0}{3\lambda_{A,B}} \left(1 - \frac{3V_c(R_0)}{2E_i} \right) \frac{1}{[1 - V_c(R_0)/E_i]}, \quad (58.79)$$

appropriate for constant mean free path λ_i .

(E, b^2) -Averaged Probability

$P^S(R_0)$ in Eq. (58.75c) at low gas density is

$$P_{A,B}(R_0) = P_{A,B}(E = k_B T, R_0). \quad (58.80)$$

Thomson Trapping Distance

When the kinetic energy gained from Coulomb attraction is assumed lost upon collision with third bodies, then bound (A, B) pairs are formed with $R \leq R_T$. Since $E = \frac{3}{2}k_B T - e^2/R$, then

$$R_T = \frac{2}{3} \left(\frac{e^2}{k_B T} \right) = \frac{2}{3} R_e. \quad (58.81)$$

Thomson Straight-Line Probability

The $E \rightarrow \infty$ limit of Eq. (58.77) is

$$P_{A,B}^T(b; R_T) = 1 - \exp[-2(R_T^2 - b^2)/\lambda_{A,B}]. \quad (58.82)$$

The b^2 -average is the Thomson probability

$$P_{A,B}^T(R_T) = 1 - \frac{1}{2X^2} [1 - e^{-2X}(1 + 2X)] \quad (58.83a)$$

for reaction of (A–B) pairs with $R \leq R_T$. As $N \rightarrow 0$

$$P_{A,B}^T(R_T) \rightarrow \frac{4}{3} X \left(1 - \frac{3}{4} X + \frac{2}{5} X^2 - \frac{1}{6} X^3 + \dots \right) \quad (58.83b)$$

and tends to unity at high N ; $X = R_T/\lambda_{A,B} = N(\sigma_0 R_T)$. These probabilities have been generalized [34] to include hyperbolic and general trajectories.

Thomson Reaction Rate

$$\hat{\alpha}_T = \pi R_T^2 \bar{v} (P_A^T + P_B^T - P_A^T P_B^T) \rightarrow \begin{cases} \frac{4}{3} \pi R_T^3 (\lambda_A^{-1} + \lambda_B^{-1}), & N \rightarrow 0 \\ \pi R_T^2 \bar{v}, & N \rightarrow \infty. \end{cases} \quad (58.84)$$

58.4 Zero-Range Methods

Zero-range methods refer to scattering models that make use of the scattering length to characterize the collision. Zero-range methods are used in ultracold collisions where the de Broglie wavelength of the atoms is much larger than the range of their interactions, and hence the scattering is well described by the S-wave scattering length, a .

The T-matrix element for S-wave scattering of two identical particles, mass m and energy $E = k^2/m$, is

$$T(k) = \frac{8\pi}{m} \frac{1}{k \cot \delta_0(k) - ik}, \quad (58.85)$$

where $\delta_0(k)$ is the S-wave phase shift. In general, one would solve numerically a couple-channel problem to compute the phase shifts for all the states of interest. In ultracold collisions, the low-energy effective range expansion of the S-wave phase shift can be utilized

$$k \cot \delta_0(k) = -1/a + \frac{1}{2}r_s k^2 + \dots \quad (58.86)$$

to simplify the scattering calculation. The effective range expansion serves to define the scattering length a and the effective range r_s . See Sect. 47.5.5 and Eq. (47.46b) in this Handbook, and [35] for details on the scattering length and effective range. For the typical ultracold collision involving alkali atoms in specific hyperfine states, the van der Waals length, ℓ_{vdW} , and energy E_{vdW} , provide natural length and energy scales, respectively

$$\ell_{\text{vdW}} = (mC_6/\hbar^2)^{1/4}, \quad (58.87a)$$

$$E_{\text{vdW}} = (m^3C_6/\hbar^6)^{-1/2}, \quad (58.87b)$$

for atom of mass m and van der Waals constant C_6 . For alkali atom collisions, the scattering lengths are [35]:

	${}^6\text{Li}(a_t)$	${}^{85}\text{Rb}(a_s)$	${}^{133}\text{Cs}(a_t)$
$a(a_0)$	-2160	2800	2400

where the subscript s or t refer to singlet or triplet states, respectively.

Contrast these large values for alkali atom collisions with the much smaller values for $e^- + \text{Rg}$ atom collisions in Sect. 47.5.5 ($\text{Rg} = \text{He} - \text{Xe}$). See Table 1 of [26] for a more complete tabulation. The elastic scattering cross section for two bosonic atoms in the same spin state is

$$\sigma_{\text{elastic}}(E) = \frac{8\pi a^2}{1 + ma^2 E}, \quad (58.88)$$

where a is the scattering length.

Shallow dimers

When $a > 0$, there is a single bound state with binding energy $E_D = 1/(ma^2)$, referred to as a shallow dimer state.

The three-body recombination rate α_s into a shallow dimer state is [26, 36]

$$\alpha_s = \frac{128\pi^2(4\pi - 3\sqrt{3})}{\sinh^2(\pi s_0) + \cosh^2(\pi s_0) \tan^2[s_0 \ln(a\kappa_*) + \gamma]} \frac{\hbar a^4}{m}, \quad (58.89)$$

where κ_* is the wave number of the shallow dimer state n_* , γ is a constant, and s_0 is the root of the transcendental equation

$$s_0 \cosh \frac{\pi s_0}{2} = \frac{8}{\sqrt{3}} \sinh \frac{\pi s_0}{6}, \quad (58.90)$$

with approximate numerical solution of $s_0 \sim 1.00624$. The phase constant γ has been computed in [37, 38] and is of order unity.

The three-body collision, at low energies in reaction Eq. (58.19), that results in the formation of dimers A_2 exhibits a universal property, wherein the spacing between adjacent energy levels of the dimer, $E_T^{(n)}$ follows an exponential scaling independent of system

$$E_T^{(n)} \rightarrow (e^{-2\pi/s_0})^{n-n_*} \frac{\hbar^2 \kappa_*^2}{m}, \quad (58.91)$$

as $n \rightarrow \infty$, and where κ_* is the wave number associated with the dimer state labeled by the integer n_* . The scaling relationship Eq. (58.91) was first described by *Efimov* [39, 40]. Further details on the universal scaling property Eq. (58.91) called the *Efimov effect* can be found in Sect. 60.6 of this Handbook, and [20, 25, 26, 41].

Deep dimers

Depending on the details of the short-range part of the dimer molecular potential, governed by the parameters a , κ_* , and the inelasticity parameter η_* , the dimer may support multiple states below threshold, called deep dimer states. See [26], and references therein, for a complete discussion of these parameters.

The three-body recombination rate α_d into a deep dimer state is [26]

$$\alpha_d = \frac{C_{\text{max}} \cosh(\pi s_0) \sinh(\pi s_0) \cosh \eta_* \sinh \eta_* \hbar a^4}{\sinh^2(\pi s_0 + \eta_*) + \sin^2[s_0 \ln(a\kappa_*) + \gamma]} \frac{\hbar a^4}{m}, \quad (58.92)$$

where η_* is the inelasticity parameter, and C_{max} is defined

$$C_{\text{max}} = \frac{128\pi^2(4\pi - 3\sqrt{3})}{\sinh^2(\pi s_0)}, \quad (58.93)$$

while s_0 and γ retain their meaning as in Eq. (58.89).

Expressions for scattering lengths and effective ranges for shallow and deep dimers can be found in Sect. 60.6.

58.5 Hyperspherical Methods

Hyperspherical methods are techniques of solving the N-body Schrödinger equation where the coupled partial differential equations are reformulated in terms of hyperspherical coordinates. See Chap. 56 of this Handbook and [20] for details on hyperspherical methods.

d-dimensional coordinates [42]

$$R = \sqrt{x_1^2 + x_2^2 + x_3^2 + \cdots + x_d^2}. \quad (58.94)$$

$$x_d = R \cos \alpha_{d-1},$$

$$x_{d-1} = R \sin \alpha_{d-1} \cos \alpha_{d-2},$$

$$x_{d-2} = R \sin \alpha_{d-1} \sin \alpha_{d-2} \cos \alpha_{d-3},$$

...

$$x_2 = R \prod_{j=1}^{d-1} \sin \alpha_j,$$

$$x_1 = R \prod_{j=2}^{d-1} \sin \alpha_j \cos \alpha_1, \quad (58.95a)$$

where R is the hyperradius, x_i the coordinates of the particles, and α_j the corresponding hyperangles. The set Eq. (58.95a) is usually termed the canonical choice and have the ranges

$$0 \leq \alpha_1 \leq 2\pi, \quad 0 \leq \alpha_i \leq \pi, \quad i = 2, \dots, d-1. \quad (58.96)$$

The nonrelativistic kinetic energy operator is then separable

$$\hat{T} = T_R + \frac{\hbar^2 \Lambda^2}{2\mu R}, \quad (58.97a)$$

$$T_R = -\frac{\hbar^2}{2\mu} \frac{1}{R^{d-1}} R^{d-1} \frac{\partial}{\partial R}, \quad (58.97b)$$

where μ is the N-body reduced mass

$$\mu = (\mu_{12}\mu_{12,3}\cdots)^{1/(N-1)}, \quad (58.98)$$

and,

$$\mu_{12} = \frac{m_1 m_2}{m_1 + m_2}, \quad (58.99a)$$

$$\mu_{12,3} = \frac{(m_1 + m_2)m_3}{m_1 + m_2 + m_3}, \quad (58.99b)$$

the usual reduced masses, while Λ is the isotropic Casimir operator

$$\Lambda^2 = -\sum_{i>j} \Lambda_{ij}^2, \quad \Lambda_{ij} = x_i \frac{\partial}{\partial x_j} - x_j \frac{\partial}{\partial x_i}. \quad (58.100)$$

Three-particle case

$$R^2 = \rho_1^2 + \rho_2^2, \quad 0 \leq R < \infty. \quad (58.101)$$

$$\vec{\rho}_1 = (\vec{r}_2 - \vec{r}_1)/\Delta, \quad (58.102a)$$

$$\vec{\rho}_2 = \Delta \left[\vec{r}_3 - \frac{m_1 \vec{r}_1 + m_2 \vec{r}_2}{m_1 + m_2} \right], \quad (58.102b)$$

with,

$$\Delta^2 = \frac{1}{\mu} \frac{m_3(m_1 + m_2)}{m_1 + m_2 + m_3}, \quad (58.103a)$$

$$\mu^2 = \frac{m_1 m_2 m_3}{m_1 + m_2 + m_3}, \quad (58.103b)$$

for particles i with mass m_i and position vector \vec{r}_i , $i = 1-3$. The mass-scaled Jacobi coordinates, $\vec{\rho}_1$ and $\vec{\rho}_2$ determine the hyperangles θ and φ in the body frame x - y plane, yielding a rescaled Schrödinger equation for three identical particles

$$\left(-\frac{1}{2\mu} \frac{\partial^2}{\partial R^2} + \frac{15}{8\mu R^2} + \frac{\Lambda^2}{2\mu R^2} + V(R, \theta, \varphi) \right) \Psi_E = E \Psi_E, \quad (58.104)$$

where the full three-particle interaction potential V is expressed in terms of the hyperradius R and hyperangles θ and φ , and the angular momentum operator Λ is given in [20, equations (22–25)].

Coupled-channel expansion

$$\Psi_{E\nu'} = \sum_{\nu} \frac{\Phi_{\nu}(R; \tilde{\omega})}{R^{(d-1)/2}} [f_{E\nu}(R) \delta_{\nu\nu'} - g_{E\nu}(R) K_{\nu\nu'}], \quad (58.105)$$

where $f_{E\nu}(R)$ and $g_{E\nu}(R)$ are the regular and irregular radial functions, respectively; $K_{\nu\nu'}$ is the real symmetric reaction matrix, and $\tilde{\omega}$ represents the set of hyperangles, while d is the dimension.

The usual technique is to solve numerically the set of coupled equations and matching to linear combinations of regular and irregular functions at a large hyperradius R_0 to obtain the reaction matrix K .

58.5.1 Three-Body Recombination Rate (Identical Particles)

$$\alpha(E) = \frac{\hbar k}{\mu} \frac{192\pi^2}{k^5} \sum_{\nu'\nu} |S_{\nu'\nu}|^2, \quad (58.106)$$

where $k = \sqrt{2\mu E/\hbar^2}$, and the S-matrix is determined from the reaction matrix using the standard expression Eq. (49.17). The sum includes all entrance channel ν three-body continuum states and exit channel ν' two-body bound states of A_2 .

58.5.2 N-Body Recombination Rate (Identical Particles)

$$\alpha_N(E) = N! \frac{\hbar k}{\mu} \left(\frac{2\pi}{k} \right)^{d-1} \frac{\Gamma(d/2)}{2\pi^{d/2}} \sum_{v'v} |S_{v'v}|^2, \quad (58.107)$$

where $\Gamma(x)$ is the Gamma function and d is the dimension.

58.6 Field-Assisted Methods

Field-assisted methods is a general term to encompass techniques used to compute recombination rates in cases where the reaction is assisted by the application of an external field. Currently, the most commonly applied field is laser-assisted recombination Eq. (58.5) in studying the spectrum in high-order harmonic generation (HHG). See Sects. 78.3, 78.4 and 80.6 in this Handbook for further details on HHG.

Differential cross section [43]

$$\frac{d\sigma_{\text{len}}^R}{d\Omega_k d\Omega_n} = \frac{4\pi^2 \omega^3}{c^3 k} |a_{\text{len}}^{\text{sc}}(k)|^2, \quad (58.108a)$$

$$\frac{d\sigma_{\text{acn}}^R}{d\Omega_k d\Omega_n} = \frac{4\pi^2 \omega}{c^3 k} |a_{\text{acn}}^{\text{sc}}(k)|^2, \quad (58.108b)$$

where σ^R is the differential cross section for Eq. (58.5), the subscripts *len* and *acn* refer to the length and acceleration form of the matrix elements, respectively; ω is the angular frequency of the released photon, k the momentum of the recombining electron, Ω_n, Ω_k the corresponding solid angles, and c the speed of light.

He

$$a_{\text{len}}^{\text{sc}}(k) = a_1 c_1 e^{i(\delta_1 + \sigma_1)} \langle u_g r \rangle u_{k1}^{\text{sc}}, \quad (58.109a)$$

$$a_{\text{acn}}^{\text{sc}}(k) = -a_1 c_1 Z_N e^{i(\delta_1 + \sigma_1)} \langle u_g \frac{1}{r^2} \rangle u_{k1}^{\text{sc}}. \quad (58.109b)$$

Rg (Ar–Xe)

$$a_{\text{len}}^{\text{sc}}(k) = a_0 c_0 e^{i(\delta_0 + \sigma_0)} \langle u_g r \rangle u_{k0}^{\text{sc}} + a_2 c_2 e^{i(\delta_2 + \sigma_2)} \langle u_g r \rangle u_{k2}^{\text{sc}} \quad (58.110a)$$

$$a_{\text{acn}}^{\text{sc}}(k) = -a_0 c_0 Z_N e^{i(\delta_0 + \sigma_0)} \langle u_g \frac{1}{r^2} \rangle u_{k0}^{\text{sc}} - a_2 c_2 Z_N e^{i(\delta_2 + \sigma_2)} \langle u_g \frac{1}{r^2} \rangle u_{k2}^{\text{sc}}, \quad (58.110b)$$

where the constants a_ℓ and c_ℓ are defined

$$a_\ell = \frac{t^\ell}{2k} \sqrt{\frac{2\ell + 1}{\pi}}, \quad (58.111a)$$

$$c_\ell = \langle Y_{\ell_g}^{m=0} \cos \theta \rangle Y_\ell^{m=0}, \quad (58.111b)$$

with Y_ℓ^m the spherical harmonics and Z_N the atomic number.

Detailed balance

$$\frac{d^2 \sigma^R}{\omega^2 d\Omega_n d\Omega_k} = \frac{d^2 \sigma^I}{k^2 c^2 d\Omega_k d\Omega_n}, \quad (58.112)$$

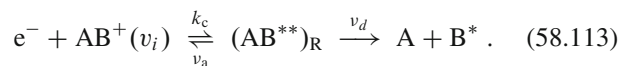
where the superscripts R and I refer to recombination and ionization, respectively.

58.7 Dissociative Recombination

58.7.1 Curve-Crossing Mechanisms

Direct Process

Dissociative recombination (DR) for diatomic ions can occur via a crossing at R_X between the bound and repulsive potential energy curves $V^+(R)$ and $V_d(R)$ for AB^+ and AB^{**} , respectively. Here, DR involves the two-stage sequence



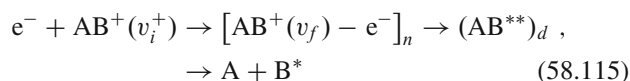
The first stage is dielectronic capture whereby the free electron of energy $\epsilon = V_d(R) - V^+(R)$ excites an electron of the diatomic ion AB^+ with internal separation R and is then resonantly captured by the ion, at rate k_c , to form a repulsive state d of the doubly excited molecule AB^{**} , which in turn can either autoionize at probability frequency ν_a , or else in the second stage, predissociate into various channels at probability frequency ν_d . This competition continues until the (electronically excited) neutral fragments accelerate past the crossing at R_X . Beyond R_X , the increasing energy of relative separation reduces the total electronic energy to such an extent that autoionization is essentially precluded, and the neutralization is then rendered permanent past the stabilization point R_X . This interpretation [44] has remained intact and robust in the current light of ab initio quantum chemistry and quantal scattering calculations for the simple diatomics (O_2^+ , N_2^+ , Ne_2^+ , etc.). Mechanism Eq. (58.113) is termed the direct process, which, in terms of the macroscopic frequencies in Eq. (58.113), proceeds at the rate

$$\hat{\alpha} = k_c P_S = k_c [\nu_d / (\nu_a + \nu_d)], \quad (58.114)$$

where P_S is probability for AB^* survival against autoionization from the initial capture at R_c to the crossing point R_X . Configuration mixing theories of this direct process are available in the quantal [45] and semiclassical-classical path formulations [46].

Indirect Process

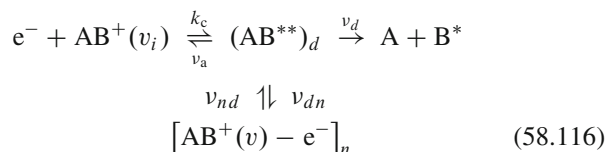
In the three-stage sequence



the so-called indirect process [45] might contribute. Here, the accelerating electron loses energy by vibrational excitation ($v_i^+ \rightarrow v_f$) of the ion and is then resonantly captured into a Rydberg orbital of the bound molecule AB^* in vibrational level v_f , which then interacts one way (via configuration mixing) with the doubly excited repulsive molecule AB^{**} . The capture initially proceeds via a small effect – vibronic coupling (the matrix element of the nuclear kinetic energy) induced by the breakdown of the Born–Oppenheimer approximation – at certain resonance energies $\varepsilon_n = E(v_f) - E(v_i^+)$ and, in the absence of the direct channel Eq. (58.113), would therefore be manifest by a series of characteristic very narrow Lorentz profiles in the cross section. Uncoupled from Eq. (58.113) the indirect process would augment the rate. Vibronic capture proceeds more easily when $v_f = v_i^+ + 1$, so that Rydberg states with $n \approx 7-9$ would be involved [for $H_2^+(v_i^+ = 0)$], so that the resulting longer periods of the Rydberg electron would permit changes in nuclear motion to compete with the electronic dissociation. Recombination then proceeds as in the second stage of Eq. (58.113), i.e., by electronic coupling to the dissociative state d at the crossing point. A multichannel quantum defect theory [47] has combined the direct and indirect mechanisms.

Interrupted Recombination

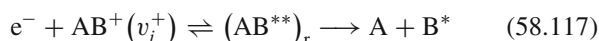
The process



proceeds via the first (dielectronic capture) stage of Eq. (58.113) followed by a two-way electronic transition with frequency ν_{dn} and ν_{nd} between the d and n states. All (n, v) Rydberg states can be populated, particularly those in low n and high v since the electronic $d-n$ interaction varies as $n^{-1.5}$ with broad structure. Although the dissociation process proceeds here via a second-order effect (ν_{dn} and ν_{nd}), the electronic coupling may dominate the indirect vibronic capture and interrupt the recombination, in contrast to Eq. (58.115) which, as written in the one-way direction, feeds the recombination. Both dip and spike structure has been observed [48].

58.7.2 Quantal Cross Section

The cross section for direct dissociative recombination



of electrons of energy ε , wavenumber k_e , and spin statistical weight 2, for a molecular ion $AB^+(v_i^+)$ of electronic statistical weight ω_{AB}^+ in vibrational level v_i^+ is

$$\begin{aligned} \sigma_{DR}(\varepsilon) &= \frac{\pi}{k_e^2} \left(\frac{\omega_{AB}^*}{2\omega^+} \right) |a_Q|^2 \\ &= \left(\frac{h^2}{8\pi m_e \varepsilon} \right) \left(\frac{\omega_{AB}^*}{2\omega^+} \right) |a_Q|^2. \end{aligned} \quad (58.118)$$

Here, ω_{AB}^* is the electronic statistical weight of the dissociative neutral state of AB^* whose potential energy curve V_d crosses the corresponding potential energy curve V^+ of the ionic state. The transition T-matrix element for autoionization of AB^* embedded in the (moving) electronic continuum of $AB^+ + e^-$ is the quantal probability amplitude

$$a_Q(v) = 2\pi \int_0^\infty V_{d\varepsilon}^*(R) [\psi_v^{+*}(R) \psi_d(R)] dR \quad (58.119)$$

for autoionization. Here, ψ_v^+ and ψ_d are the nuclear bound and continuum vibrational wave functions for AB^+ and AB^* , respectively, while

$$\begin{aligned} V_{d\varepsilon}(R) &= \langle \phi_d | \mathcal{H}_{el}(\mathbf{r}, R(t)) | \phi_\varepsilon(\mathbf{r}, \mathbf{R}) \rangle_{\mathbf{r}, \hat{\varepsilon}} \\ &= V_{\varepsilon d}^*(R) \end{aligned} \quad (58.120)$$

are the bound-continuum electronic matrix elements coupling the diabatic electronic bound state wave functions $\psi_d(\mathbf{r}, \mathbf{R})$ for AB^* with the electronic continuum state wave functions $\phi_\varepsilon(\mathbf{r}, \mathbf{R})$ for $AB^+ + e^-$. The matrix element is an average over electronic coordinates \mathbf{r} and all directions $\hat{\varepsilon}$ of the continuum electron. Both continuum electronic and vibrational wave functions are energy normalized (Sect. 58.11.3), and

$$\Gamma(R) = 2\pi |V_{d\varepsilon}^*(R)|^2 \quad (58.121)$$

is the energy width for autoionization at a given nuclear separation R . Given $\Gamma(R)$ from quantum chemistry codes, the problem reduces to evaluation of continuum vibrational wave functions in the presence of autoionization. The rate associated with a Maxwellian distribution of electrons at temperature T is

$$\hat{\alpha} = \bar{v}_e \int \varepsilon \sigma_{DR}(\varepsilon) e^{-\varepsilon/k_B T} d\varepsilon / (k_B T)^2, \quad (58.122)$$

where \bar{v}_e is the mean speed (Sect. 58.12).

Maximum Cross Section and Rate

Since the probability for recombination must remain less than unity, $|a_Q|^2 \leq 1$, so that the maximum cross section and

rates are

$$\sigma_{\text{DR}}^{\text{max}}(\varepsilon) = \frac{\pi}{k_e^2} \left(\frac{\omega_{\text{AB}}^*}{2\omega^+} \right) = \left(\frac{h^2}{8\pi m_e \varepsilon} \right) (2\ell + 1), \quad (58.123)$$

where ω_{AB}^* has been replaced by $2(2\ell + 1)\omega^+$ under the assumption that the captured electron is bound in a high-level Rydberg state of angular momentum ℓ , and

$$\hat{\alpha}_{\text{max}}(T) = \bar{v}_e \sigma_{\text{DR}}^{\text{max}}(\varepsilon = k_B T) \quad (58.124a)$$

$$\approx 5 \times 10^{-7} \left(\frac{300}{T} \right)^{1/2} (2\ell + 1) \text{ cm}^3/\text{s}. \quad (58.124b)$$

Cross section maxima of $5(2\ell + 1)(300/T) \times 10^{-14} \text{ cm}^2$ are therefore possible, being consistent with the rate Eq. (58.124b).

First-Order Quantal Approximation

When the effect of autoionization on the continuum vibrational wave function $\psi_d(R)$ for AB^* is ignored, then a first-order undistorted approximation to the quantal amplitude Eq. (58.119) is

$$T_{\text{B}}(v^+) = 2\pi \int_0^\infty V_{d\varepsilon}^*(R) [\psi_v^{+*}(R) \psi_d^{(0)}(R)] dR, \quad (58.125)$$

where $\psi_d^{(0)}$ is ψ_d in the absence of the back reaction of autoionization. Under this assumption, Eq. (58.118) reduces to

$$\sigma_c(\varepsilon, v^+) = \frac{\pi}{k_e^2} \left(\frac{\omega_{\text{AB}}^*}{2\omega^+} \right) |T_{\text{B}}(v^+)|^2, \quad (58.126)$$

which is then the cross section for initial electron capture since autoionization has been precluded. Although the Born T -matrix Eq. (58.125) violates unitarity, the capture cross section Eq. (58.126) must remain less than the maximum value

$$\sigma_c^{\text{max}} = \frac{\pi}{k_e^2} \left(\frac{\omega_{\text{AB}}^*}{2\omega^+} \right) = \left(\frac{h^2}{8\pi m_e \varepsilon} \right) \left(\frac{\omega_{\text{AB}}^*}{2\omega^+} \right), \quad (58.127)$$

since $|a_Q|^2 \leq 1$. So as to acknowledge after the fact the effect of autoionization, assumed small, and neglected by Eq. (58.125), the DR cross section can be approximated as

$$\sigma_{\text{DR}}(\varepsilon, v^+) = \sigma_c(\varepsilon, v^+) P_{\text{S}}, \quad (58.128)$$

where P_{S} is the probability of survival against autoionization on the V_d curve until stabilization takes place at some crossing point R_X .

Approximate Capture Cross Section

With the energy-normalized Winans–Stückelberg vibrational wave function

$$\psi_d^{(0)}(R) = |V_d'(R)|^{-1/2} \delta(R - R_c), \quad (58.129)$$

where R_c is the classical turning point for $(\text{A}-\text{B}^*)$ relative motion, Eq. (58.126) reduces to

$$\sigma_c(\varepsilon, v^+) = \frac{\pi}{k_e^2} \left(\frac{\omega_{\text{AB}}^*}{2\omega^+} \right) [2\pi \Gamma(R_c)] \left\{ \frac{|\psi_v^+(R_c)|^2}{|V_d'(R_c)|} \right\}, \quad (58.130)$$

where the term inside the braces in Eq. (58.130) is the effective Franck–Condon factor.

Six Approximate Stabilization Probabilities

(1)

A unitarized T -matrix is

$$T = \frac{T_{\text{B}}}{1 + \frac{1}{2}|T_{\text{B}}|^2}, \quad (58.131)$$

so that $P_{\text{S}} = |T|^2/|T_{\text{B}}|^2$ to give

$$\begin{aligned} P_{\text{S}}(\text{low } \varepsilon) &= \left(1 + \frac{1}{4}|T_{\text{B}}|^2 \right)^{-2} \\ &= \left\{ 1 + \pi^2 \left| \int_0^\infty V_{d\varepsilon}^*(R) [\psi_v^{+*}(R) \psi_d^{(0)}(R)] dr \right|^2 \right\}^{-2}, \end{aligned} \quad (58.132a)$$

which is valid at low ε when only one vibrational level v^+ , i.e., the initial level of the ion is repopulated by autoionization.

(2)

At higher ε , when population of many other ionic levels v_f^+ occurs, then

$$P_{\text{S}}(\varepsilon) = \left[1 + \frac{1}{4} \sum_f |T_{\text{B}}(v_f^+)|^2 \right]^{-2}, \quad (58.132b)$$

where the summation is over all the open vibrational levels v_f^+ of the ion. When no intermediate Rydberg $\text{AB}^*(v)$ states are energy resonant with the initial $e^- + \text{AB}^+(v^+)$ state, i.e., coupling with the indirect mechanism is neglected, then Eq. (58.128), with Eq. (58.132b), is the direct DR cross section normally calculated.

(3)

In the high- ε limit, when an infinite number of v_f^+ levels are populated following autoionization, the survival probability, with the aid of closure, is then

$$P_S = \left[1 + \pi^2 \int_{R_c}^{R_X} |V_{d\varepsilon}^*(R)|^2 |\psi_d^{(0)}(R)|^2 dR \right]^{-2}. \quad (58.133)$$

(4)

On adopting in Eq. (58.133) the JWKB semiclassical wave function for $\psi_d^{(0)}$,

$$\begin{aligned} P_S(\text{high } \varepsilon) &= \left[1 + \frac{1}{2\hbar} \int_{R_c}^{R_X} \frac{\Gamma(R)}{v(R)} dR \right]^{-2} \\ &= \left[1 + \frac{1}{2} \int_{t_c}^{t_X} v_a(t) dt \right]^{-2}, \end{aligned} \quad (58.134)$$

where $v(R)$ is the local radial speed of A–B relative motion, and where the frequency $v_a(t)$ of autoionization is Γ/\hbar .

(5)

A classical path local approximation for P_S yields

$$P_S = \exp\left(-\int_{t_c}^{t_X} v_a(t) dt\right), \quad (58.135)$$

which agrees to first order for small v with the expansion of Eq. (58.134).

(6)

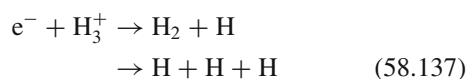
A partitioning of Eq. (58.113) yields

$$P_S = v_d/(v_a + v_d) = (1 + v_a\tau_d)^{-1}, \quad (58.136)$$

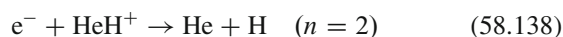
on adopting macroscopic averaged frequencies v_i and associated lifetimes $\tau_i = v_i^{-1}$. The six survival probabilities in Eqs. (58.132a), (58.132b), (58.132a), (58.133)–(58.136) are all suitable for use in the DR cross section Eq. (58.128).

58.7.3 Noncrossing Mechanism

The dissociative recombination (DR) processes

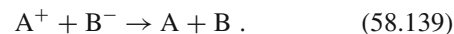


at low electron energy ε , and



have spurred renewed theoretical interest because they both proceed at respective rates of $(2 \times 10^{-7}$ to $2 \times 10^{-8}) \text{ cm}^3 \text{ s}^{-1}$ and $10^{-8} \text{ cm}^3 \text{ s}^{-1}$ at 300 K. Such rates are generally associated with the direct DR, which involves favorable curve crossings between the potential energy surfaces, $V^+(R)$ and $V_d(R)$ for the ion AB^+ and neutral dissociative AB^{**} states. The difficulty with Eqs. (58.137) and (58.138) is that there are no such curve crossings, except at $\varepsilon \geq 8 \text{ eV}$ for Eq. (58.137). In this instance, the previous standard theories would support only extremely small rates when electronic resonant conditions do not prevail at thermal energies. Theories [49–53] have been developed for application to processes such as Eq. (58.137).

58.8 Mutual Neutralization



Diabatic potentials

$V_i^{(0)}(R)$ and $V_f^{(0)}(R)$ for initial (ionic) and final (covalent) states are diagonal elements of

$$V_{if}(R) = \langle \Psi_i(\mathbf{r}, \mathbf{R}) | \mathcal{H}_{\text{el}}(\mathbf{r}, \mathbf{R}) | \Psi_f(\mathbf{r}, \mathbf{R}) \rangle_r, \quad (58.140)$$

where $\Psi_{i,f}$ are diabatic states, and \mathcal{H}_{el} is the electronic Hamiltonian at fixed internuclear distance R .

Adiabatic potentials for a two-state system

$$V^\pm(R) = V_0(R) \pm \left[\Delta^2(R) + |V_{if}(R)|^2 \right]^{1/2}, \quad (58.141a)$$

$$V_0(R) = \frac{1}{2} \left[V_i^{(0)}(R) + V_f^{(0)}(R) \right], \quad (58.141b)$$

$$\Delta(R) = \left[V_i^{(0)}(R) - V_f^{(0)}(R) \right]. \quad (58.141c)$$

For a single crossing of diabatic potentials at R_X , $V_i^{(0)}(R_X) = V_f^{(0)}(R_X)$ and the adiabatic potentials at R_X are

$$V^\pm(R_X) = V_i^{(0)}(R_X) \pm V_{if}(R_X), \quad (58.142)$$

with energy separation $2V_{if}(R_X)$.

58.8.1 Landau–Zener Probability for Single Crossing at R_X

On assuming $\Delta(R) = (R - R_X)\Delta'(R_X)$, where $\Delta'(R) = d\Delta(R)/dR$, the probability for single crossing is

$$P_{if}(R_X) = \exp[\eta(R_X)/v_X(b)], \quad (58.143a)$$

$$\eta(R_X) = \left(\frac{2\pi}{\hbar} \right) \frac{|V_{if}(R_X)|^2}{\Delta'(R_X)}, \quad (58.143b)$$

$$v_X(b) = \left[1 - V_i^{(0)}(R_X)/E - b^2/R_X^2\right]^{1/2}. \quad (58.143c) \quad (\mathbf{R}, E, L^2)\text{-distribution}$$

Overall Charge-Transfer Probability

From the incoming and outgoing legs of the trajectory,

$$P^X(E) = 2P_{if}(1 - P_{if}). \quad (58.144)$$

58.8.2 Cross Section and Rate Coefficient for Mutual Neutralization

$$\begin{aligned} \sigma_M(E) &= 4\pi \int_0^{b_X} P_{if}(1 - P_{if})b \, db \\ &= \pi b_X^2 P_M, \\ \pi b_X^2 &= \pi \left(1 - \frac{V_i^{(0)}(R_X)}{E}\right) R_X^2 \\ &= \pi \left(1 + \frac{14.4}{R_X(\text{\AA})E(\text{eV})}\right) R_X^2; \end{aligned} \quad (58.145a)$$

P_M is the b^2 -averaged probability Eq. (58.144) for charge-transfer reaction within a sphere of radius R_X .

The rate is

$$\hat{\alpha}_M = (8k_B T/\pi M_{AB})^{1/2} \int_0^\infty \epsilon \sigma_M(\epsilon) e^{-\epsilon} d\epsilon, \quad (58.146)$$

where $\epsilon = E/k_B T$.

58.9 One-Way Microscopic Equilibrium Current, Flux, and Pair Distributions

All quantities on the RHS in the Cases (a)–(e) below are to be multiplied by $\tilde{N}_A \tilde{N}_B [\omega_{AB}/\omega_A \omega_B]$, where the ω_i denote the statistical weights of species i that are not included by the density of states associated with the E, L^2 orbital degrees of freedom.

Case (a)

($i \equiv \mathbf{R}, E, L^2$).

$$\text{Current: } j_i^\pm(\mathbf{R}) = n^\pm(\mathbf{R}, E, L^2) v_R \equiv n_i^\pm v_R.$$

$$\text{Flux: } 4\pi R^2 j_i^\pm(\mathbf{R}) dE dL^2 = \frac{4\pi^2 e^{-E/k_B T}}{(2\pi M_{AB} k_B T)^{3/2}} dE dL^2. \quad (58.147)$$

This flux is independent of R . For dissociated pairs $E > 0$,

$$4\pi R^2 j_i^\pm(\mathbf{R}) dE dL^2 = [\bar{v} \epsilon e^{-\epsilon} d\epsilon] [2\pi b db]. \quad (58.148)$$

$$\begin{aligned} n(\mathbf{R}, E, L^2) d\mathbf{R} dE dL^2 \\ = \frac{(8\pi^2/v_R) e^{-E/k_B T}}{(2\pi M_{AB} k_B T)^{3/2}} \left(\frac{d\mathbf{R}}{4\pi R^2}\right) dE dL^2. \end{aligned} \quad (58.149)$$

Case (b)

($i \equiv \mathbf{R}, E, L^2$)-integrated quantities.

$$\text{Current: } j_i^\pm(\mathbf{R}) = \frac{1}{2} v n^\pm(\mathbf{R}, E) \equiv \frac{1}{2} v n_i^\pm. \quad (58.150)$$

$$\text{Flux: } 4\pi R^2 j_i^\pm(\mathbf{R}) dE = [\bar{v} \epsilon e^{-\epsilon} d\epsilon] \pi b_0^2, \quad (58.151a)$$

$$\pi b_0^2 = \pi R^2 [1 - V(R)/E]. \quad (58.151b)$$

(\mathbf{R}, E)-Distribution:

$$\begin{aligned} n(\mathbf{R}, E) d\mathbf{R} dE \\ = \frac{2}{\sqrt{\pi}} \left[\frac{E - V(R)}{k_B T}\right]^{1/2} e^{-\epsilon} d\epsilon d\mathbf{R} \\ \equiv G_{MB}(E, R) d\mathbf{R}, \end{aligned} \quad (58.151c)$$

which defines the Maxwell–Boltzmann velocity distribution G_{MB} in the presence of the field $V(R)$.

Case (c)

(E, L^2)-integrated quantities.

$$\text{Current: } j^\pm(\mathbf{R}) = \frac{1}{4} \bar{v} e^{-V(R)/k_B T}. \quad (58.152)$$

$$\text{Flux: } 4\pi R^2 j^\pm(\mathbf{R}) = \pi R^2 \bar{v} e^{-V(R)/k_B T}. \quad (58.153)$$

$$\text{Distribution: } n(R) = e^{-V(R)/k_B T}. \quad (58.154)$$

When E -integration is only over dissociated states ($E > 0$), the above quantities are

$$j_d^\pm(\mathbf{R}) = \frac{1}{4} \bar{v} [1 - V(R)/k_B T], \quad (58.155)$$

$$4\pi R^2 j_d^\pm(\mathbf{R}) = \pi R^2 \left(1 - \frac{V(R)}{k_B T}\right) \bar{v} \equiv \pi b_{\max}^2 \bar{v}, \quad (58.156)$$

$$n(R) = [1 - V(R)/k_B T]. \quad (58.157)$$

Case (d)

(E, L^2)-distribution. For bound levels

$$n(E, L^2) dE dL^2 = \frac{4\pi^2 \tau_R(E, L)}{(2\pi M_{AB} k_B T)^{3/2}} e^{-E/k_B T} dE dL^2, \quad (58.158)$$

where $\tau_R = \oint dt = (\partial J_R / \partial E)$ is the period for bounded radial motion of energy E and radial action $J_R(E, L) = M_{AB} \oint v_R dR$.

Case (e)

E -distribution. For bound levels

$$n(E)dE = \frac{2e^{-\varepsilon}}{\sqrt{\pi}} d\varepsilon \int_0^{R_A} \left(\frac{E-V}{k_B T} \right)^{1/2} dR, \quad (58.159)$$

where R_A is the turning point $E = V(R_A)$.

Example

For electron-ion bounded motion, $V(R) = -Ze^2/R$, $R_A = Ze^2/|E|$, $R_e = Ze^2/k_B T$, $\varepsilon = E/k_B T$. Then $\tau_R = 2\pi(m/Ze^2)^{1/2}(R_A/2)^{3/2}$,

$$\int_0^{R_A} \left(\frac{R_e}{R} - |\varepsilon| \right)^{1/2} dR = \frac{\pi^2}{4} R_A^{5/2} R_e^{1/2}, \quad (58.160)$$

and

$$n^s(E)dE = \left(\frac{2e^{-\varepsilon}}{\sqrt{\pi}} d\varepsilon \right) \frac{\pi^2}{4} R_A^{5/2} R_e^{1/2} \quad (58.161)$$

$$= \left(\frac{2e^{-\varepsilon}}{\sqrt{\pi}} d\varepsilon \right) \left(\frac{\pi^2 R_e^3}{4|\varepsilon|^{5/2}} \right). \quad (58.162)$$

For closely spaced levels in a hydrogenic $e^- - A^{Z+}$ system,

$$n^s(p, \ell) = n(E, L^2) \left(\frac{dE}{dp} \right) \left(\frac{dL^2}{d\ell} \right), \quad (58.163a)$$

$$n^s(p) = n(E) \left(\frac{dE}{dp} \right). \quad (58.163b)$$

Using $E = -(2p^2)^{-1}(Z^2e^2/a_0)$ and $L^2 = (\ell + 1/2)^2\hbar^2$ for level (p, ℓ) then

$$\tau_R(E, L) \frac{dE}{dp} \left(\frac{dL^2}{d\ell} \right) = \left(\frac{dJ_R}{dp} \right) \left(\frac{dL^2}{d\ell} \right) \quad (58.164)$$

$$= h((2\ell + 1)\hbar^2), \quad (58.165)$$

$$\frac{n^s(p, \ell)}{n_e N^+} = \frac{2(2\ell + 1)}{2\omega_A^+} \frac{h^3}{(2\pi m_e k_B T)^{3/2}} e^{I_p/k_B T}, \quad (58.166a)$$

$$\frac{n^s(p)}{n_e N^+} = \frac{2p^2}{2\omega_A^+} \frac{h^3}{(2\pi m_e k_B T)^{3/2}} e^{I_p/k_B T}, \quad (58.166b)$$

in agreement with the Saha ionization formula Eq. (58.28), where N^+ is the equilibrium concentration of A^{Z+} ions in their ground electronic states. The spin statistical weights are $\omega_{eA} = \omega_e = 2$.

Notation:

M_{AB} reduced mass $M_A M_B / (M_A + M_B)$

R internal separation of A–B

E orbital energy $\frac{1}{2}Mv^2 + V(R)$

L orbital angular momentum

L^2 $2MEb^2$ for $E > 0$

v_R radial speed $|\dot{R}|$

\bar{v} mean relative speed $(8kT/\pi M_{AB})^{1/2}$

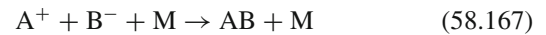
ε normalized energy $E/k_B T$

n_i pair distribution function $n_i^+ + n_i^-$

n_i^\pm component of n_i with $\dot{R} > 0$ (+) and $\dot{R} < 0$ (-).

58.10 Microscopic Methods for Termolecular Ion–Ion Recombination

At low gas density, the basic process



is characterized by nonequilibrium with respect to E . Dissociated and bound $A^+ - B^-$ ion pairs are in equilibrium with respect to their separation R , but bound pairs are not in E -equilibrium with each other; L^2 -equilibrium can be assumed for ion–ion recombination but not for ion–atom association reactions.

At higher gas densities N , there is nonequilibrium in the ion-pair distributions with respect to R , E , and L^2 . In the limit of high N , there is only nonequilibrium with respect to R . See [54] for full details.

58.10.1 Time-Dependent Method: Low Gas Density

Energy levels E_i of $A^+ - B^-$ pairs are so close that they form a quasi continuum with a nonequilibrium distribution over E_i determined by the master equation

$$\frac{dn_i(t)}{dt} = \int_{-D}^{\infty} (n_i v_{if} - n_f v_{fi}) dE_f, \quad (58.168)$$

where $n_i dE_i$ is the number density of pairs in the interval dE_i about E_i , and $v_{if} dE_f$ is the frequency of i -pair collisions with M that change the i -pair orbital energy from E_i to between E_f and $E_f + dE_f$. The greatest binding energy of the $A^+ - B^-$ pair is D .

Association Rate

$$R^A(t) = \int_{-D}^{\infty} P_i^S \left(\frac{dn_i}{dt} \right) dE_i \quad (58.169a)$$

$$= \hat{\alpha} N_A(t) N_B(t) - k n_s(t), \quad (58.169b)$$

where P_i^S is the probability for collisional stabilization (recombination) of i -pairs via a sequence of energy changing collisions with M. The coefficients for $C \rightarrow S$ recombination out of the C -block with ion concentrations $N_A(t)$, $N_B(t)$ (in cm^{-3}) into the S block of total ion-pair concentrations $n_s(t)$ and for $S \rightarrow C$ dissociation are $\hat{\alpha}$ ($\text{cm}^3 \text{s}^{-1}$) and k (s^{-1}), respectively.

One-Way Equilibrium Collisional Rate and Detailed Balance

$$C_{if} = \tilde{n}_i v_{if} = \tilde{n}_f v_{fi} = C_{fi} , \quad (58.170)$$

where the tilde denotes equilibrium (Saha) distributions.

Normalized Distribution Functions

$$\gamma_i(t) = n_i(t)/\tilde{n}_i^S , \quad \gamma_s(t) = n_s(t)/\tilde{n}_s^B(t) , \quad (58.171)$$

$$\gamma_c(t) = N_A(t)N_B(t)/\tilde{N}_A\tilde{N}_B , \quad (58.172)$$

where \tilde{n}_i^S and \tilde{n}^B are the Saha and Boltzmann distributions.

Master Equation for $\gamma_i(t)$

$$\frac{d\gamma_i(t)}{dt} = - \int_{-D}^{\infty} [\gamma_i(t) - \gamma_f(t)] v_{if} dE_f . \quad (58.173)$$

Quasi-Steady State (QSS) Reduction

Set

$$\gamma_i(t) = P_i^D \gamma_c(t) + P_i^S \gamma_s(t) \xrightarrow{t \rightarrow \infty} 1 , \quad (58.174)$$

where P_i^D and P_i^S are the respective time-independent portions of the normalized distribution γ_i , which originate, respectively, from blocks C and S . The energy separation between the C and S blocks is so large that $P_i^S = 0$ ($E_i \geq 0$, C block), $P_i^S \leq 1$ ($0 > E_i \geq -S$, \mathcal{E} block), and $P_i^S = 1$ ($-S \geq E_i \geq -D$, S block). Since $P_i^S + P_i^D = 1$, then

$$\frac{d\gamma_i(t)}{dt} = -[\gamma_c(t) - \gamma_s(t)] \int_{-D}^{\infty} (P_i^D - P_f^D) C_{if} dE_f . \quad (58.175)$$

Recombination and Dissociation Coefficients

Equation (58.174) in Eq. (58.169a) enables the recombination rate in Eq. (58.169b) to be written as

$$\hat{\alpha} \tilde{N}_A \tilde{N}_B = \int_{-D}^{\infty} P_i^D dE_i \int_{-D}^{\infty} (P_i^D - P_f^D) C_{if} dE_f . \quad (58.176)$$

The QSS condition ($dn_i/dt = 0$ in block \mathcal{E}) is then

$$P_i^D \int_{-D}^{\infty} v_{if} dE_f = \int_{-D}^E v_{if} P_f^D dE_f , \quad (58.177)$$

which involves only time-independent quantities. Under QSS, Eq. (58.176) reduces to the net downward current across bound level $-E$,

$$\hat{\alpha} \tilde{N}_A \tilde{N}_B = \int_{-E}^{\infty} dE_i \int_{-D}^{-E} (P_i^D - P_f^D) C_{if} dE_f , \quad (58.178)$$

which is independent of the energy level ($-E$) in the range $0 \geq -E \geq -S$ of block \mathcal{E} .

The dissociation frequency k in Eq. (58.169b) is

$$k \tilde{n}_s = \int_{-D}^{-E} dE_i \int_{-E}^{\infty} (P_i^S - P_f^S) C_{if} dE_f , \quad (58.179)$$

and macroscopic detailed balance $\hat{\alpha} \tilde{N}_A \tilde{N}_B = k \tilde{n}_s$ is automatically satisfied; $\hat{\alpha}$ is the direct ($C \rightarrow S$) collisional contribution (small) plus the (much larger) net collisional cascade downward contribution from that fraction of bound levels that originated in the continuum C ; k_d is the direct dissociation frequency (small) plus the net collisional cascade upward contribution from that fraction of bound levels that originated in block S .

58.10.2 Time-Independent Methods: Low Gas Density

QSS rate

Since recombination and dissociation (ionization) involve only that fraction of the bound state population that originated from the C and S blocks, respectively, recombination can be viewed as time independent with

$$N_A N_B = \tilde{N}_A \tilde{N}_B , \quad n_s(t) = 0 , \quad (58.180a)$$

$$\rho_i = n_i / \tilde{n}_i \equiv P_i^D \quad (58.180b)$$

$$\hat{\alpha} \tilde{N}_A \tilde{N}_B = \int_{-E}^{\infty} dE_i \int_{-D}^{-E} (\rho_i - \rho_f) C_{if} dE_f . \quad (58.180c)$$

QSS integral equation

$$\rho_i \int_{-D}^{\infty} v_{if} dE_f = \int_{-S}^{\infty} \rho_f v_{if} dE_f \quad (58.181)$$

is solved subject to the boundary condition

$$\rho_i = 1 (E_i \geq 0) , \quad \rho_i = 0 (-S \geq E_i \geq -D) . \quad (58.182)$$

Collisional energy-change moments

$$D^{(m)}(E_i) = \frac{1}{m!} \int_{-D}^{\infty} (E_f - E_i)^m C_{if} dE_f, \quad (58.183)$$

$$D_i^{(m)} = \frac{1}{m!} \frac{d}{dt} \langle (\Delta E)^m \rangle. \quad (58.184)$$

Averaged energy-change frequency

For an equilibrium distribution \tilde{n}_i of E_i -pairs per unit interval dE_i per second,

$$D_i^{(1)} = \frac{d}{dt} \langle \Delta E \rangle.$$

Averaged energy-change per collision

$$\langle \Delta E \rangle = D_i^{(1)} / D_i^{(0)}.$$

Time-independent dissociation

The time-independent picture corresponds to

$$n_s(t) = \tilde{n}_s, \quad \gamma_c(t) = 0, \quad \rho_i = n_i / \tilde{n}_i \equiv P_i^S, \quad (58.185)$$

in analogy to the macroscopic reduction of Eqs. (58.50a,58.50b).

Variational Principle

The QSS condition Eq. (58.174) implies that the fraction P_i^D of bound levels i with precursor C are so distributed over i that Eq. (58.176) for $\hat{\alpha}$ is a minimum. Hence P_i^D or ρ_i are obtained either from the solution of Eq. (58.181) or from minimizing the variational functional

$$\hat{\alpha} \tilde{N}_A \tilde{N}_B = \int_{-D}^{\infty} n_i dE_i \int_{-D}^{\infty} (\rho_i - \rho_f) v_{if} dE_f \quad (58.186a)$$

$$= \frac{1}{2} \int_{-D}^{\infty} dE_i \int_{-D}^{\infty} (\rho_i - \rho_f)^2 C_{if} dE_f, \quad (58.186b)$$

with respect to variational parameters contained in a trial analytic expression for ρ_i . Minimization of the quadratic functional Eq. (58.186b) has an analogy with the principle of least dissipation in the theory of electrical networks.

Diffusion-in-Energy-Space Method

Integral Eq. (58.181) can be expanded in terms of energy-change moments, via a Fokker–Planck analysis to yield the differential equation

$$\frac{\partial}{\partial E_i} \left(D_i^{(2)} \frac{\partial \rho_i}{\partial E_i} \right) = 0, \quad (58.187)$$

with the QSS analytical solution

$$\rho_i(E_i) = \left(\int_{E_i}^0 \frac{dE}{D^{(2)}(E)} \right) \left(\int_{-S}^0 \frac{dE}{D^{(2)}(E)} \right)^{-1} \quad (58.188)$$

of *Pitaevskii* [33] for ($e^- + A^+ + M$) recombination where collisional energy changes are small. This distribution does not satisfy the exact QSS condition Eq. (58.181). When inserted in the exact non-QSS rate Eq. (58.186b), highly accurate $\hat{\alpha}$ for heavy-particle recombination are obtained.

Bottleneck Method

The one-way equilibrium rate ($\text{cm}^{-3} \text{s}^{-1}$) across $-E$, i.e., Eq. (58.180c) with $\rho_i = 1$ and $\rho_f = 0$, is

$$\hat{\alpha}(-E) \tilde{N}_A \tilde{N}_B = \int_{-E}^{\infty} dE_i \int_{-D}^{-E} C_{if} dE_f. \quad (58.189)$$

This is an upper limit to Eq. (58.180c) and exhibits a minimum at $-E^*$, the bottleneck location. The least upper limit to $\hat{\alpha}$ is then $\hat{\alpha}(-E^*)$.

Trapping Radius Method

Assume that pairs with internal separation $R \leq R_T$ recombine with unit probability so that the one-way equilibrium rate across the dissociation limit at $E = 0$ for these pairs is

$$\hat{\alpha}(R_T) \tilde{N}_A \tilde{N}_B = \int_0^{R_T} dR \int_{V(R)}^0 C_{if}(R) dE_f, \quad (58.190)$$

where $V(R) = -e^2/R$, and $C_{if}(R) = \tilde{n}_i(R) v_{if}(R)$ is the rate per unit interval ($dR dE_i$) dE_f for the $E_i \rightarrow E_f$ collisional transitions at fixed R in

$$(A^+ - B^-)_{E_i,R} + M \rightarrow (A^+ - B^-)_{E_f,R} + M. \quad (58.191)$$

The concentration (cm^{-3}) of pairs with internal separation R and orbital energy E_i in the interval $dR dE_i$ about (R, E_i) is $\tilde{n}_i(R) dR dE_i$. Agreement with the exact treatment [54] is found by assigning $R_T = (0.48 - 0.55)(e^2/k_B T)$ for the recombination of equal mass ions in an equal mass gas for various ion–neutral interactions.

58.10.3 Recombination at Higher Gas Densities

As the density N of the gas M is raised, the recombination rate $\hat{\alpha}$ increases initially as N to such an extent that there are increasingly more pairs $n_i^-(R, E)$ in a state of contraction in

R than there are those $n_i^+(R, E)$ in a state of expansion; i.e., the ion-pair distribution densities $n_i^\pm(R, E)$ per unit interval $dE dR$ are not in equilibrium with respect to R in blocks C and \mathcal{E} . Those in the highly excited block \mathcal{E} , in addition, are not in equilibrium with respect to energy E . Basic sets of coupled master equations have been developed [54] for the microscopic nonequilibrium distributions $n^\pm(R, E, L^2)$ and $n^\pm(R, E)$ of expanding (+) and contracting (−) pairs with respect to A–B separation R , orbital energy E , and orbital angular momentum L^2 . With $n(\mathbf{R}, E_i, L_i^2) \equiv n_i(R)$ and using the notation defined at the beginning of Sect. 58.6, the distinct regimes for the master equations discussed in Sect. 58.10.4 are:

Low N equilibrium in R , but not in E, L^2
 → master equation for $n(E, L^2)$.

Pure Coulomb equilibrium in L^2

Attraction → master equation for $n(E)$.

High N nonequilibrium in R, E, L^2

→ master equation for $n_i^\pm(R)$.

Highest N equilibrium in (E, L^2) but not in R

→ macroscopic transport equation

Eq. (58.68a) in $n(R)$.

Normalized Distributions

For a state $|i \Rightarrow E, L^2$,

$$\begin{aligned} \rho_i(R) &= \frac{n_i(R)}{\tilde{n}_i(R)}, & \rho_i^\pm(R) &= \frac{n_i^\pm(R)}{\tilde{n}_i^\pm(R)}, \\ \rho_i(R) &= \frac{1}{2}(\rho_i^+ + \rho_i^-). \end{aligned} \quad (58.192)$$

Orbital Energy and Angular Momentum

$$E_i = \frac{1}{2}M_{AB}v^2 + V(R), \quad (58.193a)$$

$$E_i = \frac{1}{2}M_{AB}v_R^2 + V_i(R), \quad (58.193b)$$

$$V_i(R) = V(R) + \frac{L_i^2}{2M_{AB}R^2}, \quad (58.193c)$$

$$\begin{aligned} L_i &= |\mathbf{R} \times M_{AB}\mathbf{v}|, \\ L_i^2 &= (2M_{AB}E_i)b^2, \quad E_i > 0. \end{aligned} \quad (58.193d)$$

Maximum Orbital Angular Momenta

(1) A specified separation R can be accessed by all orbits of energy E_i with L_i^2 between 0 and

$$L_{im}^2(E_i, R) = 2M_{AB}R^2[E_i - V(R)]. \quad (58.194a)$$

(2) Bounded orbits of energy $E_i < 0$ can have L_i^2 between 0 and

$$L_{ic}^2(E_i) = 2M_{AB}R_c^2[E_i - V(R_c)], \quad (58.194b)$$

where R_c is the radius of the circular orbit determined by $\partial V_i/\partial R = 0$, i.e., by $E_i = V(R_c) + \frac{1}{2}R_c(\partial V/\partial R)_{R_c}$.

58.10.4 Master Equations

Master Equation for $n_i^\pm(R) \equiv n^\pm(R, E_i, L_i^2)$ [54]

$$\begin{aligned} &\pm \frac{1}{R^2} \frac{\partial}{\partial R} [R^2 n_i^\pm(R) |v_R|]_{E_i, L_i^2} \\ &= - \int_{V(R)}^{\infty} dE_f \int_0^{L_{fm}^2} dL_f^2 [n_i^\pm(R) v_{if}(R) \\ &\quad - n_f^\pm(R) v_{fi}(R)]. \end{aligned} \quad (58.195)$$

The set of master equations [54] for n_i^+ is coupled to the n_i^- set by the boundary conditions $n_i^-(R_i^\mp) = n_i^+(R_i^\mp)$ at the pericenter R_i^- for all E_i and apocenter R_i^+ for $E_i < 0$ of the E_i, L_i^2 -orbit.

Master Equations for Normalized Distributions [54]

$$\begin{aligned} \pm |v_R| \frac{\partial \rho_i^\pm}{\partial R} &= - \int_{V(R)}^{\infty} dE_f \int_0^{L_{fm}^2} dL_f^2 \\ &\quad \times [\rho_i^\pm(R) - \rho_f^\pm(R)] v_{if}(R). \end{aligned} \quad (58.196)$$

Corresponding master equations for the L^2 integrated distributions $n^\pm(R, E)$ and $\rho^\pm(R, E)$ have been derived [54].

Continuity Equations

$$J_i = [n_i^+(R) - n_i^-(R)] |v_R| = (\rho_i^+ - \rho_i^-) \tilde{j}_i^\pm, \quad (58.197)$$

$$\begin{aligned} \frac{1}{R^2} \frac{\partial}{\partial R} (R^2 J_i) &= - \int_{V(R)}^{\infty} dE_f \int_0^{L_{fm}^2} dL_f^2 \\ &\quad \times [n_i(R) v_{if}(R) - n_f(R) v_{fi}(R)], \end{aligned} \quad (58.198)$$

$$\begin{aligned} \frac{1}{2} |v_R| \frac{\partial [\rho_i^+(R) - \rho_i^-(R)]}{\partial R} \\ &= - \int_{V(R)}^{\infty} dE_f \int_0^{L_{fm}^2} dL_f^2 [\rho_i(R) - \rho_f(R)] v_{if}(R). \end{aligned} \quad (58.199)$$

58.10.5 Recombination Rate

Flux Representation

The $R_0 \rightarrow \infty$ limit of

$$\hat{\alpha} \tilde{N}_A \tilde{N}_B = -4\pi R_0^2 J(R_0) \quad (58.200)$$

has the microscopic generalization

$$\hat{\alpha} \tilde{N}_A \tilde{N}_B = \int_{V(R_0)}^{\infty} dE_i \int_0^{L_{ic}^2} dL_i^2 [4\pi R_0^2 \tilde{j}_i^{\pm}(R_0)] \times [\rho_i^-(R_0) - \rho_i^+(R_0)], \quad (58.201)$$

where L_{ic}^2 is given by Eq. (58.194b) with $R_c = R_0$ for bound states and is infinite for dissociated states, and where

$$\rho_i^-(R_0) - \rho_i^+(R_0) = \oint_{R_i}^{R_0} \rho_i(R) [v_i^b(R) + v_i^c(R)] dt, \quad (58.202)$$

with

$$\begin{aligned} \rho_i(R) v_i^b(R) &= \int_{V(R)}^{V(R_0)} dE_f \int_0^{L_{fm}^2} dL_f^2 [\rho_i(R) - \rho_f(R)] \\ &\quad \times v_{if}(R), \\ \rho_i(R) v_i^c(R) &= \int_{V(R_0)}^{\infty} dE_f \int_0^{L_{fm}^2} dL_f^2 [\rho_i(R) - \rho_f(R)] \\ &\quad \times v_{if}(R). \end{aligned} \quad (58.203a)$$

Collisional Representation

$$\hat{\alpha} \tilde{N}_A \tilde{N}_B = \int_{V(R_0)}^{\infty} dE_i \int_0^{L_{ic}^2} dL_i^2 \int_{R_i}^{R_0} \tilde{n}_i(R) dR \times [\rho_i(R) v_i^b(R)], \quad (58.204)$$

which is the microscopic generalization of the macroscopic result $\hat{\alpha} = K \rho^* v_s = \alpha_{RN}(R_0) \rho(R_0)$.

The flux for dissociated pairs $E_i > 0$ is

$$4\pi R^2 |v_R| \tilde{n}_i^{\pm}(R) dE dL^2 = [\bar{v} \varepsilon e^{-\varepsilon} d\varepsilon] [2\pi b db] \tilde{N}_A \tilde{N}_B, \quad (58.205)$$

so the rate Eq. (58.204) as $R_0 \rightarrow \infty$ is

$$\hat{\alpha} = \bar{v} \int_0^{\infty} \varepsilon e^{-\varepsilon} d\varepsilon \int_0^{b_0} 2\pi b db \oint_{R_i}^{R_0} \rho_i(R) v_i^b(R) dt, \quad (58.206)$$

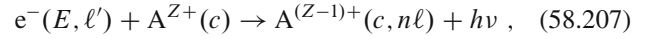
which is the microscopic generalization Eq. (58.57b) of the macroscopic result $\hat{\alpha} = k_c P^S$ of Eq. (58.56).

Reaction Rate $\alpha_{RN}(R_0)$

On solving Eq. (58.196) subject to $\rho(R_0) = 1$, according to Eq. (58.68b), $\hat{\alpha}$ determined by Eq. (58.201) is the rate $\hat{\alpha}_{RN}$ of recombination within the (A – B) sphere of radius R_0 . The overall rate of recombination $\hat{\alpha}$ is then given by the full diffusional-drift reaction rate Eq. (58.71b) where the rate of transport to R_0 is determined uniquely by Eq. (58.72).

58.11 Radiative Recombination

In the radiative recombination (RR) process



the accelerating electron e^- with energy and angular momentum (E, ℓ') is captured, via coupling with the weak quantum electrodynamic interaction $(e/m_e c) \mathbf{A} \cdot \mathbf{p}$ associated with the electromagnetic field of the moving ion, into an excited state $n\ell$ with binding energy $I_{n\ell}$ about the parent ion A^{Z+} (initially in an electronic state c). The simultaneously emitted photon carries away the excess energy $h\nu = E + I_{n\ell}$ and angular momentum difference between the initial and final electronic states. The cross section $\sigma_R^{n\ell}(E)$ for RR is calculated (a) from the Einstein A coefficient for free-bound transitions or (b) from the cross section $\sigma_I^{n\ell}(h\nu)$ for photoionization (PI) via the detailed balance (DB) relationship appropriate to Eq. (58.207).

The rates $\langle v_e \sigma_R \rangle$ and averaged cross sections $\langle \sigma_R \rangle$ for a Maxwellian distribution of electron speeds v_e are then determined from either

$$\begin{aligned} \hat{\alpha}_R^{n\ell}(T_e) &= \bar{v}_e \int_0^{\infty} \varepsilon \sigma_R^{n\ell}(\varepsilon) \exp(-\varepsilon) d\varepsilon \\ &= \bar{v}_e \langle \sigma_R^{n\ell}(T_e) \rangle, \end{aligned} \quad (58.208)$$

where $\varepsilon = E/k_B T_e$, or from the Milne DB relation Eq. (58.281) between the forward and reverse macroscopic rates of Eq. (58.207). Using the hydrogenic semiclassical σ_f^j of *Kramers* [34], together with an asymptotic expansion [55] for the g -factor of *Gaunt* [56], the quantal/semiclassical cross section ratio in Eq. (58.287), *Seaton* [57] calculated $\hat{\alpha}_R^{n\ell}$.

The rate of electron energy loss in RR is

$$\left\langle \frac{dE}{dt} \right\rangle_{n\ell} = n_e \bar{v}_e (k_B T_e) \int_0^{\infty} \varepsilon^2 \sigma_R^{n\ell}(\varepsilon) e^{-\varepsilon} d\varepsilon, \quad (58.209)$$

and the radiated power produced in RR is

$$\left\langle \frac{d(h\nu)}{dt} \right\rangle_{n\ell} = n_e \bar{v}_e \int_0^{\infty} \varepsilon h\nu \sigma_R^{n\ell}(\varepsilon) e^{-\varepsilon} d\varepsilon. \quad (58.210)$$

Standard conversions

$$E = p_e^2/2m_e = \hbar^2 k_e^2/2m_e = k_e^2 a_0^2 (e^2/2a_0) \quad (58.211a)$$

$$= \kappa^2 (Z^2 e^2/2a_0) = \varepsilon (Z^2 e^2/2a_0), \quad (58.211b)$$

$$E_v = h\nu = \hbar\omega = \hbar k_\nu c = (I_n + E) \quad (58.211c)$$

$$\equiv (1 + n^2 \varepsilon) (Z^2 e^2/2n^2 a_0), \quad (58.211d)$$

$$h\nu/I_n = 1 + n^2 \varepsilon, \quad k_e^2 a_0^2 = 2E/(e^2/a_0), \quad (58.211e)$$

$$k_\nu a_0 = (h\nu)\alpha/(e^2/a_0), \quad (58.211f)$$

$$k_\nu^2/k_e^2 = (h\nu)^2/(2Em_e c^2) \quad (58.211g)$$

$$= \alpha^2 (h\nu)^2/[2E(e^2/a_0)], \quad (58.211h)$$

$$I_H = e^2/2a_0, \quad \alpha = e^2/\hbar c = 1/137.0359895,$$

$$\alpha^{-2} = m_e c^2/(e^2/a_0), \quad I_n = (Z^2/n^2)I_H. \quad (58.211i)$$

The electron and photon wavenumbers are k_e and k_ν , respectively.

58.11.1 Detailed Balance and Recombination-Ionization Cross Sections

Cross sections $\sigma_R^{n\ell}(E)$ and $\sigma_I^{n\ell}(h\nu)$ for radiative recombination (RR) into and photoionization (PI) out of level $n\ell$ of atom A are interrelated by the detailed balance relation

$$g_e g_A^+ k_e^2 \sigma_R^{n\ell}(E) = g_\nu g_A k_\nu^2 \sigma_I^{n\ell}(h\nu), \quad (58.212)$$

where $g_e = g_\nu = 2$. Electronic statistical weights of A and A^+ are g_A and g_A^+ , respectively. Thus, using Eq. (58.211g) for k_ν^2/k_e^2 ,

$$\sigma_R^{n\ell}(E) = \left(\frac{g_A}{2g_A^+} \right) \left(\frac{(h\nu)^2}{Em_e c^2} \right) \sigma_I^{n\ell}(h\nu). \quad (58.213)$$

The statistical factors are:

(a) For $(A^+ + e^-)$ state $c[S_c, L_c; \varepsilon, \ell', m']$:

$$g_A^+ = (2S_c + 1)(2L_c + 1).$$

(b) For $A(n\ell)$ state $b[S_c, L_c; n, \ell]SL$

$$g_A = (2S + 1)(2L + 1).$$

(c) For $n\ell$ electron outside a closed shell

$$g_A^+ = 1, \quad g_A = 2(2\ell + 1).$$

Cross sections are averaged over initial and summed over final degenerate states. For case (c),

$$\sigma_I^n = \frac{1}{n^2} \sum_{\ell=0}^{n-1} (2\ell + 1) \sigma_I^{n\ell}; \quad (58.214a)$$

$$\sigma_R^n = \sum_{\ell=0}^{n-1} 2(2\ell + 1) \sigma_R^{n\ell}. \quad (58.214b)$$

58.11.2 Kramers Cross Sections, Rates, Electron Energy-Loss Rates, and Radiated Power for Hydrogenic Systems

These are all calculated from application of the detailed balance Eq. (58.212) to the original $\sigma_I^n(h\nu)$ of *Kramers* [34].

Semiclassical (Kramers) Cross Sections

For hydrogenic systems,

$$I_n = \frac{Z^2 e^2}{2n^2 a_0}, \quad h\nu = I_n + E. \quad (58.215)$$

The results below are expressed in terms of the quantities

$$b_n = \frac{I_n}{k_B T_e}, \quad (58.216)$$

$$\sigma_{10}^n = \frac{64\pi a_0^2 \alpha}{3\sqrt{3}} \left(\frac{n}{Z^2} \right) = 7.907071 \times 10^{-18} (n/Z^2) \text{ cm}^2, \quad (58.217)$$

$$\sigma_{R0}(E) = \left(\frac{8\pi a_0^2 \alpha^3}{3\sqrt{3}} \right) \frac{(Z^2 e^2/a_0)}{E}, \quad (58.218)$$

$$\hat{\alpha}_0(T_e) = \bar{v}_e \left(\frac{8\pi a_0^2 \alpha^3}{3\sqrt{3}} \right) \frac{(Z^2 e^2/a_0)}{k_B T_e}. \quad (58.219)$$

PI and RR cross sections for level n

In the Kramer (K) semiclassical approximation,

$$\kappa \sigma_I^n(h\nu) = \left(\frac{I_n}{h\nu} \right)^3 \sigma_{10}^n = \kappa \sigma_I^{n\ell}(h\nu), \quad (58.220)$$

$$\begin{aligned} \kappa \sigma_R^n(E) &= \sigma_{R0}(E) \left(\frac{2}{n} \right) \left(\frac{I_n}{I_n + E} \right) \\ &= 3.897 \times 10^{-20} \\ &\quad \times [n\varepsilon(13.606 + n^2\varepsilon^2)]^{-1} \text{ cm}^2, \end{aligned} \quad (58.221)$$

where ε is in units of eV and is given by

$$\varepsilon = E/Z^2 \equiv (2.585 \times 10^{-2}/Z^2)(T_e/300). \quad (58.222)$$

Equation (58.221) illustrates that RR into low n at low E is favored.

Cross section for RR into level $n\ell$

$$\kappa\sigma_{\text{R}}^{n\ell} = [(2\ell + 1)/n^2] \kappa\sigma_{\text{R}}^n. \quad (58.223)$$

Rate for RR into level n

$$\hat{\alpha}_{\text{R}}^n(T_e) = \hat{\alpha}_0(T_e)(2/n)b_n e^{b_n} E_1(b_n), \quad (58.224a)$$

which for large b_n (i.e., $k_{\text{B}}T_e \ll I_n$) tends to

$$\begin{aligned} \hat{\alpha}_{\text{R}}^n(T_e \rightarrow 0) &= \hat{\alpha}_0(T_e)(2/n) \\ &\times (1 - b_n^{-1} + 2b_n^{-2} - 6b_n^{-3} + \dots). \end{aligned} \quad (58.224b)$$

The Kramers cross section for photoionization at threshold is $\sigma_{\text{R}0}^n$, and

$$\sigma_{\text{R}0}^n = 2\sigma_{\text{R}0}/n; \quad \hat{\alpha}_0^n = 2\hat{\alpha}_0/n \quad (58.225)$$

provide the corresponding Kramers cross section and rate for recombination as $E \rightarrow 0$ and $T_e \rightarrow 0$, respectively.

RR Cross sections and rates into all levels $n \geq n_f$

$$\begin{aligned} \sigma_{\text{R}}^{\text{T}}(E) &= \int_{n_f}^{\infty} \sigma_{\text{R}}^n(E) dn \\ &= \sigma_{\text{R}0}(E) \ln(1 + I_f/E), \end{aligned} \quad (58.226a)$$

$$\hat{\alpha}_{\text{R}}^{\text{T}}(T_e) = \hat{\alpha}_0(T_e)[\gamma + \ln b_f + e^{b_f} E_1(b_f)]. \quad (58.226b)$$

Useful integrals

$$\int_0^{\infty} e^{-x} \ln x dx = \gamma, \quad (58.227a)$$

$$\int_b^{\infty} x^{-1} e^{-x} dx = E_1(b), \quad (58.227b)$$

$$\int_0^b e^x E_1(x) dx = \gamma + \ln b + e^b E_1(b), \quad (58.227c)$$

$$\begin{aligned} \int_0^b [1 - x e^x E_1(x)] dx \\ = \gamma + \ln b + e^b(1 - b)E_1(b), \end{aligned} \quad (58.227d)$$

where $\gamma = 0.5772157$ is Euler's constant, and $E_1(b)$ is the first exponential integral such that

$$\begin{aligned} b e^b E_1(b) \\ \xrightarrow{b \gg 1} 1 - b^{-1} + 2b^{-2} - 6b^{-3} + 24b^{-4} + \dots \end{aligned}$$

Electron Energy Loss Rate**Energy loss rate for RR into level n**

$$\left\langle \frac{dE}{dt} \right\rangle_n = n_e \hat{\alpha}_{\text{R}}^n(T_e) k_{\text{B}} T_e \left(\frac{1 - b_n e^{b_n} E_1(b_n)}{e^{b_n} E_1(b_n)} \right), \quad (58.228a)$$

which for large b_n (i.e. $(k_{\text{B}}T_e) \ll I_n$) tends to

$$n_e \hat{\alpha}_{\text{R}}^n(T_e) k_{\text{B}} T_e (1 - b_n^{-1} + 3b_n^{-2} - 13b_n^{-3} + \dots), \quad (58.228b)$$

with Eq. (58.224a) for $\hat{\alpha}_{\text{R}}^n$.

Energy loss rate for RR into all levels $n \geq n_f$

$$\begin{aligned} \left\langle \frac{dE}{dt} \right\rangle \\ = n_e k_{\text{B}} T_e \hat{\alpha}_0(T_e) [\gamma + \ln b_f + e^{b_f} E_1(b_f)(1 - b_f)] \end{aligned} \quad (58.229a)$$

$$= n_e (k_{\text{B}} T_e) [\hat{\alpha}_{\text{R}}^{\text{T}}(T_e) - \hat{\alpha}_0(T_e) b_f e^{b_f} E_1(b_f)], \quad (58.229b)$$

with Eqs. (58.226b) and (58.219) for $\hat{\alpha}_{\text{R}}^{\text{T}}$ and $\hat{\alpha}_0$.

Radiated Power**Radiated power for RR into level n**

$$\left\langle \frac{d(h\nu)}{dt} \right\rangle_n = n_e \hat{\alpha}_{\text{R}}^n(T_e) I_n [b_n e^{b_n} E_1(b_n)]^{-1}, \quad (58.230a)$$

which for large b_n (i.e. $(k_{\text{B}}T_e) \ll I_n$) tends to

$$n_e \hat{\alpha}_{\text{R}}^n(T_e) I_n (1 + b_n^{-1} - b_n^{-2} + 3b_n^{-3} + \dots). \quad (58.230b)$$

Radiated power for RR into all levels $n \geq n_f$

$$\left\langle \frac{d(h\nu)}{dt} \right\rangle = n_e \hat{\alpha}_0(T_e) I_f. \quad (58.231)$$

To allow n -summation, rather than integration as in Eq. (58.226a), $1/2\sigma_{\text{R}}^{n_f}$, $1/2\hat{\alpha}_{\text{R}}^{n_f}$, $1/2\langle dE/dt \rangle_{n_f}$, and $1/2\langle d(h\nu)/dt \rangle_{n_f}$, respectively, are added to each of the above expressions. The expressions valid for bare nuclei of charge Z are also fairly accurate for recombination to a core of charge Z_c and atomic number Z_A , provided that Z is identified as $1/2(Z_A + Z_c)$.

Differential cross sections for Coulomb elastic scattering

$$\sigma_{\text{c}}(E, \theta) = \frac{b_0^2}{4 \sin^4 \frac{1}{2}\theta}, \quad b_0^2 = (Ze^2/2E)^2. \quad (58.232)$$

The integral cross section for Coulomb scattering by $\theta \geq \pi/2$ at energy $E = (3/2)k_{\text{B}}T$ is

$$\sigma_{\text{c}}(E) = \pi b_0^2 = \frac{1}{9} \pi R_{\text{e}}^2, \quad R_{\text{e}} = e^2/k_{\text{B}}T. \quad (58.233)$$

Photon emission probability

$$P_\nu = \sigma_R^n(E)/\sigma_c(E). \quad (58.234a)$$

This is small and increases with decreasing n as

$$P_\nu(E) = \left(\frac{8\alpha^3}{3\sqrt{3}}\right) \frac{8}{n} \frac{E}{(e^2/a_0)} \left(\frac{I_n}{h\nu}\right). \quad (58.234b)$$

58.11.3 Basic Formulae for Quantal Cross Sections**Radiative Recombination and Photoionization Cross Sections**

The cross section $\sigma_R^{n\ell}$ for recombination follows from the continuum-bound transition probability P_{if} per unit time. It is also provided by the detailed balance relation Eq. (58.212) in terms of $\sigma_I^{n\ell}$, which follows from P_{fi} . The number of radiative transitions per second is

$$\begin{aligned} & \left[g_e g_A^+ \rho(E) dE d\hat{\mathbf{k}}_e \right] P_{if} \left[\rho(E_\nu) dE_\nu d\hat{\mathbf{k}}_\nu \right] \\ &= g_e g_A^+ v_e \frac{d\mathbf{p}_e}{(2\pi\hbar)^3} \sigma_R(\mathbf{k}_e) = g_\nu g_A c \frac{d\mathbf{k}_\nu}{(2\pi)^3} \sigma_I(\mathbf{k}_\nu), \end{aligned} \quad (58.235)$$

where the electron current ($\text{cm}^{-2} \text{s}^{-1}$) is

$$\frac{v_e d\mathbf{p}_e}{(2\pi\hbar)^3} = \left(\frac{2mE}{h^3}\right) dE d\hat{\mathbf{k}}_e, \quad (58.236)$$

and the photon current ($\text{cm}^{-2} \text{s}^{-1}$) is

$$c \frac{d\mathbf{k}_\nu}{(2\pi)^3} = c \frac{(h\nu)^2}{(2\pi\hbar c)^3} dE_\nu d\hat{\mathbf{k}}_\nu. \quad (58.237)$$

Time-dependent quantum electrodynamical interaction

$$\begin{aligned} V(\mathbf{r}, t) &= \frac{e}{mc} \mathbf{A} \cdot \mathbf{p} = ie \left(\frac{2\pi h\nu}{\mathcal{V}}\right)^{1/2} (\hat{\mathbf{e}} \cdot \mathbf{r}) e^{-i(\mathbf{k}_\nu \cdot \mathbf{r} - \omega t)} \\ &\equiv V(\mathbf{r}) e^{i\omega t}. \end{aligned} \quad (58.238)$$

In the dipole approximation, $e^{-i\mathbf{k}_\nu \cdot \mathbf{r}} \approx 1$.

Continuum-bound state-to-state probability

$$\begin{aligned} P_{if} &= \frac{2\pi}{\hbar} |V_{fi}|^2 \delta[E_\nu - (E + I_n)] \\ V_{fi} &= \langle \Psi_{n\ell m}(\mathbf{r}) V(\mathbf{r}) \Psi_i(\mathbf{r}, \mathbf{k}_e) \rangle. \end{aligned} \quad (58.239)$$

Number of photon states in volume \mathcal{V}

$$\rho(E_\nu, \hat{\mathbf{k}}_\nu) dE_\nu d\hat{\mathbf{k}}_\nu = \mathcal{V} (h\nu)^2 / (2\pi\hbar c)^3 dE_\nu d\hat{\mathbf{k}}_\nu \quad (58.240a)$$

$$= \mathcal{V} [\omega^2 / (2\pi c)^3] d\omega d\hat{\mathbf{k}}_\nu. \quad (58.240b)$$

Continuum-bound transition rate

On summing over the two directions ($g_\nu = 2$) of polarization, the rate for transitions into all final photon states is

$$\begin{aligned} A_{n\ell m}(E, \hat{\mathbf{k}}_e) &= \int P_{if} \rho(E_\nu) dE_\nu d\hat{\mathbf{k}}_\nu \\ &= \frac{4e^2}{3\hbar} \frac{(h\nu)^3}{(3\hbar c)^3} |\langle \Psi_{n\ell m} | \mathbf{r} | \Psi_i(\mathbf{k}_e) \rangle|^2. \end{aligned} \quad (58.241)$$

Transition frequency: alternative formula

$$A_{n\ell m}(E, \hat{\mathbf{k}}_e) = (2\pi/\hbar) |D_{fi}|^2, \quad (58.242)$$

where the dipole atom–radiation interaction coupling is

$$D_{fi}(\mathbf{k}_e) = \left(\frac{2\omega^3}{3\pi c^3}\right)^{1/2} \langle \Psi_{n\ell m} | e \mathbf{r} | \Psi_i(\mathbf{k}_e) \rangle. \quad (58.243)$$

RR cross section into level (n, ℓ, m)

$$\begin{aligned} \sigma_R^{n\ell m}(E) &= \frac{1}{4\pi} \int \sigma_R^{n\ell m}(\mathbf{k}_e) d\hat{\mathbf{k}}_e \\ &= \frac{h^3 \rho(E)}{8\pi m_e E} \int A_{n\ell m}(E, \hat{\mathbf{k}}_e) d\hat{\mathbf{k}}_e. \end{aligned} \quad (58.244)$$

RR cross section into level (n, ℓ)

$$\begin{aligned} \sigma_R^{n\ell}(E) &= \frac{8\pi^2}{3} \left(\frac{\alpha h\nu}{2(e^2/a_0)E}\right) \rho(E) R_I^{n\ell}(E), \\ R_I^{n\ell}(E) &= \int d\hat{\mathbf{k}}_e \sum_m |\langle \Psi_{n\ell m} | \mathbf{r} | \Psi_i(\mathbf{k}_e) \rangle|^2. \end{aligned} \quad (58.245)$$

Transition T-matrix for RR

$$\sigma_R^{n\ell}(E) = \frac{\pi a_0^2}{(ka_0)^2} |T_R|^2 \rho(E), \quad (58.246)$$

$$|T_R|^2 = 4\pi^2 \int \sum_m |D_{fi}|^2 d\hat{\mathbf{k}}_e. \quad (58.247)$$

Photoionization cross section

From the detailed balance in Eq. (58.235), $\sigma_I^{n\ell}$ is

$$\sigma_I^{n\ell}(h\nu) = \left(\frac{8\pi^2}{3}\right) \alpha h\nu \left(\frac{g_A^+}{g_A}\right) \rho(E) R_I^{n\ell}(E). \quad (58.248)$$

Continuum wave function expansion

$$\Psi_i(\mathbf{k}_e, \mathbf{r}) = \sum_{\ell' m'} i^{\ell'} e^{i\eta_{\ell'}} R_{E\ell'}(r) Y_{\ell' m'}(\hat{\mathbf{k}}_e) Y_{\ell' m'}(\hat{\mathbf{r}}). \quad (58.249)$$

Energy normalization

With $\rho(E) = 1$,

$$\int \Psi_i(\mathbf{k}_e; \mathbf{r}) \Psi_i^*(\mathbf{k}'_e; \mathbf{r}) d\mathbf{r} = \delta(E - E') \delta(\hat{\mathbf{k}}_e - \hat{\mathbf{k}}'_e). \quad (58.250)$$

Plane wave expansion

$$e^{i\mathbf{k}\cdot\mathbf{r}} = 4\pi \sum_{\ell=0}^{\infty} i^{\ell} j_{\ell}(kr) Y_{\ell m}^*(\hat{\mathbf{k}}) Y_{\ell m}(\hat{\mathbf{r}}), \quad (58.251)$$

$$j_{\ell}(kr) \approx \sin\left(kr - \frac{1}{2}\ell\pi\right) / (kr). \quad (58.252)$$

For bound states,

$$\Psi_{n\ell m}(\mathbf{r}) = R_{n\ell}(r) Y_{\ell m}(\hat{\mathbf{r}}). \quad (58.253)$$

RR and PI cross sections and radial integrals

$$\sigma_{\text{R}}^{n\ell}(E) = \frac{8\pi^2}{3} \left(\frac{(\alpha h\nu)^3}{2(e^2/a_0)E} \right) \rho(E) R_{\text{I}}(E; n\ell). \quad (58.254)$$

For an electron outside a closed core,

$$g_{\text{A}}^+ = 1, \quad g_{\text{A}} = 2(2\ell + 1),$$

$$\sigma_{\text{I}}^{n\ell}(h\nu) = \frac{4\pi^2 \alpha h\nu \rho(E)}{3(2\ell + 1)} R_{\text{I}}(E; n\ell), \quad (58.255a)$$

$$R_{n\ell}^{e,\ell'} = \int_0^{\infty} (R_{e\ell'} r R_{n\ell}) r^2 dr, \quad (58.255b)$$

$$R_{\text{I}}(E; n\ell) = \ell \left| R_{n\ell}^{e,\ell-1} \right|^2 + (\ell + 1) \left| R_{n\ell}^{e,\ell+1} \right|^2. \quad (58.255c)$$

For an electron outside an unfilled core (c) in the process $(\text{A}^+ + e^-) \rightarrow \text{A}(n\ell)$, the weights are

State i : $[\text{S}_{\text{c}}, L_{\text{c}}; \varepsilon]$, $g_{\text{A}}^+ = (2\text{S}_{\text{c}} + 1)(2L_{\text{c}} + 1)$.

State f : $[(\text{S}_{\text{c}}, L_{\text{c}}; n\ell)S, L]$, $g_{\text{A}} = (2S + 1)(2L + 1)$.

$$R_{\text{I}}(E; n\ell) = \frac{(2L + 1)}{(2L_{\text{c}} + 1)} \times \sum_{\ell'=\ell\pm 1} \sum_{L'} (2L' + 1) \left\{ \begin{matrix} \ell & L & L_{\text{c}} \\ L' & \ell' & 1 \end{matrix} \right\}^2 \times \ell_{\text{max}} \left| \int_0^{\infty} (R_{e\ell'} r R_{n\ell}) r^2 dr \right|^2. \quad (58.256)$$

This reduces to Eq. (58.255c) when the radial functions $R_{i,f}$ do not depend on $(\text{S}_{\text{c}}, L_{\text{c}}, S, L)$.

Cross Section for Dielectronic Recombination

$$\sigma_{\text{DLR}}^{n\ell}(E) = \frac{\pi a_0^2}{(ka_0)^2} |T_{\text{DLR}}(E)|^2 \rho(E),$$

$$|T_{\text{DLR}}(E)|^2 = 4\pi^2 \int d\hat{\mathbf{k}}_e \times \sum_j \left| \frac{\langle \Psi_f D \rangle \Psi_j \langle \Psi_j V \rangle \Psi_i(\mathbf{k}_e)}{(E - \varepsilon_j + i\Gamma_j/2)} \right|^2, \quad (58.257)$$

which is the generalization of the T -matrix Eq. (58.247) to include the effect of intermediate doubly excited autoionizing states $\langle \Psi_j$ in energy resonance to within width Γ_j of the initial continuum state Ψ_i . The electrostatic interaction $V = e^2 \sum_{i=1}^N (\mathbf{r}_i - \mathbf{r}_{N+1})^{-1}$ initially produces dielectronic capture by coupling the initial state i with the resonant states j , which become stabilized by coupling via the dipole radiation field interaction $\mathbf{D} = (2\omega^3/3\pi c^3)^{1/2} \sum_{i=1}^{N+1} (e\mathbf{r}_i)$ to the final stabilized state f . The above cross section for Eq. (58.3) is valid for isolated, nonoverlapping resonances.

Continuum Wave Normalization and Density of States

The basic formulae Eq. (58.245) for $\sigma_{\text{R}}^{n\ell}$ depends on the density of states $\rho(E)$, which in turn varies according to the particular normalization constant N adopted for the continuum radial wave,

$$R_{E\ell}(r) \approx N \sin\left(kr - \frac{1}{2}\ell\pi + \eta_{\ell}\right) / r, \quad (58.258)$$

in Eq. (58.249) where the phase is

$$\eta_{\ell} = \arg \Gamma(\ell + 1 + i\beta) - \beta \ln 2kr + \delta_{\ell}. \quad (58.259)$$

The phase corresponding to the Hartree–Fock short-range interaction is δ_{ℓ} . The Coulomb phase shift for electron motion under $(-Ze^2/r)$ is $(\eta_{\ell} - \delta_{\ell})$ with $\beta = Z/(ka_0)$.

For a plane wave $\phi_{\mathbf{k}}(\mathbf{r}) = N' \exp(i\mathbf{k} \cdot \mathbf{r})$,

$$\begin{aligned} \langle \phi_{\mathbf{k}}(\mathbf{r}) | \phi_{\hat{\mathbf{k}}'}(\mathbf{r}) \rangle d\mathbf{k} &= (2\pi)^3 |N'|^2 \rho(\mathbf{k}) d\mathbf{k} \delta(\mathbf{k} - \mathbf{k}') \\ &\equiv \left(\frac{h^3}{mp} \right) |N'|^2 \rho(E, \hat{\mathbf{k}}) dE d\hat{\mathbf{k}} \delta(E - E') \delta(\hat{\mathbf{k}} - \hat{\mathbf{k}}'). \end{aligned} \quad (58.260)$$

On integrating Eq. (58.260) over all E and $\hat{\mathbf{k}}$ for a single particle distributed over all $|E, \hat{\mathbf{k}}\rangle$ states, N' and ρ are then interrelated by

$$|N'|^2 \rho(E, \hat{\mathbf{k}}) = mp/h^3. \quad (58.261)$$

The incident current is

$$j dE d\hat{\mathbf{k}}_e = v |N'|^2 \rho(E, \hat{\mathbf{k}}) dE d\hat{\mathbf{k}}_e \quad (58.262a)$$

$$= (2mE/h^3) dE d\hat{\mathbf{k}}_e = v d\mathbf{p}_e/h^3. \quad (58.262b)$$

Radial wave connection

From Eqs. (58.249) and (58.251), $N = (4\pi N'/k)$, so that the connection between N of Eq. (58.258) and $\rho(E)$ is

$$|N|^2 \rho(E, \hat{\mathbf{k}}) = \frac{(2m/\hbar^2)}{\pi k} = \frac{(2/\pi)}{ka_0 e^2}. \quad (58.263)$$

RR Cross Sections for Common Normalization Factors of Continuum Radial Functions (Four Choices)

Choice a

$$N = 1; \quad \rho(E) = \frac{(2m/\hbar^2)}{\pi k} = \frac{(2/\pi)}{(ka_0)e^2}, \quad (58.264)$$

$$\sigma_{\text{R}}^{n\ell}(E) = \frac{8\pi^2 a_0^2}{(ka_0)^3} \int \sum_m |D_{fi}|^2 d\hat{\mathbf{k}}_e, \quad (58.265)$$

where D_{fi} of Eq. (58.243) is dimensionless.

Choice b

$$N = k^{-1}; \quad \rho(E) = (2m/\hbar^2)(k/\pi), \quad (58.266)$$

$$\sigma_{\text{R}}^{n\ell}(E) = \frac{16\pi a_0^2}{3\sqrt{2}} \left(\frac{\alpha h\nu}{e^2/a_0} \right)^3 \sqrt{\frac{(e^2/a_0)}{E}} \left(\frac{R_1}{a_0^5} \right), \quad (58.267)$$

where Eqs. (58.255b) and (58.255c) for R_1 have dimension $[L^5]$.

Choice c

$$N = k^{-1/2}; \quad \rho(E) = \frac{(2m/\hbar^2)}{\pi}, \quad (58.268)$$

$$\sigma_{\text{R}}^{n\ell}(E) = \frac{8\pi a_0^2}{3} \left(\frac{\alpha^3 (h\nu)^3}{(e^2/a_0)^2 E} \right) \left(\frac{R_1}{a_0^4} \right), \quad (58.269)$$

where R_1 has dimensions of $[L^4]$.

Choice d

$$N = (2m/\hbar^2 \pi^2 E)^{1/4}; \quad \rho(E) = 1, \quad (58.270)$$

$$\sigma_{\text{R}}^{n\ell}(E) = \frac{4(\pi a_0)^2}{3} \left(\frac{\alpha^3 (h\nu)^3}{(e^2/a_0)^2 E} \right) \left(\frac{R_1}{e^2 a_0} \right), \quad (58.271)$$

where R_1 has dimensions of $[L^2 E^{-1}]$.

58.11.4 Bound–Free Oscillator Strengths

For a transition $n\ell \rightarrow E$ to $E + dE$,

$$\frac{df_{n\ell}}{dE} = \frac{2}{3} \frac{(h\nu)}{(e^2/a_0)} \frac{1}{(2\ell + 1)} \sum_m \sum_{\ell'm'} \left| \mathbf{r}_{n\ell m}^{\ell' m'} \right|^2, \quad (58.272)$$

$$\begin{aligned} R_1(\varepsilon; n\ell) &= \int d\hat{\mathbf{k}}_e \sum_m |\langle \Psi_{n\ell m} | \mathbf{r} | \Psi_i(\mathbf{k}_e) \rangle E|^2 \\ &= \sum_{m, \ell', m'} \left| \mathbf{r}_{n\ell m}^{\ell' m'} \right|^2, \end{aligned} \quad (58.273)$$

$$\sigma_{\text{R}}^{n\ell}(E) = 2\pi^2 \alpha a_0^2 g_{\text{A}} \left(\frac{k_{\text{v}}^2}{k_{\text{e}}^2} \right) \left(\frac{e^2}{a_0} \right) \frac{df_{n\ell}}{dE}, \quad (58.274a)$$

$$\sigma_{\text{I}}^{n\ell}(h\nu) = 2\pi^2 \alpha a_0^2 g_{\text{A}}^+ \left(\frac{e^2}{a_0} \right) \frac{df_{n\ell}}{dE}. \quad (58.274b)$$

Semiclassical Hydrogenic Systems

$$g_{\text{A}} = g_{n\ell} = 2(2\ell + 1), \quad g_{\text{A}}^+ = 1,$$

$$\sigma_{\text{R}}^n(E) = \sum_{\ell=0}^{n-1} \sigma_{\text{R}}^{n\ell}(E) = 2\pi^2 \alpha a_0^2 \left(\frac{k_{\text{v}}^2}{k_{\text{e}}^2} \right) \frac{dF_n}{dE}, \quad (58.275)$$

$$\frac{dF_n}{dE} = \sum_{\ell=0}^{n-1} g_{n\ell} \frac{df_{n\ell}}{dE} = 2 \sum_{\ell, m} \frac{df_{n\ell m}}{dE}. \quad (58.276)$$

Bound–bound absorption oscillator strength

For a transition $n \rightarrow n'$,

$$F_{nn'} = 2 \sum_{\ell m} \sum_{\ell' m'} f_{n\ell m}^{n' \ell' m'} \quad (58.277a)$$

$$= \frac{2^6}{3\sqrt{3}\pi} \left[\left(\frac{1}{n^2} - \frac{1}{n'^2} \right)^{-3} \right] \frac{1}{n^3} \frac{1}{n'^3}, \quad (58.277b)$$

$$\frac{dF_n}{dE} = \frac{2^5}{3\sqrt{3}\pi} n \frac{I_n^2}{(h\nu)^3} = 2n^2 \frac{df_{n\ell}}{dE}, \quad (58.277c)$$

$$\sigma_{\text{R}}^n(E) = \frac{2^5 \alpha^3}{3\sqrt{3}} \left(\frac{n I_n^2}{E(h\nu)} \right) \pi a_0^2, \quad (58.277d)$$

$$\sigma_{\text{I}}^{n\ell}(h\nu) = \frac{2^6 \alpha}{3\sqrt{3}} \frac{n}{Z^2} \left(\frac{I_n}{h\nu} \right)^3 \pi a_0^2, \quad (58.277e)$$

$$= 7.907071 \left(\frac{n}{Z^2} \right) \left(\frac{I_n}{h\nu} \right)^3 \text{ Mb}. \quad (58.277f)$$

This semiclassical analysis yields exactly Kramers PI and associated RR cross sections in Sect. 58.8.2.

58.11.5 Radiative Recombination Rate

$$\hat{\alpha}_{\text{R}}^{n\ell}(T_e) = \bar{v}_e \int_0^{\infty} \varepsilon \sigma_{\text{R}}^{n\ell}(\varepsilon) e^{-\varepsilon} d\varepsilon \quad (58.278a)$$

$$\equiv \bar{v}_e \langle \sigma_{\text{R}}^{n\ell}(T_e) \rangle, \quad (58.278b)$$

where ε is given in Eq. (58.57c), and $\langle \sigma_{\text{R}}^{n\ell}(T_e) \rangle$ is the Maxwellian-averaged cross section for radiative recombination.

In terms of the continuum-bound $A_{n\ell}(E)$,

$$\hat{\alpha}_{\text{R}}^{n\ell}(T_e) = \frac{h^3}{(2\pi m_e k_{\text{B}} T)^{3/2}} \int_0^{\infty} \left(\frac{dA_{n\ell}}{d\varepsilon} \right) e^{-\varepsilon} d\varepsilon, \quad (58.279)$$

$$\frac{dA_{n\ell}}{dE} = \rho(E) \sum_m \int A_{n\ell m}(E, \hat{\mathbf{k}}_e) d\hat{\mathbf{k}}_e. \quad (58.280)$$

Milne Detailed Balance Relation

In terms of $\sigma_I^{n\ell}(h\nu)$,

$$\begin{aligned} \hat{\alpha}_R^{n\ell}(T_e) &= \bar{v}_e \left(\frac{g_A}{2g_A^+} \right) \left(\frac{k_B T_e}{mc^2} \right) \left(\frac{I_n}{k_B T_e} \right)^2 \langle \sigma_I^{n\ell}(T_e) \rangle, \quad (58.281) \end{aligned}$$

where, in reduced units $\omega = h\nu/I_n$, $T = k_B T_e/I_n = b_n^{-1}$, the averaged PI cross section corresponding to Eq. (58.213) is

$$\langle \sigma_I^{n\ell}(T) \rangle = \frac{e^{1/T}}{T} \int_1^\infty \omega^2 \sigma_I^{n\ell}(\omega) e^{-\omega/T} d\omega. \quad (58.282)$$

When $\sigma_I^{n\ell}(\omega)$ is expressed in Mb (10^{-18} cm²),

$$\begin{aligned} \hat{\alpha}_R^{n\ell}(T_e) &= 1.508 \times 10^{-13} \left(\frac{300}{T_e} \right)^{1/2} \left(\frac{I_n}{I_H} \right)^2 \left(\frac{g_A}{2g_A^+} \right) \\ &\times \langle \sigma_I^{n\ell}(T) \rangle \text{ cm}^3 \text{ s}^{-1}. \quad (58.283) \end{aligned}$$

When σ_I can be expressed in terms of the threshold cross section σ_0^n Eq. (58.217) as

$$\sigma_I^{n\ell}(h\nu) = (I_n/h\nu)^p \sigma_0(n); \quad (p = 0, 1, 2, 3), \quad (58.284)$$

then $\langle \sigma_I^{n\ell}(T) \rangle = S_p(T) \sigma_0(n)$, where

$$S_0(T) = 1 + 2T + 2T^2, \quad S_1(T) = 1 + T, \quad (58.285a)$$

$$S_2(T) = 1, \quad (58.285b)$$

$$S_3(T) = (e^{1/T}/T) E_1(1/T) \quad (58.285c)$$

$$\stackrel{T \ll 1}{\approx} 1 - T + 2T^2 - 6T^3. \quad (58.285d)$$

The case $p = 3$ corresponds to Kramers PI cross section Eq. (58.220) so that

$$\kappa \hat{\alpha}_R^{n\ell}(T_e) = \frac{(2\ell + 1)}{n^2} \frac{2}{n} \hat{\alpha}_0(T_e) S_3(T) \quad (58.286a)$$

$$\equiv \kappa \hat{\alpha}_R^{n\ell}(T_e \rightarrow 0) S_3(T), \quad (58.286b)$$

such that $\kappa \hat{\alpha}_R^{n\ell} \approx Z^2/(n^3 T_e^{1/2})$ as $T = (k_B T_e/I_n) \rightarrow 0$.

58.11.6 Gaunt Factor, Cross Sections, and Rates for Hydrogenic Systems

The Gaunt factor $G_{n\ell}$ is the ratio of the quantal to Kramers (K) semiclassical PI cross section such that

$$\begin{aligned} \sigma_I^{n\ell}(h\nu) &= \kappa \sigma_I^n(h\nu) G_{n\ell}(\omega); \\ \omega &= h\nu/I_n = 1 + E/I_n. \quad (58.287) \end{aligned}$$

(a) Radiative Recombination Cross Section

$$\sigma_R^{n\ell}(E) = \left(\frac{g_A}{g_A^+} \right) \left(\frac{\alpha^2 (h\nu)^2}{2E(e^2/a_0)} \right) G_{n\ell}(\omega) \kappa \sigma_I^n(h\nu) \quad (58.288a)$$

$$= G_{n\ell}(\omega) \kappa \sigma_R^{n\ell}(E) \quad (58.288b)$$

$$= \left[\frac{(2\ell + 1)}{n^2} G_{n\ell}(\omega) \right]_{\text{K}} \sigma_R^n(E), \quad (58.288c)$$

$$\sigma_R^n(E) = G_n(\omega) \kappa \sigma_R^n(E), \quad (58.288d)$$

where the quantum mechanical correction, or Gaunt factor, to the semiclassical cross sections

$$G_{n\ell}(\omega) \rightarrow \begin{cases} 1, & \omega \rightarrow 1 \\ \omega^{-(\ell+1/2)}, & \omega \rightarrow \infty \end{cases} \quad (58.289)$$

favors low $n\ell$ -states. The ℓ -averaged Gaunt factor is

$$G_n(\omega) = (1/n^2) \sum_{\ell=0}^{n-1} (2\ell + 1) G_{n\ell}(\omega). \quad (58.290)$$

Approximations for G_n : as ε increases from zero,

$$G_n(\varepsilon) = \left[1 + \frac{4}{3}(a_n + b_n) + \frac{28}{18} a_n^2 \right]^{-3/4} \quad (58.291a)$$

$$\simeq 1 - (a_n + b_n) + \frac{7}{3} a_n b_n + \frac{7}{6} b_n^2 \quad (58.291b)$$

where $E = \varepsilon(Z^2 e^2/2a_0)$, $\omega = 1 + n^2 \varepsilon$, and

$$a_n(\varepsilon) = 0.172825(1 - n^2 \varepsilon) c_n(\varepsilon), \quad (58.292a)$$

$$b_n(\varepsilon) = 0.04959 \left(1 + \frac{4}{3} n^2 \varepsilon + n^4 \varepsilon^2 \right) c_n^2(\varepsilon), \quad (58.292b)$$

$$c_n(\varepsilon) = n^{-2/3} (1 + n^2 \varepsilon)^{-2/3}. \quad (58.292c)$$

Radiative Recombination Rate

$$\hat{\alpha}_R^{n\ell}(T_e) = \kappa \hat{\alpha}_R^{n\ell}(T_e \rightarrow 0) F_{n\ell}(T), \quad (58.293)$$

$$\hat{\alpha}_R^{n\ell}(T_e \rightarrow 0) = \frac{(2\ell + 1)}{n^2} \left(\frac{2}{n} \right) \hat{\alpha}_0(T_e), \quad (58.294)$$

in accordance with Eq. (58.224b).

$$F_{n\ell}(T) = \frac{e^{1/T}}{T} \int_1^\infty \frac{G_{n\ell}(\omega)}{\omega} e^{-\omega/T} d\omega. \quad (58.295)$$

The multiplicative factors F and G convert the semiclassical (Kramers) $T_e \rightarrow 0$ rate and cross section to their quantal values. Departures from the scaling rule ($Z^2/n^3 T_e^{1/2}$) for RR rates is measured by $F_{n\ell}(T)$.

58.11.7 Exact Universal Rate Scaling Law and Results for Hydrogenic Systems

$$\hat{\alpha}_R^{n\ell}(Z, T_e) = Z \hat{\alpha}_R^{n\ell}(1, T_e/Z^2) \quad (58.296)$$

as exhibited by Eq. (58.281) with Eqs. (58.277e) and (58.282).

Recombination rates are greatest into low n levels and the $\omega^{-\ell-1/2}$ variation of $G_{n\ell}$ preferentially populates states with low $\ell \approx 2-5$. Highly accurate analytical fits for $G_{n\ell}(\omega)$ have been obtained for $n \leq 20$ so that Eq. (58.287) can be expressed in terms of known functions of fit parameters [58]. This procedure (which does not violate the S_2 sum rule) has been extended to nonhydrogenic systems of neon-like Fe XVII, where $\sigma_I^{n\ell}(\omega)$ is a monotonically decreasing function of ω .

The variation of the ℓ -averaged values

$$n^{-2} \sum_{\ell=0}^{n-1} (2\ell+1) F_{n\ell}(T)$$

is close in both shape and magnitude to the corresponding semiclassical function $S_3(T)$, given by Eq. (58.295) with $G_{n\ell}(\omega) = 1$. Hence the ℓ -averaged recombination rate is

$$\hat{\alpha}_R^n(Z, T) = (300/T)^{1/2} (Z^2/n) F_n(T), \\ \times 1.1932 \times 10^{-12} \text{ cm}^3 \text{ s}^{-1},$$

where F_n can be calculated directly from Eq. (58.295) or be approximated as $G_n(1)S(T)$. A computer program based on a three-term expansion of G_n is also available [59]. From a three-term expansion for G , the rate of radiative recombination into all levels of a hydrogenic system is

$$\hat{\alpha}(Z, T) = 5.2 \times 10^{-14} Z \lambda^{1/2} \\ \times \left(0.43 + \frac{1}{2} \ln \lambda + 0.47/\lambda^{1/2} \right), \quad (58.297)$$

where $\lambda = 1.58 \times 10^5 Z^2/T$ and $[\hat{\alpha}] = \text{cm}^3/\text{s}$. Tables [60] exist for the effective rate

$$\hat{\alpha}_E^{n\ell}(T) = \sum_{n'=n}^{\infty} \sum_{\ell'=0}^{n'-1} \hat{\alpha}_R^{n'\ell'} C_{n'\ell', n\ell} \quad (58.298)$$

of populating a given level $n\ell$ of H via radiative recombination into all levels $n' \geq n$ with subsequent radiative cascade ($i \rightarrow f$) with probability $C_{i,f}$ via all possible intermediate paths. Tables [60] also exist for the full rate

$$\hat{\alpha}_F^N(T) = \sum_{n=N}^{\infty} \sum_{\ell=0}^{n-1} \hat{\alpha}_R^{n\ell} \quad (58.299)$$

of recombination, into all levels above $N = 1, 2, 3, 4$ of hydrogen. They are useful in deducing time scales of radiative recombination and rates for complex ions.

58.12 Useful Quantities

(a) Mean speed

$$\bar{v}_e = \left(\frac{8k_B T}{\pi m_e} \right)^{1/2} = 1.076042 \times 10^7 \left(\frac{T}{300} \right)^{1/2} \text{ cm/s} \\ = 6.69238 \times 10^7 T_{\text{eV}}^{1/2} \text{ cm/s}, \\ \bar{v}_i = 2.51116 \times 10^5 \left(\frac{T}{300} \right)^{1/2} (m_p/m_i)^{1/2} \text{ cm/s},$$

where $(m_p/m_e)^{1/2} = 42.850352$, and $T = 11604.45 T_{\text{eV}}$ relates the temperature in K and in eV.

(b) Natural radius

$$|V(R_e)| = e^2/R_e = k_B T. \\ R_e = \frac{e^2}{k_B T} = 557 \left(\frac{300}{T} \right) \text{ \AA} = \left(\frac{14.4}{T_{\text{eV}}} \right) \text{ \AA}.$$

(c) Boltzmann average momentum

$$\langle p \rangle = \int_{-\infty}^{\infty} e^{-p^2/2mk_B T} dp = (2\pi m_e k_B T)^{1/2}.$$

(d) De Broglie wavelength

$$\lambda_{\text{dB}} = \frac{h}{\langle p \rangle} = \frac{h}{(2\pi m_e k_B T)^{1/2}} \\ = \frac{7.453818 \times 10^{-6} \text{ cm}}{T_e^{1/2}} \\ = 43.035 \left(\frac{300}{T_e} \right)^{1/2} \text{ \AA} = \frac{6.9194}{T_{\text{eV}}^{1/2}} \text{ \AA}.$$

References

1. Fendt, A.: *Astrophys. J. Supp. Ser.* **181**, 627 (2009)
2. Bernstein, J.: *Kinetic theory in the expanding universe*. Cambridge Univ. Press, Cambridge (1988). Chap. 8
3. Forrey, R.C.: *Phys. Rev. A* **88**, 052709 (2013)
4. Gordon, M.A., Sorochenko, R.L.: *Radio Recombination Lines. 25 Years of Investigation*. Kluwer, New York (1990)
5. Gordon, M.A., Sorochenko, R.L.: *Radio Recombination Lines: Their Physics and Astronomical Applications*. Kluwer, New York (2002)
6. Landsberg, P.T.: *Recombination in Semiconductors*. Cambridge Univ. Press, Cambridge (1991)
7. Lakhwani, G., Rao, A., Friend, R.H.: *Ann. Rev. Phys. Chem.* **65**, 557–581 (2014)
8. Del Zanna, G., Mason, H.E.: *Liv. Rev. Solar Phys.* **15**, 1–278 (2018)
9. Badnell, N.R., Del Zanna, G., Fernández-Menchero, L., Giunta, A.S., Liang, G.Y., Mason, H.E., Storey, P.J.: *J. Phys. B. At. Mol. Opt. Phys.* **49**, 094001 (2016)

10. Adamovich, et al.: *J. Phys. D* **50**, 323001 (2017)
11. Schinke, R., Grebenshchikov, S.Y., Ivanov, M.V., Fleurat-Lessard, P.: *Ann. Rev. Phys. Chem.* **57**, 625–661 (2006)
12. Burt, E.A., Ghrist, R.W., Myatt, C.J., Holland, M.J., Cornell, E.A., Wieman, C.E.: *Phys. Rev. Lett.* **79**, 337 (1997)
13. Nielsen, E., Macek, J.H.: *Phys. Rev. Lett.* **83**, 1566 (1999)
14. Ticknor, C., Rittenhouse, S.T.: *Phys. Rev. Lett.* **105**, 013201 (2010)
15. Truhlar, D.G., Wyatt, R.E.: *Ann. Rev. Phys. Chem.* **27**(1), 1–43 (1976)
16. Baer, M.: *Theory of Chemical Reaction Dynamics* vol. 1-4. CRC Press, Boca Raton, FL (1985)
17. Levine, R.D., Bernstein, R.B.: *Molecular Reaction Dynamics and Chemical Reactivity*. Oxford, New York (1987)
18. Butler, L.J.: *Ann. Rev. Phys. Chem.* **49**, 125–171 (1998)
19. Greene, S.M., Shan, X., Clary, D.C.: *Adv. Chem. Phys.* **163**, 117–149 (2018)
20. Greene, C.H., Giannakeas, P., Perez-Rios, J.: *Rev. Mod. Phys.* **89**, 035006 (2017)
21. Marcassa, L.G., Shaffer, J.P.: *Adv. At. Mol. Opt. Phys.* **63**, 47–133 (2014)
22. Scholes, G.D.: *Ann. Rev. Phys. Chem.* **54**, 57–87 (2003)
23. Flannery, M.R., Vrinceanu, D.: In: Oks, E., Pindzola, M.S. (eds.) *Atomic Processes in Plasmas*, pp. 317–333. American Institute of Physics, New York (1998)
24. Petrov, D.S., Werner, F.: *Phys. Rev. A* **92**, 022704 (2015)
25. Naidon, P., Endo, S.: *Rep. Prog. Phys.* **80**, 056001 (2017)
26. Braaten, E., Hammer, H.-W.: *Phys. Rep.* **428**, 259–390 (2006)
27. Mehta, N.P., Rittenhouse, S.T., D’Incao, J.P., von Stecher, J., Greene, C.H.: *Phys. Rev. Lett.* **103**, 153201 (2009)
28. Ferlaino, F., Knoop, S., Berninger, M., Harm, W., D’Incao, J.P., Nägerl, H.-C., Grimm, R.: *Phys. Rev. Lett.* **102**, 140401 (2009)
29. Ralchenko, Y.: *Modern Methods in Collisional-Radiative Modeling of Plasmas*. Springer, New York (2016)
30. Stevefelt, J., Boulmer, J., Delpech, J.-F.: *Phys. Rev. A* **12**, 1246 (1975)
31. Deloche, R., Monchicourt, P., Cheret, M., Lambert, F.: *Phys. Rev. A* **13**, 1140 (1976)
32. Mansbach, P., Keck, J.: *Phys. Rev.* **181**, 275 (1965)
33. Pitaevskii, L.P.: *Sov. Phys. JETP* **15**, 919 (1962)
34. Kramers, H.A.: *Philos. Mag.* **46**, 836 (1923)
35. Braaten, E., Kusunoki, M., Zhang, D.: *Ann. Phys.* **323**, 1770–1815 (2008)
36. Salomon, C., Shlyapnikov, G.V., Cugliandolo, L.F.: *Many-Body Physics with Ultracold Gases*. Oxford Univ. Press, Oxford (2013). Chap. 3
37. Bedaque, P.F., Braaten, E., Hammer, H.-W.: *Phys. Rev. Lett.* **85**, 908 (2000)
38. Braaten, E., Hammer, H.-W.: *Phys. Rev. A* **67**, 042706 (2003)
39. Efimov, V.: *Phys. Lett.* **33B**, 563 (1970)
40. Efimov, V.: *Sov. J. Nucl. Phys.* **12**, 589 (1971)
41. Braaten, E., Hammer, H.-W.: *Ann. Phys.* **322**, 120–163 (2007)
42. Avery, J.: *Hyperspherical Harmonics: Applications in Quantum Theory*. Kluwer, Norwell (1989)
43. Bhardwaj, S., Son, S.-K., Hong, K.-H., Lai, C.-J., Kärtner, F., Santra, R.: *Phys. Rev. A* **88**, 053405 (2013)
44. Bates, D.R.: *Phys. Rev.* **78**, 492 (1950)
45. Bardsley, J.N.: *J. Phys. A Proc. Phys. Soc.* **1**, 365 (1968)
46. Flannery, M.R.: In: Schultz, D.R., Strayer, M.R., Macek, J.H. (eds.) *Atomic Collisions: A Symposium in Honor of Christopher Bottcher*, pp. 53–75. American Institute of Physics, New York (1995)
47. Giusti, A.: *J. Phys. B* **13**, 3867 (1980)
48. van der Donk, P., Yousif, F.B., Mitchell, J.B.A., Hickman, A.P.: *Phys. Rev. Lett.* **68**, 2252 (1992)
49. Guberman, S.L.: *Phys. Rev. A* **49**, R4277 (1994)
50. Flannery, M.R.: *Int. J. Mass. Spectrom. Ion. Process.* **149/150**, 597 (1995)
51. Tashiro, M., Kato, S.: In: Guberman, S.L. (ed.) *Dissociative Recombination of Molecular Ions with Electrons*, pp. 243–248. Kluwer, Norwell (2003)
52. Florescu-Mitchell, A.I., Mitchell, J.B.A.: *Phys. Rep.* **430**, 277–374 (2006)
53. Johnsen, R., Guberman, S.L.: *Adv. At. Mol. Opt. Phys.* **59**, 76–128 (2010)
54. Flannery, M.R.: *J. Chem. Phys.* **95**, 8205 (1991)
55. Burgess, A.: *Mon. Not. R. Astron. Soc.* **118**, 477 (1958)
56. Gaunt, J.A.: *Philos. Trans. R. Soc. A* **229**, 163 (1930)
57. Seaton, M.J.: *Mon. Not. R. Astron. Soc.* **119**, 81 (1959)
58. Rozsnyai, B.F., Jacobs, V.L.: *Astrophys. J.* **327**, 485 (1988)
59. Flower, D.R., Seaton, M.J.: *Comp. Phys. Commun.* **1**, 31 (1969)
60. Martin, P.G.: *Astrophys. J. Supp. Ser.* **66**, 125 (1988)
61. Fontes, C.J., Zhang, H.L., Abdallah Jr, J., Clark, R.E.H., Kilcrease, D.P., Colgan, J., Cunningham, R.T., Hakel, P., Magee, N.H., Sherrill, M.E.: *J. Phys. B. At. Mol. Opt. Phys.* **48**, 144014 (2015)



Edmund J. Mansky II Edmund J. Mansky II received his PhD from Georgia Institute of Technology in 1985. His theoretical work involves statistical mechanics of dense gases. In addition, his interests are three-body recombination processes and collisions involving Rydberg states of atoms and molecules at thermal and ultracold temperatures. His day job is programming heliophysics data for the scientific community.



Michael Pindzola, Nigel Badnell, and Donald Griffin

Contents

59.1	Introduction	875
59.2	Theoretical Formulation	876
59.3	Comparisons with Experiment	877
59.3.1	Low-Z Ions	877
59.3.2	High-Z Ions and Relativistic Effects	878
59.4	Radiative-Dielectronic Recombination Interference	878
59.5	Dielectronic Recombination in Plasmas	879
	References	879

Abstract

Dielectronic recombination (DR) is a two-step process that greatly increases the efficiency for electrons and ions to recombine in a plasma. The process, therefore, plays an important role in the theoretical modeling of plasmas, whether in the laboratory or in astrophysical sources such as the solar corona. The purpose of this chapter is to present the theoretical formulation for DR and the principal methods for calculating rate coefficients. The results are compared with experiment over a broad range of low- Z ions and high- Z ions where relativistic effects become important.

Keywords

dielectronic recombination · plasmas · Rydberg series · distorted-wave approximation · autoionization rate

M. Pindzola (✉)
College of Sciences and Mathematics, Auburn University
Auburn, AL, USA
e-mail: pindzola@physics.auburn.edu

N. Badnell (✉)
Dept. of Physics, University of Strathclyde Glasgow
Glasgow, UK
e-mail: badnell@phys.strath.ac.uk

D. Griffin
Dept. of Physics, Rollins College
Winter Park, USA

59.1 Introduction

Electron-ion recombination into a particular final recombined state may be schematically represented as

$$e^- + A_i^{q+} \rightarrow A_f^{(q-1)+} + \hbar\omega, \quad (59.1)$$

and

$$e^- + A_i^{q+} \rightarrow [A_j^{(q-1)+}] \rightarrow A_f^{(q-1)+} + \hbar\omega, \quad (59.2)$$

where q is the charge on the atomic ion A , ω is the frequency of the emitted light, and the brackets in Eq. (59.2) indicate a doubly excited resonance state. The first process is called radiative recombination (RR), while the second is called dielectronic recombination (DR). Both recombination mechanisms are the inverse of photoionization. At sufficiently high electron density, three-body recombination becomes possible. The three-body mechanism is the inverse of electron impact ionization.

The review article by *Seaton and Storey* [1] includes an interesting history of the theoretical work on dielectronic recombination. The process was first referred to as dielectronic recombination by *Massey and Bates* [2], after a suggestion of its possible importance in the ionosphere by *Sayers* in 1939. However, estimates of the rate coefficient for this process indicated that DR is not an important process in the ionosphere, where the temperatures are too low to excite anything but the lower energy resonance states.

In 1961, *Unsold*, in a letter to *Seaton*, suggested that DR might account for a well-known temperature discrepancy in the solar corona. *Seaton* initially concluded that DR would not significantly increase recombination in the solar corona. However, he had only included the lower energy resonance states in his analysis; *Burgess* [3] showed that when one includes the higher members of the Rydberg series of resonance states that are populated at coronal temperatures, DR can indeed explain this discrepancy.

Dielectronic recombination has since received much theoretical attention due, in part, to its importance in modeling

high-temperature plasmas. Various approaches to the theory are discussed in a review by *Hahn* [4] and in [5]. Recently, there have been various projects aimed at the generation of large quantities of DR data for use in astrophysical and fusion plasma modeling. One such project is based on the results of the AUTOSTRUCTURE code, with both the total and partial (i.e., resolved by recombined level) DR rate coefficients being archived. The methodology is outlined in *Badnell et al.* [6]. Data are calculated for all members of an isoelectronic sequence from H to Ar, along with various ions relevant to astrophysics or fusion, namely Ca, Ti, Cr, Fe, Ni, Zn, Kr, Mo, and Xe. Work has been completed for the hydrogen [7], helium [8], lithium [9], beryllium [10], boron [11], carbon [12], nitrogen [13], oxygen [14], fluorine [15], neon [16], sodium [17], magnesium [18], aluminum [19], and argon [20] isonuclear sequences. There has also been a large quantity of data generated using a fully relativistic Dirac–Fock code [21]. These data include calculations of Na-like ions [22] and H-like through to Ne-like [23] ions of certain astrophysically important elements.

Interest in dielectronic recombination has increased dramatically in the last 20 years. *Mitchell et al.* [24] published the DR cross section for C⁺ using a merged electron–ion beams apparatus, and *Belic et al.* [25] reported on a crossed beams measurement of the DR cross section for Mg⁺. Also, *Dittner et al.* [26] published merged beams measurements of the DR cross section for the multiply charged ions B²⁺ and C³⁺. Since that time, atomic physics experiments carried out using heavy-ion traps, accelerators, and storage-cooler rings have produced high-resolution mappings of the resonance structures associated with electron–ion recombination. The experiments have been carried out using a wide range of facilities and technologies, such as the test storage ring (TSR) at Heidelberg, the experimental storage ring (ESR) at Darmstadt, the accelerator-cooler ring facility at Aarhus, the electron beam ion trap (EBIT) at Livermore, and the electron beam ion source (EBIS) at Kansas State. A good review of the dramatic experimental progress in DR measurements is again found in the NATO proceedings [5].

59.2 Theoretical Formulation

In the independent-processes approximation, the two paths for recombination are summed incoherently. The radiative recombination cross section for Eq. (59.1), in lowest-order of perturbation theory, is given by

$$\sigma_{\text{RR}} = \frac{8\pi^2}{k^3} \times \sum_{\ell_j} \sum_{JM} \sum_{M_0} \frac{1}{2g_1} \left| \langle \alpha_0 J_0 M_0 | D | \alpha_1 J_1 \ell_j J M \rangle \right|^2. \quad (59.3)$$

The set $(\alpha_1 J_1)$ represents the quantum numbers for the N -electron target ion state, $(\alpha_0 J_0 M_0)$ represents the quantum numbers for the $(N+1)$ -electron recombined ion state, $(k \ell_j)$ represents the quantum numbers for the continuum electron state, (JM) represents the quantum numbers for the $(N+1)$ -electron system of target plus free electron state, and g_1 is the statistical weight of a J_1 level. The dipole radiation field operator is given by

$$D = \sqrt{\frac{2\omega^3}{3\pi c^3}} \sum_{s=1}^{N+1} \mathbf{r}_s. \quad (59.4)$$

Continuum normalization is chosen as one times a sine function, and atomic units ($e = \hbar = m = 1$) are used. In the isolated-resonance approximation, the dielectronic recombination cross section for Eq. (59.2), in lowest-order perturbation theory, is given by

$$\sigma_{\text{DR}} = \frac{8\pi^2}{k^3} \sum_{\ell_j} \sum_{JM} \sum_{M_0} \frac{1}{2g_1} \times \sum_{\alpha_i J_i M_i} \left| \frac{\langle \alpha_0 J_0 M_0 | D | \alpha_i J_i M_i \rangle \langle \alpha_i J_i M_i | V | \alpha_1 J_1 \ell_j J M \rangle}{E_0 - E_i + i\Gamma_i/2} \right|^2, \quad (59.5)$$

where the set $(\alpha_i J_i M_i)$ represents the quantum numbers for a resonance state with energy E_i and total width Γ_i , and the electrostatic interaction between electrons is given by

$$V = \sum_{s=1}^N |\mathbf{r}_s - \mathbf{r}_{N+1}|^{-1}. \quad (59.6)$$

By the principle of detailed balance, σ_{RR} of Eq. (59.3) is proportional to the photoionization cross section from the bound state, while the energy-averaged σ_{DR} may be written as

$$\langle \sigma_{\text{DR}} \rangle = \frac{2\pi^2}{\Delta\epsilon k^2} \sum_{\alpha_i J_i M_i} \frac{1}{2g_1} \frac{A_a A_r}{\Gamma_i}, \quad (59.7)$$

where the autoionization decay rate A_a is given by

$$A_a = \frac{4}{k} \sum_{\ell_j} \sum_{JM} |\langle \alpha_1 J_1 \ell_j J M | V | \alpha_i J_i M_i \rangle|^2, \quad (59.8)$$

the radiative decay rate A_r is given by

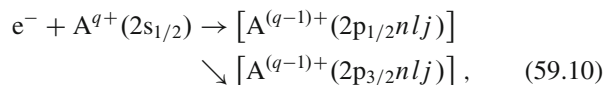
$$A_r = 2\pi \sum_{M_0} |\langle \alpha_0 J_0 M_0 | D | \alpha_i J_i M_i \rangle|^2, \quad (59.9)$$

and $\Delta\epsilon$ is the energy bin width. Each resonance level in Eq. (59.7) makes a contribution at a fixed continuum energy $k^2/2$; thus $\langle \sigma_{\text{DR}} \rangle$ plotted as a function of energy is a histogram.

59.3 Comparisons with Experiment

59.3.1 Low-Z Ions

For the most part, the agreement between the recent high-resolution measurements and theoretical calculations based on the independent-processes and isolated-resonance (IPIR) approximations is quite good [27–45]. We illustrate the agreement with experiment obtained by calculations employing the IPIR approximations with three examples from the Li isoelectronic sequence. The pathways for dielectronic capture, in terms of specific levels, are given by



where a $1s^2$ core is assumed to be present. Both Rydberg series autoionize by the reverse of the paths in Eq. (59.10), while for sufficiently high n , the $2p_{3/2}nlj$ levels may autoionize to the $2p_{1/2}$ continuum. Both series radiatively stabilize by either a $2p \rightarrow 2s$ core orbital transition or by a $nlj \rightarrow n'l'j'$ valence orbital transition, where $2p_j n'l'j'$ with $j = (1/2), (3/2)$ is a bound level.

Dielectronic recombination cross section calculations [35] in the IPIR approximation for O^{5+} are compared with experiment in Fig. 59.1. Fine-structure splitting of the two series of Eq. (59.10) is minimal for this light ion, so there appears only one Rydberg series. The $2p\ 6\ell$ resonances are located at 2.5 eV, the $2p\ 7\ell$ at 5.0 eV, and so on, accumulating at the series limit around 11.3 eV. Electric field effects on the high- n resonances are strong in O^{5+} , so that calculations were done for fields of 0, 3, 5, and 7 V/cm. Since the precise electric

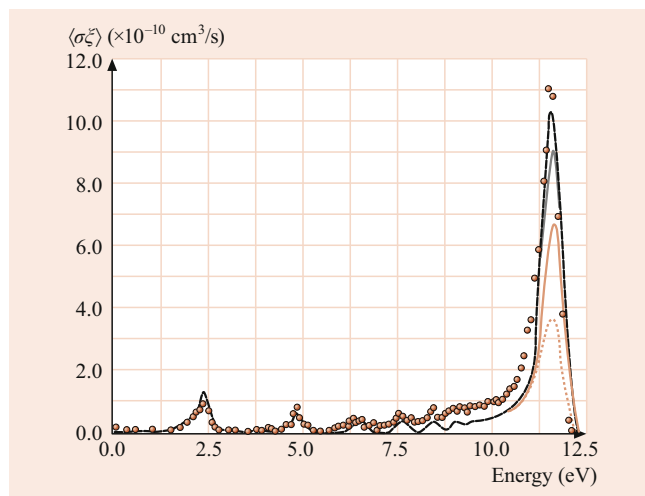


Fig. 59.1 Dielectronic recombination for O^{5+} . Calculations were performed for fields of 0 V/cm (dotted curve), 3 V/cm (dashed curve), 5 V/cm (chain curve), and 7 V/cm (solid curve)

field strength in the experiment is not known, the accuracy of an electric field-dependent theory, in this case, has yet to be determined. However, the effects of state mixing by extrinsic fields in the collision region for the dielectronic recombination of Mg^+ have been investigated both experimentally [46] and theoretically [47].

There have been a significant number of recent experiments on low- Z ions. These experiments, in general, show good agreement with theory, see *Fogle et al.* [44] and *Schnell et al.* [45]. However, it is also clear that discrepancies remain between theory and experiment for certain low-energy resonances, due to the difficulty in calculating the energy positions of such resonances. As has been pointed out in *Savin et al.* [48] and *Schippers et al.* [49], this can lead to significant uncertainties in low-temperature DR rate coefficients. Calculating such low-energy resonances to sufficient accuracy for low-temperature DR rate coefficients remains a significant challenge for theory. Some success in this area has been achieved using relativistic many-body perturbation theory, obtaining very good agreement with low-energy resonance positions for a range of systems, see, for example, *Lindroth et al.* [50], *Fogle et al.* [51], and *Tokman et al.* [52].

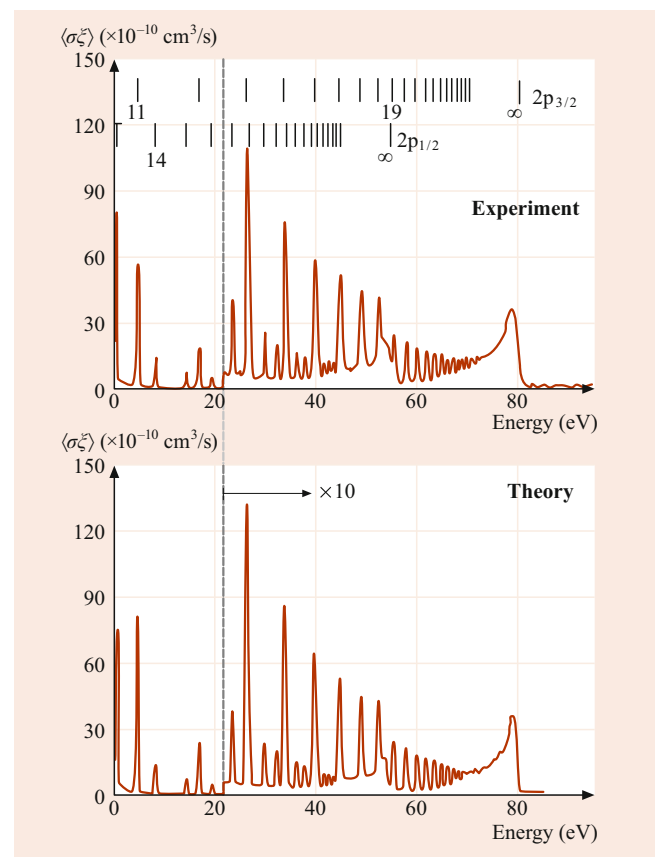


Fig. 59.2 Dielectronic recombination for Cu^{26+}

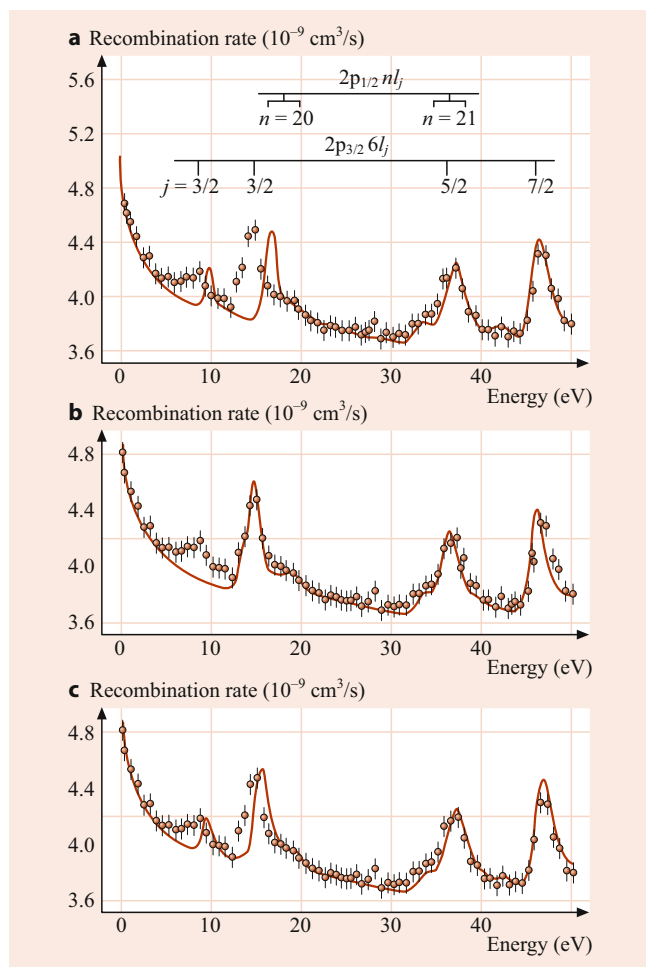


Fig. 59.3 Dielectronic recombination for Au^{76+} . The curves show (a) perturbative relativistic, (b) semirelativistic, and (c) fully relativistic calculations for the dielectronic recombination cross section

59.3.2 High- Z Ions and Relativistic Effects

Dielectronic recombination cross section calculations [38] in the IPIR approximation for Cu^{26+} are compared with experiment in Fig. 59.2. The two fine-structure Rydberg series are now clearly resolved; the fine-structure splitting is about 27 eV for Cu^{26+} . The $2p_{1/2} 13\ell$ resonances are just above threshold, while the $2p_{3/2} 11\ell$ resonances are found around 5.0 eV. Electric fields in the range 0–50 V/cm have little effect on the Cu^{26+} spectrum. Overall, the agreement between theory and experiment is excellent.

Electron–ion recombination cross section calculations [39] in the IPIR approximation for low-lying resonances in Au^{76+} are compared with experiment in Fig. 59.3. The $2p_{1/2} nlj$ series limit is at 217 eV, while the $2p_{3/2} nlj$ series limit is at 2.24 keV, yielding a fine structure splitting of 2.03 keV. QED effects alone shift the $2p_{3/2} nlj$ series limit by 22.0 eV. Thus, accurate atomic structure calculations must be made to locate the $2p_{3/2} 6lj$ resonances in the 0–50 eV

energy range of the experiment. Figure 59.3 shows that the perturbative relativistic, semirelativistic, and fully relativistic calculations for the dielectronic recombination cross section ride on top of a strong radiative recombination background. In principle, the fully relativistic theory contains the most physics, and thus it is comforting that on the whole it is in good agreement with the experiment. It is instructive, however, to see how well the computationally simpler perturbative relativistic and semirelativistic theories do for such a highly charged ion.

There have been several recent experimental measurements on high- Z ions, in particular, for astrophysically abundant species. In general, there is good agreement between theory and experiment. Examples of high- Z element DR studies include those done on Fe^{21+} and Fe^{22+} by Savin et al. [48], and on Fe^{20+} by Savin et al. [53]. There have also been recent comparisons between experiment and theory for heavy metal ions, for example W^{18+} [54], W^{19+} [55], W^{20+} [56–59], and Au^{20+} [60, 61]. Many calculations of electron–ion recombination rate coefficients and photoionization cross sections for astrophysically important species, and especially in connection with the iron project, have been carried out by Nahar et al. For recent work, see [62, 63].

59.4 Radiative–Dielectronic Recombination Interference

There has been a great deal of effort in recent years to develop a more general theory of electron–ion recombination that would go beyond the IPIR approximation to include radiative–dielectronic recombination interference and overlapping (and interacting) resonance structures [64–71]. In almost all cases, the interference between a dielectronic recombination resonance and the radiative recombination background is quite small and difficult to observe. The best possibility for observation of RR–DR interference appears to be in highly charged atomic ions. In the cases studied to date, the combination of electron and photon continuum coupling selection rules and the requirement of near energy degeneracy make the overlapping (and interacting) resonance effects small and difficult to observe. Heavy ions in relatively low stages of ionization are the best place to look, since there are resonance series attached to the large numbers of LS terms or fine structure levels.

The distorted-wave approximation (Chap. 56) has been so successful in describing dielectronic recombination cross sections for most atomic ions because, for low charged ions, the DR cross section is proportional to the radiative rate, while for highly charged ions the DR cross section is proportional to the autoionization rate. Thus, the weakness of the distorted-wave method in calculating accurate autoionization rates for low charged ions is masked by a DR cross section

that is highly dependent on radiative atomic structure. As one moves to more highly charged ions, the DR cross section becomes more sensitive to the autoionization rates, but at the same time, the distorted-wave method becomes increasingly more accurate.

59.5 Dielectronic Recombination in Plasmas

Dielectronic recombination is an important atomic process that is included in the theoretical modeling of the ionization state and emission of radiating ions, which is fundamental to the interpretation of spectral emission from both fusion and astrophysical plasmas (Chap. 86). The dielectronic recombination rate coefficient, into a particular final recombined state, is given by

$$\alpha_{\text{DR}} = \sqrt{\frac{2}{\pi T^3}} k^2 \Delta \epsilon \langle \sigma_{\text{DR}}(i \rightarrow f) \rangle \exp\left(\frac{-k^2}{2T}\right), \quad (59.11)$$

where T is the electron temperature. Dielectronic recombination rate coefficients, from the ground and metastable states of a target ion into fully resolved low-lying states and bundled high-lying states of a recombined ion, are required for a generalized collisional radiative treatment [72, 73] of highly populated metastable states, the influence of finite plasma density on excited state populations, and of ionization in dynamic plasmas. We also note that contributions to recombination in plasmas may come from high Rydberg states just below the ionization threshold [74, 75].

References

- Seaton, M.J., Storey, P.J.: In: Burke, P.G., Moiseiwitsch, B.L. (eds.) *Atomic Processes and Applications*, p. 133. North-Holland, Amsterdam (1976)
- Massey, H.S.W., Bates, D.R.: *Rep. Prog. Phys.* **9**, 62 (1942)
- Burgess, A.: *Astrophys. J.* **139**, 776 (1964)
- Hahn, Y.: *Adv. At. Mol. Phys.* **21**, 123 (1985)
- Graham, W.G., Fritsch, W., Hahn, Y., Tanis, J.A. (eds.): *New York. Recombination of Atomic Ions*, NATO ASI Ser. B, vol. 296. Plenum, New York (1992)
- Badnell, N.R., O'Mullane, M.G., Summers, H.P., Altun, Z., Bautista, M.A., Colgan, J., Gorczyca, T.W., Mitnik, D.M., Pindzola, M.S., Zatsarinny, O.: *Astron. Astrophys.* **406**, 1151 (2003)
- Zatsarinny, O., Gorczyca, T.W., Korista, K.T., Badnell, N.R., Savin, D.W.: *Astron. Astrophys.* **412**, 587 (2003)
- Colgan, J., Pindzola, M.S., Whiteford, A.D., Badnell, N.R.: *Astron. Astrophys.* **412**, 597 (2003)
- Zatsarinny, O., Gorczyca, T.W., Korista, K.T., Badnell, N.R., Savin, D.W.: *Astron. Astrophys.* **417**, 1173 (2003)
- Colgan, J., Pindzola, M.S., Badnell, N.R.: *Astron. Astrophys.* **417**, 1188 (2004)
- Altun, Z., Yumak, A., Badnell, N.R., Colgan, J., Pindzola, M.S.: *Astron. Astrophys.* **420**, 775 (2004)
- Zatsarinny, O., Gorczyca, T.W., Korista, K.T., Badnell, N.R., Savin, D.W.: *Astron. Astrophys.* **426**, 699 (2004)
- Mitnik, D.M., Badnell, N.R.: *Astron. Astrophys.* **425**, 1153 (2004)
- Zatsarinny, O., Gorczyca, T.W., Korista, K.T., Badnell, N.R., Savin, D.W.: *Astron. Astrophys.* **412**, 587 (2003)
- Zatsarinny, O., Gorczyca, T.W., Fu, J., Korista, K.T., Badnell, N.R., Savin, D.W.: *Astron. Astrophys.* **447**, 379 (2006)
- Zatsarinny, O., Gorczyca, T.W., Korista, K.T., Badnell, N.R., Savin, D.W.: *Astron. Astrophys.* **426**, 699 (2004)
- Altun, Z., Yumak, A., Badnell, N.R., Loch, S.D., Pindzola, M.S.: *Astron. Astrophys.* **447**, 1165 (2006)
- Altun, Z., Yumak, A., Yavuz, I., Badnell, N.R., Loch, S.D., Pindzola, M.S.: *Astron. Astrophys.* **474**, 1051 (2007)
- Abdel-Naby, S.A., Nikolic, D., Gorczyca, T.W., Korista, K.T., Badnell, N.R.: *Astron. Astrophys.* **537**, A40 (2012)
- Nikolic, D., Gorczyca, T.W., Korista, K.T., Badnell, N.R.: *Astron. Astrophys.* **516**, A97 (2010)
- Gu, M.F.: *Astrophys. J.* **582**, 1241 (2003)
- Gu, M.F.: *Astrophys. J.* **153**, 389 (2004)
- Gu, M.F.: *Astrophys. J.* **590**, 1131 (2003)
- Mitchell, J.B.A., Ng, C.T., Forand, J.L., Levac, D.P., Mitchell, R.E., Sen, A., Miko, D.B.: *J. Wm. McGowan: Phys. Rev. Lett.* **50**, 335 (1983)
- Belic, D.S., Dunn, G.H., Morgan, T.J., Mueller, D.W., Timmer, C.: *Phys. Rev. Lett.* **50**, 339 (1983)
- Dittner, P.F., Datz, S., Miller, P.D., Moak, C.D., Stelson, P.H., Bottcher, C., Dress, W.B., Alton, G.D., Neskovic, N.: *Phys. Rev. Lett.* **51**, 31 (1983)
- Kilgus, G., Berger, J., Blatt, P., Grieser, M., Habs, D., Hochadel, B., Jaeschke, E., Kramer, D., Neumann, R., Neureither, G., Ott, W., Schwalm, D., Steck, M., Stokstad, R., Szmola, E., Wolf, A., Schuch, R., Müller, A., Wagner, M.: *Phys. Rev. Lett.* **64**, 737 (1990)
- Pindzola, M.S., Badnell, N.R., Griffin, D.C.: *Phys. Rev. A* **42**, 282 (1990)
- DeWitt, D.R., Schneider, D., Clark, M.W., Chen, M.H., Church, D.: *Phys. Rev. A* **44**, 7185 (1991)
- Andersen, L.H., Hvelplund, P., Knudsen, H., Kvistgaard, P.: *Phys. Rev. Lett.* **62**, 2656 (1989)
- Badnell, N.R., Pindzola, M.S., Griffin, D.C.: *Phys. Rev. A* **41**, 2422 (1990)
- Andersen, L.H., Pan, G.Y., Schmidt, H.T., Badnell, N.R., Pindzola, M.S.: *Phys. Rev. A* **45**, 7868 (1992)
- Knapp, D.A., Marrs, R.E., Schneider, M.B., Chen, M.H., Levine, M.A., Lee, P.: *Phys. Rev. A* **47**, 2039 (1993)
- Ali, R., Bhalla, C.P., Cocke, C.L., Stockli, M.: *Phys. Rev. Lett.* **64**, 633 (1990)
- Griffin, D.C., Pindzola, M.S., Krylstedt, P.: *Phys. Rev. A* **40**, 6699 (1989)
- Andersen, L.H., Bolko, J., Kvistgaard, P.: *Phys. Rev. A* **41**, 1293 (1990)
- Andersen, L.H., Pan, G.Y., Schmidt, H.T., Pindzola, M.S., Badnell, N.R.: *Phys. Rev. A* **45**, 6332 (1992)
- Kilgus, G., Habs, D., Schwalm, D., Wolf, A., Badnell, N.R., Müller, A.: *Phys. Rev. A* **46**, 5730 (1992)
- Spies, W., Müller, A., Linkemann, J., Frank, A., Wagner, M., Kozhuharov, C., Franzke, B., Beckert, K., Bosch, F., Eickhoff, H., Jung, M., Klepper, O., König, W., Mokler, P.H., Moshhammer, R., Nolden, F., Schaaf, U., Spädtke, P., Steck, M., Zimmerer, P., Grün, N., Scheid, W., Pindzola, M.S., Badnell, N.R.: *Phys. Rev. Lett.* **69**, 2768 (1992)
- Badnell, N.R., Pindzola, M.S., Andersen, L.H., Bolko, J., Schmidt, H.T.: *J. Phys. B* **24**, 4441 (1991)
- Lampert, A., Habs, D., Kilgus, G., Schwalm, D., Wolf, A., Badnell, N.R., Pindzola, M.S.: *Physics* **199**(2), 537 (1992)

42. DeWitt, D.R., Schneider, D., Chen, M.H., Clark, M.W., McDonald, J.W., Schneider, M.B.: *Phys. Rev. Lett.* **68**, 1694 (1992)
43. Schneider, M.B., Knapp, D.A., Chen, M.H., Scofield, J.H., Beiersdorfer, P., Bennett, C.L., Henderson, J.R., Marrs, R.E., Levine, M.A.: *Phys. Rev. A* **45**, R1291 (1992)
44. Fogle, M., Badnell, N.R., Eklöv, N., Mohamed, T., Schuch, R.: *Astron. Astrophys.* **409**, 781 (2003)
45. Schnell, M., Gwinner, G., Badnell, N.R., Bannister, M.E., Böhm, R., Colgan, J., Klieslich, S., Loch, S.D., Mitnik, D., Müller, A., Pindzola, M.S., Schippers, S., Schwalm, D., Shi, W., Wolf, A., Zhou, S.-G.: *Phys. Rev. Lett.* **91**, 043001 (2003)
46. Müller, A., Belic, D.S., DePaola, B.D., Djuric, N., Dunn, G.H., Mueller, D.W., Timmer, C.: *Phys. Rev. Lett.* **56**, 127 (1986)
47. Bottcher, C., Griffin, D.C., Pindzola, M.S.: *Phys. Rev. A* **34**, 860 (1986)
48. Savin, D.W., Kahn, S.M., Gwinner, G., Grieser, M., Repnow, R., Saathoff, G., Schwalm, D., Wolf, A., Müller, A., Schippers, S., Zavodszky, P.A., Chen, M.H., Gorczyca, T.W., Zatzarinny, O., Gu, M.F.: *Astrophys. J. Suppl. Ser.* **147**, 421 (2003)
49. Schippers, S., Schnell, M., Brandau, C., Klieslich, S., Müller, A., Wolf, A.: *Astron. Astrophys.* **421**, 1185 (2004)
50. Lindroth, E., Danared, H., Glans, P., Pesic, Z., Tokman, M., Viktor, G., Schuch, R.: *Phys. Rev. Lett.* **86**, 5027 (2001)
51. Fogle, M., Eklöv, N., Lindroth, E., Mohamed, T., Schuch, R., Tokman, M.: *J. Phys. B* **36**, 2563 (2003)
52. Tokman, M., Eklöv, N., Glans, P., Lindroth, E., Schuch, R., Gwinner, G., Schwalm, D., Wolf, A., Hoffknecht, A., Müller, A., Schippers, S.: *Phys. Rev. A* **66**, 012703 (2002)
53. Savin, D.W., Behar, E., Kahn, S.M., Gwinner, G., Saghir, A.A., Schmitt, M., Grieser, M., Repnov, R., Schwalm, D., Wolf, A., Bartsch, T., Müller, A., Schippers, S., Badnell, N.R., Chen, M.H., Gorczyca, T.W.: *Astrophys. J. Suppl. Ser.* **138**, 337 (2003)
54. Spruck, K., Badnell, N.R., Krantz, C., Novotny, O., Becker, A., Bernhardt, D., Grieser, M., Hahn, M., Repnow, R., Savin, D.W., Wolf, A., Müller, A., Schippers, S.: *Phys. Rev. A* **90**, 032715 (2014)
55. Badnell, N.R., Spruck, K., Krantz, C., Novotny, O., Becker, A., Bernhardt, D., Grieser, M., Hahn, M., Repnow, R., Savin, D.W., Wolf, A., Müller, A., Schippers, S.: *Phys. Rev. A* **93**, 052703 (2016)
56. Schippers, S., Bernhardt, D., Müller, A., Krantz, C., Grieser, M., Repnow, R., Wolf, A., Lestinsky, M., Hahn, M., Novotny, O., Savin, D.W.: *Phys. Rev. A* **83**, 12711 (2011)
57. Badnell, N.R., Ballance, C.P., Griffin, D.C., O'Mullane, M.: *Phys. Rev. A* **85**, 052716 (2012)
58. Dzuba, V.A., Flambaum, V.V., Gribakin, G.F., Harabati, C.: *Phys. Rev. A* **86**, 022714 (2012)
59. Dzuba, V.A., Flambaum, V.V., Gribakin, G.F., Harabati, C., Kozlov, M.G.: *Phys. Rev. A* **88**, 062713 (2013)
60. Schippers, S., Bernhardt, D., Grieser, M., Hahn, M., Krantz, C., Lestinsky, M., Novotny, O., Repnow, R., Savin, D.W., Wolf, A., Müller, A.: *Phys. Scr.* **T144**, 014039 (2011)
61. Ballance, C.P., Griffin, D.C., Loch, S.D., Badnell, N.R.: *J. Phys. B* **45**, 045001 (2012)
62. Nahar, S.N.: *New Astron.* **73**, 101277 (2019)
63. Nahar, S.N.: *Mon. Not. R. Astron. Soc.* **469**, 3225 (2017)
64. Davies, P.C.W., Seaton, M.J.: *J. Phys. B* **2**, 757 (1969)
65. Trefftz, E.: *J. Phys. B* **3**, 763 (1970)
66. Bell, R.H., Seaton, M.J.: *J. Phys. B* **18**, 1589 (1985)
67. Alber, G., Cooper, J., Rau, A.R.P.: *Phys. Rev. A* **30**, 2845 (1984)
68. LaGattuta, K.J.: *Phys. Rev. A* **40**, 558 (1989)
69. Haan, S.L., Jacobs, V.L.: *Phys. Rev. A* **40**, 80 (1989)
70. Badnell, N.R., Pindzola, M.S.: *Phys. Rev. A* **45**, 2820 (1992)
71. Pindzola, M.S., Badnell, N.R., Griffin, D.C.: *Phys. Rev. A* **46**, 5725 (1992)
72. Summers, H.P., Hooper, M.B.: *Plasma Phys.* **25**, 1311 (1983)
73. Badnell, N.R., Pindzola, M.S., Dickson, W.J., Summers, H.P., Griffin, D.C.: *Astrophys. J.* **407**, L91 (1993)
74. Robicheaux, F., Loch, S.D., Pindzola, M.S., Ballance, C.P.: *Phys. Rev. Lett.* **105**, 233201 (2010)
75. Pindzola, M.S., Loch, S.D., Robicheaux, F.: *Phys. Rev. A* **83**, 042705 (2011)



Rydberg Collision Theories

60

Edmund J. Mansky II

Contents

60.1	Rydberg Collision Processes	882	60.10	Binary Encounter Approximation	903
60.2	General Properties of Rydberg States	882	60.10.1	Differential Cross Sections	903
60.2.1	Dipole Moments	882	60.10.2	Integral Cross Sections	904
60.2.2	Interaction Potentials	884	60.10.3	Classical Ionization Cross Section	906
60.2.3	Radial Integrals	885	60.10.4	Classical Charge Transfer Cross Section	906
60.2.4	Line Strengths	885	60.11	Born Approximation	907
60.2.5	Form Factors	886	60.11.1	Form Factors	907
60.2.6	Impact Broadening	887	60.11.2	Hydrogenic Form Factors	907
60.2.7	Effective Lifetimes and Depopulation Rates	887	60.11.3	Excitation Cross Sections	908
60.3	Correspondence Principles	887	60.11.4	Ionization Cross Sections	909
60.3.1	Bohr–Sommerfeld Quantization	887	60.11.5	Capture Cross Sections	909
60.3.2	Bohr Correspondence Principle	887	References		910
60.3.3	Heisenberg Correspondence Principle	888			
60.3.4	Strong Coupling Correspondence Principle	888			
60.3.5	Equivalent Oscillator Theorem	888			
60.4	Distribution Functions	888			
60.4.1	Spatial Distributions	888			
60.4.2	Momentum Distributions	889			
60.5	Classical Theory	889			
60.6	Universality Properties	890			
60.6.1	Equal Mass Case	891			
60.6.2	Unequal Mass Case	891			
60.7	Many-Body and Multiparticle Effects	891			
60.7.1	Many-Body Theory	891			
60.7.2	Dilute Bose Gas	891			
60.8	Working Formulae for Rydberg Collisions	892			
60.8.1	Inelastic n, ℓ -Changing Transitions	892			
60.8.2	Inelastic $n \rightarrow n'$ Transitions	893			
60.8.3	Quasi-Elastic ℓ -Mixing Transitions	894			
60.8.4	Elastic $n\ell \rightarrow n\ell'$ Transitions	894			
60.8.5	Inelastic $n\ell \rightarrow n\ell'$ Transitions	894			
60.8.6	Fine Structure $n\ell J \rightarrow n\ell' J'$ Transitions	895			
60.9	Impulse Approximation	896			
60.9.1	Quantal Impulse Approximation	896			
60.9.2	Classical Impulse Approximation	900			
60.9.3	Semiquantal Impulse Approximation	901			

Abstract

Collisions involving atoms or molecules in Rydberg orbitals are important in understanding a wide range of phenomena from the spectra of astrophysical objects, such as planetary nebulae and interstellar gas clouds, and industrial plasmas on Earth, to Bose-Einstein condensates and multi-qubit logic gates in quantum computing. This Chapter collects together many of the equations used to study theoretically the collisional properties of both charged and neutral particles with atoms and molecules in Rydberg states or orbitals, from thermal energies to ultracold temperatures, including the impulse approximation, binary encounter approximation and the Born approximation. Also covered are many new asymptotic methods and working formulae suitable for numerical computation, as well as models using scattering lengths and effective ranges. Readers interested in the basic quantum mechanical properties of Rydberg states may consult Chap. 15.

The theoretical techniques used to study Rydberg collisions complement and supplement the eigenfunction expansion approximations used for collisions with target atoms and molecules in their ground ($n = 1$) or first few excited states ($n > 1$), as discussed in Chap. 49. Direct application of eigenfunction expansion techniques to Rydberg collisions, wherein the target particle can be in a Rydberg orbital with principal quantum number in the range $n \geq 100$, is prohibitively difficult due to the need

E. J. Mansky II (✉)
Eikonol Research Institute
Bend, OR, USA
e-mail: mansky@mindspring.com

to compute numerically and store wave functions with n^3 , or more, nodes. For $n = 100$ this amounts to $\approx 10^6$ nodes for each of the wave functions represented in the eigenfunction expansion. Therefore, a variety of approximate scattering theories have been developed to deal specifically with the peculiarities of Rydberg collisions.

Experiments in the ultracold regime, via the use of lasers and magnetic traps, has allowed access to aspects of many-body physics using collisions of Rydberg atoms in a gas that were previously inaccessible in condensed matter and nuclear physics. For the second edition of the Handbook we have changed the title of the chapter to reflect the broader array of theories now being used, in particular, in ultra-cold collisions of Rydberg atoms and the study of their universal properties.

Keywords

binary encounter · Born approximation · impulse approximations · line strengths · correspondence principles · form factors · universality properties

60.1 Rydberg Collision Processes

(A) State-changing collisions Quasi-elastic ℓ -mixing collisions

$$A^*(n\ell) + B \rightarrow A^*(n\ell') + B. \quad (60.1)$$

Quasi-elastic J -mixing collisions: fine structure transitions with $J = |\ell \pm 1/2| \rightarrow J' = |\ell \pm 1/2|$ are

$$A^*(n\ell J) + B \rightarrow A^*(n\ell J') + B. \quad (60.2)$$

Energy transfer n -changing collisions

$$A^*(n) + B(\beta) \rightarrow A^*(n') + B(\beta'), \quad (60.3)$$

where, if B is a molecule, the transition $\beta \rightarrow \beta'$ represents an inelastic energy transfer to the rotational-vibrational degrees of freedom of the molecule B from the Rydberg atom A^* .

Elastic scattering

$$A^*(\gamma) + B \rightarrow A^*(\gamma) + B, \quad (60.4)$$

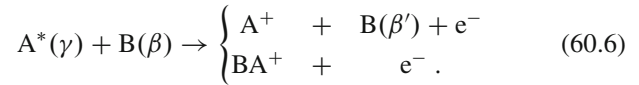
where the label γ denotes the set of quantum numbers n, ℓ or n, ℓ, J used.

Depolarization collisions

$$A^*(n\ell m) + B \rightarrow A^*(n\ell m') + B, \quad (60.5a)$$

$$A^*(n\ell JM) + B \rightarrow A^*(n\ell JM') + B. \quad (60.5b)$$

(B) Ionizing collisions Direct and associative ionization



Penning ionization

$$A^*(\gamma) + B \rightarrow A + B^+ + e^-. \quad (60.7)$$

Ion-pair formation

$$A^*(\gamma) + B \rightarrow A^+ + B^-. \quad (60.8)$$

Dissociative attachment

$$A^*(\gamma) + BC \rightarrow A^+B^- + C. \quad (60.9)$$

60.2 General Properties of Rydberg States

Figure 60.1 illustrates the range of physical phenomena where collisions of Rydberg atoms play a role from thermal molecular beams down to the ultracold regime of the Bose-Einstein condensates (BEC) and degenerate Fermi gases. The types of theories required to understand Rydberg atom collisions range from Born, binary-encounter and impulse approximations at thermal energies to hyperspherical, zero-range, and many-body theories in the cold and ultracold regimes. A good general introduction to Rydberg atom collision theories can be found in [1] and [2].

Table 60.1 displays the general n -dependence of a number of key properties of Rydberg states and some specific representative values for hydrogen.

60.2.1 Dipole Moments

Definition $D_{i \rightarrow f} = -eX_{i \rightarrow f}$, where

$$X_{i \rightarrow f} = \langle \phi_f | \sum_j e^{ik \cdot r_j} \mathbf{r}_j | \phi_i \rangle. \quad (60.10)$$

Hydrogenic dipole moments See *Bethe and Salpeter* [5] and the references by *Khandelwal* and coworkers [6–9] for details and tables.

Exact expressions In the limit $|k| \rightarrow 0$, the dipole allowed transitions summed over final states are

$$|X_{1s \rightarrow n}|^2 = \frac{2^8}{3} n^7 \frac{(n-1)^{2n-5}}{(n+1)^{2n+5}}, \quad (60.11a)$$

$$|X_{2s \rightarrow n}|^2 = \frac{2^5}{3n^3} \frac{(\frac{1}{2} - \frac{1}{n})^{2n-7}}{(\frac{1}{2} + \frac{1}{n})^{2n+7}} \left(\frac{1}{4} - \frac{1}{n^2} \right) \left(1 - \frac{1}{n^2} \right), \quad (60.11b)$$

$$|X_{2p \rightarrow n}|^2 = \frac{2^5}{144} \frac{1}{n^3} \frac{(\frac{1}{2} - \frac{1}{n})^{2n-7}}{(\frac{1}{2} + \frac{1}{n})^{2n+7}} \left(11 - \frac{12}{n^2} \right). \quad (60.11c)$$

Fig. 60.1 The world of ultracold atomic, molecular, and cluster systems [3]

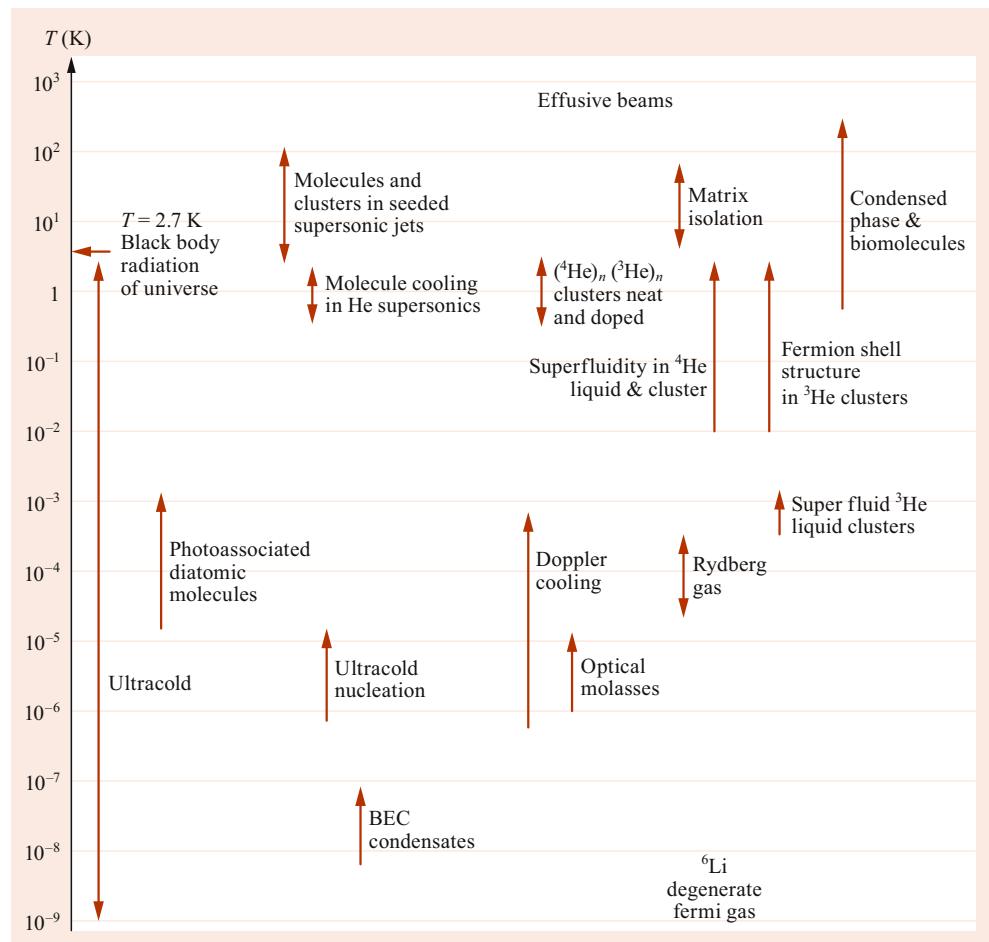


Table 60.1 General n -dependence of characteristic properties of Rydberg states. After [4]

Property	n -dependence	$n = 10$	$n = 100$	$n = 500$	$n = 1000$
Radius (cm)	$n^2 a_0 / Z$	5.3×10^{-7}	5.3×10^{-5}	1.3×10^{-3}	5.3×10^{-3}
Velocity (cm/s)	$v_B Z / n$	2.18×10^7	2.18×10^6	4.4×10^5	2.18×10^5
Area (cm ²)	$\pi a_0^2 n^4 / Z^2$	8.8×10^{-13}	8.8×10^{-9}	5.5×10^{-6}	8.8×10^{-5}
Ionization potential (eV)	$Z^2 R_\infty / n^2$	1.36×10^{-1}	1.36×10^{-3}	5.44×10^{-5}	1.36×10^{-6}
Radiative lifetime (s) ^a	$n^5 [3 \ln n - (1/4)] / (A_0 Z^4)$	8.4×10^{-5}	17	7.3×10^4	7.22 hours
Period of classical motion (s)	$2\pi / \omega_{n,n\pm 1} = \hbar n^3 / (2Z^2 R_\infty)$	1.5×10^{-13}	1.5×10^{-10}	1.9×10^{-8}	1.5×10^{-7}
Transition frequency (s ⁻¹)	$\omega_{n,n\pm 1} = 2Z^2 R_\infty / (\hbar n^3)$	4.1×10^{13}	4.1×10^{10}	3.3×10^8	4.1×10^7
Wavelength (cm)	$\lambda_{n,n\pm 1} = 2\pi c / \omega_{n,n\pm 1}$	4.6×10^{-3}	4.6	570	4.5609×10^3

^a $A_0 = [8\alpha^3 / (3\sqrt{3}\pi)] (v_B / a_0)$

Asymptotic expressions For $n \gg 1$,

$$n^3 |X_{1s \rightarrow n}|^2 \approx 1.563 + \frac{5.731}{n^2} + \frac{13.163}{n^4} + \frac{24.295}{n^6} + \frac{39.426}{n^8} + \frac{58.808}{n^{10}}, \quad (60.12a)$$

$$n^3 |X_{2s \rightarrow n}|^2 \approx 14.658 + \frac{180.785}{n^2} + \frac{1435.854}{n^4} + \frac{9341.634}{n^6} + \frac{54,208.306}{n^8} + \frac{292,202.232}{n^{10}}, \quad (60.12b)$$

$$n^3 |X_{2p \rightarrow n}|^2 \approx 13.437 + \frac{218.245}{n^2} + \frac{2172.891}{n^4} + \frac{17,118.786}{n^6} + \frac{117,251.682}{n^8} + \frac{731,427.003}{n^{10}}. \quad (60.12c)$$

60.2.2 Interaction Potentials

H(n)-H(n) long-range interactions [10]

$$V_{\rightarrow,\rightarrow}(R) = -\frac{2}{R^3}Q_1^2 - \frac{2}{R^5}[4Q_1Q_3 - 3Q_2^2] - \frac{2}{R^7}[6Q_1Q_5 - 15Q_2Q_4 + 10Q_3^2] - O(R^{-9}), \quad (60.13)$$

for parallel-aligned dipoles; and,

$$V_{\leftarrow,\rightarrow}(R) = \frac{2}{R^3}Q_1^2 + \frac{6}{R^4}Q_1Q_2 + \frac{2}{R^5}[4Q_1Q_3 + 3Q_2^2][Q_1Q_4 + 2Q_2Q_3] + \frac{2}{R^7}[6Q_1Q_5 + 15Q_2Q_4 + 10Q_3^2] - O(R^{-8}), \quad (60.14)$$

for antiparallel-aligned dipoles.

Analytical expressions for the Q_L multipole moments for $L = 0 - 5$ are provided in Table 60.2. Full expressions for L up to 10 are provided in [10].

He(2^{1,3}P)-He(2^{1,3}P) Long-range dispersion coefficients [11] Expressions for the second-order potential, $V^{(2)}$, for the first three molecular states are:

Σ molecular states

$$V^{(2)}(\Sigma, \beta; \lambda_i) = -\sum_{n \geq 3} \frac{C_{2n}(\Sigma, \beta; \lambda_i)}{R^{2n}} \quad (60.15a)$$

$$C_{2n}(\Sigma, \beta; \lambda_i) = \sum_{\substack{\ell, L, \ell', L' \geq 1 \\ \ell + L + \ell' + L' + 2 = 2n}} D_{\lambda_i}(\ell, L, \ell', L'), \quad (60.15b)$$

where the D_{λ_i} are defined

$$D_{\lambda_i}(\ell, L, \ell', L') = \frac{3\alpha^2}{8} \sum_{L_s, L_t} f_{\lambda_i}(\ell, L, L_s; L_t, \ell', L') \times (G_1 + (2-i)^{(2-i)}G_2). \quad (60.16)$$

Table 60.2 Multipoles Q_L for the Stark states $|\pm\rangle$ of H(n)

Multipole	Value	Asymptotic value
$Q_0(+)=Q_0(-)$	1	
$Q_1(+)= -Q_1(-)$	$(3/2)n(n-1)$	$(3/2)n^2$
$Q_2(+)=Q_2(-)$	$(2/2^2)n^2(n-1)(5n-7)$	$(5/2)n^4$
$Q_3(+)= -Q_3(-)$	$(5/2^3)n^3(n-1)(n-2)(7n-9)$	$(35/8)n^6$
$Q_4(+)=Q_4(-)$	$(6/2^4)n^4(n-1)(n-2)(21n^2-77n+62)$	$(63/8)n^8$
$Q_5(+)= -Q_5(-)$	$(42/2^5)n^5(n-1)(n-2)(n-3)(11n^2-39n+30)$	$(231/16)n^{10}$

Π molecular states

$$V^{(2)}(\Pi, \beta; \gamma) = -\sum_{n \geq 3} \frac{C_{2n}(\Pi, \beta; \gamma)}{R^{2n}} \quad (60.17a)$$

$$C_{2n}(\Pi, \beta; \gamma) = \sum_{\substack{\ell, L, \ell', L' \geq 1 \\ \ell + L + \ell' + L' + 2 = 2n}} D_{\beta\gamma}(\ell, L, \ell', L'), \quad (60.17b)$$

where the $D_{\beta\gamma}$ are defined

$$D_{\beta\gamma}(\ell, L, \ell', L') = \frac{9\alpha^2}{16} \sum_{L_s, L_t} [f_{1\gamma}(\ell, L, L_s; L_t, \ell', L')G_1 + f_{2\gamma}(\ell, L, L_s, L_t, \ell', L')G_2]. \quad (60.18)$$

Δ molecular states

$$V^{(2)} = -\sum_{\ell\ell'LL'} \frac{D_1(\ell, L, \ell', L')}{R^{\ell+L+\ell'+L'+2}}, \quad (60.19)$$

where the D_1 are defined

$$D_1(\ell, L, \ell', L') = \frac{1}{2\pi} \sum_{L_s, L_t} G_1(\ell, L, \ell', L', L_s, L_t) \times F_1(\ell, L, \ell', L', L_s, L_t). \quad (60.20)$$

See [11] for detailed tabulations of the dispersion coefficients C and for the (lengthy) expressions for the various $f_{\lambda_i}, f_1, f_2, F_1, G_1, G_2$ functions appearing in Eqs. (60.16), (60.18), and (60.20).

Cs-Cs and Rb-Rb pseudo-potentials [12] $V_{LS}(r)$ for $L = 0, 1$

$$V_{0S}(r) = -\frac{A}{r}e^{-\gamma r} - \frac{\alpha}{2r^4} \left(1 - e^{-(r/r_c)^6}\right) \quad (60.21a)$$

$$V_{1S}(r) = -\frac{Z_c}{r}e^{-\lambda r} - Ae^{-\gamma r} - \frac{\alpha}{2r^4} \left(1 - e^{-(r/r_c)^6}\right), \quad (60.21b)$$

where the fitted parameters for Cs and Rb are given in Table 60.3. For the case of Sr-Sr, see [13], while for e⁻-Ne, see [14].

Table 60.3 Fit parameters for Cs-Cs and Rb-Rb pseudo-potentials (from [12])

	r_0	α	λ	State	A	γ	r_c
Cs	0.01	402.2	7.2443	1S	4.5396	1.3304	1.6848
				3S	93.936	7.5397	2.6856
				1P	-3.6681	1.3195	1.8031
				3P	4.1271	2.2329	2.1294
Rb	0.01	319.2	7.4975	1S	4.5642	1.3438	1.8883
				3S	68.576	9.9898	2.3813
				1P	-4.2625	1.0055	1.8869
				3P	-1.4523	4.8733	1.8160

60.2.3 Radial Integrals

Definition

$$R_{n\ell}^{n'\ell'} \equiv \int_0^\infty R_{n\ell}(r)rR_{n'\ell'}(r)r^2dr, \quad (60.22)$$

where $R_{n\ell}(r)$ are solutions to the radial Schrödinger equation. See Chap. 9 for specific representations of $R_{n\ell}$ for hydrogen.

Exact results for hydrogen For $\ell' = \ell - 1$ and $n \neq n'$ [15],

$$\begin{aligned} R_{n\ell}^{n'\ell-1} &= \frac{a_0}{Z} \frac{(-1)^{n'-\ell} (4nn')^{\ell+1} (n-n')^{n+n'-2\ell-2}}{4(2\ell-1)!(n+n')^{n+n'}} \\ &\times \left[\frac{(n+\ell)!(n'+\ell-1)!}{(n'+\ell')!(n-\ell-1)!} \right]^{1/2} \\ &\times \left\{ {}_2F_1(-n+\ell+1, -n'+\ell; 2\ell; Y) \right. \\ &\quad \left. - \left(\frac{n-n'}{n+n'} \right)^2 \right. \\ &\quad \left. \times {}_2F_1(-n+\ell-1, -n'+\ell; 2\ell; Y) \right\}, \quad (60.23) \end{aligned}$$

where $Y = -4nn'/(n-n')^2$. For $n = n'$,

$$R_{n\ell}^{n\ell-1} = \left(\frac{a_0}{Z} \right) \frac{3}{2} n \sqrt{n^2 - \ell^2}. \quad (60.24)$$

The hypergeometric functions ${}_2F_1$ in Gordon's formulae above are increasingly difficult to compute numerically due to unavoidable roundoff errors. See Sect. 60.8 for working formulae suitable for numerical computations.

Semiclassical quantum defect representation [16]

$$\begin{aligned} |R_{n\ell}^{n'\ell'}|^2 &= \left(\frac{a_0}{Z} \right)^2 \\ &\times \left| \frac{n_c^2}{2\Delta} \left[\left(1 - \frac{\Delta\ell\ell_{>}}{n_c} \right) J_{\Delta-1}(-x) \right. \right. \\ &\quad \left. \left. - \left(1 + \frac{\Delta\ell\ell_{>}}{n_c} \right) J_{\Delta+1}(-x) \right. \right. \\ &\quad \left. \left. + \frac{2}{\pi} \sin(\pi\Delta)(1-e) \right] \right|^2, \quad (60.25) \end{aligned}$$

where

$$n_c = 2n^*n'^*/(n^* + n'^*), \quad (60.26a)$$

$$\Delta = n'^* - n^*, \quad (60.26b)$$

$$\Delta\ell = \ell' - \ell, \ell_{>} = \max(\ell, \ell'), \quad (60.26c)$$

$$x = e\Delta, e = \sqrt{1 - (\ell_{>}/n_c)^2}, \quad (60.26d)$$

and $J_n(y)$ is the Anger function.

The energies of the states $n\ell$ and $n'\ell'$ are given in terms of the quantum defects δ by

$$E_{n\ell} = -Z^2 R_\infty / n^{*2}, n^* = n - \delta_\ell, \quad (60.27a)$$

$$E_{n'\ell'} = -Z^2 R_\infty / n'^{*2}, n'^* = n' - \delta_{\ell'}. \quad (60.27b)$$

Sum rule For hydrogen

$$\sum_{n'} |R_{n\ell}^{n'\ell-1}|^2 = \sum_{n'} |R_{n\ell}^{n'\ell+1}|^2 \quad (60.28a)$$

$$= \frac{n^2 a_0^2}{2Z^2} [5n^2 + 1 - 3\ell(\ell+1)]. \quad (60.28b)$$

See §61 of [5] for additional sum rules.

Zéldovich effect [17]

$$\frac{a_B}{2\pi a_s} = -\cot \pi\delta - \frac{2}{\pi} \ln \frac{2}{\gamma x_0}, \quad (60.29)$$

where a_B is the Bohr radius of the Coulomb field, δ is the quantum defect, $\ln \gamma$ is Euler's constant, $x_0 = \sqrt{8r_0/a_B}$, and r_0 is the radius of the short-range field.

60.2.4 Line Strengths

Definition

$$S(n'\ell', n\ell) = e^2 (2\ell+1) |r_{n'\ell', n\ell}|^2 \quad (60.30a)$$

$$= e^2 \max(\ell, \ell') |R_{n\ell}^{n'\ell'}|^2, \quad (60.30b)$$

where $\ell' = \ell \pm 1$. For hydrogen,

$$S(n', n) = 32 \left(\frac{ea_0}{Z} \right)^2 (nn')^6 \frac{(n-n')^{2(n+n')-3}}{(n+n')^{2(n+n')+4}} \times \left\{ \left[{}_2F_1(-n', -n+1; 1; Y) \right]^2 - \left[{}_2F_1(-n'+1, -n; 1; Y) \right]^2 \right\}, \quad (60.31)$$

where $Y = -4nn'/(n-n')^2$.

Semiclassical representation [18]

$$S(n', n) = \frac{32}{\pi\sqrt{3}} \left(\frac{ea_0}{Z} \right)^2 \frac{(\varepsilon\varepsilon')^{3/2}}{(\varepsilon - \varepsilon')^4} G(\Delta n), \quad (60.32)$$

where $\varepsilon = 1/n^2$, $\varepsilon' = 1/n'^2$, and the Gaunt factor $G(\Delta n)$ is given by

$$G(\Delta n) = \pi\sqrt{3} |\Delta n| \mathbf{J}_{\Delta n}(\Delta n) \mathbf{J}'_{\Delta n}(\Delta n), \quad (60.33)$$

where the prime on the Anger function denotes differentiation with respect to the argument Δn . Equation (60.33) can be approximated to within 2% by the expression

$$1 - \frac{1}{4|\Delta n|}. \quad (60.34)$$

Relation to oscillator strength

$$S(n', n) = \sum_{\ell, \ell'} S(n'\ell', n\ell) = 3e^2 a_0^2 \frac{R_\infty}{\hbar\omega} \sum_{\ell, \ell'} f_{n'\ell', n\ell}. \quad (60.35)$$

Connection with radial integrals

$$-f_{n'\ell', n\ell} = \frac{\hbar\omega}{3R_\infty} \frac{\max(\ell, \ell')}{(2\ell+1)} |R_{n\ell}^{n'\ell'}|. \quad (60.36)$$

Density of line strengths For bound-free $n\ell \rightarrow E\ell'$ transitions in a Coulomb field, the semiclassical representation [4] is

$$\frac{d}{dE} S(n\ell, E) = 2n(2\ell+1) \left(\frac{R_\infty}{\hbar\omega} \right)^2 \times \left[\mathbf{J}'_{\Delta}(\mathbf{e}\Delta)^2 + \left(1 - \frac{1}{\mathbf{e}^2} \right) \mathbf{J}_{\Delta}(\mathbf{e}\Delta)^2 \right] \times \frac{e^2 a_0^2}{R_\infty}, \quad (60.37)$$

where $\Delta = \hbar\omega n^3/2R_\infty$ and $\mathbf{e} = \sqrt{1 - (\ell + (1/2))^2/n^2}$. The asymptotic expression for $\Delta \gg 1$

$$\frac{d}{dE} S(n\ell, E) = \frac{2(2\ell+1)}{3\pi^2} \left(\frac{R_\infty}{\hbar\omega} \right)^2 \frac{(\ell + \frac{1}{2})^4}{n^3} \times \left[K_{1/3}^2(\eta) + K_{2/3}^2(\eta) \right] \frac{e^2 a_0^2}{R_\infty}, \quad (60.38)$$

where $\eta = (E/R_\infty)(\ell + 1/2)^3/6$, and $K_\nu(x)$ are Bessel functions of the third kind.

Line strength of line n

$$S_n \equiv S(n) = \sum_{k \neq 0} S(n+k, n) \frac{1}{k^3}. \quad (60.39)$$

Born approximation to line strength S_n [4]

$$S_n^B = \frac{Z^2 R_\infty}{E} \left[\frac{1}{2} \ln(1 + \varepsilon_e/\varepsilon) \sum_{k \neq 0} \left(1 - \frac{1}{4k} \right) \frac{1}{k^4} + \frac{4}{3} \frac{\varepsilon_e}{\varepsilon + \varepsilon_e} \sum_{k \neq 0} \left(1 - \frac{0.60}{k} \right) \frac{1}{k^3} \right] = \frac{Z^2 R_\infty}{E} \left[0.82 \ln \left(1 + \frac{\varepsilon_e}{\varepsilon} \right) + \frac{1.47\varepsilon_e}{\varepsilon + \varepsilon_e} \right], \quad (60.40)$$

where $\varepsilon = |E_n|Z^2/R_\infty$ and $\varepsilon_e = \varepsilon/Z^2 R_\infty$.

60.2.5 Form Factors

$$F_{n'n}(Q) = \sum_{\ell, m} \sum_{\ell', m'} | \langle n\ell m | e^{i\mathbf{Q}\cdot\mathbf{r}} | n'\ell' m' \rangle |^2. \quad (60.41)$$

Connection with generalized oscillator strengths

$$f_{n'n}(Q) = \frac{Z^2 \Delta E}{n^2 Q^2 a_0^2} F_{n'n}(Q). \quad (60.42)$$

Semiclassical limit

$$\lim_{Q \rightarrow 0} f_{n'n}(Q) = \frac{32}{3n^2} \left(\frac{nn'}{\Delta n(n+n')} \right)^3 \times \Delta n \mathbf{J}_{\Delta n}(\Delta n) \mathbf{J}'_{\Delta n}(\Delta n), \quad (60.43)$$

where $J_m(y)$ denotes the Bessel function.

Representation as microcanonical distribution

$$F_{n'n\ell}(Q) = (2\ell+1) \frac{2Z^2 R_\infty}{n^3} \int d\mathbf{p} |g_{n\ell}(p)|^2 \times \delta \left(\frac{(\mathbf{p} - \hbar\mathbf{Q})^2}{2m} - \frac{p^2}{2m} - E_{n'} - E_{n\ell} \right), \quad (60.44)$$

$$F_{n'n}(Q) = \frac{4Z^2 R_\infty^2}{(nn')^3} \int \frac{d\mathbf{p} d\mathbf{r}}{(2\pi\hbar)^3} \delta \left(\frac{p^2}{2m} - \frac{Ze^2}{r} - E_n \right) \times \delta \left(\frac{(\mathbf{p} - \hbar\mathbf{Q})^2}{2m} - \frac{Ze^2}{r} - E_{n'} \right), \quad (60.45)$$

$$= \frac{2^9}{3\pi (nn')^3} \frac{\kappa^5}{(\kappa^2 + \kappa_+^2)^3 (\kappa^2 + \kappa_-^2)^3}, \quad (60.46)$$

where $\kappa = Qa_0/Z$, and $\kappa_\pm = |1/n \pm 1/n'|$.

60.2.6 Impact Broadening

The total broadening cross section of a level n is

$$\sigma_n = (\pi a_0^2 / Z^4) n^4 S_n. \quad (60.47)$$

The width of a line $n \rightarrow n+k$ is [19]

$$\gamma_{n,n+k} = n_e [\langle v\sigma_n \rangle + \langle v\sigma_{n+k} \rangle], \quad (60.48)$$

where n_e is the number density of electrons, and

$$\langle v\sigma_n \rangle = \sum_{k \neq 0} \langle v\sigma_{n+k,n} \rangle = \frac{n^4}{Z^3} K_n \quad (60.49a)$$

$$= \frac{n^4 \pi a_0^2 v_B}{Z^3 \theta^{3/2}} \int_0^\infty e^{-E/k_B T} S_n \frac{E dE}{(Z^2 R_\infty)^2}, \quad (60.49b)$$

where $\theta = k_B T / Z^2 R_\infty$. See Chap. 63 for collisional line broadening.

60.2.7 Effective Lifetimes and Depopulation Rates

Black-body radiation (BBR) depopulation rates [20]

$$\Gamma_{\text{BBR}} = \frac{1}{n_{\text{eff}}^5} \frac{2.14 \times 10^{10}}{\exp(315,780/n_{\text{eff}}^3 T) - 1} (s^{-1}), \quad (60.50)$$

where n_{eff} represents an effective quantum number for $n > 15$.

Effective sum rule

$$\sum_{n'} \omega_{nn'} f(nL \rightarrow n'L') = \frac{2}{3n_{\text{eff}}^2}. \quad (60.51)$$

For nP and nD states, Eq. (60.50) overestimates the lifetimes for intermediate quantum numbers $n \sim 20$. For those states a generalization of Eq. (60.50) using fitted parameters A , B , C , and D is appropriate,

$$\Gamma_{\text{BBR}} = \frac{A}{n_{\text{eff}}^D} \frac{2.14 \times 10^{10}}{\exp(315,780B/n_{\text{eff}}^C T) - 1} (s^{-1}). \quad (60.52)$$

Semiempirical radiative lifetimes [21]

$$\tau_0 = \tau_s n_{\text{eff}}^\delta (ns.) \quad (60.53)$$

Effective lifetimes [20]

$$\tau_{\text{eff}} = \left(\frac{1}{\tau_s n_{\text{eff}}^\delta} \frac{A}{n_{\text{eff}}^D} \frac{21.4}{\exp(315,780B/n_{\text{eff}}^C T) - 1} \right)^{-1} (ns.) \quad (60.54)$$

See [20] for extensive tables of the effective lifetimes and fitted parameters A , B , C , D , τ_s , and δ for the alkali atoms.

Depopulation rates for trapped Rydberg states [22]

$$\Gamma_{n'\ell'm\pm 1}^{n\ell m}(B) = \left(1 \mp \frac{n^2 n'^2}{n^2 - n'^2} \frac{\mu_B B}{R_\infty \hbar c} \right)^3 \Gamma_{n'\ell'm\pm 1}^{n\ell m}(0), \quad (60.55)$$

where B is the external magnetic field, μ_B is the Bohr magneton, and $\Gamma(0)$ is the field-free depopulation rate.

60.3 Correspondence Principles

Correspondence principles are used to connect quantum mechanical observables with the corresponding classical quantities in the limit of large n . See [23] for details on the equations in this section.

60.3.1 Bohr-Sommerfeld Quantization

$$A_i = J_i \Delta w_i \oint p_i dq_i = 2\pi \hbar (n_i + \alpha_i), \quad (60.56)$$

where $n_i = 0, 1, 2, \dots$ and $\alpha_i = 0$ if the generalized coordinate q_i represents rotation, and $\alpha_i = 1/2$ if q_i represents a libration.

60.3.2 Bohr Correspondence Principle

$$E_{n+s} - E_n = h\nu_{n+s,n} \approx s\hbar\omega_n, \quad s = 1, 2, \dots \ll n, \quad (60.57)$$

where $\nu_{n+s,n}$ is the line emission frequency, and ω_n is the angular frequency of classical orbital motion. The number of states with quantum numbers in the range Δn is

$$\begin{aligned} \Delta N &= \prod_{i=1}^D \Delta n = \prod_{i=1}^D (\Delta J_i \Delta w_i) / (2\pi \hbar)^D \\ &= \prod_{i=1}^D (\Delta p_i \Delta q_i) / (2\pi \hbar)^D, \end{aligned} \quad (60.58)$$

for systems with D degrees of freedom, and the mean value \bar{F} of a physical quantity $F(q)$ in the quantum state Ψ is

$$\bar{F} = \langle \Psi | F(q) | \Psi \rangle = \sum_{n,m} a_m^* a_n F_{mn}^{(q)} e^{i\omega_{mn} t}, \quad (60.59)$$

where the $F_{mn}^{(q)}$ are the quantal matrix elements between time-independent states.

The first order S -matrix is

$$S_{fi} = -\frac{i\omega}{2\pi \hbar} \int_{-\infty}^{\infty} dt \int_0^{2\pi/\omega} V[\mathbf{R}(t), r(t_1)] e^{is\omega(t_1-t)} dt_1, \quad (60.60)$$

where \mathbf{R} denotes the classical path of the projectile and r the orbital of the Rydberg electron.

60.3.3 Heisenberg Correspondence Principle

For one degree of freedom [23],

$$F_{mn}^{(q)}(\mathbf{R}) = \int_0^\infty \phi_m^*(r) F(r, \mathbf{R}) \phi_n(r) dr \quad (60.61)$$

$$= \frac{\omega}{2\pi} \int_0^{2\pi/\omega} F^{(c)}[r(t)] e^{is\omega t} dt. \quad (60.62)$$

The three-dimensional generalization is [23]

$$F_{n,n'}^{(q)} \approx F_s^{(c)}(\mathbf{J}) = \frac{1}{8\pi^3} \int F^c[\mathbf{r}(\mathbf{J}, \mathbf{w})] e^{is \cdot \mathbf{w}} d\mathbf{w}, \quad (60.63)$$

where \mathbf{n}, \mathbf{n}' denotes the triple of quantum numbers (n, ℓ, m) , (n', ℓ', m') , respectively, and $s = \mathbf{n} - \mathbf{n}'$.

The correspondence between the three-dimensional quantum and classical matrix elements in Eq. (60.63) follows from the general Fourier expansion for any classical function $F^{(c)}(\mathbf{r})$ periodic in \mathbf{r} ,

$$F^{(c)}[\mathbf{r}(t)] = \sum_s F_s^{(c)}(\mathbf{J}) \exp(-is \cdot \mathbf{w}), \quad (60.64)$$

where \mathbf{J}, \mathbf{w} denotes the action-angle conjugate variables for the motion. For the three-dimensional Coulomb problem, the action-angle variables are

$$\begin{aligned} J_n &= n\hbar, & w_n &= \left(\frac{\partial E}{\partial J_n} \right) t + \delta, \\ J_\ell &= \left(\ell + \frac{1}{2} \right) \hbar, & w_\ell &= \psi_E, \\ J_m &= m\hbar, & w_m &= \phi_E, \end{aligned} \quad (60.65)$$

where ψ_E is the Euler angle between the line of nodes and a direction in the plane of the orbit (usually taken to be the direction of the perihelion or perigee), and is constant for a Coulomb potential. The Euler angle ϕ_E is the angle between the line of nodes and the fixed x -axis. See [23] for details.

The first-order S -matrix is

$$S_{fi} = -\frac{i\omega}{2\pi\hbar} \int_0^{2\pi/\omega} dt_e \int_{-\infty}^\infty dt V[\mathbf{R}(t), r(t+t_e)] e^{is\omega t_e}, \quad (60.66)$$

with $s = i - f$, \mathbf{R} is the classical path of the projectile, and $r(t_e)$ is the classical internal motion of the Rydberg electron.

60.3.4 Strong Coupling Correspondence Principle

The S -matrix is

$$S_{fi} = \frac{\omega}{2\pi} \int_0^{2\pi/\omega} dt_e \times \exp \left\{ i(s\omega t_e) - \frac{i}{\hbar} \int_{-\infty}^\infty V[\mathbf{R}(t), r(t+t_e)] dt \right\}. \quad (60.67)$$

See [23–26] for additional details.

60.3.5 Equivalent Oscillator Theorem

$$\sum_n^f a_n(t) V_{fn}(t) e^{i\omega_f t} = \sum_{d=-f}^f a_{d+f}(t) V_d(t) e^{-id\omega t}. \quad (60.68)$$

The S -matrix is

$$\begin{aligned} S_{n',n} &= a_{n'}(t \rightarrow \infty) \\ &= \int_0^{2\pi} \frac{d\mathbf{w}}{8\pi^3} \exp \left[is \cdot \mathbf{w} - \frac{i}{\hbar} \int_{-\infty}^\infty V(\mathbf{w} + \omega t, t) dt \right]. \end{aligned} \quad (60.69)$$

60.4 Distribution Functions

The function $W_\alpha(x)dx$ characterizes the probability (distribution) of finding an electron in a Rydberg orbital α within a volume dx centered at the point x in phase space. Integration of the distribution function W_α over all phase space volumes dx yields, depending upon the normalization chosen, either unity or the density of states appropriate to the orbital α .

60.4.1 Spatial Distributions

Distribution over n, ℓ, m [4]

$$\begin{aligned} W_{n\ell m}(r, \theta) r^2 \sin \theta dr d\theta \\ = \frac{r^2 \sin \theta dr d\theta}{\pi^2 a^2 r \{ [e^2 - (1 - r/a)^2] [\sin^2 \theta - (m/\ell)^2] \}^{1/2}}, \end{aligned} \quad (60.70)$$

where $a = Ze^2/2|E| = n^2\hbar^2/mZe^2\hbar^2$ is the semimajor axis, and $e^2 = 1 - (\ell/n)^2$ is the eccentricity.

Distribution over n, ℓ

$$W_{n\ell}(r, \theta)r^2 \sin \theta dr d\theta = g(n\ell) \frac{r^2 \sin \theta dr d\theta}{2\pi a^2 r [e^2 - (1 - r/a)^2]^{1/2}}, \quad (60.71)$$

where $g(n\ell) = 2\ell$.

Distribution over n

$$W_n(r)r^2 dr = g(n) \frac{2}{\pi} \left[1 - \left(1 - \frac{r}{a} \right)^2 \right]^{1/2} \frac{r dr}{a^2}, \quad (60.72)$$

with $g(n) = n^2$.

60.4.2 Momentum Distributions

Distribution over n, ℓ [4]

$$W_{n\ell}(p)p^2 dp = g(n\ell) \frac{4}{\pi} \frac{dx}{(1+x^2)^2}, \quad (60.73)$$

where $x = p/p_n$ and $p_n^2 = 2m|E|$.

Distribution over n

$$W_n(p)p^2 dp = g(n) \frac{32}{\pi} \frac{x^2 dx}{(1+x^2)^4}. \quad (60.74)$$

Sum rules

$$\frac{1}{n^2} \sum_{\ell, m} |G_{n\ell m}(\mathbf{k})|^2 = \left(\frac{na_0}{Z} \right)^3 \frac{8}{\pi^2 (x^2 + 1)^4}, \quad (60.75a)$$

$$\frac{1}{n^2} \sum_{\ell=0}^{n-1} (2\ell + 1) |g_{n\ell}(k)|^2 k^2 = \frac{32na_0 x^2}{\pi Z (x^2 + 1)^4}, \quad (60.75b)$$

where $x = nka_0/Z$, and

$$G_{n\ell m}(\mathbf{k}) = g_{n\ell}(k) Y_{\ell m}(\hat{\mathbf{k}}), \quad (60.76a)$$

$$g_{n\ell}(k) = \left(\frac{2}{\pi} \frac{(n-\ell-1)!}{(n+\ell)!} \right)^{1/2} \left(\frac{a_0}{Z} \right)^{3/2} 2^{2(\ell+1)} n^2 \ell! \times \frac{(-ix)^\ell}{(x^2+1)^{\ell+2}} C_{n-\ell-1}^{(\ell+1)} \left(\frac{x^2-1}{x^2+1} \right), \quad (60.76b)$$

where $C_i^{(j)}(y)$ is the associated Gegenbauer polynomial. See Chap. 9 for additional details on hydrogenic wave functions.

Quantum defect representation [27]

$$g_{n\ell}(k) = - \left(\frac{2}{\pi} \frac{\Gamma(n^* - 1)}{\Gamma(n^* + \ell + 1)} \right)^{1/2} n^* (a_0/Z)^{3/2} 2^{2(\ell+1)} \times \frac{(\ell+1)! (-ix)^\ell}{(x^2+1)^{\ell+2}} J(n^*, \ell+1; X), \quad (60.77)$$

where $n^* = n - \delta$, δ being the quantum defect, and $x = n^*ka_0/Z$. The function J is given by the recurrence relation

$$J(n^*, \ell+1; X) = - \frac{1}{2(2\ell+2)} \frac{\partial}{\partial X} J(n^*, \ell; X),$$

$$J(n^*, 0; X) = - \frac{n^* \sin[n^*(\beta - \pi)]}{\sin(\beta - \pi)} - \frac{\sin n^* \pi}{\pi} \int_0^1 \frac{(1-s^2)s^{n^*}}{(1-2Xs+s^2)} ds, \quad (60.78)$$

where $X = (x^2 - 1)/(x^2 + 1)$, and $\beta = \cos^{-1} X$. In the limit $\ell \ll n^*$, Eq. (60.77) becomes

$$|g_{n\ell}(k)|^2 = 4 \left(\frac{n^* a_0}{Z} \right)^3 \frac{1 - (-1)^\ell \cos[2n^*(\beta - \pi)]}{\pi x^2 (x^2 + 1)^2}. \quad (60.79)$$

Classical density of states

$$\rho(E) = \int \delta[E - H(\mathbf{p}, \mathbf{r})] \frac{d\mathbf{p}d\mathbf{r}}{(2\pi\hbar)^3} = \frac{n^5 \hbar^2}{mZ^2 e^4}. \quad (60.80)$$

60.5 Classical Theory

The classical cross section for energy transfer ΔE between two particles, with arbitrary masses m_1, m_2 , and charges Z_1, Z_2 , is given by [28]

$$\sigma_{\Delta E}(\mathbf{v}_1, \mathbf{v}_2) = \frac{2\pi(Z_1 Z_2 e^2 V)^2}{v^2 |\Delta E|^3} \times \left(1 + \cos^2 \bar{\theta} + \frac{\Delta E}{\mu v V} \cos \bar{\theta} \right), \quad (60.81)$$

valid for $-1 \leq \cos \bar{\theta} - \Delta E/(\mu v V) \leq 1$, and $\sigma_{\Delta E}(\mathbf{v}_1, \mathbf{v}_2) = 0$ otherwise, where

$$\mathbf{v} = \mathbf{v}_1 - \mathbf{v}_2, \quad (60.82a)$$

$$\mathbf{V} = (m_1 \mathbf{v}_1 + m_2 \mathbf{v}_2)/M, \quad (60.82b)$$

$$\cos \bar{\theta} = \frac{1}{vV} \mathbf{v} \cdot \mathbf{V}, \quad (60.82c)$$

and $\mu = m_1 m_2 / M$, $M = m_1 + m_2$. If particle 2 has an isotropic velocity distribution in the lab frame, the effective cross section averaged over the direction $\hat{\mathbf{n}}_2$ of \mathbf{v}_2 is

$$v_1 \sigma_{\Delta E}^{(\text{eff})}(\mathbf{v}_1, \mathbf{v}_2) = \frac{1}{4\pi} \int d\hat{\mathbf{n}}_2 |\mathbf{v}_1 - v_2 \hat{\mathbf{n}}_2| \sigma_{\Delta E}(\mathbf{v}_1, \mathbf{v}_2). \quad (60.83)$$

If v_1 is also isotropic, then the average of Eq. (60.83), together with Eq. (60.81), gives for the special case of a Coulomb potential

$$\begin{aligned} \sigma_{\Delta E}^{(\text{eff})}(\mathbf{v}_1, \mathbf{v}_2) &= \frac{\pi(Z_1 Z_2 e^2)^2}{4|\Delta E|3v_1^2 v_2} \left[(v_1^2 - v_2^2)(v_2^2 - v_1^2)(v_l^{-1} - v_u^{-1}) \right. \\ &\quad \left. + (v_1^2 + v_2^2 + v_1^2 + v_2^2)(v_u - v_l) - \frac{1}{3}(v_u^3 - v_l^3) \right], \end{aligned} \quad (60.84)$$

where

$$v'_1 = (v_1^2 - 2\Delta E/m_1)^{1/2}, \quad (60.85)$$

$$v'_2 = (v_2^2 + 2\Delta E/m_2)^{1/2}, \quad (60.86)$$

and v_u, v_l are defined below for cases 1–4. With the definitions

$$\Delta\varepsilon_{12} = 4m_1 m_2 (E_1 - E_2)/M^2, \quad \Delta m_{12} = |m_1 - m_2|,$$

$$\Delta\tilde{\varepsilon}_{12} = \frac{4m_1 m_2}{M^2} \left(E_1 \frac{v_2}{v_1} - E_2 \frac{v_1}{v_2} \right),$$

the four cases are

1. $\Delta E \geq \Delta\varepsilon_{12} + |\Delta\tilde{\varepsilon}_{12}| \geq 0$, and $2m_2 v_2 \geq \Delta m_{12} v_1$

$$v_l = v'_2 - v'_1, \quad v_u = v'_1 + v'_2, \quad \Delta E \geq 0; \quad (60.87a)$$

$$v_l = v_2 - v_1, \quad v_u = v_1 + v_2, \quad \Delta E \leq 0. \quad (60.87b)$$

If $2m_2 v_2 < \Delta m_{12} v_1$, then $\sigma_{\Delta E}^{(\text{eff})}(v_1, v_2) = 0$,

2. $\Delta\varepsilon_{12} - \Delta\tilde{\varepsilon}_{12} \leq \Delta E \leq \Delta\varepsilon_{12} + \Delta\tilde{\varepsilon}_{12}$, and $m_1 > m_2$

$$v_l = v'_2 - v'_1, \quad v_u = v_1 + v_2, \quad \Delta E \geq 0; \quad (60.87c)$$

$$v_l = v_2 - v_1, \quad v_u = v'_1 + v'_2, \quad \Delta E \leq 0. \quad (60.87d)$$

3. $\Delta E \leq \Delta\varepsilon_{12} - |\Delta\tilde{\varepsilon}_{12}| \leq 0$, and $2m_1 v_1 \geq \Delta m_{12} v_2$

$$v_l = v_1 - v_2, \quad v_u = v_1 + v_2, \quad \Delta E \geq 0; \quad (60.87e)$$

$$v_l = v'_1 - v'_2, \quad v_u = v'_1 + v'_2, \quad \Delta E \leq 0. \quad (60.87f)$$

If $2m_1 v_1 < \Delta m_{12} v_2$, then $\sigma_{\Delta E}^{(\text{eff})}(v_1, v_2) = 0$,

4. $\Delta\varepsilon_{12} + \Delta\tilde{\varepsilon}_{12} \leq \Delta E \leq \Delta\varepsilon_{12} - \Delta\tilde{\varepsilon}_{12}$, and $m_1 < m_2$

$$v_l = v_1 - v_2, \quad v_u = v'_1 + v'_2, \quad \Delta E \geq 0; \quad (60.87g)$$

$$v_l = v'_1 - v'_2, \quad v_u = v_1 + v_2, \quad \Delta E \leq 0. \quad (60.87h)$$

If $2m_1 v_1 < \Delta m_{12} v_2$, then $\sigma_{\Delta E}^{(\text{eff})}(v_1, v_2) = 0$.

Since v'_1 and v'_2 , given by Eqs. (60.85) and (60.86), respectively, must be real, $\sigma_{\Delta E}(\mathbf{v}_1, \mathbf{v}_2) = 0$ for ΔE outside the range

$$-\frac{1}{2}m_2 v_2^2 \leq \Delta E \leq \frac{1}{2}m_1 v_1^2, \quad (60.88)$$

which simply expresses the fact that the particle losing energy in the collision cannot lose more than its initial kinetic energy.

The cross section Eq. (60.84) must be integrated over the classically allowed range of energy transfer ΔE and averaged over a prescribed speed distribution $W(v_2)$ before a comparison with experiment can be made. See [28, 29] for details.

Classical removal cross section [30] The cross section for removal of an electron from a shell is given by

$$\sigma_r(V) = \int_0^\infty f(v) \sigma_{\Delta E}(\mathbf{v}_1, \mathbf{v}_2) dv. \quad (60.89)$$

Total removal cross section [30] In an independent electron model,

$$\sigma_r^{\text{total}}(V) = N_{\text{shell}} \sigma_r(V), \quad (60.90)$$

where N_{shell} is the number of equivalent electrons in a shell. In a shielding model,

$$\sigma_r^{\text{total}}(V) = \left[1 - \frac{(N_{\text{shell}} - 1)}{4\pi \bar{r}^2} \sigma_r(V) \right] N_{\text{shell}} \sigma_r(V), \quad (60.91)$$

where \bar{r}^2 is the root mean square distance between electrons within a shell. Experiment [31] favors Eq. (60.91) over Eq. (60.90). See Fig. 4a–e of [30] for details.

Classical trajectory and Monte-Carlo methods are covered in Chap. 62.

60.6 Universality Properties

Universality properties [32, 33] have been observed in all the alkalis' atoms in ultracold Rydberg collisions where the scattering length, a , is very much greater than the effective range of the interaction, R_{eff} . The result is that details of the two-body collision are characterized by a single parameter, a , the scattering length, that is universal and independent of the details of the short-range interaction at such low energies.

In the case of three-body collisions, a universal property, first predicted in 1970 by *Efimov* [34], is that there is an infinite number of shallow three-body bound states with binding energies $E_T^{(n)}$ that has an accumulation point at $E = 0$. The *Efimov effect* of the occurrence of an infinite number of three-body bound states is present for both the case of three identical bosons, and more generally for three bodies where at least two of the three have large S-wave scattering lengths.

In the general case, the bound states appear in the spectrum at critical values of a that differ by multiplicative factors of e^{π/s_0} , where s_0 only depends on the masses and spin statistics of the particles and is the solution of the transcendental equation,

$$s_0 \cosh \frac{\pi s_0}{2} = \frac{8}{\sqrt{3}} \sinh \frac{\pi s_0}{6}. \quad (60.92)$$

The solution of Eq. (60.92) yields $s_0 \sim 1.00624$.

Asymptotic number of bound states

$$N \longrightarrow \frac{s_0}{\pi} \ln \frac{|a|}{r_0}, \quad (60.93)$$

for scattering length a and hard-core radius r_0 .

$$E_T^{(n+1)}/E_T^{(n)} \longrightarrow 1/515.03 \quad (60.94)$$

as $n \rightarrow +\infty$ and with the scattering length $a = \pm\infty$.

Asymptotic spectrum: general case

$$E_T^{(n)} \longrightarrow (e^{-2\pi/s_0})^{n-n_*} \frac{\hbar^2 \kappa_*^2}{m}. \quad (60.95)$$

60.6.1 Equal Mass Case**Asymptotic spectrum: three identical bosons**

$$E_T^{(n)} \longrightarrow \left(\frac{1}{515.03} \right)^{n-n_*} \frac{\hbar^2 \kappa_*^2}{m}, \quad (60.96)$$

with $n \rightarrow +\infty$, the scattering length $a = \pm\infty$, and where κ_* is a three-body parameter that is the zeros of

$$\sin\left(\frac{1}{2}s_0 \ln[mE_T/(\hbar^2 \kappa_*^2)]\right) = 0, \quad (60.97)$$

with s_0 being the solution of Eq. (60.92). See Table 1 of [32] for useful tabulations of scattering lengths for the alkali atoms. See §III.F of [33] for details on the ultracold experiments of the alkali atoms.

Atom-dimer scattering length (shallow dimers)

$$a_{AD} = (b_1 - b_0 \tan[s_0 \ln(a\kappa_*) + \beta])a, \quad (60.98)$$

where b_0, b_1 , and β are universal parameters, and κ_* is the three-body parameter in Eq. (60.96). The parameters in Eq. (60.98) are universal in that they hold for all identical bosons, independent of the details of their short-range interactions.

Atom-dimer scattering length a and effective range r_s (deep dimers)

$$a_{AD} = (1.46 + 2.15 \cot[s_0 \ln(a/a_*) + i\eta_*])a, \quad (60.99a)$$

$$r_{s,AD} = (1.13 + 0.73 \cot[s_0 \ln(a/a_*) + 0.98 + i\eta_*])^2 a, \quad (60.99b)$$

where a_* is the scattering length when the Efimov resonance is at the atom-dimer threshold, and is related to the three-body parameter, κ_* ; and η_* is an inelasticity parameter, generally ~ 0.1 . See §6 and 7 of [32] for a full discussion. Atom and dimer here refer to one boson scattering with a pair of bosons (dimer) in either a shallow or a deep well.

Atom-dimer cross section (deep dimers)

$$\sigma_{AD} = 84.9 \frac{\sin^2[s_0 \ln(a/a_*) - 0.97] + \sinh^2 \eta_*}{\sin^2[s_0 \ln(a/a_*)] + \sinh^2 \eta_*} \quad (60.100)$$

at $E = -E_D$, where E_D is the atom-dimer threshold Efimov resonance in which S-wave scattering dominates.

60.6.2 Unequal Mass Case

The two heavy masses are M , and the one light mass is m .

Asymptotic spectrum: two heavy – one light [35]

$$\frac{\Gamma_T^{(n)}}{E_T^{(n)}} \longrightarrow 103.0 \exp(-1.260 \sqrt{M/m}) \times \sin^2 \left[\frac{1}{2} s_0 \ln(4E_{\text{deep}}/E_T^{(n)}) \right], \quad (60.101a)$$

$$s_0 \sim 0.567142 \sqrt{M/m}, \quad (60.101b)$$

as $n \rightarrow \infty$ with $a = \pm\infty$ and $M \gg m$; $\Gamma_T^{(n)}$ and E_{deep} are the width of the Efimov trimer resonance and the binding energy of the dimer well, respectively.

60.7 Many-Body and Multiparticle Effects**60.7.1 Many-Body Theory**

Gross–Pitaevskii Equation [36, 37]

$$[T(x) - \mu]\Psi(x) + \int d^3x' V(x - x') |\Psi(x')|^2 \Psi(x) = 0, \quad (60.102)$$

where Ψ is the Bose condensate wavefunction; T and V are the kinetic and potential energy operators (respectively), and μ is the chemical potential. See the standard monographs [38–41], on many-body theory for more general details.

60.7.2 Dilute Bose Gas

The Lee-Huang-Yang equation for the second correction to the thermodynamic ground state of a dilute Bose gas has been proven in a mathematically rigorous manner [42],

$$E(\rho) \geq 4\pi\rho^2 a \left(1 + \frac{128}{15\sqrt{\pi}} \sqrt{\rho a^3} + O(\sqrt{\rho a^3}) \right), \quad (60.103)$$

where $E(\rho)$ is the energy density of the Bose gas with density ρ , and scattering length a .

Further details on the use of Rydberg states in quantum information can be found in Chap. 85 of this handbook, and [43–46].

60.8 Working Formulae for Rydberg Collisions

60.8.1 Inelastic n, ℓ -Changing Transitions

$$A^*(n\ell) + B \rightarrow A^*(n') + B + \Delta E_{n',n\ell}, \quad (60.104)$$

where $\Delta E_{n',n\ell} = E_{n'} - E_{n\ell}$ is the energy defect. The cross section for Eq. (60.104) in the quasi-free electron model [47] is

$$\sigma_{n',n\ell}(V) = \frac{2\pi a_s^2}{(V/v_B)^2 n^3} f_{n',n\ell}(\lambda), \quad \ell \ll n, \quad (60.105)$$

where a_s is the scattering length for $e^- + B$ scattering, $\lambda = n^* a_0 \omega_{n',n\ell} / V$, $\omega_{n',n\ell} = |\Delta E_{n',n\ell}| / \hbar$, $E_{n'} = -R_\infty / n'^2$, and $E_{n\ell} = -R_\infty / n^*$, with $n^* = n - \delta_\ell$. Also, v_B is the atomic unit of velocity (Chap. 1), and

$$f_{n',n\ell}(\lambda) = \frac{2}{\pi} \left[\tan^{-1} \left(\frac{2}{\lambda} \right) - \frac{\lambda}{2} \ln \left(1 + \frac{4}{\lambda^2} \right) \right]. \quad (60.106)$$

Limiting cases: $f_{n',n\ell}(\lambda) \rightarrow 1$ as $\lambda \rightarrow 0$, and $f_{n',n\ell}(\lambda) \approx 8 / (3\pi\lambda^3)$ for $\lambda \gg 1$. Then

$$\sigma_{n',n\ell} \approx \begin{cases} \frac{2\pi a_s^2}{(V/v_B)^2 n^3}, & \lambda \rightarrow 0, \\ \frac{16a_s^2 V n^3}{3v_B |\delta_\ell + \Delta n|^3}, & \lambda \gg 1. \end{cases} \quad (60.107)$$

Rate coefficients

$$\langle \sigma_{n',n\ell}(V) \rangle \equiv \langle V \sigma_{n',n\ell}(V) \rangle / \langle V \rangle \quad (60.108a)$$

$$= \frac{2\pi a_s^2}{(V_T/v_B)^2 n^3} \varphi_{n',n\ell}(\lambda_T), \quad (60.108b)$$

where $V_T = \sqrt{2k_B T / \mu}$, $\lambda_T = n^* a_0 \omega_{n',n\ell} / V_T$, $\Delta n = n' - n$, and μ is the reduced mass of A–B. The function $\varphi_{n',n\ell}(\lambda_T)$ in Eq. (60.108a) is given by

$$\varphi_{n',n\ell}(\lambda_T) = e^{\lambda_T^2/4} \operatorname{erfc} \left(\frac{1}{2} \lambda_T \right) - \frac{\lambda_T}{\pi} \int_0^\infty \frac{du}{\sqrt{u}} e^{-u} \ln \left(1 + \frac{4}{\lambda_T^2} \right) \quad (60.109a)$$

$$= \begin{cases} 1 - \frac{\lambda_T}{\sqrt{\pi}} \ln(1/\lambda_T^2), & \lambda_T \rightarrow 0, \\ 2 / (\sqrt{\pi} \lambda_T^3), & \lambda_T \gg 1, \end{cases} \quad (60.109b)$$

and $\operatorname{erfc}(x)$ is the complementary error function.

Hydrogenic For the case of hydrogen, Dewangan [48] reformulated the hypergeometric functions appearing in Gordon's formulae in terms of Jacobi polynomials $P_i^{(\alpha,\beta)}(\phi)$, a form more suitable for numerical computation

$$R_{n,\ell}^{n',\ell-1} = C_J \left[\frac{(n-\ell+1)(n-\ell)}{(n+\ell)(n+\ell-1)} P_{n-\ell+1}^{(\Delta-1, 2\ell-1)}(\cos\phi) - \sin^2 \left(\frac{1}{2} \phi \right) P_{n-\ell-1}^{(\Delta+1, 2\ell-1)}(\cos\phi) \right], \quad (60.110)$$

where the constant C_J is,

$$C_J = \left(\frac{1}{4} \sqrt{\frac{(n+\ell)!(n'+\ell-1)!}{(n-\ell-1)!(n'-\ell)!}} \cot^{2\ell+2} \left(\frac{1}{2} \phi \right) \times \sin^{\Delta+2\ell} \left(\frac{1}{2} \phi \right) \Gamma(n+\ell-1) \right)^{-1},$$

and $\Delta = n' - n \geq 1$.

Asymptotic Expressions [48]: Two Cases

(a) $n \gg n' \gg 1$ near continuum threshold The exact expression Eq. (60.110) has the following asymptotic form in terms of Airy functions $Ai(x)$

$$R_{n,\ell}^{n',\ell-1} \simeq \frac{4^\ell (n')^{\ell+1}}{n^{3/2}} \sqrt{\frac{(n'+\ell-1)!}{(n'-\ell)!}} \times \left[\frac{4n'(n'+\ell)}{(2n'+1)^{2\ell+1/3}} Ai \left(-\frac{1}{(2n'+1)^{1/3}} \right) + \frac{(2\ell-1)}{2^{2\ell-2/3}} \frac{Ai(0)}{(n')^{2\ell-2/3}} - \frac{1}{(2n'-1)^{2\ell-5/3}} Ai \left(\frac{1}{(2n'-1)^{1/3}} \right) \right] \quad (60.111)$$

suitable for practical computations, and where $\ell \ll n'$.

(b) $\Delta = n - n' \geq 1$ nearby Rydberg states

$$R_{n,\ell}^{n',\ell-1} \simeq B_J \left[J_{\Delta-1}(A_1\phi) - (n-\ell+1)(n-\ell) \frac{A_1^{\Delta-1}}{A_2^{\Delta+1}} J_{\Delta+1}(A_2\phi) \right], \quad (60.112)$$

for small Δ/n , $J_\alpha(x)$ is a Bessel function of order α , and the constants are defined

$$B_J = \sqrt{\frac{\phi}{2}} \left(\frac{1}{4} \sqrt{\frac{(n+\ell)!(n-\ell-1)!}{(n'-\ell)!(n'+\ell-1)!}} \cos^{5/2} \left(\frac{1}{2} \phi \right) \times \sin^{-3/2} \left(\frac{1}{2} \phi \right) \frac{1}{A_1^{\Delta-1}} \right) \quad (60.113a)$$

$$A_1^2 = \left(\frac{(n+n'-1)^2 - (2\ell-1)^2}{4} \right) \times \left[1 - \frac{\Delta(\Delta-2)}{3[(n+n'-1)^2 - (2\ell-1)^2]} \right], \quad (60.113b)$$

$$A_2^2 = \left(\frac{(n+n'+1)^2 - (2\ell-1)^2}{4} \right) \times \left[1 - \frac{\Delta(\Delta+2)}{3[(n+n'+1)^2 - (2\ell-1)^2]} \right]. \quad (60.113c)$$

See §4 of [48] for an extensive discussion of the numerical evaluations of both the Jacobi, and the Airy and Bessel function formulations.

Form factors for $ns \rightarrow n's$ transitions [48] The full expression from Eq. (60.41), in terms of an integral over a pair of hypergeometric functions ${}_1F_1$, is computationally difficult for large n, n' . Recast in terms of Jacobi polynomials it results in an expression that is much more suitable for practical computation

$$F_{n's,ns}(Q) = \frac{4}{Q n^{5/2} n'^{3/2}} \left(\frac{1}{\sin^2(\frac{\phi}{2})} \right)^{n-1} \times P_{n-1}^{(\Delta,1)}(\cos \phi) \operatorname{Im}(u) \quad (60.114a)$$

$$= \frac{1}{Q n^{1/2} n'^{3/2}} \sin \Theta \left(\sin \frac{1}{2} \phi \right)^\Delta \times \left(\cos \frac{1}{2} \phi \right)^2 P_{n-1}^{(\Delta,1)}(\cos \phi), \quad (60.114b)$$

where $\Delta = n' - n$, and u and Θ are defined,

$$u = \frac{(\frac{1}{n} - \frac{1}{n'} + iQ)^{n-1} (\frac{1}{n} - \frac{1}{n'} - iQ)^{n'-1}}{(\frac{1}{n} + \frac{1}{n'} - iQ)^{n+n'}} \quad (60.115)$$

$$\Theta = (n+n') \arctan \frac{Qnn'}{(n+n')} - \Delta \arctan \frac{Qnn'}{\Delta}.$$

60.8.2 Inelastic $n \rightarrow n'$ Transitions

$$A^*(n) + B \rightarrow A^*(n') + B + \Delta E_{n'n}. \quad (60.116)$$

(A) Cross sections

$$\sigma_{n'n} = \sum_{\ell\ell'} \frac{(2\ell+1)}{n^2} \sigma_{n'\ell',n\ell}, \quad (60.117)$$

$$\sigma_{n',n}(V) = \frac{2\pi a_s^2}{(V/v_B)^2 n'^3} F_{n'n}(\lambda), \quad (60.118)$$

where $\lambda = na_0\omega_{n'n}/V = |\Delta n|v_B/(n^2V)$, and

$$F_{n'n}(\lambda) = \frac{2}{\pi} \left[\tan^{-1} \left(\frac{2}{\lambda} \right) - \frac{2\lambda(3\lambda^2 + 20)}{3(4 + \lambda^2)^2} \right]. \quad (60.119)$$

Limiting cases

$$\sigma_{n'n} \approx \begin{cases} \frac{2\pi a_s^2}{(V/v_B^2 n'^3)}, & \lambda \ll 1, \\ \frac{256\sigma_{e^-B}^{\text{elastic}}(V/v_B)^3 n^7}{15\pi|\Delta n|5}, & \lambda \gg 1, \end{cases} \quad (60.120)$$

where $\sigma_{e^-B}^{\text{elastic}}$ is the elastic cross section for $e^- + B$ -scattering.

(B) Rate coefficients

$$K_{n'\ell',n\ell}(T) = \langle V\sigma_{n'\ell',n\ell} \rangle, \quad (60.121a)$$

$$K_{n'n}(T) = \sum_{\ell,\ell'} \frac{(2\ell+1)}{n^2} K_{n'\ell',n\ell}, \quad (60.121b)$$

$$K_{n'n}(T) = \frac{v_B\sigma_{e^-B}^{\text{elastic}}}{\sqrt{\pi}n^3(V_T/v_B)} \Phi_{n'n}(\lambda_T), \quad (60.121c)$$

where

$$\Phi_{n'n}(\lambda_T) = e^{\lambda_T^2/8} \left[e^{\lambda_T^2/8} \operatorname{erfc} \left(\frac{1}{2} \lambda_T \right) - \frac{\lambda_T^2}{\sqrt{2\pi}} D_{-3} \left(\frac{\lambda_T}{2} \right) - \frac{5\lambda_T}{\sqrt{\pi}} D_{-4} \left(\frac{\lambda_T}{\sqrt{2}} \right) \right] \quad (60.122a)$$

$$\approx \begin{cases} 1 - 8\lambda_T/3\sqrt{\pi}, & \lambda_T \ll 1 \\ 2^6/(\sqrt{\pi}\lambda_T^5), & \lambda_T \gg 1 \end{cases}, \quad (60.122b)$$

where $D_{-v}(y)$ denotes the parabolic cylinder function.

Limiting cases

$$K_{n'n}(T) \approx \begin{cases} \left(\frac{\mu R_\infty}{\pi m_e k_B T} \right)^{1/2} \frac{v_B\sigma_{e^-B}^{\text{elastic}}}{n^3}, & \lambda_T \rightarrow 0, \\ \frac{2^6 v_B\sigma_{e^-B}^{\text{elastic}} n^7}{\pi|\Delta n|5} \left(\frac{2k_B T}{\mu v_B^2} \right)^2, & \lambda_T \gg 1. \end{cases} \quad (60.123)$$

Born Results

$$\sigma_{n'n} = \frac{8\pi}{k^2} \frac{1}{n^2} \int_{|k-k'|}^{k+k'} F_{n'n}(Q) \frac{d(Qa_0)}{(Qa_0)^3}. \quad (60.124)$$

(A) Electron–Rydberg atom collision

$$\sigma_{n'n} = \frac{8\pi a_0^2 R_\infty}{Z^2 E n^2} \left[\left(1 - \frac{1}{4\Delta n} \right) \frac{(\varepsilon\varepsilon')^{3/2}}{(\Delta\varepsilon)^4} \ln(1 + \varepsilon_e/\varepsilon) + \left(1 - \frac{0.6}{\Delta n} \right) \frac{\varepsilon_e}{\varepsilon + \varepsilon_e} \frac{(\varepsilon')^{3/2}}{(\Delta\varepsilon)^2} \left(\frac{4}{3\Delta n} + \frac{1}{\varepsilon} \right) \right], \quad (60.125)$$

for $n' > n$, where $\varepsilon_e = E/(Z^2 R_\infty)$, $\varepsilon = 1/n^2$, $\varepsilon' = 1/n'^2$, and $\Delta\varepsilon = \varepsilon - \varepsilon'$.

(B) Heavy-particle–Rydberg atom collision

$$\sigma_{n'n} = \frac{8\pi a_0^2 Z^2}{Z^4 n^2 \varepsilon_e} \left[\left(1 - \frac{1}{4\Delta n} \right) \frac{(\varepsilon \varepsilon')^{3/2}}{(\Delta \varepsilon)^4} \ln(1 + \varepsilon_e/\varepsilon) + \left(1 - \frac{0.6}{\Delta n} \right) \frac{\varepsilon_e}{\varepsilon + \varepsilon_e} \frac{(\varepsilon')^{3/2}}{(\Delta \varepsilon)^2} \left(\frac{4}{3\Delta n} + \frac{1}{\varepsilon} \right) \right], \quad (60.126)$$

where $\varepsilon_e = m\varepsilon/MZ^2R_\infty$ with heavy-particle mass and charge denoted above by M and Z , respectively, and all other terms retain their meaning as in Eq. (60.125).

60.8.3 Quasi-Elastic ℓ -Mixing Transitions

$$\sigma_{n\ell}^{(\ell\text{-mixing})} \equiv \sum_{\ell' \neq \ell} \sigma_{n\ell', n\ell} \quad (60.127a)$$

$$\approx \begin{cases} \sigma_{\text{geo}} = 4\pi a_0^2 n^4, & n \ll n_{\text{max}}, \\ 2\pi a_s^2 v_B^2 / V^2 n^3, & n \gg n_{\text{max}}. \end{cases} \quad (60.127b)$$

The two limits correspond to strong (close) coupling for $n \ll n_{\text{max}}$ and weak coupling for $n \gg n_{\text{max}}$, and expressions Eq. (60.127b) are valid when the quantum defect δ_ℓ of the initial Rydberg orbital $n\ell$ is small; n_{max} is the principal quantum number, where the ℓ -mixing cross section reaches a maximum [49],

$$n_{\text{max}} \approx \left(\frac{v_B |a_s|}{V a_0} \right)^{2/7}. \quad (60.128)$$

For Rydberg atom–noble gas atom scattering, $n_{\text{max}} = 8$ to 20, while for Rydberg atom–alkali atom scattering $n_{\text{max}} = 15$ to 30.

60.8.4 Elastic $n\ell \rightarrow n\ell'$ Transitions

$$A^*(n\ell) + B \rightarrow A^*(n\ell') + B. \quad (60.129)$$

(A) Cross sections

$$\sigma_{ns}^{\text{elastic}}(V) = \frac{2\pi C_{ss} a_s^2}{(V/v_B)^2 n^{*4}}, \quad (60.130)$$

valid for $n^* \gg [v_B |a_s| / (4V a_0)]^{1/4}$ with

$$C_{ss} = \frac{8}{\pi^2} \int_0^{1/\sqrt{2}} [K(k)]^2 dk, \quad (60.131)$$

where $K(k)$ denotes the complete elliptic integral of the first kind.

(B) Rate coefficients [50] (three cases) With the definitions

$$v_B = v_B/v_{\text{rms}}, \quad v_{\text{rms}} = \sqrt{(8k_B T)/\mu\pi}, \quad (60.132)$$

$$f(y) = y^{-1/2}(1 - (1 - y)e^{-y}) + y^{3/2}\text{Ei}(y), \quad (60.133)$$

$$y = (v_B a_s)^2 / (4\pi a_0^2 n^{*8}), \quad (60.134)$$

$$n_1 = (|a_s| v_B / 4a_0)^{1/4}, \quad (60.135)$$

$$n_2 = 0.7 \left[|a_s| v_B^{5/6} / (\alpha_d a_0^3)^{1/6} \right]^{1/3}, \quad (60.136)$$

where α_d is the dipole polarizability of A^* , then

$$\langle \sigma_{ns}^{\text{el}} \rangle \approx \begin{cases} 8\pi a_0^2 n^{*4}, & n^* \leq n_1, \\ 4\pi^{1/2} a_0 |a_s| v_B f(y), & n_1 \leq n^* \leq n_2, \\ \begin{cases} 7(\alpha_d v_B)^{2/3} + \frac{4a_s^2 v_B^2}{n^{*4}} \\ - \frac{2.7a_s^2 v_B^2 (\alpha_d v_B)^{1/3}}{a_0 n^{*6}}, \end{cases} & n^* \geq n_2. \end{cases} \quad (60.137)$$

60.8.5 Inelastic $n\ell \rightarrow n\ell'$ Transitions**(A) Impact Parameter Theory with cutoffs [51, 52]**

$$\langle \sigma_{n\ell} \rangle = 9.93 \cdot 10^{-6} \left(\frac{\mu}{m} \right)^{1/2} \frac{D_{n\ell}}{T_e^{1/2}} \times \left\{ 11.54 + \log_{10} \left(\frac{T_e m}{D_{n\ell} \mu} \right) + 2 \log_{10} R_c \right\} \text{cm}^3/\text{sec}. \quad (60.138)$$

where μ is the reduced mass of the system, m is the electron mass, T_e is the temperature in K and,

$$D_{n\ell} = \left(\frac{Z_p}{Z_t} \right)^2 6n^2(n^2 - \ell^2 - \ell - 1) \quad (60.139)$$

with Z_p and Z_t denoting the charge of the projectile and target, respectively.

Pengelly and Seaton's expression Eq. (60.138) includes a sum over $\ell' = \ell \pm 1$, and therefore only includes the contribution of dipole transitions. See [53] and [54] for further details on the contribution of multipole transitions to the rate coefficients and line emissivities. See also [54] and [55] for tabulations of rate coefficients and line emissivities, and Eq. (14) of [54] for a modified version of Pengelly and Seaton's expression which includes more accurately the contribution from small energies.

The cutoff parameter, R_c is defined,

$$R_c = \min\{R_c^{\text{d}}, R_c^{\text{nd}}, R_D\} \quad (60.140)$$

with,

$$R_c^{\text{d}} = 0.72v\tau \quad (60.141a)$$

$$R_c^{\text{nd}} = 1.12\hbar v / \Delta E \quad (60.141b) \quad \text{where,}$$

$$R_D = \left[\frac{k_B T_e}{4\pi e^2 n_e} \right]^{1/2} \quad (60.141c)$$

where v is the projectile speed, τ , the lifetime of the initial state and ΔE is the energy difference between non-degenerate initial and final states.

The individual cutoffs R_c^{d} and R_c^{nd} for degenerate and non-degenerate states, respectively, are introduced to avoid the logarithmic divergence at large impact parameters. The third cutoff, R_D is the Debye screening length, is used to model the effect of screening at large impact parameters.

(B) Exact Classical Theory for hydrogenic collisions [56, 57] Exploiting the dynamical SO(4) symmetry of the hydrogen atom, Vranceanu and Flannery solved exactly the time-dependent classical equations for the transition probability,

$$P_{\ell'\ell}^n(\chi) = \frac{2\ell'/n^2}{\pi\hbar \sin^2(\chi/2)} \begin{cases} 0 & \mathcal{B} < 0 \\ \frac{K[\mathcal{B}/(\mathcal{B}-\mathcal{A})]}{\sqrt{\mathcal{B}-\mathcal{A}}} & \mathcal{B} > 0, \mathcal{A} < 0 \\ \frac{K[(\mathcal{B}-\mathcal{A})/\mathcal{B}]}{\sqrt{\mathcal{B}}} & \mathcal{B} > 0, \mathcal{A} > 0 \end{cases} \quad (60.142)$$

where χ is the rotation angle,

$$\cos \frac{\chi}{2} = \frac{1 + \alpha^2 \cos(\sqrt{1 + \alpha^2} \Delta\Phi)}{(1 + \alpha^2)}, \quad (60.143)$$

with $K(k)$ denoting the complete elliptic integral of the first kind, $\alpha = 3Z_p a_n v_n / 2bv$ is the Stark parameter, $\Delta\Phi$ is the polar angle swept out during the collision, and,

$$\mathcal{A}(\ell/n, \ell'/n; \chi) = \frac{\cos(u_1 + u_2) - \cos \chi}{1 - \cos \chi} \quad (60.144a)$$

$$\mathcal{B}(\ell/n, \ell'/n; \chi) = \frac{\cos(u_1 - u_2) - \cos \chi}{1 - \cos \chi} \quad (60.144b)$$

where the angles u_1 and u_2 only depend on the initial and final states, respectively,

$$\cos u_1 = 2\ell^2/n^2 - 1 \quad (60.145a)$$

$$\cos u_2 = 2\ell'^2/n^2 - 1 \quad (60.145b)$$

(C) Semiclassical Transition Probability [58]

$$P^{\text{SC}}(\ell/n, \ell'/n; \chi) = \frac{2\ell'}{\pi\hbar n^2 \sin \chi} \times \begin{cases} 0 & |\sin \chi| < |\sin(\eta_1 - \eta_2)| \\ \frac{K[\mathcal{B}/\mathcal{A}]}{\sqrt{\mathcal{A}}} & |\sin \chi| > |\sin(\eta_1 + \eta_2)| \\ \frac{K[\mathcal{A}/\mathcal{B}]}{\sqrt{\mathcal{B}}} & |\sin \chi| < |\sin(\eta_1 + \eta_2)| \end{cases} \quad (60.146)$$

$$A = \sin^2 \chi - \sin^2(\eta_1 - \eta_2) \quad (60.147a)$$

$$B = \sin^2(\eta_1 + \eta_2) - \sin^2(\eta_1 - \eta_2) \quad (60.147b)$$

and,

$$\cos \eta_1 = \ell/n \quad (60.148a)$$

$$\cos \eta_2 = \ell'/n \quad (60.148b)$$

(D) Exact Quantal Theory for hydrogenic collisions [57, 59, 60] Vranceanu and Flannery made use of the isomorphism between SO(4) and SO(3) \oplus SO(3) to solve the Schrödinger equation in the interaction picture, under assumptions of an adiabatic, dipole and classical path, to yield the transition probability on the energy shell

$$P_{\ell'\ell}^{(n)} = \frac{2\ell' + 1}{n} \sum_{L=|\ell'-\ell|}^{n-1} (2L+1) \begin{bmatrix} \ell' & \ell & L \\ j & j & j \end{bmatrix}^2 H_{jL}^2(\eta) \quad (60.149)$$

where $\{\dots\}$ denotes the 6- j symbol, and,

$$H_{jL}(\eta) = (2L)!! \sqrt{\frac{(2j+1)(2j-L)!}{(2j+L+1)!}} \left(\sin \frac{\eta}{2}\right)^L \times C_{2j-L}^{(1+L)}\left(\cos \frac{\eta}{2}\right) \quad (60.150)$$

is a standard result from group theory [61, 62], and with,

$$\cos \frac{\eta}{2} = \frac{1 + \alpha^2 \cos \sqrt{1 + \alpha^2} \Delta\Phi}{1 + \alpha^2} \quad (60.151)$$

where α and $\Delta\Phi$ have the same meanings as in (B) above. $C_n^{(\alpha)}(x)$ is the ultraspherical, or Gegenbauer polynomials of index n and order α [63]. See Table 1 of [60] for a list of exact expressions for $P_{\ell'\ell}^{(n)}$ for $n = 1-5$.

60.8.6 Fine Structure $n\ell J \rightarrow n\ell J'$ Transitions

$$A^*(n\ell J) + B \rightarrow A^*(n\ell J') + B + \Delta E_{J'J}. \quad (60.152)$$

(A) Cross sections (two cases)

$$\sigma_{n\ell J}^{n\ell J'}(V) = \frac{2J' + 1}{2(2\ell + 1)} c_{\text{norm}} 4\pi a_0^2 n^{*4}, \quad (60.153)$$

valid for $n^* \leq n_0(V)$, and

$$\sigma_{n\ell J}^{n\ell J'}(V) = \frac{2\pi C_{J'J}^{(\ell)} a_s^2 v_B^2}{V^2 n^{*4}} \varphi_{J'J}^{(\ell)}(v_{J'J}) \left(1 - \frac{n_0^8(V)}{2n^{*8}}\right), \quad (60.154)$$

valid for $n^* \geq n_0(V)$, where the quantity $n_0(V)$ is the effective principal quantum number such that the impact parameter ρ_0 of B (moving with relative velocity V) equals the radius $2n^{*2}a_0$ of the Rydberg atom A^* ; $n_0(V)$ is given by the solution to the following transcendental equation

$$n_0^8(V) = \frac{(2\ell + 1)C_{J'J}^{(\ell)}}{2(2J' + 1)c_{\text{norm}}} \left(\frac{v_B a_s}{V a_0} \right)^2 \varphi_{J'J}^{(\ell)}(v_{J'J}[n_0(V)]) . \quad (60.155)$$

The constant c_{norm} in Eq. (60.153) is equal to $5/8$ if $\sigma_{\text{geo}} = \pi \langle r^2 \rangle_{n\ell}$, or 1 if $\sigma_{\text{geo}} = 4\pi a_0^2 n^{*4}$. The function $\varphi_{J'J}^{(\ell)}(v_{J'J})$ in Eq. (60.154) is given, in general, by [64, 65]

$$\varphi_{J'J}^{(\ell)}(v_{J'J}) = \xi_{J'J}^{(\ell)}(v_{J'J}) / \xi_{J'J}^{(\ell)}(0) , \quad (60.156a)$$

$$\xi_{J'J}^{(\ell)}(v_{J'J}) = \sum_{s=0}^{\ell} A_{\ell J', \ell J}^{(2s)} \int_{v_{J'J}}^{\infty} j_s^2(z) J_s^2(z) z dz , \quad (60.156b)$$

$$v_{J'J} = |\delta_{\ell J'} - \delta_{\ell J}| \frac{v_B}{V n^*} , \quad (60.156c)$$

where $j_s(z)$ is the spherical Bessel function, and the coefficients $C_{J'J}^{(\ell)}$ and $A_{\ell J', \ell J}^{(2s)}$ in Eqs. (60.154) and (60.156b), respectively, are given in Table 5.1 of *Beigman and Lebedev* [4]. The quantum defect of Rydberg state $n\ell J$ is $\delta_{\ell J}$. For elastic scattering, $v_{JJ} = 0$, and $\varphi_{JJ}^{(\ell)}(0) = 1$.

Symmetry relation

$$\xi_{J'J}^{(\ell)}(v_{J'J}) = \frac{2J + 1}{2J' + 1} \xi_{J'J}^{(\ell)}(v_{J'J}) . \quad (60.157)$$

(B) Rate coefficients

$$\begin{aligned} \langle \sigma_{n\ell J'}^{n\ell J} \rangle &= \left(\frac{c_{\text{norm}}(2J' + 1)C_{J'J}^{(\ell)}}{2(2\ell + 1)} \right)^{1/2} \\ &\times \pi a_0^2 F(\zeta) \left(\frac{v_B |a_s|}{V_{\text{T}} a_0} \right) , \end{aligned} \quad (60.158)$$

where $\zeta = n_0^8(V_{\text{T}})/n^{*8}$, and

$$F(\zeta) \equiv \sqrt{\zeta} \left[E_2(\zeta) + \frac{1}{\zeta} (1 - e^{-\zeta}) \right] , \quad (60.159)$$

where $E_2(x)$ is an exponential integral.

Limiting cases

$$\langle \sigma_{n\ell J'}^{n\ell J} \rangle = \begin{cases} \frac{2J' + 1}{2(2\ell + 1)} c_{\text{norm}} 4\pi a_0^2 n^{*4} , & n^* \ll n_{\text{max}}^* , \\ \frac{2\pi C_{J'J}^{(\ell)} a_s^2 v_B^2}{V_{\text{T}}^2 n^{*4}} , & n^* \gg n_{\text{max}}^* , \end{cases} \quad (60.160)$$

where $n_{\text{max}}^* = (3/2)^{1/8} n_0(V)$ if $v_{J'J} \ll 1$.

60.9 Impulse Approximation

60.9.1 Quantal Impulse Approximation

Basic Formulation [66]

Consider a Rydberg collision between a projectile (1) of charge Z_1 and a target with a valence electron (3) in orbital ψ_i bound to a core (2). The full three-body wave function for the system of projectile + target is denoted by Ψ_i . The relative distance between 1 and the center-of-mass of 2–3 is denoted by σ , while the separation of 2 from the center-of-mass of 1–3 is ρ .

Formal scattering theory

$$\Psi_i^{(+)} = \Omega^{(+)} \psi_i , \quad (60.161)$$

where the Möller scattering operator $\Omega^{(+)} = 1 + G^+ V_i$, and $V_i = V_{12} + V_{13}$.

Let χ_m be a complete set of free-particle wave functions satisfying

$$(H_0 - E_m) \chi_m = 0 \quad (60.162)$$

and define operators $\omega_{ij}^+(m)$ by

$$\omega_{ij}^+(m) \chi_m = \left(1 + \frac{1}{E_m - H_0 - V_{ij} + i\epsilon} V_{ij} \right) \chi_m , \quad (60.163)$$

where V_{ij} denotes the pairwise interaction potential between particles i and j ($i, j = 1, 2, 3$). Then the action of the full Green's function G^+ on the two-body potential V_{ij} is

$$\begin{aligned} G^+ V_{ij} &= \left[\omega_{ij}^+(m) - 1 \right] \\ &+ G^+ [(E_m - E) + V_{12} + V_{13} + V_{23} - V_{ij}] \\ &\times \left[\omega_{ij}^+(m) - 1 \right] . \end{aligned} \quad (60.164)$$

Projection operators

$$b_{ij}^+(m) = \omega_{ij}^+(m) - 1 , \quad (60.165a)$$

$$b_{ij}^+ = \sum_m b_{ij}^+(m) |\chi_m\rangle \langle \chi_m| , \quad \omega_{ij}^+ = b_{ij}^+ + 1 . \quad (60.165b)$$

$$G^+ V_{ij} |\psi_i\rangle = \sum_m G^+ V_{ij} |\chi_m\rangle \langle \chi_m | \psi_i\rangle \quad (60.166a)$$

$$\begin{aligned} &= \left[b_{ij}^+ + G^+ [V_{23}, b_{ij}^+] \right. \\ &\left. + G^+ [V_{12} + V_{13} - V_{ij}] b_{ij}^+(m) \right] |\psi_i\rangle . \end{aligned} \quad (60.166b)$$

Möller scattering operator

$$\Omega^+ = (\omega_{13}^+ + \omega_{12}^+ - 1) + G^+[V_{23}, (b_{13}^+ + b_{12}^+)] + G^+(V_{13}b_{12}^+ + V_{12}b_{13}^+). \quad (60.167)$$

Exact T -matrix

$$T_{if} = \langle \psi_f | V_f | (\omega_{13}^+ + \omega_{12}^+ - 1) \psi_i \rangle + \langle \psi_f | V_f | G^+[V_{23}, (b_{13}^+ + b_{12}^+)] \psi_i \rangle + \langle \psi_f | V_f | G^+(V_{13}b_{12}^+ + V_{12}b_{13}^+) \psi_i \rangle. \quad (60.168)$$

The impulse approximation to the exact T -matrix element Eq. (60.168) is obtained by ignoring the second term involving the commutator of V_{23} ,

$$\Psi_i \longrightarrow \Psi_i^{\text{imp}} = (\omega_{13}^+ + \omega_{12}^+ - 1) \psi_i. \quad (60.169)$$

Impulse approximation: post form

$$T_{if}^{\text{imp}} = \langle \psi_f | V_f | (\omega_{13}^+ + \omega_{12}^+ - 1) \psi_i \rangle. \quad (60.170)$$

The impulse approximation can also be expressed using incoming-wave boundary conditions by making use of the prior operators

$$\omega_{ij}^-(m) \chi_m = \left(1 + \frac{1}{E_m - H_0 - V_{ij} - i\epsilon} V_{ij} \right) \chi_m, \quad (60.171a)$$

$$\omega_{ij}^- = \sum_m \omega_{ij}^-(m) |\chi_m\rangle \langle \chi_m|. \quad (60.171b)$$

The impulse approximation Eq. (60.170) is exact if V_{23} is a constant since the commutator of V_{23} vanishes in that case.

Applications [66]

(1) Electron capture $X^+ + H(i) \rightarrow X(f) + H^+$.

$$T_{if}^{\text{imp}} = \langle \psi_f | V_{12} + V_{23} (\omega_{12}^+ + \omega_{13}^+ - 1) \psi_i \rangle. \quad (60.172)$$

Wave functions: $\psi_i = e^{i\mathbf{k}_i \cdot \boldsymbol{\rho}} \varphi_i(\mathbf{r})$, $\psi_f = e^{i\mathbf{k}_f \cdot \boldsymbol{\rho}} \varphi_f(\mathbf{x})$, $\chi_m = (2\pi)^{-3} \exp[i(\mathbf{K} \cdot \mathbf{x} + \mathbf{k} \cdot \boldsymbol{\rho})]$, where the φ_n are hydrogenic wave functions.

If X above is a heavy particle, the V_{12} term in Eq. (60.172) may be omitted due to the difference in mass between the projectile 1 and the bound Rydberg electron 3. See [66] and

references therein for details. With the definitions

$$\begin{aligned} z &= \frac{4\alpha\delta^2}{(T-2\delta)(T-2\alpha\delta)}, & T &= \beta^2 + P^2, \\ \delta &= i\beta\mathbf{K} - \mathbf{p} \cdot \mathbf{K}, & v &= aZ_1/K, \\ \mathbf{t}_1 &= \mathbf{K}/a + \mathbf{v}, & N(v) &= e^{\pi v/2} \Gamma(1-iv), \\ a &= \frac{M_1}{M_1 + m_e}, & b &= \frac{M_2}{M_2 + m_e}, \\ \mathbf{k} &= a\mathbf{k}_2 - (1-a)\mathbf{k}_f, & \mathbf{K} &= a\mathbf{k}_1 - (1-a)\mathbf{k}_i, \\ \mathbf{t} &= (\mathbf{K} - \mathbf{p})/a, & \mathbf{p} &= a\mathbf{k}_f - \mathbf{k}_i, \\ \beta &= aZ_1/n, \end{aligned}$$

and n is the principal quantum number, the impulse approximation to the T -matrix becomes, in this case,

$$T_{if}^{\text{imp}} \approx \langle \psi_f | V_{23} | \omega_{13}^+ \psi_i \rangle \quad (60.173)$$

$$= \frac{-1}{2\pi^2 a^3} \int \frac{d\mathbf{K}}{t^2} N(v) g_i(\mathbf{t}_1) \mathcal{F}(f, \mathbf{K}, \mathbf{p}), \quad (60.174)$$

where, for a general final s -state,

$$\begin{aligned} \mathcal{F}(f, \mathbf{K}, \mathbf{p}) &= \int \varphi_f^*(\mathbf{x}) e^{i\mathbf{p} \cdot \mathbf{x}} \\ &\times {}_1F_1[iv, 1; i(Kx - \mathbf{K} \cdot \mathbf{x})] d\mathbf{x}, \quad (60.175) \end{aligned}$$

and $g_i(\mathbf{t}_1)$ denotes the Fourier transform of the initial state. The normalization of the Fourier transform is chosen such that momentum and coordinate space hydrogenic wave functions are related by $\varphi_n(\mathbf{r}) = (2\pi)^{-3} \int \exp(i\mathbf{t}_1 \cdot \mathbf{r}) g_n(\mathbf{t}_1) d\mathbf{t}_1$. For the case $f = 1s$,

$$\begin{aligned} \mathcal{F}(1s, \mathbf{K}, \mathbf{p}) &= -\frac{\beta^{3/2}}{\sqrt{\pi}} \frac{\partial}{\partial \beta} \mathcal{I}(v, 0, \beta, -\mathbf{K}, \mathbf{p}) \\ &= 8\sqrt{\pi} \beta^{3/2} \left[\frac{(1-iv)\beta}{T^2} \right. \\ &\quad \left. + \frac{iv(\beta - iK)}{T(T-2\delta)} \left(\frac{T}{T-2\delta} \right)^{iv} \right] \quad (60.176) \end{aligned}$$

evaluated at $\beta = aZ_1$. For the case $f = 2s$,

$$\mathcal{F}(2s, \mathbf{K}, \mathbf{p}) = -\frac{\beta^{3/2}}{\sqrt{\pi}} \left[\left(\frac{\partial}{\partial \beta} + \beta \frac{\partial^2}{\partial \beta^2} \right) \mathcal{I}(v, 0, \beta, -\mathbf{K}, \mathbf{p}) \right] \quad (60.177)$$

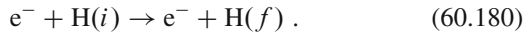
evaluated at $\beta = aZ_1/2$. For a general final ns -state f ,

$$\begin{aligned} \mathcal{I}(v, \alpha, \beta, \mathbf{K}, \mathbf{p}) &= \frac{4\sqrt{\pi}}{T} \left(\frac{T-2\alpha\delta}{T-2\delta} \right)^{iv} \\ &\times (U \cosh \pi v \pm iV \sinh \pi v), \quad (60.178) \end{aligned}$$

where the complex quantity $U + iV$ is

$$U + iV = (4z)^{iv} \frac{\Gamma(\frac{1}{2} + iv)}{\Gamma(1 + iv)} \times {}_2F_1(-iv, -iv; 1 - 2iv; 1/z). \quad (60.179)$$

(2) Electron impact excitation



Neglecting V_{12} and exchange yields the approximate T -matrix element

$$\begin{aligned} T_{if}^{\text{imp}} &\approx \langle \psi_f | V_{13} | \omega_{13}^+ \psi_i \rangle \\ &= \frac{-Z_1}{(2\pi a)^3} \int d\mathbf{x} \int d\mathbf{r} e^{iq \cdot \sigma} \phi_f^*(\mathbf{r}) \frac{1}{x} \\ &\quad \times \int d\mathbf{K} N(\nu) g_i(\mathbf{t}_1) e^{i\mathbf{t}_1 \cdot \mathbf{r}} {}_1F_1(iv, 1; i\mathbf{K}x - i\mathbf{K} \cdot \mathbf{x}) \end{aligned} \quad (60.181)$$

$$\begin{aligned} &= \frac{-Z_1}{(2\pi a)^3} \int d\mathbf{K} N(\nu) g_i(\mathbf{t}_1) g_f^*(\mathbf{t}_2) \\ &\quad \times \mathcal{I}(\nu, 0, 0, -\mathbf{K}, -\mathbf{q}), \end{aligned} \quad (60.182)$$

where

$$\begin{aligned} \mathcal{I}(\nu, 0, 0, -\mathbf{K}, -\mathbf{q}) &= \lim_{\beta \rightarrow 0} \frac{4\pi}{\beta^2 + q^2} \left(\frac{\beta^2 + q^2}{\beta^2 + q^2 + 2\mathbf{q} \cdot \mathbf{K} - 2i\beta\mathbf{K}} \right)^{iv} \\ &= \frac{4\pi}{q^2} \left| 1 + \frac{2\mathbf{K}}{q} \cos \theta \right|^{-iv} A(\cos \theta), \end{aligned} \quad (60.183)$$

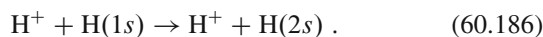
$$= \frac{4\pi}{q^2} \left| 1 + \frac{2\mathbf{K}}{q} \cos \theta \right|^{-iv} A(\cos \theta), \quad (60.184)$$

with

$$A(\cos \theta) = \begin{cases} 1, & \cos \theta > -q/2K, \\ e^{-\pi\nu}, & \cos \theta < -q/2K, \end{cases} \quad (60.185)$$

and $\cos \theta = \hat{\mathbf{K}} \cdot \hat{\mathbf{q}}$, $\mathbf{t}_2 = \mathbf{t}_1 + b\mathbf{q}$ and $\mathbf{q} = \mathbf{k}_i - \mathbf{k}_f$.

(3) Heavy-particle excitation [67]



$$\begin{aligned} T_{if}^{\text{imp}} &= -\frac{Z_1 2^{15/2} b^5}{\pi a^3 q^2} \int_0^\infty dK N(K) K^2 \int_{-1}^1 d(\cos \theta) \\ &\quad \times \left| 1 + \frac{2\mathbf{K}}{q} \cos \theta \right|^{-iv} \tilde{A}(\cos \theta), \end{aligned} \quad (60.187)$$

where

$$\begin{aligned} \tilde{A}(\cos \theta) &= \frac{2\pi}{D^4} \left(\frac{\alpha D(D - 2b^2)}{(\alpha^2 - \beta^2)^{3/2}} + \frac{8(3b^2 - D)}{(\alpha^2 - \beta^2)^{1/2}} \right. \\ &\quad - \frac{48\gamma^2 D^2 b^2}{(\gamma^2 - \delta^2)^{5/2}} + \frac{16D[\gamma D - (3\gamma + 4\alpha)b^2]}{(\gamma^2 - \delta^2)^{3/2}} \\ &\quad \left. + \frac{32(D - 3b^2)}{(\gamma^2 - \delta^2)^{1/2}} \right) A(\cos \theta), \end{aligned} \quad (60.188)$$

with $A(\cos \theta)$ given by Eq. (60.185), and

$$\alpha = b^2 + v^2 + \frac{K^2}{a^2} + \frac{K}{aq} \left(\frac{q^2}{\mu} + \Delta E \right) \cos \theta, \quad (60.189a)$$

$$\beta = \frac{K}{aq} \sin \theta \left[4v^2 q^2 - \left(\frac{q^2}{\mu} + \Delta E \right)^2 \right]^{1/2}, \quad (60.189b)$$

$$\delta = 4\beta, \quad \gamma = 4\alpha + D, \quad (60.189c)$$

$$D = \frac{4bq}{a} (q + 2K \cos \theta), \quad (60.189d)$$

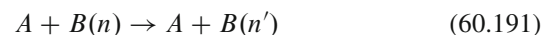
while ν and $N(\nu)$ retain their meaning from Eq. (60.173).

(4) Ionization $e^- + H(i) \rightarrow e^- + H^+ + e^-$.

$$T_{if}^{\text{imp}} \approx -\frac{4\pi}{q^2} N(\nu) g_i(\mathbf{k} - b\mathbf{q}) \left(\frac{q^2}{q^2 - 2\mathbf{q} \cdot \mathbf{K}} \right)^{iv}, \quad (60.190)$$

where $\mathbf{K} = a(\mathbf{k} - b\mathbf{q} - \mathbf{v})$ and $\mathbf{q} = \mathbf{k}_i - \mathbf{k}_f$ and exchange and V_{12} are neglected.

(5) Rydberg atom collisions [23, 68]



Consider a Rydberg collision between a projectile (3) and a target with an electron (1) bound in a Rydberg orbital to a core (2) [23, 68].

Full T -matrix element

$$T_{fi}(\mathbf{k}_3, \mathbf{k}'_3) = \langle \phi_f(\mathbf{r}_1) e^{i\mathbf{k}'_3 \cdot \mathbf{r}_3} | V(\mathbf{r}_1, \mathbf{r}_3) | \Psi_i^{(+)}(\mathbf{r}_1, \mathbf{r}_3; \mathbf{k}_3) \rangle, \quad (60.193)$$

with primes denoting quantities after the collision, and where the potential V is

$$V(\mathbf{r}_1, \mathbf{r}_3) = V_{13}(\mathbf{r}) + V_{3C}(\mathbf{r}_3 + a\mathbf{r}_1), \quad \mathbf{r} = \mathbf{r}_1 - \mathbf{r}_3, \quad (60.194)$$

with $a = M_1/(M_1 + M_2)$, while the subscript C labels the core. The impulse approximation to the full, outgoing wave function $\Psi_i^{(+)}$ is written as

$$\Psi_i^{\text{imp}} = (2\pi)^{3/2} \int g_i(\mathbf{k}_1) \Phi(\mathbf{k}_1, \mathbf{k}_3; \mathbf{r}_1, \mathbf{r}_3) d\mathbf{k}_1, \quad (60.195)$$

$$g_i(\mathbf{k}_1) = \frac{1}{(2\pi)^{3/2}} \int \phi_i(\mathbf{r}_1) e^{-i\mathbf{k}_1 \cdot \mathbf{r}_1} d\mathbf{r}_1. \quad (60.196)$$

Impulse approximation

$$T_{fi}^{\text{imp}}(\mathbf{k}_3, \mathbf{k}'_3) = \int d\mathbf{k}_1 \int d\mathbf{k}'_1 g_f^*(\mathbf{k}'_1) g_i(\mathbf{k}_1) T_{13}(\mathbf{k}, \mathbf{k}') \times \delta[\mathbf{P} - (\mathbf{k}'_1 - \mathbf{k}_1)], \quad (60.197)$$

where T_{13} is the exact off-shell T -matrix for 1–3 scattering,

$$T_{13}(\mathbf{k}, \mathbf{k}') = \langle \exp(i\mathbf{k}' \cdot \mathbf{r}) | V_{13}(\mathbf{r}) | \psi(\mathbf{k}, \mathbf{r}) \rangle. \quad (60.198)$$

The delta function in Eq. (60.197) ensures linear momentum, $\mathbf{K} = \mathbf{k}_1 + \mathbf{k}_3 = \mathbf{k}'_1 + \mathbf{k}'_3$, is conserved in 1–3 collisions, with

$$\mathbf{k}'_1 = \mathbf{k}_1 + (\mathbf{k}_3 - \mathbf{k}'_3) \equiv \mathbf{k}_1 + \mathbf{P}, \quad (60.199a)$$

$$\mathbf{k}' = \frac{M_3}{M_1 + M_3} (\mathbf{k}_1 + \mathbf{k}_3) - \mathbf{k}'_3 = \mathbf{k} + \mathbf{P}. \quad (60.199b)$$

Elastic scattering

$$T_{ii}(\mathbf{k}_3, \mathbf{k}_3) = \int g_f^*(\mathbf{k}_1) g_i(\mathbf{k}_1) T_{13}(\mathbf{k}, \mathbf{k}) d\mathbf{k}_1, \quad (60.200)$$

where $\mathbf{k} = (M_3/M)\mathbf{k}_1 + (M_1/M)\mathbf{k}_3$, and $M = M_1 + M_3$.

Integral cross section: for 3–(1,2) scattering,

$$\sigma_{if}(k_3) = \left(\frac{M_{AB}}{M_{13}} \right)^2 \frac{k'_3}{k_3} \int | \langle g_f(\mathbf{k}_1 + \mathbf{P}) | \times f_{13}(\mathbf{k}, \mathbf{k}') g_i(\mathbf{k}_1) \rangle |^2 d\hat{\mathbf{k}}'_3, \quad (60.201)$$

where M_{AB} is the reduced mass of the 3–(1,2) system, and M_{13} the reduced mass of 1–3. The 1–3 scattering amplitude f_{13} is given by

$$f_{13}(\mathbf{k}, \mathbf{k}') = -\frac{1}{4\pi} \left(\frac{2M_{13}}{\hbar^2} \right) T_{13}(\mathbf{k}, \mathbf{k}'). \quad (60.202)$$

Six Approximations to Eq. (60.197)

(1) Optical theorem

$$\begin{aligned} \sigma_{\text{tot}}(k_3) &= \frac{1}{k_3} \frac{2M_{AB}}{\hbar^2} T_{ii}(\mathbf{k}_3, \mathbf{k}'_3) \\ &= \frac{1}{v_3} \int |g_i(\mathbf{k}_1)|^2 [v_{13} \sigma_{13}^T(v_{13})] d\mathbf{k}_1, \end{aligned} \quad (60.203)$$

where σ_{13}^T is the total cross section for 1–3 scattering at relative speed v_{13} . The resultant cross section Eq. (60.203) is an upper limit and contains no interference terms.

(2) Plane-wave final state

$$\phi_f(\mathbf{r}_1) = (2\pi)^{-3/2} \exp(i\mathbf{k}'_1 \cdot \mathbf{r}_1), \quad (60.204)$$

$$g_f(\mathbf{k}'_1) = \delta(\mathbf{k}'_1 - \boldsymbol{\kappa}'_1), \quad (60.205)$$

$$T_{fi}(\mathbf{k}_3, \mathbf{k}'_3) = g_i(\mathbf{k}_1) T_{13}(\mathbf{k}, \mathbf{k}'), \quad \mathbf{k}_1 = \boldsymbol{\kappa}_1 - \mathbf{P}, \quad (60.206)$$

$$\frac{d\sigma_{if}}{d\hat{\mathbf{k}}'_3 d\mathbf{k}'_1} = \left(\frac{M_{AB}}{M_{13}} \right)^2 \frac{k'_3}{k_3} |g_i(\mathbf{k}_1)|^2 |f_{13}(\mathbf{k}, \mathbf{k}')|^2. \quad (60.207)$$

(3) Closure

$$\sum_f g_f(\mathbf{k}'_1) g_f^*(\mathbf{k}''_1) = \delta(\mathbf{k}'_1 - \mathbf{k}''_1), \quad (60.208)$$

$$\frac{d\sigma_{if}^T}{d\hat{\mathbf{k}}'_3} = \frac{\bar{k}'_3}{k_3} \left(\frac{M_{AB}}{M_{13}} \right)^2 \int |g_i(\mathbf{k}_1)|^2 |f_{13}(\mathbf{k}, \mathbf{k}')|^2 d\mathbf{k}_1, \quad (60.209)$$

where $\mathbf{k}'_1 = (M_3/M)(\mathbf{k}_1 + \mathbf{k}_3) - \mathbf{k}'_3$.

Conditions for validity of Eq. (60.209): (a) k_3 is high enough to excite all atomic bound and continuum states, and (b) $k_3^2 = (k_3^2 - 2\varepsilon_{fi}/M_{AB})$ can be approximated by k_3 , or by an averaged wavenumber $\bar{k}'_3 = (k_3^2 - 2\bar{\varepsilon}_{fi}/M_{AB})^{1/2}$, where the averaged excitation energy is

$$\bar{\varepsilon}_{fi} = \ln\{\varepsilon_{fi}\} = \sum_j f_{ij} \ln \varepsilon_{ij} \left(\sum_j f_{ij} \right)^{-1}, \quad (60.210)$$

and the f_{ij} are the oscillator strengths.

(4) Peaking approximation

$$T_{fi}^{\text{peak}}(\mathbf{k}_3, \mathbf{k}'_3) = F_{fi}(\mathbf{P}) T_{13}(\mathbf{k}, \mathbf{k}'), \quad (60.211)$$

where F_{fi} is the inelastic form factor

$$F_{fi}(\mathbf{P}) = \int g_f^*(\mathbf{k}_1 + \mathbf{P}) g_i(\mathbf{k}_1) d\mathbf{k}_1 \quad (60.212)$$

$$= \langle \psi_f(\mathbf{r}) \exp(i\mathbf{P} \cdot \mathbf{r}) | \psi_i(\mathbf{r}) \rangle. \quad (60.213)$$

(5) $T_{13} = T_{13}(\mathbf{P})$

$$T_{fi}(\mathbf{k}_3, \mathbf{k}'_3) = T_{13}(\mathbf{P}) F_{fi}(\mathbf{P}). \quad (60.214)$$

(6) $T_{13} = \text{constant}$ $f_{13} \equiv a_s = \text{constant}$ scattering length.

$$\sigma_{if}(k_3) = \frac{2\pi a_s^2}{k_3^2} \left(\frac{M_{AB}}{M_{13}} \right)^2 \int_{k_3 - k'_3}^{k_3 + k'_3} |F_{fi}(\mathbf{P})|^2 P dP, \quad (60.215)$$

$$\sigma_{\text{tot}}(k_3) = \begin{cases} 4\pi a_s^2, & v_3 \gg v_1 \\ \langle v_1 \rangle 4\pi a_s^2 / v_3, & v_3 \ll v_1. \end{cases} \quad (60.216)$$

Validity Criteria

(A) Intuitive formulation [68]

- (i) Particle 3 scatters separately from 1 and 2, i.e., $r_{12} \gg A_{1,2}$; the relative separation of (1,2) \gg the scattering lengths of 1 and 2.
- (ii) $\lambda_{13} \ll r_{12}$, i.e., the reduced wavelength for 1–3 relative motion $\ll r_{12}$. Interference effects of 1 and 2 can be ignored and 1, 2 treated as *independent* scattering centers.
- (iii) 2–3 collisions do not contribute to inelastic 1–3 scattering.
- (iv) Momentum impulsively transferred to 1 during collision (time τ_{coll}) with $3 \gg$ momentum transferred to 1 due to V_{12} , i.e.,

$$P \gg \langle \psi_{n\ell} | -\nabla V_{12} | \psi_{n\ell} \rangle \tau_{\text{coll}}. \quad (60.217)$$

For a precise formulation of validity criteria based upon the two-potential formula, see the Appendix of [68].

Two classes of interaction in A – $B(n)$ Rydberg collisions justify use of the impulse approximation for the T -matrix for 1–3 collisions: (i) quasi-classical binding with $V_{\text{core}} = \text{const.}$, and (ii) weak binding with

$$E_3 \gg \Delta E_c \approx \langle \psi_n(\mathbf{r}) | V_{1C}(\mathbf{r}) | \psi_n(\mathbf{r}) \rangle, \quad (60.218a)$$

$$\langle \psi_n(\mathbf{r}_1) | -\frac{\hbar^2}{2M_{12}} \nabla_1^2 | \psi_n(\mathbf{r}_1) \rangle \approx |\varepsilon_n|, \quad (60.218b)$$

where E_3 is the kinetic energy of relative motion of 3, and ΔE_c is the energy shift in the core. The fractional error is [69]

$$\frac{f_{13}}{\lambda} \frac{\Delta E_c}{\hbar} \left(\frac{\hbar}{E_3} + \tau_{\text{delay}} \right) \ll 1, \quad (60.219)$$

where $\lambda \approx k_3^{-1}$ is the reduced wavelength of 3, f_{13} is the scattering amplitude for 1–3 collisions, and τ_{delay} is the time delay associated with 1–3 collisions.

Special case: for nonresonant scattering with $\tau_{\text{delay}} = 0$,

$$\frac{f_{13}}{\lambda} \frac{|\varepsilon_n|}{E_3} \ll 1, \quad (60.220)$$

which follows from Eq. (60.219) upon identifying the shift in the core energy ΔE_c with the binding energy $|\varepsilon|$.

Condition Eq. (60.220) is less restrictive than Eq. (60.218a) or Eq. (60.218b) since f_{13} can be either less than or greater than λ .

60.9.2 Classical Impulse Approximation

(A) **Ionization** For electron impact on heavy particles [70], the cross section for ionization of a particle moving with velocity t by a projectile with velocity s is

$$Q(s, t) = \frac{1}{u^2} \frac{2s}{m_2} \int_1^{s^2} \frac{dz}{z^2} \left[\frac{A(z)}{z} + B(z) \right], \quad (60.221)$$

where

$$A(z) = \frac{1}{2st^3} \left[\frac{1}{3} (x_{02}^{3/2} - x_{01}^{3/2}) - 2(s^2 + t^2)(x_{02}^{1/2} - x_{01}^{1/2}) - \frac{(s^2 - t^2)^2}{2ts^3} (x_{02}^{-1/2} - x_{01}^{-1/2}) \right], \quad (60.222a)$$

$$B(z) = \frac{1}{2m_2st^3} \left[(m_1 + m_2)(s^2 - t^2)(x_{02}^{-1/2} - x_{01}^{-1/2}) - (m_2 - m_1)(x_{02}^{1/2} - x_{01}^{1/2}) \right]. \quad (60.222b)$$

For electron impact, Eq. (60.222b) is evaluated at $m_1 = 1$. The remaining terms above are given by

$$s^2 = v_2^2/v_0^2, \quad t^2 = v_1^2/v_0^2 = E_1/u,$$

$$E_2 = m_2 v_2^2,$$

$$u = v_0^2 = \text{Ionization potential of target},$$

$$x_{0i} = (s^2 + t^2 - 2st \cos \theta_i), \quad i = 1, 2,$$

$$\cos \theta_i = \begin{cases} \kappa_0 \pm \kappa_1, & |\kappa_0 \pm \kappa_1| \leq 1 \\ 1, & \kappa_0 \pm \kappa_1 > 1 \\ -1, & \kappa_0 \pm \kappa_1 < -1 \end{cases},$$

$$\kappa_0 \pm \kappa_1 = -\frac{1}{2} \left(1 - \frac{m_1}{m_2} \right) \frac{z}{st} \pm \sqrt{\left(1 + \frac{z}{t^2} \right) \left(1 - \frac{z}{s^2} \right)}.$$

Equal mass case: ($m_1 = m_2$)

$$Q(s, t) = \begin{cases} \frac{4}{3s^2} \frac{1}{u^2} \frac{2(s^2 - 1)^{3/2}}{t}, & 1 \leq s^2 \leq t^2 + 1, \\ \frac{4}{3s^2} \frac{1}{u^2} \left(2t^2 + 3 - \frac{3}{s^2 - t^2} \right), & s^2 \geq t^2 + 1. \end{cases} \quad (60.223)$$

Integrating over the speed distribution (Sect. 60.4),

$$Q(s) = \frac{32}{\pi} \frac{1}{u^2} \int_0^\infty \frac{Q(s, t) t^2 dt}{(t^2 + 1)^4}, \quad (60.224)$$

which is then numerically evaluated. For electrons, the integral can be done analytically with the result

$$Q(y) = \frac{8}{3\pi y^2(y+1)^4} \times \left[(5y^4 + 15y^3 - 3y^2 - 7y + 6)(y-1)^{1/2} + (5y^5 + 17y^4 + 15y^3 - 25y^2 + 20y) \times \tan^{-1}(y-1)^{1/2} - 24y^{3/2} \ln \left| \frac{\sqrt{y} + \sqrt{y-1}}{\sqrt{y} - \sqrt{y-1}} \right| \right],$$

with $y = s^2$.

Thomson's result

$$Q_T(y) = \frac{4}{y} \frac{1}{u^2} \left(1 - \frac{1}{y} \right). \quad (60.225)$$

(B) Electron-loss cross section [30]

$$A(V) + B(u) \rightarrow A^+ + e^- + B(f), \quad (60.226)$$

where $B(f)$ denotes that the target B is left in any state (either bound or free) after the collision with the projectile A . The initial velocity of the projectile is V , while the velocity of the Rydberg electron relative to the core is u , and the ionization potential of the target B is I .

$$\sigma_{\text{loss}} = \frac{1}{3\pi v^2} \int_{\tau/4v}^{\infty} dx \sigma_T(x\bar{u}) + \left(\frac{8vx - 1 - (v-x)^2 - 2\tau}{[1 + (v-x)^2]^3} + \frac{1}{[1 + (v+x)^2 - \tau]^2} \right), \quad (60.227)$$

where $v = V/\bar{u}$, $\tau = I/(1/2)m_e\bar{u}^2$, $\bar{u} = \sqrt{2I/m_e}$, and σ_T is the total electron scattering cross section at speed $x\bar{u}$. The cross section Eq. (60.227) is valid only for particles being stripped (or lost from the projectile), which are not strongly bound. See [30, 71, 72] for details and numerous results.

(C) Capture cross section from shell i [30]

$$\sigma_{\text{capture}}^i(V) = \frac{2^{5/2} N_i \pi}{3V^7} \int_0^{r_i} dr \int_{C(-1)}^{C(+1)} d(\cos \eta') [P_i(r)]^2 \times \frac{\sqrt{1+y^2} [4\varepsilon^2 - (\varepsilon^2 - y^2)(1 + \varepsilon^2 + a^2 - y^2)]}{r^{3/2} \varepsilon^{9/2} (1 + a^2)^3 \sqrt{y^2 - a^2}}, \quad (60.228)$$

where C denotes that the integration range $[-1, +1]$ is restricted such that the integrand is real and positive and that $|1 - \varepsilon| < \sqrt{y^2 - a^2}$. The dimensionless variables a and y above are defined as

$$y^2 = \frac{2}{m_e} |V(R)| V^2, \quad a^2 = \frac{2}{m_e} I_i V^2, \quad (60.229)$$

and with $P_i(r)/r$ representing the Hartree–Fock–Slater radial wave function for shell i , with normalization

$$\int_0^{r_i} [P_i(r)]^2 dr = 1. \quad (60.230)$$

The ionization potential and number of electrons in shell i are denoted above, respectively, by I_i and N_i .

(D) Total capture cross section [30]

$$\sigma_{\text{capture}}^{\text{total}}(V) = \sum_i \sigma_{\text{capture}}^i. \quad (60.231)$$

(E) Universal capture cross section [30] A universal curve independent of projectile mass M and charge Z is obtained from the above expressions for the capture cross section by plotting the scaled cross section

$$\tilde{\sigma}_{\text{capture}}^{\text{total}} = \frac{E^{11/4}}{M^{11/4} Z^{7/2} \lambda^{3/4}} \sigma_{\text{capture}}^{\text{total}} \quad (60.232)$$

versus the scaled energy

$$\tilde{E} = \frac{m_e E}{M I}, \quad (60.233)$$

where m_e is the mass of the particle captured, which is usually taken to be a single electron, and I is the ionization potential of the target. The term λ in Eq. (60.232) is the coupling constant in the target potential, $V(R) = m_e \lambda / R^2$, which the electron being captured experiences during the collision. See [30, Fig. 11] for details.

60.9.3 Semiquantal Impulse Approximation

Basic expression [68, 73, 74]

$$\frac{d\sigma}{d\varepsilon dP dk_1 dk d\phi_1} = \frac{k_1'^2 k_3'}{J_{55} k_3} \left(\frac{M_3}{M_{13}} \right)^2 |g_i(\mathbf{k}_1)|^2 \times |f_{13}(\mathbf{k}, \mathbf{k}')|^2. \quad (60.234)$$

J_{55} is the five-dimensional Jacobian of the transformation

$$(P, \varepsilon, k_1, k, \phi_1) \rightarrow (\hat{\mathbf{k}}_3', \mathbf{k}_1'), \quad (60.235a)$$

$$J_{55} = \frac{\partial(P, \varepsilon, k_1, k, \phi_1)}{\partial(\cos \theta_3' \phi_3', k_1', \cos \theta_1', \phi_1')}. \quad (60.235b)$$

Expression for elemental cross section [68] In the $(P, \varepsilon, k_1, k, \phi_1)$ representation,

$$d\sigma = \frac{d\varepsilon dP}{M_{13}^2 v_3^2} \left[\frac{|g_i(\mathbf{k}_1)|^2 k_1^2 dk_1 d\phi_1}{v_1} \right] \times \frac{|f_{13}(\mathbf{k}, \mathbf{k}')|^2 dg^2}{\sqrt{(g_+^2 - g^2)(g^2 - g_-^2)}}, \quad (60.236)$$

where $g_{\pm}^2 = (1/2)B \pm \sqrt{(1/4)B^2 - C}$, and

$$B = B(\varepsilon, P, v_1; v_3) = \frac{a}{(1+a)^2} \frac{P^2}{M_{13}^2} + \left(v_1^2 + v_1'^2 + v_3^2 + v_3'^2 + \frac{2\Delta_3}{M_{13}} \right) - \frac{4\varepsilon(\varepsilon + \Delta_3)}{P^2},$$

$$C = C(\varepsilon, P, v_1; v_3) = \frac{v_1^2 + av_3^2}{1+a} \frac{P^2}{M_{13}^2} + (v_1^2 - v_3^2)(v_1'^2 - v_3'^2) + \frac{2\Delta_3}{M_{13}}(v_1^2 + v_3^2) + \frac{4\Delta_3}{P^2} [v_1^2(\varepsilon + \Delta_3) - \varepsilon v_3^2],$$

$$a = \frac{M_2 M_3}{M_1(M_1 + M_2 + M_3)},$$

$$\widetilde{M}_1 = M_1(1 + M_1/M_2),$$

$$v_1'^2 = v_1^2 + \frac{2\varepsilon}{\widetilde{M}_1}, \quad v_3'^2 = v_3^2 - \frac{2(\varepsilon + \Delta_3)}{M_{AB}},$$

and Δ_3 is the change in internal energy of particle 3, while ε denotes the energy change in the target 1–2.

Hydrogenic systems $g_i(\mathbf{k}_1) = g_{nl}(\mathbf{k}_1)Y_{\ell m}(\theta_1, \phi_1)$ The g_{nl} are the hydrogenic wave functions in momentum space. See Chap. 9 for details on hydrogenic wave functions.

Elemental cross sections (m -averaged and ϕ_1 -integrated)

$$d\sigma = \frac{d\varepsilon dP}{M_{13}^2 v_3^2} \frac{W_{nl}(v_1)dv_1}{2v_1} \frac{|f_{13}(P, g)|^2 dg^2}{\sqrt{(g_+^2 - g^2)(g^2 - g_-^2)}}, \quad (60.237)$$

where the speed distribution W_{nl} is given by Eq. (60.73).

Two representations for 1–3 scattering amplitude [68]

(i) $f_{13} = f_{13}(P, g)$ is a function of momentum transferred and relative speed. Then

$$\sigma(v_3) = \frac{1}{M_{13}^2 v_3^2} \int_{\varepsilon_1}^{\varepsilon_2} d\varepsilon \int_{v_{10}}^{\infty} \frac{W_{nl}(v_1)dv_1}{v_1} \int_{P^-}^{P^+} dP \times \int_{g^-}^{g^+} \frac{|f_{13}(P, g)|^2 dg^2}{\sqrt{(g_+^2 - g^2)(g^2 - g_-^2)}}, \quad (60.238)$$

where $v_{10}^2(\varepsilon) = \max[0, (2\varepsilon/M)]$, and the limits to the P integral are

$$P^+ = P^+(\varepsilon, v_1; v_3) = \min[M(v_1' + v_1), M_{AB}(v_3' + v_3)], \quad (60.239a)$$

$$P^- = P^-(\varepsilon, v_1; v_3) = \max[M|v_1' - v_1|, M_{AB}|v_3' - v_3|], \quad (60.239b)$$

and unless $P^+ > P^-$, the P integral is zero.

(ii) $f_{13} = f_{13}(g, \psi)$ is a function of relative speed and scattering angle. Then

$$\sigma(v_3) = \frac{1}{v_3^2} \int_{\varepsilon_1}^{\varepsilon_2} d\varepsilon \int_{v_{10}}^{\infty} \frac{W_{nl}(v_1)dv_1}{v_1} \int_{g^-}^{g^+} \frac{g dg}{S(v_1, g; v_3)} \times \int_{\psi^-}^{\psi^+} \frac{|f_{13}(g, \psi)|^2 d(\cos \psi)}{\sqrt{(\cos \psi^+ - \cos \psi)(\cos \psi - \cos \psi^-)}}, \quad (60.240)$$

where

$$S(v_1, g; v_3) = \frac{M_{13}}{1+a} [(1+a)(v_1^2 + av_3^2) - ag^2]^{1/2}. \quad (60.241)$$

Scattering angle ψ -limits,

$$\cos \psi^{\pm} = \cos \psi^{\pm}(\varepsilon, v_1, g; v_3) \quad (60.242)$$

$$= \frac{g}{g' \alpha^2 + \beta^2} \left\{ \alpha(\alpha + \tilde{\varepsilon}) \pm \beta[\omega^2(\alpha^2 + \beta^2) - (\alpha + \tilde{\varepsilon})^2]^{1/2} \right\}, \quad (60.243)$$

where

$$\alpha = \alpha(v_1, g; v_3)$$

$$= \frac{1}{2} M_{13} \left[v_1^2 - v_3^2 + \left(\frac{1-a}{1+a} \right) g^2 \right],$$

$$\beta = \beta(v_1, g; v_3)$$

$$= \frac{1}{2} M_{13} \left[(2v_1^2 + 2v_3^2 - g^2)g^2 - (v_1^2 - v_3^2)^2 \right]^{1/2},$$

$$\omega = g'/g, \quad \tilde{\varepsilon} = \varepsilon + \frac{a}{1+a} \Delta_3.$$

Special case: $f_{13} = f_{13}(P)$

$$\sigma(v_3) = \frac{\pi}{M_{13}^2 v_3^2} \int_{\varepsilon_1}^{\varepsilon_2} d\varepsilon \int_{v_{10}}^{\infty} \frac{W_{nl}(v_1)dv_1}{v_1} \times \int_{P^-}^{P^+} |f_{13}(P)|^2 dP. \quad (60.244)$$

60.10 Binary Encounter Approximation

The basic assumption of the binary encounter approximation is that an excitation or ionization process is caused solely by the interaction of the incoming charged or neutral projectile with the Rydberg electron bound to its parent ion. If, for example, the cross section depends only on the momentum transfer P to the Rydberg electron (as in the Born approximation), then the total cross section is obtained by integrating σ_P over the momentum distribution of the Rydberg electron. The basic cross sections required are given in Sect. 60.10.1. For further details see [75] and references therein.

60.10.1 Differential Cross Sections

Cross Section per Unit Momentum Transfer

Let the masses, velocities, and charges of the particles be $(m_1, \mathbf{v}_1, Z_1, e)$ and $(m_2, \mathbf{v}_2, Z_2, e)$, with $\mathbf{v} = |\mathbf{v}_1 - \mathbf{v}_2|$ denoting the relative velocity, and quantities *after* the collision are denoted by primes. Then for distinguishable particles,

$$\sigma_P = \frac{8\pi Z_1^2 Z_2^2 e^4 P}{v^2} \left| \frac{\exp(i\eta_P)}{P^2} \right|^2, \quad (60.245)$$

where the phase shift η_P is

$$\eta_P = -2\gamma \ln(P/2\mu v) + 2\eta_0 + \pi, \quad (60.246)$$

and with

$$\mu = \frac{m_1 m_2}{m_1 + m_2}, \quad \gamma = \frac{Z_1 Z_2 e^2}{\hbar v}, \quad e^{2i\eta_0} = \frac{\Gamma(1 + i\gamma)}{\Gamma(1 - i\gamma)}. \quad (60.247)$$

For identical particles,

$$\sigma_P^\pm = \frac{8\pi Z_1^2 Z_2^2 e^4 P}{v^2} \left| \frac{e^{i\eta_P}}{P^2} \pm \frac{e^{i\eta_S}}{S^2} \right|^2, \quad (60.248)$$

where η_P is given by Eq. (60.246), and η_S is

$$\eta_S = -2\gamma \ln(S/2\mu v) + 2\eta_0 + \pi, \quad (60.249)$$

while η_0 is given by Eq. (60.247). The momenta \mathbf{P} and \mathbf{S} transferred by direct and exchange collisions, respectively, are given by

$$\mathbf{P} = m_1(\mathbf{v}_1 - \mathbf{v}'_1) = m_2(\mathbf{v}_1 - \mathbf{v}'_2), \quad (60.250a)$$

$$\mathbf{S} = m_1(\mathbf{v}_1 - \mathbf{v}'_2) = m_2(\mathbf{v}'_1 - \mathbf{v}_2). \quad (60.250b)$$

The collision rates (in cm^3/s) are

$$\hat{\alpha}_P = v_1 \sigma_P, \quad \hat{\alpha}_P^\pm = v_1 \sigma_P^\pm. \quad (60.251)$$

Cross Section per Unit Momentum Transferred per Unit Steradian

Differential relationships

$$\alpha_{E,P} = \frac{d^2\alpha}{dP dE} = \frac{d^2\alpha}{dP d\varphi} \frac{d\varphi}{dE} = \alpha_{P,\varphi} \frac{d\varphi}{dE}. \quad (60.252)$$

For distinguishable particles,

$$\alpha_P = 2\pi v_1 \sigma_{P,\varphi} = 2\pi \alpha_{P,\varphi}, \quad (60.253a)$$

$$\alpha_{P,\varphi} = \frac{4Z_1^2 Z_2^2 e^4 P}{v} \left| \frac{e^{i\eta_P}}{P^2} \right|^2, \quad (60.253b)$$

$$\alpha_{E,P} = v_1 \sigma_{E,P} = \frac{8Z_1^2 Z_2^2 e^4}{v_1 v_2 \sqrt{X}} \left| \frac{e^{i\eta_P}}{P^2} \right|^2. \quad (60.253c)$$

For identical particles,

$$\alpha_{P,\varphi}^\pm = \frac{4Z_1^2 Z_2^2 e^4 P}{v} \left| \frac{e^{i\eta_P}}{P^2} \pm \frac{e^{i\eta_S}}{S^2} \right|^2, \quad (60.254a)$$

$$\alpha_{E,P}^\pm = v_1 \sigma_{E,P}^\pm = \frac{8Z_1^2 Z_2^2 e^4}{v_1 v_2 \sqrt{X}} \left| \frac{e^{i\eta_P}}{P^2} \pm \frac{e^{i\eta_S}}{S^2} \right|^2, \quad (60.254b)$$

where

$$X = -\cos^2 \phi + 2(\hat{\mathbf{v}}_1 \cdot \hat{\mathbf{P}})(\hat{\mathbf{v}}_2 \cdot \hat{\mathbf{P}}) \cos \phi + 1 - (\hat{\mathbf{v}}_1 \cdot \hat{\mathbf{P}})^2 - (\hat{\mathbf{v}}_2 \cdot \hat{\mathbf{P}})^2 \quad (60.255a)$$

$$= (\cos \phi_{\min} - \cos \phi)(\cos \phi - \cos \phi_{\max}) \quad (60.255b)$$

$$= \left(\frac{v}{v_1 v_2 P} \right)^2 (E_{\max} - E)(E - E_{\min}), \quad (60.255c)$$

with ϕ being the angle between the velocity vectors \mathbf{v}_1 and \mathbf{v}_2 .

For the special case of electron impact, $M_2 = m_e$, $Z_2 = -1$, and

$$\sigma_{E,P}(\phi) = \frac{8Z_1^2 e^4}{v_1^2 v_2 P^4 \sqrt{X}}, \quad (60.256)$$

$$\sigma_{E,P}^\pm(\phi) = 8e^4 v_1^2 v_2 \sqrt{X} \times \left(\frac{1}{P^4} + \frac{1}{S^4} \frac{2 \cos(\eta_P - \eta_S)}{P^2 S^2} \right), \quad (60.257)$$

where $\eta_P - \eta_S = -2\gamma \ln(P/S) = (2e^2/\hbar v) \ln(S/P)$, and X is given by Eq. (60.255a).

Integrated Cross Sections

For incident heavy particles

$$\sigma_{E,P} = \int_0^\pi \sigma_{E,P}(\phi) \frac{1}{2} \sin \phi d\phi = \frac{4\pi Z_1^2 e^4}{v_1^2 v_2 P^4}. \quad (60.258)$$

For incident electrons

$$q\sigma_{E,P}^{\pm} = \int_0^{\pi} \sigma_{E,P}^{\pm}(\phi) \frac{1}{2} \sin \phi d\phi \quad (60.259a)$$

$$= \frac{4\pi e^4}{v_1^2 v_2} \left(\frac{1}{P^4} + \frac{v_1^2 + v_2^2 - P^2/2m_e^2 - 2E^2/P^2}{m_e^4 |v_1^2 - v_2^2 - 2E/m_e|^3} \right. \\ \left. \pm \frac{2\Phi}{m_e^2 P^2 |v_1^2 - v_2^2 - 2E/m_e|} \right), \quad (60.259b)$$

where Φ can be approximated [76] by

$$\Phi \approx \cos \left(\left| \frac{R_{\infty}}{E_3 - E_2} \right|^{1/2} \ln \left| \frac{E}{E_3 - E_2 - E} \right| \right), \quad (60.260)$$

and E_3 is defined in [76].

Cross Sections per Unit Energy

For incident heavy particles (three cases)

$$\sigma_E = \frac{2\pi Z_1^2 e^4}{m_e v_1^2} \left(\frac{1}{E^2} + \frac{2m_e v_2^2}{3E^2} \right), \quad (60.261)$$

which is valid for $2v_1 \geq v_2 + v_2'$, $E \leq 2m_e v_1(v_1 - v_2)$, or

$$\sigma_E = \frac{\pi Z_1^2 e^4}{3v_1^2 v_2 E^3} \left(4v_1^3 - \frac{1}{2}(v_2' - v_2)^2 \right), \quad (60.262)$$

which is valid for $v_2' - v_2 \leq 2v_1 \leq v_2' + v_2$, $2m_e v_1(v_1 - v_2) \leq E \leq 2m_e v_1(v_1 + v_2)$, or otherwise, $\sigma_E = 0$ for $E \geq m_e v_1(v_2' + v_2)$.

For incident electrons (two cases)

$$\sigma_E^{\pm} = \frac{2\pi e^4}{m_e v_1^2} \left(\frac{1}{E^2} + \frac{2m_e v_2^2}{3E^3} + \frac{1}{D^2} + \frac{2m_e v_2^2}{3D^3} \pm \frac{2\Phi}{ED} \right), \quad (60.263)$$

which is valid for $m_e(v_2 - v_2') \leq m_e(v_1' - v_1)$, $m_e(v_2' + v_2) \leq m_e(v_1 + v_1')$, $D \geq 0$, or

$$\sigma_E = \frac{2\pi e^4}{m_e v_1^2} \left(\frac{1}{E^2} + \frac{2m_e v_1'^2}{3E^3} + \frac{1}{D^2} \right. \\ \left. + \frac{2m_e v_1'^2}{3|D|^3} \pm \frac{2\Phi}{E|D|} \right) \frac{v_1'}{v_1}, \quad (60.264)$$

which is valid for $m_e(v_2' - v_2) \leq m_e(v_1 - v_1')$, $m_e(v_1 + v_1') \leq m_e(v_2' + v_2)$, $D \leq 0$. In the expressions above, the exchange energy D transferred during the collision is

$$D = \frac{1}{2}m_e v_1^2 - \frac{1}{2}m_e v_2^2 = \frac{1}{2}m_e v_1^2 - \frac{1}{2}m_e v_2^2 - E. \quad (60.265)$$

60.10.2 Integral Cross Sections

$$e^-(T) + A(E_2) \rightarrow e^-(E) + A^+ + e^-, \quad (60.266)$$

where T is the initial kinetic energy of the projectile electron, while the Rydberg electron, initially bound in potential U_i to the core A^+ , has kinetic energy E_2 . The cross section per unit energy E is denoted below by σ_E . See the review by *Vriens* [75] for details.

For electron impact, there are two collision models: the *unsymmetrical collision model* of Thomson and Gryzinski assumes that the incident electron has zero potential energy, and the *symmetrical collision model* of Thomas and Burgess assumes that the incident electron is accelerated initially by the target (and thereby gains kinetic energy) while losing an equal amount of potential energy.

Unsymmetrical model (two cases)

$$\sigma_E = \frac{\pi e^4}{T} \left(\frac{1}{E^2} + \frac{4E_2}{3E^3} + \frac{1}{D^2} + \frac{4E_2}{3D^3} - \frac{\Phi}{ED} \right), \quad (60.267)$$

which is valid for $D = T - E_2 - E \geq 0$, or

$$\sigma_E = \frac{\pi e^4}{T} \left(\frac{1}{E^2} + \frac{4T'}{3E^3} + \frac{1}{D^2} + \frac{4T'}{3|D|^3} - \frac{\Phi}{E|D|} \right) \\ \times \left(\frac{T'}{E_2} \right)^{1/2}, \quad (60.268)$$

which is valid for $D \leq 0$ and $T \geq E$; and where $T' \equiv T - E$.

Symmetrical model (two cases)

$$\sigma_E = \frac{\pi e^4}{T_i} \left(\frac{1}{E^2} + \frac{4E_2}{3E^3} + \frac{1}{X_i^2} + \frac{4E_2}{3X_i^3} - \frac{\Phi}{EX_i} \right), \quad (60.269)$$

which is valid for $X_i \equiv T + U_i - E \geq 0$, with $T_i \equiv T + U_i + E_2$, and

$$\sigma_E = \frac{\pi e^4}{T_i} \left(\frac{1}{E^2} + \frac{4T'_i}{3E^3} + \frac{1}{X_i^2} + \frac{4T'_i}{3|X_i|^3} - \frac{\Phi}{E|X_i|} \right) \\ \times \left(\frac{T'_i}{E_2} \right)^{1/2}, \quad (60.270)$$

which is valid for $0 \leq T'_i \leq E_2$, $T \geq 0$, with $T'_i \equiv T_i - E$, and where Φ is given by Eq. (60.260).

For incident heavy particles, the unsymmetrical model in Eq. (60.267) should be used.

Single-Particle Ionization

The total ionization cross section per atomic electron for incident heavy particles is

$$Q_i = \frac{2\pi Z_1^2 e^4}{m_e v_1^2} \left(\frac{1}{U_i} + \frac{m_e v_2^2}{3U_i^2} - \frac{1}{2m_e(v_1^2 - v_2^2)} \right), \quad (60.271)$$

which is valid for $U_i \leq 2m_e v_1(v_1 - v_2)$, or

$$Q_i = \frac{\pi Z_1^2 e^4}{m_e v_1^2} \left\{ \frac{1}{2m_e v_2(v_1 + v_2)} + \frac{1}{U_i} + \frac{m_e}{3v_2 U_i^2} \left[2v_1^3 + v_2^3 - (2U_i/m_e + v_2^2)^{3/2} \right] \right\}, \quad (60.272)$$

which is valid for $2m_e v_1(v_1 - v_2) \leq U_i \leq 2m_e v_1(v_1 + v_2)$, or otherwise $Q_i = 0$ for $U_i \geq 2m_e v_1(v_1 + v_2)$.

For electron impact,

$$Q_i = \frac{1}{2}(Q_i^{\text{dir}} + Q_i^{\text{ex}} + Q_i^{\text{int}}). \quad (60.273)$$

In the unsymmetrical model, Q_i^{ex} diverges, hence the exchange and interference terms above are omitted in the unsymmetrical model for electrons to obtain

$$Q_i^{\text{dir}} = \frac{\pi e^4}{T} \left(\frac{1}{U_i} + \frac{2E_2}{3U_i^2} - \frac{1}{T - E_2} \right), \quad (60.274)$$

which is valid for $T \geq E_2 + U_i$, or

$$Q_i^{\text{dir}} = \frac{2\pi e^4}{3T} \frac{(T - U_i)^{3/2}}{U_i^2 \sqrt{E_2}}, \quad (60.275)$$

which is valid for $U_i \leq T \leq E_2 + U_i$.

In the symmetrical model,

$$Q_i^{\text{dir}} = Q_i^{\text{ex}} = \frac{\pi e^4}{T_i} \left[\frac{1}{U_i} - \frac{1}{T} + \frac{2}{3} \left(\frac{E_2}{U_i^2} - \frac{E_2}{T^2} \right) \right], \quad (60.276)$$

$$Q_i^{\text{int}} = -\frac{\pi e^4}{T_i} \left(\frac{2\Phi'}{T + U_i} \ln \frac{T}{U_i} \right), \quad (60.277)$$

where Φ' can be approximated by [76]

$$\Phi' = \cos \left[\left(\frac{R_\infty}{E_1 + U_i} \right)^{1/2} \ln \frac{E_1}{U_i} \right], \quad (60.278)$$

and E_1 is defined in [76].

The sum of Eqs. (60.276) and (60.277) yields

$$Q_i = \frac{\pi e^4}{T_i} \left[\frac{1}{U_i} - \frac{1}{T} + \frac{2}{3} \left(\frac{E_2}{U_i^2} - \frac{E_2}{T^2} \right) - \frac{\Phi'}{T + U_i} \ln \frac{T}{U_i} \right], \quad (60.279)$$

which is also obtained by integrating the expression in Eq. (60.270) for σ_E ,

$$Q_i = \int_{U_i}^{\frac{1}{2}(T+U_i)} \sigma_E dE. \quad (60.280)$$

Ionization rate coefficients For heavy-particle impact [70],

$$\langle Q \rangle = \frac{a_0^2}{\kappa^2} \left\{ \frac{128}{9} (\kappa^3 b^3 - b^{3/2}) + \frac{1}{3} \lambda b \left(35 - \frac{58}{3} b \frac{8}{3} b^2 \right) + \frac{2}{3} \kappa a b \left[(5 - 4\kappa^2) \left(3a^2 + \frac{3}{2} a b + b^2 \right) - \lambda \kappa \left(\frac{15}{2} + 9a + 5b \right) \right] - 16\kappa a^4 \ln(4\kappa^2 1) + \theta \left[\frac{35}{6} - \kappa^2 a \left(\frac{5}{2} + 3a + 4a^2 + 8a^3 \right) \right] \right\}, \quad (60.281)$$

where

$$\begin{aligned} \kappa &= v_1/v_0, \\ \lambda &= \kappa - (4\kappa)^{-1}, \\ \theta &= \pi + 2 \tan^{-1} \lambda, \\ a &= (1 + \kappa^2)^{-1}, \\ b &= (1 + \lambda^2)^{-1}. \end{aligned}$$

$$\langle \sigma_{E,P} dP dE \rangle = \frac{64e^4 v_0^5}{3v_1^2 P^4} \left(\left| \frac{E}{P} - \frac{P}{2m_e} \right|^2 v_0^2 \right)^{-3} dP dE,$$

where $(1/2)m_e v_0^2$ is the ionization energy of H(1s).

Scaling laws Given the binary encounter cross section for ionization by protons of energy E_1 of an atom with binding energy u_a , the cross section for ionization of an atom with different binding energy u_b and scaled proton energy E'_1 can be determined to be [30]

$$\sigma_{\text{ion}}(E'_1, u_b) = \left(\frac{u_a^2}{u_b^2} \right) \sigma_{\text{ion}}(E_1, u_a), \quad (60.282)$$

$$E'_1 = (u_b/u_a) E_1, \quad (60.283)$$

where $\sigma_{\text{ion}}(E, u)$ is the ionization cross section for removal of a single electron from an atom with binding energy u by impact with a proton with initial energy E .

Double ionization See [77] for binary encounter cross section formulae for the direct double ionization of two-electron atoms by electron impact.

Excitation Excitation is generally less violent than ionization, and hence binary encounter theory is less applicable. Binary encounter theory can be applied to exchange excitation transitions, e.g., $e^- + \text{He}(n^1L) \rightarrow e^- + \text{He}(n^3L)$, with

the restriction of large incident electron velocities. The cross section is

$$\begin{aligned} Q_e^{\text{ex}} &= \int_{U_n}^{U_{n+1}} \sigma_{E,\text{ex}} dE \\ &= \frac{\pi e^4}{T_i} \left[\frac{1}{\mathcal{T}_{n+1}} - \frac{1}{\mathcal{T}_n} + \frac{2}{3} \left(\frac{E_2}{\mathcal{T}_{n+1}^2} - \frac{E_2}{\mathcal{T}_n^2} \right) \right], \end{aligned} \quad (60.284)$$

valid for $T \geq U_{n+1}$, with $\mathcal{T}_n \equiv T + U_i - U_n$ and $\mathcal{T}_{n+1} \equiv T + U_i + U_{n+1}$, or

$$\begin{aligned} Q_e^{\text{ex}} &= \int_{U_n}^T \sigma_{E,\text{ex}} dE \\ &= \frac{\pi e^4}{T_i} \left[\frac{1}{U_i} - \frac{1}{\mathcal{T}_n} + \frac{2}{3} \left(\frac{E_2}{U_i^2} - \frac{E_2}{\mathcal{T}_n^2} \right) \right], \end{aligned} \quad (60.285)$$

valid for $U_n \leq T \leq U_{n+1}$; U_n and U_{n+1} denote the excitation energies for levels n and $n + 1$, respectively.

60.10.3 Classical Ionization Cross Section

Applying the classical energy-change cross section result in Eq. (60.84) of *Gerjuoy* [28] to the case of electron-impact ionization yields the four cases [29]

$$\begin{aligned} \sigma_{\text{ion}}(v_1, v_2) &\approx \int_{\Delta E_\ell}^{\Delta E_u} \sigma_{\Delta E}^{\text{eff}}(v_1, v_2; m_1/m_2) d(\Delta E) \\ &= \frac{\pi(Z_1 Z_2 e^2)^2}{3v_1^2 v_2} \left(\frac{-2v_2^3}{(\Delta E)^2} - \frac{6v_2}{m_2 \Delta E} \right), \end{aligned} \quad (60.286)$$

which is valid for $0 < \Delta E < b$, or

$$\begin{aligned} \sigma_{\text{ion}}(v_1, v_2) &= \frac{\pi(Z_1 Z_2 e^2)^2}{3v_1^2 v_2} \\ &\times \left(\frac{4(v_1 - 2v_1')}{m_1^2 (v_1 - v_1')^2} + \frac{4(v_2 - 2v_2')}{m_2^2 (v_2 - v_2')^2} \right), \end{aligned} \quad (60.287)$$

which is valid for $b < \Delta E < a$, or

$$\sigma_{\text{ion}}(v_1, v_2) = \frac{\pi(Z_1 Z_2 e^2)^2}{3v_1^2 v_2} \left(\frac{-2v_1^3}{(\Delta E)^2} \right), \quad (60.288)$$

which is valid for $\Delta E > a$, $2m_2 v_2 > |m_1 - m_2|v_1$, or otherwise is zero for $\Delta E > a$, $2m_2 v_2 < |m_1 - m_2|v_1$.

The limits $\Delta E_{\ell,u}$ to the ΔE integration in each of the four cases is indicated in the appropriate validity conditions. The constants a and b above are given by

$$\begin{aligned} a &= \frac{4m_1 m_2}{(m_1 + m_2)^2} \left[E_1 - E_2 + \frac{1}{2} v_1 v_2 (m_1 - m_2) \right], \\ b &= \frac{4m_1 m_2}{(m_1 + m_2)^2} \left[E_1 - E_2 - \frac{1}{2} v_1 v_2 (m_1 - m_2) \right]. \end{aligned}$$

The expressions above for $\sigma_{\text{ion}}(v_1, v_2)$ must be averaged over the speed distribution of v_2 before comparison with experiment. See [29] for explicit formulae for the case of a delta function speed distribution.

60.10.4 Classical Charge Transfer Cross Section

Applying the classical energy-change cross section result in Eq. (60.84) of *Gerjuoy* [28] to the case of charge-transfer yields the four cases [29]

$$\begin{aligned} \sigma_{\text{CX}}(v_1, v_2) &\approx \int_{\Delta E_\ell}^{\Delta E_u} \sigma_{\Delta E}^{\text{(eff)}}(v_1, v_2) d\Delta E \\ &= \frac{\pi e^4}{3v_1^2 v_2} \left(-\frac{2v_2^3}{(\Delta E)^2} - \frac{6v_2/m_2}{\Delta E} \right), \end{aligned} \quad (60.289)$$

which is valid for $0 < \Delta E < b$, or

$$\begin{aligned} \sigma_{\text{CX}}(v_1, v_2) &= \frac{\pi e^4}{3v_1^2 v_2} \left(3 \frac{v_1/m_1 - v_2/m_2}{\Delta E} \right. \\ &\left. + \frac{(v_2^3 - v_1^3) - (v_1^3 + v_2^3)}{(\Delta E)^2} \right), \end{aligned} \quad (60.290)$$

which is valid for $b < \Delta E < a$, or

$$\sigma_{\text{CX}}(v_1, v_2) = \frac{\pi e^4}{3v_1^2 v_2} \left(-\frac{2v_1^2}{(\Delta E)^2} \right), \quad (60.291)$$

which is valid for $\Delta E > a$, $m_e v_2 > (m_1 - m_e)v_1$, or otherwise $\sigma_{\text{CX}} = 0$ when $\Delta E > a$, $m_e v_2 < (m_1 - m_e)v_1$. The above expressions for $\sigma_{\text{CX}}(v_1, v_2)$ must be averaged over the speed distribution $W(v_2)$ before comparison with experiment. See [29] for details. The constants a and b above are as defined in Sect. 60.10.3, and the limits $\Delta E_{\ell,u}$ are given by

$$\Delta E_\ell = \frac{1}{2} m_e v_1^2 + U_A - U_B, \quad (60.292a)$$

$$\Delta E_u = \frac{1}{2} m_e v_1^2 + U_A + U_B, \quad (60.292b)$$

$$v_2 = \sqrt{2U_A/m_e}, \quad (60.292c)$$

where $U_{A,B}$ are the binding energies of atoms A and B . The expressions above for σ_{CX} diverge for some $v_1 > 0$ if $U_A < U_B$. If $U_A = U_B$, then σ_{CX} diverges at $v_1 = 0$. To avoid the divergence, employ Gerjuoy's modification, $\Delta E_\ell = (1/2)m_e v_1^2 + U_A$.

60.11 Born Approximation

See the reviews in [78, 79], as well as any standard textbook on scattering theory, for background details on the Born approximation, and [80–85] for extensive tables of Born cross sections.

60.11.1 Form Factors

The basic formulation of the first Born approximation for high-energy heavy-particle scattering is discussed in Sect. 57.1. For the general atom–atom or ion–atom scattering process

$$A(i) + B(i') \rightarrow A(f) + B(f'), \quad (60.293)$$

with nuclear charges Z_A and Z_B , respectively, let $\hbar \mathbf{K}_i$ and $\hbar \mathbf{K}_f$ be the initial and final momenta of the projectile A , and $\hbar \mathbf{q} = \hbar \mathbf{K}_f - \hbar \mathbf{K}_i$ be the momentum transferred to the target. Then Eq. (57.4) can be written in the generalized form

$$\begin{aligned} \sigma_{if}^{i'f'} &= \frac{8\pi a_0^2}{s^2} \int_{t_-}^{t_+} \frac{dt}{t^3} \left| Z_A \delta_{if} - F_{if}^A(t) \right|^2 \\ &\times \left| Z_B \delta_{i'f'} - F_{i'f'}^B(t) \right|^2, \end{aligned} \quad (60.294)$$

where the momentum transfer is $t = qa_0$, and $s = v/v_B$ is the initial relative velocity in units of v_B . The form factors are

$$F_{if}^A(t) = \langle \Phi_f^A | \sum_{k=1}^{N_A} \exp(it \cdot \mathbf{r}_a/a_0) | \Phi_i^A \rangle, \quad (60.295)$$

where N_A is the number of electrons associated with atom A and similarly for $F_{if}^B(t)$. The limits of integration are $t_{\pm} = |K_f \pm K_i|a_0$. For heavy-particle collisions, $t_{\pm} \approx \infty$ and

$$\begin{aligned} t_- &= (K_i - K_f)a_0 \\ &\simeq \frac{\Delta E_{if}}{2s} \left(1 + \frac{m_e \Delta E_{if}}{4Ms^2} \right), \end{aligned} \quad (60.296)$$

where $M = M_A M_B / (M_A + M_B)$.

Limiting cases As discussed in Sect. 57.1, for the case $i = f$, $F_{if}^A(t) \rightarrow N_A$ as $t \rightarrow 0$, so that $Z_A - F_{if}^A(t) \rightarrow Z_A - N_A$. For the case $i \neq f$, $F_{if}^A(t) \rightarrow 0$ as $t \rightarrow 0$ and $t \rightarrow \infty$.

60.11.2 Hydrogenic Form Factors

Bound–bound transitions In terms of $\tau = t/Z$,

$$|F_{1s,1s}| = \frac{16}{(4 + \tau^2)^2}, \quad (60.297a)$$

$$|F_{1s,2s}| = 2^{17/2} \frac{\tau^2}{(4\tau^2 + 9)^3}, \quad (60.297b)$$

$$|F_{1s,2p}| = 2^{15/2} \frac{3\tau}{(4\tau^2 + 9)^3}, \quad (60.297c)$$

$$|F_{1s,3s}| = 2^4 3^{7/2} \frac{(27\tau^2 + 16)\tau^2}{(9\tau^2 + 16)^4}, \quad (60.297d)$$

$$|F_{1s,3p}| = 2^{11/2} 3^3 \frac{(27\tau^2 + 16)\tau}{(9\tau^2 + 16)^4}, \quad (60.297e)$$

$$|F_{1s,3d}| = 2^{17/2} 3^{7/2} \frac{\tau^2}{(9\tau^2 + 16)^4}. \quad (60.297f)$$

Bound–continuum transitions In terms of the scaled wave vector $\kappa = \mathbf{k}a_0/Z$ for the ejected electron,

$$|F_{1s,\kappa}|^2 = \frac{2^8 \kappa \tau^2 (1 + 3\tau^2 + \kappa^2) \exp(-2\theta/\kappa)}{3 [1 + (\tau - \kappa)^2]^3 [1 + (\tau + \kappa)^2]^3 (1 - e^{-2\pi/\kappa})}, \quad (60.298)$$

where $\theta = \tan^{-1}[2\kappa/(1 + \tau^2 - \kappa^2)]$. Expressions for the bound–continuum form factors for the L-shell ($2\ell \rightarrow \kappa$) and M-shell ($3\ell \rightarrow \kappa$) transitions can be found in [86] and [87], respectively. See also §4 of [88] for further details.

General Expressions and Trends

For final ns states

$$\begin{aligned} |F_{1s,ns}|^2 &= \frac{2^4 n [(n-1)^2 + n^2 \tau^2]^{n-1}}{\tau^2 [(n+1)^2 + n^2 \tau^2]^{n+1}} \\ &\times \sin^2(n \tan^{-1} x + \tan^{-1} y), \end{aligned} \quad (60.299)$$

where

$$x = \frac{2\tau}{n(\tau^2 + 1 - n^{-2})}, \quad y = \frac{2\tau}{\tau^2 - 1 + n^{-2}}. \quad (60.300)$$

For final $n\ell$ states [89]

$$\begin{aligned} &F_{1s,n\ell}(\tau) \\ &= (i\tau)^\ell 2^{3(\ell+1)} \sqrt{2\ell+1} (\ell+1)! \left(\frac{(n-\ell-1)!}{(n+\ell)!} \right)^{1/2} \\ &\times n^{\ell+1} \frac{[(n-1)^2 + n^2 \tau^2]^{(n-\ell-3)/2}}{[(n+1)^2 + n^2 \tau^2]^{(n+\ell+3)/2}} \\ &\times \left[a_{n\ell} C_{n-\ell-1}^{(\ell+2)}(x) - b_{n\ell} C_{n-\ell-2}^{(\ell+2)}(x) + c_{n\ell} C_{n-\ell-3}^{(\ell+2)}(x) \right], \end{aligned} \quad (60.301)$$

with coefficients $a_{n\ell}$, $b_{n\ell}$ and $c_{n\ell}$ given by

$$\begin{aligned} a_{n\ell} &= (n+1)[(n-1)^2 + n^2\tau^2], \\ b_{n\ell} &= 2n\sqrt{[(n-1)^2 + n^2\tau^2][(n+1)^2 + n^2\tau^2]}, \\ c_{n\ell} &= (n-1)[(n+1)^2 + n^2\tau^2], \end{aligned}$$

and the argument

$$x = \frac{n^2 - 1 + n^2\tau^2}{\sqrt{[(n+1)^2 + n^2\tau^2][(n-1)^2 + n^2\tau^2]}}.$$

Summation over final ℓ states

$$\begin{aligned} |F_{1s,n}|^2 &= \sum_{\ell} |F_{1s,n\ell}|^2 \\ &= 2^8 n^7 \tau^2 \left[\frac{1}{3}(n^2 - 1) + n^2\tau^2 \right] \\ &\quad \times \frac{[(n-1)^2 + n^2\tau^2]^{n-3}}{[(n+1)^2 + n^2\tau^2]^{n+3}} \end{aligned} \quad (60.302)$$

which for large n becomes

$$|F_{1s,n}|^2 \approx \frac{2^8 \tau^2 (3\tau^2 + 1)}{3n^3 (\tau^2 + 1)^6} \exp\left(\frac{-4}{(\tau^2 + 1)}\right). \quad (60.303)$$

For initial $2s$ and $2p$ states,

$$\begin{aligned} |F_{2s,n}|^2 &= 2^4 n^7 \tau^2 \left[-\frac{1}{3} + \frac{1}{2}n^2 - \frac{3}{16}n^4 + \frac{1}{48}n^6 \right. \\ &\quad \left. + n^2\tau^2 \left(\frac{1}{3} - \frac{2}{3}n^2 + \frac{19}{48}n^4 \right) \right. \\ &\quad \left. + n^4\tau^4 \left(\frac{5}{3} - \frac{7}{6}n^2 \right) + n^6\tau^6 \right] \\ &\quad \times \frac{[(\frac{1}{2}n - 1)^2 + n^2\tau^2]^{n-4}}{[(\frac{1}{2}n + 1)^2 + n^2\tau^2]^{n+4}}, \end{aligned} \quad (60.304)$$

$$\begin{aligned} |F_{2p,n}|^2 &= \frac{2^4 n^9 \tau^2}{3} \left[\frac{1}{4} - \frac{7}{24}n^2 + \frac{11}{192}n^4 \right. \\ &\quad \left. - n^2\tau^2 \left(\frac{5}{6} - \frac{23}{24}n^2 \right) + \frac{1}{4}n^4\tau^4 \right] \\ &\quad \times \frac{[(\frac{1}{2}n - 1)^2 + n^2\tau^2]^{n-4}}{[(\frac{1}{2}n + 1)^2 + n^2\tau^2]^{n+4}}. \end{aligned} \quad (60.305)$$

Power series expansion $\tau^2 \ll 1$ [7]

$$|F_{1s,ns}(\tau)|^2 = A(n)\tau^4 + B(n)\tau^6 + C(n)\tau^8 + \dots, \quad (60.306) \quad \text{with } t_-^2 = [9/(16s^2)][1 + 3m_e/(4Ms^2) + \dots].$$

where

$$\begin{aligned} A(n) &= \frac{2^8 n^9 (n-1)^{2n-6}}{3^2 (n+1)^{2n+6}}, \\ B(n) &= -\frac{2^9 n^{11} (n^2 + 11)(n-1)^{2n-8}}{3^2 5 (n+1)^{2n+8}}, \\ C(n) &= -\frac{2^8 n^{13} (313n^4 - 1654n^2 - 2067)}{3^2 5^2 7 (n+1)^{2n+10}} (n-1)^{2n-10}. \end{aligned}$$

For analytical expressions for $A(n)$, $B(n)$, and $C(n)$ for final np and nd states, see [90, 91].

General trends in hydrogenic form factors [92] The inelastic form factor $|F_{n\ell \rightarrow n'\ell'}|$ oscillates with ℓ' on an increasing background until the value

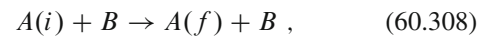
$$\ell'_{\max} = \min\left(n' - 1, n \left(\frac{2(n+3)}{(n+1)}\right)^{1/2} - \frac{1}{2}\right) \quad (60.307)$$

is reached, after which a rapid decline for $\ell > \ell'_{\max}$ occurs. See [92] for illustrative graphs.

60.11.3 Excitation Cross Sections

Atom-Atom Collisions [93, 94]

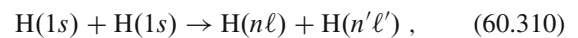
Single excitation For the process



Eq. (60.294) reduces to

$$\sigma_{if} = \frac{8\pi a_0^2}{s^2} \int_{t_-}^{\infty} \frac{dt}{t^3} |F_{if}^A|^2 |Z_B - F_{i'i'}^B|^2. \quad (60.309)$$

Double excitation For the process



$$\sigma_{1s,n\ell}^{1s,n'\ell'} = \frac{8\pi a_0^2}{s^2} \int_{t_-}^{\infty} \frac{dt}{t^3} |F_{1s,n\ell}|^2 |F_{1s,n'\ell'}|^2. \quad (60.311)$$

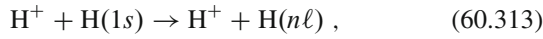
Special cases are [95]

$$\sigma_{1s,2s}^{1s,2s} = \frac{2^{30} \pi a_0^2 (880t_-^4 + 396t_-^2 + 81)}{495s^2 (4t_-^2 + 9)^{11}}, \quad (60.312a)$$

$$\sigma_{1s,2p}^{1s,2p} = \frac{2^{30} 3^4 \pi a_0^2}{11s^2 (4t_-^2 + 9)^{11}}, \quad (60.312b)$$

$$\sigma_{1s,2s}^{1s,2p} = \frac{2^{29} 3^2 (44t_-^2 + 9)}{55s^2 (4t_-^2 + 9)^{11}}, \quad (60.312c)$$

Ion–atom collisions For the proton impact process



Eq. (60.294) reduces to

$$\sigma_{1s,n\ell} = \frac{8\pi a_0^2}{s^2} \int_{t_-}^{\infty} \frac{dt}{t^3} |F_{1s,n\ell}(t)|^2, \quad (60.314)$$

with $t_- = (1 - n^{-2})/(2s)$.

Asymptotic Expansions

$$\sigma_{1s,ns} = \frac{4\pi a_0^2 (n^2 - 1) |X_{1s \rightarrow ns}|^2}{24s^2 n^2} \times \left[C_s(n) - \frac{1}{s^2} + \frac{n^2 + 11}{20n^2 s^4} + \frac{313n^4 - 1654n^2 - 2067}{8400n^4 s^6} \right], \quad (60.315)$$

$$\sigma_{1s,np} = \frac{2^{10} \pi a_0^2 n^7 (n-1)^{2n-5}}{3s^2 (n+1)^{2n+5}} \times \left[C_p(n) + \ln s^2 + \frac{n^2 + 11}{10n^2 s^2} + \frac{313n^4 - 1654n^2 - 2067}{5600n^4 s^4} \right], \quad (60.316)$$

$$\sigma_{1s,nd} = \frac{2^{11} \pi a_0^2 (n^2 - 4)n^5 (n^2 - 1)^2 (n-1)^{2n-7}}{3^2 5s^2 (n+1)^{2n+7}} \times \left[C_d(n) - \frac{1}{s^2} + \frac{11n^2 + 13}{28n^2 s^4} \right], \quad (60.317)$$

where $C_s(2) = 16/5$, $C_s(3) = 117/32$, $C_s(4) \approx 3.386$, and

$$\gamma_n C_p(n) = \frac{1.3026}{n^3} + \frac{1.7433}{n^5} + \frac{16.918}{n^7}, \quad (60.318)$$

$$\gamma_n C_d(n) = \frac{2.0502}{n^3} + \frac{7.6125}{n^5}, \quad (60.319)$$

with

$$\gamma_n \equiv \frac{2^8 n^7 (n-1)^{(2n-5)}}{3(n+1)^{(2n+5)}}. \quad (60.320)$$

Further asymptotic expansion results can be found in [6–9].

A general expression for Born excitation and ionization cross sections for hydrogenic systems in terms of a parabolic coordinate representation (Chap. 9) is given in [96, 97].

Number of independent transitions \mathcal{N}_i between levels n and n' [96, 97]

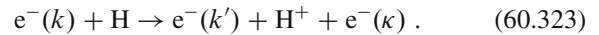
$$\mathcal{N}_i = n^2 \left[n' - \left(\frac{n}{3} \right) \right] + \left(\frac{n}{3} \right). \quad (60.321)$$

Validity criterion The Born approximation is valid provided that [98]

$$nE \gg \ln \left(\frac{4E}{J_n} \right) \quad (60.322)$$

for transitions $n \rightarrow n'$ when $n, n' \gg 1$ and $|n - n'| \approx 1$. The constant J_n is undetermined (see [98] for details) but is generally taken to be the ionization potential of level n .

60.11.4 Ionization Cross Sections



The general expression for the Born differential ionization cross section can be evaluated in closed form using screened hydrogenic wave functions. The differential cross section per incident electron scattered into solid angle $d\Omega_{k'}$, integrated over directions κ for the ejected electron (treated as distinguishable) is [99–101]

$$I(\theta, \phi) d\Omega_{k'} d\kappa' = \frac{4k'}{kq^4 a_0 \tilde{Z}_B^4} |F_{n\ell, \kappa'}|^2(q) d\Omega_{k'} d\kappa', \quad (60.324)$$

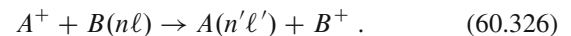
where the form factor is given by Eq. (60.299) for the case $n\ell = 1s$, with the ejected electron wavenumber κ and momentum transferred q in the collision, $\kappa' = \kappa a_0 / \tilde{Z}_B$, $\mathbf{q} = (\mathbf{k}' - \mathbf{k}) a_0 / \tilde{Z}_B$, being scaled by the screened nuclear charge \tilde{Z}_B appropriate to the $n\ell$ -shell from which the electron is ejected. The total Born ionization cross section per electron is

$$\sigma_{\text{ion}}^{\text{B}} = \int_0^{\kappa_{\text{max}}} d\kappa' \int_{k-k'}^{k+k'} I(q, \kappa') dq, \quad (60.325)$$

which is generally evaluated numerically.

60.11.5 Capture Cross Sections

Electron capture



In the Oppenheimer–Brinkman–Kramers (OBK) approximation [102],

$$\sigma_{n\ell, n'\ell'} = \frac{M^2}{2\pi \hbar^3} \frac{v_f}{v_i} \int_{-1}^1 d(\cos \theta) |F_{n\ell \rightarrow n'\ell'}|^2, \quad (60.327)$$

where $\mathbf{v}_i = v_i \hat{\mathbf{n}}_i$, $\mathbf{v}_f = v_f \hat{\mathbf{n}}_f$, θ is the angle between $\hat{\mathbf{n}}_i$ and $\hat{\mathbf{n}}_f$, $M = M_A M_B / (M_A + M_B)$, and

$$|F_{n\ell, n'\ell'}| = \iint d\mathbf{r} ds \varphi_i(\mathbf{r}) \varphi_f^*(s) \left(\frac{Z_A e^2}{r} \right) \times e^{i(\alpha \cdot \mathbf{r} + \beta \cdot \mathbf{s})}, \quad (60.328)$$

with

$$\begin{aligned} \alpha &= k_f \hat{\mathbf{n}}_f + k_i \hat{\mathbf{n}}_i \frac{M_A}{M_A + m_e}, \\ \beta &= -k_i \hat{\mathbf{n}}_i - k_f \hat{\mathbf{n}}_f \frac{M_B}{M_B + m_e}, \\ k_i &= \frac{v_f}{\hbar} \frac{M_B (M_A + m_e)}{(M_A + M_B + m_e)}, \\ k_f &= \frac{v_f}{\hbar} \frac{(M_B + m_e) M_A}{(M_A + M_B + m_e)}. \end{aligned}$$

The Jackson–Schiff correction factor [103] is

$$\begin{aligned} \gamma_{\text{JS}} &= \frac{1}{192} \left(127 + \frac{56}{p^2} + \frac{32}{p^4} \right) \\ &\quad - \frac{\tan^{-1} \frac{1}{2} p}{48 p} \left(83 + \frac{60}{p^2} + \frac{32}{p^4} \right) \\ &\quad + \frac{(\tan^{-1} \frac{1}{2} p)^2}{24 p^2} \left(31 + \frac{32}{p^2} + \frac{16}{p^4} \right), \end{aligned} \quad (60.329)$$

and the capture cross section is

$$\begin{aligned} \sigma(n_i \ell_i, n_f \ell_f) &= \frac{\gamma_{\text{JS}} \pi a_0^2}{p^2} C(n_i \ell_i, n_f \ell_f) \\ &\quad \times \int_x^\infty F(n_i \ell_i, n_f \ell_f; x) dx, \end{aligned} \quad (60.330)$$

with

$$\begin{aligned} p &= \frac{m v_i}{\hbar}, \quad a = \frac{Z_A}{n_i}, \quad b = \frac{Z_B}{n_f}, \\ x &= [p^2 + (a + b)^2][p^2 + (a - b)^2] / 4 p^2. \end{aligned}$$

The coefficients C in Eq. (60.330) are given in Table 60.4, while the functions F are given in Table 60.5 [102]. In Table 60.5, the appropriate values of a and b are indicated by the quantum numbers n_i , ℓ_i and n_f , ℓ_f .

Table 60.4 Coefficients $C(n_i \ell_i \rightarrow n_f \ell_f)$ in the Born capture cross section formula in Eq. (60.330)

$n_f \ell_f$	$C(1s \rightarrow n_f \ell_f)$
1s	$2^8 Z_A^5 Z_B^5$
2s	$2^5 Z_A^5 Z_B^5$
3s	$2^8 Z_A^5 Z_B^5 / 3^3$
2p	$2^5 Z_A^5 Z_B^7$
3p	$2^{13} Z_A^5 Z_B^7 / 3^6$
3d	$2^{15} Z_A^5 Z_B^9 / 3^9$
4s	$2^2 Z_A^5 Z_B^5$
4p	$5 Z_A^3 Z_B^7$
4d	$Z_A^5 Z_B^9$
4f	$Z_A^5 Z_B^{11} / 20$

$$C(2s \rightarrow n_f \ell_f) = C(1s \rightarrow n_f \ell_f) / 8$$

$$C(2p \rightarrow n_f \ell_f) = C(1s \rightarrow n_f \ell_f) / 24$$

Table 60.5 Functions $F(n_i \ell_i \rightarrow n_f \ell_f; x)$ in the Born capture cross section formula in Eq. (60.330)

$n_f \ell_f$	$F(n_i \ell_i, n_f \ell_f; x)$
1s	x^{-6}
2s	$(x - 2b^2)^2 x^{-8}$
2p	$(x - b^2) x^{-8}$
3s	$[x^2 - (16/3)b^2 x + (16/3)b^4]^2 x^{-10}$
3p	$(x - b^2)(x - 2b^2)^2 x^{-10}$
3d	$(x - b^2)^2 x^{-10}$
4s	$(x - 2b^2)^2 (x^2 - 8b^2 x + 8b^4)^2 x^{-12}$
4p	$(x - b^2)[x^2 - (24/5)b^2 x + (24/5)b^4]^2 x^{-12}$
4d	$(x - b^2)^2 (x - 2b^2)^2 x^{-12}$
4f	$(x - b^2)^3 x^{-12}$

$$F(2s, n_f \ell_f; x) = (x - 2a^2)^2 x^{-2} F(1s, n_f \ell_f; x)$$

$$F(2p, n_f \ell_f; x) = (x - a^2) x^{-2} F(1s, n_f \ell_f; x)$$

References

1. Connerade, J.-P.: Highly Excited Atoms. Cambridge Univ., Cambridge (1998)
2. Lebedev, V.S., Beigman, I.L.: Physics of Highly Excited Atoms and Ions. Springer, New York (1998)
3. Jortner, J., Rosenblit, M.: Ultracold Large Finite Systems. In: Advances in Chemical Physics, vol. 132, pp. 247–343. Wiley, New York (2006)
4. Beigman, I.L., Lebedev, V.S.: Phys. Rep. **250**, 95 (1995)
5. Bethe, H.A., Salpeter, E.E.: Quantum Mechanics of One- and Two-Electron Atoms. Springer, Berlin, Heidelberg (1957)
6. Khandelwal, G.S., Choi, B.H.: J. Phys. B **1**, 1220 (1968)
7. Khandelwal, G.S., Fitchard, E.E.: J. Phys. B **2**, 1118 (1969)
8. Khandelwal, G.S., Shelton, J.E.: J. Phys. B **4**, 109 (1971)
9. Khandelwal, G.S., Choi, B.H.: J. Phys. B **2**, 308 (1969)
10. Flannery, M.R., Vranceanu, D., Ostrovsky, V.N.: J. Phys. B **38**, 279–S293 (2005)
11. Zhang, J.Y., Yan, Z.C., Vranceanu, D., Babb, J.F., Sadehpour, H.R.: Phys. Rev. A **76**, 012723 (2007)

12. Khuskivadze, A.A., Chibisov, M.I., Fabrikant, I.I.: *Phys. Rev. A* **66**, 042709 (2002)
13. Santra, R., Greene, C.H.: *Phys. Rev. A* **67**, 062713 (2003)
14. Clark, W., Greene, C.H., Miecznik, G.: *Phys. Rev. A* **53**, 2248 (1995)
15. Gordon, W.: *Ann. Phys.* **2**, 1031 (1929)
16. Davidkin, V.A., Zon, B.A.: *Opt. Spectrosc.* **51**, 25 (1981)
17. Kolomeisky, E.B., Timmins, M.: *Phys. Rev. A* **72**, 022721 (2005)
18. Bureeva, L.A.: *Astron. Zh.* **45**, 1215 (1968)
19. Griem, H.: *Astrophys. J.* **148**, 547 (1967)
20. Beterov, I.I., Ryabtsev, I.I., Tretyakov, D.B., Entin, V.M.: *Phys. Rev. A* **79**, 052504 (2009)
21. Gounand, F.: *France. J. Phys.* **40**, 457 (1979)
22. Pohl, T., Sadeghpour, H.R., Schmelcher, P.: *Phys. Rep.* **484**, 181–229 (2009)
23. Flannery, M.R.: In: Stebbings, R.F., Dunning, F.B. (eds.) *Rydberg States of Atoms and Molecules*. Cambridge Univ., Cambridge (1983). Chap. 11
24. Burgess, A., Percival, I.C.: *Advances in Atomic and Molecular Physics* vol. 4. Academic Press, New York, p 109 (1968)
25. Percival, I.C.: In: Carson, T.R., Roberts, M.J. (eds.) *Atoms and Molecules in Astrophysics*. Academic Press, New York (1972)
26. Percival, I.C., Richards, D.: *Advances in Atomic and Molecular Physics* vol. 11. Academic Press, New York, p 1 (1975)
27. Matsuzawa, M.: *J. Phys. B* **8**, 2114 (1975)
28. Gerjuoy, E.: *Phys. Rev.* **148**, 54 (1966)
29. Garcia, J.D., Gerjuoy, E., Welker, J.E.: *Phys. Rev.* **165**, 66 (1968)
30. Bates, D.R., Kingston, A.E.: *Advances in Atomic and Molecular Physics* vol. 6. Academic Press, New York, p 269 (1970)
31. Khan, J.M., Potter, D.L.: *Phys. Rev.* **133**, A890 (1964)
32. Braaten, E., Hammer, H.-W.: *Phys. Rep.* **428**, 259–390 (2006)
33. Greene, C.H., Giannakeas, P., Perez-Rios, J.: *Rev. Mod. Phys.* **89**, 035006 (2017)
34. Efimov, V.: *Phys. Lett.* **33B**, 563 (1970)
35. Pen'kov, F.M.: *Phys. Rev. A* **60**, 3756 (1999)
36. Gross, E.P.: *Ann. Phys.* **4**, 57 (1958)
37. Pitaevskii, L.P.: *Sov. Phys. JETP* **9**, 830 (1959)
38. Fetter, A.L., Walecka, J.D.: *Quantum Theory of Many-Particle Systems*. McGraw-Hill, New York, pp 488–499 (1971)
39. Fetter, A.L.: *Vortices and Ions in Helium. The Physics of Liquid and Solid Helium, Part I*. Wiley, New York, p 229 (1976). Chap. 3
40. Griffin, A.: *Excitations in a Bose-Condensed Liquid*. Cambridge Univ., Cambridge (1993)
41. Salomon, C., Shlyapnikov, G.V., Cugliandolo, L.F.: *Many-Body Physics with Ultracold Gases*. Oxford University Press, Oxford (2013)
42. Fournais, S., Solovej, J.P.: *Ann. Math.* **192**, 893–976 (2020)
43. Bluvstein, D., Levine, H., Semeghini, G., Wang, T.T., Ebadi, S., Kalinowski, M., Keesling, A., Maskara, N., Pichler, H., Greiner, M., Vuletić, V., Lukin, M.D.: *Nature* **604**, 451–456 (2022)
44. Graham, T.M., Song, Y., Scott, J., Poole, C., Phuttitarn, L., Jooya, K., Eichler, P., Jiang, X., Marra, A., Grinkemeyer, B., Kwon, M., Ebert, M., Cherek, J., Lichtman, M.T., Gillette, M., Gilbert, J., Bowman, D., Ballance, T., Campbell, C., Dahl, E.D., Crawford, O., Blunt, N.S., Rogers, B., Noel, T., Saffman, M.: *Nature* **604**, 457–462 (2022)
45. Saffman M., Walker, T.G., Mølmer, K.: *Rev. Mod. Phys.* **82**, 2313–2363 (2010)
46. Byrnes, T., Llo-Okeke, E.O.: *Quantum Atom Optics*. Cambridge Univ., Cambridge
47. Lebedev, V.S., Marchenko, V.S.: *Sov. Phys. JETP* **61**, 443 (1985)
48. Dewangan, D.P.: *Phys. Rep.* **511**, 1–142 (2012)
49. Omont, A.: *J. De Phys.* **38**, 1343 (1977)
50. Kaulakys, B.: *J. Phys. B* **17**, 4485 (1984)
51. Pengelly, R.M., Seaton, M.J.: *Mon. Not. R. Astron. Soc.* **127**, 165 (1964)
52. Percival, I.C.: In: Burke, P.G., Eissner, W.B., Hummer, D.G., Percival, I.C. (eds.) *Atoms in Astrophysics*. Plenum, New York (1983). Chap. 3
53. Guzmán, F., Badnell, N.R., Williams, R.J.R., van Hoof, P.A.M., Chatzikos, M., Ferland, G.J.: *Mon. Not. R. Astron. Soc.* **459**, 3498–3504 (2016)
54. Guzmán, F., Badnell, N.R., Williams, R.J.R., van Hoof, P.A.M., Chatzikos, M., Ferland, G.J.: *Mon. Not. R. Astron. Soc.* **464**, 312–320 (2017)
55. Vrinceanu, D., Onofrio, R., Sadeghpour, H.R.: *Astrophys. J.* **780**, 2 (2014)
56. Vrinceanu, D., Flannery, M.R.: *Phys. Rev. Lett.* **85**, 4880 (2000)
57. Vrinceanu, D., Flannery, M.R.: *Phys. Rev. A* **63**, 032701 (2001)
58. Vrinceanu, D., Onofrio, R., Sadeghpour, H.R.: *Astrophys. J.* **747**, 56 (2012)
59. Vrinceanu, D., Flannery, M.R.: *J. Phys. B* **33**, L721 (2000)
60. Vrinceanu, D., Flannery, M.R.: *J. Phys. B* **34**, L1 (2001)
61. Talman, J.D.: *Special Functions: A Group Theoretic Approach*. Benjamin, New York (1968)
62. Varshalovich, D.A., Moskalev, A.N., Khersonskii, V.K.: *Quantum Theory of Angular Momentum*. World Scientific, Singapore (1988)
63. Bateman, H.: *Higher Transcendental Functions*. In: Erdélyi, A. (ed.) *Bateman Manuscript Project*, vol. 2, p. 235. Robert E. Krieger, Malabar (1981). Chap. XI
64. Lebedev, V.S.: *J. Phys. B* **25**, L131 (1992)
65. Lebedev, V.S.: *Sov. Phys. JETP* **76**, 27 (1993)
66. Coleman, J.P.: In: McDaniel, E.W., McDowell, M.R.C. (eds.) *Case Studies in Atomic Collision Physics*, vol. I, North Holland, Amsterdam (1969)
67. Coleman, J.P.: *J. Phys. B* **1**, 567 (1968)
68. Flannery, M.R.: *Phys. Rev. A* **22**, 2408 (1980)
69. Goldberger, M.L., Watson, K.M.: *Collision Theory*. Wiley, New York (1964)
70. McDowell, M.R.C.: *Proc. Phys. Soc.* **89**, 23 (1966)
71. Bates, D.R., Walker, J.C.G.: *Planet. Spac. Sci.* **14**, 1367 (1966)
72. Bates, D.R., Walker, J.C.G.: *Proc. Phys. Soc.* **90**, 333 (1967)
73. Flannery, M.R.: *Ann. Phys.* **61**, 465 (1970)
74. Flannery, M.R.: *Ann. Phys.* **79**, 480 (1973)
75. Vriens, L.: In: McDaniel, E.W., McDowell, M.R.C. (eds.) *Case Studies in Atomic Collision Physics*, vol. I, North Holland, Amsterdam (1969)
76. Vriens, L.: *Proc. Phys. Soc.* **89**, 13 (1966)
77. Roy, B.N., Rai, D.K.: *J. Phys. B* **5**, 816 (1973)
78. Holt, A.R., Moiseiwitsch, B.: *Advances in Atomic and Molecular Physics* vol. 4. Academic Press, New York, p 143 (1968)
79. Bell, K.L., Kingston, A.E.: *Advances in Atomic and Molecular Physics* vol. 10. Academic Press, New York, p 53 (1974)
80. Green, L.C., Rush, P.P., Chandler, C.D.: *Astrophys. J. Suppl. Ser.* **3**, 37 (1957)
81. Sommerville, W.B.: *Proc. Phys. Soc.* **82**, 446 (1963)
82. Burgess, A., Hummer, D.G., Tully, J.A.: *Phil. Trans. Roy. Soc. A* **266**, 255 (1970)
83. Whelan, C.T.: *J. Phys. B* **19**, 2343–2355 (1986)
84. Tanaka, H., Brunger, M.J., Campbell, L., Kato, H., Hoshino, M., Rau, A.R.P.: *Rev. Mod. Phys.* **88**, 025004 (2016)
85. Kim, Y.-K.: *Phys. Rev. A* **64**, 032713 (2001)
86. Walske, M.C.: *Phys. Rev.* **101**, 940 (1956)
87. Khandelwal, G.S., Merzbacher, E.: *Phys. Rev.* **144**, 349 (1966)
88. Merzbacher, E., Lewis, H.W.: X-ray production by heavy charged particles. In: Flügge, E. (ed.) *Handbuch der Physik*, vol. 34/2, Springer, Berlin, Heidelberg (1958)

89. Bethe, H.: Quantenmechanik der Ein- und Zwei-Elektronenprobleme. In: Flügge, E. (ed.) Handbuch der Physik, vol. 24/1, Springer, Berlin, Heidelberg (1933)
90. Inokuti, M.: Argonne National Laboratory Report No. ANL-7220, (1965)
91. Inokuti, M.: Rev. Mod. Phys. **43**, 297 (1971)
92. Flannery, M.R., McCann, K.J.: Astrophys. J. **236**, 300 (1980)
93. Bates, D.R., Griffing, G.: Proc. Phys. Soc. **66A**, 961 (1953)
94. Bates, D.R., Griffing, G.: Proc. Phys. Soc. **67A**, 663 (1954)
95. Bates, D.R., Dalgarno, A.: Proc. Phys. Soc. **65A**, 919 (1952)
96. Omidvar, K.: Phys. Rev. **140**, A26 (1965)
97. Omidvar, K.: Phys. Rev. **140**, A38 (1965)
98. Starostin, A.N.: Sov. Phys. JETP **25**, 80 (1967)
99. Burhop, E.H.S.: Proc. Camb. Phil. Soc. **36**, 43 (1940)
100. Burhop, E.H.S.: J. Phys. B **5**, L241 (1972)
101. Mott, N.F., Massey, H.S.W.: The Theory of Atomic Collisions. Clarendon Press, Oxford, pp 489–490 (1965)
102. Bates, D.R., Dalgarno, A.: Proc. Phys. Soc. **66A**, 972 (1953)
103. Jackson, J.D., Schiff, H.: Phys. Rev. **89**, 359 (1953)



Edmund J. Mansky II Edmund J. Mansky II received his PhD from Georgia Institute of Technology in 1985. His theoretical work involves statistical mechanics of dense gases. In addition, his interests are three-body recombination processes and collisions involving Rydberg states of atoms and molecules at thermal and ultracold temperatures. His day job is programming heliophysics data for the scientific community.



Jack C. Straton  and James H. McGuire

Contents

61.1	The Classical Thomas Process	913
61.2	Quantum Description	914
61.2.1	Uncertainty Effects	914
61.2.2	Conservation of Overall Energy and Momentum	914
61.2.3	Conservation of Intermediate Energy	914
61.2.4	Example: Proton–Helium Scattering	915
61.3	Off-Energy-Shell Effects	916
61.4	Dispersion Relations	916
61.5	Destructive Interference of Amplitudes	916
61.6	Recent Developments	917
	References	917

Abstract

Thomas peaks correspond to singular second-order quantum effects whose location may be determined by classical two-step kinematics. The widths of these peaks (or ridges) may be estimated using the uncertainty principle. A second-order quantum calculation is required to obtain the magnitude of these peaks. Thomas peaks and ridges have been observed in various reactions in atomic and molecular collisions involving mass transfer and also ionization.

Transfer of mass is a quasi-forbidden process. Simple transfer of a stationary mass M_2 to a moving mass M_1 is forbidden by conservation of energy and momentum. If $M_1 < M_2$, then M_1 rebounds; if $M_1 = M_2$, then M_1 stops, and M_2 continues on; and if $M_1 > M_2$, then M_2 leaves faster than M_1 . In none of these cases do M_1 and M_2 leave

together. *Thomas* [1] understood this in 1927 and further realized that transfer of mass occurs only when a third mass is present, and all three masses interact. The simplest allowable process is a two-step process now called a Thomas process [2, 3].

Quantum mechanically [4], the second Born term at high energies is the largest Born term and corresponds to the simplest allowed classical process, namely the Thomas process. While the classically forbidden first Born term is not zero (saved by the uncertainty principle), the first Born cross section varies at high v as v^{-12} , in contrast to the second Born cross section, which varies as v^{-11} , thus dominating. Higher Born terms correspond to multistep processes that are unlikely in fast collisions where there is not enough time for complicated processes. The higher Born terms ($n > 2$) are also smaller than the second Born term.

Keywords

dispersion relation · intermediate state · uncertainty principle · transfer ionization · destructive interference

61.1 The Classical Thomas Process

The basic Thomas process is shown in Fig. 61.1. Here, the entire collision is coplanar since particles 1 and 2 go off together (that is what is meant by mass transfer). We assume that all the masses and the incident velocities \mathbf{v} are known. Thus, there are six unknowns, \mathbf{v}' , \mathbf{v}_f , and \mathbf{v}_3 , each with two components. Conservation of momentum gives two equations of constraint for each collision. Conservation of overall energy gives a fifth constraint, and conservation of energy in the intermediate state (which only holds classically) gives a sixth constraint. With six equations of constraint, all six unknowns may be completely determined. The allowed values of \mathbf{v}' , \mathbf{v}_f , and \mathbf{v}_3 depend on the masses M_1 , M_2 , and M_3 . For example, in the case of the transfer of an electron from

J. C. Straton (✉)
Dept. of Physics, Portland State University
Portland, OR, USA
e-mail: straton@pdx.edu

J. H. McGuire
Dept. of Physics, Tulane University
New Orleans, LA, USA
e-mail: mcguire@tulane.edu

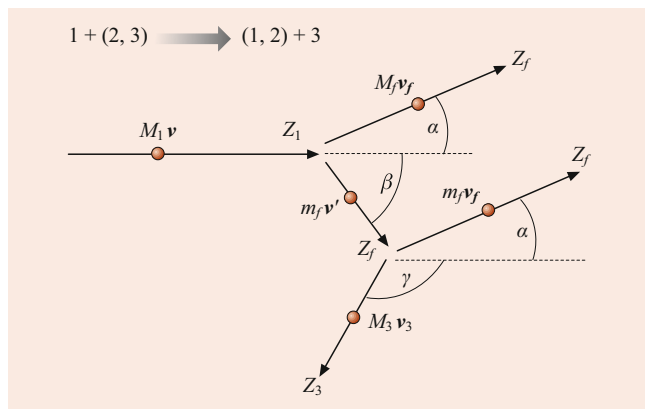


Fig. 61.1 Diagram for mass transfer via a Thomas two-step process

atomic hydrogen to a proton, i.e., $p^+ + H \rightarrow H + p^+$, it is easily verified that the angles are $\alpha = (M_2/M_1) \sin 60^\circ$, $\beta = 60^\circ$ and $\gamma = 120^\circ$, where $m' = M_2 = m_f$, and $M_1 = M_3 = M_p = 1836 m_e$. For the case $e^+ + H \rightarrow Ps + p^+$, it may be verified that $\alpha = 45^\circ$, $\beta = 45^\circ$ and $\gamma = 90^\circ$.

In general, the intermediate mass m' may be equal to M_1 , M_2 , or M_3 . We shall regard these as different Thomas processes and label them B, A, and C, respectively. The standard Thomas process (the one actually considered by Thomas in 1927) is case A and corresponds to the first example given above. Lieber diagrams for the Thomas processes A, B, and C [5] are illustrated in Fig. 61.2. In the Lieber diagram, mass regions in which solutions exist for processes A, B, and C are shown. (An equivalent diagram was given earlier by Detmann and Liebfried [3].) There are some regions in which two-step processes are forbidden. In these regions, the theory of mass transfer is not fully understood at present.

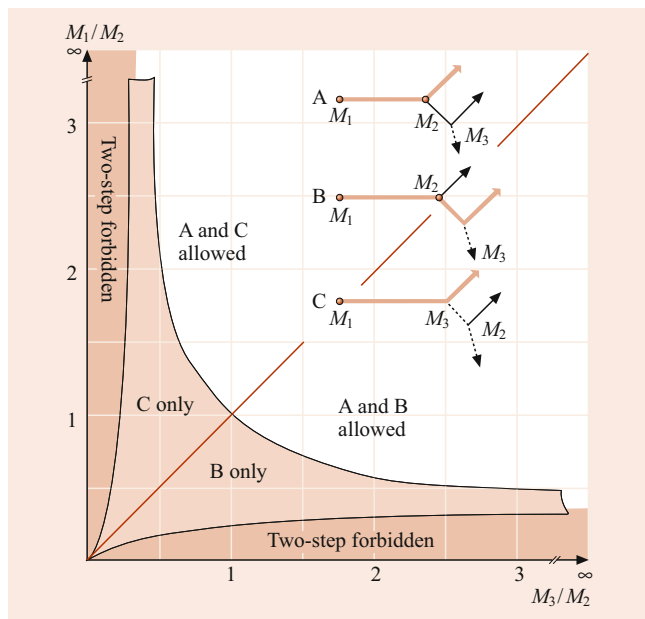


Fig. 61.2 Lieber diagram for mass transfer

61.2 Quantum Description

61.2.1 Uncertainty Effects

In quantum mechanics, energy conservation in the intermediate states may be violated within the limits of the uncertainty principle, $\Delta E \geq \hbar/\Delta t$, where Δt is the uncertainty in time of mass transfer. It is not possible to determine if mass transfer actually occurs at the beginning, in the middle, or at the end of the collision. Thus, we choose $\Delta t = \bar{r}/\bar{v}$, where \bar{r} is the size of the collision region, and \bar{v} is the mean collision velocity. Taking $\bar{r} \approx a_0/Z_{\text{target}}$ and $\bar{v} \approx v$, the projectile velocity, we have

$$\Delta E \approx \frac{\hbar}{\Delta t} = \frac{\hbar \bar{v}}{\bar{r}} = \frac{\hbar v}{a_0/Z_{\text{target}}} = \frac{\hbar Z_{\text{target}}}{a_0}. \quad (61.1)$$

Here, a_0 is the Bohr radius, and Z_{target} is the nuclear charge of the target in units of the electron charge. Within this range of energy ΔE , the constraint of energy conservation in the intermediate state does not apply.

61.2.2 Conservation of Overall Energy and Momentum

Conservation of overall energy and momentum then gives three equations of constraint on the four unknowns v_f and v_3 [6], namely,

$$M_1 v = (M_f + \tilde{M}_f) v_f + M_3 v_3, \quad (61.2)$$

$$M_1 v^2 = (M_f + \tilde{M}_f) v_f^2 + M_3 v_3^2, \quad (61.3)$$

where M_f (\tilde{M}_f) is the mass of the upper (lower) particle in the final state of the bound system shown in Fig. 61.1, in which m' is the mass of the intermediate particle M_1 , M_2 or M_3 . From Eqs. (61.2) and (61.3) it may be shown that the velocity of the recoil particle is constrained by the condition

$$2v_3 \cdot \hat{v} = 2 \cos \gamma = \frac{M_1 + M_2 + M_3}{M_1} \frac{v_3}{v} - \frac{M_2}{M_3} \frac{v}{v_3}. \quad (61.4)$$

Thus, the magnitude and the direction of v_3 are not independent. Specifying either v_3 or \hat{v}_3 is sufficient, together with the equations of constraint, to determine the energies and directions of all particles in the final state. Similarly, one may express the equations of constraint in terms of v_f and \hat{v}_f .

61.2.3 Conservation of Intermediate Energy

In a classical two-step process, the projectile hits a particle in the target, and the intermediate mass m' then propagates and subsequently undergoes a second collision. Quantum

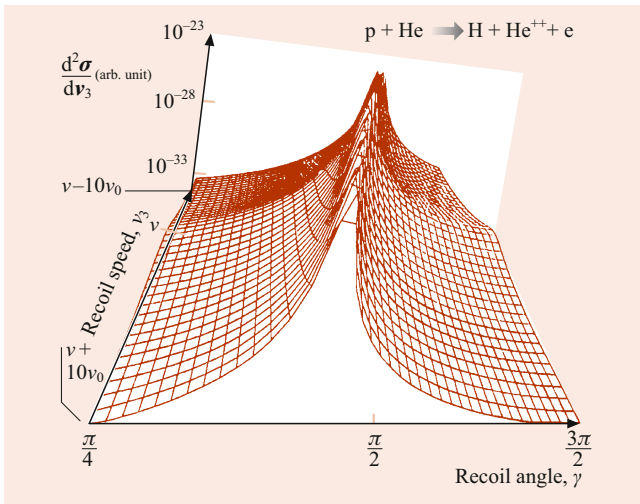


Fig. 61.3 Counting rate (or cross section) on the vertical axis versus recoil speed v_3 and recoil angle γ for a Thomas process in which a proton (projectile) picks up an electron from helium (target). The captured electron bounces off the second target electron

mechanically, this corresponds to a second Born term represented by $V_1 G_0 V_2$, where V represents an interaction and G_0 is the propagator of the intermediate state, namely,

$$G_0 = (E - H_0 + i\epsilon)^{-1} = -i\pi\delta(E - H_0) + \wp \frac{1}{E - H_0}, \quad (61.5)$$

where \wp is the Cauchy principal value of G_0 , which excludes the singularity at $E = H_0$. This singularity corresponds to conservation of energy in the intermediate state. It is this singularity that gives rise to the weaker secondary ridge in Fig. 61.3 at $v_3 = v$. The width of the secondary ridge is given approximately by $\Delta E = \hbar/\Delta t$, as discussed above. The intersection of the ridges is the Thomas peak. At very high collision velocities, the Thomas peak dominates the total cross section for mass transfer.

The constraint imposed by conservation of intermediate energy may be expressed by replacing the speed of the recoil particle v_3 by the scaled variable $K = M_3 v_3 / m'v$. Then it may be shown that the conservation of intermediate energy may be expressed in the form [6]:

$$\left(\frac{M_3 v_3}{m'v} \right)^2 \equiv K^2 = 1. \quad (61.6)$$

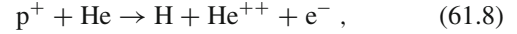
The constraints of conservation of overall energy and momentum, i.e., Eq. (61.4), may be easily written in terms of K as

$$2 \cos \gamma = r \frac{m'}{M_2} K - \frac{M_2}{m'} \frac{1}{K}, \quad (61.7)$$

where $r = (M_1 + M_2 + M_3)M_2 / (M_1 M_3)$.

61.2.4 Example: Proton–Helium Scattering

The effect of the constraints of conservation of overall energy and momentum may be seen in Fig. 61.3, where a sharp ridge is evident in the reaction



and $M_1 = M_p$, $M_2 = M_3 = m_e$. Here, v_3 is the speed of the recoiling ionized target electron, and the target nucleus is not directly involved in the reaction. The width of the sharp ridge is due to the momentum spread of the electrons in helium and may be regarded as being caused by the uncertainty principle since this momentum (or velocity) spread corresponds to $\Delta p = \hbar/\Delta r$, where Δr is taken as the radius of the helium atom.

The locus of the sharp ridge in Fig. 61.3, corresponding to conservation of overall energy and momentum, is given by Eq. (61.8). The locus of the weaker ridge, corresponding to the conservation of energy in the intermediate state, is given by Eq. (61.7). The intersection of these two loci gives the unique classical result suggested by Thomas. The width of these ridges may be estimated from the uncertainty principle as described above.

Experimental evidence for the double ridge structure has been reported by *Palinkas et al.* [7], corresponding to the calculations given in Fig. 61.3, but at a collision energy of 1 MeV, as shown below.

The data in Fig. 61.4 corresponds to a slice across the sharp ridge of Fig. 61.3 at $v = v_3$. The solid line is a second

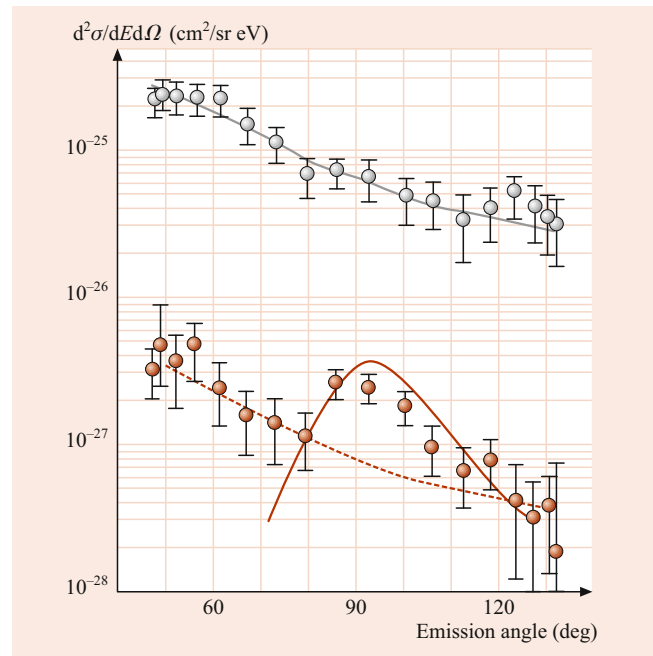


Fig. 61.4 Observation of a slice of the Thomas ridge structure in $p^+ + \text{He} \rightarrow \text{H} + \text{He}^{++} + e^-$ at 1 MeV by *Palinkas et al.* [7]

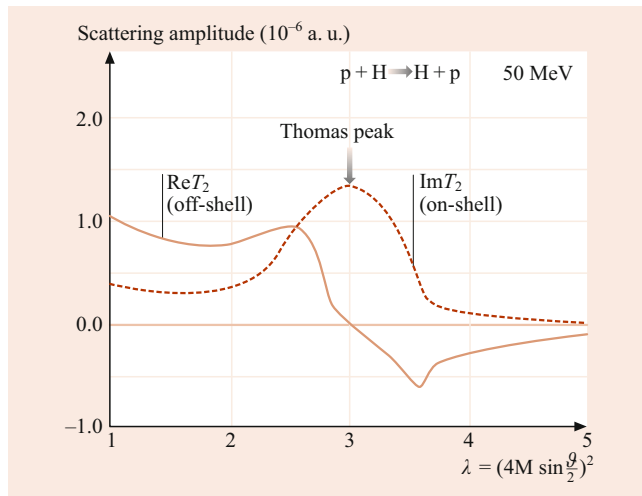


Fig. 61.5 Energy-conserving (on-shell) and energy-nonconserving contributions to the second Born scattering amplitude

Born calculation [8, 9] at 1 MeV. The bump of data above a smooth background is the indication of the ridge structure.

61.3 Off-Energy-Shell Effects

In Eq. (61.6), the Green's function G_0 contains an energy-conserving term $i\pi\delta(E - H_0)$, which is imaginary, and a real energy-nonconserving term $\wp[1/(E - H_0)]$. The latter does not occur classically; it is permitted by the uncertainty principle and represents the contribution of virtual (off-the-energy-shell or energy-nonconserving) states within $\pm\Delta E = \hbar/\Delta t$ about the classical value $E = H_0$. This quantum term also represents the effect of time-ordering in the second Born amplitude [10]. In plane wave second-Born calculations, the off-energy-shell term gives the real part of the scattering amplitude f_2 , while the on-shell (energy conserving) term gives the imaginary part of f_2 . These two contributions are shown in Fig. 61.5.

Half of the Thomas peak comes from energy-nonconserving contributions that are not included in a classical description. Also, the energy-nonconserving contribution plays a significant role in determining the shape of the standard Thomas peak, which has been observed [11].

61.4 Dispersion Relations

Because of the form of the Green's function of Eq. (61.6), the second Born contribution f_2 to the scattering amplitude has a single pole in the lower half of the complex plane. Con-

sequently, it obeys the dispersion relation

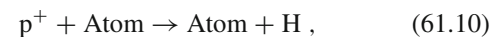
$$\begin{aligned} \operatorname{Re}[f_2(\lambda)] &= -\frac{1}{\pi} \wp \int_{-\infty}^{+\infty} \frac{\operatorname{Im}[f_2(\lambda')]}{\lambda - \lambda'} d\lambda', \\ \operatorname{Im}[f_2(\lambda)] &= \frac{1}{\pi} \wp \int_{-\infty}^{+\infty} \frac{\operatorname{Re}[f_2(\lambda')]}{\lambda - \lambda'} d\lambda', \end{aligned} \quad (61.9)$$

where $\operatorname{Re} f_2$ and $\operatorname{Im} f_2$ denote the real and imaginary parts of f_2 . Thus, the energy-nonconserving part of f_2 is related to an integral over the energy-conserving part and vice versa. In the case of the dielectric constant it is well known that the real and imaginary parts of ϵ are also related by a dispersion relation, namely the Kramers–Kronig relation [12].

Resonances are usually a function of energy E . The width of a resonance gives the lifetime τ of the resonance. Classically, τ is how long the projectile orbits the target before it leaves, corresponding to a delay or shift in time of the projectile during the interaction. If the width of the resonance is ΔE , then the lifetime is $\tau = \hbar/\Delta E$; E and τ are conjugate variables. The Thomas peak is an overdamped resonance in scattering angle, corresponding to a shift in the impact parameter of the scattering event [13]. However, unlike energy resonances, our Thomas resonance in the scattering angle seems to have no classical analog [14].

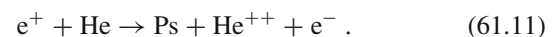
61.5 Destructive Interference of Amplitudes

It has already been noted that the location of the Thomas peaks depends on the mass of the collision partners. For the process



there are two separate Thomas peaks [2, 15] corresponding to cases A and B in the Lieber diagram (Fig. 61.2). Experimental evidence exists for both peaks. The standard Thomas peak occurs at small forward angles [11], while the second peak [16] occurs at about 60° . If the mass of the projectile is reduced, the positions of these Thomas peaks move toward one another [17], as illustrated in Fig. 61.6.

When $M_1 = M_2$, then both Thomas peaks occur at 45° . This occurs in positronium formation where $M_1 = M_2 = m_e$, i.e.,



In cases A and B of Fig. 61.2, the two $V_1 G_0 V_2$ second Born terms are of opposite sign because V_2 is of opposite sign in diagrams A and B. This leads to destructive interference for $1s - 1s$ electron capture (which is dominant at high velocities), as was first discussed by *Shakeshaft* and *Wadehra* [17].

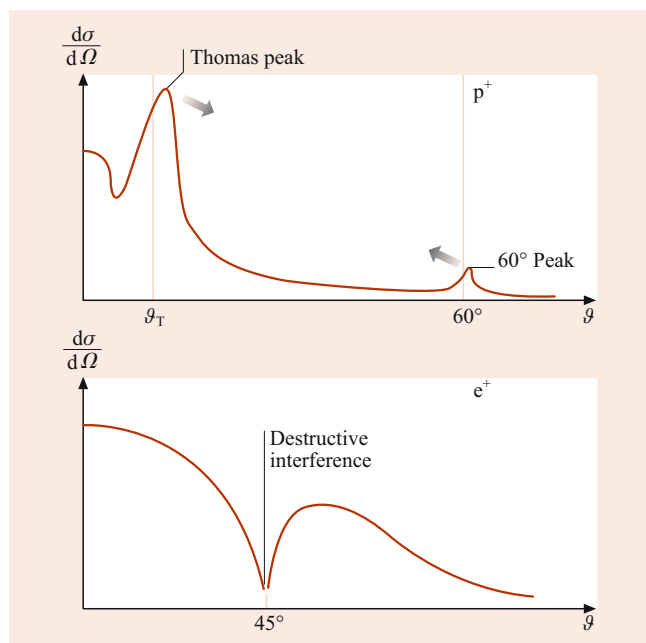


Fig. 61.6 Change of position and nature of the Thomas peaks with decreasing projectile mass

Consequently, the observed Thomas peak structure is expected [18, 19] to be quite different for e^+ impact than for impact of p^+ or other projectiles heavier than an electron. The double ridge structure for transfer ionization of helium by e^+ is expected to differ significantly from the structure shown in Fig. 61.3. Understanding such destructive interference between resonant amplitudes may give deeper insight into the physical nature of the intermediate states in this special few-body collision system.

61.6 Recent Developments

In the late 1990s, observations [20] of the Thomas peak in the case of transfer ionization (where one electron is ionized, and another is transferred) differential in the momentum of the ejected electron provided new specific detail on the kinematics of the two-step process [21]. In 2001, the Thomas peak was discussed [22] in the context of quantum time ordering. In this case, time ordering, surprisingly, is not significant at the center of the peak, in contradiction to the classical picture that there is a definite order in the two-step process for transfer ionization. However, time ordering does contribute to the shape of the Thomas peak. In 2002, the Stockholm group [23] reported that at very high velocities, the ratio of transfer ionization to total transfer approaches the same asymptotic limit as in double to single ionization in (non-Compton) photoionization, namely 1.66%. This was interpreted in terms of a common shake process occurring when the wavefunction collapses after a sudden collision.

References

1. Thomas, L.H.: Proc. Soc. A **114**, 561 (1927)
2. Shakeshaft, R., Spruch, L.: Rev. Mod. Phys. **51**, 369 (1979)
3. Detmann, K., Liebfried, G.: Z. Phys. **218**, 1 (1968)
4. Simony, P.R.: A second order calculation for charge transfer. Ph.D. Thesis. Kansas State University, Manhattan, KS, USA (1981)
5. Lieber, M.: private communication (1987)
6. McGuire, J.H., Straton, J.C., Ishihara, T.: In: Pindzola, M.S., Boyle, J.J. (eds.) The Application of Many-Body Theory to Atomic Physics. Cambridge University Press, Cambridge (1994)
7. Palinkas, J., Schuch, R., Cederquist, H., Gustafsson, O.: Phys. Rev. Lett. **22**, 2464 (1989)
8. McGuire, J.H., Straton, J.C., Axmann, W.C., Ishihara, T., Horsdal, E.: Phys. Rev. Lett. **62**, 2933 (1989)
9. Briggs, J.S., Taulbjerg, K.: J. Phys. B **12**, 2565 (1979)
10. McGuire, J.H.: Adv. At. Mol. Opt. Phys. **29**, 217 (1991)
11. Horsdal-Pederson, E., Cocke, C.L., Stöckli, M.: Phys. Rev. Lett. **57**, 2256 (1986)
12. Jackson, J.D.: Classical Electrodynamics. Wiley, New York, p 286 (1975)
13. Weaver, O.L., McGuire, J.H.: Phys. Rev. A **32**, 1435 (1985)
14. McGuire, J.H., Weaver, O.L.: J. Phys. B **17**, L583 (1984)
15. McGuire, J.H.: Indian J. Phys. **62B**, 261 (1988)
16. Horsdal-Pederson, E., Loftager, P., Rasmussen, J.L.: J. Phys. B **15**, 7461 (1982)
17. Shakeshaft, R., Wadehra, J.: Phys. Rev. A **22**, 968 (1980)
18. Igarashi, A., Toshima, N.: Phys. Rev. A **46**, R1159 (1992)
19. McGuire, J.H., Sil, N.C., Deb, N.C.: Phys. Rev. A **34**, 685 (1986)
20. Mergel, V., Dörner, R., Achler, M., Khayyat, K., Lencinas, S., Euler, J., Jagutski, O., Nüttgens, S., Unverzagt, M., Spielberger, L., Ru, W., Ali, R., Ullrich, J., Cederquist, H., Salin, A., Wood, C.J., Olson, R.E., Belkic, D., Cocke, C.L., Schmidt-Böcking, H.: Phys. Rev. Lett. **79**, 387 (1997)
21. Tolmanov, S.G., McGuire, J.H.: Phys. Rev. A **62**, 032771 (2000)
22. Godunov, A.L., McGuire, J.H., Ivanov, P.B., Shipakov, V.A., Merabet, H., Bruch, R., Hanni, J., Shakov, K.: J. Phys. B **34**, 5055 (2001)
23. Schmidt, H.T., Cederquist, H., Fardi, A., Schuch, R., Zettergren, H., Bage, L., Kallberg, A., Jensen, J., Resfelt, K.G., Mergel, V., Schmidt, L., Schmidt-Boecking, H., Cocke, C.L.: In: Burgdoerfer, J., Cohen, J.S., Datz, S., Vane, C.R. (eds.) Photonic, Electronic and Atomic Collisions, p. 720. Rinton, Princeton, NJ (2002)



Jack C. Straton Dr Straton is an Associate Professor at Portland State University, where his teaching focuses on astronomy, diversity, art, and social responsibility. His research ranges from antiracist pedagogy to nanometrology to quantum scattering theory, with a present focus on calculating the effects of laser stimulation to the attachment of a second positron to the antihydrogen atom.



James H. McGuire Dr McGuire is Murchison Mallory Professor Emeritus and past Department Chair at Tulane University. He is a past Chair of the Division of Atomic, Molecular, and Optical Physics (DAMOP) of the American Physical Society. His research interests are in electron correlation dynamics, entanglement, complexity and correlation, and quantum time.



Marcelo Ciappina , Raul O. Barrachina , Francisco Navarrete , and Ronald E. Olson

Contents

62.1	Theoretical Background	919
62.1.1	Hydrogenic Targets	919
62.1.2	Nonhydrogenic One-Electron Models	920
62.1.3	Multiply Charged Projectiles and Many-Electron Targets	920
62.2	Region of Validity	921
62.3	Applications	921
62.3.1	Hydrogenic Atom Targets	921
62.3.2	Pseudo-One-Electron Targets	922
62.3.3	State-Selective Electron Capture	922
62.3.4	Exotic Projectiles	923
62.3.5	Heavy-Particle Dynamics	923
62.3.6	Ion-Molecule Collisions	923
62.3.7	Strong Laser Field Ionization	924
62.4	Conclusions	925
	References	925

Abstract

The classical trajectory Monte Carlo (CTMC) method originated with *Hirschfelder*, who studied the $H + D_2$ exchange reaction using a mechanical calculator [1]. With the availability of computers, the CTMC method was ac-

tively applied to a large number of chemical systems to determine reaction rates and final state vibrational and rotational populations (e.g., *Karplus et al.* [2]). For atomic physics problems, a major step was introduced by *Abrines and Percival* [3], who employed Kepler's equations and the Bohr–Sommerfeld model for atomic hydrogen to investigate electron capture and ionization for intermediate velocity collisions of $H^+ + H$. An excellent description is given by *Percival and Richards* [4]. The CTMC method has a wide range of applicability to strongly coupled systems, such as collisions by multiply charged ions [5]. In such systems, perturbation methods fail, and basis set limitations of coupled-channel molecular-orbital and atomic-orbital techniques have difficulty in representing the multitude of active excitation, electron capture, and ionization channels.

Keywords

electron capture · differential cross section · target nucleus · angular scattering · classical trajectory Monte Carlo

M. Ciappina (✉)
Physics Program, Guangdong Technion – Israel Institute of Technology
Shantou, Guangdong, China
e-mail: marcelo.ciappina@gtiit.edu.cn

R. O. Barrachina
Bariloche Atomic Centre, National Atomic Energy Commission
Bariloche, Argentina
e-mail: barra@cab.cnea.gov.ar

F. Navarrete
Institute of Physics, University of Rostock
Rostock, Germany
e-mail: francisco.navarrete@uni-rostock.de

R. E. Olson
Physics Dept., University of Missouri-Rolla
Rolla, MO, USA
e-mail: olson@umr.edu

62.1 Theoretical Background

62.1.1 Hydrogenic Targets

Let us consider a simple three-body collision system comprised of a fully-stripped projectile (a), a bare target nucleus (b), and an active electron (c), where each pair of particles of charge Z_i and Z_j , and positions \mathbf{r}_i and \mathbf{r}_j , interact via a Coulomb potential $Z_i Z_j / |\mathbf{r}_i - \mathbf{r}_j|$. The classical Hamiltonian for the system is

$$H = \sum_{i=a,b,c} \frac{|\mathbf{p}_i|^2}{2m_i} + \sum_{i \neq j} \frac{Z_i Z_j}{|\mathbf{r}_i - \mathbf{r}_j|}, \quad (62.1)$$

where \mathbf{p}_i and m_i are the momenta and masses of the particles, respectively.

The initial state of the target is completely determined by five random numbers given by Kepler's equation that constrain the plane and eccentricity of the electron's orbit, and another one is used to determine the impact parameter within the range of interaction [4, 5]. From Eq. (62.1), one obtains a set of 18 coupled (this number can be reduced by energy-momentum conservation considerations) first-order differential equations that determine the time evolution of the Cartesian coordinates and momenta of each particle,

$$d\mathbf{r}_i/dt = \partial H/\partial \mathbf{p}_i \quad (62.2)$$

$$d\mathbf{p}_i/dt = -\partial H/\partial \mathbf{r}_i \quad (62.3)$$

A fourth-order Runge–Kutta integration method is suitable to solve them because of its ease of use and its ability to vary the time step size. This latter requirement is essential since the time step can typically vary by three orders of magnitude during a single trajectory.

In essence, the CTMC method is a computer experiment. Total cross sections for a particular process are determined by

$$\sigma_R = (N_R/N)\pi b_{\max}^2, \quad (62.4)$$

where N is the total number of trajectories run within a given maximum impact parameter b_{\max} , and N_R is the number of positive tests for a reaction, such as electron capture or ionization. Angle and energy differential cross sections are easily generalized from the above. As in an experiment, the cross section given by Eq. (62.4) has a standard deviation of

$$\Delta\sigma_R = \sigma_R[(N - N_R)/NN_R]^{1/2}, \quad (62.5)$$

which for large N is proportional to $1/N_R^{1/2}$. Here lies one of the major difficulties associated with the CTMC method: it takes considerable computation time to determine minor or highly differential cross sections because, to decrease the statistical error of a cross by a factor of 2, four times as many trajectories must be evaluated.

62.1.2 Nonhydrogenic One-Electron Models

For many-electron target atoms, it is sometimes adequate to treat the problem within a one-electron model and employ the independent electron approximation to approximate the atomic shell structure [6]. For an accurate calculation, it is necessary to use an interaction potential that simulates the screening of the target nucleus by the passive electrons, i.e., the electrons that do not participate in the reaction. One can simply apply a Coulomb potential with an effective charge Z_{eff} obtained from, for example, Slater's rules. Then, the computational procedure is the same as for the hydrogenic

case. However, the boundary conditions for the long and short-range interactions are poorly satisfied.

To improve the electronic representation of the target, model potentials derived from quantum mechanical calculations are now routinely used. Here, the simple solution of Kepler's equation cannot be applied. However, *Peach* et al. [7] and *Reinhold* and *Falcón* [8] have provided the appropriate methods that yield a target representation that is correct under the microcanonical distribution. The method of Reinhold and Falcón is popular because of its ease of use and generalizability. For the effective interaction potential, *Garvey* et al. [9] have performed a large set of Hartree–Fock calculations and have parametrized their results by a potential $V(R)$, which depends on the distance to the target R , as

$$V(R) = -[Z - NS(R)]/R, \quad (62.6)$$

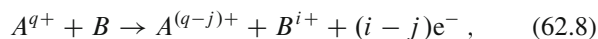
where Z and N denote the nuclear charge and number of nonactive electrons in the target core, respectively, and $S(R)$ is the screening of the core given by

$$S(R) = 1 - \{(\eta/\xi)[\exp(\xi R) - 1] + 1\}^{-1/2}, \quad (62.7)$$

where η and ξ are screening parameters. Screening parameters are given in [9] for all ions and atoms with $Z \leq 54$. This potential can also be used for the representation of partially stripped projectile ions. Even though it seems natural to think that the inclusion of more active electrons in the description of the problem would give rise to more accurate cross sections, it is worth noticing that it could also lead to unphysical autoionization, as was pointed out in [10], where a possible remedy to this problem is shown as well.

62.1.3 Multiply Charged Projectiles and Many-Electron Targets

Multiple ionization and electron capture mechanisms in energetic collisions between multiply charged ions and many-electron atoms is poorly understood because major approximations must be made to solve the many-electron problem associated with transitions between two centers. For a representative collision system such as



it is essential to use a theoretical method able to predict simultaneously the various charge states of the projectile and recoil ions, and also the energy and angular spectra of the ejected electrons. Theoretical methods based on the independent electron model fail because the varying ionization energies of the electrons are not well represented by constant values, especially for outer shells. At present, the most

successful implementation is the n CTMC method, which is a direct extension of the hydrogenic CTMC method to an n -electron system and has been able to make reasonable predictions of the cross sections and scattering dynamics of such strongly coupled systems [11]. As such, the number of coupled equations rises to $6n + 12$, where n is the number of electrons included in the calculation.

In the n CTMC technique, all interactions of the projectile and target nuclei with each other and the electrons are implicitly included in the calculations. The inclusion of all the particles then allows a direct determination of their angular scattering, along with an estimate of the energy deposition to electrons and heavy particles. Postcollision interactions are included between projectile and recoil ions with the electrons; however, electron–electron interactions are introduced only in the bound initial state via a screening factor in a central-field approximation. This theoretical model has been very successful in predicting the single and double differential cross sections for the ionized electron spectra. Moreover, since a fixed target nucleus approximation is not used, this method has been the only one available to help understand and predict the results in the field of recoil-ion momentum spectroscopy [12].

62.2 Region of Validity

The CTMC method has a demonstrated region of applicability for ion–atom collisions in the intermediate velocity regime, particularly in the elucidation of both heavy-particle and electron collision dynamics. The method can be termed a semiclassical method in that the initial conditions for the electron orbits are determined by quantum mechanically based interaction potentials with the parent nucleus. Since the method is most suitable for strongly coupled systems, it has been applied successfully to a variety of intermediate energy multiply charged ion collisions. Figure 62.1 describes pictorially and the regions of validity of various theoretical models. Both the atomic orbital (AO) and molecular orbital (MO) basis set expansion methods (Chap. 53) work well until ionization strongly mediates the collision, since the theoretical description of the ionization continuum is not well founded and relies on pseudo states to span all ejected electron energies and angles. We have arbitrarily limited these methods to a projectile charge to target charge ratio of, $Z_P/Z_T, \simeq 8$, since above this value the number of terms in the basis set becomes prohibitively large. The CTMC method does not include molecular effects, and thus it is restricted to low velocities, except in the case of high-charge-state projectiles that capture electrons into high-lying Rydberg states, which are well described classically. Likewise, at high velocities, the method is inapplicable in the perturbation regime, where quantum tunneling is important,

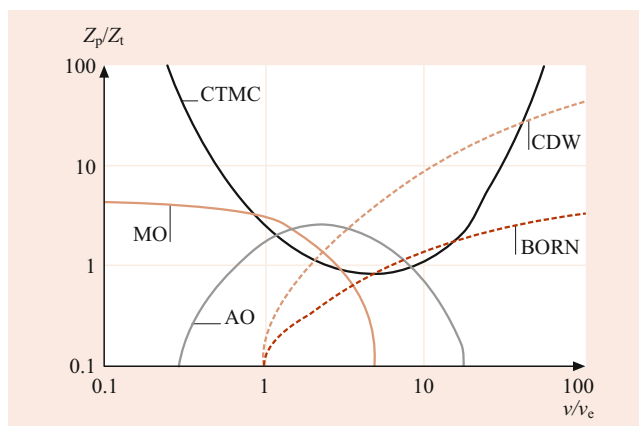


Fig. 62.1 Approximate regions of validity of various theoretical methods; Z_P/Z_T is the ratio of the projectile charge to the target charge, and v/v_e is the ratio of the collision velocity to the velocity of the active target electron. Theoretical methods: molecular orbital (MO), atomic orbital (AO), classical trajectory Monte Carlo (CTMC), continuum distorted wave (CDW), and first-order perturbation theory (BORN)

and is thus restricted to strongly coupled systems. The continuum distorted wave (CDW) method (Chap. 56) greatly extends the region of applicability of first-order perturbation methods and has demonstrated validity in high-charge state ionization collisions.

62.3 Applications

62.3.1 Hydrogenic Atom Targets

The original application of the CTMC method to atomic physics collisions was done on the $H^+ + H$ system [3]. Here, the electron capture and ionization total cross sections were found to be in very good accord with experiment. The Abrines and Percival procedure casts the coupled equations into the center-of-mass (c.m.) coordinate system to reduce the three-body problem to 12 coupled equations. However, this reduction complicates extensions of the code to laser processes and collisions in the presence of electric fields or with many electrons.

An ideal application for the CTMC method is for collisions involving excited targets. Such processes are well described classically, while basis set expansion methods show limited applicability due to computer memory constraints. Considerable early work was done on Rydberg atom collisions, including state-selective electron capture, ionization, and electric fields [13–15]. Presently, there is a resurgence of work on Rydberg atom collisions because new crossed-field experimental techniques allow the production of these atoms with specific spatial orientations and eccentricities [16, 17], and even Rydberg positronium atoms have been achieved experimentally [18].

For hydrogenic ion–ion collision processes, one must be careful to apply the CTMC method only for projectile charges $Z_P \geq Z_T$ because after the initialization of the active electron's orbit and energy, there is no classical constraint on the orbital energy of a captured electron. For a low-charge-state ion colliding with a ground state highly charged ion, one will obtain unphysical results because a captured electron will tend to preserve its original binding energy. Thus, excess probability will be calculated for electron orbits that lead to unrealistic deeply bound states of the projectile.

62.3.2 Pseudo-One-Electron Targets

Collisions involving alkali atoms are of interest because of their relevance to applied programs, such as plasma diagnostics in tokamak nuclear fusion reactors. They are also a testing ground for theoretical methods since experimental benchmarks are difficult to realize with hydrogenic targets but are amenable for such cases as alkali atoms. In such collisions, it is essential to use a theoretical formalism that correctly simulates the screening of the nucleus by the core electrons (Sect. 62.1.2), since a simple $-Z_{\text{eff}}/R$ Coulomb potential is inadequate for both large and small R .

One can also apply the methods of Sect. 62.1.2 to partially or completely filled atomic shells [19]. This works reasonably well for collisions with a low charge state ion such as a proton, but it gets less accurate as the charge of the projectile becomes greater than that of the target nucleus. The reason is that the independent electron approximation [6] must be applied to the calculated transition probabilities in order to simulate the shell structure. This latter method can only maintain its validity if the transition probability is small. Otherwise, it will greatly overestimate the multiple electron removal processes since the first ionization potential is inherently assumed for each subsequent electron that is pulled out from the shell, leading to an underestimation of the energy deposition.

62.3.3 State-Selective Electron Capture

One of the powers of the CTMC method is that it can be applied to electron capture and excitation of high-lying states that are not accessible with basis set expansion techniques [20]. For the C^{4+} colliding on Li, and C^{6+} and N^{7+} colliding on H, where AO calculations and experimental data exist, the CTMC method agrees quite favorably with both [21–23].

The procedure consists in defining first a classical number n_c related to the calculated binding energy E of the active electron to either the projectile (electron capture) or target

nucleus (excitation) as

$$E = -Z^2/(2n_c^2). \quad (62.9)$$

Then, n_c is related to the principal quantum number n of the final state by the condition [24]

$$\left[n \left(n - \frac{1}{2} \right) (n - 1) \right]^{1/3} < n_c \leq \left[n \left(n + \frac{1}{2} \right) (n + 1) \right]^{1/3}. \quad (62.10)$$

The electron's normalized classical angular momentum $l_c = (n/n_c)(\mathbf{r} \times \mathbf{k})$, is related to the orbital quantum number l of the final state by

$$l < l_c \leq l + 1. \quad (62.11)$$

The magnetic quantum number m_l is then obtained from

$$\frac{2m_l - 1}{2l + 1} \leq \frac{l_z}{l_c} < \frac{2m_l + 1}{2l + 1}, \quad (62.12)$$

where l_z is the z -projection of the angular momentum obtained from calculations [25]. In principle, it is also possible to analyze the final-state distributions from the effective quantum number

$$n^* = n - \delta_l, \quad (62.13)$$

where δ_l is the quantum defect. In this latter case, it is necessary to sort the angular momentum quantum numbers first and then sort the principal quantum numbers.

One of the main applications of the method explained in this section can be found in the description of the charge transfer of one electron from a neutral atom or molecule to an excited state of a highly charged ion, from which it deexcites by releasing electromagnetic radiation. It was uncovered in the 1970s that charge exchange (CX) reactions can be used as a diagnostic tool in nuclear fusion reactors, because the CX between impurities – constituted by multiply charged ions – and a H or D neutral beam provides a method for determining the concentration of fully stripped ions and for measuring ion temperature and plasma rotation [26]. This technique, known as charge exchange spectroscopy (XCS), has become widespread as a diagnostic in high-temperature – mostly tokamak – plasmas [27, 28]. Furthermore, the discovery in 1996 [29, 30] that comets undergo a highly efficient generation of X-rays [31–33], originated by the CX between cometary tail neutral gas and the highly charged ions from the solar wind (SWCX), opened up a vast new field of X-ray astrophysics, leading to subsequent studies that revealed many other astrophysical locations where a similar process

occurs, ranging from the heliosphere, planetary atmospheres, the interstellar medium, galaxies, and could even be linked to dark matter radiation [34]. Due to the high relevance of these applications, numerous experimental studies have been performed at the energy intervals of interest. For instance, experiments to study SWCX and CXS in the range from of 1 to 3 keV/amu and of 1 to 40 keV/amu, respectively, have been modeled using the state-selective CTMC method to successfully calculate the nl -resolved CX cross sections [35–37].

62.3.4 Exotic Projectiles

The study of collisions involving antimatter projectiles, such as positrons and antiprotons, is a field that has grown rapidly over the past two decades, spurred on by experimental advances [38, 39]. Such scattering processes are of basic interest, and they also contribute to a better understanding of normal matter–atom collisions. Antimatter–atom studies highlight the underlying differences in the dynamics of the collision, as well as on the partitioning of the overall scattering. In the Born approximation, ionization cross sections depend on the square of the projectile’s charge and are independent of its mass. Thus, the comparison of the cross sections for electron, positron, proton, and antiproton scattering from a specific target gives a direct indication of higher-order corrections to scattering theories [40, 41].

Early work using the CTMC method concentrated on the spectra of ionized electrons for antimatter projectiles [42]. Later work focused on the angular scattering of the projectiles during electron removal collisions, such as positronium formation, on ratios of the electron removal cross sections, and on ejected electron “cusp” and “anticusp” formation. Two complete reviews on antiproton and positron impact collisions, which compare various theoretical results and available experiments, are given in [43, 44].

62.3.5 Heavy-Particle Dynamics

A major attribute of the CTMC method is that it inherently includes the motion of the heavy particles after the collision. A straight-line trajectory for the projectile is not assumed, nor is the target nucleus constrained to be fixed. This allows one to compute easily the differential cross sections for projectile scattering or the recoil momenta of the target nucleus. As a computational note, the angular scattering of the projectile should be computed from the momentum components, not the position coordinates after the collision, since faster convergence of the cross sections using the projectile momenta is obtained. For recoil ion momentum transfer studies, one must initialize the target atom such that the c.m. of the nucleus plus its electrons has zero momentum so that there is

no initial momentum associated with the target. A common error is to initialize only the target nucleus momenta to zero. Then the target atom after a collision has an artificial residual momentum that is associated with the Compton profile of the electrons because target–electron interactions are included in the calculations. Examples of recoil and projectile scattering cross sections are given in [11, 12].

The field of recoil ion momentum spectroscopy rapidly expanded in the early 2000s (e.g., [45, 46]), and the CTMC theoretical method impacted on the interpretation and understanding of experimental results because it inherently provides a kinematically complete description of the collision products. For the studied systems, primarily He targets because of experimental constraints, it is necessary for the theoretical method to follow all ejected electrons and the heavy particles after a collision. As an example, it has been possible to observe the backward recoil of the target nucleus in electron capture reactions, which is due to conservation of momentum when the active electron is transferred from the target’s to the projectile’s frame [47]. Theoretical methods were tested further with magneto-optical traps (MOT) that provide frozen alkali metal atomic targets ($T \ll 1$ mK) from which to perform recoil ion studies [48].

For three and four-body systems, it is now possible to measure the momenta of all collision products. These observations provide a severe test of theory, since all projectile and target interactions must be included in the calculations. The CTMC method addresses all projectile interactions with the target nucleus and electrons. Thus, it is possible to calculate fully differential cross sections (FDCS), the most detailed accessible experimental observable. It is of interest that triply differential cross sections (TDCS) calculated using the CTMC method compare very favorably with sophisticated continuum distorted wave methods [49].

The CTMC technique allows one to incorporate electrons on both the projectile and the target nuclear centers. Furthermore, all interactions between centers are included. The only interaction that needs to be approximated is the electron–electron interaction on a given center. Here, simple screening parameters derived from Hartree–Fock calculations are employed to eliminate nonphysical autoionization. Within this many-electron model, the signatures of the electron–electron and electron–nuclear interactions on the dynamics of the collisions have been observed [50, 51]. Further, projectile ionization studies can be undertaken [52–54].

62.3.6 Ion-Molecule Collisions

Ion-molecule ionization collisions share many aspects with the processes described in 62.1.3, but its study is much more complex because, apart from being multielectronic, the target is composed of several nuclei. Due to its simplicity, the

first of these systems to be analyzed by a CTMC method was the H_2 molecule [55], for which a fixed internuclear axis (Franck–Condon approximation) randomly orientated was assumed, and the electrons initialized in terms of two one-electron microcanonical distributions constructed from the quantum mechanical ground state of the molecule. For more complex molecules, apart from the Franck–Condon approximation, which is a typical assumption, many other approximations must be performed, which give rise to different calculation methods.

Single ionization and electron capture in ion- H_2O collisions (for different projectile charges) have been successfully described by the use of one-center screened Coulomb potentials [56–58], in a similar fashion as was described for many-electron atoms in 62.3.1. In all the cases, a single active electron approximation is also invoked.

We can also mention other methods that introduce approximations on the projectile-target interaction and are based on the classical over-barrier charge transfer process [59, 60], called COB-CTMC. In COB-CTMC, electrons bound to the target molecule are included in the calculation through the course of the collision. At each time step, the internuclear ion-molecule potential is evaluated, and the most weakly bound electrons are released if its maximum is lower than the binding target energy. After this, the electrons change from being *virtual* to being an *active* part of the dynamics of the process, and a further condition is usually established to account for the spatial electron density. This method has been successfully applied to the study of ionization of DNA and RNA uracil by highly charged ion impact [61].

Finally, as was already mentioned in the first paragraph of this section, other methods describe the multicenter nature of the target by fixing the position of the nuclei but rotating the internuclear axis randomly at each trajectory calculation and have been applied to the study of the ionization by ion impact of not only H_2 [55] but also H_2O molecules [62].

62.3.7 Strong Laser Field Ionization

The study of the nonlinear electron dynamics in the ionization of atoms by intense few-cycle laser pulses has gained attention over the last years (e.g., [63]). The limitations of a quantum description for this type of processes come from the fact that perturbation theory is, in most of the cases, not applicable, and nonperturbative calculations are sometimes prohibitively expensive, from a computational viewpoint. The straightforward extension of the CTMC method to photoionization problems is a promising solution to this problem, and it consists simply of adding the external laser field to the particles Hamiltonian, while the rest of the method remains essentially the same as that derived by *Abrines* and *Percival* [3]. As a remarkable example of the power of

this method, we can mention the work of *Ho* et al. [64], who performed a fully classical self contained study of the atomic nonsequential double ionization (NSDI) [65]. Their procedure discards all quantum effects, even tunneling, but describes the dynamics in a complete form, which is a very important feature because electron–electron correlation is supposed to play an instrumental role in this process. The electrons are initialized with an energy corresponding to the two-electron quantum ground state, and then the dynamics are governed by the Coulomb interaction among the particles and their interaction with the laser electric field.

Even though the CTMC method cannot include tunneling by default, features on the cross sections found experimentally for the double ionization of He and Ne [66, 67], and single ionization of He, Ne, and Ar [68] by laser fields at high intensities, on the range of 10^{15} W/cm², have been described by nonrelativistic semiclassical CTMC methods that include an ad hoc tunneling step [69]. These theoretical works are based on a method developed by *Cohen* [70], which treats both the description of the initial state and the dynamics of the particles in the standard way. The improvement of this method on the description of the process is that, using the WKB approximation, tunneling is allowed in the direction of the field starting from classical turning points. At points \mathbf{r}_c for which $dz/dt = 0$ and $-\mathbf{E}(t) \cdot \mathbf{r}_c > 0$, being \hat{z} the polarization direction of the electric field $\mathbf{E}(t)$, the *tunneling probability* is calculated as follows:

$$P_{\text{tun}} = \exp \left\{ -2(2\mu)^{1/2} \int_0^{s_{\text{out}}} [V(\mathbf{r}_c + s\hat{z}) - V(\mathbf{r}_c)] ds \right\}, \quad (62.14)$$

where μ is the reduced mass. If this probability is greater than a random number between 0 and 1, the particle then tunnels out at the point $\mathbf{r}_c + s_{\text{out}}\hat{z}$, at which $V(\mathbf{r}_c + s_{\text{out}}\hat{z}) = V(\mathbf{r}_c)$. On the contrary, the trajectory remains unaltered. For an extension of this model, which includes references to a broad variety of applications of this method, see [71].

Finally, it is also worth giving a brief description of the extension of CTMC method to treat relativistic problems [72]. For laser intensities above 10^{18} W/cm², the motions of electrons become highly relativistic because the mass of the electron starts becoming comparable to its rest mass. Here, we can mention two methods, which are similar in that the equations of motion must be solved relativistically but treat the initial state in a different way depending on the nucleus charge. If the charge of the nucleus is lower than 10, it is possible to treat the electron nonrelativistically in its initial state [73], whereas if it is higher than that value, it needs to be treated relativistically [74]. Additionally, it is possible to study both the ion and electron dynamics driven by an ultrastrong laser field (10^{18} – 10^{26} W/cm²) by applying a fully relativistic extension of the CTMC approach [75].

62.4 Conclusions

In many ways it is surprising that a pure classical model can be successful in a quantum mechanical world, especially since the classical radial distribution for the hydrogen atom is described so poorly. However, hydrogen's classical momentum distribution is exactly equivalent to the quantum one, and since collision processes are primarily determined by velocity matching between projectile and electron, reasonable results can be expected. Moreover, the CTMC method preserves conservation of flux, energy, and momentum, and Coulomb scattering is the same in both quantal and classical frameworks.

Of significant importance is that the CTMC method is not restricted to one-electron systems and can be easily extended to more complicated systems involving electrons on both projectile and target. For these latter cases, multiple electron capture and ionization reactions can be investigated. On the projectiles side, the success of the CTMC process driven by both charged particles and photons is worth mentioning.

References

- Hirschfelder, J., Eyring, H., Topley, B.: *J. Chem. Phys.* **4**, 170 (1936)
- Karplus, M., Porter, R.N., Sharma, R.D.: *J. Chem. Phys.* **43**, 3259 (1965)
- Abrines, R., Percival, I.C.: *Proc. Phys. Soc.* **88**, 861 (1966)
- Percival, I.C., Richards, D.: *Adv. At. Mol. Phys.* **11**, 1 (1975)
- Olson, R.E., Salop, A.: *Phys. Rev. A* **16**, 531 (1977)
- McGuire, J.H., Weaver, L.: *Phys. Rev. A* **16**, 41 (1977)
- Peach, G., Willis, S.L., McDowell, M.R.C.: *J. Phys. B* **18**, 3921 (1985)
- Reinhold, C.O.: *Phys. Rev. A* **33**, 3859 (1986)
- Garvey, R.H., Jackman, C.H., Green, A.E.S.: *Phys. Rev. A* **12**, 1144 (1975)
- Jorge, A., Illescas, C., Méndez, L., Rabadán, I.: *J. Phys. Chem. A* **122**, 2523 (2018)
- Olson, R.E., Ullrich, J., Schmidt-Böcking, H.: *Phys. Rev. A* **39**, 5572 (1989)
- Cocke, C.L., Olson, R.E.: *Phys. Rep.* **205**, 153 (1991)
- Olson, R.E.: *J. Phys. B* **13**, 483 (1980)
- Olson, R.E.: *Phys. Rev. Lett.* **43**, 126 (1979)
- Olson, R.E., MacKellar, A.D.: *Phys. Rev. Lett.* **46**, 1451 (1981)
- Delande, D., Gay, J.C.: *Eur. Lett.* **5**, 303 (1988)
- Dunning, F.B., Mestayer, J.J., Reinhold, C.O., Yoshida, S., Burgdörfer, J.: *J. Phys. B* **42**, 022001 (2009)
- Wall, T.E., Alonso, A.M., Cooper, B.S., Deller, A., Hogan, S.D., Cassidy, D.B.: *Phys. Rev. Lett.* **114**, 173001 (2015)
- Sarkadi, L.: *Phys. Rev. A* **97**, 042703 (2018)
- Olson, R.E.: *Phys. Rev. A* **24**, 1726 (1981)
- Hoekstra, R., Olson, R.E., Folkerts, H.O., Wolfrum, W., Pascale, J., de Heer, F.J., Morgenstern, R., Winter, H.: *J. Phys. B* **26**, 2029 (1993)
- Jorge, A., Errea, L.F., Illescas, C., Méndez, L., Suárez, J.: *Phys. Scr.* **T156**, 014032 (2013)
- Cariatore, N.D., Otranto, S., Olson, R.E.: *Phys. Rev. A* **91**, 042709 (2015)
- Becker, R.C., MacKellar, A.D.: *J. Phys. B* **17**, 3923 (1984)
- Schippers, S., Boduch, P., van Buchem, J., Blik, F.W., Hoekstra, R., Morgenstern, R., Olson, R.E.: *J. Phys. B* **28**, 3271 (1995)
- Isler, R.C.: *Plasma Phys. Control. Fusion* **36**, 171 (1994)
- Anderson, H., von Hellermann, M.G., Hoekstra, R., Horton, L.D., Howman, A.C., König, R.W.T., Martin, R., Olson, R.E., Summers, H.P.: *Plasma Phys. Control. Fusion* **42**, 781 (2000)
- Guo, D.L., et al.: *Phys. Rev. A* **95**, 012707 (2017)
- Lisse, C.M., et al.: *Science* **274**, 205 (1996)
- Cravens, T.E.: *Geophys. Res. Lett.* **24**, 105 (1997)
- Beiersdorfer, P., Olson, R.E., Brown, G.V., Chen, H., Harris, C.L., Neill, P.A., Schweikhard, L., Utter, S.B., Widmann, K.: *Phys. Rev. Lett.* **85**, 5090 (2000)
- Beiersdorfer, P., Lisse, C.M., Olson, R.E., Brown, G.V., Chen, H.: *Astrophys. J.* **549**, 147 (2001)
- Leung, A.C.K., Kirchner, T.: *Phys. Rev. A* **93**, 052710 (2016)
- Dennerl, K.: *Space Sci. Rev.* **157**, 57 (2010)
- Mawhorter, R.J., et al.: *Phys. Rev. A* **75**, 032704 (2007)
- Fogle, M., et al.: *Phys. Rev. A* **89**, 042705 (2014)
- Otranto, S., et al.: *Phys. Rev. A* **73**, 022723 (2006)
- Kövér, Á., Laricchia, G.: *Phys. Rev. Lett.* **80**, 5309 (1998)
- Khayyat, K., et al.: *J. Phys. B* **32**, L73 (1999)
- Fiol, J., Courbin, C., Rodriguez, V.D., Barrachina, R.O.: *J. Phys. B* **33**, 5343 (2000)
- Fiol, J., Barrachina, R.O.: *J. Phys. B* **44**, 075205 (2011)
- Olson, R.E., Gay, T.J.: *Phys. Rev. Lett.* **61**, 302 (1988)
- Kirchner, T., Knudsen, H.: *J. Phys. B* **44**, 122001 (2011)
- Laricchia, G., Armitage, S., Kövér, Á., Murtagh, D.J.: *Adv. At. Mol. Opt. Phys.* **56**, 1–47 (2008)
- Ullrich, J., et al.: *Rep. Prog. Phys.* **66**, 1463–1545 (2003)
- Dörner, R., et al.: *Phys. Rep.* **330**, 95–192 (2000)
- Frohne, V., Cheng, S., Ali, R., Raphaelian, M., Cocke, C.L., Olson, R.E.: *Phys. Rev. Lett.* **71**, 696 (1993)
- Turkstra, J.W., Hoekstra, R., Knoop, S., Meyer, D., Morgenstern, R., Olson, R.E.: *Phys. Rev. Lett.* **87**, 123202 (2001)
- Fiol, J., Olson, R.E.: *J. Phys. B* **35**, 1759 (2002)
- Kollmus, H., Moshhammer, R., Olson, R.E., Hagmann, S., Schulz, M., Ullrich, J.: *Phys. Rev. Lett.* **88**, 103202 (2002)
- Fiol, J., Olson, R.E., Santos, A.C.F., Sigaud, G.M., Montenegro, E.C.: *J. Phys. B* **34**, 503 (2001)
- Olson, R.E., Watson, R.L., Horat, V., Zaharakis, K.E.: *J. Phys. B* **35**, 1893 (2002)
- Sarkadi, L., Herczku, P., Kovács, S.T.S., Kövér, A.: *Phys. Rev. A* **87**, 062705 (2013)
- Blank, I., Otranto, S., Meinema, C., Olson, R.E., Hoekstra, R.: *Phys. Rev. A* **85**, 022712 (2012)
- Meng, L., Reinhold, C.O., Olson, R.E.: *Phys. Rev. A* **40**, 3637 (1989)
- Otranto, S., Olson, R.E.: *Phys. Rev. A* **77**, 022709 (2008)
- Otranto, S., Olson, R.E., Beiersdorfer, P.: *J. Phys. B. At. Mol. Opt. Phys.* **40**, 1755 (2007)
- Errea, L.F., Illescas, L.F., Méndez, L., Pons, B., Rabadán, I., Riera, A.: *Phys. Rev. A* **76**, 040701 (2007)
- Bárány, A., Astner, G., Cederquist, H., Danared, H., Hultdt, S., Hvelplund, P., Johnson, A., Knudsen, H., Liljebj, L., Rensfelt, K.G.: *Nucl. Instrum. Methods. Phys. Res. B.* **9**, 397 (1985)
- Niehaus, A.: *J. Phys. B* **19**, 2925 (1986)
- Lekadir, H., Abbas, I., Champion, C., Fojón, O., Rivarola, R.D., Hanssen, J.: *Phys. Rev. A* **79**, 062710 (2009)
- Illescas, C., Errea, L.F., Méndez, L., Pons, B., Rabadán, I., Riera, A.: *Phys. Rev. A* **83**, 052704 (2011)
- Krausz, F., Ivanov, M.: *Rev. Mod. Phys.* **81**, 163 (2009)
- Ho, J., Panfilii, R., Haan, S.L., Eberly, J.H.: *Phys. Rev. Lett.* **94**, 093002 (2005)

65. Fittinghoff, D.N., Bolton, P.R., Chang, B., Kulander, K.C.: *Phys. Rev. Lett.* **69**, 2642 (1992)
66. Moshhammer, R., Feuerstein, B., Schmitt, W., Dorn, A., Schröter, C.D., Ullrich, J., Rottke, H., Trump, C., Wittmann, M., Korn, G., Hoffmann, K., Sandner, W.: *Phys. Rev. Lett.* **84**, 447 (2000)
67. Weber, T., Weckenbrock, M., Staudte, A., Spielberger, L., Jagutzki, O., Mergel, V., Afaneh, F., Urbasch, G., Vollmer, M., Giessen, H., Dörner, R.: *Phys. Rev. Lett.* **84**, 443 (2000)
68. Rudenko, A., Zrost, K., Schröter, C.D., de Jesus, V.L.B., Feuerstein, B., Moshhammer, R., Ullrich, J.: *J. Phys. B* **37**, L407 (2004)
69. Dimitriou, K.I., Arbó, D.G., Yoshida, S., Persson, E., Burgdörfer, J.: *Phys. Rev. A* **70**(R), 061401 (2004)
70. Cohen, J.S.: *Phys. Rev. A* **64**, 043412 (2001)
71. Shvetsov-Shilovski, N.I., Lein, M., Madsen, L.B., Räsänen, E., Lemell, C., Burgdörfer, J., Arbó, D.G., Tókési, K.: *Phys. Rev. A* **94**, 013415 (2015)
72. Di Piazza, A., Müller, C., Hatsagortsyan, K.Z., Keitel, C.H.: *Rev. Mod. Phys.* **84**, 1177 (2012)
73. Gai, L.N., Keitel, C.H.: *Phys. Rev. A* **65**, 023406 (2002)
74. Schmitz, H., Boucke, K., Kull, H.J.: *Phys. Rev. A* **57**, 467 (1998)
75. Hetzheim, H.G., Keitel, C.H.: *Phys. Rev. Lett.* **102**, 083003 (2009)



Marcelo Ciappina Dr Ciappina received his PhD from the Balseiro Institute at Argentina in 2005 and a Research Professor degree from the Czech Academy of Sciences in 2019. His academic training includes postdoctoral stays at renowned institutions in Germany, Singapore, USA, Spain and Czechia. At present, he is Associate Professor at the Guangdong Technion – Israel Institute of Technology (GTIIT), Shantou, China. His areas of interest include attosecond science and atomic collisions.



Raul O. Barrachina Dr Barrachina received his PhD from the Balseiro Institute at Argentina in 1985. His academic training also includes postgraduate studies in philosophy and the history of science, and postdoctoral stays in USA, France, Italy, and Spain. At present, he is Fellow of the Institute of Physics (IoP) and researcher of the Argentine Atomic Energy Commission (CNEA) and the Council of Scientific and Technical Research (CONICET).



Francisco Navarrete Francisco Navarrete received his PhD from Balseiro Institute, National University of Cuyo at Bariloche, Argentina in 2016. He has worked at the National Atomic Energy Commission in Argentina, at the Department of Physics of Kansas State University in the US, and at the group Quantum Theory and Many-Particle Systems at the Institute of Physics, University of Rostock in Germany, where he currently conducts his research. He has made contributions to the fields of atomic collisions and strong-field physics.



Ronald E. Olson Ronald E. Olson, Curators' Professor of Physics earned his PhD from Purdue University in 1967. He is a Fellow of the American Physics Society and a Fulbright Fellow in France. His research interests concentrate on theory of elastic and inelastic total and differential scattering cross sections and studies of multiply charged ion–atom collisions, Rydberg atom collisions, negative ion detachment mechanisms, and Penning and associative ionization.



Collisional Broadening of Spectral Lines

63

Gillian Peach

Contents

63.1	Impact Approximation	928
63.2	Isolated Lines	928
63.2.1	Semiclassical Theory	928
63.2.2	Simple Formulae	929
63.2.3	Perturbation Theory	930
63.2.4	Broadening by Charged Particles	931
63.2.5	Empirical Formulae	931
63.3	Overlapping Lines	932
63.3.1	Transitions in Hydrogen and Hydrogenic Ions	932
63.3.2	Infrared and Radio Lines	933
63.4	Quantum-Mechanical Theory	934
63.4.1	Impact Approximation	934
63.4.2	Broadening by Electrons	935
63.4.3	Broadening by Atoms	936
63.5	One-Perturber Approximation	936
63.5.1	General Approach and Utility	936
63.5.2	Broadening by Electrons	937
63.5.3	Broadening by Atoms and Molecules	938
63.6	Unified Theories and Conclusions	939
	References	939

Abstract

One-photon processes only are discussed and aspects of line broadening directly related to collisions between the emitting (or absorbing) atom and one perturber are considered. Pointers to other aspects are included and a comprehensive bibliography of work on atomic line shapes, widths, and shifts is regularly updated [1]. The perturber may be an electron, a neutral atom or an atomic ion and can interact weakly or strongly with the emitter. The emitter is either a hydrogenic or a nonhydrogenic atom that is either neutral or ionized. In general, transi-

tions in nonhydrogenic atoms can be treated as isolated, that is the separation between neighboring lines is much greater than the width of an individual line. When the emitter is hydrogen or a hydrogenic ion, the additional degeneracy of the energy levels with respect to orbital angular momentum quantum number means that lines overlap and are coupled.

Pressure broadening is a general term that describes any broadening and shift of a spectral line produced by fields generated by a background gas or plasma. The term Stark broadening implies that the perturbers are atomic ions and/or electrons, and collisional broadening implies that the ‘collision’ model is appropriate; this term is often used to describe an isolated line perturbed by electrons. Neutral atom broadening indicates neutral atomic perturbers; this implies short-range emitter–perturber interactions, which in turn influence the approximations made. The broadening of molecular lines and bands is not considered here, however *Hartmann, Boulet, and Robert* [2] have published a comprehensive review of collisional effects on molecular spectra. This includes a discussion of laboratory experiments and models with their consequences for applications.

General reviews of the theory of pressure broadening have been given [3–5], and in Chap. 2, Chap. 11, Chap. 15, Chap. 20, and Chap. 49 topics relevant to the theory of collisional broadening of spectral lines are discussed. A workshop on the topic of spectral line shapes in plasmas (SLSP) has been established to compare codes and different computational and analytic methods, see [6]. The International Conference on Spectral Line Shapes (ICSLS) and the Serbian Conference on Spectral Line Shapes in Astrophysics (SCSLSA) are devoted exclusively to this subject.

Keywords

line profile · orbital angular momentum · impact approximation · semiclassical theory · radio line

G. Peach (✉)
Dept. of Physics and Astronomy, University College London
London, UK
e-mail: g.peach@ucl.ac.uk

63.1 Impact Approximation

If the perturbers are rapidly moving, the broadening and shift of the line arise from a series of binary collisions between the atom and one of the perturbers. The theory assumes that although weak collisions may occur simultaneously, strong collisions are relatively rare and only occur one at a time. The impact approximation is valid if

$$w\tau \ll 1, \quad \bar{V}\tau/\hbar \ll 1, \quad (63.1)$$

where w is the half-width at half-maximum, τ is the average time of collision and \bar{V} is the average emitter-perturber interaction. It is not only widely applicable to electron and neutral atom broadening, but also, for certain plasma conditions, to broadening by atomic ions. The power radiated per unit time and per unit interval in circular frequency ω , in terms of the line profile $I(\omega)$, is

$$P(\omega) = \frac{4\omega^4}{3c^3} I(\omega). \quad (63.2)$$

For an isolated line produced by a transition from an upper energy level i to a lower level f , the line profile is Lorentzian with a shift d :

$$I(\omega) = \frac{1}{\pi} \langle \langle i f^* | \mathbf{A} | i f^* \rangle \rangle \frac{w}{(\omega - \omega_{if} - d)^2 + w^2}, \quad (63.3)$$

and if the profile is for a transition between an upper set of levels i, i' and a lower set f, f' with quantum numbers $J_i M_i, J_{i'} M_{i'}, J_f M_f$, and $J_{f'} M_{f'}$, then

$$I(\omega) = \frac{1}{\pi} \operatorname{Re} \left(\sum_{i' f f'} \langle \langle i f^* | \mathbf{A} | i' f'^* \rangle \rangle \times \langle \langle i' f'^* | [\mathbf{w} + i\mathbf{d} - i(\omega - \omega_{if})\mathbf{I}]^{-1} | i f^* \rangle \rangle \right), \quad (63.4)$$

where \mathbf{I} is the unit operator, and \mathbf{w} and \mathbf{d} are width and shift operators. In Eq. (63.4), \mathbf{A} is an operator corresponding to the dipole line strength defined by

$$\langle \langle i f^* | \mathbf{A} | i' f'^* \rangle \rangle \equiv q^2 \langle i | \mathbf{r} | f \rangle \cdot \langle i' | \mathbf{r} | f' \rangle, \quad (63.5)$$

where \mathbf{r} represents the internal emitter coordinates, $q^2 = e^2/(4\pi\epsilon_0)$ is the square of the electronic charge, and ϵ_0 is the permittivity of vacuum in SI units of F m^{-1} . On taking the average over all degenerate magnetic sublevels,

$$I(\omega) = \frac{1}{\pi} \operatorname{Re} \left(\sum_{i' f f'} \langle \langle i f^* | \mathbf{A} | i' f'^* \rangle \rangle \times \langle \langle i' f'^* | [\mathbf{w} + i\mathbf{d} - i(\omega - \omega_{if})\mathbf{I}]^{-1} | i f^* \rangle \rangle \right) \quad (63.6)$$

in terms of reduced matrix elements that are independent of magnetic quantum numbers. They are defined by

$$\langle \langle i f^* | \mathbf{A} | i' f'^* \rangle \rangle = D_{i f i' f'} \langle \langle i f^* | \mathbf{A} | i' f'^* \rangle \rangle, \quad (63.7)$$

where

$$D_{i f i' f'} = \sum_{\mu} (-1)^{J_i + J_{i'} - M_i - M_{i'}} \times \begin{pmatrix} J_i & 1 & J_f \\ -M_i & \mu & M_f \end{pmatrix} \begin{pmatrix} J_{i'} & 1 & J_{f'} \\ -M_{i'} & \mu & M_{f'} \end{pmatrix}, \quad (63.8)$$

$$\begin{aligned} & \langle \langle i' f'^* | [\mathbf{w} + i\mathbf{d} - i(\omega - \omega_{if})\mathbf{I}]^s | i f^* \rangle \rangle \\ &= \sum_{M_i, M_{i'}, M_f, M_{f'}} D_{i f i' f'} \\ & \times \langle \langle i' f'^* | [\mathbf{w} + i\mathbf{d} - i(\omega - \omega_{if})\mathbf{I}]^s | i f^* \rangle \rangle, \quad (63.9) \end{aligned}$$

with $s = -1, 1$. For the line profile Eq. (63.3), the width and shift each have a single element,

$$\gamma = 2w = \langle \langle i f^* | 2\mathbf{w} | i f^* \rangle \rangle, \quad d = \langle \langle i f^* | \mathbf{d} | i f^* \rangle \rangle, \quad (63.10)$$

where γ is the full width at half-maximum.

Throughout the rest of this article, it will be assumed that collisions only connect the set of upper levels i, i' or the set of lower levels f, f' , which is valid when $w \ll \omega$; pressure broadening of spectral lines is also assumed to be independent of Doppler broadening. However, for microwave spectra of molecules, w can be of the order of ω , and collisions connecting the upper to the lower levels become important; for further details, see *Ben-Reuven* [7, 8]. Also for microwave spectra, pressure broadening and Doppler broadening cannot be considered to be independent effects, and a generalized theory has been developed by *Ciurylo* and *Pine* [9].

63.2 Isolated Lines

63.2.1 Semiclassical Theory

The motion of the perturber relative to the emitter is treated classically and is assumed to be independent of the internal states of the emitter and perturber. This common trajectory is specified by an emitter-perturber separation

$$\mathbf{R} \equiv \mathbf{R}(\mathbf{b}, \mathbf{v}, t), \quad \mathbf{b} \cdot \mathbf{v} = 0, \quad (63.11)$$

where \mathbf{v} is the relative velocity, and \mathbf{b} is the impact parameter. The time-dependent wave equation for the emitter-perturber system is

$$i\hbar \frac{d\Psi}{dt} = H\Psi, \quad (63.12)$$

and the eigenfunctions ψ_i for the unperturbed emitter obey

$$H_0\psi_i = E_i\psi_i, \quad i = 0, 1, 2, \dots \quad (63.13)$$

If $\Psi(\mathbf{r}, \mathbf{R})$ is expanded in the form

$$\Psi(\mathbf{r}, \mathbf{R}) = \sum_j a_{ji}(t)\psi_j(\mathbf{r}) \exp(-iE_j t/\hbar), \quad (63.14)$$

where initially at time $t = -\infty$

$$a_{ji}(-\infty) = \delta_{ji} \quad (63.15)$$

and Eqs. (63.12)–(63.14) give

$$i\hbar \frac{da_{ji}}{dt} = \sum_k a_{ki} V_{jk} \exp(i\omega_{jk}t), \quad (63.16)$$

$$i, j, k = 0, 1, 2, \dots,$$

where

$$V_{jk}(\mathbf{R}) = \int \psi_j^*(\mathbf{r}) V(\mathbf{r}, \mathbf{R}) \psi_k(\mathbf{r}) d\mathbf{r} \quad (63.17)$$

in which $V(\mathbf{r}, \mathbf{R})$ is the emitter–perturber interaction, and

$$\hbar\omega_{jk} = E_j - E_k. \quad (63.18)$$

Integration of equations Eq. (63.16) for $-\infty \leq t \leq \infty$ gives the unitary scattering matrix \mathbf{S} , with elements

$$S_{ji}(\mathbf{b}, \mathbf{v}) \equiv a_{ji}(\infty), \quad i, j = 0, 1, 2, \dots \quad (63.19)$$

Then

$$w + id = 2\pi N \int_0^\infty v f(v) dv \times \int_0^\infty \left[\delta_{i'i} \delta_{f'f} - S_{i'i}(\mathbf{b}, \mathbf{v}) S_{f'f}^*(\mathbf{b}, \mathbf{v}) \right]_{\text{av}} b db, \quad (63.20)$$

where $J_{i'} = J_i$ and $J_{f'} = J_f$, N is the perturber density and $[\dots]_{\text{av}}$ denotes an average over all orientations of the collision and over the magnetic sublevels [Eq. (63.9)]. In (63.20), $f(v)$ is the Maxwell velocity distribution at temperature T for an emitter–perturber system of reduced mass μ :

$$f(v) = 4\pi v^2 \left(\frac{\mu}{2\pi k_B T} \right)^{3/2} \exp\left(-\frac{\mu v^2}{2k_B T} \right), \quad (63.21)$$

$$\int_0^\infty f(v) dv = 1.$$

63.2.2 Simple Formulae

Simple formulae are useful for making quick estimates but in individual cases may give results in error by a factor of 2 or more. If it is assumed in Eq. (63.17) that

$$V_{ij}(\mathbf{R}) = V_{jj}(\mathbf{R})\delta_{ij}, \quad (63.22)$$

where $V_{jj}(\mathbf{R})$ is a simple central potential

$$V_{jj}(\mathbf{R}) = \hbar C_j R^{-p}, \quad j = i, f, \quad (63.23)$$

and C_j depends only on the state j of the emitter, and if the relative motion is along the straight line

$$\mathbf{R} = \mathbf{b} + \mathbf{v}t, \quad (63.24)$$

then

$$\left[S_{i'i}(\mathbf{b}, \mathbf{v}) S_{f'f}^*(\mathbf{b}, \mathbf{v}) \right]_{\text{av}} = \exp[2i(\eta_i - \eta_f)], \quad (63.25)$$

where the phase shifts are

$$\eta_j(b, v) = -\frac{1}{2\hbar} \int_{-\infty}^{\infty} V_{jj}(R) dt, \quad j = i, f. \quad (63.26)$$

Equations (63.20)–(63.26) give

$$w + id = \pi N \bar{v} \left(\frac{\beta_p |C_p|}{\bar{v}} \right)^{2/(p-1)} \times \Gamma\left(\frac{p-3}{p-1} \right) \exp\left(\pm \frac{i\pi}{p-1} \right) \alpha_p, \quad (63.27)$$

where

$$\alpha_p = \Gamma\left(\frac{2p-3}{p-1} \right) \left(\frac{\pi}{4} \right)^{-1/(p-1)},$$

$$\beta_p = \sqrt{\pi} \frac{\Gamma(\frac{1}{2}(p-1))}{\Gamma(\frac{1}{2}p)},$$

$$C_p = C_i - C_f,$$

$$\bar{v} = \int_0^\infty v f(v) dv = \left(\frac{8k_B T}{\pi\mu} \right)^{1/2}. \quad (63.28)$$

In (63.27), the \pm sign indicates the sign of C_p , $\alpha_p \simeq 1$ for $p \geq 3$, and $\Gamma(\dots)$ is the gamma function.

The cases $p = 3, 4$ and 6 correspond to resonance, quadratic Stark and van der Waals broadening, respectively. This approximation is invalid for the dipole case ($p = 2$) for which Eq. (63.27) is not finite. The dipole–dipole interaction ($p = 3$) occurs when emitter and perturber are identical

atoms (apart from isotopic differences). If the level i is connected to the ground state by a strong allowed transition with absorption oscillator strength f_{gi} , and the perturbation of the level f can be neglected by comparison, then

$$C_3 = c_d \frac{q^2 f_{gi}}{2m_e |\omega_{gi}|},$$

$$c_d = 1 + \frac{1}{2\sqrt{3}} \ln(2 + \sqrt{3}) = 1.380173. \quad (63.29)$$

Also, if g_j is the statistical weight of level j , the constant c_d may be replaced by an empirical value

$$c_d = \frac{4}{\pi} \left(\frac{g_g}{g_i} \right)^{1/2}, \quad (63.30)$$

and this gives a width correct to about 10% [10]. Equation (63.27) does not predict a finite shift. Quadratic Stark broadening occurs when a nonhydrogenic emitter is polarized by electron perturbers. Then

$$C_4 = -\frac{q^2}{2\hbar} (\alpha_i - \alpha_f), \quad (63.31)$$

where α_i and α_f are the dipole polarizabilities of states i and f , respectively. Van der Waals broadening occurs when the emitter and perturber are nonidentical neutral atoms. If energy level separations of importance in the perturbing atom are much greater than those of the emitter (e.g., alkali spectra broadened by noble gases), C_6 is given by

$$C_6 = -\frac{q^2}{\hbar} \alpha_d (\overline{r_i^2} - \overline{r_f^2}), \quad (63.32)$$

where α_d is the dipole polarizability of the perturber. The mean square radii can be calculated from the normalized radial wave functions $\frac{1}{r} P_{n^* l_j}(r)$ or estimated from

$$\overline{r_j^2} = \int_0^\infty P_{n^* l_j}^2(r) r^2 dr$$

$$\simeq \frac{n_j^{*2} a_0^2}{2z^2} [5n_j^{*2} + 1 - 3l_j(l_j + 1)],$$

$$j = i, f, \quad (63.33)$$

in which the effective principal quantum numbers n_j^* are given by

$$E_j \equiv -\frac{z^2}{n_j^{*2}} I_h, \quad z = Z_e + 1, \quad (63.34)$$

where $I_h = hcR_\infty$ is the Rydberg energy, Z_e is the charge on the emitter, and $z = 1$ in this case.

63.2.3 Perturbation Theory

An approximate solution of Eq. (63.16) is given by [3–5, 11, 12]

$$S_{ji}(\mathbf{b}, \mathbf{v}) = \delta_{ji} - \frac{i}{\hbar} \int_{-\infty}^{\infty} V_{ji}(t) \exp(i\omega_{ji}t) dt$$

$$- \frac{1}{\hbar^2} \sum_k \left[\int_{-\infty}^{\infty} V_{jk}(t) \exp(i\omega_{jk}t) dt \right.$$

$$\left. \times \int_{-\infty}^t V_{ki}(t') \exp(i\omega_{ki}t') dt' \right]. \quad (63.35)$$

This gives a cross section for the collisional transition $i \rightarrow j$:

$$\sigma_{ij}(v) = 2\pi \int_0^\infty [P_{ij}(\mathbf{b}, \mathbf{v})]_{\text{av}} b db,$$

$$i, j = 0, 1, 2, \dots, \quad (63.36)$$

where

$$P_{ij}(\mathbf{b}, \mathbf{v}) = |\delta_{ji} - S_{ji}(\mathbf{b}, \mathbf{v})|^2, \quad (63.37)$$

$$2 \operatorname{Re}[1 - S_{ii}(\mathbf{b}, \mathbf{v})] = \sum_j P_{ij}(\mathbf{b}, \mathbf{v}), \quad (63.38)$$

correct to second-order in $V(\mathbf{r}, \mathbf{R})$ on both sides. Using Eqs. (63.10), (63.20), and (63.36)–(63.38), the full width is

$$\gamma = N \int_0^\infty v f(v) dv$$

$$\times \left[\sum_{j \neq i} \sigma_{ij}(v) + \sum_{j \neq f} \sigma_{fj}(v) + \tilde{\sigma}_{if}(v) \right], \quad (63.39)$$

where the sums are taken over all energy-changing transitions, the tilde indicates an interference term, and

$$\tilde{\sigma}_{if}(v) = 2\pi \int_0^\infty [\tilde{P}_{if}(\mathbf{b}, \mathbf{v})]_{\text{av}} b db, \quad (63.40)$$

in which

$$\tilde{P}_{if}(\mathbf{b}, \mathbf{v}) = \left| \frac{1}{\hbar} \int_{-\infty}^{\infty} [V_{ii}(t) - V_{ff}(t)] dt \right|^2. \quad (63.41)$$

63.2.4 Broadening by Charged Particles

The total emitter–perturber interaction is

$$\frac{zZ_p q^2}{R} - \frac{Z_p q^2}{|\mathbf{R} - \mathbf{r}|} \simeq V_0(R) + V(\mathbf{r}, \mathbf{R}), \quad (63.42)$$

where Z_p is the charge on the perturber, and

$$V_0(R) = \frac{Z_e Z_p q^2}{R}, \quad V(\mathbf{r}, \mathbf{R}) = -Z_p q^2 \frac{\mathbf{r} \cdot \mathbf{R}}{R^3}. \quad (63.43)$$

If $Z_e = 0$, the relative motion is described by Eq. (63.24), but if $Z_e \neq 0$, the trajectory is hyperbolic and is given by

$$\mu \frac{d^2 \mathbf{R}}{dt^2} = -\nabla V_0 = \frac{Z_e Z_p q^2}{R^3} \mathbf{R}, \quad (63.44)$$

with the resulting hyperbola characterized by a semimajor axis a and an eccentricity ϵ , where

$$b^2 = a^2(\epsilon^2 - 1), \quad a = \frac{|Z_e Z_p| q^2}{\mu v^2}. \quad (63.45)$$

On using Eqs. (63.17), (63.20), (63.36)–(63.41), and (63.43),

$$V_{ii}(t) = 0, \quad \tilde{P}_{if}(\mathbf{b}, \mathbf{v}) = 0, \quad \tilde{\sigma}_{if}(v) = 0, \quad (63.46)$$

and

$$w + id = 2\pi N \int_0^\infty v f(v) dv \quad (63.47)$$

$$\times \left[\int_0^\infty \sum_{j \neq i} Q_{ij}(b, v) + \sum_{j \neq f} Q_{fj}(b, v) \right] b db,$$

where

$$Q_{ij}(v) = \frac{4Z_p^2 I_h^2 a_0^2}{\hbar m_e |\omega_{ij}|} \frac{f_{ij}}{b^2 v^2} [A(\beta, \xi) + iB(\beta, \xi)],$$

$$2 \operatorname{Re}[Q_{ij}(v)] = [P_{ij}(\mathbf{b}, \mathbf{v})]_{\text{av}}. \quad (63.48)$$

If

$$\xi \equiv \frac{a|\omega_{ij}|}{v}, \quad \beta \equiv \xi \epsilon, \quad \delta \equiv \frac{\epsilon^2 - 1}{\epsilon^2}, \quad (63.49)$$

the functions $A(\beta, \xi)$ and $B(\beta, \xi)$ in Eq. (63.48) are given by

$$A(\beta, \xi) = \delta \exp(\mp \pi \xi) \beta^2 \times \left[|K'_{i\xi}(\beta)|^2 + \delta |K_{i\xi}(\beta)|^2 \right], \quad (63.50)$$

$$B(\beta, \xi) = \frac{2\beta}{\pi} \wp \int_0^\infty \frac{A(\beta', \xi) d\beta'}{(\beta^2 - \beta'^2)}, \quad (63.51)$$

where $K_{i\xi}(\beta)$ is a modified Bessel function. In Eq. (63.50), the \mp sign corresponds to $Z_e Z_p = \pm |Z_e Z_p|$, and in

Eq. (63.51), \wp indicates the Cauchy principal value. If $Z_e = 0$, then

$$\xi = 0, \quad \beta = b \frac{|\omega_{ij}|}{v}, \quad \delta = 1 \quad (63.52)$$

in Eqs. (63.50) and (63.51).

Approximation Eq. (63.48) breaks down at small values of b because of assumption Eq. (63.43) and the lack of unitarity of \mathbf{S} as given by Eq. (63.35). This problem is discussed elsewhere [3, 11, 12], and all methods used involve choosing a cutoff at $b = b_0$, where $b_0^2 \gtrsim \bar{r}_f^2$, and using Eq. (63.48) only for $b > b_0$. For $b \leq b_0$, an effective constant probability is introduced, and the method works well as long as the contribution from $b \leq b_0$ is small. For $b > b_0$ (or $\beta > \beta_0$), the contribution to $\sigma_{ij}(v)$ in Eq. (63.39) is evaluated using Eqs. (63.47)–(63.50) and (63.52), where

$$\int_{b_0}^\infty A(\beta, \xi) \frac{db}{b} = -e^{\mp \pi \xi} \beta_0 K'_{i\xi}(\beta_0) K_{i\xi}(\beta_0). \quad (63.53)$$

A similar treatment exists for the quadrupole contribution to $V(\mathbf{r}, \mathbf{R})$ in Eq. (63.43) [3, 11, 12].

63.2.5 Empirical Formulae

An empirical formula based on the theory of Sect. 63.2.4 for the width of an atomic line Stark broadened by electrons has been developed [13]. *Konjević* [14] has reviewed the data available for nonhydrogenic lines and has provided simple analytical representations of the experimental results for widths and shifts.

The full half-width is given by Eq. (63.39), where $\tilde{\sigma}_{if} = 0$, and

$$\int_0^\infty v f_e(v) \sum_{k \neq j} \sigma_{jk}(v) dv = \frac{8\pi^2}{3\sqrt{3}} \left(\frac{\hbar}{m_e} \right)^2 v^{-1}$$

$$\times \left[T_j g(x_j) + \sum_{l' = l_j \pm 1} \tilde{T}_{jj'} \tilde{g}(x_{jj'}) \right], \quad j = i, f, \quad (63.54)$$

where

$$\overline{v^{-1}} = \int_0^\infty v^{-1} f_e(v) dv = \left(\frac{2m_e}{\pi k_B T} \right)^{1/2}, \quad (63.55)$$

and $f_e(v) = f(v)$ with $\mu = m_e$. In Eq. (63.54),

$$T_j = \left(\frac{3n_j^*}{2z} \right)^2 \frac{1}{9} [n_j^{*2} + 3l_j(l_j + 1) + 11], \quad (63.56)$$

$$\tilde{T}_{jj'} = \frac{l_{>}}{(2l_j + 1)} R_{jj'}^2(n_{l_{>}}^*, n_{l_{<}}^*, l_{>}), \quad (63.57)$$

$$l_{<} = \min(l_j, l_{j'}), \quad l_{>} = \max(l_j, l_{j'}),$$

with

$$R_{jj'}(n_{l_>}^*, n_{l_<}^*, l_>) \equiv a_0^{-1} \int_0^\infty P_{n_{l_>}^* l_>}(r) r P_{n_{l_<}^* l_<}(r) dr. \quad (63.58)$$

The radial matrix element Eq. (63.58) can be written as

$$\begin{aligned} R_{jj'}(n_{l_>}^*, n_{l_<}^*, l_>) &= \widetilde{R}_{jj'}(n_{l_>}^*, l_>) \phi(n_{l_>}^*, n_{l_<}^*, l_>) \\ &\equiv \frac{3n_{l_>}^*}{2z} (n_{l_>}^* - l_>)^{1/2} \phi(n_{l_>}^*, n_{l_<}^*, l_>), \end{aligned} \quad (63.59)$$

and $\phi(n_{l_>}^*, n_{l_<}^*, l_>)$ is tabulated elsewhere [15]. The effective principal quantum numbers $n_{l_>}^*$ and $n_{l_<}^*$ of the states j and j' in Eqs. (63.57)–(63.59) both correspond to principal quantum number n_j and $\phi \simeq 1$ for $(n_{l_>}^* - n_{l_<}^*) \ll 1$. The effective Gaunt factors $g(x)$ and $\widetilde{g}(x)$ are given by

$$\widetilde{g}(x) = 0.7 - 1.1/z + g(x), \quad x = \frac{3k_B T}{2\Delta E}, \quad (63.60)$$

where

x	≤ 2	3	5	10	30	100
$g(x)$	0.20	0.24	0.33	0.56	0.98	1.33

is used for $x < 50$, and for $x > 50$

$$\widetilde{g}(x) = g(x) = \frac{\sqrt{3}}{\pi} \left[\frac{1}{2} + \ln \left(\frac{4}{3z} \frac{|E|}{I_h} x \right) \right], \quad (63.61)$$

with Eqs. (63.60) and (63.61) joined smoothly near $x = 50$. The energy $E = E_j$ is given by Eq. (63.34), and x_j and $x_{j'}$ in Eq. (63.54) are evaluated using

$$\Delta E_j = \frac{2z^2}{n_j^{*3}} I_h, \quad \Delta E_{jj'} = |E_j - E_{j'}|. \quad (63.62)$$

For $Z_e = 2$ and 3, Eq. (63.54) is generally accurate to within $\pm 30\%$ and $\pm 50\%$. For $Z_e \geq 4$, Eq. (63.54) is less accurate, as relativistic effects and resonances become more important. Accuracy increases for transitions to higher Rydberg levels as long as the line remains isolated.

Tables in Appendices IV and V of [3] give widths for atoms with $Z_e = 0, 1$, and other semiempirical formulas based on detailed calculations have been developed by *Seaton* [16, 17] for use in the Opacity Project where simple estimates of many thousands of line widths are required.

63.3 Overlapping Lines

63.3.1 Transitions in Hydrogen and Hydrogenic Ions

The most important case is that of lines of hydrogenic systems emitted by a plasma with overall electrical neutrality, broadened by perturbing electrons and atomic ions. The line profile is given by Eqs. (63.4)–(63.9) in which Eq. (63.20) is generalized to give

$$\begin{aligned} \langle \langle i' f'^* \| \mathbf{w} + i\mathbf{d} \| i f^* \rangle \rangle &= 2\pi N \int_0^\infty v f(v) dv \\ &\times \int_0^\infty \left[\delta_{i'i} \delta_{f'f} - S_{i'i}(\mathbf{b}, \mathbf{v}) S_{f'f}^*(\mathbf{b}, \mathbf{v}) \right]_{\text{av}} b db. \end{aligned} \quad (63.63)$$

The superscripts and suffixes e and i will be used to denote electronic and ionic quantities respectively, and *em* indicates that averaging over magnetic quantum numbers has not been carried out. In the impact approximation, electron and ion contributions evaluated using (63.63) are additive, and the matrix to be inverted is of order $n_i n_f$. However, under typical conditions in a laboratory plasma, e.g., a hydrogen plasma with $N_e = N_i = 10^{22} \text{ m}^{-3}$, perturbing atomic ions cannot be treated using the impact approximation. The ions collectively generate a static field at the emitter that produces first-order Stark splitting of the upper and lower levels. The ions are randomly distributed around the emitter, and the field distribution $W(\mathbf{F})$ used assumes that each ion is Debye screened by electrons; allowance is made for these heavy composite perturbers interacting with each other as well as with the emitter. If the ion field has a slow time variation, ion dynamic effects can produce significant changes in the line shape, see [3, 4, 6, 18].

The shift produced by electron perturbers is very small, and the usual model adopted is to assume that the ions split the line into its Stark components, and that each component is broadened by electron impact. In both cases, only the dipole interactions in Eq. (63.43) are included, and the profile is symmetric. Then (63.4) takes the form

$$\begin{aligned} I(\omega) &= \frac{1}{\pi} \text{Re} \int W(\mathbf{F}) d\mathbf{F} \sum_{ii'ff'} \langle \langle i f^* | \Delta | i' f'^* \rangle \rangle \\ &\times \left\langle \left\langle i' f'^* \left| [\mathbf{w} + i\mathbf{d} - i(\omega - \omega_{if}) \mathbf{I}]^{-1} \right| i f^* \right\rangle \right\rangle, \end{aligned} \quad (63.64)$$

and the destruction of the degeneracy by the ion field means that the matrix to be inverted in Eq. (63.64) is of order $(n_i n_f)^2$. Inclusion of higher multipoles in $V(\mathbf{r}, \mathbf{R})$ in

Eq. (63.43) introduces small asymmetries. The Stark representation for the hydrogenic wave functions is often used because it diagonalizes the shift matrix in Eq. (63.64). The transformation is given by (see Chap. 9.1.2 and Chap. 14.4.2)

$$|n_j K_j m_j\rangle = \sum_{l_j=|m_j|}^{n_j-1} (-1)^K (2l_j + 1)^{1/2} \times \begin{pmatrix} N & N & l_j \\ M_1 & M_2 & -m_j \end{pmatrix} |n_j l_j m_j\rangle, \quad (63.65)$$

$j = i, i', f, f',$

where quantum number K_j replaces l_j , and

$$\begin{aligned} n_j &= K_j + K'_j + |m_j| + 1, \quad N = \frac{1}{2}(n_j - 1), \\ K &= \frac{1}{2}(2K'_j + |m_j| + m_j) + 1, \\ 0 &\leq K_j \leq (n_j - 1), \\ M_1 &= \frac{1}{2}(m_j + K'_j - K_j), \\ M_2 &= \frac{1}{2}(m_j + K_j - K'_j). \end{aligned} \quad (63.66)$$

For the electron impact broadening, it is convenient to separate the energy-changing and the zero energy-change transitions, so that Eq. (63.39) is generalized to give

$$\gamma_{em} = \gamma_{em}^0 + \tilde{\gamma}_{em} \equiv \langle\langle i' f'^* | 2\mathbf{w}_e | i f^* \rangle\rangle, \quad (63.67)$$

where

$$\begin{aligned} \gamma_{em}^0 &\equiv \langle\langle i' f'^* | 2\mathbf{w}_e^0 | i f^* \rangle\rangle = N_e \int_0^\infty v f_e(v) dv \\ &\times \left[\sum_{j \neq i} \sigma_{ij}^{em}(v) + \sum_{j \neq f} \sigma_{fj}^{em}(v) \right] \delta_{i'i'} \delta_{f'f'}, \end{aligned} \quad (63.68)$$

$$\begin{aligned} \tilde{\gamma}_{em} &\equiv \langle\langle i' f'^* | 2\tilde{\mathbf{w}}_e | i f^* \rangle\rangle \\ &= N_e \int_0^\infty v f_e(v) dv \tilde{\sigma}_{i'f'if}^{em}(v). \end{aligned} \quad (63.69)$$

In Eq. (63.68), $|n_i - n_j| \neq 0$ and $|n_f - n_j| \neq 0$ in the first and second terms, respectively, and in Eq. (63.69) $(n_{i'} - n_i) = (n_{f'} - n_f) = 0$. The matrix element Eq. (63.68) can be evaluated using Eqs. (63.36), (63.48), (63.50), and (63.52) as before. In Eq. (63.68),

$$\begin{aligned} \sigma_{ij}^{em}(v) &= 2\pi \int_0^\infty \left[P_{ij}^e(\mathbf{b}, \mathbf{v}) \right]_{\text{av}_0} b db, \\ &i, j = 0, 1, 2, \dots, \end{aligned} \quad (63.70)$$

and in Eq. (63.69)

$$\tilde{\sigma}_{i'f'if}^{em}(v) = 2\pi \int_0^\infty \left[\tilde{P}_{i'f'if}^e(\mathbf{b}, \mathbf{v}) \right]_{\text{av}_0} b db \quad (63.71)$$

by analogy with Eqs. (63.36) and (63.40), where av_0 indicates an average over all orientations of the collision only. On using Eqs. (63.48)–(63.50), (63.59), and (63.8) with $j_i = l_i$, $j_{i'} = l_{i'}$, $j_f = l_f$, and $j_{f'} = l_{f'}$,

$$\begin{aligned} &\left[\tilde{P}_{i'f'if}^e(\mathbf{b}, \mathbf{v}) \right]_{\text{av}_0} \\ &= \frac{8I_h a_0^2}{3m_e b^2 v^2} D_{if i' f'} \tilde{R}_{i' f' i f} A(0, 0), \end{aligned} \quad (63.72)$$

where

$$\begin{aligned} \tilde{R}_{i' f' i f} &\equiv \left[\sum_{l_j=l_i \pm 1} \tilde{R}_{ij}^2(n_i, l_{i>}) + \sum_{l_j=l_f \pm 1} \tilde{R}_{fj}^2(n_f, l_{f>}) \right] \\ &\times \delta_{l_{i'} l_i} \delta_{l_{f'} l_f} \\ &- 2\tilde{R}_{i'i}(n_i, l_{i>}) \tilde{R}_{f'f}(n_f, l_{f>}) \delta_{l_{i'} l_i \pm 1} \delta_{l_{f'} l_f \pm 1}. \end{aligned} \quad (63.73)$$

From Eqs. (63.45) and (63.49)–(63.53)

$$A(0, 0) = \delta,$$

$$\int_{b_0}^{b_1} A(0, 0) \frac{db}{b} = \begin{cases} \ln(\epsilon_1/\epsilon_0), & Z_e \neq 0, \\ \ln(b_1/b_0), & Z_e = 0. \end{cases} \quad (63.74)$$

The impact approximation neglects electron–electron correlations and the finite duration of collisions, so the long-range dipole interaction leads to a logarithmic divergence at large impact parameters in Eq. (63.74). Therefore, a second cutoff parameter is introduced, which is chosen to be the smaller of the Debye length b_D and $v\tau$:

$$b_1 = \min \left[b_D \equiv \left(\frac{k_B T}{4\pi q^2 N_e} \right)^{1/2}, v\tau \right], \quad (63.75)$$

but estimating τ in this case is not straightforward; it depends on the splitting of the Stark components [3].

63.3.2 Infrared and Radio Lines

If the density N_i is low enough, the impact approximation becomes valid for the perturbing atomic ions, and since impact

shifts are unimportant, Eq. (63.6) gives

$$I(\omega) = \frac{1}{\pi} \operatorname{Re} \sum_{i'f'f''} \langle \langle i'f'^* \| \Delta \| i'f'^* \rangle \rangle \times \langle \langle i'f'^* \| [\mathbf{w}_e + \mathbf{w}_i - i(\omega - \omega_{if})\mathbf{I}]^{-1} \| if^* \rangle \rangle, \tag{63.76}$$

where in Eq. (63.76)

$$\gamma_{e,i} = \gamma_{e,i}^0 + \tilde{\gamma}_{e,i} \equiv \langle \langle i'f'^* \| 2\mathbf{w}_{e,i} \| if^* \rangle \rangle, \tag{63.77}$$

$$\gamma_{e,i}^0 \equiv \langle \langle i'f'^* \| 2\mathbf{w}_{e,i}^0 \| if^* \rangle \rangle = N_{e,i} \int_0^\infty v f_{e,i}(v) dv \times \left[\sum_{j \neq i} \sigma_{ij}^{e,i}(v) + \sum_{j \neq f} \sigma_{fj}^{e,i}(v) \right] \delta_{i'i} \delta_{f'f}, \tag{63.78}$$

$$\tilde{\gamma}_{e,i} \equiv \langle \langle i'f'^* \| 2\tilde{\mathbf{w}}_{e,i} \| if^* \rangle \rangle = N_{e,i} \int_0^\infty v f_{e,i}(v) dv \tilde{\sigma}_{i'f'if}^{e,i}(v). \tag{63.79}$$

In general, cross sections for electron and heavy-particle impact are roughly comparable for the same velocity and, hence, different impact energies. Therefore, using Eqs. (63.78) and (63.79),

$$\gamma_e^0 \gg \gamma_i^0, \quad \tilde{\gamma}_e \ll \tilde{\gamma}_i, \tag{63.80}$$

and this result is consistent with approximation Eq. (63.64) for high-density plasmas. If $(n_i - n_f) = 1, 2$, say, as n_f increases, the relative contributions from Eqs. (63.78) and (63.79) decrease because there is increasing coherence, and, hence, cancelation in $\tilde{\sigma}_{i'f'if}^e(v)$ and $\tilde{\sigma}_{i'f'if}^i(v)$ between the effects of levels i, i' and f, f' .

Radio lines of hydrogen are observed in galactic HII regions where principal quantum numbers are of the order of $n_f \simeq 100$, temperatures are $T_e = T_i \simeq 10^4$ K, and densities are $N_e = N_i \simeq 10^9 \text{ m}^{-3}$. For a comprehensive review of the theory and observation of radio recombination lines, see *Gordon and Sorochenko* [19].

If γ is the full half-width and $\tilde{\gamma}$ is the full half-width when only contributions Eq. (63.79) are retained, the effect of cancelation is illustrated by

$n_i - n_f = 1$	Electrons	Protons + Electrons
n_f	$\tilde{\gamma}/\gamma$	$\tilde{\gamma}/\gamma$
5	0.82	0.99
10	0.40	0.95
15	0.17	0.86
20	0.08	0.73
25	0.05	0.59
50	0.00	0.17
100	0.00	0.01

Further details are given by *Peach* [20].

63.4 Quantum-Mechanical Theory

63.4.1 Impact Approximation

The scattering amplitude for a collisional transition $i \rightarrow j$ is given in terms of elements of the transition matrix $\mathbf{T} = \mathbf{1} - \mathbf{S}$ by

$$f(\mathbf{k}_j, \mathbf{k}_i) \equiv f(\chi_j M_j \mathbf{k}_j, \chi_i M_i \mathbf{k}_i) = \frac{2\pi i}{(k_i k_j)^{1/2}} \sum_{lm'l'm'} i^{l-l'} Y_{lm}^*(\hat{\mathbf{k}}_i) Y_{l'm'}(\hat{\mathbf{k}}_j) \times T(\chi_j M_j l' m'; \chi_i M_i l m), \tag{63.81}$$

where the quantities $\mathbf{k}_i l m$ and $\mathbf{k}_j l' m'$ refer to the motion of the perturber relative to the emitter before and after the collision, and χ_i and χ_j represent all nonmagnetic quantum numbers associated with the unperturbed states i and j of the emitter. The total energy of the emitter-perturber system is given by

$$E_J = E_j + \varepsilon_j, \quad \varepsilon_j = \frac{\hbar^2}{2\mu} k_j^2, \tag{63.82}$$

$$(J, j) = (I, i), (F, f),$$

and for an isolated line, γ is given by Eq. (63.39), where

$$\sigma_{ij}(v) = \frac{k_j}{k_i} \frac{1}{4\pi g_i} \times \sum_{M_i M_j} \int |f(\chi_j M_j \mathbf{k}_j, \chi_i M_i \mathbf{k}_i)|^2 d\hat{\mathbf{k}}_i d\hat{\mathbf{k}}_j, \tag{63.83}$$

$$k_i = \mu v / \hbar,$$

and the interference term $\tilde{\sigma}_{if}(v) \equiv \tilde{\sigma}_{ifif}(v)$ is given by

$$\tilde{\sigma}_{if}(v) = \frac{1}{4\pi} \sum_{\substack{M_i M_i' \\ M_f M_f'}} D_{if i' f'} \int |f(\chi_i M_i \mathbf{k}', \chi_i M_i \mathbf{k}) - f(\chi_f M_f \mathbf{k}', \chi_f M_f \mathbf{k})|^2 d\hat{\mathbf{k}} d\hat{\mathbf{k}}', \tag{63.84}$$

with $k = k' = \mu v / \hbar$. From Eqs. (63.8) and (63.20),

$$w + id = \pi \left(\frac{\hbar}{\mu} \right)^2 N \int_0^\infty \frac{1}{v} f(v) dv \times \sum_{l=0}^\infty (2l+1) \left[1 - S_{ii}(l, v) S_{ff}^*(l, v) \right], \tag{63.85}$$

where

$$(\mu vb)^2 \implies \hbar^2 l(l+1), \quad (63.86)$$

and the integral over b has been replaced by a summation over l . In Eq. (63.85), $S_{ii}(l, v)S_{ff}^*(l, v)$ is given by

$$\begin{aligned} S_{ii}(l, v)S_{ff}^*(l, v) &= \frac{1}{(2l+1)} \sum_{\substack{M_i M'_i M_f M'_f \\ mm'}} D_{if i' f'} S_I(\chi_{i'} M_{i'} l m'; \chi_i M_i l m) \\ &\times S_F^*(\chi_{f'} M_{f'} l m'; \chi_f M_f l m), \end{aligned} \quad (63.87)$$

and subscripts I and F are introduced to emphasize that the S -matrix elements correspond to different total energies E_I and E_F defined by Eq. (63.82). If scattering by the emitter in a state j is treated using a central potential, the amplitude for elastic scattering is

$$f(k', k) = \frac{i}{2k} \sum_{l=0}^{\infty} (2l+1) T_{jj}(l, v) P_l(\hat{\mathbf{k}}' \cdot \hat{\mathbf{k}}), \quad (63.88)$$

where

$$1 - T_{jj}(l, v) = S_{jj}(l, v) = \exp[2i\eta_j(l, k)], \quad j = i, f, \quad (63.89)$$

[Eqs. (63.23), (63.25), and (63.26)]. For the case of overlapping lines, Eq. (63.63) becomes

$$\begin{aligned} \langle\langle i' f'^* \| \mathbf{w} + i\mathbf{d} \| i f^* \rangle\rangle &= \pi \left(\frac{\hbar}{\mu} \right)^2 N \int_0^{\infty} \frac{1}{v} f(v) dv \\ &\times \sum_{l=0}^{\infty} (2l+1) \left[\delta_{i'i} \delta_{f'f} - S_{ii}(l, v) S_{ff}^*(l, v) \right] \end{aligned} \quad (63.90)$$

on generalizing Eq. (63.85) and using Eq. (63.87). Formulae Eqs. (63.85) and (63.90) have been obtained by assuming that a collision produces no change in the angular momentum of the relative emitter–perturber motion. This corresponds to the assumption of a common trajectory in semiclassical theory and means that the total angular momentum of the emitter–perturber system is not conserved. This assumption is removed in the derivation of the more general expressions given in the following sections.

63.4.2 Broadening by Electrons

Different coupling schemes can be used to describe the emitter–perturber collision. For LS coupling,

$$\chi_j M_j \implies \chi_j^0 L_j M_j S M_S, \quad j = i, i', f, f', \quad (63.91)$$

in Eq. (63.81), where χ_j^0 denotes all other quantum numbers required to describe state j that do not change during the collision. Then

$$\begin{aligned} \left| L_j M_j S M_S l m \frac{1}{2} m_s \right\rangle &= \sum_{L_j^T M_j^T S^T M_S} C_{M_j M_S}^{L_j l L_j^T} C_{M_S m_s M_S}^{S \frac{1}{2} S^T} \\ &\times \left| L_j S l \frac{1}{2} L_j^T M_j^T S^T M_S^T \right\rangle, \end{aligned} \quad (63.92)$$

where $C_{m_1 m_2 m_3}^{j_1 j_2 j_3}$ is a vector coupling coefficient, the superscript T denotes quantum numbers of the emitter–perturber system, and $\frac{1}{2}, m_s$ are the spin quantum numbers of the scattered electron. On using Eq. (63.92), Eq. (63.90) is replaced by

$$\begin{aligned} \langle\langle i' f'^* \| \mathbf{w} + i\mathbf{d} \| i f^* \rangle\rangle &= \pi (\hbar/m_e)^2 N \\ &\times \sum_{L_i^T L_i'^T S^T l l'} (-1)^{L_i + L_i' + l + l'} (2L_i^T + 1) (2L_i'^T + 1) \\ &\times \frac{(2S^T + 1)}{2(2S + 1)} \left\{ \begin{matrix} L_f^T & L_i^T & 1 \\ L_i & L_f & l \end{matrix} \right\} \left\{ \begin{matrix} L_f^T & L_i^T & 1 \\ L_i' & L_f' & l' \end{matrix} \right\} \\ &\times \int_0^{\infty} \frac{1}{v} f_e(v) dv \left[\delta_{l'l'} \delta_{L_i' L_i} \delta_{L_f' L_f} \right. \\ &- S_I \left(L_i' S l' \frac{1}{2} L_i^T S^T; L_i S l \frac{1}{2} L_i^T S^T \right) \\ &\left. \times S_F^* \left(L_f' S l' \frac{1}{2} L_f^T S^T; L_f S l \frac{1}{2} L_f^T S^T \right) \right], \end{aligned} \quad (63.93)$$

where, for an isolated line, the width and shift are given by Eq. (63.93) with $L_{i'} = L_i$ and $L_{f'} = L_f$. For hydrogenic systems, where states i, i' and f, f' with different angular momenta are degenerate, a logarithmic divergence occurs for large values of l and l' [Eq. (63.74)], and must be removed by using Eqs. (63.75) and (63.86).

If a jj coupling scheme is used $\chi_j M_j \implies \chi_j^0 J_j M_j$, $j = i, i', f, f'$ in Eq. (63.81), and

$$\begin{aligned} \left| J_j M_j l m \frac{1}{2} m_s \right\rangle &= \sum_{J_j^T M_j^T j m'} C_{M_j M_j^T}^{J_j j J_j^T} C_{m m_s m'}^{l \frac{1}{2} j} \left| J_j l j J_j^T M_j^T \right\rangle, \end{aligned} \quad (63.94)$$

then Eq. (63.93) becomes

$$\begin{aligned} \langle\langle i' f'^* \| \mathbf{w} + i\mathbf{d} \| i f^* \rangle\rangle &= \pi (\hbar/m_e)^2 N \\ &\times \sum_{J_i^T J_i'^T j j' l l'} (-1)^{J_i + J_i' + 2J_f^T + j + j'} \frac{1}{2} (2J_i^T + 1) (2J_f^T + 1) \end{aligned}$$

$$\begin{aligned}
& \times \left\{ \begin{array}{ccc} J_f^T & J_i^T & 1 \\ J_i & J_f & j \end{array} \right\} \left\{ \begin{array}{ccc} J_f^T & J_i^T & 1 \\ J_{i'} & J_{f'} & j' \end{array} \right\} \\
& \times \int_0^\infty \frac{1}{v} f_e(v) dv \left[\delta_{l'l} \delta_{j'j} \delta_{J_i J_i'} \delta_{J_f J_f'} \right. \\
& \left. - S_I(J_{i'} l' j' J_i^T; J_i l j J_i^T) S_F^*(J_{f'} l' j' J_f^T; J_f l j J_f^T) \right], \quad (63.95)
\end{aligned}$$

where $J_{i'} = J_i$ and $J_{f'} = J_f$ for an isolated line. If the spectrum of the emitter is classified using LS coupling, it is often sufficient to use energies defined by

$$E_{L_j S} = \sum_{J_j} \frac{(2J_j + 1)}{(2L_j + 1)(2S_j + 1)} E_{L_j S J_j} \quad (63.96)$$

and obtain the S -matrix elements in an LS coupling scheme. They are then transformed to jj coupling by using the algebraic transformation

$$\begin{aligned}
& S(J_{i'} l' j' J_i^T; J_j l j J_j^T) \\
& = [(2J_j + 1)(2J_{j'} + 1)(2j + 1)(2j' + 1)]^{1/2} \\
& \times \sum_{L_j^T S^T} (2L_j^T + 1)(2S^T + 1) \\
& \times \left\{ \begin{array}{ccc} L_j & l & L_j^T \\ S & \frac{1}{2} & S^T \\ J_j & j & J_j^T \end{array} \right\} \left\{ \begin{array}{ccc} L_{j'} & l' & L_{j'}^T \\ S & \frac{1}{2} & S^T \\ J_{j'} & j' & J_{j'}^T \end{array} \right\} \\
& \times S\left(L_{j'} S l' \frac{1}{2} L_j^T S^T; L_j S l \frac{1}{2} L_j^T S^T\right), \quad (63.97)
\end{aligned}$$

and introducing the splitting of the fine structure components in Eq. (63.4) or (63.6). If in LS coupling the line is isolated, but nevertheless the broadened fine structure components overlap significantly, then the interference terms in Eq. (63.6) must be included.

63.4.3 Broadening by Atoms

The formal result is very similar to Eq. (63.95), but in this case, the relative motion only gives rise to orbital angular momentum. Thus,

$$\begin{aligned}
& \langle\langle i' f'^* \| \mathbf{w} + i\mathbf{d} \| i f^* \rangle\rangle = \pi (\hbar/\mu)^2 N \\
& \times \sum_{J_i^T J_f^T l l'} (-1)^{J_i + J_{i'} + 2J_f^T + l + l'} (2J_i^T + 1)(2J_f^T + 1) \\
& \times \left\{ \begin{array}{ccc} J_f^T & J_i^T & 1 \\ J_i & J_f & l \end{array} \right\} \left\{ \begin{array}{ccc} J_f^T & J_i^T & 1 \\ J_{i'} & J_{f'} & l' \end{array} \right\}
\end{aligned}$$

$$\begin{aligned}
& \times \int_0^\infty \frac{1}{v} f(v) dv [\delta_{l'l} \delta_{J_i J_i'} \delta_{J_f J_f'} \\
& - S_I(J_{i'} l' J_i^T; J_i l J_i^T) S_F^*(J_{f'} l' J_f^T; J_f l J_f^T)]. \quad (63.98)
\end{aligned}$$

For many cases of practical interest, transitions of type $J_i \rightarrow J_f$ are isolated and so have line profiles given by Eqs. (63.3), (63.10), and (63.98), where $J_i = J_{i'}$ and $J_f = J_{f'}$ [10]. In order to obtain the S -matrix elements in Eq. (63.98), it is usually sufficient to use adiabatic potentials for the emitter–perturber system that have been calculated neglecting fine structure. Since T is typically a few hundred degrees, only coupling between adiabatic states that tend to the appropriate separated-atom limit are retained in the scattering problem. The coupled scattering equations are then solved with fine structure introduced by applying an algebraic transformation to the adiabatic potentials, and using the observed splittings of the energy levels. The Born–Oppenheimer approximation is valid, and details are given in [21].

63.5 One-Perturber Approximation

63.5.1 General Approach and Utility

If only one perturber is effective in producing broadening, $I(\omega)$ can be obtained by considering a dipole transition between initial and final states I and F of the emitter–perturber system. Then $P(\omega)$ is given by Eq. (63.2), where

$$\begin{aligned}
I(\omega) & = [\delta(\omega - \omega_{IF}) \langle\langle IF^* | \mathbf{A} | IF^* \rangle\rangle]_{av}, \\
\hbar\omega_{IF} & = E_I - E_F, \quad (63.99)
\end{aligned}$$

and av denotes an average over states I and a sum over states F [4]. Wave functions Ψ_J are given by

$$\Psi_J(\mathbf{r}, \mathbf{R}) = \mathcal{O} \sum_j \psi_j(\mathbf{r}) \phi(\mathbf{k}_j, \mathbf{k}_{j_0}; \mathbf{R}), \quad (63.100)$$

where $J = I, F$, and \mathcal{O} is an operator that takes account of any symmetry properties of the emitter–perturber system. The energies E_I and E_F are given by Eq. (63.82). The perturber wave functions for initial state j_0 and final state j are expanded in the form

$$\begin{aligned}
\phi(\mathbf{k}_j, \mathbf{k}_{j_0}; \mathbf{R}) & = 2\pi i \sum_{l_{j_0} m_{j_0} l_j m_j} i^{l_{j_0}} k_{j_0}^{-1/2} Y_{l_{j_0} m_{j_0}}^*(\hat{\mathbf{k}}_{j_0}) \\
& \times Y_{l_j m_j}(\hat{\mathbf{R}}) \frac{1}{R} F(\Gamma_j, \Gamma_{j_0}; R), \quad (63.101)
\end{aligned}$$

where Γ_j denotes a channel characterized by

$$\Gamma_j = \chi_j M_j l_j m_j, \quad j = 0, 1, 2, \dots, \quad (63.102)$$

[Eq. (63.81)]. In Eq. (63.101), the radial perturber wave function has the limiting forms

$$F(\Gamma_j, \Gamma_{j_0}; R) \underset{R \rightarrow 0}{\approx} R^{l_j+1} \underset{R \rightarrow \infty}{\approx} k_j^{-1/2} \left[\delta_{\Gamma_j \Gamma_{j_0}} \exp(-i\theta_j) - S_j(\Gamma_j; \Gamma_{j_0}) \exp(i\theta_j) \right], \quad (63.103)$$

with

$$\theta_j = k_j R - \frac{1}{2} l_j \pi - \frac{z}{k_i} \ln(2k_j R) + \arg \Gamma \left(l_j + 1 + i \frac{z}{k_j} \right), \quad z = \frac{\mu q^2}{\hbar^2} Z_c Z_p. \quad (63.104)$$

The coupled equations obtained by using Eqs. (63.12), (63.13), (63.100), and (63.101), where

$$\Psi(\mathbf{r}, \mathbf{R}, t) = \Psi_j(\mathbf{r}, \mathbf{R}) \exp(-iE_j t / \hbar) \quad (63.105)$$

are integrated to give functions $F(\Gamma_j, \Gamma_{j_0}; R)$. Using Eqs. (63.100) and (63.101), Eq. (63.99) becomes

$$I(\omega) = \frac{1}{2} N \sum_{\Gamma_{i_0} \Gamma_i \Gamma_{i'} \Gamma_{j_0} \Gamma_f \Gamma_{f'}} u_{i_0} \langle \langle \Gamma_i \Gamma_{f'}^* | \mathbf{A} | \Gamma_{i'} \Gamma_{f'}^* \rangle \rangle \times \int_0^\infty \frac{1}{v} f(v) dv \mathcal{F}(\Gamma, v), \quad (63.106)$$

where

$$\mathcal{F}(\Gamma, v) = \int_0^\infty F^*(\Gamma_i, \Gamma_{i_0}; R) F(\Gamma_f, \Gamma_{f_0}; R) dR \times \int_0^\infty F(\Gamma_{i'}, \Gamma_{i_0}; R) F^*(\Gamma_{f'}, \Gamma_{f_0}; R) dR, \quad (63.107)$$

$$u_{i_0} = g_{i_0} / \sum_{i'_0} g_{i'_0}, \quad v = \frac{\hbar k_{i_0}}{\mu}. \quad (63.108)$$

The one-perturber approximation is valid when

$$\Delta\omega \equiv |\omega - \omega_{if}| \gg w; \quad V \gg \bar{V}, \quad (63.109)$$

where V is the effective interaction potential required to produce a shift $\Delta\omega$. In the center of the line, many-body effects are always important, and the one-perturber approximation diverges as $\Delta\omega \rightarrow 0$. In many cases, there is a region of overlap where criteria Eqs. (63.1) and (63.109) are all valid, but when $\Delta\omega \tau \gg 1$, Eq. (63.99) is a static approximation, since the average time between collisions is $\Delta\omega^{-1}$.

63.5.2 Broadening by Electrons

If LS coupling is used, definition of channel Γ_j in Eq. (63.104) is replaced by

$$\Gamma_j = L_j S l_j \frac{1}{2} L_j^T S^T, \quad j = i_0, i, i', f_0, f, f', \quad (63.110)$$

[cf. Eqs. (63.91) and (63.92)]. Then assuming that the weights u_{i_0} of all the levels i_0 that effectively contribute to the line are the same, Eq. (63.106) becomes

$$I(\omega) = \frac{1}{2} N_e \sum_{\substack{\Gamma_{i_0} \Gamma_i \Gamma_{i'} \\ \Gamma_{f_0} \Gamma_f \Gamma_{f'}}} \langle \langle L_i S (L_f S)^* | \mathbf{A} | L_{i'} S (L_{f'} S)^* \rangle \rangle \times \delta_{i_l f_l} \delta_{i'_l f'_l} \delta_{L_{i_0}^T L_i^T} \delta_{L_{f_0}^T L_f^T} \delta_{L_{i_0}^T L_{i'}^T} \delta_{L_{f_0}^T L_{f'}^T} \times (-1)^{L_i + L_{i'} + l_i + l_{i'}} \frac{(2S^T + 1)}{2(2S + 1)} \times (2L_i^T + 1)(2L_{f'}^T + 1) \times \begin{Bmatrix} L_f^T & L_i^T & 1 \\ L_i & L_f & l \end{Bmatrix} \begin{Bmatrix} L_f^T & L_{i'}^T & 1 \\ L_{i'} & L_{f'} & l_{i'} \end{Bmatrix} \times \int_0^\infty \frac{1}{v} f_e(v) dv \mathcal{F}(\Gamma, v), \quad (63.111)$$

where $\mathcal{F}(\Gamma, v)$ is defined by Eqs. (63.107) and (63.111). If the functions $F(\Gamma_j, \Gamma_{j_0}; R)$ in Eq. (63.107) are replaced by their asymptotic forms Eq. (63.103), then

$$\mathcal{F}(\Gamma, v) \simeq \Delta\omega^{-2} (\hbar/m_e)^2 \times \left[\delta_{\Gamma_{i_0} \Gamma_i} \delta_{\Gamma_{f_0} \Gamma_f} - S_I(\Gamma_i; \Gamma_{i_0}) S_F^*(\Gamma_f; \Gamma_{f_0}) \right] \times \left[\delta_{\Gamma_{i_0} \Gamma_{i'}} \delta_{\Gamma_{f_0} \Gamma_{f'}} - S_I^*(\Gamma_{i'}; \Gamma_{i_0}) S_F(\Gamma_{f'}; \Gamma_{f_0}) \right]. \quad (63.112)$$

On substituting Eq. (63.112) into Eq. (63.111), summing over Γ_{i_0} and Γ_{f_0} and using the unitary property of the S -matrix,

$$I(\omega) = \frac{1}{\pi \Delta\omega^2} \sum_{L_i^T L_f^T S^T l l'} \langle \langle L_i S (L_f S)^* | \mathbf{A} | L_{i'} S (L_{f'} S)^* \rangle \rangle \times \langle \langle i' f'^* | \mathbf{w} | i f^* \rangle \rangle, \quad (63.113)$$

where $\langle \langle i' f'^* | \mathbf{w} | i f^* \rangle \rangle$ is given by Eq. (63.93). Line shape Eq. (63.113) is identical to that obtained from Eq. (63.6) when $\Delta\omega \gg w$. If the jj coupling scheme specified by Eq. (63.94) is used, and channel Γ_j is defined by

$$\Gamma_j = J_j l_j j_j J_j^T, \quad j = i_0, i, i', f_0, f, f', \quad (63.114)$$

Equation (63.106) becomes [cf. Eq. (63.95)]

$$\begin{aligned}
I(\omega) &= \frac{1}{2} N_e \sum_{\Gamma_{i_0} \Gamma_i \Gamma_{i'} \Gamma_{f_0} \Gamma_f \Gamma_{f'}} \langle \langle J_i(J_f)^* \parallel \Delta \parallel J_{i'}(J_{f'})^* \rangle \rangle \\
&\times \delta_{l_i l_f} \delta_{l_{i'} l_{f'}} \delta_{j_i j_f} \delta_{j_{i'} j_{f'}} \delta_{J_{i_0}^T J_i^T} \delta_{J_{f_0}^T J_f^T} \delta_{J_{i_0}^T J_{i'}^T} \delta_{J_{f_0}^T J_{f'}^T} \\
&\times (-1)^{J_i + J_{i'} + 2J_f^T + j_i + j_{i'}} \\
&\times \frac{1}{2} (2J_i^T + 1) (2J_f^T + 1) \\
&\times \left\{ \begin{array}{ccc} J_f^T & J_i^T & 1 \\ J_i & J_f & j_i \end{array} \right\} \left\{ \begin{array}{ccc} J_f^T & J_{i'}^T & 1 \\ J_{i'} & J_{f'} & j_{i'} \end{array} \right\} \\
&\times \int_0^\infty \frac{1}{v} f_e(v) dv \mathcal{F}(\Gamma, v), \quad (63.115)
\end{aligned}$$

where $\mathcal{F}(\Gamma, v)$ is given by Eqs. (63.107) and (63.114).

63.5.3 Broadening by Atoms and Molecules

In the wings of a line where $\hbar|\Delta\omega| \simeq |E_{J_i} - E_{J_{i'}}|$, $j = i_0, i, i', f_0, f, f'$, coupling between the fine structure levels is important. If channel Γ_j is defined by

$$\Gamma_j = J_j l_j J_j^T, \quad j = i_0, i, i', f_0, f, f', \quad (63.116)$$

Equation (63.106) becomes [cf. Eq. (63.115)]

$$\begin{aligned}
I(\omega) &= \frac{1}{2} N \sum_{\Gamma_{i_0} \Gamma_i \Gamma_{i'} \Gamma_{f_0} \Gamma_f \Gamma_{f'}} \langle \langle J_i(J_f)^* \parallel \Delta \parallel J_{i'}(J_{f'})^* \rangle \rangle \\
&\times \delta_{l_i l_f} \delta_{l_{i'} l_{f'}} \delta_{J_{i_0}^T J_i^T} \delta_{J_{f_0}^T J_f^T} \delta_{J_{i_0}^T J_{i'}^T} \delta_{J_{f_0}^T J_{f'}^T} \\
&\times (-1)^{J_i + J_{i'} + 2J_f^T + l_i + l_{i'}} (2J_i^T + 1) (2J_f^T + 1) \\
&\times \left\{ \begin{array}{ccc} J_f^T & J_i^T & 1 \\ J_i & J_f & l_i \end{array} \right\} \left\{ \begin{array}{ccc} J_f^T & J_{i'}^T & 1 \\ J_{i'} & J_{f'} & l_{i'} \end{array} \right\} \\
&\times \int_0^\infty \frac{1}{v} f(v) dv \mathcal{F}(\Gamma, v), \quad (63.117)
\end{aligned}$$

where $\mathcal{F}(\Gamma, v)$ is given by Eqs. (63.107) and (63.116). In the far wings, where $\hbar|\Delta\omega| \gg |E_{J_i} - E_{J_{i'}}|$, $j = i_0, i, i', f_0, f, f'$, an adiabatic approximation is valid. Adiabatic states of the diatomic molecule formed by the emitter-perturber system are considered in which the total spin is assumed to be decoupled from the total orbital angular momentum of the electrons. The coupling between rotational and electronic angular momentum can also be neglected, because, typically, contributions to the line profile come from

$0 \leq l_j \lesssim 400$, whereas $\Lambda_j \lesssim 2$. Therefore, transitions take place between channels defined by

$$\Gamma_j = \Lambda_j L_j S L_j, \quad j = i, f, \quad (63.118)$$

where the unperturbed emitter in state j has quantum numbers $L_j S$, the quantum number Λ_j represents the projection of the orbital angular momentum on the internuclear axis, and Eq. (63.100) is replaced by

$$\Psi_J(\mathbf{r}, \mathbf{R}) = \mathcal{O} \sum_j \psi_j(\mathbf{r}; \mathbf{R}) \phi(\mathbf{k}_j, \mathbf{k}_{j_0}; \mathbf{R}), \quad (63.119)$$

where $k_j = k_{j_0}$, and $\psi_j(\mathbf{r}; \mathbf{R})$ is the wave function for molecular state Λ_j . In Eq. (63.119), the only molecular states retained are those that correlate with emitter states i and f . The scattering is described by

$$\begin{aligned}
\left[\frac{d^2}{dR^2} - \frac{l_j(l_j + 1)}{R^2} - \frac{2z}{R} - \frac{2\mu}{\hbar^2} V_{\Lambda_j}(R) + k_j^2 \right] \\
\times F_j(R) = 0, \quad (63.120)
\end{aligned}$$

where $k_j = k_{j_0}$ and

$$\begin{aligned}
F_j(R) &= P_{v_j l_j}(R) \text{ or} \\
F_j(R) &\equiv F(\Gamma_j, \Gamma_j; R) = F_{k_i l_i}(R) \quad (63.121)
\end{aligned}$$

for vibrational or free states, respectively, and $V_{\Lambda_j}(R)$ is the potential energy of state Λ_j . Free-free transitions always contribute to the line profile, but bound-free and free-bound transitions only contribute on the red and blue wings, respectively. On using Eqs. (63.82), (63.99), and (63.109), $\hbar\Delta\omega = \varepsilon_i - \varepsilon_f$, and ε_j becomes the energy of bound state j with vibrational quantum number v_j when $\varepsilon_j < 0$. If

$$\mathcal{G}(\Gamma, \varepsilon_i, \varepsilon_f) \equiv \left| \int_0^\infty F_i^*(R) \bar{\Delta}(R) F_f(R) dR \right|^2 \quad (63.122)$$

[cf. Eq. (63.107)], where

$$\bar{\Delta}(R) = -q \int \psi_i^*(\mathbf{r}; \mathbf{R}) \mathbf{r} \psi_f(\mathbf{r}; \mathbf{R}) d\mathbf{r} \quad (63.123)$$

is the dipole moment, then using Eq. (63.119), the free-free contribution is given by

$$\begin{aligned}
I_0(\omega) &= \frac{N}{2} \sum_{\Gamma_i \Gamma_f} u_{\Lambda_i} \delta_{l_i l_f} (2l_i + 1) \\
&\times \int_0^\infty \frac{f(v)}{v} dv \mathcal{G}(\Gamma, \varepsilon_i, \varepsilon_f), \quad (63.124)
\end{aligned}$$

where $\varepsilon_i = \frac{1}{2}\mu v^2$, and u_{Λ_i} is the relative weight of state Λ_i [cf. Eqs. (63.106)–(63.108)]. The bound–free contribution is

$$I_1(\omega) = \frac{N}{2} \sum_{\Gamma_i \Gamma_f} u_{\Lambda_i} \delta_{l_i l_f} (2l_i + 1) \times \sum_i g(\varepsilon_i) \mathcal{G}(\Gamma, \varepsilon_i, \varepsilon_f), \quad (63.125)$$

and the free–bound contribution is

$$I_2(\omega) = \frac{1}{2} N \sum_{\Gamma_i \Gamma_f} u_{\Lambda_i} \delta_{l_i l_f} (2l_i + 1) \exp\left(-\frac{\hbar \Delta \omega}{k_B T}\right) \times \sum_f g(\varepsilon_f) \mathcal{G}(\Gamma, \varepsilon_i, \varepsilon_f), \quad (63.126)$$

where

$$g(\varepsilon) = 2\pi \left(\frac{\hbar}{\mu}\right)^2 \frac{f(v)}{v^2} = 8\pi^2 \left(\frac{\hbar}{\mu}\right)^2 \left(\frac{\mu}{2\pi k_B T}\right)^{3/2} \exp\left(-\frac{\varepsilon}{k_B T}\right), \quad (63.127)$$

on using Eq. (63.21) with $\varepsilon = \frac{1}{2}\mu v^2$. The full line profile is then given by Eqs. (63.124)–(63.126), so that

$$I(\omega) = \sum_{j=0}^2 I_j(\omega). \quad (63.128)$$

The satellite features that are often seen in line wings arise because turning points in the difference potential $[V_{\Lambda_i}(R) - V_{\Lambda_f}(R)]$ produce a phenomenon analogous to the formation of rainbows in scattering theory. The JWKB approximation is often used for the functions $F_{k_j l_j}(R)$ and can be shown to lead to the correct static limit in which transitions take place at fixed values of R called ‘‘Condon points’’, i.e., the Franck–Condon principle is valid. Further details are given in [4, 5, 22–24].

63.6 Unified Theories and Conclusions

The pressure broadening of spectral lines is, in general, a time-dependent many-body problem and as such cannot be solved exactly. After all, even the problem of two free electrons scattered by a proton is still a subject of active research. There is no practical theory that leads to the full static profile in the limit of high density (or low temperature) and to the full impact profile in the limit of low density (or high temperature). As with so many problems in physics, it is the intermediate problem that is intractable because no particular feature can be singled out as providing a weak perturbation on a known physical situation. However, much progress has

been made over the last 30 years in developing theories that take into account many of the key features of the intermediate problem, and they are often successful in predicting line profiles for practical applications [3–5, 22–24]. More recently, time-dependent many-body problems have been tackled using computer-oriented approaches that invoke Monte Carlo and other simulation methods to study line broadening in dense, high-temperature plasmas, see, for example, [25]. In this chapter, the emphasis has been on aspects of the subject that relate directly to electron–atom and low-energy atom–atom scattering. Many experts in the fields of electron–atom and atom–atom collisions are still not exploiting the direct applicability of their work to line broadening. It is hoped that this contribution will encourage more research workers to study these fascinating problems that not only provide links with plasma physics and, in particular, with the physics of fusion plasmas, but also with a quite distinct body of laboratory-based experimental data.

References

1. Kramida, A., Fuhr, J.R.: Atomic Spectral Line Broadening Bibliographic Database, Version 3.0. National Institute of Standards and Technology, Washington, D.C. (2017)
2. Hartmann, J.-M., Boulet, C., Robert, D.: Collisional Effects on Molecular Spectra. Elsevier, Amsterdam (2008)
3. Griem, H.R.: Spectral Line Broadening in Plasmas. Academic Press, New York (1974)
4. Peach, G.: Adv. Phys. **30**, 367 (1981)
5. Allard, N., Kielkopf, J.R.: Rev. Mod. Phys. **54**, 1103 (1982)
6. Stambulchik, E., Calisti, A., Chung, H.-K., González, M.Á. (eds.): Spectral Line Shapes in Plasmas. MDPI, Basel, Switzerland (2015)
7. Ben-Reuven, A.: Phys. Rev. **145**, 7 (1966)
8. Ben-Reuven, A.: Adv. Atom. Molec. Phys. **5**, 201 (1969)
9. Ciuryło, R., Pine, A.S.: J. Quant. Spectrosc. Radiat. Transf. **67**, 375 (2000)
10. Lewis, E.L.: Phys. Rep. **58**, 1 (1980)
11. Sahal-Bréchet, S.: Astron. Astrophys. **1**, 91 (1969)
12. Sahal-Bréchet, S.: Astron. Astrophys. **2**, 322 (1969)
13. Dimitrijević, M.S., Konjević, N.: J. Quant. Spectrosc. Radiat. Transf. **24**, 451 (1980)
14. Konjević, N.: Phys. Rep. **316**, 339 (1999)
15. Oertel, G.K., Shomo, L.P.: Astrophys. J. Suppl. **16**, 175 (1969)
16. Seaton, M.J.: J. Phys. B **21**, 3033 (1988)
17. Seaton, M.J.: J. Phys. B **22**, 3603 (1989)
18. Kogan, V.I., Lisitsa, V.S., Sholin, G.V.: Rev. Plasma Phys. **13**, 261 (1987)
19. Gordon, M.A., Sorochenko, R.L.: Radio Recombination Lines. Springer, New York (2009)
20. Peach, G.: J. Astrophys. Astr. **36**, 555 (2015)
21. Leo, P.J., Peach, G., Whittingham, I.B.: J. Phys. B **28**, 591 (1995)
22. Szudy, J., Baylis, W.E.: J. Quant. Spectrosc. Radiat. Transf. **15**, 641 (1975)
23. Szudy, J., Baylis, W.E.: J. Quant. Spectrosc. Radiat. Transf. **17**, 269 (1977)
24. Szudy, J., Baylis, W.E.: Phys. Rep. **266**, 127 (1996)
25. Calisti, A., Godbert, L., Stamm, R., Talin, B.: J. Quant. Spectrosc. Radiat. Transf. **51**, 59 (1994)

Part E
Scattering Experiment

Part E focuses on the experimental aspects of scattering processes. Recent developments in the field of photodetachment are reviewed, with an emphasis on accelerator-based investigations of the photodetachment of atomic negative ions. The theoretical concepts and experimental methods for the scattering of low-energy photons, proceeding primarily through the photoelectric effect, are given. The main photon–atom interaction processes in the intermediate energy range are outlined. The atomic response to inelastic photon scattering is discussed; essential aspects of radiative and radiationless transitions are described in

the two-step approximation. Advances such as cold-target recoil-ion momentum spectroscopy are also touched upon. Electron–atom and electron–molecule collision processes, which play a prominent role in a variety of systems, are presented. The discussion is limited to electron collisions with gaseous targets, where single collision conditions prevail, and to low-energy impact processes. The involving neutral molecules at chemical energies is presented. Applications of single-collision scattering methods to the study of reactive collision dynamics of ionic species with neutral partners are discussed.



Contents

64.1	Negative Ions	943
64.2	Photodetachment	944
64.2.1	Photodetachment Cross Sections	944
64.2.2	Threshold Behavior	945
64.2.3	Structure in Continuum	946
64.2.4	Photoelectron Angular Distributions	946
64.2.5	Higher-Order Processes	946
64.3	Experimental Procedures	947
64.3.1	Production of Negative Ions	947
64.3.2	Interacting Beams	947
64.3.3	Light Sources	948
64.3.4	Detection Schemes	948
64.4	Measuring Properties of Negative Ions	948
64.4.1	Electron Affinities	948
64.4.2	Bound States	949
64.4.3	Continuum Processes	949
64.5	Investigation of Fundamental Processes	950
64.5.1	Threshold Studies	950
64.5.2	Photodetachment Using Short Laser Pulses	950
64.6	Observations and Applications of Negative Ions	950
64.6.1	Natural Occurrence of Negative Ions	950
64.6.2	Applications of Negative Ions	951
	References	951

Abstract

Investigations of photon–ion interactions have grown rapidly over the past few decades, primarily due to the increased availability of laser and synchrotron light sources. At photon energies below about 1 keV, the dominant radiative process is the electric dipole induced photoelectric

effect. In the gaseous phase, the photoelectric effect is referred to as either photoionization (atoms and positive ions) or photodetachment (negative ions). This chapter reviews the basics of negative ions, photodetachment, and the experimental methods used when the photodetachment process is applied to the study of negative ions. Negative ions of molecules and cluster exist, but this article covers only atomic negative ions. The monographs of *Massey* [1] and *Smirnov* [2] and a review by *Bates* [3] offer good introductions to the subject of negative ions. The focus will be on accelerator-based measurements. Reviews of experimental methods used to investigate the properties of negative ions have been published by, for example, *Andersen* [4], *Pegg* [5], and *Rienstra-Kiracofe* [6].

Keywords

photodetachment · laser photodetachment threshold spectroscopy · Wigner law · doubly excited states · Fano resonance profile · photoelectron angular distributions · resonance ionization spectroscopy · anomalous threshold behavior · collinear laser-ion beam geometry · neutral atom detection

64.1 Negative Ions

Interest in negative ions stems from the fact that their structure and dynamics are qualitatively different from those of isoelectronic atoms and positive ions. This can be traced to the nature of the force that binds the outermost electron. In the case of atoms and positive ions, the outermost electron moves asymptotically in the long-range Coulomb field of the positively charged core. The relatively strong $1/r$ potential is able to support an infinite spectrum of bound states that converge on the ionization limit. In contrast, the outermost electron in a negative ion experiences the short-range induced-dipole field of the atomic core. The relatively weak $1/r^4$ polarization potential can typically sup-

D. Pegg (✉)
Dept. of Physics, University of Tennessee
Knoxville, TN, USA
e-mail: djpegg@utk.edu

D. Hanstorp (✉)
Dept. of Physics, University of Gothenburg
Gothenburg, Sweden
e-mail: dag.hanstorp@physics.gu.se

port only a single bound state. The weakness of the attractive force is reflected in the binding energies of the outermost electron, i.e., the electron affinities, which are typically an order of magnitude smaller than the ionization energies of atoms. Weakly bound systems such as negative ions are ideally suited for investigations of the effects of electron correlation, which plays an important role in determining the structure and dynamics of many-electron systems [7]. As a result of the more efficient shielding of the nucleus by the atomic core, the electron–electron interactions become relatively more important than the electron–nucleus interaction. A major goal of photodetachment experiments is to measure correlation-sensitive quantities such as electron affinities, the energies and widths of resonant states, and asymmetry parameters describing photoelectron angular distributions. These quantities provide sensitive tests of the ability to incorporate electron correlation into theoretical models. The stimulating interplay between experiment and theory continues to help elucidate the role of many-electron effects in the structure and dynamics of atomic systems.

There exist a number of bound excited states of negative ions, but most of them have the same parity as the ground state [8]. As such, they are long lived and radiate via electric dipole-forbidden transitions. Dipole-allowed transitions have been observed in a few ions. In these cases, excited states connect to the ground state or other excited states of opposite parity [9–12]. Multiple excitations in a negative ion leads to the production of states embedded in continua lying above the detachment limits. Such quasi-discrete states are unbound and decay rapidly via the allowed process of Coulomb autodetachment. Most negative ions exhibit a rich spectrum of these short-lived states [5]. They are manifested as resonance structures at well-defined energies in photodetachment spectra.

Most, but not all, elements form stable negative ions. Exceptions are, for instance, the noble gases, nitrogen and magnesium. Here, the degree of correlation is insufficient to attach an extra electron. Negative ions of other atoms such as Ca have ground states that are very weakly bound and, therefore, easily destroyed [13, 14]. Some negative ions, such as Be^- [15], are formed in states that are embedded in continua but are metastable due to violations of the selection rules for Coulomb autodetachment. A prominent example is the $1s2s2p^4P$ metastable state of He^- [16, 17], which has a binding energy of 77 meV relative to the $1s2s^3S$ metastable state of He. Its decay via autodetachment is strongly suppressed by the selection rule on spin.

64.2 Photodetachment

Pioneering photodetachment experiments using lasers began in the mid 1960s with the work of *Hall* and coworkers [18–20]. The use of a tunable dye laser by *Lineberger* and

coworkers [21, 22] followed soon after. Essentially all information on the structure and dynamics of negative ions comes from controlled experiments in which electrons are detached from the ions when they interact with photons or other particles. Photodetachment is the preferred method since the energy resolution associated with such measurements is typically much higher than that attainable in any particle-induced detachment process. Generally, one or more electrons can be detached from a negative ion following the absorption of one or more photons in the photodetachment process. To date most measurements of the structure of negative ions involve the simplest process of single-electron detachment following single-photon absorption. In this process, the photon transfers energy and angular momentum to the negative ion, which subsequently breaks up into a neutral atom and an electron. The initial energy and angular momentum are conserved and shared in the final state by the residual atom and the free electron.

64.2.1 Photodetachment Cross Sections

The total cross section for photodetachment is proportional to the probability of detaching one electron while leaving the residual atom in its ground state or any of its excited states. The partial cross section describes the detachment probability for leaving the atom in a specific state, which could be either the ground or an excited state. The differential cross section, finally, represents the angular distribution of the detached electrons. Examples of the photon energy dependence of these three types of cross sections are shown in Fig. 64.1.

Fermi's golden rule predicts the photodetachment cross section to be proportional to the product of the square of the dipole matrix element connecting the initial and final states and the density of final states. The general behavior of a photodetachment cross section is that it starts at zero at threshold, rises to a peak that occurs at an energy of a few, to as much as tens of, eV above threshold, and then asymptotically approaches zero at higher energies. In Fig. 64.1a, the total cross section for the photodetachment of Na^- is given as an example. The increase in the probability of detachment just above threshold depends on the density of final states and the ability of the outermost electron to overcome a possible centrifugal barrier. The decrease in the cross section at higher energies is due to the declining overlap between the initial bound state wave function and the rapidly oscillating wave function representing the emitted electron. On top of the otherwise smooth behavior of the photodetachment cross sections different structures occur. One prominent feature that can be observed in certain special cases is called a Wigner cusp (see the sharp peak around 2.7 eV in Fig. 64.1a). This structure arises at the opening of an excited state channel when there

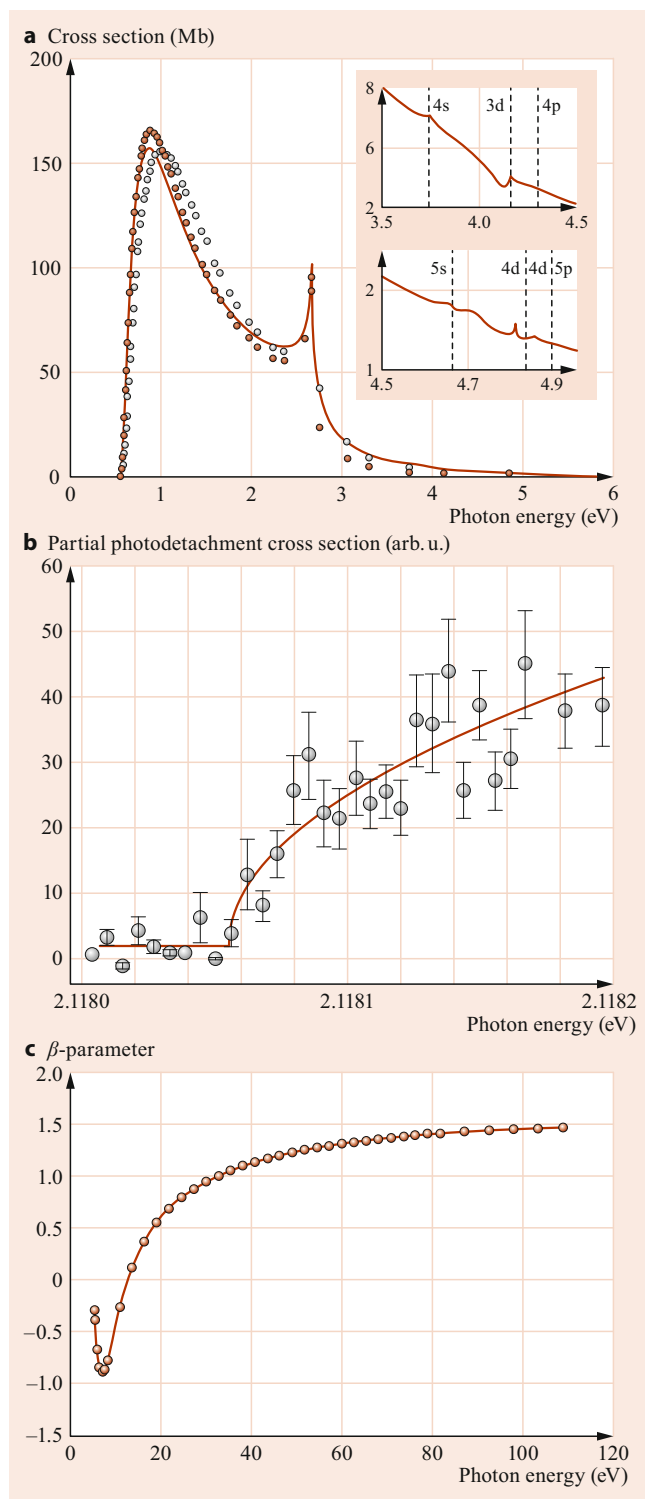


Fig. 64.1 Typical photodetachment cross sections. **a** The *solid line* shows the calculated total cross section for photodetachment of Na^- by Liu and Starace [23], whereas the *opened (filled) circles* indicate the dipole length (velocity) results of Moores and Norcross [24]. The *inset* shows a magnification of the region from 3.5–4.9 eV where resonances can be observed. The figure is reprinted with permission from [23]. Copyright 1999 by American Physical Society. **b** Measured partial cross section for $4p_{3/2}$ photodetachment channel of K^- . The *solid line* is a fit to the Wigner law (Eq. (64.1)), which is used to extract the threshold position from the data. Reprinted with permission from [25]. Copyright 2000 by American Physical Society. **c** Theoretical differential cross section for F^- expressed as the asymmetry parameter β [26]. The figure is reprinted with permission from [26]. Copyright 1987 by American Physical Society ◀

64.2.2 Threshold Behavior

Theoretical aspects of the general subject of threshold laws has been reviewed by Rau [27]. Cross sections for photodetachment are zero at threshold, in contrast to the finite value characteristic of photoionization cross sections. The threshold behavior for systems without Coulomb interaction is determined by the dynamics of the residual atom and the emitted electron. In general terms, Wigner demonstrated that for a two-body final state, the near-threshold cross section depends only on the dominant long-range interaction between the two product particles. The *Wigner law* [28] determines the energy dependence of the near-threshold cross section for the photodetachment of a single electron from an atomic negative ion. It can be written as

$$\sigma = Ak^{2l+1} = B(E - E_{\text{th}})^{l+1/2}, \quad (64.1)$$

where A and B are constants, and k and l represent the wavenumber and angular momentum quantum number of the detached electron, respectively; E is the photon energy, and E_{th} is the threshold energy for the photodetachment process. As a result of the electric dipole selection rules, the detached electron is represented, in general, by two partial waves $l = l_0 + 1$ and $l_0 - 1$, where l_0 is the angular momentum of the bound electron in the negative ion prior to detachment. In the case of photodetachment involving electrons with $l > 0$, the angular momentum dependence arises from the centrifugal force, $l(l + 1)/r^2$. The $1/2$ exponent is associated with the density of continuum states. Shorter-range final state interactions, such as those due to the electric dipole polarizability of the residual atom, will not change the form of the threshold behavior, as long as the potential falls off faster than $1/r$. They will, however, limit the range of validity of the Wigner law. The polarizability of the atom increases rapidly with the degree of excitation, making the range of validity correspondingly smaller. There is no a priori way of determining the range of validity of the Wigner law in any particular experiment. Measured threshold data is usually fit to the Wigner law in order to determine the threshold energy, as is shown in Fig. 64.1b in the case of K^- . It is possible to extend the range of the fit beyond that of the Wigner law.

is a strong configuration interaction between the ground state and excited state final continuum channels [23]. Other, more common, structures called resonances are the result of multiple excitation in the negative ion (see the inset of Fig. 64.1a). Cusps and resonances will be discussed in more detail in Sects. 64.2.2 and 64.2.3, respectively.

O'Malley [29], for example, considered the effects of atomic multipole forces on threshold behavior. *O'Malley's* formalism does not treat polarization explicitly. This is, however, accounted for in the modified effective range theory of *Watanabe* and *Greene* [30]. Anomalous threshold behavior can be observed in cases where there is a coupling of two final state channels as a result of configurational mixing. For example, a sharp feature has been observed in the partial cross section for the photodetachment of Na^- via the p-wave channel as a result of the strong coupling between this channel and the s-wave channel. The sharp peak at threshold in the p-wave channel is called a Wigner cusp, as can be seen in Fig. 64.1a.

64.2.3 Structure in Continuum

Photodetachment cross sections are often modulated by resonance structure at certain photon energies. The structure arises when more than one electron, or a core electron, is excited. These unbound quasi-discrete states are embedded in the continua above the first (or higher) detachment limit and are, therefore, subject to decay via the spontaneous process of autodetachment. The allowed autodetachment process is induced by the relatively strong electrostatic interaction between the outermost electrons. This process causes quasi-discrete continuum states to be very short lived. The decay of a quasi-discrete state in the continuum by autodetachment is manifested as a resonance structure in the detachment cross section, as can be seen in the inset of Fig. 64.1a. The shape of a resonance is determined by the interference between the two pathways for reaching the same final continuum state: direct detachment and detachment via the quasi-discrete state embedded in the continuum. A resonance can be parametrized by fitting it to a Fano profile [31]

$$\sigma(\omega) = \sigma_0 \frac{(q + \varepsilon)^2}{1 + \varepsilon^2}, \quad (64.2)$$

$$\varepsilon = \frac{\hbar\omega - E_r}{\Gamma/2}, \quad (64.3)$$

where σ denotes the cross section, σ_0 the nonresonant cross section, $\hbar\omega$ the photon energy, E_r the resonance energy, Γ the resonance width, and q a shape parameter. The resonance parameters (E_r , Γ) can be extracted from a fit to Eq. (64.2). If the selection rules on the allowed Coulomb-induced process are violated, the state may live much longer. Such metastable states eventually decay via autodetachment induced by weaker higher-order interactions.

64.2.4 Photoelectron Angular Distributions

For an unpolarized target, such as an ion beam, the angular distribution of the photoelectrons, i.e., the differential cross

section can, within the dipole approximation, be written in the form

$$\frac{d\sigma}{d\Omega} = \frac{\sigma}{4\pi} [1 + \beta P_2(\cos\theta)]. \quad (64.4)$$

Here, σ represents the total cross section, θ is the angle between the directions of the linear polarization vector of the photons and the momentum of the outgoing electrons, and $P_2(\cos\theta)$ is the second-order Legendre polynomial. The asymmetry parameter, β , characterizes the angular distribution or anisotropy of the photoelectrons. The angular distribution of the free electrons in the photodetachment process has been treated theoretically by *Cooper* and *Zare* [32]. They showed that the β parameter, in a central-potential model, can be described by

$$\beta = \frac{l(l-1)\sigma_{l-1}^2 + (l+1)(l+2)\sigma_{l+1}^2 - 6l(l+1)\sigma_{l-1}\sigma_{l+1}\cos(\delta_{l+1} - \delta_{l-1})}{(2l+1)l\sigma_{l-1}^2 + (l+1)\sigma_{l+1}^2}, \quad (64.5)$$

where l is the angular momentum of the electron prior to photodetachment, σ and δ are the dipole radial matrix elements and the residual phase shift of the interfering waves, respectively. A bound electron in an s-orbital ($l=0$) yields an outgoing electron represented by a pure p-wave. In this case, $\beta=2$ for all photon energies and the angular distribution has a pure $\cos^2\theta$ distribution. If, however, the bound state electron is in a p-orbital ($l=1$) prior to detachment, the outgoing electron will be represented by both s-waves and d-waves. Close to threshold the d-wave is suppressed due to the centrifugal barrier, and the s-wave dominates. In this case, $\beta=0$, and the angular distribution is isotropic. At higher energies, the value of β will be determined by the relative amplitudes of the s-waves and the d-waves, as well as their relative phases. This behavior can be seen in Fig. 64.1c, in the case of F^- . Most angular distribution measurements have been performed with a crossed laser and ion beams geometry [33, 34]. However, *Hanstorp* et al. [35] investigated the interference between s-waves and d-waves arising from the photodetachment of O^- using a collinear beams geometry. They introduced an approximation in the analysis of a measurement of the energy dependence of the β parameter. They showed that the phase difference between the s-waves and d-waves can be determined from the value of β at the minimum. A β -value of -1 means that the two waves are completely out of phase.

64.2.5 Higher-Order Processes

With the advent of high-power pulsed lasers, it has become possible to observe multiphoton detachment processes. Here, a single electron is ejected following the absorption of two or more photons. *Hall* et al. [18] performed the first such measurement on I^- . Early work in this area has been reviewed by

Blondel [36]. More recently, Bergues et al. [37] used a short-pulse, high-intensity laser to study photodetachment in the strong field regime.

In contrast, multielectron detachment involves the detachment of two or more electrons following the absorption of a single photon. This process, which appears to be initiated by the detachment of an inner shell electron, requires photons with energies higher than can be generated by conventional lasers. Such measurements can, however, be performed at synchrotron radiation [38–40] and free-electron laser sites [41].

64.3 Experimental Procedures

Experimental investigations of negative ions have been performed using ion traps [16], linear accelerators [42], and storage rings [43]. The focus of this article is on the use of photodetachment in accelerated-based measurements, which is by far the most commonly used method.

64.3.1 Production of Negative Ions

Negative ions are created in exoergic attachment processes when an electron is captured by an atom or molecule. These quantum systems are weakly bound with diffuse outer orbitals. As a consequence, they are easily destroyed in collisions with other particles. The production of negative ions with a density sufficiently high for spectroscopic studies poses a challenge to the experimentalist since processes involved in their creation must compete with more probable destruction processes. The most versatile source for the production of negative ions for accelerator-based experiments is the Cs sputter ion source [44]. This source has been used to generate a wide variety of atomic, molecular, and cluster negative ions. Alternatively, negative ions can be produced in a plasma source, either by direct extraction [45] or by extraction of positive ions that are converted to negative ions through a sequential double-charge transfer in an alkali vapor [15].

64.3.2 Interacting Beams

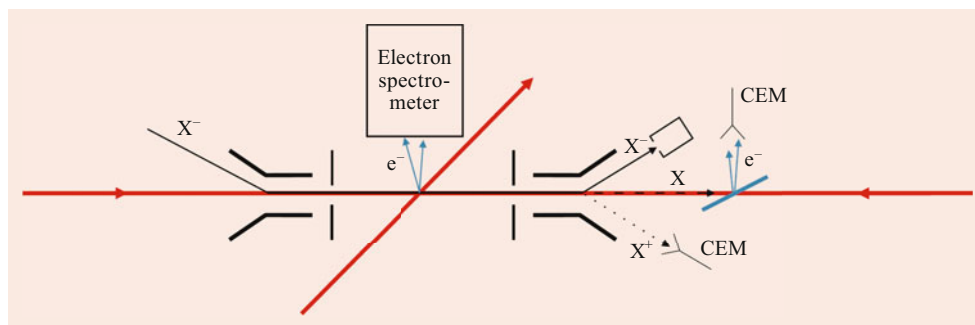
The most common method used for spectroscopic studies of negative ions is to form a unidirectional beam in an accelerator. Here, the ions are extracted from the ion source and focused to form a collimated beam that is accelerated to a desired energy of typically 1–30 keV. A bending magnet is used to select a single mass beam that is essentially monoenergetic. The ions then drift to the interaction region through a beamline that is maintained at low pressure to minimize destructive collisions with the residual gas. Negative ions have also been injected into storage rings, where repeated passes through the interaction region take place.

The well-defined spatial dimensions of an ion beam readily permit an efficient overlap with a beam of photons. Figure 64.2 schematically shows two different geometries that have been used in photodetachment measurements. If the ion and laser beam are merged collinearly, the product particle that is usually detected is the residual atom [46]. In this geometry, the laser beam can be either copropagating or counterpropagating with respect to the ion beam. If, however, the two beams are crossed with respect to each other, either the residual atom or the photoelectrons are detected.

The crossed beam arrangement is best suited for spectroscopic and angular distribution studies of the detached photoelectrons since they are, in this case, collected from a spatially well-defined interaction region. Further, crossed beams are advantageously used for absolute cross section measurements using the so-called animated beams method [47]. Here, the overlap of the ion and photon beam is determined by sweeping the laser beam through the ion beam.

The collinear beam arrangement, on the other hand, yields the best energy resolution. In almost all collinear beam experiments, the residual atoms have constituted the signal. The sensitivity of a measurement is significantly enhanced by the use of the large interaction volume defined by the collinear laser and ion beams. The energy resolution is determined by the convolution of the laser bandwidth and the Doppler broadening. Doppler broadening is the result of the divergence of both the ion and laser beams and the longitudinal velocity spread of the ions that originates from the motion

Fig. 64.2 Schematic showing both the crossed and collinear beam geometries. Negative ions (solid black line) are bent twice using two electrostatic deflectors. The trajectories of positive ions (dotted black line), neutral atoms (dashed black line), photoelectrons (blue lines), and the laser beam (red lines) are also shown. CEM represents “channel electron multiplier” detectors



of the ions in the ion source. The broadening due to the divergences of the two beams is greatly reduced by the use of a collinear interaction geometry. In this case, the derivative of the Doppler angle is zero since the two beams are superimposed at a crossing angle of zero. Furthermore, the longitudinal velocity spread is compressed in the collinear geometry [48]. In collinear beam experiments, the energy resolution will essentially be determined by the bandwidth of the light source. There will remain, however, a Doppler shift of the center-of-mass energy arising from the fast-moving ions. This energy shift can be determined experimentally by performing separate experiments, one with the ion and laser beams parallel and another with them antiparallel. The corrected energy can then be determined, to all orders, by taking the geometric mean of the two results [49].

64.3.3 Light Sources

Most photodetachment experiments to date have been performed using lasers. CW lasers have been used for high-resolution studies but, nowadays, pulsed lasers are most often preferred. The large peak powers characteristic of pulsed lasers are a necessity in, for example, multiphoton experiments. Lasers, in combination with nonlinear techniques such as frequency doubling or optical parametric oscillators, are used in photodetachment experiments to span a wavelength range from the ultraviolet to the infrared. Optical parametric oscillators have also become available commercially. In order to investigate inner shell excitation and detachment processes it is necessary to access the VUV or X-ray region. These regions are still outside the limits of conventional lasers and can only be accessed at synchrotron radiation or free-electron laser facilities.

64.3.4 Detection Schemes

Photodetachment events are usually monitored by detecting the particles (electrons, atoms, or positive ions) produced in the breakup of the negative ion. The heavy residual particles, atoms or positive ions, can be detected in both crossed and collinear beam experiments. The neutral atoms are efficiently detected by allowing them to impact on a solid target [50]. The secondary electrons thus produced can then be detected and used as the signal. The major source of background arises from collisions of the negative ions with the atoms and molecules of the residual gas in the vacuum chamber. By maintaining a high vacuum, typically 10^{-9} mbar or better, the background contribution can be kept at a tolerable level. The signal-to-noise ratio can be further enhanced by using time-gated detection, which becomes possible if a pulsed laser is used. The selectivity and sensitivity of a measurement is im-

proved significantly if the residual atoms are state-selectively detected, i.e., by performing a partial cross section measurement. This can be achieved using the method of resonance ionization spectroscopy [42]. Here, a second laser is used to excite the residual atom to a state near the ionization limit. This resonance step is followed by electric field ionization of the high-lying, Rydberg state. In this case, the resulting positive ions constitute the signal.

An alternative scheme for monitoring photodetachment events involves the detection of photoelectrons. This method is the most efficient if the laser and ion beams are perpendicularly crossed. The total cross section is measured by detecting the yield of photoelectrons, whereas the partial and differential cross sections are obtained by measuring their energy and angular distributions, respectively. Initially, electrostatic analyzers [51] and time-of-flight (TOF) spectrometers [52] were used in such studies. However, more recent measurements have favored a velocity mapping imaging (VMI) technique [53]. In a VMI spectrometer, an electric field is applied to the interaction region to guide all of the emitted electrons onto a position-sensitive detector. Velocity and angular information can be determined from the position on the detector, allowing both energy-resolved and angle-resolved measurements with a detection efficiency approaching 100%.

64.4 Measuring Properties of Negative Ions

64.4.1 Electron Affinities

Initially, most electron affinities (EA) were determined using photoelectron spectroscopy since such experiments could be conducted with a fixed-frequency laser, as long as the photon energy exceeded the EA . More recent EA measurements, however, involve the laser photodetachment threshold (LPT) method. Here, the normalized yield of residual atoms arising from photodetachment is recorded as a function of the photon energy in the near-threshold region of the cross section. The threshold position is obtained by fitting the Wigner law (Eq. (64.1)) to the data. The threshold can be accurately determined if a p-orbital electron is detached into a pure s-wave continuum. Then, according to the Wigner law, a sharp $E^{1/2}$ energy dependence at threshold is predicted. For many elements, however, an s-wave threshold is either not accessible within the energy range of the available laser, or the lowest energy process involves the detachment of an s-orbital electron. In the latter case, the cross section near threshold will exhibit a slowly rising onset, characteristic of a p-wave continuum. Under such circumstances, a high-resolution study of the EA would require access to an excited state threshold in order to detach into an s-wave continuum. The residual atom will then be left in a specific excited state, which can be detected using the RIS method, as was the case of K^- , shown

in Fig. 64.1b. This technique has been applied, for example, to negative ions of the alkalis [25], alkaline earths [42], and helium [17]. Until recently, all LPT measurements involved stable negative ions. However, the method has now been used at the CERN facility to make the first measurements of the electron affinity of a radioactive atom, in this case the radioactive isotope ^{128}I [54] and ^{211}At [55].

The LPT method has been used to accurately determine the electron affinities of many atoms. However, the most accurate affinity measurements to date have been performed using the photodetachment microscope method, pioneered by *Blondel* et al. [56]. Here, the photodetachment takes place in the presence of a weak electric field that provides two paths for the detached electron to travel from the interaction region to a position sensitive detector. In addition to yielding the highest resolution, the method also provides a beautiful demonstration of quantum interference.

The electron affinities of the atoms of the elements was last reviewed in 1999 by *Andersen, Haugen, and Hotop* [8]. *Blondel* is currently maintaining an updated list [57].

64.4.2 Bound States

Long-lived excited states of negative ions with the same parity as the ground state are known to exist. For example, the simplest, associated with the ground state configuration, would be excited fine structure levels and those arising from term splitting. More highly excited metastable states, with different electron configurations but the same parities as the ground state, are also present in a number of negative ions. The energy of such states has been determined using electron spectroscopy [58]. These states are long lived since they can only radiate via forbidden radiative transitions driven by M1, E2, or even higher-order processes. The principal method of measuring the lifetimes of these long-lived states is to use an ion storage ring. The time-varying population of the excited state due to radiative decay can be sampled by laser photodetachment on each trajectory around the ring [59]. The latest measurements have been performed at DESIREE in Stockholm, which is cryogenically cooled to an operating temperature of 13 K, resulting in an extremely low background pressure of 10^{-14} mbar. Such an environment greatly reduces the destruction of the negative ions by particle collisions. The longest lifetime observed so far, obtained in a study of S^- , is 503 ± 54 s [43]. More recently such experiments are now also conducted at the CSR storage ring in Heidelberg [60].

Until relatively recently, it was thought that bound excited states of negative ions that were able to radiate via allowed electric dipole transitions, were nonexistent. Now, however, it has been shown that such states are present in at least three ions, Os^- , [9] Ce^- [10], La^- [11] and Th^- [12]. The first clear observation of a bound-bound transition in a negative

ion was made on Os^- by *Bilodeau and Haugen* [9]. La^- was first studied using photoelectron spectroscopic methods to determine the energies of several of these bound states [61]. In a more recent photodetachment experiment, *Walter* et al. [11] used a crossed beams geometry to identify excited bound states in La^- . A two-step process was employed in which the first photon was used to excite the ion to an intermediate bound state, and a second photon was used to detach an electron from the ion in this state. One of the observed resonances was identified with the intermediate $^3\text{D}_1$ odd parity state that was excited from the $^3\text{F}_2$ even parity ground state. More recently, *Kellerbauer* et al. [62] showed, by performing a high resolution experiment, that this transition is a promising candidate for laser cooling. In 2019 *Tang* et al. [12] showed that also in Th^- there exist an electric dipole transition. Laser cooling of negative ions is of considerable interest to the antimatter physics community since, potentially, it could be used to sympathetically cool antiprotons.

64.4.3 Continuum Processes

Detachment continua contain a wealth of structure, and many Feshbach resonances in negative ions have been studied. The simplest negative ion is the two-electron H^- ion. This three-body Coulomb system is fundamentally important in our understanding of the role played by electron correlation in the atomic structure. The pioneering measurements of the photodetachment of one and two electrons from the H^- ion were performed by *Bryant* and coworkers [63, 64]. In this work, the ion-frame photon energy was scanned by Doppler tuning the angle between a relativistic H^- beam and a laser beam. ASTRID (Aarhus Storage Ring Denmark) was later used in two measurements of resonance structure in H^- with much higher resolution than the previous measurements [65, 66]. Subsequent, collinear beam experiments by *Hanstorp* and coworkers revealed resonance structure in the photodetachment continua of the metastable He^- ion [67] and the alkali-metal negative ions [68, 69].

Synchrotron radiation has been used over the past few years in order to study how negative ions respond to the absorption of high-energy photons. Photons in the VUV and X-ray regions will excite and/or detach inner shell electrons. Multiple electron detachment appears to be initiated by the excitation of a core electron. This process triggers the ejection of one or more valence electrons, either by shake-off or by interactions of the detached core electron with the valence electrons as it leaves the atom. For example, measurements of the absolute cross sections for the detachment of two electrons from the closed shell ions Cl^- [38] and Li^- [39] have been reported. The Advanced Light Source (ALS) has been used to investigate resonance structure and multielectron detachment processes, where, for instance, resonances

associated with the photodetachment of inner-shell electrons have been observed in K^- [70] and He^- [71]. Currently, the most intense light source in the UV regime is the free-electron laser (FEL). *Pedersen* and coworkers used a FEL to study the branching of single-to-double detachment in the photodetachment of O^- [41]. The intense light pulse from the FEL permitted the photoelectron spectrum to be studied using a magnetic bottle spectrometer. More recently, multiphoton detachment of negative ions are also conducted at the PETRA III synchrotron radiation source [40].

64.5 Investigation of Fundamental Processes

A weakly bound quantum system such as a negative ion allows one to study fundamental photon-ion interactions in atomic physics.

64.5.1 Threshold Studies

The photodetachment threshold, as described by Wigner (Eq. (64.1)), is unique in the sense that an atomic process can be described with a very simple analytical expression. Small deviations from this law can be used to observe various physical processes. For example, *Larson* and coworkers applied this approach to negative ions in order to study the fundamental problem of particle breakup in magnetic [72] and electrical [73] fields. Small oscillations in the threshold cross sections were observed superimposed on the normal Wigner behavior.

Atomic dipole polarizabilities are normally positive (as would be expected from a classical model of a dipole in an electric field). However, in certain special cases, an atomic polarizability can be negative, which can only be explained in a quantum context. In recent experiments involving the photodetachment of K^- [74] and Na^- [75], anomalous threshold behavior was observed in which the onset of the photodetachment process occurred at a photon energy well above the predicted threshold energy. This was attributed to the fact that the highest members of a manifold of excited states in alkali atoms have a negative polarizability. In such cases, the Wigner law is no longer valid.

64.5.2 Photodetachment Using Short Laser Pulses

The combination of a weakly bound quantum system such as a negative ion and the strong electric fields associated with intense laser radiation is suitable for fundamental investigations of multiphoton detachment processes. The internal structures of the negative ions of hydrogen and the halogens

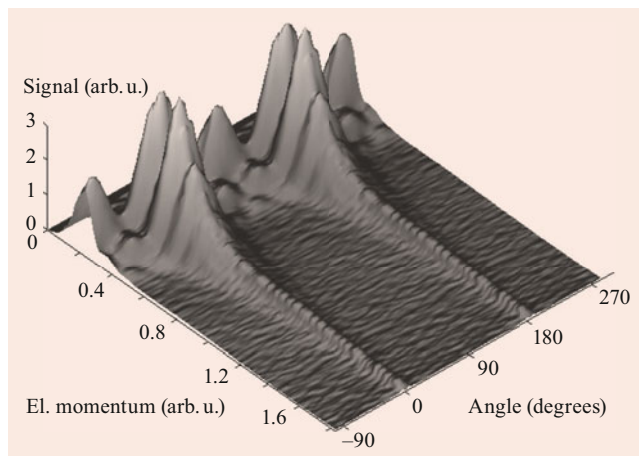


Fig. 64.3 Momentum and angular distributions observed in the strong laser field-induced photodetachment of Br^- . Reprinted with permission from [76]. Copyright 2008 by American Physical Society

are particularly suited for such experiments since the initial state is well defined. In addition, long-range $1/r$ potentials are absent in the final state arising from photodetachment.

Kiyan et al. [53] conducted a number of experiments on multiphoton detachment using a velocity-mapping imaging technique. For example, they used intense femtosecond laser pulses to study excess photon detachment (EPD) in the F^- ion, in which many more photons were absorbed than were necessary to reach the detachment threshold [37]. It was also observed that the angular distribution of the ejected photoelectrons became highly directional along the laser polarization vector, as can be seen in the case of EPD of Br^- shown in Fig. 64.3 [76].

Kiyan et al. also used the photodetachment process to create a ground state atom in carbon [77] and silicon [78] that was in a superposition of its fine structure levels. In this superposition state, the atom exhibited spatial oscillations. The oscillations were monitored by applying a second laser, in a pump-probe arrangement, to photoionize the atom.

64.6 Observations and Applications of Negative Ions

Negative ions occur naturally, in both astrophysical environments (plasma state) and terrestrial environments (matter in the liquid and gaseous phases). They also play a role in numerous applications.

64.6.1 Natural Occurrence of Negative Ions

Negative ions are difficult to detect in natural environments due to the rarity of bound excited states and, consequently, the lack of emission/absorption spectra. One of the first iden-

tifications of negative ions in nature was made by *Wildt* in 1939 [79]. He suggested that absorption seen in the black-body radiation spectrum from the sun was the result of photodetachment of H^- in the photosphere. This prediction was confirmed in subsequent calculations and experiments by *Branscomb* and *Smith* [80]. In 2006, the CH_6^- ion was detected in the interstellar medium [81]. This first identification was followed by the observation of other ions in the following years [82]. In addition, negative ions occur in abundance both in liquids, where Cl^- ions in the sea is the most obvious example, and in gases, such as in the Earth's atmosphere.

64.6.2 Applications of Negative Ions

Negative ions have a role in numerous applications. Several applications are based on the fact that the outermost electron in a negative ion is weakly bound and, therefore, easy to remove. For example, in the field of thermonuclear fusion, a commonly used method of heating the plasma in a tokamak reactor is to inject an intense, high-energy beam of neutralized D^- ions. The removal of the outermost electron has so far been achieved by the use of particle collisions; however, the process could be made more efficient if photodetachment were used [83]. The same neutralization principle has also been used to produce fast beams of atoms for particle collision experiments [84]. Currently, one of the most important applications of negative ions is in the field of accelerator mass spectrometry (AMS) [85], which is the most sensitive method for trace element analysis. AMS is based on a tandem accelerator, in which a beam of negative ions produced at the low-energy end of the accelerator is converted into positive ions at the high-voltage terminal. In many cases, however, a major limitation on sensitivity is the presence of interfering atomic isobars in the beam leaving the ion source. The photodetachment process has the potential to overcome such problems by overlapping the negative ions beam with a laser beam prior to injection into the tandem accelerator. The interfering isobar can then be removed from the ion beam by photodetachment provided that the EA of the isobar of interest is larger than the interfering isobar. However, photodetachment cross sections are, unfortunately, typically small due to the nonresonant nature of the bound-free process. As a consequence, only a small fraction of the interfering isobar will normally be detached, even when a powerful laser is employed in a collinear geometry. One viable solution to this problem is to slow down the ion beam in an RF cooler in order to increase the interaction time. It has been shown that using photodetachment in combination with an RF cooler can reduce the presence of an interfering isobar by many orders of magnitude [86]. A successful proof-of-principle of this method has been performed at the VERA facility in Vienna, [87].

References

1. Massey, H.S.: *Negatives Ions*. Cambridge University Press, Cambridge (1976)
2. Smirnov, B.M.: *Negative Ions*. McGraw-Hill, New York (1982)
3. Bates, D.R.: *Negative Ions: Structure and Spectra*. *Adv. At. Mol. Opt. Phys.* **27**, 1–80 (1991)
4. Andersen, T.: Atomic negative ions: Structure, dynamics and collisions. *Phys. Rep.* **394**(4-5), 157–313 (2004)
5. Pegg, D.J.: Structure and dynamics of negative ions. *Rep. Prog. Phys.* **67**(6), 857–905 (2004)
6. Rienstra-Kiracofe, J.C., Tschumper, G.S., Schaefer, H.F., Nandi, S., Ellison, G.B.: Atomic and molecular electron affinities: photoelectron experiments and theoretical computations. *Chem. Rev.* **102**(1), 231–282 (2002)
7. Fano, U.: Correlations of two excited electrons. *Rep. Prog. Phys.* **46**(2), 97–165 (1983)
8. Andersen, T., Haugen, H.K., Hotop, H.: Binding energies in atomic negative ions: III. *J. Phys. Chem. Ref. Data* **28**(6), 1511–1533 (1999)
9. Bilodeau, R.C., Haugen, H.K.: Experimental studies of Os^- : Observation of a bound-bound electric dipole transition in an atomic negative ion. *Phys. Rev. Lett.* **85**(3), 534–537 (2000)
10. Walter, C.W., Gibson, N.D., Janczak, C.M., Starr, K.A., Snedden, A.P., Field, R.L., Andersson, P.: Infrared photodetachment of Ce^- : threshold spectroscopy and resonance structure. *Phys. Rev. A* **76**(5), 052702 (2007)
11. Walter, C.W., Gibson, N.D., Matyas, D.J., Crocker, C., Dungan, K.A., Matola, B.R., Rohlén, J.: Candidate for laser cooling of a negative ion: observations of bound-bound transitions in La^- . *Phys. Rev. Lett.* **113**(6), 063001 (2014)
12. Tang, R., Si, R., Fei, Z., Fu, X., Lu, Y., Brage, T., Liu, H., Chen, C., Ning, C.: Candidate for laser cooling of a negative ion: High-resolution photoelectron imaging of Th^- . *Phys. Rev. Lett.* **123**(20), 203002 (2019)
13. Pegg, D.J., Thompson, J.S., Compton, R.N., Alton, G.D.: Evidence for a stable negative ion of calcium. *Phys. Rev. Lett.* **59**(20), 2267–2270 (1987)
14. Petrunin, V.V., Andersen, H.H., Balling, P., Andersen, T.: Structural properties of the negative calcium ion: Binding energies and fine-structure splitting. *Phys. Rev. Lett.* **76**(5), 744–747 (1996)
15. Tang, C.Y., Wood, J.R., Pegg, D.J., Dellwo, J., Alton, G.D.: Photodetachment and autodetachment of the Be^- ion. *Phys. Rev. A* **48**(3), 1983–1986 (1993)
16. Reinhd, P., Orbán, A., Werner, J., Rosén, S., Thomas, R.D., Kashperka, I., Johansson, H.A.B., Misra, D., Brännholm, L., Björkhaug, M., Cederquist, H., Schmidt, H.T.: Precision lifetime measurements of He^- in a cryogenic electrostatic ion-beam trap. *Phys. Rev. Lett.* **103**(21), 213002 (2009)
17. Kristensen, P., Pedersen, U.V., Petrunin, V.V., Andersen, T., Chung, K.T.: Binding energy of the metastable He^- ion. *Phys. Rev. A* **55**(2), 978–983 (1997)
18. Hall, J.L., Robinson, E.J., Branscomb, L.M.: Laser double-quantum photodetachment of I. *Phys. Rev. Lett.* **14**(25), 1013–1017 (1965)
19. Brehm, B., Gusinow, M.A., Hall, J.L.: Electron affinity of helium via laser photodetachment of its negative ion. *Phys. Rev. Lett.* **19**(13), 737–741 (1967)
20. Hall, J.L., Siegel, M.W.: Angular dependence of the laser photodetachment of the negative ions of carbon, oxygen, and hydrogen. *J. Chem. Phys.* **48**(2), 943–945 (1968)
21. Lineberger, W.C., Woodward, B.W.: High resolution photodetachment of S^- near threshold. *Phys. Rev. Lett.* **25**(7), 424 (1970)
22. Hotop, H., Patterson, T.A., Lineberger, W.C.: High-resolution photodetachment study of Se^- ions. *Phys. Rev. A* **8**(2), 762–774 (1973)

23. Liu, C.-N., Starace, A.F.: Photodetachment of Na. *Phys. Rev. A* **59**(5), 3643–3654 (1999)
24. Moores, D.L., Norcross, D.W.: Alkali-metal negative ions. I. Photodetachment of Li^- , Na^- , and K. *Phys. Rev. A* **10**(5), 1646–1657 (1974)
25. Andersson, K.T., Sandström, J., Kiyani, I.Y., Hanstorp, D., Pegg, D.J.: Measurement of the electron affinity of potassium. *Phys. Rev. A* **62**(2), 022503 (2000)
26. Radojević, V., Kelly, H.P., Johnson, W.R.: Photodetachment of negative halogen ions. *Phys. Rev. A* **35**(5), 2117–2121 (1987)
27. Rau, A.R.P.: Threshold laws. *Comments At. Mol. Phys.* **14**, 285–306 (1984)
28. Wigner, E.P.: On the behavior of cross sections near thresholds. *Phys. Rev.* **73**(9), 1002–1009 (1948)
29. O'Malley, T.F.: Effect of long-range final-state forces on the negative-ion photodetachment cross section near threshold. *Phys. Rev.* **137**(6A), 1668–1672 (1965)
30. Watanabe, S., Greene, C.H.: Atomic polarizability in negative-ion photodetachment. *Phys. Rev. A* **22**(1), 158–169 (1980)
31. Fano, U.: Effects of configuration interaction on intensities and phase shifts. *Phys. Rev.* **124**(6), 1866–1878 (1961)
32. Cooper, J., Zare, R.N.: Angular distribution of photoelectrons. *J. Chem. Phys.* **48**, 942–943 (1968)
33. Thompson, J.S., Pegg, D.J., Compton, R.N., Alton, G.D.: Angular distributions of electrons from the photodetachment of metastable He^- . *J. Phys. B: At. Mol. Opt. Phys.* **23**, L15–L19 (1990)
34. Lee, D.H., Brandon, W.D., Pegg, D.J., Hanstorp, D.: Cross section for photodetachment of the excited C^- (2D) ion using fast ion-laser-beam electron spectroscopy. *Phys. Rev. A* **56**(2), 1346–1350 (1997)
35. Hanstorp, D., Bengtsson, C., Larson, D.J.: Angular distributions in photodetachment from O^- . *Phys. Rev. A* **40**(2), 670 (1989)
36. Blondel, C.: Recent experimental achievements with negative ions. *Phys. Scr.* **T58**, 31–42 (1995)
37. Bergues, B., Ansari, Z., Hanstorp, D., Kiyani, I.Y.: Photodetachment in a strong laser field: An experimental test of Keldysh-like theories. *Phys. Rev. A* **75**(6), 063415 (2007)
38. Aguilar, A., Thompson, J., Calabrese, D., Covington, A., Cisneros, C., Davis, V., Gulley, M., Halka, M., Hanstorp, D., Sandström, J., McLaughlin, B., Pegg, D.: Double photodetachment from the Cl^- ion. *Phys. Rev. A* **69**(2), 022711 (2004)
39. Kjeldsen, H., Andersen, P., Folkmann, F., Kristensen, B., Andersen, T.: Inner-shell photodetachment of Li^- . *J. Phys. B: At. Mol. Opt. Phys.* **34**(10), L353–L357 (2001)
40. Perry-Sassmannshausen, A., Buhr, T., Martins, M., Reinwardt, S., Trinter, F., Müller, A., Fritzsche, S., Schippers, S.: Multiple photodetachment of silicon anions via K -shell excitation and ionization. *Phys. Rev. A* **104**, 053107 (2021)
41. Harbo, L.S., Becker, A., Dziarzhyski, S., Domesle, C., Guerasimova, N., Wolf, A., Pedersen, H.B.: Single and double electron photodetachment from the oxygen anion at 41.7 nm. *Phys. Rev. A* **86**(2), 023409 (2012)
42. Petrunin, V.V., Voldstad, J.D., Balling, P., Kristensen, P., Andersen, T., Haugen, H.K.: Resonant ionization spectroscopy of Ba^- : Metastable and stable ions. *Phys. Rev. Lett.* **75**(10), 1911–1914 (1995)
43. Bäckström, E., Hanstorp, D., Hole, O.M., Kaminska, M., Nascimento, R.F., Blom, M., Björkhage, M., Källberg, A., Löfgren, P., Reinhd, P., Rosén, S., Simonsson, A., Thomas, R.D., Mannervik, S., Schmidt, H.T., Cederquist, H.: Storing keV negative ions for an hour: the lifetime of the metastable $^2P_{1/2}^o$ level in $^{32}\text{S}^-$. *Phys. Rev. Lett.* **114**(14), 143003 (2015)
44. Middleton, R.: A versatile high intensity negative ion source. *Nucl. Instrum. Methods Phys. Res.* **214**(2-3), 139–150 (1983)
45. Mead, R.D., Hefter, U., Schulz, P.A., Lineberger, W.C.: Ultrahigh resolution spectroscopy of C^{2-} : The $\text{A}2\text{-}\pi\text{-u}$ state characterized by deperturbation methods. *J. Chem. Phys.* **82**(4), 1723–1731 (1985)
46. Hanstorp, D.: An ion beam apparatus for collinear photodetachment experiments. *Nucl. Instrum. Methods Phys. Res. B* **100**, 165–175 (1995)
47. Génévriez, M., Urbain, X.: Animated-beam measurement of the photodetachment cross section of H. *Phys. Rev. A* **91**(3), 033403 (2015)
48. Kaufman, S.L.: High-resolution laser spectroscopy in fast beams. *Opt. Commun.* **17**(3), 309–312 (1976)
49. Juncar, P., Bingham, C.R., Bounds, J.A., Pegg, D.J., Carter, H.K., Mlekodaj, R.L., Cole, J.D.: New method to measure the relativistic doppler shift: first results and a proposal. *Phys. Rev. Lett.* **54**(1), 11–13 (1985)
50. Hanstorp, D.: A secondary emission detector capable photoelectric effect induced by pulsed. *Meas. Sci. Technol.* **3**, 523–527 (1992)
51. Frey, P., Breyer, F., Hotop, H.: High resolution photodetachment from the rubidium negative ion around the $\text{Rb}(5p\ 1/2)$ threshold. *J. Phys. B: At. Mol. Phys.* **11**(19), L589–L594 (1978)
52. Haefliger, G., Ljungblad, U., Kiyani, I.Y., Hanstorp, D.: Fine structure of As^- . *Z. Phys.* **D**, 4 (1997)
53. Kiyani, I.Y., Helm, H.: Production of Energetic Electrons in the Process of Photodetachment Process of F^- . *Phys. Rev. Lett.* **90**(18), 183001 (2003)
54. Rothe, S., Sundberg, J., Welander, J., Chrysalidis, K., Day Goodacre, T., Fedosseev, V., Fiotakis, S., Forstner, O., Heinke, R., Johnston, K., Kron, T., Köster, U., Liu, Y., Marsh, B., Ringvall-Moberg, A., Rossel, R.E., Seiffert, C., Studer, D., Wendt, K., Hanstorp, D.: Laser photodetachment of radioactive $^{128}\text{I}^-$. *J. Phys. G: Nucl. Part. Phys.* **44**(10), 104003 (2017)
55. Leimbach, D., Karls, J., Guo, Y., Ahmed, R., Ballof, J., Bengtsson, L., Boix Pamies, F., Borschevsky, A., Chrysalidis, K., Eliav, E., Fedorov, D., Fedosseev, V., Forstner, O., Galland, N., Garcia Ruiz, R.F., Granados, C., Heinke, R., Johnston, K., Koszorus, A., Köster, U., Kristiansson, M.K., Liu, Y., Marsh, B., Molkanov, P., Pašteka, L.F., Ramos, J.P., Renault, E., Reponen, M., Ringvall-Moberg, A., Rossel, R.E., Studer, D., Vernon, A., Warbinek, J., Welander, J., Wendt, K., Wilkins, S., Hanstorp, D., Rothe, S.: The electron affinity of astatine. *Nature. Comm.* **11**(1) 3824 (2020)
56. Blondel, C., Delsart, C., Dulieu, F.: The photodetachment microscope. *Phys. Rev. Lett.* **77**(18), 3755–3758 (1996)
57. Blondel, C.: https://en.wikipedia.org/wiki/Electron_affinity_data_page
58. Feiglerle, C.S., Corderman, R.R., Bobashev, S.V., Lineberger, W.C.: Binding energies and structure of transition metal negative ions. *J. Chem. Phys.* **74**(3), 1580–1598 (1981)
59. Ellmann, A., Schef, P., Lundin, P., Royen, P., Mannervik, S., Fritioff, K., Andersson, P., Hanstorp, D., Froese Fischer, C., Österdahl, F., Pegg, D., Gibson, N., Danared, H., Källberg, A.: Radiative lifetime of a bound excited state of Te^- . *Phys. Rev. Lett.* **92**(25), 253002 (2004)
60. Müll, D., Grussie, F., Blaum, K., George, S., Göck, J., Grieser, M., von Hahn, R., Harman, Z., Kálosi, Á., Keitel, C.H., Krantz, C., Lyu, C., Novotný, O., Nuesslein, F., Paul, D., Schmidt, V.C., Singh, S., Sunil Kumar, S., Urbain, X., Wolf, A., Kreckel, H.: Metastable states of Si^- observed in a cryogenic storage ring. *Phys. Rev. A* **104**, 032811 (2021)
61. Covington, A.M., Calabrese, D., Thompson, J.S., Kvale, T.J.: Measurement of the electron affinity of lanthanum. *J. Phys. B: At. Mol. Opt. Phys.* **31**, L855–L860 (1998)
62. Jordan, E., Cerchiari, G., Fritzsche, S., Kellerbauer, A.: High-resolution spectroscopy on the laser-cooling candidate La^- . *Phys. Rev. Lett.* **115**(11), 113001 (2015)

63. Bryant, H.C., Dieterle, B.D., Donahue, J., Sharifian, H., Tootoonchi, H., Wolfe, D.M., Gram, P.A.M., Yates-Williams, M.A.: Observation of resonances near 11 eV in the photodetachment cross section of the H^- ion. *Phys. Rev. Lett.* **38**(5), 228–230 (1977)
64. Harris, P.G., Bryant, H.C., Mohagheghi, A.H., Reeder, R.A., Tang, C.Y., Donahue, J.B., Quick, C.R.: Observation of doubly excited resonances in the H^- ion. *Phys. Rev. A* **42**(11), 6443–6465 (1990)
65. Balling, P., Kristiansen, P., Pedersen, U.V., Petrunin, V.V., Præstegaard, L., Haugen, H.H., Andersen, T.: Vacuum ultraviolet spectroscopy of H^- in a heavy ion storage ring; the region near $H(n=2)$. *Phys. Rev. Lett.* **77**(14), 2905–2908 (1996)
66. Balling, P., Andersen, H., Brodie, C., Pedersen, U., Petrunin, V., Raarup, M., Steiner, P., Andersen, T.: High-resolution VUV spectroscopy of H^- in the region near the $H(n=2)$ threshold. *Phys. Rev. A* **61**(2), 022702 (2000)
67. Klinkmüller, A.E., Haeffler, G., Hanstorp, D., Kiyani, I.Y., Berzinsh, U., Pegg, D.J.: Photodetachment study of quartet resonances below the thresholds. *J. Phys. B: At. Mol. Opt. Phys.* **31**(11), 2549–2557 (1998)
68. Berzinsh, U., Haeffler, G., Hanstorp, D., Klinkmüller, A.E., Lindroth, E., Ljungblad, U., Pegg, D.J.: Resonance structure in the Li^- photodetachment cross section. *Phys. Rev. Lett.* **74**(24), 4795–4798 (1995)
69. Kiyani, I.Y., Berzinsh, U., Sandström, J., Hanstorp, D., Pegg, D.: Spectrum of doubly excited states in the K^- ion. *Phys. Rev. Lett.* **84**(26), 5979–5982 (2000)
70. Covington, A.M., Kraus, R.G., Emmons, E.D., Duvvuri, S.S., Davis, V.T., Calabrese, D., Davis, D.D., Cisneros, C., Schlachter, A.S., Gulley, M.S., Hanstorp, D., Thompson, J.S., Pegg, D.J.: Inner-shell photodetachment from the K^- ion. *J. Phys. B: At. Mol. Opt. Phys.* **40**(5), 935–942 (2007)
71. Bilodeau, R.C., Bozek, J.D., Aguilar, A., Ackerman, G.D., Turri, G., Berrah, N.: Photoexcitation of He^- hollow-ion resonances: Observation of the $2s2p\ 4P$ state. *Phys. Rev. Lett.* **93**(19), 193001 (2004)
72. Elmquist, R.E., Edge, C.J., Fletcher, G.D., Larson, D.J.: Observation of resolved Zeeman thresholds in photodetachment in a magnetic field. *Phys. Rev. Lett.* **58**(4), 333–336 (1987)
73. Gibson, N.D., Davies, B.J., Larson, D.J.: s-wave photodetachment in a static electric field. *Phys. Rev. A* **47**(3), 1946–1952 (1993)
74. Lindahl, A.O., Rohlén, J., Hultgren, H., Kiyani, I.Y., Pegg, D.J., Walter, C.W., Hanstorp, D.: Threshold photodetachment in a repulsive potential. *Phys. Rev. Lett.* **108**(3), 033004 (2012)
75. Rohlén, J., Lindahl, A.O., Hultgren, H., Thomas, R.D., Pegg, D.J., Hanstorp, D.: Threshold behaviour in photodetachment into a final state with large negative polarizability. *Europhys. Lett.* **106**(5), 53001 (2014)
76. Bergues, B., Kiyani, I.Y.: Two-electron photodetachment of negative ions in a strong laser field. *Phys. Rev. Lett.* **100**(14), 143004 (2008)
77. Hultgren, H., Eklund, M., Hanstorp, D., Kiyani, I.Y.: Electron dynamics in the ground state of a laser-generated carbon atom. *Phys. Rev. A* **87**(3), 031404 (2013)
78. Eklund, M., Hultgren, H., Hanstorp, D., Kiyani, I.Y.: Orbital alignment in atoms generated by photodetachment in a strong laser field. *Phys. Rev. A* **88**(2), 023423 (2013)
79. Wildt, R.: Negative ions of hydrogen and the opacity of stellar atmospheres. *Astrophys. J.* **90**, 611–620 (1939)
80. Branscomb, L.M., Smith, S.J.: Experimental cross section for photodetachment of electrons from H^- and D^- . *Phys. Rev.* **98**(4), 1028–1034 (1955)
81. McCarthy, M.C., Gottlieb, C.A., Gupta, H., Thaddeus, P.: Laboratory and astronomical identification of the negative molecular ion C_6H . *ApJ* **652**(2), L141–L144 (2006)
82. Millar, T.J., Walsh, C., Field, T.A.: Negative ions in space. *Chem. Rev.* **117**(3), 1765–1795 (2017)
83. Simonin, A., Agnello, R., Bechu, S., Bernard, J.M., Blondel, C., Boeuf, J.P., Bresteau, D., Cartry, G., Chaibi, W., Drag, C., Duval, B.P., De Esch, H.P.L., Fubiani, G., Furno, I., Grand, C., Guittienne, Ph., Howling, A., Jacquier, R., Marini, C., Morgal, I.: Negative ion source development for a photoneutralization based neutral beam system for future fusion reactors. *New J. Phys.* **18**(12), 125005 (2016)
84. Bruhns, H., Kreckel, H., Miller, K., Lestinsky, M., Serezyuk, B., Mitthumsiri, W., Schmitt, B.L., Schnell, M., Urbain, X., Rappaport, M.L., Havener, C.C., Savin, D.W.: A novel merged beams apparatus to study anion-neutral reactions. *Rev. Sci. Instrum.* **81**, 013112 (2010)
85. Kutschera, W.: Progress in isotope analysis at ultra-trace level by AMS. *Int. J. Mass. Spectrom.* **242**(2–3), 145–160 (2005)
86. Andersson, P., Lindahl, A.O., Hanstorp, D., Havener, C.C., Liu, Y., Liu, Y.: Nearly complete isobar suppression by photodetachment. *J. Appl. Phys.* **107**(2), 026102 (2010)
87. Martschini, M., Hanstorp, D., Lachner, J., Marek, C., Priller, A., Steier, P., Wasserburger, P., Golser, R.: The ILIAMS project – An RFQ ion beam cooler for selective laser photodetachment at VERA. *Nucl. Instrum. Methods Phys. Res.* **456**, 213–217 (2019)



David Pegg holds a BSc (Manchester, 1963) and a PhD (New Hampshire, 1970). He has worked at the University of Tennessee, Knoxville (1970–2006) with a research base at Oak Ridge National Laboratory (1971–2000). His research interests lie in the structure and dynamics of positive and negative ions. He has taken part in collaborative research at Lund, Lyon, Brookhaven, and Lawrence Berkeley National Laboratories and is in long-term collaboration with the University of Gothenburg.



Dag Hanstorp received his PhD at the University of Gothenburg in 1992 and now holds a professorship at the same university. He was Chairman of the Scientific Council for Natural and Engineering Sciences at the Swedish Research Council 2019–2021. His research is focused on laser spectroscopy of negative ions and optical levitation.



Denise Caldwell and Manfred Krause

Contents

65.1	Theoretical Concepts	955
65.1.1	Differential Analysis	956
65.1.2	Electron Correlation Effects	958
65.2	Experimental Methods	960
65.2.1	Synchrotron Radiation Source	961
65.2.2	Photoelectron Spectrometry	961
65.2.3	Resolution and Natural Width	963
65.3	Additional Considerations	964
References		965

Abstract

Theoretical and experimental aspects of the atomic photoelectric effect at photon energies up to about 1 keV are presented. Relevant formulae and interpretations are given for the various excitation and decay processes. Techniques and results of photoelectron spectrometry in conjunction with synchrotron radiation are emphasized.

Keywords

photoelectric effect · partial cross section · double ionization · natural width · Auger decay

65.1 Theoretical Concepts

Scattering of low-energy photons proceeds predominantly through the photoelectric effect. In this process a photon γ of

D. Caldwell (✉)
 Physics Division, National Science Foundation
 Alexandria, VA, USA
 e-mail: dcaldwel@nsf.gov

M. Krause
 Oak Ridge National Laboratory
 Oak Ridge, TN, USA
 e-mail: altefritz@comcast.net

energy $h\nu$, angular momentum $j_\gamma = 1$, and parity $\pi_\gamma = -1$ interacts with a free atom or molecule A , having total energy E_i , angular momentum J_i , and parity π_i to produce an electron of energy ε , spin $s = 1/2$, orbital angular momentum ℓ , total angular momentum j , and parity $\pi_e = (-1)^\ell$ and an ion A^+ with final total energy E_f , angular momentum J_f , and parity π_f . This process can be written as the reaction

$$\gamma(h\nu, j_\gamma = 1, \pi_\gamma = -1) + A(E_i, J_i, \pi_i) \rightarrow A^+(E_f, J_f, \pi_f) + e^-[\varepsilon, \ell s j, \pi_e = (-1)^\ell] . \quad (65.1)$$

Conservation laws require that

$$\begin{aligned} h\nu + E_i &= \varepsilon + E_f , \\ \mathbf{J}_i + \mathbf{j}_\gamma &= \mathbf{J}_f + \mathbf{s} + \boldsymbol{\ell} , \\ \pi_i \cdot \pi_\gamma &= \pi_f \cdot \pi_e = (-1)^\ell \cdot \pi_f . \end{aligned} \quad (65.2)$$

Since $E_f - E_i$ becomes quite large for inner shells or deep core levels, scattering of low-energy photons involves the removal of an electron from a valence or shallow core level. In the low-energy regime, from the first ionization threshold to $h\nu \approx 1$ keV, the photoelectric effect accounts for more than 99.6% of the photon interactions in the elements, with elastic scattering contributing the remainder [1, 2]. Ionization by inelastic scattering, the Compton effect, assumes increasing importance with the higher photon energies and the lower Z elements. Above the first ionization potential, the total photoabsorption cross section and the photoionization cross section are essentially equivalent at the lower photon energies.

The cross section σ_{if} for producing a given final ionic state in the photoionization process is given by

$$\sigma_{if} = \frac{4\pi^2\alpha^2}{k} \sum |\langle \Psi_f | \hat{T} | \Psi_i \rangle|^2 , \quad (65.3)$$

where k is the photon momentum, \hat{T} is the transition operator, Ψ_i and Ψ_f are the wave functions of the initial and final states, and the summation includes an average over all initial

states and a summation over all the unobserved variables in the final state. A detailed derivation of this expression, including the different forms for \hat{T} , is given in the articles by *Fano* and *Cooper* [3] and *Starace* [4] and in Chap. 25. The total cross section is given by the sum of all these different partial cross sections, σ_{if} .

65.1.1 Differential Analysis

Detailed information about the photoionization process can be obtained most directly in emission measurements, especially those involving the photoelectron. The resulting photoelectron spectrum yields the energy and intensity for a given interaction. Further differentiation is obtained by varying the angle of observation and by a spin analysis of the photoelectron. Hence, electron emission analysis can reveal all energetically allowed photoprocesses connecting an initial atomic state i to a final ionic state f and yield their dynamic properties. When averaged over the spin, the differential cross section $d\sigma_{if}/d\Omega$ is given in terms of the partial cross section σ_{if} and an expression involving an expansion in Legendre polynomials of order n with the coefficients B_n

$$\frac{d\sigma_{if}}{d\Omega} = \left(\frac{\sigma_{if}}{4\pi}\right) \sum_n B_n P_n(\cos\theta), \quad (65.4)$$

where the angle θ is measured between the direction of the emitted electron and the unpolarized incoming photon beam. In the *dipole* approximation, which describes the dominant process at low energy, only the terms containing P_0 and P_2 contribute. Then Eq. (65.4) reduces, for a photon beam with linear polarization p , to

$$\frac{d\sigma_{if}}{d\Omega} = \left(\frac{\sigma_{if}}{4\pi}\right) \left[1 + \frac{\beta_{if}}{4}(1 + 3p \cos 2\theta)\right], \quad (65.5)$$

where the angle θ lies in the plane perpendicular to the direction of propagation and is measured with respect to the major axis of the polarization ellipse [5]. Then, the differential cross section, or photoelectron angular distribution, is characterized by the single angular distribution or anisotropy parameter β_{if} for a particular process $i \rightarrow f$. For observation at the so-called pseudomagic angle θ_m , defined as

$$\theta_m = \frac{1}{2} \cos^{-1}\left(\frac{-1}{3p}\right), \quad (65.6)$$

the differential cross section $d\sigma_{if}/d\Omega$ becomes proportional to the angle-integrated, or partial, cross section σ_{if} .

In the absence of correlation effects, the partial cross section σ_{if} for the production of an individual final state and the corresponding anisotropy parameter β_{if} are given by simple

expressions derived from a single-particle model [1, 4]. For the central field potential,

$$\sigma_{if} = \frac{4\pi^2\alpha}{3} a_0^2 N_{n\ell} h\nu \times \left[\left(\frac{\ell}{2\ell+1}\right) R_-^2 + \left(\frac{\ell+1}{2\ell+1}\right) R_+^2 \right], \quad (65.7)$$

where $N_{n\ell}$ is the occupation number of the subshell, and

$$\beta_{if} = \frac{\ell(\ell-1)R_-^2 + (\ell+1)(\ell+2)R_+^2}{(2\ell+1)[\ell R_-^2 + (\ell+1)R_+^2]} - \frac{6\ell(\ell+1)R_+R_- \cos\Delta}{(2\ell+1)[\ell R_-^2 + (\ell+1)R_+^2]}. \quad (65.8)$$

The subscripts $+$ and $-$ refer to the $(\ell+1)$ and $(\ell-1)$ channels respectively, and $\Delta = \delta_+ - \delta_-$ is the difference in phase shift between these two allowed outgoing waves. The parameter R_{\pm} is the radial dipole matrix element connecting the electron in the bound orbital with orbital angular momentum ℓ with the outgoing wave having orbital angular momentum $\ell \pm 1$.

Effects of the electron correlation on the direct photoionization process can result in values for β which are not reproduced by the Cooper–Zare expression in Eq. (65.8) [4]. The contribution of the different partial waves to the outgoing wave function can, however, be ascertained through the angular momentum transfer formalism developed by *Fano* and *Dill* [6]. In this approach, one defines the angular momentum transferred from the photon to the unobserved variables j_t as

$$\mathbf{j}_t = \mathbf{j}_\gamma - \ell = \mathbf{J}_f + \mathbf{s} - \mathbf{J}_i, \quad (65.9)$$

where the second portion of the equality results from the conservation of angular momentum. For each allowed value of j_t the associated transfer can be defined as either parity favored or parity unfavored according to whether the product $\pi_i \pi_f$ is equal to $+(-1)^{j_t}$ or $-(-1)^{j_t}$ respectively. (All symbols have the same definition as in Eq. (65.1).) Calculation of the partial cross section for the production of a given final state characterized by the values \mathbf{J}_f and \mathbf{s} is then determined from the cross section corresponding to each angular momentum transfer according to

$$\sigma_{if} = \sum_{j_t} \sigma(j_t). \quad (65.10)$$

The associated anisotropy parameter β_{if} is derived from a similar sum

$$\sigma_{if} \beta_{if} = \sum_{j_t=\text{fav}} \sigma(j_t)_{\text{fav}} \beta(j_t)_{\text{fav}} - \sum_{j_t=\text{unfav}} \sigma(j_t)_{\text{unfav}}. \quad (65.11)$$

The second equation derives from the fact that $\beta(j_i)$ for each parity-favored value must be calculated separately, whereas for the parity-unfavored case $\beta(j_i) = -1$ always.

The physical effect described by the angular momentum transfer approach is the interaction between an electron and the anisotropic distribution of the other electrons in the atom. Thus, it becomes most useful in the case of ionization from an open-shell atom having an extra electron or a hole in a shell with $\ell \neq 0$. An illustrative example is the 3s ionization of chlorine. Here $\beta_{if} = 2$ identically in Eq. (65.8) because only the single value $\ell = 1$ is allowed in the single-particle model. However, the three possible values, $j_t = 0, 1, 2$ are allowed, of which only the first corresponds to the Cooper–Zare or single-particle, central field result [4]. That $\beta \neq 2$ for 3s ionization of atomic chlorine has been demonstrated experimentally [7].

It is generally the case for ionization of elements which are found naturally in the atomic state that there is an equal population in all the fine-structure components of the initial state. This is because of the relatively small energies associated with the fine-structure splitting. (This does not necessarily apply to atomic species generated through a process of molecular dissociation or high-temperature metal vaporization.) Thus, the determination of all cross sections and angular distributions involves an average over these fine-structure components. However, it is possible to generate atoms in which one of the fine-structure components is preferentially populated. In this case there can also be a preferential ionization to a particular J -component of the final ionic state even in the limit in which the electron correlation is neglected, i.e., the geometrical limit. The partial intensities for the production of a given ionic state characterized by the angular momenta $L_f S_f J_f$ by removal of an electron from an orbital ℓ of a state characterized by $L_i S_i J_i$ are given by

$$R_\ell^{L_f S_f J_f} = \frac{[J_f][L_f][S_f]}{[1/2][\ell]} g(\ell, L_i, S_i, L_f, S_f) \times \sum_{j=\ell-1/2}^{j=\ell+1/2} [j] \left\{ \begin{array}{ccc} \ell & 1/2 & j \\ L_i & S_i & J_i \\ L_f & S_f & J_f \end{array} \right\}^2. \quad (65.12)$$

Here the term in curly brackets is a 9- j symbol, and the notation $[J] = 2J + 1$ is used. The quantities $g(\ell, L_i, S_i, L_f, S_f)$ are weighting factors determined solely by the initial-state wave function. For the case in which ℓ represents a closed shell, these factors are equal to unity [8].

In situations in which the target atoms possess an initial orientation, i.e., have an average value $\langle J_z \rangle \neq 0$, or if the ionization is performed with circularly polarized radiation, the electrons which are produced have a net spin [9, 10]. It is also possible that unpolarized atoms which are ionized by unpolarized photons can have a net spin, provided that the

detection is carried out at a specific angle, and the ionization is from a given fine-structure component of the initial state to a given fine-structure component of the final state. In the latter case, the transverse spin polarization is given by

$$P = \frac{-2\xi \sin \theta \cos \theta}{1 + \beta P_2(\cos \theta)}, \quad (65.13)$$

for linearly polarized radiation, and by

$$P = \frac{2\xi \sin \theta \cos \theta}{2 - \beta P_2(\cos \theta)}, \quad (65.14)$$

for unpolarized radiation [11, 12]. The angle θ is the same as in the angular distribution measurement; the parameter ξ is the spin parameter analogous to β ; and $P_2(\cos \theta)$ is the Legendre polynomial of order 2.

Yet another parameter which describes the differentiation inherent in the photoionization process is the alignment A , which reflects an anisotropy in the quadrupole distribution of the angular momentum J_f of the ion [12]. For the cylindrically symmetric coordinate system appropriate to dipole photon excitation, only one moment A_0 of the distribution is nonzero. This is defined by

$$A_0 = \frac{\sum_{m_j} [3m_j^2 - J_f(J_f + 1)] \sigma(m_j)}{J_f(J_f + 1) \sum_{m_j} \sigma(m_j)}, \quad (65.15)$$

where $\sigma(m_j)$ is the partial cross section for production of a given m_j component of J_f . A very useful approach to the interpretation of the alignment can be obtained through the angular-momentum-transfer formalism [13]. In this approach the angular momentum transfer j_t is defined as

$$\mathbf{j}_t = \mathbf{j}_\gamma - \mathbf{J}_f. \quad (65.16)$$

In contrast to the case of the electron angular distribution, it is possible to derive an alignment for each value of j_t as a function of the angular momentum J_f of the ion. The net alignment is then the incoherent sum of the contributions corresponding to each

$$A_0 = \sum_{j_t} A_0(j_t) \sigma(j_t) / \sum_{j_t} \sigma(j_t). \quad (65.17)$$

If the photoionization produces an ion in an excited state which decays by photoemission, the parameter A_0 is reflected either in the angular distribution of the fluorescence photons $I(\theta)$ or the linear polarization P measured at one angle, typically 90° , according to

$$I(\theta) = I_0 \left[1 - \frac{1}{2} h^{(2)} A_0 P_2(\cos \theta) + \frac{3}{4} h^{(2)} A_0 \sin^2 \theta \cos(2\chi) \cos(2\eta) \right] \quad (65.18)$$

or, for $\theta = \pi/2$ and $\chi = 0$,

$$P = \frac{I(\eta = 0) - I(\eta = \pi/2)}{I(\eta = 0) + I(\eta = \pi/2)} = \frac{3h^{(2)}A_0}{4 + h^{(2)}A_0}, \quad (65.19)$$

respectively. The angle θ is the angle at which the fluorescence is determined, and the angle χ is measured between the axis of the polarization selected by the detector and the quantization axis. The polarization of the fluorescence is given by $\zeta = (\cos \eta, i \sin \eta, 0)$. The quantity $h^{(2)}$ is a ratio of $6-j$ symbols depending on the angular momenta J_f of the intermediate ion and the final state J'_f

$$h^{(2)} = (-1)^{J_f - J'_f} \times \left\{ \begin{matrix} J_f & J_f & 2 \\ 1 & 1 & J'_f \end{matrix} \right\} / \left\{ \begin{matrix} J_f & J_f & 2 \\ 1 & 1 & J_f \end{matrix} \right\}. \quad (65.20)$$

When it is energetically allowed, a hole in a shallow inner-shell will preferentially undergo Auger decay, emitting an electron with an energy ε_A determined by the energy difference between the energy E_f of the ion and E'_f of the state of the doubly-charged ion to which the decay occurs. Angular analysis of the Auger electrons reflects the alignment of the intermediate ionic state, which is different from, and does not bear a one-to-one relationship to, the angular distribution parameter β of the photoelectrons. Normally, Auger decay is regarded as a two-step process in which the first step is the production of the hole and the release of the primary photoelectron, followed by the decay and the release of the second electron. Within this approximation [14], the angular distribution of the Auger electrons takes on the simple form

$$I(\theta) = \left(\frac{I_0}{4\pi} \right) [1 + \alpha_2 A_0 P_2(\cos \theta)]. \quad (65.21)$$

Here $P_2(\cos \theta)$ is the second-order Legendre polynomial, and α_2 is the matrix element corresponding to the Auger decay. For the specific case in which the Auger decay is to a final ionic state of 1S_0 symmetry, α_2 is purely geometric, and a measurement of the angular distribution leads directly to a determination of the alignment. Correspondingly, if the alignment of a specific state can be determined through such a decay, then analysis of the angular distribution of the decay to other states provides a value for α_2 .

65.1.2 Electron Correlation Effects

The primary focus of advanced studies in photoionization is to determine the role played by electron correlation in the structure and dynamics of electron motion above the lowest ionization threshold. Because the form of the interaction potential for the Coulomb interaction is very well

known, theory can focus on the many-body aspects of the process (Chap. 24). Electron correlation manifests itself in many ways. Most prominent are the appearance of autoionization structure due to the excitation of one or two electrons, the production of correlation satellites due primarily to the ionization of one electron accompanied by the excitation of another, and the creation of two continuum electrons in a double ionization process.

Autoionization resonances are perhaps the oldest known features associated with electron correlation (Chap. 26). These features arise when the absorption of a photon creates a localized state which lies in energy above at least one ionization limit. This state is then degenerate in energy with a state of an electron in the continuum, and the interaction between these states results in the decay of the quasi-localized state into the continuum. Such resonance states appear in an absorption spectrum in the form of strong, localized variations over an energy range characteristic of the width Γ of the feature, which is in turn related to the lifetime τ of the state by

$$\Gamma = \hbar/\tau. \quad (65.22)$$

In contrast to absorption features between bound states, autoionization resonances are characterized by having an asymmetric line shape. When only one localized state and one continuum are involved, these line shapes can be derived analytically, as first shown by *Fano* [15] and later by *Shore* [16], resulting in simple parametrized forms which are suitable for numerical calculation of overlap integrals for determining widths. For the Fano profile

$$\sigma(\epsilon) = \sigma_a \frac{(\epsilon + q)^2}{\epsilon^2 + 1} + \sigma_b, \quad (65.23)$$

with

$$\epsilon = \frac{E - E_r}{(\Gamma/2)}, \quad (65.24)$$

the parameter q describes the asymmetry of the line, E_r is the resonance position, and Γ is the width of the line. The parameters σ_a and σ_b reflect the relative contributions to states in the continuum which do and do not interact with the autoionizing state respectively. The energy E_r does not correspond to the peak energy E_m of the resonance feature but is related to the maximum through

$$E_m = E_r + \frac{\Gamma}{2q}. \quad (65.25)$$

The Shore profile,

$$\sigma(\epsilon) = C(\epsilon) + \frac{A\epsilon + B}{\epsilon^2 + 1}, \quad (65.26)$$

describes the same phenomenon except that the interpretation of the parameters A and B is different. In this case, they represent products of dipole and Coulomb matrix elements. $C(\epsilon)$ is the continuum contribution.

From an experimental point of view, the parametrized forms for the Fano and Shore profiles are very useful as a basis for fitting autoionization spectra. However, they both have the limitation that they only describe the interaction of an isolated state with the continuum. While they can be extended to include several continua [4], they do not allow for an interaction among two or more localized states [17, 18]. Nevertheless, it is possible to use these functions to achieve often good fits of states which do interact with each other, as these functions are mathematical representations of localized resonances in a continuous spectral distribution. If this is done, the parameters no longer have the physical meaning which they have for the noninteracting case.

Mixing of discrete ionization channels with competing continuum channels adds complexity to the photoionization process, not just in the classical autoionization regime but also in the vicinity of inner shells [19–21]. In a rigorous application of the Mies formalism [17], feasible with modern computer power, even complex experimental spectra can now be satisfactorily interpreted and reproduced. A case in point is the excitation spectrum from the 2p level of the open-shell chlorine atom [19].

The process of autoionization is discussed in more detail in Chap. 26. In Fig. 65.1 an example is shown of the set of $2s^2 2p^3(^4S) \rightarrow 2s 2p^3 np$, $n \geq 3$ autoionization resonances which decay into the 3P ground state of the N^+ ion [22]. The energies E_n of these resonances are related to the ionization limit E_∞ of the series by the Rydberg formula

$$E_n = E_\infty - R_\infty / (n - \mu_s)^2, \quad (65.27)$$

where n is the principal quantum number and μ_s is the quantum defect characteristic of a given series and reflecting the short-range electrostatic interactions of the electron with the ion core. Values of μ_s for s, p, d, and f electrons have been calculated for atoms and ions up to $Z = 50$ [23]. For high precision work, the reduced Rydberg constant

$$R_M = \frac{R_\infty}{1 + 5.485\,799 \times 10^{-4} / (M_A - m_e)} \quad (65.28)$$

should be used instead of the value R_∞ for infinite nuclear mass (Chap. 1). The atomic mass M_A and the electron mass m_e are in a.u.

A process closely related to the autoionization phenomenon is resonant Auger decay. This process differs from the ordinary Auger process [24] in that an electron from an inner shell is not ionized but excited to either a partially filled or an empty subshell. It may be viewed either as an Auger process or as autoionization. Such an inner-shell excited state

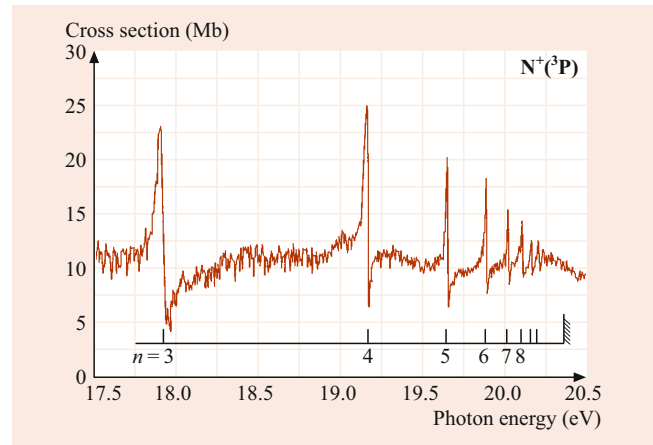


Fig. 65.1 Autoionization resonances $2s^2 2p^3(^4S) \rightarrow 2s 2p^3 np$ in atomic nitrogen

of a neutral atom (molecule) lies above one or more of the ionization limits of the singly ionized species and consequently must decay by electron emission unless the decay is forbidden by selection rules. As a result, resonance structure will appear superimposed on the continua of direct photoionization from the various subshells. From a most general point of view, the resonant Auger process can be considered as resonances in the continua of single photoionization, while the ordinary Auger process can be regarded as resonances in the continua of double photoionization. If excitation proceeds to a partially filled subshell *within* a principal shell, as, for example, Mn 3p \rightarrow 3d [20], interference between the direct photoionization channels and the indirect resonance channel may be strong, and the lineshapes are given by Eq. (65.23) with arbitrary q values and σ_a/σ_b ratios. If, however, the excitation proceeds to an empty shell, as, for example, Mg 2p \rightarrow ns or nd, $n \geq 4$, interference with the direct channels is likely to be negligible, and the resulting resonances are distinguished by essentially Lorentzian line shapes (as for normal Auger lines) with $q \gg 1$ and $\sigma_a/\sigma_b \gg 1$ in Eq. (65.23). For a given excitation state a number of resonance peaks may arise because more than one ionization channel is usually available and, in addition, the excited electron can change its orbital from n to $n' = n \pm 1, 2, \dots$ in a shakeup or shakedown process [25].

As a consequence of the electron–electron interactions which occur simultaneously with the electron–photon interaction, ions are produced in states which do not correspond to those which would be expected based on an interpretation using an independent particle model, which allows for only a single-electron transition (Chap. 25). Evidence for these states appears as correlation satellites in the photoelectron spectrum, the Auger electron spectrum or the X-ray spectrum [26]. Figure 65.2 [27] presents as an example the photoelectron spectrum of argon produced by photons with $h\nu = 60.6$ eV. In addition to the 3s main line of single electron

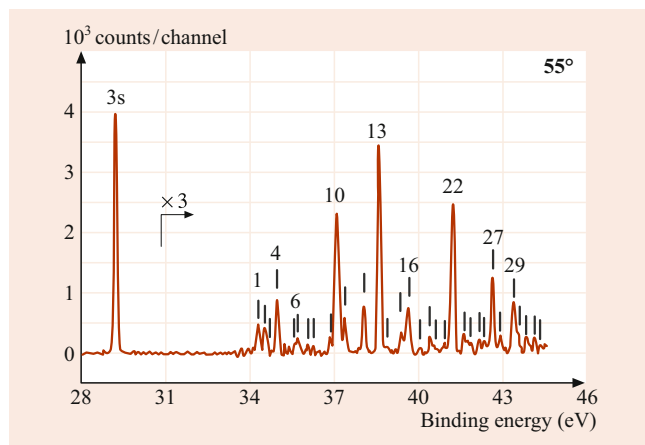


Fig. 65.2 Photoelectron spectrum (PES) of 3s, 3p satellites in argon at a photon energy of 60.6 eV. Note the reduced intensity of the satellites compared to the 3s main line

photoionization (and the 3p main lines not shown) numerous satellite lines are seen as the manifestation of two-electron transitions involving ionization-with-excitation correlations. It is convenient to categorize the satellites in a photoelectron spectrum according to various electron correlations, as, for example, initial state interactions which mix different configurations into the initial state, and final state interactions, which include core relaxation and electron–electron interactions in the final ionic state, electron–continuum, and continuum–continuum interactions. While initial-state correlations are essentially independent of the photon energy, final-state correlations depend on the energy of the photon through the interactions with the continuum channels. However, the heuristic value of placing correlation effects into a strict classification scheme is limited by the fact that their relative strengths depend on the basis set used in a particular theoretical model and its expansion into a *fully correlated* system within a given gauge [3, 4, 28, 29] (see also Chap. 25).

Another manifestation of double-electron processes is the simultaneous excitation of two electrons to bound states. These states may decay by electron or photon emission and are seen as resonance structures above the thresholds of inner-shell ionization or near autoionizing members of Rydberg series. As single or double ionization continua are usually strong in the spectral range of the double excitations, interference occurs, and the lineshapes can display dispersion forms. Typically, the cross section for the sum of all correlation processes is between 10 and 30% of that for single photoionization, but may exceed this range considerably in special cases.

Photon scattering near thresholds is complex because of the possibility of strong interactions between the various particles created and the different modes of deexcitation (Chap. 66). In the case of ionization-with-excitation pro-

cesses, the threshold cross section is finite, as it is for single electron photoionization, in accord with Wigner’s theorem [30] (Sect. 64.2.2). In the case of double photoionization, the cross section is zero at threshold and then rises according to Wannier’s law [31] (Chap. 56). For the motion of two electrons with essentially zero kinetic energies in the field of the ionic core,

$$\sigma \propto E^{(2\mu-1)/4}, \quad (65.29)$$

where μ depends on the value of the nuclear charge Z through

$$\mu = \frac{1}{2} \left(\frac{(100Z - 9)}{(4Z - 1)} \right)^{\frac{1}{2}}. \quad (65.30)$$

For $Z = 1$ the Wannier exponent has the value 1.127.

In the case of Auger decay following ionization at threshold, interaction between the two electrons results in a shift in the energy of the Auger electron and a corresponding shift in that of the photoelectron (to conserve energy), as well as an asymmetry in the shape of the Auger electron peak and a corresponding asymmetry in the photoelectron peak shape. In this so-called post-collision interaction (Chap. 66), the lineshape, averaged over angles, has the form [32]

$$K(\varepsilon) = \frac{(\Gamma/2\pi)}{(\varepsilon - \varepsilon_A)^2 + (\Gamma/2)^2} f(\varepsilon) \quad (65.31)$$

with

$$f(\varepsilon) = \frac{\pi \psi}{\sinh(\pi \psi)} \exp \left[2\psi \tan^{-1} \left(\frac{\varepsilon - \varepsilon_A}{(\Gamma/2)} \right) \right]. \quad (65.32)$$

In the above equations, ε is the energy of the Auger line, ε_A is the nominal Auger energy, Γ is the initial hole-state width, and the parameter $\psi = 1/\sqrt{2\varepsilon_e} - 1/\sqrt{2\varepsilon_A}$, with ε_e being the energy of the photoelectron, and $\varepsilon_A \geq \varepsilon_e$.

65.2 Experimental Methods

An overview of the experimental approaches to the study of photon interactions at low energies is given in Fig. 65.3. The sketch emphasizes the interaction of a polarized photon beam with a small static or particle-beam target of atoms, ions, molecules, or clusters, and the detection of the reaction products at various angles in a plane perpendicular to the direction of propagation of the photon beam, where the general equation in Eq. (65.5) is valid. Emission products, such as electrons, ions, or photons, may be studied by way of the total yields, which can be related to the total photoionization cross section, or by differential analysis in a spectrometer according to energy, intensity, emission angle, and polarization.

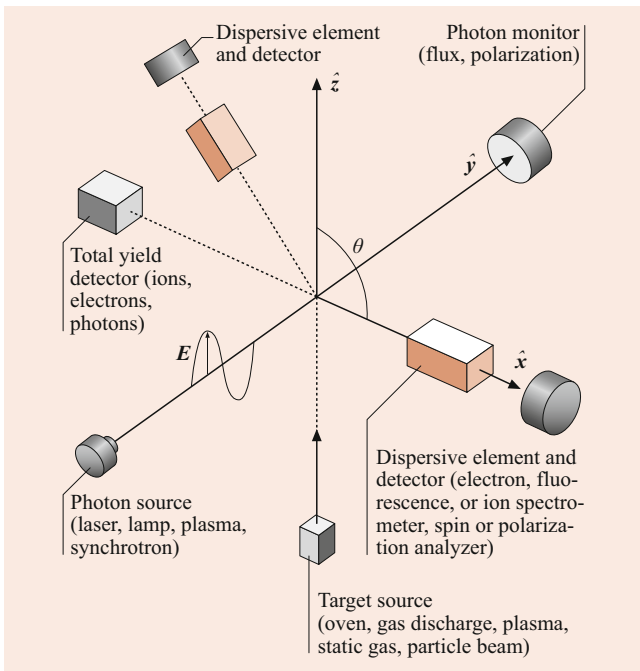


Fig. 65.3 Generic arrangement for detection of particles in an emission measurement. The incoming radiation is assumed to be linearly polarized along the z -axis

The various particles may be measured independently, simultaneously, or in coincidence. The photon monitor provides the information for normalization of the data with regard to flux and polarization. The photon monitor can also be used for a measurement of the total photoionization cross section, equivalent to the photoabsorption or photoattenuation coefficient at low photon energies. For this purpose, the size of the target source is advantageously increased in the direction of the photon beam. While experimental apparatus differs, sometimes drastically, for the photon sources as well as for the spectrometry of electrons, ions, and fluorescence photons, many features are common, and the relationships of the measured quantities to basic properties of the atoms and the photon–atom interaction are similar. Thus, the following will place emphasis only on the roles of the synchrotron radiation source and photoelectron spectrometry, whereas specific references to other methods can be found elsewhere [5, 33–38].

65.2.1 Synchrotron Radiation Source

The primary source of photons over a broad energy range for experiments in the VUV and soft X-ray region of the spectrum is the synchrotron radiation source [39, 40]. In a synchrotron or electron storage ring, radiation is produced as the electrons are bent to maintain the closed orbit. Such bending magnet radiation is emitted in a broad continuous spectrum which begins in the infra-red and ends sharply

at a critical photon energy given by $h\nu_c = \kappa E_e^2$, where E_e is the energy of the electrons in the ring and κ is a constant characteristic of the ring. Synchrotron radiation can also be generated by introducing additional magnetic field structures [41] into the ring, such as undulators or wigglers, which produce a deviation of the electron motion from a straight path in a well-defined manner. Wiggler radiation has the same spectrum as a bending magnet, except that the critical energy is generally much higher because the effective magnetic fields can be larger than those of the bending magnet. Undulator radiation is very different in that it consists of a sharp spiked profile of about a 1% bandwidth at energies determined by the magnetic field within the undulator and by the electron beam energy in the storage ring.

Synchrotron radiation, no matter what the magnetic field structure of the source, requires monochromatization before it can be used for experiments. For the wavelengths of interest in low-energy photon scattering, this can be achieved by using grating instruments with a metallic coating on the grating surface. The highest resolution possible is obtained through the use of a normal incidence monochromator (NIM) with a plane grating set at normal incidence. However, because the reflectivity of the metallic coating at normal beam incidence decreases drastically as the photon energy increases, use of a NIM has an upper limit of about 40 eV. At energies above this, up to about 1 keV, gratings can still be used but must be mounted at grazing incidence. There is a number of functional designs for these grazing-incidence instruments which vary in the shape of the grating – spherical, toroidal, or plane surfaces (SGM, TGM, PGM) – and the associated optics. Above 1 keV, gratings are no longer suitable, and crystal diffraction must be used. While the radiation emerging from a beamline which couples the monochromator to a bending magnet, wiggler, or undulator has a high degree of linear polarization, varying from 80 to 99% in the plane of the electron orbit, a useful flux of circularly polarized radiation can be derived from out-of-plane radiation [33], by the use of multiple reflection optics, or from a helical undulator.

65.2.2 Photoelectron Spectrometry

The primary particle emitted in photoionization is the photoelectron. Hence, a photoelectron spectrum provides a detailed view of the photon interaction by (a) specifying the individual processes from an initial state i to a final state f by way of the electron energy, (b) determining their differential and partial cross sections by recording the number of electrons as a function of emission angle, and (c) measuring the polarization of the electrons by a spin analysis (spin polarimetry). The experimental approach is governed largely by the relations in Eqs. (65.3), (65.5), and (65.6). The num-

ber of electrons N_{if} (e) detected per unit time at an angle θ within an energy interval $d\varepsilon$ and within a solid angle $d\Omega$ is given by

$$N_{if}(e) = GN(h\nu)N(A)f(h\nu)f(\varepsilon)\frac{d\sigma_{if}}{d\Omega}d\varepsilon \quad (65.33)$$

where G is a geometry factor, which includes the source dimensions, $N(h\nu)$ the number of photons, $N(A)$ the number of atoms in the source, $f(h\nu)$ and $f(\varepsilon)$ efficiency factors depending, respectively, on photon and electron kinetic energies, and $d\sigma_{if}/d\Omega$ is the differential cross section for a particular transition $i \rightarrow f$. Equation (65.33) assumes that $d\Omega$ and $d\varepsilon$ are sufficiently small that integration over the pertinent parameters is not needed. Since $N_{if} \propto d\sigma_{if}/d\Omega$, a measurement at two angles, e.g., $\theta = 0^\circ$ and 90° , yields the electron angular distribution parameter β_{if} according to Eq. (65.5), and a measurement at θ_m in Eq. (65.6) yields the partial cross section σ_{if} . In the case of closed-shell atoms, $n\ell j$ notation is sufficient to designate single ionization to an $\varepsilon\ell$ continuum, e.g., $3p_{1/2,3/2} \rightarrow \varepsilon s$ or εd in argon, but for open-shell atoms LSJ notation is required, e.g., $3P^5(2P^0_{3/2}) \rightarrow 3P^4(3P^e_{2,1,0}, 1D^e_2, 1S^e_0)\varepsilon\ell(2D^e, 2P^e, 2S^e)$ in chlorine. Similarly, for ionization-with-excitation transitions, the final state requires an open-shell designation.

The sum of the partial cross sections is equal to the total photoionization or absorption cross section

$$\sigma_{\text{tot}} = \sum_{i,f} \sigma_{if} \quad (65.34)$$

where the σ_{if} encompass (a) single ionization events in all energetically accessible subshells $n\ell j$, or the LSJ multiplet components, (b) ionization-with-excitation events (shakeup or shakedown), and (c) double ionization events (shakeoff). All σ_{if} can be determined from a photoelectron spectrum from its discrete peaks (cf. Fig. 65.2) and from the continuum distribution of multiple ionization. However, the latter process is measured more readily by observing the multiply charged ions in a mass spectrometer.

The differentiation afforded by measuring the various partial cross sections, and the associated β parameters, can be augmented by differentiating the continuum channels according to the spin using a spin polarimeter [33]. In closed-shell atoms, this allows for an experimental determination of the relevant matrix elements and phase shifts, and hence for a direct comparison with theory at the most basic level [34, 35]. In a more global measurement, the cross section σ_{tot} is obtained by ion or mass spectrometry from

$$\sigma_{\text{tot}} = \sigma(A^+) + \sigma(A^{2+}) + \sigma(A^{3+}) + \dots \quad (65.35)$$

Generally, the charge states can be correlated with the various initial photoionization processes if allowance is made for

Auger transitions and the fluorescence yield upon exceeding the binding energies of core levels.

If the charge states are not distinguished, as in a total ion yield measurement, σ_{tot} is obtained directly. Similarly, a direct measurement of the global quantity σ_{tot} is obtained by the total electron yield, although care must be exercised to avoid discrimination by angular distribution effects. At photon energies below about 1 keV, ionization, absorption, and attenuation are virtually equivalent, and σ_{tot} can also be determined in an ion chamber setup [36] or in a photoabsorption measurement in which the number of photons ΔN absorbed in a source of length d and having an atom density n is given by

$$\Delta N = N(\text{ph})[1 - \exp(-\sigma_{\text{tot}}nd)] \quad (65.36)$$

with $N(\text{ph})$ being the flux of incident photons. As a rule, in all experiments employing the relation in Eq. (65.5), the total, partial, or differential cross sections are determined on a relative rather than an absolute scale because it is very difficult to know accurately such factors as the geometry of the source volume and the number density. However, once a single absolute value of σ_{tot} or any σ_{if} is available, all relative values of the other quantities can be converted to absolute values.

An electron spectrometric experiment can be carried out in three different operational modes, as defined in Fig. 65.4. In the most conventional mode, PES, the photon energy is fixed, and a scan of the electron kinetic energy reveals all the electron-emission processes possible and yields their properties. The CIS (constant ionic state) mode is especially suited to follow continuously a selected process as a function of photon energy by locking onto a given state $E_f - E_i$ (denoted by E_B) which requires a strict synchronization of the photon energy ($h\nu$) and electron kinetic energy (ε) during a scan. This mode is particularly advantageous to elucidate resonance features, such as autoionization resonances. Finally, a CKE (constant kinetic energy) scan allows one to access various processes sequentially or, most importantly, follow a process of fixed energy, such as an Auger transition, as a function of photon energy. This description also includes the technique of zero-kinetic-energy measurements. Most frequently, the PES and CIS modes are employed, and Fig. 65.5 gives a self-explanatory example of an actual experiment directed at the characterization of the argon $3s \rightarrow np$ autoionizing resonances. It should be stressed that the cross section σ_{tot} can be partitioned into its components by CIS scans that differentiate between the $3p_{1/2}$ and $3p_{3/2}$ doublet states.

Energy analysis can be performed either by electrostatic energy analyzers or by time-of-flight techniques. The latter is well-suited to those electrons which have very low ki-

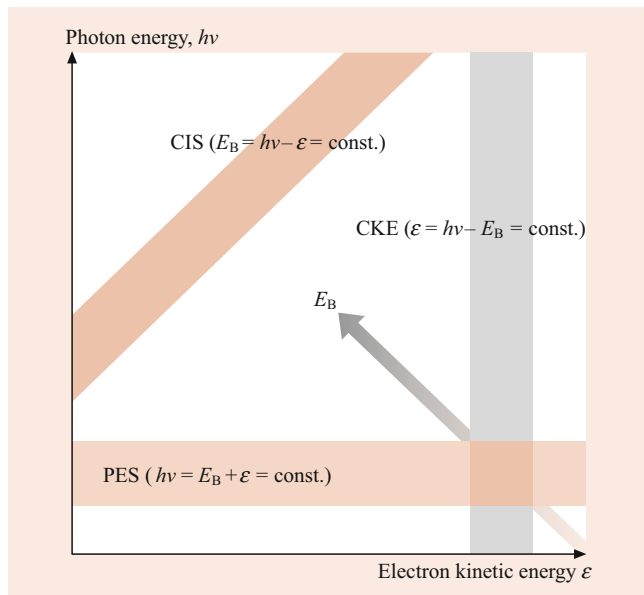


Fig. 65.4 Energy relationship among the three different operational modes of the technique of photoelectron spectrometry. E_B is the binding energy of the level

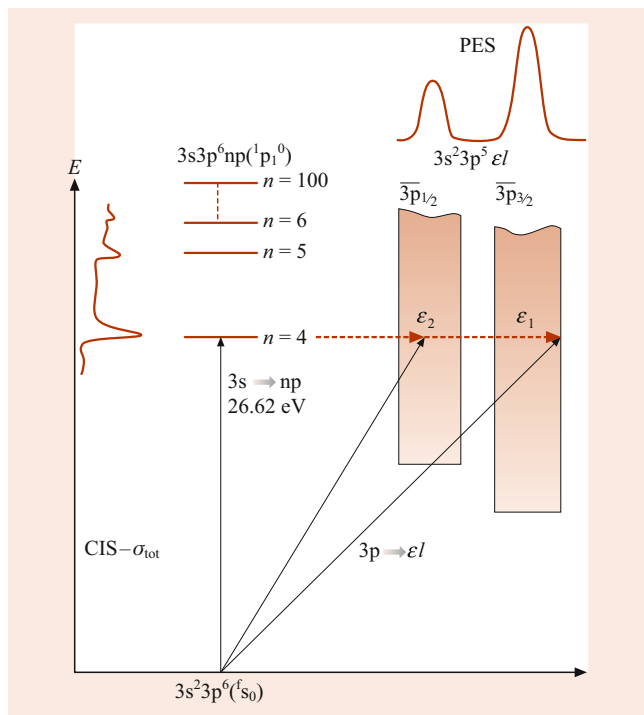


Fig. 65.5 Connection between the PES and CIS techniques as illustrated by the $3s \rightarrow np$ autoionization resonances in argon

netic energy, including threshold electrons with $\varepsilon \approx 0$ eV. Of the electrostatic energy analyzers now in use, two designs are prevalent, the cylindrical mirror analyzer (CMA) and the hemispherical analyzer, where the latter readily lends itself to the application of multichannel detectors.

65.2.3 Resolution and Natural Width

The details that can be gleaned from an experiment using photons depend on the resolution achievable with the particular photon source and spectrometry used, the particular excitation or analysis modes and the target conditions chosen, and, ultimately, on the natural width of either the levels or transitions examined as well as any fine structure present. Generally, the instrumental and operational resolution should approach, but need not exceed by much, the natural width inherent in the photoprocess under scrutiny. The demands are most severe for processes involving outer levels because of their typically very narrow widths, and are relatively mild for processes involving inner levels [5, 35]. It is desirable that in the former case the resolving power (the inverse of the resolution) of the instrument exceed 10^5 , while in the latter case 10^4 may suffice. If the target atoms move randomly, a resolution limit is set by the thermal motion, namely

$$\Delta\varepsilon = 0.723 (\varepsilon T/M)^{1/2} \text{ (meV)}, \quad (65.37)$$

where, in an experiment involving photoelectron spectrometry, ε is the kinetic energy of the photoelectron in eV, T the temperature in K, and M the mass in a.u. of the target atom. This contribution can be limited in first order by employing a suitably directed atomic beam.

The experimental peak-width and shape generally contain the natural width; the extent to which instrumental factors enter depends on the specific experiment. In a measurement of the total or partial photoionization cross section in which either the fluorescence photons, the electrons, or the ions are monitored, the resolution of the photon source (often called the bandpass) is the only instrumental contributor. This applies specifically to the CIS mode of electron spectrometry, in which features are scanned in photon energy and the electron serves solely as a monitor. However, in such a CIS study, or a corresponding fluorescence study, the resolution of the electron or fluorescence spectrometer must be adequate to be able to distinguish adjacent processes. For the example of Fig. 65.5, the $3p_{3/2}$ and $3p_{1/2}$ levels of Ar need to be separated if the partial photoionization cross sections are to be determined across the resonances. In such a case of more than one open ionization channel, the natural widths of the features will be identical in all channels [4], but the shapes may be different. In emission processes subsequent to initial photoionization, namely electron (Auger) decay or photon (X-ray) emission, the resolution of only the spectrometer performing the detection counts on the instrumental side. In the PES mode (Fig. 65.4) the observed lines contain contributions from all sources, the photon source or photon monochromator, the electron analyzer, thermal broadening, and the natural level width. In the special case of photo-

processes near inner thresholds, the post-collision interaction influences the position and shape of photoelectron and Auger lines (Chap. 66).

Excluding threshold regions and the resonant Raman effect, the line profile observed in the various experiments is given by the Voigt function

$$V(\omega, \omega_0) = \int L(\omega' - \omega)G(\omega' - \omega_0)d\omega'. \quad (65.38)$$

In this the Lorentzian function L represents the natural level or transition profile, and the Gaussian function G is representative of the window functions of the dispersive apparatus. Although the integral representing the Voigt profile has no analytic form, it can be represented for practical purposes by the analytic Pearson-7 function [42]

$$P_7(\varepsilon) = A \left(1 + \frac{(\varepsilon - \varepsilon_0)^2}{B^2 C} \right)^{-C}, \quad (65.39)$$

where A is the peak height, ε_0 the peak position, B the nominal half-width-half-maximum of the peak, and C the shape of the peak. In the limit in which $C = 1$, this function is identically a Lorentzian; in the limit $C \rightarrow \infty$, the function is essentially Gaussian. Use of this function allows one to fit the resulting photoelectron spectrum using standard numerical techniques. If the width of the feature is the only quantity of interest, the simple approximate expression

$$\frac{\Gamma_L}{\Gamma_V} = 1 - \left(\frac{\Gamma_G}{\Gamma_V} \right)^2 \quad (65.40)$$

which relates the Voigt width Γ_V with the Lorentzian width Γ_L and the Gaussian width Γ_G can be used to determine either Γ_L or Γ_G from the measured Γ_V [5]. Often the observed feature exhibits a dispersive shape given by the Fano or Shore profile. In this instance the instrumental function must be convoluted with the resonance profiles given by Eq. (65.23) or (65.26) in order to fit the data and to extract the parameters [43].

For the special case of resonant Auger decay in which the bandpass of the exciting radiation is very narrow compared with the natural width of the excited state, the experimental linewidth is governed by the width of the exciting radiation, and will be more narrow than the natural width of the line. The resulting lineshape in this resonant Raman effect is then the simple product [24]

$$L'(\omega, \omega_0) = L(\omega)G(\omega - \omega_0), \quad (65.41)$$

where $L(\omega)$ is the line profile as determined by the natural width, typically Lorentzian for resonant Auger decay, and $G(\omega - \omega_0)$ is the, usually, Gaussian function representing the bandpass of the exciting radiation.

65.3 Additional Considerations

Although low-energy photon interactions are well described nonrelativistically in the dipole approximation, relativistic and higher multipole effects which become increasingly important at higher energies cannot be ignored even below 1 keV. Spin-orbit effects [44] and relativistic effects [45] are of special significance even at low energies in Cooper minima, where one of the transition matrix elements becomes zero. Moreover, the use of intermediate coupling, which includes both the spin-orbit and electrostatic interactions [46], is required in open-shell systems, as exemplified for the halogen atoms and atomic oxygen [47]. Level energies of heavy elements also require a relativistic treatment [48] (Chap. 23), and it is natural to employ relativistic formulations for calculating the spin parameters appearing in photoionization [49].

Although low energy photon scattering is dominated by the dipole contribution, experiments and theory have shown higher multipole effects to be present at $h\nu < 1$ keV [50–57]. As a result, measurements that take the dipole formulations as a basis in Eqs. (65.5) and (65.6) can incur a discernible error in both the differential cross sections $d\sigma_{if}/d\Omega$ and the partial cross sections σ_{if} . A more accurate determination of $d\sigma_{if}/d\Omega$ can be made [51, 55, 56] on the basis of the equation

$$\frac{d\sigma_{if}}{d\Omega} = \left(\frac{\sigma_{if}}{4\pi} \right) \left[1 + \beta P_2(\cos \theta) + (\delta + \gamma \cos^2 \theta) \sin \theta \cos \phi \right], \quad (65.42)$$

using linearly polarized radiation, where $P_2(\cos \theta)$ is the second-order Legendre polynomial, θ is the angle between the electron emission direction and the electric vector, ϕ is the angle between the electron and photon directions, β is the angular distribution parameter related to B_2 , and the parameters δ and γ are related to B_1 and B_3 in Eq. (65.4). Figure 65.6 shows the geometry for the relationship between the photoelectron momentum vector, the polarization vector, and the photon momentum vector,

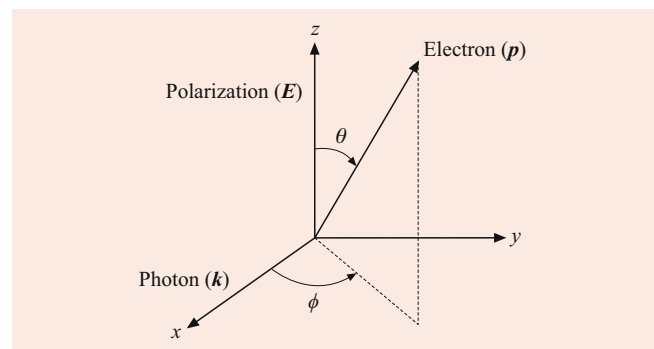


Fig. 65.6 Geometry of the relationship between the photoelectron momentum p , the polarization vector E , and the photon momentum k . (Courtesy of O. Hemmers)

and the photon propagation vector as used in Eq. (65.42). It serves as the template for the arrangement and motion of the electron detector, or, for added efficiency and accuracy, several detectors [51–53, 56]. The parameters β , δ , and γ have been calculated for most subshells of the noble gases for photoelectron energies between 100 eV and 5 keV [55] and 20 eV to 5 keV [57]. Generally, the electric quadrupole (E2) and magnetic dipole (M1) photoionization channels are the most important beyond the dipole (E1) photoionization channel. Similar to the dipole angular distribution parameter β , the parameter γ may also be subject to interchannel coupling and relativistic effects, as demonstrated for xenon 5s photoionization [51].

References

1. Veigele, W.J.: *At. Data Nucl. Data Tables* **5**, 51 (1973)
2. Hubbell, J.H., Berger, M.J.: Photon cross section, attenuation coefficients, and energy absorption coefficients. In: Jaeger, R.G. (ed.) *Engineering Compendium on Radiation Shielding*, vol. 1, p. 167. Springer, Berlin (1968)
3. Fano, U., Cooper, J.W.: *Rev. Mod. Phys.* **40**, 441 (1963)
4. Starace, A.F.: Theory of photoionization. In: Flügge, S., Mehlhorn, W. (eds.) *Handbuch der Physik*, vol. XXI, p. 1. Springer, Berlin (1982)
5. Krause, M.O.: Electron spectrometry of atoms and molecules. In: Winick, H., Doniach, S. (eds.) *Synchrotron Radiation Research*. Plenum, New York (1980). Chap. 5
6. Fano, U., Dill, D.: *Phys. Rev. A* **6**, 185 (1972)
7. Whitfield, S.B., Kehoe, K., Krause, M.O., Caldwell, C.D.: *Phys. Rev. Lett.* **84**, 4818 (2000)
8. Schirmer, J., Cederbaum, L.S., Kiessling, J.: *Phys. Rev. A* **22**, 2696 (1990)
9. Hughes, V.W., Long Jr., R.L., Lubell, M.S., Posner, M., Raith, W.: *Phys. Rev. A* **5**, 195 (1972)
10. Fano, U.: *Phys. Rev.* **178**, 131 (1969)
11. Cherepkov, N.A.: *Adv. At. Mol. Phys.* **19**, 395 (1983)
12. Fano, U., Macek, J.H.: *Rev. Mod. Phys.* **45**, 553 (1973)
13. Greene, C.H., Zare, R.N.: *Phys. Rev. A* **25**, 2031 (1982)
14. Mehlhorn, W.: Auger-electron spectrometry of core levels in atoms. In: Crasemann, B. (ed.) *Atomic Inner-Shell Physics*. Plenum, New York (1985). Chap. 4
15. Fano, U.: *Phys. Rev.* **124**, 1866 (1961)
16. Shore, B.: *J. Opt. Soc. Am.* **57**, 881 (1967)
17. Mies, F.H.: *Phys. Rev.* **175**, 164 (1968)
18. Connerade, J.P., Lane, A.M.: *Rep. Prog. Phys.* **51**, 1439 (1988)
19. Martins, M.: *J. Phys. B* **34**, 1321 (2001)
20. Whitfield, S.B., Krause, M.O., van der Meulen, P., Caldwell, C.D.: *Phys. Rev. A* **50**, 1269 (1994)
21. Gorczyca, T.W., McLaughlin, B.M.: *J. Phys. B* **33**, 859 (2000)
22. Schaphorst, S.J., Whitfield, S.B., Saha, H.P., Caldwell, C.D., Azuma, Y.: *Phys. Rev. A* **47**, 3007 (1993)
23. Theodosiou, C.E., Inokuti, M., Manson, S.T.: *At. Data Nucl. Data Tables* **35**, 473 (1986)
24. Åberg, T., Howat, G.: Theory of the Auger effect. In: Flügge, S., Mehlhorn, W. (eds.) *Handbuch der Physik*, vol. XXI, p. 469. Springer, Berlin (1982)
25. Whitfield, S.B., Tulkki, J., Åberg, T.: *Phys. Rev. A* **44**, R6985 (1994)
26. Krause, M.O.: *J. Phys. (Paris)* **32**, C4–67 (1971)
27. Krause, M.O., Whitfield, S.B., Caldwell, C.D., Wu, J.-Z., van der Meulen, P., de Lange, C.A., Hansen, R.W.C.: *J. Elec. Spectros. Rel. Phen.* **58**, 79 (1992)
28. Martin, R.L., Shirley, D.A.: *Phys. Rev. A* **13**, 1475 (1976)
29. Åberg, T.: *Nucl. Instrum. Methods* **B87**, 5 (1994)
30. Wigner, E.P.: *Phys. Rev.* **73**, 1002 (1948)
31. Wannier, G.H.: *Phys. Rev.* **90**, 817 (1953)
32. Kuchiev, M.Y., Sheinermann, S.A.: *Sov. Phys. JETP* **63**, 986 (1986)
33. Heinzmann, U.: *J. Phys. B* **13**, 4353 (1980)
34. Schmidt, V.: *Rep. Prog. Phys.* **55**, 1483 (1992)
35. Becker, U., Shirley, D.A. (eds.): *VUV and Soft X-ray Radiation Studies*. Plenum, New York (1996)
36. Samson, J.A.R.: Atomic photoionization. In: Flügge, S., Mehlhorn, W. (eds.) *Handbuch der Physik*, vol. XXI, p. 123. Springer, Berlin (1982)
37. Sonntag, B., Zimmermann, P.: *Rep. Prog. Phys.* **55**, 911 (1992)
38. de Lange, C.A.: *Adv. Chem. Phys.* **117**, 1 (2001)
39. Winick, H., Brown, G.: *Nucl. Instrum. Methods* **195**, 1 (1987)
40. Koch, E.E.: *Handbook of Synchrotron Radiation*. North-Holland, Amsterdam (1983)
41. Clarke, J.A.: *The Science, Technology of Undulators, Wigglers*. Oxford University Press, Oxford (2004)
42. Whitfield, S.B., Caldwell, C.D., Huang, D.X., Krause, M.O.: *J. Phys. B* **25**, 4755 (1992)
43. Jiménez-Mier, J.: *J. Quant. Spectros. Radiat. Transf.* **51**, 741 (1994)
44. Fano, U.: *Phys. Rev.* **178**, 131 (1969)
45. Manson, S.T., Lee, Z.J., Pratt, R.H., Goldberg, I.B., Tambe, B.R., Ron, A.: *Phys. Rev. A* **28**, 2885 (1983)
46. Cowan, R.D.: *The Theory of Atomic Structure and Spectra*. Univ. of California Press, Berkeley (1981)
47. Caldwell, C.D., Krause, M.O.: *Rad. Phys. Chem.* **70**, 43 (2004)
48. Grant, I.P.: *Aust. J. Phys.* **39**, 649 (1986)
49. Huang, K.N., Johnson, W.R., Cheng, K.T.: *At. Data Nucl. Data Tables* **26**, 33 (1981)
50. Tseng, H.K., Pratt, R.H., Yu, S., Ron, A.: *Phys. Rev. A* **17**, 1060 (1978)
51. Hemmers, O., Guillemin, R., Lindle, D.W.: *Rad. Phys. Chem.* **70**, 123 (2004)
52. Martin, N.L.S., Thompson, D.B., Bauman, R.P., Caldwell, C.D., Krause, M.O., Frigo, S.P., Wilson, M.: *Rev. Lett.* **81**, 1199 (1998)
53. Dunford, R.W., Kanter, E.P., Krässig, B., Southworth, S.H., Young, L.: *Rad. Phys. Chem.* **70**, 149 (2004)
54. Krause, M.O.: *Phys. Rev.* **177**, 151 (1969)
55. Cooper, J.W.: *Phys. Rev. A* **47**, 1841 (1993)
56. Shaw, P.S., Arp, U., Southworth, S.H.: *Phys. Rev. A* **54**, 1463 (1996)
57. Derevianko, A., Johnson, W.R., Cheng, K.T.: *At. Data Nucl. Data Tables* **73**, 153 (1999)



Denise Caldwell Dr Caldwell is the Division Director of the Physics Division at the National Science Foundation. She was awarded her Ph.D. by Columbia University in 1976. She then held a postdoc at the University of Bielefeld and a junior faculty position at Yale University. In 1985 she joined the faculty at the University of Central Florida, where she maintained a research program on atomic photoionization using synchrotron radiation. In 1998 she left full-time academia to become a permanent staff member of the NSF. She is a Fellow of the American Physical Society.



Manfred Krause Dr. Krause was a Senior Scientist at the Oak Ridge National Laboratory working primarily in the field of photoelectron spectrometry of atoms with the use of synchrotron radiation. He received his Dr. rer. nat. in physics at the Technische Universität and the Max Planck Institut für Metallforschung in Stuttgart in 1954. He joined the Oak Ridge National Laboratory in 1963 and retired in 1995. He is a Fellow of the American Physical Society, and was a Professeur d'Echange at the University of Paris in 1975 and an Alexander von Humboldt awardee at the University of Freiburg in 1976.



Photon–Atom Interactions: Intermediate Energies 66

Michael W. J. Bromley

Contents

66.1	Overview	967
66.2	Scattering Cross Sections	968
66.2.1	Applications of Atomic Cross Sections	970
66.3	Experimental Progress	971
66.3.1	Inelastic Processes	972
66.4	Theory, Computation, and Data	974
66.4.1	Databases	974
66.4.2	Bulk Modeling	974
66.5	Future Directions	975
	References	975

Abstract

This chapter provides an overview of our understanding of photon–atom interactions involving soft x-rays, hard x-rays, and gamma-rays with “intermediate” photon energies roughly between 1 keV to 1 MeV (37 a.u. to 37×10^3 a.u.). These energies correspond to wavelengths of 1.2 nm to 1.2 pm, where the electronic shell structure of a multielectron atom can be probed, and resonant excitations and deexcitations can be important. Here, we will emphasize the cross sections of various processes, which are independent of the intensity of the incoming electromagnetic field. We explore elastic Rayleigh scattering and inelastic scattering, including photoionization, Auger, Raman, and Compton processes. We describe various experimental methods, Monte Carlo approaches and other applications of the sets of atomic data, all spanning the intermediate energy range.

M. W. J. Bromley (✉)
University of Southern Queensland
Toowoomba, QLD, Australia
e-mail: atombrom@expolife.com

Keywords

photon · x-ray · atom · scattering · cross section · absorption · hard · soft · keV · MeV

66.1 Overview

The photon–atom interactions through the intermediate 1 keV to 1 MeV regime are broadly classified into elastic and inelastic processes, depending on whether the outgoing photon energy changes [1, 2]. The interactions are also classified into coherent or incoherent processes [3]. In this chapter, we will explore the physics of each process through the intermediate energy regime.

The atom–photon interaction Hamiltonian in this regime involves the quantized radiation field corresponding to a photon of frequency ω , wave vector \mathbf{k} , and polarization vector $\boldsymbol{\epsilon}^{(\alpha)}$, which couples to the electron position \mathbf{r} , via [4]

$$\mathbf{A}_{k\alpha}(\mathbf{r}, t) \propto c \sqrt{\frac{\hbar}{2\omega}} \boldsymbol{\epsilon}^{(\alpha)} e^{i(\mathbf{k}\cdot\mathbf{r}-\omega t)}, \quad (66.1)$$

with speed of light c . The quantized radiation field operator is then built through creation and annihilation operators over field modes

$$\hat{\mathbf{A}}(\mathbf{r}, t) = \sum_{\mathbf{k}, \alpha} [\hat{a}_{k\alpha} \mathbf{A}_{k\alpha}(\mathbf{r}, t) + \hat{a}_{k\alpha}^\dagger \mathbf{A}_{k\alpha}^*(\mathbf{r}, t)], \quad (66.2)$$

which gives the interaction Hamiltonian, H_{int} , by summing over $j = 1, N$ electrons with momentum \mathbf{p}_j

$$H_{\text{int}} = \sum_j \left[\frac{e^2}{2m_e c^2} \hat{\mathbf{A}}(\mathbf{r}_j, t)^2 - \frac{e}{m_e c} \mathbf{p}_j \cdot \hat{\mathbf{A}}(\mathbf{r}_j, t) \right], \quad (66.3)$$

where e and m_e are the charge and mass of the electron. This form assumes that $\mathbf{p}_j \cdot \hat{\mathbf{A}}(\mathbf{r}_j, t) = \hat{\mathbf{A}}(\mathbf{r}_j, t) \cdot \mathbf{p}_j$ as per the Coulomb gauge [4].

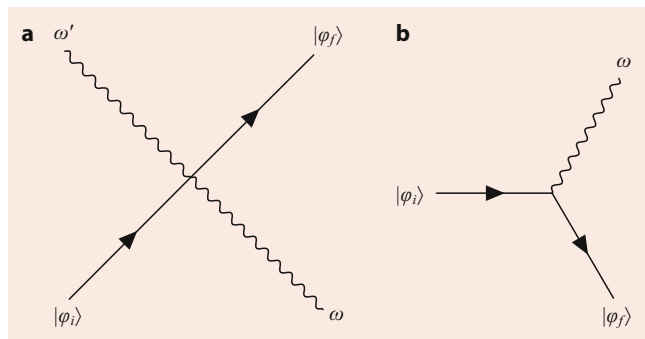


Fig. 66.1 Feynman diagram vertices for the photon interaction in the Hamiltonian H_{int} (Eq. (66.3)). The *solid lines* represent the electronic states of the atom, the *squiggly lines* are the interacting photons [5]

The two terms in the interaction Hamiltonian in Eq. (66.3) are best visualized through the two Feynman vertices shown in Fig. 66.1. The A^2 term shown in Fig. 66.1a only couples to the position of the electron. This permits instantaneous two-photon absorption, emission, and scattering processes, which begin to dominate at intermediate photon energies [5]. The $\mathbf{p} \cdot \mathbf{A}$ term shown in Fig. 66.1b couples to both the position and momentum of the electron and allows for single-photon absorption and emission processes (including via an intermediate state). The solution to the $\mathbf{p} \cdot \mathbf{A}$ term in the Hamiltonian in Eq. (66.3) is normally undertaken with perturbation theory, where the number of interacting photons determines the order of the process, e.g., first order are single-photon absorption and emission processes, and second order are scattering processes.

66.2 Scattering Cross Sections

For time-dependent scattering processes such as absorption, emission, and scattering, the photon contributes to both real and virtual transitions between atomic states, including the atomic continuum, and must also be systematically included [4]. Using time-dependant perturbation theory, the scattering of a photon by an atom can be considered through transition amplitudes, \mathcal{T}_{fi} between atomic states either discrete or through a continuum [6]. The photon scattering transition rate $\Gamma_{i \rightarrow f}$ and the cross section $\sigma_{i \rightarrow f}$ are [7]

$$\Gamma_{i \rightarrow f} \propto \int \frac{|\mathcal{T}_{fi}|^2}{T} d^3k, \quad \sigma_{i \rightarrow f} \propto \int \frac{|\mathcal{T}_{fi}|^2}{|\Phi_i|T} d^3k, \quad (66.4)$$

where d^3k is a differential of the outgoing photon frequency, Φ_i is the incoming photon flux, and T is the duration of the interaction. The differential cross sections, $d\sigma/d\Omega$, are usually computed through the Kramers–Heisenberg–Waller formula, which includes both A^2 and $\mathbf{p} \cdot \mathbf{A}$ terms [4]. From a time-independent viewpoint, off-resonant interactions pro-

duce successive Stark corrections of the eigenstates and eigenenergies of the unperturbed atomic system described through the (frequency dependent) polarizability [8].

An example of the cross sections of various processes for atomic hydrogen is shown in Fig. 66.2. Such cross section data are often tabulated as photon mass attenuation coefficients, (μ/ρ) , which describe the decay of the photon beam of intensity I (given incoming intensity I_0) as [9–11]

$$\frac{I}{I_0} = \exp(-\mu d) = \exp\left[-\left(\frac{\mu}{\rho}\right)x\right] = \exp\left[-\left(\frac{\sigma}{m}\right)x\right], \quad (66.5)$$

where μ is the attenuation coefficient, d is the thickness of the material, ρ is the nominal density of the material, $x \equiv (\rho d)$ is the mass thickness, which are all related to σ , the relevant atomic scattering cross section, through the atomic mass $m \equiv uA$ where u is the atomic mass unit, and A the relative atomic mass. An illustrative way to gauge the scale of the various cross sections is to compare them, as can be seen in Fig. 66.2, relative to the Thomson (free-electron) scattering cross section,

$$\sigma_{\text{Th}} = \frac{8\pi}{3} \alpha^4 a_0^2 = 6.652\,458\,7321(60) \times 10^{-29} \text{ m}^2, \quad (66.6)$$

where a_0 is the Bohr radius, and the classical electron radius $r_e = a_0 \alpha^2 \approx 2.8$ fm. The error brackets indicate the standard uncertainty in the last two digits of the 2018 CODATA value [12]; $\sigma_{\text{Th}} \approx 6.65 \times 10^{-25} \text{ cm}^2 = 0.665 \text{ barn} = 66.5 \text{ fm}^2$, which is much smaller than the scale of an atomic cross section of πa_0^2 , due to the factor of $\alpha^4 \approx 3 \times 10^{-9}$. This dictates that away from thresholds and resonances the photon–atom coupling strength is weaker than typical electron–atom interactions, e.g., the electron–hydrogen threshold elastic scattering cross section is around $30\pi a_0^2$ [13]. Instead, as the size of r_e suggests, σ_{Th} is on the order of typical nucleon–nucleon interactions, e.g., the low-energy proton–aluminium total cross section is about 0.65 barn, whilst the fundamental proton–proton cross section is smaller at about 0.04 barn [14].

We now discuss several aspects that Fig. 66.2 highlight:

1. *Elastic photon–atom scattering* (solid line in Fig. 66.2), also known as Rayleigh scattering [3], shows the classic ω^4 dependence for sub-10 eV energies before hitting the atomic $1s \rightarrow np \rightarrow 1s$ excitation resonances between 10.2–13.6 eV. If the wavelength of the incoming photon is large compared to the dimensions of the atom, the dipole approximation $e^{i\mathbf{k} \cdot \mathbf{r}} \approx 1$ holds. In this regime, the vector potential $\mathbf{A}_{k\alpha}(\mathbf{r}, t)$ (Eq. (66.1)) does not significantly depend on the position of the electron \mathbf{r} ; this means that the A^2 term does not directly couple with the atom. Therefore, the $\mathbf{p} \cdot \mathbf{A}$ term dominates for transitions at lower incoming photon energies [5]. An analytic solution

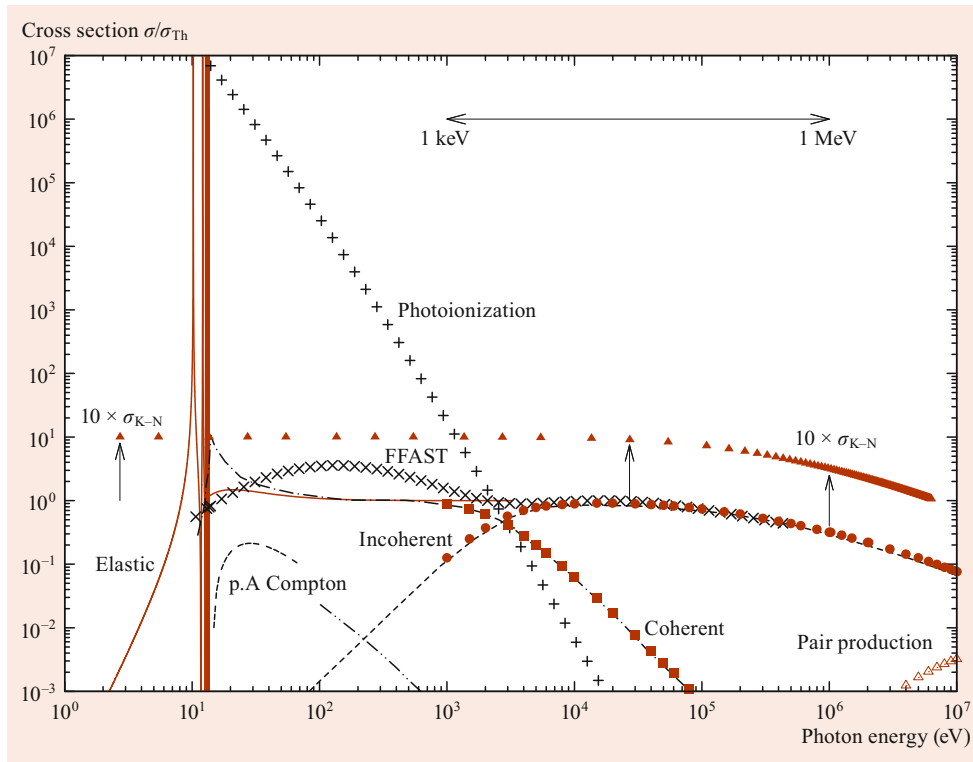


Fig. 66.2 Theoretical (total) cross sections for photon–atomic hydrogen scattering given incoming photon energy in eV, and dimensionless cross sections, $\sigma/\sigma_{\text{Th}}$, are scaled by the Thomson cross section σ_{Th} . The nonrelativistic elastic (Rayleigh) scattering result is the *solid line* (shown up to 100 a.u. = 2.7 keV) and includes resonances. The FFAST [11] database results are included as the + symbols (photoionization) and × symbols (coherent + incoherent). The XCOM [9] results above 1 keV are the *solid squares* (coherent), *solid circles* (incoherent), and *open triangles* (pair-production processes). The Bergstrom et al. [15] results are shown as the *dot-dash line* (coherent), *dashed line* (incoherent), *dash-dot-dot line* ($\mathbf{p} \cdot \mathbf{A}$ Compton). The Drukarev et al. $\mathbf{p} \cdot \mathbf{A}$ Compton calculations [16] are shown as the *three-dash line*. The *filled triangles* are the $\sigma_{\text{K-N}}$ Klein–Nishina cross section (scaled by 10 since it otherwise lies over the other data above 10^5 eV perfectly, indicated by the *vertical arrows*)

to the Kramers–Heisenberg equation exists for hydrogen [17, 18], which approaches the Thomson scattering cross section (the cross section of a photon interacting with an electron in vacuum) at around 100 eV energy. Elastic scattering is classified as “coherent”, shown in Fig. 66.2 for FFAST [11] and XCOM [9] theoretical data, where relativistic effects are important by around 1 keV, which will be discussed further shortly.

There is also, for high- Z atoms, the nuclear (Thomson) scattering of the photon from the nuclear charge that also contributes to the elastic cross section [19–21]. At intermediate photon energies, the nucleus interacts like a point charge, and so the nuclear contribution to the total cross section is [19]

$$\sigma_N = Z^4 \left(\frac{m_e}{M} \right)^2 \sigma_{\text{Th}}, \quad (66.7)$$

where M is the mass of the nucleus. For light atoms, this is very small, e.g., for hydrogen $\sigma_N \approx 3 \times 10^{-7} \sigma_{\text{Th}}$, which is well below the range shown in Fig. 66.2.

2. *Inelastic single-photon photoionization* (the + symbols in Fig. 66.2) dominates above the ionization threshold. As it

is a first-order process, in this energy regime, it is orders of magnitude above the scale of the other processes shown but then reduces with increasing photon energy. The photoionization process is both inelastic and incoherent [22]. For hydrogenic systems, there are analytic results [23], and there are systematic calculations and databases of photoionization cross sections [24], which will be discussed later. Not shown are small radiative corrections to the photoionization cross sections [25], which, above the ionization threshold, are on the same order as the Rayleigh contributions [15].

3. *Inelastic Compton scattering* (shown in Fig. 66.2) is considered to be “incoherent” and is also an inelastic contribution to the cross section [22]. This process requires that the photon have enough energy to photoionize the atom and eject an electron, however, with an associated emission of a photon with a lower frequency than the incident [7, 26]. Compton scattering involves both $\mathbf{p} \cdot \mathbf{A}$ and \mathbf{A}^2 Hamiltonian terms [16]. Figure 66.2 shows the calculations for hydrogen by Drukarev et al. [16] (the line with three dashes) and Bergstrom et al. [15] (the dot-dot-dash line), where only the $\mathbf{p} \cdot \mathbf{A}$ terms were included and shows

a relatively small contribution between onset at 13.6 eV up to about 500 eV. The differences between these two calculations can be explained by the different numerical cut-offs applied that truncate the infrared divergence [27]. The A^2 term represents the dominant method of transferring momentum during Compton scattering [28]. It dominates at keV and above incoming photon energies [5], where atomic recoil is more important, and the dipole approximation is increasingly not valid. This is seen in the incoherent scattering results in Fig. 66.2 from Bergstrom et al. [15] (line with small dashes), which rises up from 100 eV and crosses over the $\mathbf{p} \cdot \mathbf{A}$ Compton cross section and at 1 keV connects with the incoherent XCOM database results [9] (the large dots in Fig. 66.2). Including the A^2 term only is known as the impulse approximation [5].

Not shown in Fig. 66.2 is (inelastic) Raman scattering [29], which has $1s-np-ns$ resonances [30]; for hydrogen these behave similarly to those seen for Rayleigh scattering in Fig. 66.2. However, the Raman cross sections are generally smaller than the Rayleigh and Compton cross sections above the ionization threshold.

4. *Relativistic scattering* of a photon from a free-electron has an analytic result given by the Klein–Nishina formula [27, 31, 32], which, in dimensionless form, is

$$\frac{\sigma_{K-N}}{\sigma_{Th}} = \frac{3}{4} \left[\frac{(1+\epsilon)}{\epsilon^3} \left(\frac{2\epsilon(1+\epsilon)}{(1+2\epsilon)} - \ln(1+2\epsilon) \right) + \frac{\ln(1+2\epsilon)}{2\epsilon} - \frac{(1+3\epsilon)}{(1+2\epsilon)^2} \right], \quad (66.8)$$

where $\epsilon = E/m_e c^2 \approx \hbar\omega/511$ keV. This is also shown in Fig. 66.2, where at energies about 10^4 eV, there begins a significant departure from the Thomson value, σ_{Th} . The curve tracks the hydrogen calculations almost perfectly through the keV to MeV energies, compared to the database and numerical cross sections. Note that the relativistic treatment of photon-particle scattering includes virtual particle creation [4].

The inclusion of relativistic effects on the photon–atom scattering cross sections is mostly clearly seen in the decrease of the coherent XCOM database results [9] starting at energies from 1 keV and above (large squares in Fig. 66.2). They rely on relativistic atomic form factors such that Rayleigh scattering cross sections are approximated as [33],

$$\sigma_{coh} = \frac{3}{8} \sigma_{Th} \int_{-1}^1 (1 + \cos^2 \theta) [F(x, Z)]^2 d(\cos \theta), \quad (66.9)$$

where Z is the atomic number and $x = \sin(\frac{1}{2}\theta)/\lambda$ of wavelength, λ . Numerical methods to compute $F(x, Z)$

rely on the density distribution of the electron/s, whilst $F(x, Z) \rightarrow 0$ and, thus, $\sigma_{coh} \rightarrow 0$ at keV energies (large x). Attempts to improve the form-factor approximation hit some limitations [3], however, calculations using the relativistic impulse approximation show that the Compton scattering cross sections are in general agreement with the Klein–Nishina formula at keV–MeV energies [34]. It is possible to systematically include relativistic, retardation, and higher multipole effects [15, 35].

For all atoms through the intermediate keV to MeV energy regime, photoionization tends to dominate all scattering cross sections, but there is a cross-over point where incoherent inelastic scattering processes begin to dominate. The cross-over point generally increases with the atomic number, e.g., for copper atoms, it crosses over at around 100 keV [2].

5. *Nuclear scattering* processes contribute towards both the elastic and inelastic scattering amplitudes [3]. As mentioned above, there is elastic (nuclear) Thomson scattering, but there are other high-energy processes that can exceed that of (bound electron/s) Rayleigh scattering cross sections around the GeV and above energy range. XCOM data (glimpsed at GeV energies in the bottom-right corner of Fig. 66.2), shows the scattering cross section for electron–positron pair production in the field of the atomic nucleus (starting at $2m_e c^2 \approx 2 \times 511$ keV) [9]. This is one of the phenomena classified as Delbrück nuclear scattering [36], which is considered as an inelastic contribution where the pairs are produced. There is also a smaller contribution due to elastic scattering off the vacuum polarization, with annihilation of the virtual pair created [3], which is not included in XCOM [9]. There is also a contribution due to pair production in the field of the atomic electrons, which is also presented in XCOM tabulations [9]. For light atoms, the pair-production contribution from the electron/s can be larger than the nuclear contribution at energies above hundreds of GeV. For heavy atoms, the nuclear contribution is significantly larger [36]. For all atoms, XCOM shows that these processes at well above GeV photon energies are the largest cross sections and approach an asymptotic limit. XCOM does not include photonuclear resonance scattering, two-photon Delbrück scattering, or other higher-energy inelastic processes [37, Fig. 1].

66.2.1 Applications of Atomic Cross Sections

Photon–atom cross sections are used throughout the physical sciences [38]. Intermediate energy photon scattering has a wide range of applications in both medical and biological contexts, i.e., radiological physics and radiation dosimetry [39], including medical diagnosis [40]. Another

important area is nondestructive testing and 3-D imaging, such as for detecting explosives [41] and food contaminants [42], as well as archaeology [43].

Some of the example photon energy regimes are:

- 10 keV – materials science using x-ray elastic diffraction (XRD) to probe crystal and other material structures
- 10–150 keV – high-resolution medical imaging using x-ray and computed tomography (CT) [44]
- 28–60 keV – x-ray back-scattering-based airport security [45]
- 1–15 MeV – megavoltage x-rays are used in external beam radiation therapy (EBRT), i.e., photon therapy.

With so many diverse applications, it is infeasible to collect experimental data for each one. These applications are designed through the simulation of photon transport through techniques such as Monte-Carlo codes and radiation hydrodynamics, which are discussed later. In such radiation transport simulations, the frequency of the photon ω tends to decrease with successive collisions, depositing energy into the material. Individual photons are tracked as they interact with a material and tend to lose energy to the atoms/molecules they interact with for each collision. For example, cross sections are used to the combined attenuation and buildup factors, for energies into the GeV regime and distances (10 cm) relevant in photon-based treatments [46].

Photon–atom scattering cross sections are the main ingredient in characterizing the opacity of a material through different temperatures and phases and with photons of varying energy [47]. The input cross section data is computed by various approximations, requiring major data compilations and software developed by large collaborations, including the Opacity Project [48], as well as at Los Alamos [49]. The focus of the input cross sections is in single-photon physics, including photoionization and core excitations [48], but does include low-energy Rayleigh scattering [49]. There is a vast number of applications of opacity data [47], ranging from sub-keV photon energies (greenhouse gas and stellar structure) through to GeV energies (nuclear and high-temperature plasma modeling).

Atomic cross sections in the intermediate energy regime are found throughout astrophysics [50]. There have been many space-based x-ray detecting missions, since the Earth’s atmosphere absorbs x-rays, and the satellites need to orbit outside the Earth’s radiation belts. Some examples of active satellites, their launch dates, and x-ray observation ranges are [51]

- 1999 – XMM-Newton observatory, low-mid energy x-rays 0.1–15 keV
- 1999 – Chandra x-ray observatory, high-resolution spectroscopy < 0.5 keV or > 2 keV

- 2007 – AGILE, x-rays 18–60 keV, gamma-rays 350 keV–100 MeV, 30 MeV–50 GeV
- 2017 – Insight, hard x-ray modulation telescope (HXMT), 20–250 keV, 5–30 keV, 1–15 keV
- 2019 – Spektr-RG, medium-band 0.3–10 keV and 4–30 keV.

Theoretical knowledge of spectroscopic lines and cross sections is critical to their design and, subsequently, to understanding their astrophysical observations.

66.3 Experimental Progress

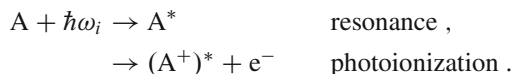
X-rays can be produced on demand through several means; primarily, through synchrotrons. Secondly, electroluminescence using an x-ray tube where the collision of high-energy electrons in a material with core electrons can produce a photon flux with well-defined energies. Thirdly, radioactive sources that emit with well-defined energies both through the x-ray and gamma ray regimes. Fourthly, like electroluminescence but using proton beams colliding with a material at core-electron excitation and subsequent emission. For x-ray manipulation, generally diffraction gratings are used for the soft x-ray range, whereas perfect Bragg crystal optics are utilized in the hard x-ray range [52]. The *X-Ray Booklet* is a regularly updated collection of both data and articles that summarizes various technological advances used for x-ray production and also x-ray measurement (updated v3 in 2009) [53]. Another regularly updated x-ray resource is the massive *International Tables for Crystallography, Volume C* (3rd edition 2004) [54], with a new x-ray-related Volume I in preparation <https://it.iucr.org/>.

Experimental total absorption cross sections have been in broad agreement with theory over a wide range of energies for many years. For example, see the total cross section comparisons in 1980 shown in Figs. 1/2/3 (for C/Cu/Pb) in [36]. The experimental data in those figures consist of 90, 116, and 121 independent measurements, tracking the theoretical core-electron structure due to photoionization, then the incoherent dominated region around 1 MeV, and then the pair-production cross section above MeV energies. Measurements of high-energy Rayleigh scattering tend to be above the energy ranges considered, i.e., in above 1 MeV, where the nuclear effects begin to dominate [20].

The 1 keV to 1 GeV x-ray regime presents challenges and opportunities for using photon–atom studies that probe the core electron/s in various ways. The primary experimental data needed are the transition energies, defined as the energies at which the possibility of a core electron being excited to the continuum by a photon exists. Experimental data has been combined with theoretical data in an extensive data review by *Deslattes et al.* [55].

There are several well-developed techniques now routinely employed (with acronyms deployed) such as:

- XRD – x-ray elastic diffraction – experimental information of the long-range order in the material that an atom is surrounded by can be obtained, with wavelengths $1 \text{ keV} \equiv 8.07 \times 10^6 \text{ cm}^{-1} \equiv 1.24 \text{ nm}$ being on the order of the spacing in materials (note $1 \text{ MeV} \equiv 8.07 \times 10^9 \text{ cm}^{-1} \equiv 0.00124 \text{ nm}$). Whilst (Rayleigh) elastic scattering of photons from an isolated atom is coherent, the presence of nearby atoms generates Bragg–Laue coherent scattering, which gives peaks and profiles and enables both x-ray diffraction and, thus, crystallography. However, thermal effects can result in thermal diffuse scattering (TDS), where a more complicated interference structure arises due to the incoherence between scattering events [54].
- XAS – x-ray absorption spectroscopy – is a broad set of methods where the x-ray photon is absorbed by an electron with enough energy to transition into an excited state or photoionize and place it above the Fermi-level of the material, which does not need to have long-range material order [56]. When an atom interacts with a photon of frequency ω_i , the first-order absorption processes are



Thus, the photon is removed from the beam, which is then seen as a signal loss as a function of incident frequency. This is initially seen as a series of edges where the absorption rapidly rises when there is more incoming photon energy than the core electron binding energy, and it photoionizes to the continuum (with nomenclature K for removal of a $1s$ core electron, L for $2s$ or $2p$ core electron, etc. [2]). XAS also is used to encompass the absorption both through the “pre-edge” energy region and below it. XAS includes XANES, EXAFS, XAFS, and XERT, which are discussed individually below. The XAS field and range of applications have exploded in the last decade [52, 57].

- XANES – x-ray absorption near-edge structure – are the lowest energy XAS absorption signatures, resulting from the transition of the core electron to (unoccupied) bound states. For example, chromium has valence states of $3d^5 4s^1$, so the lowest energy absorption peak series seen at the K -edge is from $1s \rightarrow 3d$, then $1s \rightarrow 4s$, then $1s \rightarrow 4p$, etc. [56]. As the energy levels are modified by the chemical environment that the atom is in, there are changes in the measured spectra that can be interpreted [58].
- EXAFS – extended x-ray absorption fine structure – is also XAS but is performed in the region of energy above XAFS. XAS absorption signature where the absorption,

for example, for the K -shell, is above the $1s \rightarrow n\ell$ (Rydberg) bound state series and into the $1s \rightarrow \varepsilon p$ continuum. This EXAFS regime is where the photoionization process involves the relatively slow emission of a photoelectron, which can have a de Broglie wavelength on the order of the surrounding material, and, thus, a particular interference pattern due to the local chemistry is observed as a function of incoming photon frequency.

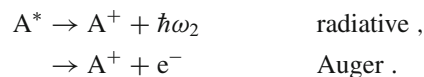
- XAFS – x-ray fine structure absorption spectroscopy – represents both XANES and EXAFS, i.e., the overall XAS structures spanning the valence and low-lying continuum at a core-excitation edge [59].
- DAFS – diffraction anomalous fine structure – is a combined XRD and XAS technique that relies on the long-range order in the material with a high brightness of the source [57].
- XERT – x-ray extended-range technique – is XAFS used with multiple measurements taken with varying material thicknesses, which is used to reduce errors [60, 61]. Given improved synchrotron and detector resolution below the linewidth of atomic transitions, XAFS is able to resolve the (atomic fine-structure) level splitting (e.g., between $p_{\frac{1}{2}}$ and $p_{\frac{3}{2}}$ core states in the L edge) and is sensitive to quantum electrodynamics (QED)-level correction physics [62].

66.3.1 Inelastic Processes

The initial suggestion of inelastic photon scattering with quantized emission was made by *Smekal* [63] and was experimentally observed in the optical regime by *Raman* [64], with the suggestion that a similar mechanism should be seen in x-rays. Inelastic (Smekal–Raman) x-ray scattering was spectroscopically observed in 1958 along with Rayleigh scattering from the core electrons, as well as Compton scattering [65].

There are now many methods relying on inelastic x-ray scattering (IXS). IXS covers a broad set of methods where the photon is absorbed with resulting excitation or photoionization, resulting in a secondary process, which is experimentally involved with the spectroscopic detection of outgoing photon/s with a different energy to the incident (or correlated electron/s) [66]. This, along with the momentum transfer, provides information about the materials surrounding the atom [67].

When an atom (or ion) is placed in an excited state A^* with a hole in a core shell, this can decay through either radiative or radiationless (Auger) processes



Each of these processes is restricted to the usual quantum selection rules, which, in LS -coupling, are all conserved for Auger processes [2]

$$\Delta J = \Delta M_J = \Delta L = \Delta M_L = \Delta S = \Delta M_S = 0, \quad (66.10)$$

where the total angular momentum of the A^* wave function is $J = L + S$, and the initial wave function parity is the same as the final ($\pi_i = \pi_f$). For radiative processes via electric dipole allowed transitions,

$$\begin{aligned} \Delta J &= 0, \pm 1 \quad (\text{but not } J_i = 0 \rightarrow J_f = 0), \\ \Delta M_J &= 0, \pm 1, \quad \pi_i = -\pi_f. \end{aligned} \quad (66.11)$$

Within LS -coupling, if it is a single-electron transition then $\Delta L = \pm 1$, and if $\Delta S = 0$, then $\Delta L = 0, \pm 1$ (but not $L_i = 0 \rightarrow L_f = 0$). In most atoms, when a core electron has been removed, these selection rules mean that many more Auger transitions are allowed than radiative transitions [2].

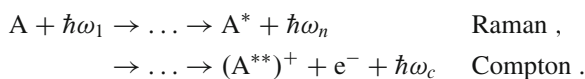
The probability of each (allowed) decay pathway occurring depends on their transition matrix elements, which, to compute them accurately, requires complicated wave functions with many-body correlations. However, simpler approximations such as Wentzel’s independent particle approximation are often an illustrative, if not always accurate, starting point. For an Auger process, the probability is related to the Coulomb matrix element [68–70]

$$P \propto \left\langle \left\langle n_c \ell_c j_c, \varepsilon \ell_\varepsilon j_\varepsilon \left| \frac{1}{r_1 - r_2} \right| n_a \ell_a j_a, n_b \ell_b j_b \right\rangle \right\rangle^2, \quad (66.12)$$

with a and b denoting the two initial electrons, c the final state core orbital, and ε the continuum orbital, which is the (Auger) ejected electron. Such two-body matrix elements must include both direct and exchange contributions [2] and obey the above total angular momentum selection rules. The (ionized) continuum electron carries off the energy that the remaining electron/s require to be released to drop down into the core shell. The (x-ray fluorescence emission) radiative dipole transition matrix elements in their reduced form look like $\langle n_c \ell_c j_c || r \cos \theta || n_a \ell_a j_a \rangle$, which can provide a good description of these decay pathways [70].

Atoms tend to decay predominantly via Auger processes [2, 69], which can involve cascades of multiple states [71, 72]. An initial state (i) has partial widths for radiative decay, $\Gamma_R(i)$, and for Auger $\Gamma_A(i)$. The fluorescence yield for this state is then given by $\Gamma_R(i)/(\Gamma_R(i) + \Gamma_A(i))$ since decay rates are additive [68].

Raman and Compton scattering are heuristically



The notation “...” indicates that, as per Fig. 66.1, either the first-order A^2 interaction will skip straight to the final state or the second-order consecutive $p \cdot A$ operations proceed through a complete set of intermediate states. In Raman processes, each emitted photon is from the set of frequencies $\{\omega_n\}$, which are based on an available quantized relaxation transition to a lower bound state. In contrast, the photoionization-based Compton process emits a photon from the continuous distribution of energetically available photon frequencies ω_c . These are often grouped together as inelastic “Raman–Compton” scattering [66].

Capturing x-ray emission yields information about the atoms and their local environment [57]. Some techniques (and their acronyms) are:

- XES – x-ray emission spectroscopy – a broad set of techniques that measures the outgoing photon frequencies using x-ray spectrometry [57]. XES is an intrinsic part of both XAS and XAFS, i.e., the emission/fluorescence spectroscopy forms the toolkit.
- XRS – x-ray Raman spectroscopy/scattering – is a specific type of XES that involves inelastic Raman scattering, detecting photons at characteristic energies that have been emitted at a different frequency to the incident [59]. Note that the final state (A^* as above) can be a continuum state above the Fermi level [67].
- RIXS – resonant inelastic x-ray scattering – is the second-order $p \cdot A$ -dominated Raman scattering process, which is enhanced during absorption of the photon to a continuum state near threshold, which is observed through emission at discrete frequencies $\{\omega_n\}$ [67]. This is also known as resonant Auger scattering [73], RRS (resonant Raman scattering) [74], or RXES (resonant XES) [75].

Some key experiments using different photon generation schemes that measured inelastic scattering are the following.

- 1989 – Synchrotron-generated tunable x-ray beams of energy between a few keV up to 19 keV, detector tunable, e.g., at 6 keV with 0.155 eV resolution [76, 77]. Scattering off Zr (whose K-shell binding energy is close to 18 keV) measured “Raman–Compton” and Rayleigh scattering and the infrared divergence.
- 1989 – Radioactive ^{137}Cs source that emits 662 keV photons, an x-ray detector, e.g., operating at 80 keV with resolution of 0.7 keV for fluorescent photon in coincidence with a gamma-ray detector for the scattered photon for Compton scattering studies of Pb [78].
- 1996 – X-ray tube with W-anode (the $K\alpha_1$ line is 59.32 keV), with a detector at 60 keV with resolution 0.4 keV for Compton scattering off Cu in coincidence with fluorescence photons [79].

- 2006 – Resonant Raman study with incident synchrotron beam scanned across the energy range near the Si K-absorption edge (1.840 keV) with a beam width of 6 eV and a high-resolution (0.9 eV) spectrometer measuring the emitted photons at the fluorescence line (1.740 keV) [74].
- 2010 – 1 MeV proton beam, which irradiates Mg, Al, and Si targets to form soft-x-ray beams of 1.235, 1.486, and 1.740 keV, which then target the same materials, measuring resonant Raman scattering [80, 81].
- 2010 – Benchmark IXS experiments have been performed with Compton scattering on He with synchrotron radiation using a detector fixed at 9.88968 keV with energy resolution down to 70 meV [82].

66.4 Theory, Computation, and Data

Excellent introductory tutorials covering both soft and hard x-ray interactions with atoms have been given by *Pratt* [83] and *Santra* [70]. The *Hopersky* and *Yavna* monograph presents the general many-body theory of x-ray photon-atom interactions, with an emphasis on computation of both atoms and molecules [84]. Detailed theoretical approaches to resonant x-ray Auger/Raman scattering emphasizing Kramers-Heisenberg and Weisskopf-Wigner descriptions can be found in [73, 75, 85].

Overviews of the fundamental theories used in inelastic scattering calculations can be found in [86, 87]. The most successful computational approach remains the relativistic S-matrix with independent particle approximation, which goes beyond the impulse approximation [88]. Accurate calculations require solving challenging many-body problems, which presents problems even when computing the underlying atomic structure [55].

Beyond single-atom physics, computing the effects of the local material requires a combination of approaches since x-ray absorption involves a description of the chemical interactions between the valence orbitals, the conduction band, and phonon-like excitations.

This is challenging for the theoretical and computational modeling of experimental XAS/EXAFS/XANES data where multiple-particle scattering effects need to be included [89, 90], and chemistry-based methods such as density functional theory (DFT) are now routinely applied [58]. High-performance computing software is now readily available to solve a broad range of such physics and systems. For example, several programs have been developed in recent decades that have a lot of versatility, e.g., the GNXAS suite, which handles XAS data analysis including the molecular/crystal structure [91], the FDMNES suite models XANES and RXS [92], whilst the FEFF suite can handle XAS, Compton, NRIXS (nonresonant IXS) [93].

66.4.1 Databases

The history of photon cross section calculations, as used in databases, is discussed by *Hubbell* [38]. Three photon-atom scattering cross section databases at NIST are part of their Atomic and Molecular Physics component of the Standard Reference Data (SRD) program:

- **SRD 8** XCOM/XGAM: Photon Cross Sections Database [9, 94],
- **SRD 66** FFAST: x-ray Form Factor, Attenuation and Scattering Tabulation [95],
- **SRD 126** XAAMDI: x-ray Attenuation and Absorption for Materials of Dosimetric Interest [10].

Lawrence Livermore National Laboratories (LLNL) have had a long history of photon-atom database development. As was mentioned earlier, the XDB x-ray Data Booklet contains a massive regularly updated set of data [53]. It appears that their standalone RTAB database for Rayleigh scattering cross sections [21] is no longer publicly available via URL. They produced the Evaluated Photon Data Library (EPDL), which is part of the Evaluated Nuclear Data File ENDF/B-VI photon interaction library, which covers photons in the energy range 10 eV–100 MeV interacting with elements $Z = 1-100$ [96]. This was revised in 2018 as ENDF/B-VIII.0 [97, 98].

These databases, which focus on x-ray through γ -ray photon energies, find application through fundamental physics, materials sciences, and medical physics [39, 99].

66.4.2 Bulk Modeling

The tracking of how intermediate energy photons propagate through bulk material is extremely challenging due to the aforementioned inelastic channels that are open. Radiation transport is handled through *Monte-Carlo* simulations that can consider first and second-order photon scattering processes [100, 101]. Some examples of programs are GEANT4 Geometry and Tracking [102, 103], PENELOPE [104, 105], EGS5 [106], EGSnrc [107], FLUKA [108, 109], ROSI Roentgen Simulation [110], MRED Radiative Energy Deposition [111], and ARCHER [112].

A popular alternative to the above tracking-based Monte-Carlo schemes is to use *radiation hydrodynamics*, which treats the flow of radiation as a fluid [113]. This uses as input the first-order atom-photon interactions, such as the opacity, where emission and absorption processes are considered as distinct. Codes such as FLYCHK [114] and PURGATORIO [115] have been used to model extreme material environments involving intense pulses of several keV x-rays [116]. Such experiments are able to extract information

about extreme temperatures of stellar interiors and high-energy density plasmas using x-rays in the laboratory [117].

66.5 Future Directions

Finally, we mention a few areas of recent activity with a view towards the future.

Continuing improvements in synchrotron brightness and spectrometer resolution [52, 53, 57] will enable the next generation of x-ray reaction microscopes, e.g., for coincidence measurements of photons from cascades and photoelectrons from gas phase targets.

For even a relatively simple atom like Si [118], XAFS experimental measurements have, as yet, unresolved errors on the order of 5% between theory and experiment [62]. There has been a call for experimental XAFS benchmarking between facilities to identify the error sources [119]. RIXS experiments have become increasingly sophisticated, with precision spectroscopy (sub-1eV detector resolution) involving multiple channels with gas phase targets presenting challenges for theory to keep up with [120], especially where more than one electron is involved in the absorption/emission process [121].

Pratt previously summarized some outstanding theoretical issues [22], which remain relevant and should be pursued. Very recently, a promising new computational approach to x-ray processes was developed and released [122]; it uses MCDHF (multiconfiguration Dirac–Hartree–Fock) calculations to model the atomic structure and is designed to compute atomic cascades and the time evolution of density matrices. The availability of new high-performance computing codes using configuration interaction such as GRASP [123], and with particle-hole excitations and with over five valence particles, e.g., AMBIT [124, 125], opens up the ability to compute the atomic levels, x-ray transition probabilities, and Auger physics to even higher-accuracy than MCDHF systematically across the periodic table. These codes are also systematically able to compute and quantify isotope and QED effects that are able to be resolved in x-ray experiments with highly-charged ions in electron beam ion traps (EBITs) [62], and a major effort should be undertaken for the ab-initio computation of atomic processes involving keV to MeV photons.

The nonlinear response of atoms and ions interacting with intense electromagnetic fields is useful in a wide-range of applications throughout the physical sciences [126]. Nonlinear x-ray optics presents a new frontier to probe atoms and materials, with the latest generation of synchrotron sources capable of reaching such brightness, especially if applied in intense ultrashort pulses. New theoretical work has begun to appear to describe Rayleigh scattering of two x-ray photons by an atom [127] and to develop a time-dependent QED ap-

proach to x-ray nonlinear Compton scattering (XNCS) [128], where the independent photon model breaks down. Applications to multielectron systems present a theoretical, computational, and experimental challenge.

All of the NIST database calculations are not ab-initio and are generally thought to work best above the keV photon regime [95]. The development of improved intermediate-energy approximations towards improved modeling of photon transport as the photons drop from the GeV and down into the sub-keV would be welcome. For example, a side-by-side comparison of Monte-Carlo ROSI and GEANT4 calculations with x-rays at 100 keV, 400 keV, 1 GeV, and higher, showed that the use of the different input data sets makes observable differences in the outputs [129].

There are other extreme facilities available for x-ray studies, such as ZAPP, The Z Astrophysical Plasma Properties collaboration [130]. This has enabled benchmarking photoionized plasma models and validating extreme radiation transport models in laboratory astrophysics [131].

For the future of x-ray astrophysics, there are a couple of main missions in planning: for 2022 launch of the x-ray Imaging and Spectroscopy Mission (XRISM) to measure 0.3–12 keV x-rays with 5–7 eV energy resolution, and in 2031 the launch of the next generation ATHENA telescope with spectroscopic imaging in the energy range of 0.2–12 keV [132].

Acknowledgments The author would like to thank Dr Swaantje Grunefeld, Dr Emily Kahl, Gian Carlo Ruzzi Villacres, and Corey Hanrahan for many discussions and for providing Fig. 66.1 and the Rayleigh data in Fig. 66.2. He further thanks Dr Ivan Mikhaylov for providing the [16] data in Fig. 66.2 and Professor Christopher Chantler for helpful suggestions. This work was partially supported through an Australian Research Council Future Fellowship FT100100905 at The University of Queensland.

References

1. Crasemann, B.: Photon-Atom Interactions: 1 keV – 1 MeV. American Institute of Physics, New York, pp 701–711 (1996). Ch. 60
2. Crasemann, B.: Photon-Atom Interactions: Intermediate Energies. Springer, New York, pp 915–927 (2006) <https://doi.org/10.1007/978-0-387-26308-3>. Ch. 62
3. Kissel, L., Pratt, R.H.: Rayleigh Scattering: Elastic Photon Scattering by Bound Electrons. Springer US, Boston, p 465 (1985) <https://doi.org/10.1007/978-1-4613-2417-1>. Ch. 11
4. Sakurai, J.J.: Advanced Quantum Mechanics. Addison-Wesley (1967)
5. Eisenberger, P., Platzman, P.M.: Compton scattering of x rays from bound electrons. Phys. Rev. A **2**, 415 (1970). <https://doi.org/10.1103/PhysRevA.2.415>
6. Weissbluth, M.: Photon–Atom Interactions. Academic Press, San Diego (1989) <https://doi.org/10.1016/C2009-0-22193-3>
7. Cohen-Tannoudji, C., Dupont-Roc, J., Grynberg, G.: Atom–Photon Interactions: Basic Processes and Applications. Wiley, New York, USA (1992) <https://doi.org/10.1002/9783527617197>

8. Mitroy, J., Safronova, M.S., Clark, C.W.: Theory and applications of atomic and ionic polarizabilities. *J. Phys. B* **43**, 202001 (2010). <https://doi.org/10.1088/0953-4075/43/20/202001>
9. Berger, M.J., Hubbell, J.H., Seltzer, S.M., Chang, J., Coursey, J.S., Sukumar, R., Zucker, D.S., Olsen, K.: XCOM: Photon Cross Section Database (version 1.5) (2010). <http://physics.nist.gov/xcom>
10. Hubbell, J.H., Seltzer, S.M.: Tables of X-ray Mass Attenuation Coefficients and Mass Energy-Absorption Coefficients (version 1.4) (2004). <http://physics.nist.gov/xaamdi>
11. Chantler, C., Olsen, K., Dragoset, R., Chang, J., Kishore, A., Kotochigova, S., Zucker, D.: X-Ray Form Factor, Attenuation and Scattering Tables (version 2.1) (2005). <http://physics.nist.gov/ffast>
12. Tiesinga, E., Mohr, P.J., Newell, D.B., Taylor, B.N.: The 2018 CODATA Recommended Values of the Fundamental Physical Constants (Web Version 8.1) (2020). <http://physics.nist.gov/constants>. database developed by J. Baker, M. Douma, and S. Kotochigova
13. Bederson, B., Kieffer, L.J.: Total electron-atom collision cross sections at low energies - a critical review. *Rev. Mod. Phys.* **43**, 601 (1971). <https://doi.org/10.1103/RevModPhys.43.601>
14. Bugg, D.V., Salter, D.C., Stafford, G.H., George, R.F., Riley, K.F., Tapper, R.J.: Nucleon-nucleon total cross sections from 1.1 to 8 GeV/c. *Phys. Rev.* **146**, 980 (1966). <https://doi.org/10.1103/PhysRev.146.980>
15. Bergstrom, P.M., Surić, T., Pisk, K., Pratt, R.H.: Compton scattering of photons from bound electrons: Full relativistic independent-particle-approximation calculations. *Phys. Rev. A* **48**, 1134 (1993). <https://doi.org/10.1103/PhysRevA.48.1134>
16. Drukarev, E.G., Mikhailov, A.I., Mikhailov, I.A.: Low-energy K-shell Compton scattering. *Phys. Rev. A* **82**, 023404 (2010). <https://doi.org/10.1103/PhysRevA.82.023404>
17. Gavrilin, M.: Analytic evaluation of the Kramers-Heisenberg matrix element for coherent scattering of photons by atomic hydrogen. *Rev. Roum. Phys.* **12**, 745 (1967)
18. Gavrilin, M.: Elastic scattering of photons by a hydrogen atom. *Phys. Rev.* **163**, 147 (1967). <https://doi.org/10.1103/PhysRev.163.147>
19. Moon, P.B.: The hard components of scattered gamma-rays. *Proc. Phys. Soc. A* **63**, 1189 (1950). <https://doi.org/10.1088/0370-1298/63/11/301>
20. Kissel, L., Pratt, R.H., Roy, S.C.: Rayleigh scattering by neutral atoms, 100 eV to 10 MeV. *Phys. Rev. A* **22**, 1970 (1980). <https://doi.org/10.1103/PhysRevA.22.1970>
21. Kissel, L.: RTAB: the Rayleigh scattering database. *Rad. Phys. Chem.* **59**, 185 (2000). [https://doi.org/10.1016/S0969-806X\(00\)00290-5](https://doi.org/10.1016/S0969-806X(00)00290-5)
22. Pratt, R.H.: Photon absorption and photon scattering - What we do not know and why it matters. *Rad. Phys. Chem.* **95**, 4 (2014). <https://doi.org/10.1016/j.radphyschem.2013.10.018>
23. Sobelman, I.I.: Atomic Spectra and Radiative Transitions, 2nd edn. Springer, Berlin (1996) <https://doi.org/10.1007/978-3-642-76907-8>. Corrected Second Edition
24. Scofield, J.H.: Theoretical photoionization cross sections from 1 to 1500 keV., Tech. rep. Lawrence Livermore Laboratory (1973) <https://doi.org/10.2172/4545040>
25. Botto, D.J., Gavrilin, M.: Radiative corrections to atomic photoeffect and tip bremsstrahlung. III. *Phys. Rev. A* **26**, 237 (1982). <https://doi.org/10.1103/PhysRevA.26.237>
26. Dick, R., Advanced Quantum Mechanics: Materials and Photons, 2nd edn. Graduate Texts in Physics. Springer (2016) <https://doi.org/10.1007/978-3-319-25675-7>
27. Heitler, W.: The Quantum Theory of Radiation. Clarendon Press, Oxford (1954)
28. Brouder, C.: Angular dependence of X-ray absorption spectra. *J. Phys. Cond. Matter* **2**, 701 (1990). <https://doi.org/10.1088/0953-8984/2/3/018>
29. Band, Y.B.: Light and matter (electromagnetism, optics, spectroscopy and lasers). Wiley, Hoboken, NJ, Chichester, England (2006). <http://www.wiley.com/remtitle.cgi?ISBN=9780471899310>
30. Sadeghpour, H.R., Dalgarno, A.: Rayleigh and Raman scattering by hydrogen and caesium. *J. Phys. B* **25**, 4801 (1992). <https://doi.org/10.1088/0953-4075/25/22/015>
31. Klein, O., Nishina, Y.: Über die Streuung von Strahlung durch freie Elektronen nach der neuen relativistischen Quantendynamik von Dirac. *Z. Phys.* **52**, 853 (1929). <https://doi.org/10.1007/BF01366453>
32. Klein, O., Nishina, Y.: On the Scattering of Radiation by Free Electrons According to Dirac's New Relativistic Quantum Dynamics. World Scientific, Singapore, p 253 (2014) https://doi.org/10.1142/9789814571616_0015, translated by Dr Lars Bergström
33. Hubbell, J.H., Overbo, I.: Relativistic atomic form factors and photon coherent scattering cross sections. *J. Phys. Chem. Ref. Data* **8**, 69 (1979). <https://doi.org/10.1063/1.555593>
34. Stutz, G.E.: Compton scattering cross section for inner-shell electrons in the relativistic impulse approximation. *Nucl. Instrum. Methods Phys. Res. B* **319**, 8 (2014). <https://doi.org/10.1016/j.nimb.2013.11.001>
35. Costescu, A., Spanulescu, S.: Retardation, multipole, and relativistic kinematics effects for x- and γ -ray Compton scattering from K-shell electrons. *Phys. Rev. A* **73**, 022702 (2006). <https://doi.org/10.1103/PhysRevA.73.022702>
36. Hubbell, J.H., Gimm, H.A., Øverbø, I.: Pair, triplet, and total atomic cross sections (and mass attenuation coefficients) for 1 MeV-100 GeV photons in elements Z=1 to 100. *J. Phys. Chem. Ref. Data* **9**, 1023 (1980). <https://doi.org/10.1063/1.555629>
37. Hirayama, H.: Lecture Note on Photon interactions and Cross Sections, Tech. rep., KEK High Energy Accelerator Research Organization (2000). http://rcwww.kek.jp/research/shield/photon_r.pdf, Accessed 2015
38. Hubbell, J.H.: Review and history of photon cross section calculations. *Phys. Med. Biol.* **51**, R245 (2006). <https://doi.org/10.1088/0031-9155/51/13/r15>
39. Hubbell, J.H.: Review of photon interaction cross section data in the medical and biological context. *Phys. Med. Biol.* **44**, R1 (1999). <https://doi.org/10.1088/0031-9155/44/1/001>
40. Guzzardi, R., Licitra, G.: A critical review of Compton imaging. *Crit. Rev. Biomed. Eng.* **15**, 237 (1987). <http://www.ncbi.nlm.nih.gov/pubmed/3329596>
41. Harding, G.: X-ray scatter tomography for explosives detection. *Rad. Phys. Chem.* **71**, 869 (2004). <https://doi.org/10.1016/J.RADPHYSHEM.2004.04.111>
42. Bull, C.R., Zwiggelaar, R., Speller, R.D.: Review of inspection techniques based on the elastic and inelastic scattering of x-rays and their potential in the food and agricultural industry. *J. Food. Eng.* **33**, 167 (1997). [https://doi.org/10.1016/S0260-8774\(97\)88544-5](https://doi.org/10.1016/S0260-8774(97)88544-5)
43. Harding, G., Harding, E.: Compton scatter imaging: a tool for historical exploration. *Appl. Rad. Iso.* **68**, 993 (2010). <https://doi.org/10.1016/j.apradiso.2010.01.035>
44. Müller, B.: Recent trends in high-resolution x-ray tomography. *Dev. X-ray Tomogr. Xi* **10391**, 1039102 (2017). <https://doi.org/10.1117/12.2275580>
45. Rez, P., Metzger, R.L., Mossman, K.L.: The dose from compton backscatter screening. *Rad. Prot. Dos.* **145**, 75 (2011). <https://doi.org/10.1093/rpd/ncq358>
46. Angelopoulos, A., Perris, A., Sakellariou, K., Sakelliou, L., Sari-geannidis, K., Zarris, G.: Accurate Monte Carlo calculations of the combined attenuation and build-up factors, for energies (20-1500 keV) and distances (0-10 cm) relevant in brachytherapy. *Phys.*

- Med. Biol. **36**, 763 (1991). <https://doi.org/10.1088/0031-9155/36/6/005>
47. Huebner, W.F., Barfield, W.D.: *Opacity. Astrophysics and Space Science Library*, vol. 402. Springer, New York (2014) <https://doi.org/10.1007/978-1-4614-8797-5>
 48. Badnell, N.R., Bautista, M.A., Butler, K., Delahaye, F., Mendoza, C., Palmeri, P., Zeippen, C.J., Seaton, M.J.: Updated opacities from the Opacity Project. *MNRAS* **71**, 458 (2005). <https://doi.org/10.1111/j.1365-2966.2005.08991.x>
 49. Colgan, J., Kilcrease, D.P., Magee, N.H., Sherrill, M.E., Abdallah Jr., J., Hakel, P., Fontes, C.J., Guzik, J.A., Mussack, K.A.: A new generation of Los Alamos opacity tables. *Ap. J.* **817**, 116 (2016). <https://doi.org/10.3847/0004-637X/817/2/116>
 50. Ghisellini, G.: *Radiative Processes in High Energy Astrophysics. Lecture Notes in Physics*, vol. 873. Springer, Switzerland (2013) <https://doi.org/10.1007/978-3-319-00612-3>
 51. Wikipedia: X-ray space telescopes (2019). https://en.wikipedia.org/wiki/List_of_X-ray_space_telescopes. retrieved 2nd October 2019
 52. Evans, J.: *X-Ray Absorption Spectroscopy for the Chemical and Materials Sciences*. John Wiley & Sons (2017) <https://doi.org/10.1002/9781118676165>
 53. Thompson, A., Attwood, D., Gullikson, E., Howells, M., Kim, K., Zirz, J., Kortright, J., Lindau, I., Liu, Y., Pianetta, P., Robinson, A., Scofield, J., Underwood, J., Williams, G., Winick, H.: X-ray Data Booklet, Tech. rep., Lawrence Berkeley National Laboratory, LBNL/PUB-490 Rev 3 (2009). <https://xdb.lbl.gov/>
 54. Prince, E. (ed.): *International Tables for Crystallography. Mathematical, Physical and Chemical Tables*, vol. C. Wiley (2006) <https://doi.org/10.1107/97809553602060000103>. 1st online edition based on 3rd print edition (2004)
 55. Deslattes, R.D., Kessler, E.G., Indelicato, P., de Billy, L., Lindroth, E., Anton, J.: X-ray transition energies: new approach to a comprehensive evaluation. *Rev. Mod. Phys.* **75**, 35 (2003). <https://doi.org/10.1103/RevModPhys.75.35>
 56. Young, N.A.: The application of synchrotron radiation and in particular X-ray absorption spectroscopy to matrix isolated species. *Coord. Chem. Rev.* **277–278**, 224 (2014). <https://doi.org/10.1016/j.ccr.2014.05.010>
 57. van Bokhoven, J.A., Lamberti, C. (eds.): *X-Ray Absorption and X-Ray Emission Spectroscopy: Theory and Applications*. John Wiley & Sons (2016) <https://doi.org/10.1002/9781118844243>
 58. Rehr, J.J., Ankudinov, A.L.: Progress in the theory and interpretation of XANES. *Coord. Chem. Rev.* **249**, 131 (2005). <https://doi.org/10.1016/j.ccr.2004.02.014>
 59. Bergmann, U., Glatzel, P., Cramer, S.P.: Bulk-sensitive XAS characterization of light elements: From X-ray Raman scattering to X-ray Raman spectroscopy. *Microchem. J.* **71**, 221 (2002). [https://doi.org/10.1016/S0026-265X\(02\)00014-0](https://doi.org/10.1016/S0026-265X(02)00014-0)
 60. Chantler, C.T., Barnea, Z., Tran, C.Q., Tiller, J.B., Paterson, D.: Precision X-ray optics for fundamental interactions in atomic physics, resolving discrepancies in the X-ray regime. *Opt. Quantum Electron.* **31**, 495 (1999). <https://doi.org/10.1023/A:1006923329884>
 61. Chantler, C.T., Tran, C.Q., Paterson, D., Cookson, D., Barnea, Z.: X-ray extended-range technique for precision measurement of the X-ray mass attenuation coefficient and $\text{Im}(f)$ for copper using synchrotron radiation. *Phys. Lett. A* **286**, 338 (2001). [https://doi.org/10.1016/S0375-9601\(01\)00444-3](https://doi.org/10.1016/S0375-9601(01)00444-3)
 62. Chantler, C.T.: Accurate measurement and physical insight: the X-ray extended range technique for fundamental atomic physics, condensed matter research and biological sciences. *Rad. Phys. Chem.* **79**, 117 (2010). <https://doi.org/10.1016/j.radphyschem.2009.07.022>
 63. Smekal, A.: Quantentheorie der Dispersion. *Naturwissenschaften* **11**, 873 (1923). <https://doi.org/10.1007/BF01576902>
 64. Raman, C.V.: A new radiation. *Ind. J. Phys.* **2**, 387 (1928). <http://repository.ias.ac.in/70648/>
 65. Das Gupta, K.: Smekal-Raman type modified x-ray scattering. *Phys. Rev. Lett.* **3**, 38 (1959). <https://doi.org/10.1103/PhysRevLett.3.38>
 66. Kane, P.P.: Inelastic scattering of X-rays and gamma rays. *Rad. Phys. Chem.* **75**, 2195 (2006). <https://doi.org/10.1016/j.radphyschem.2006.08.001>
 67. Krisch, M., Sette, F.: Scattering, inelastic: X-ray (methods and applications). In: Bassani, F., Liedl, G.L., Wyder, P. (eds.) *Encyclopedia of Condensed Matter Physics*, p. 220. Elsevier, Oxford (2005) <https://doi.org/10.1016/B0-12-369401-9/00649-5>
 68. Bambynek, W., Crasemann, B., Fink, R.W., Freund, H., Mark, H., Swift, C.D., Price, R.E., Rao, P.V.: X-ray fluorescence yields, Auger, and Coster-Kronig transition probabilities. *Rev. Mod. Phys.* **44**, 716 (1972). <https://doi.org/10.1103/RevModPhys.44.716>
 69. Mehlhorn, W.: 70 years of Auger spectroscopy, a historical perspective. *J. Electron Spectrosc. Relat. Phenom.* **93**, 1 (1998). [https://doi.org/10.1016/S0368-2048\(98\)00153-4](https://doi.org/10.1016/S0368-2048(98)00153-4)
 70. Santra, R.: Concepts in x-ray physics. *J. Phys. B* **42**, 023001 (2009). <https://doi.org/10.1088/0953-4075/42/2/023001>
 71. Levin, J.C., Armen, G.B.: Studies of fluorescence and Auger decay following inner-shell photoionization. *Rad. Phys. Chem.* **70**, 105 (2004). <https://doi.org/10.1016/j.radphyschem.2003.12.008>
 72. Kabachnik, N.M., Fritzsche, S., Grum-Grzhimailo, A.N., Meyer, M., Ueda, K.: Coherence and correlations in photoinduced Auger and fluorescence cascades in atoms. *Phys. Rep.* **451**, 155 (2007). <https://doi.org/10.1016/j.physrep.2007.07.005>
 73. Armen, S.B., Aksela, A., Åberg, T., Aksela, S.: The resonant Auger effect. *J. Phys. B* **33**, R49 (2000). <https://doi.org/10.1088/0953-4075/33/2/201>
 74. Szlachetko, J., Dousse, J., Hoszowska, J., Pajek, M., Barrett, R., Berset, M., Fennane, K., Kubala-Kukus, A., Szlachetko, M.: High-resolution study of X-ray resonant Raman scattering at the K edge of silicon. *Phys. Rev. Lett.* **97**, 073001 (2006). <https://doi.org/10.1103/PhysRevLett.97.073001>
 75. Glatzel, P., Alonso-Mori, R., Sokaras, D.: Hard x-ray photon-in/photon-out spectroscopy: Instrumentation, theory and applications. In: van Bokhoven, J.A., Lamberti, C. (eds.) *X-Ray Absorption and X-Ray Emission Spectroscopy: Theory and Applications*, p. 125. John Wiley & Sons (2016) <https://doi.org/10.1002/9781118844243.ch6>. Ch. 6
 76. Briand, J.P., Simionovici, A., Chevallier, P., Indelicato, P.: Infrared divergence of the resonant Raman-Compton scattering. *Phys. Rev. Lett.* **62**, 2092 (1989). <https://doi.org/10.1103/PhysRevLett.62.2092>
 77. Simionovici, A., Briand, J.P., Indelicato, P., Chevallier, P.: Resonant Raman-Compton scattering on zirconium. *Phys. Rev. A* **41**, 3707 (1990). <https://doi.org/10.1103/PhysRevA.41.3707>
 78. Wolff, W., Wolf, H.E., Coelho, L.F.S., de Barros, S., Eichler, J.: Compton scattering of 662-keV photons from K electrons of lead. *Phys. Rev. A* **40**, 4378 (1989). <https://doi.org/10.1103/PhysRevA.40.4378>
 79. Laukkanen, J., Hämäläinen, K., Manninen, S.: The absolute double-differential Compton scattering cross section of Cu 1s electrons. *J. Phys. Condens. Matter* **8**, 2153 (1996). <https://doi.org/10.1088/0953-8984/8/13/007>
 80. Sokaras, D., Müller, M., Kolbe, M., Beckhoff, B., Zarkadas, C., Karydas, A.G.: Resonant Raman scattering of polarized and unpolarized x-ray radiation from Mg, Al, and Si. *Phys. Rev. A* **81**, 012703 (2010). <https://doi.org/10.1103/PhysRevA.81.012703>
 81. Sokaras, D., Zarkadas, C., Beckhoff, B., Fliegau, R., Zarkadas, C., Karydas, A.G.: Proton induced quasi-monochromatic x-ray

- beams for soft x-ray spectroscopy studies and selective x-ray fluorescence analysis. *Rev. Sci. Instrum.* **83**, 123102 (2012). <https://doi.org/10.1063/1.4768735>
82. Xie, B.P., Zhu, L.F., Yang, K., Zhou, B., Hiraoka, N., Cai, Y.Q., Yao, Y., Wu, C.Q., Wang, E.L., Feng, D.L.: Inelastic x-ray scattering study of the state-resolved differential cross section of Compton excitations in helium atoms. *Phys. Rev. A* **82**, 032501 (2010). <https://doi.org/10.1103/PhysRevA.82.032501>
 83. Pratt, R.H.: Tutorial on fundamentals of radiation physics: interactions of photons with matter. *Radiat. Phys. Chem.* **70**, 595 (2004). <https://doi.org/10.1016/j.radphyschem.2003.12.032>
 84. Hoppersky, A.N., Yavna, V.A.: Scattering of Photons by Many-Electron Systems, Springer Series on Atomic, Optical and Plasma Physics, vol. 58. Springer (2010) <https://doi.org/10.1007/978-3-642-04256-0>
 85. Ågren, H., Gel'mukhanov, F.: Kramers–Heisenberg and Weisskopf–Wigner descriptions of resonant x-ray Raman scattering. *J. Electron Spectrosc. Relat. Phenom.* **110**, 153 (2000). [https://doi.org/10.1016/S0368-2048\(00\)00162-6](https://doi.org/10.1016/S0368-2048(00)00162-6)
 86. Kane, P.P.: Inelastic scattering of X-rays and gamma rays by inner shell electrons. *Phys. Rep.* **218**, 67 (1992). [https://doi.org/10.1016/0370-1573\(92\)90050-A](https://doi.org/10.1016/0370-1573(92)90050-A)
 87. Bergstrom, P.M., Pratt, R.H.: An overview of the theories used in Compton scattering calculations. *Radiat. Phys. Chem.* **50**, 3 (1997). [https://doi.org/10.1016/S0969-806X\(97\)00022-4](https://doi.org/10.1016/S0969-806X(97)00022-4)
 88. Pratt, R.H., LaJohn, L.A., Florescu, V., Surić, T., Chatterjee, B.K., Roy, S.C.: Compton scattering revisited. *Radiat. Phys. Chem.* **79**, 124 (2010). <https://doi.org/10.1016/j.radphyschem.2009.04.035>
 89. Filippini, A., Di Cicco, A., Natoli, C.R.: X-ray-absorption spectroscopy and n-body distribution functions in condensed matter. I. Theory. *Phys. Rev. B* **52**, 15122 (1995). <https://doi.org/10.1103/PhysRevB.52.15122>
 90. Sébilleau, D., Hatada, K., Ebert, H. (eds.): Multiple Scattering Theory for Spectroscopies, Springer Proceedings in Physics vol. 204. Springer (2016) <https://doi.org/10.1007/978-3-319-73811-6>
 91. Iesari, F., Hatada, K., Trapananti, A., Minicucci, M., Di Cicco, A.: GNXAS: Advances in the suite of programs for multiple-scattering analysis of x-ray absorption data, Ch. 8. In: Sébilleau, D., Hatada, K., Ebert, H. (eds.) Multiple Scattering Theory for Spectroscopies, Springer Proceedings in Physics, vol. 204. Springer (2016) https://doi.org/10.1007/978-3-319-73811-6_8
 92. Bunão, O., Joly, Y.: Self-consistent aspects of x-ray absorption calculations. *J. Phys. Condens. Matter* **21**, 345501 (2009). <https://doi.org/10.1088/0953-8984/21/34/345501>
 93. Rehr, J., Kas, J., Vila, F.D., Prange, M.P., Jorissen, K.: Parameter-free calculations of x-ray spectra with FEFF9. *Phys. Chem. Chem. Phys.* **12**, 503 (2010). <https://doi.org/10.1039/B926434E>
 94. Berger, M.J., Hubbell, J.H.: XCOM: Photon cross sections on a personal computer, Tech. rep. National Bureau of Standards (1973) <https://doi.org/10.2172/6016002>
 95. Chantler, C.T.: Detailed tabulation of atomic form factors, photoelectric absorption and scattering cross section, and mass attenuation coefficients in the vicinity of absorption edges in the soft x-ray ($Z=30-36$, $Z=60-89$, $E=0.1$ keV–10 keV), addressing convergence issues of earlier work. *J. Phys. Chem. Ref. Data* **29**, 597 (2000). <https://doi.org/10.1063/1.1321055>
 96. Cullen, D.E., Perkins, S.T., Seltzer, S.M.: Photon and electron data bases and their use in radiation transport calculations. *Appl. Radiat. Isot.* **44**, 1343 (1993). [https://doi.org/10.1016/0969-8043\(93\)90084-N](https://doi.org/10.1016/0969-8043(93)90084-N)
 97. Brown, D.A., et al.: ENDF/B-VIII.0: The 8th major release of the nuclear reaction data library with CIELO-project cross sections, new standards and thermal scattering data. *Nucl. Data Sheets* **148**, 1 (2018). <https://doi.org/10.1016/j.nds.2018.02.001>
 98. Cullen, D.E.: ENDF/B-VIII versus ENDF/B-VII: What is Different?, Tech. rep., IAEA Nuclear Data Services, iNDC(NDS)-0759 (2018). <https://www-nds.iaea.org/publications/indc/indc-nds-0759/>
 99. Chantler, C.T.: Theoretical form factor, attenuation and scattering tabulation for $Z = 1 - 92$ from $E = 1 - 10$ eV to $E = 0.4 - 1.0$ MeV. *J. Phys. Chem. Ref. Data* **24**, 71 (1995). <https://doi.org/10.1063/1.555974>
 100. Jenkins, T.M., Nelson, W.R., Rindi, A.: Monte Carlo Transport of Electrons and Photons. Plenum Press, New York (1988) <https://doi.org/10.1007/978-1-4613-1059-4>
 101. Salvat, F., Fernández-Varea, J.M.: Overview of physical interaction models for photon and electron transport used in Monte Carlo codes. *Metrologia* **46**, 112 (2009). <https://doi.org/10.1088/0026-1394/46/2/S08>
 102. Asai, M., Dotti, A., Verderi, M., Wright, D.H.: The Geant4 Collaboration, Recent developments in Geant4. *Ann. Nucl. Energy* **82**, 19 (2015). <https://doi.org/10.1016/j.anucene.2014.08.021>
 103. Allison, J., Amako, K., Apostolakis, J.: The Geant4 Collaboration, recent developments in Geant4. *Nucl. Instrum. Methods Phys. Res. A* **835**, 186 (2016). <https://doi.org/10.1016/j.nima.2016.06.125>
 104. Baró, J., Sempau, J., Fernández-Varea, J.M., Salvat, F.: PENELOPE: An algorithm for Monte Carlo simulation of the penetration and energy loss of electrons and positrons in matter. *Nucl. Instrum. Methods Phys. Res. B* **100**, 31 (1995). [https://doi.org/10.1016/0168-583X\(95\)00349-5](https://doi.org/10.1016/0168-583X(95)00349-5)
 105. Salvat, F., Fernández-Varea, J.M., Roma, J.S.: PENELOPE-2008: A Code System for Monte Carlo Simulation of Electron and Photon Transport. Tech. rep., OECD, nEA 6416 (2009). <http://hdl.handle.net/2117/9265>
 106. Hirayama, H., Namito, Y., Bielajew, A.F., Wilderman, S.J., Nelson, W.R.: The EGS5 Code System, Tech. rep. Stanford Linear Accelerator Center (2005) <https://doi.org/10.2172/877459>
 107. Kawrakow, I., Mainegra-Hing, E., Rogers, D.W.O., Tessier, F., Walters, B.R.B.: The EGSnrc Code System: Monte Carlo Simulation of Electron and Photon Transport, Tech. rep., National Research Council Canada (2015). <https://nrc-cnrc.github.io/EGSnrc/>
 108. Ferrari, A., Sala, P.R., Fasso, A., Ranft, J.: FLUKA: A multi-particle transport code, Tech. rep., CERN, INFN, SLAC, cERN-2005-010, INFN TC05/11, SLAC-R-773 (2005). <https://www.slac.stanford.edu/pubs/slacreports/reports16/slac-r-773.pdf>
 109. Battistoni, G., Boehlen, T., Cerutti, F., Chin, P.W., Esposito, L.S., Fassò, A., Ferrari, A., Lechner, A., Empl, A., Mairani, A., Merighetti, A., Ortega, P.G., Ranft, J., Roesler, S., Sala, P.R., Vlachoudis, V., Smirnov, G.: Overview of the FLUKA code. *Ann. Nucl. Energy* **82**, 10 (2015). <https://doi.org/10.1016/j.anucene.2014.11.007>
 110. Giersch, J., Weidemann, A., Anton, G.: ROSI – an object-oriented and parallel-computing Monte Carlo simulation for X-ray imaging. *Nucl. Instrum. Methods Phys. Res. A* **509**, 151 (2003). [https://doi.org/10.1016/S0168-9002\(03\)01564-X](https://doi.org/10.1016/S0168-9002(03)01564-X)
 111. Reed, R.A., Weller, R.A., Mendenhall, M.H., Fleetwood, D.M., Warren, K.M., Sierawski, B.D., King, M.P., Schrimpf, R.D., Auden, E.C.: Physical processes and applications of the Monte Carlo radiative energy deposition (MRED) code. *IEEE Trans. Nucl. Sci.* **62**, 1441 (2015). <https://doi.org/10.1109/TNS.2015.2454446>
 112. Xu, X.G., Liu, T., Su, L., Du, X., Riblett, M., Ji, W., Gu, D., Carothers, C.D., Shephard, M.S., Brown, F.B., Kalra, M.K., Liu, B.: ARCHER, a new Monte Carlo software tool for emerging heterogeneous computing environments. *Ann. Nucl. Energy* **82**, 2 (2015). <https://doi.org/10.1016/j.anucene.2014.08.062>
 113. Castor, J.I.: Radiation Hydrodynamics. Cambridge University Press, Cambridge (2004) <https://doi.org/10.1017/CBO9780511536182>

114. Chung, H., Morgan, W.L., Lee, R.W.: FLYCHK: an extension to the K-shell spectroscopy kinetics model FLY. *J. Quant. Spectrosc. Radiat. Transf.* **81**, 107 (2003). [https://doi.org/10.1016/S0022-4073\(03\)00064-5](https://doi.org/10.1016/S0022-4073(03)00064-5)
115. Wilson, B., Sonnad, V., Sterne, P., Isaacs, W.: PURGATORIO – a new implementation of the INFERNO algorithm. *J. Quant. Spectrosc. Radiat. Transf.* **99**, 658 (2006). <https://doi.org/10.1016/j.jqsrt.2005.05.053>
116. Gregori, G., Glenzer, S.H., Fournier, K.B., Campbell, K.M., Dewald, E.L., Jones, O.S., Hammer, J.H., Hansen, S.B., Wallace, R.J., Landen, O.L.: X-ray scattering measurements of radiative heating and cooling dynamics. *Phys. Rev. Lett.* **101**, 045003 (2008). <https://doi.org/10.1103/PhysRevLett.101.045003>
117. Nagayama, T., Bailey, J.E., Loisel, G., Hansen, S.B., Rochau, G.A., Mancini, R.C., MacFarlane, J.J., Golovkin, I.: Control and diagnosis of temperature, density, and uniformity in x-ray heated iron/magnesium samples for opacity measurements. *Phys. Plasmas* **21**, 056502 (2014). <https://doi.org/10.1063/1.487232421>
118. Tran, C.Q., Chantler, C.T., Barnea, Z.: X-ray mass attenuation coefficient of silicon: Theory versus experiment. *Phys. Rev. Lett.* **90**, 257401 (2003). <https://doi.org/10.1103/PhysRevLett.90.257401>
119. Chantler, C.T., Bunker, B.A., Abe, H., Kimura, M., Newville, M., Welter, E.: A call for a round robin study of XAFS stability and platform dependence at synchrotron beamlines on well defined samples. *J. Synch. Rad.* **25**, 935 (2018). <https://doi.org/10.1107/S1600577518003752>
120. Kavciv, M., Zitnik, M., Bucar, K., Mihelic, A., Stuhec, M., Szlachetko, J., Cao, W., Alonso Mori, R., Glatzel, P.: Separation of two-electron photoexcited atomic processes near the inner-shell threshold. *Phys. Rev. Lett.* **102**, 143001 (2009). <https://doi.org/10.1103/PhysRevLett.102.143001>
121. Kanter, E.P., Ahmad, I., Dunford, R.W., Gemmell, D.S., Krässig, B., Southworth, S.H., Young, L.: Double K-shell photoionization of silver. *Phys. Rev. A* **73**, 022708 (2006). <https://doi.org/10.1103/PhysRevA.73.022708>
122. Fritzsche, S.: A fresh computational approach to atomic structures, processes and cascades. *Comp. Phys. Comm.* **240**, 1 (2019). <https://doi.org/10.1016/j.cpc.2019.01.012>
123. Froese Fischer, C., Gaigalas, G., Jönsson, P., Bieroń, J.: GRASP2018 - A Fortran 95 version of the general relativistic atomic structure package. *Comp. Phys. Comm.* **237**, 184 (2019). <https://doi.org/10.1016/j.cpc.2018.10.032>
124. Berengut, J.C.: Particle-configuration interaction and many-body perturbation theory: Application to Hg^+ . *Phys. Rev. A* **94**, 012502 (2016). <https://doi.org/10.1103/PhysRevA.94.012502>
125. Kahl, E.V., Berengut, J.C.: AMBIT: A programme for high-precision relativistic atomic structure calculations. *Comp. Phys. Comm.* **238**, 232 (2019). <https://doi.org/10.1016/j.cpc.2018.12.014>
126. Boyd, R.W.: *Nonlinear Optics*. Academic Press, Amsterdam (2008). <http://www.sciencedirect.com/science/book/9780123694706>
127. Hopersky, A.N., Nadolinsky, A.N., Novikov, S.A.: Rayleigh scattering of two x-ray photons by an atom. *Phys. Rev. A* **93**, 052709 (2016). <https://doi.org/10.1103/PhysRevA.93.052701>
128. Krebs, D., Reis, D.A., Santra, R.: Time-dependent QED approach to x-ray nonlinear Compton scattering. *Phys. Rev. A* **99**, 022120 (2019). <https://doi.org/10.1103/PhysRevA.99.022120>
129. Kiunke, M., Stritt, C., Schielein, R., Sukowski, F., Hölzing, A., Zabler, S., Hofmann, J., Flisch, A., Kasperl, S., Sennhauser, U., Hanke, R.: ROSI and GEANT4 - A comparison in the context of high energy X-ray physics. *Nucl. Instrum. Methods Phys. Res. B* **377**, 50 (2016). <https://doi.org/10.1016/j.nimb.2016.04.029>
130. Rochau, G.A., Bailey, J.E., Falcon, R.E., Loisel, G.P., Nagayama, T., Mancini, R.C., Hall, I., Winget, D.E., Montgomery, M.H., Liedahl, D.A.: ZAPP: The Z Astrophysical Plasma Properties collaboration. *Phys. Plasmas* **21**, 056308 (2014). <https://doi.org/10.1063/1.4875330>
131. Loisel, G.P., Bailey, J.E., Liedahl, D.A., Fontes, C.J., Kallman, T.R., Nagayama, T., Hansen, S.B., Rochau, G.A., Mancini, R.C., Lee, R.W.: Benchmark experiment for photoionized plasma emission from accretion-powered x-ray sources. *Phys. Rev. Lett.* **119**, 075001 (2017). <https://doi.org/10.1103/PhysRevLett.119.075001>
132. Nandra, K., et al.: The hot and energetic universe: a white paper presenting the science theme motivating the athena+ mission, arXiv (2013). <http://arxiv.org/abs/astro-ph/1306.2307>



Dr Michael Bromley is currently an honorary Research Fellow at the University of Southern Queensland and was a Senior Lecturer in Physics and ARC Future Fellow at The University of Queensland, Australia and an Associate Professor at San Diego State University, USA. His group's research interests are in computational physics with a focus on photon-atom and positron-atom systems and designing Bose-Einstein condensate-based technologies.



Isik Kanik, William McConkey , and Sandor Trajmar

Contents

67.1	Basic Concepts	982
67.1.1	Electron Impact Processes	982
67.1.2	Definition of Cross Sections	982
67.1.3	Scattering Measurements	982
67.2	Collision Processes	984
67.2.1	Total Scattering Cross Sections	984
67.2.2	Elastic Scattering Cross Sections	984
67.2.3	Momentum Transfer Cross Sections	985
67.2.4	Excitation Cross Sections	985
67.2.5	Dissociation Cross Sections	986
67.2.6	Ionization Cross Sections	986
67.3	Coincidence and Superelastic Measurements	987
67.4	Experiments with Polarized Electrons	989
67.5	Electron Collisions with Excited Species	990
67.6	Electron Collisions in Traps	990
67.7	Current Applications	990
67.8	Emerging Applications	991
	References	991

Abstract

Electron–atom and electron–molecule collision processes play a prominent role in a variety of physical systems such

I. Kanik (✉)
Jet Propulsion Laboratory, California Institute of Technology
Pasadena, CA, USA
e-mail: isik.kanik@jpl.nasa.gov

W. McConkey
Dept. of Physics, University of Windsor
Windsor, ON, Canada
e-mail: mcconk@uwindsor.ca

S. Trajmar
Jet Propulsion Laboratory, California Institute of Technology
Redwood City, CA, USA
e-mail: strajmar@comcast.net

as electrical discharges, electron-beam lasers, plasma processing, and fusion devices. They are also significant in various environments, such as planetary atmospheres and astrophysical and solar plasmas. Early studies of these interactions contributed significantly to the understanding of the quantum nature of matter. Experimental activities in this field, initiated by *Franck* and *Hertz* [1], flourished in the 1930s and, after a dormant period of about a quarter of a century, had a renaissance in the latter half of the century. More recently, sophisticated developments in experimental and theoretical techniques have led to increased physical insight and data production.

When electrons collide with atomic or molecular targets, a large variety of reactions can take place (Sect. 67.1.1). We limit our discussion to electron collisions with neutral atoms and molecules, where single collision conditions prevail. Furthermore, we discuss only low-energy (threshold to few hundred eV) impact processes where the interaction between the valence-shell electrons of the target and the free electron dominates.

Comprehensive discussions on electron–atom (molecule) collision physics can be found in the books of *Massey* et al. [2], *McDaniel* [3], and the volumes of *Advances in Atomic and Molecular* (since 1990 *Atomic, Molecular and Optical*) *Physics*. The latest developments are usually published in *Physical Review Letters*, *Physical Review A*, *Journal of Physics B*, *Journal of Chemical Physics*, *European Physics Journal D* and *Journal of Physical and Chemical Reference Data*, and are presented at the biannual International Conference on Photonic, Electronic and Atomic Collisions (ICPEAC).

Keywords

ionization cross section · scatter cross section · electron collision · excitation cross section · integral cross section

67.1 Basic Concepts

67.1.1 Electron Impact Processes

Low-energy electrons can very effectively interact with the valence-shell electrons of atoms and molecules, in part because they have similar speeds. In elastic scattering, the continuum electron changes direction and transfers momentum to the target. Inelastic collisions also include a transfer of kinetic energy to the target, such as excitation of valence electrons to discrete energy levels, to the ionization continuum, and, in the case of molecules, excitation of nuclear motion (rotational, vibrational), and excitation to states that dissociate into neutral or ionic fragments. Various combinations of these processes are also possible, e.g., dissociative attachment, excitation, or ionization. Excitation of more than one valence electron at the same time, or excitation of electrons from intermediate and inner shells, may also occur, but these processes are more likely at impact energies of a few keV. These excitations lie above the first ionization limit and, therefore, with high probability lead to autoionization, except for heavy elements where X-ray emission is an important competing process.

67.1.2 Definition of Cross Sections

The parameters that characterize collision processes are the cross sections. Electron collision cross sections depend on impact energy E_0 and scattering polar angles θ and ϕ . The differential cross section (DCS), for a specific well-defined excitation process indicated by the index n , is defined as

$$\frac{d\sigma_n(E_0, \Omega)}{d\Omega} = \frac{k_f}{k_i} |f_n(E_0, \Omega)|^2, \quad (67.1)$$

where Ω is the polar angle of detection, k_i and k_f are the initial and final electron momenta, and f_n is the complex scattering amplitude ($n = 0$ refers to elastic scattering). Integration over the energy-loss profile is assumed. If the energy-loss spectrum is broad, differentiation with respect to energy loss also has to be included. For certain processes it may be necessary to define DCSs with respect to angle and energy for both primary and secondary particles.

Integration over all scattering angles yields the integral cross sections

$$\sigma_n(E_0) = \int_0^{2\pi} \int_0^\pi \frac{d\sigma_n(E_0, \Omega)}{d\Omega} \sin \theta \, d\theta \, d\phi. \quad (67.2)$$

In the case of elastic scattering, the momentum transfer cross section is defined as

$$\sigma_0^M(E_0) = \int_0^{2\pi} \int_0^\pi \frac{d\sigma_0(E_0, \Omega)}{d\Omega} (1 - \cos \theta) \sin \theta \, d\theta \, d\phi. \quad (67.3)$$

The total electron scattering cross section is obtained by summing all integral cross sections

$$\sigma_{\text{tot}}(E_0) = \sum_n \sigma_n(E_0) + \sum_m \sigma_m(E_0), \quad (67.4)$$

where σ_m are the cross sections for other possible channels. Experimental cross sections typically represent averages over indistinguishable processes (e.g., magnetic sublevels, hyperfine states, rotational states, etc.). The cross section obtained this way corresponds to an average over initial and sum over final indistinguishable states with equal weight given to the initial states. (This may not always be true, as discussed later.) If the target molecules are randomly oriented, the cross section averaged over these orientations is independent of ϕ . In addition, there is an averaging over the finite energy and angular resolution of the apparatus. It is important, therefore, to specify clearly the nature of the measured cross section, otherwise their utilization and comparison with other experimental and theoretical cross sections become meaningless. We denote the conventionally measured differential and integral cross sections by $D_n(E_0, \theta)$ and $Q_n(E_0)$, with the various averagings implied. Similarly, $Q^M(E_0)$ and $Q_{\text{tot}}(E_0)$ are the corresponding momentum transfer and total scattering cross sections.

The collision strength for a process $i \rightarrow j$, which is the particle equivalent of the oscillator strength, is defined by

$$\Omega_{ij}(E_0) = q_i E_0 \sigma_{ij}(E_0), \quad (67.5)$$

where q_i is the statistical weight of the initial state [$q_i = (2L_i + 1)(2J_i + 1)$], E_0 is in Rydbergs, and σ_{ij} is in units of πa_0^2 .

The rate for a specific collision process (e.g., excitation) for electrons of energy E_0 is given as

$$R_{ij}(E_0) = NI(E_0)\sigma_{ij}(E_0), \quad (67.6)$$

where N is the density of the target particles (m^{-3}), and $I(E_0)$ is the electron flux ($\text{m}^{-2} \text{s}^{-1}$); σ_{ij} is in m^2 , yielding R_{ij} in units of $\text{m}^{-3} \text{s}^{-1}$. For nonmonoenergetic electron beams, Eq. (67.6) must be integrated over E_0 to get the average rate.

67.1.3 Scattering Measurements

Most scattering experiments are carried out in a beam–beam arrangement (Fig. 67.1). A beam of nearly monoenergetic electrons is formed by extracting electrons from a hot filament and selecting a narrow segment of the thermal energy distribution. For the formation and control of the electron beam, electrostatic lenses are used, and the energy selection is achieved with electrostatic energy selectors. A magnetic field may also be applied to obtain a magnetically collimated

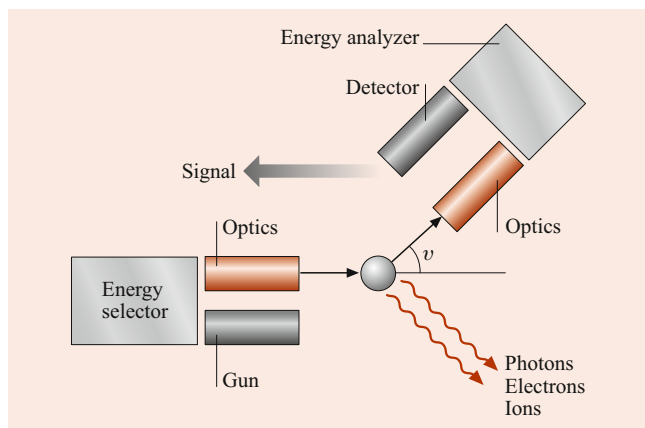


Fig. 67.1 A schematic diagram for electron scattering measurements

electron beam. The target beam is formed by letting the sample gas effuse from an orifice, tube or capillary array with various degrees of collimation. Target species that are in the condensed phase at room temperature need to be placed in a crucible and evaporated by heating. An extensive discussion of this technique was given by *Scoles* [4]. The electron beam intersects the target beam at a 90° angle, and electrons scattered into a specific direction, over a small solid angle ($\approx 10^{-3}$ sr), are detected. However, the scattered electron is not necessarily the same as the incoming electron. Exchange with the target electrons may occur and is required for spin-forbidden transitions in light elements. The detector system consists of electron lenses and energy analyzers similar to those used in the electron gun. The actual detector is an electron multiplier that generates a pulse for each electron. In the scattering process, secondary species (electrons, photons, ions, neutral fragments) may also be generated and can be detected individually or in various coincidence schemes. The experiments are carried out in a vacuum chamber, and it is important to minimize stray electric and magnetic fields. More details about the apparatus and procedures can be found in a review by *Trajmar* and *Register* [5]. The primary information gained in these experiments is the energy and angular distribution of the scattered electrons.

There are several methods used to carry out scattering measurements. In the most commonly used energy-loss mode, the impact energy and scattering angle are fixed, and the scattering signal as a function of energy lost by the electron is measured by applying pulse counting and multi-channel scaling techniques. The result of such an experiment is an energy-loss spectrum. The elastic scattering feature appears at zero energy loss; the other features correspond to various excitation processes and to ionization. Energy-loss spectra can also be generated in the constant residual energy mode. In this case, the detector is set to detect only electrons with a specific residual energy $E_R = E_0 - \Delta E$ at a fixed scattering angle, and E_0 and ΔE are simultaneously varied. Each feature in the energy-loss spectrum is then obtained at

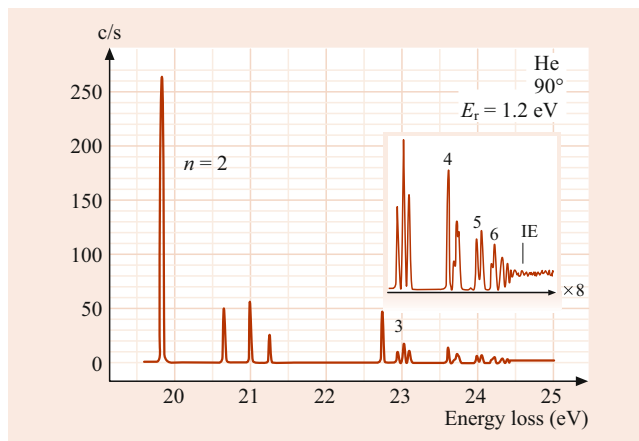


Fig. 67.2 Energy-loss spectrum of He at a constant residual energy of 1.2 eV and scattering angle of 90° . The inelastic features with the corresponding principal quantum numbers are shown. IE is the ionization potential of He (24.58 eV). No background is subtracted, and true signal zero is indicated by a dotted line under the expand portion of the spectrum m. (Taken from *Allen* [6])

the same energy above its own threshold. An example, taken from the work of *Allen* [6], is shown in Fig. 67.2.

The energy loss spectrum becomes equivalent to the photoabsorption spectrum in the limit of small momentum transfer \mathbf{K} , where $\mathbf{K} = \mathbf{k}_f - \mathbf{k}_i$ (i.e., high impact energy, small scattering angle). The equivalence of electrons and photons in this limit follows from the Born approximation, and it can be used to obtain optical absorption and ionization cross sections. The correspondence is defined through the limit theorem

$$\lim_{\mathbf{K} \rightarrow 0} f_n^G(\mathbf{K}) = f_n^{\text{opt}}, \quad (67.7)$$

$$f_n^G(\mathbf{K}) = \frac{\Delta E}{2} \frac{k_i}{k_f} \mathbf{K}^2 \frac{d\sigma_n}{d\Omega}(\mathbf{k}), \quad (67.8)$$

where f_n^G is the generalized oscillator strength for excitation process n , and f_n^{opt} is the corresponding optical f -value. Equation (67.7) was originally derived by *Bethe* [7] from the Born cross section. It was later extended by *Lassette* et al. [8] to cases where the Born approximation does not hold. In this case, $f_n^G(\mathbf{K})$ is replaced by $f_n^{\text{app}}(\mathbf{K})$, the apparent generalized oscillator strength. The limit theorem implies that, in the limit of small \mathbf{K} , optical selection rules apply to electron impact excitation. The practical problem is that the limit is nonphysical and the extrapolation to zero \mathbf{K} involves some arbitrariness. When \mathbf{K} is significantly different from zero, optical-type selection rules do not apply to electron-impact excitation. Spin and/or symmetry forbidden transitions then readily occur and can be an efficient way of producing metastable species.

Selection rules for electron impact excitations can be derived from group theoretical arguments [9, 10]. For atoms, the selection rule $S_g \leftrightarrow S_u$ applies in general, and scattering to 0° and 180° is forbidden if $(L_i + \Pi_i + L_f + \Pi_f)$ is odd.

Here, L_i and L_f are the angular momenta and Π_i , and Π_f are the parities. For molecules, selection rules can be derived under two special conditions: (a) rules concerning 0° and 180° scattering for arbitrary orientation of the molecule and (b) rules concerning scattering to any angle but for specific orientation of the molecule. An important example of the first case is the $\Sigma^- \leftrightarrow \Sigma^+$ selection rule for linear molecules at 0° and 180° scattering angles.

The energy dependence of cross sections is obtained by fixing the energy-loss value (scattering channel) and studying the variation of scattering signals with impact energy at a given angle or integrated over all scattering angles. In general, cross sections associated with spin forbidden and optically allowed transitions peak near and at several times the threshold impact energy respectively, and they usually vary smoothly with impact energy. However, resonances may appear at certain specific impact energies. These sudden changes are associated with temporary electron capture and are the result of quantum mechanical interference between two indistinguishable paths.

Integral cross sections can be obtained from extrapolation of the measured $D_n(E_0, \theta)$ to 0° and 180° scattering angles and integration over all angles. Recently, incorporation of an *angle-changing* device has enabled measurements to be extended over the whole range of scattering angles [11, 12]. In certain cases, it is possible to measure integral cross sections directly by detecting secondary products such as photons and ions. These procedures and the resulting cross sections will be discussed in some detail in Sect. 67.2.

67.2 Collision Processes

In addition to the basic elastic and inelastic processes defined in Sect. 67.1.2, we now also explicitly include dissociation (to neutral and charged fragments) cross sections $Q_D(E_0)$; and ionization cross sections $Q_I(E_0)$. Each of these is now considered separately.

67.2.1 Total Scattering Cross Sections

Total electron scattering cross sections represent the sum of all integral cross sections

$$Q_{\text{tot}}(E_0) = \sum_n Q_n(E_0) + Q_I(E_0) + Q_D(E_0), \quad (67.9)$$

$Q_{\text{tot}}(E_0)$ are useful for checking the validity of scattering theories, and the consistency of available data, for normalization of integral and differential cross sections, and as input to the Boltzmann equation. At low impact energies, elastic scattering dominates, while at intermediate and high impact

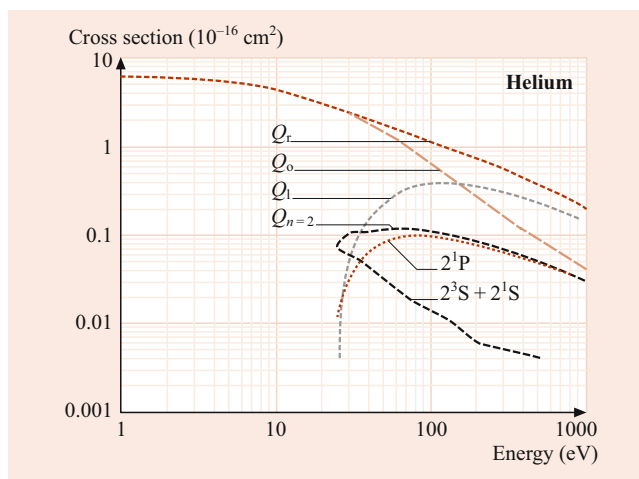


Fig. 67.3 Cross sections for various processes in the electron–helium collision (see text for data sources)

energies, electronic excitations and ionization become major contributors to Q_{tot} . Figure 67.3 shows the various cross sections for electron–helium collisions. The data are from the recommended values of *Trajmar* and *Kanik* [13].

Two methods are commonly used for measuring $Q_{\text{tot}}(E_0)$: the transmission method and the target recoil method (for details, [5, 14]). Total scattering cross sections measured by these techniques are, in general, accurate to within a few percent. The extensive reviews by *Zecca* and coworkers [15–17] should be noted.

67.2.2 Elastic Scattering Cross Sections

Elastic scattering cross sections $Q_0(E_0)$ are not as readily available as $Q_{\text{tot}}(E_0)$. They are obtained from differential scattering experiments over limited angular ranges by extrapolation and integration of the measured values. Typical error limits are 5 to 20%. For molecular species, rotational excitation is usually not resolved but is included in the $D_0(E_0, \theta)$ and $Q_0(E_0)$ values. In order to obtain the absolute $D_0(E_0, \theta)$ directly from the scattering signal, one has to know the electron flux, the number of scattering species, the scattering geometry, and the overall response function of the apparatus. A direct measurement of these parameters can be made at high energies (> 100 eV). However, at low electron energies, this approach is not feasible. A number of methods have been devised to derive relative $D_0(E_0, \theta)$ from the measured scattering intensities and then to normalize the $D_0(E_0, \theta)$ to the absolute scale. Here, we briefly outline only the most commonly used procedure.

The most practical and reliable method of obtaining the absolute $D_0(E_0, \theta)$ is the relative flow technique in which scattering signals for a known standard gas and an unknown test gas are compared at each energy and angle [5, 18–20].

The He elastic cross section is the natural choice of standard since it is known accurately over a wide energy and angular range, and He is experimentally easy to handle. Only the relative electron beam flux and molecular beam densities (and their distributions) need be known in the two measurements. The flow rate of the test gas is adjusted so that the flux and density distribution patterns of the two gases are identical, and all geometrical factors cancel in the scattering intensity ratios. The absolute $D_0(E_0, \theta)$ for the sample gas is obtained from the measured scattering intensity, target density, and electron beam intensity ratios, and the standard $D_0(E_0, \theta)$ value. See [5, 20, 21] for a detailed discussion of this technique.

67.2.3 Momentum Transfer Cross Sections

The $Q^M(E_0)$ can be obtained both from the elastic DCSs (differential cross sections) and from swarm measurements. At low electron-impact energies (from 0.05 to a few eV), where only a few collision channels are open, the electron swarm technique is the most accurate ($\approx 3\%$) way to determine the momentum transfer cross sections. Beam–beam experiments are mandatory at higher energies. A detailed discussion of these techniques is given by *Trajmar* and *Reg-ister* [5].

67.2.4 Excitation Cross Sections

The $D_n(E_0, \theta)$ and $Q_n(E_0)$ can be derived from energy-loss spectra obtained in beam–beam scattering experiments. The relative $D_n(E_0, \theta)$ is usually normalized to $D_0(E_0, \theta)$, which in turn is normalized to the helium $D_0(E_0, \theta)$ by the relative flow technique described in Sect. 67.2.2. There are, however, complications and uncertainties associated with this technique because of the sensitivity of the instrument response function to the residual energy of the scattered electrons. For more details, see *Trajmar* and *McConkey* [21]. Data obtained by this procedure are rather limited, partly due to experimental difficulties and partly due to the time required to carry out such measurements.

For cases where an excited state j is formed, which can radiatively decay by means of a short-lived (dipole-allowed) transition to a lower lying state i , the intensity of the resultant radiation is directly related to the cross section for production of the excited state in the original collision process. An optical emission cross section, $Q_{ji}(E_0)$, is defined by

$$Q_{ji}(E_0) = \frac{N_j \Gamma_{ji}}{I n_0 \tau_j}, \quad (67.10)$$

where N_j and n_0 are the densities in the excited and ground states, respectively, Γ_{ji} is the branching ratio for radiative

decay from state j to state i , I is the electron beam flux, and τ_j is the natural radiative lifetime of state j . Since the excited state may be produced either by direct electron impact or by cascade from higher-lying states k , also formed in the collision process, we may define the direct excitation cross section $Q_j^d(E_0)$ by

$$Q_j^d(E_0) = \sum_i Q_{ji}(E_0) - \sum_k Q_{kj}(E_0). \quad (67.11)$$

The last term subtracts the cascade contribution from higher-lying states. The quantity $Q_j^a(E_0) = \sum_i Q_{ji}(E_0)$ is known as the apparent excitation cross section for level j . Clearly, to obtain $Q_j^d(E_0)$ from $Q_j^a(E_0)$, the cascade contribution must be known.

In Eq. (67.10), $N_j \Gamma_{ji} / \tau_j$ gives the steady-state number of $j \rightarrow i$ photons per unit time per unit volume emitted from the interaction region. Since observation is made in a particular direction care must be taken to correct for any anisotropy in the radiation pattern. Alternatively, if observation is made at the so-called *magic* angle ($54^\circ 44'$) to the electron beam direction, the emission intensity per unit solid angle is equal to the average intensity per unit solid angle irrespective of the polarization of the emitted radiation. However, even at this magic angle, care must be taken to avoid problems with polarization sensitivity of the detection equipment [22, 23].

The phenomenon of radiation trapping is often a problem if the radiative decay channels of the excited state include a dipole allowed channel to the ground state. Repeated absorption and re-emission of the radiation can occur and can lead to a diffuse emitting region much larger than the original interaction region, and the polarization of the emitted light can also be altered. Often, a study of the variation of the emitted intensity or polarization with the target gas pressure is sufficient to reveal the presence of radiation trapping or other secondary effects.

The emission cross sections of certain lines have been measured with great care and now serve as benchmarks for other work. Examples of these are the measurements of *van Zyl* et al. [24] on the n^1S levels of He in the visible spectral region or the measurements of the cross section for production of Lyman α from H_2 in the VUV region ([25, 26] for a full discussion of this including many references). Use of secondary standards is particularly important when crossed-beam measurements are being carried out because of the cancellation of geometrical and other effects that occur.

The Bethe–Born theory [27] provides a convenient calibration of the detection system for optically allowed transitions of known oscillator strength. At sufficiently high energies, the excitation cross section, Q_n , of level n is given by

$$Q_n = \frac{4\pi a_0^2}{E_0/R_\infty} \frac{f_n^{\text{opt}}}{\Delta E_n/R_\infty} \ln\left(\frac{4c_n E_0}{R_\infty}\right). \quad (67.12)$$

Here, ΔE_n is the excitation energy, and c_n is a constant dependent on the transition. A plot of $Q_n E_0$ versus $\ln E_0$ is a straight line with a slope proportional to f_n^{opt} and the intercept with the $\ln E_0$ axis yields an experimental value for c_n independent of the normalization. For example, the He n^1P – 1^1S optical oscillator strengths are very accurately known, as are cascade contributions. Thus, accurate normalization of the slope of the Bethe plot can be made, yielding accurate excitation cross sections.

As was mentioned above, the excitation cross sections display characteristic shapes as a function of energy. For optically allowed transitions, the cross section rises relatively slowly from threshold to a broad maximum approximately five times the threshold energy. At higher energies, the $(\ln E_0)/E_0$ dependence of the cross section predicted by Eq. (67.12) is observed. For exchange processes, e.g., a triplet excited state from a singlet ground state, the cross section peaks sharply close to threshold and falls off at high energy as E^{-3} . If the excitation is spin allowed but optically forbidden, e.g., He n^1D from 1^1S , then the Bethe theory predicts an E^{-1} dependence of the cross section at high energies.

When excitation occurs to a long-lived (metastable or Rydberg) state following electron impact, it is often possible to detect the excited particle directly. Time-of-flight (TOF) techniques are used to distinguish the long-lived species from other products, e.g., photons, produced in the collisions.

67.2.5 Dissociation Cross Sections

Dissociation of a molecular target can result in fragments that may be excited or ionized. Such processes may be studied using the techniques discussed in the previous section or in the following section, where charged particle detection is considered. Because a repulsive state of the molecule is accessed, the fragments can leave the interaction region with considerable kinetic energy (several eV). If the fragment is in a long-lived metastable or Rydberg state, TOF techniques may be used to distinguish the long-lived species from other products such as photons, and also to measure the energies of the excited fragments, and thus provide information on the repulsive states responsible for the dissociation. For a further discussion, see the reviews by *Compton and Bardsley* [28], *Freund* [29], and *Zipf* [30]. If the detector can be made sensitive to a particular excited species, its excitation can be isolated and studied. Examples are the work of *McConkey* and coworkers [31, 32] on O($1S$) and S($1S_0$) production from various molecules. The detection of unexcited neutral fragments is more challenging. One early method was to trap selectively the dissociation products using a getter and measure the resulting pressure decrease. In a more sophisticated approach, *Cosby* [33] produced a fast (≈ 1 keV) target molecular beam by resonant charge exchange and sub-

jected it to electron-impact dissociation. The fast dissociation products were detected by conventional particle detectors in a time-correlated measurement. Laser techniques, such as laser-induced fluorescence or multiphoton ionization, were also used recently to detect the dissociation products.

The Franck–Condon principle largely governs molecular dissociation. The principle states that if the excitation takes place on a time scale that is short compared with vibrational motion of the atomic nuclei, the transition occurs vertically between potential energy curves. Since dissociation rapidly follows a vertical transition to the repulsive part of a potential energy curve, compared with the period of molecular rotation, the dissociation products tend to move in the direction of vibrational motion. Since the excitation probability depends on the relative orientation of the electron beam and the molecule, dissociation products often demonstrate pronounced anisotropic angular distributions. The angular distributions have been analyzed by *Dunn* [34] using symmetry considerations.

67.2.6 Ionization Cross Sections

Some 90 years ago, *Tate and Smith* [35] developed the basic techniques for measuring total ionization cross sections. These were later improved by *Rapp and Englander-Golden* [36]. Full details of the experimental methods are given in the reviews and books already cited. *Märk and Dunn* [37] reviewed the situation as it existed in the mid 1980s. In the basic *parallel plate* method, the electron beam is directed through a beam or a static target gas between collector plates that detect the resultant ions. Unstable species can be studied by the *fast neutral beam* technique [38], in which the neutral target species is formed by charge neutralization from a fast ion beam, and is subsequently ionized by a crossed electron beam. For the determination of partial ionization cross sections specific to a given ion species in a given ionization stage, mass spectroscopic (quadrupole mass spectrometer, electrostatic, or magnetic charged particle analyzer or time-of-flight) methods are used. Fourier transform mass spectrometry (FTMS) has also been used effectively to study fragmentation with formation of both positive and negative ions. A recent example of this can be found in [39]. Absolute total ionization cross sections have been measured for a large number of species with an accuracy of better than 10%. *Christophorou* and colleagues have presented helpful compilations of ionization and other data of particular relevance to the plasma processing industry, [40, and earlier references in this journal].

A large number of mechanisms can contribute to the ionization of atoms and molecules by electron impact. For targets with only a few atomic electrons, the dominant process is single ionization of the outer shell, with the resultant ion being left in its ground state. The process is direct and

is characterized by large impact parameters b and small momentum transfers. The cross section varies with incident electron energy in a way very similar to the optically allowed excitation processes discussed in Sect. 67.2.4. Processes involving ionization of more than one outer-shell electron become more important as the size of the target increases. These events are associated with small b , and electron–electron correlations are usually strong. Autoionization increases in significance for heavier targets. Here, also, collisions with small b dominate and electron–electron correlations are strong. For heavier targets, inner-shell effects, such as Auger electron or X-ray emission, become progressively more important. For molecular targets, dissociative ionization (either directly or through a highly excited intermediate state) and ion-pair formation also play a significant role.

In addition to the measurement of gross ion production, it is also possible to study the ionization process by monitoring the electron(s) ejected or scattered inelastically. Conventional electron spectroscopic techniques are used for this purpose. The addition of coincidence techniques (e–2e measurements) in which the momenta of all the electrons involved are completely specified has allowed many of the fine details of the ionization process to be extracted [41].

A major advance in the study of dissociative ionization has come with the development of so-called “reaction microscopes” [42–45] and “velocity slice imaging” spectrometers [46–48]. These allow 4π detection of fragment ions but also bring the possibility of complete momentum and angular distribution analysis of the fragment ions even from quite complicated polyatomic targets. *Slaughter et al.* [49] provide a recent review of how these and advanced theoretical techniques have been applied successfully in the case of dissociative attachment.

Dissociative attachment studies have featured prominently in the field of electron collisions ever since the early work [50] by Sanche’s group demonstrated that this process could lead to strand-breaking in DNA molecules. Since production of electrons in biological material following high-energy radiation input is governed by ionization processes, there has been much work on these as well [51]. A recent paper [52] provides an update on recent work on DNA bases together with references to relevant earlier studies. A recent discussion of absolute cross section evaluations following low-energy electron impact on DNA and the formation of transient anions is given in [53].

67.3 Coincidence and Superelastic Measurements

The cross section measurements described so far do not yield complete information on electron scattering processes. As was mentioned in Sect. 67.1.2, these cross sections do not

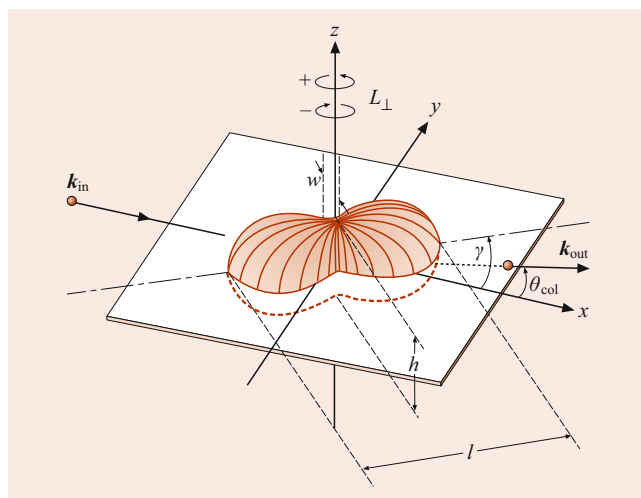


Fig. 67.4 Collisionally induced charge cloud in a p -state atom. The scattering plane is fixed by the direction of incoming \mathbf{k}_{in} and outgoing \mathbf{k}_{out} momentum vectors of the electrons. The atom is characterized by the relative length (l), width (w), and height (h) of the charge cloud, by its alignment angle γ , and by its inherent angular momentum L_{\perp} . The coordinate frame is the natural frame with the z -axis perpendicular to the scattering plane and with the x and y -axes defined as shown in the figure relative to \mathbf{k}_{in} and \mathbf{k}_{out}

distinguish magnetic sublevels, electron spin, etc., and represent summation of cross sections over these experimentally indistinguishable processes (summation of the square moduli of the corresponding scattering amplitudes). The quantum mechanical description of a scattering process is given in terms of scattering amplitudes and under certain conditions requires summing up amplitudes and squaring the sum. This leads to interference terms that arise from the coherent nature of the scattering process. A complete characterization of a scattering process, therefore, requires knowledge of the complex scattering amplitudes.

Sophisticated experimental techniques have been developed in recent years, which go beyond the conventional scattering cross section measurements and yield information on magnetic sublevel specific scattering amplitudes and the polarization (alignment and orientation) of the excited atomic ensemble. The experimental techniques fall into two main categories: a) electron–photon coincidence measurements and b) superelastic scattering measurements involving coherently excited species. (We still consider unpolarized electron beams in the description of these two techniques here and will address the question of spin polarization in the following section.)

In electron–photon coincidence measurements, the radiation pattern emitted by the excited atom is determined for a given direction of the scattered electron. A scattering plane is defined by \mathbf{k}_i and \mathbf{k}_f , and hence the symmetry is lowered from cylindrical (around the incident beam direction) to planar, see Fig. 67.4.

It is now possible to determine, at least in principle, both the atomic alignment (i.e., the shape of the excited state

charge cloud and its alignment in space) and its orientation (i.e., the angular momentum transferred to the atom during the course of the collision). Complete sets of excitation amplitudes for the coherently excited atomic states and their relative phases have been measured in some cases. A comparison with theory can then be made at the most fundamental level. See [54] for a full discussion and analysis.

The electron–photon coincidence measurements can be carried out in two ways: (1) measuring polarization correlations and (2) measuring angular correlations. In (1), polarization analysis of the emitted photon in a given direction occurs, while in (2), the angular distribution of the emitted photons is determined without polarization analysis. We will describe here only method (1) in some detail.

Method (1) has the advantage that it directly measures the angular momentum (perpendicular to the scattering plane) transferred in the collision. For P -state excitation from a 1S_0 ground state, four parameters plus a cross section are needed to describe the collisionally excited P -state fully. The natural parameters introduced by Andersen et al. [54] are defined as follows (Fig. 67.4): γ is the alignment angle of the excited state charge cloud relative to the electron beam axis, P_ℓ^+ is the linear polarization in the scattering plane, L_\perp^+ is the orbital angular momentum perpendicular to the scattering plane that is transferred to the atom in the collision, and ρ_{00} is the relative height of the charge cloud perpendicular to the scattering plane at the point of origin. The $+$ superscript indicates positive reflection symmetry with respect to the scattering plane.

In polarization correlation experiments, one typically measures two linear (P_1, P_2) and one circular (P_3) polarization correlation parameters perpendicular to the scattering plane. One additional linear polarization correlation parameter P_4 is measured in the scattering plane. Each parameter is the result of two intensity measurements for different orientations of the polarization analyzer

$$\begin{aligned} P_1 &= \frac{I(0^\circ) - I(90^\circ)}{I(0^\circ) + I(90^\circ)} \beta^{-1}, \\ P_2 &= \frac{I(45^\circ) - I(135^\circ)}{I(45^\circ) + I(135^\circ)} \beta^{-1}, \\ P_3 &= \frac{I^R - I^L}{I^R + I^L} \beta^{-1}, \\ P_4 &= \frac{I(0^\circ) - I(90^\circ)}{I(0^\circ) + I(90^\circ)} \beta^{-1}. \end{aligned} \quad (67.13)$$

Here, $I(\alpha)$ denotes the photon intensity measured for a polarizer orientation α with respect to the electron beam axis, I^R and I^L refer to right and left-handed circularly polarized light, and β denotes the polarization sensitivity of the polarization analyzer. The relationships between the experimentally determined polarization correlation parameters and

the natural parameters are given by

$$\begin{aligned} \gamma &= \frac{1}{2} \tan^{-1}(P_2/P_1), \\ P_1^+ &= (P_1^2 + P_2^2)^{1/2}, \\ L_\perp^+ &= -P_3, \\ \rho_{00} &= \frac{(1 + P_1)(1 - P_4)}{4 - (1 - P_1)(1 - P_4)}. \end{aligned} \quad (67.14)$$

The total polarization P_{tot}^+ , which is defined as

$$\begin{aligned} P_{\text{tot}}^+ &= \left[(P_1^+)^2 + (L_\perp^+)^2 \right]^{1/2} \\ &= (P_1^2 + P_2^2 + P_3^2)^{1/2}, \end{aligned} \quad (67.15)$$

is a measure for the degree of coherence in the excitation process. In the absence of atomic depolarizing effects due to, for example, fine and/or hyperfine interactions, a value of $P_{\text{tot}}^+ = +1$ for the emitted radiation indicates total coherence of the excitation process.

Much of the earlier work involved excitation of helium n^1P states. Here, the situation is simplified as L – S coupling applies strictly: $P_4 = 1$, and ρ_{00} is zero. Excitation of the 2^1P state, for example, is fully coherent, and hence the excitation is completely specified by just two parameters, γ and L_\perp (or P_1 since $P_1 = (1 - L_\perp^2)^{1/2}$). More recently, the techniques have been applied to heavier targets and more complicated excitation processes [55–59].

The superelastic scattering experiments could be looked at as time-inverse electron–photon coincidence experiments (although this is not exactly the case). In these experiments, a laser beam is utilized to prepare a coherently excited, polarized ensemble of target atoms for the electron scattering measurement. The superelastic scattering intensity is then measured as a function of laser-beam polarization and/or angle with respect to a reference direction. Linearly polarized laser light produces an aligned target (uneven population in magnetic sublevels for quantum numbers of different $|M_J|$ values). Circularly polarized laser light produces oriented targets (uneven population in $M_J = +m$ and $M_J = -m$ magnetic sublevels). From these measurements, the same electron impact coherence parameters can be deduced as from the coincidence experiments. The big advantage of these experiments over the coincidence ones is that the data production rates are much higher, often by many orders of magnitude. When the technique is combined with the use of the magnetic angle changing device (MAC) [60], the coherence parameters can be obtained for the complete range of electron scattering angles. The MAC device is basically a coil system generating variable magnetic fields without disturbing a free flow of atomic and electron beams. The B-field steers the incident electron beam into the interaction region, and the electrons change angle as they pass into the MAC

device, which is a direct consequence of the B-field changing from negative to positive. This superelastic scattering approach has been applied to atomic species (mainly metal atoms) that are conveniently excited with available lasers. Detailed descriptions of the experimental techniques, the underlying theoretical background, and the interpretation of the experimental data are given in [61–70].

It should be noted that electron scattering by coherently excited atoms can be utilized not only to obtain electron impact coherence parameters for inelastic processes originating from ground state but for elastic, inelastic, and superelastic transitions involving excited states. These measurements yield information on the creation, destruction, and transfer of alignment and orientation in electron collision processes, which is needed, e.g., in the application of plasma polarization spectroscopy [71].

67.4 Experiments with Polarized Electrons

So far, we have considered the utilization of unpolarized electron beams that yield spin-averaged cross sections. Little information on spin-dependent interactions is gained from these experiments. However, these interactions can be studied using polarized electron beam techniques. Developments on both the production and detection of spin-polarized electron beams have resulted in a wide range of elegant experiments probing these effects. The theory is also highly developed. For a detailed discussion, see the work of Kessler [72, 73], Blum and Kleinpoppen [74], Hanne [75–77], and Andersen et al. [57, 58] and the references therein. Some basic concepts are presented here.

The degree of polarization P of an electron beam is given by

$$P = \frac{N(\uparrow) - N(\downarrow)}{N(\uparrow) + N(\downarrow)}, \quad (67.16)$$

where $N(\uparrow)$ and $N(\downarrow)$ are the numbers of electrons with spins parallel and antiparallel, respectively, to a particular quantization direction. Measurements of P both before and after the collision enable one to probe directly for specific spin-dependent processes. For example, in elastic scattering from heavy spinless atoms, any changes in the polarization of the electrons must be caused by spin–orbit interactions alone since, in this instance, it is not possible to alter the polarization of the electron beam by electron exchange. Measurements have been carried out for Hg and Xe for both direct (f) and spin-flip (g) scattering amplitudes, as well as their phase differences [73].

The spin–orbit interaction for the continuum electron caused by the target nucleus leads to different scattering potentials and, consequently, to different cross sections for

spin-up and spin-down electrons (called Mott scattering). Consequently, an initially unpolarized electron beam can become spin polarized after scattering by a specific angle according to

$$\mathbf{P}' = S_p(\theta)\hat{\mathbf{n}}, \quad (67.17)$$

where $\hat{\mathbf{n}}$ is the unit vector normal to the scattering plane, $S_p(\theta)$ is the polarization function, and \mathbf{P}' is the polarization of the scattered beam. For the same reasons, when a spin-polarized electron beam is scattered by an angle θ to the left and to the right, an asymmetry is found in the scattering cross sections. Furthermore, an existing polarization \mathbf{P}' can be detected through the left–right asymmetry A in the differential cross section, which is given by

$$A \equiv \frac{\sigma_l(\theta) - \sigma_r(\theta)}{\sigma_l(\theta) + \sigma_r(\theta)} = S_A(\theta)\mathbf{P}' \cdot \hat{\mathbf{n}}, \quad (67.18)$$

where $\sigma_l(\theta)$ and $\sigma_r(\theta)$ are the differential cross sections for scattering at an angle θ relative to the incident beam axis to the left and to the right, respectively. For elastic scattering, the polarization function S_p , and the asymmetry function S_A are identical and are called the Sherman function.

When electron exchange is studied under conditions where other explicitly spin-dependent forces can be neglected, the cross sections for the scattering of polarized electrons from polarized atoms depend on the relative orientation of the polarization vectors. According to [73]

$$\sigma(\theta) = \sigma_u(\theta)[1 - A_{\text{ex}}(\theta)\mathbf{P}_e \cdot \mathbf{P}_A], \quad (67.19)$$

where \mathbf{P}_e and \mathbf{P}_A are the electron and atom polarization vectors, and $\sigma_u(\theta)$ is the cross section for unpolarized electrons. Hence, an *exchange asymmetry* $A_{\text{ex}}(\theta)$ can be defined by

$$A_{\text{ex}}(\theta)\mathbf{P}_e \cdot \mathbf{P}_A = \frac{\sigma_{\uparrow\downarrow}(\theta) - \sigma_{\downarrow\uparrow}(\theta)}{\sigma_{\uparrow\downarrow}(\theta) + \sigma_{\downarrow\uparrow}(\theta)}, \quad (67.20)$$

where $\sigma_{\uparrow\uparrow}(\theta)$ and $\sigma_{\uparrow\downarrow}(\theta)$ denote the cross sections for parallel and antiparallel polarization vectors, respectively. As Bartschat [78] points out, an asymmetry can occur even if the scattering angle is not defined. In this case, the function $A_{\text{ex}}(\theta)$ is averaged over all angles. Differential and integral measurements of this kind have been performed for elastic scattering, excitation, and ionization.

For heavy target systems it is necessary to consider a combination of effects together with a description of the target states in the intermediate or fully coupled scheme. Consequently, the number of independent parameters can become very large, and the *complete* experiments, which disentangle the various contributions to any observed asymmetry in the scattering, are rarely possible.

Even for very light target atoms, where conventional Mott scattering is negligible, *Hanne* [75] has shown that the *fine structure* effect, in which electron scattering from individual fine structure levels of a multiplet occurs, can lead to polarization effects. In fact, it can be a dominating effect for inelastic collision processes.

For full details of these various mechanisms and how density matrix theory and other theoretical techniques have been applied to scattering involving polarization effects, the reader is referred to the review articles cited, particularly *Andersen* et al. [57].

In certain cases, experiments involving spin-polarized electron beams coupled with coincidence (or superelastic) measurements allow one to extract the maximum possible information for a given process and are termed complete or perfect in the sense defined by *Bederson* [79–81].

It has also been possible to use spin-polarized electron beams to extract the fine details of electron–atom and electron–molecule interactions, where the detection of photons or ions rather than electrons occurs (e.g., [82, 83]).

67.5 Electron Collisions with Excited Species

There are many plasma systems where electron collisions with excited atoms and molecules play a prominent role, e.g., electron beam and discharge pumped lasers, and planetary and astrophysical plasmas. Especially important are electron collisions with metastable species because of the long lifetime, large cross section, and large amount of excitation energy associated with them. Electron collision studies and cross section data in this area are scarce, mainly due to experimental difficulties associated with the production of target beams with sufficiently high densities of excited species. With the application of lasers for the preparation of the excited species, this problem can be overcome. However, this approach has not yet been extensively exploited. Reviews of this field are given by *Lin* and *Anderson* [84], *Trajmar* and *Nickel* [85], and *Christophorou* and *Olthoff* [86].

Since electron collisions with excited species necessarily involve a method of preparation, they are two-step processes. Excitation and ionization in these cases are frequently referred to as stepwise excitation and ionization. The target preparation leads to mixed beams containing both ground and excited atoms or molecules. Preparation of excited atoms is achieved by electron impact or photoabsorption. Fast metastable beams can be produced by near-resonance charge exchange. For more details, see [85, 87, 88]. Electron impact excitation is simple and effective but highly nonspecific, and characterization of the composition of the mixture is difficult. Laser excitation is more involved but very well defined. Specific fine and hyperfine levels of individual isotopes can be excited. When laser excitation is used in conjunction with su-

perelastic electron scattering, an energy resolution of 10^{-8} eV is easily achieved, compared with the 10^{-2} eV resolution possible in conventional electron scattering.

Depending on the method of preparation, the population distribution in the magnetic sublevels of the target atoms may be uneven and some degree of polarization (alignment or orientation) may be present. The scattering will then be ϕ -dependent. For polarized target atoms the measured electron collision cross sections do not correspond to the conventional cross sections (which are summed over final and averaged over initial experimentally indistinguishable states, with equal populations in the initial states). One, therefore, has to characterize precisely the state of the target beam in order to be able to deduce a well-defined, meaningful cross section. Polarization of atoms can be conveniently controlled, in the case of excitation with laser light, through the control of the laser light polarization (as discussed in Sect. 67.3). Since the atomic ensemble is coherently excited in this case, the scattering cross sections will depend on the azimuthal scattering angle ϕ . These considerations also come into play when one tries to relate measured inelastic and corresponding inverse superelastic cross sections by the principle of detailed balancing.

67.6 Electron Collisions in Traps

A technique that has recently begun to be exploited involves collisions with trapped atoms. Pioneered by *Lin* and colleagues [89, 90], using Rb targets, the technique has many advantages over more conventional techniques, not the least of which is the fact that the absolute number density of the target need not be known. Cross section data are obtained from measurements of trap loss and electron beam current density. Because up to half of the atoms in the trap can be in the excited state, it is possible to make measurements of cross sections involving excited states as well [91, 92]. Measurements involving Cs targets have also been reported [93].

67.7 Current Applications

Electron-impact driven processes have been identified as being of fundamental importance in many diverse areas, including waste remediation and environmental cleanup [94], and medical [95], technological [96], and space applications. For example, one of the most important environmental applications is terrestrial “space weather”. This can affect the accurate functioning of spaceborne and ground-based communication systems, have a negative impact on infrastructure and technology, as well as endanger human health. Space weather is created by N_2 , the most abundant constituent of the Earth’s atmosphere. Nitrogen molecules collide with

low-energy secondary electrons generated by collision processes involving high-energy particles from the “solar wind”. Line (band) intensities (cross sections) from atmospheric species (such as N_2 in the case of the Earth) are widely used as indirect probes of atomic and molecular concentrations and are, thus, used as a diagnostic tool in atmospheric chemistry [97].

In the medical field, investigations on low-energy electrons and their role in DNA damage have been carried out; see Sect. 63.2.6 for more details. A comprehensive understanding of data of this nature has a vital importance in the modeling of radiation damage to biological tissues and in cancer treatment. [95].

In the technology area, for example, atomic and molecular collision processes play an important role in the edge region of fusion plasmas for understanding the plasma–wall interactions that govern fueling and recycling processes. This leads to optimization in designing a new generation of fusion reactors [98]. Recent advancements in the availability of reliable data for electron impact collisions with atoms and molecules have also enabled development of high-efficiency lasers [99].

In space environments, the modeling of planetary plasmas (energy budget and general behavior), interpretation of optical observations, electron flux and energy distributions require accurate dissociative and direct electron impact excitation cross sections for processes involving the atmospheric and ionospheric constituents of planetary bodies. A large fraction of these electrons are energetic enough to cause further ionization and, thus, produce a large number of secondary electrons. In addition, charged particles accelerated in the magnetic field of planets can contribute significantly to the planetary plasma by ionizing collisions. These secondary electrons are very effective in various collision processes because both the cross sections and the electron energy distributions peak at low energies (from a few tenths of an eV to about 100 eV). The auroral phenomenon in the atmospheres of Earth [97, 100], Venus [101], and Mars [102], the electroglow in the ionosphere of giant planets [103], the oxygen emission features prominent in the far ultraviolet (FUV) airglow spectrum of Europa [104] and Ganymede [105], the UV emission from the Io plasma torus [106], and the UV emission from Titan [107, 108] all clearly demonstrate the importance of the electron impact excitation and emission processes from atomic and molecular species (and their ions) such as O, S, O_2 , CO, N_2 , H_2 , CO_2 , and SO_2 .

67.8 Emerging Applications

Electron collisions with atoms, molecules, ions, and surfaces have formed the basis of many areas of science and technology and will continue to empower new, emerging applications [109]. Next-generation laser development and

micro and nanotechnology-based microprocessor fabrication are exciting emerging applications of electron collisions.

Recently, the international community has been investing heavily in high-powered (kW-class) diode-pumped alkali laser (DPAL) development research, with particular interest in scaling for defense, power beaming, and industrial applications. Key alkali laser processes require accurate ionization and recombination data [110]. Electron collisions in intense laser field situations is also an exciting field that is rapidly expanding [111, 112].

Plasma-using technologies such as the remote plasma etching (RPE) technique in fabricating next generation microprocessors require accurate and comprehensive sets of electron collision data. Further development and optimization of the RPE technique is critically dependent on the quality of fundamental electron and ion scattering data [113]. Developments in large-scale supercomputing capabilities have opened the door to calculations involving large molecules, which could not even have been contemplated a few years ago. Electron-initiated dissociation of large molecules can act as a catalyst for reactive chemistry in environmentally sensitive situations.

References

1. Franck, J., Hertz, G.: *Verh. Dtsch. Phys. Ges.* **16**, 457 (1914)
2. Massey, H.S.N., Burhop, E.H.S., Gilbody, H.B.: *Electronic and Ionic Impact Phenomena* vol. 1 & 2. Clarendon Press, Oxford (1969)
3. McDaniel, E.W.: *Atomic Collisions, Electron and Photon Projectiles*. John Wiley & Sons, New York (1989)
4. Scoles, G.: *Atomic and Molecular Beam Methods* vol. 1. Oxford University Press, New York (1988)
5. Trajmar, S., Register, D.F.: Experimental techniques for cross section measurements. In: Shimamura, I., Takayanagi, K. (eds.) *Electron Molecule Collisions*. Plenum, New York (1984)
6. Allen, M.: *J. Phys. B* **25**, 1559 (1992)
7. Bethe, H.A.: *Ann. Phys.* **5**, 325 (1930)
8. Lassetre, E.N., Skerbele, A., Dillon, M.A.: *J. Chem. Phys.* **50**, 1829 (1969)
9. Cartwright, D.C., Trajmar, S., Williams, W., Huestis, D.L.: *Phys. Rev. Lett.* **27**, 704 (1971)
10. Goddard, W.A., Huestis, D.L., Cartwright, D.C., Trajmar, S.: *Chem. Phys. Lett.* **11**, 329 (1971)
11. Zubek, M., Mielewska, B., Channing, J., King, G.C., Read, F.H.: *J. Phys. B* **32**, 1351 (1996)
12. Channing, J., Read, F.H.: *Rev. Sci. Instr.* **67**, 2372 (1996)
13. Trajmar, S., Kanik, I.: Elastic and excitation electron collisions with atoms. In: Janev, R.K., Winter, H.P., Fritsch, W. (eds.) *Atomic and Molecular Processes in Fusion Edge Plasmas*. Plenum, New York (1995)
14. Bederson, B., Kieffer, L.J.: *Rev. Mod. Phys.* **43**, 601 (1971)
15. Zecca, A., Carwasz, G.P., Brusa, R.S.: *Riv. Nuovo Cim.* **19**(3), 1 (1996)
16. Carwasz, G.P., Brusa, R.S., Zecca, A.: *Riv. Nuovo Cim.* **24**(1), 1 (2001)
17. Carwasz, G.P., Brusa, R.S., Zecca, A.: *Riv. Nuovo Cim.* **24**(4), 1 (2001)

18. Srivastava, S., Chutjian, A., Trajmar, S.: *J. Chem. Phys.* **63**, 2659 (1975)
19. Nickel, J.C., Mott, C., Kanik, I., McCollum, D.C.: *J. Phys. B* **21**, 1867 (1988)
20. Nickel, J.C., Zetner, P., Shen, G., Trajmar, S.: *J. Phys. E* **22**, 730 (1989)
21. Trajmar, S., McConkey, J.W.: *Adv. At. Mol. Opt. Phys.* **33**, 63 (1994)
22. Clout, P.N., Heddle, D.W.O.: *J. Opt. Soc. Am.* **59**, 715 (1969)
23. Donaldson, F.G., Hender, M.A., McConkey, J.W.: *J. Phys. B* **5**, 1192 (1972)
24. van Zyl, B., Dunn, G.H., Chamberlain, G., Heddle, D.W.O.: *Phys. Rev. A* **22**, 1916 (1980)
25. Filippelli, A.R., Lin, C.C., Anderson, L.W., McConkey, J.W.: *Adv. At. Mol. Opt. Phys.* **33**, 1 (1994)
26. McConkey, J.W., Malone, C.P., Johnson, P.V., Winstead, C., McKoy, V., Kanik, I.: *Phys. Rep.* **466**, 103 (2008)
27. Inokuti, M.: *Rev. Mod. Phys.* **43**, 297 (1971)
28. Compton, R.N., Bardsley, J.N.: Dissociation of molecules by slow electrons. In: Shimamura, I., Takayanagi, K. (eds.) *Electron Molecule Collisions*. Plenum, New York (1984)
29. Freund, R.S.: In: Stebbings, R.F., Dunning, F.B. (eds.) *Rydberg States of Atoms and Molecules*. Cambridge University Press, Cambridge (1983)
30. Zipf, E.C.: Dissociation of molecules by electron impact. In: Christophorou, L.G. (ed.) *Electron-Molecule Interactions and Their Applications*, vol. 1, Academic Press, New York (1984)
31. LeClair, L.R., McConkey, J.W.: *J. Chem. Phys.* **99**, 4566 (1993)
32. McConkey, J.W., Kedzierski, W.: *Adv. At. Mol. Opt. Phys.* **63**, 1 (2014)
33. Cosby, P.C.: *J. Chem. Phys.* **98**(7804), 9544–9560 (1993)
34. Dunn, G.H.: *Phys. Rev. Lett.* **8**, 62 (1962)
35. Tate, J.T., Smith, P.T.: *Phys. Rev.* **39**, 270 (1932)
36. Rapp, D., Englander-Golden, P.: *J. Chem. Phys.* **43**, 1464 (1965)
37. Märk, T.D., Dunn, G.H.: *Electron Impact Ionization*. Springer, Vienna, New York (1985)
38. Dixon, A.J., Harrison, M.F.A., Smith, A.C.H.: *J. Phys. B* **9**, 2617 (1986)
39. Jaio, C.Q., DeJoseph, C.A., Garscadden, A.: *J. Phys. Chem.* **107**, 9040 (2003)
40. Christophorou, L.G., Olthoff, J.K.: *J. Phys. Chem. Ref. Data* **31**, 971 (2002)
41. Ehrhardt, H., Jung, K., Knoth, G., Schlemmer, P.: *Z. Phys.* **D**(1), 3 (1986)
42. Ulrich, J., Moshhammer, R., Dorn, A., Dörner, R., Schmidt, L.P.H., Schmidt-Bocking, H.: *Rep. Prog. Phys.* **66**, 1463 (2003)
43. Dörner, R., et al.: *Phys. Rep.* **330**, 95 (2000)
44. Adaniya, H., Slaughter, D.S., Osipov, T., Weber, T., Belkacem, A.: *Rev. Sci. Instrum.* **83**, 023106 (2012)
45. Moradmand, A., Williams, J.B., Landers, A.L., Fogel, M.: *Rev. Sci. Instrum.* **84**, 033104 (2013)
46. Chandler, D.W., Houston, P.L.: *J. Chem. Phys.* **87**, 1445 (1987)
47. Nandi, D., Prabhudesai, V.S., Krishnakumar, E., Chatterjee, A.: *Rev. Sci. Instrum.* **76**, 053107 (2005)
48. Wu, B., Xia, L., Li, K.H., Zeng, X.J., Xi, T.: *Rev. Sci. Instrum.* **83**, 013108 (2012)
49. Slaughter, D.S., Belkamen, A., McCurdy, C.W., Rescigno, T.N., Haxton, D.J.: *J. Phys. B* **49**, 222001 (2016)
50. Boudaiffa, B., Cloutier, P., Hunting, D., Huels, M.A., Sanche, L.: *Science* **287**, 1658 (2000)
51. Gomez-Tejedor, G.G., Fuss, M.C. (eds.): *Radiation damage in Biomolecular systems*. Springer, New York (2012)
52. Rahman, M.A., Krishnakumar, E.: *J. Chem. Phys.* **144**, 161102 (2016)
53. Chen, W., Chen, S., Dong, Y., Cloutier, P., Zheng, Y., Sanche, L.: *Phys. Chem. Chem. Phys.* **18**, 32762 (2016)
54. Andersen, N., Gallagher, J.W., Hertel, I.V.: *Phys. Rep.* **165**, 1 (1988)
55. Becker, K., Crowe, A., McConkey, J.W.: *J. Phys. B* **25**, 3885 (1992)
56. Sohn, M., Hanne, G.F.: *J. Phys. B* **25**, 4627 (1992)
57. Andersen, N., Bartschat, K., Broad, J.T., Hertel, I.V.: *Phys. Rep.* **279**, 251 (1997)
58. Andersen, N., Bartschat, K.: *Polarization, Alignment, and Orientation in Atomic Collisions*. Springer, Berlin (2001)
59. Herting, C., Hanne, G.F.: Correlation and polarization in photonic, electronic and atomic collisions. *AIP Conf. Proc.* **697**, 181 (2004)
60. Hussey, M., Murray, A., MacGillivray, W., King, G.: *J. Phys. B* **41**, 055202 (2008)
61. Hertel, I.V., Stoll, W.: *Adv. At. Mol. Phys.* **13**, 113 (1977)
62. Zetner, P.W., Trajmar, S., Csanak, G.: *Phys. Rev. A* **41**, 5980 (1990)
63. Fano, U.: *Rev. Mod. Phys.* **29**, 74 (1957)
64. Blum, K.: *Density Matrix Theory and Applications*. Plenum, New York (1981)
65. Fano, U., Macek, J.H.: *Rev. Mod. Phys.* **45**, 553 (1973)
66. Macek, J.H., Hertel, I.V.: *J. Phys. B* **7**, 2173 (1974)
67. MacGillivray, W.R., Standage, M.C.: *Phys. Rep.* **168**, 1 (1988)
68. Karaganov, V., Bray, I., Teubner, P.J.O.: *Phys. Rev. A* **57**, 208 (1998)
69. Stockman, K.A., Karaganov, V., Bray, I., Teubner, P.J.O.: *J. Phys. B* **34**, 1105 (2001)
70. Zetner, P.W., Johnson, P.V., Li, Y., Csanak, G., Clark, R.E.H., Abdallah, J.: *J. Phys. B* **34**, 1619 (2001)
71. Kazantsev, S.A., Hénoux, J.-C.: *Polarization Spectroscopy of Ionized Gases*. Kluwer, Dordrecht (1995)
72. Kessler, J.: *Polarized Electrons*, 2nd edn. Springer, Berlin, Heidelberg, p 2 (1985)
73. Kessler, J.: *Adv. At. Mol. Opt. Phys.* **27**, 81 (1991)
74. Blum, K., Kleinpoppen, H.: *Adv. At. Mol. Phys.* **19**, 187 (1983)
75. Hanne, G.F.: *Phys. Rep.* **95**, 95 (1983)
76. Hanne, G.F.: In: Beyer, H.J., Blum, K., Hippler, R. (eds.) *Coherence in Atomic Collision Physics*, p. 41. Plenum, New York (1988)
77. Hanne, G.F.: Collisions of polarized electrons with atoms and molecules. In: MacGillivray, W.R., McCarthy, I.E., Standage, M.C. (eds.) *Proceedings of the 17th ICPEAC, Electronic and Atomic Collisions*, p. 199. Hilger, Bristol (1992)
78. Bartschat, K.: *Comments At. Mol. Phys.* **27**, 239 (1992)
79. Bederson, B.: *Comments At. Mol. Phys.* **1**, 41 (1969)
80. Yu, D.H., Williams, J.F., Chen, X.J., Hayes, P.A., Bartschat, K., Zeman, V.: *Phys. Rev. A* **67**, 032707 (2003)
81. Al-Khateeb, H.M., Birdsey, B.G., Gay, T.J.: *Phys. Rev. Lett.* **85**, 4040 (2000)
82. Gay, T.J.: *Adv. At. Mol. Opt. Phys.* **57**, 157 (2009)
83. Dreiling, J.M., Gay, T.J.: *Phys. Rev. Lett.* **113**, 118103 (2014)
84. Lin, C.C., Anderson, L.W.: *Adv. At. Mol. Opt. Phys.* **29**, 1 (1992)
85. Trajmar, S., Nickel, J.C.: *Adv. At. Mol. Opt. Phys.* **30**, 45 (1993)
86. Christophorou, L.G., Olthoff, J.K.: *Adv. At. Mol. Opt. Phys.* **44**, 156 (2001)
87. Boffard, J.B., Lagus, M.E., Anderson, L.W., Lin, C.C.: *Rev. Sci. Instrum.* **67**, 2738 (1996)
88. Boffard, J.B., Gehrke, M.F., Lagus, M.E., Anderson, L.W., Lin, C.C.: *Eur. J. D* **8**, 193 (2000)
89. Schappe, R.S., Walker, T., Anderson, L.W., Lin, C.C.: *Europhys. Lett.* **29**, 439 (1995)
90. Schappe, R.S., Walker, T., Anderson, L.W., Lin, C.C.: *Phys. Rev. Lett.* **76**, 4328 (1996)
91. Keeler, M.L., Anderson, L.W., Lin, C.C.: *Phys. Rev. Lett.* **85**, 3353 (2000)

92. Uhlmann, L.J., Dall, R.G., Truscott, A.G., Hoogerland, M.D., Baldwin, K.G.H., Buckman, S.J.: *Phys. Rev. Lett.* **94**, 173201 (2005)
93. MacAskill, J.A., Kedzierski, W., McConkey, J.W., Domyslawska, J., Bray, I.: *J. Electron Spectrosc. Relat. Phenom.* **123**, 173 (2002)
94. Garrett, B.C., Dixon, D.A., Camaioni, D.M., Chipman, D.M., Johnson, M.A.: *Chem. Rev.* **105**, 355 (2005)
95. Hunniford, C.A., McCullough, R.W., Davies, R.J.H., Timson, D.J.: *Biochem. Soc. Trans.* **37**(4), 893 (2009)
96. Becker, K.H., McCurdy, C.W., Orlando, T.M., Resigno, T.N.: *Electron-Driven Processes: Scientific Challenges and Technological Opportunities*. US DOE Report, Washington, DC (2000)
97. Young, J.A., Malone, C.P., Johnson, P.V., Ajello, J.M., Liu, X., Kanik, I.: *J. Phys. B* **43**, 135201 (2010)
98. Hey, J.D., Brezinsek, S., Mertens, Ph., Unterberg, B.: *AIP Conf. Proc.* **876**, 235 (2006). <https://doi.org/10.1063/1.2406033>
99. Markosyan, A.H.: *Opt. Lett.* **42**, 4295 (2017)
100. Meier, R.R., Picone, J.M., Drob, D., Bishop, J., Emmert, J.T., Lean, J.L., Stephan, A.W., Strickland, D.J., Christensen, A.B., Paxton, L.J., Morrison, D., Kil, H., Wolven, B., Woods, T.N., Crowley, G., Gibson, S.T.: *Earth Space Sci.* **2**, 1–37 (2015). <https://doi.org/10.1002/2014EA000035>
101. Gérard, J.-C., Bougher, S.W., pez-Valverde, M.A.L., Pätzold, M., Drossart, P., Piccioni, G.: *Space Sci. Rev.* **212**, 1617 (2017)
102. Stiepen, A., Gérarda, J.-C., Bougherb, S., Montmessinc, F., Huberta, B., Bertauxc, J.-L.: *Icarus* **245**, 295 (2015)
103. Badman, S.V.: *Space Sci. Rev.* **187**, 1 (2015)
104. Roth, L., Saur, J., Retherford, K.D., Strobel, D.F., Feldman, P.D., McGrath, M.A., Spencer, J.R., Blöcker, A., Ivchenko, N.: *J. Geophys. Res. Space Phys.* **121**, 2143 (2016)
105. Eviatar, A.: *ApJ* **555**, 1013 (2001)
106. Nerney, E.G., Bagenal, F., Steffl, A.J.: *J. Geophys. Res. Space Phys.* **122**(727), 744 (2017)
107. Ajello, J.M., West, R.A., Gustin, J., Larsen, K., Stewart, A.I.F., Esposito, L.W., McClintock, W.E., Holsclaw, G.M., Bradley, E.T.: *J. Geophys. Res.* **117**, A12315 (2012)
108. Stevens, M.H., Gustin, J., Ajello, J.M., Evans, J.S., Meier, R.R.: *J. Geophys. Res.* **116**, A5304 (2011). <https://doi.org/10.1029/2010JA016284>
109. Board on Physics and Astronomy: *National Research Council Report on Plasma Science: Advancing Knowledge in the National Interest*. The National Academies Press, Washington, DC (2007). Ch. 2
110. Anderson, G.A., Anderson, M.D.: *Appl. Phys. Rev.* **4**, 041101 (2017). <https://doi.org/10.1063/1.5006913>
111. Niikura, H., Légaré, F., Hasbani, R., Ivanov, M.Y., Villeneuve, D.M., Corkum, P.B.: *Nature* **421**, 826 (2003)
112. Weckenbrock, M., Becker, A., Staudte, A., Kammer, S., Smolarski, M., Bhardwaj, V.R., Rayner, D.M., Villeneuve, D.M., Corkum, P.B., Dorner, R.: *Phys. Rev. Lett.* **91**, 123004 (2003)
113. Bartschat, K., Kushner, M.J.: *Proc. Natl. Acad. Sci. U.S.A.* **113**, 26 (2016)



Bill McConkey Bill McConkey obtained his PhD at Queen's University, Belfast. He has spent time at the Sorbonne, the University of Windsor, and at NASA's Jet Propulsion Laboratory in California. His research involves processes that occur in planetary atmospheres or astrophysical sources. Bill is the author of over 180 papers in the refereed scientific literature. His awards include the Gold Medal of CAP and the APS Will Allis Prize.



Sandor Trajmar Dr Sandor Trajmar received his PhD in Physical Chemistry from the University of California at Berkeley, California. He was Head of the Electron collision Physics Group, Jet Propulsion Laboratory, California Institute of Technology, Pasadena, California. He retired in January 1997.



Charles Havener , Ruitian Zhang , and Ronald Phaneuf

Contents

68.1	Low-Energy Ion–Atom Collision Processes	995
68.2	Experimental Methods for Total Cross Section Measurements	997
68.2.1	Gas-Target Beam Attenuation Method	997
68.2.2	Gas-Target Product Growth Method	997
68.2.3	Crossed Ion and Thermal Beams Method	998
68.2.4	Fast Merged Beams Method	998
68.2.5	Trapped Ion Method	999
68.2.6	Swarm Method	999
68.3	Methods for State-Selective Measurements	999
68.3.1	Photon Emission Spectroscopy	999
68.3.2	Translational Energy Spectroscopy	999
68.3.3	Electron Emission Spectroscopy	1000
68.3.4	Recoil-Ion Momentum Spectroscopy	1000
References	1000

Abstract

This chapter outlines the physical principles and experimental methods used to investigate low energy ion–atom collisions. A low-energy collision is here defined as one in which the initial ion–atom relative velocity v is less than the mean orbital velocity $\langle v_e \rangle$ of the active electrons during the collision. For outer or valence electrons, $\langle v_e \rangle \simeq v_B$, where $v_B = 2.1877 \times 10^8$ cm/s is the Bohr velocity. In terms of the energy of a projectile ion, v_B corresponds to 24.8 keV/u.

C. Havener (✉)
Physics Division, Oak Ridge National Laboratory
Oak Ridge, TN, USA
e-mail: havenercc@ornl.gov

R. Zhang
Institute of Modern Physics, Chinese Academy of Sciences
Lanzhou, China
e-mail: zhangrtimp@hotmail.com

R. Phaneuf
Dept. of Physics, University of Nevada, Reno
Reno, NV, USA
e-mail: phaneuf@unr.edu

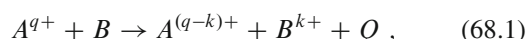
The theory and results of ion–atom scattering studies are further discussed in other chapters of the book. The focus here is on the experimental techniques. Since several of these depend on the characteristics of a specific process, the following section presents a summary of the physics of low-energy ion–atom collisions.

Keywords

electron capture · single-electron capture · relative collision energy · total cross section · measurement · model charge transfer

68.1 Low-Energy Ion–Atom Collision Processes

For the low-energy region, electron capture between charged ions and atoms is the most important and widely studied inelastic collision process. Electron capture, also referred to as charge exchange or charge transfer, is a process where one or several target electrons are captured by the projectile ion and is described by



where Q is the potential energy difference between the initial and final states.

For an exoergic process, $Q > 0$, and this energy appears as excess kinetic energy of the products after the collision. For an endoergic process, $Q < 0$ and must be provided by the initial kinetic energy of the reactants, so that the corresponding cross section is usually small at low collision energies. If Q is zero or very small, it is a resonant or near-resonant electron capture process, and the resulting cross section is appreciable even at very low energies.

Electron capture by multiply charged ions from atoms is predominantly an exoergic process, for which cross sections

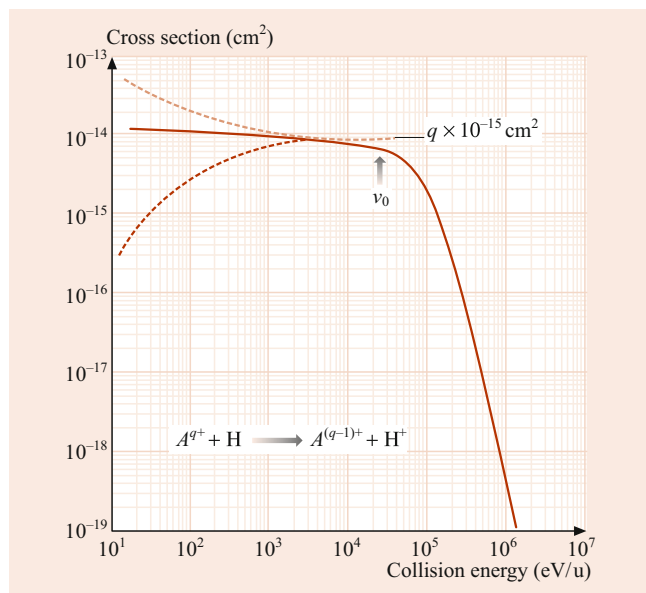


Fig. 68.1 Typical cross section variation with collision energy for electron capture by a multiply charged ion from hydrogen. The low-energy behavior depends on the structure of the quasi molecule formed during the collision

may also be large at low energies. In this case, electrons are preferentially captured into excited levels of $A^{(q-k)+}$. As shown in Fig. 68.1, the typical cross section behavior for single-electron capture ($k = 1$) by a multiply charged ion from atomic hydrogen is described by the $q \times 10^{-15} \text{ cm}^2$ scaling law. At intermediate and high collision energies, the initial ionic charge is no longer the major determinant of the cross section, whereas at low energies, the cross section strongly depends on the structure of the transient quasi molecule formed during the collision. For the thermal energy region (not shown in Fig. 68.1), the cross section shows a $1/v$ dependence (v is the collision velocity) due to the attractive ion-induced dipole [1]. Several techniques like gas target, crossed ion beam, merged beam methods, etc., have been developed for total cross section measurements.

For a multiply charged ion collision with a neutral atom, as shown in Fig. 68.2, electron capture reaction channels that are moderately exoergic produce curve crossings at internuclear separations where there is sufficient overlap of the electron clouds for electron capture to be a likely process. The Landau–Zener curve-crossing model [2], the classical over-barrier model for single capture [3], and the extended classical over-barrier model for multiple capture [4] are useful in predicting the important final product states, and in providing a semiquantitative interpretation. In the case of single-electron capture by a bare multiply charged ion (of charge $q = Z$) from a hydrogen atom, the principal quantum number n_p of the most probable final ionic state is given in

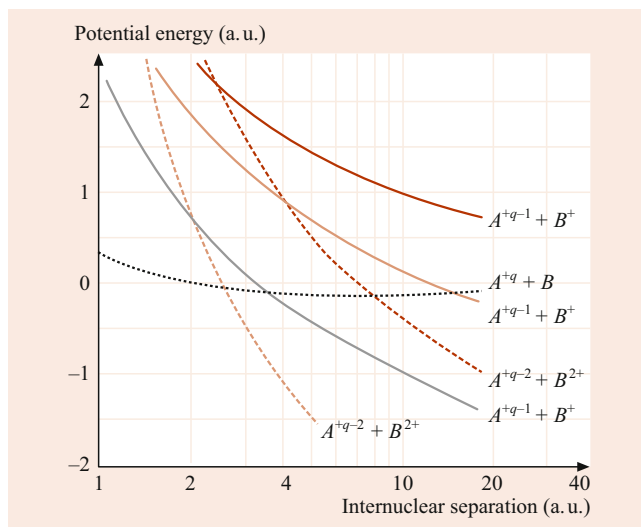


Fig. 68.2 Potential energy curves for the collision of a multiply charged ion A^{q+} with a multielectron atom B

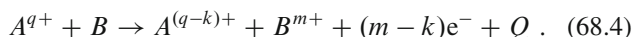
this model [3] by

$$n_p = \sqrt{\frac{2Z^{1/2} + 1}{Z + 2Z^{1/2}}} \quad (68.2)$$

The internuclear separation R_p at which the potential curves cross in this case is given by

$$R_p = \frac{2(Z - 1)}{Z^2/n_p^2 - 1} \quad (68.3)$$

Multiple electron capture ($k > 1$) from multielectron atoms occurs predominantly into multiply excited levels, which stabilize either radiatively, leading to stabilized or *true* double capture, or via autoionization. The latter process is usually referred to as transfer ionization,



At low energies, transfer ionization is particularly important in collisions of highly charged ions with multielectron atoms. There has been much discussion of the role of electron correlation in the multiple-electron capture process. An issue is the relative importance of the mechanism whereby several electrons are transferred (in a correlated manner) at a single curve crossing compared with electrons transferred sequentially at different curve crossings.

Measurements of the distribution of final product electronic states as well as its angular scattering can provide insight into electron capture collision mechanisms [5]. This motivated the development of experimental detection techniques beyond the total cross section measurement for measuring the nl -resolved differential cross sections (n and l

are the principal quantum number and angular momentum quantum number, respectively) and angular differential cross sections. To this end, traditional electron spectroscopy, energy gain spectroscopy, photon emission spectroscopy, as well as recoil ion momentum spectroscopy, etc., have been developed [6]. A lot of progress has been achieved by measuring nl -resolved differential cross sections. There have been some measurements of the electron dipole and current density following electron transfer [7, 8]. The next generation of electron capture experiment would be expected to measure nlm -resolved differential cross sections (m is the magnetic substate quantum number), i.e., the captured electron is initially prepared in a specific nlm state.

Other inelastic ion-atom collision processes, such as direct electronic excitation and ionization, are endothermic, with relatively small cross sections that fall off with decreasing energy below a few tens of keV/u. Exceptions are collisions involving Rydberg atoms and collisional excitation of fine structure transitions, for which the required energy transfer is relatively small. There is only a small amount of experimental data available for direct excitation and ionization processes at low collision energies.

68.2 Experimental Methods for Total Cross Section Measurements

In the present context, a total cross section measurement refers to an integration or summation over scattering angles, product kinetic energies and (frequently) electronic states. The total cross section is usually measured as a function of relative collision energy or velocity.

68.2.1 Gas-Target Beam Attenuation Method

The attenuation of a collimated ion beam of incident intensity I_0 in a differentially pumped gas target cell or gas jet is related to the collision cross section σ by

$$I = I_0 e^{-\sigma NL}, \quad (68.5)$$

where I is the intensity after traversing an effective length L of the target gas, and N is the number density of target atoms. For a gas target cell with entrance and exit apertures of diameter d_1 and d_2 , which are much less than the physical length z of the gas cell, L is given to a good approximation by $z + (d_1 + d_2)/2$. This is valid under molecular flow conditions, for which the mean free path between collisions of target atoms is much larger than the dimensions of the gas cell.

In designing the gas cell for measurements of total cross sections, d_2 and the beam detector must be large enough that elastic scattering may be eliminated as a contributor to the measured attenuation. Usually d_2 is made larger than d_1 . Measurement of the gas pressure in a target cell is usually made using a capacitance manometer connected to the cell via a tube whose conductance is much larger than that of the gas cell apertures so that, to a good approximation, the pressure will be the same in both the manometer and the gas cell. For gas jet targets, the effective target thickness NL is usually determined by in-situ normalization to some well-known cross section.

The quantity σ in Eq. (68.5) refers to an effective cross section for removing projectile ions from the incident beam, which is the sum of cross sections for all such processes. In many cases, a single process (e.g., electron capture) is dominant, and σ primarily describes that process. Whether or not a collision process removes a projectile ion from the reactant beam depends on the configuration of the experiment. For example, the projectile particle may remain physically in the beam after passing through the target, but with a changed charge due to a collision. This would be registered as an attenuation of the primary ion beam if the beam is charge analyzed after the reaction.

68.2.2 Gas-Target Product Growth Method

The product growth method is similar to the beam attenuation method; the major difference is that the growth of reaction products is measured rather than the loss of reactant projectiles. The products may be derived from either the projectile beam or the gas target, or both. The main advantage of this method is its higher degree of selectivity of a specific collision process. In addition, the reactants and products can usually be registered simultaneously, or in some cases in coincidence, eliminating the sensitivity of the measurement to temporal variation of ion beam intensity.

An important criterion is that the density of the target gas be low enough that single collision conditions prevail (i.e., that the likelihood of an ion passing through the gas target and interacting with more than one target atom is negligibly small). This must, in general, be satisfied in order for Eq. (68.5) to correctly relate the measured attenuation to the collision cross section of interest and is critical to the product growth method [9]. In this case, under single-collision conditions, one may set the number of products $I_p = I_0 - I$, and Eq. (68.5) may then be written as

$$\frac{I_p}{I_0} = 1 - e^{-\sigma NL} \approx \sigma NL. \quad (68.6)$$

The approximate expression is useful for $\sigma NL \ll 1$, which is a requirement for single-collision conditions. It is also important that the products not be lost in a subsequent collision in the gas cell, so the magnitudes of cross sections for the loss of products in the target gas must also be considered. The products in such an experiment may be derived from either the projectile beam or the target gas (e.g., collection of slow product ions in a gas cell), or from both in coincidence to enhance the specificity of the method. The method may, in principle, be used to determine either total or differential cross sections, depending on the degree of selectivity of collision products.

68.2.3 Crossed Ion and Thermal Beams Method

Replacement of the gas target cell by an effusive thermal beam is advantageous for studying collisions of ions with reactive species such as atomic hydrogen, as well as for collecting slow ion products. The use of accelerating electrodes or grids for slow charged products allows coincident detection of fast and slow products, permitting measurement of ionization as well as electron-capture cross sections. The use of an effusive source or gas jet precludes accurate measurement of the effective target thickness, and in-situ normalization to the cross section for some well-known process is usually employed. A comprehensive discussion of such methods as applied to collisions of multiply charged ions with atomic hydrogen is given by *Gilbody* [9].

68.2.4 Fast Merged Beams Method

Cross sections for ion–atom collision processes at very low energies have been measured by merging fast beams of ions and neutral atoms [10], as in Fig. 68.3. In this case, σ is determined from experimental parameters by

$$\sigma = \frac{R}{\epsilon} \frac{qe}{I_+ I_0} \frac{v_+ v_0}{|v_+ - v_0|} \frac{1}{L \Omega}, \quad (68.7)$$

where R is the number of products detected per second, ϵ is the product detection efficiency, q is the charge state of projectile ion, e is the electronic charge, I_+ is the ion current, I_0 is the neutral “current” (number/second) of atoms, v_+ and v_0 the laboratory velocities of the ion and atom beams, v_{rel} their relative velocity, and Ω is the overlap integral and is a measure of the spatial overlap of the two beams along the merged path L . Rigorously, the overlap of the beams should be determined by integrating the product of the current density j_+ and j_0 of the two beams at every point along the merged path

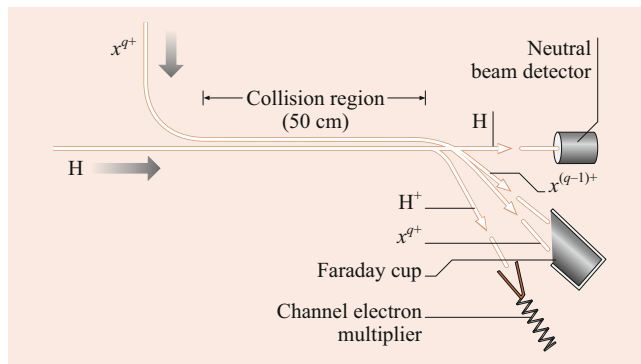


Fig. 68.3 The merged beams arrangement used at the multicharged ion research facility at Oak Ridge National Laboratory to study low-energy electron capture collisions of multicharged ions with H [10]

and is given by

$$\Omega = \frac{\iiint j_+(x, y, z) j_0(x, y, z) dx dy dz}{\iiint j_+(x, y, z) dx dy dz \iiint j_0(x, y, z) dx dy dz}. \quad (68.8)$$

A variety of three-dimensional and approximate schemes have been developed to measure the overlap of the two beams (Chap. 4 in [6] and references therein).

The relative collision energy E_{rel} in eV/u is given by

$$\frac{E_{\text{rel}}}{\mu} = \frac{E_+}{m_+} + \frac{E_0}{m_0} - 2 \sqrt{\frac{E_+}{m_+} \frac{E_0}{m_0}} \cos \theta, \quad (68.9)$$

where E_+ , m_+ , and E_0 , m_0 are the energies and masses of the ion and atom, respectively, and μ is their reduced mass. For collinear merged beams, $\theta = 0$ and E_{rel} can be reduced to zero by making the two beam velocities the same. In practice, the finite divergences of the beams place a lower limit on the energy and the energy resolution. The fast neutral atom beam can be created by neutralizing an accelerated positive ion in a gas via electron capture, or by electron detachment of a negative ion beam either in a gas, or by using a laser. In gas collisions, a small fraction of the neutral beam is produced in excited n -levels (with an n^{-3} distribution), which may influence the measurements.

With fast colliding beams, the maximum effective beam densities are invariably much smaller than the background gas density, even under ultrahigh vacuum conditions. For example, a typical 10 keV proton beam with a circular cross section of diameter 3 mm and a current $I = 10 \mu\text{A}$ has an average effective density $n = I/(eav) = 1.6 \times 10^6 \text{ cm}^{-3}$ (a is the beam cross sectional area, and v is its velocity). It is, therefore, necessary either to modulate the beams or to use coincidence techniques to separate signal events due to beam–beam collisions from background events produced by collisions of either beam with residual gas. A typical two-beam modulation scheme is described in [10]. To eliminate

the production of spurious signals, the signal detector is gated “on” a short time after the beams are switched, and the beam modulation period is made much shorter than the pressure time constant of the vacuum system.

Absolute electron-capture cross sections have been measured for $\text{Si}^{4+} + \text{D}$ collisions to energies below 1 eV/u, where the attractive ion-induced-dipole (polarization) interaction is expected to play a role [1]. The inverse velocity dependence of the cross section in this region is suggestive of the classical Langevin orbiting model for ion–neutral collisions [11].

68.2.5 Trapped Ion Method

The trapped ion method is used to determine rate coefficients and effective cross sections for ion–atom collisions at near thermal energies. The technique involves storing ions in an electrostatic or electromagnetic trap and measuring the rate of loss of ions from the trap after a small quantity of neutral gas is admitted [12]. Like the beam attenuation method, the trap technique cannot distinguish different processes that cause ions to be lost from the trap. The mean collision energy is estimated from an analysis of the ion dynamics in the trap. Collisions at temperatures of a few K and below have been achieved in, e.g, a magneto-optical (MOT) trap.

68.2.6 Swarm Method

The swarm method, using the flowing afterglow, drift tube, or selected-ion flow tube, has been used successfully to study ion–atom collisions at very low energies [13]. Ions are injected into a homogeneous electric field and drift through a suitable low-density buffer gas such as helium. The ions move as a swarm whose mean energy depends on the applied electric field and on collisions with the buffer gas and can be varied from the near-thermal region to tens of eV. The method involves measuring the additional attenuation of the directed ion swarm by a known quantity of added reactant gas and is the major technique that has been used for the study of ion–atom collisions at near-thermal energies [14]. As with ion beam attenuation and ion trap methods, the drift tube is not selective of the process that leads to attenuation of the ion swarm.

68.3 Methods for State-Selective Measurements

Four principal methods have been developed and applied to the measurement of partial cross sections for the population of specific product electronic states in ion–atom collisions involving electron capture [15]. These are photon emission, translational energy gain, electron emission, and cold target

recoil ion momentum spectroscopy (COLTRIMS) in collisions of ion beams with gas targets.

68.3.1 Photon Emission Spectroscopy

At low energies, electron capture from an atom by a charged ion usually populates excited levels. Since the timescale of photon emission deexcitation is several orders of magnitude larger than the collision time, and photon emissions usually show discrete spectroscopic structure, the measured photon spectra contain state-selective information. For example, photon emission spectra can be used to measure emission cross sections and electron capture state-selectivity involving angular momentum quantum states [16, 17]. A calibrated grating or crystal spectrometer can be used to record spectra. By summing the signal under a peak area in the spectra, the emission cross sections can be calculated via the relation

$$\sigma_{\text{em}}\lambda = \frac{4\pi}{\omega} \frac{q}{K(\lambda)Q_c} \frac{S(\lambda)}{NL}, \quad (68.10)$$

where σ_{em} is the emission cross section, ω is the solid angle of observation, q is the charge of the projectile ions, Q_c is the accumulated ion charge, $K(\lambda)$ is the wavelength dispersive quantum yield of the detection system, $S(\lambda)$ is the measured signal, N is the effective target density, and L is the observation length.

Similar measurements have also been performed with an x-ray quantum microcalorimeter (XQC) detector based on cryogenic techniques [18], with which the photon spectral range is extended beyond the visible and vacuum ultraviolet to the X-ray region. The measurements are able to cover all direct and many possible cascade emissions. Complementary, with an electron beam ion trap, those X-ray emissions due to charge exchange arising from forbidden transitions can be observed [19–21]. These long-lived transitions are not accessible with the traditional ion extraction mode.

68.3.2 Translational Energy Spectroscopy

Translational energy loss or energy gain spectroscopy provides a convenient method to determine the distribution of final states in low-energy ion–atom collisions that are either endoergic or exoergic ($Q \neq 0$). For example, this method has been used extensively by the Belfast group [22] to study the predominantly exoergic process of electron capture by multiply charged ions from hydrogen atoms. An ion beam with a well-defined energy is directed through a gas target, and the energy of the product ion beam is energy analyzed after the collision. Since the energy gain or loss to be measured is only a very small fraction of the initial kinetic energy, it is

usually necessary to reduce the initial energy spread to a few tenths of an eV by decelerating the reactant ion beam prior to energy selection by an electrostatic analyzer. If the scattering angle of the ion is very small, its energy change is approximately equal to Q . Since the ion beam is attenuated by deceleration and energy analysis, cross sections for collisionally populating specific states are determined by normalizing the measured product-state distributions to total cross section data. The attainable state resolution is not as good as for photon emission spectroscopy.

68.3.3 Electron Emission Spectroscopy

As noted in Sect. 68.1, multiple-electron capture by multiply charged ions from atoms at low energies occurs primarily into multiply excited states, which decay either radiatively or via autoionization [5]. The latter decay pathway (transfer ionization) provides an experimental method to determine the product ionic states by ejected-electron spectroscopy. Analysis of electrons emitted into the forward (ion beam) direction (zero degree spectroscopy) offers significant advantages for analysis of low-energy electrons with high resolution [23]. Since a gas jet is often employed, and absolute electron collection and spectrometer efficiencies are difficult to determine, some normalization procedure is usually employed to determine state-selective cross sections by this method. Electrons and product projectile or recoil ions have also been detected in coincidence to increase the specificity of the method.

68.3.4 Recoil-Ion Momentum Spectroscopy

Over the past 20 years, a significant experimental technique development in ion–atom collisions is cold-target recoil ion momentum spectroscopy [24, 25], also called a *reaction microscope*. Its powerful multifold differential measurements have advanced ion–atom electron capture to the point where the details of state-selectivity become available. It has also been used to identify molecular or cluster geometry configurations and dissociation dynamics.

As shown in Fig. 68.4, the core components of a COLTRIMS apparatus are a time-of-flight (TOF) spectrometer, an ultracold supersonic gas jet, and two-dimensional position sensitive detectors (PSD). For an ion–atom electron capture collision, an energetic ion beam interacts with a precooled and localized supersonic gas jet at a right angle in the center of the TOF spectrometer, which consists of a homogenous electric field acceleration-region and field-free drift region. The slow recoil ions produced are accelerated by the electric field away from the collision zone towards a recoil-ion PSD. The charge changed projectile ions are separated from

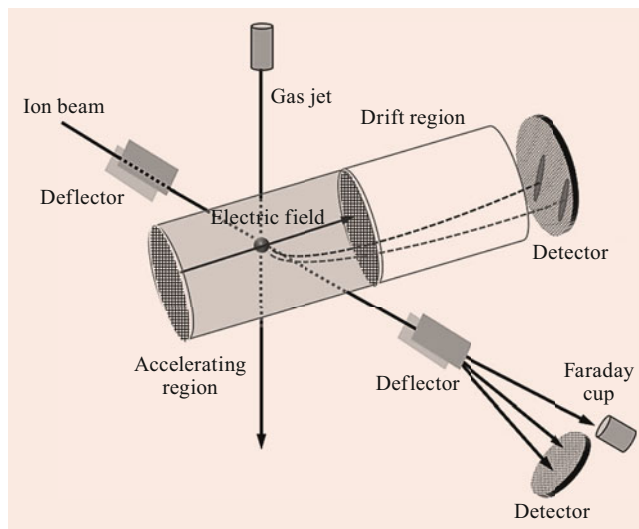


Fig. 68.4 Schematic of the COLTRIMS apparatus used for ion–atom electron capture

the primary beam by the electrostatic deflector downstream of the collision zone and directed to a projectile PSD, while the primary beam is collected by a Faraday cup. The PSD detectors can record time and position information of the recoil ions and projectile ions. By making a time coincidence between the recoil ions and scattered projectile ions, the desired electron capture process can be identified, and background events are suppressed. Three-dimensional momentum vectors of the recoil ions can be constructed using kinematical expressions. The binding energy difference of the active electrons in the state-selective electron capture is reflected in the measured longitudinal momentum distributions of recoil ions. Angular differential information is obtained by the measured transversal momentum of the recoil ions, which is equivalent to that of the scattered projectile ions according to momentum conservation.

More recently, COLTRIMS was updated by replacing the supersonic gas jet with a MOT trap where more targets are available by laser cooling. This updated COLTRIMS is the so-called MOTRIMS [26], with which electron capture measurements have achieved an unprecedented resolution in low-energy ion–atom collisions. In addition, it is promising to combine x-ray detecting techniques with COLTRIMS, with which the spectroscopy of charged ions as well as collision dynamics can be studied in electron capture processes [27].

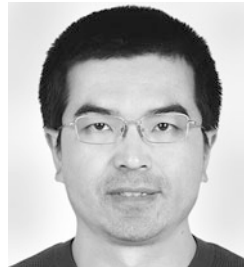
References

1. Pieksma, M., Gargaud, M., McCarroll, R., Havener, C.C.: *Phys. Rev. A* **54**, R(13) (1996)
2. Salop, A., Olson, R.E.: *Phys. Rev. A* **13**, 1312 (1976)
3. Ryufuku, H., Sasaki, K., Watanabe, T.: *Phys. Rev. A* **23**, 745 (1980)

4. Niehaus, A.: *J. Phys. B* **19**, 2925 (1986)
5. Barat, M., Roncin, P.: *J. Phys. B* **25**, 2205 (1992)
6. Shafroth, S.M., Austin, J.C.: *Accelerator-based Atomic Physics Techniques and Applications*. AIP Press, Woodbury (1997)
7. Havener, C.C., Westerveld, W.B., Risley, J.S., Tolk, N.H., Tully, J.C.: *Phys. Rev. Lett.* **48**, 926 (1982)
8. Havener, C.C., Rouze, N., Westerveld, W.B., Tully, J.C.: *Phys. Rev. Lett.* **53**, 1049 (1984)
9. Gilbody, H.B.: *Adv. At. Mol. Phys.* **22**, 143 (1986)
10. Havener, C.C., Huq, M.S., Krause, H.F., Schulz, P.A., Phaneuf, R.A.: *Phys. Rev. A* **39**, 1725 (1989)
11. Gioumousis, G., Stevenson, D.P.: *J. Chem. Phys.* **29**, 294 (1958)
12. Church, D.A.: *Phys. Rep.* **228**, 254 (1993)
13. Kaneko, Y.: *Comm. At. Mol. Phys.* **10**, 145 (1981)
14. Lindinger, W.: *Phys. Scr. T* **3**, 115 (1983)
15. Janev, R.K., Winter, H.: *Phys. Rep.* **117**, 266–387 (1985)
16. Van Zyl, B., Dunn, G.H., Chamberlain, G., Heddl, D.W.O.: *Phys. Rev. A* **22**, 1916 (1980)
17. Ćirić, D., Brazuk, A., Dijkamp, D., de Heer, F.J., Winter, H.: *J. Phys. B* **18**, 3639 (1985)
18. McCammon, D., Almy, R., Apodaca, E., Bergmann Tiest, W., Cui, W., Deiker, S., Galeazzi, M., Juda, M., Lesser, A., Mihara, T., Morgenthaler, J.P., Sanders, W.T., Zhang, J.: *Astrophys. J.* **576**, 188 (2002)
19. Beiersdorfer, P., Olson, R.E., Brown, G.V., Chen, H., Harris, C.L., Neill, P.A., Schweikhard, L., Utter, S.B., Widmann, K.: *Phys. Rev. Lett.* **85**, 5090 (2000)
20. Allen, F.I., Biedermann, C., Radtke, R., Fussmann, G., Fritzsche, S.: *Phys. Rev. A* **78**, 032705 (2008)
21. Tawara, H., Takács, E., Suta, T., Makónyi, K., Ratliff, L.P., Gillaspay, J.D.: *Phys. Rev. A* **73**, 012704 (2006)
22. Gilbody, H.B.: *Adv. At. Mol. Opt. Phys.* **32**, 149 (1994)
23. Stolterfoht, N.: *Phys. Rep.* **146**, 316 (1987)
24. Dörner, R., Mergel, V., Jagutzki, O., Spielberger, L., Ullrich, J., Moshhammer, R., Schmidt-Böcking, H.: *Phys. Rep.* **330**, 95 (2000)
25. Ullrich, J., Moshhammer, R., Dorn, A., Dörner, R., Schmidt, L.P.H., Schmidt-Böcking, H.: *Rep. Prog. Phys.* **66**, 1463 (2003)
26. DePaola, B., Morgenstern, R., Andersen, N.: *Adv. At. Mol. Opt. Phys.* **55**, 139 (2008)
27. Ali, R.: *AIP Conf. Proc.* **926**, 216 (2007)



Charles Havener Charles Havener received his PhD in Physics from North Carolina State University in 1983. This was followed by a postdoc and research staff position at Oak Ridge National Laboratory. The merged-beam apparatus he developed measures charge exchange cross sections from meV to keV collision energies for ions on atomic H and is currently used to measure high-resolution x-ray spectra.



Ruitian Zhang Ruitian Zhang received his PhD from the Lanzhou University in 2013. He worked at Helmholtz Centre for Heavy Ion Research in Germany, at Oak Ridge National Laboratory and Columbia University in the City of New York, and at the Institute of Modern Physics, Chinese Academy of Sciences in China. He is currently working on experimental atomic collision physics, focusing on heavy ion-atom collision dynamics.



Ronald Phaneuf Phaneuf earned a PhD in Physics from the University of Windsor (1973) and has since been engaged in experimental research on interactions of ions with electrons, photons, atoms, and molecules using merged-beams and crossed-beams techniques. He was a postdoctoral fellow at JILA and researcher and program manager for atomic physics and plasma diagnostics for fusion at Oak Ridge National Laboratory. He is Professor Emeritus (University of Nevada).



Michael Schulz  and Lew Cocke

Contents

69.1	Basic One-Electron Processes	1003
69.1.1	Perturbative Processes	1003
69.1.2	Nonperturbative Processes	1009
69.2	Multielectron Processes	1009
69.3	Electron Spectra in Ion–Atom Collisions	1012
69.3.1	General Characteristics	1012
69.3.2	High-Resolution Measurements	1013
69.4	Quasi-Free Electron Processes in Ion–Atom Collisions	1013
69.4.1	Radiative Electron Capture	1014
69.4.2	Resonant Transfer and Excitation	1014
69.4.3	Excitation and Ionization	1014
69.5	Some Exotic Processes	1014
69.5.1	Molecular Orbital X-Rays	1014
69.5.2	Positron Production from Atomic Processes	1015
	References	1015

Abstract

This chapter deals with inelastic processes that occur in collisions between fast, often highly charged, ions and atoms. Fast collisions are here defined to be those for which $V/v_e \geq 1$, where V is the projectile velocity and v_e the orbital velocity of this electron. For processes involving outer-shell target electrons, this implies $V \gtrsim 1$ a.u., or the projectile energy $\gtrsim 25$ keV/a.m.u. For inner-shell electrons, typically, $V \gtrsim Z_2/n$ a.u., where Z_2 is the target nuclear charge and n the principal quantum number of the active electron. A useful relationship is $V = 6.35\sqrt{E/M}$, where V is in a.u., E is in MeV, and M is in a.m.u. Fast

collisions involving outer-shell processes can be studied using relatively small accelerators, while those involving inner-shell processes require larger van de Graaffs, LINACs (linear accelerators), etc. Because the motion of the inner-shell electrons is dominated by the nuclear Coulomb field of the target, and because transitions involving these electrons take place rather independently of what transpires with the outer-shell electrons, it has proven to be somewhat easier to understand one-electron processes involving inner-shell electrons. Thus, for a long time, a great deal of the work on fast ion–atom collisions concentrated on inner-shell processes involving heavy-target atoms. However, more recently, new experimental techniques have led to a shift of this focus to inelastic processes involving light-target atoms. Furthermore, present investigations go beyond the one-electron picture to include the influence of the electron–electron interaction. The present chapter outlines some of the developments in this area over a very active past few decades. The literature is vast, and only a small sampling of references is given. Emphasis is on experimental results (for the theory, see Part D of this book).

Keywords

double ionization · Compton profile · recoil peak · plane wave bear approximation · single-ionization cross section

M. Schulz (✉)
Dept. of Physics, Missouri University of Science & Technology
Rolla, MO, USA
e-mail: schulz@mst.edu

L. Cocke
Dept. of Physics, Kansas State University
Manhattan, KS, USA
e-mail: cocke@phys.ksu.edu

69.1 Basic One-Electron Processes

69.1.1 Perturbative Processes

Inner-Shell Ionization of Heavy Targets

For ion–atom collisions involving projectile and target nuclear charges Z_1 and Z_2 , respectively, the parameters $\eta_1 = [\hbar V/(Z_1 e^2)]^2$ and $\eta_2 = [\hbar v_e/(Z_2 e^2)]^2$ are useful in characterizing the strength of the interaction between Z_1 , Z_2 , and

the target electron. If $\eta_2 \ll \eta_1$, (i.e., $Z_1/Z_2 \ll V/v_e$), the effect of the projectile on the target wave function can be treated perturbatively. Perturbation treatments of inner-shell ionization by lighter projectiles have been extensively studied and reviewed [1–8]. Two well-known formulations have been used: the plane wave Born approximation (PWBA) [1–4] and the semiclassical approximation (SCA) [9, 10]. The former represents the nuclear motion with plane waves, while the latter is formulated in terms of the impact parameter b with the nuclear motion treated classically. For straight line motion of the nuclei, the results are equivalent [11]. The total cross section for ionizing the K-shell of a target of charge Z_2 by a projectile of charge Z_1 is given within the PWBA by

$$\sigma_i = (8\pi Z_1^2/Z_2^4 \eta_2) f(\theta_2, \eta_2) a_0^2, \quad (69.1)$$

where $\theta_2 = 2u_k n^2/Z_2^2$, and u_k is the target binding energy. The function f rises rapidly for $V < v_e$, reaching a value near unity near $V = v_e$ and falling very slowly thereafter. Tables of f for K and L-shell ionization are given in [3, 4]. Figure 69.1 shows a comparison of experimental data for K vacancy production by protons with PWBA calculations, and with a classical binary encounter approximation [12] for a large range of proton data [6]. For larger Z_1 , corrections to the PWBA and SCA must be made for the effective increase of u_k due to the presence of the projectile during the ionization, for nuclear projectile deflection, for relativistic corrections, and for the polarization of the electron cloud, as reviewed in [13–17]. Total cross section measurements for inner-shell vacancy production in the perturbative region are reviewed in [15, 16].

In the SCA treatment, the heavy-particle motion is taken to be classical, and the evolution of the electronic wave function under the influence of the projectile field is calculated by time-dependent perturbation theory. The assumption of classical motion is valid if the Bohr parameter $K = 2Z_1 Z_2 e^2 / (\hbar V)$ is much larger than unity [18]. If this condition is satisfied, the projectile scattering angle can be associated with a particular b through a classical deflection function. For K-shell ionization, the action occurs typically at sufficiently small b that a screened Coulomb potential is sufficient for calculating the deflection. In the absence of screening, $\theta = r_0/b$, where $r_0 = Z_1 Z_2 e^2 / E$ with θ and E expressed in either the laboratory or center of mass system. Calculations for K and L-shell ionization have been carried out [10]. The typical ionization probability $P(b)$ for $V \approx v_e$ and $b = 0$ is $P(0) \approx (Z_1/Z_2)^2$. For $V < v_e$, $P(b)$ decreases with increasing b with a characteristic scale length of $r_{\text{ad}} = V/\omega$, the *adiabatic radius*, where ω is the transition energy. For $V > v_e$, $P(b)$ cuts off near the K-shell radius of the target. A more sophisticated relativistic SCA program has been written [19] and is widely used for calculating $P(b)$,

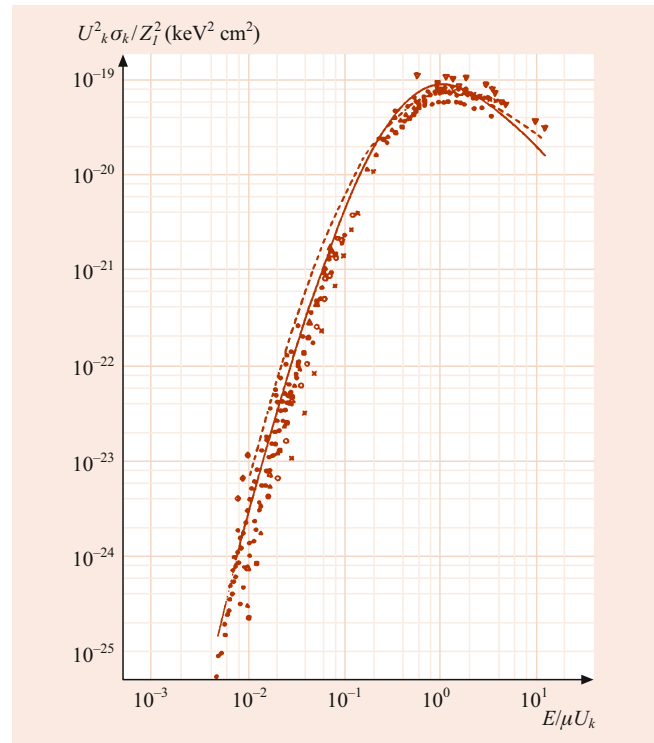


Fig. 69.1 Comparison of experimental cross sections for K-shell vacancy production with PWBA (*dashed line*) and binary encounter (*solid line*) theories; U_k is the target binding energy in keV and λ the projectile/electron mass ratio [6]

cross sections, and probabilities differential in the final electron energy and angle. Experimentally, the probability $P(b)$ for inner-shell ionization can be determined from

$$P(b) = \frac{1}{\epsilon \omega \Delta \Omega} \left(\frac{Y}{N[\theta(b)]} \right), \quad (69.2)$$

where Y is the coincidence yield for the scattering of $N(\theta)$ ions into a well-defined angle $\theta(b)$ accompanied by X-ray (or Auger electron) emission with fluorescence yield ω into a detector of efficiency ϵ and solid angle $\Delta \Omega$ [20]. The necessary ω can be obtained from calculations for neutral targets [21] (Chap. 66). However, they must be corrected for changes due to extensive outer-shell ionization during the collision. Such corrections are particularly important for targets with low fluorescence yields, for Z_2 below 30, and for collisions in which the L-shell is nearly depleted in the collision [15, 16]. Values of $P(b)$ have been measured for many systems and generally show good agreement (better than 10%) with the SCA for fast light projectiles such as protons, with increasing deviation as higher Z_1 or slower V are used [22]. Examples of $P(b)$ for K vacancy production for several systems are shown in Fig. 69.2, showing the evolution away from the SCA as the collision becomes less perturbative.

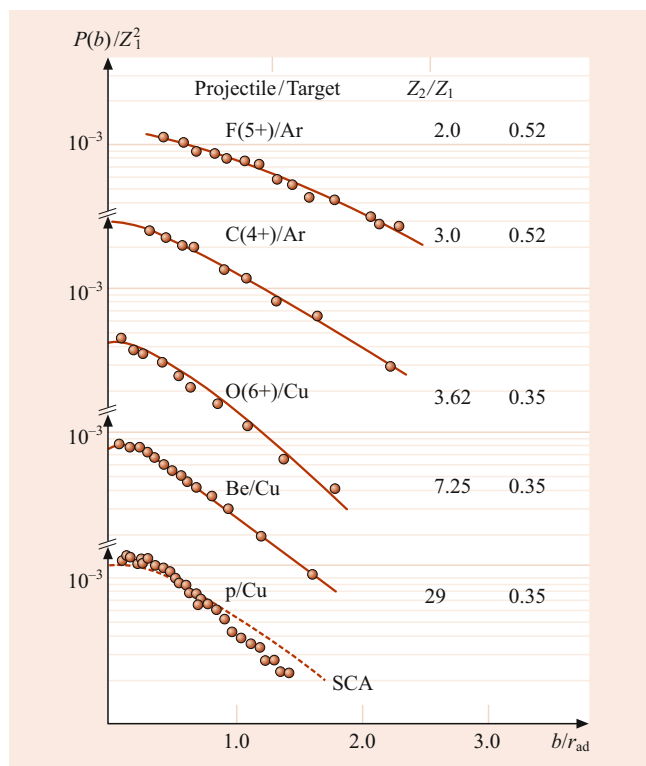


Fig. 69.2 $P(b)$ for K-shell vacancy production versus b/r_{ad} for several systems (see text). The ratio V/v_e is designated as V here. For protons p , agreement with the SCA theory is found [10], while for higher Z_1/Z_2 , $P(b)$ moves to larger impact parameters as one leaves the perturbative region [22]

Ionization of light-target Atoms

Ionization of light-target atoms by bare ion impact is a particularly suitable process to study the atomic few-body problem. In the case of an atomic hydrogen target the collision represents a three-body system, i.e., the simplest system for which the Schrödinger equation is not analytically solvable. However, because of the experimental difficulties associated with atomic hydrogen, measurements with this target species are rare [23, 24] and experimental studies have focused on helium targets. Here, the collision still constitutes a relatively simple four-body system. With regard to the few-body problem, studies of ionization processes have the important advantage that, in contrast to pure excitation and capture processes, the final state involves at least three independently moving particles.

Detailed information about the few-body dynamics in a collision can be extracted from multiply differential measurements. This can be accomplished by measuring the kinematic properties (e.g., energy, momentum, ejection angle) of one or more of the collision fragments. The first experimental multiply differential single-ionization cross sections were obtained by studying the ionized electron spectra as a function of energy and ejection angle. Such studies were reviewed by *Rudd et al.* [25] and are discussed in more detail in

Sect. 69.3. More recently, complementary multiply differential data were obtained by measuring projectile energy-loss spectra as a function of the scattering angle in $p + \text{He}$ and $p + \text{H}$ collisions [24, 26, 27].

A comprehensive picture of ionizing collisions can be obtained from kinematically complete experiments. In such a study, the momentum vectors of all collision fragments need to be determined. However, in the case of single ionization, it is sufficient to directly measure the momentum vectors of any two particles in the final state; the third one is then readily determined by momentum conservation. For ionization by electron impact, this has been accomplished by momentum-analyzing the scattered and the ejected electrons ([28] for a review). For ion impact, this approach is difficult because of the very small scattering angles and energy losses (relative to the initial collision energy) resulting from the large projectile mass. Consequently, the only kinematically complete experiments involving a direct projectile-momentum analysis were reported for light ions at relatively low projectile energies [29]. For heavy-ion impact at high projectile energies, in contrast, the complete determination of the final space state is only possible through a direct measurement of the ejected electron and recoil-ion momenta [30].

The technology to measure recoil-ion momenta with sufficient resolution, and therefore to perform kinematically complete experiments for heavy-ion impact, has only become available over the last 2 decades ([31–33] for reviews). Figure 69.3 shows measured (top) and calculated (bottom) three-dimensional angular distributions of electrons ionized in 100 MeV/a.m.u. $\text{C}^{6+} + \text{He}$ collisions for fully determined kinematic conditions [34]. The arrows labeled p_o and q indicate the direction of the initial projectile momentum and the momentum transfer defined as the difference between p_o and the final projectile momentum p_f . This plot is rich in information about the dynamics of the ionization process. The main feature is a pronounced peak in the direction of q . It can be explained in terms of a binary interaction between the projectile and the electron, i.e., a first-order process, and is thus dubbed the *binary peak*. A second, significantly smaller, structure is a contribution centered on the direction of $-q$ (called the *recoil peak*). This has been interpreted as a two-step mechanism where the electron is initially kicked by the projectile in the direction of q and then backscattered by the residual target ion by 180° . Although this process involves two interactions of the electron, it is nevertheless a first-order process in the projectile–target atom interaction. Therefore, as expected for this very large value of $\eta_1 = 100$ (in a.u.), the ionization cross sections are dominated by first-order contributions.

The basic features of the data in Fig. 69.3 are well reproduced even by the relatively simple first Born approximation (FBA). Furthermore, the calculation shown at the bottom

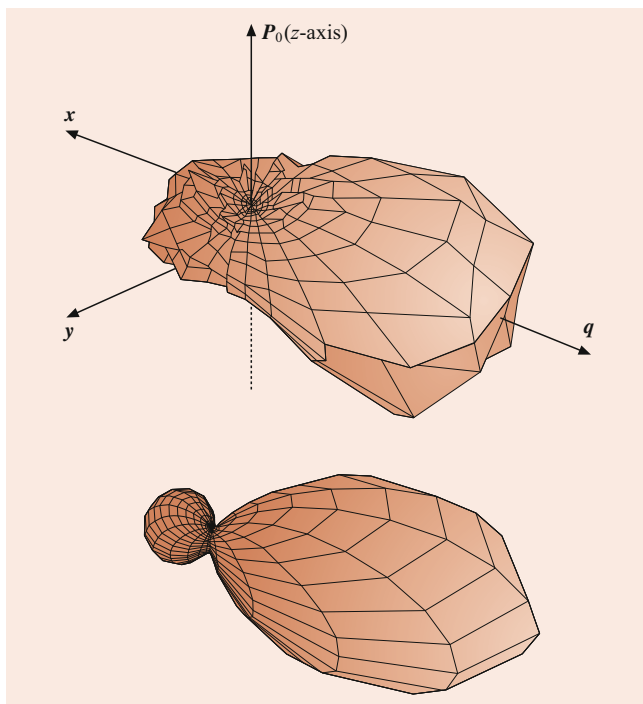


Fig. 69.3 Three-dimensional angular distribution for fully determined kinematic conditions of electrons ionized in 100 MeV/a.m.u. $C^{6+} + He$ collisions. *Top*, experimental data; *bottom*, CDW calculation (see text)

of Fig. 69.3, which is based on the more sophisticated continuum distorted wave approach (CDW) ([35–37], also Chap. 56), yields practically identical results to the FBA. In the CDW method, higher-order contributions are accounted for in the final-state scattering wavefunction. Apart from this good overall agreement, a closer inspection of the comparison between experiment and theory also reveals some significant discrepancies. While in the calculation the binary and recoil peaks are sharply separated by a minimum near the origin, in the data, this minimum is almost completely filled up, giving rise to a *ring-like* shape of the recoil peak. This was explained by a higher-order ionization mechanism involving an interaction between the projectile and the residual target ion [34, 37, 38]. Although the contribution of this process to the total cross section is negligible, it is a very surprising result that for selected kinematic conditions higher-order processes can be important even at large projectile energies. A sobering conclusion of recent research on ionization of light-target atoms is that even well inside the perturbative regime the atomic few-body problem is not nearly as well understood as was previously assumed based on studies for restricted collision geometries. At large perturbation, the lack of understanding is dramatic [39].

Part of these discrepancies may be related to a realization that was recently made in studies of ionization of H_2 by proton impact at a much smaller projectile energy. There it was found that interference structures are present in the scattering angle-dependent cross sections when the incoming

projectiles are coherent relative to the dimension of the target molecule but absent if the projectiles are incoherent [40]. The coherence properties of the projectiles, in turn, are basically determined by the width of the projectile wave packet in momentum space. If the momentum spread is too large, the phase relation between the overlapping amplitudes is not well defined, and no interference structure is observable. In contrast, in scattering theory, it is usually assumed that the incoming projectiles can be described in terms of a plane wave or a distorted wave, which corresponds to a sharp momentum, i.e., to fully coherent projectiles. Therefore, theory may predict interference structures that are not observable in experiments if the projectiles are incoherent.

In the ionization of atomic targets interference can arise from the superposition of different (nonobservable) impact parameters leading to the same (observable) scattering angle. Formally, this type of interference is reflected in the Fourier transform, which converts an impact parameter transition amplitude to a scattering angle-dependent amplitude. If the projectile is represented by a broad wave packet in momentum space, rather than, e.g., a plane wave, the Fourier transform can be altered considerably. Even in the coherent case, the interference resulting from the Fourier transform is not necessarily reflected by an oscillating pattern in the cross sections. Nevertheless, the effect of the momentum wave packet on the Fourier transform could explain differences between cross sections for coherent and incoherent projectiles and, thereby, the aforementioned discrepancies between theory and experiment on ionization of atomic targets.

This interpretation seemed to be confirmed by a study of ionization for a similar collision system as 100 MeV/a.m.u. $C^{6+} + He$, but for projectiles with a much higher degree of transverse coherence [41]. There, the discrepancies to theory were drastically reduced. Furthermore, this interpretation is supported by theoretical analyses [42, 43]. Another experimental study, also performed for a collision system with a perturbation parameter similar to 100 MeV/a.m.u. $C^{6+} + He$, was consistent with calculations assuming coherent projectiles [44]. However, there the smallest coherence length realized in the experiment was several orders of magnitude larger than for 100 MeV/a.m.u. C^{6+} and larger than the size of the target atom. A theoretical study showed that under these circumstances, much smaller decoherence effects are to be expected than for 100 MeV/a.m.u. C^{6+} collisions [43]. Nevertheless, further studies on the role of the projectile coherence properties are needed for collisions with small perturbation parameters. While for much slower collisions coherence effects have been reported for several cases ([45] for a recent review), the question of the extent to which the discrepancies between experiment and theory for the 100 MeV/a.m.u. $C^{6+} + He$ collision system can be explained by such effects has not yet been settled.

Initially, recoil-ion and electron-momentum spectrometers were operated in conjunction with supersonic gas jets

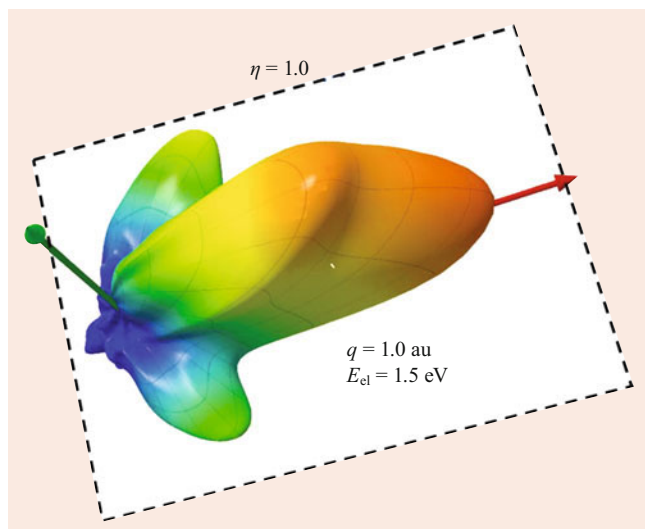


Fig. 69.4 Fully differential, three-dimensional angular distribution of electrons ejected in $7\text{ MeV Li}^{2+} + \text{Li}$ collisions

delivering target beams with a temperature around 1 K. While these setups made kinematically complete experiments possible, which, in turn, led to major advances in our understanding of the few-body dynamics, they also entail some drawbacks compared to conventional approaches. These include: a) the recoil-ion momentum resolution is limited by the achievable temperature that can be reached in supersonic gas jets. b) The energies of electrons detected simultaneously with the recoil ions is limited by the extraction voltage on the spectrometer. For the large voltages required to detect large-energy electrons with sufficiently large solid angle, the recoil-ion momentum resolution is compromised. c) The method is restricted to molecular and noble gas targets. However, the recoil-ion momentum resolution gets worse with increasing target mass. As a result, many applications are actually restricted to H_2 and He targets.

While the second problem is inherent to the spectrometer design, the first and third problems can be addressed by a different target design. A successful approach was to replace the supersonic jet with a gas target cooled in a magneto-optical trap (MOT). Initially, this method was only used in conjunction with momentum spectroscopy of the recoil ions, but no ejected electrons were momentum analyzed [46, 47]. Target temperatures reduced by about two orders of magnitude compared to gas jets were achieved, resulting in drastically improved recoil-ion momentum resolution. Furthermore, in principle, recoil ions can be momentum analyzed with much improved resolution for any target that can be optically pumped, independent of the target mass.

One enormous challenge posed by a MOT target is the momentum analysis of ejected electrons. Conventional setups operating with supersonic gas jets use a magnetic field in order to detect electrons for a sufficiently large momen-

tum space. In order to achieve good momentum resolution this field needs to be as uniform as possible, which seems to be in conflict with the requirement of a field gradient in order to trap the target atoms magnetically. This problem was overcome with a sophisticated switching device so that the trapping magnetic field can be turned off during a brief electron detection period [48]. With this apparatus, the only fully differential cross sections for ion impact ionization of targets other than He or H_2 were measured, and the resolution was improved by about a factor of 3. In Fig. 69.4, a measured fully differential three-dimensional angular distribution of electrons ejected in $7\text{ MeV Li}^{2+} + \text{Li}$ collisions is shown [49]. In the region of the binary peak, the data reveal a considerably richer structure than for $100\text{ MeV/a.m.u C}^{6+} + \text{He}$. This was explained in terms of a combination of the nodal structure of the initial state wave function and the interaction between the nuclei of the collision partners.

Excitation

Inner-shell excitation can be treated within the same perturbative framework, which leads to a cross section given in terms of the generalized oscillator strength for the transition [50–52]. For inner-shell vacancy production by light projectiles, excitation is generally much smaller than ionization, since the oscillator strengths are strongest for transitions to low-lying occupied orbitals, as reviewed by *Inokuti* [51]. Excitation cross sections can be deduced from photon production cross sections and from inelastic energy-loss experiments. An example of the cross section for excitation of the $n = 2$ level of H by protons, measured by the latter technique, is shown in Fig. 69.5 [53].

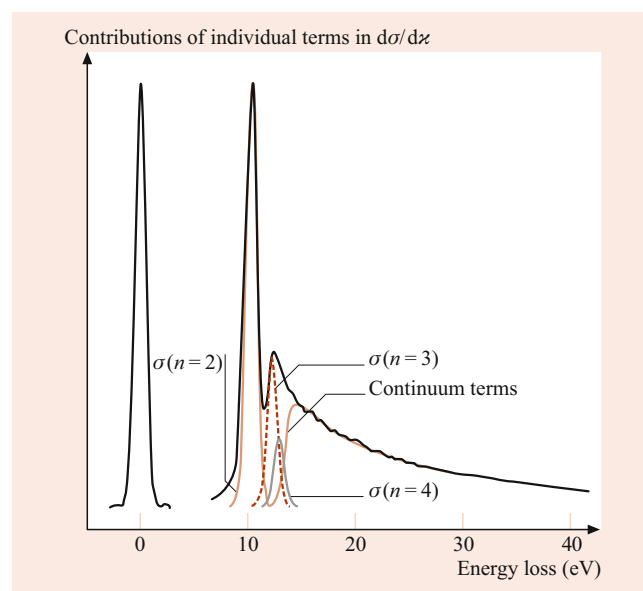


Fig. 69.5 Energy loss spectrum for 50 keV protons in atomic hydrogen, showing excitation to discrete states in H proceeding smoothly into ionization at the continuum limit [53]

Capture

As Z_1/Z_2 is raised, the probability for direct transfer of inner-shell electrons from the projectile to the target becomes competitive with, and can even exceed, that for ionization of the target electron into the continuum. The first-order perturbation treatment for electron capture, given by *Oppenheimer* [54] and by *Brinkman* and *Kramers* [55] (OBK) [11, p. 379] results in a cross section per atom

$$\sigma_{\text{OBK}} = 2^9 \pi (Z_1 Z_2)^5 / 5 V^2 v^5 n^3 \beta^5 a_0^2, \quad (69.3)$$

from a filled shell ν to all final states n , where

$$\beta = \frac{1}{4} V^2 \left[V^4 + 2V^2 (Z_2^2 / \nu^2 + Z_1^2 / n^2) + (Z_2^2 / \nu^2 - Z_1^2 / n^2)^2 \right]. \quad (69.4)$$

Both the PWBA/SCA and the OBK cross sections maximize near the matching velocity, but the OBK falls off much more strongly with increasing V beyond this, eventually falling as V^{-12} , while the ionization cross section only falls as $V^{-2} \ln V$. The OBK amplitude for capture is simply the momentum space overlap of the initial wave function with the final state wave function, where the latter is simply a bound state on the projectile but moving at a velocity V relative to the initial bound state. The integral is done only over the transverse momentum, since the longitudinal momentum transfer is fixed by energy conservation [11]. This capture amplitude thus depends heavily on there being enough momentum present in the initial and/or final wave function to enable the transfer, and the loss of this match is what leads to the steep decrease in the OBK cross section above velocity matching. Cross sections for K-shell capture have been measured by detection of K Auger electrons and K X-rays in coincidence with charge capture by the projectiles [22, 56, 57]. On the basis of these and much other data on electron capture, the OBK is a factor of approximately 3 too large [56–59]. This factor comes from a fundamental failure of first-order perturbation theory for electron capture. As was pointed out already in 1927 by *Thomas* [60], who proposed a classical two-collision mechanism for capture, it is essential that the electron interacts with both nuclei during the collision in order to be captured (Chap. 61). In quantum theories, this corresponds to the fundamental need to include second-order terms (and higher) in the capture amplitude. In the limit of large V , the second-order cross section decreases more slowly than the OBK term, as V^{-10} , and is, thus, asymptotically larger than the first-order term [61]. At large V , the coefficient of the V^{-12} term, the dominant one at most experimentally reachable V , is 0.29 times the OBK cross section, when the theory is carried out to second order in the projectile potential [61, 62]. Roughly speaking, this provides an explanation for the factor of 3. Much more sophisticated treatments of high-velocity capture are now available [63–

71]. The underlying role of the second-order scattering process was confirmed experimentally by the detection of the Thomas peak in the angular distribution of protons capturing electrons from He and H [72, 73] (Chap. 61).

In spite of the basic importance of second-order amplitudes in perturbative capture, the OBK gives an excellent account of the relative contributions from and to different final shells over a large range of V above v_e , and is thus, when appropriately reduced, still useful as an estimate for perturbative capture cross sections between well-defined ν and n for large V .

For electron capture, as in the case of ionization (see Sect. 69.1.1, *Inner-Shell Ionization of Heavy Targets*), the development of recoil-ion momentum spectroscopy (RIMS) has enabled much more detailed studies of the collision dynamics. The transverse (perpendicular to the beam direction) recoil-ion momentum component p_{\perp} reflects the closeness of the collision both relative to the target nucleus and the electrons. The longitudinal (parallel to the beam direction) component p_z , on the other hand, is related to the internal energy transfer Q in the collision by (in a.u.)

$$p_z = -Q/V - nV/2, \quad (69.5)$$

where n is the number of captured electrons. A measurement of p_z is, therefore, equivalent to a measurement of Q . The advantage over measuring Q from the projectile energy loss is that at large collision energies, a much better energy resolution is achievable. A sample Q measurement with RIMS is shown in Fig. 69.6 [74]. Very recently, RIMS was applied to study capture processes in collisions with an atomic hydrogen target [75]. This could be an important breakthrough in advancing our understanding of the atomic

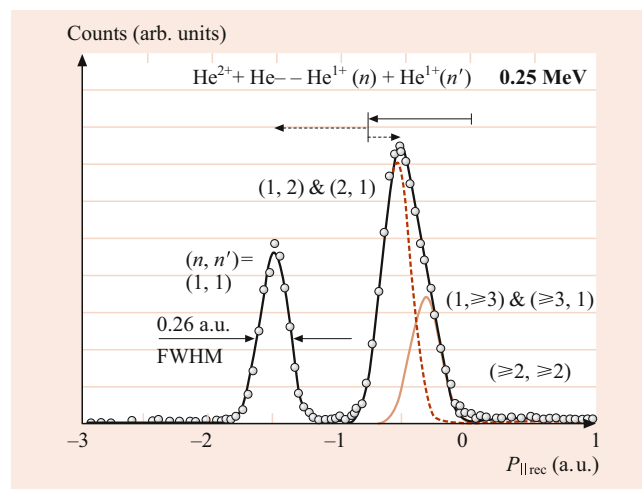


Fig. 69.6 Longitudinal momentum spectrum of recoil ions from 0.25 MeV He^{2+} capturing a single electron from a cold He target, showing clear resolution of capture to $n = 1$ from that which leaves target or projectile excited [74]

few-body problem as it opens the possibility to perform kinematically complete experiments on the true three-body system $X^{Z+} + H$, where X can be any bare projectile.

69.1.2 Nonperturbative Processes

Fano–Lichten Model

When the collision becomes increasingly perturbative, either due to a decreased V or increased Z_1/Z_2 , higher-order effects become generally more important. One approach to account for such contributions is the continuum distorted wave–eikonal initial state (CDW-EIS) model ([35, 36, 76], see also Chap. 56 and Sect. 69.1.1). The range of validity of CDW-EIS is roughly given by $Z_1/V^2 \ll 1$ [35]. Therefore, if the perturbation is large due to the projectile charge, the collision may still be treated perturbatively provided that the collision energy is sufficiently large. Otherwise, the perturbation treatment is replaced by a molecular orbital treatment.

Fano and Lichten [77] pointed out that the ratio V/v_e can be small for inner orbitals even for V of several a.u., and thus an adiabatic picture of the collision holds. K vacancy production cross sections become much larger than the perturbation treatments above predict and extend to much larger b . In the molecular orbital picture, the collision system is described in terms of time-dependent molecular orbitals (MO) formed when the inner shells of the systems overlap. Vacancy production occurs due to rotational, radial, and potential coupling terms between these orbitals during the collision. The independent electron model is used, but the results in any specific collision are quite sensitive to the occupation numbers (or vacancies) in the initial orbitals. These are very difficult to control in ion–atom collisions in solids and even problematic in gases, since outer-shell couplings can produce vacancies at large internuclear distances, which then enable transfers at smaller distances. Numerous reviews of the subject are available, including [78–82]. The most famous MO ionization mechanism involves the promotion of the $4f\sigma$ orbital in a symmetric collision (Fig. 69.7), which promotes both target and projectile L electrons to higher energies where they are easily lost to the continuum during the collision. There are now many treatments of inner-shell vacancy production mechanisms based on MO expansions (Chaps. 53, 55). For the case of K vacancy production in quasi-symmetric collisions, an important MO mechanism is the transfer of L vacancies in the projectile to the K-shell of the target through the rotational coupling between $2p\pi$ and $2p\sigma$ orbitals, which correlate to the L and K-shells, respectively, of the separated systems (Fig. 69.7) [83, 84]. The process can be dynamically altered by the sharing at large b between L vacancies of target and projectile through a radial coupling mechanism [85, 86]. This sharing mechanism can also give rise to the direct transfer of K vacancies from

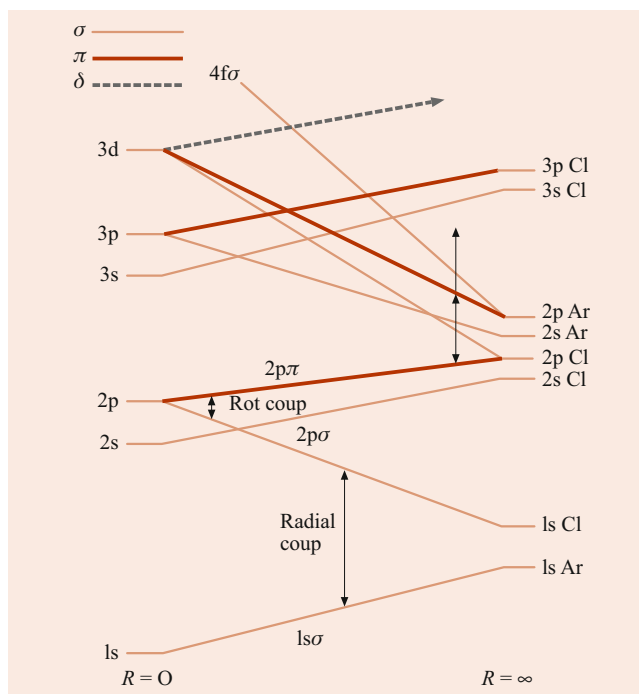


Fig. 69.7 Schematic correlation diagram for the Cl–Ar system, indicating the rotational coupling and radial couplings important for K vacancy production and the $4f\sigma$ orbital whose promotion leads to L vacancy production [89]

projectile to target (KK sharing). In symmetric systems, the KK sharing results in an oscillation of the K vacancy back and forth between target and projectile during the collision and leads to an oscillatory behavior of the transfer probability with V and b [87, 88]. Both of the above vacancy production mechanisms are electron transfer processes rather than direct ionization processes in that no inner-shell electron need be liberated into the continuum. Between the perturbation region and the full MO region the importance of transfer increases relative to ionization. While the MO correlation diagrams and mechanisms are qualitatively useful, actual close-coupling calculations for both inner and outer-shell processes are often carried out using atomic orbitals instead of molecular orbitals, as well as other basis sets (Chaps. 53, 55).

69.2 Multielectron Processes

In a single collision between multielectron partners, two or more electrons may be simultaneously excited or ionized. The electric fields created during a violent ion–atom collision are so large that at small impact parameters the probability of such multielectron processes can be of order unity. While there are many similarities between ion–atom collisions and the interaction of atoms with photons (X-rays or short laser pulses) or electrons, the dominance of multielectron processes is very much less common in the photon and

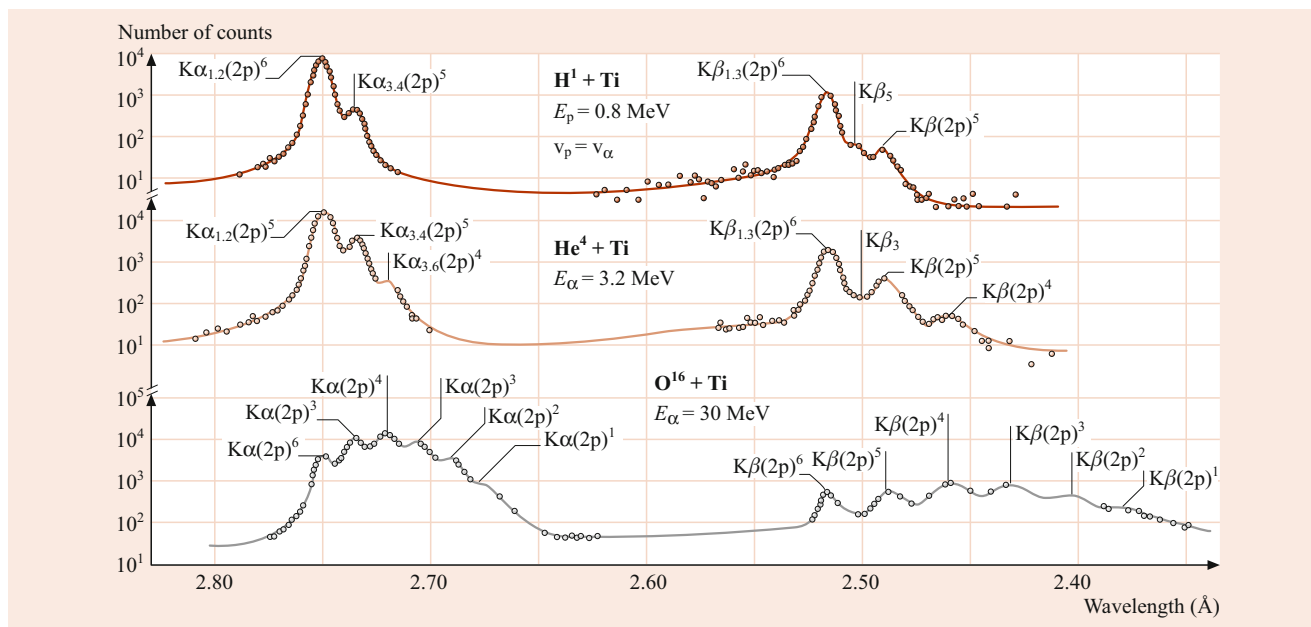


Fig. 69.8 K X-ray spectrum of Ti for various projectiles showing dominance of multielectron transitions when K vacancies are collisionally produced by heavily ionizing projectiles (^{16}O beam) [90]

electron cases. As an example, when a K-shell electron is removed from a target atom (which is selective on small impact parameters) by the passage of a fast highly charged ion through its heart, the probability that L-shell electrons will be removed at the same time can be large. This gives rise to target X-ray and Auger-electron spectra that are dominated by satellite structure [20]. For example, the spectrum of X-rays from Ti bombarded by 30 MeV oxygen shows that the production of the K vacancy is accompanied by multiple L vacancy production and that the dominant K X-rays are those of systems that are missing several L electrons [90] (Fig. 69.8).

When a gas target is used, the recoil target ion is heavily ionized and/or excited electronically without receiving much translational kinetic energy. In the impulse approximation the transverse momentum Δp_{\perp} received by the target from a projectile passing at impact parameter b is given in a.u. by $\Delta p_{\perp} = 2Z_1Z_2/bV$. This expression ignores the exchange of electronic translational momentum but gives a good estimate. The resulting recoil energies are typically quite small, ranging from thermal to a few eV. This subject was reviewed in [74, 91]. These slow moving recoils have been used to provide information about the primary collision dynamics, and as secondary highly charged ions from a fast-beam-pumped ion source. Such an ion source has, for moderately charged ions, a high brightness and has been used extensively for energy-gain measurements. The primary recoil production process is difficult to treat without the independent electron model, and even in this model, the nonperturbative nature of the collision makes the theory difficult. The most successful treatments have been the CTMC (Chap. 62) and a solution of the Vlasov equation [75].

Studies of many-electron transitions in collisions of bare projectiles with a He target are particularly suitable to investigate the role of electron–electron correlation effects because such collisions represent the simplest systems where the electron–electron interaction is present. Such studies have been performed extensively for a variety of processes, such as double ionization, transfer-ionization, double excitation, transfer-excitation, or double capture ([92–94] for reviews). It is common to distinguish (somewhat artificially) between such correlations in the initial state, the final state, and during the transition (dynamic correlation). From a theoretical point of view, the biggest challenge is to describe electron–electron correlation effects and the dynamics of the two-center potential generated by the projectile and the target nucleus simultaneously with sufficient accuracy.

In the case of double ionization, an experimental method, based on the so-called correlation function [95], was developed to analyze electron–electron correlations independently of the collision dynamics. Here, a measured two-electron spectrum (for example, the momentum difference spectrum of both ejected electrons) is normalized to the corresponding spectrum one would obtain for two independent electrons. An example of such a correlation function R is shown in Fig. 69.9 for three very different collision systems (η_1 ranging from 0.05 to 100 and η_2 from 0.01 to 0.5 in a.u.). The similarity in these three data sets illustrates that R is remarkably insensitive to the collision dynamics. Rather, the shape of R is determined predominantly by correlations in the final state [95, 97]. However, for selected kinematic conditions, R can also be sensitive to initial-state correlations [98]. Clear signatures of initial-state correlations

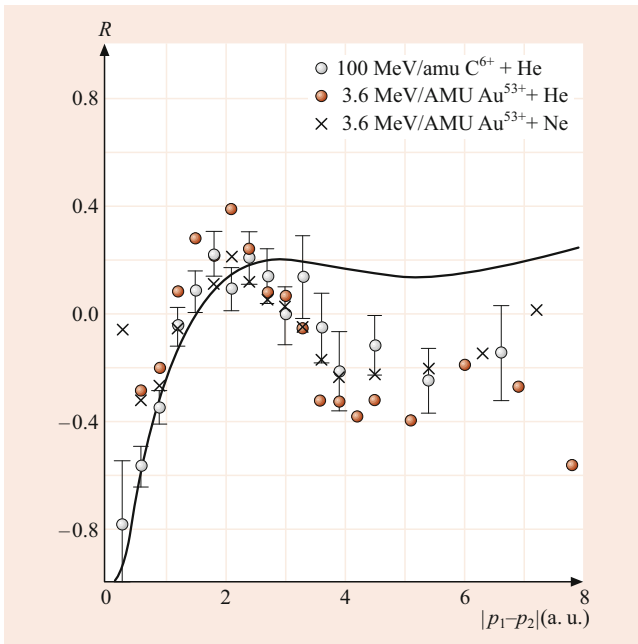


Fig. 69.9 Correlation function R for double ionization in the collisions indicated in the legend as a function of the momentum difference between the two electrons [95]; R is defined as $R = I_{\text{exp}}/I_{\text{IEM}} - 1$, where I_{exp} is the directly measured momentum spectrum and I_{IEM} the one obtained for independent electrons

were found in the recoil-ion momentum spectra for transfer-ionization [99].

Early attempts to identify dynamic correlations were based on measurements of the ratio of double to single-ionization cross sections [100, 101]. From such studies, it was found that at small V , double ionization is dominated by an uncorrelated mechanism involving two independent interactions of the projectile with both electrons. In contrast, at large V , the double to single ionization ratio asymptotically approaches a common value for all collision systems [102]. This is indicative of the dominance of first-order double-ionization mechanisms, where the projectile interacts with only one electron, and the second electron is ionized through an electron–electron correlation effect. This may either be a rearrangement process of the target atom adjusting to a new Hamiltonian (shake-off, an initial-state correlation) or a direct interaction with the first electron (i.e., dynamic correlation). However, a recent, nearly kinematically complete experiment on double ionization in $p + \text{He}$ collisions revealed that even at large V , higher-order contributions are not negligible [96]. In Fig. 69.10, the ejection angles of both electrons are plotted against each other for almost completely determined kinematics. For comparison, the bottom part of Fig. 69.10 shows the corresponding spectra for elec-

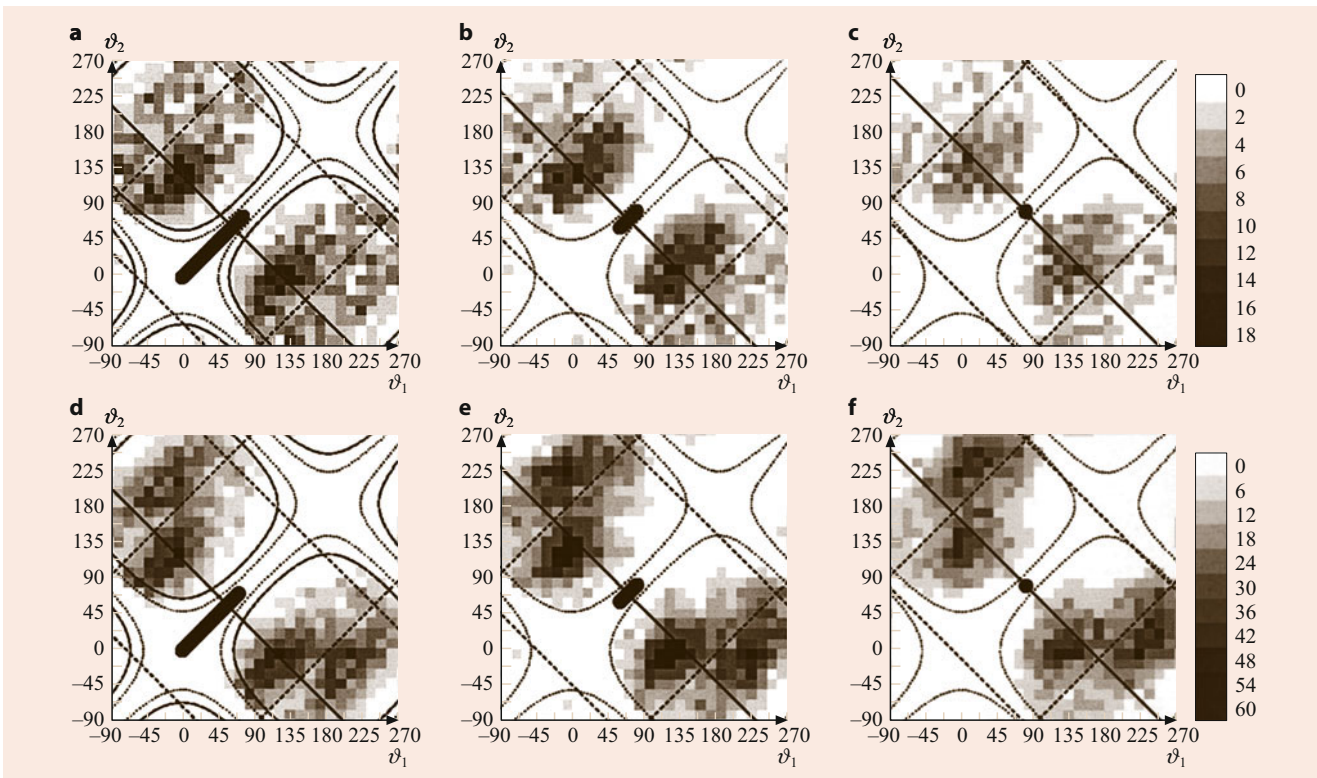


Fig. 69.10 Differential double-ionization cross sections in 6 MeV $p + \text{He}$ (a–c) and 2 keV $e^- + \text{He}$ (d–f) collisions as a function of the polar emission angle of both electrons, which are emitted into the scattering plane. The electrons have equal energy, and data are shown for small (a,d), medium (b,e), and large momentum transfers (c,f) [96]

tron impact at the same V [103]. For both projectiles, the basic features of these spectra are determined by the electric dipole selection rules, which again is indicative of dominating first-order contributions. However, a closer inspection of the comparison between the proton and electron impact data shows some nonnegligible differences. Since in a first-order treatment, the cross sections should be identical for both projectile species, this demonstrates that higher-order contributions cannot be ignored.

Another efficient method to distinguish different double-ionization mechanisms, like e.g., first from higher-order processes, is to analyze four-particle Dalitz (4-D) plots [104]. Here, the data are presented in a tetrahedral coordinate system, where each tetrahedron plane represents one final-state particle (i.e., the scattered projectile, the two ejected electrons, and the residual target ion). The quantities that are plotted are the relative squared momenta $\epsilon_i = p_i^2 / \Sigma p_j^2$ so that $\Sigma \epsilon_i = 1$. For a given data point, each ϵ_i for the four particles is given by the distance of that data point from the corresponding tetrahedron plane.

An example of such a 4-D plot for double ionization in 6 MeV $p + \text{He}$ collisions is shown in Fig. 69.11 [105]. The spectrum is dominated by a strong peak structure at the intersection line between the planes representing the two ejected electrons. This intersection line corresponds to events for which both ejected electrons have a small momentum compared to the heavy particles, i.e., momentum exchange occurs mostly between the nuclei. This shows that a higher-order mechanism involving the nucleus–nucleus interaction plays an important role even at this relatively large projectile energy. Further information about the underlying double-ionization mechanism was obtained from a comparison with various theoretical models [105]. In fact, a new mechanism,

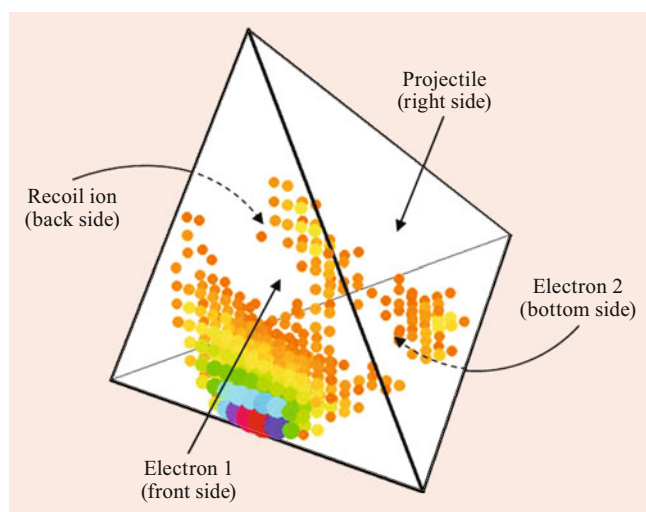


Fig. 69.11 Four-particle Dalitz plot for double ionization of helium by 6 MeV proton impact

which can be viewed as a hybrid between a correlated and an uncorrelated process, could be identified. Here, the projectile only ejects one electron directly; the second electron is ejected by an interaction with the first electron (like in the correlated mechanism). Nevertheless, the projectile does interact with the second electron as well (like in the uncorrelated mechanism), but only after the latter has already been promoted to the continuum.

69.3 Electron Spectra in Ion–Atom Collisions

69.3.1 General Characteristics

An ionizing collision between a single ion and a neutral atom ejects electrons into the continuum via two major processes. Electrons ejected during the collision form broad features or continua and are traditionally referred to as delta rays; electrons ejected after the collisions from the Auger decay of vacancies created during the collision form sharp lines in the spectra. The distributions of energy and the angle of all electrons determine the electronic stopping power and characteristics of track formation of ions in matter, and the study of these distributions in the binary encounter of one ion with one atom forms the basis of any detailed understanding of these averaged quantities. Figure 69.12 shows a typical electron spectrum from the collision of a fast O ion with O_2 [106, 107]. Electrons from the projectile can be identified in the cusp peak (electron loss, P) or ELC, and the O-K-Auger (P) peak. Electrons from the target include the soft (large b) collision electrons (T), which are ejected directly by Coulomb ionization by the projectile, the binary collision (or encounter) electrons coming from hard collisions between projectile and quasi-free target electrons, and the target O-K-Auger (T) electrons. The electron loss peak is widely called the *cusp* peak because the doubly differential cross section in the laboratory $d^2\sigma/dEd\Omega$ becomes infinite, in principle, if it is finite in the projectile frame. In general, this peak may also contain capture to the continuum. All of these features have been heavily studied; some reviews can be found in [108, 109]. Capture to the continuum [109] is an extension of normal capture into the continuum of the projectile and is not a weak process. Both it and ELC produce a heavy density of events in the electron-momentum space centered on the projectile velocity vector and, thus, appear strongly only at or near zero degrees in the laboratory and at $v_e \simeq V$.

The binary encounter electrons at forward angles occur at $v_e \simeq 2V$. For relatively slow collisions, it was found that the ELC and binary peaks are just part of a more general and complex structure of the electron spectra [110]. Additional peaks in the forward direction were found for $v_e \simeq nV$, where

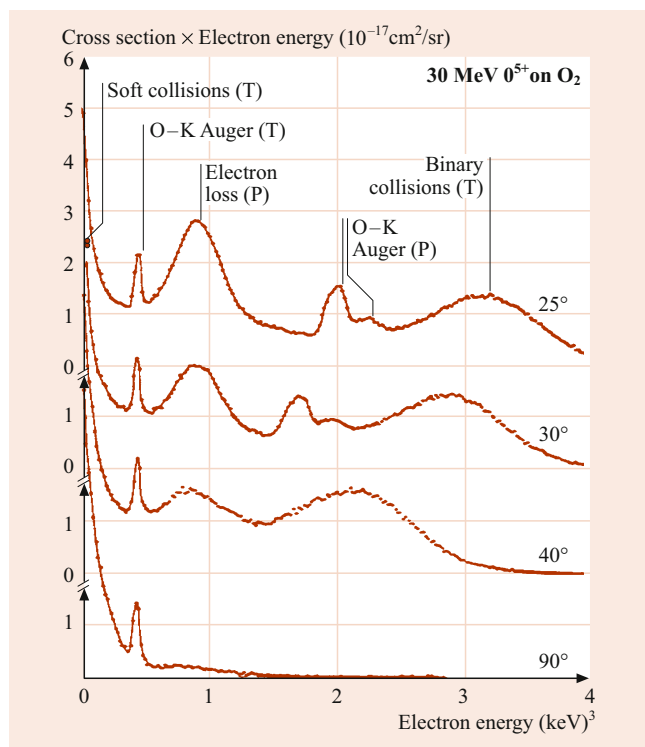


Fig. 69.12 Electron spectrum from 30 MeV O on molecular oxygen. See text for an explanation of features [106, 107]

n can, in principle, be any integer number. These structures reflect a *bouncing back and forth* (known as the Fermi shuttle) between the projectile and the target core before the electron eventually gets ejected from the collision system.

In electron spectra for molecular targets, additional structures were found that were not observed for atomic targets [111]. These were initially interpreted as an interference effect. The electronic wavefunction has maxima at the atomic centers of the molecule. Since in the experiment, it cannot be distinguished from which center the electron is ionized, both possibilities have to be treated coherently. However, more recent studies showed that at small electron energies the structures in the electron spectra reflect vibrational excitation of the molecule [112].

69.3.2 High-Resolution Measurements

The Auger electron spectra provide detailed information about inner-shell vacancy production mechanisms. When coupled with fluorescence yields, Auger electron production probabilities, and cross sections can be converted into the corresponding quantities for vacancy production [15, 108]. This is best done when sufficient resolution can be obtained to isolate individual Auger lines. The Auger spectra in ion-atom collisions are often completely different from those obtained from electron or photon bombardment because of

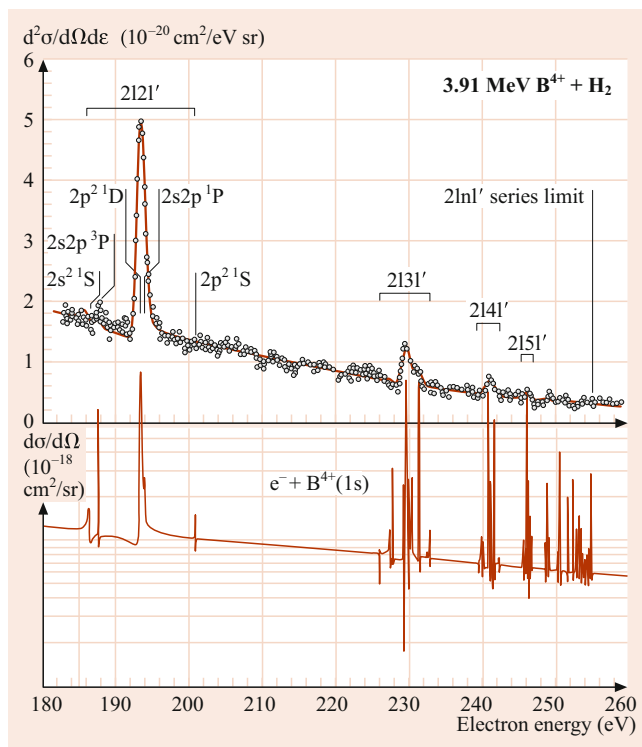


Fig. 69.13 High-resolution Auger electron spectrum from H-like B on H_2 , showing resolved lines from doubly excited projectile states lying on top of a continuum due to electron elastic scattering [115]. The *bottom part* shows an R-matrix calculation, which does not account for the experimental resolution. The *smooth line* in the *upper figure* is the R-matrix calculation convoluted with the experimental spectrometer resolution

the multiple outer-shell ionization that attends the inner-shell vacancy producing event, in close analogy to X-ray spectra (see Sect. 69.2). Projectile Auger electron spectra suffer from kinematic broadening due to the finite solid angle of the spectrometer and velocity of the emitter, but at 0° to the beam this problem vanishes, and the resolution in the emitter frame is actually enhanced by the projectile motion, such that for electrons with eV energies in the projectile frame, resolutions in the meV region are possible [113, 114]. The highest resolution Auger lines from ion-atom collisions have been recorded for electrons ejected from projectiles. A sample spectrum is shown in Fig. 69.13. From such high resolution spectra, one-electron processes in which one electron is excited, captured, or ionized can be distinguished from the configuration of the emitting state.

69.4 Quasi-Free Electron Processes in Ion-Atom Collisions

At sufficiently low V , those electrons not actively involved in a transition play only a passive role in screening the Coulomb potential between the nuclei and, thereby, create

a coherent effective potential for their motion. However, at high V , the colliding electrons begin behaving as incoherent quasi-free particles capable of inducing transitions directly via the electron–electron interaction. Such processes signal their presence through their free-particle kinematics, as if the parent nucleus were not present. For example, a projectile ionization process requiring energy U has a threshold at $(1/2)m_e V^2 \simeq U$, in collisions with light targets where the quasi-free picture is meaningful. The threshold is not sharp, due to the momentum distribution or Compton profile of the target electrons. Within the impulse approximation, the cross section for any free electron process can be related to the corresponding cross section for the ion–atom process by folding the free electron cross section into the Compton profile [115–117].

69.4.1 Radiative Electron Capture

The first quasi-free electron process to be observed was radiative electron capture (REC), the radiative capture of a free electron by an ion. Conservation of energy and momentum is achieved by the emission of a photon that carries away the binding energy. The cross section exceeds that for bound-state capture at high V . Radiative electron capture was observed through the X-ray spectra from fast heavy projectiles for which the electrons of light targets appear to be *quasi free*. The corresponding free electron process was seen [118] and has recently been heavily studied in EBIT [119], cooler [120], and storage rings [121]. Total cross sections for REC have also been deduced from measured total capture cross sections at large V , where REC dominates the bound-state capture [122]. At high velocities, the cross section for radiative capture to the K-shell of a bare projectile is given approximately by

$$\sigma_n = [n / (\kappa^{-2} + \kappa^{-4})] \times 2.1 \times 10^{-22} \text{ cm}^2, \quad (69.6)$$

where [123] $\kappa = \sqrt{E_B/E_0}$, E_B is the binding energy of the captured electron, E_0 the energy of the initial electron in the ion frame, and n the principal quantum number of the captured electron. The theory seems to be in good agreement with experiment for capture to all shells of fast bare projectiles, although a small unexplained discrepancy between theory and experiment exists for capture to the K-shell [121].

69.4.2 Resonant Transfer and Excitation

Dielectronic recombination in electron–ion collisions is the process whereby an incident electron excites one target electron and, having suffered a corresponding energy loss, drops

into a bound state on the projectile (Chap. 59). If the doubly excited state so populated decays radiatively, resonant radiative recombination is achieved (DR); if it Auger decays, resonant elastic scattering has occurred. The process has long been known to be important as a recombination process in hot plasmas [124] but was not observed in the laboratory until 1983 [125–127]. The corresponding ion–atom process, known as resonant transfer and excitation (RTE), was seen a bit earlier by *Tanis* et al. [128]; see [129, 130] for reviews of both DR and RTE.

69.4.3 Excitation and Ionization

Excitation and ionization of inner shells of fast projectile ions by the quasi-free electrons of light targets (usually He or H₂) have been identified and studied. This process competes with excitation and ionization by the target nucleus [131–133], and special signatures must be sought to distinguish the processes. In the case of excitation, the e–e excitation populates states through the exchange part of the interaction, which is excluded for the nuclear excitation, and this has been used to separate this mechanism [134]. For ionization, enhancements of the ionization cross section above the Born result for nuclear ionization [135], coincident charge exchange measurements [136], and projectile [137] and recoil-ion momentum spectroscopy [138, 139] have been used to distinguish the two processes. Rapid development in the production of good sources of beams of highly charged ions (EBIS/T, ECR; [140]) have made these studies possible. Continued study of this field in heavy-ion storage rings is now achieving resolutions of meV and is opening broad new opportunities for data of unprecedented high quality for electron–ion collisions [141].

Recently, the first kinematically complete experiment on projectile ionization by quasi-free electrons was reported [142]. The observed features are qualitatively similar to those found for ionization of neutral target atoms by free electron impact.

69.5 Some Exotic Processes

69.5.1 Molecular Orbital X-Rays

A typical time duration for an ion–atom encounter is $\approx 10^{-17}$ s, which is much shorter than Auger and X-ray lifetimes, so that hard characteristic radiation is emitted by the products long after the collision. There remains, however, a small but finite probability that X-rays or Auger electrons can be emitted during the collision, in which case the radiation proceeds between the time-dependent molecular orbitals formed in the collision and reflects the time evolution of the

energies and transition strengths between the orbitals. Such molecular orbital X-radiation (MOX) has now been observed in many collision systems [143] and is reviewed in [144–146]. MOX spectra have been studied in total cross sections as well as a function of impact parameter. In the latter case, oscillating structures in the MOX spectra are seen [145, 147], due to the interference between amplitudes for the emission of X-rays with the same energy on the incoming and outgoing parts of the trajectory.

The formation of transient molecular orbitals in close collisions between highly charged ions provides opportunities for studying the electrodynamics of very highly charged systems [148]. For example, two uranium nuclei passing within one K-shell radius of each other form a transient molecule whose energy levels resemble those of an atom of charge 184.

69.5.2 Positron Production from Atomic Processes

Investigating the MOX interference patterns in such exotic systems offers the interesting prospect of performing spectroscopy on superheavy ions.

Reinhart et al. [149] predicted that, for such highly charged species, the binding energy of the united atom K-shell exceeds twice the rest mass energy of the electron, and that if a K vacancy is either brought into the collision or created during it, spontaneous electron–positron pair production occurs (the decay of the charged vacuum) with the electron filling the K-hole. However, further analysis showed that the dominant mechanism for positron production (other than those resulting from the decay of nuclear excitations) likely results from the dynamic time dependence of the fields during the collision [150]. Experiments showed evidence for such positron production in collisions at 6 MeV/u [151], but reported sharp lines in the positron spectra were later attributed to an error in the data analysis.

Present theories for the production of lepton pairs in the close collision of two highly charged systems predict that the cross section grows rapidly with the collision energy. Electrons produced in such a process may end up in bound states on either collision partner, and thus represent a new charge-changing mechanism. At highly relativistic velocities, the cross section for this process exceeds that for any other charge-changing process. In a heavy-ion collider, such as RHIC, this process could limit the ultimate storage time for the counterpropagating beams, since charge-exchanged ions are lost. The cross section has been measured recently by Vane et al. [152], for 6.4 TeV S on several targets (the highest energy ion–atom collision experiment performed to date) and are in good agreement with theory [153]. The bound-

state capture was measured at lower energy by Belkacem et al. [154], with similarly good agreement. The extension of ion–atom collisions to such extreme velocities has opened the field for the study of processes that not even imagined a short time ago.

References

- Merzbacher, E., Lewis, H.W.: *Handbuch der Physik* vol. 34. Springer, Berlin, p 166 (1958)
- Madison, D., Merzbacher, E.: Theory of charge–particle excitation. In: Craseman, B. (ed.) *Atomic Inner Shell Processes*. Academic Press, New York (1975)
- Khandelwal, B.S., Choi, B.H., Merzbacher, E.: *At. Data* **15**, 103 (1969)
- Khandelwal, B.S., Choi, B.H., Merzbacher, E.: *At. Data* **5**, 291 (1973)
- Crasemann, B. (ed.): *Atomic Inner Shell Processes*. Academic Press, New York (1975)
- Garcia, J.D., Fortner, R.J., Kavanagh, T.M.: *Rev. Mod. Phys.* **45**, 111 (1973)
- Richard, P.: *Atomic physics: Accelerators*. In: Williams, L. (ed.) *Meth. Expt. Physics*, vol. 17, Academic Press, New York (1980)
- Williams, D.: *Spectroscopy*. In: *Meth. Expt. Physics*, vol. 13, Academic Press, New York (1976)
- Bang, J., Hansteen, J.M.: *K. Dan. Vidensk. Mat. Fys. Medd.* **31**, 13 (1973)
- Hansteen, J.M., Johnsen, O.M., Kocbach, L.: *At. Data Nucl. Data Tables* **15**, 305 (1975)
- McDowell, M.R.C., Coleman, J.P.: *Introduction to the Theory of Ion–Atom Collisions*. North Holland, Amsterdam (1970)
- Garcia, J.D.: *Phys. Rev. A* **4**, 955 (1971)
- Anholt, R.: *Phys. Rev. A* **17**, 983 (1978)
- Basbas, G., Brandt, W., Laubert, R.: *Phys. Rev. A* **7**, 983 (1973)
- Gray, J.T.: *Meth. Expt. Physics*. Academic Press, New York, p 193 (1980)
- Paul, H., Muhr, J.: *Phys. Rep.* **135**, 47 (1986)
- Brandt, W., Lapicki, G.: *Phys. Rev. A* **10**, 474 (1974)
- Bohr, N.: *K. Dan. Vidensk. Selsk. Mat. Fys. Medd.* **18**, No. 8 (1948)
- Pauli, M., Trautmann, D.: *J. Phys. B* **11**(667), 2511 (1978)
- Kauffman, R.L., Richard, P.: *Meth. Expt. Physics* vol. 17. Academic Press, New York, p 148 (1980)
- Bambynek, W., Crasemann, C., Fink, R.W., Freund, H.-U., Mark, H., Swift, C.D., Price, R.E., Rao, P.V.: *Rev. Mod. Phys.* **44**, 716 (1972)
- Cocke, C.L.: *Meth. Expt. Physics* vol. 17. Academic Press, New York, p 303 (1980)
- Park, J.T., Aldag, J.E., George, J.M., Peacher, J.L., McGuire, J.H.: *Phys. Rev. A* **15**, 508 (1977)
- Laforge, A.C., Egodapitiya, K.N., Alexander, J.S., Hasan, A., Ciappina, M.F., Khakoo, M.A., Schulz, M.: *Phys. Rev. Lett.* **103**, 053201 (2009)
- Rudd, M.E., Kim, Y.-K., Madison, D.H., Gay, T.J.: *Rev. Mod. Phys.* **64**, 441 (1992)
- Schulz, M., Vajnai, T., Gaus, A.D., Htwe, W., Olson, R.E.: *Phys. Rev.* **54**, 2951 (1996)
- Vajnai, T., Gaus, A.D., Brandt, J.A., Htwe, W., Madison, D.H., Olson, R.E., Peacher, J.L., Schulz, M.: *Phys. Rev. Lett.* **74**, 3588 (1995)

28. Ehrhardt, H., Jung, K., Knoth, G., Schlemmer, P.: *Z. Phys.* **D1**, 3 (1986)
29. Maydanyuk, N.V., Hasan, A., Foster, M., Tooke, B., Nanni, E., Madison, D.H., Schulz, M.: *Phys. Rev. Lett.* **94**, 243201 (2005)
30. Moshhammer, R., Ullrich, J., Unverzagt, M., Schmidt, W., Jardin, P., Olson, R.E., Mann, R., Dörner, R., Mergel, V., Buck, U., Schmidt-Böcking, H.: *Phys. Rev. Lett.* **73**, 3371 (1994)
31. Dörner, R., Mergel, V., Jagutzki, O., Spielberger, L., Ullrich, J., Moshhammer, R., Schmidt-Böcking, H.: *Phys. Rep.* **330**, 95 (2000)
32. Ullrich, J., Moshhammer, R., Dorn, A., Dörner, R., Schmidt, L.P.H., Schmidt-Böcking, H.: *Rep. Prog. Phys.* **66**, 1463 (2003)
33. Cocke, C.L.: *Phys. Scr.* **T110**, 9 (2004)
34. Schulz, M., Moshhammer, R., Fischer, D., Kollmus, H., Madison, D.H., Jones, S., Ullrich, J.: *Nature* **422**, 48 (2003)
35. Crothers, D.S.F., McCann, J.F.: *J. Phys.* **B16**, 3229 (1983)
36. Madison, D.H., Schulz, M., Jones, S., Foster, M., Moshhammer, R., Ullrich, J.: *J. Phys.* **B35**, 3297 (2002)
37. Madison, D.H., Fischer, D., Foster, M., Schulz, M., Moshhammer, R., Jones, S., Ullrich, J.: *Phys. Rev. Lett.* **91**, 253201 (2003)
38. Schulz, M., Moshhammer, R., Fischer, D., Ullrich, J.: *J. Phys.* **B36**, L311 (2003)
39. Schulz, M., Moshhammer, R., Perumal, A.N., Ullrich, J.: *J. Phys.* **B35**, 161L (2002)
40. Egodapitiya, K.N., Sharma, S., Hasan, A., Laforge, A.C., Madison, D.H., Moshhammer, R., Schulz, M.: *Rev. Lett.* **106**, 153202 (2011)
41. Wang, X., Schneider, K., LaForge, A., Kelkar, A., Grieser, M., Moshhammer, R., Ullrich, J., Schulz, M., Fischer, D.: *J. Phys. B* **45**, 211001 (2012)
42. Navarrete, F., Ciappina, M.F., Sarkadi, L., Barrachina, R.O.: *Nucl. Instrum. Methods Phys. Res. B* **508**, 165 (2017)
43. Jarai-Szabo, F., Borbely, S., Nagy, L.: *J. Phys. Conf. Ser.* **635**, 022037 (2015)
44. Gassert, H., Chuluunbaatar, O., Waitz, M., Trinter, F., Kim, H.-K., Bauer, T., Laucke, A., Müller, C., Voigtsberger, J., Weller, M., Rist, J., Pitzer, M., Zeller, S., Jahnke, T., Schmidt, L.P.H., Williams, J.B., Zaytsev, S.A., Bulychev, A.A., Kouzakov, K.A., Schmidt-Böcking, H., Dörner, R., Popov, Y.V., Schöffler, M.S.: *Phys. Rev. Lett.* **116**, 073201 (2016)
45. Schulz, M.: in “: In: Arimondo, E., Lin, C.C., Yelin, S. (eds.) *Advances in Atomic, Molecular, and Optical Physics*, vol. 66, pp. 508–543. Elsevier, Amsterdam (2017)
46. Wolf, S., Helm, H.: *Phys. Rev. A* **56**, R4385 (1997)
47. Zhu, G., Schuricke, M., Steinmann, J., Albrecht, J., Ullrich, J., Ben-Itzhak, I., Zouros, T.J.M., Colgan, J., Pindzola, M.S., Dorn, A.: *Phys. Rev. Lett.* **103**, 103008 (2009)
48. Hubele, R., Schuricke, M., Goullon, J., Lindenblatt, H., Ferreira, N., Laforge, A., Brühl, E., de Jesus, V.L.B., Globig, D., Kelkar, A., Misra, D., Schneider, K., Schulz, M., Sell, M., Song, Z., Wang, X., Zhang, S., Fischer, D.: *Rev. Sci. Instrum.* **86**, 033105 (2015)
49. Hubele, R., Laforge, A.C., Schulz, M., Goullon, J., Wang, X., Najjari, B., Ferreira, N., Grieser, M., de Jesus, V.L.B., Moshhammer, R., Schneider, K., Voitkiv, A.B., Fischer, D.: *Phys. Rev. Lett.* **110**, 133201 (2013)
50. Mott, N.F., Massey, S.N.: *The Theory of Atomic Collisions*. Oxford University Press, Oxford (1965)
51. Inokuti, M.: *Rev. Mod. Phys.* **43**, 297 (1971)
52. Bethe, H.: *Ann. Phys.* **5**, 325 (1930)
53. Park, J.T., Aldag, J.E., Geroge, J.M., Peacher, J.L.: *Phys. Rev. A* **14**, 608 (1976)
54. Oppenheimer, J.R.: *Phys. Rev.* **31**, 349 (1928)
55. Brinkman, H.S., Kramers, H.A.: *Proc. Acad. Sci. Amsterdam* **33**, 973 (1930)
56. Rödbro, M., Horsdal Pedersen, E., Cocke, C.L., Macdonald, J.R.: *Phys. Rev. A* **19**, 1936 (1979)
57. Macdonald, J.R.: *Meth. Expt. Physics* vol. 17. Academic Press, New York, p 303 (1980)
58. Nikolaev: *Zh. Eksp. Teor. Fiz.* **51**, 1263 (1966)
59. Nikolaev: *Sov. Phys. JETP* **24**, 847 (1967)
60. Thomas, L.H.: *Proc. R. Soc. Lond. A* **114**, 561 (1927)
61. Shakeshaft, R., Spruch, L.: *Rev. Mod. Phys.* **51**, 369 (1979)
62. Bransden, B.H., Cheshire, I.M.: *Proc. Phys. Soc.* **81**, 820 (1963)
63. Simony, P.R., McGuire, J.H.: *J. Phys. B* **14**, L737 (1981)
64. Macek, J., Alston, S.: *Phys. Rev. A* **26**, 250 (1982)
65. Macek, J., Taulbjerg, K.: *Phys. Rev. Lett.* **46**, 170 (1981)
66. Ford, A.L., Reading, J.R., Becker, R.L.: *Phys. Rev. A* **23**, 510 (1981)
67. Belkic, D., Salin, A.: *J. Phys. B* **11**, 3905 (1978)
68. Eichler, J., Chan, T.: *Phys. Rev. A* **20**, 104 (1978)
69. Dewangan, D.P., Eichler, J.: *Comm. At. Mol. Phys.* **27**, 317 (1992)
70. Marxer, H., Briggs, J.S.: *J. Phys. B* **18**, 3823 (1992)
71. Briggs, J.S., Macek, J.H., Taulbjerg, K.: *Comments At. Mol. Phys.* **12**, 1 (1983)
72. Horsdal-Pedersen, E., Cocke, C.L., Stöckli, M.: *Phys. Rev. Lett.* **50**, 1910 (1983)
73. Vogt, H., Schuch, R., Justiniano, E., Schultz, M., Schwab, W.: *Phys. Rev. Lett.* **57**, 2256 (1986)
74. Mergel, V., Dörner, R., Ullrich, J., Jagutzki, O., Lencinas, S., Nüttgens, S., Spielberger, L., Unverzagt, M., Cocke, C.L., Olson, R.E., Schulz, M., Buck, U., Zanger, E., Theisinger, W., Isser, M., Geis, S., Schmidt-Böcking, H.: *Phys. Rev. Lett.* **74**, 220 (1995)
75. Edgu-Fry, E., Cocke, C.L., Stuhlman, J.: *Bull. Am. Phys. Soc.* **48**, 12 (2003)
76. Fainstein, P.D., Gulyas, L., Salin, A.: *J. Phys.* **B27**, L259 (1994)
77. Fano, U., Lichten, W.: *Phys. Rev. Lett.* **14**, 627 (1965)
78. Wille, U., Hippler, R.: *Phys. Rep.* **132**, 131 (1986)
79. Kessel, Q., Fastrup, B.: *Case Stud. At. Phys.* **3**, 137 (1973)
80. Briggs, J.: *Rep. Prog. Phys.* **39**, 217 (1976)
81. Meyerhof, W.E., Taulbjerg, K.: *Ann. Rev. Nucl. Sci.* **27**, 279 (1977)
82. Sellin, I.A. (ed.): *Structure and Collisions of Ions and Atoms. Topics in Current Physics*, vol. 5. Springer, Berlin (1975)
83. Taulbjerg, K., Briggs, J.S.: *J. Phys. B* **8**, 1895 (1975)
84. Briggs, J.S., Macek, J.: *J. Phys. B* **5**, 579 (1972)
85. Demkov, Y.: *Sov. Phys. JETP* **18**, 138 (1964)
86. Meyerhof, W.E.: *Phys. Rev. Lett.* **31**, 1341 (1973)
87. Lockwood, G.T., Everhart, E.: *Phys. Rev.* **125**, 567 (1962)
88. Hagmann, S., Cocke, C.L., Macdonald, J.R., Richard, P., Schmidt-Böcking, H., Schuch, R.: *Phys. Rev. A* **25**, 1918 (1982)
89. Cocke, C.L., Randall, R.R., Varghese, S.L., Curnutte, B.: *Phys. Rev. A* **14**, 2026 (1976)
90. Moore, C.F., Senglaub, M., Johnson, B., Richard, P.: *Phys. Rev. Lett.* **40**, 107 (1972)
91. Sellin, I.A.: *Extensions of beam-foil spectroscopy*. In: Sellin, I.A. (ed.) *Topics in Current Physics 5: Structure and Collisions of Ions and Atoms*. Springer, Berlin (1978). Chap. 7
92. McGuire, J.H.: *Adv. At. Mol. Phys.* **29**, 217 (1992)
93. Schulz, M.: *Int. J. Mod. Phys. B* **9**, 3269 (1995)
94. McGuire, J.H.: *Electron correlation dynamics in atomic collisions*. In: McGuire, J.H. (ed.) *Cambridge Monographs on Atomic, Molecular, and Chemical Physics*, vol. 8, Cambridge University Press, Cambridge (1997)
95. Schulz, M., Moshhammer, R., Schmitt, W., Kollmus, H., Feuerstein, B., Mann, R., Hagmann, S., Ullrich, J.: *Phys. Rev. Lett.* **84**, 863 (2000)
96. Fischer, D., Moshhammer, R., Dorn, A., Crespo López-Urrutia, J.R., Feuerstein, B., Höhr, C., Schröter, C.D., Hagmann, S., Kollmus, H., Mann, R., Bapat, B., Ullrich, J.: *Phys. Rev. Lett.* **90**, 243201–243201 (2003)
97. Gerchikov, L.G., Sheinerman, S.A.: *J. Phys.* **B34**, 647 (2001)

98. Schulz, M., Moshhammer, M., Gerchikov, L.G., Sheinerman, S.A., Ullrich, J.: *J. Phys.* **B34**, L795 (2001)
99. Mergel, V., Dörner, R., Khayyat, K., Achler, M., Weber, T., Jagutzki, O., Lüdde, H.J., Cocke, C.L., Schmidt-Böcking, H.: *Phys. Rev. Lett.* **86**, 2257 (2001)
100. Andersen, L.H., Hvelplund, P., Knudsen, H., Møller, S.P., Elsener, K., Rensfelt, K.-G., Uggerhøj, E.: *Phys. Rev. Lett.* **57**, 2147 (1986)
101. Giese, J.P., Horsdal, E.: *Phys. Rev. Lett.* **60**, 2018 (1988)
102. Ullrich, J., Moshhammer, R., Berg, H., Mann, R., Tawara, H., Dörner, R., Schmidt-Böcking, H., Hagmann, S., Cocke, C.L., Unverzagt, M., Lencinas, S., Mergel, V.: *Phys. Rev. Lett.* **71**, 1697 (1993)
103. Dorn, A., Kheifets, A., Schröter, C.D., Najjari, B., Höhr, C., Moshhammer, R., Ullrich, J.: *Phys. Rev. Lett.* **86**, 3755 (2001)
104. Schulz, M., Fischer, D., Ferger, T., Moshhammer, R., Ullrich, J.: *J. Phys. B* **40**, 3091 (2007)
105. Schulz, M., Ciappina, M.F., Kirchner, T., Fischer, D., Moshhammer, R., Ullrich, J.: *Phys. Rev. A* **79**, 042708 (2009)
106. Stolterfoht, N., Schneider, D., Burch, D., Wieman, H., Risely, J.S.: *Phys. Rev. Lett.* **33**, 59 (1974)
107. Stolterfoht, N., Schneider, D., Burch, D., Wieman, H., Risely, J.S.: *Phys. Rev. Lett.* **64**, 441 (1992)
108. Stolterfoht, N.: Electronic screening in heavy-ion–atom collisions. In: Sellin, I.A. (ed.) *Topics in Current Physics*, vol. 5, Springer, Berlin (1978)
109. Crooks, G.B., Rudd, M.E.: *Phys. Rev. Lett.* **25**, 1599 (1970)
110. Sulik, B., Koncz, C., Tokési, K., Orbán, A., Berényi, D.: *Phys. Rev. Lett.* **88**, 073201 (2002)
111. Stolterfoht, N., Sulik, B., Hoffmann, V., Skogvall, B., Chesnel, J.Y., Rangama, J., Frémont, F., Hennecart, D., Cassimi, A., Husson, X., Landers, A.L., Tanis, J.A., Galassi, M.E., Rivarola, R.D.: *Phys. Rev. Lett.* **87**, 023201 (2001)
112. Dimopoulou, C., Moshhammer, R., Fischer, D., Höhr, C., Dorn, A., Fainstein, P.D., Urrutia, J.R.C.L., Schröter, C.D., Kollmus, H., Mann, R., Hagmann, S., Ullrich, J.: *Phys. Rev. Lett.* **93**, 123203 (2004)
113. Itoh, A., Schneider, T., Schiwietz, G., Roller, Z., Platten, H., Nolte, G., Schneider, D., Stolterfoht, N.: *J. Phys. B* **16**, 3965 (1983)
114. Lee, D.H., Richard, P., Zouros, T.J.M., Sanders, J.M., Shimpugh, J.L., Hidmi, H.: *Phys. Rev. A* **41**, 4816 (1990)
115. Richard, P.: In: Carlson, T. (ed.) *Proceedings of 15th International Conference on X-Ray and Inner Shell Processes, 1990*. American Institute of Physics, New York (1990)
116. Cocke, C.L.: Recent trends in ion–atom collisions. In: MacCarty, I.E., MacGillivray, W.R., Standage, M.C. (eds.) *Electronic and Atomic Collisions, Invited Papers, XVII ICPEAC, Book of Abstracts*, p. 49. Adam Hilger, Bristol, Philadelphia and New York (1992)
117. Sellin, I.A.: In: Berényi, D., Hock, D. (eds.) *High-Energy Ion-Atom Collisions. Lecture Notes in Physics*, vol. 376. Springer, Berlin (1990)
118. Schnopper, H.W., Betz, H.D., Delvaille, J.P., Kalata, K., Sohval, A.R., Jones, K.W., Wegner, H.E.: *Phys. Rev. Lett.* **29**, 898 (1972)
119. Marrs, R.W.: *Phys. Rev. Lett.* **60**, 1757 (1988)
120. Andersen, L.H., Bolko, J.: *J. Phys. B* **23**, 3167 (1990)
121. Stöhlker, T., Kozhuharov, C., Livongston, A.E., Mokler, P.H., Stachura, Z., Warczak, A.: *Z. Phys. D* **23**, 121 (1992)
122. Gould, H., Greiner, D., Lindstrom, P., Symons, T.J.M., Crawford, H.: *Phys. Rev. Lett.* **52**, 180 (1984)
123. Bethe, H.A., Salpeter, E.E.: In: *Fluegge, S. (ed.) Encyclopidia of Physics*, vol. 35, p. 408. Springer, Berlin (1957)
124. Burgess, A.: *Astrophys. J.* **139**, 776 (1964)
125. Mitchell, J.B.A., Ng, C.T., Forand, J.L., Levac, D.P., Mitchell, R.E., Sen, A., Miko, D.B., McGowan, J.W.: *Phys. Rev. Lett.* **50**, 335 (1983)
126. Belic, D.S., Dunn, G.H., Morgan, T.J., Mueller, D.W., Timmer, C.: *Phys. Rev. Lett.* **50**, 339 (1983)
127. Dittner, P.F., Datz, S., Miller, P.D., Moak, C.D., Stelson, P.H., Bottcher, C., Dress, W.B., Alton, G.D., Neskovic, N., Fou, C.M.: *Phys. Rev. Lett.* **51**, 31 (1983)
128. Tanis, J.A., Shafroth, S.M., Willis, J.E., Clark, M., Swenson, J., Strait, E.N., Mowat, J.R.: *Phys. Rev. Lett.* **47**, 828 (1981)
129. Graham, W.G., Fritsch, W., Hahn, Y., Tanis, J.H. (eds.): *Recombination of Atomic Ions*. NATO ASI Ser. B. Plenum, New York, p. 296 (1992)
130. Tanis, J.A.: Resonant transfer excitation (RTE) associated with single X-ray emission. In: Graham, W.G., Fritsch, W., Hahn, Y., Tanis, J.H. (eds.) *Recombination of Atomic Ions*. NATO ASI Series B, vol. 296, p. 241. Plenum, New York (1992)
131. Bates, D.R., Griffing, G.: *Proc. Phys. Soc. Lond. A* **66**, 961 (1955)
132. Bates, D.R., Griffing, G.: *Proc. Phys. Soc. Lond. A* **67**, 663 (1954)
133. Bates, D.R., Griffing, G.: *Proc. Phys. Soc. Lond. A* **68**, 90 (1955)
134. Zouros, T., Lee, D.H., Richard, P.: *Proceedings of the XVI International Conference on the Physics of Electronic and Atomic Collisions*, New York, 1989. In: Dalgarno, A., Freund, R.S., Lubell, M.S., Lucatorto, T.B. (eds.) *AIP Conference Proceedings No. 205*, p. 568. AIP, New York (1990)
135. Meyerhof, W.E., Hülskötter, H.-P., Dai, Q., McGuire, J.H., Wang, Y.D.: *Phys. Rev. A* **43**, 5907 (1991)
136. Montenegro, E.C., Melo, W.S., Meyerhof, W.E., de Pinho, A.G.: *Phys. Rev. Lett.* **69**, 3033 (1992)
137. Montenegro, E.C., Belkacem, A., Spooner, D.W., Meyerhof, W.E., Shah, M.B.: *Phys. Rev. A* **47**, 1045 (1993)
138. Wu, W., Wong, K.L., Ali, R., Chen, C.Y., Cocke, C.L., Frohne, V., Giese, J.P., Raphaelian, M., Walch, B., Dörner, R., Mergel, V., Schmidt-Böcking, H., Meyerhof, W.E.: *Phys. Rev. Lett.* **72**, 3170 (1994)
139. Dörner, R., Mergel, V., Ali, R., Buck, U., Cocke, C.L., Froschauer, K., Jagutzki, O., Lencinas, S., Meyerhof, W.E., Nüttgens, S., Olson, R.E., Schmidt-Böcking, H., Spielberger, L., Tökési, K., Ullrich, J., Unverzagt, M., Wu, W.: *Phys. Rev. Lett.* **72**, 3166 (1994)
140. Cocke, C.L.: Progress in atomic collisions with multiply charged ions. In: Lin, C.D. (ed.) *Review of Fundamental Processes and Application of Ions and Atoms*, p. 138. World Scientific, Singapore (1993)
141. Schuch, R.: Cooler storage rings: New tools for atomic physics. In: Lin, C.D. (ed.) *Review of Fundamental Processes and Application of Ions and Atoms*, p. 169. World Scientific, Singapore (1993)
142. Kollmus, H., Moshhammer, R., Olson, R.E., Hagmann, S., Schulz, M., Ullrich, J.: *Phys. Rev. Lett.* **88**, 103202–103201 (2002)
143. Saris, F.W., van der Weg, W.F., Tawara, H., Laubert, R.: *Phys. Rev. Lett.* **28**, 717 (1972)
144. Mokler, P.O.: Quasi molecular radiation. In: Sellin, I.A. (ed.) *Topics in Current Physics*, vol. 5, p. 245. Springer, Berlin (1978)
145. Schuch, R., Meron, M., Johnson, B.M., Jones, K.W., Hoffmann, R., Schmidt-Böcking, H., Tserruya, I.: *Phys. Rev. A* **37**, 3313 (1988)
146. Anholt, R.: *Rev. Mod. Phys.* **57**, 995 (1985)
147. Tserruya, I., Schuch, R., Schmidt-Böcking, H., Barrette, J., Dahai, W., Johnson, B.M., Meron, M., Jones, K.W.: *Phys. Rev. Lett.* **50**, 30 (1983)
148. Pieper, W., Geiner, W.: *Z. Phys.* **218**, 126 (1969)
149. Reinhardt, J., Müller, U., Müller, B., Greiner, W.: *Z. Phys. A* **303**, 173 (1981)
150. Soff, G., Reinhardt, J., Müller, B., Greiner, W.: *Z. Phys. A* **294**, 137 (1980)
151. Müller-Nehrer, U., Soff, G.: Electron excitations in superheavy quasi-molecules. *Phys. Rep.* **246**, 101 (1994)

152. Vane, C.R., Datz, S., Dittner, P.F., Krause, H.F., Bottcher, C., Strayer, M., Schuch, R., Gao, H., Hutton, R.: Phys. Rev. Lett. **69**, 1911 (1992)
153. Bottcher, C., Strayer, M.: Phys. Rev. A **39**, 4 (1989)
154. Belkacem, A., Gould, H., Feinberg, B., Bossingham, R., Meyerhof, W.E.: Phys. Rev. Lett. **71**, 1514 (1993)



Michael Schulz Michael Schulz received his PhD from Heidelberg University in 1987. After positions at ORNL and Kansas State University, he joined Missouri S&T in 1990. He is Curators' Distinguished Professor and Director of the Laboratory for Atomic, Molecular, and Optical Research. His research focuses on the atomic few-body problem. He is a Fellow of the APS and received a Distinguished Scientist Fellowship from the Chinese Academy of Sciences.



Hongwei Li , Arthur G. Suits , and Yuan T. Lee

Contents

70.1	Introduction	1019
70.2	Experimental Methods	1020
70.2.1	Molecular Beam Sources	1020
70.2.2	Reagent Preparation	1020
70.2.3	Detection of Neutral Products	1021
70.2.4	A Typical Signal Calculation	1023
70.3	Experimental Configurations	1024
70.3.1	Crossed-Beam Rotatable Detector	1024
70.3.2	Laboratory to Center-of-Mass Transformation	1025
70.3.3	Product Imaging	1026
70.4	Elastic and Inelastic Scattering	1028
70.4.1	The Differential Cross Section	1028
70.4.2	Rotationally Inelastic Scattering	1028
70.4.3	Vibrationally Inelastic Scattering	1029
70.4.4	Electronically Inelastic Scattering	1029
70.5	Reactive Scattering	1029
70.5.1	Harpoon and Stripping Reactions	1029
70.5.2	Rebound Reactions	1030
70.5.3	Long-Lived Complexes	1030
70.6	Recent Developments	1031
	References	1032

Abstract

This chapter presents the experimental aspects of reactive scattering from neutral–neutral chemical reactions under single-collision conditions. It begins with a discussion of the principle of molecular beam sources, developments of reagent preparation, various detection methods of neutral products, and a typical signal calculation. Two main crossed-beam configurations are also summarized here: one with a rotatable ionizer mass spectrometer detector and the other one with velocity-map ion-imaging detection. The differential cross section is introduced and discussed in application to elastic, inelastic, and reactive scattering. Various mechanisms are illustrated in reactive scattering, such as harpoon, stripping, rebound, and long-lived complexes mechanisms. In the last part, recent developments and advances are summarized to show the power of crossed-beam techniques to study the chemical reaction dynamics.

Keywords

differential cross section · Newton diagram · velocity-map imaging · relative velocity vector · supersonic beam

H. Li (✉)
State Key Laboratory of Molecular Reaction Dynamics, Dalian
Institute of Chemical Physics, Chinese Academy of Sciences
Dalian, Liaoning, China
e-mail: lihw@dicp.ac.cn

A. G. Suits
Dept. of Chemistry, University of Missouri
Columbia, MO, USA
e-mail: suitsa@missouri.edu

Y. T. Lee
Institute of Atomic and Molecular Science, Academia Sinica
Taipai, Taiwan
e-mail: ytleee@gate.sinica.edu.tw

70.1 Introduction

This chapter presents a résumé of the methods commonly employed in scattering experiments involving neutral molecules at chemical energies, i.e., less than about 10 eV. These experiments include the study of intermolecular potentials, the transfer of energy in molecular collisions, and elementary chemical reaction dynamics. Closely related material is presented in Chaps. 37, 39, and 40, as well as in other chapters on quantum optics.

70.2 Experimental Methods

70.2.1 Molecular Beam Sources

The development of molecular beam methods has transformed the study of chemical physics [1]. Supersonic molecular beam sources allow one to prepare reagents possessing a very narrow velocity distribution with very low internal energies, ideal for use in detailed studies of intermolecular interactions. Early experiments generally employed continuous beam sources, but since the 1980s more intense pulsed beam sources have come into common usage [2]. The advantages of pulsed beams primarily arise from the lower gas loads associated with their use, hence reduced demands on the pumping system. If any component of the experiment is pulsed (pulsed laser detection, for example), then considerable advantages may be obtained by also pulsing the beam. Although the theoretical descriptions of pulsed and continuous expansions are essentially equivalent, in practice, some care is required in employing pulsed beams because the temperature and velocity distributions may change dramatically through the course of the pulse. Free jet expansions are supersonic because the dramatic drop in the local temperature in the beam is associated with a drop in the local speed of sound. A detailed description of the supersonic expansion may be found in [3–5]. In practice, many of the detailed features associated with a supersonic expansion may be ignored, and one may assume an isentropic expansion into the vacuum. For an isentropic nozzle expansion of an ideal gas, the maximum terminal velocity is given by

$$v_{\max} = \sqrt{2\hat{C}_p T_0}, \quad (70.1)$$

where, for an ideal gas, the heat capacity is

$$\hat{C}_p = \left(\frac{\gamma}{\gamma - 1}\right) \frac{R}{m}, \quad (70.2)$$

R is the gas constant, m is the molar molecular mass, T_0 is the temperature in the stagnation region, and γ is the heat capacity ratio. For ideal gas mixtures, and assuming C_p independent of temperature for the range encountered in the expansion, one may use

$$\bar{C}_p = \sum_i X_i C_{p_i} = \sum_i X_i \left(\frac{\gamma_i}{\gamma_i - 1}\right) R, \quad (70.3)$$

and the average molar mass

$$\bar{m} = \sum_i X_i m_i, \quad (70.4)$$

where X_i is the mole fraction of component i , to obtain an estimate of the maximum velocity for a mixture:

$$v_{\max} = \sqrt{\frac{2\bar{C}_p T_0}{\bar{m}}}. \quad (70.5)$$

Table 70.1 Collision numbers for coupling between different modes. V, R, and T refer to vibrational, rotational, and translational energy, respectively. Each entry is the typical range of Z_{A-B}

	V	R	T
V	10^{5-3}	10^{3-4}	10^{5-6}
R		10^{0-1}	10^{2-3}

By seeding heavy species in light gases one may accelerate them to superthermal energies. Supersonic beams are characterized by the speed ratio, i.e., the mean velocity divided by the velocity spread:

$$S \equiv \frac{v}{\sqrt{2kT/m}}, \quad (70.6)$$

where T is the local translational temperature, or by the Mach number

$$M \equiv \frac{v}{\sqrt{\gamma kT/m}}. \quad (70.7)$$

For the purpose of order-of-magnitude calculations, the number density on axis far from the nozzle may be estimated as

$$n \approx n_0 \left(\frac{d}{x}\right)^2, \quad (70.8)$$

where n_0 is the number density in the stagnation region, d is the nozzle diameter, and x is the distance from the nozzle. The number density versus speed distribution of a nozzle beam is well described as a Gaussian characterized by the speed ratio S and a parameter $\alpha = v_0/S$, where v_0 is the most probable velocity:

$$n(v) = v^2 \exp\left[-\left(\frac{v}{\alpha} - S\right)^2\right]. \quad (70.9)$$

Cooling efficiencies for the various internal degrees of freedom correlate with the efficiency of coupling of these modes with translation, hence they vary widely. Coupling of modes A and B are expressed by the collision number Z_{A-B} :

$$Z_{A-B} \equiv Z \tau_{A-B}, \quad (70.10)$$

where τ_{A-B} is the bulk relaxation time and Z the collision frequency. This represents the number of collisions between effective inelastic events. Typical values are summarized in Table 70.1. R-T coupling is relatively efficient, while V-T coupling is quite inefficient, so that vibrational excitation may not be effectively cooled in the expansion.

70.2.2 Reagent Preparation

Molecular beam methods may be used in conjunction with a variety of other techniques to prepare atoms or molecules in excited or polarized initial states (Chap. 48), to generate unstable molecules or radicals [6, 7], or to produce

beams of refractory materials such as transition metals or carbon [8, 9]. Some of the common techniques are outlined below. Optical pumping of atoms to excited electronic states is a useful means of reagent preparation, and this topic is presented in detail in Chap. 11. This technique further allows one, using polarized lasers, to explore the influence of angular momentum polarization in the reagents on the collision dynamics [10]. Most of these studies have been performed using alkali and alkaline earth metals since there exist strong electronic transitions and convenient narrowband visible lasers suitable for use with these systems. Laser excitation may also be used to generate vibrationally excited molecules in their ground electronic states. The techniques employed include direct IR excitation using an HF chemical laser [11], population depletion methods [12], and various Raman techniques [13]. Adiabatic passage techniques, such as stimulated Raman adiabatic passage (STIRAP), Stark-induced Raman adiabatic passage (SARP), and rapid adiabatic passage (RAP), opened new opportunities for coherent laser control of atomic and molecular processes and were applied to prepare molecules in a single excited rovibrational level in their ground electronic states with near 100% efficiency. They are applied to use for different molecules with differing advantages. STIRAP allows efficient population transfer through a third upper electronic intermediate state [14]. SARP can be used for molecules that have no vibrational transition moment and no conveniently accessible excited states, like H_2 [15]. RAP only requires a single laser but is only applicable for molecules that possess a strongly allowed vibrational transition [16]. Stimulated emission pumping (SEP) [17] is an alternative technique for preparing very highly excited vibrational states, which does not require a coherent laser but needs convenient electronically excited states, as is the case for NO.

Metastable atoms may also be prepared by laser photolysis of a suitable precursor. $\text{O}(^1D)$ is readily prepared by photolysis of ozone or N_2O , for example [18]. Alternatively, RF or microwave discharges may be used to produce metastable species or reactive atoms or radicals [19]. These techniques may also be used to prepare ground-state atoms; for example, hot H atom beams are frequently produced by photolysis of HI or H_2S [20]. Such atomic or molecular radical beams may also be generated by pyrolysis in the nozzle. In this case, care must be taken to minimize recombination through careful choice of the temperature, nozzle geometry, and transit time through the heated region. Beams of refractory materials are now commonly generated using laser ablation sources [8, 9]. Typically, these employ a rod or disk of the substrate of interest, which is simultaneously rotated and translated to provide a fresh surface for ablation at each laser pulse. A laser beam is focused on the substrate and timed to fire just as a carrier gas pulse passes over. Laser power and wavelength must be optimized for a given sub-

strate. Lasers operating in the IR, visible, and UV have all been employed. Aligned or oriented molecules have been prepared using multipole focusing [21, 22], and more recently using strong electric fields (“brute force”) [23]. In the former case, specific quantum states are focused by the field. In the latter case, so-called pendular states are prepared from the low rotational levels of molecules possessing large dipole moments and small rotational constants. The ability to orient these molecules can be estimated on the basis of the Stark parameter $\omega = \mu E/B$, where μ is the dipole moment, E the electric field strength, and B the rotational constant. Orientation is feasible for low rotational levels of molecules when the Stark parameter is on the order of 10 or higher [23]. Manipulating the motion or control over the velocity of molecules in a molecular beam is achieved by concepts from charged-particle accelerator physics. Stark [24, 25] and Zeeman [26, 27] decelerators have been developed to control the motion of molecules that possess an electric or magnetic dipole moment using time-varying electric and magnetic fields, respectively. These decelerator techniques can not only slow the molecular beam to a narrow distribution of velocities but also select molecules into a single rotational quantum state.

70.2.3 Detection of Neutral Products

Broadly speaking, detection of neutral molecules is accomplished either by optical (spectroscopic) or nonoptical techniques. Nonoptical methods usually involve nonspecific ionization of neutral particles, most commonly by electron impact, followed by mass selection and ion counting. Thermal detectors such as cryogenic bolometers are also finding widespread application in molecular beam experiments owing to their remarkable sensitivity [28]. In general, optical methods may rely on resonant or nonresonant processes, hence they may or may not enjoy quantum-state selectivity. Both photoionization and laser-induced fluorescence methods are now in common usage, usually in applications where quantum-state resolved information is desired. The advantage of nonoptical methods is primarily one of generality: all neutral molecules may be detected and branching into different channels readily measured. Quantum-state resolution is more difficult to achieve using nonoptical detection methods, but both vibrationally and rotationally resolved measurements have been obtained by these means [29, 30].

The primary advantage of spectroscopic detection is the aforementioned possibility of quantum-state specificity. Another unique opportunity afforded by spectroscopic probes is the measurement of product alignment and orientation. In addition, in some cases, background interference may be reduced or eliminated using state-specific probes, thereby affording enhanced signal-to-noise ratios.

Nonoptical Techniques

Detectors based on nonspecific ionization remain the most commonly used in molecular beam experiments, owing to the ease of subsequent mass selection, and the convenience and sensitivity of ion detection. Surface ionization is a sensitive means of detecting alkali atoms and other species exhibiting low ionization potentials [31]. Surface ionization occurs when a neutral atom or molecule with a low ionization potential sticks on a surface with a high work function and is subsequently desorbed. Typically, these detectors employ a hot platinum or oxidized tungsten wire or ribbon for formation and subsequent desorption of the ions, which is surrounded by an ion collector. They are very efficient for the detection of alkali atoms and molecules whose ionization potentials are $\lesssim 6$ eV.

All neutral gas molecules may be ionized by collision with energetic electrons, and electron beam ionizers may be produced that couple conveniently to quadrupole mass spectrometers [32]. Collision of a molecule with a 100–200 eV electron leads predominantly to formation of the positive ion and a secondary electron. Other processes also occur and can be very significant: doubly or triply charged ions may be formed and, importantly, molecules can fragment yielding many daughter ions in addition to the parent ion. These fragmentation patterns vary with different molecules and may further show a strong dependence on molecular internal energy, so particular care must be taken to determine the role of these phenomena in each particular application. It is often necessary to record data for the parent ion and daughter ions for a given product channel and compare them to eliminate contributions arising from cracking of the parent molecule or other species [33]. Electron impact ionization probabilities for most species exhibit a similar dependence on electron energy, rising rapidly from the ionization potential to a peak at 80–100 eV, then falling more slowly with increasing collision energy. The ionization cross section for different species scales with molecular polarizability according to a well-established empirical relation [34]:

$$\sigma_{\text{ion}} = 36\sqrt{\alpha} - 18, \quad (70.11)$$

where σ_{ion} is in \AA^2 and α , the molecular polarizability, is in \AA^3 . This relation can be used to estimate branching ratios in the absence of any other means of calibrating the relative contributions of two different channels. The ionization rate is given by

$$\frac{d[M^+]}{dt} = I_e \sigma [M], \quad (70.12)$$

where I_e is the electron beam intensity, typically 10 mA/cm^2 or 6×10^{16} electrons/($\text{cm}^2 \text{ s}$), and $[M]$ is the number density of molecules M in the ionizer. If one assumes an ionization

cross section σ_{ion} of 10^{-16} cm^2 for collision with 150 eV electrons (a typical value for a small molecule), the ionization probability for molecules residing in the ionizer is then

$$\frac{d[M^+]}{dt} \frac{1}{[M]} = I_e \sigma = 6 \times 10^{16} \times 10^{-16} = 6 \text{ s}^{-1}. \quad (70.13)$$

However, product molecules arriving in the detector are not stationary. Typically, product velocities are on the order of 500 m/s. If the ionization region has a length of 1 cm, the residence time τ of a product molecule is on the order of 2×10^{-5} s. Consequently, the ionization probability of product molecules passing through the ionizer is

$$\frac{d[M^+]}{dt} \frac{\tau}{[M]} = 2 \times 10^{-5} \times 6 = 1.2 \times 10^{-4}. \quad (70.14)$$

Although this does not appear very efficient (indeed, it is four orders of magnitude less so than surface ionization), nevertheless, if the background count rate is sufficiently low, then good statistics may be obtained with signal levels as low as 1 Hz. Thus, for detection based on electron impact ionization, a key factor determining the sensitivity of the experiment is the background count rate at the masses of interest.

Spectroscopic Detection

Spectroscopic detection methods usually involve either laser-induced fluorescence (LIF) or resonant photoionization (REMPI) (Chap. 46). Alternative techniques such as laser-induced grating methods and nonresonant vacuum ultraviolet (VUV) photoionization are also being applied to scattering experiments. VUV photoionization can detect molecules and radicals with ionization energy lower than the photon energy that provides universal detection ability but does not resolve any vibrational or rotational information. Essential to the use of spectroscopic methods for reactive scattering studies is an understanding of the spectrum of the species of interest. This may be challenging for many reactive systems because the products may be produced in highly excited vibrational or electronic states that may not be well characterized. Additional spectroscopic data may be required. Franck–Condon factors are necessary to compare the intensities of different product vibrational states, while a calibration of the relative intensities of different electronic bands requires a measure of the electronic transition moments. In some cases, one must include the specific dependence of the electronic transition moment on the internuclear distance by integrating over the vibrational wave function. Populations corresponding to different rotational lines may be compared after the appropriate correction, which is represented by the Hönl–London factors, only for isotropic irradiation and detection. This is certainly not the case for most laser-based experiments. Generally, the detailed dependence of the excitation and detection on the relevant magnetic sublevels must be

considered [35–37]. Caution is required in using any spectroscopic method involving a level that is predissociated. This may lead to a dramatic decrease in the associated fluorescence or photoionization yield if the predissociation rate approaches or exceeds the rate of fluorescence or subsequent photoionization. An important question in any experiment based on spectroscopic detection is whether product flux or number density is probed. This question is considered in detail in several articles [13, 38]. It depends on the lifetime of the state that is probed, the relative time that the molecule is exposed to the probe laser field, and its residence time in the interaction region. Saturation phenomena are also important, yet not necessarily easily anticipated. Complete saturation does not readily occur because excitation in the wings of the laser beam profile becomes more significant as the region in the center of the beam becomes saturated [39].

LIF was a widely used spectroscopic technique in inelastic and reactive scattering experiments [35, 40, 41] in the 1980s to 1990s. It has been used to measure state-resolved total cross sections [42] and differential cross sections in electronic [43], vibrational, and rotationally inelastic scattering [12], as well as reactive scattering [44]. With the development of high-power tunable lasers and the broad use of imaging methods, REMPI is becoming a more general technique [45, 46]. REMPI has the advantages associated with ion detection, namely considerable convenience in mass selection and efficient detection, in addition to the capability of quantum-state selectivity. Disadvantages associated with REMPI arise primarily from higher laser power employed compared with LIF. Caution is required in attempting to extract quantitative information from REMPI spectra if one or several of the steps involved in the ionization process are saturated. This is of particular concern at the high laser powers necessary for multiple photon transitions. Another disadvantage, similar to LIF measurement, is the lack of available spectroscopic information for larger molecules, which limits its versatility in terms of universal detection. An alternative to direct photoionization involves excitation of products to metastable Rydberg states, followed by field ionization some distance from the interaction region. This technique has the advantage of very low background and is capable of extraordinary time-of-flight resolution. One example is the H atom Rydberg time-of-flight (HRTOF) method [47, 48] pioneered by the late *Karl Welge* and coworkers [49] for the hydrogen exchange reaction, $D + H_2$. This approach employs a conventional scattering geometry and is suitable only for experiments yielding product H or D atoms. Despite this narrow focus, owing to the general importance of hydrogen elimination reactions and the remarkable resolution of the technique, this has been an important development. The H or D atom products are excited to long-lived high- n Rydberg states in a $1 + 1'$ excitation scheme at the interaction region. They fly through a field-free region and impinge upon a rotat-

able field-ionization detector. The result is very high velocity resolution, largely because the spreads in the beam velocities make a negligible contribution to the product velocity spread since the H atoms are moving so fast. In addition, the dimensions of the scattering volume and ionization region may easily be made small relative to the flight length. Using this technique, Welge and coworkers achieved fully rotationally resolved differential cross sections for the hydrogen exchange reaction. Now, this technique has also been widely applied by the Yang group in studying the benchmark systems such as $F + H_2$ and $Cl + H_2$ [50–52]. They were able to observe quantum effects from the reactive resonances trapped in the transition-state region of those reactions.

70.2.4 A Typical Signal Calculation

For a crossed-beam system in which a beam of atoms A collides with a beam of molecules B yielding products C and D, the rate of formation of C is given by

$$\frac{dN_C}{dt} = n_A n_B \sigma_r g \Delta V, \quad (70.15)$$

where n_A and n_B are the number densities of the respective reagents at the interaction region, σ_r is the reaction cross section, g the magnitude of the relative velocity between the reactants, and ΔV the volume of intersection of the beams. For a typical experiment employing continuous supersonic beams, the number densities of the atomic and molecular reactants are $\approx 10^{11}$ – 10^{12} cm^{-3} and the scattering volume 10^{-2} cm^3 . For $g = 10^5$ cm/s and $\sigma_r = 10^{-15}$ cm^2 , the rate of product formation $dN_C/dt = 10^{11}$ molecules/s. The kinematics and energetics of the reaction then determines the range of laboratory angles into which the products scatter and the magnitude of the scattered signal.

If the products scatter into 1 sr of solid angle, and the detector aperture is 3×10^{-3} sr (roughly 1° in both directions perpendicular to the detector axis), then the detector receives 3×10^7 product molecules/s. Given the detection probability obtained above, 3600 product ions/s are detected. This is adequate to obtain very good statistics in a short time, as long as the background count rate is not considerably higher.

For a nonspecific detection technique, such as electron bombardment ionization coupled with mass filtering, it is necessary to use ultrahigh vacuum ($\approx 10^{-10}$ Torr) in the detector region to minimize interference from background gases. The residual gases are then primarily H_2 and CO, with number densities on the order of 10^6 cm^{-3} . Differential pumping stages, each of which may reduce the background by two orders of magnitude, are generally used to lower the background from gases whose partial pressures are lower than the ultrahigh vacuum limit of the detector chamber. However, this differential pumping helps only for those molecules that

do not follow a straight trajectory through the detector. The contribution from the latter is given by

$$n' = \frac{nA}{4\pi x^2}, \quad (70.16)$$

where n is the number density of molecules effusing from an orifice of area A , and n' is their number density at a distance x on the axis downstream. For a distance of 30 cm and a main chamber pressure of 3×10^{-7} Torr, this corresponds to a steady-state density of 10^5 molecules/cm³ at the ionizer, a reduction of six orders of magnitude. Three stages of differential pumping are, thus, the most useful under these conditions, since the primary source of background is then molecules following a straight trajectory from the main chamber. A liquid helium-cooled surface opposite the detector entrance may then be useful to minimize scattering of background molecules into the ionizer.

70.3 Experimental Configurations

70.3.1 Crossed-Beam Rotatable Detector

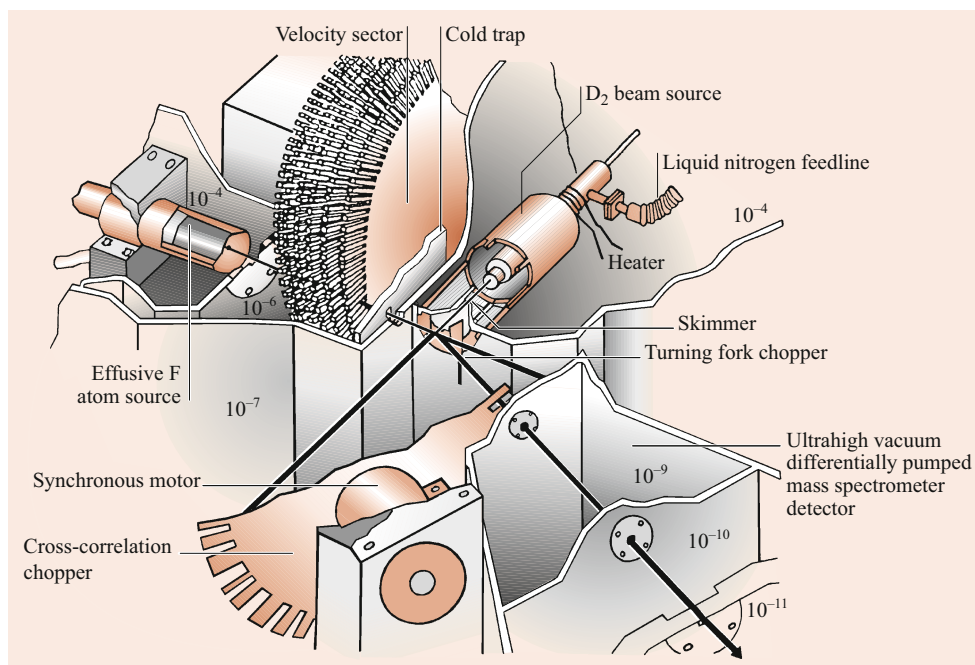
The configuration illustrated in Fig. 70.1 represents a standard, now widely used [32], usually with two continuous beams fixed at 90°. The molecular beam sources are differentially pumped and collimated to yield an angular divergence of about 2°. The beams cross as closely as possible to the nozzles, with a typical interaction volume of 3 mm³. Scattered products pass through an aperture on the front of the detector, thence through several stages of differential

pumping before reaching the ionizer. Ions formed by electron impact on the neutral products are then extracted into a quadrupole mass spectrometer with associated ion counter. A chopper wheel is generally used at the entrance to the detector to provide a time origin for recording time-of-flight spectra.

Pseudo-random sequence chopper disks provide optimal counting statistics while maintaining a high-duty cycle (50%) [53]. The detector may be rotated about the interaction region, typically through a range of 120° or so, allowing one to examine products scattered at a range of laboratory angles. In addition to time-of-flight detection, one of the beams may be gated on and off for background subtraction, and the detector moved to record the integrated signal at each laboratory angle.

Two kinds of measurements are typically made in these experiments: time-of-flight spectra and angular distributions. Usually, one is interested in obtaining the complete product-flux versus velocity contour map, since this contains full details of the scattering process. This is obtained by measuring a full angular distribution as well as time-of-flight data at many laboratory angles. The results are then simulated using a forward convolution fitting procedure to obtain the underlying contour map [54–56]. Because scattering of isotropic reagents exhibits cylindrical symmetry about the relative velocity vector, it is sufficient to measure products scattered in any plane containing this vector to determine the product distribution. This is not true for structured particles (e.g., involving atoms in P states); however, this azimuthal anisotropy has been used to explore the impact parameter dependence of the reaction dynamics [57].

Fig. 70.1 Experimental arrangement for $F + D_2 \rightarrow DF + F$ reactive scattering. Pressure (in Torr) indicated in each region



In a typical reactive scattering experiment, $A + BC \rightarrow AB + C$, either of the two products may be detected. Conservation of linear momentum requires that the center-of-momentum (CM) frame momenta of the two products must sum to zero. It is, thus, only necessary to obtain the contour map for one of the products. The choice of detected product is usually dictated by kinematic considerations, although one may choose to detect a product that is kinematically disfavored if its partner happens to have a mass with a large natural background in the detector. Kinematic considerations can be critical in assessing the suitability of a given system for study. It is very important that one of the products be scattered entirely within the viewing range of the detector in order to obtain a complete picture of the reaction dynamics.

The advantages of crossed beams employed in conjunction with an electron impact ionizer-mass spectrometer detector derive primarily from the universality of the detector. No spectroscopic information is required, and there are no invisible channels, such as may occur with spectroscopic detection methods. In addition, the resolution of these machines may be increased almost arbitrarily; indeed, even rotationally inelastic scattering has been studied [58]. The disadvantages are complementary to the advantages: the universal detector implies that quantum-state resolution is not achieved directly, although in favorable cases, the product vibrational states may be resolved in the translational energy distributions [29, 59]. In addition, if the product of interest represents a mass that receives interference from one of the beam masses, background interference may be problematic. The kinematic considerations mentioned above may also preclude study of certain systems. However, the kinematic requirements for the imaging approach discussed below are complementary to those of the rotatable-detector configuration.

70.3.2 Laboratory to Center-of-Mass Transformation

Angular and velocity distributions measured in the laboratory frame must be transformed to the CM frame for theoretical interpretation. Accounts of this transformation and details concerning the material presented below may be found in [60–63], among others. The Newton diagram is useful to aid in visualizing the transformation and in understanding the kinematics of a given collision system. For the scattering of $F + D_2$, for example, shown in Fig. 70.2, a beam of fluorine atoms with a velocity \mathbf{v}_F is crossed by a beam of D_2 , velocity \mathbf{v}_{D_2} , at 90° . The relative velocity between the two reactants is $\mathbf{g} = \mathbf{v}_F - \mathbf{v}_{D_2}$, and the velocity of the CM of the entire system is

$$\mathbf{V}_{\text{CM}} = \frac{M_F \mathbf{v}_F + M_{D_2} \mathbf{v}_{D_2}}{M_F + M_{D_2}}; \quad (70.17)$$

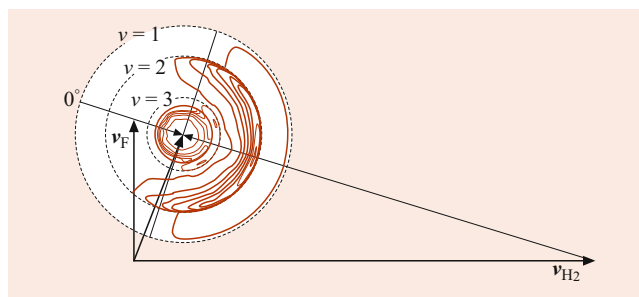


Fig. 70.2 Newton diagram for collision of F with H_2 with superimposed CM flux versus velocity contour map

\mathbf{V}_{CM} divides the \mathbf{g} into two segments corresponding to the CM velocities of the two reagents. The magnitude of these vectors, u_F and u_{D_2} , are inversely proportional to the respective masses. If scattered DF products are formed with a laboratory scattering angle Θ and a laboratory velocity \mathbf{v}_{DF} , as shown in Fig. 70.2, this corresponds to DF *backscattered* with respect to the incident F atom, in the CM system. It is common to refer the scattering frame direction to the atomic reagent in an $A + BC \rightarrow AB + C$ reaction, for example, to make clear the dynamics of the process. In this case, the backscattered DF arises as a result of a direct rebound collision. Some useful kinematic quantities are summarized here. For beams A and BC intersecting at 90° , the angle of the CM velocity vector with respect to A is given by

$$\Theta_{\text{CM}} = \arctan \frac{M_{\text{BC}} v_{\text{BC}}}{M_A v_A}. \quad (70.18)$$

For an arbitrary Newton diagram with angle α between the two beams, the magnitude of the relative velocity is

$$g^2 = v_A^2 + v_{\text{BC}}^2 - 2v_A v_{\text{BC}} \cos \alpha, \quad (70.19)$$

the relative velocity vector is

$$\mathbf{g} = \mathbf{v}_A - \mathbf{v}_{\text{BC}}, \quad (70.20)$$

and the collision energy is

$$E_{\text{coll}} = \frac{1}{2} \mu_i g^2, \quad (70.21)$$

where μ_i is the reduced mass of the initial collision system. The magnitude of the CM frame velocity of particle A before collision is

$$\mathbf{u}_A = \frac{m_{\text{BC}}}{m_A + m_{\text{BC}}} \mathbf{g}. \quad (70.22)$$

The final relative velocity is

$$\mathbf{g}' = \mathbf{v}_{\text{AB}} - \mathbf{v}_C, \quad (70.23)$$

with magnitude

$$g' = \sqrt{\frac{2E_{\text{avail}}}{\mu_{\text{F}}}}, \quad (70.24)$$

where the available energy E_{avail} is

$$E_{\text{avail}} = E_{\text{coll}} + E_{\text{int, reac}} + E_{\text{exo}} - E_{\text{int, prod}}, \quad (70.25)$$

in which $E_{\text{int, reac}}$ is the internal energy of the reactants, E_{exo} is the exoergicity of the reaction, and $E_{\text{int, prod}}$ is the internal energy of the products.

One must transform the laboratory intensity $I(\Omega) \equiv d^2\sigma/d^2\Omega$ into $I(\omega) (\equiv d^2\sigma/d^2\omega)$, the corresponding CM quantity. For the crossed-beam configuration described in Sect. 70.3.1, the laboratory distributions are distorted by a transformation Jacobian that arises because the laboratory detector views different CM frame solid angles, depending on the scattering angle and recoil velocity. For the spectroscopic experiments described in Sect. 70.3.3, the Jacobian is unity (the CM velocity represents a simple frequency offset of the Doppler profiles, for example); however, the transformation of the scattering distributions from the recorded quantities (two-dimensional projections or intensity versus wavelength) to recoil velocity distributions may be complex. Two cases must be considered for the configuration discussed in Sect. 70.3.1: one in which discrete velocities result (such as elastic or state-resolved scattering experiments), and one in which continuous final velocities are measured. For the first case, the laboratory and CM differential cross sections are independent of the respective product velocities v and u , and these quantities are related by

$$\frac{d^2\sigma}{d^2\Omega} = J \frac{d^2\sigma}{d^2\omega}, \quad (70.26)$$

so that the transformation Jacobian is given by

$$J = \frac{d^2\omega}{d^2\Omega}. \quad (70.27)$$

For discrete recoil velocities, the CM solid angle is

$$d^2\omega = \frac{dA}{u^2}, \quad (70.28)$$

where dA is a surface element of the product Newton sphere. The laboratory solid angle corresponding to this quantity is

$$d^2\Omega = \frac{\cos(\mathbf{u}, \mathbf{v})}{v^2} dA, \quad (70.29)$$

so that the Jacobian for the first case is given by

$$J = \frac{v^2}{u^2 \cos(\mathbf{u}, \mathbf{v})}. \quad (70.30)$$

For the case of continuous final velocities, the σ are velocity dependent and are related by

$$\frac{d^3\sigma}{d^2\Omega dv} = J \frac{d^3\sigma}{d^2\omega du}, \quad (70.31)$$

so that here the Jacobian is given by

$$J = \frac{d^2\omega du}{d^2\Omega dv}. \quad (70.32)$$

In this case, we consider a recoil volume element $d\tau$ (in velocity space), which must be the same in both coordinate frames:

$$d\tau_{\text{CM}} = u^2 du d^2\omega = d\tau_{\text{lab}} = v^2 dv d^2\Omega, \quad (70.33)$$

so that the Jacobian is

$$J = \frac{v^2}{u^2}. \quad (70.34)$$

The laboratory intensity is then related to that in the CM frame by

$$I_{\text{lab}}(v, \Theta) = \left(\frac{v^2}{u^2}\right) I_{\text{CM}}(u, \theta). \quad (70.35)$$

For a mass spectrometer detector with electron bombardment ionizer, one measures the number density of particles rather than the flux, so that the recorded signal is given by

$$N_{\text{lab}}(v, \Theta) = \frac{I_{\text{lab}}(v, \Theta)}{v} = \frac{v}{u^2} I_{\text{CM}}(u, \theta). \quad (70.36)$$

The usual flux versus velocity contour map is a polar plot of the quantity $I_{\text{CM}}(u, \theta)$. The product velocity distributions are then

$$I(u) = \iint I(\theta, u) \sin \theta d\theta d\phi = 2\pi \int_0^\pi I(u, \theta) \sin \theta d\theta, \quad (70.37)$$

and the translational energy distributions are

$$I(E_{\text{T}}) = I(u) \left| \frac{du}{dE_{\text{T}}} \right|. \quad (70.38)$$

70.3.3 Product Imaging

An important approach now is based on direct imaging of the scattered product distribution. The technique was first used to record state-resolved angular distributions of methyl radicals from the photodissociation of methyl iodide [64] and

has since been widely employed to study unimolecular photodissociation dynamics [65]. In 1993, *Houston* and coworkers first applied imaging detection in a crossed-beam experiment to record state-resolved inelastic scattering of NO with argon [66]. Since then, velocity map imaging combined with crossed-beam apparatus has been widely used to measure inelastic and reactive scattering of bimolecular reactions [67]. The crossed-beam configuration coupled with velocity map imaging detection, which was first used by *Houston* and coworkers and now widely adopted to use by many research groups, is shown schematically in Fig. 70.3. The two skimmed supersonic beams cross at right angles, and scattered products are state-selectively ionized on the axis of a time-of-flight mass spectrometer using resonant photoionization (or ionized by a VUV nonresonant photoionization without state selectivity). The ion cloud thus formed continues to expand with its nascent recoil velocity as it drifts through the flight tube. The ions then strike a microchannel plate coupled to a phosphor screen. The latter is viewed by a video camera gated to record the signal at the mass of interest. The images are, thus, two-dimensional projections of the nascent three-dimensional product distributions. From this projection, it is necessary to generate the three-dimensional distribution. This is a tomographic reconstruction, achieved using an inverse Abel transform or related method, as widely used in photodissociation studies [68–70]. It is a direct inversion procedure feasible for cases in which the image is the projection of a cylindrically symmetric object, with its axis of symmetry parallel to the image plane. This analysis yields a unique product contour map directly from the image, but it is difficult to incorporate apparatus functions, and it is sensitive to noise in the data. The problem of the noise or uncertainty induced from the reconstruction process was overcome by an important innovation in ion imaging, time slicing, in the early twenty-first century. Time slicing was first reported by *Kit-sopoulos* and coworkers [71] using delayed pulsed extraction in 2001, followed by two closely related velocity mapping versions in 2003: “DC slicing” [72] and “time-sliced imaging” [73]. Ideally, DC slice-imaging techniques do not require any reconstruction procedure in the analysis; however, in practice, most slice-imaging experiments achieve a velocity slice width of 10–25% or more around the center of the distribution due to the limited experimental conditions. This will carry significant out-of-plane elements that can blur the spectrum, lose fine resolution, and underestimate the contribution from slow recoiling products. To overcome these limitations, a finite-slice analysis (FINA) slice reconstruction method was recently developed [74, 75] to remove these out-of-plane elements from a sliced image. This method allows reconstruction procedure at any velocity slice width and can even be applied to nonsliced or conventional images.

The advantages of the imaging method again derive from its reliance on a spectroscopic probe, so that quantum-state

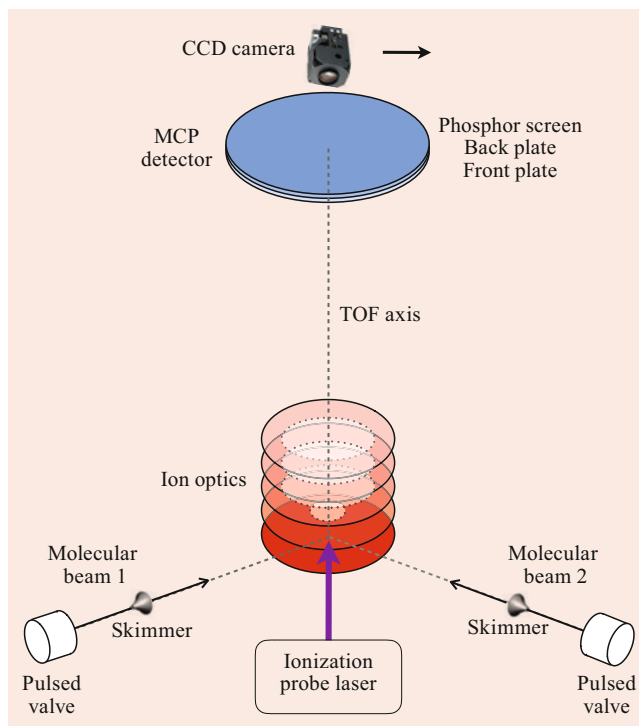


Fig. 70.3 Crossed molecular beam apparatus with product imaging detection

resolution is possible, and background interference may be avoided. In addition, it possesses a multiplexing advantage since the velocity distribution is recorded for all angles simultaneously. Imaging relies exclusively on photoionization, unlike the Doppler methods, which may use either photoionization or LIF. This is somewhat disadvantageous since the available photoionization schemes are limited, and often high laser power is necessary to achieve adequate signal intensity. As a result, background ions can be a problem. In general, resonantly enhanced two-photon ionization, i.e., $[1 + 1]$, detection schemes are thus preferable. As we mentioned earlier in the spectroscopic detection in Sect. 70.2.3, nonresonant VUV photoionization is an alternative ionization method for the velocity map imaging technique when a REMPI scheme is not available for probed products. VUV photoionization does not have quantum-state resolution but provides universal detection that can ionize all molecules and radicals with their ionization energy lower than the VUV photon energy. VUV photoionization from an excimer laser serves as a convenient and powerful probe with crossed beams for a variety of systems [76]. This combination of crossed molecular beam experiment with a high-resolution velocity map imaging technique directly measures the product velocity-flux contour map that reflects the underlying dynamics of the bimolecular reaction. High-resolution product images provide coupling information between scattering angles, i.e., the differential cross section and the energy partitioning into translational and internal degrees of freedom

of the products [77–79]. The velocity map imaging technique has been a powerful probe tool and been used in many crossed-beam studies, as discussed in Sect. 70.6.

70.4 Elastic and Inelastic Scattering

When particles collide, they may exchange energy or recouple it into different modes, they may change their direction of motion, and they may even change their identity. The study of these processes reveals a great deal of information about the forces acting between the particles and their internal structure. It is useful to begin with a summary of the dominant features of elastic and inelastic scattering.

70.4.1 The Differential Cross Section

Figure 70.4 illustrates the relation between the deflection function χ and the impact parameter b for a realistic potential containing an attractive well and a repulsive core. For large b there is no interaction, hence no deflection. At smaller values of b , the attractive part of the potential is experienced, and some positive deflection results. At a smaller value of b , b_r , the influence of the attractive component of the potential reaches a maximum, giving the greatest positive deflection: this is the *rainbow angle* by analogy with the optical phenomenon. There is another value of the b for which point the attractive and repulsive parts of the potential balance, yielding no net deflection. This is the *glory* impact parameter b_g . For yet smaller values of b , the interaction is dominated by the repulsive core, and rebound scattering gives a negative deflection function.

The important expressions related to the differential cross section are summarized here [80]. For scattering involving an isotropic potential, the deflection angle is $\Theta = |\chi|$. The

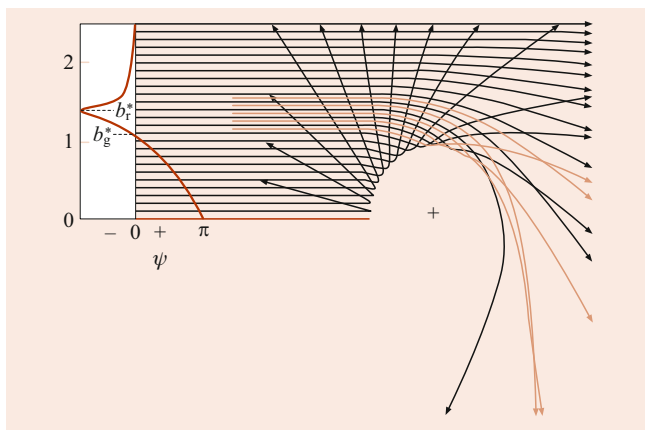


Fig. 70.4 Schematic diagram showing the relation between impact parameter b and deflection function χ

differential cross section $d\sigma$ gives the rate of all collisions leading to deflection angles in the solid angle element $d\omega$:

$$\frac{dN(\theta)}{dt} \propto I(\theta) d\omega = I(\theta) 2\pi \sin(\theta) d\theta. \quad (70.39)$$

The incremental cross section is $d\sigma = I(\theta) d\omega = 2\pi b db$, so

$$I(\theta) = \frac{b}{\sin \theta (d\theta/db)}. \quad (70.40)$$

For classical particles, the relation between the deflection function and the potential is

$$\chi = \pi - 2b \int_{R_0}^{\infty} \frac{dR}{R^2} \left[1 - \frac{V(R)}{E_T} - \frac{b^2}{R^2} \right]^{-1/2}, \quad (70.41)$$

where $V(R)$ is the potential as a function of interparticle distance R , R_0 is the turning point of the collision, and E_T the collision energy.

In the high energy limit, for large $b \approx R_0$,

$$\chi(b, E_T) \propto \frac{V(b)}{E_T}. \quad (70.42)$$

For a long-range potential $V(R)$ proportional to R^{-s} ,

$$E_T^{2/s} \theta^{2(1+1/s)} I(\theta) = \text{const.} \quad (70.43)$$

For a potential exhibiting a minimum, the rainbow angle θ_r is proportional to the collision energy and clearly resolved when the collision energy is three to five times the well depth. In addition, supernumary rainbows and quantum-mechanical “fast oscillations” occur in the $d\sigma$, and these provide a sensitive probe of the interaction. Accurate interatomic potentials are routinely obtained from elastic scattering experiments [62, 81].

70.4.2 Rotationally Inelastic Scattering

Classical scattering involving an anisotropic potential results in another rainbow phenomenon, distinct from that seen in pure elastic scattering and notable in that it does not require an attractive component in the potential. These rotational rainbows are equivalently seen in a plot of integral cross section against change in rotational angular momentum Δj or in the differential cross section for a particular value of Δj . The rotational rainbow peaks arise from the range of possible orientation angles γ in a collision involving an anisotropic potential. When there is a minimum in $d\gamma/d\theta$ for a given Δj , the differential cross section reaches

a maximum [82]. The rotational rainbow peak occurs at the most forward classically allowed value of the scattering angle, and $d\sigma$ drops rapidly at smaller angles. The rainbow moves to more backward angles with increasing Δj because the larger j -changing collisions require greater momentum transfer and, hence, must arise from lower impact parameter collisions. For heteronuclear molecules, two rainbow peaks may be observed, corresponding to scattering off either side of the molecule. One can relate the location of the rainbow peak to the shape of the potential using a classical hard ellipsoid model [83]:

$$A - B = \frac{j}{p_0} \left[2 \sin \left(\frac{\theta_{r,cl}}{2} \right) \right]^{-1}, \quad (70.44)$$

where j is the rotational angular momentum, p_0 is the initial linear momentum, $\theta_{r,cl}$ is the classical rainbow position, and A and B are the semimajor and semiminor axes of a hard ellipse potential. The classical rainbow positions occur somewhat behind the quantum-mechanical and experimental rainbow positions, so the classical rainbow may be estimated as the point at which the peak has fallen to 44% of the experimental value. Real molecular potentials may be far from ellipsoids, however, such detailed quantitative insight into the potential requires a comparison of scattering data with quantum-mechanical calculations. The open-shell, close-coupled quantum-mechanical (CC QM) scattering calculations have been proved successfully in the rotationally inelastic scattering of NO with rare gases. Interesting phenomena, like scattering resonances [84], diffraction oscillations [85], and stereodynamic effects [86], have been observed in the joint work of high-resolution imaging detection with crossed-beam experiments and CC QM calculations.

70.4.3 Vibrationally Inelastic Scattering

There has been no direct observation of the differential cross section of T-V or V-T energy transfer involving neutral molecules owing to the small cross sections for these processes. Integral cross section data are available, however. Above threshold, the latter has shown a linear dependence of σ on collision energy for $\Delta v = 1$, quadratic for $\Delta v = 2$ and cubic for $\Delta v = 3$ [87]. In addition, a great deal of information on vibrational relaxation processes has been obtained in cell experiments [88].

70.4.4 Electronically Inelastic Scattering

A wealth of information is available on electronically inelastic scattering systems, since these in general exhibit much

larger cross sections than V-T processes [89, 90]. In addition, spectroscopic methods may be used to overcome some of the background problems that hamper the study of the latter. Often, quenching of electronically excited states involves curve crossing mechanisms, so that very effective coupling of electronic to vibrational energy may occur. Spin-orbit changing collisions of Ba(1P) with O₂ or NO, for example, occur by a near-resonant process and result in almost complete conversion of electronic energy to vibrational excitation of the product [91]. The analogous collisions with N₂ and H₂, however, reveal very repulsive energy release with little concomitant vibrational excitation. Both processes likely occur via curve crossings of the relevant electronic states, but the near-resonant mechanism occurs by way of an ionic intermediate.

70.5 Reactive Scattering

Reactive differential cross sections reveal several distinct aspects of the chemical encounter. The angular distributions themselves may be used to infer the lifetime of the collision intermediate: long-lived complexes exhibit forward-backward symmetry along the relative velocity vector. In this case, “long-lived” means on the order of several rotational periods. The rotational period of the complex may thus be used as a clock to study the energy dependence of the intermediate’s lifetime. The angular distributions further reveal the relation of initial and final orbital angular momentum. Sharply peaked angular distributions generally indicate strongly correlated initial and final orbital angular momentum vectors. Finally, the product translational energy release contains the details of the energy disposal and reveals a wealth of information about the thermodynamics of the process, the existence of barriers, and sometimes even the geometry of the transition state. Together, the angular and translational energy distributions reveal many of the details of the potential energy surface.

The dynamics of reactive collisions fall broadly into three main categories characterized by distinct angular and energy distributions. The three categories are harpoon/stripping reactions, rebound reactions, and long-lived complex formation. Some reactions may exhibit more than one of these mechanisms at once, or the dynamics may change from one to another as the collision energy is varied.

70.5.1 Harpoon and Stripping Reactions

It was known in the 1930s that collisions of alkali atoms with halogen molecules exhibit very large cross sections and yield highly excited alkali halide products. These observations were accounted for by the *harpoon* mechanism proposed by

M. Polanyi. Because alkali atoms have low ionization potentials and halogen molecules large electron affinities, as the alkali atom approaches the molecule, electron transfer may occur at long range. These processes are considered in detail in Chap. 52 [92, 93]. The harpooning distance R_c at which this curve crossing takes place may be estimated simply as the distance at which the Coulomb attraction of the ion pair is sufficient to compensate for the endoergicity of the electron transfer:

$$R_c = \frac{e^2}{I_P - A_e}, \quad (70.45)$$

where I_P and A_e represent the ionization potential and electron affinity of the electron donor and recipient, respectively. For R in Å and E in eV, this relation is

$$R_c = \frac{14.4}{I_P - A_e}. \quad (70.46)$$

Due to the large Coulombic attraction between the ion pair, reaction proceeds immediately following electron transfer. The crossing distance may then be used to estimate the effective reaction cross section. The vertical A_e is not necessarily the appropriate value to use in estimating these crossing distances; stretching of the halogen bond may occur during approach, so the effective A_e is generally somewhere between the vertical and adiabatic values. Often, there exists some repulsion between the atoms in the resulting halogen molecular ion, so that electron transfer is accompanied by dissociation of the molecule in the strong field of the ion pair. The alkali ion, having sent out the electron as the “harpoon”, then reels in the negative ion, leaving the neutral halogen atom nearly undisturbed as a spectator. Because these events occur at long range, there is no momentum transfer to the spectator atom, and it is a simple matter to estimate the anticipated angular and translational energy distributions in this *spectator-stripping* limit. The product molecule is scattered forward (relative to the direction of the incident atom), and for the reaction $A + BC \rightarrow AB + C$, the final CM velocity for the product AB is given by

$$\mathbf{u}'_{AB} = \frac{-M_C \mathbf{u}_{BC}}{M_{AB}}, \quad (70.47)$$

where \mathbf{u}_{BC} is the initial CM velocity of the BC molecule. This spectator-stripping mechanism may occur in systems other than harpoon reactions, and it is useful to remember it as a limiting case.

The likelihood of electron transfer at these crossings may be estimated using a simple Landau–Zener model [93] (Chap. 52). For relative velocity g , impact parameter b , and crossing distance R_c , the probability for undergoing a transition from one adiabatic curve to another (that is, the

probability for remaining on the diabatic curve) is given by

$$p = 1 - e^{-\delta}, \quad (70.48)$$

where

$$\delta = \frac{2\pi H_{12}^2 R_c^2}{g} \left[1 - \frac{b^2}{R_c^2} \right]^{-\frac{1}{2}}, \quad (70.49)$$

and H_{12} is the coupling matrix element between the two curves; H_{12} may be estimated from an empirical relation that is accurate within a factor of three over a range of ten orders of magnitude [94]. In atomic units,

$$H_{12} = \sqrt{I_1 I_2} R_c^* e^{-0.86 R_c^*}, \quad (70.50)$$

where

$$R_c^* = (\sqrt{I_1} + \sqrt{I_2}) \quad (70.51)$$

is the reduced crossing distance, and I_1 and I_2 are the initial and final ionization potentials of the transferred electron. One finds electron transfer probabilities near unity for curve crossing distances below about 5 Å, dropping to zero for crossing at distances greater than about 8 Å. These estimates are based on electron transfer in atom–atom collisions, and it is important to remember that atom–molecule collisions occur on surfaces rather than curves, so the crossing seam may cover a broad range of internuclear distances.

70.5.2 Rebound Reactions

Another common direct reaction mechanism is the *rebound* reaction exemplified by $F + D_2 \rightarrow DF + D$ [29]. The CM product flux versus velocity contour map obtained for this reaction is shown in Fig. 70.2. Due to the favorable kinematics and energetics in this case, the FD product vibrational distribution is clearly resolved and peaks at $v = 2$. The dominant $v = 2$ product peaks at a CM angle of 180° (referred to the direction of the incident F atom). This rebound scattering is characteristic of reactions exhibiting a barrier in the entrance channel. Rebound scattering implies small b collisions, and this serves to couple the translational energy efficiently into overcoming the barrier. Small b collisions necessarily have smaller cross sections however, since the cross section scales quadratically with b .

70.5.3 Long-Lived Complexes

A third, important reaction mechanism involves the formation of an intermediate that persists for some time before dissociating to give products. If the collision complex survives

for many rotational periods ($\approx 10^{-11}$ s), then the CM angular distribution exhibits a characteristic forward–backward symmetry, usually with peaking along the poles. The latter occurs because the initial and final orbital angular momenta tend to be parallel (and perpendicular to the initial relative velocity vector). When there exist dynamical constraints enforcing some other relation, as in the case $F + C_2H_4$, then sideways scattering may be observed, despite a lifetime of several rotational periods [95–97]. For some systems exhibiting this long-lived behavior, the rotational period may be used as a *molecular clock* to monitor the lifetime of the complex. By increasing the collision energy until the distribution begins to lose its forward–backward symmetry, one can investigate the internal energy of the system just when its lifetime is on the order of a rotational period.

Systems that have an inherent symmetry may exhibit this forward–backward symmetry in the scattering distributions despite lifetimes that are considerably shorter than a rotational period. This is the case for $O(^1D)$ reacting with H_2 , for example [98]. This reaction involves insertion of the O atom into the H_2 bond, resulting in an intermediate that accesses the deep H_2O well and contains considerable vibrational excitation. Trajectory calculations show that the complex dissociates after a few vibrational periods, but the distribution exhibits forward–backward symmetry because the O atom is equally likely to depart with either H atom.

70.6 Recent Developments

Astonishing progress in reactive scattering methods have continued in the past decade, and a few highlights are summarized here. These advances have taken the form of improvements in detection methods, or in some cases, entirely new experimental approaches and new achievements that people have made from crossed-beam experiments.

One of the most important of these is the high-resolution H/D-atom Rydberg tagging time-of-flight (HRTOF) technique in the crossed molecular beam experiment, which is suitable for the study of bimolecular reaction yielding product H or D atoms. Yang and coworkers applied this method to systematically study the benchmark reaction of $F + H_2$ and look for reactive resonances in this elementary bimolecular reaction. The lowest barrier height for the $F + H_2$ reaction is $1.63 \text{ kcal mol}^{-1}$, [99]; however, H products were probed when collision energies were lower than the barrier height that indicates some tunneling effects here [100]. Based on the conservation of the linear momentum, such high-resolution H-atom TOF spectra of the H atom products resolve the rovibrational states of the HF ($v' = 1, 2, 3, j'$) coproducts. Pronounced forward-scattered HF products in the $v' = 2$ vibrational state were clearly observed at the collision energy of $0.52 \text{ kcal mol}^{-1}$. Full quantum scattering calculations

based on an accurately constructed potential energy surface indicate that this is attributed to the Feshbach resonances trapped in the peculiar HF($v' = 3$) – H' vibrationally adiabatic potential (VAP) and decay to the HF($v' = 2$) product channel via strong coupling between HF($v' = 3$) – H' and HF($v' = 2$) – H' adiabatic curves [100–102].

The advantage of HRTOF is its very high resolution, but it can only detect H/D products at one angle each time and requires rotating the detector in order to get full differential cross section (DCS) information. This could be improved by combining it with velocity map imaging (VMI) detection, since VMI can measure the product angular distribution (proportional to DCS distribution) at all angles together and can measure the translational energy distribution simultaneously. The problem for imaging the H/D-atom is that the H/D-atom is light, and electron recoil will blur the image and result in spectrum resolution that is not good. Very recently, Wang and coworkers applied the $1 + 1'$ REMPI threshold ionization technique to eliminate the electron recoil for H(D)-atom detection that gives rise to a high-resolution time-sliced velocity map ion imaging apparatus [103]. Such a high-resolution experiment allowed them to observe the geometric phase effect in the $H + HD \rightarrow H_2 + D$ reaction for the first time.

Compelling applications of time-sliced VMI with crossed beams can be found in the work of Liu and coworkers on state-resolved detection on methyl radicals following reactions of methane with X (X: F, Cl, $O(^3P)$, and OH) [104–106]. Unlike an atom detected in HRTOF, polyatomic molecules/radicals have vibrational and rotational excitation when they are first produced. In general, their REMPI schemes are not available for all vibrational and rotational states, i.e., the methyl radical only has the origin bands and the umbrella-mode excited bands known in its first REMPI spectrum [107]. Nevertheless, the methyl ion images provide quantum-state correlated differential cross sections for this type of reactions directly, allowing comparison to theory at an unprecedented level of detail [108–111].

Another significant new direction in detection strategies is the use of near-threshold VUV product ionization, especially for larger molecules whose REMPI probe schemes are not available. This is a universal approach, in that little advance spectroscopic information is required, but it is selective in that dissociative ionization is minimized, and sometimes isomer-selective detection may be achieved. This approach has been used in synchrotron-based studies of Cl atom reactions [112], radical–radical reactions [113] and in transition metal reactions [114, 115], and in product imaging studies of oxygen and chlorine atom reactions using the F_2 excimer at 157 nm [77, 79, 116]. Inspired by the threshold VUV detection methods, Casavecchia and coworkers recently advanced the use of near-threshold electron impact ionization in a conventional universal crossed-beam config-

uration [117]. Their recent results show the great promise of this technique to deliver higher signal-to-noise ratio and to minimize fragmentation processes in the detection step that may obscure the underlying dynamics [118].

A final note concerns developments in the study of chemical dynamics in the cold and ultracold regime with crossed beams. Quantum phenomena such as resonances dominate at low temperatures where few partial waves contribute to the collision. One can reduce the collision energy by slowing the beams with a Stark decelerator [119], merged beams [120, 121], or by making the small intersection angles of the two beams as shown in Eq. (70.19) [122–124]. These approaches are ushering in a new era in scattering studies, and reactive applications of these methods hold promise for interesting new effects.

References

- Lee, Y.T.: *Science* **236**, 793 (1987)
- Gentry, W.R.: Chap. 3. In: Scoles, G. (ed.) *Atomic and Molecular Beam Methods*, p. 54. Oxford University Press, New York (1988)
- Anderson, J.B., Andres, R.P., Fenn, J.B.: *Adv. Chem. Phys.* **10**, 275 (1966)
- Miller, D.R.: Chap. 2. In: Scoles, G. (ed.) *Atomic and Molecular Beam Methods*, p. 14. Oxford University Press, New York (1988)
- Campargue, R.: *J. Phys. Chem.* **88**, 275 (1984)
- Davis, H.F., Kim, B., Johnston, H.S., Lee, Y.T.: *J. Phys. Chem.* **97**, 2172 (1993)
- Chen, P.: Chap. 8. In: Ng, C.Y., Baer, T., Powis, I. (eds.) *Unimolecular and Bimolecular Reaction Dynamics*, p. 371. John Wiley & Sons, New York (1994)
- Smalley, R.E.: *Laser Chem.* **2**, 167 (1983)
- Morse, M.D., Hopkins, J.B., Langridge-Smith, P.R.R., Smalley, R.E.: *J. Chem. Phys.* **79**, 5316 (1983)
- Hertel, I.V., Stoll, W.: *Adv. At. Mol. Phys.* **13**, 113 (1978)
- Pruett, J.G., Zare, R.N.: *J. Chem. Phys.* **64**, 1774 (1976)
- Bergmann, K., Hefter, U., Witt, J.: *J. Chem. Phys.* **72**, 4777 (1980)
- Bergmann, K.: Chap. 12. In: Scoles, G. (ed.) *Atomic and Molecular Beam Methods*. Oxford University Press, New York (1988)
- Broers, B., van Linden van den Heuvell, H.B., Noordam, L.D.: *Phys. Rev. Lett.* **69**, 2062 (1992)
- Perreault, W.E., Mukherjee, N., Zare, R.N.: *Nat. Chem.* **10**, 561 (2018)
- Avrillier, S., Raimond, J.M., Borde, C.J., Bassi, D., Scoles, G.: *Opt. Commun.* **39**, 311 (1981)
- Yang, X., Wodtke, A.M.: *J. Chem. Phys.* **92**, 116 (1990)
- Brouard, M., Duxon, S., Enriquez, P.A., Simons, J.P.: *J. Chem. Soc. Faraday Trans.* **89**, 1435 (1991)
- Sibener, S.J., Buss, R.J., Cassavecchia, P., Hirooka, T., Lee, Y.T.: *J. Chem. Phys.* **72**, 4341 (1980)
- Continetti, R.E., Balko, B.A., Lee, Y.T.: *J. Chem. Phys.* **93**, 5719 (1990)
- Brooks, P.R.: *Science* **193**, 11 (1976)
- Stolte, S.: *Ber. Bunsenges. Phys. Chem.* **86**, 413 (1982)
- Friedrich, B., Herschbach, D.R.: *Nature* **353**, 412 (1991)
- Bethlem, H.L., Berden, G., Meijer, G.: *Phys. Rev. Lett.* **83**, 1558 (1999)
- van de Meerakker, S.Y.T., Bethlem, H.L., Vanhaecke, N., Meijer, G.: *Chem. Rev.* **112**, 4828 (2012)
- Vanhaecke, N., Meier, U., Andrist, M., Meier, B.H., Merkt, F.: *Phys. Rev. A* **75**, 031402 (2007)
- Plomp, V., Gao, Z., Cremers, T., van de Meerakker, S.Y.T.: *Phys. Rev. A* **99**, 033417 (2019)
- Bassi, D., Boschetti, A., Scotoni, M., Zen, M.: *Appl. Phys. B.* **26**, 99 (1981)
- Neumark, D.M., Wodtke, A.M., Robinson, G.N., Hayden, C.C., Shobatake, K., Sparks, R.K., Schaefer, T.P., Lee, Y.T.: *J. Chem. Phys.* **82**, 3067 (1985)
- Faubel, M.: *Adv. At. Mol. Phys.* **19**, 345 (1983)
- Touw, T.R., Trischka, J.W.: *J. Appl. Phys.* **34**, 3635 (1963)
- Lee, Y.T., McDonald, J.D., LeBreton, P.R., Herschbach, D.: *Rev. Sci. Instrum.* **40**, 1402 (1969)
- Lee, Y.T.: Chap. 22. In: Scoles, G. (ed.) *Atomic and Molecular Beam Methods*, p. 563. Oxford University Press, New York (1988)
- Center, R.E., Mandl, A.: *J. Chem. Phys.* **57**, 4104 (1972)
- Greene, C.H., Zare, R.N.: *J. Chem. Phys.* **78**, 6741 (1983)
- Case, D.A., McLelland, G.M., Herschbach, D.R.: *Mol. Phys.* **35**, 541 (1978)
- Hall, G., Houston, P.: *Ann. Rev. Phys. Chem.* **40**, 375 (1989)
- Sonnenfroh, D.M., Liu, K.: *Chem. Phys. Lett.* **176**, 183 (1991)
- Billy, N., Girard, B., Gouédard, G., Vigué, J.: *Mol. Phys.* **61**, 65 (1987)
- Zare, R.N., Dagdigian, P.J.: *Science* **185**, 739 (1974)
- Altcorn, R., Zare, R.N.: *Ann. Rev. Phys. Chem.* **35**, 265 (1984)
- Joswig, H., Andresen, P., Schinke, R.: *J. Chem. Phys.* **85**, 1904 (1986)
- Mestdagh, J.M., Visticot, J.P., Suits, A.G.: In: Liu, K., Wagner, W. (eds.) *The Chemical Dynamics and Kinetics of Small Radicals*. World Scientific, Singapore (1994)
- Jons, S.D., Shirley, J.E., Vonk, M.T., Giese, C.F., Gentry, W.R.: *J. Chem. Phys.* **92**, 7831 (1992)
- Feldman, D.L., Lengel, R.K., Zare, R.N.: *Chem. Phys. Lett.* **52**, 413 (1977)
- Marinero, E.E., Rettner, C.T., Zare, R.N.: *J. Chem. Phys.* **80**, 4142 (1984)
- Schnieder, L., Seekamp-Rahn, K., Wrede, E., Welge, K.H.: *J. Chem. Phys.* **107**, 6175 (1997)
- Strazisar, B., Lin, C., Davis, H.F.: *Science* **290**, 958 (2000)
- Schneider, L., Seekamp-Rahn, K., Liedeker, F., Stewe, H., Welge, K.H.: *Farad. Discuss. Chem. Soc.* **91**, 259 (1991)
- Yang, X.: *Int. Rev. Phys. Chem.* **24**, 37 (2005)
- Yang, X., Zhang, D.H.: *Acc. Chem. Res.* **41**, 981 (2008)
- Wang, T., Yang, T., Xiao, C., Sun, Z., Zhang, D., Yang, X., Weichman, M.L., Neumark, D.M.: *Chem. Soc. Rev.* **47**, 6744 (2018)
- Comsa, G., David, R., Schumacher, B.J.: *Rev. Sci. Instrum.* **52**, 789 (1981)
- Entemann, E., Herschbach, D.R.: *J. Chem. Phys.* **55**, 4872 (1971)
- Buss, R.: Ph. D. thesis. University of California, Berkeley (1972)
- Pack, R.T.: *J. Chem. Phys.* **81**, 1841 (1984)
- Suits, A.G., Hou, H., Davis, H.F., Lee, Y.T.: *J. Chem. Phys.* **95**, 8207 (1991)
- Faubel, M., Kohl, K.-H., Toennies, J.P., Tang, K.T., Yung, Y.Y.: *Faraday Discuss. Chem. Soc.* **73**, 205 (1982)
- Continetti, R.E., Balko, B.A., Lee, Y.T.: *J. Chem. Phys.* **93**, 5719 (1990)
- Warnock, T.T., Bernstein, R.B.: *J. Chem. Phys.* **49**, 1878 (1968)
- Helbing, R.K.B.: *J. Chem. Phys.* **48**, 472 (1968)
- Toennies, J.P.: Chap. 5. In: Jost, W. (ed.) *Physical Chemistry, an Advanced Treatise*, vol. VIA, Academic Press, New York (1974)
- Faubel, M., Toennies, J.P.: *Adv. At. Mol. Phys.* **13**, 229 (1978)
- Chandler, D.W., Houston, P.L.: *J. Chem. Phys.* **87**, 1445 (1987)
- Eppink, A.T.J.B., Parker, D.H.: *Rev. Sci. Instrum.* **68**, 3457 (1997)
- Bontuyan, L.S., Suits, A.G., Houston, P.L., Whitaker, B.J.: *J. Phys. Chem.* **97**, 6342 (1993)

67. Kitsopoulos, T.A., Baldwin, D.P., Buntine, M.A., Zare, R.N., Chandler, D.W.: *Science* **260**, 1605 (1993)
68. Strickland, R.N., Chandler, D.W.: *Appl. Opt.* **30**, 1811 (1990)
69. Castleman, K.R.: *Digital Image Processing*. Prentice Hall, Englewood Cliffs (1979)
70. Dribinski, V., Ossadtchi, A., Mandelshtam, V.A., Reisler, H.: *Rev. Sci. Instrum.* **73**, 2634 (2002)
71. Gebhardt, C.R., Rakitzis, T.P., Samartzis, P.C., Ladopoulos, V., Kitsopoulos, T.N.: *Rev. Sci. Instrum.* **72**, 3848 (2001)
72. Townsend, D., Minitti, M.P., Suits, A.G.: *Rev. Sci. Instrum.* **74**, 2530 (2003)
73. Lin, J.J., Zhou, J., Shiu, W., Liu, K.: *Rev. Sci. Instrum.* **74**, 2495 (2003)
74. Thompson, J.O.F., Amarasinghe, C., Foley, C.D., Suits, A.G.: *J. Chem. Phys.* **147**, 013913 (2017)
75. Thompson, J.O.F., Amarasinghe, C., Foley, C.D., Rombes, N., Gao, Z., Vogels, S.N., van de Meerakker, S.Y.T., Suits, A.G.: *J. Chem. Phys.* **147**, 074201 (2017)
76. Willis, P.A., Stauffer, H.U., Hinrichs, R.Z., Davis, H.F.: *Rev. Sci. Instrum.* **70**, 2606 (1999)
77. Joalland, B., Shi, Y., Estillore, A.D., Kamasah, A., Mebel, A.M., Suits, A.G.: *J. Phys. Chem. A* **118**, 9281 (2014)
78. Joalland, B., Shi, Y., Kamasah, A., Suits, A.G., Mebel, A.M.: *Nat. Comm.* **5**, 4064 (2014)
79. Li, H., Kamasah, A., Matsika, S., Suits, A.G.: *Nat. Chem.* **11**, 123 (2019)
80. Levine, R.D., Bernstein, R.B.: *Molecular Reaction Dynamics and Chemical Reactivity*. Oxford University Press, New York (1987). Chap. 3
81. Farrar, J.M., Schafer, T.P., Lee, Y.T.: In: Kestin, J. (ed.) *AIP Conference Proceedings No. 11, Transport Phenomena*. American Institute of Physics, New York (1973)
82. Schinke, R., Bowman, J.: In: Bowman, J. (ed.) *Molecular Collision Dynamics*. Springer, Berlin (1983)
83. Bosanac, S.: *Phys. Rev. A* **22**, 2617 (1980)
84. Vogels, S.N., Onvlee, J., Chefdeville, S., van der Avoird, A., Groenenboom, G.C., van de Meerakker, S.Y.T.: *Science* **350**, 787 (2015)
85. von Zastrow, A., Onvlee, J., Vogels, S.N., Groenenboom, G.C., van der Avoird, A., van de Meerakker, S.Y.T.: *Nat. Chem.* **6**, 216 (2014)
86. Heid, C.G., Walpole, V., Brouard, M., Jambrina, P.G., Aoiz, F.J.: *Nat. Chem.* **11**, 662 (2019)
87. Hall, G., Liu, K., McAuliffe, M.J., Giese, C.F., Gentry, W.R.: *J. Chem. Phys.* **81**, 5577 (1984)
88. Yang, X., Wodtke, A.: *Int. Rev. Phys. Chem.* **12**, 123 (1993)
89. Hertel, I.V.: *Adv. Chem. Phys.* **50**, 475 (1982)
90. Breckenridge, W.H., Umamoto, H.: *Adv. Chem. Phys.* **50**, 325 (1982)
91. Suits, A.G., de Pujo, P., Sublemontier, O., Visticot, J.P., Berlande, J., Cuvellier, J., Gustavsson, T., Mestdagh, J.M., Meynadier, P., Lee, Y.T.: *J. Chem. Phys.* **97**, 4094 (1992)
92. Los, J., Kleyn, A.W.: Chap. 8. In: Davidovits, P., McFadden, D.L. (eds.) *Alkali Halide Vapors*. Academic Press, New York (1979)
93. Gislason, E.A.: Chap. 13. In: Davidovits, P., McFadden, D.L. (eds.) *Alkali Halide Vapors*. Academic Press, New York (1979)
94. Olson, R.E., Smith, F.T., Bauer, E.: *Appl. Opt.* **10**, 1848 (1971)
95. Miller, W.B., Safran, S.A., Herschbach, D.R.: *Discuss. Faraday Soc.* **44**, 108 (1967)
96. Miller, W.B.: Ph.D. thesis. Harvard University, Cambridge (1969)
97. Farrar, J.M., Lee, Y.T.: *J. Chem. Phys.* **65**, 1414 (1976)
98. Buss, R.J., Casavecchia, P., Hirooka, T., Lee, Y.T.: *Chem. Phys. Lett.* **82**, 386 (1981)
99. Werner, H.J., Kallay, M., Gauss, J.: *J. Chem. Phys.* **128**, 034305 (2008)
100. Qiu, M., Ren, Z., Che, L., Dai, D., Harich, S.A., Wang, X., Yang, X., Xu, C., Xie, D., Gustafsson, M., Skodje, R.T., Sun, Z., Zhang, D.H.: *Science* **311**, 1440 (2006)
101. Ren, Z., Che, L., Qiu, M., Wang, X., Dong, W., Dai, D., Wang, X., Yang, X., Sun, Z., Fu, B., Lee, S.-Y., Xu, X., Zhang, D.H.: *Proc. Natl. Acad. Sci. U. S. A.* **105**, 12662 (2008)
102. Wang, T., Yang, T., Xiao, C., Sun, Z., Zhang, D., Yang, X., Weichman, M., Neumark, D.M.: *Chem. Soc. Rev.* **47**, 6744 (2018)
103. Yuan, D., Guan, Y., Chen, W., Zhao, H., Yu, S., Luo, C., Tan, Y., Xie, T., Wang, X., Sun, Z., Zhang, D.H., Yang, X.: *Science* **362**, 1289 (2018)
104. Zhou, J., Lin, J.J., Liu, K.: *J. Chem. Phys.* **119**, 8289 (2003)
105. Pan, H., Liu, K., Caracciolo, A., Casavecchia, P.: *Chem. Soc. Rev.* **46**, 7517 (2017)
106. Liu, K.: *Annu. Rev. Phys. Chem.* **67**, 91 (2016)
107. Hudgens, J.W., DiGiuseppe, T.G., Lin, M.C.: *J. Chem. Phys.* **79**, 571 (1983)
108. Zhang, W., Kawamata, H., Liu, K.: *Science* **325**, 303 (2009)
109. Wang, F., Lin, J.S., Liu, K.: *Science* **331**, 900 (2011)
110. Pan, H., Wang, F., Czako, G., Liu, K.: *Nat. Chem.* **9**, 1175 (2017)
111. Liu, K.: *Annu. Rev. Phys. Chem.* **67**, 91 (2016)
112. Blank, D.A., Hemmi, N., Suits, A.G., Lee, Y.T.: *Chem Phys* **231**, 261 (1998)
113. Sun, Y.L., Huang, W.J., Lee, S.H.: *J. Phys. Chem. A* **121**, 9687 (2017)
114. Willis, P.A., Stauffer, H.U., Hinrichs, P.Z., Davis, H.F.: *J. Chem. Phys.* **108**, 2665 (1998)
115. Proctor, D., Davis, H.F.: *Proc. Natl. Sci. U. S. A* **105**, 12673 (2008)
116. Ahmed, M., Peterka, D.S., Suits, A.G.: *Phys. Chem. Chem. Phys.* **2**, 861 (2000)
117. Capozza, G., Segoloni, E., Lenori, F., Volpi, G.G., Casavecchia, P.: *J. Chem. Phys.* **120**, 4557 (2004)
118. Casavecchia, P., Leonori, F., Balucani, N.: *Int. Rev. Phys. Chem.* **34**, 161 (2015)
119. van de Meerakker, S.Y.T., Bethlem, H.L., Vanhaecke, N., Meijer, G.: *Chem. Rev.* **112**, 4828 (2012)
120. Hesnson, A.B., Gersten, S., Shagam, Y., Narevicius, J., Narevicius, E.: *Science* **338**, 234 (2012)
121. Jankunas, J., Osterwalder, A.: *Ann. Rev. Phys. Chem.* **66**, 241 (2015)
122. Chefdeville, S., Kalugina, Y., van de Meerakker, S.Y.T., Naulin, C., Lique, F., Costes, M.: *Science* **341**, 1094 (2013)
123. Bergeat, A., Onvlee, J., Naulin, C., van der Avoird, A., Costes, M.: *Nat. Chem.* **7**, 349 (2015)
124. Amarasinghe, C., Li, H., Perera, C.A., Besemer, M., van der Avoird, A., Groenenboom, G.C., Xie, C., Guo, H., Suits, A.G.: *J. Phys. Chem. Lett.* **10**, 2422 (2019)



Hongwei Li Hongwei Li received his PhD in 2016 from the University of Pennsylvania. He then joined the Suits group at the University of Missouri as a postdoctoral fellow. He is now a professor at Dalian Institute of Chemical Physics, CAS, China. His research focuses on generating different radical sources to investigate their reaction dynamics and kinetics with other molecules.



Arthur G. Suits Arthur G. Suits obtained his PhD in 1991 with Yuan T. Lee at Berkeley. He has held positions at Lawrence Berkeley and Brookhaven National Laboratories and faculty positions at Stony Brook and Wayne State. He is now Curators' Distinguished Professor of Chemistry at the University of Missouri. He has devoted his career to studying the detailed dynamics of elementary chemical reactions.



James M. Farrar

Contents

71.1	Introduction	1035
71.2	Specification of Cross Sections	1036
71.3	Instrumentation	1037
71.3.1	Reactant Ion Preparation	1037
71.3.2	Reactant Mass Selection	1037
71.3.3	The Collision Region	1038
71.3.4	Product Detection	1038
71.3.5	Imaging Methods in Velocity Space	1039
71.4	Kinematics	1039
71.5	Recent Examples of State-Resolved Measurements	1040
71.5.1	Velocity-Angle Differential Cross Sections $\sigma(V'_{\text{rel}}, \theta V_{\text{rel}})$	1040
71.5.2	State-Resolved Cross Sections $\sigma(n' n, V_{\text{rel}})$ and Rate Constants $k(n' n, T)$	1040
71.6	The Future of the Field	1042
	References	1042

Abstract

Ionized matter is ubiquitous in Nature, occurring over a large range of length scales and energy densities, in environments ranging from plasmas to condensed phases. In the gas phase, collisions that occur between ions and neutral atoms and molecules provide important microscopic routes for the formation of species that influence the macroscopic behavior of chemical and physical systems such as flames and planetary atmospheres. The term “ion–molecule” reactions generally applies to an entire class of gas phase collision phenomena in which electrons and atoms can be transferred among the approaching reactants to form products with new chemical bonds and distributions of charge. Such reactions are generally regarded as low energy phenomena, occurring over a collision energy range from thermal up to several eV.

J. M. Farrar (✉)
Dept. of Chemistry, University of Rochester
Rochester, NY, USA
e-mail: farrar@chem.rochester.edu

Keywords

state-resolved products · mass spectrometry · cross section · reaction dynamics · total cross section · flux distribution · vibrational state · total reaction cross section · collision complex

71.1 Introduction

Mass spectrometry has played a crucial role in the discovery and the study of ion–molecule reactions. At the beginning of the twentieth century, *J.J. Thomson* discovered that operating his positive ray parabola apparatus in a hydrogen atmosphere produced signals at a mass to charge ratio of 3, which he correctly attributed to the species H_3 [1]. Later experiments by *Hogness* and *Lunn* [2] employing mass spectrometry with a high-pressure ion source demonstrated unequivocally that this species was produced by a very fast reaction between the primary ionization product H_2^+ and molecular hydrogen.

The pioneering work of *Tal'rose* in Moscow on ion formation in methane gas irradiated by electrons [3, 4] initiated the study of ion–molecule reactions as a distinct discipline within the field of chemical kinetics and established the central role of such reactions in radiation chemistry. The same reactions were also observed by *Stevenson* and coworkers [5–7] in the ion source of a laboratory mass spectrometer. Their analysis [8] via an orbiting collision model [9] predicted that ion–molecule reactions proceed with encounter-controlled rates in excess of $10^{-9} \text{ cm}^3 \text{ molecule}^{-1} \text{ s}^{-1}$, corresponding to thermal energy cross sections of magnitude $10^{-16}–10^{-15} \text{ cm}^2$. This recognition and its confirmation by experiment has made ion–molecule reactions critical contributors to the modeling of planetary atmospheres, interstellar chemistry, and reactive plasmas. Studies of chemical dynamics that focus on how reactant energy is consumed and how available energy appears in products have highlighted the

importance of scattering processes and the critical role that features of multidimensional potential surfaces play to control reaction dynamics.

This chapter builds on the relationship between ion–molecule reactions and advances in mass spectrometry. Under single-collision conditions, which may be achieved when a collimated ion beam interacts with neutral reactants also formed into a beam, the experimental data for product formation take the form of one of a number of quantities called “cross sections”. In its simplest, phenomenological form, the total cross section σ parameterizes the attenuation of an ion beam with a collision gas of number density n and interaction length L according to Eq. (71.1)

$$\sigma = (nL)^{-1} \ln \frac{I_0}{I} . \quad (71.1)$$

In this expression, I_0 denotes the initial ion beam intensity, and I is the intensity measured after attenuation. Although Eq. (71.1) defines a cross section including all processes that scatter reactant ions from the beam, it is useful to think of the more specific cross section for chemical reaction as a major contributor to σ , providing a means to estimate the total rate of product formation

$$\frac{dN_{\pm}}{dt} = \sigma V_{\text{rel}} n_1 n_2 \Delta V . \quad (71.2)$$

In this expression, σ is the total reaction cross section, V_{rel} is the relative speed of the collision partners, n_1 is the number density of the primary (ion) beam, n_2 is the number density of the collision gas, and ΔV is the collision volume defined by the overlap of the ion beam with the target gas. This expression can be converted to a particularly useful form for computing signal levels from experimental parameters such as ion beam current I_{\pm} , cross section σ , neutral number density n_2 , and attenuation length L as follows

$$\frac{dN_{\pm}}{dt} = 6.25 \times 10^{-7} \sigma I_{\pm} n_2 L , \quad (71.3)$$

where σ is expressed in \AA^2 , I_{\pm} in units of 10^{-9} A, n_2 in cm^{-3} , and L , the attenuation length, in cm. An ion beam of current 1×10^{-9} A, intersecting a target of length 1 cm at a pressure of 10^{-3} Torr, corresponding to a number density of $3.5 \times 10^{13} \text{ cm}^{-3}$, and reacting with a cross section of 1 \AA^2 yields a total rate of product formation of $2 \times 10^7 \text{ s}^{-1}$. The cross section σ used to estimate total product formation rates is phenomenological, and in order to understand measurements, we need to define a hierarchy of cross sections based on the incident velocities and quantum states of reactants, as well as the quantum states, relative velocities, and scattering angles of products. Experimental conditions

may also require us to consider quantities that are averages over initial states, sums over final states, or are averaged over initial and final velocity distributions. The next section provides assistance in interpreting cross sections for these less well-specified processes.

71.2 Specification of Cross Sections

An “ideal” experiment is one in which reactants with well-specified quantum numbers, collectively denoted \mathbf{n} , collide at a precisely defined relative velocity V , resolving products in quantum states \mathbf{n}' scattered through center of mass scattering angle θ . Technological advances, particularly in laser preparation of quantum state-selected reactants and in state-specific product detection, have made this goal a near-reality in favorable circumstances, particularly in neutral–neutral interactions, e.g., in experiments on $\text{H} + \text{H}_2$ and its isotopic variants. Most experiments, however, require the experimenter to settle for a less precisely defined system in which one carries out partial averages over initial conditions or partial summations over final states. Figure 71.1 shows that the detailed differential cross section described above and denoted $\sigma(\mathbf{n}', \theta | \mathbf{n}, V_{\text{rel}})$ can be averaged over scattering angle to yield a state-to-state cross section at a fixed collision velocity V_{rel} denoted as $\sigma(\mathbf{n}' | \mathbf{n}, V_{\text{rel}})$. Averaging this cross section over a Maxwell–Boltzmann distribution of molecular speeds at a specified temperature T yields the detailed state-to-state rate constant $k(\mathbf{n}' | \mathbf{n}, T)$, while summation over the final states \mathbf{n}' and averaging over the initial states \mathbf{n} yields the thermal rate constant $k(T)$. The rate constant is a thermally averaged, multiple-collision property and not the subject of this chapter, although $k(T)$ plays an important role in modeling applications. Less detailed differential cross sections $\sigma(\mathbf{n}', \theta | \mathbf{n}, V_{\text{rel}})$ arise from averaging over initial states \mathbf{n} and summing over final states \mathbf{n}' to yield cross sections dependent on product velocity V'_{rel} and scattering angle at fixed collision velocity, denoted by $\sigma(V'_{\text{rel}}, \theta | V_{\text{rel}})$. An average over scattering angles and product velocities yields the velocity dependent total cross section $\sigma(V_{\text{rel}})$, and its average over the Maxwell–Boltzmann reactant speed distribution produces the thermal rate constant $k(T)$ once again. As one moves from more highly averaged quantities to the detailed cross sections, more sophisticated reactant preparation and product detection schemes are required to extract the desired information content. More highly specified cross sections lead to lower signal levels as defined in Eq. (71.3). The subject of this chapter will be a discussion of the various cross sections σ shown in Fig. 71.1, emphasizing new experimental methods and results that focus on the determination of cross sections for state-selected reactants and for state-to-state processes.

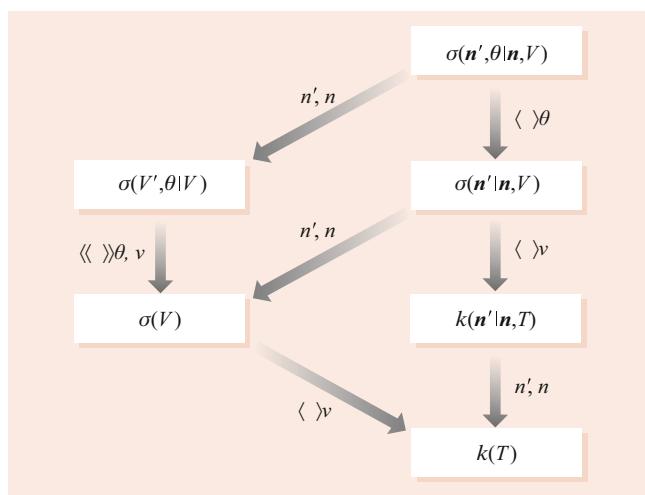


Fig. 71.1 Relationships among differential and total cross sections, and rate constants. *Brackets* denote averages over indicated variables or averages over initial states and summations over final states

71.3 Instrumentation

Instrumentation to study ion–molecule reactions is quite diverse, and numerous literature sources are available for further discussion [10, 11]. A typical instrument has an ionization source that may allow for some degree of reactant state specification, a primary mass selector, a collision region, and a detector, consisting of a mass spectrometer or employing a spectroscopic technique allowing product quantum state and molecular identification. The “traditional” method for determining high-resolution/high-information content cross sections employs continuous ion and neutral beams in a crossed beam configuration. Product detection with an energy/mass analyzer that rotates about the collision center allows pointwise construction of the velocity space distribution of reaction products. In principle, with adequate resolution, product vibrational state-resolved angular distributions may be measured. Experiments conducted at Rochester on the $\text{O}^- + \text{D}_2$ reactive system [12, 13] and at Freiburg on the $\text{H}^- + \text{D}_2$ system [14, 15] have approached this limit. However, except for optical detection of reaction products, rotational state resolution has yet to be achieved. These limitations reflect the low signal levels associated with increasing resolution.

Significant progress in extending the scope of high-resolution experiments has come from the application of pulsed methods of reactant preparation and pulsed techniques for product detection. Matching the time structures for reactant formation and product detection has yielded promising results for measuring cross sections with enhanced information content and for extending the range of chemical complexity of reactants and products. Elegant methods employing ions trapped by electrodynamic poten-

tials and probed optically have also led to major advances in the quest to measure state-to-state cross sections.

71.3.1 Reactant Ion Preparation

Ion–molecule reactions were the first chemical reactions for which initial quantum state selection was achieved. Photoionization has been the method of choice for vibrational and vibrational–rotational state selection of molecular ions. Historically, single-photon VUV ionization methods played a special role in illustrating fundamental concepts of reactivity. The selective role of reactant vibrational excitation in overcoming potential energy barriers to endothermic chemical reactions was first demonstrated in the pioneering work of *Chupka* and coworkers on the $\text{H}_2^+ + \text{He}$ system [16]. Many more studies on systems of comparable complexity have followed; the recent development of pulsed-field ionization – photoelectron secondary ion coincidence (PFI-PESICO) on this same system and others [17, 18] provides a picture of the high resolution that is now accessible to simple ion–molecule systems. In systems of greater complexity, *Anderson* and colleagues [19–21] applied guided beam methods to reactions of polyatomic ions prepared by photoionization to demonstrate “mode-selective” chemistry. *Ng* and coworkers demonstrated recently [22] that single rotational states in H_2O^+ can be prepared and that significant dynamical effects can be observed in the reactions with D_2 .

Laser-based multiphoton ionization methods have also been applied to the production of state-selected ions. Measurements of photoelectron spectra of emitted electrons are often necessary to assess the vibrational state purity of the photoions, as demonstrated by *Zare* and coworkers [23] on NH_3^+ prepared in the ν_2 umbrella bending mode. Although such methods are, in principle, capable of producing usable populations of state-selected ions, examples are relatively few in number [20, 24]. State selection of N_2^+ , for example, to produce rovibronic ground-state ions has been accomplished by $(2 + 1)$ multiphoton ionization of N_2 via the $a''^1 \sum_g^+ v' = 0, J' = 2$ intermediate state [25].

Less selective ionization methods forming a range of internally excited states have been teamed with ion trapping methods that contain excited ions in a small volume with a cold collision gas to cool them to the lowest vibrational state. Examples will be discussed below.

71.3.2 Reactant Mass Selection

“Traditional” mass selection methods using deflecting fields are continuous in nature. To complement the quantum-state selection methods described above, which are intrinsically pulsed, time-of-flight methods are ideally suited to add mass

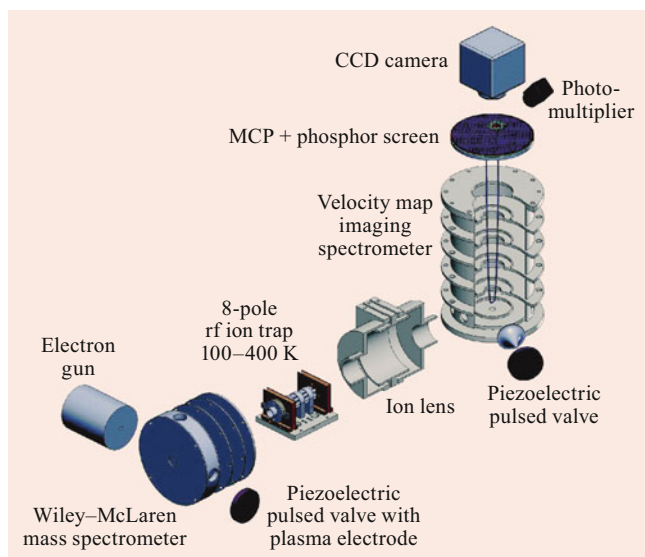


Fig. 71.2 Schematic view of the Innsbruck ion–molecule crossed-beam imaging spectrometer. (Reprinted from [27] with permission from the PCCP Owner Societies)

selection to reactant ion preparation schemes. The standard Wiley–McLaren time-of-flight (TOF) method [26] produces a train of spatially compressed, time-separated ions with the proper time structure to mate with pulsed methods for neutral reactant preparation and time-dependent methods for product detection. *Wester* and coworkers have combined these methods in instrumentation in the last few years [27]. Figure 71.2 shows a schematic of this instrument, illustrating the formation of a pulsed beam of mass selected ions by a Wiley–McLaren TOF mass spectrometer, cooling of the ions in a multipole trap, and injection of those ions into the collision region along with pulsed neutral reactants. The collision region, the dimensions of which are controlled by the spatial extent of the overlap of the pulsed reactant beams, is monitored by a velocity map imaging (VMI) detector, which is also intrinsically pulsed. The operation of such a detection scheme will be discussed in a later section.

71.3.3 The Collision Region

The potential difference between the volume where ions are created and where they undergo reaction generally determines the incident collision energy of an ion–molecule system. In a “traditional” experiment with continuous beams, the collision volume is typically held at a constant potential, most often ground potential. With pulsed beams, the collision volume can be held at ground potential when the pulsed reactant beams intersect but can be pulsed to a nonzero potential to extract product ions into an imaging detector, for example. Constraints on such extraction pulses will be discussed in a later section.

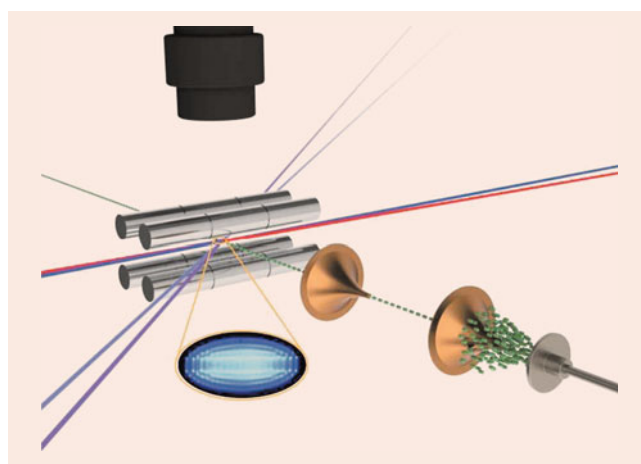


Fig. 71.3 Collision- and state-controlled ion–molecule reactions. Schematic of the experimental setup of the Basel instrument. N_2^+ ions were prepared in their rotational–vibrational ground state using a threshold-photoionization scheme and were sympathetically cooled into a Coulomb crystal of laser-cooled Ca^+ ions (*inset*). The state-selected N_2^+ ions were exposed to rotationally cold neutral N_2 molecules introduced into the ion trap via a doubly skimmed supersonic molecular beam. (Reproduced from [11] by permission of John Wiley & Sons Ltd)

Significant progress in the study of ion–molecule collisions has also been achieved by allowing reaction to occur within the volume of a multipole ion trap such that all product ions are collected and analyzed. *Willitsch* and collaborators [11, 25, 28] have made noteworthy use of the idea of “sympathetic cooling”, as shown in Fig. 71.3, to produce state-selected ions whose reactions can be initiated by pulsing a reactant gas into the trap. Further details are discussed below.

71.3.4 Product Detection

Mass spectrometry and angle-resolved product energy and mass analysis have opened the door to cross section measurements of product-state resolved ion–molecule reactions. The ability to determine product state-resolved cross sections via product kinetic energy analysis is determined by the kinetic energy resolution of the detection system. The majority of extant crossed-beam experimental studies construct three-dimensional velocity space distributions with a series of one-dimensional sections through the full distribution such that, in any interval of time, only a single detection element in velocity space can be measured. Typically, kinetic energy distributions at N energy points are collected at M different scattering angles, yielding a dataset of dimension $N \times M$. Acquisition of the product signal occurs in a pointwise manner, in which any given measurement interval only collects signals in a single element of the velocity space. The total signal level calculated by Eq. (71.2) must be distributed among all $N \times M$ elements of velocity space,

providing a practical limit on this method's abilities. As described below, imaging methods allow all $N \times M$ velocity space elements to be measured in a single time window.

71.3.5 Imaging Methods in Velocity Space

Originally proposed in the late 1980s by *Paul Houston* and *David Chandler* [29] to study the velocity distributions of the products of pulsed laser photolysis of molecules such as CH_3I , methods for reconstructing velocity space flux distributions have undergone significant development since that time. The velocity focusing method of *Parker* and *Ep-pink* [30] is a particularly important improvement: the use of an additional electrostatic lens after the extraction region allows all points in the plane of the intersecting beams with the same V_x and V_y components to be imaged to a single point. Such a geometry is particularly useful in crossed beam applications. In this geometry, two pulsed beams of reactants intersect in a small volume, and the reactive products separate with their characteristic velocities. The locus of points in the center of the mass coordinates for each product quantum state is distributed, perhaps nonuniformly, on the surface of a sphere. After the beams intersect, a repeller plate pushes the ions up a drift tube. During this drift time, a given product-state sphere grows in coordinate space, until the sphere is flattened on the MCP detector. Spheres associated with individual quantum states of a single product of unique mass are “nested”, having a common origin, and produce concentric rings of intensity on the MCP detector. Figure 71.4 shows a schematic of an instrument that illustrates the imaging prin-

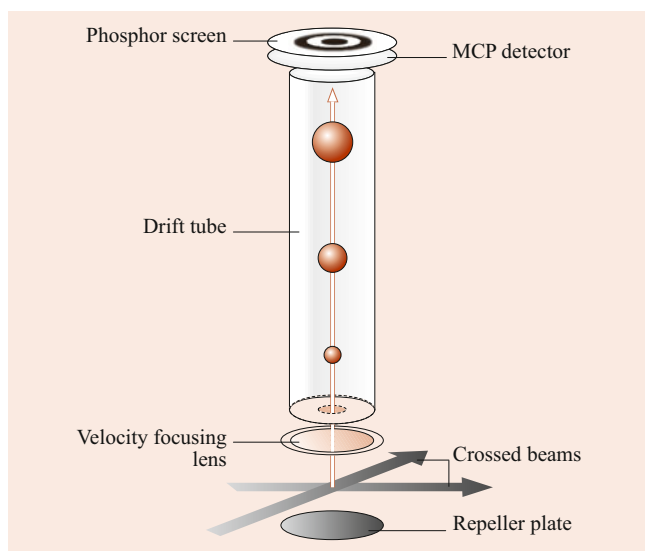


Fig. 71.4 Schematic of crossed beam imaging instrument. Product flux extracted from the collision volume with a single center-of-mass speed describes a sphere in velocity space. This flux is projected onto a multichannel plate/phosphor screen detector and recorded with a CCD camera

ciple. Products with different masses describe spheres with different delay times, providing mass-selective detection of products via temporal gating of the MCP detector. Electrons from the MCP are accelerated into a phosphor screen, the light from which is detected by a CCD camera. The signal detected on the phosphor screen is a two-dimensional representation of the three-dimensional distribution. One method for recovering the true three-dimensional distribution employs inverse Abel transformation of the data [31]. Time-sliced methods have also been developed that gate the imaging detector such that slices of the product spheres can be analyzed [32]. The azimuthal symmetry of the flux distribution about the relative velocity vector is sufficient to ensure that equatorial slices represent the full distribution.

One limitation of the simplest version of VMI is its inherent two-dimensional focusing capability. The thickness of the collision volume along the focusing direction can degrade resolution. Three-dimensional imaging methods that correlate arrival position and time have been applied successfully to reduce this “chromatic aberration” contribution to this degradation of resolution [27, 33].

71.4 Kinematics

The sliced or inverse Abel-transformed images represent product ion flux in laboratory Cartesian velocity coordinates [34, 35] (v_x, v_y), and a simple velocity shift to the center of mass

$$\mathbf{u} = \mathbf{v} - \mathbf{C} \quad (71.4)$$

yields barycentric distributions in Cartesian coordinates, symbolized by $P(u_x, u_y)$. Barycentric recoil speed and scattering angle are given by the following expressions

$$u = (u_x^2 + u_y^2)^{1/2}, \quad (71.5)$$

$$\theta = \tan^{-1} \frac{u_y}{u_x}. \quad (71.6)$$

The relationship between Cartesian and polar flux intensity is given by the following expression

$$I_{\text{c.m.}}(u, \theta) = u^2 P(u_x, u_y). \quad (71.7)$$

Product angular and kinetic energy distributions, computed by averaging the flux distribution over recoil speed and scattering angle, respectively, and denoted by the bracket notation below, require integration over the Cartesian flux. The angle-averaged relative translational energy distribution of products, $P(E'_T)$, is given by the following expression

$$\langle P(E'_T) \rangle_\theta = \int_0^\pi d\theta \sin \theta u P(u_x, u_y). \quad (71.8)$$

Integration over specific angular regions provides a means to assess how energy disposal may depend on scattering angle. For example, the angular distribution for a particular product may arise from a superposition of long-lived complex decay with flux distributed symmetrically about the relative velocity vector, and direct reaction, with an asymmetric flux distribution.

The speed-averaged angular distribution is computed as follows

$$\langle g(\theta) \rangle_u = \int_0^\infty du u^2 P(u_x, u_y). \quad (71.9)$$

The kinetic energy and angular distributions described in Eqs. (71.8) and (71.9) are the primary quantities that are subject to comparison with theory. Depending on the resolution of a given experiment, the limits of integration in Eq. (71.8), for example, can be controlled to allow relative vibrational state populations to be extracted from experimental data. Most often, dynamical calculations in the form of quasi-classical trajectories or an appropriate approximation in quantum theory can be undertaken with a parametrized potential energy surface, in order to probe a particular region of the surface or to test a particular dynamical approximation.

71.5 Recent Examples of State-Resolved Measurements

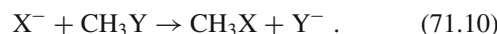
The study of ion–molecule reactions in the context of scattering or collision phenomena is a technologically dependent activity. As single-collision methods have advanced from crossed-beam geometries to configurations in which reactant states may be controlled and/or selected, and products can be detected state-selectively, either kinematically or optically, information content has increased, and tests of theory have become more stringent. In the final section of this chapter, examples of a few of the more recent and advanced experiments will be presented. They should be viewed as a representative sampling rather than an exhaustive compilation of recent advances in the field of ion–molecule reactions.

71.5.1 Velocity-Angle Differential Cross Sections $\sigma(V'_{\text{rel}}, \theta | V_{\text{rel}})$

Implementing VMI detection in a crossed beam experiment with a continuous ion beam and a pulsed neutral beam has led to a number of new results. The $\text{C}^+ + \text{NH}_3$ reaction, important in circumstellar shells, has been studied in the author's lab, [36] providing one of the first examples of a system in

which more than a single reaction product has been detected by VMI. Figure 71.5 shows images for the NH_3^+ product and the HCNH^+ product at a collision energy of 1.5 eV. The NH_3^+ charge transfer product appears in velocity space in the vicinity of the neutral NH_3 beam, consistent with long-range electron transfer that results in negligible momentum transfer to the ionic product. The formation of HCNH^+ around the centroid indicates that this product arises from a long-lived collision complex. Product images are readily separated in time since the extraction process acts like a TOF mass spectrometer, with the lower mass NH_3^+ products arriving at the detection plane before the heavier HCNH^+ products. The detector is gated to allow only a single product to be imaged at a time. This instrument has also been used with free-radical reactants, yielding the first crossed beam VMI studies of ion-radical reactions [37, 38].

Wester and coworkers [27] have used the instrument shown in Fig. 71.2 to study ion–molecule interactions with an emphasis on increased reactant complexity. A long-standing interest of the group is the second-order nucleophilic $\text{S}_{\text{N}}2$ reaction of the form



Among the recent examples from the group is a series of studies in which $\text{X} = \text{OH}$ and $\text{Y} = \text{I}$, with the incoming nucleophile OH^- solvated by a variable number of H_2O molecules [39]. Such studies are critical in making the connection between the gas phase and the solution phase in which nucleophilic substitution is a benchmark reaction in organic chemistry. Figure 71.6 shows product images for the $\text{I}^- (\text{H}_2\text{O})_{1,2}$ products of the reactions



at collision energies of 0.5 and 1.5 eV [27]. The images show significant dynamical signatures that depend both on collision energy and degree of solvation. Most important, the data provide evidence of the degree of chemical complexity that may be probed in contemporary experiments.

71.5.2 State-Resolved Cross Sections $\sigma(n'|n, V_{\text{rel}})$ and Rate Constants $k(n'|n, T)$

Measurements of state-to-state total cross sections as a function of initial relative velocity have advanced significantly in the past decade. Improved resolution in photoionization, advances in methods for confinement of ions in multipole traps, and the use of sympathetic cooling techniques have been responsible for these advances.

Until recently, photoionization methods were limited to elucidation of the role of reactant vibrational excitation in

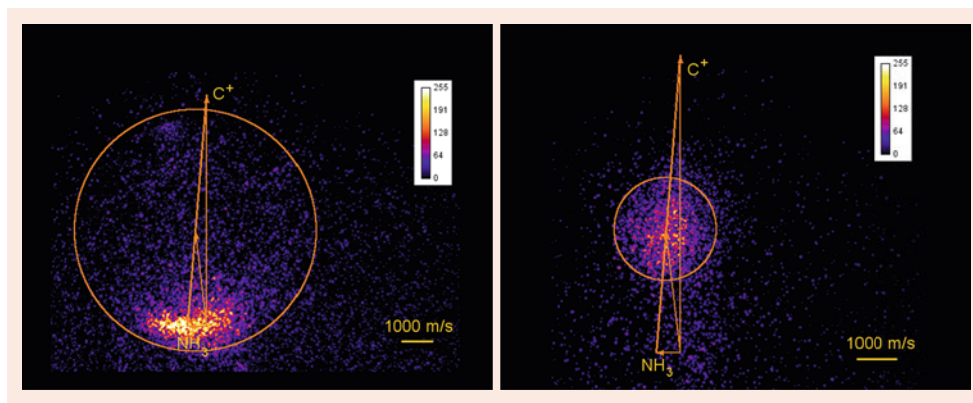


Fig. 71.5 Product images for charge transfer and C–N bond formation from the $C^+ + NH_3$ reaction, superimposed on the most probable Newton diagrams at a collision energy of 1.5 eV. The *left-hand image* corresponds to the formation of NH_3^+ by charge transfer, and the *right-hand image* corresponds to the formation of $HCNH^+$ products by C–N

bond formation. The *circles* denote the loci of center of mass speeds that correspond to the maximum product values allowed by energy conservation. (Reprinted with permission from [36]. Copyright 2012, American Institute of Physics)

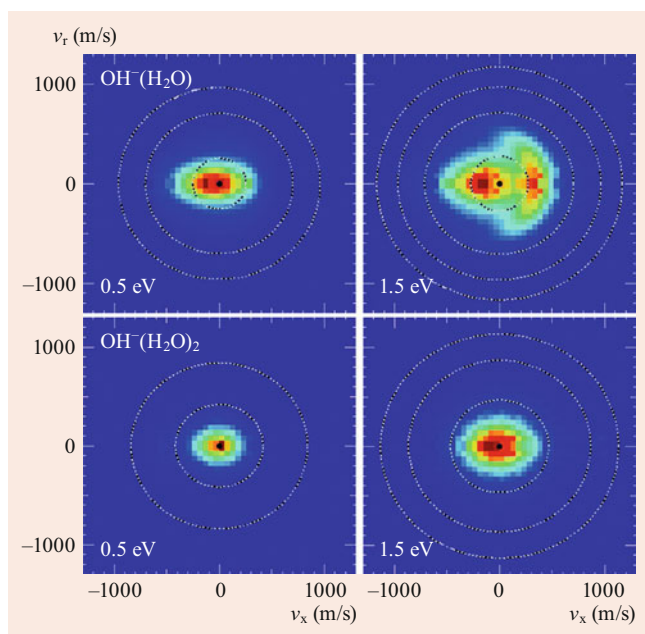
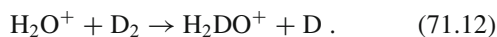


Fig. 71.6 Crossed-beam reactive scattering images of the I^- reaction product for the reaction of $OH^- (H_2O)$ and $OH^- (H_2O)_2$ with CH_3I . The translational energy difference between adjacent rings is 1 eV, the *outer rings* again mark the kinematic cutoff. (Reprinted from [27] with permission from the PCCP Owner Societies)

promoting reactivity. A recent example from the laboratory of N_g at UC Davis [22] has provided convincing evidence for the role of reactant rotational excitation in promoting atom transfer in the system



The reactant H_2O^+ species was prepared in the 2_{11} , 1_{11} , and 0_{00} asymmetric rotor states by vacuum ultraviolet (VUV) photoionization, and was transported to the interaction re-

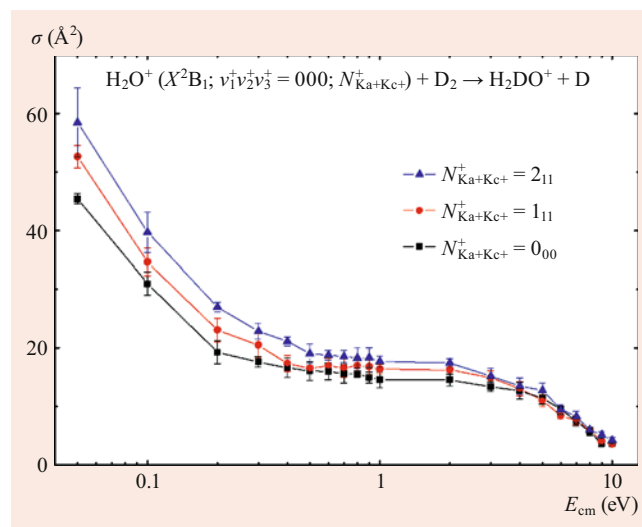


Fig. 71.7 Comparison of the σ values for the reaction $H_2O^+(X^2B_1; v_1^+v_2^+v_3^+ = 000; N_{Ka+Kc}^+ + D_2 \rightarrow H_2DO^+ + D$ in the E_{cm} range of 0.05–10.00 eV. (Reprinted with permission from [22]. Copyright 2012, American Institute of Physics)

gion with a quadrupole mass filter. The collision region consists of a gas cell where ions are confined by an octupole trap, and products are mass-analyzed by another quadrupole mass filter. The geometry allows absolute total cross sections to be measured. Figure 71.7 shows plots of energy-dependent total cross sections from 0.05 to 10 eV, indicating a strong rotational state dependence at the lowest collision energies. Relative to ground-state ions, rotational excitation enhances the cross section by as much as 30%. Quasi-classical trajectory studies [40] have shown that rotational excitation reorients the H_2O^+ ion to allow the oxygen atom to achieve the necessary orientation with respect to H_2 , thereby accessing the transition state that leads to the $H_3O^+ \cdots H$ complex and subsequent product formation.

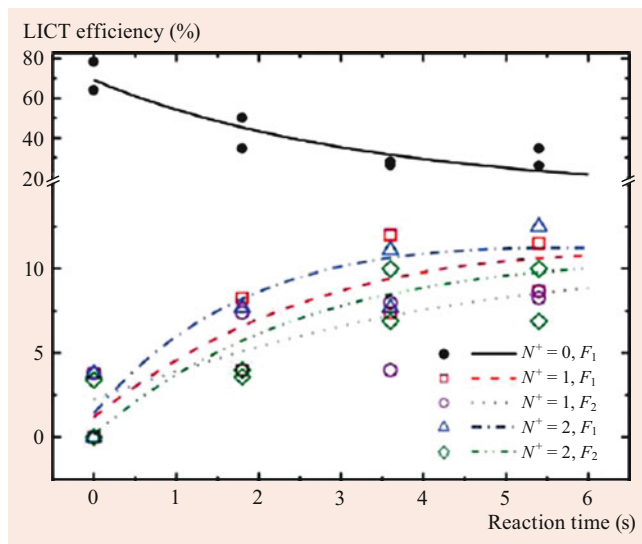


Fig. 71.8 Dynamics of the populations in different spin-rotational states N^+ , $F_{1,2}$ of sympathetically cooled N_2^+ ions as a function of the time of exposure to the molecular beam of neutral N_2 molecules. The populations in the different states have been probed by laser-induced charge transfer (LICT) with Ar atoms. (Reproduced from [11] by permission of John Wiley & Sons Ltd)

The high degree of control that can be achieved in ion-molecule reactions studied in ion trapping configurations is illustrated beautifully in recent work by Willitsch and coworkers. By preloading the multipole trap with Ca^+ , cooling those ions, and establishing a “Coulomb crystal” [28] in which the individual trapped ions are arranged in a regular spatial pattern, reactions of Ca^+ ions with CH_3F , CH_2F_2 , and CH_3Cl have been studied [41, 42]. Ground-state N_2^+ ions produced by multiphoton ionization may also be injected into the trap and cooled by the process of sympathetic cooling to form a bicomponent Coulomb crystal, as shown in Fig. 71.3. The individual trapped N_2^+ ions may then be reacted with rotationally cooled N_2 molecules to produce rotationally excited product N_2^+ ions. Rotational excitation cross sections may be detected by employing a laser-induced charge transfer (LICT) method. Photoexcitation of the reaction products with a 787 nm laser pumps rotationally excited N_2^+ , via the first electronically excited state, into vibrationally excited N_2^+ , which selectively undergoes LICT with Ar. This detection scheme results in time-dependent depletion of the ground rotational state of N_2^+ , and growth of excited rotational state populations, as shown in Fig. 71.8. The data yield cross sections $\sigma(n'|n, T)$ and rate constants $k(n'|n, T)$ for rotational excitation in $N_2^+-N_2$ collisions. Equally impressive is the fact that these cross sections may be determined for the reactions of single ions.

71.6 The Future of the Field

Compared to the examples covered in the last edition of the Handbook, many experimental methods such as ion imaging have reached maturity, and the potential of new methods, particularly ion trapping and cooling, is just beginning to be realized. New methods have allowed collision studies to be carried out with single ions and at very low collision energies, approaching 1 K. In a field as technologically dependent as collision physics and chemistry, there is every expectation that new phenomena in the quantum regime will be discovered and that new chemistry with ultracold reagents will be elucidated. In the same way that single-molecule methods have revolutionized the study of condensed matter, we also expect that the ability to “pick apart the ensemble” in gas phase collisions will yield new insights into reactivity and provide exciting theoretical challenges for many years to come.

References

1. Thomson, J.J.: Rays of Positive Electricity. Longman, Green, and Company, Essex, p 116 (1913)
2. Hogness, T.R., Lunn, E.G.: Phys. Rev. **26**, 0044 (1925)
3. Frankevich, E.L., Tal'rose, V.L.: Dokl. Akad. Nauk. SSSR **119**, 1174 (1958)
4. Tal'rose, V.L., Frankevich, E.L.: Dokl. Akad. Nauk. SSSR **111**, 376 (1956)
5. Schissler, D.O., Stevenson, D.P.: J. Chem. Phys. **24**, 926 (1956)
6. Stevenson, D.P.: J. Phys. Chem. **61**, 1453 (1957)
7. Stevenson, D.P., Schissler, D.O.: J. Chem. Phys. **23**, 1353 (1955)
8. Gioumousis, G., Stevenson, D.P.: J. Chem. Phys. **29**, 294 (1958)
9. Langevin, P.: Ann. Chim. Phys. **5**, 245 (1905)
10. Farrar, J.M., Saunders, J.W.H.: Technique for the Study of Ion-Molecule Reactions. John Wiley & Sons, New York (1988)
11. Willitsch, S.: In: Rice, S.A., Dinner, A.R. (eds.) Advances in Chemical Physics, vol. 162, p. 307. (2017)
12. Carpenter, M.A., Farrar, J.M.: J. Phys. Chem. A. **101**, 6475 (1997)
13. Carpenter, M.A., Farrar, J.M.: J. Phys. Chem. A. **101**, 6870 (1997)
14. Zimmer, M., Linder, F.: Chem. Phys. Lett. **195**, 153 (1992)
15. Zimmer, M., Linder, F.: J. Phys. B At. Mol. Opt. Phys. **28**, 2671 (1995)
16. Chupka, W.A., Russell, M.E.: J. Chem. Phys. **49**, 5426 (1968)
17. Qian, X.M., Zhang, T., Chang, C., Wang, P., Ng, C.Y., Chiu, Y.H., Levandier, D.J., Miller, J.S., Dressler, R.A., Baer, T., Peterka, D.S.: Rev. Sci. Instrum. **74**, 4096 (2003)
18. Zhang, T., Qian, X.M., Tang, X.N., Ng, C.Y., Chiu, Y., Levandier, D.J., Miller, J.S., Dressler, R.A.: J. Chem. Phys. **119**, 10175 (2003)
19. Chiu, Y.H., Fu, H.S., Huang, J.T., Anderson, S.L.: J. Chem. Phys. **101**, 5410 (1994)
20. Anderson, S.L.: Accounts Chem. Res. **30**, 28 (1997)
21. Qian, J., Green, R.J., Anderson, S.L.: J. Chem. Phys. **108**, 7173 (1998)
22. Xu, Y.T., Xiong, B., Chang, Y.C., Ng, C.Y.: J. Chem. Phys. **137**, 241101 (2012)

23. Morrison, R.J.S., Conaway, W.E., Ebata, T., Zare, R.N.: *J. Chem. Phys.* **84**, 5527 (1986)
24. Green, R.J., Anderson, S.L.: *Int. Rev. Phys. Chem.* **20**, 165 (2001)
25. Tong, X., Nagy, T., Reyes, J.Y., Germann, M., Meuwly, M., Willitsch, S.: *Chem. Phys. Lett.* **547**, 1 (2012)
26. Wiley, W.C., McLaren, I.H.: *Rev. Sci. Instrum.* **26**, 1150 (1955)
27. Wester, R.: *Phys. Chem. Chem. Phys.* **16**, 396 (2014)
28. Willitsch, S.: *Int. Rev. Phys. Chem.* **31**, 175 (2012)
29. Chandler, D.W., Houston, P.L.: *J. Chem. Phys.* **87**, 1445 (1987)
30. Eppink, A., Parker, D.H.: *Rev. Sci. Instrum.* **68**, 3477 (1997)
31. Dribinski, V., Ossadtchi, A., Mandelstam, V.A., Reisler, H.: *Rev. Sci. Instrum.* **73**, 2634 (2002)
32. Townsend, D., Minitti, M.P., Suits, A.G.: *Rev. Sci. Instrum.* **74**, 2530 (2003)
33. Trippel, S., Stei, M., Cox, J.A., Wester, R.: *Phys. Rev. Lett.* **110**, 163201 (2013)
34. Wolfgang, R., Cross, R.J.: *J. Phys. Chem.* **73**, 743 (1969)
35. Friedrich, B., Herman, Z.: *Collect. Czech. Chem. Commun.* **49**, 570 (1984)
36. Pei, L., Farrar, J.M.: *J. Chem. Phys.* **136**, 204305 (2012)
37. Pei, L.S., Carrascosa, E., Yang, N., Falcinelli, S., Farrar, J.M.: *J. Phys. Chem. Lett.* **6**, 1684 (2015)
38. Pei, L.S., Farrar, J.M.: *J. Phys. Chem. A* **120**, 6122 (2016)
39. Otto, R., Brox, J., Trippel, S., Stei, M., Best, T., Wester, R.: *J. Phys. Chem. A* **117**, 8139 (2013)
40. Song, H.W., Li, A.Y., Guo, H., Xu, Y.T., Xiong, B., Chang, Y.C., Ng, C.Y.: *Phys. Chem. Chem. Phys.* **18**, 22509 (2016)
41. Willitsch, S., Bell, M.T., Gingell, A.D., Procter, S.R., Softley, T.P.: *Phys. Rev. Lett.* **100**, 043203 (2008)
42. Gingell, A.D., Bell, M.T., Oldham, J.M., Softley, T.P., Harvey, J.N.: *J. Chem. Phys.* **133**, 194302 (2010)



James Farrar James Farrar received his PhD degree from The University of Chicago in 1974. He is currently Professor Emeritus at the University of Rochester, where he served as Professor of Chemistry from 1976 to 2018. His research has been concerned with the application of mass spectrometry, molecular beams, and computational chemistry to the study of ion–molecule interactions.

Part F
Quantum Optics

Part F presents a coherent collection of the main topics and issues found in quantum optics. Optical physics, which is concerned with the dynamical interactions of atoms and molecules with electromagnetic fields, is first discussed within the context of semiclassical theories, and then extended to a fully quantized version. The theoretical techniques used to describe absorption and emission spectra using density matrix methods are developed. Applications of the dark state in laser physics is briefly mentioned. The basic concepts common to all lasers, such as gain, threshold, and electromagnetic modes of oscillation are described. Recent developments in laser physics, including single-atom lasers, two-photon lasers, and the generation of attosecond pulses are also introduced. The current status of the development of different types of lasers – including nanocavity, quantum-cascade, and free-electron lasers – are summarized. The important operational characteristics, such as frequency range and output power, are given for each of the types of lasers described. Nonlinear processes arising from the modifications of the optical properties of a medium due to the passage of intense light beams are discussed. Additional processes that are enabled by the use of ultrashort or ultra-intense laser pulses are presented. The concept of coherent optical transients in atomic and molecular systems is reviewed; homogeneous and inhomogeneous relaxation in the theory are properly distinguished. Multiphoton and strong-field pro-

cesses are given a theoretical description. A discussion of the generation of sub-femtosecond pulses is also included. General and specific theories for the control of atomic motion by light are presented. Various traps used for the cooling and trapping of charged and neutral particles and their applications are discussed. The fundamental physics of dilute quantum degenerate gases is outlined, especially in connection with Bose–Einstein condensation. de Broglie optics, which concerns the propagation of matter waves, is presented with a concentration on the underlying principles and the illustration of these principles. The fundamentals of the quantized electromagnetic field and applications to the broad area of quantum optics are discussed. A detailed description of the changes in the atom–field interaction that take place when the radiation field is modified by the presence of a cavity is given. The basic concepts needed to understand current research, such as the EPR experiment, Bell’s inequalities, squeezed states of light, the properties of electromagnetic waves in cavities, and other topics depending on the nonlocality of light are reviewed. Applications to cryptography, tunneling times, and gravity wave detectors are included, along with recent work on “fast light” and “slow light”. Correlations and quantum superpositions, which can be exploited in quantum information processing and secure communication, are delineated. Their link to quantum computing and quantum cryptography is given explicitly.



Pierre Meystre

Contents

72.1	Multipole Expansion	1047
72.1.1	Electric Dipole (E1) Interaction	1048
72.1.2	Electric Quadrupole (E2) Interaction	1048
72.1.3	Magnetic Dipole (M1) Interaction	1049
72.2	Lorentz Atom	1049
72.2.1	Complex Notation	1049
72.2.2	Index of Refraction	1049
72.2.3	Beer's Law	1050
72.2.4	Slowly Varying Envelope Approximation	1050
72.3	Two-Level Atoms	1050
72.3.1	Hamiltonian	1050
72.3.2	Rotating Wave Approximation	1051
72.3.3	Rabi Frequency	1051
72.3.4	Dressed States	1051
72.3.5	Optical Bloch Equations	1053
72.4	Relaxation Mechanisms	1053
72.4.1	Relaxation Toward Unobserved Levels	1053
72.4.2	Relaxation Toward Levels of Interest	1053
72.4.3	Optical Bloch Equations with Decay	1054
72.4.4	Density Matrix Equations	1054
72.5	Rate Equation Approximation	1054
72.5.1	Steady State	1055
72.5.2	Saturation	1055
72.5.3	Einstein A and B Coefficients	1055
72.6	Light Scattering	1055
72.6.1	Rayleigh Scattering	1055
72.6.2	Thomson Scattering	1056
72.6.3	Resonant Scattering	1056
	References	1056

cal physics, while quantum optics treats the interaction of atoms or molecules with quantized electromagnetic fields. A significant part of optical physics and quantum optics is the study of near-resonant atom–field interactions and concentrates on nonperturbative dynamics, where the effects of the optical fields have to be kept to all orders. The atomic properties themselves are assumed to be known.

The vast majority of problems in light–matter interactions can be treated quite accurately within semiclassical theories. However, an important class of problems where this is not the case is presented in Chaps. 82–84. While much of optical physics and quantum optics ignores the effects of the electromagnetic fields on the center-of-mass motion of the atoms, important topics such as atomic trapping and cooling (Chap. 79) and de Broglie optics (Chap. 81) rely in an essential way on such mechanical effects of light. The present chapter deals with more *traditional* aspects of optical physics, where these effects are ignored.

Keywords

Rabi frequency · multipole expansion · rotating wave approximation · atomic coherence · optical Bloch equations · dressed states · Einstein A and B coefficients · Lorentz atom · two-level atom

Abstract

Optical physics is concerned with the dynamical interactions of atoms and molecules with electromagnetic fields. Semiclassical theories, which study the interaction of atoms with classical fields, are often said to comprise opti-

72.1 Multipole Expansion

Consider a test charge q of mass m localized within an atom and acted upon by an external electromagnetic field with electric field $\mathbf{E}(\mathbf{r}, t)$ and magnetic field $\mathbf{B}(\mathbf{r}, t)$. In the multipole expansion formalism [1, 2], the electric and magnetic interaction energies between the charge and the electromagnetic field are

$$V_e = V_{E0}(t) - q \int_0^r ds \cdot \mathbf{E}(\mathbf{R} + \mathbf{s}, t), \quad (72.1)$$

P. Meystre (✉)
University of Arizona
Tucson, AZ, USA
e-mail: pierre.meystre@optics.arizona.edu

$$V_m = -q \int_0^r ds \cdot \mathbf{v} \times \mathbf{B}(\mathbf{R} + \mathbf{s}, t), \quad (72.2)$$

respectively. (The material of this chapter is discussed in detail in a number of texts and review articles. We cite such references rather than the original sources whenever possible.) These energies correspond to the work done by the electric and magnetic components of the Lorentz force in first moving the charge to a stationary origin of coordinates at a point \mathbf{R} and then to a location \mathbf{r} relative to \mathbf{R} . Here, $V_{E0}(t)$ represents the energy of the charge when located at the reference point \mathbf{R} . It may be expressed in terms of the electrostatic potential $\phi(\mathbf{R}, t)$ as $V_{E0}(t) = +q\phi(\mathbf{R}, t)$.

A Taylor series expansion of $V_e(t)$ and $V_m(t)$ about $\mathbf{r} = 0$ yields

$$V_e(t) = V_{E0}(t) - q \sum_{n=1}^{\infty} \frac{1}{n!} \left(\mathbf{r} \cdot \frac{\partial}{\partial \mathbf{R}} \right)^{n-1} \mathbf{r} \cdot \mathbf{E}(\mathbf{R}, t), \quad (72.3)$$

$$V_m(t) = -\frac{q\hbar}{m} \sum_{n=1}^{\infty} \frac{n}{(n+1)!} \left(\mathbf{r} \cdot \frac{\partial}{\partial \mathbf{R}} \right)^{n-1} \boldsymbol{\ell} \cdot \mathbf{B}(\mathbf{R}, t), \quad (72.4)$$

where $\hbar\boldsymbol{\ell} = \mathbf{r} \times \mathbf{p}$ is the angular momentum of the test charge relative to the coordinate origin \mathbf{R} . Here, use of the mechanical momentum $\mathbf{p} = m\dot{\mathbf{r}}$, instead of the canonical momentum, neglects the electromagnetic component of the momentum responsible for diamagnetic effects.

In addition to the electromagnetic interaction, electrons and nuclei are characterized by a spin magnetic moment $\mathbf{m}_s = (q\hbar/2m)g_s\mathbf{s}$, where \mathbf{s} is the spin of the test charge and g_s its gyromagnetic factor, equal to 2.002... for electrons. The factor $q\hbar/2m$ is the particle's magneton. The spin magnetic moment yields an additional term to the magnetic energy V_m , which becomes

$$V_m(t) = -\frac{e\hbar}{2m} \sum_{n=1}^{\infty} \frac{1}{n!} \left(\mathbf{r} \cdot \frac{\partial}{\partial \mathbf{R}} \right)^{n-1} \times \left(\frac{2}{n+1} g_\ell \boldsymbol{\ell} + g_s \mathbf{s} \right) \cdot \mathbf{B}(\mathbf{R}, t), \quad (72.5)$$

where the orbital g -factor is $g_\ell = q/e$ ($g_\ell = -1$ for an electron). For an ensemble $\{\alpha\}$ of charged particles q_α in an atom, these expressions are to be summed over all particles. Thus, the electric energy becomes

$$\begin{aligned} V_e(t) &= \sum_{\alpha} q_{\alpha} \phi(\mathbf{R}, t) - \sum_{i=1}^3 \sum_{\alpha} q_{\alpha} r_i(\alpha) E_i(\mathbf{R}, t) \\ &\quad - \frac{1}{2} \sum_{i,j=1}^3 \left[\sum_{\alpha} q_{\alpha} r_i(\alpha) r_j(\alpha) \right] \\ &\quad \times \frac{\partial}{\partial R_j} E_i(\mathbf{R}, t) + \dots \\ &\equiv V_{E0}(t) + V_{E1}(t) + V_{E2}(t) + \dots, \end{aligned} \quad (72.6)$$

and the magnetic energy becomes

$$\begin{aligned} V_m(t) &= \sum_{i=1}^3 B_i(\mathbf{R}, t) \\ &\quad \times \sum_{\alpha} \frac{e\hbar}{2m_{\alpha}} [g_{\ell}(\alpha) \ell_i(\alpha) + g_s(\alpha) s_i(\alpha)] \\ &\quad - \sum_{i,j=1}^3 \frac{\partial B_i(\mathbf{R}, t)}{\partial R_j} \sum_{\alpha} \frac{e\hbar}{2m_{\alpha}} \left[\frac{2}{3} g_{\ell}(\alpha) \ell_i(\alpha) r_j(\alpha) \right. \\ &\quad \left. + g_s(\alpha) s_i(\alpha) \right] + \dots \\ &\equiv V_{M1}(t) + V_{M2}(t) + \dots. \end{aligned} \quad (72.7)$$

72.1.1 Electric Dipole (E1) Interaction

For optical fields whose wavelength is large compared with the interacting atom, only the first few terms in the Taylor expansions of $V_e(t)$ and $V_m(t)$ need to be retained. The first term, $V_{E0}(t)$, of $V_e(t)$ is the net charge of the atom, which vanishes for neutral atoms. The second term, $V_{E1}(t)$, is the electric dipole interaction energy. Introducing the electric dipole (E1) moment,

$$\mathbf{d} = \sum_{\alpha} q_{\alpha} \mathbf{r}(\alpha), \quad (72.8)$$

or

$$\mathbf{d} = \int d^3r \rho(\mathbf{r}) \mathbf{r}, \quad (72.9)$$

for a charge distribution, this contribution to the interaction energy may be re-expressed as

$$V_{E1}(t) = -\mathbf{d} \cdot \mathbf{E}(\mathbf{R}, t). \quad (72.10)$$

The E1 term dominates most optical phenomena.

72.1.2 Electric Quadrupole (E2) Interaction

The $V_{E2}(t)$ contribution to $v_e(t)$ describes electric quadrupole (E2) interactions. In terms of the quadrupole tensor

$$Q = 3 \int d^3r \rho(\mathbf{r}) r_i r_j, \quad (72.11)$$

$V_{E2}(t)$ becomes

$$V_{E2}(t) = -\frac{1}{6} \sum_{i,j=1}^3 Q_{ij} \frac{\partial}{\partial R_i} E_j(\mathbf{R}, t). \quad (72.12)$$

Alternatively, E2 interactions can be expressed in terms of the traceless quadrupole tensor $Q_{ij}^{(2)} = \int d^3r \rho(\mathbf{r}) \times (3r_i r_j -$

$\delta_{ij} r^2$). E2 interactions are typically weaker than E1 interactions by a factor a_0/λ , where a_0 is the Bohr radius, and λ is the wavelength of the transition. Since a_0/λ is very small for optical transitions, E2 interactions are typically neglected in quantum optics.

72.1.3 Magnetic Dipole (M1) Interaction

The first term in the multipole expansion of the magnetic interaction (Sect. 72.6) is the magnetic dipole M1 interaction,

$$V_{M1} = -\mathbf{m} \cdot \mathbf{B}(\mathbf{R}, t), \quad (72.13)$$

of a magnetic moment \mathbf{m} in a magnetic field, where

$$\begin{aligned} \mathbf{m} &= \sum_{\alpha} \left(\frac{q_{\alpha} \hbar}{2m_{\alpha}} \right) [g_{\ell}(\alpha) \boldsymbol{\ell}(\alpha) + g_s(\alpha) \mathbf{s}(\alpha)] \\ &= -\mu_B (\mathbf{L} + 2\mathbf{S}), \end{aligned} \quad (72.14)$$

and we have used the fact that for electrons $g_{\ell} = -1$ and $g_s \simeq -2$. The Bohr magneton μ_B is

$$\mu_B = \frac{e\hbar}{2mc} = \frac{\alpha e a_0}{2}, \quad (72.15)$$

where α is the fine structure constant. Thus, M1 interactions tend to be smaller than E1 interactions by a factor of order $\alpha/2$. The connection between \mathbf{m} and angular momentum \mathbf{J} is $\mathbf{m} = \gamma \mathbf{J}$, where γ is the gyromagnetic ratio.

72.2 Lorentz Atom

The Lorentz atom consists of a classical electron harmonically bound to a proton. It provides a framework for understanding a number of elementary aspects of the electric dipole interaction between a single atom and light [3–7]. Assuming that the center of mass (CM) motion of the atom is unaffected by the field, and neglecting magnetic effects, the equation of motion of the electron is

$$\left(\frac{d^2}{dt^2} + \frac{\Gamma_0}{2} \frac{d}{dt} + \omega_0^2 \right) \mathbf{r} = -\frac{e}{m} \mathbf{E}(\mathbf{R}, t), \quad (72.16)$$

where ω_0 is the electron's natural oscillation frequency, and Γ_0 represents a frictional decay rate that accounts for the effects of radiative damping. For the classical Lorentz atom

$$\Gamma_0 = 2\omega_0^2 r_0 / 3c, \quad (72.17)$$

where $r_0 = e^2 / 4\pi\epsilon_0 m c^2$ is the classical electron radius. This damping arises physically from the radiation reaction of the field radiated by the atom on itself. In the E1 approximation, the electric field is evaluated at the location \mathbf{R} of the atomic c.m.

72.2.1 Complex Notation

The study of light–matter interactions is simplified by the introduction of complex variables [8–11]. For example, an electric field

$$\mathbf{E}(\mathbf{R}, t) = \sum_{n,\mu} \boldsymbol{\epsilon}_{\mu} \mathcal{E}_n \cos(\omega_n t), \quad (72.18)$$

where $\boldsymbol{\epsilon}_{\mu}$ is the polarization vector of the field Fourier component at frequency ω_n , is expressed as

$$\mathbf{E}(\mathbf{R}, t) = \mathbf{E}^+(\mathbf{R}, t) + \mathbf{E}^-(\mathbf{R}, t), \quad (72.19)$$

where the *positive frequency part* of the field is

$$\mathbf{E}^+(\mathbf{R}, t) = \frac{1}{2} \sum_{n,\mu} \boldsymbol{\epsilon}_{\mu} \mathcal{E}_n \exp[i(\mathbf{k}_n \cdot \mathbf{R} - \omega_n t)]. \quad (72.20)$$

Due to the linearity of Eq. (72.16), it is sufficient to study the response of the Lorentz atom to a plane monochromatic electric field of frequency ω , complex amplitude \mathcal{E} and polarization $\boldsymbol{\epsilon}$. Introducing the *complex dipole moment*

$$\mathbf{d} = -e\mathbf{r} = \boldsymbol{\epsilon} \mathcal{P} \exp[i(\mathbf{k} \cdot \mathbf{R} - \omega t)] + \text{c.c.}, \quad (72.21)$$

where \mathcal{P} is in general complex for \mathcal{E} real, and the complex polarizability $\alpha(\omega)$ via $\mathcal{P} = \alpha(\omega)\mathcal{E}$, then

$$\alpha(\omega) = \frac{e^2/m}{\omega_0^2 - \omega^2 - i\Gamma_0\omega}. \quad (72.22)$$

72.2.2 Index of Refraction

From the Maxwell wave equation

$$\left(\nabla^2 - \frac{1}{c^2} \frac{\partial^2}{\partial t^2} \right) \mathbf{E}(\mathbf{R}, t) = \frac{1}{\epsilon_0 c^2} \frac{\partial^2 \mathbf{P}(\mathbf{R}, t)}{\partial t^2}, \quad (72.23)$$

where $\mathbf{P}(\mathbf{R}, t)$ is the electric polarization, given by the electric dipole density of the medium $\mathbf{P} = N\mathbf{d}$, N being the atomic density, the plane wave dispersion relation is

$$k^2 = \frac{\omega^2}{c^2} n^2(\omega), \quad (72.24)$$

where the index of refraction $n(\omega)$ is

$$n(\omega) = \sqrt{1 + \frac{N\alpha(\omega)}{\epsilon_0}}. \quad (72.25)$$

72.2.3 Beer's Law

Since the polarizability $\alpha(\omega)$ is normally complex, so is the index of refraction. Its real part leads to dispersive effects, while its imaginary part leads to absorption. Specifically, $\text{Re}[n(\omega)] - 1$ has the form of a standard dispersion curve, positive for $\omega - \omega_0 < 0$ and negative for $\omega - \omega_0 > 0$, while $\text{Im}[n(\omega)]$ is a Lorentzian curve peaked at $\omega = \omega_0$. The intensity absorption coefficient $a(\omega)$ is

$$\begin{aligned} a(\omega) &= 2 \text{Im}[n(\omega)]\omega/c \\ &= \frac{2\omega}{c} \text{Im} \left[1 + \left(\frac{Ne^2}{m\epsilon_0} \right) \frac{i\gamma\omega + (\omega_0^2 - \omega^2)}{(\omega_0^2 - \omega^2)^2 + \gamma^2\omega^2} \right]^{1/2}. \end{aligned} \quad (72.26)$$

For atomic vapors, the corrections to the vacuum index of refraction are normally small, so that the square root in Eq. (72.26) can be expanded to first order, giving

$$a(\omega) = \left(\frac{Ne^2}{\epsilon_0 mc} \right) \frac{\gamma\omega^2}{(\omega_0^2 - \omega^2)^2 + \gamma^2\omega^2}. \quad (72.27)$$

The intensity of a monochromatic field propagating along the z -direction through a gas of Lorentz atoms is, therefore, attenuated according to *Beer's law* given by

$$I(\omega, z) = I(\omega, 0) e^{-a(\omega)z}. \quad (72.28)$$

If the index of refraction at a given frequency becomes purely imaginary, no electromagnetic wave can propagate inside the medium. In a plasma this is the case for field frequencies smaller than the plasma frequency

$$\omega_p = \sqrt{\frac{Ne^2}{m\epsilon_0}}. \quad (72.29)$$

While the Lorentz atom model gives an adequate description of absorption and dispersion in a weakly excited absorbing medium, it fails to predict the occurrence of important phenomena such as saturation and light amplification. This is because, in this model, the phase of the induced atomic dipoles with respect to the incident field is always such that the polarization field adds destructively to the incident field. The description of light amplification requires a quantum treatment of the medium, which gives a greater flexibility to the possible relative phases between the incident and polarization fields.

72.2.4 Slowly Varying Envelope Approximation

Light-matter interactions often involve quasi-monochromatic fields for which the electric field (taken to propagate along

the z -axis) can be expressed in the form

$$\mathbf{E}(\mathbf{R}, t) = \frac{1}{2} \boldsymbol{\epsilon} \mathcal{E}^+(\mathbf{R}, t) e^{i(kz - \omega t)} + \text{c.c.}, \quad (72.30)$$

such that

$$\left| \frac{\partial \mathcal{E}^+}{\partial t} \right| \ll \omega |\mathcal{E}^+|, \quad \left| \frac{\partial \mathcal{E}^+}{\partial z} \right| \ll k |\mathcal{E}^+|. \quad (72.31)$$

It is further consistent within this approximation to assume that the polarization takes the form

$$\mathbf{P}(\mathbf{R}, t) = \frac{1}{2} \boldsymbol{\epsilon} \mathcal{P}^+(\mathbf{R}, t) e^{i(kz - \omega t)} + \text{c.c.}, \quad (72.32)$$

with

$$\left| \frac{\partial \mathcal{P}^+}{\partial t} \right| \ll \omega |\mathcal{P}^+|. \quad (72.33)$$

Under these conditions, known as the *slowly varying envelope approximation* [5], Maxwell's wave equation reduces to

$$\left(\frac{\partial}{\partial z} + \frac{1}{c} \frac{\partial}{\partial t} \right) \mathcal{E}^+(z, t) = -\frac{k}{2i\epsilon_0} \mathcal{P}^+(z, t). \quad (72.34)$$

Hence, in the slowly varying envelope approximation, we ignore the backward propagation of the field [12]. The slowly varying amplitude and phase approximation is essentially the same, except that it expresses the electric field envelope in terms of a real amplitude and phase.

72.3 Two-Level Atoms

A large number of optical phenomena can be understood by considering the interaction between a quasi-monochromatic field of central frequency ω and a two-level atom, which simulates a (dipole-allowed) atomic transition [5, 7, 10, 11, 13–17]. This approximation is well justified for near-resonant interactions; i.e., $\omega \simeq \omega_0$. The next three sections discuss the model Hamiltonian for this system in the *semiclassical* approximation where the electromagnetic field can be described classically. The formal results are then extended to the case of a quantized field, where the electric field is treated as an operator.

72.3.1 Hamiltonian

In the absence of dissipation mechanisms, the dipole interaction between a quasi-monochromatic classical field and a two-level atom is

$$H = \hbar\omega_e |e\rangle\langle e| + \hbar\omega_g |g\rangle\langle g| - \mathbf{d} \cdot \mathbf{E}(\mathbf{R}, t), \quad (72.35)$$

where $|e\rangle$ and $|g\rangle$ label the upper and lower atomic levels, of frequencies ω_e and ω_g , respectively, with $\omega_e - \omega_g = \omega_0$, and \mathbf{R} is the location of the center of mass of the atom. The electric dipole operator Eq. (72.8) couples the excited and ground levels and may be expressed as

$$\mathbf{d} = \epsilon_d d (|e\rangle\langle g| + |g\rangle\langle e|), \quad (72.36)$$

where ϵ_d is a unit vector in the direction of the dipole and d the matrix element of the electric dipole operator between the ground and excited state, which we take to be real for simplicity. We also neglect the vector character of \mathbf{d} and $\mathbf{E}(\mathbf{R}, t)$ in the following, assuming, for example, that both ϵ_d and ϵ are parallel to the x -axis. The Hamiltonian Eq. (72.35) may then be expressed as

$$H = \hbar\omega_e |e\rangle\langle e| + \hbar\omega_g |g\rangle\langle g| - d(|e\rangle\langle g| + |g\rangle\langle e|) \times [E^+(\mathbf{R}, t) + E^-(\mathbf{R}, t)], \quad (72.37)$$

where we have generalized the notation of Eq. (72.20) in an obvious way. One can introduce the *pseudo-spin operators*

$$\begin{aligned} s_z &= (|e\rangle\langle e| - |g\rangle\langle g|)/2, \\ s_+ &= s_-^\dagger = |e\rangle\langle g|, \end{aligned} \quad (72.38)$$

and redefine the zero of atomic energy to introduce the commonly used form

$$H = \hbar\omega_0 s_z - d(s_+ + s_-)[E^+(\mathbf{R}, t) + E^-(\mathbf{R}, t)]. \quad (72.39)$$

72.3.2 Rotating Wave Approximation

Under the influence of a monochromatic electromagnetic field of frequency ω , atoms undergo transitions between their lower and upper states by interacting with either the positive or the negative frequency part of the field. The corresponding contributions to the atomic dynamics oscillate at frequencies $\omega_0 - \omega$ and $\omega_0 + \omega$, respectively, and their contributions to the probability amplitudes involve denominators containing this same frequency dependence. For near-resonant atom-field interactions, the rapidly oscillating contributions lead to small corrections, the first-order one being the Bloch–Siegert shift, whose value near resonance is, for $\omega \simeq \omega_0$, [17].

$$\delta\omega_{eg} = -\frac{(d|E^+|/\hbar)^2}{4\omega} \quad (72.40)$$

to lowest order in $dE/\hbar\omega$. The neglect of these terms is the rotating wave approximation (RWA). Note that it is normally inconsistent to regard an atom as a two-level system and not

to perform the RWA. In the RWA, the atomic system is described by the Hamiltonian

$$H = \hbar\omega_0 s_z - d[s_+ E^+(\mathbf{R}, t) + s_- E^-(\mathbf{R}, t)], \quad (72.41)$$

or, in a frame rotating at the frequency ω of the field,

$$H = \hbar\Delta s_z - \frac{1}{2}d(s_+ \mathcal{E} e^{ik\cdot\mathbf{R}} + \text{h.c.}), \quad (72.42)$$

where $\Delta = \omega_0 - \omega$ is the atom–light detuning. (Note that the alternate definition $\delta = \omega - \omega_0$ is frequently used in the literature.) In the rest of this chapter, we consider atoms placed at $\mathbf{R} = 0$.

72.3.3 Rabi Frequency

The dynamics of the two-level atom is conveniently expressed in terms of its density operator ρ , whose evolution is given by the Schrödinger equation

$$\frac{d\rho}{dt} = -\frac{i}{\hbar}[H, \rho], \quad (72.43)$$

where $\rho_{ee} = \langle e|\rho|e\rangle$ and $\rho_{gg} = \langle g|\rho|g\rangle$ are the upper and lower state populations P_e and P_g , respectively, while the off-diagonal matrix elements $\rho_{eg} = \langle e|\rho|g\rangle = \rho_{ge}^*$ are called the atomic coherences, or simply coherences, between levels $|e\rangle$ and $|g\rangle$. These coherences play an essential role in optical physics and quantum optics, since they are proportional to the expectation value of the electric dipole operator.

The evolution of $P_g(t)$ and $P_e(t) = 1 - P_g(t)$, is characterized by oscillations at the generalized Rabi frequency

$$\Omega = (\Omega_1^2 + \Delta^2)^{1/2}, \quad (72.44)$$

where the *Rabi frequency* Ω_1 is $\Omega_1 = dE/\hbar$, (or $\Omega_1 = dE(\epsilon_d \cdot \epsilon)/\hbar$ when the vector character of the electric field and dipole moment are included). Specifically, assuming that the atom is initially in its ground state $|g\rangle$, the probability that it is in the excited state $|e\rangle$ at a subsequent time t is given by Rabi's formula

$$P_e(t) = (\Omega_1/\Omega)^2 \sin^2(\Omega t/2). \quad (72.45)$$

At resonance ($\Delta = 0$), the generalized Rabi frequency Ω reduces to the Rabi frequency Ω_1 . (In addition to the texts on quantum optics already cited, see also [18].)

72.3.4 Dressed States

Semiclassical Case

The atomic dynamics can alternatively be described in terms of a *dressed states* basis instead of the *bare states* $|e\rangle$ and

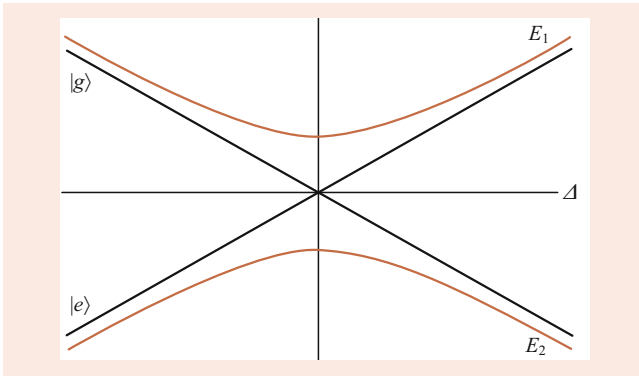


Fig. 72.1 Dressed levels of a two-level atom driven by a classical monochromatic field as a function of the detuning $\Delta = \omega_0 - \omega$

$|g\rangle$ [17]. The dressed states $|1\rangle$ and $|2\rangle$ are eigenstates of the Hamiltonian Eq. (72.42), and, by convention, the state $|1\rangle$ is the one with the greatest energy. They are conveniently expressed in terms of the bare states via the Stückelberg angle $\theta/2$ as

$$\begin{aligned} |1\rangle &= \sin \theta |g\rangle + \cos \theta |e\rangle, \\ |2\rangle &= \cos \theta |g\rangle - \sin \theta |e\rangle, \end{aligned} \quad (72.46)$$

where $\sin(2\theta) = -\Omega_1/\Omega$, $\cos(2\theta) = \Delta/\Omega$. The corresponding eigenenergies are

$$\begin{aligned} E_1 &= +\frac{1}{2}\hbar\Omega, \\ E_2 &= -\frac{1}{2}\hbar\Omega. \end{aligned} \quad (72.47)$$

These energies are illustrated in Fig. 72.1 as a function of the field frequency ω . The dressed levels repel each other and form an anticrossing at resonance $\omega = \omega_0$. As the detuning Δ varies from positive to negative values, state $|1\rangle$ passes continuously from the excited state $|e\rangle$ to the bare ground state $|g\rangle$, with both bare states having equal weights at resonance. The distances between the perturbed levels and their asymptotes for $|\Delta| \gg \Omega_1$ represent the AC Stark shifts, or light shifts, of the atomic states when coupled to the laser. From Fig. 72.1, the AC Stark shift of $|g\rangle$ is positive for $\Delta < 0$ and negative for $\Delta > 0$, while the $|e\rangle$ state shift is negative for $\Delta < 0$ and positive for $\Delta > 0$.

Quantized Field

The concept of dressed states can readily be generalized to a two-level atom interacting with a single-mode quantized field in the dipole and rotating wave approximations. The atom and its dipole interaction with the field are still described by the Hamiltonian Eq. (72.41), except that the positive and negative frequency components of the field are now operators, and the free field Hamiltonian must be

included. The Hamiltonian of the total atom–field system becomes

$$H = \hbar\omega_0 s_z + \hbar\omega \left(a^\dagger a + \frac{1}{2} \right) + \hbar g (s_+ a + a^\dagger s_-), \quad (72.48)$$

where the creation and annihilation operators a^\dagger and a obey the boson commutation relation $[a, a^\dagger] = 1$ (Chap. 6), and the coupling constant

$$g = d \sqrt{\frac{\omega}{2\epsilon_0 \hbar V}} \quad (72.49)$$

is the vacuum Rabi frequency, with V being a photon normalization volume. This Hamiltonian defines the Jaynes–Cummings model, [7, 19] which is discussed in more detail in Chap. 83.

The dressed states of the atom–field system are the eigenstates of the Jaynes–Cummings model. Since, in the RWA, the dipole interaction only couples states of same *excitation number*, e.g., $|e, n\rangle$ and $|g, n+1\rangle$, where $|n\rangle$ is an eigenstate of the photon number operator, $a^\dagger a |n\rangle = n |n\rangle$, with n an integer, the diagonalization of the Jaynes–Cummings model reduces to that of the semiclassical driven two-level atom in each of these manifolds. Hence, the dressed states are

$$\begin{aligned} |1, n\rangle &= \sin \theta_n |g, n+1\rangle + \cos \theta_n |e, n\rangle, \\ |2, n\rangle &= \cos \theta_n |g, n+1\rangle - \sin \theta_n |e, n\rangle, \end{aligned} \quad (72.50)$$

with

$$\tan(2\theta_n) = -2g\sqrt{n+1}/\Delta. \quad (72.51)$$

(The factor of 2 difference between this and the semiclassical case is due to the use of a running waves quantization scheme, while the semiclassical discussion was for standing waves.) The corresponding eigenenergies are

$$\begin{aligned} E_{1n} &= \hbar(n+1)\omega - \hbar R_n, \\ E_{2n} &= \hbar(n+1)\omega + \hbar R_n, \end{aligned} \quad (72.52)$$

where

$$R_n = \frac{1}{2} \sqrt{\Delta^2 + 4g^2(n+1)}. \quad (72.53)$$

Chapter 83 shows that by including the effects of spontaneous emission, this picture yields a straightforward interpretation of a number of effects, including the Burshtein–Mollow resonance fluorescence spectrum. Dressed states also help to elucidate the interaction between two-level atoms and quantized single-mode fields, as occur, for example, in cavity QED ([19] and Chap. 83). Their generalization to the case of moving atoms offers simple physical interpretations of several aspects of laser cooling, see Chap. 79 and [20].

72.3.5 Optical Bloch Equations

Introducing the density operator matrix elements $\rho_{ab} = \langle a|\rho|b\rangle$, where a, b can be either e or g , as well as the real quantities

$$\begin{aligned} U &= \rho_{eg} e^{i\omega t} + \text{c.c.} , \\ V &= i\rho_{eg} e^{i\omega t} + \text{c.c.} , \\ W &= \rho_{ee} - \rho_{gg} , \end{aligned} \quad (72.54)$$

the equations of motion for the density matrix elements $\rho_{ij} = \langle i|\rho|j\rangle$ may be expressed, with Eq. (72.43), as

$$\begin{aligned} \frac{dU}{dt} &= -\Delta V , \\ \frac{dV}{dt} &= \Delta U + \Omega_1 W , \\ \frac{dW}{dt} &= -\Omega_1 V . \end{aligned} \quad (72.55)$$

These are the optical Bloch equations, as discussed extensively in [5, 17]. Physically, U describes the component of the atomic coherence in phase with the driving field, V the component in quadrature with the field, and W the atomic inversion. The optical Bloch equations have a simple geometrical interpretation offered by thinking of U , V , and W as the three components of a vector called the Bloch vector \mathbf{U} , whose equation of motion is

$$\frac{d\mathbf{U}}{dt} = \boldsymbol{\Omega} \times \mathbf{U} , \quad (72.56)$$

where $\boldsymbol{\Omega} = (-\Omega_1, 0, \Delta)$. Thus, \mathbf{U} precesses about $\boldsymbol{\Omega}$, of length Ω , while conserving its length. The evolution of a two-level atom driven by a monochromatic field is, thus, mathematically equivalent to that of a spin- $\frac{1}{2}$ system in two magnetic fields \mathbf{B}_0 and $2\mathbf{B}_1 \cos \omega t$, which are parallel to the z - and x -axis, respectively, and whose amplitudes are such that the Larmor spin precession frequencies around them are ω and $2\Omega_1 \cos \omega t$, respectively. In optics, this vectorial picture is often referred to as the Feynman–Vernon–Hellwarth picture [21]. It is very useful in discussing the coherent transient phenomena discussed in Chap. 77.

72.4 Relaxation Mechanisms

In addition to their coherent interaction with light fields, atoms suffer incoherent relaxation mechanisms, whose origin can be as diverse as elastic and inelastic collisions and spontaneous emission. Collisional broadening is discussed in Chap. 63, while a QED microscopic discussion of spontaneous emission is described in Chap. 83 in terms of reservoir

theory. One advantage of describing the atomic state in terms of a density operator ρ is that the physical interpretation of its elements allows us phenomenologically to add various relaxation terms directly to its elements.

72.4.1 Relaxation Toward Unobserved Levels

If the relaxation mechanisms transfer populations or atomic coherences toward uninteresting or unobserved levels, their description can normally be given in terms of a Schrödinger equation, but with a complex Hamiltonian. In contrast, if all levels involved in the relaxation mechanism are observed, a more careful description, e.g., in terms of a master equation, is required. Specifically, in the case of relaxation to unobserved levels, the evolution of the atomic density operator, restricted to the levels of interest, is of the general form [16]

$$\frac{d\rho}{dt} = -\frac{i}{\hbar} (H_{\text{eff}}\rho - \rho H_{\text{eff}}^\dagger) , \quad (72.57)$$

where

$$H_{\text{eff}} = H + \hat{\Gamma} , \quad (72.58)$$

H being the atom–field Hamiltonian and $\hat{\Gamma}$ the non-Hermitian relaxation operator, defined by its matrix elements

$$\langle n|\hat{\Gamma}|m\rangle = \frac{\hbar}{2i} \gamma_n \delta_{nm} . \quad (72.59)$$

Both inelastic collisions and spontaneous emission to unobserved levels can be described by this form of evolution. In the framework of this chapter, inelastic, or strong, collisions are defined as collisions that can induce atomic transitions into other energy levels.

72.4.2 Relaxation Toward Levels of Interest

A master equation description is necessary when all levels involved are observed [7, 17]. This master equation can rapidly take a complicated form if more than two levels are involved. We give results only for the case of a two-level atom and upper to lower-level spontaneous decay and elastic or soft collisions; i.e., collisions that change the separation of energy levels during the collision but leave the level populations unchanged. In that case, the atomic master equation takes the form

$$\begin{aligned} \frac{d\rho}{dt} &= -\frac{i}{\hbar} [H, \rho] - \frac{\Gamma}{2} (s_+ s_- \rho + \rho s_+ s_- - 2s_- \rho s_+) \\ &\quad - \frac{1}{2} \gamma_{\text{ph}} \rho + 2\gamma_{\text{ph}} s_z \rho s_z , \end{aligned} \quad (72.60)$$

where the free-space spontaneous decay rate Γ is found from QED to be

$$\Gamma = \frac{1}{4\pi\epsilon_0} \frac{4d^2\omega_0^3}{3\hbar c^3}, \quad (72.61)$$

and γ_{ph} is the decay rate due to elastic collisions.

It is possible to express the classical decay rate Eq. (72.17) in terms of the quantum spontaneous emission rate Eq. (72.61) as

$$\Gamma = \Gamma_{\text{cl}} f_{ge}, \quad (72.62)$$

where f_{ge} is the oscillator strength of the transition. The various oscillator strengths characterizing the dipole-allowed transitions from a ground state $|e\rangle$ to excited levels $|g\rangle$ obey the Thomas–Reiche–Kuhn sum rule

$$\sum_e f_{ge} = 1, \quad (72.63)$$

where the sum is on all levels dipole-coupled to $|g\rangle$. Assuming that \mathbf{d} and the polarization of the field are both parallel to the x -axis, this gives

$$f_{ge} = \frac{2m\omega_0}{\hbar} |\langle g|x|e\rangle|^2. \quad (72.64)$$

72.4.3 Optical Bloch Equations with Decay

In general, the optical Bloch equations cannot be generalized to cases where relaxation mechanisms are present. There are, however, two notable exceptions corresponding to the following situations.

1. The upper level spontaneously decays to the lower level only, while the atom undergoes only elastic collisions.
2. Spontaneous emission between the upper and lower levels can be ignored in comparison with decay to unobserved levels, which occur at equal rates $\gamma_e = \gamma_g = 1/T_1$.

Under these conditions, Eq. (72.55) generalizes to

$$\begin{aligned} \frac{dU}{dt} &= -U/T_2 - \Delta V, \\ \frac{dV}{dt} &= -V/T_2 + \Delta U + \Omega_1 W, \\ \frac{dW}{dt} &= -(W - W_{\text{eq}})/T_1 - \Omega_1 V, \end{aligned} \quad (72.65)$$

where we have introduced the longitudinal and transverse relaxation times T_1 and T_2 , with $T_1 = 1/\Gamma$ and $T_2 = (1/2T_1 + \gamma_{\text{ph}})^{-1}$ in the first case, and $T_2 = (1/T_1 + \gamma_{\text{ph}})^{-1}$ in the second case. The equilibrium inversion W_{eq} is equal to zero in the second case since the decay is to unobserved levels.

72.4.4 Density Matrix Equations

In the general case, it is necessary to consider the density operator equation (72.43) instead of the optical Bloch equations. The equations of motion for the components of ρ become, for the general case of complex Ω_1 ,

$$\begin{aligned} \frac{d\rho_{ee}}{dt} &= -\gamma_e \rho_{ee} - \frac{1}{2}(i\Omega_1^* \tilde{\rho}_{eg} + \text{c.c.}), \\ \frac{d\rho_{gg}}{dt} &= -\gamma_g \rho_{gg} + \frac{1}{2}(i\Omega_1^* \tilde{\rho}_{eg} + \text{c.c.}), \\ \frac{d\tilde{\rho}_{eg}}{dt} &= -(\gamma + i\Delta)\tilde{\rho}_{eg} - i\frac{\Omega_1}{2}(\rho_{ee} - \rho_{gg}), \end{aligned} \quad (72.66)$$

where $\gamma = (\gamma_e + \gamma_g)/2 + \gamma_{\text{ph}}$, and $\tilde{\rho}_{eg} = \rho_{eg} e^{i\omega t}$. In the case of spontaneous decay from the upper to the lower level, these equations become

$$\begin{aligned} \frac{d\rho_{ee}}{dt} &= -\Gamma \rho_{ee} - \frac{1}{2}(i\Omega_1^* \tilde{\rho}_{eg} + \text{c.c.}), \\ \frac{d\rho_{gg}}{dt} &= +\Gamma \rho_{ee} + \frac{1}{2}(i\Omega_1^* \tilde{\rho}_{eg} + \text{c.c.}), \\ \frac{d\tilde{\rho}_{eg}}{dt} &= -(\gamma + i\Delta)\tilde{\rho}_{eg} - i\frac{\Omega_1}{2}(\rho_{ee} - \rho_{gg}), \end{aligned} \quad (72.67)$$

where $\gamma = \Gamma/2 + \gamma_{\text{ph}}$. Equations (72.67) are completely equivalent to the optical Bloch equations (72.65).

72.5 Rate Equation Approximation

If the coherence decay rate γ is dominated by elastic collisions, and hence is much larger than the population decay rates γ_e and γ_g , $\tilde{\rho}_{eg}$ can be adiabatically eliminated from the equations of motion Eqs. (72.66) and (72.67) to obtain the rate equations (Sect. 72.2)

$$\begin{aligned} \frac{d\rho_{ee}}{dt} &= -\gamma_e \rho_{ee} - R(\rho_{ee} - \rho_{gg}), \\ \frac{d\rho_{gg}}{dt} &= -\gamma_g \rho_{gg} + R(\rho_{ee} - \rho_{gg}), \end{aligned} \quad (72.68)$$

and

$$\begin{aligned} \frac{d\rho_{ee}}{dt} &= -\Gamma \rho_{ee} - R(\rho_{ee} - \rho_{gg}), \\ \frac{d\rho_{gg}}{dt} &= +\Gamma \rho_{gg} + R(\rho_{ee} - \rho_{gg}), \end{aligned} \quad (72.69)$$

respectively, where the transition rate is

$$R = |\Omega_1|^2 \mathcal{L}(\Delta)/(2\gamma), \quad (72.70)$$

and we have introduced the dimensionless Lorentzian

$$\mathcal{L}(\Delta) = \gamma^2/(\gamma^2 + \Delta^2). \quad (72.71)$$

The transitions between the upper and lower state are, thus, described in terms of simple rate equations.

Adding phenomenological pumping rates Λ_e and Λ_g on the right-hand side of Eq. (72.68) provides a description of the excitation of the upper and lower levels from some distant levels, as would be the case in a laser. The equations then form the basis of conventional, single-mode laser theory. In the absence of such mechanisms, the atomic populations eventually decay away.

72.5.1 Steady State

In the case of upper to lower-level decay, the state populations reach a steady state with inversion [5, 17]

$$W_{\text{st}} = -\frac{\Gamma}{\Gamma + 2R} = -\frac{1}{1 + s}, \quad (72.72)$$

where s is the saturation parameter. In the case of pure radiative decay, $\gamma_{\text{ph}} = 0$, s is given by

$$s = \frac{\Omega_1^2/2}{\Gamma^2/4 + \Delta^2}. \quad (72.73)$$

In steady state, the other two components of the Bloch vector U are given by

$$U_{\text{st}} = -\frac{2\Delta}{\Omega_1} \left(\frac{s}{1 + s} \right) \quad (72.74)$$

and

$$V_{\text{st}} = \frac{\Gamma}{\Omega_1} \left(\frac{s}{1 + s} \right); \quad (72.75)$$

U_{st} varies as a dispersion curve as a function of the detuning Δ , while V_{st} is a Lorentzian of power-broadened half-width at half-maximum $(\Gamma^2/4 + \Omega_1^2)^{1/2}$.

72.5.2 Saturation

As the intensity of the driving field, or Ω_1^2 , increases, U_{st} and V_{st} first increase linearly with Ω_1 , reach a maximum, and finally tend to zero as $\Omega_1 \rightarrow \infty$. The inversion W_{st} , which equals -1 for $\Omega_1 = 0$, first increases quadratically and asymptotically approaches $W_{\text{st}} = 0$ as $\Omega_1 \rightarrow \infty$. At this point, where the upper and lower state populations are equal, the transition is said to be saturated, and the medium becomes effectively transparent, or bleached. (This should not be confused with self-induced transparency, which is discussed in Chap. 77.) The inversion is always negative, which, in particular, means that no steady-state light amplification can be achieved in this system. This is one reason why external pump mechanisms are required in lasers.

72.5.3 Einstein A and B Coefficients

When atoms interact with broadband radiation instead of the monochromatic fields considered so far, Eq. (72.69) still apply, but the rate R becomes

$$R \rightarrow B_{eg}\varrho(\omega), \quad (72.76)$$

where $\varrho(\omega)$ is the spectral energy density of the inducing radiation. Einstein's A and B coefficients apply to an atom in thermal equilibrium with the field, which is described by Planck's blackbody radiation law

$$\varrho(\omega) = \frac{\hbar\omega^3}{\pi^2 c^3} \frac{1}{e^{\hbar\omega/k_B T} - 1}, \quad (72.77)$$

where T is the temperature of the source, and k_B is Boltzmann's constant. Invoking the principle of detailed balance, which states that at thermal equilibrium, the average number of transitions between arbitrary states $|i\rangle$ and $|k\rangle$ must be equal to the number of transitions between $|k\rangle$ and $|i\rangle$, one finds

$$\frac{A_{ki}}{B_{ki}} = \frac{\hbar\omega^3}{\pi^2 c^3}, \quad (72.78)$$

where A_{ki} is the rate of spontaneous emission from $|k\rangle$ to $|i\rangle$, and $\Gamma_k = \sum_i A_{ki}$ is the level width.

72.6 Light Scattering

Far from resonance, the approximation of a two-level or few-level atom is no longer adequate. Two limiting cases, which are always far from resonance, are Rayleigh scattering for low frequencies and Thomson scattering for high frequencies.

72.6.1 Rayleigh Scattering

Rayleigh scattering is the elastic scattering of a monochromatic electromagnetic field of frequency ω , wave vector \mathbf{k} , and polarization $\boldsymbol{\epsilon}$ by an atomic system in the limit where ω is very small compared with its excitation energies [4, 17]. To second order in perturbation theory, the Rayleigh scattering differential cross section into the solid angle Ω' about the wave vector \mathbf{k}' with $k' = k$, and polarization $\boldsymbol{\epsilon}'$ is

$$\frac{d\sigma}{d\Omega'} = r_0^2 \omega^4 (\boldsymbol{\epsilon} \cdot \boldsymbol{\epsilon}')^2 \left(\sum_e \frac{f_{ge}}{\omega_{eg}^2} \right)^2, \quad (72.79)$$

where r_0 is the classical electron radius, the sum is over all states $|e\rangle$, f_{ge} is the E1 oscillator strength Eq. (72.64), and

ω_{ge} is the transition frequency. The corresponding total cross section is

$$\sigma = \frac{8\pi r_0^2 \omega^4}{3} \left(\sum_e \frac{f_{ge}}{\omega_{eg}^2} \right)^2. \quad (72.80)$$

72.6.2 Thomson Scattering

Thomson scattering is the corresponding elastic photon scattering by an atom in the limit where ω is very large compared with the atomic ionization energy, yet small enough compared to $\alpha mc^2/\hbar$, that the dipole approximation can be applied. The differential cross section for this process is [4, 17]

$$\frac{d\sigma}{d\Omega'} = r_0^2 (\boldsymbol{\epsilon} \cdot \boldsymbol{\epsilon}')^2, \quad (72.81)$$

and the total cross section is

$$\sigma = \frac{8}{3} \pi r_0^2. \quad (72.82)$$

This is a completely classical result, which exhibits no frequency dependence.

72.6.3 Resonant Scattering

We finally consider elastic scattering in the limit where ω is close to the transition frequency ω_0 between $|g\rangle$ and $|e\rangle$. Provided that no other level is near resonant with the ground state, the resonant scattering differential cross section is [6, 17]

$$\frac{d\sigma}{d\Omega'} = \frac{9}{16\pi^2} \lambda_0^2 (\boldsymbol{\epsilon} \cdot \boldsymbol{\epsilon}')^2 \frac{(\Gamma/2)^2}{\Delta^2 + (\Gamma/2)^2}, \quad (72.83)$$

where $\lambda_0 = 2\pi c/\omega_0$ is the wavelength of the transition, and Γ is the spontaneous decay rate Eq. (72.61). The total elastic scattering cross section is

$$\sigma = \frac{3}{2\pi} \lambda_0^2. \quad (72.84)$$

In contrast to the nonresonant Rayleigh and Thomson scattering cross sections, which scale as the square of the classical electron radius, the resonant scattering cross section scales as the square of the wavelength. For optical frequencies, $\lambda_0/r_0 \simeq 10^4$, giving a *resonant enhancement* of about eight orders of magnitude. This illustrates why near-resonant phenomena, which form the bulk of the following chapters, are so important in optical physics and quantum optics.

References

1. Shore, B.W.: The Theory of Coherent Atomic Excitation. Wiley, New York (1990)
2. Cohen-Tannoudji, C., Dupont-Roc, J., Grynberg, G.: Photons and Atoms: Introduction to Quantum Electrodynamics. Wiley, New York (1989)
3. Sommerfeld, A.: Optics. Academic Press, New York (1967)
4. Jackson, J.D.: Classical Electrodynamics. Wiley, New York (1975)
5. Allen, L., Eberly, J.H.: Optical Resonance and Two-Level Atoms. Dover, New York (1987)
6. Milonni, P.W., Eberly, J.H.: Laser Physics. Wiley, New York (1988)
7. Meystre, P., Sargent III, M.: Elements of Quantum Optics, 4th edn. Springer, Berlin, Heidelberg (2007)
8. Born, M., Wolf, E.: Principles of Optics, 4th edn. Pergamon, Oxford (1970)
9. Glauber, R.J.: Optical coherence and photon statistics. In: DeWitt, C., Blandin, A., Cohen-Tannoudji, C. (eds.) Quantum Optics and Electronics. Gordon and Breach, New York (1965)
10. Mandel, L., Wolf, E.: Optical Coherence and Quantum Optics. Cambridge University Press, Cambridge (1995)
11. Zubairy, M.S., Scully, M.O.: Quantum Optics. Cambridge University Press, Cambridge (1997)
12. Shen, Y.R.: The Principles of Nonlinear Optics. Wiley, New York (1984)
13. Orszag, M.: Quantum Optics, 3rd edn. Springer, Berlin, Heidelberg (2016)
14. Schleich, W.P.: Quantum Optics in Phase Space. Wiley-VCH, Weinheim (2001)
15. Sargent III, M., Scully Jr., M.O., Lamb, W.E.: Laser Physics. Wiley, Reading (1977)
16. Stenholm, S.: Foundations of Laser Spectroscopy. Wiley, New York (1984)
17. Cohen-Tannoudji, C., Dupont-Roc, J., Grynberg, G.: Atom-Photon Interactions: Basic Processes and Applications. Wiley, New York (1992)
18. Knight, P.L., Milonni, P.W.: Phys. Rep. **66**, 21 (1980)
19. Berman, P.P. (ed.): Cavity QED. Academic Press, Boston (1994)
20. Cohen-Tannoudji, C.: Atomic motion in laser light. In: Dalibard, J., Raimond, J.M., Zinn-Justin, J. (eds.) Fundamental Systems in Quantum Optics. North-Holland, Amsterdam (1992)
21. Feynman, R.P., Vernon, F.L., Hellwarth, R.W.: J. Appl. Phys. **28**, 49 (1957)



Pierre Meystre's research ranges from theoretical quantum optics and ultracold science to quantum optomechanics. He is a recipient of the Senior Scientist Research Prize of the Humboldt Society, the R.W. Wood Prize, and the Willis E. Lamb Award. He is an Emeritus Regents Professor at the University of Arizona and a Honorary Professor at East China Normal University.



Stig Stenholm

Contents

73.1	Introduction	1057
73.2	Index of Refraction	1057
73.3	Density Matrix Treatment of the Two-Level Atom	1058
73.4	Line Broadening	1059
73.5	The Rate Equation Limit	1060
73.6	Two-Level Doppler-Free Spectroscopy	1062
73.7	Three-Level Spectroscopy	1064
73.8	Special Effects in Three-Level Systems	1065
73.9	Summary of the Literature	1067
	References	1067

Abstract

This chapter develops theoretical techniques to describe absorption and emission spectra, using concepts introduced in Chap. 72, and density matrix methods from Chap. 7. The simplest cases are treated, compatible with the physics involved, and more realistic applications are referred to in other chapters. Vector notation is not used, but it can be inserted as required. Only steady-state spectroscopy is covered; for time-resolved transient techniques see Chap. 77.

Laser technology has greatly expanded the potential of atomic and molecular spectroscopy, but the same techniques for describing the interaction of light with matter also apply to the traditional arc lamps and flash discharges, and the more recent synchrotron radiation sources.

Keywords

density matrix · rotate wave approximation · hole burning · density matrix element · radiation trapping

73.1 Introduction

In many cases, departures from the thin sample limit, such as beam attenuation, light scattering and radiation trapping (Sect. 73.3) may be important. However, the properties of laser devices themselves depend in an essential way on these effects, making a self-consistent treatment of their properties necessary.

At the other extreme, the spectroscopy of dilute gases is well characterized by ensemble averages over the properties of the individual particles, interrupted by occasional brief collisions. Ensemble averages, however, may no longer apply to recent experiments probing a single atomic particle in a trap, as discussed in Chap. 79.

73.2 Index of Refraction

As discussed in Sect. 72.2.2, the complex index of refraction for a medium containing harmonically bound charges (electrons) [1] with natural frequency ω_0 is

$$\begin{aligned}
 n(\omega) &= \sqrt{1 + \frac{N\alpha(\omega)}{\epsilon_0}} \approx 1 + \frac{N\alpha(\omega)}{2\epsilon_0} \\
 &= 1 + \frac{Ne^2}{2m\epsilon_0} \left(\frac{i\gamma\omega + (\omega_0^2 - \omega^2)}{(\omega_0^2 - \omega^2)^2 + \gamma^2\omega^2} \right) \\
 &= n' + i n'' .
 \end{aligned} \tag{73.1}$$

The expansion is valid when the density of atoms N is low. A plane wave can be written in the form

$$\mathcal{E} \propto e^{ikz} = e^{i\omega n z/c} = e^{i\omega n' z/c} e^{-\omega n'' z/c} . \tag{73.2}$$

The absorption of light through the medium then shows a resonant behavior near $\omega \approx \omega_0$ determined by

$$\begin{aligned} n'' &= \frac{Ne^2}{2m\epsilon_0} \left(\frac{\gamma\omega}{(\omega_0^2 - \omega^2)^2 + \gamma^2\omega^2} \right) \\ &\approx \frac{\pi Ne^2}{4m\epsilon_0\omega_0} \left(\frac{\gamma/2\pi}{(\omega - \omega_0)^2 + \gamma^2/4} \right). \end{aligned} \quad (73.3)$$

This is called an absorptive lineshape. When the single electron is harmonically bound, its interaction with radiation is found in this response. For a real atom, the response of the electron is divided among the various transitions to other states. The fraction assigned to one single transition is characterized by the oscillator strength f_n as discussed in Sect. 72.4.2.

In ordinary linear spectroscopy, the laser is tuned through the resonance $\omega \approx \omega_0$, and the value of ω_0 is determined from the lineshape Eq. (73.3). Several closely spaced resonances can be *resolved* if their spacing is larger than their widths

$$\left| \omega_0^{(1)} - \omega_0^{(2)} \right| > \gamma. \quad (73.4)$$

This defines the *spectral resolution* (Chap. 11).

The velocity of light in the medium is seen to be given by the expression

$$c_{\text{eff}} = \frac{c}{n'} \approx c \left[1 - \frac{Ne^2}{2m\epsilon_0} \left(\frac{\omega_0^2 - \omega^2}{(\omega_0^2 - \omega^2)^2 + \gamma^2\omega^2} \right) \right]. \quad (73.5)$$

This expression shows a *dispersive behavior* around the position $\omega = \omega_0$, where the modification of the velocity disappears. Below resonance $\omega < \omega_0$, the velocity of light is lower than in vacuum. This derives from the fact that the polarization is in phase with the driving field. Thus, by storing the incoming energy, the driving field retards the propagation of the radiation.

For a harmonically bound charge, the refractive index Eq. (73.1) always stays absorptive and it is independent of the intensity of the laser radiation. This no longer holds for discrete level atomic systems. In order to see this, we consider the *two-level atom* in Sect. 73.3.

73.3 Density Matrix Treatment of the Two-Level Atom

The response of atoms to light is conveniently expressed in terms of the density matrix ρ . In addition to the direct physical meaning of the density matrix elements discussed in Sect. 72.3.3, the density matrix formalism is advantageous because the various relaxation mechanisms effecting the atomic resonances can be introduced phenomenologically

into its equations of motion, and theoretical derivations often provide *master equations* for the density matrix (Chap. 7).

The two-level Hamiltonian Eq. (72.35) can be written as

$$\mathbf{H} = \begin{bmatrix} \hbar\omega_0/2 & -d\mathcal{E}(R, t) \\ -d\mathcal{E}(R, t) & -\hbar\omega_0/2 \end{bmatrix}. \quad (73.6)$$

The equation of motion for the density matrix Eq. (72.67) is then

$$\begin{aligned} \frac{d}{dt}\rho_{ee} &= -\Gamma\rho_{ee} + \frac{id\mathcal{E}}{\hbar} \cos\omega t (\rho_{ge} - \rho_{eg}), \\ \frac{d}{dt}\rho_{gg} &= \Gamma\rho_{ee} - \frac{id\mathcal{E}}{\hbar} \cos\omega t (\rho_{ge} - \rho_{eg}), \\ \frac{d}{dt}\rho_{eg} &= -(\gamma + i\omega_0)\rho_{eg} + \frac{id\mathcal{E}}{\hbar} \cos\omega t (\rho_{gg} - \rho_{ee}). \end{aligned} \quad (73.7)$$

Here Γ is the spontaneous decay rate given by Eq. (72.61) and

$$\gamma = \Gamma/2 + \gamma_{\text{ph}}, \quad (73.8)$$

where γ_{ph} derives from all processes that tend to randomize the phase between the quantum states $|e\rangle$ and $|g\rangle$, such as collisions (Chaps. 7 and 20), noise in the laser fields and thermal excitation of the environment in solid state spectroscopy. The Greek letters Γ and γ correspond to the longitudinal relaxation rate (T_1 -process) and the transverse relaxation rate (T_2 -process), respectively.

In the rotating wave approximation (RWA) the density matrix equations Eq. (73.7) become identical to Eq. (72.67) with

$$\rho_{eg} = \tilde{\rho}_{eg} e^{-i\omega t}. \quad (73.9)$$

Using the condition of conservation of probability

$$\rho_{ee} + \rho_{gg} = 1, \quad (73.10)$$

the steady state solutions to Eq. (72.67) are [2]

$$\rho_{ee} = \frac{\Omega_1^2 \gamma}{2\Gamma} \left(\frac{1}{\Delta^2 + \gamma^2 + \Omega_1^2 \gamma / \Gamma} \right), \quad (73.11)$$

$$\begin{aligned} \tilde{\rho}_{eg} &= \frac{i\Omega_1}{2} \frac{(\rho_{gg} - \rho_{ee})}{\gamma + i\Delta} \\ &= \frac{i\Omega_1}{2} \left(\frac{\gamma - i\Delta}{\Delta^2 + \gamma^2 + \Omega_1^2 \gamma / \Gamma} \right), \end{aligned} \quad (73.12)$$

where Ω_1 is the Rabi frequency from Eq. (72.44), and $\Delta = \omega_0 - \omega$ is the detuning. The induced polarization is then

$$\begin{aligned} \mathcal{P} &= N \text{Tr}(\hat{d}\rho) = N \text{Tr} \left[\begin{pmatrix} 0 & d \\ d & 0 \end{pmatrix} \begin{pmatrix} \rho_{ee} & \rho_{eg} \\ \rho_{ge} & \rho_{gg} \end{pmatrix} \right] \\ &= Nd (e^{-i\omega t} \tilde{\rho}_{eg} + e^{i\omega t} \tilde{\rho}_{ge}) \\ &= N (\alpha \mathcal{E}^{(+)} + \alpha^* \mathcal{E}^{(-)}), \end{aligned} \quad (73.13)$$

where N is the density of active two-level atoms. Setting

$$\mathcal{E}^{(+)} = \frac{1}{2} \mathcal{E} e^{-i\omega t}, \quad (73.14)$$

the complex polarization is

$$\alpha(\omega) = \frac{d^2}{\hbar} \left(\frac{i\gamma + \Delta}{\Delta^2 + \gamma^2 + \Omega_1^2\gamma/\Gamma} \right), \quad (73.15)$$

and from Eq. (73.1), the complex index of refraction is

$$\begin{aligned} n(\omega) &= 1 + \frac{N\alpha(\omega)}{2\varepsilon_0} \\ &= 1 + \frac{\pi N e^2}{4\varepsilon_0 m \omega_0} \left(\frac{f_0}{\pi} \right) \frac{i\gamma + \Delta}{\Delta^2 + \gamma^2 + \Omega_1^2\gamma/\Gamma}, \end{aligned} \quad (73.16)$$

where $f_0 = 2d^2 m \omega_0 / \hbar e^2$ is the oscillator strength. Summing over all possible transitions yields the f-sum rule Eq. (72.63), (Chap. 22).

The imaginary part of Eq. (73.16) shows exactly the same absorptive behavior as in the harmonic oscillator model of Sect. 73.2 [see Eq. (73.3)]. However, the additional factor of $(\Omega_1^2\gamma/\Gamma)$ in the denominator makes the line appear broader than in the harmonic case; the line is power broadened. Physically, this derives from a saturation of the two-level system in which the population of the upper level becomes an appreciable fraction of that of the lower level. In the limit $\Omega_1 \rightarrow \infty$, Eq. (73.16) shows that $n(\omega) \rightarrow 1$ and the atom-field interaction effectively vanishes. In this limit, $\rho_{ee} \rightarrow \frac{1}{2}$ Eq. (73.11), and the field induces as many upward transitions as downward transitions.

When radiation at the frequency ω propagates in a medium of two-level atoms, the energy density is

$$I(z) \propto \mathcal{E}^* \mathcal{E} \propto \exp \left[- \left(\frac{N d^2 \omega}{\hbar \varepsilon_0 c} \right) \frac{\gamma z}{(\omega - \omega_0)^2 + \gamma^2} \right]. \quad (73.17)$$

Far from resonance ($|\omega - \omega_0| \gg \gamma$), the medium is transparent; but near resonance, damping is observed. The impinging radiation energy is deposited in the medium and propagation is impeded. This is called radiation trapping. In spectroscopy, the phenomenon is seen as a prolongation of the radiative decay time; the spontaneously emitted energy is seen to emerge from the sample more slowly than the single atom lifetime implies.

73.4 Line Broadening

The effective width of a spectral line from Eq. (73.16) is

$$\gamma_{\text{eff}} = \sqrt{\gamma^2 + \Omega_1^2 \frac{\gamma}{\Gamma}} \simeq \frac{1}{2} \Gamma + \gamma_{\text{ph}} + \frac{\Omega_1^2}{2\Gamma} + O(\Omega_1^4). \quad (73.18)$$

The various contributions are as follows [3]. The term γ contains all the transverse relaxation mechanisms. If decay to

additional levels occurs, these must be included (Sect. 73.5). The term γ_{ph} contains all perturbing effects effecting each single atom. For low enough pressures, collisional perturbations are proportional to the density of perturbing atoms so that

$$\gamma_{\text{ph}} = \eta_{\text{coll}} p, \quad (73.19)$$

where p is the pressure of the perturbing gas and η_{coll} is a constant of proportionality. This is called *collision* or *pressure broadening* (Chap. 63), whose order of magnitude can be estimated to be the inverse of the average free time between collisions. For high pressure (usually of the order of torrs), the linearity in Eq. (73.19) breaks down. When identical atoms collide, *resonant exchange* of energy may also take place. The third term in Eq. (73.18) is the *power broadening* term. It derives from the effect of the laser field on each individual atom. All such relaxation processes that are active on each and every individual atom separately are called *homogeneous broadening* processes. For a detailed discussion of *line broadening*, consult Chap. 20.

In contrast to homogeneous broadening, Doppler broadening is characterized by an atomic velocity parameter v which varies over the observed assembly. In a thermal assembly at temperature T (e.g., a gas cell), the velocity distribution is

$$P(v) = \frac{1}{\sqrt{2\pi}u^2} \exp\left(-\frac{v^2}{2u^2}\right), \quad (73.20)$$

where $u^2 = k_B T / M$. A particular atom with velocity v in the direction of the optical beam with wave vector k then experiences the Doppler-shifted frequency $\omega - kv$ relative to a stationary atom, and the effective detuning becomes

$$\Delta' = \Delta + kv, \quad (73.21)$$

replacing Δ . The population in the lower level from Eq. (73.11) is then

$$\rho_{gg} = 1 - \frac{\Omega_1^2 \gamma}{2\Gamma} \left(\frac{1}{(\Delta + kv)^2 + \gamma^2 + \Omega_1^2 \gamma / \Gamma} \right). \quad (73.22)$$

The atoms in the lower level, originally distributed according to Eq. (73.20), are now depleted from the velocity group around

$$v = (\omega - \omega_0) / k. \quad (73.23)$$

The width of the depleted region is given by γ_{eff} of Eq. (73.18). This region is called a *Bennett hole*. When the laser frequency ω is tuned, the hole sweeps over the velocity distribution of the atoms. The atomic response is saturated at the velocity group of the hole, indicating that *spectral hole burning* has occurred.

The observed spectrum is obtained by averaging the single atom response Eq. (73.15) over the velocity distribution. From the imaginary part, the absorption response is

$$\alpha''(\omega) = \frac{d^2}{\hbar\sqrt{2\pi}u^2} \int_{-\infty}^{+\infty} \frac{\gamma e^{-v^2/2u^2}}{(\Delta + kv)^2 + \gamma^2 + \Omega_1^2\gamma/\Gamma} dv. \quad (73.24)$$

In the limits $\Omega_1 \rightarrow 0$ (no saturation), and $\gamma \ll ku$ (the Doppler limit), the Lorentzian line shape sweeps over the entire velocity profile, finding a resonant velocity group according to Eq. (73.23) as long as $v \leq u$. Thus, the linear spectroscopy sees a *Doppler broadened line* of width ku . This is called *inhomogeneous broadening*.

In the unsaturated regime, the atomic response function Eq. (73.24) is proportional to the imaginary part of the function

$$V(z) = \frac{1}{\sqrt{2\pi}\sigma^2} \int_{-\infty}^{+\infty} \frac{\exp(-x^2/2\sigma^2)}{z - x} dx, \quad (73.25)$$

at $z = -\Delta - i\gamma$ and $\sigma = ku$. This is the Hilbert transform of the Gaussian, and its shape is called a *Voigt profile* [4]. For $\gamma \ll ku$, it traces over the Gaussian, but for large detunings it always goes to zero as slowly as the Lorentzian, i.e., as Δ^{-1} . The profile has been widely used to interpret the data of *linear spectroscopy*. The function is tabulated [5] and its expansion is

$$V(z) = \sqrt{-\frac{\pi}{2\sigma^2}} \sum_{n=0}^{\infty} \frac{(iz/\sqrt{2}\sigma)^n}{\Gamma(1 + n/2)}, \quad (73.26)$$

and it has the continued fraction representation,

$$V(z) = \frac{1}{z - \frac{\sigma^2}{z - \frac{2\sigma^2}{z - \frac{3\sigma^2}{z - \frac{4\sigma^2}{z - \dots}}}}} \quad (73.27)$$

In addition to velocity, any other parameter shifting the individual atomic resonance frequencies ω_0 by different amounts for the different individuals leads to *inhomogeneous broadening*. The detuning Δ is then different for different members of the observed assembly, and a line shape similar to Eq. (73.24) applies. The distribution function must be replaced by the one relevant for the problem. In practice a Gaussian is almost always assumed.

An example of inhomogeneous broadening is the influence of the lattice environment on impurity spectroscopy

in solids. The resonant light selectively excites atoms at those particular positions which make the atoms resonant. Thus only these spatial locations are saturated, and the phenomenon of *spatial hole burning* occurs. This has been investigated as a method for storing information, signal processing, and volume holography.

It is, however, possible that the effects of collisions can counteract the inhomogeneous broadening. In order to see this we observe that the induced atomic dipole is proportional to the induced density matrix element, from Eq. (73.9),

$$\rho_{eg} = \tilde{\rho}_{eg} e^{i(kz(t) - \omega t)} \propto e^{ikvt}. \quad (73.28)$$

If the atoms now experience collisions characterized by an average free time of flight τ , the phase $kv t$ cannot build up coherently for times longer than this duration, the atomic velocity is quenched on the average, and the full Doppler profile cannot be observed. To see how this comes about, consider a time $t \gg \tau$. During this period the atom experiences on the average $\bar{n} = t/\tau$ collisions. Assuming a Poisson distribution, the probability of n collisions in time t is

$$p_n = \frac{e^{-\bar{n}} \bar{n}^n}{n!}. \quad (73.29)$$

Taking the average of Eq. (73.28) over the time $t = n\tau$ with the distribution p_n yields

$$\begin{aligned} \bar{\rho}_{eg} &\propto \sum_{n=0}^{\infty} e^{ikv n\tau} \left(\frac{e^{-\bar{n}} \bar{n}^n}{n!} \right) \\ &= e^{-\bar{n}} \exp(\bar{n} e^{ikv\tau}) \\ &\approx e^{ikvt} \exp\left(-\frac{1}{2} t k^2 v^2 \tau\right). \end{aligned} \quad (73.30)$$

This heuristic derivation suggests that for long enough interaction times ($t \gg \tau$), the large velocity components are suppressed. This tends to prevent the tails of the velocity distribution from contributing to the observed spectral profile. The effect is called *collisional narrowing* or *Dicke narrowing*. It is an observable effect, but the narrowing cannot be very large. To overcome the Doppler broadening one has to turn to nonlinear laser methods (Sect. 73.6).

73.5 The Rate Equation Limit

Consider now a generalized theory for the case of several incoming electromagnetic fields of the form

$$\mathcal{E}(R, t) = \sum_i \frac{1}{2} \mathcal{E}_i(R) e^{-i\omega_i t + i\varphi_i} + \text{c.c.} \quad (73.31)$$

The index i may range over several laser sources, the output of a multimode laser or the multitude of components of

a flashlight or a thermal source. Each component carries its own amplitude \mathcal{E}_i .

In steady state, the generalization of Eq. (73.12) becomes

$$\rho_{eg} = \frac{i}{2} \sum_i \frac{d\mathcal{E}_i}{\hbar} \frac{(\rho_{gg} - \rho_{ee})}{\gamma + i\Delta_i} e^{-i\omega_i t + i\varphi_i}, \quad (73.32)$$

where the detuning is

$$\Delta_i = \omega_0 - \omega_i. \quad (73.33)$$

The response of the atom now separates into individual contributions oscillating at the various frequencies ω_i according to

$$\rho_{eg} = \sum_i \rho_{eg}^{(i)} e^{-i\omega_i t + i\varphi_i}. \quad (73.34)$$

This resolution is of key importance to the theory.

With the multimode field, Eq. (72.67) for the level occupation probabilities become

$$\begin{aligned} \frac{d}{dt} \rho_{ee} &= -\frac{d}{dt} \rho_{gg} \\ &= -\Gamma \rho_{ee} + \frac{i}{2} \sum_i \\ &\quad \times \left(\frac{d\mathcal{E}_i}{\hbar} e^{-i\omega_i t + i\varphi_i} \rho_{ge} - \text{c.c.} \right). \end{aligned} \quad (73.35)$$

Insertion of the steady state result Eq. (73.32) into this equation yields a closed set of equations for the level occupation probabilities. These are called *rate equations*.

To justify the above steps, consider the single frequency case again. The off-diagonal time derivatives can be neglected when

$$\left| \frac{d}{dt} \rho_{eg} \right| \ll |\gamma + i\Delta| |\rho_{eg}|. \quad (73.36)$$

This can be surmised to hold when the phase relaxation contributions to γ are large Eq. (73.8) or the detuning $|\Delta|$ is large. Insertion of Eq. (73.32) into Eq. (73.35) for the single mode case gives

$$\frac{d}{dt} \rho_{ee} = -\Gamma \rho_{ee} - W (\rho_{ee} - \rho_{gg}), \quad (73.37)$$

where the rate coefficient is given by

$$W = 2\pi \left(\frac{d\mathcal{E}}{2\hbar} \right)^2 \frac{\gamma/\pi}{\Delta^2 + \gamma^2}. \quad (73.38)$$

Multiplying Eq. (73.37) by the density of active atoms N then produces the conventional rate equations for the populations $N_{ee} = N\rho_{ee}$ and $N_{gg} = N\rho_{gg}$.

Two physical effects can be discerned in Eq. (73.37): *induced* and *spontaneous emission*. The term with Γ gives

the spontaneous emission which forces the entire population to the lower level. The terms proportional to W describe induced emission, with upward transitions proportional to $W\rho_{gg}$ and downward transitions proportional to $W\rho_{ee}$. In the absence of spontaneous emission, they strive to equalize the population of the two levels. Using Eq. (73.10), the steady-state solution is

$$\begin{aligned} \rho_{ee} &= \frac{W}{\Gamma + 2W} \\ &= \frac{1}{2} \left(\frac{d\mathcal{E}}{\hbar} \right)^2 \frac{\gamma}{\Gamma \Delta^2 + \gamma^2 + (d\mathcal{E}/\hbar)^2 \gamma/\Gamma}. \end{aligned} \quad (73.39)$$

This is clearly seen to agree with the solution Eq. (73.11) as is expected in steady state.

Although the rate equations were derived in the limit Eq. (73.36), the rate coefficient Eq. (73.38) has a special significance in the limit $\gamma \rightarrow 0$. In this limit, the factor

$$\begin{aligned} \frac{1}{\hbar} \lim_{\gamma \rightarrow 0} \left(\frac{\gamma/\pi}{\Delta^2 + \gamma^2} \right) &= \frac{1}{\hbar} \delta(\Delta) \\ &= \delta(\hbar\omega - \hbar\omega_0), \end{aligned} \quad (73.40)$$

enforces energy conservation in the transition. Using the field in Eq. (73.14), and the interaction from Eq. (73.6), the off-diagonal matrix element is

$$|\langle e|H|g\rangle| = \frac{1}{2} d\mathcal{E}. \quad (73.41)$$

With these results, Eq. (73.38) can be written in the form of *Fermi's Golden Rule*

$$W = \frac{2\pi}{\hbar} |\langle e|H|g\rangle|^2 \delta(\hbar\omega - \hbar\omega_0), \quad (73.42)$$

usually derived from time dependent perturbation theory.

Returning to the multimode rate equations, an incoherent *broad band light source* has many components that contribute to the sum over field frequencies. In the case of flash pulses, thermal light sources, or free-running multimode lasers the spectral components are uncorrelated. Inserting Eq. (73.32) into Eq. (73.35) yields

$$\begin{aligned} \frac{d}{dt} \rho_{ee} &= -\frac{d}{dt} \rho_{gg} \\ &= -\Gamma \rho_{ee} + \frac{d^2}{2\hbar^2} (\rho_{gg} - \rho_{ee}) \\ &\quad \times \sum_{i,j} \mathcal{E}_i \mathcal{E}_j e^{i(\omega_j - \omega_i)t} e^{i(\varphi_i - \varphi_j)} \frac{\gamma}{\Delta_{j,j}^2 + \gamma^2}. \end{aligned} \quad (73.43)$$

The contributions from the different terms $i \neq j$ average to zero either by beating at the frequencies $|\omega_i - \omega_j|$ or by incoherent effects from the random phases φ_j . Thus, only the coherent sum survives to give

$$\begin{aligned} \frac{d}{dt} \rho_{ee} &= -\frac{d}{dt} \rho_{gg} \\ &= -\Gamma \rho_{ee} \times \sum_i W^{(i)} (\rho_{gg} - \rho_{ee}), \end{aligned} \quad (73.44)$$

where the rate coefficients $W^{(i)}$ are given by Eq. (73.38) with the appropriate detunings $\Delta_j = \omega_0 - \omega_j$. This is a *rate equation* in the limit of many uncorrelated components of light, i.e., for a *broad band light source*. In this case the incoherence between the different components justifies the use of a rate approach, and no assumption like Eq. (73.36) is needed. Thus, the limit $\gamma \rightarrow 0$ Eq. (73.40) is legitimate, and the $W^{(i)}$ can be calculated in time dependent perturbation theory from Fermi's Golden Rule.

In the limit of an incoherent broad band light source, the sum in Eq. (73.44) can be replaced by an integral. In particular, this is allowed for incandescent light sources as used in *optical pumping* experiments [6]. Pumping of lasers by strong lamps or flashes are also describable by the same rate equations.

In amplifiers and lasers, the atoms must be brought into states far from equilibrium by incoherent optical excitation or resonant transfer of excitation energy in collisions (Chap. 74). In the two-level description, the atomic levels are constantly replenished. The normalization condition Eq. (73.10) is then no longer appropriate; often the density matrix is normalized so that $\text{Tr}(\rho)$ directly gives the density of active atoms.

With pumping into the levels, one must allow for decay out of the two-level system in order to prevent the atomic density from growing in an unlimited way. This decay takes the atom to unobserved levels. In the rate equation approximation, the pumping and decay processes can be described by terms added to the equations of the form Eq. (72.68)

$$\begin{aligned} \frac{d}{dt}\rho_{ee} &= \lambda_e - \gamma_e\rho_{ee}, \\ \frac{d}{dt}\rho_{gg} &= \lambda_g - \gamma_g\rho_{gg}. \end{aligned} \quad (73.45)$$

In a laser, the level $|g\rangle$ is usually not the ground state of the system.

From Eq. (73.45), the steady state population is

$$\rho_{gg}^{(0)} - \rho_{ee}^{(0)} = \lambda_g/\gamma_g - \lambda_e/\gamma_e. \quad (73.46)$$

A *population inversion* exists when this is negative. The population difference Eq. (73.46) is modified when the effects of spontaneous and induced processes are added, as in Eq. (73.37). Then the transitions saturate because of the *induced processes*.

Using Eq. (73.46) in Eq. (73.12), the calculated polarizability without saturation is

$$\alpha(\omega) = \left(\frac{d^2}{\hbar}\right) \left(\frac{i\gamma + \Delta}{\gamma^2 + \Delta^2}\right) (\rho_{gg}^{(0)} - \rho_{ee}^{(0)}). \quad (73.47)$$

According to Eq. (73.1), the index of refraction is

$$\begin{aligned} n'(\omega) &= 1 + \frac{N\alpha'(\omega)}{2\varepsilon_0} \\ &= 1 - \left(\frac{Nd^2}{2\varepsilon_0\hbar}\right) \frac{(\omega - \omega_0)}{(\omega - \omega_0)^2 + \gamma^2} (\rho_{gg}^{(0)} - \rho_{ee}^{(0)}). \end{aligned} \quad (73.48)$$

For weakly excited atoms, $\rho_{gg} \approx 1$, and Eq. (73.47) agrees with the unsaturated limit of Eq. (73.16). The dispersion of a light signal behaving according to Eq. (73.48) is called *normal*, i.e., according to the harmonic model in Sect. 73.2. Below resonance ($\omega < \omega_0$), n' is larger than unity, implying a reduction of the velocity of light. As a function of ω , the curve Eq. (73.48) starts above unity, and passes below unity for $\omega > \omega_0$. This is *normal dispersion*.

However, for an *inverted medium* ($\rho_{gg}^{(0)} < \rho_{ee}^{(0)}$), n' is less than unity for low frequencies and goes through unity with a positive slope. This is called *anomalous dispersion* and signifies the presence of a *gain profile*. In such a medium, $\alpha'' = \text{Im}[\alpha(\omega)]$ is of opposite sign, as seen from Eq. (73.47); in the inverted medium, α'' becomes negative near $\Delta = 0$. From Eq. (73.2), this indicates a growing electromagnetic field, i.e., an *amplifying medium*. The amplitude grows, and the assumption of a small signal becomes invalid. Then saturation has to be included, either at the rate equation level or by performing a full density matrix calculation. This regime describes a laser with *saturated gain*. In steady state, the two levels become nearly equally populated ($\rho_{ee} \approx \rho_{gg}$), and the operation is stable. The theory of the laser is discussed in detail in Chap. 74.

73.6 Two-Level Doppler-Free Spectroscopy

The *linear absorption* of a scanned laser signal defines *linear spectroscopy* and gives information characterizing the sample. However, Sect. 73.4 shows that inhomogeneous broadening masks the desired information by dominating the line shape. The availability of laser sources has made it possible to overcome this limitation, and to use the *saturation* properties of the medium to perform *nonlinear spectroscopy*. This section discusses how Doppler broadening can be eliminated to achieve *Doppler-free spectroscopy*. Similar techniques may be used to overcome other types of *inhomogeneous line broadening*; a general name is then *hole-burning spectroscopy* (see the discussion in Sect. 73.4). Other aspects of nonlinear matter-light interaction are found in Chap. 76.

Equation (73.24) shows that a single laser cannot resolve beyond the Doppler width. However, if a strong laser is used to pump the transition, a weak *probe signal* can see the hole burned into the spectral profile by the pump. This technique is called *pump-probe spectroscopy*. Because the probe

is taken to be weak, perturbation theory may be used to calculate the induced polarization to lowest order in the probe amplitude only.

In the field expansion Eq. (73.31), define the strong pump amplitude to be \mathcal{E}_1 and the weak probe \mathcal{E}_2 at frequency ω_2 . From the resolution Eq. (73.34), the component $\rho_{eg}^{(2)}$ carries the information about the linear response at frequency ω_2 . If the field \mathcal{E}_2 propagates in a direction opposite to that of \mathcal{E}_1 , its detuning is

$$\Delta'_2 = \Delta_2 - kv \quad (73.49)$$

(as compared with $\Delta'_1 = \Delta_1 + kv$ for \mathcal{E}_1). Since $\omega_1 \simeq \omega_2$, the two k -vectors are nearly equal in magnitude.

The linear response now becomes

$$\rho_{eg}^{(2)} = \left(\frac{id\mathcal{E}_2}{2\hbar} \right) \frac{1}{\gamma + i(\Delta_2 - kv)} (\rho_{gg} - \rho_{ee}). \quad (73.50)$$

With only the signal \mathcal{E}_1 present, the population difference follows directly from Eq. (73.22). The linear response at frequency ω_2 is then

$$\begin{aligned} \rho_{eg}^{(2)} &= \left(\frac{d\mathcal{E}_2}{2\hbar} \right) \frac{i\gamma + (\Delta_2 - kv)}{\gamma^2 + (\Delta_2 - kv)^2} \\ &\times \left[1 - \frac{\Omega_1^2 \gamma}{\Gamma} \left(\frac{1}{(\Delta_1 + kv)^2 + \gamma^2 + \Omega_1^2 \gamma / \Gamma} \right) \right]. \end{aligned} \quad (73.51)$$

This is the linear response of atoms moving with velocity v . To obtain the polarization of the whole sample, we must average over the velocity distribution using the Gaussian weight Eq. (73.20). The first term in Eq. (73.51) gives the linear response in the form of a *Voigt profile*, as discussed in Sect. 73.4. This part of the response carries no Doppler-free information. The second terms contain the nonlinear response. This shows the details of the homogeneous features under the Doppler line shape. For simplicity we assume the Doppler limit, $\gamma \ll kv$, and neglect the variation of the Gaussian over the atomic line shape. We also neglect the power broadening due to the field \mathcal{E}_1 and obtain, using Eqs. (73.13), (73.20), and (73.51),

$$\begin{aligned} \alpha''(\omega) &= - \left(\frac{d^2}{\hbar} \right) \frac{\Omega_1^2 \gamma^2}{\sqrt{2\pi} \Gamma u} \\ &\times \int_{-\infty}^{+\infty} \frac{dv}{\left[(\Delta_2 - kv)^2 + \gamma^2 \right] \left[(\Delta_1 + kv)^2 + \gamma^2 \right]} \\ &= - \left(\frac{d^2}{\hbar} \right) \frac{\sqrt{2\pi} \Omega_1^2}{4\Gamma ku} \frac{\gamma}{(\omega - \omega_0)^2 + \gamma^2}. \end{aligned} \quad (73.52)$$

This denotes the energy absorbed from the field \mathcal{E}_1 , as induced nonlinearly by the intensity \mathcal{E}_1^2 . The resonance is still at $\omega = \omega_0$, but with a homogeneous atomic line shape. In the Doppler limit, the Doppler broadening is only seen in the prefactor

$$\frac{\Omega_1^2}{\Gamma ku} = \left(\frac{\Omega_1^2}{\Gamma \gamma} \right) \frac{\gamma}{ku}, \quad (73.53)$$

which shows that only the fraction (γ/ku) of all atoms can contribute to the resonant response. The first factor on the right-hand side of Eq. (73.53) is the dimensionless saturation factor.

The Doppler-free character of this spectroscopy derives from the fact that the two fields burn their two separate Bennett holes at the velocities

$$kv_1 = -\Delta_1, \quad \text{and} \quad kv_2 = \Delta_2. \quad (73.54)$$

When these two groups coincide, i.e., when $v_1 = v_2$, the probe \mathcal{E}_2 sees the absorption saturated by the pump field \mathcal{E}_1 and a decreased absorption is observed. For $\omega_1 = \omega_2$, the two holes meet in the middle at zero velocity. With two different frequencies, one can make the holes meet at a nonzero velocity to one side of the Doppler profile. The decreased absorption seen in these experiments is called an *inverted Lamb dip* Chap. 74.

The results derived here are based on a simplified view of the pump-probe response which in turn is based on the rate equation approach. Certain coherent effects are neglected, which would considerably complicate the treatment [2]. Section 73.7 discusses these effects in the three-level system where they are more important.

In addition to measuring the probe absorption induced by the pump field, it is also possible to observe the dispersion of the probe signal caused by the saturation induced by the pump. Assuming that the pump introduces the velocity dependent population difference

$$\rho_{ee} - \rho_{gg} = \Delta\rho(v), \quad (73.55)$$

then from Eq. (73.50), $\text{Re}(n)$ is

$$n' = 1 + \frac{Nd^2}{2\hbar\epsilon_0} \int \frac{\Delta_2 - kv}{(\Delta_2 - kv)^2 + \gamma^2} \Delta\rho(v) dv. \quad (73.56)$$

From Eq. (73.2), the phase of the electromagnetic signal feels the value of n' through the factor

$$\mathcal{E} \propto \exp(i\omega n' z/c). \quad (73.57)$$

Thus, by modifying $\Delta\rho(v)$, a pump laser can control the phase acquired by light traversing the sample, and thereby control the optical length of the sample.

A real atom has magnetic sublevels, which are coupled to light in accordance with *dipole selection rules* (see the

discussion in Chap. 35). If a pump laser is used to affect populations in the various sub-levels differently, the optical paths experienced by the differently circularly polarized components of a linearly polarized probe signal are different. Thus, its plane of polarization will turn, corresponding to the *Faraday effect*. By tuning the pump and the probe over the spectral lines of the sample, the turning of the probe polarization provides a signal to investigate the atomic level structure. This method of *polarization spectroscopy* can be used both with two-level and three-level systems [7].

73.7 Three-Level Spectroscopy

New nonlinear phenomena appear when one of the levels in the two-state configuration, $|e\rangle$ say, is coupled to a final level $|f\rangle$ by a weak probe. This may be above the level $|e\rangle$ (the cascade configuration denoted by \mathcal{E}) or below $|e\rangle$ (the lambda configuration Λ) (if the third level were coupled to $|g\rangle$ we would talk about the inverted lambda or V configuration) [8]. For simplicity, only the \mathcal{E} configuration is discussed here.

Assume that the level pair $|g\rangle \leftrightarrow |e\rangle$ is pumped by the field \mathcal{E}_1 and its effect probed by the field \mathcal{E}_2 coupling $|e\rangle \leftrightarrow |f\rangle$. The dipole matrix element is $d_2 = \langle f|H|e\rangle$. The RWA is now achieved by introducing slowly varying quantities through the definitions

$$\begin{aligned}\rho_{fe} &= e^{i(k_2z - \omega_2t)} \tilde{\rho}_{fe}, \\ \rho_{fg} &= e^{i[(k_1+k_2)z - (\omega_1+\omega_2)t]} \tilde{\rho}_{fg},\end{aligned}\quad (73.58)$$

and omitting all components oscillating at multiples of the optical frequencies. From the equation of motion for the density matrix, the steady state equations are [2]

$$\begin{aligned}(\Delta_2 + k_2v - i\gamma_{fe})\tilde{\rho}_{fe} &= \frac{d_2\mathcal{E}_2}{2\hbar}\rho_{ee} - \frac{d_1\mathcal{E}_1}{2\hbar}\tilde{\rho}_{fg}, \\ [(\Delta_1 + \Delta_2) + (k_1 + k_2)v - i\gamma_{fg}]\tilde{\rho}_{fg} &= \frac{d_2\mathcal{E}_1}{2\hbar}\tilde{\rho}_{eg} - \frac{d_1\mathcal{E}_1}{2\hbar}\tilde{\rho}_{fe},\end{aligned}\quad (73.59)$$

where the second step detuning is now

$$\Delta_2 = \omega_{fe} - \omega_2. \quad (73.60)$$

These equations contain the lowest order response proportional to \mathcal{E}_2 , including some coherence effects. The coherence effects remain to lowest order, even when the last term

in Eq. (73.59) is neglected; in that case, the solution is

$$\begin{aligned}\tilde{\rho}_{fe} &= \left(\frac{d_2\mathcal{E}_2}{2\hbar}\right)\frac{\rho_{ee}}{\Delta_2 + k_2v - i\gamma_{fe}} \\ &\quad - \left(\frac{d_1\mathcal{E}_1}{2\hbar}\right)\left(\frac{d_2\mathcal{E}_2}{2\hbar}\right) \\ &\quad \times \frac{\tilde{\rho}_{eg}}{(\Delta_2 + k_2v - i\gamma_{fe})} \\ &\quad \times \frac{1}{[(\Delta_1 + \Delta_2) + (k_1 + k_2)v - i\gamma_{fg}]}. \quad (73.61)\end{aligned}$$

The result to lowest order in \mathcal{E}_2 follows by replacing the density matrix elements for the two-level system $|e\rangle \leftrightarrow |g\rangle$ by their results calculated without this field. This shows that the polarization induced at the frequency ω_2 consists of two parts: one induced by the population excited to level $|e\rangle$ by the field \mathcal{E}_1 proportional to ρ_{ee} , and the other one is induced by the coherence $\tilde{\rho}_{eg}$ created by the pump. Retaining only the former produces a rate equation approximation, called a *two-step process*. This misses important physical features which are included in the second term called a *two-photon or coherent process*.

In order to see the effects of the two terms most clearly, consider the two-level matrix elements from Eqs. (73.11) and (73.12) in lowest perturbative order with respect to the pump field \mathcal{E}_1 , i.e.,

$$\begin{aligned}\rho_{ee} &= \left(\frac{d_1\mathcal{E}_1}{\hbar}\right)^2 \frac{\gamma_{eg}}{2\gamma_{ee}} \frac{1}{(\Delta_1 + k_1v)^2 + \gamma_{eg}^2}, \\ \tilde{\rho}_{eg} &= \frac{d_1\mathcal{E}_1}{2\hbar} \frac{1}{\Delta_1 + k_1v - i\gamma_{eg}}\end{aligned}\quad (73.62)$$

From Eq. (73.61), these matrix elements give

$$\begin{aligned}\tilde{\rho}_{fe} &= -\left(\frac{A}{\Delta_1 + k_1v - i\gamma_{eg}}\right) \\ &\quad \times \left[\left(\frac{2\gamma_{eg}}{\gamma_{ee}}\right)\frac{1}{(\Delta_1 + k_1v + i\gamma_{eg})(\Delta_2 + k_2v - i\gamma_{fe})}\right. \\ &\quad \left. - \frac{1}{(\Delta_2 + k_2v - i\gamma_{fe})}\right] \\ &\quad \times \frac{1}{[(\Delta_1 + \Delta_2) + (k_1 + k_2)v - i\gamma_{fg}]}, \quad (73.63)\end{aligned}$$

where

$$A = -\left(\frac{d_2\mathcal{E}_2}{2\hbar}\right)\left(\frac{d_1\mathcal{E}_1}{2\hbar}\right)^2. \quad (73.64)$$

The imaginary part of this yields the absorptive part of the polarization at the frequency ω_2 . The first term becomes the product of two Lorentzians, and is an incoherent rate contribution. It dominates when the induced population ρ_{ee} decays

much more slowly than the induced coherence $\tilde{\rho}_{eg}$, i.e., when $\gamma_{ee} \ll \gamma_{eg}$.

The significance of the second term in Eq. (73.63) is evident in the limit when no phase perturbing processes intervene, so that

$$\begin{aligned} \gamma_{ee} &= \Gamma, & \gamma_{eg} &= \frac{1}{2}\Gamma, \\ \gamma_{fg} &= \frac{1}{2}\gamma_{ff}, & \gamma_{fe} &= \frac{1}{2}(\gamma_{ff} + \Gamma). \end{aligned} \quad (73.65)$$

For $v = 0$, $\tilde{\rho}_{fe}$ becomes

$$\tilde{\rho}_{fe} = -\frac{A}{\Delta_1^2 + (\Gamma/2)^2} \left(\frac{1}{\Delta_1 + \Delta_2 - i\frac{1}{2}\gamma_{ff}} \right). \quad (73.66)$$

Neglecting the decay of the final level $|f\rangle$, $\gamma_{ff} \rightarrow 0$, the absorption becomes proportional to

$$\text{Im}(\tilde{\rho}_{fe}) = \frac{\pi|A|}{\Delta_1^2 + (\Gamma/2)^2} \delta(\Delta_1 + \Delta_2). \quad (73.67)$$

In this limit, strict energy conservation between the ground state and the final state must prevail; the final state must be reached by the absorption of exactly two quanta. The delta function in Eq. (73.67) indicates precisely this:

$$\begin{aligned} \Delta_1 + \Delta_2 &= \omega_{fe} + \omega_{eg} - (\omega_1 + \omega_2) \\ &= \omega_{fg} - \omega_1 - \omega_2 \\ &= 0. \end{aligned} \quad (73.68)$$

The detuning and the width of the intermediate state affect the total transition rate, but not the condition of energy conservation. The presence of the second term in Eq. (73.63) makes the resonance contributions at

$$\Delta_2 = \omega_{fg} - \omega_2 = 0 \quad (73.69)$$

cancel approximately. Only a *two-photon transition* remains; in the Λ configuration this would be a *Raman process* (Chaps. 66 and 76).

If the velocity dependence in Eq. (73.63) is retained, the nonlinear response of an atomic sample must be averaged over the velocity distribution given by the Gaussian Eq. (73.20). The computations become involved, but the results show more or less well resolved resonances around the two positions Eqs. (73.68) and (73.69), i.e., the *coherent two-photon process* and the single step rate process $|e\rangle \rightarrow |f\rangle$ appearing due to a previous single step process $|g\rangle \rightarrow |e\rangle$; this is the *two-step process*.

A special situation arises when the intermediate step is detuned so much that no velocity group is in resonance, i.e., $|\Delta_1| \approx |\Delta_2| \gg kv$ for all velocities contributing significantly to the spectrum. Then the second coherent term of

Eq. (73.63) can be written in the form

$$\tilde{\rho}_{fe} = -\frac{A}{\Delta_1^2} \left(\frac{1}{(\Delta_1 + \Delta_2) + (k_1 + k_2)v - i\gamma_{fg}} \right). \quad (73.70)$$

If the two fields \mathcal{E}_1 and \mathcal{E}_2 have the same frequency but are counterpropagating, then $k_1 + k_2 = 0$, and no velocity dependence occurs in Eq. (73.70) for the two-photon resonance. All atoms in the sample contribute to the strength of the resonance, and then polarization is obtained directly by multiplication with the total atomic density. Equation (73.13) then gives

$$\alpha_2'' = \frac{d_2^2}{\hbar} \left(\frac{d_1 \mathcal{E}_1}{2\hbar \Delta_1} \right)^2 \frac{\gamma_{fg}}{(2\omega - \omega_{fg})^2 + \gamma_{fg}^2}. \quad (73.71)$$

This is a sharp *Doppler-free resonance* on the two-photon transition ω_{fg} . The advantage is that all atoms contribute with the sharp line width γ_{fg} , which is not easily affected by phase perturbations because of the two-photon nature of the transition. The disadvantage is the weakness of the transition, which is caused by the large detuning, making $d_1 \mathcal{E}_1 / |\Delta_1| \ll 1$ in most cases. With tunable lasers, however, this Doppler-free spectroscopy method has been used successfully in many cases.

73.8 Special Effects in Three-Level Systems

We continue our considerations of a three-level system but this time in the V -configuration. Thus, we have a ground state $|g\rangle$ coupled to a doublet of excited states $\{|e\rangle, |f\rangle\}$ through the interaction

$$V = \Omega_1 |g\rangle \langle e| + \Omega_2 |g\rangle \langle f| + \text{h.c.}, \quad (73.72)$$

where the couplings are due to radiation fields and given by

$$\Omega_i = \frac{d_i \mathcal{E}_i}{2\hbar}. \quad (73.73)$$

We use the rotating wave approximation and set the detunings to

$$\Delta\omega_e = \omega_e - \omega_1 \quad \text{and} \quad \Delta\omega_f = \omega_f - \omega_2, \quad (73.74)$$

where the frequency ω_i derives from the coupling field \mathcal{E}_i . The energy $E_g = 0$.

The time-dependent Schrödinger equation for this system is then written as

$$i\dot{c}_g = \Omega_1 c_e + \Omega_2 c_f, \quad (73.75)$$

$$i\dot{c}_e = \Delta\omega_e c_e + \Omega_1 c_g, \quad (73.76)$$

$$i\dot{c}_f = \Delta\omega_f c_f + \Omega_2 c_g. \quad (73.77)$$

We now introduce the two new variables

$$c_C = \bar{\Omega}^{-1}(\Omega_1 c_e + \Omega_2 c_f) \quad (73.78)$$

$$c_{NC} = \bar{\Omega}^{-1}(\Omega_2 c_e - \Omega_1 c_f), \quad (73.79)$$

where

$$\bar{\Omega}^2 = \Omega_2^2 + \Omega_1^2. \quad (73.80)$$

The equations of motion follow:

$$\begin{aligned} i\dot{c}_{NC} &= \left(\frac{\Omega_2}{\bar{\Omega}} \Delta\omega_e c_e - \frac{\Omega_1}{\bar{\Omega}} \Delta\omega_f c_f \right) \\ &= \frac{1}{\bar{\Omega}^2} \left[\Omega_1 \Omega_2 (\Delta\omega_e - \Delta\omega_f) c_C \right. \\ &\quad \left. + (\Delta\omega_e \Omega_2^2 + \Delta\omega_f \Omega_1^2) c_{NC} \right], \end{aligned} \quad (73.81)$$

$$\begin{aligned} i\dot{c}_C &= \left(\frac{\Omega_1}{\bar{\Omega}} \Delta\omega_e c_e + \frac{\Omega_2}{\bar{\Omega}} \Delta\omega_f c_f \right) + \bar{\Omega} c_g \\ &= \frac{1}{\bar{\Omega}^2} \left[(\Delta\omega_e \Omega_1^2 + \Delta\omega_f \Omega_2^2) c_C \right. \\ &\quad \left. + \Omega_1 \Omega_2 (\Delta\omega_e - \Delta\omega_f) c_{NC} \right] + \bar{\Omega} c_g. \end{aligned} \quad (73.82)$$

We notice that c_{NC} is not coupled to the ground state, but, in general, its coupling to the state c_C provides an indirect coupling. This indirect coupling, however, can be made to disappear, if we set $\Delta\omega_e = \Delta\omega_f \equiv \Delta\omega$. Then we find the equations

$$\begin{aligned} i\dot{c}_{NC} &= \Delta\omega c_{NC}, \\ i\dot{c}_C &= \Delta\omega c_C + \bar{\Omega} c_g, \\ i\dot{c}_g &= \bar{\Omega} c_C. \end{aligned} \quad (73.83)$$

This describes a pair of coupled quantum levels and a single uncoupled level. Thus, if we start in the ground state, this latter level can never be populated. It remains unpopulated and is called a dark state. This state corresponds to the superposition

$$|NC\rangle = \frac{1}{\bar{\Omega}}(\Omega_2|e\rangle - \Omega_1|f\rangle). \quad (73.84)$$

Using the coupling operator Eq. (73.72), we find the matrix element

$$\langle g|V|NC\rangle = 0. \quad (73.85)$$

We also notice that the dark state can be found if the states $|e\rangle$ and $|f\rangle$ are the lower ones, i.e., we have the Λ -configuration.

Alternatively, if we start the system off in the dark state, it will never be able to get out of this state. This is also taken to hold true if we let the couplings depend slowly on time.

In this case, we may let Ω_1 come on later than Ω_2 . Then we may have

$$\begin{aligned} \lim_{t \rightarrow -\infty} \left(\frac{\Omega_1}{\sqrt{\Omega_2^2 + \Omega_1^2}} \right) &= 0, \\ \lim_{t \rightarrow -\infty} \left(\frac{\Omega_2}{\sqrt{\Omega_2^2 + \Omega_1^2}} \right) &= 1 \end{aligned} \quad (73.86)$$

and

$$\begin{aligned} \lim_{t \rightarrow \infty} \left(\frac{\Omega_1}{\sqrt{\Omega_2^2 + \Omega_1^2}} \right) &= 1, \\ \lim_{t \rightarrow \infty} \left(\frac{\Omega_2}{\sqrt{\Omega_2^2 + \Omega_1^2}} \right) &= 0. \end{aligned} \quad (73.87)$$

Both couplings are thus pulses, but they occur with a slight time delay. If we now start the system in the state $|e\rangle$, we find from Eq. (73.84) that

$$\lim_{t \rightarrow -\infty} |NC\rangle = |e\rangle, \quad (73.88)$$

and

$$\lim_{t \rightarrow +\infty} |NC\rangle = -|f\rangle. \quad (73.89)$$

Thus, by keeping the system in this uncoupled state we can adiabatically transfer its population between the states without involving any population of the intermediate state $|g\rangle$. Especially if this is an upper state, which may decay and dephase rapidly, the proposed population transfer may be greatly advantageous. Because it is usually applied in the Λ -configuration, it is termed Stimulated Raman Adiabatic Passage (STIRAP).

The dark state has found a wide range of applications in laser physics. As we may use the method to pass radiation through a medium without any absorption, it has led to the phenomenon of light-induced transparency. It can also be used to affect the index of refraction without having the accompanying absorption. The absorptive part of a resonance normally manifests itself as a quantum noise; utilizing the dark state idea one may reduce the noise in quantum devices. The dressing of the levels due to the special features of the interaction has also made it possible to achieve lasing without an inversion of the bare levels. These topics, however, will not be treated here.

A special application of the method to affect the refractive index deserves a more detailed consideration. We look at the relationship between the electric field vectors in the medium:

$$D(\omega) = \varepsilon_0 E + N\alpha(\omega)E(\omega) = \chi(\omega)\varepsilon_0 E(\omega), \quad (73.90)$$

where $\chi(\omega)$ is the susceptibility of the medium. From Maxwell's equations we find the relation Eq. (72.24)

$$k^2 = n^2(\omega) \frac{\omega^2}{c^2} = \frac{\omega^2}{c^2} [1 + \chi(\omega)]. \quad (73.91)$$

If we take the real parts of the quantities, this describes the propagation of waves in the medium.

Now we may use the relations Eq. (73.16) to estimate the function $\alpha(\omega)$ in the case when we have two weak fields exciting the three-level system in the V -configuration. We assume that both couplings have the same frequency, $\omega_1 = \omega_2 = \omega$. We write

$$\chi(\omega) \approx \Lambda \left(\frac{(\omega - \omega_e)}{(\omega - \omega_e)^2 + \gamma^2} + \frac{(\omega - \omega_f)}{(\omega - \omega_f)^2 + \gamma^2} \right); \quad (73.92)$$

in the weak field limit we may assume the two processes to add independently. The parameter

$$\Lambda = \frac{Nd^2}{2\hbar\epsilon_0} \quad (73.93)$$

has the dimension of a frequency and indicates the strength of the interaction. It is clear that tuning the frequency between the levels may give rise to a value of zero for the susceptibility. For a large enough γ , we write, in the neighbourhood of the zero,

$$\chi(\omega) \approx \frac{2\Lambda}{\gamma^2} (\omega - \bar{\omega}), \quad (73.94)$$

where $\bar{\omega} = \frac{1}{2}(\omega_e + \omega_f)$.

We now have the relation Eq. (73.91) to determine the dispersion relation, and assuming the effect of the medium to be substantial, we may derive an expression for the group velocity in the medium

$$v_g^{-1} = \frac{\partial k}{\partial \omega}. \quad (73.95)$$

We find

$$\frac{2k}{v_g} = \frac{2\omega}{c^2} (1 + \chi) + \frac{\omega^2}{c^2} \left(\frac{2\Lambda}{\gamma^2} \right). \quad (73.96)$$

Even though $\chi = 0$ near the point $\bar{\omega}$, we still have $\omega \approx ck$, so that

$$v_g = \frac{c}{1 + \frac{\Lambda\omega}{\gamma^2}} \approx c \left(\frac{\gamma^2}{\Lambda\omega} \right) \ll c. \quad (73.97)$$

The last inequality follows from the fact that in all cases $\gamma \ll \omega$.

We have thus found that utilizing the interference of two near quantum levels, the refractive index may acquire a very strong dependence on frequency. This may manifest itself in

an exceedingly slow propagation of light pulses. Such slow light has been shown to travel at only a few kilometers per hour, which is a most remarkable result. The drawback is, however, that this can only occur over a very narrow frequency range, as follows from the assumption of a strong dependence on frequency.

73.9 Summary of the Literature

Much of the material needed to formulate the basic theory of interaction between light and matter can be found in the text book [2]. A comparison between the harmonic model and the two-level model is given by *Feld* [1]. The density matrix formulation is presented in detail in [2]. The influence of various line broadening mechanisms on laser spectroscopy is discussed in the book [3]. The Voigt profile is related to the error function, which is treated in the compilation [5]. The numerical evaluation of the Voigt profile is discussed in [4]. Rate equations are commonly used in laser theory and they are derived for optical pumping and laser-induced processes in the lectures [6]. The Doppler-free spectroscopy was developed in the 1960s and 1970s by many authors following the initial discovery of the Benett hole by Bill R. Bennett Jr. and the Lamb dip by Willis E. Lamb Jr. Much of the pioneering work can be found in the book [3]. The three-level work has been reviewed by *Chebotayev* [8]. Various applications of lasers in spectroscopy are treated by *Levenson* and *Kano* [7]. For references to other topics, we refer to the specialized chapters of the present book.

Many features of the quantum dynamics of a few-level system are found in [9, 10]. The theoretical methods to treat such systems are presented in detail in [11]. The ensuing physical processes are presented in [12] with much additional material on quantum optics phenomena. The basic theory of the dark state and many of its applications in spectroscopy and laser physics are found in [13]. A rather complete review of adiabatic processes induced by delayed pulses is the article [14]. The slowing down and stopping of light is reviewed in [15]. A very recent article with earlier references is [16].

References

1. Feld, M.S.: In: Balian, R., Haroche, S., Liberman, S. (eds.) *Frontiers in Laser Spectroscopy*, p. 203. North-Holland, Amsterdam (1977)
2. Stenholm, S.: *Foundations of Laser Spectroscopy*. Wiley, New York (1984)
3. Letokhov, V.S., Chebotayev, V.P.: *Nonlinear Laser Spectroscopy*. Springer, Berlin, Heidelberg (1977)
4. Thompson, W.J.: *Comp. Phys.* **7**, 627 (1993)
5. Abramowitz, M., Stegun, I.E.: *Handbook of Mathematical Functions*. Dover, New York (1970)

6. Cohen-Tanoudji, C.: In: Balian, R., Haroche, S., Liberman, S. (eds.) *Frontiers in Laser Spectroscopy*, p. 1. North-Holland, Amsterdam (1977)
7. Levenson, M.D., Kano, S.S.: *Introduction to Nonlinear Laser Spectroscopy*. Academic Press, New York (1988)
8. Chebotae, V.P.: In: Shimoda, K. (ed.) *High-Resolution Spectroscopy*. Springer, Berlin, Heidelberg (1976)
9. Shore, B.W.: *Simple Atoms and Fields. The Theory of Coherent Atomic Excitation*, vol. 1. Wiley, New York (1990)
10. Shore, B.W.: *Multilevel Atoms and Incoherence. The Theory of Coherent Atomic Excitation*, vol. 2. Wiley, New York (1990)
11. Cohen-Tannoudji, C., Dupont-Roc, J., Grynberg, G.: *Atom-Photon Interactions, Basic Processes and Applications*. Wiley, New York (1992)
12. Mandel, L., Wolf, E.: *Optical Coherence and Quantum Optics*. Cambridge University Press, Cambridge (1995)
13. Scully, M.O., Zubairy, M.S.: *Quantum Optics*. Cambridge University Press, Cambridge (1997)
14. Vitanov, N.V., Fleischauer, M., Shore, B.W., Bergmann, K.: In: Bederson, B., Walther, H. (eds.) *Advances of Atomic, Molecular and Optical Physics*, vol. 46, p. 55. Academic Press, New York (2001)
15. Matsko, A.B., Kocharovskaya, O., Restoutsev, Y., Welch, G.R., Zibrov, A.S., Scully, M.O.: In: Bederson, B., Walther, H. (eds.) *Advances in Atomic, molecular, and Optical Physics*, vol. 46, p. 191. Academic Press, New York (2001)
16. Bajcsy, M., Zibrov, A.S., Lukin, M.D.: *Nature* **26**, 368 (2003)



Stig Stenholm Stig Stenholm was Professor of Laser Physics and Quantum Optics at the Royal Institute of Technology, Stockholm. He studied Technical Physics at the Helsinki Institute of Technology and Mathematics. He worked at the Research Institute for Theoretical Physics in Helsinki until 1997, when moving to Stockholm. His research included spectroscopy, quantum optics, and informatics. He passed away in 2017.



Contents

74.1	Gain, Threshold, and Matter–Field Coupling	1069
74.2	Continuous Wave, Single-Mode Operation	1071
74.3	Laser Resonators and Transverse Modes	1074
74.4	Photon Statistics	1076
74.5	Multimode and Pulsed Operation	1077
74.6	Instabilities and Chaos	1079
	References	1079

Abstract

Despite their great variety and range of size, power, wavelength, and temporal, spatial, and polarization characteristics, all lasers involve certain basic concepts, such as gain, threshold, and electromagnetic modes of oscillation [1–6]. In addition to these universal characteristics are features, such as Gaussian beam modes, that are important to such a wide class of devices and must be included in any reasonable compendium of important laser concepts and formulas. We have, therefore, included here both generally applicable results as well as some more specific but widely applicable ones.

Keywords

gain coefficient · laser resonators · Gaussian beams · laser linewidth · frequency stabilization · ultrashort laser pulses

R. Menzel (✉)
 Dept. of Physics, University of Potsdam
 Potsdam, Germany
 e-mail: menzel@uni-potsdam.de

P. W. Milonni
 Theoretical Division, Los Alamos National Laboratory
 Los Alamos, NM, USA

74.1 Gain, Threshold, and Matter–Field Coupling

All lasers involve some medium that amplifies an electromagnetic field within some band of frequencies. At the simplest level of description, the amplifying medium changes the intensity I of a field according to the equation

$$\frac{dI}{dz} = gI, \quad (74.1)$$

where z is the coordinate along the direction of propagation, and g is the gain coefficient, typically expressed in cm^{-1} . Amplification occurs as a consequence of stimulated emission of radiation from the upper state (or band of states) of a transition for which a population inversion exists, i.e., for which an upper state has greater likelihood of occupation than a lower state. Different types of lasers may be classified by the pump mechanisms used to achieve population inversion (Chap. 75). In the case that the amplifying transition involves two discrete energy levels, E_1 and $E_2 > E_1$, the gain coefficient at the frequency ν is given by

$$g(\nu) = \frac{\lambda^2 A}{8\pi n^2} \left(N_2 - \frac{g_2}{g_1} N_1 \right) S(\nu). \quad (74.2)$$

Here, $\lambda = c/\nu$ is the transition wavelength, A (s^{-1}) is the Einstein A coefficient for spontaneous emission for the transition, and g_2, g_1 are the degeneracies of the upper and lower energy levels. In nearly every case, these quantities are fixed characteristics of the medium, independent of the laser intensity or the pump mechanism; N_2 and N_1 are the population densities (cm^{-3}) of the upper and lower levels, respectively, and $S(\nu)$ is the normalized transition lineshape function (Chap. 20); n is the refractive index at frequency ν and has contributions from all nonlasing transitions and from the host medium. Equations (74.1) and (74.2) describe either amplification or absorption, depending on whether the population inversion $N_2 - (g_2/g_1)N_1$ is positive or negative.

Equation (74.2) is a standard expression for the gain coefficient [2], which can also be written in terms of the stimulated emission cross section [4] or the oscillator strength of the laser transition [5].

By far the most common configuration is that in which the gain medium is contained in a cavity bounded on two sides by reflecting surfaces. The mirrors, defining what is called the laser resonator or cavity, allow feedback, i.e., the redirection of the field back into the gain medium for multipass amplification and sustained laser action. The two mirrors allow the field to build up along the directions parallel to the *optical axis* and to form a pencil-like beam of light. The design of the resonator determines the spectral, spatial, temporal, and polarization properties of the laser radiation within the limitations set by the properties of the chosen laser medium. In order to sustain laser action, the gain in intensity due to stimulated emission must equal or exceed the loss due to transmission through the mirrors, scattering, absorption in the host medium, and diffraction.

Transmission through at least one of the mirrors is, of course, required to obtain a usable laser beam, and it is typically the dominant field loss mechanism. If the mirror reflectivities are r_1 and r_2 , then the intensity I is reduced by the factor $r_1 r_2$ in a round-trip pass through the cavity, while according to Eq. (74.1) the gain medium causes the intensity to increase by a factor $\exp(2g\ell)$ in the two passes through the gain medium of length ℓ . Equating of the gain and loss factors leads to the threshold condition for laser oscillation: $g \geq g_t$, where the threshold gain is

$$g_t = -\frac{1}{2\ell} \ln(r_1 r_2) + a, \quad (74.3)$$

a being an attenuation coefficient associated with any loss mechanisms that may exist in addition to reflection losses at the mirrors.

Suppose, for example, that a laser has a 50 cm gain cell and mirrors with reflectivities 0.99 and 0.97, and that absorption within the host medium of the gain cell is negligible. Then the threshold gain is $g_t = 4 \times 10^{-4} \text{ cm}^{-1}$. If the lasing transition is the 6328 Å Ne transition of the He-Ne laser, $A \cong 1.4 \times 10^6 \text{ s}^{-1}$, $n \cong 1.0$ and, assuming a pure Doppler lineshape,

$$S(\nu) = \left(\frac{4 \ln 2}{\pi} \right)^{1/2} \frac{1}{\delta\nu_D} \quad (74.4)$$

at line center, where $\delta\nu_D$ is the width (FWHM) of the Doppler lineshape (Sect. 73.4). For $T = 400 \text{ K}$ and the Ne atomic weight, $\delta\nu_D \cong 1500 \text{ MHz}$ and $S(\nu) \cong 6.3 \times 10^{-10} \text{ s}$. Then the threshold population difference required for laser oscillation is

$$\left(N_2 - \frac{g_2}{g_1} N_1 \right)_t = \frac{8\pi n^2 g_t}{\lambda^2 A S(\nu)} \cong 2.8 \times 10^9 \text{ cm}^{-3}. \quad (74.5)$$

This is a typical result: the population *inversion* required for laser oscillation tends to be relatively small compared with the total population.

Calculations of population inversions and other properties of the gain medium are based on rate equations, or more generally, the density matrix ρ . This density matrix and, thus, the gain coefficient g can be functions of time, space, frequency, and polarization of the laser light. However, in many instances, the laser process in the medium is fairly well described in terms of two energy eigenstates, other states appearing only indirectly through pumping and decay channels. In this case, ρ is a 2×2 matrix whose elements satisfy (Chap. 72)

$$\begin{aligned} \dot{\rho}_{22} &= -(\Gamma_2 + \Gamma)\rho_{22} - \frac{1}{2}i(\Omega^* \rho_{21} - \Omega \rho_{12}), \\ \dot{\rho}_{11} &= -\Gamma_1 \rho_{11} + \Gamma \rho_{22} + \frac{1}{2}i(\Omega^* \rho_{21} - \Omega \rho_{12}), \\ \dot{\rho}_{21} &= -(\gamma + i\Delta)\rho_{21} - \frac{1}{2}i\Omega(\rho_{22} - \rho_{11}), \end{aligned} \quad (74.6)$$

with $\rho_{12} = \rho_{21}^*$. Here, Γ_2 and Γ_1 are, respectively, the rates of decay of the upper and lower states due to all processes other than the spontaneous decay from state 2 to state 1 described by the rate $\Gamma = A$. γ , which is 2π times the homogeneous linewidth (HWHM) of the transition, is the rate of decay of off-diagonal coherence due to both elastic and inelastic processes; in general, $\gamma \geq (\Gamma_1 + \Gamma_2 + \Gamma)/2$. $\Omega = \mathbf{d}_{21} \cdot \mathcal{E}/\hbar$ is the Rabi frequency (Chaps. 72 and 77). (The Rabi frequency is often defined as $2\mathbf{d}_{21} \cdot \mathcal{E}/\hbar$.) \mathcal{E} is the complex amplitude of the electric field; i.e., the electric field is

$$\mathbf{E}(\mathbf{r}, t) = \text{Re} [\mathcal{E}(\mathbf{r}, t) e^{i(\mathbf{k} \cdot \mathbf{r} - \omega t)}] \cong \text{Re} [\epsilon \mathcal{E}(\mathbf{r}, t) e^{i\mathbf{k} \cdot \mathbf{z}} e^{-i\omega t}]. \quad (74.7)$$

It is assumed that \mathcal{E} is slowly varying in time compared with the oscillations at frequency ω ($= 2\pi\nu$), and that the wave vector \mathbf{k} is approximately $k\hat{\mathbf{z}} = (n\omega/c)\hat{\mathbf{z}}$, where $\hat{\mathbf{z}}$ is a unit vector pointing in the direction of propagation. Finally, $\Delta = \omega_0 - \omega$ in Eq. (74.6) is the detuning of ω from the central transition frequency $\omega_0 = (E_2 - E_1)/\hbar$ of the lasing transition. Rapidly oscillating terms involving $\omega_0 + \omega$ are ignored in the rotating-wave approximation that pervades nearly all of laser theory (Chap. 72).

In most lasers, γ is so large compared with the diagonal decay rates that the off-diagonal elements of ρ may be assumed to relax quickly to the quasi-steady values obtained by setting $\dot{\rho}_{12} = 0$ in Eq. (74.6). Then the diagonal density matrix elements satisfy the rate equations

$$\begin{aligned} \dot{\rho}_{22} &= -(\Gamma_2 + \Gamma)\rho_{22} - \frac{|\Omega|^2 \gamma / 2}{\Delta^2 + \gamma^2} (\rho_{22} - \rho_{11}), \\ \dot{\rho}_{11} &= -\Gamma_1 \rho_{11} + \Gamma \rho_{22} + \frac{|\Omega|^2 \gamma / 2}{\Delta^2 + \gamma^2} (\rho_{22} - \rho_{11}). \end{aligned} \quad (74.8)$$

Such rate equations, usually expressed equivalently in terms of population densities N_2, N_1 rather than occupation probabilities ρ_{22}, ρ_{11} , are the basis of most practical models of laser oscillation. These equations, or, more generally, the density matrix equations, must also include terms accounting for the pump mechanism. In the simplest model of pumping, one adds a constant pump rate Λ_2 to the right-hand side of the equation for ρ_{22} to obtain

$$\dot{\rho}_{22} = \Lambda_2 - (\Gamma_2 + A)\rho_{22} - \frac{|\Omega|^2\gamma/2}{\Delta^2 + \gamma^2}(\rho_{22} - \rho_{11}). \quad (74.9)$$

In the case of an inhomogeneously broadened laser transition, equations of the type Eqs. (74.6) and (74.8) apply separately to each detuning Δ arising from the distribution of atomic or molecular transition frequencies. In writing these equations, we have assumed a nondegenerate electric dipole transition. The generalization to magnetic or multiphoton transitions, or to a case where the amplification is due, for instance, to a Raman process, is straightforward but of less general interest.

A more realistic treatment of the electromagnetic field than that based on Eq. (74.1) proceeds from the Maxwell equations, which, for a homogeneous and nonmagnetic medium, lead to the equation

$$\frac{1}{2ik} \nabla_T^2 \mathcal{E} + \left(\frac{\partial}{\partial z} + \frac{1}{c} \frac{\partial}{\partial t} \right) \mathcal{E} = \frac{4\pi i \omega}{nc} N \mu^* \rho_{21}. \quad (74.10)$$

Here, N is the density of active atoms, $\mu^* \equiv (\mathbf{d}_{12} \cdot \boldsymbol{\epsilon})$, and $\nabla_T^2 \equiv \partial^2/\partial x^2 + \partial^2/\partial y^2$. This result assumes the validity of the rotating-wave approximation as well as the assumption that \mathcal{E} is slowly varying compared with $\exp(ikz)$ and $\exp(-i\omega t)$. In the plane-wave approximation, Eq. (74.10) becomes

$$\left(\frac{\partial}{\partial z} + \frac{1}{c} \frac{\partial}{\partial t} \right) \mathcal{E} = \frac{4\pi i \omega}{nc} N \mu^* \rho_{21}. \quad (74.11)$$

(More generally, the velocity c on the left-hand sides of Eqs. (74.10) and (74.11) should be replaced by the group velocity v_g associated with nonresonant transitions. If there is substantial group velocity dispersion, it is sometimes necessary to include a term involving the second derivative of \mathcal{E} with respect to t .) Equations (74.6) or (74.8) and (74.10) or (74.11) are coupled matter–field equations whose self-consistent solutions determine the operating characteristics of the laser. The density matrix or rate equations must be modified to include pumping, as in Eq. (74.9), and the field equations must be supplemented by boundary conditions and loss terms. Laser media based on more complicated energy-level schemes (e.g., “three-level” and “four-level” lasers [2–6]) are described similarly with more general rate or density-matrix equations. With these modifications, the

equations are the basis of semiclassical laser theory, wherein the particles constituting the gain medium are treated quantum mechanically whereas the field is treated according to classical electromagnetic theory. Aside from fundamental linewidth considerations and photon statistics (Sects. 74.2 and 74.4), very few aspects of lasers require the quantum theory of radiation.

74.2 Continuous Wave, Single-Mode Operation

In the case of steady-state, continuous-wave (CW) operation, the appropriate matter–field equations are those obtained by setting all time derivatives equal to zero. Equation (74.11), for instance, becomes

$$\frac{d\mathcal{E}}{dz} = \frac{2\pi\omega N |d|^2}{3n\hbar c} \frac{1}{\gamma + i\Delta} (\rho_{22} - \rho_{11}) \mathcal{E}, \quad (74.12)$$

or, in terms of the intensity I ,

$$\begin{aligned} \frac{dI}{dz} &= \frac{4\pi\omega N |d|^2}{3n\hbar c} \frac{\gamma}{\Delta^2 + \gamma^2} (\rho_{22} - \rho_{11}) I \\ &= \frac{\lambda^2 A}{8\pi n^2} (N_2 - N_1) S(\nu) I = g(\nu) I, \end{aligned} \quad (74.13)$$

for the nondegenerate case under consideration. Here, $|d|^2 = 3|\mathbf{d}_{12} \cdot \boldsymbol{\epsilon}|^2$, $N_j = N\rho_{jj}$, $S(\nu) = 2\pi \times (\gamma/\pi)/(\Delta^2 + \gamma^2)$ is the Lorentzian lineshape function for homogeneous broadening, and $A = 4\omega^3 |d|^2 n / 3\hbar c^3$ is the spontaneous emission rate in the host medium of (real) refractive index n . Local (Lorentz–Lorenz) field corrections will, in general, modify these results, but such corrections are ignored here [7].

The steady-state solution of the density matrix or rate equations gives, similarly,

$$g(\nu) = \frac{g_0(\nu)}{1 + I/I_{\text{sat}}}, \quad (74.14)$$

where the saturation intensity I_{sat} , like the small-signal gain coefficient $g_0(\nu)$, depends on decay rates and other characteristics of the lasing species. Thus, in the plane-wave approximation, the growth of intensity in a homogeneously broadened laser medium is typically described by the equation

$$\frac{dI}{dz} = \frac{g_0(\nu) I}{1 + I/I_{\text{sat}}}. \quad (74.15)$$

This equation, supplemented by boundary conditions at the mirrors and possibly other terms on the right-hand side to account for any distributed losses within the medium, determines the intensity in CW, single-mode operation.

The simplest model for calculating output intensity assumes that the intensity is uniform throughout the laser cavity. In steady state, the gain exactly compensates for the loss; i.e., $g(\nu) = g_t$, the ‘‘gain clamping’’ condition for CW lasing. Equation (74.14) then implies that the steady-state intracavity intensity is

$$I = I_{\text{sat}}[g_0(\nu)/g_t - 1]. \quad (74.16)$$

If I is assumed to be the sum of the intensities of waves propagating in the $+z$ and $-z$ -directions, i.e., $I = I_+ + I_-$, then the output intensity from the laser is

$$I_{\text{out}} = t_2 I_+ + t_1 I_-, \quad (74.17)$$

where t_2, t_1 are the mirror transmissivities at the right and left mirrors, respectively. The uniform intensity approximation implies that $I_+ = I_- = I/2$, and

$$I_{\text{out}} = \frac{1}{2}(t_2 + t_1)I_{\text{sat}}[g_0(\nu)/g_t - 1]. \quad (74.18)$$

Suppose one of the mirrors is perfectly reflecting, so that $t_1 = 0$ and $t_2 = t$. If the reflectivity r of the transmitting mirror is close to unity, then $g_t \cong (1/2\ell)(1-r) = (1/2\ell)(t+s)$, where s is the fraction of the incident beam power that is scattered or absorbed at the output mirror. Then

$$I_{\text{out}} \cong \frac{1}{2}I_{\text{sat}}t \left(\frac{2g_0(\nu)\ell}{t+s} - 1 \right), \quad (74.19)$$

and it follows that the optimal output coupling, i.e., the transmissivity that maximizes the output intensity, is

$$t_{\text{opt}} = \sqrt{2g_0(\nu)\ell s} - s. \quad (74.20)$$

This output coupling gives the output intensity

$$I_{\text{out}}^{\text{max}} = I_{\text{sat}} \left[\sqrt{g_0(\nu)\ell} - \sqrt{s/2} \right]^2; \quad (74.21)$$

$g_0(\nu)I_{\text{sat}}$ is the largest possible power per unit volume extractable as output laser radiation at the frequency ν .

More generally, when mirror reflectivities are not necessarily close to unity, $I_+ \neq I_-$ and both I_+ and I_- vary with the axial coordinate z . In this more general case, Eqs. (74.14) and (74.15) are replaced by

$$g(\nu, z) = \frac{g_0(\nu)}{1 + [I_+(z) + I_-(z)]/I_{\text{sat}}} \quad (74.22)$$

and

$$\frac{dI_+}{dz} = g(\nu, z)I_+, \quad \frac{dI_-}{dz} = -g(\nu, z)I_-, \quad (74.23)$$

where it is assumed that $g_0(\nu)$ is independent of z , and that all cavity loss processes occur at the mirrors. The solution of these equations with the boundary conditions $I_-(L) =$

$r_2 I_+(L)$, $I_+(0) = r_1 I_-(0)$ for mirrors at $z = 0$ and $z = L$ gives, for $I_{\text{out}} = t_1 I_-(0) + t_2 I_+(L)$, the formula [5, 8]

$$I_{\text{out}} = I_{\text{sat}} \left(t_2 + \sqrt{\frac{r_2}{r_1}} t_1 \right) \frac{\sqrt{r_1}}{(\sqrt{r_1} + \sqrt{r_2})(1 - \sqrt{r_1 r_2})} \times [g_0(\nu)\ell + \ln \sqrt{r_1 r_2}]. \quad (74.24)$$

Analysis of this result gives an optimal output coupling that reduces to Eq. (74.19) in the limit $t + s \ll 1$. Curves for optimal output coupling and I_{out} as a function of g_0 and s are given by *Rigrod* [8]. These results are based on several assumptions and approximations: the gain medium is assumed to be homogeneously broadened and to saturate according to the formula Eq. (74.14); g_0 and I_{sat} are taken to be constant throughout the medium; the field is approximated as a plane wave; field loss processes occur only at the mirrors; and interference between the left and right-going waves is ignored.

Interference of the counterpropagating waves in a standing-wave, single-mode laser modifies the gain saturation formula Eq. (74.14) as follows:

$$g(\nu, z) = \frac{g_0(\nu)}{1 + (2I_+/I_{\text{sat}}) \sin^2 kz} \quad (74.25)$$

in the case of small output coupling, where $I_+ \cong I_-$ as assumed in Eq. (74.18). (The general case of arbitrary output coupling with spatial interference of counterpropagating waves is somewhat complicated and is not considered here.) The $\sin^2 kz$ term is responsible for spatial hole burning: *holes* are *burned* in the curve of $g(\nu, z)$ versus z at points where $\sin^2 kz$ is largest. This spatially dependent saturation of the gain acts to reduce the output intensity, typically by as much as about 30%, compared with the case where interference of counterpropagating waves is absent or ignored. Spatial hole burning tends to be washed out by atomic motion in gas lasers and is absent entirely in pure traveling-wave ring lasers. If complete spatial hole burning based on Eq. (74.25) is assumed, the output intensity is

$$I_{\text{out}} = \frac{t}{2} I_{\text{sat}} \left(\frac{g_0(\nu)}{g_t} - \frac{1}{4} - \sqrt{\frac{g_0(\nu)}{2g_t} + \frac{1}{16}} \right) \quad (74.26)$$

in the case where one mirror is perfectly reflecting.

In inhomogeneously broadened media, the gain coefficient is obtained by integrating the contributions from all possible values of ν_0 . The different contributions saturate differently, depending on the detuning of ν_0 from the cavity mode frequency ν . If spatial hole burning and power broadening are ignored, then, to a good approximation, the gain saturates as

$$g(\nu) = \frac{g_0(\nu)}{\sqrt{1 + I/I_{\text{sat}}}} \quad (74.27)$$

in typical inhomogeneously broadened media.

Oscillation on a single longitudinal mode (Sect. 74.3) may be realized simply by making the cavity length L small enough that the mode spacing $c/2nL$ (Eq. (74.28)) exceeds the spectral width of the gain curve. This is possible in many gas lasers where the spectral width is small, and in semiconductor lasers, where L is very small. More generally, the gain clamping condition $g(\nu) = g_t$ implies that the cavity mode frequency having the largest small-signal gain $g_0(\nu)$ saturates the gain $g(\nu)$ down to the threshold value g_t , while the gain at all other mode frequencies then lies below g_t . In other words, the gain clamping condition implies single-mode oscillation. However, this conclusion assumes homogeneous broadening and also that spatial hole burning is negligible, so that the gain saturates uniformly throughout the cavity. High-pressure gas lasers, where the line broadening is due primarily to collisions and is, therefore, homogeneous, tend to oscillate on a single mode because spatial hole burning is largely washed out by atomic motion. On the other hand, homogeneously broadened solid-state lasers can be multimode as a consequence of spatial hole burning.

Single-mode oscillation in inhomogeneously broadened media is generally more difficult to achieve because of spectral hole burning, which makes the simple gain clamping argument inapplicable. However, single-mode oscillation can be enforced in any case by introducing, in effect, an additional loss mechanism for all mode frequencies except one. This is commonly done with a Fabry–Pérot etalon inside the cavity having a free spectral range that is large compared with the spectral width of the gain curve. By choosing the tilt angle appropriately, a particular resonant frequency of the etalon can be brought close to the center of the gain curve, while all other resonance frequencies lie outside the gain bandwidth.

Laser oscillation at a fixed polarization can likewise be achieved by discriminating against the orthogonal polarization, as is done when Brewster angles are employed.

Laser oscillation, in general, does not occur precisely at one of the allowed cavity mode frequencies. Associated with the $\sin kz$ dependence of the intracavity field is the condition $kL = N\pi$, or

$$\nu = N \frac{c}{2nL} \quad (N \text{ an integer}), \quad (74.28)$$

for the cavity mode frequencies in the plane-wave approximation. If the gain medium of refractive index n does not fill the entire length L between the mirrors, then Eq. (74.28) is replaced by

$$\nu = \frac{Nc/2}{L_{\text{opt}}}, \quad (74.29)$$

or

$$\frac{\ell}{L}[n(\nu) - 1]\nu = \nu_N - \nu, \quad (74.30)$$

where L is the geometrical distance between the resonator mirrors, ℓ ($\leq L$) is the length of the gain medium, $L_{\text{opt}} = n\ell + (L - \ell)$ is the optical length of the cavity, and $\nu_N = Nc/2L$ is an empty-cavity mode frequency. The laser oscillation frequency will, therefore, be different, in general, from any of the allowed empty-cavity mode frequencies. If the refractive index $n(\nu)$ here is attributable primarily to the lasing transition, as opposed to the host material, or other nonlasing transitions, then the following relation between $n(\nu)$ and $g(\nu)$ may be used in the case of homogeneous broadening (for instance [5]):

$$n(\nu) - 1 = -\frac{\lambda_0}{4\pi} \frac{\nu_0 - \nu}{\delta\nu_0} g(\nu), \quad (74.31)$$

where λ_0 , ν_0 , and $\delta\nu_0$ are the wavelength, frequency, and homogeneous linewidth (HWHM), respectively, of the lasing transition. This implies that

$$\nu = \frac{\nu_0 \delta\nu_c + \nu_N \delta\nu_0}{\delta\nu_c + \delta\nu_0}, \quad (74.32)$$

for the laser oscillation frequency ν , where

$$\delta\nu_c \equiv \frac{cg(\nu)\ell}{4\pi L} \quad (74.33)$$

is the cavity bandwidth. Thus, the actual lasing frequency is not simply one of the allowed empty-cavity frequencies ν_N , but is rather *pulled* away from ν_N toward the center of the gain profile. This is called frequency pulling.

If spatial hole burning is absent, then $g(\nu) = g_t$ in steady-state oscillation, and the cavity bandwidth $\delta\nu_c = cg_t\ell/4\pi L$ is the largest for lossy cavities. Most lasers fall into the *good cavity* category, that is, $\delta\nu_c \ll \delta\nu_0$, so that Eq. (74.32) may be approximated by

$$\nu \cong \nu_N + (\nu_0 - \nu_N)\delta\nu_c/\delta\nu_0. \quad (74.34)$$

Similar results apply to inhomogeneously broadened lasers. For a Doppler broadened medium, for instance, the frequency pulling formula is

$$\nu \cong \nu_N + (\nu_0 - \nu_N)(\delta\nu_c/\delta\nu_D)\sqrt{4 \ln \frac{2}{\pi}}, \quad (74.35)$$

for good cavities. These results show that frequency pulling is most pronounced in lasers with large peak gain coefficients and narrow gain profiles, such as the 3.51 μm He-Xe laser, as observed experimentally [9].

Spectral hole burning leads to especially interesting consequences in Doppler-broadened gas lasers. Since two traveling waves propagating in opposite ($\pm z$) directions will strongly saturate spectral packets of atoms with oppositely Doppler-shifted frequencies, a standing-wave field will burn

two holes on opposite sides of the peak of the Doppler profile. When the mode frequency is exactly at the center of the Doppler profile, however, the two holes merge, the field now being able to saturate strongly only those atoms with zero velocity along the z -direction. In this case, since the field feeds off a single spectral packet of more strongly saturated atoms, there is a dip in the output power compared with the case when the mode frequency is detuned from the line center. This dip in the output power at the line center is called the Lamb dip. It can be used to determine whether a gas laser is Doppler broadened, and more importantly, to stabilize the laser frequency to the center of the dip. High-precision measurements often require that a laser operate at a very stable frequency, in spite of mirror vibrations and other noise processes. Lamb-dip frequency stabilization is based on an “error signal” that is the difference between the measured output intensity and the intensity at the center of the Doppler gain profile. A feedback circuit controls the bias voltage across a piezoelectric element used to vary the cavity length so as to minimize the error signal and thereby to stabilize the laser frequency. Fractional frequency stabilities of about 1 part in 10^{10} can be obtained by Lamb-dip stabilization.

The widely used *Pound–Drever–Hall* frequency stabilization technique employs a Fabry–Pérot cavity to provide an error signal proportional to the intensity reflected when the field frequency differs from a cavity resonance frequency. This method has the advantage that it is not restricted to stabilization of laser frequencies near that of a laser material resonance [10–13]. With high-finesse etalons it has been possible to obtain short-time fractional frequency stabilities $\approx 10^{-16}$ and laser linewidths < 40 mHz [13].

Semiclassical laser theory suggests that CW laser radiation could ideally be perfectly monochromatic, since the amplitude and phase of the field given by Eq. (74.7) are time-independent. However, when quantum electrodynamic considerations are built into laser theory, it is found that spontaneous emission, which adds to the number of photons put in the lasing mode by stimulated emission, causes a phase diffusion that results in a Lorentzian linewidth (FWHM)

$$\Delta\nu = \frac{N_2}{N_2 - N_1} \frac{8\pi h\nu}{P_{\text{out}}} \left[\frac{\delta\nu_c}{n_g + 1 + \delta\nu_c/\delta\nu_0} \right]^2, \quad (74.36)$$

where P_{out} is the output laser power and $n_g = d(n\omega)/d\omega$ is the group index associated with nonlasing transitions in the laser medium. In the *bad cavity* limit in which $\delta\nu_c \gg \delta\nu_0$, this reduces to the expression originally derived by *Schawlow* and *Townes* [14] when it is assumed that the contribution (n_g) from nonlasing transitions is negligible:

$$\Delta\nu = \frac{N_2}{N_2 - N_1} \frac{8\pi h\nu}{P_{\text{out}}} (\delta\nu_0)^2. \quad (74.37)$$

In the more common case of a *good cavity*,

$$\Delta\nu = \frac{N_2}{N_2 - N_1} \frac{8\pi h\nu}{P_{\text{out}}} (\delta\nu_c)^2. \quad (74.38)$$

The “Schawlow–Townes linewidth” $\Delta\nu$ is a fundamentally quantum-mechanical, finite linewidth that persists no matter how small various sources of “technical noise”, such as mirror jitter, are made. Although it has been observed in highly stabilized gas lasers, it is negligible compared with technical noise in conventional lasers. However, in free-running semiconductor lasers, L is very small and, consequently, $\delta\nu_c$ is large, and the fundamental lower limit $\Delta\nu$ to the laser linewidth can be the dominant contribution to the laser linewidth.

However, linewidths 10–100 MHz observed in semiconductor lasers are too large to be explained by these expressions for $\Delta\nu$, and two modifications are necessary, each of them involving a multiplication of the Schawlow–Townes linewidth $\Delta\nu$ by a certain factor:

$$\Delta\nu \rightarrow \Delta\nu' = (1 + \alpha^2)K\Delta\nu; \quad (74.39)$$

α is called the *Henry α parameter* and is associated with a coupling between phase and intensity fluctuations above the laser threshold [15, 16]. Values of α between about 4 and 6 are typical in semiconductor injection lasers, and consequently, the correction to the Schawlow–Townes linewidth due to the Henry α parameter is substantial. The K factor [17–19] arises as a consequence of the deviation from the spatially uniform intracavity intensity assumed in the derivation of the Schawlow–Townes formula [20, 21]. (Intracavity intensities along the optical axis are approximately uniform only in the case of low output couplings.) The fundamental quantum-mechanical linewidth under consideration can be associated with vacuum field fluctuations, which, according to general fluctuation–dissipation theory, will increase as the cavity loss increases. This explains why the *Petermann K factor* deviates increasingly from unity as the output coupling (cavity loss) increases. Values of K between 1 and 2 appear to be typical for lossy, stable resonators [22, 23], but much larger values are possible for unstable resonators [24].

74.3 Laser Resonators and Transverse Modes

The assumption that the complex field amplitude $\mathcal{E}(\mathbf{r}, t)$ is slowly varying in z compared with $\exp(ikz)$ leads to the paraxial wave equation Eq. (74.10),

$$\nabla_T^2 \mathcal{E} + 2ik \frac{\partial \mathcal{E}}{\partial z} = 0, \quad (74.40)$$

for a monochromatic field in vacuum. If $\mathcal{E}(x, y, z)$ is specified in the plane $(x, y, z = 0)$, it follows that

$$\mathcal{E}(x, y, z) = -\frac{i}{\lambda z} \iint dx' dy' \times \mathcal{E}(x', y', 0) e^{ik[(x-x')^2 + (y-y')^2]/2z}. \quad (74.41)$$

Thus, in the case of a laser resonator, the field $\mathcal{E}(x, y, L)$ at the mirror at $z = L$ is related to the field $\mathcal{E}(x, y, 0)$ at the mirror at $z = 0$ by

$$\begin{aligned} \mathcal{E}(x, y, L) &= -\frac{i}{\lambda L} \iint dx' dy' \\ &\times \mathcal{E}(x', y', 0) e^{ik[(x-x')^2 + (y-y')^2]/2L} \\ &\equiv \iint dx' dy' K(x, y; x', y') \mathcal{E}(x', y', 0). \end{aligned} \quad (74.42)$$

Similarly, the field at $z = 0$ after one round-trip pass through the resonator is

$$\begin{aligned} \mathcal{E}(x, y, 0) &= \iint dx' dy' K(x, y; x', y') \mathcal{E}(x', y', L) \\ &= \iint dx' dy' K(x, y; x', y') \\ &\times \iint dx'' dy'' K(x', y'; x'', y'') \mathcal{E}(x'', y'', 0) \\ &\equiv \iint dx'' dy'' \tilde{K}(x, y; x'', y'') \mathcal{E}(x'', y'', 0). \end{aligned} \quad (74.43)$$

By definition, a mode of the resonator is a field distribution that does not change on successive round-trip passes through the resonator. More precisely, since an empty cavity is assumed, a mode will be such that the field spatial pattern remains the same except for a change in amplitude per pass. A longitudinal mode is defined by the value of k in $\exp(ikz)$, whereas a transverse mode is defined by the corresponding (x, y) dependence and satisfies the integral equation

$$\gamma \mathcal{E}(x, y, z) = \iint dx' dy' \tilde{K}(x, y; x', y') \mathcal{E}(x', y', z), \quad (74.44)$$

where z defines any plane between the mirrors, and γ accounts for the change per pass of the complex field amplitude. Iterative numerical solutions of this equation for laser resonator modes were first presented by Fox and Li [25].

Laser resonators may be classified as stable or unstable according to whether a paraxial ray traced back and forth through the resonator remains confined in the resonator or escapes. This leads to the condition

$$0 \leq g_1 g_2 \leq 1, \quad (74.45)$$

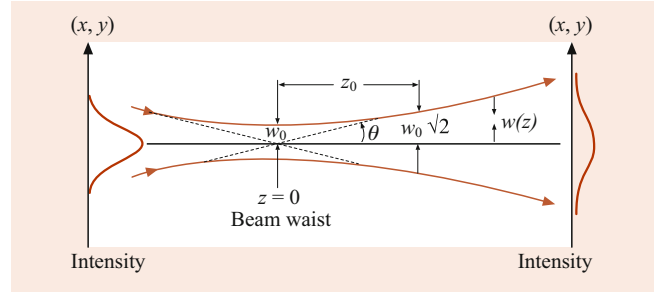


Fig. 74.1 Variation of the beam radius $w(z)$ of a Gaussian beam with the propagation distance z from the beam waist

for stable resonators, where the g parameters are defined in terms of the (spherical) mirror curvatures R_i and the mirror separation L by $g_i \equiv 1 - L/R_i$; R_i is defined as positive or negative depending on whether the mirror i is concave or convex, respectively, with respect to the interior of the resonator. Plane-parallel mirrors ($R_i \rightarrow \infty$) can be used, but they are difficult to keep aligned and have large diffractive losses.

Among stable configurations, the symmetric confocal resonator with $R_1 = R_2 = L$ has the smallest beam radii at the mirrors, while the concentric resonator with $R_1 = R_2$ slightly greater than $L/2$, has the smallest beam waist (Fig. 74.1). The hemispherical resonator ($R_1 = \infty$, R_2 slightly greater than L) is relatively easy to keep aligned and allows the beam radius w at mirror 2 to be adjusted by slight changes in L .

The fundamental Gaussian beam modes of stable resonators may be constructed from the free-space solutions of the paraxial wave equation. The most important (lowest-order) solution for this purpose is

$$\mathcal{E}(x, y, z) = \frac{A e^{-i\phi(z)} e^{ik(x^2 + y^2)/2R(z)} e^{-(x^2 + y^2)/w^2(z)}}{\sqrt{1 + z^2/z_0^2}}, \quad (74.46)$$

where A is a constant, $\phi(z) = \tan^{-1}(z/z_0)$, and $R(z)$, $w(z)$, and z_0 are the radius of curvature of surfaces of constant phase, the beam radius, and the Rayleigh range, respectively. The confocal parameter, $2z_0$, is also used to characterize Gaussian beams. Here, $z_0 \equiv \pi w_0^2/\lambda$, where w_0 is the beam radius at the waist at $z = 0$ (Fig. 74.1), and $R(z)$ and $w(z)$ vary with the distance z as follows:

$$R(z) = z + z_0^2/z, \quad w(z) = w_0 \sqrt{1 + z^2/z_0^2}. \quad (74.47)$$

The divergence angle of a Gaussian beam (Fig. 74.1) is $\theta = \lambda/\pi w_0$.

The ABCD law for Gaussian beams [2–6] allows the effects of various optical elements on Gaussian beam propagation to be calculated in a relatively simple fashion. For instance, a Gaussian beam incident on a lens of focal length f at its waist is focused to a new waist at a distance $d =$

$f/(1 + f^2/z_0^2)$ behind the lens, and the beam radius at the new waist is

$$w'_0 = \frac{f\lambda}{\pi w_0} \frac{1}{\sqrt{1 + f^2/z_0^2}}, \quad (74.48)$$

which is approximately $f\lambda/\pi w_0 = f\theta$ for tight focusing. This shows that a Gaussian beam can be focused to a very small spot, on the order of a wavelength. On the other hand, beam expanders consisting of two appropriately spaced lenses may be used to increase the beam radius by the ratio of the focal lengths in order to realize very small divergence angles.

Gaussian beam modes of laser resonators have radii of curvature $R(z)$ that match in magnitude those at the positions of mirrors. The beam radii at the mirrors and the location of the beam waist with respect to the mirrors may be expressed in terms of λ , L , and g_1g_2 . The empty-cavity mode frequencies are given by

$$\nu_N = \frac{c}{2L} \left(N + \frac{1}{\pi} \cos^{-1} \sqrt{g_1g_2} \right), \quad (74.49)$$

where N is an integer. For a host medium of refractive index n , $c/2L$ is replaced by $c/2nL$, and Eq. (74.49) then generalizes the plane wave result Eq. (74.28) to account for both longitudinal and transverse effects in the determination of the cavity mode frequencies.

The assumption of Gaussian modes presupposes that the resonator mirrors are large enough to intercept the entire beam without any spillover; i.e., that $a \gg w_1, w_2$, where w_1, w_2 are the beam radii at the mirrors, and a is an effective mirror cross sectional radius; this is very easy to realize. This implies that the Fresnel number $N_F \equiv a^2/\lambda L \gg 1$. Diffraction losses generally increase with decreasing Fresnel numbers.

Higher-order Gaussian modes, where the Gaussian functions of x and y in Eq. (74.46) are replaced by higher-order Hermite (or Laguerre) polynomials, or combinations of them (hybrid modes) [4], can be produced via suitable resonator designs and may be used in special applications.

In general, it is not possible to write closed-form expressions for laser modes. There are at least two reasons for this, the first being that the gain medium cannot, in general, be regarded as a simple amplifying element that preserves the basic empty-cavity mode structure. In general, the gain coefficient and the refractive index of the laser material, especially in the high-power regime, are functions of space, time, frequency, and light intensity. In low-power gas lasers, the spatial variations of the gain and refractive index are sufficiently mild that the lasing modes can be accurately described as Gaussians. However, there can be strong gain and index variations that themselves play an important role in determining the modes of the laser, as in *index-guided* and *gain-guided* semiconductor lasers or in fiber lasers.

Secondly, the resonator structure itself may introduce complications that preclude closed-form solutions even for the empty cavity. This is generally true, for instance, of unstable resonators, where iterative numerical solutions of the integral equation (Eq. (74.44)) are necessary for accurate predictions of modes. In such computer simulations, the mode structure must be determined self-consistently with the numerical solutions of the density matrix or, more commonly, rate equations for the gain medium.

The diffraction-limited divergence angle of the ideal lowest-order (TEM₀₀) Gaussian mode, $\theta = \lambda/\pi w_0$, may be difficult to realize in practice. The deviation from the ideal diffraction-limited field is characterized by a beam quality M^2 defined by writing the actual divergence angle of the output field as

$$\theta_M = M^2 \lambda / \pi w_0. \quad (74.50)$$

For the lowest-order Hermite–Gaussian mode $M^2 = 1$ by definition, whereas for the first-order mode $M^2 = 3$ and increases to 13 for the sixth-order mode, for example. Comparable values are obtained for the circularly symmetric Gauss–Laguerre modes [4]. For a low-power gas laser, M^2 might be around 1.1, whereas for a high-power laser, it might be ≈ 10 or more. The *brightness* L of a laser beam, defined as the power per unit area per unit solid angle, is, therefore, inversely proportional to M^2 and may be defined as [4]

$$L = \frac{P}{\lambda^2 (M^2)^2}, \quad (74.51)$$

where P is the beam power.

Unstable resonators, although inherently lossy, offer some important advantages for high-gain and high-power lasers. Thus, whereas the Gaussian modes of stable resonators typically involve small beam radii, the distinctly non-Gaussian modes of unstable resonators often have large mode volumes and make more efficient use of the available gain volume. Phase conjugation mirrors can be used to improve the beam quality of high-power lasers [4].

74.4 Photon Statistics

Optical fields may be characterized and distinguished by their photon statistical properties (Chap. 82 and [26–30]). In a photon counting experiment, the number of photons registered at a photodetector during a time interval T is measured and used to infer the probability $P_n(T)$ that n photons are counted in a time interval T . If the probability of counting a photon at the time t in the interval dt is denoted $\eta I(t)dt$, where $I(t)$ is the intensity of the field, and η is a factor depending on the microscopic details of the photon absorption

process and on the photodetector geometry, then it may be shown from largely classical considerations that [5, 28, 29]

$$P_n(T) = \left\langle \frac{1}{n!} \left[\eta \int_0^T dt' I(t') \right]^n e^{-\eta \int_0^T dt' I(t')} \right\rangle, \quad (74.52)$$

where the average $\langle \dots \rangle$ is over the intensity variations during the counting interval. (The fully quantum-mechanical treatment involves normally ordered products of electric field operators [28, 29].) In the simplest case of constant intensity, P_n follows the Poisson distribution:

$$P_n = \bar{n}^n e^{-\bar{n}} / n!, \quad (74.53)$$

where $\bar{n} = \eta IT$. Since a single-mode laser field can be thought of approximately as a classical stable wave [29], it is not surprising that its photocount distribution is found both theoretically and experimentally to satisfy Eq. (74.53), which is characteristic of a coherent state of the field (Chap. 82). Because of spontaneous emission a laser cannot produce exactly a coherent state of the field but, if the phase diffusion due to spontaneous emission is sufficiently slow, laser radiation on sufficiently short time scales can be treated in effect as a coherent-state field to a very good approximation.

A thermal light source, by contrast, follows the Bose–Einstein distribution,

$$P_n = \bar{n}^n / (1 + \bar{n})^{n+1}, \quad (74.54)$$

if the time interval T is short compared with the coherence time of the light; i.e., if $T\Delta\nu \ll 1$, where $\Delta\nu$ is the bandwidth. If $T\Delta\nu \gg 1$, P_n is again Poissonian. Thus, if a quasi-monochromatic beam of light is made from a natural source by spatial and spectral filtering, it has measurably different photon counting statistics from a single-mode laser beam of exactly the same bandwidth and average intensity. These differences are exhibited, for example, in measurements of intensity correlations of the Brown–Twiss type [28–30]. In such experiments, thermal photons (or more generally photons from a “chaotic” source [29]) have a statistical tendency to arrive in pairs (“photon bunching”), whereas the photons from a laser arrive independently.

74.5 Multimode and Pulsed Operation

Multimode laser theory is generally much more complicated than single-mode theory, particularly in the case of inhomogeneous broadening with both spectral and spatial hole burning. In certain situations, however, considerable simplification is possible. For instance, when the cavity mode frequency spacing is small compared with the homogeneous

linewidth $\delta\nu_0$, the gain tends to saturate homogeneously, and the total output power on all modes is well described by the analysis outlined in Sect. 74.2.

Pulsed laser operation adds the further complication of temporal variations to the CW theory outlined in the preceding sections. It is possible, nevertheless, to understand some of the most important types of multimode and pulsed operation using relatively simple models.

One method of obtaining short, high-power laser pulses is Q switching [31]. In a very lossy cavity, the gain can be pumped to large values before the threshold condition is met and gain saturation occurs. If the cavity loss is suddenly decreased via an optical switch, there will be a rapid buildup of intensity because the gain is far above the (now reduced) threshold value. The switching of the cavity loss is called Q switching, the quality factor Q being defined as $\nu/2\delta\nu_c$. The buildup time for a Q -switched pulse is typically on the order of the cavity round-trip time [4], resulting in pulses of duration on the order of 10 ns for solid-state lasers, for example. Q switching requires that the gain medium be capable of retaining a population inversion over a time much larger than the Q -switched pulse duration, and, in particular, that the spontaneous emission lifetime be relatively long. The pulse duration can be reduced to approximately a single cavity round-trip time by Q switching from low reflectivity mirrors to 100% reflectivities, and then switching the reflectivity of the outcoupling mirror from 100% to 0% at the peak of the amplified pulse. In addition to this pulsed transmission mode is cavity dumping, where both mirrors have nominally 100% reflectivity and the intracavity power is “dumped” by an acousto-optic or electro-optic intracavity element that deflects the light out of the cavity. The pulse duration achieved in this way is again roughly a round-trip time. Cavity dumping can be employed with CW lasers and does not require the long energy storage times necessary for ordinary Q switching.

Shorter pulses can be realized by mode locking, where the phases of N longitudinal cavity modes are locked together. (The evolution of the mode-locking technique is reviewed in [32].) In the simplest model, assuming equal amplitudes and phases of the individual modes, the net field amplitude is proportional to

$$\begin{aligned} X(t) &= \sum_{n=-(N-1)/2}^{(N-1)/2} X_0 \sin[(\omega_0 + n\Delta)t + \phi_0] \\ &= X_0 \sin(\omega_0 t + \phi_0) \frac{\sin(N\Delta t/2)}{\sin(\Delta t/2)}. \end{aligned} \quad (74.55)$$

The temporal variation described by this function for large N is a train of spikes of amplitude NX_0 at times $t_m = 2\pi m/\Delta$, $m = 0, \pm 1, \pm 2, \dots$, the width of each spike being $2\pi/(N\Delta)$. In the case of a mode-locked laser, $\Delta = 2\pi(c/2L)$, and the

output field consists of a train of pulses separated in time by $T = 2\pi/\Delta = 2L/c$. The peak amplitude of the spikes is proportional to N , and the duration of each spike is approximately $2L/cN$. The spectrum of such a field may be described as a “comb” of frequencies with “teeth” separated by the angular frequency Δ . The regular, controllable comb of frequencies in the output of a mode-locked laser serves as a “ruler” for measurements of absolute optical frequencies (optical frequency metrology) [33–35].

The maximum number N_{\max} of modes that can actually be phase-locked is limited by the spectral width $\Delta\nu_g$ of the gain curve:

$$N_{\max} = \frac{\Delta\nu_g}{c/2L} = \frac{2L}{c} \Delta\nu_g. \quad (74.56)$$

Similarly, the shortest pulse duration is

$$\tau_{\min} = \frac{2L}{cN_{\max}} = \frac{1}{\Delta\nu_g}. \quad (74.57)$$

Mode locking thus requires a gain bandwidth large compared with the cavity mode spacing, and the shortest and most intense mode-locked pulse trains are obtained in gain media having the largest gain bandwidths. Trains of picosecond pulses are routinely obtained with liquid dye and solid gain media having gain bandwidths $\Delta\nu_g \approx 10^{12} \text{ s}^{-1}$ or more.

Various techniques, employing acoustic or electro-optic modulation or saturable absorbers, are used to achieve mode locking. The different methods all basically rely on the fact that a modulation of the gain or loss at the mode separation frequency $c/2L$ tends to cause the different modes to oscillate in phase. Such a modulation is achieved *passively* when a saturable absorber is placed in the laser cavity; because of the intensity-dependent loss caused by the saturable absorber, the multimode intensity oscillates with a beat frequency that is impressed on the saturated loss coefficient.

Kerr lens mode locking (KLM) [36–38] is based on the self-focusing of a field in a medium with a nonlinear refractive index (Chap. 76)

$$n = n_0 + n_2 I. \quad (74.58)$$

With such a nonlinear index the field can be strongly self-focused (assuming $n_2 > 0$) where the intensity I is largest. The basic idea in KLM is that there is an intensity-dependent loss, as in a saturable absorber. However, this intensity-dependent loss now occurs within the laser medium; the extent to which the field is susceptible to diffractive losses depends on the degree of self-focusing and, therefore, the intracavity intensity. Megawatt mode-locked pulses with durations and repetition rates on the order of femtoseconds and 100 MHz, respectively, are routinely produced with KLM Ti:sapphire lasers (Chap. 75).

Ultrashort pulse generation is possible with other nonlinear techniques. The colliding-pulse laser [39] is a three-mirror ring laser in which two mode-locked pulse trains

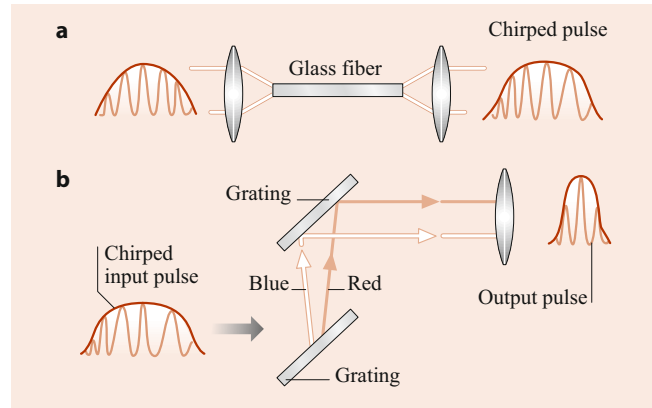


Fig. 74.2 Nonlinear pulse compression by frequency chirping. In (a), the nonlinear refractive index of a glass fiber results in a time-dependent frequency of the transmitted pulse, and in (b), a pair of diffraction gratings is used to produce frequency-dependent path delays such as to temporally compress the pulse

propagate in opposite senses and overlap in a very thin ($\approx 10 \mu\text{m}$) saturable absorber placed in the ring in addition to the gain cell. The cavity loss is least when the two pulses synchronize to produce the highest intensity, and, therefore, the lowest loss coefficient in the saturable absorber. The short length of the absorbing cell forces the pulses to overlap within a very small distance and, therefore, to produce very short pulses ($10 \mu\text{m}/c \approx 30 \text{ fs}$ pulse duration with a $c/L \approx 100 \text{ MHz}$ repetition rate).

Another method of ultrashort pulse generation relies on, i.e., a time dependent shift of the frequency of an optical pulse [40–43]. In a medium (e.g., a glass fiber) with a nonlinear refractive index (Eq. (74.58)), a field experiences an instantaneous phase shift $\phi(t)$ that depends on the instantaneous intensity. Therefore, as $I(t)$ increases toward the peak intensity of the pulse, $\phi(t)$ increases (assuming $n_2 > 0$), whereas $\phi(t)$ decreases as $I(t)$ decreases from its peak value. The frequency shift $\dot{\phi}(t)$ is such that the instantaneous frequency of the pulse is smaller at the leading edge and larger at the trailing edge of the pulse (Fig. 74.2), resulting in a stretching of the pulse bandwidth. Following this spectral broadening by the nonlinear medium, the pulse can be compressed in time by means of a frequency-dependent delay line such that the smaller frequencies, say, are delayed more than the higher frequencies. The trailing edge of the pulse can, therefore, catch up to the leading edge, resulting in a shorter pulse whose duration is given by the inverse of the chirp bandwidth. The delay line can be realized with a pair of diffraction gratings (Fig. 74.2). More than two decades ago this pulse compression technique was used to compress 40 fs amplified pulses from a colliding pulse laser to 8 fs, corresponding to about four optical cycles [44].

One of the most important techniques in ultrashort, high-power laser pulse generation is chirped pulse amplification (CPA) [45, 46] in which a laser pulse is chirped, temporally

stretched, and then passed through one or more amplifiers. The lengthening in time of the pulse by factors typically $\approx 10^3$ – 10^4 prior to amplification allows greater energy extraction from the amplifier and avoids optical damage and nonlinear effects causing spatiotemporal pulse distortion. After amplification, pulse compression is performed with a grating pair. The Ti:sapphire (Ti:Al₂O₃) amplifier is particularly attractive for femtosecond CPA because of its very large spectral width and high saturation fluence.

The wavelength dependence of the linear refractive index n_0 in Eq. (74.58) results in a group velocity

$$v_g = c \left[n_0 - \lambda \frac{dn_0}{d\lambda} \right]^{-1} \quad (74.59)$$

that, if $dn_0/d\lambda < 0$, is such that higher frequencies propagate more rapidly than lower frequencies. Assuming $n_2 > 0$, on the other hand, the nonlinear part of the index causes a delay of higher frequencies with respect to lower ones, as discussed above. This leads to soliton solutions of the wave equation, such that the opposing effects of the linear and nonlinear dispersion are balanced, and the pulse propagates without distortion. Soliton lasers, with pulse durations ranging from picoseconds down to ≈ 100 fs, depending on the fiber length, have been made with solid-state lasers and intracavity optical fibers [47].

The generation of coherent, extreme ultraviolet and x-ray radiation by creating a population inversion and gain (Eq. (74.2)) on atomic transitions is impractical due to the very short lifetimes and large energies required to populate excited levels of such transitions; there is the additional problem that conventional optical components like mirrors and lenses are unavailable at x-ray wavelengths. Such radiation is generated in free electron “lasers” (FELs) by undulator radiation from relativistic electron beams in a “wiggler” magnetic field [48, 49]. (For reviews of FEL developments and x-ray FELs: [50, 51].)

The high intensities produced with mode locking and chirped pulse amplification allow highly nonlinear atom–field interactions, such as the generation of high harmonics of the central frequency of an incident pulse. This has made possible the generation of *attosecond* pulses [52, 53]. High-harmonic generation (HHG) has been achieved by focusing high-intensity, femtosecond infrared pulses onto atoms with high ionization potentials (inert gases), resulting in the generation of coherent extreme ultraviolet pulses and *tabletop* x-ray “lasers” [54]. HHG has been explained by a classical “three-step” model [55, 56] involving (i) ionization of the atom by the field, (ii) the field drives the freed electron back to the ion, and (iii) the emission of high-harmonic radiation by the accelerated electron. General features of the classical model are recovered in fully quantum-mechanical theory [57].

74.6 Instabilities and Chaos

Mode-locked pulses and solitons exemplify an ordered dynamics, as opposed to the erratic and seemingly random intensity fluctuations that are sometimes observed in the output of a laser. In fact, it is possible, under certain circumstances, for laser oscillation to exhibit deterministic chaos; i.e., an effectively random behavior that can nevertheless be described by purely deterministic equations of motion. Extensive experimental and theoretical work on unstable and chaotic behavior in a wide variety of laser systems has been reported [58–61]. Instabilities of single transverse mode dynamics have also been studied, especially in connection with spontaneous spatial pattern formation [61]. The high gain and strong nonlinearities of diode lasers can result in chaotic behavior, which is of interest for possible applications including secure communications and random number generation [62].

References

- Sargent III, M., Scully, M.O., Lamb Jr., W.E.: *Laser Physics*. Addison-Wesley, Reading, Massachusetts (1974)
- Yariv, A.: *Quantum Electronics*, 3rd edn. Wiley, New York (1989)
- Siegman, A.E.: *Lasers*. University Science Books, Mill Valley (1986)
- Menzel, R.: *Photonics. Linear and Nonlinear Interactions of Laser Light and Matter*, 2nd edn. Springer, Berlin (2007)
- Milonni, P.W., Eberly, J.H.: *Laser Physics*. Wiley, Hoboken (2010)
- Svelto, O.: *Principles of Lasers*, 5th edn. Springer, New York (2010)
- DiBartolo, B.: *Optical Interactions in Solids*. Wiley, New York (1968)
- Rigrod, W.W.: *J. Appl. Phys.* **36**, 27 (1965)
- Casperson, L.W., Yariv, A.: *Appl. Phys. Lett.* **17**, 259 (1970)
- Drever, R.W.P., Hall, J.L., Kowalski, F.V., Hough, J., Ford, G.M., Munley, A.J., Ward, H.: *Appl. Phys. B.* **31**, 97 (1983)
- Black, E.D.: *Am. J. Phys.* **69**, 79 (2001)
- Alnis, J., Matveev, A., Kolachevsky, N., Udem, Th., Hänsch, T.W.: *Phys. Rev. A* **77**, 053809 (2008)
- Kessler, T., Hagemann, C., Grebing, C., Legero, T., Sterr, U., Riehle, F., Martin, M.J., Chen, L., Ye, J.: *Nat. Photon.* **6**, 687 (2012)
- Schawlow, A.L., Townes, C.H.: *Phys. Rev.* **112**, 1940 (1958)
- Lax, M.: *Phys. Rev.* **160**, 290 (1967)
- Henry, C.H.: *IEEE J. Quantum Electron.* **18**, 259 (1982)
- Petermann, K.: *IEEE J. Quantum Electron.* **19**, 1391 (1979)
- Siegman, A.E.: *Phys. Rev. A* **39**, 1253 (1989)
- Siegman, A.E.: *Phys. Rev. A* **39**, 1264 (1989)
- Goldberg, P., Milonni, P.W., Sundaram, B.: *Phys. Rev. A* **44**, 1969 (1991)
- Goldberg, P., Milonni, P.W., Sundaram, B.: *Phys. Rev. A* **44**, 4556 (1991)
- Hamel, W.A., Woerdman, J.P.: *Phys. Rev. Lett.* **64**, 1506 (1990)
- Eijkelenborg, M.A., Lindberg, A.M., Thijssen, M.S., Woerdman, J.P.: *Phys. Rev. A* **55**, 4556 (1997)
- Cheng, K.-J., Mussche, P., Siegman, A.E.: *IEEE J. Quantum Electron.* **30**, 1498 (1994)
- Fox, A.G., Li, T.: *Bell Syst. Tech. J.* **40**, 453 (1961)

26. Glauber, R.J.: Phys. Rev. **130**, 2529 (1963)
27. Glauber, R.J.: Phys. Rev. **131**, 2766 (1963)
28. Mandel, L., Wolf, E.: Optical Coherence and Quantum Optics. Cambridge University Press, Cambridge (1995)
29. Loudon, R.: The Quantum Theory of Light, 3rd edn. Clarendon, Oxford (2000)
30. Meystre, P., Sargent III, M.: Elements of Quantum Optics, 2nd edn. Springer, Berlin, Heidelberg (1991)
31. McClung, F.J., Hellwarth, R.W.: J. Appl. Phys. **33**, 828 (1962)
32. Haus, H.A.: IEEE J. Sel. Top. Quantum. Electron. **6**, 1173 (2000)
33. Hall, J.L.: Rev. Mod. Phys. **78**, 1279 (2006)
34. Hänsch, T.W.: Rev. Mod. Phys. **78**, 1297 (2006)
35. Cundiff, S.T., Ye, J.: Rev. Mod. Phys. **75**, 325 (2003)
36. Spence, D.E., Kean, P.N., Sibbett, W.: Opt. Lett. **16**, 42 (1991)
37. Brabec, T., Spielmann, Ch., Curley, P.F., Krausz, F.: Opt. Lett. **17**, 1292 (1992)
38. Yefet, S., Pe'er, A.: Appl. Sci. **3**, 694 (2013)
39. Fork, R.L., Greene, B.I., Shank, C.V.: Appl. Phys. Lett. **38**, 671 (1981)
40. Treacy, E.B.: IEEE J. Quantum Electron. **5**, 454 (1969)
41. Grischkowsky, D., Balant, A.C.: Appl. Phys. Lett. **41**, 1 (1982)
42. Mollenauer, L.F., Stolen, R.H., Gordon, J.P., Tomlinson, W.J.: Opt. Lett. **8**, 289 (1983)
43. Fujimoto, J.G., Weiner, A.M., Ippen, E.P.: Appl. Phys. Lett. **44**, 832 (1984)
44. Shank, C.V.: Science **233**, 1276 (1986). and references therein
45. Strickland, D., Mourou, G.: Opt. Commun. **56**, 219 (1985)
46. Maine, P., Strickland, D., Bado, P., Pessot, M., Mourou, G.: IEEE J. Quantum Electron. **24**, 398 (1988)
47. Mollenauer, L.F., Stolen, R.H.: Opt. Lett. **9**, 13 (1984)
48. Madey, J.: J. Appl. Phys. **42**, 1906 (1971)
49. Deacon, D.A.G., Elias, L.R., Madey, J.M.J., Ramian, G.J., Schwettman, H.A., Smith, T.I.: Phys. Rev. Lett. **38**, 892 (1977)
50. Pellegrini, C.: Eur. Phys. J. H **37**, 659 (2012)
51. Huang, Z., Kim, K.-J.: Phys. Rev. Special Top. Accel. Beams **10**, 034801 (2007)
52. Krausz, F., Ivanov, M.: Rev. Mod. Phys. **81**, 163 (2009)
53. Gallmann, L., Cirelli, C., Keller, U.: Annu. Rev. Phys. Chem. **63**, 447 (2012)
54. Popmintchev, T., et al.: Science **336**, 1287 (2012)
55. Kulander, K.C., Schafer, K.J., Krause, J.L.: eds. In: Piraux, B., L'Huillier, A., Rzążewski, K.K. (eds.) Super-Intense Laser-Atom Physics. Plenum, New York (1993)
56. Corkum, P.B.: Phys. Rev. Lett. **71**, 1994 (1993)
57. Lewenstein, M., Balcou, P., Ivanov, M.Y., L'Huillier, A., Corkum, P.B.: Phys. Rev. A **49**, 2117 (1994)
58. Caspersen, L.W.: Spontaneous pulsations in lasers. In: Harvey, J.D., Walls, D.F. (eds.) Laser Physics. Springer, Berlin, Heidelberg (1983)
59. Milonni, P.W., Shih, M.-L., Ackerhalt, J.R.: Chaos in Laser-Matter Interactions. World Scientific, Singapore (1987)
60. Abraham, N.B., Arecchi, F.T., Lugiato, L.A. (eds.): Instabilities and Chaos in Quantum Optics II. Plenum, New York (1988)
61. Lugiato, L., Prati, F., Brambilla, M.: Nonlinear Optical Systems. Cambridge University Press, Cambridge (2015)
62. Sciamanna, M., Shore, K.A.: Nat. Photon. **9**, 151 (2015)



Ralf Menzel Ralf Menzel studied physics, received his PhD from the Humboldt University, Berlin, in 1978, and finished his Habilitation in Physical Chemistry at the Technical University, Berlin, in 1989. In 1994 he became a full Professor for Experimental Physics in Photonics at the University of Potsdam. His research interests are in the fields of lasers, nonlinear optics, measurement techniques for biological and medical applications, and quantum optics.



Peter Milonni Peter Milonni received his PhD from the University of Rochester in 1974. He is currently a Laboratory Fellow and Guest Scientist at Los Alamos National Laboratory and a Research Professor at the University of Rochester. He previously had positions with the US Air Force, the Perkin-Elmer Corporation, and the University of Arkansas. His research interests include quantum optics and electrodynamics.



Types of Lasers

75

Richard S. Quimby and Richard C. Powell

Contents

75.1	Introduction	1081
75.2	Single-Atom Transitions	1082
75.2.1	Neutral Atom Gas Lasers	1082
75.2.2	Ion Lasers	1083
75.2.3	Metal Vapor Lasers	1083
75.2.4	Rare-Earth Ion Lasers	1083
75.2.5	Transition Metal Ion Lasers	1086
75.3	Molecular Transitions	1088
75.3.1	Molecular Vibrational Lasers	1088
75.3.2	Dye Lasers	1089
75.3.3	Excimer Lasers	1089
75.4	Solid-State Transitions	1090
75.4.1	Semiconductor Lasers	1090
75.4.2	Quantum Cascade Lasers	1091
75.5	Free Electron Lasers	1092
75.6	Nonlinear Optical Processes	1092
75.6.1	Raman Lasers	1093
75.6.2	Optical Parametric Oscillators	1093
75.6.3	Frequency Conversion	1093
75.6.4	High Harmonic Generation	1094
	References	1094

Abstract

The availability of coherent light sources has revolutionized atomic, molecular, and optical science. Since its invention in 1960, the laser has become the basic tool for atomic and molecular spectroscopy and for elucidating fundamental properties of optics and optical interactions with matter. The unique properties of laser light have found many practical applications as well, and the laser

has become an essential component of industries such as telecommunications, manufacturing, medicine, and photonics. The various types of lasers can be categorized in a number of different ways; for example, in terms of spectral range, temporal characteristics, pumping mechanism, or by the phase (solid, liquid, gas, plasma) of the laser gain medium. In keeping with a handbook on atomic, molecular and optical physics, the types of lasers will be organized here more fundamentally, according to the type of quantum states involved in the lasing transition. Lasing can arise, for example, from transitions between quantum states that are primarily associated with either a single atom, a single molecule, or an extended solid. But it can also arise from stimulated scattering and nonlinear parametric processes that do not require population inversion between the energy levels of a medium.

Keywords

fiber laser · solid state laser · color center · laser emission · pulsed lasers

75.1 Introduction

Various types of lasers are listed in Table 75.1. The list is not comprehensive but illustrates the variety and properties of the most important lasers that are currently of interest for applications. Included in the table are examples of specific lasers of a given type, the type of lasing medium, and the typical spectral range. Also indicated is the nature of the transition: between electronic states, between vibrational states, a combination of electronic and vibrations, or not involving transitions between discrete energy levels of the medium (nonlinear processes). In this chapter, the emphasis will be on understanding the basic operational principles of and differences between the laser types, with details of a few representative lasers as space allows. For a more comprehensive discussion of different laser types, the reader is

R. S. Quimby (✉)
Dept. of Physics, Worcester Polytechnic Institute
Worcester, MA, USA
e-mail: rsquimby@WPI.EDU

R. C. Powell
Optical Sciences Center, University of Arizona
Tucson, AZ, USA
e-mail: rcpowell@email.arizona.edu

Table 75.1 Overview of laser types, organized by the nature of the lasing transition

Laser type	Typical lasers	Host	Transition type	Spectral range
Single-atom transitions				
Neutral atom gas lasers	He-Ne	Low-pressure gas	Elec	Vis/IR
Ion gas lasers	Ar ⁺	Low-pressure gas	Elec	Vis/IR
Metal vapor lasers	Cu vapor	High-temp metal	Elec	UV/vis
Rare-earth ion lasers	Er:YAG Yb:silica glass fiber Yb thin disk lasers	Dielectric crystal glass fiber thin disk crystal	Elec	UV/vis/IR
Transition metal ion lasers	Ti:sapphire Cr:ZnSe/S	Dielectric crystal semiconductor	Elec-vib	IR tunable
Molecular transitions				
Molecular vibrational lasers (IR)	CO ₂	Gas mixture	Vib	IR
Dye lasers (visible)	Rhodamine 6G	Liquid (ethanol)	Elec-vib	Vis
Excimer lasers (UV)	ArF	Gas discharge	Elec-vib	UV
Solid-state transitions				
Semiconductor lasers	Double heterostructure quantum well VCSEL	III/V semiconductor II/VI semiconductor	E-h interband transition	Near IR-vis
Quantum cascade lasers	QCL	III/V semiconductor II/VI semiconductor	Intraband transition	IR
Free electron lasers	Synchrotron facility linac facility	High-energy electron beam in vacuum	Radiation from electron oscillations	IR-vis-UV-Xray
Nonlinear optical processes				
Raman lasers	Phosphosilicate fiber Yb fiber laser pump	Glass optical fiber	Stimulated scattering	Near IR-vis
Optical parametric oscillators	OPA & OPO	Transparent dielec- tric crystal	Parametric process	Near-mid IR
Frequency conversion	Frequency doubling frequency difference generation	Transparent dielec- tric crystal	Parametric process	Mid IR THz
High harmonic generation	Table-top XUV soft X-ray source	Noble gas	High field ↔ atom interaction	Extreme UV soft X-ray

referred to textbooks on lasers [1–5], general handbooks on lasers [6–11], books on specialized laser types [12–17], and authoritative websites [18].

75.2 Single-Atom Transitions

The simplest type of laser transition, and the one usually considered when explaining or learning about laser theory, is a transition between energy levels associated with a single atom. As discussed in the previous chapter, it is generally necessary to have population inversion (more atoms in the upper level than in the lower level) in order to have amplification of light in the medium, and thus lasing. There are exceptions to this general rule, however. For example, atomic transitions can occur between two energy level manifolds, with a quasi-thermal distribution of population within each manifold. This can lead to unequal absorption and emission cross sections at the lasing wavelength, relaxing the requirement of population inversion. Another exception occurs when two closely spaced lower levels are put into a coherent superposition state, such that absorption to a higher level is

suppressed relative to emission. This makes “lasing without inversion” [19] possible (see also Sect. 78.2.7).

For our purpose, transitions will be considered single-atom type even if the atoms are not completely isolated or in the gaseous or plasma phase. Certain atoms, such as the rare-earth or transition metals, can occur as ionic impurities in an insulating dielectric solid, and they have optical transitions that are between energy levels of one atom. The host solid does interact with the impurity atom, perturbing its energy levels to various degrees, but nonetheless the transition can be described as between these perturbed levels of a single atom.

75.2.1 Neutral Atom Gas Lasers

The signature laser of this type is the He-Ne laser, one of the first lasers to be developed in the early 1960s, and still in use today. Although the lasing medium is a mixture of two gases, only Ne is involved in the lasing transition, He serving only to populate the 3s levels of Ne by collisional energy transfer. Lasing occurs on Ne transitions from the excited 3s levels to the lower 3p levels in the infrared (3.39 μm),

and also to the lower 2p levels in the visible (543.3, 594.1, and 632.8 nm) and infrared (1.15, 1.529 μm). For operation at the visible wavelengths, it is necessary to suppress lasing on the much stronger 3.39 μm transition, for example by using end mirrors with less than 0.5% reflectivity at that wavelength. The gas mixture ($\approx 10\%$ Ne) is excited in a low pressure (4–7 mbar) discharge tube of small diameter (0.5–2 mm), with 1–5 kV and 4–11 mA. The tube diameter is limited because of the need for wall collisions to return the Ne to the ground state, and this limits the practical output power to tens of mW. Although not scalable to high power, He-Ne lasers are still relevant for applications such as interferometry, where long coherence lengths are needed. For typical tube lengths of 20–50 cm, there is simultaneous lasing of two to three longitudinal modes, and this limits the coherence length to ≈ 20 cm. However, operation on a single longitudinal mode and frequency stabilization can result in coherence lengths greater than 1 km. Although diode lasers have replaced He-Ne lasers for many applications, these long coherence lengths along with the nearly diffraction-limited output of the He-Ne laser remain distinct advantages, and it continues to be relevant for interferometry and educational instruction.

75.2.2 Ion Lasers

Ion lasers operate on transitions between energy levels of ionized noble gas atoms such as Ar or Kr. The noble gas (argon, for example) is excited in a high voltage (100–400 V) and high current (5–30 A) electrical discharge. The upper laser level is excited by a two-step process: first, the neutral argon atom is ionized by electron collisions (≈ 16 eV), and then the Ar^+ ions are raised to an excited electronic state (≈ 20 eV) by further electron collisions. Lasing occurs on the Ar^+ $4p \rightarrow 4s$ transition (≈ 2 eV). The gas pressure is carefully adjusted to give the greatest possible density of argon atoms, while at the same time allowing the electron mean free path to be great enough to give the electrons sufficient kinetic energy when they collide with Ar atoms. Even with optimum tube pressure, the gain coefficients are small, and this requires long cavity lengths, very high mirror reflectivities, and low cavity losses. To minimize reflection losses at the plasma tube windows, they are tilted at Brewster's angle (Brewster windows) and must be kept very clean. The spectral output of argon lasers is a series of green and blue lines, most prominently at 514.5 and 488 nm, which can be selected by an intracavity prism. Krypton lasers ($5p \rightarrow 5s$ transition) emit in the green and red, most prominently at 521, 568, and 647 nm. The wall-plug efficiency is quite low ($\approx 0.1\%$), and for output powers greater than 1 W, water cooling is needed to extract the waste heat. Ion lasers were at one time the most important source of high-power laser light in the visible but have decreased in

popularity due to competition from frequency-doubled solid-state lasers such as Nd:YAG.

75.2.3 Metal Vapor Lasers

These lasers are similar in operation to the neutral atom gas or ion lasers discussed above, except that the excitation process begins with vaporizing a solid or liquid to produce the gas for lasing, then followed by normal electrical discharge pumping. A typical ion laser of this class is the helium–cadmium laser. For the excitation processes, metallic Cd is evaporated and mixed with He. Then a DC electric discharge excites the He atoms and ionizes the Cd. The excited He atoms transfer their energy to the Cd ions, and lasing occurs between electronic levels of the Cd ion. The main emission lines are 441.6 and 325 nm, with CW output powers in the range 10–150 mW. The wall-plug efficiency is low, between 0.002% and 0.02%.

A typical neutral atom laser of this type is the copper vapor laser, with emission lines at 510.5 and 578.2 nm. These lasers operate only in the pulsed mode since the lower levels of the laser transitions are metastable and the transition is self-terminating. These lasers have high gain (10–30%/cm), and high wall-plug efficiency ($\approx 1.0\%$), but require high temperatures to create the vapor.

75.2.4 Rare-Earth Ion Lasers

This section and the next (Sect. 75.2.5) discuss lasers in which the gain medium is a dielectric solid (crystal or glass), doped with metal impurity ions to form an optically active center. The solid host itself is not usually optically active, and this type of laser has come to be referred to as a “solid-state laser”. This is in contrast to the case of semiconductor lasers (Sect. 75.4), in which the solid itself is the optically active material. Although semiconductor lasers might be considered a kind of “solid-state laser” (they are, after all, a laser that is in the solid state), conventional terminology is to reserve the term “solid-state laser” for those based on impurity-doped dielectric solids.

When elements of the lanthanide series (Ce, Pr, Nd, Pm, Sm, Eu, Gd, Tb, Dy, Ho, Er, Tm, Yb) are doped as impurities into an dielectric crystal or glass, they typically become triply ionized, e.g., Er^{3+} . These rare-earth ions have atomic-like transitions between levels of the same $(4f)^n$ configuration, where n ranges from 1 for Ce to 13 for Yb [20]. The host matrix perturbs these levels only weakly, due to the shielding of the optically active inner 4f shell by the filled outer 5s and 5p shells. The intermediate coupling scheme applies here, where spin–orbit interactions are small but not negligible compared to electrostatic interactions [21]. In this

case, the LS Russell–Saunders states with the same J are mixed, forming states that are linear combinations of different LS with a common value of J . The notation used to identify a given level is that of the principal LSJ component (i.e., $^{2S+1}L_J$). The local electric field from surrounding atoms in the host splits the $(2J + 1) M_J$ levels of each LSJ state through the Stark effect, resulting in a manifold of closely spaced sublevels [22]. For even values of n , there are $2J + 1$ Stark levels, but for odd n , there are $(2J + 1)/2$ levels, due to Kramer's degeneracy. The three types of splittings of the $4f$ states differ from each other by roughly an order of magnitude: electrostatic ($\approx 10^4 \text{ cm}^{-1}$), spin–orbit ($\approx 10^3 \text{ cm}^{-1}$), and Stark effect ($\approx 10^2 \text{ cm}^{-1}$).

Radiative $(4f)^n \rightarrow (4f)^n$ transitions are not electric dipole allowed by parity, and although magnetic dipole and quadrupole transitions are allowed, they are very weak. However, the local electric field mixes some of the higher $5d$ levels into the nominal $4f$ states, allowing so-called “forced electric dipole” transitions with an oscillator strength of $\approx 10^{-6}$ [23]. Typical absorption and emission cross sections are on the order of $\approx 10^{-20} \text{ cm}^2$, and with rare-earth ion concentrations of $\approx 10^{20} \text{ cm}^{-3}$ ($\approx 1\%$ doping), the gain coefficient can be as high as $\approx 1 \text{ cm}^{-1}$. This is intermediate between the very low gain typical of gas lasers and the very high gain of semiconductor lasers.

There are many varieties of rare-earth-doped lasers, and they have become one of the most important lasers for a variety of applications. The main characteristics that distinguish the different types are the nature of the optical pump, the type of solid host, the geometry of the host, and, of course, the selection of a particular rare-earth ion. In what follows, each of these aspects will be examined to illustrate the large and still growing variety of rare-earth-doped lasers.

Rare-earth doped lasers are excited optically and were originally pumped by lamps. However, the brightness of lamps is limited, and their spectral output does not couple efficiently with the narrow absorption lines of the rare earth. These issues were overcome with the advent of efficient and powerful diode lasers for pumping (Sect. 75.4.1), and today diode laser pumping of solid-state lasers has largely replaced lamp pumping [24].

The first host materials used in solid-state lasers were oxide crystals such as Al_2O_3 (sapphire) and $\text{Y}_3\text{Al}_5\text{O}_{12}$ (YAG). Fluoride crystals such as LiYF_3 (YLF) were found to have desirable properties, such as lower nonradiative relaxation between levels, which allows transitions further into the infrared. Glass hosts were tried early on [25], but the low thermal conductivity presented thermal management problems. It was not until the advent of fiber lasers, with a very small diameter that allows efficient cooling, that glass hosts began to compete seriously with crystal hosts. Just as with crystals, it was found that fluoride-based glasses such as ZBLAN [26] exhibit lower nonradiative relaxation, and hence the potential

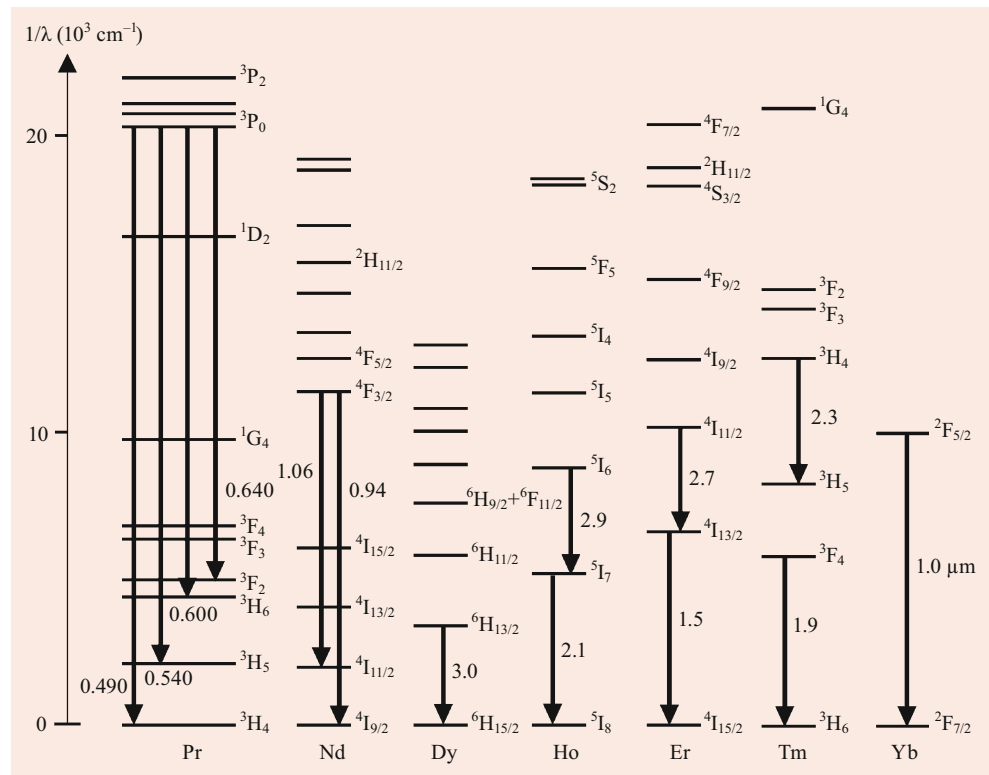
for lasing further into the infrared. A major difference between crystal and glass hosts is the smoothness of the optical spectra. Crystals provide similar crystal field sites for every dopant ion, while the disorder associated with glass structure gives many different types of local crystal field sites for the dopant ions, leading to inhomogeneous broadening of the spectral lines. As a result, absorption and emission spectra for rare earths in crystals show a great deal of structure [22], while in glasses, the spectra are significantly smoothed out, which is an advantage for tunable lasers. More recently, there has been a developing interest in glass ceramics [27], where active ions embedded in nanocrystals see essentially a crystalline environment, while on a macroscopic scale, the material is amorphous and can be molded and drawn into shapes like a glass. This topic is under active development.

The classic geometry of the gain medium is a cylindrical rod, typically 5–15 cm long and a few mm in diameter. This is still a common geometry, although for higher powers, rectangular slabs with Brewster's angle ends are sometimes used [14]. At high powers where thermal lensing limits the output power of traditional rod or slab geometries, there is increasing interest in thin-disk lasers [14], which have the active medium in the form of a thin disk mounted directly on a reflecting element and heat sink. Both pumping and lasing occur perpendicularly to the plane of the disk, which is efficiently cooled with the temperature gradient in the direction of lasing, avoiding thermal lensing issues.

Fiber lasers take the opposite geometric approach – instead of being short with large diameter like a disk, they are long and have a small diameter [28, 29]. In both cases, the surface-to-volume ratio is large, leading to efficient cooling. Comparing the two approaches, fiber lasers are better suited for high CW power, whereas thin-disk lasers are better for pulses with high peak power. In a fiber laser, the fiber core is doped with the active ion, while the cladding is undoped. It is usually end-pumped with another laser, most often with a diode laser but sometimes with another fiber laser. For very high power operation, the diode laser sources that are available do not provide a Gaussian beam that can be coupled into the core of a single-mode fiber. In this case, a double-clad fiber is used, which has a second inner cladding into which the pump light is launched and guided. The fraction of pump light absorbed per unit length is smaller than in core pumping, but for a sufficiently long fiber, most of the pump light can be absorbed. This amounts to a brightness converter, in which low brightness pump light is converted into high brightness lasing light.

The output power in a fiber laser is ultimately limited by nonlinear optical effects, due to the confinement of significant power in the very small mode area of the core. This led to the development of large-mode-area (LMA) fibers [30], which reduce the light intensity in the core. Another approach is hollow core fibers, a special class of photonic

Fig. 75.1 Low-lying energy levels of selected rare-earth 3+ ions, showing the wavelength of important lasing transitions in μm



crystal fibers in which the light propagates mostly in air, avoiding nonlinear effects in the glass [30]. The guiding of light in such fibers is due to the photonic bandgap effect, rather than the index guiding characteristic of traditional optical fibers. Although optical fibers are typically made of glass, there is increasing interest in single-crystal fibers (SCF), especially for very high power ultrashort pulse amplification [31]. These can have diameters from $\approx 100 \mu\text{m}$ to as large as $\approx 1 \text{ mm}$, approaching the dimensions of a traditional rod but with guiding of the pump light much as in a traditional fiber amplifier.

There are many possible laser transitions for the 12 optically active rare-earth ions, but only a few important examples can be mentioned here. A more comprehensive listing can be found elsewhere [11, 20, 23]. Figure 75.1 shows the more important lasing transitions in the visible (Pr), near-IR (Nd, Yb, Er), and mid-IR (Dy, Ho, Er, Tm). The development of efficient GaN diode lasers [32–34] at 440 nm has made practical the direct pumping of the Pr 3P levels to give visible lasers in the blue (490 nm), green (540 nm), and red (600, 640 nm). Typical hosts for these lasers are fluorozirconate glass (ZBLAN) and the crystal LiYF_4 (LYF). In the near-IR, the Nd:YAG laser has been and continues to be one of the most widely used solid-state lasers for scientific, industrial, and medical applications, operating most efficiently at 1064 nm, but also at 946, 1123, and 1319 nm. Originally pumped with lamps, it is now mostly pumped with high power diode lasers. When the 1064 beam is frequency

doubled (Sect. 75.6.3), the 532 nm output has replaced the 514.5 nm line of the more bulky and less efficient argon ion laser for many applications. The Nd:YAG laser is now, in turn, gradually being replaced by the more compact and efficient Yb fiber laser, which operates in the same $\approx 1 \mu\text{m}$ wavelength region. These Yb lasers have been scaled to the kW range and higher in recent years, pumped by increasingly efficient and powerful diode laser stacks [35].

Also important in the near-IR is the $\text{Er}^{3+} \ ^4I_{13/2} \rightarrow \ ^4I_{15/2}$ transition at 1.5–1.6 μm , which falls right at the wavelength of minimum attenuation in silica glass fibers. With Er doped in silica fiber, this transition forms the basis for the erbium-doped fiber amplifier (EDFA), which is largely responsible for the explosive growth in telecommunications bandwidths in the past two decades [28, 36]. The EDFA can be pumped with diode lasers at 980 or 1480 nm, the latter having a higher potential efficiency due to a smaller quantum defect (difference between pump and lasing photon energy). In the case of 980 nm pumping, the fiber is sometimes codoped with Yb, which absorbs the pump more strongly and transfers the energy to Er nonradiatively. Output powers can be several to $\approx 100 \text{ W CW}$ [11]. Er-doped crystals also operate with high power on this transition, for example, Er:YAG at $\approx 1645 \text{ nm}$.

For operation in the $\approx 2 \mu\text{m}$ region, both Tm (1.9 μm) and Ho (2.1 μm) have transitions that terminate on the ground-state manifold (three-level systems). Tm has an especially large tuning range of up to $\approx 250 \text{ nm}$ in a fiber and $\approx 300 \text{ nm}$ in a crystal. Another unique advantage of Tm is the cross-

relaxation that occurs at high ($> 2\%$) Tm concentrations when the $^3\text{H}_4$ level is pumped at 790 nm [37]. In this process, the excited Tm^{3+} exchanges energy nonradiatively with a neighboring Tm^{3+} in the ground state, leaving both ions in the $^3\text{F}_4$. The result is two ions in the upper laser level for a single pump photon absorbed – a quantum efficiency of 200%. Another mid-IR transition in Tm is the $^3\text{H}_4 \rightarrow ^3\text{H}_5$ transition at 2.3 μm , which can also be pumped at 790 nm. In this case, however, the Tm concentration is kept below 2% because cross-relaxation would have the undesirable effect of depleting the upper laser level.

The first excited state of Ho^{3+} is a bit lower in energy than that of Tm^{3+} , and its ground state transition is somewhat longer in wavelength, $\approx 2.1 \mu\text{m}$. Unfortunately, Ho^{3+} does not have a convenient wavelength for high power diode laser pumping, so Tm is often codoped to efficiently absorb the pump light at 790 nm. The excited Tm^{3+} cross relaxes as described above, and then the Tm^3F_4 level transfers its energy to a nearby Ho^{3+} in the ground state, exciting it to the $^5\text{I}_7$. This process can be efficient with proper adjustment of the Tm and Ho concentrations [38].

In the $\approx 3 \mu\text{m}$ spectral region, there are transitions in Dy, Ho, and Er that have proven successful in fiber and crystalline solid-state lasers. For these lasers, fluoride hosts are preferred due to decreased multiphonon quenching of the laser transition and increased host transparency. The Dy ($^6\text{H}_{13/2} \rightarrow ^6\text{H}_{15/2}$) transition is three-level, whereas the Ho ($^5\text{I}_6 \rightarrow ^5\text{I}_7$) and Er ($^4\text{I}_{11/2} \rightarrow ^4\text{I}_{13/2}$) transitions are four-level. The four-level transitions have the disadvantage of a lower laser level that is metastable with a long (ms) lifetime, and this limits the output power due to accumulation of population in the excited states. Three techniques that have been used to reduce this problem are codoping with a quencher ion, energy transfer upconversion (ETU), and cascade lasing. An example of the first method is codoping Pr into a Ho-doped host, which results in energy transfer from the lower laser level of Ho ($^5\text{I}_7$) to a nearby Pr ion, recycling the Ho ion to the ground state [39]. Similarly, codoping of Pr into an Er-doped host depopulates the lower laser level of Er ($^4\text{I}_{13/2}$). An important example of the second method (ETU) occurs in highly doped Er materials [40], whereby two neighboring Er ions both in the lower laser level ($^4\text{I}_{13/2}$) exchange energy, leaving one in the ground state ($^4\text{I}_{15/2}$) and the other in the excited state ($^4\text{I}_{9/2}$). The ($^4\text{I}_{9/2}$) then relaxes nonradiatively to the ($^4\text{I}_{11/2}$). This has a double benefit: the lower laser level is quenched while the upper level population is simultaneously increased. A similar ETU process can occur in highly doped Ho systems [41]. In the third method, simultaneous lasing (cascade lasing) is established on, for example, both the Ho ($^5\text{I}_6 \rightarrow ^5\text{I}_7$) transition at 2.9 μm , and the ($^5\text{I}_7 \rightarrow ^5\text{I}_8$) transition at 2.1 μm [42]. For Er, cascade lasing can be established on the ($^4\text{I}_{11/2} \rightarrow ^4\text{I}_{13/2}$) and ($^4\text{I}_{13/2} \rightarrow ^4\text{I}_{15/2}$) transitions [43]. This method is especially advantageous for high-power op-

eration, because it not only solves the population bottleneck problem, but also reduces the heat load and cooling requirements. In contrast to Ho and Er, a Dy 3 μm laser does not suffer from population bottlenecks. As a three-level system, however, it requires high pump intensity to reach lasing threshold, and, therefore, the fiber geometry with fluoride glass is most efficient.

75.2.5 Transition Metal Ion Lasers

When transition metal elements of the fourth row of the periodic table (Ti, V, Cr, Mn, Fe, Co, Ni, Cu, and Zn) are doped as impurities into an dielectric crystal or glass, they can take on various oxidation states, such as 2+, 3+, or 4+. In the oxidation process, they first lose the two outer 4s electrons and then the 3d electrons according to the oxidation state. Example electron configurations for the optically active electrons are $(3d)^1$ for Ti^{3+} , and $(3d)^3$ for Cr^{3+} . Unlike the case of the rare-earth ions, there is little shielding of these optically active 3d states from external electric fields, and the energy level positions are strongly influenced by the host. The quantum states become characterized by the symmetry of the ion's crystallographic site, rather than by the atomic states of an isolated ion [44, 45].

This strong ion–host interaction leads to broadly tunable optical transitions, best understood in terms of a “configurational coordinate diagram” [21]. In this picture, the collective motion of all nearby host atoms is represented by a single coordinate Q , and the Born–Oppenheimer approximation is used to separate the degrees of freedom into electronic (fast) and nuclear (slow) parts. The energies of the ion's different electronic levels are calculated assuming a stationary Q and then plotted as a function of Q as shown in Fig. 75.2. For each electronic state, there is a minimum energy at some value of Q , about which the system oscillates with a frequency given by the curvature of $E(Q)$. This gives rise to vibrational sublevels superimposed on the electronic states, with the total quantum state now characterized by the electronic state and an integer number of vibrational quanta. Optical transitions are nearly vertical in this diagram, because the electron motion is much faster than the nuclear motion during the transition. During the optical transition, the atoms of the host can be thought of as “frozen in position” (the Franck–Condon principle). When the minima for the two electronic states occur at different values of Q , there is a shift to lower energy (longer wavelength) between absorption and emission, known as the “Stokes shift”. Both the absorption and emission spectra are then broadened and shifted as shown in Fig. 75.3. When the two minima occur at nearly the same Q , however, as is the case for rare-earth 4f transitions and certain pairs of transition metal states, the op-

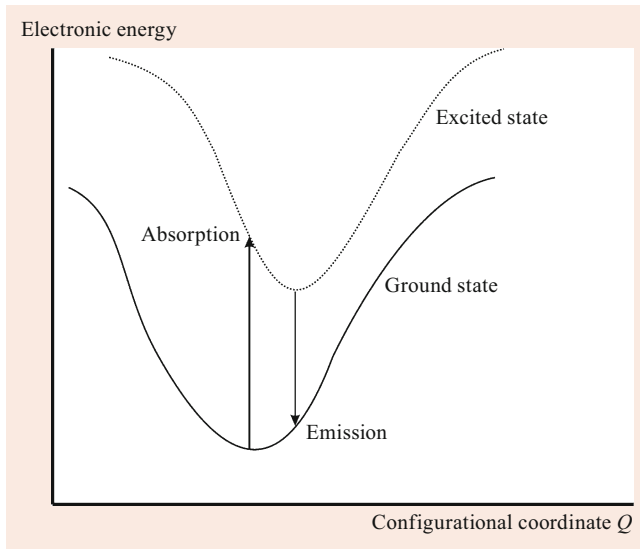


Fig. 75.2 Configuration coordinate diagram for strong electron-lattice interaction

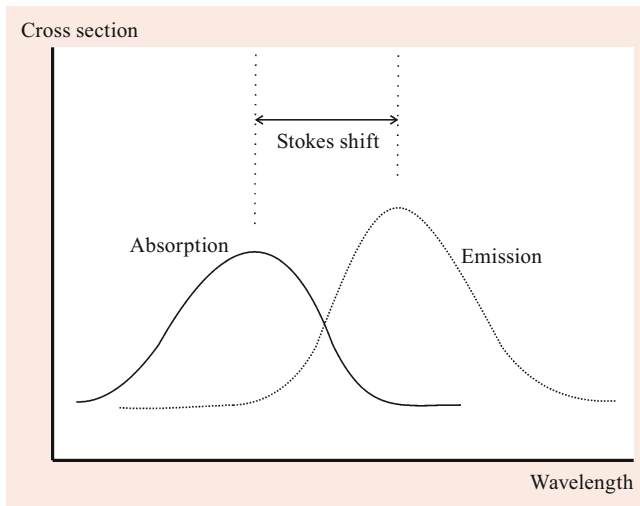


Fig. 75.3 Stokes shift between absorption and emission

tical transition is mostly purely electronic (“zero-phonon”), with a very weak phonon sideband.

Taking Cr^{3+} as an example, Fig. 75.4 shows how the energy E/B of different atomic orbitals in a site having octahedral symmetry vary with the crystal field strength Dq/B , relative to the ground state. This is known as a Tanabe–Sugano diagram [21]. For certain states (2E , 2T), the energy difference with the ground state changes little as the field strength changes, indicating weak ion–lattice coupling. At sufficiently high field strength, these are the lowest-lying excited states, leading to sharp spectral absorption and emission for transitions to and from the ground state. This explains why the ruby laser ($\text{Cr}^{3+}:\text{Al}_2\text{O}_3$), the first laser to be demonstrated in 1960, operates at a single wavelength of 694 nm, with no tunability. Other crystalline hosts for Cr^{3+} provide a “low field” envi-

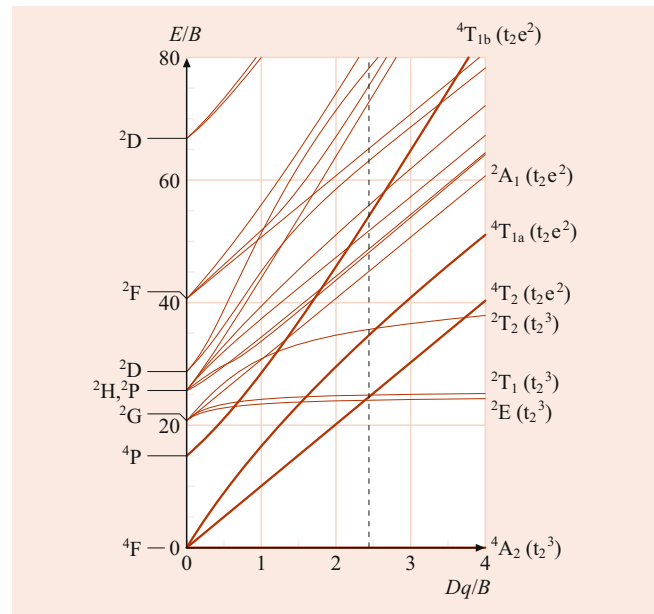


Fig. 75.4 Energy E/B of transition metal ion states versus crystal field strength Dq/B [11]

ronment, such that the 4T_2 level lies lower in energy than the 2E . The first tunable laser based on Cr^{3+} was $\text{Cr}^{3+}:\text{BeAl}_2\text{O}_4$ (alexandrite), which is tunable from 700–820 nm with good efficiency and thermal properties [46]. Other hosts for Cr^{3+} that are similarly tunable have been demonstrated, such as LiCaAlF_6 and LiSrAlF_6 , but these have poorer crystal properties and lower power output than alexandrite [47].

The really significant advance in tunable lasers after alexandrite was the introduction of the Ti-sapphire laser ($\text{Ti}^{3+}:\text{Al}_2\text{O}_3$) in 1982 [10, 48]. The $(3d)^1$ configuration for Ti^{3+} leads to a very simple energy level diagram, with a single absorption band from 450–550 nm and tuning range from 670–1100 nm. This wide tunability, along with the lack of excited-state absorption, high slope efficiency ($\approx 60\%$), high crystal thermal conductivity, scalability to high power, and good mechanical and chemical hardness, have made the Ti-sapphire laser one of the most important and commercially successful of all solid-state lasers. The same broad emission bandwidth that gives wide tunability also allows ultrashort mode-locked pulses, and pulse widths of ≈ 5 fs have been achieved. Pumping was originally with an Ar ion laser in the blue/green, and then with frequency-doubled Nd:YAG lasers at 532 nm. Recent progress in high-power blue diode lasers based on GaN (Sect. 75.4.1) now allows direct diode laser pumping [34], which permits a much more compact and efficient Ti-sapphire laser.

Other valence states of Cr are possible for tunable solid-state lasers, in particular Cr^{4+} and Cr^{2+} . Cr^{4+} has the $(3d)^2$ configuration, and the best hosts are found to be YAG ($\text{Y}_3\text{Al}_5\text{O}_{12}$) with $1350 < \lambda < 1550$ nm, and Mg_2SiO_4 , with $1200 < \lambda < 1350$ nm. The main drawbacks of Cr^{4+} systems

are excited-state absorption (ESA) at the lasing wavelength and nonradiative relaxation that reduces the quantum efficiency. Furthermore, careful material preparation is needed to make sure that only the Cr^{4+} oxidation state is present and not Cr^{3+} [49]. More promising is the divalent state Cr^{2+} , most notably $\text{Cr}^{2+}:\text{ZnSe}$, which has a lasing transition tunable from 2.0–3.1 μm [50]. The many advantages of this system include high absorption and emission cross sections ($\approx 10^{-18} \text{ cm}^2$) due to the tetrahedral site symmetry, near unity quantum efficiency due to the low phonon energy of the chalcogenide host, and no significant ESA because all relevant ESA transitions are spin-forbidden. For all these reasons, the $\text{Cr}^{2+}:\text{ZnSe}$ laser has come to be called the “Ti-sapphire laser of the mid-IR”, and has been commercialized [35].

A rather new type of impurity-doped solid-state laser is the bismuth-doped fiber laser. Although bismuth is not actually a transition metal ion, it is discussed here because its optical properties in the near-IR, like those of transition metal ions, depend strongly on the host. The actual nature of the Bi-related near-IR emitting centers is not yet understood, despite extensive research. The emitting center may be not a single ion, but rather clusters of ions of some valence (Bi^{5+} , Bi^{3+} , Bi^{2+} , and Bi^{+}), perhaps in association with an oxygen vacancy. Despite this current lack of understanding, such fiber lasers were first demonstrated in the range 1140–1215 nm using Bi-doped aluminosilicate fibers, and subsequent work has extended the range to include 1270–1800 nm using newly developed phosphogermanosilicate, germanosilicate, and silica fibers [51, 52]. Although these are not currently as efficient as rare-earth-doped fiber lasers, a better understanding of the nature of the optical centers may allow improved efficiency.

75.3 Molecular Transitions

This section considers lasers involving transitions between the quantum states associated with a molecule. Vibrational transitions in a gas (e.g., the carbon dioxide laser) are discussed in Sect. 75.3.1, electronic-vibrational transitions in a liquid (e.g., dye lasers) in Sect. 75.3.2, and electronic-vibrational transitions in a gas (e.g., excimer lasers) in Sect. 75.3.3.

75.3.1 Molecular Vibrational Lasers

The flagship laser of this type is the carbon dioxide (CO_2) laser, operating on transitions between different vibrational states of the CO_2 molecule [14]. It was developed at Bell Laboratories by Patel in 1964, and while the basic operational principles have changed little over the years, the applications have evolved as newer types of lasers have been developed. Once the go-to laser for cutting, welding,

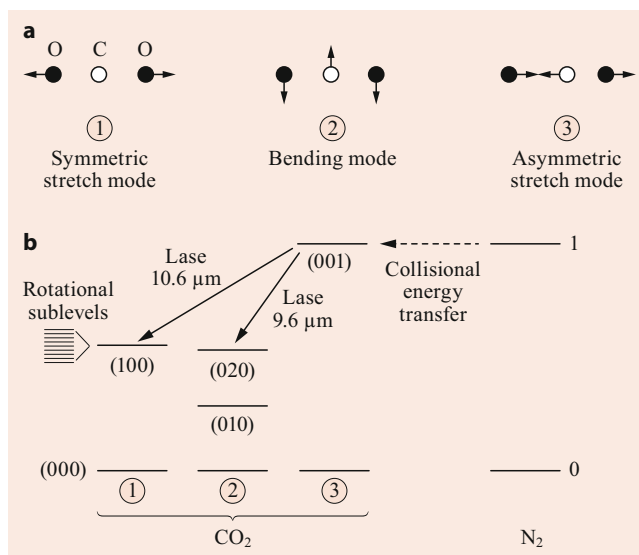


Fig. 7.5 Vibrational modes (a) and laser transitions (b) in a CO_2 laser [4]

marking, surface treatments, as well as spectroscopy in the 9.2–11 μm region, it now faces competition with high-power Yb fiber lasers in the 1 μm region, and quantum cascade lasers (Sect. 75.4.1) in the 2–12 μm region. However, the CO_2 laser still remains relevant for certain applications [53] because of its unique combination of longer wavelengths ($\approx 10 \mu\text{m}$), high power (kW CW), good beam quality (often diffraction limited), and spectral purity (linewidth $< 1 \text{ kHz}$).

CO_2 is a linear molecule and has three vibrational modes, as indicated in Fig. 7.5. Transitions from the asymmetric stretch mode to the symmetric stretch or bending modes give rise to the two principle laser transitions around 10.6 and 9.6 μm , each having a number of closely spaced ($\approx 10 \text{ GHz}$) rotational sidebands. Rotational states with quantum number J have energies $\propto J(J+1)$, and vibrational-rotational transitions obey the selection rule $J_{\text{final}} = J_{\text{initial}} \pm 1$, with the result that the rotational sideband energies are evenly spaced in frequency. The so-called P branch has $J_{\text{final}} = J_{\text{initial}} + 1$, and the R branch has $J_{\text{final}} = J_{\text{initial}} - 1$ [1, 54]. Tuning the laser to discrete lines in the range 9.2–11 μm region is possible using a diffraction grating in place of the end mirror. With no wavelength selection, lasing occurs on the 10P branch with $J \approx 20$. Since the thermal population of the different rotational states depends on gas temperature, cooling of the gas is needed for stable high-power operation.

Excitation of the CO_2 vibrational levels occurs in a high-voltage ($\approx 15 \text{ kV/m}$) gas discharge tube, either sealed or with flowing gases. The gas mixture contains CO_2 , N_2 , and He, with approximate ratios 1, 2, and 8, respectively. The N_2 serves to selectively enhance excitation of the CO_2 upper laser level by collisional energy transfer, while the He helps depopulate the lower CO_2 laser level and also cool the gas due to its high thermal conductivity. Other gases that are

sometimes added include Xe (few %), which absorbs fast electrons in the discharge that would otherwise disassociate the CO₂ molecules. The wall-plug efficiency is rather high ($\approx 10\text{--}15\%$) for a gas laser, and output power scales with increasing tube length ($\approx 80\text{ W/m}$). Tube diameters are limited to $\approx 5\text{--}10\text{ mm}$ due to limits on heat extraction.

Other vibrational transition lasers include the carbon monoxide (CO) laser operating at $5\text{--}6.5\ \mu\text{m}$, and the nitrous oxide (NO₂) laser operating at $10\text{--}11\ \mu\text{m}$, although these are much less commonly used. Some vibrational lasers utilize a chemical reaction to achieve an excited vibrational state, and are termed chemical lasers. Examples are the hydrogen fluoride (HF) laser operating at $2.6\text{--}3.3\ \mu\text{m}$, and the deuterium fluoride (DF) laser operating at $3.5\text{--}4.2\ \mu\text{m}$.

75.3.2 Dye Lasers

Dye molecules consist of a hydrocarbon backbone chain terminated by a more complicated structure on each end. The electrons in the conjugate double bonds give broad and efficient absorption and emission spectra in the visible, making them useful for lasers as well as decorative coloration. Developed by Sorokin and Lankard in 1966, dye lasers became very popular during the next three decades as one of the few sources of widely tunable visible and near-IR laser light [55]. The optically active electrons in the conjugate double bonds are strongly coupled to vibrational modes of the molecule, and the configurational coordinate diagram of Fig. 75.2 can be used to understand the large Stokes shift between absorption and emission, as previously discussed for transition metal ions (Sect. 75.2.5). A typical tuning range for one particular dye is $50\text{--}60\text{ nm}$, and by sequentially choosing different dyes it is possible to cover the range $300\text{--}1200\text{ nm}$ [56]. The wide emission bandwidth makes dye lasers attractive for mode-locking, and they have played an important role in developing ultrashort pulse technology, first in the ps and then the fs region [57].

Dye lasers have desirable properties in the frequency as well as time domain. With CW pumping (Ar ion laser or frequency-doubled Nd:YAG, for example), spectral linewidths in the tens of kHz can be obtained on a single longitudinal cavity mode [58]. To avoid spatial hole burning, which would otherwise cause multimode output, an etalon or a ring laser configuration can be used. In pulsed operation (e.g. flashlamp, N₂ laser, excimer laser) the linewidth is longer, typically hundreds of MHz.

Despite the dye laser's desirable properties, it does have some drawbacks that have decreased its popularity in the past two decades. One issue is the need to avoid triplet quenching, in which an excited-state population accumulates in the lowest triplet spin level, followed by excited-state absorption, which quenches laser action [55]. In pulsed operation, this is

not a problem, because the triplet states can relax back to the ground state between pulses. For CW operation, however, it is necessary to circulate the dye and move it rapidly through a small nozzle in a thin jet of flowing liquid across the optically pumped area. This limits the ability to make the laser compact and robust. Eventually, the dye degrades and needs to be replaced for both continuous wave (CW) and pulsed operation. Most significantly, perhaps, are the safety and convenience issues dealing with messy and, in many cases, carcinogenic dyes. Because of these drawbacks, newer options such as frequency-doubled solid-state lasers or fiber lasers are now often seen as more desirable for applications once served by the dye laser. Dye lasers do, however, continue to serve in niche applications such as laser isotope separation [59] and laser guide stars at large terrestrial telescopes [60].

75.3.3 Excimer Lasers

The excimer laser was developed in the 1970s and operates in the UV region in a pulsed mode [61]. The lasing transition is between electronic energy states of an “excited dimer” molecule, or excimer, which has the interesting property that bound states only exist when the molecule is in the excited state. When the molecule returns to the ground state, it dissociates, breaking up into two separate atoms.

Taking KrF as a typical example, the lasing process is illustrated in Fig. 75.6, which shows the electronic energy of a KrF “molecule” as a function of the separation of the two nuclei. This is similar in concept to the configurational coordinate diagram of Fig. 75.2, where Q is now simply the internuclear separation R . When an atom of Kr and F are brought together, each in their ground state, the energy of the system increases monotonically due to Coulomb repulsion, and the “molecule” is unbound. This is characteristic of the noble gases (He, Ne, Ar, Kr, and Xe), which are gener-

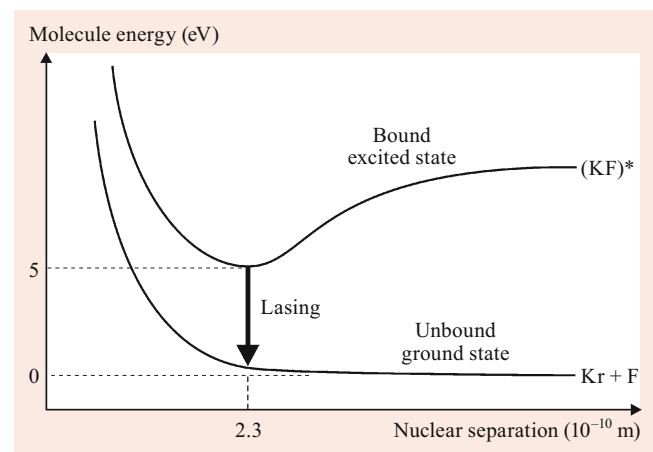


Fig. 75.6 An excimer laser operates on a bound \rightarrow unbound transition [4]

ally unreactive and not inclined to form stable molecules. If the KrF molecule is promoted to the next-highest electronic state, however (by electron bombardment in an electrical discharge, for example), then the energy curve has a minimum at $R = 0.23$ nm. This gives rise to a bound state at this value of R , which remains stable as long as the molecule remains in the excited state (≈ 10 ns for KrF). During this excited-state lifetime, lasing can occur on the transition from the bound excited state to the unbound ground state. Since there is no stable population in the lower laser level, this is an example of a perfect four-level system.

In KrF, lasing occurs at a wavelength of 248 nm. Other noble-gas-halide pairs operate in the same fashion, for example XeCl at 309 nm, XeF at 351 nm, and ArF at 193 nm. Excimer lasers have moderately high efficiencies (≈ 1 –4%), short pulse duration (≈ 10 ns), high pulse energies (0.1–1 J), and can be scaled up to high average power (100 W). They have numerous applications, including photolithography [62], materials processing, and ophthalmology (LASIK – laser-assisted in situ keratomileusis). The short wavelengths are strongly absorbed by most materials, a distinct advantage for precision cutting. The principal disadvantage of these lasers is the need to work with highly reactive gases such as fluorine, which requires proper ventilation and safety precautions. Typically, the gases are circulated through the electrical discharge chamber to maintain the purity of the reactants. A high concentration of helium (about 2 atm pressure) is added as a buffer gas to facilitate the reactions between noble and halide gases.

75.4 Solid-State Transitions

This section considers lasers based on transitions between extended, band-like states in a solid. These can be divided into two categories: semiconductor lasers, in which the transitions occur between conduction and valence band, and quantum cascade lasers (QCL), in which transitions occur between electronic sublevels of the conduction band. Semiconductor lasers are typically pumped by an electric current, in which case, they are also referred to as diode lasers. When the semiconductor is pumped optically (the optically pumped semiconductor laser, OPSL), it is often configured in the thin-disk geometry for high-power operation, similar to that of the thin-disk solid-state laser [63]. Semiconductor lasers have high gain coefficients ($\approx 10^3$ cm⁻¹), which allows for compact photonic devices.

75.4.1 Semiconductor Lasers

The fundamental light emission process in semiconductor lasers arises from radiative recombination of electrons

and holes. In the simplest case, this occurs at the junction of an n -type material having excess electrons (e.g., n -Al_{*x*}Ga_{1-*x*}As) and a p -type material having excess holes (e.g., p -Al_{*x*}Ga_{1-*x*}As). At this p - n junction, there is an electric field that keeps the charges separated until they are “injected” by an applied voltage into the depletion region, where light emission occurs. A double-heterostructure (DH) laser [64, 65] improves the performance by introducing a middle layer of a different composition (e.g., GaAs) sandwiched between the original p and n -type materials. This provides several advantages over the single homojunction laser: (1) a well-defined recombination region (given by the thickness of the middle layer) that confines the carriers, reducing lasing threshold and improving temperature stability, (2) index guiding of the emitted light due to the index difference between middle and outer layers, and (3) reduced reabsorption of emitted light in the outer layers, due to the higher bandgap there. In choosing materials for these heterostructures, lattice matching at the junctions is important to minimize strain. Common III-V compound families that exhibit good lattice matching and have wavelengths of interest for photonic applications include Al_{*x*}Ga_{1-*x*}In_{*y*}P_{1-*y*} (635–670 nm), Al_{*x*}Ga_{1-*x*}As (720–850 nm), In_{*x*}Ga_{1-*x*}As (900–1100 nm), and In_{*x*}Ga_{1-*x*}As_{*y*}P_{1-*y*} (1000–1650 nm). Most recently there has been significant progress in developing high-power blue diode lasers, based on the In_{*x*}Ga_{1-*x*}N family [32], with operation at 380, 405, 450, and 470 nm. This permits efficient diode laser pumping of certain solid-state lasers, as discussed in Sects. 75.2.4 and 75.2.5.

Quantum well (QW) structures are often used to improve the diode laser performance [66]. These are thin (≈ 10 nm) regions within the active gain region that have a smaller bandgap than the surrounding material, forming a potential well for charge carriers. The quantum states become localized in the well, resulting in a ladder of discrete energy levels that is similar to the familiar “particle in a box” of elementary quantum mechanics. The laser wavelength then depends not only on the host material but also on the width of the wells. This flexibility, along with improved device performance, has made QW structures common in commercially available laser diodes.

There are a number of configurations and geometries for the semiconductor laser cavity [14, 65]. In an edge emitter, laser light propagates along the plane of the thin semiconductor layers and is emitted from the edge of the semiconductor chip. The simplest of these is the Fabry–Perot (FP) laser, in which Fresnel reflections from the cleaved semiconductor end facets suffice for reaching the lasing threshold, due to the very high gain coefficient. Another option is a feedback mirror external to the semiconductor, which allows insertion of an intracavity element for modulation or control of polarization. Single-frequency operation can be obtained in a distributed feedback (DFB) laser, which has an undulat-

ing element of period Λ incorporated throughout the gain region of the waveguide. The laser frequency is then given by the Bragg condition $\nu = c/(2n\Lambda)$, where n is the effective waveguide index of refraction. A variation of this is the distributed Bragg reflector (DBR) laser, where the Bragg reflection occurs only at the cavity ends, separate from the gain region.

The gain region in an edge emitter is usually confined in the lateral dimension to a width $\approx 10\ \mu\text{m}$, known as the stripe geometry. This improves stability at high powers by confining both light and charge carriers to a smaller, well-defined area. For high-power applications, multiple stripes are incorporated in a single layer of a diode laser, and for even higher powers, a number of multistripe lasers are packaged in a linear array, in a diode laser bar. These bars can be stacked to provide a planar array with very high ($\approx \text{kW}$) power suitable for pumping high-power solid-state lasers [14].

In contrast to the edge emitters, there is an entirely different class of semiconductor laser in which the emission is perpendicular to the plane of the semiconductor chip [67]. These “vertical cavity surface emitting lasers” (VCSELs) consist of a small circular active region of thickness $\leq 1\ \mu\text{m}$ and diameter $\approx 10\ \mu\text{m}$, with Bragg reflecting mirrors above and below formed by a series of dielectric layers with alternating refractive index. Since the fractional gain in one pass through the active region is only $\approx 1\%$, the Bragg reflectors must have a reflectivity $R > 99.5\%$. The small cavity length L has the advantage of naturally promoting single-frequency operation, since the mode spacing $c/(2nL)$ is greater than the width of the gain spectrum. VCSELs have a number of other advantages, including a symmetrical emission pattern with diffraction-limited divergence, suitable for efficient coupling to single-mode optical fibers. They can be modulated up to $\approx 25\ \text{GHz}$ due to the small surface area (and small capacitance) and formed into arrays that are individually modulable. CW lasers can have linewidths of $\approx 200\ \text{MHz}$. A practical advantage of VCSELs is that thousands of individual devices can be processed on a single wafer and tested at various stages of the manufacturing process, increasing reliability and yield.

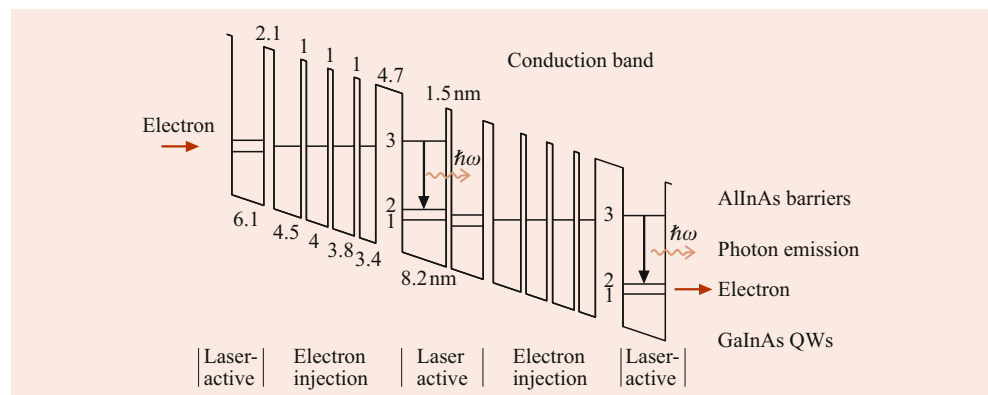
Closely related to the VCSEL is the vertical external-cavity surface-emitting laser (VECSEL), in which one of the Bragg reflecting elements is replaced by an external mirror in an extended cavity. This allows intracavity elements such as saturable absorbers for mode-locking or nonlinear crystals for second harmonic generation (SHG). VECSELs have potential as a compact high-power fs laser source [68].

75.4.2 Quantum Cascade Lasers

In the quantum cascade Laser (QCL), light generation arises not from electron–hole recombination but rather from electron transitions from one quantum-well (QW) state to another, all within the conduction band [69]. The bandgap and valence band states play no role, in contrast to a conventional semiconductor laser. The gain medium consists of alternate layers of higher and lower bandgap material, forming a series of closely spaced QWs. A voltage is applied across the device, which causes the electron’s potential energy to vary linearly with position, as shown in Fig. 75.7. There is no p–n junction, so in a circuit, the device behaves much like a resistor. It is termed a unipolar circuit element, because its operation depends on only one type of charge carrier (i.e., the electron). Conventional laser diodes, in contrast, are bipolar circuit elements.

As electrons flow through the QCL opposite to the electric field direction, they lose potential energy, not continuously, but in steps, as they jump from one QW to the next. Electrons in the lowest energy level of each QW see a potential barrier on both sides but can tunnel through with a probability that depends on the barrier height and width. In the lasing process, an electron first tunnels through a number of QWs in the “electron injection” region, as shown in Fig. 75.7, and then tunnels into a higher state of the laser active QW. Light is emitted as the electron relaxes to the lower level, followed by tunneling into the next injection region. This process is repeated many times (typically 20–25) during the transit of a single electron across the device, so that a single electron gives rise to many individual photons.

Fig. 75.7 Electron energy levels in a quantum cascade laser [11]



The most important application of the QCL is as a light source in the mid-IR wavelength range (4–12 μm) [69]. For a conventional diode laser, this would require working with materials with a very small bandgap energy, which is problematic due to the high levels of thermally generated electrons and holes. Since the photon energy in the QCL is independent of the band gap, wide bandgap materials can be used in the layers for better performance. The lasing wavelength can be selected simply by choosing the proper QW width and spacing. In fact, it is possible to operate the QCL laser at multiple wavelengths simultaneously, by varying the QW energy levels across the device. QCLs have also been operated in the THz region [70].

A variation of the QCL concept is the interband cascade laser (ICL), which differs from the QCL in that the lasing transition is from QW states in the conduction band to QW states in the valence band. However, unlike a traditional interband transition, the transition in the ICL is between QW states in adjacent layers of the material. There must be sufficient overlap between the wavefunctions of the QW states in the two adjacent layers for this method to work. These lasers operate in the 3–6 μm range and can have advantages in terms of power dissipation [71].

75.5 Free Electron Lasers

The free electron laser (FEL) is very different from the other lasers discussed so far; the electrons emitting the radiation are not bound to any atom. A beam of high-energy (relativistic) electrons in a vacuum is sent through an undulator (or “wiggler”), where they are deflected by a transverse magnetic field that periodically reverses direction. The resulting oscillatory motion of the electrons creates a dipole radiation pattern in the electron rest frame, which becomes a beam of light colinear with the electron beam in the laboratory frame. The light beam has wavelength $\lambda \cong \Lambda/(2\gamma^2)$, where Λ is the undulation period, and γ is the relativistic factor. Varying the electron beam kinetic energy $(\gamma - 1)m_e c^2$ changes the emission wavelength, and this leads to a very wide tunability, a hallmark of the FEL. By using different combinations of beam energy and undulation period, FELs have been demonstrated with wavelengths from the microwave region ($\approx \text{mm}$) to hard X-rays ($\approx 0.1 \text{ nm}$) [72, 73].

Free electron lasers can be operated as either an amplifier or an oscillator, depending on the availability of reflecting optics at the laser wavelength. In the oscillator configuration, reflecting elements are placed at each end of the undulation region, and laser action proceeds much in the same way as in a traditional laser. Spontaneous emission provides the seed light for subsequent amplification, and very high gain is not required since the light makes multiple passes through the cavity. In the absence of mirrors, the device acts as a single-

pass amplifier, which amplifies either a seed pulse that is injected from one end or spontaneous emission. High gain is desirable in this case. With seed pulse injection, the system is referred to as a master oscillator power amplifier, or MOPA, which has the advantage of preserving the spectral and noise properties of the seed, while increasing its power in the undulator region. With no seed pulse, the output is actually superradiance rather than lasing, termed amplified spontaneous emission (ASE) in general laser theory or self-amplified spontaneous emission (SASE) in connection with FELs. This has less temporal coherence than laser oscillation but still has high spatial (transverse) coherence, and therefore high brightness (brilliance). The main drawback of the FEL is the need for a high-energy electron accelerator, found only at a few large facilities around the world [73]. Both linear accelerator (linac-based) and storage ring facilities are available with FEL sources, and users must schedule time at the facility that meets their requirements for wavelength, power, temporal structure of output, etc.

There is increasing interest in an X-ray FEL (XFEL), a spectral region where few other laser sources are available [74]. Due to a lack of suitable mirrors, the XFEL operates in the single-pass amplifier mode. An important figure-of-merit is the single-pass gain, which can be as high as 10^7 for $\lambda < 1 \text{ nm}$. Preliminary success has led to governmental support of a number of linac facilities, including the Linac Coherent Light Source (LCLS) in the US, the SPring-8 Compact SASE Source (SACLA) in Japan, the European X-FEL in Germany, and the SwissFEL XFEL in Switzerland. All of these use a room-temperature LINAC except for the Swiss facility, which uses superconducting accelerator technology that enables orders of magnitude higher brilliance. The LCLS operates in the hard X-ray wavelength range 0.12–1 nm, with pulse energies of 1–3 mJ and pulse duration from 40–500 fs. The SACLA produces 0.06 nm hard X-ray pulses with pulse energies $\approx 0.5 \text{ mJ}$ and pulse duration 2–10 fs.

75.6 Nonlinear Optical Processes

The final section of this chapter is concerned with various types of nonlinear optical processes that can be used to extend the wavelength range of available lasers. These processes arise from the optical behavior of materials at high light intensity and are discussed from a theoretical viewpoint in the next chapter. In these processes, the medium plays a different role than in a conventional laser, where the medium stores energy in electronic or vibrational energy states, with lasing occurring due to transitions between those states. Instead, nonlinear processes such as stimulated Raman scattering, optical parametric amplification and oscillation, second harmonic generation (SHG), and difference

frequency generation (DFG) use the medium as an intermediary, by which two or more optical waves can interact with each other. High-harmonic generation is a special case of extreme nonlinearity, in which electrons are forced to emit radiation by an incident pump beam but in a manner quite different from that of a conventional laser.

75.6.1 Raman Lasers

In Raman scattering, a pump photon of frequency ν_p is incident on a molecule or solid with vibrational modes of frequency f_v . After scattering, the photon has frequency $\nu_s = \nu_p - f_v$, which is lower than that of the incident photon because some of the photon's energy was converted into vibrational energy. This process occurs spontaneously with low efficiency, but at sufficiently high incident intensity, stimulated emission of the scattered light can occur, making the process more efficient. The gain (fractional increase per unit length) of the scattered "signal" light is proportional to the intensity of the incident "pump" light and is described by a third-order nonlinear process (Sect. 76.5.1). To make a Raman laser, the gain medium is placed between mirrors with high reflectivity at the signal frequency ν_s and high transmission at the pump frequency ν_p . The pump beam comes in along the cavity axis from a separate laser. Optical fiber is an ideal medium for a CW Raman laser because of its good light confinement (high intensity) over a long path length [75]. Typical frequency shifts for fluoride glass fiber are 550–650 cm^{-1} (16.5–19.5 THz), while for phosphosilicate glass, the shift is as high as 1330 cm^{-1} (≈ 40 THz). The conversion efficiency in a fiber can be so high that cascaded Raman shifts are possible, where the first-order Raman shift becomes the pump for the second-order Raman shift, and so on, up to six to seven orders [76].

Raman conversion can also be accomplished in bulk crystals, especially diamond, which has a high Raman gain and excellent thermal properties. CW Raman lasing in diamond has been achieved with a pump threshold of 11 W at 1064 nm [77].

75.6.2 Optical Parametric Oscillators

In an optical parametric oscillator (OPO), a high-intensity pump beam of frequency ν_p incident on a crystal inside an optical resonator creates two additional optical beams, a signal beam of frequency ν_s and an idler beam of frequency ν_i [78, 79]. There is no physical distinction between signal and idler, but by convention the signal is the higher of the two frequencies. This three-wave mixing process is mediated by the second-order nonlinear susceptibility $\chi^{(2)}$ of the crystal, which is nonzero only for crystals that lack inversion sym-

metry (Sect. 76.3). The signal light originates from quantum fluctuations (optical parametric fluorescence), with no need to seed the oscillator with an external signal. The optical cavity can be resonant with only ν_s (singly resonant oscillator – SRO) or with both ν_s and ν_i (doubly resonant oscillator – DRO), the latter having a lower pump threshold for lasing.

An important requirement for efficient parametric amplification is that both energy and crystal momentum be conserved, a condition known as phase matching (Sect. 76.2.2). In a single crystal, this can be accomplished by varying the angle of a birefringent crystal (critical phase matching) or varying the temperature of the crystal at fixed angle (noncritical phase matching). An alternative to these perfect phase matching schemes is quasi-phase-matching (QPM), in which the nonlinear crystal is periodically modified in the direction of light propagation. In this scheme, the accumulated phase mismatch in one section is reversed in the next section, giving an average conversion efficiency somewhat smaller than for perfect phase matching, but still good. This approach has the advantage of allowing more flexibility in the choice of crystal axis and polarization, so a higher value of $\chi^{(2)}$ may be used. A commonly used QPM material with high $\chi^{(2)}$ is periodically poled lithium niobate (LiNbO_3) or PPLN [80].

75.6.3 Frequency Conversion

Two other parametric processes that depend on $\chi^{(2)}$ are second harmonic generation (SHG), outlined in Sect. 76.3.2, and difference frequency generation (DFG), outlined in Sect. 76.3.4. Phase matching is required for both of these. In SHG (also known as frequency doubling), high-intensity light at frequency ν_p is incident on a crystal, resulting in a newly generated lightwave at frequency $2\nu_p$. Efficient SHG requires high incident intensity, which tends to be naturally available in pulsed operation. For CW operation, the nonlinear crystal can be located inside a laser cavity, to take advantage of the high intracavity intensity there [81], or inside a separate resonator tuned to the harmonic wavelength [82]. An important example is frequency doubling of the Nd:YAG laser ($\lambda = 1064$ nm) to green light at 532 nm [83], which has played a large role in advancing the technology of Ti:sapphire lasers (Sect. 75.2.5).

The difference-frequency generation process is similar to that of the OPO, except that two strong beams at frequencies ν_p and ν_s are incident on the crystal, rather than just one at ν_p . A third beam at $\nu_i = \nu_p - \nu_s$ is generated, which, in spite of being labeled the "idler", is actually the desired output. DFG is often used to generate mid-IR light from near-IR lasers. For example, tunable coherent light in the range 6.4–7.5 μm has been generated by mixing a Tm fiber laser at 2010 nm with a Yb-fiber-pumped OPO in orientation-patterned GaAs [84]. DFG can also be used to generate THz

radiation, using two lasers with closely spaced frequencies, incident on a semiconductor.

75.6.4 High Harmonic Generation

High harmonic generation (HHG) is of interest as a coherent source of extreme ultraviolet (XUV, 30–100 nm) and soft X-ray (0.2–30 nm) radiation and is generated by focusing intense ($\approx 10^{14}$ W/cm²) femtosecond laser pulses on a gaseous target. This process involves an extreme (nonperturbative) atom–laser interaction, in which the electric field of the pump light is comparable to the Coulomb field of the atom. The light generation process can be understood as occurring in three steps. First, an electron in the atom's bound state tunnels through the potential barrier that has been lowered by the strong laser field, freeing the electron from the atom. Second, the electron is accelerated by the laser field, first away from the parent ion and then back to it when the laser field reverses its direction in the second half-cycle. Third, the electron recombines with the ion, releasing the kinetic energy it has acquired and the binding energy as an optical pulse. Since this process repeats every half-cycle of the fundamental field, it gives rise to a series of attosecond pulses that create a harmonic spectrum going up to very high order [85]. The photon energy of the maximum harmonic component scales with pump intensity I and wavelength λ as $h\nu_{\max} \propto I\lambda^2$. This allows table-top generation of X-ray pulses in the few nm region and is a more accessible technology for many researchers than the use of large free electron facilities. Although HHG naturally results in a pulse train, single attosecond pulses can be obtained in a number of ways by careful control of the spectral phase [86]. Thus, HHG not only allows table-top access to these short wavelengths but also opens the door to the optical investigation of phenomena on an attosecond timescale.

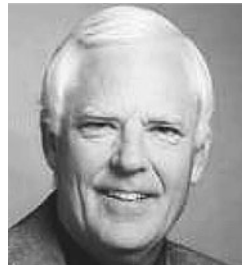
References

- Siegman, A.E.: *Lasers*. Univ. Science Books (1986)
- Svelto, O.: *Principles of Lasers*. Plenum, New York (1998)
- Silfvast, W.T.: *Laser Fundamentals*. Cambridge University Press (2004)
- Quimby, R.S.: *Photonics and Lasers*. Wiley (2006)
- Milonni, P.W., Eberly, J.H.: *Laser Physics*. Wiley (2010)
- Bass, M., Stitch, M.L. (eds.): *Laser Handbook vol. 5*. North Holland, Amsterdam (1985)
- Weber, M.J. (ed.): *Handbook of Laser Science and Technology*. CRC, Boca Raton (1991)
- Meyers, R.A. (ed.): *Encyclopedia of Lasers and Optical Technology*. Academic Press, San Diego (1991)
- Weber, M.J.: *Handbook of Laser Wavelengths*. CRC Press, Boca Raton (1999)
- Weber, M.J.: *Handbook of Lasers*. CRC Press, Boca Raton (2001)
- Trager, F. (ed.): *Handbook of Lasers and Optics*. Springer, New York (2012)
- Cheo, P.K. (ed.): *Handbook of Solid State Lasers*. Marcel Dekker, New York (1989)
- Duarte, F.J.: *Tunable Lasers Handbook*. Academic Press, San Diego (1995)
- Injeyan, H., Goodno, G.D. (eds.): *High Power Laser Handbook*. McGraw-Hill, New York (2011)
- Denker, B., Shklovsky, E. (eds.): *Handbook of Solid-State Lasers*. Woodhead (2013)
- Jaeschke, E., Khan, S., Schneider, J.R., Hastings, J.B. (eds.): *Synchrotron Light Sources and Free-Electron Lasers*. Springer, New York (2016)
- Koehner, W.: *Solid-State Laser Engineering*. Springer, Berlin, Heidelberg (1996)
- RP-Photonics: <https://www.rp-photonics.com>
- Scully, M.O., Zhu, S.-Y., Gavrielides, A.: *Phys. Rev. Lett.* **62**, 2813 (1989)
- Dieke, G.H.: *Spectra and Energy Levels of Rare Earth Ions in Crystals*. Wiley, New York (1968)
- Henderson, B., Imbusch, G.F.: *Optical Spectroscopy of Inorganic Solids*. Clarendon, Oxford (1989)
- Kaminskii, A.A.: *Laser Crystals*, 2nd edn. Springer (1990)
- Gorriller-Walrand, C., Binneemans, K.: *Handbook on the Physics and Chemistry of Rare Earths*, 25, 167 (1998)
- Scheps, R.: *Introduction to Laser Diode-Pumped Solid State Lasers*. SPIE (2002)
- Snitzer, E.: *Phys. Rev. Lett.* **7**, 444 (1961)
- Aggarwal, I.D., Lu, G. (eds.): *Fluoride Glass Fiber Optics*. Academic Press, N.Y (1991)
- Fedorov, P.P., Luginina, A.A., Popov, A.I.: *J. Fluor. Chem.* **172**, 22 (2015)
- Digonnet, M.J.F. (ed.): *Rare-Earth-Doped Fiber Lasers and Amplifiers*, 3rd edn. CRC (2018)
- Dutta, N.K.: *Fiber Amplifiers and Fiber Lasers*. World Scientific (2014)
- Mendez, A., Morse, T.F. (eds.): *Specialty Optical Fibers Handbook*. Academic Press (2007)
- Lesparre, F., Gomes, J.T., Delen, X., Martial, I., Didierjean, J., Pallmann, W., Resan, B., Eckerle, M., Graf, T., Ahmed, M.A., Druon, F., Balembos, F., Georges, P.: *Opt. Lett.* **40**, 2517 (2015)
- Nakamura, S., Fasol, G., Pearton, S.J.: *The Blue Laser Diode*, 2nd edn. Springer (2000)
- Hashimoto, K., Kannari, F.: *Opt. Lett.* **32**, 2493 (2007)
- Durfee, C.G., Storz, T., Garlick, J., Hill, S., Squier, J.A., Kirchner, M., Taft, G., Shea, K., Kapteyn, H., Murnane, M., Backus, S.: *Opt. Exp.* **20**, 13677 (2012)
- IPG Photonics: www.ipgphotonics.com
- Deen, M., Kumar, S.: *Fiber Optic Communications*. Wiley (2014)
- Jackson, S.D.: *Opt. Commun.* **230**, 197 (2004)
- Jackson, S.D.: *Opt. Lett.* **32**, 241 (2007)
- Jackson, S.D.: *Opt. Lett.* **24**, 2327 (2009)
- Pollnau, M., Spring, R., Ghisler, C., Wittwer, S., Lüthy, W., Weber, H.P.: *IEEE J. Quantum Electron.* **32**, 657 (1996)
- Jackson, S.D.: *Electron. Lett.* **40**, 1400 (2004)
- Li, J., Hudson, D.D., Jackson, S.D.: *Opt. Lett.* **3642**, 36 (2011)
- Jackson, S.D., Pollnau, M., Li, J.: *IEEE J. Quantum Electron.* **47**, 471 (2011)
- Griffith, J.S.: *The Theory of Transition-Metal Ions*. Cambridge University Press (1961)
- Sugano, S., Tanabe, Y., Kamimura, H.: *Multiplets of Transition-Metal Ions in Crystals*. Academic Press (1970)
- Lai, S.T., Shand, M.L.: *J. Appl. Phys.* **54**, 5642 (1983)
- Payne, S.A., Chase, L.L., Newkirk, H.W., Smith, L.K., Krupke, W.F.: *IEEE J. Quantum Electron.* **24**, 2243 (1988)

48. Moulton, P.F.: *Opt. News* **8**, 9 (1982)
49. Kück, S.: *Appl. Phys. B.* **72**, 515 (2001)
50. Sorokin, E., Sorokina, I.T.: *Appl. Phys. Lett.* **80**, 3289 (2002)
51. Firstov, S.V., Alyshev, S.V., Riumkin, K.E., Khagai, A.M., Kharakhordin, A.V., Melkumov, M.A., Dianov, E.M., Evgeny, M.: *IEEE J. Sel. Top. Quantum Electron.* **24**, 0902415 (2018)
52. Dianov, E.M.: *Laser Focus World* **51**, 49 (2015)
53. Zhang, Y., Killeen, T.: *Laser Focus World* **52**, 29 (2016)
54. Witteman, W.J.: *The CO2 Laser*. Springer (1987)
55. Schäfer, F.P. (ed.): *Dye Lasers*. Springer, Berlin, Heidelberg (1990)
56. Maeda, M.: *Laser Dyes*. Academic Press, New York (1984)
57. Diels, J.-C.: Femtosecond dye lasers. In: Duarte, F.J., Hillman, L.W. (eds.) *Dye Laser Principles*, pp. 41–132. Academic Press, New York (1990)
58. Hollberg, L.W.: CW dye lasers. In: Duarte, F.J., Hillman, L.W. (eds.) *Dye Laser Principles*, pp. 185–238. Academic Press, New York (1990)
59. Bokhan, P.A., Buchanov, V.V., Fateev, N.V., Kalugin, M.M., Kazaryan, M.A., Prokhorov, A.M., Zakrevskii, D.E.: *Laser Isotope Separation in Atomic Vapor*. Wiley-VCH, Weinheim (2006)
60. Pique, J., Farinotti, S.: *J. Opt. Soc. Am. B.* **20**, 2093–2101 (2003)
61. Basting, D., Marowsky, G. (eds.): *Excimer Laser Technology*. Springer (2005)
62. Pätzelt, R., Stamm, U.: Excimer lasers for microlithography. In: Basting, D., Marowsky, G. (eds.) *Excimer Laser Technology*, pp. 98–103. Springer, Berlin, Heidelberg (2005). Chap. 6
63. Rudin, B., Rutz, A., Hoffmann, M., Maas, D., Bellancourt, A.R., Sudmeyer, E., Sudmeyer, T., Keller, U.: *Opt. Lett.* **33**, 2719 (2008)
64. Alferov, Z.I.: *The Double Heterostructure Concept and its Applications in Physics, Electronics, and Technology*. Wiley, Weinheim (2001). Nobel Lecture
65. Chow, W.W., Koch, S.W.: *Semiconductor-Laser Fundamentals*. Springer, Berlin (1999)
66. Zory, P.S. (ed.): *Quantum Well Lasers*. Academic Press, New York (1993)
67. Michalzik, R. (ed.): *VCSELs. Fundamentals, Technology, and Applications*. Springer (2014)
68. Waldburger, D., Link, S.M., Mangold, M., Alfieri, C.G.E., Gini, E., Golling, M., Tilma, B.W., Keller, U.: *Optica* **3**, 844 (2016)
69. Federico, C.: *Opt. Eng.* **49**, 111102 (2010)
70. Kumar, S.: *IEEE J. Sel. Top. Quantum Electron.* **17**, 38 (2011)
71. Kim, M., Bewley, W.W., Canedy, C.L., Kim, C.S., Merritt, C.D., Abell, J., Vurgafman, I., Meyer, J.R.: *Opt. Exp.* **23**, 9664 (2015)
72. Freund, H.P., Antonsen Jr., T.M.: *Principles of Free Electron Lasers*, 3rd edn. Springer (2018)
73. The WWW Virtual Library: http://sbfel3.ucsb.edu/www/vl_fel.html
74. Galayda, J.N., Arthur, J., Ratner, D.F., White, W.E.: *J. Opt. Soc. Am. B.* **27**, B106 (2010)
75. Yao, T., Nilsson, J.: *J. Opt. Soc. Am. B.* **31**, 882 (2014)
76. Han, Y.-G., Kim, C.-S., Kang, J.U., Paek, U.-C., Chung, Y.: *IEEE Photonics Technol. Lett.* **15**, 383 (2003)
77. Kitzler, O., McKay, A., Mildren, R.P.: *Opt. Lett.* **37**, 2790 (2012)
78. Byer, R.L.: Optical parametric oscillators. In: Rabin, H., Tang, C.L. (eds.) *Quantum Electronics, Nonlinear Optics*, vol. 1, Academic Press, New York (1975)
79. Sutherland, R.L.: *Handbook of Nonlinear Optics*. Marcel Dekker, New York (1996)
80. Bosenberg, W.R., Drobshoff, A., Alexander, J.I., Myers, L.E., Byer, R.L.: *Opt. Lett.* **21**, 1336 (1996)
81. Stolzenburg, C., Schule, W., Zawischa, I., Killi, A., Sutter, D.: *Proc. SPIE* **7578**, 75780A (2010)
82. Paschotta, R., Kurz, P., Henking, R., Schiller, S., Mlynek, J.: *Opt. Lett.* **19**, 1325 (1994)
83. Liu, Y.S., Dentz, D., Belt, R.: *Opt. Lett.* **9**, 76 (1984)
84. Devi, K., Schunemann, P.G., Ebrahim-Zadeh, M.: *Opt. Lett.* **39**, 6751 (2014)
85. Hadrich, S., Krebs, M., Rothhardt, J., Carstens, H., Demmler, S., Limpert, J., Tunnermann, A.: *Opt. Exp.* **20**, 19374 (2011)
86. Chini, M., Zhao, K., Chang, Z.: *Nat. Photonics* **8**, 178 (2014)



Richard Quimby Richard Quimby received his PhD from the University of Wisconsin, Madison in 1979. After a stay at the Center for Laser Studies at the University of Southern California, he joined the Physics Department at Worcester Polytechnic Institute in 1982. His research interests include radiative and nonradiative processes in rare-earth doped glasses and crystals, for laser and optical amplifier applications.



Richard Powell Richard Powell was educated in physics at the United States Naval Academy and Arizona State University. He has been a research scientist and professor at Air Force Cambridge Research Laboratories, Sandia National Laboratory, and Lawrence Livermore National Laboratory, Oklahoma State University, and the University of Arizona. He has authored two textbooks and over 260 scientific papers on laser spectroscopy and solid-state laser development.



Contents

76.1	Nonlinear Susceptibility	1098	76.5	Stimulated Light Scattering	1106
76.1.1	Tensor Properties	1098	76.5.1	Stimulated Raman Scattering	1106
76.1.2	Nonlinear Refractive Index	1098	76.5.2	Stimulated Brillouin Scattering	1106
76.1.3	Quantum Mechanical Expression for $\chi^{(n)}$	1099	76.6	Other Nonlinear Optical Processes	1107
76.1.4	Hyperpolarizability	1099	76.6.1	High-Order Harmonic Generation	1107
76.2	Wave Equation in Nonlinear Optics	1100	76.6.2	Electro-Optic Effect	1108
76.2.1	Coupled-Amplitude Equations	1100	76.6.3	Photorefractive Effect	1108
76.2.2	Phase Matching	1100	76.7	New Regimes of Nonlinear Optics	1108
76.2.3	Manley–Rowe Relations	1101	76.7.1	Ultrafast and Intense-Field Nonlinear Optics	1108
76.2.4	Pulse Propagation	1101	76.7.2	Nonlinear Plasmonics and Epsilon-Near-Zero Effects	1109
76.3	Second-Order Processes	1101	References		1110
76.3.1	Sum-Frequency Generation	1101			
76.3.2	Second Harmonic Generation	1102			
76.3.3	Parametric Amplification and Oscillation	1102			
76.3.4	Difference-Frequency Generation	1102			
76.3.5	Two-Mode Squeezing	1102			
76.3.6	Spontaneous Parametric Down-Conversion	1103			
76.3.7	Focused Beams	1104			
76.4	Third-Order Processes	1104			
76.4.1	Third-Harmonic Generation	1104			
76.4.2	Self-Phase and Cross-Phase Modulation	1104			
76.4.3	Four-Wave Mixing	1105			
76.4.4	Self-Focusing and Self-Trapping	1105			
76.4.5	Saturable Absorption	1105			
76.4.6	Two-Photon Absorption	1105			
76.4.7	Nonlinear Ellipse Rotation	1106			

R. W. Boyd (✉)
Dept. of Physics, University of Ottawa
Ottawa, ON, Canada
Institute of Optics, University of Rochester
14627 Rochester, NY, USA
e-mail: boydrw@mac.com

A. L. Gaeta
Applied Physics and Applied Mathematics, Columbia University
New York, NY, USA
e-mail: a.gaeta@columbia.edu

E. Giese
Institut für Angewandte Physik, Technische Universität Darmstadt
Darmstadt, Germany
e-mail: enno.a.giese@gmail.com

Abstract

Nonlinear optics is concerned with the propagation of intense beams of light through a material system. The optical properties of the medium can be modified by the intense light beam, leading to new processes not present in a material that responded linearly to an applied optical field. These processes can lead to the modification of the spectral, spatial, or polarization properties of the light beam or the creation of new frequency components. More complete accounts of nonlinear optics including the origin of optical nonlinearities can be found in [1–4].

Both the Gaussian and MKS system of units are commonly used in nonlinear optics. Thus, we have chosen to express the equations in this chapter in both the Gaussian and MKS systems. Each equation can be interpreted in the MKS system as written or in the Gaussian system by omitting the prefactors (e.g., $1/4\pi\epsilon_0$) that appear in square brackets at the beginning of the expression on the right-hand-side of the equation.

Keywords

nonlinear refractive index · stimulate Brillouin scattering · nonlinear susceptibility · difference-frequency generation · nonlinear polarization

76.1 Nonlinear Susceptibility

In linear optics it is customary to describe the response of a material in terms of a macroscopic polarization $\tilde{\mathbf{P}}$ (i.e., dipole moment per unit volume) that is linearly related to the applied electric field $\tilde{\mathbf{E}}$ through the linear susceptibility $\chi^{(1)}$. In order to extend the relationship between $\tilde{\mathbf{P}}$ and $\tilde{\mathbf{E}}$ into the nonlinear regime, the polarization is expanded in a power series of the electric field strength. We express this relationship mathematically by first decomposing the field and the polarization into their frequency components such that

$$\tilde{\mathbf{E}}(\mathbf{r}, t) = \sum_l \mathbf{E}(\mathbf{r}, \omega_l) e^{-i\omega_l t}, \quad (76.1)$$

$$\tilde{\mathbf{P}}(\mathbf{r}, t) = \sum_l \mathbf{P}(\mathbf{r}, \omega_l) e^{-i\omega_l t}, \quad (76.2)$$

where the summations are performed over both positive and negative frequencies. The reality of $\tilde{\mathbf{E}}$ and $\tilde{\mathbf{P}}$ is then assured by requiring that $\mathbf{E}(\mathbf{r}, \omega_l) = \mathbf{E}^*(\mathbf{r}, -\omega_l)$ and $\mathbf{P}(\mathbf{r}, \omega_l) = \mathbf{P}^*(\mathbf{r}, -\omega_l)$. In this case, the general expression for the Cartesian component i of the polarization at frequency ω_σ is given by

$$\begin{aligned} P_i(\omega_\sigma) = [\epsilon_0] & \left[\sum_j \chi_{ij}^{(1)}(\omega_\sigma) E_j(\omega_\sigma) \right. \\ & + \sum_{jk} \sum_{(mn)} \chi_{ijk}^{(2)}(\omega_\sigma; \omega_m, \omega_n) \\ & \times E_j(\omega_m) E_k(\omega_n) \\ & + \sum_{jkl} \sum_{(mno)} \chi_{ijkl}^{(3)}(\omega_\sigma; \omega_m, \omega_n, \omega_o) \\ & \left. \times E_j(\omega_m) E_k(\omega_n) E_l(\omega_o) + \dots \right], \quad (76.3) \end{aligned}$$

where $ijkl$ refer to field components, and the notation (mn) , for example, indicates that the summation over n and m should be performed such that $\omega_\sigma = \omega_m + \omega_n$ is held constant. Inspection of Eq. (76.3) shows that the $\chi^{(n)}$ can be required to satisfy intrinsic permutation symmetry, i.e., the Cartesian components and the corresponding frequency components [e.g., (j, ω_j) but not (i, ω_σ)] associated with the applied fields may be permuted without changing the value of the susceptibility. For example, for the second-order susceptibility,

$$\chi_{ijk}^{(2)}(\omega_\sigma; \omega_m, \omega_n) = \chi_{ikj}^{(2)}(\omega_\sigma; \omega_n, \omega_m). \quad (76.4)$$

If the medium is lossless at all the field frequencies taking part in the nonlinear interaction, then the condition of full permutation symmetry is necessarily valid. This condition states that the pair of indices associated with the Cartesian component and the frequency of the nonlinear polarization

[i.e., (i, ω_σ)] may be permuted along with the pairs associated with the applied field components. For example, for the second-order susceptibility, this condition implies that

$$\chi_{ijk}^{(2)}(\omega_\sigma; \omega_m, \omega_n) = \chi_{kji}^{(2)}(-\omega_n; \omega_m, -\omega_\sigma). \quad (76.5)$$

If full permutation symmetry holds, and in addition all the frequencies of interest are well below any of the transition frequencies of the medium, the $\chi^{(n)}$ are invariant upon free permutation of all the Cartesian indices. This condition is known as the Kleinman symmetry condition.

76.1.1 Tensor Properties

The spatial symmetry properties of a material can be used to predict the tensor nature of the nonlinear susceptibility. For example, for a material that possesses inversion symmetry, all the elements of the even-ordered susceptibilities must vanish (i.e., $\chi^{(n)} = 0$ for n even). The number of independent elements of the nonlinear susceptibility for many materials can be substantially fewer than the total number of elements. For example, in general, $\chi^{(3)}$ consists of 81 elements, but for the case of isotropic media such as gases, liquids, and glasses, only 21 elements are nonvanishing, and only three of these are independent. The nonvanishing elements consist of the following types: $\chi_{iijj}^{(3)}$, $\chi_{ijij}^{(3)}$, and $\chi_{ijji}^{(3)}$, where $i \neq j$. In addition, it can be shown that

$$\chi_{iiii}^{(3)} = \chi_{iijj}^{(3)} + \chi_{ijij}^{(3)} + \chi_{ijji}^{(3)}. \quad (76.6)$$

76.1.2 Nonlinear Refractive Index

For many materials, the refractive index n is intensity-dependent such that

$$n = n_0 + n_2 I, \quad (76.7)$$

where n_0 is the linear refractive index, n_2 is the nonlinear refractive index coefficient, and $I = [4\pi\epsilon_0]n_0c|E|^2/2\pi$ is the intensity of the optical field. For the case of a single, linearly polarized light beam traveling in an isotropic medium or along a crystal axis of a cubic material, n_2 is related to $\chi^{(3)}$ by

$$n_2 = \left[\frac{1}{16\pi^2\epsilon_0} \right] \frac{12\pi^2}{n_0^2 c} \chi_{iiii}^{(3)}(\omega; \omega, \omega, \omega, -\omega). \quad (76.8)$$

For the common situation in which n_2 is measured in units of cm^2/W , and $\chi^{(3)}$ is measured in Gaussian units, the relation becomes

$$n_2 \left(\frac{\text{cm}^2}{\text{W}} \right) = \frac{12\pi^2 \times 10^7}{n_0^2 c} \chi_{iiii}^{(3)}(\omega; \omega, \omega, \omega, -\omega). \quad (76.9)$$

There are various physical mechanisms that can give rise to a nonlinear refractive index. For the case of induced molecular orientation in CS₂, $n_2 = 3 \times 10^{-14} \text{ cm}^2/\text{W}$. If the contribution to the nonlinear refractive index is electronic in nature (e.g., glass), then $n_2 \approx 2 \times 10^{-16} \text{ cm}^2/\text{W}$.

76.1.3 Quantum Mechanical Expression for $\chi^{(n)}$

The general quantum mechanical perturbation expression for the $\chi^{(n)}$ in the nonresonant limit is

$$\begin{aligned} \chi_{i_0 \dots i_n}^{(n)}(\omega_\sigma; \omega_1, \dots, \omega_n) &= \left[\frac{1}{\varepsilon_0} \right] \frac{N}{\hbar^n} \mathcal{P}_F \sum_{g a_1 \dots a_n} \rho_0(g) \\ &\times \frac{1}{(\omega_{a_1 g} - \omega_1 - \dots - \omega_n)} \\ &\times \frac{\mu_{g a_1}^{i_0} \mu_{a_1 a_2}^{i_1} \dots \mu_{a_{n-1} a_n}^{i_{n-1}} \mu_{a_n g}^{i_n}}{(\omega_{a_2 g} - \omega_2 - \dots - \omega_n) \dots (\omega_{a_n g} - \omega_n)}, \end{aligned} \quad (76.10)$$

where $\omega_\sigma = \omega_1 + \dots + \omega_n$, N is the density of atoms or molecules that compose the material, $\rho_0(g)$ is the probability that the atomic or molecular population is initially in the state g in thermal equilibrium, $\mu_{a_1 a_2}^{i_1}$ is the i_1 -th Cartesian component of the $(a_1 a_2)$ dipole matrix element, $\omega_{a_1 g}$ is the transition frequency between the states a_1 and g , and \mathcal{P}_F is the full permutation operator that is defined such that the expression that follows it is to be summed over all permutations of the pairs (i_0, ω_σ) , $(i_1, \omega_1) \dots (i_n, \omega_n)$ and divided by the number of permutations of the input frequencies. Thus, the full expression for $\chi^{(2)}$ consists of six terms and that for $\chi^{(3)}$ consists of 24 terms. (Under conditions of resonant excitation, relaxation phenomena must be included in the treatment, and the density matrix formalism must be used [4]. The resulting equation for the nonlinear susceptibility is then more complicated.)

In the limit in which the frequencies of all the fields are much smaller than any resonance frequency of the medium, the value of $\chi^{(n)}$ can be estimated to be

$$\chi^{(n)} \approx \left[\frac{1}{\varepsilon_0} \right] \left(\frac{2\mu}{\hbar\omega_0} \right)^n N\mu, \quad (76.11)$$

where μ is a typical value for the dipole transition moment, and ω_0 is a typical value of the transition frequency between the ground state and the lowest-lying excited state. For the case of $\chi^{(3)}$ in Gaussian units, the predicted value is $\chi^{(3)} = 3 \times 10^{-14}$, which is consistent with the measured values of many materials (e.g., glass) in which the nonresonant electronic nonlinearity is the dominant contribution.

76.1.4 Hyperpolarizability

The nonlinear susceptibility relates the macroscopic polarization \mathbf{P} to the electric field strength \mathbf{E} . A related microscopic quantity is the hyperpolarizability, which relates the dipole moment \mathbf{p} induced in a given atom or molecule to the electric field \mathbf{E}^{loc} (the Lorentz local field) that acts on that atom or molecule. The relationship between \mathbf{p} and \mathbf{E}^{loc} is

$$\begin{aligned} p_i(\omega_\sigma) &= [\varepsilon_0] \left[\sum_j \alpha_{ij}(\omega_\sigma) E_j^{\text{loc}}(\omega_\sigma) \right. \\ &+ \sum_{jk} \sum_{(mn)} \beta_{ijk}(\omega_\sigma; \omega_m, \omega_n) E_j^{\text{loc}}(\omega_m) E_k^{\text{loc}}(\omega_n) \\ &+ \sum_{jkl} \sum_{(mno)} \gamma_{ijkl}(\omega_\sigma; \omega_m, \omega_n, \omega_o) \\ &\left. \times E_j^{\text{loc}}(\omega_m) E_k^{\text{loc}}(\omega_n) E_l^{\text{loc}}(\omega_o) + \dots \right], \end{aligned} \quad (76.12)$$

where α_{ij} is the linear polarizability, β_{ijk} is the first hyperpolarizability, and γ_{ijkl} is the second hyperpolarizability. The nonlinear susceptibilities and hyperpolarizabilities are related by the number density of molecules N and by local-field factors, which account for the fact that the field \mathbf{E}^{loc} that acts on a typical molecule is not, in general, equal to the macroscopic field \mathbf{E} . Under many circumstances, it is adequate to relate \mathbf{E}^{loc} to \mathbf{E} through use of the Lorentz approximation

$$\mathbf{E}^{\text{loc}}(\omega) = \mathbf{E}(\omega) + \left[\frac{1}{4\pi\varepsilon_0} \right] \frac{4\pi}{3} \mathbf{P}(\omega). \quad (76.13)$$

To a good approximation, one often needs to include only the linear contribution to $\mathbf{P}(\omega)$, and thus the local electric field becomes

$$\mathbf{E}^{\text{loc}}(\omega) = \mathcal{L}(\omega) \mathbf{E}(\omega), \quad (76.14)$$

where $\mathcal{L}(\omega) = \{[\varepsilon_0^{-1}]\varepsilon(\omega) + 2\}/3$ is the local field correction factor, and $\varepsilon(\omega)$ is the linear dielectric constant. Since $\mathbf{P}(\omega) = N \mathbf{p}(\omega)$, Eqs. (76.3) and (76.12) through Eq. (76.14) relate the $\chi^{(n)}$ to the hyperpolarizabilities through

$$\chi_{ij}^{(1)}(\omega_\sigma) = \mathcal{L}(\omega_\sigma) N \alpha_{ij}(\omega_\sigma), \quad (76.15)$$

$$\begin{aligned} \chi_{ijk}^{(2)}(\omega_\sigma; \omega_m, \omega_n) &= \mathcal{L}(\omega_\sigma) \mathcal{L}(\omega_m) \mathcal{L}(\omega_n) \\ &\times N \beta_{ijk}(\omega_\sigma; \omega_m, \omega_n), \end{aligned} \quad (76.16)$$

$$\begin{aligned} \chi_{ijkl}^{(3)}(\omega_\sigma; \omega_m, \omega_n, \omega_o) &= \mathcal{L}(\omega_\sigma) \mathcal{L}(\omega_m) \mathcal{L}(\omega_n) \mathcal{L}(\omega_o) \\ &\times N \gamma_{ijkl}(\omega_\sigma; \omega_m, \omega_n, \omega_o). \end{aligned} \quad (76.17)$$

For simplicity, the analysis above ignores the vector character of the interacting fields in calculating $\mathcal{L}(\omega)$. A generalization that does include these effects is given in [5].

76.2 Wave Equation in Nonlinear Optics

76.2.1 Coupled-Amplitude Equations

The propagation of light waves through a nonlinear medium is described by the wave equation

$$\nabla^2 \tilde{\mathbf{E}} - \frac{1}{c^2} \frac{\partial^2 \tilde{\mathbf{E}}}{\partial t^2} = \left[\frac{1}{4\pi\epsilon_0} \right] \frac{4\pi}{c^2} \frac{\partial^2 \tilde{\mathbf{P}}}{\partial t^2}. \quad (76.18)$$

For the case in which $\tilde{\mathbf{E}}$ and $\tilde{\mathbf{P}}$ are given by Eq. (76.1), the field amplitudes associated with each frequency component can be decomposed into their plane wave components such that

$$\begin{aligned} \mathbf{E}(\mathbf{r}, \omega_l) &= \sum_n \mathbf{A}_n(\mathbf{r}, \omega_l) e^{i\mathbf{k}_n \cdot \mathbf{r}}, \\ \mathbf{P}(\mathbf{r}, \omega_l) &= \sum_n \mathbf{P}_n(\mathbf{r}, \omega_l) e^{i\mathbf{k}_n \cdot \mathbf{r}}, \end{aligned} \quad (76.19)$$

where $k_n = n(\omega_l)\omega_l/c$ is the magnitude of the wave-vector \mathbf{k}_n . The amplitudes \mathbf{A}_n and \mathbf{P}_n are next decomposed into vector components whose linear optical properties are such that the polarization associated with them does not change as the field propagates through the material. For example, for a uniaxial crystal these eigenpolarizations could correspond to the ordinary and extraordinary components. In order to describe the propagation and the nonlinear coupling of these eigenpolarizations, the vector field amplitudes are expressed as

$$\begin{aligned} \mathbf{A}_n(\mathbf{r}, \omega_l) &= \hat{\mathbf{u}}_{ln} A_n(\mathbf{r}, \omega_l), \\ \mathbf{P}_n(\mathbf{r}, \omega_l) &= \hat{\mathbf{u}}_{ln} P_n(\mathbf{r}, \omega_l), \end{aligned} \quad (76.20)$$

where $\hat{\mathbf{u}}_{ln}$ is the unit vector associated with the eigenpolarization of the spatial mode n at frequency ω_l . If the fields are assumed to travel along the z -direction, and the slowly-varying amplitude approximation $\partial^2 A_n / \partial z^2 \ll 2k_n \partial A_n / \partial z$ is made, the change in the amplitude of the field as it propagates through the nonlinear medium with no linear absorption is described by the differential equation

$$\frac{dA_n(\omega_l)}{dz} = \pm \left[\frac{1}{4\pi\epsilon_0} \right] \frac{i2\pi\omega_l}{n(\omega_l)c} P_n^{\text{NL}}(\omega_l), \quad (76.21)$$

where P_n^{NL} is the nonlinear contribution to the polarization amplitude P_n , $n(\omega_l)$ is the linear refractive index at frequency ω_l , and the plus (minus) sign indicates propagation in the positive (negative) z -direction. Sections 76.3 and 76.4 give expressions for the P_n^{NL} for various second- and third-order nonlinear optical processes. Equation (76.21) is used to determine the set of coupled-amplitude equations describing a particular nonlinear process. For example, for the case of sum-frequency generation, the two fields of frequency

ω_1 and ω_2 are combined through second-order nonlinear interaction to create a third wave at frequency $\omega_3 = \omega_1 + \omega_2$. Assuming full permutation symmetry, the amplitudes of the nonlinear polarization for each of the waves are

$$P^{\text{NL}}(z, \omega_1) = [\epsilon_0] 2\chi_{\text{eff}}^{(2)} A(z, \omega_3) A^*(z, \omega_2) e^{-i\Delta k z}, \quad (76.22)$$

$$P^{\text{NL}}(z, \omega_2) = [\epsilon_0] 2\chi_{\text{eff}}^{(2)} A(z, \omega_3) A^*(z, \omega_1) e^{-i\Delta k z}, \quad (76.23)$$

$$P^{\text{NL}}(z, \omega_3) = [\epsilon_0] 2\chi_{\text{eff}}^{(2)} A(z, \omega_1) A(z, \omega_2) e^{i\Delta k z}, \quad (76.24)$$

where $\Delta k = k_1 + k_2 - k_3$ is the wave-vector mismatch (Sect. 76.2.2), and $\chi_{\text{eff}}^{(2)}$ is given by

$$\chi_{\text{eff}}^{(2)} = \sum_{ijk} \chi_{ijk}^{(2)} (\hat{\mathbf{u}}_1^*)_i (\hat{\mathbf{u}}_2)_j (\hat{\mathbf{u}}_3)_k, \quad (76.25)$$

where $(\hat{\mathbf{u}}_i)_i$ is the i -th Cartesian component of $\hat{\mathbf{u}}_i$. For simplicity, the subscripts on each of the field amplitudes have been dropped, since only one spatial mode at each frequency contributed. The resulting coupled-amplitude equations are

$$\frac{dA(\omega_1)}{dz} = \left[\frac{1}{4\pi} \right] \frac{i4\pi\omega_1 \chi_{\text{eff}}^{(2)}}{n(\omega_1)c} A(\omega_3) A^*(\omega_2) e^{-i\Delta k z}, \quad (76.26)$$

$$\frac{dA(\omega_2)}{dz} = \left[\frac{1}{4\pi} \right] \frac{i4\pi\omega_2 \chi_{\text{eff}}^{(2)}}{n(\omega_2)c} A(\omega_3) A^*(\omega_1) e^{-i\Delta k z}, \quad (76.27)$$

$$\frac{dA(\omega_3)}{dz} = \left[\frac{1}{4\pi} \right] \frac{i4\pi\omega_3 \chi_{\text{eff}}^{(2)}}{n(\omega_3)c} A(\omega_1) A(\omega_2) e^{i\Delta k z}. \quad (76.28)$$

76.2.2 Phase Matching

For many nonlinear optical processes (e.g., harmonic generation) it is important to minimize the wave-vector mismatch in order to maximize the efficiency. For example, if the field amplitudes $A(\omega_1)$ and $A(\omega_2)$ are constant and $\chi_{\text{eff}}^{(2)}$ does not depend upon z , the solution to Eq. (76.28) yields for the output intensity

$$\begin{aligned} I(L, \omega_3) &= \left[\frac{1}{64\pi^3 \epsilon_0} \right] \\ &\times \frac{32\pi^3 \left[\chi_{\text{eff}}^{(2)} \right]^2 \omega_3^2 I(\omega_1) I(\omega_2) L^2}{n(\omega_1) n(\omega_2) n(\omega_3) c^3} \\ &\times \text{sinc}^2(\Delta k L / 2), \end{aligned} \quad (76.29)$$

in terms of $\text{sinc } x = (\sin x)/x$, where $I(L, \omega_3) = (4\pi\epsilon_0)n(\omega_3)c|A(L, \omega_3)|^2/2\pi$, and $I(\omega_1)$ and $I(\omega_2)$ are the corresponding input intensities. Clearly, the effect of the wave-vector mismatch is to reduce the efficiency of the generation of the sum-frequency wave. The maximum propagation distance over which efficient nonlinear coupling can

occur is given by the coherence length

$$L_c = \frac{2}{\Delta k}. \quad (76.30)$$

As a result of the dispersion in the linear refractive index that occurs in all materials, achieving phase matching over typical interaction lengths (e.g., 5 mm) is nontrivial. For the case in which the nonlinear material is birefringent, it is sometimes possible to achieve phase matching by insuring that the interacting waves possess some suitable combination of ordinary and extraordinary polarization. Other techniques for achieving phase matching include quasi-phase matching [5], which relies on a $\chi_{\text{eff}}^{(2)}$ that varies in the propagation direction z , and the use of the mode dispersion in waveguides [6].

However, the phase-matching condition is automatically satisfied for certain nonlinear optical processes, such as two-photon absorption (Sect. 76.4.6) and Stokes amplification in stimulated Raman scattering (Sect. 76.5.1). One can tell when the phase-matching condition is automatically satisfied by examining the frequencies that appear in the expression for the nonlinear susceptibility. For a nonlinear susceptibility of the sort $\chi^{(3)}(\omega_1; \omega_2, \omega_3, \omega_4)$, the wave-vector mismatch in the corresponding set of coupled differential equations is given, in general, by $\Delta \mathbf{k} = \mathbf{k}_2 + \mathbf{k}_3 + \mathbf{k}_4 - \mathbf{k}_1$. Thus, for the example of Stokes amplification in stimulated Raman scattering, the nonlinear susceptibility is given by $\chi^{(3)}(\omega_1; \omega_1, \omega_0, -\omega_0)$, where ω_0 (ω_1) is the frequency of the pump (Stokes) wave, and, consequently, the wave-vector mismatch vanishes identically.

76.2.3 Manley–Rowe Relations

Under conditions of full permutation symmetry, there is no flow of power from the electromagnetic fields to the medium, and thus the total power flow of the fields is conserved. The flow of energy among the fields can be described by the Manley–Rowe relations. For example, for the case of sum-frequency generation, one can deduce from Eqs. (76.26)–(76.28) that

$$\frac{d}{dz} \left[\frac{I(\omega_1)}{\omega_1} \right] = \frac{d}{dz} \left[\frac{I(\omega_2)}{\omega_2} \right] = -\frac{d}{dz} \left[\frac{I(\omega_3)}{\omega_3} \right]. \quad (76.31)$$

The expressions in square brackets are proportional to the flux of photons per unit area per unit time and imply that the creation of a photon at ω_3 must be accompanied by the annihilation of photons at both ω_1 and ω_2 . Similar relations can be formulated for other nonlinear optical processes that are governed by a nonlinear susceptibility that satisfies full permutation symmetry. Since this behavior occurs at the photon level, nonlinear optical processes can lead to the generation

of light fields that have esoteric quantum statistical properties (Chaps. 82 and 84).

A nonlinear optical process that satisfies the Manley–Rowe relations is called a parametric process. Conversely, a process for which field energy is not conserved, and thus Manley–Rowe relations cannot be formulated, is said to be nonparametric. Thus, parametric processes are described by purely real $\chi^{(n)}$, whereas nonparametric processes are described by complex $\chi^{(n)}$.

76.2.4 Pulse Propagation

If the optical field consists of ultrashort (< 100 ps) pulses, it is more convenient to work with the temporally varying amplitude, rather than with the individual frequency components. Thus, for a linearly polarized plane wave pulse propagating along the z -axis, the field is decomposed into the product of a slowly varying amplitude $A(z, t)$ and a rapidly varying oscillatory term such that

$$\tilde{E}(\mathbf{r}, t) = A(z, t) e^{i(k_0 z - \omega_0 t)} + \text{c.c.}, \quad (76.32)$$

where $k_0 = n_0 \omega_0 / c$. For a pulse propagating in a material with an intensity-dependent refractive index, the propagation can be described by the nonlinear Schrödinger equation

$$\frac{\partial A}{\partial z} + \frac{i\beta_2}{2} \frac{\partial^2 A}{\partial \tau^2} = i\gamma |A|^2 A, \quad (76.33)$$

where $\beta_2 = (d^2 k / d\omega^2)|_{\omega=\omega_0}$ is the group velocity dispersion parameter, $\tau = t - z/v_g$ is the local time for the pulse, $v_g = [(dk/d\omega)|_{\omega=\omega_0}]^{-1}$ is the group velocity, and $\gamma = [4\pi\epsilon_0]n_2 n_0 \omega_0 / 2\pi$ is the nonlinear refractive index parameter.

76.3 Second-Order Processes

Second-order nonlinear optical processes occur as a consequence of the second term in expression Eq. (76.3), i.e., processes whose strength is described by $\chi^{(2)}(\omega_\sigma; \omega_m, \omega_n)$. These processes entail the generation of a field at frequency $\omega_\sigma = \omega_m + \omega_n$ in response to applied fields at (positive and/or negative) frequencies ω_m and ω_n . Several examples of such processes are described in this section.

76.3.1 Sum-Frequency Generation

Sum-frequency generation produces an output field at frequency $\omega_3 = \omega_1 + \omega_2$ for ω_1 and ω_2 both positive. It is useful, for example, for the generation of tunable radiation in the UV

if ω_1 and/or ω_2 are obtained from tunable lasers in the visible range. Sum-frequency generation is described in detail in Sects. 76.2.1–76.2.3.

76.3.2 Second Harmonic Generation

Second harmonic generation is routinely used to convert the output of a laser to a higher frequency. It is described by $\chi^{(2)}(2\omega; \omega, \omega)$. Let η be the power conversion efficiency from frequency ω to 2ω . Assuming that phase matching is perfect, and the pump wave has the fundamental frequency ω , a derivation analogous to that for Eq. (76.29) yields

$$\eta = \tanh^2(z/l), \quad (76.34)$$

where the characteristic conversion length l is given by

$$l = [4\pi] \frac{c \sqrt{n(\omega)n(2\omega)}}{4\pi\omega\chi^{(2)}|A_1(0)|}. \quad (76.35)$$

Note that the conversion efficiency asymptotically approaches unity. In practice, conversion efficiencies exceeding 80% can be achieved.

76.3.3 Parametric Amplification and Oscillation

Under the assumption that the pump at ω_3 in a second-order process is undepleted and strong, the system of coupled differential Eqs. (76.26) and (76.27) can be solved analytically. The solution for $A(\omega_j) = A_j$ and up to a global phase factor is [4]

$$A_{1,2}(z) = A_{1,2}(0) \left(\cosh gz + i \frac{\Delta k}{2g} \sinh gz \right) - i \sqrt{\frac{n_{2,1}\omega_{1,2}}{n_{1,2}\omega_{2,1}}} \frac{\kappa}{g} \frac{A_3}{|A_3|} A_{2,1}^*(0) \sinh gz, \quad (76.36)$$

where the gain κ for conditions of perfect phase matching is given by

$$\kappa^2 = \left[\frac{1}{16\pi^2} \right] \frac{16\pi^2 [\chi^{(2)}]^2 \omega_1^2 \omega_2^2}{k_1 k_2 c^4} |A_3|^2, \quad (76.37)$$

and the generalized gain for arbitrary phase matching is

$$g^2 = \kappa^2 - (\Delta k/2)^2. \quad (76.38)$$

Equation (76.36) shows simultaneous (and exponential) amplification of the two fields A_1 and A_2 , often called signal and idler. The process is referred to as parametric amplification. It is a direct consequence of the Manley–Rowe

relations, as described above in Sect. 76.2.3. Because of the relation $\omega_3 = \omega_1 + \omega_2$, the annihilation of an ω_3 photon must be accompanied by the simultaneous creation of photons ω_1 and ω_2 . From Eq. (76.36) it is apparent that the intensity of the generated fields depends on the phase relations among the three incoming fields, and the amplification is, therefore, a phase sensitive process.

An optical parametric oscillator can be constructed by placing the nonlinear optical material inside an optical resonator that provides feedback at ω_1 and/or ω_2 . When such a device is excited by a wave at ω_3 , it can produce output frequencies ω_1 and ω_2 that satisfy $\omega_1 + \omega_2 = \omega_3$. Optical parametric oscillators are of considerable interest as sources of broadly tunable radiation [7].

76.3.4 Difference-Frequency Generation

Difference-frequency generation can be used to create light in the infrared and far infrared by generating the difference frequency $\omega_2 = \omega_3 - \omega_1$ (where ω_3 and ω_1 are positive, and $\omega_3 > \omega_1$) of two incident lasers. Consider the case in which a strong (undepleted) pump wave at frequency ω_3 and a weak (signal) wave at ω_1 are incident on a nonlinear medium described by $\chi^{(2)}(\omega_2; \omega_3, -\omega_1) = \chi^{(2)}(\omega_1; \omega_3, -\omega_2)$. The amplitude A_3 of the strong wave can be taken as a constant, and Eq. (76.36) describes the solution to a system of coupled differential equations. Since there is no incident idler field, we have $A_2(0) = 0$, and the solution reduces to

$$A_1(z) = A_1(0) \left(\cosh gz + \frac{i\Delta k}{2g} \sinh gz \right), \quad (76.39)$$

$$A_2(z) = -i \sqrt{\frac{n_1\omega_2}{n_2\omega_1}} \frac{A_3}{|A_3|} A^*(0, \omega_1) \frac{\kappa}{g} \sinh gz. \quad (76.40)$$

Equation (76.40) describes the spatial growth of the difference-frequency signal.

76.3.5 Two-Mode Squeezing

To describe the quantum mechanical properties of light–matter interactions, one has to quantize the electromagnetic fields participating in the nonlinear interaction. However, the Heisenberg equations of motion of the respective field operators are very similar to their classical counterparts from Eqs. (76.26)–(76.28), and one can just replace $A_j \rightarrow \text{const.} \times \sqrt{\omega_j/n_j} \hat{a}_j$ and A_j^* by the Hermitian conjugate of this operator. Note that the photon annihilation operators \hat{a}_j are defined per field mode, and the proportionality factor depends on the quantization volume. Note further that the commutation relation $[\hat{a}_j, \hat{a}_j^\dagger] = \delta_{j,l}$ is preserved upon propagation of the quantum field. For an undepleted and strong pump, the so-

lution to the Heisenberg equations of motion is in analogy to Eq. (76.36) the Bogoliubov transformation [8]

$$\hat{a}_{1,2}(z) = u\hat{a}_{1,2}(0) + v\hat{a}_{2,1}^\dagger(0), \quad (76.41)$$

with the coefficients

$$u = \cosh gz + i\frac{\Delta k}{2g} \sinh gz \quad (76.42)$$

$$v = -ie^{i\phi_3} \frac{\kappa}{g} \sinh gz, \quad (76.43)$$

where ϕ_3 is the phase of the pump wave, and g as well as κ are defined as in Eqs. (76.38) and (76.37), respectively. Note that $|u|^2 - |v|^2 = 1$, which ensures unitarity of the amplification process. This transformation leads to a squeezing of the quadratures, as demonstrated in the following.

The two-mode quadratures of the electromagnetic field are defined by $\hat{x}_\pm = [\hat{a}_1 \pm \hat{a}_1^\dagger + \hat{a}_2 \pm \hat{a}_2^\dagger]/\sqrt{\pm 8}$. They correspond to the quantum analog of the real and imaginary parts of the electric fields. From Eq. (76.41) with $\phi_3 = \pi/2$ and $\Delta k = 0$ (for phase matching), we find that the two-mode quadratures are amplified or deamplified according to [9]

$$\hat{x}_\pm(z) = e^{\pm\kappa z} \hat{x}_\pm(0). \quad (76.44)$$

Hence, the variances $\Delta^2 x_\pm = \langle (\hat{x}_\pm - \langle \hat{x}_\pm \rangle)^2 \rangle$ of these quadrature operators can be written as $\Delta^2 x_\pm(z) = e^{\pm 2\kappa z} \Delta^2 x_\pm(0)$ and are amplified and suppressed, respectively. Since the variances correspond to the intrinsic noise of the electric fields, the squeezing process can lead to its suppression. Therefore, squeezed light is used to increase the sensitivity of interferometers and gives a sensitivity below the shot-noise level. Single-mode squeezing and the associated squeezing operator are discussed in Chaps. 82 and 84.

76.3.6 Spontaneous Parametric Down-Conversion

With the results from the preceding section, it is possible to look at the squeezing of vacuum input states and the limit of a small coupling κz , which leads to spontaneous parametric down-conversion (SPDC). In this process, a pump photon is spontaneously converted into one signal and one idler photon, without the process being seeded by input fields. The two generated photons always appear pairwise and are, therefore, often used as a source of single photons. The detection of an idler photon implies that there is a single photon in the signal field.

For any uncorrelated input state, it is easy to show with Eq. (76.41) and the commutation relations that the expectation value $n_j = \langle \hat{a}_j^\dagger \hat{a}_j \rangle$ of the photon number is

$$n_{1,2}(z) = |u|^2 n_{1,2}(0) + |v|^2 [n_{2,1}(0) + 1]. \quad (76.45)$$

Unlike for the case of its classical counterpart, the output photon number $n_{1,2}(z) = |v|^2$ is nonvanishing even for a vacuum input $n_{1,2}(0) = 0$ because of the noncommutativity of the photon creation and annihilation operators. This means that one can not only squeeze input light, but also the vacuum itself. Moreover, a weak nonlinear interaction or a weak pump field leads to spontaneous emission. In this case, $\kappa \ll \Delta k/2$ and Eq. (76.45) reduces to

$$n_{1,2}^{\text{SPDC}}(L) = \kappa^2 L^2 \text{sinc}^2(\Delta k L/2), \quad (76.46)$$

for a bulk crystal of length L . A more sophisticated treatment shows that there are not only photons spontaneously emitted, but they are strongly correlated. The photons are always generated in pairs and share common properties, a feature that is called entanglement. There have been numerous experimental verifications of polarization entanglement, but also entanglement of continuous variables such as energy and time or transverse position and momentum, discussed in Chap. 84. Position-momentum entanglement is a direct consequence of the shape of the crystal and the pump beam in SPDC. The two-photon wave function $\psi(\mathbf{q}_1, \mathbf{q}_2)$ of signal and idler photons with a transverse momentum \mathbf{q}_1 and \mathbf{q}_2 , respectively, is proportional to [10]

$$\psi(\mathbf{q}_1, \mathbf{q}_2) \propto A_3(\mathbf{q}_1 + \mathbf{q}_2) e^{i\Delta k L/2} \text{sinc}(\Delta k L/2), \quad (76.47)$$

with $\Delta k = k_3(\mathbf{q}_1 + \mathbf{q}_2) - k_1(\mathbf{q}_1) - k_2(\mathbf{q}_2)$. Here, k_j corresponds to the longitudinal component of the respective wave vector. $A_3(\mathbf{q}_3)$ is the angular distribution of the pump field. For degenerate down-conversion ($\omega_1 = \omega_2$), we find in the paraxial regime that $\Delta k = \lambda_3(\mathbf{q}_1 - \mathbf{q}_2)^2/(4\pi)$. For a plane wave pump, $A_3(\mathbf{q}_3)$ becomes very narrow and the transverse wave vectors become anticorrelated, which is implied by momentum conservation. The squared modulus of Eq. (76.47) is proportional to the coincidence count rate of signal and idler photons with the respective momenta.

With a Fourier transform, the two-photon wave function from Eq. (76.47) is transformed into position space, and it may reveal that the transverse positions are correlated. The combination of position correlation and momentum anticorrelation can lead to the apparent violation of a Heisenberg uncertainty relation for a linear combination of the two positions and momenta, which is a clear witness of continuous-variable entanglement. In fact, a photon pair that is not entangled cannot have correlated positions of the signal and idler photons and simultaneously anticorrelated momenta, as these are two conjugate variables. However, for an entangled photon pair, quantum correlations allow for simultaneous position correlation and momentum anticorrelation [11, 12].

76.3.7 Focused Beams

For conceptual clarity, much of the discussion so far has assumed that the interacting beams are plane waves. In practice, the incident laser beams are often focused into the nonlinear material to increase the field strength within the interaction region and, consequently, to increase the nonlinear response. However, it is undesirable to focus too tightly, because doing so leads to a decrease in the effective length of the interaction region. In particular, if w_0 is the radius of the laser beam at the beam waist, the beam remains focused only over a distance of the order $b = 2\pi w_0^2/\lambda$, where λ is the laser wavelength measured in the nonlinear material. For many types of nonlinear optical processes, the optimal nonlinear response occurs if the degree of focusing is adjusted so that b is several times smaller than the length L of the nonlinear optical material.

76.4 Third-Order Processes

A wide variety of nonlinear optical processes are possible as a result of the nonlinear contributions to the polarization that are third-order in the applied field. These processes are described by $\chi^{(3)}(\omega_\sigma; \omega_m, \omega_n, \omega_o)$ as defined in Eq. (76.3) and can lead not only to the generation of new field components (e.g., third-harmonic generation) but can also result in a field affecting itself as it propagates (e.g., self-phase modulation). Several examples are described in this section.

76.4.1 Third-Harmonic Generation

Assuming full-permutation symmetry, the nonlinear polarization amplitudes for the fundamental and third-harmonic beams are

$$\begin{aligned} \mathcal{P}^{\text{NL}}(z, \omega) &= [\varepsilon_0] 3\chi_{\text{eff}}^{(3)} A(z, 3\omega) [A^*(z, \omega)]^2 e^{-i\Delta k z}, \\ \mathcal{P}^{\text{NL}}(z, 3\omega) &= [\varepsilon_0] \chi_{\text{eff}}^{(3)} [A(z, \omega)]^3 e^{i\Delta k z}, \end{aligned} \quad (76.48)$$

where $\Delta k = 3k(\omega) - k(3\omega)$ and $\chi_{\text{eff}}^{(3)}$ is the effective third-order susceptibility for third-harmonic generation and is defined in a manner analogous to the $\chi_{\text{eff}}^{(2)}$ in Eq. (76.25). If the intensity of the fundamental wave is not depleted by the nonlinear interaction, the solution for the output intensity $I(L, 3\omega)$ of the third-harmonic field for a crystal of length L is

$$\begin{aligned} I(L, 3\omega) &= \left[\frac{1}{256\pi^4 \varepsilon_0^2} \right] \frac{48\pi^2 \omega^2 [\chi_{\text{eff}}^{(3)}]^2}{n(3\omega)n(\omega)^3 c^4} \\ &\times I(\omega)^3 L^2 \text{sinc}^2 \left[\frac{\Delta k L}{2} \right], \end{aligned} \quad (76.49)$$

where $I(\omega)$ is the input intensity of the fundamental field. As a result of the typically small value of $\chi_{\text{eff}}^{(3)}$ in crystals, it is generally more efficient to generate the third harmonic by using two $\chi^{(2)}$ crystals in which the first crystal produces second harmonic light, and the second crystal combines the second harmonic and the fundamental beams via sum-frequency generation. It is also possible to use resonant enhancement of $|\chi^{(3)}|$ in gases to increase the efficiency of third-harmonic generation [13].

76.4.2 Self-Phase and Cross-Phase Modulation

The nonlinear refractive index leads to an intensity-dependent change in the phase of the beam as it propagates through the material. If the medium is lossless, the amplitude of a single beam at frequency ω propagating in the positive z -direction can be expressed as

$$A(z, \omega) = A(0, \omega) e^{i\phi^{\text{NL}}(z)}, \quad (76.50)$$

where the nonlinear phase shift $\phi^{\text{NL}}(z)$ is given by

$$\phi^{\text{NL}}(z) = \frac{\omega}{c} n_2 I z, \quad (76.51)$$

and $I = [4\pi\varepsilon_0] n_0 c |A(0, \omega)|^2 / 2\pi$ is the intensity of the laser beam. If two fields at different frequencies ω_1 and ω_2 are traveling along the z -axis, the two fields can affect each other's phase; this effect is known as cross-phase modulation. The nonlinear phase shift $\phi_{1,2}^{\text{NL}}(z)$ for each of the waves is given by

$$\phi_{1,2}^{\text{NL}}(z) = \frac{\omega_{1,2}}{c} n_2 (I_{1,2} + 2I_{2,1}) z. \quad (76.52)$$

For the case of a light pulse, the change in the phase of the pulse inside the medium becomes a function of time. In this case, the solution to Eq. (76.33) shows that in the absence of group-velocity dispersion (GVD) (i.e., $\beta_2 = 0$), the time-varying amplitude $A(z, \tau)$ is of the form of Eq. (76.50), except that the temporal intensity profile $I(\tau)$ replaces the steady-state intensity I in Eq. (76.51). As the pulse propagates through the medium, its frequency becomes time dependent, and the instantaneous frequency shift from the central frequency ω_0 is given by

$$\delta\omega(\tau) = -\frac{\partial\phi^{\text{NL}}(\tau)}{\partial\tau} = -\frac{\omega_0 n_2 z}{c} \frac{\partial I}{\partial t}. \quad (76.53)$$

This time-dependent self-phase modulation leads to a broadening of the pulse spectrum and to a frequency chirp across the pulse.

If the group velocity dispersion parameter β_2 and the nonlinear refractive index coefficient n_2 are of opposite sign, the

nonlinear frequency chirp can be compensated by the chirp due to group velocity dispersion, and Eq. (76.33) admits soliton solutions. For example, the fundamental soliton solution is

$$A(z, t) = \sqrt{\frac{1}{|\gamma L_D|}} \operatorname{sech}\left(\frac{\tau}{\tau_p}\right) e^{-iz/2L_D}, \quad (76.54)$$

where τ_p is the pulse duration, and $L_D = \tau_p^2/\beta_2$ is the dispersion length. As a result of their ability to propagate in dispersive media without changing shape, optical solitons show a great deal of promise in applications such as optical communications and optical switching. For further discussion of optical solitons, see [14].

76.4.3 Four-Wave Mixing

Various types of four-wave mixing processes can occur among different beams. One of the most common geometries is backward four-wave mixing used in nonlinear spectroscopy and optical phase conjugation. In this interaction, two strong counterpropagating pump waves with amplitudes A_1 and A_2 and with equal frequencies $\omega_{1,2} = \omega$ are injected into a nonlinear medium. A weak wave, termed the probe wave, (with frequency ω_3 and amplitude A_3) is also incident on the medium. As a result of the nonlinear interaction among the three waves, a fourth wave with an amplitude A_4 is generated, which is counterpropagating with respect to the probe wave and with frequency $\omega_4 = 2\omega - \omega_3$. For this case, the third-order nonlinear susceptibilities for the probe and conjugate waves are given by $\chi^{(3)}(\omega_{3,4}; \omega, \omega, -\omega_{4,3})$. For constant pump wave intensities and full permutation symmetry, the amplitudes of the nonlinear polarization for the probe and conjugate waves are given by

$$\begin{aligned} P^{\text{NL}}(z, \omega_{3,4}) \\ = \pm[\varepsilon_0]6\chi^{(3)}[(|A_1|^2 + |A_2|^2)A_{3,4} + A_1A_2A_{4,3}^* e^{i\Delta kz}], \end{aligned} \quad (76.55)$$

where $\Delta k = k_1 + k_2 - k_3 - k_4$ is the phase mismatch, which is nonvanishing when $\omega_3 \neq \omega_4$. For the case of optical phase conjugation by degenerate four-wave mixing (i.e., $\omega_3 = \omega_4 = \omega$, and $A_4(L) = 0$), the phase conjugate reflectivity R_{PC} is

$$R_{\text{PC}} = \frac{|A_4(0)|^2}{|A_3(0)|^2} = \tan^2(\kappa L), \quad (76.56)$$

where $\kappa = [1/16\pi^2\varepsilon_0][24\pi^2\omega\chi^{(3)}/(n_0c)^2]\sqrt{I_1I_2}$ and $I_{1,2}$ are the intensities of the pump waves. Phase-conjugate reflectivities greater than unity can be routinely achieved by performing four-wave mixing in atomic vapors or photorefractive media.

76.4.4 Self-Focusing and Self-Trapping

Typically, a laser beam has a transverse intensity profile that is approximately Gaussian. In a medium with an intensity-dependent refractive index, the index change at the center of the beam is different from the index change at the edges of the beam. The gradient in the refractive index created by the beam can allow it to self-focus for $n_2 > 0$. For this condition to be met, the total input power of the beam must exceed the critical power P_{cr} for self-focusing, which is given by

$$P_{\text{cr}} = \frac{\pi(0.61\lambda)^2}{8n_0n_2}, \quad (76.57)$$

where λ is the vacuum wavelength of the beam. For powers much greater than the critical power, the beam can break up into various filaments, each with a power approximately equal to the critical power. For a more extensive discussion of self-focusing and self-trapping, see [15, 16].

76.4.5 Saturable Absorption

When the frequency ω of an applied laser field is sufficiently close to a resonance frequency ω_0 of the medium, an appreciable fraction of the atomic population can be placed in the excited state. This loss of population from the ground state leads to an intensity-dependent saturation of the absorption and the refractive index of the medium (for a more detailed discussion: Chap. 73.3) [4]. The third-order susceptibility as a result of this saturation is given by

$$\chi^{(3)} = \left[\frac{1}{\varepsilon_0}\right] \frac{|\mu|^2 T_1 T_2 \alpha_0 c}{3\pi\omega_0 \hbar^2} \frac{\delta T_2 - i}{[1 + (\delta T_2)^2]^2}, \quad (76.58)$$

where μ is the transition dipole moment, T_1 and T_2 are the longitudinal and transverse relaxation times, respectively (Chap. 72.4.3), α_0 is the line-center weak-field intensity absorption coefficient, and $\delta = \omega - \omega_0$ is the detuning. For the $3s \leftrightarrow 3p$ transition in atomic sodium vapor at 300°C, the nonlinear refractive index $n_2 \approx 10^{-7} \text{ cm}^2/\text{W}$ for a detuning $\delta T_2 = 300$.

76.4.6 Two-Photon Absorption

When the frequency ω of a laser field is such that 2ω is close to a transition frequency of the material, it is possible for two-photon absorption (TPA) to occur. This process leads to a contribution to the imaginary part of $\chi^{(3)}(\omega; \omega, \omega, -\omega)$. In the presence of TPA, the intensity $I(z)$ of a single, linearly polarized beam as a function of propagation distance is

$$I(z) = \frac{I(0)}{1 + \beta I(0)z}, \quad (76.59)$$

where $\beta = [1/16\pi^2\varepsilon_0]24\pi^2\omega \text{Im}[\chi^{(3)}]/(n_0c)^2$ is the TPA coefficient. For wide-gap semiconductors such as ZnSe at 800 nm, $\beta \approx 10^{-8}$ cm/W.

76.4.7 Nonlinear Ellipse Rotation

The polarization ellipse of an elliptically polarized laser beam rotates but retains its ellipticity as the beam propagates through an isotropic nonlinear medium. Ellipse rotation occurs as a result of the difference in the nonlinear index changes experienced by the left-circular and right-circular components of the beam, and the angle θ of rotation is

$$\begin{aligned} \theta &= \frac{1}{2}\Delta n\omega z/c \\ &= \left[\frac{1}{16\pi^2\varepsilon_0} \right] \frac{12\pi^2}{n_0^2c} \chi_{xyyx}^{(3)}(\omega; \omega, \omega, -\omega)(I_+ - I_-)z, \end{aligned} \quad (76.60)$$

where I_{\pm} are the intensities of the circularly polarized components of the beam with unit vectors $\hat{\sigma}_{\pm} = (\hat{x} \pm i\hat{y})/\sqrt{2}$. Nonlinear ellipse rotation is a sensitive technique for determining the nonlinear susceptibility element $\chi_{xyyx}^{(3)}$ for isotropic media and can be used in applications such as optical switching.

76.5 Stimulated Light Scattering

Stimulated light scattering occurs as a result of changes in the optical properties of the material that are induced by the optical field. The resulting nonlinear coupling between different field components is mediated by some excitation (e.g., acoustic phonon) of the material that results in changes in its optical properties. The nonlinearity can be described by a complex susceptibility and a nonlinear polarization that is of third order in the interacting fields. Various types of stimulated scattering can occur. Discussed below are the two processes that are most commonly observed.

76.5.1 Stimulated Raman Scattering

In stimulated Raman scattering (SRS), the light field interacts with a vibrational mode of a molecule. The coupling between the two optical waves can become strong if the frequency difference between them is close to the frequency ω_v of the molecular vibrational mode. If the pump field at ω_0 and another field component at ω_1 are propagating in the same direction along the z -axis, the steady-state nonlinear polarization amplitudes for the two field components are given by

$$P^{\text{NL}}(z, \omega_{0,1}) = [\varepsilon_0]6\chi_{\text{R}}(\omega_{0,1})|A(z, \omega_{1,0})|^2A(z, \omega_{0,1}), \quad (76.61)$$

where $\chi_{\text{R}}(\omega_{0,1}) \equiv \chi^{(3)}(\omega_{0,1}; \omega_{0,1}, \omega_{1,0}, -\omega_{1,0})$, the Raman susceptibility, actually depends only on the frequency difference $\Omega = \omega_0 - \omega_1$ and is given by

$$\chi_{\text{R}}(\omega_{0,1}) = \left[\frac{1}{\varepsilon_0} \right] \frac{N(\partial\alpha/\partial q)_0^2}{6\mu_M} \frac{1}{\omega_v^2 - \Omega^2 \mp 2i\gamma\Omega}, \quad (76.62)$$

where the minus (plus) sign is taken for the ω_0 (ω_1) susceptibility, μ_M is the reduced nuclear mass, and $(\partial\alpha/\partial q)_0$ is a measure of the change of the polarizability of the molecule with respect to a change in the intermolecular distance q at equilibrium. If the intensity of the pump field is undepleted by the interaction with the ω_1 field and is assumed to be constant, the solution for the intensity of the ω_1 field at $z = L$ is given by

$$I(L, \omega_1) = I(0, \omega_1) e^{G_{\text{R}}}, \quad (76.63)$$

where the SRS gain parameter G_{R} is

$$\begin{aligned} G_{\text{R}} &= \left[\frac{1}{16\pi^2\varepsilon_0} \right] 48\pi^2 \frac{\omega_1}{(n_1c)^2} \text{Im}[\chi_{\text{R}}(\omega_1)]I_0L \\ &= g_{\text{R}}I_0L, \end{aligned} \quad (76.64)$$

g_{R} is the SRS gain factor, and I_0 is the input intensity of the pump field. For $\omega_1 < \omega_0$ ($\omega_1 > \omega_0$), the ω_1 field is termed the Stokes (anti-Stokes) field, and it experiences exponential amplification (attenuation). For sufficiently large gains (typically $G_{\text{R}} \gtrsim 25$), the Stokes wave can be seeded by spontaneous Raman scattering and can grow to an appreciable fraction of the pump field. For a complete discussion of the spontaneous initiation of SRS, see [17]. For the case of CS₂, $g_{\text{R}} = 0.024$ cm/MW.

Four-wave mixing processes that couple a Stokes wave having $\omega_1 < \omega_0$ and an anti-Stokes wave having $\omega_2 > \omega_0$, where $\omega_1 + \omega_2 = 2\omega_0$, can also occur [4]. In this case, additional contributions to the nonlinear polarization are present and are characterized by a Raman susceptibility of the form $\chi^{(3)}(\omega_{1,2}; \omega_0, \omega_0, -\omega_{2,1})$. The technique of coherent anti-Stokes Raman spectroscopy is based on this four-wave mixing process [18].

76.5.2 Stimulated Brillouin Scattering

In stimulated Brillouin scattering (SBS), the light field induces and interacts with an acoustic wave inside the medium. The resulting interaction can lead to extremely high amplification for certain field components (i.e., Stokes wave). For many optical media, SBS is the dominant nonlinear optical process for laser pulses of duration > 1 ns. The primary applications for SBS are self-pumped phase conjugation and pulse compression of high-energy laser pulses.

If an incident light wave with wave vector \mathbf{k}_0 and frequency ω_0 is scattered from an acoustic wave with wave vector \mathbf{q} and frequency Ω , the wave vector and frequency of the scattered wave are determined by conservation of momentum and energy to be $\mathbf{k}_1 = \mathbf{k}_0 \pm \mathbf{q}$ and $\omega_1 = \omega_0 \pm \Omega$, where the (+) sign applies if $\mathbf{k}_0 \cdot \mathbf{q} > 0$ and the (-) applies if $\mathbf{k}_0 \cdot \mathbf{q} < 0$. Here, Ω and \mathbf{q} are related by the dispersion relation $\Omega = v|\mathbf{q}|$ where v is the velocity of sound in the material. These Bragg scattering conditions lead to the result that the Brillouin frequency shift $\Omega_B = \omega_1 - \omega_0$ is zero for scattering in the forward direction (i.e., in the \mathbf{k}_0 direction) and reaches its maximum for scattering in the backward direction given by

$$\Omega_B = 2\omega_0 v n_0 / c, \quad (76.65)$$

where n_0 is the refractive index of the material.

The interaction between the incident wave and the scattered wave in the Brillouin-active medium can become nonlinear if the interference between the two optical fields can coherently drive an acoustic wave, either through electrostriction or through local density fluctuations resulting from the absorption of light and consequent temperature changes. The following discussion treats the more common electrostriction mechanism.

Typically, SBS occurs in the backward direction (i.e., $\mathbf{k}_0 = k_0 \hat{z}$ and $\mathbf{k}_1 = -k_1 \hat{z}$), since the spatial overlap between the Stokes beam and the laser beam is maximized under these conditions and, as mentioned above, no SBS occurs in the forward direction. The steady-state nonlinear polarization amplitudes for backward SBS are

$$\mathcal{P}^{\text{NL}}(z, \omega_{0,1}) = [\varepsilon_0] 6\chi_B(\omega_{0,1}) |A(z, \omega_{1,0})|^2 A(z, \omega_{0,1}), \quad (76.66)$$

where $\chi_B(\omega_{0,1}) \equiv \chi^{(3)}(\omega_{0,1}; \omega_{0,1}, \omega_{1,0}, -\omega_{1,0})$, the Brillouin susceptibility, depends only on $\Omega = \omega_0 - \omega_1$ and is given by

$$\chi_B(\omega_{0,1}) = \left[\frac{1}{\varepsilon_0} \right] \frac{\omega_0^2 \gamma_e^2}{24\pi^2 c^2 \rho_0} \frac{1}{\Omega_B^2 - \Omega^2 \mp i\Gamma_B \Omega}, \quad (76.67)$$

where the minus (plus) sign is taken for the ω_0 (ω_1) susceptibility, γ_e is the electrostrictive constant, ρ_0 is the mean density of the material, and Γ_B is the Brillouin linewidth given by the inverse of the phonon lifetime. If the pump field is undepleted by the interaction with the ω_1 field and is assumed to be constant, the solution for the output intensity of the ω_1 field at $z = 0$ is given by

$$I(0, \omega_1) = I(L, \omega_1) e^{G_B}, \quad (76.68)$$

where the Brillouin gain coefficient G_B is given by

$$G_B = \left[\frac{1}{16\pi^2 \varepsilon_0} \right] 48\pi^2 \frac{\omega_1}{(n_0 c)^2} \text{Im}[\chi_B(\omega_1)] I_0 L$$

$$\begin{aligned} &= g_0 \frac{\Omega \Omega_B \Gamma_B^2}{[\Omega_B^2 - \Omega^2]^2 + (\Omega \Gamma_B)^2} I_0 L \\ &= g_B I_0 L, \end{aligned} \quad (76.69)$$

g_B is the SBS gain factor, I_0 is the input intensity of the pump field, and

$$g_0 = \left[\frac{1}{\varepsilon_0^2} \right] \frac{\omega_0^2 \gamma_e^2}{n_0 c^3 \rho_0 v \Gamma_B} \quad (76.70)$$

is the line-center (i.e., $\Omega = \pm \Omega_B$) SBS gain factor. For $\Omega > 0$ ($\Omega < 0$), the ω_1 field is termed the Stokes (anti-Stokes) field, and it experiences exponential amplification (attenuation). For sufficiently large gains (typically $G_B \gtrsim 25$), the Stokes wave can be seeded by spontaneous Brillouin scattering and can grow to an appreciable fraction of the pump field. For a complete discussion of the spontaneous initiation of SBS, see [19]. For CS_2 , $g_0 = 0.15 \text{ cm/MW}$.

76.6 Other Nonlinear Optical Processes

76.6.1 High-Order Harmonic Generation

If full permutation symmetry applies, and the fundamental field ω is not depleted by nonlinear interactions, then the intensity of the q -th harmonic is given by

$$\begin{aligned} I(z, q\omega) &= \left[\frac{1}{4\pi(4\pi\varepsilon_0)^{(q-1)/2}} \right] \\ &\times \frac{2\pi q^2 \omega^2}{n^2(q\omega)c} \left[\frac{2\pi I(\omega)}{n(\omega)c} \right]^q \\ &\times |\chi^{(q)}(q\omega; \omega, \dots, \omega) J_q(\Delta k, z_0, z)|^2, \end{aligned} \quad (76.71)$$

where $\Delta k = [n(\omega) - n(q\omega)]\omega/c$,

$$J_q(\Delta k, z_0, z) = \int_{z_0}^z \frac{e^{i\Delta k z' dz'}}{(1 + 2iz'/b)^{q-1}}, \quad (76.72)$$

$z = z_0$ at the input face of the nonlinear medium, and b is the confocal parameter (Sect. 76.3.7) of the fundamental beam. Defining $L = z - z_0$, the integral J_q can be easily evaluated in the limits $L \ll b$ and $L \gg b$. The limit $L \ll b$ corresponds to the plane-wave limit in which case

$$|J_q(\Delta k, z_0, z)|^2 = L^2 \text{sinc}^2\left(\frac{\Delta k L}{2}\right). \quad (76.73)$$

The limit $L \gg b$ corresponds to the tight-focusing configuration in which case

$$J_q(\Delta k, z_0, z) = \begin{cases} 0, & \Delta k \leq 0, \\ \frac{\pi b}{(q-2)!} \left(\frac{b\Delta k}{2}\right)^{q-2} e^{-b\Delta k/2}, & \Delta k > 0. \end{cases} \quad (76.74)$$

Note that in this limit, the q -th harmonic light is only generated for positive phase mismatch. *Reintjes* et al. [20, 21] observed both the fifth and seventh harmonics in helium gas, which exhibited a dependence on $I(\omega)$, which is consistent with the $I^q(\omega)$ dependence predicted by Eq. (76.71). However, more recent experiments in gas jets have demonstrated the generation of extremely high-order harmonics, which do not depend on the intensity in this simple manner (Chap. 78 for further discussion of this nonperturbative behavior).

76.6.2 Electro-Optic Effect

The electro-optic effect corresponds to the limit in which the frequency of one of the applied fields approaches zero. The linear electro-optic effect (or Pockels effect) can be described by a second-order susceptibility of the form $\chi^{(2)}(\omega; \omega, 0)$. This effect produces a change in the refractive index for light of certain polarizations, which depends linearly on the strength of the applied low-frequency field. More generally, the linear electro-optic effect induces a change in the amount of birefringence present in an optical material. This electrically controllable change in birefringence can be used to construct amplitude modulators, frequency shifters, optical shutters, and other optoelectronic devices. Materials commonly used in such devices include KDP and lithium niobate [22]. If the laser beam is propagating along the optic axis (i.e., z -axis) of the material of length L , and the low-frequency field E_z is also applied along the optic axis, the nonlinear index change $\Delta n = n_y - n_x$ between the components of the electric field polarized along the principal axes of the crystal is given by

$$\Delta n = \left[\frac{1}{4\pi} \right] n_0^3 r_{63} E_z, \quad (76.75)$$

where r_{63} is one of the electro-optic coefficients.

The quadratic electro-optic effect produces a change in the refractive index that scales quadratically with the applied DC electric field. This effect can be described by a third-order susceptibility of the form $\chi^{(3)}(\omega; \omega, 0, 0)$.

76.6.3 Photorefractive Effect

The photorefractive effect leads to an optically induced change in the refractive index of a material. In certain ways,

this effect mimics that of the nonlinear refractive index described in Sect. 76.1.2, but it differs from the nonlinear refractive index in that the change in refractive index is independent of the overall intensity of the incident light field and depends only on the degree of spatial modulation of the light field within the nonlinear material. In addition, the photorefractive effect can occur only in materials that exhibit a linear electro-optic effect and contain an appreciable density of trapped electrons and/or holes that can be liberated by the application of a light field. Typical photorefractive materials include lithium niobate, barium titanate, and strontium barium niobate.

A typical photorefractive configuration might be as follows: two beams interfere within a photorefractive crystal to produce a spatially modulated intensity distribution. Bound charges are ionized with greater probability at the maxima than at the minima of the distribution and, as a result of the diffusion process, carriers tend to migrate away from regions of large light intensity. The resulting modulation of the charge distribution leads to the creation of a spatially modulated electric field that produces a spatially modulated change in refractive index as a consequence of the linear electro-optic effect. For a more extensive discussion, see [23].

76.7 New Regimes of Nonlinear Optics

76.7.1 Ultrafast and Intense-Field Nonlinear Optics

Additional nonlinear optical processes are enabled by the use of ultrashort (< 1 ps) or ultraintense laser pulses. For reasons of basic laser physics, ultraintense pulses are necessarily of short duration, and, thus, these effects normally occur together. Ultrashort laser pulses possess a broad frequency spectrum, and, therefore, the dispersive properties of the optical medium play a key role in the propagation of such pulses. The three-dimensional nonlinear Schrödinger equation must be modified when treating the propagation of these ultrashort pulses by including contributions that can be ignored under other circumstances [24, 25]. These additional terms lead to processes such as space–time coupling, self-steepening, and shock-wave formation [26, 27]. The process of self-focusing is significantly modified under short-pulse (pulse duration shorter than approximately 1 ps) excitation. For example, temporal splitting of a pulse into two components can occur; this pulse splitting lowers the peak intensity and can lead to the arrest of the usual collapse of a pulse undergoing self-focusing [28]. Moreover, optical shock formation, the creation of a discontinuity in the intensity evolution of a propagating pulse, leads to supercontinuum generation, the creation of a light pulse with

an extremely broad frequency spectrum [29]. Shock effects and the generation of supercontinuum light can also occur in one-dimensional systems, such as a microstructure optical fiber. The relatively high peak power of the ultrashort pulses from a mode-locked laser oscillator and the tight confinement of the optical field in the small ($\approx 2 \mu\text{m}$) core of the fiber yield high intensities and strong self-phase modulation, which results in a spectral bandwidth that spans more than an octave of the central frequency of the pulse [30]. Such a coherent octave-spanning spectrum allows for the stabilization of the underlying frequency comb of the mode-locked oscillator and has led to a revolution in the field of frequency metrology [31]. Multiphoton absorption [32] constitutes an important loss process that becomes important for intensities in excess of $\approx 10^{13} \text{ W/cm}^2$. In addition to introducing loss, the electrons released by this process can produce additional nonlinear effects associated with their relativistic motion in the resulting plasma [33, 34]. For very large laser intensities (greater than approximately 10^{16} W/cm^2), the electric field strength of the laser pulse can exceed the strength of the Coulomb field that binds the electron to the atomic core, and nonperturbative effects can occur. A dramatic example is that of high-harmonic generation [35–37]. Harmonic orders as large as the 341-st have been observed, and simple conceptual models have been developed to explain this effect [38]. Under suitable conditions, the harmonic orders can be suitably phased so that attosecond pulses are generated [39].

76.7.2 Nonlinear Plasmonics and Epsilon-Near-Zero Effects

Despite their intrinsic loss, plasmonic materials (i.e., metals) have shown stronger nonlinear effects than insulators or dielectrics [40]. The optical properties of such materials are determined by the dynamics of quasi-free electrons in the conduction band and can be understood in terms of the Drude model for sufficiently low frequencies. In this model, the permittivity

$$\epsilon(\omega) = \epsilon_\infty - \omega_p^2 / (\omega^2 + i\gamma\omega) \quad (76.76)$$

shows a strong dependence on the frequency ω and is determined by the high-frequency permittivity ϵ_∞ , a damping constant γ , and the plasma frequency

$$\omega_p^2 = [1/(4\pi\epsilon_0)] 4\pi N e^2 / m^* . \quad (76.77)$$

Here, N is the electron density, and m^* the effective mass of the electrons in the conduction band, $-e$ denotes the el-

ementary charge. Note that for most plasmonic materials the optical response deviates significantly from the Drude model due to interband transitions at optical frequencies. However, the model can be improved by including additional contributions to the permittivity that arise in a Lorentz-oscillator description of bound electrons. Even though such models give a better quantitative description of the response, Eq. (76.76) describes the qualitative behavior of plasmonic materials very well [41].

The permittivity from Eq. (76.76) has some remarkable features. For example, the real part of ϵ can take negative values. Moreover, it may even vanish for $\omega^2 = \omega_p^2 / \epsilon_\infty$ (neglecting terms of the order of γ^2). This resonance gives rise to a new class of epsilon-near-zero (ENZ) materials, which possess unique nonlinear optical properties. For a vanishing real part of ϵ , the real part of the refractive index becomes small and, following Eq. (76.8), the nonlinear refractive index n_2 is enhanced [42, 43]. This heuristic explanation captures some features of the outstanding optical response of some plasmonic materials. Other nonlinear mechanisms that dominate in such materials [44–47] are (i) saturable absorption due to the filling of the conduction band, (ii) quantum-size effects for small particles where the electrons in the conduction band are confined to a small volume and, thus, not completely free, (iii) ponderomotive effects in Fermi–Dirac metals where the electron density is depleted by high intensities, and (vi) hot-electron effects where the distribution of electrons in the conduction band is modified by the absorption of heat from high intensities. The latter effect leads to a shift of the frequency where the real part of the permittivity vanishes, which can be easily understood in terms of Eq. (76.77), since a modified distribution changes the effective mass m^* and by that ω_p . Note that such thermal effects are not instantaneous and depend relatively strongly on the laser pulse parameters.

A field of magnitude $|E_0|$ incident on such an ENZ medium is also significantly enhanced inside the material. Since the perpendicular component of the electric displacement is continuous at the interface, the electric field inside a material depends on the inverse of the permittivity. For an angle of incidence ϕ , the magnitude of the field $|E_{\text{mat}}|$ within the material is

$$|E_{\text{mat}}| = |E_0| (\cos^2 \phi + \epsilon^{-1} \sin^2 \phi)^{1/2} \quad (76.78)$$

and, therefore, enhanced for an oblique angle of incidence and small values of ϵ . In fact, the field enhancement leads to an angle-dependence for the nonlinear optical response of ENZ materials [42].

References

1. Bloembergen, N.: *Nonlinear Optics*. Benjamin, New York (1964)
2. Shen, Y.R.: *Nonlinear Optics*. Wiley, New York (1984)
3. Butcher, P.N., Cotter, D.: *The Elements of Nonlinear Optics*. Cambridge University Press, Cambridge (1990)
4. Boyd, R.W.: *Nonlinear Optics*, 3rd edn. Academic Press, Boston (2008)
5. Armstrong, J.A., Bloembergen, N., Ducuing, J., Pershan, P.S.: *Phys. Rev.* **127**, 1918 (1962)
6. Stegeman, G.I.: In: Agrawal, G.P., Boyd, R.W. (eds.) *Contemporary Nonlinear Optics*. Academic Press, Boston (1992). Chap. 1
7. See for example the Special Issue on: *Optical Parametric Oscillation and Amplification*. *J. Opt. Soc. Am. B.* **10** (1993)
8. Klyshko, D.N.: *Photons and Nonlinear Optics*. Gordon and Breach, New York (1989)
9. Loudon, R., Knight, P.L.: *J. Mod. Opt.* **34**, 709 (1987)
10. Walborn, S.P., Monken, C.H., Pádua, S., Souto Ribeiro, P.H.: *Phys. Rep.* **495**, 87 (2010)
11. Howell, J.C., Bennink, R.S., Bentley, S.J., Boyd, R.W.: *Phys. Rev. Lett.* **92**, 210403 (2004)
12. D'Angelo, A., Kim, Y.-H., Kulik, S.P., Shih, Y.: *Phys. Rev. Lett.* **92**, 233601 (2004)
13. Miles, R.B., Harris, S.E.: *IEEE J. Quant. Electron.* **9**, 470 (1973)
14. Agrawal, G.P.: *Nonlinear Fiber Optics*. Academic Press, Boston (1989)
15. Akhmanov, S.A., Khokhlov, R.V., Sukhorukov, A.P.: In: *Arecchi, F.T., Schulz-Dubois, E.O. (eds.) Laser Handbook*. North-Holland, Amsterdam (1972)
16. Marburger, J.H.: *Prog. Quant. Electr.* **4**, 35 (1975)
17. Raymer, M.G., Walmsley, I.A.: In: *Wolf, E. (ed.) Progress in Optics*, vol. 28, North-Holland, Amsterdam (1990)
18. Levenson, M.D., Kano, S.: *Introduction to Nonlinear Spectroscopy*. Academic Press, Boston (1988)
19. Boyd, R.W., Rzazewski, K., Narum, P.: *Phys. Rev. A* **42**, 5514 (1990)
20. Reintjes, J., She, C.Y., Eckardt, R.C., Karangelen, N.E., Elton, R.C., Andrews, R.A.: *Phys. Rev. Lett.* **37**, 1540 (1976)
21. Reintjes, J., She, C.Y., Eckardt, R.C., Karangelen, N.E., Elton, R.C., Andrews, R.A.: *Appl. Phys. Lett.* **30**, 480 (1977)
22. Kaminow, I.P.: *An Introduction to Electro-Optic Devices*. Academic Press, New York (1974)
23. Günter, P., Huignard, J.-P. (eds.): *Photorefractive Materials and Their Applications*. Springer, Berlin, Heidelberg (1989). Part I (1988), Part II (1989)
24. Brabec, T., Krausz, F.: *Phys. Rev. Lett.* **78**, 3283 (1997)
25. Ranka, J.K., Gaeta, A.L.: *Opt. Lett.* **23**, 534 (1998)
26. Rothenberg, J.E.: *Opt. Lett.* **17**, 1340 (1992)
27. Yang, G., Shen, Y.R.: *Opt. Lett.* **9**, 510 (1984)
28. Ranka, J.K., Schirmer, R., Gaeta, A.L.: *Phys. Rev. Lett.* **77**, 3783 (1996)
29. Gaeta, A.L.: *Phys. Rev. Lett.* **84**, 3582 (2000)
30. Ranka, J.K., Windeler, R.S., Stentz, A.J.: *Opt. Lett.* **25**, 25 (2000)
31. Jones, D.J., Diddams, S.A., Ranka, J.K., Stentz, A., Windeler, R.S., Hall, J.L., Cundiff, S.T.: *Science* **288**, 635 (2000)
32. Kaiser, W., Garrett, C.G.B.: *Phys. Rev. Lett.* **7**, 229 (1961)
33. Sprangle, P., Tang, C.-M., Esarey, E.: *IEEE Trans. Plasma Sci.* **15**, 145 (1987)
34. Wagner, R., Chen, S.-Y., Maksemchak, A., Umstadter, D.: *Phys. Rev. Lett.* **78**, 3125 (1997)
35. Agostini, P., Fabre, F., Mainfray, G., Petite, G., Rahman, N.K.: *Phys. Rev. Lett.* **42**, 1127 (1979)
36. Chang, Z.: *Phys. Rev. Lett.* **79**, 2967 (1997)
37. Chang, Z.: *Phys. Rev. Lett.* **82**, 2006 (1999)
38. Corkum, P.B.: *Phys. Rev. Lett.* **71**, 1994 (1993)
39. Kienberger, H.R., Spielmann, C., Reider, G.A., Milosevic, N., Brabec, T., Corkum, P., Heinzmann, U., Drescher, M., Krausz, F.: *Nature* **414**, 509 (2001)
40. Maier, S.A.: *Plasmonics: Fundamentals and Applications*. Springer, New York (2007)
41. Vial, A., Grimault, A.S., Macías, D., Barchiesi, D., Lamy De La Chapelle, M.: *Phys. Rev. B* **71**, 085416 (2005)
42. Alam, M.Z., De Leon, I., Boyd, R.W.: *Science* **352**, 795 (2016)
43. Reshef, O., Giese, E., Alam, M.Z., De Leon, I., Upham, J., Boyd, R.W.: *Opt. Lett.* **42**, 3225 (2017)
44. Hache, F., Ricard, D., Flytzanis, C.: *J. Opt. Soc. Am. B* **3**, 1647 (1986)
45. Hache, F., Ricard, D., Flytzanis, C., Kreibig, U.: *Appl. Phys. A Mater. Sci. Process.* **47**, 347 (1988)
46. Boyd, R.W., Shi, Z., De Leon, I.: *Opt. Commun.* **326**, 74 (2014)
47. Clerici, M., et al.: *Nat. Commun.* **8**, 15829 (2017)



Robert Boyd Robert Boyd received the BS degree in Physics from MIT and the PhD degree from UC Berkeley under the supervision of Charles Townes. Dr Boyd holds faculty appointments at the University of Rochester and University of Ottawa. His research interests include optical physics and quantum effects in nonlinear optics. He has written two textbooks.



Alexander L. Gaeta Alexander Gaeta received his BS, MS, and PhD in Optics from the University of Rochester in Rochester, NY in 1983, 1985, and 1991, respectively. He remained there as a postdoctoral associate from 1991 to 1992. Gaeta joined Columbia Engineering as the David M. Rickey Professor of Applied Physics and Materials Science in 2015. Prior to that, Gaeta was the Samuel B. Eckert Professor of Engineering at Cornell University and was Chair of the School of Applied and Engineering Physics from 2011 to 2014. He is a Fellow of the American Physical Society, the Institute of Electrical and Electronics Engineers, and of Optica (formerly the Optical Society of America) and is also the founding Editor-in-Chief of the journal *Optica*.



Enno Giese Enno Giese received his Dr rer nat from Ulm University in 2015 and subsequently worked on quantum nonlinear optics, quantum imaging, and nonlinear interferometry in the Department of Physics, University of Ottawa. His current position is at the Technical University of Darmstadt, where he focuses on matter wave optics and interferometry in microgravity and in curved space–time for tests of relativity.



Coherent Transients

77

Joseph H. Eberly and Carlos R. Stroud Jr.

Contents

77.1	Introduction	1112
77.2	Origin of Relaxation	1112
77.3	State Evolution	1113
77.4	Numerical Estimates of Parameters	1114
77.5	Homogeneous Relaxation	1114
77.5.1	Rabi Oscillations	1114
77.5.2	Bloch Vector and Bloch Sphere	1114
77.5.3	Pi Pulses and Pulse Area	1115
77.5.4	Adiabatic Following	1115
77.6	Inhomogeneous Relaxation	1116
77.6.1	Free Induction Decay	1116
77.6.2	Photon Echoes	1117
77.7	Resonant Pulse Propagation	1117
77.7.1	Maxwell–Bloch Equations	1117
77.7.2	Index of Refraction and Beer’s Law	1117
77.7.3	The Area Theorem and Self-Induced Transparency	1118
77.8	Multilevel Generalizations	1118
77.8.1	Rydberg Packets and Intrinsic Relaxation	1118
77.8.2	Multiphoton Resonance and Two-Photon Bloch Equations	1119
77.8.3	Pump-Probe Resonance and Dark States	1120
77.8.4	Induced Transparency	1121
77.9	Disentanglement and “Sudden Death” of Coherent Transients	1121
	References	1123

Abstract

Coherent transients are excited in atomic and molecular systems when a phase relation is able to persist at least

J. H. Eberly (✉)
Dept. of Physics and Astronomy, University of Rochester
Rochester, NY, USA
e-mail: eberly@pas.rochester.edu

C. R. Stroud Jr.
The Institute of Optics, University of Rochester
Rochester, NY, USA
e-mail: stroud@optics.rochester.edu

semistably between an exciting light field and the system’s response. A steady state can occur whenever the multiplicity of “reservoir” effects in the background has reached a stable average. The theory of coherent transients typically makes an important distinction between two types of average, labeled either *homogeneous* or *inhomogeneous*. The terms refer to the type of randomness existing over the experimental “system” and originating in the system’s environment.

An example of inhomogeneous randomness and relaxation to a steady state is found in the distribution of transition frequencies of otherwise identical atoms or molecules trapped as impurities in a host crystal and arising from the host crystal’s random strain fields, which induce a permanent energy-level shift in each of the impurities under study. These unchanging level shifts allow, in principle, the experimenter to assign permanent energy-level information in a one-by-one way to system members.

Examples of homogeneous randomness are also common. For example, because of continuing collisions, energy-level shifts throughout a vapor cell are random and are constantly changing. Their effect is individually transient, and any consequent relaxation effects are observable only homogeneously over the entire sample, allowing no information to be retained about individual atoms and molecules.

We remark at the end of this chapter that the existence of vector-space non factorization, called “quantum entanglement” by Schrödinger in 1935, leads to nonintuitive effects in transients that are currently still under some discussion as not being completely explained. One example is the predicted, and multiply observed, phenomenon labelled ESD, which stands for entanglement sudden death.

Keywords

wave packet · Rabi frequency · free induction decay · Rabi oscillation · Bloch sphere · photon echo · Area theorem · qubit

77.1 Introduction

When an electromagnetic field is incident on matter it polarizes the matter by causing a displacement between the electrons and the nuclei. As the electromagnetic field oscillates the induced polarization also oscillates. The nature of this induced oscillation is determined by both the incident field and the internal dynamics of the matter. This same physics occurs whether the matter is made of isolated atoms or molecules, dopant atoms, quantum dots, or color centers in a host medium, or bulk matter: an insulator, semiconductor or metal. The bulk matter might even be an electronic circuit in the form of a radio receiver or a superconducting quantum interference device (SQUID).

For all of these systems, the energy is exchanged between the field and the matter according to

$$\frac{dW_m}{dt} = \int d^3r \mathbf{J} \cdot \mathbf{E}, \quad (77.1)$$

where W_m is the energy of the matter, \mathbf{J} is the induced current, and \mathbf{E} is the electric field. This relation holds both for classical variables and the corresponding quantum operators. For most cases of interest, the dipole approximation is appropriate. The atoms, molecules, and quantum dots are small compared with the wavelength of optical fields, and the circuits are small compared with the wavelength of the microwave fields with which they interact. The electric field is then constant over the integration region and can be taken outside the integral. The integral over the current density can then be carried out reducing the energy absorption integral to

$$\frac{dW_m}{dt} = \frac{d\mathbf{p}}{dt} \cdot \mathbf{E}, \quad (77.2)$$

where \mathbf{p} is the dipole moment associated with the absorber.

If both the field and the induced dipole are oscillatory, then whether the matter is absorbing or emitting energy depends on the phase relation between the two. Coherent optical transients are excited in a quantum system when a stable phase relation persists between (typically) an exciting electric field and the system's electronic response. The extreme sensitivity of phase-dependent effects is responsible for the many applications of optical transient techniques in atomic, molecular and optical (AMO) physics [1–7]. While all of our discussion thus far applies equally to many classical or quantum systems, we must specialize somewhat to discuss the dynamic response of the induced polarization. We will assume that our dipole is associated with a single resonance in a quantum system. A quantum resonance is associated with two energy levels. We can usually ignore all of the other levels of quantum system and reduce our consideration to a “two-level atom”, equivalently in modern context in an atomic “qubit”. Even in the case of a superconducting cir-

cuit, the bias voltage can be adjusted to form such a two-level quantum system [8].

The coherent oscillations of the induced dipole are subject to the influence of the environment. One way that the dipole interacts with the environment is through the field that the dipole itself generates. This field interacts back on the dipole, causing damping and a frequency shift. In classical circuits, we refer to this as the *impedance of free space* and the frequency shift as *self-inductance* [9]. The impedance of free space is given exactly by

$$Z = \sqrt{\mu_0/\epsilon_0} = 120\pi \text{ (Ohms)}, \quad (77.3)$$

and the self-inductance depends on the exact shape of the dipole radiator. In the case of a circuit, this resistance and inductance will be a part of the impedance in the circuit. In the case of an atomic or molecular dipole, the impedance of free space will lead directly to the Einstein A-coefficient damping and the Lamb shift of the quantum transition. If the radiator is placed in a cavity, the self-field of the dipole radiator will be modified leading to the Purcell-effect-enhanced damping rate [10] and modification of the Lamb shift.

77.2 Origin of Relaxation

We will examine the transient effects that are present as a result of interactions that lead to relaxation. The first step is to mention the two types of relaxation, homogeneous and inhomogeneous, and to distinguish between coherent and incoherent evolution. Relaxation occurs whenever the environment of a physical system fluctuates randomly, that is, it is too irregular and too complex to be treated fundamentally. Typically, such fluctuation leads to degradation of some degree of regularity in the evolution of a particular subsystem of interest. The inability to track short-term irregularities requires signal-smoothing of some kind, and this means a loss of microscopic coherence. The time scales of environmental fluctuations determine the division between homogeneous and inhomogeneous decoherences, as follows.

When environmental fluctuations are sufficiently rapid that all dynamical systems in a macroscopic sample experience the whole range of fluctuations in a time that is short compared with the time scale of interest, the resultant relaxation is called homogeneous. If environmental differences exist randomly over a macroscopic sample, but change relatively slowly in time, then the relaxation is called inhomogeneous. As examples, weak distant collisions are experienced constantly by all atoms at thermal equilibrium in a vapor cell and give rise to homogeneous relaxation. If the vapor is sufficiently dilute, the same atoms may nevertheless retain their own individual velocities and, thus, transition frequencies for long times. These transition frequencies are

relatively fixed in time, as are the frequency shifts experienced by impurity atoms in crystal lattices. However, they are random over a distribution of shifts and give rise to inhomogeneous relaxation. Fundamentally, the distinction between homogeneous and inhomogeneous relaxation is artificial, depending on a separation of timescales that may not always exist. Nevertheless, when it exists, the distinction provides an extremely useful way to classify coherent transients. It is one of the foundations of the subject.

77.3 State Evolution

A very weakly excited dipole transition in a ground-state quantum system responds linearly to an applied time-dependent electric field. This is the case when transitions to upper quantum levels are negligibly excited, and this is the basis for classical and linear Lorentzian dielectric theory in Chap. 72. However, the generally unequal spacing of dipole-allowed levels introduces the possibility of partial or even complete transfer of occupation probability from the ground level to just one of the upper levels. If the transition frequency ω_0 between upper and lower levels is nearly resonant with ω , the frequency of the exciting electric field, one can, to first approximation ignore other levels and deal with a much-simplified “two-level” quantum system. Its wave function is then simply written in terms of lower and upper (ground and excited) states $|g\rangle$ and $|e\rangle$ and two complex time-dependent coefficients:

$$|\Psi(t)\rangle = c_g(t)|g\rangle + c_e(t)|e\rangle. \quad (77.4)$$

We will adopt the Hamiltonian described for such a two-state system in Eqs. (72.38)–(72.41):

$$H = \frac{\hbar\omega_0}{2}(|e\rangle\langle e| - |g\rangle\langle g|) - d\left[|e\rangle\langle g|E^+(t) + |g\rangle\langle e|E^-(t)\right], \quad (77.5)$$

and apply the Schrödinger equation $i\hbar\frac{\partial}{\partial t}|\Psi(t)\rangle = H|\Psi(t)\rangle$ to obtain equations of motion for the quantum state amplitudes. Some minor algebra leads to

$$i\hbar\dot{c}_g = -\frac{\hbar\omega_0}{2}c_g - dE^-(t)c_e, \quad (77.6)$$

$$i\hbar\dot{c}_e = -\frac{\hbar\omega_0}{2}c_e - dE^+(t)c_g, \quad (77.7)$$

where the positive and negative frequency radiation fields are defined in Eq. (72.30):

$$E^\pm(t) = \frac{1}{2}\mathcal{E}^\pm(t)e^{\mp i\omega t}, \quad (77.8)$$

with the understanding that $\mathcal{E}^\pm(t)$ is a field amplitude that is very slowly varying in comparison to the applied field’s carrier frequency oscillations $e^{\pm i\omega t}$.

Equations (77.6) and (77.7) for the level amplitudes can be used to obtain the equations of motion for the level probabilities $|c_g(t)|^2$ and $|c_e(t)|^2$, with an important conservation equation as a consequence:

$$\frac{d}{dt}\left(|c_g(t)|^2 + |c_e(t)|^2\right) = 0, \quad (77.9)$$

indicating that all of the initial probability remains confined to those two levels. Under these approximations, pure state evolution is fully conservative.

However, as indicated in Chap. 72, it is usually impossible to describe fully an interacting two-level system by a state vector such as Eq. (77.4) simply because of environmental fluctuations. There is no way, consistent with the two-level model, to add damping terms such as $-i\hbar\gamma c_e$ to a state amplitude equation such as Eq. (77.6) and (77.7) to account for the relaxation due to those fluctuations. The density matrix approach is required. The pure state Eq. (77.4) is equivalent to the fully coherent density matrix ρ_{coh} :

$$\begin{aligned} \rho_{\text{coh}} &\equiv |\Psi(t)\rangle\langle\Psi(t)| \\ &= \left(c_g(t)|g\rangle + c_e(t)|e\rangle\right)\left(\langle g|c_g^*(t) + \langle e|c_e^*(t)\right), \end{aligned} \quad (77.10)$$

with matrix elements $(\rho_{\text{coh}})_{ge} = c_g^*c_e$, etc. The actual density matrix is the same as the one in Eq. (77.10), after it has been averaged over environmental randomness:

$$\rho(t) = \begin{pmatrix} \rho(t)_{gg} & \rho(t)_{ge} \\ \rho(t)_{eg} & \rho(t)_{ee} \end{pmatrix}, \quad (77.11)$$

where $\rho(t)_{ge} = [c_g(t)c_e^*(t)]_{\text{avg.}}$, etc.

We note that restriction to two levels implies full conservation of level probability: $\rho_{gg} + \rho_{ee} = 1$, and the Hermitian character of ρ means that $\rho_{ge} = \rho_{eg}^*$, so that three real variables are sufficient to exhibit the entire temporal evolution of the two-level system’s density matrix. As in Chap. 72, we will denote by U and V the amplitudes of the components of the time-dependent dipole expectation value that are, respectively, in-phase and in-quadrature with the field. That is, U and V are given by

$$-\langle ex(t) \rangle = -\langle\Psi(t)|ex|\Psi(t)\rangle = \text{Re}\{d(U - iV)e^{-i\omega t}\}, \quad (77.12)$$

where d is the matrix element of the transition dipole. Still following Chap. 72, for simplicity both dipole moment matrix element and field amplitude have been taken to be real scalars. The complications of vector notation add little to a discussion of the principles of coherent transients.

Chapter 72.3.5 shows that U and V are dynamically coupled to each other and to the inversion W through three equations introduced by Felix Bloch initially for spin resonance theory and now called “optical Bloch equations” and commonly abbreviated as OBE:

$$\begin{aligned}\frac{dU}{dt} &= -\Delta V, \\ \frac{dV}{dt} &= \Delta U + \Omega_1 W, \\ \frac{dW}{dt} &= -\Omega_1 V.\end{aligned}\quad (77.13)$$

Furthermore, Bloch showed that weak Markovian interactions with environmental oscillators had the effect of decohering the evolution of U , V , and W in specific ways. These decohering influences can be accounted for by adding damping terms into the U , V , and W (i.e., density matrix) equations, rather than into the state vector equations. Chap. 72 shows that when Bloch’s damping terms are included, the OBEs are given by Eq. (72.55):

$$\begin{aligned}\frac{dU}{dt} &= -\Delta V - U/T_2, \\ \frac{dV}{dt} &= \Delta U + \Omega_1 W - V/T_2, \\ \frac{dW}{dt} &= -\Omega_1 V - (W - W_{\text{eq}})/T_1,\end{aligned}\quad (77.14)$$

where $\Delta = \omega_0 - \omega$ is the detuning, and the so-called Rabi frequency Ω_1 is given by $\hbar\Omega_1 = d\mathcal{E}$. These are the key equations of the theory of optical transients [1, 2].

Clearly, Ω_1 is, in frequency units, the dipole interaction energy between the electric field and the quantum system, but it has a significance beyond this, as is discussed in Sect. 77.5.2.

77.4 Numerical Estimates of Parameters

The nature of the coherent interaction between a quantum system and a time-dependent electric field is controlled by the relative size of a number of frequencies or rates. In the case of single-photon transitions, they include Δ and Ω_1 , the detuning and Rabi frequency defined above, $1/T_2$ the transverse, and $1/T_1$ the longitudinal damping rates, given in Eq. (77.14) and $1/T^*$ the inhomogeneous linewidth, and $2\pi/\tau_p$ the transform bandwidth of the exciting field or pulse. All of these frequencies are defined in Chap. 2, with the exception of the last, so we should mention its effect.

A wide excitation bandwidth can overcome the two-level assumption by leading to excitation of several or many levels beyond the single one we have been calling “upper”. This can occur with any exciting pulse, from radio and microwave to X-ray frequencies, if the pulse is short enough to provide

a bandwidth that engages some or many other “resonances”. For perspective, in the atomic case, one can note that with $\tau_p \geq 1$ ns and with an intensity less than about 1 GW/cm², a laser pulse can be tuned to an isolated atomic resonance, and the interaction can be described in terms of a simple two-level theory. However, laser pulses as short as a few fs in duration, or with intensities greater than 10²⁰ W/cm², are available, and such pulses can quasi-resonantly excite many more than just one upper level. For example, if a 1 ps pulse (bandwidth approximately 20 cm⁻¹) were tuned so that it resonantly excited the $n = 95$ Rydberg state of an atom, it would also simultaneously and coherently excite all the levels from $n = 67$ to the continuum limit, while a 10 fs pulse would excite all the levels from $n = 4$ to the continuum. In other extended cases, in which multiphoton transitions are possible, or simultaneous excitation by a number of near-resonant fields occurs, the appropriately generalized versions of these same parameters apply.

77.5 Homogeneous Relaxation

Homogeneous relaxation is ubiquitous and can be dominant when the wave function phase is rapidly and irregularly interrupted, as from quantum acoustic or other collisional interactions. In the absence of an exciting field (i.e., $\Omega_1 = 0$), the solutions of the OBEs are

$$\begin{aligned}(U - iV) &= (U_0 - iV_0) e^{-(1/T_2 + i\Delta)t}, \\ W &= -1 + (W_0 + 1) e^{-t/T_1},\end{aligned}\quad (77.15)$$

where the subscripts denote values at $t = 0$. Then the roles of T_1 and T_2 as relaxation times are clear. They are homogeneous because they apply to each atom individually.

77.5.1 Rabi Oscillations

The OBEs predict damped, although well-defined (coherent, many-period) oscillations of the inversion W with the angular frequency Ω_1 even in the presence of T_1 and T_2 if Ω_1 is large enough: $\Omega_1 T_1 \gg 1$ and $\Omega_1 T_2 \gg 1$. These are usually called *Rabi oscillations* and were originally called *optical nutations* following the terminology of nuclear magnetic resonance. Figure 77.1 shows the behavior of the Bloch variables undergoing Rabi oscillations in a representative case.

77.5.2 Bloch Vector and Bloch Sphere

Coherent dynamical behavior is simplest for times much shorter than the relaxation times T_1 and T_2 . In this case, the

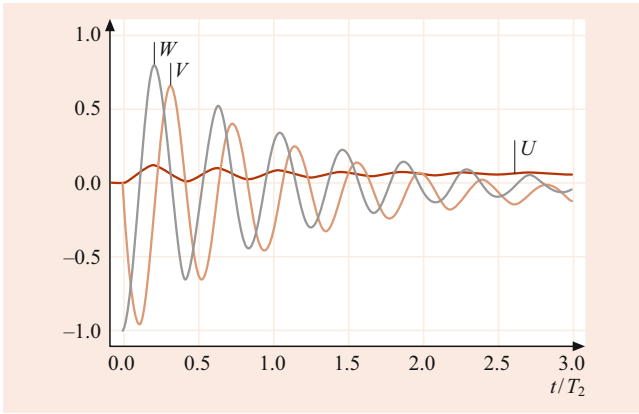


Fig. 77.1 Damped Rabi oscillations of the atomic variables after sudden turn-on of the field. In this example, $T_1 = T_2$, $\Delta T_2 = 1$, and $\Omega_1 T_2 = 15$

damping terms can be dropped from the OBEs and the resulting equations can be written in the form (Chap. 72.3.5)

$$\frac{d\mathbf{U}}{dt} = \boldsymbol{\Omega} \times \mathbf{U} \quad \text{with} \quad \boldsymbol{\Omega} = (-\Omega_1, 0, \Delta), \quad (77.16)$$

where $\mathbf{U} = (U, V, W)$ is the Bloch vector, and $\boldsymbol{\Omega}$ acts as a torque vector defining the axis and rate of precession. Conservation of probability is reflected in the unit length of the undamped Bloch vector: $\mathbf{U} \cdot \mathbf{U} = 1$.

All possible states of an undamped two-level quantum system can be mapped onto a unit sphere in U - V - W space. Conventionally, W defines the polar axis with the ground state at the south pole, and the excited state at the north pole. Points on the sphere surface between the poles represent coherent superpositions of the two states. The azimuthal angle ϕ represents the phase between the expectation value of the quantum dipole moment and the incident field. In Fig. 77.2, the solutions to Eq. (77.16) are shown for the case of a square pulse applied to the system in its ground state at $t = 0$. The solutions in this case are

$$\begin{aligned} U(t, \Delta) &= \frac{\Omega_1}{\Omega} \sin \Omega t, \\ V(t, \Delta) &= -\frac{\Delta \Omega_1}{\Omega^2} (1 - \cos \Omega t), \\ W(t, \Delta) &= -1 + \frac{\Omega_1^2}{\Omega^2} (1 - \cos \Omega t). \end{aligned} \quad (77.17)$$

For any Δ , the solution orbit is a circle on the surface of the sphere with the orbit passing through the south pole. The rate at which the system precesses about the circle is given by the *generalized Rabi frequency* $\Omega \equiv \sqrt{\Delta^2 + \Omega_1^2}$.

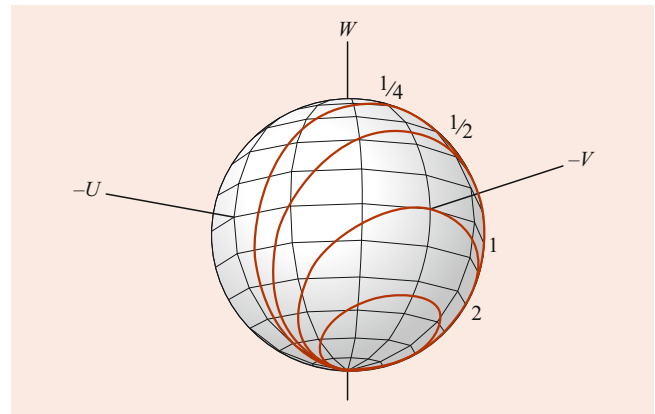


Fig. 77.2 Orbits of the Bloch vector on the unit sphere for various ratios of the detuning Δ to the Rabi frequency Ω_1

77.5.3 Pi Pulses and Pulse Area

The exactly resonant ($\Delta = 0$) undamped OBEs can be solved analytically even for arbitrarily time-dependent exciting pulse envelopes. The solutions are

$$\begin{aligned} U(t, 0) &= 0, \\ V(t, 0) &= -\sin \theta(t), \\ W(t, 0) &= -\cos \theta(t), \end{aligned} \quad (77.18)$$

a rotation of the Bloch vector in the V - W plane. The rotation angle θ is called the *pulse area*, defined by the integrale

$$\theta(t) \equiv \int_{-\infty}^t dt' \Omega_1(t') = \frac{d}{\hbar} \int_{-\infty}^t dt' \mathcal{E}(t'). \quad (77.19)$$

The area under the envelope of the Rabi frequency is the same as the angle through which an exactly-resonant Bloch vector turns due to the pulse. If $\theta = \pi$, the system is driven from the ground state exactly to the excited state. This is “ π -pulse” inversion. A “ 2π -pulse” takes the system from the lower state through the excited state and back to the lower state. The Bloch vector rotation angle does not depend upon the shape of the field pulse, only on the area of the pulse.

77.5.4 Adiabatic Following

The Bloch vector picture for fixed Δ and Ω_1 can be used for semiquantitative predictions even if Δ and Ω_1 are time dependent, if they change slowly. For example, if $\boldsymbol{\Omega}$ is moved slowly, the Bloch vector follows closely. It is possible to achieve complete inversion smoothly in this way. If the field is initially tuned far below resonance so Δ is large and negative, then $\boldsymbol{\Omega}$ points approximately toward the south pole of the Bloch sphere. As shown in Fig. 77.3, the Bloch vector

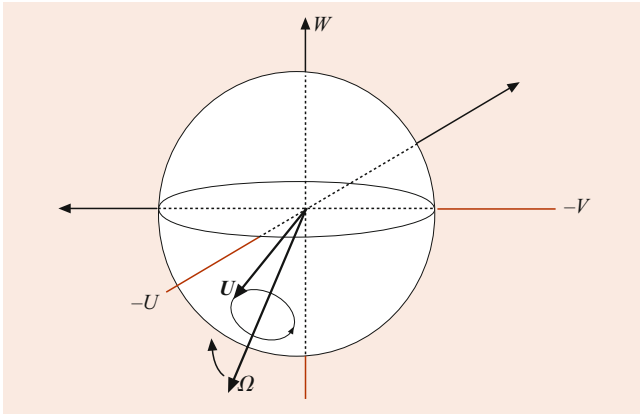


Fig. 77.3 In adiabatic inversion, the Bloch vector precesses in a small cone about the torque vector as the torque vector goes from straight down to straight up

then precesses about the torque vector in a very small circle near the south pole. If the field frequency is now slowly changed (chirped) so that Δ goes from a large negative value to a large positive value, then every atomic Bloch vector will continue to precess rapidly around the torque vector and follow it as it proceeds from pointing nearly straight down to pointing nearly straight up. In this way, the population can be transferred from lower to upper levels.

77.6 Inhomogeneous Relaxation

The fact that individual otherwise identical quantum systems in a sample may have slightly different resonance frequencies produces a number of notable phenomena. Given a distribution $g(\Delta)$ of detunings in a dilute sample of density N , the macroscopic collective polarization can be written as

$$P(t) = -N \langle ex(t) \rangle = Nd \int g(\Delta) \text{Re} [(U - iV) e^{-i\omega t}] d\Delta . \quad (77.20)$$

77.6.1 Free Induction Decay

Free induction refers to evolution of the polarization in the absence of an exciting field. For $\Omega_1 = 0$, the Bloch vector of a system with $\Delta < 0$ precesses counterclockwise in the “transverse” $U-V$ plane. In a macroscopic sample, there are many values of Δ , and about as many are positive as negative. Thus, a collection of Bloch vectors, all pointing in the V direction at $t = 0$, will rapidly fan out in the $U-V$ plane due to differing positive and negative Δ precession rates, and after a short time, the net U and V values will be zero. This is free induction decay (FID) of polarization and is indicated in the top row of Fig. 77.4.

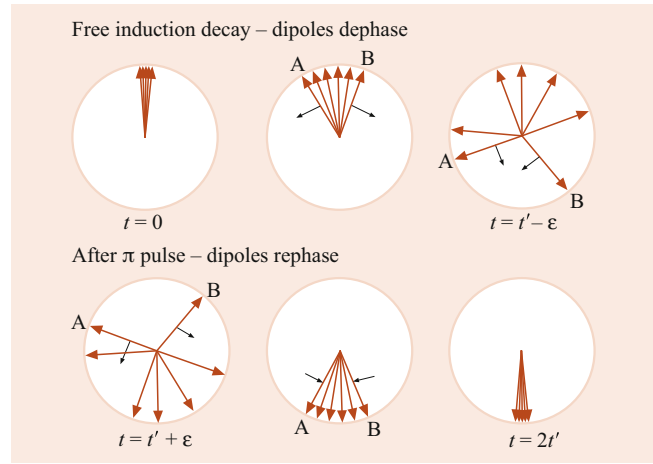


Fig. 77.4 The ensemble of dipole moments spreads due to the distribution of resonance frequencies. The distribution of Bloch vectors in the $U-V$ plane is shown at various times after the initial short-pulse excitation. By the time t' , the dipoles have spread uniformly around the unit circle. A π -pulse then flips the relative orientation of the dipoles, so that they subsequently rephase

More specifically, if all systems are first exposed to a θ_0 pulse, so that at $t = 0$

$$\begin{aligned} U(0, \Delta) &= 0 , \\ V(0, \Delta) &= -\sin \theta_0 , \\ W(0, \Delta) &= -\cos \theta_0 , \end{aligned} \quad (77.21)$$

then if $\mathcal{E} = 0$ for $t > 0$, an individual system with detuning Δ evolves according to Eq. (77.15):

$$U - iV = i \sin \theta_0 e^{-(1/T_2 - i\Delta)t} . \quad (77.22)$$

The macroscopic polarization is found by summing the individual $(U - iV)$ values over the detuning distribution $g(\Delta)$.

If we temporarily ignore competition from homogeneous decay (take $1/T_2 \approx 0$) and assume the most common inhomogeneous lineshape (i.e., Doppler–Maxwellian):

$$g(\Delta) = \frac{T^*}{\sqrt{2\pi}} e^{-(\Delta - \Delta_0)^2 T^{*2}/2} , \quad (77.23)$$

where $1/T^*$ is defined as the width (standard deviation) of the Doppler distribution, and Δ_0 is the detuning of the zero-velocity atoms, then the collective result is

$$P(t) = Nd \sin \theta_0 \sin \omega t e^{i\Delta_0 t} \exp(-t^2/2T^{*2}) . \quad (77.24)$$

The detuning “inhomogeneity” in the sample leads to dephasing of the collective dipole moment at the rate $1/T^*$, so the inhomogeneous relaxation time is obviously T^* . This is illustrated by the decrease of collective alignment of Bloch vectors in the top row of Fig. 77.4. The Doppler effect for

atoms makes a common example, and in a typical room temperature gas, a visible transition has a Doppler width given by $1/(2\pi T^*) \approx 1.5$ GHz so that $T^* \approx 10^{-10}$ s.

77.6.2 Photon Echoes

A photon echo is generated by pulse-induced *recovery* of a nonzero $P(t)$ after free induction decay (FID) and $P(t) \rightarrow 0$. This analog of the spin echo effect is possible when each near-resonant quantum system retains its own detuning for a relatively long time, i.e., up to an average collision time T_2 .

During FID, the U - V projection of every atom's Bloch vector precesses steadily clockwise or counterclockwise, depending on the sign of its Δ . Thus, the Bloch vectors could be rephased, if they could all be forced at the same moment to reverse their relative sense of precession. The prototypical echo scenario begins with FID at $t = 0$, as an established $P(t)$ approaches zero for $t \gg T^*$. This is followed by injection of a π -pulse at the time t' , where $t' \gg T^*$. The effect of the π -pulse is to reverse the sign of V and W (recall Eq. (77.21)), in effect flipping the equatorial plane of the Bloch sphere upside-down. Thus, for $t \gg t'$, we have Bloch vectors fanning back together. The macroscopic polarization obeys

$$P(t) = Nd \sin \theta_0 \sin \omega t \exp[-(t - 2t')^2/2T^{*2}] e^{-t/T_2}, \quad (77.25)$$

where the last factor reinserts the effect of homogeneous dipole damping. We require $T_2 \gg t' \gg T^*$ for a strong echo signal in the neighborhood of $t = 2t'$.

The result is illustrated in Fig. 77.4. An "echo" of the initial excitation at $t = 0$ appears at the time $t = 2t'$. After this, FID occurs again. This second decay can also be reversed by applying another π -pulse, and so on, until $t \approx T_2$, at which time the inevitable and irreversible homogeneous relaxation cannot be avoided. The scenario employing π -pulse reversal is only the most ideal, leading to the most complete echo, and other pulse areas will also lead to echoes. A more important factor is that the reversing pulse must be short enough that negligible dephasing takes place during its application.

77.7 Resonant Pulse Propagation

77.7.1 Maxwell–Bloch Equations

Time-dependent atomic dipole moments created by applied fields are themselves a source of fields, another form of coherent transient. We limit discussion to plane-wave propagation in the z -direction. Note that we use z rather than Z for convenience, although in the dipole approximation, the coordinate entering our equations is the coordinate of the center

of mass of the atom rather than the internal electron coordinate. The field is generalized from Eq. (77.2) to

$$E(t, z) = \frac{1}{2} [\mathcal{E}(t, z) e^{i(Kz - \omega t)} + \text{c.c.}], \quad (77.26)$$

and the macroscopic polarization is the correspondingly generalized form of Eq. (77.20):

$$P(t, z) = Nd \int g(\Delta) \text{Re}\{(U - iV) e^{i(Kz - \omega t)}\} d\Delta. \quad (77.27)$$

The difference between K and $k = \omega/c$ indicates that the refractive index is nonzero. The traveling-pulse rotating frame is also obtained by replacing ωt by $\omega t - Kz$.

If the field envelope \mathcal{E} is slowly varying, its second derivatives can be dropped when $E(t, z)$ is substituted into Maxwell's wave equation. The resulting dispersive and absorptive *reduced wave equations* are

$$\begin{aligned} [K^2 - k^2] \mathcal{E} &= 4\pi k^2 Nd \int g(\Delta) U(t, z, \Delta) d\Delta, \\ \left[K \frac{\partial}{\partial z} + k \frac{\partial}{\partial(ct)} \right] \mathcal{E} &= 2\pi k^2 Nd \int g(\Delta) V(t, z, \Delta) d\Delta. \end{aligned} \quad (77.28)$$

The Bloch equations along with these reduced wave equations form the *self-consistent Maxwell–Bloch equations* that are used to treat resonant propagation problems in quantum optics and laser theory [1, 2, 5, 11].

77.7.2 Index of Refraction and Beer's Law

If a weak field propagates in a ground-state medium ($W \approx -1$), the Bloch equations have simple quasi-steady-state solutions

$$U = \frac{\Omega_1 \Delta}{\Delta^2 + 1/T_2^2}, \quad (77.29)$$

$$V = \frac{-\Omega_1/T_2}{\Delta^2 + 1/T_2^2}. \quad (77.30)$$

When U and V are substituted back into the reduced wave equations Eq. (77.28), the dispersive equation gives the index of refraction $n = K/k$:

$$n^2 - 1 = \frac{4\pi Nd^2}{\hbar} \int \frac{\Delta g(\Delta)}{\Delta^2 + 1/T_2^2} d\Delta, \quad (77.31)$$

and the absorptive equation predicts steady-state field attenuation during propagation:

$$\frac{\partial}{\partial z} \mathcal{E} = -\frac{1}{2} \alpha_B \mathcal{E}. \quad (77.32)$$

The constant α_B given by

$$\alpha_B = \frac{4\pi N d^2 \omega}{\hbar c T_2} \int \frac{g(\Delta)}{\Delta^2 + 1/T_2^2} d\Delta \quad (77.33)$$

is called the *extinction coefficient* or the *reciprocal Beer's length*.

Since field intensity $I(z)$ is proportional to \mathcal{E}^2 , the solution to the absorptive equation is

$$I(z) = I(0) e^{-\alpha_B z} . \quad (77.34)$$

This relation is called Beers law. Both the dispersive and absorptive results are familiar from classical physics [12], with the important distinction that here the quantum \hbar -dependence is apparent in the oscillator strength, which is only an empirical parameter in Lorentzian dielectric theory [11, 12].

77.7.3 The Area Theorem and Self-Induced Transparency

A form of pulse propagation with no classical analog arises in the short-pulse limit. By integration over the entire pulse, the absorptive Maxwell equation becomes an equation for $\partial\theta/\partial z$, where θ is the pulse area defined in Eq. (77.19). In the short-pulse limit, the relaxation terms in the OBEs can be ignored and when substituting from the OBEs we obtain the *McCall–Hahn area theorem* [1]:

$$\frac{\partial}{\partial z} \theta(z) = -\frac{1}{2} \alpha_B \sin \theta(z) . \quad (77.35)$$

When $\sin \theta \approx \theta$, this predicts the same exponential attenuation as Eq. (77.32) for the case of a small area pulse, $\theta(z) \ll \pi$, but in the case of larger area pulses, the behavior dictated by Eq. (77.35) is quite different. The area decreases during propagation for areas in the range $0 < \theta(z) < \pi$, but it *increases* for areas $\pi < \theta(z) < 2\pi$. As seen from Fig. 77.5, this change of area with propagation causes the pulse area to evolve to one of the stable values $0, 2\pi, 4\pi, \dots$

There is one special pulse, a *soliton* solution with area exactly 2π , which propagates without shape change in the short-pulse limit, given by

$$\mathcal{E}(t, z) = \frac{2\hbar}{\tau d} \operatorname{sech}\left(\frac{t - z/v}{\tau}\right) , \quad (77.36)$$

where τ is the pulse duration, which is arbitrary but must satisfy the short-pulse inequality $\tau \ll T_1, T_2$. The soliton's group velocity is determined by the dispersive wave equation to be

$$v = \frac{c}{1 + \frac{1}{2} \alpha_B c \tau} . \quad (77.37)$$

The group velocity can be slower than the speed of light by orders of magnitude if $\alpha_B c \tau \gg 1$.

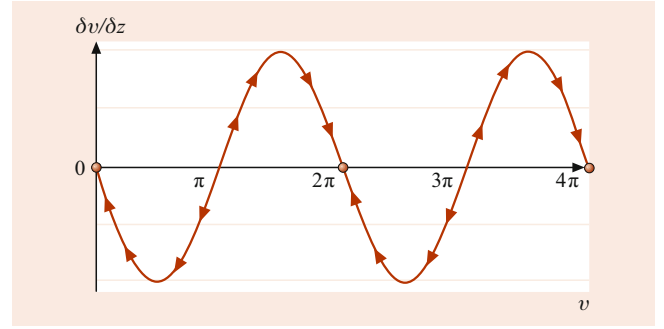


Fig. 77.5 McCall–Hahn area theorem for an absorbing medium. On propagation the area of the pulse will follow the arrows toward one of the stable values, $0, 2\pi, 4\pi, \dots$

77.8 Multilevel Generalizations

77.8.1 Rydberg Packets and Intrinsic Relaxation

A short laser pulse can populate a band of excited states, and their probability amplitudes will exhibit mutual coherence [13]. This single-atom coherence is transient, even without collisions or other external perturbations to disrupt it, and its decay can be called *intrinsic relaxation*. The decay is basically a dephasing. The dipole moments associated with the excited band interfere due to the wide variety of resonance frequencies of the states in the superposition. Because of the discreteness of the energy levels of any bound quantum system, this relaxation has its own unique characteristics, including similarities with both homogeneous and inhomogeneous decay.

The wave function for a coherently excited system can be expressed in the interaction picture in the form [13]

$$\Psi(r, t) = a(t) \psi_g(r) + \sum_n b_n(t) e^{-i\omega_n t} \psi_n(r) , \quad (77.38)$$

where $\psi_g(r)$ is the ground-state wave function, and n labels the states in an upper band with excitation frequencies $\omega_n \approx \omega$. If $|\omega_n - \omega| \ll \omega_n$, the transition frequency ω_n can be expanded about the principal quantum number \bar{n} of the resonant excited state $E_{\bar{n}} = \hbar\omega$ to obtain

$$\begin{aligned} \omega_n &= \omega_{\bar{n}} + (n - \bar{n}) \frac{\partial \omega_n}{\partial n} + \frac{1}{2!} (n - \bar{n})^2 \frac{\partial^2 \omega_n}{\partial n^2} + \dots \\ &= \omega_{\bar{n}} + (n - \bar{n}) \frac{2\pi}{T_K} + (n - \bar{n})^2 \frac{2\pi}{T_R} + \dots \end{aligned} \quad (77.39)$$

Thus, $2\pi/T_K$ is the mean frequency separating neighboring levels, i.e., $T_K/2\pi = \hbar\rho(E)$, where $\rho(E)$ is the density of excited states, and $2\pi/T_R$ is the mean change in this frequency separation; T_K is the same as the *Kepler period* of a classical orbit, and T_R is the *revival time*. Substituting the Bohr frequencies into the definitions for T_K and T_R yields $T_R = \bar{n}T_K/3$.

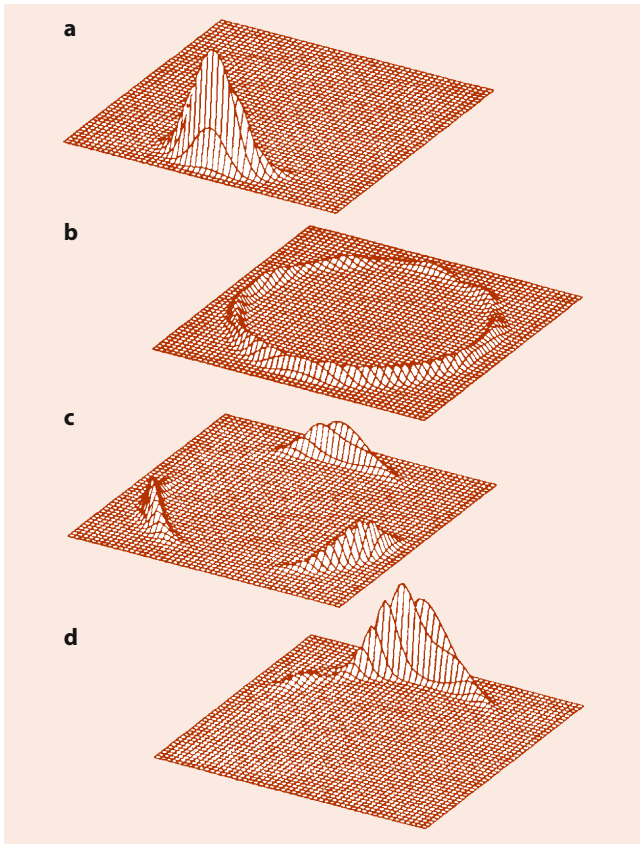


Fig. 77.6 The free evolution of a Rydberg wave packet made up of a superposition of circular-orbit states centered about $n = 360$. (a) Initially, the wave packet is to good approximation a minimum uncertainty wave packet in all three dimensions, but after 12 orbits, (b) the packet has spread all the way around the orbit so that the head and tail of the wave packet overlap, producing interference fringes. (c) After 40 orbits, $t = T_R/3$, the fringes have produced the one-third fractional revival in which three miniature replicas of the original wave packet are equally spaced around the orbit. (d) After 120 orbits, $t = T_R$, the complete wave packet revival occurs

For times $t \leq T_R$, the expansion can be truncated after the third term. Then the wave function is given approximately by

$$\Psi(r, t) \approx a(t)\psi_g(r) + e^{-i\omega\pi t} \sum_m b_{\bar{n}+m}(t) e^{-i2\pi m t/T_K} \times e^{-i2\pi m^2 t/T_R} \psi_{\bar{n}+m}(r), \quad (77.40)$$

where $m = n - \bar{n}$. For high Rydberg states, $\bar{n} \gg 1$, the timescales associated with the two exponentials inside the sum are quite different. For times $t \ll T_K$, the individual levels are not resolved, thus the laser excites what is effectively a continuum with a density of states $\rho(E)$. In that case, the ground-state population simply decays exponentially at the rate given by first-order perturbation theory, $\Gamma = (2\pi/\hbar)d^2\mathcal{E}^2\rho(E)$. At longer times $t \approx T_K$, the first exponential contributes, but the second does not, giving a simple Fourier series time dependence. In this regime, the evolution of the wave function is just periodic motion of a wave packet around a Kepler orbit, as is illustrated in Fig. 77.6a.

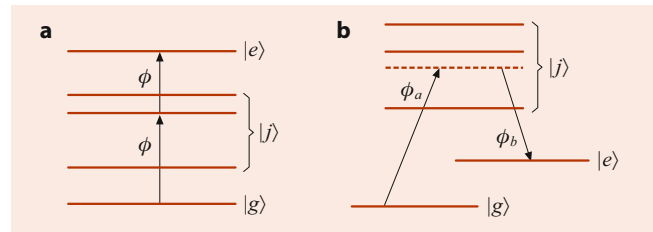


Fig. 77.7 Model two-photon resonances. Two photons couple the ground state $|g\rangle$ with an excited state $|e\rangle$. Many intermediate nonresonant levels $|j\rangle$ are present. In (a) we have the cascade system and in (b) the Λ pump-probe system

The coherent quantum wave packet behaves like a classical particle for many Kepler periods, gradually spreading out as the second exponential in the sum Eq. (77.40) begins to contribute. This spreading of the wave packet produces the intrinsic relaxation of the collective dipole moments from the various transitions. However, because the levels are discrete, this decay is not permanent but is reversed and leads to a spontaneous “revival” of the original wave packet [6], without the need for a π -pulse to produce an “echo”.

In its evolution toward the revival, the wave packet passes through a number of *fractional revivals* in which miniature replicas of the original wave packet are equally spaced around the orbit, each traveling at the velocity of a particle traveling in a corresponding classical Kepler orbit. This complex time evolution arises from the spreading of the wave packet all the way around the orbit, so that the head and tail of the packet interfere with each other, producing interference fringes. The further evolution of this fringe pattern produces the various revival phenomena shown in Fig. 77.6.

77.8.2 Multiphoton Resonance and Two-Photon Bloch Equations

Multiphoton transitions (Fig. 77.7a) introduce new coherent transient phenomena. If levels $|g\rangle$ and $|e\rangle$ have the same parity, two photons from the same laser field are sufficient to excite level $|e\rangle$. For simplicity, we regard $|e\rangle$ as a single state, but any number of intermediate levels $|j\rangle$ of opposite parity may be present.

Substituting the state vector

$$|\Psi(t)\rangle = a_g(t)|g\rangle + \sum_j b_j(t) e^{-i\omega t} |j\rangle + a_e(t) e^{-i2\omega t} |e\rangle \quad (77.41)$$

into the Schrödinger equation yields

$$i \frac{da_g}{dt} = -\frac{1}{2} \sum_j \Omega_{gj} b_j, \quad (77.42)$$

$$i \frac{db_j}{dt} = \Delta_{jg} b_j - \frac{1}{2} [\Omega_{jg} a_g + \Omega_{je} a_e], \quad (77.43)$$

$$i \frac{da_e}{dt} = \Delta_{eg} a_e - \frac{1}{2} \sum_j \Omega_{ej} b_j, \quad (77.44)$$

where the Δ s are the detunings, and the Ω s are the Rabi frequencies for the dipole-allowed transitions. For example, $\Omega_{gj} = d_{gj} \mathcal{E} / \hbar$, and $\Delta_{jg} = (E_j - E_g) / \hbar - \omega$ and $\Delta_{eg} = (E_e - E_g) / \hbar - 2\omega$.

If the states $|j\rangle$ are not too close to resonance, the b_j oscillate rapidly and to a first approximation average to zero. A better approximation is to retain the small nonzero solution for b_j obtained by setting $db_j/dt = 0$ in Eq. (77.43) to obtain

$$b_j = -\frac{[\Omega_{jg} a_g + \Omega_{je} a_e]}{2\Delta_{jg}}, \quad (77.45)$$

which can be used to eliminate b_j from the equations for a_g and a_e . This is called *adiabatic elimination* of dipole coherence. In this approximation, levels $|g\rangle$ and $|e\rangle$ are directly coupled to each other, and *two-photon coherence* arises. The coupling of levels $|g\rangle$ and $|e\rangle$ is similar to the two-level coupling described in Sects. 77.3–77.6, and *two-photon Bloch equations* analogous to Eq. (77.16) are the result:

$$\begin{aligned} \frac{dU^{(2)}}{dt} &= -\Delta^{(2)} V^{(2)}, \\ \frac{dV^{(2)}}{dt} &= \Delta^{(2)} U^{(2)} + \Omega^{(2)} W^{(2)}, \\ \frac{dW^{(2)}}{dt} &= -\Omega^{(2)} V^{(2)}. \end{aligned} \quad (77.46)$$

Here the superscript (2) indicates that the variables are identified with the two-photon $|g\rangle \rightarrow |e\rangle$ transition.

The various coefficients are similarly generalized [14]. For example, the two-photon Rabi frequency is given by

$$\Omega^{(2)} \equiv \frac{1}{2} \sum_j \frac{d_{gj} d_{je}}{\hbar^2 \Delta_{jg}} \mathcal{E}^2, \quad (77.47)$$

and the *two-photon detuning* $\Delta^{(2)}$ incorporates the laser-induced level shifts

$$\begin{aligned} \Delta^{(2)} &\equiv \Delta_{ej} + \Delta_{jg} \\ &+ \frac{1}{4} \sum_j \frac{|d_{ej}|^2 \mathcal{E}^2(t)}{\hbar^2 \Delta_{ej}} + \frac{1}{4} \sum_j \frac{|d_{jg}|^2 \mathcal{E}^2(t)}{\hbar^2 \Delta_{jg}}. \end{aligned} \quad (77.48)$$

The last two terms give the difference in the *AC Stark shifts* of the upper and lower levels produced by the laser field.

As before, $W^{(2)}$ is the inversion, but $U^{(2)}$ and $V^{(2)}$ are somewhat different. They cannot be directly tied to the expectation value of a dipole moment because here levels $|g\rangle$ and

$|e\rangle$ have the same parity. Thus, the quantity $U^{(2)} - iV^{(2)}$ is the two-photon analog of $U - iV$ in the original OBEs; however, it cannot serve as a source term in the Maxwell equation.

In the case of continuous wave (CW) applied fields, the solutions to the two-photon OBEs are formally identical to those for a two-level atom. In the case of pulsed fields, however, the detuning $\Delta^2(t)$ is automatically “chirped” in frequency by the Stark shifts. This chirping may significantly modify the dynamics. Multiphoton generalizations of the Bloch equations can be made for other arrangements and numbers of levels. The two-photon version applies to three-level **A** and **V** configurations as well as to the *cascade* system shown in Fig. 77.7a, for which they were derived.

77.8.3 Pump-Probe Resonance and Dark States

Dark states or *trapping states* occur whenever a field-dependent linear combination of active levels is dynamically disconnected from the other levels. This occurs, e.g., in a pump-probe interaction, which fits the scenario of Fig. 77.7b, if two lasers instead of one are used to excite level $|e\rangle$ from the ground level via two-photon resonance. A strong steady laser a is applied for the $|g\rangle \rightarrow |j\rangle$ transitions and a weak tunable “probe” laser b for the $|j\rangle \rightarrow |e\rangle$ transitions. In the simplest format, $\Delta_{eg} = 0$, and all the $|j\rangle$ levels can be combined into a single level labeled $|2\rangle$.

The three-level state vector can be written in terms of field-free states

$$|\Psi(t)\rangle = a_g |g\rangle + b_2 |2\rangle + a_e |e\rangle, \quad (77.49)$$

or, in terms of field-dependent dressed states,

$$|\Psi(t)\rangle = A_T |T\rangle + b_2 |2\rangle + A_S |S\rangle, \quad (77.50)$$

where $\Omega|T\rangle \equiv \Omega_a |e\rangle - \Omega_b |g\rangle$, $\Omega|S\rangle \equiv \Omega_a |g\rangle + \Omega_b |e\rangle$ and

$$A_S(t) \equiv \Omega^{-1} [\Omega_a a_g + \Omega_b a_e], \quad (77.51)$$

$$A_T(t) \equiv \Omega^{-1} [\Omega_a a_e - \Omega_b a_g]. \quad (77.52)$$

The normalizing factor is $\Omega \equiv \sqrt{\Omega_a^2 + \Omega_b^2}$.

The state $|T\rangle$ is an eigenvector of the three-level rotating wave approximation (RWA) Hamiltonian, with eigenvalue zero, and the amplitude $A_T(t)$ is a constant of motion. Thus, $|T\rangle$ is termed a *trapping state*, and the population in $|T\rangle$ is inaccessible to the (possibly very strong) laser fields. At two-photon resonance, this conclusion is robust, not depending strongly on the idealized conditions assumed here. In fact, A_T , the trapping state amplitude, is an adiabatic invariant, remaining constant to first order even under slow changes in Ω_a and Ω_b . In a pump-probe experiment, this trapping state is observed as an abrupt drop in probe absorption, as

the probe frequency is tuned through two-photon resonance. Since only two-photon resonance is required (both transitions can be equally detuned) this coherent transient effect has no analog in two-level physics.

The ideal method for exciting the trapping state from the ground state uses another coherent transient process called *counterintuitive pulse sequencing* in which pulse b is turned on first. The trapping state $|T\rangle$ is essentially the ground state $|g\rangle$ if $\Omega_a = 0$. Thus, if Ω_b is turned on first, and then Ω_a is turned on later, the ground state adiabatically becomes the trapping state, and all initial probability flows smoothly with it.

An essential point is the ease with which pump-probe adiabaticity is maintained, particularly for strong fields on resonance, in contrast to one-photon adiabaticity, which is never achieved at strong-field resonance. In the pump-probe case, one must only satisfy the inequality

$$\left| \frac{d\Omega_a}{dt} \Omega_b - \frac{d\Omega_b}{dt} \Omega_a \right| \ll (\Omega_a^2 + \Omega_b^2)^{3/2}, \quad (77.53)$$

which is automatically accomplished by counterintuitive pulse sequencing. The inequality allows one to tolerate a rapid change of Ω_b while $\Omega_a = 0$. Then after Ω_b has reached a high value, Ω_a can also be turned on very rapidly because the right-hand side of Eq. (77.53) is already very large. This is “counterintuitive” excitation because if the population is in level $|g\rangle$, it is “natural” to turn on pulse Ω_a first, not Ω_b . It can be dramatically beneficial to use counterintuitive excitation when it is important to avoid relaxation associated with level $|2\rangle$.

77.8.4 Induced Transparency

The foregoing results for three-level excitation can be extended to resonant pulse propagation in three-level media. The equations governing simultaneous two-pulse evolution in the local-time coordinates $cT \equiv ct - z$ and $\zeta \equiv z$ are

$$\frac{\partial \Omega_a}{\partial \zeta} = i\mu_a a_g^* a_2, \quad (77.54)$$

$$\frac{\partial \Omega_b}{\partial \zeta} = i\mu_b a_e^* a_2, \quad (77.55)$$

where, as before,

$$\mu_a = \frac{4\pi d_a^2 N \omega_a}{\hbar c}, \quad \text{etc.} \quad (77.56)$$

Note that the bilinear combination $2a_g^* a_2$ corresponds to $U - iV$ in Eq. (77.27).

Soliton-like pulses can propagate in three-level media. Both pulses must compete for interaction with level $|2\rangle$. They

depend only on a single variable $Z \equiv \zeta - uT$, where u is the pulse’s constant velocity in the moving frame. Soliton solutions are given (for $\mu_a = \mu_b$) by

$$\Omega_a = A \operatorname{sech} KZ, \quad \Omega_b = B \tanh KZ, \quad (77.57)$$

and

$$\begin{aligned} a_g &= -\tanh KZ, \\ a_2 &= \frac{-2iKu}{A} \operatorname{sech} KZ, \\ a_e &= \frac{B}{A} \operatorname{sech} KZ, \end{aligned} \quad (77.58)$$

where the parameters A, B, Ku are nonlinearly related to the pulse length τ :

$$Ku \equiv 1/\tau \quad \text{and} \quad (2/\tau)^2 = A^2 - B^2. \quad (77.59)$$

The moving frame velocity is given by $1/u = 2\mu/A^2$, and the expression for the lab frame velocity V is $1/V = 1/c + 2\mu/A^2$.

If $B \rightarrow 0$, then $A \rightarrow 2/\tau$, which is the exact McCall–Hahn formula for the two-level one-pulse soliton amplitude [1]. No adiabatic condition was invoked in obtaining the soliton solutions. The physical measure of adiabaticity comes from the pulse duration τ . If τ is short, an appreciable population appears transiently in level $|2\rangle$, but if τ is long (an adiabatic pulse), the population skips level $|2\rangle$ and goes directly from $|g\rangle$ to $|e\rangle$ and back again during the pulse.

Note that the sech and tanh functions are ideally counterintuitive, with pulse b starting infinitely far ahead of pulse a . In practice, the infinite leading edge of the tanh function plays no role and can be truncated to several times τ without appreciable change in the character of the pulse pair.

77.9 Disentanglement and “Sudden Death” of Coherent Transients

The existence of entanglement (nonseparability) of states is the most prominent evidence that quantum mechanics allows possibilities not known in classical physics. This has consequences for coherent transients, allowing them to exhibit nonintuitive effects unlike any discussed up to this point. An example that directly illustrates this point shows that two entangled atoms whose inversion and coherences decay exponentially can have an entanglement that does not decay similarly smoothly and reaches zero long *before* the atoms reach their final states. This shows that transients of an entangled pair of atoms can be very different from the transients affecting the atoms separately.

We imagine the situation sketched in Fig. 77.8, two two-level atoms A and B of the type discussed at length already,

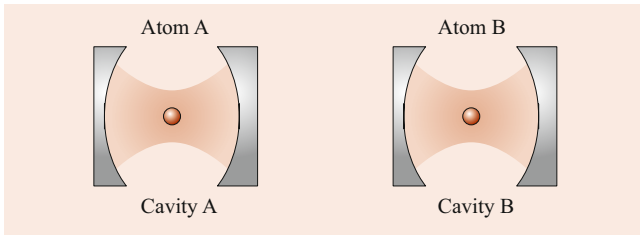


Fig. 77.8 Illustration of a setup in which two partially excited atoms A and B are located inside two spatially separated cavities that are possibly very remote from each other. The two atoms are assumed to initially be entangled, but they have no interaction

prepared by an earlier interaction in a partially excited entangled mixed state and subsequently located remotely from each other, without further interaction. They each must eventually, because of spontaneous emission, come to their ground states, creating the final joint state $|g\rangle_A \otimes |g\rangle_B$, which is clearly not entangled, a factored simple product. The question is, what is the manner of evolution by which the entanglement of the pair evolves toward zero?

The standard master equation methods [15] for investigating spontaneous emission [16] can be applied to each atom separately since they are not interacting with each other. For any initial state $\rho^{AB}(0)$, the density operator at t can be expressed as

$$\rho^{AB}(t) = \sum_{\mu=1}^4 K_{\mu}(t)\rho^{AB}(0)K_{\mu}^{\dagger}(t), \quad (77.60)$$

where the so-called Kraus operators [17] $K_{\mu}(t)$ are available in closed form in this case [18].

For illustration purposes, we will choose a partially coherent initial state, expressed by a two-atom density matrix with a single free parameter a :

$$\rho^{AB}(0) = \frac{1}{3} \begin{pmatrix} a & 0 & 0 & 0 \\ 0 & 1 & 1 & 0 \\ 0 & 1 & 1 & 0 \\ 0 & 0 & 0 & 1-a \end{pmatrix}. \quad (77.61)$$

Here, the convention is to label the rows and columns in the “inverted” order ee, eg, ge, gg . That is, the probabilities are $a/3$ that both atoms are in state $|e\rangle$ at $t = 0$ and $(1-a)/3$ in state $|g\rangle$, and with probability $1/3$, they are in either one of the opposite pair states, with the sum equaling 1, of course. Local transient decay, e.g., of either atom’s inversion W , can be evaluated separately from their reduced density matrices, $\rho^A \equiv \text{Trace}_B\{\rho^{AB}\}$, etc. For example,

$$\begin{aligned} \rho^A &= {}_B\langle e|\rho^{AB}|e\rangle_B + {}_B\langle g|\rho^{AB}|g\rangle_B \\ &= \frac{1}{3} \begin{pmatrix} 1+a & 0 \\ 0 & 2-a \end{pmatrix}, \end{aligned} \quad (77.62)$$

and the upper level occupation of atom A can be found to decay exactly as expected: $\rho_{ee}^A(t) = \frac{a+1}{3} e^{-t/\tau_0}$, where τ_0 is the usual spontaneous emission lifetime.

For nonlocal transients, we need a time-dependent measure of entanglement, and there are several options [19], all related to the joint entropy of the two-atom system. We will use the concurrence $C(t)$ of Wootters [20], which has the convenient normalization $1 \geq C(t) \geq 0$, where $C = 1$ represents completely entangled atoms (such as in a pure Bell state, for example), and $C = 0$ denotes the complete absence of entanglement.

For the specific case $a = 1$, one finds for the state Eq. (77.61) the initial concurrence $C(0) = \frac{2}{3}$, indicating a state with partial two-party coherence (incomplete entanglement). At time t , one then finds:

$$C^{AB}(t) = \frac{2}{3} \max\{0, e^{-t/\tau_0} f(t)\}, \quad (77.63)$$

where $f(t) = 1 - \sqrt{2\omega^2 + \omega^4}$, and $\omega \equiv 1 - e^{-t/\tau_0}$. The strikingly nonintuitive consequence of this transient is that $C(t)$ reaches 0 abruptly after a finite time (disentanglement suffers a “sudden death”), if $2\omega^2 + \omega^4 \geq 1$. In fact, only a minor algebraic rearrangement shows that this strange condition must occur, and that the finite sudden death time t_0 is given by

$$\frac{t_0}{\tau_0} \equiv \ln \left[\frac{2 + \sqrt{2}}{2} \right] \approx 0.53. \quad (77.64)$$

The nonlocal coherent transient behavior of entanglement for the entire range of allowed a values [18] is shown in Fig. 77.9. This shows that the concurrence undergoes familiar smooth and infinitely long decay only for a values in the limited range $\frac{1}{3} > a \geq 0$. Otherwise, sudden (finite-time) death occurs sooner or later. In our example, nonlocal coherence becomes zero most abruptly after a finite time for $a = 1$, the case that was calculated in Eq. (77.63). It appears that these results are not exceptional. Sudden termination of entanglement has also been predicted for two-party continuum

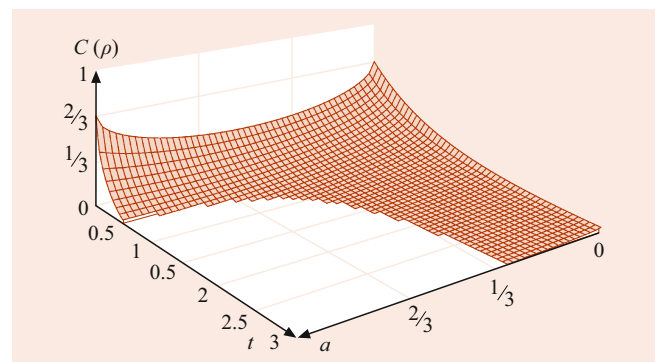
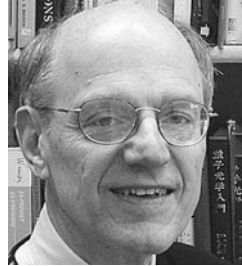


Fig. 77.9 Effect of spontaneous emission on concurrence of two two-level atoms, given the initially entangled mixed state Eq. (77.61) depending on the single parameter $1 \geq a \geq 0$

states, as well as for qubit pairs experiencing only T_2 decay, in contrast to the combined T_1 and T_2 decay appropriate to spontaneous emission as treated here.

References

1. Allen, L., Eberly, J.H.: *Optical Resonance and Two-Level Atoms*. Dover, New York (1987)
2. Shore, B.W.: *Theory of Coherent Atomic Excitation* vol. 1 & 2. Wiley, New York (1990)
3. Meystre, P., Sargent III, M.: *Elements of Quantum Optics*. Springer, New York (1990)
4. Cohen-Tannoudji, C., Dupont-Roc, J., Grynberg, G.: *Atom-Photon Interactions*. Wiley, New York (1992)
5. Scully, M.O., Zubairy, M.S.: *Quantum Optics*. Singapore, Cambridge (1997)
6. Schleich, W.P.: *Quantum Optics in Phase Space*. Wiley-VCH, New York (2001)
7. Gerry, C.C., Knight, P.L.: *Introductory Quantum Optics*. Singapore, Cambridge (2005)
8. M. H. Devoret, A. Wallraff, and J. M. Martinis: arXiv:cond-mat/0411174 (2004).
9. Stratton, J.: *Electromagnetic Theory*. McGraw-Hill, New York (1941)
10. Purcell, E.M.: *Phys. Rev.* **69**, 681 (1946)
11. Milonni, P.W., Eberly, J.H.: *Lasers*. Wiley, New York (1988)
12. Jackson, J.D.: *Classical Electrodynamics*, 2nd edn. Wiley, New York (1975)
13. Fedorov, M.V.: *Atomic and Free Electrons in a Strong Light Field*. World Scientific, New York (1997)
14. Faisal, F.H.M.: *Theory of Multiphoton Processes*. Plenum, New York (1987)
15. This citation is intended for cross-reference to the location in the Handbook where the Master Equation approach to density matrix evolution is explained.
16. This citation is intended for cross-reference to the location in the Handbook where spontaneous emission is treated systematically.
17. Daffer, S., Wódkiewicz, K., McIver, J.K.: A complete discussion of Kraus operators appropriate to Bloch vector evolution is given in. *J. Mod. Opt.* **51**, 1843 (2004)
18. Yu, T., Eberly, J.H.: *Phys. Rev. Lett.* **93**, 140404 (2004)
19. This citation is intended to refer to the chapter on Quantum Information.
20. Wootters, W.K.: *Phys. Rev. Lett.* **80**, 2245 (1998)



Joseph H. Eberly Joseph H. Eberly is Andrew Carnegie Professor of Physics and Professor of Optics at the University of Rochester. He has published more than 400 research and review papers as well as several books dealing with a variety of topics in quantum and classical optics, including spontaneous revivals in cavity QED, photon-atom interactions, non-diffracting beams, entanglement versus duality, high-field atomic attophysics, and nonlinear propagation of short optical pulses.



Carlos R. Stroud Jr. Carlos R. Stroud Jr. is Professor of Optics, Professor of Physics, and Director of the Center for Quantum Information at the University of Rochester where he works in a variety of areas of experimental and theoretical quantum optics and atomic physics. His group pioneered the area of Rydberg electron wave-packet physics observing localization, decays, revivals, and interferometry with a single electron.



Marcelo Ciappina , Alexis A. Chacon S. , and Maciej Lewenstein

Contents

78.1	Introduction	1125
78.2	Weak-Field Multiphoton Processes	1126
78.2.1	Perturbation Theory	1126
78.2.2	Resonant-Enhanced Multiphoton Ionization	1127
78.2.3	Multielectron Effects	1127
78.2.4	Autoionization	1127
78.2.5	Coherence and Statistics	1127
78.2.6	Effects of Field Fluctuations	1128
78.2.7	Excitation with Multiple Laser Fields	1128
78.2.8	Waveforms	1128
78.3	Strong-Field Multiphoton Processes	1129
78.3.1	Nonperturbative Multiphoton Ionization	1129
78.3.2	Tunneling Ionization	1129
78.3.3	Multiple Ionization	1130
78.3.4	Above Threshold Ionization	1130
78.3.5	High-Order Harmonic Generation	1131
78.3.6	Stabilization of Atoms in Intense Laser Fields	1133
78.3.7	Molecules in Intense Laser Fields	1133
78.3.8	Microwave Ionization of Rydberg Atoms	1134
78.4	Strong-Field Computational Techniques	1135
78.4.1	Floquet Theory	1135
78.4.2	Direct Integration of the TDSE	1135
78.4.3	Volkov States	1136
78.4.4	Strong-Field Approximations	1136
78.4.5	phase-space Averaging Method	1136

78.5	Atto-Nano Physics	1137
------	------------------------------------	------

References	1138
-----------------------------	------

Abstract

The excitation of atoms by intense laser pulses can be divided into two broad regimes: the first regime involves relatively weak optical laser fields of long duration, and the second involves strong fields of short duration. In the first case, the intensity is presumed to be high enough for multiphoton transitions to occur. The resulting spectroscopy is not limited by the single-photon selection rules for radiative transitions. However, the intensity is still low enough for a theoretical description based on perturbations of field-free atomic states to be valid, and the time dependence of the field amplitude does not play an essential role. In the second case, the field intensities are too large to be treated by perturbation theory, and the time dependence of the pulse must be taken into account. In addition to a detailed picture of the two subjects described above, we include a discussion on the generation of attosecond pulses and applications of both high-order harmonic generation (HHG) and above-threshold ionization (ATI). Furthermore, we incorporate a brief summary about the incipient field of atto-nano physics.

Keywords

strong laser fields · Rydberg atoms · multiphoton ionization · multiphoton processes · attosecond physics

M. Ciappina (✉)
Physics Program, Guangdong Technion – Israel Institute of
Technology
Shantou, Guangdong, China
e-mail: marcelo.ciappina@gtit.edu.cn

A. A. Chacon S.
Dept. of Physics, Pohang University of Science and Technology and
Max Planck Research Initiative/Korea
Pohang, Korea, Republic of
e-mail: achacon@postech.ac.kr

M. Lewenstein
The Barcelona Institute of Science and Technology, Quantum Optics
Theory, ICFO and ICREA
Av. Carl Friedrich Gauss 3, 08860 Castelldefels, Spain
e-mail: maciej.lewenstein@icfo.es

78.1 Introduction

The excitation of atoms by intense laser pulses can be divided into two broad regimes determined by the characteristics of the laser pulse relative to the atomic response. The first regime involves relatively weak optical laser fields of long

duration (> 1 ns), and the second involves strong fields of short duration (< 10 ps). These will be referred to as the weak-long (WL) and strong-short (SS) cases, respectively.

In the case of atomic excitation by WL pulses, the intensity is presumed to be high enough for multiphoton transitions to occur. The resulting spectroscopy of absorption to excited states is potentially much richer than single-photon excitation because it is not limited by the single-photon selection rules for radiative transitions. However, the intensity is still low enough for a theoretical description based on perturbations of field-free atomic states to be valid, and the time dependence of the field amplitude does not play an essential role.

The SS case is fundamentally different in that the atomic electrons are strongly driven by fields too large to be treated by perturbation theory, and the time dependence of the pulse as it switches on and off must be taken into account. Atoms may absorb hundreds of photons, leading to the emission of one or more electrons, as well as photons of both lower and higher energy. Because the flux of incident photons is high, a classical description of the laser field is adequate, but the time-dependent Schrödinger equation (TDSE) must be solved directly to obtain an accurate representation of the atom–field interaction.

For SS pulses of optical wavelength, it is sufficient in most cases to consider only the electric dipole (E1) interaction term defined in Chap. 72. The atom–field interaction can then be expressed in either the length gauge or the velocity gauge [1] (Chap. 22). In the length gauge, the TDSE is

$$i\hbar \frac{\partial \Psi(\mathbf{r}, t)}{\partial t} = [H_0 + e\mathbf{r} \cdot \mathbf{E}(t)]\Psi(\mathbf{r}, t), \quad (78.1)$$

where H_0 is the field-free atomic Hamiltonian, \mathbf{r} the collective coordinate of the electrons, and $\mathbf{E}(t)$ the electric field of the laser given by

$$\mathbf{E}(t) = \mathcal{E}(t)[\hat{\mathbf{x}} \cos(\omega t + \varphi) + \epsilon \hat{\mathbf{y}} \sin(\omega t + \varphi)]. \quad (78.2)$$

Here, $\mathcal{E}(t)$ defines the envelope, φ is the so-called carrier envelope phase (CEP), and ϵ characterizes the polarization: linear if $\epsilon = 0$ and circular if $|\epsilon| = 1$. In the velocity gauge, the TDSE is

$$i\hbar \frac{\partial \psi(\mathbf{r}, t)}{\partial t} = \left[H_0 - \frac{ie\hbar}{mc} \mathbf{A}(t) \cdot \nabla + \frac{e^2}{2mc^2} A^2(t) \right] \psi(\mathbf{r}, t). \quad (78.3)$$

Here, $\mathbf{A}(t) = -c \int^t \mathbf{E}(t') dt'$ is the vector potential of the laser field. The solutions of Eqs. (78.1) and (78.3) are related by the phase transformation

$$\Psi(\mathbf{r}, t) = \exp \left[\frac{ie}{\hbar c} \mathbf{r} \cdot \mathbf{A}(t) \right] \psi(\mathbf{r}, t). \quad (78.4)$$

Since lasers must usually be focused to reach the strong-field regime, measured electron and ion yields include contributions from a distribution of field strengths. The photoemission spectrum, on the other hand, contains a coherent component due to the macroscopic polarization of all the atoms and is, therefore, sensitive also to the laser phase variations within the focal volume. In this chapter, methods for solving Eqs. (78.1) and (78.3) are discussed along with details of the atomic emission processes.

Three relevant books provide excellent introductions to this subject [1–3]. Further developments are well described in the proceedings of the International Conferences on Multiphoton Physics [4–7] and the NATO workshop on Super-Intense Laser-Atom Physics [8, 9].

78.2 Weak-Field Multiphoton Processes

78.2.1 Perturbation Theory

Since atomic ionization energies are generally $\gtrsim 10$ eV, while optical photons have energies of only a few eV, several photons must be absorbed to produce ionization, or even electronic excitation in the case of the noble gases. For WL pulses, the electronic states are only weakly perturbed by the electromagnetic field. The rate of an n -photon transition can then be calculated using the n -th order perturbation theory for the atom–field interaction. For an incident photon number flux ϕ of frequency ω , the rate is

$$W_{i \rightarrow f}^{(n)} = 2\pi \left(\frac{2\pi\alpha\phi\omega}{e^2} \right)^n \left| T_{i \rightarrow f}^{(n)} \right|^2 \delta(\omega_i + n\omega - \omega_f), \quad (78.5)$$

where

$$T_{i \rightarrow f}^{(n)} = \langle f | d G[\omega_i + (n-1)\omega] \times d G[\omega_i + (n-2)\omega] \cdots d G[\omega_i + \omega] d | i \rangle, \quad (78.6)$$

$|i\rangle$ is the i -th eigenstate of the field-free atomic Hamiltonian, $d = e\hat{\mathbf{e}} \cdot \mathbf{r}$, with $\hat{\mathbf{e}}$ the polarization direction, and

$$G(\omega) = \sum_j \frac{|j\rangle\langle j|}{(\omega - \omega_j + i\Gamma_j/2)}. \quad (78.7)$$

The sum over j includes an integration over the continuum for all sequences of E1 transitions allowed by angular momentum and parity selection rules. Methods for calculating cross sections and rates in the weak-field regime are described in [1, 10] and in Chap. 25.

78.2.2 Resonant-Enhanced Multiphoton Ionization

For multiphoton ionization, ω can be continuously varied because the final state in Eq. (78.5) lies in the continuum. If ω is tuned so that $\omega_i + m\omega \cong \omega_j$ for some contributing intermediate state $|j\rangle$ in Eq. (78.7), then in that state lies an integer m photons above the initial state, and the corresponding denominator vanishes (to within the level width Γ_j), producing a strongly peaked resonance. Since it takes $k = n - m$ additional photons for ionization, the process is called m, k resonant-enhanced multiphoton ionization (REMPI). Measurements of the photoelectron angular distribution are useful in characterizing the resonant intermediate state.

Calculations using the semi-empirical multichannel quantum defect theory to provide the needed matrix elements have been very successful in describing experimental results. This technique is discussed in more detail in Chap. 49.

The perturbation equation Eq. (78.5) indicates that the rate for nonresonant multiphoton ionization scales as ϕ^n for an n -photon process [11]. However, this is not the case for REMPI since the resonant transition saturates, and Eq. (78.5) no longer applies. Then the rate can be controlled either by the m -photon resonant excitation step or by the number of photons k needed for the ionization step.

78.2.3 Multielectron Effects

Multiply excited states can play a role in multiphoton excitation dynamics. These states are particularly important if their energies are below or not too far above the first ionization potential. Configuration expansions including these states have been used successfully in studies, for example, of the alkaline earth atoms, which have many low-lying doubly excited states. The presence of these states can also enhance the direct double ionization of an atom [12].

78.2.4 Autoionization

The configuration interaction between a bound state and an adjacent continuum leads to an absorption profile in the single photon ionization spectrum with a Fano lineshape. The actual lineshape reflects the interference between the two pathways to the continuum. Autoionizing states can also be probed via multiphoton excitation [13, 14]. Because, in the strong-field regime, coupling strengths and phases change with intensity, the lineshapes can be strongly distorted by changing the incident intensity. At particular intensities, the phases of the excited levels can be manipulated to prevent autoionization completely. Then a trapped population with energy above the ionization limit can be created [15].

78.2.5 Coherence and Statistics

Real laser fields exhibit various kinds of fluctuations and so are never perfectly coherent. The effects of such fluctuations on the complex electric field amplitude

$$E(t) = \mathcal{E}(t) \exp[-i\omega t + \varphi(t)] \quad (78.8)$$

can be modeled by a variety of stochastic processes [16], depending on the conditions [10, 17–20], as follows.

For continuum wave (CW) lasers, a phase diffusion model (PDM) is often used, for which $\mathcal{E}(t) = \mathcal{E} = \text{const.}$ and

$$\dot{\varphi}(t) = \sqrt{2b}F(t), \quad (78.9)$$

where $F(t)$ describes white noise by a real Gaussian function [16] characterized by the averaged values $\langle F(t) \rangle = 0$, $\langle F(t)F(t') \rangle = 2b\delta(t - t')$. The stochastic electric field then has an exponential autocorrelation function

$$\langle E(t)E^*(t') \rangle = \mathcal{E}^2 \exp[-b|t - t'| - i\omega(t - t')], \quad (78.10)$$

and a Lorentzian spectrum of width b . Far-off resonance, such a Lorentzian spectrum often gives unrealistic results, and the model Eq. (78.9) is then replaced by an Ornstein-Uhlenbeck process,

$$\ddot{\varphi}(t) = -\beta\dot{\varphi}(t) + \sqrt{2b\beta}F(t), \quad (78.11)$$

where the parameter β for $\beta \ll b$ plays the role of a cutoff of the Lorentzian spectrum.

A multimode laser with a large number M of independent modes has a field of the form $E(t) = \sum_{j=1}^M \mathcal{E}_j \exp[-i\omega_j t + i\varphi_j(t)]$, and according to the central limit theorem [16], can be described for large M as a complex Gaussian process defined to be a chaotic field,

$$\dot{E}(t) = -(b + i\omega)E(t) + \sqrt{2b|E(t)|^2}F(t), \quad (78.12)$$

where $F(t)$ is now a complex white noise, and ω is the central frequency of the field. The field, Eq. (78.12) has an exponential autocorrelation function and a Lorentzian spectrum of width b .

Various other stochastic models have been discussed in the literature. These include Gaussian fluctuations of the real amplitude of the field $\mathcal{E}(t)$; Gaussian chaotic fields with non-Lorentzian spectra; non-Gaussian, nonlinear diffusion processes (that describe for instance a laser close to threshold [16]); multiplicative stochastic processes (that describe a laser with pump fluctuations [18]) and jump-like Markov processes [21–23]. Statistical properties of laser fields can sometimes be controlled experimentally to a great extent [19, 20].

78.2.6 Effects of Field Fluctuations

Since the response of systems undergoing multiphoton processes is, in general, a nonlinear function of the field intensity (and, in particular, of the field amplitude), it depends in a complex manner on the statistics of the field. The enhancement of the nonresonant multiphoton ionization rate illustrates the point. According to the perturbation equation Eq. (78.5), the rate of an n -photon process is proportional to ϕ^n ; i.e., to I^n , where I is the field intensity. For fluctuating fields, the average response is thus

$$W_{i \rightarrow f}^{(n)} \propto \langle I^n \rangle \propto \langle |E(t)|^{2n} \rangle. \quad (78.13)$$

Phase fluctuations (as described by PDM) do not affect the average. On the other hand, for complex chaotic fields, the average is

$$\langle I^n \rangle \cong n! \langle I \rangle^n, \quad (78.14)$$

i.e., there exists a significant enhancement of the rate for $n > 1$.

Field fluctuations lead to more complex effects in resonant processes. Two well-studied examples are the enhancement of the AC Stark shift in resonant multiphoton ionization [24], and the spectrum of double optical resonance – a process in which the AC Stark splitting of the resonant line is probed by a slightly detuned fluctuating laser field [18]. Double optical resonance is very sensitive not only to the bandwidth of the probing field but also to the shape of its frequency spectrum.

78.2.7 Excitation with Multiple Laser Fields

The simultaneous application of more than one laser field produces interesting and novel effects. If a laser and its second (2ω) or third (3ω) harmonic are combined and the relative phase between the fields controlled, product state distributions and yields can be altered dramatically. The effects include reducing the excitation or ionization rates in the $\omega - 3\omega$ case [25] or altering the photoelectron angular distributions and the harmonic emission parity selection rules using a $\omega - 2\omega$ laser source [26].

A laser field can dress or strongly mix the field-free excited states, including the continuum, of an atom. This can produce a number of effects depending on how the dressed system is probed. By coupling a bound, excited state with the continuum, ionization strengths and dynamics are altered, resulting in new resonance-like structures where none existed before. This effect is called laser-induced continuum structure, or LICS [15, 27]. This general idea has been exploited to design schemes for lasers without

inversion [28] in which the dressed atom can have an inverted population, allowing gain, even though in terms of the undressed states, the lower level has the largest population. A laser can produce dramatic changes in the index of refraction of an atomic medium [29], creating, at specific frequencies, laser-induced transparency for a second, probe laser field. Multistep ionization, where each step is driven by a laser at its resonant frequency, has resulted in two useful applications. These are: efficient atomic isotope separation [23]; and the detection of small numbers of atoms in a sample, called single-atom detection. This technique is extremely sensitive because the use of exact resonance for each step yields very large cross sections for ionization, and the efficiency of collecting ions is high [30].

78.2.8 Waveforms

One step beyond would be to drive the atomic or molecular system with a so-called multicolor laser field, i.e., with a laser source created starting from different laser frequencies, not necessarily a multiple of each other (these sources are also known as waveforms or light-field transients). Waveform-controlled light transients with a bandwidth spanning almost two octaves have been demonstrated at microjoule energy and gigawatt peak power levels. These particular sources allow temporal confinement of optical radiation to less than 1 fs in subcycle waveforms. With their power substantially enhanced, these extreme waveforms may open up a new stage in nonlinear optics and attoscience. This is mainly due to, among other things, the feasibility of suppressing ionization up to unprecedented peak intensities and instantaneous ionization rates approaching optical frequencies, respectively. A prototypical three-color few-cycle system is already available, and it offers a conceptually simple route to scaling multioctave optical waveform synthesis to the multiterawatt regime (e.g., [31]). To this end, with the three channels delivering few-cycle pulses in the visible (VIS), $0.45 \approx 0.65 \mu\text{m}$, near-infrared (NIR), $0.7 \approx 1.3 \mu\text{m}$, and mid-infrared (MIR), $1.6 \approx 2.7 \mu\text{m}$, spectral ranges are recombined using a set of dichroic chirped mirrors to yield one single beam. Additionally, the feasibility of superoctave optical waveform synthesis was recently demonstrated in the NIR-VIS-ultraviolet (UV) spectral range by seeding a three-channel and, more recently, a four-channel, synthesizer consisting of broadband chirped mirrors with a continuum originating from a Ti:sapphire-laser-driven hollow-fiber/chirped-mirror compressor. Further degrees of freedom for waveform sculpting can be introduced by shaping the amplitude and phase of the spectra of the individual channels, e.g., via an acousto-optic pulse shaper and/or a spatial light modulator (for a recent review see, e.g., [32]).

78.3 Strong-Field Multiphoton Processes

Recently developed laser systems can produce very short pulses, some as short as a few to tens of femtoseconds, while at the same time maintaining the pulse energy so that the peak power becomes very high. In this regard, e.g., focused intensities up to 10^{19} W/cm² have been achieved. Because the pulses are short, atoms survive to much higher intensities before ionizing, making possible studies of laser–atom interactions in an entirely new regime [33]. A discussion of the status of short-pulse laser development is given in Chap. 75 and in [34].

With increasing intensity, higher-order corrections to Eq. (78.6) contribute to the transition rate. The next order correction comes from transitions involving two additional photons, one absorbed and one emitted, leading to the same final state. One effect of these terms is to shift the energies of the excited states in response to the oscillating field. This is called the dynamic or AC Stark shift. The AC Stark shift of the ground state tends to be small because of the large detuning from the excited states for long wavelength photons. On the other hand, in strong fields, the shift of the higher states and the continuum can become appreciable. Electrons in highly excited states respond to the oscillating field in the same manner as a free electron. Their energies shift with the continuum by the amount

$$U_p = \frac{(1 + \epsilon)e^2 \mathcal{E}^2}{4m\omega^2}, \quad (78.15)$$

where U_p is the cycle-averaged kinetic energy of a free electron in the field, and ϵ defines the polarization of the field Eq. (78.2); U_p is called the ponderomotive or quiver energy of the electron. For strong laser fields, U_p can be several eV or more, meaning that during a pulse, many states shift through resonance as their energies change by an amount larger than the incident photon energy. The resulting intensity-induced resonances can dominate the ionization dynamics.

Electrons promoted into the continuum acquire the ponderomotive energy, oscillating in phase with the field. In a linearly polarized field, the amplitude of the quiver motion of a free electron, given by $e\mathcal{E}/m\omega^2$, can become many times larger than the bound-state orbitals. If the initial velocity of an electron is small after ionization, it can be accelerated by the laser electric field and back into the vicinity of the ion core, when the field reverses its direction. The subsequent rescattering process, amongst other effects, changes the photoelectron energy and angular distributions, and allows the emission of high-energy photons [35, 36]. This simple dynamical picture forms the basis of the current understanding of many strong-field multiphoton processes.

78.3.1 Nonperturbative Multiphoton Ionization

The breakdown of perturbation theory for n th-order multiphoton processes occurs when the higher-order correction terms become comparable to the n -th-order term. Assuming that the dipole strength is $\propto ea_0$, where a_0 is the Bohr radius, and the detuning is $\delta \propto \omega$, the ratio of an $(n + 2)$ -order contribution to the n -th-order term from Eq. (78.6) is [1]

$$R_{n+2,n} \approx \left(\frac{2\pi\alpha\phi\omega}{e^2} \right) \left(\frac{ea_0}{\omega} \right)^2 = \left(\frac{I}{I_\gamma} \right) \left(\frac{\omega_a}{2\omega} \right)^2, \quad (78.16)$$

where $\hbar\omega_a \approx 27.2114$ eV is the atomic unit of energy e^2/a_0 , and $I_\gamma \approx 3.50945 \times 10^{16}$ W/cm² is the intensity corresponding to an atomic unit of field strength, given by $E_a = \alpha c(m/a_0^3)^{1/2} \approx 5.1422 \times 10^9$ V/cm. The atomic unit of intensity itself is defined by

$$I_a = \phi_a \hbar\omega_a = \alpha c E_a^2, \quad (78.17)$$

which is $6.436414(4) \times 10^{15}$ W/cm². Thus, $I_\gamma = I_a/(8\pi\alpha)$. For photon energies of 1 eV, $R_{n+2,n}$ becomes unity for $I \approx 10^{14}$ W/cm². Because of the large number of $(n + 2)$ -order terms, perturbation theory actually fails for $I > 10^{13}$ W/cm². Above this critical intensity, nonresonant n -photon ionization ceases to scale with the ϕ^n dependence predicted by perturbation theory.

78.3.2 Tunneling Ionization

At sufficiently high intensity and low frequency, a tunneling mechanism changes the character of the ionization process. For lasers in the infrared (IR) or optical range, a strongly bound electron can respond to the instantaneous laser field since the oscillating electric field varies slowly on the timescale of the electron. The Coulomb attraction of the ion core combines with the laser electric field to form an oscillating barrier through which the electron can escape by tunneling, if the amplitude of the laser field is large enough. The DC rate for this process is $e\mathcal{E}/\sqrt{2mI_p}$, where I_p is the ionization potential of the electron. When this rate is comparable to the laser frequency, tunneling becomes the most probable ionization mechanism [37–39]. The ratio of the incident laser frequency to the tunneling rate is called the Keldysh parameter and is given by

$$\gamma = \sqrt{I_p/2U_p}, \quad (78.18)$$

which is less than unity ($\gamma \ll 1$) when tunneling dominates and larger than unity ($\gamma \gg 1$) when multiphoton ionization

governs the laser–matter process. Interestingly, many experiments are carried out in an intermediate or *crossover* region, defined by $\gamma \approx 1$. Another way to interpret γ is to note that we can write $\gamma = \tau_T/\tau_L$, where τ_T is the Keldysh time (defined as $\tau_T = \sqrt{2I_p/F}$) and $\tau_L = 2\pi/\omega$ is the laser period. Hence, γ serves as a measure of nonadiabaticity by comparing the response time of the electron wavefunction to the period of the laser field.

78.3.3 Multiple Ionization

Excitation and ionization dynamics are dominated by single-electron transitions in the strong-field regime. Although atoms can lose several electrons during a single pulse, the electrons are released sequentially. There is no convincing evidence of significant collective excitation in atoms in strong fields, even though it has been extensively sought. Once one electron is excited in an atom, the remaining electrons have much higher binding energies. As a result, the laser field is unable to affect them significantly until it reaches a much higher intensity. By that time, the first electron has already been emitted.

Simultaneous ejection of two electrons occurs as a minor channel (< 1%) in strong-field multiple ionization. Although it is possible that doubly excited states of atoms could assist in the double ionization, in the helium and neon cases studied, these states are unlikely to be contributors [40].

Correlated multi-electron ionization became a very hot subject over the past 20 years. Various mechanisms were proposed and demonstrated theoretically and experimentally. Perhaps the most important is the recollision mechanism, in which one electron tunnels out and is driven back to the nucleus by the laser field, where it recollides and releases a second atomic or molecular electron [41].

78.3.4 Above Threshold Ionization

In strong optical and IR laser fields, electrons can gain more than the minimum amount of energy required for ionization. Rather than forming a single peak, the emitted electron energy spectrum contains a series of peaks separated by the photon energy. This is called above-threshold-ionization, or ATI [42–45]. The peaks appear at the energies

$$E_s = (n + s)\hbar\omega - I_p, \quad (78.19)$$

where n is the minimum number of photons needed to exceed I_p , and $s = 0, 1, \dots$ is called the number of excess photons or above threshold photons carried by the electron. Calculations in the perturbative regime for ATI are given for hydrogen in [11].

Peak Shifting

As the intensity approaches the nonperturbative regime, the AC Stark shift of the atomic states begins to play a significant role in the structure of the ATI spectrum. The first effect is a shift of the ionization potential, given roughly by the ponderomotive energy U_p . Additional photons may then be required in order to free the electron from the atom, i.e., enough to exceed $I_p + U_p$. If the emitted electron escapes from the focal volume while the laser is still on, it is accelerated by the gradient of the field. The quiver motion is converted into radial motion, increasing the kinetic energy by U_p and exactly canceling the shift of the continuum. In this situation, the electron energies are still given by Eq. (78.19). However, when U_p exceeds the photon energy, the lowest ATI peaks disappear from the spectrum. In this long pulse limit, no electron is observed with energy less than U_p . This is called peak shifting and names the situation where the dominant peak in the ATI spectrum moves to higher order as the intensity increases.

ATI Resonance Substructure

If the laser pulse is short enough (< 1 ps for the typical laser focus), the field turns off before the electron can escape from the focal volume. Then the quiver energy is returned to the field, and the ATI spectrum becomes much more complicated. The observed electron energy can now be computed by

$$E_s \text{ (short pulse)} = (n + s)\hbar\omega - (I_p + U_p), \quad (78.20)$$

which results shifted an amount U_p with respect to the long pulses case Eq. (78.19). Electrons from different regions of the focal volume are thus emitted with different ponderomotive shifts, introducing a substructure in the spectrum, which can be directly associated with AC Stark-shifted resonances [42, 43].

ATI in Circular Polarization

The above discussion is particularly appropriate for the case of linear polarization, where the excited states of the atom can play a significant role in the excitation. On the contrary, in a circularly polarized field, the orbital angular momentum L must increase one unit with each photon absorbed, so that multiphoton ionization is allowed only to states that have high L , and, hence, a large centrifugal barrier. The lower energy scattering states thus cannot penetrate into the vicinity of the initial state. Thus, the ATI spectrum in circular polarization peaks at high energy and is very small near threshold.

ATI Applications

In the few-cycle regime, a precise knowledge of the CEP is instrumental to adequately characterize the subsequent nonlinear laser–matter phenomena. Then, the CEP plays

a major role in, for instance, the production and control of single attosecond pulses and the investigation of nonsequential double-electron ionization [46–48], amongst others. Recently, experimental observations of ATI driven by few-cycle IR-laser pulses have demonstrated that using a so-called “stereo” technique measurement of electrons emitted on the left and on the right with respect to the linear laser polarization, it is possible to extract the CEP of the driving laser [49].

In addition, another important application is to use energetic rescattered ATI electrons to estimate the bond distance in molecules. For instance, recent measurements in acetylene (C_2H_2) [50] have proved that it is entirely possible to extract structural information of the chemical internuclear distance between the carbon atoms in the C–C pair and the carbon and hydrogen atoms in the C–H one, both with unprecedented high accuracy. This singular technique is named laser-induced electron diffraction (LIED) and promises to lead the time-resolved studies in complex molecules [51].

The two above-mentioned examples, namely the few-cycle CEP characterization and the LIED technique, show the capabilities of ATI to interrogate nature and answer fundamental questions about both the electron dynamics and molecular structure, just to name a few. Hence, ATI provides a powerful tool to not only give light about time-dependent atomic and molecular processes but also to configure an invaluable ally for extracting information of the driving laser itself [49].

78.3.5 High-Order Harmonic Generation

High-order harmonic generation (HHG) in noble gases is a rapidly developing field of laser physics [33, 52–54]. When an SS pulse interacts with an atomic gas, the atoms respond in a nonlinear way, emitting coherent radiation at frequencies that are integral multiples of the laser frequency. Due to the inversion symmetry of the atom, only odd harmonics of the fundamental are emitted. In the high-intensity ($> 10^{13}$ W/cm²), low-frequency regime, the harmonic strengths fall off for the first few orders, followed by a broad plateau of nearly constant conversion efficiency and then a rather sharp cutoff [52, 53]. The plateau extends to well beyond the hundredth order of the 800–1000 nm incident wavelengths, using the light noble gases as the active medium. Moreover, there has also been experimental evidence of HHG from ions. Considering the laser-induced electron dynamics behind HHG natively develops on a sub-fs timescale, HHG provides a source of very bright, short-pulse, coherent XUV radiation, which can have several advantages over the other known sources, such as the synchrotron.

Plateau and Cutoff

The well-known three-step model [35, 36], which in 2018 turned 25 years old and combines quantum and classical aspects of laser-atom physics, accounts for many strong-field phenomena. In this model, the electron first tunnels out [55] from the ground state of the atom through the barrier formed by the Coulomb potential and the laser field. Its subsequent motion can be treated classically, and primarily consists of oscillatory motion in phase with the laser field. If the electron returns to the vicinity of the nucleus with kinetic energy \mathcal{T} , it may recombine into the ground state with the emission of a photon of energy $(2n + 1)\hbar\omega \leq \mathcal{T} + I_p$, where n is an integer. (The relation of this recombination process to atomic photoionization is discussed briefly in Chap. 25.) The maximum kinetic energy of the returning electron turns out to be $\mathcal{T} \approx 3.2U_p$, resulting in a cutoff in the harmonic spectrum at the harmonic of order

$$N_{\max} \approx (I_p + 3.2U_p)/\hbar\omega. \quad (78.21)$$

Theoretical Methods

Calculation of harmonic strengths requires the evaluation of the time-dependent dipole moment of the atom,

$$\mathbf{d}(t) = \langle \Psi(t) | e\mathbf{r} | \Psi(t) \rangle. \quad (78.22)$$

The strength of harmonics emitted by a single atom are then related to the Fourier components of $\mathbf{d}(t)$, or more precisely, its second time derivative, $\ddot{\mathbf{d}}(t)$.

The induced dipole moment $\mathbf{d}(t)$ can be directly evaluated from the numerical [56] or Floquet [26] solutions of the TDSE. Good agreement with numerical and experimental data is also obtained using the strong-field approximation discussed below and a Landau–Dykhne formula. This latter approach can be considered to be a quantum mechanical implementation of the three-step model [57].

Propagation and Phase-Matching Effects

A single atom response is not sufficient to determine the macroscopic response of the atomic medium. Because different atoms interact with different parts of the focused laser beam, they feel different peak field intensities and phases (which actually undergo a rapid π shift close to the focus, due to geometrical effects). The total harmonic signal results from coherently adding contributions from single atoms, accounting for propagation and interference effects. The latter effects can wipe out the signal completely if a constructive phase matching does not take place.

The propagation and phase-matching effects in the strong-field regime [58] can be studied by solving Maxwell’s equations for a given harmonic component of the electric

field $\mathcal{E}_M(\mathbf{r})$ Eq. (72.23),

$$\nabla^2 \mathcal{E}_M(\mathbf{r}) + n_M(\mathbf{r}) \mathcal{E}_M(\mathbf{r}) = -\frac{1}{\epsilon_0} \left(\frac{M\omega}{c} \right)^2 \mathcal{P}_M(\mathbf{r}), \quad (78.23)$$

where $n_M(\mathbf{r})$ is the refractive index of the medium (which depends on atomic, electronic, and ionic dipole polarizabilities), while $\mathcal{P}_M(\mathbf{r})$ is the polarization induced by the fundamental field only. The latter can be expressed as

$$\mathcal{P}_M(\mathbf{r}) \propto N(\mathbf{r}) d_M M(\mathbf{r}) \exp[-iM\Delta(\mathbf{r})], \quad (78.24)$$

where $N(\mathbf{r})$ is the atomic density, $d_M(\mathbf{r})$ is the M -th Fourier component of the induced dipole moment, and $\Delta(\mathbf{r})$ is a phase shift coming from the phase dependence of the fundamental beam due to focusing. All of these quantities may have a slow time dependence, reflecting the temporal envelope of the laser pulse.

Typically, phase matching is the most efficient in the forward direction. In general, the strength and spatial properties of a harmonic depend in a very complex way on the focal parameters, the medium length, and the coherence length of a given harmonic. Propagation and phase-matching effects can lead to a shift of the location of the cutoff in the harmonic spectrum [59].

Harmonic Generation by Elliptically Polarized Fields

The three-step model implies that for harmonic emission it is necessary that the tunneling electrons return to the nucleus and recombine into their initial state. According to classical mechanics, there are many trajectories in a linearly polarized field that involve one or more returns to the origin. However, there are practically no such trajectories in elliptically polarized fields. As a result, the three-step model predicts a strong decrease of the harmonic strengths as a function of the laser ellipticity. This prediction has been already confirmed experimentally [60].

The Generation of Attosecond XUV Pulses

Manipulation of generated harmonics by allowing the temporal beating of superposed high-order harmonics can produce a train of intense and very short spikes, on the order of ≈ 100 as and shorter, where $1 \text{ as} = 10^{-18} \text{ s}$ [61–63]. The structural characteristics of the generated pulse trains depend on the relative phases of the harmonics combined. Employing driving pulses that were themselves only a few femtoseconds long, experimental groups in Vienna [64] and Paris [65] reported the first observations and measurements of such subfemtosecond UV/XUV light pulse trains. Very recently, a new world record was set in Florida, where a single 53-attosecond X-ray pulse, with a photon energy enough to reach the carbon K-edge, was measured [66]. The scientific

importance of breaking the femtosecond barrier is obvious: the timescale necessary for probing the motion of an electron in a typical bound, the valence state, is measured in attoseconds (atomic unit of time $\equiv 24$ as). Attosecond pulses will allow the study of the time-dependent dynamics of correlated electron systems by freezing the electronic motion, in essence exploring the structure with ultrafast snapshots. A crucial aspect for all attosecond pulse generation is the control of spectral phases. Measurements of the timing of the attosecond peaks relative to the absolute phase of the IR driving field have been accomplished [67]. This provides insight into the recollision, the key step in the harmonic generation process. Also, the control of the group velocity phase relative to the envelope of the few-cycle driving pulses allows the production of reproducible pulse trains [68]. Thus, the highly nonperturbative, nonlinear multiphoton interactions of very short IR or visible light pulses with atoms or molecules is becoming a novel, powerful, and unique source for studies of the fastest quantum electronic processes known to date.

HHG Applications

One of the singular aspects of HHG is the possibility to produce and control both trains of and single attosecond pulses. These ultrashort light sources are extremely important for the investigation of the ultrafast process in atomic and molecular systems. The Auger decay, the delay in the photoemission absorption via an XUV source and double-electron ionization are examples of phenomena that occur on the subfemtosecond time domain. HHG allows not only to get knowledge about the ultrafast electron dynamics inside atoms and molecules, but it also has also been demonstrated that it configures an indispensable tool to extract atomic and molecular structural information [69, 70].

The fascinating technological advances of pump-probe experiments, where attosecond pulses and delayed IR lasers are being employed to firstly trigger the system and later interrogate its dynamical time evolution, have allowed us to address unexplored questions on the above-mentioned processes. The extension of these techniques to more complex systems, such as solid structures and biological materials, is already in the pipeline.

HHG in Bulk Matter

So far, the cornerstone of attosecond science applications has been the HHG phenomenon in gases. However, there still exists a clear disadvantage of HHG due to its poor conversion efficiency—the ratio between the outgoing XUV and incoming IR photon fluxes. Recent advances in light sources within the mid-infrared (MIR) domain, $1.7 \approx 7 \mu\text{m}$, have opened a new avenue in the investigation of HHG using condensed matter materials [71]. In particular, the control of such MIR sources allows us to overcome the low-efficiency problem and substantially increase the photon flux per produced at-

tosecond pulse. This characteristic could lead to unexplored physical processes in that condensed matter phase.

As is known, in an insulator, there exists the concept of band energy dispersion for electrons in its valence or conduction bands. For instance, the HHG in semiconductors (dielectrics) is governed by electron or holes bound wavefunctions that are not spatially (or energetically) localized. Holes, in addition, also have the possibility to move on their own valance band while, on the other hand, the electron dynamics takes place entirely in the conduction band. This leads to two main contributions to the HHG process, namely, one dictated by an intraband oscillation and other by an interband electron–hole current [72, 73].

This emerging field is attracting the attention of both the attosecond science and condensed matter communities. Joint efforts are being carried out to address fundamental questions such as how particle collisions can be mimicked in a solid through HHG processes [74] or how Bloch oscillations might be observed in real time [75]. Additionally, questions related to topological insulators and how their features might affect the harmonic emissions were recently brought up [76, 77].

78.3.6 Stabilization of Atoms in Intense Laser Fields

It has been argued [78] that in very intense laser fields of high frequency, atoms undergo dynamical stabilization and do not ionize. The stabilization effect can be explained by gauge transforming the TDSE Eq. (78.1) to the Kramers–Henneberger (K–H) frame; i.e., a noninertial oscillating frame that follows the motion of the free electron in the laser field. The K–H transformation consists of replacing $\mathbf{r} \rightarrow \mathbf{r} + \boldsymbol{\alpha}(t)$, where, for the linearly polarized monochromatic laser field, $\boldsymbol{\alpha}(t) = \hat{\mathbf{x}}\alpha_0 \cos(\omega t - \varphi)$; $\alpha_0 = eE/(m\omega^2)$ is the excursion amplitude of a free electron, and $\hat{\mathbf{x}}$ is the polarization direction. The TDSE in the K–H frame is

$$i\hbar \frac{\partial \Psi(\mathbf{r}, t)}{\partial t} = \left\{ -\frac{\hbar^2 \nabla^2}{2m} + V[\mathbf{r} + \boldsymbol{\alpha}(t)] \right\} \Psi(\mathbf{r}, t), \quad (78.25)$$

i.e., it describes the motion of the electron in an oscillatory potential. In the high-frequency limit, this potential may be replaced by its time average

$$V_{\text{K-H}}(\mathbf{r}) = \frac{\omega}{2\pi} \int_0^{2\pi/\omega} dt V[\mathbf{r} + \boldsymbol{\alpha}(t)], \quad (78.26)$$

and the remaining Fourier components of $V[\mathbf{r} + \boldsymbol{\alpha}(t)]$ treated as a perturbation. When α_0 is large, the effective potential Eq. (78.26) has two minima close to $\mathbf{r} = \pm \hat{\mathbf{x}}\alpha_0$. The corresponding wave functions of the bound states are centered

near these minima, thus exhibiting a dichotomy. The ionization rates from the K–H bound states are induced by the higher Fourier components of $V(\mathbf{r} + \boldsymbol{\alpha}(t))$. For large enough α_0 , the rates decrease, if either the laser intensity increases, or the frequency decreases.

Numerical solutions of the TDSE [79, 80] show that stabilization, indeed, occurs for laser field strengths and frequencies of the order of one atomic unit. More importantly, stabilization is possible even when the laser excitation is not monochromatic but, rather, is produced by a short laser pulse. Physically, free electrons in a monochromatic laser field cannot absorb photons due to the constraints imposed by energy and momentum conservation. Absorption is possible only in the vicinity of a potential, such as the Coulombic attraction of the nucleus. In the case of a strong excitation, i.e., when α_0 is much larger than the Bohr radius, the electron spends most of the time very far from the nucleus, and, therefore, does not absorb energy from the laser beam. Therefore, stabilization, as viewed from the K–H frame, has a classical analog. Other mechanisms of stabilization based on the quantum mechanical effects of destructive interference between various ionization paths have also been proposed [81].

Due to classical scaling (Sect. 78.3.8) stabilization is predicted to occur for much lower laser frequencies, if the atoms are initially prepared in highly excited states. If additionally, the initial state has a large orbital angular momentum corresponding to classical trajectories that do not approach the nucleus, stabilization is even more easily accomplished. For instance, the stabilization of a 5g Rydberg state of neon has been reported [82].

Although recently interest in stabilization in intense laser fields became very limited, the K–H transformation and the stabilization effect have been discussed in a completely different situation. In [83, 84], the stabilization of atoms in a shaken trap Bose–Einstein condensate was proposed. In fact, recently, a K–H trick was used to develop an experimental simulator of ultrafast processes in strong laser fields using ultracold trapped atoms [85].

78.3.7 Molecules in Intense Laser Fields

Molecular systems are much more complex than atoms because of the additional degrees of freedom resulting from nuclear motion. Even in the presence of a laser field, the electron and nuclear degrees of freedom can be separated by the Born–Oppenheimer approximation, and the dynamics of the system can be described in terms of motions on potential energy surfaces. In strong fields, the Born–Oppenheimer states become dressed, or mixed by the field, creating new molecular potentials. Because of avoided crossings between the dressed molecular states, the field induces new potential wells in which the molecules become trapped.

These states, known as laser-induced bound states, are stable against dissociation, but exist only while the laser field is present [86]. Their existence affects the spectra of photoelectrons, photons, and the fragmentation dynamics. If the field is strong enough, many electrons can be ejected from a molecule before dissociation, producing highly charged, energetic fragments [87]. Such experiments are similar to beam-foil Coulomb explosion studies of molecular structure. However, because of changes from the field-free equilibrium geometries in laser dissociation, the energies of the fragments lie systematically below the corresponding values from Coulomb explosion studies. Additionally to the latter, a similar phenomenon was intensively studied with atomic clusters [88].

78.3.8 Microwave Ionization of Rydberg Atoms

Similar phenomena appear in the ionization of highly excited hydrogen-like (Rydberg) atoms by microwave fields [89, 90], but the dynamical range of the parameters involved is different from the case of tightly bound electrons. Recent developments have greatly extended techniques for the preparation and detection of Rydberg states. Since, according to the equivalence principle, highly excited Rydberg states exhibit many classical properties, a classical perspective of ionization yields useful insights (Sect. 78.4.5).

Classical Scaling

The classical equations of motion for an electron in both a Coulomb field and a monochromatic laser field polarized along the z -axis are invariant with respect to the following scaling transformations:

$$\begin{aligned} p &\propto n_0^{-1} \tilde{p}, & r &\propto n_0^2 \tilde{r}, \\ t &\propto n_0^3 \tilde{t}, & \varphi &\propto \tilde{\varphi}, \\ \omega &\propto n_0^{-3} \tilde{\omega}, & \mathcal{E} &\propto n_0^{-4} \tilde{\mathcal{E}}. \end{aligned} \quad (78.27)$$

In the scaled units, the Hamiltonian $\tilde{H} = n_0^{-2} H$ of the system becomes

$$\tilde{H} = \frac{\tilde{p}^2}{2m} - \frac{1}{\tilde{r}} + \tilde{z} e \tilde{\mathcal{E}} \cos(\tilde{\omega} \tilde{t} + \tilde{\varphi}), \quad (78.28)$$

i.e., it depends only on $\tilde{\omega}$ and $\tilde{\mathcal{E}}$. In experiments, the principal quantum number n_0 of the prepared initial state typically ranges from 1 to 100.

Classical scaling extends to the fields of other polarizations and to pulsed excitations, provided that the number of cycles in the rise, top, and fall of the pulse is kept fixed. This scaling does not hold for a quantum Hamiltonian, unless one also rescales Planck's constant, $\tilde{\hbar} = \hbar/n_0$. In practice, increasing n_0 , keeping $\tilde{\mathcal{E}}$ and $\tilde{\omega}$ constant, corresponds to

a decrease in the effective \hbar toward the classical limit. In view of this classical scaling, experimental and theoretical results are usually analyzed in terms of the scaled variables. Since the classical dynamics generated by the Hamiltonian Eq. (78.28) exhibits chaotic behavior in some regimes, the dynamics of the corresponding quantum system is frequently referred to as an example of quantum chaos [91–93].

Regimes of Response

By varying the initial n_0 , several regimes of the scaled parameters can be covered. The experimentally measured response of Rydberg atoms in microwave fields can be divided into six categories:

The tunneling regime

For $\tilde{\omega} \leq 0.07$, the response of the system is accurately represented as tunneling through the slowly oscillating potential barrier composed of the Coulomb and microwave potentials.

The low-frequency regime

For $0.05 \leq \tilde{\omega} \leq 0.3$, the ionization probability exhibits distinct structures (bumps, steps, changes of slope) as a function of the field strength. The quantum probability curves might be lower or higher than the corresponding classical counterparts, calculated with the aid of the phase averaging method (Sect. 78.4.5).

The semiclassical regime

For $0.1 \leq \tilde{\omega} \leq 1.2$, the ionization probabilities agree well for most frequencies with the results obtained from the classical theory. In particular, the onset of ionization and appearance intensities (i.e., the intensities at which a given degree of ionization is achieved) coincide with the onset of chaos in the classical dynamics. In the ionization probabilities, resonances appear that correspond to the classical trapping resonances [91–94].

The transition region

For $1 \leq \tilde{\omega} \leq 2$, the differences between the quantum and classical results are visible. Quantum ionization probabilities are frequently lower and appearance intensities higher than their classical counterparts.

The high-frequency regime

For $\tilde{\omega} \geq 2$, quantum results for ionization probabilities are systematically lower and appearance intensities higher than their classical counterparts. This apparent stability of the quantum system has been attributed to three kinds of effects: quantum localization [94], quantum scars [95], and perhaps the stabilization of atoms in intense laser fields (Sect. 78.3.6).

The photoeffect regime

When the scaled frequency becomes greater than the single-photon ionization threshold, the system undergoes single-photon ionization (the photoeffect).

Quantum Localization

The classical dynamics changes as the field increases. Chaotic trajectories start to fill the phase space and, as the KAM tori (describing periodic orbits) [91–93] break down, the motion becomes stochastic, resembling a random walk. This process, in which the mean energy grows linearly in time, is termed diffusive ionization. In quantum theory, diffusion corresponds to a random walk over a ladder of suitably chosen quantum levels. However, both diagonal and off-diagonal elements of the evolution operator, which describe quantum mechanical amplitudes for transitions between the levels, depend in a quasi-periodic manner on the quantum numbers of the levels involved. Such quasiperiodic behavior is quite analogous to a random one. Electronic wave packets, which initially spread in accordance with the classical laws, tend to remain localized for longer times due to destructive quantum-interference effects. Quantum localization is an analog of the Anderson localization of electronic wave functions propagating in random media [94].

Quantum Scars

Even in the fully chaotic regime, classical phase space contains periodic, although unstable, orbits. Nevertheless, quantum mechanical wave-function amplitudes can become localized around these unstable orbits, resulting in what are called quantum scars. The increased stability of the hydrogen atom at $\tilde{\omega} \approx 1.3$ has, in fact, been attributed [95] to the effects of quantum scars. These effects are very sensitive to fluctuations in the driving laser field. Control of the laser noise, therefore, provides a powerful spectroscopic tool to study such quantal phenomena [96]. Using this tool, it has become possible to demonstrate the effects of quantum scars in the intermediate regime of scaled frequencies, i.e., for values less than but close to 1.

78.4 Strong-Field Computational Techniques

The SS pulse regime requires a nonperturbative solution of the TDSE. We describe here two of the most used approaches: the explicit numerical solution of the TDSE and the Floquet expansion technique. In addition to these, several approximate methods have been proposed.

78.4.1 Floquet Theory

The excitation and ionization dynamics of an atom in a strong laser field can be determined by turning the problem

into a time-independent eigenvalue problem [26, 97]. From Floquet's theorem, the eigenfunctions for a perfectly periodic Hamiltonian of the form

$$H = H_0 + \sum_{N \neq 0} H_N e^{-iN\omega t} \quad (78.29)$$

can be expressed as

$$\Psi(t) = e^{-iXt/\hbar} \sum_N e^{-iN\omega t} \psi_N. \quad (78.30)$$

Putting this into the time-dependent Schrödinger equation results in an infinite set of coupled Floquet equations for the harmonic components ψ_N . In the velocity gauge, the Floquet equations are

$$(X + N\hbar\omega - H_0)\psi_N = V_+ \psi_{N-1} + V_- \psi_{N+1}, \quad (78.31)$$

where, for a vector potential of amplitude \mathcal{A} ,

$$V_+ = -\frac{e}{2mc} \mathcal{A} \cdot \mathbf{p}, \quad (78.32)$$

and $V_- = V_+^\dagger$. The Eq. (78.31) has been solved, after truncation to a manageable number of terms, using many techniques to provide what are called the quasi-energy states of the laser-atom system. The eigenvalues X of these equations are complex, with $\text{Im}(X)$ giving the decay or ionization rate for the system. The generated rates are found to be very accurate as long as the pulse length of the laser field is not too short, at least hundreds of cycles. The eigenfunctions provide the amplitudes for the photoelectron energy spectra, and the time-dependent dipole of the state can be related to the photoemission spectrum of the system. Yields for slowly varying pulses can be constructed by combining the results from the individual, fixed-intensity calculations [26].

The Floquet method can be applied for any periodic Hamiltonian. In strong enough fields of high frequency, the Floquet equations can be truncated to a very small set in the K–H frame [78].

78.4.2 Direct Integration of the TDSE

Methods for the direct solution of the time-dependent Schrödinger equation (TDSE) are described in general in Chap. 8 and in [98, 99] for multiphoton processes. The wave functions are defined on spatial grids or in terms of an expansion in basis functions. The time evolution is obtained by either explicit or implicit time propagators. All these methods are capable of generating numerically exact results for an atom with a single electron in a short pulsed field for a wide range of pulse shapes, wavelengths, and intensities. The solutions are time-dependent wave functions for the electrons,

which can be analyzed to obtain excitation and ionization rates, photoelectron energies, angular distributions, and photoemission yields. The ability to generate an explicit solution of the TDSE allows the study of arbitrary pulse shapes and provides insight into the excitation dynamics.

For multielectron atoms, one generally has to limit the calculations to that for a single electron in effective potentials, which represent, as well as possible, the influences of the remaining atomic electrons. This approach is called the single-active electron (SAE) approximation, and it gives generally accurate results for systems with no low-lying doubly excited states, for example, the noble gases [98]. In these cases, the excitation dynamics is dominated by the sequential promotion of a single electron at a time.

78.4.3 Volkov States

A laser interacting with a free electron superimposes an oscillatory motion on its drift motion in response to the field. The wave function for an electron with drift velocity $\mathbf{v} = \hbar\mathbf{k}/m$ is given by

$$\begin{aligned} \Psi_V(\mathbf{r}, t) &= \exp\left(-\frac{i}{2m\hbar} \int^t \left[\hbar\mathbf{k} - \frac{e}{c}\mathbf{A}(t')\right]^2 dt'\right) e^{i[\mathbf{k} - e\mathbf{A}(t)/\hbar c] \cdot \mathbf{r}}, \end{aligned} \quad (78.33)$$

where $\mathbf{A}(t) = -c \int^t \mathbf{E}(t') dt'$ is the vector potential of the field; Ψ_V is called a Volkov state. In a linearly polarized field, the electron oscillates along the direction of polarization with an amplitude $\alpha_0 = e\hbar\mathcal{A}/(mc\omega)$. In the strong-field regime, this amplitude can greatly exceed the size of a bound-state orbital. Volkov states provide a useful tool that can be applied in various strong-field approximations discussed in Sect. 78.4.4.

78.4.4 Strong-Field Approximations

There have been several attempts to solve the TDSE in the strong-field limit using approximate but analytic methods. Such strong-field approximations (SFA) typically neglect all the bound states of the atom except for the initial state. In the tunneling regime ($\gamma < 1$), and a quasi-static limit ($\omega \rightarrow 0$), one can use a theory [55] in which the ionization occurs due to the tunneling through the Coulomb barrier distorted by the electric field of the laser. The wave function is constructed as a combination of a bare initial wave function of the electron (close to the nucleus) and a wave function describing a motion of the electron in a quasi-static electric field (far from the nucleus). In a second approach [37–39], the elements of the scattering matrix \hat{S} are calculated assuming that initially the

electronic wave function corresponds to a bare bound state. On the other hand, the final, continuum states of the electron are described by dressed wave functions that account for the free motion of the electron in the laser field. In the simplest case, such dressed states are Volkov states Eq. (78.33). Alternatively, the time-reversed \hat{S} -matrix is obtained by dressing the initial state and using field-free scattering states for the final state.

Yet another method consists of expanding the electronic continuum–continuum dipole matrix elements in terms corresponding to matrix elements for free electrons plus corrections due to the potential [57]. In the latter version of the SFA, the amplitude of the electronic wave function $b(\mathbf{p})$, corresponding to an outgoing momentum \mathbf{p} , is given by

$$b(\mathbf{p}) = i \int_0^{t_F} dt \mathbf{d}[\mathbf{p} - e\mathbf{A}(t)/c] \cdot \mathbf{E}(t) \exp[-iS(t_F, t)/\hbar]. \quad (78.34)$$

Here, $\mathbf{d}[\mathbf{p} - e\mathbf{A}(t)/c]$ denotes the dipole matrix element for the transition from the initial bound state to the continuum state in which the electron has the kinetic momentum $\mathbf{p} - e\mathbf{A}(t)/c$, t_F is the switch-off time of the laser pulse, and

$$S(t_F, t) = \int_t^{t_F} dt' \left[\frac{[\mathbf{p} - e\mathbf{A}(t')/c]^2}{2m} + I_P \right] \quad (78.35)$$

is a quasi-classical action for an electron that is born in the continuum at t and propagates freely in the laser field. The form of the expression Eq. (78.34) is generic to the SFA.

78.4.5 phase-space Averaging Method

The methods of classical mechanics are particularly useful in describing the microwave excitation of highly excited (Rydberg) atoms [89, 90] (Sect. 78.3.8), but have also been applied to describe HHG, stabilization of atoms in super-intense fields, and two-electron ionization [100–102].

The classical phase-space averaging method [103] solves Newton's equations of motion

$$\dot{\mathbf{r}} = \frac{\mathbf{p}}{m}, \quad (78.36)$$

$$\dot{\mathbf{p}} = -\nabla V(\mathbf{r}) - e\mathbf{E}(t), \quad (78.37)$$

for an electron interacting with an ion core and an external laser field. A distribution of initial conditions in phase space is chosen to mimic the initial quantum mechanical state of the system, and a sample of classical trajectories is generated. Quantum mechanical averages of physical observables are then identified with ensemble averages of those observables

over the initial distribution. Since the dynamics of multiphoton processes is very complex, the neglected phases in this approach generally cause negligible errors, and the results can be in quite good agreement with quantum calculations. Additionally, an examination of the trajectories provides details of the excitation dynamics, which are often difficult to extract from a complex time-dependent wave function.

78.5 Atto-Nano Physics

The interaction of ultrashort strong laser pulses with larger systems has recently received much attention; it has led to a consequent advance in our understanding of the attosecond to few-femtosecond electronic and nuclear dynamics. For instance, the interaction of atomic clusters with strong ultrafast laser fields has long been known to lead to the formation of nanoplasmas in which there is, on the one hand, a high degree of charge localization and ultrafast dynamics and, on the other hand, the emission of both very energetic (multiple keV) electrons and highly charged ions (in the MeV energy range). Interestingly, the most recent utilization of ultrashort few-cycle pulses (≈ 10 fs) to trigger the laser–matter processes has succeeded in isolating the electron dynamics from the longer ion dynamics timescale (which can essentially be considered as frozen) revealing a higher degree of fragmentation anisotropy in both electrons and ions compared to the isotropic distributions found from much longer (multicycle) pulses (100 fs).

Additionally, interactions of intense lasers with nanoparticles, such as micron and submicron scale liquid droplets, lead to hot plasma formation. An important role is found for enhanced local fields on the surface of these droplets, the so-called hot spots. Furthermore, studies of driving bound and free charges in larger molecules, e.g., collective electron dynamics in fullerenes and in graphene-like structures, proton migration in hydrocarbon molecules, charge migration in proteins and biomolecules, amongst others, could be included in this category. In addition, biological applications of atto-nano physics could be envisaged as well, e.g., to explain the DNA-protein interactions in solutions of living cells, study the induced covalent crosslink between aromatic amino acids and peptides, and characterize the protein–protein interactions in living cells. In turn, laser-driven broadband electron wavepackets have been used for static and dynamic diffraction imaging of molecules, obtaining structural information with subnanometer spatial and subfemtosecond temporal resolution (Sect. 78.3.4).

Tailored ultrashort and intense fields have also been used to drive electron dynamics and electron or photon emission from (nanostructured) solids (for a recent compilation: [104]). The extraordinary progress seen recently has been largely driven by advances in both experimental, e.g., laser technology, and engineering, e.g., nanofabrication, tech-

niques. Amongst the remarkable achievements in just the most recent years are the demonstration of driving electron currents and switching the conductivity of dielectrics with ultrashort pulses, controlling the light-induced electron emission from nanoparticles and nanotips, and the subcycle-driven photon emission from solids. Furthermore, the intrinsic electron propagation and photoemission processes have been investigated on their natural, attosecond timescales.

A key feature of light-nanostructure interactions is the enhancement, by several orders of magnitude, of the electric near-field and its local confinement on a subwavelength scale. From a theoretical viewpoint, this field localization presents a unique challenge: we have at our disposal strong fields that change on a comparable spatial scale of the oscillatory electron dynamics that are initiated by those same fields. This peculiar property entails profound consequences in the underlying physics of the conventional strong-field phenomena. In particular, it violates one of the main assumptions that the modeling of strong-field interactions is based upon: the spatial homogeneity of laser fields in the volume of the electronic dynamics under scrutiny (this hypothesis was *per se* considered in all the previous sections of this chapter).

Interestingly, an exponential growing attraction in strong-field phenomena induced by plasmonic-enhanced fields was sparked by the controversial work of Kim et al. [105]. These authors claimed having observed efficient HHG from noble-gas atoms driven by the plasmonic-enhanced field generated by bow-tie metallic nanostructures. Although later on the interpretation of the outcomes was demonstrated to be incorrect [106], Kim's paper definitively stimulated a steadily constant interest in the plasmonic-enhanced HHG and ATI. We should mention, however, a very recent result of the same group, which clearly seems to be well justified and, as such, opens new perspectives and ways toward efficient HHG using nanostructures [107]. In this recent contribution, the authors demonstrate experimentally plasmonic-driven HHG by devising a metal-sapphire nanostructure that provides a solid tip as the HHG emitter instead of gaseous atoms. Measured EUV spectra show odd-order harmonics up to 60-nm wavelengths, without the plasma atomic lines typically seen when using gaseous atoms as the HHG-driven media. This experimental data confirm that the plasmonic HHG approach is a promising way to make real coherent EUV sources for nanoscale near-field applications in spectroscopy, microscopy, lithography, and attosecond physics (for another recent related experiment, see, e.g., [108]).

Within the conventional assumption, both the laser electric field, $\mathbf{E}(\mathbf{r}, t)$, and the corresponding vector potential, $\mathbf{A}(\mathbf{r}, t)$, are spatially homogeneous in the region where the electron moves and only their time dependence is considered, i.e., $\mathbf{E}(\mathbf{r}, t) = \mathbf{E}(t)$ in Eq. (78.2) and $\mathbf{A}(\mathbf{r}, t) = \mathbf{A}(t)$ in Eq. (78.4). This is a genuine assumption considering the usual electron excursion α_0 is bounded roughly by a few nanometers in the NIR, for typical laser intensities, and sev-

eral tens of nanometers for MIR sources (note that $\alpha_0 \propto \mathcal{E}\lambda^2$, where λ is the wavelength of the driving laser and $\mathcal{E} = \sqrt{I}$, where I is the laser intensity). Hence, electron excursions are very small relative to the spatial variation of the field in the absence of local (or nanoplasmonic) field enhancement. On the contrary, the fields generated using surface plasmons are spatially dependent on a nanometric region. As a consequence, all the standard theoretical tools in the strong-field ionization toolbox described previously, ranging from purely classical to frequently used semiclassical and complete quantum mechanical descriptions, have to be reexamined. For a comprehensive review about atto-nano physics see, e.g., [109]

Acknowledgments ML acknowledges support from: ERC AdG NOQIA; Agencia Estatal de Investigación (R&D project CEX2019-000910-S, funded by MCIN/AEI/10.13039/501100011033, Plan National FIDEUA PID2019-106901GB-I00, FPI, QUANTERA MAQS PCI2019-111828-2, Proyectos de I+D+I “Retos Colaboración” QUSPIN RTC2019-007196-7), MCIN via European Union NextGenerationEU (PRTR-C17.I1); Fundació Cellex; Fundació Mir-Puig; Generalitat de Catalunya through the European Social Fund FEDER and CERCA program (AGAUR Grant No. 2017 SGR 134, QuantumCATU16-011424, co-funded by ERDF Operational Program of Catalonia 2014–2020); EU Horizon 2020 FET-OPEN OPTologic (Grant No 899794); National Science Centre, Poland (Symfonia Grant No. 2016/20/W/ST4/00314); European Union’s Horizon 2020 research and innovation programme under the Marie-Sklodowska-Curie grant agreement No 101029393 (STREDCH) and No 847648 (“La Caixa” Junior Leaders fellowships ID100010434: LCF/BQ/PI19/11690013, LCF/BQ/PI20/11760031, LCF/BQ/PR20/11770012, LCF/BQ/PR21/11840013). MFC acknowledges financial support from the Guangdong Province Science and Technology Major Project (Future functional materials under extreme conditions – 2021B0301030005).

References

- Faisal, F.H.M.: Theory of Multiphoton Processes. Plenum, New York (1987)
- Gavrila, M. (ed.): Atoms in Intense Laser Fields. Academic Press, San Diego (1992)
- Mittleman, M.H.: Theory of Laser–Atom Interactions, 2nd edn. Plenum, New York (1993)
- Lambropoulos, P., Smith, S.J. (eds.): Proceedings of the International Conference of Multiphoton Processes III, 1984 vol. 2. Springer, Berlin, Heidelberg (1984)
- Smith, S.J., Knight, P.L. (eds.): Proceedings of the International Conference on Multiphoton Processes IV, 1988 vol. 8. Cambridge University Press, Cambridge (1988)
- Mainfray, G., Agostini, P. (eds.): Proceedings of the International Conference on Multiphoton Processes V, 1991. Centre d’Etudes de Saclay, Saclay (1991)
- DiMauro, L.F., Freeman, R.R., Kulander, K.C. (eds.): *Proceedings of the International Conference of Multiphoton Processes VIII*, AIP Conference Proceedings vol. 525. American Institute of Physics, Melville (2000)
- Piroux, B., L’Huillier, A., Rzążewski, K. (eds.): Super-Intense Laser–Atom Physics vol. 316. Plenum, New York (1993)
- Piroux, B., Rzążewski, K. (eds.): *Super-Intense Laser-Atom Physics*, NATO ASI Series II vol. 12. Kluwer Academic, The Netherlands (2001)
- Lambropoulos, P.: Adv. At. Mol. Phys. **12**, 87–158 (1976)
- Gontier, Y., Trahin, M.: J. Phys. B **13**, 4383 (1980)
- Tang, X., Lambropoulos, P.: Phys. Rev. Lett. **58**, 108 (1987)
- Eberly, J.H.: Phys. Rev. Lett. **47**, 408 (1981)
- Lambropoulos, P., Zoller, P.: Phys. Rev. A **24**, 379 (1981)
- Knight, P.L., Lauder, M.A., Dalton, B.J.: Phys. Rep. **190**, 1 (1990)
- Risken, H.: In: Haken, H. (ed.) The Fokker–Planck Equation: Methods of Solution and Applications. Springer, Berlin, Heidelberg (1984)
- Eberly, J.H.: In: Walther, H., Rothe, K.W. (eds.) Laser Spectroscopy, p. 80. Springer, Berlin, Heidelberg (1979)
- Zoller, P.: In: Lambropoulos, P., Smith, S.J. (eds.) Proceedings of the International Conference of Multiphoton Processes III, 1984, vol. 2, pp. 68–75. Springer, Berlin, Heidelberg (1984)
- Elliot, D.S.: In: Lambropoulos, P., Smith, S.J. (eds.) Proceedings of the International Conference of Multiphoton Processes III, 1984, vol. 2, pp. 76–81. Springer, Berlin, Heidelberg (1984)
- Elliot, D.S., Hamilton, M.W., Arnett, K., Smith, S.J.: Phys. Rev. A **32**, 887 (1985)
- Burshtein, A.I.: Sov. Phys. JETP **21**, 597 (1965)
- Burshtein, A.I.: Sov. Phys. JETP **22**, 939 (1966)
- Shore, B.W.: The Theory of Coherent Atomic Excitation. Wiley, New York (1990)
- Lompré, L.A., Mainfray, G., Manus, C., Marinier, J.P.: J. Phys. B **14**, 4307 (1981)
- Chen, C., Elliot, D.S.: Phys. Rev. Lett. **65**, 1737 (1990)
- Potvliege, R.M., Shakeshaft, R.: In: Gavrilu, M. (ed.) Atoms in Intense Laser Fields, pp. 373–434. Academic Press, San Diego (1992)
- Faucher, O., et al.: Phys. Rev. Lett. **70**, 3004 (1993)
- Field, J.E., Harris, S.E.: Phys. Rev. Lett. **66**, 1154 (1991)
- Harris, S.E.: Phys. Rev. Lett. **70**, 552 (1993)
- Hurst, G.S., Payne, M.G., Kramer, S.D., Young, J.P.: Rev. Mod. Phys. **52**, 767 (1979)
- Wirth, A., Hassan, M.T., Grguraš, I., Gagnon, J., Moulet, A., Luu, T.T., Pabst, S., Santra, R., Alahmed, Z.A., Azzeer, A.M., Yakovlev, V.S., Pervak, V., Krausz, F., Goulielmakis, E.: Science **334**, 195 (2011)
- Fattahi, H., Barros, H.G., Gorjan, M., Nubbemeyer, T., Alsaif, B., Teisset, C.Y., Schultze, M., Prinz, S., Haefner, M., Ueffing, M., Alismail, A., Vámos, L., Schwarz, A., Pronin, O., Brons, J., Geng, X.T., Arisholm, G., Ciappina, M.F., Yakovlev, V., Kim, D.-E., Azzeer, A.M., Karpowicz, N., Sutter, D., Major, Z., Metzger, T., Krausz, F.: Optica **1**, 45 (2014)
- Lewenstein, M., L’Huillier, A.: Strong Field Laser Physics. In: Brabec, T. (ed.) Springer Series in Optical Sciences, vol. 137, pp. 147–183. Springer, Berlin (2008)
- Perry, M.D., Mourou, G.: Science **264**, 917 (1994)
- Kulander, K.C., Schafer, K.J., Krause, J.L.: Super-Intense Laser-Atom Physics. In: Piroux, B., Rzążewski, K. (eds.) NATO ASI Series II, vol. 12, pp. 95–110. Kluwer Academic, The Netherlands (2001)
- Corkum, P.B.: Phys. Rev. Lett. **73**, 1995 (1993)
- Keldysh, L.V.: Sov. Phys. JETP **20**, 1307 (1965)
- Reiss, H.R.: Phys. Rev. A **22**, 1786 (1980)
- Faisal, F.: J. Phys. B **6**, 312 (1973)
- Fittinghoff, D., Bolton, P.R., Chang, B., Kulander, K.C.: Phys. Rev. A **49**, 2174 (1994)
- Becker, W., Liu, X., Ho, P.J., Eberly, J.H.: Rev. Mod. Phys. **84**, 1011–1043 (2012)

42. Muller, H.G., Agostini, P., Petite, G.: In: Gavrilu, M. (ed.) *Atoms in Intense Laser Fields*, pp. 1–42. Academic Press, San Diego (1992)
43. Freeman, R.R., et al.: In: Gavrilu, M. (ed.) *Atoms in Intense Laser Fields*, pp. 43–65. Academic Press, San Diego (1992)
44. Eberly, J.H., Javanainen, J., Rzążewski, K.: *Phys. Rep.* **204**, 331 (1991)
45. Milosević, D.B., Paulus, G.G., Bauer, D., Becker, W.: *J. Phys. B* **39**, R202–R262 (2006)
46. Hentschel, M., Kienberger, R., Spielmann, C., Reider, G.A., Milošević, N., Brabec, T., Corkum, P., Heinzmann, U., Drescher, M., Krausz, F.: *Nature* **414**, 509 (2001)
47. Sola, I.J., Mével, E., Elouga, L., Constant, E., Strelkov, V., Poletto, L., Villoresi, P., Benedetti, E., Caumes, J.-P., Stagira, S., Vozzi, C., Sansone, G., Nisoli, M.: *Nat. Phys.* **2**, 319 (2006)
48. Bergues, B., Kübel, M., Kling, N.G., Burger, C., Kling, M.F.: *IEEE J. Sel. Top. Quantum Electron.* **21**, 8701009 (2015)
49. Paulus, G.G., Grasbon, F., Walther, H., Villoresi, P., Nisoli, M., Stagira, S., Priori, E., De Silvestri, S.: *Nature* **414**, 182 (2001)
50. Wolter, B., Pullen, M.G., Le, A.-T., Baudisch, M., Doblhoff-Dier, K., Senfleben, A., Hemmer, M., Schröter, C.D., Ullrich, J., Pfeifer, T., Moshhammer, R., Gräfe, S., Vendrell, O., Lin, C.D., Biegert, J.: *Science* **354**, 308 (2016)
51. Sciaini, G., Miller, R.J.D.: *Rep. Prog. Phys.* **74**, 096101 (2011)
52. L’Huillier, A., Lompré, L.-A., Mainfray, G., Manus, C.: In: Gavrilu, M. (ed.) *Atoms in Intense Laser Fields*, pp. 139–205. Academic Press, San Diego (1992)
53. Liang, Y., Ammosov, M.V., Chin, S.L.: *J. Phys. B* **27**, 1269 (1994)
54. Salières, P., L’Huillier, A., Antoine, P., Lewenstein, M.: In: Bederson, B., Walther, H. (eds.) *Advances of Atomic and Molecular Physics*, 41st edn., pp. 83–142. Academic Press, New York (1999)
55. Ammosov, M.V., Delone, N.B., Krainov, V.P.: *Sov. Phys. JETP* **64**, 1191 (1986)
56. Krause, J.L., Schafer, K.J., Kulander, K.C.: *Phys. Rev. A* **45**, 4998 (1992)
57. Lewenstein, M., Balcou, P., Ivanov, M.Y., L’Huillier, A., Corkum, P.: *Phys. Rev. A* **49**, 2117 (1994)
58. L’Huillier, A., Schafer, K.J., Kulander, K.C.: *J. Phys. B* **24**, 3315 (1991)
59. L’Huillier, A., Lewenstein, M., Salières, P., Balcou, P., Larsson, J., Wahlström, C.G.: *Phys. Rev. A* **48**, 4091 (1993)
60. Budil, K.S., Salières, P., L’Huillier, A., Ditmire, T., Perry, M.D.: *Phys. Rev. A* **48**, 3437 (1993)
61. Harris, S.E., Macklin, J.L., Hänsch, T.W.: *Opt. Comm.* **100**, 487 (1993)
62. Krausz, F., Ivanov, M.: *Rev. Mod. Phys.* **81**, 163 (2009)
63. Corkum, P.B., Krausz, F.: *Nat. Phys.* **3**, 381 (2007)
64. Drescher, M., Hentschel, M., Kienberger, R., Tempea, G., Spielmann, C., Reider, G.A., Corkum, P.B., Krausz, F.: *Science* **291**, 1923 (2001)
65. Paul, P.M., Toma, E.S., Breger, P., Mullot, G., Aug, F., Balcou, P., Muller, H.G., Agostini, P.: *Science* **292**, 1689 (2001)
66. Li, J., Ren, X., Yin, Y., Zhao, K., Chew, A., Cheng, Y., Cunningham, E., Wang, Y., Hu, S., Wu, Y., Chini, M., Chang, Z.: *Nat. Commun.* **8**, 186 (2017)
67. Dinu, L.C., Muller, H.G., Kazamias, S., Mullot, G., Aug, F., Balcou, P., Paul, P.M., Kovačev, M., Breger, P., Agostini, P.: *Phys. Rev. Lett.* **91**, 063901 (2003)
68. Baltuška, A., Udem, T., Uiberacker, M., Hentschel, M., Goulielmakis, E., Gohle, C., Holzwarth, R., Yakovlev, V.S., Scrinzi, A., Hänsch, T.W., Krausz, F.: *Nature* **421**, 611 (2003)
69. Itatani, J., Levesque, J., Zeidler, D., Niikura, H., Pépin, H., Kieffer, J.C., Corkum, P.B., Villeneuve, D.M.: *Nature* **432**, 867 (2004)
70. Lein, M.: *J. Phys. B* **40**, R135 (2007)
71. Ghimire, S., DiChiara, A.D., Sistrunk, E., Agostini, P., DiMauro, L.F., Reis, D.A.: *Nat. Phys.* **7**, 138 (2011)
72. Vampa, G., Brabec, T.: *J. Phys. B* **50**, 083001 (2017)
73. Vampa, G., Hammond, T.J., Thiré, N., Schmidt, B.E., Légaré, F., McDonald, C.R., Brabec, T., Corkum, P.B.: *Nature* **522**, 462 (2015)
74. Hohenleutner, M., Langer, F., Schubert, O., Knorr, M., Huttner, U., Koch, S.W., Kira, M., Huber, R.: *Nature* **523**, 572 (2015)
75. Schubert, O., Hohenleutner, M., Langer, F., Urbanek, B., Lange, C., Huttner, U., Golde, D., Meier, T., Kira, M., Koch, S.W., Huber, R.: *Nat. Phot.* **8**, 119 (2014)
76. Liu, H., Li, Y., You, Y.S., Ghimire, S., Heinz, T.F., Reis, D.A.: *Nat. Phys.* **13**, 262 (2017)
77. Luu, T.T., Wörner, H.J.: *Nat. Comm.* **9**, 916 (2018)
78. Gavrilu, M.: In: Gavrilu, M. (ed.) *Atoms in Intense Laser Fields*, pp. 435–510. Academic Press, San Diego (1992). and references therein
79. Su, Q., Eberly, J.H., Javanainen, J.: *Phys. Rev. Lett.* **64**, 862 (1990)
80. Kulander, K.C., Schafer, K.J., Krause, J.L.: *Phys. Rev. Lett.* **66**, 2601 (1991)
81. Fedorov, M.V.: *Super-Intense Laser-Atom Physics*. In: Piraux, B., Rzążewski, K. (eds.) *NATO ASI Series II*, vol. 12, pp. 245–259. Kluwer Academic, The Netherlands (2001)
82. de Boer, M.P., Hoogenraad, J.H., Vrijen, R.B., Noordam, L.D., Muller, H.: *Phys. Rev. Lett.* **71**, 3263 (1993)
83. Dum, R., Sanpera, A., Suominen, K.-A., Brewczyk, M., Kuś, M., Rzążewski, K., Lewenstein, M.: *Phys. Rev. Lett.* **80**, 3899 (1998)
84. Sala, S., Förster, J., Saenz, A.: *Phys. Rev. A* **95**, 011403 (2017)
85. R. Senaratne, S. V. Rajagopal, T. Shimasaki, P. E. Dotti, K. M. Fujiwara, K. Singh, Z. A. Geiger, D. M. Weld: *arXiv:1711.02654* (2017)
86. Bandrauk, A.D. (ed.): *Molecules in Laser Fields*. Dekker, New York (1994)
87. Normand, D., Cornaggia, C.: *Super-Intense Laser-Atom Physics*. In: Piraux, B., Rzążewski, K. (eds.) *NATO ASI Series II*, vol. 12, pp. 351–362. Kluwer Academic, The Netherlands (2001)
88. Fennel, T., Meiwes-Broer, K.-H., Tiggesbäumker, J., Reinhard, P.-G., Dinh, P.M., Suraud, E.: *Rev. Mod. Phys.* **82**, 1793 (2010)
89. Koch, P.M.: *Super-Intense Laser-Atom Physics*. In: Piraux, B., Rzążewski, K. (eds.) *NATO ASI Series II*, vol. 12, pp. 305–316. Kluwer Academic, The Netherlands (2001)
90. Koch, P.M.: *Proceedings of the Eighth South African Summer School in Physics*. Heidelberg, vol. 1993. Springer, Berlin (1993)
91. Gutzwiller, M.C.: *Chaos in Classical and Quantum Mechanics*. Springer, Berlin, Heidelberg (1990)
92. Haake, F.: *Quantum Signatures of Chaos*. Springer, Berlin, Heidelberg (1991)
93. Casati, G., Chirikov, B., Shepelyansky, D.L., Guarneri, I.: *Phys. Rep.* **154**, 77 (1987)
94. Casati, G., Guarneri, I., Shepelyansky, D.L.: *Phys. A* **163**, 205 (1990). and references therein
95. Jensen, R.V., Sanders, M.M., Saraceno, M., Sundaram, B.: *Phys. Rev. Lett.* **63**, 2771 (1989)
96. Sirko, L., Bellermand, M.R.W., Haffmans, A., Koch, P.M., Richards, D.: *Phys. Rev. Lett.* **71**, 2895 (1993)
97. Chu, S.I.: *Adv. Chem. Phys.* **73**, 739 (1989)
98. Kulander, K.C., Schafer, K.J., Krause, J.L.: In: Gavrilu, M. (ed.) *Atoms in Intense Laser Fields*, pp. 247–300. Academic Press, San Diego (1992)
99. Burnett, K., Reed, V.C., Knight, P.L.: *J. Phys. B* **26**, 561 (1993)
100. Lewenstein, M., Rzążewski, K., Salières, P.: *Super-Intense Laser-Atom Physics*. In: Piraux, B., Rzążewski, K. (eds.) *NATO ASI Series II*, vol. 12, pp. 425–434. Kluwer Academic, The Netherlands (2001)

101. Lerner, P.B., LaGattuta, K., Cohen, J.S.: Super-Intense Laser-Atom Physics. In: Piraux, B., Rzażewski, K. (eds.) NATO ASI Series II, vol. 12, pp. 413–424. Kluwer Academic, The Netherlands (2001)
102. Vèniard, V., Maquet, A., Mènis, T.: Super-Intense Laser-Atom Physics. In: Piraux, B., Rzażewski, K. (eds.) NATO ASI Series II, vol. 12, pp. 225–232. Kluwer Academic, The Netherlands (2001)
103. Leopold, J.G., Percival, I.C.: *J. Phys. B* **12**, 709 (1979)
104. Hommelhoff, P., Kling, M.F.: *Attosecond Nanophysics: from Basic Science to Applications*. Wiley, Berlin (2015)
105. Kim, S., Jin, J., Kim, Y.-J., Park, I.-Y., Kim, Y., Kim, S.-W.: *Nature* **453**, 757 (2008)
106. Sivis, M., Duwe, M., Abel, B., Ropers, C.: *Nat. Phys.* **9**, 304 (2013)
107. Han, S., Kim, H., Kim, Y.W., Kim, Y.-J., Kim, S., Park, I.-Y., Kim, S.-W.: *Nat. Commun.* **7**, 13105 (2016)
108. Vampa, G., Ghamsari, B.G., Siadat Mousavi, S., Hammond, T.J., Olivieri, A., Lisicka-Skrek, E., Naumov, A.Y., Villeneuve, D.M., Staudte, A., Berini, P., Corkum, P.B.: *Nat. Phys.* **13**, 659 (2017)
109. Ciappina, M.F., Pérez-Hernández, J.A., Landsman, A.S., Okell, W.A., Zherebtsov, S., Förg, B., Schötz, J., Seiffert, L., Fennel, T., Shaaran, T., Zimmermann, T., Chacón, A., Guichard, R., Zair, A., Tisch, J.W.G., Marangos, J.P., Witting, T., Braun, A., Maier, S.A., Roso, L., Krüger, M., Hommelhoff, P., Kling, M.F., Krausz, F., Lewenstein, M.: *Rep. Prog. Phys.* **80**, 054401 (2017)



Marcelo Ciappina Dr Ciappina received his PhD from the Balseiro Institute at Argentina in 2005 and a Research Professor degree from the Czech Academy of Sciences in 2019. His academic training includes postdoctoral stays at renowned institutions in Germany, Singapore, USA, and Spain. At present, he is Senior Researcher at ELI-Beamlines. His areas of interest include attosecond science and atomic collisions.



Alexis A. Chacon S. Alexis A. Chacon S. obtained his PhD in Quantum Optics-Physics at Universidad de Salamanca-Spain (2015). He then moved to QIT group led by Lewenstein at ICFO to expand his background to electron and photon emissions from atoms and solids. Alexis joined LANL-USA in 2017 and is currently Group Leader at MPI-Korea pursuing ultrafast physics in quantum materials.



Maciej Lewenstein Maciej Lewenstein received his PhD in Essen, Germany, in 1983. He has worked at the Center for Theoretical Physics, Harvard University, CEA Saclay, and Leibniz University, Hannover. In 2005 he became ICREA Professor and Group Leader at ICFO in Castelldefels. His interests include quantum optics, quantum physics, quantum information, many-body theory, attophysics, and statistical physics. He is also an acclaimed jazz writer and critic.



Juha Javanainen

Contents

79.1	Notation	1141
79.2	Control of Atomic Motion by Light	1142
79.2.1	General Theory	1142
79.2.2	Two-State Atoms	1144
79.2.3	Multistate Atoms	1147
79.3	Magnetic Trap for Atoms	1148
79.3.1	Evaporative Cooling	1148
79.4	Trapping and Cooling of Charged Particles	1149
79.4.1	Paul Trap	1149
79.4.2	Penning Trap	1150
79.4.3	Collective Effects in Ion Clouds	1151
79.5	Experimental	1152
79.5.1	Free Particles	1152
79.5.2	Trapped Particles	1152
79.6	Applications	1153
79.6.1	Cold Molecules	1153
79.6.2	Quantum Systems of Internal and CM States	1154
	References	1154

Abstract

Interactions of light with an atomic particle are accompanied by exchange of momentum between the electromagnetic field and the atom. Narrowband resonance radiation from tunable lasers enhances the ensuing mechanical effects of light to the extent that it is possible to stop atoms emanating from a thermal gas and to trap atoms with light. We will also discuss charged ions trapped by types of electromagnetic fields other than light, and possibly cooled with light. The emphasis is on basic theoretical concepts and experimental procedures. Cooling and trapping of atomic particles is now a basic tool and large swaths of modern AMO physics depend on it, so the discussion of applications is necessarily cursory.

J. Javanainen (✉)
Department of Physics, University of Connecticut
Storrs, CT, USA
e-mail: juha.javanainen@uconn.edu

At the time of writing, the book [1] appears to be the standard reference on cooling and trapping of atoms. Reviews of various vintages with a substantial component on trapped particles include [2–5]. Optical lattices binding atoms, discussed in a tutorial manner in [6], is presently a prominent frontier. Additional references ranging from pioneering works to representative recent examples are given as leads into specific topics. No assignment of credit or priority is implied.

Keywords

spontaneous emission · Wigner function · trap particle · laser cool · Paul trap

79.1 Notation

In this chapter, the lower and upper states of an optical transition are denoted by the respective labels g and e , for *ground* and *excited*. The notation $J_g \rightarrow J_e$ stands for a transition in which the lower and upper levels have the angular momentum degeneracies $2J_g + 1$ and $2J_e + 1$. The resonance frequency of the transition is ω_0 .

The detuning of the driving monochromatic light of frequency ω from the atomic resonance is defined as

$$\Delta = \omega - \omega_0 . \quad (79.1)$$

Spontaneous emission is taken to be the sole mechanism of line broadening, so that the rate of spontaneous emission Γ and the half-width half-maximum (HWHM) linewidth of the transition are related by $\gamma = \Gamma/2$. The Rabi frequency is $\Omega = \mathcal{D}\mathcal{E}/\hbar$, where \mathcal{D} is the reduced dipole moment matrix element that would apply to a transition with unit Clebsch–Gordan coefficient, and \mathcal{E} is the electric field amplitude of the laser. The corresponding intensity scale is the saturation

Table 79.1 Laser cooling parameters for the lowest $S_{1/2}-P_{3/2}$ transition of hydrogen and most alkalis (the D_2 line). Also shown are the nuclear spin I and the ground state hyperfine splitting $\Delta\nu_{\text{hfs}}$

Parameter	^1H	^6Li	^7Li	^{23}Na	^{39}K	^{40}K	^{85}Rb	^{87}Rb	^{133}Cs	Units
m	1.67	9.99	11.7	38.2	64.7	66.4	141	144	221	10^{-27} kg
λ	121.6	671.0	671.0	589.2	766.7	766.7	780.2	780.2	852.3	nm
v_r	326	9.89	8.48	2.95	1.34	1.30	0.602	0.588	0.352	cm/s
Γ	99.7	5.87	5.87	9.79	6.05	6.05	6.07	6.07	5.22	2π MHz
T_D	2390	141	141	235	145	145	146	146	125	μK
ε_r	13,400	73.7	63.2	25.0	8.71	8.49	3.86	3.77	2.07	2π kHz
T_r	643	3.54	3.03	1.20	0.418	0.408	0.185	0.181	0.0992	μK
I_s	14,500	5.08	5.08	12.5	3.51	3.51	3.34	3.34	2.20	mW/cm ²
I	1/2	1	3/2	3/2	3/2	4	5/2	3/2	7/2	
$\Delta\nu_{\text{hfs}}$	1420	228.2	803.5	1772	461.7	1286	3036	6835	9193	2π MHz

intensity

$$I_s = \frac{4\pi^2\hbar c\Gamma}{3\lambda^3}, \quad (79.2)$$

defined in such a way that the light intensity I satisfies

$$\Omega = \Gamma \Rightarrow I = I_s. \quad (79.3)$$

If multiple laser beams are explicitly mentioned, laser intensity and Rabi frequency are quoted for one of the equally intense beams.

The momentum of a photon with the wave vector \mathbf{k} is $\hbar\mathbf{k}$. The recoil velocity

$$v_r = \frac{\hbar k}{m} \quad (79.4)$$

equals the change of the velocity of an atom of mass m when it absorbs a photon with wave number $k = 2\pi/\lambda$. The kinetic energy of an atom with velocity v_r and the corresponding frequency,

$$E_r = \frac{1}{2}mv_r^2, \quad \varepsilon_r = \frac{E_r}{\hbar}, \quad (79.5)$$

are referred to as recoil energy and recoil frequency. Two temperatures, the Doppler limit T_D and the recoil limit T_r , are often cited in laser cooling. They are

$$T_D = \frac{\hbar\gamma}{k_B}, \quad T_r = \frac{E_r}{k_B}, \quad (79.6)$$

where k_B is the Boltzmann constant.

Table 79.1 lists numerical values of pertinent parameters for laser cooling and trapping using the D_2 line for most stable and long-lived alkali isotopes and hydrogen. Except for the spontaneous decay rates Γ (and the derived quantities T_D , I_s), data greatly exceeding the displayed precision are widely available. The spontaneous decay rate is taken either from [7] or [8].

79.2 Control of Atomic Motion by Light

79.2.1 General Theory

The Hamiltonian

The mechanical effects of light may be derived from the Hamiltonian

$$\hat{H} = \hat{H}_A + \hat{H}_{\text{CM}} + \hat{H}_F - \hat{\mathbf{d}} \cdot \hat{\mathbf{E}}(\hat{\mathbf{r}}), \quad (79.7)$$

where \hat{H}_A , \hat{H}_{CM} , and \hat{H}_F are the Hamiltonians for the internal degrees of freedom of the atom, center-of-mass (CM) motion of the atom, and free electromagnetic field. The quantized electric field is $\hat{\mathbf{E}}(\hat{\mathbf{r}})$, where $\hat{\mathbf{r}}$ is the CM position operator. The dipole operator $\hat{\mathbf{d}}$ acts on the internal degrees of freedom of the atom. Since the $\hat{\mathbf{d}} \cdot \hat{\mathbf{E}}(\hat{\mathbf{r}})$ term couples all degrees of freedom, the possibility of influencing CM motion by light immediately follows. The inclusion of the quantized CM motion is the essential ingredient not contained in traditional theories of light–matter interactions. For an atom with mass m trapped in a possibly anisotropic harmonic oscillator potential with frequencies ν_i ($i = x, y, z$), the CM Hamiltonian is

$$H_{\text{CM}} = \frac{\hat{\mathbf{p}}^2}{2m} + \sum_{i=x,y,z} \frac{m\nu_i^2 \hat{r}_i^2}{2}, \quad (79.8)$$

where $\hat{\mathbf{p}}$ is the CM momentum operator. For a free atom, $\nu_i = 0$.

Master Equation

With the aid of Markov and Born approximations, the vacuum modes of the electromagnetic field may be eliminated as described in Chap. 7.1.6. This gives a master equation for the reduced density operator $\hat{\rho}$ that contains the internal and CM degrees of freedom of the atom. Relaxation terms proportional to Γ and γ are all that is left of the quantized fields.

Consider as an example a two-state atom in a traveling wave of light with the electric field strength

$$E(\mathbf{r}, t) = \frac{1}{2}E e^{i(\mathbf{k}\cdot\mathbf{r}-\omega t)} + \text{c.c.} \quad (79.9)$$

Master equations are conveniently written using *Wigner functions* to represent the CM motion. Given the internal-state labels i and $j = g$ or e , and the three-dimensional variables \mathbf{r} , \mathbf{p} , the Wigner functions are defined as

$$\rho_{ij}(\mathbf{r}, \mathbf{p}) = \frac{1}{(2\pi\hbar)^3} \int d^3u e^{i\mathbf{u}\cdot\mathbf{p}/\hbar} \times \left\langle \mathbf{r} - \frac{1}{2}\mathbf{u} | \langle i | \hat{\rho} | j \rangle | \mathbf{r} + \frac{1}{2}\mathbf{u} \right\rangle. \quad (79.10)$$

The Wigner function is one of the quantum mechanical quasi-probability distributions, Chap. 82.5, with the special property that the marginal distribution of \mathbf{r} obtained by integrating over \mathbf{p} coincides with the correct quantum probability density function for position, and vice versa with \mathbf{r} and \mathbf{p} interchanged. In the rotating wave approximation, Chap. 72.3.2, the master equations are

$$\frac{d}{dt} \rho_{ee}(\mathbf{p}) = -\Gamma \rho_{ee}(\mathbf{p}) + i \frac{\Omega}{2} \left[e^{i\mathbf{k}\cdot\mathbf{r}} \hat{\rho}_{ge} \left(\mathbf{p} - \frac{1}{2}\hbar\mathbf{k} \right) - e^{-i\mathbf{k}\cdot\mathbf{r}} \hat{\rho}_{eg} \left(\mathbf{p} - \frac{1}{2}\hbar\mathbf{k} \right) \right], \quad (79.11)$$

$$\frac{d}{dt} \rho_{gg}(\mathbf{p}) = \Gamma \int d^2n W(\hat{\mathbf{n}}) \rho_{ee}(\mathbf{p} + \hbar\mathbf{k}\hat{\mathbf{n}}) - \frac{i\Omega}{2} \times \left[e^{i\mathbf{k}\cdot\mathbf{r}} \hat{\rho}_{ge} \left(\mathbf{p} + \frac{1}{2}\hbar\mathbf{k} \right) - e^{-i\mathbf{k}\cdot\mathbf{r}} \hat{\rho}_{eg} \left(\mathbf{p} + \frac{1}{2}\hbar\mathbf{k} \right) \right], \quad (79.12)$$

$$\frac{d}{dt} \hat{\rho}_{ge}(\mathbf{p}) = -(\gamma + i\Delta) \hat{\rho}_{ge}(\mathbf{p}) - \frac{i\Omega}{2} \times \left[e^{-i\mathbf{k}\cdot\mathbf{r}} \rho_{gg} \left(\mathbf{p} - \frac{1}{2}\hbar\mathbf{k} \right) - e^{i\mathbf{k}\cdot\mathbf{r}} \rho_{ee} \left(\mathbf{p} + \frac{1}{2}\hbar\mathbf{k} \right) \right], \quad (79.13)$$

$$\frac{d}{dt} \hat{\rho}_{eg}(\mathbf{p}) = -(\gamma - i\Delta) \hat{\rho}_{eg}(\mathbf{p}) + \frac{i\Omega}{2} \times \left[e^{i\mathbf{k}\cdot\mathbf{r}} \rho_{gg} \left(\mathbf{p} - \frac{1}{2}\hbar\mathbf{k} \right) - e^{-i\mathbf{k}\cdot\mathbf{r}} \rho_{ee} \left(\mathbf{p} + \frac{1}{2}\hbar\mathbf{k} \right) \right]. \quad (79.14)$$

Here, the convective derivative that describes the motion of the atom in the absence of light is

$$\frac{d}{dt} = \frac{\partial}{\partial t} + \frac{\mathbf{p}}{m} \cdot \frac{\partial}{\partial \mathbf{r}} - \sum_i m v_i r_i \frac{\partial}{\partial p_i}; \quad (79.15)$$

cf. H_{CM} in Eq. (79.8); $W(\hat{\mathbf{n}})$ is the angular distribution of spontaneous photons, and the integral runs over the unit

sphere. Representative expressions for $W(\hat{\mathbf{n}})$ are

$$W(\hat{\mathbf{n}}) = \frac{1}{4\pi}, \quad \frac{3}{8\pi} [1 - (\hat{\mathbf{e}} \cdot \hat{\mathbf{n}})^2], \quad \frac{3}{16\pi} [1 + (\hat{\mathbf{e}} \cdot \hat{\mathbf{n}})^2]. \quad (79.16)$$

These apply, respectively, for isotropic spontaneous emission, for spontaneous emission in a $\Delta m = 0$ transition, and in $\Delta m = \pm 1$ transitions; $\hat{\mathbf{e}}$ stands for the unit vector in the direction of the quantization axis for angular momentum. Only the \mathbf{p} dependence has been denoted explicitly in the Wigner functions, as the recoil effects displayed on the right-hand sides of Eqs. (79.11)–(79.14) take place at a fixed position \mathbf{r} .

Semiclassical Theory

Suppose that $v_{\text{CM}} \gg v_r$ and $\tau \ll \tau_{\text{CM}}$, where τ and τ_{CM} are the timescales for light-driven changes of the internal state and CM motion of the atom. Then the internal degrees of freedom may be eliminated adiabatically from the master equations in favor of the position-momentum distribution for the CM motion,

$$f(\mathbf{r}, \mathbf{p}, t) = \sum_i \rho_{ii}(\mathbf{r}, \mathbf{p}, t), \quad (79.17)$$

where the sum runs over the internal states of the atom. Technically, the recoil velocity v_r is treated as an asymptotically small expansion parameter. The result is the Fokker–Planck equation for the CM motion

$$\frac{d}{dt} f = -\frac{\partial}{\partial \mathbf{p}} \cdot (\mathbf{F} f) + \sum_{i,j} \frac{\partial^2}{\partial p_i \partial p_j} (D_{ij} f). \quad (79.18)$$

In this semiclassical theory, the CM motion of the atom is regarded as classical. The atom moves under the optical force $\mathbf{F}(\mathbf{r}, \mathbf{p}, t)$, which models the coarse-grained flow of momentum between the electromagnetic field and the atom; $D_{ij}(\mathbf{r}, \mathbf{p}, t)$, with $i, j = x, y, z$, is the diffusion tensor. Diffusion is an attempt to model quantum mechanics with a classical stochastic process, including discreteness of recoil kicks, random directions of spontaneous photons, and random timing of optical absorption and emission processes.

A general prescription exists for calculating the force and the diffusion tensor for an arbitrary atomic level scheme and light field [9]. However, the formally correct analysis of diffusion has not proven to be particularly useful, and here only the force is considered at length. Let $\hat{V}(\mathbf{r})$ be the dipole interaction operator coupling the driving field and the internal state for an atom at position \mathbf{r} . By assumption, $\hat{V}(\mathbf{r})$ has been rendered slowly varying in time with the aid of a suitable rotating wave approximation. To compute the force, one takes

an atom that travels along a hypothetical trajectory unperturbed by light in such a way that at time t it arrives at the phase space point (\mathbf{r}, \mathbf{p}) , whereupon the density operator of the internal degrees of freedom is $\hat{\rho}$. The force is then

$$F_i(\mathbf{r}, \mathbf{p}, t) = -\text{Tr}\left(\hat{\rho} \frac{\partial \hat{V}}{\partial r_i}\right). \quad (79.19)$$

Quantum Theory

When either $v_{\text{CM}} \lesssim v_r$ or $\tau \gtrsim \tau_{\text{CM}}$, the full quantum theory of cooling and trapping is needed. Master equations such as Eqs. (79.11)–(79.14) must then be solved without the assumption that v_r is small. For instance, a truncated basis of plane waves may be used to expand the CM state. Density matrix equations are then solved numerically either directly or by resorting to quantum Monte-Carlo simulations [10]. Such solutions for free ($v_i = 0$) particles are very few. Our approach and terminology are, therefore, semiclassical by default.

Qualitative origin of laser cooling

Velocity-dependent dissipative forces are needed for cooling. They arise because the evolution of the internal state of a moving atom has a finite response time τ . The atom conveys the memory of the field it has sampled over the length $\ell = v\tau$ on its past trajectory. If $\ell \ll \lambda$, a nonequilibrium component proportional to ℓ is present in the density operator of the internal state of the atom. Further interactions with light convert this component into a velocity-dependent force of the form

$$F = -m\beta v, \quad \beta \propto I\tau. \quad (79.20)$$

If the damping constant β is positive, Eq. (79.20) describes exponential damping of the velocity on the timescale β^{-1} . In the contrary case $\ell \gg \lambda$, when the atom travels many wavelengths during the memory time, linear dependence of force on velocity breaks down. The watershed is the critical velocity or velocity capture range

$$v_c \approx \frac{\lambda}{\tau}. \quad (79.21)$$

One-dimensional considerations

Most specific results cited here are one-dimensional. By default, the propagation direction of light and the direction of vector quantities other than light polarization is $\hat{\mathbf{e}}_x$. The relevant components of position, velocity, and momentum are denoted by x , v , and p .

The general one-dimensional Fokker–Planck equation for a particle trapped in a harmonic oscillator potential with a CM oscillation frequency ν is

$$\left(\frac{\partial}{\partial t} + \frac{p}{m} \frac{\partial}{\partial x} - mv^2 x \frac{\partial}{\partial p}\right) f = -\frac{\partial}{\partial p}(Ff) + \frac{\partial^2}{\partial p^2}(Df). \quad (79.22)$$

For the force in Eq. (79.20) with constant $\beta = \beta_0$ and $D(z, p) = D_0$, the steady state of the Fokker–Planck equation is a thermal distribution of the form

$$f(x, p) = K \exp\left[-\frac{\beta_0 m}{D_0} \left(\frac{p^2}{2m} + \frac{mv^2 x^2}{2}\right)\right], \quad (79.23)$$

where K is a normalization constant.

Since Wigner functions give correct quantum mechanical marginal distributions for \mathbf{r} and \mathbf{p} , expectation values of kinetic and potential energy may be calculated from the distribution function Eq. (79.23) as if it were a classical phase space density. For a free atom with $v = 0$, the temperature is directly proportional to the kinetic energy,

$$T = \frac{D_0}{\beta_0 m k_B}. \quad (79.24)$$

However, for a trapped particle with $v \neq 0$ the Fokker–Planck equation may be valid all the way to the quantum mechanical zero-point energy. Then, temperature and energy are no longer directly proportional to one another. For a trapped particle, the safe interpretation of Eq. (79.23) is that the total CM energy of the particle is

$$E = \frac{D_0}{\beta_0 m}. \quad (79.25)$$

79.2.2 Two-State Atoms

A two-state or two-level atom, discussed in detail in Chap. 72.3, stands for a closed (cycling) transition with one lower state and one excited state. In practice, a two-state system is often realized by driving a $J \rightarrow J + 1$ transition with circularly polarized light. This leads to optical pumping to the states with the maximal (or minimal) component of angular momentum along the quantization axis, say, to the transition $m = J \rightarrow m' = J + 1$.

Two types of force are generally distinguished: light pressure, or scattering force, or spontaneous force, and dipole, or gradient, or induced force. However, the distinction is neither exclusive, nor exhaustive. Here, the two types of force are approached by way of examples.

Traveling Waves

Light pressure

Consider a cycle of absorption and spontaneous emission. In the absorption, the atom receives a photon recoil kick in the direction of the laser beam, while in the spontaneous emission the recoil kick has a random direction and zero average. The atom is, on the average, left with a velocity change equal

to v_r . The rate of such processes equals $\Gamma\rho_{ee}$, which gives the force along \mathbf{k} and equal to

$$F = F_m \frac{\Omega^2/2}{\gamma^2 + \Delta^2(v) + \Omega^2/2} \quad (79.26)$$

in magnitude. Here, the maximum of light pressure force, a convenient scale for optical forces, is

$$F_m = \frac{1}{2} m v_r \Gamma, \quad (79.27)$$

and

$$\Delta(v) = \Delta - kv \quad (79.28)$$

is the effective detuning, which includes the Doppler shift experienced by the moving atom.

Diffusion

For a traveling wave, the diffusion coefficient accompanying light pressure is

$$\frac{D}{\hbar^2 k^2 \Gamma} = \frac{(1 + \alpha)\Omega^2}{4[\Delta^2(v) + \gamma^2 + \Omega^2/2]} - \frac{[\Delta^2(v) - 3\gamma^2]\Omega^4}{4[\Delta^2(v) + \gamma^2 + \Omega^2/2]^3}, \quad (79.29)$$

where

$$\alpha = \int d^2n W(\hat{\mathbf{n}})(\hat{\mathbf{e}}_x \cdot \hat{\mathbf{n}})^2 \quad (79.30)$$

depends on $W(\hat{\mathbf{n}})$, see Eq. (79.16). Representative values are $\alpha = 1/3$ for isotropic spontaneous emission, and $\alpha = 2/5$ ($\alpha = 3/10$) for spontaneous emission with $\Delta m = 0$ ($\Delta m = \pm 1$) with respect to a quantization axis that is perpendicular (parallel) to the direction $\hat{\mathbf{e}}_x$.

The expression Eq. (79.29) is the formally complete result from the expansion in recoil velocity. The first term on the right is easily obtained by computing the variance of the atomic momentum in a cycle of absorption and spontaneous emission and multiplying it by the rate of such processes $\Gamma\rho_{ee}$. The second term, rarely seen in theoretical analyses and henceforth ignored, is related to photon antibunching: The subsequent spontaneous emissions do not happen independently of one another at the rate $\Gamma\rho_{ee}$, but after an emission, there is some delay before the atom gets excited and can emit again.

Spontaneously emitted photons cover all of the 4π solid angle, and so do the directions of photon recoil kicks on the atom. Absorption from a light wave traveling in a particular direction leads to transverse diffusion also in the orthogonal directions, which is not accounted for by the one-dimensional Eq. (79.29).

Phenomenology in Multimode Fields

Doppler cooling in standing waves

Next, take an atom in two counterpropagating plane waves of light. At low intensity, $\Omega \ll \Gamma$, forces of the form Eq. (79.26) for the two beams may be added when averaged over a wavelength. For velocities well below the critical velocity

$$v_{c,D} = \frac{\Gamma}{k}, \quad (79.31)$$

the wavelength-averaged force is of the form of Eq. (79.20),

$$F = -m\bar{\beta}v, \quad \bar{\beta} = -\frac{4\Omega^2\gamma\Delta}{(\Delta^2 + \gamma^2)^2} \varepsilon_r. \quad (79.32)$$

When light is tuned below the atomic resonance (*red detuning* with $\Delta < 0$), exponential damping of the atomic velocity with the time constant $\bar{\beta}^{-1}$ ensues. No matter which way the atom moves, it is always Doppler tuned toward resonance with the light wave that propagates opposite to its velocity, and away from resonance with the light wave that propagates along its velocity. Net momentum transfer, therefore, opposes the motion of the atom. This is known as Doppler cooling.

Optical molasses

For three pairs of counterpropagating waves in three orthogonal directions, Eq. (79.32) is valid in all coordinate directions, and, hence, as a vector equation between the force \mathbf{F} and velocity \mathbf{v} . For $\Delta < 0$, an atom experiences an isotropic viscous damping force, as if it were moving in a thick liquid. Such a field configuration is dubbed optical molasses. Two counterpropagating beams make a one-dimensional optical molasses.

Limit of Doppler cooling

Under the conditions of Eq. (79.32), the diffusion coefficients for the two counterpropagating beams averaged over a wavelength may be added, and the $v = 0$ form suffices for slow atoms. This yields

$$\frac{\bar{D}(v=0)}{\hbar^2 k^2 \Gamma} = \frac{(1 + \alpha)\Omega^2}{2(\Delta^2 + \gamma^2)}. \quad (79.33)$$

The random diffusive motion of the atom corresponds to diffusive heating that competes with Doppler cooling. In equilibrium, the temperature is

$$T = \frac{\bar{D}(v=0)}{m\bar{\beta}k_B} = \frac{\hbar\gamma}{4k_B}(1 + \alpha) \left(\frac{|\Delta|}{\gamma} + \frac{\gamma}{|\Delta|} \right). \quad (79.34)$$

Equation (79.34) also applies to three-dimensional Doppler cooled molasses, provided one uses $\alpha = 1$ corresponding

to added transverse diffusion. The minimum temperature is reached at

$$|\Delta| = \gamma = \frac{\Gamma}{2}. \quad (79.35)$$

For three-dimensional molasses, the Doppler limit T_D of Eq. (79.6) is obtained.

For $\Omega > \Gamma$, the performance of Doppler cooling deteriorates. Qualitatively, power broadening increases the effective linewidth γ .

Dipole forces

Dipole forces are the resonant analog of the ponderomotive forces discussed in Chap. 78.3. They arise from successions of absorption and induced emission driven by photons with different momenta. Such processes occur only if there is more than one wave vector present in the field, i.e., if there is an intensity gradient. For a zero-velocity, two-state atom, the gradient force in a monochromatic field with the local total intensity $I(\mathbf{r})$ is

$$\mathbf{F}_g(\mathbf{r}) = -\frac{4\hbar\Delta\gamma^2}{\Delta^2 + \gamma^2[1 + 2I(\mathbf{r})/I_s]} \frac{\nabla I(\mathbf{r})}{I_s}. \quad (79.36)$$

The dipole force may be derived from the potential energy

$$V_g(\mathbf{r}) = 2\hbar\Delta \ln\left(1 + \frac{2\gamma^2 I(\mathbf{r})/I_s}{\Delta^2 + \gamma^2}\right). \quad (79.37)$$

The atoms are strong-field seekers for red detuning ($\Delta < 0$) and weak-field seekers for blue detuning ($\Delta > 0$).

Suppose the amplitude of the dipole moment induced on the atom equals $d = \alpha \mathcal{E}(\mathbf{r})$, where $\mathcal{E}(\mathbf{r})$ is a slowly varying (or stationary) local electric field amplitude, and α is the polarizability. This is true in the limit of a large detuning or a low light intensity, in the case when the response of the atom is isotropic. In the limit of large detunings, the dipole moment is also either in phase ($\Delta \rightarrow -\infty$) or π out of phase with the electric field, so the polarizability is real. Then, there is a general expression for the dipole force,

$$\mathbf{F}_g(\mathbf{r}) = \frac{1}{4}\alpha \nabla |\mathcal{E}(\mathbf{r})|^2, \quad (79.38)$$

with the obvious potential energy. For a CO₂ or Nd-YAG laser, the static polarizability of the atom serves as a practical approximation for α .

Optical trap and optical lattice

Dipole forces are utilized in an optical trap for atoms, and even molecules. A common configuration is the crossed-beam dipole force trap, two crossing laser beams tuned below resonance, and focused to the same spot. The frequencies of

the beams may be deliberately offset to average out extraneous standing wave patterns. Very intense lasers with a large detuning, including CO₂ and Nd-YAG, can be used. As the optical force and the rate of spontaneous emission scale, respectively, as I/Δ and I/Δ^2 , the heating from spontaneous emission may be negligible.

A standing wave of light makes a periodic array of optical traps called an optical lattice. Optical lattices may be set up in 1-D, 2-D, and 3-D configurations.

Induced diffusion

Random motion of atoms in velocity space owing to absorptions and induced emissions of photons with different momenta leads to induced diffusion. Contrary to diffusion in a traveling wave as in Eq. (79.29), induced diffusion does not saturate at high intensity. Instead, the diffusion coefficient continues to grow linearly with I . Induced diffusion is another reason why the lowest Doppler cooling temperatures are generally reached at low ($I < I_s$) light intensities.

Sisyphus effect

In a standing wave at high intensity and large detuning, another kind of optical force becomes important that cannot be categorized either as light pressure or gradient force.

As explained in Chap. 72.3.4, one may diagonalize the Hamiltonian to obtain the dressed atom-field states. Because the light field depends on position, so do the energies of the dressed states and their decompositions into plain atomic states. In Fig. 79.1 drawn for $\Delta > 0$, the dressed state with a minimum (maximum) at the field nodes coincides with the bare ground state (excited state) at the nodes. At the antinodes, the admixtures of ground and excited states are evened out to some extent.

The energy of a dressed state acts as potential energy for the CM motion of an atom residing in that particular state. In fact, the gradient force is the force derived from these potential energies, averaged over the occupation probabilities of the dressed states. The occupation probability is larger for the dressed state with a larger ground-state admixture. From Fig. 79.1 one, therefore, sees that the atom predominantly resides in the dressed state that has a minimum of energy at the antinodes. The atom is a weak-field seeker, as it should for $\Delta > 0$.

Spontaneous emission remains to be considered. It gives rise to transitions between the dressed states. These transitions may go both ways between the dressed states because the states are, in general, superpositions of the bare ground state and the excited state. The rate of spontaneous transitions from one dressed state to another increases (decreases) with the excited (ground) state admixture of the initial state.

In reference to Fig. 79.1, suppose that the atom is coming from the left in the upper dressed state. The probability that the atom makes a transition to the lower dressed state,

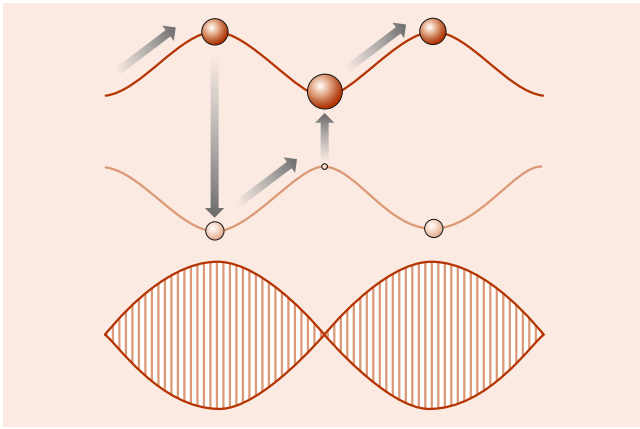


Fig. 79.1 Qualitative origin of the Sisyphus effect. The *hatched pattern* represents a standing light wave. The energies of the two dressed states are drawn as a function of position, along with a few *filled circles* representing the admixture of the ground state in each dressed state at selected field positions. *Larger circles* correspond to larger ground-state admixtures, and hence, larger equilibrium populations of the dressed state. This figure applies for tuning of the laser above the atomic resonance (blue detuning)

as marked by the downward vertical arrow, is largest at the antinode. If this transition takes place, near the next node the most probable transition is as shown by the upward vertical arrow. In this manner, the atom spends most of its time at an uphill climb against the potential, and is, therefore, slowed down. In reference to Greek mythology, this is called the Sisyphus effect. In the two-state model atom, cooling takes place when the laser frequency is higher than the atomic resonance frequency.

Semiclassical Versus Quantum Theory

When $\gamma \gg \varepsilon_r$, the root-mean-square (RMS) velocity of a cooled two-state atom is always $\gg v_r$, and semiclassical theory is valid. Under the same condition $\gamma \gg \varepsilon_r$, the Doppler-limit RMS velocity is also less than the critical velocity $v_{c,D}$ from Eq. (79.31). Velocity expansions such as in Eqs. (79.32) and (79.33) are then justified.

In the contrary case, $\gamma \lesssim \varepsilon_r$, the full quantum theory of trapping and cooling must be employed. The cooled velocity distribution cannot be expected to be thermal and temperature is ill defined, but on dimensional grounds, one expects that the minimum kinetic energy for cooled free atoms is comparable to the recoil energy E_r .

79.2.3 Multistate Atoms

Energy levels of atomic systems usually have angular momentum degeneracy. In addition, the polarization of light, in general, depends on position. A combination of these aspects leads to phenomena beyond the two-state atomic model.

Polarization Gradient Cooling

As explained in connection with Eq. (79.20), a finite memory time of the internal atomic state may lead to damping of the CM motion. For a two-state atom, internal equilibration arises from spontaneous emission. The timescale is $\tau_D \approx \Gamma^{-1}$, and Doppler cooling ensues. However, an atom whose ground state has angular momentum degeneracy is also subject to optical pumping. If the polarization of light varies as a function of position, optical pumping is needed to reach local equilibrium. The pumping timescale $\tau_p \propto I^{-1}$ then becomes relevant for a moving atom. The associated cooling is known as polarization gradient cooling. Its hallmark is that, for low I , the damping coefficient $\beta \propto I \tau_p$ is independent of intensity.

Two detailed mechanisms of polarization gradient cooling have been described [11], although in three-dimensional light fields they are intertwined. The Sisyphus effect works like the Sisyphus effect for a two-state atom, except that it relies on light shifts and optical pumping within the ground state manifold. Induced orientation cooling is analogous to Doppler cooling. Velocity dependence of optical pumping in counterpropagating waves leads to pumping to a state for which the force due to the wave propagating opposite to the atom exceeds the force due to the wave propagating along with the atom.

$\sigma^+ - \sigma^-$ molasses

As an example consider one-dimensional $\sigma^+ - \sigma^-$ molasses, which consists of two counterpropagating waves with opposite circular polarizations. The net polarization is linear everywhere, but the direction of polarization rotates as the point of observation is displaced along the propagation axis; hence the name corkscrew molasses. At low intensity and low velocity, the force on an atom with a $1 \rightarrow 2$ transition is

$$F = \frac{60}{17} \frac{\Delta \gamma}{5\gamma^2 + \Delta^2} \hbar k^2 v. \quad (79.39)$$

In this configuration, only induced orientation cooling contributes. Cooling again takes place for $\Delta < 0$, and the resulting temperature is

$$T = \frac{29\Delta^2 + 1045\gamma^2}{300(\Delta^2 + \gamma^2)} \left(\frac{2I\Gamma}{I_s|\Delta|} \right) T_D. \quad (79.40)$$

Experimental molasses

For $I\Gamma/I_s|\Delta| < 1$ and $|\Delta| \gg \Gamma$, the temperature Eq. (79.40) reduces to the form

$$T = C \frac{\hbar \Omega^2}{k_B |\Delta|} = C \frac{2I\Gamma}{I_s |\Delta|} T_D. \quad (79.41)$$

Under these conditions, the same I/Δ scaling is approximately observed also in three-dimensional, six-beam optical

molasses operating with atoms that have a degenerate ground state. The constant C depends on the degeneracy of the transitions and on the polarizations of the molasses beams. On dimensional-analysis grounds, one expects $C \approx 1$; values in the range $0.25 < C < 0.5$ have been reported [12].

Limit of cooling

While the expressions in Eqs. (79.40) and (79.41) suggest that T goes all the way to zero as $I \rightarrow 0$ or $\Delta \rightarrow -\infty$, in practice there is a lower limit of T reached in polarization gradient cooling. This is because the velocity capture range falls below the speeds of the would-be cooled atoms. The temperature eventually starts to rise abruptly when $|\Delta|$ is increased, or I is decreased. The empirical rule of thumb is that $T \approx 10 T_r$ is the lowest temperature one can expect.

Magneto-Optical Trap

Since spontaneous forces may be strong already at modest light intensities, $I \approx I_s$, the use of light pressure to trap neutral atoms appears desirable. However, the optical Earnshaw theorem states that (in the limit of low I) the spontaneous force on a two-state atom is sourceless. While confinement may be possible in some directions, escape routes for atoms remain open in others. Three-dimensional trapping of a two-state atom with light pressure is not possible.

A magneto-optical trap (MOT) defeats the Earnshaw theorem by relying on angular momentum degeneracy. Consider an atom with a $0 \rightarrow 1$ transition in a magnetic field \mathbf{B} that depends linearly on position around the zero at $x = 0$. Suppose that the gradient of \mathbf{B} is chosen in such a way that the $m = 1$ ($m = -1$) magnetic substate of the excited state has the higher (lower) energy for $x > 0$, and that the atom is illuminated by σ^\pm polarized beams propagating in the $\pm x$ -directions, tuned below resonance. When the atom is displaced from $x = 0$ in either direction, it is closer to resonance with the beam that pushes it back toward $x = 0$. This makes the restoring force responsible for trapping.

A magneto-optical trap can be set up also in three dimensions. A quadrupole magnetic field of the form

$$\mathbf{B}(\mathbf{r}) \approx \left. \frac{\partial B_z}{\partial z} \right|_{r=0} \left(z \hat{\mathbf{e}}_z - \frac{1}{2} x \hat{\mathbf{e}}_x - \frac{1}{2} y \hat{\mathbf{e}}_y \right) \quad (79.42)$$

is produced by reversing the direction of current in one of the two Helmholtz coils. Three orthogonal pairs of light beams, each in the $\sigma^+ - \sigma^-$ configuration, complete the trap. The magnetic field is sourceless. To compensate for the ensuing signs of the field gradients, one of the $\sigma^+ - \sigma^-$ corkscrews has the opposite handedness from the other two (with the $+x$, $+y$ and $+z$ -directions as the reference for handedness).

The mechanism of the magneto-optical trap for the $0 \rightarrow 1$ configuration is the same as the mechanism for Doppler cooling, except that position-dependent level shifts of the excited

states take the place of velocity-dependent Doppler shifts. The restoring force and the damping coefficient of Doppler cooling are closely related. For the coordinate directions $u = x, y, z$, the relation is

$$F_u = -\kappa_u u, \kappa_u = \beta \frac{mg_e \mu_B}{\hbar k} \left| \frac{\partial B_u}{\partial u} \right|, \quad (79.43)$$

where g_e is the Landé factor of the excited state.

A magneto-optical trap may similarly be based on the induced-orientation mechanism of polarization gradient cooling. This might actually be the mechanism of many magneto-optical traps.

Atoms in a well-aligned magneto-optical trap reside near the zero of \mathbf{B} , so that the magnetic field has little effect on polarization gradient cooling. Trapping and cooling are achieved simultaneously.

79.3 Magnetic Trap for Atoms

The magnitude $B(\mathbf{r})$ of a magnetic field may have a minimum in free space, as in Eq. (79.42). A particle with a magnetic dipole moment $\boldsymbol{\mu}$ then experiences a trapping potential $U(\mathbf{r}) = \boldsymbol{\mu} \cdot \mathbf{B}(\mathbf{r})$ if $\boldsymbol{\mu}$ and \mathbf{B} are antiparallel; $\boldsymbol{\mu}$ remains locked antiparallel to \mathbf{B} if the field seen by the moving dipole satisfies the adiabatic condition

$$\frac{1}{B} \left| \frac{dB}{dt} \right| \ll \frac{\mu B}{\hbar} \quad (79.44)$$

(cf. Sect. 77.5.4). However, if $B(\mathbf{r}) = 0$ at the minimum, the adiabatic condition is violated, and the dipole may flip (Majorana transition). The particle may end up in a repulsive potential and get expelled from the trap. This could become a problem at low temperatures, when the particles accumulate near the minimum of the potential. Trap configurations are, therefore, designed in which $B(\mathbf{r}) \neq 0$ at the minimum.

79.3.1 Evaporative Cooling

A magnetic trap is often combined with evaporative cooling. The most energetic atoms from the tail of the thermal distribution escape from the trap, whereupon the average energy of the remaining atoms decreases. The atoms then thermalize to a lower temperature. Successful operation of evaporative cooling requires a high enough rate of elastic collisions so that the atoms thermalize in a time short compared with the lifetime of the sample. In order to sustain the evaporation, the effective depth of the trap is typically lowered as the atoms cool.

79.4 Trapping and Cooling of Charged Particles

Since the potential $\Phi(\mathbf{r})$ of a static electric field satisfies Laplace's equation, $\Phi(\mathbf{r})$ cannot have an extremum in free space. A static electric field, therefore, cannot serve as an ion trap (Earnshaw's theorem). Paul and Penning traps circumvent this limitation by making use of an alternating electric field and a magnetic field, respectively. Cooling is often employed to assist trapping.

Before going any further, it should be noted that neutral atoms trapped in sufficiently deep far-off resonance optical dipole traps and optical lattices may behave essentially like ions in a Paul trap. They are, therefore, subject to similar cooling and detection methods.

79.4.1 Paul Trap

Trapping

Configuration

Consider an ideal trap whose surfaces are hyperboloids of revolution; see Fig. 79.2. The two *endcaps* and the intervening *ring* are equipotential surfaces of the quasi-static electric potential

$$\Phi(x, y, z) = \frac{\Phi_0(t)(2z^2 - x^2 - y^2)}{2\varrho_0^2}, \quad (79.45)$$

where ϱ_0 is the distance from the center to the ring, $z_0 = \varrho_0/\sqrt{2}$ is the distance to the endcaps, and $\Phi_0(t)$ is a voltage applied between the endcaps and the ring,

$$\Phi_0(t) = U - V \cos \tilde{\omega}t. \quad (79.46)$$

Motion of an ion

In the ideal three-dimensional Paul trap, Newton's equations of motion for the coordinates $u = x, y, \text{ or } z$ may be recast as Mathieu's equations,

$$\frac{d^2u}{d\tau^2} + (a_u - 2q_u \cos 2\tau)u = 0, \quad (79.47)$$

where $\tau = \tilde{\omega}t/2$ is a dimensionless quantity proportional to time, the parameters are

$$a_z = -2a_{x,y} = -\frac{8qU}{m\tilde{\omega}^2\varrho_0^2}, \quad (79.48)$$

$$q_z = -2q_{x,y} = -\frac{4qV}{m\tilde{\omega}^2\varrho_0^2}, \quad (79.49)$$

and m and q are the mass and charge of the particle. Stable trapping ensues when a_u and q_u are such that the motion

of the ion is stable in all directions. A Paul trap normally operates in the first stability region of Eq. (79.47).

Stable motion may be qualitatively divided into forced micromotion at the frequency $\tilde{\omega}$ of the external drive, and slower secular motion of the center of the micromotion. If $U = 0$, the secular motion takes place in an effective ponderomotive potential U_P , Sect. 78.3, equal to the cycle-averaged kinetic energy in the micromotion. Explicitly,

$$U_P(\mathbf{r}) = \frac{q^2 \mathcal{E}^2(\mathbf{r})}{4m\tilde{\omega}^2} = \frac{q^2 V^2 (x^2 + y^2 + 4z^2)}{4m\tilde{\omega}^2 \varrho_0^4}, \quad (79.50)$$

where $\mathcal{E}(\mathbf{r})$ is the AC field amplitude. This is an anisotropic harmonic oscillator potential characterized by the oscillation frequencies

$$\nu_z = 2\nu_{x,y} = \frac{\sqrt{2}qV}{m\tilde{\omega}\varrho_0^2}. \quad (79.51)$$

Quantization of CM motion

The separation of micromotion and secular motion is excellent, and the trap is stable, when $\nu_{x,y,z} \ll \tilde{\omega}$. Ignoring the micromotion, the CM motion of the ions in the potential $U_P(\mathbf{r})$ may be quantized readily. The energy of a state with $n_{x,y,z}$ quanta in the coordinate directions x, y, z is

$$E = \sum_{i=x,y,z} \hbar \nu_i \left(n_i + \frac{1}{2} \right). \quad (79.52)$$

Variations of the Paul trap

Usually, little practical advantage arises from realization of the ideal shape. Even a single electrode with an applied AC voltage may work as a Paul trap. A linear trap is basically a two-dimensional Paul trap with an added static longitudinal potential to prevent escape of the ions from the ends of the trap. A closed race track Paul trap is obtained by bending a linear trap into a ring.

Cooling

Origin of laser cooling

The Wigner function formalism in Eqs. (79.11)–(79.14) is exact as long as the trapping forces are harmonic, but occasionally it is more convenient to think in terms of harmonic oscillator eigenstates of a trapped particle instead of position and momentum. In this view, a plane wave of light can effect transitions between motional states because the position of the ion is regarded as a quantum mechanical operator. The coupling matrix element between two harmonic oscillator eigenstates n_1 and n_2 due to light is proportional to

$$K_{n_1 n_2} = \langle n_2 | e^{ik \cdot \hat{r}} | n_1 \rangle;$$

$|K_{n_1 n_2}|^2$ may be viewed as the Franck–Condon factor for the transition $n_1 \rightarrow n_2$.

Laser cooling in one dimension

Consider the motion of the ion in one of the principal-axis directions x, y, z , with ν denoting the corresponding CM frequency. In the common case where $\gamma \gg \nu$, Doppler cooling basically works as with a free atom. In the contrary case, $\nu \gg \gamma$, cooling may be achieved by tuning the laser to $\omega = \omega_0 - \nu$. Resonant photoabsorption starting with n quanta in the CM motion decreases the quantum number from n to $n - 1$, and the subsequent spontaneous emission, on the average, leaves the CM energy nearly untouched. The net effect is reduction of the CM energy by $\hbar\nu$ in such a Raman process. Since the oscillating ion sees a frequency-modulated laser with sidebands, this method of cooling is called sideband cooling. For one-dimensional motion of a two-state ion in a traveling light wave at low I , the velocity damping rate for tuning below resonance, $\Delta < 0$, is

$$\beta = \frac{2\Omega^2\gamma|\Delta|}{[(\Delta + \nu)^2 + \gamma^2][(\Delta - \nu)^2 + \gamma^2]} \varepsilon_r, \quad (79.53)$$

and the expectation value of the CM energy is

$$E = \frac{\hbar}{4|\Delta|} \times \left(\Delta^2 + \gamma^2 + \nu^2 + \alpha \frac{[(\Delta - \nu)^2 + \gamma^2][(\Delta + \nu)^2 + \gamma^2]}{\Delta^2 + \gamma^2} \right), \quad (79.54)$$

where α characterizes the angular distribution of spontaneous emission, see Eq. (79.30). The result in Eq. (79.54) is useful when either $\varepsilon_r \ll \gamma$ or $\varepsilon_r \ll \nu$. The case with $\varepsilon_r, \nu \ll \gamma$ is for Doppler cooling; the temperature from Eq. (79.54) coincides with Eq. (79.34) for a free atom. The case with $\varepsilon_r, \gamma \ll \nu$ corresponds to sideband cooling in the Lamb–Dicke regime, in which the cooled ion is confined to a region much smaller than λ .

In connection with sideband cooling, it is convenient to cite the expectation number of harmonic oscillator quanta $\langle n \rangle$ instead of energy or temperature; the latter are

$$E = \hbar\nu \left(\langle n \rangle + \frac{1}{2} \right), \quad T = \frac{\hbar\nu}{k_B} [\ln(1 + \langle n \rangle^{-1})]^{-1}. \quad (79.55)$$

For optimal sideband cooling, $\nu \gg \gamma$ and $\Delta = -\nu$, the result is

$$\langle n \rangle = \frac{1}{4}(1 + 4\alpha) \left(\frac{\gamma}{\nu} \right)^2 + O \left[\left(\frac{\gamma}{\nu} \right)^4 \right]. \quad (79.56)$$

In principle, by decreasing the linewidth γ , the ion may be put arbitrarily close to the ground state of the CM harmonic oscillator. Such a tuning of linewidth is not practical

in a given two-state system, but there is a workaround. After Doppler cooling on one transition, the experiment may switch to sideband cooling using another, narrower, transition. A narrow resonance may also be achieved by using the two-photon resonance in a three-state Λ configuration as an effective two-state system, see Chap. 77.8.2.

Laser cooling in three dimensions

Either by design or chance, no two of the ν_i are precisely degenerate. If the damping rate β and the trap frequencies ν_i satisfy

$$\beta \lesssim |\nu_i - \nu_j|, \quad i \neq j, \quad (79.57)$$

the motion of the ion in each principal axis direction of the trap is cooled independently of the other directions. For $\gamma \gg \nu_{x,y,z}$, a single laser beam propagating approximately in the direction $(1/\sqrt{3})(\hat{e}_x + \hat{e}_y + \hat{e}_z)$ suffices to cool all components of the secular motion.

Energy in micromotion

Possibly with the aid of compensating static electric fields, one cooled ion may be confined near the zero of the trapping AC electric fields. The energy in the micromotion is then comparable to the energy in the secular motion.

79.4.2 Penning Trap

Trapping

Configuration

A Penning trap might use the same hyperboloid-shape electrodes as an ideal Paul trap. However, a DC voltage U is applied between the endcaps and the ring, and a constant magnetic field \mathbf{B} in the direction of the trap axis z is added. The magnetic field forces an ion escaping toward the ring to turn back.

Motion of an ion

The motion of an ion is a superposition of three periodic components. For the hyperboloid-shape trap, Eq. (79.45) and Fig. 79.2, the three components are completely decoupled. Firstly, in the axial direction, the ion executes oscillations at the axial frequency

$$\nu_z = \left(\frac{2qU}{mQ_0^2} \right)^{1/2}. \quad (79.58)$$

Secondly, the ion undergoes cyclotron motion in the plane perpendicular to the trap axis. As a result of the electric field,

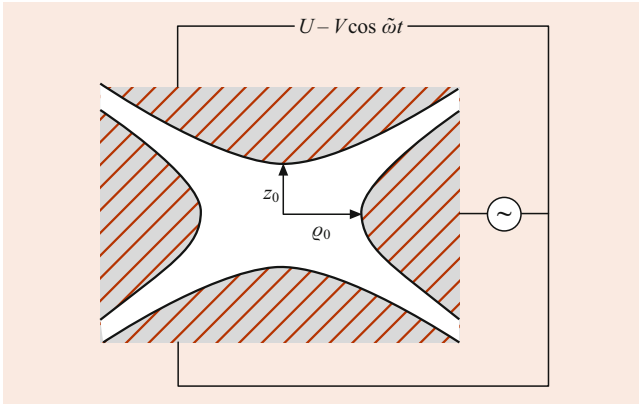


Fig. 79.2 Electrode configuration and voltages of an ideal hyperboloid Paul trap

the frequency of the cyclotron motion

$$\nu'_c = \frac{1}{2}\nu_c + \left(\frac{1}{4}\nu_c^2 - \frac{1}{2}\nu_z^2\right)^{1/2} \quad (79.59)$$

is displaced from the cyclotron frequency $\nu_c = qB/m$ of a free ion. Thirdly, the guiding center of cyclotron motion rotates about the trap axis at the magnetron frequency

$$\nu_m = \frac{1}{2}\nu_c - \left(\frac{1}{4}\nu_c^2 - \frac{1}{2}\nu_z^2\right)^{1/2}. \quad (79.60)$$

The frequencies typically satisfy

$$\nu_m \ll \nu_z \ll \nu'_c. \quad (79.61)$$

Magnetron motion has unusual properties. It takes up the majority of the electrostatic energy in the transverse directions, which in the absence of the magnetic field would lead to expulsion of the ion. Relative to a stationary ion at the trap center, the energy of the magnetron motion is bounded from above by zero. The radius, as well as velocity and kinetic energy of magnetron motion, decreases with increasing total energy. The energy for a state with n_c , n_z , and n_m quanta in the cyclotron, axial, and magnetron motions is, therefore,

$$E = \hbar\nu'_c\left(n_c + \frac{1}{2}\right) + \hbar\nu_z\left(n_z + \frac{1}{2}\right) - \hbar\nu_m\left(n_m + \frac{1}{2}\right). \quad (79.62)$$

Cooling

Laser cooling

For ions in a practical Penning trap, the frequencies ν'_c , ν_z and ν_m are $< \gamma$. If \mathbf{k} is not orthogonal to either the cyclotron motion or the axial motion, Doppler cooling proceeds

essentially as for a free atom. However, energy should be added to the magnetron motion in order to reduce the magnetron radius and velocity. The solution is to aim a finite-size laser beam off the center of the trap in such a way that an ion experiences a higher (lower) intensity over the part of its magnetron orbit in which it travels in the direction of (opposite to) the laser beam. With a proper choice of the parameters, the ensuing addition of energy overcomes Doppler cooling of the magnetron motion.

Other cooling methods

Precision measurements are carried out in Penning traps with objects that do not have an internal level structure suitable for laser cooling, and, thus, other cooling methods are used.

For light particles such as electrons, characteristic times of radiative damping of the cyclotron motion are in the sub-second regime, and, hence, so are the equilibration times with blackbody radiation. Cooling is accomplished by enclosing the trap in a low-temperature (e.g., liquid helium) environment. For protons and heavier particles, the equilibration times of the cyclotron motion with the environment are impracticably long, and the same applies to the axial and magnetron motions even for electrons.

A workable cooling scheme for the axial motion is based on the charges that the oscillating particle induces on the endcaps. The charges generate currents in an external circuit connecting the endcaps. The endcaps are coupled to a cooled resonant circuit tuned to the axial frequency, and axial motion relaxes to thermal equilibrium with the resonant circuit. A variant of this resistive cooling, in which the ring is split into electrically insulated segments, is used to cool the cyclotron motion of protons and heavier ions.

Magnetron motion of an electron or proton is cooled by sideband cooling. An electric field with components in both the z -direction and xy -plane, and tuned to $\omega = \nu_z + \nu_m$, drives transitions that may either increase or decrease the number of quanta in each mode. However, the matrix elements favor transitions with $\Delta n_z = 1$ and $\Delta n_m = -1$. Pumping of the axial motion is canceled by axial cooling, while an equilibrium with low kinetic energy ensues for the magnetron motion. Ideally, the ratio of kinetic energies becomes

$$\frac{\mathcal{T}_{\text{kin},m}}{\mathcal{T}_{\text{kin},z}} = \frac{\nu_m}{\nu_z}. \quad (79.63)$$

79.4.3 Collective Effects in Ion Clouds

As soon as there is more than one ion in the trap, Coulomb interactions between the ions profoundly shape the physics [13].

Ion Crystal

In the standard Paul trap, radio frequency heating [14] due to transfer of energy from micromotion to secular motion limits the number of ions that can be cooled efficiently by a laser. Nevertheless, if a low enough temperature is reached, the ions settle to equilibrium positions corresponding to a minimum of the joint trapping and Coulomb potentials and form a *crystal*.

Strongly Coupled Plasma

Cooling of a large number of ions is possible in a Penning trap. However, magnetron motion becomes uniform rotation of the entire cloud, and Coulomb interactions set a lower limit on the attainable radius of the cloud. This leads to a lower limit on the kinetic energy and second-order Doppler shift.

In a corotating frame, the ions behave like a one-component plasma on a neutralizing background. The characteristic parameter for a one-component plasma with charge per particle q and density n is

$$\Gamma_P = \left(\frac{4\pi n}{3} \right)^{1/3} \frac{q^2}{4\pi\epsilon_0 k_B T}, \quad (79.64)$$

essentially the ratio of the Coulomb energy between two nearest-neighbor ions divided by the thermal kinetic energy. $\Gamma_P > 1$ indicates a strongly coupled plasma; for $\Gamma_P > 2$ and $\Gamma_P > 170$ liquid and solid phases are expected in an infinite plasma. Experiments with a Penning trap have produced $\Gamma_P \gtrsim 300$. Concentric shells of ions or various more or less crystalline arrangements are seen, depending on the experimental conditions.

Sympathetic Cooling

In a trap that holds two or more species of charged particles, cooling of the motion of one species is transferred by the Coulomb interactions to the other species. This sympathetic cooling broadens the selection of species accessible to ion cooling methods.

79.5 Experimental

79.5.1 Free Particles

Historically, the focus has been on alkali metal vapors, to a large extent because the required laser frequencies can be generated using inexpensive diode lasers. Hyperfine structure of the ground state of the alkalis complicates experiments because the atoms may end up in an inert hyperfine level outside the active cooling/trapping transitions. To counteract this, appropriately tuned repumper light is added to

return such atoms to circulation. Other species such as alkaline earths (Sr) and lanthanides (Yb) are occasionally used. They offer very narrow optical transitions and isotopes with varying hyperfine structures (including none).

Originally the experiments often started with a longitudinal deceleration and cooling of an atomic beam by a counterpropagating laser beam. To compensate for the change of the Doppler shift of the atoms while they slowed down, the position-dependent magnetic field of a tapered solenoid shifted the transition frequency of the atoms to keep them near resonance while they moved down the solenoid. A magneto-optical trap then scooped up some atoms, cooled them further, and held them. Nowadays, this Zeeman slower is mostly supplanted by various schemes in which a MOT directly captures atoms from the low-velocity wing of the thermal distribution. Depths of neutral-atom traps are far below 1 K. Storage times in a MOT are typically on the order of seconds, limited at high densities by exothermic binary collisions and at low densities by collisions with the atoms of the background gas.

Absorption imaging of the atom cloud is the standard diagnostic tool, giving both (the projection to a plane of) the spatial distribution of the atoms, and after proper calibration, the number of the atoms. If cooling and trapping is suddenly turned off, the atom cloud flies apart ballistically, and the velocity distribution gets converted into a position distribution. Analysis of time-delayed absorption images, thus, gives the momentum distribution.

The evolution of the experimental techniques during the era of laser cooling and trapping has been nothing short of spectacular. Acousto-optic and electro-optic modulators enable control of temporal variations and frequencies of the light; the spatial shape of the light field may be tailored using spatial light modulators such as digital micromirror devices; by moving an optical trap of light around quickly, one can “paint” a nearly arbitrary time-averaged optical potential energy for the atoms [15]; it is possible to assemble an arbitrary defect-free 2-D array of atoms one atom at a time [16], and so on. Digital control of the apparatus, data acquisition, and data analysis is an indispensable element in the experiments.

79.5.2 Trapped Particles

Both Paul and Penning traps behave like a conservative potential and scatter rather than confine a particle coming from the outside. One method to load a trap is to generate the ions in situ, e.g., by letting a beam of atoms and electrons collide inside the trap. Time-dependent electric potentials are another loading method. The trapped species is injected through a hole in the endcap, and the opposing endcap is raised to an electric potential that makes the entering parti-

cles stop. The potential is then lowered before it ejects the particles. A single electron, positron, proton, antiproton, or ion may be loaded. Typical depths of ion traps are ≈ 1 eV or $\approx 10^4$ K. With the aid of cooling, the storage time may be made infinite for all practical purposes.

Trap frequencies are measured by observing the resonances excited by added AC fields. For instance, an electric field near the axial resonance frequency may be coupled between the ring and one endcap. A resonance circuit coupled between the ring and the other endcap is used to detect the resonance. Alternatively, ejection of the driven ions is monitored.

For an ion with a dipole-allowed resonance transition, fluorescence of a single ion is readily detected. Even absorption of a single ion may be measurable. Various methods of finding the temperature have been devised. At temperatures of 1 K and higher, Doppler broadening of a dipole-allowed optical transition is observable. The size of the single-ion cloud is a measure of temperature. Finally, motional sidebands in the absorption of a narrow transition ($\gamma \ll \nu$), not necessarily the same transition as the one used for cooling, may be measured to find $\langle n \rangle$. In the Lamb–Dicke regime, only the carrier absorption at $\Delta = 0$ and sidebands at $\Delta = \pm \nu$ are significant, and the ratios of the peak absorptions are

$$\alpha_- : \alpha_0 : \alpha_+ = \langle n \rangle \frac{\epsilon_r}{\nu} : 1 : (1 + \langle n \rangle) \frac{\epsilon_r}{\nu}. \quad (79.65)$$

Fluorescence carries similar information.

In an ion crystal, the ions have collective vibration modes akin to phonons, instead of the three vibration modes along the principal axes of the trap of a single ion. Doppler cooling and sideband cooling work for such collective modes much like they work for the vibration modes of a single ion.

Ion traps and optical dipole traps make it possible to isolate an individual atom scale particle for studies for a practically infinite time, which enables clean experiments on various fundamental aspects of quantum mechanics and quantum electrodynamics. Quantum jumps are a case in point. Suppose that, in addition to an optically driven two-level system, a single ion has a third “shelving” state. Suppose further that the ion infrequently makes a transition to the shelving state, stays there for a long time compared with the timescale of spontaneous emission of the active system, and then returns to the two-level system. When the ion makes a transition to the shelving state, fluorescence from the two-level system suddenly ceases, and the fluorescence reappears equally abruptly when the ion returns to the two-level system. These jumps in light scattering are the quantum jumps [17]. They are a method to detect a weak transition with an enormous amplification; a single transition to or from the shelving state may mean the difference between the presence or absence of billions of fluorescence photons.

79.6 Applications

Trapping and cooling offer increased interaction times between the atoms/ions and the light. This leads to reduced transit time broadening, and, indeed, to macroscopic (> 1 s) interaction times. Laser cooling in a magneto-optical trap routinely gives temperatures so low that the Doppler width is below the natural linewidth of the cooling transition. A homogeneously broadened atomic sample is thus prepared. Cooling also enables reduction of the second-order Doppler effect. Spectroscopy and various frequency measurements have traditionally been the primary beneficiary. Potential applications range from detection of the change of natural constants over time (Chap. 30) to such feats of technology as the Global Positioning System.

Another broad area drawing from low temperatures is experiments, and in the future possibly technologies, that rely on quantum mechanical behavior of either light or atoms. Nowadays, nearly all cutting-edge experiments in quantum optics start with laser cooling. Trapping and manipulation of individual atomic particles is also an established practice.

In this chapter we, by necessity, limit the discussion of applications to very few topics in which the interplay between the internal degrees of freedom and the CM motion is the central theme. At the moment, the most prominent broad application area of laser cooling and trapping is probably quantum gases under conditions when the particle statistics matters, such as the use of optical lattices as quantum simulators of condensed matter systems. These are taken up separately in Chap. 80.

79.6.1 Cold Molecules

Ultralow-temperature molecules may be produced by starting with an ultralow-temperature atomic gas or gases, and using photoassociation or Feshbach resonances to convert pairs of atoms into diatomic molecules [18]. Direct laser cooling of molecules was long thought impossible because of the proliferation of vibrational and rotational states. In general, there is no closed transition that allows enough cycles of absorption and spontaneous emission so that the net exchange of momentum between light and the molecules would be comparable to the momentum of a room-temperature molecule. However, in certain molecules, such as CaF and SrF, there are diagonal transitions between vibrational states with the Franck–Condon factor very close to unity, giving a simulacrum of a closed two-level system. One still has to compensate for the leakage from the almost-closed transition because the Franck–Condon factors of the unwanted transitions are not exactly zero, branching between hyperfine levels is possible as in atoms, and so on. A number of

laser frequencies may be needed to repump the molecule into the desired transition. Nonetheless, the basic program of laser cooling and trapping has been demonstrated for diatomic molecules [19]. One of the foreseeable goals is a Bose–Einstein condensate of polar molecules, a novel system because of the strong anisotropic long-range electric dipole interactions between the molecules.

79.6.2 Quantum Systems of Internal and CM States

A vibrational mode of a trapped ion and an effective two-state system for the internal degrees of freedom make a realization of the Jaynes–Cummings model (discussed in detail in Chap. 83.4.1) possible. Moreover, sideband cooling enables the experimenter to put the mode cleanly in its lowest quantum state. These observations have inspired quantum-state engineering with the objective of generating an arbitrary state of the vibrational motion of the ion [20]. In many-ion crystals, the collective vibration modes may be used to couple and entangle the internal degrees of freedom of two or more ions. As discussed in Chap. 85, quantum information processing has been demonstrated in this manner.

Fully coherent manipulation of joint internal and CM states of free atoms is also possible. For instance, two motional states of a ground-state atom with the velocities v and $v + 2v_r$ can be coupled by two light pulses with opposite propagation directions. If both pulses are off resonance from a transition between the ground and excited state of the atom, and their frequency difference matches the difference of the kinetic energies $\frac{1}{2}mv^2$ and $\frac{1}{2}m(v + 2v_r)^2$, a Raman scheme is set up that may transfer the atom between the two motional states. Variations of this Bragg diffraction technique have been used to coherently split an atomic wave packet to components with the velocities differing by tens of recoil velocities [21]. Recombining the wave packet makes an interferometer that is sensitive to the forces, real and inertial, that acted on the atom while the wave packet was split. Analogous atom interferometers are being developed for purposes such as gravimetry. The hope is improved sensitivity; in the literature one sees claims of fundamental scaling of the sensitivity between atom interferometers and light interferometers with $mc^2/\hbar\omega_0$.

More generally in the way of coupling between internal and CM degrees of freedom, a field called (in the atomic context maybe confusingly) spin–orbit coupling [22] emerged during the past decade and has inspired much theoretical and experimental work. In an elementary example, consider a two-level atom without damping moving in the x -direction in the plane wave of light with the amplitude proportional to e^{ikx} . Using the vector-matrix representation for the internal states $\{|e\rangle, |g\rangle\}$ and in the convention that the zero of the en-

ergy in the rotating frame lies halfway between the states, the Hamiltonian reads

$$H = \begin{bmatrix} \frac{\hat{p}_x^2}{2m} - \frac{\hbar\Delta}{2} & -\frac{\hbar\Omega}{2}e^{ikx} \\ -\frac{\hbar\Omega}{2}e^{-ikx} & \frac{\hat{p}_x^2}{2m} + \frac{\hbar\Delta}{2} \end{bmatrix}. \quad (79.66)$$

After a unitary transformation generated by

$$U = \begin{bmatrix} e^{-ikx/2} & 0 \\ 0 & e^{ikx/2} \end{bmatrix}, \quad (79.67)$$

the Hamiltonian may be written in terms of Pauli spin matrices as

$$H = \frac{1}{2m} \left(\hat{p}_x + \frac{\hbar k}{2} \sigma_z \right)^2 - \frac{\hbar\Omega}{2} \sigma_x - \frac{\hbar\Delta}{2} \sigma_z. \quad (79.68)$$

The term $\propto \hat{p}_x \sigma_z$ that arises from the expansion of the square is the spin–orbit coupling, seemingly a direct coupling between motional and internal states of the atom. A Raman scheme with two beams propagating in opposite directions and the intermediate state far-off resonance offers a potential realization. A main goal here, again, is clean AMO physics simulations of prominent systems in condensed matter physics. A similar topic, synthetic gauge fields that arise from coupling between internal and motional states of an atom, is discussed at some length in Chap. 80.

References

1. Metcalf, H., van der Straten, P.: *Laser Cooling and Trapping*. Springer, New York (1999)
2. Wineland, D., Itano, W.M., Van Dyck Jr, R.: High-resolution spectroscopy of stored ions. *Adv. At. Mol. Phys.* **19**, 135–186 (1983)
3. Brown, L.S., Gabrielse, G.: Geonium theory: Physics of a single electron or ion in a Penning trap. *Rev. Mod. Phys.* **58**, 233–311 (1986). <https://doi.org/10.1103/RevModPhys.58.233>
4. Stenholm, S.: The semiclassical theory of laser cooling. *Rev. Mod. Phys.* **58**, 699–739 (1986). <https://doi.org/10.1103/RevModPhys.58.699>
5. Knoop, M., Madsen, N., Thompson, R.C. (eds.): *Physics with Trapped Charged Particles*. Imperial College Press, London (2014)
6. Morsch, O., Oberthaler, M.: Dynamics of Bose–Einstein condensates in optical lattices. *Rev. Mod. Phys.* **78**, 179–215 (2006). <https://doi.org/10.1103/RevModPhys.78.179>
7. (2018). <http://steck.us/alkalidata>
8. (2018). https://physics.nist.gov/PhysRefData/ASD/lines_form.html
9. Javanainen, J.: Density-matrix equations and photon recoil for multistate atoms. *Phys. Rev. A* **44**, 5857–5880 (1991). <https://doi.org/10.1103/PhysRevA.44.5857>
10. Castin, Y., Mølmer, K.: Monte Carlo wave-function analysis of 3D optical molasses. *Phys. Rev. Lett.* **74**, 3772–3775 (1995). <https://doi.org/10.1103/PhysRevLett.74.3772>
11. Dalibard, J., Cohen-Tannoudji, C.: Laser cooling below the Doppler limit by polarization gradients: Simple theoretical models. *J. Opt. Soc. Am. B* **6**, 2023–2045 (1989). <https://doi.org/10.1364/JOSAB.6.002023>

12. Gerz, C., Hodapp, T.W., Jessen, P., Jones, K.M., Phillips, W.D., Westbrook, C.I., Molmer, K.: The temperature of optical molasses for two different atomic angular momenta. *EPL* **21**, 661 (1993)
13. Bollinger, J.J., Wineland, D.J., Dubin, D.H.E.: Non-neutral ion plasmas and crystals, laser cooling, and atomic clocks. *Phys. Plasmas* **1**, 1403–1414 (1994). <https://doi.org/10.1063/1.870690>
14. Nam, Y., Weiss, D., Blümel, R.: Explicit, analytical radio-frequency heating formulas for spherically symmetric nonneutral plasmas in a Paul trap. *Phys. Lett. A* **381**(40), 3477–3481 (2017). <https://doi.org/10.1016/j.physleta.2017.09.001>
15. Henderson, K., Ryu, C., MacCormick, C., Boshier, M.G.: Experimental demonstration of painting arbitrary and dynamic potentials for Bose–Einstein condensates. *New J. Phys.* **11**, 043030 (2009)
16. Barredo, D., de Léséleuc, S., Lienhard, V., Lahaye, T., Browaeys, A.: An atom-by-atom assembler of defect-free arbitrary two-dimensional atomic arrays. *Science* **354**, 1021–1023 (2016). <https://doi.org/10.1126/science.aah3778>
17. Blatt, R., Zoller, P.: Quantum jumps in atomic systems. *Eur. J. Phys.* **9**, 250 (1988)
18. Danzl, J.G., Mark, M.J., Haller, E., Gustavsson, M., Hart, R., Aldegunde, J., Hutson, J.M., Nägerl, H.-C.: An ultracold high-density sample of rovibronic ground-state molecules in an optical lattice. *Nat. Phys.* **6**, 265 (2010)
19. Barry, J.F., McCarron, D.J., Norrgard, E.B., Steinecker, M.H., DeMille, D.: Magneto-optical trapping of a diatomic molecule. *Nature* **512**, 286 (2014)
20. Leibfried, D., Blatt, R., Monroe, C., Wineland, D.: Quantum dynamics of single trapped ions. *Rev. Mod. Phys.* **75**, 281–324 (2003). <https://doi.org/10.1103/RevModPhys.75.281>
21. Müller, H., Chiow, S.-W., Long, Q., Herrmann, S., Chu, S.: Atom interferometry with up to 24-photon-momentum-transfer beam splitters. *Phys. Rev. Lett.* **100**, 180405 (2008). <https://doi.org/10.1103/PhysRevLett.100.180405>
22. Zhai, H.: Degenerate quantum gases with spin–orbit coupling: A review. *Rep. Prog. Phys.* **78**, 026001 (2015)



Juha Javanainen Juha Javanainen is Professor of Physics at the University of Connecticut. He has worked on a number of topics in theoretical quantum optics.



Juha Javanainen

Contents

80.1	Introduction	1157
80.2	Elements of Quantum Field Theory	1158
80.2.1	Bosons	1158
80.2.2	Fermions	1159
80.2.3	Bosons Versus Fermions	1159
80.3	Basic Properties of Degenerate Gases	1160
80.3.1	Atoms Are Trapped	1160
80.3.2	Atom–Atom Interactions	1160
80.3.3	Model Hamiltonian	1160
80.3.4	Bosons	1160
80.3.5	Meaning of the Macroscopic Wave Function	1164
80.3.6	Fermions	1165
80.4	Experimental	1165
80.4.1	Preparing a BEC	1165
80.4.2	Preparing a Degenerate Fermi Gas	1166
80.4.3	Monitoring Degenerate Gases	1166
80.5	BEC Superfluid	1167
80.5.1	Vortices	1167
80.5.2	Superfluidity	1167
80.6	Optical Lattice as Quantum Simulator	1168
80.6.1	Basics of the Optical Lattice	1168
80.6.2	Strongly Correlated Systems	1169
80.6.3	Topological Phases of Matter	1170
	References	1172

Abstract

The purpose of this chapter is to summarize the physics of dilute quantum degenerate gases. Given the broad activity in the field, many choices have to be made regarding the topics to include and the style of the discussion. Emphasis is on AMO physics, as opposed to condensed-matter physics. Two related choices are that virtually nothing is said about temperature dependence, and that the focus is on one-particle and mean-field theories as opposed to

strongly correlated systems. Inside AMO physics the approach is in the vein of quantum optics, as opposed to atomic/molecular structure and collisions. For the most part, the coverage is on elementary concepts and basic material. The exception is Sect. 80.6, where a few topical issues are addressed.

The article [1] has become the standard reference on the mean-field physics of a Bose–Einstein condensate (BEC), [2] is particularly explicit about the excitations of a BEC, and [3] reviews the basics of the concurrent condensed-matter approach to quantum degenerate gases. The monograph [4] is a recent broad overview of BEC physics. Here, references are usually not given for topics that are discussed in these sources or where a full discussion can be traced from them. Otherwise, references are meant to be entries to the literature. Assignment of credit or priority is never implied.

Keywords

magnetic trap · optical trap · Feshbach resonance · phase space density · condensate wave function

80.1 Introduction

Bose–Einstein condensation in dilute alkali metal vapors has realized a source of atoms with properties analogous to the properties of laser light, and ultralow-temperature Fermi gases have also come under study. Quantum degenerate gases have become a main theme in AMO physics. Dilute-vapor systems are weakly interacting and subject to a degree of experimental control not seen before in traditional low-temperature condensed-matter systems. Ultralow-temperature gases thereby reinvigorated, say, investigations of superfluids. More recently, the main thrust has been to use AMO techniques to simulate experimentally condensed-

J. Javanainen (✉)
Department of Physics, University of Connecticut
Storrs, CT, USA
e-mail: juha.javanainen@uconn.edu

matter systems, some of which have been subject to much theoretical study in the past but have lacked clean implementations. This applies, in particular, to various lattice systems [5, 6].

80.2 Elements of Quantum Field Theory

A Bose–Einstein condensate and a degenerate Fermi gas are both consequences of particle statistics, exchange symmetries of the many-particle wave function. It is possible, in principle, to deal directly with the wave functions, but in practice, analyses of many-body systems are usually carried out using the methods of second quantization and field theory. In first quantization, the particles are labeled as if each one had a unique tag on it, and the wave function for more than one indistinguishable particle must be symmetrized explicitly. In second quantization, the question is how many particles are in a given one-particle state without any distinction between identical particles. The exchange symmetries are then taken care of automatically. Here, we briefly summarize [7] elementary features of quantum field theories for both bosons and fermions.

80.2.1 Bosons

Particles with an integer value of the angular momentum obey the Bose–Einstein statistics. The characteristic property is that a one-particle state can accommodate an arbitrary number of bosons.

State Space for Bosons

Specifically, first consider one particle whose states are completely specified by a set of quantum numbers k . As a notational device for the purposes of the present chapter, all of the quantum numbers are assumedly mapped in a one-to-one fashion to nonnegative integers, and, correspondingly, the quantum numbers are written $k = 0, 1, 2, \dots$. The quantum numbers incorporate a description of the state of the center-of-mass (CM) motion of the particle. We, therefore, have an orthonormal basis of wave functions to represent any state of a particle, $\{u_k(\mathbf{x})\}_k$, where \mathbf{x} stands for the CM coordinate.

Given the one-particle states, the postulate is that the Fock states $|n_0, n_1, \dots, n_\infty\rangle$ with $n_k = 0, 1, 2, \dots$ particles in the states $k = 0, 1, 2, \dots$ form an orthonormal basis for the many-body system.

Second-Quantized Operators for Bosons

The annihilation operator for the state k , a_k , is defined by

$$\begin{aligned} a_k |n_0, n_1, \dots, n_k, \dots, n_\infty\rangle \\ = \sqrt{n_k} |n_0, n_1, \dots, n_k - 1, \dots, n_\infty\rangle. \end{aligned} \quad (80.1)$$

Its Hermitian conjugate, the creation operator, behaves as

$$a_k^\dagger |\dots, n_k, \dots\rangle = \sqrt{n_k + 1} |\dots, n_k + 1, \dots\rangle. \quad (80.2)$$

It follows that

$$a_k^\dagger a_k |\dots, n_k, \dots\rangle = n_k |\dots, n_k, \dots\rangle, \quad (80.3)$$

and so $\hat{n}_k = a_k^\dagger a_k$ is called the number operator for the state k . Correspondingly,

$$\hat{N} = \sum_k a_k^\dagger a_k \quad (80.4)$$

is the operator for the total number of particles in the system. The annihilation and the creation operators have the usual boson commutators,

$$[a_k, a_{k'}] = [a_k^\dagger, a_{k'}^\dagger] = 0, \quad [a_k, a_{k'}^\dagger] = \delta_{kk'}. \quad (80.5)$$

The boson field operator is defined as

$$\hat{\psi}(\mathbf{x}) = \sum_k u_k(\mathbf{x}) a_k. \quad (80.6)$$

The commutator for the field operator,

$$[\hat{\psi}(\mathbf{x}), \hat{\psi}^\dagger(\mathbf{x}')] = \delta(\mathbf{x} - \mathbf{x}'), \quad (80.7)$$

follows from boson commutators and the completeness of the wave functions $\{u_k(\mathbf{x})\}_k$. The orthonormality of the wave functions gives the expression

$$\hat{N} = \int d^3x \hat{\psi}^\dagger(\mathbf{x}) \hat{\psi}(\mathbf{x}), \quad (80.8)$$

for the particle number operator. The positive operator

$$\hat{n}(\mathbf{x}) = \hat{\psi}^\dagger(\mathbf{x}) \hat{\psi}(\mathbf{x}) \quad (80.9)$$

evidently represents the density of the particles at the position \mathbf{x} .

The second-quantized operators introduced thus far can be used to express all observables acting on indistinguishable bosons. The most relevant here are the one and two-particle operators. One-particle operators, such as kinetic energy, act on one particle at a time, while two-particle operators, such as atom–atom interactions, refer to two particles. In first quantization, these are of the form

$$O_1 = \sum_n V(\mathbf{x}_n), \quad O_2 = \frac{1}{2} \sum_{n \neq n'} u(\mathbf{x}_n, \mathbf{x}_{n'}), \quad (80.10)$$

where the sums run over the labels of the particles. The corresponding second-quantized operators are

$$\hat{O}_1 = \int d^3x \hat{\psi}^\dagger(\mathbf{x}) V(\mathbf{x}) \hat{\psi}(\mathbf{x}), \quad (80.11)$$

$$\hat{O}_2 = \frac{1}{2} \int d^3x d^3x' \hat{\psi}^\dagger(\mathbf{x}) \hat{\psi}^\dagger(\mathbf{x}') u(\mathbf{x}, \mathbf{x}') \hat{\psi}(\mathbf{x}') \hat{\psi}(\mathbf{x}). \quad (80.12)$$

When the particles have internal degrees of freedom in addition to the CM motion, such as hyperfine and Zeeman states, it is convenient for the present purposes to regard particles in each internal state as a separate species. Thus, if the quantum number breaks up into $k \equiv \{p, \alpha\}$, where p stands for quantum numbers of the center of the mass and α for the quantum numbers of the internal state, it is expedient to define a quantum field for each species α as

$$\hat{\psi}_\alpha(\mathbf{x}) = \sum_p u_{p\alpha}(\mathbf{x}) a_{p\alpha}. \quad (80.13)$$

Mechanisms that cause transitions between the internal states couple the fields $\hat{\psi}_\alpha(\mathbf{x})$ with different α .

States of Bosons

To complete the transformation from wave function quantum mechanics to second quantization, the state of the system must be specified in second quantization. For instance, take the Hamiltonian \hat{H} and the particle number operator \hat{N} . According to statistical mechanics a system characterized by the temperature T and chemical potential μ is in the state with the density operator $\hat{\rho} = e^{-(\hat{H} - \mu\hat{N})/k_B T} / \mathcal{Z}$, where the grand partition function is $\mathcal{Z} = \text{Tr} e^{-(\hat{H} - \mu\hat{N})/k_B T}$.

Bose–Einstein Condensate

The state of a boson system of particular interest here is the BEC. In an ideal gas, condensation entails a macroscopic fraction of the particles occupying the ground state of the CM motion. Condensation is a phase transition that occurs when either the density of the gas is increased, or the temperature is lowered. In a homogeneous ideal Bose gas, the governing parameter is the phase space density ζ , defined in three spatial dimensions as

$$\zeta = \left(\frac{2\pi\hbar^2}{mk_B T} \right)^{3/2} n, \quad (80.14)$$

where m is the mass of the condensing atoms, T is the temperature, and n is the density of the condensing species. For the purposes of quantum degeneracy, each internal state of an atom behaves as a separate species. Bose–Einstein condensation takes place when the phase space density satisfies $\zeta = 2.612$. Depending on whether density or temperature is

regarded as a constant, Eq. (80.14) may be regarded as an equation for the critical temperature T_c or the critical density n_c for Bose–Einstein condensation.

80.2.2 Fermions

Particles with a half-integer angular momentum obey the Fermi–Dirac statistics. Each Fock state may then only have the occupation numbers $n_k = 0, 1$. The conventional definition of the annihilation operator contains a phase factor,

$$a_k |n_0, n_1, \dots, n_k, \dots, n_\infty\rangle \\ = n_k (-1)^{\sum_{p=0}^{k-1} n_p} |n_0, n_1, \dots, n_k - 1, \dots, n_\infty\rangle, \quad (80.15)$$

and fermion operators are governed by the anticommutator

$$[A, B]_+ \equiv AB + BA \quad (80.16)$$

rather than the commutator. For instance,

$$[a_k, a_{k'}]_+ = 0, \quad [a_k, a_{k'}^\dagger]_+ = \delta_{kk'}. \quad (80.17)$$

Except for the use of anticommutators in lieu of commutators, all formal expressions for field operators and one and two-particle operators written down for bosons in Sect. 80.2.1 remain valid as stated.

Degenerate Fermi Gas

A degenerate Fermi gas realized in a dilute atom vapor is the fermion counterpart of a BEC. The basic parameter of a free noninteracting Fermi gas is the Fermi energy, the chemical potential at zero temperature. It is given by

$$\epsilon_F = \frac{\hbar^2 k_F^2}{2m}; \quad k_F = (6\pi^2 n)^{1/3}, \quad (80.18)$$

where n once more is the density for the relevant fermion species. In the limit of zero temperature, the Fermi gas makes a Fermi sea; the states below the Fermi energy are filled with one particle each, the states above the Fermi energy are empty. The gas begins to show substantial deviations from the Maxwell–Boltzmann statistics and may be regarded as degenerate when the temperature is below the Fermi temperature, $T \lesssim T_F = \epsilon_F/k_B$. Except for a numerical factor, in terms of density and temperature, the condition $T = T_F$ is the same as the condition for Bose–Einstein condensation.

80.2.3 Bosons Versus Fermions

Isotopes of alkali metals with an odd mass number (${}^7\text{Li}$, ${}^{23}\text{Na}$, ${}^{39}\text{K}$, ${}^{85}\text{Rb}$, ${}^{87}\text{Rb}$, ${}^{133}\text{Cs}$) make Bose–Einstein gases,

while isotopes with an even mass number (${}^6\text{Li}$, ${}^{40}\text{K}$) make Fermi–Dirac gases. Atoms are composite particles consisting of fermions, and how they may act as bosons is a legitimate question. Whether a satisfactory formal answer to this question exists may be debated, but in practice, atoms seem to obey the correct statistics in processes that do not expose their individual constituents.

When two bosonic atoms with integer angular momenta combine into a molecule, the molecule has an integer angular momentum and behaves as a boson. On the other hand, two fermionic atoms also make a bosonic molecule. Models for the latter type of system are basically ad hoc since, at this point in time, no microscopic theory for such a rearrangement of the statistics appears to exist. Nonetheless, empirically, diatomic molecules formed by combining two fermionic atoms indeed appear to be bosons.

80.3 Basic Properties of Degenerate Gases

80.3.1 Atoms Are Trapped

Quantum degenerate alkali vapors are typically prepared in an atom trap. Close to the bottom almost every trap is a three-dimensional harmonic oscillator potential completely characterized by the principal-axis directions and the corresponding trap frequencies ω_i , the (angular) frequencies at which a single atom would oscillate back and forth in the given principal-axis direction. In the principal-axis coordinate system the trapping potential reads

$$V(\mathbf{x}) = \frac{1}{2} \sum_{i=1}^3 m \omega_i^2 x_i^2. \quad (80.19)$$

It is convenient to introduce the characteristic harmonic-oscillator frequency scale and the corresponding harmonic-oscillator length scale as

$$\bar{\omega} = (\omega_1 \omega_2 \omega_3)^{1/3}, \quad \ell = \sqrt{\frac{\hbar}{m \bar{\omega}}}. \quad (80.20)$$

80.3.2 Atom–Atom Interactions

At low temperatures/energies, only s -wave collisions are significant. In the theory of quantum degenerate gases, these are frequently represented by a pseudopotential tailored to give the correct s -wave phase shift. Except for a mathematical subtlety that is usually ignored, for two atoms the pseudopotential is

$$u(\mathbf{x}_1, \mathbf{x}_2) = \frac{4\pi \hbar^2 a}{m} \delta(\mathbf{x}_1 - \mathbf{x}_2), \quad (80.21)$$

where a is the s -wave scattering length. Qualitatively, the scattering length is positive (negative) if the interaction is repulsive (attractive).

80.3.3 Model Hamiltonian

Quantum field theory for a single-component Bose gas usually starts with the Hamiltonian

$$\hat{H} = \int d^3x \hat{\mathcal{H}}(\mathbf{x}), \quad (80.22)$$

where the Hamiltonian density is

$$\begin{aligned} \hat{\mathcal{H}}(\mathbf{x}) = & \hat{\psi}^\dagger(\mathbf{x}) \left[-\frac{\hbar^2}{2m} \nabla^2 + V(\mathbf{x}) \right] \hat{\psi}(\mathbf{x}) \\ & + \frac{2\pi \hbar^2 a}{m} \hat{\psi}^\dagger(\mathbf{x}) \hat{\psi}^\dagger(\mathbf{x}) \hat{\psi}(\mathbf{x}) \hat{\psi}(\mathbf{x}). \end{aligned} \quad (80.23)$$

As in Sect. 80.2.1, $\hat{\psi}(\mathbf{r})$ is the boson field operator, the kinetic energy $-\hbar^2 \nabla^2 / 2m$ and trapping potential $V(\mathbf{x})$ are one-particle operators, and atom–atom interactions are governed by the two-particle operator u of Eq. (80.21). Analogous models can be written down for multicomponent boson and fermion fields, for conversion between atoms and molecules, and so on.

80.3.4 Bosons

Gross–Pitaevskii Equation

Mean-field approximation

Conventionally, the next step for bosons is to go over to the corresponding classical field theory. The result is referred to as mean-field theory or semiclassical theory.

Formally, one first writes down explicitly the Heisenberg equation of motion for the boson field $\hat{\psi}$,

$$i\hbar \frac{\partial}{\partial t} \hat{\psi}(\mathbf{x}, t) = [\hat{\psi}(\mathbf{x}, t), \hat{H}], \quad (80.24)$$

and then declares that in the equations of motion, $\hat{\psi} \rightarrow \psi$ is a classical field and no longer a quantum field. We call ψ the macroscopic wave function of the condensate. This approximation is precisely analogous to using the classical instead of the quantum description for the electric and magnetic fields of the light coming out of a laser.

Time-dependent Gross–Pitaevskii equation

The ensuing time-dependent Gross–Pitaevskii equation (GPE) is

$$i\hbar \frac{\partial}{\partial t} \psi(\mathbf{r}, t) = \left[-\frac{\hbar^2}{2m} \nabla^2 + V(\mathbf{r}) \right] \psi(\mathbf{r}, t) + \frac{4\pi\hbar^2 a}{m} |\psi(\mathbf{r}, t)|^2 \psi(\mathbf{r}, t). \quad (80.25)$$

This equation is nonlinear, and normalization of the macroscopic wave function ψ is important. Quantum mechanically, the particle number operator is given by Eq. (80.8), so the normalization for a system with N particles naturally reads

$$\int d^3x |\psi(\mathbf{x}, t)|^2 = N. \quad (80.26)$$

Time evolution under Eq. (80.25) preserves the normalization. Obviously, and in accordance with Eq. (80.9),

$$n(\mathbf{x}) = |\psi(\mathbf{x})|^2 \quad (80.27)$$

is the local density of the gas.

Time-independent Gross–Pitaevskii equation

Solutions to the time-dependent GPE of the form $\psi(\mathbf{x}, t) = \phi(\mathbf{x})e^{-i\mu t/\hbar}$ are stationary states with no time evolution in the physics. The analog μ of the energy of a stationary state in ordinary quantum mechanics is called chemical potential. The corresponding wave function ϕ satisfies the time-independent GPE

$$\mu\phi = \left(-\frac{\hbar^2}{2m} \nabla^2 + V \right) \phi + \frac{4\pi\hbar^2 a}{m} |\phi|^2 \phi. \quad (80.28)$$

Both GPEs are nonlinear variants of the Schrödinger equation, and in other contexts they are often referred to as nonlinear Schrödinger equations. The nonlinear term approximates the interaction energy of an atom with the other atoms in an averaged way based on the local density of the atoms, hence the term mean-field theory.

Sign of scattering length

The qualitative properties of a condensate, as per the GPE, depend on the sign of the scattering length. For repulsive atom–atom interactions or no atom–atom interactions, $a \geq 0$, both the time-dependent and the time-independent forms are mathematically well behaved. Unless otherwise noted, below the scattering length is always assumed nonnegative.

In the case of a negative scattering length, a BEC may, in principle, decrease its energy without a bound by collapsing to a point. Mechanisms such as three-body recombination and molecule formation would eventually set in as the density increases, and the collapse would stop, but the

condensate must then be presumed lost. In the absence of an external potential, a condensate with a negative scattering length is unconditionally unstable against collapse. For a bounded condensate, the increase in the kinetic energy coming with the decreasing size may hold off the collapse, provided the number of atoms in the condensate is sufficiently small. Simple dimensional-analysis arguments give the condition of stability in a harmonic trap as $N|a| \lesssim \ell$.

Behavior attributed to a collapse has been observed in ^7Li with a negative scattering length. By using a Feshbach resonance it is also possible to adjust the scattering length, see Eq. (80.66), which has led to further demonstrations of collapse-like physics.

Healing length

Consider the time-independent GPE Eq. (80.28) without an external potential and scale the various quantities:

$$\begin{aligned} \phi &= \sqrt{n} \bar{\phi}, \quad \mu = \bar{\mu} \frac{4\pi\hbar^2 n a}{m}, \\ \mathbf{x} &= \xi \bar{\mathbf{x}}; \quad \xi = \frac{1}{\sqrt{8\pi n a}}. \end{aligned} \quad (80.29)$$

Here, n is the density scale for the gas, and the length scale is ξ . In terms of these new variables, the time-independent GPE reads

$$\bar{\mu} \bar{\phi} = -\bar{\nabla}^2 \bar{\phi} + |\bar{\phi}|^2 \bar{\phi}. \quad (80.30)$$

There is a solution in all of space with $\bar{\mu} = 1$, $\bar{\phi} = 1$. If for some reason, such as an edge of the sample, the condensate wave function must vanish, the length scale over which the wave function grows back to one (in the scaled units) is on the order of unity. In fact, Eq. (80.30) has the solution $\bar{\phi}(\bar{\mathbf{x}}) = \tanh(\bar{z}/\sqrt{2})$ in the half-space $\bar{z} \geq 0$. The quantity ξ is the minimum length scale over which a condensate wave function can build up to the density n . It is called the healing length.

Thomas–Fermi approximation

Without atom–atom interactions, the ground state of the trapping potential $V(\mathbf{x})$ would be the lowest-energy (lowest μ) solution to Eq. (80.28). However, experience has shown that even modest repulsive atom–atom interactions ($a > 0$) spread out the macroscopic wave function of the condensate a great deal. With increasing size comes decreasing kinetic energy, according to the Heisenberg uncertainty principle. This suggests the Thomas–Fermi approximation, in which the kinetic energy term in Eq. (80.28) is simply ignored. The density of the gas is then easily solved to be

$$n(\mathbf{x}) = \begin{cases} \frac{m[\mu - V(\mathbf{x})]}{4\pi\hbar^2 a}, & \mu > V(\mathbf{x}) \\ 0, & \text{otherwise,} \end{cases} \quad (80.31)$$

an inverted image of the trapping potential. The normalization Eq. (80.26) can be used to find the relation between chemical potential and particle number, and all of the unknown quantities may, in principle, be found.

For a harmonic potential the Thomas–Fermi approximation can be worked out explicitly with the results

$$\begin{aligned} \mu &= \frac{1}{2} \hbar \bar{\omega} \left(\frac{15Na}{\ell} \right)^{2/5}, & R &= \ell \left(\frac{15Na}{\ell} \right)^{1/5}, \\ n(0) &= \frac{1}{8\pi\ell^3} \frac{\ell}{a} \left(\frac{15Na}{\ell} \right)^{2/5}. \end{aligned} \quad (80.32)$$

The quantity R represents the size of the condensate. In particular, it equals the radius of the spherical condensate if the trap is isotropic with $\omega_1 = \omega_2 = \omega_3$. Finally, $n(0)$ is the central, maximum, density of the atoms.

The relevant dimensionless parameter is Na/ℓ , which can easily be much larger than unity in the experiments. When the Thomas–Fermi approximation is accurate, the chemical potential exceeds the typical level spacing of the harmonic-oscillator trap, and the condensate is larger than the ground-state wave function of the harmonic oscillator would be. Ordinarily, the condensate is also much larger than the healing length.

Small Excitations in a BEC

Linearizing the GPE

The time-dependent GPE is nonlinear but may be linearized around a stationary solution. Consider the special case without a trapping potential, $V(\mathbf{x}) \equiv 0$. The stationary solutions are plane waves,

$$\phi(\mathbf{x}) = \sqrt{n} e^{i\mathbf{p}\cdot\mathbf{x}}. \quad (80.33)$$

This corresponds to a flow of the gas at the velocity $\mathbf{v} = \hbar\mathbf{p}/m$ and with a momentum $\hbar\mathbf{p}$ per atom. The chemical potential of such a mode is

$$\frac{\mu}{\hbar} = \epsilon_p + \frac{1}{2}\epsilon_0, \quad (80.34)$$

where

$$\epsilon_p = \frac{\hbar p^2}{2m}, \quad \epsilon_0 = \frac{mc^2}{\hbar}, \quad c = \frac{\hbar\sqrt{8\pi na}}{m} = \frac{\hbar}{m\xi} \quad (80.35)$$

are the dispersion relation of free atoms, a peculiar analog of the rest energy, and the speed of sound in the BEC.

The ansatz for small deviations from the stationary solution is written as

$$\psi(\mathbf{x}, t) = \sqrt{n} e^{i(\mathbf{p}\cdot\mathbf{x} - \frac{\mu}{\hbar}t)} \left[1 + u e^{i(\mathbf{q}\cdot\mathbf{x} - \nu t)} + v^* e^{-i(\mathbf{q}\cdot\mathbf{x} - \nu^* t)} \right], \quad (80.36)$$

where $\hbar\mathbf{q}$ and $\hbar\nu$ are the momentum and energy associated with the excitation relative to the momentum and energy of the original flow. The GPE mixes the field ψ and its complex conjugate ψ^* , so that two small amplitudes u and v are needed for the excitations. The ansatz Eq. (80.36) is a solution to the time-dependent GPE to the lowest nontrivial order in u and v if these amplitudes and the frequency of the excitation satisfy the eigenvalue equation

$$\begin{pmatrix} \epsilon_q + \epsilon_0 + \mathbf{q}\cdot\mathbf{v} & \epsilon_0 \\ \epsilon_0 & \epsilon_q + \epsilon_0 - \mathbf{q}\cdot\mathbf{v} \end{pmatrix} \begin{pmatrix} u \\ v \end{pmatrix} = \nu \begin{pmatrix} u \\ -v \end{pmatrix}. \quad (80.37)$$

The remaining problem is that the eigenvalue equation has two solutions for each \mathbf{q} , which gives twice as many small-excitation modes as there are degrees of freedom. The extra modes are the penalty one pays for the linearization of the GPE. The criterion $|u|^2 - |v|^2 > 0$ picks out the correct small-excitation modes. The corresponding dispersion relation for the excitations is

$$\nu(\mathbf{q}) = \mathbf{q}\cdot\mathbf{v} + \sqrt{\epsilon_q(\epsilon_q + 2\epsilon_0)}. \quad (80.38)$$

For a stationary BEC with $\mathbf{v} = 0$ and in the limit $q \rightarrow 0$, Eq. (80.38) gives $\nu \approx cq$. This confirms the identification of c as the speed of sound.

In the BEC experiments the condensates are usually trapped, but in principle the same analysis of small-excitation modes may be carried out both numerically and in a myriad of analytical approximations. The generic result is that the trap frequencies lend their frequency scale to small excitations. At low enough temperatures, excitation frequencies calculated in this way agree well with the experiments.

Within the mean-field approximation, small excitations may be analyzed similarly in all boson systems, for instance, in a multicomponent Bose–Einstein condensate or a joint atom–molecule condensate. The evolution frequencies may be complex, which signals a dynamical instability of the stationary configuration; there are small-excitation modes that grow exponentially. The instability of a free gas with a negative scattering length, which is apparent in Eq. (80.38) for $\epsilon_0 < 0$, is a simple example.

Bogoliubov theory

Bogoliubov theory is the many-body quantum version of the analysis of small excitations. The idea is to treat the condensate mode ψ_0 , containing n_0 atoms, separately in the field operator,

$$\hat{\psi} = \sqrt{n_0} \psi_0 + \delta\hat{\psi}, \quad (80.39)$$

expand the Hamiltonian in the lowest nontrivial (second) order in the remnant quantum field $\delta\hat{\psi}$, and diagonalize.

The result is small-excitation modes with the annihilation operators A_k , where k stands for the appropriate quantum numbers. It turns out that the core mathematics of Bogoliubov theory is the same as the mathematics of small excitations, but two features are added. First, Bogoliubov theory explicitly shows that the coefficients u and v in the analog of Eq. (80.37) need to satisfy $|u|^2 - |v|^2 = 1$ to ensure boson commutators for the operators A_k . Second, with quantum fluctuations, atom–atom interactions force atoms out of the condensate even at zero temperature. In a homogeneous (untrapped) condensate, in the limit $na^3 \ll 1$, at $T = 0$, the fraction of noncondensate atoms is

$$\frac{N - n_0}{N} = \frac{8}{3} \sqrt{\frac{na^3}{\pi}}. \quad (80.40)$$

When the so-called gas parameter na^3 is much smaller than unity, at low enough temperatures most of the atoms are in the condensate. Mean-field theory and the GPE are expected to apply, and empirically, they do.

Numerical Methods for GPE

Mathematical properties of the GPE

Let us momentarily assume that, by separation of variables or by some fiat, the problem of solving the time-independent GPE has been rendered one-dimensional. The ordinary Schrödinger equation is linear, and any constant multiple of a solution is also a solution. One parameter, e.g., the logarithmic derivative of the wave function at a given point in space, determines a stationary state completely. This does not hold for the corresponding GPE, for which the values of the wave function and its derivative can be specified independently at (almost) every fixed point in space. As a result of the added flexibility, and unlike the Schrödinger equation, the GPE has bounded solutions for continuous ranges of the values of the chemical potential μ .

However, the time-independent GPE Eq. (80.28) comes with the added normalization condition Eq. (80.26). Normalization quantizes the values of μ for the bound states. In practice one might, for instance, find a solution that satisfies the boundary conditions for a given μ with the shooting method, then adjust the value of μ until the normalization holds. Techniques used in the first numerical analyses of the time-independent GPE in the context of atom vapor condensates were variations of this theme. Such schemes are not feasible in spatial dimensions greater than one.

In general, there is one solution to the time-independent GPE that can be chosen to be positive everywhere, the ground state with the lowest chemical potential. Excited steady states exist, but only a few, such as the flowing states of Eq. (80.33) and vortices discussed in Sect. 80.5.1, have obvious physical meanings. As the GPE is nonlinear, excited states are not the same as small excitations.

Split-step Fourier method

The superposition principle does not hold for the solutions of the time-dependent GPE, and the excited states are usually not orthogonal to one another in any useful sense. Methods based on eigenstate expansions for solving the time-dependent GPE are cumbersome at best. Instead, one often simply integrates the GPE as a partial differential equation in time. A number of different methods are used, but here we only discuss an elementary split-step Fourier method [8]. This is an exceedingly popular algorithm for parabolic equations, which is easy to implement and with minor modifications also solves the time-independent GPE in any number of dimensions.

Thus, consider integration of Eq. (80.25) forward in time over a step from t to $t + \Delta t$. For this purpose, assume first that $|\psi|^2$ in the GPE were a constant equal to its value at time t , then the evolution over the time step Δt would be given by

$$\psi(\mathbf{x}, t + \Delta t) = \exp\left[-i\Delta t\left(-\frac{\hbar\nabla^2}{2m} + U(\mathbf{x})\right)\right]\psi(\mathbf{x}, t), \quad (80.41)$$

where $U(\mathbf{x})$ is a known function of position. In the algorithm the exponential is first split approximately, for instance, as

$$\begin{aligned} & \exp\left[-i\Delta t\left(-\frac{\hbar\nabla^2}{2m} + U(\mathbf{x})\right)\right] \\ & \approx \exp\left(i\frac{\Delta t}{2}\frac{\hbar\nabla^2}{2m}\right)\exp[-i\Delta t U(\mathbf{x})]\exp\left(i\frac{\Delta t}{2}\frac{\hbar\nabla^2}{2m}\right) \\ & \equiv \tilde{T}\tilde{U}\tilde{T}. \end{aligned} \quad (80.42)$$

The exponential of the kinetic-energy operator is diagonal in the Fourier representation. Consequently, carrying out the Fourier transformation \mathcal{F} and its inverse gives the split-step algorithm

$$\psi(t + \Delta t) = \mathcal{F}^{-1}\tilde{T}\mathcal{F}\tilde{U}\mathcal{F}^{-1}\tilde{T}\mathcal{F}\psi(t), \quad (80.43)$$

with an efficient implementation using the fast Fourier transformation. For the GPE, $U(\mathbf{x})$ includes the mean-field contribution that depends on the wave function ψ itself, so the question arises as to which approximation of ψ to use when one operates with \tilde{U} . The maybe surprising answer is that the very ψ that emerges from the first step $\mathcal{F}^{-1}\tilde{T}\mathcal{F}\psi(t)$ leads to the lowest order of error in Δt [9]. The split-step algorithm preserves the normalization of the macroscopic wave function, and features an accurate compact approximation of the exponential function of the kinetic-energy operator.

Integration in imaginary time

The split-step algorithm also provides a global method to find the ground state. To this end, the time-dependent GPE is integrated in imaginary time, i.e., replacing $\Delta t \rightarrow -i\Delta t$, starting

from a more or less random initial wave function and normalizing after every step. For the Schrödinger equation, this process would increase the amplitude of the lowest-energy component in the wave function with respect to the other components exponentially in the imaginary time, and eventually leave only the ground state. It is not clear that the same should hold for the nonlinear GPE, but often it does. However, in nonlinear problems split-operator methods often exhibit spurious behavior. Successful use of these techniques requires experience and skill in the art of numerical methods.

Local-Density Approximation

While an experimental BEC is usually trapped, it is often much easier to study the theory for a formally infinite homogeneous condensate. As long as the phenomena under investigation involve length scales much smaller than the size of the condensate, trapping cannot affect the behavior of the gas locally. Under such conditions, one may analyze the gas at each position \mathbf{x} as if it were homogeneous, and at the end of the calculations average over the density distribution. The unit-normalized distribution of the density of the gas used in the averaging is

$$P(\varrho) = \frac{\int \delta[\varrho - n(\mathbf{x})] n(\mathbf{x}) d^3x}{\int n(\mathbf{x}) d^3x}. \quad (80.44)$$

For instance,

$$P(\varrho) = \frac{15\sqrt{n(0) - \varrho} \varrho}{4[n(0)]^{5/2}} H(\varrho) H(n(0) - \varrho) \quad (80.45)$$

holds for the Thomas–Fermi approximation with the maximum density $n(0)$. The Heaviside step functions H restrict the density to the correct range $0 \leq \varrho \leq n(0)$. As an example, the average density in the Thomas–Fermi model is

$$\int \varrho P(\varrho) d\varrho = \frac{4}{7} n(0). \quad (80.46)$$

80.3.5 Meaning of the Macroscopic Wave Function

Here, the macroscopic wave function ψ has been introduced by replacing a boson field theory with a classical field theory.

The intuitive interpretation is that, for interacting particles, the atoms condense not to the ground state of the confining potential but to the one-body state whose wave function is the macroscopic wave function. This notion may be criticized on various grounds, but in practice it makes a useful picture.

A precise formal meaning of the macroscopic wave function, and of Bose–Einstein condensation for interacting systems, is found by considering the one-particle density matrix

$$\rho(\mathbf{x}, \mathbf{x}') = \langle \hat{\psi}^\dagger(\mathbf{x}) \hat{\psi}(\mathbf{x}') \rangle, \quad (80.47)$$

which is sufficient to determine the expectation value of any one-particle operator. This is the position representation of a positive operator with the trace equal to particle number (or technically, its expectation value) N . Therefore, an orthonormal set of eigenfunctions $\{\psi_k(\mathbf{x})\}_k$ and the corresponding nonnegative eigenvalues n_k with

$$\sum_k n_k = N \quad (80.48)$$

exist such that the one-particle density matrix may be put in the form

$$\rho(\mathbf{x}, \mathbf{x}') = \sum_k n_k \psi_k(\mathbf{x}) \psi_k(\mathbf{x}'). \quad (80.49)$$

The system is a BEC if in the thermodynamic limit at least one eigenvalue n_k is on the order of the number of particles (if the thermodynamic limit exists and is sensible). The usual case is that only one state, call it $k = 0$, has such a large eigenvalue. The macroscopic wave function is essentially the corresponding eigenfunction, $\psi \equiv \sqrt{n_0} \psi_0$, and n_0 gives the number of condensate atoms. If there is more than one macroscopic eigenvalue, the condensate is called fragmented.

Another interpretation of the macroscopic wave function comes from statistical mechanics. In a continuous (second-order) phase transition typically a symmetry of the system is spontaneously broken. For example, below the Curie temperature, a single-domain ferromagnet magnetizes in some specific direction, and the state has a lower symmetry than the rotationally invariant Hamiltonian of an isotropic ferromagnet. Any quantity that appears in a continuous phase transition and characterizes the breaking of the symmetry may be called an order parameter. The macroscopic wave function can be viewed as the order parameter associated with spontaneous breaking of the global phase or *gauge* symmetry of quantum mechanics. Specifically, in quantum mechanics, the state of the system is unchanged if the wave function is multiplied by an arbitrary complex phase factor $e^{i\varphi}$. However, to write the wave function as $\psi(\mathbf{x})$ already implies a preferred phase, and likewise even if the wave function is adorned with random but, for any given condensate, fixed phase, as in $e^{i\varphi} \psi(\mathbf{x})$.

For one condensate the random phase is inconsequential. Suppose, however, that two BECs with the wave functions $e^{i\varphi_1} \psi_1(\mathbf{x})$ and $e^{i\varphi_2} \psi_2(\mathbf{x})$ are combined. If the macroscopic

wave functions behave as wave functions should, the combination of two condensates displays the density $n(\mathbf{x}) = |e^{i\varphi_1}\psi_1(\mathbf{x}) + e^{i\varphi_2}\psi_2(\mathbf{x})|^2$. There should be an interference pattern between the condensates. Two BECs indeed produce an interference pattern when they are combined.

From the quantum optics viewpoint, a condensate is a given number of atoms in a given one-particle state, a number state, and cannot possess any phase at all. This seems to contradict the observations of an interference pattern. The resolution is that the process of measuring the phase difference in itself creates a phase difference, even if there initially was none [10].

80.3.6 Fermions

Static Fermi Gas

Thomas–Fermi approximation

Consider an ideal single-species Fermi gas of trapped atoms. The original Thomas–Fermi approximation (Chap. 21) was formulated for fermions, namely, electrons, and in the present case, it is modified as follows. For the atom density $n(\mathbf{x})$ at position \mathbf{x} , at a low temperature, the corresponding local chemical potential is approximated according to Eq. (80.18) as

$$\epsilon_F(\mathbf{x}) = \frac{\hbar^2 [6\pi^2 n(\mathbf{x})]^{2/3}}{2m}. \quad (80.50)$$

Given the trapping potential $V(\mathbf{x})$, the density of the gas adjusts in such a way that the sum of the external potential energy and the local chemical potential, the Fermi energy, is a constant across the gas,

$$V(\mathbf{x}) + \frac{\hbar^2 [6\pi^2 n(\mathbf{x})]^{2/3}}{2m} = \mu, \quad (80.51)$$

the global chemical potential. One may solve the density for a given chemical potential as

$$n(\mathbf{x}) = \begin{cases} \frac{\sqrt{2}m^{3/2} [\mu - V(\mathbf{x})]^{3/2}}{3\pi^2 \hbar^3}, & V(\mathbf{x}) < \mu; \\ 0, & \text{otherwise.} \end{cases} \quad (80.52)$$

Finally, the integral of the density over all space should equal the atom number, which gives an equation to determine the chemical potential μ .

For a harmonic trap, this program can be carried out exactly, analytically, with the result that

$$\mu = 6^{1/3} N^{1/3} \hbar \bar{\omega}, \quad R = 2^{2/3} 3^{1/3} N^{1/6} \ell, \quad (80.53)$$

$$n(0) = \frac{2\sqrt{N}}{\sqrt{3}\pi^2 \ell^3}.$$

The quantities $\bar{\omega}$, ℓ , R , and $n(0)$ have the same meaning as in the BEC case. The Thomas–Fermi approximation for fermions should be applicable whenever $N \gg 1$.

In a one-component Fermi gas at low temperature, atom–atom interactions are typically negligible for a multitude of reasons. There is no s -wave scattering, and the presence of the Fermi sea tends to suppress repulsive interactions. However, in the case of attractive interactions between two species, the Fermi sea may be thermodynamically unstable; the energy may be lowered by pairing fermions into Cooper pairs. This is the mechanism behind the BCS theory of superconductivity. BCS theory is a mean-field theory and also allows one to describe a superconductor or a fermion superfluid with a wave function.

Excitations in a Fermi Gas

If the interactions do not render a fermion system into a BCS superfluid, the elementary excitations of a degenerate weakly interacting Fermi gas with short-range interactions are basically atom–hole pairs. Both the static Fermi gas and its excitations have been major themes throughout the history of quantum physics, and we will not attempt a more detailed discussion.

80.4 Experimental

80.4.1 Preparing a BEC

In a trapped gas, the density $n(\mathbf{x})$ is self-determined from the atom number N , and the condition for a BEC in an ideal gas is most readily expressed in terms of the total number of atoms as

$$k_B T_c = 0.94 \hbar \bar{\omega} N^{1/3}. \quad (80.54)$$

In practice, at the bottom of the trap, the conditions on temperature and density for a BEC are similar to the conditions for a BEC in a free gas. In the thermodynamic limit, such that $\bar{\omega} \rightarrow 0$, $N \rightarrow \infty$ with $\bar{\omega} N^{1/3}$ held constant, below the critical temperature T_c , the fraction of condensate atoms behaves as a function of temperature T as

$$\frac{n_0}{N} = 1 - \left(\frac{T}{T_c}\right)^3. \quad (80.55)$$

The experimental realizations of alkali vapor condensates are based on techniques of laser cooling and trapping of atoms. The following discussion overlaps with, and is supplemented by, the material in Chap. 79.

A BEC in a dilute atomic gas is typically prepared using a two-stage process. First, a magneto-optical trap is used to capture a sample of cold atoms and to cool it to a temperature of the order of a few tens of microkelvin. The atoms are

then transferred to a magnetic or optical trap for evaporative cooling that leads to condensation.

A magnetic trap is based on a combination of two ideas. First, if an atom that starts out with its magnetic moment antiparallel to the magnetic field moves slowly enough in a position-dependent magnetic field, its magnetic moment remains adiabatically locked antiparallel to the magnetic field. The energy of the atom is then a minimum where the magnetic field is a minimum. Second, the absolute value of the magnetic field may have a minimum in free space. The minimum is then a trap for atoms whose magnetic moments are suitably oriented. The downside is that only atoms in the right magnetic (Zeeman) states are trapped.

While the atoms cool down, they accumulate at the center of the trap. The center should not be a zero of the magnetic field, because at zero field an atom would lose the lock between the directions of the magnetic moment and the magnetic field. In a time-orbiting potential (TOP) trap, a time-dependent magnetic field is added in such a way that the zero of the magnetic field orbits around the center of the trap. If the frequency at which the zero moves is high enough, the atoms see a time-averaged effective potential with a minimum at the center of the trap, and do not dwell around the zero of the magnetic field. Alternatively, it is possible to wind a coil in such a way that it makes a magnetic field whose absolute value has a minimum that is not zero. In this kind of Ioffe–Pritchard trap, the winding of the wire resembles the seams on a US baseball.

It is also possible to condense atoms trapped in a far-off resonant optical trap based on the dipole forces of light, instead of the magnetic trap. For tuning below the resonance, the atoms are strong-field seekers. An arrangement with two crossed laser beams focused to the same spot is typical. With extreme off-resonant light from, say, a CO₂ or a Nd:YAG laser, absorption of photons, and the associated photon recoil kicks and heating, may be negligible. The frequencies of the two beams may be made slightly different by using, for instance, an acousto-optic modulator, whereby a potentially harmful standing-wave pattern averages out. The advantage of a far-off resonant optical trap is that it is not particularly sensitive to the Zeeman state, so that it can hold atoms in many states.

The idea of evaporative cooling is that the most energetic atoms escape from the trap, and then the remaining atoms thermalize to a lower temperature. Some atoms are lost in the process, but with the decreasing temperature, the density at the trap center nonetheless tends to increase, and the phase space density increases even more due to the cooling.

Evaporative cooling is forced by actually or effectively lowering the depth of the trap. For instance, a radio frequency field is applied to the atoms. The transition frequency between the Zeeman states depends on the magnetic field and increases toward the edges of the trap. Atoms are re-

moved where the radio frequency (RF) is on resonance and drives transitions to untrapped Zeeman states. Thus, while the atoms cool and concentrate at the center, the radio frequency is swept down in such a way that the “RF knife” removing the atoms slides in from the edge of the trap. At some point along the evaporation, a condensate abruptly emerges. The temperature can be further lowered by continuing evaporative cooling, albeit at the expense of loss of atoms. A typical time needed to prepare a condensate is on the order of a second, and a condensate may live for tens of seconds in a good vacuum.

80.4.2 Preparing a Degenerate Fermi Gas

A single-species, very low-temperature Fermi gas is usually an uninteresting system, as the Fermi–Dirac statistics forbids *s*-wave interactions between the atoms, and the gas is nearly ideal. In the experiments the gas usually has two or more species, different states of the same atom. The interactions between the species are then comparable in strength to the interactions between bosonic atoms. Evaporative cooling works in a two-species gas and can be used to prepare a degenerate Fermi gas either in an optical or a magnetic trap. One can also use a gas of bosons, and, indeed, a BEC, as a refrigerator. The lowest attainable temperatures with direct cooling are on the order of $0.1 T_F$. In the quest toward lower temperatures, methods have been devised to reduce the entropy of the atoms rather than the energy.

80.4.3 Monitoring Degenerate Gases

Orders of Magnitude

As a rule of thumb, the trapping frequencies in a magnetic trap are $\bar{\omega} \approx 2\pi \times 10$ Hz, while the frequencies in an optical trap may reach into the kHz regime. A typical oscillator length is $\ell \approx 1$ μ m. A usual number of atoms is $N \approx 10^7$. Scattering lengths are of the order of $a \approx 10$ nm. The size of a degenerate gas is in the neighborhood of $R \approx 0.1$ mm, the maximum density is about $n(0) \approx 10^{15}$ cm⁻³, and the BEC transition temperature and the Fermi temperature are of the order of $T_c \approx T_F \approx 1$ μ K. However, much lower temperatures are readily reached in a BEC.

Time-of-Flight Imaging

Usually the observation of a degenerate gas in an experiment is by time-of-flight imaging. The trap is suddenly removed, whereupon the gas expands freely. After the atom cloud has grown to a size large enough compared to the wavelength of the resonant light used to monitor the gas, an absorption image of the cloud is taken. This gives the projection of the density of the gas onto a plane perpendicular to the direction

of propagation of the imaging light. Except for the effects of atom–atom interactions, after a sufficiently long time of free flight the density reflects the initial momentum distribution of the atoms. Time-of-flight images bear the signs of both condensation in a Bose gas and quantum degeneracy in a Fermi gas. Nontrivially, other features of interest such as vortex cores are also preserved and can be detected after the free expansion. The downside is that the time-of-flight method is destructive. After each snapshot, the sample will have to be prepared again.

80.5 BEC Superfluid

80.5.1 Vortices

Flow Velocity in a Superfluid

By manipulating the Heisenberg equations of motion for a Bose field under the Hamiltonian Eq. (80.22) it is easy to derive the equation of continuity for the atoms,

$$\frac{\partial}{\partial t} \hat{n} + \nabla \cdot \hat{\mathbf{j}} = 0, \quad (80.56)$$

$$\hat{n} = \hat{\psi}^\dagger \hat{\psi}, \quad \hat{\mathbf{j}} = i \frac{\hbar}{2m} (\hat{\psi} \nabla \hat{\psi}^\dagger - \hat{\psi}^\dagger \nabla \hat{\psi}). \quad (80.57)$$

This identifies \hat{n} and $\hat{\mathbf{j}}$ as the operators for atom density and atom current density. The corresponding mean-field quantities are again obtained when the boson fields are replaced with the corresponding classical fields. Writing the classical field in terms of the density $n(\mathbf{x}, t)$ and phase $\varphi(\mathbf{x}, t)$ in the form

$$\psi = \sqrt{n} e^{i\varphi}, \quad (80.58)$$

the local flow velocity $\mathbf{v} = \mathbf{j}/n$ becomes

$$\mathbf{v} = \frac{\hbar}{m} \nabla \varphi. \quad (80.59)$$

The velocity field is irrotational.

Quantization of Circulation

Integration of the flow velocity around an arbitrary loop gives

$$\oint d\mathbf{l} \cdot \mathbf{v} = \frac{\hbar}{m} \Delta\varphi = p \frac{2\pi\hbar}{m}, \quad (80.60)$$

$$p = 0, \pm 1, \pm 2, \dots,$$

since the change of the phase $\Delta\varphi$ around a closed loop must be an integer multiple of 2π . Equation (80.60) expresses the quantization of circulation in a superfluid. A medium described by a macroscopic wave function, such as a BEC, cannot sustain arbitrary flow velocities.

Vortices

As an example, in a fluid rotating as a whole at the angular velocity Ω , the line integral around a loop at the distance r from the axis of rotation would be $2\pi r^2 \Omega$, which is not permitted for an arbitrary r . Instead, upon an attempt to make a BEC rotate, the angular velocity will be carried by vortex lines. These are lines through the condensate, entering and exiting at the surface, such that each vortex carries a quantum of circulation. At the core of a vortex, the flow velocity should be infinite to sustain a finite circulation, which is physically impossible. Nature solves this problem by making the vortex core normal (not BEC), so that the macroscopic wave function does not apply. The diameter of the vortex core is of the order of the healing length ξ , given by Eq. (80.29).

When the trapping potential on the atoms is rotated, it is convenient to study the physics in the corotating frame. Given a frame rotating at the angular velocity Ω and the angular momentum operator $\mathbf{L} = \mathbf{x} \times \mathbf{p}$ per particle, transformation to the rotating frame adds the one-particle term

$$H_r = -\Omega \cdot \mathbf{L} \quad (80.61)$$

to the Hamiltonian. Any particular configuration of vortices is a thermodynamically stable equilibrium if it is the minimum of energy in the corotating frame. For a trapped condensate, at zero rotation velocity the state without vortices is the energy minimum, and increasing the rotation speed makes states with an increasing number of vortices the stable configuration. However, a vortex configuration may be metastable and live for a long time even if it is not the minimum of energy. Conversely, even the energy-minimum configuration of vortices must first be nucleated. Since the circulation can only have quantized values, it cannot change in a continuous process. It takes a zero condensate density somewhere to create or destroy a vortex.

These alternatives provide a large number of experimental scenarios involving rotation of the trap or stirring of the condensate, condensation of a rotating normal gas by taking it across the transition temperature, and so forth. For instance, when a trap containing a BEC is rotated, vortices are generated at the surface where they start their lives as dynamical instabilities. The vortices then drift in and form a regular vortex array. When the rotation is halted, the vortices drift out to the surface and disappear.

80.5.2 Superfluidity

A BEC also has the remarkable property that it may sustain persistent currents that are completely immune to viscosity. The qualitative reason may be seen from the dispersion relation of small excitations Eq. (80.38). As long as the flow

speed $|v|$ is less than the speed of sound c , all excitation energies are positive, so that the flowing state is the state of lowest energy and is thermodynamically stable. On the other hand, when the flow velocity exceeds the speed of sound, the system has excitations that lower the energy, $v(\mathbf{q}) < 0$ for some \mathbf{q} . The flowing state is then not a minimum of energy. The flow is not thermodynamically stable, and it decays when it interacts with an environment by sending off small excitations. The speed of sound gives the Landau critical velocity for superfluidity.

The critical velocity c tends to zero when the atom–atom interactions vanish with $a \rightarrow 0$. While the condensate wave function may be written down whether or not the atoms interact, superfluidity and persistent flows rely on the interactions. The same applies to vortices, as in the limit of a noninteracting gas the healing length and the radius of the vortex core tend to infinity.

The conventional picture is that superfluid flow in an inhomogeneous medium is thermodynamically unstable if the local flow velocity somewhere exceeds the local (density-dependent) speed of sound. In practice, in liquid He experiments and numerical simulations of dilute condensates, the supercurrent often dissipates by shedding vortices when it flows past an obstacle. Persistent flow in a toroidal geometry would be an ideal test case for superfluidity, and such experiments have, in fact, been carried out with dilute atomic condensates [11]. Nonetheless, no clear picture of the quantitative limits to the flow velocity of a superfluid has emerged from these experiments.

80.6 Optical Lattice as Quantum Simulator

Lattice models have been, and are, widely studied in condensed-matter physics. Even though they may look deceptively simple, quantum systems with interactions between the particles usually cannot be solved exactly even with massive numerical computations. Certain static properties of bosonic systems are accessible to quantum Monte Carlo methods even in fairly large models, but less so for fermions because of the notorious “sign problem” [12]; and exact numerical solutions of time dependence in, say, boson lattice models are restricted to the scale of about ten sites with ten particles. The thermodynamic limit of a strongly interacting system is typically addressed with in-principle uncontrolled approximations, such as a judicious mean-field theory.

However, progress in AMO physics has given us materially flawless optical lattices to hold the atoms, lattice parameters may be controlled by varying the parameters of the lattice lasers, and even the strength of the atom–atom interactions may be tuned using Feshbach resonances. In addition, it is possible to monitor the atoms with single-site resolution. In most experiments, the optical lattice is raised

adiabatically in a cold gas and captures atoms without undue heating of the CM motion, but with a random number of atoms at random lattice sites. Nevertheless, loading of the desired initial configuration atom by atom has also been demonstrated [13]. Such developments have lent credence to the idea of using an optical lattice system as a quantum simulator [5, 6, 14]—basically as an analog quantum computer.

80.6.1 Basics of the Optical Lattice

Dipole forces of standing-wave fields of light generate a periodic potential, an optical lattice, on the atoms [15]. If the light is detuned far enough from atomic resonances, absorption and spontaneous emission are negligible, and the potential is conservative. In one dimension, the prototypical potential energy for the motion of the atoms is of the form

$$V(x) = V_0 \sin^2 kx, \quad (80.62)$$

where k is the wave number of the lattice light, and the depth of the lattice V_0 can be inferred from the known parameters of the atoms and the light as explained in Chap. 79.2.2. With multiple laser beams propagating in different directions and having different polarizations, a wide variety of 2-D and 3-D optical lattices may be set up analogously.

As is usual with periodic potentials, the one-particle energy eigenstates are characterized by a quasimomentum or lattice momentum \mathbf{q} , and group into bands λ typically separated by bandgaps. In an experimental technique called band mapping, the lattice potential is adiabatically removed, whereupon such Bloch states get converted into eigenstates of ordinary momentum. Upon further free evolution, momenta get mapped into observable positions of the atoms. In this way, the distribution of the atoms among the quasimomenta and bands may be determined.

Bose–Hubbard Model

Consider as an example a 1-D optical lattice that holds spin-0 atoms, with the sites labeled by an integer n . The simplified Hamiltonian, the Bose–Hubbard model, reads

$$\frac{\hat{H}}{\hbar} = \frac{1}{2} \sum_n \left[-J (a_{n+1}^\dagger a_n + a_{n-1}^\dagger a_n) + U a_n^\dagger a_n^\dagger a_n a_n \right]. \quad (80.63)$$

The operator a_n annihilates and the operator a_n^\dagger creates an atom at the site n , so the terms $\propto J$ describe tunneling of the bosons from a site to a neighboring site. The term $\propto U$ models the interactions of the atoms that are in the same site. Boundary conditions ordinarily matter little for a long lattice; for convenience, we assume periodic boundary conditions for a lattice with L sites, so that the sites n and $n + L$ are

regarded as the same. This case could be physically realized by making a 1-D ring lattice.

The key consideration in the physics of the Bose–Hubbard model is the competition between tunneling $\propto J$ and atom–atom interactions $\propto U$.

Tuning of the Parameters

Without the interactions, the model Eq. (80.63) corresponds to the tight-binding approximation to the band structure of a 1-D solid, with the energies in the single Bloch band ranging from $-\hbar J$ to $\hbar J$. The wave functions of the states annihilated by a_n are the corresponding Wannier states $\phi_n(x)$. We use vector notation for the position since in reality the lattice is confined in the transverse directions, making a wave function in 3-D, and the atom–atom interactions depend on the volume density of the atoms anyway. For the standard contact interaction Eq. (80.21) characterized by the scattering length a , we have

$$U = \frac{4\pi\hbar a}{m} \int d^3x |\phi_n(x)|^4. \quad (80.64)$$

On the other hand, the exact band structure for the potential energy Eq. (80.62) of an optical lattice comes from the Mathieu equation. A comparison of the width of the first band with the tight-binding approximation gives the estimate

$$J = \frac{8}{\sqrt{\pi}} \frac{E_r}{\hbar} \left(\frac{V_0}{E_r} \right)^{3/4} \exp\left(-2\sqrt{\frac{V_0}{E_r}}\right), \quad (80.65)$$

where E_r is the photon recoil energy, and we assume that $V_0 \gtrsim E_r$. Since the depth of the optical lattice V_0 is proportional to the intensity of the lattice light and the tunneling amplitude J depends strongly on V_0 , J may be varied over a wide range by changing the intensity of the lattice light.

Near a Feshbach resonance at the magnetic field B_0 , the scattering length varies with the magnetic field applied to the atoms, B , as

$$a = a_0 \left(1 - \frac{\Delta B}{B - B_0} \right), \quad (80.66)$$

where a_0 , B_0 , and ΔB are constants depending on the atomic species and the Feshbach resonance in question. Under favorable conditions, it may be possible to vary the scattering length over a wide range, and even to change its sign, by varying the magnetic field applied to the atoms.

Discrete Nonlinear Schrödinger Equation

The mean-field counterpart of the Bose–Hubbard model is found in the usual way, by positing that in the Heisenberg equations of motion the operators a_n are no longer boson operators but instead complex numbers α_n . Furthermore, we

scale these numbers so that the average of $|\alpha_n|^2$ over the lattice equals 1, which brings in the average site occupation $\bar{n} = N/L$ for a total of N bosons in a lattice of length L . The result, an analog of the GPE,

$$\frac{d}{dt}\alpha_n = -\frac{1}{2}J(\alpha_{n+1} + \alpha_{n-1}) + \bar{n}U|\alpha_n|^2\alpha_n, \quad (80.67)$$

is often called the discrete nonlinear Schrödinger equation (DNLS).

DNLS has interesting properties of its own. For instance, for attractive ($a < 0$) atom–atom interactions, it may have solutions called gap solitons, clusters of atoms that propagate along the lattice (or stand still) while retaining their shape. They are “gap solitons” because formally their energies are outside of the energies of the Bloch bands, i.e., in the bandgaps.

80.6.2 Strongly Correlated Systems

Superfluid–Mott Insulator Transition

In generic terms, a many-body system that cannot be adequately described by a mean-field theory is called strongly correlated. In particular, the mean-field version of the Bose–Hubbard model Eq. (80.67) misses an essential piece of physics that emerges when the interactions become sufficiently strong. When tunneling dominates, the system is in what is referred to as the superfluid phase. Fluctuations of the atom number between the sites are relatively large. On the other hand, if atom–atom interactions dominate, fluctuations in atom number become costly in energy; a configuration with zero atoms in one site and two in the next site has a much higher energy than a configuration with one atom in both sites. The same number of atoms in each site corresponds to the Mott insulator phase. According to calculations carried out using the so-called Gutzwiller ansatz, the ground state of an optical lattice inserted in an atom trap then consists of regions with the same integer number of atoms at the lattice sites within each region [16]. When the parameters of the system are varied, in what is known as a quantum phase transition [17] the system should abruptly switch between the phases.

This superfluid–Mott insulator transition has been observed experimentally [18]. The observation of the transition is by means of phase coherence. In the superfluid phase, the system is characterized by a global macroscopic wave function. When the atoms are abruptly released from the lattice, atoms originating from different sites are capable of interference, and the interference pattern reflects the lattice structure. On the other hand, in the Mott insulator phase, the lattice sites are in number states with little phase coherence between them, and there is no interference pattern.

Quantum Gas Microscope

The superfluid–Mott insulator transition has established optical lattices as viable simulators of lattice models and has inspired much current following [5, 6, 14]. As an example of the ongoing technical advances, we describe cursorily the quantum gas microscope [19]. This is literally a microscope, one with an objective lens that has a very large (effectively 0.8) numerical aperture. This entails resolution close to a wavelength. The microscope views a 2-D lattice of the atoms. However, in this particular experiment, the lattice is not produced by added standing waves but by imaging a judiciously designed mask backwards through the objective to the plane of the atoms. The lattice is turned on slowly and collects cold atoms from a suitable trap. The physics experiment then commences.

After the experiment, the lattice is switched much deeper. It then confines the atoms to its individual potential wells, and facilitates a measurement of the number of the atoms at each lattice site; or at least the parity of the atom numbers, since the trapped atoms experience pairwise laser-assisted exothermic collisions and are lost from the trap until only one or zero atoms per site remains. Laser beams forming an optical molasses illuminate the atoms, and the atoms fluoresce. The deep confinement and a tuning of the laser conducive to cooling eliminate heating from photon recoil kicks, so that the atoms stay in place and send out a number of fluorescence photons. This improves the signal-to-noise ratio to the extent that an individual atom can be detected at the resolution of a single lattice site. Not only atom density, but also position correlations of the atoms can be recorded for comparison with theory. By making use of resonance spectroscopy, the spins of the atoms and the correlations of the spins between the sites may also be determined.

Phase Diagrams in Lattice Systems

There is, for all practical purposes, an infinity of lattice systems to study: different lattice structures; bosons versus fermions, various spins, real, or simulated with internal states of the atoms; short-range on-site interactions versus long-range coupling of the spins via magnetic or (for polar molecules) electric dipole interactions; and so on. A number of implementations relying on AMO techniques have been considered and are being considered. In the tradition of condensed-matter physics, the goal is to find the phases and phase diagrams; either to compare with existing theoretical arguments, or to discover new phases experimentally. We will say nothing further about this kind of work.

Time Dependence

As was mentioned already, time dependence in large, strongly interacting many-body quantum systems usually overwhelms the theoretical tools that we have available today, including exact numerical computations. Quench ex-

periments, in which a steady-state system is suddenly altered and then let evolve, have the potential to deliver reliable results not available in any other way.

The broad experience in physics is that, when left alone, a large system thermalizes and can then be described by statistical mechanics, at least to the extent permitted by the conserved quantities. The issue is, does this always happen, and how; especially in isolated systems when it is not possible to appeal to the interactions with the environment as the cause of the thermalization. Time evolution in well-controlled lattice systems [20] is an enterprise with potential for breakthroughs in our understanding of the foundations of statistical mechanics.

80.6.3 Topological Phases of Matter

As another current line of development, also a spin-off from condensed-matter physics, we discuss topological band structures and topological phases of matter [14, 21].

Phase of Tunneling in a Lattice

Consider as a preparatory example a static magnetic field acting on a charged free particle. In the minimum coupling substitution, the Hamiltonian reads

$$H = \frac{1}{2m} [\hat{p} - q\mathbf{A}(\mathbf{x})]^2. \quad (80.68)$$

If there actually is no magnetic field so that the vector potential satisfies $\mathbf{B} = \nabla \times \mathbf{A} = 0$, the vector potential may be “gauged away” with the canonical transformation

$$\psi(\mathbf{x}) \rightarrow \tilde{\psi}(\mathbf{x}) = \exp \left[\frac{iq}{\hbar} \int_{\mathbf{x}_0}^{\mathbf{x}} d\mathbf{l} \cdot \mathbf{A} \right] \psi(\mathbf{x}), \quad (80.69)$$

where \mathbf{x}_0 is an arbitrary reference point. With $\nabla \times \mathbf{A} = 0$, the integral is independent of the path. In particular, the integral vanishes over any closed path.

In contrast, if a magnetic field is present, the integral depends on the path, and the canonical transformation as written in Eq. (80.69) is ill defined. The integral becomes a phase factor $e^{i\Phi}$, where the phase $\Phi(P, \mathbf{x}_0, \mathbf{x})$ depends on the path P . If a wave packet ψ is split at \mathbf{x}_0 and the components are sent along two different paths to recombine at \mathbf{x} , they will have a phase difference modifying the interference

$$\Delta\Phi = \frac{q}{\hbar} \int_S d\Omega \cdot \mathbf{B} \quad (80.70)$$

proportional to the magnetic flux through an arbitrary surface S with the paths of the two wave packets as its edge. This is how the Aharonov–Bohm effect comes about.

By making use of the interplay between internal and CM degrees of freedom of an atom, it is possible to realize a Hamiltonian of the form Eq. (80.68) also for a neutral atom whose CM motion does not directly couple to electromagnetic fields, and even with $\nabla \times \mathbf{A} \neq 0$. This is the idea of synthetic gauge fields [22].

Suppose now that in a 1-D lattice, there is a change of phase φ of the wave function when an atom tunnels from site n to the site $n + 1$. The counterpart of the Bose–Hubbard model would be

$$\frac{\hat{H}}{\hbar} = \frac{1}{2} \sum_n \left[-J (e^{i\varphi} a_{n+1}^\dagger a_n + e^{-i\varphi} a_{n-1}^\dagger a_n) + U a_n^\dagger a_n^\dagger a_n a_n \right]. \quad (80.71)$$

A priori such a phase change is inconsequential, as one can remove it by redefining the inconsequential phases of the states corresponding to an atom at different sites n . However, if it is possible to have a closed loop among the lattice sites and the phase changes do not add up to an integer multiple of 2π along the way, the phases φ cannot be gauged away in this way. This could happen in a 1-D ring lattice. Among the consequences is a nontrivial ground state in which the atoms flow around the ring.

Here, the emphasis is on 2-D lattice systems. It could correspondingly happen, for instance, that in a square lattice the phase changes in a loop around a plaquette of the four atoms at the corners of a unit cell add up to something other than 0 or another integer multiple of 2π .

A phase change in tunneling can be engineered by having external light drive a transition between the sites, instead of the ordinary tunneling. This is because the phase of the light gets imprinted on the transition. In practice, complicated arrangements are needed [23, 24] to effect a nontrivial accumulation of phase around a closed loop, for one thing because the phase changes of a laser field itself add up to zero around a closed loop; but it has been achieved experimentally. Modulation of the lattice potential, e.g., by shaking the lattice, is another approach to the same effect [25, 26]. We do not go into the details of either type of idea, but stipulate that an effective magnetic field with a nontrivial phase accumulation can be achieved. The effective magnetic field can be enormous compared to the real magnetic fields that can be reached in a laboratory.

Topological Band Structure

As an example, we briefly consider a recent experiment [24]. The starting point here is (conceptually) a square lattice with a lattice constant a in the xy plane. The reciprocal lattice is also square, with the lattice constant $2\pi/a$, and so is the first Brillouin zone that contains the values of the lattice momenta \mathbf{q} for the lowest energy band. By using optical fields, an accumulated phase $\Delta\Phi = \pi/2$ is put in each loop around

a four-site plaquette. This means that the translation that leaves the lattice unchanged is not a , but $2a$. Since the unit cell has become two times as big, the Brillouin zone is half the size, and 1/4 in area. The result is that the original lowest band splits into (in principle) four energy bands.

Moreover, as a result of the accumulated phases, the topology of these bands may be nontrivial. The topology is characterized by an invariant called the Chern number. Suppose one first solves for the one-body Bloch states in an energy band, $u(q_x, q_y)$, and forms the Berry curvature

$$\Omega = i(\langle \partial_{q_x} u | \partial_{q_y} u \rangle - \langle \partial_{q_y} u | \partial_{q_x} u \rangle), \quad (80.72)$$

then the Chern number is computed as an integral over the first Brillouin zone,

$$C = \frac{1}{2\pi} \int \Omega d^2q. \quad (80.73)$$

The value would be zero for a topologically trivial band, while in the experiments actually three bands are found (one with twice as many states as the other two) with the Chern numbers 1, -2 , and 1.

It is not possible to modify the Hamiltonian continuously in such a way that the Chern number suddenly changes between integer values unless “something drastic” happens along the way. In this case, the drastic event is that the gap between bands closes. In the experiments, there is an auxiliary control variable to take the system across such a topological phase transition.

One way of detecting the Chern number is to apply a force that moves the atoms. As one might expect from the analogy between the engineered phases and a magnetic field, in an analog of the Hall effect, the atoms get translated also in the direction perpendicular to the applied force. This translation may be measured and is proportional to the Chern number (under the particular experimental conditions), which gives a measurement of the latter.

Significance of Topology

The circulation of a superfluid around the core of a vortex is a topological property, characterized by discrete values. A vortex is, therefore, resilient; it vanishes if the density of the superfluid vanishes, but small perturbations will not change its circulation. The same applies to the Chern number, which will not change unless the perturbations of the lattice are so drastic that a bandgap closes. The integer quantum Hall effect with a precisely determined quantized value of the Hall conductance occurs because the Hall conductance is equal to the product of a Chern number and a combination of natural constants [21].

In practice, there is no such thing as an infinite lattice. A finite 2-D lattice with a topologically nontrivial band structure is believed to have chiral edge modes. They are localized

at the edges of the lattice, are chiral in that the atoms propagate in one direction around the lattice only (in analogy with cyclotron motion), and are topologically protected, i.e., their character does not change in small perturbations of the lattice or of the edge.

From the AMO perspective, the long-term goal is to use topologically protected variables, hopefully insensitive to decoherence, for quantum computations.

References

- Dalfovo, F., Giorgini, S., Pitaevskii, L.P., Stringari, S.: Theory of Bose–Einstein condensation in trapped gases. *Rev. Mod. Phys.* **71**, 463–512 (1999). <https://doi.org/10.1103/RevModPhys.71.463>
- Fetter, A.L.: Bose–Einstein condensates in dilute trapped atomic gases. *J. Low Temp. Phys.* **129**, 263–321 (2002). <https://doi.org/10.1023/A:1021408428662>
- Bloch, I., Dalibard, J., Zwirger, W.: Many-body physics with ultracold gases. *Rev. Mod. Phys.* **80**, 885–964 (2008). <https://doi.org/10.1103/RevModPhys.80.885>
- Pitaevskii, L., Stringari, S.: Bose–Einstein Condensation and Superfluidity. International Series of Monographs in Physics. Oxford University Press, Oxford (2016)
- Lewenstein, M., Sanpera, A., Ahufinger, V.: Ultracold Atoms in Optical Lattices: Simulating Quantum Many-Body Systems. Oxford University Press, Oxford (2012)
- Gross, C., Bloch, I.: Quantum simulations with ultracold atoms in optical lattices. *Science* **357**, 995–1001 (2017). <https://doi.org/10.1126/science.aal3837>
- Fetter, A.L., Walecka, J.D.: Quantum Theory of Many-Particle Systems. Dover, Mineola (2003)
- Feit, M.D., Fleck Jr., J.A., Steiger, A.: *J. Comp. Phys.* **47**, 412 (1982)
- Javanainen, J., Ruostekoski, J.: Symbolic calculation in development of algorithms: Split-step methods for the Gross–Pitaevskii equation. *J. Phys. A* **39**, L179 (2006)
- Javanainen, J., Yoo, S.M.: Quantum phase of a Bose–Einstein condensate with an arbitrary number of atoms. *Phys. Rev. Lett.* **76**, 161–164 (1996). <https://doi.org/10.1103/PhysRevLett.76.161>
- Kumar, A., Eckel, S., Jendrzejewski, F., Campbell, G.K.: Temperature-induced decay of persistent currents in a superfluid ultracold gas. *Phys. Rev. A* **95**, 021602 (2017). <https://doi.org/10.1103/PhysRevA.95.021602>
- Wikipedia contributors: Numerical sign problem – Wikipedia (2019)
- Barredo, D., de Léséleuc, S., Lienhard, V., Lahaye, T., Browaeys, A.: An atom-by-atom assembler of defect-free arbitrary two-dimensional atomic arrays. *Science* **354**, 1021–1023 (2016). <https://doi.org/10.1126/science.aah3778>
- Goldman, N., Budich, J.C., Zoller, P.: Topological quantum matter with ultracold gases in optical lattices. *Nat. Phys.* **12**, 639 (2016)
- Morsch, O., Oberthaler, M.: Dynamics of Bose–Einstein condensates in optical lattices. *Rev. Mod. Phys.* **78**, 179–215 (2006). <https://doi.org/10.1103/RevModPhys.78.179>
- Jaksch, D., Bruder, C., Cirac, J.I., Gardiner, C.W., Zoller, P.: Cold bosonic atoms in optical lattices. *Phys. Rev. Lett.* **81**, 3108–3111 (1998). <https://doi.org/10.1103/PhysRevLett.81.3108>
- Sachdev, S.: Quantum Phase Transitions, 2nd edn. Cambridge University Press, New York (2011)
- Greiner, M., Mandel, O., Esslinger, T., Hänsch, T.W., Bloch, I.: Quantum phase transition from a superfluid to a Mott insulator in a gas of ultracold atoms. *Nature* **415**, 39 (2002)
- Bakr, W.S., Gillen, J.I., Peng, A., Fölling, S., Greiner, M.: A quantum gas microscope for detecting single atoms in a Hubbard-regime optical lattice. *Nature* **462**, 74 (2009)
- Trotzky, S., Chen, Y.-A., Flesch, A., McCulloch, I.P., Schollwöck, U., Eisert, J., Bloch, I.: Probing the relaxation towards equilibrium in an isolated strongly correlated one-dimensional Bose gas. *Nat. Phys.* **8**, 325–330 (2012). <https://doi.org/10.1038/nphys2232>
- Xiao, D., Chang, M.-C., Niu, Q.: Berry phase effects on electronic properties. *Rev. Mod. Phys.* **82**, 1959–2007 (2010). <https://doi.org/10.1103/RevModPhys.82.1959>
- Dalibard, J., Gerbier, F., Juzeliūnas, G., Öhberg, P.: Colloquium: Artificial gauge potentials for neutral atoms. *Rev. Mod. Phys.* **83**, 1523–1543 (2011). <https://doi.org/10.1103/RevModPhys.83.1523>
- Jaksch, D., Zoller, P.: Creation of effective magnetic fields in optical lattices: The Hofstadter butterfly for cold neutral atoms. *New J. Phys.* **5**, 56–56 (2003). <https://doi.org/10.1088/1367-2630/5/1/356>
- Aidelsburger, M., Lohse, M., Schweizer, C., Atala, M., Barreiro, J.T., Nascimbène, S., Cooper, N.R., Bloch, I., Goldman, N.: Measuring the Chern number of Hofstadter bands with ultracold bosonic atoms. *Nat. Phys.* **11**, 162 (2014)
- Struck, J., Ölschläger, C., Weinberg, M., Hauke, P., Simonet, J., Eckardt, A., Lewenstein, M., Sengstock, K., Windpassinger, P.: Tunable gauge potential for neutral and spinless particles in driven optical lattices. *Phys. Rev. Lett.* **108**, 225304 (2012). <https://doi.org/10.1103/PhysRevLett.108.225304>
- Goldman, N., Dalibard, J.: Periodically driven quantum systems: Effective Hamiltonians and engineered gauge fields. *Phys. Rev. X* **4**, 031027 (2014). <https://doi.org/10.1103/PhysRevX.4.031027>



Juha Javanainen Juha Javanainen is Professor of Physics at the University of Connecticut. He has worked on a number of topics in theoretical quantum optics.



Contents

81.1	Wave-Particle Duality	1173
81.2	The Hamiltonian of de Broglie Optics	1174
81.2.1	Gravitation and Rotation	1174
81.2.2	Charged Particles	1175
81.2.3	Magnetic Moments	1175
81.2.4	Atoms	1175
81.3	Evolution of De Broglie Waves	1177
81.3.1	Light Optics Analogy	1177
81.3.2	WKB Approximation	1177
81.3.3	Phase and Group Velocity	1178
81.3.4	Paraxial Approximation	1178
81.3.5	Raman–Nath Approximation	1178
81.4	Refraction and Reflection	1178
81.4.1	Atomic Mirrors	1179
81.4.2	Atomic Cavities	1179
81.4.3	Atomic Lenses	1180
81.4.4	Atomic Waveguides	1180
81.5	Diffraction	1180
81.5.1	Fraunhofer Diffraction	1180
81.5.2	Fresnel Diffraction	1181
81.5.3	Near-Resonant Kapitza–Dirac Effect	1181
81.5.4	Atom Beam Splitters	1181
81.6	Interference	1182
81.6.1	Interference Phase Shift	1182
81.6.2	Internal-State Interferometry	1184
81.6.3	Manipulation of Cavity Fields by Atom Interferometry	1184
81.7	Coherence of Scalar Matter Waves	1184
81.7.1	Atomic Sources	1185
81.7.2	Atom Decoherence	1185
	References	1186

C. Henkel (✉) · M. Wilkens (✉)
Institute of Physics and Astronomy, University of Potsdam
Potsdam, Germany
e-mail: carsten.henkel@uni-potsdam.de

M. Wilkens
e-mail: mwilkens@uni-potsdam.de

Abstract

De Broglie optics concerns the propagation of quantum mechanical particle waves, their reflection, refraction, diffraction, and interference. The basic principles of De Broglie optics, which are quite similar to the principles of ordinary light optics, do not depend much on the specific nature of the sort of particles under consideration – electron, neutron, atom, ion, or molecule, but the focus in this chapter is on the De Broglie optics of atoms and molecules. This sort of particle comes with a variety of internal degrees of freedom, which are easily addressed and manipulated with electromagnetic fields, in particular laser fields, and thereby allow for quite a broad spectrum of different applications in lithography, imaging, and precision measurement.

Keywords

atomic beam · matter wave · Fresnel zone plate · Sagnac effect · atom optics

81.1 Wave-Particle Duality

The wave-particle duality of quantum mechanics states that freely traveling material particles of mass M and momentum p are properly described by a plane wave of wavelength $\lambda_{\text{dB}} = 2\pi\hbar/p$, named in honor of Prince Victor Louis De Broglie, and frequency $\omega = \hbar k^2/(2M)$, with k the wavenumber $k = 2\pi/\lambda_{\text{dB}}$.

Originally meant to account for the orbitals of a Coulomb-bound electron, the ultimate wave character of particles has meanwhile been confirmed for all fundamental particles, but also for the center-of-mass (CM) motion of composite particles like ions, atoms, and even large molecules. These waves have been dubbed matter waves, although they do not encode

a density variation or the like, but rather a probability amplitude for the center-of-mass degree of freedom of the particle under consideration.

The optics of matter waves comprises, among others, electron optics and electron microscopy [1], electron holography [2], neutron optics and neutron imaging [3], in particular neutron interferometry [4], and atom optics [5].

Being strongly driven by the progress of laser cooling – see Chap. 79 on cooling and trapping – but also nanofabrication, the subject of atom optics is relatively new, and applications are currently being developed in atom interferometry [6], atom lithography, [7] and atom imaging [8]. These days, the wave character of particles has been confirmed for molecules with more than 430 atoms [9], and atom optics is promoted as a competitive method for the determination of the gravitational redshift [10], a particle’s proper time [11], Newton gravitational constant [12], gravimetry [13], inertial sensing [14], and even the exploration of possible manifestations of dark energy [15]. Interference experiments with atoms and molecules have been suggested to explore the boundaries between quantum and classical mechanics [16, 17]. In this domain, processes called decoherence or localization are expected to change the behavior of particles; quantal features like superpositions and particle-wave duality are fading out, and the particles start to behave as expected from classical kinetic theory [18].

In terms of the Bohr radius a_0 , the fine-structure constant α , and the electron mass m_e ,

$$\lambda_{\text{dB}} = \frac{2\pi\alpha a_0}{(v/c)(M/m_e)} = 2\pi \left(\frac{E_h m_e}{2\mathcal{T} M} \right)^{1/2} a_0, \quad (81.1)$$

where $v = p/M$ is the velocity, $\mathcal{T} = (1/2)Mv^2$ is the kinetic energy, and E_h is the atomic unit of energy (Table 1.4 of Sect. 1.2). For electrons, $\lambda_{\text{dB}} \approx 1.226426 \text{ nm}/(\mathcal{T}/\text{eV})^{1/2}$.

For thermal samples, the mean kinetic energy is of the order of $k_B T$, and, thus, the mean momentum scales $\propto \sqrt{T}$, and Eq. (81.1) is replaced by the thermal De Broglie wavelength, which is defined in Eq. (81.76). In terms of the atomic mass unit u : $\lambda_{\text{th}} = 1.74(5) \text{ nm} (M/u)^{-1/2} (T/\text{K})^{-1/2}$. At room temperature, the thermal De Broglie wavelength of atomic samples is sub-Å, but for temperatures on the micro or nano-Kelvin scale, even in dilute samples the wavelength may well exceed the mean interparticle spacing, in which case, the quantum statistical effects of indistinguishability become manifest – see Chap. 80 on quantum degenerate gases.

However, even in the nondegenerate regime, the physics of de Broglie waves differs from that of light waves in a number of regards. First, the dispersion relation of free particles is quadratic in the wavenumber, giving rise to spatial spreading of wave packets even in one-dimensional configurations. Second, particles may be brought to rest, which is impos-

sible for photons. Finally, particles in beams are subject to pair interactions, giving rise to nonlinear optical phenomena. Electrons and ions, for example, experience a particle density-dependent Coulomb broadening in the focus of a lens (Boersch effect [2]). Similarly, atoms or molecules interact via short range interparticle van der Waals forces, giving rise to density-dependent nonlinear effects, see Sect. 81.2.4 “Atom Optical Nonlinearity”, below.

81.2 The Hamiltonian of de Broglie Optics

A typical de Broglie optical experiment involves a source, a beam of particles produced by that source, an array of optical elements, possibly a probe, other optical elements placed behind the probe, and, finally, a detector. Optical elements are collimators, apertures, lenses, mirrors, and beam splitters. A probe could be a crystal, a biological sample, or just another unknown optical element whose properties are to be investigated. To avoid proliferation of notation, we refer to any object placed in the beam path simply as an *optical element*.

Here, we shall assume that the particles are far from quantum degeneracy, and the effects of particle interactions can safely be ignored. A large class of optical elements is then well described by a Hamiltonian model in which the ensemble of particles is described by a wave function $\psi(\mathbf{x}, t) = \langle \mathbf{x} | \psi(t) \rangle$ whose time evolution is governed by the Schrödinger equation

$$i\hbar \frac{\partial}{\partial t} |\psi(t)\rangle = H(t) |\psi(t)\rangle, \quad (81.2)$$

with a one-particle Hamiltonian of the generic form

$$H(t) = \frac{[\hat{\mathbf{p}} - \mathcal{A}(\hat{\mathbf{x}}, t)]^2}{2M} + \mathcal{U}(\hat{\mathbf{x}}, t). \quad (81.3)$$

Here, $\hat{\mathbf{p}}$ and $\hat{\mathbf{x}}$ denote the canonically conjugate operators of the center of mass momentum and position, respectively. The Cartesian components of $\hat{\mathbf{p}}$ and $\hat{\mathbf{x}}$ obey the fundamental commutation relation

$$[\hat{x}_i, \hat{p}_j] = i\hbar \delta_{ij}. \quad (81.4)$$

The vector potential $\mathcal{A}(\mathbf{x}, t)$ and scalar potential energy $\mathcal{U}(\mathbf{x}, t)$ account for the interaction of the particle with all the optical elements, probes, and samples that are placed between the source and the detector, including the effects of gravitation and rotation.

81.2.1 Gravitation and Rotation

All particles are subject to the influence of gravitation and rotation, which may both be viewed as being special cases

of an accelerated frame of reference. The effects of uniform gravitation are described by

$$\mathcal{U}(\mathbf{x}) = -M \mathbf{g} \cdot \mathbf{x}, \quad \mathcal{A}(\mathbf{x}) = 0, \quad (81.5)$$

where \mathbf{g} describes the direction and magnitude of gravitational acceleration. The effects of uniform rotation are described by

$$\mathcal{U}(\mathbf{x}) = -\frac{M}{2}(\boldsymbol{\Omega} \times \mathbf{x})^2, \quad \mathcal{A}(\mathbf{x}) = M(\boldsymbol{\Omega} \times \mathbf{x}), \quad (81.6)$$

where the direction and magnitude of $\boldsymbol{\Omega}$ refer to the orientation of the axis of rotation and the angular velocity, respectively. Here, $\mathcal{U}(\mathbf{x})$ is the potential of the centrifugal force, while $\mathcal{A}(\mathbf{x})$ is the potential of the Coriolis force.

81.2.2 Charged Particles

The interaction of charged particles (electrons, ions) with the electromagnetic field is described by

$$\mathcal{U}(\mathbf{x}, t) = q\Phi(\mathbf{x}, t), \quad \mathcal{A}(\mathbf{x}, t) = qA(\mathbf{x}, t), \quad (81.7)$$

where q is the particle charge ($q = -e$ for electrons), and A and Φ denote the gauge potentials of the electric field strength \mathbf{E} and magnetic induction \mathbf{B} , respectively,

$$\mathbf{E}(\mathbf{x}, t) = -\frac{\partial}{\partial t}A(\mathbf{x}, t) - \nabla\Phi(\mathbf{x}, t), \quad (81.8)$$

$$\mathbf{B}(\mathbf{x}, t) = \nabla \times A(\mathbf{x}, t). \quad (81.9)$$

The quantum mechanics of charged particles is invariant under a gauge transformation $A \mapsto A' = A + \nabla\chi$, $\Phi \mapsto \Phi' = \Phi - \dot{\chi}$ combined with a local phase transformation of the wave function, $\psi \mapsto \psi' = e^{iq\chi/\hbar}\psi$. In particular, all measurable quantities in the De Broglie optics of charged particles, including the phase shift in the Aharonov–Bohm effect, are independent of the gauge – see Sect. 81.6.1 “Aharonov–Bohm Effect” below.

81.2.3 Magnetic Moments

The interaction of a magnetic dipole moment $\hat{\boldsymbol{\mu}}$ with the electromagnetic field is described by

$$\begin{aligned} \hat{\mathcal{U}}(\mathbf{x}, t) &= -\hat{\boldsymbol{\mu}} \cdot \mathbf{B}(\mathbf{x}, t), \\ \hat{\mathcal{A}}(\mathbf{x}, t) &= \frac{\hat{\boldsymbol{\mu}} \times \mathbf{E}(\mathbf{x}, t)}{c^2}. \end{aligned} \quad (81.10)$$

Here, the vector potential is due to the motional correction of the magnetic dipole interaction. Usually, it is neglected. However, it does play an important role for the Aharonov–Casher effect (Sect. 81.6.1).

81.2.4 Atoms

Many optical elements in atom optics are based on the mechanical effects of the radiation interaction. In the electric dipole approximation, the interaction of a single atom with the electromagnetic field is described by

$$\begin{aligned} \hat{\mathcal{U}}(\mathbf{x}, t) &= -\hat{\mathbf{d}} \cdot \mathbf{E}(\mathbf{x}, t), \\ \hat{\mathcal{A}}(\mathbf{x}, t) &= \mathbf{B}(\mathbf{x}, t) \times \hat{\mathbf{d}}, \end{aligned} \quad (81.11)$$

where $\hat{\mathbf{d}}$ is the operator of electric dipole transition. The vector potential $\hat{\mathcal{A}}$ is due to the motional correction of the electric dipole interaction. Usually it is neglected; see however, the paragraph “Electric dipole phase” in Sect. 81.6.1.

For a monochromatic field of frequency ω

$$\mathbf{E}(\mathbf{x}, t) = \mathbf{E}^{(+)}(\mathbf{x})e^{-i\omega t} + \text{h.c.}, \quad (81.12)$$

where $\mathbf{E}^{(+)}(\mathbf{x})$ defines both polarization and spatial characteristics of the field. A standing-wave laser field with optical axis in the x -direction and linear polarization $\boldsymbol{\epsilon}$, for example, is described by

$$\mathbf{E}^{(+)}(\mathbf{x}) = \boldsymbol{\epsilon} \mathcal{E}_0 f(x, y, z) \cos(kx), \quad (81.13)$$

where \mathcal{E}_0 is the electric field amplitude, $k = \omega/c$ is the wavenumber, and the slowly varying function $f(x, y, z)$ accounts for the transverse profile of the laser field.

Essential state approximation

The electric dipole operator $\hat{\mathbf{d}}$ acts in the Hilbert space of electronic states of the atom. In the particular case that the polarization of the laser field is spatially uniform and that spontaneous emission does not play a role, two states are generally sufficient, and the atom may be modeled by a two-level atom with electronic levels $|e\rangle$ and $|g\rangle$ of energy E_e and E_g , respectively ($E_e > E_g$). With the pseudo-spin representation

$$|e\rangle \mapsto \begin{pmatrix} 1 \\ 0 \end{pmatrix}, \quad |g\rangle \mapsto \begin{pmatrix} 0 \\ 1 \end{pmatrix}, \quad (81.14)$$

the electric dipole operator assumes the form

$$\hat{\mathbf{d}} \mapsto d \boldsymbol{\epsilon}_d \begin{pmatrix} 0 & 1 \\ 1 & 0 \end{pmatrix}, \quad (81.15)$$

where d is the matrix element of the dipole transition, and $\boldsymbol{\epsilon}_d$ denotes its polarization. The prefix “pseudo” of a pseudo spinor indicates that it does not transform in the spin-(1/2) representation of the physical rotation group.

The laser field is assumed to be near resonant with the $e \leftrightarrow g$ transition at $\omega_0 = (E_e - E_g)/\hbar$, and we denote by

$\Delta \equiv \omega_0 - \omega$ the atom-laser detuning. Using the rotating-wave approximation (Sect. 72.3.2) in an interaction picture with respect to the laser frequency, the Hamiltonian describing the atomic dynamics – both internal and center-of-mass – is given by

$$H = \frac{\hat{\mathbf{p}}^2}{2M} - \frac{\hbar}{2} \begin{pmatrix} -\Delta & \Omega_1(\hat{\mathbf{x}}) \\ \Omega_1^\dagger(\hat{\mathbf{x}}) & \Delta \end{pmatrix}, \quad (81.16)$$

where

$$\Omega_1(\mathbf{x}) = \frac{2d \boldsymbol{\epsilon}_d \cdot \mathbf{E}^{(+)}(\mathbf{x})}{\hbar} \quad (81.17)$$

is the spatially dependent bare Rabi frequency. In the field Eq. (81.13), $\Omega_1(\mathbf{x})$ is cosinusoidal with peak value $\Omega_0 = 2d\mathcal{E}_0/\hbar$.

The Hamiltonian Eq. (81.16) may be written in the form

$$H = \frac{\hat{\mathbf{p}}^2}{2M} + \frac{\hbar}{2} \boldsymbol{\Omega}(\hat{\mathbf{x}}) \cdot \hat{\boldsymbol{\sigma}}, \quad (81.18)$$

where $\hat{\boldsymbol{\sigma}}$ is the vector of Pauli matrices and

$$\boldsymbol{\Omega}(\mathbf{x}) = (-\text{Re}[\Omega_1(\mathbf{x})], \text{Im}[\Omega_1(\mathbf{x})], \Delta). \quad (81.19)$$

As it stands, the Hamiltonian Eq. (81.18) describes the precession and center-of-mass motion of the *atomic pseudo spin* in an external *fictitious magnetic field* $\boldsymbol{\Omega}(\mathbf{x})$ [Eq. (81.10)]. Spatial variations of this field give rise to the atom-optical Stern–Gerlach effect, i.e., the splitting of the atomic center of mass wave function (Sect. 81.5.3).

Adiabatic approximation

In the position representation, the Hamiltonian Eq. (81.16) acts on state vectors of the form of a pseudo spinor

$$\Psi(\mathbf{x}, t) = \begin{pmatrix} \psi_e(\mathbf{x}, t) \\ \psi_g(\mathbf{x}, t) \end{pmatrix}. \quad (81.20)$$

Alternatively, this state vector may be expanded in terms of the local eigenvectors $\alpha_\pm(\mathbf{x})$, $\beta_\pm(\mathbf{x})$ of the interaction matrix, also called dressed states,

$$\Psi(\mathbf{x}, t) = \psi_+(\mathbf{x}, t) \begin{pmatrix} \alpha_+(\mathbf{x}) \\ \beta_+(\mathbf{x}) \end{pmatrix} + \psi_-(\mathbf{x}, t) \begin{pmatrix} \alpha_-(\mathbf{x}) \\ \beta_-(\mathbf{x}) \end{pmatrix}, \quad (81.21)$$

where

$$\hat{\mathcal{U}}(\mathbf{x}) \begin{pmatrix} \alpha_\pm(\mathbf{x}) \\ \beta_\pm(\mathbf{x}) \end{pmatrix} = \pm \frac{\hbar \Omega(\mathbf{x})}{2} \begin{pmatrix} \alpha_\pm(\mathbf{x}) \\ \beta_\pm(\mathbf{x}) \end{pmatrix}, \quad (81.22)$$

with eigenvalues determined by the dressed Rabi frequency

$$\Omega(\mathbf{x}) = \sqrt{|\Omega_1(\mathbf{x})|^2 + \Delta^2}, \quad (81.23)$$

and coefficients (we suppress the \mathbf{x} -dependence for notational clarity)

$$\begin{pmatrix} \alpha_+ & \alpha_- \\ \beta_+ & \beta_- \end{pmatrix} = \begin{pmatrix} \cos \frac{\vartheta}{2} & -e^{-i\varphi} \sin \frac{\vartheta}{2} \\ e^{i\varphi} \sin \frac{\vartheta}{2} & \cos \frac{\vartheta}{2} \end{pmatrix} \equiv \hat{S}. \quad (81.24)$$

Here, the Stückelberg angle $\vartheta \equiv \vartheta(\mathbf{x})$ and phase angle $\varphi \equiv \varphi(\mathbf{x})$ are defined in terms of the polar representation of the fictitious magnetic field

$$\boldsymbol{\Omega} = \Omega (\cos \varphi \sin \vartheta, \sin \varphi \sin \vartheta, \cos \vartheta). \quad (81.25)$$

In the dressed state basis, the transformed Hamiltonian assumes the form

$$\tilde{H} \equiv \hat{S}^\dagger H \hat{S} = \frac{[\hat{\mathbf{p}} - \hat{\mathcal{A}}(\hat{\mathbf{x}})]^2}{2M} + \frac{\hbar}{2} \Omega(\hat{\mathbf{x}}) \sigma_3, \quad (81.26)$$

with matrix-valued vector potential

$$\hat{\mathcal{A}}(\mathbf{x}) = i\hbar S^\dagger(\mathbf{x}) [\nabla S(\mathbf{x})]. \quad (81.27)$$

This matrix is not diagonal; its off-diagonal elements describe nonadiabatic transitions between the dressed states. If the detuning is sufficiently large, and the atom moves sufficiently slowly, these nonadiabatic transitions may be neglected in a first approximation. In such an approximation, which is akin to the Born–Oppenheimer approximation in molecular physics, the dynamics of the atom is described by two decoupled Hamiltonians of the generic form Eq. (81.3), with scalar potentials \mathcal{U} given by

$$\mathcal{U}(\mathbf{x}) = \pm \frac{\hbar}{2} \Omega(\mathbf{x}), \quad (81.28)$$

and vector potentials $\mathcal{A}(\mathbf{x})$ given by the diagonal elements of Eq. (81.27). The vector potential is usually neglected. If included, it describes the Berry phase of the mechanical effects of the radiation interaction of a two-level atom.

The idea behind the adiabatic approximation is that the internal state of the atom, which is described by any of the locally varying dressed states, has enough time to adjust smoothly to the motion of the atom. For the important case of strong detuning $|\Delta| \gg |\Omega_1(\mathbf{x})|$, this assumption is usually well justified. In this case, an atom in the dressed ground state experiences a potential that is approximately given by

$$\mathcal{U}(\mathbf{x}) = -\frac{\hbar |\Omega_1(\mathbf{x})|^2}{4\Delta}. \quad (81.29)$$

For red detuning, we have $\Delta > 0$, in which case the atom is attracted towards regions of high intensity (high-field seeker). For blue detuning, the atom is repelled from such regions (low-field seeker). A potential similar to Eq. (81.29) also applies for complex particles like molecules whose transitions are detuned far from the light frequency. The potential is proportional to the dynamic polarizability $\alpha(\omega)$ and the field intensity.

Atom optical nonlinearity

In atom optics, nonlinear phenomena occur due to atom–atom interactions in the ensemble, the nature of which may be significantly influenced by laser light [19]. In the presence of laser light, atom–atom interactions mainly result from photon exchange, which, in most cases, leads to a repulsive interaction. Details of the microscopic basis of atom–atom interactions, in particular those concerning cold collisions, are presented in Chap. 54. Characteristic effects of nonlinear atom optics like four-wave mixing [20] and parametric amplification [21] have been observed with the highly dense samples provided by Bose–Einstein degenerate gases (Chap. 80).

81.3 Evolution of De Broglie Waves

Since the Schrödinger equation is a linear partial differential equation, de Broglie optics shares most of its principles with principles of other wave phenomena, and in particular with the optical principles of electromagnetic waves.

81.3.1 Light Optics Analogy

The analogy of de Broglie optics and light optics becomes particularly transparent for monoenergetic beams of scalar particles. Such beams are described by a time harmonic wave function $\psi(\mathbf{x}, t) = e^{-iEt/\hbar} \psi_E(\mathbf{x})$, where $\psi_E(\mathbf{x})$ obeys the stationary Schrödinger equation

$$H \psi_E = E \psi_E . \quad (81.30)$$

Setting $\mathcal{A}(\mathbf{x}) = 0$ in Eq. (81.3) for simplicity, this equation assumes the form

$$\left[\nabla^2 + k_0^2 \left(1 - \frac{U(\mathbf{x})}{E} \right) \right] \psi_E(\mathbf{x}) = 0 , \quad (81.31)$$

where the wavenumber k_0 is related to the energy E via the dispersion relation

$$E \equiv \frac{\hbar^2 k_0^2}{2M} . \quad (81.32)$$

If $U = 0$ at the entrance to the interaction region, E is the kinetic energy of the freely traveling de Broglie wave, and k_0 is the related wavenumber.

Comparing Eq. (81.31) with the scalar Helmholtz equation of electromagnetic theory and identifying

$$n_E(\mathbf{x}) \equiv \left[\frac{E - U(E)}{E} \right]^{1/2} \quad (81.33)$$

as an index of refraction for matter waves, one observes the complete analogy of scalar optics of stationary matter waves and monochromatic light waves. This analogy can be generalized for spinor-valued wave functions, which would correspond to vector wave optics in anisotropic index media. However, in contrast to light, spinor-valued wave functions do not obey a transversality condition.

In Eqs. (81.31)–(81.33), the parameter E describes the kinetic energy of the incoming beam. Thus, E is positive, and, therefore, $n_E < 1$ for positive values of the potential, while $n_E > 1$ for negative values of the potential. For neutrons, one generally has $n_E < 1$. This contrasts to the index of refraction for light waves, which is generally larger than 1. For electrons, ions, and atoms both $n_E < 1$ and $n_E > 1$ may be realized.

81.3.2 WKB Approximation

Waves are described by amplitude and phase. Particles are described by position and momentum. The link between these concepts is provided by Hamilton's ray optics. For scalar matter waves, a ray follows a classical trajectory. The optical signature of the ray is the phase associated with it. The quantum mechanical version of Hamilton's ray optics is obtained in the WKB (Wenzel, Kramers, and Brillouin) approximation of the stationary Schrödinger equation (Eq. (81.30)).

Any solution of Eq. (81.30) may be written in the form

$$\psi_E(\mathbf{x}) = A(\mathbf{x}) e^{iW(\mathbf{x})} , \quad (81.34)$$

with real-valued $A(\mathbf{x})$ and $W(\mathbf{x})$. In the WKB approximation, $A(\mathbf{x})$ is slowly varying, and

$$W(\mathbf{x}) = k_0 \int_{P_i}^P n_E(s) ds + \hbar^{-1} \int_{x_i}^x \mathcal{A}(\mathbf{x}') \cdot d\mathbf{x}' , \quad (81.35)$$

which is called eikonal in Hamilton's ray optics. In this expression, $n_E(s) \equiv n_E(\mathbf{x}(s))$, where $\mathbf{x}(s)$ denotes the classical trajectory of energy E connecting the point P_i with the point P , x_i and x are the coordinates of P_i and P , respectively, and $ds \equiv |d\mathbf{x}|$ is the element of arc length measured

along the classical trajectory. Note that the second contribution in Eq. (81.35) is generally gauge dependent. However, for closed loops, which are frequently encountered in interferometry, the gauge-dependence disappears by virtue of Stokes theorem, which transforms the path integral into an area integral over the rotor of \mathcal{A} .

The eikonal Eq. (81.35) may also be written in the form of a reduced action

$$W(\mathbf{x}) = \frac{1}{\hbar} \int_{x_i}^{\mathbf{x}} \mathbf{p}(\mathbf{x}') \cdot d\mathbf{x}' = \int_{x_i}^{\mathbf{x}} \mathbf{k}(\mathbf{x}') \cdot d\mathbf{x}', \quad (81.36)$$

where $\mathbf{p}(\mathbf{x})$ is the local value of the canonical momentum of the particle, $\mathbf{k}(\mathbf{x}) \equiv \mathbf{p}(\mathbf{x})/\hbar$ is the corresponding wave vector, and the integral is evaluated along the classical trajectory of the particle. Note that in the presence of a vector potential, $\mathbf{p}(\mathbf{x})$ and $d\mathbf{x}$ are no longer parallel as a result of the difference between canonical momentum \mathbf{p} and kinetic momentum $M d\mathbf{x}/dt \equiv \mathbf{p} - \mathcal{A}$.

The WKB approximation becomes invalid in the vicinity of caustics where neighboring rays intersect, and the amplitude $A(\mathbf{x})$ becomes large. There, connection formulae are used to find the proper phase factors picked up by the ray in traversing the caustics. Depending on the topology of the intersecting rays, different classes of diffraction integrals provide uniform approximations for the wave amplitude near caustics. For further details, see [22].

81.3.3 Phase and Group Velocity

The velocity of a particle that traverses a region of negative potential increases so that $p(\mathbf{x}) > p_0$, and the phase advances: $\delta W = \int [\mathbf{p}(\mathbf{x}) - \mathbf{p}_0] \cdot d\mathbf{x} > 0$. In quantum mechanics, the classical velocity corresponds to the group velocity, while the evolution of the phase is determined by the phase velocity. The phase and group velocities of de Broglie waves are given by

$$v_p(\mathbf{x}) \equiv \frac{E}{p(\mathbf{x})} = \frac{1}{n_E(\mathbf{x})} \sqrt{\frac{E}{2M}}, \quad (81.37)$$

$$v_g(\mathbf{x}) \equiv \frac{\partial E}{\partial p(\mathbf{x})} = n_E(\mathbf{x}) \sqrt{\frac{2E}{M}}, \quad (81.38)$$

respectively. Note that the product $v_p v_g = E/M$ is independent of $n_E(\mathbf{x})$.

81.3.4 Paraxial Approximation

The paraxial approximation is useful in describing the evolution of wave-like properties and/or distortion of wavefronts in the immediate neighborhood of an optical ray.

Let the z -axis be the central optical axis of symmetry along which the optical elements are aligned. Using the ansatz $\psi_E(\mathbf{x}) = e^{ik_0 z} \phi(x, y; z)$ and dropping $\partial^2 \phi / \partial z^2$ in a slowly varying envelope approximation one obtains

$$i\hbar v_0 \frac{\partial}{\partial z} \phi(x, y; z) = \left[-\frac{\hbar^2}{2M} \nabla_{\perp}^2 + \mathcal{U}(x, y; z) \right] \phi(x, y; z), \quad (81.39)$$

where $\nabla_{\perp}^2 = \partial^2 / \partial x^2 + \partial^2 / \partial y^2$, and $v_0 = \hbar k_0 / M$ is the longitudinal velocity of incoming particles. This equation has exactly the form of a time-dependent Schrödinger equation in two dimensions, with z/v_0 playing the role of a fictitious time t . With this interpretation, the spatial evolution of phase fronts along z can be analyzed in dynamical terms of particles moving in the xy -plane.

81.3.5 Raman–Nath Approximation

In the Raman–Nath approximation (also called the short-time, thin-hologram, or thin-lens approximation), the ∇_{\perp}^2 term in Eq. (81.39) is neglected. The potential $\mathcal{U}(x, y; z)$ then acts as a pure phase structure, and the solution of Eq. (81.39) becomes

$$\phi(x, y; z) = \exp \left[-\frac{i}{\hbar v_0} \int_{z_i}^z dz' \mathcal{U}(x, y; z') \right] \phi(x, y; z_i). \quad (81.40)$$

In terms of a classical particle moving under the influence of \mathcal{U} , the approximation loses validity for $(1/2)M v_{\perp}^2 \gtrsim \mathcal{U}$, which is just a quarter cycle for a harmonic oscillator.

81.4 Refraction and Reflection

Consider a particle beam of energy E incident on a medium with constant index of refraction n_E . The boundary plane at $z = 0$ in Fig. 81.1 divides the vacuum from the medium. At the boundary, the beam is partially reflected and partially transmitted, with the angles determined by Snell's law of refraction

$$\sin \alpha = n_E \sin \beta, \quad (81.41)$$

and the law of reflection

$$\alpha = \alpha'. \quad (81.42)$$

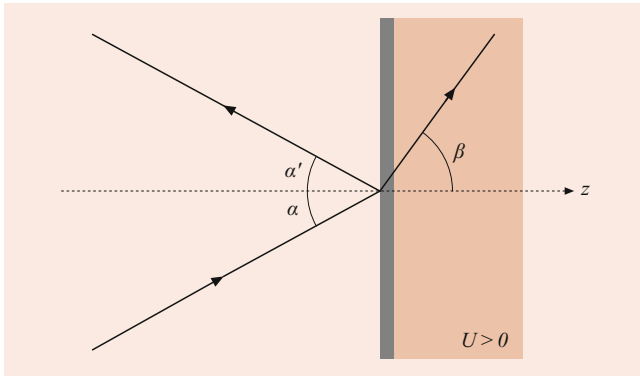


Fig. 81.1 Reflection geometry

The coefficients of reflectivity R , and transmittivity $T = 1 - R$ are given by the Fresnel formula

$$R = \left| \frac{\cos \alpha - n_E \cos \beta}{\cos \alpha + n_E \cos \beta} \right|^2. \quad (81.43)$$

For $n_E > 1$, the interface is *attractive*, and $R \ll 1$, with $R \rightarrow 1$ only for glancing incidence $\alpha \rightarrow \pi/2$. For $n_E < 1$, the interface is *repulsive*, and total reflection ($R = 1$) occurs for $\alpha \geq \tilde{\alpha}_c$, where $\tilde{\alpha}_c = \sin^{-1} n_E$ is the critical angle. For $\alpha > \tilde{\alpha}_c$, the de Broglie wave becomes evanescent, with $\psi_E(z > 0) \approx e^{-\kappa z}$ inside the medium ($z > 0$), where

$$\kappa = k_0 (\sin^2 \alpha - \sin^2 \tilde{\alpha}_c)^{1/2}. \quad (81.44)$$

If $E < \mathcal{U}$, then n_E is imaginary, and total reflection occurs for all α . In neutron optics, this total mirror reflection requires ultracold neutrons ($T \approx 0.5$ mK). It has important applications for the storage of ultracold neutrons in material cavities, and neutron microscopy using spherical mirrors. For details, see [3].

81.4.1 Atomic Mirrors

Inelastic processes, such as diffuse scattering and adsorption, inhibit coherent reflection of atoms from bare surfaces. The surface must, therefore, be coated either with material of low adsorptivity (noble gas), or electromagnetic fields (evanescent light or magnetic fields, see below).

Reflection of atoms by evanescent laser light

Evanescent light fields are produced by total internal reflection of a light beam at a dielectric–vacuum interface. In the vacuum ($z \geq 0$), the field decays exponentially away from the interface on a characteristic length κ^{-1} , where

$$\kappa = k(n^2 \sin^2 \theta_i - 1)^{1/2}. \quad (81.45)$$

Here, n is the light index of refraction of the dielectric, k is the wave number of the light beam in vacuo, and θ_i is its angle of incidence.

If the light is blue-detuned from the atomic resonance, an incident beam of ground state atoms experiences the repulsive potential

$$\mathcal{U}(x) = \frac{\hbar}{2} \left[(\Omega_0^2 e^{-2\kappa z} + \Delta^2)^{1/2} - |\Delta| \right]. \quad (81.46)$$

For $\alpha > \tilde{\alpha}_c$, the evanescent field acts as a nearly perfect mirror, the imperfections being due to nonadiabatic transitions into the *wrong* dressed state, possible spontaneous emission, and scattering off an inhomogeneous potential, inherited from the roughness of the dielectric–vacuum interface. Reflection of atoms by evanescent laser light was demonstrated by *Balykin et al.* [23] at grazing incidence and by *Kasevich et al.* [24] at normal incidence.

Reflection of atoms by magnetic near fields

Magnetic near fields are produced above substrates with a spatially modulated permanent magnetization or close to arrays of stationary currents. In the vacuum above the substrate, the field decays approximately exponentially over a length comparable to the scale of the magnetic modulation. The motion of atoms that cross such inhomogeneous magnetic fields sufficiently slowly is governed by the analog of the adiabatic potential described in Sect. 81.2.4

$$\mathcal{U}(x) = -\mu \frac{m_s}{s} |\mathbf{B}(x)|, \quad (81.47)$$

where μ is the magnetic moment, and m_s is the (conserved) projection of the atomic spin s onto the local magnetic field direction. A repulsive mirror potential is achieved for spin states with $\mu m_s < 0$; these weak field seekers are repelled from the strong fields close to the substrate.

Experiments have used magnetic recording media like magnetic tapes or hard disks, arrays of current-carrying wires, or amorphous magnetic substrates, see [25].

81.4.2 Atomic Cavities

Atomic reflections are used in the two kinds of cavities proposed so far: the trampoline cavity and bicolored traps.

The trampoline cavity, also called the gravito-optical cavity, consists of a single evanescent mirror facing upwards, the second mirror being provided by gravitation [26]. A stable cavity is realized with the evanescent laser field of a parabolically shaped dielectric–vacuum interface, see the experiment by *Aminoff et al.* [27]. A cavity with transverse confinement provided by a hollow blue-detuned laser beam was demonstrated by *Hammes et al.* [28]. By combining red and

blue-detuned beams guided by an optical fiber, one can form an array of traps, as shown by *Vetsch et al.* [29].

81.4.3 Atomic Lenses

De Broglie waves may be focused by refraction from a parabolic potential or by diffraction, e.g., by a Fresnel zone plate (Sect. 81.5.2). Consider focusing by the parabolic potential

$$\mathcal{U}(x, y; z) = \begin{cases} \frac{1}{2}M\omega_f^2(x^2 + y^2), & -w \leq z \leq 0 \\ 0, & \text{otherwise.} \end{cases} \quad (81.48)$$

For ground-state atoms, such a potential is realized in the vicinity of the node of a blue-detuned standing-wave laser field of transverse width w . In this case,

$$\omega_f = \Omega_0 \left(\frac{\omega_{\text{rec}}}{|\Delta|} \right)^{1/2}, \quad (81.49)$$

where $\omega_{\text{rec}} = \hbar k^2/2M$ is the recoil frequency.

The comparison of the Raman–Nath approximation Eq. (81.40) at $z = 0$ with the phase fronts of a spherical wave converging towards a point $\mathbf{x}_f = (0, 0, f)$, shows that \mathcal{U} describes a lens of focal length

$$f = \frac{v_0^2}{w\omega_f^2}. \quad (81.50)$$

The Raman–Nath approximation is only valid for a thin lens $w \ll f$ and breaks down for $w > w_{\text{RN}} = \pi v_0/2\omega_f$. In the latter case, oscillations of the particles in the harmonic potential become relevant, a phenomenon sometimes called channeling. Channeling may be used to realize thick lenses with focal length $f = w_{\text{RN}}$ corresponding to a quarter oscillation period.

Focusing of a metastable helium beam using the antinode of a large period standing-wave laser field has been demonstrated [30]. Such a field is produced by reflecting a laser beam from a mirror under glancing incidence. The standing wave forms normal to the mirror surface. Similar interference patterns provide arrays of thick lenses that have been exploited in atom lithography to focus an atomic beam onto a substrate [7].

81.4.4 Atomic Waveguides

Atomic waveguides can be realized with potentials that confine atoms in one or two dimensions [26, 31, 32]. These devices are key elements for integrated atom optics, a field

that has seen a rapid evolution recently [33]. A planar waveguide is provided by the one-dimensional confinement in an optical standing wave or an atomic mirror combined with gravity. The discrete nature of the waveguide modes in that case was demonstrated by lowering an absorbing object [34]. Linear waveguides can be modeled by the parabolic transverse potential Eq. (81.48) that now extends along the waveguide axis (the z -axis). Physical realizations include hollow, blue-detuned laser beams, hollow fibers whose inner wall is coated with blue-detuned evanescent light [35], interference patterns from three or four far-detuned beams (also known as optical lattices) [36], and magnetic field minima along current-carrying wires, possibly combined with homogeneous bias fields [37]. With typical thermal atomic ensembles, these waveguides operate in a multimode regime, and coherent operation has been demonstrated only with Bose–Einstein condensates. A strong transverse confinement that facilitates monomode operation, can be achieved with miniaturized wire networks deposited on a solid substrate. This approach has led to the fabrication of atom chips [38, 39], and integrated atomic interferometers were demonstrated in [40, 41].

81.5 Diffraction

The diffraction of matter waves is described by the solution of the Schrödinger equation (Eq. (81.30)) subject to the boundary conditions imposed by the diffracting object. For a plane screen Σ made of opaque portions and apertures, the solution in the source-free region behind the screen is given by the Rayleigh–Sommerfeld formulation of the Huygens principle

$$\psi_E(\mathbf{x}) = \frac{k_0}{i} \int_{\Sigma} \frac{d\xi d\eta}{2\pi} \frac{e^{ik_0 R}}{R} \times \left(1 + \frac{i}{k_0 R} \right) \frac{\mathbf{n} \cdot \mathbf{R}}{R} \psi(\xi), \quad (81.51)$$

where $\xi = (\xi, \eta, \zeta)$ denotes coordinates of points on Σ , \mathbf{n} is an inwardly directed normal to Σ at a point ξ , and $\mathbf{R} = \mathbf{x} - \xi$.

A diffraction pattern only becomes manifest in the diffraction limit $r \gg d$, where r is the distance to the observation point, and d is the length scale of the diffracting system. The two diffraction regimes are then the Fraunhofer limit $r \gg d^2/\lambda_{\text{dB}}$ and the Fresnel regime $r \approx d^2/\lambda_{\text{dB}}$, also called near-field optics.

81.5.1 Fraunhofer Diffraction

In the Fraunhofer limit, the field at position (x, y) on a screen at a distance L downstream from the diffracting object is

given by

$$\psi(x, y; L) = k_0 \frac{e^{ik_0 L}}{iL} \int \frac{d\xi d\eta}{2\pi} \times e^{-i(k_x \xi + k_y \eta)} \psi(\xi, \eta; 0), \quad (81.52)$$

where $k_x = k_0 x/L$, $k_y = k_0 y/L$. The field at the observation screen is thus given by the Fourier transform of the field in the object plane; i.e., the momentum representation of the diffracted state. Since most diffraction experiments in atom optics are performed in the Fraunhofer limit, most calculations are done in the momentum representation.

Atomic diffractions from microfabricated transmission gratings [42] and double slits [43] have been observed. Recent experiments have extended de Broglie wave diffraction to heavier, complex particles like fullerenes (C_{60}) [44] and even larger molecules [9].

81.5.2 Fresnel Diffraction

Typical applications of Fresnel diffraction are Fresnel zone plates and the effects of Talbot and Lau. Fresnel zone plates are microfabricated concentric amplitude structures that act like lenses. They are frequently employed in optics of α -particles and neutrons. In atom optics, focusing with a Fresnel zone plate was first demonstrated by *Carnal* et al. [45].

The Talbot effect and the related Lau effect refer to the self-imaging of a grating of period d , which appears downstream at distances that are integral multiples of the Talbot length $L = 2d^2/\lambda_{dB}$. For a discrete set of distances smaller than the Talbot length, images of the grating appear with smaller periods d/n , $n = 2, 3, \dots$ For applications in matter-wave interferometry, see [46].

81.5.3 Near-Resonant Kapitza–Dirac Effect

The near-resonant Kapitza–Dirac effect refers to the diffraction of two-level atoms from a standing-wave laser field with a spatially uniform polarization. The dynamics of the effect is described by the Hamiltonian Eq. (81.16) with the mode function of the laser field given by Eq. (81.13). Consider atoms traveling predominantly in the z -direction, i.e., orthogonal to the axis of the laser field, with energy $(1/2)Mv_0^2 \gg \hbar\Omega_0$ (Fig. 81.2). Kapitza–Dirac diffraction is then observed in transmission, which in the theory of diffraction is called Laue geometry. In the paraxial approximation (Sect. 81.3.4) for motion in the z -direction, and assuming that the laser profile is homogeneous in the y -direction, the description reduces to an effectively one-dimensional model for the quantum mechanical motion along the x -axis of the laser field.

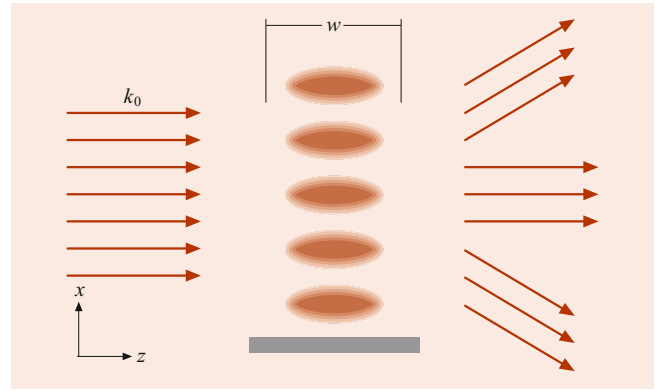


Fig. 81.2 Geometry of the Kapitza–Dirac effect

Due to the periodicity of the standing-wave light field, the transverse momenta of the transmitted atom waves differ by multiples of $\hbar k$ from the transverse momentum of the undiffracted wave. For the important case of strong detuning, and assuming that the incoming atoms are in their electronic ground state moving with transverse momentum $p_x = 0$, the p_x -distribution of the outgoing wave is given in the Raman–Nath approximation (Sect. 81.3.5) by

$$\text{Prob}(p_x = 2n\hbar k) \propto \left| J_n \left(\frac{\Omega_0^2}{8|\Delta|} \tau \right) \right|^2, \quad (81.53)$$

where J_n is a Bessel function of order n , $\tau = w/v_0$ is an effective interaction time, w being the width of the laser field, and v_0 the longitudinal velocity of the atoms. The distribution Eq. (81.53) was observed by *Gould* et al. [47].

For $\tau \gtrsim \tau_{RN}$, where $\tau_{RN} = (\omega_{rec} \Omega_0^2 / |\Delta|)^{-1/2}$, the Raman–Nath approximation becomes invalid. As a result of Doppler related phase-mismatch, the momentum spread saturates and shows a sequence of collapse and revival as a function of τ .

If the detuning is too small to allow for a scalar description, the two-level character of the atoms must be taken into account. For the particular case of $\Delta = 0$, the ground state evolves into an equal superposition of the two diabatic states $1/\sqrt{2}(|e\rangle \pm |g\rangle)$ while entering the interaction region. Inside the interaction region, these states experience potentials that differ only by their sign. For atomic beams with a small spatial spread $\delta x \ll 2\pi/k$, the diabatic states experience opposite forces, leading to a splitting of the atomic beam called the atom-optical Stern–Gerlach effect [48].

Diffraction similar to the Kapitza–Dirac effect is also possible with other polarizable particles. Experiments with molecules have been demonstrated by *Gerlich* et al. [49].

81.5.4 Atom Beam Splitters

Beam splitters are optical devices that divide an incoming beam into two outgoing beams traveling in different direc-

tions. For thermal neutrons, beam splitters may be realized by diffraction from perfect crystals in Laue geometry. For atoms, they can be realized using diffraction from crystalline surfaces, microfabricated structures (Sect. 81.5.1), or by using diffraction from an optical standing wave.

The Kapitza–Dirac effect, for example, may be exploited to split an atomic beam coherently using Bragg reflection at the *lattice planes* provided by the periodic intensity variations of a standing-wave laser field [50]. This process is resonant for an incoming atomic beam traveling with transverse momentum $p_x = \hbar k$ because it is energetically degenerate with the diffracted beam traveling with transverse momentum $\bar{p}_x = -\hbar k$. This level degeneracy is lifted while the atoms enter the interaction region. In the Bragg regime, the lifting happens slowly enough that only the momentum states $|\pm \hbar k\rangle$ participate in the diffraction (two-beam resonance), and their populations show Pendellösung-type oscillations as a function of the transit time. The frequency of the oscillations is given by $\delta E/\hbar$, where δE is the energy splitting of the two beams inside the interaction region. For a transit time given by a quarter period of the Pendellösung, a 50% beam splitting is observed [50]. In principle, Bragg resonances may also be realized for higher diffraction order $p_x = n\hbar k \leftrightarrow \bar{p}_x = -n\hbar k$. However, in this case, intermediate momentum states become populated (multibeam resonance), which makes the higher-order Bragg resonances less suitable for beam splitting purposes.

More promising for the realization of an atomic beam splitter is the magneto-optical diffraction which refers to the diffraction of three-level atoms from a laser field with a periodic polarization gradient (lin \perp lin configuration) (Chap. 79), and a magnetic field aligned parallel to the optical axis of the laser field. This configuration realizes an interaction potential in the form of a blazed grating, i.e., a phase grating with an approximately triangular variation of phase. In an experiment by Pfau et al., transverse splitting of a beam of metastable helium by $42\hbar k$ was observed [51].

Diffraction from an evanescent standing wave involves Bragg reflection of atoms under glancing incidence from the periodic grating of a blue detuned evanescent standing-wave laser field [52]. Diffraction at normal incidence has been demonstrated with sufficiently slow atoms [53, 54] and can be described by a generalization of the Raman–Nath approximation (Sect. 81.3.5).

81.6 Interference

While the overall phase of a wave function ψ is not observable, interferometry makes detectable the relative phases of two components ψ_1, ψ_2 in a superposition $\psi = \psi_1 + \psi_2$. Two types of interferometers are most common: the Young double-slit as a paradigm for interferometers based on di-

vision of wavefront, and the Mach–Zehnder interferometer as a paradigm for interferometers based on division of amplitude. In de Broglie optics, the latter type is realized in the form of a three-grating interferometer, since division of amplitude is achieved by diffraction at gratings rather than by semitransparent mirrors. Experiments with this geometry have been reported for atoms [55] and recently for more massive, complex molecules [56].

81.6.1 Interference Phase Shift

From a fundamental point of view, any interferometer is a ring. At the entrance port of a three-grating interferometer displayed in Fig. 81.3, for example, the wave function is split into two coherent parts that evolve spatially along different paths and, subsequently, come together at the exit port where they are superimposed to produce two outgoing waves

$$\psi_{\pm} = \frac{1}{\sqrt{2}}(\psi_1 \pm \psi_2), \quad (81.54)$$

where the components from path 1 and 2 are given by

$$\begin{aligned} \psi_1 &= A_1 \exp(iW_1), \\ \psi_2 &= A_2 \exp(iW_2). \end{aligned} \quad (81.55)$$

For simplicity, assume $A_1 = A_2 = A_0/\sqrt{2}$. The relative flux of the outgoing waves is then

$$I_{\pm} = \frac{1}{2}(1 \pm \cos \chi), \quad (81.56)$$

where $\chi = W_1 - W_2$ is the relative phase of the two components. The sinusoidal variations of I_{\pm} with varying χ are called interference fringes, and $\chi/2\pi$ is called the fringe order number.

In the WKB approximation, the phases W_1 and W_2 are given by

$$W_i = W_0 + \int_i \mathbf{k}(\mathbf{x}) \cdot d\mathbf{x}, \quad i = 1, 2, \quad (81.57)$$

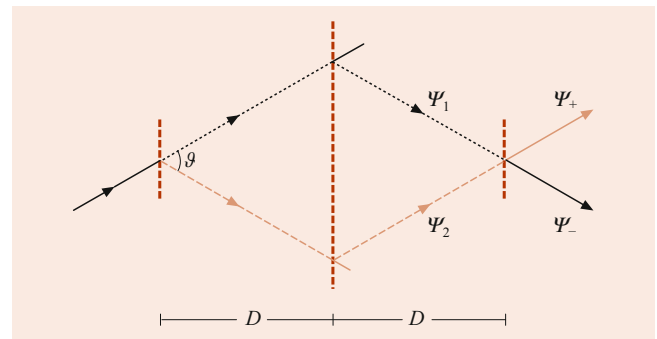


Fig. 81.3 Geometry of the three-grating interferometer

where the integrals extend over the classical paths 1 and 2, respectively, and $d\mathbf{x}$ is an element of displacement along the paths. Using Eq. (81.57), the relative phase is

$$\chi = \int_C \mathbf{k}(\mathbf{x}) \cdot d\mathbf{x} , \quad (81.58)$$

where C is the closed interferometer loop. Note that on path 2, the path element $d\mathbf{x}$ in Eq. (81.58) and \mathbf{k} are antiparallel.

Usually, the absolute value of χ is not measured, but only variations, called phase shifts, which result from displacements of the diffraction gratings or placement of optical elements into the beam path. Phase shifts come in two categories: dispersive and geometric. If a phase shift χ depends on v_0 , it is called dispersive, otherwise it is called geometric. Geometric phases depend only on the geometry of the interferometer loop. The Sagnac effect (see below), for example, may be geometric. A phase that depends neither on v_0 nor on the geometry of the interferometer loop is called topological. The Aharonov–Bohm effect (see below) is topological.

Using Eq. (81.35), χ becomes

$$\chi = \chi_0 + \chi\{\mathcal{U}\} + \chi\{\mathcal{A}\} , \quad (81.59)$$

where for weak potentials \mathcal{U} and \mathcal{A} ,

$$\chi_0 = \frac{Mv_0}{\hbar}(L_1 - L_2) , \quad (81.60)$$

$$\chi\{\mathcal{U}\} = -\frac{1}{\hbar v_0} \oint \mathcal{U}[\mathbf{x}(s)] ds , \quad (81.61)$$

$$\chi\{\mathcal{A}\} = \frac{1}{\hbar} \oint \mathcal{A}(\mathbf{x}) \cdot d\mathbf{x} , \quad (81.62)$$

and L_i is the geometric length of the path i . For a constant potential \mathcal{U}_0 intersecting the interferometer on a length w , $\chi\{\mathcal{U}\}$ is given by

$$\chi\{\mathcal{U}\} = -\frac{\mathcal{U}_0 w}{\hbar v_0} . \quad (81.63)$$

Using Stokes' theorem, $\chi\{\mathcal{A}\}$ may be written in the manifestly gauge-invariant form

$$\chi\{\mathcal{A}\} = \frac{1}{\hbar} \int [\nabla \times \mathcal{A}(\mathbf{x})] \cdot d\mathbf{a} , \quad (81.64)$$

where the integral extends over the area enclosed by the interferometer, and $d\mathbf{a}$ is an infinitesimal area element.

Dispersive phase shifts. Atom interferometers have been able to measure phase shifts of the form Eq. (81.61) due to, for example, the atomic level shift in an electric field (Stark effect) or to coherent forward scattering by background gas atoms, see [6].

Sagnac effect. The Sagnac effect refers to $\chi\{\mathcal{A}\}$ in a rotating interferometer. Inserting Eq. (81.6) into Eq. (81.64) and assuming that the axis of rotation is oriented perpendicular to the plane of the interferometer, the Sagnac phase shift is given by

$$\chi_{\text{Sa}} = \frac{4M\Omega A}{\hbar} , \quad (81.65)$$

where A is the geometric area enclosed by the interferometer loop; χ_{Sa} may be dispersive or geometric depending on the type of interferometer. In a Young double-slit, A is independent of energy, and χ_{Sa} is geometric. In a three-grating interferometer, the area is $A \approx \vartheta D^2$, where ϑ is the splitting angle; see Fig. 81.3. In this case, χ_{Sa} is dispersive because of the velocity dependence of $\vartheta \approx 2\hbar k / M v_0$. The Sagnac effect for de Broglie waves was first observed by *Werner et al.* [57] using a neutron interferometer.

Aharonov–Bohm effect. The Aharonov–Bohm effect refers to the $\chi\{\mathcal{A}\}$ of charged particles encircling a magnetic flux line [58]. Inserting \mathcal{A} from Eq. (81.7) into Eq. (81.64), and assuming the particles of charge q encircle a line of flux Φ once, one finds

$$\chi_{\text{AB}} = \frac{q\Phi}{\hbar} . \quad (81.66)$$

A characteristic feature of the Aharonov–Bohm effect is that the particles actually never *see* the magnetic field of the flux line, which is confined to some region inaccessible to the particles; χ_{AB} is strictly topological and only depends on the linking number of the interferometer loop and the flux line. Its appearance is characteristic for all gauge theories. For further details and a summary on its experimental verification, see [2].

Aharonov–Casher effect. The Aharonov–Casher effect refers to $\chi\{\mathcal{A}\}$ of a magnetic spin encircling an electric line charge [59]. Inserting \mathcal{A} from Eq. (81.10) into Eq. (81.64), one obtains for proper alignment of $\boldsymbol{\mu}$ and \mathbf{E} ,

$$\chi_{\text{AC}} = 2\pi \frac{|\boldsymbol{\mu}| r_0}{\mu_B \xi} , \quad (81.67)$$

where r_0 is the classical electron radius, μ_B is the Bohr magneton, $\xi = e/\rho_{\text{el}}$, ρ_{el} being the electric line charge density; χ_{AC} is topological only if the spin is aligned parallel to the electric line charge, and both are oriented perpendicular to the plane of the interferometer; χ_{AC} for atoms has been observed by *Sangster et al.* [60].

Electric dipole phase. Electric dipole phase refers to the $\chi\{\mathcal{A}\}$ of an electric dipole moment encircling a magnetic line charge [61]. Inserting \mathcal{A} from Eq. (81.11) into

Eq. (81.64), one obtains for proper alignment of \mathbf{d} and \mathbf{B}

$$\chi_{\text{dE}} = 2\pi \frac{|\mathbf{d}| a_0}{e a_0 \xi}, \quad (81.68)$$

where a_0 is the Bohr radius, and $\xi = \Phi_0/\varrho_{\text{mg}}$, Φ_0 being the magnetic flux unit, and ϱ_{mg} being the magnetic line charge density. In analogy to the Aharonov–Casher effect, χ_{dE} is topological, provided that \mathbf{d} is aligned parallel to the magnetic line charge, and both are oriented perpendicular to the interferometer plane. The electric dipole phase has been experimentally measured using atom interferometry [62].

81.6.2 Internal-State Interferometry

Manipulation of the internal state of atoms by means of electromagnetic fields makes it possible to realize interferometric setups that involve separation of paths in internal space rather than in real space. Examples of such interferometers are the optical Ramsey interferometer [63], the stimulated Raman interferometer [64], and interferometers using static electric and magnetic fields [65, 66].

81.6.3 Manipulation of Cavity Fields by Atom Interferometry

The entanglement of atomic states and quantized field states opens novel possibilities for manipulating and/or measuring nonclassical field states in a cavity. In the adiabatic limit, for example, and assuming sufficient detuning between the atom and the cavity field, the interaction and CM motion of an atom traversing a cavity is well described by the potential Eq. (81.29)

$$\mathcal{U}(\mathbf{x}) = -\hbar \frac{g^2}{\Delta} f(\mathbf{x})^2 a^\dagger a, \quad (81.69)$$

where g is the vacuum Rabi frequency, $f(\mathbf{x})$ is a cavity mode function, and a, a^\dagger denote cavity photon annihilation and creation operators, respectively (see Chap. 82).

Because of the presence of the photon-number operator $a^\dagger a$ in Eq. (81.69), the deflection and phase shift of an atom traversing the cavity is quantized, displaying essentially the photon number statistics in the cavity. The quantized deflection is sometimes called the inverse Stern–Gerlach effect.

Due to the entanglement of atom and cavity states, and the position dependence of the interaction strength, the phase shift induced by $\mathcal{U}(\mathbf{x})$ in a standing-wave cavity may be used to measure either the atomic position via homodyne detection of the cavity field or the photon statistics via atom interferometry. In a ring cavity, the entanglement of CM motion and cavity field may be used to measure the atomic

momentum via homodyne detection of the cavity field. For further details, see [67] and Chap. 82.

81.7 Coherence of Scalar Matter Waves

The general solution of the free Schrödinger equation (Eq. (81.2)) may be written in the form

$$\psi(\mathbf{x}, t) = \int d^3\mathbf{k} a(\mathbf{k}) e^{i(\mathbf{k}\cdot\mathbf{x} - \omega(\mathbf{k})t)}, \quad (81.70)$$

where $\omega(\mathbf{k}) \equiv E/\hbar = \hbar\mathbf{k}^2/2M$. If the coefficients $a(\mathbf{k})$ are known, the state represented by $\psi(\mathbf{x}, t)$ is called a pure state. Otherwise it is called a mixed state, and physical quantities are obtained by an ensemble average over the possible realizations of $a(\mathbf{k})$.

The degree of coherence of matter waves is described by the autocorrelation function of $\psi(\mathbf{x}, t)$

$$\Gamma(\mathbf{x}, t; \mathbf{x}', t') \equiv \overline{\psi(\mathbf{x}', t')^* \psi(\mathbf{x}, t)}, \quad (81.71)$$

where the overline ($\overline{\dots}$) denotes the ensemble average over the possible realizations of $a(\mathbf{k})$. In light optics, $\Gamma(\mathbf{x}, t; \mathbf{x}', t')$ is called the mutual coherence function. In particular, for equal times, $\Gamma(\mathbf{x}, t; \mathbf{x}', t)$ describes the spatial coherence, and for equal positions, $\Gamma(\mathbf{x}, t; \mathbf{x}, t')$ describes the temporal coherence.

For a beam of particles, coherence may be either longitudinal (measured along the beam) or transverse (measured across the beam). In contrast to light optics, there is no simple relation between longitudinal coherence and temporal coherence because the dispersion relation of matter waves is quadratic in the wavenumber.

The spatial coherence function is intimately related to the quantum mechanical density operator of the particles (Chap. 7)

$$\rho(t) = \overline{|\psi(t)\rangle\langle\psi(t)|}. \quad (81.72)$$

In the position representation, one has

$$\langle\mathbf{x}|\rho(t)|\mathbf{x}'\rangle \equiv \rho(\mathbf{x}, \mathbf{x}'; t) = \Gamma(\mathbf{x}, t; \mathbf{x}', t). \quad (81.73)$$

Longitudinal and temporal coherence of a particle beam is determined mainly by the source of the beam. The thermal fission reactors used in neutron optics and the ovens used in atom optics are analogous to black-body sources in light optics. In contrast, the transverse coherence is mainly determined by the way the particles are extracted from the oven to form a beam.

81.7.1 Atomic Sources

To describe thermal sources, consider a single particle in an oven of temperature T and volume V , assuming that $a(\mathbf{k})$ and $a(\mathbf{k}')$ are statistically independent

$$\overline{a(\mathbf{k})^* a(\mathbf{k}')} = \rho(k) \delta(\mathbf{k} - \mathbf{k}'), \quad (81.74)$$

where

$$\rho(k) = \frac{\lambda_{\text{th}}^3}{V} \exp\left(-\frac{\hbar^2 k^2}{2Mk_{\text{B}}T}\right) \quad (81.75)$$

accounts for the thermal distribution of wavenumbers, and

$$\lambda_{\text{th}} = \left(\frac{2\pi\hbar^2}{Mk_{\text{B}}T}\right)^{1/2} \quad (81.76)$$

denotes the thermal de Broglie wavelength.

Using Eqs. (81.74)–(81.76) in Eq. (81.71), the mutual coherence function becomes

$$\Gamma(\mathbf{x}, t; \mathbf{x}', t') = \frac{1}{V} \frac{1}{\{1 + i(t - t')/\tau_{\text{th}}\}^{3/2}} \times \exp\left\{-\pi \frac{(\mathbf{x} - \mathbf{x}')^2 / \lambda_{\text{th}}^2}{1 + i(t - t')/\tau_{\text{th}}}\right\}, \quad (81.77)$$

where

$$\tau_{\text{th}} = \frac{\hbar}{k_{\text{B}}T}, \quad (81.78)$$

is the thermal coherence time.

According to Eq. (81.77), the spatial coherence of a thermal state falls off in a Gaussian manner on a scale given by λ_{th} . The temporal coherence, in contrast, falls off algebraically on a timescale given by τ_{th} . Expressed in physical units, one has

$$\lambda_{\text{th}} = \frac{1.74(5) \text{ nm}}{\sqrt{(M/\text{u})(T/\text{K})}}, \quad \tau_{\text{th}} = \frac{7.63 \text{ ps}}{(T/\text{K})}, \quad (81.79)$$

where u is the atomic mass unit.

Atomic Beams

Effusive beams. Effusive beams are produced from thermal sources by a suitable set of collimators placed in front of the opening of the oven. This produces a Maxwell–Boltzmann distribution of atomic velocities in the longitudinal direction. The coherence properties in the transverse direction are described by the van Cittert–Zernike theorem [68]; for details see any textbook on classical optics.

Supersonic beams. Supersonic beams are produced by supersonic expansion of a high-pressure gas that is forced through an appropriately designed nozzle. The expansion produces a velocity distribution in the longitudinal direction, which is approximately Gaussian with a velocity ratio $v/\delta v \approx 10\text{--}20$.

Pulsed beams. Pulsed beams are produced by chopping any of the beams described above. Important applications for pulsed beams are the resolution of temporal coherence and the mapping of the relative phases of the $a(\mathbf{k})$ in matter-wave interferometry.

Laser-like source of atoms. In these sources, many atoms with integral spin (Bosons) occupy one and the same quantum state of motion. Their operational principle is rooted in the quantum statistical effects of indistinguishability. It may be viewed in close analogy to the operational principle of an ordinary laser (Chap. 74) and the mechanism underlying Bose–Einstein condensation (Chap. 80). Laser-like sources have, indeed, been achieved by letting a small current of atoms leak out of a trapped Bose–Einstein condensate [69].

81.7.2 Atom Decoherence

In any interferometer, the contrast of the interference fringes quantitatively measures the coherence of the wave involved. Partially coherent beams show an output flux given by

$$I_{\pm} = \frac{1}{2} [1 \pm \text{Re}(C e^{i\chi})], \quad (81.80)$$

instead of Eq. (81.56), with a complex number C . One has $|C| \leq 1$, with the maximum achieved for a pure state; the phase of C is measured by scanning the interferometer phase shift χ .

In de Broglie interferometry, coherence can be lost when the interfering matter wave gets entangled with other systems. This happens for atoms, for example, due to the emission or scattering of photons, as soon as the detection of these photons permits, in principle, the resolution of spatially separated paths in the interferometer. In fact, the width of $\Gamma(\mathbf{x}, t; \mathbf{x}', t)$ as a function of $\mathbf{x} - \mathbf{x}'$, also called the spatial coherence length, is reduced to the photon wavelength after a single scattering event; see [70]. Interference can be restored when the emitted photons are detected and correlated with the atom output [71, 72]. Collisions with background gas atoms between the optical elements of a three-grating interferometer also reduce coherence, as has been shown with fullerene molecules [73]. Furthermore, coherence is lost when atoms interact with random electromagnetic fields. This has become relevant for atom reflection from evanescent light because of the roughness of the dielectric surface

used [74]. The coherent operation of integrated atom optics near metallic surfaces is limited by thermally excited electromagnetic near fields [75], as shown in experiments by Harber et al. [76]. Finally, there are suggestions that decoherence may be ever more efficient for particles with larger masses, due to the interaction with the gravitational field or internal degrees of freedom [17, 18]. Interferometer experiments with large molecules [16] and nanoparticles [77] have been proposed to resolve this issue.

References

- Pozzi, G.: *Particles and Waves in Electron Optics and Microscopy*. Academic Press, Cambridge (2016)
- Tonomura, A.: *Electron Holography*. In: Shimoda, K. (ed.) *Springer Series in Optical Sciences*, vol. 70, Springer, Berlin, Heidelberg (1993)
- Utsuro, M., Ignatovich, V.K. (eds.): *Handbook of Neutron Optics*. John Wiley & Sons, Hoboken (2010)
- Rauch, H., Werner, S.A.: *Neutron Interferometry*. Clarendon Press, Oxford (2000)
- Meystre, P.: *Atom Optics*. Springer, Berlin, Heidelberg (2001)
- Cronin, A.D., Schmiedmayer, J., Pritchard, D.E.: *Optics and interferometry with atoms and molecules*. *Rev. Mod. Phys.* **81**, 1051 (2009)
- Rohwedder, B.: Resource Letter AON-1: Atom optics, a tool for nanofabrication. *Am. J. Phys.* **75**, 394 (2007)
- Witham, P.W., Sanchez, E.: A simple approach to neutral atom microscopy. *Rev. Sci. Instr.* **82**, 103705 (2011)
- Gerlich, S., Eibenberger, S., Tomandl, M., Nimmrichter, S., Hornberger, K., Fagan, P.J., Tüxen, J., Mayor, M., Arndt, M.: Quantum Interference of Large Organic Molecules. *Nat. Commun.* **2**, 263 (2011)
- Müller, H., Peters, A., Chu, S.: A precision measurement of the gravitational redshift by the interference of matter waves. *Nature* **463**, 926 (2010)
- Lan, S.-Y., Kuan, P.-C., Estey, B., English, D., Brown, J.N., Hohenstein, M.A., Müller, H.: A clock directly linking time to a particle's mass. *Science* **339**, 554 (2013)
- Rosi, G.: Precision measurement of the Newton gravitational constant using cold atoms. *Nature* **510**, 518 (2014)
- dos Santos, F.P., Bonvalot, S.: *Cold-Atom Absolute Gravimetry*. In: Grafarend, E. (ed.) *Encyclopedia of Geodesy*. Springer, Cham (2016)
- Barrett, B., Antoni-Micollier, L., Chichet, L., Battellier, B., Lévêque, T., Landragin, A., Bouyer, P.: Dual matter-wave inertial sensors in weightlessness. *Nat. Commun.* **7**, 13786 (2016)
- Hamilton, P., et al.: Atom-interferometry constraints on dark energy. *Science* **349**, 849 (2015)
- Arndt, M., Hornberger, K.: Testing the limits of quantum mechanical superpositions. *Nat. Phys.* **10**, 271 (2014)
- Pikovski, I., Zych, M., Costa, F., Brukner, C.: Universal decoherence due to gravitational time dilation. *Nat. Phys.* **11**, 668 (2015)
- Joos, E., Zeh, H.D., Kiefer, C., Giulini, D., Kupsch, J., Stamatescu, I.-O.: *Decoherence and the Appearance of a Classical World in Quantum Theory*, 2nd edn. Springer, Berlin, Heidelberg (2003)
- Anderson, B.P., Meystre, P.: Nonlinear atom optics. *Contemp. Phys.* **44**, 473 (2003)
- Deng, L., et al.: Four-wave mixing with matter waves. *Nature* **398**, 218 (1999)
- Inouye, S., et al.: Phase-coherent amplification of atomic matter waves. *Nature* **402**, 641 (1999)
- Berry, M.V., Upstill, C.: Catastrophe optics: morphology of caustics and their diffraction patterns. In: Wolf, E. (ed.) *Progress in Optics*, vol. XVIII, pp. 259–346. North-Holland, Amsterdam (1980)
- Balykin, V.I., Letokhov, V.S., Ovchinnikov, Y.B., Sidorov, A.I.: Quantum-state-selective mirror reflection of atoms by laser light. *Phys. Rev. Lett.* **60**, 2137 (1988)
- Kasevich, M.A., Weiss, D.S., Chu, S.: Normal-incidence reflection of slow atoms from an optical evanescent wave. *Opt. Lett.* **15**, 607 (1990)
- Wang, Y., et al.: Magnetic lattices for ultracold atoms and degenerate quantum gases. *Sci. Bull.* **61**(14), 1097 (2016)
- Dowling, J.P., Gea-Banacloche, J.: Evanescent light-wave atom mirrors, resonators, waveguides, and traps. In: Berman, P.R. (ed.) *Adv. At. Mol. Opt. Phys.*, vol. 37, pp. 1–94. Academic Press, New York (1997)
- Aminoff, C.G., et al.: Cesium atoms bouncing in a stable gravitational cavity. *Phys. Rev. Lett.* **71**, 3083 (1993)
- Hammes, M., et al.: Optical and evaporative cooling of caesium atoms in the gravito-optical surface trap. *J. Mod. Opt.* **47**, 2755 (2000)
- Vetsch, E., et al.: Optical interface created by laser-cooled atoms trapped in the evanescent field surrounding an optical nanofiber. *Phys. Rev. Lett.* **104**, 203603 (2010)
- Sleator, T., Pfau, T., Balykin, V., Mlynek, J.: Imaging and focusing of an atomic beam with a large period standing light wave. *Appl. Phys. B* **54**, 375 (1992)
- Balykin, V.I.: Atom waveguides. In: Bederson, B., Walther, H. (eds.) *Adv. At. Mol. Opt. Phys.*, vol. 41, pp. 181–260. Academic Press, San Diego (1999)
- Hinds, E.A., Hughes, I.G.: Magnetic atom optics: mirrors, guides, traps, and chips for atoms. *J. Phys. D Appl. Phys.* **32**, R199 (1999)
- Amico, L., et al.: Roadmap on Atomtronics, AVS Quantum. *Sci.* **3**, 039201 (2021)
- Nesvizhevsky, V.V., et al.: Quantum states of neutrons in the Earth's gravitational field. *Nature* **415**, 297 (2002)
- Ito, H., et al.: Laser spectroscopy of atoms guided by evanescent waves in micron-sized hollow optical fibers. *Phys. Rev. Lett.* **76**, 4500 (1996)
- Bloch, I.: Ultracold quantum gases in optical lattices. *Nat. Phys.* **1**, 23 (2005)
- Schmiedmayer, J.: Guiding and trapping a neutral atom on a wire. *Phys. Rev. A* **52**, R13 (1995)
- Reichel, J., Vuletić, V. (eds.): *Atom Chips*. Wiley-VCH, Weinheim (2011)
- Keil, M., Amit, O., Zhou, S., Groswasser, D., Japha, Y., Folman, R.: Fifteen years of cold matter on the atom chip: promise, realizations, and prospects. *J. Mod. Opt.* **63**, 1840 (2016)
- Wang, Y.-J., et al.: Atom Michelson interferometer on a chip using a Bose–Einstein condensate. *Phys. Rev. Lett.* **94**, 090405 (2005)
- Berrada, T., van Frank, S., Bücker, R., Schumm, T., Schaff, J.-F., Schmiedmayer, J.: Integrated Mach–Zehnder interferometer for Bose–Einstein condensates. *Nat. Commun.* **4**, 2077 (2013)
- Keith, D.W., Schattenburg, M.L., Smith, H.I., Pritchard, D.E.: Diffraction of atoms by a transmission grating. *Phys. Rev. Lett.* **61**, 1580 (1988)
- Carnal, O., Mlynek, J.: Young's double-slit experiment with atoms: a simple atom interferometer. *Phys. Rev. Lett.* **66**, 2689 (1991)
- Arndt, M., et al.: Wave-particle duality of C₆₀ molecules. *Nature* **401**, 680 (1999)
- Carnal, O., et al.: Imaging and focusing of atoms by a Fresnel zone plate. *Phys. Rev. Lett.* **67**, 3231 (1991)

46. Clauser, J.F., Reinsch, M.: New theoretical and experimental results in Fresnel optics with applications to matter-wave and X-ray interferometry. *Appl. Phys. B* **54**, 380 (1992)
47. Gould, P.L., Ruff, G.A., Pritchard, D.E.: Diffraction of atoms by light: the near-resonant Kapitza–Dirac effect. *Phys. Rev. Lett.* **56**, 827 (1986)
48. Sleator, T., et al.: Experimental demonstration of the optical Stern–Gerlach effect. *Phys. Rev. Lett.* **68**, 1996 (1992)
49. Gerlich, S., et al.: A Kapitza–Dirac–Talbot–Lau interferometer for highly polarizable molecules. *Nat. Phys.* **3**, 711 (2007)
50. Martin, P.J., Oldaker, B.G., Miklich, A.H., Pritchard, D.E.: Bragg scattering of atoms from a standing light wave. *Phys. Rev. Lett.* **60**, 515 (1988)
51. Pfau, T., et al.: Magneto-optical beam splitter for atoms. *Phys. Rev. Lett.* **71**, 3427 (1993)
52. Henkel, C., et al.: Theory of atomic diffraction from evanescent waves. *Appl. Phys. B* **69**, 277 (1999)
53. Landragin, A., et al.: A reflection grating for atoms at normal incidence. *Europhys. Lett.* **39**, 485 (1997)
54. Stehle, C., Bender, H., Zimmermann, C., Kern, D., Fleischer, M., Slama, S.: Plasmonically tailored micropotentials for ultracold atoms. *Nat. Photon.* **5**, 494 (2011)
55. Keith, D.W., Ekstrom, C.R., Turchette, Q.A., Pritchard, D.E.: An interferometer for atoms. *Phys. Rev. Lett.* **66**, 2693 (1991)
56. Juffmann, T., Ulbricht, H., Arndt, M.: Experimental methods of molecular matter-wave optics. *Rep. Progr. Phys.* **76**, 086402 (2013)
57. Werner, S.A., Staudenmann, J., Colella, R.: Effect of Earth’s rotation on the quantum mechanical phase of the neutron. *Phys. Rev. Lett.* **42**, 1103 (1979)
58. Aharonov, Y., Bohm, D.: Significance of electromagnetic potentials in the quantum theory. *Phys. Rev.* **115**, 485 (1959)
59. Aharonov, Y., Casher, A.: Topological quantum effects for neutral particles. *Phys. Rev. Lett.* **53**, 319 (1984)
60. Sangster, K., Hinds, E.A., Barnett, S.M., Riis, E.: Measurement of the Aharonov–Casher phase in an atomic system. *Phys. Rev. Lett.* **71**, 3641 (1993)
61. Wilkens, M.: Quantum phase of a moving dipole. *Phys. Rev. Lett.* **72**, 5 (1994)
62. Lepoutre, S., Gauguier, A., Tréneç, G., Büchner, M., Vigué, J.: He–McKellar–Wilkens topological phase in atom interferometry. *Phys. Rev. Lett.* **109**, 120404 (2012)
63. Bordé, C.J.: Atomic interferometry with internal state labelling. *Phys. Lett. A* **140**, 10 (1989)
64. Kasevich, M., Chu, S.: Atomic interferometry using stimulated Raman transitions. *Phys. Rev. Lett.* **67**, 181 (1991)
65. Sokolov, Y.L., Yakovlev, V.P.: Measurement of the Lamb shift in the hydrogen atom ($n = 2$). *Sov. Phys. JETP* **56**, 7 (1982)
66. Robert, J., et al.: Atomic interferometry with metastable hydrogen atoms. *Europhys. Lett.* **16**, 29 (1991)
67. Haroche, S., Raimond, J.M.: Manipulation of non classical field states by atom interferometry. In: Berman, P.R. (ed.) *Cavity Quantum Electrodynamics*, *Adv. At. Mol. Opt. Phys.*, suppl. 2, pp. 123–170. Academic Press, Boston (1994)
68. Taylor, B., Scherthanner, K.J., Lenz, G., Meystre, P.: The van Cittert–Zernike theorem in atom optics. *Opt Commun* **110**, 569 (1994)
69. Köhl, M., Hänsch, T.W., Esslinger, T.: Measuring the temporal coherence of an atom laser beam. *Phys. Rev. Lett.* **87**, 160404 (2001)
70. Pfau, T., et al.: Loss of spatial coherence by a single spontaneous emission. *Phys. Rev. Lett.* **73**, 1223 (1994)
71. Chapman, M.S., et al.: Photon scattering from atoms in an atom interferometer: coherence lost and regained. *Phys. Rev. Lett.* **75**, 3783 (1995)
72. Kurtsiefer, C., et al.: Observation of correlated atom-photon pairs on the single particle level. *Phys. Rev. A* **55**, R2539 (1997)
73. Hackermüller, L., et al.: Decoherence in a Talbot–Lau interferometer: the influence of molecular scattering. *Appl. Phys. B* **77**, 781 (2003)
74. Landragin, A., et al.: Specular versus diffuse reflection of atoms from an evanescent-wave mirror. *Opt. Lett.* **21**, 1591 (1996)
75. Henkel, C., Wilkens, M.: Heating of trapped atoms near thermal surfaces. *Europhys. Lett.* **47**, 414 (1999)
76. Harber, D.M., McGuirk, J.M., Obrecht, J.M., Cornell, E.A.: Thermally induced losses in ultra-cold atoms magnetically trapped near room-temperature surfaces. *J. Low. Temp. Phys.* **133**, 229 (2003)
77. Romero-Isart, O., et al.: Large quantum superpositions and interference of massive nanometer-sized objects. *Phys. Rev. Lett.* **107**, 020405 (2011)



Carsten Henkel Carsten Henkel is Docteur en Sciences at the Université Paris-Sud Orsay. In 1997, he went to the University of Potsdam where he was appointed Professor (apl.) of Quantum Optics in 2015. His research interests are in nano-optics and ultracold atoms.



Martin Wilkens Martin Wilkens received his PhD in Physics from Essen University. He spent his postdoctoral years in Warsaw, Tucson, and Konstanz. He has been Professor of Quantum Theory at the University of Potsdam since 1997. His research interests are in degenerate quantum gases, quantum information processing, and general relativity.



Da-Wei Wang  and Girish S. Agarwal

Contents

82.1	Introduction	1189
82.2	Quantization of the Electromagnetic Field	1190
82.3	Quantum States	1190
82.4	Field Observables: Quadratures	1192
82.5	Phase-Space Representations of the Light: P, Q, and Wigner Functions	1192
82.6	Squeezed State	1194
82.7	Detection of Quantum Light by Array Detectors	1196
82.8	Two-Mode Squeezed States	1197
82.9	Quantum Entanglement	1198
82.10	Non-Gaussian Nonclassical States	1199
82.11	Beam Splitter, Interferometer, and Measurement Sensitivity	1200
	References	1203

Abstract

This article focuses on the understanding of issues where the quantumness of the radiation field is important. To this end, we introduce the experimental signatures of the strict quantum character of the radiation field. Besides the fundamental interest in quantumness, we discuss the important consequences of it, especially in beating the standard quantum noise limit. The quantum character of the field can be used for achieving unprecedented sensitivity. This article is focused on the radiation field, but

many of these ideas are applicable to spin systems, two-level systems, and many other bosonic systems, like ionic motion and mechanical (phonon) degrees of freedom in optomechanical systems. An extensive discussion of the quantumness and its applications in quantum metrology can be found in the book [1]; the summary in this Handbook chapter is tailored along the lines of this book. We start with a historical introduction to the quantum theory of radiation.

Keywords

quantum entanglement · coherent state · squeezed state · CAT states · Nonclassical light · Quantum sensing · Standard quantum noise limit · Heisenberg limit · Detection of quantum fields

82.1 Introduction

The quantum theory of light has its beginnings in the work of Max Planck in 1900. After a tedious struggle in explaining the black-body radiation, Planck found that in order to fit the thermal radiation curve, he had to assume the exchange of energy between a black body and the radiation fields with an undividable unit of energy, $\hbar\omega$, where $\hbar = 1.06 \times 10^{-34}$ J s is the Planck constant and ω is the circular frequency of the light. However, Planck did not regard light itself as being composed of particles with this unit energy. The idea of light quanta was proposed by Einstein in 1905. In studying the thermal dynamic properties of light, Einstein realized that the thermal dynamic equations of light allow a corpuscular theory of light, i.e., the energy of light is carried in discrete quantized packets.

Let us first see how the quantum nature of light affects its thermal statistical distribution. If light behaves like classical waves, the intensity distribution at a certain temperature is

$$P(I) = \frac{1}{\langle I \rangle} e^{-I/\langle I \rangle}, \quad (82.1)$$

D.-W. Wang (✉)
Department of Physics, Zhejiang University
Hangzhou, China
e-mail: dwwang@zju.edu.cn

G. S. Agarwal
Institute for Quantum Science and Engineering, Texas A&M
University
College Station, TX, USA
e-mail: girish.agarwal@tamu.edu

where $\langle I \rangle$ is the average intensity. Quantum theory requires that the probability that the light field contains n photons is, given by the Bose–Einstein distribution,

$$p_n = \frac{1}{1 + \langle n \rangle} \left(\frac{\langle n \rangle}{1 + \langle n \rangle} \right)^n, \quad (82.2)$$

where Planck's law gives the average photon number $\langle n \rangle = 1/[\exp(\hbar\omega/k_B T) - 1]$ at the frequency ω with k_B the Boltzmann constant, and T is the temperature. In the large photon number limit, $\langle n \rangle \gg 1$,

$$p_n \approx \frac{1}{\langle n \rangle} \exp\left(-\frac{n}{\langle n \rangle}\right), \quad (82.3)$$

which is identical to Eq. (82.1) since $\langle I \rangle \propto \langle n \rangle$. However, in the low-temperature limit, when $\langle n \rangle \approx 1$ or smaller than 1, p_n drops to zero much faster than Eq. (82.1).

Another drastic difference is in the fluctuations of the fields. From Eq. (82.1), the variance of the intensity $\Delta I^2 = \langle I \rangle^2$, while the fluctuation in the photon numbers according to Eq. (82.2) is $\Delta n^2 = \langle n \rangle^2 + \langle n \rangle$. Einstein called $\langle n \rangle^2$ and $\langle n \rangle$ the particle and wave parts of the fluctuations, respectively. At the low-temperature limit, the fluctuation of the photon numbers is larger than that of the classical statistics. In a remarkable experiment [2], the moments of the Bose–Einstein distribution were measured down to the mean number of the order of unity with deviation in the second moment less than 10%.

The nature of the quantization of the electromagnetic field was not fully understood until Dirac found the second quantization after quantum mechanics was formulated by Heisenberg and Schrödinger in 1925–1926. The wave nature of the light is governed by the Maxwell equations, which give the mode function for the electromagnetic modes. In each of the modes, the amplitude of the field is quantized using the fact that photons obey Bose statistics.

82.2 Quantization of the Electromagnetic Field

According to the Maxwell equations, which characterize the wave nature of the electromagnetic fields, the electromagnetic fields in free space can be written with the vector potential \mathbf{A} ,

$$\mathbf{E} = -\frac{1}{c} \frac{\partial \mathbf{A}}{\partial t}, \quad \mathbf{B} = \nabla \times \mathbf{A}, \quad (82.4)$$

where \mathbf{E} and \mathbf{B} are the electric field and the magnetic field, respectively. We employ CGS units because the physics community uses these widely. In a volume V , \mathbf{A} can be

decomposed into plane waves with wave vector \mathbf{k} and polarization s ,

$$\mathbf{A} = \sum_{\mathbf{k}, s} \frac{A_{\mathbf{k}s}}{\sqrt{V}} \boldsymbol{\epsilon}_{\mathbf{k}s} e^{i\mathbf{k}\cdot\mathbf{r} - i\omega_{\mathbf{k}}t} + \text{c.c.}, \quad (82.5)$$

where the mode functions of the plane wave satisfy the orthogonal condition, $(1/V) \int_V d^3r e^{i\mathbf{k}\cdot\mathbf{r} - i\mathbf{k}'\cdot\mathbf{r}} = \delta(\mathbf{k} - \mathbf{k}')$.

The energy of the electromagnetic fields, $U = (1/8\pi) \int_V [E^2(\mathbf{r}, t) + B^2(\mathbf{r}, t)] d^3r$ can be written in terms of the vector potential,

$$U = \frac{1}{2\pi} \sum_{\mathbf{k}, s} \left(\frac{\omega_{\mathbf{k}}^2}{c^2} \right) |A_{\mathbf{k}s}|^2. \quad (82.6)$$

What was revealed in Planck's black-body radiation is that the above energy should be quantized, $U = \sum_{\mathbf{k}, s} n_{\mathbf{k}s} \hbar\omega_{\mathbf{k}}$, where $n_{\mathbf{k}s}$ is the number of quanta in the mode $\mathbf{k}s$. By making comparison between these two expressions of the energy, we realize the correspondence,

$$\frac{\omega_{\mathbf{k}}}{2\pi\hbar c^2} |A_{\mathbf{k}s}|^2 \leftrightarrow n_{\mathbf{k}s}. \quad (82.7)$$

This is the quantization of the field amplitudes. This quantization is done by introducing the annihilation and creation operators for the electromagnetic field, $a_{\mathbf{k}s}$ and $a_{\mathbf{k}s}^\dagger$, with the commutation relations

$$\begin{aligned} [a_{\mathbf{k}s}, a_{\mathbf{k}'s'}^\dagger] &= \delta_{\mathbf{k}, \mathbf{k}'} \delta_{s, s'}, \\ [a_{\mathbf{k}s}, a_{\mathbf{k}'s'}] &= 0. \end{aligned} \quad (82.8)$$

The number operator can be written as,

$$n_{\mathbf{k}s} = a_{\mathbf{k}s}^\dagger a_{\mathbf{k}s}. \quad (82.9)$$

From Eqs. (82.7) and (82.9), we can relate $A_{\mathbf{k}s} = \sqrt{2\pi\hbar c^2/\omega_{\mathbf{k}}} a_{\mathbf{k}s}$, and the vector potential can be rewritten as $\mathbf{A} = \sum_{\mathbf{k}, s} \boldsymbol{\epsilon}_{\mathbf{k}s} \sqrt{2\pi\hbar c^2/(\omega_{\mathbf{k}} V)} a_{\mathbf{k}s} e^{i\mathbf{k}\cdot\mathbf{r} - i\omega_{\mathbf{k}}t} + \text{H.c.}$, where H.c. stands for Hermitian conjugate. With \mathbf{A} , it is straightforward to write \mathbf{E} and \mathbf{B} in the form of a and a^\dagger . Most importantly, the total energy of the electromagnetic fields, i.e., the Hamiltonian can be written as

$$H = \sum_{\mathbf{k}, s} \hbar\omega_{\mathbf{k}} \left(n_{\mathbf{k}s} + \frac{1}{2} \right). \quad (82.10)$$

82.3 Quantum States

After the field is quantized, it is natural to ask what kind of quantum states photons can possess. In the following, we first introduce several photonic states that people frequently encounter, i.e., the Fock states, the coherent states and the thermal states.

The Fock state. The quantization of the electromagnetic field is most obviously represented by the quantized value of the number operator $a^\dagger a$, which is directly related to the Hamiltonian of the electromagnetic fields through Eq. (82.10). Fock states $|n\rangle$ are the eigenstates of the number operators,

$$a^\dagger a |n\rangle = n |n\rangle . \quad (82.11)$$

For a single mode, the commutation relation in Eq. (82.8) reduces to $[a, a^\dagger] = 1$. It is easy to find that $a |n\rangle$ is also an eigenstate of the number operator,

$$a^\dagger a a |n\rangle = (a a^\dagger - 1) a |n\rangle = (n - 1) a |n\rangle . \quad (82.12)$$

Therefore, $a |n\rangle = c |n - 1\rangle$ with c being a constant, which can be determined from the inner product $\langle n | a^\dagger a |n\rangle = \langle n - 1 | c^* c |n - 1\rangle$ that $c = \sqrt{n}$. This then leads to

$$|n\rangle = \frac{a^{\dagger n}}{\sqrt{n!}} |0\rangle . \quad (82.13)$$

Obviously, there is a lower limit of the number in the number states,

$$a |0\rangle = 0 . \quad (82.14)$$

Here, $|0\rangle$ is also called the vacuum state, which is also an eigenstate of the annihilation operator. Note that $\langle 0 | H |0\rangle = \hbar\omega/2$ for a single mode. This is called the zero-point energy of the mode. It diverges for infinitely many-mode fields. This cannot be measured, and hence no physical consequence exists. However, the differences of the zero-point energy are finite and are related to the Casimir force and the van der Waals force.

In the following, we are going to introduce a more general form of the eigenstate of the annihilation operator.

The coherent state. A coherent state is an eigenstate of the annihilation operator a ,

$$a |\alpha\rangle = \alpha |\alpha\rangle , \quad (82.15)$$

and in the basis of the number states,

$$|\alpha\rangle = \sum_n e^{-|\alpha|^2/2} \frac{\alpha^n}{\sqrt{n!}} |n\rangle . \quad (82.16)$$

The photon number distribution

$$p_n = e^{-\langle n \rangle} \frac{\langle n \rangle^n}{n!} , \quad (82.17)$$

is Poissonian with the mean value $\langle n \rangle = |\alpha|^2$. The variance is equal to its mean value,

$$\langle \Delta n^2 \rangle = \langle n^2 \rangle - \langle n \rangle^2 = \langle n \rangle . \quad (82.18)$$

One important property of the coherent state is that they form a complete set,

$$\frac{1}{\pi} \int d^2\alpha |\alpha\rangle \langle \alpha| = 1 , \quad (82.19)$$

where $\alpha = x + iy$ and $d^2\alpha = dx dy$ with x and y being real numbers. However, different from the complete set formed by the number states, the basis states of the coherent states are not orthogonal,

$$\langle \alpha | \beta \rangle = \exp\left(\alpha^* \beta - \frac{|\alpha|^2}{2} - \frac{|\beta|^2}{2}\right) . \quad (82.20)$$

The nonorthogonality of the coherent states leads to an important property of the coherent state, namely, we can represent a coherent state in the form of other coherent states,

$$|\alpha\rangle = \frac{1}{\pi} \int \langle \beta | \alpha \rangle |\beta\rangle d^2\beta . \quad (82.21)$$

Any coherent state can be generated by the displacement of the vacuum state,

$$|\alpha\rangle = D(\alpha) |0\rangle , \quad (82.22)$$

where $D(\alpha)$ is the displacement operator

$$D(\alpha) = \exp(\alpha a^\dagger - \alpha^* a) . \quad (82.23)$$

The displacement operator has the following important properties,

$$\begin{aligned} D^{-1}(\alpha) &= D^\dagger(\alpha) = D(-\alpha) , \\ D^\dagger(\alpha) G(a, a^\dagger) D(\alpha) &= G(a + \alpha, a^\dagger + \alpha^*) , \\ D(\alpha) D(\beta) &= D(\alpha + \beta) \exp[(\alpha\beta^* - \alpha^*\beta)/2] . \end{aligned} \quad (82.24)$$

Here, G is any function of annihilation and creation operators.

The thermal state. The Fock states and the coherent states are both pure states. In contrast, thermal states are mixed states and can only be represented by the density matrices,

$$\rho_T = \frac{\exp(-\beta \hbar \omega a^\dagger a)}{\text{Tr}[\exp(-\beta \hbar \omega a^\dagger a)]} , \quad (82.25)$$

where $\beta = 1/k_B T$. In terms of the Fock states,

$$\rho_T = \sum_{n=0}^{\infty} \frac{\langle n \rangle^n}{(1 + \langle n \rangle)^{n+1}} |n\rangle \langle n| , \quad (82.26)$$

where the average photon number $\langle n \rangle = 1/[\exp(\beta \hbar \omega) - 1]$, which is Planck's law.

82.4 Field Observables: Quadratures

The above three kinds of states are different in their quantum statistical properties, which can be measured by physical observables of the fields. However, the annihilation and creation operators are not Hermitian or directly measurable. Instead, the measurable quantities in experiments are, besides the photon number distributions, the amplitudes and phases of the fields, e.g., the real and imaginary parts of the electric fields. These are called in-phase and out-of-phase quadratures, which can be measured by homodyne detection. We can define two Hermitian quadrature operators, X and Y ,

$$X = \frac{a + a^\dagger}{\sqrt{2}}, Y = \frac{a - a^\dagger}{\sqrt{2}i}. \quad (82.27)$$

The commutation relation between X and Y is

$$[X, Y] = i, \quad (82.28)$$

analogous to the position-momentum commutation relation. Therefore, we can represent the operator Y with $Y = -i(\partial/\partial X)$. The Hamiltonian $H = \hbar\omega(a^\dagger a + 1/2)$ can be rewritten as $H = (X^2 + Y^2)/2$, which is similar to the one of the harmonic oscillators. The number state can be represented with variable X in a similar way as in the harmonic oscillator,

$$\Psi_n(X) = \langle X|n\rangle = (2^n n! \sqrt{\pi})^{-1/2} H_n(X) e^{-X^2/2}, \quad (82.29)$$

where $H_n(X)$ is the Hermite polynomial of degree n .

The variance of the quadratures reflects the fluctuations in the amplitudes and phases of the fields,

$$\begin{aligned} \langle \Delta X^2 \rangle &= \frac{\langle a^2 \rangle + \langle a^{\dagger 2} \rangle}{2} + \langle n \rangle + \frac{1}{2} - \frac{\langle a + a^\dagger \rangle^2}{2} \\ \langle \Delta Y^2 \rangle &= -\frac{\langle a^2 \rangle + \langle a^{\dagger 2} \rangle}{2} + \langle n \rangle + \frac{1}{2} + \frac{\langle a - a^\dagger \rangle^2}{2} \end{aligned} \quad (82.30)$$

For Fock states or thermal states, $\langle \Delta X^2 \rangle = \langle \Delta Y^2 \rangle = \langle n \rangle + 1/2$. For coherent states, $\langle \Delta X^2 \rangle = \langle \Delta Y^2 \rangle = 1/2$. The coherent states are the minimum uncertainty states as the product $\langle \Delta X \Delta Y \rangle$ takes the minimum value $1/2$.

82.5 Phase-Space Representations of the Light: P , Q , and Wigner Functions

The quantum nature of light is evidently represented by the number states. On the other hand, in classical electromagnetic theory, according to the Maxwell equations,

light can be represented by harmonic oscillations of the fields. Classically, we can describe the center of mass of a particle with its position and momentum. For an ensemble of particles, we can define a probability distribution $P(x, p)$ (phase-space distribution) to study their statistics. However, in quantum mechanics, x and p do not commute, and thus cannot have definite values at the same time. E. Wigner tried to incorporate quantum mechanics into the classical statistics. By doing this, the noncommutative nature in quantum mechanics is demonstrated by negative values of the Wigner quasi probability. The same problem exists in a probability description of the light field with respect to its amplitude and phase. In this section, we are going to introduce several representations of light in phase space.

P -representation. Glauber and Sudarshan proposed to use the coherent states as a basis to describe the light field [3, 4]. The coherent state basis, even though composed by states that are nonorthogonal, can represent any radiation field

$$\rho = \int P(\alpha) |\alpha\rangle \langle \alpha| d^2\alpha, \quad (82.31)$$

with the normalization condition $\int P(\alpha) d^2\alpha = 1$. This representation is called Glauber–Sudarshan P -representation. The $P(\alpha)$ is not necessarily positive, and thus cannot be simply regarded as a probability. For the Fock states, $\rho = |n\rangle \langle n|$, the P -function is highly singular,

$$P_n(\alpha) = e^{|\alpha|^2} \frac{1}{n!} \frac{\partial^{2n}}{\partial \alpha^n \partial \alpha^{*n}} \delta^2(\alpha). \quad (82.32)$$

For a coherent state $|\alpha_0\rangle$, the P -function is completely classical,

$$P_c(\alpha) = \delta^{(2)}(\alpha - \alpha_0). \quad (82.33)$$

Likewise for a thermal state $\rho_T = \exp(-\beta\hbar\omega a^\dagger a) / \text{Tr}[\exp(-\beta\hbar\omega a^\dagger a)]$, the P -function is classical [3],

$$P_T(\alpha) = \frac{1}{\pi \langle n \rangle} \exp\left(-\frac{|\alpha|^2}{\langle n \rangle}\right). \quad (82.34)$$

The P -representation is convenient to evaluate normally ordered quantities, such as

$$\langle a^{\dagger m} a^n \rangle = \int P(\alpha) \alpha^{*m} \alpha^n d^2\alpha. \quad (82.35)$$

We will use the singularity or negativity of the P -function to characterize the strict quantum nature of the field. This is because the experimentally measured observables correspond to the normally ordered moments like $\langle a^{\dagger m} a^n \rangle$.

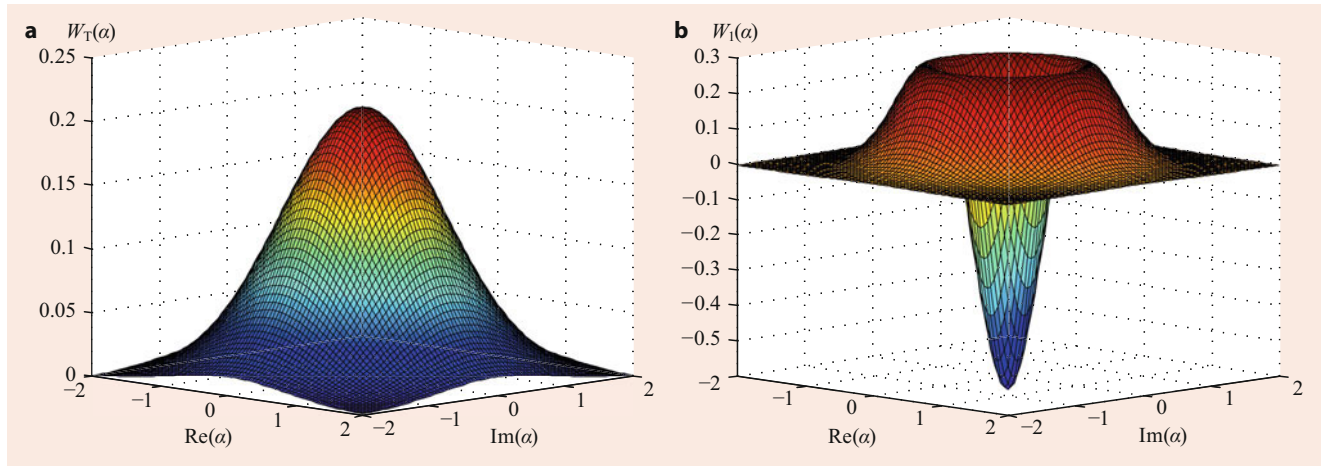


Fig. 82.1 The Wigner function of a thermal state (a) and single-photon state (b)

***Q*-representation.** Different from the *P*-functions, the *Q*-function has the properties of a classical probability distribution,

$$Q(\alpha) = \frac{1}{\pi} \langle \alpha | \rho | \alpha \rangle. \quad (82.36)$$

Q-functions are convenient to evaluate antinormally ordered moments of a and a^\dagger ,

$$\begin{aligned} \langle a^n a^{\dagger m} \rangle &= \text{Tr} \left(\frac{1}{\pi} \int a^n | \alpha \rangle \langle \alpha | a^{\dagger m} \rho d^2 \alpha \right) \\ &= \frac{1}{\pi} \int \alpha^n \alpha^{*m} \langle \alpha | \rho | \alpha \rangle d^2 \alpha \\ &= \int \alpha^n \alpha^{*m} Q(\alpha) d^2 \alpha. \end{aligned} \quad (82.37)$$

By substituting Eq. (82.31) in Eq. (82.36), we obtain the relation between the *P* and *Q*-functions,

$$Q(\alpha) = \frac{1}{\pi} \int P(\beta) \exp(-|\alpha - \beta|^2) d^2 \beta. \quad (82.38)$$

The *Q*-function of a thermal field is

$$Q_T(\alpha) = \frac{1}{\pi(1 + \langle n \rangle)} \exp\left(-\frac{|\alpha|^2}{1 + \langle n \rangle}\right), \quad (82.39)$$

which is Gaussian.

The *P* and *Q*-functions can be written as integrals of their characteristic functions,

$$\begin{aligned} P(\alpha) &= \frac{1}{\pi^2} \int d^2 \beta e^{-\beta \alpha^* + \beta^* \alpha} C_P(\beta), \\ Q(\alpha) &= \frac{1}{\pi^2} \int d^2 \beta e^{-\beta \alpha^* + \beta^* \alpha} C_Q(\beta), \end{aligned} \quad (82.40)$$

where $C_P(\beta) = \text{Tr}(e^{\beta \alpha^\dagger} e^{-\beta^* a} \rho)$ and $C_Q(\beta) = \text{Tr}(e^{-\beta^* a} e^{\beta \alpha^\dagger} \rho)$. Other phase-space representations can be

obtained by using different characteristic functions, such as the Wigner function in the following.

The Wigner representation. We next discuss the Wigner function. This function has great practical utility as it always exists and can be experimentally measured, and, thus, nonclassical aspects are easily accessible via the Wigner function. The Wigner function is defined as

$$W(\alpha) = \frac{1}{\pi^2} \int d^2 \beta \text{Tr}[\rho D(\beta)] e^{-\beta \alpha^* + \beta^* \alpha}, \quad (82.41)$$

where $D(\beta)$ is the displacement operator. The characteristic function of the Wigner function is $C_W = \text{Tr}[\rho D(\beta)]$. For a coherent state $|\gamma\rangle$, the Wigner function is

$$W_c(\alpha) = \frac{2}{\pi} \exp(-2|\alpha - \gamma|^2), \quad (82.42)$$

which is a Gaussian distribution with a width $1/2$. The Wigner function is related to the *P*-function,

$$W(\alpha) = \frac{2}{\pi} \int P(\gamma) \exp(-2|\alpha - \gamma|^2) d^2 \gamma. \quad (82.43)$$

The Wigner function of a thermal state is

$$W_T(\alpha) = \frac{1}{\pi(\langle n \rangle + 1/2)} \exp\left[-\frac{|\alpha|^2}{\langle n \rangle + 1/2}\right], \quad (82.44)$$

which is Gaussian as shown in Fig. 82.1a.

The Wigner function of a Fock state is more complicated,

$$W_n(\alpha) = \frac{2}{\pi} (-1)^n e^{-2|\alpha|^2} L_n(4|\alpha|^2), \quad (82.45)$$

where $L_n(x)$ is the n -th order Laguerre polynomial. Obviously, Wigner functions can be negative. Shown in Fig. 82.1b

is the Wigner function of the single-photon number state

$$W_1(\alpha) = \frac{2}{\pi} e^{-2|\alpha|^2} (4|\alpha|^2 - 1), \quad (82.46)$$

which is clearly maximally negative at $|\alpha| = 0$.

For an arbitrary state, the Wigner function at the zero point is used in many tests of nonclassicality,

$$W(0) = \frac{2}{\pi} \sum_{n=0}^{\infty} \rho_{nn} (-1)^n = \frac{2}{\pi} \langle \exp(i\pi a^\dagger a) \rangle, \quad (82.47)$$

which is related to the average value of the parity operator or $\exp(i\pi a^\dagger a)$. For a single-photon Fock state $W(0) = -2/\pi$. Another important property is that the Wigner function is square-integrable,

$$\text{Tr} \rho^2 = \pi \int d^2\alpha W^2(\alpha) \leq 1. \quad (82.48)$$

The negativity of the Wigner function at the origin has been used to test the nonclassicality. *Haroche* and collaborators [5] measured the negativity of the Wigner function for the Fock state $|1\rangle$ using cavity QED. More recently, this was measured for ionic motion (boson) [6]. Further, the negativity of the Wigner function for a set of states equivalent to non-Gaussian states including Fock states is measured [7].

82.6 Squeezed State

One of the most important nonclassical fields is the squeezed state, which was discovered by *Yuen* [8]. It only gained popularity after *Caves* proposed its great advantage in measurements beyond the standard quantum noise limit (SQL) [9]. The effectiveness of the squeezed states was first demonstrated by *Kimble's* group by a 3-dB sensitivity enhancement [10]. We will discuss this issue later. Here, we first discuss the measurable properties of the squeezed states.

Squeezing operator. We have shown that the coherent state can be generated by applying a displacement operator on the vacuum state. The squeezed state $|\xi\rangle$ can also be generated by applying a squeezing operator $S(\xi)$ on the vacuum state,

$$|\xi\rangle = S(\xi)|0\rangle, \quad (82.49)$$

where

$$S(\xi) = \exp(\xi a^{\dagger 2}/2 - \xi^* a^2/2), \quad (82.50)$$

and $\xi = r e^{i\phi}$ is a complex number.

The expansion of the squeezed state in the Fock-state basis is given by

$$|\xi\rangle = \frac{1}{\sqrt{\cosh r}} \sum_{n=0}^{\infty} e^{in\phi} (\tanh r)^n \frac{\sqrt{(2n)!}}{n! 2^n} |2n\rangle, \quad (82.51)$$

where all the Fock states with odd numbers are missing.

The action of the squeezing operator to the annihilation operator yields

$$a(\xi) = S^\dagger(\xi) a S(\xi) = a \cosh r + a^\dagger e^{i\phi} \sinh r. \quad (82.52)$$

Note that Eq. (82.52) also represents the Bogoliubov transformation. The squeezed state is the vacuum state of the transformed annihilation operator

$$a(-\xi)|\xi\rangle = 0. \quad (82.53)$$

To see the effect of squeezing, let us define a general quadrature X_θ ,

$$X_\theta = \frac{a e^{-i\theta} + a^\dagger e^{i\theta}}{\sqrt{2}}, \quad (82.54)$$

which is conjugate to $X_{\theta+\pi/2}$ and satisfies the commutation relation $[X_\theta, X_{\theta+\pi/2}] = i$. The variance of $X_{\phi/2}$ of a squeezed state $|\xi\rangle$ is

$$(\Delta X_{\phi/2})^2 = \frac{1}{2} e^{2r}, \quad (82.55)$$

while for the conjugate quadrature, $(\Delta X_{\phi/2+\pi/2})^2 = (1/2) e^{-2r}$. Therefore, the squeezed state has a squeezed quadrature $X_{\phi/2+\pi/2}$ and a stretched quadrature $X_{\phi/2}$. To see the nonclassicality of the squeezed state, we introduce the squeezing parameter [8]

$$S_\theta = \langle : (X_\theta)^2 : \rangle - \langle X_\theta \rangle^2, \quad (82.56)$$

where $::$ stands for the normal ordering of the operators between them; S is related to the variance of the quadrature by $S_\theta = (\Delta X_\theta)^2 - 1/2$. The negative value of S is a sufficient condition for nonclassicality. Obviously, for the squeezed state, $S_{\phi/2-\pi/2} = -(1 - e^{-2r})/2 < 0$, which is a signature of the nonclassicality of the squeezed vacuum.

The representation of the squeezed state in the quadrature- X space can be obtained from Eq. (82.53),

$$\Psi_\xi(X) = \Psi^{(0)} \exp\left(-\frac{1}{2} X^2 \frac{\cosh r - e^{i\phi} \sinh r}{\cosh r + e^{i\phi} \sinh r}\right), \quad (82.57)$$

which is a Gaussian wavefunction with chirped width (due to the complex parameter in the exponent).

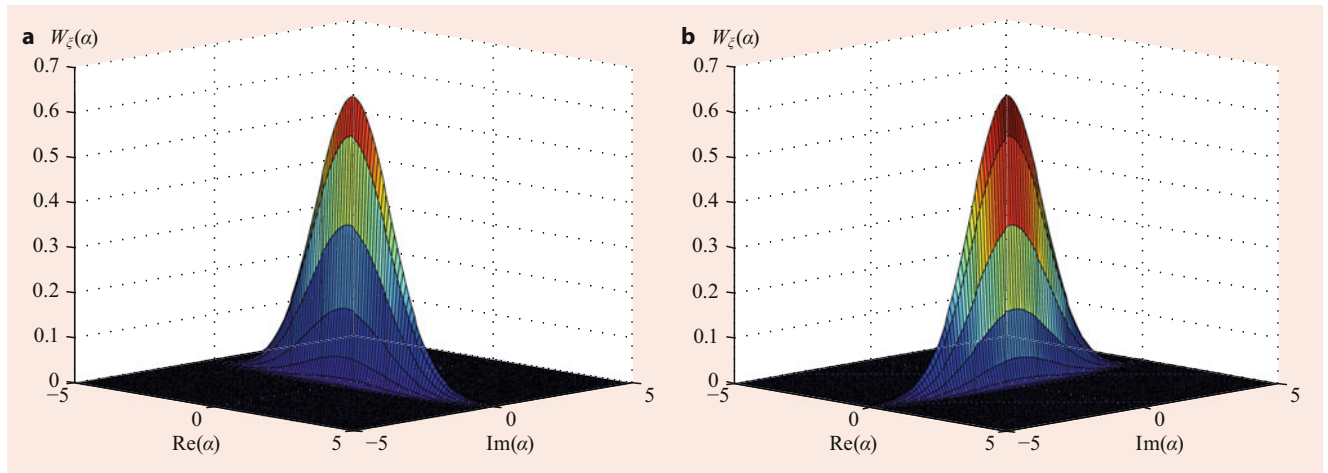


Fig. 82.2 The Wigner function of a squeezed state with $r = 1$, $\phi = 0$ (a), and $\phi = \pi$ (b)

Phase-space representations. While the P -function of the squeezed states does not exist, the Q -function and Wigner function are

$$Q_{\xi}(\alpha) = \frac{1}{\pi \cosh r} \exp\left[\frac{\tanh r}{2}(e^{i\phi}\alpha^{*2} + e^{-i\phi}\alpha^2) - |\alpha|^2\right], \quad (82.58)$$

and

$$W_{\xi}(\alpha) = \frac{2}{\pi} \exp(-2|\alpha \cosh r - \alpha^* e^{i\phi} \sinh r|^2). \quad (82.59)$$

The Wigner functions of a squeezed state with the same squeezing amplitude but different squeezing angles are plotted in Fig. 82.2. The Wigner function for the squeezed states is Gaussian and does not exhibit a nonclassical nature, which is truly reflected by the P -function.

The squeezed coherent state. The squeezed coherent state is defined by first squeezing the vacuum state and then displacing it,

$$|\xi, \beta\rangle = D(\beta)S(\xi)|0\rangle. \quad (82.60)$$

The annihilation operator transforms under these two operations,

$$\begin{aligned} a(\xi, \beta) &= S^{\dagger}(\xi)D^{\dagger}(\beta)aD(\beta)S(\xi) \\ &= a \cosh r + a^{\dagger} e^{i\phi} \sinh r + \beta. \end{aligned} \quad (82.61)$$

The Q -function and Wigner function of $|\xi, \beta\rangle$ are

$$\begin{aligned} Q_{\xi\beta}(\alpha) &= Q_{\xi}(\alpha - \beta), \\ W_{\xi\beta}(\alpha) &= W_{\xi}(\alpha - \beta). \end{aligned} \quad (82.62)$$

The squeezed thermal state. The squeezed thermal state can be obtained by applying the squeezing operator to the thermal state density matrix,

$$\rho = S(\xi)\rho_T S^{\dagger}(\xi). \quad (82.63)$$

The Wigner function of the squeezed thermal state is

$$\begin{aligned} W_{\rho}(\alpha) &= \frac{2}{\pi(2\langle n \rangle + 1)} \\ &\times \exp\left(-\frac{2}{2\langle n \rangle + 1}|\alpha \cosh r - \alpha^* e^{i\phi} \sinh r|^2\right). \end{aligned} \quad (82.64)$$

Nonclassicality. To characterize the nonclassicality of the squeezed states, we need to introduce a physical quantity that can tell us its quantum feature. Mandel observed that the photon number distribution of the coherent state is Poissonian and realized that a state with narrower variance is the feature of a nonclassical field. He introduced the parameter [11],

$$Q_M = \frac{\langle (a^{\dagger}a)^2 \rangle - \langle a^{\dagger}a \rangle^2 - \langle a^{\dagger}a \rangle}{\langle a^{\dagger}a \rangle} \quad (82.65)$$

to quantify the nonclassicality of the field [12–15]. The P -function of a coherent field is a delta function, which is in accord with the classical probability distribution. The Q_M of a classical field is zero. In contrast, there are singularities in the P -function of the number states. The Q_M of a number state is -1 . The negativity of Q_M is a sufficient condition for a nonclassical field.

While the Mandel Q_M factor is super-Poissonian for a squeezed state, $Q_M(\xi) = 1 + 2 \sinh^2 r = 1 + 2\langle a^{\dagger}a \rangle$, the Q_M factor for a squeezed coherent state, e.g., with phase

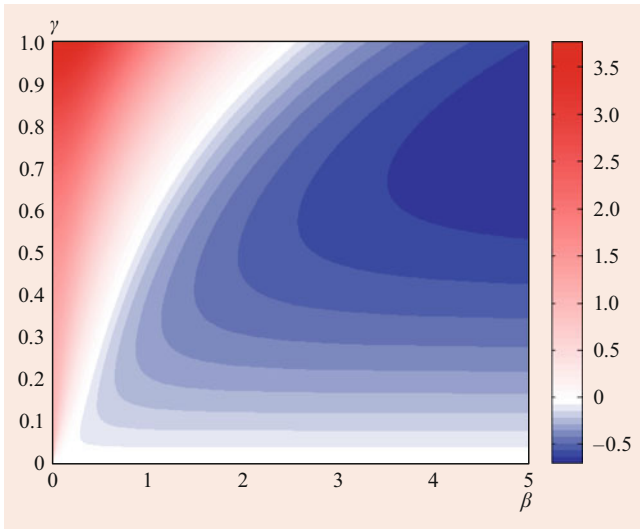


Fig. 82.3 The Mandel Q_M -factor as a function of r and β for the squeezed coherent state $|\xi, \beta\rangle$, $\phi = \pi$

$\phi = \pi$,

$$Q_M(\xi, \beta) = \frac{\sinh^4 r + 2\beta^2 \sinh^2 r + \sinh^2 r \times \cosh^2 r - 2\beta^2 \sinh r \cosh r}{\beta^2 + \sinh^2 r}, \quad (82.66)$$

can be negative, as shown in Fig. 82.3.

82.7 Detection of Quantum Light by Array Detectors

In this section, we discuss only the array detectors that have recently become in vogue in the study of the statistics of quantum fields although photon counting devices have been extensively used in past. The characterization of quantum light requires the detection of photons. However, ideal photon-number-resolving measurement devices are typically not available. For example, avalanche photodiodes in the Geiger mode can only distinguish between the presence (“click” or “on”) and the absence (“no click” or “off”) of photons. To overcome this deficiency, different measurement schemes have been proposed and implemented. One of the most successful approaches is the multiplexed detection of photons [16]. In such a measurement layout, a beam of light is split into N beams with equal and reduced intensities. Subsequently, experimentally accessible on–off detectors, such as avalanche photodiodes, can be used to measure the resulting quantum light fields.

Typically, the photon-number distribution takes the form of a quantum version of a Poisson distribution. However, the theory of multiplexing layouts with N on–off detectors

yields statistics resembling a binomial distribution [17],

$$c_k = \frac{N!}{k!(N-k)!} \langle : \pi^{N-k} (1-\pi)^k : \rangle, \quad (82.67)$$

where $::$ denotes the normal ordering, k is the number of recorded clicks, and $\hat{\pi}$ describes the measurement operator for a click of a single on–off detector including its imperfections. In fact, coherent light, describing a classical radiation field, yields a true binomial distribution. Consequently, non-classical light can be identified via the binomial parameter as follows [18],

$$Q_B = N \frac{(\Delta k)^2}{\bar{k}(N-\bar{k})} - 1 < 0, \quad (82.68)$$

where \bar{k} and $(\Delta k)^2$ are the mean value and the variance of the click-counting distribution c_k , respectively. The binomial parameter generalizes the Mandel Q -parameter [11] to the case of measurements with on–off detectors. Moreover, in the limit of an infinite number of detectors, the binomial click statistics converges to the actual Poisson distribution of the photons.

As an example, let us consider the click-counting statistics of an n -photon state measured with N on–off detectors with a quantum efficiency η . This scenario yields $Q_B = (N-1)([1-2\eta/N]^n - [1-\eta/N]^{2n})(1-[1-\eta/N]^n)^{-1}[1-\eta/N]^{-n}$, which is negative for all efficiencies $\eta > 0$ ($N \geq 2$ and $n \geq 1$). This means that an n -photon state represents a sub-binomial, i.e., nonclassical, state of light [18]. For a large number of detectors ($N \gg 1$), we approach the well-known Mandel parameter for photons, $Q_B \approx -\eta(1-1/N)$, as was mentioned previously. This example demonstrates the direct application of the method for verifying quantum properties of quantized radiation fields, as shown in Fig. 82.4a. Furthermore, the click-counting theory can be directly employed to analyze data and characterize experiments [19–22].

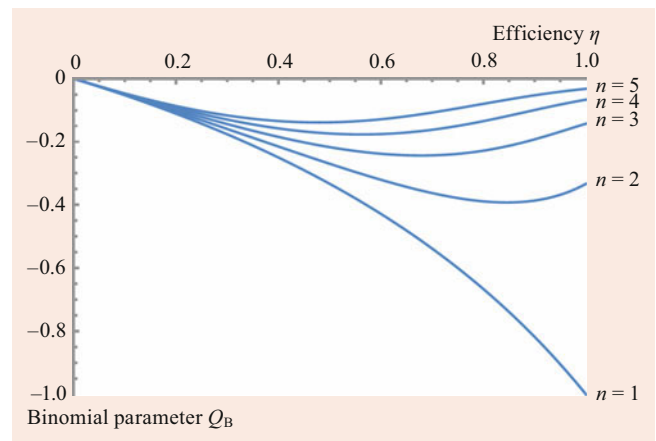


Fig. 82.4 $Q_B < 0$ certifies the nonclassicality of n -photon states as a function of η for only two on–off detectors ($N = 2$)

Besides the applications to certify quantum properties based on the photon-number statistics, the click-counting theory additionally allows for more advanced techniques to characterize and manipulate quantum light. For example, employing multiplexing detectors in interferometers [23] uncovers the click-counting counterpart of squeezing [24]. In addition, click-counting detectors can be used to implement advanced multiphoton heralding, addition, and subtraction protocols to generate nonclassical quantum states [25]. For instance, the heralding is based on the conditional click-counting statistics of a two-mode light field, which has been experimentally compared with the joint click-counting statistics [26].

82.8 Two-Mode Squeezed States

The squeezing operator can be generated in parametric downconversion (PDC) into the same optical modes. More generally, if the generated modes are different, the PDC process results in the two-mode squeezing.

The two-mode squeezing operator. The two-mode squeezed state can be generated from the operator

$$S(\xi) = \exp(\xi a^\dagger b^\dagger - \xi^* ab), \quad (82.69)$$

where $\xi = r e^{i\phi}$ is a complex number. We apply $S(\xi)$ to the two-mode vacuum state $|0, 0\rangle$,

$$\begin{aligned} |\xi\rangle &= S(\xi)|0, 0\rangle = \frac{1}{\cosh r} \exp(e^{i\phi} \tanh r a^\dagger b^\dagger) |0, 0\rangle \\ &= \frac{1}{\cosh r} \sum_{n=0}^{\infty} e^{in\phi} (\tanh r)^n |n, n\rangle. \end{aligned} \quad (82.70)$$

The interesting property of the two-mode squeezed states is that the two modes must contain the same number of photons. The operators a and b transform under two-mode squeezing

$$\begin{aligned} a(\xi) &= S^\dagger(\xi) a S(\xi) = a \cosh r + b^\dagger e^{i\phi} \sinh r, \\ b(\xi) &= S^\dagger(\xi) b S(\xi) = b \cosh r + a^\dagger e^{i\phi} \sinh r, \end{aligned} \quad (82.71)$$

which is a two-mode Bogoliubov transformation. By introducing two linearly combinational modes of a and b ,

$$d = \frac{a+b}{\sqrt{2}}, \quad c = \frac{a-b}{\sqrt{2}}, \quad (82.72)$$

we obtain the two-mode squeezing operator

$$\begin{aligned} \exp(\xi a^\dagger b^\dagger - \xi^* ab) &= \exp\left(\frac{\xi}{2} d^{\dagger 2} - \frac{\xi^*}{2} d^2\right) \\ &\quad \times \exp\left(-\frac{\xi}{2} c^{\dagger 2} + \frac{\xi^*}{2} c^2\right), \end{aligned} \quad (82.73)$$

which is a product of two single-mode squeezing operators.

The Q -function of the two-mode squeezed states is

$$\begin{aligned} Q_\xi(\alpha, \beta) &= \frac{1}{\pi} |\langle \alpha, \beta | \xi \rangle|^2 \\ &= \frac{1}{\pi \cosh^2 r} \\ &\quad \times \exp\left[e^{i\phi} \tanh r \alpha^* \beta^* + \text{c.c.}\right] - |\alpha|^2 - |\beta|^2, \end{aligned} \quad (82.74)$$

which is a Gaussian distribution of $\text{Re}\alpha$, $\text{Re}\beta$, $\text{Im}\alpha$, and $\text{Im}\beta$.

The Wigner function of the two-mode squeezed vacuum is

$$\begin{aligned} W_\xi(\alpha, \beta) &= \frac{4}{\pi^2} \exp(-2|\alpha \cosh r - \beta^* \sinh r e^{i\phi}|^2 \\ &\quad - 2|-\alpha^* \sinh r e^{i\phi} + \beta \cosh r|^2). \end{aligned} \quad (82.75)$$

The quadrature representation is

$$\begin{aligned} \Psi(X_a, X_b) &= \langle X_a, X_b | \xi \rangle \\ &= \frac{1}{\cosh r} \sum_{n=0}^{\infty} e^{in\phi} \tanh^n r \frac{1}{2^n n! \sqrt{\pi}} \\ &\quad \times H_n(X_a) H_n(X_b) e^{-(X_a^2 + X_b^2)/2} \\ &= \frac{1}{\sqrt{(1-\eta^2)\pi \cosh^2 r}} \\ &\quad \exp\left[\frac{2X_a X_b \eta - (X_a^2 + X_b^2)\eta^2}{1-\eta^2} - \frac{1}{2}(X_a^2 + X_b^2)\right], \end{aligned} \quad (82.76)$$

where $\eta = e^{i\phi} \tanh r$. This distribution of the quadratures is plotted in Fig. 82.5.

Cauchy–Schwarz inequality. The nonclassicality of the two-mode squeezed states can be measured by the Cauchy–Schwarz inequalities. For two well-defined functions f and g , the Cauchy–Schwarz inequality is $\langle f^* f \rangle \langle g^* g \rangle \leq |\langle f^* g \rangle|^2$ if the average is made with positive probability distributions. Considering the P -representation of the two-mode density matrix $\rho = \int P(\alpha, \beta) |\alpha, \beta\rangle \langle \alpha, \beta| d^2\alpha d^2\beta$, letting $f = \alpha^* a$ and $g = \beta^* b$, the Cauchy–Schwarz inequality in phase-space distribution is

$$\langle a^{\dagger 2} a^2 \rangle \langle b^{\dagger 2} b^2 \rangle \leq |\langle a^\dagger a b^\dagger b \rangle|^2. \quad (82.77)$$

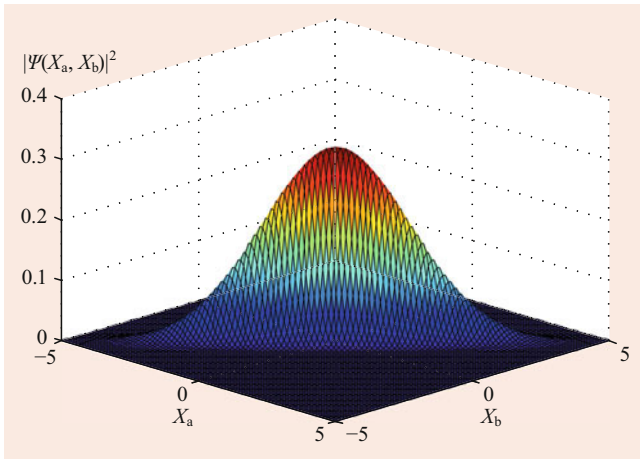


Fig. 82.5 Quadrature distribution of a two-mode squeezed state $|\Psi(X_a, X_b)|^2$ for $r = 1$ and $\phi = 0$

A violation of this inequality can be regarded as a sufficient condition of nonclassicality. We define a parameter [27–29]

$$I = \frac{\sqrt{\langle a^{\dagger 2} a^2 \rangle \langle b^{\dagger 2} b^2 \rangle}}{\langle a^{\dagger} a b^{\dagger} b \rangle} - 1 \quad (82.78)$$

to measure this deviation. The quantity I has been used to measure the nonclassicality of both photons [30–32] and matter waves [33]. More recently, such a violation of nonclassicality using Eq. (82.78) was studied in phonon–photon interactions [34]; obviously, for a coherent state $I = 0$. For the two-mode squeezed states,

$$I = -\frac{\langle a^{\dagger} a \rangle}{\langle (a^{\dagger} a)^2 \rangle} = -\operatorname{sech} 2r < 0. \quad (82.79)$$

Therefore, the two-mode squeezed state is essentially nonclassical.

82.9 Quantum Entanglement

The two-mode states that cannot be written as a direct product of two quantum states, such as the two-mode squeezed states $|\xi\rangle \neq |\Psi_a\rangle |\Psi_b\rangle$, are called entangled states. Historically, entanglement was proposed by *Einstein, Podolsky, and Rosen* to challenge the completeness of quantum theory [35]. The entangled nonseparable states indicate that the measurement of one particle will project the other particle to a certain quantum state, even if the other particle is far away. They suggested the existence of hidden variables to explain the “spooky action at a distance” between entangled particles. *Bell* proposed an inequality to distinguish the predictions between the theories of hidden variables and quantum entanglement [36]. Many experiments have been done, and the results overwhelmingly support the quantum theory [37–41].

Entanglement has been widely used in quantum information [42–44]. We briefly introduce the basic properties of entanglement in the following.

Using the Peres–Horodecki criterion [45, 46] on the negativity of the partial transpose of the density matrix, we can measure the entanglement by the logarithmic negativity,

$$E_N(\rho) = \log_2[1 + 2N(\rho)]. \quad (82.80)$$

Here, $N(\rho)$ is the absolute value of the sum of the negative eigenvalues of the partial transpose density matrix ρ^{PT} , which is obtained by taking the transpose of the operators associated with the mode b . In the following, we calculate the parameter $E_N(\rho)$ for the state in Eq. (82.70). The density matrix is

$$\rho = \sum_{nm} c_n c_m^* |nn\rangle \langle mm|. \quad (82.81)$$

Its partial transpose is

$$\rho^{\text{PT}} = \sum_{nm} c_n c_m^* |nm\rangle \langle mn|. \quad (82.82)$$

This matrix can be block-diagonalized within the basis states $|mn\rangle$ and $|nm\rangle$ for any combination $n \neq m$, and the eigenvalues are $\pm |c_n c_m|$. The negativity is

$$E_N(\rho) = \log_2 \left(1 + \sum_{n \neq m} |c_n c_m| \right) = \log_2 \left(\sum_n |c_n| \right)^2. \quad (82.83)$$

For the two-mode squeezed vacuum state $|c_n| = (\tanh r)^n / \cosh r$, we obtain

$$E_N(\rho) = \log_2(e^{2r}). \quad (82.84)$$

The entanglement is measured by the squeezing parameter.

The reduced density matrix of mode a after tracing over the mode b is

$$\rho^{(a)} = \operatorname{Tr}_b |\xi\rangle \langle \xi| = \frac{1}{\cosh^2 r} \sum_{n=0}^{\infty} \tanh^{2n} r |n\rangle \langle n|, \quad (82.85)$$

which is a thermal state. Therefore, by measuring one mode, we lose the nonclassicality of the other mode. In particular, if we measure b and obtain a Fock state $|n\rangle$, we immediately know that the a -mode is also in the state $|n\rangle$. This is extensively used in experiments of generating single photons, which is called the heralded source of single photons.

Parametric downconversion. We can use parametric downconversion to generate two-mode squeezed states by considering a three-wave mixing process with the Hamiltonian

$$H = \hbar(Gfa^\dagger b^\dagger + \text{H.c.}), \quad (82.86)$$

where the frequency of the mode f is $\omega_f = \omega_a + \omega_b$, G is related to $\chi^{(2)}$, and the geometric factors of the crystal. If $\omega_a = \omega_b$, the Hamiltonian is reduced to one containing the a^2 -term, which describes single-mode squeezing.

The squeezing parameter $r = gt$ is proportional to the interaction time t , and g is an effective coupling constant. The evolution of the two mode operators is described by Eq. (82.71). The evolution of the quadratures of the combinational mode operators c and d in Eq. (82.72) obeys,

$$\begin{aligned} \frac{d(t) \pm d^\dagger(t)}{\sqrt{2}} &= e^{\pm r} \frac{d \pm d^\dagger}{\sqrt{2}}, \\ \frac{c(t) \pm c^\dagger(t)}{\sqrt{2}} &= e^{\mp r} \frac{c \pm c^\dagger}{\sqrt{2}}. \end{aligned} \quad (82.87)$$

After having passed through the crystal, the operators are obtained by scaling the ones input into the crystal. No quantum noise terms are added. This property is useful in phase-sensitive amplifiers, since one quadrature is amplified, while the other quadrature is attenuated. The signal-to-noise ratio of the quadrature,

$$\frac{\langle X_d(t) \rangle}{\sqrt{\langle X_d^2(t) \rangle - \langle X_d(t) \rangle^2}} = \frac{\langle X_d \rangle}{\sqrt{\langle X_d^2 \rangle - \langle X_d \rangle^2}}, \quad (82.88)$$

where $X_d = (d + d^\dagger)/\sqrt{2}$ does not change with time.

Type II parametric downconversion is widely used to generate entangled photons. The Hamiltonian can be written as

$$H = i\hbar g(e^{i\phi_1} a_H^\dagger b_V^\dagger + e^{i\phi_2} a_V^\dagger b_H^\dagger - \text{H.c.}), \quad (82.89)$$

where the photons with orthogonal polarizations travel in different directions. To first order in the coupling, the photons generated are entangled,

$$|\psi\rangle = \frac{|H_1, V_2\rangle + e^{i\chi}|V_1, H_2\rangle}{2}, \quad (82.90)$$

where χ is a phase factor. Such entangled states have been realized in experiments for up to 10 photons [47, 48]. Currently, the entanglement is widely used in the fields of quantum information science and quantum technology.

82.10 Non-Gaussian Nonclassical States

In this section, we introduce the quantum properties of two important non-Gaussian nonclassical states: the cat state and the single-photon added state.

Cat states. In 1935, Schrödinger proposed a thought experiment, which contains a radioactive atom, a vial of cyanide, and a cat. The electron emitted during the decay of the atom can trigger some mechanical device, which finally results in the release of the cyanide and kills the cat. However, a quantum mechanical description of the atom allows a superposition of the decayed and undecayed states. Consequently, the cat is in a superposition of dead and alive states. This later became known as Schrödinger's cat and led to a lively debate over the completeness of quantum mechanics.

When the excitation number is large, a classical state of a harmonic oscillator is naturally described by a coherent state. A superposition of two different coherent states is, therefore, thought of as a superposition of two classical states and traditionally called the cat states,

$$|\alpha_0\rangle_c = N^{-1}(|\alpha_0\rangle + e^{-i\phi} |-\alpha_0\rangle), \quad (82.91)$$

where $N = (2 + 2e^{-2|\alpha_0|^2} \cos \phi)^{1/2}$ is a normalization factor. Typically, a nonlinear medium like the Kerr medium can produce such cat states provided that the nonlinearity is strong. The Kerr medium can also produce a superposition of many coherent states lying on a circle [49]. The strong Kerr interaction can be realized in cavity QED and related setups. Such cat states have been created in trapped ions [6], and cavity quantum electrodynamic systems [50] with a dispersive cavity [51]. Multicomponent cat states as a superposition of several coherent states have also been realized in superconducting qubit systems [52, 53].

The coherent superposition of the two states results in interference of the wavefunction in the quadrature space,

$$\begin{aligned} |\Psi_c(x)|^2 &= |\langle x|\alpha_0\rangle_c|^2 \\ &= N^{-2} \pi^{-1/2} \\ &\quad \times \left[e^{-(x-x_0)^2} + e^{-(x+x_0)^2} \right. \\ &\quad \left. + 2e^{-(x^2+x_0^2)} \cos(\phi - 2y_0x) \right], \end{aligned} \quad (82.92)$$

where we have written $\alpha_0 = (x_0 + iy_0)/\sqrt{2}$. The oscillation of the probability appears in the complementary way of x and y . When $y_0 = 0$, $\Psi_c(x)$ does not oscillate, but the wavefunction with the conjugate variable $\Psi_c(y)$ oscillates.

The nonclassicality of the cat states can be shown by its Wigner function,

$$\begin{aligned} W_c(\alpha) &= \frac{2N^{-2}}{\pi} \\ &\quad \times \left[e^{-2|\alpha-\alpha_0|^2} + e^{-2|\alpha+\alpha_0|^2} \right. \\ &\quad \left. + 2e^{-2|\alpha|^2} \cos(\phi + 4\text{Im}\alpha_0^* \alpha) \right], \end{aligned} \quad (82.93)$$

where the oscillation of the cosine function results in negativity of the Wigner function, as is shown in Fig. 82.6.

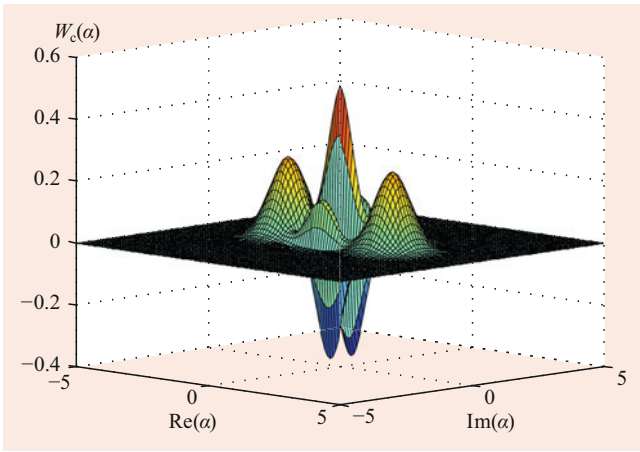


Fig. 82.6 The Wigner function of a cat state with $\alpha_0 = 2$ and $\phi = 0$

Single-photon-added states. If we add a photon to a classical state, we can generate a nonclassical state [54]. A simple example is the vacuum state. By adding a photon, it becomes a single-photon state, which is highly nonclassical. The density matrix of a single-photon-added state is related to the original density matrix by

$$\rho^{(a)} = \frac{a^\dagger \rho a}{\text{Tr}(a^\dagger \rho a)}. \tag{82.94}$$

The Q -function and P -function are related to the original one by

$$\begin{aligned} Q^{(a)}(\alpha) &= \frac{\langle \alpha | a^\dagger \rho a | \alpha \rangle}{\langle a a^\dagger \rangle} = \frac{|\alpha|^2}{\langle a a^\dagger \rangle} Q(\alpha), \\ P^{(a)}(\alpha) &= \frac{e^{|\alpha|^2}}{\langle a a^\dagger \rangle} \frac{\partial^2}{\partial \alpha \partial \alpha^*} P(\alpha) e^{-|\alpha|^2}. \end{aligned} \tag{82.95}$$

It is clear that the Q -function can become zero (for the vacuum state) and the P -function can become negative, even if the original functions are classical. For example, it is easy to calculate the P -function of the single-photon-added thermal state [55],

$$P_T^{(a)}(\alpha) = \frac{1 + \langle n \rangle}{\langle n \rangle^2} \left[|\alpha|^2 - \frac{\langle n \rangle}{1 + \langle n \rangle} \right] P_T(\alpha). \tag{82.96}$$

For $|\alpha|^2 < \langle n \rangle / (1 + \langle n \rangle)$, $P_T^{(a)}(\alpha) < 0$.

The P -function for a single-photon-added coherent state is singular. It is more convenient to use the Wigner function to characterize its nonclassical behavior. The general relation between the Wigner functions after adding the single photon is,

$$W^{(a)}(\alpha) = \frac{1}{\langle a a^\dagger \rangle} \left(\alpha^* - \frac{1}{2} \frac{\partial}{\partial \alpha} \right) \left(\alpha - \frac{1}{2} \frac{\partial}{\partial \alpha^*} \right) W(\alpha). \tag{82.97}$$

For a photon-added coherent state, the result is

$$\begin{aligned} W_c^{(a)}(\alpha) &= \frac{2}{\pi(1 + |\alpha_0|^2)} \\ &\times [4|\alpha|^2 - 2(\alpha^* \alpha_0 + \alpha \alpha_0^*) - 1 + |\alpha_0|^2] \\ &\times e^{-2|\alpha - \alpha_0|^2}, \end{aligned} \tag{82.98}$$

which can be negative.

The quadrature representation of the single-photon-added coherent classical state is

$$\Psi_c^{(a)}(x) = \frac{\langle x | a^\dagger | \alpha \rangle}{\sqrt{1 + |\alpha|^2}} = \frac{1}{\sqrt{2}} \frac{2x - \sqrt{2}\alpha}{\sqrt{1 + |\alpha|^2}} \Psi_c(x), \tag{82.99}$$

which has a zero at $x = \alpha / \sqrt{2}$. Here we have used $a^\dagger = (x - \partial/\partial x) / \sqrt{2}$.

The single-photon-added coherent states [56–58] and thermal states [59] have been realized in experiments, and several properties, as originally predicted [54, 55], have been measured. The negativity of the Wigner function mentioned above has been tested using the photon addition or subtraction on Gaussian states [60].

82.11 Beam Splitter, Interferometer, and Measurement Sensitivity

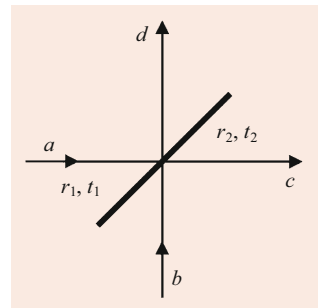
Beam splitter. At a beam splitter as shown in Fig. 82.7, the input modes a and b are transformed to the output modes c and d by

$$\begin{pmatrix} c \\ d \end{pmatrix} = \begin{pmatrix} t_1 & r_2 \\ r_1 & t_2 \end{pmatrix} \begin{pmatrix} a \\ b \end{pmatrix} = U \begin{pmatrix} a \\ b \end{pmatrix}, \tag{82.100}$$

where $r_{1,2}$ and $t_{1,2}$ are the two reflection and transmission coefficients at the two sides of the beam splitter. The lossless beam splitter has the requirement that U is unitary, which leads to,

$$|t_1|^2 + |r_1|^2 = |t_2|^2 + |r_2|^2 = 1, t_1^* r_2 + r_1^* t_2 = 0. \tag{82.101}$$

Fig. 82.7 Beam splitter



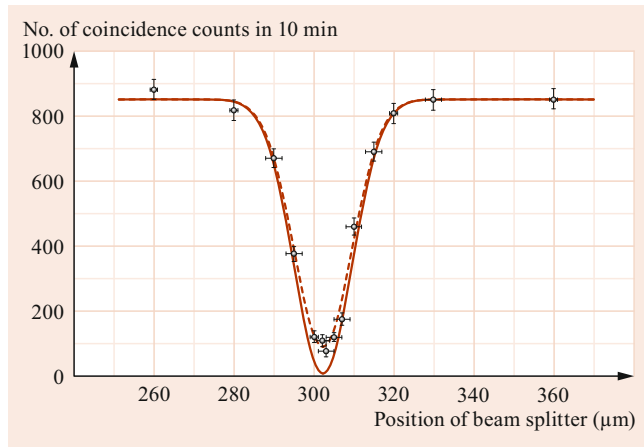


Fig. 82.8 The second-order correlation function as a function of the time delay (controlled by the position of the beam splitter) between the two single photons. Adopted from [61]

For a symmetric beam splitter, $r_1 = r_2$, $t_1 = t_2$, we can rewrite U as

$$U = \begin{pmatrix} \cos \theta & i \sin \theta \\ i \sin \theta & \cos \theta \end{pmatrix}. \quad (82.102)$$

When $\theta = \pi/2$, it is a 50–50 beam splitter.

A remarkable feature of the beam splitter is the Hong–Ou–Mandel effect [61]. Two photons incident at a 50–50 beam splitter simultaneously bunch together to come out from either one of the output modes. This can be easily seen by

$$\begin{aligned} |1, 1\rangle_{\text{out}} &= \frac{1}{2}(c^\dagger + id^\dagger)(d^\dagger + ic^\dagger)|0\rangle \\ &= \frac{i}{\sqrt{2}}(|2, 0\rangle + |0, 2\rangle). \end{aligned} \quad (82.103)$$

Two single photons get entangled to become a two-photon NOON state [62] at a beam splitter, i.e., two detectors cannot click at the same time, if the two single photons arrive at the beam splitter simultaneously. Note that a NOON state is one in which N photons can exist either in one mode or the other mode, i.e., it has the structure $(|N, 0\rangle + |0, N\rangle)/\sqrt{2}$. The second-order correlation function $g^{(2)}(\tau)$ as a function of the time delay between the two single-photon pulses was measured in the original Hong–Ou–Mandel experiment, as shown in Fig. 82.8.

However, if $n > 1$, we cannot obtain an n -photon NOON state, although the output state is still entangled.

Mach–Zehnder interferometer. The Mach–Zehnder interferometer is composed of two successive beam splitters. The two output modes of the first beam splitter are directed to the two input modes of the second beam splitter by two mirrors,

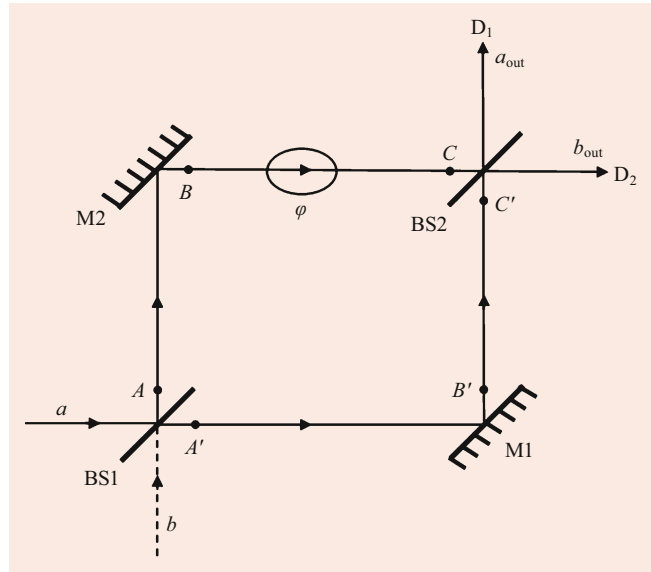


Fig. 82.9 Mach–Zehnder interferometer. Adopted from [1]

as shown in Fig. 82.9. In one of the two split light paths, we have a tunable phase ϕ . The output fields at detectors D_1 and D_2 are,

$$\begin{aligned} a_{\text{out}}(D_1) &= \frac{1}{\sqrt{2}} \left(-\frac{a+ib}{\sqrt{2}} - ie^{-i\phi} \frac{b+ia}{\sqrt{2}} \right) \\ &= (-ie^{-i\phi/2}) \left(a \sin \frac{\phi}{2} + b \cos \frac{\phi}{2} \right), \\ b_{\text{out}}(D_2) &= \frac{1}{\sqrt{2}} \left(-e^{-i\phi} \frac{b+ia}{\sqrt{2}} - i \frac{a+ib}{\sqrt{2}} \right) \\ &= (-ie^{-i\phi/2}) \left(a \cos \frac{\phi}{2} - b \sin \frac{\phi}{2} \right). \end{aligned} \quad (82.104)$$

If one of the input modes, e.g., b , is the vacuum state, the output photon numbers are

$$\begin{aligned} \langle a_{\text{out}}^\dagger a_{\text{out}} \rangle &= \sin^2 \frac{\phi}{2} \langle a^\dagger a \rangle, \\ \langle b_{\text{out}}^\dagger b_{\text{out}} \rangle &= \cos^2 \frac{\phi}{2} \langle a^\dagger a \rangle. \end{aligned} \quad (82.105)$$

Therefore, the phase can be measured by the detectors.

Sensitivity of the interferometer. Now we calculate the sensitivity of the Mach–Zehnder interferometer with respect to the phase ϕ . We take the signal to be the difference between the intensities of the a_{out} and b_{out} modes. We assume that mode a is in a coherent state $|\alpha\rangle$, and the mode b is either in vacuum or squeezed vacuum state, then

$$\begin{aligned} S &= \langle b_{\text{out}}^\dagger b_{\text{out}} \rangle - \langle a_{\text{out}}^\dagger a_{\text{out}} \rangle \\ &= (\langle b^\dagger b \rangle - |\alpha|^2) \cos \phi \\ &\approx \delta\phi (|\alpha|^2 - \langle b^\dagger b \rangle), \end{aligned} \quad (82.106)$$

for small $\delta\phi$ around $\phi = \pi/2$, i.e., $\phi = \pi/2 + \delta\phi$. We next calculate the noise in the measured signal

$$(\Delta S)^2 = \langle S^2 \rangle - \langle S \rangle^2. \quad (82.107)$$

The calculation based on the properties of the squeezed vacuum and coherent states shows that

$$\begin{aligned} (\Delta S)^2 &= (|\alpha|^2 \langle (be^{i\theta} + b^\dagger e^{-i\theta})^2 \rangle + \sinh^2 r) \\ &= (|\alpha|^2 e^{-2r} + \sinh^2 r), \quad \alpha = |\alpha| e^{-i\theta}. \end{aligned} \quad (82.108)$$

We chose the phases such that the quadrature $be^{i\theta} + b^\dagger e^{-i\theta}$ is squeezed. Thus, the signal-to-noise ratio becomes

$$\begin{aligned} \frac{S}{N} &= \frac{\langle b^\dagger b - a^\dagger a \rangle}{\sqrt{\langle (b^\dagger b - a^\dagger a)^2 \rangle - \langle b^\dagger b - a^\dagger a \rangle^2}} \\ &= \frac{(|\alpha|^2 - \sinh^2 r) \delta\phi}{(|\alpha|^2 e^{-2r} + \sinh^2 r)^{1/2}}, \end{aligned} \quad (82.109)$$

which for $r = 0$ is $(S/N) = |\alpha| \delta\phi$ leading to the shot noise limit or the standard quantum noise limit (SQL) of the phase sensitivity $\delta\phi = 1/(|\alpha|)$. Clearly, the above equation, Eq. (82.109), shows that with squeezed light applied to one of the ports, the phase sensitivity improves considerably

$$\delta\phi \approx \frac{1}{|\alpha| e^r} \quad \text{if } |\alpha|^2 \gg \sinh^2 r. \quad (82.110)$$

We say that we have sensitivity better than the SQL.

For 3-dB squeezing of the field $e^{-2r} = 1/2$, the SQL is beaten by a factor $\sqrt{2}$. This was the proposal of *Caves* [9], first experimentally implemented by *Kimble* [10]. The great utility of using squeezed light in advanced LIGO has been extensively considered [63]. *Schnabel's* group reported a direct measurement of 15-dB squeezed vacuum states of light at 1064 nm from a doubly resonant, type I optical parametric amplifier operated below threshold. They managed to push down the noise levels from various contributing sources [64].

Heisenberg limited sensitivity. Thus, the discussion above shows that the SQL can be beaten by illuminating the vacuum port in conventional interferometer by squeezed vacuum. In addition, we can have the interferometer where both input ports are illuminated with two-mode squeezed vacuum. This leads to several advantages, as shown both theoretically [65] and experimentally [66]. Besides beating the SQL it is also possible to achieve Heisenberg limited sensitivity, i.e.,

$$\delta\phi \approx \frac{1}{|\alpha|^2} \quad (82.111)$$

by using the SU(1,1) interferometers [67–69].

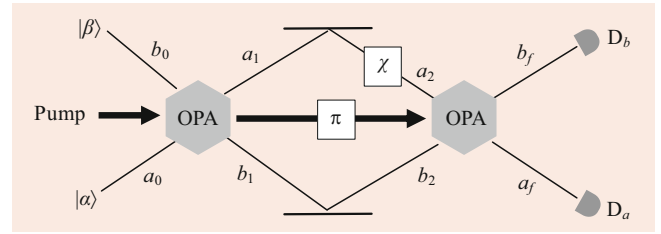


Fig. 82.10 Mach-Zehnder interferometer with two OPAs as the beam splitter

Instead of half-reflection mirrors, we use two optical parametric amplifiers (OPAs) (Fig. 82.10) to mix the fields in the two interfering paths. The same pumping field pumps the two OPAs. The idler fields and signal fields after the first OPA is,

$$\begin{aligned} a_1 &= \mu a_0 + \nu b_0^\dagger, \\ b_1 &= \mu b_0 + \nu a_0^\dagger, \end{aligned} \quad (82.112)$$

with $\mu = \cosh r$ and $\nu = e^{i\phi} \sinh r$. The object in one of the interfering paths brings a phase factor, $a_2 = e^{i\chi} a_1$ and $b_2 = b_1$. The second OPA transforms a_2 and b_2 to

$$\begin{aligned} a_f &= \mu a_2 - \nu b_2^\dagger, \\ b_f &= \mu b_2 - \nu a_2^\dagger. \end{aligned} \quad (82.113)$$

There is a relative phase π between the two OPA transformations. The relation between the input fields and output fields is

$$\begin{aligned} a_f &= e^{i\chi} (A a_0 + B b_0^\dagger), \\ b_f &= A b_0 + B a_0^\dagger, \end{aligned} \quad (82.114)$$

where $A = \mu^2 - |\nu|^2 e^{-i\chi}$ and $B = \mu\nu(1 - e^{-i\chi})$. Since $|A|^2 - |B|^2 = 1$, the input fields and the output fields are related by a Bogoliubov transformation, which is dependent on χ . If the input field is a vacuum state, we obtain,

$$\langle a_f^\dagger a_f \rangle = \langle b_f^\dagger b_f \rangle = |B|^2. \quad (82.115)$$

We define the signal as

$$S \equiv \langle a_f^\dagger a_f + b_f^\dagger b_f \rangle = 8|\mu|^2 |\nu|^2 \sin^2\left(\frac{\chi}{2}\right). \quad (82.116)$$

The variance of the signal is

$$\Delta S = \sqrt{\langle (a_f^\dagger a_f + b_f^\dagger b_f)^2 \rangle - S^2} = 2\sqrt{|B|^2 + |B|^4}. \quad (82.117)$$

At the point $\chi = 0$, we obtain the sensitivity

$$\Delta\chi = \frac{\Delta S}{|\partial S / \partial \chi|} = \frac{1}{2|\mu\nu|}. \quad (82.118)$$

Since the average photon number in each OPA arm is around $|\nu\mu|$, this result yields the Heisenberg limited sensitivity. This interferometer was realized by *Jing et al.* [70]. The SU(1,1) interferometer and its variants are currently gaining momentum in the ultrasensitive measurements of phase [71, 72]. Besides being of great utility, the two-mode squeezed states in metrology may also turn out to be of special importance in bioimaging. Two-photon excitation microscopy (TPEM) is the most widely used technique for optically imaging tissues at depths up to several cell layers below the surface. However, because two-photon absorption is such a weak effect, and scattering in biological tissues is so strong, TPEM requires excitation with high-power lasers that can damage or disrupt biological function. It is known that the use of entangled light leads to two-photon absorption that is proportional to intensity [73–75]. *Goodson's* group reported that two-photon absorption in some molecules can be significantly enhanced when the two incident photons are energy-time entangled with one another [76]. Clearly, the real advantages of entangled photon excitation are just beginning to appear now [77, 78] and should have far-reaching consequences for bioimaging.

We mention that the nonclassical states for atoms like squeezed states and cat states have been introduced [79–81]. The review by *Pezzè et al.* [82] discusses in detail the metrological applications of the nonclassical states of atoms.

We also note that many of the ideas of nonclassicality from the radiation field are being applied to general bosonic degrees of freedom. An important example of mesoscopic systems is the optomechanical interactions involving mechanical mirrors in high-quality cavities. Squeezing of mechanical mirrors and Fock states of mirrors have been realized [83, 84]. The entanglement of mirrors has also been reported [85, 86]. The field of optomechanics is likely to remain very active in the nonclassical properties of mechanical mirrors.

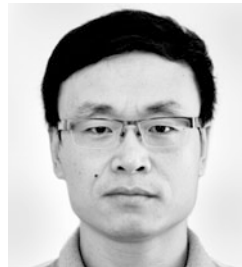
Acknowledgments GSA thanks Barnabas Kim and Jan Sperling for help in preparing this article. He also thanks his collaborators who worked on nonclassical aspects of the radiation fields, two-level systems, and general bosonic systems. DWW thanks Wei Feng for technical help and support. The work of GSA is supported by the Air Force Office of Scientific Research [Award Nos. FA 9550-18-1-0141, FA 9550-20-1-0366] and The Welch Grant award No. [A-1943-20180324]. DWW is supported by National Natural Science Foundation of China [No. 11874322] and the Basic Science Research Funding of Zhejiang University.

References

1. Agarwal, G.S.: Quantum Optics. Cambridge University Press, New York (2012)
2. Arecchi, F.T.: Measurement of the statistical distribution of Gaussian and laser sources. Phys. Rev. Lett. **15**, 912 (1965)
3. Glauber, R.J.: Photon correlations. Phys. Rev. Lett. **10**, 84 (1963)
4. Sudarshan, E.C.G.: Equivalence of semiclassical and quantum mechanical descriptions of statistical light beams. Phys. Rev. Lett. **10**, 277 (1963)
5. Noguees, G., Rauschenbeutel, A., Osnaghi, S., Berter, P., Brune, M., Raimond, J.M., Haroche, S., Lutterbach, L.G., Davidovich, L.: Measurement of a negative value for the Wigner function of radiation. Phys. Rev. A **62**, 054101 (2000)
6. Ding, S., Maslennikov, G., Hablützel, R., Loh, H., Matsukevich, D.: Quantum Parametric Oscillator with Trapped Ions. Phys. Rev. Lett. **119**, 150404 (2017)
7. Stoklasa, B., Motka, L., Rehacek, J., Hradil, Z., Sánchez-Soto, L.L., Agarwal, G.S.: Experimental violation of a Bell-like inequality with optical vortex beams. New J. Phys. **17**, 113046 (2015)
8. Yuen, H.P.: 2-photon coherent states of radiation-field. Phys. Rev. A **13**, 2226 (1976)
9. Caves, C.M.: Quantum-mechanical noise in an interferometer. Phys. Rev. D **23**, 1693 (1981)
10. Xiao, M., Wu, L.-A., Kimble, H.J.: Precision measurement beyond the shot-noise limit. Phys. Rev. Lett. **59**, 278 (1987)
11. Mandel, L.: Sub-poissonian photon statistics in resonance fluorescence. Opt. Lett. **4**, 205 (1979)
12. Short, R., Mandel, L.: Observation of sub-poissonian photon statistics. Phys. Rev. Lett. **51**, 384 (1983)
13. Hong, C.K., Mandel, L.: Experimental realization of a localized one-photon state. Phys. Rev. Lett. **56**, 58 (1986)
14. Lounis, B., Moerner, W.E.: Single photons on demand from a single molecule at room temperature. Nature **407**, 491 (2000)
15. Chen, Y., Muller, J.D., So, P.T.C., Gratton, E.: The photon counting histogram in fluorescence fluctuation spectroscopy. Biophys. J. **77**, 553 (1999)
16. Silberhorn, C.: Detecting quantum light. Contemp. Phys. **48**, 143 (2007)
17. Sperling, J., Vogel, W., Agarwal, G.S.: True photocounting statistics of multiple on-off detectors. Phys. Rev. A **85**, 023820 (2012)
18. Sperling, J., Vogel, W., Agarwal, G.S.: Sub-binomial light. Phys. Rev. Lett. **109**, 093601 (2012)
19. Bartley, T.J., Donati, G., Jin, X.-M., Datta, A., Barbieri, M., Walmsley, I.A.: Direct observation of sub-binomial light. Phys. Rev. Lett. **110**, 173602 (2013)
20. Sperling, J., Vogel, W., Agarwal, G.S.: Correlation measurements with on-off detectors. Phys. Rev. A **88**, 043821 (2013)
21. Sperling, J., Bohmann, M., Vogel, W., Harder, G., Brecht, B., Ansari, V., Silberhorn, C.: Uncovering quantum correlations with time-multiplexed click detection. Phys. Rev. Lett. **115**, 023601 (2015)
22. Sperling, J., Clements, W.R., Eckstein, A., Moore, M., Renema, J.J., Kolthammer, W.S., Nam, S.W., Lita, A., Gerrits, T., Vogel, W., Agarwal, G.S., Walmsley, I.A.: Detector-independent verification of quantum light. Phys. Rev. Lett. **118**, 163602 (2017)
23. Lipfert, T., Sperling, J., Vogel, W.: Homodyne detection with on-off detector systems. Phys. Rev. A **92**, 053835 (2015)
24. Sperling, J., Vogel, W., Agarwal, G.S.: Balanced homodyne detection with on-off detector systems: Observable nonclassicality criteria. Europhys. Lett. **109**, 34001 (2015)
25. Sperling, J., Vogel, W., Agarwal, G.S.: Quantum state engineering by click counting. Phys. Rev. A **89**, 043829 (2014)
26. Sperling, J., Bartley, T.J., Donati, G., Barbieri, M., Jin, X.-M., Datta, A., Vogel, W., Walmsley, I.A.: Quantum correlations from the conditional statistics of incomplete data. Phys. Rev. Lett. **117**, 083601 (2016)
27. Loudon, R.: Review article: Non-classical effects in the statistical properties of light. Rep. Prog. Phys. **43**, 913 (1980)
28. Reid, M.D., Walls, D.F.: Violations of classical inequalities in quantum optics. Phys. Rev. A **34**, 1260 (1986)

29. Agarwal, G.S.: Nonclassical statistics of fields in pair coherent states. *J. Opt. Soc. Am. B* **5**, 1940 (1988)
30. Du, S., Kolchin, P., Belthangady, C., Yin, G.Y., Harris, S.E.: Sub-natural linewidth biphotons with controllable temporal length. *Phys. Rev. Lett.* **100**, 183603 (2008)
31. Srivathsan, B., Gulati, G.K., Chng, B., Maslennikov, G., Matsukevich, D., Kurtsiefer, C.: Narrow band source of transform-limited photon pairs via four-wave mixing in a cold atomic ensemble. *Phys. Rev. Lett.* **111**, 123602 (2013)
32. Marino, A.M., Boyer, V., Lett, P.D.: Violation of the Cauchy–Schwarz inequality in the macroscopic regime. *Phys. Rev. Lett.* **100**, 233601 (2008)
33. Kheruntsyan, K.V., Jaskula, J.C., Deuar, P., Bonneau, M., Partridge, G.B., Ruaudel, J., Lopes, R., Boiron, D., Westbrook, C.I.: Violation of the cauchy-schwarz inequality with matter waves. *Phys. Rev. Lett.* **108**, 260401 (2012)
34. Riedinger, R., Hong, S., Norte, R.A., Slater, J.A., Shang, J., Krause, A.G., Anant, V., Aspelmeyer, M., Gröblacher, S.: Non-classical correlations between single photons and phonons from a mechanical oscillator. *Nature* **530**, 313 (2016)
35. Einstein, A., Podolsky, B., Rosen, N.: Can quantum-mechanical description of physical reality be considered complete? *Phys. Rev.* **47**, 777 (1935)
36. Bell, J.S.: On the Einstein Podolsky Rosen paradox. *Physics* **1**, 195 (1964)
37. Freedman, S.J., Clauser, J.F.: Experimental test of local hidden-variable theories. *Phys. Rev. Lett.* **28**, 938 (1972)
38. Aspect, A., Dalibard, J., Roger, G.: Experimental test of Bell’s inequalities using time-varying analyzers. *Phys. Rev. Lett.* **49**, 1804 (1982)
39. Giustina, M., Versteegh, M.A.M., Wengerowsky, S., Handsteiner, J., Hochrainer, A., Phelan, K., Steinlechner, F., Kofler, J., Larsson, J.A., Abellan, C., Amaya, W., Pruneri, V., Mitchell, M.W., Beyer, J., Gerrits, T., Lita, A.E., Shalm, L.K., Nam, S.W., Scheidl, T., Ursin, R., Wittmann, B., Zeilinger, A.: Significant-loophole-free test of Bell’s theorem with entangled photons. *Phys. Rev. Lett.* **115**, 250401 (2015)
40. Hensen, B., Bernien, H., Dreau, A.E., Reiserer, A., Kalb, N., Blok, M.S., Ruitenberg, J., Vermeulen, R.F.L., Schouten, R.N., Abellan, C., Amaya, W., Pruneri, V., Mitchell, M.W., Markham, M., Twitche, D.J., Elkouss, D., Wehner, S., Taminiau, T.H., Hanson, R.: Loophole-free Bell inequality violation using electron spins separated by 1.3 kilometres. *Nature* **526**, 682 (2015)
41. Shalm, L.K., Meyer-Scott, E., Christensen, B.G., Bierhorst, P., Wayne, M.A., Stevens, M.J., Gerrits, T., Glancy, S., Hamel, D.R., Allman, M.S., Coakley, K.J., Dyer, S.D., Hodge, C., Lita, A.E., Verma, V.B., Lambrocco, C., Tortorici, E., Migdall, A.L., Zhang, Y.B., Kumor, D.R., Farr, W.H., Marsili, F., Shaw, M.D., Stern, J.A., Abellan, C., Amaya, W., Pruneri, V., Jennewein, T., Mitchell, M.W., Kwiat, P.G., Bienfang, J.C., Mirin, R.P., Knill, E., Nam, S.W.: Strong loophole-free test of local realism. *Phys. Rev. Lett.* **115**, 250402 (2015)
42. Bennett, C.H., Brassard, G.: Quantum cryptography: Public key distribution and coin tossing. *Theor. Comput. Sci.* **560**, 7 (2014)
43. Liao, S.K., Cai, W.Q., Liu, W.Y., Zhang, L., Li, Y., Ren, J.G., Yin, J., Shen, Q., Cao, Y., Li, Z.P., Li, F.Z., Chen, X.W., Sun, L.H., Jia, J.J., Wu, J.C., Jiang, X.J., Wang, J.F., Huang, Y.M., Wang, Q., Zhou, Y.L., Deng, L., Xi, T., Ma, L., Hu, T., Zhang, Q., Chen, Y.A., Liu, N.L., Wang, X.B., Zhu, Z.C., Lu, C.Y., Shu, R., Peng, C.Z., Wang, J.Y., Pan, J.W.: Satellite-to-ground quantum key distribution. *Nature* **549**, 43 (2017)
44. Ren, J.G., Xu, P., Yong, H.L., Zhang, L., Liao, S.K., Yin, J., Liu, W.Y., Cai, W.Q., Yang, M., Li, L., Yang, K.X., Han, X., Yao, Y.Q., Li, J., Wu, H.Y., Wan, S., Liu, L., Liu, D.Q., Kuang, Y.W., He, Z.P., Shang, P., Guo, C., Zheng, R.H., Tian, K., Zhu, Z.C., Liu, N.L., Lu, C.Y., Shu, R., Chen, Y.A., Peng, C.Z., Wang, J.Y., Pan, J.W.: Ground-to-satellite quantum teleportation. *Nature* **549**, 70 (2017)
45. Peres, A.: Separability criterion for density matrices. *Phys. Rev. Lett.* **77**, 1413 (1996)
46. Horodecki, P.: Separability criterion and inseparable mixed states with positive partial transposition. *Phys. Lett. A* **232**, 333 (1997)
47. Pan, J.-W., Chen, Z.-B., Lu, C.-Y., Weinfurter, H., Zeilinger, A., Zukowski, M.: Multiphoton entanglement and interferometry. *Rev. Mod. Phys.* **84**, 777 (2012)
48. Wang, X.-L., Chen, L.-K., Li, W., Huang, H.L., Liu, C., Chen, C., Luo, Y.H., Su, Z.E., Wu, D., Li, Z.D., Lu, H., Hu, Y., Jiang, X., Peng, C.Z., Li, L., Liu, N.L., Chen, Y.-A., Lu, C.-Y., Pan, J.-W.: Experimental ten-photon entanglement. *Phys. Rev. Lett.* **117**, 210502 (2016)
49. Tara, K., Agarwal, G.S., Chaturvedi, S.: Production of Schrödinger macroscopic quantum-superposition states in a Kerr medium. *Phys. Rev. A* **47**, 5024 (1993)
50. Brune, M., Hagley, E., Dreyer, J., Maître, X., Maali, A., Wunderlich, C., Raimond, J.M., Haroche, S.: Observing the progressive decoherence of the “meter” in a quantum measurement. *Phys. Rev. Lett.* **77**, 4887 (1996)
51. Brune, M., Haroche, S., Raimond, J.M., Davidovich, L., Zagury, N.: Manipulation of photons in a cavity by dispersive atom-field coupling: Quantum-nondemolition measurements and generation of “Schrödinger cat” states. *Phys. Rev. A* **45**, 5193 (1992)
52. Vlastakis, B., Kirchmair, G., Leghtas, Z., Nigg, S.E., Frunzio, L., Girvin, S.M., Mirrahimi, M., Devoret, M.H., Schoelkopf, R.J.: Deterministically encoding quantum information using 100-photon schrödinger cat states. *Science* **342**, 607 (2013)
53. Song, C., Xu, K., Li, H., Zhang, Y., Zhang, X., Liu, W., Guo, Q., Wang, Z., Ren, W., Hao, J., Feng, H., Fan, H., Zheng, D., Wang, D., Wang, H., Zhu, S.: Observation of multi-component atomic Schrödinger cat states of up to 20 qubits. *Science* **365**, 574 (2019)
54. Agarwal, G.S., Tara, K.: Nonclassical properties of states generated by the excitations on a coherent state. *Phys. Rev. A* **43**, 492 (1991)
55. Agarwal, G.S., Tara, K.: Nonclassical character of states exhibiting no squeezing or sub-Poissonian statistics. *Phys. Rev. A* **46**, 485 (1992)
56. Zavatta, A., Viciani, S., Bellini, M.: Quantum-to-classical transition with single-photon-added coherent states of light. *Science* **306**, 660 (2004)
57. Parigi, V., Zavatta, A., Kim, M., Bellini, M.: Probing quantum commutation rules by addition and subtraction of single photons to/from a light field. *Science* **317**, 1890 (2007)
58. Kumar, R., Barrios, E., Kupchak, C., Lvovsky, A.I.: Experimental characterization of bosonic creation and annihilation operators. *Phys. Rev. Lett.* **110**, 130403 (2013)
59. Zavatta, A., Parigi, V., Kim, M.S., Jeong, H., Bellini, M.: Experimental demonstration of the bosonic commutation relation via superpositions of quantum operations on thermal light fields. *Phys. Rev. Lett.* **103**, 140406 (2009)
60. Walschaers, M., Fabre, C., Parigi, V., Treps, N.: Entanglement and Wigner function negativity of multimode non-Gaussian states. *Phys. Rev. Lett.* **119**, 183601 (2017)
61. Hong, C.K., Ou, Z.Y., Mandel, L.: Measurement of subpicosecond time intervals between two photons by interference. *Phys. Rev. Lett.* **59**, 2044 (1987)
62. Boto, A.N., Kok, P., Abrams, D.S., Braunstein, S.L., Williams, C.P., Dowling, J.P.: Quantum interferometric optical lithography: Exploiting entanglement to beat the diffraction limit. *Phys. Rev. Lett.* **85**, 2733 (2000)

63. LIGO Scientific Collaboration: Enhanced sensitivity of the LIGO gravitational wave detector by using squeezed states of light. *Nat. Photonics* **7**, 613 (2013)
64. Vahlbruch, H., Mehmet, M., Danzmann, K., Schnabel, R.: Detection of 15 dB squeezed states of light and their application for the absolute calibration of photoelectric quantum efficiency. *Phys. Rev. Lett.* **117**, 110801 (2016)
65. Kolkiran, A., Agarwal, G.S.: Quantum interferometry using coherent beam stimulated parametric down-conversion. *Opt. Express* **16**, 6479 (2008)
66. Pooser, R.C., Lawrie, B.: Ultrasensitive measurement of micro-cantilever displacement below the shot-noise limit. *Optica* **2**, 393 (2015)
67. Yurke, B., McCall, S.L., Klauder, J.R.: SU(2) and SU(1,1) interferometers. *Phys. Rev. A* **33**, 4033 (1986)
68. Plick, W.N., Dowling, J.P., Agarwal, G.S.: Coherent-light-boosted, sub-shot noise, quantum interferometry. *New J. Phys.* **12**, 083014 (2010)
69. Chekhova, M.V., Ou, Z.Y.: Nonlinear interferometers in quantum optics. *Adv. Opt. Photon.* **8**, 104 (2016)
70. Jing, J.T., Liu, C.J., Zhou, Z.F., Ou, Z.Y., Zhang, W.P.: Realization of a nonlinear interferometer with parametric amplifiers. *Appl. Phys. Lett.* **99**, 011110 (2011)
71. Anderson, B.E., Gupta, P., Schmittberger, B.L., Horrom, T., Hermann-Avigliano, C., Jones, K.M., Lett, P.D.: Phase sensing beyond the standard quantum limit with a variation on the SU(1,1) interferometer. *Optica* **4**, 752 (2017)
72. Hudelist, F., Kong, J., Liu, C.J., Jing, J.T., Ou, Z.Y., Zhang, W.P.: Quantum metrology with parametric amplifier-based photon correlation interferometers. *Nat. Commun.* **5**, 3049 (2014)
73. Gea-Banacloche, J.: Two-photon absorption of nonclassical light. *Phys. Rev. Lett.* **62**, 1603 (1989)
74. Javanainen, J., Gould, P.L.: Linear intensity dependence of a two-photon transition rate. *Phys. Rev. A* **41**, 5088 (1990)
75. Georgiades, N. P., Polzik, E.S., Edamatsu, K., Kimble, H.J., Parkins, A.S.: Nonclassical excitation for atoms in a squeezed vacuum. *Phys. Rev. Lett.* **75**, 3426 (1995)
76. Varnavski, O., Pinsky, B., Goodson III, T.: Entangled photon excited fluorescence in organic materials: An ultrafast coincidence detector. *J. Phys. Chem. Lett.* **8**, 388 (2017)
77. Dorfman, K.E., Schlawin, F., Mukamel, S.: Nonlinear optical signals and spectroscopy with quantum light. *Rev. Mod. Phys.* **88**, 045008 (2016)
78. Qu, K., Agarwal, G.S.: Ramsey spectroscopy with squeezed light. *Opt. Lett.* **38**, 2563 (2013)
79. Agarwal, G.S., Puri, R.R.: Cooperative behavior of atoms irradiated by broadband squeezed light. *Phys. Rev. A* **41**, 3782 (1990)
80. Agarwal, G.S., Puri, R.R., Singh, R.P.: Atomic Schrödinger cat states. *Phys. Rev. A* **56**, 2249 (1997)
81. Kitagawa, M., Ueda, M.: Squeezed spin states. *Phys. Rev. A* **47**, 5138 (1993)
82. Pezzè, L., Smerzi, A., Oberthaler, M.K., Schmied, R., Treutlein, P.: Quantum metrology with nonclassical states of atomic ensembles. *Rev. Mod. Phys.* **90**, 035005 (2018)
83. Hong, S., Riedinger, R., Marinković, I., Wallucks, A., Hofer, S.G., Norte, R.A., Aspelmeyer, M., Gröblacher, S.: Hanbury Brown and Twiss interferometry of single phonons from an optomechanical resonator. *Science* **358**, 203 (2017)
84. Wollman, E.E., Lei, C.U., Weinstein, A.J., Suh, J., Kronwald, A., Marquardt, F., Clerk, A.A., Schwab, K.C.: Quantum squeezing of motion in a mechanical resonator. *Science* **349**, 952 (2015)
85. Riedinger, R., Wallucks, A., Marinković, I., Löschnauer, C., Aspelmeyer, M., Hong, S., Gröblacher, S.: Remote quantum entanglement between two micromechanical oscillators. *Nature* **556**, 473 (2018)
86. Ockeloen-Korppi, C.F., Damskägg, E., Pirkkalainen, J.-M., Asjad, M., Clerk, A.A., Massel, F., Woolley, M.J., Sillanpää, M.A.: Stabilized entanglement of massive mechanical oscillators. *Nature* **556**, 478 (2018)



Da-Wei Wang Da-Wei Wang obtained his PhD from the Chinese University of Hong Kong in 2012. He worked at Texas A&M University as a postdoc, Research Assistant Professor, and Research Associate Professor from 2012 to 2017. He joined Zhejiang University, China, in 2017 and works on quantum optics and quantum information with atoms and superconducting circuits.



Girish S. Agarwal Girish S. Agarwal received his PhD in 1969 from Rochester. He is Fellow of the Royal Society UK and author of a book and 700 research papers. His work has been recognized by receiving the Max-Born Prize of the Optical Society of America, the Physics Prize of the World Academy, a Humboldt Research Award, and honorary doctorates.



Entangled Atoms and Fields: Cavity QED

83

Qiongyi He , Wei Zhang , Dieter Meschede, and Axel Schenzle

Contents

83.1	Introduction	1208	83.7	Cavity QED for Cold Atomic Gases	1222
83.2	Atoms and Fields	1208	83.7.1	Atomic Ensembles in a Cavity	1222
83.2.1	Two-Level Atoms	1208	83.7.2	Bose–Einstein Condensate in a Cavity	1223
83.2.2	Electromagnetic Fields	1208	83.7.3	Cavity Optomechanics with Cold Atoms	1225
83.2.3	Dipole Coupling of Fields and Atoms	1209	83.8	Applications of Cavity QED	1225
83.3	Weak Coupling in Cavity QED	1210	83.8.1	Quantum Nondemolition (QND) Counting of Photons	1225
83.3.1	Radiating Atoms in Waveguides	1210	83.8.2	Detecting and Trapping Atoms Through Strong Coupling	1226
83.3.2	Trapped Radiating Atoms and Their Mirror Images	1210	83.8.3	Single-Photon Sources	1227
83.3.3	Radiating Atoms in Resonators	1211	83.8.4	Generation of Entanglement	1227
83.3.4	Radiative Shifts and Forces	1212	References		1228
83.3.5	Experiments on Weak Coupling	1213			
83.3.6	Cavity QED and Dielectrics	1213			
83.4	Strong Coupling in Cavity QED	1213			
83.4.1	The Jaynes–Cummings Model	1214			
83.4.2	Fock States, Coherent States, and Thermal States	1215			
83.4.3	Vacuum Splitting	1216			
83.4.4	Strong Coupling in Experiments	1216			
83.5	Micromasers	1217			
83.5.1	Maser Threshold	1218			
83.5.2	Nonclassical Features of the Field	1218			
83.5.3	Trapping States	1219			
83.5.4	Atom Counting Statistics	1219			
83.6	Cavity Cooling	1220			
83.6.1	Master Equation	1220			
83.6.2	Cavity Cooling Experiments	1221			

Q. He (✉)
School of Physics, Peking University
Beijing, China
e-mail: qiongyihe@pku.edu.cn

W. Zhang
Dept. of Physics, Renmin University of China
Beijing, China
e-mail: wzhangl@ruc.edu.cn

D. Meschede
Inst. f. Applied Physics, Rheinische Friedrich-Wilhelm Universität
Bonn
Bonn, Germany
e-mail: meschede@iap.uni-bonn.de

Abstract

Although the concept of a *free atom* is of use as a first approximation, a full quantum description of the interaction of atoms with an omnipresent electromagnetic radiation field is necessary for a proper account of spontaneous emission and radiative level shifts such as the Lamb shift. This chapter is concerned with the changes in the atom–field interaction that take place when the radiation field is modified by the presence of a cavity. An atom in the vicinity of a plane perfect mirror serves as an example of cavity quantum electrodynamics [1–5].

The interaction between atom and intracavity light field can significantly change the spontaneous and stimulated emission of light and induce transitions of the atom between different quantum states. In the case of strong coupling, it also becomes possible for a single atom to control the transmission of light through the cavity, and for a single photon to deterministically change the state of the atom.

Keywords

cavity mode · photon number · Rydberg state · Casimir force · Rydberg atom

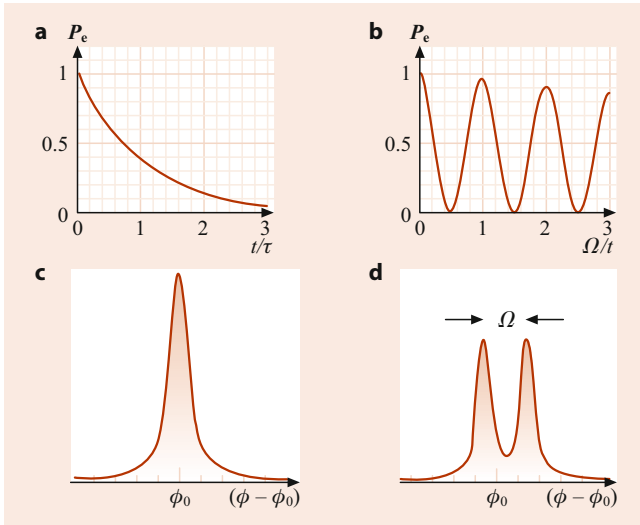


Fig. 83.1 Upper row: excitation probability of an excited atom. (a) Exponential decay in free space or bad cavities in the weak coupling limit. (b) Oscillatory evolution in good cavities or in the strong coupling case. Lower row: the spectral signature of exponential decay is a Lorentzian line shape (c), while the so-called vacuum Rabi splitting (d) is observed in the strong coupling case

83.1 Introduction

In the weak coupling regime, the coupling of an excited atom to a broad continuum of radiation modes leads to exponential decay (Fig. 83.1a), as first described by *Weisskopf* and *Wigner* [6]. Spontaneous emission may be enhanced or suppressed in structures such as waveguides or *bad* cavities. Cavities also introduce van der Waals forces and the subtle Casimir level shifts [7].

In the strong coupling regime, the excited atom is strongly coupled to an isolated resonant cavity mode. In the absence of damping, an oscillatory exchange of energy between the atom and the field replaces exponential decay (Fig. 83.1b) with a coherent evolution in time. Experimental investigations of these effects began [8] with the development of suitable resonators and techniques for producing atoms with long-lived excited states and strong dipole transition moments.

83.2 Atoms and Fields

83.2.1 Two-Level Atoms

Most of the essential features of cavity QED can be elucidated by the two-level model atom discussed in Chaps. 72, 74, and 81 (also [9]). A ground state $|g\rangle$ and an excited state $|e\rangle$ are coupled to the radiation field by a dipole interaction. Using the formal equivalence to a spin-1/2 system, the Pauli

spin operators are

$$\begin{aligned}\sigma_x &= \sigma_+ + \sigma_-, \\ \sigma_y &= -i(\sigma_+ - \sigma_-), \\ \sigma_z &= \sigma_+\sigma_- - \sigma_-\sigma_+ = [\sigma_+, \sigma_-],\end{aligned}\quad (83.1)$$

with $\sigma_+ = |e\rangle\langle g|$ and $\sigma_- = |g\rangle\langle e|$. The quadratures (out-of-phase components) of the atomic polarization are given by σ_x and σ_y , while σ_z is the occupation number difference. The free atom Hamiltonian is

$$\mathcal{H}_{\text{atom}} = \frac{1}{2}\hbar\omega_0\sigma_z, \quad (83.2)$$

where $\hbar\omega_0 = E_e - E_g$ is the transition energy.

83.2.2 Electromagnetic Fields

Classical Fields

Classical electromagnetic fields have longitudinal and transverse components

$$\mathbf{E}(\mathbf{r}, t) = \mathbf{E}^l(\mathbf{r}, t) + \mathbf{E}^t(\mathbf{r}, t). \quad (83.3)$$

In the Coulomb gauge, the longitudinal part is the instantaneous electric field. The transverse part is the radiation field that obeys the wave equation

$$\left(\nabla^2 - \frac{1}{c^2}\frac{\partial^2}{\partial t^2}\right)\mathbf{E}^t(\mathbf{r}, t) = \frac{1}{\epsilon_0 c^2}\frac{\partial}{\partial t}\mathbf{j}(\mathbf{r}, t). \quad (83.4)$$

In empty space, the driving current density $\mathbf{j}(\mathbf{r}, t)$ vanishes, and the field may be expanded in a set of orthogonal modes as

$$\mathbf{E}^t(\mathbf{r}, t) = \sum_{\mu} E_{\mu}(t)e^{-i\omega_{\mu}r}\mathbf{u}_{\mu}(\mathbf{r}) + \text{c.c.}, \quad (83.5)$$

with slowly varying amplitudes $E_{\mu}(t)$. The spatial distributions $\mathbf{u}_{\mu}(\mathbf{r})$ obey the vector Helmholtz equation

$$\left[\nabla^2 + \left(\frac{\omega_{\mu}}{c}\right)^2\right]\mathbf{u}_{\mu}(\mathbf{r}, t) = 0, \quad (83.6)$$

depending on geometric boundary conditions as imposed by conductive or dielectric mirrors, waveguides, and resonators. In free space, plane wave solutions $\mathbf{u}_{\mu}(\mathbf{r}, t) = \mathbf{u}_{\epsilon}e^{i\mathbf{k}\cdot\mathbf{r}}$ have a continuous index $\mu = (\mathbf{k}, \epsilon)$ with wave vector \mathbf{k} and an index ϵ for the two independent polarizations. The orthogonality relation

$$\frac{1}{V}\int_V \mathbf{u}_{\mu} \cdot \mathbf{u}_{\nu}^* d^3\mathbf{r} = \delta_{\mu\nu} \quad (83.7)$$

applies. For a closed cavity, V is the resonator volume. In waveguides and free space, an artificial boundary is introduced and then increased to infinity at the end of a calculation, such that the final results do not depend on V . Many of the properties of cavity QED can be described by a classical theory [10] where the classical fields interact with electric dipoles via the so-called dipole approximation.

Quantum Fields

The quantum analog of the classical transverse field in Eq. (83.4) is obtained through a quantization of its harmonic modes leading to a number state expansion. Field operators obey standard commutation relations $[a_\mu, a_\nu^\dagger] = \delta_{\mu,\nu}$, and for a single mode with index μ , the amplitude E_μ in Eq. (83.5) is replaced by the corresponding operator

$$E_\mu(t) = \mathcal{E}_\mu a_\mu e^{-i\omega t}, \quad E_\mu^\dagger(t) = \mathcal{E}_\mu^* a_\mu^\dagger e^{i\omega t}. \quad (83.8)$$

The normalization factor \mathcal{E}_μ is chosen such that the energy difference between number states $|n\rangle_\mu$ and $|n+1\rangle_\mu$ in the volume V is $\hbar\omega_\mu$, giving

$$\mathcal{E}_\mu \mathcal{E}_\mu^\dagger = \frac{\hbar\omega_\mu}{2\epsilon_0 V}. \quad (83.9)$$

The Hamiltonian of the free field is

$$\mathcal{H}_{\text{Field}} = \sum_\mu \hbar\omega_\mu \left(a_\mu^\dagger a_\mu + \frac{1}{2} \right). \quad (83.10)$$

In the Coulomb gauge, the vector potential $\mathbf{A}(\mathbf{r})$ is related to the electric field $\mathbf{E} = -\partial\mathbf{A}/\partial t$ by

$$\mathbf{A}_\mu(\mathbf{r}, t) = -\frac{\mathcal{E}_\mu}{\omega_\mu} \left(a_\mu e^{-i\omega t} + a_\mu^\dagger e^{i\omega t} \right) \mathbf{u}_\mu(\mathbf{r}). \quad (83.11)$$

The ground state $|0\rangle_\mu$ is called the vacuum state. While the expectation value $\langle n|\mathbf{E}|n\rangle = 0$ for a number state, the variance is not zero, since $\langle n|\mathbf{E}\mathbf{E}^*|n\rangle > 0$, giving rise to non-vanishing *fluctuations* of the free electromagnetic field.

83.2.3 Dipole Coupling of Fields and Atoms

The combined system of atoms and fields can be described by the product quantum states $|a, n\rangle$ of atom states $|a\rangle$ and field states $|n\rangle$. The interaction Hamiltonian \mathcal{H}_I of the atom and the radiation field is given by (The A^2 -term plays an important role in energy shifts and can only be neglected when radiative processes involving energy exchange are considered.)

$$\mathcal{H}_I = -\frac{q}{m} \mathbf{p} \cdot \mathbf{A}(\mathbf{r}) + \frac{q^2}{2m} A^2(\mathbf{r}). \quad (83.12)$$

This interaction causes the atom to exchange energy with the radiation field. In the dipole approximation, the interaction can be reduced to the commonly used form of $\mathbf{p} \cdot \mathbf{E}$ [11], with the coupling strength proportional to the component of the atomic dipole moment $\mathbf{d}_{eg} = q\langle e|\mathbf{r}_{eg}|g\rangle$ along the electric field. The coupling constant

$$g_\mu(\mathbf{r}) = |\mathbf{d}_{eg} \cdot \mathbf{u}_\mu(\mathbf{r}) \mathcal{E}_\mu|/\hbar. \quad (83.13)$$

In the rotating-wave approximation (RWA) (Chaps. 72 and 74),

$$\mathcal{H}_{\text{RWA}} = \sum_\mu \hbar \left(g_\mu \sigma_+ a_\mu + g_\mu^* a_\mu^\dagger \sigma_- \right), \quad (83.14)$$

where we have used the atomic operators of Eq. (83.1).

For the simplest scenario of a two-level atom interacting with a monomode cavity, the Hamiltonian under RWA reduces to the Jaynes–Cummings (JC) model

$$\mathcal{H}_{\text{JC}} = \frac{1}{2} \hbar\omega_0 \sigma_z + \hbar\omega_C a^\dagger a + \hbar(g\sigma_+ a + g^* a^\dagger \sigma_-), \quad (83.15)$$

where ω_C denotes the cavity mode frequency, and the zero-point energy of the field is neglected. Note that the JC model is valid only if the RWA can be employed to describe the coherent dipole interaction between the atom and the field mode. This usually requires that the coupling constant g is relatively much smaller than the energy scales of ω_0 and ω_C . Research beyond the RWA has been conducted in the regime where the coupling constant g is comparable with the atomic and field frequencies.

In a continuous electromagnetic spectrum, the atom interacts with a large number of modes having quantum numbers μ , yielding exponential decay of an excited atomic level at the rate [6]

$$\Gamma_{eg} = \frac{2\pi}{\hbar^2} \sum_{\tilde{\mu}} \sum_{\mathbf{k}} |g_\mu|^2 \delta(\omega_\mu - \omega_0). \quad (83.16)$$

Here, we have separated the discrete ($\tilde{\mu}$) and the continuous part (wave vector \mathbf{k}) of the mode index μ . If g_μ Eq. (83.13) does not vary much across a narrow resonance, then

$$\Gamma_{eg} \simeq 2\pi |g_\mu(\omega_0)|^2 \sum_{\tilde{\mu}} \rho_{\tilde{\mu}}(\omega_0). \quad (83.17)$$

The density of states corresponding to the continuous mode index \mathbf{k} of dimension ν can be evaluated on a ν -dimensional fictitious volume $V^{(\nu)}$ as

$$\rho_{\tilde{\mu}} = \sum_{\mathbf{k}} \delta(\omega_{\tilde{\mu},\mathbf{k}} - \omega) \rightarrow \frac{V^{(\nu)}}{(2\pi)^\nu} \int_0^\infty d^\nu k \delta(\omega_{\tilde{\mu},\mathbf{k}} - \omega), \quad (83.18)$$

provided that $\omega(\mathbf{k})$ is known, and by converting the sum over plane wave vectors \mathbf{k} into an integral. (This is formally accomplished by taking the limit of $\Delta k = 2\pi/l$ for large l , where l is a linear dimension of an artificial resonator, and the resonator volume is $V = l^3$. If the relation between mode spacing Δk and geometric dimension is nonlinear in a more complex geometry, this analysis can be very complicated.)

The Rate of Spontaneous Emission

In free space [$\omega(\mathbf{k})^2 = (c\mathbf{k})^2$], the sum in Eq. (83.17) contributes a factor of 2, due to polarization, to the total density of states in free space, $\rho_{\text{free}}(\omega) = V\omega^2/\pi^2c^3$. When the vector coupling of atom and field Eq. (83.13) is replaced by its average in isotropic free space, that is, by 1/3, the result

$$\Gamma_{eg} = A_{eg} = \frac{e^2 r_{eg}^2 \omega^3}{3\pi\epsilon_0 \hbar c^3} \quad (83.19)$$

is obtained for the decay rate A_{eg} as measured by the natural linewidth Γ_{eg} .

83.3 Weak Coupling in Cavity QED

The regime of weak cavity QED generally applies when an atom is coupled to a continuum of radiation modes. This is always the case with mirrors, waveguides, or bad cavities. The signatures of weak cavity QED are modifications of the rate of spontaneous emission, as well as the existence of van der Waals and Casimir forces. Formally, this regime is well described by perturbation theory.

83.3.1 Radiating Atoms in Waveguides

Within the continuous spectrum of a waveguide, the radiative decay of an excited atomic level remains exponential, and Γ_{eg} may be determined as in the preceding section. We now consider the modifications of spontaneous decay in a parallel plate waveguide. According to Eq. (83.17), the theoretical problem is reduced to a geometric evaluation of mode densities. Between a pair of mirrors it is convenient to distinguish TE_{nk} and TM_{nk} modes, where n is the number of half-waves across the gap of width d . The dispersion relation $\omega(\mathbf{k})$ reflects the discrete standing-wave part ($n\pi/d$) and a running-wave part as in free space,

$$\omega_{n,k}^2 = c^2(|\mathbf{k}|^2 + n\pi/d)^2 \quad \begin{array}{l} n = 0, 1, 2, \dots \quad \text{TM} \\ n = 1, 2, \dots \quad \text{TE} \end{array} \quad (83.20)$$

The average mode density [$d\mathbf{u} = 1$, Eq. (83.13)] is evaluated [Eq. (83.18), $\nu = 2$] with an appropriate quantization volume

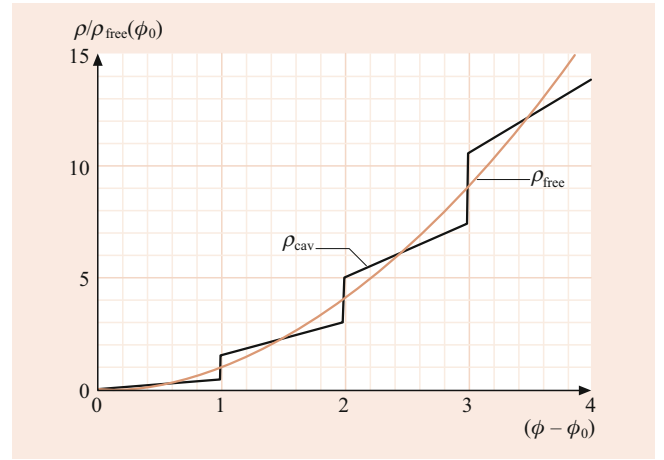


Fig. 83.2 Modification of the average vacuum spectral density ($\rho^{\text{TE}} + \rho^{\text{TM}}$) in a parallel plate cavity (thick line) compared with free space (thin line)

containing the area of the plates, $V = Ad$, giving

$$\begin{aligned} \rho^{\text{TE}}(\omega) &= \frac{\omega_c[\omega]}{2\omega_c^2} \rho_{\text{free}}(\omega_c), \\ \rho^{\text{TM}}(\omega) &= \frac{\omega_c[\omega + 1]}{2\omega_c^2} \rho_{\text{free}}(\omega_c), \end{aligned} \quad (83.21)$$

where $[x]$ is the largest integer in x , and $\omega_c = \pi c/d$ gives the waveguide cutoff frequency. Below ω_c , the TE-mode density clearly vanishes and, with the pictorial notion of turning off the vacuum introduced by Kleppner [12], inhibition of radiative decay is obvious. Figure 83.2 shows the calculated mode density for a parallel plate waveguide. The decay rate can be calculated from Eq. (83.17), with the spatial variation of g_μ included. This configuration was used for the first experiments, which showed the suppression of spontaneous emission in both the microwave and the near optical frequency domain [13, 14] with atomic beams.

83.3.2 Trapped Radiating Atoms and Their Mirror Images

Boundary conditions imposed by conductive surfaces may also be simulated by appropriately positioned image charges. Inspired by classical electrodynamics, this image charge model can be successfully used to determine the modifications of radiative properties in confined spaces. In the simplest case, an atom is interacting with its image produced by a plane mirror. Trapped atoms and ions allow one to control their relative position with respect to a mirror to distances below the wavelength of light. Hence they are ideal objects for studying the spatial dependence of the mirror-induced modifications of their radiative properties. In an experiment with a single trapped ion (Fig. 83.3), its radiation field was

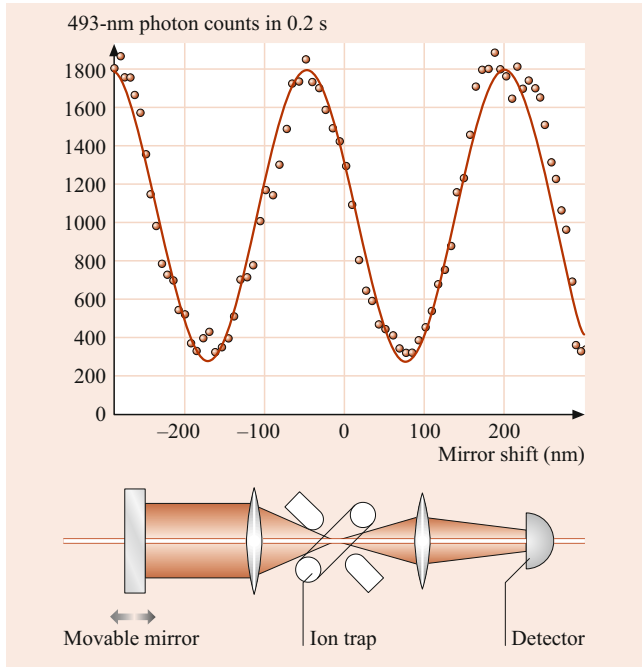


Fig. 83.3 Sinusoidal variation of the $\lambda = 493$ nm spontaneous emission rate of a single trapped Ba ion caused by self-interference from a retroreflecting mirror. The experimental arrangement is sketched at the bottom [15]

superposed onto its mirror image [15, 16], yielding a sinusoidal variation of both the spontaneous decay rate and the mirror-induced level shift with excellent contrast.

83.3.3 Radiating Atoms in Resonators

Resonators

In a resonator, the electromagnetic spectrum is no longer continuous, and the discrete mode structure can also be resolved experimentally. While a resonator is only weakly coupled to external electromagnetic fields, it still interacts with a large thermal reservoir through currents induced in its walls. The total damping rate is due to resistive losses in the walls (κ_{wall}) and also due to transmission at the radiation ports, $1/\tau_{\mu} = \kappa_{\mu} = \kappa_{\text{wall}} + \kappa_{\text{out}}$. An empty resonator stores energy for times

$$\tau_{\mu} = \frac{Q}{\omega_{\mu}}, \quad (83.22)$$

and the power transmission spectrum is a Lorentzian with width $\Delta\omega_{\mu} = \omega_{\mu}/Q_{\mu}$. The index μ , for instance, represents the TE_{lm} and TM_{lm} modes of a *pillbox* microwave cavity, or the TEM_{klm} modes of a Fabry–Perot (FP) interferometer (Fig. 83.4).

When cavity damping remains strong, $\Gamma_{\mu} \gg \Gamma_{eg}$, the atomic radiation field is *immediately* absorbed, and Weisskopf–Wigner perturbation theory remains valid. In this so-called bad cavity limit, resonator damping can be accounted

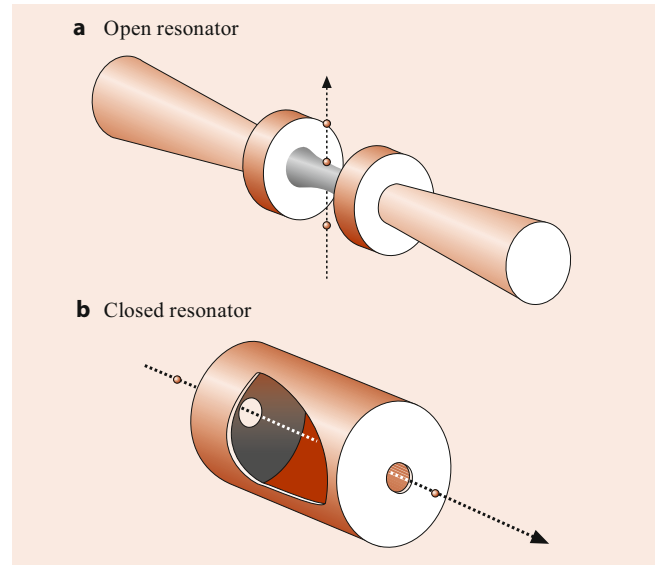


Fig. 83.4 Two frequently used resonator types for cavity QED: (a) open Fabry–Perot (FP) optical cavity; (b) closed *pillbox* microwave cavity

for by an effective mode density of Lorentzian width $\Delta\omega_{\mu}$ for a single isolated mode,

$$\rho_{\mu}(\omega) = \frac{1}{\pi} \frac{\omega_{\mu}/2Q_{\mu}}{(\omega - \omega_{\mu})^2 + (\omega_{\mu}/2Q_{\mu})^2}. \quad (83.23)$$

Bad and Good Cavities

The modification of spontaneous decay is again calculated from Eq. (83.17). For an atomic dipole aligned parallel to the mode polarization, and right at resonance, $\omega_{\mu} = \omega_0$, the enhancement of spontaneous emission is found to be proportional to the Q -value of a selected resonator mode

$$\frac{\Gamma_{eg}^{\text{cav}}}{\Gamma_{eg}^{\text{free}}} = \frac{\rho_{\mu}|\mathbf{u}(\mathbf{r})|}{\rho_{\text{free}}} = \frac{3Q\lambda^3}{4\pi^2V} |\mathbf{u}(\mathbf{r})|^2 = \frac{3Q\lambda^3}{4\pi^2V_{\text{eff}}}, \quad (83.24)$$

where the effective mode volume is $V_{\text{eff}} = V/|\mathbf{u}(\mathbf{r})|^2$. The lowest possible value $V_{\text{eff}} \simeq \lambda^3$ is obtained for ground modes of a closed resonator. For an atom located at the waist of an open FP cavity with length L , it is much larger. Special limiting cases for concentric and confocal cavities are $V_{\text{eff}}^{\text{conc}} = \lambda^2 L(R/D)$ and $V_{\text{eff}}^{\text{conf}} = \lambda L^2/2\pi$, respectively, where (R/D) gives the ratio of mirror radius to cavity diameter.

At resonance, the atomic decay rate Γ_{μ} grows with Q_{μ} , whereas the resonator damping time constant κ_{μ} is reduced. Eventually, the energy of the atomic radiation field is stored for such a long time that reabsorption becomes possible. Perturbative Weisskopf–Wigner theory is no longer valid in this good cavity limit, which is separated from the regime of bad cavities by the more formal condition

$$\Gamma_{eg}^{\text{cav}} > \kappa_{\mu}. \quad (83.25)$$

The strong coupling case is considered explicitly in Sect. 83.4.

Antenna Patterns

Since the reflected radiation field of an atomic radiator is perfectly coherent with the source field, the combined radiation pattern modifies the usual dipole distribution of a radiating atom. The new radiation pattern can be understood in terms of antenna arrays [17]. For a single atomic dipole in front of a reflecting mirror, for example, one finds a quadrupole-type pattern due to the superposition of a second, coherent image antenna. In some of the earliest experimental investigations on radiating molecules in cavities, modifications of the radiation pattern were observed [18].

83.3.4 Radiative Shifts and Forces

When the radiation field of an atom is reflected back onto its source, an energy or radiative shift is caused by the corresponding self-polarization energy. An atom in the vicinity of a plane mirror (Fig. 83.5) again makes a simple model system. Since the energy shift depends on the atom wall separation z , it is equivalent to a dipole force F_{dip} whose details depend on the role of retardation. Here, we distinguish between the two cases where no radiation energy is exchanged between the atom and the field (van der Waals, Casimir forces), and where the atomic radiation causes forces by self-interference.

The Unretarded Limit: van der Waals Forces

When the radiative round-trip time $t_r = 2z/c$ is short compared with the characteristic atomic revolution period $2\pi/\omega_{\text{eg}}$, retardation is not important. In this quasi-static limit, van der Waals energy shifts for decaying atomic dipoles vary as z^{-3} with the atom–wall separation. Such a shift is also present for a nonradiating atom in its ground

state. In perturbation theory, the van der Waals energy shift of an atomic level $|a\rangle$ is

$$\Delta_{\text{vdW}} = -\frac{\langle a|q^2[(\mathbf{d}^2 \cdot \hat{\mathbf{x}}_1)^2 + 2(\mathbf{d}^2 \cdot \hat{\mathbf{z}})^2]|a\rangle}{64\pi\epsilon_0 z^3}. \quad (83.26)$$

Since the van der Waals force is anisotropic for electronic components parallel ($\hat{\mathbf{z}}$) and perpendicular ($\hat{\mathbf{x}}_1$) to the mirror normal, the degeneracy of magnetic sublevels in an atom is lifted near a surface. The total energy shift is ≈ 1 kHz for a ground-state atom at $1 \mu\text{m}$ separation and is very difficult to detect. However, the energy shifts grow as n^4 since the transition dipole moment scales as n^2 . With Rydberg atoms, van der Waals energy shifts have been successfully observed in spectroscopic experiments [19].

The Retarded Limit: Casimir Forces

At large separation, retardation becomes relevant, since the contributions of individual atomic oscillation frequencies in Eq. (83.26) cancel by dephasing, thus reducing the Δ_{vdW} . A residual Casimir–Polder [20] shift may be interpreted as the polarization energy of a slowly fluctuating field with squared amplitude $\langle E^2 \rangle = 3\hbar c/64\epsilon_0 z^4$ originating from the vacuum field noise

$$\Delta_{\text{CP}} = -\frac{1}{4\pi\epsilon_0} \frac{3\hbar c \alpha_{\text{st}}}{8\pi z^4}, \quad (83.27)$$

where α_{st} is the static electric polarizability. The vacuum field noise Δ_{CP} replaces Δ_{vdW} at distances larger than characteristic wavelengths and is even smaller. Only indirect observations have been possible to date, relying on a deflection of polarizable atoms by this force [21, 22]. The Casimir–Polder force can also be regarded as an ultimate, cavity-induced consequence of the mechanical action of light on atoms [23]. It is an example of the conservative and dispersive dipole force, which is even capable of binding a polarizable atom to a cavity [24].

Radiative Self-Interference Forces

Spontaneous emission of atoms in the vicinity of a reflecting wall also provides an example of cavity-induced modification of the dissipative type of light forces, or radiation pressure. If the returning field is reabsorbed, the spontaneous emission rate is reduced, and a recoil force directed away from the mirror is exerted. If the returning radiation field causes enhanced decay, a recoil towards the mirror occurs due to stimulated emission.

If the photon is detected at some angle with respect to the normal vector connecting the atom with the mirror surface, two paths for the photon are possible: it can reach a detector directly or following a reflection off the wall. At small atom–mirror separation, these paths are indistinguishable, the atom is thus left in a superposition of two recoil momentum states.

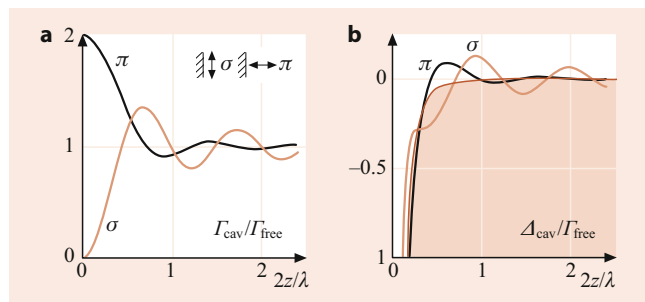


Fig. 83.5 (a) Normalized rate of modified spontaneous emission in the vicinity of a perfectly reflecting wall for σ and π orientation of the radiating dipole. (b) Corresponding energy shift of the resonance frequency. The shaded area indicates contribution of static van der Waals interaction

83.3.5 Experiments on Weak Coupling

Perhaps the most dramatic experiment in a weak coupling cavity QED is the total suppression of spontaneous emission. For the experiments that were carried out with Rydberg atoms and for a low-lying near-infrared atomic transition [13, 14], it is essential to prepare atoms in a single decay channel. In addition, the atoms must be oriented in such a way that they are only coupled to a single decay mode (see the model waveguide in Fig. 83.4). This may be interpreted as an anisotropy of the electromagnetic vacuum or as a specific antenna pattern.

An important problem in detecting the modification of radiative properties – changes in emission rates as well as radiative shifts – arises from their inhomogeneity due to the dependence on atom–wall separation. This difficulty has been overcome by controlling the atom–wall separation at microscopic distances through light forces [19], or by using well localized trapped ions [15, 16]. Furthermore, spectroscopic techniques that are only sensitive to a thin layer of surface atoms [25] have been used to clearly detect van der Waals shifts.

An atom emitting a radiation field in the vicinity of a reflecting wall will experience an additional dipole optical force caused by its radiation field. This force has been observed as a modification of the trapping force holding an ion at a fixed position with respect to the reflector [26].

Conceptually most attractive and experimentally most difficult to detect is the elusive Casimir interaction. Only for atomic ground states is this effect observable, free from other much larger shifts. The influence of the corresponding Casimir force on atomic motion was observed in a variant of a scattering experiment, confirming the existence of this force in neutral atoms [21, 22].

The success of this experiment shows that spectroscopic techniques involving the exchange of photons are not suitable for the Casimir problem. A notable exception could be Raman spectroscopy of the magnetic substructure in the vicinity of a surface. In general, scattering or atomic interferometry experiments are more promising methods. The experiment by Brune et al. [27] may be interpreted in this way.

83.3.6 Cavity QED and Dielectrics

There are two variants of dielectric materials employed to study light–matter interaction in confined space: conventional materials, such as glass or sapphire, and artificial materials called photonic materials or metamaterials.

While dielectric materials are theoretically more difficult to treat than perfect mirrors, since the radiation at least partially enters the medium, they have a similar influence on radiative decay processes. One new aspect is, however, the

coupling of atomic excitations to excitations of the medium, which was observed for the case of a surface-polariton in [28].

Cavities with dimensions comparable to the wavelength promise the most dramatic modification of radiative atomic properties, but micrometer-sized cavities for optical frequencies with highly reflecting walls are difficult to manufacture. So-called whispering gallery modes of spherical microcavities [29] have been intensely studied, but no simple way of coupling atoms to these resonator modes has yet been found.

On the other hand, dielectric materials with a periodic modulation of the index of refraction may exhibit photonic bandgaps in analogy with electronic bandgaps in periodic crystals [30, 31]. Electronic phenomena of solid-state physics can then be transferred to photons. For example, excited states of a crystal dopant or a quantum dot cannot radiate into a photonic bandgap, the radiation field cannot propagate, and the excitation energy remains localized. The bandgap behaves like an empty resonator, and if a resonator structure is integrated into the device, the regime of strong coupling [32, 33] can be achieved with such photonic structures. An overview of suitable systems can be found in [34].

83.4 Strong Coupling in Cavity QED

Strong coupling of atoms and fields is realized in a good cavity when $\Gamma_\mu < \Gamma_{eg}$ Eq. (83.25). The Hilbert space of the combined system is then the product space of a single two-level atom and the countable set of Fock states of the field,

$$\mathcal{H} = \mathcal{H}_{\text{atom}} \otimes \mathcal{H}_{\text{field}}, \quad (83.28)$$

which is spanned by the states

$$|n; a\rangle = |n\rangle|a\rangle. \quad (83.29)$$

The interaction of a single-cavity mode with an isolated atomic resonance is now characterized by the Rabi nutation frequency, which gives the exchange frequency of the energy between atom and field. For an amplitude \mathcal{E} corresponding to n photons,

$$\Omega(n) = g_\mu \sqrt{n+1}. \quad (83.30)$$

This is the simplest possible situation of a strongly coupled atom–field system. The new energy eigenvectors are conveniently expressed in the dressed-atom model [35]

$$\begin{aligned} |+, n\rangle &= \cos \theta |g, n+1\rangle + \sin \theta |e, n\rangle, \\ |-, n\rangle &= -\sin \theta |g, n+1\rangle + \cos \theta |e, n\rangle, \end{aligned} \quad (83.31)$$

with $\tan 2\theta = 2g_\mu \sqrt{n+1}/(\omega_0 - \omega_\mu)$. The separate energy structures of free atom and empty resonator are now replaced

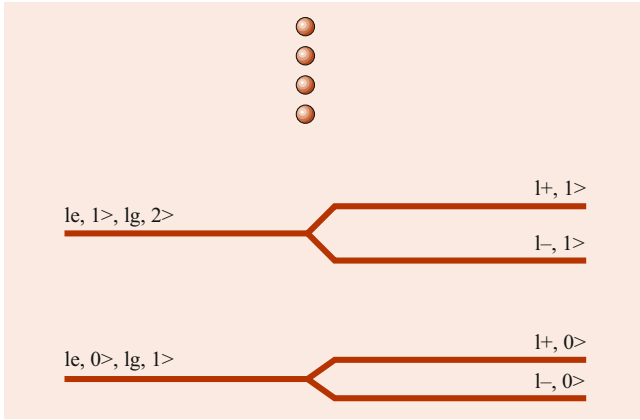


Fig. 83.6 Level diagram for the combined states of noninteracting atoms and fields (*left*) which are degenerate at resonance. Degeneracy is lifted by strong coupling of atoms and fields (*right*) yielding new dressed eigenstates

by the combined system of Fig. 83.6. At resonance, the new eigenstates are separated by $2\hbar\Omega_R$, where $\Omega_R = g_\mu$ is the vacuum Rabi frequency.

83.4.1 The Jaynes-Cummings Model

In a microscopic laser, simple atoms are strongly coupled to a single mode of a resonant or near-resonant radiation field. Collecting atomic and field operators from Eqs. (83.2), (83.10), and (83.14), this situation is described by the Jaynes–Cummings model Hamiltonian Eq. (83.15) [36, 37]

$$\begin{aligned} \mathcal{H}_{\text{JC}} &= \mathcal{H}_{\text{atom}} + \mathcal{H}_{\text{field}} + \mathcal{H}_{\text{RWA}} \\ &= \frac{1}{2}\hbar\omega_0\sigma_z + \hbar\omega_\mu a_\mu^\dagger a_\mu + \hbar(g_\mu\sigma_+ a_\mu + g_\mu^* a_\mu^\dagger \sigma_-). \end{aligned} \quad (83.32)$$

The JC model Eq. (83.32) represents the most basic and, at the same time, the most informative model of strong coupling in quantum optics. It consists of a single two-level atom interacting with a single mode of the quantized cavity field. The time evolution of the system is determined by

$$i\hbar\frac{\partial\psi}{\partial t} = H\psi. \quad (83.33)$$

This model can be solved exactly due to the existence of the additional constant of motion

$$N = a^\dagger a + \sigma_z + 1, \quad (83.34)$$

i.e., conservation of the *number of excitations*. Its eigenvalues are the integers N , which are twofold degenerate except for $N = 0$. The simultaneous eigenstates of H and N are the pairs of dressed states defined in Eq. (83.31), which are

not degenerate with respect to the energy H . The initial state problem corresponding to Eq. (83.33) is solved by elementary methods in terms of the expansion

$$|\Psi(t)\rangle = \sum_{n=0}^{\infty} \sum_{j=1}^2 C_n^j(t) |n, j\rangle, \quad (83.35)$$

where the expansion coefficients are

$$\begin{aligned} C_n^1(t) &= \left(C_n^1(0) \left\{ \cos[\Omega(n)t] - i \frac{\delta}{2\Omega(n)} \sin[\Omega(n)t] \right\} \right. \\ &\quad \left. - i \frac{\sqrt{n}g_\mu}{\Omega(n)} C_{n-1}^2(0) \sin[\Omega(n)t] \right) \\ &\quad \times \exp\left[-i\omega_\mu\left(n - \frac{1}{2}\right)t\right] \end{aligned} \quad (83.36)$$

and

$$\begin{aligned} C_n^2(t) &= \left(C_n^2(0) \left\{ \cos[\Omega(n+1)t] \right. \right. \\ &\quad \left. \left. + i \frac{\delta}{2\Omega(n+1)} \sin[\Omega(n+1)t] \right\} \right. \\ &\quad \left. - i \frac{g_\mu\sqrt{n+1}}{\Omega(n+1)} C_{n+1}^1(0) \sin[\Omega(n+1)t] \right) \\ &\quad \times \exp\left[-i\omega_\mu\left(n + \frac{1}{2}\right)t\right], \end{aligned} \quad (83.37)$$

with $\delta = \omega_\mu - \omega_0$ the detuning between the atom and cavity, and $\Omega(n) = (1/2)(\delta^2 + 4g_\mu^2 n)^{1/2}$ is the generalized Rabi frequency. The coefficients $C_n^j(0)$ are determined by the initial preparation of atom and cavity mode. The result simplifies considerably for $\delta = 0$ to

$$\begin{aligned} |\Psi(t)\rangle &= \sum_{m=0}^{\infty} \left\{ C_m^1(0) e^{-i\omega_\mu(m-1/2)t} \right. \\ &\quad \times [\cos(g_\mu\sqrt{m}t)|m; 1\rangle \\ &\quad \left. - i \sin(g_\mu\sqrt{m}t)|m-1; 2\rangle] \right. \\ &\quad \left. + C_m^2(0) e^{-i\omega_\mu(m+1/2)t} \right. \\ &\quad \times [\cos(g_\mu\sqrt{m+1}t)|m; 2\rangle \\ &\quad \left. - i \sin(g_\mu\sqrt{m+1}t)|m+1; 1\rangle] \right\}. \end{aligned} \quad (83.38)$$

The coefficients $C_n^j(0)$ represent any initial state of the system, from uncorrelated product states to entangled states of atom and field. There exist numerous generalizations of this model that include more atomic levels and several coherent fields.

83.4.2 Fock States, Coherent States, and Thermal States

We now illustrate the properties of the Jaynes–Cummings model by specifying the initial state. Assume that the atom and field are brought into contact at time $t = 0$ and that all correlations that might exist due to previous interactions are suppressed.

Rabi Oscillations

If the atom is initially in the excited state, and the field contains precisely m quanta, then

$$C_n^j(t=0) = \delta_{n,m} \delta_{j,2}. \quad (83.39)$$

The solution of Eq. (83.33) assumes the form

$$\begin{aligned} |\Psi(t)\rangle &= e^{-i\omega_\mu(m+1/2)t} \\ &\times \left[\cos(g_\mu \sqrt{m+1}t) |m; 2\rangle \right. \\ &\quad \left. - i \sin(g_\mu \sqrt{m+1}t) |m+1; 1\rangle \right]. \end{aligned} \quad (83.40)$$

The occupation probabilities of the atomic states evolve in time according to

$$\begin{aligned} n_2(t) &= \langle \Psi(t) | 2 \rangle \langle 2 | \Psi(t) \rangle \\ &= \cos^2(g_\mu \sqrt{m+1}t), \end{aligned} \quad (83.41)$$

$$\begin{aligned} n_1(t) &= \langle \Psi(t) | 1 \rangle \langle 1 | \Psi(t) \rangle \\ &= \sin^2(g_\mu \sqrt{m+1}t). \end{aligned} \quad (83.42)$$

The photon number and its variance are

$$\begin{aligned} \langle n(t) \rangle &= \langle \Psi(t) | a^\dagger a | \Psi(t) \rangle \\ &= m + \sin^2(g_\mu \sqrt{m+1}t), \end{aligned} \quad (83.43)$$

$$\begin{aligned} \langle \Delta^2 n \rangle &= \langle \Psi(t) | (a^\dagger a - \langle a^\dagger a \rangle)^2 | \Psi(t) \rangle \\ &= \frac{\sin^2(2g_\mu \sqrt{m+1}t)}{4}. \end{aligned} \quad (83.44)$$

In the limit of large m , $g_\mu \sqrt{m+1}$ is proportional to the field amplitude, and the classical Rabi oscillations in a resonant field are recovered. The nonclassical features of the states are characterized by Mandel's parameter

$$Q_M = \frac{\langle \Delta^2 n \rangle - \langle n \rangle}{\langle n \rangle} \geq -1. \quad (83.45)$$

For the present example,

$$Q_M = -1 + \frac{1}{4} \frac{\sin^2(2g_\mu \sqrt{m+1}t)}{m + \sin^2(g_\mu \sqrt{m+1}t)}; \quad (83.46)$$

$Q_M \geq 0$ indicates the classical regime, while $Q \leq 0$ can only be reached by a quantum process.

The Coherent State

Consider the case where the field is initially prepared in a coherent state

$$|\alpha\rangle = \exp(\alpha a^\dagger - \alpha^* a) |0\rangle = e^{-|\alpha|^2/2} \sum_{n=0}^{\infty} \frac{\alpha^n}{\sqrt{n!}} |n\rangle, \quad (83.47)$$

while the atom starts from the excited state

$$C_n^j(0) = e^{-|\alpha|^2/2} \frac{|\alpha|^n}{\sqrt{n!}} \delta_{j,2}. \quad (83.48)$$

In this case, the general solution specializes to

$$\begin{aligned} |\Psi(t)\rangle &= \sum_{n=0}^{\infty} \frac{\alpha^n}{\sqrt{n!}} e^{-i\omega(n+1/2)t} e^{-|\alpha|^2/2} \\ &\times \left[\cos(g_\mu \sqrt{n+1}t) |n; 2\rangle \right. \\ &\quad \left. - i \sin(g_\mu \sqrt{n+1}t) |n+1; 1\rangle \right], \end{aligned} \quad (83.49)$$

and the occupation probability of the excited state is

$$n_2(t) = \frac{1}{2} \left[1 + \sum_{n=0}^{\infty} \frac{|\alpha|^{2n}}{n!} e^{-|\alpha|^2} \cos(2g_\mu \sqrt{n+1}t) \right]. \quad (83.50)$$

From here, detailed quantitative results can only be obtained by numerical methods [38]. However, if the coherent state contains a large number of photons $|\alpha|^2 \gg 1$, the essential dynamics can be determined by elementary methods. Initially, the population oscillates with the Rabi frequency $\Omega_1 \approx g_\mu |\alpha|$, which is proportional to the average amplitude of the field, as expected from its classical counterpart. With increasing time, the coherent oscillations tend to cancel due to the destructive interference of the different Rabi frequencies in the sum

$$n_2(t) = \frac{1}{2} \left[1 + \cos(2g_\mu |\alpha| t) e^{-(g_\mu t)^2/2} \right]. \quad (83.51)$$

However, strictly aperiodic relaxation of $n_2(t)$ is impossible since the exact expressions, Eqs. (83.35) and (83.36), represent a quasi-periodic function which, given enough time, approaches its initial value with arbitrary accuracy.

For short times, the oscillating terms in the sum cancel each other due to the slow evolution of their frequency with n . However, consecutive terms interfere constructively for larger times t_r , such that the phases satisfy

$$\phi_{n+1}(t_r) - \phi_n(t_r) = 2\pi. \quad (83.52)$$

For $|\alpha|^2 \gg 1$, the increment of the arguments is

$$\phi_{n+1} - \phi_n = \frac{g_\mu t_r}{|\alpha|}, \quad (83.53)$$

and, therefore, the first revival of the Rabi oscillations occurs approximately at $t_r = \pi |\alpha| / g_\mu$. A clear distinction of Rabi

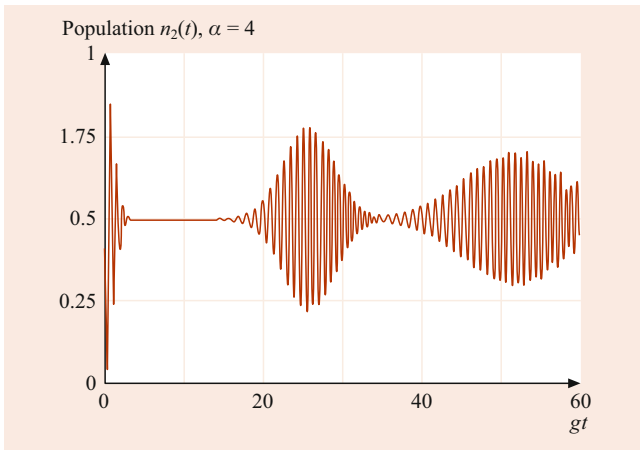


Fig. 83.7 Rabi oscillations, dephasing, and quantum revival

oscillation, collapses, and revivals requires a clear separation of the three timescales

$$t_1 \ll t_2 \ll t_3, \quad (83.54)$$

where $t_1 \approx (g_\mu |\alpha|)^{-1}$ for Rabi oscillation, $t_2 \approx g_\mu^{-1}$ for collapse, and $t_3 \approx |\alpha|/g_\mu$ for revival.

The discovery of the collapse and revival of Rabi oscillations is one of the key demonstrations of photons [38–40]. The typical features of the transient evolution starting from a coherent state are shown in Fig. 83.7. With time increasing even further, revivals of higher order occur, which spread in time and finally can no longer be separated order by order. It is also proposed that by carefully manipulating the initial states and atom–light coupling during evolution, arbitrary Fock states can be created with prechosen evolution time [41].

The Thermal State

Consider a microwave resonator brought into thermal contact with a reservoir, inducing loss on a timescale κ^{-1} and thermal excitation. The dissipative time evolution is described by the master equation

$$\begin{aligned} \dot{\rho} &= (L_0 + L)\rho \\ &\equiv \frac{i[H, \rho]}{\hbar} + \kappa(n_{\text{th}} + 1)\{[a, \rho a^\dagger] + [a\rho, a^\dagger]\} \\ &\quad + \kappa n_{\text{th}}\{[a^\dagger, \rho a] + [a^\dagger \rho, a]\}, \end{aligned} \quad (83.55)$$

where $n_{\text{th}} = [\exp(\beta\hbar\omega) - 1]^{-1}$, at $T = k_B\beta^{-1}$, is the equilibrium population of the cavity mode, L_0 symbolizes the unitary evolution according to the Jaynes–Cummings dynamics, and L is a dissipation term.

The solution of this model can be expressed in terms of an eigenoperator expansion of the equation

$$L\rho = -\lambda\rho. \quad (83.56)$$

The eigenvalues λ that determine the relaxation rates, as well as the eigenoperators, are known in closed form for the case

of vanishing temperature [42]. Since energy is exchanged between the nondecaying atom and the decaying cavity mode, cavity damping is modified in a characteristic way due to the presence of the atom. The technical details can be found in [43].

83.4.3 Vacuum Splitting

In the classical case, the eigenvalues of the interaction-free Hamiltonian are degenerate at resonance. The atom–field interaction splits the eigenvalues and determines the Rabi frequency of oscillation between the two states. One consequence is the existence of sidebands in the resonance fluorescence spectrum [44]. In the quantum case, the field itself is treated as a quantized dynamical variable determined from a self-consistent solution for the complete system of atom plus field. The vacuum Rabi frequency $\Omega_{\text{vac}} = g_\mu$ remains finite and accounts for the spontaneous emission of radiation from an excited atom placed in a vacuum. In the limiting case of a single atom interacting with the quantized field, the photon number n can only change by ± 1 , and the population oscillates with the frequency $\Omega(n)$ given by Eq. (83.30). For an ensemble of N atoms, n can, in principle, change by up to $\pm N$. However, if the field and atoms are only weakly excited, the collective frequency of the ensemble is determined by the linearized Maxwell–Bloch equations. The eigenfrequencies are given by

$$\lambda^\pm = \frac{1}{2} \left[i(\gamma_\perp + \kappa) \pm \sqrt{4g_\mu^2 N - (\gamma_\perp - \kappa)^2} \right], \quad (83.57)$$

where γ_\perp^{-1} is the phase relaxation time of the atom and κ^{-1} the decay time of the resonator. This is the polariton dispersion relation in the neighborhood of the polariton gap. The spectral transmission

$$T(\omega) = T_0 \left| \frac{\kappa[\gamma + i(\omega_0 - \omega)]}{(\omega - \lambda^+)(\omega - \lambda^-)} \right|^2 \quad (83.58)$$

of an optical cavity containing a resonant atomic ensemble of N atoms reveals the internal dynamics of the coupled system and a splitting of the resonance line occurs; T_0 is the peak transmission of the empty cavity. The splitting increases either with the number of photons, approaching $\sqrt{n+1}$ in the presence of a single atom or with the number of atoms, approaching \sqrt{N} in the resonator when the field is weak. The latter case is demonstrated in Fig. 83.8 [45] for an optical resonator with 1–10 atoms interacting with a field that contains, on average, much less than a single photon.

83.4.4 Strong Coupling in Experiments

In order to achieve strong coupling experimentally, it is necessary to use a high- Q resonator in combination with a small

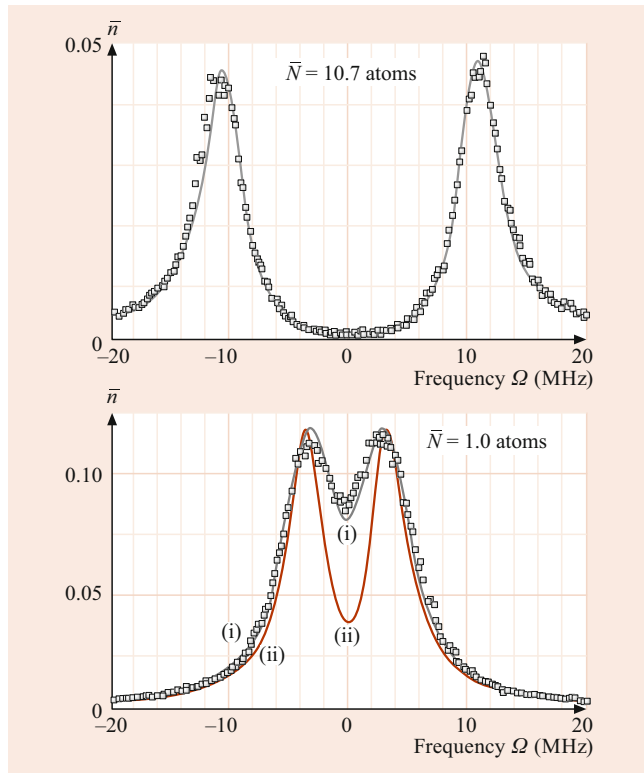


Fig. 83.8 Intracavity photon number (measured from a transmission experiment, [45]) as a function of probe frequency detuning, and for two values of N , the average number of atoms in the mode. *Thin lines* give theoretical fits to the data, including atomic number and position fluctuations. *Curve (ii)* in the lower graph is for a single intracavity atom with optimal coupling g_μ

effective mode volume. This condition was first realized for ground modes of a closed microwave cavity [8] and later also for open-cavity optical resonators (Fig. 83.6) [45]. It is interesting to control the interaction time of the atoms with the cavity field. In earlier experiments, this was typically achieved by selecting the passage time for an atom transiting the cavity. The advancement of atom-trapping methods has also led to the observation of a truly one-atom laser at optical frequencies [46].

More recently, this situation has also been realized for artificial atoms including superconducting systems [47, 48] and quantum dots [32, 33].

Rydberg Atoms and Microwave Cavities

At microwave frequencies, very low-loss superconducting niobium cavities are available with $Q \approx 10^{10}$. Resonator frequencies are typically several tens of GHz and can be matched by atomic dipole transitions between two highly excited Rydberg states. By selective field ionization, the excitation level of Rydberg atoms can be detected, and hence it is possible to measure whether a transition between the levels involved has occurred. The efficiency of this method approaches unity, so that experiments can be performed at

the single-atom level. The interaction or transit time T is usually much shorter than the lifetime τ_{Ry} of the Rydberg states involved. For this reason, circular Rydberg states with quantum numbers $l = m = n - 1$ are particularly suitable.

Rydberg atoms [49] are prepared in an atomic beam, selectively excited to an upper level, and then sent through a microwave cavity where the upper and lower levels are coupled by the electromagnetic field. If the atom is detected in the lower of the coupled levels as it leaves the resonator, the excitation energy has been stored in the resonator field. Thus, the evolution of the resonator field is recorded as a function of the atomic interaction.

A microwave cavity in interaction with a single or a few Rydberg atoms is called a micromaser (formerly a one-atom maser) [8]. The experimental conditions may be summarized as

$$g_\mu > \frac{1}{T} > \frac{1}{\tau_{\text{Ry}}} > \kappa_\mu. \quad (83.59)$$

Strong Coupling in Open Optical Cavities

At optical wavelengths, a cavity with small V_{eff} in Eq. (83.24) is clearly more difficult to construct than at centimeter wavelengths. However, dielectric coatings that allow very low damping rates ω_μ/Q_μ for optical cavities are now available. Very high finesse $\mathcal{F} \simeq 10^7$ (which is a more convenient measure for the damping rate of an optical FP interferometer) has been achieved. By reducing the volume of such a high- Q cavity mode, strong coupling of atoms and fields at optical frequencies has been demonstrated [45].

In open structures, the atoms can still decay into the continuum states with a rate γ . Therefore, the condition for strong coupling in such systems is usually given as

$$\frac{g_\mu^2}{\kappa_\mu \gamma} > 1. \quad (83.60)$$

83.5 Micromasers

Sustained oscillations of a cavity mode in a microwave resonator can be achieved by a weak beam of Rydberg atoms excited to the upper level of a resonant transition. For a cavity with a $Q \approx 10^{10}$, much less than a single atom at a time, on average, suffices to balance the cavity losses. Operation of a single atom maser has been demonstrated [8]. The atoms enter the cavity at random times, according to the Poisson statistics of a thermal beam, and interact with the field only for a limited time. In order to restrict the fluctuations of the atomic transit time, the velocity spread is reduced. This is achieved either by Fizeau chopping techniques or by making use of Doppler velocity selection in the initial laser excitation process. Since most of the time no atom is present, it is natural to separate the dynamics into two parts [50]:

1. For the short time while an atom is present, the state evolves according to the Jaynes–Cummings dynamics, where H is defined in Eq. (83.32),

$$\dot{\rho}(t) = \frac{i[H, \rho]}{\hbar}, \quad (83.61)$$

and damping can safely be neglected. The formal solution is abbreviated by $\rho(t) = F(t - t_0)\rho(t_0)$.

2. During the time interval between successive atoms, the cavity field relaxes freely toward the thermal equilibrium according to Eq. (83.55) with $L_0 = 0$

$$\dot{\rho}(t) = L\rho, \quad (83.62)$$

with the formal solution $\rho(t) = \exp[L(t - t_0)]\rho(t_0)$.

The time development of the micromaser, therefore, consists of an alternating sequence of unitary $F(t)$ and dissipative $e^{(Lt)}$ evolutions. Atoms enter the cavity one by one at random times t_i . Until the next atom enters at time t_{i+1} , the evolution t_i is given by

$$\rho(t_{i+1}) = \exp(Lt_p)F(\tau)\rho(t_i), \quad (83.63)$$

where $t_p = t_{i+1} - t_i - \tau$, and τ is the transit time. If $\tau \ll t_{i+1} - t_i$ on average, then $t_p \approx t_{i+1} - t_i$. After averaging Eq. (83.63) over the Poisson distribution $P(t) = R \exp(-Rt_p)$ for t_p , where R is the injection rate, the mean propagator from atom to atom is

$$\langle \rho(t_{i+1}) \rangle = \frac{R}{R - L} F(\tau) \langle \rho(t_i) \rangle. \quad (83.64)$$

After excitation, the reduced density matrix of the field alone becomes diagonal after several relaxation times κ^{-1}

$$\langle n | \text{Tr}_{\text{atom}}(\rho) | m \rangle = P_n \delta_{n,m}. \quad (83.65)$$

Due to the continuous injection of atoms, the field never becomes time independent but may relax toward a stroboscopic state defined by

$$\langle \rho(t_{i+1}) \rangle = \langle \rho(t_i) \rangle. \quad (83.66)$$

The state of the cavity field can be determined in closed form by iteration

$$P_n = N \prod_{k=1}^n \frac{n_{\text{th}}\kappa + A_k}{(n_{\text{th}} + 1)\kappa}, \quad (83.67)$$

where N guarantees normalization of the trace, and $A_k = (R/n) \sin^2(g_\mu \tau \sqrt{n})$, and exact resonance between cavity mode and atom is assumed. Since all off-diagonal elements vanish in steady state, Eq. (83.67) provides a complete description for the photon statistics of the field.

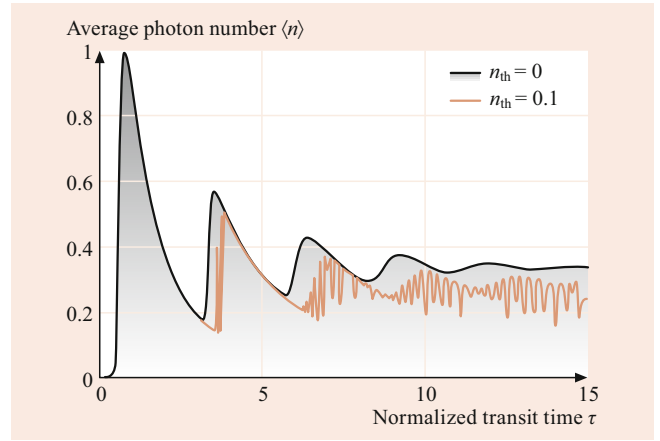


Fig. 83.9 Average photon number as a function of the normalized transit time defined by Eq. (83.69)

83.5.1 Maser Threshold

The steady-state distribution determines the mean photon number of the resonator as a function of the operating conditions

$$\langle n \rangle = \sum_{n=0}^{\infty} n P_n. \quad (83.68)$$

A suitable dimensionless control parameter is

$$\Theta = \frac{1}{2} g_\mu \tau \sqrt{\frac{R}{\kappa}}. \quad (83.69)$$

For $\Theta \ll 1$, the energy input is insufficient to counterbalance the loss of the cavity, effectively resulting in a negligible photon number. With increasing pump rate R , a threshold is reached at $\Theta \simeq 1$, where $\langle n \rangle$ increases rapidly with R . In contrast to the behavior of the usual laser, the single-atom maser displays multiple thresholds with a sequence of minima and maxima of $\langle n \rangle$ as a function of Θ [51]. This can be related to the rotation of the atomic Bloch vector. When the atom undergoes a rotation of about π during the transit time τ , a maximum of energy is transferred to the cavity, and $\langle n \rangle$ is maximized. The converse applies if the average rotation is a multiple of 2π . This behavior is shown in Fig. 83.9. The minima in $\langle n \rangle$ are at $\Theta \simeq 2n\pi$.

83.5.2 Nonclassical Features of the Field

Fluctuations can be of classical or of quantum origin. The variance of the photon number

$$\sigma^2 = (\langle n^2 \rangle - \langle n \rangle^2) \quad (83.70)$$

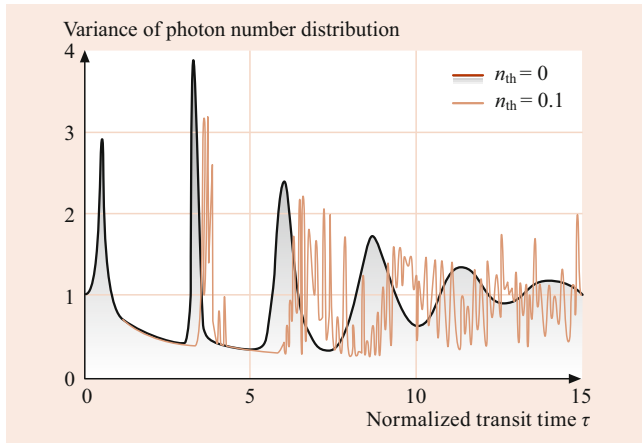


Fig. 83.10 Variance normalized on the average photon number $\sigma^{2(n)}/\langle\sigma\rangle$. Values below unity indicate regions of nonclassical behavior

is a measure of the randomness of the field intensity. Classical Poisson statistics require that $\sigma^2 \geq \langle n \rangle$. A value below unity indicates quantum behavior, which has no classical analog. In Fig. 83.10, the variance is plotted as a function of Θ . Regions of enhanced fluctuations $\sigma^2 > \langle n \rangle$ alternate with regions with sub-Poissonian character $\sigma^2 < \langle n \rangle$ [52]. When $\langle n \rangle$ approaches a local maximum, it is accompanied by large fluctuations, while at points of minimum field strength, the fluctuations are reduced below the classical limit. This feature is repeated with a period of $\Theta \simeq 2\pi$ but finally washes out at large values of Θ .

The large variance of n is caused by a splitting of the photon distribution P_n into two peaks, which gives rise to bistability in the transient response [53]. The sub-Poissonian behavior of the field is reflected in an increased regularity of the atoms leaving the cavity in the ground state.

83.5.3 Trapping States

If cavity losses are neglected, operating conditions exist which lead directly to nonclassical, i.e., Fock states. If the cavity contains precisely n_q photons, an atom that enters the resonator in the excited state leaves it again in the same state provided the condition [54]

$$g_\mu \tau \sqrt{n_q + 1} = 2q\pi \quad (83.71)$$

is satisfied, i.e., the Bloch vector of the atom undergoes q complete rotations. Such a photon Fock state $|n_q\rangle$ is referred to as a trapping state in the literature of maser. Note that the same term is also used in other contexts with very different definitions. If the maser happens to reach a trapping state $|n_q\rangle$, the photon number n_q can no longer increase irrespective of the flux of pump atoms. With the inclusion of cavity damping

at zero temperature, n_q still represents an upper barrier that cannot be overcome, since damping only causes downward transitions. Even in the presence of dissipation, generalized trapping states exist with a photon distribution that vanishes for $n > n_q$ and has a tail towards smaller photon numbers $n \leq n_q$. However, thermal fluctuations at finite temperatures destabilize the trapping states since they can momentarily increase the photon number and allow the distribution to jump over the barrier $n = n_q$. Nevertheless, even for $n_{\text{th}} < 10^{-7}$, remnants of the trapping behavior persist and can be seen in the transient response of the micromaser (Sect. 83.5.4).

83.5.4 Atom Counting Statistics

Direct measurements of the field in a single-atom maser resonator are not possible because detector absorption would drastically degrade its quality. However, the field can be deduced from the statistical signature of the atoms leaving the resonator.

The probability $P(n)$ of finding n atoms in a beam during an observation interval t is given by the classical Poisson distribution

$$P(n) = \frac{(Rt)^n e^{-Rt}}{n!}. \quad (83.72)$$

Information on the field inside is then revealed by the conditional probability $W(n, |g\rangle, m, |e\rangle, T)$ of finding n atoms in the ground state and m atoms in the excited state during a time t . Since there are only two states, it is sufficient to determine the probability

$$W(n, |g\rangle, t) = \sum_{m=0}^{\infty} W(n, |g\rangle, m, |e\rangle, t) \quad (83.73)$$

for being in the ground state [55]. For $n = 0$, the probability of observing no atom in the ground state during the period t is

$$\begin{aligned} W(0, |g\rangle, t) &= \text{Tr}(\rho_{\text{stst}} \exp\{L + R[O_{|g}\rangle + (1 - \eta)O_{|e}\rangle - 1]t\}) , \\ & \quad (83.74) \end{aligned}$$

where $O_{|j}\rangle = \langle j | F(\tau) | j \rangle$ Eq. (83.61) and ρ_{stst} is the steady state of the maser field. This probability is closely related to the waiting time statistic $P_2(0, |g\rangle, t)$ between two successive ground-state atoms, a property that is easily determined in a start–stop experiment. For an atom detector with finite quantum efficiency η for state selective detection, the waiting time probability is

$$\begin{aligned} P_2(0, |g\rangle, t) &= \frac{\text{Tr}(\rho_{\text{stst}}) O_{|g}\rangle \exp[L + R[O_{|g}\rangle + (1 - \eta)O_{|e}\rangle - 1]T] O_{|g}\rangle}{[\text{Tr}(\rho_{\text{stst}}) O_{|g}\rangle]^2} . \\ & \quad (83.75) \end{aligned}$$

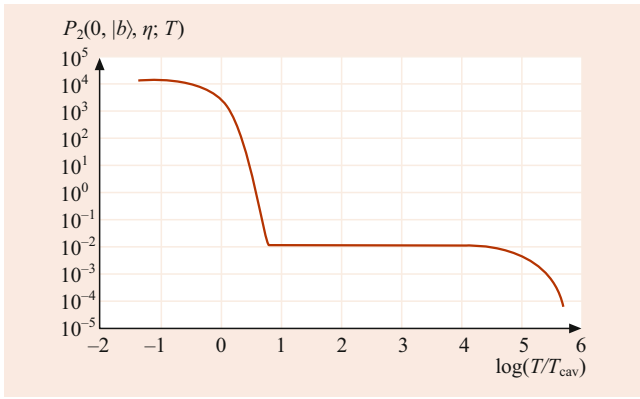


Fig. 83.11 Waiting time probability for atoms in the ground state while the cavity is operated at the vacuum trapping-state condition

How a specific field state is reflected in the atom counting statistics will be illustrated for two situations: the region of sub-Poisson statistics and the region where the trapping condition is satisfied. Increased regularity of the cavity field $Q_M \leq 0$ manifests itself in increased regularity of ground-state atoms in the beam. The statistical behavior exhibits *antibunching*, i.e., $P_2(0, |g), t$ has a maximum at finite t , indicating *repulsion* between successive atoms in comparison with a Poissonian beam. If the transit time τ is chosen in such a way that $g\tau \simeq 2\pi$, the chance of observing an initially excited atom in the ground state is negligible. At some point, however, an unlikely thermal fluctuation occurs, adding a photon. The rotation angle of the Bloch vector suddenly increases to $2\pi\sqrt{2} \simeq 3\pi$, and the atoms tend to leave the cavity in the ground state. After a typical cavity lifetime, the field decays, and the trapping condition is restored again. Under this operation condition, the statistics of ground-state atoms is governed by two time constants:

1. A short interval, in which successive atoms leave the cavity in the ground state after a thermal fluctuation
2. A long time interval, in which the trapping condition is maintained, and all atoms leave the resonator in their excited state until the next fluctuation occurs.

The probability $P_2(0, |g), t$ is plotted in Fig. 83.11. The plot clearly shows the two time regimes that govern the imperfect trapping situation.

83.6 Cavity Cooling

In previous sections, we presented some important aspects of cavity QED by examining the effect of coupling between a single-cavity photon and the atomic (pseudo-)spin degree of freedom. However, an experimental realization and a perfect control of such coupling requires very cold atoms

trapped at a specific position. Thus, the external degree of freedom associated with the kinetic motion of atoms needs to be taken into account to achieve a complete description of the system. As an example, the cavity modes can exert light forces on moving atoms and induce a significant effect in transmission spectroscopy measurements [56–58].

Another important example and one of the most promising applications of the cavity QED dynamics involving atomic motion is the realization of cavity cooling, i.e., the dissipation of kinetic energy through the cavity photon-loss channel in a controlled manner. The realization of cavity cooling has been proved to be an essential step for the experimental achievement of strongly coupled cavity QED systems with sufficiently long interaction times and precise control of atomic motion. In the weak coupling regime, the atom can be cooled by coupling with cavity photons if the pumping is red-detuned with $\omega_p - \omega_C < 0$, in which case the average frequency of emitted photons is higher than that of the pumping laser due to the increase of mode density around the cavity frequency. The energy, hence, has to be compensated by the loss in kinetic energy of the atomic center-of-mass (CM) motion. In the strong-coupling regime, however, the atom–light scattering process becomes complicated with the nonnegligible photon reabsorption. For a high-finesse FP cavity, the dynamic cavity cooling effect in this case can be interpreted in the frequency domain with a Sisyphus-type mechanism using the dressed-state picture [59]. For the case of a ring cavity, the intuitive photon scattering picture can still be used but with a full velocity dependence on the radiation pressure [60].

83.6.1 Master Equation

As a simplest example, we consider a system of a single two-level atom trapped in a single-mode optical cavity, which is driven by a monochromatic pumping laser. Under the dipole approximation and the RWA, the Hamiltonian of the system can be written as

$$\mathcal{H} = \mathcal{H}_{\text{GJC}} + \mathcal{H}_{\text{CoM}} + \mathcal{H}_{\text{pump}}. \quad (83.76)$$

The generalized Jaynes–Cummings (GJC) term is similar to the JC model in Eq. (83.15)

$$\begin{aligned} \mathcal{H}_{\text{GJC}} = & \frac{1}{2} \hbar \omega_0(\mathbf{r}) \sigma_z + \hbar \omega_C a^\dagger a \\ & + \hbar [g f(\mathbf{r}) \sigma_+ a + g^* f^*(\mathbf{r}) a^\dagger \sigma_-], \end{aligned} \quad (83.77)$$

where the atomic frequency $\omega_0(\mathbf{r})$ acquires explicit dependence on the CM coordinate \mathbf{r} of the atom owing to a differential AC-Stark shift induced by a far-detuned external trapping potential exerted on the atom. Besides, the

atom–photon coupling strength is spatially modulated with a function $f(\mathbf{r})$ according to the electric field strength of cavity mode. For a standing-wave mode in an FP cavity, the coupling modulates in magnitude with $f(\mathbf{r}) = \cos(kx)$, while for a propagating-wave mode in a ring cavity, the coupling modulates in phase with $f(\mathbf{r}) = e^{i\pi kx}$. In both cases, the intracavity mode is assumed without loss of generality to be along the x -direction. The motion of the atomic CM degree of freedom is described by the term

$$\mathcal{H}_{\text{CoM}} = \frac{\mathbf{p}^2}{2m} + V_{\text{trap}}(\mathbf{r}), \quad (83.78)$$

where m is the atomic mass, and $V_{\text{trap}}(\mathbf{r})$ denotes the trapping potential. If pumped by a driving laser at frequency ω_p , the pumping Hamiltonian takes the form

$$\begin{aligned} \mathcal{H}_{\text{pump}} = & i\hbar\eta(a^\dagger - a)e^{-i\omega_p t} \\ & + i\hbar\Omega_p(\mathbf{r})e^{-i\omega_p t}(\sigma_+ - \sigma_-), \end{aligned} \quad (83.79)$$

where the first term describes a pumping laser applied along the cavity direction to couple the cavity mode with amplitude η , and the second corresponds to a driving directly on the atomic spin degree of freedom at a position-dependent Rabi frequency $\Omega_p(\mathbf{r})$.

The dynamics of the system can be described by the density operator ρ , which satisfies the master equation

$$\frac{d\rho}{dt} = -\frac{i}{\hbar}[\mathcal{H}, \rho] + \mathcal{L}_{\text{cav}}\rho + \mathcal{L}_{\text{atom}}\rho, \quad (83.80)$$

where the Liouville operators are introduced to describe the dissipation of cavity photons and atoms. If the environment is Markovian, this photon decay can be approximated by

$$\mathcal{L}_{\text{cav}}\rho = -\kappa(a^\dagger a \rho + \rho a^\dagger a - 2a\rho a^\dagger), \quad (83.81)$$

with κ the cavity decay rate. Another decay channel of the system is the spontaneous decay of atom from the excited to the ground state, accompanied by the emission of a photon into the environment. This process takes the form

$$\begin{aligned} \mathcal{L}_{\text{atom}}\rho = & -\gamma[\sigma_+\sigma_-\rho + \rho\sigma_+\sigma_- \\ & - 2\int d^2\hat{\mathbf{r}}_\perp h(\hat{\mathbf{r}}_\perp)\sigma_-\epsilon^{-ik_0 r_\perp}\rho\epsilon^{ik_0 r_\perp}\sigma_+], \end{aligned} \quad (83.82)$$

where γ is the spontaneous decay rate, $\hat{\mathbf{r}}_\perp$ is the directional unit vector in the transversal plane, $r_\perp = \mathbf{r} \cdot \hat{\mathbf{r}}_\perp$ is the projection, and $k_0 = \omega_0/c$ is the recoil wave vector of the atom. The function $h(\hat{\mathbf{r}}_\perp)$ is present to describe the directional distribution of spontaneous decay of specific atomic transition.

In general, it is not possible to solve the master equation (83.80) analytically, even for a single atom. If the population of the atomic excited state is negligible, one

can significantly simplify the Hamiltonian Eq. (83.76) by adiabatically eliminating the atomic excited state. This approximation is valid provided that the atomic transition between the two internal spin states is far detuned from the pumping laser or has a large spontaneous decay rate. In either case, the atomic operator can be approximated as

$$\sigma_- \approx \frac{gf(\mathbf{r})a + \Omega_p(\mathbf{r})}{-i(\omega_p - \omega_0) + \gamma}. \quad (83.83)$$

By substituting the expressions of σ_- and $\sigma_+ = \sigma_-^\dagger$ back into Eq. (83.76), we obtain an effective Hamiltonian in which the CM motion of the atom is coupled to the cavity mode

$$\begin{aligned} \mathcal{H}_{\text{eff}} = & \frac{\mathbf{p}^2}{2m} + V_{\text{trap}}(\mathbf{r}) \\ & - \hbar[(\omega_p - \omega_C) - U_0|f(\mathbf{r})|^2]a^\dagger a \\ & + \hbar\eta_{\text{eff}}(\mathbf{r})[f^*(\mathbf{r})a^\dagger + f(\mathbf{r})a], \end{aligned} \quad (83.84)$$

where the position-dependent effective pumping strength is given by

$$\eta_{\text{eff}}(\mathbf{r}) = \frac{(\omega_p - \omega_0)g\Omega_p(\mathbf{r})}{(\omega_p - \omega_0)^2 + \gamma^2}. \quad (83.85)$$

In this effective model, one can see clearly that the cavity photons provide a trapping potential $\hbar U_0|f(\mathbf{r})|^2 a^\dagger a$ to the atomic CM motion with

$$U_0 = \frac{g^2(\omega_p - \omega_0)}{(\omega_p - \omega_0)^2 + \gamma^2}. \quad (83.86)$$

The gradient of this effective potential acts as a force exerted on the atom. This force acquires an explicit dependence on the amplitude of the cavity mode, which depends not only on the momentary position of the atom but has a memory effect owing to the finite decay rate κ . The force, hence, becomes velocity dependent, which, in a semiclassical theory of atomic motion, leads to an effective viscous friction that can cool the atom.

83.6.2 Cavity Cooling Experiments

Cavity cooling of single atoms was first demonstrated with ^{85}Rb atoms trapped in an FP cavity [61]. In this experiment, the trapping field was red-detuned with respect to the atom, while the cooling laser was a blue-detuned probing field with frequency $\omega_p > \omega_0$. From Eqs. (83.84) and (83.86), the interaction between the probing laser and the atom induces to a blueshift of the cavity frequency by an amount of $U_0|f(\mathbf{r})|^2$, which then leads to an increase of the energy stored in the cavity field with a cost of kinetic energy

of the atoms. The cooling effect was demonstrated via the observation of extended storage times and improved localization of ^{85}Rb atoms from time-resolved measurement of the cavity transmission signal. As a result, a cooling rate of $\beta/m = 21$ kHz is achieved, which exceeds the estimated value of 4 kHz for blue-detuned Sisyphus cooling of a two-level atom in free space, or with the Doppler cooling rate of 1.5 kHz at equivalent atomic saturation.

With the advanced progresses of free-space laser cooling and trapping, other achievements have been obtained in the exploration and applications of single-atom cavity QED systems. These include the high-precision measurements demonstrated the basic cavity QED model in the optical domain [62, 63], the quantum anharmonic domain of the Jaynes–Cummings spectrum [64, 65], the generation of squeezed light [66], the development of a deterministic single-photon source [67, 68], the realization of the long-time sought atom–photon quantum interface [69, 70] and single-atom quantum memory [71], and the realization of electromagnetically induced transparency with a single atom [72].

83.7 Cavity QED for Cold Atomic Gases

Another new research direction in cavity QED is about the hybrid system of cold and ultracold atomic ensembles and high-finesse optical resonators. With the common coupling of atoms to the cavity field, there exists a long-range interatomic interaction mediated by coherent scattering of cavity photons, an ingredient which is usually absent in free-space cold atom experiments. As a result, this strongly interacting many-body system can present novel quantum phenomena with strong correlation. Besides, the coupling between the cavity mode and the atomic motion can induce a frequency shift of the cavity frequency and its backaction on mechanical motion, which may lead to a self-organization of atoms and an implementation of cavity optomechanics.

83.7.1 Atomic Ensembles in a Cavity

The interatomic interaction in a cavity is mediated by the cavity mode by its direct coupling to the atomic electric-dipole moments. However, the nature is inherently different from the induced dipole–dipole interaction, i.e., the van der Waals interaction in free space. In a cavity, the interaction strength does not decay with the interatomic separation and depends only on the local coupling of the atoms to the cavity field. More importantly, the interaction is a global coupling with the ensemble of atoms collectively coupling to the cavity field and experiencing the resulting backaction. Thus, even in cases where the interaction between a single atom and cavity mode is not strong enough, the collective interac-

tion energy can still be enhanced coherently within an atomic ensemble. Next, we discuss the character of the cavity-mediated interatomic interaction in two different pumping geometries, namely, pumping the cavity either directly or indirectly via light scattering off the laser-driven atoms.

In the case of cavity pumping, the detuning between the driving laser and the dispersively shifted cavity resonance depends on the position of all atoms, which, in turn, experience the optical dipole force of the intracavity field. Under the adiabatic approximation with small atomic velocities and low saturation, the interaction potential among the ensemble of N atoms takes the form [73]

$$V(\mathbf{r}_1, \dots, \mathbf{r}_N) = \frac{\hbar(\omega_p - \omega_0)|\eta|^2}{(\omega_p - \omega_0)\kappa + (\omega_p - \omega_C)\gamma} \times \tan^{-1} \frac{\gamma\kappa - (\omega_p - \omega_0)(\omega_p - \omega_C + g_{\text{eff}}^2)}{(\omega_p - \omega_0)\kappa + (\omega_p - \omega_C)\gamma}. \quad (83.87)$$

The collective coupling strength g_{eff} depends on the spatial distribution of the N atoms. This cavity-mediated long-range interatomic interaction gives rise to an asymmetric deformation of the normal-mode splitting, which has been observed experimentally [74].

The situation drastically changes if the system is atom pumped by a driving laser from a direction perpendicular to the cavity axis. In this case, photons are Rayleigh scattered by atoms into the cavity mode. Photons scattered from different atoms will interfere either destructively or constructively, depending on the relative positions of the atoms. Consider as a simple example, two atoms trapped in a cavity. If the two atoms are separated by odd integer multiples of the half-wavelength, the photons scattered into the cavity have the same magnitude but opposite signs, resulting in destructive interference and a vanishing cavity field intensity. On the other hand, if the two atoms are separated by even integer multiples of the half-wavelength, the photons scattered off the two atoms interfere constructively to yield a fourfold enhancement of the field intensity. This collective enhancement of scattering photons from multiple atoms is referred to as superradiance [75, 76].

Approximately, in the limit of $U_0 \rightarrow 0$, the collective potential of the atomic ensemble reads

$$V(\mathbf{r}_1, \dots, \mathbf{r}_N) = \frac{\hbar(\omega_p - \omega_C)|\eta_{\text{eff}}|^2}{(\omega_p - \omega_C)^2 + \kappa^2} \times \left[\sum_{j=1}^N \cos(kx_j) \cos(kz_j) \right]^2. \quad (83.88)$$

Here, we assume that the cavity mode and the pumping laser are both standing waves along the x and z -directions, respectively. Notice that if one moves along the cavity direction

over a wavelength, the potential varies from its maximal value to zero, leading to a contrast of unity regardless of the atom–cavity coupling constant g . This is clearly distinct from the case of cavity pumping, where the atoms cause only a small modulation of the cavity intensity as $g \rightarrow 0$. This observation suggests that significant many-body effects can be encountered even in the weak-coupling regime in the atom pumping geometry.

The long-range interaction between atoms is the origin of various collective dynamical effects. As an example, a thermal cloud of cold atoms interacting with a single-mode FP cavity shows a phase transition upon tuning the atomic pumping power P from a direction perpendicular to the cavity axis [77, 78]. For pumping power less than a critical value P_{cr} , the atoms distribute uniformly to minimize its kinetic energy. The light scattered from atoms in different positions then interferes destructively, and the average intensity of the cavity field is zero. When the pumping power $P > P_{\text{cr}}$, however, the atoms arrange themselves to form a checkerboard pattern to compensate the long-range interaction energy, so that the light interferes constructively to achieve a macroscopic cavity field.

The self-organization of atoms in a transversally driven FP cavity was first demonstrated in 2003 [79]. In that experiment, a total of $N \approx 10^7$ Cs atoms prepared at a temperature of 6 μK were pumped by a strong enough red-detuned laser to achieve collective emission of light into the cavity. As a result, the emission rate exceeded the free-space single-atom Rayleigh scattering rate by a factor of up to 10^3 , and the spatial configuration of atoms featured a spontaneous symmetry breaking into either the odd or even sites of a checkerboard pattern, which was revealed by measuring π jumps in the phase of emitted cavity field relative to the pumping laser. In a ring-cavity with two propagating-wave modes, the self-organization of atoms was also observed with transverse pumping [80]. However, the system spontaneously breaks a continuous translational symmetry rather than a discrete \mathbb{Z}_2 symmetry as in the FP cavity.

83.7.2 Bose–Einstein Condensate in a Cavity

As compared to a thermal cloud of cold atoms, the system of a Bose–Einstein condensate (BEC) coupling with an optical cavity is of particular importance as it corresponds to some conceptually fundamental models of atoms coupling to a single-mode light field. When the atoms are Bose condensed into a single motional quantum state, the number of degrees of freedom required to describe the system can be substantially reduced. Therefore, the experimental platform can be used to mimic some model Hamiltonians of matter–light interaction, including the Tavis–Cummings or the Dicke

model, as well as the generic model for cavity optomechanics.

Under the mean-field approximation, which is valid in the presence of a cavity-mediated global coupling among all atoms, the condensate wave function and the cavity field are assumed by their amplitudes of expectation

$$\begin{aligned}\Psi(\mathbf{r}, t) &\rightarrow \sqrt{N_c} \phi(\mathbf{r}, t), \\ a(t) &\rightarrow \alpha(t),\end{aligned}\quad (83.89)$$

where N_c is the number of condensed atoms, and $\phi(\mathbf{r})$ is the normalized wave function. These mean fields for atoms and cavity field satisfy the Gross–Pitaevskii-like equations

$$\begin{aligned}i\hbar\partial_t\phi(\mathbf{r}, t) &= \left\{ -\frac{\hbar^2\nabla^2}{2m} + V_{\text{trap}}(\mathbf{r}) \right. \\ &\quad + N_c g_{\text{atom}} |\phi(\mathbf{r}, t)|^2 + \hbar U_0 |\alpha(t)|^2 \cos^2(kz) \\ &\quad \left. + \hbar\eta_{\text{eff}} [\alpha(t) + \alpha^*(t)] \cos(kx) \cos(kz) \right\} \phi(\mathbf{r}, t), \\ i\partial_t\alpha(t) &= [\omega_C - \omega_p + N_c U_0 \langle \phi | \cos^2(kz) | \phi \rangle - i\kappa] \alpha(t) \\ &\quad + i\eta + N_c \eta_{\text{eff}} \langle \phi | \cos(kx) \cos(kz) | \phi \rangle,\end{aligned}\quad (83.90)$$

where the interatomic contact interaction $g_{\text{atom}} = 4\pi\hbar^2 a_s/m$ with a_s the s -wave scattering length. On the one hand, the dynamics of the cavity field involves spatial averages over the condensate density distribution. On the other hand, the atoms are also affected by the backaction from the cavity field according to the potential-like terms, which depend on the amplitude α and intensity $|\alpha|^2$ of the cavity field in the Gross–Pitaevskii equation for atoms. The mean-field equations are usually solved numerically to obtain the time-evolution of the system and the steady-state solutions for both atoms and cavity field [81].

As in a thermal atomic ensemble, the BEC trapped inside a cavity can also self-organize to emit an intracavity field collectively. The key difference in the case of BEC is that the atomic motion is also quantized, and the transition is now between a uniform distribution and a periodic array of atoms in the cavity-induced lattice potential. As a consequence, the transition point is determined by the competition of kinetic energy and potential energy associated with the spatial modulation of atomic density.

Under the mean-field approximation, the steady state of the system can be determined by the numerical solutions of the Gross–Pitaevskii-like equations for both the cavity field α and the atomic mode $\phi(\mathbf{r})$. By assuming for simplicity that the atomic motion is only along the cavity axis and the cavity pumping $\eta = 0$, one can define an order parameter $\Theta = \langle \phi | \cos(kx) | \phi \rangle$, which describes the nonuniform spatial

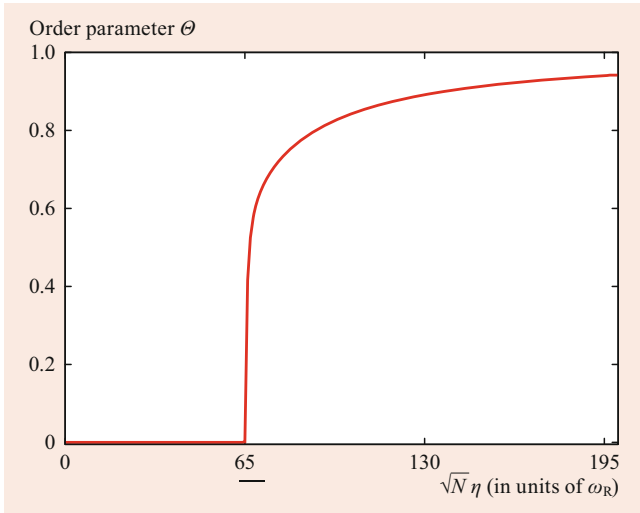


Fig. 83.12 The steady-state order parameter Θ plotted as a function of the effective cavity pumping strength η_{eff} , indicating the self-organization of a Bose–Einstein condensate in an FP cavity [81]

modulation of the atoms. As can be seen from a typical result of the numerical solution shown in Fig. 83.12, the order parameter takes a nonzero value beyond a critical pumping strength η_{eff} , indicating self-organization of the density of atoms.

Self-organization of a BEC was experimentally achieved in 2010 [82]. In that experiment, a BEC of about 10^5 atoms was trapped inside a high-finesse FP cavity and was illuminated from a transversal direction by a far red-detuned standing-wave laser beam. By gradually increasing the power of the transverse laser beam beyond a critical value, a sharp rise of the intracavity field intensity and a macroscopic populations in the atomic momentum states $(px, pz) = (\pm\hbar k, \pm\hbar k)$ were observed, indicating a transition to the self-organization phase. Above this critical pump power, the relative phase $\Delta\phi$ between pump field and cavity field was observed to stay constant, which demonstrates that the system reached a steady state.

Self-organization of a laser-driven BEC in an optical cavity can also be considered as a realization of the Dicke quantum-phase transition in an open system, where the quantized atomic motion acts as a macroscopic spin, which strongly couples to the cavity field. The Dicke model, or equivalently, the Tavis–Cummings model, is proposed to study the collective interaction between a set of two-level atoms and a single light mode

$$\mathcal{H}_{\text{Dicke}} = \frac{1}{2}\hbar\omega_0 \sum_{j=1}^N \sigma_z^{(j)} + \hbar\omega_C a^\dagger a + \hbar g \sum_{j=1}^N (\sigma_+^{(j)} a + a^\dagger \sigma_-^{(j)}), \quad (83.91)$$

which contains a sum over all atoms with index j that couple to the field mode. It is instructive to introduce the collective spin operators

$$S_z = \frac{1}{2} \sum_{j=1}^N \sigma_z^{(j)},$$

$$S_\pm = \sum_{j=1}^N \sigma_\pm^{(j)}, \quad (83.92)$$

together with the total spin operator $\mathbf{S} = (S_x, S_y, S_z)$, where N is the number of atoms, $S_\pm = S_x \pm iS_y$, and $\sigma^{(j)}$ are the Pauli spin operators for the j -th atoms. In this notation, the Dicke Hamiltonian becomes

$$\mathcal{H}_{\text{Dicke}} = \hbar\omega_0 S_z + \hbar\omega_C a^\dagger a + \hbar g (S_+ a + a^\dagger S_-). \quad (83.93)$$

Here, we assumed that all atoms have the same frequency ω_0 and that they are coupled with the same strength g . Note that the eigenstates of the Dicke Hamiltonian are highly degenerate, reflecting the fact that there are many possible ways to accommodate a fixed number of excitations.

The eigenstates of the Dicke Hamiltonian, usually referred to as Dicke states, can be labeled by the quantum numbers of the spin operators $S^2|J, M\rangle = J(J+1)|J, M\rangle$ and $S_z|J, M\rangle = M|J, M\rangle$, where $J = 0, 1, \dots, N/2$, and $M = -J, -J+1, \dots, J$. In the weak excitation limit of $J+M \ll N$, the Dicke states behave like a harmonic oscillator, as can be seen from

$$|\langle J, M+1|S_+|J, M\rangle|^2 = (J+M+1)(J-M) \approx (J+M+1)N. \quad (83.94)$$

Thus, in this regime, the Dicke model can be regarded as a pair of harmonic oscillators coupled at a rate of $\sqrt{N}g$. If there is only one excitation in the system, the eigenstate is equivalent to that of the JC model, except that the coupling strength is collectively enhanced by a factor of \sqrt{N} . However, for the case of more than one excitation, the energy spectrum acquires a significant difference of anharmonicity.

For the case of large number of excitations, the Dicke Hamiltonian has been investigated extensively in the context of superradiance, during which process a macroscopic number of the atomic ensemble decays collectively and emits a large pulse of radiation. This can be seen from

$$S_+ S_- |J, M\rangle = (J+M)(J-M+1)|J, M\rangle, \quad (83.95)$$

which is proportional to the spontaneous emission rate of the ensemble. For the case of $M=J$, the emission rate is proportional to N as $J=N/2$. For the case of $M=0$, however, it is proportional to N^2 . This increase can be understood as

a result of strong correlations between the atoms in the ensemble during the emission process.

The self-organization of a BEC-cavity system can be regarded as the Dicke model by considering a pair of motional states as two pseudo-spin states [82, 83]. The two motional states are given by the uniform condensate mode $|p_x, p_z\rangle = |0, 0\rangle$ and the coherent superposition of the four momentum states $|\pm\hbar k, \pm\hbar k\rangle$, where x and z denote the cavity and pump directions, respectively. Coherent light scattering between the transverse pump beam and the cavity mode couples these two momentum states via two distinguishable Raman channels, resulting in a tunable interaction between the cavity mode and the corresponding collective spin degree of freedom. Experimentally, the phase boundary was mapped out as a function of pump-cavity detuning $\omega_p - \omega_C$ as shown in Fig. 83.13 [82].

83.7.3 Cavity Optomechanics with Cold Atoms

The hybrid atom-cavity system can also be used to study an important model of cavity optomechanics, where a harmonically suspended mechanical element interacts with an intracavity single-mode field. In certain limiting cases, where the motional degrees of freedom of atoms can be reduced to a single-mode harmonic oscillator [84], the effective Hamiltonian of Eq. (83.84) can be significantly simplified, leading to a generic form of the cavity optomechanics Hamiltonian

$$\mathcal{H}_{\text{OM}} = \hbar\omega_m c^\dagger c - \hbar \left[(\omega_p - \omega_C) - \frac{G}{2}(c^\dagger + c) \right] a^\dagger a + i\hbar\eta(a^\dagger - a), \quad (83.96)$$

where c^\dagger and c denote creation and annihilation operators of the mechanical oscillator at frequency ω_m , G is the dispersive shift of the cavity frequency induced by the atomic density modulation, and η is the pumping strength along the cavity axis.

The key ingredient of the experimental realization of the cavity optomechanics Hamiltonian Eq. (83.96) is that the cavity field must affect and sense predominantly a single collective motional mode of the atomic ensemble, which hence can be regarded as the harmonically suspended mechanical element. One possible way to realize this condition is to trap ultracold atoms in a far-detuned intracavity lattice potential such that the atoms form a stack of tightly confined atom clouds [85]. Each atom cloud is harmonically suspended with oscillation frequency ω_m and extends along the cavity axis by only a fraction of the optical wavelength. A cavity mode, whose periodicity differs from that of the trapping lattice potential, couples strongly to a single collective center-of-mass mode of the atomic stack. All remaining collective modes are

detuned from the cavity field and hence contribute as a heat bath.

Another route to realize the cavity optomechanics Hamiltonian is reported in 2008 [86]. In that experiment, a BEC is prepared in an external harmonic trapping potential, extending over several periods of the cavity standing-wave mode structure. Initially, all condensate atoms are prepared in the zero-momentum state $|p = 0\rangle$. The dispersive interaction with the cavity field diffracts atoms into the symmetric superposition of momentum states $|\pm 2\hbar k\rangle$ along the cavity axis. If the diffraction into higher-order momentum modes can be neglected, the dynamics of the coupled system can be well described by the optomechanics Hamiltonian Eq. (83.96).

83.8 Applications of Cavity QED

83.8.1 Quantum Nondemolition (QND) Counting of Photons

When the object of interest consists of only a few atoms and a few photons, the puzzling consequences of quantum mechanical measurement become visible. In the case of the micromaser, the information on the state of the field is imprinted in a subtle way on the atomic beam. While photon counting is normally a destructive operation, the dispersive part of the photon-atom interaction may be used to determine the photon number inside a resonator without altering it on average. Dispersive effects shift the phase of an oscillating atomic dipole without changing its state.

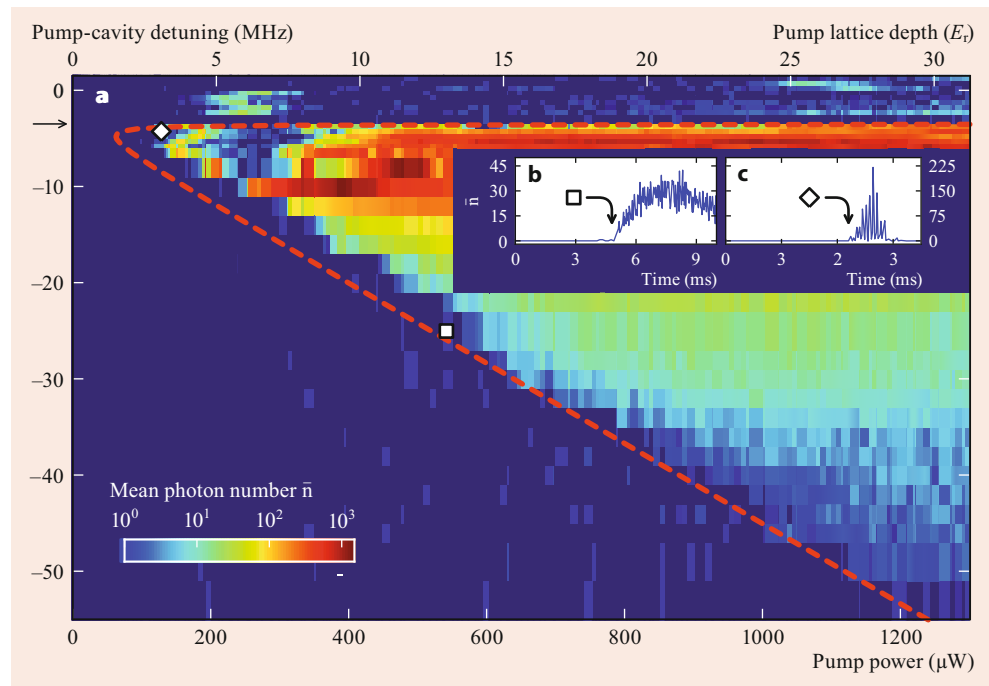
The phase shift due to the field in the resonator can be measured in a Ramsey-type experiment [87]. Consider an atom with two transitions $|g\rangle \rightarrow |e\rangle$ and $|e\rangle \rightarrow |i\rangle$. The first is far from resonance with the cavity, and the second is close to resonance but with a detuning $\delta_{ie} = \omega - \omega_{ie}$ large enough so as not to change the cavity photon number as the atom passes through. The dynamic Stark effect of the $|g\rangle \rightarrow |e\rangle$ transition frequency due to state $|i\rangle$ is then

$$\Delta\omega_{eg} = \frac{[g_{ie}\sqrt{n+1}]^2}{\delta_{ie}}. \quad (83.97)$$

If the resonator is now placed between the two Ramsey cavities, which are tuned to $\omega_R \approx \omega_{eg}$, such that the polarization of the $|e\rangle \rightarrow |g\rangle$ transition is rotated by $\approx \pi/2$, then the additional phase shift $\Delta\omega_{eg}\tau$ and, hence, the photon number n can be measured. Here, τ is the transit time through the optical resonator. Since Rydberg states have a large coupling constant g_μ , the phase shift due to a single atom is detectable [87].

This proposal was demonstrated experimentally in 2007 at ENS [88]. With the ability of developing super high-

Fig. 83.13 Dicke-model phase diagram. The mean-intracavity photon number is finite in the superradiant phase with large pumping power and small pump-cavity detuning [82]



quality microwave cavity, the experimental group successfully performs a QND measurement on single photons via dispersive interaction of single atoms in circular Rydberg states. The atoms have a high principal quantum number $n = 50$, and the highest possible angular and magnetic quantum numbers ($l = n - 1$, $|m_l| = n - 1$), hence acquire a life time of the order $\tau = 30$ ms. The experiment can witness the birth, life, and death of a photon nondestructively.

A complete measurement of n requires a sequence of N atoms because a single Ramsey measurement only determines whether the atom is in state $|e\rangle$ or $|g\rangle$, and hence $\Delta\omega_{eg}\tau$ to within $\pm\pi/2$. Since each measurement provides one binary bit of information, a sequence of N measurements can, in principle, distinguish 2^N possible Fock states for the photon field. However, with a monoenergetic beam, integral multiples of 2π remain undetermined. A distribution of velocities, and hence transit times, is, therefore, desirable. An entropy reduction strategy for selecting an optimal velocity distribution, based on the outcome of previous measurements, is described in [89]. The experimental demonstration was also reported in 2007 by the same group at ENS [90], where the experimental setup was refined to distinguish states with photon number $n \leq 7$.

As a consequence of the uncertainty principle, a measurement of the photon number destroys all information about the phase of the field. In the present case, the noise in the conjugate variable (the phase) is prevented from coupling back on the measured one, and hence the measurement is called a quantum nondemolition experiment. Many other aspects of phase diffusion, entangled states, and quantum measurements in the micromaser are discussed in [91].

83.8.2 Detecting and Trapping Atoms Through Strong Coupling

One of the key ingredients of cavity QED experiments is to deterministically localize atoms at desired positions in a cavity, where the atom–photon coupling can be well calculated and tuned. From Fig. 83.8 it is obvious that an atom traveling through the cavity will modify the transmission properties of this cavity. The ability of tuning strong coupling, thus, enables the experimenter to detect the presence of a single atom dispersively by monitoring cavity transmission or reflection. Laser-cooled atoms have low velocities and spend sufficient time in the cavity even in free flight to generate the transmission signal shown in Fig. 83.14. The signals correspond to individual atom transits, and the shape depends on the detuning of the probe laser from the resonantly interacting cavity–atom system [56, 92]. Thus, the strongly coupled cavity QED system can work as a sensitive single-atom detector, and can help us to extract the temperature and the statistical properties of cold atoms, which have great potential in time-resolved atom–cavity microscopy and in tracking single-atom trajectories.

The same scheme can also be applied to monitor a specific collective motion in an atomic ensemble [85, 93, 94]. In these experiments, the cavity mode is shifted in frequency by the strong interaction with the center-of-mass motion of the atomic ensemble. This provides the ability to realize continuous nondestructive measurement of a quantum many-body system.

The strong coupling between atom and cavity mode can also be used to trap atoms at specified positions. If an atom

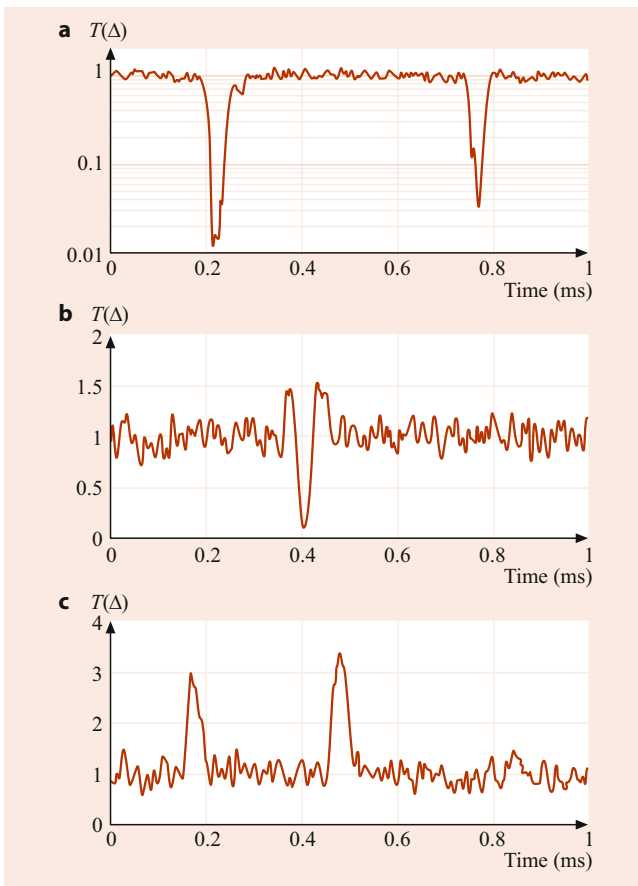


Fig. 83.14 Transmission of a strongly coupled cavity for individual atom transits. Cesium atoms and cavity are in perfect resonance at $\lambda = 852$ nm, while the probe laser is increasingly detuned to the red side of the resonance from top to bottom [125]

absorbs a photon inside the cavity, a strong dipole force can be exerted due to the inhomogeneous field distribution of the cavity mode. Trapping of atoms with a single photon was achieved [92], and from the time variation of the cavity transmission, a reconstruction of atomic trajectories became possible. A similar mechanism is also implemented in a hybrid system of ion trap and optical cavity to localize single ions [95, 96]. This has allowed for very long trapping times of more than 90 min, as well as excellent control over the position of trapped ions within a subwavelength precision [97]. Recently, position control was also demonstrated individually for two ions trapped in the same cavity [98].

83.8.3 Single-Photon Sources

Coherent laser fields are considered the ultimate source of classical radiation fields, and they are characterized by the random arrival time of photons. Nonclassical light sources with, for instance, a regularized stream of photons offer interesting properties for low-noise measurement applications.

Cavity-QED systems offer an attractive light–matter process for the generation of such *photon-bit-streams*, or single-photon sources [99]. In such devices, a single-photon state can, for instance, be created by Raman processes involving a classical field, which serves as the control parameter for the process, and the vacuum field of the optical resonator. The Raman process leaves a single photon in the cavity, which only weakly interacts with the atom. If the resonator has suitable transmission properties, this photon will then escape with predetermined frequency, shape, and propagation direction. Deterministic single-photon sources have been realized with quantum dots [100, 101], single molecules [102], and also with slow [103, 104] or trapped [105, 106] cold atoms and ions [97, 107] inside optical cavities.

The high efficiency of photon sources also paves the route towards quantum memory and quantum network, which is essential for providing cluster states in one-way quantum computing [92] and for the quantum simulation of complex solid-state systems [93]. Successive operations of photon generation, photon storage, and photon retrieval were successfully demonstrated in a hybrid atom–cavity system [71].

83.8.4 Generation of Entanglement

In the middle of the 1990s, it was realized that fully controlled quantum systems can be used to implement a revolutionary type of information processing, now called quantum computing [108]. From the beginning, cavity QED has conceptually played an important role for experimental realizations, since it offers a route to manipulate, in principle, all physical parameters of a coherently interacting system. With the well-established microwave-cavity–Rydberg–atom system, it was proven that the generation of correlated and nonlocal, so-called *entangled* quantum states, is possible [109].

The first *application* of cavity QED was the transfer of the strong coupling idea to the combined internal and motional quantum states of trapped ions [110]. Here, the harmonic oscillation of the ion replaces the electric field of the conventional cavity-QED system. This quantum gate was realized with a system of two trapped ions coupled to each other by Coulomb forces [111].

Ideas about how to use the strong coupling of atoms and photons [112–114] for the generation of atom–photon, photon–photon, or atom–atom systems (by insertion of more than one atom) abound and become possible with the aid of experimental capabilities in the preparation and control of atoms in high-finesse cavities.

Atom–Photon Entanglement

A key advantage of the hybrid atom–cavity QED system is the potential to work as a quantum interface through which

the quantum state can be faithfully transferred from one medium to another. By driving a vacuum-stimulated Raman adiabatic passage into a superposition of two atomic ground states, for example with different orientations of the atomic spin of ^{87}Rb atoms [70], the internal state of a single atom can be entangled with the polarization state of a single photon.

Photon–Photon Entanglement

Starting from the atom–photon entangled state, one can drive another vacuum-simulated Raman adiabatic passage into a single atomic ground state with a well-defined spin orientation to map the quantum state of the atom into a second single photon. This process disentangles the atom and the light and creates an entangled photon pair. The two photons are emitted one after the other into the same spatial mode, hence have never overlapped with each other [115].

Atom–Atom Entanglement

By reversing the role of field and atom, the atom–photon entanglement can also be transferred to a second atom to create atom–atom entanglement. Multiparticle entanglement is considered as a crucial resource of quantum simulation, quantum computation, and quantum-enhanced metrology. The largest number of atoms ever to be entangled in an FP cavity is about 3000 [116] and is more than 40 in an optical fiber cavity [117]. The entanglement between two ions and two atomic ensembles via coupling to cavity mode were also demonstrated in experiments [118, 119].

Quantum Network

Using the aforementioned atom–photon entangled state as building blocks, an elementary quantum network can be implemented with two fiber-linked optical cavities, each containing a single trapped atom as a stationary quantum node. This scheme offers a clear perspective of both addressability and scalability because the atoms are trapped in their corresponding cavities, and more constituent cavities can be added to an existing network without much apparent complication. Besides, the component cavities can, in principle, be arranged in any geometry and two-party links can be established at will, both in time and space.

Elementary quantum network links implementing teleportation protocols between remote trapped atoms and atom–photon quantum-gate operations have been demonstrated in experiments [115, 120–122]. Besides, quantum networking between two cavities has also been experimentally demonstrated with atomic ensembles [123, 124]. These achievements represent a big step towards the goal of realizing an elementary quantum network and a feasible quantum computing system.

References

- Haroche, S.: Cavity QED is reviewed in detail. In: Dalibard, J. (ed.) *Fundamental Systems in Quantum Optics*. Elsevier, Amsterdam (1992)
- Meschede, D.: *Phys. Rep.* **211**(5), 201–250 (1992)
- Berman, P. (ed.): *Cavity Quantum Electrodynamics*. Academic Press, Amsterdam (1994)
- Milonni, P. (ed.): *The Quantum Vacuum*. Academic Press, Boston (1994)
- Berman, P. (ed.): *Cavity Quantum Electrodynamics*. Academic Press, Boston (1994)
- Weisskopf, V., Wigner, E.: *Z. Phys.* **63**, 54 (1930)
- Levin, F., Micha, D. (eds.): *Long-Range Casimir Forces*. Plenum, New York (1993)
- Meschede, D., Walther, H., Müller, G.: *Phys. Rev. Lett.* **54**, 551 (1985)
- Allen, L., Eberly, J.: *Optical Resonance and Two-Level-Atoms*. Dover, New York (1987). reprint of the original 1975 edn.
- Tanji-Suzuki, H., Leroux, I.D., Schleier-Smith, M.H., Cetina, M., Grier, A.T., Simon, J., Vuletić, V.: *Adv. At. Mol. Opt. Phys.* **60**, 201 (2011)
- Power, E.A., Thirunamachandran, T.: *Am. J. Phys.* **46**, 370 (1978)
- Kleppner, D.: *Phys. Rev. Lett.* **47**, 233 (1981)
- Hulet, R.G., Hilfer, E., Kleppner, D.: *Phys. Rev. Lett.* **55**, 2137 (1985)
- Jhe, W., Anderson, A., Hinds, E., Meschede, D., Moi, L., Haroche, S.: *Phys. Rev. Lett.* **58**, 666 (1987)
- Eschner, J., Raab, Ch., Schmidt-Kaler, F., Blatt, R.: *Nature* **413**, 495 (2001)
- Wilson, M.A., Bushev, P., Eschner, J., Schmidt-Kaler, F., Becher, C., Blatt, R., Dorner, U.: *Phys. Rev. Lett.* **91**, 213602 (2003)
- Dowling, J.: In: Tombesi, P., Walls, D. (eds.) *Quantum Measurements in Optics*. Plenum, New York (1992)
- Drexhage, K.H.: In: Wolf, E. (ed.) *Progress in Optics*, vol. 12, North-Holland, Amsterdam (1974)
- Sandoghar, V., Sukenik, C., Hinds, E., Haroche, S.: *Phys. Rev. Lett.* **68**, 3432 (1992)
- Casimir, H., Polder, D.: *Phys. Rev.* **73**, 360 (1948)
- Sukenik, C., Boshier, M., Cho, D., Sandoghar, V., Hinds, E.: *Phys. Rev. Lett.* **70**, 560 (1993)
- Shih, A., Raskin, D., Kusch, P.: *Phys. Rev. A* **9**, 652 (1974)
- Cohen-Tannoudji, C.: In: Dalibard, J. (ed.) *Fundamental Systems in Quantum Optics*. Elsevier, Amsterdam (1992)
- Haroche, S., Brune, M., Raimond, J.M.: *Europhys. Lett.* **14**, 19 (1991)
- Chevrollier, M., Fichet, M., Oria, M., Rahmat, G., Bloch, D., Ducloy, M.: *J. Phys. (Paris)* **2**, 631 (1992)
- Bushev, P., Wilson, A., Eschner, J., Raab, C., Schmidt-Kaler, F., Becher, C., Blatt, R.: *Phys. Rev. Lett.* **92**, 223602 (2004)
- Brune, M., Nussenzveig, P., Schmidt-Kaler, F., Bernadot, R., Maali, A., Raimond, J.M., Haroche, S.: *Phys. Rev. Lett.* **72**, 3339 (1994)
- Failache, H., Saltiel, S., Fischer, A., Bloch, D., Ducloy, M.: *Phys. Rev. Lett.* **88**, 243603 (2002)
- von Klitzing, W., Long, R., Ilchenko, V.S., Hare, J., Lefèvre-Seguin, V.: *Opt. Lett.* **26**, 166 (2001)
- Yablonovitch, E.: *Phys. Rev. Lett.* **58**, 2059 (1987)
- Inoue, K., Ohtaka, K. (eds.): *Photonic Crystals*. Springer, Berlin, Heidelberg (2004)
- Reithmaier, J.P., Sek, G., Löffler, A., Hofmann, C., Kuhn, S., Reitzenstein, S., Keldysh, L.V., Kulakovskii, V.D., Reinecke, T.L., Forchel, A.: *Nature* **432**, 197 (2004)

33. Yoshie, T., Scherer, A., Hendrickson, J., Khitrova, G., Gibbs, H.M., Rupper, G., Ell, C., Shchekin, O.B., Deppe, D.G.: *Nature* **432**, 200 (2004)
34. Vahala, K.: *Nature* **424**, 839 (2003)
35. Cohen-Tannoudji, C.: In: Balian, R. (ed.) *Frontiers in Laser Spectroscopy*. North-Holland, Amsterdam (1977)
36. Jaynes, E.T., Cummings, F.W.: *Proc. IEEE* **51**, 89 (1963)
37. Paul, H.: *Ann. Phys.* **11**, 411 (1963)
38. Eberly, J.H., Narozhny, N.B., Sanchez-Mondragon, J.J.: *Phys. Rev. Lett.* **44**, 1323 (1980)
39. Narozhny, N.B., Sanchez-Mondragon, J.J., Eberly, J.H.: *Phys. Rev. A* **23**, 236 (1981)
40. Knight, P.L., Radmore, P.M.: *Phys. Rev. A* **26**, 676 (1982)
41. Law, C.K., Eberly, J.H.: *Phys. Rev. Lett.* **76**, 1055 (1996)
42. Briegel, H.J., Englert, B.G.: *Phys. Rev. A* **47**, 3311 (1993)
43. Ginzl, C., Briegel, H.J., Martini, U., Englert, B.G., Schenzle, A.: *Phys. Rev. A* **48**, 732 (1993)
44. Mollow, B.R.: *Phys. Rev.* **188**, 1969 (1969)
45. Thompson, R., Rempe, G., Kimble, H.: *Phys. Rev. Lett.* **68**, 1132 (1992)
46. McKeever, J., Boca, A., Boozer, A.D., Buck, J.R., Kimble, H.J.: *Nature* **425**, 268 (2003)
47. Chiorescu, I., Bertet, P., Semba, K., Nakamura, Y., Harmans, C.J.P.M., Mooij, J.E.: *Nature* **431**, 159 (2004)
48. Wallraff, A., Schuster, D.I., Blais, A., Frunzio, L., Huang, R.-S., Majer, J., Kumar, S., Girvin, S.M., Schoelkopf, R.J.: *Nature* **431**, 164 (2004)
49. Stebbings, R.F., Dunning, F.B. (eds.): *Rydberg States of Atoms and Molecules*. Cambridge University Press, Cambridge (1983)
50. Filipowicz, P., Javanainen, J., Meystre, P.: *Phys. Rev. A* **34**, 3077 (1986)
51. Rempe, G., Walther, H.: *Phys. Rev. A* **42**, 1650 (1990)
52. Rempe, G., Schmidt-Kaler, F., Walther, H.: *Phys. Rev. Lett.* **64**, 2783 (1990)
53. Benson, U., Raithel, G., Walther, H.: *Phys. Rev. Lett.* **72**, 3506 (1994)
54. Meystre, P., Rempe, G., Walther, H.: *Opt. Lett.* **13**, 1078 (1988)
55. Wagner, C., Schenzle, A., Walther, H.: *Opt. Commun.* **107**, 318 (1994)
56. Mabuchi, H., Turchette, Q.A., Chapman, M.S., Kimble, H.J.: *Opt. Lett.* **21**, 1393 (1996)
57. Hood, C.J., Chapman, M.S., Lynn, T.W., Kimble, H.J.: *Phys. Rev. Lett.* **80**, 4153 (1998)
58. Münstermann, P., Fischer, T., Maunz, P., Pinkse, P.W.H., Rempe, G.: *Phys. Rev. Lett.* **82**, 3791 (1999)
59. Horak, P., Hechenblaikner, G., Gheri, K.M., Stecher, H., Ritsch, H.: *Phys. Rev. Lett.* **79**, 4974 (1997)
60. Murr, K.: *Phys. Rev. Lett.* **96**, 253001 (2006)
61. Maunz, P., Puppe, T., Schuster, I., Syassen, N., Pinkse, P.W.H., Rempe, G.: *Nature* **428**, 50 (2004)
62. Boca, A., Miller, R., Birnbaum, K.M., Boozer, A.D., McKeever, J., Kimble, H.J.: *Phys. Rev. Lett.* **93**, 233603 (2004)
63. Maunz, P., Puppe, T., Schuster, I., Syassen, N., Pinkse, P.W.H., Rempe, G.: *Phys. Rev. Lett.* **94**, 033002 (2005)
64. Kubanek, A., Ourjoumtsev, A., Schuster, I., Koch, M., Pinkse, P.W.H., Murr, K., Rempe, G.: *Phys. Rev. Lett.* **101**, 203602 (2008)
65. Schuster, I., Kubanek, A., Fuhrmanek, A., Puppe, T., Pinkse, P.W.H., Murr, K., Rempe, G.: *Nat. Phys.* **4**, 382 (2008)
66. Ourjoumtsev, A., Kubanek, A., Koch, M., Sames, C., Pinkse, P.W.H., Rempe, G., Murr, K.: *Nature* **474**, 623 (2011)
67. Kuhn, A., Hennrich, M., Rempe, G.: *Phys. Rev. Lett.* **89**, 067901 (2002)
68. McKeever, J., Boca, A., Boozer, A.D., Miller, R., Buck, J.R., Kuzmich, A., Kimble, H.J.: *Science* **303**, 1992 (2004)
69. Boozer, A.D., Boca, A., Miller, R., Northup, T.E., Kimble, H.J.: *Phys. Rev. Lett.* **98**, 193601 (2007)
70. Wilk, T., Webster, S.C., Kuhn, A., Rempe, G.: *Science* **317**, 488 (2007)
71. Specht, H.P., Nölleke, C., Reiserer, A., Uphoff, M., Figueroa, E., Ritter, S., Rempe, G.: *Nature* **473**, 190 (2011)
72. Kampschulte, T., Alt, W., Brakhane, S., Eckstein, M., Reimann, R., Widera, A., Meschede, D.: *Phys. Rev. Lett.* **105**, 153603 (2010)
73. Fischer, T., Maunz, P., Puppe, T., Pinkse, P.W.H., Rempe, G.: *New J. Phys.* **3**, 11 (2001)
74. Münstermann, P., Fischer, T., Maunz, P., Pinkse, P.W.H., Rempe, G.: *Phys. Rev. Lett.* **84**, 4068 (2000)
75. Dicke, R.H.: *Phys. Rev.* **93**, 99 (1954)
76. DeVoe, R.G., Brewer, R.G.: *Phys. Rev. Lett.* **76**, 2049 (1996)
77. Domokos, P., Ritsch, H.: *Phys. Rev. Lett.* **89**, 253003 (2002)
78. Asbóth, J.K., Domokos, P., Ritsch, H., Vukics, A.: *Phys. Rev. A* **72**, 053417 (2005)
79. Black, A.T., Chan, H.W., Vuletić, V.: *Phys. Rev. Lett.* **91**, 203001 (2003)
80. Nagy, D., Asbóth, J.K., Domokos, P., Ritsch, H.: *Europhys. Lett.* **74**, 254 (2006)
81. Nagy, D., Szirmai, G., Domokos, P.: *Eur. Phys. J. D* **48**, 127 (2008)
82. Baumann, K., Guerlin, C., Brennecke, F., Esslinger, T.: *Nature* **464**, 1301 (2010)
83. Nagy, D., Kónya, G., Szirmai, G., Domokos, P.: *Phys. Rev. Lett.* **104**, 130401 (2010)
84. Kippenberg, T.J., Vahala, K.J.: *Science* **321**, 1172 (2008)
85. Gupta, S., Moore, K.L., Murch, K.W., Stamper-Kurn, D.M.: *Phys. Rev. Lett.* **99**, 213601 (2007)
86. Brennecke, F., Ritter, S., Donner, T., Esslinger, T.: *Science* **322**, 235 (2008)
87. Brune, M., Haroche, S., Lefevre, V., Raimond, J.M., Zagury, N.: *Phys. Rev. Lett.* **65**, 976 (1990)
88. Gleyzes, S., Kuhr, S., Guerlin, C., Bernu, J., Deléglise, S., Hoff, U.B., Brune, M., Raimond, J.-M., Haroche, S.: *Nature* **446**, 297 (2007)
89. Schack, R., Breitenbach, A., Schenzle, A.: *Phys. Rev. A* **45**, 3260 (1992)
90. Guerlin, C., Bernu, J., Deléglise, S., Sayrin, C., Gleyzes, S., Kuhr, S., Brune, M., Raimond, J.-M., Haroche, S.: *Nature* **448**, 889 (2007)
91. Wagner, C., Schenzle, A., Walther, H.: *Phys. Rev. A* **47**, 5068 (1993)
92. Doherty, A.C., Lynn, T.W., Hood, C.J., Kimble, H.J.: *Phys. Rev. A* **63**, 013401 (2001). and references therein
93. Brennecke, F., Donner, T., Ritter, S., Bourdel, T., Köhl, M.: *Nature* **450**, 268 (2007)
94. Colombe, Y., Steinmetz, T., Dubois, G., Linke, F., Hunger, D., Reichel, J.: *Nature* **450**, 272 (2007)
95. Guthöhrlein, G.R., Keller, M., Hayasaka, K., Lange, W., Walther, H.: *Nature* **414**, 49 (2001)
96. Mundt, A.B., Kreuter, A., Becher, C., Leibfried, D., Eschner, J., Schmidt-Kaler, F., Blatt, R.: *Phys. Rev. Lett.* **89**, 103001 (2002)
97. Keller, M., Lange, B., Hayasaka, K., Lange, W., Walther, H.: *Nature* **431**, 1075 (2004)
98. Steiner, M., Meyer, H.M., Deutsch, C., Reichel, J., Möhl, M.: *Phys. Rev. Lett.* **110**, 043003 (2013)
99. Law, C.K., Kimble, H.J.: *J. Mod. Opt.* **44**, 2067 (1997)
100. Michler, P., Kiraz, A., Becher, C., Schoenfeld, W.V., Petroff, P.M., Lidong Zhang, E.H., Imamoglu, A.: *Science* **290**, 2282 (2000)
101. Santori, C., Pelton, M., Solomon, G., Dale, Y., Yamamoto, Y.: *Phys. Rev. Lett.* **86**, 1502 (2001)
102. Lounis, B., Moerner, W.E.: *Nature* **407**, 491 (2000)
103. Kuhn, A., Hennrich, M., Rempe, G.: *Phys. Rev. Lett.* **89**, 067901 (2002)

104. Wilk, T., Webster, S.C., Specht, H.P., Rempe, G., Kuhn, A.: *Phys. Rev. Lett.* **98**, 063601 (2007)
105. McKeever, J., Boca, A., Boozer, A.D., Miller, R., Buck, J.R., Kuzmich, A., Kimble, H.J.: *Science* **303**, 1992 (2004)
106. Hijlkema, M., Weber, B., Specht, H.P., Webster, S.C., Kuhn, A., Rempe, G.: *Nat. Phys.* **3**, 253 (2007)
107. Barros, H.G., Stute, A., Northup, T.E., Russo, C., Schmidt, P.O., Blatt, R.: *New J. Phys.* **11**, 103004 (2009)
108. DiVincenzo, D.P.: *Fortschr. Phys.* **48**, 771–783 (2000)
109. Raimond, J.M., Brune, M., Haroche, S.: *Rev. Mod. Phys.* **73**, 565 (2001)
110. Cirac, J.I., Zoller, P.: *Phys. Rev. Lett.* **74**, 4091 (1995)
111. Schmidt-Kaler, F., Häffner, H., Riebe, M., Gulde, S., Lancaster, G.P.T., Deuschle, T., Becher, C., Roos, C.F., Eschner, J., Blatt, R.: *Nature* **422**, 408 (2003)
112. Pellizari, T., Gardiner, S.A., Cirac, J.I., Zoller, P.: *Phys. Rev. Lett.* **75**, 3788 (1995)
113. Soerensen, A.S., Moelmer, K.: *Phys. Rev. Lett.* **91**, 097905 (2003)
114. You, L., Yi, X.X., Su, X.H.: *Phys. Rev. A* **67**, 032308 (2003)
115. Weber, B., Specht, H.P., Müller, T., Bochmann, J., Mücke, M., Moehring, D.L., Rempe, G.: *Phys. Rev. Lett.* **102**, 030501 (2009)
116. McConnell, R., Zhang, H., Hu, J., Čuk, S., Vuletić, V.: *Nature* **519**, 439 (2015)
117. Haas, F., Volz, J., Gehr, R., Reichel, J., Estève, J.: *Science* **344**, 180 (2014)
118. Casabone, B., Stute, A., Friebe, K., Brandstätter, B., Schüppert, K., Blatt, R., Northup, T.E.: *Phys. Rev. Lett.* **111**, 100505 (2013)
119. Simon, J., Tanji, H., Ghosh, S., Vuletić, V.: *Nat. Phys.* **3**, 765 (2007)
120. Ritter, S., Nölleke, C., Hahn, C., Reiserer, A., Neuzner, A., Uphoff, M., Mücke, M., Figueroa, E., Bochmann, J., Rempe, G.: *Nature* **484**, 195 (2012)
121. Nölleke, C., Neuzner, A., Reiserer, A., Hahn, C., Rempe, G., Ritter, S.: *Phys. Rev. Lett.* **110**, 140403 (2013)
122. Reiserer, A., Kalb, N., Rempe, G., Ritter, S.: *Nature* **508**, 237 (2014)
123. Choi, K.S., Deng, H., Laurat, J., Kimble, H.J.: *Nature* **452**, 67 (2008)
124. Matsukevich, D.N., Chaneilière, T., Jenkins, S.D., Lan, S.-Y., Kennedy, T.A.B., Kuzmich, A.: *Phys. Rev. Lett.* **96**, 030405 (2006)
125. Hood, C.J., Chapman, M.S., Lynn, T.W., Kimble, H.J.: *Phys. Rev. Lett.* **80**, 4157 (1998)



Qiongyi He Qiongyi He received her PhD from Jilin University in Changchun, China in 2007 and then worked at the University of Queensland in Brisbane, at Swinburne University of Technology in Melbourne, Australia, and at Peking University in China. She now works on quantum optics and information, with a focus on quantum entanglement, nonlocality, and quantum information applications.



Wei Zhang Wei Zhang received his PhD from Georgia Institute of Technology in 2006 and then worked at the University of Michigan at Ann Arbor and at Renmin University of China. He now works on quantum simulation and computation in artificial quantum systems, including cold quantum gases, optical microcavities, and trapped ions.



Dieter Meschede Professor Dieter Meschede teaches at the Institute for Applied Physics in Bonn. After his studies in Hanover and Cologne and having been awarded his Dr rer nat in Munich in 1984, he first worked at Yale University. Then he became Senior Scientist at the MPI for Quantum Optics, Garching. He has been Professor of Physics since 1990, first in Hanover and since 1994 in Bonn.



Axel Schenzle Professor Schenzle worked on various aspects of theoretical quantum optics, the description of classical and quantum-mechanical noise in microscopic and mesoscopic systems, Bose–Einstein condensation, quantum information theory, and quantum computing and decoherence. He was Deputy Rector of the University of Munich and Dean for many years. He passed away in 2016.



Quantum Optical Tests of the Foundations of Physics

84

L. Krister Shalm, Aephraim M. Steinberg, Paul G. Kwiat, and Raymond Y. Chiao

Contents

84.1	Introduction: The Photon Hypothesis	1232	84.6.2	Bell's Inequalities as a Game	1241
84.2	Quantum Properties of Light	1232	84.6.3	Loopholes in Bell Tests	1242
84.2.1	Vacuum Fluctuations: Cavity QED	1232	84.6.4	Closing the Loopholes in Bell Tests	1242
84.2.2	Two-Photon Light Sources	1233	84.6.5	Polarization-Based Entangled Sources	1243
84.2.3	Squeezed States of Light	1233	84.6.6	Other Entanglement Sources for Bell Tests	1244
84.3	Nonclassical Interference	1234	84.6.7	Advanced Experimental Tests of Nonlocality	1245
84.3.1	Single-Photon and Matter-Wave Interference	1234	84.6.8	Nonlocality Without Inequalities	1246
84.3.2	"Nonlocal" Interference Effects and Energy-Time Uncertainty	1235	84.6.9	Connection to Quantum Information	1246
84.3.3	Two-Photon Interference	1235	84.7	Single-Photon Tunneling Time	1247
84.4	Complementarity and Coherence	1236	84.7.1	An Application of EPR Correlations to Time Measurements	1247
84.4.1	Wave-Particle Duality	1236	84.7.2	Superluminal Tunneling Times	1247
84.4.2	Quantum Eraser	1236	84.7.3	Tunneling Delay in a Multilayer Dielectric Mirror	1248
84.4.3	Vacuum-Induced Coherence	1237	84.7.4	Interpretation of Tunneling Time	1249
84.4.4	Suppression of Spontaneous Parametric Downconversion	1237	84.7.5	Other Fast and Slow Light Schemes	1250
84.5	Measurements in Quantum Mechanics	1238	84.8	Gravity and Quantum Optics	1250
84.5.1	Quantum (Anti-)Zeno Effect	1238	84.8.1	Gravitational Wave Detection	1250
84.5.2	Quantum Nondemolition	1238	84.8.2	Gravity and Quantum Information	1251
84.5.3	Quantum Interrogation	1239	References		1251
84.5.4	Weak Measurements	1239			
84.5.5	Direct Measurements of a Wave Function	1240			
84.6	The EPR Paradox and Bell's Inequalities	1240			
84.6.1	Generalities	1240			

L. K. Shalm (✉)
 Dept. of Physics, University of Colorado at Boulder
 Boulder, CO, USA
 e-mail: lynden.shalm@colorado.edu

A. M. Steinberg
 Dept. of Physics, University of Toronto
 Toronto, ON, Canada
 e-mail: steinberg@physics.utoronto.ca

P. G. Kwiat
 Dept. of Physics, University of Illinois at Urbana-Champaign
 Urbana, IL, USA
 e-mail: kwiat@illinois.edu

R. Y. Chiao
 Departments of Physics and Engineering, University of California
 Merced
 Merced, CA, USA
 e-mail: chiao@physics.berkeley.edu

Abstract

Quantum mechanics began with the solution of the problem of blackbody radiation by Planck's quantum hypothesis: in the interaction of light with matter, energy can only be exchanged between the light in a cavity, and the atoms in the walls of the cavity by the discrete amount $E = h\nu$, where h is Planck's constant, and ν is the frequency of the light. Einstein, in his treatment of the photoelectric effect, reinterpreted this equation to mean that a beam of light consists of particles ("light quanta") with energy $h\nu$. The Compton effect supported this particle viewpoint of light by demonstrating that photons carried momentum, as well as energy. In this way, the wave-particle duality of quanta made its first appearance in connection with the properties of light.

It might seem that the introduction of the concept of the photon as a particle would necessarily also introduce the concept of locality into the quantum world. However, in view of observed violations of Bell's inequalities, exactly the opposite seems to be true. Here, we review some

recent results in quantum optics, which elucidate nonlocality and other fundamental issues in physics.

Keywords

wave packet · entangle state · beamsplitter · Bell inequality · weak measurement

84.1 Introduction: The Photon Hypothesis

In spite of the successes of quantum electrodynamics, and of the standard model in particle physics, there was for a time considerable resistance to the concept of the photon as a particle. Many papers have been written trying to explain all optical phenomena semiclassically, i.e., with the light viewed as a classical wave, and the atoms treated quantum mechanically [1–4]. We first present some quantum optics phenomena that exclude this semiclassical viewpoint.

In an early experiment, Taylor reduced the intensity of a thermal light source in Young’s two-slit experiment, until, on the average, there was only a single photon passing through the two slits at a time. He then observed a two-slit interference pattern, which was identical to that for a more intense classical beam of light. In Dirac’s words, the apparent conclusion is that “each photon then interferes only with itself” [5]. However, a coherent state, no matter how strongly attenuated, always remains a coherent state (Sect. 83.4.2); since a thermal light source can be modeled as a statistical ensemble of coherent states, a stochastic classical wave model yields complete agreement with Taylor’s observations. The one-by-one darkening of grains of film can be explained by treating the matter alone quantum mechanically [2]; consequently, the concept of the photon need not be invoked, and the claim that this experiment demonstrates quantum interference of individual photons is unwarranted [6].

This weakness in Taylor’s experiment can be removed by the use of nonclassical light sources; as discussed by Glauber [7], classical predictions diverge from quantum ones only when one considers counting statistics or photon *correlations*. In particular, two-photon light sources, combined with coincidence detection, allow the production of single-photon ($n = 1$ Fock) states with near certainty. In the first such experiment [8], two photons, produced in an atomic cascade within nanoseconds of each other, impinged on two beamsplitters and were then detected in coincidence by means of four photomultipliers placed at all possible exit ports.

In a simplified version of this experiment [9], one of the beamsplitters and its two detectors are replaced with a single detector D_1 (Fig. 84.1). We define the anticorrelation parameter

$$\alpha \equiv N_{123}N_1/N_{12}N_{13}, \quad (84.1)$$

where N_{123} is the rate of triple-coincidences between detectors D_1 , D_2 , and D_3 ; N_1 is the singles rate at D_1 ; and N_{12} and N_{13} are double-coincidence rates. Then from Schwarz’s inequality [6, 9, 10], $\alpha \geq 1$ for any classical wave. In essence, since the wave divides smoothly, the coincidence rate between D_2 and D_3 is never smaller than the “accidental” coincidence rate, even when measurements are conditioned on an event at D_1 . (The Hanbury-Brown and Twiss experiment [11] can be explained classically, because thermal fluctuations lead to “bunching”, or a mean coincidence rate, which is *greater* than the mean accidental rate; cf. Sect. 74.4.) By contrast, the indivisibility of the photon leads to strong anticorrelations between D_2 and D_3 , making α arbitrarily small. In agreement with this quantum mechanical picture, Grangier et al. observed a 13-standard-deviation violation of the inequality [9], corroborating the notion of the “collapse of the wave packet” as proposed by Heisenberg [12].

84.2 Quantum Properties of Light

84.2.1 Vacuum Fluctuations: Cavity QED

The above considerations necessitate the quantization of the electromagnetic field, which in turn leads to the concept of vacuum fluctuations [4] (Sect. 82.2). Difficulties with this idea, such as the implied infinite zero-point energy of the universe, have led some researchers to attempt to dispense with this concept altogether, along with that of the photon, in every explanation of electromagnetic interactions with matter. Of course, it is impossible to explain all phenomena, such as spontaneous emission and the Lamb shift, without some kind of fluctuating electromagnetic fields (Chap. 70), but one can go a long way with an *ad hoc* ambient classical electromagnetic noise-field filling all of space, in conjunction with the radiation reaction [1, 4].

In particular, even the Casimir attraction between two conducting plates can be explained semiclassically in terms of dipole forces between electrons in each plate as they undergo zero-point motion and induce image charges in the other plate. Nevertheless, the effects of cavity QED (Chap. 71) [13, 14], including the influence of cavity-induced

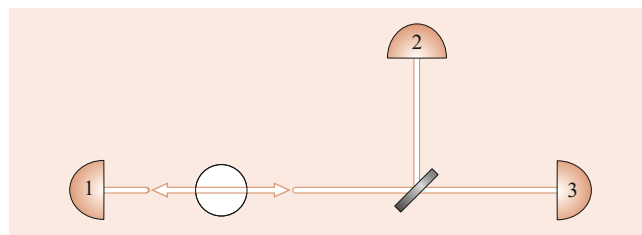


Fig. 84.1 Triple-coincidence setup of Grangier et al. [9]

boundary conditions on energy levels and spontaneous emission rates, are most easily unified via quantization of the electromagnetic field.

By coupling highly excited Rydberg atoms to photons in a high-finesse superconducting microwave cavity, *Brune et al.* observed single-photon-driven Rabi oscillations [15] and used these to study decoherence effects [16], atom-photon entanglement [17], and quantum nondemolition measurements [18] (Sect. 84.5.2). *Kimble et al.* [19] and *Rempe et al.* [20] performed similar experiments, coupling atoms to small optical cavities, and even trapping the atoms with light fields at the single-photon level [21, 22]. By monitoring the amplitude of the light transmitted through the cavity (which depends on the precise location of the atom inside the cavity volume), the trajectory of the atom can be determined with ultrahigh resolution, much smaller than an optical wavelength [23, 24].

84.2.2 Two-Photon Light Sources

The quantum aspects of electromagnetism are made more striking with a two-photon light source, for example, when two highly correlated photons are produced in spontaneous parametric downconversion, or parametric fluorescence [25–27], or four-wave mixing. In this process, a “pump” photon produced in a laser spontaneously decays inside a crystal with a $\chi^{(2)}$ nonlinearity into two highly correlated lower energy photons, conventionally called the “signal” and the “idler” (Sect. 76.3.6). (The quantum state of the light is more correctly written as $|\psi\rangle \propto |\text{vacuum}\rangle + \epsilon|1\rangle_s|1\rangle_i + \epsilon^2|2\rangle_s|2\rangle_i$, but since the amplitude of the downconversion process itself is very weak (ϵ is of order 10^{-4} to 10^{-6}), one often neglects the terms containing two or more pairs. However, recent experiments have begun to exploit these higher-order terms, e.g., to investigate multiphoton quantum entangled states of up to 10 and 12 photons [28].). As shown in Fig. 84.2, a rainbow of colored cones is produced around an axis defined by the direction of the pump beam (for the case of type-I phase-matching), with the correlated downconversion photons always emitted on opposite sides of the pump (Sect. 76.2.2). Their emission times are within femtoseconds of each other, so that detection of one photon implies with near certainty that there is exactly one quantum present in the conjugate mode [29]. In type-I phase-matching, the correlated photons share the same polarization, while in type-II phase-matching, they have orthogonal polarizations (Sect. 76.2.2). We will see below (Sect. 84.6.5) how both of these can enable the production of photons that are entangled in polarization, as well as in other degrees of freedom. Downconversion can only take place in a crystal having inversion symmetry; otherwise $\chi^{(2)} = 0$. However, the next order nonlinearity ($\chi^{(3)}$) can occur in any optical material, although it

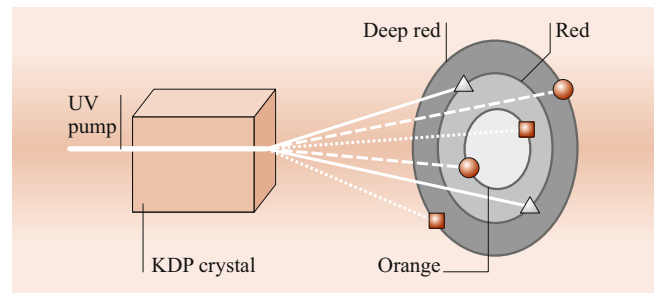


Fig. 84.2 Conical emissions of downconversion from a nonlinear crystal. Photon energy depends on the cone opening angle, and conjugate photons lie on opposite sides of the axis, e.g., the inner “circle” orange photon is conjugate to the outer “circle” deep-red photon, etc.

is a weaker effect. Using this third-order nonlinearity, it is possible to create a correlated signal and idler photon pair through the annihilation of two pump photons in a process known as four-wave mixing.

84.2.3 Squeezed States of Light

The creation of correlated photon pairs is closely related to the process of quadrature-squeezed light production (Sect. 82.6 and the review in [30]). For example, when the gain arising from parametric amplification in a downconversion crystal becomes large, there is a transition from spontaneous to stimulated emission of pairs. This gain is dependent on the phase of amplified light relative to the phase of the pump light. As a result, the vacuum fluctuations are reduced (“squeezed”) below the standard quantum limit in one quadrature but increased in the other, in such a way as to preserve the minimum uncertainty-principle product [31]. This periodicity of the fluctuations at 2ω is a direct consequence of the fact that the light is a superposition of states differing in energy by $2\hbar\omega$ – the quadrature-squeezed vacuum state

$$|\xi\rangle = \exp\left(\frac{1}{2}\xi^*aa - \frac{1}{2}\xi a^\dagger a^\dagger\right)|0\rangle \quad (84.2)$$

represents a vacuum state transformed by the creation ($a^\dagger a^\dagger$) and destruction (aa) of photons two at a time. Essentially any optical processes operating on photon pairs (e.g., four-wave mixing [32, 33]) can also produce such squeezing.

Amplitude squeezing involves preparation of states with a well-defined photon number, i.e., states lacking the Poisson fluctuations of the coherent state. The possibility of producing such states (e.g., via a constant-current-driven semiconductor laser [34], or more recently a quantum dot-based source [35–38]) demonstrates that “shot noise” in photodetection should not be thought of as merely the result of the probabilistic (à la Fermi’s Golden Rule; Sect. 73.5) excitation of quantum mechanical atoms in a classical field but

as representing real properties of the electromagnetic field, accessible to experimental control. This longstanding field of fundamental research has at long last begun to be applied to gravitational-wave detection (Sect. 84.8) and to quantum metrology [39].

84.3 Nonclassical Interference

84.3.1 Single-Photon and Matter-Wave Interference

The first truly one-photon interference experiment [9] used the cascade source discussed in Sect. 84.1. One of the photons was directed to a “trigger” detector, while the other, thus prepared in an $n = 1$ Fock state, was sent through a Mach–Zehnder interferometer. The output photon, detected in coincidence with the trigger photon, showed fringes with a visibility $> 98\%$. Dirac’s statement that a single photon interferes with itself is thus verified.

The pioneering atomic matter-wave interferometry experiments of Pritchard used standing-light gratings and nanofabricated diffraction gratings to construct Mach–Zehnder-type interferometers for sodium atoms [40] and molecules [41] from a supersonic source. Chu and Kasevich significantly advanced the field by the use of STIRAP (stimulated Raman pulses) to produce coherent beamsplitters for cold atomic beams, also in a Mach–Zehnder-type interferometer, but whose source were cesium atoms cooled in and launched from a magneto-optical trap (MOT) [42]. Matter-wave interferometry has since been applied to precision measurements of the acceleration g due to Earth’s gravity [43], gravity gradiometry [44], and Sagnac matter-wave gyroscopes [45, 46].

To date some of the largest molecular systems to display quantum interference of this sort are large molecules like carbon 60 (“buckyball”) and carbon 70 [47]. These are significant in that the average de Broglie wavelength of the molecules, emitted from an oven, was 2.8 pm, actually about 350 times *smaller* than the molecule itself. Multislit diffraction has also been demonstrated with the biological molecule porphyrin and with fluorofullerenes ($C_{60}F_{48}$) [48]. With a mass of 1632 amu, the latter are currently the largest single objects to display interference. *Marshall, Simon, Penrose*, and *Bouwmeester* separately suggested that it may be possible to put a micron-scale mirror (with $\approx 10^{14}$ atoms) into a superposition of resolvable spatial locations [49] – the mirror, part of a high-finesse optical cavity forming one arm of a Michelson interferometer, could be mounted on a high-quality mechanical oscillator, whereby the interaction with a single photon would change the frequency of the oscillator. During the last decade, progress along these lines has been dramatic. The quantum optical control of nano and micromechanical devices through motional coupling to optical cavity

fields or superconducting circuits, i.e., quantum optomechanics, has now been firmly established [50–52]. Recent examples include ground-state laser cooling of the center of mass motion of a micromechanical device comprising up to 10^{11} atoms [53], as well as the generation of quantum-squeezed states [54–56] and of non-Gaussian states [57, 58] of motion. Regarding interference phenomena, Ramsey interference has been observed with a micromechanical device coupled to a superconducting qubit [57], and quantum entanglement comprising one [59] and two [60–62] mechanical resonators has been demonstrated, including the violation of a Bell inequality [63]. Still, while masses of these solid-state resonators comprise the collective motion of up to 10^{15} atoms, the displacement involved in the demonstrated interference experiments is minute (specifically, on the order of one or a few mechanical quanta, which translates to nuclear-scale spatial displacements). Larger spatial displacements may be possible using levitated solid-state systems coupled to cavities [64], which is now becoming a focus of intense research and which holds even the promise of matter-wave interference in this extreme large-mass regime [65, 66].

Two other systems, demonstrating Bose–Einstein condensation (BEC), have also produced evidence of macroscopic quantum coherence. In the experiments of *Andrews* et al., atoms from two different atomic vapor BEC clouds were allowed to fall onto the same detection region, and displayed interference fringes [67] (more recently interference from an array of 30 independent BECs was observed [68]). In some ways, this is the matter-wave equivalent of the famous Pflieger–Mandel experiment [69], in which light from two separate lasers displays interference, even when attenuated to the single-photon level. The explanation in terms of the indistinguishability of the underlying processes is that one cannot ascertain from which laser source a given photon originated. However, this explanation must be applied carefully to the situation of the two atomic BECs; unlike the lasers, the BEC clouds can – at least in principle – be prepared with a definite number of atoms, and it would therefore seem that one could, in principle, determine which cloud emitted a given detected atom. However, this determinacy is rapidly lost after a few atoms are detected [70]. Once the number becomes uncertain, a well-defined relative phase of the two BECs is established, according to the number-phase uncertainty relation $\Delta(N_2 - N_1)\Delta(\phi_2 - \phi_1) \geq 1/2$.

Finally, quantum coherence (although not explicitly spatial interference as in the previous examples) has been detected in the operation of a Josephson-junction linked superconducting loop. Specifically, the group of Mooij was able to prepare a superposition of clockwise and counter-clockwise circulating electrical currents [71]. The $\approx 0.5 \mu\text{A}$ currents corresponded to the motion of millions of Cooper pairs. This superconducting system has become a major focus of quantum computing efforts (Chap. 85), with many groups and

companies around the world making rapid progress with superconducting quantum bits [72–83].

84.3.2 “Nonlocal” Interference Effects and Energy-Time Uncertainty

The energy-time uncertainty principle, $\Delta E \Delta t \geq \hbar/2$ has been tested in a downconversion interference experiment [84]. The downconversion process conserves energy and momentum:

$$\hbar\omega_0 = \hbar\omega_1 + \hbar\omega_2, \quad (84.3)$$

$$\hbar\mathbf{k}_0 \approx \hbar\mathbf{k}_1 + \hbar\mathbf{k}_2, \quad (84.4)$$

where $\hbar\omega_0$ ($\hbar\mathbf{k}_0$) is the energy (momentum) of the parent photon, and $\hbar\omega_1$ ($\hbar\mathbf{k}_1$) and $\hbar\omega_2$ ($\hbar\mathbf{k}_2$) are the energies (momenta) of the daughter photons; \mathbf{k}_1 and \mathbf{k}_2 sum to \mathbf{k}_0 to within an uncertainty given by the reciprocal of the crystal length [85]. Since there are many ways of partitioning the parent photon’s energy, each daughter photon may have a broad spectrum, and hence a wave packet narrow in time; indeed, detecting one of the photons with a fast detector will localize the other to a narrow pulse. However, $\omega_1 + \omega_2 = \omega_0$ is extremely well defined, so that the *difference* in the daughter photons’ arrival times and the *sum* of their energies can be simultaneously known to high precision. Thus, the daughter photons of a parent photon of sharp energy E_0 are in an energy-entangled state, a nonfactorizable sum of product states [86]:

$$|\Psi\rangle = \int_0^{E_0} dE A(E) |E\rangle |E_0 - E\rangle, \quad (84.5)$$

where $A(E)$ is the probability amplitude for the production of two photons of energies E and $E_0 - E$. Measuring the energy of one of the photons to be E_1 “collapses” the system to the state $|E_1\rangle |E_0 - E_1\rangle$, implying an instantaneous increase of the width of the other photon’s wave packet. In the experiment, one photon was used as a trigger, while the other was sent into an adjustable Michelson interferometer (Fig. 84.3) used to measure its coherence length. If the trigger photon was detected after passing through an interference filter F1 of narrow width ΔE , then the conjugate photon occupied a broad wave packet of duration $\Delta t \approx \hbar/\Delta E$ and displayed interference. When there was no trigger, no fringes were observed, implying a much shorter wave packet. This is a nonlocal effect in that the photons can be arbitrarily far away from each other when the collapse occurs.

84.3.3 Two-Photon Interference

In the above experiments, interference occurs between two paths taken by a *single* photon. An early experiment to

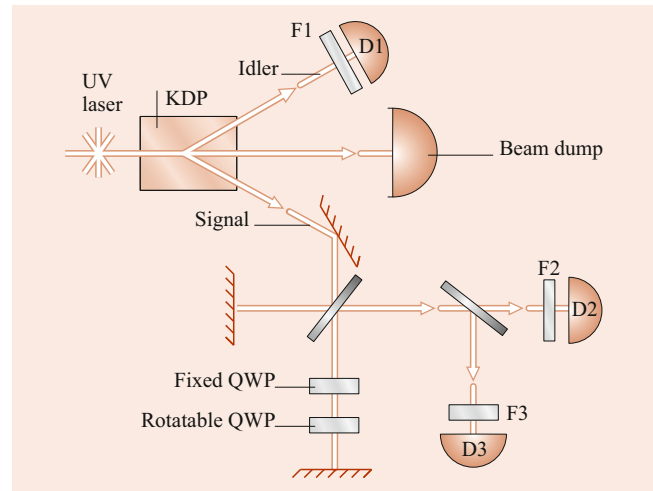


Fig. 84.3 The energy–time uncertainty relation and wave-function collapse were studied by investigating the effect of various filters before the detectors in a single-photon interference experiment [9, 84]

demonstrate *two*-photon interference using the downconversion light source was performed by Ghosh and Mandel [88]. They looked at the counting rate of a detector illuminated by both of the twin beams. No interference was observed at the detector, because although the sum of the phases of the two beams emitted in parametric fluorescence is well defined (by the phase of the pump), their *difference* is not, due to the number-phase uncertainty principle. However, when Ghosh and Mandel looked at the rate of *coincidence* detections between two such detectors whose separation was varied, they observed high-visibility interference fringes. Whereas in the standard two-slit experiment, interference occurs between the two paths a single photon could have taken to reach a given point on a screen, in this case, it occurs between the possibility that the signal photon reached detector 1 and the idler photon detector 2, and the possibility that the reverse happened. This experiment provides a manifestation of quantum nonlocality; interference occurs between alternate global histories of a system, not between local fields. At a null of the coincidence fringes, the detection of one photon at detector 1 excludes the possibility of finding the conjugate photon at detector 2.

Such interference becomes clearer in the related interferometer of Hong, Ou, and Mandel [89] (Fig. 84.4). The identically polarized conjugate photons from a downconversion crystal are directed to opposite sides of a 50–50 beamsplitter, such that the transmitted and reflected modes overlap. If the difference in the path lengths ΔL prior to the beamsplitter is larger than the two-photon correlation length (of the order of the coherence length of the downconverted light), the photons behave independently at the beamsplitter, and coincidence counts between detectors in the two output ports are observed half of the time – the other half of the time, both photons travel to the same detector. However, when

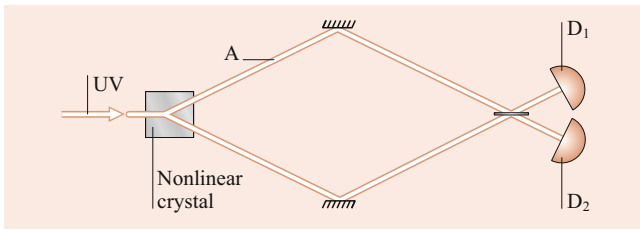


Fig. 84.4 Simplified setup for a Hong–Ou–Mandel (HOM) interferometer [89]. Coincidences may result from both photons being reflected or both being transmitted. When the path lengths to the beamsplitter are equal, these processes destructively interfere, causing a null in the coincidence rate. In a modified scheme, a half-waveplate in one arm of the interferometer (at “A”) serves to distinguish these otherwise interfering processes, so that no null in coincidences is observed. Using polarizers before the detectors one can “erase” the distinguishability, thereby restoring interference [108]. (Sections 84.4.2 and 84.6.5)

$\Delta L \approx 0$, such that the photon wave packets overlap at the beamsplitter, the probability of coincidences is reduced, in principle to zero if $\Delta L = 0$. One can explain the coincidence null at zero path-length difference using the Feynman rules for calculating probabilities: add the probability amplitudes of *indistinguishable* processes that lead to the same final outcome, and then take the absolute square. The two indistinguishable processes here are both photons being reflected at the beamsplitter (with Feynman amplitude $r \cdot r$) and both photons being transmitted (with Feynman amplitude $t \cdot t$). The probability of a coincidence detection is then

$$P_c = |r \cdot r + t \cdot t|^2 = \left| \frac{i}{\sqrt{2}} \cdot \frac{i}{\sqrt{2}} + \frac{1}{\sqrt{2}} \cdot \frac{1}{\sqrt{2}} \right|^2 = 0, \quad (84.6)$$

assuming a real transmission amplitude, and where the factors of i come from the phase shift upon reflection at a beamsplitter [90, 91].

The possibility of a perfect null at the center of the dip is indicative of a nonclassical effect. Indeed, classical field predictions allow a maximum coincidence-fringe visibility of only 50% [92]. The tendency of the photons to travel off together at the beamsplitter can be thought of as a manifestation of the Bose–Einstein statistics for the photons [93]. In practice, the bandwidth of the photons, and hence the width of the null, is determined by filters and/or irises before the detectors [85]. Widths as small as $5 \mu\text{m}$ have been observed, corresponding to time delays of only 15 fs [94]. Consequently, one application is the determination of single-photon propagation times with extremely high time resolution (Sect. 84.7). The dependence of the dip visibility on the indistinguishability of the photons is now commonly used to characterize quantum light sources [95–98].

84.4 Complementarity and Coherence

84.4.1 Wave-Particle Duality

The complementary nature of wave-like and particle-like behavior is frequently interpreted as follows: due to the uncertainty principle, any attempt to measure the position (particle aspect) of a quantum leads to an uncontrollable, irreversible disturbance in its momentum, thereby washing out any interference pattern (wave aspect) [99, 100]. This picture is incomplete though; no “state reduction”, or “collapse”, is necessary to destroy interference, and measurements that do not involve reduction can be reversible. One must view the loss of coherence as arising from an *entanglement* of the system wave function with that of the measuring apparatus (MA) [101]. Previously interfering paths can thereby become distinguishable, such that no interference is observed. Consider the simplest experiment, a Mach–Zehnder interferometer with a 90° polarization rotator in arm 1. If horizontally polarized light is input, the state before the recombining beamsplitter is $(|1\rangle|V\rangle + |2\rangle|H\rangle)/\sqrt{2}$, where $|1\rangle$ and $|2\rangle$ label the path of the photon. Because the polarization – playing the role of the MA – labels the path, no interference is observed at the output. Englert [102] has introduced a generalized relation quantifying the interplay between the wave-like attributes of a system (as measured by the fringe visibility V) and the particle-like character (as measured by the distinguishability D of the underlying quantum processes):

$$V^2 + D^2 \leq 1. \quad (84.7)$$

The equality holds for *pure* input states. This relation has now been well verified in optical systems like that described above [103], as well as in atom interferometry (Sect. 81.6) [104]. In the latter, the role of the polarization was played by internal energy states of an atom diffracted off a standing light wave.

84.4.2 Quantum Eraser

The interference lost to entanglement may be regained if one manages to “erase” the distinguishing information. This is the physical content of quantum erasure [105, 106]. The primary lesson is that one must consider the total physical state, including any MA with which the interfering quantum has become entangled, even if that MA does not allow accessible which-path information [107]. If the coherence of the MA is maintained, then interference may be recovered.

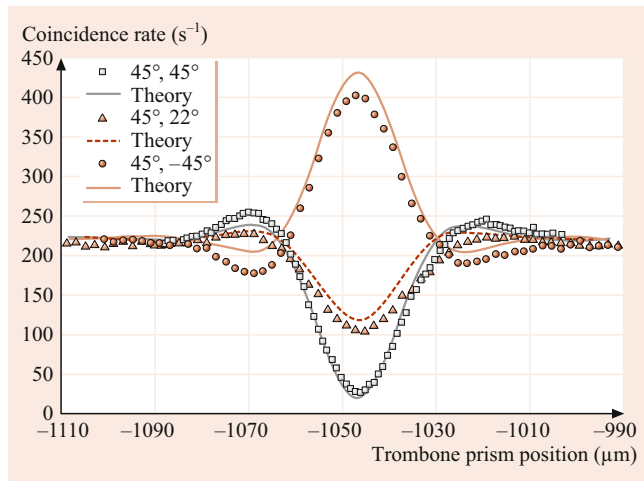


Fig. 84.5 Experimental data and scaled theoretical curves (adjusted to fit observed visibility of 91%) with polarizer 1 at 45° and polarizer 2 at various angles. Far from the dip, there is no interference, and the angle is irrelevant [108]

The first demonstration of a quantum eraser was based on the interferometer in Fig. 84.4 [108]. A half-waveplate inserted into one of the paths before the beamsplitter serves to rotate the polarization of light in that path. In the extreme case, the polarization is made orthogonal to that in the other arm, and the $r \cdot r$ and $t \cdot t$ processes become distinguishable; hence, the destructive interference that led to a coincidence null does not occur. The distinguishability can be erased, however, by using polarizers just before the detectors. In particular, if the initial polarization of the photons is horizontal, and the waveplate rotates one of the photon polarizations to vertical, then polarizers at 45° before both detectors restore the original interference dip. If one polarizer is at 45° and the other at -45° , interference is once again seen but now in the form of a peak instead of a dip (Fig. 84.5). There are four basic measurements possible on the MA (here the polarization) – two of which yield which-path information, one of which recovers the initial interference fringes (here the coincidence dip), and one of which yields interference antifringes (the peak instead of the dip). In some implementations, the decision to measure wave-like or particle-like behavior may even be delayed until *after detection* of the original quantum, an irreversible process [114, 115]. However, in all cases, one must correlate the results of measurements on the MA with the detection of the originally interfering system. This requirement precludes any possibility of superluminal signaling. This is an extension of the original delayed-choice discussion by *Wheeler* [109] and the experiments by *Hellmuth et al.*, *Alley et al.*, *Jacques et al.*, and *Kim et al.* [110–113], in which the decision to display wave-like or particle-like aspects in a light beam may be delayed until after the beam has been split by the appropriate optics.

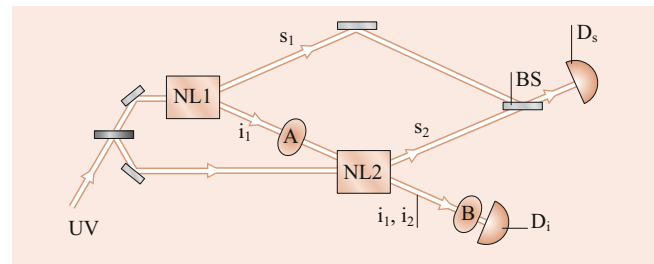


Fig. 84.6 Setup used in [117]. The idler photons from the two crystals are indistinguishable; consequently, interference fringes may be observed in the signal singles rate at detector D_s . Additional elements at A and B can be used to make a quantum eraser

84.4.3 Vacuum-Induced Coherence

A somewhat different demonstration [116, 117] of complementarity involves two downconversion crystals, NL1 and NL2, aligned such that the trajectories of the idler photons from each crystal overlap (Fig. 84.6). A beamsplitter acts to mix the signal modes. If the path lengths are adjusted correctly, and the idler beams overlap precisely, there is no way to tell, even in principle, from which crystal a photon detected at D_s originated. Interference appears in the signal *singles* rate at D_s , as any of the path lengths is varied. If the idler beam from crystal NL1 is prevented from entering crystal NL2, then the interference vanishes, because the presence or absence of an idler photon at D_i then “labels” the parent crystal. Thus, one explanation for the effect of blocking this path is that coherence is established by the idler-mode *vacuum* field seen by both crystals.

Experiments have also been performed in which a *time-dependent* gate is introduced in the idler arm between the two crystals [118]. As one expects, the presence or absence of interference depends on the earlier state of the gate, at the time when the idler photon amplitude was passing through it.

84.4.4 Suppression of Spontaneous Parametric Downconversion

A modification [119] of this two-crystal experiment uses only a single nonlinear crystal (Fig. 84.7). A given pump photon may downconvert in its initial rightward passage through the crystal or in its left-going return trip (or not at all, the most likely outcome). As in the previous experiment, the idler modes from these two processes are made to overlap; moreover, the signal modes are also aligned to overlap. Thus, the left-going and right-going production processes are indistinguishable and interfere. The result is that fringes are observed in all of the counting rates (i.e., the coincidence rate and both singles rates) as any of the mirrors is translated. A different interpretation is as a change in the spontaneous emission of the downconverted photons, akin to the suppression of spon-

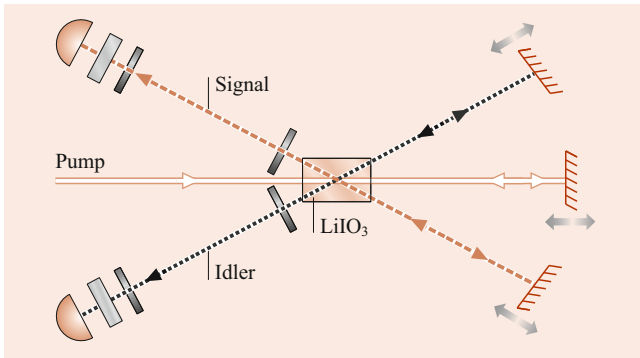


Fig. 84.7 Experiment to demonstrate enhancement and suppression of spontaneous downconversion [119]

taneous emission in cavity QED demonstrations, discussed in Sects. 84.2.1 and 83.3. Subsequent work has shown that, in a sense, there are always photons between the downconversion crystal and the mirrors, even in the case of complete suppression of the spontaneous emission process [120]. This same conclusion should also apply in the atom case, although in contrast to that system, for the downconversion experiment, the distances to the mirrors are much longer than the coherence lengths of the spontaneously emitted photons.

One recent application of this phenomenon is to study effective nonlinearities at the single-photon level [121]. Finally, with the inclusion of waveplates to label the photons' paths and polarizers to erase this information, an improved quantum eraser experiment was also completed, in which the which-path information for one photon was carried by the other photon [115].

84.5 Measurements in Quantum Mechanics

84.5.1 Quantum (Anti-)Zeno Effect

A strong measurement of a quantum system will project it into one of its eigenstates [101]. If the system evolves slowly out of its initial state: $|\Psi(t=0)\rangle = |\Psi_0\rangle \rightarrow \sqrt{1-t^2/\tau^2}|\Psi_0\rangle + t/\tau|\Psi_1\rangle$, then repeated measurements with an interval much less than τ can inhibit this evolution. If there are N total measurements within τ , then the probability for the system to still be in the initial state is $P(\tau) = (1 - (\tau/N)^2/\tau^2)^N \rightarrow 1$ as $N \rightarrow \infty$. This phenomenon, known as the quantum Zeno effect [122], has been experimentally observed using three levels in a ${}^9\text{Be}^+$ ion [123]. The ion was prepared in state $|i\rangle$ and weakly coupled to state $|f\rangle$ via RF radiation that induced a slow Rabi oscillation between the two states. Thus, in the absence of any intervening measurements, the ion evolved sinusoidally into state $|f\rangle$. When rapid measurements were made (by a laser strongly coupling state $|f\rangle$ to readout state $|r\rangle$, hence leading to strong fluorescence only if the atom was in state $|f\rangle$), the effect was to inhibit the $|i\rangle \rightarrow |f\rangle$ transition.

Note that here it was the *absence* of fluorescent photons that projected the state at each measurement back into the state $|i\rangle$.

Kofman and Kurizki pointed out that the above inhibition phenomenon depends on there being a bounded number of final states (the ion example had only one). If, instead, the measurement process actually *increases* the number of accessible final states $|f\rangle$, then one obtains the “anti-Zeno” effect, in which the $|i\rangle \rightarrow |f\rangle$ rate is enhanced rather than suppressed by frequent measurements [124]. For example, in the ion example, this would be the case if the $|i\rangle \rightarrow |f\rangle$ transition were spontaneous (allowing all frequencies) instead of driven (proceeding only at the driving Rabi frequency). The anti-Zeno effect has been observed by monitoring the survival time (against tunneling escape) of atoms trapped in an accelerating far-detuned standing wave of light [125].

84.5.2 Quantum Nondemolition

The uncertainty principle between the number of quanta N and phase ϕ of a beam of light,

$$\Delta N \Delta \phi \geq 1/2, \quad (84.8)$$

implies that to know the number of photons exactly, one must give up all knowledge of the phase of the wave. In theory, a *quantum nondemolition* (QND) process is possible [126]: without annihilating any of the light quanta, one can count them. It might seem that this would make possible successive measurements on noncommuting observables of a single photon, in violation of the uncertainty principle; it is the unavoidable introduction of phase uncertainty by any number measurement that prevents this.

QND schemes [127] often employ the intensity-dependent index of refraction arising from the optical Kerr effect (Sect. 76.4.3) – the change in the index due to the intensity of the “signal” beam changes the optical phase shift on a “probe” beam [128–131]. Other proposals include using the Aharonov–Bohm effect to sense photons via the phase shift their fields induce in passing electrons [132, 133]. Two classic experimental realizations [18] of a QND measurement – of the photon number in a microwave cavity – were performed by passing Rydberg atoms [134, 135] in a superposition of ground and excited state through the cavity. The interaction with the cavity photon is equivalent to a 2π -pulse (Sect. 83.8). The result is that, in the absence of any photon, the quantum state of the atoms after the cavity was unchanged; with a photon in the cavity, the ground state acquired an extra relative phase of π , which was then detected by measuring the atom's quantum state. Using similar schemes, successful nondemolition measurements have now been performed on microwave photons in microwave circuits [136, 137].

84.5.3 Quantum Interrogation

The previous section described techniques to measure the presence of a photon without absorbing it. Now we discuss a method – quantum interrogation – to optically detect the presence of an object without absorbing or scattering a photon. The possibility that the *absence* of a detection event – a “negative-result” measurement – can lead to wave-packet reduction was first discussed by *Renninger* [138] and later by *Dicke* [139]. Here, we consider the *gedanken* experiment proposed by *Elitzur* and *Vaidman*, a simple single-particle interferometer, with particles injected one at a time [140]. The path lengths are adjusted so that all the particles leave a given output port (A) and never the other (B). Now suppose that a nontransmitting object is inserted into one of the interferometer’s two arms – to emphasize the result, we consider an infinitely sensitive “bomb”, such that interaction with even a single photon will cause it to explode. By classical intuition, any attempt to check for the presence of the bomb involves interacting with it in some way, and by hypothesis this will inevitably set it off.

Quantum mechanics, however, allows one to be certain some fraction of the time that the bomb is in place, *without* setting it off. After the first beamsplitter of the interferometer, a photon has a 50% chance of heading towards the bomb and, thus, exploding it. On the other hand, if the photon takes the path without the bomb, there is no more interference, since the *nonexplosion* of the bomb provides *welcher Weg* (“which way”) information (Sect. 84.4.1). Thus, the photon reaches the final beamsplitter and chooses randomly between the two exit ports. Some of the time (25%), it leaves by output port B, something that never happened in the absence of the bomb. This immediately implies that the bomb (or some object) is in place – even though (since the bomb is unexploded) it has not interacted with any photon; *Elitzur* and *Vaidman* termed this an “interaction-free measurement”. (We prefer the more general description “quantum interrogation”, which then includes cases – e.g., detecting a semitransparent or quantum object – where it may not be possible to logically exclude the possibility of an interaction.) It is the possibility that the bomb *could* have interacted with a photon that destroys interference. An initial experimental implementation of these ideas [141] used downconversion to prepare the single photon states (Sect. 84.1) and a single-photon detector as the “bomb”. Subsequently, the technique was implemented incorporating focusing lenses, which would enable the image (more correctly, the silhouette) of an object to be determined with less than one photon per “pixel” being absorbed [142].

By adjusting the beamsplitter reflectivities in the above example, one can achieve at most a 50% fraction of measurements that are interaction free. An improved method, relying on the quantum Zeno effect [122] (Sect. 84.5.1), was discovered with which one can, in principle, make this fraction

arbitrarily close to 1 [141]. For example, consider a photon initially in cavity #1 of two identical cavities coupled by a lossless beamsplitter whose reflectivity $R = \cos^2(\pi/2N)$. If the photon’s coherence length is shorter than the cavity length, after N cycles, the photon will with certainty be located in cavity #2, due to an interference effect. However, if cavity #2 instead contains an absorbing object (e.g., the ultrasensitive bomb), at each cycle there is only a small chance ($= 1 - R$) that the photon will be absorbed; otherwise, the *nonabsorption* projects the photon wave packet entirely back onto cavity #1. After all N cycles, the total probability for the photon to be absorbed by the object is $1 - R^N$, which goes to 0 as N becomes large. In practice, unavoidable losses in the system limit maximum number of cycles and, hence, the achievable performance [143]. The photon effectively becomes trapped in cavity #1, thus indicating unambiguously the presence of the object in cavity #2.

This quantum-Zeno version of interrogation was first implemented using the inhibited rotation of a photon’s polarization (the object to be detected blocked one arm of a polarizing interferometer through which the photon was repeatedly cycled), achieving an efficiency of 75% [143]. A cavity-based implementation, in which the presence of the absorbing object inside a high-finesse cavity vastly increased the reflection off the cavity [144], detected the presence of the object with only 0.15 photons on average being absorbed or scattered [145].

84.5.4 Weak Measurements

Aharonov, *Albert*, and *Vaidman* extended quantum measurement theory by introducing “weak measurement”, a procedure that determines a physical property of a quantum system belonging to an ensemble that is both preselected and *postselected* [146, 147]. In the standard theory, a quantum system is measured by entangling its eigenstates with distinguishable pointer states of a measurement device, completely resolving the observable spectrum. The measurement can be weakened by increasing the overlap of the pointer states, consequently reducing the resolution of the eigenstates. When performed between two measurements this can give surprising results – in contrast to ordinary expectation values, the pointer can lie *outside* the range of the eigenvalue spectrum of the measured observable \mathbf{O} . The “weak value” $\mathbf{O}_w = \langle \Psi_{\text{fin}} | \mathbf{O} | \Psi_{\text{ini}} \rangle / \langle \Psi_{\text{fin}} | \Psi_{\text{ini}} \rangle$ between preselected $|\Psi_{\text{ini}}\rangle$ and postselected $|\Psi_{\text{fin}}\rangle$ states completely characterizes the outcome of the weak measurement. Weak measurements do not disturb each other, so that the weak values of noncommuting observables can be measured simultaneously [148].

Weak measurements have played an important role in addressing many fundamental issues in quantum mechanics, from the tunneling time [149, 150] (Sect. 84.7) to Hardy’s

paradox [151, 152] (Sect. 84.6.8) to the role of momentum disturbance in complementarity experiments [153] to verification of Ozawa's precision-disturbance relationship [154], which shows that a measurement need not disturb a system as much as predicted by a naive reading of the Heisenberg relation [155]. They have also permitted the study of negative kinetic energies [156], by postselecting a particle in a classically forbidden region, the direct reconstruction of the Bohmian trajectories of particles in a two-slit experiment [157], and a demonstration that a single postselected "shutter" can block two slits at once [158].

One other potentially powerful application of weak measurements is the amplification of weak signals, which was first demonstrated by amplifying the birefringence-induced small displacement of optical fields [159]. More recently it was used to detect very small deflections of an optical beam ($< \text{frad}$), much less than the intrinsic spread of the beam [160]. While it is true that weak amplification does not give a signal-to-noise ratio better than an optimal strong projection measurement if a system is quantum noise limited [161, 162], weak measurements can be advantageous in the typical case of dominant systematic noise [163, 164]. Recently, it was shown that the nonlinear effect of a single properly postselected photon on a probe beam could be amplified by a factor of 8, based on this principle [165]. Additionally, one could amplify a 5 nm displacement to 5 μm , which could then be easily observed, even if the measuring device measures an intrinsic jitter of 500 nm (ten times larger). Weak measurements also arise naturally in fiber optics telecom networks, due to polarization-mode dispersion and polarization-dependent losses [166].

84.5.5 Direct Measurements of a Wave Function

One particularly fundamental use of weak measurement is to directly measure an arbitrary unknown quantum wave function $|P s i_{\text{ini}}\rangle$ [167]. Here, one weakly measures whether the particle is at a particular position $X = x$, i.e., observable $\pi = |x\rangle\langle x|$, and then subsequently measures momentum, P . In the subset of trials that have outcome $P = p$, the weak value is $\pi_w = \langle p|x\rangle\langle x|\Psi_{\text{ini}}\rangle / \langle p|\Psi_{\text{ini}}\rangle$. For $p = 0$, this reduces to $\pi_w = C \langle x|\Psi_{\text{ini}}\rangle = \Psi_{\text{ini}}(x)$, where C is a complex constant that is independent of x , which can be found through calibration or normalization [167]. Hence, the weak value is directly proportional to the position wave function. In contrast to the standard method of quantum-state estimation, quantum tomography, a mathematical reconstruction or fitting is not required. Instead, the pointer directly indicates the real and imaginary parts of the wave function. An experiment used this concept to demonstrate the measurement of the transverse spatial wave function of a photon [167].

The concept has since been extended to general (e.g., mixed) quantum states [168–170]. More generally, this is an example of the aforementioned use of weak measurement to jointly measure complementary observables, and, thus, applies to any quantum system, whether it be discrete or continuous. Experiments have gone on to demonstrate the direct measurement of discrete states such as photon polarization [171] and orbital angular momentum [172]. In this context, the quantum-state estimation of systems with a high dimensionality d is greatly simplified, as has been experimentally demonstrated [173, 174]. Whereas tomography typically requires measurements in d different bases, this procedure requires only two (e.g., x and p). This advantage is multiplied when the direct measurement is applied to estimating processes [175], which would require d^2 experimental settings with tomography.

84.6 The EPR Paradox and Bell's Inequalities

84.6.1 Generalities

Nowhere is the nonlocal character of the quantum mechanical entangled state as evident as in the "paradox" of *Einstein, Podolsky, and Rosen* (EPR) [176], the version of *Bohm* [177], and the related inequalities by *Bell* [178, 179]. Consider two photons traveling in opposite directions, described by the entangled state

$$|\psi^-\rangle = (|H_1, V_2\rangle - |V_1, H_2\rangle) / \sqrt{2}, \quad (84.9)$$

where the letters denote horizontal (H) or vertical (V) polarization, and the subscripts denote photon propagation direction. This state, analogous to the singlet state of a pair of spin-1/2 particles, has the same form regardless of what polarization basis is used to describe it. Measurement of any polarization component for one of the particles will yield a count with 50% probability; individually, each particle is unpolarized. Nevertheless, if one measures the polarization component of particle 1 in any basis, one can predict with certainty the polarization of particle 2 in the same basis – either both photons will pass through their respective (aligned) polarizers or both will be reflected. Quantum mechanics predicts that this will happen no matter how far apart the polarizers are separated. According to EPR, to prevent faster-than-light influences between the two particles, there must be some extra information or variables that the photons carry locally with them that correlates their polarization state in every basis. These variables may be hidden or inaccessible to us, and are, therefore, referred to as local hidden variables (LHV). Quantum mechanics is a statistical theory that does not include in its formulation any such LHV, and, therefore, EPR argued that quantum theory is an incomplete description

of reality. For two entangled particles, a local hidden variable (LHV) theory can be made, which correctly describes perfect correlations or anticorrelations (i.e., measurements made in the same polarization basis). It was thought for many years that LHV theories and quantum mechanics yield the same predictions, and, consequently, the choice of an LHV theory versus quantum mechanics was a purely philosophical choice and not a physical one. However, in 1964 *John Bell* [178] discovered that QM gives different statistical predictions than does any LHV theory, for situations of imperfect correlations (i.e., analyzers at intermediate angles). Bell's inequality (BI) constrains various joint probabilities given by any local realistic theory and was later generalized to include any model incorporating locality [180, 181], and also extended to apply to real experimental situations [182, 183], and to systems with higher dimensionality [184–188]. Bell's theorem means that there is an experimental method to test whether local hidden variables are a fundamental aspect of nature.

84.6.2 Bell's Inequalities as a Game

A Bell test can be thought of as a game that two parties, Alice and Bob, play. Alice and Bob are isolated from one another and given a sequence of particles (e.g., photons in our case) to independently measure. Their goal is to correlate their outcomes in the way demanded by the rules of the game as much as possible. While they cannot communicate during the game, they are allowed to devise a shared secret strategy beforehand to try to maximize the number of times they win. Such a strategy can be thought of as a local hidden variable model (local in the sense that Alice and Bob are isolated from one another and must act independently).

In photonic Bell tests, it is often convenient for Alice and Bob to measure the polarization degree of freedom of their individual photons. To perform their measurements, Alice and Bob each have a polarizer that is randomly switched between two different angles every time they receive a photon. Alice has her polarizer set randomly to either angle a or a' , while Bob's polarizer is set to angles b or b' . Alice and Bob cannot know ahead of time what each other's polarizer setting is. If a particle is transmitted through the polarizer, a $+$ is recorded, and if it is reflected, a $-$ is recorded. This leaves four possible joint measurement settings ($ab, ab', a'b,$ and $a'b'$) as well as four possible measurement outcomes for each setting ($++, +-, -+,$ and $--$). The game proceeds in the following way. To win, we demand that if Alice and Bob happen to choose settings ab, ab' , or $a'b$, they report a correlated result (either $++$ or $--$), and if they choose setting $a'b'$ that they report an anticorrelated result (either $+-$ or $-+$). Each time they report a correct outcome for their particular measurement setting they receive a score of $+1$, but if they are wrong, they receive a score of -1 . Alice and Bob

play the game many times and then tabulate their joint score. To keep track of the score, we look at the average correlation as a function of the settings. For a given setting xy , the normalized correlation function $E(xy)$ is:

$$E(xy) = \frac{N_{++}(xy) - N_{+-}(xy) - N_{-+}(xy) + N_{--}(xy)}{N(xy)}, \quad (84.10)$$

where, for example, $N_{+-}(xy)$ is the number of times that Alice records a $+$ and Bob records a $-$ outcome when Alice sets her polarizer to $x \in a, a'$ and Bob sets his polarizer to $y \in b, b'$. This score is normalized by the total number of occurrences, $N(xy)$, resulting in the term $E(xy)$ taking on a value that ranges from -1 to 1 . The total joint correlation score, S , between Alice and Bob is then:

$$S = E(ab) + E(ab') + E(a'b) - E(a'b'). \quad (84.11)$$

This form of a Bell inequality was first proposed by *Clauser, Horne, Shimony, and Holt* (CHSH) [182, 183].

There are many optimal hidden variable strategies, but one of the simplest optimal approaches is for each photon to always be detected as $+$ regardless of the measurement setting. Therefore, Alice and Bob will report the correct result for three of the four possible settings' choices, but give the incorrect result when they perform the setting $a'b'$, resulting in an average score of 2 ($= 1 + 1 + 1 - 1$). The problem is that when Alice chooses to measure in setting b' , she does not know whether Bob is setting his polarizer to angle a or a' , and, therefore, is not sure whether to report a correlated or anticorrelated result. In general, for any local hidden variable model, the average score from Eq. (84.11) is bounded between $|S| \leq 2$. This form of Bell's inequalities was formulated in 1969 by Clauser, Horne, Shimony, and Holt (CHSH) and holds for any set of polarizer angles that Alice and Bob choose.

Surprisingly, if Alice and Bob are instead sent a pair of polarization-entangled photons, such as the singlet state in Eq. (84.9), and choose the appropriate measurement angles, then it is possible for them to achieve a maximum score of $2\sqrt{2}$. This means that quantum mechanics predicts correlations that are stronger than those permitted by local hidden variables. A Bell test is an experiment designed to test this contradiction. If a value of $S > 2$ is observed, this rules out any local hidden variable description of the experiment. Strictly speaking, in a Bell test, we are never able to prove that quantum mechanics is correct, but rather we are only trying to falsify the notion that local hidden variables are fundamental to nature. The stronger correlations in quantum systems not only have important philosophical implications about the structure of reality but are part of the reason why emerging technologies like quantum computers should have

a massive performance advantage over classical computers in certain situations. It should also be noted that, in principle, the maximum achievable score in this Bell game is 4 for a perfectly correlated system, which is even greater than what quantum mechanics allows for. While we do not have any evidence that the universe permits correlations stronger than quantum mechanics, models of such systems, known as PR boxes [189], can serve as a useful theoretical tool.

84.6.3 Loopholes in Bell Tests

To unambiguously violate a Bell inequality one must experimentally satisfy several conditions. The first experiments to violate Bell's inequalities were carried out by *John Clauser* [190] and later by *Aspect* and colleagues [191], but due to technological limitations needed to make additional assumptions. These extra assumptions open up “loopholes” that could allow a local hidden variable theory to replicate the stronger correlations predicted by quantum mechanics. Strictly speaking, these experiments could only rule out a subset of local hidden variable models. If Alice and Bob are close together, then there is the possibility that hidden variables controlling Alice and Bob's photons could signal one another to coordinate their outcomes. To prevent this, Alice and Bob must be far enough apart so that their measurements can be individually completed before any such signals traveling at the speed of light could influence the outcomes. If this condition is not satisfied, it opens the so-called “locality loophole”. There is a subset of the locality loophole, sometimes referred to as “freedom of choice”, where Alice and Bob must assume that their measurement choices are independent of one another and the source of photons. This is usually addressed through the use of independent random number generators at Alice and Bob, but strictly speaking they can never guarantee that something in their shared past light cones did not correlate their settings choices. The extreme example of this is “superdeterminism”, the idea that the universe is deterministic with its entire history set in stone at beginning of time. Such theories are not testable, and therefore exist outside the realm of experimental physics.

Because a Bell test is statistical in nature, if there is too much loss, it is possible for a local hidden variable to appear to violate a Bell inequality. A local hidden variable could bias the observed correlations by preferentially discarding, through nondetection, certain outcomes. In this way, the detected events would appear to violate Bell's inequalities, but the total ensemble of detected and undetected events would not. To prevent this, at least 2/3 of the photons sent to Alice and Bob must be detected. If this efficiency threshold cannot be met, then one must assume that the detected events are fairly sampled from the total ensemble leading to the “fair-sampling” loophole (also known as the “detector loop-

hole”). All of the experiments discussed above that closed the locality loophole were unable to simultaneously close the fair-sampling loophole. In order to understand the detection loophole, it is convenient to consider the Clauser–Horne (CH) form of the Bell inequality [183]. This form of the inequality incorporates loss directly and is convenient because it only requires Alice and Bob to use one detector each. Now Alice and Bob must report either the detection of a photon (+) or no detection (0) every trial (any – outcomes are now just mapped to 0). The CH inequality is:

$$N_{++}(a, b) + N_{++}(a, b') + N_{++}(a', b) - N_{++}(a', b') \leq N_+(a) + N_+(b). \quad (84.12)$$

The left-hand side of this equation is the number of coincidence events where in a given trial Alice and Bob both detect a photon. The term $N_+(a)$ ($N_+(b)$) on the right-hand side represent the total number of photons Alice (Bob) detects while in setting a (b) irregardless of what the other party measures. For certain choices of a , a' , b , and b' , quantum mechanics predicts that the left-hand side of the CH inequality can exceed the right-hand side. However, in practice, this is very difficult to observe, since the probability of detecting a coincidence falls as η^2 (η is the detection efficiency), compared to the singles counts on the right-hand side, which fall only as η . For a maximally entangled state, such as the one described in Eq. (84.9), a detection efficiency $\eta \geq 83\%$ is required to violate the CH inequality [192]. If one uses a nonmaximally entangled state of the form:

$$|\Psi\rangle = \cos(\theta)|H_1, V_2\rangle - \sin(\theta)|V_1, H_2\rangle, \quad (84.13)$$

then the required detection efficiency may be reduced to 67% as θ goes to 0 for the appropriate analysis settings [193, 194]. Finally, the CH inequality in Eq. (84.12) can be converted into a “hypothesis test”. Doing so can prevent additional forms of potential statistical manipulation. For example, if Alice and Bob normalize their correlations by the total number of counts, they are implicitly making the assumption that every trial was independent and identical. Instead, by using an appropriate hypothesis-testing framework it is possible to avoid these subtle analysis assumptions. In the hypothesis-testing framework, a p-value is reported which is the probability that, if local realism is true, it would be able to produce a violation of the Bell inequality greater than or equal to the observed violation.

84.6.4 Closing the Loopholes in Bell Tests

In 1982, *Aspect* et al. used entangled photons from an atomic cascade to perform the first Bell test where Alice and Bob were separated far enough apart (12 m) that their measurement outcomes satisfied the locality constraints [191]. This

was followed up by a first attempt to have Alice and Bob vary their measurement settings while the photons were in flight towards the measurement stations (early experiments used passive components that could be interpreted as allowing the photons to make the decisions as to how they would be measured). In this experiment, function generators at Alice and Bob produced a periodic voltage to drive home-built acoustic optic modulators that switched the incoming photons between two different measurement setups. However, because the generators used to drive the measurement switching were periodic, the locality loophole could not be fully addressed. In 1998, Weihs et al. were able to fully close the locality loophole by using entangled photons generated by the process of spontaneous parametric downconversion along with fast random number generators that drove electronic polarization analyzers. The photons were sent to measurement stations 400 m apart, and while they were in flight, the measurement basis was randomly and independently set to ensure space-like separated observers [195]. However, in that experiment, the detection efficiency was less than 5%. Currently, the locality loophole has been closed on a continental scale—in 2018, Yin et al. performed a Bell test with Alice and Bob separated by 1203 km using an entangled source of photons on board a satellite in low Earth orbit [196].

The first experiment to close the detection loophole was the entangled-ion experiment of Rowe et al. [197] in 2001. In this experiment the entangled variables were the hyperfine energy levels of ${}^9\text{Be}^+$ ions. By employing a cycling transition that leads to the emission of many photons if the atom is in one of the states, a detection efficiency in excess of 98% was achieved, allowing an $8\text{-}\sigma$ Bell inequality violation. However, because the ions were separated by only $3\ \mu\text{m}$ in the same linear Paul trap, and in fact were measured using the same laser pulse, there was no possibility of closing the locality loophole. A decade later the detection loophole was finally closed using photons in two experiments [198, 199] that utilized superconducting transition edge detectors with efficiencies $> 98\%$. These detectors use a superconducting material operating near the transition point to measure the energy deposited by one or more photons. However, in these experiments the detectors used for Alice and Bob were cooled in the same cryostat, preventing the locality loophole from being closed.

It wasn't until 2015, 51 years after Bell's original paper, that three groups were able to independently close these loopholes at the same time in the same experiment. At TU Delft Hensen et al. used entangled spins in Nitrogen-vacancies in diamonds separated by 1.3 km to violate a Bell inequality with a value of $S = 2.42 \pm 0.20$ [200]. This corresponds to a p-value of 0.039 for refuting local realism. The other two experiments were performed using entangled photons. At the National Institute of Standards and Technologies in Boulder, Shalm et al. were able to close

all the loopholes with $> 5\sigma$ confidence, and violate a Bell inequality with a p-value of 5.3×10^{-9} [201], while in Vienna a loophole-free Bell test was conducted at the Hofburg Imperial Palace by Giustina et al., measuring a p-value of 3.74×10^{-31} [202]. In 2016 a fourth loophole-free Bell test used entangled Rb^{87} atoms separated by 398 m by Rosenfeld et al. in Munich to obtain a violation of $S = 2.221 \pm 0.033$, corresponding to a p-value of 2.57×10^{-9} [203].

While in principle it is not possible to close the freedom-of-choice loophole due to super determinism, with some additional assumptions one is able to push back the earliest time that a local hidden variable could have correlated Alice's and Bob's measurement choices by using light from distant stars or quasars to choose the measurement settings used. This requires the assumption that the detectors, telescopes, and other electronic equipment used by Alice and Bob are not correlated with one another, and that the mechanisms that produce the light in the stellar objects are short-lived. For example, it might take a photon 100,000 years to escape the deep plasma core of a star due to the short mean-free path [204, 205], but an unimpeded neutrino could escape at a much earlier time to carry the information to the Earth. Recently, in 2018 Li et al. were able to perform a loophole-free Bell test using polarization entangled photons that used the random arrival times of light from nearby stars to make Alice and Bob's measurement choices. This pushes the earliest point at which Alice's and Bob's measurement choices could be correlated to 11 years in the past [206]. A similar experiment, albeit not loophole-free, used high-redshifted light from distant quasars to choose Alice's and Bob's settings, and pushing back the earliest time a local hidden variable model could have exerted an influence to approximately 7.8 billion years ago (corresponding to 96% of the space-time volume in the past light cone of the experiment) [207]. Taken together these experiments provide convincing proof that local realism is not a viable theory of nature.

84.6.5 Polarization-Based Entangled Sources

The process of downconversion (see Sect. 76.3.6) provides a convenient way to generate entangled pairs of polarization-entangled photons. To create entangled photons, two different processes need to interfere with one another. For example, consider two identical type-I phase-matched crystals placed back-to-back, but with the second crystal rotated by 90° . The first crystal will downconvert a H -polarized pump into V -polarized pairs while the second crystal downconverts a V -polarized pump into H -polarized pairs. By coherently pumping the two crystals with light polarized at $|45\rangle = (|V\rangle + |H\rangle)/\sqrt{2}$, there is an equal probability of producing a pair of photons in either the first or second crystal. Since there is no knowledge of which process took place,

one obtains the entangled state $(|HH\rangle + e^{i\varphi}|VV\rangle)/\sqrt{2}$ [208]. More generally, pumping $\alpha|V\rangle + e^{i\varphi}\beta|H\rangle$ produces arbitrary nonmaximally entangled states of the form $\alpha|HH\rangle + e^{i\varphi}\beta|VV\rangle$ [209].

Using type-II phase-matching one also can produce polarization entanglement from a single crystal [210]. One member of each downconversion pair is emitted along an ordinary polarized cone while the other is emitted along an extraordinary polarized cone. If the photons happen to be emitted along the intersection of the two cones, neither photon will have a definite polarization – they will be in the state $(|HV\rangle + |VH\rangle)/\sqrt{2}$. This entanglement source has now been used in a variety of quantum investigations, including Bell inequality tests [195, 210], quantum cryptography [211, 212] (Sect. 85.2.1) and teleportation [213, 214], and as a resource for studying entanglement of more than two photons [215–218].

84.6.6 Other Entanglement Sources for Bell Tests

The advent of parametric downconversion has also led to the appearance of several nonpolarization-based BI tests, using, for example, an entanglement of the photon momenta (Fig. 84.8) [219]. By the use of small irises (labeled ‘A’ in Fig. 84.8), only four downconversion modes are examined: 1s, 1i, 2s, and 2i. Beams 1s and 1i correspond to one pair of conjugate photons; beams 2s and 2i correspond to a different pair. Photons in beams 1s and 2s have the same wavelength, as do photons in beams 1i and 2i. With proper alignment, after the beamsplitters there is no way to tell whether a pair of photons came from the 1s-1i or the 2s-2i paths. Consequently, the coincidence rates display interference, although the singles rates at the four detectors indicated in Fig. 84.8 remain constant. This interference depends on the difference of phase shifts induced by rotatable glass plates P_i and P_s in paths 1i and 2s, respectively, and is formally equivalent to the polarization case considered above, in which it is the difference of polarization-analyzer angles that is rele-

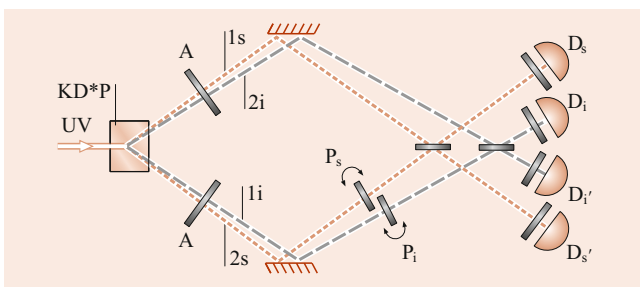


Fig. 84.8 Outline of apparatus used to demonstrate a violation of a Bell’s inequality based on momentum entanglement [219]

vant. By measuring the coincidence rates for two values for each of the phase shifters – a total of four combinations – the experimenters were able to violate an appropriate BI. One interpretation is that the paths taken by a given pair of photons are not elements of reality.

Momentum conservation in the downconversion process (Eq. (84.4)) also leads to entanglement directly in the spatial modes in the correlated photons. For example, *Zeilinger et al.* [220, 221] and *Langford et al.* [222] demonstrated entanglement between the *orbital* angular momentum of the photons, of the form $(|+1, -1\rangle + \epsilon|0, 0\rangle + |-1, +1\rangle)$, where 0 and ± 1 , respectively, denote modes with no orbital angular momentum (Gaussian spatial profiles) and $\pm\hbar$ (Laguerre–Gauss vortex modes). Note that this enables one to investigate correlations for degrees of freedom that reside in larger Hilbert spaces than do the two-level systems (e.g., polarization) discussed above. The nonlocal spatial correlations of the downconversion photons have also given rise to many interesting experiments in the area of quantum imaging [223–226], where one is able to obtain spatial resolution beyond that predicted by the usual \sqrt{N} shot-noise limitations.

Several groups [227, 228] have implemented a different BI proposal [229], based on energy-time entanglement of the photons. One member of each downconverted pair is directed into an unbalanced Mach–Zehnder-like interferometer, allowing both a short and a long path to the final beamsplitter; the other photon is directed into a separate but similar interferometer. There arises interference between the indistinguishable processes (“short-short” and “long-long”), which could lead to coincidence detection. Using fast detectors to select out only these processes, the reduced state (Eq. (84.9)) is

$$|\psi\rangle = \frac{1}{\sqrt{2}}(|S_1, S_2\rangle - e^{i\phi}|L_1, L_2\rangle), \quad (84.14)$$

where the letters indicate the short or the long path, and the phase is the sum of the relative phases in each interferometer. Although no fringes are seen in any of the singles count rates, the high-visibility coincidence fringes (Fig. 84.9) lead to a violation of an appropriate BI. One conclusion is that it is incorrect to ascribe to the photons a definite time of emission from the crystal, or even a definite energy, unless these observables are explicitly measured. A more general interpretation, applicable to all violations of Bell’s inequalities, is that the predictions of QM cannot be reproduced by any completely local theory. It must be that the results of measurements on one of the photons depend on the results for the other, and these correlations are not merely due to a common cause at their creation [230, 231].

This same sort of arrangement, modified to work with a pulsed pump, has been used to demonstrate a violation of local realism with photons separated by 10.9 km [232].

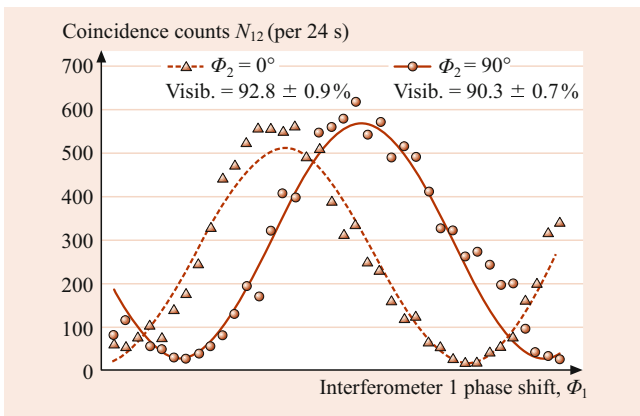


Fig. 84.9 High-visibility coincidence fringes in a Franson dual-interferometer experiment [229] for two values of the phase in interferometer 2 as the phase in interferometer 1 is slowly varied. The curves are sinusoidal fits

In a related experiment, a similar system was used to place limits on the “speed of collapse” of the two-photon wave function, i.e., how fast a nonlocal “signal” would need to propagate from one side of the experiment to the other to account for the measured nonclassical correlations. Depending on some assumptions about the detection process and which inertial frame of reference is considered, the nonlocal influence speed was constrained to be at least 10^4c to 10^7c [233]. In one interesting variant, the researchers arranged to have *moving* detectors, such that in the local reference frame of each detector, it was the *other* detector that initiated the collapse. Due to the experimental difficulty of accelerating actual detectors to high velocities, a rapidly rotating absorbing disk was placed close to one output port of a polarizing beamsplitter; following ideas discussed in Sect. 84.5.3, the *nonabsorbance* of the photon by the absorber was deemed sufficient to cause a reduction of the wave function. As expected, the measured correlations were in no way reduced, but this experiment did rule out one alternative theory of nonlocal collapse [234].

Finally, by using more than two possible creation times, one can also demonstrate entanglement in higher dimensional Hilbert spaces. For instance, using a mode-locked pulsed laser, *Gisin’s* group demonstrated entanglement for a two-photon state at least of dimension 11 [235].

84.6.7 Advanced Experimental Tests of Nonlocality

The previously described tests of Bell’s inequality actually have little to do with quantum mechanics per se, other than that it is quantum correlations that enable a violation; the conclusions of such a violation only say that no local realistic description is sufficient to explain the results. Just as the

CHSH inequality [183] bounds the observable correlations of a local realistic description to $|S| \leq 2$, *Tsirelson* [236] showed that, according to quantum theory, $|S|$ has an upper bound of $2\sqrt{2} \approx 2.82843$. One immediate question is how close experimental realizations have come to reaching this value. The loophole-free experiments discussed in Sect. 84.6.4 have values of S that, while larger than the local realistic bound of 2, are still far from the maximum possible value permitted by quantum mechanics. A recent experiment [237] that did not attempt to close the detection and locality loopholes provides the best test of the upper bound to date, using photon pairs in a maximally entangled state of polarization to obtain $S = 2.82759 \pm 0.00051$.

Other generalizations to the Bell inequality have been studied and have obtained some counterintuitive results. For example, one modified Bell inequality has the property that the maximum quantum violation can only be obtained using partially entangled states [238], and another cannot be violated at all by a maximally entangled state. Experimental violations [239] of these modified inequalities have been observed, with results matching the (quantum) theoretical predictions extremely well, thus illustrating the phenomenon of “more nonlocality with less entanglement” [238, 240, 241].

In fact, the four correlation functions that make up S (Eq. (84.11)) are each bounded by 1, and *Popescu* and *Rohrlich* showed that the no-signaling principle that prevents superluminal communication is compatible with values up to $S = 4$ [242]; a theoretical ultra-nonlocal construct that enables one to achieve this maximal value is called a “PR box” after its originators. A 2.828 maximal quantum violation of the CHSH inequality could, thus, be interpreted as arising from a 41% contribution of a PR box and a 59% contribution from a local theory: $2\sqrt{2} = (0.59 \times 2) + (0.41 \times 4)$, where the 2 and 4 represent the maximum values for S attainable with a local theory or nonsignaling nonlocal theory, respectively. One can instead consider a “chained Bell inequality” [243, 244] in which the usual two measurement settings on either side are replaced by a value $n > 2$; in this case, as n increases, the quantum violation approaches the bound imposed by the no-signaling principle. Consequently, one can place a stronger bound on the “nonlocal” content that would be required to achieve the observed results. In the experiment reported in [239], nonlocal resources (such as PR boxes) would be needed in $87.4 \pm 0.1\%$ of the experimental rounds in order to match the observed chained Bell inequality violation; this represents the most nonlocal correlations ever produced experimentally (this experiment did not attempt to close the detector or locality loophole). A subsequent experiment using ${}^9\text{Be}^+$ ions closed the detection loophole in a chained-Bell inequality while certifying that the nonlocal content consistent with their results was at least 67.3% [245]. A remaining challenge is performing a fully loophole-free chained Bell inequality.

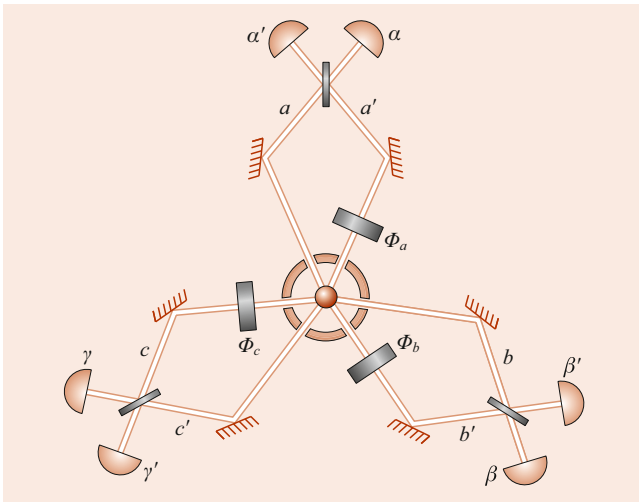


Fig. 84.10 A three-particle gedankenexperiment to demonstrate the inconsistency of quantum mechanics and any local realistic theory. All beamsplitters are 50–50 [116]

84.6.8 Nonlocality Without Inequalities

In the above experiments for testing nonlocality, the disagreement between quantum predictions and Bell’s constraints on local realistic theories are only statistical. Greenberger, Horne, and Zeilinger (GHZ) pointed out that in some systems involving *three* or more entangled particles [246, 247], a contradiction could arise even at the level of perfect correlations. A schematic of one version of the GHZ *gedankenexperiment* is shown in Fig. 84.10. The source at the center is posited to emit trios of correlated particles. Just as the Rarity-Tapster experiment selected two pairs of photons (Fig. 84.8), the GHZ source selects two trios of photons; these are denoted by abc and $a'b'c'$. Hence, the state coming from the source may be written as

$$|\psi\rangle = (|abc\rangle + |a'b'c'\rangle)/\sqrt{2}. \quad (84.15)$$

After passing through a variable phase shifter (e.g., ϕ_a), each primed beam is recombined with the corresponding unprimed beam at a 50–50 beamsplitter. Detectors (denoted by Greek letters) at the output ports signal the occurrence of triple coincidences. The following simplified argument conveys the spirit of the GHZ result.

Given the state Eq. (84.15), one can calculate from standard QM the probability of a triple coincidence as a function of the three phase shifts:

$$P(\phi_1, \phi_2, \phi_3) = \frac{1}{8}[1 \pm \sin(\phi_a + \phi_b + \phi_c)], \quad (84.16)$$

where the plus sign applies for coincidences between all unprimed detectors, and the minus sign for coincidences between all primed detectors. For the case in which all phases

are 0, it will occasionally happen (1/8-th of the time) that there will be a triple coincidence of all primed detectors. Using a “contrafactual” approach, we ask what would have happened if ϕ_a had been $\pi/2$ instead. By the locality assumption, this would not change the state from the source, nor the fact that detectors β' and γ' went off. However, from Eq. (84.16), the probability of a triple coincidence for primed detectors is zero in this case; therefore, we can conclude that detector α would have “clicked” if ϕ_a had been $\pi/2$. Similarly, if ϕ_b or ϕ_c had been $\pi/2$, then detectors β or γ would have clicked. Consequently, if all the phases had been equal to $\pi/2$, we would have seen a triple coincidence between unprimed detectors. However, according to Eq. (84.16), this is impossible: the probability of triple coincidences between unprimed detectors when all three phases are equal to $\pi/2$ is strictly zero! Hence, if one believes the quantum mechanical predictions for these cases of perfect correlations, it is not possible to have a consistent local realistic model.

Downconversion experiments have enabled the production of three and four-photon GHZ states, with results in good agreement with theory (the all-or-nothing arguments given above become inequalities in any real experiment) [215, 216, 248]. In 2014, Erven et al. were able to close the locality loophole while violating the Mermin inequality by $9\text{-}\sigma$, although they were unable to close the detector loophole simultaneously.

By similar arguments, *Hardy* has shown the inconsistency of quantum mechanics and local realism in a *gedankenexperiment* with just two particles [249, 250]. When the arguments are suitably modified to deal with real experiments, inequalities once again result; these have also been experimentally violated, using nonmaximally entangled states from downconversion [251, 252], underscoring the vast disagreement between quantum theory and locality.

84.6.9 Connection to Quantum Information

The properties of entangled photons and the nonlocal correlations they share play a critical role in many quantum information applications. The information carried by photons cannot be cloned perfectly, which has led to protocols for securely exchanging one-time pads for use in cryptography [211, 212, 253–260]. The stronger correlations present between entangled photon-pairs can also be exploited to transfer two bits of information using a single photon [261–263], a process known as superdense coding. Since it is not possible to perfectly clone a quantum state, techniques have been devised to use an entangled pair of photons to instead “teleport” or move quantum information from one location to another through the use of Bell state measurements and classical communications [213, 264–267]. This process of teleportation may form a fundamental building block in fu-

ture quantum networks, allowing quantum information to be transmitted over long distances [268]. Such a network would enable networked quantum computing, connecting quantum circuits based on solid-state or matter quantum bits using light. Finally, loophole-free Bell tests are a fundamental component in new types of security protocols. A hacker or attacker who wishes to control or predict the outcome of a Bell test has at their disposal a set of tools equivalent to those of a hidden-variable theory. They are hoping to use their added knowledge, perhaps hidden from the experimenter, to manipulate the results. However, if a loophole-free Bell violation can be obtained, one can rule out the influence of such an attacker even if they control part of the equipment used. For this reason, protocols based on loophole-free Bell tests are referred to as being “device-independent” [269–273]. In 2017, the first fully device-independent protocol was carried out to generate certifiably secure random numbers using the loophole-free Bell test developed at NIST in Boulder, CO [274]. As the technology behind loophole-free Bell tests improves, a wider-range of device-independent applications promises to become more prevalent.

As an indicator of the importance of these fundamental tests of (non)locality, the 2022 Nobel prize in physics was awarded to John F. Clauser, Alain Aspect, and Anton Zeilinger “for experiments with entangled photons, establishing the violation of Bell inequalities and pioneering quantum information science,” i.e., based on the research described above [182, 183, 190, 191, 195, 213, 268].

84.7 Single-Photon Tunneling Time

84.7.1 An Application of EPR Correlations to Time Measurements

In this section, we discuss experiments involving the quantum propagation of light in matter. Due to the sharp time correlations of the paired photons from spontaneous downconversion, one can use the HOM interferometer (Sect. 84.3.3, Fig. 84.4) to measure very short relative propagation delay times for the signal and idler photons. One early application was, therefore, to confirm that single photons in glass travel at the group velocity [94]. At least until recently, the only quantum theory of light in dispersive media was an *ad hoc* one [275]. The shift of the interference dip resulting from a medium introduced into one of the interferometer arms can be accurately measured by determining how much the path lengths must be changed to compensate the shift and recover the dip. This result suggests that when looking for a microscopic description of dielectrics, it is unnecessary to consider the medium as being polarized by an essentially classical electric field due to the collective action of all photons present, and reradiating accordingly. Linear di-

electric response is not a collective effect in this sense – each photon interferes only with itself (as per Dirac’s dictum) as it is partially scattered from the atoms in the medium. The single-photon group velocity thus demonstrates “wave-particle unity”.

The standard limitation for measurements of short-time phenomena is that to have high time-resolution, one needs short pulses (or at least short coherence lengths), but these, in turn, require broad bandwidths and are, therefore, very susceptible to dispersive broadening. It is a remarkable consequence of the EPR energy correlations of the downconversion photons (Sect. 84.3.2) that time measurements made with the HOM interferometer are essentially immune to such broadening [94, 276, 277]. In effect, the measurement is sensitive to the *difference* in emission times while the broadening is sensitive to the *sum* of the frequencies. While frequency and time cannot both be specified for a given pulse, the crucial feature of EPR correlations such as those exhibited by downconverted photons is that this difference and this sum correspond to commuting observables and both may be arbitrarily well defined. The photon that reaches detector 1 could either have traversed the dispersive medium and been transmitted or traversed the empty path and been reflected, leaving its twin to traverse the medium. The medium, thus, samples *both* of the (anticorrelated) frequencies, leading to an automatic cancelation of any first-order (and in fact, all odd-order) dispersive broadening. Measurements can be more than five orders of magnitude more precise than would be possible via electronic timing of direct detection events, and in principle, better than those performed with nonlinear autocorrelators (which rely on the same fundamental physics as downconversion but do not benefit from a cancelation of dispersive broadening).

84.7.2 Superluminal Tunneling Times

Another well-known problem in the theory of quantum propagation is the delay experienced by a particle as it tunnels. There are difficulties associated with calculating the “duration” of the tunneling process, since evanescent waves do not accumulate any phase [278–280]. First, the kinetic energy in the barrier region is negative, so the momentum is imaginary. Second, the transit time of a wave-packet peak through the barrier, defined in the stationary phase approximation by

$$\tau^{(\phi)} \equiv \partial[\arg t(\omega)e^{ikd}]/\partial\omega, \quad (84.17)$$

tends to a constant as the barrier thickness diverges, in seeming violation of relativistic causality. It is shown in [91] that such saturation of the delay time is a natural consequence of time-reversal symmetry, and in [281] that one can deduce

from the principle of causality itself that *every* system possesses a superluminal group delay, at least at the frequency where its transmission is a minimum. For example, the transmission function for a rectangular barrier,

$$t(k, \kappa) = \frac{e^{-ikd}}{\cosh \kappa d + i \frac{\kappa^2 - k^2}{2k\kappa} \sinh \kappa d}, \quad (84.18)$$

leads in the opaque limit ($\kappa d \gg 1$) to a traversal time of $2m/\hbar k \kappa$, independent of the barrier width d . The same result applies to photons undergoing frustrated total internal reflection [91], when the mass m is replaced by $n^2 \hbar \omega / c^2$, and similar results apply to other forms of tunneling.

Some researchers have, therefore, searched for some more meaningful “interaction time” for tunneling, which might accord better with relativistic intuitions and perhaps have implications for the ultimate speed of devices relying on tunneling [282]. The “semiclassical time” corresponds to treating the *magnitude* of the (imaginary) momentum as a real momentum. This time is of interest mainly because it also arises in Büttiker and Landauer’s calculation of the critical timescale in problems involving oscillating barriers, which they take to imply that it is a better measure of the duration of the interaction than is the group delay [278]. The Larmor time [283] is one of the early efforts to attach a “clock” to a tunneling particle, in the form of a spin aligned perpendicular to a small magnetic field confined to the barrier region. The basic idea is that the amount of Larmor precession experienced by a transmitted particle is a measure of the time spent by that particle in the barrier. This clock turns out to contain components corresponding both to the distance-independent “dwell time” and the linear-in-distance semiclassical time. Experiments are being done with cold atoms, which have begun to resolve these two contributions [284]. Curiously, the most common theories for tunneling times become superluminal in certain cases anyway, whether or not they deal with the motion of wave packets. Pioneering tests of tunneling times included both optical and solid-state approaches [285]. In recent years, new experimental results have begun to appear both in attosecond strong-field ionization measurements and in cold-atoms experiments [286–289], but there is still disagreement about their interpretation. Below, in Sect. 84.7.4, we discuss theoretical status of different tunneling-time proposals.

Here, we will restrict ourselves to discussing the time of appearance of a peak of a single-photon wave packet. Optical tests offer certain unique advantages [290], including the ease of construction of a barrier with no dissipation, very little energy dependence, and a superluminal group delay. The transmitted wave packets suffer little distortion and are essentially indistinguishable from the incident wave packets. At a theoretical level, the fact that photons are described by Maxwell’s (fully relativistic) equations is an important argu-

ment against interpreting superluminal tunneling predictions as a mere artifact of the nonrelativistic Schrödinger equation. Also, one is denied the recourse suggested by some workers [291] of interpreting the superluminal appearance of transmitted peaks to mean that only the high-energy components (which, for matter waves, traveled faster even before reaching the barrier [292]) were transmitted.

84.7.3 Tunneling Delay in a Multilayer Dielectric Mirror

A suitable optical tunnel barrier can be a standard multilayer dielectric mirror. The alternating layers of low and high index material, each one quarter-wave thick at the design frequency of the mirror, lead to a photonic bandgap [293] analogous to that in the Kronig–Penney model of solid state physics (Sect. 83.3.6). The gap represents a forbidden range of energies, in which the multiple reflections will interfere constructively so as to exponentially damp any incident wave. The analogy with tunneling in nonrelativistic quantum mechanics arises because of the exponential decay of the field *envelope* within the periodic structure, i.e., the imaginary value of the quasi momentum. The same qualitative features arise for the transmission time: for thick barriers, it should saturate at a constant value, as was verified in a recent experiment employing short *classical* pulses [300]. A more direct analogy, that of waveguides beyond cutoff, yielded similar results in a classical microwave experiment [294], while another paper reported superluminal effects related to the penetration of diffracted or “leaky” microwaves into a shadow region [295]. All these experiments involve very small detection probabilities, just as in *Chu* and *Wong*’s pioneering experiment on propagation within an absorption line [296]. However, it has been predicted that superluminal propagation could occur *without* high loss or reflection [297–299] by operating outside the resonance line of an *inverted* medium (Sect. 74.1). One can understand the effect as off-resonance “virtual amplification” of the leading edge of a pulse.

The phenomenon was investigated at the single-photon level by using the high time-resolution techniques discussed in Sect. 84.7.1 to measure the relative delay experienced by downconversion photons [301] when such a tunnel barrier (consisting of 11 layers) was introduced into one arm of a HOM interferometer. The transmissivity of the barrier was relatively flat throughout the bandgap (extending from 600 to 800 nm; Fig. 84.11), with a value of 1% at the gap center (700 nm), where the experiment was performed. The HOM coincidence dip was measured both with the barrier (and its substrate) and with the substrate alone (Fig. 84.12). Each dip was subsequently fitted to a Gaussian, and the difference between their centers was calculated. When several such runs

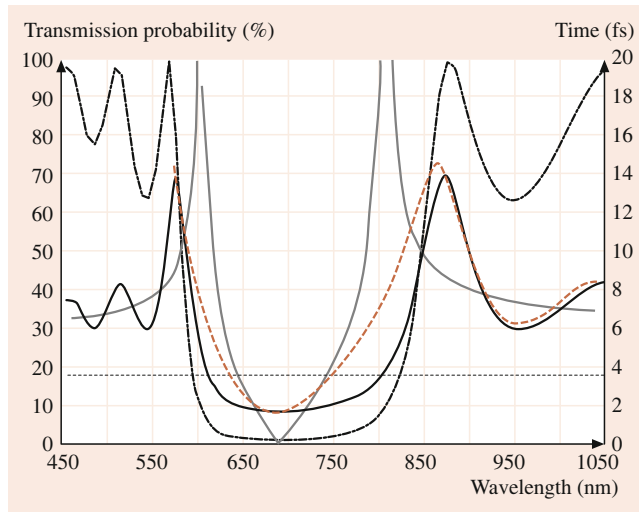


Fig. 84.11 Transmission probability for the tunnel barrier used in [301] (light solid curve); heavy, dashed, and dotted curves show group delay, Larmor time, and semiclassical time; $d/c = 3.6$ fs is shown for comparison

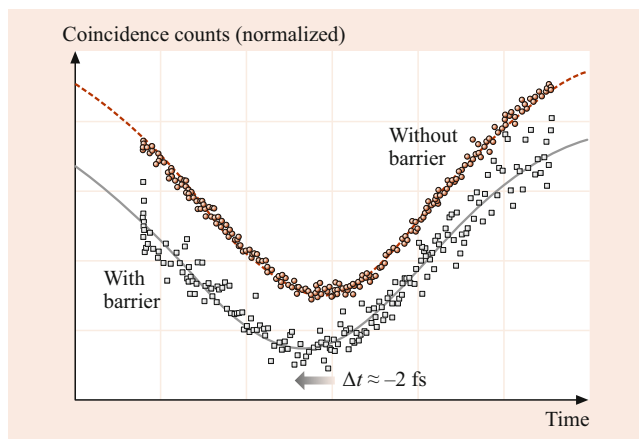


Fig. 84.12 Coincidence profiles with and without the tunnel barrier map out the single-photon wave packets. The lower profile shows the coincidences with the barrier; this profile is shifted by ≈ 2 fs to negative times relative to the one with no barrier (upper curve): the average particle which tunnels arrives earlier than the one which travels the same distance in air

were combined, it was found that the tunneling peak arrived 1.47 ± 0.21 fs earlier than the one traveling through air, in reasonable agreement with theoretical prediction of approximately 1.9 fs. Taking into account the $1.1 \mu\text{m}$ thickness of the barrier, this implies an effective photon tunneling velocity of $1.7c$. The results exclude the “semiclassical” time but are consistent with the group delay. A recent investigation of the energy dependence of the tunneling time was performed by angling the dielectric mirror, thus shifting its bandgap [150]. The data confirm the group delay in this limit as well and rule out identification of Büttiker’s Larmor time with a peak propagation time.

84.7.4 Interpretation of Tunneling Time

Even though a wave-packet peak may appear on the far side of a barrier sooner than it would under allowed propagation, it is important to stress that no information is transmitted faster than c , nor, on average, is any energy. These effects occur in the limit of low transmission, where the transmitted wave packet can be considered as a “reshaped” version of the leading edge of the incident pulse [285, 296, 302, 303]. At a physical level, the reflection from a multilayer dielectric is due to destructive interference among coherent multiple reflections between the different layers. At times before the field inside the structure reaches its steady-state value, there is little interference, and a nonnegligible fraction of the wave is transmitted. This preferential treatment of the leading edge engenders a sort of “optical illusion”, shifting the transmitted peak earlier in time. A signal, such as a sharp onset, relies on high-frequency components, which would not benefit from this illusion but instead travel more slowly than c . Even for a smooth wave packet, no energy travels faster than light; most is simply reflected by the barrier. Only if one considers the Copenhagen interpretation of quantum mechanics, with its instantaneous collapse, does one find superluminal propagation of those particles that happen to be transmitted. This leads to the question of whether it is possible to ask which part of a wave packet a given particle comes from.

In one paper it was argued that transmitted particles do, in fact, stem only from the leading edge of the wave packet [304]. While it is true that the transmission only depends on causally connected portions of the incident wave packet, further analysis revealed that simultaneous discussion of such particle-like questions and the wave nature of tunneling ran afoul of the complementarity principle [305]. In essence, labeling the initial positions of a tunneling particle destroys the careful interference by which the reshaping occurs (as in the quantum eraser). However, one picture in which the transmitted particles really do originate earlier is the Bohm–de Broglie model of quantum mechanics [306, 307]. This theory considers Ψ to be a real field (residing, however, in configuration space, thus incorporating non-locality) that guides point-like particles in a deterministic manner. It reproduces all the predictions of quantum mechanics without incorporating any randomness; the probabilistic predictions of QM arise from a range of initial conditions. Bohm’s equation of motion has the form of a fluid-flow equation, $\mathbf{v}(\mathbf{x}) = \hbar \nabla \arg \Psi(\mathbf{x}) / m$, implying that particle trajectories may never cross, as velocity is a single-valued function of position. Consequently, all transmitted particles originate earlier in the ensemble than all reflected particles [305, 308]. This approach yields trajectories with well-defined (and generally subluminal) dwell times in the barrier region. However, the fact that the mean tunneling delay of Bohm particles diverges as the incident bandwidth becomes

small, along with other interpretational issues [309, 310], leaves open the question of whether time scales as defined by the Bohm model have any physical meaning.

The “weak measurement” approach of Aharonov et al. [146, 147] or equivalently, complex conditional probabilities obeying Bayes’s theorem [149, 311], can be used to address the question of tunneling interaction times in an experimentally unambiguous way. The real part of the resulting complex times determines the effect a tunneling particle would have on a “clock” to which it coupled, while the imaginary part indicates the clock’s backaction on the particle. They unify various approaches such as the Larmor and Büttiker–Landauer times, as well as Feynman path methods. In addition, they allow one to discuss separately the *histories* of particles that have been transmitted or reflected by a barrier, rather than discussing only the wave function as a whole. Interestingly, these calculations do *not* support the assertion that transmitted particles originate in the leading edge of a wave packet.

84.7.5 Other Fast and Slow Light Schemes

In addition to the case of tunneling described already, apparently superluminal propagation was observed in a Bessel beam geometry [312], and in the case of an inverted medium [313], as described in [297–299]. While the former case may be explained geometrically, the latter – in which superluminal group velocities occur without significant gain, loss, or distortion – raises difficult questions about the speeds of propagation of both energy and information. For two contrasting perspectives, see [314] and [315]. Much more work has followed [313], including theoretical treatments of the role of quantum noise in preventing superluminal information transfer [316] and attempts to experimentally compare the velocity of information transfer with the group velocity [317]. The latter work seemed to verify the claim, previously tested only in an electronic analog [318], that even in the regime of superluminal propagation, new information was limited to causal speeds. Some dispute has persisted [319], and it seems clear that a more rigorous definition of information velocity is required; somewhere between the idealized extremes of infinitely sharp signal fronts and strictly finite signal bandwidths lies the real world, and neither the front velocity nor the group velocity should be expected to completely describe the behavior of actual information-carrying pulses. At the same time, the definition of the energy velocity in active media cannot be resolved without reviving the long-standing conundrum about how to apportion energy between the propagating field and energy stored in the medium [320, 321].

Since 1999 there has actually been much more excitement over so-called “slow light” than over “fast light” [322].

Building on the concepts of electromagnetically induced transparency [323], two groups succeeded in that year in utilizing the steep dispersion curves that can be generated by extremely narrow holes in absorption lines to slow light by a remarkable factor, to speeds as low as 17 m/s [324, 325]. Two experiments succeeded in bringing light to a *standstill* [326, 327] 2 years later. This can be understood in terms of a “dark-state polariton” model, in which the propagating photon is adiabatically converted into a (stationary) metastable atomic excitation. In addition to the obvious possibilities for storage of optical pulses [328, 329], there have been several proposals and demonstrations of generating extremely strong optical nonlinearities at the single-photon level that may be directly applicable to quantum information processing [330–337]. For a review on anomalous optical propagation velocities, see [338].

84.8 Gravity and Quantum Optics

84.8.1 Gravitational Wave Detection

According to general relativity, gravitational waves can be produced and detected by moving mass distributions [339–341]. However, gravitational waves are coupled only to time-varying mass *quadrupole* moments in lowest order, since the mass dipole moment is $\sum_j m_j \mathbf{r}_j = M \mathbf{R}_{\text{cm}}$ and \mathbf{R}_{cm} , for a closed system can only exhibit uniform rectilinear motion. Current efforts focus on detecting gravitational waves (typically at 100 Hz to 1 kHz) from astrophysical sources, such as supernovae or collapsing binary stellar systems. For example, it is expected that in the nearby Virgo cluster of galaxies, several such events should occur per year, each yielding a fractional strain ($\Delta L/L$) of 10^{-21} on Earth.

The first major effort to detect gravitational waves began in the 1960s and utilized a large cylindrical mass (sometimes known as a “Weber bar”, after its inventor) whose fundamental mode of acoustical oscillation is resonantly excited by time-varying tidal forces produced by the passage of a gravitational wave [341]. However, these devices were not sensitive enough to detect gravitational waves. More recently, a large amount of research has been devoted to using optical interferometry to detect gravitational waves. A passing gravitational wave alters the relative path length in the arms of a Michelson interferometer, thereby slightly shifting the output fringes. Although the effective gravitational mass of the light is much smaller than that of the Weber bar, very long interferometer arms (2–4 km, with a Fabry–Perot cavity in each arm to increase the effective length) more than make up for this disadvantage. The signal-to-noise ratio for the detection of a fringe shift depends on the power of the light. The US initiative, called Advanced LIGO (Laser Interferometer Gravitational-Wave Observatory [342]) uses 20 W

from a Nd:YAG laser and an additional external mirror to recirculate the unmeasured light, thus increasing the stored light power up to 100 kW. There are three LIGO interferometers, located in Hanford, Washington (with both a 2-km and a 4-km version), and Livingston, Louisiana (4-km version), respectively. The registration of coincident events at the separated interferometers allows one to rule out terrestrial artifacts, but many problems involving seismic and thermal isolation, absorption and heating, intrinsic thermal noise, and optical quality had to be addressed. In September 2015, both the Louisiana and Hanford LIGO interferometers registered the first direct terrestrial observation of gravitational waves. The signal, which was coincident at both detection site, swept up from 35 Hz to 250 Hz, and corresponded to a peak gravitational strain of 1.0×10^{-21} [343]. The gravitational waves were most likely produced by the merger of two black holes that converted ≈ 3 solar masses worth of energy into gravitational waves. This discovery was awarded the 2017 Nobel prize. Since then several other binary black hole mergers have been detected, and in August 2017 gravitational waves were detected from the inspiral of two binary neutron stars [344]. Currently, a world-wide network of gravitational wave detectors is coming online with operational locations in Italy (VIRGO) and Germany (GEO600), along with planned detectors in Japan (KAGRA) and India (IndIGO).

Because the standard quantum noise limit of these detectors is ultimately determined by the vacuum fluctuations incident on the unused input ports of the interferometers, it is, in principle, possible to achieve reduced noise levels by using *squeezed* vacuum instead [341, 345] (Sect. 84.2.3). Currently, at lower frequencies, it is the radiation pressure of the circulating light in the interferometers at LIGO that set the noise floor—adding more power to the laser will not lead to a simple gain in sensitivity. Using squeezed light instead could circumvent this problem by yielding increased sensitivity at current power levels. At the GEO600 gravitational detector in Hanover, Germany, squeezed light has been used to improve the observable volume of the universe by approximately a factor of 2 [346], and plans are underway to incorporate this technology in future versions of LIGO [347]. A more ambitious project aims to establish an interferometric gravitational wave detector in space using a network of satellites, where the fundamental baseline can be several million kilometers long, allowing the device to detect gravity waves with much lower frequencies than ground-based systems [348].

It has also been suggested that matter waves that interact with gravity waves inside a matter-wave interferometer (Sect. 84.3.1) could lead to a sensitive method to detect gravitational waves [349]. Such a “Matter-Wave Interferometric Gravitational-Wave Observatory” (MIGO) may allow the detection of primordial gigahertz gravity waves arising from the Big Bang [350]. Moreover, quantum mechanical detec-

tors based on the use of macroscopically coherent entangled states may enable quantum transducers that can interconvert between electromagnetic and gravitational waves, based on time-reversal symmetry [351].

84.8.2 Gravity and Quantum Information

A fundamental connection between black holes and quantum information was suggested recently [352–354]. The basic idea is that every physical object, including a black hole, can be thought of as a computer that unitarily transforms input states to output states; i.e., “in” quantum bits (“qubits”) can always be *reversibly* interconverted into “out” qubits, thus obeying time-reversal symmetry. Hawking blackbody radiation from a black hole, thus, contains as much information in an evaporating black hole as originally fell into it, when this process is viewed as a *reversible* quantum-scattering problem. To resolve the paradox of the apparent loss of information of matter falling into a black hole, Lloyd and Ng propose that pairs of entangled photons can materialize at the event horizon of a black hole. One member of the photon pair flies outward to become the Hawking radiation; the other falls into the black hole and hits the singularity together with the matter that formed the hole. The annihilation of the infalling photon acts a measurement on the infalling matter in a quantum teleportation-like process, transporting the information contained in the infalling matter to the outgoing Hawking radiation, using the Horowitz–Maldacena mechanism [355].

References

1. Jaynes, E.T.: Phys. Rev. A **2**, 260 (1970)
2. Clauser, J.F.: Phys. Rev. A **6**, 49 (1972)
3. Barut, A.O., Dowling, J.P.: Phys. Rev. A **41**, 2284 (1990)
4. Milonni, P.W.: The Quantum Vacuum: An Introduction to Quantum Electrodynamics. Academic Press (1994)
5. Dirac, P.A.M.: The Principles of Quantum Mechanics. Oxford University Press, Oxford (1958)
6. Aspect, A., Grangier, P., Roger, G.: J. Opt. **20**, 119 (1989)
7. Glauber, R.J.: In: DeWitt, C. (ed.) Quantum Optics and Electronics (1964)
8. Clauser, J.F.: Phys. Rev. D **9**, 853 (1974)
9. Grangier, P., Roger, G., Aspect, A.: Europhys. Lett. **1**, 173 (1986)
10. Chiao, R.Y., Kwiat, P.G., Deutsch, I.H., Steinberg, A.M.: In: Inguva, R. (ed.) Recent Developments in Quantum Optics. Plenum Press (1993)
11. Hanbury-Brown, R., Twiss, R.Q.: Proc. R. Soc. Lond. A **248**, 199 (1958)
12. Heisenberg, W.: The Physical Principles of the Quantum Theory. Dover (1930)
13. Sukenik, C.I., Boshier, M.G., Cho, D., Sandoghdar, V., Hinds, E.A.: Phys. Rev. Lett. **70**, 560 (1993)
14. Rempe, G., Thompson, R.J., Kimble, H.J.: Phys. Scr. **T51**, 67 (1994)
15. Brune, M., et al.: Phys. Rev. Lett. **76**, 1800 (1996)
16. Maitre, X., et al.: J. Mod. Opt. **44**, 2023 (1997)

17. Raimond, J.M., Brune, M., Haroche, S.: *Rev. Mod. Phys.* **73**, 565 (2001)
18. Nogues, G., Rauschenbeutel, A., Osnaghi, S., Brune, M., Haroche, J.M.R.S.: *Nature* **400**, 239 (1999)
19. Mabuchi, H., Ye, J., Kimble, H.J.: *Appl. Phys. B* **68**, 1095 (1999)
20. Münstermann, P., Fischer, T., Maunz, P., Pinkse, P.W.H., Rempe, G.: *Phys. Rev. Lett.* **82**, 3791 (1999)
21. Doherty, A.C., Lynn, T.W., Hood, C.J., Kimble, H.J.: *Phys. Rev. A* **63**, 013401 (2000)
22. Pinkse, P.W.H., Fischer, T., Maunz, P., Rempe, G.: *Nature* **404**, 365 (2000)
23. Hood, C.J., Lynn, T.W., Doherty, A.C., Parkins, A.S., Kimble, H.J.: *Science* **287**, 1457 (2000)
24. Fischer, T., Maunz, P., Pinkse, P.W.H., Rempe, T.P.G.: *Phys. Rev. Lett.* **88**, 163002 (2002)
25. Burnham, D.C., Weinberg, D.L.: *Phys. Rev. Lett.* **25**, 84 (1970)
26. Harris, S.E., Oshman, M.K., Byer, R.L.: *Phys. Rev. Lett.* **18**, 732 (1967)
27. Klyshko, D.N.: *Sov. Phys. JETP* **6**, 490 (1967)
28. Wang, X., Chen, L., Li, W., Huang, H.-L., Liu, C., Chen, C., Luo, Y.-H., Su, Z.-E., Wu, D., Li, Z.-D., Lu, H., Hu, Y., Jiang, X., Peng, C.-Z., Li, L., Liu, N.-L., Chen, Y.-A., Lu, C.-Y., Pan, J.-W.: *Phys. Rev. Lett.* **117**, 210502 (2016)
29. Hong, C.K.: *L. M. Phys. Rev. Lett.* **56**, 58 (1986)
30. Kimble, H.J., Walls, D.F.: *J. Opt. Soc. Am. B* **4**, 1450 (1987)
31. Rarity, J.G., Tapster, P.R., Levenson, J.A., Garreau, J.C., Abram, I., Mertz, J., Debuisschert, T., Heidmann, A., Fabre, C., Giacobino, E.: *Appl. Phys. B* **55**, 250 (1992)
32. Slusher, R.E., Hollberg, L.W., Yurke, B., Mertz, J.C., Valley, J.F.: *Phys. Rev. Lett.* **55**, 2409 (1985)
33. Lambrecht, A., Coudreau, T., Steinberg, A.M., Giacobino, E.: In: Eberly, J., Mandel, L., Wolf, E. (eds.) *Coherence and Quantum Optics VII*. Plenum (1995)
34. Machida, S., Yamamoto, Y., Itaya, Y.: *Phys. Rev. Lett.* **58**, 1000 (1987)
35. Santori, C., Fattal, D., Vuckovic, J., Solomon, G.S., Yamamoto, Y.: *Nature* **419**, 594 (2002)
36. Dousse, A., Suffczynski, J., Beveratos, A., Krebs, O., Lemaître, A., Sagnes, I., Bloch, J., Voisin, P., Senellart, P.: *Nature* **466**, 217 (2010)
37. Gazzano, O., Michaelis de Vasconcellos, S., Arnold, C., Nowak, A., Galopin, E., Sagnes, I., Lanco, L., Lemaître, A., Senellart, P.: *Nat. Commun.* **4**(1), 1425 (2013)
38. Somaschi, N., Giesz, V., De Santis, L., Loredò, J.C., Almeida, M.P., Hornecker, G., Portalupi, S.L., Grange, T., Antón, C., Demory, J., Gómez, C., Sagnes, I., Lanzillotti-Kimura, N.D., Lemaître, A., Auffèves, A., White, A.G., Lanco, L., Senellart, P.: *Nat. Photonics* **10**(5), 340–345 (2016)
39. Giovannetti, V., Lloyd, S., Maccone, L.: *Nat. Photonics* **5**(4), 222–229 (2011)
40. Keith, D.E., Ekstrom, C.R., Turchette, Q.A., Pritchard, D.E.: *Phys. Rev. Lett.* **66**, 2693 (1991)
41. Chapman, M.S., et al.: *Phys. Rev. Lett.* **74**, 4783 (1995)
42. Kasevich, M.A., Chu, S.: *Phys. Rev. Lett.* **67**, 181 (1991)
43. Peters, A., Chung, K.Y., Chu, S.: *Metrologia* **38**, 25 (2001)
44. McGuirk, J.M., Foster, G.T., Fixler, J.B., Snadden, M.J., Kasevich, M.A.: *Phys. Rev. A* **65**, 033608 (2002)
45. Riehle, F., Kisters, T., Witte, A., Helmcke, J., Bordé, C.: *Phys. Rev. Lett.* **67**, 177 (1991)
46. Gustavson, T.L., Landragin, A., Kasevich, M.A.: *Class. Quantum Gravity* **17**, 2385 (2000)
47. Arndt, M., et al.: *Nature* **401**, 680 (1999)
48. Hackermüller, L., et al.: *Phys. Rev. Lett.* **91**, 090408 (2003)
49. Marshall, W., Simon, C., Penrose, R., Bouwmeester, D.: *Phys. Rev. Lett.* **91**, 130401 (2003)
50. Aspelmeyer, M., Kippenberg, T.J., Marquardt, F.: *Rev. Mod. Phys.* **86**, 1391–1452 (2014)
51. Poot, M., van der Zant, H.S.J.: *Phys. Rep.* **511**(5), 273–335 (2012)
52. Aspelmeyer, M., Meystre, P., Schwab, K.: *Phys. Today* **65**(7), 29–35 (2012)
53. Chan, J., Alegre, T.P.M., Safavi-Naeini, A.H., Hill, J.T., Krause, A., Gröblacher, S., Aspelmeyer, M., Painter, O.: *Nature* **478**(7367), 89–92 (2011)
54. Wollman, E.E., Lei, C.U., Weinstein, A.J., Suh, J., Kronwald, A., Marquardt, F., Clerk, A.A., Schwab, K.C.: *Science* **349**(6251), 952–955 (2015)
55. Pirkkalainen, J.M., Damskägg, E., Brandt, M., Massel, F., Sillanpää, M.A.: *Phys. Rev. Lett.* **115**, 243601 (2015)
56. Lecocq, F., Clark, J.B., Simmonds, R.W., Aumentado, J., Teufel, J.D.: *Phys. Rev. X* **5**, 041037 (2015)
57. O’Connell, A.D., Hofheinz, M., Ansmann, M., Bialczak, R.C., Lenander, M., Lucero, E., Neeley, M., Sank, D., Wang, H., Weides, M., Wenner, J., Martinis, J.M., Cleland, A.N.: *Nature* **464**(7289), 697–703 (2010)
58. Hong, S., Riedinger, R., Marinković, I., Wallucks, A., Hofer, S.G., Norte, R.A., Aspelmeyer, M., Gröblacher, S.: *Science* **358**(6360), 203–206 (2017)
59. Palomaki, T.A., Teufel, J.D., Simmonds, R.W., Lehnert, K.W.: *Science* **342**(6159), 710–713 (2013)
60. Lee, K.C., Sprague, M.R., Sussman, B.J., Nunn, J., Langford, N.K., Jin, X.-M., Champion, T., Michelberger, P., Reim, K.F., England, D., Jaksch, D., Walmsley, I.A.: *Science* **334**(6060), 1253–1256 (2011)
61. Riedinger, R., Wallucks, A., Marinković, I., Löschnauer, C., Aspelmeyer, M., Hong, S., Gröblacher, S.: *Nature* **556**(7702), 473–477 (2018)
62. Ockeloen-Korppi, C.F., Damskägg, E., Pirkkalainen, J.-M., Asjad, M., Clerk, A.A., Massel, F., Woolley, M.J., Sillanpää, M.A.: *Nature* **556**(7702), 478–482 (2018)
63. Marinković, I., Wallucks, A., Riedinger, R., Hong, S., Aspelmeyer, M., Gröblacher, S.: *Phys. Rev. Lett.* **121**, 220404 (2018)
64. Kiesel, N., Blaser, F., Delić, U., Grass, D., Kaltenbaek, R., Aspelmeyer, M.: *Proc. Natl. Acad. Sci.* **110**(35), 14180–14185 (2013)
65. Romero-Isart, O., Pflanzner, A.C., Blaser, F., Kaltenbaek, R., Kiesel, N., Aspelmeyer, M., Cirac, J.I.: *Phys. Rev. Lett.* **107**, 020405 (2011)
66. Pino, H., Prat-Camps, J., Sinha, K., Venkatesh, B.P., Romero-Isart, O.: *Quantum Sci. Technol.* **3**(2), 025001 (2018)
67. Andrews, M.R., et al.: *Science* **275**, 637 (1997)
68. Hadzibabic, Z., et al.: *Phys. Rev. Lett.* **93**, 180403 (2004)
69. Pflieger, R.L., Mandel, L.: *Phys. Rev.* **159**, 1084 (1967)
70. Javanainen, J., Yoo, S.M.: *Phys. Rev. Lett.* **76**, 161 (1996)
71. van der Wal, C., et al.: *Science* **290**, 773 (2000)
72. Niskanen, A.O., Harrabi, K., Yoshihara, F., Nakamura, Y., Lloyd, S., Tsai, J.S.: *Science* **316**(5825), 723–726 (2007)
73. Motzoi, F., Gambetta, J.M., Rebentrost, P., Wilhelm, F.K.: *Phys. Rev. Lett.* **103**, 110501 (2009)
74. Chow, J.M., Córcoles, A.D., Gambetta, J.M., Rigetti, C., Johnson, B.R., Smolin, J.A., Rozen, J.R., Keefe, G.A., Rothwell, M.B., Ketchen, M.B., Steffen, M.: *Phys. Rev. Lett.* **107**, 080502 (2011)
75. Chow, J.M., Gambetta, J.M., Córcoles, A.D., Merkel, S.T., Smolin, J.A., Rigetti, C., Poletto, S., Keefe, G.A., Rothwell, M.B., Rozen, J.R., Ketchen, M.B., Steffen, M.: *Phys. Rev. Lett.* **109**, 060501 (2012)
76. Barends, R., Kelly, J., Megrant, A., Sank, D., Jeffrey, E., Chen, Y., Yin, Y., Chiaro, B., Mutus, J., Neill, C., O’Malley, P., Roushan, P., Wenner, J., White, T.C., Cleland, A.N., Martinis, J.M.: *Phys. Rev. Lett.* **111**, 080502 (2013)

77. Heeres, R.W., Reinhold, P., Ofek, N., Frunzio, L., Jiang, L., Devoret, M.H., Schoelkopf, R.J.: *Nat. Commun.* **8**(1), 94 (2017)
78. Kelly, J., Barends, R., Fowler, A.G., Megrant, A., Jeffrey, E., White, T.C., Sank, D., Mutus, J.Y., Campbell, B., Chen, Y., Chen, Z., Chiaro, B., Dunsworth, A., Hoi, I.-C., Neill, C., O'Malley, P.J.J., Quintana, C., Roushan, P., Vainsencher, A., Wenner, J., Cleland, A.N., Martinis, J.M.: *Nature* **519**, 66 (2015)
79. Narla, A., Shankar, S., Hatridge, M., Leghtas, Z., Sliwa, K.M., Zalusky-Geller, E., Mundhada, S.O., Pfaff, W., Frunzio, L., Schoelkopf, R.J., Devoret, M.H.: *Phys. Rev. X* **6**, 031036 (2016)
80. Gambetta, J.M., Chow, J.M., Steffen, M.: *npj Quantum Inf.* **3**(1), 2 (2017)
81. Boixo, S., Isakov, S.V., Smelyanskiy, V.N., Babbush, R., Ding, N., Jiang, Z., Bremner, M.J., Martinis, J.M., Neven, H.: *Nat. Phys.* **14**(6), 595–600 (2018)
82. Axline, C.J., Burkhardt, L.D., Pfaff, W., Zhang, M., Chou, K., Campagne-Ibarcq, P., Reinhold, P., Frunzio, L., Girvin, S.M., Jiang, L., Devoret, M.H., Schoelkopf, R.J.: *Nat. Phys.* **14**(7), 705–710 (2018)
83. Rosenblum, S., Gao, Y.Y., Reinhold, P., Wang, C., Axline, C.J., Frunzio, L., Girvin, S.M., Jiang, L., Mirrahimi, M., Devoret, M.H., Schoelkopf, R.J.: *Nat. Commun.* **9**(1), 652 (2018)
84. Chiao, R.Y., Kwiat, P.G., Steinberg, A.M.: In: Han, D., Kim, Y.S., Zachary, W.W. (eds.) *Workshop on Squeezed States and Uncertainty Relations*. NASA Conference Publication 3135 (1991)
85. Joobeur, A., Saleh, B., Teich, M.: *Phys. Rev. A* **50**, 3349 (1994)
86. Schrödinger, E.: *Proc. Am. Phil. Soc.* **124**, 323 (1980)
87. Kwiat, P.G., Chiao, R.Y.: *Phys. Rev. Lett.* **66**, 588 (1991)
88. Ghosh, R.L.M.: *Phys. Rev. Lett.* **59**, 1903 (1987)
89. Hong, C.K., Ou, Z.Y., Mandel, L.: *Phys. Rev. Lett.* **59**, 2044 (1987)
90. Ou, Z.Y.L.M.: *Phys. Rev. Lett.* **57**, 66 (1989)
91. Steinberg, A.M., Chiao, R.Y.: *Phys. Rev. A* **49**, 3283 (1994)
92. Mandel, L.: *Phys. Rev. A* **28**, 929 (1983)
93. Fearn, H.: In: Barut, A.O. (ed.) *New Frontiers in Quantum Electronics and Quantum Optics*. Plenum Press (1990)
94. Steinberg, A.M., Kwiat, P.G., Chiao, R.Y.: *Phys. Rev. Lett.* **68**, 2421 (1992)
95. Santori, C., Fattal, D., Vučković, J., Solomon, G.S., Yamamoto, Y.: *Nature* **419**(6907), 594–597 (2002)
96. Mosley, P.J., Lundeen, J.S., Smith, B.J., Wasylczyk, P., U'Ren, A.B., Silberhorn, C., Walmsley, I.A.: *Phys. Rev. Lett.* **100**, 133601 (2008)
97. Lang, C., Eichler, C., Steffen, L., Fink, J.M., Woolley, M.J., Blais, A., Wallraff, A.: *Nat. Phys.* **9**(6), 345–348 (2013)
98. Kaneda, F., Garay-Palmett, K., U'Ren, A.B., Kwiat, P.G.: *Opt. Express* **24**(10), 10733 (2016)
99. Bohr, N.: In: Wheeler, J.A., Zurek, W.H. (eds.) *Quantum Theory and Measurement*. Princeton University Press, Princeton (1983)
100. Feynman, R.P., Leighton, R.B., Sands, M.: *The Feynman Lectures on Physics*. Addison-Wesley (1965)
101. von Neumann, J.: *Mathematical Foundations of Quantum Mechanics*. Princeton University Press, Princeton (1955)
102. Englert, B.G.: *Phys. Rev. Lett.* **77**, 2154 (1996)
103. Schwindt, P.D.D., Kwiat, P.G., Englert, B.G.: *Phys. Rev. A* **60**, 4285 (1999)
104. Dürr, S., Nonn, T., Rempe, G.: *Phys. Rev. Lett.* **81**, 5705 (1998)
105. Hillery, M., Scully, M.O.: In: Meystre, P., Scully, M.O. (eds.) *Quantum Optics, Experimental Gravitation, and Measurement Theory*. Plenum Press (1983)
106. Scully, M.O., Englert, B.G., Walther, H.: *Nature* **351**, 111 (1991)
107. Kwiat, P.G., Englert, B.-G.: *Science and Ultimate Reality: Quantum Theory, Cosmology, and Complexity*. Cambridge University Press, Cambridge (2004)
108. Kwiat, P.G., Steinberg, A.M., Chiao, R.Y.: *Phys. Rev. A* **45**, 7729 (1992)
109. Wheeler, J.A.: In: diFrancia, G.T. (ed.) *Problems in the Formulation of Physics* (1979)
110. Hellmuth, T., Walther, H., Zajonc, A., Schleich, W.: *Phys. Rev. A* **35**, 2532 (1987)
111. Alley, C.O., Jakubowicz, O.G., Wickes, W.C.: ed. by. In: Namiki, M. (ed.) *Proceedings of the Second International Symposium on the Foundations of Quantum Mechanics*. Physical Society of Japan (1986)
112. Jacques, V., Wu, E., Grosshans, F., Treussart, F., Grangier, P., Aspect, A., Roch, J.-F.: *Science* **315**(5814), 966–968 (2007)
113. Kim, Y.-H., Yu, R., Kulik, S.P., Shih, Y., Scully, M.O.: *Phys. Rev. Lett.* **84**, 1–5 (2000)
114. Kwiat, P.G., Steinberg, A.M., Chiao, R.Y.: *Phys. Rev. A* **49**, 61 (1994)
115. Herzog, T., Kwiat, P.G., Weinfurter, H., Zeilinger, A.: *Phys. Rev. Lett.* **75**, 3034 (1995)
116. Greenberger, D.M., Horne, M.A., Zeilinger, A.: *Phys. Today* **46**, 8–22 (1993) DOI: <https://doi.org/10.1063/1.881360>
117. Zou, X.Y., Wang, L.J., Mandel, L.: *Phys. Rev. Lett.* **67**, 318 (1991)
118. Wang, L.J., Rhee, J.K.: *Phys. Rev. A* **59**, 1654 (1999)
119. Herzog, T.J., Rarity, J.G., Weinfurter, H., Zeilinger, A.: *Phys. Rev. Lett.* **72**, 629 (1994)
120. Weinfurter, H., et al.: In: Greenberger, D.M., Zeilinger, A. (eds.) *Fundamental Problems on Quantum Theory*, vol. 755, *Ann. N. Y. Acad. Sci.* (1995)
121. Resch, K.J., Lundeen, J.S., Steinberg, A.M.: *Phys. Rev. Lett.* **87**, 123603 (2001)
122. Misra, B., Sudarshan, E.C.G.: *J. Math. Phys.* **18**, 756 (1977)
123. Itano, W.M., Heinzen, D.J., Bollinger, J.J., Wineland, D.J.: *Phys. Rev. A* **41**, 2295 (1990)
124. Kofman, A.G., Kurizki, G.: *Nature* **405**, 546 (2000)
125. Fischer, M.C., Gutiérrez-Medina, B., Raizen, M.G.: *Phys. Rev. Lett.* **87**, 040402 (2001)
126. Braginsky, V.B., Vorontsov, Y.I., Thorne, K.S.: *Science* **209**, 547 (1980)
127. Roch, J.F., Roger, G., Grangier, P., Courty, J., Reynaud, S.: *Appl. Phys. B* **55**, 291 (1992)
128. Imoto, N., Haus, H.A., Yamamoto, Y.: *Phys. Rev. A* **32**, 2287 (1985)
129. Kitagawa, M., Yamamoto, Y.: *Phys. Rev. A* **34**, 3974 (1986)
130. Grangier, P., Poizat, J.P., Roch, J.F.: *Phys. Scr.* **T51**, 51 (1994)
131. Sinclair, N., Heshami, K., Deshmukh, C., Oblak, D., Simon, C., Tittel, W.: *Nat. Commun.* **7**, 13454 (2016)
132. Chiao, R.Y.: *Phys. Lett. A* **33**, 177 (1970)
133. Lee, B., Yin, E., Gustafson, T.K., Chiao, R.Y.: *Phys. Rev. A* **45**, 4319 (1992)
134. Haroche, S., Brune, M., Raimond, J.M.: In: Walther, H., Hänsch, T.W., Niezart, D. (eds.) *Atomic Physics 13*. American Institute of Physics (1993)
135. Walther, H.: In: Walther, H., Hänsch, T.W., Niezart, D. (eds.) *Atomic Physics 13*. American Institute of Physics (1993)
136. Johnson, B.R., Reed, M.D., Houck, A.A., Schuster, D.I., Bishop, L.S., Ginossar, E., Gambetta, J.M., DiCarlo, L., Frunzio, L., Girvin, S.M., Schoelkopf, R.J.: *Nat. Phys.* **6**, 663 (2010)
137. Besse, J.-C., Gasparinetti, S., Collodo, M.C., Walter, T., Kurpiers, P., Pechal, M., Eichler, C., Wallraff, A.: *Phys. Rev. X* **8**, 021003 (2018)
138. Renninger, M.: *Z. Phys.* **158**, 417 (1960)
139. Dicke, R.H.: *Am. J. Phys.* **49**, 925 (1981)
140. Elitzur, A.C., Vaidman, L.: *Found. Phys.* **23**, 987 (1993)
141. Kwiat, P.G., Weinfurter, H., Herzog, T., Zeilinger, A., Kasevich, M.A.: *Phys. Rev. Lett.* **74**, 4763 (1995)

142. White, A.G., Mitchell, J.R., Nairz, O., Kwiat, P.G.: *Phys. Rev. A* **58**, 605 (1998)
143. Kwiat, P.G., et al.: *Phys. Rev. Lett.* **83**, 4725 (1999)
144. Paul, H., Pavicic, M.: *Int. J. Theor. Phys.* **35**, 2085 (1996)
145. Tsegaye, T., et al.: *Phys. Rev. A* **57**, 3987 (1998)
146. Aharonov, Y., Albert, D.Z., Vaidman, L.: *Phys. Rev. Lett.* **60**, 1351 (1988)
147. Aharonov, Y., Vaidman, L.: *Phys. Rev. A* **41**, 11 (1990)
148. Schulz, O., et al.: *Phys. Rev. Lett.* **90**, 177901 (2003)
149. Steinberg, A.M.: *Phys. Rev. Lett.* **74**, 2405 (1995)
150. Steinberg, A.M., Chiao, R.Y.: *Phys. Rev. A* **51**, 3525 (1995)
151. Aharonov, Y., Botero, A., Popescu, S., Reznik, B., Tollaksen, J.: *Phys. Rev. A* **301**, 130 (2002)
152. Yokota, K., Yamamoto, T., Koashi, M., Imoto, N.: *New J. Phys.* **11**(3), 033011 (2009)
153. Mir, R., Lundeen, J.S., Mitchell, M.W., Steinberg, A.M., Garretson, J.L., Wiseman, H.M.: *New J. Phys.* **9**(8), 287 (2007)
154. Ozawa, M.: *Phys. Rev. A* **67**, 042105 (2003)
155. Rozema, L.A., Darabi, A., Mahler, D.H., Hayat, A., Soudagar, Y., Steinberg, A.M.: *Phys. Rev. Lett.* **109**, 100404 (2012)
156. Aharonov, Y., Popescu, S., Rohrlich, D., Vaidman, L.: *Phys. Rev. A* **48**, 4084 (1993)
157. Kocsis, S., Braverman, B., Ravets, S., Stevens, M.J., Mirin, R.P., Shalm, L.K., Steinberg, A.M.: *Science* **332**(6034), 1170–1173 (2011)
158. Okamoto, R., Takeuchi, S.: *Sci. Rep.* **6**, 35161 EP – (2016)
159. Ritchie, N.W.M., Story, J.G., Hulet, R.G.: *Phys. Rev. Lett.* **66**, 1107 (1991)
160. Dixon, P.B., Starling, D.J., Jordan, A.N., Howell, J.C.: *Phys. Rev. Lett.* **102**, 173601 (2009)
161. Ferrie, C., Combes, J.: *Phys. Rev. Lett.* **112**, 040406 (2014)
162. Combes, J., Ferrie, C., Jiang, Z., Caves, C.M.: *Phys. Rev. A* **89**, 052117 (2014)
163. Feizpour, A., Xing, X., Steinberg, A.M.: *Phys. Rev. Lett.* **107**, 133603 (2011)
164. Harris, J., Boyd, R.W., Lundeen, J.S.: *Phys. Rev. Lett.* **118**, 070802 (2017)
165. Hallaji, M., Feizpour, A., Dmochowski, G., Sinclair, J., Steinberg, A.M.: *Nat. Phys.* **13**, 540 EP – (2017)
166. Brunner, N., Acín, A., Collins, D., Gisin, N., Scarani, V.: *Phys. Rev. Lett.* **91**, 180402 (2003)
167. Lundeen, J.S., Sutherland, B., Patel, A., Stewart, C., Bamber, C.: *Nature* **474**(7350), 188–191 (2011)
168. Lundeen, J.S., Bamber, C.: *Phys. Rev. Lett.* **108**, 070402 (2012)
169. Bamber, C., Lundeen, J.S.: *Phys. Rev. Lett.* **112**, 070405 (2014)
170. Thekkadath, G.S., Giner, L., Chalich, Y., Horton, M.J., Banker, J., Lundeen, J.S.: *Phys. Rev. Lett.* **117**, 120401 (2016)
171. Salvail, J.Z., Agnew, M., Johnson, A.S., Bolduc, E., Leach, J., Boyd, R.W.: *Nat. Photon.* **7**(4), 316–321 (2013)
172. Malik, M., Mirhosseini, M., Lavery, M.P.J., Leach, J., Padgett, M.J., Boyd, R.W.: *Nat. Comm.* **5**, 3115 (2014)
173. Shi, Z., Mirhosseini, M., Margiewicz, J., Malik, M., Rivera, F., Zhu, Z., Boyd, R.W.: *Optica* **2**(4), 388–392 (2015)
174. Mirhosseini, M., Magaña Loaiza, O.S., Hashemi Rafsanjani, S.M., Boyd, R.W.: *Phys. Rev. Lett.* **113**, 090402 (2014)
175. Kim, Y., Kim, Y.-S., Lee, S.-Y., Han, S.-W., Moon, S., Kim, Y.-H., Cho, Y.-W.: *Nat. Commun.* **9**(1), 192 (2018)
176. Einstein, A., Podolsky, B., Rosen, N.: *Phys. Rev.* **47**, 777 (1935)
177. Bohm, D.: In: Wheeler, J.A., Zurek, W.H. (eds.) *Quantum Theory and Measurement*. Princeton University Press, Princeton (1983)
178. Bell, J.S.: *Physics* **1**, 195 (1964)
179. Bell, J.S.: *Speakable and Unsayable in Quantum Mechanics*. Cambridge University Press, Cambridge (1987)
180. Stapp, H.P.: *Phys. Rev. D* **3**, 1303 (1971)
181. Eberhard, P.H.: *Nuovo Cimento B* **38**, 75 (1977)
182. Clauser, J.F., Horne, M.A., Shimony, A., Holt, R.A.: *Phys. Rev. Lett.* **23**, 880 (1969)
183. Clauser, J.F., Horne, M.A.: *Phys. Rev. D* **10**, 526 (1974)
184. Peres, A.: *Phys. Rev. A* **46**, 4413–4414 (1992)
185. Kaszlikowski, D., Gnaniński, P., Żukowski, M., Miklaszewski, W., Zeilinger, A.: *Phys. Rev. Lett.* **85**, 4418–4421 (2000)
186. Collins, D., Gisin, N., Linden, N., Massar, S., Popescu, S.: *Phys. Rev. Lett.* **88**, 040404 (2002)
187. Dada, A.C., Leach, J., Buller, G.S., Padgett, M.J., Andersson, E.: *Nat. Phys.* **7**(9), 677–680 (2011)
188. Erhard, M., Fickler, R., Krenn, M., Zeilinger, A.: *Light. Sci. Appl.* **7**(3), 17146 (2018)
189. Rohrlich, P.S.D.: *Found. Phys.* **24**, 379 (1994)
190. Freedman, S.J., Clauser, J.F.: *Phys. Rev. Lett.* **28**, 938 (1972)
191. Aspect, A., Dalibard, J., Roger, G.: *Phys. Rev. Lett.* **49**, 1804 (1982)
192. Clauser, J.F., Shimony, A.: *Rep. Prog. Phys.* **41**, 1881 (1978)
193. Eberhard, P.H.: *Phys. Rev. A* **47**, R747 (1993)
194. Kwiat, P.G., Eberhard, P.H., Steinberg, A.M., Chiao, R.Y.: *Phys. Rev. A* **49**, 3209 (1994)
195. Weihs, G., Jennewein, T., Simon, C., Weinfurter, H., Zeilinger, A.: *Phys. Rev. Lett.* **81**, 5039 (1998)
196. Yin, J., Cao, Y., Li, Y.-H., Liao, S.-K., Zhang, L., Ren, J.-G., Cai, W.-Q., Liu, W.-Y., Li, B., Dai, H., Li, G.-B., Lu, Q.-M., Gong, Y.-H., Xu, Y., Li, S.-L., Li, F.-Z., Yin, Y.-Y., Jiang, Z.-Q., Li, M., Jia, J.-J., Ren, G., He, D., Zhou, Y.-L., Zhang, X.-X., Wang, N., Chang, X., Zhu, Z.-C., Liu, N.-L., Chen, Y.-A., Lu, C.-Y., Shu, R., Peng, C.-Z., Wang, J.-Y., Pan, J.-W.: *Science* **356**(6343), 1140–1144 (2017)
197. Rowe, M.A., et al.: *Nature* **409**, 791 (2001)
198. Christensen, B.G., McCusker, K.T., Altepeter, J.B., Calkins, B., Gerrits, T., Lita, A.E., Miller, A., Shalm, L.K., Zhang, Y., Nam, S.W., Brunner, N., Lim, C.C.W., Gisin, N., Kwiat, P.G.: *Phys. Rev. Lett.* **111**(13), 130406 (2013)
199. Giustina, M., Mech, A., Ramelow, S., Wittmann, B., Kofler, J., Beyer, J., Lita, A., Calkins, B., Gerrits, T., Nam, S.W., Ursin, R., Zeilinger, A.: *Nature* **497**, 227 (2013)
200. Hensen, B., Bernien, H., Dréau, A.E., Reiserer, A., Kalb, N., Blok, M.S., Ruitenberg, J., Vermeulen, R.F.L., Schouten, R.N., Abellán, C., Amaya, W., Pruneri, V., Mitchell, M.W., Markham, M., Twitche, D.J., Elkouss, D., Wehne, S., Taminiau, T.H., Hanson, R.: *Nature* **526**, 682–686 (2015) DOI: <https://doi.org/10.1038/nature15759>
201. Shalm, L.K., et al.: *Phys. Rev. Lett.* **115**(25), 250402 (2015)
202. Giustina, M., et al.: *Phys. Rev. Lett.* **115**(25), 250401 (2015)
203. Rosenfeld, W., Burchardt, D., Garthoff, R., Redeker, K., Ortel, N., Rau, M., Weinfurter, H.: *Phys. Rev. Lett.* **119**(1), 10402 (2017)
204. Gould, R.J., Schröder, G.P.: *Phys. Rev.* **155**, 1408–1411 (1967)
205. Mitalas, R., Sills, K.R.: *ApJ* **401**, 759 (1992)
206. Li, M.-H., Wu, C., Zhang, Y., Liu, W.-Z., Bai, B., Liu, Y., Zhang, W., Zhao, Q., Li, H., Wang, Z., You, L., Munro, W.J., Yin, J., Zhang, J., Peng, C.-Z., Ma, X., Zhang, Q., Fan, J., Pan, J.-W.: *Phys. Rev. Lett.* **121**, 080404 (2018)
207. Rauch, D., Handsteiner, J., Hochtner, A., Gallicchio, J., Friedman, A.S., Leung, C., Liu, B., Bulla, L., Ecker, S., Steinlechner, F., Ursin, R., Hu, B., Leon, D., Benn, C., Ghedina, A., Cecconi, M., Guth, A.H., Kaiser, D.I., Scheidl, T., Zeilinger, A.: *Phys. Rev. Lett.* **121**, 080403 (2018)
208. Kwiat, P.G., Waks, E., White, A.G., Appelbaum, I., Eberhard, P.H.: *Phys. Rev. A* **60**, R773 (1999)
209. White, A.G., James, D.F.V., Eberhard, P.H., Kwiat, P.G.: *Phys. Rev. Lett.* **83**, 3103 (1999)
210. Kwiat, P.G., et al.: *Phys. Rev. Lett.* **75**, 4337 (1995)
211. Jennewein, T., Simon, C., Weihs, G., Weinfurter, H., Zeilinger, A.: *Phys. Rev. Lett.* **84**, 4729 (2000)

212. Poppe, A., Fedrizzi, A., Ursin, R., Böhm, H.R., Lorünser, T., Maurhardt, O., Peev, M., Suda, M., Kurtsiefer, C., Weinfurter, H., Jennewein, T., Zeilinger, A.: *Opt. Express* **12**(16), 3865–3871 (2004)
213. Bouwmeester, D., et al.: *Nature* **390**, 575 (1997)
214. Boschi, D., Branca, S., De Martini, F., Hardy, L., Popescu, S.: *Phys. Rev. Lett.* **80**, 1121 (1998)
215. Bouwmeester, D., Pan, J.W., Daniell, M., Weinfurter, H., Zeilinger, A.: *Phys. Rev. Lett.* **82**, 1345 (1999)
216. Pan, J.W., Daniell, M., Gasparoni, S., Weihs, G., Zeilinger, A.: *Phys. Rev. Lett.* **86**, 4435 (2001)
217. Zhao, Z., et al.: *Nature* **430**, 54 (2004)
218. Eisenberg, H.S., Khoury, G., Durkin, G.A., Simon, C., Bouwmeester, D.: *Phys. Rev. Lett.* **93**, 193901 (2004)
219. Rarity, J.G., Tapster, P.R.: *Phys. Rev. Lett.* **64**, 2495 (1990)
220. Mair, A., Vaziri, A., Weihs, G., Zeilinger, A.: *Nature* **412**, 313 (2001)
221. Vaziri, A., Weihs, G., Zeilinger, A.: *Phys. Rev. Lett.* **89**, 240401 (2002)
222. Langford, N.K.: *Phys. Rev. Lett.* **93**, 053601 (2004)
223. Abouraddy, A.F., Saleh, B.E.A., Sergienko, A.V., Teich, M.C.: *Phys. Rev. Lett.* **87**, 123602 (2001)
224. Abouraddy, A.F., Saleh, A., Sergienko, B.E.A., Sergienko, V., Teich, M.C.: *Opt. Express* **9**, 498 (2001)
225. Lugiato, L.A., Gatti, A., Brambilla, E.: *J. Opt. B: Quantum Semicl. Opt.* **4**, 176 (2002)
226. Navez, P., Brambilla, E., Gatti, A., Lugiato, L.A.: *Phys. Rev. A* **65**, 013813 (2002)
227. Brendel, J., Mohler, E., Martienssen, W.: *Europhys. Lett.* **20**, 575 (1992)
228. Kwiat, P.G., Steinberg, A.M., Chiao, R.Y.: *Phys. Rev. A* **47**, R2472 (1993)
229. Franson, J.D.: *Phys. Rev. Lett.* **62**, 2205 (1989)
230. Jarrett, J.: *Nous* **18**, 569 (1984)
231. Shimony, A.: *An Exposition of Bell's Theorem*. Plenum Press (1990)
232. Tittel, W., Brendel, J., Zbinden, H., Gisin, N.: *Phys. Rev. Lett.* **81**, 3563 (1998)
233. Zbinden, H., Brendel, J., Gisin, N., Tittel, W.: *Phys. Rev. A* **63**, 022111 (2001)
234. Suarez, A., Scarani, V.: *Phys. Lett. A* **232**, 9 (1997)
235. Riedmatten, H., Marcikic, I., Zbinden, H., Gisin, N.: *Quantum Inf. Comp.* **2**, 425 (2002)
236. Cirel'son, B.S.: *Lett. Math. Phys.* **4**, 93 (1980)
237. Poh, H.S., Joshi, S.K., Cerè, A., Cabello, A., Kurtsiefer, C.: *Phys. Rev. Lett.* **115**, 180408 (2015)
238. Liang, Y.-C., Vértesi, T., Brunner, N.: *Phys. Rev. A* **83**, 022108 (2011)
239. Christensen, B.G., Liang, Y.-C., Brunner, N., Gisin, N., Kwiat, P.G.: *Phys. Rev. X* **5**, 041052 (2015)
240. Junge, M., Palazuelos, C.: *Commun. Math. Phys.* **306**(3), 695 (2011)
241. Vidick, T., Wehner, S.: *Phys. Rev. A* **83**, 052310 (2011)
242. Popescu, S., Rohrlich, D.: *Found. Phys.* **24**(3), 379–385 (1994)
243. Braunstein, S.L., Caves, C.M.: *Ann. Phys.* **202**(1), 22–56 (1990)
244. Stuart, T.E., Slater, J.A., Colbeck, R., Renner, R., Tittel, W.: *Phys. Rev. Lett.* **109**, 020402 (2012)
245. Tan, T.R., Wan, Y., Erickson, S., Bierhorst, P., Kienzler, D., Glancy, S., Knill, E., Leibfried, D., Wineland, D.J.: *Phys. Rev. Lett.* **118**, 130403 (2017)
246. Mermin, N.D.: *Phys. Rev. Lett.* **65**, 1838 (1990)
247. Greenberger, D.M., Horne, M.A., Shimony, A., Zeilinger, A.: *Am. J. Phys.* **58**, 1131 (1990)
248. Pan, J.W., Bouwmeester, D., Daniell, M., Weinfurter, H., Zeilinger, A.: *Nature* **403**, 515 (2000)
249. Hardy, L.: *Phys. Rev. Lett.* **68**, 2981 (1992)
250. Hardy, L.: *Phys. Lett. A* **167**, 17 (1992)
251. Torgerson, J., Branning, D., Mandel, L.: *Appl. Phys. B* **60**, 267 (1995)
252. White, A.G., James, D.F.V., Eberhard, P.H., Kwiat, P.G.: *Phys. Rev. Lett.* **83**, 3103 (1999)
253. Brassard, G.: In: Brassard, G. (ed.) *Modern Cryptology: A Tutorial* (1998)
254. Ekert, A.K.: *Phys. Rev. Lett.* **67**, 661 (1991)
255. Bennett, C.H.: *Phys. Rev. Lett.* **68**, 3121 (1992)
256. Gisin, N., Ribordy, G., Tittel, W., Zbinden, H.: *Rev. Mod. Phys.* **74**, 145 (2002)
257. Naik, D.S., Peterson, C.G., White, A.G., Berglund, A.J., Kwiat, P.G.: *Phys. Rev. Lett.* **84**, 4733 (2000)
258. Enzer, D.G., Hughes, R.J., Peterson, C.G., Kwiat, P.G.: *Focus Issue on Quantum Cryptography*. *New J. Phys.* **4**, 45 (2002)
259. Tittel, W., Brendel, J., Zbinden, H., Gisin, N.: *Phys. Rev. Lett.* **84**, 4737 (2000)
260. Marcikic, I., et al.: *Phys. Rev. Lett.* **93**, 180502 (2004)
261. Bennett, C., Wiesner, S.J.: *Phys. Rev. Lett.* **69**, 2881 (1992)
262. Braunstein, S.L., Mann, A., Revzen, M.: *Phys. Rev. Lett.* **68**, 3259 (1992)
263. Mattle, K., Weinfurter, H., Kwiat, P.G., Zeilinger, A.: *Phys. Rev. Lett.* **76**, 4656 (1996)
264. Bennett, C.H., Brassard, G., Crépeau, C., Jozsa, R., Peres, A., Wootters, W.K.: *Phys. Rev. Lett.* **70**, 1895 (1993)
265. Riebe, M., et al.: *Nature* **429**, 734 (2004)
266. Barrett, M.D., et al.: *Nature* **429**, 737 (2004)
267. Jennewein, T., Weihs, G., Pan, J.W., Zeilinger, A.: *Phys. Rev. Lett.* **88**, 017903 (2002)
268. Briegel, H.J., Dür, W., Cirac, J.I., Zoller, P.: *Phys. Rev. Lett.* **81**, 5932–5935 (1998)
269. Pironio, S., Acín, A., Massar, S., de la Giroday, A.B., Matsukevich, D.N., Maunz, P., Olmschenk, S., Hayes, D., Luo, L., Manning, T.A., Monroe, C.: *Nature* **464**, 1021–1024 (2010)
270. Colbeck, R., Kent, A.: *Mathematical and Theoretical. J. Phys. A* **44**(9), 095305 (2011)
271. Acín, A., Masanes, L.: *Nature* **540**, 213 (2016)
272. Pironio, S., Massar, S.: *Phys. Rev. A* **87**, 012336 (2013)
273. Miller, C.A., Shi, Y.: *J. ACM* **63**(4), 33:1–33:63 (2016)
274. Bierhorst, P., Knill, E., Glancy, S., Zhang, Y., Mink, A., Jordan, S., Rommal, A., Liu, Y.-K., Christensen, B., Nam, S.W., Stevens, M.J., Shalm, L.K.: *Nature* **556**(7700), 223–226 (2018)
275. Glauber, R.J., Lewenstein, M.: *Phys. Rev. A* **43**, 467 (1991)
276. Franson, J.D.: *Phys. Rev. A* **45**, 3126 (1992)
277. Steinberg, A.M., Kwiat, P.G., Chiao, R.Y.: *Phys. Rev. A* **45**, 6659 (1992)
278. Büttiker, M.R.L.: *Phys. Rev. Lett.* **49**, 1739 (1982)
279. Hauge, E.H., Stovngeng, J.A.: *Rev. Mod. Phys.* **61**, 917 (1989)
280. Wigner, E.P.: *Phys. Rev.* **98**, 145 (1955)
281. Bolda, E.L., Chiao, R.Y., Garrison, J.C.: *Phys. Rev. A* **48**, 3890 (1993)
282. Büttiker, M.R.L.: *Phys. Scr.* **32**, 429 (1985)
283. Büttiker, M.: *Phys. Rev. B* **27**, 6178 (1983)
284. Ramos, R., Spierings, D., Racicot, I., Steinberg, A.M.: *International Conference on Atomic Physics* vol. 573. (2018)
285. Chiao, R.Y., Steinber, A.M.: *Tunneling Times and Superluminality*. Elsevier, pp 347–406 (1997)
286. Eckle, P., Pfeiffer, A.N., Cirelli, C., Staudte, A., Dörner, R., Müller, H.G., Büttiker, M., Keller, U.: *Science* **322**(5907), 1525–1529 (2008)
287. Fortun, A., Cabrera-Gutiérrez, C., Condon, G., Michon, E., Billy, J., Guéry-Odelin, D.: *Phys. Rev. Lett.* **117**, 010401 (2016)
288. Zimmermann, T.C.V., Mishra, S., Doran, B.R., Gordon, D.F., Landsman, A.S.: *Phys. Rev. Lett.* **116**, 233603 (2016)

289. Camus, N., Yakaboylu, E., Fechner, L., Klaiber, M., Laux, M., Mi, Y., Hatsagortsyan, K.Z., Pfeifer, T., Keitel, C.H., Moshhammer, R.: *Phys. Rev. Lett.* **119**, 023201 (2017)
290. Martin, T.R.L.: *Phys. Rev. A* **45**, 2611 (1992)
291. Dumont, R.S., Marchioro II, T.L.: *Phys. Rev. A* **47**, 85 (1993)
292. Hauge, E.H., Falck, J.P., Fjeldly, T.A.: *Phys. Rev. B* **36**, 4203 (1987)
293. Yablonovitch, E.: *J. Opt. Soc. Am. B* **10**, 283 (1993)
294. Enders, A., Nimtz, G.: *J. Phys.* **3**, 1089 (1993)
295. Ranfagni, A., Fabeni, P., Pazzi, G.P., Mugnai, D.: *Phys. Rev. E* **48**, 1453 (1993)
296. Chu, S., Wong, S.: *Phys. Rev. Lett.* **48**, 738 (1982)
297. Chiao, R.Y.: *Phys. Rev. A* **48**, R34 (1993)
298. Steinberg, A.M., Chiao, R.Y.: *Phys. Rev. A* **49**, 2071 (1994)
299. Bolda, E.L., Garrison, J.C., Chiao, R.Y.: *Phys. Rev. A* **49**, 2938 (1994)
300. Spielmann, C., Szipöcs, R., Stingl, A., Krausz, F.: *Phys. Rev. Lett.* **73**, 2308 (1994)
301. Steinberg, A.M., Kwiat, P.G., Chiao, R.Y.: *Phys. Rev. Lett.* **71**, 708 (1993)
302. Garrett, C.G.B., McCumber, D.E.: *Phys. Rev. A* **1**, 305 (1970)
303. Siegman, A.E.: *Lasers*. University Science Books (1986)
304. Deutch, J.M., Low, F.E.: *Ann. Phys.* **228**, 184 (1993)
305. Steinberg, A.M., Kwiat, P.G., Chiao, R.Y.: *Found. Phys. Lett.* **7**, 223 (1994)
306. Bohm, D., Hiley, B.J.: *The Undivided Universe: An Ontological Interpretation of Quantum Mechanics*. Routledge (1993)
307. Holland, P.R.: *The Quantum Theory of Motion*. Cambridge University Press, Cambridge (1993)
308. Leavens, C.R., Aers, G.C.: In: Wiesendanger, R., Güntherodt, H.-J. (eds.) *Scanning Tunneling Microscopy III*. Springer (1993)
309. Englert, B.G., Scully, M.O., Süßmann, G., Walther, H.: *Z. Naturforsch. A* **47**, 1175 (1992)
310. Dewdney, C., Hardy, L., Squires, E.J.: *Phys. Lett. A* **184**, 6 (1993)
311. Steinberg, A.M.: *Phys. Rev. A* **52**, 32 (1995)
312. Mugnai, D., Ranfagni, A., Ruggeri, R.: *Phys. Rev. Lett.* **84**, 4830 (2000)
313. Wang, L.J., Kuzmich, A., Dogariu, A.: *Nature* **406**, 277 (2000)
314. Nimtz, G., Heitmann, W.: *Prog. Quantum Electron.* **21**, 81 (1997)
315. Chiao, R.Y., Steinberg, A.M.: *Prog. Opt.* **37**, 345 (1997) DOI: [https://doi.org/10.1016/S0079-6638\(08\)70341-X](https://doi.org/10.1016/S0079-6638(08)70341-X)
316. Kuzmich, A., Dogariu, A., Wang, L.J., Milonni, P.W., Chiao, R.Y.: *Phys. Rev. Lett.* **86**, 3925 (2001)
317. Stenner, M.D., Gauthier, D.J., Neifeld, M.A.: *Nature* **425**, 695 (2003)
318. Mitchell, M.W., Chiao, R.Y.: *Phys. Lett. A* **230**, 133 (1997)
319. Nimtz, G.: *Nature* **429**, 40 (2004)
320. Diener, G.: *Phys. Lett. A* **235**, 118 (1997)
321. Goenner, H.: *Ann. Phys.* **7**, 774 (1998)
322. Milonni, P.W.: *Fast Light, Slow Light, and Left-Handed Light*. Institute of Physics (2004)
323. Marangos, J.P.: *J. Mod. Opt.* **45**, 471 (1998)
324. Hau, L.V., Harris, S.E., Dutton, Z., Behroozi, C.H.: *Nature* **397**, 594 (1999)
325. Kash, M.M., et al.: *Phys. Rev. Lett.* **82**, 5229 (1999)
326. Liu, C., Dutton, Z., Behroozi, C.H., Hau, L.V.: *Nature* **409**, 490 (2001)
327. Phillips, D.F., Fleischhauer, A., Mair, A., Walsworth, R.L., Lukin, M.D.: *Phys. Rev. Lett.* **86**, 783 (2001)
328. Turukhin, A.V., et al.: *Phys. Rev. Lett.* **88**, 023602 (2002)
329. Bigelow, M.S., Lepeshkin, N.N., Boyd, R.W.: *Science* **301**, 200 (2003)
330. van der Wal, C.H., et al.: *Science* **301**, 196 (2003)
331. Harris, S.E., Hau, L.V.: *Phys. Rev. Lett.* **82**, 4611 (1999)
332. Lukin, M.D., et al.: *Phys. Rev. Lett.* **87**, 037901 (2001)
333. Bajcsy, M., Hofferberth, S., Balic, V., Peyronel, T., Hafezi, M., Zibrov, A.S., Vuletić, V., Lukin, M.D.: *Phys. Rev. Lett.* **102**, 203902 (2009)
334. Feizpour, A., Hallaji, M., Dmochowski, G., Steinberg, A.M.: *Nat. Phys.* **11**, 905–909 (2015)
335. Tiarks, D., Schmidt, S., Rempe, G., Dürr, S.: *Sci. Adv.* **2**(4), e1600036 (2016) doi: <https://doi.org/10.1126/sciadv.1600036>
336. Bhaskar, M.K., Sukachev, D.D., Sipahigil, A., Evans, R.E., Burek, M.J., Nguyen, C.T., Rogers, L.J., Siyushev, P., Metsch, M.H., Park, H., Jelezko, F., Lončar, M., Lukin, M.D.: *Phys. Rev. Lett.* **118**, 223603 (2017)
337. Liang, Q.-Y., Venkatramani, A.V., Cantu, S.H., Nicholson, T.L., Gullans, M.J., Gorshkov, A.V., Thompson, J.D., Chin, C., Lukin, M.D., Vuletić, V.: *Science* **359**(6377), 783–786 (2018)
338. Boyd, R.W., Gauthier, D.J.: *Prog. Opt.* **43**, 497 (2002)
339. Weinberg, S.: *Gravitation and Cosmology*. Wiley (1972)
340. Misner, C.W., Thorne, K.S., Wheeler, J.A.: *Gravitation*. Freeman (1987)
341. Thorne, K.S.: In: Hawking, S.W., Israel, W. (eds.) *Three Hundred Years of Gravitation*. Cambridge University Press, Cambridge (1987)
342. Barish, B.C., Weiss, R.: *Phys. Today* **52**, 44 (1999)
343. Abbott, B.P., et al.: *Phys. Rev. Lett.* **116**, 061102 (2016)
344. Abbott, B.P., et al.: *Phys. Rev. Lett.* **119**, 161101 (2017)
345. Caves, C.M.: *Phys. Rev. D* **23**, 1693 (1981)
346. Grote, H., Danzmann, K., Dooley, K.L., Schnabel, R., Slutsky, J., Vahlbruch, H.: *Phys. Rev. Lett.* **110**, 181101 (2013)
347. Aasi, J., et al.: *Nat. Photonics* **7**, 613 (2013)
348. (2020)
349. Chiao, R.Y., Speliotopoulos, A.D.: *J. Mod. Opt.* **51**, 861 (2004)
350. Foffa, S., Gasparini, A., Papucci, M., Sturani, R.: *Phys. Rev. D* **73**, 022001 (2006)
351. Chiao, R.Y., Boyce, J., Garrison, J.C.: *Ann. N. Y. Acad. Sci.* **755**, 400 (1995)
352. Lloyd, S., Ng, Y.J.: *Sci. Am.* **291**, 52 (2004)
353. Hayden, P., Preskill, J.: *J. High Energy Phys.* **2007**(09), 120 (2007)
354. Lloyd, S., Preskill, J.: *J. High Energy Phys.* **2014**(8), 126 (2014)
355. Horowitz, G.T., Maldacena, J.: *J. High Energy Phys.* **02008**, 00 (2004)



L. Krister Shalm Krister is a Sr. Research Associate at the University of Colorado, Boulder and an Associate of the National Institute of Standards and Technologies. He uses photons to study quantum networking as well as perform fundamental tests of quantum mechanics. When he isn't in the lab he can be found swing dancing.



Paul G. Kwiat Paul G. Kwiat is the Bardeen Chair in Physics, at the University of Illinois, in Urbana-Champaign. A Fellow of the American Physical Society and the Optical Society of America, he studies the phenomena of entanglement, quantum interrogation, quantum erasure, and optical implementations of quantum information protocols. He can't resist a good swing dance.




Aephraim M. Steinberg Aephraim Steinberg works on experimental quantum optics and laser cooling, with specific emphasis on foundational questions in quantum mechanics (especially quantum measurement) and on quantum information. His obsession is with tunneling times; in 1994, and in 2005, he demonstrated (with Kwiat and Chiao) the superluminal tunneling of photons; he is starting an experiment to probe tunneling times for Bose-condensed atoms through optical barriers.



Raymond Y. Chiao Professor Chiao was awarded his PhD by MIT in 1965. He has been Professor of Physics at Berkeley since 1977. His research interests are nonlinear and quantum optics, low-temperature physics as applied to astrophysics, and the relationship between general relativity and macroscopic quantum matter. He is writing a book with J.C. Garrison on quantum optics.



Daniel F. V. James, Peter L. Knight , and Stefan Scheel

Contents

85.1	Entanglement and Information	1260
85.1.1	Testing for and Quantifying Entanglement	1260
85.2	Simple Quantum Protocols	1262
85.2.1	Quantum Key Distribution	1262
85.2.2	Quantum Teleportation	1262
85.3	Quantum Logic	1263
85.3.1	Single-Qubit Operations	1263
85.3.2	Two-Qubit Operations	1264
85.3.3	Multiqubit Gates and Networks	1264
85.3.4	Cluster-State Quantum Computing	1264
85.4	Quantum Algorithms	1265
85.4.1	Deutsch–Jozsa Algorithm	1265
85.4.2	Grover’s Search Algorithm	1265
85.4.3	Shor’s Factor-Finding Algorithm	1266
85.4.4	Other Algorithms	1266
85.5	Error Correction	1266
85.6	The DiVincenzo Checklist	1267
85.6.1	Qubit Characterization, Scalability	1267
85.6.2	Initialization	1267
85.6.3	Long Decoherence Times	1268
85.6.4	Universal Set of Quantum Gates	1268
85.6.5	Qubit-Specific Measurement	1268
85.7	Physical Implementations	1268
85.7.1	Linear Optics	1268
85.7.2	Trapped Ions	1269
85.8	Outlook	1269
	References	1270

D. F. V. James (✉)
Dept. of Physics, University of Toronto
Toronto, ON, Canada
e-mail: dfvj@physics.utoronto.ca

P. L. Knight
Dept. of Physics, Imperial College London
London, UK
e-mail: p.knight@imperial.ac.uk

S. Scheel
Institute of Physics, University of Rostock
Rostock, Germany
e-mail: stefan.scheel@uni-rostock.de

Abstract

Since its inception over a century ago, quantum mechanics has been an indispensable tool for understanding atomic structure and has been used very successfully in the calculation energy levels, natural lifetimes, and cross sections; but for the most part, the philosophical interpretation of quantum mechanics has been left to others. However, after the work of Bell in the 1960s showed that the peculiarly nonlocal nature of quantum correlations could be tested in the lab, a number of atomic physicists turned to the experimental study of entanglement and quantum measurement. By the mid 1990s, it was becoming increasingly apparent that the peculiar quantum correlations and quantum superpositions might be exploited in *quantum information processing*, and that practical devices to exploit this potential might well be within the grasp of current experimental techniques. This led to an explosive growth of the subject over the past 25 years, fueled by the long-term prospects of quantum computing, quantum-enhanced metrology, and quantum cryptography. Today, quantum information is a vast area, embracing physics, chemistry, electrical engineering, material science, mathematics, and computer science. In this chapter, we introduce some of the basics of the subject, with an emphasis on atomic, molecular, and optical physics.

Keywords

entangled state · quantum teleportation · quantum information processing · quantum gate · dense coding

The fundamental resource in quantum information processing is generally considered to be *entanglement* between spatially separated subsystems. Entanglement is a quantum-mechanical effect and has led to numerous speculations about the validity of quantum mechanics itself for its apparent paradoxical implications. Most, if not all, of these difficulties have been resolved and can be mostly attributed

to the simple fact that paradoxical behavior is incompatible with common sense or everyday experience. These quantum-mechanical correlations have numerous applications in quantum key distribution (QKD), quantum communication, dense coding, and act as the main resource in quantum computing. We will briefly touch upon some mathematical issues concerning separability and quantification of entanglement before describing how quantum key distribution and teleportation work. After that, a brief discussion of single-qubit and two-qubit quantum gates follows, before we describe some simple quantum algorithms. The issues of error correction and fault tolerant computation as well as DiVincenzo's checklist (which any realization should satisfy) provide the background for the discussion of some physical implementations, of which we will pay most attention to those involving atomic, molecular, and atomic physics.

We are acutely aware of the fact that we can give only a brief introduction into what has become a major field of investigation over the last quarter-century. There are a number of textbooks available that cover the vast literature on this subject. Perhaps the most well-known is the widely cited quantum information textbook by *Nielsen and Chuang* [1]; a number of more recent works are also recommended as starting points for more in-depth study [2–7].

85.1 Entanglement and Information

As was already noted, entanglement comes about if a quantum-mechanical system can be divided into two or more distinguishable parts. (Distinguishability of the subsystems is important for applications of entanglement and is implicit in Schrödinger's original definition of the term [8]; systems such as the two-electron ground state of helium form a spin-singlet system, but the two electrons are not distinguishable, thus strictly speaking are not entangled.) As an example, consider a two-photon emission process from a spin-zero particle by which two photons escape in opposite directions. Given that the photons are spin-one particles, their spin projections onto some axis must be mutually opposite. As there is no prior information about the actual orientation of the spin, the part of the photon wave function associated with the spin degree is, therefore,

$$|\psi\rangle = \frac{1}{\sqrt{2}}(|\uparrow\downarrow\rangle - |\downarrow\uparrow\rangle). \quad (85.1)$$

The striking feature of this type of quantum state is that it describes correlations of two spatially separated particles. If the polarization state of one photon is measured in any basis (e.g., linear polarization, circular polarization, etc.), the state of the other photon, which can be far away, is then instantly predetermined. This nonlocal correlation of purely quantum

origin is called entanglement. (Classical entanglement, i.e., an electromagnetic field, which is nonfactorizable in some representation, has received some attention in the last few years ([9] and references therein); although there are interesting parallels with quantum entanglement, the key difference is the significance of the quantum wavefunction and the collapse of multipartite states due to measurement, which is fundamentally quantum mechanical.) An important and inviolable principle of special relativity is that no information can be transmitted faster than the speed of light. Because the (classical) information concerning the measurement result on one particle needs to be transmitted via a causal classical channel, this experiment respects the letter of the law; however, the instantaneous collapse of the distant photon's state can be said to violate the spirit of the law. This issue of nonlocality has been seen as a vital part in understanding the foundations of quantum mechanics itself (Chap. 84). In 1935, *Einstein, Podolsky, and Rosen* argued on the basis of entangled states that quantum mechanics is incomplete [10]. They were most concerned about the existence of elements of reality within strongly correlated quantum systems and initiated the debate on quantum nonlocality. The nonexistence of so-called local hidden variable theories for the description of states like Eq. (85.1) was demonstrated by *John Stewart Bell* [11]. He showed that maximally entangled states violate certain inequalities (now called Bell's inequalities), which local hidden variable models would have obeyed. Later experiments showed the correctness of Bell's demonstration [12–16].

In classical information theory, the unit of information is called a bit, which can be defined as the amount of information contained in a yes–no question. As a matter of fact, “bit” is the abbreviation for “binary digit” and refers to Boolean algebra in which the allowed states of a system are the logical 0 and the logical 1. Therefore, by abuse of language, one bit (as a unit) is the information carried by one bit (as a binary digit) [18].

In quantum mechanics, however, due to its inherent linearity, two “quantum bits” (or “qubits” – this word, which has now been included the *Oxford English Dictionary*, seems to have been first used in [17] can be in superpositions of the logical states $|01\rangle$ and $|10\rangle$ (or $|\uparrow\downarrow\rangle$ and $|\downarrow\uparrow\rangle$, as in the example above). This typical example of an entangled state shows that quantifying the amount of information contained in a quantum state is different from what is known in classical information theory because of the superposition property.

85.1.1 Testing for and Quantifying Entanglement

From the above it is clear that entangled states play a major role in defining the differences between classical and

quantum information. Thus, it is clearly useful to be able to determine whether or not a particular state is entangled. Consider a quantum state of two distinct subsystems A and B . Note that these subsystems themselves might consist of ensembles of particles, in which case we are looking at a bipartite cut through the whole system. Suppose subsystem A is described by an orthonormal basis set $\{|\alpha_i\rangle, i = 1, 2, \dots, N_A\}$ and subsystem B by an orthonormal basis set $\{|\beta_k\rangle, k = 1, 2, \dots, N_B\}$, then the most general state of the bipartite system can be written as

$$|\Psi_{AB}\rangle = \sum_{i=1}^{N_A} \sum_{k=1}^{N_B} c_{ik} |\alpha_i\rangle |\beta_k\rangle, \quad (85.2)$$

where c_{ik} are probability amplitudes, which form the elements of a $N_A \times N_B$ matrix. Using the singular value decomposition on this matrix [19], the state may be rewritten in a simpler manner known as the Schmidt decomposition, i.e.,

$$|\Psi_{AB}\rangle = \sum_{n=1}^N \sqrt{p_n} |u_n\rangle |v_n\rangle, \quad (85.3)$$

where $\{p_n, n = 1, 2, \dots, N\}$ are real, positive valued constants, such that $\sum_{n=1}^N p_n = 1$; $\{|u_n\rangle, n = 1, 2, \dots, N\}$ and $\{|v_n\rangle, v = 1, 2, \dots, N\}$ are sets of orthonormal vectors in subsystems A and B , respectively. The constants p_n and the vectors $\{|u_n\rangle\}$ are, respectively, the eigenvalues and the eigenvectors of the $N_A \times N_A$ Hermitian, positive-definite matrix $\mathcal{A}_{ij} = \sum_{k=1}^{N_B} c_{ik} c_{jk}^*$, and N is the number of nonzero eigenvalues; similarly, the $N_B \times N_B$ Hermitian, positive-definite matrix $\mathcal{B}_{kl} = \sum_{i=1}^{N_A} c_{ik} c_{il}^*$ has eigenvectors $\{|v_n\rangle\}$; the eigenvalues of \mathcal{A}_{ij} and \mathcal{B}_{kl} are identical, hence if $N_B < N_A$, then some of the eigenvalues of \mathcal{B}_{kl} will be zero, and vice versa). The Schmidt number must be greater than or equal to 1, and at most, equal to the smaller of the two subsystem dimensions N_A and N_B . If (and only if) the Schmidt number of the state is 1 the state of the combined system can be written as a simple product of a state of subsystem A and a state of subsystem B ; such states are called *separable*. If the Schmidt number is greater than 1, no such factorization exists, and the state is then *entangled*.

In order to find some notion of the extent of the entanglement of a state, let us now suppose we were to discard subsystem B and concentrate our attention on subsystem A . How could we describe the state of this system? If we assume that the Schmidt number is greater than 1, then there can be no pure state description, and one must consider the reduced density operator for subsystem A , viz.

$$\begin{aligned} \hat{\rho}_A &= \text{Tr}_B\{|\Psi_{AB}\rangle\langle\Psi_{AB}|\} = \sum_{i,j=1}^N \mathcal{A}_{ij} |\alpha_i\rangle\langle\alpha_j| \\ &= \sum_{n=1}^N p_n |u_n\rangle\langle u_n|, \end{aligned} \quad (85.4)$$

where, to account for the uncertainty of the state of subsystem B , we have averaged out all its possible states; mathematically this is described by taking a partial trace over subsystem B . A simple and useful measure of how mixed a state is given by the trace of the square of its density matrix, called the *purity*, defined as

$$P(\hat{\rho}) = \text{Tr}\{\hat{\rho}^2\}. \quad (85.5)$$

The purity has the maximum value of 1, corresponding to pure states; its smallest value is $1/N$, (where N is the dimensionality of $\hat{\rho}$), corresponding to maximally mixed states. As we have seen, a pure reduced density matrix implies a separable state, for which the entanglement is zero; for a maximally entangled state, we would expect the reduced density matrix to be maximally mixed, corresponding to complete randomness. In this case, the entanglement is so strong and comprehensive that discarding subsystem B has resulted in a completely random state for subsystem A . Hence, it is natural to define a measure of entanglement for the pure state $|\Psi_{AB}\rangle$ as:

$$\begin{aligned} C(\Psi_{AB}) &= \sqrt{\frac{N}{N-1}(1 - P(\hat{\rho}_A))} \\ &= \sqrt{\frac{N}{N-1} \left(1 - \sum_{n=1}^N p_n^2\right)}. \end{aligned} \quad (85.6)$$

This quantity is called the *concurrence* [20, 21]. By definition, it takes values between 0 (separable states) and 1 (maximally entangled states). For the simplest nontrivial case, that of two qubits, the concurrence of the state $|\Psi_{AB}\rangle = \alpha|\downarrow\downarrow\rangle + \beta|\downarrow\uparrow\rangle + \gamma|\uparrow\downarrow\rangle + \delta|\uparrow\uparrow\rangle$ is given by $C = 2|\alpha\delta - \beta\gamma|$; for the state Eq. (85.1), $C = 1$, implying that it is maximally entangled.

We have concentrated here on bipartite entanglement of pure states. This is a major simplification and ignores a great body of work on the entanglement both of mixed states and of multipartite states. The fundamental issue when dealing with mixed states is that one must somehow separate the inherent mixture of the state as a whole from the mixture induced by discarding one of the subsystems; for pure states, the former is zero. Since quantum information usually assumes devices that are prepared in pure states, and their performance rapidly degrades as their systems undergo decoherence, the taxonomy of mixed-state entanglement measures, while fascinating, is at best tangential to the main thrust of this article; the interested reader should consult some of the recent review articles on the topic [22, 23].

85.2 Simple Quantum Protocols

In this section, we describe the historically first and simplest quantum protocols – quantum key distribution and quantum teleportation – that make use of inherently “quantum” properties of quantum-mechanical systems. These are either entanglement or, in the case of the simplest version of quantum key distribution, properties of the quantum-mechanical measurement process. We should mention here the pioneering work of *Holevo* [24], who showed that there are fundamental limits on the amount of information that can be extracted by measurements. The application of his ideas to channel capacity and communication [25, 26] are well described in [1], and space limitations prevent us from elaborating on it in this chapter.

85.2.1 Quantum Key Distribution

Historically, the earliest protocol that used quantum-mechanical features in order to realize some specific task that could not have been performed classically was a protocol for secure distribution of a key in cryptography, known as the BB84 protocol after its inventors *Bennett* and *Brassard* and the year of its invention [27]. Although it is commonly referred to as the first example of quantum information processing, it does not make use of entanglement; an entanglement-based method for quantum key distribution was introduced some years later by *Ekert* [28]. The BB84 protocol works in the following way. The sender, generically called Alice, prepares a random sequence (or string) of single photons in a polarization state, which is chosen out of a set of four basis states, horizontally and vertically (H and V) polarized, and diagonal (45°) and antidiagonal (135°) (D and A) polarized. In each of the two basis sets $\{H, V\}$, $\{D, A\}$, one of the states is used to encode the logical value 0 (say in H and D), and the other states encode the logical value 1 (V and A). The random sequence is sent to the receiver, Bob, who performs measurements on the sequence of signals by randomly choosing analogous basis states. The result will be another string of 0’s and 1’s that generically does not coincide with the original string. To rectify this problem, sender and receiver communicate over a classical public channel, where the sender announces the sequence of basis sets in which the photon states were prepared. The receiver compares its sequence of randomly chosen basis states with the announced string and keeps all measurement results for which the choice of basis had been the same. In that way, a common secret key is established (Table 85.1).

The security against eavesdropping of this simple protocol comes from the fact that even by knowing the measurement basis (say $\{H, V\}$) no information has been revealed about the choice of the actual bit value (H or V). Hence, it

Table 85.1 BB84 protocol for secret key distribution. “Alice” sends information encoded in either of two basis sets. “Bob” randomly chooses a measurement basis that is publicly communicated. For those cases when sender and receiver chose the same basis, the receiver’s measurement yields a secure bit

Sender (Alice)	Receiver (Bob)	Generated key
D	$\{H, V\}$	None
V	$\{H, V\}$	0
A	$\{H, V\}$	None
H	$\{H, V\}$	1
D	$\{D, A\}$	0
V	$\{D, A\}$	None
A	$\{D, A\}$	1
H	$\{D, A\}$	None

is the quantum-mechanical measurement process itself that provides security of the protocol. Nor can any eavesdropper (generically known as Eve) hope to intercept the signal without being detected: individual photons can neither be split in a beam splitter (the photon will either go to Bob, so Eve cannot see it, or to Eve, in which case Bob does not receive it), nor can it be cloned by some device [29] without inducing a detectable increase in the error rate. The first quantum key distribution experiments were reported in [30]. However, imperfections in the generation and detection of photons, transmission losses, and polarization drift cause an actual experimental realization to be far from ideal. In practice, encodings other than polarization may be used (for example, a time-binned interferometric basis). Despite these error sources, unconditionally secure quantum key distribution has been demonstrated and implemented over distances of up to 100 km in both fibers and free space. For reviews of theoretical and experimental aspects of quantum cryptography, see [31, 32].

85.2.2 Quantum Teleportation

An important utilization of entanglement as a necessary resource can be found in quantum teleportation. The task of teleportation is to transmit the complete information of an arbitrary unknown quantum state to a spatially different location with the aim of recreating it. The simplest and most obvious way to perform this task would be to take the quantum object that is prepared in the original state and physically transport it to a different location. However, sometimes this is not possible because, for example, an ion needs to be stored in a trap and cannot be moved. The next obvious thing to do would be to measure the quantum state and to recreate it at a different position using the classical information obtained during the measurement. However, single measurements on a quantum system yield only partial information and multiple measurements on many identically prepared copies would have to be performed.

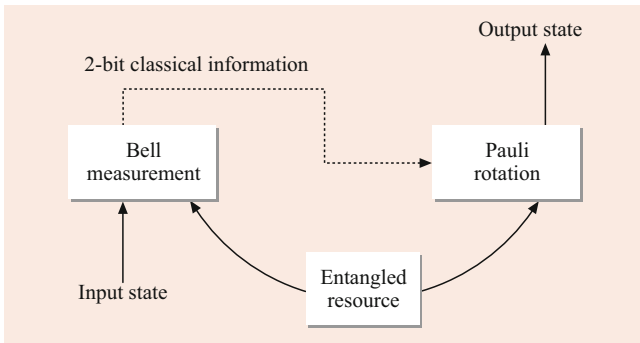


Fig. 85.1 Outline of an ideal teleportation protocol

The protocol (Fig. 85.1), which was originally proposed in [33], makes use of the existence of maximally entangled states. Let the unknown quantum state that is to be teleported be a qubit superposition state of the form:

$$|\psi\rangle = \alpha|0\rangle + \beta|1\rangle, \quad |\alpha|^2 + |\beta|^2 = 1. \quad (85.7)$$

Then one prepares a maximally entangled state $|\Psi^+\rangle = (1/\sqrt{2})(|01\rangle + |10\rangle)$, which is one of the four orthonormal Bell states, defined by

$$\begin{aligned} |\Psi^\pm\rangle &= \frac{1}{\sqrt{2}}(|01\rangle \pm |10\rangle), \\ |\Phi^\pm\rangle &= \frac{1}{\sqrt{2}}(|00\rangle \pm |11\rangle). \end{aligned} \quad (85.8)$$

We then form the tensor product state $|\psi_A\rangle|\Psi_{BC}^+\rangle$ as

$$\begin{aligned} |\psi_A\rangle|\Psi_{BC}^+\rangle &= \frac{1}{\sqrt{2}}(\alpha|0_A0_B1_C\rangle + \alpha|0_A1_B0_C\rangle \\ &\quad + \beta|1_A0_B1_C\rangle + \beta|1_A1_B0_C\rangle), \\ &= \frac{1}{2} [|\Psi_{AB}^+\rangle(\alpha|0_C\rangle + \beta|1_C\rangle) \\ &\quad + |\Psi_{AB}^-\rangle(\alpha|0_C\rangle - \beta|1_C\rangle) \\ &\quad + |\Phi_{AB}^+\rangle(\alpha|1_C\rangle + \beta|0_C\rangle) \\ &\quad + |\Phi_{AB}^-\rangle(\alpha|1_C\rangle - \beta|0_C\rangle)], \end{aligned} \quad (85.9)$$

where we have explicitly indexed the relevant subsystems. After performing a joint measurement on subsystems A and B in the Bell basis (this is called a Bell-state measurement), one obtains one of four possible results. If the measurement result was $|\Psi_{AB}^+\rangle$, then the subsystem C is, indeed, prepared in the original unknown quantum state $|\psi\rangle$, and hence the state has been “teleported” from subsystem A to C . For all other measurement results the outcome is not exactly the same quantum state as intended, but the difference is just a unitary transformation, which is uniquely determined by the outcome of the Bell measurement. For example, measuring $|\Psi_{AB}^-\rangle$ means one has to perform a $\hat{\sigma}_z$ -operation on qubit

C , that flips the sign of the state $|1\rangle$, whereas on obtaining $|\Phi_{AB}^+\rangle$ or $|\Phi_{AB}^-\rangle$ the operations to be applied have to be $\hat{\sigma}_x$ or $\hat{\sigma}_z\hat{\sigma}_x = i\hat{\sigma}_y$, respectively.

Note that this quantum teleportation protocol works with perfect fidelity only if a maximally entangled state has been used. In the course of the Bell measurement, the quantum information is used up, and two classical bits of information (the measurement result) have to be communicated to C in order to restore the original quantum state. In this sense, entanglement can be regarded as a resource or “fuel” for certain tasks in quantum information processing.

The first experimental demonstrations of teleportation of qubits were performed using photons as qubits by the groups of *Zeilinger* in Vienna and *De Martini* in Rome [34, 35], although these could not implement a complete Bell-state measurement (i.e., they could only distinguish one or two of the four Bell states). The first experiments to demonstrate full teleportation with highly entangled states, strong projective measurement, and complete state reconstruction were performed by the groups of *Blatt* at Innsbruck, Austria and, independently, *Wineland* at Boulder in Colorado USA, both using trapped ions [36, 37]. Since then, it has been implemented on other systems and over longer distances; in 2017 a collaboration headed by *Pan* demonstrated the teleportation of photons over distances of up to 1400 km from a ground station to a satellite in low Earth orbit [38].

85.3 Quantum Logic

As we have seen, quantum information relies on devices consisting of qubits. In order to perform any quantum information processing task, one must implement unitary operations on them collectively, in order to create the desired quantum state. For a large number of qubits, this would seem a task daunting in its complexity; fortunately, it has been demonstrated that all unitary operations on a large qubit register can be broken down into single-qubit operations and operations involving pairs of qubits.

85.3.1 Single-Qubit Operations

It is instructive to give an example of how to classify all possible unitary operations that can act on a single qubit. A unitary operation acting upon the basis states $\{|0\rangle, |1\rangle\}$ can be represented by a unitary (2×2) -matrix, and hence is a matrix that represents an element of the unitary group $U(2)$. This group has four generators, the identity matrix and the three Pauli matrices. All unitary (2×2) -matrices are linear combinations of those four matrices. Given the way they

act upon basis states, they can be written as

$$\begin{aligned} \hat{I} &= |0\rangle\langle 0| + |1\rangle\langle 1| \\ \hat{\sigma}_x &= |0\rangle\langle 1| + |1\rangle\langle 0| \\ \hat{\sigma}_z &= |0\rangle\langle 0| - |1\rangle\langle 1| \end{aligned} \tag{85.10}$$

and, by virtue of the commutation rules for $U(2)$ -generators, $\hat{\sigma}_y = i\hat{\sigma}_x\hat{\sigma}_z$. Sometimes, the short-hand notation $\hat{X} = \hat{\sigma}_x$, etc., is used.

A particularly useful single-qubit gate that is not just one of the Pauli operators is the Hadamard gate \hat{H} . In terms of Pauli operators, it is defined as $\hat{H} = (1/\sqrt{2})(\hat{X} + \hat{Z})$. Its purpose is to transform each basis state into equal superpositions of basis states, i.e., $|0\rangle \rightarrow (1/\sqrt{2})(|0\rangle + |1\rangle)$ and $|1\rangle \rightarrow (1/\sqrt{2})(|0\rangle - |1\rangle)$. The Hadamard gate is used to initialize an equal superposition of all possible N -qubit basis states from the state $|0\rangle^{\otimes N}$ (i.e., the tensor product of N qubits in state $|0\rangle$). Hence,

$$\bigotimes_{i=1}^N \hat{H}_i |0\rangle^{\otimes N} = \frac{1}{\sqrt{2^N}} \sum_k |x_k\rangle, \tag{85.11}$$

where the $|x_k\rangle$ are all 2^N possible N -digit binary numbers.

85.3.2 Two-Qubit Operations

Similarly to the single-qubit case, one can write down all possible unitary operations on two qubits by noting that they constitute a representation of $U(4)$; the 16 generators of this group can be found by forming the tensor products of pairs the four generators of $U(2)$, listed above; all possible two-qubit operators can be written as a linear combination of these generators.

Particular examples of nontrivial two-qubit gates are the controlled-NOT and the controlled-phase gate, defined in terms of Pauli operators as

$$\begin{aligned} \hat{C}_{12} &= |0_1\rangle\langle 0_1| \otimes \hat{I}_2 + |1_1\rangle\langle 1_1| \otimes \hat{X}_2, \\ \hat{P}_{12} &= |0_1\rangle\langle 0_1| \otimes \hat{I}_2 + |1_1\rangle\langle 1_1| \otimes \hat{Z}_2, \end{aligned} \tag{85.12}$$

where in both cases, qubit 1 acts as the ‘‘control’’ and qubit 2 acts as the ‘‘target’’ (Fig. 85.2). The net effect of the

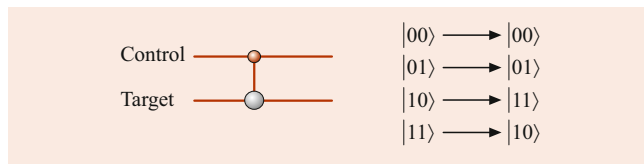


Fig. 85.2 Symbol and truth table of the controlled-NOT gate. The target qubit is flipped depending on the state of the control qubit

controlled-NOT gate is to interchange the states $|10\rangle \leftrightarrow |11\rangle$, whereas the controlled-phase gate changes the phase of the basis state $|11\rangle$ by π and leaves all other states unchanged. The controlled-NOT gate has an interpretation as a sum gate in that it performs a mapping $|x, y\rangle \rightarrow |x, x \oplus y\rangle$, where the addition has to be taken modulo 2. Moreover, it acts as an entangling gate when acting on tensor products of superpositions.

85.3.3 Multiqubit Gates and Networks

To realize a unitary operation on many qubits for a particular algorithm one would need a network of single-particle and multiparticle quantum gates. Quantum networks enable a prepared input state to be transformed by the appropriate unitary operator to a final state, which is then measured. Deutsch’s model of quantum networks enables us to decompose the network into component gates in diagrammatic form [39]. The task is then to optimize the sequence of gates. One can treat quantum gates acting on N qubits as being elements of the group, which has generators. This, however, is not a particularly transparent or useful way of looking at these gates. Much more useful, and of immense practical importance, is a result essentially from linear algebra, which states that every N -qubit gate can be generated by a network that consists only of very few elementary building blocks consisting of one or two-qubit operations, the so-called universal set of quantum gates [40]. This set contains all possible single-qubit rotations and one nontrivial two-qubit gate, such as the controlled-NOT or controlled-phase gate mentioned above.

85.3.4 Cluster-State Quantum Computing

The original paradigm for a quantum computer was a register of qubits, on which unitary operations would be performed, and eventually the answer would be read out by performing a measurement on some or all of the qubits. A system of N qubits in a pure entangled state would be a quantum system of 2^N dimensions; however the readout could at most procure N bits of information. This indicates both the potential and the drawbacks of the scheme: a quantum computer has an enormous memory on which parallel operations might be performed most efficiently; however, only a small amount of the information present in that memory can ever be accessed.

An important new paradigm for quantum computing was introduced by *Raussendorf* and *Briegel* in 2001 [41]. Cluster-state quantum computing (also called one-way quantum computing, or measurement-based quantum computing) envisions the initial creation of an entangled state of a very

large number of qubits, called a cluster state. If the algorithm one wishes to implement requires N register qubits to store information and M quantum gates to process it, then the size of the cluster state needs to be $N \times M$ physical qubits. The quantum algorithm may then be implemented by measurements of a subset of the qubits, followed by a series of single-qubit operations conditioned on the outcome of those measurements, followed by another series of measurements and conditional single-qubit operations, and so on. The resultant final state can be shown to be equivalent to the output state of a traditional, circuit-based quantum computer.

85.4 Quantum Algorithms

The search for algorithms that would run faster on a quantum computer than on any classical computer is a formidable task. By “faster”, we actually mean that the number of elementary tasks required to perform a given computation should be drastically reduced. The hope is that eventually one will find algorithms that provably run exponentially faster on a quantum computer compared to a classical computer. Here, we briefly discuss three well-known algorithms; investigation of other useful quantum algorithms remains an area of intense on-going research (for reviews: [42–44]).

85.4.1 Deutsch–Jozsa Algorithm

Let us give a particularly instructive example due to *Deutsch* and *Jozsa* [45]. Suppose one is given a function $f(x)$, which is Boolean (i.e., $f(x)$ has only two possible values: 0 or 1), and whose argument is a N -bit number, (i.e., $x \in \{0, 1, \dots, 2^N - 1\}$). From the start it is assumed $f(x)$ is either constant (i.e., it always has the value 0 or 1) or that it is balanced, (i.e., it returns the value 0 and 1 with equal probability). The task is to find out whether $f(x)$ is constant or balanced.

Although this seems a contrived problem, it serves to illustrate the potential power of quantum computers. Classically, to be certain of getting the correct answer, one needs to evaluate the function at least $2^{N-1} + 1$ times to find the answer (i.e., half of the possible values of x , plus 1). With a quantum computer, only a single evaluation of the function is required. First, N qubits are prepared in a superposition of all possible input states, using the Hadamard gate from Eq. (85.11); and a single qubit is prepared in the state $|y\rangle = (1/\sqrt{2})(|0\rangle - |1\rangle)$; then a unitary operator that evaluates the function $f(x)$ is applied, i.e., $\hat{U}_f|x\rangle|y\rangle = |x\rangle|y \oplus f(x)\rangle$. Since the N qubits containing the value of the argument x are in a superposition of all possible values, a single evaluation of the function suffices (Fig. 85.3). The following state

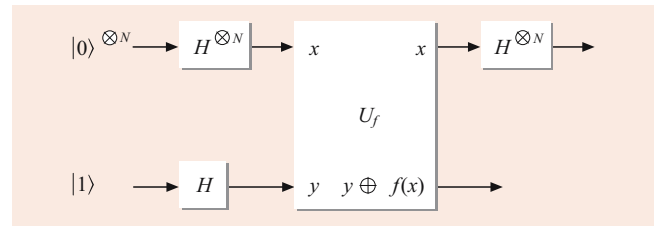


Fig. 85.3 Gate network for implementing the Deutsch–Jozsa algorithm

is the result:

$$\begin{aligned} & \frac{1}{\sqrt{2^{N+1}}} \sum_k |x_k\rangle (|f(x_k)\rangle - |1 \oplus f(x_k)\rangle) \\ & = \left(\frac{1}{\sqrt{2^N}} \sum_k (-1)^{f(x_k)} |x_k\rangle \right) |y\rangle, \end{aligned} \quad (85.13)$$

where we have used the fact that $f(x)$ can only take the value 0 or 1 in order to simplify the result. The final step is to repeat the Hadamard single-qubit unitaries of the argument register qubits and perform a measurement on all of these qubits; the probability of all the output qubits being in state $|0\rangle$ can be shown to be $|(1/\sqrt{2^N}) \sum_k (-1)^{f(x_k)}|^2$, which will be 1 if the function is constant, and 0 if it is balanced. Thus, a measurement outcome other than 0 on any of the N argument qubits then tells that the function $f(x)$ is balanced.

This quantum parallelism is at the heart of the increase in speed that occurs in quantum computation. The Deutsch–Jozsa algorithm involving a few qubits has been implemented on various platforms, most compellingly using ion traps [46].

85.4.2 Grover’s Search Algorithm

In contrast to the preceding example, which always gives the desired answer after exactly one trial, the quantum search algorithm by *Grover* [47] uses a procedure that amplifies the sought after result by a method called “inversion about average”. The goal of Grover’s algorithm is to search an unsorted database with $2N$ entries out of which only one entry fulfills a given criterion; for example, searching through an alphabetic telephone directory to find the person who has some specific telephone number. As in the Deutsch–Jozsa algorithm described above, the query is simultaneously run on all 2^N possible N -qubit basis states, being prepared in an equal superposition. It is assumed that the state that satisfies the search criterion will acquire a phase shift of π . After this step, the inversion about average is carried out. It is represented by a diffusion operator $\hat{D} = 2\hat{P} - \hat{I}$, where \hat{I} is the identity operator, and \hat{P} is a projection operator that averages each input vector with respect to its components. Compared to the previous average value of probability amplitudes, after each of

these steps, the magnitude of the desired state increases by $O(2^{-N/2})$. This procedure is repeated, and after only $O(2^{N/2})$ steps, a projective measurement yields the desired result with probability of $O(1)$, or more precisely, of more than a half. This is a quadratic increase in speed compared to classical search algorithms, which need $O(2^N)$ steps.

85.4.3 Shor's Factor-Finding Algorithm

Suppose one were given an integer n known to be the product of two primes, a and b . A systematic way to determine a and b would be to attempt to divide n by all the prime numbers less than \sqrt{n} . If n , written in binary, has L digits (i.e., $L = \lceil \log_2(n) \rceil$), then the prime number theorem [48, p. 47] implies that one must perform this division $O(2^{(L/2)+1}/L)$ times; in other words, the complexity of finding factors is exponential in the size of the number to be factored. While more efficient algorithms exist, they all have this unfortunate exponential scaling. This mathematical fact is central to the security of public-key encryption systems [48, pp. 212–217], and thus an algorithm that can find factors more efficiently will have far-reaching implications.

Shor's algorithm for quantum computers provides just such an algorithm [49]. The basic idea is to exploit conventional number theory to convert the factor finding to finding the period of particular modular exponential function. While a conventional computer would require multiple evaluations to determine the period of a function, a quantum computer, using the sort of parallelism we have already seen in the Deutsch–Jozsa algorithm, would require a single evaluation. A quantum Fourier transform (analogous to the fast Fourier transform executed on quantum registers) followed by measurement allows the period of the function to be determined with high probability. Once the period of this modular exponential function is determined, the factors of n may be deduced straightforwardly. The total number of operations required is a polynomial function of the number of bits L in the number to be factored.

Implementation of simplified versions of Shor's algorithm, using various tricks and short-cuts, have been reported using various platforms [50–53]; the first potentially scalable experimental demonstration (albeit on a small scale, i.e., factoring 15, using 5 qubits) was reported by Blatt and co-workers in 2016 using trapped ions [54].

85.4.4 Other Algorithms

Other algorithms that are attracting considerable attention and are being pursued both theoretically and experimentally include *quantum simulations* [55, 56], i.e., the use of quantum devices to emulate physical systems with prescribed

microscopic interactions to study the emergence of macroscopic behavior ([57, 58], for some recent experiments); the efficient calculations of molecular energy spectra in *Quantum Chemistry* [59–61]; *Boson Sampling*, the interference of harmonic oscillator modes in nonclassical states (typically single-photon states) in a large interferometer, the output of which can be shown to be related to computational intractable problems such as the calculation of permanents of matrices [62–64]; and *Quantum Machine Learning* [65], plus many others.

A significant milestone in the development of viable quantum computing was passed in 2019 with the demonstration of *quantum supremacy* using a 53 qubit quantum processor developed by the team at Google led by John Martinis [66]. They carried out a calculation in about 200 seconds which, had a conventional computer been used, would have required 10 000 years.

85.5 Error Correction

As we have discussed, the essence of quantum information processing is the use of quantum superpositions, interference, and entanglement. However, quantum interference is fragile. It appears in practice that it is very difficult to maintain a superposition of states of many particles in which each particle is physically separated from all the others. Entanglement turns out to be incredibly delicate. The reason for this is that all systems, quantum or classical, are not isolated; they interact with everything around them: local fluctuating electromagnetic fields, the presence of impurity ions, coupling to unobserved degrees of freedom of the system containing the qubit, etc. These fluctuations destroy quantum interference. A simple analogy is the interference of optical waves in Young's double-slit experiment. In that apparatus, waves from two spatially separated portions of a beam are brought together. If the two parts of the beam have the same phase, then the fringe pattern remains stable. However, if the phase of one part of the beam is drifting with respect to the other, then the fringe pattern will be washed out. And the more slits there are in the screen, the lower the visibility for the same amount of phase randomization per pair of slits. The sensitivity of an N -qubit register to decoherence is even worse, as a maximally entangled N -particle state decoheres at a rate N times faster than a single particle [67], one of the reasons why the world around us appears so classical. A single bit of information lost to an unobserved degree of freedom will result in the reduction of the quantum superposition to a mixed state. Yet, correcting errors due to environmental interactions is essential if a quantum computer is to be constructed; to do "fault tolerant" computing we need to be able to execute many gate operations coherently within the decoherence time

if we are to have a chance of building a scalable quantum register [68].

It might appear that the problem of stabilizing a register of qubits is hopeless, like trying to balance several pencils on their tips on the deck of a ship in a storm. Yet, amazingly, quantum mechanics provides a way to solve this problem, through the use of even higher levels of entanglement. In 1996, *Steane* and, independently, *Shor* and coworkers, showed that encoding information in entangled sets of qubits offered the opportunity to execute quantum error correction [69, 70]. That one can do this is a remarkable consequence of entanglement. In classical information processing, inevitable environmental noise is dealt with by error correction. In its simplest form, this involves repeating the message transmission or calculation until a majority result is obtained.

However, there are more efficient ways, for example, the use of a parity check on a block of bits. It turns out that a similar notion can be applied to a quantum register. However, the application is not straightforward because the contents of a register cannot be measured without destroying the superposition state encoded in it. The problem then is to determine what errors might be present in a quantum register without looking at the qubits. The elegant solution is to entangle the qubits in question with those in an ancillary register and measure the ancillary register. Because the two registers are correlated, the results of the measurement of the ancilla reveal any errors present in the processing register without destroying any coherent superpositions in the processing register itself.

The first experimental demonstration of quantum error correction used liquid-state nuclear magnetic resonance (NMR) techniques [71]; but given the highly mixed nature of the “pseudo-pure” quantum states in NMR, which precludes the existence of any entanglement [72], this work had limited implications for quantum information processing. In 2004, *Wineland’s* group in Boulder succeeded in implementing quantum error correction in an entangled system using trapped ions [73, 74]; since then, multiple, repetitive error correction has been demonstrated by *Blatt’s* group. Another way to prevent the register coherence from falling apart is to know a little about the sort of noise that is acting on it. If the noise has some very slow components (or those with very long wavelengths), then it is sometimes possible to find certain combinations of qubit states for which the noise on one qubit exactly cancels the noise on another. These qubit states live in a “decoherence-free subspace” (DFS) [75–77]. A computer will then be immune to environmental perturbations if all the computational states lie in this DFS. Decoherence-free subspaces were first realized experimentally using photonic qubits by *Kwiat* and coworkers in 2000 [78].

A remarkable result, which has important implications for the long-term viability of quantum information processing, is the quantum threshold theorem, which states in essence that

if a qubit can be realized with a high enough degree of protection against environmental errors, then through the process of concatenation (i.e., encoding one logical qubit using noisy qubits; each of which might be encoded on another set of qubits, and so on), quantum computations can be performed with arbitrary accuracy [79]. As in the field of quantum algorithms, fault-tolerant quantum computing remains a highly active area of research ([80], for a recent overview).

85.6 The DiVincenzo Checklist

So much for the theory of what we would like to with quantum computers; there remains the vexatious topic of how they might be realized in practice. The short answer is that no one knows for certain how (or, indeed, if) practical quantum computers might be realized. *DiVincenzo* has given a list of requirements that a physical implementation must fulfill in order to qualify as a sensible candidate for an implementation of quantum information processing [81]; we will review these here and then use them to assess how various technologies are developing. We will concentrate on those implementations that currently seem the most promising, rather than discuss every proposal that initially seem promising but has over the years fallen by the wayside.

85.6.1 Qubit Characterization, Scalability

Each physical implementation must be tested upon how qubits should be encoded. For a qubit being essentially a two-level system, this task is generally not too difficult. Several candidates, such as electronic or nuclear spin, photon polarization, and choice of path in an interferometer, degenerate ground states of an atom or ion, charge or flux states in superconducting quantum interference devices (SQUIDS), or exciton population, have all been explored. Much more challenging will be the question as to whether there are fundamental or technological limitations of having many of those qubits being operated upon separately, hence whether the system can be scaled up to contain potentially many qubits.

85.6.2 Initialization

Once the qubits have been specified, each quantum information processing or quantum computation task needs to be able to start from a well-defined state. This can be basically any quantum state of the many-qubit system as long as it is a product state and can be prepared error-free. Commonly, this state is then called the ground state and is denoted by $|0\rangle^{\otimes N}$.

85.6.3 Long Decoherence Times

In order to ensure error-free computation without loss of purity of quantum superpositions, the decoherence times that are relevant for the quantum operation should be much longer than the gate operation time itself. In most situations, decoherence limits the number of qubits that can be worked on simultaneously, thus affecting the scalability of the system. Typical examples of decoherence processes are heating mechanisms in ultracold systems, such as ion-trap or atom-chip experiments, spin relaxation in NMR-type experiments, or absorption in linear optical elements. Generally, decoherence is unavoidable due to the basic principles upon which quantum information processing is supposed to work. Avoiding decoherence means isolating the system from the outside world, the environment. However, controlling the interaction between subsystems always has the negative effect of bringing the system in contact with the environment and, therefore, necessarily introduces decoherence. Once one has accepted that decoherence is unavoidable, ways have to be found to guard against it. Several error-correction schemes have been proposed that can correct for certain small amounts of decoherence as described in Sect. 85.5.

85.6.4 Universal Set of Quantum Gates

A necessary prerequisite for quantum information processing and quantum computing is the ability to generate a set of quantum gates that can be considered universal. With such a set, it will then be possible to generate all other quantum gates by concatenating them to form suitably arranged networks. The choice of which set out of the many possible is taken depends on the physical implementation itself. Basically, it is determined by the operations that are intrinsically simple for the given interaction Hamiltonian. In some applications, such as the ion-trap experiments, the controlled-NOT gate is preferred as the nontrivial two-qubit gate, whereas in linear optical networks, one rather works with the controlled-phase gate.

85.6.5 Qubit-Specific Measurement

The last requirement is to be able to read out the result of the computation. That is, there has to be a way of providing a selective projective measurement. This proves to be a major challenge in most proposals for implementing quantum computing. Examples of the challenges involved are the necessity to provide photon-number resolving photodetectors, single-electron charge measurement devices, or single-spin measurements.

85.7 Physical Implementations

Over the past quarter of a century, a number of architectures capable of attempting an assault on the rigors of the DiVincenzo criteria have been proposed and tested; many have fallen by the wayside, a few have persevered. In general, atomic and optical systems based on nonclassical light (e.g., single photons) [82] or cold trapped atoms [83, 84] have led the way, since these had been studied for many years for their intrinsic scientific interest, and had already the proven capability to produce entangled quantum states and/or the high degree of protection against environmental decoherence necessary for quantum computation. In what follows, we will concentrate our attention on these. However, they possess a decided *disadvantage* as a scalable architecture for a full-scale quantum computer with say 10^5 qubits and capable of performing useful tasks: in order that computation technology be robust and durable, it is taken for granted that a solid-state-based architecture will ultimately be necessary. Such architectures, based on quantized magnetic flux in superconducting circuits [85, 86] or on individual spin impurities in a semiconductor host [87, 88], have also shown considerable promise. In such a rapidly developing field, the relative merits of the various technological implementations may well reverse themselves within the space of a few years.

85.7.1 Linear Optics

The use of photons as carriers of quantum information seems to be a straightforward matter: they are easy to produce in numbers; much of the technology to store and to manipulate photons in mature due to its dominance in conventional telecommunications; they show both spin-like behavior (i.e., polarization) and boson-like behavior, making them versatile quantum systems. The first serious proposal for a quantum logic gate was made using photons as qubits in 1989 [89]. The major drawback for photons as qubits is the lack of strong nonlinearities at the single-photon level needed to implement two-qubit logic gates.

However, a different approach, based on a generalization of the well-known quantum-optical Hong–Ou–Mandel interference effect [90], was proposed in 2001 [91, 92]. In this scheme, information is encoded in number states (also called *Fock states*): one photon can be in one of two distinct modes of free space or of a photonic waveguide. Since photons are bosons, there is a natural tendency to bunch together in interference experiments, which in a sense is a nonlinearity on the level of single or few photons. The trick is to use conditional measurements or measurement-induced nonlinearities. The idea was first realized experimentally in [93], where a polarization encoding was used. Fig. 85.4 shows the schematic

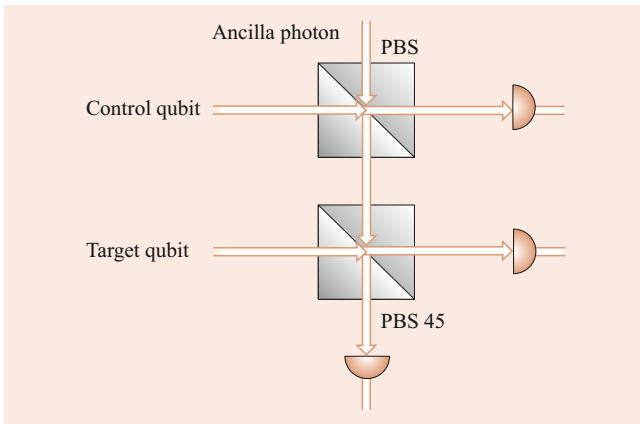


Fig. 85.4 Setup of an all-optical controlled-NOT gate. Control and target qubits are encoded in the polarization of single photons. These are fed into polarizing beam splitters (PBS), one of which is rotated by 45°

setup of a simplified version of a controlled-NOT gate with one single ancilla photon (after [94]).

Measurement-induced nonlinearities make use of the fact that unitary transformations in a larger Hilbert space, e.g., with added auxiliary photon modes combined with photodetection, can yield effective nonlinearities [95]. The drawback is, however, that the wanted nonlinearity is conditioned on the appearance of a certain measurement pattern, which means that these schemes work only with a certain probability [96].

The set of quantum gates that can be considered fundamental differs slightly from most other physical implementations. Within the qubit encoding in photon number states, the gates that can actually be implemented efficiently are those that act within Fock layers (subspaces of fixed total photon number), such as the controlled-phase gate, or the swap gate. Other gates that do not fall into this class require excessively more resources unless other types of qubit encodings are used simultaneously. Gate operation times can be very fast and are only limited by the gating times of the photodetectors. Other attractive features of this approach are that devices can work at room temperature and can readily be integrated into photonic waveguides. However, a major experimental challenge is mode matching in larger networks and interferometric setups, as well as scalability [96]. The cluster state approach discussed above (Sect. 85.3.4) is actively being pursued using linear optical implementations.

85.7.2 Trapped Ions

The most advanced method of quantum information processing in terms of the number of qubits and the number of gates

that have been unequivocally demonstrated is the ultracold-ions scheme proposed by *Cirac* and *Zoller* in 1995 [97]. The ions are stored in a linear Paul trap, in which radio frequency electric quadrupole fields are used to generate confining potentials [98, 99]. The ions are cooled into their motional ground states by Doppler cooling [100] and further cooled to the quantum ground state by resolved sideband cooling [101]. Since the ions are strongly coupled by their mutual Coulomb repulsion, their oscillations are resolved into a number of normal modes, rather like pendulums connected by springs [102]; each of these normal modes are quantum harmonic oscillators that interact with all of the ions in the trap, enabling a quantum data bus to connect the ion qubits.

The qubits are encoded into two long-lived electronic states of individual ions, either transitions to metastable excited states (i.e., with lifetimes of a second or more, since decays are dipole forbidden) or Raman coupling between sublevels of the ground state, thereby avoiding the decoherence that an upper-state lifetime, or laser phase drift can generate. Lasers focused on individual ions are then used to control both the internal states of individual qubits and, by detuning, to couple the qubits to the quantum oscillation modes of the ions, thereby enabling two-qubit quantum logic gates. Readout is performed by observation of fluorescence from individual ions. To date 20 qubits have been trapped, cooled, coherently manipulated, and shown to be entangled [103].

85.8 Outlook

We have discussed the basic ideas behind quantum information and described a few possible applications. However, the immense wealth of ideas and possible routes have barely been touched upon. In the past few years, the field has generated tremendous excitement, with many new strands of investigation evolving rapidly. Quantum key distribution is becoming a commercial technology. For quantum computing, only one or two dozen qubits have been entangled and manipulated experimentally so far, and a deployable quantum computer remains decades away, although new algorithm research suggests that demonstrations of the quantum advantage in computation may be a reality in a much shorter time.

Acknowledgements We like to thank A. Al-Quasimi, A. Beige, R. Blatt., J. Eisert, E. A. Hinds, V. Kendon, P. G. Kwiat, W. J. Munro, M. B. Plenio, A. G. White and many others for numerous stimulating discussions on this exciting subject. Funding by the Natural Science Engineering Research Council (Canada), UK Engineering and Physical Sciences Research Council (EPSRC), the Royal Society, the European Commission, and the Alexander von Humboldt foundation are gratefully acknowledged.

References

1. Nielsen, M.A., Chuang, I.L.: *Quantum Computation and Quantum Information*. Cambridge University Press, Cambridge (2000)
2. Vedral, V.: *Introduction to Quantum Information Science*. Oxford University Press (2006)
3. Kaye, P., Laflamme, R., Mosca, M.: *An Introduction to Quantum Computing*, 1st edn. Oxford University Press (2008)
4. Barnett, S.M.: *Quantum Information*. Oxford University Press (2009)
5. Lipton, R.J., Regan, K.W.: *Quantum Algorithms via Linear Algebra: A Primer*, 1st edn. MIT Press (2014)
6. Hayashi, M., et al.: *Introduction to Quantum Information Science*. Springer (2015). English edition
7. Wilde, M.M.: *Quantum Information Theory*, 2nd edn. Cambridge University Press (2017)
8. Schrödinger, E.: *Math. Proc. Camb. Philos. Soc.* **31**, 555 (1935)
9. Eberly, J.H., et al.: *Phys. Scr.* **91**, 063003 (2016)
10. Einstein, A., Podolsky, B., Rosen, N.: *Phys. Rev.* **47**, 777 (1935)
11. Bell, J.S.: *Speakable and Unsayable in Quantum Mechanics: Collected Papers on Quantum Philosophy*. Cambridge University Press, Cambridge (2004)
12. Freedman, S.J., Clauser, J.F.: *Phys. Rev. Lett.* **28**, 938 (1972)
13. Aspect, A., Grangier, P., Roger, G.: *Phys. Rev. Lett.* **47**, 460 (1981)
14. Hensen, B., et al.: *Nature* **526**, 682–686 (2015)
15. Giustina, M., et al.: *Phys. Rev. Lett.* **115**, 250401 (2015)
16. Shalm, L.K., et al.: *Phys. Rev. Lett.* **115**, 250402 (2015)
17. Schumacher, B.: *Phys. Rev. A* **51**, 2738 (1995)
18. Cover, T.M., Thomas, J.A.: *Elements of Information Theory*. Wiley, New York (1991)
19. Strang, G.: *Linear Algebra and Its Applications*. Thomson Brooks/Cole, Belmont (2006). 6.3.
20. Hill, S., Wootters, W.K.: Concurrence was introduced as a measure of entanglement for two qubits. *Phys. Rev. Lett.* **78**, 5022 (1997)
21. Wootters, W.K.: The formula presented here is a straightforward generalization for larger systems. *Phys. Rev. Lett.* **80**, 2245 (1998)
22. Horodecki, R., et al.: *Rev. Mod. Phys.* **81**, 865 (2009)
23. Streltsov, A., Adesso, G., Plenio, M.B.: *Rev. Mod. Phys.* **89**, 041003 (2017)
24. Holevo, A.S.: *Proceedings of the Second Japan–USSR Symposium on Probability Theory*. Springer, Berlin, Heidelberg, pp 104–119 (1973)
25. Holevo, A.S.: *IEEE Trans. Inf. Theory* **44**, 269 (1998)
26. Schumacher, B., Westmoreland, M.D.: *Phys. Rev. A* **56**, 131 (1997)
27. Bennett, C.H., Brassard, G.: *Proceedings of IEEE Int. Conf. on Computers Systems, Signal Processing*. IEEE, Bangalore, India, pp 175–179 (1984)
28. Ekert, A.K.: *Phys. Rev. Lett.* **67**, 661 (1991)
29. Zurek, W.H., Wootters, W.K.: *Nature* **299**, 802 (1981)
30. Bennett, C.H., et al.: *J. Crypt.* **5**, 3 (1992)
31. Gisin, N., et al.: *Rev. Mod. Phys.* **74**, 145 (2002)
32. Diamanti, E., et al.: *npj Quantum Inf.* **2**, 16025 (2016)
33. Bennett, C.H., et al.: *Phys. Rev. Lett.* **70**, 1895 (1993)
34. Bouwmeester, D., et al.: *Nature* **390**, 575 (1997)
35. Boschi, D., et al.: *Phys. Rev. Lett.* **80**, 1121 (1998)
36. Riebe, M., Häffner, H., Roos, C.F., Hänsel, W., Benhelm, J., Lancaster, G.P.T., Körber, T.W., Becher, C., Schmidt-Kaler, F., James, D.F.V., Blatt, R.: *Nature* **429**, 734 (2004)
37. Barrett, M., Chiaverini, J., Schaetz, T., Britton, J., Itano, W.M., Jost, J.D., Knill, E., Langer, C., Leibfried, D., Ozeri, R., Wineland, D.J.: *Nature* **429**, 737 (2004)
38. Ren, J.-G., et al.: *Nature* **549**, 70 (2017)
39. Deutsch, D.: *Proc. R. Soc. A* **425**, 73 (1989)
40. DiVincenzo, D.P.: *Phys. Rev. A* **51**, 1015 (1995)
41. Raussendorf, R., Briegel, H.J.: *Phys. Rev. Lett.* **86**, 5188 (2001)
42. Childs, A., van Dam, W.: *Rev. Mod. Phys.* **82**, 1 (2010)
43. Bacon, D., van Dam, W.: *Commun. ACM* **53**, 84 (2010)
44. Montanaro, A.: *npj Quantum Inf.* **2**, 15023 (2016)
45. Deutsch, D., Jozsa, R.: *Proc. R. Soc. A* **439**, 553 (1992)
46. Gulde, S., et al.: *Nature* **421**, 48 (2003)
47. Grover, L.: *Phys. Rev. Lett.* **79**, 325 (1997)
48. Rosen, K.H.: *Elementary Number Theory and its Applications*. Addison-Wesley, Reading (1984)
49. Shor, P.W.: *Proceedings of the 35th Annual Symposium on Foundations of Computer Science*, 1994, Los Alamitos. IEEE Computer Society Press, New York, pp 124–134 (1994)
50. Vandersypen, L.M.K., et al.: *Nature* **414**, 883 (2001)
51. Lu, C.-Y., et al.: *Phys. Rev. Lett.* **99**, 250504 (2007)
52. Lanyon, B.P., et al.: *Phys. Rev. Lett.* **99**, 250505 (2007)
53. Martin-Lopez, E., et al.: *Nat. Photon.* **6**, 773 (2012)
54. Monz, T., et al.: *Science* **351**, 1068 (2016)
55. Feynman, R.P.: *Int. J. Theor. Phys.* **21**, 467 (1982)
56. Lloyd, S.: *Science* **273**, 1073 (1996)
57. Lanyon, B.P., et al.: *Science* **334**, 57 (2011)
58. Britton, J.W., et al.: *Nature* **484**, 489 (2012)
59. Aspuru-Guzik, A., et al.: *Science* **309**, 1704 (2005)
60. Lanyon, B.P., et al.: *Nat. Chem.* **2**, 106 (2010)
61. Hempel, C., et al.: *Phys. Rev. X* **8**, 031022 (2018)
62. Aaronson, S., Arkhipov, A.: *Theory Comput.* **9**, 143 (2013)
63. Broome, M., et al.: *Science* **339**, 794 (2013)
64. Spring, J., et al.: *Science* **339**, 798 (2013)
65. Schuld, M., Sinayskiy, I., Petruccione, F.: *Contemp. Phys.* **56**, 172 (2014)
66. Arute, F., et al.: Quantum supremacy using a programmable superconducting processor. *Nature* **574**, 505–510 (2019)
67. Zurek, W.H.: *Rev. Mod. Phys.* **75**, 715 (2003)
68. Preskill, J.: *Proc. R. Soc. A* **454**, 385 (1998)
69. Steane, A.: *Phys. Rev. Lett.* **77**, 793 (1996)
70. Calderbank, A.R., Shor, P.W.: *Phys. Rev. A* **54**, 1098 (1996)
71. Cory, D.G., et al.: *Phys. Rev. Lett.* **81**, 2152 (1998)
72. Braunstein, S.L., et al.: *Phys. Rev. Lett.* **83**, 1054 (1999)
73. Chiaverini, J., et al.: *Nature* **432**, 602 (2004)
74. Schindler, P., et al.: *Science* **332**, 1059 (2011)
75. Palma, G.A., Suominen, K.-A., Ekert, A.K.: *Proc. R. Soc. A* **452**, 567 (1996)
76. Duan, L.-M., Guo, G.-C.: *Phys. Rev. Lett.* **79**, 1953 (1997)
77. Zanardi, P., Rasetti, M.: *Phys. Rev. Lett.* **79**, 3306 (1997)
78. Kwiat, P.G., et al.: *Science* **290**, 498 (2000)
79. Knill, E., Laflamme, R., Zurek, W.H.: *Science* **279**, 342 (1998)
80. Campbell, E.T., Terhal, B.M., Vuillot, C.: *Nature* **549**, 172 (2017)
81. DiVincenzo, D.P.: *Fortschr. Phys.* **48**, 7718 (2000). For a recent discussion, see <http://blog.qutech.nl/index.php/2018/02/22/looking-back-at-the-divincenzo-criteria/>
82. Ralph, T.C., Pryde, G.J.: *Prog. Opt.* **54**, 209 (2010)
83. Häffner, H., Roos, C.F., Blatt, R.: *Phys. Rep.* **469**, 155–203 (2008)
84. Monroe, C., Kim, J.: *Science* **339**, 1164 (2013)
85. Devoret, M.H., Schoelkopf, R.J.: *Science* **339**, 1169 (2013)
86. Wendin, G.: *Rep. Prog. Phys.* **80**, 106001 (2017)
87. Kane, B.E.: *Nature* **393**, 133 (1998)
88. Broome, M.A., et al.: *Nat. Commun.* **9**, 980 (2018)
89. Milburn, G.J.: *Phys. Rev. Lett.* **62**, 2124 (1989)
90. Hong, C.K., Ou, Z.Y., Mandel, L.: *Phys. Rev. Lett.* **59**, 2044 (1987)
91. Knill, E., Laflamme, R., Milburn, G.J.: *Nature* **409**, 46 (2001)
92. Koashi, M., Yamamoto, T., Imoto, N.: *Phys. Rev. A* **63**, 030301 (2001)

93. Pittman, T.B., Jacobs, B.C., Franson, J.D.: Phys. Rev. Lett. **88**, 257902 (2002)
94. Pittman, T.B., Fitch, M.J., Jacobs, B.C., Franson, J.D.: Phys. Rev. A **68**, 032316 (2003)
95. Scheel, S., Nemoto, K., Munro, W.J., Knight, P.L.: Phys. Rev. A **68**, 032310 (2003)
96. Kok, P., et al.: Rev. Mod. Phys. **79**, 135 (2007)
97. Cirac, J.I., Zoller, P.: Phys. Rev. Lett. **74**, 4094 (1995)
98. Paul, W., Osberghaus, O., Fischer, E.: Forschungsberichte des Wirtschafts und Verkehrsministeriums Nordrhein-Westfalen Nr. 415. Westdeutscher Verlag, Köln (1958)
99. Neuhauser, W., Hohenstatt, M., Toschek, P.E., Dehmelt, H.G.: Phys. Rev. A **22**, 1137 (1980)
100. Wineland, D.J., Drullinger, R., Walls, D.F.: Phys. Rev. Lett. **40**, 1639 (1978)
101. Wineland, D.J., Dehmelt, H.G.: Bull. Am. Phys. Soc. **20**, 637 (1975)
102. James, D.F.V.: Appl. Phys. B **66**, 181 (1998)
103. Friis, N., et al.: Phys. Rev. X **8**, 021012 (2018)



Daniel James Daniel James was born in Manchester, UK. He received his PhD from the University of Rochester in 1992, supervised by Professor Emil Wolf. He was a staff member in the Theoretical Division, Los Alamos National Laboratory (1994–2005), after which he joined the faculty of the University of Toronto. He has been engaged in quantum information research since 1995.



Peter Knight Peter Knight is Emeritus Professor at Imperial, a past President of the Institute of Physics, 2004 President of the Optical Society of America, Chair of the UK National Quantum Technology Programme Strategy Advisory Board and chairs the Quantum Metrology Institute at the National Physical Laboratory. His research centres on quantum technology.



Stefan Scheel Stefan Scheel received his PhD (Dr rer nat) from the Friedrich Schiller University, Jena, Germany, in 2001. He worked in the Quantum Optics and Laser Science Group at Imperial College London until 2012, when he moved to Rostock, Germany as a Full Professor. His research interests include QED in dielectrics, fluctuation-induced phenomena, integrated waveguide quantum optics, and Rydberg physics with atoms and semiconductor excitons.

Part G
Applications

Part G is concerned with the various applications of atomic, molecular, and optical physics. A summary of the processes that take place in photoionized gases, collisionally ionized gases, the diffuse interstellar medium, molecular clouds, circumstellar shells, supernova ejecta, shocked regions, and the early universe are presented. The principal atomic and molecular processes that lead to the observed cometary spectra, as well as the needs for basic atomic and molecular data in the interpretation of these spectra, are focused on. The basic methods used to understand planetary atmospheres are given. The structure of atmospheres and their interac-

tion with solar radiation are detailed, with an emphasis on ionospheres. Atmospheric global change is then studied in terms of the applicable atomic and molecular processes responsible for these changes. Various applications of atomic and molecular physics to phenomena that occur at surfaces are reviewed; particular attention is placed on the application of electron-atom and photon-atom scattering processes to obtain surface specific structural and spectroscopic information. The effect of finite nuclear size on the electronic energy levels of atoms is also detailed; and conversely, the electronic structure effects in nuclear physics are discussed.



Applications of Atomic and Molecular Physics to Astrophysics

86

Stephen Lepp, Phillip C. Stancil, and Alexander Dalgarno

Contents

86.1	Introduction	1275
86.2	Photoionized Gas	1276
86.3	Collisionally Ionized Gas	1278
86.4	Diffuse Molecular Clouds	1278
86.5	Dark Molecular Clouds	1280
86.6	Circumstellar Shells and Stellar Atmospheres	1281
86.7	Supernova Ejecta	1282
86.8	Shocked Gas	1283
86.9	The Early Universe	1283
86.10	Atacama Large Millimeter/Submillimeter Array	1284
86.11	Recent Developments	1285
86.12	Other Reading	1285
	References	1286

Abstract

The range of physical conditions of density, temperature, and radiation fields encountered in astrophysical environments is extreme and can rarely be reproduced in a laboratory setting. It is not only reliable data on known processes that are needed but also a deep understanding so that the relevant processes can be identified and the influence of the conditions in which they occur fully taken into account.

We present here a summary of the processes that take place in photoionized gas, collisionally ionized gas, the diffuse interstellar medium, molecular clouds, circumstel-

lar shells, supernova ejecta, shocked regions, and the early universe.

Keywords

charge exchange · dielectronic recombination · early universe · molecular cloud · photoionization · planetary nebula · radiative association · recombination · supernova remnant · three-body recombination · Wilkinson microwave anisotropy probe

86.1 Introduction

Almost all our information about the universe reaches us in the form of photons, though neutrinos, cosmic rays, and, recently, gravitational waves provide additional insight. Traditional observational astronomy is based on measurements of the distribution in frequency and intensity of the photons that are emitted by astronomical objects and detected by instrumentation on ground-based and space-borne telescopes. Information about the earliest stages in the evolution of the universe before galaxies and stars had formed is carried to us by blackbody background photons that attended the beginning of the universe. The photons that are the signatures of astronomical phenomena are the result of a plethora of physical and chemical processes reaching into a host of disciplines, including nuclear physics; plasma physics; solid-state physics or surface sciences; and atomic, molecular, and optical physics. The processes that modify the photons on their journey from distant origins through intergalactic and interstellar space to the Earth belong mostly to the domain of atomic, molecular, and optical physics, as do the instruments that detect and measure the arriving photons and their spectral distribution. The spectra are used to classify galaxies and stars and to identify other astronomical entities and phenomena such as quasars, active galactic nuclei, gravitational lensing, jets and outflows, pulsars, supernovae, novae, supernova remnants, nebulae, masers, protostars, shocks,

S. Lepp (✉)
Dept. of Physics & Astronomy, University of Nevada, Las Vegas
Las Vegas, NV, USA
e-mail: lepp@unlv.nevada.edu

P. C. Stancil
Dept. of Physics & Astronomy, The University of Georgia
Athens, GA, USA
e-mail: pstancil@uga.edu

molecular clouds, circumstellar shells, accretion disks, protoplanetary disks (PPDs), galaxy clusters, and black holes.

Quantitative analyses of the spectra of astronomical sources of photons and of the atomic, molecular, and optical processes that populate the atomic and molecular energy levels and give rise to the observed absorption and emission require accurate data on transition frequencies and wavelengths, oscillator strengths, cross sections for electron impact, rate coefficients for radiative, dielectronic, and dissociative recombination, and cross sections for heavy-particle collisions involving charge transfer, excitation, ionization, dissociation, fine structure and hyperfine transitions, collision-induced absorption, and line broadening. Data on ion–molecule and neutral particle reaction rate coefficients are central to the interpretation of measurements of chemical composition in molecular clouds, circumstellar shells, PPDs, and supernova ejecta.

The range of physical conditions of density, temperature, and radiation fields encountered in astrophysical environments is extreme and can rarely be reproduced in a laboratory setting. It is not only reliable data on known processes that are needed but also a deep understanding of the microphysics so that the relevant processes can be identified and their influence on the environments in which they occur fully taken into account.

We present here a summary of the processes that take place in photoionized gas, collisionally ionized gas, the diffuse interstellar medium, molecular clouds, circumstellar shells, PPDs, supernova ejecta, kilonovae, shocked regions, and the early universe.

86.2 Photoionized Gas

The universe contains copious sources of energetic photons, most often due to radiation from hot stars. As a consequence, much of the baryonic material of the universe exists as photoionized gas. Photoionized gas produces the visible emission from emission nebulae, planetary nebulae, nova shells, starburst galaxies, and probably active galactic nuclei [1].

Emission nebulae are extended regions of luminosity in the sky. They arise from the absorption of stellar radiation by the gas surrounding one or more hot stars. The gas is ionized by the photons and excited and heated by the electrons released in the photoionizing events. A succession of ionization zones is created in which highly ionized regions give way to less ionized gas with increasing distance from the central star as the photon flux is diminished by geometrical dilution and by absorption. The outer edge of a nebula is a front of ionization pushing out into the neutral interstellar gas. The densities are typically between 100 and 10,000 cm⁻³, with temperatures between 5000 and 15,000 K. Nebulae are also called HII regions. At low densities, the lu-

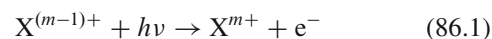
minosity is low, but the ionized regions can still be detected by radio observations.

Planetary nebulae are smaller in extent and denser. They have a passing similarity in appearance to planets. Planetary nebulae are produced by the photoionization of shells of gas that have been ejected from the parent star as it evolved to its final white dwarf stage. Because the core of the parent star is very hot, the irradiated gas is more highly ionized than are emission nebulae and has a distinctive spectrum.

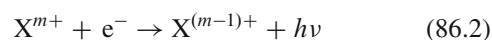
Photoionized gas is also found around novae. Novae are stars that have undergone spasmodic outbursts, and they are surrounded by faint shells of ejected gas, photoionized and excited by the stellar radiation. Some supernova remnants, which are what remains after a massive star has exploded, have spectra that also appear to be emanating from photoionized gas. The source of ionization may be synchrotron radiation. Figure 86.1 shows the X-ray emission spectrum of a supernova remnant.

The nuclei of starburst galaxies have spectra like those of emission nebulae. They result from gas photoionized by radiation from hot stars created in a period of rapid star formation. Active galactic nuclei, such as quasars, have a different spectrum characterized by broad lines indicating a large range of velocities. Photoionized gas is the most likely interpretation, although the ionizing source may be an accretion disk around a compact object, such as a black hole.

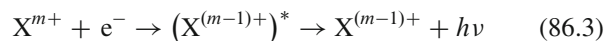
The ionization structure in a photoionized gas is determined by a balance of photoionization



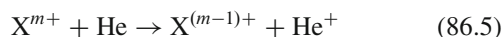
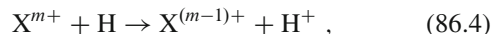
and radiative



and dielectronic



recombination, while in plasmas with a significant population of neutral hydrogen and helium, charge transfer recombination



may also play a role. Many detailed calculations of the ionization structure of photoionized regions have been carried out [1].

The ionizing source spectra of hot stars can be obtained from calculations of stellar atmospheres; see Sect. 86.6. Approximate values of cross sections for photoionization for a wide range of atomic and ionic systems in many stages of ionization are available [3–6]. Calculations of higher precision and reliability that incorporate the contributions

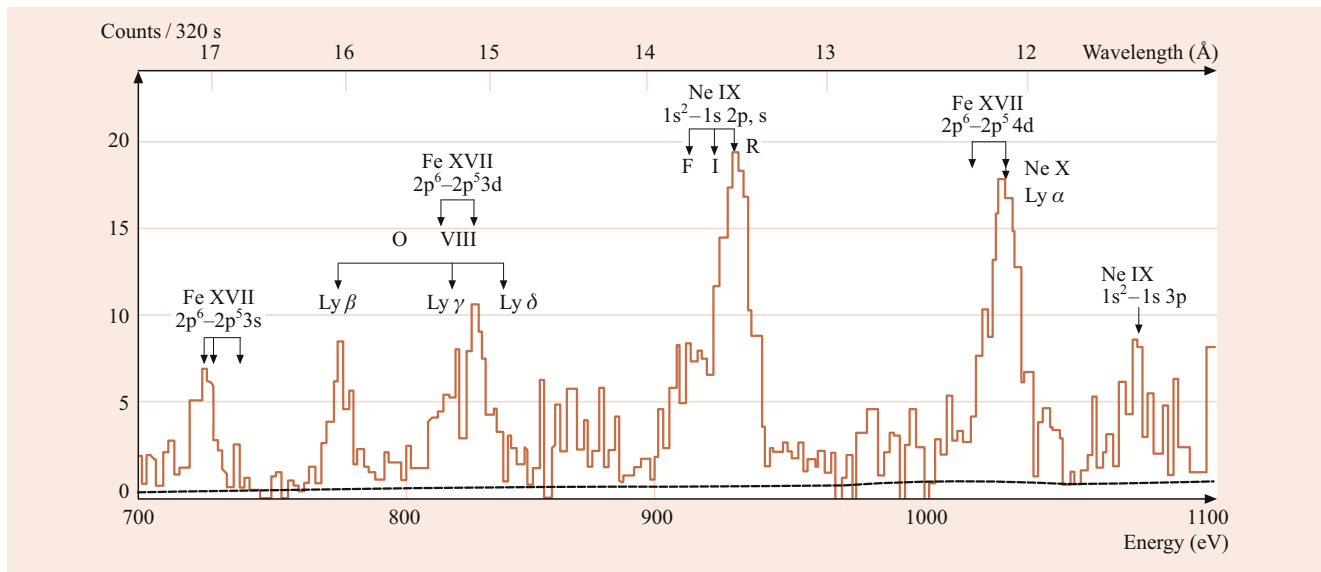


Fig. 86.1 X-ray spectrum of the supernova remnant Puppis A as observed by the Einstein satellite. Note the high level of ionization with hydrogen-like ions of oxygen and neon, suggesting a high temperature. After [2]

from autoionizing resonance structures exist for specific systems [7]. They are undergoing continual improvements as increasingly more powerful computational techniques are brought to bear on the calculations.

The cross sections for radiative recombination are obtained by summing the cross sections for capture into the ground and excited states of the recombining system, typically by applying detailed balance to the state-resolved photoionization cross sections. Because of the contribution from highly excited states that are nearly hydrogenic, the rate coefficients are similar for different ions of the same excess nuclear charge. They vary slowly with temperature. In contrast, dielectronic recombination is a specific process whose efficiency depends on the energy level positions of the resonant states. For nebular temperatures, the rate coefficients vary exponentially with temperature. Explicit calculations have been carried out for many ionic systems [8–10]. Because the photoionization cross sections of the major cosmic gases hydrogen and helium diminish rapidly at high frequencies, multiply charged ions and neutral gas coexist in cosmic plasmas produced by energetic photons and charge-transfer recombination may control the ionization structure. For multiply charged ions with excess charge, greater than 2, charge transfer is rapid. For doubly charged and singly charged ions, the cross sections are sensitive to the details of the potential energy curves of the quasi molecule formed in the approach of the ion and the neutral particle and the interaction mechanism. Few reliable data exist. Some recent calculations may be found in the papers [11–13].

Photoionized gas is heated by collisions of the energetic photoelectrons and cooled by electron impact excitation of metastable levels, principally of O^+ and O^{2+} , N^+ and N^{2+} ,

and S^+ and S^{2+} , followed by emission of photons that escape from the nebula. Considerable attention has been given to the determination of the rate coefficients [14]. The resulting cooling rates increase exponentially with temperature and keep the temperature of the gas between narrow limits. Some contribution to cooling occurs from recombination and from free-free emission by electrons moving in the field of the positive ions.

The luminosity of the photoionized gas comes from the photons emitted in the cooling processes and from radiative and dielectronic recombination. The radiative recombination spectrum of hydrogen extends from the $Ly \alpha$ line at 121.6 nm to radio lines at meter wavelengths.

The recombination spectrum can be predicted to high accuracy, and calculations for a wide range of temperature, density, and radiation environments have been carried out for diagnostic purposes [15–18]. Electron impact and proton impact-induced transitions are important in determining the energy-level populations and the resulting spectrum. Stimulated emission often affects the intensities of the radio lines, especially those from extragalactic sources. Comparisons of the predicted intensities in the visible and infrared with theoretical predictions yield information on interstellar extinction in the nebula and along the line of sight.

The relative intensities of the lines emitted by different metastable levels depend exponentially on the temperature. The relative intensities of the lines at 500.7 and 436.3 nm originating in the 1D_2 and 1S_0 levels of O^{2+} vary as $\exp(33,170/T)$, and are commonly used to derive the temperature T .

The electron density can be inferred from the lines emitted from neighboring levels with different radiative lifetimes

for which there occurs a competition between spontaneous emission and quenching by impact with thermal electrons. There are many possible combinations of lines. The lines at 372.89 and 372.62 nm emitted by the $^2D_{3/2}$ and $^2D_{5/2}$ levels of N^+ are readily observable, and their relative intensity can be used to estimate the electron density.

Radiative and dielectronic recombination lines are often seen in the spectra, as are a few lines due to charge transfer recombination. Fluorescence of starlight and resonance fluorescence of lines emitted in the nebula, called Bowen fluorescence by astronomers, also contribute to the spectra of photoionized gases. A large variety of data are needed to adequately interpret the observations.

Two X-ray satellites, Chandra and XMM-Newton, both launched in 1999, have greatly increased our ability to detect hot ionized gas in stars, supernova remnants, active galaxies, and other regions [19]. In particular, Chandra has allowed us for the first time to directly observe the hot gas between galaxies [20]. The state of modeling photoionized clouds has been reviewed by *Ferland* [21]. He also highlights the great need for atomic and molecular data for analyzing these clouds.

86.3 Collisionally Ionized Gas

Hot gas is found in the coronae of stars and, particularly, the Sun, and in young supernova remnants, in the hot phase of the interstellar medium, and in intergalactic space. In a hot gas, the ionization is produced by impact ionization due to the fast thermal electrons and removed by recombination, both radiative and dielectronic [22]. The rate coefficients for electron impact ionization and for recombination for any given ionization stage are functions only of temperature, and hence so is the resulting ionization distribution. When ionization and recombination balance, coronal equilibrium is attained, in which the ionization structure is specified by the temperature.

Recombination at high temperatures is dominated by dielectronic recombination. At high temperatures, dielectronic recombination is stabilized by transitions in which the core electrons are the active electrons. The associated emission lines lie close in frequency to that of the resonant transition of the parent ion, resulting in so-called satellite lines. Together with lines generated by electron impact excitation, they provide a powerful diagnostic probe of density and temperature. In many circumstances, such as in supernova remnants, coronal equilibrium does not hold, and the ionization and recombination must be followed as functions of time, a situation referred to as nonequilibrium ionization. The temperature also evolves as the hot plasma is cooled by electron impact excitation and ionization.

The recombining gas produces X-rays and extreme UV radiation, which modify the ionization structure. There is a par-

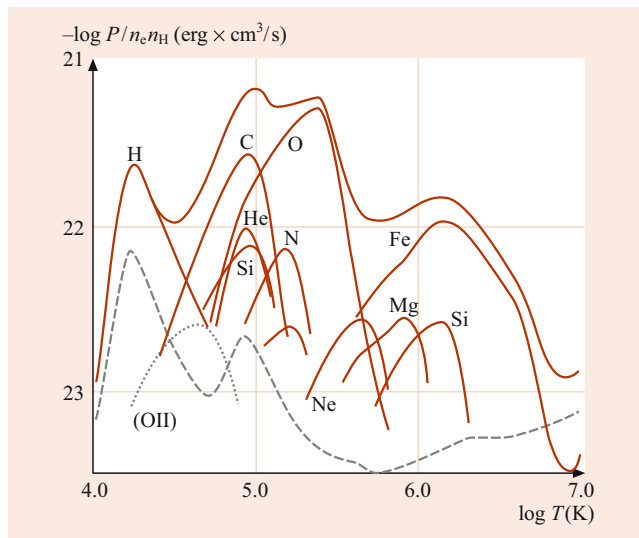


Fig. 86.2 Total emissivity and emissivity by element as a function of temperature in coronal equilibrium. The *heavy solid curve* is total emissivity, and the *lighter lines* are contributions from individual elements. After [23]

ticular need for more reliable data on high-energy photoionization cross sections, on collision cross sections for electrons and positive ions, and on the energy levels and transition probabilities of highly stripped complex ions. In particular, for M-shell ions, dielectronic recombination becomes important at low temperatures, but the reliability of theoretical rate coefficients are uncertain due to a large number of near threshold resonances. Currently, available atomic data have been used to update coronal ionization equilibrium calculations [24]. Figure 86.2 shows the emissivity of coronal gas.

86.4 Diffuse Molecular Clouds

Diffuse molecular clouds are intermediate between the hot phase of the galaxy and the giant molecular clouds where much of the gas resides. They are called diffuse because they have optical depths of order unity, or less, allowing photons to penetrate from outside the cloud and affect the chemical composition. The atoms and molecules are observed in absorption against background stars. Translucent clouds, defined to have optical depths between about 2 and 5 are intermediate between diffuse and dark clouds where photons from the outside still affect the chemistry. They can be observed both in absorption against a background source or in emission in the radio.

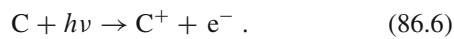
The gas temperature is 100–200 K at the edges of a diffuse cloud with a density of about 100 cm^{-3} . In a typical diffuse cloud, the temperature decreases to about 30 K at the center, while the density increases to about $300\text{--}800 \text{ cm}^{-3}$. The chemistry is driven by ionization from interstellar UV photons and from cosmic rays, composed mostly of high-energy protons.

Interstellar UV photons ionize species that have ionization potentials less than that of atomic hydrogen. Atomic hydrogen is so pervasive in the galaxy that UV photons with energies higher than 13.6 eV are absorbed near the source. The UV flux is a very important parameter in determining the composition of a diffuse cloud. Photodissociation provides destruction that limits the buildup of more complex species, and so diffuse clouds are typically dominated by simpler diatomic species. However, a number of polyatomic molecules, including SO₂, H₂CO, and C₃H₂, have been observed in diffuse clouds, while the so-called diffuse interstellar bands suggest the presence of large organic molecules. Understanding the origin of these large molecules in diffuse clouds remains an important area of research [25].

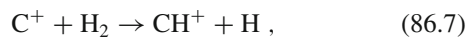
Species with ionization potentials greater than hydrogen are mainly ionized by cosmic rays. Cosmic rays are high-energy nuclei that stream through the galaxy. The cosmic-ray ionization rate, the number of cosmic-ray ionizations per second per particle, is an important parameter in interstellar chemistry. A lower limit to the cosmic-ray ionization rate may be set by measured high-energy cosmic rays reaching Earth, giving an ionization rate of $\approx 10^{-17} \text{ s}^{-1}$. More realistic estimates of the cosmic-ray ionization rate from looking at recombination lines suggest values of a few $\times 10^{-17} \text{ s}^{-1}$. Earlier work by studying recombination lines suggests values of a few $\times 10^{-17} \text{ s}^{-1}$. However, more recent studies based on observations of molecular ions in the galactic disk indicate a much higher rate of $\approx 5.3 \times 10^{-16} \text{ s}^{-1}$, although with only marginal evidence for a decrease in the rate with extinction into diffuse clouds [26].

On the other hand, the hydroxyl radical OH is produced in a manner similar to that discussed below in Sect. 86.6 and removed by photodissociation. Thus, in diffuse clouds, OH may be used to measure the cosmic-ray ionization rate, subject to uncertainties in the OH photodissociation rate and the H₃⁺ dissociative recombination rate. The OH abundances give rates of several $\times 10^{-17} \text{ s}^{-1}$ for many diffuse clouds.

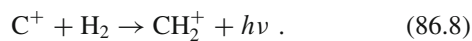
The carbon chemistry begins with the ionization of C by UV photons:



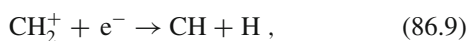
The carbon ion cannot react directly with H₂ by



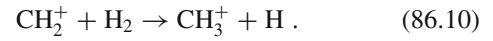
as this reaction is endothermic by 0.4 eV. Instead, the chemistry proceeds by the slow radiative association process



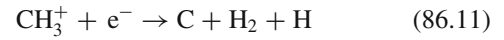
The CH₂⁺ ion may either dissociatively recombine



or react with molecular hydrogen



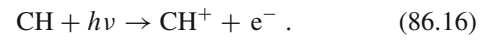
The CH₃⁺ then undergoes dissociative recombination



where the products are listed in order of decreasing likelihood. The CH is removed by photodissociation



and by photoionization



CH may also be removed by reactions with oxygen or nitrogen atoms to form CO and CN, respectively.

One of the outstanding problems in diffuse clouds is to understand the large abundance of CH⁺ relative to CH. The difficulty is in finding a mechanism that can produce sufficient CH⁺ without producing additional CH. Since most reaction paths go through reaction Eq. (86.7), this is the most likely candidate. What is needed is some extra energy to overcome the endothermicity. This energy must come from either hot C⁺ or from hot or vibrationally excited H₂. The most popular model is gas heated by a shock, possibly a magnetic shock, in which ions stream relative to the neutrals, giving a high effective energy. Unfortunately, although these shock models can reproduce the CH⁺ abundances, they also predict relative velocities between the CH⁺ and CH, which are not often observed. Recently, there have been suggestions that turbulence in the cloud could account for the CH⁺ abundance.

The most comprehensive models of diffuse clouds are by *van Dishoeck and Black* [27]. A collection of photodissociation rates and photoionization rates is given by *Roberge et al.* [28], and a more recent compilation has been made by *Heays et al.* [29].

The UV flux is predominantly from stars and may be as much as 10⁵ times larger near an HII region (Sect. 86.2) than it is in the general interstellar medium. Regions in which the chemistry is dominated by photons are referred to as *photon-dominated regions* or *photodissociation regions* (PDRs) [30]. In the presence of high UV flux, the cloud is much warmer than in a typical diffuse cloud. Temperatures may reach 1000 K near the edge of the cloud and 100 K far into the cloud. The chemistry differs from traditional diffuse cloud chemistry in that the high temperatures allow endothermic reactions to proceed. *Sternberg and Dalgarno* [31] have published a comprehensive model of photodominated regions.

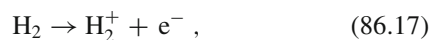
86.5 Dark Molecular Clouds

Much of the mass of the galaxy is in the form of dark molecular clouds. The molecular clouds are sites of new star formation. They are composed primarily of hydrogen, with about 10% helium and trace amounts of heavier elements. They have densities of approximately 10^3 or 10^4 cm^{-3} and temperatures between 10 and 20 K, and often contain denser clumps. The clouds are optically thick, and so photons from the outside are absorbed on the surface of the clouds. The interiors are heated and ionized by cosmic rays that penetrate deep into the cloud.

The temperatures are too low to sustain much neutral chemical activity in the clouds, and cosmic-ray ionization is important in driving the chemistry. In dense clouds, the cosmic rays both initiate the chemistry and limit it through the production of He^+ and through cosmic-ray induced photons.

Currently, about 200 molecules have been detected in the interstellar medium, many of which have also been found in other galaxies. Table 86.1 gives a partial list, ranging from simple diatomics to the largest being C_{70} . Most molecules, except H_2 , are formed in the gas phase by ion–molecule reaction sequences initiated by a cosmic-ray ionization. The fact that isomers, such as HCN and HNC, are seen in approximately equal abundances suggests a low density gas phase environment. Reactions on surfaces and the formation of grains are not well understood but are surely important. It does appear that many complex organic molecules, such as dimethyl ether, are primarily formed on ice mantles [32]. The Infrared Space Observatory (ISO) has provided a tremendous amount of data on cold regions in our own galaxy and allowed us to directly observe the icy mantles of dust grains [33].

The chemistry of molecular clouds is dominated by ion–molecule reactions driven by cosmic-ray ionization. The cosmic rays primarily ionize H_2 :



producing both H_2^+ and fast electrons. The fast electrons produce additional ionizations. The H_2^+ quickly reacts with H_2 to form H_3^+ ,



The H_3^+ reacts with other species by proton transfer, which then drives much of the interstellar chemistry.

As an example of the production of more complex molecules in interstellar chemistry, we examine the reaction networks leading to the production of water H_2O and the hydroxyl radical OH. The H_3^+ ions formed by cosmic-ray ionization react with atomic oxygen to form OH^+

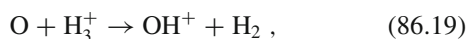
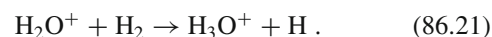
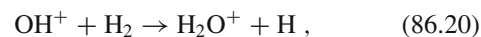


Table 86.1 Molecules observed in interstellar clouds

H_2	Hydrogen
CH^+	Methylidyne ion
C_2	Carbon
CO	Carbon monoxide
NH	Amidogen
CS	Carbon monosulfide
SO	Sulphur monoxide
NS	Nitrogen sulfide
PN	Phosphorus nitride
SiN	Silicon nitride
H_2O	Water
HCN	Hydrogen cyanide
HCO	Formyl
N_2H^+	Protonated nitrogen
HNO	Nitroxyl
SO_2	Sulfur dioxide
C_2O	Carbon suboxide
N_2O	Nitrous oxide
H_2CO	Formaldehyde
NH_3	Ammonia
HNCO	Isocyanic acid
C_3H	Propynylidyne
C_3S	Tricarbon sulfide
C_2H_2	Acetylene
HCNH^+	Protonated hydrogen cyanide
CH_4	Methane
HCOOH	Formic acid
HC_3N	Cyanoacetylene
HCCNC	Ethynyl isocyanide
NH_2CH	Cyanamide
CH_2NH	Methanimine
H_2CCCC	Butatrienylidene
C_5H	Pentynylidyne
CH_3OH	Methyl alcohol
NH_2CHO	Formamide
CH_2CHCN	Vinyl cyanide
C_6H	Hexatrienyl
CH_3CHO	Acetaldehyde
$\text{CH}_3\text{C}_3\text{N}$	Methyl cyanoacetylene
$(\text{CH}_3)_2\text{O}$	Dimethyl ether
HC_7N	Cyanoheptatriyne
HC_9N	Cyano-nonaheptatriyne

which quickly reacts with H_2 to form H_3O^+ in an abstraction sequence



The H_3O^+ then undergoes dissociative recombination to form water and OH

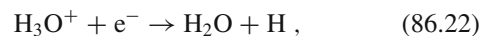
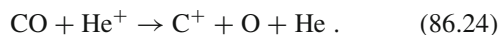


Table 86.1 (Continued)

CH	Methylidyne
OH	Hydroxyl
CN	Cyanogen
CO ⁺	Carbon monoxide ion
NO	Nitric oxide
SiO	Silicon monoxide
SO ⁺	Sulfur monoxide ion
SiS	Silicon sulfide
HCl	Hydrogen chloride
NH ₂	Amino radical
C ₂ H	Ethynyl
HNC	Hydrogen isocyanide
HCO ⁺	Formyl ion
H ₂ S	Hydrogen sulfide
OCS	Carbonyl sulfide
HCS ⁺	Thioformyl ion
C ₂ S	Dicarbon sulfide
H ₂ CN	Methylene amidogen
H ₂ CS	Thioformaldehyde
HCNS	Isothiocyanic acid
HOCO ⁺	Protonated carbon dioxide
C ₃ N	Cyanoethynyl
C ₃ O	Tricarbon monoxide
H ₃ O ⁺	Hydronium ion
C ₃ H ₂	Cyclopropenylidene
H ₂ CCC	Propadienylidene
CH ₂ CO	Ketene
HNCCC	Cyanoacetylene isomer
C ₄ H	Butadynyl
CH ₂ CN	Cyanomethyl radical
CH ₃ CH	Methyl cyanide
CH ₃ SH	Methyl mercaptan
HCC ₂ HO	Propynal
HC ₃ NH ⁺	Protonated cyanoacetylene
CH ₃ C ₂ H	Methyl acetylene
HC ₅ N	Cyanodiacetylene
CH ₃ NH ₂	Methylamine
HCOOCH ₃	Methyl formate
CH ₃ C ₄ H	Methyl diacetylene
CH ₃ CH ₂ CN	Ethyl cyanide
CH ₃ CH ₂ OH	Ethyl alcohol
HC ₁₁ N	Cyano-decapenta-yne

The water is removed by reactions with neutral or ionized carbon, which eventually lead to the production of CO. OH is primarily removed by reactions with atomic oxygen, leading to O₂. The CO and O₂ are removed by reactions with He⁺. The He⁺, generated by cosmic-ray ionization of helium, does not react with H₂ and is available to remove species by reactions such as



Water and OH are also removed by UV photons generated within the cloud. The clouds are too thick for external UV

photons to penetrate, but cosmic rays excite H₂ into electronically excited states that decay through emission of UV photons. These internally generated photons play an important role in determining the composition of the cloud. *Gredel et al.* [34] compiled a list of the photodissociation and photoionization rates for cosmic-ray induced photons.

Modern chemical networks for molecular clouds include several hundred species and several thousand reactions. Standard sets of reaction rates are provided by the UMIST (University of Manchester Institute of Science and Technology) dataset [35, 36] and the KInetic Database for Astrochemistry (KIDA) [37]. The datasets may be obtained from the UMIST Astrochemistry (udfa.ajmarkwick.net) and KIDA (kida.obs.u-bordeaux1.fr) home pages.

The clouds also contain dust particles as evidenced by the extinction curves with the observed depletions of heavier elements. The importance of surface chemistry on these dust particles to interstellar clouds is still uncertain. Dust particles are the best candidates for the sites of molecular hydrogen formation because known gas phase reactions fail to produce H₂ in the quantities observed.

86.6 Circumstellar Shells and Stellar Atmospheres

The continuum emission from a star is very nearly that of a blackbody at the photosphere. This emission is then absorbed and redistributed by the atmosphere of the star. The spectrum of the star is, thus, determined by its atmosphere. In the hottest stars, most of the material is ionized, and the absorption lines are predominantly those of ions, while in the coldest stars, molecular lines are prominent. *Kurucz* has calculated models with continuum spectra and the inclusion of a large number of absorption lines [38]. There are two major projects for calculating the required atomic data. In 1984, an international collaboration named the *Opacity Project* was set up to calculate accurate atomic data needed for opacity calculations [39, 40]. The other earlier project is called OPAL. The two sources of data are compared in [41, 42]. The Opacity Project data was updated by *Badnell et al.* [43], while another set of opacity data is available from Los Alamos [44].

Low and intermediate mass stars eject circumstellar envelopes in their red giant phase near the end of their evolution. Circumstellar envelopes are an important part of astronomy, and they are a likely location for dust formation. They provide an interesting environment for studying molecules because they represent a transition between very high-density stellar atmosphere environments to low-density interstellar environments. These objects evolve to become planetary nebulae (Sect. 86.2).

We are fortunate in having one example, IRC +10216, which is very close to the Sun. The brightest 10 μm source

beyond the solar system, IRC +10216 is a carbon-rich star surrounded by the dust and gas it ejected in a strong stellar wind. The central star is so shielded that it is almost undetectable at optical wavelengths and was not discovered until the 2 μ m survey. IRC +10216 is where most of the circumstellar molecules are detected and has greatly increased our understanding of circumstellar envelopes.

The envelopes are ejected by the red giant in its final phase of evolution, the asymptotic giant branch (AGB). The mass loss rates increase to $\approx 10^{-4}$ solar masses per year, and temperatures in the envelope are of order 1000 K. Close to the star, the density is high, and the chemistry is characteristic of thermal equilibrium. The situation is quite unlike any interstellar environments. For example, in IRC +10216, the HNC is over 100 times less abundant than HCN, whereas in molecular clouds, they have about the same abundance.

If the star is oxygen-rich, such as the AGB star IK Tau, large amounts of H₂O are formed, and if it is carbon-rich, C₂H₂ and other hydrocarbons are abundant. This high-temperature environment forms both molecules and grains. The high obscuration of the central source indicates that grains are formed in these envelopes. Polycyclic aromatic hydrocarbons (PAHs) or similar carbonaceous species, are observed in carbon-rich planetary nebulae. These large molecules must have been produced when the object was in the AGB phase.

As the material flows out from the star, the density and temperature decrease. As the density becomes lower, three-body reactions become less important, and at some point the products of these reactions are frozen out in a similar manner to the evolution of molecules in the early universe (Sect. 86.12). In the outermost portions of the circumstellar envelope, molecules are dissociated by interstellar UV photons. The penetrating UV radiation is shielded by dust, H₂, and CO. The relative abundances can vary rapidly with radius, and observations provide abundances and radial distributions, a wealth of data for modelers. Circumstellar chemistry was reviewed by *Omont* [45], and recent chemical models are given in [46–48].

86.7 Supernova Ejecta

A supernova, the explosion of a massive star following core collapse, is one of the most spectacular displays in the universe. The explosion occurs when the iron core of a massive star collapses to form a neutron star, and the rebound shock and neutrino flux eject the outer portion of the star. The ejected portions of the star are rich in heavy elements produced in the interior of the progenitor star.

We are fortunate to have had in our lifetime a supernova that was close and in an unobscured line of sight. Supernova 1987A, the first supernova observed in 1987, went off in the

Large Magellanic Cloud, a small satellite galaxy close to our own. It was the first supernova visible to the naked eye in nearly 400 years (since the Kepler supernova in 1604). Using the full range of modern astronomical instruments has allowed us to get detailed spectra of the evolving ejecta, which has greatly increased our knowledge of supernovae. We will use SN1987A as an example of supernova ejecta.

Initially the temperature of the ejecta of SN1987A was high, $\approx 10^6$ K, but it quickly cooled through adiabatic expansion and radiation from the photosphere. The temperature leveled off at several thousand degrees because of heating by radioactive nuclei, first ⁵⁶Ni and then ⁵⁶Co, formed in the explosion. The dynamics is homologous free expansion: the velocity scales linearly with the radius $r(t) = vt$, where v is the velocity and t the time since the explosion.

The ejecta were at first optically thick, and the spectrum resembled that of a hot-star continuum with absorption lines from the surface. After a few days, the temperature dropped, but the ejecta remained optically thick and continued to show strong continuum emission. As the ejecta expanded, the temperature dropped, the ejecta became optically thin, and the resulting spectrum was dominated by strong emission lines, superficially resembling an emission nebula (Sect. 86.3). The emission is dominated by neutral atoms and singly ionized species.

The gas is heated and ionized by gamma rays from radioactive decay. The gamma rays Compton scatter, producing X-rays and fast electrons. The X-rays further ionize the gas and produce multiply charged ions through the Auger process. These multiply charged ions recombine through charge transfer with neutral atoms. Further charge transfer determines the relative ionization of different species, with the lowest ionization potential species more ionized than the higher ionization potential species. The development of the infrared and optical spectrum of Supernova 1987A was reviewed by *McCray* [49].

One of the great surprises in the spectrum of Supernova 1987A was the discovery of molecules in the infrared region. CO, SiO, and possibly H₃⁺ have been identified. In the absence of grains, molecules must be formed through either three-body or radiative processes. In the supernova ejecta, the densities are too low for three-body processes to be effective, and molecules are formed through radiative association reactions. The molecules are removed by reactions with He⁺, and the molecular abundances put a constraint on how much helium can be mixed back into the region with carbon and oxygen [50].

Since the detection of molecules in SN 1987A, there have been many more observations of CO molecules in Type II supernova, and they may even occur in every Type II [51]. CO has also been observed in a Type Ic supernova [52]. It remains a puzzle as to why the molecules are not rapidly removed by helium ions. A calculation of the O + He⁺

system [53] found that radiative charge transfer is much faster than direct charge transfer for temperatures below 10^6 K but still too slow to significantly reduce the helium ion abundance in supernova ejecta. The most likely explanation remains that mixing is not complete in supernova ejecta, and the molecules survive in regions of relatively low helium abundance. More recent observations have detected H_2 [54], and the Atacama Large Millimeter/submillimeter Array (ALMA) has also detected HCO^+ and SO , which are discussed in Sect. 86.10.

86.8 Shocked Gas

Shock waves occur in compressible fluids when the pressure gradients are large enough to generate supersonic motion, or when a disturbance is propagating through the fluid at supersonic velocities. Because information about the disturbance cannot propagate upstream in the fluid faster than the speed of sound, the fluid cannot respond dynamically until the shock arrives. The shock then compresses, heats, and accelerates the fluid. The boundary separating the hot compressed gas and the upstream gas is the shock front in which the energy of directed motion of the shock is converted to random thermal energy.

Shocks are ubiquitous in the interstellar medium where they are driven by the ionization fronts of expanding HII regions or nebulae, by outflowing gas accompanying stellar birth and evolution, and by supernova explosions. If the shock velocity is above 50 km/s, the shock gas is excited, dissociated, and ionized. The subsequent recombination and cooling radiation produces photons that may ionize and dissociate the gas components ahead of and behind the shock. This precursor radiation modifies the effects of the shock and influences its dynamical and thermal evolution. Fast shocks destroy all molecules by dissociating H_2 by collisions with H, H_2 and He and with electrons. Exchange reactions with H atoms destroy the other molecular species. At low densities, radiative stabilization occurs, and dissociation is less efficient. Molecules reform in the cooling postshock gas. Slower shocks do not cause ionization or dissociation, but the chemical composition and the ion composition are modified by reactions taking place in the warm gas. The response of the interstellar gas to slow shocks is significantly affected by the presence of a magnetic field. In some ionization conditions, a magnetic precursor may occur in which a magnetosonic wave carries information about the shock, and the ionized and neutral components of the gas react differently to the shock. Many different kinds of shocks have been identified [55].

A very fast shock with a velocity of hundreds of km/s, such as are driven by supernova explosions, creates a hot dilute cavity in the interstellar medium with a temperature of millions of degrees. The density is low, and the gas cools and

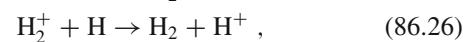
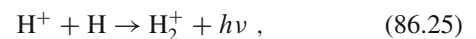
recombines slowly. Overlapping supernova-induced cavities may be responsible for the hot gas that occupies a considerable volume of the interstellar medium in the Galaxy and in some external galaxies. The conditions are far from coronal equilibrium as the gas cools more rapidly than it recombines. The cooling radiation appears as soft X-rays and UV emission lines with a characteristic spectrum.

As the gas cools below 10,000 K, molecular formation occurs. Molecular hydrogen is formed on the surfaces of grains as in molecular clouds and by the negative ion sequence that is effective in the early universe (Sect. 86.9). With the formation of H_2 in a still warm gas, the chemistry is driven by exothermic and endothermic reactions with H_2 . Thus, OH is produced by the reaction of O atoms, and H_2O by the further reaction of OH with H_2 . Enhanced abundances of other neutral and ionic molecules are the products of subsequent reactions with OH. The reactions of S^+ and S with OH lead to SO^+ and SO , and their simultaneous presence may be an indicator of a dissociative shock. There are, in addition, physical indicators of shocks, such as asymmetric line profiles indicating high velocities.

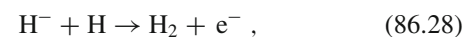
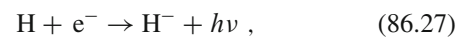
In a nondissociative shock in a molecular gas, reactions with warm H_2 dominate the chemistry as it does in the cooling zone of a dissociative shock. The composition is controlled by the post shock temperature and the H/ H_2 ratio. The warm H_2 changes the ionic composition by converting C^+ into CH^+ . Evidence for a nondissociative shock is the infrared emission from H_2 . The thermal emission from collisionally excited vibrational levels in shock-heated gas is readily distinguished from that discussed in Sect. 86.4 arising from UV pumping in a PDR. Emission from H_2 has been detected in numerous objects in the Galaxy and in many distant external galaxies. In external galaxies, X-rays may contribute to the H_2 infrared spectrum through heating the gas and through excitation by photoelectron pumping to excited states followed by a downward cascade [56, 57].

86.9 The Early Universe

Molecules appeared first in the universe after the adiabatic expansion had reduced the matter and radiation temperature to a few thousand degrees, and recombination occurred, creating a nearly neutral universe. The small fractional ionization that remained was essential to the formation of molecules. Molecular hydrogen formed through the sequences



and



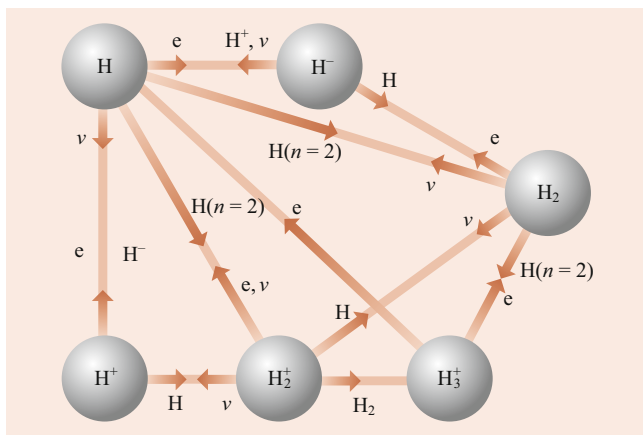
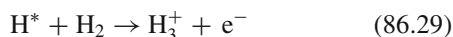


Fig. 86.3 Diagram showing the important reactions in the production of hydrogen molecules in the early universe

the protons and electrons acting as catalysts. Many other atomic and molecular processes occurred (Fig. 86.3), some involving excited hydrogen atoms. Thus,

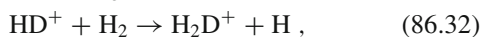
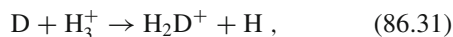


was a source of H_3^+ .

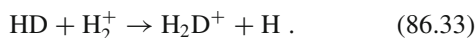
The universe contained trace amounts of deuterium and ${}^7\text{Li}$ nuclei with which heteronuclear molecules could be made. Molecules with dipole moments may leave an imprint on the cosmic blackbody background radiation that permeates the universe. The deuterated molecule HD forms from



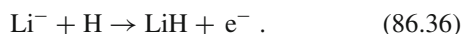
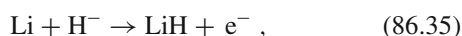
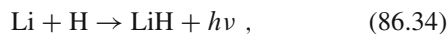
and H_2D^+ from



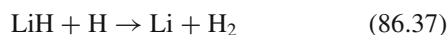
and



Lithium hydride is formed through



There are many destruction processes, of which



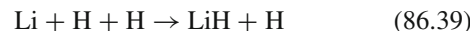
may be the most severe, although its rate coefficient is uncertain. The chemistry of the early universe is summarized in [58].

The formation of molecules was a crucial step in the fragmentation of the first gravitationally collapsing objects,

which separated out of the cosmic flow. Three-body recombination reactions such as



[59] and



were likely major sources of molecules as the density increased.

The Wilkinson Microwave Anisotropy Probe (WMAP) has given us the best map of the universe at the time of recombination and given us general confirmation of the big bang model. Perhaps the most surprising result is that stars seem to have formed much sooner than would have been expected, about 180 million years after the big bang [60]. This makes it even more difficult to understand how the universe evolves from the relative uniformity at the time of recombination to the collapse and formation of the first objects so quickly, a problem that is certainly controlled by atomic and molecular processes. The relevant atomic and molecular processes have been reviewed by the authors [61].

86.10 Atacama Large Millimeter/Submillimeter Array

Breakthroughs in astronomy are often driven by major improvements in instrumentation [62]. The Atacama Large Millimeter/Submillimeter Array (ALMA) provides angular resolution and sensitivity improvements of over an order of magnitude leading to quicker and better resolved spectra for many astrophysical environments. To fully interpret these spectra will require additional work in laboratory astrophysics so that breakthroughs in understanding may occur. It is expected that ALMA will revolutionize our understanding of astrophysical environments. Some early ALMA results are highlighted in this section.

By using the improved spatial resolution of ALMA, observations were able to resolve the dust production and show that Supernova 1987A produced about 0.2 solar masses of dust [63]. These observations demonstrated that the dust was formed in the inner ejecta and has not yet been processed through the shock front. If the dust survives the processing of the shock, then supernova are an important cosmological source of dust. In addition, a molecular line survey for Supernova 1987A detected both HCO^+ and SO in the ejecta of a supernova for the first time [64]. The spectral resolution of the molecular survey is also helping to understand the mixing that occurs in the expanding ejecta.

Using ALMA astronomers were able to resolve the millimeter size dust grains around a young A-type star Oph IRS

48 [65]. By comparing this strongly asymmetric distribution of millimeter grains to that of smaller dust particles and molecules, both of which are symmetric about the orbit, the authors infer that the larger grains may be trapped. In their model, the trapping is due to a larger preexisting planet in the system. This trap could allow the dust grains to keep growing to sizes that allow for additional planet formation.

With improved sensitivity, ALMA has detected additional building-blocks-of-life molecules in the interstellar medium, including iso-propyl cyanide [66] in the star-forming region of Sagittarius B2 and methyl isocyanate in the solar-type protostar IRAS16293-2422 B [67]. The detection of these potential precursors to biological molecules is interesting and hints at the proposed idea that life and self-replicating molecules formed first in the interstellar medium and then rained down on the surfaces of planets. With its increased sensitivity, ALMA may give insight into this idea for the appearance of life.

86.11 Recent Developments

In 2015, a new era opened up when gravitational waves from a binary black hole merger were detected for the first time [68]. More recently, a merger between two neutron stars was observed [69]. The neutron star merger, known as a kilonova, was also observed as a gamma-ray burst, and transient emission was observed in several electromagnetic bands [70]. The observations confirmed a long standing prediction that the violent collision between neutron stars could lead to gamma-ray bursts and the production of heavy elements [71]. This start to multimessenger astronomy, combining the electromagnetic and gravitational waves along with recent theoretical studies [72], suggests that a binary neutron star merger is a major source for production of gold and other heavy elements.

The Herschel Space Observatory, a far infrared and submillimeter telescope active 2009 through 2013, greatly increased our knowledge of molecular astrochemistry. A special issue of *Astronomy and Astrophysics* was released in 2010 with Herschel's first results with papers on observations of the solar system, star formation, interstellar medium, galaxy evolution, and cosmology [73]. Herschel had four main objectives: to study the formation of galaxies in the early universe, the creation of stars and their interaction with the interstellar medium, the observation of chemical composition of solar system objects, and the molecular chemistry in the universe. The observatory made the first multiline detection of molecular oxygen in space [74, 75].

Another rapidly expanding field involves planets outside our solar system. The detection and characterization of molecules in exoplanets will be critical to understanding how they formed, and what the planets are like. It will be an im-

portant factor in the search for life on these planets. So far, CO and H₂O have been detected [76], as well as TiO [77]. However, further detections should be forthcoming, particularly with the launch of the James Webb Space Telescope. A database of molecular line lists for species that might be detected in exoplanet atmospheres is currently being maintained and updated [78].

In summary, satellite data along with continued ground observations continually raise new astrophysical puzzles, puzzles that are controlled and probed by atomic and molecular processes. The astrophysical community owes a great debt to both atomic and molecular laboratory measurements and theoretical models of energy levels, reaction rates, and transition probabilities. In order to continue to progress in our understanding of the universe we will need to continue to fund the work needed for the understanding of the atomic and molecular processes that control it.

86.12 Other Reading

Astronomy is one of the oldest sciences and one of the fastest evolving. Advances in technology are rapidly increasing the sensitivity and resolution of our instruments, and so new observations and more sophisticated models lead to an ever greater understanding of the universe. This means that books will often be somewhat dated when they appear. However, the series *Annual Review of Astronomy and Astrophysics* is a good source of recent review articles.

In addition, the following books are recommended as good introductions or overviews of a particular field [1, 79–86]:

- *Astrophysical Quantities* by Allen
- *Astrophysical Formula* by Lang
- *Interstellar Chemistry* by Duley and Williams
- *Physical Processes in the Interstellar Medium* by Spitzer
- *Astrophysics of Gaseous Nebula and Active Galactic Nuclei* by Osterbrock and Ferland
- *Spectroscopy of Astrophysical Environments* edited by Dalgarno and Layzer
- *Molecular Astrophysics* edited by Hartquist
- *The Physics and Chemistry of the Interstellar Medium* by Tielens
- *The Physics of the Interstellar and Intergalactic Medium* by Draine.

Many sources of atomic and molecular data are listed and discussed in a special issue of *Revista Mexicana de Astronomia y Astrofisica*, 23 March 1992 [7]. For details on atomic spectroscopy, the books [87, 88]:

- *The Theory of Atomic Structure and Spectra* by Cowan
- *Atomic Spectra and Radiative Transitions* by Sobelman.

For details on molecular spectroscopy, the books [89, 90]:

- *Molecular Spectra and Molecular Structure* by Herzberg
- *Spectra of Atoms and Molecules* by Bernath.

References

- Osterbrock, D.E., Ferland, G.J.: *Astrophysics of Gaseous Nebulae and Active Galactic Nuclei*. University Science Books, Mill Valley (2006)
- Winkler, P.F., Clark, G.W., Markert, T.H., Kalata, K., Schnopper, H.W., Canizares, C.R.: *Astrophys. J. Lett.* **246**, 27L (1981)
- Reilman, R.F., Manson, S.T.: *Astrophys. J. Suppl. Ser.* **40**, 815 (1979)
- Henke, B.L., Lee, P., Tanaka, T.J., Shimabukoro, R.L., Fujikawa, B.K.: *Atom. Nucl. Data Tables* **27**, 1 (1982)
- Balucinska-Church, M., McCammon, D.: *Astrophys. J.* **400**, 699 (1992)
- Verner, D.A., Yakovlav, D.G., Band, J.M., Trzhaskavskaya, A.B.: *Atom. Nucl. Data Tables* **55**, 233 (1993)
- Special issue of *Revista Mexicana de Astronomia y Astrofisica*, March 23 (1992)
- Nussbaumer, H., Storey, P.J.: *Astron. Astrophys.* **178**, 324 (1978)
- Ramadan, H.R., Hahn, Y.: *Phys. Rev. A* **39**, 3350 (1989)
- Badnell, N.R.: *Phys. Scr. T* **28**, 33 (1989)
- Bacchus-Montabonel, M.C., Amezian, K.: *Z. Phys. D* **25**, 323 (1993)
- Honvault, P., Bacchus-Montabonel, M.C., McCarroll, R.: *J. Phys. B* **27**, 3115 (1994)
- Herrero, B., Cooper, I.L., Dickinson, A.S., Flower, D.R.: *J. Phys. B* **28**, 711 (1995)
- Mendoza, C.: In: Flower, D.R. (ed.) *Planetary Nebulae IAU Symp.* 103, p. 143. Reidel, Dordrecht (1983)
- Brocklehurst, M., Salem, M.: *Comput. Phys. Commun.* **13**, 39 (1977)
- Salem, M., Brocklehurst, M.: *Astrophys. J. Suppl. Ser.* **39**, 633 (1979)
- Martin, P.G.: *Astrophys. J. Suppl. Ser.* **66**, 125 (1988)
- Storey, P.J., Hummer, D.G.: *Mon. Not. R. Astron. Soc.* **272**, 41 (1995)
- Paerels, F., Kahn, S.: *Ann. Rev. Astron. Astrophys.* **41**, 291 (2003)
- Nicastro, F., et al.: *Nature* **433**, 495 (2005)
- Ferland, G.: *Ann. Rev. Astron. Astrophys.* **41**, 517 (2003)
- Arnaud, M., Rothenflug, R.: *Astron. Astrophys. Suppl.* **60**, 425 (1985)
- Gaetz, T.J., Salpeter, E.E.: *Astrophys. J. Suppl. Ser.* **52**, 155 (1983)
- Bryans, P., Landi, E., Savin, D.W.: *Astrophys. J.* **691**, 1540 (2009)
- Snow, T.P., McCall, B.J.: *Ann. Rev. Astron. Astrophys.* **44**, 367 (2006)
- Neufeld, D.A., Wolfire, M.G.: *Astrophys. J.* **845**, 163 (2017)
- van Dishoeck, E., Black, J.: *Astrophys. J. Suppl. Ser.* **62**, 109 (1987)
- Roberge, W.G., Jones, D., Lepp, S., Dalgarno, A.: *Astrophys. J. Suppl. Ser.* **77**, 287 (1991)
- Heays, A., Bosman, A.D., van Dishoeck, E.F.: *Astron. Astrophys.* **602**, A105 (2017)
- Hollenbach, D.J., Tielens, A.G.G.M.: *Rev. Mod. Phys.* **71**, 173 (1999)
- Sternberg, A., Dalgarno, A.: *Astrophys. J. Suppl. Ser.* **99**, 565 (1995)
- Hall, P., Millar, T.J.: *Astron. Astrophys.* **517**, A1 (2010)
- Cesarsky, C., Salama, A.: *ISO Science Legacy: A compact review of ISO major Achievements*. Springer (2005)
- Gredel, R., Lepp, S., Dalgarno, A., Herbst, E.: *Astrophys. J.* **347**, 289 (1989)
- Millar, T.J., Bennett, A., Rawlings, J.M.C., Brown, P.D., Charnley, S.B.: *Astron. Astrophys. Suppl.* **87**, 585 (1991)
- Farquhar, P.R.A., Millar, T.J.: *CCP7 Newsletter* **18**, 6 (1993)
- Wakelam, V., et al.: *Astrophys. J. Suppl. Ser.* **199**, 21 (2012)
- Kurucz, R.L.: *Astrophys. J. Suppl. Ser.* **40**, 1 (1979)
- Seaton, M.J.: *J. Phys. B* **20**, 6363 (1987)
- Lynas-Gray, A.E., Seaton, M.J., Storey, P.J.: *J. Phys. B* **28**, 2817 (1995)
- Seaton, M.J., Yan, Y., Mihalas, B., Pradhan, A.K.: *Mon. Not. R. Astron. Soc.* **266**, 805 (1994)
- Iglesias, C.A., Rogers, F.J.: *Astrophys. J.* **443**, 460 (1995)
- Badnell, N.R., et al.: *Mon. Not. R. Astron. Soc.* **360**, 458 (2005)
- Colgan, J., et al.: *Astrophys. J.* **817**, 116 (2016)
- Omont, A.: *Circumstellar Chemistry*. In: Greenberg, J.M., Pirronello, V. (eds.) *Chemistry in Space*, p. 171. Kluwer Academic, Dordrecht (1991)
- Mamon, G.A., Glassgold, A.E., Omont, A.: *Astrophys. J.* **323**, 306 (1987)
- Nejad, L.A.M., Millar, T.J.: *Astron. Astrophys.* **183**, 279 (1987)
- Millar, T.J., Herbst, E.: *Astron. Astrophys.* **288**, 561 (1994)
- McCray, R.: *Ann. Rev. Astron. Astrophys.* **31**, 175 (1993)
- Liu, W., Lepp, S., Dalgarno, A.: *Astrophys. J.* **396**, 679 (1992)
- Spyrimilo, J., Leibundgut, B., Gilmozzi, R.: *Astron. Astrophys.* **376**, 188 (2001)
- Gerardy, C., et al.: *Publ. Astron. Soc. Jpn.* **54**, 905 (2002)
- Zhao, L.B., et al.: *Astrophys. J.* **615**, 1063 (2004)
- Fransson, C., et al.: *Astrophys. J.* **821**, L5 (2016)
- Draine, B.T., McKee, C.F.: *Ann. Rev. Astron. Astrophys.* **31**, 373 (1993)
- Lepp, S., McCray, R.: *Astrophys. J.* **269**, 560 (1983)
- Gredel, R., Dalgarno, A.: *Astrophys. J.* **446**, 852 (1995)
- Dalgarno, A., Fox, J.: *Ion Chemistry in Atmospheric and Astrophysical Plasmas*. In: Ng, C.-Y., Baer, T., Powis, I. (eds.) *Unimolecular and Bimolecular Reaction Dynamics*. Wiley, New York (1994)
- Forrey, R.C.: *Astrophys. J.* **773**, L25 (2013)
- Bennett, C.L., et al.: *Astrophys. J. Suppl.* **148**, 1 (2003)
- Lepp, S., Stancil, P., Dalgarno, A.: *J. Phys. B* **35**, R57 (2002)
- Harwit, M.: *Phys. Today* **56**(11), 38 (2003)
- Indebetouw, R., Matsuura, M., et al.: *Astrophys. J. Lett.* **782**(1), L2 (2014)
- Matsuura, M., Indebetouw, R., et al.: *Mon. Not. R. Astron. Soc.* **469**, 3347 (2017)
- van der Marel, N., van Dishoeck, E.F., et al.: *Science* **340**, 1199 (2013)
- Belloch, A., Garrod, R., Holger, S., Muller, P., Menten, K.M.: *Science* **345**, 1584 (2014)
- Martin-Domenech, R., Rivilla, V.M., Jimenez-Serra, I., Quenard, D., Testi, L., Martin-Pintado, J.: *Mon. Not. R. Astron. Soc.* **469**, 2230 (2017)
- Abbott, B.P., et al.: *Phys. Rev. Lett.* **116**, 061102 (2016)
- Abbott, B.P., et al.: *Phys. Rev. Lett.* **119**, 161101 (2017)
- Abbott, B.P., et al.: *Astrophys. J. Lett.* **848**, L12 (2017)
- Eichler, M., Livio, M., Piran, T., Schramm, D.N.: *Nature* **340**, 126 (1989)
- Siegel, D., Metzger, B.D.: *Phys. Rev. Lett.* **119**, 231102 (2017)
- Walmsley, C.M., et al.: *Astron. Astrophys.* **518**, 1 (2010)
- Goldsmith, P.F., et al.: *Astrophys. J.* **737**, 96 (2011)
- Liseau, R., et al.: *Astron. Astrophys.* **541**, 73 (2012)
- Madhusudhan, N., Agundez, M., Moses, J.I., Hu, Y.: *Space Sci. Rev.* **205**, 285 (2016)
- Sedaghati, E., Boffin, H., MacDonald, R., Gandhi, S., Madhusudhan, N.: *Nature* **549**, 238 (2016)

78. Tennyson, J., Yurchenko, S.N.: *Atoms* **6**, 26 (2018)
79. Allen, C.W.: *Astrophysical Quantities*. Athlone, London (1973)
80. Lang, K.R.: *Astrophysical Formulae*. Springer, Berlin, Heidelberg (1980)
81. Duley, W.W., Williams, D.A.: *Interstellar Chemistry*. Academic Press, London (1984)
82. Spitzer, L.: *Physical Processes in the Interstellar Medium*. Wiley, New York (1978)
83. Dalgarno, A., Layzer, D.R.: *Spectroscopy of Astrophysical Plasmas*. Cambridge University Press, Cambridge (1987)
84. Hartquist, T.: *Molecular Astrophysics*. Cambridge University Press, Cambridge (1990)
85. Tielens, A.G.G.M.: *The Physics and Chemistry of the Interstellar Medium*. Cambridge University Press, Cambridge (2005)
86. Draine, B.T.: *The Physics of the Interstellar and Intergalactic Medium*. Princeton University Press, Princeton (2011)
87. Cowan, R.D.: *The Theory of Atomic Structure and Spectra*. University of California Press, Berkeley (1981)
88. Sobelman, I.I.: *Atomic Spectra and Radiative Transitions*. Springer, Berlin, Heidelberg (1979)
89. Herzberg, G.: *Molecular Spectra and Molecular Structure*. Prentice-Hall, New York (1939)
90. Bernath, P.F.: *Spectra of Atoms and Molecules*. Oxford University Press, Oxford (1995)

Paul D. Feldman 

Contents

87.1	Introduction	1289
87.2	Observations	1290
87.3	Excitation Mechanisms	1291
87.3.1	Basic Phenomenology	1291
87.3.2	Fluorescence Equilibrium	1292
87.3.3	Swings and Greenstein Effects	1293
87.3.4	Bowen Fluorescence	1294
87.3.5	Electron Impact Excitation	1294
87.3.6	Prompt Emission	1294
87.3.7	OH Level Inversion	1295
87.4	Cometary Models	1295
87.4.1	Photolytic Processes	1295
87.4.2	Density Models	1296
87.4.3	Radiative Transfer Effects	1296
87.5	Summary	1297
	References	1297

Abstract

Prior to spacecraft missions to comets, beginning with the *Giotto* and *Vega* spacecraft to comet 1P/Halley (the *P* signifies a periodic comet) in March 1986, determinations of the volatile composition of a cometary coma were derived from spectroscopic analyses. Detailed modeling was then used to infer the volatile composition of the cometary nucleus. Since then there have been additional missions, including *Deep Impact* (2005), *Stardust* (2006), *EPOXI* (2010), and most recently, *Rosetta*, that flew along with comet 67P/Churyumov-Gerasimenko for over 2 years, that have greatly advanced our knowledge of the physics, chemistry, and geology of comets. Only a few comets have been studied this way, but the results provide a framework, or “ground truth”, for remote observations from Earth and spaceborne observatories, both past and future. This chapter focuses on the principal atomic and molecular processes that lead to the observed spectrum as well as the needs for basic atomic and molecular data in the interpretation of these spectra. The largely collision-

less and low-density coma, with no gravity or magnetic field, is a unique spectroscopic laboratory, and in recent decades, observations of comets have expanded over the entire electromagnetic spectrum, from X-ray to the submillimeter and millimeter. Although *Rosetta* has elucidated many key questions, issues concerning the basic molecular composition and the elemental abundances of both the volatile and refractory components of the cometary nucleus, as well as the comet-to-comet variation (particularly between *new* and evolved periodic comets) of these quantities still remain to be solved. A recent (although slightly out-of-date) compendium covering all aspects of cometary science is the *Comets II* book [1], while a review of coma chemistry is given by *Mumma* and *Charnley* [2].

Keywords

comets · cometary coma · spectroscopy · ultraviolet · fluorescence

87.1 Introduction

Comets are small bodies of the solar system believed to be remnants of the primordial solar disk. As long-period comets are believed to have formed near the orbits of Uranus and Neptune and were subsequently ejected into an *Oort cloud* of some 40,000 AU in extent, these objects likely preserve a record of the volatile composition of the early outer solar system and so are of great interest for the physical and chemical modeling of solar system formation. The comets arrive in the inner solar system as a result of galactic perturbations. The cometary volatiles are vaporized as their orbits bring them closer to the Sun, and it is solar radiation that initiates all of the processes that lead to the extended coma. Gas vaporization also leads to the release of dust into the coma, and the scattering of sunlight by dust is the major source of the visible coma and dust tail of comets. Somewhat fainter, and much more extended, is the plasma tail, resulting from

photoionization by solar extreme UV radiation of the neutral volatiles and their subsequent interaction with the solar wind.

87.2 Observations

In a review in 1965, *Arpigny* [3] summarized the known molecular and atomic emissions detected in the visible region of the spectrum (here defined as 3000 to 11,000 Å) as follows:

radicals:	OH, NH, CN, CH, C ₃ , C ₂ , and NH ₂ ,
ions:	OH ⁺ , CH ⁺ , CO ₂ ⁺ , CO ⁺ , and N ₂ ⁺ ,
metals:	Na, Fe.

The only known atomic feature was the O I forbidden red doublet at 6300 and 6364 Å. From the radicals and ions, one could infer the presence of their progenitor *parent* molecules such as H₂O, NH₃, HCN, CO, and CO₂, directly vaporizing from the comet's nucleus. The metals, seen only in comets passing close to the Sun, were assumed to come from the vaporization of refractory grains. The inventory of metals was soon expanded to include K, Ca⁺, Ca, V, Cr, Mn, Ni, and Cu, from observations of the Sun-grazing comet Ikeya-Seki (C/1965 S1) [4, 5], and H₂O⁺ was identified in comet Kohoutek (C/1973 E1). This latter comet was also the first to be extensively studied at wavelengths both shortward and longward of the visible spectral range.

The first parent molecule to be directly identified was CO, which fluoresces in the Fourth Positive system ($A^1\Pi_u - X^1\Sigma^+$) in the VUV [6]. In principle, the molecular species should be detectable through their radio and sub-mm rotational transitions or through the detection of vibrational bands or individual rovibrational lines in the near IR. Water was first directly detected through rovibrational lines near 2.7 μm in comet Halley and in many subsequent comets [7]. The detection of species such as H₂CO, H₂S and CH₃OH was made possible by the development of more sensitive instrumental techniques. More than two dozen parent molecules have been identified spectroscopically [8, 9]. Many more parent species, including O₂ and N₂, were detected by the ROSINA mass spectrometer on *Rosetta* [10]. Isotope ratios, particularly the D/H ratio, in molecules such as HDO have been determined from IR and submillimeter observations [11].

The ultimate result of solar photolysis (and to a lesser degree, the interaction with the solar wind) is the reduction of all of the cometary volatiles to their atomic constituents. The atomic inventory is somewhat easier to derive as the resonance transitions of the cosmically abundant elements H, O, C, N, and S all lie in the VUV and, in principle, the total content of these species in the coma can be determined by an instrument with a suitably large field of view. Of course, a fraction of the atomic species of each element will be pro-

duced directly in ionic form and will not be counted using this approach. In addition, another fraction exists in the coma in the solid grains, and this component will not be included either, except for a small amount volatilized by evaporation or sputtering by energetic particles. The composition of the grains, although not the absolute abundance, has been determined from in situ measurements made by the Halley encounter spacecraft [12] and can be inferred, although not unambiguously, from reflection spectroscopy of cometary dust in the 3–5 μm range.

The advent of spaceborne platforms for observations in the VUV has produced a wealth of new information about the volatile constituents of the coma. The $A^2\Sigma^+ - X^2\Pi$ (0, 0) band of the OH radical at ≈ 3085 Å was well known from ground-based spectroscopic observations, but as this wavelength lies very close to the edge of the atmospheric transparency window, the strength of this feature (relative to that of other species) was not appreciated until 1970, when comet Bennett (C/1969 Y1) was observed from space by the Orbiting Astronomical Observatory (OAO-2). The OAO-2 spectrum also showed a very strong, broadened H I Ly- α emission from H, the other principal dissociation product of H₂O. The broad shape of Ly- α seen in the OAO-2 spectrum is due to the large spatial extent of the atomic H envelope, the result of a high velocity acquired in the photodissociation process and a long lifetime against ionization. Later, at the apparition of comet Kohoutek (C/1973 E1), atomic O and C were identified in the spectra, and direct UV images of the H coma, as well as of the O I and C I emissions, were obtained from sounding rocket experiments.

Between 1978 and 1996, over 50 comets were observed spectroscopically over the wavelength range 1200–3400 Å by the International Ultraviolet Explorer (IUE) satellite observatory [13, 14]. Most of the spectra were obtained at moderate resolution ($\Delta\lambda = 6$ – 10 Å), although high-dispersion echelle spectra ($\Delta\lambda = 0.2$ – 0.3 Å) are useful for some studies, particularly those of fluorescence equilibrium (Sect. 87.3.2). The launch of the *Hubble Space Telescope* (HST) in 1990, together with subsequent enhancements to the spectroscopic instrumentation that were made on-orbit, marked another advance in sensitivity as well as the ability to observe in a small field-of-view very close to the nucleus. This yielded the first detection of CO Cameron band emission, a direct measure of CO₂ being vaporized from the nucleus [15]. Both the *Space Telescope Imaging Spectrograph*, installed in 1997, and the *Cosmic Origins Spectrograph*, installed in 2009, enabled high-resolution observations of the CO Fourth Positive System [16, 17]. An example of a STIS (Space Telescope Imaging Spectrograph) spectral image of the region of the CO Fourth Positive system is shown in Fig. 87.1 [16]. The geocentric distance of comet 153P/Ikeya-Zhang was 0.43 AU so that the image, top to bottom, spans 2800 km on either side of the nucleus.

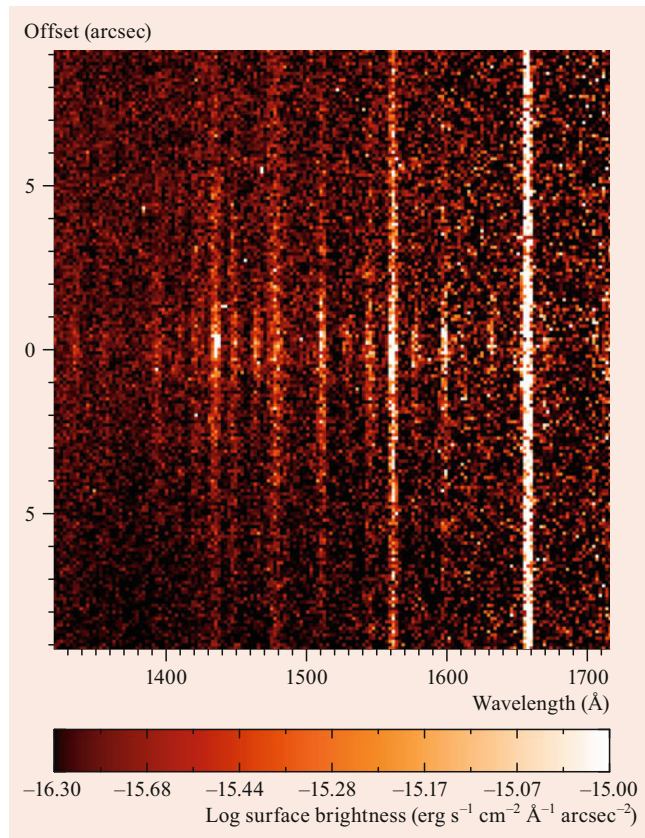


Fig. 87.1 STIS spectral image of comet 153P/Ikeya-Zhang, showing the brightness variations along the slit. The spectral region containing the strong geocoronal H I λ 1216 and O I λ 1302 has been excluded. The carbon multiplets at 1561 Å and 1657 Å are the strongest features and appear relatively constant, as they are dissociation products extending far into the coma. The zero point in the vertical direction marks the location of the nucleus. From [16]

The launch of the *Far Ultraviolet Spectroscopic Explorer* (FUSE) in 1999 provided access to the spectral region between 900 and 1200 Å at very high spectral resolution and has led to the detection of H₂ (Sect. 87.3.4), upper limits on Ar and N₂, and some three dozen emission lines identified as solar Lyman- α pumped H₂ fluorescence from vibrationally excited H₂ resulting from the photodissociation of H₂CO. [18, 19].

Several other satellite observatories have contributed unique cometary observations in the UV and sub-mm spectral windows. The *Solar and Heliospheric Observatory* (SOHO) has two valuable instruments: the SWAN (Solar Wind Anisotropies) instrument provides sky maps in H I Ly- α at 1° resolution and has observed over 20 comets since 1996 [20]. The UVCS (Ultraviolet Coronagraph Spectrometer) provides far-UV spectra and images of comets close to the Sun, where HST and FUSE are prohibited from observing, and has recently detected C²⁺ in the tail of comet C/2002 X5 (Kudo-Fujikawa) [21]. The direct detection of H₂O in the fundamental rotational line at 557 GHz in sev-

eral comets was made by the *Submillimeter Wave Astronomy Satellite* (SWAS) [22], the *Odin satellite* [23], and the *Herschel* observatory [24]. This line cannot be observed from ground-based telescopes because of the strong absorption by water vapor in the terrestrial atmosphere.

Prior to 1996, X-rays had not been detected in comets, and the conventional wisdom was that they were unlikely to be produced in the cold, rather thin cometary atmosphere. The discovery of soft X-ray emission ($E < 2$ keV) from comet Hyakutake (C/1996 B2) by the *Röntgen Satellite* (ROSAT) thus came as a surprise [25]. Since then, X-ray emission has been detected from over a dozen comets using ROSAT and four other space observatories, the *Extreme Ultraviolet Explorer*, *BeppoSAX*, the *Chandra X-ray Observatory* (CXO), and *Newton-XMM* [26]. The earliest observations were at very low spectral resolution, making it difficult to select amongst the possible excitation mechanisms: charge exchange, scattering of solar photons by attogram dust particles, energetic electron impact and bremsstrahlung, collisions between cometary and interplanetary dust, and solar X-ray scattering and fluorescence. The more recent CXO observations, at higher spectral resolution, favor the charge exchange of energetic minor solar wind ions such as O⁶⁺, O⁷⁺, C⁵⁺, C⁶⁺, and others, with cometary gas, principally H₂O, CO, and CO₂, as the primary mechanism. This mechanism would explain why the X-ray intensity appears to be independent of the gas production rate of the comet, and that the peak emission is offset from the location of the comet's nucleus. This conclusion is also supported by recent laboratory work on the charge transfer of highly ionized species with cometary molecules [27] and by theoretical calculations of state-specific cascades [28]. The X-ray emission thus tells us more about the solar wind than about the gaseous composition of comets.

87.3 Excitation Mechanisms

87.3.1 Basic Phenomenology

Coma abundances may be derived from spectrophotometric measurements of either the total flux or the surface brightness in a given spectral feature. The uncertainty in the derived abundances includes not only the measurement uncertainty, but also uncertainties in the atomic and molecular parameters and, in the case of surface brightness measurements, uncertainties in the model parameters used. Thus, relative abundances, derived from observations of different comets with the same instrument and under similar geometrical conditions, are often more reliable.

Atoms and ions in the cometary coma emit radiation primarily by means of resonance re-radiation of solar photons. For the cosmically abundant elements H, C, N, O, and S, their

strongest resonance transitions are in the VUV. The few exceptions are noted below. Assume that the coma is optically thin in these transitions. The total number of species i in the coma is

$$M_i = Q_i \tau_i(r), \quad (87.1)$$

where Q_i is the production rate (atoms or molecules s^{-1}) of species i , and $\tau_i(r)$ is its lifetime at heliocentric distance r , $\tau_i(r) = \tau_i(1 \text{ AU})r^2$. The r dependence arises from photolytic destruction processes induced by solar UV radiation and to a lesser degree by the solar wind, as described in Sect. 87.4.1.

The luminosity, in photons s^{-1} , in a given transition at wavelength λ , is then

$$L_{i\lambda} = M_i g_{i\lambda}(r), \quad (87.2)$$

where the fluorescence efficiency, or g -factor, $g_{i\lambda}(r) = g_{i\lambda}(1 \text{ AU})r^{-2}$, is

$$g_{i\lambda}(1 \text{ AU}) = \frac{\pi e^2}{mc^2} \lambda^2 f_\lambda \pi F_\odot \tilde{\omega} \quad \text{photons s}^{-1} \text{atom}^{-1}, \quad (87.3)$$

where f_λ is the absorption oscillator strength, πF_\odot is the solar flux per unit wavelength interval at 1 AU, and $\tilde{\omega}$ is the albedo for single scattering, defined for a line in an atomic multiplet as

$$\tilde{\omega} = \frac{A_j}{\sum_j A_j}, \quad (87.4)$$

where A_j is the decay rate. If a given multiplet is not resolved, then $\tilde{\omega} = 1$. For diatomic molecules, fluorescence to other vibrational levels becomes important, and the evaluation of $\tilde{\omega}$ depends on the physical conditions in the coma, as discussed in Sect. 87.3.2. Thus, for a comet at a geocentric distance Δ , the total flux from the coma for the transition is

$$F_{i\lambda} = \frac{L_{i\lambda}}{4\pi\Delta^2} = \frac{Q_i g_{i\lambda}(r) \tau_i(r)}{4\pi\Delta^2}, \quad (87.5)$$

and the product $g_{i\lambda}(r) \tau_i(r)$ is independent of r .

Unfortunately, the scale lengths (the product of lifetime and outflow velocity) of almost all of the species of interest in the UV are $\approx 10^5$ – 10^6 km at 1 AU. Thus, total flux measurements require fields of view ranging from several arc-minutes to a few degrees. This has been done only in the case of a few isolated sounding rocket experiments. Most information about the UV spectra comes from observations made by orbiting satellite observatories whose spectrographs have small apertures (e.g., $10'' \times 20''$ for IUE) and, thus, sample only a very small part of the total coma. In this case, again assuming an optically thin coma, the measured flux $F'_{i\lambda}$ in the aperture can be converted to an average surface brightness $B_{i\lambda}$ (in units of Rayleighs):

$$B_{i\lambda} = 4\pi 10^{-6} F'_{i\lambda} \Omega^{-1}, \quad (87.6)$$

where Ω is the solid angle subtended by the aperture. The brightness, in turn, is related to \bar{N}_i , the average column density of species i within the field of view by

$$B_{i\lambda} = 10^{-6} g_{i\lambda}(r) \bar{N}_i. \quad (87.7)$$

The evaluation of Q_i from \bar{N}_i requires the use of a model of the density distribution of the species i (Sect. 87.4.2).

A similar treatment can be applied to the excitation of the near-infrared vibrational transitions of cometary parent molecules since the direct pumping by solar IR radiation far exceeds the indirect pumping of ground state vibrational levels through electronic transitions excited by the solar UV flux [8]. However, this does not apply to the rotational transitions, which are controlled by collisional excitation, primarily collisions with H_2O . In this case, the observed rotational temperature may be regarded as a reliable measure of the kinetic temperature of the coma gas.

87.3.2 Fluorescence Equilibrium

In the case of low-resolution spectroscopy, where an atomic multiplet or molecular band is unresolved, the evaluation of the g -factor Eq. (87.3) does not require knowledge of the population of either atomic fine structure levels or molecular rotational levels in the ground state of the transition. Furthermore, the assumption that the solar flux does not vary over the multiplet or band allows us to use the total transition oscillator strength. This assumption is more often than not invalid because of the Fraunhofer structure of the solar spectrum in the near-UV and visible region and the emission line nature of the spectrum below 2000 Å. For high-resolution spectra, the g -factors for each individual line must be calculated separately, and the relative populations of the ground state levels must be included. There are three cases to be considered:

1. The g -factor, or probability of absorption of a solar photon, is less than the probability that the species will be dissociated or ionized, i.e., $g_{i\lambda} < (\tau_i)^{-1}$. In this case, the ground-state population is not affected by fluorescence, and a Boltzmann distribution at a suitable temperature (typically ≈ 200 K at 1 AU) corresponding to the production of the species may be used. This is often the case in the far-UV, where the solar flux is low, such as for the Fourth Positive band system of CO. For atomic transitions from triplet ground states, such as is found with O, C and S, downward fine-structure transitions are fast enough to effectively depopulate all but the lowest fine structure level.
2. The species undergoes many photon absorption and emission cycles in its lifetime, and the ground-state population is determined (usually after five or six cycles) by the fluorescence branching ratios. This is the condition of

fluorescence equilibrium, which applies for almost all radicals observed in the visible and near-UV regions. The general procedure is to solve a set of coupled equations of the form

$$\frac{dn_a}{dt} = -n_a \sum_{b=1}^N p_{ab} + \sum_{b=1}^N n_b p_{ba}, \quad (87.8)$$

where n_a is the relative population of level a , and p_{ab} and p_{ba} are transition rates out of and into this level, respectively. The n_a are normalized to unity. The steady state, obtained after many cycles, is given by $dn_a/dt = 0$. Since the downward transition rates are determined only by quantum mechanics, while the absorption rates depend on the magnitude of the solar flux, the steady-state population varies with distance from the Sun with higher rotational levels (as for the case of CN [3]) populated closer to the Sun. In some cases, where only a few cycles occur, the equations are integrated numerically. As the g -factor varies with time, it also effectively varies with the position of a species in the coma. Care must also be taken when spectra taken with small apertures are analyzed, as the transit time for an atom or molecule to cross the aperture may be $\lesssim g_{i\lambda}(r)^{-1}$. In practice, these considerations are often not important.

3. The same as 2., except that the density is sufficiently high that collisional transitions must be included in addition to the radiative transitions between levels. However, as the collisional rates are poorly known, in practice a *collision sphere* is defined such that a molecule traveling radially outward from this sphere suffers only one collision with other molecules or atoms. Outside this sphere, fluorescence equilibrium is assumed to hold, while inside, a thermal distribution of ground-state levels is used. A rough estimate of the radius R_c of the collision sphere, based on the radial outflow model of Sect. 87.4.2, is given by [29, 30]

$$R_c = 10^3 \frac{Q}{10^{29}} \text{ km}, \quad (87.9)$$

where Q is the total production rate in molecules s^{-1} .

87.3.3 Swings and Greenstein Effects

Swings [31] first pointed out that because of the Fraunhofer absorption lines in the visible region of the solar spectrum, the absorption of solar photons in a molecular band would vary with the comet's heliocentric velocity \dot{r} , leading to differences in the structure of a band at different values of \dot{r} when observed at high resolution. In Eq. (87.8), this corresponds to evaluating the $p_{ba} = p_{ba}(\dot{r})$. For typical comets observed near 1 AU, \dot{r} can range from -30 to

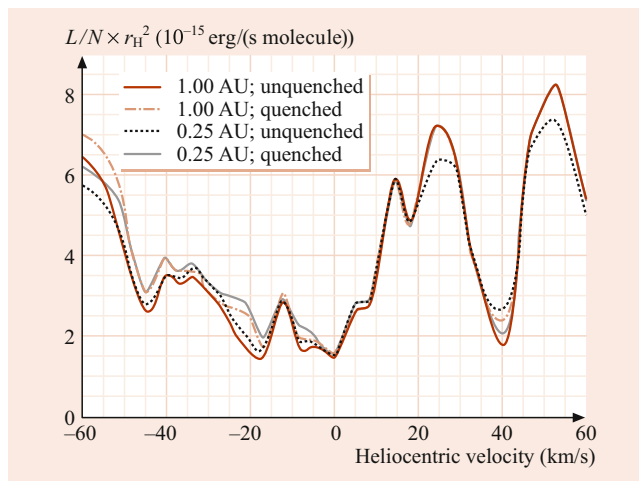


Fig. 87.2 OH (0,0) band g -factor as a function of heliocentric velocity. After [32]

+30 km/s, while in certain cases of comets with small perihelia, the range can be twice as large. This effect of the Doppler shift between the Sun and the comet is commonly referred to as the *Swings effect*. Even for observations at low resolution, the Swings effect must be taken into account in the calculation of the total band g -factor, and this has been done for a number of important species such as OH, CN, and NH. A particularly important case, that of the OH $A^2\Sigma^+ - X^2\Pi$ (0,0) band at $\approx 3085 \text{ \AA}$, which is often used to derive the water production rate of a comet, is illustrated in Fig. 87.2, which also shows the dependence of fluorescence equilibrium on heliocentric distance [32].

While this effect was first recognized in the spectra of radicals in the visible range, a similar phenomenon occurs in the excitation of atomic multiplets below 2000 \AA , where the solar spectrum makes a transition to an emission line spectrum. For example, the three lines of the O I $\lambda 1302$ multiplet have widths of $\approx 0.1 \text{ \AA}$, corresponding to a velocity of $\approx 25 \text{ km/s}$, so that knowledge of exact solar line shapes is essential for a reliable evaluation of the g -factor for this transition [33]. A similar effect occurs for the Si I multiplets at 1429 and 1479 \AA [17].

A differential Swings effect occurs in the coma since atoms and molecules on the sunward side of the coma, flowing outward towards the Sun, have a net velocity that is different from those on the tailward side, and so, if the absorption of solar photons takes place on the edge of a line, the g -factors will be different in the two directions. Differences of this type appear in long-slit spectra in which the slit is placed along the Sun–comet line (the *Greenstein effect* [34]). Again, an analogue in the far-UV has been observed in the case of O I $\lambda 1302$ [35]. Although it is also possible to explain the observation by nonuniform outgassing, this was considered unlikely, as all of the other observed emissions had symmetric spatial distributions. The measurement of the

Greenstein effect immediately leads to a determination of the mean outflow velocity of the given species.

87.3.4 Bowen Fluorescence

For heliocentric velocities > 30 km/s, the Doppler shift reduces the solar flux at the center of the absorption line to a very small value, so that the O I $\lambda 1302$ line is expected to appear weakly, if at all, in the observed spectrum. Thus, it was a surprise that this line appeared fairly strongly in two comets, Kohoutek (C/1973 E1) and West (C/1975 V1), whose values of \dot{r} were both > 45 km/s at the times of observation. The explanation invoked the accidental coincidence of the solar H I Ly- β line at 1025.72 \AA with the O I $^3\text{D}-^3\text{P}$ transition at 1025.76 \AA , cascading through the intermediate ^3P state to the ^3S upper level of the 1302 \AA multiplet [33]. This mechanism, well known in the study of planetary nebulae, is referred to as *Bowen* fluorescence [36]. The g -factor due to Ly- β pumping is an order of magnitude smaller than that for resonance scattering but is sufficient to explain the observations and to confirm that H₂O is the dominant source of the observed oxygen in the coma.

Ly- β is also coincident with the P1 line of the (6,0) band of the H₂ Lyman system ($B^1\Sigma_u^+ - X^1\Sigma_g^+$) leading to fluorescence in the same line of several (6, v'') bands, the strongest being that of the (6,13) band at 1608 \AA [37]. This line is, however, difficult to observe because of the nearby strong CO Fourth Positive bands. Recently, the shorter wavelength (6,1), (6,2), and (6,3) bands have been detected in three comets using FUSE, and the derived H₂ column abundance was found to be consistent with a water photodissociation source [18]. Another interesting example occurs for Ne I, where the second resonance transition at 629.74 \AA coincides with the strong solar O V line at 629.73 \AA . This line was used to set a sensitive upper limit on the Ne abundance in the coma of comet Hale-Bopp (C/1995 O1) [38].

87.3.5 Electron Impact Excitation

The photoionization of parent molecules and their dissociation products leads to the formation of a cometary ionosphere whose characteristics are only now known as a result of measurements by the Rosetta Plasma Consortium [39]. In principle, electron impact excitation, which is often the dominant source of airglow in the atmospheres of the terrestrial planets, also contributes to the observed emissions, particularly in the UV, and so must be accounted for in deriving column densities from the observed emission brightnesses. However, one can use a very simple argument, based on the known energy distribution of solar UV photons, to demonstrate that electron impact excitation is only a minor source for the principal

emissions. Since the photoionization rate of water (and of the important minor species such as CO and CO₂) is $\approx 10^{-6} \text{ s}^{-1}$ at 1 AU, and the efficiency for converting the excess electron energy into excitation of a single emission is of the order of a few percent, the effective excitation rate for any emission will be $\approx 10^{-8} \text{ s}^{-1}$ or less at 1 AU [40]. Since the efficiencies for resonance scattering or fluorescence for almost all the known cometary emissions are much larger, electron impact may be safely neglected except in a few specific cases.

The cases of interest are those of forbidden transitions, where the oscillator strength, and consequently the g -factor, is very small. The primary example is the O I $^5\text{S}_2 - ^3\text{P}_{2,1}$ doublet at 1356 \AA , which was observed faintly in several bright comets such as Hyakutake and Hale-Bopp. This emission appeared very conspicuously in measurements of the coma of 67P/Churyumov-Gerasimenko made by the Alice far-ultraviolet spectrograph on *Rosetta* and was found concentrated within a few km of the nucleus, a region usually not resolvable from Earth-based observations [41]; O I $\lambda 1356$ is produced by dissociative electron impact of the principal molecular species H₂O, CO₂, and O₂, with the brightness of this multiplet relative to O I $\lambda 1304$, C I $\lambda 1657$, and H I Ly- β , diagnostic of the composition of the near-nucleus coma [42]. However, calculations of excitation rates require electron impact cross sections at energies where the electron flux is high, usually near threshold [39], and these are poorly known.

87.3.6 Prompt Emission

In cases where the dissociation or ionization of a molecule leaves the product atom or molecule in an excited state, the decay of this state with the prompt emission of a photon provides a useful means for tracing the spatial distribution of the parent molecule in the inner coma. The products of interest for the water molecule are described in Sect. 87.4.1. Prompt emission includes both allowed radiative decays (such as from the $A^2\Sigma^+$ state of OH) as well as those from metastable states such as O(¹D), since the latter will move ≈ 150 km (for a comet at a geocentric distance of 1 AU, 1 arc-second corresponds to a projected distance of 725 km) in its lifetime. The O I $^1\text{D} - ^3\text{P}$ transition at 6300 and 6364 \AA has been used extensively as a ground-based monitor of the water production rate with the caveat that other species such as OH, CO and CO₂ may also contribute to the observed red line emission. In addition, when the density of H₂O is sufficient to produce observable red line emission, it is also sufficient to produce collisional quenching of the ¹D state, and this must also be considered in the interpretation of the observations. The analogous $^1\text{D} - ^3\text{P}$ transitions in carbon occur at 9823 and 9849 \AA and provide similar information about the production rate of CO. Carbon atoms in the ¹D state, whose lifetime is ≈ 4000 s, are known to be present from the observation of the resonantly

scattered $^1\text{P}^0 - ^1\text{D}$ transition at 1931 Å [43], and the 9849 Å line has been detected in comet Hale-Bopp [44].

The OH $A^2\Sigma^+ - X^2\Pi$ prompt emission competes with that produced by the resonance fluorescence of OH and is difficult to detect, except close to the nucleus (inside 100 km) where the density of water molecules exceeds that of OH by a few orders of magnitude [45]. Again, the reason is that at the wavelengths below the threshold for simultaneous dissociation and excitation, the Sun has much less flux than at the resonance wavelength. On the other hand, only a few rotational lines are excited in fluorescence equilibrium [32], while the prompt emission is characterized by a very *hot* rotational distribution, so in principle the two components may be separated although observations at very high spatial and spectral resolution are required. OH prompt emission has also recently been detected in the infrared at 3.28 μm [46].

87.3.7 OH Level Inversion

An important consequence of fluorescence equilibrium in the OH radical is the UV pumping of the hyperfine and Λ -doublet levels of the $X^2\Pi_{3/2}(J = 3/2)$ ground state, which results in a deviation of the population from statistical equilibrium [32]. Depending on the heliocentric velocity, this departure may be either *inverted* or *anti-inverted*, giving rise to either stimulated emission or absorption against the galactic background at 18-cm wavelength. This technique has been used extensively since 1974 to monitor the OH production rate in comets, even of those that appear close to the Sun [47]. The resulting radio emissions are easily quenched by collisions with molecules and ions, the latter giving rise to a fairly large R_c that must be accounted for in interpreting the derived OH column density. Nevertheless, the radio and UV measurements give reasonably consistent results [47].

87.4 Cometary Models

87.4.1 Photolytic Processes

As an example of the photolytic destruction processes occurring in the coma, consider the dominant molecular species, water. Water vapor is assumed to leave the surface of the nucleus with some initial velocity v_0 and flow radially outward, expanding into the vacuum, and increasing its velocity according to thermodynamics [48]. Even though collisions are important at distances typically up to 10^4 km (depending on the density and, consequently, on the total gas production rate), the net flow of H_2O molecules is radially outward, such that the density varies as R^{-2} near the nucleus, where R is the cometocentric distance. This is the basis for spherically symmetric coma models (the number of particles flowing through

a spherical surface is conserved), which assume isotropic gas production but appears to hold equally well for the case of Halley, which clearly was not outgassing uniformly over its surface [49].

The photolysis of H_2O can proceed by:

<i>a</i>	$\text{H}_2\text{O} + h\nu \rightarrow \text{OH} + \text{H}$	2424.6 Å
<i>a'</i>	$\rightarrow \text{OH}(A^2\Sigma^+) + \text{H}$	1357.1 Å
<i>b</i>	$\rightarrow \text{H}_2 + \text{O}(^1\text{D})$	1770 Å
<i>b'</i>	$\rightarrow \text{H}_2 + \text{O}(^1\text{S})$	1450 Å
<i>b''</i>	$\rightarrow \text{H} + \text{H} + \text{O}(^3\text{P})$	1304 Å
<i>c</i>	$\rightarrow \text{H}_2\text{O}^+ + \text{e}^-$	984 Å
<i>d</i>	$\rightarrow \text{H} + \text{OH}^+ + \text{e}^-$	684.4 Å
<i>e</i>	$\rightarrow \text{H}_2 + \text{O}^+ + \text{e}^-$	664.4 Å
<i>f</i>	$\rightarrow \text{OH} + \text{H}^+ + \text{e}^-$	662.3 Å

The right-hand column gives the energy threshold for each reaction, in wavelength units. The products are subsequently removed by:

<i>g</i>	$\text{OH} + h\nu \rightarrow \text{O} + \text{H}$	2823.0 Å
<i>h</i>	$\rightarrow \text{OH}^+ + \text{e}^-$	928 Å
<i>i</i>	$\text{H}_2 + h\nu \rightarrow \text{H} + \text{H}$	844.79 Å
<i>j</i>	$\rightarrow \text{H}_2^+ + \text{e}^-$	803.67 Å
<i>k</i>	$\rightarrow \text{H} + \text{H}^+ + \text{e}^-$	685.8 Å
<i>l</i>	$\text{O} + h\nu \rightarrow \text{O}^+ + \text{e}^-$	910.44 Å
<i>m</i>	$\text{H} + h\nu \rightarrow \text{H}^+ + \text{e}^-$	911.75 Å

Reactions *l* and *m* can also occur by resonant charge exchange with solar wind protons. Reactions *a'*, *b*, and *b'* correspond to the production of prompt emission, as discussed in Sect. 87.3.6. The determination of column densities of H, O, and OH simultaneously was convincing evidence that the dominant volatile species in the cometary nucleus was H_2O , long before the direct infrared detection of this species in the coma.

Detailed cross sections for the absorption of UV photons by each of the reactants, including proper identification of the final product states, is necessary for the evaluation of the photodestruction rate in the solar radiation field of each of the above reactions. These rates are evaluated at 1 AU using whole disk measurements of the solar flux by integrating the cross section

$$J_d = \int_0^{\lambda_{\text{th}}} \pi F_{\odot} \sigma_d d\lambda. \quad (87.10)$$

Another quantity of interest in coma modeling is the excess velocity (or energy) of the dissociation or ionization

products, and this requires knowledge of the partitioning of energy between internal and translational modes for each reaction [50].

Qualitatively, the photodissociation and photoionization rates can be estimated from the threshold energies given in the table above, since the solar flux is decreasing very rapidly to shorter wavelengths. It is customary to specify the lifetime against photodestruction τ_i , of species i , which is just

$$(\tau_i)^{-1} = \sum_j (J_d)_j, \quad (87.11)$$

where the sum is over all possible reaction channels, as well as the lifetimes into specific channels. Processes with thresholds near 3000 Å have lifetimes $\approx 10^4$ s, those with thresholds near 2000 Å an order of magnitude longer, while those with thresholds below Ly- α , such as most photoionization channels, have lifetimes $\approx 10^6$ s, all at 1 AU. In addition to uncertainties in the details of the absorption cross sections, further uncertainty is introduced into the calculation of J_d by the lack of knowledge of the solar flux at the time of a given observation due to the variability of the solar radiation below 2000 Å, and most importantly, below Ly- α , where there have not been continuous space observations for more than a decade. The solar UV flux is known to vary considerably both with the 27-day solar rotation period and with the 11-year solar activity cycle. Also, at any given point in its orbit, a comet sees a different hemisphere of the Sun than what is seen from Earth. Huebner et al. [51] have compiled an extensive list of useful photodestruction rates using mean solar fluxes to represent the extreme conditions of solar minimum and solar maximum. They also include the excess energies of the dissociation products. A detailed analysis of the rates for H₂O and OH, using surrogate solar indices such as the 10.7 cm solar radio flux, or the equivalent width of the He I line at 1.083 μ m, is in good agreement with observations [52]. Similar analyses still remain to be carried out for other important species, such as CO and NH₃.

87.4.2 Density Models

For parent molecules produced directly by sublimation from the surface of the comet, a spherically symmetric radial outflow model is often adopted. Such a model assumes a steady-state gas production rate Q_i and a constant outflow velocity v , and gives rise to a density distribution as a function of cometocentric distance R given by

$$n_i(R) = \frac{Q_i}{4\pi v R^2} e^{-R/\beta_i}, \quad (87.12)$$

where $\beta_i = v\tau_i$ is the scale length of species i . The basic validity of this model was demonstrated by the *Giotto* neutral mass spectrometer measurements of H₂O and CO₂ [49],

although detailed analysis revealed that the velocity of the water molecules increased from 0.8 km/s at about 1000 km from the nucleus to 1.1 km/s at a radial distance of 10,000 km. The dependence of outflow velocity on heliocentric distance remains uncertain, although Delsemme [53] has suggested an $r^{-1/2}$ -dependence based on thermodynamic arguments. Submillimeter observations of H₂O have sufficient spectral resolution to permit the mapping of outflow velocities along various lines-of-sight to the comet [23].

For the dissociation products, the modeling is more complex. The simplest model assumes continued radial outflow, although at a different velocity, such as to maintain a constant flux of the initial particle across an arbitrary spherical surface surrounding the nucleus [54]. This model, which is valid only at distances equal to a few β_i , is widely used, as the densities can be easily expressed in analytical form. However, as surface brightness measurements are often made with small fields of view close to the nucleus, this model can lead to a factor of 2 error from the neglect of the dissociation kinematics. Since the solar photodissociation often leaves the product fragments with 1–2 eV of kinetic energy [50, 51], the resultant motion (which is assumed to be isotropic in the parent molecule's rest frame), will contain a large non-radial component. Several approaches have been developed to account properly for the kinematics; notably, the vectorial model of Festou [55] and the average random walk model (a Monte Carlo method) of Combi and Delsemme [56]. The latter model has been extended to include time-dependent gas kinetics so as to properly account for regions of the coma where the gas is not in local thermodynamic equilibrium [57].

In addition to the photodestruction chains, chemical reactions, particularly ion–molecule reactions, can alter the composition within the collision zone defined in Sect. 87.3.2. While such reactions may produce numerous minor species, they do not erase the signatures of the original parent molecules. In fact, detailed chemical models have clearly demonstrated the need for complex molecules to serve as the parents of the observed C₂ and C₃ radicals in the coma, strengthening the connection between comet formation and molecular cloud abundances. Thus, the photochemical chains provide a valid means of relating the coma composition to that of the nucleus.

87.4.3 Radiative Transfer Effects

The results of a model calculation for the density of a species must be integrated over the line of sight to obtain the column density at a given projected distance from the nucleus and then integrated over the instrumental field of view for comparison with the observed average surface brightness or derived average column density \overline{N}_i . This assumes that the

coma is optically thin, and that all atoms or molecules have an equal probability of absorbing a solar photon. In practice, this is true for all molecular emissions except perhaps within 1000 km of the nucleus (i.e., for observations made at better than 1'' resolution). Since the cross sections at line center can be very large for an atomic resonance transition, the optical depth for the abundant species can exceed unity, and radiative transfer along both the line of sight to the Sun and that to the Earth must be considered. This is not a trivial problem, as the velocity distribution of the atoms, particularly the component due to the excess energy of the photodestruction process, must be well known, as must be the shape of the exciting solar line. The most thoroughly studied case to date is that of H I Ly- α , whose angular extent, in direct images, can exceed several degrees on the sky [58].

An interesting case arises for resonance transitions between an excited 3S_1 state and the ground $^3P_{2,1,0}$ state, as for O and S, particularly the latter, as its concentration near the nucleus can be quite large due to the rapid decay of one of its parents, CS₂. For S I the three lines at 1807, 1820, and 1826 Å are not observed to have their statistical intensity ratio of 5 : 3 : 1, except at large distances from the nucleus. This is explained by noting that fine structure transitions will lead to all of the S atoms reaching the $J = 2$ ground state in a time short compared with that for absorbing a solar photon, and that the emitted 1807 Å photons will be reabsorbed and can then branch into the other two lines. The detailed solution to this problem has led to the conclusion that H₂S was the primary source of sulfur rather than CS₂, whose other product, CS, was simultaneously observed in the UV [59]. Millimeter and submillimeter observations of comet Hale-Bopp (C/1995 O1) subsequently showed that SO, SO₂, and OCS were also minor sources of atomic sulfur, comparable in abundance to CS₂ [60]. Another minor source is S₂, initially observed in only one comet, IRAS-Araki-Alcock (C/1983 H1) [61], but recently seen in three additional comets by HST. The origin of S₂ in the cometary nucleus has been discussed in the context of *Rosetta* mass spectrometer measurements of this species [62].

87.5 Summary

This brief chapter can only hint at the wealth of observational data spanning the entire electromagnetic spectrum now routinely acquired at almost every comet apparition allowing for a statistically significant assessment of comet diversity and formation scenarios. The *Rosetta* mission has revolutionized our knowledge of comets [63] and will serve as a benchmark for inferring the properties of comets from remote observations. Nevertheless, since space missions to comets are rare, Earth-based observations of comets will continue to play an important role in understanding the physical and chemical

environments of these objects left over from the formation of the solar system, as well as the diversity of comets, as spacecraft missions are not able to visit long-period comets.

References

1. Festou, M.C., Weaver, H.A., Keller, H.U. (eds.): Comets II. Univ. Arizona Press, Tucson (2004)
2. Mumma, M.J., Charnley, S.B.: *Ann. Rev. Astron. Astrophys.* **49**, 471 (2011)
3. Arpigny, C.: *Ann. Rev. Astron. Astrophys.* **3**, 351 (1965)
4. Preston, G.W.: *Astrophys. J.* **147**, 718 (1967)
5. Slaughter, C.D.: *Astron. J.* **74**, 929 (1969)
6. Feldman, P.D., Brune, W.H.: *Astrophys. J. Lett.* **209**, L45 (1976)
7. Mumma, M.J., Weaver, H.A., Larson, H.P., Davis, D.S., Williams, M.: *Science* **232**, 1523 (1986)
8. Bockelée-Morvan, D., Crovisier, J., Mumma, M.J., Weaver, H.A.: In: Festou, M.C., Weaver, H.A., Keller, H.U. (eds.) Comets II. Univ. Arizona Press, Tucson (2004)
9. Crovisier, J., Bockelée-Morvan, D., Colom, P., Biver, N.: *C. R. Phys.* **17**, 985 (2016)
10. Le Roy, L., Altwegg, K., Balsiger, H.: *Astron. Astrophys.* **583**, A1 (2015)
11. Bockelée-Morvan, D., Calmonte, U., Charnley, S.: *Space Sci. Rev.* **197**, 47 (2015)
12. Jessberger, E.K., Kissel, J.: In: Newburn, R.L., Neugebauer Jr., M., Rahe, J. (eds.) Comets in the Post-Halley Era, p. 1075. Kluwer, Dordrecht (1989)
13. Festou, M.C., Feldman, P.D.: In: Kondo, Y. (ed.) Exploring the Universe with the IUE Satellite, p. 101. Reidel, Dordrecht (1987)
14. Festou, M.C.: International Ultraviolet Explorer – Uniform Low Dispersion Data Archive Access Guide: Comets. ESA SP-1134. ESA, Noordwijk (1990)
15. Weaver, H.A., Feldman, P.D., McPhate, J.B., A'Hearn, M.F., Arpigny, C., Smith, T.E.: *Astrophys. J.* **422**, 374 (1994)
16. Lupu, R.E., Feldman, P.D., Weaver, H.A., Tozzi, G.-P.: *Astrophys. J.* **670**, 1473 (2007)
17. Feldman, P.D., Weaver, H.A., A'Hearn, M.F., Combi, M.R., Dello Russo, N.: *Astron. J.* **155**, 193 (2018)
18. Feldman, P.D., Weaver, H.A., Burgh, E.B.: *Astrophys. J. Lett.* **576**, L91 (2002)
19. Feldman, P.D.: *Astrophys. J.* **812**, 115 (2015)
20. Mäkinen, J.T.T., Bertaux, J.-L., Pulkkinen, T.I., Schmidt, W., Kyrölä, E., Summanen, T., Quémerais, E., Lallement, R.: *Astron. Astrophys.* **368**, 292 (2001)
21. Povich, M.S., Raymond, J.C., Jones, G.H., Uzzo, M., Ko, Y.-K., Feldman, P.D., Smith, P.L., Marsden, B.G., Woods, T.N.: *Science* **302**, 1949 (2003)
22. Neufeld, D.A., et al.: *Astrophys. J. Lett.* **539**, L151 (2000)
23. Lecacheux, A., et al.: *Astron. Astrophys.* **402**, L55 (2003)
24. Hartogh, P., Crovisier, J., de Val-Borro, M.: *Astron. Astrophys.* **518**, L150 (2010)
25. Lisse, C.M., et al.: *Science* **274**, 205 (1996)
26. Cravens, T.E.: *Science* **296**, 1042 (2002)
27. Greenwood, J.B., Williams, I.D., Smith, S.J., Chutjian, A.: *Phys. Rev. A* **63**, 62707 (2001)
28. Kharchenko, V., Dalgarno, A.: *Astrophys. J. Lett.* **554**, L99 (2001)
29. Festou, M.C., Rickman, H., West, R.M.: *Astron. Astrophys. Rev.* **4**, 363 (1993)
30. Festou, M.C., Rickman, H., West, R.M.: *Astron. Astrophys. Rev.* **5**, 37 (1993)
31. Swings, P.: *Lick. Obs. Bull.* **131**, xix (1941)
32. Schleicher, D.G., A'Hearn, M.F.: *Astrophys. J.* **331**, 1058 (1988)

33. Feldman, P.D., Opal, C.B., Meier, R.R., Nicolas, K.R.: The Study of Comets. In: Donn, B., Mumma, M., Jackson, W., A'Hearn, M., Harrington, R. (eds.) NASA SP-393, p. 773. NASA, Washington (1976)
34. Greenstein, J.L.: *Astrophys. J.* **128**, 106 (1958)
35. Dymond, K.F., Feldman, P.D., Woods, T.N.: *Astrophys. J.* **338**, 1115 (1989)
36. Bowen, I.S.: *Publ. Astron. Soc. Pac.* **59**, 196 (1947)
37. Feldman, P.D., Fastie, W.G.: *Astrophys. J. Lett.* **185**, L101 (1973)
38. Krasnopolsky, V.A., Mumma, M.J., Abbott, M., Flynn, B.C., Meech, K.J., Yeomans, D.K., Feldman, P.D., Cosmovici, C.B.: *Science* **277**, 1488 (1997)
39. Galand, M., Héritier, K.L., Odelstad, E.: *Mon. Not. R. Astron. Soc.* **462**, 331 (2016)
40. Cravens, T.E., Green, A.E.S.: *Icarus* **33**, 612 (1978)
41. Feldman, P.D., A'Hearn, M.F., Bertaux, J.-L.: *Astron. Astrophys.* **583**, A8 (2015)
42. Feldman, P.D., A'Hearn, M.F., Bertaux, J.-L.: *Astron. J.* **155**, 9 (2018)
43. Tozzi, G.P., Feldman, P.D., Festou, M.C.: *Astron. Astrophys.* **330**, 753 (1998)
44. Oliverson, R.J., Doane, N., Scherb, F., Harris, W.M., Morgenthaler, J.P.: *Astrophys. J.* **581**, 770 (2002)
45. Bertaux, J.-L.: *Astron. Astrophys.* **160**, L7 (1986)
46. Mumma, M.J., et al.: *Astrophys. J.* **546**, 1183 (2001)
47. Gérard, E.: *Astron. Astrophys.* **230**, 489 (1990)
48. Mendis, D.A., Houppis, H.L.F., Marconi, M.L.: *Fund. Cosm. Phys.* **10**, 1 (1985)
49. Krankowsky, D.: In: Newburn, R.L., Neugebauer Jr., M., Rahe, J. (eds.) *Comets in the Post-Halley Era*, p. 855. Kluwer, Dordrecht (1989)
50. Okabe, H.: *The Photochemistry of Small Molecules*. Wiley, New York (1978)
51. Huebner, W.F., Keady, J.J., Lyon, S.P.: *Solar Photo Rates for Planetary Atmospheres and Atmospheric Pollutants*. Springer, New York (1992)
52. Budzien, S.A., Festou, M.C., Feldman, P.D.: *Icarus* **107**, 164 (1994)
53. Delsemme, A.H.: In: Wilkening, L.L. (ed.) *Comets*, p. 85. Univ. Arizona Press, Tucson (1982)
54. Haser, L.: *Bull. Acad. R. Sci. Liège* **43**, 740 (1957)
55. Festou, M.C.: *Astron. Astrophys.* **95**, 69 (1981)
56. Combi, M.R., Delsemme, A.H.: *Astrophys. J.* **237**, 633 (1980)
57. Combi, M.R.: *Icarus* **123**, 207 (1996)
58. Richter, K., Combi, M.R., Keller, H.U., Meier, R.R.: *Astrophys. J.* **531**, 599 (2000)
59. Meier, R., A'Hearn, M.F.: *Icarus* **125**, 164 (1997)
60. Bockelée-Morvan, D., Lis, D.C., Wink, J.E., Despois, D., Crovisier, J., Bachiller, R., Benford, D.J., Biver, N., Colom, P., Davies, J.K., Gérard, E., Germain, B., Houde, M., Mehringer, D., Moreno, R., Paubert, G., Phillips, T.G., Rauer, H.: *Astron. Astrophys.* **353**, 1101 (2000)
61. A'Hearn, M.F., Feldman, P.D., Schleicher, D.G.: *Astrophys. J. Lett.* **274**, L99 (1983)
62. Mousis, O., Ozgurel, O., Lunine, J.I.: *Astrophys. J.* **835**, 134 (2017)
63. Taylor, M.G.G.T., Altobelli, N., Buratti, B.J., Choukroun, M.: *Philos. Trans. R. Soc. A* **375**, 20160262 (2017)



Paul Feldman Dr Feldman was Professor Emeritus of Physics and Astronomy at the Johns Hopkins University, where he has been since 1967. He received his PhD in Physics from Columbia University in 1964. His last work was in space ultraviolet astronomy and spectroscopy with a focus on the study of the atmospheres of comets, planets, and the Galilean satellites.



Jane L. Fox

Contents

88.1	Basic Structure of Atmospheres	1299
88.1.1	Introduction	1299
88.1.2	Atmospheric Regions	1300
88.2	Density Distributions of Neutral Species	1304
88.2.1	The Continuity Equation	1304
88.2.2	Diffusion Coefficients	1305
88.3	Interaction of Solar Radiation with the Atmosphere 1305	
88.3.1	Introduction	1305
88.3.2	The Interaction of Solar Photons with Atmospheric Gases	1306
88.3.3	Interaction of Energetic Electrons with Atmospheric Gases	1309
88.4	Ionospheres	1311
88.4.1	Ionospheric Regions	1311
88.4.2	Sources of Ionization	1312
88.4.3	Nightside Ionospheres	1317
88.4.4	Ionospheric Density Profiles	1320
88.4.5	Ion Diffusion	1322
88.5	Neutral, Ion, and Electron Temperatures	1323
88.6	Luminosity	1325
88.7	Planetary Escape	1332
	References	1334

Abstract

We describe here the neutral and ionic structures of atmospheres, including the processes that determine the atmospheric layers, the distributions of the species, and the temperature profiles. We focus on the upper atmosphere, which comprises the thermosphere and the ionosphere, two regions that overlay and interact with each other. We describe the interaction of near and extreme ultraviolet solar photons and energetic electrons with the atmosphere and their role in ionization and dissociation of

atmospheric species. We also review the production and loss processes that are important in the formation of the different layers of the dayside and nightside ionospheres, including ion and neutral diffusion. The processes that determine the neutral, ion, and electron temperatures are discussed. We review the processes that are important in the production of the luminosity of the upper atmospheres, including dayglow, nightglow, and auroras. Finally, we describe atmospheric escape processes, including thermal and nonthermal mechanisms.

Keywords

solar zenith angle · terrestrial planet · outer planet · dissociative recombination · suprathermal electron

88.1 Basic Structure of Atmospheres

88.1.1 Introduction

In a stationary atmosphere, the force of gravity is balanced by the plasma pressure gradient force in the vertical direction, and the variation of pressure $P(z)$ with altitude above the surface z is governed by the hydrostatic relation

$$\frac{dP(z)}{dz} = -\rho(z)g(z), \quad (88.1)$$

where $\rho(z) = n(z)m(z)$ is the mass density, $n(z)$ is the number density, and $m(z)$ is the weighted average mass of the atmospheric constituents. In general, variables such as P , T , ρ , g , n , and even m are functions of altitude, although it will often not be shown explicitly in the equations that follow for the sake of compactness. The acceleration of gravity g is usually taken to be the vector sum of the gravitational attraction per unit mass and the centrifugal acceleration due to the rotation of the planet

$$g(r) = \frac{GM}{r^2} - \omega^2 r \cos^2 \phi, \quad (88.2)$$

J. L. Fox (✉)
Dept. of Physics, Wright State University
Dayton, OH, USA
e-mail: jane.fox@wright.edu

where $r = r_0 + z$ is the distance from the center of the planet, r_0 is the planetary radius, M is the planetary mass, $G = 6.670 \times 10^{-8} \text{ dyn cm}^2 \text{ g}^{-2}$ is the gravitational constant, ϕ is the latitude, and ω is the angular velocity of the planet.

When the hydrostatic relation Eq. (88.1) is combined with the ideal gas law in the form

$$P = nk_{\text{B}}T, \quad (88.3)$$

where k_{B} is Boltzmann's constant, and T is the temperature, and integrated, the barometric formula

$$P(z) = P_0 \exp\left(-\int_{z_0}^z \frac{1}{H(z')} dz'\right), \quad (88.4)$$

for the pressure $P(z)$ above a reference level (denoted by the subscript 0) as a function of altitude results. The pressure scale height $H(z)$ is defined as

$$H(z) = \frac{k_{\text{B}}T}{mg}. \quad (88.5)$$

In the lower and middle atmosphere, the mass m in Eq. (88.5) is the weighted average mass of the atmospheric constituents.

When the ideal gas law Eq. (88.3) is substituted into the barometric formula Eq. (88.4), the altitude distribution

$$n(z) = n_0 \frac{T_0}{T(z)} \exp\left(-\int_{z_0}^z \frac{1}{H(z')} dz'\right), \quad (88.6)$$

for the number density $n(z)$ above a reference altitude is obtained. Integration of Eq. (88.1) or Eq. (88.6) from z to infinity shows that the column density above that altitude is approximately $N(z) = n(z)H(z)$. Thus, the scale height can be thought of as the effective thickness of the atmosphere.

Throughout the atmosphere, gravity exerts a force on each particle that is proportional to its mass. Below the homopause, however, the tendency of the species to separate out under the force of gravity is overpowered by large scale mixing processes, such as turbulence and/or convection. Thus in its lower and middle regions, the homosphere, the atmosphere is well-mixed. The upper boundary of this region is called the homopause (or turbopause). Above this level, the major transport process is diffusion, and each species is distributed according to its own scale height. The homopause is defined as the level at which the time constants for mixing and diffusion are equal, and usually occurs at $n(z) \approx 10^{11} - 10^{13} \text{ cm}^{-3}$, depending on the strength of vertical mixing for a given planet. Since molecular diffusion coefficients vary from one species to another, the exact altitude of the homopause is species-dependent, with smaller species (or those that have smaller momentum transfer colli-

sion frequencies) having lower homopause altitudes. It must also be borne in mind that the homopause is not a sharp boundary, and that the transition from mixing to diffusion occurs gradually. In the terrestrial atmosphere, the homopause is near 100 km at $n(z) \approx 10^{13} \text{ cm}^{-3}$. Below the homopause, the mixing ratios (or fractions by number) of the constituent gases, apart from those minor or trace species whose density profiles are determined by photochemistry or physical loss processes, are fairly constant with altitude. Characteristics of the homopauses of the planets are presented in Table 88.1.

88.1.2 Atmospheric Regions

The division of atmospheres into regions is based on the temperature structure of the terrestrial atmosphere, which is shown in Fig. 88.1. In the troposphere of a planet, above the boundary layer, T decreases at close to the adiabatic lapse rate (Γ) for the constituent gases from the surface to the tropopause. For an atmosphere that is a mixture of ideal gases, $\Gamma = g/c_p$, where c_p is the specific heat of the gas mixture at constant pressure. The presence of a condensible constituent, such as water vapor in the terrestrial troposphere and that of other planets, such as Mars and the outer planets, and ammonia, C_2 - or higher hydrocarbons in the atmospheres of the outer planets and satellites, decreases Γ because upward motion leads to cooling and condensation, which releases latent heat. On Earth, the dry adiabatic lapse rate is about 10 K km^{-1} , and the moist adiabatic lapse rate is about $4-6 \text{ K km}^{-1}$ in the lower to middle troposphere. The average lapse rate is about 6.5 K km^{-1} , and the altitude of the tropopause varies from about 9 to 16 km from the poles to the equator. The composition of the lower atmosphere of the Earth is given in Table 88.2.

Above the terrestrial tropopause lies the stratosphere, a region of increasing T that is terminated at the stratopause, near 50 km. This increase in T is caused by absorption of solar near-UV radiation by ozone in the Hartley bands and continuum (200–310 nm). In the terrestrial mesosphere, which lies above the stratosphere, T decreases again to an absolute minimum at the mesopause, where $T \approx 180 \text{ K}$ and $n(z) \approx 10^{14} \text{ cm}^{-3}$. Above the mesopause, in the thermosphere, T increases rapidly to a constant value, the exospheric temperature, T_{∞} . The value of T_{∞} in the terrestrial atmosphere depends on solar activity and is usually between about 700 and 1500 K. Figure 88.1a also shows altitude profiles of the noon and midnight thermospheric temperature for four values of the $F_{10.7}$ index (the 2800 MHz flux in units of $10^{-22} \text{ W m}^{-2} \text{ Hz}^{-1}$ at 1 AU), which represent different levels of solar activity. Analogous temperature profiles of other planetary bodies as a function of pressure are shown in Fig. 88.1b. It can be seen that the temperature profiles above some of the tropopauses do not reach a maximum value that signals the stratopause. In

Table 88.1 Homopause characteristics of planets and other solar system bodies

Planet	Altitude (km)	K ($\text{cm}^2 \text{s}^{-1}$)	T (K)	n_1 (cm^{-3})	P (μbar)	Composition (fraction by number)
Venus ^b	135	4(7) ^a	199	1.4(11)	4.7(−3)	CO ₂ (76%), N ₂ (7.6%), O(9.3%), CO(6.7%), N(0.16%), C(0.01%)
Earth ^c	100	1(6)	185	1.3(13)	0.3	N ₂ (77%), O ₂ (18%), O(3–4%), Ar(0.7%), He(9.5 ppm), H(1.3 ppm)
Mars ^d	130–140	2.3(8)	≈ 163	2.8(10)	≈ 6.2(−4)	CO ₂ (86%), N ₂ (4.3%), Ar(2.7%), O(3.2%), CO(3.1%), NO(40 ppm), H ₂ (22 ppm)
Jupiter ^e	500 ^f	2(6)	600	1.4(13)	0.4	H ₂ (95%), He(4.1%), H(0.055%), CH ₄ (200 ppb), C ₂ H ₂ (1.2 ppb), C ₂ H ₄ (2.5 ppb), C ₂ H ₆ (0.12 ppb)
Saturn ^g	1010 ^f (900–1400)	3(7) (3–7)(7)	≈ 325	6(11)	2.7(−2)	H ₂ (96–99%), He(1.2–3.1%), CH ₄ (16 ppm), H(0.17–3.7%)
Uranus ^g	350 ^f	5(3)	137	1.93(15)	≈ 36	H ₂ (93%), He(6.7%), H(17 ppm), CH ₄ (0.8%), C ₂ H ₂ (0.83 ppb), C ₂ H ₆ (0.46 ppb)
Neptune ^g	700 ^f	5(6)	210	2.8(12)	≈ 0.83	H ₂ (96.6%), He(3.42%), CH ₄ (0.48 ppm), H≈(30 ppm), C ₂ H ₆ ≈(0.4 ppb)
Titan ^h	1010 (1000–1100)	4(8) (1.2(8)–1.8(9))	150–180	≈ 3.2(9)	6.4(−5)	N ₂ (94–96%), H ₂ (3.4%), CH ₄ (2.1%), C ₂ H ₂ (0.034%), C ₂ H ₄ (0.04%), HCN(0.024%), C ₂ H ₆ (60.5 ppm)
Triton ⁱ	30–40	(2–8)(3)	50	3.7(14)	2.7	N ₂ (99.9%), CH ₄ (3 ppm), H ₂ (70 ppm)
Pluto ^j	0–12	(1–4)(3)	40–50	1.85(15) (5(14)–2(15))	11.5	N ₂ (99.7%), CH ₄ (0.3%), C ₂ H ₂ (274 ppb), C ₂ H ₆ (230 ppm), C ₂ H ₄ (700 ppb)

^a Read as 4×10^7 ^b K from *von Zahn* et al. [1] and model atmosphere from *Hedin* et al. [2], for 1500 h, 15° N latitude, $F_{10.7} = 150$ ^c From The US Standard Atmosphere [3]^d Fit to MAVEN model for $F_{10.7} = 120$, near subsolar point^e From photochemical model of *Kim* [4]^f Altitude above the 1 bar level^g From *Vervack, Jr.* and *Moses* [5]^h From *Magee* et al. [6]ⁱ From *Strobel* and *Zhu* [7]^j From *Young* et al. [8]**Table 88.2** Molecular weights and fractional composition of dry air in the terrestrial atmosphere^a

Species	Molecular weight (g mol^{-1})	Fraction by volume
N ₂	28.0134	0.78084
O ₂	31.9988	0.209476
Ar	39.948	0.00934
CO ₂	44.00995	0.00042099 ^b
Ne	20.183	0.00001818
He	4.0026	0.00000524
Kr	83.80	0.00000114
Xe	131.30	0.000000087
CH ₄	16.04303	0.000002
H ₂	2.01594	0.0000005

^a Taken from The US Standard Atmosphere [3], except as noted^b 2022 June global averaged data value. The CO₂ mixing ratio is increasing at an average annual rate of 0.489%. Value from Earth System Research Laboratory Global Monitoring Division of the National Oceanic and Atmospheric Administration (NOAA) (website <http://gml.noaa.gov/ccgg/trends>)

these atmospheres, the region between the tropopause and the mesopause is usually called the mesosphere for the inner planets and the stratosphere for the outer planets.

The exosphere is assumed to be a nearly collisionless region of the thermosphere that is bounded from below by

a level called the “exobase”. The assumption involved in deriving the altitude of the exobase is that a particle traveling upward at or above the exobase will, with high probability, escape from the gravitational field of the planet. The exobase on Earth is located at about 450–500 km, depending upon solar activity. The properties of the classical exobase will be discussed in the context of escape of species from atmospheres in Sect. 88.7.

The surface P and T on Mars are about 6 mbar and 230 K, respectively. Due to the effect of dust storms, the extent of the Martian troposphere is highly variable, with a lapse rate that is 2–3 K km^{−1} compared with the adiabatic lapse rate of 4.5 K km^{−1} and a variable thickness of 20–50 km [11]. The atmosphere of Mars, like many planetary atmospheres, does not have a stratopause. A roughly isothermal mesosphere extends from the tropopause to the base of the thermosphere at about 90 km. Sometimes a peak in the temperature between the tropopause and the mesosphere is caused by the absorption of solar radiation by dust that is lifted to high altitudes by dust storms, which are most common at perihelion. The thermospheric T is sensitive to solar activity and, since Mars has a very eccentric orbit, to heliocentric distance; T_∞ varies from about 180 to 350 K. Near the surface of Venus, $T \gtrsim 700$ K, and $P \approx 95$ bar; T decreases with a mean lapse rate of 7.7 K km^{−1},

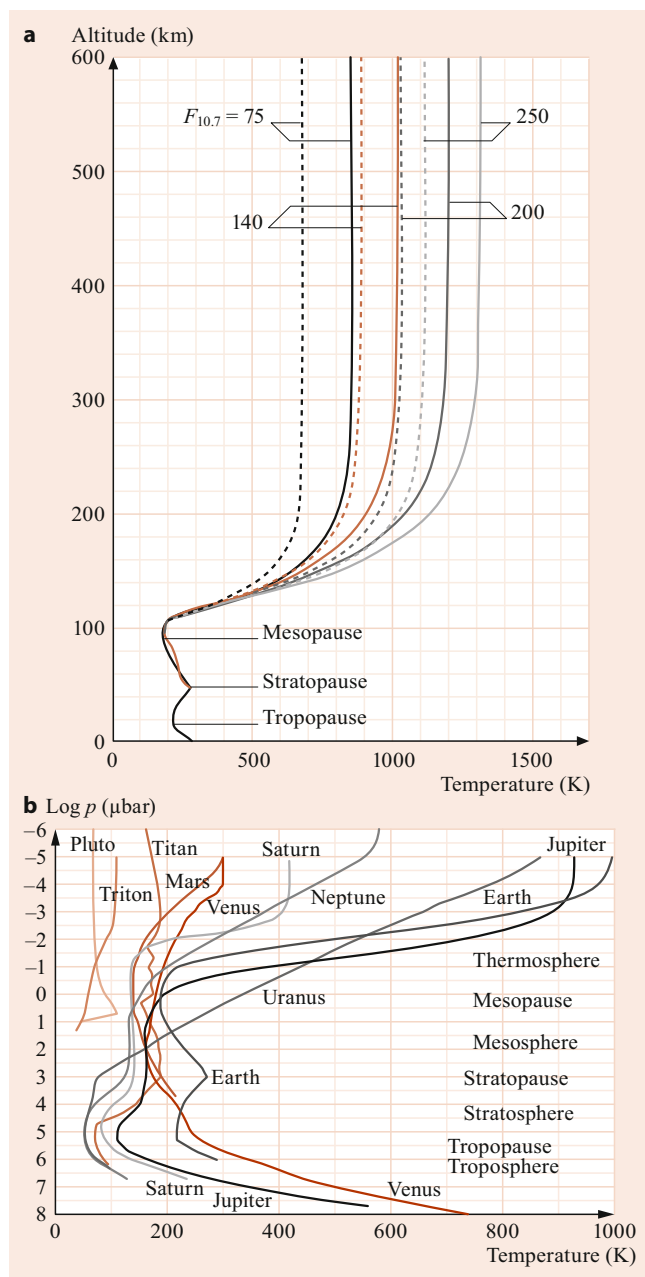


Fig. 88.1 (a) Vertical distribution of temperature in the terrestrial atmosphere. The altitudes of the tropopause, stratopause, and mesopause are indicated. The thermospheric temperatures depend on solar activity, and profiles are shown for four values of the $F_{10.7}$ index, from 75 (low solar activity) to 250 (high solar activity). The *solid* and *dashed curves* are for noon and midnight, respectively. After the MSIS model of Hedin [9]. (b) Vertical distribution of neutral temperatures of planets and satellites plotted on a common pressure scale. The regions of the atmospheres that are analogous to the terrestrial atmosphere are shown. From Strobel [10]

compared with the adiabatic lapse rate of 8.9 K km^{-1} , from the surface to about 50 km. The region from 50 to 60 km contains the major cloud layer, and the tropopause is usually considered to be at about 60 km. In the mesosphere, between about 60 and 85 km, T decreases slowly from about 250 to 180 K

Table 88.3 Composition of the lower atmospheres of Mars and Venus

Species	Mixing ratio	
	Mars	Venus ⁱ
CO ₂	0.949 ^a	0.965
N ₂	0.0279 ^a	0.035
⁴⁰ Ar	0.0208 ^a	20–50 ppm ^b
O ₂	0.0013 ^a	0.3 ppm
CO	0.00174 ^a	20–30 ppm
H ₂ O	0.0003 ^c	(30±10) ppm ^d
He	(10±6) ppm ^e	(9±6) ppm ^e
Ne	2.5 ppm ^f	5–13 ppm
Kr	0.3 ppm ^f	0.02–0.4 ppm
Xe	0.08 ppm ^f	–
H ₂	(15±5) ppm ^g	>0.1 ppm ^h
CH ₄	0.69 ppm ⁱ	–
SO ₂	–	150 ppm
H ₂ S	–	1–3 ppm

^a From Franz et al. [12]

^b Includes all isotopes of Ar

^c Highly variable. From Jakosky and Haberle [13]

^d Value applies to altitudes below the cloud deck. From [14] and Taylor et al. [15]

^e From Krasnopolsky and Gladstone [16]

^f Owen [17]

^g At base of thermosphere; Krasnopolsky and Feldman [18]

^h From the lower atmosphere model of Yung and DeMore [19] at 100 km; value is almost certainly higher

ⁱ Variable. Background value measured at Gales Crater by Webster et al. [20]

^j From Lodders and Fegley, Jr. [21] except as noted

and is nearly constant from 85 km to the mesopause at 100 km. The daytime exospheric temperature is only weakly dependent on solar activity, varying from about 230 to 300 K from low to high solar activity. The slow retrograde rotation of the planet, which results in a period of darkness that lasts 58 Earth days, leads to the relative isolation of the nightside thermosphere, where T is found to decrease above the mesopause to a constant value of $T_{\infty} \approx 100 \text{ K}$. Because of this, the nightside Venus thermosphere has been called the *cryosphere*. The compositions of the lower atmospheres of Mars and Venus are given in Table 88.3.

The giant planets, Jupiter, Saturn, Uranus, and Neptune do not have solid surfaces, so their atmospheric regions are defined either in terms of pressure, altitude above the cloud tops, or more commonly, altitude above the 1 bar level. The temperature structures of all but Uranus are influenced by internal heat sources that the terrestrial planets do not possess. The temperature structures near the tropopause can be determined from IR observations and radio occultation data, and at thermospheric altitudes from ultraviolet solar and stellar occultations performed by various spacecraft.

Below 300 mbar on Jupiter, the lapse rate is close to adiabatic (1.9 K km^{-1}); T at 1 bar is about 165 K, and the tropopause occurs near 140 mbar, where $T \approx 110 \text{ K}$. At 1 mbar, T again reaches 160–170 K. Temperature inversions

Table 88.4 Composition of the lower atmospheres of Jupiter and Saturn

Species	Mixing ratio	
	Jupiter	Saturn
H ₂	0.864 ^b	0.881 ^b
He	0.136 ^b	0.119 ^b
CH ₄	0.00181 ^b	0.0047 ^d
NH ₃	0.00061 ^b	0.00016 ^c
H ₂ O	520 ppm ^b	2–20 ppb ^b
C ₂ H ₆	5.8 ppm ^a	7.0 ppm ^b
PH ₃	1.1 ppm ^a	4.5 ppm ^b
C ₂ H ₂	0.11 ppm ^a	0.3 ppm ^b
C ₂ H ₄	7 ppb ^b	0.2 ppb ^b
²⁰ Ne	21 ppm ^c	
³⁶ Ar	16 ppm ^c	
⁸⁴ Kr	8 ppb ^c	
¹³² Xe	8 ppb ^c	

^a After Strobel [23]^b After Lodders and Fegley, Jr. [21]^c After Niemann et al. [24]^d After Fletcher et al. [25]

have been reported in the stratosphere and are probably due to absorption of solar radiation by dust or aerosols. Temperatures derived from the Voyager UV stellar and solar occultations show that T increases from about 200 K near 1 μ bar to an exospheric value of about 1000 K [22].

For $P > 500$ mbar on Saturn, the lapse rate approaches the adiabatic value of 0.9 K km^{-1} , and the tropopause, near the 100 mbar level, is characterized by $T \approx 80$ K. Above the tropopause, the temperature increases to about 140 K near a $P \approx 1$ mbar, and above this altitude, the temperature is essentially constant. Above 1000 km, T increases to a $T_{\infty} \approx 400\text{--}500$ K, e.g. [22]; T_{∞} appears to increase with latitude (Vervack, Jr. and Moses [5]). The mixing ratios of the species in the lower atmospheres of Jupiter and Saturn are given in Table 88.4.

The tropopauses on both Uranus and Neptune occur near 100 mbar, where $T \approx 50$ K. The lapse rates in the troposphere are 0.7 and 0.85 K km^{-1} for Uranus and Neptune, respectively. The temperatures in the Uranus thermosphere range from 500 K near 10^{-7} bar (about 1000 km above the 1 bar level) to an exospheric value of about 700–800 K. In the range 300 to 600 km on Neptune, T is characterized by a nearly constant value of 160–180 K. Above 600 km, where $P \approx 1 \mu$ bar, T increases again to a value that is probably about 700 K [26, 27]. The compositions of the lower atmospheres of Uranus and Neptune are given in Table 88.5.

Titan, which is a satellite of Saturn, has an N₂/CH₄ atmosphere of intermediate oxidation state. The mixing ratios of components of the lower atmosphere are given in Table 88.6. The surface P and T are 1.5 bar and 94 K, respectively; T decreases above the surface to about 70 K at the tropopause, which occurs at an altitude of 42 km and

Table 88.5 Composition of the lower atmospheres of Uranus and Neptune^a

Species	Mixing ratio	
	Uranus	Neptune
H ₂	≈ 0.825	≈ 0.80
He	≈ 0.152	≈ 0.19
CH ₄	≈ 0.023	$\approx 0.01\text{--}0.02$
HD	≈ 148 ppm	≈ 192 ppm
CH ₃ D	≈ 8.3 ppm	≈ 12 ppm
C ₂ H ₆	$\approx (10 \pm 1)$ ppb	≈ 1.5 ppm
C ₂ H ₂	≈ 10 ppb	≈ 60 ppb
CO	< 27 ppb	$0.6\text{--}2.2$ ppm
NH ₃	< 100 ppb	< 600 ppb

^a After Lodders and Fegley, Jr. [21]**Table 88.6** Composition of the lower atmosphere of Titan^a

Species	Mixing ratio ^b
N ₂	0.951–0.984
CH ₄	0.049
H ₂	9.6×10^{-4}
CO	47 ppm
⁴⁰ Ar	43 ppm
C ₂ H ₆	13 ppm
C ₃ H ₈	0.6 ppm
C ₂ H ₂	3.7 ppm
C ₂ H ₄	0.11–0.22 ppm
C ₄ H ₂	1.18–4.2 ppb
HCN	0.15 ppm
H ₂ O	≈ 0.4 ppb ^c

^a From measurements obtained by the Cassini spacecraft, including the Huygens probe, except as noted^b From Lodders and Fegley, Jr. [21], except as noted^c Value pertains to an altitude of 400 km. From the Infrared Space Observatory (ISO) measurements of Coustenis et al. [28]

a pressure of 128 mbar. A reanalysis of the Voyager 1 solar occultation experiment showed that, above the tropopause, the temperature increases to a peak value of about 176 K at an altitude of about 300 km. The temperature then decreases to a T_{∞} of 153–158 K [29]. The Huygens Atmospheric Structure Instrument (HASI) on the Cassini spacecraft measured temperature profiles that exhibited wave-like structure in the range 200–1400 km (Fulchignoni et al. [30]). A review of the thermal structure and dynamics of the upper atmosphere of Titan has been presented by Yelle et al. [31].

Triton is a satellite of Neptune. It also has an N₂ atmosphere with small amounts of methane, CO, H₂, H, N, C, and HCN. The mixing ratios at 10 km are given in Table 88.7. The surface P is about 19 μ bar, and the surface temperature is about 37 K. Methane in the troposphere is in equilibrium with a surface methane frost at about 38–50 K. The temperature decreases with a lapse rate of about 0.1 K km^{-1} from the surface to the tropopause. The tropopause temperature is about 36 K, and occurs in the 8–12 km region. The middle

Table 88.7 Composition of the atmosphere of Triton^a

Species	Mixing ratio	Comments
N ₂	0.99 ± 0.01	Below ≈ 200 km
CO	0.0016	At surface; uncertain by a factor of 3 ^b
CH ₄	600 ppm	At surface ^b
H ₂	75 ppm	From model
N	3.8 × 10 ⁻⁵ ppm	From model
N	290 ppm	100 km; from model
H	1 ppm	30 km; from model

^a From [32]. Values are at 10 km, except as noted

^b From *Lellouch et al.* [33]

Table 88.8 Number densities of neutral and ion species at the surface of Mercury^a

Species	Number density (cm ⁻³)	Scale height (km)
Na ^b	(1 × 10 ³ –1 × 10 ⁵)	75–110
Mg ^b	(5–50)	300–2000
Ca ^b	(6.6–4)	1000–2500
H ^b	70–140	600–800
Al ^b	0.2–0.6	515–675
Fe	Detected	Scale height not measured
Mn	Detected	Not measured
Ca ⁺	Detected	Not measured
K	Detected	Not measured

^a For references, see *Killen et al.* [35]; *McClintock et al.* [36]

^b Variable spatially and temporally

atmosphere is isothermal with a temperature of about 52 K from 25 to 50 km, increasing to 78 K near 150 km [34]; T then rises to a constant maximum T_∞ in the range 80–100 K above 450 km.

Mercury does not have a troposphere, mesosphere, or stratosphere; the surface of the planet is the exobase. Nevertheless, several atomic species and ions have been identified previous to and during the recent MESSENGER mission. They are listed in Table 88.8. Among the possible sources of atmospheric species are interactions with the incoming solar wind, dust, and meteoroids. There are also a number of sources that act to release of atoms from the surface and include radiation pressure, thermal desorption, impact vaporization, photon-stimulated desorption, ion sputtering, and chemical sputtering (*Killen et al.* [35]; *McClintock et al.* [36]). Ions produced by photoionization of neutrals may be picked up by the solar wind and lost from the atmosphere.

The dwarf planet Pluto forms a binary system with its satellite Charon. The radius of Pluto is 1190 km, and that of Charon is about 617 km. The atmosphere of Pluto is mostly N₂, with small amounts of methane, the C-2 hydrocarbons C₂H₂, C₂H₄, and C₂H₆, and haze (Table 88.9), which were detected by the solar occultations carried out by the New

Table 88.9 Composition of the lower atmosphere of Pluto^a

Species	Mixing ratio
N ₂	0.997
CH ₄	0.0031
C ₂ H ₆	20 ppm
C ₂ H ₂	5 ppm
C ₂ H ₄	6 ppm
H ₂ O	≈ 100 ppb ^b
HCN	10–100 ppb ^c
CO	(515±40) ppm ^d

^a From *Young et al.* [8] and *Hinson et al.* [37] at 100 km

^b From the model of *Strobel and Zhu* [7]

^c Below 100 km, increases at higher altitudes. From *Lellouch et al.* [38]

^d At surface. From *Lellouch et al.* [38]

Horizons spacecraft (e.g., *Young et al.* [8]). The appearance of haze is common to atmospheres in which methane is present, even in small abundance; it signals the presence of higher hydrocarbons, including benzene, and for Pluto, Titan, and Triton, large nitrogen-containing organic compounds. The mixing ratio of CO was measured as ≈ 515 ppm and is evenly mixed in the atmosphere of Pluto; HCN was detected by the interferometer on the ALMA (Atacama Large Millimeter Array). Below 100 km, a mixing ratio for HCN of 0.01–0.1 ppm was found, rising to 40 ppm at 800 km (*Lellouch et al.* [38]). H₂O with an abundance of 0.1 ppm at the surface was inferred in order to explain the observed temperature profile (*Strobel and Zhu* [7]).

The surface pressure and temperature on Pluto are ≈ 11.5 μbar and ≈ 45 K, respectively. The thermal structure of the atmosphere is influenced by the large thermal escape flux at the top of the atmosphere, by adiabatic cooling, and by H₂O rotational cooling. The temperature profile shows a shallow (if any) troposphere, above which T increases to a maximum (stratopause) temperature of about 110 K at an altitude of ≈ 30 km, due to absorption of solar UV radiation. Above that altitude, T decreases to form a broad minimum of about 63 K, before rising to an exospheric temperature of ≈ 70 K. Charon has no apparent atmosphere.

88.2 Density Distributions of Neutral Species

88.2.1 The Continuity Equation

The density distribution of a minor neutral species j in an atmosphere is determined by the continuity equation

$$\frac{\partial n_j}{\partial t} + \nabla \cdot \Phi_j = P_j - L_j, \quad (88.7)$$

where Φ_j is the flux of species j , and P_j and L_j are the chemical production and loss rates, respectively. If only the

vertical direction is considered, the divergence of the flux becomes $\partial\Phi_j/\partial z$, and $\Phi_j = n_j w_j$, where w_j is the vertical velocity of the species, and n_j is its number density. In one-dimensional models, transport due to turbulence and other macroscopic motions of air masses is often parametrized like molecular diffusion, using an eddy diffusion coefficient K in place of the molecular diffusion coefficient D_j . The total transport velocity w_j is then the sum of the diffusion velocity w_j^D and the eddy diffusion velocity w_j^K

$$w_j = w_j^D + w_j^K. \quad (88.8)$$

If there are no net flows of major constituents, w_j^D and w_j^K satisfy the equations

$$w_j^D = -D_j \left(\frac{1}{n_j} \frac{dn_j}{dz} + \frac{1}{H_j} + \frac{(1 + \alpha_j^T)}{T} \frac{dT}{dz} \right), \quad (88.9)$$

$$w_j^K = -K \left(\frac{1}{n_j} \frac{dn_j}{dz} + \frac{1}{H_{\text{avg}}} + \frac{1}{T} \frac{dT}{dz} \right). \quad (88.10)$$

In these expressions, α_j^T is the thermal diffusion factor (the ratio of the thermal diffusion coefficient to the molecular diffusion coefficient), and the pressure scale height H_{avg} for a mixed atmosphere is given by Eq. (88.5) with $m = m_{\text{avg}}$, the average molecular mass.

For a stationary atmosphere, if molecular diffusion greatly exceeds eddy diffusion, and if photochemistry can be neglected, then $w_j^D = 0$. The resulting number density distribution is called diffusive equilibrium, and is given by

$$n_j(z) = n_j(z_0) \left(\frac{T_0}{T} \right)^{(1+\alpha_j^T)} \exp \left(- \int_{z_0}^z \frac{dz'}{H_j} \right). \quad (88.11)$$

When mixing processes dominate, and $w_j^K = 0$, the distribution is given by Eq. (88.6), with $m = m_{\text{avg}}$ in the definition of the scale height H (Eq. (88.5)).

88.2.2 Diffusion Coefficients

In the thermosphere of a planet, above the homopause, the major transport mechanism is diffusion or transport by random molecular motions. The characteristic time τ_D for molecular diffusion is approximately H_j^2/D_j . The diffusion coefficient for a species j in a multicomponent mixture is usually taken as a weighted mean of inverse binary diffusion coefficients D_{jk}

$$\frac{1}{D_j} = \sum_{k \neq j} \frac{f_k}{D_{jk}}, \quad (88.12)$$

where f_k is the mixing ratio of species k . The binary diffusion coefficient can be expressed as

$$D_{jk} = \frac{3k_B T}{16n_t \mu_{jk} \Omega_{jk}}, \quad (88.13)$$

where μ_{jk} is the reduced mass

$$\mu_{jk} = \frac{m_j m_k}{m_j + m_k}, \quad (88.14)$$

and $n_t = n_j + n_k$ is the total number density. The collision integral Ω_{jk} is given by

$$\Omega_{jk} = \frac{1}{2\pi^{1/2}} \left(\frac{\mu}{2k_B T} \right)^{5/2} \times \int_0^\infty Q^D(v) v^5 \exp \left(\frac{-\mu v^2}{2k_B T} \right) dv, \quad (88.15)$$

where v is the relative velocity of the particles, $Q^D(v)$ is the diffusion or momentum transfer cross section

$$Q^D(v) = 2\pi \int_0^\pi \sigma_{jk}^{\text{el}}(\theta, v) (1 - \cos \theta) \sin \theta d\theta, \quad (88.16)$$

and $\sigma_{jk}^{\text{el}}(\theta, v)$ is the differential cross section for elastic scattering of species j and k through angle θ in the center-of-mass frame. In practice, D_{jk} is often expressed as b_{jk}/n_t , where n_t is the total number density, and b_{jk} is the binary collision parameter, which is usually given in tabulations in the semiempirical form $b = AT^s$. Here, A and s ($0.5 \lesssim s \lesssim 1.0$) are parameters that are fitted to the data. The binary collision parameter appears, for example, in the expression for the diffusion limited flux of a light species to the “exosphere” of a planet (e.g., *Hunten* [40]) (Sect. 88.7).

88.3 Interaction of Solar Radiation with the Atmosphere

88.3.1 Introduction

The source for all atmospheric processes is ultimately the interaction of solar radiation, either photons or particles, with atmospheric gases. Since visible photons arise from the photosphere of the sun, which is characterized by $T \approx 6000$ K, the solar spectrum in the visible and IR is similar to that of a black body at 6000 K. At longer (radio) and shorter (UV and X-ray) wavelengths, the photons arise from parts of the chromosphere and corona where the temperatures are higher ($10^4 - 10^6$ K). Thus, the photon fluxes differ substantially from those that would be predicted for a 6000 K black body. Photons in the extreme and far UV regions of the spec-

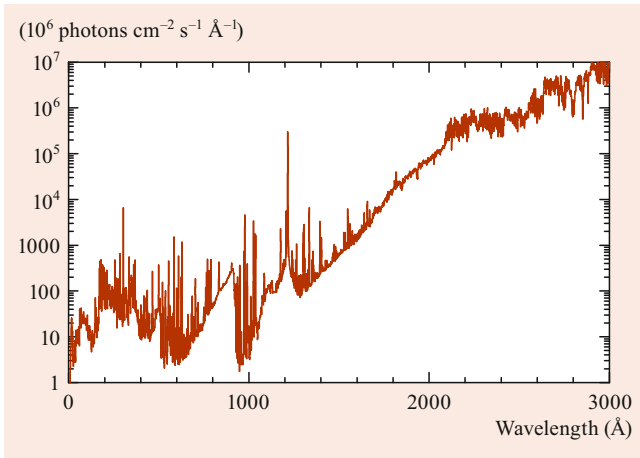


Fig. 88.2 Solar fluxes in units of $10^6 \text{ photons cm}^{-2} \text{ s}^{-1} \text{ Å}^{-1}$ at 1 AU for 1–3000 Å at a resolution of 1 Å. From *Eparvier* [41]. See also *Chamberlin et al.* [39]

trum are absorbed in the terrestrial thermosphere and X-rays in the lower thermosphere and mesosphere. The solar Lyman α line at 1216 Å penetrates through a window in the O_2 absorption cross sections to about 75 km. Near-UV photons are absorbed by ozone in the stratosphere, and visible radiation is not appreciably attenuated by the atmosphere.

The wavelength ranges that are most important for aeronomy are the UV and X-ray regions. A solar spectrum in the UV and X-ray regions at moderate solar activity ($F_{10} = 120$) is presented in Fig. 88.2. The ratio of high solar activity fluxes to low solar activity fluxes is near unity at wavelengths longward of 2000 Å but increases to factors that range between 2 and 3 over much of the extreme UV. At wavelengths between about 100 and 550 Å, the ratio of high to low solar activity fluxes reaches values as high as 100. The fluxes at X-ray wavelengths arise principally from solar flares and can increase by orders of magnitude from low to high solar activity.

The sun also emits a stream of charged particles, the solar wind, which flows radially outward in all directions, and consists mostly of protons, electrons, and alpha particles. The average number density of solar wind protons is about 5 cm^{-3} , and the average speed is about 400–450 km s^{-1} at Earth orbit (1 AU). The interaction of these particles with the magnetic field (either induced or intrinsic) of a planet, and ultimately with the atmosphere, is the source of auroral activity. Terrestrial auroras arise mostly from precipitation of electrons with energies in the kilovolt range, although measured spectra vary widely. An example of a primary electron auroral spectrum is shown in Fig. 88.3. Terrestrial auroral emissions maximize in the midnight sector, but dayside cusp auroras are produced by lower energy electrons, and diffuse proton auroras are also observed.

Since charged particles are constrained to move along magnetic field lines, for planets with intrinsic dipole fields,

auroras are usually found in an oval around the magnetic poles, where the dipole field lines enter the atmosphere. On Venus and Mars, diffuse and variable auroras are observed on the nightside. Since Mars has a remanent crustal magnetic field, discrete auroras are also seen on the nightside. On Earth, low-latitude auroras, which arise from heavy particle precipitation, have also been observed. The primary particles that are responsible for the Jovian aurora may be electrons, protons, or heavy ions originating from its satellite Io. The latter source produces a well-defined “footprint” near the auroral oval. Due to charge transfer, heavy particles spend part of their lifetime as neutral species, and their paths may then diverge from magnetic field lines. In any case, a large fraction of the effects of auroral precipitation is due to secondary electrons, regardless of the identity of the primary particles. In addition to producing emissions of atmospheric species in the visible UV and IR portions of the spectrum, auroral particles ionize and dissociate atmospheric species and contribute to heating the neutrals, ions, and electrons.

88.3.2 The Interaction of Solar Photons with Atmospheric Gases

The number flux of solar photons in a small wavelength interval around λ at an altitude z can, for the most part, be computed from the Beer–Lambert absorption law

$$F_\lambda(z) = F_\lambda^\infty \exp[-\tau(\lambda, z)], \quad (88.17)$$

where F_λ^∞ is the solar photon flux outside the atmosphere, and $\tau(\lambda, z)$ is the optical depth which, in the plane parallel approximation, is given by

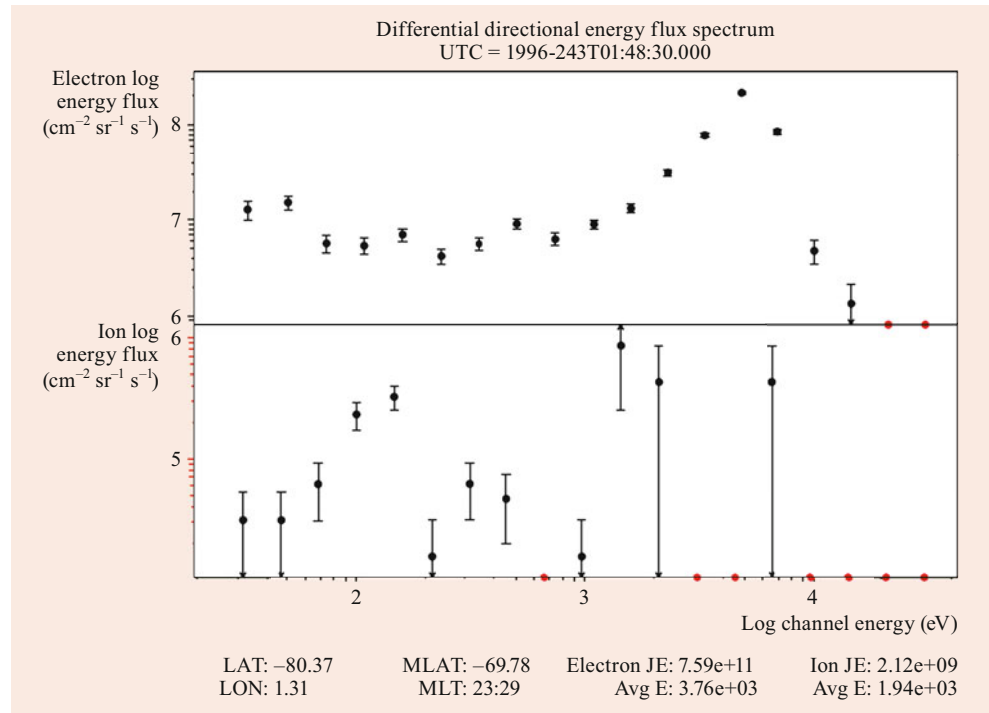
$$\tau(\lambda, z) = \sum_j \int_z^\infty n_j(z') \sigma_j^a(\lambda) \sec \chi \, dz'. \quad (88.18)$$

Here, $\sigma_j^a(\lambda)$ is the absorption cross section of species j at wavelength λ , and the solar zenith angle χ is the angle of the sun with respect to the local vertical.

For χ greater than about 75° , the variation of the solar zenith angle (SZA) along the path of the radiation cannot be neglected; the optical depth must be computed by numerical integration along this path in spherical geometry. For $\chi \leq 90^\circ$, the optical depth is

$$\tau(\lambda, z) = \sum_j \int_z^\infty n_j(z') \sigma_j^a(\lambda) \times \left[1 - \left(\frac{r_o + z}{r_o + z'} \right)^2 \sin^2 \chi \right]^{-0.5} dz'. \quad (88.19)$$

Fig. 88.3 Sample of energy spectrum of precipitating auroral electrons and ions (protons) as measured by the Defense Meteorology Satellite Program (DMSP) satellite. The abscissa is log (base-10) of the energy in electron-volts, and the ordinates are log (base 10) of the energy fluxes of the electrons (*top*) and protons (*bottom*). Also shown are the universal time (UT) geographic latitude (LAT) and longitude (LON), magnetic latitude (MLAT) and longitude (MLT), the integrated energy flux (Electron JE) and ion flux (Ion JE), and average energy (Avg E) of the electrons and ions. From Paxton [42]



For χ larger than 90° , the optical depth is given by

$$\tau(\lambda, z) = \sum_j \left\{ 2 \int_{z_s}^{\infty} n_j(z') \sigma_j^a(\lambda) \times \left[1 - \left(\frac{r_o + z_s}{r_o + z'} \right)^2 \sin^2 90^\circ \right]^{-0.5} dz' - \int_z^{\infty} n_j(z') \sigma_j^a(\lambda) \times \left[1 - \left(\frac{r_o + z}{r_o + z'} \right)^2 \sin^2 \chi \right]^{-0.5} dz' \right\}, \quad (88.20)$$

where z_s is the tangent altitude, the point at which the solar zenith angle is 90° for the path of solar radiation through the atmosphere. Of course, we need not write $\sin 90^\circ$ explicitly in Eq. (88.20), but its inclusion helps to elucidate the origin of the equation.

In a one-species atmosphere, the rate of absorption of solar photons of wavelength λ is

$$q^a(\lambda) = F_\lambda \sigma^a(\lambda) n. \quad (88.21)$$

For an isothermal atmosphere in which $H(z)$ is approximately constant, the absorption maximizes where $\tau(\lambda, z) = 1$. This is a fairly good approximation even for regions of the atmosphere where the $H(z)$ is not constant. The altitude of unit optical depth is shown for wavelengths from X-rays to

the near UV for overhead sun in the terrestrial atmosphere in Fig. 88.4a. Note the accidental window in the O_2 photoabsorption cross sections at Lyman alpha (1216 \AA), which was mentioned above.

Similar plots for Venus, Mars, Jupiter, and Saturn are shown in Fig. 88.4b–e, respectively. N_2 does not absorb longward of about 105 nm, so in the terrestrial atmosphere, O_2 and O_3 are the primary absorbers between 100 and 220 nm, while ozone dominates the absorption for wavelengths in the range 220–320 nm. On Venus and Mars, CO_2 is the main absorber of FUV and EUV radiation, although at wavelengths less than about 100 nm, N_2 , CO, and O also contribute.

On Jupiter and Saturn, H_2 absorbs radiation in the 842–1116 \AA range in discrete transitions to rovibrational levels of excited states, which decay either to rovibrational levels or to the continuum of the ground state. Since the cross sections vary by several orders of magnitude, this leads to oscillations in the depths of penetration, especially in the wings of the lines and gaps between groups of lines. The photons are abruptly stopped near the methane homopause, when the hydrocarbon densities are large enough to absorb the photons.

Similarly, in the thermospheres of Titan and Pluto, absorption by N_2 in the range 850–1020 \AA is like that of H_2 ; it undergoes discrete line absorption to predissociating states. Methane and hydrocarbon hazes are the primary absorbers of UV radiation between 1600 \AA and the effective absorption threshold of N_2 of about 12.14 eV (Strobel and Zhu [7]; Zhang et al. [45]). The threshold for photoabsorption of CH_4 is effectively near 1600 \AA , above which the cross sections are very small (e.g., Huebner et al. [46]). Higher hydrocarbons,

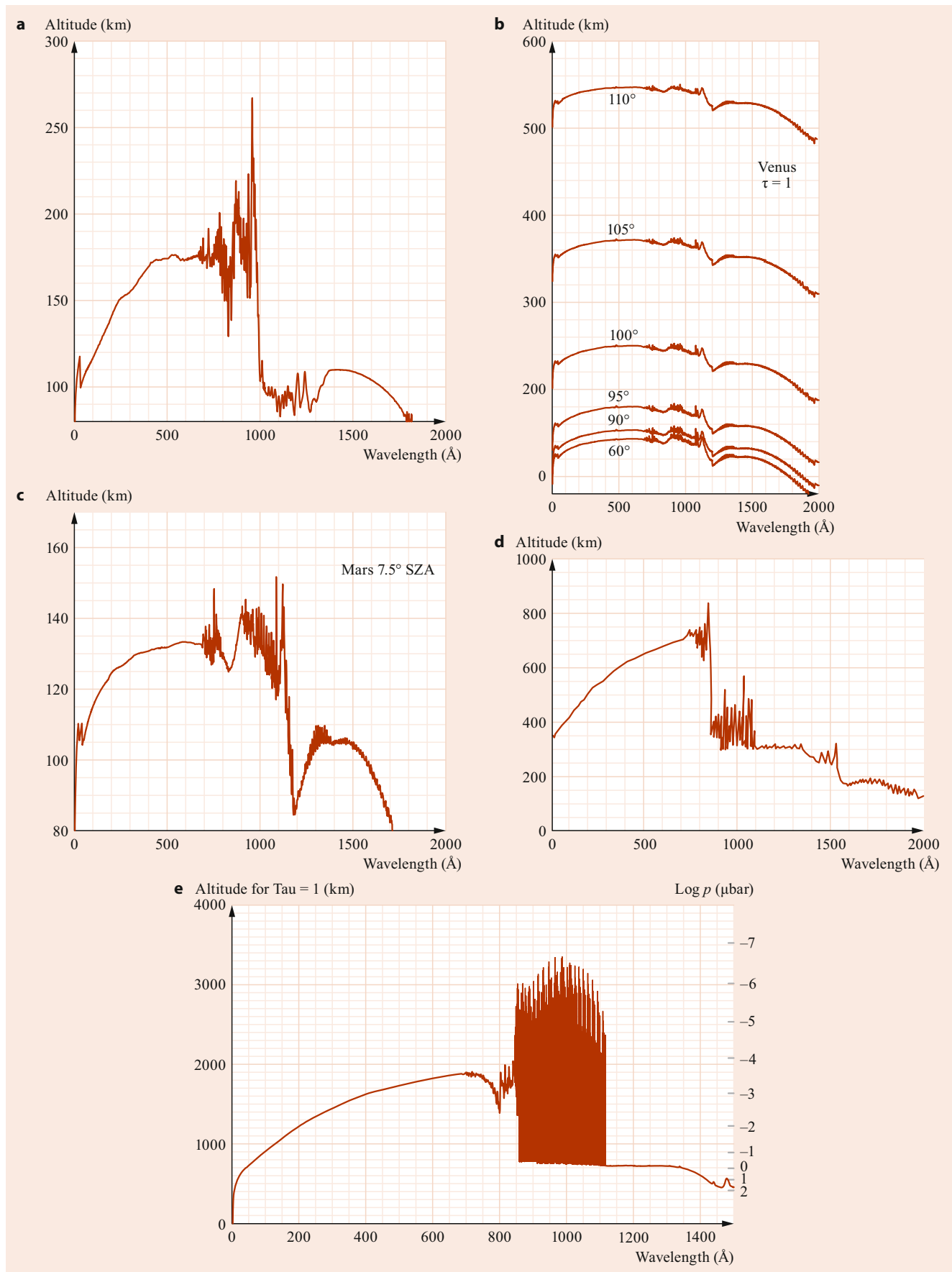
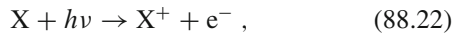


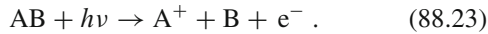
Fig. 88.4 The altitude where $\tau = 1$ versus wavelength: (a) Earth, (b) Venus. The optical depths for various solar zenith angles (SZA) from 60° to 110° . The solar zenith angle is the angle that the line of sight to the sun makes with the vertical. (c) Mars, for near-subsolar conditions (SZA = 5° – 10°) and moderate solar activity, (d) Jupiter [43], (e) Saturn, wavelength range 1–1500 Å, high-resolution values for SZA = 27° . The oscillations in the 842–1116 Å range are characteristic of the high-resolution photoabsorption cross sections of H₂. In this region, the photons can be seen to penetrate to the region of hydrocarbon absorption, where they are abruptly absorbed. Soft X-rays with wavelengths in the range 40–150 Å are absorbed in the altitude range of 700–1000 km above the 1-bar level, from Kim et al. [44] ◀

however, such as C₂H₂, C₂H₄, and C₂H₆, which are formed chemically subsequent to photoabsorption of methane, absorb longward of 1600 Å.

The interaction of UV photons with atmospheric gases produces ions and photoelectrons through photoionization, which may be represented as



and photodissociative ionization



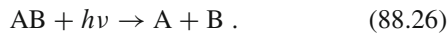
In these equations, X represents any atmospheric species; A is either an atom or a molecular fragment, and AB is a molecule. The energy of the photoelectron in reaction Eq. (88.22) is given by

$$E_{pe} = h\nu - I_X - E_{ex}, \quad (88.24)$$

and in reaction Eq. (88.23) it is

$$E_{pe} = h\nu - E_d - I_A - E_{ex}, \quad (88.25)$$

where I_j is the ionization potential of species j , E_d is the dissociation energy of molecule AB, and E_{ex} is the sum of the internal energy states of the products. Neutral fragments, which may be reactive radicals, are also produced in photodissociation



The rate of ionization of a species j by a photon of wavelength λ at an altitude z is given by

$$q_j^i(\lambda, z) = F_\lambda(z)\sigma_j^i(\lambda)n_j(z), \quad (88.27)$$

where $\sigma_j^i(\lambda)$ is the photoionization cross section. The rate for photodissociation is given by a similar expression, with the photoionization cross section replaced by the photodissociation cross section. The expression above must be integrated over the solar spectrum to give the total rate. In addition, it is often necessary to take into account ionization and/or dissociation to different final internal states of the products, so the partial cross sections or yields are needed.

In the atmospheres of magnetic planets, photoelectrons may travel upward along the magnetic field lines to the conjugate point, where the field line re-enters the atmosphere. In

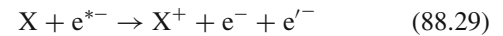
order to model this effect, the differential (with respect to angle) cross sections for photoionization $\sigma_j^i(\lambda, \theta)$ are necessary. The differential cross section is sometimes expressed as

$$\sigma_j^i(\lambda, \theta) = \frac{\sigma_j^i(\lambda)}{4\pi} \left[1 - \frac{1}{2}\beta(\lambda)P_2(\cos\theta) \right], \quad (88.28)$$

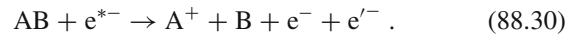
where θ is the angle between the incident photon beam and the ejected electron, P_2 is a Legendre polynomial, and β is an asymmetry parameter.

88.3.3 Interaction of Energetic Electrons with Atmospheric Gases

Suprathermal electrons, which are here denoted e^{*-} and include both energetic photoelectrons and auroral primary electrons, can also ionize species through electron-impact ionization



and electron-impact dissociative ionization

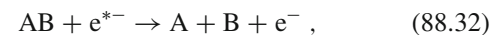


In these reactions, e^- represents the energy degraded photoelectron or primary electron, and e'^- the secondary electron. The energy of the secondary electron $E_{e'}$ in an electron-impact ionization process Eq. (88.29) is given by

$$E_{e'} = E_{e^*} - I_X - E_{ex} - E_e, \quad (88.31)$$

where E_{e^*} is the energy of the primary or photoelectron, E_e is the energy of the degraded primary or photoelectron, and E_{ex} is the internal excitation energy of the product ion or neutral fragments. For the dissociative ionization process Eq. (88.30) the dissociation energy of the molecule must also be subtracted as well.

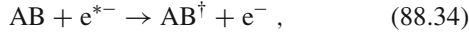
Energetic electrons can also dissociate atmospheric species. In this process,



the energy of the degraded electron is

$$E_e = E_{e^*} - D_{AB} - E_{ex}, \quad (88.33)$$

where D_{AB} is the dissociation energy of molecule AB. Collisions with suprathermal electrons can also promote species to excited electronic, vibrational, or rotational states



where the dagger denotes internal excitation. The energy lost by the electron is, thus, the excitation energy of the species.

In determining the rate of ionization, dissociation, and excitation by photoelectrons, the local energy loss approximation, that is, the assumption that the electrons lose their energy at the same altitude where they are produced, is fairly good near the altitude of peak photoelectron production. The mean free path of an electron near 150 km on Earth is about 30 m. Substantially above the altitude of peak production of photoelectrons, transport of electrons from below is important, and use of the local energy loss assumption causes the excitation, ionization, and dissociation rates to be underestimated. For keV auroral electrons, the computation of the energy deposition of the electrons must consider their transport through the atmosphere. Thus, the elastic total and differential cross sections for electrons colliding with neutral species must be employed, as well as the inelastic cross sections, and the angles through which the electrons scatter must be taken into account.

In general, the excitation rate $q_j^k(z)$ of a species j to an excited level k with a threshold energy E_k at an altitude z by electron impact is given by

$$q_j^k(z) = n_j(z) \int_{E_k}^{\infty} \sigma_j^k(E) \frac{dF(z, E)}{dE} dE , \quad (88.35)$$

where $\sigma_j^k(E)$ is the excitation cross section at electron energy E , and $dF(z, E)/dE$ is the differential flux of electrons (between energies E and $E + dE$). The ionization rate $q_j^i(z)$ of a species with ionization potential I_j due to electron impact is given by

$$q_j^i(z) = n_j(z) \int_{I_j}^{\infty} \int_0^{(E-I_j)/2} \frac{d\sigma_j^i(E)}{dW_s} \frac{dF(z, E)}{dE} dW_s dE , \quad (88.36)$$

where $d\sigma_j^i(E)/dW_s$ is the differential cross section for production of a secondary electron with energy W_s by a primary electron with energy E . The integral over secondary energies W_s terminates at $(E - I_j)/2$ because the secondary electron is by convention considered to be the one with the smaller energy. Since the average energy of photoelectrons is less than 20 eV, the error incurred in cutting off the integrals in Eqs. (88.35) and (88.36) at 200 eV or so, rather than

$(E - I_j)/2$, is not serious, although for high-energy auroral electrons, a larger upper limit may be required.

An estimate of the number of ionizations in a gas produced by a primary electron with energy E_p is E_p/W_{ip} , where W_{ip} is the energy loss per ion pair produced, which approaches a constant value as the energy of the electron increases. This constant is also found to increase as a function of fractional ionization because of the larger amount of energy lost to thermal electrons as the fractional ionization increases. Empirical values are available for W_{ip} for many gases, and usually fall in the range 30–40 eV [47].

The total loss function or stopping cross section for an electron with incident energy E in a gas j is given by the expression

$$L_j(E) = \sum_k \sigma_j^k(E) W_j^k + \int_0^{(E-I_j)/2} (I_j + W_s) \frac{d\sigma_j^i(E)}{dW_s} dW_s , \quad (88.37)$$

where W_j^k is the energy loss associated with excitation of species j to excited state k . The differential cross section is usually adopted from an empirical formula that is normalized so that

$$\sigma_j^i(E) = \int_0^{(E-I_j)/2} \frac{d\sigma_j^i(E)}{dW_s} dW_s , \quad (88.38)$$

where $\sigma_j^i(E)$ is the total ionization cross section at primary electron energy E . One formula in common use is that employed by *Opal* et al. [48] to fit to their data

$$\frac{d\sigma_j^i(E)}{dW_s} = \frac{A(E)}{1 + (W_s/\bar{W})^{2.1}} , \quad (88.39)$$

where $A(E)$ is a normalization factor, and \bar{W} is an empirically determined constant, which has been found to be equal to within a factor of about 50% to the ionization potential for a number of species.

For energy loss due to elastic scattering by thermal electrons, an analytic form of the loss function such as that proposed by *Swartz* et al. [49] may be used

$$L_e(E) = \frac{3.37 \times 10^{-12}}{E^{0.94} n_e^{0.03}} \left(\frac{E - k_B T_e}{E - 0.53 k_B T_e} \right)^{2.36} , \quad (88.40)$$

where T_e is the electron temperature and n_e is the number density of ambient thermal electrons.

For high-energy auroral electrons, the rate of energy loss per electron per unit distance over the path s of the electrons

in the atmosphere can be estimated using the continuous slowing down approximation (CSDA) as

$$-\frac{dE}{ds} = \sum_j n_j(z) L_j(E) \sec \theta + n_e(z) L_e(E) \sec \theta, \quad (88.41)$$

where θ is the angle between the path of the primary electron s and the local vertical. In the CSDA, all the electrons of a given energy are assumed to lose their energy continuously and at the same rate. The rate of energy loss ($-dE/ds$) is integrated numerically over the path of the electron, which degrades in energy until it is thermalized. In this approximation, inelastic processes are assumed to always scatter the electrons forward, so cross sections that are differential in angle are not required. Because electrons actually lose energy at different rates, however, and because elastic and inelastic scattering processes do change the direction of the electrons, the CSDA gives an estimate for the rates of electron energy loss processes that is increasingly inaccurate as the energy of the electron decreases.

In practice, discrete energy loss of electrons can be easily treated numerically if the local energy loss approximation is valid. The spectrum of electrons must be divided into energy bins that are smaller than the energy losses for the processes, and the integrals in Eqs. (88.35) and (88.36) are replaced by sums over energy bins. Since elastic scattering of electrons by neutrals changes mostly the direction of the incident electron, and not its energy, only inelastic processes need be considered. In order to compute excitation and dissociation rates, only integral cross sections are required; the scattering angle is unimportant. For ionization, of course, the energy distribution of the secondary electrons must be considered but not the scattering angles of either the primary or secondary electrons. Below the lowest thresholds for excitations, energetic electrons lose their energy in elastic collisions with thermal electrons. The process of energy loss to thermal electrons is often approximated as continuous, rather than discrete.

The collision frequency ν_j^k for a discrete electron-impact excitation process k of a species j is given by

$$\nu_j^k(E) = n_j(z) v_e(E) \sigma_j^k(E). \quad (88.42)$$

For energy loss due to elastic scattering from thermal electrons, a pseudo-collision frequency ν_e may be defined as

$$\nu_e(E) = \frac{1}{\Delta E} \left(-\frac{dE}{dt} \right), \quad (88.43)$$

where ΔE is the grid spacing in the calculation, and the energy loss rate is

$$-\frac{dE}{dt} = \nu_e(E) n_e L_e(E), \quad (88.44)$$

where L_e is taken from, for example, Eq. (88.40).

Since the energy bins should be smaller than the typical energy loss in order to obtain accurate rates for the excitation processes, it is often convenient to treat rotational excitation also as a continuous process, with a pseudo-collision frequency similar to that for elastic scattering from ambient electrons Eq. (88.43) with

$$-\frac{dE}{dt} = \nu_e(E) n_j L_j^{\text{rot}}(E), \quad (88.45)$$

where the loss function for rotational excitation is given by

$$L_j^{\text{rot}}(E) = \sum_J \eta_j^J \sum_{J'} \sigma_j^{J,J'}(E) W_j^{J,J'}. \quad (88.46)$$

In this expression, η_j^J is the fraction of molecules j in the rotational level J , and $\sigma_j^{J,J'}$ is the measured or computed cross section for electron-impact excitation of species j from rotational state J to rotational state J' , and $W_j^{J,J'}$ is the associated energy loss.

The slowing down of high energy auroral primary or the concomitant high energy secondary electrons arises from both elastic and inelastic scattering processes and cannot be treated using the local energy loss approximation. In solving the equations for electron transport, the angle through which the primary electron is scattered, as well as the change in energy of the primary electron and the production of any secondaries, must be taken into account. Thus, differential cross sections for the elastic and inelastic scattering of electrons by neutral species are required. The detailed equations for electron transport have been presented by, for example, *Rees* [50].

Several methods for approximating the energy deposition of auroral electrons are currently in use. The CSDA has already been discussed, but it provides only a rough approximation to the depth of penetration of the electrons, and the rates of excitation, ion production, and other energy loss processes. In the two-stream approximation, the electrons are assumed to be scattered in either the forward or the backward direction [51]. Implementation of this method requires only the backscattering probabilities, rather than complete differential cross sections. The method has been generalized to multistream models, in which the solid angle range of the electrons is divided into 20 or more intervals, so more or less complete differential cross sections are required [52, 53]. Monte Carlo methods have also been used to model auroral electron precipitation [54].

88.4 Ionospheres

88.4.1 Ionospheric Regions

The division of the dayside ionosphere into regions is based on the structure of the terrestrial ionosphere, which consists of overlapping layers of ions. These layers are the result of

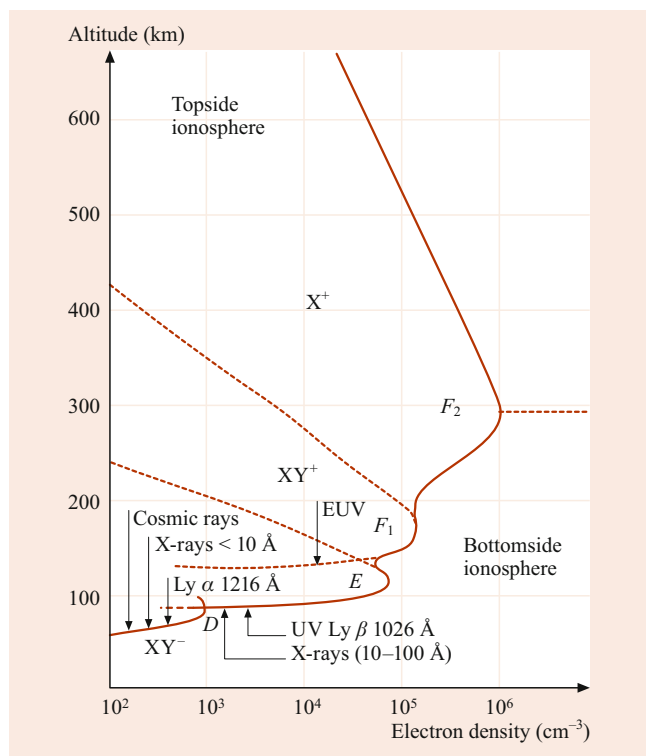


Fig. 88.5 Ionospheric regions and primary ionization sources. After Bauer [55]

changes both in the composition of the thermosphere and in the sources of the ionization, and are shown schematically in Fig. 88.5. The major molecular ion layer is the F_1 layer, which is produced by absorption of EUV (100–1000 Å) photons by the major thermospheric species, and occurs where the ion production maximizes. The E layer is below the F_1 layer and is produced by shorter and longer wavelength photons that are absorbed deeper in the atmosphere: soft X-rays and Lyman β , which can ionize O_2 and NO (Fig. 88.4a). In the D region, the densities of negative ions become appreciable, and large densities of positive cluster ions appear. These ions are produced by harder X-rays, with $\lambda \lesssim 10$ Å, and Lyman α , which penetrates to about 75 km, where it ionizes NO . The highest altitude peak in the terrestrial ionosphere is the F_2 peak, which occurs near or slightly below 300 km, where the major ion is O^+ . In the ionospheres of the outer planets, an F_2 peak is formed from H^+ . The F_1 region is formed from H_3^+ , and near or below that layer by hydrocarbon ions, as shown for Saturn in Fig. 88.10e. The peak density in the F_2 region occurs where the chemical lifetime of the (atomic) ion is comparable to the characteristic time for transport by diffusion ($\approx H^2/D$).

88.4.2 Sources of Ionization

As discussed in Sect. 88.3, ionization can be produced either by solar photons and photoelectrons during the daytime or

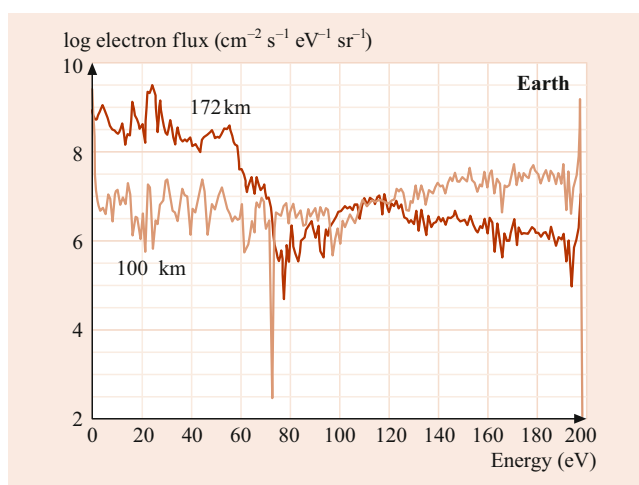


Fig. 88.6 Primary photoelectron spectrum for the terrestrial atmosphere at 172 km (near the F_1 peak) and at 100 km. The spectrum at 100 km is significantly harder than that at 172 km

by energetic particles and secondary electrons during auroral events. Photoelectrons have sufficient energy to carry out further ionization if they are produced by photons with $\lambda \lesssim 500$ Å. These photons penetrate further and exhibit larger solar activity variations than longer-wavelength ionizing photons. Thus, the ionization rate due to photoelectrons peaks below the main photoionization peak. Primary flux spectra of photoelectrons produced near the F_1 peak (172 km) and below the ion peak (100 km) are shown in Fig. 88.6. The primary spectrum at the ion peak consists mostly of lower-energy electrons, whereas at 100 km, the lower-energy electrons are depleted, and there are relatively larger fluxes of electrons with $E \gtrsim 50$ eV. Figure 88.7 shows the primary and steady-state photoelectron spectra near the ion peaks on Venus and Titan.

The major ions produced in the ionospheres of the Earth and planets are usually those from the major thermospheric species: N_2^+ , O_2^+ , and O^+ on Earth; CO_2^+ , O^+ , N_2^+ , and CO^+ on Venus and Mars; H_2^+ , H^+ , CH_4^+ , and He^+ on the outer planets; N_2^+ , N^+ , and CH_4^+ (and higher hydrocarbon ions) in the ionospheres of Titan and Pluto; and N_2^+ , N^+ , CH_4^+ , and C^+ in the ionosphere of Triton. In the presence of sufficient neutral densities, however, ion–molecule reactions transform ions whose parent neutrals have high ionization potentials to ions whose parent neutrals have low ionization potentials. This is a rigorous rule only for charge transfer reactions, but it applies more often than not in other ion–molecule reactions as well.

Because of transformations by ion–molecule reactions, the major ions in the F_1 regions of the dayside ionospheres of Earth, Venus, and Mars are O_2^+ and NO^+ , despite the large differences in composition between the thermosphere of the Earth and the thermospheres of Venus and Mars. A diagram illustrating the ion chemistry in the ionospheres of the terrestrial planets is shown in Fig. 88.8. The vertical positions of the ions in this figure represent the relative ionization po-

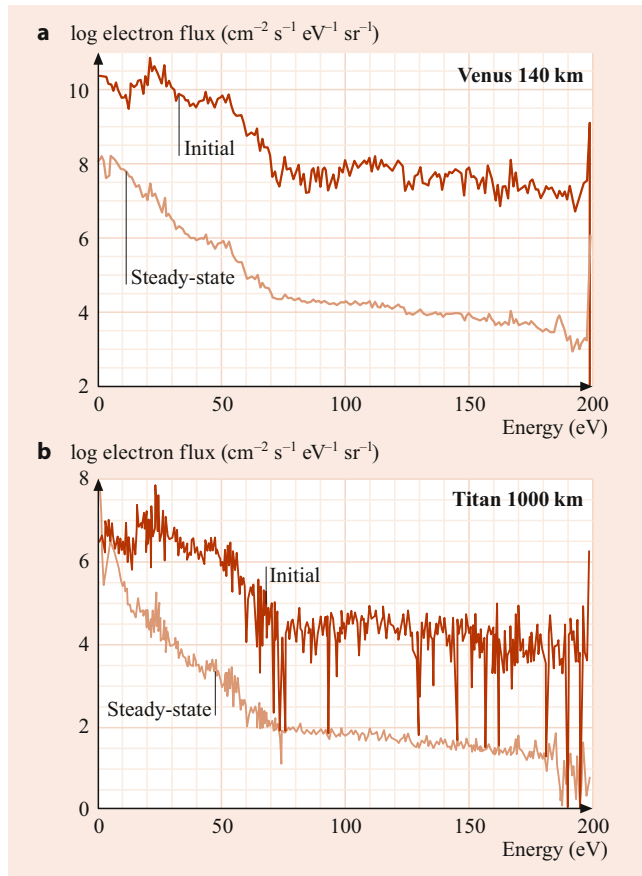


Fig. 88.7 Computed primary and steady-state spectra for photoelectrons near the F_1 peak on Venus at 1 eV resolution (a), and Titan at 0.5 eV resolution (b). For Titan, no precipitation of electrons from Saturn's magnetosphere is assumed. The steady-state spectra are averaged over three intervals in both plots

tentials of the parent neutrals. In regions where there are sufficient neutral densities the ionization flows downward.

Table 88.10 shows ionization potentials (I_p) for several major and minor species present in planetary thermospheres. Major atmospheric species generally have $I_p \gtrsim 12\text{--}16$ eV ($\lambda < 775\text{--}1000$ Å). Only a few species can be ionized by the strong solar Lyman alpha line (1216 Å, 10.2 eV), including NO, and a few hydrocarbon radicals and stable species, such as CH₃, C₂H₅, C₄H₂, and benzene. Metal atoms, which are produced in the lower thermospheres and mesospheres of planets from ablation of meteors, have very low ionization potentials, and some can be ionized by photons with wavelengths longer than 2000 Å.

In ionospheres where hydrogen and sufficient neutral densities are present, ionization flows from protonated species whose parent neutrals have small proton affinities to species formed by protonation of neutrals that have large proton affinities. There are no *in situ* measurements of the ion composition of the outer planets, but models predict that H₃⁺ and hydrocarbon ions dominate the lower ionospheres. In regions where meteor ablation occurs, metal ions may also be found.

Table 88.10 Ionization potentials (I_p) of common atmospheric species (computed with data taken from [56], except as noted)

High I_p		Medium I_p		Ionized by Ly α	
Species	I_p (eV)	Species	I_p (eV)	Species	I_p (eV)
He	24.59	H ₂ O	12.612	C ₄ H ₂	10.18
Ne	21.56	CH ₄	12.51	CH ₃	9.73
N ₂	15.58	O ₂	12.07	NO	9.264
H ₂	15.43	C ₂ H ₆	11.52	C ₂ H ₅	8.13
N	14.53	C ₂ H ₂	11.40	HCO	8.10
CO	14.01	C	11.26	C ₃ H ₇	8.09
CO ₂	13.76	C ₃ H ₈	10.95	Mg	7.65
O	13.62	CH	10.64	<i>trans</i> -HCNH	7.0 ^a
H	13.60	C ₂ H ₄	10.51	<i>cis</i> -HCNH	6.8 ^a
HCN	13.60	CH ₂	10.40	Ca	6.11
OH	13.00	S	10.35	Na	5.14

^a From [57]

Many ion–molecule reactions proceed at or near gas kinetic (or collision) rates. The interaction of an ion with a nonpolar molecule is dominated by the ion–induced dipole interaction, for which the interaction potential is $-\frac{1}{2}\alpha_d q^2/r^4$, where α_d is the polarizability of the neutral, q is the charge on the ion, and r is the distance between the particles. The Langevin–Gioumousis–Stevenson (LGS) or merely the Langevin rate coefficient, k_L , is then given by

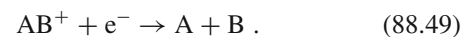
$$k_L = 2\pi q \left(\frac{\alpha_d}{\mu} \right)^{1/2}, \quad (88.47)$$

where μ is the reduced mass of the two species. For a singly charged ion, with α_d in Å³ and μ in atomic mass units, this formula reduces to $2.34 \times 10^{-9}(\alpha_d/\mu)^{1/2}$. The rate coefficient for an ion with a polar molecule is

$$k_d = \frac{2\pi q}{\mu^{1/2}} \left[\alpha_d^{1/2} + c\mu_d \left(\frac{2}{\pi k_B T} \right)^{1/2} \right], \quad (88.48)$$

where μ_d is the dipole moment, and c is a constant that is unity in the locked dipole approximation and is about 0.1 in the average dipole orientation (ADO) theory. The value of c has been shown to be a function of $\mu_D/\alpha^{1/2}$ and can be determined either experimentally or graphically, as proposed by *Su* and *Bowers* [58]. Proton transfer reactions in particular have been shown to proceed at rates that are close to the Langevin (or capture) rates. Theories for ion–quadrupole interactions have also been developed, and the resulting formulas can be found in, for example, the review by *Su* and *Bowers* [58]. Measured rate coefficients for ion–molecule reactions have been compiled by *Anicich* et al. [59], *Ikezo* et al. [60], and *Anicich* [61].

Loss of ionization in planetary atmospheres proceeds mainly by dissociative recombination of molecular ions, which may be represented by



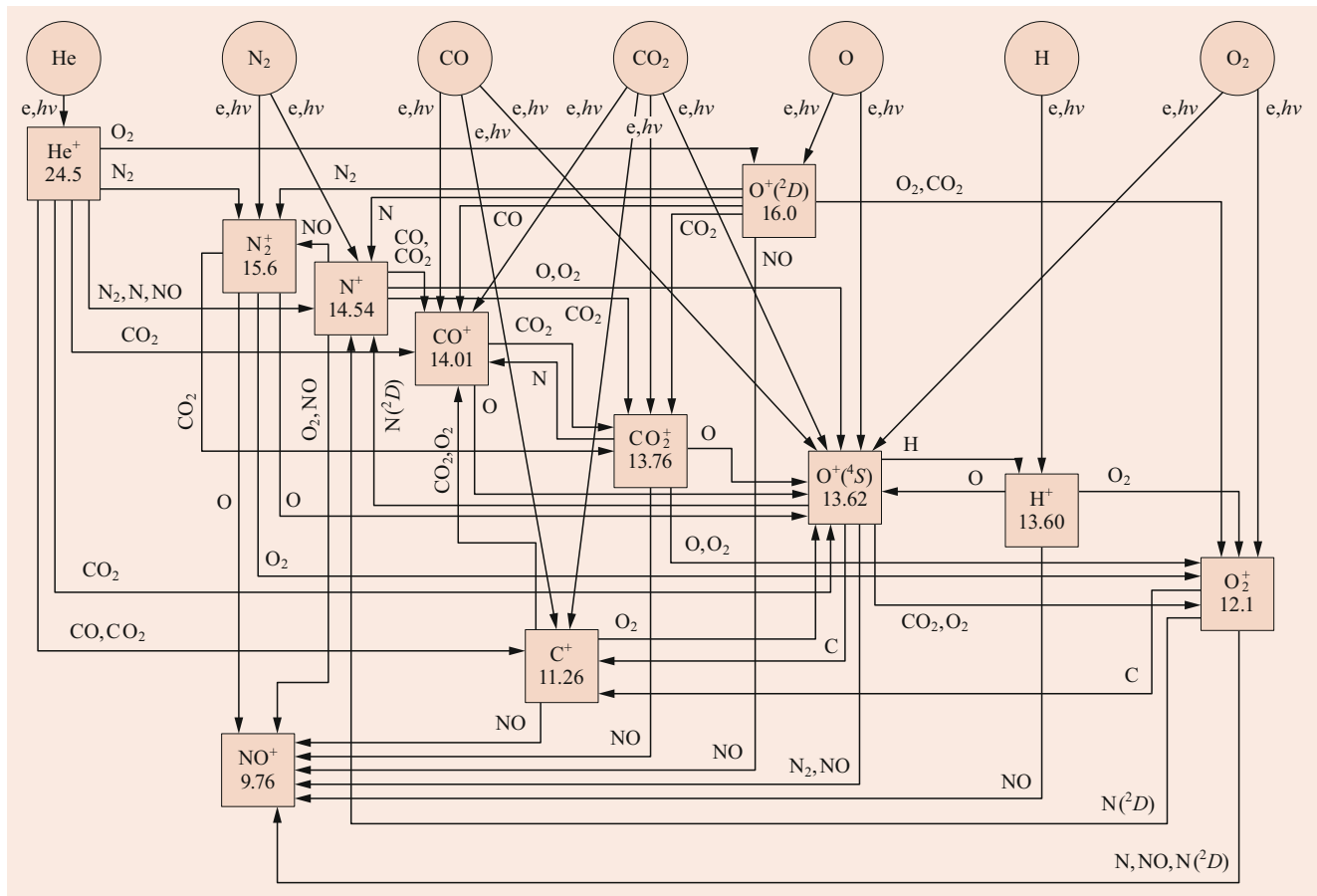


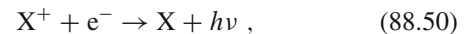
Fig. 88.8 Ion chemistry in the ionospheres of the terrestrial planets. The numbers under the names of the ions indicate the ionization potentials of the parent neutral. In the presence of sufficient neutral densities, the ionization flows downward, and the importance of dissociative recombination for the molecular ions increases as the ionization potentials of the parent neutrals decrease

Dissociative recombination coefficients are characteristically large, about $10^{-7} \text{ cm}^3 \text{ s}^{-1}$, at the electron temperatures T_e typical of planetary ionospheres, which are usually within a factor of a few of the neutral $T \approx 150\text{--}800 \text{ K}$ near the molecular ion density peak. Daytime peak electron densities tend to be in the range $10^4\text{--}10^6 \text{ cm}^{-3}$; fractional ionizations are small, about 10^{-5} , near the F_1 peak.

The relative importance of ion–molecule reactions and dissociative recombination in the destruction of a particular ion is determined by the relative densities of electrons and neutrals with which the ions can react. In general, molecular ions whose parent neutrals have high I_P are transformed by ion–molecule reactions preferentially to loss by dissociative recombination, and their peak densities occur higher in the atmosphere. Ions for which dissociative recombination is an important loss mechanism near the ion peaks of the terrestrial planets include NO^+ and O_2^+ , and in the atmospheres of the outer planets, H_3^+ and hydrocarbon ions. For ions whose parent neutrals have very high I_P , such as N_2^+ and H_2^+ , dissociative recombination is rarely important as a loss process, except at very high altitudes. They may, however, be im-

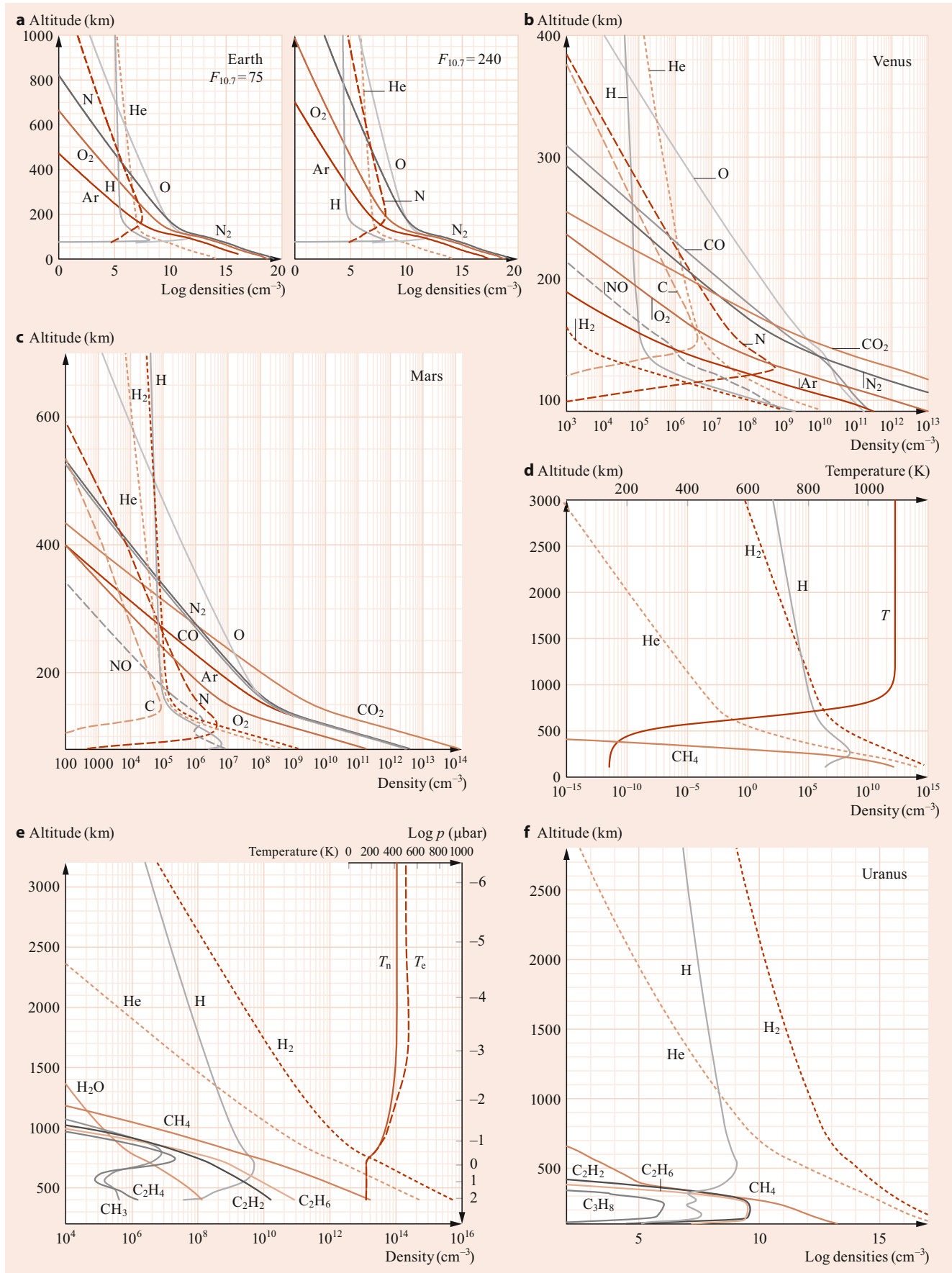
portant as a source of vibrationally or electronically excited fragments or hot atoms.

Atomic ions may be destroyed by radiative recombination



but the rate coefficients are small, less than $10^{-12} \text{ cm}^3 \text{ s}^{-1}$ at the typical T_e of planetary ionospheric peaks [62], and decrease with increasing electron temperature. Atomic ions may dominate at high altitudes, where neutral densities are low, but in such regions, loss by diffusion may be more important than chemical recombination. The ions diffuse downward to altitudes where the neutral densities are higher and are then destroyed in ion–molecule reactions. The major ions in the topside ionospheres of the planets tend to be atomic ions: O^+ in the ionospheres of Earth and Venus and H^+ in the ionospheres of the outer planets. On Mars, however, the O^+ peak density appears not to exceed that of O_2^+ even at high altitudes.

Model thermospheres for Earth and selected planets and satellites are shown in Fig. 88.9a–j. Measured or computed



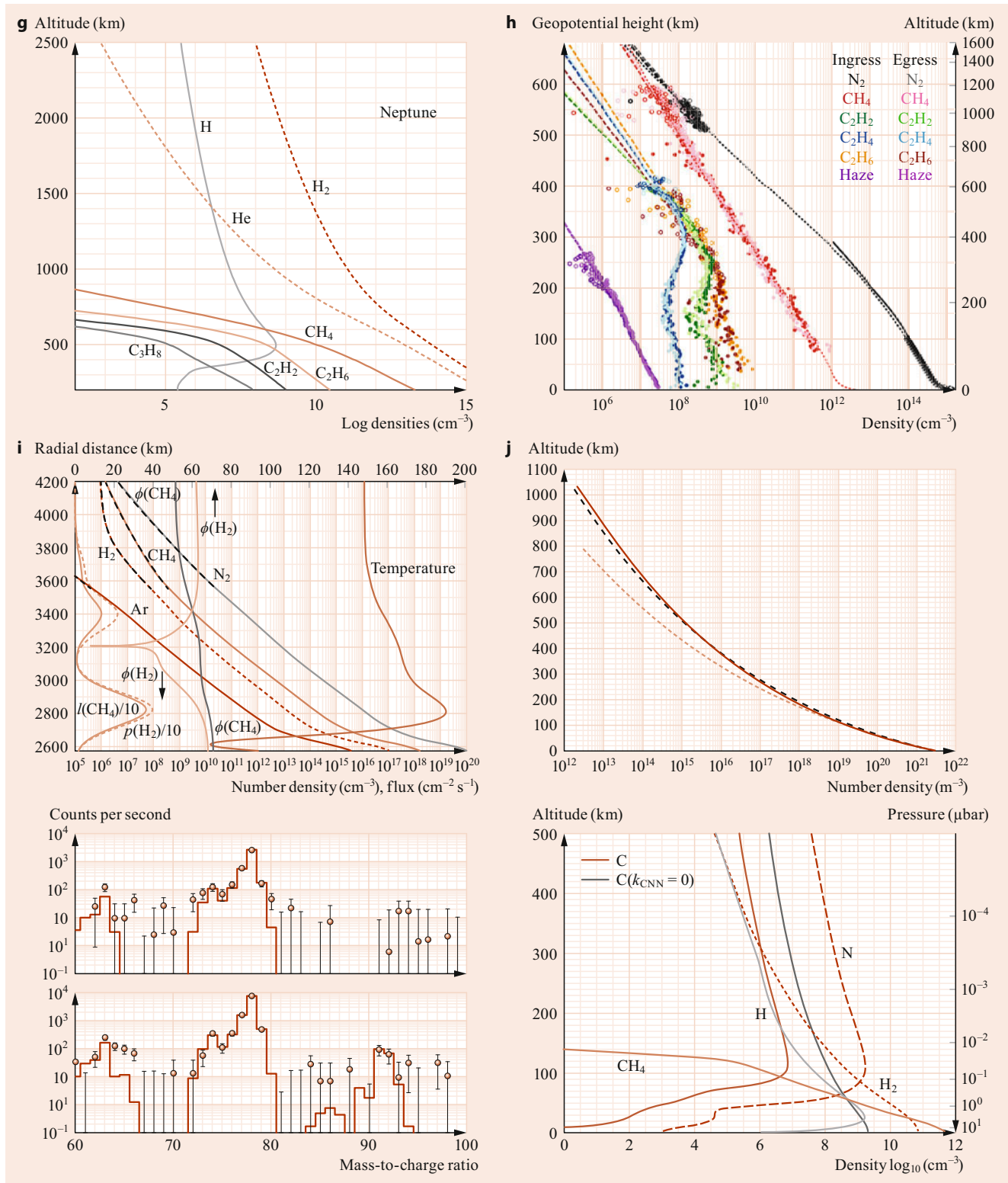


Fig. 88.9 Model thermospheres for the Earth, planets, and satellites. The curves are number density profiles and are labeled by the species they represent. (a) Earth, based on the NRLMSIS model of [9] for a latitude of 0° and a local time of noon for low (*left*) and high (*right*) solar activities. (b) High solar activity model of Venus, based on the model of [2] for 15° N latitude 15:00 LT. (c) Moderate ($F_{10.7} = 120$) solar activity model of Mars, based on MAVEN NGIMS (Neutral Gas and Ion Mass Spectrometer) measurements that are averaged over 5 km bins from March, April, and May 2015 for the SZA range of 5° – 10° . The CO_2 , O, N_2 , CO, Ar, and He profiles (*solid curves*) are fitted to data. The N, C, and NO profiles (*dashed curves*) are computed self-consistently from a model, as are the H and H_2 profiles. (d) Jupiter, basic JGITM (Jupiter Global Ionosphere-Thermosphere Model) after Egert et al. [63]. (e) Saturn, after Kim et al. [44] from the model from Vervack and Moses [5]. The neutral and electron temperatures are also shown, as well as C-1 and C-2 hydrocarbons and H_2O . (f) Uranus, plotted with model data from Moses and Poppe [64]. (g) Neptune, plotted with model data from Moses and Poppe [64]. (h) Pluto. Densities of species derived from line-of-sight integrated densities obtained from solar occultations of the New Horizons spacecraft as a function of geopotential height and altitude. The species are labeled by the color-coded names in the upper right corner. The circles are from data, and the dashed curves, as well as the dotted curves for N_2 and CH_4 are from a model. The N_2 densities at altitudes below about 110 km are from the radio occultation profiles carried out by the New Horizons REX instrument. Also shown (in purple) are the extinction coefficients multiplied by 10^{15} of the hazes. Both ingress and egress values are shown. From Young et al. [8]. (i) (top) Titan model, after Strobel [65]. The measured densities of N_2 , Ar, CH_4 , and H_2 are shown with dashed curves for radial distances above about 3500 km. (The radius of the surface is 2575 km.) The solid curves of these species' densities are from a model. Also shown are the upward fluxes of CH_4 and upward and downward fluxes of H_2 , denoted by $\phi(\text{CH}_4)$, and $\phi(\text{H}_2)$, respectively, and the adopted temperature profile. The loss rates of methane and production rates of H_2 are also shown in units of $\text{cm}^{-3} \text{s}^{-1}$ divided by 10. (bottom) The diversity of neutral species with mass/charge ratios of 60–99, in counts s^{-1} found in the atmosphere of Titan by the Ion and Neutral Mass Spectrometer (INMS) instrument on the Cassini spacecraft. The range of mass/charge is adapted for investigations of benzene and its derivatives. Masses less than 60 amu are not shown but are also present due to the presence of higher hydrocarbons that are ultimately formed from photolysis of methane. The points are the averaged values over the 960–980 km range, and the solid line is from a model. From Vuitton et al. [66]. (j) (top) Triton total neutral densities (largely N_2) as a function of altitude, after Strobel and Zhu [7]. The three curves represent models with different neutral temperature profiles. The red (solid), black (long dashes), and brown (short dashes) curves are those for exospheric temperatures of 97, 90, and 75 K, respectively. Note that the units of number density are SI units of m^{-3} rather than the traditional cm^{-3} . (bottom) Density profiles of minor species on Triton, including H_2 , N, H, and CH_4 . The two profiles that represent C densities are for slight differences in the chemistry ◀

ion density profiles for the Earth and selected planets and satellites are shown in Fig. 88.10a–j.

88.4.3 Nightside Ionospheres

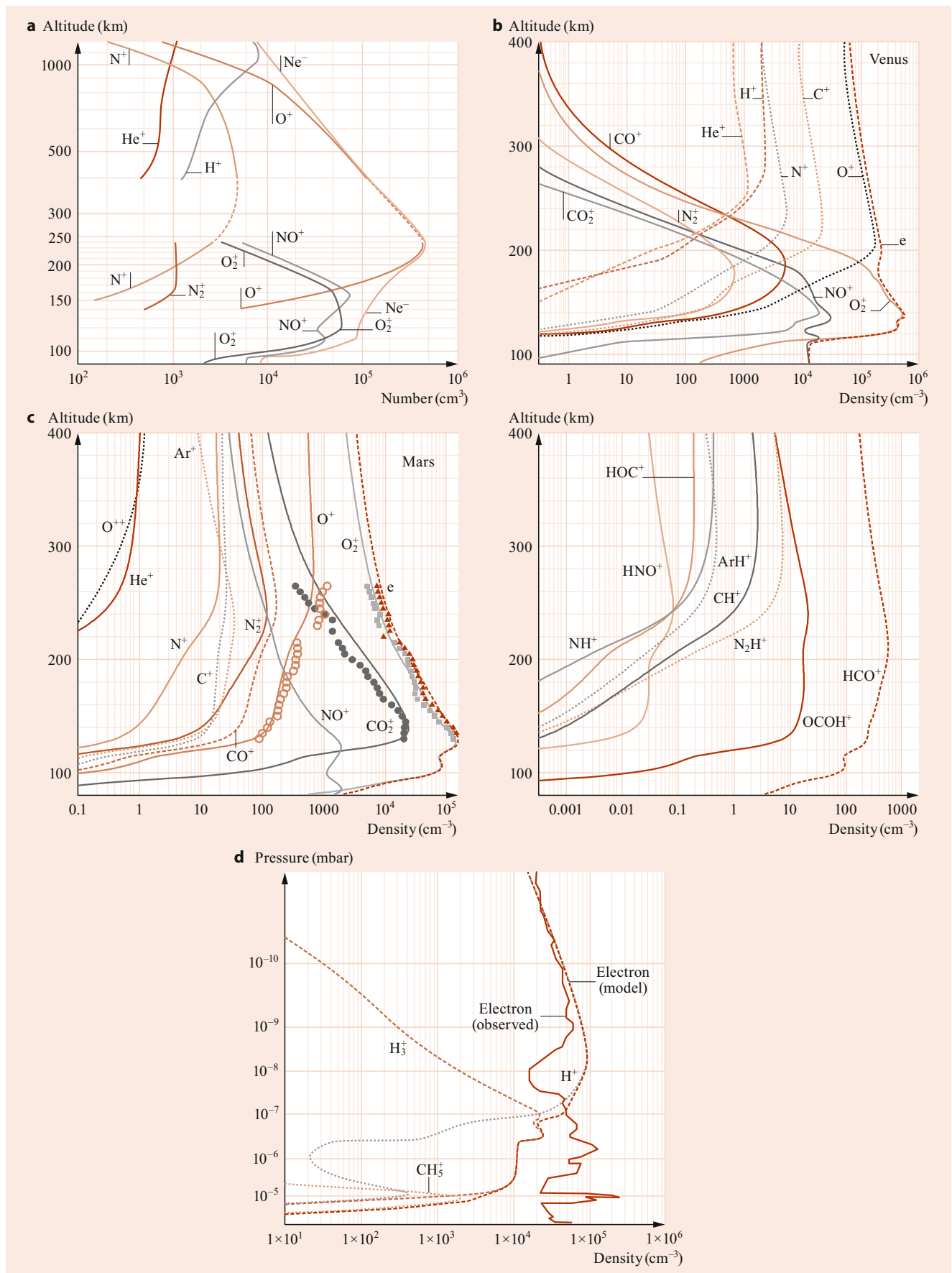
Nightside ionospheres can result from several sources, including remnant ionization from the dayside, like O^+ in the terrestrial ionosphere. While the lower molecular ion layers recombine, the F_2 peak persists through the night, although it rises, and the peak density is reduced by a factor of 10. Electron density profiles for day and night at high and low solar activities are shown in Fig. 88.11. In the auroral regions of the Earth, the precipitating electrons may also produce significant ionization, which maximizes in the midnight sector of the auroral oval.

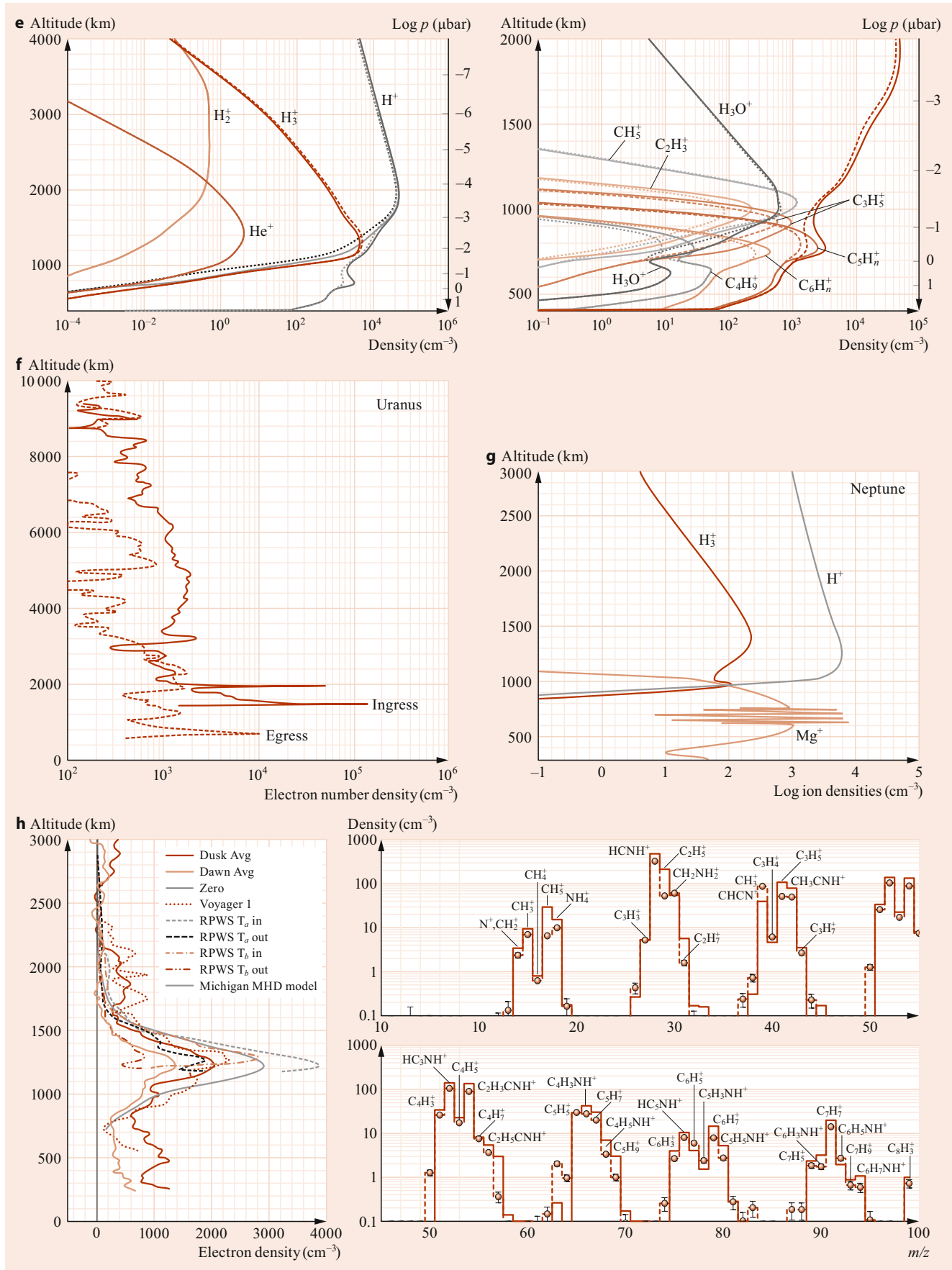
The nightside ionosphere of Venus is highly variable but has been shown to contain the same ions as the dayside ionosphere. The ion and electron densities are, however, smaller by factors of 10 or more than those of the dayside ionosphere, and the average peak in the electron density profile is about $(1\text{--}2) \times 10^4 \text{ cm}^{-3}$. It is produced by a combination of precipitation of suprathermal electrons that have been observed at high altitudes in the umbra, and transport of atomic ions (mostly O^+) at high altitudes from the dayside. For Mars, geometry limits the solar zenith angle probed by radio occultation (RO) measurements beyond the terminator of the nightside to values of about 130° . The

ionosphere is sunlit to about 105° SZA. The nightside ionosphere has been probed by radio occultation experiments on the Mariner 9 orbiter, the Viking spacecraft [76], and by the Mars Global Surveyor (MGS) spacecraft radio sciences (RS) experiment [77]. Until recently, there was no composition information about the nightside ionosphere of Mars.

More recently, however, the Neutral Gas and Ion Mass Spectrometer (NGIMS) on the MAVEN spacecraft has measured ion densities in situ on Mars from periapsis of about 150 km (with occasional “deep dips” down to 125–130 km) to ≈ 500 km at all SZAs, including the nightside. On both the dayside and the nightside of Mars, in addition to the major ions found on the dayside, populations of protonated species, including water-group ions, that is, those that contain only H and O were measured (e.g., Benna et al. [78]; Fox [79]; Fox et al. [80]).

The nightside ion densities for SZAs from 110° to 120° were shown to be smaller by an order of magnitude or more than those of the near-terminator dayside 75° – 80° SZA, and the composition in the lower ionosphere changed from O_2^+ and CO_2^+ to O_2^+ , NO^+ , and HCO^+ , the latter three of which have longer chemical lifetimes than CO_2^+ . For long-lived molecular ions, the major loss process is usually dissociative recombination, but the dissociative recombination coefficient of HCO^+ is particularly uncertain. As for all the known nightside ionospheres, the nightside ion densities have been shown to be quite variable (Girazian et al. [81]).





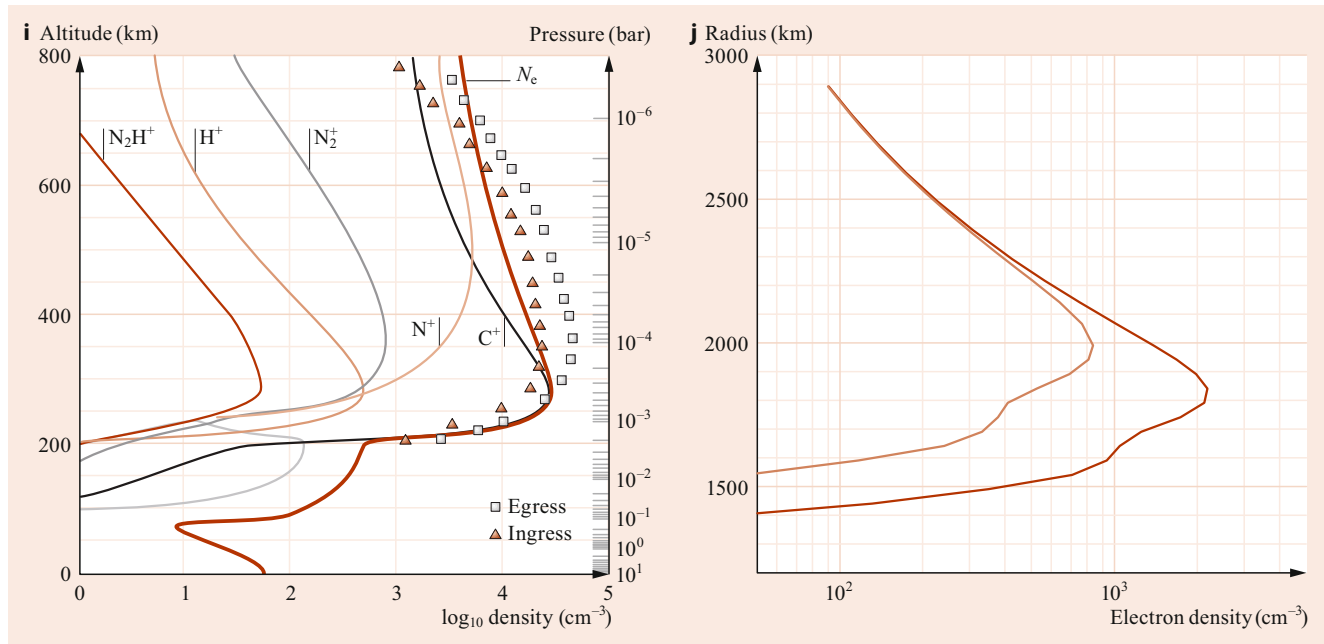


Fig. 88.10 Ionospheric density profiles. (a) Measured ion density profiles for Earth [67]. (b) Computed ion density profiles for Venus, for high solar activity and a solar zenith angle of 45° . (c) Ion density profiles for Mars, for moderate solar activity ($F_{10.7} = 120$) and a SZA range of 5° – 10° . (Left) major ions and (right) protonated species. The model densities of the major ions O_2^+ , O^+ , and CO_2^+ are compared to the MAVEN NGIMS measurements. Not shown are the density profiles of water ions (H^+ , H_2^+ , H_3^+ , OH^+ , OH_2^+ , H_3O^+). The model has no ambient water other than that produced through ion chemistry. (d) Jupiter, precomet impact model without hydrocarbon ion chemistry. After *Maurellis and Cravens* [68]. (e) Saturn, after *Kim et al.* [44], who adopted the model of *Vervack, Jr. and Moses* [5]. The total electron density profiles are shown with a thick curve. The SZA is 27° , and the magnetic dip angle is 45° . (Left) model density profiles of the H-containing ions and He^+ . (Right) model density profiles of hydrocarbon ions and H_3O^+ . (f) Uranus. Voyager 2 radio occultation electron density profiles for ingress and egress. From *Lindal et al.* [69]. (g) Neptune. From a model of *Lyons* [70], also [71]. (h) (Left) Titan. Electron density profiles measured by various instruments including the Voyager 1 radio occultation and in situ measurements of electron densities by the Cassini RPWS (Radio and Plasma Wave Science) LP (Langmuir probe) on the first two flybys, Ta and Tb, along with the dawn and dusk averages from the Cassini radio occultations, and one model. From *Kliore et al.* [72]. (Right) Titan. Cassini INMS (Ion and Neutral Mass Spectrometer) ion density measurements compared to a model at 1100 km. The abscissa is the mass/charge ratios from 0 to 55 is shown on the upper panel, and those from 45 to 100 are shown on the lower panel. From the review by *Vuitton et al.* [73]. (i) Triton. From the model of *Strobel and Summers* [74]. (j) Pluto. Upper limits to electron density profiles from a model (*Hinson et al.* [37]). That for the subsolar point (SZA = 0°) is shown in red, and that for the terminator region is in orange. No ionosphere was detected, however, by the New Horizons' radio science experiment

On satellites whose trajectories take them into the magnetospheres of the planet that they orbit, such as Titan around Saturn, or Triton around Neptune, ionization on the dayside or nightside may be produced by the impact of energetic electrons from these magnetospheres. The nightside ion densities of Titan have been shown to be a factor of ≈ 4 smaller than those of the dayside (*Ågren et al.* [82]).

At this time, there is no information available about the nightside ionospheres of the outer planets. Radio occultations can only probe the near-terminator ionospheres because of geometrical considerations. Just as on the dayside, only modeling can predict the identity of the major ions.

88.4.4 Ionospheric Density Profiles

Density profiles of molecular ions have often been approximated as idealized Chapman layers. A Chapman layer of ions is one in which the ions are produced by photoionization and

lost locally by dissociative recombination. The ionization rate q^i in a one-species Chapman layer for monochromatic radiation is given by

$$q^i = F\sigma^i n, \quad (88.51)$$

where σ^i is the ionization cross section, and $F = F^\infty \exp[-\tau(z)]$ is the local solar flux. For an isothermal atmosphere, the scale height is approximately constant and, therefore, $n = n_0 \exp(-z/H)$. Sometimes an ionization efficiency η^i is defined such that

$$\sigma^i = \eta^i \sigma^a. \quad (88.52)$$

Near threshold, the ionization efficiency for molecules is usually about 0.3–0.7, but it increases rapidly to 1.0 at shorter wavelengths, usually less than $\approx 600 \text{ \AA}$.

Since the maximum ionization rate in an isothermal atmosphere occurs where the optical depth ($\tau = nH\sigma^a \sec \chi$)

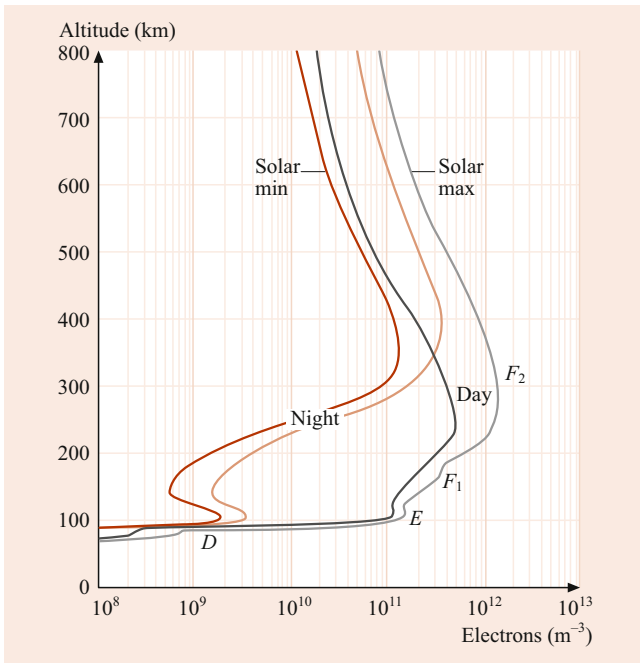


Fig. 88.11 Typical midlatitude ionospheric electron density profiles for sunspot maximum and minimum, day and night. After *Richmond* [75]

is unity and, therefore, $n = 1/(\sigma^a H \sec \chi)$, the maximum ionization rate in a Chapman layer is

$$q_{\max,\chi}^i = \frac{F^\infty}{e} \frac{\sigma^i}{\sigma^a H \sec \chi} = \frac{q_{\max,0}^i}{\sec \chi}. \quad (88.53)$$

If the altitude of maximum ionization for overhead sun is defined as $z = 0$, then $n_0 = (\sigma^a H)^{-1}$, and, expressing F^∞ in terms of $q_{\max,0}^i$, the ionization rate is

$$q^i(z) = q_{\max,0}^i \exp\left(1 - \frac{z}{H} - \sec \chi e^{-z/H}\right). \quad (88.54)$$

It is apparent that at high altitudes ($z \rightarrow \infty$), the ionization profile follows that of the neutral density, and below the peak ($z \rightarrow -\infty$), the ionization rate rapidly approaches zero. As the solar zenith angle increases, the peak rises, and the magnitude of the density maximum decreases. Figure 88.12 shows a production profile for an idealized Chapman layer on both linear and semilog plots. The asymmetry with respect to the maximum is more obvious for the semilog plot.

If photochemical equilibrium prevails, the production rate of the major molecular ion is equal to the loss rate due to dissociative recombination

$$q^i(z) = \alpha_{\text{dr}} n_i n_e = \alpha_{\text{dr}} n_i^2, \quad (88.55)$$

where α_{dr} is the dissociative recombination coefficient, n_i is the ion density, and n_e is the electron density. Therefore, the

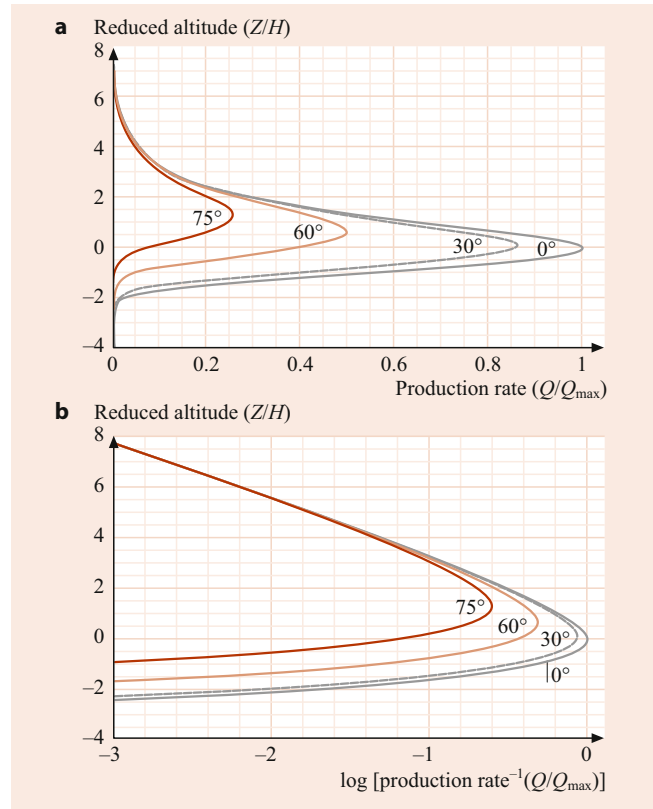


Fig. 88.12 Chapman production profile as a function of altitude on linear (a) and semilog plots (b). The production rate is divided by the maximum production rate and the altitude by the scale height H , which is assumed to be constant. The origin on the altitude scale corresponds to the point of maximum absorption for overhead sun

density of an ion in a Chapman layer (in the photochemical equilibrium region) is given by

$$\begin{aligned} n_i(z) &= \left(\frac{q^i(z)}{\alpha_{\text{dr}}}\right)^{1/2} \\ &= \left(\frac{q_{\max,0}^i}{\alpha_{\text{dr}}}\right)^{1/2} \exp\left(\frac{1}{2} - \frac{z}{2H} - \frac{1}{2} \sec \chi e^{-z/H}\right). \end{aligned} \quad (88.56)$$

Actual ion density profiles differ from the idealized Chapman profile for several reasons. First, ionization is produced by photons over a range of wavelengths, which do not all reach unit optical depth at the same altitude. Second, thermospheres are usually not isothermal near the altitude of peak ion production. Third, photoionization is supplemented by photoelectron-impact ionization, which peaks lower in the atmosphere. Fourth, the major ion produced is often transformed by ion–molecule reactions before it can recombine dissociatively; finally, the underlying neutral atmosphere undergoes changes with SZA. Nonetheless, the idealized concept of the Chapman profile is useful in attaining a general understanding of the shape of ion profiles and their behavior as the solar zenith angle changes. In addition, ion

layers produced by auroral precipitation may take on a similar appearance to a Chapman-type layer, although energetic electrons are not extinguished, as are photons, in ion production. Although attempts have been made to express real ionospheric profiles in terms of Chapman layer theory, ion layers rarely, if at all, fit true, or even slightly modified Chapman layers.

88.4.5 Ion Diffusion

Above the photochemical equilibrium layer of the ionosphere, upward and downward transport of ions must be considered. The motions of ions, neutrals, and electrons are coupled, and the momentum equation, which determines the fluxes or velocities of the ions must take into account these interactions. The interaction of an ion, denoted by a subscript i , with a neutral species denoted by a subscript n , is through the ion-induced dipole attraction or, for the diffusion of an ion through its parent neutral, by resonant charge transfer. For the former process, the ion-neutral diffusion coefficient is given by

$$D_{in} = \frac{k_B T}{m_i \bar{v}_{in}}, \quad (88.57)$$

where m_i is the mass of the ion, and the ion-neutral momentum transfer collision frequency

$$\bar{v}_{in} = 2.21 \pi \frac{n_n m_n}{m_i + m_n} \left(\frac{\alpha_n e^2}{\mu_{in}} \right)^{1/2}, \quad (88.58)$$

where α_n is the polarizability of the neutral species (*Dalgarno et al. [83], Schunk and Nagy [84]*). For the resonant charge transfer interaction, the diffusion coefficient is

$$D_{in}^{ct} = \frac{3(\pi/2)^{1/2}}{8n_n \bar{Q}_{in}^{ct}} \left(\frac{k_B T_i}{m_i} \right)^{1/2} \frac{1}{(1 + T_n/T_i)^{1/2}}, \quad (88.59)$$

where \bar{Q}_{in}^{ct} is the average charge transfer cross section [85]. It should be noted that the forgoing effect does not apply to accidental resonances, since it arises from the indistinguishability of the nuclei.

The momentum transfer collision frequency for Coulomb interactions between an ion i and another ion or electron denoted by the subscript s is

$$\bar{v}_{is} = \frac{16\pi^{1/2}}{3} \frac{n_s m_s}{m_i + m_s} \left(\frac{\mu_{is}}{2k_B T_{is}} \right)^{3/2} \frac{e_i^2 e_s^2}{\mu_{is}^2} \ln \Lambda, \quad (88.60)$$

where e_s is the charge on species s , $\ln \Lambda$ is related to the Debye shielding length, and $T_{is} = (m_s T_i + m_i T_s)/(m_i + m_s)$

is a reduced temperature. Numerically, $\ln \Lambda$ is about 15, and the collision frequency is approximately [84]

$$\bar{v}_{is} = 1.27 \frac{Z_i^2 Z_s^2 \mu_{is}^{1/2} n_s}{m_i T_{is}^{3/2}}, \quad (88.61)$$

where Z is the species charge number, μ and m are in amu, and the number density is in units of cm^{-3} .

The ion densities can be computed by solving the ion continuity equation, which is similar to Eq. (88.7) for neutral species, and in one dimension is

$$\frac{\partial n_i}{\partial t} + \frac{\partial \Phi_i}{\partial z} = P_i - L_i, \quad (88.62)$$

where the ion flux is given by $\Phi_i = n_i w_i$. In general, it is impossible to solve the momentum equation for the ion diffusion velocity w_i in closed form, except for the special cases of a single major ion and of a minor ion moving through a dominant ion species. If only motion of the ions parallel to magnetic field lines is considered, the vertical velocity of a dominant ion (for which $n_i \approx n_e$) moving through a stationary neutral atmosphere is

$$w_i = -D_a \sin^2 I \times \left(\frac{1}{n_i} \frac{dn_i}{dz} + \frac{m_i g}{k(T_e + T_i)} + \frac{1}{T_e + T_i} \frac{d(T_e + T_i)}{dz} \right), \quad (88.63)$$

where I is the magnetic dip angle, and the ambipolar diffusion coefficient is defined as

$$D_a = \frac{k_B(T_e + T_i)}{m_i \bar{v}_{in}}. \quad (88.64)$$

For a minor ion i diffusing through a major ion species j , its velocity is given by

$$w_i = -\frac{k_B T_i / m_i}{\bar{v}_{ij} + \bar{v}_{in}} \times \left(\frac{1}{n_i} \frac{dn_i}{ds} + \frac{T_e / T_i}{n_e} \frac{dn_e}{ds} + \frac{m_i g}{k_B T_i} + \frac{1}{T_i} \frac{d(T_e + T_i)}{ds} \right) - \frac{\bar{v}_{ij} w_j}{\bar{v}_{ij} + \bar{v}_{in}}. \quad (88.65)$$

For regions in which there are large gradients in the ion or electron temperatures, thermal diffusion may also be important in determining the ion density profiles, especially those of light ions such as H^+ and He^+ . Equations for ion distributions in which thermal diffusion is included have been presented by, for example, *Schunk and Nagy [84]*; see also references therein.

88.5 Neutral, Ion, and Electron Temperatures

The temperature distribution in planetary thermospheres/ionospheres can be modeled by solving the equation for conservation of energy, which, in a simplified form in the vertical direction is

$$n_m \frac{\mathcal{N}}{2} k_B \frac{\partial T_m}{\partial t} - \frac{\partial}{\partial z} \left(\kappa_m \frac{\partial T_m}{\partial z} \right) = Q_m - L_m \quad (88.66)$$

where \mathcal{N} is the number of degrees of freedom (three for an atom and five for a diatomic molecule), the subscript m refers to the neutrals, ions or electrons, κ_m is the thermal conductivity, Q_m is the volume heating rate, and L_m is the volume cooling rate. If horizontal variations are considered, the model becomes multidimensional, and advective terms must be added to the equations. The values of T_m are also affected by compression or expansion due to subsidence or upwelling, respectively. Viscous heating may be a factor where there are local regions of intense energy input, such as in auroral arcs. These terms are not shown in the energy equation above but may be found in standard aeronomy texts, such as *Banks and Kockarts* [85], *Whitten and Popoff* [86], *Rees* [50], and *Schunk and Nagy* [87]. For planets with intrinsic magnetic fields, the electrons and ions are constrained to move along magnetic field lines, and the second term on the left-hand side of Eq. (88.66) must be multiplied by a factor $\sin^2 I$.

The neutral thermospheres of planets are mostly heated by absorption of solar radiation in the 10–2000 Å range, although on planets with powerful auroras, electron precipitation may be an important source of heat. Absorption of EUV radiation (100–1000 Å) largely results in ionization of the major thermospheric species, in which most of the excess energy is carried away by the photoelectron. The photoelectron, however, may produce further dissociation or excitation of neutral species along the path to thermalization, and these processes may result in neutral heating. Photons near and longward of ionization thresholds in the FUV may lose their energy in photodissociation, in which the excess energy of the photon appears as kinetic or internal energy of the fragments.

Chemical reactions that follow ionization or dissociation release much of the absorbed solar energy as heat. Although the partitioning of kinetic energy released between the product species can easily be determined by conservation of energy and momentum, the fraction of energy that appears as internal or kinetic energy must be determined by measurements or theoretical calculations. If vibrationally or electronically excited states are produced in these interactions, however, the energy may be radiated to space, thus producing cooling. This may occur promptly if the radiative lifetime is short, or subsequent to an energy transfer process from a long-lived metastable species to a species for which radiation to a lower state is allowed. If the metastable species is quenched, however, its energy can also appear as

heat. Thus, the energy partitioning in chemical reactions and in the interactions of photons and photoelectrons with atmospheric species is important in understanding the temperature structure of thermospheres.

A heating efficiency ϵ is often defined as the fraction of energy absorbed at a given altitude that appears locally as heat. The heating efficiencies are in the range 30%–40% in the terrestrial lower thermosphere. Above 200 km, the heating efficiency decreases because the energy of the important metastable species $O(^1D)$ is lost as radiation rather than by quenching [88]. The heating efficiencies in the thermospheres of Venus and Mars are about 20% from 100 to 200 km [89, 90], and on Titan, they range from 20% to 30% from 800 to 2000 km. A column averaged heating efficiency for the Jovian thermosphere has been computed as 53% [91].

On Venus and Mars, CO_2 is the major absorber of far UV radiation, whereas on the Earth, O_2 plays that role. In the F_1 regions of the ionospheres of the terrestrial planets, dissociative recombination of molecular ions tends to be the major source of heating. Below the F_1 peak, photodissociation and neutral–neutral reactions, including quenching of metastable species, dominate. Since CH_4 is a very strong absorber, the major heating mechanisms in the thermosphere of Titan are photodissociation and neutral–neutral reactions, both above and below the F_1 peak. The few data that exist suggest that electron-impact dissociation is unimportant as a source of neutral heating, although further measurements would certainly be of benefit. Profiles of the heat sources in the terrestrial thermosphere and those of Mars and Titan are also shown in Fig. 88.13.

Important cooling processes in planetary thermospheres include downward transport of heat by molecular and eddy conduction and infrared cooling from rotational and vibrational excitation of IR active species such as NO, CO, and CO_2 . Excitation of the fine structure levels of atomic oxygen and subsequent emission at 63 and 147 μm also plays a role in cooling the neutral species in the thermospheres of the terrestrial planets. In the outer planets and their satellites, hydrocarbon molecules such as CH_4 and C_2H_2 are the primary thermospheric IR radiators. The global circulation may play a role in redistributing the heat that is deposited in the dayside or auroral thermosphere [95, 96].

In order to model heating rates, cross sections for processes in which solar photons or photoelectrons interact with neutral species, and rate coefficients and product yields for chemical reactions of ions and neutral atmospheric species are necessary. In addition, it is necessary to know, for example, how much of the energy released appears as internal energy of the products in chemical reactions and how much appears as kinetic energy of the products. Knowledge of energy transfer processes, including vibration–vibration (V–V) and translation–vibration (T–V) transfer between atmospheric species is also important. For example, a particularly

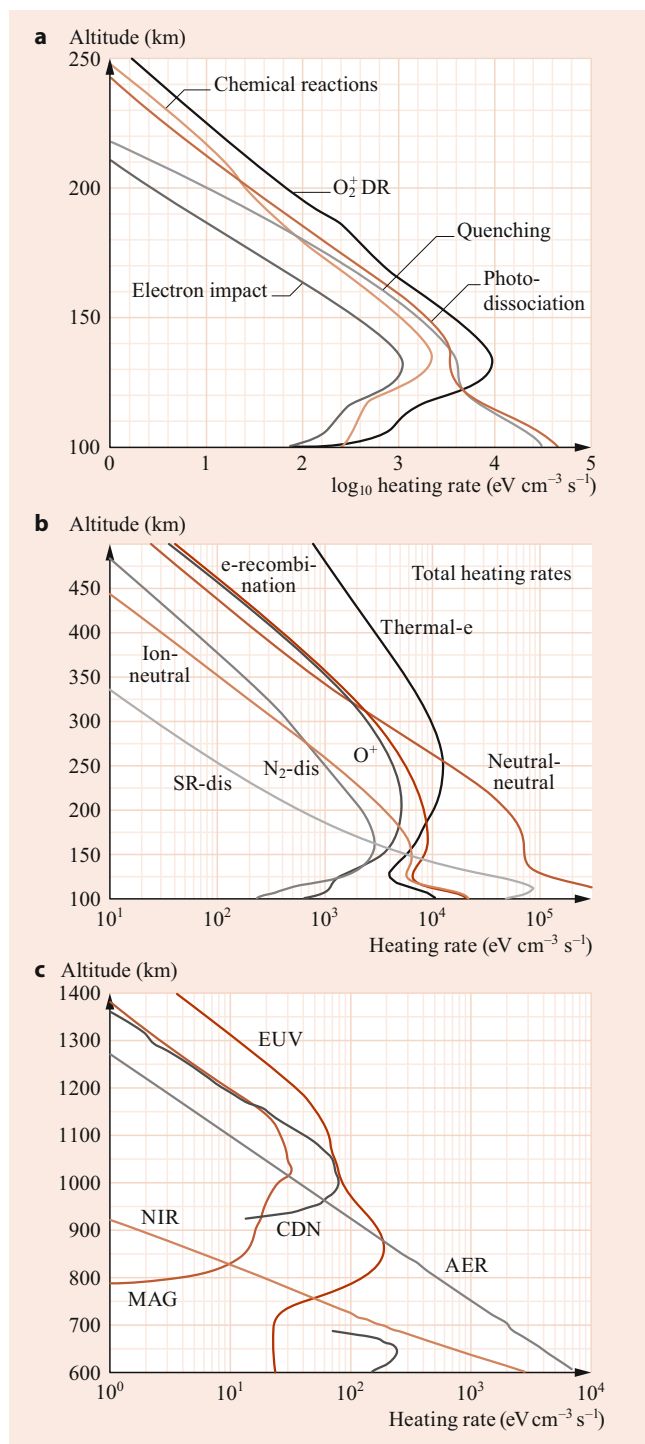


Fig. 88.13 Heating rates for the thermospheres of (a) Mars, (b) Earth, and (c) Titan. In (b), the curve labeled “Thermal-e” is the heating rate due to collisions between the neutrals and electrons, “O⁺” is the heating rate due to reactions of O⁺ with neutrals; “ion-neutral” is the heating rate due to other exothermic neutral-ion reactions. “Neutral-neutral” is the heating rate due to neutral-neutral chemical reactions; “e-recombination” is the heating rate due to dissociative recombination reactions; N₂-dis is the heating rate due to dissociation of N₂; SR-dis is the heating rate due to absorption by O₂ in the Schuman–Runge bands and continuum. From Richards [92]. In (c), the heating rates in the atmosphere of Titan due to five sources are shown. EUV represents solar heating, CDN represents heating due to thermal conduction, AER represents heating by aerosols, MAG is the heating due to magnetospheric ion precipitation, NIR is the heating due to absorption of the near infrared bands of CH₄. After Snowden [93]; see also Snowden and Yelle [94] ◀

important cooling process for the thermospheres of the terrestrial planets is excitation of the CO₂ 15 μm ν₂ bending mode in collisions with energetic O, and subsequent radiation [97]. The deexcitation rate coefficient is several percent of gas kinetic, which is anomalously large for a V–T process [98].

In the lower ionosphere, the electrons and ions are in thermal equilibrium with the neutral species, but at higher altitudes the plasma temperatures deviate from the neutral tem-

peratures. Near the F₁ peak, T_e is usually larger than T_i, but T_i begins to diverge from T_e at higher altitudes. The source for the energetic electrons on the dayside is largely photoionization, which, as discussed above, produces photoelectrons with average energies in the 15–20 eV range. In slowing down, these electrons lose their energy in inelastic processes with neutrals until E ≈ 1–2 eV. At this point, elastic scattering by the thermal electron population becomes the dominant energy loss process for the suprathermal electrons and the major source of heat for the thermal electrons. Other heating mechanisms for thermal electrons include deactivation of electronically or vibrationally excited species, and, for the terrestrial planets, quenching of the fine structure levels of O.

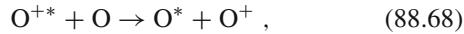
As for the neutrals, heat in the electron gas is redistributed by conduction at a rate that depends on the electron thermal conductivity. This quantity is inversely proportional to the sum of the momentum transfer collision frequencies of electrons with ions, neutrals, and ambient electrons. Cooling mechanisms for thermal electrons include Coulomb collisions with ions, rotational excitation of molecules, and, for the terrestrial planets, excitation of the fine structure levels of O. Because of the large mass difference, elastic collisions between neutrals and electrons are not effective in transferring kinetic energy.

In the ionosphere, T_i is elevated above T_n at high altitudes principally because of Coulomb collisions of ions with energetic electrons. Another potentially important source of heat input to the ions near the ion peak is exothermic ion–neutral reactions, including quenching of metastable ions, such as O⁺(²D), by neutrals. In the presence of electric fields, Joule heating may be important and can cause T_i to exceed T_e.

The ions cool in elastic collisions and resonant charge transfer with neutral species, which are characterized by lower temperatures than the ions. The cooling rate for elastic collisions is

$$L_{\text{in}} = -2n_i \frac{m_i}{m_i + m_n} \bar{v}_{\text{in}} \frac{3}{2} k_B (T_i - T_n). \quad (88.67)$$

Collisions between ions and neutrals (other than their parents) are dominated by the ion-induced dipole interaction. The momentum transfer collision frequency $\bar{\nu}_{in}$ is, thus, given by Eq. (88.58). Resonant charge transfer between an ion and its parent neutral, such as



leads to very effective ion cooling, which dominates at sufficiently high temperatures.

Examples of T_i and T_e profiles are shown in Fig. 88.14a–f for various bodies, including Earth, Venus, Mars, Titan, and Saturn. The International Reference Ionosphere (IRI) temperature profiles for the terrestrial thermosphere show the close coupling between the electrons, ions, and neutrals at low altitudes and the ions and electrons at high altitudes; T_i increases with increasing solar activity at low altitudes and approaches T_e at high altitudes. The values of T_e and T_i are about 2000–3000 K at 1000 km on the dayside and slightly smaller on the nightside [105]. Electron and ion temperatures in the terrestrial ionosphere have been discussed by Rees [50], Banks and Kockarts [85], Whitten and Popoff [86], and Schunk and Nagy [106].

In the Venus atmosphere, T_e and T_i were measured by instruments on the PVO, including the Langmuir Probe (LP) (e.g., Brace et al. [107]) and the Retarding Potential Analyzer (ORPA) (e.g., Miller et al. [99]). The values of T_i were found to be in the range 2000–2500 K at high altitudes and to be insensitive to the solar zenith angle, except beyond about 150° SZA, where T_i increases to values of 5000–6000 K [99]. Measured values of T_e do not vary appreciably with the solar zenith angle; the high altitude values are in the range 4000–6000 K [108].

The STATIC (Superthermal and Thermal Ion Composition) experiment on the MAVEN spacecraft found that T_i on Mars decouples from the T_n near 180–200 km and approaches values of about 1000–1200 K at high altitudes (McFadden [100]). The electron temperatures on Mars have been measured by the LPW (Langmuir Probe and Waves) instrument on the MAVEN spacecraft (e.g. Ergun et al. [101]); T_e is predicted to diverge from the T_n in the lower ionosphere (120–130 km) and has been found to approach values of 3000–4000 K at high altitudes.

The plasma temperatures on Titan have been measured and predicted by models. Electrons from Saturn's magnetosphere may interact with the Titan ionosphere during the part of its orbit that is within Saturn's magnetosphere. In this case, T_e is predicted to increase to values that are about 5000 K near 2000 km. The models of Richard et al. [103] showed that the predicted altitude profiles of the ion and electron temperatures depend greatly on the magnetic field orientation near a given location. Their computed results are shown in Fig. 88.14d and e. They deviate significantly from the val-

ues measured by the Cassini Plasma Spectrometer (CAPS) and the Radio and Plasma Wave Science/Langmuir Probe (RPWS/LP) on the Cassini spacecraft (Ågren et al. [82]; Crary et al. [102]).

88.6 Luminosity

The luminosity that originates in the atmospheres of the planets is generally classified as dayglow, nightglow, or aurora. Dayglow is the luminosity of the dayside atmosphere that occurs as a more or less direct result of the interaction of solar radiation with atmospheric gases. Among the sources of dayglow are photodissociative excitation and simultaneous photoionization and excitation. Dayglow may also include scattering of solar radiation by processes that are selective, such as resonance scattering by atoms and fluorescent scattering by molecules, but the term generally excludes nonselective scattering processes, such as Rayleigh scattering.

In resonance scattering, the absorption of a photon by an atom in the ground state causes a (usually dipole allowed) transition to a higher electronic state



followed by the emission of a photon as the state decays back to the ground state



The wavelength of the emitted radiation is very nearly the same as that of the radiation absorbed. The cross section for absorption of a line in the solar spectrum is

$$\sigma_{12}^a(\nu) = \frac{\varpi_2}{\varpi_1} \frac{c^2}{8\pi\nu^2} A_{21} \phi(\nu), \quad (88.71)$$

where the subscript 1 indicates the lower state and 2 the upper state, ϖ is the statistical weight of the state, and $\nu = c/\lambda$ is the frequency of the transition; A_{21} is the Einstein A coefficient for the transition, and $\phi(\nu)$ is the lineshape function, which in this equation is normalized so that the integral over all frequencies is unity.

If the linewidth is determined by the spread of velocities of the species, the lineshape $\phi(\nu)$ is a Doppler (Gaussian) profile

$$\phi_D(\nu) = \frac{c}{u\nu_0\sqrt{\pi}} \exp\left[-\left(\frac{\nu - \nu_0}{\nu_0}\right)^2 \frac{c^2}{u^2}\right], \quad (88.72)$$

where ν_0 is the frequency at the line center. The variable $u = (2k_B T/m)^{1/2}$ is the modal velocity of a gas in thermal

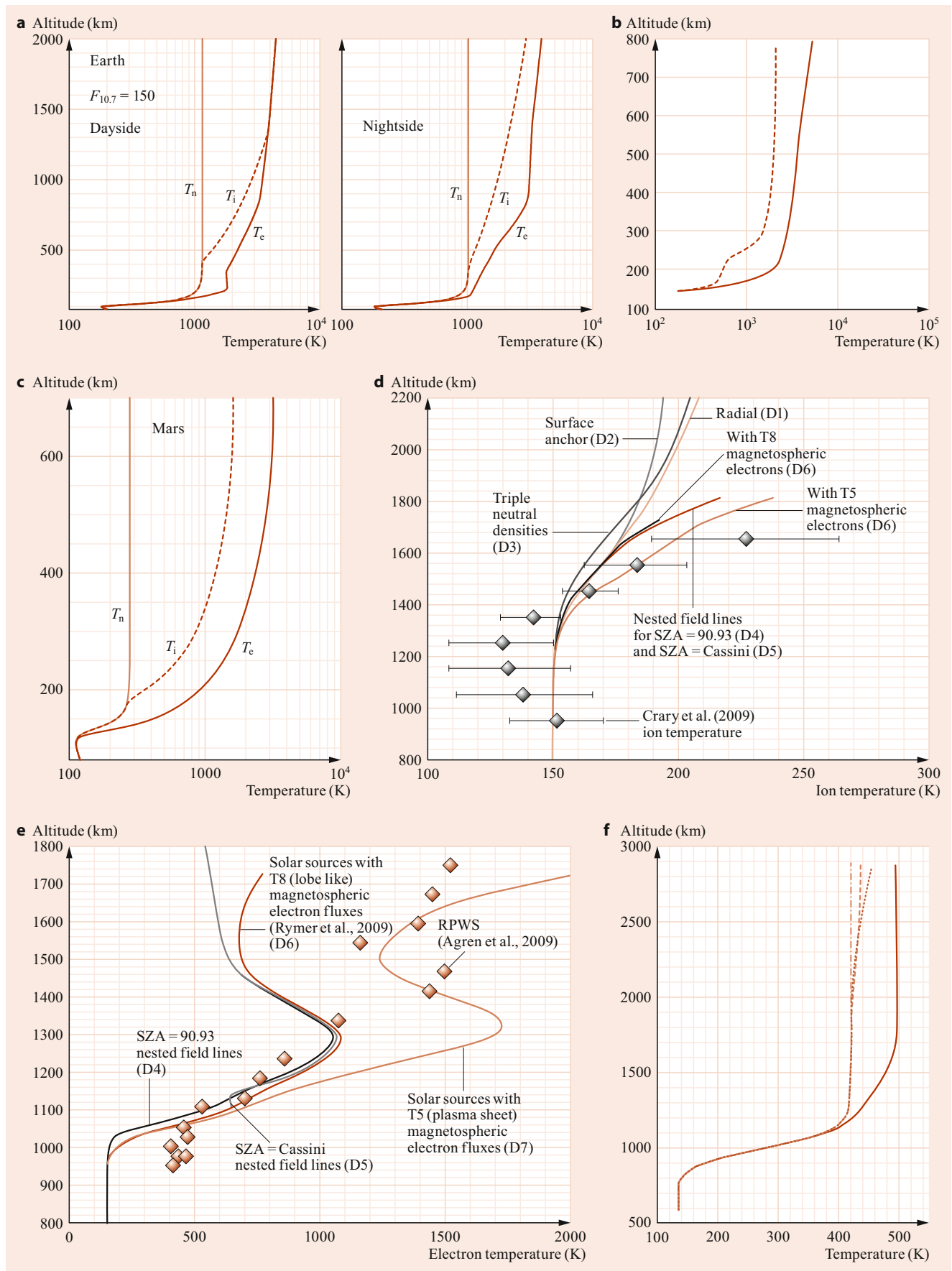


Fig. 88.14 Neutral (T_n), ion (T_i), and electron (T_e) temperature profiles for selected planets. (a) For the dayside terrestrial ionosphere from the International Reference Ionosphere (IRI) for equinox, noon, and moderate solar activity ($F_{10.7} = 150$). (Left) dayside; (right) nightside. The T_e is found to not vary substantially with SZA. Downloaded from the IRI website irmodel.org. (b) Smoothed median ion (dashed curve) and electron (solid curve) temperatures in the Venus ionosphere as measured by the Pioneer Venus (PV) retarding potential analyzer and the Langmuir probe, respectively. The electron temperature profile is essentially constant with the solar zenith angle. The ion temperature profile applies to solar zenith angles between 0 and 90°. After [99]. (c) Mars. Temperatures fit to the MAVEN model for $F_{10.7} = 120$; T_n is fit to the CO₂ density profile; T_i is fit to the ion temperatures at 200 km and at high altitudes *McFadden* [100]. It is assumed to deviate smoothly from the neutral temperature profile at 180 km. The T_e profile is based on that of *Ergun et al.* [101] at 200 km and above and adjusted smoothly to converge with the value of T_n at 125 km. (d) Titan T_i dayside models for various magnetic field configurations compared to measurements of the Cassini spacecraft (*Cravay et al.* [102]). From *Richard et al.* [103]. (e) Titan (T_e) dayside models for various magnetic field configurations compared to measurements of the Cassini RPWS/LP (*Ågren et al.* [82]). From *Richard et al.* [103]. (f) Saturn, T_n , T_i , and T_e for 07:00 LT (local time). The dash-dot curve is the T_n profile. The solid curve is the T_e profile, and the dotted and dashed curves are for H⁺ and H₃⁺, respectively. From *Moore et al.* [104] ◀

equilibrium at temperature T . The width of the line at half maximum, $\Delta\nu_D$ is

$$\Delta\nu_D = \frac{2\nu_0 u}{c} (\ln 2)^{1/2}. \quad (88.73)$$

If the linewidth is determined by the natural lifetime, the profile is a Lorentzian

$$\phi_L(\nu) = \frac{\Delta\nu_L/2\pi}{(\nu - \nu_0)^2 + (\Delta\nu_L/2)^2}, \quad (88.74)$$

where $\Delta\nu_L = \Gamma_R/2\pi$ is the linewidth at half-maximum, and

$$\Gamma_R = \Gamma_2 + \Gamma_1, \quad (88.75)$$

where Γ_2 and Γ_1 are the inverse radiative lifetimes of the levels 2 and 1, respectively. Collisional broadening also results in a Lorentzian lineshape. If both Doppler and natural broadening mechanisms are important, the lineshape is a convolution of the two profiles, called a Voigt profile

$$\phi_V(\nu) = \int_{-\infty}^{\infty} \phi_D(\nu') \phi_L(\nu - \nu') d\nu'. \quad (88.76)$$

The absorption cross section σ_{12}^a integrated over all frequencies is proportional to the absorption oscillator strength f_{12}

$$\int_0^{\infty} \sigma_{12}^a(\nu) d\nu = \frac{\pi e^2}{m_e c} f_{12}, \quad (88.77)$$

where m_e is the mass of the electron; A_{21} is related to the oscillator strength through

$$A_{21} = \frac{\omega_1}{\omega_2} \frac{8\pi^2 e^2 \nu^2}{m_e c^3} f_{12} = \frac{\omega_1}{\omega_2} \frac{8\pi^2 e^2}{m_e c \lambda^2} f_{12}. \quad (88.78)$$

The excitation rate q_2 of an upper level 2 by resonance scattering is given by

$$q_2 = F(\nu) \frac{\pi e^2}{m_e c} f_{12} = F(\lambda) \frac{\omega_2}{\omega_1} \frac{\lambda^4}{8\pi c} A_{21}, \quad (88.79)$$

where $F(\nu)$ is the solar flux in units of photons $\text{cm}^{-2} \text{s}^{-1} \text{Hz}^{-1}$, and $F(\lambda)$ is the flux in units of photons $\text{cm}^{-2} \text{s}^{-1}$ per unit wavelength interval. It should be noted that for radiative transfer purposes, the photon flux that we have called $F(\nu)$ is sometimes denoted $\pi F(\nu)$. It is customary in aeronomy to define a *g-factor*, which is the probability per atom that a photon will be resonantly scattered in a particular transition

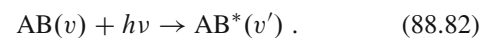
$$g_{21} = \frac{q_2 A_{21}}{\sum_i A_{2i}}, \quad (88.80)$$

where the sum in the denominator is over all the lower states i that are accessible from the upper state 2. The *g-factor* for unattenuated solar radiation is often quoted at the mean sun–Earth distance or at a particular planet. The volume emission rate $\varepsilon_{21}(z)$ for resonance scattering of a solar photon is then given by

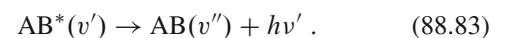
$$\varepsilon_{21}(z) = g_{21} n_1(z), \quad (88.81)$$

where $n_1(z)$ is the number density of atoms in level 1.

In fluorescent scattering, a photon is absorbed by a molecule in a vibrational state ν producing an excited electronic state with a vibrational quantum number ν'



This is followed by emission, at wavelengths that are usually the same as or longer than that of the absorbed photon, to a range of vibrational levels ν'' of a lower state



The volume emission rate of a transition from a level ν' of the upper electronic state to a vibrational level ν'' of a lower electronic state at an altitude z is given by

$$\varepsilon_{\nu'\nu''}(z) = n(z) g_{\nu'\nu''} = n(z) q_{\nu'} \frac{A_{\nu'\nu''}}{\sum_{\nu} A_{\nu'\nu}}, \quad (88.84)$$

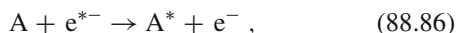
where $A_{\nu'\nu''}$ is the transition probability, $n(z)$ is the number density of the molecular species at altitude z , and $q_{\nu'}$ is the

excitation rate of vibrational level v' of the upper electronic state from a range of lower states v . The latter quantity is

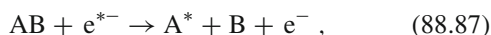
$$q_{v'} = \sum_v \eta_v F(\lambda) \frac{\pi e^2}{m_e c^2} \lambda^2 f_{vv'} , \quad (88.85)$$

where η_v is the fraction of molecules in the v vibrational level. A pedagogical review of these quantities and the relationships between them can be found in *Hilborn* [109] (erratum in *Hilborn* [110]).

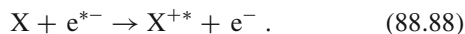
Dayglow also includes emissions that are the result of the interaction of atmospheric species with the photoelectrons produced in solar photoionization, either by direct excitation



or by simultaneous dissociation and excitation



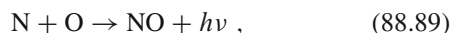
or ionization and excitation



Electron impact processes are particularly important in producing excited states that are connected to the ground state by dipole forbidden transitions, whereas resonance and fluorescent scattering are largely limited to transitions that are dipole allowed. Dayglow emissions may also result from prompt chemiluminescent reactions, which occur when fragments or ions produced by dissociation or ionization recombine with the emission of a photon.

As an example, the dayglow spectrum of the Earth from 1200 to 9000 Å is shown in Fig. 88.16. An ultraviolet spectrum of Mars as measured by the MAVEN Imaging Ultraviolet Spectrometer (IUVS) is shown in Fig. 88.17a; that of Saturn as measured by the Ultraviolet Imaging Spectrograph (UVIS) on Cassini (Fig. 88.17b); the UV dayglow of Saturn and Uranus, which were measured by the Voyager spacecraft, are compared in Fig. 88.17c; and the dayglow of N₂, along with NII and NI lines on Titan in Fig. 88.17d.

Nightglow arises from chemiluminescent reactions of species whose origin can be traced to species produced during the daytime or that have been transported from the dayside. For example, on Venus, O and N produced on the dayside are transported by the subsolar to antisolar circulation to the nightside, where they subside and radiatively associate



producing emission in the δ and γ bands of NO (e.g., *Stewart et al.* [119]). The point on the disk of maximum intensity is

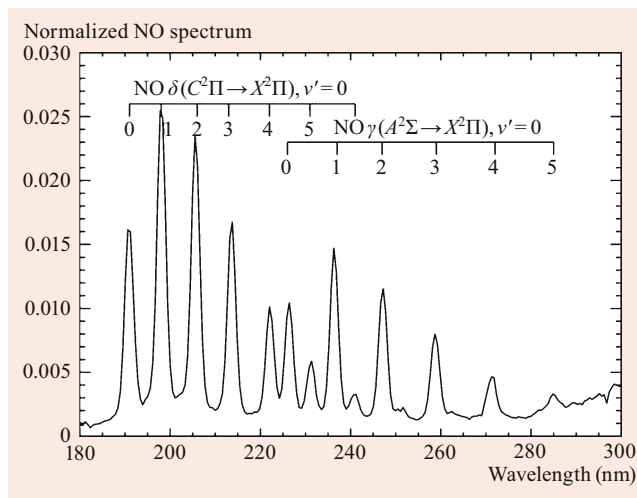


Fig. 88.15 Far ultraviolet NO nightglow spectrum of Venus obtained with the SPICAV (Spectroscopy for the Investigation of the Characteristics of the Atmosphere of Venus) instrument on the Venus Express spacecraft. Show is an average of 771 spectra obtained during orbit 516 when the tangent altitude was between 90 and 120 km. The sum of all the intensities is normalized to 1. The NO δ ($C^2\Pi \rightarrow X^2\Pi$) and γ ($A^2\Sigma \rightarrow X^2\Pi$) bands are shown. From *Royer et al.* [118]

a tracer of day-to-night transport and is found near 2 am just south of the equator. The normalized NO nightglow spectrum as measured by the SPICAV (Spectroscopy for the Investigation of the Characteristics of the Atmosphere of Venus) instrument on the Venus Express is shown in Fig. 88.15 (*Royer et al.* [118]). Similar phenomena have recently been observed by the ultraviolet spectrometer on the Mars Express spacecraft [120], and by the MAVEN UVIS, but the circulation seems to be mostly pole to pole, or equator to pole, depending upon the season. In any case, the day-to-night circulation seems to be much more complicated than that of Venus.

Auroral emissions are defined here as those produced by the impact of particles other than photoelectrons. Although auroras are usually thought of as confined to the polar regions of the Earth and the outer planets, Venus, which does not have an intrinsic magnetic field, exhibits UV emissions on the nightside that are highly variable and cannot be explained as nightglow. It has been proposed that the emissions are produced by precipitation of soft electrons into the nightside thermosphere, and the auroras are seen as diffuse and variable emissions on the nightside of the planet [121]. Mars, which has only a remanent crustal magnetic field, mostly in the southern hemisphere, exhibits discrete emissions that are concentrated over magnetic field anomalies, and more diffuse auroral emissions, which are seen over more extended regions. The SPICAM instrument on the Mars Express (e.g., *Bertaux et al.* [122], *Gérard et al.* [123]), and the IUVS instrument on the MAVEN spacecraft (*Schneider et al.* [124]) have observed both diffuse and discrete aurorae.

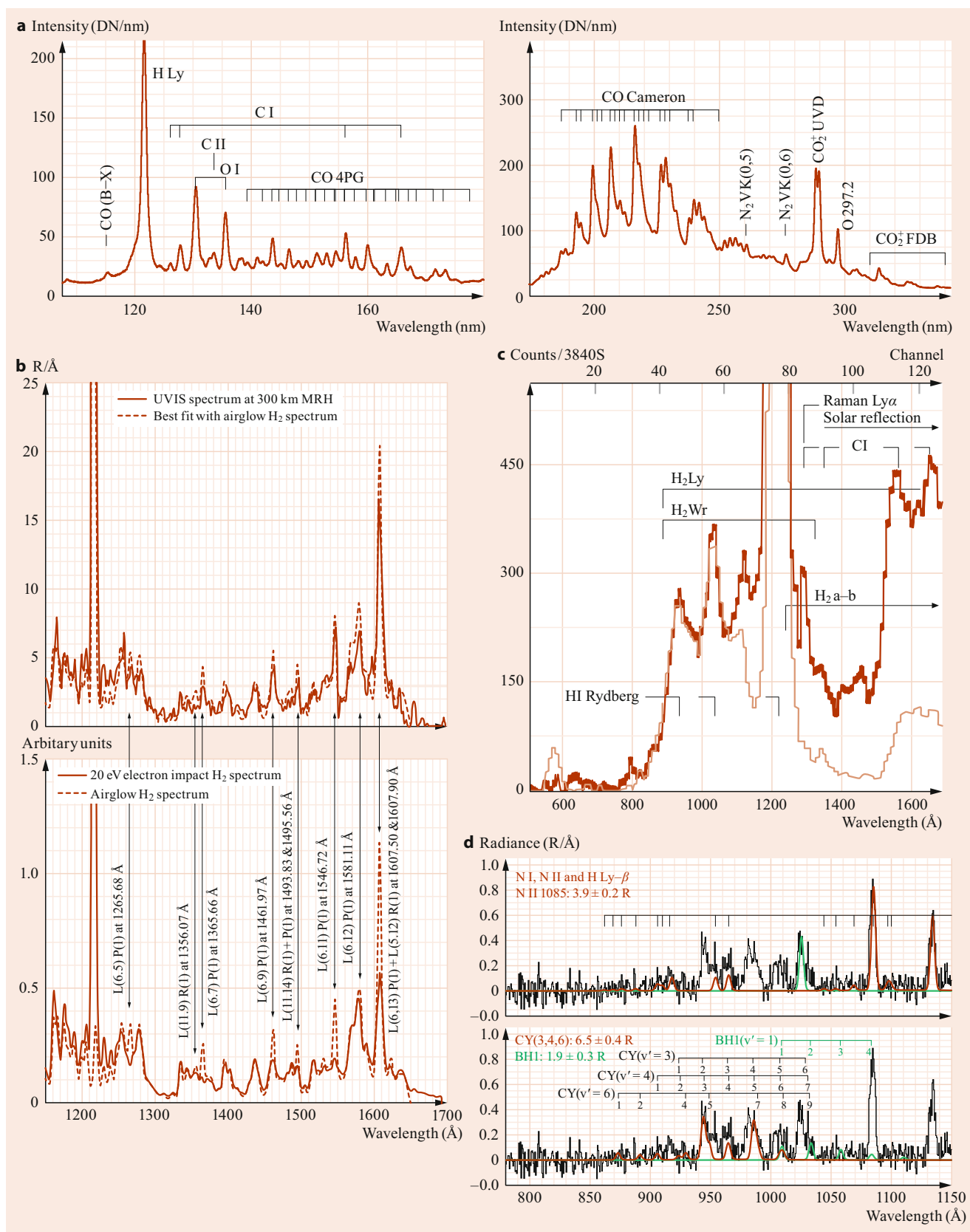


Fig. 88.17 Dayglow spectra of selected planets. **(a)** Martian dayglow spectrum (intensity as a function of wavelength) in the FUV to NUV, as measured by the MAVEN IUVS. The major features are labeled on the plot. From *Jain* [113, 114]. **(b)** (Top) Saturn airglow spectrum, as measured by the Cassini UVIS at a minimum ray height (MRH) of 300 km, compared to a fitted airglow H₂ spectrum. (Bottom) spectrum produced by the impact of 20 eV electrons compared to the airglow spectrum. From *Gustin* et al. [115]. **(c)** Comparison of dayglow spectra from Uranus (heavy line) and Saturn (thin line) recorded by Voyager 2 [116]. **(d)** Titan. Ultraviolet airglow of Titan in the wavelength range from about 780 to 1150 Å. (Top) Some atomic lines of NI, NII, and Lyman-beta are identified. (Bottom) Some bands of the N₂ Carroll-Yoshino (CY) and Birge-Hopfield 1 (BHI) systems. From *Stevens* et al. [117]

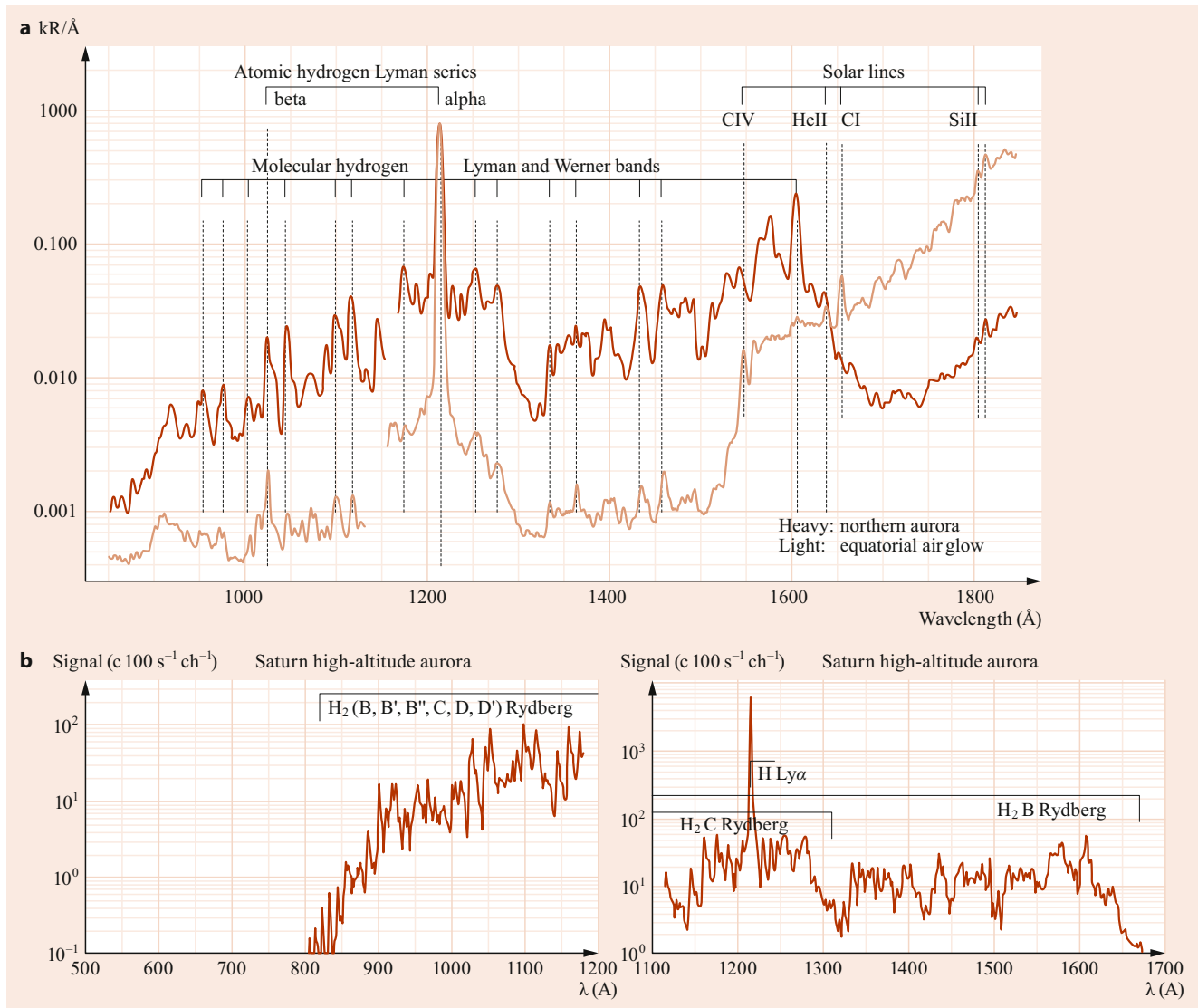


Fig. 88.18 (a) Spectra of the northern aurora (*heavy line*) and the equatorial airglow of Jupiter (*light line*) taken by the UVIS spectrometer the Cassini spacecraft on closest approach on 30 December 2000. In both spectra, the Lyman and Werner bands of molecular hydrogen are prominent. They are excited by photoelectron impact in the airglow and by primary and secondary auroral electrons. Locations of some of the brighter bands are indicated by *dotted lines*. Also shown are the Lyman-alpha and beta lines of atomic hydrogen. At wavelengths longer than 1550 Å, the airglow spectrum is swamped by reflected UV sunlight; some solar lines are indicated. At shorter wavelengths, UV sunlight is absorbed by methane and acetylene, rather than reflected. The solar signal is much weaker in the auroral spectrum than in the equatorial, due to the higher angles of incidence and emission in the former [125]. (b) Auroral synthetic spectrum of Saturn as predicted for the Cassini Ultraviolet Imaging Spectrograph in the EUV (*left*) and FUV (*right*); H₂ bands and H emissions are shown. From Esposito et al. [126]

The intensities of airglow and aurora are usually measured in units of brightness called Rayleighs. One Rayleigh is an apparent column emission rate at the source of 10^6 photons $\text{cm}^{-2} \text{s}^{-1}$ integrated over all angles or $10^6/4\pi$ photons $\text{cm}^{-2} \text{s}^{-1} \text{sr}^{-1}$. A comparison of auroral and dayglow emissions as measured by the Cassini UVIS as the spacecraft flew by Jupiter is shown in Fig. 88.18a (Stewart [125]).

A discussion of terrestrial airglow and auroral emissions can be found in Rees [50]. Meier [127] has reviewed

spectroscopy and remote sensing of the terrestrial ultraviolet emissions. The airglows of Mars and Venus have been reviewed by Barth [11], Fox [128], and Paxton and Anderson [129]. Airglow and auroral emissions on the outer planets have been reviewed by Atreya et al. [130], Atreya [22], and Strobel [116]. Airglow in the atmospheres of the planets has been reviewed by Slanger and Wolven [131]. Airglow and aurorae of solar system bodies have been reviewed by Slanger et al. [132].

88.7 Planetary Escape

The escape of species from atmospheres can occur by thermal and nonthermal mechanisms. Thermal processes include Jeans escape and hydrodynamic escape. Jeans escape is essentially evaporation of the energetic tail of the Maxwell–Boltzmann distribution, while hydrodynamic escape is a large-scale expansion of the atmosphere that occurs when the average molecular velocity is near or above the escape velocity. Although Jeans escape still occurs for light species in the thermospheres of small solar system bodies, until recently, hydrodynamic escape was thought to have been operative only in the early history of the smaller solar system bodies when the solar flux in the UV was higher. Now, hydrodynamic escape has been postulated to occur for light species in the atmospheres of comets, or, for example, for H₂ escape from Titan (*Strobel* [133]). There is an intermediate region between Jeans and hydrodynamic escape called “slow hydrodynamic escape”. The transition from hydrodynamic to Jeans escape is discussed by *Volkov et al.* [134]. Nonthermal escape mechanisms, which dominate for heavy species on smaller bodies such as Mars and Titan and for all species on Venus and Earth, include both photochemical and mechanical processes. A pedagogical discussion of escape processes can be found in *Chamberlain and Hunten* [135].

Because of the exponential rate of change of density with altitude in thermospheres, escape is sometimes assumed to occur only in the exosphere, that is, at or above an altitude historically called the “exobase” or “critical level”. The classically defined exobase is the altitude where the mean free path of a species, $l = (n\sigma^c)^{-1}$ (where σ^c is the collision cross section), is equal to the atmospheric scale height. The probability that a particle, moving upward from the exobase with sufficient velocity will actually escape without suffering another collision is then $1/e$. The condition $l = H$, therefore, reduces to $nH\sigma^c = 1$ or, equivalently, to $N = (\sigma^c)^{-1}$, where N is the column density. A typical collision cross section has been assumed to be about 3×10^{-15} cm², which places the “exobase” at the altitude above which the column density is about 3.3×10^{14} cm⁻³. Thus, the “exosphere” defined in this way is not a truly collisionless region.

Whether the trajectory of a particle moving upward at a given altitude is ballistic (bound) or escaping (free) in a collision-free region is determined by its total energy E , which is the sum of its kinetic and potential energies

$$E = \frac{1}{2}mv_c^2 + \int_{\infty}^{r_c} \frac{mGM}{r^2} dr, \quad (88.90)$$

where the symbols have the same meaning as in Eq. (88.2), and the subscript c refers to the critical level, the base of the assumed collision-free region. If $E < 0$, the particle is bound.

Equation (88.90) reduces to

$$E = \frac{1}{2}mv_c^2 - mg_c r_c, \quad (88.91)$$

where g_c is the gravitational acceleration at the critical level. The escape velocity at the exobase, v_{esc} , is then defined by the condition $v_{esc} = (2g_c r_c)^{1/2}$. In the “exobase” approximation, particles with velocities greater than the escape velocity are assumed to escape if their velocity vectors are oriented in the upward hemisphere and if they undergo no further collisions. In this approximation, the angular distribution of the products of collisions is assumed to be isotropic, and therefore half of the sufficiently energetic particles meet this criterion. The exobase approximation has been shown not to be valid for photochemical escape mechanisms by, for example, *Fox and Hač* [136].

In reality, the elastic and inelastic cross sections for collisions of different pairs of species vary over nearly an order of magnitude and are functions of energy in the relevant hyperthermal energy region (≈ 1 –10 eV), however, and thus the location of the exobase should vary from species to species. In addition, for similar mass species pairs, the angular differential cross sections in the center-of-mass frame for the hyperthermal energy region are also strongly forward peaked, and escape of atoms, such as O from the Martian thermosphere, originate over a large range of altitudes that extends from well below to above the theoretical exobase. Measurements of angular differential cross sections, however, show that the collisions of comparable mass particles are strongly forward-peaked, so the nonthermal escape of a given species occurs over a range of altitudes, which varies from several scale heights above to well below the “exobase”. Use of the exobase approximation has been shown to be in error for photochemical escape of O, C, and N on Mars (e.g., *Fox and Hač* [136]) but may have some relevance for thermal escape mechanisms. It also useful as a reference altitude that shows the escape region to within several scale heights above and below it. The radius, gravitational acceleration, escape velocity, and scale heights at the equatorial “exobases” of the planets are given in Table 88.11.

In the thermal Jeans process, escape occurs when particles in the high-energy tail of the Maxwellian distribution attain the escape velocity. The escape flux, Φ_J is given by

$$\Phi_J = \frac{n_c u}{2\sqrt{\pi}} (1 + \lambda_c) \exp(-\lambda_c), \quad (88.92)$$

where $u = (2k_B T/m)^{1/2}$ is the modal velocity, and λ is the gravitational potential energy in units of $k_B T$

$$\lambda = \frac{GMm}{rk_B T} = \frac{mgr}{k_B T} = \frac{r}{H}. \quad (88.93)$$

Sometimes, a correction factor is applied to the expression for the escape flux to account for the suppression of the tail

Table 88.11 Exobase properties of solar system bodies

Planet	r_c^a (km)	g_c^a (cm s^{-2})	$v_{\text{esc},c}^a$ (km s^{-1})	$H_{\text{avg}}^{a,b}$ (km)
Mercury ^c	2440	371	4.25	–
Venus ^d	6250	831	10.2	17
Earth ^e	6878	841	10.8	71
Mars ^f	3605	331	4.74	21.8
Jupiter ^g	73 000	2236	57.2	250
Saturn ^h	62 968	821	32.2	192
Uranus ⁱ	31 800	561	18.9	66
Neptune ⁱ	27 300	919	22.4	250
Titan ^j	4000	56.1	2.12	85
Triton ^k	2203	29.5	1.14	90
Pluto ^k	≈2900	10.3	0.774	253

^a Values given are those at the equatorial exobase and assume that the thermosphere corotates with the planet

^b Average value computed from $H_{\text{avg}} = k_B T / m_{\text{avg}} g$ but does not represent the local pressure scale height, except for cases where there is one major constituent

^c Exobase is at the surface

^d Model from *Hedin et al.* [2] for $F_{10.7} = 150$, 45° solar zenith angle.

^e MSIS model for $F_{10.7} = 150$, equator, 45° solar zenith angle [9]

^f Model fit to MAVEN data for $F_{10.7} = 120$ conditions; April 2015, 7.5° solar zenith angle

^g Model from [4, 22]

^h From *Koskinen et al.* [137] and from *Vervack, Jr. and Moses* [5]

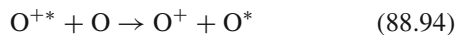
ⁱ Model from *Moses and Poppe* [64]

^j Model from *Strobel* [133], *Strobel* [65]

^k Model from *Strobel and Zhu* [7]

of the distribution due to the escape of the energetic particles [138, 139].

Photochemical processes that produce energetic fragments include photodissociation and photodissociative ionization, photoelectron impact dissociation and dissociative ionization, as well as exothermic chemical reactions. The most important example of the latter are dissociative recombination reactions, which are very exothermic and tend to produce neutral fragments with large kinetic energies. Charge transfer processes such as



or



can produce fast neutrals if the ion temperature is larger than the neutral temperature, as is usually the case at altitudes well above the exobase of a planet, or if solar wind heavy ions, including protons, directly impact the atmosphere. In modeling these processes, the kinetic energy distribution (in the laboratory frame) of the product species is important, as well as the cross sections or reaction rates.

Physical or collisional escape mechanisms include sputtering and *knock-on*. Sputtering can occur when a heavy ion

picked up by the solar wind (the projectile) collides with an atmospheric species (the target) and in the process produces a *back-splash* in which the accelerated neutral may be ejected from the atmosphere. Since for comparably sized species, there is no backscattering in the laboratory frame, either the collision must be glancing or the process must involve multiple collisions. The sputtering phenomenon has been described in detail in the monograph by *Johnson* [140]. In knock-on, hot atmospheric neutral species, such as O atoms produced in exothermic chemical reactions at sufficiently high altitudes can collide with a (usually) lighter species, such as H, imparting sufficient kinetic energy to allow it to escape. Modeling these processes requires knowledge of the ion–neutral and neutral–neutral elastic, inelastic, and angular differential collision cross sections.

The escape rate of a light species from a planetary atmosphere may be limited by diffusion of the species from the lower atmosphere to the exosphere, rather than by the escape process itself [141]. The limiting upward flux, ϕ_i of a species i with mixing ratio f_i can be estimated as

$$\phi_i \approx \frac{b_i f_i}{H_a}, \quad (88.96)$$

where H_a is the scale height that is based on the average mass of the constituents of the thermosphere at the homopause, and b_i is the binary collision parameter introduced in Sect. 88.2.2. Equation (88.96) above is usually evaluated at the homopause, with the mixing ratio taken from a suitable altitude in the middle atmosphere, but above the cold trap (where the species condenses, if one exists). The limiting flux obtains, if and only if the mixing ratio is constant with altitude. The effect of photochemistry can be accounted for if all chemical forms of the species are considered in the calculation of f_i (*Hunten* [40]). For example, on Titan, H_2 sometimes escapes hydrodynamically and sometimes by Jeans escape at the diffusion limit, but CH_4 escapes at 75% of its diffusion limiting rate. On Triton, the mixing ratio of CH_4 near the surface is much smaller than that in the lower atmosphere of Titan. It is chemically destroyed in the lower atmosphere before it can escape (e.g., *Strobel* [65]). On Pluto, CH_4 escapes with significant rates, exceeding 10^{25} s^{-1} ; H and H_2 escape at their diffusion limit (*Strobel* [10]).

Even if energetic particles released near the exobase of a planet do not have enough energy to escape, they may travel to great heights along ballistic orbits before falling back to the atmosphere. These particles are said to form hot atom coronas. Hot H and O coronas surround Earth, Venus, and Mars (Fig. 88.19). In addition, hot C and hot N coronas have been detected or predicted to surround Venus and Mars. Since the escape velocities of the giant planets are so large (tens of km s^{-1}), escape of even H is not possible. Non-thermal processes at high altitudes may, however, lead to the formation of hot H coronas. Reviews of the H and O coronas

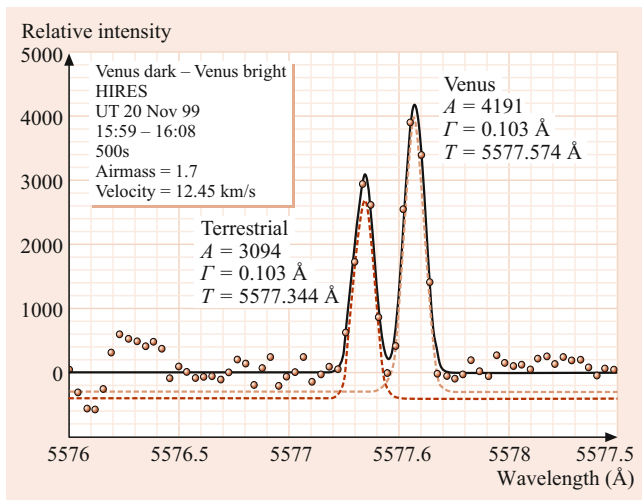


Fig. 88.19 Spectrum of the oxygen green line taken on the nightside of Venus by the Keck/HIRES on 20 November 1999. The individual terrestrial and Doppler-shifted Venusian components are shown by the dashed lines (from *Slanger et al.* [142])

of Venus have been presented by *Fox and Bougher* [96] and by *Nagy et al.* [143]. The exospheres of various solar system bodies and the coronas of Mars, Venus, and Titan have been reviewed by *Futaana et al.* [144]. See *Chamberlain and Hunten* [135] for a detailed discussion of planetary coronal population processes.

References

- von Zahn, U., Kumar, S., Niemann, J., Prinn, R.: Composition of the Venus atmosphere. In: Hunten, D.M., Colin, L., Donahue, T.M., Moroz, V.I. (eds.) *Venus*. Univ. Arizona Press, Tucson (1983)
- Hedin, A.E., Neimann, H.B., Kasprzak, W.T., Seiff, A.: *J. Geophys. Res.* **88**, 73 (1983)
- The U.S. Standard Atmosphere: U.S. Government Printing Office. National Oceanic and Atmospheric Administration (1976)
- Kim, Y.H.: The Jovian Ionosphere. Ph.D. Thesis. State University of New York at Stony Brook, New York (1991)
- Vervack Jr., R.J., Moses, J.I.: *Icarus* **258**, 135 (2015)
- Magee, B.A., Waite, J.H., Mandt, K.E., Westlake, J., Bell, J., Gell, D.A.: *Planet. Space Sci.* **57**, 1895 (2009)
- Strobel, D.F., Zhu, X.: *Icarus* **291**, 55 (2017)
- Young, L.A.: and 25 co-authors. *Icarus* **300**, 174 (2018)
- Hedin, A.E.: *J. Geophys. Res.* **96**, 1159 (1991)
- Strobel, D.: private communication (2018)
- Barth, C.A., Stewart, A.I.F., Bougher, S.W., Hunten, D.M., Bauer, S.J., Nagy, A.F.: Aeronomy of the current Martian atmosphere. In: Kiefer, H., Jakosky, B.M., Snyder, C.W., Matthews, M.S. (eds.) *Mars*. Univ. Arizona Press, Tucson (1992)
- Franz, H.B. and 13 co-authors: *Planet. Space Sci.* **138**, 44 (2017)
- Jakosky, B.M., and Haberle, R.M.: In: Kieffer, H.H., Jakosky, B.M., Snyder, C.W., Matthews, M.S. (eds.) *Mars*, pp. 969–1016. Univ. Arizona Press, Tucson (1992)
- Donahue, T.M., Hodges Jr., R.R.: *Geophys. Res. Lett.* **20**, 591 (1993)
- Taylor, F.W., Crisp, D. and Bézard, B. In: Bougher, S., Hunten, D., Phillips, R.J. (eds.) *Venus II. Geology, Geophysics, Atmosphere and Solar Wind Environment*. University of Arizona Press (1997)
- Krasnopolsky, V.A., Gladstone, G.R.: *J. Geophys. Res.* **101**, 15765 (1996)
- T. Owen: in *Mars*, edited by H.H. Kieffer, B.M. Jakosky, C. W. Snyder, and M. S. Matthews, Univ. of Arizona press, Tucson 818–834 (1992)
- Krasnopolsky, V.A., Feldman, P.D.: *Science* **294**, 1914 (2001)
- DeMore, W.B.: *Icarus* **51**, 199 (1982)
- C. R. Webster, and 32 coauthors: *Science Express*, <https://doi.org/10.1126/Science.126173> (2014)
- Lodders, K., Fegley Jr., B.: *Chemistry of the Solar System*. Royal Society of Chemistry, Cambridge (2011)
- Atreya, S.K.: *Atmospheres and Ionospheres of the Outer Planets and Their Satellites*. Springer, New York (1986)
- Strobel, D.F.: In: Levine, J.S. (ed.) *The Photochemistry of Atmospheres: Earth, the Other Planets, and Comets*. Academic, New York (1985)
- Niemann, H.B., et al.: *J. Geophys. Res.* **103**, 22831 (1998)
- Fletcher, L.N., Orton, G.S., Teanby, N.A., Irwin, P.G.J., Bjoraker, G.L.: *Icarus* **199**, 351 (2009)
- Broadfoot, A.L., Atreya, S.K., Bertaux, J.L., Blamont, J.E., Dessler, A.J., Donahue, T.M., Forrester, W.T., Hall, D.T., Herbert, F., Holberg, J.B., Hunter, D.M., Krasnopolsky, V.A., Linick, S., Lunine, J.I., McConnell, J.C., Moos, H.W., Sandel, B.R., Schneider, N.M., Shemansky, D.E., Smith, G.R., Strobel, D.F., Yelle, R.V.: *Science* **246**(4936), 1459–1466 (1989)
- Herbert, F., Sandel, B.R., Yelle, R.V., Holberg, J.B., Shemansky, D.E., Broadfoot, A.L., Atreya, S.K., Romani, P.N.: The upper atmosphere of Uranus: EUV occultations observed by Voyager 2. *J. Geophys. Res.* **92**, 15093–15109 (1987)
- Coustenis, A., Salama, A., Lellouch, E., Encrenaz, T., Bjoraker, G.J., Samuelson, R.E., de Graauw, T.: *Astron. Astrophys.* **336**, L85 (1998)
- Vervack Jr., R.J., Sandel, B.R., Strobel, D.F.: *Icarus* **170**, 91 (2004)
- Fulchignoni, M.F., Ferri, F., Angrilli, F., Ball, A.J.: *Nature* **438**, 785 (2005)
- Yelle, R.V., Snowden, D.S., Müller-Wodarg, I.C.F.: In: Müller-Wodarg, I.C.F., Griffith, C., Lellouch, E., Cravens, T.E. (eds.) in *Titan: Interior, Surface, Atmosphere, and Space Environment*, pp. 322–375. Cambridge University Press, New York, NY (2014)
- Krasnopolsky, V.A., Sandel, B.R., Herbert, F., Vervack, R.J.: *J. Geophys. Res.* **98**, 3065 (1993)
- Lellouch, E., de Bergh, C., Sicardy, B., Ferron, S., Käuff, H.-U.: *Astron. Astrophys.* **512**, 1 (2010)
- Elliot, J.L., Person, M.J., Qu, S.: *Astron. J.* **126**, 1041 (2003)
- Killen, R.M., Burger, M.H., Vervack Jr., R.J., Cassidy, T.A.: In: Solomon, S.C., Nittler, L.R., Anderson, B.J. (eds.): Chapter 15. In: *Mercury: the View After MESSENGER*, Cambridge University Press, Cambridge (2018)
- McClintock, W.E., Cassidy, T.A., Merkel, A.W., Killen, R.M., Burger, M.H., Vervack Jr., R.J.: In: Solomon, S.C., Nittler, L.R., Anderson, B.J. (eds.): Chapter 14. In: *Mercury: the View After MESSENGER*, Cambridge University Press, Cambridge (2018)
- Hinson, D.P., Linscott, I.R., Strobel, D.F., Tyler, G.L., Bird, M.K., Pätzold, M., Summers, M.E., Stern, S.A., Ennico, K., Gladstone, G.R., Olkin, C.B., Weaver, H.A., Woods, W.W., Young, L.A. and the New Horizons Science Team: *Icarus* **307**, 17 (2018)
- Lellouch, E. and 18 co-authors: *Icarus* **286**, 289 (2017)
- Chamberlin, P.C., Eparvier, F.G., Knoer, V., Leise, H.G., Pankratz, A., Snow, M., Templeman, B., Thiemann, E.M.R., Woodraska,

- D.L., Woods T.N.: Space Weather (2020) <https://doi.org/10.1029/2020SW002588>
40. D. M. Hunten: in *Atmospheres in the Solar System: Comparative Aeronomy*, ed. by M. Mendillo, A. Nagy, J. H. Waite, Geophysical Monograph 130, AGU Press, Washington (2002)
 41. Eparvier, F.G.: private communication (2018)
 42. Paxton, L.J.: private communication (2018)
 43. Y. H. Kim: unpublished.
 44. Kim, Y.H., Fox, J.L., Black, J.H., Moses, J.I.: *J. Geophys. Res. Space Phys.* **119**(A11), 1 (2014)
 45. Zhang, X., Strobel, D.F., Imanaka, H.: *Nature* **551**, 352 (2017)
 46. Huebner, W.F., Keady, J.J., Lyon, S.P.: *Astrophys. Space Sci.* **195**, 1 (1992)
 47. Valentine, J.M., Curran, S.C.: *Rep. Prog. Phys.* **21**, 1 (1958)
 48. Opal, C.B., Peterson, W.K., Beaty, E.C.: *J. Chem. Phys.* **55**, 4100 (1971)
 49. Swartz, W.E., Nisbet, J.S., Green, A.E.S.: *J. Geophys. Res.* **74**, 6415 (1971)
 50. Rees, M.H.: *Physics and Chemistry of the Upper Atmosphere*. Cambridge University Press, Cambridge (1989)
 51. Nagy, A.F., Banks, P.M.: *J. Geophys. Res.* **75**, 6260 (1970)
 52. Porter, H.S., Varosi, F., Mayr, H.G.: *J. Geophys. Res.* **92**, 5933 (1987)
 53. Strickland, D.J., Daniell, R.E., Basu, B., Jasperse, J.R.: *J. Geophys. Res.* **98**, 21533 (1993)
 54. Solomon, S.C.: *Geophys. Res. Lett.* **20**, 185 (1993)
 55. Bauer, S.J.: *Physics of Planetary Ionospheres*. Springer, New York (1973)
 56. S. G. Lias, J. E. Bartmess, J. F. Liebman, J. L. Holmes, R. D. Levin, W. G. Mallard: *Gas-phase ion, and neutral thermochemistry*, *J. Phys. Chem. Ref. Data* **17**, Suppl. 1 (1988)
 57. Nesbitt, F.L., Marston, G., Stief, L.J., Wickramaaratchi, M.A., Tao, W., Klemm, R.B.: *J. Phys. Chem.* **95**, 7613 (1991)
 58. Su, T., Bowers, M.T.: *Classical ion–molecule collision theory*. In: by M. T. Bowers (ed.) *Gas Phase Ion Chemistry*, vol. 1, Academic Press, New York (1979)
 59. Anicich, V.G.: *Astrophys. J. Suppl. Ser.* **84**, 215 (1993)
 60. Ikezoe, Y., Matsuoka, S., Takabe, M., Viggiano, A.: *Gas Phase Ion–Molecule Rate Constants Through 1986*. Maruzen Co, Tokyo (1986)
 61. V. G. Anicich: *An index of the literature for bimolecular gas phase cation–molecule reaction kinetics*, JPL Publication 03 (2003)
 62. Bates, D.R., Dalgarno, A.: *Electronic recombination*. In: Bates, D.R. (ed.) *Atomic and Molecular Processes*, pp. 245–271. Academic Press, New York (1962)
 63. Egert, A., Waite Jr., J.H., Bell, J.: *J. Geophys. Res. Space Phys.* **122**, 2210 (2016)
 64. Moses, J.I., Poppe, A.R.: *Icarus* **297**, 33 (2017)
 65. Strobel, D.F.: *Can. J. Phys.* **90**, 795 (2012)
 66. Vuitton, V., Yelle, R.V., Cui, J.: *J. Geophys. Res.* **113**, 1 (2008)
 67. Johnson, C.Y.: *J. Geophys. Res.* **71**, 330 (1966)
 68. Maurellis, A.N., Cravens, T.E.: *Icarus* **154**, 350 (2001)
 69. Lindal, G.F., Lyons, J.R., Sweetnam, D.N., Eshleman, V.R., Hinson, D.P., Tyler, G.L.: *J. Geophys. Res.* **92**, 987 (1987)
 70. J. R. Lyons: private communication
 71. Lyons, J.R.: *Nature* **267**, 648 (1995)
 72. Kliore, A.J., Nagy, A.F., Marouf, E.A., French, R.G., Flasar, F.M., Rappaport, N.J., Anabtawi, A., Asmar, S.M., Kahann, D.S., Barbini, E., Goltz, G.L., Fleischman, D.U., Rochblatt, D.J.: *J. Geophys. Res.* **113**, A09317–1 (2008)
 73. Vuitton, V., Yelle, R.V., McEwan, M.J.: *Icarus* **191**, 722 (2007)
 74. Strobel, D.F., Summers, M.E.: *Triton’s upper atmosphere and ionosphere*. In: Cruikshank, D.P. (ed.) *Neptune and Triton*, pp. 1107–1148. University of Arizona Press (1995)
 75. Richmond, A.D.: *The ionosphere*. In: Akasofu, S.-I., Kamide, Y. (eds.) *The Solar Wind and the Earth*. Terra Scientific Publishing Co, Tokyo (1987)
 76. Zhang, M.H.G., Luhmann, J.G., Kliore, A.J.: *J. Geophys. Res.* **95**, 17095 (1990)
 77. D. P. Hinson and the Mars Radio Science team: *Public access to MGS RS Standard electron density profiles* (2007). <https://pds-geosciences.wustl.edu/missions/mgs.rsdata.html>
 78. Benna, M., Mahaffy, P.R., Grebowsky, J.M., Fox, J.L., Yelle, R.V., Jakosky, B.M.: *Geophys. Res. Lett.* **42**, 8958 (2015)
 79. Fox, J.L.: *Icarus* **252**, 366 (2015)
 80. Fox, J.L., Benna, M., Mahaffy, P., Jakosky, B.M.: *Geophys. Res. Lett.* **42**, 8977 (2015)
 81. Girazian, Z., Mahaffy, P.R., Lillis, R.J., Benna, M., Elrod, M., Jakosky, B.M.: *J. Geophys. Res. Space Phys.* **122**, 4712 (2017)
 82. Ågren, K., Wahlund, J.-E., Garnier, P., Modolo, R., Cui, J., Galand, M., Müller-Wodarg, I.: *Planet. Space Sci.* **57**, 1821 (2009)
 83. Dalgarno, A., McDowell, M.R.C., Williams, A.: *Phil. Trans. Roy. Soc. Lond. Ser. A* **250**, 411 (1958)
 84. Schunk, R.W., Nagy, A.F.: *Rev. Geophys. Space Phys.* **18**, 813 (1980)
 85. Banks, P.M., Kockarts, G.: *Aeronomy*. Academic Press, New York (1973)
 86. Whitten, R.C., Poppoff, I.G.: *Fundamentals of Aeronomy*. Wiley, New York (1971)
 87. Schunk, R.W., Nagy, A.F.: *Ionospheres: Physics, Plasma Physics and Chemistry*. Cambridge University Press, Cambridge (2000)
 88. Roble, R.G., Ridley, E.C., Dickinson, R.E.: *J. Geophys. Res.* **92**, 8745 (1987)
 89. Fox, J.L.: *Planet. Space Sci.* **37**, 36 (1988)
 90. Fox, J.L., Zhou, P., Bougher, S.W.: *Adv. Space Res.* **17**, 203 (1995)
 91. Waite, J.H., Cravens, T.E., Kozyra, J., Nagy, A.F., Atreya, S.K., Chen, R.H.: *J. Geophys. Res.* **88**, 6143 (1983)
 92. Richards, P.G.: *Can. J. Phys.* **90**, 759 (2012)
 93. C. Snowden, private communication
 94. Snowden, C., Yelle, R.V.: *Icarus* **228**, 64 (2014)
 95. Roble, R.G.: *Rev. Geophys.* **21**, 217 (1983)
 96. Fox, J.L., Bougher, S.W.: *Space Sci. Rev.* **55**, 357 (1991)
 97. Bougher, S.W., Hunten, D.M., Roble, R.G.: *J. Geophys. Res.* **99**, 14609 (1994)
 98. Wintersteiner, R.P., Picard, R.H., Sharma, R.D., Winick, J.R., Joseph, R.A.: *J. Geophys. Res.* **97**, 18083 (1992)
 99. Miller, K.L., Knudsen, W.C., Spenner, K., Whitten, R.C., Novak, V.: *J. Geophys. Res.* **85**, 7759 (1980)
 100. McFadden, J.: private communication (2017)
 101. Ergun, R.E., Morooka, M.W., Andersson, L.A., Fowler, C.M., Delory, G.T., Andrews, D.J., Eriksson, A.I., McEnulty, T., Jakosky, B.M.: *Geophys. Res. Lett.* **42**, 8846 (2015)
 102. Crary, F.J., Magee, B.A., Mandt, K., Waite Jr., J.H., Westlake, J., Young, D.T.: *Planet. Space Sci.* **57**, 1847 (2009)
 103. Richard, M.S., Cravens, T.E., Robertson, I.P., Waite, J.H., -E, J.: Wahlund F. J. Crary A. J. Coates: *J. Geophys. Res.* **116**(A09310), 1 (2011)
 104. Moore, L., Galand, M., Müller-Wodarg, I., Yelle, R., Mendillo, M.: *J. Geophys. Res.* **113**, A10306 (2008)
 105. Bilitza, D., Hoegy, W.R.: *Adv. Space Res.* **10**, 81 (1990)
 106. Schunk, R., Nagy, A.F.: *Ionospheres*, 2nd edn. Cambridge University Press, Cambridge (2009)
 107. Brace, L.R.F., Niemann, H.B., Mayr, H.G., Hoegy, W.R., Nagy, A.F.: *Science* **205**, 102 (1979)
 108. Theis, R.F., Brace, L.H., Mayr, H.G.: *J. Geophys. Res.* **85**, 7787 (1980)
 109. Hilborn, R.C.: *Am. J. Phys.* **50**, 982 (1982)
 110. Hilborn, R.C.: *Am. J. Phys.* **51**, 471 (1983)

111. Broadfoot, A.L., Sandel, B.R., Knecht, D., Viereck, R., Murad, E.: *Appl. Opt.* **31**, 3083 (1992)
112. G. Sims, and 20 coauthors: *Pub. Astron. Soc. Pacific*, **124**, 637 (2012)
113. S. K. Jain, Private communication
114. Jain, S.K., Stewart, A.I.F., Schneider, N.M., Deighan, J., Stiepen, A., Evans, J.S., Stevens, M.H., Chaffin, M.S., Crismani, M., McClintock, W.E., Clarke, J.T., Holsclaw, G.M., Lo, D.Y., Lefèvre, F., Montmessin, F., Thiemann, E.M.B., Eparvier, F., Jakosky, B.M.: *Geophys. Res. Lett.* **42**, 9023 (2015)
115. Gustin, J., Stewart, I., Gérard, J.-C., Esposito, L.: *Icarus* **210**, 270 (2010)
116. Strobel, D.F., Yelle, R.V., Shemansky, D.E., Atreya, S.K.: The upper atmosphere of Uranus. In: Bergstrahl, J.T., Miner, E.D., Matthews, M.S. (eds.) *Uranus*. Univ. Arizona Press, Tucson (1991)
117. Stevens, M.H., Gustin, J., Ajello, J.M., Evans, J.S., Meier, R.R., Kochenash, A.J., Stephan, A.W., Stewart, A.I.F., Esposito, L.W., McClintock, W.E., Holsclaw, G., Bradley, E.T., Lewis, B.R., Heays, A.N.: *J. Geophys. Res.* **116**(A05304), 1 (2011)
118. Royer, E., Montmessin, F., Bertaux, J.-L.: *Planet. Space Sci.* **58**, 1314 (2010)
119. Stewart, A.I.F., Gerard, J.-C., Rusch, D.W., Bougher, S.W.: *J. Geophys. Res.* **85**, 7861 (1980)
120. Bertaux, J.L., Leblanc, F., Perrier, S.V., Quemerais, E., Korablev, O., Dimarellis, E., Reberac, A., Forget, F., Simon, P.C., Sandel, B.: Nightglow in the upper atmosphere of Mars and implication for atmospheric transport. *Science* **307**(5709), 566 (2005)
121. Fox, J.L., Stewart, A.I.F.: *Geophys. Res.* **96**, 9829 (1991)
122. Bertaux, J.L., Leblanc, F., Witasse, O., Quemerais, E., Lilienstein, J., Stern, S.A., Sandel, B., Korablev, O.: *Nature* **435**(7043), 790 (2005)
123. Gérard, J.-C., Soret, L., Libert, L., Lundin, R., Stepien, A., Radioti, A., Bertaux, J.-L.J.: *Geophys. Res.: Space Phys.* **120**, 6749 (2015)
124. Schneider, N.M., Jain, S.K., Deighan, J., Nasr, C.R., Brain, D.A., Larson, D., Lillis, R., Rahmati, A., Halekas, J.S., Lee, C.O., Chaffin, M.S., Stiepen, A., Crismani, M., Evans, J.S., Stevens, M.H., Lo, D.Y., McClintock, W.E., Stewart, A.I.F., Yelle, R.V., Clarke, J.T., Holsclaw, G.M., Lefevre, F., Montmessin, F., Jakosky, B.M.: *Geophys. Res. Lett.* **45**, 7391 (2018)
125. Stewart, A.I.F.: private communication (2004)
126. Esposito, L.W. and 18 coauthors: *Space Sci. Rev.* **115**, 299–361 (2004)
127. Meier, R.R.: *Space Sci. Rev.* **58**, 1 (1991)
128. Fox, J.L.: Airglow and aurora in the atmospheres of Venus and Mars. In: Luhmann, J.G., Tatrallay, M., Pepin, R.O. (eds.) *Venus and Mars: Atmospheres, Ionospheres and Solar Wind Interactions*, Geophysical Monograph, vol. 66, pp. 191–222. American Geophysical Union, Washington, D.C. (1992)
129. Paxton, L.J., Anderson, D.E.: Far ultraviolet remote sensing of Venus and Mars. In: Luhmann, J.G., Tatrallay, M., Pepin, R.O. (eds.) *Venus and Mars: Atmospheres, Ionospheres and Solar Wind Interactions*, Geophysical Monograph, vol. 66, pp. 113–190. American Geophysical Union, Washington, D.C. (1992)
130. Atreya, S.K., Waite Jr., J.H., Donahue, T.M., Nagy, A.F., McConnell, J.C.: Theory, measurements, and models of the upper atmosphere and ionosphere of Saturn. In: Gehrels, T., Matthews, M.S. (eds.) *Saturn*. Univ. Arizona Press, Tucson (1984)
131. Slanger, T.G., Wolven, B.C.: Airglow processes in planetary atmospheres. In: *Atmospheres in the Solar System: Comparative Aeronomy*. Geophysical Monograph, vol. 130. AGU, Washington, D.C. (2002)
132. Slanger, T.G., Cravens, T.E., Crovisier, J., Miller, S., Strobel, D.F.: Photoemission phenomena in the solar system, *Space Sci. Rev.* **139**, 267–310 (2008)
133. Strobel, D.F.: *Icarus* **193**, 588 (2008)
134. Volkov, A., Johnson, R.E., Tucker, O.J., Erwin, J.T.: *Astrophys. J. Lett.* **729**, L24 (2011)
135. Chamberlain, J.W., Hunten, D.M.: *Theory of Planetary Atmospheres*. Academic Press, New York (1987)
136. J. L. Fox, and A. Hać, *Icarus*, **204**, 527 (2009)
137. Koskinen, T.T., Sandel, B.R., Yelle, R.V., Capalbo, F.J., Holsclaw, G.M., McClintock, W.E., Edgington, S.: *Icarus* **226**, 1318 (2013)
138. Chamberlain, J.W.: *Planet. Space Sci.* **11**, 901 (1963)
139. Hunten, D.M.: *Planet. Space Sci.* **30**, 773 (1982)
140. Johnson, R.E.: *Energetic charged particle interactions with atmospheres and surfaces*. Springer, Berlin (1990)
141. Hunten, D.M.: *J. Atmos. Sci.* **30**, 1481 (1973)
142. Slanger, T.G.: Private communication
143. Nagy, A.F., Kim, J., Cravens, T.E.: *Ann. Geophys.* **8**, 251 (1990)
144. Futaana, Y., Chaufray, J.-Y., Smith, H.T., Garnier, P., Lichtenegger, H., Delva, M., Gröller, H., Mura, A.: *Space Sci. Rev.* **162**, 213 (2011)



Jane Fox Jane Fox received her PhD in Chemical Physics from Harvard University and has held positions at the State University of New York at Stony Brook and the Harvard/Smithsonian Astrophysical Observatory. She is a Fellow of the American Geophysical Union. Her research has focuses on the chemistry, luminosity, heating of the thermospheres/ionospheres of the planets, and their evolution.



Applications of Atomic and Molecular Physics to Global Change

89

Gonzalo González Abad , Kelly Chance , and Kate P. Kirby

Contents

89.1	Overview	1337
89.1.1	Global Change Issues	1337
89.1.2	Structure of the Earth's Atmosphere	1338
89.2	Atmospheric Models and Data Needs	1339
89.2.1	Modeling the Thermosphere and Ionosphere	1339
89.2.2	Heating and Cooling Processes	1339
89.2.3	Atomic and Molecular Data Needs	1340
89.3	Tropospheric Warming/Upper Atmosphere Cooling	1340
89.3.1	Incoming and Outgoing Energy Fluxes	1340
89.3.2	Tropospheric "Global" Warming	1340
89.3.3	Upper Atmosphere Cooling	1341
89.4	Stratospheric Ozone	1342
89.4.1	Production and Destruction	1342
89.4.2	The Antarctic Ozone Hole	1343
89.4.3	Arctic Ozone Loss	1344
89.4.4	Global Ozone Depletion	1344
89.5	Atmospheric Measurements	1344
	References	1345

Abstract

While there has been a general understanding and appreciation of the science involved in both global warming and stratospheric ozone depletion by atmospheric scientists for some time, a detailed understanding and rigorous proof have often been lacking. Over the last 20 years, there have been many advances made in filling in the

details, and there will continue to be rapid advances in the future. This means that any article or book discussing this topic becomes out of date as soon as it is written. Nevertheless, several recent references on these topics are recommended [1–3].

Atomic and molecular structure and spectroscopy, as well as collision processes involving atoms, molecules, ions and electrons, are important to the study of all planetary atmospheres.

Keywords

polar vortex · sulfate aerosol · ozone layer · total ozone column · ozone monitoring instrument · air quality · global warming · greenhouse effect · stratospheric ozone depletion

89.1 Overview

89.1.1 Global Change Issues

Over the last several decades there has been increasing concern about the global environment and the effect of human perturbations on it. This whole area, which involves a wide range of scientific disciplines, has become known as *global change*. Knowledge of processes taking place in the atmosphere, oceans, land masses, and plant and animal populations, as well as the interactions between these various Earth–system components is essential to an overall understanding of global change – both natural and human induced.

The processes of atomic and molecular physics find greatest application in the area of atmospheric global change. The three major issues that have received significant attention in both the media and the scientific literature are: (1) global warming, due to the buildup of infrared-active gases; (2) stratospheric ozone depletion due to an enhancement of de-

G. González Abad (✉)
Harvard-Smithsonian Center for Astrophysics
Cambridge, MA, USA
e-mail: ggonzalezabad@cfa.harvard.edu

K. Chance
Harvard-Smithsonian Center for Astrophysics
Cambridge, MA, USA
e-mail: kchance@cfa.harvard.edu

K. P. Kirby
American Physical Society
College Park, MD, USA
e-mail: kirby@aps.org

structive catalytic cycles; and (3) air quality and tropospheric pollution. These three problems are thought to be largely caused by atmospheric pollutants due to industrialized human society. However, the general problem of air pollution and its direct effects on plant and animal populations will not be addressed here.

89.1.2 Structure of the Earth's Atmosphere

The vertical temperature structure of the Earth's atmosphere shown in Fig. 89.1 provides an important nomenclature that is widely used [4]. The atmosphere is divided into regions called “-spheres”, in which the sign of the temperature gradient with respect to altitude, dT/dz , is constant. The regions in which the temperature gradient changes sign are called “-pauses”. The precise altitude pertaining to each of these regions can vary depending upon latitude and the time of year.

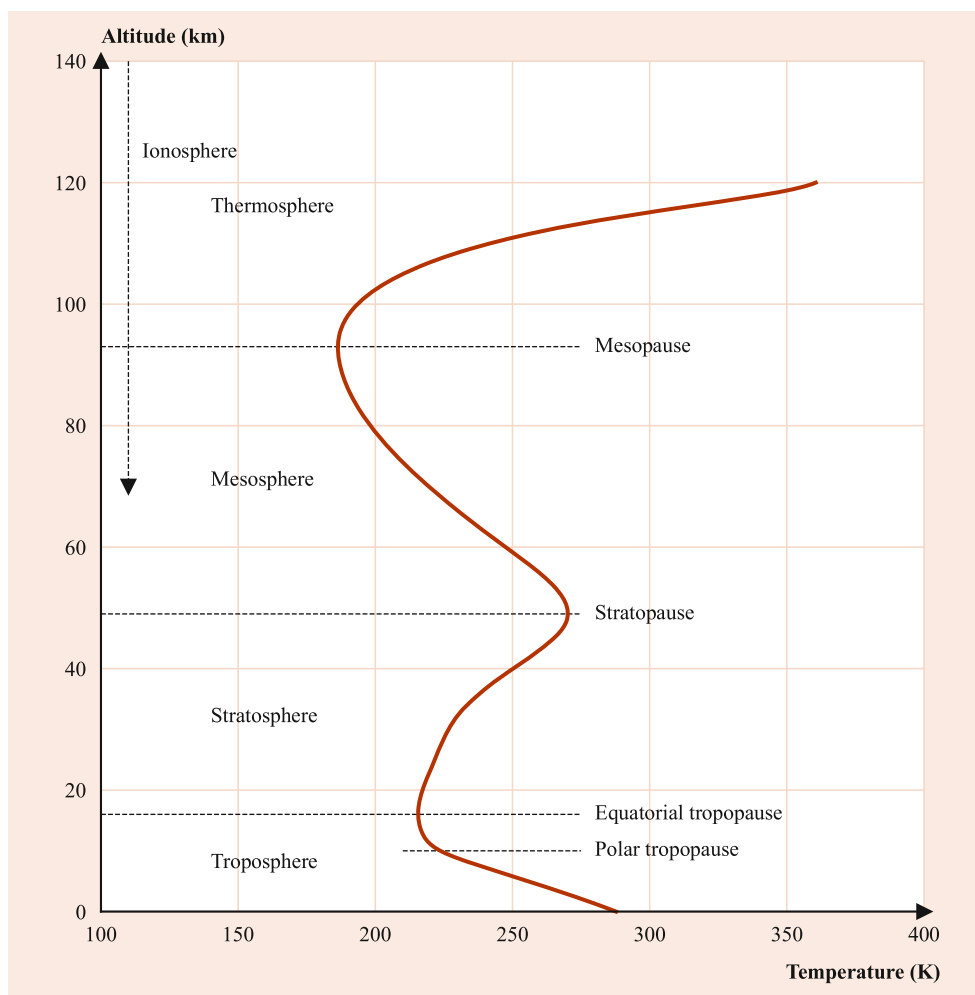
In the troposphere, covering the range from 0 to ≈ 15 km above the Earth surface. The temperature steadily decreases with altitude. This is the most complex region of the atmo-

sphere, as it interacts directly with plant and animal life, land masses, and the oceans. It is the region in which weather occurs.

The change in sign of the temperature gradient at the tropopause to a positive dT/dz in the stratosphere is due to heating by absorption of solar ultraviolet radiation, which photodissociates O_2 and O_3 . The stratosphere, extending from ≈ 15 to 50 km above the Earth, contains the ozone layer, which shields the Earth's surface from harmful ultraviolet radiation in the range 280–320 nm.

At the stratopause, the heating processes have become too weak to compete with the cooling processes, and throughout the mesosphere, approximately 50–85 km, the temperature again decreases with increasing altitude. Cooling processes, which will be discussed in Sect. 89.2.2, involve collisional excitation of molecular vibrational modes, which decay by radiating to space. The coldest temperatures in the atmosphere are found at the mesopause, where the temperature gradient once again becomes positive. From approximately 70 km upward, a very diffuse plasma called the ionosphere exists due to photoionization of atoms and molecules by short wavelength (UV and EUV) solar radiation.

Fig. 89.1 Vertical temperature profile of the atmosphere



Throughout the thermosphere, which extends from approximately 90 km upward, heating occurs because the atmosphere has become so thin that there are very few collisions and, thus, inefficient equilibration of the highly translationally excited atoms and ions with the molecular species, which can radiate in the infrared. This “bottleneck” for energy loss causes increased heating. In the thermosphere and ionosphere, the thermal inertia is very small, and there are huge temperature variations, both diurnally and with respect to solar activity.

The densities are low enough in the thermosphere, ionosphere, and mesosphere that the primary processes determining the chemical and physical characteristics of these regions are two-body processes and “half-collision events” discussed elsewhere in this volume: dissociative recombination, photoionization, photodissociation, charge transfer, and collisional excitation of molecular rotation and vibration. As the altitude decreases, the density increases. Then, three-body interactions, interactions on surfaces (of aerosols and ices), and complex chemical cycles together with dynamical effects such as winds determine the chemical and physical characteristics of the stratosphere and troposphere.

89.2 Atmospheric Models and Data Needs

While models are absolutely essential to the study of any system as complex as the Earth’s atmosphere, they play a particularly fundamental role in exploring global change issues. Models not only provide predictions of future changes but also allow exploration of sensitivities to particular parameters. Comparing the results of a model with observations ultimately tests and challenges scientific understanding. Of critical importance is the atomic and molecular data that goes into the models.

Generally, atmospheric models become increasingly complex as altitude decreases. General circulation models (GCMs), incorporating thousands of chemical reactions, global wind patterns, and abundances of large numbers of trace species, require supercomputers in order to model aspects of the troposphere and stratosphere [5]. Tropospheric chemistry and transport models, such as GEOS-CHEM [6], and CAM-Chem [7] model the sources, evolution, transport, and sinks of pollution, as well as the oxidative capacity of the troposphere.

89.2.1 Modeling the Thermosphere and Ionosphere

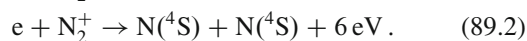
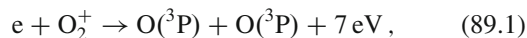
The data necessary for modeling of the thermosphere and ionosphere are described here. The primary components of

such a model include: a solar spectrum of photon fluxes as a function of wavelength, concentrations of neutral species, and photoabsorption, photodissociation, and photoionization cross sections as functions of wavelength. The computer code brings all these elements together, calculating opacity as the solar radiation propagates downward through the atmosphere, keeping track of ion production and electron production. Additional steps are required to calculate the abundances of trace species such as NO^+ , necessitating the inclusion of all relevant ion–neutral reactions. Electron energy degradation can be tracked by including inelastic collisions of electrons with ions, atoms, and molecules.

The primary neutral species are N_2 , O_2 , O , and He . Below about 100 km, the atmosphere is fully mixed by turbulence in the ratio 78% N_2 , 21% O_2 , and 1% trace species such as O_3 and CO_2 . Above 100 km, turbulence dies out, and the atmospheric species are in diffusive equilibrium, distributed by their molecular weight, with atomic oxygen dominating above ≈ 150 km and He dominating much higher. The major ions are N_2^+ , O_2^+ , O^+ , and NO^+ .

89.2.2 Heating and Cooling Processes

In the upper atmosphere, heating occurs through absorption of short wavelength solar radiation to produce ionization and dissociation and is mediated by collisions between electrons, ions, and neutrals. Ions and electrons are created during the daytime and to a great extent disappear during the night with the absence of solar radiation. Processes such as dissociative recombination, the primary electron loss mechanism, heat the gas:



Cooling takes place when the kinetic energy of the gas is transformed through collisions into internal energy, which can then be radiated away. The primary coolant above ≈ 200 km is the fine structure transition of atomic oxygen, $\text{O}(^3\text{P}_1) \xrightarrow{h\nu} \text{O}(^3\text{P}_2)$, which is excited by thermal collisions and radiates at $63 \mu\text{m}$. From approximately 120 to 200 km, the fundamental band of NO , $v = 1 \rightarrow v = 0$, which is excited by collisions with atomic oxygen and radiates at $5.3 \mu\text{m}$, dominates the cooling. Below 120 km and throughout the mesosphere and stratosphere, the primary coolant is the ν_2 band of CO_2 radiating at $15 \mu\text{m}$. This transition is excited by collisions of CO_2 and atomic oxygen. Cooling throughout most of the atmosphere is accomplished through trace species because the major molecular species, N_2 and O_2 , are not infrared active.

89.2.3 Atomic and Molecular Data Needs

Knowledge of rate coefficients for ion–neutral and neutral–neutral reactions as functions of vibrational and rotational excitation of the reactants is becoming increasingly important, as there is recent evidence of more internal excitation of molecular species than had previously been thought [8]. Accurate photoabsorption, photodissociation, and photoionization cross sections as functions of wavelength for all the relevant species are important parameters determining the reliability and ultimate accuracy of an atmospheric model. Compilations of data, such as that by *Conway* [9] and *Kirby et al.* [10] are very useful but can rapidly become outdated. The Smithsonian Astrophysical Observatory maintains the world standard database, HITRAN, for molecular line parameters and absorption cross sections from the microwave through the ultraviolet for analysis of atmospheric spectra [11]. Discussions of the needs for atomic and molecular data in the context of space astronomy, but including applications to atmospheric physics, can be found in a book edited by *Smith and Wiese* [12]. Atomic and molecular data are available at the Virtual Atomic and Molecular Data Center Consortium [13].

89.3 Tropospheric Warming/Upper Atmosphere Cooling

89.3.1 Incoming and Outgoing Energy Fluxes

The overall temperature of a planet is determined by a balance between incoming and outgoing energy fluxes. In a steady state, the planet must radiate as much energy as it absorbs from the sun. The Earth, radiating as a black body at an effective temperature T_E , obeys the Stefan–Boltzmann law in which the energy emitted is expressed as $\sigma T_E^4 4\pi R_E^2$, with σ the Stefan–Boltzmann constant, and R_E the radius of the Earth. An equation expressing the equality of energy absorbed and energy emitted can be written as [14]

$$F_s \pi R_E^2 (1 - A) = \sigma T_E^4 4\pi R_E^2, \quad (89.3)$$

where A is the albedo of the Earth (the fraction of solar radiation reflected from, rather than absorbed by, the Earth), F_s is the solar flux at the edge of the Earth’s atmosphere, and πR_E^2 is the Earth’s area normal to the solar flux. Solving this equation for T_E , one obtains $T_E \approx 255 \text{ K}$ (-18°C).

The sun, which has a surface temperature of approximately 6000 K, emits most of its radiation in the 0.2–4.0 μm region of the spectrum (200–4000 nm). The upper atmosphere of the Earth (thermosphere, ionosphere, mesosphere, and stratosphere) absorbs all the solar radiation shortward of 320 nm. The atmosphere of the Earth absorbs only weakly in the visible region of the spectrum where the solar flux peaks.

The Earth, with an effective radiating temperature of 255 K, emits mainly long-wavelength radiation in the 4–100 μm region. Molecules naturally present in the atmosphere in trace amounts, such as carbon dioxide, water, and methane, absorb strongly in this wavelength region [15]. Radiation coming from the Earth is thus absorbed, reradiated back to the surface and thermalized through collisions with the ambient gas. This trapping of the radiation produces an additional warming of 33 K. Thus, the mean surface temperature of the Earth is 288 K, not 255 K as found for T_E above. This effect of the Earth’s atmosphere is known as the greenhouse effect. The greenhouse effect is what makes Earth habitable for life as we know it. Gases, both natural and manmade, which absorb strongly in the 4–100 μm region, are known collectively as greenhouse gases.

89.3.2 Tropospheric “Global” Warming

According to the Intergovernmental Panel on Climate Change (IPCC) Fifth Assessment Report (AR5) the “globally averaged combined land and ocean surface temperature data as calculated by a linear trend, show a warming of 0.85 [0.65 to 1.06] $^\circ\text{C}$, over the period 1880 to 2012.” The IPCC has also concluded that “Human influence on the climate system is clear. This is evident from the increasing greenhouse gas concentrations in the atmosphere, positive radiative forcing, observed warming, and understanding of the climate system” [16]. The Arctic region has warmed by an estimated 1 $^\circ\text{C}$ in the past two decades, leading to substantial changes in the cryosphere. Antarctic sea ice was stable from 1840 to 1950 but has since declined sharply. The extent of sea ice shows a 20% decline since about 1950 [17, 18].

From air bubbles trapped at different depths in polar ice, it is possible to determine carbon dioxide and methane concentrations several thousand years ago. In 2011, CO_2 levels reached 390.5 ppm, 40% greater than in 1750 [19]. In 2013, CO_2 levels passed the 400 ppm threshold for the first time. Over the next century, the total amount of CO_2 in the atmosphere since 1900 is expected to double to as much as 600 ppm [20]. This increase is due primarily to the burning of fossil fuels.

Although methane is present at levels several orders of magnitude less than CO_2 , it is increasing much more rapidly. Methane concentrations have more than doubled over the last 200 years due to industrial processes, fuels, and agriculture [19].

The manmade chlorofluorocarbons (CFCs), which have been widely used as refrigerants and in industry, increased in the atmosphere at a rate of over 5% per year between the 1970s and the 1990s. Due to the Montreal Protocol there has been a reduction or inversion of this trend [21].

Ozone, which is a primary component of chemical smog, is a pollutant when it occurs in the troposphere and an ef-

fective greenhouse gas. It has been increasing worldwide as well. This buildup of CO₂, CH₄, CFCs, and tropospheric O₃ causes a problem. In much of the spectral region from 5–100 μm, there is 100% absorption of radiation by the atmosphere – due mainly to naturally occurring water vapor. There is, however, a region of rather weak absorption, from ≈ 7–15 μm, known as the “atmospheric window”. Increased concentrations of the greenhouse gases strengthen the absorption in this region, tending to “close” this window, thus increasing the infrared opacity of the atmosphere. The increased opacity causes an immediate decrease in the thermal radiation from the planet–atmosphere system, forcing the temperature to rise until the energy balance is restored [22].

It is difficult to prove that the buildup of greenhouse gases is the cause of the observed temperature rise. Other possible causes include slight changes in solar activity and irradiance, and changes in ocean currents, which may have a profound effect on global temperature and climate. These are areas of active research.

Given the increase in concentrations of greenhouse gases that has occurred and is predicted to continue, the change in radiative heating of the troposphere can be calculated. Models generally predict an increase in tropospheric temperatures ranging from 1.5 to 5 °C, considering different emission scenarios over the next century [23]. The 3.5 °C range in temperature is due to the ways that different models incorporate climate feedbacks. Climate feedbacks include water vapor, snow and sea ice, and aerosols and clouds. Rising temperatures increase the concentration of water vapor, which is itself a greenhouse gas, producing further warming. Rising temperatures reduce the extent of reflective snow and ice, thus reducing the Earth’s albedo. This leads to increased absorption of solar radiation, further increasing temperatures. Clouds and aerosols both contribute to the albedo, thereby reducing the solar flux reaching the Earth, and absorb infrared radiation causing temperatures to rise. The modeling of clouds and aerosols and their radiative properties is very difficult and is one of the largest sources of uncertainty in the climate models. Understanding the role that the ocean, with its giant heat capacity, plays in global warming and identifying and quantifying the various interactions occurring at the ocean–atmosphere interface are vital areas of research, which will affect the size of the predicted temperature increase. At present, there are few obvious opportunities for traditional atomic and molecular physics to play a significant part in global-warming research.

89.3.3 Upper Atmosphere Cooling

The buildup of CO₂ has an even greater effect on the temperature in the upper atmosphere than on that in the troposphere [24]. As discussed in Sect. 89.2.2, CO₂ is a coolant

in the stratosphere, mesosphere, and thermosphere, but as a greenhouse gas it is involved in heating the troposphere. The explanation for this revolves around the collision physics issue of quenching versus radiating.

In the troposphere, CO₂ absorbs infrared radiation coming from the Earth, exciting the ν_2 vibrational bending mode at 15 μm. The excited molecule can either reradiate or collisionally de-excite. In the lower atmosphere, where densities are large, the lifetime against collisions is very short, and the excited molecule is rapidly quenched. This transfer of energy from radiation through collisions into the kinetic energies of the colliding partners results in a net heating.

In the stratosphere and above, atomic oxygen collisions with CO₂ excite this same bending mode, but at these higher altitudes, densities are lower and quenching is greatly reduced. The excited molecule radiates, and the radiation escapes into space. A net cooling results because the opacity is low at these altitudes. The cooling of the stratosphere has also been linked with ozone trends [25].

Roble and coworkers [26, 27] investigated the doubling of CO₂ and CH₄ concentrations (as predicted for the twenty-first century) in the mesosphere and at the lower boundary of the thermosphere. Using sophisticated atmospheric general circulation models, they predict that the stratosphere, mesosphere, and thermosphere will show significant cooling – the largest cooling of 40–50 °C occurring in the thermosphere.

The extent of this cooling very much depends on the rate coefficient for the O + CO₂ excitation of the ν_2 bending mode. *Rishbeth* and *Roble* [26] assumed a value for this rate coefficient of 1×10^{-12} cm³/s, intermediate between the value of *Sharma* and *Wintersteiner* [28] (6×10^{-12} cm³/s) and an earlier value of 2×10^{-13} cm³/s used by *Dickinson* [29]. The *Sharma* and *Wintersteiner* value, based on observations of 15 μm emission in the atmosphere around 100–150 km, was recently confirmed by *Rodgers* et al. [30], but *Pollock* et al. [31] obtained a value of 1.2×10^{-12} cm³/s in laboratory experiments. Using the larger rate coefficient would result in even greater cooling [32].

The overall consequences of such a large temperature decrease in the upper atmosphere have not been fully explored – particularly the question as to how the dynamics of the atmosphere will be affected. Since many chemical reactions depend on temperature, there may be considerable readjustments in the vertical distribution of minor species in the atmosphere. Cooler temperatures cause the atmosphere to contract, reducing densities and, consequently, satellite drag. Cooler temperatures may also increase the occurrence of polar stratospheric clouds, thereby affecting ozone depletion (Sect. 89.4).

Most significantly, tropospheric warming and upper atmosphere cooling both result from a buildup of CO₂. The size of the predicted cooling is greater by an order of magnitude than the amount of the predicted heating. Thus, it may be

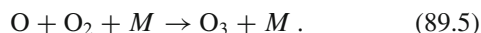
possible to monitor the global warming trend by observing the predicted cooling in the upper atmosphere.

There is evidence of this cooling in the stratosphere and mesosphere. *Keckhut* and coworkers [33] found cooling rates of 1.1 ± 0.6 K at 25 km, 1.7 ± 0.7 K between 35–50 km and 3.3 ± 0.9 K at 60 km per decade, while *Santer* and coworkers linked these changes in the thermal structure of the atmosphere with human activities [34]. *Gadsden* [35] also found that the frequency of occurrence of noctilucent clouds, the highest-lying clouds in the atmosphere, has more than doubled over the last 25 years. He calculated that this change could result from a decrease in the mean temperature at the mesopause of 6.4°C during this time period. However, increased concentrations of water produced by oxidation of increased amounts of methane may be responsible for the more frequent appearance of these clouds. This is an ongoing area of research.

89.4 Stratospheric Ozone

89.4.1 Production and Destruction

Ozone production takes place continually in the stratosphere during daylight hours, as molecular oxygen is photodissociated, and the resulting oxygen atoms undergo three-body recombination with O_2 :



Ozone can be destroyed through photodissociation:

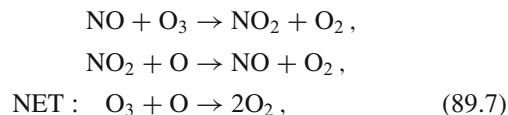


but because an oxygen atom is produced, which immediately recombines with another O_2 to form O_3 , no net loss of O_3 results. The photodissociations of O_2 and O_3 are important heating processes in the stratosphere.

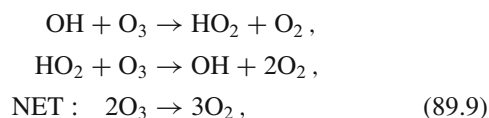
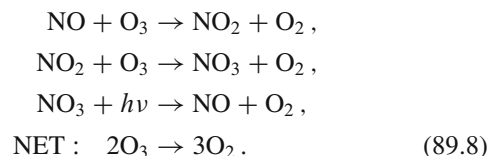
The amount of ozone in the stratosphere is quite variable, changing significantly with the seasons and with latitude. In the lower stratosphere, much of the ozone is created over the equatorial regions and then transported toward the poles.

In addition to being photodissociated, O_3 is destroyed by reactions with radicals that are involved in catalytic cycles. The shorthand notation for the major cycles, NO_x , HO_x , and ClO_x (BrO_x) refers to the catalytically active forms involved in the cycles. Our knowledge about the relative importance of these catalytic cycles in ozone destruction has increased dramatically over the last decades. A number of these cycles are given below, with the ozone-destroying step listed first, and the rate-limiting step closing the catalytic cycle and regenerating the ozone-destroying radical listed last. The net effect

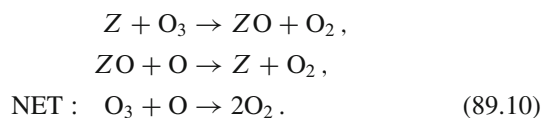
in each of these cases is to convert ozone and atomic oxygen (otherwise known as odd-oxygen) into molecular oxygen:



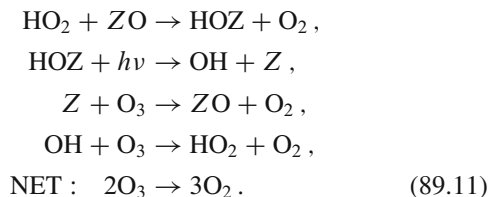
and



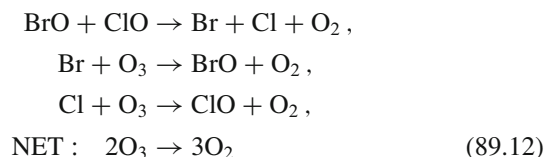
and the halogen cycle, in which $Z = \text{Cl}$ or Br :



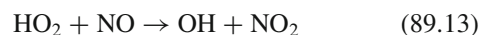
The following series of reactions couples the HO_x and halogen cycles:



Finally, the reaction set



is also important in the halogen destruction cycle. The coupling between these different cycles by reactions such as



turns out to be very important in understanding the details of ozone destruction, such as how much each mechanism contributes to the destruction as a function of altitude and in the presence of aerosols. *Wennberg* et al. [36] recently showed that catalytic destruction by NO_2 , which for two decades was considered to be the predominant loss process, accounted for

less than 20% of the O_3 removal in the lower stratosphere during May 1993. They further showed that the cycle involving the hydroxyl radical accounted for nearly 50% of the total O_3 removal, and the halogen-radical chemistry was responsible for the remaining 33%.

The NO_x and HO_x cycles occur naturally, whereas the ClO_x and BrO_x cycles are due mainly to manmade chemicals – CFCs and halons. The amplification that takes place through a catalytic cycle is the reason that these chemicals, which are only present at the level of parts per trillion, can have such a destructive effect.

It is useful to think in terms of a total chemical budget for a radical, such as Cl, that enters into a cycle. Chlorine is put into the stratosphere when chemicals such as CF_2Cl_2 are released into the atmosphere. Such compounds are chemically inert and insoluble in water, and therefore are not easily cleansed out of the lower atmosphere. In the stratosphere, however, the CF_2Cl_2 is subjected to solar UV radiation and is photodissociated, producing the Cl radical. Chlorine exists in the upper atmosphere in catalytically active forms, Cl and ClO, as well as in stable, reservoir species, HCl and ClONO₂. The total chlorine budget consists of both the catalytically active plus reservoir species. Reactions that reduce the formation of reservoir species, or convert reservoir species to catalytically active forms, contribute to the ozone destruction. Photolysis of stable reservoir species, such as ClONO₂, can produce catalytically active forms. Bromine has an identical cycle to that of chlorine but is 50 to 100 times more destructive than Cl because it does not react readily to go into its reservoir form, HBr. A knowledge of the photodestruction rates of all such species is important for an understanding of the overall ozone photochemical depletion problem.

Studies of the Antarctic ozone hole show that gas phase photochemical cycles, as given above, are not the whole story with respect to ozone depletion. Heterogeneous chemistries taking place on the surfaces of ice crystals and sulfate aerosols also play an important role. These are discussed briefly in Sects. 89.4.2 and 89.4.4.

89.4.2 The Antarctic Ozone Hole

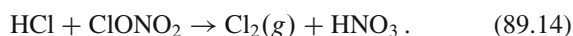
The ozone depletion problem was largely theoretical until the discovery of the ozone hole over Antarctica. Following the 1985 announcement by *Farman et al.* [37] of ground-based observations of significant decline in O_3 concentrations during springtime in the Southern Hemisphere, it was possible to map this event using archived satellite data beginning in 1979. The data depict a worsening event throughout the early 1980s. In 1987, 70% of the total O_3 column over Antarctica was lost during September and early October, and the areal extent of the hole was $\approx 10\%$ of the Southern Hemisphere. The ozone hole continued to grow in depth and width dur-

ing the 1990s [38]. Recent data shows that this phenomenon continues, but due to the implementation of the Montreal protocol there are signs of decline in the Antarctic ozone depletion [39, 40].

The link between the release and buildup of manmade CFCs and the ozone hole over Antarctica was convincingly established by *Anderson et al.* [41] through in situ observations from high altitude aircraft flights into the polar vortex during the end of the polar night and the beginning of Antarctic spring in 1987.

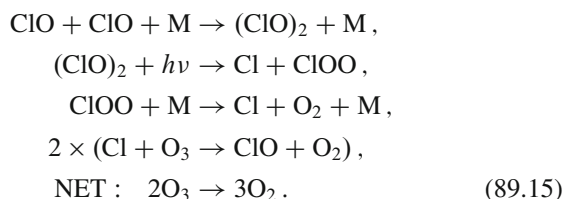
The polar vortex is a stream of air circling Antarctica in the winter, creating an isolated region that becomes very cold during the polar night. Flights into the vortex were able to document a heightened, increasing level of ClO and a monotonically decreasing O_3 concentration over a 3–4 week time period during late September and early October.

The mechanism repartitioning the chlorine from its reservoir form into its catalytically active form is a heterogeneous process occurring on the surfaces of polar stratospheric clouds. At the cold temperatures during the polar night, polar stratospheric clouds form, consisting of ice and nitric acid trihydrate. Gaseous ClONO₂ collides with HCl that has been adsorbed onto the surface of the cloud crystals. Chlorine gas is liberated, and the nitric acid formed in the reaction remains in the ice [41]:

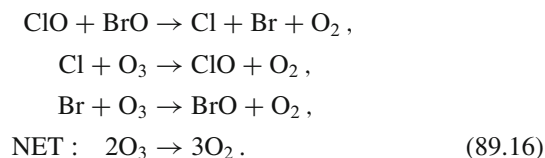


As solar radiation starts to penetrate the region at the beginning of spring, the Cl_2 molecules are rapidly photodissociated, producing Cl atoms, which initiate the catalytic destruction of O_3 . As there are few oxygen atoms available to complete the catalytic cycles, several mechanisms for regenerating the Cl and Br radicals that involve only the ClO and BrO molecules themselves have been proposed.

Mechanism I [42]



Mechanism II [43]



While Mechanism I accounts for 75% of the observed ozone loss, the sum of I and II yields a destruction rate in harmony with the observed O_3 loss rates [41].

89.4.3 Arctic Ozone Loss

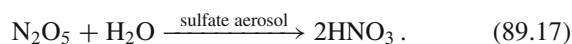
The region around the North Pole does not appear to exhibit an ozone hole as severe as that found in the Antarctic. Several factors lessen the probability of a significant ozone hole developing in the Arctic. First, a stable polar vortex does not get well established due to increased atmospheric turbulence from the greater land surface area in the Northern Hemisphere. Second, temperatures during the Arctic winter do not get as cold as during the Antarctic winter, so that polar stratospheric clouds (PSCs) do not form as easily. As seen in the preceding section, the surfaces of PSCs play an essential role in the O₃ destruction mechanisms in the Antarctic.

However, ozone levels are showing 20–25% reductions during February and March [44] over a much larger area around the North Pole than in the South. Thus, ozone destruction is taking place during the transition from polar winter to spring in the Arctic, but the phenomenon is more widespread, diffuse, and not as well contained as in the Antarctic.

89.4.4 Global Ozone Depletion

Over the last four decades, satellite instruments have measured the total ozone column in the atmosphere. During this time ozone levels decreased globally. Only recently have they stabilized as a consequence of the policies introduced in Montreal protocol agreements. A recent analysis indicates the first evidence of recovery of stratospheric ozone levels, with diminished rates of ozone loss at altitudes of 35–45 km, coupled with a slowdown in the increase in stratospheric loading of chlorine [38].

Heterogeneous reactions on aerosol surfaces, as well as the homogeneous gas phase chemical cycles mentioned earlier, must be invoked to explain the global decline in ozone levels. A particularly important reaction appears to be the hydrolysis of N₂O₅ on sulfate aerosols. This occurs very rapidly, converting reactive nitrogen, NO₂, into its reservoir species HNO₃:



The N₂O₅ is formed at night by reaction of NO₂ and NO₃. Following the hydrolysis of N₂O₅, there is less reactive NO₂ available to convert ClO into its reservoir species, ClONO₂, and less NO₂ around to convert OH into the reservoir species, HNO₃. A heightened sensitivity of the ozone to increasing levels of CFCs develops. It has been shown that certain regions of significantly depleted ozone also show high concentrations of sulfate aerosols [45]. In addition, measurements of the ratio of catalytically active nitrogen to

total nitrogen can be reproduced using the above heterogeneous reaction, and not by using gas phase processes alone. The study of further mechanisms at varying altitudes and latitudes is an active area of research.

Record low global ozone measurements, 2 to 3% lower than any previous year, were reported beginning in 1992 [46] and continuing well into 1993. The increase in naturally occurring aerosols due to the eruption of Mount Pinatubo in June 1991 appears to explain this decline. During the winter of 1993–1994, the total ozone levels returned to levels slightly above normal [47], presumably because the excess aerosols had been removed from the stratosphere by natural sedimentation processes.

The continuing buildup of CO₂ is predicted to contribute to increase cooling of the stratosphere. Declining temperatures in the stratosphere may increase the frequency of formation of polar stratospheric clouds that drive the destructive heterogeneous chemistry creating the Antarctic ozone hole. An increased occurrence of these clouds outside of the polar regions could affect ozone levels globally. There are also indications that certain ozone depletion chemistries taking place on the surface of sulfate aerosols may also be enhanced by lower temperatures [45].

Ozone itself is the dominant heat source in the lower stratosphere. Decreasing the amount of ozone drives temperatures still lower [48]. It is unfortunate that the two most significant atmospheric global change effects – the buildup of CO₂ and the enhanced ozone destruction due to manmade CFCs – both cause decreasing temperatures in the stratosphere, which may further enhance the destructiveness of the ozone's photochemical cycles.

89.5 Atmospheric Measurements

Ground-based observations, as well as measurements made by instruments carried aloft in satellites, balloons, rockets, and high-flying aircraft, allow to explore the atmosphere.

Measurements may be made either in situ or by remote sensing techniques. The region of the atmosphere from ≈ 60 to 120 km, encompassing the mesosphere and lower thermosphere and ionosphere, is studied by in situ measurements using sounding rockets as it is too high for balloons and aircraft and too low (i.e., too much drag) for satellites. A comprehensive description of rocket measurements is provided by *Larsen* [49]. Remote sensing experiments are essential to observe the upper atmosphere. A comprehensive book on the subject is recommended [50].

Most of the instruments used to make atmospheric measurements were developed in molecular physics and spectroscopy laboratories. Even experiments utilizing sophisticated techniques, such as laser-induced fluorescence, and instruments, such as Fourier transform spectrometers, are be-

ing flown on payloads. An excellent compendium of satellite instruments for stratospheric research has been assembled by Grant [51]. A detailed description of past satellite instruments can be found in the *Encyclopedia of Atmospheric Science* [52–60].

A combination of good laboratory experiments, theoretical calculations, and ingenuity is necessary to extract accurate information from measurements made in the atmosphere. For instance, in order to understand the complicated interactions of the different photochemical cycles involved in ozone chemistry, spectroscopic emissions and absorptions of the many trace species are used to measure concentration profiles. An accurate knowledge of the emission spectroscopy of species such as OH, HO₂, H₂O₂, H₂O, O₃, HNO₃, NO₂, N₂O, N₂O₅, HNO₃, ClONO₂, BrO, HCl, HOCl, and ClO is essential. Such measurements provide a rigorous test of atmospheric models. The NASA EOS Aura satellite, launched in 2004, carries instruments making global measurements of a number of these species [61–63]. One year before, in August 2003, the Canadian Space Agency launched the ACE-FTS instrument [64]. Taking advantage of the high signal-to-noise measurements inherent to the solar occultation technique it was able to measure vertical profile distributions of more than 60 molecules and isotopologues globally.

In order to analyze the data and deconvolve some of the line profiles to give information on concentrations as a function of altitude, molecular data such as line strengths and pressure broadening coefficients are needed [11].

Until recently, it was impossible for remote sensing experiments to distinguish between ozone occurring in the stratosphere (where it is formed naturally) and ozone occurring in the troposphere (where it is a pollutant). Satellite instruments such as the ESA Global Ozone Monitoring Experiment (GOME), the Scanning Imaging Absorption Spectrometer for Atmospheric Cartography (SCIAMACHY), and the Ozone Monitoring Instrument (OMI) have a broad enough spectral coverage and a high enough resolution that the temperature dependence of the ozone absorption features from 300–340 nm, known as the Huggins bands, can be used to separate out the ozone concentrations in the middle and lower atmospheres [65, 66].

The future of atmospheric remote sensing from space looks very promising. Projects around the world are increasing the number and quality of observations, allowing scientists to investigate the time and spatial scales previously out of reach. The Sentinel-5 Precursor satellite launched by the European Space Agency in 2017 carrying the TROPOMI instrument [67] is starting to show what future geostationary instruments, like the US Tropospheric Emissions: Monitoring of Pollutants (TEMPO) [68], the Korean Geostationary Environment Spectrometer (GEMS), and the European Space Agency's Sentinel-4 instrument, each having even higher spatial resolution, will be capable of. To keep track

of past and current satellite missions, as well as instrumental techniques for atmospheric observation, the NASA Earth Science site (<https://www.nasa.gov/topics/earth/index.html>) and the ESA Earth Observation site (https://www.esa.int/Our_Activities/Observing_the_Earth) are extremely useful.

References

- Houghton, J.: *Global Warming: The Complete Briefing*, 5th edn. Cambridge University Press, Cambridge (2015)
- Staelin, J., Harris, N.R.P., Appenzeller, C., Eberhard, J.: Ozone trends: a review. *Rev. Geophys.* **39**(2), 231–290 (2001)
- Graedel, T.E., Crutzen, P.J., Freeman, W.H.: *Atmospheric Change: An Earth System Perspective*. *J. Chem. Educ.* **70**(9), A252 (1993)
- Roble, R.G.: *Atmospheric Structure*. In: *Digital Encyclopedia of Applied Physics*, pp. 201–224. American Cancer Society (2003)
- Brasseur, G.P., Jacob, D.J.: *Modeling of Atmospheric Chemistry*. Cambridge University Press, Cambridge (2017)
- Bey, I., et al.: Global modeling of tropospheric chemistry with assimilated meteorology: Model description and evaluation. *J. Geophys. Res. Atmos.* **106**(D19), 23073–23095 (2001)
- Lamarque, J.-F., et al.: CAM-chem: description and evaluation of interactive atmospheric chemistry in the Community Earth System Model. *Geosci. Model Dev.* **5**(2), 369–411 (2012)
- Armstrong, P.S., Lipson, S.J., Dodd, J.A., Lowell, J.R., Blumberg, W.A.M., Nadile, R.M.: Highly rotationally excited NO(ν ,J) in the thermosphere from CIRRIS 1A limb radiance measurements. *Geophys. Res. Lett.* **21**(22), 2425–2428 (1994)
- Conway, R. R.: *Photoabsorption and Photoionization Cross Sections of O, O₂, and N₂ for Photoelectron Production Calculations: A Compilation of Recent Laboratory Measurements*. (1988)
- Kirby, K., Constantinides, E.R., Babeu, S., Oppenheimer, M., Victor, G.A.: Photoionization and photoabsorption cross sections of He, O, N₂ and O₂ for aeronomic calculations. *At. Data Nucl. Data Tables* **23**(1), 63–81 (1979)
- Gordon, I.E., et al.: The HITRAN2016 molecular spectroscopic database. *J. Quant. Spectrosc. Radiat. Transf.* **203**, 3–69 (2017)
- Smith, P.L., Wiese, W.L. (eds.): *Atomic and Molecular Data for Space Astronomy: Needs, Analysis, and Availability*. Springer, New York (1992)
- Dubernet, M.L., et al.: The virtual atomic and molecular data centre (VAMDC) consortium. *J. Phys. B. At. Mol. Opt. Phys.* **49**(7), 074003 (2016)
- Wayne, R.P.: *Chemistry of Atmospheres: An Introduction to the Chemistry of the Atmospheres of Earth, the Planets, and their Satellites*, 3rd edn. Oxford University Press, Oxford, New York (2000)
- Mitchell, J.F.B.: The 'Greenhouse' effect and climate change. *Rev. Geophys.* **27**(1), 115–139 (1989)
- Intergovernmental Panel on Climate Change: Summary for Policymakers. In: *Climate Change 2013 – The Physical Science Basis: Working Group I Contribution to the Fifth Assessment Report of the Intergovernmental Panel on Climate Change*, pp. 1–30. Cambridge University Press (2014)
- Curran, M.A.J., van Ommen, T.D., Morgan, V.I., Phillips, K.L., Palmer, A.S.: Ice Core Evidence for Antarctic Sea Ice Decline Since the 1950s. *Science* **302**(5648), 1203–1206 (2003)
- Wolff, E.W.: Whither Antarctic Sea Ice? *Science* **302**(5648), 1164–1164 (2003)
- Intergovernmental Panel on Climate Change: Observations: Atmosphere and Surface. In: *Climate Change 2013 – The Physical Science Basis: Working Group I Contribution to the Fifth Assess-*

- ment Report of the Intergovernmental Panel on Climate Change, pp. 159–254. Cambridge University Press (2014)
20. Firor, J.: *The Changing Atmosphere*. Yale University Press, New Haven (1990)
 21. Montzka, S.A., Butler, J.H., Elkins, J.W., Thompson, T.M., Clarke, A.D., Lock, L.T.: Present and future trends in the atmospheric burden of ozone-depleting halogens. *Nature* **398**(6729), 690–694 (1999)
 22. Hansen, J., et al.: Climate impact of increasing atmospheric carbon dioxide. *Science* **213**(4511), 957–966 (1981)
 23. Intergovernmental Panel on Climate Change: Long-term Climate Change: Projections, Commitments and Irreversibility Pages 1029 to 1076. In: *Climate Change 2013 – The Physical Science Basis: Working Group I Contribution to the Fifth Assessment Report of the Intergovernmental Panel on Climate Change*, pp. 1029–1136. Cambridge University Press (2014)
 24. Cicerone, R.J.: Greenhouse cooling up high. *Nature* **344**(6262), 104–105 (1990)
 25. Thompson, D.W.J., Solomon, S.: Understanding Recent Stratospheric Climate Change. *J. Climate* **22**(8), 1934–1943 (2009)
 26. Rishbeth, H., Roble, R.G.: Cooling of the upper atmosphere by enhanced greenhouse gases – modelling of thermospheric and ionospheric effects. *Planet. Space. Sci.* **40**(7), 1011–1026 (1992)
 27. Roble, R.G., Dickinson, R.E.: How will changes in carbon dioxide and methane modify the mean structure of the mesosphere and thermosphere? *Geophys. Res. Lett.* **16**(12), 1441–1444 (1989)
 28. Sharma, R.D., Wintersteiner, P.P.: Role of carbon dioxide in cooling planetary thermospheres. *Geophys. Res. Lett.* **17**(12), 2201–2204 (1990)
 29. Dickinson, R.E.: Infrared radiative cooling in the mesosphere and lower thermosphere. *J. Atmos. Terr. Phys.* **46**(11), 995–1008 (1984)
 30. Rodgers, C.D., Taylor, F.W., Muggenridge, A.H., López-Puertas, M., López-Valverde, M.A.: Local thermodynamic equilibrium of carbon dioxide in the upper atmosphere. *Geophys. Res. Lett.* **19**(6), 589–592 (1992)
 31. Pollock, D.S., Scott, G.B.I., Phillips, L.F.: Rate constant for quenching of CO₂(010) by atomic oxygen. *Geophys. Res. Lett.* **20**(8), 727–729 (1993)
 32. Bougher, S.W., Hunten, D.M., Roble, R.G.: CO₂ cooling in terrestrial planet thermospheres. *J. Geophys. Res. Planets* **99**(E7), 14609–14622 (1994)
 33. Keckhut, P., Schmidlin, F.J., Hauchecorne, A., Chanin, M.L.: Stratospheric and mesospheric cooling trend estimates from u.s. rocketsondes at low latitude stations (8°S–34°N), taking into account instrumental changes and natural variability. *J. Atmos. Sol. Terr. Phys.* **61**(6), 447–459 (1999)
 34. Santer, B.D., et al.: Human and natural influences on the changing thermal structure of the atmosphere. *PNAS* **110**(43), 17235–17240 (2013)
 35. Gadsden, M.: A secular change in noctilucent cloud occurrence. *J. Atmos. Terr. Phys.* **52**(4), 247–251 (1990)
 36. Wennberg, P.O., et al.: Removal of Stratospheric O₃ by Radicals: In Situ Measurements of OH, HO₂, NO, NO₂, ClO, and BrO. *Science* **266**(5184), 398–404 (1994)
 37. Farman, J.C., Gardiner, B.G., Shanklin, J.D.: Large losses of total ozone in Antarctica reveal seasonal ClO_x/NO_x interaction. *Nature* **315**(6016), 207–210 (1985)
 38. Scientific Assessment of Ozone Depletion: 2014, World Meteorological Organization, Global Ozone Research and Monitoring Project-Report No. 55. World Meteorological Organization (WMO), Geneva (2014)
 39. Kuttippurath, J., Nair, P.J.: The signs of Antarctic ozone hole recovery. *Sci Rep* **7**(1), 585 (2017)
 40. Strahan, S.E., Douglass, A.R.: Decline in Antarctic Ozone Depletion and Lower Stratospheric Chlorine Determined From Aura Microwave Limb Sounder Observations. *Geophys. Res. Lett.* **45**(1), 382–390 (2018)
 41. Anderson, J.G., Toohey, D.W., Brune, W.H.: Free Radicals Within the Antarctic Vortex: The Role of CFCs in Antarctic Ozone Loss. *Science* **251**(4989), 39–46 (1991)
 42. Molina, L.T., Molina, M.J.: Production of chlorine oxide (Cl₂O₂) from the self-reaction of the chlorine oxide (ClO) radical. *J. Phys. Chem.* **91**(2), 433–436 (1987)
 43. Prather, M.J., Watson, R.T.: Stratospheric ozone depletion and future levels of atmospheric chlorine and bromine. *Nature* **344**(6268), 729–734 (1990)
 44. Manney, G.L., et al.: Chemical depletion of ozone in the Arctic lower stratosphere during winter 1992–93. *Nature* **370**(6489), 429–434 (1994)
 45. Fahey, D.W., et al.: In situ measurements constraining the role of sulphate aerosols in mid-latitude ozone depletion. *Nature* **363**(6429), 509–514 (1993)
 46. Gleason, J.F., et al.: Record Low Global Ozone in 1992. *Science* **260**(5107), 523–526 (1993)
 47. Hofmann, D.J., et al.: Recovery of stratospheric ozone over the United States in the winter of 1993–1994. *Geophys. Res. Lett.* **21**(17), 1779–1782 (1994)
 48. Ramaswamy, V., et al.: Stratospheric temperature trends: observations and model simulations. *Rev. Geophys.* **39**(1), 71–122 (2001)
 49. Larsen, M.F.: OBSERVATIONS PLATFORMS – Rockets. In: North, G.R., Pyle, J., Zhang, F. (eds.) *Encyclopedia of Atmospheric Sciences*, 2nd edn., pp. 285–289. Academic Press, Oxford (2015)
 50. Houghton, J.T., Taylor, F.W., Rodgers, C.D.: *Remote Sounding of Atmospheres*. Cambridge University Press, Cambridge (1984)
 51. Grant, W.B.: *Ozone Measuring Instruments for the Stratosphere*. Optical Society of America, Washington D.C. (1989)
 52. Dudhia, A.: SATELLITE REMOTE SENSING – Temperature Soundings. In: Holton, J.R. (ed.) *Encyclopedia of Atmospheric Sciences*, pp. 1985–1998. Academic Press, Oxford (2003)
 53. Fischer, H., Hase, F.: OBSERVATIONS FOR CHEMISTRY (REMOTE SENSING) – IR/FIR. In: Holton, J.R. (ed.) *Encyclopedia of Atmospheric Sciences*, pp. 1499–1508. Academic Press, Oxford (2003)
 54. Hays, P.B., Skinner, W.R.: SATELLITE REMOTE SENSING – Wind, Middle Atmosphere. In: Holton, J.R. (ed.) *Encyclopedia of Atmospheric Sciences*, pp. 2012–2024. Academic Press, Oxford (2003)
 55. Healy, S.B.: SATELLITE REMOTE SENSING – GPS Meteorology. In: Holton, J.R. (ed.) *Encyclopedia of Atmospheric Sciences*, pp. 1965–1972. Academic Press, Oxford (2003)
 56. King, M.D., Herring, D.D.: SATELLITES – Research (Atmospheric Science). In: Holton, J.R. (ed.) *Encyclopedia of Atmospheric Sciences*, pp. 2038–2047. Academic Press, Oxford (2003)
 57. Shepherd, G.G.: OPTICS, ATMOSPHERIC – Optical Remote Sensing Instruments. In: Holton, J.R. (ed.) *Encyclopedia of Atmospheric Sciences*, pp. 1595–1601. Academic Press, Oxford (2003)
 58. Stolarski, R.S., McPeters, R.D.: SATELLITE REMOTE SENSING – TOMS Ozone. In: Holton, J.R. (ed.) *Encyclopedia of Atmospheric Sciences*, pp. 1999–2005. Academic Press, Oxford (2003)
 59. Vaughan, G.: OBSERVATIONS FOR CHEMISTRY (REMOTE SENSING) – Lidar. In: Holton, J.R. (ed.) *Encyclopedia of Atmospheric Sciences*, pp. 1509–1516. Academic Press, Oxford (2003)
 60. Waters, J.: OBSERVATIONS FOR CHEMISTRY (REMOTE SENSING) – Microwave. In: Holton, J.R. (ed.) *Encyclopedia of Atmospheric Sciences*, pp. 1516–1528. Academic Press, Oxford (2003)

61. Levelt, P.F., et al.: The Ozone Monitoring Instrument: overview of 14 years in space. *Atmos. Chem. Phys.* **18**(8), 5699–5745 (2018)
62. Beer, R.: TES on the aura mission: scientific objectives, measurements, and analysis overview. *IEEE Trans. Geosci. Remote. Sens.* **44**(5), 1102–1105 (2006)
63. Waters, J.W., et al.: The Earth observing system microwave limb sounder (EOS MLS) on the aura satellite. *IEEE Trans. Geosci. Remote. Sens.* **44**(5), 1075–1092 (2006)
64. Bernath, P.F.: The Atmospheric Chemistry Experiment (ACE). *J. Quant. Spectrosc. Radiat. Transf.* **186**, 3–16 (2017)
65. Liu, X., et al.: Ozone profile and tropospheric ozone retrievals from the Global Ozone Monitoring Experiment: Algorithm description and validation. *J. Geophys. Res.* **110**(D20), D20307 (2005)
66. Liu, X., Bhartia, P.K., Chance, K., Spurr, R.J.D., Kurosu, T.P.: Ozone profile retrievals from the Ozone Monitoring Instrument. *Atmos. Chem. Phys.* **10**(5), 2521–2537 (2010)
67. Veefkind, J.P., et al.: TROPOMI on the ESA Sentinel-5 Precursor: A GMES mission for global observations of the atmospheric composition for climate, air quality and ozone layer applications. *Remote. Sens. Environ.* **120**, 70–83 (2012)
68. Zoogman, P., et al.: Tropospheric emissions: Monitoring of pollution (TEMPO). *J. Quant. Spectrosc. Radiat. Transf.* **186**, 17–39 (2017)



Gonzalo Gonzalez Abad Gonzalo Gonzalez Abad works as a physicist at the Harvard-Smithsonian Center for Astrophysics, where he is member of the Tropospheric Emissions: Monitoring of Pollution satellite instrument science team for measuring North American air pollution hourly from geostationary orbit (tempo.si.edu). He measures Earth's atmosphere composition from aircraft, the ground, and satellites, with a special interest in pollution and air quality.



Kelly Chance Kelly Chance heads the Tropospheric Emissions: Monitoring of Pollution satellite instrument for measuring North American air pollution hourly from geostationary orbit (tempo.si.edu). He measures Earth's atmosphere from balloons, aircraft, the ground, and satellites, including the stratospheric ozone layer, greenhouse gases, and atmospheric pollution. He is an author a textbook on spectroscopy and radiative transfer of planetary atmospheres.



Kate Kirby Kate Kirby has a PhD in Chemical Physics from the University of Chicago and is currently Director of the Institute for Theoretical Atomic, Molecular, and Optical Physics. Her research interests center on theoretical studies of ultracold molecule formation and atomic and molecular structure and processes that are of interest to astronomy and atmospheric physics. Such processes include photoionization, photodissociation, radiative association, charge transfer, and line-broadening.



Erik T. Jensen

Contents

90.1	Low Energy Electrons and Surface Science	1349
90.2	Electron–Atom Interactions	1350
90.2.1	Elastic Scattering: Low Energy Electron Diffraction (LEED)	1350
90.2.2	Inelastic Scattering: Electron Energy Loss Spectroscopy	1351
90.2.3	Auger Electron Spectroscopy	1351
90.3	Photon–Atom Interactions	1352
90.3.1	Ultraviolet Photoelectron Spectroscopy (UPS)	1352
90.3.2	Inverse Photoemission Spectroscopy (IPES)	1353
90.3.3	X-Ray Photoelectron Spectroscopy (XPS)	1353
90.3.4	X-Ray Absorption Methods	1355
90.4	Atom–Surface Interactions	1357
90.4.1	Physisorption	1357
90.4.2	Chemisorption	1357
90.5	Recent Developments	1357
	References	1358

Abstract

This chapter describes various applications of atomic and molecular physics to phenomena that occur at surfaces. Particular attention is placed on the application of electron- and photon-atom scattering processes to obtain surface specific structural and spectroscopic information.

The study of surfaces and interfaces touches on many fields of pure and applied science. In particular there are applications in the fields of semiconductor processing, thin film growth, catalysis, corrosion and fundamental physics in two-dimensions. A number of recent texts cover surface physics in general [1–4] as well as specific areas such as experimental techniques [5], surface electron spectroscopies [6, 7], and the application of synchrotron radiation to surface science [8]. Also a number

of book series that deal with areas of particular interest are published at regular intervals, such as surface chemistry [9], surface vibrations [10] and stimulated desorption processes [11].

Keywords

Auger electron spectroscopy · electron energy loss spectroscopy · resonant scattering · surface sensitivity · core hole · electron diffraction · electron-molecule collisions · photoelectron spectroscopy · X-ray absorption · atom scattering

90.1 Low Energy Electrons and Surface Science

To obtain information specific to the first few layers of atoms at the surface of a solid, techniques must be devised that discriminate between signals from the surface and from the bulk of the material. If a solid has dimensions of $\approx 1 \text{ cm}^3$, then only approximately one atom in 10^7 is located at the surface. This makes the application of bulk techniques to the study of surfaces (e.g. X-ray diffraction [12]) problematic.

There are several experimental approaches to achieving surface sensitivity. If the probe used is an atom or molecule that can be scattered from or desorbed from the surface, then these species can be analyzed by techniques such as mass spectrometry or resonant ionization. A more recent innovation has been the use of scanning probe microscopies [13] (e.g., the scanning tunneling microscope and its variants) which exploit a surface sensitivity such as the surface valence electron density. However the most common surface analytical techniques use the intrinsic surface sensitivity of low energy (10–2000 eV) electrons.

The surface specificity of low energy electrons arises from the very short inelastic mean free path (MFP) for these electrons in a solid. This property can be seen in Fig. 90.1 which

E. T. Jensen (✉)
Dept. of Physics, University of Northern British Columbia
Prince George, BC, Canada
e-mail: ejensen@unbc.ca

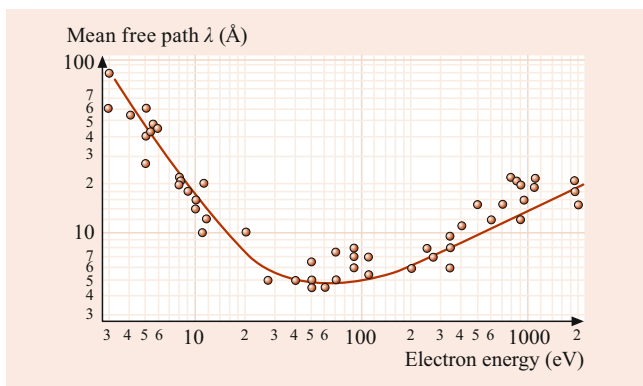


Fig. 90.1 The variation of the inelastic mean free path with electron kinetic energy (*universal curve*). Based on *Briggs and Seah* [14]

plots measured values of the inelastic MFP for a number of materials and electron energies between 1 and 2000 eV. The curve is called *universal* because the same general trend of short inelastic MFP is observed for nearly all materials [14]. The dominant energy loss mechanisms are valence band excitations (plasmons and electronic excitations), and since most materials have similar valence electron densities, the resultant inelastic scattering MFP is to a good approximation, material independent.

The very short inelastic MFPs for low energy electrons has the result that any that escape from the solid without having undergone inelastic scattering can only have originated very close to the surface, usually within a few atomic layer spacings. Many of the surface analysis techniques described in this chapter use this surface sensitivity to obtain surface structural and spectroscopic information. The same techniques are easily applicable to conducting and semiconducting materials, and can also be applied to insulating materials, if the charging effects are dealt with in some manner.

90.2 Electron–Atom Interactions

90.2.1 Elastic Scattering: Low Energy Electron Diffraction (LEED)

The elastic scattering of low energy (20–500 eV) electrons at surfaces is historically important in physics as the experiments of Davisson and Germer provided early experimental evidence of the wave nature of electrons. After these initial experiments, the technique was largely unused until the advent of cleaner ultra-high vacuum systems and surface preparation techniques in the 1960's. LEED is one of the most important and widely used surface characterization techniques due to its surface sensitivity and wide utility [5].

Diffraction from a two-dimensional net of scatterers results in a two-dimensional array of reciprocal lattice *rods* oriented normal to the surface. All kinematically allowed

rods intersect the Ewald sphere at all energies—unlike the case in bulk X-ray diffraction. The short inelastic MFP for scattering low energy electrons yields the surface sensitivity of LEED for a crystal surface. The kinematic theory used in X-ray diffraction is not directly applicable to LEED since the low energy electrons can undergo several elastic collisions in the surface region. The elastic MFPs for low energy electrons are comparable in magnitude to the inelastic mean free paths shown in Fig. 90.1. This *multiple scattering* does not affect the positions of the diffraction beams, but does alter their intensities due to interference effects.

Kinematic analysis is sufficient to determine the diffraction beam positions for a proposed structure, and this is the most common use for LEED. A diffraction pattern is often sufficient to determine the surface periodicity and unit mesh size. However determining the surface crystal basis from the intensities of the diffracted LEED beams requires moderately sophisticated calculations to be performed for proposed structures.

Quantitative LEED generally compares measured $I(V)$ curves (the intensity I of a particular diffraction beam as a function of electron energy measured in volts) with a calculated $I(V)$ profile for a proposed surface crystal structure. These calculations determine the propagating electron wave functions Ψ_{LEED} that take into account electron-ion core scattering cross sections and phase shifts, available multiple scattering pathways, inelastic scattering cross sections and Debye-Waller effects. The structural parameters are varied systematically until agreement can be reached with the experimental $I(V)$ curves [15, 16]. These calculations can yield surface atom positions to better than 0.1 Å vertically and 0.2 Å horizontally. Over 1000 surface structures have been determined using LEED and associated techniques [17].

Clean surfaces often have a different crystallography than simple termination of the bulk crystal structure. Due to the absence of neighbors above the surface, the surface atoms can undergo both relaxation (change in interlayer spacing) and reconstruction (changes in periodicity and bonding) [2]. While relaxation and reconstruction do occur on all types of surfaces, the reconstructions found on semiconductors are most striking. The strong covalent bonds that are broken when a semiconductor is cleaved give rise to high energy *dangling bonds*. The surface energy is minimized by having the surface reconstruct to reduce the total number of these bonds. The resultant structure is formed through a balance between eliminating as many dangling bonds as possible and the resultant stress caused in other bonds due to the displacements of the surface atoms. One example of this is the clean Si(111) surface, in which 49 surface atoms form a new periodic arrangement to make up the reconstructed Si(111)–(7×7) unit cell [2]. The number of dangling bonds is thereby reduced from 49 to 19.

90.2.2 Inelastic Scattering: Electron Energy Loss Spectroscopy

Low energy surface excitations such as phonons, plasmons and electron-hole pair excitations can be studied using inelastic electron scattering. High resolution electron energy loss spectroscopy (HREELS) [18] uses incident electron beam energies of 1–300 eV with energy resolutions of 1–10 meV. Inelastic scattering phenomenon are divided into three types: dipole, impact and resonant scattering. Surface vibrations are also studied using infra-red absorption spectroscopy and inelastic atomic beam scattering techniques [19].

Dipole Scattering

In dipole scattering HREELS, the incident electron ($1 < E_i < 20$ eV) undergoes a long range Coulomb interaction with dipole fields associated with a dynamic dipole moment. The main characteristic of dipole scattering is that the inelastically scattered electrons have an angular distribution that is strongly peaked (width $\Delta\theta \approx \hbar\omega/E_i$) close to the specular direction ($\theta_i = \theta_f$). In this limit there is no momentum exchange with the surface vibrational mode (i.e., $\mathbf{k}_{\parallel} = 0$ in the bandstructure), so dipole scattering HREELS is similar to infrared spectroscopy in that only ir active vibrational modes at the zone center can be studied. At the surface of a conductor, dielectric screening guarantees that only ir active modes having a component perpendicular to the surface are visible—modes having dipole moments parallel to the surface are screened by the surface and so cannot be excited by dipole scattering. This *quasi-selection rule* allows the site symmetry for some systems to be decided [18]. Dipole scattering is most commonly used in the study of vibrations of molecules on surfaces, which often have dipole-active vibrational modes that are both intrinsic and caused by adsorption (i.e., frustrated translations and rotations).

Impact Scattering

In impact scattering, the incident electron samples the short-range interatomic potential, and is not restricted to dipole-active vibrational modes [18]. Higher electron energies are used ($30 < E_i < 300$ eV) since the cross section for impact scattering generally increases with energy. The inelastically scattered electrons are distributed at all angles, and so there can be exchange of parallel momentum (\mathbf{k}_{\parallel}) with the surface, allowing the mapping of surface excitation bandstructure $\hbar\omega(\mathbf{k}_{\parallel})$. The cross sections for impact scattering HREELS can be calculated using an approach similar to LEED, but now considering the normal displacements of atoms from equilibrium positions. The scattering potential $V(\mathbf{r}, [\mathbf{R}])$ (where $[\mathbf{R}]$ is the set of position vectors of the N atoms in

the surface region) can be expanded in terms of the normal displacements μ_i from equilibrium according to

$$V(\mathbf{r}, [\mathbf{R}]) = V(\mathbf{r}, [\mathbf{R}_0]) + \sum_{i=1}^N \left(\nabla_{\mu_i} V(\mathbf{r}, [\mathbf{R}]) \right) \Big|_{[\mathbf{R}_0]} \cdot \mu_i + \dots \quad (90.1)$$

The first term is responsible for elastic scattering (LEED) and the second term is the dominant term for impact scattering. The inelastic cross section for mode i is then [20]

$$\frac{d\sigma}{d\Omega} = \left| \left\langle \Psi_{\text{LEED}}^*(\mathbf{k}_f) \left| \frac{\partial V}{\partial \mu_i} \right| \Psi_{\text{LEED}}(\mathbf{k}_i) \right\rangle \right|^2 \quad (90.2)$$

using electron wave functions calculated using the same formalism as LEED. The symmetry properties of this matrix element can be used to determine the polarization direction of surface vibrational modes by searching for systematic absences in the inelastic intensity in particular high symmetry direction of the surface [20]. Impact scattering studies are most commonly made in the study of surface phonon bandstructure and the vibrational modes of adsorbed molecules that are not dipole-active.

Resonant Scattering

Resonant electron scattering at surfaces [21, 22] is usually applied to the study of adsorbed molecules, and has much in common with resonant scattering from gas-phase atoms and molecules (see Chap. 49). In resonant scattering, the incident electron combines with a target molecule to form a short-lived molecular ion, which subsequently decays and can leave the molecule vibrationally or electronically excited. The cross sections for this process have a typical profile. For example, in a shape resonance the formation of the temporary negative ion intermediate corresponds to adding the incident electron to a particular unoccupied orbital of the target molecule. The study of the angular dependence of resonance scattering cross sections [22] can yield information on the orientation of molecules on surfaces, since the electron capture and emission cross sections are fixed by the molecular orientation and the resonance symmetry.

90.2.3 Auger Electron Spectroscopy

Auger electron spectroscopy (AES) is one of the most widely used surface science techniques due to its chemical and surface sensitivity [5, 14, 23]. Core holes are created in near surface atoms using a high energy electron beam (2–5 keV, 1–100 μA) or less commonly, an X-ray source. For these low

binding energy core holes, the Auger decay mode is highly probable (Sects. 26.1.1 and 66.3.1). Although the Auger energy and lineshape can give spectroscopic information, in surface science this is seldom used—rather it is the chemical fingerprint of the atoms which is of interest.

Auger electron spectroscopy is a surface sensitive technique by virtue of the low kinetic energy (50–1000 eV) of the emitted Auger electrons. Auger electrons from atoms more than a few Ångströms below the surface are inelastically scattered and so not detected by the energy selective detector. The kinetic energy of the Auger electrons is

$$\mathcal{T}_e = E_A - E_B - E_C - U \quad (90.3)$$

where E_A is the binding energy of the initial core electron and E_B , E_C are the binding energies of the other electrons (one or both are valence levels) involved in the Auger process. Energy shifts and relaxation are accounted in the term U which includes hole-hole interactions and atomic and solid state (dielectric) screening of the holes, and hence can be sensitive to the local chemical environment.

Auger spectra are typically obtained in derivative mode [i.e., $N'dN(E)/dE$] to separate the Auger transitions from the secondary electron background, and comparison is made to reference spectra [24]. The raw chemical sensitivity of AES is very high, and surface concentrations of $\approx 1\%$ of many common chemical species can be detected. Semiquantitative measurements may be made by comparison to these reference spectra, but such comparisons only give atomic concentrations within a factor of 2 (or worse) since the measured AES signal can be modified by a number of factors. More precise quantitative measurements can be made by calibration of the AES intensity for the atomic constituents at a surface [5]. The AES sensitivity to atoms A on a clean substrate (atoms B) can be determined if the absolute quantity of A can be established by some other means.

The chemical sensitivity of AES can also be exploited as a form of chemical microscopy (scanning Auger microscopy) since the exciting electron beam that is used may be focused to a very small size. The Auger signal from the small target volume can be analyzed for specific chemical components. By rastering the incident electron beam, a chemical map of the surface can be made.

90.3 Photon–Atom Interactions

90.3.1 Ultraviolet Photoelectron Spectroscopy (UPS)

Photoelectron spectroscopy (PES) (Sect. 65.1) has been historically divided into UV photoelectron spectroscopy for low photon energies (generally the study of valence electron

states) and X-ray photoelectron spectroscopy (study of core electron levels). The use of low energy photons ($5 < h\nu < 50$ eV) for PES of solids has the advantage that the photons have a negligible momentum ($\mathbf{k} \approx 0$). This allows straightforward mapping since the transitions are vertical in momentum space:

$$h\nu = E_f(\mathbf{k} + \mathbf{G}) - E_i(\mathbf{k}) \quad (90.4)$$

where \mathbf{k} is the electron state wavevector and \mathbf{G} is a reciprocal lattice vector.

Most UPS studies are done using angle-resolved photoelectron detection (also called angle resolved photoelectron spectroscopy or ARPES). The kinetic energy \mathcal{T}_e and emission angle θ of the photoelectrons are measured, allowing the initial state binding energy and momentum parallel to the surface (\mathbf{k}_{\parallel}) to be determined from

$$k_{\parallel} = \sqrt{\frac{2m\mathcal{T}_e}{\hbar^2}} \sin \theta. \quad (90.5)$$

The mean free path of the photoelectrons from valence levels allows both surface and bulk electron states to be studied. Separation of the surface from bulk bands can be accomplished in several ways [5]. Since a crystal surface has two-dimensional symmetry, only the \mathbf{k}_{\parallel} component of momentum is a good quantum number for the surface states. Also, in transporting the surface or bulk state photoelectron of momentum \mathbf{k} through the surface to the detector, only the \mathbf{k}_{\parallel} component is conserved. A bulk state disperses in three-dimensions, requiring knowledge of $\mathbf{k} = \mathbf{k}_{\parallel} + \mathbf{k}_{\perp}$. The magnitude of \mathbf{k}_{\perp} cannot be determined unless the inner potential (change in potential normal to the surface) is known by some other means. This property allows bulk and surface states to be distinguished since surface states remain fixed in energy for a constant \mathbf{k}_{\parallel} , while bulk states disperse if \mathbf{k}_{\perp} is changed while \mathbf{k}_{\parallel} is kept constant. This is done by measuring the photoelectron spectrum for a range of UV photon energies at a fixed value of \mathbf{k}_{\parallel} (often at $\theta = 0$ so $\mathbf{k}_{\parallel} = 0$). Bulk states disperse since \mathbf{k}_{\perp} varies as the photon energy is changed, but the surface states remain at a fixed binding energy in the photoelectron spectrum.

The photoelectron transition matrix element between initial and final states $|i\rangle$ and $|f\rangle$ due to the incident photon vector potential \mathbf{A} is

$$I \propto |\langle f | \mathbf{A} \cdot \mathbf{p} + \mathbf{p} \cdot \mathbf{A} | i \rangle|^2 \approx |\langle f | 2\mathbf{A} \cdot \mathbf{p} | i \rangle|^2. \quad (90.6)$$

The spatial variation of \mathbf{A} near the surface (the surface photoeffect) can be neglected, although this is not strictly valid at these low photon energies [25].

Due to the low photoelectron kinetic energies in most UPS work, precise calculation of photoelectron spectrum intensities is rather difficult due to multiple scattering and phase

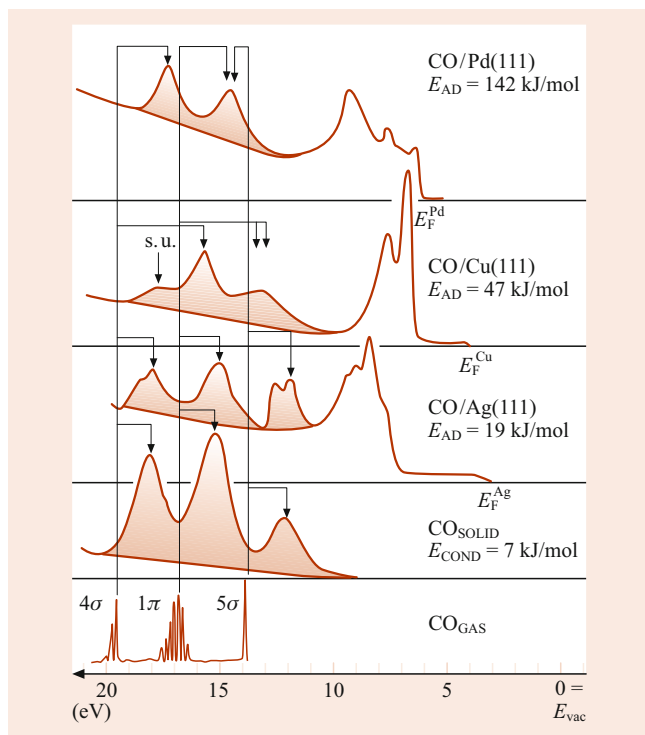


Fig. 90.2 A set of UPS spectra for CO adsorbed on various surfaces, as well as gas phase and solid CO. The peak labeled *su* is a shake-up satellite peak. After [26]

shifts sensitive to valence electrons. However, the initial electron state symmetries can be determined using the symmetry properties of the matrix element Eq. (90.6). Selection rules allow the state symmetries to be determined by measuring the photoemission spectrum along high symmetry directions of the surface using polarized UV radiation [5].

The valence electron states of adsorbed molecules can also be studied using UPS. Peaks in the photoelectron spectrum due to valence levels of adsorbed molecules tend to have larger linewidths (≈ 1 eV typically) than in the gas phase due to solid state and instrumental effects, so vibrational structure is seldom resolved. The positions of the molecular valence states are shifted in energy due to the surface work function and solid state relaxation (dielectric screening) effects. In addition to these rigid shifts, chemical shifts are also observed due to bonding (chemisorption) interactions between the molecule and surface. The molecular character of the valence orbitals is often retained from the gas phase, so the shifted levels can be identified by using the symmetry properties of the photoemission matrix element. For example, photoemission from gas phase CO shows three valence states: 5σ , 1π and 4σ in order of increasing binding energy. A series of photoemission spectra [26] for gas phase CO, solid CO and CO chemisorbed on several transition metal surfaces (in order of increasing CO–surface binding energy) is shown in Fig. 90.2. For solid CO and

weakly chemisorbed CO/Ag(111) all three valence orbitals of molecular CO are well resolved, though the adsorbed CO spectrum is shifted rigidly in energy by relaxation effects. Since CO is chemisorbed more strongly on Cu(111) and Pd(111), the 1π and 5σ valence states shift relative to one another. The strongly overlapping 1π and 5σ states observed for chemisorbed CO can be individually resolved by using the photoemission selection rules and linearly polarized UV radiation [26]. The origin of the chemical shift between the 5σ and 1π levels has been ascribed to bond formation involving the CO 5σ level and σ -symmetry d-electron states on the transition metal surfaces [2].

90.3.2 Inverse Photoemission Spectroscopy (IPES)

Inverse photoemission spectroscopy is properly classified as an incident electron technique but is included here as a natural companion to UPS. IPES utilizes low energy electrons (5–50 eV) incident on a surface. Transitions from a high-lying initial electron state in the continuum to a lower unoccupied state cause a UV photon to be emitted. By detecting the emitted photon intensity as a function of energy, the joint density of states is measured [7]. IPES is used to study the unoccupied portion of surface and bulk band-structure, particularly the region between the Fermi level and the vacuum level, which is difficult to access by other means. This allows the study of unoccupied states of adsorbed molecules (e.g., antibonding molecular levels) as well as intrinsic surface states such as the Rydberg-like states of electrons trapped in the image potential at the surface [7].

90.3.3 X-Ray Photoelectron Spectroscopy (XPS)

X-ray photoelectron spectroscopy allows the study of the energy of atomic core levels via the Einstein photoelectric equation $\mathcal{T}_e = h\nu - E_b$, where \mathcal{T}_e is the kinetic energy of the photoemitted electron and E_b is the binding energy of the core level. Atoms bound in different chemical environments (e.g., at particular sites on a surface) experience different chemical shifts, and so are measured at slightly different binding energies. This sensitivity to chemical environment allows XPS to characterize the different types of binding sites for similar atoms, and measure their abundance by measuring the relative intensities of XPS emission from different species.

Shifts in \mathcal{T}_e arise from two sources: intra-atomic and inter-atomic relaxation shifts. The intra-atomic relaxation E_a is due to screening of the core hole by other electrons in the emitter atom. The inter-atomic relaxation E_r is important in solids (particularly for metals) and is due to screening of the core hole by the dielectric response of the surrounding

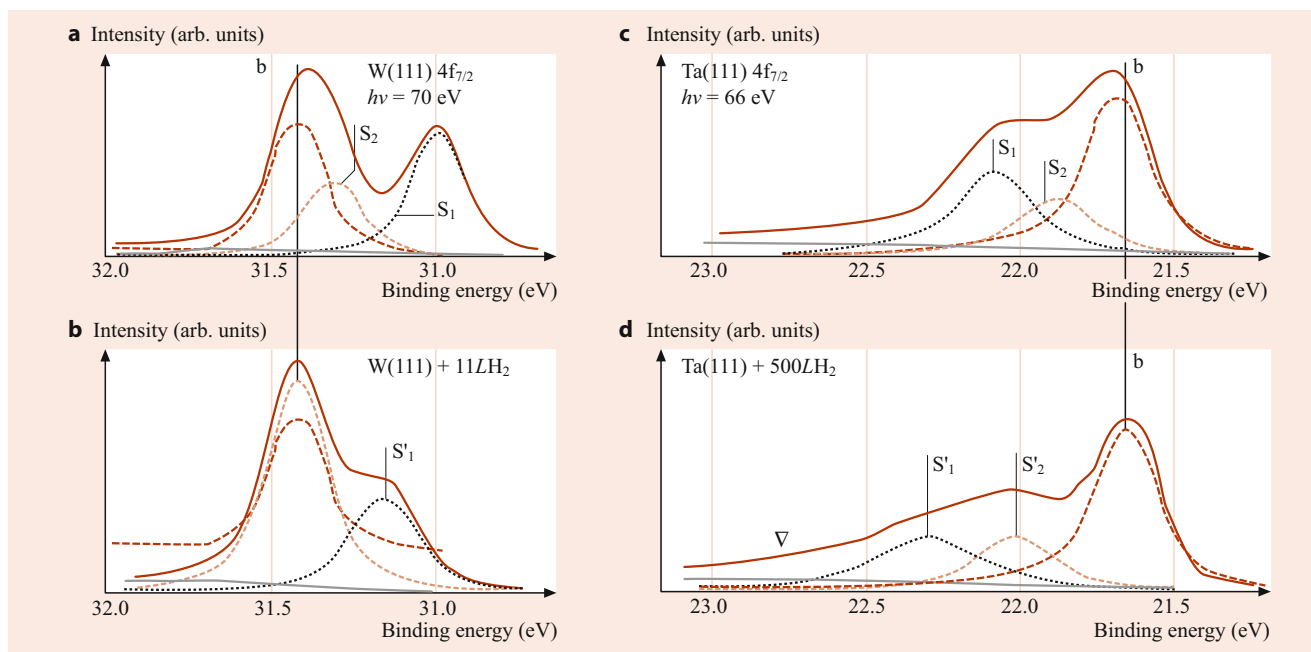


Fig. 90.3 XPS spectra of the $4f_{7/2}$ states of W(111) and Ta(111). Contributions from the bulk (b) and surface (S1,S2) atoms can be distinguished, and the surface atom peaks are shifted by the adsorption of hydrogen. After [27]

medium. These relaxation shifts (on the order of a few eV) tend to increase the kinetic energy of the emitted photoelectron, so the kinetic energy in the adiabatic limit is

$$\mathcal{T}_e = h\nu - E_b + E_a + E_r. \quad (90.7)$$

Since photoemission is a rapid process, nonadiabatic processes lead to shakeup and shakeoff features in which other electrons are excited to higher energy levels, causing the photoelectron to have lower kinetic energy [5] (see Sect. 65.1.2). It is also possible to excite discrete excitations of the solid, such as plasmons and a continuum of low energy electron-hole excitations, causing the XPS peak to have an asymmetric lineshape. The overall XPS distributions of \mathcal{T}_e thus contain contributions from the adiabatic channel, and lower energy photoelectrons in a series of discrete peaks or a continuum from nonadiabatic processes.

The chemical abundance of a species can be determined from the sum rule that the total XPS cross section is proportional to the sum of the adiabatic peak and all the shake-up and shake-off components. However it is usually only convenient to measure the intensity of the adiabatic peak. If comparisons are made between chemical species in different chemical environments, the shake-up and shake-off intensities may differ. Hence the adiabatic channel intensities might not reflect the true abundance. Very often this problem can be minimized by careful calibration, and chemical analyses can be made to an accuracy of a few percent.

The surface sensitivity of XPS is due to the short inelastic MFP for the photoelectrons, which can be made to have

energies in the range 10–1000 eV by appropriate choice of the X-ray wavelength. The XPS signal is proportional to $\exp[-z/(\lambda \cos \theta)]$, where z is the depth of the emitter, λ is the inelastic mean free path of the photoelectron and θ is the angle measured from the surface normal.

The popularity of XPS as a surface analysis technique is due to the availability of convenient and sufficiently intense monochromatic X-rays from lab sources (usually Al and Mg K_α X-ray lines at 1486.6 and 1253.6 eV). The increasing availability of continuously tunable X-rays from synchrotron radiation sources allows improved measurements due to the ability to tune the X-rays to slightly above threshold, where the XPS cross sections are maximized, the inelastic MFP is shorter (hence more surface specific) and electron monochromators can operate with higher resolution [5].

As an example of the chemical sensitivity of XPS, photoelectron spectra of the $4f_{7/2}$ core levels of W(111) and Ta(111) are shown in Fig. 90.3. The spectra show discrete peaks from both bulk and surface atoms. The binding energies of the surface atoms are affected by the adsorption of hydrogen.

XPS can also be used to give local structural information due to elastic scattering of the photoemitted electron in the region near the emitter [5]. One form of this is the use of forward scattering from a buried emitter. A high energy XPS photoelectron is focused in the direction of nearby atoms due to a lower effective potential close to the atomic core. Angular scanning of the XPS detector will then detect a more intense signal along the bond axis. This method has proved useful in studying the orientation of adsorbed molecules and the structure of hetero-epitaxial thin films [28].

90.3.4 X-Ray Absorption Methods

X-ray absorption methods [8] measure the decay of the core hole rather than the intensity of emitted photoelectrons, since that XPS process is complicated by a number of possible final state processes, as discussed above. To obtain surface sensitivity, the X-ray absorption is measured using a low energy electron emitting channel such as an Auger electron emission or the total electron yield, which are proportional to the overall X-ray absorption. These methods require an intense and tunable source of monochromatic x-radiation near the excitation edge for the core level of a particular atom, and so are usually performed using synchrotron radiation. Synchrotron sources have the additional benefit of linearly polarized light, which is crucial for NEXAFS and useful for SEXAFS discussed next.

SEXAFS: Measurement of Bond Lengths

The surface extended X-ray absorption fine structure (SEXAFS) technique is most commonly used to measure the bond lengths for atoms adsorbed on a surface. SEXAFS utilizes the elastic backscattering of the emitted XPS photoelectron from nearby atoms that surround the emitter. Elastically scattered waves arrive back at the emitter and add coherently (constructively and destructively) to the outgoing wave, thus modifying the matrix element for the transition to the final state [29]. Experimentally, the cross section $\sigma(h\nu)$ for X-ray absorption above the threshold photon energy is modified by an oscillatory structure. The *atomic* contribution to the absorption cross section can be removed using

$$\chi = \frac{\sigma - \sigma_0}{\sigma_0}, \quad (90.8)$$

where σ and σ_0 are the measured surface and free atom X-ray absorption cross sections. If only single scattering events are involved in backscattering to the emitter then the fine structure function χ is

$$\chi(k) = \sum_{i=1}^N A_i(k) \sin [2kR_i + \phi_i(k)], \quad (90.9)$$

where k is the magnitude of the photoelectron wavevector and the sum is done for N shells of atoms surrounding the emitter. The distance R_i is the radius of the i -th shell and $2kR_i$ is the associated phase factor for the backscattered photoelectron, with an amplitude $A_i(k)$. The phase shift $\phi_i(k)$ is required due to the backscattering path through the potential surrounding the emitter and scattering from the atom at R_i . If the ϕ_i could be ignored, then a simple Fourier transform of $\chi(k)$ would reveal the radial distribution function and the bond lengths R_i [29]. In practice, the phase shifts cannot be neglected, but very often these can be found by studying chemically similar systems in which the bond lengths

are known. The phase shifts for photoelectrons well above the absorption edge (having kinetic energies greater than ≈ 50 eV) are dominated by the atomic ion cores, and so are not sensitive to the valence electronic structure. The phase shifts can also be calculated in a straightforward way since this problem is essentially the same as done in LEED multiple scattering calculations.

The amplitudes $A_i(k)$ due to scattering from shell i at distance R_i from a point source emitter are [29]

$$A_i(k) = \frac{N_i^*}{kR_i^2} |f_i(\pi, k)| \exp(-2\langle u^2 \rangle_i k^2) \times \exp(-2R_i/\lambda), \quad (90.10)$$

where N_i^* is an effective number of atoms and $\langle u^2 \rangle_i$ is the mean-square displacement of the atoms in shell i . The backscattering amplitude $|f_i(\pi, k)|$ has been separated from its phase factor $\phi_i(k)$ in Eq. (90.9). The inelastic mean free path for the photoelectrons reduces the contribution from successive shells by a factor $\exp(-2R_i/\lambda)$, and it is this term that allows the kinematic single-scattering approach to be used. Multiple scattering paths involve longer trajectories and so are more strongly attenuated by this exponential factor. If the near-edge energy region of the absorption cross section is not included in the analysis, then the scheme outlined in Eqs. (90.9) and (90.10) is reasonable. The near-edge region (within ≈ 50 eV of the absorption edge) is troublesome, not only because of multiple scattering, but also because the phase shifts $\phi_i(k)$ for low energy photoelectrons are more sensitive to valence electron distributions, and so are more sensitive to the details of the local chemical environment.

The SEXAFS method is illustrated with the data of Fig. 90.4 for iodine adsorbed on Cu(111). Panel (a) shows the measured X-ray absorption $\sigma(h\nu)$ for both the surface system Cu(111)-I and bulk CuI. The extracted $\chi(k)$ and their Fourier transforms are shown in (b) and (c). The Cu-I nearest neighbor bondlength is clearly shown by the peak in (c), and is found to be 0.07 \AA longer than in bulk CuI. SEXAFS is most commonly applied to atomic adsorption systems since molecular systems are difficult to analyze, as they can contain several similar bond lengths, and the shells containing different atoms are difficult to model.

NEXAFS: Molecular Orientation at Surfaces

In SEXAFS, the X-ray absorption close to the excitation edge is avoided due to the problems of multiple scattering, and phase shifts that are chemically sensitive to valence electrons. The study of near-edge X-ray absorption fine structure (NEXAFS) can avoid these difficulties by using only the symmetry properties of the transition matrix element without concern for the absolute amplitudes [31]. For isolated molecules, unoccupied molecular states having σ or π symmetry are very commonly found close to or just below the

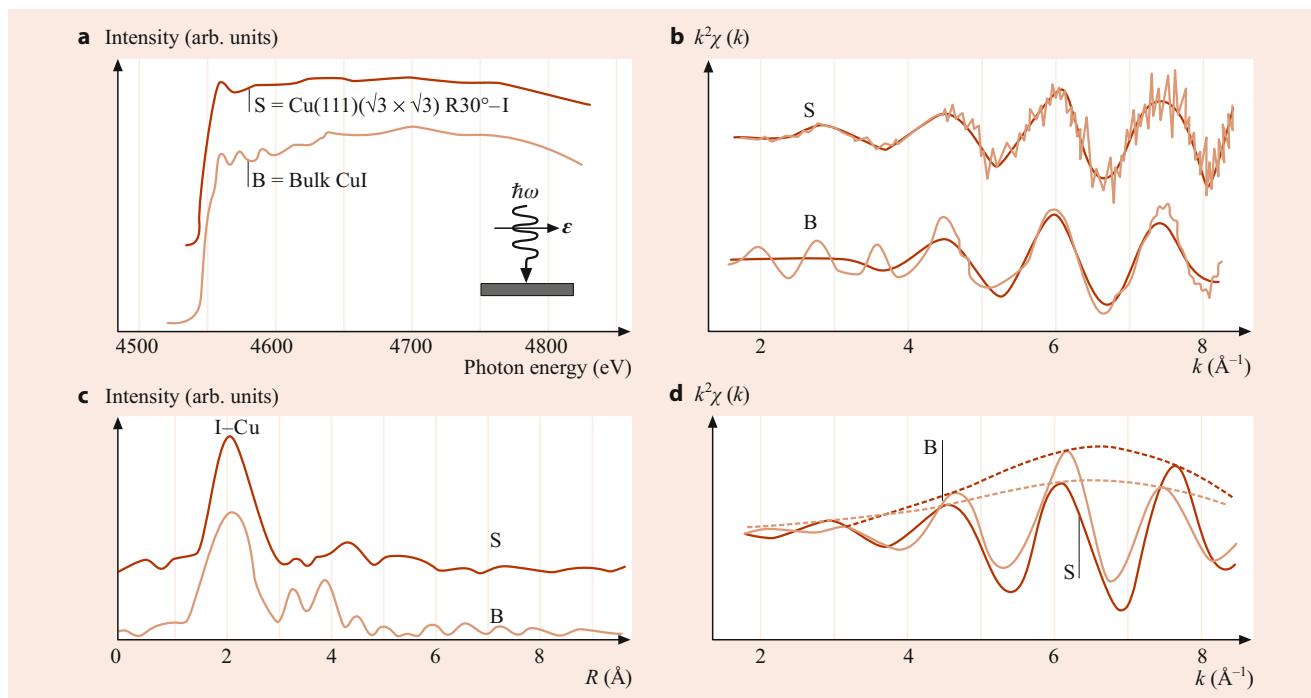


Fig. 90.4 (a) X-ray absorption data taken near the iodine edge for bulk CuI and Cu(111)-I. (b) The extracted fine structure function $\chi(k)$, shown multiplied by k^2 to enhance the high k structure. (c) The Fourier transform of $\chi(k)$ showing the location of the first shell of Cu atoms from the I emitters. (d) Back-transformed $k^2\chi(k)$ after applying a filter to extract the nearest neighbor data. After [30]

threshold for photoemission. These *molecular resonances* often remain for adsorbed molecules, and the symmetry properties of the absorption intensity $I \propto |\langle f | \mathbf{A} \cdot \mathbf{p} | i \rangle|^2$ can be used to determine the molecular orientation.

For the overall matrix element to be nonzero, it must be totally symmetric. Using linearly polarized synchrotron radiation, the direction of polarization \mathbf{A} can be varied by rotating the crystal. For example, the K-edge X-ray absorption of CO on the Ni(100) surface in Fig. 90.5 shows final state resonances A (π -symmetry) and B (σ -symmetry). The intensity of these features depends of the direction of polarization of the incident X-rays. X-rays with a polarization vector parallel to the surface ($\theta = 90^\circ$) strongly excite the π -symmetry absorption while the σ -symmetry absorption is absent. For grazing incidence X-rays polarized normal to the surface, the σ -resonance is prominent. From dipole selection rules, this polarization dependence of the X-ray absorption is evidence that the CO molecule is adsorbed with its bond perpendicular to the plane of the Ni(100) surface.

The σ -resonance final state in NEXAFS corresponds to multiple scattering of the photoelectron along the bond axis. The overall phase shift for this final state is approximately

$$\int \sqrt{E - V(r)} dr \approx \sqrt{E - V(r)} R = \text{const.} \quad (90.11)$$

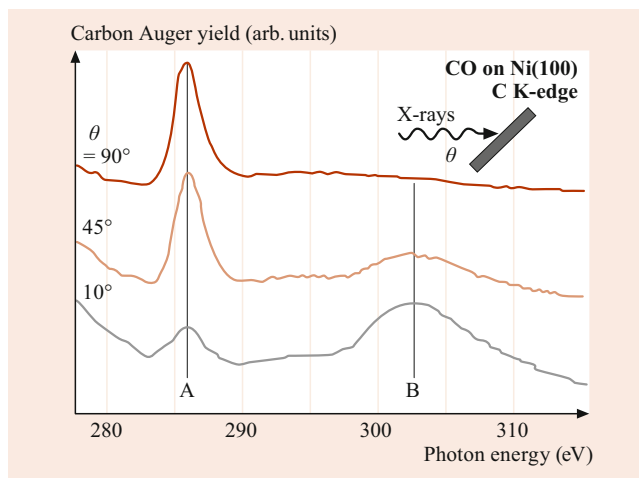


Fig. 90.5 Near-edge X-ray absorption data from the C K-edge from CO adsorbed on Ni(100) as function of incident photon angle θ . The molecular π (peak A) and σ (peak B) resonances are observed. The polarization dependence of the absorption allows the CO orientation to be determined. After [32]

where R is the bond length. This sensitivity of the final state phase shift to bond lengths allows the σ -resonance energy to be used as a measure the molecular bond length [33]. A plot of the σ -resonance energy versus $1/R^2$ shows a linear relationship, as is found in the case of simple hydrocarbons in the gas phase and adsorbed on a Cu(100) surface [31].

90.4 Atom–Surface Interactions

90.4.1 Physisorption

The binding interactions between atoms and surfaces can be classified as physisorption (long range attractive dispersion forces) and chemisorption, in which chemical bonds are formed. The long-range dispersion force between a polarizable atom and a conducting surface give rise to the leading term of the van der Waals potential $V(z) \propto -1/z^3$. At smaller atom-surface separations, the location of the reference image plane needs to be included, resulting in an attractive potential $V(z) = -C_v/|z - z_i|^3$ where z_i is the distance from the last atomic plane to the image plane, typically 2–3 Å. In principle, the constant C_v is calculable from the dielectric properties of the substrate and the atomic polarizability, but experiments have found values of C_v 40% less than expected [34]. The cause of this discrepancy has not been clarified, although contributions from surface roughness have been suggested.

At larger atom-surface separations, retardation effects must be taken into account in the dispersion interaction (the Casimir–Polder force, Sect. 83.3.4), and here theory predicts a $1/z^4$ interaction potential. This form for the potential has been confirmed experimentally [35].

As the atom approaches the surface, wave function overlap eventually causes repulsion. In the absence of chemical bond formation, the repulsive potential is simply proportional to the surface electron density $n(z)$, resulting in the overall physisorption potential

$$V(z) = Kn(z) - \frac{C_v}{|z - z_i|^3}. \quad (90.12)$$

The surface charge density $n(z)$ decreases exponentially above the surface [2], and the constant K can be determined to reasonable accuracy by an effective medium theoretical approach [36]. This shallow physisorption potential well has been studied experimentally in atomic beam (often He) scattering experiments. Under certain scattering conditions, it is possible for an incident atom to be *selectively adsorbed* on the surface by making transitions into and out of bound states of the potential well of Eq. (90.12). The incident atom with wavevector \mathbf{k} is diffracted by a surface reciprocal lattice vector \mathbf{G}_{hk} into a bound state E_n of the potential well [2]. The diffracted atomic beam intensities due to scattering via selective adsorption show strong variations which can be related to the quantum numbers (n, h, k) , and give information on the shape of the physisorption potential well.

90.4.2 Chemisorption

Many atoms and molecules will chemisorb when brought sufficiently close to a surface, forming chemical bonds (co-

valent or ionic) that are much stronger than the physisorption bond [3]. In chemisorption, there is charge transfer between the adsorbate and the surface, modifying the electronic structure of both. Valence electronic levels of the adsorbate are shifted in energy and also broadened by resonant interactions with the delocalized valence electrons at the surface (e.g., free electron-like s–p states). For many transition metal surfaces, interactions with the more localized d-states are also important.

The adsorbate-surface bond energies are most commonly studied by thermal desorption spectroscopy (TDS) [37, 38]. In this method, the adsorbate covered surface is heated using a linear temperature ramp, and the desorption rate of a particular species is measured using a mass spectrometer. By using a range of heating rates β , not only can the desorption energy be measured, but the kinetics governing the desorption process can be uncovered. For example, in the simplest case of a coverage-independent adsorption energy and first order kinetics, if the peak desorption rate occurs at a temperature T_0 then [39]

$$\frac{\nu}{\beta} = \frac{E_d}{k_B T_0^2} \exp\left(\frac{E_d}{k_B T_0}\right) \quad (90.13)$$

where E_d is the desorption energy and ν is the *attempt frequency* for desorption. Since both ν and E_d are unknown, values for both can be found by measuring TDS spectra using two different heating rates β or by estimating ν (often $\nu \approx 10^{13} \text{ s}^{-1}$). More complex desorption kinetics are studied by utilizing the full desorption profile, and a range of heating rates and initial adsorbate coverages. These kinetic data are also applicable to adsorption if the adsorption and desorption are reversible processes. For irreversible adsorption systems, it is possible to measure the adsorption energies directly [40] by monitoring the ir radiation emitted from a surface as a submonolayer quantity of atoms or molecules is adsorbed.

90.5 Recent Developments

Surface Physics has both rapidly matured and expanded its connections with other disciplines in the last eight years. A number of notable review works have been published recently [41–45]. The application of surface science techniques has expanded rapidly in a number of technological areas, such as semiconductor devices, catalysis, and magnetic materials. The emerging field of nanotechnology has drawn heavily from the techniques of surface science. Important advances have been made in a large number of areas, including biosurfaces [46, 47], cluster science [48], carbon fullerene materials [49, 50], electrochemistry [51], and surface photochemistry [52].

Continuing advances have been made in the application of light from synchrotron radiation sources—so much so that a complete catalog of applicable techniques would be difficult to compile. Many new facilities have been constructed, with higher brightness sources allowing the development of a large number of new techniques using synchrotron radiation from the ir through the soft and hard X-ray regimes [53, 54].

References

- Ertl, G., Küppers, J.: *Low Energy Electrons and Surface Chemistry*, 2nd edn. VCH, Weinheim (1985)
- Zangwill, A.: *Physics at Surfaces*. Cambridge University Press, Cambridge (1988)
- Bortolani, V., March, N.H., Tosi, M.P. (eds.): *Interaction of Atoms and Molecules with Solid Surfaces*. Plenum, New York (1990)
- Lüth, H.: *Surfaces and Interfaces of Solids*. Springer, Berlin, Heidelberg (1993)
- Woodruff, D.P., Delchar, T.A.: *Modern Techniques of Surface Science*, 2nd edn. Cambridge University Press, Cambridge (1994)
- Kevan, S.D. (ed.): *Angle-Resolved Photoemission: Theory and Current Applications*. Elsevier, Amsterdam (1992)
- Fuggle, J.C., Inglesfield, J.E.: *Unoccupied Electronic States*. Springer, Berlin, Heidelberg (1992)
- Bachrach, R.Z. (ed.): *Synchrotron Radiation Research: Advances in Surface and Interface Science*, vol. 1. Plenum, New York (1992)
- King, D.A., Woodruff, D.P. (eds.): *Chemical Physics of Solid Surfaces and Heterogeneous Catalysis*. Elsevier, New York (1990)
- Chabal, Y.J., Hoffmann, F.M., Williams, G.P. (eds.): *Vibrations at Surfaces*. Elsevier, Amsterdam (1990)
- Burns, A.R., Stechel, E.R., Jennison, D.R.: *Desorption Induced by Electronic Transitions, DIET V*. Springer, Berlin, Heidelberg (1993)
- Fuoss, P.H., Liang, K.S., Eisenberger, P.: In: Bachrach, R.Z. (ed.) *Synchrotron Radiation Research: Advances in Surface and Interface Science*, vol. 1. Plenum, New York (1992)
- Wiesendanger, R., Güntherodt, H.-J.: *Scanning Tunneling Microscopy*. Springer, Berlin, Heidelberg (1993)
- Briggs, D., Seah, M.P.: *Practical Surface Analysis: Auger and X-Ray Photoelectron Spectroscopy*, vol. 1. Wiley, Chichester (1990)
- Rous, P.J.: *Prog. Surf. Sci.* **39**, 3 (1992)
- Van Hove, M.A.: *Low-Energy Electron Diffraction*. Springer, Berlin, Heidelberg (1986)
- MacLaren, J.M., Pendry, J.B., Rous, P.J., Saldin, D.K., Somorjai, G.A., Van Hove, M.A., Vvedensky, D.: *Surface Crystallographic Information Service: A Handbook of Surface Structures*. Reidel, Dordrecht (1987)
- Ibach, H., Mills, D.L.: *Electron Energy Loss Spectroscopy and Surface Vibrations*. Academic Press, New York (1982)
- Ibach, H.: In: Bortolani, V., March, N.H., Tosi, M.P. (eds.) *Interaction of Atoms and Molecules with Solid Surfaces*. Plenum, New York (1990)
- Tong, S.Y., Li, C.H., Mills, D.L.: *Phys. Rev. B* **24**, 806 (1981)
- Sanche, L.: *J. Phys. B* **23**, 1597 (1990)
- Palmer, R.E., Rous, P.J.: *Rev. Mod. Phys.* **64**, 383 (1992)
- Bryant, C.L., Messmer, R.P. (eds.): *Auger Electron Spectroscopy*. Academic Press, New York (1988)
- Davis, L.E., MacDonald, N.C., Palmberg, P.W., Riach, G.E., Weber, R.E.: *Handbook of Auger Spectroscopy*. Physical Electronics Div, Perkin Elmer (1976)
- Kliwer, K.L.: In: Feuerbacher, B., Fitton, B., Willis, R.F. (eds.) *Photoemission and the Electronic Properties of Surfaces*. Wiley, Chichester (1978)
- Freund, H.J., Neumann, M.: In: Kevan, S.D. (ed.) *Angle-Resolved Photoemission*, p. 319. Elsevier, Amsterdam (1992)
- Eastman, D.E., Himpsel, F.J., van der Veen, J.F.: *J. Vac. Sci. Technol.* **20**, 609 (1982)
- Woodruff, D.P.: In: Kevan, S.D. (ed.) *Angle-Resolved Photoemission*. Elsevier, Amsterdam (1992)
- Rowe, J.E.: In: Bachrach, R.Z. (ed.) *Synchrotron Radiation Research*, vol. 1, p. 117. Plenum, New York (1992)
- Citrin, P.H., Eisenberger, P., Hewitt, R.C.: *Phys. Rev. Lett.* **45**, 1948 (1980)
- Bianconi, A., Marcelli, A.: In: Bachrach, R.Z. (ed.) *Synchrotron Radiation Research: Advances in Surface and Interface Science*, vol. 1, p. 63. Plenum, New York (1992)
- Stöhr, J., Baberschke, K., Jaeger, R., Treichler, R., Brennan, S.: *Phys. Rev. Lett.* **47**, 381 (1981)
- Stöhr, J., Sette, F., Johnson, A.L.: *Phys. Rev. Lett.* **53**, 1684 (1984)
- Shih, A., Parsegian, V.A.: *Phys. Rev. A* **12**, 835 (1975)
- Sukenik, C.I., Boshier, M.G., Cho, D., Sandoghdar, V., Hinds, E.A.: *Phys. Rev. Lett.* **70**, 560 (1993)
- Norskov, J.K., Lang, N.D.: *Phys. Rev. B* **21**, 2136 (1980)
- Menzel, D.: In: Vanselow, R., Howe, R. (eds.) *Chemistry and Physics of Solid Surfaces IV*, p. 102. Springer, Berlin, Heidelberg (1982)
- Kreuzer, H.J., Payne, S.H.: In: Rettner, C.T., Ashfold, M.N.R. (eds.) *Dynamics of Gas-Surface Interactions*, p. 220. Royal Society of Chemistry, Cambridge (1991)
- Redhead, P.A.: *Vacuum* **12**, 203 (1962)
- Stuckless, J.T., Al-Sarraf, N., Warnaby, C., King, D.A.: *J. Chem. Phys.* **99**, 2202 (1993)
- Kolasinski, K.W.: *Surface Science: Foundations of Catalysis and Nanoscience*. Wiley, New York (2002)
- Somorjai, G.A.: *Introduction to Surface Chemistry and Catalysis*. Wiley, New York (1994)
- Duke, C.B. (ed.): *Surface Science: The First Thirty Years*. Elsevier, New York (1994)
- Bonnell, D. (ed.): *Scanning Probe Microscopy and Spectroscopy: Theory, Techniques, and Applications*. Wiley-VCH, Berlin (2000)
- Bruch, L.W., Cole, M.W., Zaremba, E.: *Physical Adsorption: Forces and Phenomena*. Oxford University Press, Oxford (1997)
- Castner, D.G., Ratner, B.D.: *Surf. Sci.* **500**, 28 (2002)
- Tirrell, M., Kokkoli, E., Biesalski, M.: *Surf. Sci.* **500**, 61 (2002)
- Eberhardt, W.: *Surf. Sci.* **500**, 242 (2002)
- Dai, H.: *Surf. Sci.* **500**, 218 (2002)
- Knupfer, M.: *Surf. Sci. Rep.* **42**, 1 (2001)
- Kolb, D.M.: *Surf. Sci.* **500**, 722 (2002)
- Dai, H.L., Ho, W. (eds.): *Laser Spectroscopy and Photochemistry on Metal Surfaces*. World Scientific, Singapore (1995)
- Lamberti, C.: *Surf. Sci. Rep.* **53**, 1 (2004)
- Baraldi, A., et al.: *Surf. Sci. Rep.* **49**, 169 (2003)



James S. Cohen and John D. Morgan III

Contents

91.1	Introduction	1359
91.2	Nuclear Size Effects in Atoms	1360
91.2.1	Nuclear Size Effects on Nonrelativistic Energies	1360
91.2.2	Nuclear Size Effects on Relativistic Energies	1361
91.2.3	Nuclear Size Effects on QED Corrections	1362
91.3	Electronic Structure Effects in Nuclear Physics	1362
91.3.1	Electronic Effects on Closely Spaced Nuclear Energy Levels	1362
91.3.2	Electronic Effects on Tritium Beta Decay	1362
91.3.3	Electronic Screening of Low-Energy Nuclear Reactions	1362
91.3.4	Atomic and Molecular Effects in Relativistic Ion–Atom Collisions	1363
91.4	Muon-Catalyzed Fusion	1363
91.4.1	The Catalysis Cycle	1365
91.4.2	Muon Atomic Capture	1365
91.4.3	Muonic Atom Deexcitation and Transfer	1367
91.4.4	Muonic Molecule Formation	1368
91.4.5	Fusion	1370
91.4.6	Sticking and Stripping	1370
91.4.7	Prospectus	1372
	References	1372

Abstract

For an atom with a small to moderately large atomic number Z , the typical length scale a_0/Z of the innermost core orbitals is so much larger than typical nuclear length scales that the corrections to the energy levels and wave functions arising from the nonzero electric charge radius of the nucleus can accurately be computed using first-order perturbation theory, as is described in Sect. 91.2.

J. S. Cohen (✉)
Atomic and Optical Theory, Los Alamos National Laboratory
Los Alamos, NM, USA
e-mail: cohen@mailaps.org

J. D. Morgan III
Dept. of Physics & Astronomy, University of Delaware
Newark, DE, USA
e-mail: jdmorgan@udel.edu

Nonetheless, these relatively small shifts can sometimes have a profound effect on processes in atomic and/or nuclear physics, particularly if two or more energy levels are very close. For example, as is discussed in Sect. 91.3, the presence of the electron cloud makes energetically possible the β -decay of ^{187}Re to ^{187}Os and significantly modifies the energy distribution of products in the β -decay of tritium in various chemical environments. Also, electronic screening can greatly enhance the cross sections of low-energy nuclear reactions relative to what they would be for bare nuclei.

In isotopes of hydrogen, the replacement of an electron by a muon, with $m_\mu \approx 207m_e$, results in a tiny neutral *atom* that can closely approach another nucleus, thereby catalyzing nuclear fusion. For example, the rate of deuterium–tritium fusion is enhanced by 77 orders of magnitude if a single electron is replaced by a muon. A rich variety of bound-state properties and scattering processes for these exotic atoms and molecules has been extensively investigated, as is reviewed in Sect. 91.4.

Keywords

muonic atom · sticking probability · muon transfer · muonic molecule · molecular wave function

91.1 Introduction

That nuclei are not infinitesimally small, structureless particles causes small but perceptible shifts in the electronic structure of atoms and molecules. Even for nuclei with a small atomic number Z , the effects are readily detectable through modern high-precision spectroscopy, and their magnitude grows as $Z^{14/3}$. Conversely, the presence of electrons tightly bound to atomic nuclei can alter the ordering of nuclear energy levels or make them unstable to β decay. Atomic effects can also influence nuclear branching ratios into the product

channels. Nominally small atomic effects have been shown to affect the complicated chain of nuclear reactions responsible for the generation of energy in the sun. Setting bounds to the rest mass of the neutrino from the endpoint of the β -decay spectrum of tritium requires a precise understanding of atomic and molecular structure and scattering processes.

The great disparity between nuclear scales of energy (several MeV) and distance (10^{-5} to 10^{-4} Å) and the corresponding atomic scales (several eV and 1 Å, respectively) usually allows the separate treatment of nuclear and atomic effects. However, since not absolute energies but energy differences determine the magnitudes of perturbative effects, near coincidences in energy differences can greatly enhance the interplay between the two regimes. Such comparable differences of energies account for the important role of nuclear structure in the Lamb shift splitting between the $2s_{1/2}$ and $2p_{1/2}$ states of the hydrogen atom (Chap. 28) and the influence of atomic structure on nuclear processes (Sects. 91.2 and 91.3).

For the case of muonic atoms and molecules, the interplay is enhanced by the much larger mass of a muon relative to an electron. This decreases the distance scale by a factor of m_e/m_μ and increases the energy scale by a factor of m_μ/m_e . Small corrections such as the vacuum polarization part of the Lamb shift are amplified even more ($\approx (m_\mu/m_e)^3$ for low Z).

Besides the areas where atomic physics effects play an important role in nuclear physics, or vice versa, it is worth remembering that atomic and molecular physicists and nuclear physicists can benefit from knowing the theoretical techniques that have been developed in each others' fields. For example, it is well known that group theoretical methods are widely employed in formulating and solving many-body problems in nuclear, atomic, and molecular physics. To take another case, the coupled-cluster method, which was first proposed in the late 1950s by *Coester* and *Kümmel* in the context of nuclear theory [1–3], was applied a decade later to electronic structure problems in atomic and molecular physics and quantum chemistry by *Cizek*, *Paldua*, and *Shavitt* [4–6], and in the 1980s was widely developed by Rod Bartlett and coworkers at the University of Florida and by John Pople and coworkers at Carnegie Mellon University. *Quantum halos*, which are very loosely bound states for which most of the probability density is spread diffusely over the classically forbidden region, have been treated in a unified manner for both nuclear and molecular systems [7].

91.2 Nuclear Size Effects in Atoms

91.2.1 Nuclear Size Effects on Nonrelativistic Energies

Interest in the influence of a finite nuclear charge distribution on the energy levels of the hydrogen atom goes back

to the measurement of the Lamb shift [8–11], and to even earlier indications that the fine structure of hydrogen did not quite agree with the predictions of the Dirac equation for a point nucleus [12–15]. The finite proton size does, in fact, raise the energy of the $2s_{1/2}$ state relative to $2p_{1/2}$, but the shift is only $\approx 0.012\%$ of the dominant electron self-energy contribution (Chap. 28). It must nevertheless be taken into account in high-precision tests of QED. A long-standing disagreement in the proton size between values obtained from electron-based measurements and muon-based measurements has now been resolved [16], resulting in the value $r_p = 0.833(10)$ fm, in excellent agreement with the muonic value $r_p = 0.84087(39)$ fm [17, 18].

Early derivations were given by several authors [19–22] and generalized by *Zemach* [23] (also [24]) to a form involving integrals over the nuclear electric and magnetic form factors. The basic result is illustrated by the following argument. Let $\rho(\mathbf{r})$ be the electron density, which may have no spatial symmetry properties in the particular case of a polyatomic molecule, and $\rho_n(\mathbf{r}_n)$ be the charge density of a nucleus, which obeys

$$\int d^3r_n \rho_n(\mathbf{r}_n) = Z. \quad (91.1)$$

Assume that $\rho_n(\mathbf{r}_n)$ has no permanent electric dipole moment, so that

$$\int d^3r_n \mathbf{r}_n \rho_n(\mathbf{r}_n) = \mathbf{0}. \quad (91.2)$$

By writing the Coulomb potential for a point-like nucleus as

$$-\frac{Z}{r} = -\int d^3r_n \frac{Z\delta^{(3)}(\mathbf{r}_n)}{|\mathbf{r} - \mathbf{r}_n|}, \quad (91.3)$$

the first-order shift of the electronic energy due to the replacement of the point-like nucleus by an extended nucleus is

$$\Delta E_{\text{nuc}} = \int d^3r \int d^3r_n \frac{Z\delta^{(3)}(\mathbf{r}_n) - \rho_n(\mathbf{r}_n)}{|\mathbf{r} - \mathbf{r}_n|} \rho(\mathbf{r}). \quad (91.4)$$

Since the Fourier transform, defined by

$$\hat{\rho}_n(\mathbf{k}) = \int d^3r_n e^{-i\mathbf{k}\cdot\mathbf{r}_n} \rho_n(\mathbf{r}_n), \quad (91.5)$$

preserves inner products within a factor of $(2\pi)^3$ and maps convolutions to simple products, the integral in Eq. (91.4) reduces to

$$(2\pi)^3 \int d^3k [Z - \hat{\rho}_n(\mathbf{k})] \frac{4\pi}{k^2} \hat{\rho}(\mathbf{k}), \quad (91.6)$$

where the hats denote the Fourier transforms of the densities, and $4\pi/k^2$ is the Fourier transform of the Coulomb potential $1/r$. Since $Z = \int d^3r_n \rho_n(\mathbf{r}_n)$, the energy shift can be

reexpressed as

$$(2\pi)^3 \int d^3k \int d^3r_n (1 - e^{-i\mathbf{k}\cdot\mathbf{r}_n}) \rho_n(\mathbf{r}_n) \frac{4\pi}{k^2} \hat{\rho}(\mathbf{k}), \quad (91.7)$$

which is still an exact first-order perturbation expression. Since typical nuclear length scales are much smaller than typical nonrelativistic atomic length scales, it is legitimate to expand the exponential in a Taylor series. The zeroth-order term, -1 , is canceled by the $+1$. The linear term, $i\mathbf{k}\cdot\mathbf{r}_n$, contributes nothing by the hypothesis that the nuclear charge distribution has no permanent electric dipole moment. The first nonvanishing term is

$$(2\pi)^3 \int d^3k \int d^3r_n \frac{1}{2}(\mathbf{k}\cdot\mathbf{r}_n)^2 \rho_n(\mathbf{r}_n) \frac{4\pi}{k^2} \hat{\rho}(\mathbf{k}). \quad (91.8)$$

If $\rho(\mathbf{r})$ is nonzero at the nucleus, then for large k , the leading behavior of $\hat{\rho}(\mathbf{k})$ is that of a spherically symmetric s -wave with a radial dependence proportional to k^{-4} . The angular integration in the variable \mathbf{k} leads to the replacement of $(\mathbf{k}\cdot\mathbf{r}_n)^2$ by its average value $(1/3)k^2r_n^2$, so the expression Eq. (91.8) reduces to

$$\frac{2\pi}{3} (2\pi)^3 \int d^3k \hat{\rho}(\mathbf{k}) \int d^3r_n r_n^2 \rho_n(\mathbf{r}_n), \quad (91.9)$$

which can be further simplified by observing that

$$(2\pi)^3 \int d^3k \hat{\rho}(\mathbf{k}) = (2\pi)^3 \int d^3k e^{i\mathbf{0}\cdot\mathbf{k}} \hat{\rho}(\mathbf{k}) = \rho(0), \quad (91.10)$$

and by definition

$$\int d^3r_n r_n^2 \rho_n(\mathbf{r}_n) = Z\langle r_n^2 \rangle, \quad (91.11)$$

thus yielding the final expression

$$\Delta E_{\text{nuc}} = \frac{2\pi}{3} Z e^2 \rho(0) \langle r_n^2 \rangle, \quad (91.12)$$

with

$$\rho(0) = \left(\frac{\mu}{m_e}\right)^3 \frac{Z^3}{\pi n^3} a_0^{-3} \quad (91.13)$$

for a hydrogenic ion with reduced mass μ . This derivation is independent of the specific nuclear model or the assumption of spherical symmetry of the electron density. Since $\langle r_n^2 \rangle$ scales as $Z^{2/3}$, ΔE_{nuc} then scales as $Z^{14/3}$. For a molecule with several nuclei, the contributions Eq. (91.12) from each nucleus should be summed.

For the helium atom, $\rho(0) = \langle \delta(\mathbf{r}_1) + \delta(\mathbf{r}_2) \rangle$ can be accurately calculated from high-precision variational wave functions (Chap. 12). For the $1s_2 \ ^1S_0$ ground state, $\rho(0) \simeq$

$(\mu/m_e)^3 [3.6208586 - 0.18237(\mu/M)] a_0^{-3}$, where M is the nuclear mass. Results for other states up to $n = 10$ are tabulated in [25]. Combined with high-precision isotope shift measurements, the results can be used to extract differences in nuclear radii for pairs such as $^3\text{He}/^4\text{He}$, $^6\text{Li}/^7\text{Li}$, and H/D [26–29]. The method has been applied to the short-lived, neutron-rich nuclei ^6He , ^8Li , and ^9Li [30, 31].

Equation (91.12) works well for atoms with small Z , since relativistic corrections to the electron density are small. However, it breaks down for heavier nuclei, for which relativistic wave functions are needed.

91.2.2 Nuclear Size Effects on Relativistic Energies

The preceding analysis breaks down for relativistic wave functions because they are singular at a point nucleus, making $\rho(\mathbf{0})$ infinite. In this case, the Dirac equations with Hamiltonians H_0 and H for the point nucleus and distributed nucleus cases, respectively, can be combined to obtain

$$(E - E_0)\Psi^\dagger\Psi_0 = \Psi^\dagger H\Psi_0 - \Psi^\dagger H_0\Psi_0. \quad (91.14)$$

If a finite radius r_s is now chosen such that $H = H_0$ outside the sphere $r = r_s$, then this equation can be integrated from r_s outward to yield [32]

$$\Delta E_{\text{nuc}} = \frac{\hbar c (gf_0 - fg_0)_{r=r_s}}{\int_{r_s}^{\infty} (gg_0 + ff_0) dr}, \quad (91.15)$$

where f_0 and f are the large radial components of Ψ_0 , and Ψ and g_0 and g are their small radial components (Chap. 9), and the numerator is the surface term that remains after integrating by parts the $c\boldsymbol{\alpha}\cdot\mathbf{p}$ term in H . The units are $\hbar c/a_0 = \alpha m_e c^2$. The solutions can be further expanded in terms of Bessel functions, or the Dirac equation can simply be integrated numerically.

For hydrogenic ions up to moderately large Z , the results are reasonably well represented by [33, 34]

$$\Delta E_{\text{nuc}} = \frac{2}{3n^3} (Z\alpha)^2 m_e c^2 \times [\delta_{\ell,0} + C_2(Z\alpha)^2] (Z^2 \langle r_n^2 \rangle / a_0^2)^\gamma, \quad (91.16)$$

with $\gamma = [1 - (Z\alpha)^2]^{1/2}$, and $C_2 \simeq 0.50, 1.38$, and 0.1875 for the $1S_{1/2}$, $2S_{1/2}$, and $2P_{1/2}$ states, respectively. Extensions to higher-order terms are discussed in [35]. The above formula was used in the tabulations of *Mohr* [34] for $10 \leq Z \leq 40$, while *Johnson* and *Soff* [36] used the numerical integration method for Z up to 110. The nuclear electric and magnetization density distributions are tabulated in [37], nuclear moments in [38], and nuclear masses in [39]. In the absence

of better data, the root-mean-square nuclear radius can be estimated from $\langle r_n^2 \rangle^{1/2} \approx 0.777A^{1/3} + 0.778 \pm 0.06$ fm, where A is the atomic mass number.

91.2.3 Nuclear Size Effects on QED Corrections

The progress in the experimental study of transition energies in heavy ions stripped of most of their electrons [40–42] has inspired theoretical work on modifications of QED corrections due to an extended nuclear charge distribution. Calculations based on propagators expanded in terms of basis splines [43–45] (Sect. 8.1.1) have led to relatively rapid convergence with the number of angular functions.

91.3 Electronic Structure Effects in Nuclear Physics

91.3.1 Electronic Effects on Closely Spaced Nuclear Energy Levels

The presence of a nearby cloud of electrons can significantly affect nuclear processes involving closely spaced nuclear energy levels. One of the most dramatic cases involves the β -decay process $^{187}\text{Re} \rightarrow ^{187}\text{Os} + e^- + \bar{\nu}_e$, which is energetically forbidden by about 12 keV for bare nuclei but becomes allowed for the neutral atoms when the difference in electronic binding energies is included. The nuclear charges are $Z = 75$ for ^{187}Re and $Z = 76$ for ^{187}Os . There is also the possibility of the electron being captured into a bound state of ^{187}Os , as opposed to the continuum β -decay process.

The total electronic binding energies of heavy neutral atoms can be roughly estimated using the large- Z expansion for $E(Z)$ given by Eq. (21.31) in Chap. 21. The difference between the energies of two neutral atoms with atomic numbers $Z + 1$ and Z , respectively, is then given approximately by

$$\begin{aligned} E(Z + 1) - E(Z) &\simeq \frac{dE}{dZ} \\ &\simeq (-48.83Z^{4/3} + 27.21Z^{3/3} \\ &\quad - 12.24Z^{2/3}) \text{ eV}, \end{aligned} \quad (91.17)$$

which amounts to about -13.6 keV at $Z = 75$. This is sufficient to overcome the 12 keV energy deficit in the otherwise energetically forbidden β -decay of ^{187}Re .

The general theory of bound state β -decay is discussed by *Bahcall* [46], who also calculated the ratio ρ of bound state β -decay to continuum β -decay for bare nuclei. In the case of $^{187}\text{Re} \rightarrow ^{187}\text{Os}$, ρ is of importance in estimating changes in the half-life for β -decay of ^{187}Re under various conditions of ionization, since the measured isotope ratios $^{187}\text{Re}/^{188}\text{Re}$

and $^{187}\text{Os}/^{188}\text{Os}$ from terrestrial rocks and meteorites can be used to determine not only the age of the solar system but also the age of our galaxy [47, 48]. Estimates based on a modified Thomas–Fermi (TF) model [49] indicate that $\rho \simeq 0.01$, and further multiconfiguration Dirac–Fock calculations give $\rho = 0.005$ to 0.007 [50–52]. See [50–52] for further details and references.

91.3.2 Electronic Effects on Tritium Beta Decay

The mass of the neutrino, normally taken to be zero in the Standard Model, can be determined in principle from analysis of the β -decay process $^3\text{T} \rightarrow ^3\text{He}^+ + e^- + \bar{\nu}_e$. An early measurement based on this method [53–55] yielded a neutrino mass of ≈ 25 eV. Several independent tests of this result were initiated soon thereafter. Since the experiments are performed not on bare tritons but on tritium gases and solids under various conditions, it is essential to understand quantitatively the atomic and molecular processes that affect the distribution of the highest-energy electrons produced from various initial states [56, 57].

Martin and *Cohen* [58] used a Stieltjes imaging technique to calculate shakeup and shakeoff probabilities for the β -decay of T_2 into $^3\text{HeT}^+$. Simultaneously, extensive calculations were carried out by *Kolos*, *Jeziorski*, *Szalewicz*, *Monkhorst*, et al. [59–63] using potential energy curves for the reactant T_2 and TH molecules and the product $^3\text{HeT}^+$ and $^3\text{HeH}^+$ molecules and accounting for the production of electronically and rovibrationally ground and excited final states, as well as resonant states. Nuclear motion was found to have a small but detectable effect on the results, and solid-state effects for frozen T_2 were also investigated and found to be small. These calculations played a crucial role in the interpretation of the experiments [64–68], which indicated that the neutrino mass is less than ≈ 10 eV. In 1998, there was published evidence from the super-Kamiokande experiment that the three flavors of neutrinos oscillate, as further confirmed by the Sudbury Neutrino Observatory. This implies that neutrinos have a nonzero rest mass [69]. Subsequently, upper bounds of the order of a few eV to the neutrino mass have been derived from measurements of tritium beta decay [70, 71] and from cosmological considerations [72]. As of 2018 the best upper bound from tritium beta decay experiments was about 2 eV [73].

91.3.3 Electronic Screening of Low-Energy Nuclear Reactions

The cross section $\sigma(E)$ for a nuclear reaction involving charged reactants drops very rapidly for collision energies E below the Coulomb barrier. A WKB treatment shows that

for low collision energies, the dependence of $\sigma(E)$ can be conveniently expressed as

$$\sigma(E) = S(E) E^{-1} e^{-2\pi\eta}, \quad (91.18)$$

where $S(E)$ is the astrophysical factor, and

$$\eta = Z_1 Z_2 \alpha c (\mu/2E)^{1/2} \quad (91.19)$$

is the Sommerfeld parameter, which depends on the charge numbers Z_1 and Z_2 of the projectile and target nuclides, their reduced mass μ , and the center-of-mass energy E . For nuclear reactions involving light nuclei, it is found that $S(E)$ typically varies slowly with E except close to resonances. Thus, an accurate determination of $S(E)$ at moderately low E can be used to extrapolate $\sigma(E)$ to much lower energies, which are beyond the reach of laboratory experiments but are of great relevance to the nuclear reactions that occur in stars.

However, electron screening effects can greatly enhance cross sections for nuclear reactions as measured in the laboratory at low energy [74], because at least the target nucleus is almost always surrounded by a cloud of electrons that screen the Coulomb repulsion between nuclei. The effect has been observed in various low-energy reactions such as ${}^3\text{He}(d, p){}^4\text{He}$, ${}^6\text{Li}(p, \alpha){}^3\text{He}$, ${}^6\text{Li}(d, \alpha){}^4\text{He}$, and ${}^6\text{Li}(p, \alpha){}^4\text{He}$ [75–78]. Since reactions in stars involve bare nuclei, the laboratory data must be carefully corrected for screening effects.

Analysis of the data for the ${}^3\text{He}(d, p){}^4\text{He}$ reaction indicates that the effect of screening is always greater than that predicted in the adiabatic limit [79–81]. A more general theoretical treatment of the $d + {}^2\text{H}$ and $d + {}^3\text{He}$ reactions [82], using a time-dependent Hartree–Fock method for the electrons screening and classical motion for the nuclei found less enhancement than that observed. An improved treatment taking account of electron correlation and quantum-mechanical effects on the nuclear motion will likely be needed. This remains an important area of development for the future.

For some work on the subject of electronic screening of low-energy nuclear reactions, see [83–88].

91.3.4 Atomic and Molecular Effects in Relativistic Ion–Atom Collisions

High-energy accelerators can now produce beams of atomic ions partly or completely stripped of their electrons, even for Z as high as 92. The collisions of such beams of highly charged ions with fixed targets involve a broad array of atomic and molecular processes, such as excitation, ionization, charge transfer, and, in the extreme relativistic case, pair production. A similarly broad array of theoretical techniques is required to study these topics. A thorough review of these,

including comparisons with experimental data where available, is given in [89, 90].

A topic of particular interest is the first experimental observation of the capture of electrons from electron–positron pair production in the extreme relativistic collision of a 0.96 GeV/nucleon U^{92+} beam with gold, silver, copper, and Mylar targets [91]. The energy and angular distributions of the positrons were also measured. For the gold target, the cross section for capture was nearly as large as that for pair production without capture, and it was found to vary with the nuclear charge Z_t of the target nucleus roughly as $Z_t^{2.8(\pm 0.25)}$. Neither the dependence on Z_t nor the relatively great probability for capture is in agreement with perturbation theory, which highlights the need for further exploration of this exotic system.

91.4 Muon-Catalyzed Fusion

Exotic muonic atoms and molecules are more suitable subjects than electronic atoms and molecules for probing some physical effects. The muon μ^- is a leptonic elementary particle like the electron, except that it is 206.768 times more massive and has a finite lifetime ($\tau_0 = 1/\lambda_0$, where λ_0 is the rate of decay) of 2.197 μs . This lifetime is amply long for most experiments. In normal atoms, the fine-structure splitting (due to $\mathbf{L} \cdot \mathbf{S}$ coupling) is much larger than the hyperfine splitting (due to $\mathbf{s}_{\text{nuc}} \cdot \mathbf{s}_e$ coupling); this relation is reversed in muonic atoms. Likewise, vacuum polarization, relativistic, finite-nuclear-size, and nonadiabatic effects are enhanced. (*Note:* the muonic Bohr radius $\hbar^2/m_\mu e^2 \approx (1/207) a_0$ is similar in size to the Compton wavelength $\hbar/m_e c \approx (1/137) a_0$.) Remarkably, muonic molecules make nuclear fusion possible at room temperature. In the phenomenon of muon-catalyzed fusion (μCF), there are both indirect and direct interactions between the atomic and molecular physics and the nuclear physics. Indirectly, the atomic and molecular densities and transition rates control the nuclear fusion rates, and, in turn, the kinetic energies of the fusion products affect the atomic and molecular kinetics. Directly, the nuclear structure affects some molecular energy levels that determine important resonant rates and the boundary condition on the muonic wave functions used to calculate the muon *sticking* loss.

The phenomenon of μCF was actually discussed theoretically [92–94] before it was experimentally observed [95]. Shortly after its observation, its possible use for energy production was discussed [96]. This was an attractive prospect, since hot fusion schemes are made difficult by the electrostatic (Coulomb) repulsion between nuclei. In the two conventional approaches to controlled fusion, magnetic and inertial confinement, this barrier is partially surmounted by energetic collisions. (*Note:* the particle densities N and con-

finement times τ in the hot plasmas ($T \gtrsim 10^8$ K) are typically more than ten orders of magnitude different for these two schemes, but the product of the two required for d-t fusion is $N\tau \gtrsim 10^{14}$ s/cm³ in either case. For muon-catalyzed fusion, effectively $N\tau \approx 10^{25}$ s/cm³, but this criterion does not tell the real story.) In contrast, in μ CF, the objective is for the nuclei to tunnel through the barrier without the benefit of kinetic energy. This feat is enabled by binding two hydrogenic nuclei (p, d, or t) in an exotic molecule like H_2^+ with the electron replaced by a negative muon.

Since the molecular size is inversely proportional to the mass of the binding particle, the average distance between nuclei in $pp\mu$ is $\approx 1/200$ Å (500 fm) instead of 1 Å as in ppe (i.e., H_2^+). This distance, which would be reached in a d + d collision at ≈ 3 keV ($\approx 3 \times 10^7$ K), is still large compared with the separation of a few fm where the nuclear strong forces cause fusion, but fusion occurs rapidly because of the increased vibrational frequency and, more importantly, the increased probability of tunneling per vibration. The vibrational frequency is $(m_\mu/m_e)^{3/2} \approx 3 \times 10^3$ times faster than for the corresponding electronic molecule. (Note: for comparison, the muonic/electronic energy scales as m_μ/m_e and the rotational energy scales as $(m_\mu/m_e)^2$. These relations [97] are based on the Born–Oppenheimer approximation, which is not very accurate for muonic molecules.) The effect on the tunneling probability depends on the nuclear masses; for $dt\mu$, which has the largest nuclear matrix element (astrophysical S factor, Sect. 91.3.3), the increase is by a factor of $\approx 10^{77}$ compared with DT, and the consequential fusion rate is $\lambda_{dt\mu}^f \approx 10^{12}$ s⁻¹.

Just on the basis of the fusion rate, one would expect a yield of $\lambda_{dt\mu}^f/\lambda_0 \approx 10^6$ muon-catalyzed d-t fusions for the average muon. While this number indeed provides an upper limit, the actual average number of fusions, ≈ 150 for $dt\mu$, is much smaller and is determined by the atomic and molecular physics of the catalysis cycle (although the energy released in the nuclear fusion does play an important role here). Some of the atomic and molecular processes in the μ CF cycle are quite ordinary, but others, like atomic capture and resonant molecular formation, have no counterpart with normal atoms.

Muon-catalyzed fusions of all pairs of hydrogen isotopes, except two protons, have been observed. Based on the experiments and theory, the dominant reaction products are [98–103]:

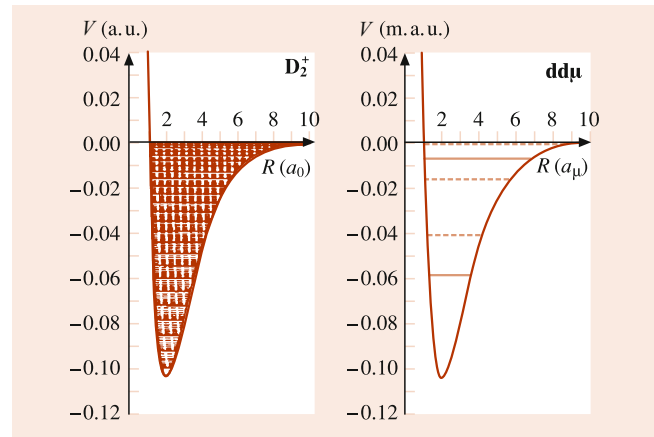
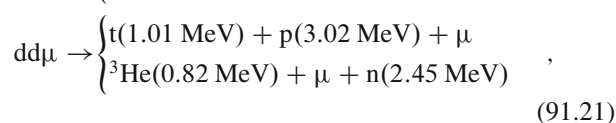
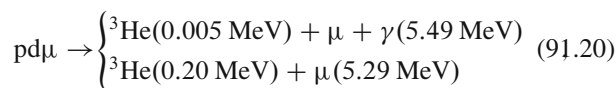
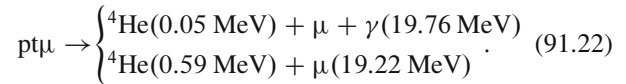
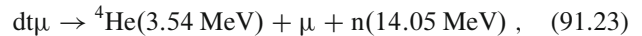


Fig. 91.1 Rovibrational energy levels for D_2^+ and $dd\mu$. The $J = 0$ levels are shown as solid lines, and the $J > 0$ levels are shown as dashed lines. For D_2^+ , all 28 vibrational levels are displayed, but the associated rotational levels are displayed only up to the next higher vibrational level. All levels of $dd\mu$ are displayed; the $(J = 1, v = 1)$ level is barely discernible below the $V = 0$ axis



(Note: A channel producing ${}^4\text{He}$ and a e^+e^- pair was theoretically predicted to be significant [104] but seems to be ruled out by experimental results published in 2012 [105].)



In these reactions, a μ without an energy designated is a spectator; i.e., it serves to bring the nuclei together but plays no significant role in the kinematics of the reaction – such a μ may actually be bound (stuck) to one of the product nuclei.

Each reaction is of special interest in its own right: $pd\mu$ and $pt\mu$ for the contribution of μ conversion, and $tt\mu$ for the correlation of the two final state neutrons. Only the $dd\mu$ and $dt\mu$ molecular formations are resonant; i.e., their formation can occur in a one-body state because they, and only they, possess a loosely bound state such that the muonic binding energy can go into rovibrational energy of the electronic molecule. That the existence of such a state really is fortuitous can be seen in Fig. 91.1 where the bound rovibrational states of $dd\mu$ (1 m.a.u. = 5626.5 eV) are compared with the rovibrational states of D_2^+ (1 a.u. = 27.2 eV). Although both $dd\mu$ and $dt\mu$ can be formed resonantly, $dt\mu$ is unique in having a rapid (as compared with muon decay) formation rate and also in having a small sticking loss. The sticking loss is due to the possibility that the negatively charged muon may form a bound state with the positively charged fusion product. The relatively low branching fraction ($< 1\%$) for $dt\mu \rightarrow {}^4\text{He}\mu + n$ is due simply to the high speed of the outgoing ${}^4\text{He}$ (α particle).

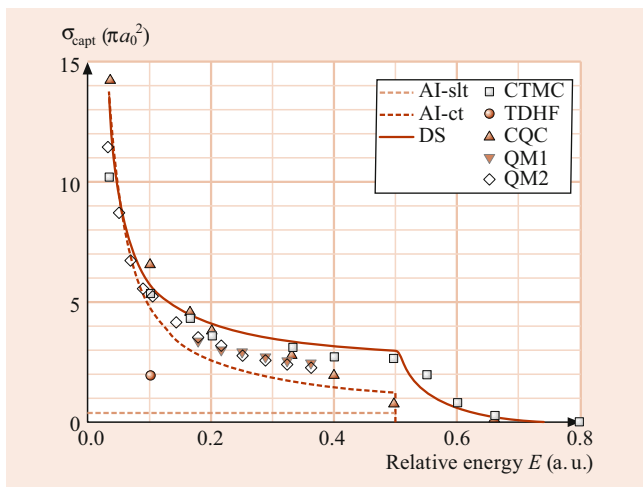


Fig. 91.3 Comparison of different capture cross sections for $\mu^- + \text{H}$ collisions: adiabatic ionization with straight-line trajectories (AI-slt), adiabatic ionization with curved trajectories (AI-ct), diabatic states with polarized orbital (DS), classical-trajectory Monte Carlo (CTMC), time-dependent Hartree–Fock (TDHF), classical-quantal coupling (CQC), quantum mechanical wavepacket (QM1), and Chew–Goldberger integral equation (QM2)

Early calculations were done using the Born or Coulomb–Born approximation [112]. These methods are not very accurate for μ^- at velocities below 1 a.u., but, more importantly, their implementation treated slowing down and capture inconsistently. The upshot was prediction of capture of muons at kinetic energies of hundreds of eV, whereas it turns out that most captures actually do not occur until the muon is slowed to energies below 100 eV.

The perturbative methods failed because of the great electron charge redistribution that occurs during the capture process. Other approaches have led to progressively more accurate treatment:

1. Adiabatic ionization with straight-line trajectories (AI-slt) [113]
2. Adiabatic ionization with curved trajectories (AI-ct) [114, 115]
3. Diabatic states (DS) [116, 117]
4. Classical-trajectory Monte Carlo (CTMC) [115]
5. Time-dependent Hartree–Fock (TDHF) [118]
6. Classical-quantal coupling (CQC) [119]
7. Quantum mechanical wavepacket (QM1) [120]
8. Chew–Goldberger integral equation (QM2) [121].

Results for the capture cross sections are shown in Fig. 91.3.

The early study by *Wightman* [113] shed a great deal of light on the capture process. His method, known as adiabatic ionization (AI), followed from the observation of *Fermi and Teller* [122] that there exists a critical value of the dipole moment eR_c , formed by the negative muon and positive proton at distance $R_c = 0.639 a_0$, for binding the electron. In colli-

sions where the μ^- approaches closer than this distance, the electron is assumed to escape adiabatically, and, if the electron carries off more energy than the muon’s initial kinetic energy, the $\mu\mu$ atom is formed. This cross section is thus

$$\sigma_{\text{AI-slt}} = \pi R_c^2, \quad (91.29)$$

and μ^- capture results if and only if $E < 0.5$ a.u., the target ionization energy.

The AI-slt model has three major shortcomings: (1) it does not take into account trajectory curvature, which is caused by the Coulomb attraction of the negative muon toward the positive nucleus and can be large at the low-trajectory velocities where capture usually occurs, (2) the adiabatically escaping electron takes off no kinetic energy, and (3) ionization occurs with unit probability if the approach is closer than R_c . The first failing is easy to remedy. The cross section with curved adiabatic trajectories (AI-ct) is just [115]

$$\sigma_{\text{AI-ct}} = \frac{\pi R_c^2}{E} \left(E + \frac{1}{R_c} - 0.5 \text{ a.u.} \right), \quad (91.30)$$

as long as the collision energy E in the center-of-mass system is greater than 0.03 a.u. (0.8 eV). Hence, trajectory curvature increases the capture cross section by a factor $1 + (1.06/E)$ (for E in a.u.), which is over a factor of 3 even at the highest collision energy (0.5 a.u.) where adiabatic capture can occur. For $E < 0.03$ a.u., the centrifugal barrier in the effective potential,

$$V_{\text{a(eff)}}(R, b) = V_{\text{a}}(R) + \frac{b^2}{R^2} E, \quad (91.31)$$

restricts penetration and reduces the cross section below the value given by Eq. (91.30) [114].

Cures for the second and third failings are less trivial. These two assumptions were first avoided by using the diabatic-states (DS) model [116, 117]. The adiabatic electronic potential energy no longer increases once it reaches the continuum ceiling; however, in view of the μ^- acceleration by the Coulomb attraction, the electron cloud actually does not have enough time to adjust adiabatically. In recognition of this situation, the diabatic treatment yields an electronic potential energy that crosses into the continuum at a distance larger than R_c and continues to rise smoothly. The concomitant probability of ionization is given by the ionization width, obtained from a Fermi-golden-rule-like formula. The next method applied was classical-trajectory Monte Carlo (CTMC) [115], discussed in Chap. 62. The CTMC method treats the dynamics of all particles exactly but classically. The classical approximation was later eliminated by using the time-dependent Hartree–Fock (TDHF) method discussed in Sect. 53.3 [118]. However, the improvement was open to question since it was achieved at the expense of

neglecting correlation, which turns out to be important in the present problem. This deficiency was remedied by the classical-quantal coupling (CQC) method, which makes only the seemingly well-justified approximation of treating the muon classically while retaining the quantum treatment of the electron [119]. Since then, there have been two rigorous quantum-mechanical calculations [120, 121] using time-dependent methods. These calculations have been limited to collision energies below 10 eV (0.37 a.u.). At very low energies, especially in view of the resonance behavior found [120], the time-dependent methods require quite time-consuming computations. Recently, the capture cross section was also calculated quantum mechanically by the time-independent R -matrix method, which was able to better characterize the resonances; this calculation was done only for very low energies (below 1 eV) [123]. Except for the adiabatic ionization and TDHF methods, the results of the various methods are generally in fairly good agreement, although calculations for $E_{\text{cm}} > 0.5$ a.u. are more challenging, and the classical results have yet to be confirmed by completely quantum mechanical calculations.

Real μ^- capture experiments (and μCF) are generally done with molecules (H_2 , DT , etc.). The naive notion, once accepted, that the H_2 cross section is simply twice that of H is quite unrealistic for slow ($v \ll 1$ a.u.) collisions. The capture by hydrogen molecules, which is the first step in μCF , is now theoretically much better understood [124]. The molecular cross section is greatly enhanced, primarily due to the molecular vibrational degree of freedom, which enables the molecule to capture μ^- at collision energies up to ≈ 40 eV in hydrogenic states with principal quantum number $n \gtrsim 9$, whereas atomic capture cuts off above ≈ 14 eV with $n \gtrsim 14$. There is a corresponding isotope effect in the molecule, which is absent in the atom.

91.4.3 Muonic Atom Deexcitation and Transfer

The muon is captured in a highly excited state but normally must reach the $1s$ configuration of the heavier isotope (in the case of mixtures like D/T) before the muonic molecule is formed. In the $1s$ configuration, there are two hyperfine levels – the ground state with the nuclear and μ^- spins antiparallel and an excited state with spins parallel. Resonant molecular formation rates in the two states can be quite different and also depend strongly on the atom's kinetic energy. Thus, there are several types of muonic atom collisions that must be taken into account: (1) elastic scattering in the ground and excited states, (2) isotopic transfer in excited states, (3) deexciting transitions (which may also occur radiatively), (4) isotopic transfer in the $1s$ state, and (5) hyperfine transitions. Cross sections for most of these processes have been calculated. The bulk of the calcula-

tions have been done by expanding in adiabatic (or modified adiabatic) eigenfunctions, but there also exist some calculations using the coupled-rearrangement-channel, Faddeev, hyperspherical, and variational approaches ([97, 107] for references).

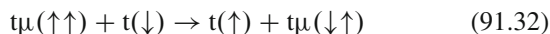
The cascade of the initially formed muonic atom, especially in mixtures, is a complicated process [125]. It constitutes a crucial part of the d - t μCF cycle in that it determines the parameter q_{1s} in Eq. (91.26). This parameter is essential to experimental analysis, but it was evident that early calculations yielded values of q_{1s} too small to be consistent with experiments. Theoretical calculations suggest the explanation is that the excited muonic atoms are not thermalized [126–128]. Epithermal atoms have three effects here: (1) the normal transfer rates are smaller, (2) the transfer is reversible down to lower principal quantum numbers n where E still exceeds the threshold for excitation of the next-higher level, and (3) excited-state [from $(t\mu)^*$] resonant formation of $(d\mu)^*$ molecules that can predissociate back to $d\mu$ is enhanced [129]. (*Note:* the isotopic energy splittings are $134.7/n^2$ for $d\mu$ - $p\mu$, $182.8/n^2$ for $t\mu$ - $p\mu$, and $48.0/n^2$ for $t\mu$ - $d\mu$.) The parameter q_{1s} is determined by competition between transfer and deexcitation, which depend on the kinetic energies that result from further competition between superelastic deexcitation and thermalizing elastic collisions. It appears that the stage of the cascade most crucial for q_{1s} is $n \approx 4$ for normal muon transfer and $n = 2$ for the resonant sidepath.

In contrast with electrons, for muons the elastic cross sections are more difficult to calculate than the inelastic ones. The inelastic transitions occur at short range (a few a_μ) where the effects of electronic structure are negligible. However, electronic effects are not negligible for low-energy (< 1 eV) elastic scattering where $\lambda_{\text{dB}} \approx 1 a_0$. They have been taken into account for ground state but not yet excited-state scattering. In doing so, it is not necessary to solve the general problem directly because of the following simplifications: (1) this energy is below the vibrational threshold, so the molecular target can be taken as a rigid rotor, and (2) the relative smallness of the muonic atoms makes the sudden approximation adequate.

If the $1s$ state is reached without muon transfer to the heavier isotope already having occurred, the transfer takes significant time and plays an important role in determining the tritium fraction c_t that optimizes the fusion yield. All of the $1s$ isotopic-exchange cross sections display the characteristic $\approx 1/v$ velocity dependence at thermal energies, so that the corresponding rate $v\sigma$ is independent of temperature.

In muon-catalyzed d - d and d - t fusions, the resonant molecular formation rates in different hyperfine structure (HFS) states can differ by two or more orders of magnitude at low T due to their different energy levels. The HFS also has important effects on thermalization and diffusion

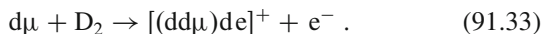
via the different elastic cross sections. Under usual μCF experimental conditions, the hyperfine quenching (or *spin flip*) is irreversible; the HFS splittings are 0.1820, 0.0485, and 0.2373 eV for $p\mu$, $d\mu$, and $t\mu$, respectively. Theoretically, it is expected that transitions between HFS levels mainly occur in symmetric collisions since muon exchange suffices in such collisions [130]; e.g.,



(the usual terminology here is *muon exchange*, although it might seem more logical to refer to the reaction as *triton exchange* since it is the identity of the tritons that enables the reaction). As in the case of the isotopic exchange cross sections, the behavior is $\approx 1/v$ at thermal energies, so the rates are nearly independent of temperature.

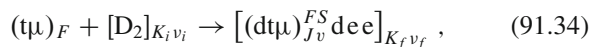
91.4.4 Muonic Molecule Formation

Until the prediction by *Vesman* [131] of a resonant formation for $dd\mu$, it was thought that all muonic molecules were formed by an Auger process of the type



Unlike the resonant process for $dd\mu$ and $dt\mu$, the nonresonant process generally depends weakly on the temperature of the target, the hyperfine state of the muonic atom, and the *spectator* atom X in the molecule DX , where X can be H, D, or T. The nonresonant rate at low (liquid hydrogen) temperature for $dd\mu$ formation is about $3 \times 10^4 \text{ s}^{-1}$, and for $dt\mu$ it is about $6 \times 10^5 \text{ s}^{-1}$. These rates are competitive with the resonant rates at low T for $d\mu(\uparrow\downarrow) + D_2$ and $t\mu(\uparrow\uparrow) + D_2$, but are two and three orders of magnitude smaller than the resonant rates for $d\mu(\uparrow\uparrow) + D_2$ and $t\mu(\uparrow\downarrow) + D_2$, respectively. The $(\uparrow\downarrow)$ state is the ground state; thus HFS quenching plays an important role in low-temperature experiments, especially for $dd\mu$. At room temperature, resonant formation is dominant for both the ground and excited hyperfine states of $d\mu$ and $t\mu$.

In the *Vesman* mechanism, the binding energy of the muonic molecule goes into rovibrational excitation of the electronic host molecule instead of into ionization of a molecular electron. The process is resonant since the collision energy must be tuned to match the energy of the final discrete state. For the compound molecule formed, two sets of rovibrational quantum numbers are needed, e.g.,



where (K_i, v_i) and (K_f, v_f) are the initial and final rovibrational quantum numbers of the electronic molecule, (J, v)

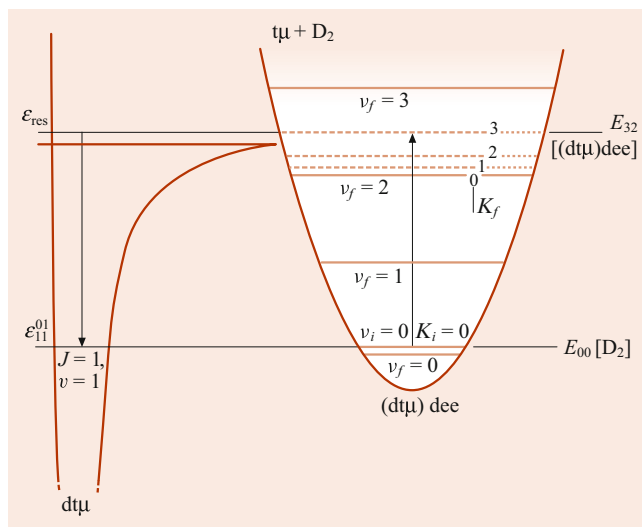


Fig. 91.4 Energy levels for the resonant reaction $t\mu + [D_2]_{K_i=0, v_i=0} \rightarrow [(dt\mu)_{J=1, v=1}^{F=0, S=1} \text{de}]_{K_f v_f}$. The rovibrational quantum numbers are designated by (J, v) for the muonic molecule and (K, v) for the electronic molecules

are the quantum numbers of the muonic molecule, F is the spin of the muonic atom, and S is the total spin of the muonic molecule. The energetics of this process is shown in Fig. 91.4.

The resonant condition is achieved at the collision energy

$$\epsilon_{\text{res}}(t\mu + D_2) = \epsilon_{11}^{FS} [dt\mu] + E_{K_f v_f} [(dt\mu)\text{de}] - E_{K_i 0} [D_2] , \quad (91.35)$$

where it is explicitly recognized that $(J, v) = (1, 1)$ is the only muonic level that can satisfy the resonant energy condition and that only $v_i = 0$ is populated at ordinary temperatures. Accurate calculations require values of ϵ_{res} to within about 0.1 meV. The rovibrational energies $E_{K v}$ of the electronic molecule, as well as the Coulomb contributions to the binding energy of the muonic molecule, ϵ_{11}^{FS} , are now known to this high accuracy. However, ϵ_{11}^{FS} is subject to corrections due to relativity, vacuum polarization, nuclear charge distributions and polarizabilities, the hyperfine interaction, and the finite size and shape of the muonic molecule in the complex. The present overall accuracy is ≈ 1 meV. Some of the resulting values of ϵ_{res} are given in Table 91.1. The calculated cross section for reaction Eq. (91.34) is sharply peaked at E_{res} but must be averaged over a kinetic energy distribution (e.g., Maxwellian) to obtain the observable rate. Still, the rate will display a characteristic resonant dependence on T .

Because the E_{res} are different for each target molecule (D_2, DT, T_2, \dots), the effective molecular formation rate in a mixture depends on the molecular composition in addition to the isotopic fractions (c_d, c_t, \dots) if the target is not in chemical equilibrium.

Table 91.1 Resonant (quasiresonant if negative) collision energies ϵ_{res} (in meV) calculated using Eq. (91.35)^a

$d\mu + D_2$		$t\mu + D_2$		$t\mu + DT$	
$[(dd\mu)_{11}dee]_{v_f=7}$		$[(dt\mu)_{11}dee]_{v_f=2}$		$[(dt\mu)_{11}tee]_{v_f=3}$	
F, S, K_i, K_f	ϵ_{res}	F, S, K_i, K_f	ϵ_{res}	F, S, K_i, K_f	ϵ_{res}
$\frac{1}{2}, \frac{1}{2}, 0, 1$	52.7	0, 1, 0, 1	-14.0	0, 1, 0, 1	277.1
$\frac{1}{2}, \frac{3}{2}, 0, 1$	76.9	0, 1, 0, 2	-4.3	1, 0, 0, 1	223.5
$\frac{3}{2}, \frac{1}{2}, 0, 1$	4.2	0, 1, 0, 3	10.3	1, 1, 0, 1	226.9
$\frac{3}{2}, \frac{3}{2}, 0, 1$	28.4	0, 1, 1, 2	-11.7	1, 2, 0, 1	233.3
$\frac{1}{2}, \frac{1}{2}, 1, 0$	40.9	0, 1, 1, 3	2.9		
$\frac{1}{2}, \frac{3}{2}, 1, 0$	65.1				
$\frac{1}{2}, \frac{1}{2}, 1, 2$	54.1				
$\frac{1}{2}, \frac{3}{2}, 1, 2$	78.3				

^a Note: $kT = 1$ meV for $T = 11.6$ K

The rate of resonant molecular formation is given by

$$\lambda^{mf}(T) = N \sum_f \int \left\{ d\epsilon 2\pi |\langle i | \hat{V} | f \rangle|^2 \times f(\epsilon, T) I(\epsilon - \epsilon_{if}, T) \right\}, \quad (91.36)$$

where N is the target density, $f(\epsilon, T)$ is the collisional energy distribution, ϵ_{if} is the energy of the unperturbed resonance, $I(\Delta\epsilon, T)$ is the intensity at energy $\Delta\epsilon$ relative to the unperturbed energy, and $\langle i | \hat{V} | f \rangle$ is the transition matrix element, with \hat{V} the Coulomb perturbation operator in the *post* form of the rearrangement-collision Hamiltonian using the $dt\mu$ bound state as the zeroth-order Hamiltonian; \hat{V} can be expressed as a multipolar expansion beginning with

$$\hat{V} = e^2 \mathbf{d} \cdot \mathbf{E} + \dots, \quad (91.37)$$

where \mathbf{d} is the dipole operator of the $dt\mu$ (or $dd\mu$) system, and \mathbf{E} is the electric field at the $dt\mu$ (or $dd\mu$) center of mass due to the *spectator* nucleus and electrons [132]. A calculation has been done including the quadrupole term [133], but the dipole term is dominant. In the dipole approximation [134] conservation of angular momentum requires [135]

$$\mathbf{L} + \mathbf{K}_i = \mathbf{J} + \mathbf{K}_f, \quad (91.38)$$

where \mathbf{L} is the orbital angular momentum of relative motion for $t\mu + D_2$ in reaction Eq. (91.34). At low T , $L = 0$ is predominant, so that $K_f = K_i \pm 1$. This is simply the case for $d\mu + D_2 \rightarrow (dd\mu)dee$, where the most probable transition is $(K, v) = (0, 0) \rightarrow (1, 7)$. For $dt\mu$, the vibrational state of the electronic molecule changes by only $\Delta v_i = 2$ or 3 instead of 7, so the matrix element of Eq. (91.37) and the resulting rate are considerably larger than for $dd\mu$. However, it can be seen in Fig. 91.4 that if D_2 is in its ground state ($K_i = 0$), the first level energetically accessible for $(dt\mu)dee$ has $K_f = 3$. If, as proves to be adequate in the case of $dd\mu$, the intensity

distribution I is taken to be a δ function, the lower levels are eliminated from Eq. (91.36). There are two possible solutions to this problem, whose relative importance has not been fully determined: (1) the less likely $L > 0$ collisions contribute, or (2) the levels with smaller K_f play a role even though they lie *below threshold*.

The latter case is termed *quasi resonant*. Theoretically, the levels below threshold can contribute (1) directly if they are broadened so that they extend to positive energy [136–138], or (2) indirectly if configurations with different K_f are mixed [139]. Broadening can occur either inhomogeneously due to the finite lifetime (mainly with respect to Auger emission of an electron in the complex) or homogeneously due to collisions with neighboring molecules. Interactions with neighboring molecules can also mix the different K_f states, so the $K_f = 3$ state may *borrow* some intensity from the lower K_f states. Three-body molecular formation facilitated by neighboring molecules leads to a density dependence of the formation rate (normalized to LHD) that has been observed in experiments.

There have been a number of measurements of the $dd\mu$ molecular-formation rate for various target densities and temperatures. However, the epithermal effect due to nonthermalized $d\mu$ may be significant and makes a full understanding of the temperature dependence a little difficult, especially at low temperatures. Further measurements have been carried out [140, 141] by controlling the initial molecular state (K_i) with the use of ortho- D_2 ($K_i = 0, 2, \dots$) and normal or even para-rich ($K_i = 1, 3, \dots$) D_2 . These measurements have clarified the dependence on the molecular state and the density. The resonant formation rate with ortho- D_2 was found to be much larger than with normal D_2 in the gas around 35 K, while its rate is reduced by nearly half at liquid density, even smaller than for normal- D_2 . This finding indicates that the resonance with ortho- D_2 must be very close to the threshold, and that the target density could be affecting its shift or broadening.

The resonant $dd\mu$ formation has now been observed directly [142]. Previously, the experimental evidence for this

in the zero-density limit since R is still finite in this limit.) The net sticking is then

$$\omega_s = \omega_s^0(1 - R). \quad (91.43)$$

Since the nuclear reaction is very rapid compared with the atomic and molecular dynamics, the probability of sticking in a given state ν is given adequately by the sudden approximation,

$$P_\nu = |\langle \psi_\nu^{(f)} | \psi^{(i)} \rangle|^2, \quad (91.44)$$

where the initial wave function $\psi^{(i)}$ is the normalized molecular wave function in the limit $r_{\text{dt}} \rightarrow 0$, and the final wave function $\psi_\nu^{(f)}$ is given by

$$\psi_\nu^{(f)} = \phi_{n\ell m}(\mathbf{r}) e^{i\mathbf{q}\cdot\mathbf{r}}, \quad (91.45)$$

in which $\phi_{n\ell m}$ is an atomic wave function of $({}^4\text{He}\mu)^+$, and the plane wave with momentum \mathbf{q} represents its motion with respect to the initial molecule (recoil determined by conservation of energy and momentum). The total sticking is then

$$\omega_s^0 = \sum_\nu P_\nu. \quad (91.46)$$

The $({}^4\text{He}\mu)^+$ wave function is known analytically since it is hydrogenic. Most of the labor goes into determination of the muonic molecule wave function. In the Born–Oppenheimer approximation this is simply $({}^5\text{He}\mu)^+$ and results in $(\omega_s^0)_{\text{BO}} = 1.20\%$ for $\text{dt}\mu$ [151]. More accurate nonadiabatic calculations show that the muonic motion lags behind that of the nuclei and reduces ω_s^0 to 0.886% [152, 153]. After inclusion of nuclear effects, the best current theoretical value of ω_s^0 is 0.912% [149, 154].

Since the ground-state $(\text{He}\mu)^+$ ion is bound by 11 keV, it takes a quite energetic collision to strip off the muon. The reactivation fraction R is determined basically by competition between collisional processes that slow down the muonic ion and those that lead to stripping. Calculation of R requires a full kinetic treatment of the fast $(\text{He}\mu)^+$ ion, starting with its distribution among various states (1s, 2s, 2p, \dots , $n \approx 10$). The most important processes are stopping power (due mainly to ionization of the medium) and muon ionization or transfer in collisions of the $(\text{He}\mu)^+$ ion with an isotope of H, but inelastic (excitation and deexcitation), Auger deexcitation, and ℓ -changing collisions, as well as radiative deexcitation are also involved. The initial sticking occurs mostly in the 1s state (77% of the $\alpha\mu$'s from $\text{dt}\mu$ fusion), but the excited states have larger ionization cross sections. Most of the muons stripped from $\alpha\mu$ originally stuck in the 1s state, but a significant number is promoted to excited states before being ionized (so-called *ladder ionization*). The

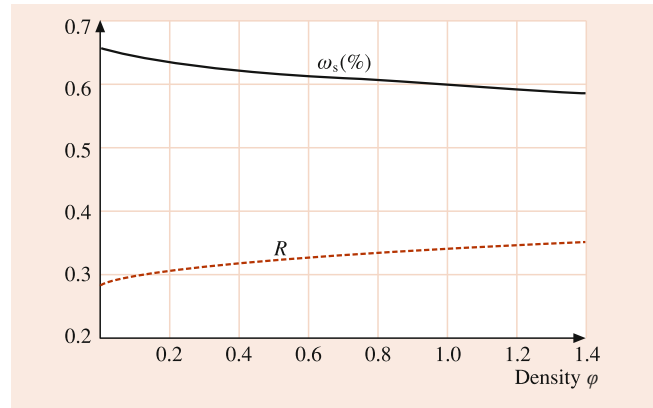


Fig. 91.5 Theoretical sticking fraction (solid curve) and reactivation probability (dashed curve) for d-t μCF

metastable 2s state is significant for its role in prolonging the excited-state populations. The resulting values of R and ω_s are shown as a function of density in Fig. 91.5.

Most experiments on d-t μCF have been done with neutron detection [155–157], where λ_c and the muon loss probability per cycle W can be deduced from the time structure of the neutron emissions. The analysis is indirect and requires a theoretical model. What is actually measured is the product $W\phi\lambda_c$; the extraction of ω_s requires corrections for other loss mechanisms and separate determination of λ_c . Thus, it is desirable to have other experimental diagnostics. Two types of corroborating experiments detect either X-rays from the $\alpha\mu$ formed by sticking or detect the species $(\alpha)^{2+}$ and $(\alpha\mu)^+$ by the different effects of their double and single electrical charges.

The theoretical sticking is compared in Table 91.2 with that from all three types of experiments. For a more meaningful comparison of measurements at different densities ϕ , the theoretical R has been used to convert all values to ω_s^0 . The theoretical values are slightly, but significantly, higher than the observations. This discrepancy has not yet been resolved.

One suggested explanation for the lower-than-predicted value of ω_s may be that a significant fraction of the fusions might occur in muonically excited bound or resonant states for which the initial sticking is lower than in the ground state [158].

A 2003 experiment systematically studied muon-catalyzed fusion in solid deuterium and tritium mixtures as a function of temperature and tritium concentration [159]. An unexpected decrease in the muon cycling rate (λ_c) and an increase in the muon loss (W) were observed. The former is likely due to the freezing out of phonons contributing to the resonance energy. The latter is especially intriguing. It is inconceivable that ω_s^0 for fusion in a given state of $\text{dt}\mu$ could depend on temperature, but this observation could imply either an unexpected effect of temperature on the muonic state in which fusion occurs or an unpredicted temperature

Table 91.2 Comparison of sticking values^a

Source	ϕ	ω_s (%)	ω_s^0 (%)
Theory			
[149, 154]	1.2	0.59	0.91
Neutron experiments			
LANL [165]	≈ 1	$0.43 \pm 0.05 \pm 0.06$	0.66
PSI [166]	≈ 1	$0.48 \pm 0.02 \pm 0.04$	0.74
KEK [167]	1.2	0.51 ± 0.004	0.78
RAL [168]	1.24	0.532 ± 0.030	0.82
RAL [168]	1.45	0.515 ± 0.030	0.79
X-ray experiments			
PSI [169]	1.2	0.39 ± 0.10	0.60
KEK [167]	1.2	0.34 ± 0.13	0.52
$\alpha/\alpha\mu$ experiments			
RAL [170]	0.001	–	$0.80 \pm 0.15 \pm 0.12$
PSI [171]	0.17	0.56 ± 0.04	0.80

^a Experimental values of ω_s^0 without error bars were obtained assuming the theoretical stripping [172, 173].

In cases of two error estimates, the first is statistical and the second is systematic.

The extraction of ω_s^0 from the X-ray experiments requires theoretical scaling

dependence of the thermalization kinetics (e.g., due to ion channeling). It should be noted that the experimental analysis does not reject the possibility of some correlation between the extracted values of λ_c and W [158].

91.4.7 Prospectus

Muon-catalyzed d-d fusion in D₂ and HD gases has now been investigated in a wide temperature range, with all the main observables in the reaction chain accurately measured [101, 160]. The energy of the loosely bound dd μ was extracted with high precision [101], and it is in impressive agreement with the latest theoretical results. The experimental knowledge of parameters for p-t μ CF [105] and t-t μ CF [103] have also been advanced.

The d-t μ CF is now fairly well understood [102], but investigations under broader conditions of temperature and density are still desirable; in particular, three-body effects on molecular formation at high densities, the excited-state cross sections and kinetics that go into the determination of the cascade factor q_{1s} , and the remaining discrepancy in the sticking factor ω_s , which might have a theoretical or experimental resolution. Experimentally it is of interest to push on to higher temperatures and densities to see whether more surprises lurk there. There have been a few schemes proposed to enhance stripping of stuck muons artificially, but none has been subjected to experiments yet.

The currently observed yield of about 150 d-t fusions (releasing 17.6 MeV each) per muon produces an energy return 25 times the rest-mass energy of the muon but is only about

one-third of that required for breakeven in a pure-fusion reactor. This conclusion is based on the estimated energy cost of producing a muon, ≈ 8 GeV [161, 162]. Other possible practical uses of μ CF include a hybrid (fusion–fission) reactor [161, 162] or an intense 14 MeV neutron source [163, 164].

Apart from such technological applications, the study of μ CF is fruitful for a number of reasons, including (1) bridging the gap between atomic and nuclear physics, (2) enabling nuclear reactions *including* p-waves at room temperature, (3) allowing precise studies under unusual physical conditions, (4) observing a compound electronic-muonic molecular environment, and (5) exhibiting phenomena spanning nine orders of magnitude in distance and energy. The experimental possibilities are far from exhausted even though the holy grail of pure fusion energy now appears just beyond reach.

Acknowledgement J.D.M. is grateful to the Institute for Nuclear Theory of the University of Washington for making it possible for him to spend a productive semester there in the spring of 1993. This work has also been supported by National Science Foundation grant PHY-9215442.

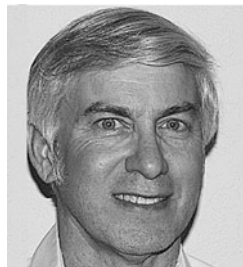
References

- Coester, F.: Nucl. Phys. **7**, 421 (1958)
- Coester, F., Kümmel, H.: Nucl. Phys. **17**, 477 (1960)
- Kümmel, H.: Nucl. Phys. **22**, 177 (1969)
- Cizek, J.: J. Chem. Phys. **45**, 4256 (1966)
- Cizek, J.: Adv. Chem. Phys. **14**, 35 (1969)
- Paldus, J., Cizek, J., Shavitt, I.: Phys. Rev. A **5**, 50 (1972)
- Jensen, A.S., Riisager, K., Fedorov, D.V., Garrido, E.: Rev. Mod. Phys. **76**, 215 (2004)
- Lamb, W.E., Retherford, R.C.: Phys. Rev. **72**, 241 (1950)
- Lamb, W.E., Retherford, R.C.: Phys. Rev. **79**, 549 (1950)
- Lamb, W.E., Retherford, R.C.: Phys. Rev. **81**, 222 (1951)
- Lamb, W.E., Retherford, R.C.: Phys. Rev. **86**, 1014 (1952)
- Houston, W.V., Hsieh, Y.M.: Phys. Rev. **45**, 263 (1934)
- Houston, W.V.: Phys. Rev. **51**, 446 (1937)
- Williams, R.C.: Phys. Rev. **54**, 558 (1938)
- Pasternack, S.: Phys. Rev. **54**, 1113 (1938)
- Bezginov, N., Valdez, T., Horbatsch, M., Marsman, A., Vutha, A.C., Hessels, E.A.: Science **365**, 1007 (2019)
- Pohl, R., et al.: Nature **466**, 213 (2010)
- Antognini, A., et al.: Science **339**, 417 (2013)
- Kemble, E.C., Present, R.D.: Phys. Rev. **44**, 1031 (1933)
- Karplus, R., Klein, A., Schwinger, J.: Phys. Rev. **86**, 301 (1951)
- Lamb, W.E.: Phys. Rev. **85**, 276 (1952)
- Salpeter, E.E.: Phys. Rev. **89**, 95 (1953)
- Zemach, A.C.: Phys. Rev. **104**, 1771 (1956)
- Flügge, S.: Practical Quantum Mechanics vol. I. Springer, New York, pp 191–192 (1971)
- Drake, G.W.F., Yan, Z.-C.: Phys. Rev. A **46**, 2378 (1992)
- Shiner, D., Dixon, R., Vedantham, V.: Phys. Rev. Lett. **74**, 3553 (1995)
- Riis, E., Sinclair, A.G., Poulsen, O., Drake, G.W.F., Rowley, W.R.C., Levick, A.P.: Phys. Rev. A **49**, 207 (1994)
- Pachucki, K., Weitz, K.M., Hänsch, T.W.: Phys. Rev. A **49**, 2255 (1994)
- Huber, A., Udem, T., Gross, B., Reichert, J., Kourogi, M., Pachucki, K., Weitz, M., Hänsch, T.W.: Phys. Rev. Lett. **80**, 468 (1998)

30. Wang, L.-B., Mueller, P., Bailey, K., Drake, G.W.F., Greene, J.P., Henderson, D., Holt, R.J., Janssens, R.V.F., Jiang, C.L., Lu, Z.-T., O'Connor, T.P., Pardo, R.C., Paul, M., Rehm, K.E., Schiffer, J.P., Tang, X.D.: *Phys. Rev. Lett.* **93**, 142501 (2004)
31. Ewald, G., Nörtershäuser, W., Dax, A., Göte, S., Kirchner, R., Kluge, H.-J., Kühl, T., Sanchez, R., Wojtaszek, A., Bushaw, B.A., Drake, G.W.F., Yan, Z.-C., Zimmermann, C.: *Phys. Rev. Lett.* **93**, 113002 (2004)
32. Schawlow, A.L., Townes, C.H.: *Phys. Rev.* **100**, 1273 (1955)
33. Bodmer, A.R.: *Proc. Phys. Soc. A* **66**, 1041 (1953)
34. Mohr, P.J.: *At. Data Nucl. Data Tables* **33**, 456 (1983)
35. Friar, J.L.: *Ann. Phys.* **122**, 151 (1979)
36. Johnson, W.R., Soff, G.: *At. Data Nucl. Data Tables* **33**, 407 (1985)
37. de Jager, C.W., de Vries, H., de Vries, C.: *At. Data Nucl. Data Tables* **14**, 479 (1974)
38. Raghaven, P.: *At. Data Nucl. Data Tables* **42**, 189 (1989)
39. Wapstra, A.H., Audi, G.: *Nucl. Phys. A* **432**, 1 (1985)
40. Seely, J.F., Ekberg, J.O., Brown, C.M., Feldman, U., Behring, W.E., Reader, J., Richardson, M.C.: *Phys. Rev. Lett.* **57**, 2924 (1986)
41. Cowan, T.E., Bennett, C.L., Dietrich, D.D., Bixler, J.V., Hailey, C.J., Henderson, J.R., Knapp, D.A., Levine, M.A., Marrs, R.E., Schneider, M.B.: *Phys. Rev. Lett.* **66**, 1150 (1991)
42. Schweppe, J., Belkacem, A., Blumenfeld, L., Claytor, N., Feinberg, B., Gould, H., Kostroune, V.E., Levy, L., Misawa, S., Mowat, J.R., Prior, M.H.: *Phys. Rev. Lett.* **66**, 1434 (1991)
43. Blundell, S.A., Snyderman, N.J.: *Phys. Rev. A* **44**, R1427 (1991)
44. Blundell, S.A.: *Phys. Rev. A* **46**, 3762 (1992)
45. Cheng, K.T., Johnson, W.R., Sapirstein, J.: *Phys. Rev. A* **47**, 1817 (1993)
46. Bahcall, J.N.: *Phys. Rev.* **124**, 495 (1961)
47. Clayton, D.D.: *Astrophys. J.* **139**, 637 (1964)
48. Woosley, S.E., Fowler, W.A.: *Astrophys. J.* **233**, 411 (1979)
49. Williams, R.D., Fowler, W.A., Koonin, S.E.: *Astrophys. J.* **281**, 363 (1984)
50. Chen, Z., Rosenberg, L., Spruch, L.: *Phys. Rev. A* **35**, 1981 (1987)
51. Chen, Z., Rosenberg, L., Spruch, L.: *Adv. At. Mol. Opt. Phys.* **26**, 297 (1989)
52. Chen, Z., Spruch, L.: *AIP Conference Proceedings # 189, Relativistic, Quantum Electrodynamics, and Weak Interaction Effects in Atoms*. AIP, New York, pp 460–478 (1989)
53. Lubimov, V.A., Novikov, E.G., Nozik, V.Z., Tretyakov, E.F., Kozik, V.S.: *Phys. Lett. B* **94**, 266 (1980)
54. Boris, S., Golutvin, A., Laptin, L., Lubimov, V., Nagovizin, V., Nozik, V., Novikov, E., Soloshenko, V., Tihomirov, I., Tretjakov, E., Myasoedov, N.: *Phys. Rev. Lett.* **58**, 2019 (1987)
55. Boris, S.D., Golutvin, A.I., Laptin, L.P., Lyubimov, V.A., Myasoedov, N.F., Nagovitsyn, V.V., Nozik, V.Z., Novikov, E.G., Soloshchenko, V.A., Tikhomirov, I.N., Tretyakov, E.F.: *Pis'ma Zh. Eksp. Teor. Fiz.* **45**, 267 (1987). *Sov. Phys. JETP Lett.* **45**, 333 (1987)
56. Bergkvist, K.-E.: *Phys. Scr.* **4**, 23 (1971)
57. Bergkvist, K.-E.: *Nucl. Phys. B* **39**(317), 371 (1972)
58. Martin, R.L., Cohen, J.S.: *Phys. Lett. A* **110**, 95 (1985)
59. Kolos, W., Jeziorski, B., Szalewicz, K., Monkhorst, H.J.: *Phys. Rev. A* **31**, 551 (1985)
60. Fackler, O., Jeziorski, B., Kolos, W., Monkhorst, H.J., Szalewicz, K.: *Phys. Rev. Lett.* **55**, 1388 (1985)
61. Jeziorski, B., Kolos, W., Szalewicz, K., Fackler, O., Monkhorst, H.J.: *Phys. Rev. A* **32**, 2573 (1985)
62. Szalewicz, K., Fackler, O., Jeziorski, B., Kolos, W., Monkhorst, H.J.: *Phys. Rev. A* **35**, 965 (1987)
63. Kolos, W., Jeziorski, B., Rychlewski, J., Szalewicz, K., Monkhorst, H.J., Fackler, O.: *Phys. Rev. A* **37**, 2297 (1988)
64. Fritschi, M., Holzschuh, E., Kundig, W., Petersen, J.W., Pixley, R.E., Stussi, H.: *Phys. Lett. B* **173**, 485 (1986)
65. Wilkerson, J.F., Bowles, T.J., Browne, J.C., Maley, M.P., Robertson, R.G.H., Cohen, J.S., Martin, R.L., Knapp, D.A., Helffrich, J.A.: *Phys. Rev. Lett.* **58**, 2023 (1987)
66. Robertson, R.G.H., et al.: *Phys. Rev. Lett.* **67**, 957 (1991)
67. Holzschuh, E., Fritschi, M., Kündig, W.: *Phys. Lett. B* **287**, 381 (1992)
68. Weinheimer, C., Przyrembel, M., Backe, H., Barth, H., Bonn, J., Degen, B., Edling, T., Fischer, H., Fleischmann, L., Gross, J.U., Haid, R., Hermann, A., Kube, G., Leiderer, P., Loeken, T., Molz, A., Moore, R.B., Osipowicz, A., Otten, E.W., Picard, A., Schrader, M., Steininger, M.: *Phys. Lett. B* **300**, 210 (1993)
69. Fukuda, Y., et al.: *Phys. Rev. Lett.* **81**, 1562 (1998)
70. Weinheimer, C., Degen, B., Bleile, A., Bonn, J., Bornschein, L., Kazachenko, O., Kovalik, A., Otten, E.W.: *Phys. Lett. B* **460**, 219 (1999)
71. Bonn, J., Bornschein, B., Bornschein, L., Fickinger, L., Flatt, B., Kazachenko, O., Kovalik, A., Kraus, C., Otten, E.W., Schall, J.P., Ulrich, H., Weinheimer, C.: *Nucl. Phys. B* **91**, 273 (2001)
72. Hannestad, S.: *Phys. Rev. D* **66**, 125011 (2002)
73. Robertson, R.G.H.: *Nucl. Part. Phys. Proc.* **265/266**, 7–12 (2015). arXiv:1502.00144. NOW14, Neutrino Oscillation Workshop, Conca Specchiulla (Otranto, Lecce, Italy) Sept. 7–14, 2014
74. Assenbaum, H.J., Langanke, K., Rolfs, C.: *Z. Phys. A* **327**, 461 (1987)
75. Engstler, S., Krauss, A., Neldner, K., Rolfs, C., Schröder, U., Langanke, K.: *Phys. Lett. B* **202**, 179 (1988)
76. der Schr, U., Engstler, S., Krauss, A., Neldner, K., Rolfs, C., Somorjai, E., Langanke, K.: *Nucl. Instrum. Methods B* **40/41**, 466 (1989)
77. Engstler, S., Raimann, G., Angulo, C., Greife, U., Rolfs, C., Schröder, U., Somorjai, E., Kirch, B., Langanke, K.: *Phys. Lett. B* **279**, 20 (1992)
78. Engstler, S., Raimann, G., Angulo, C., Greife, U., Rolfs, C., Schröder, U., Somorjai, E., Kirch, B., Langanke, K.: *Z. Phys. A* **342**, 471 (1992)
79. Blüge, G., Langanke, K., Reusch, H.G., Rolfs, C.: *Z. Phys. A* **333**, 219 (1989)
80. Langanke, K., Lukas, D.: *Ann. Phys. (Leipzig)* **1**, 332 (1992)
81. Langanke, K.: *Adv. Nucl. Phys.* **21**, 179 (1994)
82. Shoppa, T.D., Koonin, S.E., Langanke, K., Seki, R.: *Phys. Rev. C* **48**, 837 (1993)
83. Shoppa, T.D., Jeng, M., Koonin, S.E., Langanke, K., Seki, D.: *Nucl. Phys. A* **605**, 387 (1996)
84. Bahcall, J.N., Chen, X., Kamionkowski, M.: *Phys. Rev. C* **57**, 2756 (1998)
85. Strieder, F., Rolfs, C., Spitaleri, C., Corvisiero, P.: *Naturwissenschaften* **88**, 461 (2001)
86. Zavatarelli, S., Corvisiero, P., Costantini, H., Moroni, P.G.P., Prati, P., Bonetti, R., Guglielmetti, A., Broggin, C., Campajola, L., Formicola, A., Gialanella, L., Imbriani, G., Ordine, A., Roca, V., Romano, M., D'Onofrio, A., Terrasi, F., Gervino, G., Gustavino, C., Junker, M., Rogalla, D., Rolfs, C., Schumann, F., Strieder, F., Trautvetter, H.P.: *Nucl. Phys. A* **688**, 514 (2001)
87. Aliotta, M., Raiola, E., Gyurky, G., Formicola, A., Bonetti, R., Broggin, C., Campajola, L., Corvisiero, P., Costantini, H., D'Onofrio, A., Fulop, Z., Gervino, G., Gialanella, L., Guglielmetti, A., Gustavino, C., Imbriani, G., Junker, M., Moroni, P.G., Ordine, A., Prati, P., Roca, V., Rogalla, D., Rolfs, C., Romano, M., Schumann, F., Somorjai, E., Straniero, O., Strieder, F., Terrasi, F., Trautvetter, H.P., Zavatarelli, S.: *Nucl. Phys. A* **690**, 790 (2001)
88. Kimura, S., Takigawa, N., Abe, M., Brink, D.M.: *Phys. Rev. C* **022801**(R), 67 (2003)
89. Eichler, J.: *Phys. Rep.* **193**, 165 (1990)

90. Anholt, R., Gould, H.: *Adv. At. Mol. Phys.* **22**, 315 (1986)
91. Belkacem, A., Gould, H., Feinberg, B., Bossingham, R., Meyerhof, W.E.: *Phys. Rev. Lett.* **71**, 1514 (1993)
92. Frank, F.C.: *Nature* **160**, 525 (1947)
93. Sakharov, A.D.: *Otchet Fiz. Inst. Akad. Nauk*, 1 (1948). (in Russian) translated into English in *Muon Catal. Fusion* **4**, 235 (1989)
94. Zel'dovich, Y.B.: *Dokl. Akad. Nauk. SSSR* **95**, 493 (1954)
95. Alvarez, L.W., et al.: *Phys. Rev.* **105**, 1127 (1957)
96. Jackson, J.D.: *Phys. Rev.* **106**, 330 (1957)
97. Cohen, J.S.: Chap. 2. In: Lin, C.D. (ed.) *Review of Fundamental Processes and Applications of Atoms and Ions*, pp. 61–110. World Scientific, Singapore (1993)
98. Ackerbauer, P., Breunlich, W.H., Fuchs, M., Fussy, S., Jeitler, M., Kammel, P., Lauss, B., Marton, J., Prymas, W., Werner, J., Zmeskal, J., Lou, K., Petitjean, C., Baumann, P., Daniel, H., Hartmann, F.J., Schott, W., Vonegidy, T., Wojciechowski, P., Chatellard, D., Egger, J.P., Jeannot, E., Case, T., Crowe, K.M., Sherman, R.H., Markushin, V.: *Hyperfine Interact.* **82**, 243 (1993)
99. Balin, D.V., Baturin, V.N., Chestnov, Y.A., Ilyin, A.I., Kapinos, P.A., Maev, E.M., Petrov, G.E., Petrov, L.B., Semenchuk, G.G., Smirenin, Y.A., Vorobyov, A.A., Voropaev, N.I.: *Muon Catal. Fusion* **5/6**, 163–169 (1991)
100. Baumann, P., Daniel, H., Grunewald, S., Hartmann, F.J., Lipowsky, R., Moser, E., Schott, W., Vonegidy, T., Ackerbauer, P., Breunlich, W.H., Fuchs, M., Jeitler, M., Kammel, P., Marton, J., Nagele, N., Werner, J., Zmeskal, J., Bossy, H., Crowe, K.M., Sherman, R.H., Lou, K., Petitjean, C., Markushin, V.E.: *Phys. Rev. Lett.* **70**, 3720 (1993)
101. Balin, D.V., Ganzha, V.A., Kozlov, S.M., Maev, E.M., Petrov, G.E., Soroka, M.A., Schapkin, G.N., Semenchuk, G.G., Trofimov, V.A., Vasiliev, A.A., Vorobyov, A.A., Voropaev, N.I., Petitjean, C., Gartner, B., Lauss, B., Marton, J., Zmeskal, J., Case, T., Crowe, K.M., Kammel, P., Hartmann, F.J., Faifman, M.P.: *Phys. Part. Nucl.* **42**, 185 (2011)
102. Bom, V.R., Demin, A.M., Demin, D.L., van Eijk, C.W.E., Faifman, M.P., Filchenkov, V.V., Golubkov, A.N., Grafov, N.N., Grishchkin, S.K., Gritsaj, K.I., Klevtsov, V.G., Konin, A.D., Kuryakin, A.V., Medved, S.V., Musyaev, R.K., Perevozchikov, V.V., Rudenko, A.I., Sadetsky, S.M., Vinogradov, Y.I., Yukhimchuk, A.A., Yukhimchuk, S.A., Zinov, V.G., Zlatoustovskii, S.V.: *Zh. Eksp. Theor. Fiz.* **127**, 152 (2005). *Sov. Phys. JETP* **100**, 663 (2005)
103. Bogdanova, L.N., Bom, V.R., Demin, A.M., Demin, D.L., van Eijk, C.W.E., Filchagin, S.V., Filchenkov, V.V., Grafov, N.N., Grishchkin, S.K., Gritsaj, K.I., Konin, A.D., Kuryakin, A.V., Medveda, S.V., Musyaev, R.K., Rudenko, A.I., Tumkin, D.P., Vinogradov, Y.I., Yukhimchuk, A.A., Yukhimchuk, S.A., Zinov, V.G., Zlatoustovskii, S.V.: *Zh. Eksp. Theor. Fiz.* **135**, 242 (2009). *Sov. Phys. JETP* **108**, 216 (2009)
104. Bogdanova, L., Markushin, V.: *Nucl. Phys. A* **508**, 29c (1990)
105. Bogdanova, L.N., Demin, D.L., Duginov, V.N., Filchenkov, V.V., Gritsaj, K.I., Konin, A.D., Mamedov, T.N., Rudenko, A.I., Stolupin, V.A., Vinogradov, Y.I., Volnykh, V.P., Yukhimchuk, A.A.: *Phys. Part. Nucl. Lett.* **9**, 605 (2012)
106. Breunlich, W.H., Kammel, P., Cohen, J.S., Leon, M.: *Ann. Rev. Nucl. Part. Sci.* **39**, 311 (1989)
107. Gershtein, S.S., Petrov, Y.V., Ponomarev, L.I.: *Usp. Fiz. Nauk* **160**, 3 (1990). *Sov. Phys. Usp.* **33**, 591 (1990)
108. Froelich, P.: *Adv. Phys.* **41**, 405 (1992)
109. Petitjean, C.: *Nucl. Phys. A* **543**, 79 (1992)
110. Nagamine, K.: *Introductory Muon Science*. University Press, Cambridge (2007)
111. Cohen, J.S.: *Rep. Prog. Phys.* **67**, 1769 (2004)
112. Haff, P.K., Tombrello, T.A.: *Ann. Phys.* **86**, 178 (1974)
113. Wightman, A.S.: *Phys. Rev.* **77**, 521 (1950)
114. Cohen, J.S.: *Proceedings of the International School of Physics of Exotic Atoms*, 5th Course, Erice, Sicily, 1989. In: Simons, L.M., Horvath, D., Torelli, G. (eds.) *Electromagnetic Cascade and Chemistry of Exotic Atoms*, pp. 1–22. Plenum, New York (1990)
115. Cohen, J.S.: *Phys. Rev. A* **27**, 167 (1983)
116. Cohen, J.S., Martin, R.L., Wadt, W.R.: *Phys. Rev. A* **24**, 33 (1981)
117. Cohen, J.S., Martin, R.L., Wadt, W.R.: *Phys. Rev. A* **27**, 1821 (1983)
118. Garcia, J.D., Kwong, N.H., Cohen, J.S.: *Phys. Rev. A* **35**, 4068 (1987)
119. Kwong, N.H., Garcia, J.D., Cohen, J.S.: *J. Phys. B* **22**, L633 (1989)
120. Sakimoto, K.: *Phys. Rev. A* **66**, 032506 (2002)
121. Tong, X.M., Shirahama, T., Hino, K., Tushima, N.: *Phys. Rev. A* **75**, 052711 (2007)
122. Fermi, E., Teller, E.: *Phys. Rev.* **72**, 406 (1947)
123. Sakimoto, K.: *Phys. Rev. A* **81**, 012511 (2010)
124. Cohen, J.S.: *Phys. Rev. A* **59**, 1160 (1999)
125. Markushin, V.E.: *Hyperfine Interact.* **119**, 11 (1999)
126. Czaplinski, W., Gula, A., Kravtsov, A., Mikhailov, A., Popov, N.: *Phys. Rev. A* **50**, 525 (1994)
127. Pohl, R., Biraben, F., Conde, C.A.N., Donche-Gay, C., Haensch, T.W., Hartmann, F.J., Hauser, P., Hughes, V.W., Huot, O., Indelicato, P., Knowles, P.E., Kottmann, F., Liu, Y.-W., Markushin, V.E., Mulhauser, F., Nez, F., Petitjean, C., Rabinowitz, P., dos Santos, J.M.F., Schaller, L.A., Schnewly, H., Schott, W., Taqqu, D., Veloso, J.F.C.A.: *Lecture Notes in Physics* vol. 570. Springer, Berlin, p 454 (2001)
128. Jensen, T.S., Markushin, V.E.: *Lecture Notes in Physics* vol. 627. Springer, Berlin, p 37 (2003)
129. Froelich, P., Wallenius, J.: *Phys. Rev. Lett.* **75**, 2108 (1995)
130. Cohen, J.S.: *Phys. Rev. A* **43**, 4668 (1991)
131. Vesman, E.A.: *Pis'ma Zh. Eksp. Fiz.* **5**, 113 (1967). *JETP Lett.* **5**, 91 (1967)
132. Cohen, J.S., Martin, R.L.: *Phys. Rev. Lett.* **53**, 738 (1984)
133. Faifman, M.P., Strizh, T.A., Armour, E.A.G., Harston, M.R.: *Hyperfine Interact.* **101/102**, 179 (1996)
134. Faifman, M.P., Menshikov, L.I., Strizh, T.A.: *Muon Catal. Fusion* **4**, 1 (1989)
135. Leon, M.: *Phys. Rev. Lett.* **52**, 605 (1984)
136. Y.V. Petrov: *Phys. Lett. B* **163**, 28 (1985)
137. Menshikov, L.I., Ponomarev, L.I.: *Phys. Lett. B* **167**, 141 (1986)
138. Cohen, J.S., Leon, M.: *Phys. Rev. A* **39**, 946 (1989)
139. Leon, M.: *Phys. Rev. A* **39**, 5554 (1989)
140. Toyoda, A., Ishida, K., Shimomura, K., Nakamura, S.N., Matsuda, Y., Higemoto, W., Matsuzaki, T., Nagamine, K.: *Phys. Rev. Lett.* **90**, 23401 (2003)
141. Imao, H., Ishida, K., Kawamura, N., Matsuzaki, T., Matsuda, Y., Toyoda, A., Strasser, P., Iwasaki, M., Nagamine, K.: *Phys. Lett. B* **658**, 120 (2008)
142. Fujiwara, M.C., Adamczak, A., Bailey, J.M., Beer, G.A., Beveridge, J.L., Faifman, M.P., Huber, T.M., Kammel, P., Kim, S.K., Knowles, P.E., Kunselman, A.R., Maier, M., Markushin, V.E., Marshall, G.M., Martoff, C.J., Mason, G.R., Mulhauser, F., Olin, A., Petitjean, C., Porcelli, T.A., Wozniak, J., Zmeskal, J.: *Phys. Rev. Lett.* **85**, 1642 (2000)
143. Bystritsky, V.M., Dzhelepov, V.P., Ershova, Z.V., Filchenkov, V.V., Kapyshev, V.K., Mukhamet-Galeeva, S.M., Nadezhdin, V.S., Rivkis, L.A., Rudenko, A.I., Satarov, V.I., Sergeeva, N.V., Somov, L.N., Stolupin, V.A., Zinov, V.G.: *Phys. Lett. B* **94**, 476 (1980)
144. Bogdanova, L.N.: *Muon Catal. Fusion* **3**, 359 (1988)
145. Bogdanova, L.N., Markushin, V.E., Melezhih, V.S., Ponomarev, L.I.: *Yad. Phys.* **34**, 1191 (1981). *Sov. J. Nucl. Phys.* **34**, 662 (1981)

146. Kamimura, M.: In: Jones, S.E., Rafelski, J., Monkhurst, H.J. (eds.) AIP Conference Proceedings 181, Muon-Catalyzed Fusion, p. 330. AIP, New York (1989)
147. Struensee, M.C., Hale, G.M., Pack, R.T., Cohen, J.S.: Phys. Rev. A **37**, 340 (1988)
148. Szalewicz, K., Jeziorski, B., Scrinzi, A., Zhao, X., Moszynski, R., Kolos, W., Froelich, P., Monkhurst, H.J., Velenik, A.: Phys. Rev. A **42**, 3768 (1990)
149. Hu, C.-Y., Hale, G.M., Cohen, J.S.: Phys. Rev. A **49**, 4481 (1994)
150. Hale, G.M.: Muon Catal. Fusion **5/6**, 227–229 (1991)
151. Bracci, L., Fiorentini, G.: Nucl. Phys. A **364**, 383 (1981)
152. Haywood, S.E., Monkhurst, H.J., Szalewicz, K.: Phys. Rev. A **37**, 3393 (1988)
153. Haywood, S.E., Monkhurst, H.J., Alexander, S.A.: Phys. Rev. A **43**, 5847 (1991)
154. Jeziorski, B., Szalewicz, K., Scrinzi, A., Zhao, X., Moszynski, R., Kolos, W., Velenik, A.: Phys. Rev. A **43**, 1640 (1991)
155. Jones, S.E., Anderson, A.N., Caffrey, A.J., Vansiclen, C.D., Watts, K.D., Bradbury, J.N., Cohen, J.S., Gram, P.A.M., Leon, M., Maltrud, H.R., Paciotti, M.A.: Phys. Rev. Lett. **56**, 588 (1986)
156. Breunlich, W.H., Cargnelli, M., Kammel, P., Marton, J., Naegele, N., Pawlek, P., Scrinzi, A., Werner, J., Zmeskal, J., Bistirlich, J., Crowe, K.M., Justice, M., Kurck, J., Petitjean, C., Sherman, R.H., Bossy, H., Daniel, H., Hartmann, F.J., Neumann, W., Schmidt, G.: Phys. Rev. Lett. **58**, 329 (1987)
157. Nagamine, K., Matsuzaki, T., Ishida, K., Hirata, Y., Watanabe, Y., Kadono, R., Miyake, Y., Nishiyama, K., Jones, S.E., Maltrud, H.R.: Muon Catal. Fusion **1**, 137 (1987)
158. Froelich, P., Flores-Riveros, A.: Phys. Rev. Lett. **70**, 1595 (1993)
159. Kawamura, N., Nagamine, K., Matsuzaki, T., Ishida, K., Nakamura, S.N., Matsuda, Y., Tanase, M., Kato, M., Sugai, H., Kudo, K., Takeda, N., Eaton, G.H.: Phys. Rev. Lett. **90**, 043401 (2003)
160. Baluev, V.V., Bogdanova, L.N., Bom, V.R., Demin, D.L., van Eijk, C.W.E., Filchenkov, V.V., Grafov, N.N., Grishechkin, S.K., Gritsaj, K.I., Konin, A.D., Mikhailuykov, K.L., Rudenko, A.I., Vinogradov, Y.I., Volnykh, V.P., Yukhimchuk, A.A., Yukhimchuk, S.A.: Zh. Eksp. Theor. Fiz. **140**, 80 (2011). Sov. Phys. JETP **113**, 68 (2011)
161. Petrov, Y.V.: Nature **285**, 466 (1980)
162. Petrov, Y.V.: Muon Catal. Fusion **3**, 525 (1988)
163. Kase, T., Konashi, K., Sasao, N., Takahashi, H., Hirao, Y.: Muon Catal. Fusion **5/6**, 521–529 (1991)
164. Anisimov, V.V., Arkhangel'sky, V.A., Ganchuk, N.S., Yukhimchuk, A.A., Cavalleri, E., Karmanov, F.I., Konobeyev, Y.A., Slobodtchouk, V.I., Latysheva, L.N., Pshenichnov, I.A., Ponomarev, L.I., Vecchi, M.: Fusion Technol. **39**, 198 (2001)
165. Jones, S.E., Taylor, S.F., Anderson, A.N.: Hyperfine Interact. **82**, 303 (1993)
166. Petitjean, C., Balin, D.V., Baturin, V.N., Baumann, P., Breunlich, W.H., Case, T., Crowe, K.M., Daniel, H., Grigoriev, Y.S., Hartmann, F.J., Ilyin, A.I., Jeitler, M., Kammel, P., Lauss, B., Lou, K., Maev, E.M., Marton, J., Muhlbauer, M., Petrov, G.E., Prymas, W., Schott, W., Semenchuk, G.G., Smirenin, Y.V., Vorobyov, A.A., Voropaev, N.I., Wojciechowski, P., Zmeskal, J.: Hyperfine Interact. **82**, 273 (1993)
167. Nagamine, K., Ishida, K., Sakamoto, S., Watanabe, Y., Matsuzaki, T.: Hyperfine Interact. **82**, 343 (1993)
168. Ishida, K., Nagamine, K., Matsuzaki, T., Kawamura, N., Nakamura, S.N., Matsuda, Y., Kato, M., Sugai, H., Tanase, M., Kudo, K., Takeda, N., Eaton, G.H.: Hyperfine Interact. **138**, 225 (2001)
169. Bossy, H., Daniel, H., Hartmann, F.J., Neumann, W., Plendl, H.S., Schmidt, G., Vonegidy, T., Breunlich, W.H., Cargnelli, M., Kammel, P., Marton, J., Naegele, N., Scrinzi, A., Werner, J., Zmeskal, J., Petitjean, C.: Phys. Rev. Lett. **59**, 2864 (1987)
170. Paciotti, M.A., Baker, O.K., Bradbury, J.N., Cohen, J.S., Leon, M., Maltrud, H.R., Sturgess, L.L., Jones, S.E., Li, P., Rees, L.M., Sheely, E.V., Shurtleff, J.K., Taylor, S.F., Anderson, A.N., Caffrey, A.J., Zabriskie, J.M., Brooks, F.D., Cilliers, W.A., Davies, J.D., England, J.B.A., Pyle, G.J., Squier, G.T.A., Bertin, A., Bruschi, M., Piccinini, M., Vitale, A., Zoccoli, A., Bom, V.R., van Eijk, C.W.E., de Haan, H., Eaton, G.H.: In: Jones, S.E., Rafelski, J., Monkhurst, H.J. (eds.) AIP Conference Proceedings 181, Muon-Catalyzed Fusion, p. 38. AIP, New York (1989)
171. Case, T., Crowe, K.M., Lou, K., Petitjean, C., Breunlich, W.H., Jeitler, M., Kammel, P., Lauss, B., Marton, J., Prymas, W., Zmeskal, J., Balin, D.V., Baturin, V.N., Grigoriev, Y.S., Ilyin, A.I., Maev, E.M., Petrov, G.E., Semenchuk, G.G., Smirenin, Y.V., Vorobyov, A.A., Voropaev, N.I., Baumann, P., Daniel, H., Hartmann, F.J., Muhlbauer, M., Schott, W., Wojciechowski, P.: Hyperfine Interact. **82**, 295 (1993)
172. Struensee, M.C., Cohen, J.S.: Phys. Rev. A **38**, 44 (1988)
173. Stodden, C.D., Monkhurst, H.J., Szalewicz, K., Winter, T.G.: Phys. Rev. A **41**, 1281 (1990)



James S. Cohen Dr Cohen is Group Leader of the Atomic and Optical Theory Group in the Theoretical Division of Los Alamos National Laboratory and a Fellow of the American Physical Society. He received a PhD in Physics from Rice University in 1973. His general area of research is theoretical atomic and molecular physics, with a special interest in exotic muonic and antiprotonic species.



John D. Morgan III Dr Morgan, Associate Professor, obtained his BS from The George Washington University, his MSc in Theoretical Chemistry from Oxford University, and his PhD in Chemistry from Berkeley. He has served on the editorial boards of the *Journal of Mathematical Physics* and the *International Journal of Quantum Chemistry*. His interests include the application of sophisticated mathematical techniques to assist the accurate calculation of properties of atoms and molecules.

Index

- π and 2π pulse, 1115
 - 3- j coefficients, 29
 - explicit forms, 31
 - limiting properties and asymptotic forms, 34
 - recurrence relations, 33
 - special cases, 65
 - symmetries, 33
 - tabulation of, 65
 - 6- j coefficients, tabulation of, 66
 - 6- j symbol, 895
 - 9- j coefficients, 44
 - algebraic form, 46
 - definition, 45
 - Hilbert space, tensor operator actions, 44
 - reduction to 6- j coefficients, 46
 - relations to 3- j coefficients, 45
 - relations to 6- j coefficients, 45
 - symmetry relations, 46
 - 9- j , invariant operators, 44

 - A**
 - ABCD law, 1075
 - Abel transform, 1027
 - ablation, laser, 1021
 - above threshold ionization (ATI), 1130
 - (CEP) characterization, 1130
 - in circular polarization, 1130
 - laser-induced electron diffraction, 1130
 - peak shifting, 1130
 - resonance substructure, 1130
 - absorption, 1050
 - coefficient, 290, 545, 1050
 - discrete, 187
 - optical, 262
 - oscillator strength, 262, 652
 - spectrum, 247
 - absorptive lineshape, 1058
 - abstraction, atom, 601
 - accelerator mass spectrometry(AMS), 951
 - ACME experiment, 475
 - ACT theory, 588
 - action variable, 244, 245
 - principal, 244
 - active set of orbitals, 320
 - Adams–Bashforth formula, 138
 - Adams–Moulton formula, 138
 - ADAS, 166
 - addition of angular momentum, magic squares, 59
 - adiabatic
 - approximation, 774, 1176
 - energy-modified, 744
 - in atom optics, 1176
 - capture theory, 585, 1366
 - correction, 489
 - elimination, 1054, 1120, 1143
 - following, 1115, 1148
 - Hamiltonian, 774
 - ionization, 1366
 - lapse rate, 1300
 - nuclei approximation, 742, 744
 - passage, of Rydberg atoms, 236
 - PES, 774
 - potential, 586
 - charge transfer, 996
 - two-state system, 860
 - vibrational, 555
 - state, 284, 489
 - electronic, 774
 - vibronic, 783
 - switching, 105
 - transition, 1030
- adjoint action, 96
 - adsorption, 1357
 - Aharonov–Bohm effect, 1170, 1183
 - Aharonov–Casher effect, 1175, 1183
 - air quality, 1338
 - Airy function, 249, 892
 - Al₂O₃, 1084
 - albedo, 1340
 - AlGaAs, 1090
 - alignment, 218, 713
 - angle, 122
 - atomic, 987
 - density matrix formalism, 124
 - in molecular beams, 1021
 - in photoionization, 957
 - alkali atom
 - electron scattering by, 371
 - laser cooling parameters, 1142
 - molecular beams, 1021
 - Rydberg states of, 236
 - scattering by, 922, 1030
 - alkali metal cluster, 610
 - alkali-like spectra, 178
 - allowed and forbidden lines, 324
 - amplified spontaneous emission (ASE), 1092
 - amplifying medium, 1062
 - analytical
 - quantum ropagators, 686
 - anapole moment, 473, 474
 - Anderson localization, 1135
 - Anger function, 885
 - angular correlation, 988

- density matrix formalism, 124
- angular distribution, 986, 1028
- angular momentum
 - abstract, 15
 - cone (diagram), 517
 - coupling scheme, 179, 312
 - coupling schemes, 318
 - differential operator realizations of, 26
 - orbital, 12
 - cartesian representation, 12
 - spherical polar coordinates, 14
 - transfer, 122
 - transfer formalism, 957
- anisotropy parameter, 957
- annihilation operator, 72, 88, 99, 111, 114, 1158, 1159, 1190
- anomalous dispersion, 262, 1062
- anomalous magnetic moment, 223
 - effects in helium, 205
- antenna patterns, 1212
- anticommutator, 1159
- antihydrogen, 477
- antiproton scattering, 788, 923
- antiprotonic helium, 477
- anti-Zeno effect, 1238
- apparent excitation cross section, 985
- Appell function, 160
- applied field
 - crossed, 242
 - parallel, 242
- arbitrarily normalized decay curve (ANDC) method, 266
- ArF, 1090
- argon, photoionization of, 389
- aromaticity rule, 614
- array detector, 1196
- Arrhenius rate law, 585
- artificial magnetism, 809
- ASE, 1092
- association rate, 863
- associative detachment, 598, 602
- associative ionization, 882
- astronomy
 - comets, 1290
 - submillimeter and far-infrared, 645
- astrophysical factor, 1363, 1370
- astrophysics, 1275
- AstroPy, 168
- asymmetric hybrid model, 815
- asymmetric top, 509, 541
 - Hamiltonian, 528
 - transition moments for, 550
- asymmetry parameter, 386, 391
- asymptotic expansion, 162
- asymptotic expansion method, for atomic energies, 210
- ATLAS software, 171
- atmosphere
 - effective thickness of, 1300
 - far-infrared and submillimeter spectroscopy of, 646
 - heating efficiency, 1323
 - ion and electron temperature profile, 1327
 - luminosity of, 1325
 - planetary escape mechanism, 1332
 - pressure and density variations in, 1299
 - temperature distribution model, 1323
- atmospheric measurement, 1344
- atmospheric model, 1339
- atom
 - abstraction, 601
 - counting statistics, 1219
 - decoherence, 1185
 - diffraction, 1180
 - interferometry, 463, 466, 481
 - optics, 1174
 - optics, nonlinear, 1177
- atomic beam, 1180
 - beam splitters, 1181
- atomic cascade, source of nonclassical light, 1232
- atomic clock, 450, 463, 467, 478, 482
- atomic ensemble in cavity QED, 1222
- atomic fountain, 450
- atomic frame, 714
- atomic ionization, 830
 - in collisions with a bare nucleus, 832
- atomic lens, 1180, 1181
 - thick, 1180
 - thin, 1180
- atomic mirror, 1179
 - evanescent wave mirror, 1179
 - magnetic mirror, 1179
- atomic scattering software, 166
- atomic structure
 - eigenvector composition, 182
 - eigenvector purity, 182
 - ground level tabulation, 184
 - ground state, 183
 - Hartree–Fock theory, 311
 - helium, 199
 - hierarchy of, 179
 - hydrogenic, 149
 - many-body perturbation theory, 99, 363
 - notation and nomenclature, 178–180
 - relativistic, 331, 335
 - software, 166
 - Thomas–Fermi theory, 297
- atomic unit, 3
- atomic waveguide, 1180
- atomic/ionic form factor, 831
- atom–surface interactions, 1357
- attachment
 - dissociative, 598, 882
 - theory, 742
 - electron, 598
- atto-nano physics, 1137
- attosecond pulses, 1132
- Auger
 - decay, 972
 - emission, 987
 - process, 395, 958, 1012
 - calculation of width, 370
 - resonant, 959
- auroral activity, 1306
- autocorrelation function, 560
- autodetachment, 395, 604
- autoionization, 325, 395, 600, 958, 987
 - electron capture, 996
 - formation of states, 396
 - H⁻(¹S) resonance calculation, 398
 - He⁻(1s2s²2S) autodetachment state, 397
 - in multiphoton processes, 1127
 - MCHF variational method for, 321
 - minimax method for, 321

- of core excited states, 396
- of Rydberg atoms, 239
- of two-electron systems, 403
- other applications of, 403
- resonant excitation, double, 396
- saddle-point method for, 321
- scattering resonances, 396
- sum rule, 397
- automorphism, 77
- AUTOSTRUCTURE, 166
- average energy, 313
- avoided crossing, 229, 246, 775, 807, 808
- axion, 462

- B**
- Baker–Campbell–Hausdorff identity, 35
- balance, microscopic
 - coronal, 847
 - improper, 847
 - proper, 846
 - radiative, 847
- ballistic atom pump, 250
- band mapping, 1168
- baryogenesis, 462
- baryon asymmetry, 475
- basis expansion method
 - basis generator method, 790
 - molecular, 790
 - one-and-a-half centered, 790
 - single-centered, 789
 - triple-centered, 790
 - two-centered, 790
- basis function
 - adiabatic and diabatic, 775
 - Gaussian, 791
 - Hylleraas, 204
 - Laguerre, 791
 - molecular orbital, 495, 540
 - radial scattering, 732
 - Slater, 322
 - Slater-type, 791
 - spline, 322
 - Sturmian, 150, 791
- basis generator method, 790
- BBK theory, 819
- beam
 - attenuation method, 997
 - effusive, 1185
 - quality, 1076
 - splitter, 1181, 1200
 - supersonic, 1185
- beam–foil spectroscopy, 266, 269
 - lifetime measurement, 266
- BEC, 1157
 - Bogoliubov theory, 1162
 - critical density, 1159
 - critical temperature, 1159, 1165
 - dynamical instability, 1162
 - excitations, 1162
 - fragmented, 1164
 - free gas, 1159
 - gas parameter, 1163
 - interference, 1165
 - mean-field theory, 1160
 - noncondensate fraction, 1163
 - optical lattice, 1168
 - orders of magnitude, 1166
 - persistent current, 1167
 - quantization of circulation, 1167
 - speed of sound, 1162
 - superfluid, 1167
 - superfluidity, 1167
 - trapped gas, 1165
 - vortex, 1167
 - wavefunction, 891
- Beer’s law, 1050, 1118
 - atmospheric application of, 1306
- Beer’s length, 1118
- Bell’s inequalities, 1260
- Bell’s inequality, 1240
 - apparatus to demonstrate, 1244
 - cosmic Bell test, 1243
 - detection loophole, 1242
 - energy-time entanglement, 1244
 - freedom of choice, 1242
 - locality loophole, 1242
 - nonpolarization-based tests of, 1244
 - super determinism, 1243
- Bennett hole, 1059, 1063
- Bernoulli number, 96
- Berry phase, 499, 1176
- Bethe logarithm, 412
 - asymptotic expansion for, 207
 - electric field effect, 229
 - two-electron, 205
- Bethe ridge, 833
- Bethe–Born approximation, normalization to, 985
- Bethe–Salpeter equation, 409, 416, 429
- Biedenharn–Elliott identity, 41, 47
- bifurcation, 248
- billiard ball, 246
- binary coupling theory
 - combinatorics, 52
 - intermediate angular momenta, 53
 - types of coupling, 53
- binary encounter approximation (BEA), 903
 - double ionization, 905
- binary peak, 1005
- binary reaction, 600
 - ion–molecule, 602
 - ion–neutral, 601
 - temperature dependence, 603
- binary-encounter electron, 833
- bismuth-doped fiber laser, 1088
- blackbody decay rate, 234
- blackbody radiation, 234, 545, 1055
- BLAS software, 171
- Blatt–Jackson formula, 693
- bleaching, 1055
- Bloch equations
 - optical, 1114
 - two-photon, 1120
- Bloch operator, 732
- Bloch sphere, 1114
- Bloch states, 1168
- Bloch vector, 1053, 1114
 - adiabatic inversion, 1116
 - orbits of (diagram), 1114
 - spreading of (diagram), 1116

- Bloch–Siegert level shift, 1051
 blocking temperature, 611
 blue diode laser, 1090
 body-fixed
 coordinates, 28, 539, 540, 558, 577
 frame, 774
 Boersch effect, 1174
 Bogoliubov theory, 1162
 Bogoliubov transformation, 1103, 1194
 Bohm–de Broglie deterministic quantum mechanics, 1249
 Bohr
 correspondence principle, 887
 formula, 232
 magneton, 1049
 Bohr–Sommerfeld quantization, 887
 bolometer, 1021
 Boltzmann average momentum, 873
 Boltzmann distribution, definition, 849
 Boost libraries, software, 168
 Born approximation, 736, 907, 1366
 capture cross section, 909
 dispersion relation, 916
 elastic cross section, 695
 excitation cross section, 908
 for alignment in scattering, 721
 for charge transfer, 815
 for electron capture, 837
 for heavy particle scattering, 788, 789, 792
 for line strength S_n , 886
 for radiative capture, 839
 ionization cross section, 909
 test of, 923
 Thomas process, 913
 Born sequence, 106
 Born series, 106, 142, 736
 Born–Huang ansatz, 488
 Born–Huang–Dalgarno adiabatic correction, 809
 Born–Oppenheimer approximation, 488, 546, 556, 742, 1086, 1176, 1371
 Born–Huang ansatz, 488
 breakdown of, 489
 in scattering theory, 742
 Born–Oppenheimer electronic energies, 807
 Bose–Einstein condensate, 1157
 in cavity QED, 1223
 Bose–Einstein distribution, 1076
 Bose–Einstein statistics, 1158
 two-photon interference, 1236
 Bose–Hubbard model, 1168
 boson, 72, 88, 112, 1158
 commutation relations, 111
 commutators, 1158
 field operator, 1158
 operator, 19
 bosonic realization of $U(4)$, 88
 bottleneck method
 for ion–dipole reactions, 587
 for recombination processes, 864
 boundary conditions, 244, 245
 boundary-corrected Born approximation, 838
 bound–bound pair production, 843
 bound–free pair production, 842
 bow ties, 263
 Bowen fluorescence, 1278
 in comets, 1294
 bracketing theorem, 98
 Bragg
 diffraction, 1154
 reflection, 1182
 regime, 1182
 scattering conditions, optical, 1107
 branching fraction, 189, 261
 branching ratio
 in highly ionized atoms, 264
 radiative, 264
 branching rule, group, 74, 75
 Breit interaction, 474
 relativistic, 339
 Breit–Pauli interaction, 309, 310, 340, 497, 729
 in MCHF calculations, 321
 Breit–Wigner line shape, 400
 Bremsstrahlung, 377
 Brewster angle, 1073
 Brewster’s angle, 1083
 brightness, 1076, 1084, 1092
 brilliance, 1092
 Brillouin frequency shift, 1107
 Brillouin gain coefficient, 1107
 Brillouin linewidth, 1107
 Brillouin scattering, stimulated, 1106
 anti-Stokes field, 1107
 Stokes field, 1107
 Brillouin susceptibility, 1107
 Brillouin’s theorem, 315, 320, 357
 broadband light source, 1061
 Brueckner approximation, 411
 Brueckner equation, 408
 B-spline, 315, 414
 Hartree–Fock software, 166
 R-matrix software, 166
 buckminsterfullerene, 613
 bunching, photon, 1232
 Burshtein–Mollow spectrum, 1052
- C**
 C_2 symmetry, character table, 513
 $C_2H_2^+ + H_2 \rightarrow C_2H_3^+ + H$, 591
 C_6H_6 spectrum, rotational, 514
 C_{60} spectrum, rotational, 514
 caloric curve, 618
 CAM-Chem, 1339
 canonical reduction, 75
 Cantor set, 250
 capture theory, 587
 Born approximation for, 909
 carbon chemistry, in molecular clouds, 1279
 carbon cluster, 613
 Cartan–Weyl form, 72
 cascade, 985
 lasing, 1086
 Casimir effect, 1232
 Casimir force, 208
 retarded limit, 1212
 Casimir operator, 72, 74, 78
 of $SO(3)$ and $SO(2)$, 82
 cat states, 1199
 catalysis, muon, 1364
 Cauchy–Schwartz inequality, 1197
 causality

- superluminal group delays, 1248
- Wigner condition for scattering, 693
- caustic, 243, 248
 - in WKB approximation, 1178
- cavity bandwidth, 1073
- cavity cooling, 1220
- cavity dumping, 1076
- cavity effect, 234
 - excitation probability diagram, 1208
- cavity enhanced transmission spectroscopy, piezo-electric transducer (PZT), 661
- cavity field, manipulation of, 1184
- cavity limit, bad and good, 1211
- cavity optomechanics with cold atoms, 1225
- cavity QED, 1194, 1207, 1208, 1232
 - applications of, 1226
 - dielectrics, 1213
 - resonator types for, 1211
 - strong coupling, 1213
 - weak coupling, 1210
- cavity ring-down spectroscopy (CRDS), 658
 - photodetector, 658
- cavity, atomic, 1179
 - gravito-optical, 1179
 - trampoline, 1179
- cavity-enhanced spectroscopy, 657, 660
 - absorption spectroscopy, 661
 - Levenberg–Marquardt (LM), 660
 - ring-down spectroscopy, 657
 - transmission spectroscopy, 661
- cavity-enhanced transmission spectroscopy
 - free spectral range (FSR), 661
 - frequency modulation (FM), 662
 - locked, 662
- $\text{CCH} + \text{H}_2 \rightarrow \text{C}_2\text{H}_2 + \text{H}$, 591
- center of mass, separation, 250
- central potential model, 82, 340
 - for photoionization, 386
 - SO(4) symmetry of, 77
- CeNTREX, 477
- centrifugal barrier, 585, 1366
 - effect on adiabatic capture, 1366
 - effect on multiphoton ionization, 1130
 - effect on Rydberg states, 232
- centrifugal coupling tensor, 515
- centrifugal potential, 578
- CF_4 spectrum, 519
 - rovibrational, 518
- CFC, 1343
- $\text{CH}(X^2\Pi) + \text{N}_2(X^1\Sigma_g^+)$ reaction, 502
- chalcogenide, 1088
- channel
 - coupled-channel method, 789, 791
 - decay, 262, 325
 - exoergic, 591, 601
 - function, 726
 - inelastic, projection operator, 397
 - photoionization, 385, 956
 - reaction, 502, 593, 601, 602
 - scattering, 726
- channeling in de Broglie optics, 1180
- chaos, 1079
 - in Rydberg atoms, 1134
- chaotic laser, 1079
- Chapman layer, 1320
- Chapman production profile, 1321
- Chapman–Enskog formula, 692
- characteristic conversion length, 1102
- charge conjugation, 475
- charge exchange, 601
 - excitation, 990
- charge solvation, 621
- charge transfer, 601, 602, 786, 805, 814
 - amplitudes, 790
 - recombination, 1276
 - resonant, 1322
 - symmetrical, 602
- charge-coupled device, 676
- charmonium, 86
- Chebyshev interpolation, 133
- chemical kinetics, 599
- chemical potential, 1161
- chemical reaction
 - gas phase, 583, 598
 - ionic, 598
- chemiluminescent reaction, 1328
- chemisorption, 612, 616, 1357
- chemistry of clusters, 612, 616
- CHIANTI, 166
- chiral edge modes, 1171
- chirped pulse amplification, 1077
- chirping, 1077
- chi-square curve fitting, 134
- Christoffel–Darboux formula, 161
- chronological operator, 105
- Clang software, 170
- classical
 - action, 247
 - action variable, 245
 - chaos, 241, 242, 246
 - density, 244
 - dynamics
 - integrable, 242
 - regular, 242
 - separable, 242, 246
 - electron radius, 1049, 1055
 - Hamilton–Jacobi equation, 245, 246
 - oscillator approximation, 284
 - over-barrier model, charge transfer, 996
 - scaling, 1134
 - scattering theory, 696, 889, 1028
 - charge transfer, 906
 - electron removal cross section, 890
 - impulse approximation, 900
 - ionization, 906
 - Thomas process, 913
 - trajectory Monte Carlo (CTMC) method, 919, 1366
 - n*CTMC, 921
 - trajectory Monte Carlo calculation, 834
 - trapping resonance, 1134
- classically forbidden, 245
- classical-quantal coupling, 1366
- Clebsch–Gordan coefficient, 77, 578
- Clebsch–Gordan series, 29
- Clifford algebra, 87, 91
- Clifford number, 88
- close-coupling method, 726
 - convergent, 792
 - for heavy particle scattering, 789, 791
- closed shell, 397, 405, 407, 411, 414

- cluster, 609
 - adsorbate binding energy, 612
 - alkali metal, 610
 - binding energy of, 611
 - carbon, 613
 - chemistry of, 612, 616, 617
 - classical models, 611
 - copper, 611
 - doped, 619, 620
 - electronic properties of, 610, 616, 618, 621
 - electronic spectra of, 611
 - elliptical distortions, 611
 - expansion, 103
 - geometric structures, 610, 612, 615, 618, 620
 - giant, 615
 - helium, 619
 - ionic, 615
 - ionization potentials, 618
 - magnetic moment of, 611
 - magnetic properties of, 610
 - mercury, 611
 - metal, 610
 - molecular, 620
 - noble gas, 618
 - noble metal, 610
 - phase change in, 618, 621
 - phase dynamics, 620
 - quantum calculations for, 610
 - reaction rates in, 612
 - semiconductor, 616
 - silicon and germanium, 616
 - spectroscopy of, 610, 617, 619, 620
 - transition to bulk, 610
 - wetting, 619
- cluster-state quantum computing, 1264
- CO₂ laser, 1088
- CO₂ spectrum, rovibrational, 518
- coherence
 - and statistics, 1127
 - atomic, 1051
 - in three-level processes, 1064
 - induced by the vacuum, 1237
 - length, 1101
 - spatial, 1185
 - wave-function collapse, 1235
 - of matter waves, 1184
 - of projectile beam, 793
 - off-diagonal, 1070
 - parameter, 988
 - time, thermal, 1185
 - two-photon, 1120
- coherent
 - anti-Stokes Raman scattering, 656
 - electron emission, 820
 - excitation, 125, 714, 718
 - scattering, photon, 967
 - state, 219, 1076, 1191, 1215
 - superposition, 819
 - transients, 1112
 - multilevel generalizations, 1118
 - two-dimensional spectroscopy, 570
- coincidence
 - electron–photon, 123, 127
 - fringes in a Franson interferometer, 1245
 - measurement, 987
 - profile, 1249
 - triple, of Grangier, 1232
- cold molecule, 1153
- collective effects, in ion traps, 1151
- collective excitation, 611
- colliding pulse laser, 1078
- collision
 - action, 698
 - complex, 1030
 - delay time, 698
 - density matrix representation, 716
 - dynamics and antimatter, 923
 - frame, 714
 - frequency, 1311
 - number, 1020
 - orientation and alignment in, 713
 - process, 1337
 - processes, 984
 - strength, 727
 - strong and weak, 1053
 - theory, *see also* scattering theory
- collisional association, 598
- collisional narrowing, 1060
- collisionally ionized gas, 1278
- comets, 598, 1289
 - atomic and molecular processes in, 1291
 - density model, 1296
 - dust tail, 1289
 - excitation mechanisms, 1291
 - g*-factor as a function of heliocentric velocity, 1293
 - model, 1295
 - observational data, 1290
 - phenomenology, 1291
 - photodissociation in, 1295
 - photoionization in, 1295
 - photolytic processes in, 1295
 - plasma tail, 1289
 - radiative transfer effects, 1296
- complementarity, 115
 - principle, 1236
 - quantum eraser, 1236
- complete active space, 320
 - perturbation theory, 494
 - reduced form, 321
 - wave function, 493
- complete scattering experiment, 989
- complex
 - collisional stabilization of, 584
 - of atomic states, 320
 - probabilities in quantum theory, 1250
 - radiative stabilization of, 591
 - rotation, 400
 - rotation method, 400
 - scattering, 1030
- composite rotor, 528
- Compton scattering, 969, 973
- concurrence, 1261
- conditional probabilities in quantum theory, 1250
- Condon oscillation, 289
- conducting sphere, 611
- configuration interaction, 100, 311
 - expansion, 493
 - limited, 90
 - method, contracted, 494
- configuration state function, 311, 312, 491

- configurational coordinate diagram, 1086, 1089
- configuration-interaction, software, 166
- confluent hypergeometric function, 157
- confocal parameter, 1075
- conical intersection, 499, 504
 - points of, 504
- conjugation operator, 114
- connected cluster theorem, 102
- connected diagram, 102
- conservation law, 245
 - approximate, 244
- constant ionic state mode, 964
- constant kinetic energy mode, 964
- continuity equation
 - and recombination, 853
 - atmospheric, 1304
- continuous slowing down approximation (CSDA), 1311
- continuum distorted wave (CDW), 814
 - amplitude, 815
 - and Monte Carlo techniques, 921
 - ionization theory, 817
 - perturbation series, 815
 - projectile, 815
 - relativistic, 816
 - second-order, 815
 - target, 815
 - theory, magnetically quantized, 818
 - variational, 816
 - wave function, 815
- continuum radiation, atomic, 195, 630, 668, 958, 1128
- continuum radiation, stellar, 1281
- continuum wave function, 151, 325, 726
 - Dirac equation, 156
 - normalization of, 691, 870
 - variational, 733, 816
- continuum-distorted-wave model for radiative electron capture, 840
- contraction of operators, 99
- contravariant four-vector, 333
- convergence acceleration, 163
- convergent close-coupling (CCC) method, 735
- cooling
 - axial motion, 1151
 - critical velocity, 1144, 1145
 - cyclotron motion, 1151
 - damping coefficient, 1144, 1145, 1147, 1148, 1150
 - diffusion, 1143, 1145, 1146
 - diffusive heating, 1145
 - dissipative force, 1144
 - Doppler, 1145, 1150
 - Doppler limit, 1142
 - evaporative, 1148, 1166
 - induced diffusion, 1146
 - induced orientation, 1147
 - induced-orientation, 1148
 - ion crystal, 1152
 - magnetron motion, 1151
 - many ions, 1151
 - optical molasses, 1145
 - parameters, laser, 1142
 - polarization gradient, 1147
 - quantum theory, 1144, 1147
 - recoil limit, 1142
 - resistive, 1151
 - semiclassical theory, 1143, 1147
 - sideband, 1150, 1151
 - Sisyphus, 1147
 - effect, 1147
 - sympathetic, 1152
 - temperature of trapped particle, 1144, 1145, 1147, 1150
 - transverse diffusion, 1145, 1146
 - velocity capture range, 1144, 1145
- Cooper minimum, 387
- coordinate system, scattering, 714
- copper cluster, 611
- core
 - excited states, 396
 - penetration, 179
 - potential, 242
 - scattering, 246, 249
- Coriolis coupling, 508, 579, 777, 1175
- correlation
 - angular, 124, 988
 - analysis of, 716
 - dynamic, 493
 - decay curve analysis, 266
 - electron-electron, 787
 - internal or static, 493
 - of symmetry types, 514
 - Pauli, 788
 - photon, 1077, 1232
 - polarization, 988
 - static and dynamic, 789
 - valence, 321
 - vector, in photodissociation, 557
- correlation energy, 100, 318
 - definition of, 318
 - diagrammatic expression for, 368
 - Thomas–Fermi $Z^{-1/3}$ expansion for, 302
- correlation function, 1201
 - scattering, 726
- correlation potential, 726
 - exchange, 495
 - Lee, Yang, Parr expression for, 303
- correspondence principle
 - Bohr, 887
 - Bohr–Sommerfeld quantization, 887
 - equivalent oscillator theorem, 888
 - Heisenberg, 888
 - in Rydberg collisions, 887
 - strong-coupling, 888
- cosmic rays, 1279
- Coulomb
 - boundary conditions, 814, 817
 - crystal, 1042
 - explosion, 1134
 - function, 151
 - gauge, 384, 967
 - phase shift, 870
 - repulsion, 1363
 - scattering, 705, 868
 - modified, effective range formula, 693
 - trajectory, 786
- Coulomb–Born approximation, 1366
- Coulomb–Stark potential, 234, 235
- counterintuitive pulse sequencing, 1121
- counting statistics, 1232
- coupled cluster (CC), 103
 - approximation, 405
 - calculations, 359
 - expansion, 103, 342

- method, 103, 492
 - coupled-channel
 - dynamics, 786
 - method, 789, 791, 834, 836
 - coupled-channels optical (CCO) method, 736
 - coupled-cluster method, 474, 475
 - coupling
 - electronic and rotational, 500
 - coupling scheme
 - term symbols, 180
 - coupling, atomic
 - $J_1 j$ or $J_1 J_2$, 181
 - $J_1 l$ or $J_1 L_2 (J_1 K)$, 182
 - jj , 180
 - LS (Russell–Saunders), 179
 - $LS_1 (LK)$, 182
 - covariant four-vector, 333
 - CPAN, 168
 - CPT symmetry, 477
 - CP-violation, 475
 - Cr2+, 1087, 1088
 - Cr3+, 1087
 - Cr4+, 1087
 - creation operator, 72, 88, 99, 111, 114, 1158, 1190
 - critical
 - angle for total reflection, 1179
 - density, 1159
 - field, 840
 - laser intensity, 1129
 - temperature, 1159
 - velocity, 1168
 - cross section, 696, 726, 934
 - classical, 696, 889, 1028
 - collision strength, 982
 - density matrix formalism for, 126, 715
 - differential, 690, 726, 737, 738, 787, 982, 1028
 - binary encounter approximation, 903
 - for Coulomb scattering, 868
 - double differential, 738
 - doubly-differential, 791
 - elastic scattering, 696
 - for multipolar relaxation, 219
 - frame transformation, 539, 1025
 - integral, 738, 982
 - moments of, 728, 864
 - momentum transfer, 982
 - Rutherford, 151, 706, 868
 - selection rules, 983
 - total, 787
 - total scattering, 727, 887, 984
 - triple differential, 738, 824
 - triply differential, 791
 - crossed beam, 1024
 - dipole force trap, 1146
 - ion-laser, 265
 - trap, 1166
 - crossing distance, 1030
 - cross-relaxation, 1086
 - Crothers semiclassical approximation, 825
 - Cs atomic clock, 480
 - Cs PNC experiment, 473
 - Cu²⁶⁺ dielectronic recombination, 877
 - cubic graphs, classes of, 56
 - cubic spline, 132
 - cuboid crystal, 615
 - curve crossing, 556, 857, 860, 1029
 - curve fitting, 133
 - chi-square, 134
 - least squares, 134
 - cusp conditions, Kato, 200
 - cylindrical mirror analyzer, 962
 - Cython, 171
- D**
- D_2 symmetry
 - character table, 514
 - correlation with C_2 , 514
 - damping rate
 - longitudinal, 1114
 - transverse, 1114
 - dark
 - energy, 461, 466
 - matter, 461, 466, 474, 482
 - state, 1066, 1120
 - Darwin term, 311, 729
 - David Bates, 808
 - dayglow, 1325
 - spectra of selected planets, 1330
 - terrestrial spectrum, 1329
 - De Broglie optics
 - gravitation, 1174
 - Hamiltonian, 1174
 - rotation, 1174
 - De Broglie wavelength, 796, 873
 - thermal, 1185
 - Debye screening length, 895
 - decay
 - free induction, 1116
 - purely radiative, 1055
 - β -decay
 - general theory, 1362
 - $^{187}\text{Re} \rightarrow ^{187}\text{Os}$, 1362
 - tritium, 1362
 - decay rate, 249
 - inelastic collisions, 1054
 - spontaneous, 213, 1054
 - decoherence, 1174, 1261
 - Dedalus software, 168
 - deflection function, 687, 696, 1028
 - formulae, 696
 - deflection parameter, 669
 - degeneracy, 246
 - group (algebra), 81
 - degenerate Fermi gas, 1159
 - delay time, collisional, 698
 - delayed choice, in quantum measurement, 1237
 - Delbrück scattering, 970
 - delocalization, 821
 - delta function, electric field effect on matrix elements, 229
 - delta rays, 1012
 - density functional theory, 91, 92, 303, 494
 - locality, 304
 - time-dependent, 788
 - density matrix, 119, 120, 217, 1191
 - diagonal representation, 218
 - equation of motion, 1058
 - for polarized beams, 719
 - for relaxation processes, 121
 - for thermal equilibrium, 121

- from Stokes vector, 716
 - full, 122
 - reduced, 122, 788
 - reduced spin, 126
 - two-level atom, 1054, 1058, 1070, 1071
- density of states
 - classical, 889
 - photon, 213
- density operator, 120
 - irreducible components, 123
 - time evolution, 120
- depolarization, 125
 - in Rydberg atom collisions, 882
 - postcollisional, 716
- depopulation rates, 887
 - in external B fields, 887
- derivative coupling, 496
- derivative, numerical approximation of, 136
- desorption, 1357
- detailed balance, 649, 857, 867, 872, 1055
- detailed balancing, 990
- detection operator, 220
- detector, 675
 - charge-coupled device, 676
 - far-infrared, 645
 - microchannel plate, 675
 - neutral particles, 1021
 - nonoptical, 1022
 - photomultiplier tube, 675
 - silicon photodiode, 675
 - spectroscopic, 1021, 1022
 - surface ionization, 1022
- deterministic chaos, 1079
- detuning, 1051, 1058, 1070, 1105, 1114, 1129, 1141, 1175, 1214
 - two-photon, 1120
- adiabatic
 - coupling matrix element, 808
 - electronic state, 774
 - Hamiltonian, 774
 - passage, of Rydberg atoms, 236
 - PES, 774
 - potential for mutual neutralization, 860
 - state, 489, 1181, 1366
- diagrammatic technique, 102, 363
- diamagnetic system, 476
- diatomic molecule, 819
 - binding with noble gases, 500
 - dissociative electron–ion recombination, 604
 - electron scattering by, 742
 - noncrossing rule, 490
 - nonrigid, 89
 - one-electron, 86
 - radiative transitions in, 541
 - rigid, 89
 - symmetric top structure, 508
 - Thomas–Fermi *no binding* result, 298
 - vibrational structure, 499
- dichroism, 465
- Dicke model, 1223
- Dicke narrowing, 1060
- dielectric screening, 796
- dielectric, cavity QED in, 1213
- dielectronic recombination, 846, 875, 1014, 1276
 - Au⁷⁶⁺, 878
 - cross section, 870
 - Cu²⁶⁺, 877
 - data generation, 875
 - in plasmas, 879
 - O⁵⁺, 877
- difference frequency generation (DFG), 1093, 1102
- differencing algorithm, 138
- differential cross section, 962, 982
- differential equation
 - numerical methods, 137
 - ordinary, 137
 - power series solution, 142
- different-orbitals-for-different-spins (DODS), 104
- diffraction, 248, 1180
 - anomalous fine structure (DAFS), 972
 - atom, 1180
 - electron, 1180
 - Fraunhofer limit, 1180
 - Fresnel regime, 1180
 - Laue geometry, 1181
 - limit, 1180
 - neutron, 1180
 - small-angle, 700
 - superluminal group delays, 1248
- diffraction-limited field, 1076
- diffusion
 - coefficient, 853, 1305
 - cross section, *see* momentum transfer cross section
 - induced, 1146
- diffusion method
 - for recombination processes, 864
- diffusional-drift, in recombination processes, 853
- diode laser, 1090
- diode laser pump, 1084, 1090
- dipole
 - approximation, 956, 1049
 - coupling, of atoms and fields, 1209
 - critical strength, 1366
 - force, 1144, 1146
 - moment, 104, 1048
 - potential, 597
 - scattering, 708, 1351
- Dirac energy levels, 442
- Dirac equation, 333, 836
 - boundary conditions
 - near nucleus, 345
 - singular points, 345
 - characterizing states, 334
 - charge–current continuity, 335
 - charge–current four-vector, 334
 - Coulomb Green’s function, 156
 - finite nuclear model, 346
 - free electron, 348
 - hydrogenic, 85, 153
 - dynamical effects, 347
 - hydrogenic solution, radial moments, 347
 - in scattering theory, 729
 - interpretation of spectrum, 335
 - magnetic field, 224
 - many–electron atom model, 356
 - many–electron model
 - atomic state function (ASF), 356, 357
 - configuration state function (CSF), 356
 - CSF interaction matrix, 357
 - four–component orbitals, 356
 - Slater determinant, 356

- nonrelativistic limit, 346
 - numerical approximation
 - acceptable trial functions, 350, 352
 - Bloch operator, 354
 - B-splines, 353
 - Galerkin equations, 354
 - G-spinors, 353
 - L-spinors, 352
 - S- and G-spinor exponents, 353
 - S-spinors, 352
 - bound state stability, 350
 - expansion methods, 350
 - Rayleigh quotient, 350
 - variational methods, 350
 - point nucleus, 346
 - radial boundary conditions, 346
 - limit-circle case, 346
 - limit-point case, 346
 - radial equations
 - finite difference approximation, 354
 - self-adjointness, 349
 - radial Bloch operator, 349
 - self-consistent fields
 - bound state stability, 356
 - Dirac–Hartree–Fock–Breit model, 357, 358
 - Fock matrix, 358
 - spherical symmetry, 342
 - angular distribution, 344
 - eigenstates, 344
 - jj -coupling subshells, 344
 - radial density distribution, 344
 - square integrable solutions, 346
 - Dirac field
 - normal ordered operator, 336
 - vacuum state, 336
 - zero-point energy, 336
 - Dirac gamma matrices, 334
 - Dirac matrices, 831
 - DIRAC software, 167
 - Dirac “sea”, 841
 - Dirac–Coulomb Hamiltonian, 309, 310
 - Dirac–Coulomb–Breit Hamiltonian, 309, 310
 - Dirac–Hartree–Fock equation, 315
 - Dirac–Hartree–Fock method, 313, 1362
 - Dirac–Pauli matrices, 88
 - direct charge transfer, 805
 - direct dynamics, 563
 - direct excitation cross section, 985
 - direction cosine matrix elements, 21
 - discharge
 - flash, 670
 - H₂, D₂, 670
 - discrete nonlinear Schrödinger equation, 1169
 - discretization of the continuum, 791
 - dispersion
 - anomalous, 1062
 - normal, 1062
 - optical, 262
 - quantum mechanical cancelation, 1247
 - dispersion relation, 1177
 - for Thomas scattering, 916
 - dispersive behaviour, 1058
 - dispersive phase, 1183
 - displacement operator, 1191
 - dissociation, 584, 598
 - electron impact, 986
 - probabilities, 852
 - spontaneous, 584
 - dissociative attachment, 598, 742, 743
 - in Rydberg atom collisions, 882
 - dissociative ionization, 1309
 - dissociative recombination, 598, 846, 857, 1279, 1313, 1321
 - of diatomic ions, 857
 - polyatomic, 588
 - distinct row table, 90
 - distorted-wave
 - approximation, 737
 - for dielectronic recombination, 878
 - method
 - continuum distorted waves, 789, 792
 - model, 834
 - model for electron capture, 839
 - distribution function, use of in Rydberg collisions, 888
 - DNA, 822
 - Doppler broadening, 1060, 1153
 - Doppler cooling, 1145, 1150
 - Doppler-free resonance, 1065
 - Doppler-free spectroscopy, 452, 1062
 - double excitation, 960
 - double ionization, 818, 958, 959
 - binary encounter approximation for, 905
 - by antiprotons, 789
 - by protons, 789
 - double Pfaffians, skew symmetric matrices, 61
 - double-clad fiber, 1084
 - doubly excited states, 396
 - down-conversion
 - from a nonlinear crystal (diagram), 1233
 - spontaneous, 1103
 - four-wave mixing, 1233
 - suppression of spontaneous, 1237
 - dressed atom, two-level, 1052
 - dressed state, 1051
 - in electron scattering, 744
 - Drude model, 1109
 - Dy³⁺, 1085
 - dynamical
 - algebra, 81
 - group, noncompact, 82
 - symmetry, 508, 544
 - tunneling, 511
 - Dyson equation, 106, 405, 407, 410–412
 - Dyson orbital, 371
- E**
- e–2e measurement, 987
 - e[–]–Cs scattering phase shift, 797
 - Eagle mount, 673
 - Earnshaw theorem, 1149
 - earth’s atmosphere, 1338
 - EDFA, 1085
 - edge modes, 1171
 - EDWIN software, 168
 - effective
 - Hamiltonian, 104
 - lifetimes, 887
 - range, 855
 - range theory, 796
 - range, in elastic scattering, 693
 - thickness of the atmosphere, 1300
 - effusive beam, 1185
 - Efimov effect, 855, 890
 - Ehrenfest theorem, 689
 - eigenfunction, semiclassical, 244

- eigenpolarization, 1100
- eigentorus, 245
- eigentrajectory, 244, 245
- eikonal
 - Born series, 737, 746
 - criterion, 814
 - distorted state, 817
 - in de Broglie optics, 1177
- eikonal method
 - for forward reactive scattering, 696
 - for heavy particle scattering, 787, 791
 - for heavy-particle scattering, 816
- Einstein *A* and *B* coefficients, 233, 262, 290, 1055, 1069
 - molecular, 545
- Einstein–Podolsky–Rosen (EPR) paradox, 1240
- elastic cross section, two bosons, 855
- elastic scattering, 696, 725, 786, 787, 984, 1028
 - Born approximation, 695
 - cross section, 372, 696
 - effective range formulae, 693
 - in reactive systems, 695
 - intermediate and high energy, 735
 - intermediate and high-energy, 735
 - low energy, 725
 - of electrons, 725
 - thermal energy loss function, 1310
 - small-angle, 701
- elastic target mode of ion–atom collisions, 835
- electric dipole interaction, 214, 384, 1048
 - finite nuclear mass effect, 214
 - length, velocity and acceleration forms, 384
 - molecular, 542
 - motional correction, 1175
 - two-level atom, 1051
- electric dipole moment, 214, 463, 467, 475, 882, 1048
 - molecular, 547
- electric dipole phase, 1183
- electric dipole transition, 188, 324, 384
 - finite nuclear mass effect, 214
 - helium results, 214
 - hydrogenic matrix elements, 882
 - molecular, 542, 547
 - selection rules, 385
 - Stokes parameters for, 127
- electric field
 - atoms in, 227
 - hydrogenic wave functions in, 227
 - static, 241, 242
- electric multipole, 258, 1047
- electric polarization, 1049
- electric quadrupole transition, 187, 188
- electromagnetic field, 1208
 - quantized, 336
- electron affinity, 324, 328
 - of cluster, 611, 617
- electron attachment, 600, 604
- electron beam ion trap, 273
- electron capture, 984, 1008
 - Born approximation for, 909
 - from hydrogen, 996
 - Monte Carlo method for, 919, 920
 - state-selective, 922
 - Thomas double-scattering, 815
 - to the projectile continuum, 833
- electron collisions with trapped atoms, 990
- electron configuration, 178
- electron correlation, 89, 100
 - density functional theory, 494
 - Green’s function techniques for, 405
 - in heavy particle scattering, 788
 - many-body perturbation theory of, 359, 368
 - photoionization effects, 383, 956
 - wave function methods for, 491
- electron diffraction, 1180, 1350
- electron EDM, 475
- electron energy loss, 1311, 1350
 - spectroscopy, 1351
- electron impact processes, 982
- electron optics, 1174
- electron scattering
 - by complex atoms, 746
 - by ions, 746
- electron self-energy, 359
- electron shell, 178
- electron shelving, 1153
- electron transition moment, molecular, 547
- electron translation factor, 790, 814
- electron translational factor, 837
- electron–atom collisions, 725, 982
 - benchmark measurement, 985
 - collisions with excited species, 990
 - diagrammatic perturbation theory, 364
 - excitation cross sections, 985
 - in a laser field, 744, 746
- electron–electron interaction operator
 - Breit, 339
 - Coulomb, 339
 - Feynman, 339
 - Gaunt, 339
- electronic translation factors, 810
- electron–ion collisions, 725
- electron–ion recombination, 597, 604
 - working formulae, 850
- electron–molecule collisions
 - inelastic, 1029
 - theory, 741
- electron–photon coincidence
 - geometry of, 127
 - measurement, 987
- electron–photon excitation, simultaneous, 744
- electron–positron field, 335
 - quantization, 335
- electron–positron pair production, 840
- electro-optic effect, 1108
 - linear, 1108
 - quadratic, 1108
- ellipse eccentricity, 244
- Elliptic integral $K(k)$, 895
- emission intensity, 187
- endoergic reaction, 805
- endohedral complexes, 615
- energy disposal in elementary reactions, 1025
- energy level repulsion, 246
- energy loss, 983
 - electron, 1311
 - spectrum, 983, 1007
- energy spectrum of two-electron systems, 792
- energy transfer
 - cross section, 890
 - upconversion, 1086

- energy–intensity model, of molecular transition strengths, 539
enhancement factor, 810
entangled states, 1184, 1235, 1240
entanglement, 1198, 1259
 entangled state, 1198
 generation of, 1227
 position-momentum, 1103
enthalpy change, 598
entropy
 change, 598
 reduction, 1226
 Shannon's information, 229
epsilon near zero, 1109
Epstein–Nesbet perturbation theory, 100
equation of continuity, 1167
equation-of-motion method, 104
equilibrium constant, 599
equivalent
 electron, 178
 oscillator theorem, 888
 width, 187
Er³⁺, 1085
erbium-doped fiber amplifier, 1085
Euler's method, 137
Euler's theorem, 614
evanescent light, 1179
evanescent matter wave, 1179
evaporative cooling, 1148, 1166
evolution operator, 105
exchange
 asymmetry, 989
 operator, 787
 potential, 726, 727
 gradient corrected, 303
 local, 742
 reaction, Monte Carlo method for, 919, 920
exchange–correlation potential, 303
 validity tests, 304
excitation
 projectile, 786
 target, 786
excitation in Fermi gas, 1165
excitation-ionization, 786
excited atomic states, 321
excited-state absorption (ESA), 1088, 1089
exohedral complexes, 615
exosphere, terrestrial, 1301
exothermic reaction, 805
extended x-ray absorption fine structure (EXAFS), 972
extinction coefficient, 1118
- F**
F + D₂ scattering, 1025, 1030
Fabry–Pérot etalon, 1073
Fabry–Perot resonator, 651
factorization lemma, 102
Fano profile, 946, 958
Fano–Feshbach resonance, 797
Fano–Lichten model, 1009
Faraday effect, 1064
far-infrared (FIR) spectroscopy, 641
 detector, 645
 instrumental resolution, 643
 spectrometer (diagram), 643
 tunable sources, 642
feedback, 1070
Felgett advantage, in Fourier transform spectroscopy, 631
femtosecond laser pulses, 670, 1077, 1129
femtosecond measurement, single photon, 1247
Fermi
 contact term, 327
 energy, 1159
 gas, 1159
 degenerate, 1159
 excitations, 1165
 Thomas–Fermi approximation, 1165
 sea, 1159
 temperature, 1159
 vacuum, 100
Fermi–Dirac statistics, 1159
fermion, 72, 88, 112
 anticommutator, 1159
 commutation relations, 111
Fermi's golden rule, 213, 325, 944, 1061
Feshbach projection operator, 396, 730, 736, 743
Feshbach resonance, 396, 398, 400, 561, 730, 949, 1153, 1161, 1169
 vibrational predissociation and radiative stabilization mechanism, 592
Feynman causal propagator, 336, 338
Feynman diagram, 100, 363
 photon scattering, 968
Feynman–Vernon–Hellwarth picture, 1053
field
 atoms in, 223
 classical, 1208
 dipole coupling, 1209
 electromagnetic, 1208
 nonclassical features, 1218
 operator, 1158
 quantum, 1209
 shift, 256, 326
 theory, classical, 1160
filter, optical, 676
fine structure
 atomic, 179
 depolarization effects of, 716
 effect, 990
 on electron scattering, 990
 on low temperature reactions, 587
Hamiltonian, 310
of helium, 215
rotational, 513, 515, 519
transition
 cross sections for in Rydberg collisions, 894
 measurement of, 641
 rates, in Rydberg collisions, 894
finite basis set method, 226, 735
finite element method, 140
finite group action, 22, 24
finite matrix method, atoms, 358
first-order perturbation theory, 830
Floquet theory, 747, 1135
 for atoms in a laser field, 746
fluctuation potential, 337
fluorescence efficiency, 1292
fluorescence process, 958
 in comets, 1292
fluorescent scattering, 1327
fluorozirconate, 1085

- flux-velocity contour map, 1026
 - Fock
 - exchange operator, 787
 - expansion, 200
 - state, 1158, 1191, 1215
 - Fokker–Planck equation, 1143
 - forbidden band, 289
 - forbidden transition, 187, 188
 - molecular, 551
 - forced impulse method, 789
 - form factor, 886
 - connection with generalized oscillator strength, 886
 - expressions for discrete transitions, 908
 - general trends, 908
 - power series expansion for, 907
 - representation as microcanonical distribution, 886
 - semiclassical limit, 886
 - FORTRAN, 170
 - forward convolution analysis, 1024
 - Fourier analysis, 135
 - Fourier transform (FT), 247, 830
 - discrete, 135
 - fast, 135, 790
 - mass spectrometry, 986
 - spectroscopy (FTS), 263, 630, 641
 - alignment techniques, 634
 - spectrum generation, 632
 - four-potential of the electromagnetic field, 830
 - four-wave mixing, 1105, 1233
 - optical phase conjugation, 1105
 - fractal, 250
 - epistrophic, 250
 - fractional parentage, 113–115
 - coefficients of, 113
 - fractional revival, 1119
 - fragmented condensate, 1164
 - frame transformation, 539, 1025
 - theory, 751
 - Franck–Condon
 - factor, 546
 - effective, for dissociative recombination, 859
 - sum rule, 546
 - mapping, 561
 - overlap, 601
 - principle, 288, 546, 560, 939, 986, 1086
 - region, 560
 - Fraunhofer
 - diffraction, 1180
 - black sphere, 696
 - limit, 1180
 - free electron
 - gas, 303
 - laser, 1079, 1092
 - free induction decay, 1116
 - free pair production, 841
 - free, bound–free, bound–free pair production, 841
 - frequency
 - pulling, 1073
 - standard, 186, 450
 - frequency chirping, 1078
 - frequency comb, 453
 - optical, 656
 - application to spectroscopy, 656
 - frequency doubling, 1093
 - Fresnel
 - diffraction, 1181
 - formula, 1179
 - integral, 249
 - number, 1075, 1076
 - regime, 1180
 - zone plate, 1181
 - Fröhlich Hamiltonian, 801
 - frozen correlation approximation, 789
 - fullerene, 613, 614
 - buckled, 617
 - endohedral complexes, 615
 - formation, 614
 - rotational spectrum of, 523
 - function, representation of, 132
 - fundamental constants, 5, 449, 455
 - furnace method, 262
 - Furry bound interaction picture, 335, 419
 - fusion, nuclear, 1363
 - f*-value, 187–189
- G**
- GaAs, 1090
 - gain clamping, 1071, 1072
 - gain coefficient, 1069
 - gain media, 1069, 1070
 - homogeneously broadened, 1071–1073
 - inhomogeneously broadened, 1072, 1073
 - gain saturation, 1071, 1072
 - Galerkin method, 140, 315
 - GAMESS software, 167
 - GaN (blue), 1090
 - gap soliton, 1169
 - gas phase collisions and chemistry, 583, 598
 - astrophysical applications, 1275, 1289, 1305
 - clusters, 610
 - gauge
 - invariance, 405, 1175
 - length and velocity, 213, 384, 744
 - symmetry, 1164
 - transformation, 223
 - gauge field, synthetic, 1171
 - Gaunt factor, 872
 - semiclassical representation, 886
 - Gaussian
 - beam, 1075
 - chaotic field, 1127
 - quadrature, 136
 - GBT theorem, 315
 - gcc software, 170
 - Gegenbauer polynomial, 15, 163, 889, 895
 - Gel'fand tableaux, 87
 - Gel'fand–Paldus tableau, 90
 - Gel'fand–Tsetlin canonical chain, 87
 - Gell-Mann and Low formula, 105
 - general circulation, 1339
 - generalized gradient approximation (GGA), 303, 304
 - generalized oscillator strength, 983, 1007
 - connection with form factor, 886
 - generator
 - atomic operator as, 72
 - commuting, 73
 - lowering, 86
 - raising, 86
 - weight, 86

- geometric magnetism, 809
geometric phase, 1183
GEOS-CHEM, 1339
germanium cluster, 616
g-factor
 electron, 437
 hydrogenic carbon, 438
 hydrogenic silicon, 438
gfortran software, 170
ghost recurrence, 249
giant cluster, 615
Gibbs free energy, 598
GitHub software, 169
glass ceramics, 1084
Glauber approximation, 737, 789
global change, 1337
 issue, 1337
global warming, 1337
glory and rainbow scattering, 697, 700, 701, 939, 1028
 glory diffraction oscillations, 701
 rotational rainbow, 1028
GNU autotools software, 170
godparent, 113
Goldstone diagram, 101
Gordon's formula, 885
 in terms of Jacobi polynomials, 892
gradient force, 1144, 1146
grand-canonical ensemble, 1159
GRASP2K software, 166
Grassman algebra, 91
gravitational
 Aharonov-Bohm effect, 481
 redshift anomaly, 479
 wave detection, 482, 1250
 wave detector, 1250
gravity, possible link to quantum information, 1251
Green function, 420
greenhouse, 1340
Green's function, 106, 398, 405, 419, 730
 continuum distorted wave, 814, 815
 Coulomb, 154
 Coulomb Dirac, 156
 four-point, 409
 Hartree-Fock propagator, 369
 in formal scattering theory, 142
 potential scattering, 106
 propagator, 338
 radiative corrections, 412
 radiative transitions, 410
 Thomas process, 914
 two-point, 406
Greenstein effect, in comets, 1293
Gross-Pitaevskii equation (GPE), 797, 891, 1160, 1223
 numerical methods, 1163
group
 Abelian, 72
 dynamical, 81
 noncompact, 82
 Euclidean, 83
 Lie, 333
 Lorentz, 83, 333
 molecular symmetry, 509
 octahedral, 513
 orthogonal, 509
 parametrized $SO(3, \mathbf{R})$ representations, 19
 parametrized $SU(2)$ representations, 19
 Poincaré, 333
 representation theory, 86
 rotation, 73, 82, 509
 semisimple, 72
 simple, 72
 $SU(2)$
 parametrization of representation functions, 17
 representation functions, 19
 representation, orthogonality properties, 20
 representation, symmetry relations, 21
 solid harmonics, 56
 $SO(3)$
 Euler-Rodrigues parameters of representation functions, 17, 19
 representation, orthogonality properties, 20
 representation, symmetry relations, 21
 symplectic, 73
 tetrahedral, 513
 $U(2)$ spin, 89
 $U(2n)$ spin-orbital, 90
 $U(n)$ orbital, 90
 unitary, 72
group action
 Hilbert spaces, 25
 matrix group actions, 24
 relation to angular momentum theory, 25
group and Lie algebra realizations, 25
group delay
 definition, 1247
group generator, 71, 73
group reduction, 75
group velocity, 1071, 1118, 1178
 dispersion
 cancelation of, 1247
 pulse propagation, 1101
 in dispersive medium, 1067
 single photon, 1247
 superluminal, 1247
GSL software, 171
GUASSIAN software, 167
gyromagnetic ratio, 1049
- ## H
- $H + H_2$ reaction, 590
 H_2 , Monte Carlo method for, 924
hadronic weak interactions, 473
halfway house VCDW, 817
halogen molecule scattering, 1030
halon, 1343
haloscope, 466
Hamilton optics, 1177
Hamilton-Jacobi equation, 245, 246, 823
Hanbury-Brown and Twiss effect, 1077, 1232
Hanle effect, 126, 264
harmonic generation, 1102, 1131
 by elliptically polarized fields, 1132
 conversion efficiency, 1102
 higher-order, 1107, 1108
 third, 1104
harmonic oscillator, length scale, 1160
harmonic plateau, 1131
harmonium, 86
harpoon mechanism, 1029
harpooning distance, 1030

- Hartree term, 408
- Hartree–Fock
- approximation, 100, 311, 313, 405
 - diagram, 367
 - multiconfiguration, 318, 320
 - time-dependent, 1363, 1366
- diagram, 101
- method, 313
- time-dependent, 787
- operator, 314
- software, 166
- Hartree–Fock–Slater approximation, 791
- Hausdorff formula, 103
- He₂ diatomic molecule, 619
- healing length, 1161
- heat capacity, ideal gas, 1020
- heat of formation, 598
- heavy particle scattering, 786
- coupled-channel method, 789
 - finite difference method, 790
 - Fourier collocation method, 790
 - independent event model, 789
 - independent particle model, 787
 - many-electron treatments, 787
 - numerical lattice calculations, 790, 792
- heavy-ion storage ring, 277
- heavy-particle scattering, 814
- dynamics of, 923
- height parameter, 717
- Heisenberg correspondence principle, 888
- Heisenberg limited sensitivity, 1202
- helicity, photon, 715
- helioscope, 465
- helium
- 2s2p ¹P⁰ autoionization states, 397
 - cluster, 619
 - electron scattering processes, 984
 - energy structure and notation, 179
 - ground-state expectation values (table), 208
 - high-precision calculations for, 199
 - ionization energy (table), 209
 - isotope shift (table), 207
 - nonrelativistic eigenvalue (table), 206
 - nonrelativistic energies for He-like ions, 208
 - oscillator strength (table), 214
 - quantum defect extrapolation (table), 211
 - singlet-triplet mixing (table), 215
 - threshold ionization of, 824, 825
 - total energies for, 205
- helium-like ion, 304
- energy structure and notation, 179
- Hellmann–Feynman theorem, 304
- Helmholtz equation, 1177
- hemispherical analyzer, 962
- He–Ne laser, 1082
- Henry α parameter, 1074
- Hessian matrix, 489
- Hg EDM experiment, 476
- HHG in solids, 1132
- hidden variable, 1241
- high field seeker, 1177
- high multipole order radiation, 277
- high-energy ion–atom collisions, 829
- high-harmonic generation (HHG), 570, 1093
- highly stripped ion, 264, 269, 1363
- in astrophysics, 1278
- Hilbert transform, 1060
- HITRAN, 1340
- Ho3+, 1085
- Hohenberg–Kohn theorem, 494
- Hohenberg–Kohn variational principle, 302
- hole burning, 654
- spatial, 1060, 1072, 1073, 1076
 - spectral, 1059, 1073, 1076
- hollow cathode, 670
- lamp, 263
- Holstein–Biberman theory, 290
- homogeneous broadening, 1059, 1071, 1072, 1153
- homologous sequence, 186
- $SU(2) \rightarrow SO(3, \mathbf{R})$, 10
- homonuclear molecule, 819
- homopause, 1300
- characteristics of planets and other solar system bodies, 1301
- homosphere, 1300
- HONDO software, 167
- Hong–Ou–Mandel effect, 1201
- Hong–Ou–Mandel interference, 1268
- Hong–Ou–Mandel interferometer, 1235, 1236
- ultrafast measurement, 1247
- Hönl–London factor, 548
- sum rules, 548
- Hook method, 262
- HRTOF, 1019
- Hubble Space Telescope, 1290
- Hugenholtz diagram, 101
- Hund’s coupling cases, 549
- Huygens principle, 1180
- hybrid ion trap, 810
- hydrodynamic escape mechanism, 1332
- hydrogen, 441
- atom, 454
 - atomic beam, 1021
 - electron capture, 996
 - electron impact excitation of, 719
 - group theory of, 77, 82
 - infrared lines of, 933
 - O(4) symmetry, 152
 - radio lines of, 933
 - SO(4) symmetry, 83
 - SO(4,2) symmetry, 83
- hydrogenic atom, 185
- algebraic approach to, 85
 - electric dipole transition integrals, 883
 - excited state energies in magnetic fields (table), 226
 - expectation values (table), 212
 - ground state energies in magnetic fields (table), 226
 - Monte Carlo calculations for, 921
 - N -dimensional, 85
 - nuclear size correction (table), 226
 - perturbations of, 85
 - structure and notation, 178
- hydrogenic ion, 185, 189
- Hylleraas function, 201, 397
- Hamiltonian matrix elements, 204
 - integral recursion relations, 204
 - integrals involving, 202
- Hylleraas–Undheim–MacDonald theorem, 201, 312, 791
- hyperfine structure, 253, 276, 327, 520, 1368
- anomalies, 259
 - depolarization effects of, 716

energy splittings, 254
 intensities, 255
 normal, 257
 tetrahedral nuclear, 518
 hypergeometric function, 32, 157
 numerical evaluation, 885
 hypergeometric series form of WCG coefficients, 33
 hyperpolarizability, 1099
 hyperradius, 822
 hyperspherical coordinates, 403, 822

I

idler beam, 1093
 imaginary time, 1163
 imaging methods, 1039
 impact parameter, 243, 807
 approximation, 814
 method, 787
 impedance of free space, 1112
 impulse approximation, 896
 for electron capture, 838
 for radiative capture, 840
 quantal, weak binding condition, 900
 semiquantal, 901
 IMSL software, 171
 independent
 event model, 789
 particle model, 787
 processes approximation, 877
 index of refraction, 1049, 1057, 1117
 complex, 1059, 1062
 inelastic target mode of ion-atom collisions, 835
 infinitesimal generator, 11
 infrared spectral region, definition, 186, 626
 infrared spectroscopy, 626
 InGaAs, 1090
 InGaAsP, 1090
 InGaN, 1090
 inhomogeneous broadening, 1060, 1071, 1072
 inner-shell processes, 1003
 inner-shell vacancy rearrangement, 390
 Innsbruck experiment, schematic of, 1238
 instability, thermodynamical, 1165
 integral approximation, 135
 adaptive quadrature, 136
 composite quadrature, 136
 Gaussian quadrature, 136
 polynomial quadrature, 135
 integral cross section, 982
 integral equation, 142
 numerical methods, 137
 integral transform, 142
 integral, atomic and molecular, 99
 integration in imaginary time, 1163
 intensity quantities, 188
 atomic
 multiplet values, 188
 regularities, scaling, 189
 systematic trends, sequences, 189
 molecular, 540
 fits to experiment, 542
 interaction picture, 105, 120
 interaction potentials
 Cs-Cs, 884
 H(n)-H(n), 884
 He-He, 884
 Rb-Rb, 884
 Sr-Sr, 884
 interaction-free measurement
 quantum interrogation
 quantum theory of measurement empty waves observable effects
 of, 1239
 interband cascade laser, 1092
 interference
 effects, 819, 821
 Feynman rules, 1236
 filter, 677
 fringes, 1182
 in de Broglie optics, 1182
 low-intensity, 1232
 matter-wave, 1234
 patterns, 820
 single-photon, 1234
 two-photon, or fourth-order, 1235
 interferometer
 division of amplitude, 1182
 division of wavefront, 1182
 Hong-Ou-Mandel, 1235
 loop, 1183
 Mach-Zehnder, 1182
 optical Ramsey, 1184
 scanning Michelson, 630
 stimulated Raman, 1184
 three-grating, 1182
 Young double-slit, 1182
 intermediate coupling, 182
 internal conversion in predissociation, 556
 International System of Units (SI), 3
 International Ultraviolet Explorer, 1290
 interpolated function, derivatives of, 137
 interpolation, 132
 Chebyshev, 133
 cubic spline, 133
 iterated, 132
 Lagrange, 132
 orthogonal function, 133
 rational function, 133
 intersection, conical, 504
 interstellar gas cloud, 598
 molecules observed in, 1280
 intersystem transition, atomic, 179
 intrinsic relaxation, 1118
 invariance group (algebra), 81
 inverse Abel transformation, 1039
 inversion symmetry, 509
 of wave functions, 538
 inverted medium optical pumping, 1062
 Ioffe-Pritchard trap, 1166
 ion beam spectroscopy, 269
 ion crystal, 1152
 ion-atom collisions, 807
 electron spectroscopy, 1000
 electron spectrum, 1012, 1013
 multielectron, 1009
 nonperturbative processes, 1009
 perturbative processes, 1003
 photon spectroscopy, 999
 quasi-free electron, 1013
 recoil momentum spectroscopy, 1000

relativistic, 1363
state selective, 999
translational energy spectroscopy, 999

ion–atom interchange, 601

ion–dipole reactions, 586

ionic cluster, 615

ionic reactions, table of, 598

ionization, 817, 1003, 1014
adiabatic, 1366
classical, 235
scaling, 1134
cross section
Born series method, 740
distorted wave method, 740
exterior complex scaling (ECS) method, 739
pseudostate method, 738
time-dependent close-coupling method, 739
differential, 791
diffusive, 1135
double, 786, 788, 818
binary encounter approximation for, 905
electron impact, 986, 1022, 1309
empirical formula for, 1022
electron scattering theory of, 737
field, 235, 237
in heavy particle scattering, 786, 791
mechanism, 986
Monte Carlo method for, 919, 920
multiphoton (REMPI), 1022, 1023, 1127
multiple, 1130
multistep, 1128
nonperturbative, 1129
of light-target atoms, 1005
of molecular targets, 819
potential
in Hartree–Fock approximation, 318
of cluster, 611
of clusters, 616, 617
of ground state atoms (table), 183, 184
single, 786
stabilization in intense laser fields, 1133
Stark, 236
state-selective field, 236
strong-field approximations, 1136
surface, 1022
tunneling, 235, 1129

ionizing radiation, charged particles, 1003

ion–lattice coupling, 1087

ion–molecule reaction, 585, 586, 603, 1035, 1313
atmospheric, 1312
in interstellar clouds, 1280

ion–neutral reaction, 597, 601

ionosphere, electron density profile, 1320, 1321

ionospheric
density profile, 1320
regions, 1311

ion-pair formation, in Rydberg collisions, 882

ion-pair molecule, 799

ion–quadrupole interactions, 1313

IPCC, 1340

irreducible representation, 74
of $SO(2,1)$, 82

irreducible tensor operator, 35, 123, 220
algebra of, 36
examples, 37

unit tensor operators, 37
Wigner–Eckart theorem, 37

irreversible process, 121

isentropic expansion, 1020

isobaric nuclei, 1362

isoelectronic sequence, 186

isoionic sequence, 186

isolated pentagon rule, 614

isolated resonance approximation, 877

isolating integral, 245

isomer shift, 256

isomers, 613, 614, 616

isonuclear sequence, 186

isoscalar factor, 78

isotope separation, 1128

isotope shift, 256, 326, 328
residual, 257

isotope-dependent charge exchange reaction, 811

isotopic labeling, 602

isotropic harmonic oscillator, 84

J

Jackson–Schiff correction factor, in electron capture, 910

Jacobi coordinates, 559

Jacobi polynomials, 15, 892
relation to $SU(2)$ group representations, 19

Jacobian, frame transformation, 1026

Jacquinet advantage, in Fourier transform spectroscopy, 633

Jacquinet stop, 633

Jahn–Teller effect, 556

Jaynes–Cummings model, 1052, 1209, 1214

Jeans escape mechanism, 1332

Jeffrey–Born phase function, 698

Jeffreys’ connection formula, 823, 824

Jellium model, 610

jj coupling, 181
allowed J -values for, 180

Jost functions, 810

K

KAM torus, 1135

Kapitza–Dirac effect, 1182
geometry of, 1181
near-resonant, 1181

Kato cusp condition, 200
in Thomas–Fermi theory, 301

Keldysh parameter, 1130

Kepler
ellipse, perturbed, 244, 245
orbit, 920
realization of $SO(4)$, 83

kernel function, 142

Kerr lens mode locking, 1078

kinematics, 1039

Klein–Gordon equation, 85

Kleinman symmetry, 1098

Klein–Nishina formula, 970

Klots unimolecular decay theory, 589

K -matrix, 727

Kohn variational method, 733, 823

Kohn–Sham method, 303, 495

Kohn–Sham scheme, 788

Kolmogorov–Arnold–Moser (KAM) theorem, 245

- Koopman's theorem, 314, 357
 Kramers cross section, for photoionization, 868
 Kramers–Heisenberg–Waller formula, 968
 Kramers–Henneberger frame transformation, 747, 1133
 Kramers–Kronig relation, 916
 KrF, 1089
 Krieger–Li–Iafate approximation, 788
 Kroll–Watson formula, 746
 Kronecker product, 75
 reduction, 29
 krypton, one-electron, 264
- L**
- ladder operator, 82
 Lagrange interpolation, 132
 Lagrange multiplier, in Hartree–Fock theory, 313
 Lagrangian manifold, 244
 Laguerre polynomial, 160
 Lamb dip, 655, 1073
 frequency stabilization, 1073
 inverted, 1063
 stabilization, 1073
 Lamb shift, 415, 421
 Lamb–Dicke regime, 1150
 Landau critical velocity, 1168
 Landau level, 224
 relativistic, 224
 Landau–Dykhne formula, 1131
 Landau–Lifshitz cross section, 705
 Landau–Zener, 807
 Landau–Zener model, 807, 1030
 charge transfer, 996
 transition probability, 237, 860
 Landé g -value, 183, 225
 Langevin orbiting, 806, 999
 Langevin rate coefficient, 586, 854, 1313
 LAPACK software, 171
 Laplace–Runge–Lenz vector, 83, 244
 large molecule, 822
 Larmor precession, used as a clock, 1248
 laser
 alexandrite, 1087
 beam quality, 650
 bismuth-doped, 1088
 carbon dioxide, 1088
 carbon monoxide, 1089
 chemical, 1089
 coherent states, 1076
 configuration, 649
 copper vapor, 1083
 design, 651
 dye, 1089
 excimer, 1089
 excitation, 990
 field, collisions in, 744
 fixed frequency (table), 653
 fluctuations, 1127
 free electron, 1092
 frequency conversion techniques, 671
 difference-frequency mixing, 671
 stimulated anti-Stokes Raman scattering, 671
 sum-frequency mixing, 671
 third harmonic generation, 672
 gain, 650
 gain media (tables), 653
 GaN (blue), 1085, 1087
 guide stars, 1089
 helium–cadmium, 1083
 He–Ne, 1082
 hydrogen fluoride (HF), 1089
 interaction with matter, 652
 interferometry, 467
 ion, 1083
 isotope separation, 1089
 linewidth, 1074
 magnetic resonance (LMR) spectrometer, 644
 metal vapor, 1083
 mode
 Fox–Li computations, 1074
 frequencies, 1073
 Gaussian, 1075
 longitudinal, 1072, 1074
 transverse, 1074
 multimode, 1076
 Nd, YAG, 1085, 1093
 optically pumped semiconductor, 1090
 oscillator and beam parameters, 650
 oscillator geometry, 650
 output intensity, 1071
 photodetachment threshold (LPT) method, 948
 photolysis in molecular beams, 1021
 population inversion, 649
 principles of operation, 649
 pumping method, 652
 quantum cascade (QCL), 1088, 1090, 1091
 Raman, 1093
 rare-earth ion, 1083
 resonator, 651, 1074
 concentric, 1075
 hemispherical, 1075
 stable, 1074, 1076
 symmetric confocal, 1074
 unstable, 1074, 1076
 ring, 652
 ruby, 1087
 selective excitation, 265
 semiconductor, 1083, 1090
 single-mode, 1071
 solid-state, 1083
 spectroscopy
 far-infrared, 642
 ultraviolet, 667
 visible region, 649
 stability parameters, 651
 sub-picosecond, 652
 theory, semiclassical, 1071, 1073
 thin-disk, 1084, 1090
 Ti-sapphire, 1087, 1093
 type, He–Ne, 1070
 vacuum ultraviolet, 671
 without inversion, 1128
 X-ray, 1092
 Yb fiber, 1085, 1088
 laser-induced
 bound states, 1134
 charge transfer (LICT), 1042
 continuum structure, 1128
 fluorescence (LIF), 1022
 detector, 1023

- transparency, 1128
- laser-produced plasma, 670
- LASIK, 1090
- lattice matching, 1090
- lattice permutation, 75
- Lau effect, 1181
- Laue geometry, 1181
- Layzer complex, 319
- leap-frogging, 263
- least dissipation, principle of, 864
- least squares, method of, 134
- Lee-Huang-Yang formula, 891
- Legendre function, 163
- Legendre polynomial, 957
- Lennard-Jones potential, 586
 - scattering by, 702
- lens, atomic, 1180, 1181
- lepton charge, 406, 407
- level shift
 - ac Stark, 1052
 - and width, 654
 - Bloch-Siegert, 1051
 - light, 1052
 - operator, 96
 - transformation, 96
- level-crossing method, 264
- Levinson's theorem, 693
- Lie algebra, 72
 - classification of, 72
 - realization, 82
 - semisimple, 72
- Lie algebra action, 24
 - Hilbert spaces, 25
 - matrix group actions, 24
 - relation to angular momentum theory, 25
- Lie group, 73, 333
- Lieber diagram, 914
- ligand shell, 613
- light
 - pressure, 1144
 - scattering
 - Rayleigh, 1055
 - resonant, 1056
 - stimulated, 1106
 - shift, 1052
 - source
 - infrared, 630
 - ultraviolet, 668
 - velocity of, 1058
- light transients, 1128
- light-cone approximation, 834
- light-matter interaction, 744, 1047
 - quantized fields, 1047
 - semiclassical, 1047
- light-shining-through-a-wall, 464
- LIGO gravitational wave observatory, 1250
- limit theorem, for generalized oscillator strength, 983
- Lindemann mechanism, 584
- line
 - atomic spectral, 179
 - intensity, 187
 - isotope shift, 326
 - profile, Voigt function, 964
 - radiation source, 670
- line broadening, 97, 283, 927
 - adiabatic approximation, 936, 938
 - asymmetric line shapes, 286
 - bound states and other quantum effects, 289
 - bound-free and free-bound transitions, 938
 - by atom-atom collisions, 936, 938
 - by charged particles, 931
 - by electrons, 932, 935, 937
 - by field of static ions, 932
 - classical oscillator approximation, 284
 - coefficient, 287
 - collisional, 927, 1059
 - collisional narrowing, 1060
 - cross section, 930
 - Doppler, 194, 286, 1059, 1060
 - effective Gaunt factor, 932
 - empirical formulae, 931
 - impact approximation, 285, 928, 933, 934
 - and line strength s_n , 887
 - in hydrogen and hydrogenic ions, 932
 - inhomogeneous, 1060
 - interaction potentials, 284
 - ion impact, 932
 - neutral atom, 927
 - one-perturber, 936
 - overlapping lines, 927
 - perturbation theory for, 930
 - power, 1059
 - pressure, 194, 283, 927
 - unified theories of, 939
 - quadratic Stark, 930
 - quasistatic approximation, 288
 - quasistatic theory, 286
 - resonance, 194, 930
 - satellite features, 289
 - semiclassical theory, 928
 - shift and width operator for, 928
 - simple formulae, 929
 - Stark, 195, 927, 929
 - widths, hydrogen, 195
 - van der Waals, 195, 929
 - Voigt profile, 1063
 - width and shift, 935
 - matrices, 928
 - WKB approximation, 939
- line emissivities, 894
- line shape
 - Breit-Wigner, 400
 - Doppler, 284, 1059, 1070
 - Fano, 399, 964
 - Gaussian, 194, 964
 - Lorentzian, 194, 284, 650, 928, 964, 1050, 1060, 1071, 1211
 - Shore, 958
 - Voigt, 284, 964
 - profile, 1060
- line strength, 187, 324, 885
 - connection with oscillator strength, 886
 - hyperfine structure, 255
 - molecular, 538
 - semiclassical representation, 886
- line width
 - Doppler, 1070
 - homogeneous, 1070
 - inhomogeneous, 1114
 - Lorentzian, 1073
- linear algebra, computational, 143

- linear algebraic equations method, 735
 linear response, 801
 linear spectroscopy, 1058
 linear-response method, 104
 lineshape
 Doppler, 1325
 Fano, 1127
 Lorentzian, 1327
 linkage, of transition rates, 263
 linked cluster theorem, 342
 linked diagram, 102
 Liouville
 equation, 120
 operator, 219
 space, 219
 Lippmann–Schwinger equation, 106, 734
 distorted wave, 815
 lithium-like ion, dielectronic recombination, 877
 LLVM software, 170
 local density approximation (LDA), 303
 local realism
 disproof of without inequalities, 1246
 three-particle gedankenexperiment, 1246
 local thermodynamic equilibrium (LTE), 263
 local-density approximation, 1164
 locked dipole approximation, 586, 600, 709, 1313
 locking, of magnetic moment, 612
 locking-radius model, 713
 logarithmic negativity, 1198
 long-range interactions, 368
 capture theories, 585
 loopholes in Bell tests, 1242
 Lorentz
 approximation, 1099
 atom, 1049
 group, 333
 homogeneous, 83
 proper, 333
 local field, 1099
 symmetry violation, 478
 transformation, 332
 boosts, 332
 discrete, 332
 infinitesimal, 333
 rotations, 332
 transformation matrix, 831
 triplet, 225
 Lorentzian line shape, 928, 1060
 Lorentz–Lorenz corrections, 1071
 LoSurdo–Stark effect, 86
 low field seeker, 1177
 luminosity, atmosphere, 1325
 lunar laser ranging, 481
- M**
 Mach number, 1020
 Mach–Zehnder interferometer, 1182, 1201
 Mackay icosahedra, 618
 macroscopic wave function, 1160, 1164
 magic angle, 221, 985
 pseudomagic, 956
 magic number, 610, 620
 magic square, addition of angular momentum, 59
 magnetic
 dipole interaction, 1047, 1049
 motional correction, 1175
 dipole transition, 187, 188
 field
 atoms in, 223
 in neutron stars, 226
 static, 241, 242
 mirror, 1179
 moment
 electron, 437
 of clusters, 611
 multipole, 258, 1047
 trap, 1148, 1166
 white dwarf, presence of helium in, 229
 magnetometry, 463, 467, 478, 480
 magneton, 1048
 magneto-optical
 diffraction, 1182
 trap (MOT), 452, 1148, 1152
 magneto-optical traps (MOT), 882
 magnetron cooling, 1151
 magnetron motion, 1151
 Majorana transition, 1148, 1166
 Mandel Q_M factor, 1195
 Mandel’s formula, for photon counting, 1076
 Manley–Rowe relations, 1101
 many-body perturbation theory (MBPT), 99, 359, 363, 405, 474
 configuration mixing, 370
 correspondence rules, 365
 diagram, 364
 effective interelectron interaction, 372
 electron and vacancy states, 366
 electron scattering, 371
 electron–vacancy states, 373
 Hartree–Fock approximation, 367
 one-particle states, 369
 photoionization diagram, 388
 photon emission, 377
 role of the Pauli principle, 366, 370
 software, 166
 summation of sequences, 367
 many-body theory, 99, 891
 relativistic, 339
 many-electron wave function, 311
 Markov approximation, 121
 maser threshold, 1218
 Maslov index, 244, 245
 mass determination, 438
 mass polarisation, 326
 mass polarization, 200
 mass shift, 200, 256, 326
 normal, 200, 256, 326
 reduced, 257
 specific, 200, 256, 326
 mass transfer cross section, 913
 Massey parameter, 774
 Massey–Mohr cross section, 705
 master equation, 121, 1053, 1058, 1142, 1220
 recombination theory, 865
 master oscillator power amplifier (MOPA), 1092
 master theorem
 MacMahon form, 60
 Schwinger form, 60
 mathematical function, digital library of, 149
 matter waves, 481

- Maxwell equation
 - absorptive, 1117
 - dispersive, 1117
- Maxwell–Bloch equations, 1117
- McCall–Hahn area theorem, 1118
- mean speed, thermal, 873
- mean-field theory, 1160, 1163
- measurement of the wave function, 1240
- measurement, quantum theory of, 1235
- mechanical effects of radiation, 1175
- mercury cluster, 611
- merged beam method, 876, 998
- mesopause, 1338
- mesosphere, 1338
 - terrestrial, 1300
- metal cluster, 610
 - molecule, 612
- metal–fullerene cluster, 615
- metal–insulator–metal (MIM) diode, 642
- metallocarbohedrenes, 612
- metallofullerenes, 614
- metastable atom, 325
 - electron scattering by, 990
 - in atomic beams, 983, 986, 990, 1021, 1180
 - in comets, 1294
 - in planetary atmospheres, 1323
- method of perturbed stationary states (PSS), 809
- Metropolis algorithm, 146
- Michelson interferometer
 - (diagram), 630
 - distribution of modulation frequencies, 632
- microcanonical ensemble, 921
- microchannel plate, 675
- micromaser, 1217
 - quantum nondemolition experiment, 1238
- microwave cavities, 1217
- Milky Way galaxy, age, 1362
- Milne detailed balance, 872
- minimax method for autoionizing states, 321
- Minkowski space, 332
- mirror images, radiating atoms and, 1210
- mirror, atomic, 1179
- mixed states, 119
- mobility
 - coefficient, 853
 - of ions in a gas, 692
- mode locking, 1077
- mode pulling, 1073
- model potentials
 - scattering results for, 707
 - table of, 707
- mode-locked pulses, 1087
- modulation
 - cross-phase, 1104
 - self-phase, 1104
- MOLCAS software, 167
- molecular and heavy-particle scattering software, 168
- molecular beam, 984, 1019, 1020
 - angular momentum polarization studies, 1021
 - beam splitters, 1181
 - reagent preparation, 1020
 - sources, 1020
- molecular clock, 1030
- molecular cloud
 - carbon chemistry of, 1279
 - dark, 1280
 - diffuse, 1278
- molecular cluster, 620
- molecular double-slit, 819
- molecular dynamics, 507, 557
- molecular formation, resonant, 1364
- molecular fragmentation, 557, 850, 1022, 1134
 - fragmentation pattern, 1022
- molecular imaging, 1132
- molecular ion, 476
- molecular orbital close-coupling (MOCC), 808
- molecular orbital X-rays, 1014
- molecular spectra, 507
 - measurement of, 641
- molecular structure, 487
 - approximation methods, 487
 - fitting experimental energies, 541
 - nuclear motion, 499
 - rotation, 487
 - rotational–vibrational, 500
 - software, 167
 - vibration, 487
 - wave function, 101, 488, 538
 - weakly interacting systems, 495, 500
- molecular symmetry, 507, 538
- molecule, compound, 1368
- molecules in intense laser fields, 1133
- MOLPRO software, 167
- Møller operator (matrix), 817
- Møller–Plesset perturbation theory, 100, 492
- momentum space
 - ejected-electron distribution, 791
 - wave function, 791
 - quantum defect representation, 889
 - wave packet, 793
- momentum transfer
 - collision frequency, 1322
 - cross section, 728, 982, 985, 1305
 - in collision, 832
 - vector, 791
- momentum–vector field, 244, 246
- Monte Carlo integration, 146
 - relation to random number distributions, 146
- Monte Carlo method, 144
 - classical trajectory, 919
 - exotic projectiles, 923
 - heavy-particle dynamics, 923
 - hydrogenic targets, 919, 921
 - many-electron targets, 920
 - multiply charged projectiles, 920
 - nonhydrogenic one-electron models, 920
 - pseudo-one-electron targets, 921
 - state-selective electron capture, 922
 - for line broadening, 939
- Morse potential, scattering by, 710
- MOT, 882, 1148, 1152
- motional correction, magnetic dipole interaction, 1175
- Mott insulator, 1169
- Mott scattering, 989
- MR CC
 - state selective, 104
 - state universal, 104
 - valence universal, 104
- multibeam resonance, 1182
- multichannel quantum defect theory, multiphoton processes, 1127

- multiconfiguration (Dirac) Hartree–Fock approximation, 319
 - multiconfiguration Dirac–Fock software, 166
 - multiconfiguration Hartree–Fock approximation, 318, 320
 - Breit–Pauli interaction, 321
 - multiconfiguration Hartree–Fock software, 166
 - multiconfigurational self-consistent field theory, 493
 - multielectron transitions, 1010
 - multilayer coating, 677
 - multiphonon quenching, 1086
 - multiphoton process, 654, 1119, 1125
 - multi-electron effects, 1127
 - rate enhancement, 1128
 - strong-field, 1129
 - weak field, 1126
 - multiple lasers, excitation by, 1128
 - multiple path occupation, 514
 - multiplet, 179
 - multiplex advantage, in Fourier transform spectroscopy, 631
 - multiplexed detection, 267, 631
 - multiplicity, 178, 179
 - multipole
 - effects, 965
 - expansion, 1047
 - moment, 217
 - multireference (MR), 320
 - CC theory, 104
 - configuration interaction theory, 494
 - muon, 1363
 - atomic capture, 1365
 - lifetime, 1363
 - muon-catalyzed fusion, 1363
 - cycle, 1365
 - experimental methods, 1371
 - muon loss, 1370
 - reactions and energy release, 1364
 - muonic atom
 - cascade, 1367
 - elastic scattering, 1367
 - formation, 1365
 - helium, 1370
 - hydrogen, 1365
 - hyperfine transitions, 1368
 - isotopic transfer, 1367
 - sticking, 1370
 - stripping, 1371
 - muonic molecule
 - Auger formation, 1368
 - energy corrections, 1368
 - nuclear fusion rate, 1370
 - resonant formation, 1368
 - rovibrational energy levels, 1364
 - scaling, 1364
 - three-body formation, 1369
 - mutual neutralization, 597, 598, 605, 846, 860
 - cross section, 861
 - Landau–Zener probability, 860
 - rate coefficient, 861
- N**
- NAG software, 171
 - nanocapsules, 615
 - nanocrystal, 1084
 - nanoengineering, 1138
 - natural
 - coordinate system, 123
 - frame, 714
 - orbital expansion, 321
 - unit, 5
 - width, 964
 - N-body recombination, 848
 - formula, 857
 - Nd, YAG laser, 1085
 - Nd³⁺, 1085
 - near-edge X-ray absorption fine structure (NEXAFS), 1355
 - nearest-neighbor statistics, 246
 - near-fields, 1138
 - negative ion, 372, 600, 943
 - asymmetry parameters, 944
 - auto-detachment, 944
 - autodetachment from, 325, 395
 - cluster, 621
 - collinear beam arrangement, 947
 - Doppler broadening, 947
 - electron affinity, 944
 - electron correlation, 944
 - harpoon mechanism, 1030
 - ion storage ring measurement, 949
 - multiple excitations, 944
 - optical parametric oscillators, 948
 - photodetachment from, 390, 998
 - photoelectron angular distributions, 944
 - synchrotron radiation, 948
 - neutral–molecule reactions, 585
 - neutral–neutral reactions, 586
 - neutrino mass, 1362
 - neutron
 - diffraction, 1180
 - EDM, 476
 - optics, 1174
 - skin, 472
 - stars, magnetic fields, 226
 - ultracold, 1179
 - Neville’s algorithm, 132
 - Newton diagram, 1025
 - NH₃⁺ + H₂ → NH₄⁺ + H, 591
 - nightglow, 1325
 - spectrum of Venus, 1328
 - nightside ionospheres, 1317
 - noble gas
 - cluster, 618
 - compounds with diatoms, 500
 - electron scattering by, 371
 - harmonic generation in, 1131
 - photoionization, 388, 965
 - scattering lengths for, 694
 - noble metal cluster, 610
 - no-exchange R-matrix software, 166
 - non-Abelian gauge potentials, 809
 - nonadiabatic
 - coupling, 774, 775
 - coupling matrix, 809
 - scattering theory, 744
 - transition, 556, 1176
 - relativistically induced, 497
 - nonclassicality, 1194, 1195
 - noncrossing rule, 490, 775, 860
 - nonfine structure, Hamiltonian, 310
 - noniterative integral equation method (NIEM) software, 166
 - nonlinear

- atom optics, 1177
- optics, 655, 1097
 - enabled by ultraintense laser pulses, 1108
 - enabled by ultrashort laser pulses, 1108
 - focused beam effects, 1104
 - wave equation, 1099
- plasmonics, 1109
- polarization, 1098
- refractive index, 1098
 - coefficient, 1098
 - in an atomic vapor, 1105
 - intensity-dependent, 1098
 - mechanisms, 1099
- Schrödinger equation, pulse propagation, 1101
- Schrödinger equation, 1161
- susceptibility, 655, 1098
 - quantum mechanical expression, 1099
 - relation to hyperpolarizability, 1099
 - tensor properties, 1098
- nonlocality, 1260
- nonlocality, in quantum measurement, 1240
- nonradiative electron capture in high-energy collisions, 836
- nonradiative relaxation, 1084, 1088
- nonreactive scattering, 575
- nonrelativistic limit, 832
- nonrelativistic orbital, 311
- NOON state, 1201
- normal congruence, 244
- normal ordering operator, 99
- normal product of operators, 99
- normal product with contractions, 99
- normalization
 - incoming wave, 385
 - of continuum wave functions, 870
 - of continuum wavefunctions, 691
- normally ordered, 1192
 - antinormally ordered, 1193
- novae, 1276
- nuclear charge distribution, 345
- nuclear electric quadrupole moment, 258, 327
- nuclear magnetic dipole moment, 255, 258, 327
- nuclear mass, 250
- nuclear motion
 - in molecular scattering, 742
 - in molecules, 499
- nuclear reaction
 - astrophysical factor, 1363, 1370
 - Coulomb barrier, 1362
 - cross sections, 1362
 - electronic screening of, 1363
- nuclear size effect, 326
 - for hydrogenic atoms (table), 226
 - in atoms, 1360
 - quantum electrodynamic, 1362
 - relativistic, 1361
- nuclear spin and statistics in molecules, 543
- nuclei, isobaric, 1362
- nucleobases, 822
- number operator, 1158
- numerical
 - differentiation, 136
 - integration, 143
 - method, 315
 - solution on a lattice, 834
- Numerov method, 137, 232
- NumPy, 168
- Nyquist frequency, 135
- O**
- O symmetry
 - character table, 516
 - correlations with C_n , 517
- O(4) symmetry, of hydrogen, 152
- O(1D) + H₂ scattering, 1031
- O(1D) preparation, 1021
- O(n) representation theory, 87
- O⁵⁺ dielectronic recombination, 877
- Ochkur approximation, 737
- octahedral rotor, semirigid, 515
- octahedral symmetry, molecular, 514
- OH level inversion, 1295
- one-and-a-half centered expansion, 790
- one-particle density operator, 1164
- one-particle operator, 1158
- onions, 615
- Oort cloud, 1289
- opacity project, 1281
- open shell, 397
- operator
 - annihilation/creation, 72, 88, 111, 114, 336
 - commutation relations, 336
 - conjugation, 114
 - non-commuting, 336
 - normal ordering, 336
 - ordering, normal, 99, 336
 - quasiparticle, 116
 - representation of, 112
 - time evolution, 120
- OPO, 1093
- Oppenheimer–Brinkman–Kramers (OBK) approximation, 815, 909, 1008
- optical
 - Bloch equations, 1053, 1114
 - with decay, 1054
 - cavities, strong cavities, 1217
 - depth, 1307
 - Earnshaw theorem, 1148
 - emission cross section, 985
 - excitation, 233
 - fiber
 - double-clad, 1084
 - hollow core, 1084
 - large-mode-area (LMA), 1084
 - photonic crystal, 1085
 - single-crystal, 1085
 - force, 1143
 - frequency comb, 656
 - lattice, 1146, 1168
 - parameters, 1169
 - material, 676
 - coating, 677
 - interference filter, 677
 - multichannel plate, 676
 - multilayer coating, 677
 - polarizer, 677
 - thin film, 676
 - window, 676
 - molasses, 1145, 1147
 - $\sigma^+ - \sigma^-$, 1147, 1148

- corkscrew, 1147
 - nutaton, 1114
 - parametric fluorescence, 1093
 - parametric oscillation (OPO), 1092
 - parametric oscillator, 655, 1102
 - potential, 396, 695, 730, 736
 - second order, 736
 - pumping, 217, 220
 - in molecular beams, 1021
 - theorem, 692
 - in quantal impulse approximation, 899
 - trap, 1146, 1166
 - optics
 - near-field, 1180
 - normal congruence, 244
 - orbital collapse, 317
 - orbitally forbidden transitions, 551
 - orbiting
 - and spiraling collisions, 698
 - Astronomical observatory, 1290
 - collision model, 1035
 - orbit–orbit interaction, 311
 - order parameter, 1164
 - orientation, 218, 713
 - atomic, 987
 - density matrix formalism, 124
 - from spin-orbit interaction, 125
 - in molecular beams, 1021
 - Ornstein–Uhlenbeck process, 1127
 - oscillator strength, 187, 188, 262, 324, 1054, 1059
 - absorption, 187, 930
 - bound–free, 871
 - connection with line strength, 886
 - definition, 213
 - finite nuclear mass effects, 213
 - generalized, 886, 983
 - helium (table), 214
 - length and velocity forms, 213
 - measurement of, 262, 263
 - molecular, 545
 - sum rule, 545
 - sum rules, 205
 - time-resolved measurement, 265
 - Ostwald’s step rule, 621
 - output coupling, 1072
 - over the barrier model, 806
 - overtone bands, 547
 - oxygen
 - green, spectrum of Venus, 1333
 - quenching reactions, 502
 - ozone depletion, 1337, 1344
 - ozone layer, 1338
- P**
- Padé approximation, 133
 - pair correlation, 323
 - pair production
 - electron–positron, 1363
 - photon–atom scattering, 970
 - Paldus tableau, 90
 - Pandas, 168
 - papier mâché, 615
 - parabolic coordinates, 150, 227
 - parabolic quantum number, 234
 - paramagnetic cluster, 612
 - paramagnetic system, 475
 - parametric
 - amplification, 1102
 - oscillation, 1102
 - process, 1101
 - parametric downconversion, 1197, 1199
 - paraxial approximation in de Broglie optics, 1178
 - paraxial wave equation, 1074
 - parent term, atomic structure, 180
 - parity, 178, 577
 - combined with rotations, 509
 - molecular structure and selection rules, 542
 - selection rule, 955
 - parity nonconservation, 463, 472
 - parity transformation, 471
 - partial
 - cross section, 962
 - wave expansion, 690, 726
 - wave phase shift, 809
 - particle–hole interaction
 - in photoionization, 388
 - interchannel interactions, 389
 - intrachannel interactions, 388
 - virtual double excitations, 389
 - partition correlation function interaction, 323
 - partition sum, 121
 - Paschen–Back effect, 225
 - relativistic, 225
 - Paul trap, 1149
 - electrode configuration and voltages, 1151
 - Pauli
 - correlations (blocking), 788
 - exclusion principle, 841
 - matrices, 10, 88
 - principle, 513
 - pseudo-spin operator, 1051
 - Pauli-induced rotational blockade, 801
 - peaking approximation in quantal impulse approximation, 899
 - Pearson-7 function, 964
 - Pendellösung oscillations, 1182
 - pendular states, 1021
 - Penning ionization, 882
 - Penning trap, 1150
 - Peres-Horodecki criterion, 1198
 - perfect scattering experiment, 128, 713, 715
 - periodic orbit, 561
 - periodically poled lithium niobate, 1093
 - Perl, 168, 171
 - XS extension, 171
 - permutation symmetry
 - full, 1098
 - intrinsic, 1098
 - of wave functions, 538
 - persistent current, 1167
 - perturbation theory, 95, 363
 - central field, 85
 - continuum distorted wave, third-order, 815
 - diagrammatic, 100, 363
 - Epstein–Nesbet, 100
 - expansion, 96, 98, 102
 - for state multipoles, 125
 - large-order, 85
 - many-body, 99, 363
 - matrix, 95

- Møller–Plesset, 100
- multiphoton processes, 1126
- open-shell case, 341
- principal term, 98
- Rayleigh–Schrödinger, 98, 340
- renormalization term, 98
- time-independent, 95
- Z-dependent, 318
- Peterkop semiclassical theory, 822
- Peterkop theorem, 738
- Petermann *K* factor, 1074
- Pfaffians, skew symmetric matrices, 61
- P*-function, 1193
 - P*-representation, 1192
- phase
 - diffusion, 1074
 - model, 1127
 - matching, 655, 1093, 1131
 - of nonlinear optical processes, 1100
 - shift, 691, 728, 1183
 - binary encounter approximation, 903
 - Born S-wave, 694
 - dispersive, 1183
 - effective range expansion, 693, 728
 - eigenphase sum, 730
 - geometric, 1183
 - near resonances, 730
 - quantum defect equation, 728
 - topological, 1183
 - space, 244, 245
 - space averaging method, 1136
 - space theory
 - of gas phase reactions, 587
 - topological, 1170
 - velocity, 1178
- phonon sideband, 1087
- photoabsorption
 - 4d¹⁰ subshell threshold, 375
 - by ionic clusters, 616
- photoassociation, 1153
- photochemical escape processes, atmospheric, 1333
- photodetachment, 944
 - anomalous threshold behavior, 950
 - dipole polarizability, 950
 - double electron, 825
 - from H⁻, He⁻, and K⁻, 825
 - H⁻, 951
 - metastable states, 946
 - mirroring of resonance profiles in alternative partial cross sections, 391
 - multi-electron detachment, 947
 - multiphoton detachment, 946
 - of H⁻, Li⁻, and Na⁻, 391
 - of the *K*-shell of He⁻ and Li⁻, 391
 - photodetachment cross section, 944
 - resonance structure, 946
 - threshold behavior, 945
 - Wigner law, 945
- photodissociation, 1309
 - absorption cross section, 557
 - anisotropy parameter, 557
 - branching ratios, 557
 - direct, 555
 - experimental techniques, 558
 - in comets, 1295
 - indirect, 555
 - interstellar, 1278
 - molecular, 555
 - partial cross section, 557
 - predissociation
 - electronic, 556
 - rotational, 555
 - vibrational, 555
 - quantum yields, 557
 - rates of, 1279
 - selection rules, 556
 - state-resolved, 1026
- photodissociative ionization, 1309
- photoelectric effect, 955
 - angular distribution, 956
 - dipole approximation, 955
 - experimental methods, 960
 - open-shell atom, 957
 - spin analysis, 956, 957
- photoelectron
 - angular distribution, 958
 - energy analysis, 960
 - spectrometry, 961
 - spectroscopy
 - operational modes, 963
 - spectrum, 956
 - spectrum, 964
 - correlation satellites, 959
- photoionization, 383, 819, 969, 971, 1022, 1023, 1276, 1309, 1338
 - 5s² electrons, 375
 - angular distribution, 956
 - anisotropy parameter, 957
 - asymmetry parameter, 391
 - anisotropy parameter, 956
 - configuration interaction effects, 959
 - Cooper minimum, 387
 - cross section, 386, 390
 - delayed maximum, 387
 - diagrammatic perturbation theory, 364
 - double photoionization of He, 391
 - electron correlation effects, 958
 - field-induced oscillatory structure, 236
 - high photon energy behavior of the partial cross sections, 387, 388
 - in comets, 1295
 - interaction Hamiltonian, 383
 - mirroring of resonance profiles in alternative partial cross sections, 391
 - multiple excitation, 377
 - multiple ionization processes, 960
 - nondipole effects, 391
 - of positive ions, 391
 - of Rydberg atoms, 236, 237
 - particle–hole interaction effects, 388
 - polarization effects, 390
 - post collision interactions, 960
 - random phase approximation for, 374
 - rates of, 1279
 - relativistic and spin-dependent effects, 390, 964
 - relaxation effects, 390
 - resonances, 389, 958
 - theoretical methods for, 374, 390
 - threshold laws, 960
 - wave function boundary conditions, 385
- photoionized gas, processes in, 1276
- photolithography, 1090

- photomultiplier tube, 675
- photon
 - bandpass, 964
 - bunching, 1076
 - correlations, 1232
 - counting, Mandel's formula, 1076
 - density of states, 213
 - echo, 1117
 - indivisibility, 1232
 - number
 - average, 1218
 - intracavity, 1217
 - variance normalized, 1219
 - occupation number, 234
 - recoil effects, 1142
 - scattering, hydrogen, 968
 - sources, single, 1227
 - statistics, 1076
 - Bose–Einstein distribution, 1076
 - Poisson distribution, 1076
- photon–atom scattering, 967
 - applications, 971
 - elastic, 967, 969
 - experimental, 971
 - relativistic, 970
 - inelastic, 967
 - interaction Hamiltonian, 967
- photonic bandgap, 1085, 1213
 - superluminal tunneling, 1248
- photonic crystal fiber, 1085
- photons, 1268
- photorefractive effect, 1108
- physisorption, 612, 1357
- Planck's law, 1191
- plane wave Born approximation (PWBA), 1004
- planetary atmosphere, 598
- planetary nebulae, 1276
- planets, exobase properties (table), 1333
- plasma
 - diagnostics, 922
 - frequency, 1050, 1109
- plasmonics, 1138
- plasmonics-enhanced fields, 1138
- plethysm, 75
- Pluvinage wave function, 818
- Pockels effect, 1108
- Poincaré
 - sphere, 716
 - transformation, 333
- Poisson distribution, 1060, 1076
- Poisson sum formula, 702
- Poissonian, 1191
 - super-Poissonian, 1195
- polar stratospheric cloud, 1344
- polarizability, 104, 806, 1146
 - complex, 1049
 - frequency dependent, 369, 968
 - hydrogenic, 211, 228
 - relativistic, for hydrogen, 228
 - static, 1146
- polarization, 218, 985
 - correlation, 988
 - effect, 990
 - ellipse, 714
 - nonlinear rotation, 1106
 - in heavy atom scattering, 719
 - in optical transitions, 264
 - interaction, 999
 - optical, 121, 127, 715
 - particle scattering phenomena, 122, 713
 - photon, 336
 - potential, 693, 727, 728, 795
 - redistribution, 289
 - relaxation, 217
 - spectroscopy, 1064
 - spin, 121, 126
- polarized
 - atom, 218
 - beams, collisions involving, 121, 718, 989
 - electron, 989
 - light, 1049
 - and atomic multipoles, 220
 - production of, 669, 677
 - orbital, software, 166
 - target, 989
- polarizer, 677
- polyatomic molecule, electron scattering by, 744
- polynomial quadrature, 135
- POLYRATE software, 168
- ponderomotive energy, 1129, 1146, 1149
- population
 - inversion, 1062, 1069, 1082
 - representation, 218
 - trapping, 1127
- positron pair production, 1363
- positron production, 1015
- positron scattering, 761, 923
 - annihilation, 762
 - angular correlation, 762
 - atomic hydrogen, 765
 - resonances, 765
 - atoms, 766
 - Born approximation, 763
 - close-coupling approximation, 764
 - convergent close-coupling method, 764
 - eikonal-Born series, 764
 - ionization, 764, 818
 - Wannier threshold law, 764
 - noble gases, 765
 - Ramsauer minimum, 765
 - optical potentials, 764
 - Ore gap, 762
 - positronium formation, 762
 - potential scattering, 763
 - variational method, 764
 - Wigner cusp, 764
- positronium, 762
 - Thomas peak, 916
- post and prior forms of the transition amplitude, 836
- post collision interaction, photoionization, 960
- postion sensitive detector (PSD), 267
- post–prior discrepancy, 837
- potential
 - complex absorbing, 791
 - correlation, 788
 - exchange, 788
 - soft-core, 791
 - time-dependent Kohn–Sham, 788
- potential energy curve (PEC), 774, 776
- potential energy surface (PES), 487, 540, 555, 774, 776, 1029

- analytic derivative technique, 491
- intersection of, 490
- perturbations of, 495
- potential scattering, 1028
 - hard-core, 694
 - laser field effects, 744
 - modified Coulomb, 693
 - polarization potential, 693
 - van der Waals, 693
- Pound–Drever–Hall stabilization, 1074
- power broadening, 1055, 1059
- PPLN, 1093
- PQS software, 167
- Pr3+, 1085
- precision measurement, 471
- predissociation, 555
- pressure broadening, 283
- product
 - growth method, 997
 - imaging, 1019, 1026
 - detection, 1026
 - kinetic energy distribution, 1026
 - quantum-state distribution, 1026
- projectile continuum distorted wave approximation (PCDW), 815
- projectile-electron loss, 830, 834
- projection operator, 95, 96, 730, 736
 - formalism, 396
 - hole, 398
 - quasi projectors, 398
- propagator, 410, 686
 - electron, 338
 - one-body, 406
 - photon, 338
 - two-body, 409
 - two-point, 412
- propensity rules, 713
- properties of HF solutions, 317
- proton
 - EDM, 476
 - size, 1360
 - transfer, 601
- proton–helium scattering, 915
- pseudo crossing, 775
- pseudo state, 790, 791
 - interpretation problem, 793
 - two-electron, 792
- pseudomomentum, 250
- pseudopotential, 302, 796, 1160
 - method, 400, 402
 - results, 403
- pseudostate expansion, 735
- pulse area theorem, 1115
- pulse compression, 1077
- pulse propagation, resonant, 1117
- pump mechanism, 1069, 1070
- pump-probe experiment, 1132
- pump-probe resonance, 1120
- pump-probe scheme, 568
- Purcell effect, 1112
- P-wave electron–atom scattering, 798
- P-wave shape resonance, 799
- PyPI software, 168
- PySCF software, 167
- Python, 168, 171
 - Cython, 171
- Q**
 - Q switching, 1076, 1077
 - Q -function, 1193
 - Q -representation, 1193
 - quadrature, 1192
 - operator, 1103
 - quadrature operator, 1192
 - quadrature- X space, 1194
 - quadrupole
 - interaction, electric, 1048
 - moment, 104
 - potential, 597
 - tensor, 1048
 - quantization
 - of action variables, 244, 245
 - of circulation, 1167
 - quantum
 - beats, 125, 267
 - time integration of, 125
 - cascade laser, 1088, 1091
 - chaos, 241, 246, 247, 1134
 - control, 571
 - defect, 185, 210, 233, 235, 237, 242, 318, 922, 1085
 - analytic continuation, 728
 - definition of, 210
 - in momentum space wave functions, 889
 - multichannel, 746
 - parameters, 318
 - relativistic and finite mass corrections to, 210
 - Rydberg series, 317
 - semiclassical representation, 885
 - theory, 231
 - use in radial integrals, 885
 - defect theory, 751
 - degenerate gas, 1157
 - electrodynamics, 309, 415, 1362
 - equations of motion, 335
 - helium-like ions, 205
 - perturbation theory, 336
 - eraser, 1236, 1237
 - field theory, 405, 1158
 - fluid, 620
 - gas microscope, 1170
 - Hall effect, 1171
 - jumps, 1153
 - liquid, 618
 - localization, 1135
 - network, 1228
 - nondemolition experiment, 1226, 1238
 - gravitational radiation detection, 1250
 - number, 178, 414
 - molecular, 540
 - principal, 244
 - optics, 1047
 - phase transition, 1169
 - propagator, 686
 - quench, 1170
 - reactive scattering software, 168
 - scars, 1135
 - state selection, 1037
 - theory of measurement, 1225
 - nonlocality of, 1235
 - transition amplitude, 830, 831
 - transport in molecular gases, software, 168
 - well, 1091

- well laser, 1090
 - Zeno effect, 1238
 - quantum key distribution, 1262
 - quantum teleportation, 1262
 - quantum-classical correspondence, 242
 - quantumness, 1189
 - quartz oscillator, 480
 - quasi-elastic collisions, ℓ - and J -mixing, 882
 - quasi-electron, 371
 - quasi-free electron model of Rydberg atom collisions, 892
 - quasiparticle, 116
 - quasi-phase-matching, 1093
 - quasi-projection operator, 398
 - quasispin, 76
 - boson, 113
 - conjugation, 114
 - dependence on electron number, 114
 - fermion, 113
 - half-filled shell, 115
 - spin-quasispin interchange, 115
 - triple tensor, 114
 - quasi-steady state, 850
 - qubit, 1112
 - qubits, 1260
 - quench, 1170
- R**
- Rabi frequency, 1051, 1058, 1070, 1114, 1176
 - generalized, 1051, 1115
 - power dependent, 654
 - two-photon, 1120
 - vacuum, 1052
 - Rabi oscillations, 1114, 1215, 1216
 - damped, 1115
 - Racah
 - coefficients
 - fundamental identities, 41
 - orthogonality, 40
 - recurrence relations, 43
 - relation to hypergeometric series, 43
 - relation to Wigner–Clebsch–Gordan coefficients, 40
 - Schwinger–Bargmann generating function, 41
 - symmetries, 42
 - coefficients, definition, 40
 - commutation relations, 112
 - invariant operator, 39
 - lemma, 78
 - operators, Biedenharn–Elliott identity, 46
 - reciprocity relation, 78
 - radial coupling, 777
 - radial Dirac equation
 - free electron
 - progressive waves, 348
 - standing waves, 348
 - radial Dirac equation for bound states
 - finite difference methods
 - deferred correction, 355
 - marching, 355
 - radial integral
 - asymptotic expressions, 892
 - Gordon’s formula, 885
 - hydrogenic, for dipole transitions, 883
 - in terms of Jacobi polynomials, 892
 - semiclassical quantum defect representation, 885
 - radial wave function for H and Na, 232
 - radiating atom
 - and mirror images, 1210
 - in resonators, 1211
 - in waveguides, 1210
 - radiation reaction, 1049
 - radiation theory, semiclassical, 1071
 - radiation trapping, 290, 985, 1059
 - multiple component lines, 292
 - radiative association, 584, 591, 603, 805, 1279
 - thermal model, 592
 - modified, 593
 - radiative charge transfer, 805
 - radiative damping, Lorentz atom, 1049
 - radiative electron capture, 1014
 - in high-energy collisions, 839
 - radiative force, 1212
 - radiative lifetime, 189, 233, 264
 - cavity effects, 234, 1208
 - finite temperature effects, 234
 - measurement of, 265
 - np^2P_J states, 265
 - radiative line strength, 187
 - radiative recombination, 598, 840, 846, 866, 1276, 1314
 - collisional, 849, 850
 - cross sections for, 867, 869, 871
 - electron energy loss rate, 866, 868
 - Gaunt factor, 872
 - normalization of continuum wave function, 870
 - photon emission probability, 869
 - radiated power, 866, 868
 - rate, 866, 871
 - scaling laws, 873
 - three-body collisional, 846
 - radiative self-interference force, 1212
 - radiative shift, 1212
 - radiative stabilization, 396, 591, 600, 996
 - radiative transition, 187, 213, 360
 - molecular, 541
 - moment matrix, 541
 - rate, 187, 188
 - hydrogen (table), 194
 - hydrogenic matrix elements, 882
 - selection rules, 187
 - theory, 213
 - radio frequency heating, 1152
 - rainbow angle, 243, 704, 1028
 - Raman process, 1065
 - Raman scattering, 655, 973, 1093
 - stimulated, 656, 1106
 - anti-Stokes field, 1106
 - Stokes field, 1106
 - stimulated, Stokes amplification in, 1101
 - Raman–Nath approximation, 1178
 - Rampsberger–Rice–Karplus–Marcus (RRKM) theory, 562, 590
 - Ramsauer–Townsend effect, 694
 - random number generation, 145
 - Metropolis algorithm, 146
 - nonuniform, 145
 - rejection method, 145
 - transformation method, 145
 - random phase approximation, 369, 405
 - rare-earth ion laser, 1083
 - rate coefficient, 576, 598, 599
 - rate equation, 121

- approximation, 1054, 1060, 1062, 1070, 1071
 - chemical, 599
- rate law, 583
- Rayleigh (unit), 1331
- Rayleigh scattering, 970, 1055
- Rayleigh–Ritz variational principle, 140, 200
- r*-centroid, 547
- reactance matrix, 576
- reaction, 1019
 - association, 591
 - barrier, 585
 - bimolecular, 585
 - competition with association, 593
 - complex, 584
 - coordinate, 585
 - energetics, 598
 - ion–molecule, 585
 - ion–neutral, 597
 - neutral–molecule, 585
 - path, 501
 - curvature, 502
 - spontaneity, 599
 - termolecular, 584
 - unimolecular, 584
- reactive scattering, 696, 1019, 1029
- reactive sphere model, for recombination processes, 851
- rebound reaction, 1030
- recoil
 - ion momentum spectroscopy (RIMS), 923, 1008
 - peak, 1005
- recombination, 604
 - computer codes, 850
 - destruction rates, 849
 - dielectronic, 875
 - differential cross section, 857
 - distributions used in, 862
 - Efimov effect, 855
 - electron–ion, 875
 - vibrational populations in, 605
 - four-body experiment, 848
 - high gas density theory, 864
 - diffusional-drift, 853
 - high-order harmonic generation, 846
 - ion–ion, 605
 - Langevin rate, 854
 - LTE equations, 847
 - microscopic methods, 862
 - bottleneck method, 864
 - diffusion theory, 864
 - master equations, 865
 - time-dependent, 862
 - time-independent, 863
 - trapping radius method, 864
 - N-body, 848
 - formula, 857
 - neutral–neutral reactions, 847
 - NLTE equations, 847
 - nonequilibrium theory, 864
 - production rates, 849
 - radiative, 875
 - rate, 854
 - deep dimers, 855
 - shallow dimers, 855
 - theory
 - hyperspherical methods, 856
 - macroscopic methods, 850
 - zero-range methods, 855
 - Thomson theory of, 854
 - three-body, 846, 875
 - tidal, 846
 - variational principle for, 864
 - working formulae, 850, 853
- recoupling theory
 - and $3n-j$ coefficients
 - composite systems, 51
 - commutation and association of symbols, 55
 - construction of transformation coefficients, 54
 - unsolved problems, 55
- recurrence
 - amplitude, 247
 - relations, $d_{m'm}^j(\beta)$ functions, 21
 - spectroscopy, 247–249
 - strength, 247
- red giant, 1281
- reduced mass, electronic, for light nuclei, 207
- reflection
 - critical angle, 1179
 - law of, 1178
 - principle, 561
 - symmetry, 714
 - conservation of in scattering, 717
 - total, 1179
 - total mirror, 1179
- reflectivity, coefficient of, 1179
- refraction, 248
 - law of, 1178
- refractive index, 1070, 1073, 1076
 - nonlinear, 1078
- Regge generating function, 32
- regions of nonadiabatic coupling (NAR), 774
- relative flow technique, 984, 985
- relativistic atomic structure, electron correlation, 359
 - biorthogonal orbital sets, 359
 - configuration interaction, 359
 - correlation orbitals, 359
 - multi-configuration Dirac–Hartree–Fock model, 359
 - QED and other corrections, 359
 - radiative transitions, 360
 - gauge dependence, 360
- relativistic binding energy, 226
- relativistic correction, 454
 - asymptotic expansions for, 212
 - Darwin term, 729
 - for helium, 205
 - hydrogenic atoms in strong fields, 227
 - mass-correction term, 729
 - spin–orbit potential, 729
- relativistic effect
 - magnetic field, 224
 - Thomas–Fermi theory for, 304
- relativistic effective Hamiltonian
 - Breit–Pauli, 340
 - Dirac–Coulomb, 340
 - Dirac–Coulomb–Breit, 340
 - nonrelativistic limit, 340
- relativistic Hamiltonian, 309
- relativistic orbital, 312
- relativistic recoil, Hamiltonian for, 207
- relaxation, 1053, 1112
 - density matrix formalism, 121

- effective Hamiltonian, 1053
- homogeneous, 1114
- inhomogeneous, 1116
- intrinsic, 1118
- observed levels, 1053
- operator, 1053
- unobserved levels, 1053
- relaxation rate
 - longitudinal, 1054, 1058
 - transverse, 1054, 1058
- Renner–Teller effect, 499, 556
- renormalization, 337
- representation theory
 - bosonic, 88
 - fermionic, 88
 - universal enveloping algebra, 90
- resolution
 - in Fourier transform spectroscopy, 633
 - in photon experiments, 963
- resolvent operator, 97, 341
- resonance
 - Auger, 959
 - autoionizing, 396, 958
 - Bragg, 1182
 - Breit–Wigner parameters, 400
 - double, 1128
 - Feshbach, 579
 - fluorescence, 264
 - giant, 374, 611
 - in electron scattering, 984
 - intensity-induced, 1129
 - isolated, 876
 - laser, 1051, 1058, 1105, 1113, 1127, 1145
 - electric/magnetic, 644
 - line broadening, 194, 929
 - mirroring of resonance profiles, 391
 - overlapping, 878
 - photoionization, 390, 958
 - pump-probe, 1120
 - quasi-Landau, 237
 - scattering, 396, 729, 1325
 - on surfaces, 1351
 - shape, 579
 - shape parameter, 398
 - strong field mixing, 236
 - theory, 396, 742
 - multichannel, 729
 - Thomas peak, 916
 - two-beam, 1182
 - two-photon (diagram), 1119
 - width and shift, 398, 730, 1212
- resonant
 - capture-stabilization model, 850
 - charge transfer, 805
 - enhanced multiphoton photoionization (REMPI), 1023
 - inelastic x-ray scattering (RIXS), 973
 - photoionization detector, 1022, 1023
 - pulse propagation, 1117
 - Raman effect, 964
 - transfer, 1014
- resonant-enhanced multiphoton photoionization (REMPI), 1022, 1127
- resonant-mass detector, 1250
- resonators, radiating atoms in, 1211
- rigid rotor, 28, 508
 - asymmetric, 509
 - symmetry analysis, 513
 - eigenvalue graph, 511
 - symmetric, 27
 - representation function, 27
- ring-down spectroscopy, 659
 - acousto-optic modulator (AOM), 659
 - analytical chemistry, 663
 - Brewster’s angle, 660
 - continuous-wave, 659
 - diode laser, 659
 - evanescent-wave, 663
 - predissociation dynamics, 659
 - pulsed, 659
- Ritz formula, 185
- R*-matrix, 1370
 - fixed nuclei, 743
 - method, 732
 - software, 166
- R*-matrix-Floquet method, 746
- rock salt lattice, 615
- Rodrigues formula, 161
- Rosen–Demkov model, 807
- rotating frame
 - molecular, 539
 - optical, 237, 1051
- rotating-wave approximation, 1051, 1058, 1070, 1143, 1176, 1209
- rotation
 - dynamics, semiclassical, 511
 - group
 - Clebsch–Gordan series, 342
 - irreducible representations (irreps), 342
 - Lie algebra $SO(3)$, 82
 - $SU(2)$ group ($SO(3, \mathbf{R})$), 10
 - matrices, 17, 539
 - as generalized Fourier transforms, 509
 - as rigid rotor eigenfunctions, 508
 - parametrization, Euler angles, 18
- rotational branch
 - molecular, 542
 - strengths, 547
- rotational energy surface, 511
 - asymmetrical gyro-rotor, diagram, 532
 - diagram, 510, 516
 - multiple, 528
 - octahedral and tetrahedral, 515
 - quadrupole, 529
 - scalar monopole, 529
 - spherical gyro-rotor, diagram, 529, 531–534
 - vector dipole, 529
- rotational excitation, theory, 742
- rotational invariants, solid harmonic expansions, 13
- rotational scattering, 1028
- rotational sidebands, 1088
- rotational structure, 513
 - octahedral and tetrahedral, 515
- rotational symmetry, molecular, 539
- rovibrational coupling, 508
- rovibrational structure, 88, 518
 - diagram, 519
- Rowland circle, 673
- Runge–Kutta method, 138
- Runge–Lenz vector, 77, 244
- Russell–Saunders (*LS*) coupling, 179, 180
 - allowed *LS* terms, 179
- Russian doll, 518, 615

- Rutherford cross section, 706
- Rydberg atom, 1217
- in electric fields, 234
 - in magnetic fields, 236
 - in microwave fields, 237
 - microwave ionization, 1134
 - optical excitation, 233
 - radiative lifetimes, 233
 - wave functions for, 231
- Rydberg atom collisions, 238, 882
- binary encounter approximation, 903
 - Born approximation, 908
 - capture, 909
 - classical impulse approximation, 900
 - classical scattering theory for, 889
 - depopulation rates, 887
 - depopulation rates in external B fields, 887
 - effective lifetimes, 887
 - Efimov effect, 890
 - elastic $n\ell \rightarrow n\ell'$ transitions, 894
 - fine structure transitions, 894
 - impact parameter theory, 894
 - inelastic $n \rightarrow n'$ transitions, 893
 - Born results for, 893
 - inelastic n, ℓ changing transitions, 892
 - inelastic $n\ell \rightarrow n\ell'$ transitions, 894
 - interaction potentials, 884
 - momentum distribution functions, 889
 - practical formulae, 892
 - quantal impulse approximation, 896, 900
 - quasi-elastic ℓ mixing transitions, 894
 - quasifree electron model, 892
 - semiclassical radiative lifetimes, 887
 - semiquantal impulse approximation, 901
 - spatial distribution functions, 888
 - types of collision processes, 882
 - universality properties, 890
 - Zeldovich effect, 885
- Rydberg Bose polaron, 200
- Rydberg chemistry, 799
- Rydberg dimers, trimers, tetramers, 801
- Rydberg formula, 185, 959
- Rydberg l -mixing, 799
- Rydberg state, 875
- autoionizing, 239
 - basic properties, 882
 - high ℓ , 233, 235
 - in clusters, 619
 - in laser fields, 746
 - in static fields, 241
 - quantum nondemolition experiment, 1238
- Rydberg wave packet, 1118
- free evolution (diagram), 1119
- S**
- saddle-point method for autoionizing states, 321
- Sagnac effect, 1183
- Saha distribution, definition, 849
- sapphire, 1084
- SASE, 1092
- satellite lines, 939
- saturable absorption, optical nonlinearities, 1105
- saturation, 1055
- in ion–molecule reactions, 603
 - laser, 1062
 - parameter, 1055
 - spectroscopy, 1062
 - saturation intensity, 1071
 - SBECROSS software, 168
 - scale height, 1300
 - scaling law, 242, 248
 - scaling transformation, 84
 - scattering, *see* collisions; light scattering; particular processes
 - angle, 243
 - chaotic, 250
 - elastic, 242
 - electron
 - by atoms in laser field, 746
 - by ions in laser field, 746
 - matrix, 576
 - signal calculation, 1023
 - spectral line shift, 796
 - two-dimensional, 242, 243
 - scattering amplitude, 690, 695, 700, 702, 706, 726, 727, 934, 982, 987, 989
 - Born, second, 916
 - capture, 1008
 - continuum distorted wave, 824
 - for polarization phenomena, 720
 - impulse approximation for, 899
 - spin flip, 720
 - scattering length, 728, 855, 1160, 1161
 - in elastic scattering, 693
 - sign, 1161
 - S-wave, 796
 - use of, in Rydberg collisions, 892
 - values for alkali atoms, 855
 - values for noble gas atoms, 694
 - scattering theory
 - adiabatic nuclei approximation, 742
 - angular momentum recoupling, 728
 - atom–atom collisions, 785
 - autodetachment, 395
 - autoionization, 395
 - basic definitions, 773
 - Born, 735, 736
 - charge transfer, 813
 - classical, 696, 882, 889, 895, 1028
 - classical trajectory method, 919
 - close-coupling, 726
 - continuum distorted wave method, 813
 - coordinate systems, 714
 - density matrix formalism, 122, 715
 - distorted wave, 737
 - elastic, 696, 1028
 - quantum amplitudes for, 690
 - electron–atom, 371, 725
 - electron–ion recombination, 846, 875
 - laser-assisted, 846
 - electron–molecule, 741
 - energy transfer cross section, for Coulomb potentials, 890
 - identical particles, 692
 - impact parameter theory, 894
 - intermediate and high-energy, 735
 - ion–atom collisions, 785
 - ion–molecule collisions, 789
 - laboratory frame representation, 741
 - line broadening, 283, 927
 - linear algebraic equations method, 735

- mass transfer, 913
- model potential formulae, 707
- molecular frame representation, 742
- Monte Carlo method, 919
- normalization choices, 691, 870
- optical potential, 736
- orbiting and spiraling collisions, 698
- orientation and alignment, 119, 713
- photoionization, 383
- potential scattering, 106, 693
- reactive, 583, 1029
 - ionic, 598
- recombination, 846, 875
- regions of validity (diagram), 921
- relativistic effects, 728
- resonances, 751
- resonant, 395
- R**-matrix, 732, 735, 743
- Rydberg atom collisions, 881
- semiclassical, 698, 882
- Thomas process, 913
- variational methods, 733
- Wannier method, 822
- Schawlow–Townes linewidth, 1074
- Schiff moment, 476
- Schiff’s theorem, 475
- Schmidt model, 454
- Schrödinger equation, 103, 231, 309
 - asymptotic form, 200
 - cusp conditions for, 200
 - for Zeeman effect, 224
 - hydrogenic, 149
 - mathematical properties of, 200
 - momentum space, 152
 - nonlinear, 797
 - parabolic coordinates, 150
 - radial solutions of, 691
 - spherical coordinates, 149
 - three body, 199
 - computational methods for, 200
 - time-dependent, 787, 1126
 - direct integration of, 1135
 - solution of, 744
 - two-electron, 199
- Schrödinger Hamiltonian, 310
- Schwinger
 - generating function, 32, 42
 - g-value, 185
 - variational method, 734
- Schwinger–Bargmann generating function, 41
- Schwinger–Wu generating function, 47
- SciPy, 168
- screening and antiscreening effects of atomic electrons in pair production, 842
- second harmonic generation (SHG), 1092, 1093
- second quantization, 99
- second-order nucleophilic SN2 reaction, 1040
- selection rule
 - for electron impact excitation, 983
 - for molecular radiative transitions, 542
 - for nonadiabatic coupling, 777
 - for photoionization, 385
 - for radiative transitions, 187
- self impedance, 1112
- self-consistent field method
 - energy derivatives, 491
 - for molecules, 491
- self-focusing, 1105
 - critical power, 1105
- self-imaging, 1181
- self-induced transparency, 1055
- self-organization in cavity QED, 1223
- self-similarity, 250
- self-trapping, 1105
- semiclassical
 - and quasi-classical, 579
 - propagator, 687
 - quantum defect representation, 885
 - theory, Young’s two slit experiment, exclusion of, 1232
 - transition amplitude, 830, 832
- semiclassical approximation, 242, 702, 823, 830, 882, 1004, 1047
 - for heavy particle scattering, 786, 789, 791
 - for ionization, 824
 - Monte Carlo, 921
- semiclassics, 685
- semiconductor cluster, 616, 617
- semiconductor laser, 1074, 1075, 1083, 1090
 - distributed Bragg reflector (DBR), 1091
 - distributed feedback (DFB), 1090
 - double-heterostructure (DH), 1090
 - edge emitter, 1090
 - Fabry–Perot (FP), 1090
 - quantum cascade (QCL), 1091
 - quantum well, 1090
 - VCSEL, 1091
 - VECSEL, 1091
- semirigid rotor, 508
- seniority, 76, 113, 311, 357
- sensitive dependence on initial conditions, 246
- sensitivity, 1201
- separatrix curve, 512
- series limit, 185
- Seya–Namioka design, 673
- SF₆ spectrum, rotational, 514
- shakedown process, 959
- shakeoff process, 962, 1362
- shakeup process, 959, 1362
- shallowest ascent path, 489
- Shannon’s information entropy, 229
- shape resonance, 403
 - in surface scattering, 1351
- Shavitt graph, 90
- shell structure
 - group theory of, 76
 - mixed configuration, 76
- shelving state, 1153
- Sherman function, 989
- shocked gas, interstellar, 1283
- Shore profile, 959
- shot noise, 1233
- SiF₄ spectrum, spin- $\frac{1}{2}$ basis states for, 520
- Sil variational principle, 816
- silicon
 - cluster, 616
 - photodiode, 675
- single active electron approximation, 787
- single, double, triple, quadruple (SDTQ) replacements, 320
- single-active electron approximation, 1136
- single-atom detection, 1128
- single-centered expansion, 789

- single-ion trap, 451
- single-particle model, 956
- single-photon sources, 1227
- single-photon-added states, 1200
- singlet–triplet mixing
 - helium mixing angles, 215
 - scattering phase difference, 719
 - spin-flip cross section, 693
- sinusoidal variation, 1211
- Sisyphus effect, 1147
 - origin of, 1147
- size extensivity, 492
- Slater
 - determinant, 112, 491
 - integral, 313
 - rule, 100
- Slater-type orbital, 322
- slice imaging, 1019
- slow light, 1067, 1250
- slowly varying envelope approximation, 1050
 - in de Broglie optics, 1178
- S -matrix, 727, 934
 - impact parameter, 929
 - near a resonance, 730
- SN1987A (supernova), 1282
- Snell's law, 1178
- $SO(3, \mathbf{R})$ and $SU(2)$ solid harmonics, 57
- $SO(4)$ dynamical symmetry, 895
- sodium, energy levels of, 233
- soft-electron peak, 833
- software
 - ADAS, 166
 - ATLAS, 171
 - atomic structure, 166
 - AUTOSTRUCTURE, 166
 - BLAS, 171
 - B-spline Hartree–Fock, 166
 - B-spline R-matrix, 166
 - CHIANTI, 166
 - configuration-interaction (CI), 166
 - DIRAC, 167
 - EDWIN, 168
 - GAMESS, 167
 - GRASP2K, 166
 - GSL, 171
 - GUASSIAN, 167
 - Hartree–Fock, 166
 - HONDO, 167
 - IMSL, 171
 - LAPACK, 171
 - many-body perturbation theory, 166
 - MOLCAS, 167
 - MOLPRO, 167
 - Multi-configuration Dirac–Fock, 166
 - Multi-configuration Hartree–Fock, 166
 - NAG, 171
 - no-exchange R-matrix, 166
 - non-iterative integral equation method (NIEM), 166
 - polarized orbital, 166
 - POLYRATE, 168
 - PQS, 167
 - PySCF, 167
 - quantum reactive scattering, 168
 - quantum Transport in molecular gases, 168
 - R-matrix, 166
 - SBECROSS, 168
 - TRIATOM, 167
 - VIBREQ, 168
- solar
 - corona, emissivity of, 1278
 - radiation, interaction with the atmosphere, 1305
 - wind, 1306
- solid harmonics, 12
 - orthogonality, 13
 - product, 13
 - table, 65
 - vector addition rule, 13
- solid, impurity spectroscopy in, 1060
- solid-state laser, 1083
- soliton
 - in dispersive nonlinear media, 1105
 - laser, 1079
 - optical pulse, 1118, 1121
- solvent shell, 619, 621
- Sommerfeld parameter, 1363
- space shuttle environment, 598
- space-fixed coordinates, 577
- space-fixed frame, 774
- spark, 670
- spatial coherence length, 1185
- spatial laser modes, 1076
- spatially inhomogeneous fields, 1138
- special function, 156
- spectator stripping, 1030
- spectra
 - irregular, 246
 - regular, 246
 - width weighted, 249
- spectral
 - aliasing, 631
 - density, 1210
 - line series, 185
 - linewidth, 1089
 - method, analysis of data, 135
 - redistribution, 289
 - resolution, 95
- spectrometer, 657, 673
 - absorption, 657
 - Fourier transform, 630, 657, 674
 - grazing incidence grating, 674
 - light intensity, 657
 - normal incidence grating, 673
 - selectivity, 657
 - sensitivity, 657
- spectrometry, photoelectron, 961
- spectroscopic
 - data, atomic, 196
 - factor, 369
 - notation, 178–180
- spectroscopy, 463, 467, 478
 - accelerator based, 265, 269, 1363
 - atomic, 177
 - Auger, 1351
 - beam-foil, 269
 - beam-gas, 270
 - beam-laser, 271
 - Doppler, 559
 - Doppler-free, 1062
 - electron emission, 1000
 - electron energy loss, 1351

- Fourier transform, 630, 641
- hole-burning, 655, 1062
- infrared, 626
- intensity versus line position, 537
- ion trap, 272
- Lamb dip, 655
- laser, 649
 - electric resonance (LER), 642
 - magnetic resonance (LMR), 642, 644
- linear, 1060
- nonlinear, 1062
- of clusters, 610
- photoelectron, 956
 - angle-resolved, 1352
 - ultraviolet, 1352
 - X-ray, 1353
- polarization, 1063
- pump/probe, 1062
- Raman, 1106
- recoil-ion momentum, 923, 1000, 1008
- saturation, 1062
- scaled variable, 248
- selection rules, 187
- Stark, 234
- submillimeter and far-infrared, 641
- three-level, 1064
- time-resolved, 559, 669
- translational energy, 999
- two-level, 1062
- two-photon, 1064
- ultraviolet, 667
- wavelength and frequency standards, 186
- wavelength ranges, 186
- spectrum generating algebra, 81
- spherical harmonics
 - angular momentum operator actions, 49
 - definition, 15
 - spinor, 49
 - table of, 65
 - tensor, 48
 - vector, 49
- spherical top, 514
 - Hamiltonian for, 509
- spin group $\text{spin}(m)$, 87
- spin magnetic moment, 1048
- spin polarimetry, 961
- spin-dependent effects
 - in collisions, 125
 - on radiative transitions in helium, 215
 - on scattering, 989
 - molecular, 551
- spin-dependent operator, 91
- spin-exchange cross section, 797
- spin-flip amplitude, 693, 719, 989
- spinor representation, 87
- spin-orbit coupling, 1154
- spin-orbit interaction, 178, 311, 340, 989
- spinorial invariant, 14
- spin-polarized projectiles, scattering of, 126, 718, 989
- spin-rotation Hamiltonian, 540
- spline, cubic, 132
- split-step method, 1163
- spontaneous decay, 1058
- spontaneous emission, 1061
 - rate of, 213, 1210
 - suppression of, 1208, 1213
- spontaneous symmetry breaking in molecules, 516, 521
- spontaneously broken symmetry, 1164
- squeezed state, 1194
 - gravitational radiation detection, 1250
 - squeezed coherent state, 1195
 - squeezed quadrature, 1194
 - squeezed thermal state, 1195
 - squeezing operator, 1194
 - squeezing parameter, 1194
 - two-mode squeezed states, 1197
 - two-mode squeezing operator, 1197
 - two-mode, or twin-beam, 1233
- squeezing, two-mode, 1102
- standard model, 472, 474, 477
 - extension, 478
- standard quantum noise limit, 1202
- Stark
 - effect, 246
 - motional, 250
 - interference method, 473
 - ionization, 227
 - parameter, 1021
 - representation, 933
 - shift, 227, 235, 509
 - dynamic (AC), 1052, 1120, 1129
 - hydrogenic, 86
 - linear, 227
 - quadratic, 228
 - third order, 228
 - spectroscopy, 234
 - switching, 236
- Stark parameter, 895
- state multipole
 - definition, 123
 - for coupled systems, 124
 - symmetry properties, 123
 - time evolution, 125
 - transformation properties, 123
- state-resolved measurement, 1040
- states of a moving atom, 837
- stationary phase approximation, 288, 702
 - superluminal group delays, 1247
- statistical
 - adiabatic channel model (SACM), 783
 - analysis of data, 135
 - weight (level, term), 188
- steepest descent, method of, 162
- Stefan-Boltzmann, 1340
- stellar atmosphere, 1281
 - circumstellar shells, 1281
- Stern-Gerlach effect
 - atom optical, 1176
 - atom-optical, 1181
 - inverse, 1184
- Stieltjes imaging, 1362
- stimulated emission, 1069, 1070
- stimulated Raman adiabatic passage (STIRAP), 1066
- stimulated Raman scattering, 1092
- stochastic model, laser, 1127
- Stokes amplification, stimulated Raman scattering, 1101
- Stokes parameter, 122, 127, 715
 - angle-differential, 122, 127
 - definition, 127, 128
 - generalized, 122, 127

- integrated, 122, 127
 - Stokes shift, 1086, 1089
 - Stokes vector, 715
 - density matrix representation, 716
 - stopping power, 1012
 - straight-line trajectory, 830
 - stratopause, 1338
 - stratosphere, 1338
 - terrestrial, 1300
 - stratospheric ozone, 1342
 - stripping reaction, 1029
 - strong coupling
 - cavity QED, 1213
 - correspondence principle, 888
 - detecting and trapping atoms, 1227
 - in experiments, 1216
 - open optical cavities, 1217
 - strong CP problem, 462
 - strong-field processes, 1125
 - strongly correlated system, 1169
 - strontium, Rydberg states of, 239
 - Stückelberg angle, 1052, 1176
 - STU*-parameter, 720
 - definition, 126
 - generalized, 126, 127
 - Sturmian functions, 150
 - SU(1,1) interferometer, 1202
 - submillimeter spectroscopy, 641
 - sudden approximation, 836
 - sum rule, 397
 - momentum space wave function, 889
 - oscillator strength, 205
 - radial integral, 885
 - sum-frequency generation, 1100, 1101
 - nonlinear polarization, 1100
 - SunPy, 168
 - superconducting quantum interference detector (SQUID), 1250
 - supercontinuum light, generation of, 1108
 - supercontinuum radiation, 670
 - superelastic scattering, 987, 988
 - superfine splitting, 512
 - superfine structure, 511, 516, 520
 - octahedral, 517
 - superfluid, 1167
 - superfluid–Mott insulator transition, 1169
 - superhyperfine structure, 520
 - superluminal group delays, 1247
 - superluminal velocity in tunneling, 1247
 - supermultiplet, 179
 - supernova, 1282
 - ejecta, 1282
 - SN1987A, 1282
 - X-ray spectrum of, 1277
 - superradiance, 1092
 - in cavity QED, 1222
 - supersonic beam, 1020, 1185
 - supersonic expansion, 1020
 - supersymmetry, 475, 477
 - surface
 - extended X-ray absorption fine structure (SEXAFS), 1355
 - ionization detector, 1022
 - of intersection, 498
 - physics, 1349
 - surface-hopping approximation, 782
 - surfaces, atomic processes on, 1350, 1357
 - adsorption and desorption, 1357
 - Auger spectroscopy, 1351
 - chemisorption, 1357
 - impact scattering, 1351
 - inverse photoemission spectroscopy, 1353
 - photoelectron spectroscopy, 1352
 - resonance scattering, 1351
 - X-ray absorption, 1355
 - X-ray photoelectron spectroscopy, 1353
 - swarm method, 999
 - s*-wave, 1160
 - s*-wave scattering, 810
 - Swings effect, in comets, 1293
 - symmetric eikonal model, 836
 - symmetric rotator
 - angular momentum operators, 28
 - body frame components, 28
 - inertial frame components, 28
 - wave functions, 28
 - symmetric top, 508, 541
 - energy levels, 508
 - Hamiltonian, 508
 - transition moments for, 550
 - symmetry
 - breaking, 1164
 - cylindrical, 249
 - dynamical, 81
 - group (algebra), 81
 - molecular, 509, 513, 543
 - oscillations, 692
 - time, 249
 - sympathetic cooling, 1038
 - synchrotron radiation, 668, 669, 961, 971
 - monochromator, 961
 - polarization property, 669
 - spectral property, 668
 - temporal property, 668
 - undulator, 669
 - wiggler, 669
 - synthetic gauge field, 1154, 1171
 - synthetic magnetism, 809
- ## T
- tableaux, outer product, 75
 - Talbot effect, 1181
 - target continuum distorted wave approximation (TCDW), 815
 - target recoil method, for electron scattering, 984
 - target, excited, scattering from, 987
 - Tavis–Cummings model, 1223
 - Taylor expansion, 132
 - Taylor-series algorithm, 138
 - tensor construction, 112
 - tensor coupled form, 112
 - tensor harmonics (table), 65
 - tensor operator
 - algebra, 35
 - coupling of tensor operator, 36
 - properties of tensor operator, 36
 - tensor operator, 35
 - universal enveloping algebra, 36
 - Wigner operators, 37
 - Wigner–Eckart theorem, 37
 - for coupled systems, 124
 - irreducible, 35, 123

- tensor representation, 87
- tensor spherical harmonics, angular momentum operator actions, 48
- term dependence, 317
- term series, 185
- term value, 185
- term, atomic structure, 178, 179
- termolecular recombination, 846
- ternary reactions, ion–molecule, 603
- test of gravity, 481
- tetrahedral symmetry, molecular, 514
- thermal
 - beam method, 998
 - coherence time, 1185
 - equilibrium, density matrix for, 121
 - lensing, 1084
 - model of radiative association, 592
 - state, 1191, 1216
 - wavelength, 1185
- thermodynamical instability, 1165
- thermosphere, terrestrial, 1300
- thin-disk laser, 1084
- Thomas peak, 815, 915–917
- Thomas process, 913
 - classical, 913
 - diagram for mass transfer, 914
 - equations of constraint, 914
 - interference effects, 916
 - off-energy-shell, 916
 - quantum, 914
- Thomas ridge, 915
- Thomas–Fermi approximation, 1161, 1165
- Thomas–Fermi theory, 297, 1362
 - Dirac exchange correction, 301
 - gradient expansion for the kinetic energy, 300, 303
 - no binding result for molecules, 297
 - nonrelativistic energy expansion, 302
 - relativistic effects, 304
 - von Weizsäcker correction, 300
- Thomas–Reiche–Kuhn sum rule, 205, 1054
- Thomson scattering, 969, 1056
- Thomson theory of recombination, 854
- three-body distorted-wave model, 836
- three-body nonadditive interactions, 800
- three-level processes, 1064
- three-level system, 1065
 - special effects in, 1065
- three-point vertex
 - irreducible, 410
 - reducible, 410
- three-wave mixing, 1093
- threshold cross section
 - for photodetachment, 390
 - for photoionization, 387, 388, 390, 868, 960
 - Auger decay effect, 960
 - delayed maximum, 387, 389
- threshold law
 - Wannier, 737, 822, 960
 - Wigner, 822, 960
- threshold, analytic continuation through, 728
- threshold, laser
 - condition for, 1070
 - gain, 1070
 - population difference, 1070
- threshold, maser, 1218
- throughput advantage, in Fourier transform spectroscopy, 633
- THz radiation, 1094
- Ti³⁺, 1087
- tidal recombination, 846
- tight-binding approximation, 1169
- tilting transformation, 84
- time evolution operator, 120
- time reversal, 475
 - symmetry, 538
- time-dependent perturbation, 566
- time-evolution operator, 790
- time-independent perturbation theory, 95
- time-of-flight (TOF)
 - analyzer, 962
 - imaging, 1166
 - technique, 986
- time-orbiting potential trap, 1166
- time-ordered operator, 105, 337
- time-resolved spectroscopy, 567
- Ti-sapphire laser, 1087
- Tm³⁺, 1085
- T*-matrix, 727, 787, 934
- tokamak, 922
- tomographic reconstruction, 1027
- Tomonaga–Schwinger equation, 105
- TOP trap, 1166
- topological band structure, 1171
- topological phase, 1170, 1183
 - transition, 1171
- torsion pendulum, 463, 467
- torsion-balance experiment, 481
- torus, 244–246
- total
 - angular momentum of the composite system
 - SU*(2) transformation properties, 51
 - uncoupled and coupled basis vectors, 51
 - cross section, 982
 - internal reflection, frustrated, 1248
 - ionization cross section, 833
 - photoionization cross section, 962
- trajectory
 - chaotic, 245, 246
 - closed, 247
 - helix, 245
 - in Monte Carlo calculations, 923
 - periodic, 247
 - regular, 244, 245
- transfer ionization, 996
- transfer-excitation, 786
- transfer-ionization, 786
- transient absorption, 568
- transit time broadening, 1153
- transition array, 179
- transition data, 324
- transition moment matrix, orbital and spin selection rules, 544
- transition probability, 808
- transition probability, collisional
 - double passage, 780
 - molecular, 540
 - multiple passage, 782
 - Nikitin model, 778
 - single passage, 778
- transition state, 597
 - barrier, 585
 - loose, 589
 - theory, 250

- bimolecular statistical, 588
 - unimolecular statistical, 589
 - tight, 589
 - translational energy spectroscopy, 999
 - transmission matrix, 576
 - transmission method, for electron scattering, 984
 - transmittivity, coefficient of, 1179
 - transparency
 - induced, 1121
 - self-induced, 1118
 - transverse diffusion, 1145, 1146
 - trap
 - crossed beam, 1166
 - frequency, 1160
 - optical, 1166
 - trapped ion, 478, 1269
 - method, 999
 - trapping
 - atom, 1146, 1148, 1152, 1166
 - axial motion, 1150
 - cyclotron motion, 1150
 - diffusion, 1143
 - dipole force, 1146
 - Earnshaw theorem, 1148, 1149
 - Ioffe–Pritchard trap, 1166
 - ion crystal, 1152
 - Lamb–Dicke regime, 1150
 - linear trap, 1149
 - magnetic, 1148, 1166
 - magneto-optical, 1148, 1152
 - magnetron motion, 1151
 - many ions, 1151
 - micromotion, 1149, 1150
 - molecule, 1146
 - of charged particles, 1149, 1150
 - Penning trap, 1150
 - quantization of motion, 1149
 - quantum theory, 1144, 1147
 - race track, 1149
 - radius method, for recombination processes, 864
 - secular motion, 1149, 1150
 - semiclassical theory, 1143, 1147
 - state, 1120, 1219
 - sympathetic cooling, 1152
 - time-orbiting potential trap, 1166
 - TOP trap, 1166
 - trap frequencies, 1149, 1153
 - TRIATOM software, 167
 - triple tensor, 114
 - triple-centered expansion, 790
 - triplet quenching, 1089
 - tritium, β -decay, 1362
 - tropopause, 1338
 - troposphere, 1338
 - terrestrial, 1300
 - tropospheric warming, 1340
 - tunneling, 921, 1364
 - dynamic, 511, 512
 - matrix eigenvector table, 518
 - Hamiltonian matrix for, 512
 - in binary reaction, 601
 - ionization, 235, 1129
 - multilayer dielectric mirror experiment, 1248
 - phase, 1170
 - reaction mechanism, 590
 - RRKM correction, 590
 - superluminal delay time, 1247
 - transmission probability for, 1249
 - Wigner correction to, 590
 - tunneling time
 - definitions, 1248
 - interpretation of, 1249
 - weak measurement approach, 1249
 - two-beam resonance, 1182
 - two-center coupled-channel methods, 839
 - two-centered expansion, 790
 - two-effective center, 819
 - two-level atom, 1050
 - density matrix, 1058
 - model Hamiltonian, 1050, 1058
 - steady state, 1055
 - two-particle operator, 1158
 - two-photon
 - absorption, 1105
 - coherence, 1120
 - excitation microscopy, 1203
 - process, 1064
 - resonance, 1119
 - two-state approximation for collisions, 775
 - two-step mechanism for heavy particle scattering, 788
 - two-step process, 1065
- ## U
- $U(n)$ Casimir operator, 87
 - $U(n)$ representation theory, 86
 - $U(n)$ solid harmonics, 60
 - ultra-long range Rydberg molecule, 798
 - ultrashort pulse generation
 - chirped pulse amplification, 1078
 - Kerr lens mode locking, 1078
 - Ultraspherical polynomial, 895
 - ultraviolet spectral region
 - definition, 667
 - near ultraviolet, 667
 - uncertainty principle
 - energy-time form, 1235
 - number-phase form, 1238
 - undulator, 669, 961
 - undulatory Born–Oppenheimer potentials, 798
 - unimolecular decay, 588, 590
 - thermal, 590
 - unimolecular reaction, 563
 - unit
 - in atomic spectroscopy, 178
 - tensor operators, coupling laws, 38
 - tests software, 172
 - unitary group approach (UGA), 86, 491
 - unitary group $U(n)$, 86
 - generators of, 86, 491
 - unitary irreducible representations, 17
 - universality of free fall, 481
 - universality properties, 890
 - universe, early, molecular processes in, 1283
 - unrestricted Hartree–Fock (UHF), 104
 - upper atmosphere cooling, 1340
 - uranium, fully stripped, 1363

V

- vacancy production, 1005
 - K*-shell, 1004
 - rotational coupling, 1009
 - vacuum
 - birefringence, 465
 - diagram, 101
 - fluctuations, 1232
 - polarization, 336, 359, 424
 - current, 336
 - splitting, 1216
 - van Cittert–Zernike theorem, 1185
 - van der Waals
 - energy scale, 855
 - force, 286, 591, 618
 - in neutral–neutral reactions, 586
 - unretarded limit, 1212
 - interaction, 796
 - length scale, 855
 - variation of constants method, 107
 - variational method, 140
 - for capture rate, 586
 - Kohn, 733
 - Kohn–Sham, 303
 - Schwinger, 734
 - transition state, 589
 - variational principle
 - for bound state wave functions, 200, 312
 - for charge transfer, 816
 - for recombination processes, 864
 - Hohenberg–Kohn, 302
 - Rayleigh–Ritz, 200
 - Sil, 816
 - vector
 - coupling coefficients, 29
 - of zero length, 14
 - solid harmonics, angular momentum operator actions, 50
 - velocity distribution, thermal, 1059
 - velocity map imaging, 1038
 - velocity mapping, 1019
 - vibrational
 - excitation, theory, 742
 - scattering, 1029
 - states, 1086, 1088, 1089
 - structure, 499
 - transitions, 547
 - VIBREQ software, 168
 - vibron model, 88
 - Virgo gravitational wave observatory, 1250
 - virial theorem, 300
 - virus coat, symmetry of, 523
 - Voigt
 - function, 964
 - line shape, 284, 1060
 - profile, 1063
 - Volkov state, 1136
 - Volkov wave function, 745
 - von Neumann rejection method, for random numbers, 145
 - vortex, 1167
 - vortices
 - in atomic collisions, 792
- W**
- Wadsworth mount, 673
 - waiting time probability, 1220
 - Wang transformation, 541
 - Wannier exciton, 619, 620
 - Wannier method, 822
 - ridge, 822
 - threshold law, 737, 822, 825, 960
 - water cluster, 621
 - Watson Hamiltonian, 500
 - wave function
 - coupled cluster expansion for, 103
 - irregular, 246
 - regular, 244
 - wave operator, 341
 - wave packet, 566
 - coherent, 1119
 - continuum, 791, 792
 - in momentum space, 793
 - waveforms, 1128
 - wave-function
 - collapse, 1249
 - collapse, energy-time uncertainty relation, 1235
 - waveguide, 663
 - atomic, 1180
 - radiating atoms in, 1210
 - wavelength standards, 186
 - wave-packet collapse, 1232
 - wave-particle duality, 1236
 - weak
 - charge, 472, 474
 - coupling, experiments on, 1213
 - equivalence principle, 481
 - hadronic interactions, 474
 - interactions, 472
 - measurement, 1239
 - mixing angle, 472
 - Weber bar, 1250
 - weight, highest and vector, 86
 - Weizsäcker–Williams approximation, 841
 - welcher Weg information, 1239
 - Weyl dimension formula, 86
 - white noise, 1127
 - Wick’s theorem, 99, 338, 342, 418
 - wiggler, 669, 961
 - Wigner
 - causality condition, 693
 - distribution, 246, 1247
 - function, 1143, 1193
 - Wigner quasi probability, 1192
 - Wigner representation, 1193
 - law, 945
 - threshold behavior, 810
 - threshold law, 822, 960
 - tunneling correction, 590
 - Wigner–Clebsch–Gordan coefficients, 29
 - combinatorial definition, 57
 - discretized representation functions, 34
 - Kronecker product reduction, 30
 - Racah’s form, 31
 - tensor product space construction, 31
 - Van der Warden’s form, 31
 - Wigner’s form, 31
 - Wigner–Eckart theorem, 37, 77, 114, 124
 - Wiley–McLaren time-of-flight, 1038
 - Winans–Stückelberg vibrational wave function, 859
 - window, optical, 676

WKB approximation, [1177](#), [1362](#)
in de Broglie optics, [1177](#)
work function, [611](#)

X

XeCl, [1090](#)
XeF, [1090](#)
xenon, photoionization of, [391](#)
XFEL, [1092](#)
x-ray
absorption, [1355](#)
absorption near-edge structure (XANES), [972](#)
absorption spectroscopy (XAS), [972](#)
elastic diffraction (XRD), [972](#)
emission spectroscopy (XES), [973](#)
extended-range technique (XERT), [972](#)
fine structure absorption spectroscopy (XAFS), [972](#)
free-electron laser (XFEL), [571](#)
laser, [1079](#)
Raman spectroscopy (XRS), [973](#)
XUV coherent radiation, [1132](#)

Y

Y3Al5O12, [1084](#)
YAG, [1084](#)
YAG (Y3Al5O12), [1087](#)
Yb fiber laser, [1085](#), [1088](#)
Yb3+, [1085](#)

Yb⁺ octupole clock, [480](#)
YLF, [1084](#)
YLF (LiYF4), [1085](#)
Young double-slit, [1182](#)
Young tableau, [74–76](#)

Z

Z boson, [472](#)
ZBLAN, [1084](#), [1085](#)
Zeeman effect, [85](#), [225](#), [236](#), [509](#)
anomalous, [225](#)
classification of energy levels, [225](#)
energy tabulation, [226](#), [227](#)
Landé *g*-value, [225](#)
nonrelativistic theory, [224](#)
normal, [225](#)
quadratic, [226](#)
quadratic relativistic, [226](#)
strong field, [226](#)
weak field, [225](#)
intermediate-coupling *g*-value, [185](#)
Landé *g*-value, [183](#)
Lorentz unit, [183](#)
magnetic splitting factor *g*, [183](#)
Schwinger *g*-value, [185](#)
Zeeman slower, [1152](#)
Zeldovich effect, [885](#)
zone plate, [1181](#)